

ASM HANDBOOK[®]

VOLUME

8

*Mechanical
Testing and
Evaluation*



Publication Information and Contributors

Introduction

Mechanical Testing and Evaluation was published in 2000 as Volume 8 of the *ASM Handbook*. The Volume was prepared under the direction of the ASM Handbook Committee.

Volume Coordinator

The Volume Coordinators were Howard Kuhn, Concurrent Technologies Corporation and Dana Medlin, The Timkin Company.

Authors and Contributors

- **LAMET**
UFRGS
- **John A. Bailey**
North Carolina State University
- **John Barsom**
Barsom Consulting Limited
- **Peter Blau**
Oak Ridge National Laboratory
- **Kenneth Budinski**
Eastman Kodak Company
- **Vispi Bulsara**
Cummins Engine Company
- **Leif Carlsson**
Florida Atlantic University
- **Norm Carroll**
Applied Test Systems, Inc.
- **Srinivasan Chandrasekar**
Purdue University
- **P. Dadras**

Wright State University

- **K.L. DeVries**

University of Utah

- **George E. Dieter**

University of Maryland

- **James Earthman**

University of California, Irvine

- **Horatio Espinosa**

Northwestern University

- **Henry Fairman**

MQS Inspection, Inc.

- **Thomas Farris**

Purdue University

- **Andrew R. Fee**

Consultant

- **William W. Gerberich**

University of Minnesota

- **Jeffrey Gibeling**

University of California, Irvine

- **Amos Gilat**

The Ohio State University

- **Peter P. Gillis**

University of Kentucky

- **William Glaeser**

Battelle Memorial Institute

- **Blythe Gore**

Northwestern University

- **George (Rusty) Gray III**
Los Alamos National Laboratory
- **Amitava Guha**
Brush Wellman Inc.
- **Gary Halford**
NASA Glenn Research Center at Lewis Field
- **John Harding**
Oxford University
- **Jeffrey Hawk**
Albany Research Center
- **Jennifer Hay**
Applied Nano Metrics, Inc.
- **Robert Hayes**
Metals Technology Inc.
- **K.H. Herter**
University of Stuttgart
- **John (Tim) M. Holt**
Alpha Consultants and Engineering
- **Joel House**
Air Force Research Laboratory
- **Roger Hurst**
Institute for Advanced Materials (The Netherlands)
- **Ian Hutchings**
University of Cambridge
- **Michael Jenkins**
University of Wyoming
- **Steve Johnson**

Georgia Institute of Technology

- **Serope Kalpakjian**

Illinois Institute of Technology

- **Y. Katz**

University of Minnesota

- **Kevin M. Kit**

University of Tennessee

- **Brian Klotz**

The General Motors Corporation

- **Howard A. Kuhn**

Concurrent Technologies Corporation

- **John Landes**

University of Tennessee

- **Bradley Lerch**

NASA Glenn Research Center at Lewis Field

- **Peter Liaw**

University of Tennessee

- **John Magee**

Carpenter Technology Corporation

- **Frank N. Mandigo**

Olin Corporation

- **Michael McGaw**

McGaw Technology, Inc.

- **Lothar Meyer**

Technische Universität Chemnitz

- **James Miller**

Oak Ridge National Laboratory

- **Farghalli A. Mohamed**
University of California
- **William C. Mohr**
Edison Welding Institute
- **Charles A. Moyer**
The Timken Company (retired)
- **Yukitaka Murakami**
Kyushu University
- **Sia Nemat-Nasser**
University of California, San Diego
- **Vitali Nesterenko**
University of California, San Diego
- **Todd M. Osman**
U.S. Steel
- **F. Otremba**
University of Stuttgart
- **T. Ozkai**
Olin Brass Japan, Inc.
- **George M. Pharr**
The University of Tennessee
- **Paul Phillips**
The University of Tennessee
- **Martin Prager**
Welding Research Council and Materials Properties Council
- **Lisa Pruitt**
University of California, Berkeley
- **George Quinn**

National Institute of Standards and Technology

- **J.H. Rantala**

Institute for Advanced Materials (The Netherlands)

- **Suran Rao**

Applied Research Laboratories

- **W. Ren**

Air Force Research Laboratory

- **Gopal Revankar**

Deere & Company

- **Robert Ritchie**

University of California, Berkeley

- **Roxanne Robinson**

American Association for Laboratory Accreditation

- **E. Roos**

University of Stuttgart

- **Clayton Rudd**

Pennsylvania State University

- **Jonathan Salem**

NASA Glenn Research Center at Lewis Field

- **P. Sandberg**

Outokumpu Copper

- **Ashok Saxena**

Georgia Institute of Technology

- **Eugene Shapiro**

Olin Corporation

- **Ralph S. Shoberg**

R.S. Technologies Ltd.

- **M.E. Stevenson**
The University of Alabama
- **Ghatu Subhash**
Michigan Technological University
- **Ed Tobolski**
Wilson Instruments
- **N. Tymiak**
University of Minnesota
- **George Vander Voort**
Buehler Ltd.
- **Howard R. Voorhees**
Materials Technology Corporation
- **Robert Walsh**
Florida State University
- **Robert Waterhouse**
University of Nottingham
- **Mark Weaver**
University of Alabama
- **Dale Wilson**
The Johns Hopkins University
- **David Woodford**
Materials Performance Analysis, Inc.
- **Dan Zhao**
Johnson Controls, Inc.

Reviewers

- **Julie Bannantine**
Consultant

- **Raymond Bayer**
Tribology Corporation
- **Peter Blau**
Oak Ridge National Laboratory
- **Toni Brugger**
Carpenter Technology Corporation
- **Prabir Chaudhury**
Concurrent Technologies Corporation
- **Richard Cook**
National Casein of California
- **Dennis Damico**
Lord Corporation Chemical Products Division
- **Craig Darragh**
The Timken Corporation
- **Mahmoud Demeri**
Ford Research Laboratories
- **Dez Demianczuk**
LTV Steel
- **George E. Dieter**
University of Maryland
- **James Earthman**
University of California/Irvine
- **Kathy Faber**
Northwestern University
- **Henry Fairman**
MQS Inspection, Inc.
- **Gerard Gary**

Polytechnique Institute (France)

- **Thomas Gibbons**

Consultant

- **William Glaeser**

Battelle Memorial Institute

- **Jennifer Hay**

Applied Nano Metrics, Inc.

- **Robert Hayes**

Metals Technology, Inc.

- **David Heberling**

Southwestern Ohio Steel

- **Kent Johnson**

Engineering Systems Inc.

- **Brian Klotz**

The General Motors Corporation

- **Howard A. Kuhn**

Concurrent Technologies Corporation

- **Lonnie Kuntz**

Mar-Test, Inc.

- **David Lambert**

Air Force Research Laboratory

- **John Landes**

University of Tennessee

- **Iain LeMay**

Metallurgical Consulting Services

- **John Lewandowski**

Case Western Reserve University

- **David Lewicki**
NASA Glenn Research Center at Lewis Field
- **Alan Male**
University of Kentucky
- **John Makinson**
University of Nebraska, Lincoln
- **William Mankins**
Metallurgical Services, Inc.
- **Frank Marsh**
Consultant
- **Dana Medlin**
The Timken Company
- **Gary Miller**
Allegheny Ludlum Corporation
- **Sia Nemat-Nasser**
University of California, San Diego
- **Robert Neugebauer**
Mar-Test, Inc.
- **Theodore Nicholas**
Air Force Research Laboratory, Wright-Patterson Air Force Base
- **William Nix**
Stanford University
- **Todd M. Osman**
U.S. Steel
- **Philip Pearson**
The Torrington Company
- **J. Michael Pereira**

NASA Research Center at Lewis Field

- **Joy Ransom**

Fatigue Technology, Inc.

- **Gopal Revankar**

Deere & Company

- **Clare Rinnac**

Case Western Reserve University

- **Earl Ruth**

Tinius Olsen Testing Machine Company, Inc.

- **Ghatu Subhash**

Michigan Technological University

- **Yuki Sugimura**

Harvard University

- **Eric Taleff**

The University of Texas at Austin

- **Ed Tobolski**

Wilson Instruments

- **George Vander Voort**

Buehler Ltd.

- **Kenneth S. Vecchio**

University of California, San Diego

Foreword

The new edition of *ASM Handbook, Volume 8, Mechanical Testing and Evaluation* is a substantial update and revision of the previous volume. This latest edition of Volume 8 contains over 50 new articles, and the scope of coverage has been broadened to include the mechanical testing of alloys, plastics, ceramics, composites, and common engineering components such as fasteners, gears, bearings, adhesive joints, and welds. This new scope is also complemented by substantial updates and additions in the coverage of traditional quasi-static testing, hardness testing, surface testing, creep deformation, high strain rate testing, fracture toughness, and fatigue testing.

The efforts of many people are to be commended for creating this useful, comprehensive reference on mechanical testing. The ASM Handbook Committee, the editors, the authors, the reviewers, and ASM staff

have collaborated to produce a book that meets high technical standards for the benefit of engineering communities everywhere. To all who contributed to the completion of this task, we extend our sincere thanks.

ASH Khare

President, ASM International

Michael J. DeHaemer

Managing Director, ASM International

Preface

At least three major trends have occurred since the last edition of Volume 8 in 1984. First, concurrent engineering is growing in importance in the industrial world, and mechanical testing plays a major role in concurrent engineering through the measurement of properties of product design, as well as for deformation processing. *ASM Handbook*, Volume 20, *Materials Selection and Design* (1997) reflects this focus in concurrent engineering and the broadening spectrum of involvement of materials engineers. Second, new methods of measurement have evolved such as strain measurement by vision systems and ultrasonic methods for measurement of elastic properties. This area will continue to grow as miniaturized sensors and computer vision technologies mature. Third, computer modeling capabilities, based on fundamental continuum principles and numerical methods, have entered the mainstream of everyday engineering. The validity of these computer models depends heavily on the availability of accurate material properties from mechanical testing.

Toward this end, this revision of *ASM Handbook*, Volume 8 is intended to provide up-to-date, practical information on mechanical testing for metals, plastics, ceramics, and composites. The first section, "Introduction to Mechanical Testing and Evaluation," covers the basics of mechanical behavior of engineering materials and general engineering aspects of mechanical testing including coverage on the accreditation of testing laboratories, mechanical tests in metalworking operations, and the general mechanical tests of plastics and ceramics. The next three sections are organized around the basic modes of loading of materials: tension, compression bending, shear, and contact loads. The first four modes (tension, compression, bending, and shear) are the basic simple loading types for determination of bulk properties of materials under quasi-static or dynamic conditions.

The third section, "Hardness Testing," describes the various methods for indentation testing, which is a relatively inexpensive test of great importance in manufacturing quality control and materials science. This section includes new coverage on instrumented (nano-indentation) hardness testing and the special issues of hardness testing of ceramics. Following the section on hardness testing, the fourth section addresses the mechanical evaluation of surfaces in terms of adhesion and wear characteristics from point loading and contact loading. These methods, often in conjunction with hardness tests, are used to determine the response of surfaces and coatings to mechanical loads.

The next four sections cover mechanical testing under important dynamic conditions of slow strain rates (i.e., creep deformation and stress relaxation), high strain rate testing, dynamic fracture, and fatigue. These four sections cover the nuances of testing materials under the basic loading types but with the added dimension of time as a factor. Very long-term, slow rate of loading (or unloading) in creep and stress relaxation is a key factor in many high-temperature applications and the testing of viscoelastic materials. On the opposite end of the spectrum, high strain rate testing characterizes material response during high-speed deformation processes and dynamic loading of products. Fracture toughness and fatigue testing are the remaining two sections covering engineering dynamic properties. These sections include coverage on the complex effects of temperature and environmental degradation on crack growth under cyclic or sustained loads.

Finally, the last section focuses on mechanical testing of some common types of engineering components such as gears, bearings, welds, adhesive joints, and mechanical fasteners. A detailed article on residual stress measurements is included, as residual stress from manufacturing operations can be a key factor in some forms of mechanical performance such as stress corrosion cracking and fatigue life analysis. Coverage of fiber-reinforced composites is also included as a special product form with many special and unique testing and evaluation requirements.

In this extensive revision, the end result is over 50 new articles and an all-new Volume 8 of the *ASM Handbook* series. As before, the key purpose of this Handbook volume is to explain test set-up, common testing problems and solutions, and data interpretations so that reasonably knowledgeable, but inexperienced, engineers can understand the factors that influence proper implementation and interpretation. Easily obtainable and

recognizable standards and research publications are referenced within each article, but every attempt is made to provide sufficient clarification so that inexperienced readers can understand the reasons and proper interpretation of published industrial test standards and research publications.

In this effort, we greatly appreciate the knowledgeable guidance and support of all the section editors in developing content requirements and author recommendations. This new content would not have been possible without their help: Peter Blau, Oak Ridge National Laboratory; James C. Earthman, University of California, Irvine; Brian Klotz, General Motors Corporation; Peter K. Liaw, University of Tennessee; Sia Nemat-Nasser, University of California, San Diego; Todd M. Osman, U.S. Steel Research; Gopal Revankar, Deere & Company; Robert Ritchie, University of California at Berkeley. Finally, we are all especially indebted to the volunteer spirit and devotion of all the authors, who have given us their time and effort in putting their expertise and knowledge on paper for the benefit of others. This work would not have been possible without them.

Howard Kuhn

Concurrent Technologies Corporation

Dana Medlin

The Timken Company

General Information

Officers and Trustees of ASM International (1997 - 1998)

Officers

- **Ash Khare**, President and Trustee, National Forge Company
- **Aziz I. Asphahani**, Vice President and Trustee, Carus Chemical Company
- **Michael J. DeHaemer**, Secretary and Managing Director, ASM International
- **Peter R. Strong**, Treasurer, Buehler Krautkrämer
- **Hans H. Portisch**, Immediate Past President, Krupp VDM Austria GmbH

Trustees

- **E. Daniel Albrecht**, Advanced Ceramics Research, Inc.
- **W. Raymond Cribb**, Brush Wellman Inc.
- **Gordon H. Geiger**, University of Arizona-Tucson Office & Consultant, T.P. McNulty & Associates
- **Walter M. Griffith**, Wright-Patterson Air Force Base
- **Jennie S. Hwang**, H-Technologies Group Inc.
- **C. "Ravi" Ravindran**, Ryerson Polytechnic University
- **Thomas G. Stoebe**, University of Washington
- **Robert C. Tucker, Jr.**, Praxair Surface Technologies, Inc.
- **James C. Williams**, The Ohio State University

Members of the ASM Handbook Committee (1984–1985)

- **Craig V. Darragh**

(Chair 1999-; Member 1989-)

The Timken Company

- **Bruce P. Bardes** (1993-)

Materials Technology Solutions Company

- **Rodney R. Boyer** (1982-1985; 1995-)

Boeing Commercial Airplane Group

- **Toni M. Brugger** (1993-)
Carpenter Technology Corporation
- **Henry E. Fairman** (1993-)
MQS Inspection Inc.
- **Michelle Gauthier** (1990-)
Raytheon Systems Company
- **Larry D. Hanke** (1994-)
Materials Evaluation and Engineering Inc.
- **Jeffrey A. Hawk** (1997-)
U.S. Department of Energy
- **Dennis D. Huffman** (1982-)
The Timken Company
- **S. Jim Ibarra, Jr.** (1991-)
Amoco Corporation
- **Dwight Janoff** (1995-)
FMC Corporation
- **Kent L. Johnson** (1999-)
Engineering Systems, Inc.
- **Paul J. Kovach** (1995-)
Stress Engineering Services Inc.
- **Peter W. Lee** (1990-)
The Timken Company
- **Donald R. Lesuer** (1999-)
Lawrence Livermore National Laboratory
- **Huimin Liu** (1999-)
Citation Corporation

- **William L. Mankins**(1989-)
Metallurgical Services Inc.
- **Dana J. Medlin** (1998-)
The Timken Company
- **Mahi Sahoo** (1993-)
CANMET
- **Srikanth Raghunathan** (1999-)
Nanomat Inc.
- **Karl P. Staudhammer** (1997-)
Los Alamos National Laboratory
- **Kenneth B. Tator** (1991-)
KTA-Tator Inc.
- **George F. Vander Voort** (1997-)
Buehler Ltd.
- **Dan Zhao** (1996-)
Johnson Controls Inc.

Previous Chairs of the ASM Handbook Committee

- **R. J. Austin**
(1992–1994) (Member, 1984-)
- **L.B. Case**
(1931–1933) (Member, 1927–1933)
- **T.D. Cooper**
(1984-1986) (Member 1981-1986)
- **E.O. Dixon**
(1952–1954) (Member, 1947–1955)
- **R.L. Dowdell**
(1938–1939) (Member, 1935–1939)

- **M.M. Gauthier**
(Chair 1997-1998; Member 1990-)
- **J.P. Gill**
(1937) (Member, 1934–1937)
- **J.D. Graham**
(1966–1968) (Member, 1961–1970)
- **J.F. Harper**
(1923–1926) (Member, 1923–1926)
- **C.H. Herty, Jr.**
(1934–1936) (Member, 1930–1936)
- **D.D. Huffman**
(1986-1990) (Member 1982-)
- **J.B. Johnson**
(1948–1951) (Member, 1944–1951)
- **L.J. Korb**
(1983) (Member, 1978–1983)
- **R.W.E. Leiter**
(1962–1963) (Member, 1955–1958, 1960–1964)
- **G.V. Luerssen**
(1943–1947) (Member, 1942–1947)
- **G.N. Maniar**
(1979–1980) (Member, 1974–1980)
- **W.L. Mankins**
(1994-1997) (Member 1989-)
- **J.L. McCall**
(1982) (Member, 1977–1982)
- **W.J. Merten**

(1927–1930) (Member, 1923–1933)

- **D.L. Olson**

(1990–1992) (Member 1982–1988, 1989–1992)

- **N.E. Promisel**

(1955–1961) (Member, 1954–1963)

- **G.J. Shubat**

(1973–1975) (Member, 1966–1975)

- **W.A. Stadler**

(1969–1972) (Member, 1962–1972)

- **R. Ward**

(1976–1978) (Member, 1972–1978)

- **M.G.H. Wells**

(1981) (Member, 1976–1981)

- **D.J. Wright**

(1964–1965) (Member, 1959–1967)

Staff

ASM International staff who contributed to the development of the Volume included Steven R. Lampman, Project Editor; Bonnie R. Sanders, Manager of Production; Nancy Hrivnak and Carol Terman, Copy Editors; Kathleen Dragolich, Production Supervisor; and Candace Mullet and Jill Kinson, Production Coordinators. Editorial Assistance was provided by Erika Baxter, Kelly Ferjutz, Heather Lampman, Pat Morse, and Mary Jane Riddlebaugh. The Volume was prepared under the direction of Scott D. Henry, Assistant Director of Reference Publications and William W. Scott, Jr., Director of Technical Publications.

Conversion to Electronic Files

ASM Handbook, Volume 8, *Mechanical Testing and Evaluation* was converted to electronic files in 2003. The conversion was based on the First printing (2000). No substantive changes were made to the content of the Volume, but some minor corrections and clarifications were made as needed.

ASM International staff who contributed to the conversion of the Volume to electronic files included Sally Fahrenholz-Mann, Sue Hess, Bonnie Sanders, and Scott Henry. The electronic version was prepared under the direction of Stanley Theobald, Managing Director.

Copyright Information (for Print Volume)

Copyright © 2000 by ASM International
All rights reserved

No part of this book may be reproduced, stored, in a retrieval system, or transmitted, in any form or by any means, electronic, mechanical, photocopying, recording, or otherwise, without the written permission of the copyright owner.

First printing, October 2000

This book is a collective effort involving hundreds of technical specialists. It brings together in one book a wealth of information from world-wide sources to help scientists, engineers, and technicians to solve current and long-range problems.

Great care is taken in the compilation and production of this volume, but it should be made clear that no warranties, express or implied, are given in connection with the accuracy or completeness of this publication, and no responsibility can be taken for any claims that may arise.

Nothing contained in the ASM Handbook shall be construed as a grant of any right of manufacture, sale, use, or reproduction, in connection with any method, process, apparatus, product, composition, or system, whether or not covered by letters patent, copyright, or trademark, and nothing contained in the ASM Handbook shall be construed as a defense against any alleged infringement of letters patent, copyright, or trademark, or as a defense against any liability for such infringement.

Comments, criticisms, and suggestions are invited, and should be forwarded to ASM International.

Library of Congress Cataloging-in-Publication Data (for Print Volume)

ASM Handbook.

Includes bibliographical references and indexes.

Contents: v. 1. Properties and selection—v. 2. Properties and selection—nonferrous alloys and puremetals—[etc.]—v. 8. Mechanical testing.

1. Metals—Handbooks, manuals, etc. 2. ASM International. Handbook Committee.

TA459.M43 1990 620.1'6 90-115

SAN 204-7586

ISBN 0-87170-389-0

ASM International

Materials Park, OH 44073-0002

www.asminternational.org

Copyright © ASM International®. All Rights Reserved.

Introduction to the Mechanical Behavior of Metals

Todd M. Osman, U.S. Steel Research; Joseph D. Rigney, General Electric Aircraft Engines

Introduction

THE SUCCESSFUL EMPLOYMENT OF METALS in engineering applications relies on the ability of the metal to meet design and service requirements and to be fabricated to the proper dimensions. The capability of a metal to meet these requirements is determined by the mechanical and physical properties of the metal. Physical properties are those typically measured by methods not requiring the application of an external mechanical force (or load). Typical examples of physical properties are density, magnetic properties (e.g., permeability), thermal conductivity and thermal diffusivity, electrical properties (e.g., resistivity), specific heat, and coefficient of thermal expansion. Mechanical properties, the primary focus of this Volume, are described as the relationship between forces (or stresses) acting on a material and the resistance of the material to deformation (i.e., strains) and fracture. This deformation, however, may or may not be evident in the metal after the applied load is removed. Different types of tests, which use an applied force, are employed to measure properties, such as elastic modulus, yield strength, elastic and plastic deformation (i.e., elongation), hardness, fatigue resistance, and fracture toughness. Typical specimens for these evaluations are shown in Fig. 1.

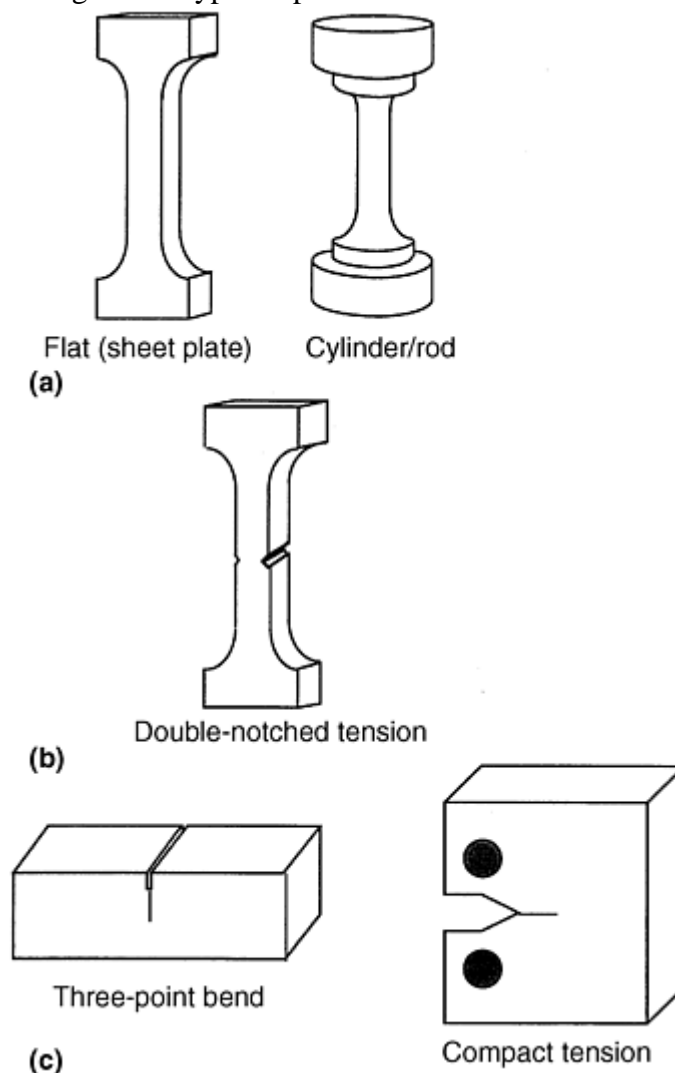


Fig. 1 Typical specimens for (a) tension testing, (b) notched tension testing, and (c) fracture toughness testing

As will be highlighted throughout the discussion below, mechanical properties are highly dependent on microstructure (e.g., grain size, phase distribution, second phase content), crystal structure type (i.e., the arrangement of atoms), and elemental composition (e.g., alloying element content, impurity level). A common illustration of the relationship between micro-structure and mechanical performance is the often observed increase in yield stress with a decrease in grain size. Relationships like these between metal structure and performance make mechanical property determination important for a wide variety of structural applications in metal working, in failure analysis and prevention, and in materials development for advanced applications. The following discussions are designed to briefly introduce typical relationships between metallurgical features (such as crystal structures and microstructures) and the mechanical behavior of metals. Using basic examples, deformation and fracture mechanisms are introduced. Typical properties measured during mechanical testing are then related to these deformation mechanisms and the microstructures of metals.

Introduction to the Mechanical Behavior of Metals

Todd M. Osman, U.S. Steel Research; Joseph D. Rigney, General Electric Aircraft Engines

Structure of Metals

At the most basic level, metallic materials (as well as many nonmetallic ones) are typically crystalline solids, although it is possible to produce amorphous metals (i.e., those with random atomic arrangement) in limited quantities. The basic building block of the crystal lattice is the unit cell, some examples of which are shown in Fig. 2(a) through (d). By repeating this arrangement in three dimensions, a crystal lattice is formed (see Fig 2.). Although the arrangement of atoms in space can be of fourteen different types (or Bravais lattices), most metals have face-centered cubic (fcc) (e.g., nickel, aluminum, copper, lead), body-centered cubic (bcc) (e.g., iron, niobium, tungsten, molybdenum), or hexagonal close-packed (hcp) (e.g., titanium, magnesium, zinc) structures as the unit cell structure. In very specific applications, materials can be used as single crystals where an entire component is fabricated with one spatial orientation repeating throughout. More often than not, however, engineering materials usually contain many crystals, or grains, as shown in Fig. 3. Depending on the composition and thermomechanical processing, these grains are typically approximately 1 to 1000 μm in size (although finer grain sizes can be produced via other techniques). While the crystal lattice within a grain is consistent, the crystalline orientations vary from one grain to another.

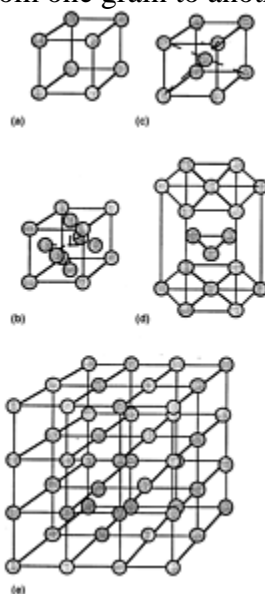


Fig. 2 Examples of crystal structures. Unit cells: (a) simple cubic, (b) face-centered cubic, (c) body-centered cubic, and (d) hexagonal close-packed. A crystal lattice: (e) three-dimensional simple cubic

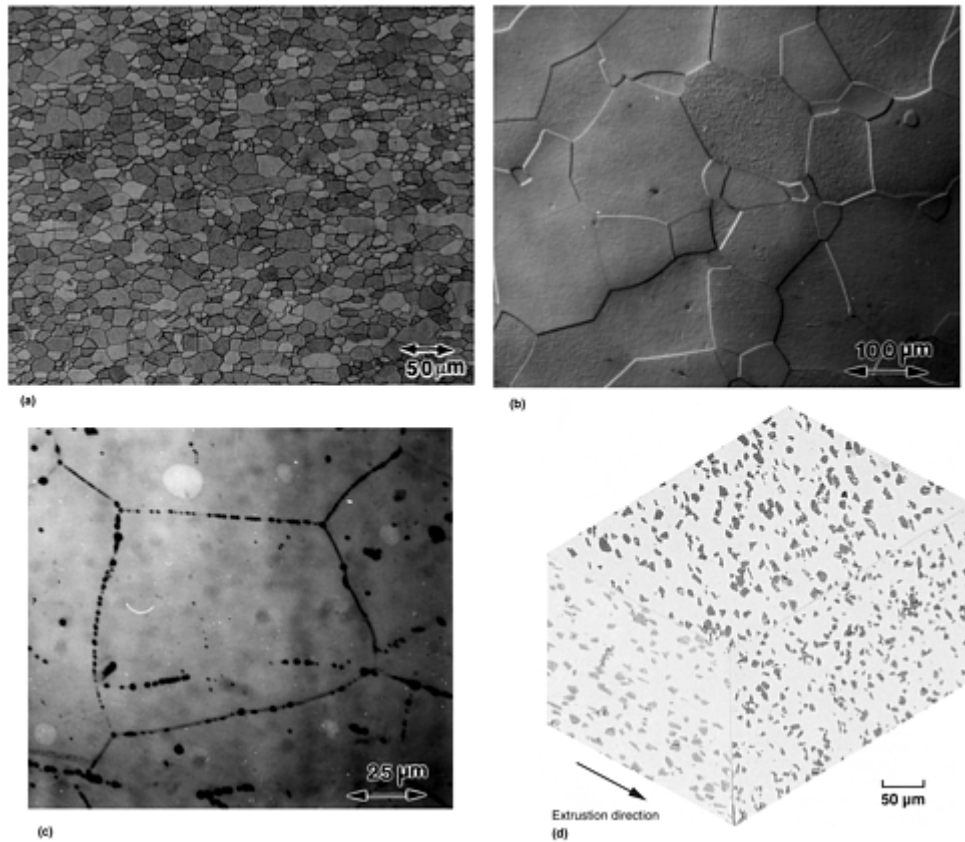


Fig. 3 Examples of metallic microstructures: (a) Grains in an ultralow-carbon steel. Courtesy of U.S. Steel. (b) Grains in pure niobium. (c) Precipitates at grain boundaries in niobium. (d) Discontinuously reinforced metal matrix composite (silicon carbide particles in an aluminum matrix). Source:Ref 1. Note: the grains in a–c are highlighted through the use of a chemical etchant.

Although some nonstructural applications may require pure metals because of certain physical property advantages, additions of alloying elements are usually made for purposes of enhancing the mechanical properties or other material characteristics (e.g., corrosion resistance). Metal alloys may consist of over ten different elements in specific concentrations with the purpose to optimize a variety of properties. Minor alloying additions typically do not alter the basic crystal structure as long as the elements remain in solid solution. At sufficiently high concentrations, other phases (either with the same or different crystallographic forms) may precipitate within the base metal (at grain boundaries or in the grain interior) as shown in Fig. 3. Phase diagrams are used by metallurgists and materials engineers to understand equilibrium solubility limits in engineering alloys and predict the phases which may form during thermomechanical processing (Ref 2). As will be discussed later, solid solution elements and precipitates/particles are often used during alloy design to improve the strength of a metal.

Metal matrix composites can also be fabricated in which dissimilar constituents (e.g., ceramics and intermetallics) are incorporated into the metallic microstructure in order to enhance mechanical properties. The example microstructure in Fig. 3 shows the reinforcement material to be dispersed throughout a continuous metallic matrix with the metal representing 50% or greater of the total volume. Although the example shows particles as the reinforcement, these materials can be designed with whiskers, short fibers, or long fibers (e.g., rods or filaments). Processing of these composites typically entails the incorporation of the reinforcement material into the metal using ingot metallurgy or powder metallurgy techniques (Ref 3).

To the structural engineer, or in the macroscopic view ($1\times$), most metals appear to be continuous, homogeneous, and isotropic. Continuity assumes that structures do not contain voids; homogeneity assumes that the microstructure (in views at $\sim 100\text{--}1000\times$) and properties will be identical in all locations; isotropic behavior assumes that the properties are identical in all orientations. While these assumptions have been used in continuum mechanics to study the strength of materials and structures under load, engineering materials are often inhomogeneous and anisotropic. While it is desirable to minimize such inhomogeneities, it is often impossible to completely eliminate them. As discussed above, microstructural evaluation typically shows that

materials are comprised of an aggregate of grains of unique crystal structure and usually have second phases (with different properties) dispersed throughout the parent structure. Typically, materials will have variations in grain size, second phase size and distribution, and chemical composition, especially in binary and higher-order alloys. Fabrication route may also play a key role in affecting the preferred crystallographic orientation (or texture) of the grains, further contributing to the inhomogeneity and anisotropy of the microstructure. As will be shown later, all of these microstructural features can greatly influence the properties measured during mechanical testing.

When metals are subject to an external force, the response will depend on a number of factors. The type of loading (e.g., tension, compression, shear, or combinations thereof) is one key factor. The strain rate, temperature, nature of loading (monotonic versus alternating fatigue stresses), and presence of notches will also affect the deformation response of the metal. Chemical influences, such as those associated with stress-corrosion cracking (SCC) and hydrogen embrittlement, as well as physical alterations, such as those resulting from radiation damage, may affect the deformation behavior. Finally, the specimen size and surface preparation can influence the response observed during mechanical testing.

All of these factors are important and will be covered in various articles contained within this Volume. For simplicity, the remainder of this section focuses on basic examples to illustrate the relationship between the structure of a metal and the properties measured during mechanical testing.

References cited in this section

1. T.M. Osman, J.J. Lewandowski, and W.H. Hunt, Jr., *Fabrication of Particulates Reinforced Metal Composites*, ASM International, 1990, p 209
2. Alloy Phase Diagrams, Vol 3, *ASM Handbook*, ASM International, 1992
3. D. Hull, *An Introduction to Composite Materials*, Cambridge University Press, 1975

Introduction to the Mechanical Behavior of Metals

Todd M. Osman, U.S. Steel Research; Joseph D. Rigney, General Electric Aircraft Engines

Deformation of Metals

The basic principles of deformation and fracture can be described through the use of a uniaxial tension (or tensile) test. A detailed review of tension testing is presented later in this Volume; therefore, only a brief description is presented for the purpose of introducing deformation and fracture mechanisms in metals. In general, tensile tests are performed on cylindrical specimens (e.g., rods) or parallel-piped specimens (e.g., sheet and plate) as shown in Fig. 1(a). The samples are loaded uniaxially, along the length of the specimen. The applied load and extension (or change in length) of the sample are simultaneously measured.

The load and displacement are used to calculate engineering stress (s) and engineering strain (e) using Eq 1 and Eq 2 :

$$S = P/A_0 \quad (\text{Eq 1})$$

$$e = \Delta L/L_0 = (L_i - L_0)/L_0 \quad (\text{Eq 2})$$

where P is the applied load, L_0 is the initial gage length, L_i is the instantaneous gage length, A_0 is the initial gage cross-sectional area, and ΔL is the change in length. This analysis facilitates the comparison of results obtained when testing samples that differ in thickness or geometry. (For validity, the samples need to conform to certain design specifications as detailed later in this Volume.) Although these engineering values are adequate, the best measures of the response of a material to loading are the true stress (σ) and true strain (ϵ) determined by the instantaneous dimensions of the tensile specimen in Eq 3 and Eq 4:

$$\sigma = P/A_i = S(1 + e) \quad (\text{Eq 3})$$

$$\varepsilon = \ln(L_i/L_0) = (1 + e)$$

(Eq 4)

Because the instantaneous dimensions of the specimen are not typically measured, the true stress and true strain may be estimated using the engineering stress and engineering strain (see Eq 1 and Eq 2). It is noted that these estimations are only valid during uniform elongation (see Fig. 4) and are not applicable throughout the entire deformation range.

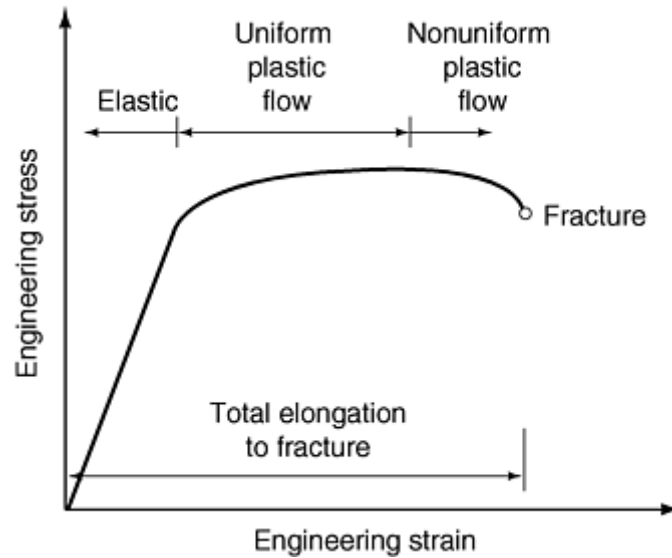


Fig. 4 Typical engineering stress-versus-engineering strain curve

Figure 4 depicts a typical engineering stress-versus-engineering strain curve produced in a uniaxial tension test. In the initial stages of deformation, generally stress varies linearly with the strain. In this region, all deformation is considered to be elastic because the sample will return to its original shape (i.e., dimensions) when the applied stress is removed. If, however, the sample is not unloaded and deformation continues, the stress-versus-strain curve becomes nonlinear. At this point, plastic deformation begins, causing a permanent elongation that will not be recovered after unloading of the specimen. The stress at which a permanent deformation occurs is called the elastic (or proportional) limit; however, an offset yield strength (e.g., 0.2% offset) is typically used to quantify the onset of plastic deformation due to the ease and standardization of measurement. The tensile yield strength of most alloys is on the order of 10^2 to 10^3 MPa:

- 135 to 480 MPa (20–70 ksi) for low-carbon steels
- 200 to 480 MPa (30–70 ksi) for aluminum alloys
- 1200 to 1650 MPa (175–240 ksi) for high-strength steels

To understand the different deformation modes, the structure of a metal must be considered. Elastic deformation can be conceptualized by considering the bonds between individual atoms to be springs. As mentioned above, a metal will stretch under the application of a load, but will return to its original shape after the removal of that load if only elastic deformation occurs. Just as a spring constant relates the force to the applied displacement (i.e., $F = kx$), the elastic modulus (E) relates the tensile stress to the applied tensile strain (i.e., $\sigma = E\varepsilon$) and is simply the slope of the linear portion of the tensile stress-versus-tensile strain curve produced in the tension test. Differences in the measured elastic moduli for different metals can therefore be rationalized in part by the differences in the atomic bonds between the individual atoms within the crystal lattice.

Plastic deformation results in a permanent change of shape, meaning that after the load is removed, the metal will not return to its original dimensions. This implies a permanent displacement of atoms within the crystal lattice. If a perfect crystal is assumed, this deformation could only occur by breaking all of the bonds at once between two planes of atoms and then sliding one row (or plane) of atoms over another. Based on calculations using the theoretical bond strengths, this process would result in yield strengths on the order of 10^4 to 10^5 MPa. These strengths are much greater than those typically observed in actual metals (10^2 MPa); therefore, deformation must occur via a different method.

Even under the most ideal crystal growth conditions, metals are not crystallographically perfect, as shown in Fig. 2. Instead, the lattice may contain many imperfections. One such imperfection is an edge dislocation, which, for simple cubic structures, can be considered to be the extra half plane of atoms shown schematically in Fig. 5. Regions surrounding the dislocation may be a perfect array of atoms; however, the core of the dislocation is shown as a localized distortion of the crystal lattice. While it may appear that this structure is unfavorable, dislocations are necessary in metals. For example, at grain boundaries, dislocations are “geometrically necessary” to allow the individual grains of different orientations to match.

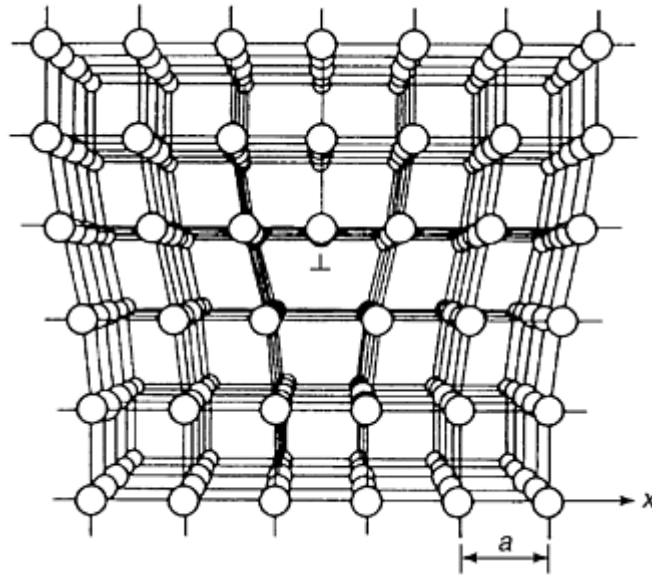


Fig. 5 Schematic of an edge dislocation

The nature and quantity of the dislocations become an integral aspect of plastic deformation. There are two generic types of dislocations, edge and screw, which are primarily differentiated by the manner in which each may traverse through the metallic crystal (Ref 4). It is noted that dislocations of mixed character (i.e., partially edge and partially screw) are most commonly observed. In general, both types of dislocations entail the stepwise movement of the dislocation across the crystal lattice as opposed to the displacement of an entire plane over another. This means that only one set of bonds is broken at a time as opposed to an entire plane. Motion now occurs on a distinct set of slip systems, which are combinations of planes—denoted as $\{uvw\}$ or (uvw) —and directions—denoted as $\langle hkl \rangle$ or $[hkl]$ —based on the closest packing of atoms within the crystal structure (see Fig. 6 for an example of crystallographic planes and directions) (Ref 5). For example, motion will predominantly occur on $\{111\} \langle 110 \rangle$ slip systems in fcc metals and on $\{110\} \langle 111 \rangle$, $\{112\} \langle 111 \rangle$, or $\{123\} \langle 111 \rangle$ slip systems in bcc metals. As a result, differences in the plastic behavior of a given type of metal (e.g., aluminum-killed versus fully stabilized steels) can in part be rationalized by which slip systems are active during deformation. Likewise, differences in the properties between different metal types (e.g., bcc iron versus fcc aluminum versus hcp titanium) can be related to the active slip systems in each metal and the relative ease with which dislocations can move within the slip systems.

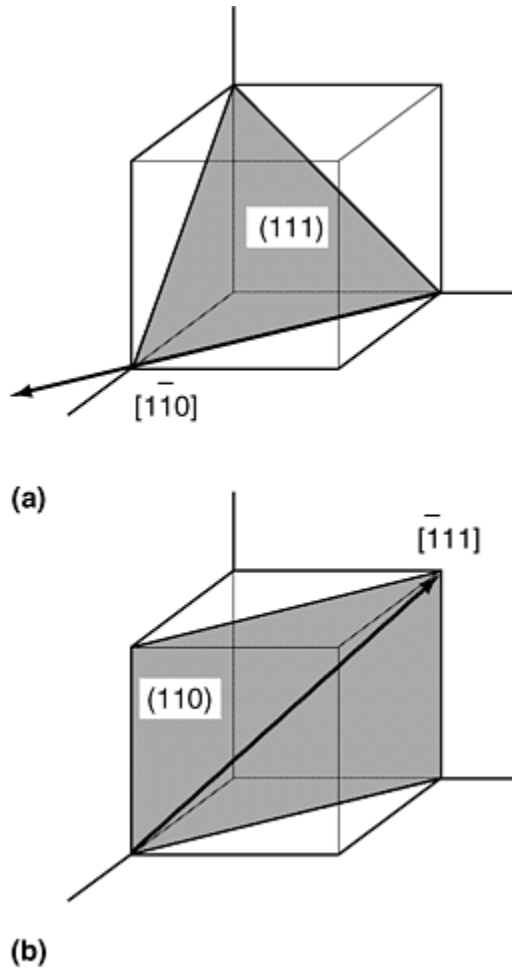


Fig. 6 Examples of crystallographic planes and directions. (a) $(111)[\bar{1}\bar{1}0]$ and (b) $(110)(\bar{1}\bar{1}1)$

Motion within a slip system is governed by the critical resolved shear strength (τ_{CRSS}). As shown schematically in Fig. 7 for a single crystal, the attainment of τ_{CRSS} on a given slip system is related to the geometric relationship between the applied load and the slip system. This relationship is described mathematically by Schmid's law.

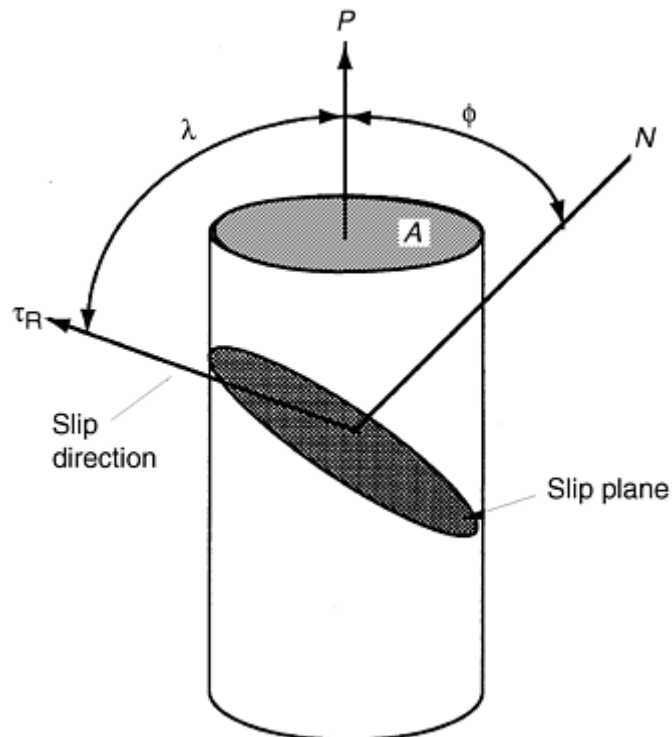


Fig. 7 Schmid's law. $\tau_R = (P/A) \text{COS } \phi \text{COS } \lambda$. Note: plastic flow on a given slip system will initiate when $\tau_R > \tau_{CRSS}$

In polycrystalline metals, plastic flow typically does not occur at a constant stress. In contrast, an increased stress must be applied to produce additional deformation, as shown in Fig 4. This trend can be rationalized by considering the motion, interaction, and multiplication of dislocations. As plastic flow continues, the number of dislocations increases, typically in a parabolic fashion (Ref 6). These dislocations begin to interact with each other and with interfaces such as grain boundaries. When a dislocation encounters a grain boundary, motion is usually halted. Although direct transmission to the neighboring grain may occur (Ref 7, 8, 9), more typically dislocations start to build up at the grain boundary and dislocation tangles may be created. As this buildup continues, a back stress develops that opposes the motion of additional dislocations, giving rise to work hardening (i.e., the increase in strength with straining shown in Fig. 4) (Ref 7).

Typically, the work hardening of a metal is calculated by assuming a parabolic fit to the true stress-versus-true strain data as suggested by Eq 5:

$$\sigma = K\varepsilon^n \quad (\text{Eq 5})$$

where K is the strength coefficient and n is the strain-hardening exponent. The true stress and true strain measured (or calculated from Eq 1 Eq 2 Eq 3 Eq 4) can be used to determine the strain-hardening exponent (n -value). This exponent is simply the slope calculated after plotting the logarithm of true stress versus the logarithm of true strain:

$$\log \sigma = n \log \varepsilon + \log K \quad (\text{Eq 6})$$

As will be discussed later in this Volume, the value of the strain-hardening exponent becomes important when predicting the response of metals to straining during primary metalworking as well as forming operations for final components.

As shown in Fig. 4, there is a point in the stress-versus-strain curve where the work hardening can no longer compensate for the increase in local stress arising from the reduced cross-sectional area. At this point, nonuniform plastic flow occurs in which deformation is concentrated in one region, called a neck. Necking in the tensile specimen usually coincides with the maximum stress (i.e., the ultimate tensile strength) in an engineering stress-versus-engineering strain curve.

Figure 7 introduces the influence of crystallographic orientation on the deformation of single crystals. Although this relationship becomes more complex in polycrystalline metals, the deformation will still depend on the orientation of the load with respect to the active slip systems. For example, the tensile properties of a highly oriented (i.e., textured anisotropic) metallic sheet product will be different when measured parallel (longitudinal), normal (transverse), or at 45° (diagonal) to the rolling direction. The variation in plastic deformation in different orientations can be defined in terms of Lankford values (Ref 10). The individual Lankford values in Eq 7 are calculated using strains measured in a tensile test:

$$r = \varepsilon_w / \varepsilon_t = -\varepsilon_w / (\varepsilon_l + \varepsilon_w) \quad (\text{Eq 7})$$

where ε_w , ε_t , and ε_l are width, thickness, and longitudinal true strains measured from a parallel-sided tensile specimen, respectively. The mean plastic anisotropy (r_m) and normal plastic anisotropy (Δr) can be calculated using Eq 8 and Eq 9, respectively:

$$r_m = \frac{(r_0 + 2r_{45} + r_{90})}{4} \quad (\text{Eq 8})$$

$$\Delta r = \frac{(r_0 - 2r_{45} + r_{90})}{2} \quad (\text{Eq 9})$$

where r_0 , r_{45} , and r_{90} are the r -values calculated from sheet tensile specimens oriented at 0° (parallel), 45° (diagonal), and 90° (normal) to the rolling direction, respectively. As may be expected, Lankford values depend on the crystal structure. Figure 8 relates the calculated Lankford values with crystallographic texture for a low-carbon steel as measured using X-ray diffraction techniques, further highlighting the influence of metallic structure on mechanical behavior.

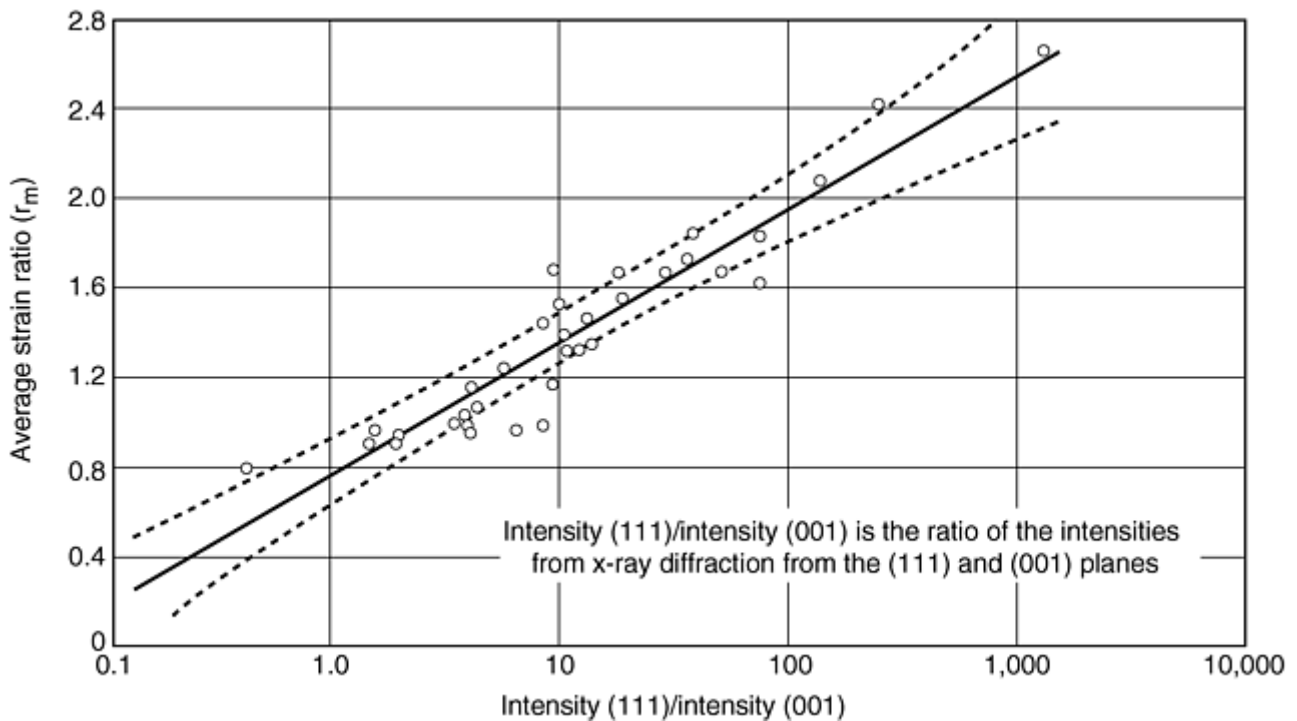


Fig. 8 Relationship between average (mean) plastic strain ratio (r_m) and crystallographic texture.
Source: Ref 11

References cited in this section

4. R.W.K. Honeycombe, *The Plastic Deformation of Metals*, 2nd ed., Edward Arnold, London, 1984
5. D. Hull and D.J. Bacon, *Introduction to Dislocations*, Pergamon Press, London, 1984
6. A.S. Keh, *Direct Observations of Imperfections in Crystals*, J.B. Newbrick and J.H. Wernick, Ed., Interscience Publishers, New York, 1962, p 213–238
7. A.N. Stroh, *Proc. R. Soc. (London)*, Vol 223, 1954, p 404
8. Z. Shen, R.H. Wagoner, and W.A.T. Clark, *Acta Metall.*, Vol 36, 1988, p 3231
9. T.C. Lee, I.M. Robertson, and H.K. Birnbaum, *Metall. Trans. A*, Vol 21, 1990, p 2437
10. W.T. Lankford, S.C. Snyder, and J.A. Bauscher, *Trans. ASM*, Vol 42, 1950, p 1197–1228
11. J.F. Held, *Proc. Mechanical Working and Steel Processing Conference*, Vol 4, AIME, New York, 1965, p 3

Introduction to the Mechanical Behavior of Metals

Todd M. Osman, U.S. Steel Research; Joseph D. Rigney, General Electric Aircraft Engines

Strength of Metals

Thus far, the mechanical properties of crystalline metals have been discussed only in relationship to the crystal lattice. Because most metals are comprised of many grains (see Fig. 2), properties such as yield strength and ductility (i.e., elongation to fracture) are also highly dependent on the microstructure. Once again, the influence

of both of these factors can be rationalized by considering the motion of dislocations. The strength of a metal is related to the ease, or conversely the difficulty, of dislocation motion. If dislocation motion is uninhibited (i.e., motion is initiated easily and continues without hindrance), the strength will be low and relatively little work hardening will occur. In contrast, the presence of obstacles, or barriers, within the microstructure slow dislocation motion, resulting in an increase in strength.

Grain boundaries provide an obstacle to dislocation motion. As the grain size is decreased, the strength (σ) of the metal typically increases according to the Hall-Petch relationship given in Eq 10 and illustrated in Fig. 9 (Ref 12, 13):

$$\sigma = \sigma_0 + kd^{1/2} \quad (\text{Eq 10})$$

where σ_0 is the intrinsic strength of the metal, k is a coefficient, and d is the grain diameter. At small grain sizes, there is a larger probability of dislocation-dislocation interactions (e.g., dislocation “pile-up” at the grain boundaries), leading to a larger resistance to dislocation motion. As the grain size increases, the opposition to dislocation motion, due to back stresses associated with dislocation tangles at grain boundaries, lessens due to the larger distances between grain boundaries. Therefore, the lower strength of a large-grained metal when compared to a small-grained metal can be rationalized by a decrease in the resistance to dislocation motion.

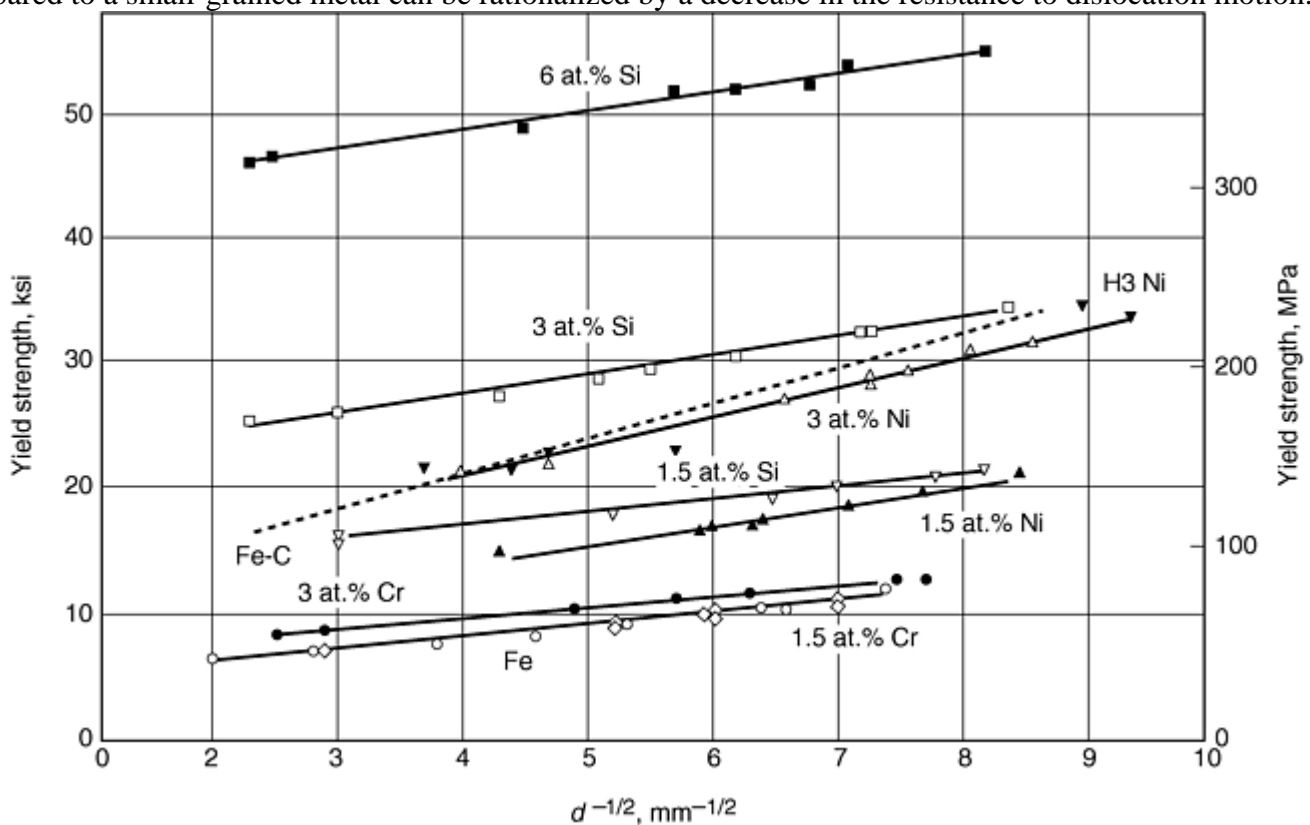


Fig. 9 Influence of grain size diameter (d) on yield strength for α -iron alloys. Source: Ref 12

The strength of a metal will also be related to the impurity content. Sometimes elements are intentionally added to metals, such as adding nickel to copper or phosphorus to steel. Other times, the presence of impurities, such as inclusions (e.g., oxides) in copper or solute carbon in steel, may be undesired. In order to rationalize these statements, the effect of each on plastic flow in metals needs to be considered. Figure 10 schematically illustrates two scenarios for incorporating atoms into a metallic matrix. Substitutional atoms (see Fig. 10a) take the place of matrix atoms. Because of the mismatch in atomic size between the substitutional atom and the matrix atom, the lattice may become locally strained. This lattice strain may impede dislocation motion and is conventionally considered to be the source of solid solution strengthening in metals. In general, the strengthening increment varies proportionally with the mismatch in atomic size and properties (specifically modulus) between the solute and solvent atoms, as shown in Fig. 11 (Ref 14).

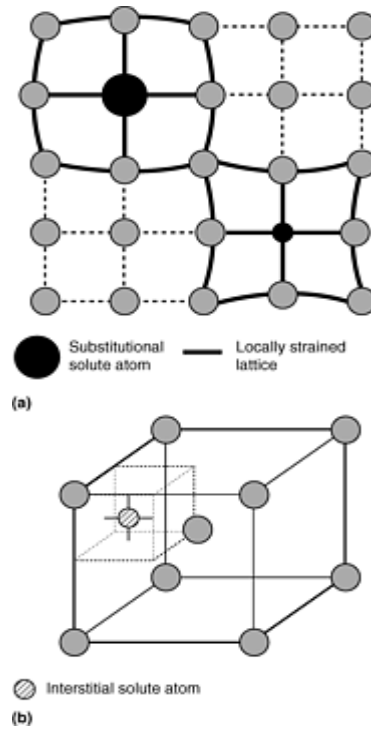


Fig. 10 Two scenarios of incorporating atoms into a metal matrix. (a) Substitutional atoms and (b) an interstitial atom in a body-centered cubic unit cell

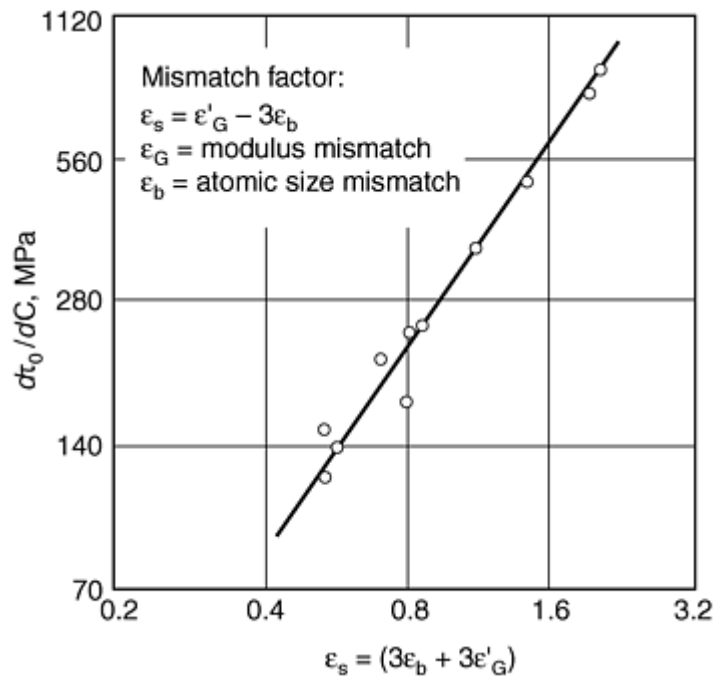


Fig. 11 Relationship between mismatch factor and strengthening increment ($\Delta\tau_0/\Delta C$) for solute atoms in copper alloys. Source: Ref 14

Interstitial atoms can also be present within the metal (see Fig. 10b). In this case, the atom is much smaller than the matrix atoms and is located in the gaps (or interstices) in the crystal lattice. Most often, interstitial atoms can diffuse to the dislocation core (see Fig. 5) due to the more open structure and the local tensile stresses in this region of the crystal lattice. The presence of the interstitial can inhibit dislocation motion, leading to dislocation “locking.” This locking necessitates larger applied stresses to produce dislocation motion and further plastic deformation (Ref 15). In the classic example of carbon in iron, such a mechanism can result in discontinuous yielding as shown in Fig. 12. Deformation is not continuous, and a sharp upper yield point is typically observed followed by yielding at a constant stress. The serrations in the stress-versus-strain curve in

Fig. 12 are most often attributed to the breakaway of dislocations from the solute carbon atoms. If the physical appearance of the tensile specimen is considered, localized distortions, called Lüders fronts (local regions of yielded material), will traverse the length of the specimen during yield-point elongation, and continuous plastic flow under an increasing load will not commence until the entire gage section has yielded. The extent of the yield-point elongation will depend on the density of mobile dislocations (i.e., those which are not “locked”) and the ease with which these dislocations can move once initiated (Ref 16).

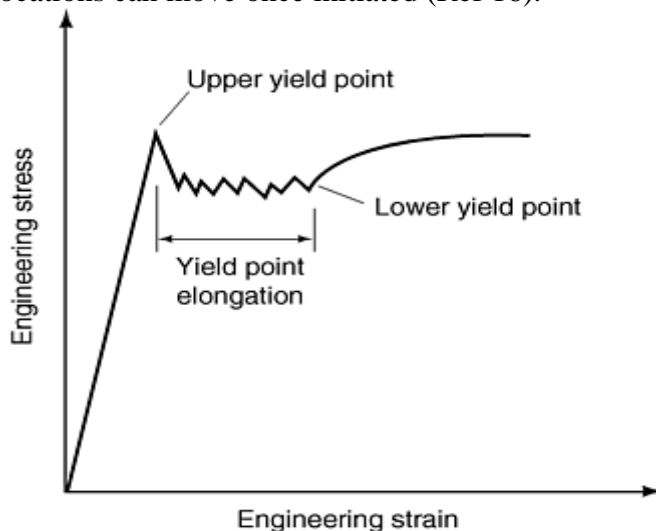


Fig. 12 Discontinuous yielding

Impurity atoms and interstitial alloy additions can often cause second phase particles or precipitates to be present in the structure. A fine dispersion of small particles generally produces a higher strength than a coarse dispersion of large particles, as suggested in Fig. 13. At each volume fraction, small particles (10 Å) produce a higher strength than large (100 Å) particles. The strengthening increase is related to two factors: (a) a higher probability of the mobile dislocation intersecting the particles due to the smaller interparticle spacing and (b) the higher fracture resistance of smaller particles. Conversely, as the size of the particles increases at a constant volume fraction, the interparticle spacing increases, causing the particles to become less effective strengtheners (i.e., barriers to dislocation motion) (Ref 18). This effect can be observed in hot-rolled, low-carbon steels. At low coiling temperatures, finer carbides (e.g., Fe₃C and NbC) are typically produced, resulting in increased strength. At higher coiling temperatures, the carbide particles coarsen at a constant volume fraction, which typically results in a lower strength.

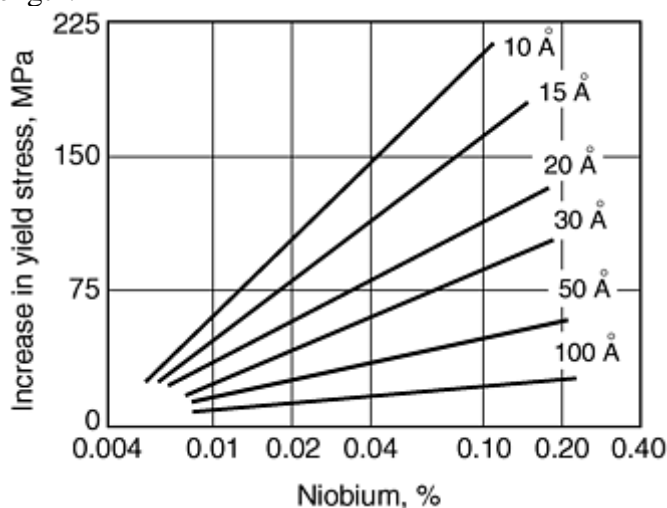


Fig. 13 Influence of particle size on yield strength (NbC in an HSLA steel). Source: Ref 17

A similar scenario occurs with age-hardenable aluminum alloys. The strength of these alloys varies as a function of time at temperature as shown in Fig. 14. The yield strength initially increases proportionally with time, but eventually reaches a maximum. Longer aging times then result in decreased yield strength. These

trends are once again directly related to the mechanisms of particle hardening. At short aging times, small coherent precipitates form that are effective strengtheners. Overaging (i.e., soaking past the maximum yield strength) causes the particles to coarsen, and the interparticle spacing increases, resulting in the decreased strength.

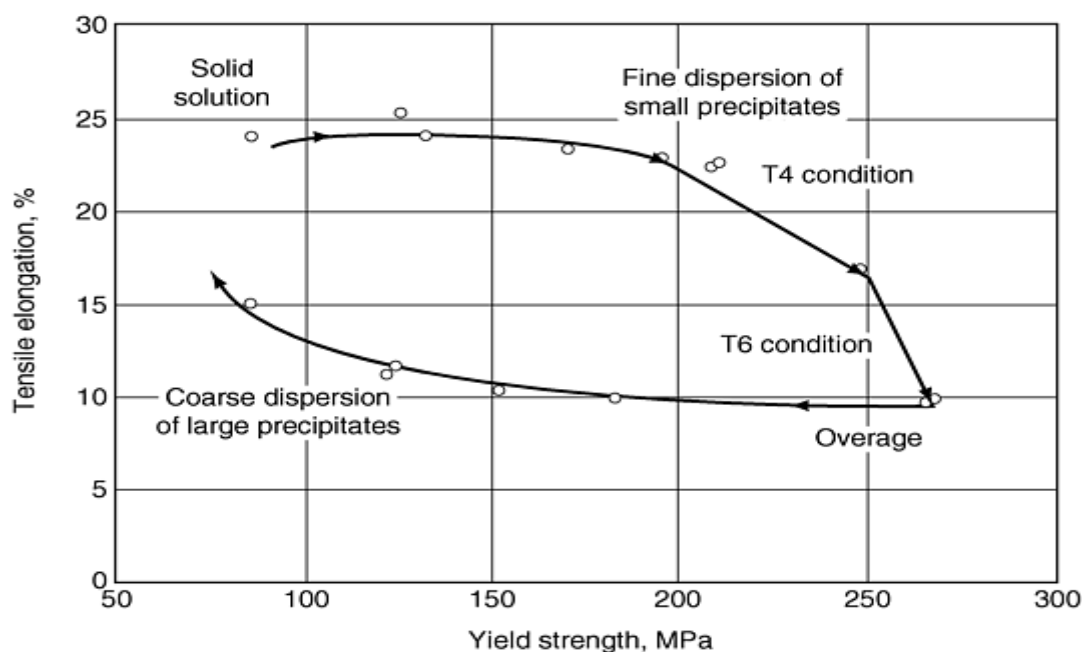


Fig. 14 Effect of aging heat treatment on ductility for a 2036 aluminum alloy. Source:Ref 19

Figure 14 also provides evidence that the ductility (i.e., the elongation prior to failure) of a metal will also be influenced by microstructural changes. Typically, there is an inverse relationship between strength and ductility. In order to rationalize this observation, the failure modes for metals need to be considered. In general, failure is classified as either ductile or brittle. There are many ways to differentiate the two types of failures, as illustrated in Table 1 and Fig. 15.

Table 1 Distinguishing characteristics of brittle versus ductile behavior depending on the scale of observation

Scale of observation	Brittle	Ductile
Structural engineer	Applied stress at failure is less than the yield stress	Applied stress at failure is greater than the yield stress
By eye (1×)	No necking, shiny facets, crystalline, granular	Necked, fibrous, woody
Macroscale (<50×)	“Low” RA or ductility	Medium to high RA
Microscale, scanning electron microscopy (100–10,000×)	Brittle microprocess, cleavage (see Fig. 15b), intergranular (see Fig. 15c)	Ductile microprocess, microvoid coalescence (see Fig. 15a)
Transmission electron microscopy (>10,000×)	May have a large level of local plasticity	High amount of plasticity globally

RA, reduction of area

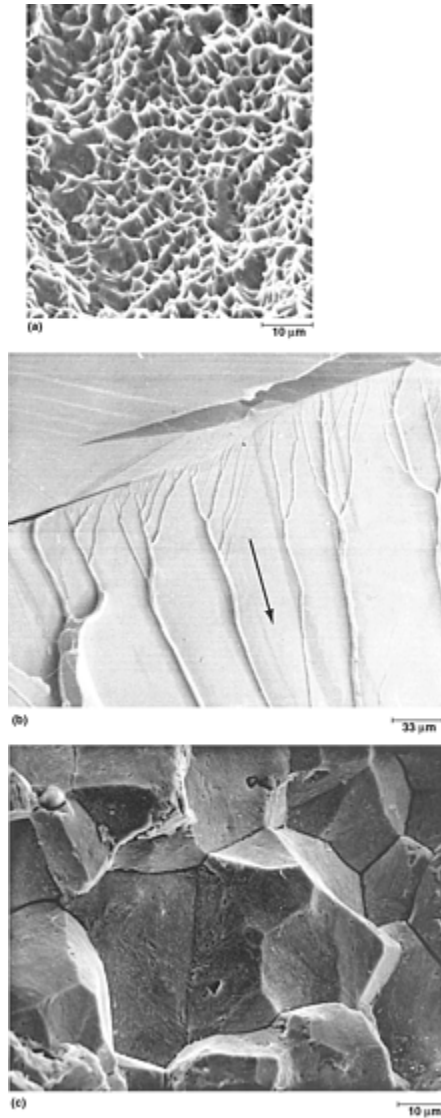


Fig. 15 Examples of fracture surfaces of metals failing by (a) microvoid coalescence, (b) cleavage, and (c) intergranular fracture. Source: Ref 20

Ductile fracture is generally preceded by stresses that exceed the yield stress, and specimens failing with high reductions of area and by shear or microvoid coalescence. The process of ductile fracture by microvoid coalescence has been described by several authors (Ref 21, 22, and 23). Microvoids nucleate predominantly at particles (e.g., inclusions, precipitates) that are present in nearly all metals. The particle size and shape, the particle-matrix interfacial strength, and the matrix flow strength influence the mechanism of void formation. In general, void nucleation by particle cracking is favored by increasing particle size, higher interfacial strengths, and the presence of nonequiaxed particles. By contrast, void nucleation by interfacial decohesion is more likely with smaller particles, weaker interfaces, and lower matrix flow strength (Ref 23). After nucleation, the voids will grow in the direction of the applied tensile stress and secondary voids can also nucleate at smaller particles. During necking, expansion of the voids can occur, leading to coalescence by void impingement (resulting in higher uniform strain) or by void sheet formation (lower, more local strain). After failure, a “dimpled” fracture surface is typically observed, as shown in Fig. 15(a).

As a result, the ductility of a metal typically decreases with increasing particle content, as shown in Fig. 16. An increase in particle volume fraction results in a larger number of potential void nucleation sites. Furthermore, there is an increased probability for the linkage of neighboring voids (impingement).

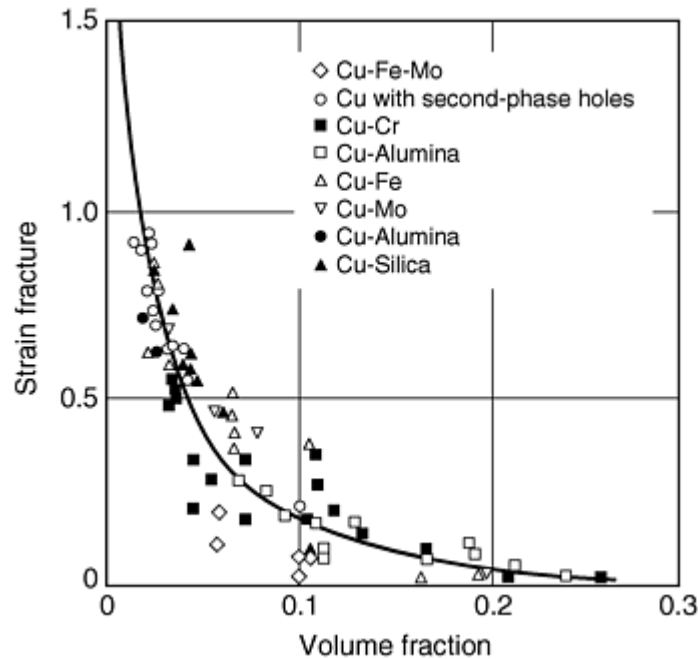


Fig. 16 Influence of particle content on ductility. Source: Ref 24

According to the descriptions in Table 1, brittle behavior is generally classified by failure at stresses below the yield strength and low reductions in area (little uniform strain) (Ref 25). Although this fracture process may be initiated by some dislocation activity, the levels generally detected are far below those found in a material exhibiting ductile behavior. Cleavage fracture, one of the brittle fracture modes, is distinguished by separation of individual grains along low index crystallographic planes in a transgranular manner—for example, iron cleaves along (100) planes. As shown in Fig. 15(b), lines on the cleavage facets, as seen in the scanning electron microscope (SEM), provide postmortem evidence of the direction of crack growth (i.e., the lines trace back to the origin of the failure origin). Each “line” is actually a step created between fractures propagating along parallel low index planes but separated by a small step. For pure cleavage, a step created on each side of the fracture surface should fit together except for some discrepancy that may occur due to some plasticity at the step. Another brittle fracture mode is intergranular fracture. In this case, a crack is initiated at grain boundaries and propagates along them. The grain-boundary facets appear to be “glassy smooth” as in Fig. 15(c). There may be evidence of local plasticity with tearing evident at the grain-boundary corners. It should be noted that intergranular microvoid coalescence, which is locally ductile fracture in grain boundary regions, can also occur.

References cited in this section

12. W.B. Morrison and W.C. Leslie, *Metall. Trans.*, Vol 4, 1973, p 379
13. N.J. Petch, *J. Iron Steel Inst. Jpn.*, Vol 173, 1953, p 25
14. Fleischer, *Acta Metall.*, Vol 11, 1963, p 203
15. J. Heslop and N.J. Petch, *Philos. Mag.*, Vol 2, 1958, p 649
16. G.T. Hahn, *Acta Metall.*, Vol 10, 1962, p 727
17. W.J. Murphy and R.G.B. Yeo, *Met. Prog.*, Sept 1969, p 85
18. J.W. Martin, *Micromechanisms in Particle Hardened Alloys*, Cambridge University Press, 1980
19. L.B. Morris et al., *Formability of Aluminum Sheet Alloys, Aluminum Transformation Technology and Applications*, C.A. Pampillo et al., Ed., American Society for Metals, 1982, p 549

20. V. Kerlins and A. Philips, Modes of Fracture, *Fractography*, Vol 12, ASM Handbook, ASM International, 1987, p 12–71
21. I. Kirman, *Metall. Trans.*, Vol 2, 1971, p 1761
22. R.H. Van Stone, T.B. Cox, J.R. Low, and J.A. Psioda, *Int. Met. Rev.*, Vol 30, 1985, p 157
23. W.M. Garrison, Jr. and N.R. Moody, *J. Phys. Chem. Solids*, Vol 48, 1987, p 1035
24. B.I. Edelson and W.M. Baldwin, *Trans. ASM*, Vol 55, 1962, p 230
25. G.E. Dieter, *Mechanical Metallurgy*, 3rd ed., McGraw-Hill, 1986

Introduction to the Mechanical Behavior of Metals

Todd M. Osman, U.S. Steel Research; Joseph D. Rigney, General Electric Aircraft Engines

Special Conditions in Flow: Temperature and Strain Rate

Many of the most widely employed structural metals have bcc lattices (e.g., steels, refractory metals) or fcc lattices (e.g., aluminum, copper). The strength of fcc metals is relatively insensitive to test temperature; however, the properties of bcc metals are typically highly dependent on testing conditions. This dissimilar behavior is related to the nature of dislocation motion with the individual crystal lattices. Face-centered cubic metals are more closely “packed” (i.e., a shorter distance exists between atoms in the unit cell of Fig. 2) than body-centered cubic metals. A common slip system (i.e., $\{111\} \langle 110 \rangle$) prevails across temperature regimes for fcc metals; however, dislocations have been found to move on different slip systems in bcc metals (e.g., $\{110\} \langle 111 \rangle$, $\{112\} \langle 111 \rangle$, or $\{123\} \langle 111 \rangle$ for α -iron), depending on temperature (Ref 5, 25, and 26).

In bcc metals, a substantial increase in flow stress (or strength) can be observed at temperatures less than one-fifth the melting temperature of the metal. Under these conditions, the internal resistance to dislocation motion can greatly increase. If the barriers to dislocation motion are considered further, they can be separated into athermal (i.e., not influenced by temperature) and thermal (i.e., dependent upon temperature) components (Ref 5). Athermal barriers, such as long-range interaction of dislocations, are too large to be overcome by gliding dislocations utilizing only thermal fluctuations and the applied stress to move from one site to another. In contrast, thermal barriers, such as solute atoms and precipitates, are surmountable by dislocations with the assistance of this thermal energy and an applied stress.

At low temperatures, the thermal activation of dislocations is minimal; therefore, a large applied stress is required for deformation. At higher temperatures, thermal activation will assist in dislocation motion “around” the thermal barriers. The applied stress necessary for plastic flow is lowered, which reduces the measured strength. Above a critical temperature, thermal activation provides a substantial portion of the driving force for dislocation motion, such that the strength of the material will be primarily determined by athermal barriers.

The previous discussion assumes that plastic flow will take place and that there is a constancy of fracture mechanism. Such an assumption is not necessarily valid for bcc metals. These metals show a transition in fracture mode from ductile (microvoid coalescence or shear) to brittle (e.g., cleavage) with decreasing temperature. This transition can be conceptualized using a simple Orowan-type construction (Ref 27) such as the one shown in Fig. 17. The brittle fracture stress (the cleavage stress) varies weakly with temperature and may be considered to be approximately independent of temperature. The yield strength, however, will increase with decreasing temperatures as discussed previously. The temperature where the two curves intersect (T_1 in Fig. 17) is considered to be the ductile-to-brittle transition temperature (DBTT) for the metal. Above this temperature, the metal will yield prior to fracture, while below the DBTT, cleavage occurs without macroscopic yielding.

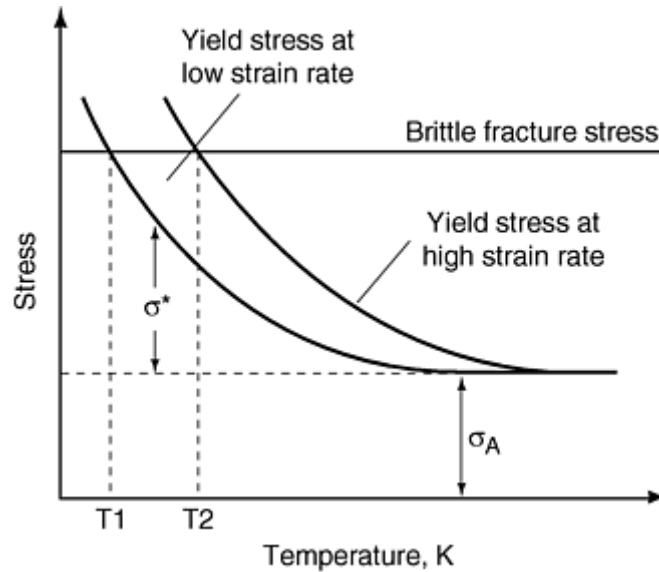


Fig. 17 Schematic illustration of the ductile-to-brittle transition in body-centered cubic metals

In addition to temperature, the rate of loading (i.e., strain rate) during testing will also greatly affect the measured mechanical properties of bcc metals. In general, an increase in strain rate is analogous to a decrease in temperature. The combined effect of strain rate ($\dot{\epsilon}$) and temperature (T) can be seen in Eq 11 (Ref 5):

$$\dot{\epsilon} = \dot{\epsilon}_0 \exp\left[\frac{-\Delta G^*(\tau^*)}{kT}\right] \quad (\text{Eq 11})$$

where ΔG^* is the Gibbs free energy associated with the shear stress (τ^*) required to overcome short-range obstacles and $\dot{\epsilon}_0$ is the product of the mobile dislocation density, the vibration frequency for the dislocation segment, and the Burgers vector for the dislocation, the distance that the dislocation may “jump.” This relationship illustrates that sufficiently high temperatures or low enough strain rates increase the probability for exciting dislocation motion through a thermal activation event in the presence of an applied load. On the other hand, low temperatures and high strain rates can lead to significant strengthening due to smaller contributions by thermal activation.

For bcc metals, which exhibit a ductile-to-brittle transition, increasing the strain rate can have an additional effect. As discussed previously and shown schematically in Fig. 17, the yield strength increases at a higher strain rate. This shifts the temperature dependence of yield strength, resulting in an intersection with the brittle fracture stress at a higher temperature (T_2 in Fig. 17). The end result is that the measured DBTT will be greater at a higher strain rate (T_2) than at a lower strain rate (T_1).

References cited in this section

5. D. Hull and D.J. Bacon, *Introduction to Dislocations*, Pergamon Press, London, 1984
25. G.E. Dieter, *Mechanical Metallurgy*, 3rd ed., McGraw-Hill, 1986
26. U.F. Kocks, A.S. Argon, and M.F. Ashby, *Thermodynamics of Slip*, Pergamon Press, New York, 1975
27. J.F. Knott, *Fundamentals of Fracture Mechanics*, Butterworths, London, 1981

Introduction to the Mechanical Behavior of Metals

Todd M. Osman, U.S. Steel Research; Joseph D. Rigney, General Electric Aircraft Engines

Special Conditions in Fracture: Notches and Cracks

The deformations and processes governing fracture in metals are affected by both the stresses and strains experienced in the specimen. In a simple tension test, the stresses are designed to be uniform throughout the cross section of the sample. When stress is applied to a component with a notch, crack, or other stress concentration, regions in the vicinity of these features will always experience much higher stresses compared to unaffected regions, and the strains produced can be very different from what would be predicted by the stresses. The stress fields created around stress concentrations are controlled by three factors: (a) the extent of deformation prior to failure, (b) the mode of loading (i.e., the relative orientation of the applied load with respect to the plane of the crack), and (c) the constraints, if any, on the cracked body (Ref 25, 27).

As a result, the mechanical properties measured when testing specimens with notches (see Fig. 1b) or cracks (see Fig. 1c) will be much different than those observed in uniaxial tension tests. For the case of notched tensile specimens, the measured tensile yield strength often will be greater than that observed in a uniaxial tension test. However, the ductility and load-carrying capacity will be decreased. As the sample is loaded, the notched region will yield first due to the elevated local stresses and strains associated with the notches. The maximum stress ahead of the notch will be a function of the geometry of the notch and the applied loading (Ref 28, 29). Furthermore, the stresses are no longer purely uniaxial (such as is developed in a tensile test), but now become triaxial (i.e., tensile stresses in the three primary directions of space). If ductile fracture via microvoid coalescence is reconsidered, the elevated stress and strain fields may accelerate the nucleation of secondary voids. The void growth rate will also increase proportionally to the level of the triaxial stresses, resulting in reduced ductility for notched samples compared to smooth, uniaxial tensile specimens (Ref 30, 31).

A more severe stress concentration will occur in cracked specimens, such as those used to determine fracture toughness (see Fig. 1c). In the most limiting case (e.g., opening of a sharp crack or Mode I loading), the component is highly constrained (with the level of constraint dependent on mechanical properties and component size). Under these conditions and with the application of a sufficient load, the peak tensile stresses around the crack tip can reach levels as high as five times the yield strength of the metal. As in the case of notched specimens, this change in stress state reduces the measured fracture strains due to a local acceleration of the fracture process.

To understand effects of cracks in ductile metals, the interactions between microstructural features and the elevated stress fields around the crack tip need to be considered. Ahead of a sharp crack, a finite volume of material is subjected to deformations at high stress values. To a first-order approximation, this volume of material, or the “plastic zone” in plane strain, can be represented as the radius of a circle as described by Eq 12 (Ref 25, 27):

$$r_p = \frac{1}{6\pi} \left(\frac{K_I}{\sigma_{ys}} \right)^2 \quad (\text{Eq 12})$$

where r_p is the distance from the crack to the elastic-plastic boundary, K_I is the stress intensity calculated from the geometry and loading conditions, and σ_{ys} is the uniaxial yield strength of the material. The highly constrained regions experiencing the triaxial stress state are located within this volume. As a result, the size of this zone relative to the microstructural features becomes a key factor influencing the measured properties of cracked specimens.

In general, the stresses are highest in a plastically deforming material ahead of the crack tip. In contrast, the plastic strains are highest at the notch tip and decrease after a critical distance, which is approximately equivalent to the crack-opening displacement (i.e., the relative displacement of the “mouth” of the crack) (Ref 27). The extent of the strained region often becomes comparable to microstructural features (grain size, interparticle particle spacing, etc.) and can initiate failure. When large strains are required for fracture, the crack-opening displacement must reach a critical size as to envelop the microstructural features responsible for void nucleation. Depending on the intrinsic fracture resistance of the metal, void growth and failure will occur when this zone becomes 1.0 to 2.7 times the microstructural feature responsible for fracture (e.g., the grain size or the mean spacing of second-phase particles) (Ref 32, 33).

An example of this type of fracture process can be seen in the case of metal matrix composites (i.e., a ductile metal matrix with brittle reinforcement particles). Crack growth in such a material is schematically shown in Fig. 18. When a crack in the ductile matrix is loaded, the large stresses ahead of the notch promote void nucleation by particle fracture or interface decohesion. This void nucleation limits the straining capacity of the metal in the vicinity of the crack tip. The high strain field ahead of the tip then allows for continued growth of

the nucleated voids to the point of instability, as the blunted crack links with the microcrack. This process of microcracking, crack-tip blunting, and failure of the matrix (void formation) between the particles continues as the crack propagates. This mechanism gives cracks an easy path for failure and clearly shows that the presence of a stress raiser exacerbates the processes of fracture compared to the case of uniaxial tension.

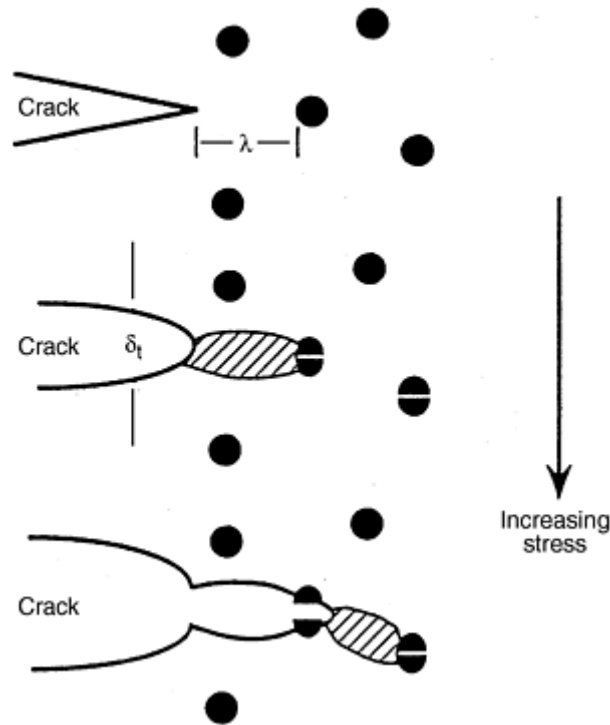


Fig. 18 Rice and Johnson model for failure in ductile matrix composites. Top: sharp crack blunts. Middle: particle cracking occurs followed by ductile tearing. Bottom: crack propagation. λ is the interparticle spacing; δ_t is the crack opening displacement. Source: Ref 32

The interaction between the microstructure of a metal and the resulting properties measured during mechanical testing is further illustrated by Fig. 18. In this example, crack propagation from a notch or crack tip is related to the spacing of microstructural features. As a result, a metal with a reduced volume fraction of particles (and the assumed increased interparticle spacing) can exhibit a greater resistance to fracture than a metal with a larger amount of particles (in agreement with Fig. 16).

References cited in this section

25. G.E. Dieter, *Mechanical Metallurgy*, 3rd ed., McGraw-Hill, 1986
27. J.F. Knott, *Fundamentals of Fracture Mechanics*, Butterworths, London, 1981
28. D.J.F. Ewing and R. Hill, *J. Mech. Phys. Solids*, Vol 5, 1957, p 115
29. W.D. Pilkey, *Peterson's Stress Concentration Factors*, 2nd ed., John Wiley & Sons, Inc., New York, 1997
30. J.R. Rice and D.M. Tracey, *J. Mech. Phys. Solids*, Vol 17, 1969, p 201
31. P.F. Thomason, *Ductile Fracture of Metals*, Pergamon Press, Oxford, 1990
32. J.R. Rice and M.A. Johnson, *Inelastic Behavior of Solids*, M.F. Kanninen, Ed., McGraw-Hill, New York, 1970, p 641

Introduction to the Mechanical Behavior of Metals

Todd M. Osman, U.S. Steel Research; Joseph D. Rigney, General Electric Aircraft Engines

Summary

The previous discussions were designed to provide a brief introduction to the influence of microstructure on the mechanical behavior of metals. The mechanisms of elastic and plastic flow have been highlighted along with the response of metals to stress raisers such as notches. The properties measured during mechanical testing can be rationalized by considering the effect of microstructural features, such as grain size and particle content, on deformation mechanisms. During quality-control testing, a larger-than-normal strength (or hardness) for a given metal during testing might be the result of grain refinement during processing. A lower strength observed for an age-hardenable metal might be the result of particle coarsening during overaging in heat treatment. Likewise, a dramatic drop in ductility might be the result of an increased inclusion content (or, in some cases, from embrittlement due to impurity segregation to the grain boundaries).

The relationship between microstructure and mechanical properties is also important when designing processing conditions, as well as in material selection for various applications. If increased strength in the final product is desired, solid-solution strengtheners may be added (e.g., adding nickel to copper), or the thermomechanical processing may be changed to produce a finer distribution of particles (e.g., lowering the coiling temperature for hot-rolled steel). If the final application has notches, it may be beneficial to use a metal with a lower inclusion content.

The remaining articles in this Volume will continue to build on this theme. In particular, the design of mechanical testing procedures and the analysis of resultant data will be highly dependent on the structure of the metal. Small variations in this structure may result in large changes in mechanical properties. As highlighted above, these changes are a direct consequence of the relationship between the metallurgical features and the mechanisms of deformation and fracture.

Introduction to the Mechanical Behavior of Metals

Todd M. Osman, U.S. Steel Research; Joseph D. Rigney, General Electric Aircraft Engines

References

1. T.M. Osman, J.J. Lewandowski, and W.H. Hunt, Jr., *Fabrication of Particulates Reinforced Metal Composites*, ASM International, 1990, p 209
2. Alloy Phase Diagrams, Vol 3, *ASM Handbook*, ASM International, 1992
3. D. Hull, *An Introduction to Composite Materials*, Cambridge University Press, 1975
4. R.W.K. Honeycombe, *The Plastic Deformation of Metals*, 2nd ed., Edward Arnold, London, 1984
5. D. Hull and D.J. Bacon, *Introduction to Dislocations*, Pergamon Press, London, 1984

6. A.S. Keh, *Direct Observations of Imperfections in Crystals*, J.B. Newbrick and J.H. Wernick, Ed., Interscience Publishers, New York, 1962, p 213–238
7. A.N. Stroh, *Proc. R. Soc. (London)*, Vol 223, 1954, p 404
8. Z. Shen, R.H. Wagoner, and W.A.T. Clark, *Acta Metall.*, Vol 36, 1988, p 3231
9. T.C. Lee, I.M. Robertson, and H.K. Birnbaum, *Metall. Trans. A*, Vol 21, 1990, p 2437
10. W.T. Lankford, S.C. Snyder, and J.A. Bauscher, *Trans. ASM*, Vol 42, 1950, p 1197–1228
11. J.F. Held, *Proc. Mechanical Working and Steel Processing Conference*, Vol 4, AIME, New York, 1965, p 3
12. W.B. Morrison and W.C. Leslie, *Metall. Trans.*, Vol 4, 1973, p 379
13. N.J. Petch, *J. Iron Steel Inst. Jpn.*, Vol 173, 1953, p 25
14. Fleischer, *Acta Metall.*, Vol 11, 1963, p 203
15. J. Heslop and N.J. Petch, *Philos. Mag.*, Vol 2, 1958, p 649
16. G.T. Hahn, *Acta Metall.*, Vol 10, 1962, p 727
17. W.J. Murphy and R.G.B. Yeo, *Met. Prog.*, Sept 1969, p 85
18. J.W. Martin, *Micromechanisms in Particle Hardened Alloys*, Cambridge University Press, 1980
19. L.B. Morris et al., *Formability of Aluminum Sheet Alloys, Aluminum Transformation Technology and Applications*, C.A. Pampillo et al., Ed., American Society for Metals, 1982, p 549
20. V. Kerlins and A. Philips, Modes of Fracture, *Fractography*, Vol 12, ASM Handbook, ASM International, 1987, p 12–71
21. I. Kirman, *Metall. Trans.*, Vol 2, 1971, p 1761
22. R.H. Van Stone, T.B. Cox, J.R. Low, and J.A. Psioda, *Int. Met. Rev.*, Vol 30, 1985, p 157
23. W.M. Garrison, Jr. and N.R. Moody, *J. Phys. Chem. Solids*, Vol 48, 1987, p 1035
24. B.I. Edelson and W.M. Baldwin, *Trans. ASM*, Vol 55, 1962, p 230
25. G.E. Dieter, *Mechanical Metallurgy*, 3rd ed., McGraw-Hill, 1986
26. U.F. Kocks, A.S. Argon, and M.F. Ashby, *Thermodynamics of Slip*, Pergamon Press, New York, 1975
27. J.F. Knott, *Fundamentals of Fracture Mechanics*, Butterworths, London, 1981
28. D.J.F. Ewing and R. Hill, *J. Mech. Phys. Solids*, Vol 5, 1957, p 115
29. W.D. Pilkey, *Peterson's Stress Concentration Factors*, 2nd ed., John Wiley & Sons, Inc., New York, 1997
30. J.R. Rice and D.M. Tracey, *J. Mech. Phys. Solids*, Vol 17, 1969, p 201

31. P.F. Thomason, *Ductile Fracture of Metals*, Pergamon Press, Oxford, 1990
32. J.R. Rice and M.A. Johnson, *Inelastic Behavior of Solids*, M.F. Kanninen, Ed., McGraw-Hill, New York, 1970, p 641
33. J. R. Rice, *Fracture—An Advanced Treatise*, H. Liebowitz, Ed., Academic Press, New York, 1968, p 191

Introduction to the Mechanical Behavior of Metals

Todd M. Osman, U.S. Steel Research; Joseph D. Rigney, General Electric Aircraft Engines

Selected References

Structure of Metals

- D.A. Porter and K.E. Easterling, *Phase Transformations in Metals and Alloys*, Van Nostrand Reinhold, Birkshire, UK, 1987
- C.R. Barrett, W.D. Nix, and A.S. Tetelman, *The Principles of Engineering Materials*, Prentice-Hall, Inc., Englewood Cliffs, New Jersey, 1973
- W. Hume-Rothery and G.V. Raynor, *The Structure of Metals and Alloys*, The Institute of Metals, London, 1956
- D. Hull and D.J. Bacon, *Introduction to Dislocations*, Pergamon Press, London, 1984
- P.B. Hirsch, Ed., Defects, Vol 2, *The Physics of Metals*, Cambridge University Press, Cambridge, 1975
- U.F. Kocks, C.N. Tome, and H.-R. Wenk, *Texture and Anisotropy*, Cambridge University Press, Cambridge, 1998
- D. Hull, *An Introduction to Composite Materials*, Cambridge University Press, 1975

Deformation of Metals and Strength of Metals

- M.A. Meyers and K.K. Chawla, *Mechanical Metallurgy: Principles and Applications*, Prentice Hall, Inc., 1984
- J.M. Gere and S.P. Timoshenko, *Mechanics of Materials*, 2nd ed., PWS Publishers, 1984
- T.H. Courtney, *Mechanical Behavior of Materials*, McGraw-Hill, New York, 1990
- J.W. Martin, *Micromechanisms in Particle Hardened Alloys*, Cambridge University Press, 1980
- P.F. Thomason, *Ductile Fracture of Metals*, Pergamon Press, Oxford, 1990
- R.W.K. Honeycombe, *The Plastic Deformation of Metals*, 2nd ed., Edward Arnold, London, 1984

Special Conditions in Flow and Fracture

- J.F. Knott, *Fundamentals of Fracture Mechanics*, Butterworths, 1981
- B.R. Lawn and T.R. Wilshaw, *Fracture of Brittle Solids*, Cambridge University Press, 1975
- H.L. Ewalds and R.J.H. Wanhill, *Fracture Mechanics*, Edward Arnold, London, 1985
- D. Broek, *Elementary Engineering Fracture Mechanics*, Martinus Nishoff Publishers, 4th ed., Dordrecht, Netherlands, 1987

Introduction to the Mechanical Behavior of Nonmetallic Materials

M.L. Weaver and M.E. Stevenson, The University of Alabama, Tuscaloosa

Introduction

MANY DIFFERENT types of materials are used in applications where a resistance to mechanical loading is necessary. The type of material used depends strongly upon a number of factors including the type of loading that the material will experience and the environment in which the materials will be loaded. Collectively known as *engineering materials* (Ref 1), they can be pure elements, or they can be combinations of different elements (alloys and compounds), molecules (polymers), or phases and materials (composites). All solid materials are typified by the presence of definite bonds between component atoms or molecules. Ultimately, it is the type of bonding present that imparts each class of materials with distinct microstructural features and with unique mechanical and physical properties.

Crystalline solids exhibit atomic or molecular structures that repeat over large atomic distances (i.e., they exhibit long-range-ordered, LRO, structures) whereas noncrystalline solids exhibit no long-range periodicity. The atomic and molecular components of both crystalline and noncrystalline solids are held together by a series of strong *primary* (i.e., ionic, covalent, and metallic) and/or weak *secondary* (i.e., hydrogen and Van der Waals) bonds. Primary bonds are usually more than an order of magnitude stronger than secondary bonds. As a result, *ceramics* and *glasses*, which have strong ionic-covalent chemical bonds, are very strong and stiff (i.e., they have large elastic moduli). They are also resistant to high temperatures and corrosion, but are brittle and prone to failure at ambient temperatures. In contrast, thermoplastic *polymers* such as polyethylene, which have weak secondary bonds between long chain molecules, exhibit low strength, low stiffness, and a susceptibility to creep at ambient temperatures. These polymers, however, tend to be extremely ductile at ambient temperatures.

In this article, some of the fundamental relationships between microstructure and mechanical properties are reviewed for the major classes of nonmetallic engineering materials. The individual topics include chemical bonding, crystal structures, and their relative influences on mechanical properties. The present article has been derived in structure and content from the article “Fundamental Structure-Property Relationships in Engineering Materials,” in *Materials Selection and Design*, Volume 20 of *ASM Handbook* (Ref 2). In light of the bewildering number of different engineering materials within each class, discussions were limited to a number of general examples typifying the general features of the major classes of nonmetallic materials.

References cited in this section

1. N.E. Dowling, *Mechanical Behavior of Materials: Engineering Methods for Deformation, Fracture, and Fatigue*, 2nd ed., Prentice Hall, 1999, p 23
2. T.H. Courtney, *Materials Selection and Design*, Vol 20, *ASM Handbook*, ASM International, 1997, p 336–356

Introduction to the Mechanical Behavior of Nonmetallic Materials

M.L. Weaver and M.E. Stevenson, The University of Alabama, Tuscaloosa

General Characteristics of Solid Materials

Engineering materials can be conveniently grouped into five broad classes: metals, ceramics and glasses, intermetallic compounds, polymers, and composite materials. Metals, ceramics and glasses, polymers, and composites represent the most widely utilized classes of engineering materials, whereas intermetallic compounds (i.e., intermetallics), which are actually subcategories of metals and ceramics, are an emerging class of monolithic materials. The general features of five major classes of materials are summarized in Fig. 1 and are described in the following sections. Though this article deals with the properties of nonmetallic materials, a brief discussion of the general characteristics of metallic materials is included where pertinent.

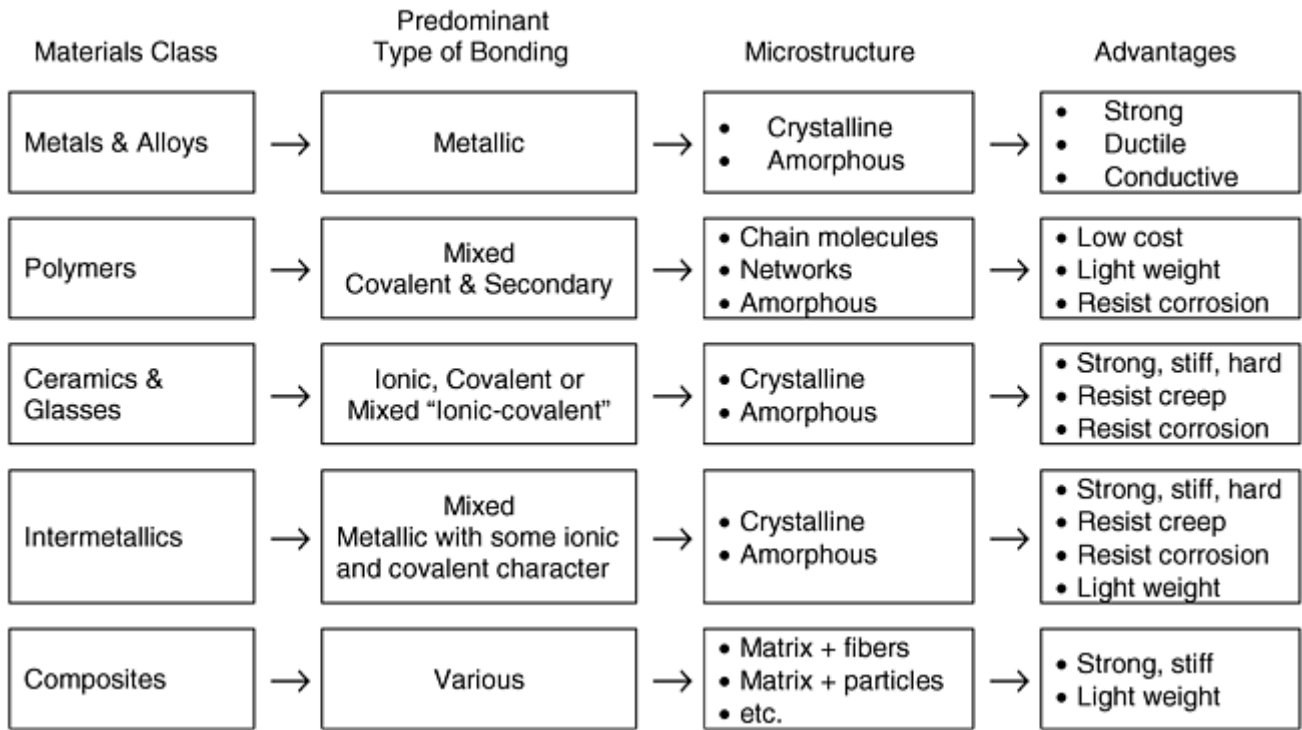


Fig. 1 General characteristics of major classes of engineering materials. Adapted from Ref 3

Metals

Metals represent the majority of the pure elements and form the basis for the majority of the structural materials. The mechanical behavior of metals depends on a combination of microstructural and macrostructural features, which ultimately depend upon bonding, chemical composition, and mode of manufacture. Metals are held together by metallic bonds. Metallic bonds arise because on an atomic scale, the outer electron shells in metals are less than half full. As a result, each atom donates its available outer shell (i.e., valence) electrons to an electron cloud that is collectively shared by all of the atoms in the solid. This is referred to as *metallic bonding* and is responsible for the high elastic moduli and the high thermal and electrical conductivity exhibited by metals. Many metals also exhibit a limited solid solubility for other atoms (i.e., one metal can dissolve into another). Consequently, engineers can often vary their properties by varying composition. In terms of atomic arrangements, metals also have large coordination numbers (CNs), typically 8 to 12, which account for their relatively high densities. Metals, by their nature, tend to be ductile in comparison to other engineering materials and exhibit a high tolerance for stress concentrations. As such, many metals can deform locally to redistribute load. Structurally, metals are generally crystalline, though amorphous structures (i.e., metallic glasses) are possible using special processing techniques. Further information concerning structure-property relationships in metals is provided in the article "Introduction to the Mechanical Behavior of Metals" in this volume.

Ceramics and Glasses

Ceramics and glasses include a broad range of inorganic materials containing nonmetallic and metallic elements. Like metals, these materials can be formed directly from the melt or via powder processing techniques (e.g., sintering or hot isostatic pressing) and their mechanical properties depend on structural (i.e., microstructural and macrostructural) features and chemical composition. They differ from metals in that strong ionic, covalent, or intermediate bonds, which often result in higher hardness, stiffness, and melting temperatures compared with metals, hold them together.

Ionic bonding occurs in compounds containing electropositive (i.e., metals, atoms on the left side of the periodic table) and electronegative (i.e., nonmetals, atoms on the right side of the periodic table) elements. This type of bonding involves the transfer of electrons whereby electropositive elements readily donate their valence electrons to the electronegative elements, allowing the establishment of stable outer shell configurations in each element. Figure 2 depicts ordinary table salt, NaCl, which is a perfect example of an ionically bonded solid. In

ionic solids, the coordination number (CN), which is defined as the number of cation/anion (i.e., positive ion/negative ion) nearest neighbors, are typically lower than those in metals, which accounts for their slightly lower densities compared with metals. Ionic solids are typically hard and brittle, and electrically and thermally insulative (i.e., with lower electrical and thermal conductivity than metals). The insulative properties are a direct result of the electron configurations within the ionic bond. Ionic solids usually form only in stoichiometric proportions (e.g., NaCl and Al_2O_3), which cause them to have little tolerance for alloying.

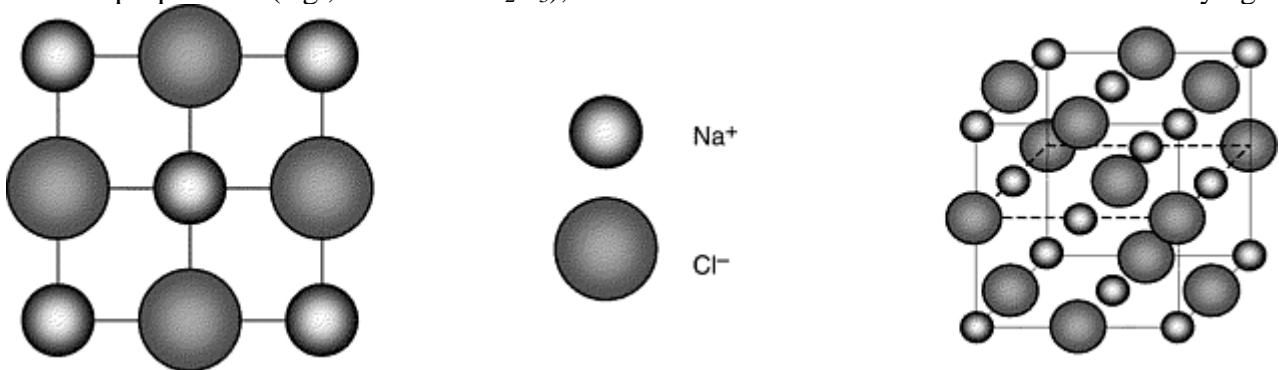


Fig. 2 Schematic representation of ionic bonding in NaCl. Note that this structure consists of Na^+ and Cl^- ions sitting on interpenetrating fcc Bravais lattices.

Covalent bonding occurs in compounds containing electronegative elements. Covalent bonding involves the sharing of valence electrons with specific neighboring atoms. This is schematically illustrated for methane (CH_4) in Fig. 3. For a covalent bond to occur between C and H, for example, each atom must contribute at least one electron to the bond. These electrons are shared by both atoms, resulting in a strong directional bond between atoms. The number of covalent bonds that form depends on the number of valence atoms that are available in each atom. In methane, carbon has four valence electrons, while each hydrogen atom has only one. Thus, each hydrogen atom can acquire one valence electron to fill its outer orbital shell. Similarly, each carbon atom can accommodate four valence electrons to fill its outer shell. This type of bonding makes covalent solids strong, brittle, and highly insulative because electrons are incapable of detaching themselves from their parent and moving freely through the solid. Covalent solids also have lower CNs due to this localized electron sharing resulting in lower densities. For example, diamond, which is an elemental covalent compound, has a CN of 4 (Fig. 4). Like ionic solids, covalent solids tend to exhibit very narrow composition ranges and exhibit little tolerance for alloying additions. Examples of covalent molecules, elements, and compounds include H_2O , HNO_3 , H_2 , diamond, silicon, GaAs, and SiC.

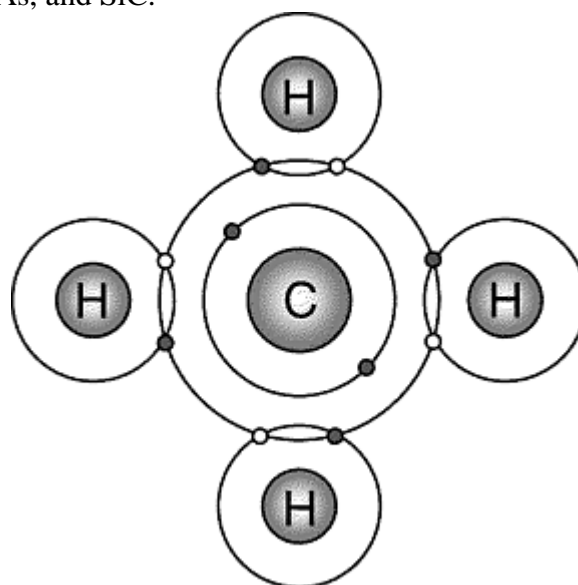


Fig. 3 Schematic representation of covalent bonding in methane (CH_4)

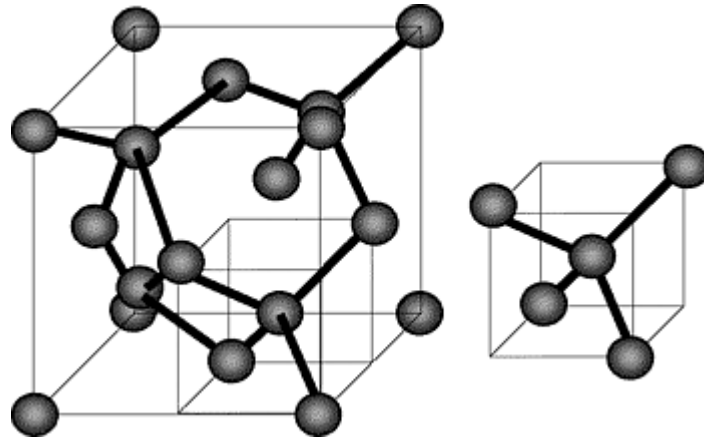


Fig. 4 An example of perfect covalent bonding in diamond

In general, most ceramic compounds exhibit a mixture of ionic and covalent bonding, the degree of which depends on the positions of the constituent elements on the periodic table. For elements exhibiting a greater difference in electronegativity, bonding tends to be more ionic, while for elements with smaller differences, bonding tends to be more covalent. Solids that exhibit mixed bonding, which are termed polar covalent solids, often exhibit high melting points and elastic moduli. Silica (SiO_2) is a good example of a polar covalent solid. Ceramics and glasses have higher elastic moduli than most metals and exhibit extremely high strengths when deformed in compression. The presence of strong ionic and covalent bonds allows these materials to retain their strength to high temperature and makes them extremely resistant to corrosion. However, these same bonds render ceramics and glasses brittle at ambient temperatures, resulting in little tolerance for stress concentrations (e.g., holes, cracks, and flaws) and usually in catastrophic failure during tensile or shear loading.

Intermetallic Compounds

In some cases, intermetallic compounds can form within alloys. These materials are composed of two or more metallic or metalloid constituents and exhibit crystal structures that are distinctly different from its constituents. Unlike solid solution alloys, these mixtures form stoichiometric compounds (e.g., NiAl , Ni_3Al , TiAl , and Ti_3Al), and their bonding is typically a combination of metallic, ionic, and/or covalent types. In terms of mechanical and physical properties, intermetallics occupy a position between metals and ceramics. As in the case of ionic and covalent solids, extremely strong bonds exist between unlike constituents, which imparts intermetallics with lower CNs and densities than metals, highly directional properties, higher stiffness and strength, and good resistance to temperatures or chemical attack. These materials, which have intrinsically high strengths and elastic moduli, are often used in precipitate form to strengthen commercial alloys (e.g., Ni_3Al in Ni-base superalloys), and their low densities and high microstructural stability makes them attractive for use in high-temperature structural applications such as turbine blades, exhaust nozzles, and automotive valves. Examples of some typical intermetallic compounds are illustrated in Fig. 5. Of the more than 25,000 known intermetallic compounds, recent emphasis has focused on the development of NiAl , FeAl , Ni_3Al , TiAl , and MoSi_2 base alloys for use as monolithic alloys in structural applications (Ref 4). As in the cases of ceramics and glasses, the same bonds that impart intermetallics with high strengths render most of them with low ductility and fracture toughness at ambient temperatures.

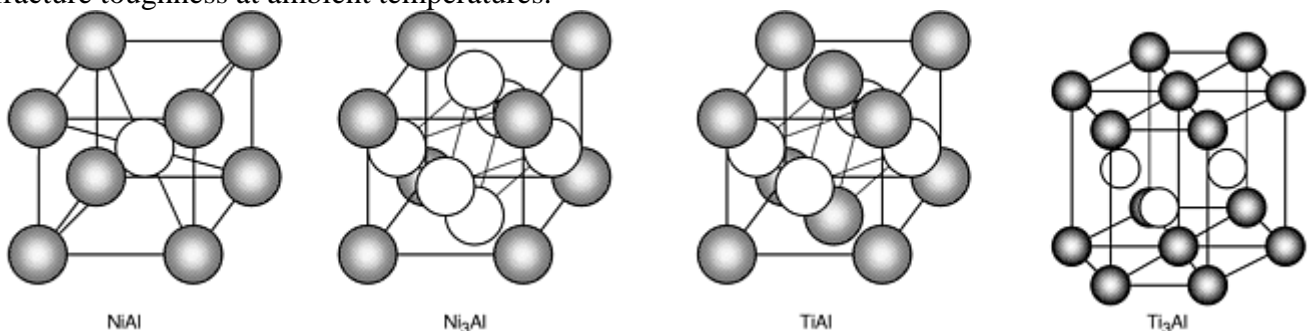


Fig. 5 Some simple intermetallic crystal structures

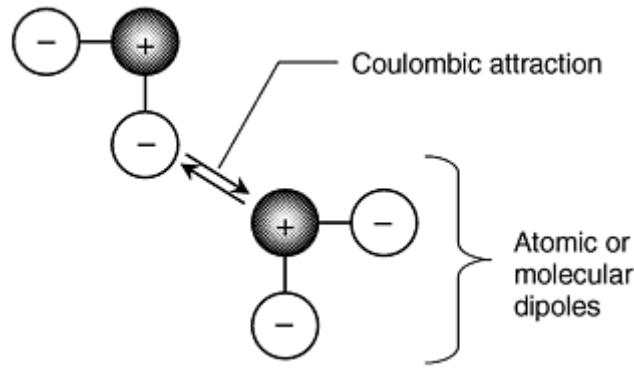


Fig. 7 Schematic representation of secondary bonding between two molecular dipoles

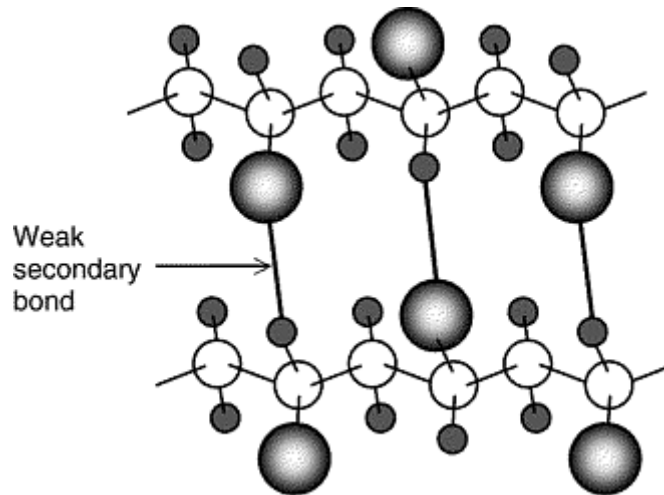


Fig. 8 Schematic representation of secondary bonding between two polymer chains

In comparison to metals, intermetallics, and ceramics and glasses, polymers have very low CNs, which is part of the cause for their low densities; however, they also consist primarily of light atoms such as C and H, which tends to result in lower density. The localized nature of electrons in polymers renders them good electrical insulators and poor thermal conductors.

There are three categories of polymers: thermoplastics, thermosetting plastics, and elastomers. Thermoplastics have linear chain configurations where chains are joined by weak secondary bonds as described above. These materials often melt upon heating but return to their original solid condition when cooled. In thermosetting polymers, covalent cross-links or strong hydrogen bonds occur between polymer chains resulting in three-dimensional networks of cross-linked molecular chains. Phenol formaldehyde, or Bakelite, is a good example. Thermosettings change chemically during processing and will not melt upon reheating. Instead, they will remain strong until they break down chemically via charring or burning. Elastomers differ from thermoplastics and thermosetting polymers in that they are capable of rubbery behavior and are capable of very large amounts of recoverable deformation (often in excess of 200%). Structurally, these materials consist of networks of heavily coiled and heavily cross-linked polymer chains, which impacts higher strengths than thermoplastics by inhibiting the sliding of polymer chains past each other. Elastomers are typified by natural rubber and by a series of synthetic polymers exhibiting similar mechanical behavior (e.g., polyisoprene).

Composites

Composites are relatively macroscopic arrangements of phases or materials designed to take advantage of the most desirable aspects of each. As a result, the strengths and/or physical properties of composites are usually an average of the strengths and/or properties of the individual constituents/phases. Most composites are composed of a compliant, damage-tolerant matrix and a strong reinforcing phase/constituent, usually filaments, fibers, or whiskers, that are too brittle for use in a monolithic form. In composites with brittle matrices (e.g., ceramic matrix composites), the reinforcing constituent may toughen the material more than strengthen it.

References cited in this section

3. N.E. Dowling, *Mechanical Behavior of Materials: Engineering Methods for Deformation, Fracture, and Fatigue*, 2nd ed., Prentice Hall, 1999, p 24
4. G. Sauthoff, *Intermetallics*, VCH Publishers, New York, 1995
5. W.D. Callister, *Materials Science and Engineering—An Introduction*, 4th ed., John Wiley & Sons, 1997, p 21

Introduction to the Mechanical Behavior of Nonmetallic Materials

M.L. Weaver and M.E. Stevenson, The University of Alabama, Tuscaloosa

Structures of Materials

Depending upon the application, engineering materials can be pure elements such as silicon, compounds such as aluminum oxide (Al_2O_3) or gamma titanium aluminide ($\gamma\text{-TiAl}$), or combinations of different molecules (polymers) or materials (composites). All materials are composed of a three-dimensional arrangement of atoms, the general details of which are described subsequently.

Inorganic Crystalline Solids

The basic building blocks of crystalline solids are unit cells, which represent the smallest repeating unit within a crystal. When stacked together, these repeating unit cells form a *space lattice*, which is a repeating three-dimensional array of atoms. Due to geometrical considerations, atoms can only have one of 14 possible arrangements, known as Bravais lattices (Fig. 9). Most metals and metallic alloys crystallize with face-centered cubic (fcc), hexagonal close-packed (hcp), or body-centered cubic (bcc) crystal structures. However, the structures in nonmetallic solids tend to be more complicated.

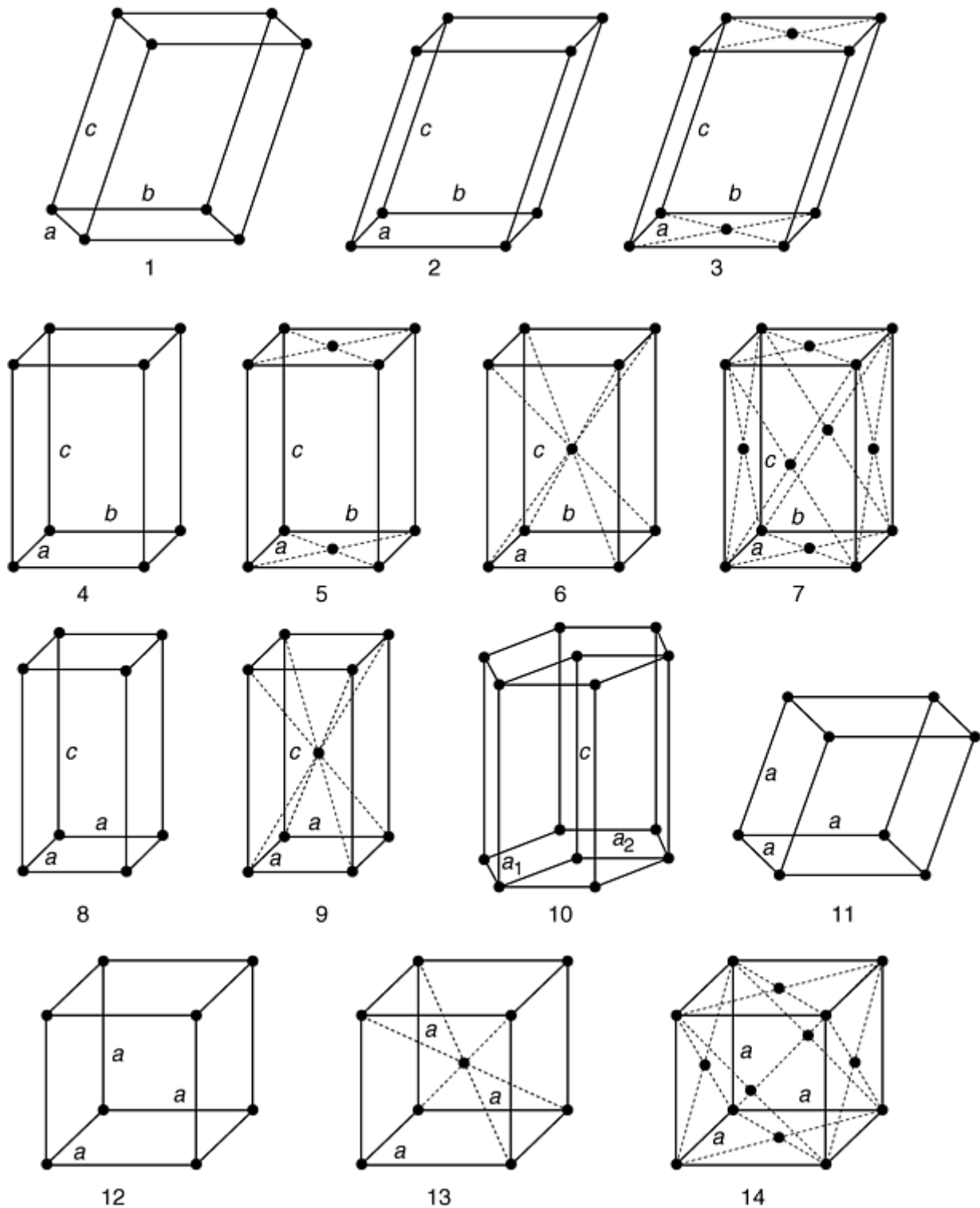


Fig. 9 The 14 Bravais lattices illustrated by a unit cell of each: 1, triclinic, primitive; 2, monoclinic, primitive; 3, monoclinic, base centered; 4, orthorhombic, primitive; 5, orthorhombic, base centered; 6, orthorhombic, body centered; 7, orthorhombic, face centered; 8, tetragonal, primitive; 9, tetragonal, body centered; 10, hexagonal, primitive; 11, rhombohedral, primitive; 12, cubic, primitive; 13, cubic, body centered; 14, cubic, face centered. Source: Ref 6

Crystalline ceramics and intermetallics have crystal structures consisting of multiple interpenetrating Bravais lattices, each of which is occupied by a specific atomic constituent. For example, common table salt (NaCl) consists of two fcc (cubic F) Bravais lattices, slightly offset and overlaid on top of each other. One Bravais lattice contains Cl⁻ ions and is centered at origin, 0 0 0, while the second Bravais lattice contains Na⁺ ions and is centered at 0 ½ 0 (Fig. 10). The structure of the intermetallic compound β-NiAl, which is often called an ordered

bcc structure, actually consists of two simple cubic (primitive) Bravais lattices, one containing Ni atoms centered at 0 0 0 and the second containing Al atoms centered at $\frac{111}{222}$.

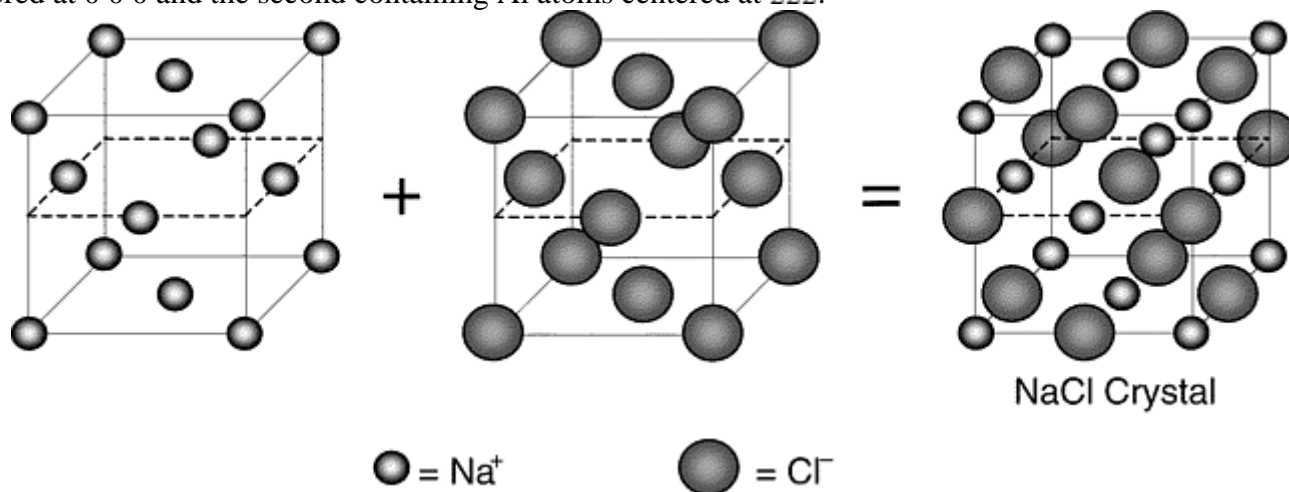


Fig. 10 Schematic illustration of the construction of NaCl from two interpenetrating fcc Bravais lattices

Inorganic Noncrystalline Solids

Not all solids are crystalline. Unlike their crystalline counterparts, noncrystalline materials do not display long-range order. Instead, these solids exhibit some local order (i.e., short-range order) where atomic or molecular subunits repeat over short distances. This group of materials, often collectively referred to as glasses, includes many high molecular weight polymers, some polar-covalent ceramics, and some metallic alloys. Amorphous structures arise because the mobility of atoms within these materials is restricted such that low energy configurations (crystalline) cannot be reached.

To fully describe the nature of glassy materials, it is useful to consider the structure and properties of commercial inorganic glasses. When cooling from the liquid state, materials may solidify in two different ways. If the cooling rate is sufficiently slow, the liquid may freeze in the form of a crystalline solid. If the cooling rate is extremely high, the liquid may pass through the freezing range without crystallizing so that it becomes a supercooled liquid, which transforms to glass at lower temperatures. The critical cooling rate required for glass formation in common inorganic glass is very low ($\leq 10^{-1}$ K/s), which means that it is very easy to form inorganic glasses with these compositions. In metallic alloys, glass formation is more difficult and requires cooling rates in excess of 10^5 K/s (Ref 7).

The supercooled liquid transforms to glass at the glass transition point, T_g in Fig. 11(a). At this point, the temperature dependence of the specific volume of the liquid changes. In glassy materials, there is little or no change in volume upon cooling below the melting point, T_{mp} . In contrast, crystallization is accompanied by a sharp decrease in volume below T_{mp} . At temperatures below T_g , the slopes of both the glass and crystallized solid curves are the same; however, the volume of glass is greater than the crystalline solid at all temperatures where both forms can exist. The volume difference and the glass transition temperature depend on the cooling rate, as illustrated in Fig. 11(b). The volume difference is related to the more open structure in the glass. The difference is usually very small, in the range of a few percent for silicate glasses. In metallic glasses, it is usually less than one percent (Ref 7).

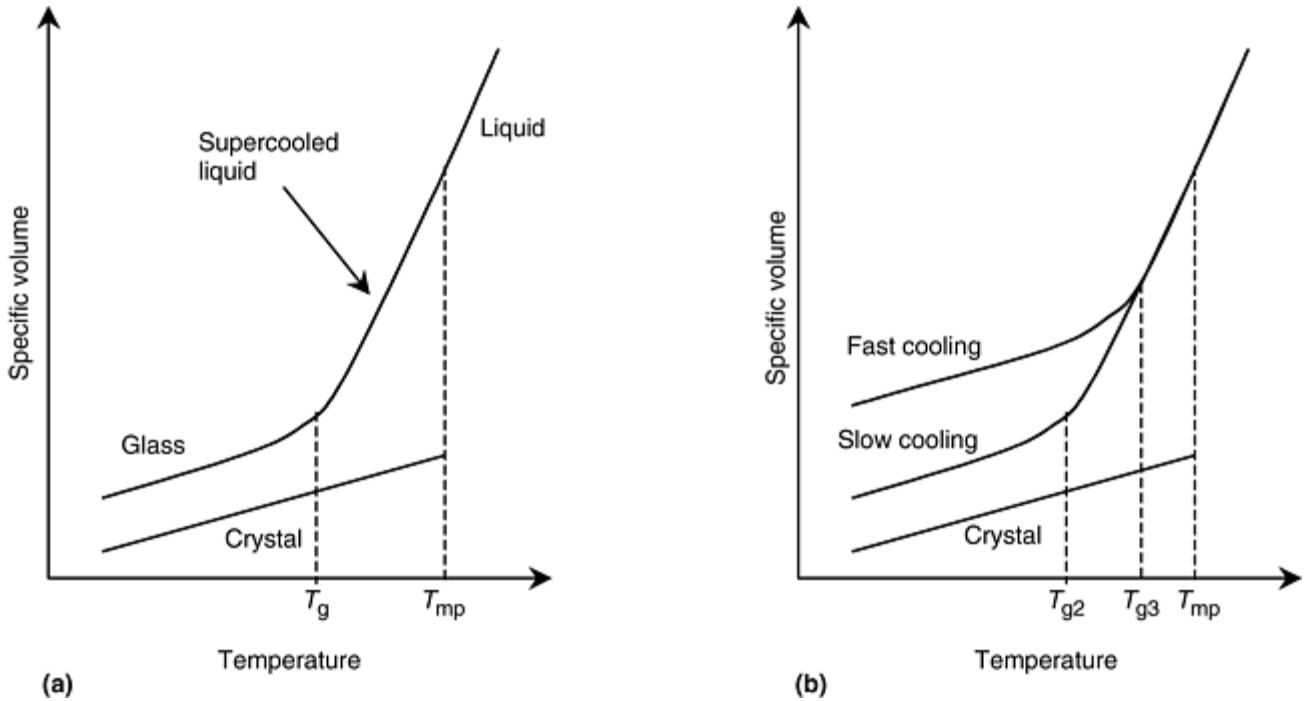


Fig. 11 Schematic representation of (a) the specific volume of liquid, glass, and crystal versus temperature, and (b) the effect of cooling rate

The transition from supercooled liquid to glass during cooling is believed to be caused by a rapid rise in the viscosity of the supercooled liquid during cooling. Empirical relationships have been derived to describe the viscosity of glass as a function of temperature. The simplest relationship is (Ref 8):

$$\eta = \eta_0 \exp\left(\frac{B}{T - T_0}\right) \quad (\text{Eq 1})$$

where η is the viscosity, T is the absolute temperature, and η_0 , B , and T_0 are constants.

Below the glass transition point, viscous flow of the supercooled liquid becomes so slow that the liquid begins to behave as though it was elastic. In other words, the supercooled liquid structure existing at the glass transition temperature becomes frozen in place below T_g .

Most common inorganic glasses are based on the silicate tetrahedron shown in Fig. 12(a). A three-dimensional solid forms when the corner oxygen atoms join with the adjacent tetrahedra. In the glassy state (Fig. 12b), the tetrahedra join randomly, whereas in the crystalline state the tetrahedra take on long-range order, as illustrated in Fig. 12(c). Pure silica glass exhibits a high glass transition temperature, making it suitable for elevated temperature applications but also making it viscous and difficult to work. To overcome this problem, network modifiers, such as CaO or Na₂O, are usually added to commercial glasses. The network modifiers introduce positive ions to the structure, which are accommodated by breaking up the three-dimensional network (Fig. 12d).

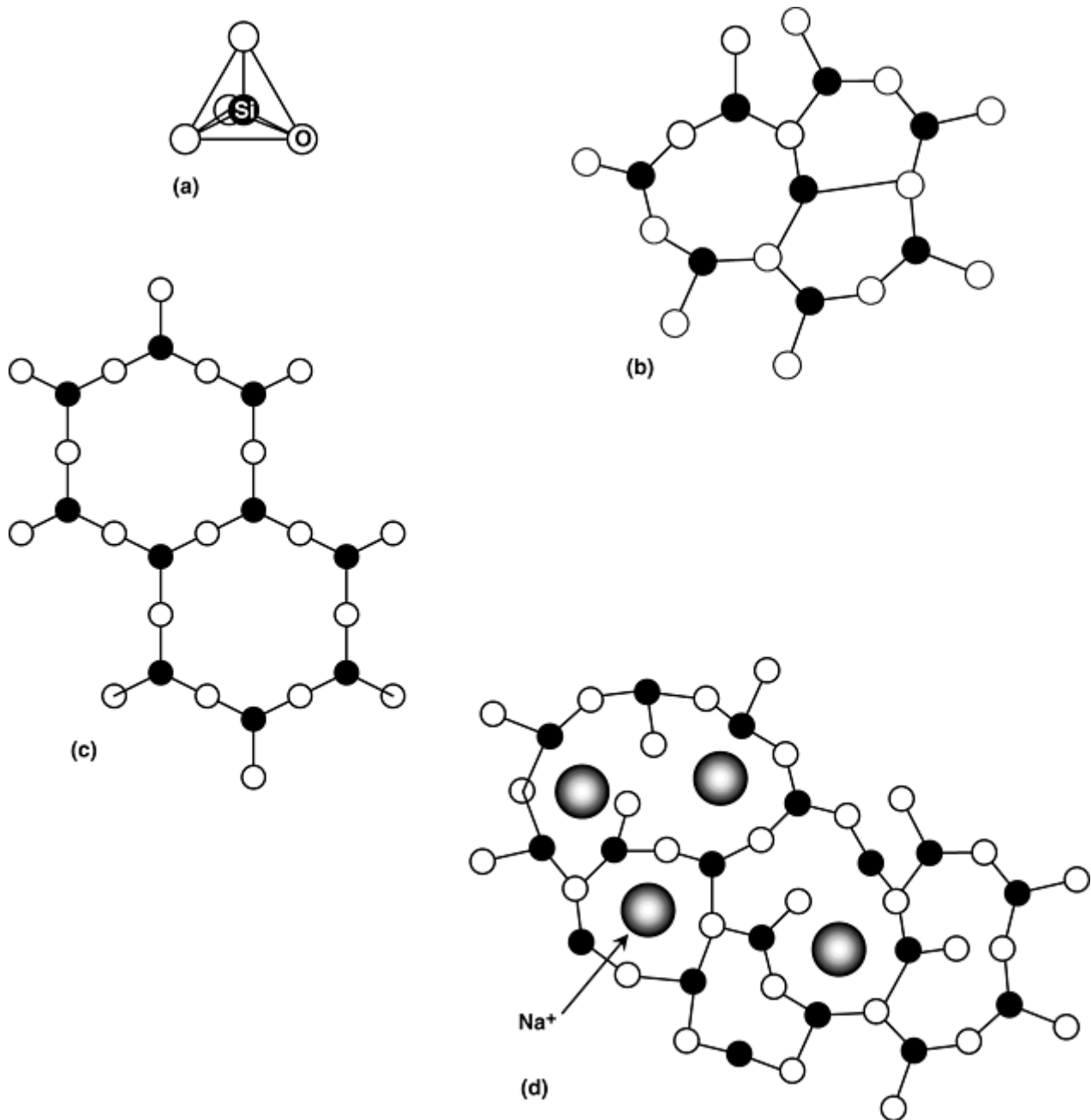


Fig. 12 Two-dimensional diagram of the structure of silica. (a) Silica tetrahedron. (b) In the form of glass. (c) In the form of an ordered quartz crystal. (d) In the form of a Na^+ modified glass

Metallic glasses exhibit many unique physical and mechanical properties. Some of these materials exhibit high strength coupled with high ductility, and high corrosion resistance. Metallic glasses deform by homogeneous shear above their glass transition temperatures. In this type of flow, every atom or molecule responds to the applied shear stress and participates in deformation. Homogeneous shear flow is a common deformation mechanism in liquids. Above T_g , metallic glasses behave like liquids. Below T_g , the deformation is inhomogeneous and occurs via the formation of localized shear bands. Each band is accompanied by extensive local offsets. The formation of multiple shear bands can produce extensive ductility.

Polymers

As noted previously, polymers are composed of covalently bonded long-chain molecules, which are joined together by secondary bonds or covalent cross links. Under applied stresses, polymer chains slide over each other, and failure occurs by separation of chains rather than by breaking of interchain bonds. This type of motion is relatively easy where secondary bonds join molecules. However, most polymers have side branches or bulky side groups on their chains and are not strictly linear. Side branches alter the properties of polymers by

inhibiting interchain sliding. Cross-linking also influences the properties of polymers. Cross-linking can occur, for example, when unsaturated carbon bonds (e.g., double bonds) exist between the atoms making up the backbone of the polymer chain that can be broken, allowing individual atoms or molecules to link to adjacent chains. Heavily cross-linked polymers can develop rigid three-dimensional network structures that inhibit interchain sliding, resulting in increased strength and decreased ductility.

Structurally, most polymers are amorphous and consist of a random arrangement of molecules, as illustrated in Fig. 13. Examples of amorphous polymers include polyvinyl chloride (PVC), polymethyl methacrylate (PMMA), and polycarbonate (PC).

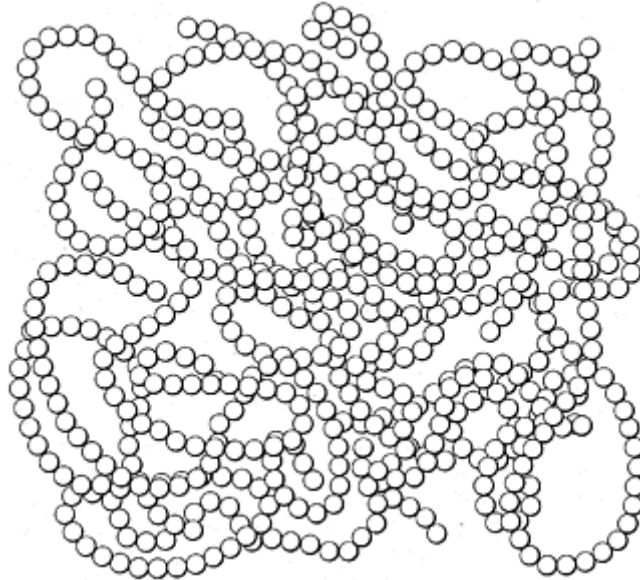


Fig. 13 Schematic representation of a polymer. The spheres represent the repeating units of the polymer chain, not individual atoms. Source: Ref 9

Some polymers can exhibit limited crystallinity. This occurs when the polymer chains arrange themselves in a regular manner. Crystalline polymers are characterized by a degree of crystallinity, which is a measure of the extent of long-range three-dimensional order. In general, simple polymers, such as polyethylene with little or no side branching crystallize very easily whereas in heavily cross-linked polymers, such as polyisoprene, and in polymers containing bulky side groups, crystallization is inhibited. As such, thermoset polymers are seldom crystalline. In polymers containing side groups, the degree of crystallinity is often to the location of the side group. Polystyrene (PS), for example, is amorphous in its *atactic* form where benzene ring substitution is random within each repeating unit of the molecule. However, PS is crystalline in the *isotactic* form where substitution occurs at the same location within each repeating unit. The regular structure of the isotactic form promotes crystallinity. Crystalline structures are also likely in polymers that are *syndiotactic*, where the side groups alternate positions in a regular manner. Examples of atactic, isotactic, and syndiotactic arrangements are schematically illustrated in 14 14Fig. 14.

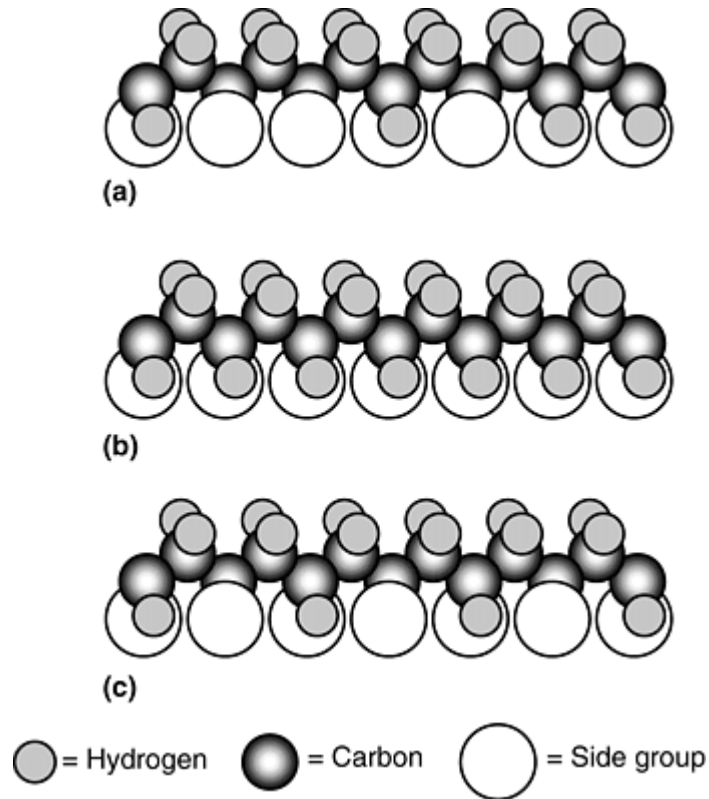


Fig. 14 Schematic representation of the possible side group arrangements in a simple vinyl polymer: (a) atactic (random), (b) isotactic (all on same side), and (c) syndiotactic (regularly alternating). Source: Ref 10

Amorphous polymers are normally used near or below their glass transition temperatures. Above this temperature, the elastic modulus decreases rapidly, and creep effects become pronounced. Below this temperature, they tend to be glassy and brittle with elastic moduli on the order of 3 GPa. Crystalline polymers are, in general, less brittle than amorphous polymers. In addition, they retain their strength and stiffness more effectively than amorphous polymers at elevated temperatures.

Some polymers, known as *network polymers* or *cross-linked thermosets*, form three-dimensional structures via *cross-linking* between chains. Common examples include Bakelite, polyester resins, and epoxy adhesives. In Bakelite, cross-links form by means of phenol rings, which are integral parts of each chain. The structure of Bakelite is schematically illustrated in Fig. 15. Unlike thermoplastic polymers, thermosets do not have real glass-transition temperatures and thus will not melt during heating. Instead, they tend to degrade (depolymerize) at elevated temperatures.

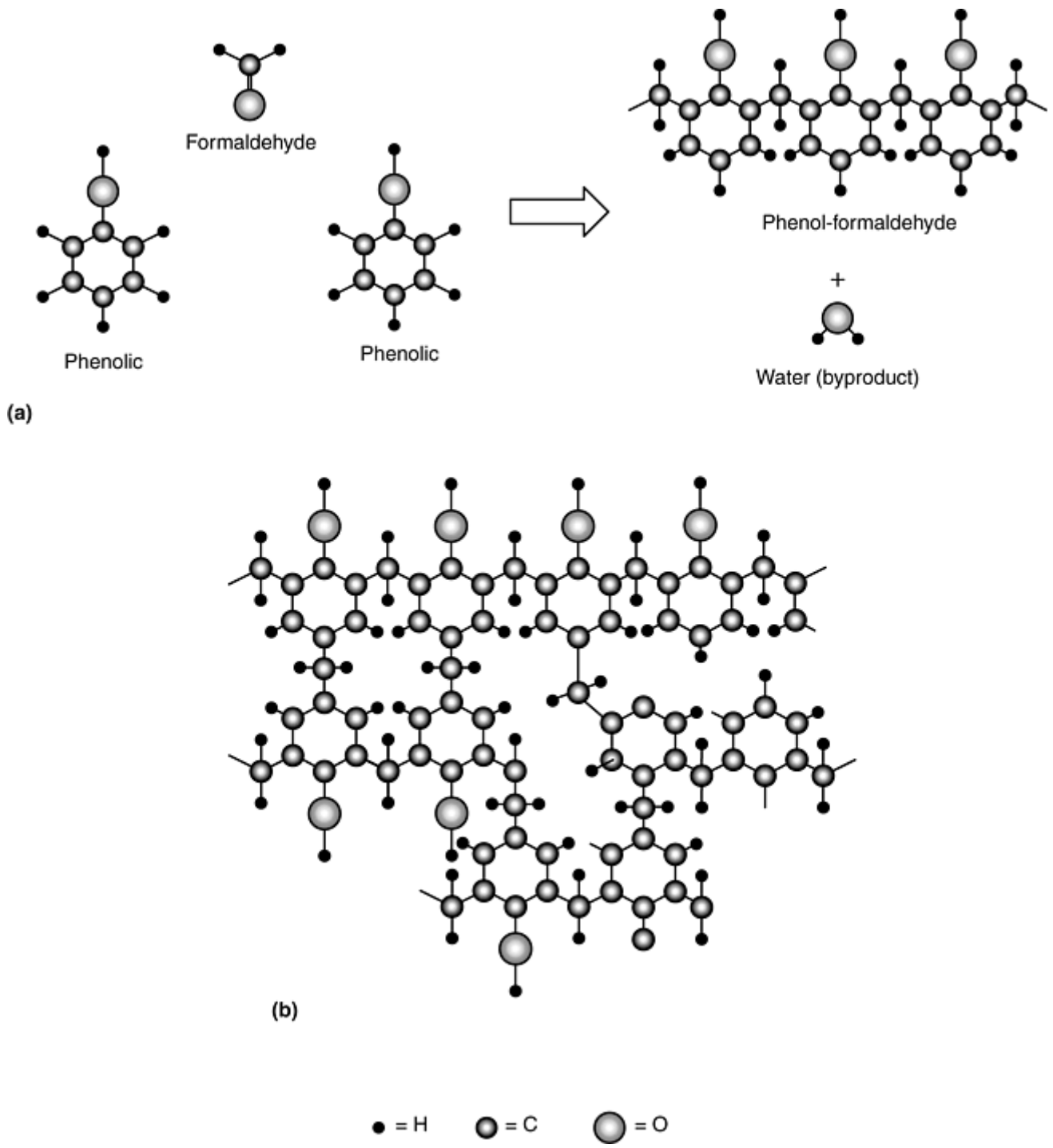


Fig. 15 Schematic representation of the structure of a phenol formaldehyde. (a) Two phenol rings join with a formaldehyde molecule to form a linear chain polymer and molecular by-product. (b) Excess formaldehyde results in the formation of a network, thermosetting polymer due to cross-linking.

Elastomers are another class of polymers that include natural rubber and a variety of other synthetic polymers exhibiting similar mechanical properties. Elastomers also form via cross linking between chains, and most behave like thermosets. Polyisoprene, for example, is a synthetic polymer with the same basic structure as natural rubber, but without the impurities found in natural rubber. The addition of sulfur along with heat (~140 °C) and pressure causes sulfur cross-links to form. As the degree of cross-linking increases, the polymer becomes harder. This particular process is known as *vulcanization*. A schematic representation of these cross-linking arrangements is shown in Fig. 16. Sometimes curved polymer chains can also evolve due to the arrangement of bonds between the atoms forming the backbone of each chain. This is schematically represented in Fig. 17. In this example, the molecule or atom, R, is placed on an unsaturated carbon chain in either a cis or trans position. In the cis position, the unsaturated bonds lie on the same side of the chain. In the trans position, they lie on opposite sides of the chain. The cis structure makes the molecule tend to coil rather than remain

linear. This coiling is believed to be responsible for the extensive elasticity observed in elastomers (e.g., rubber).

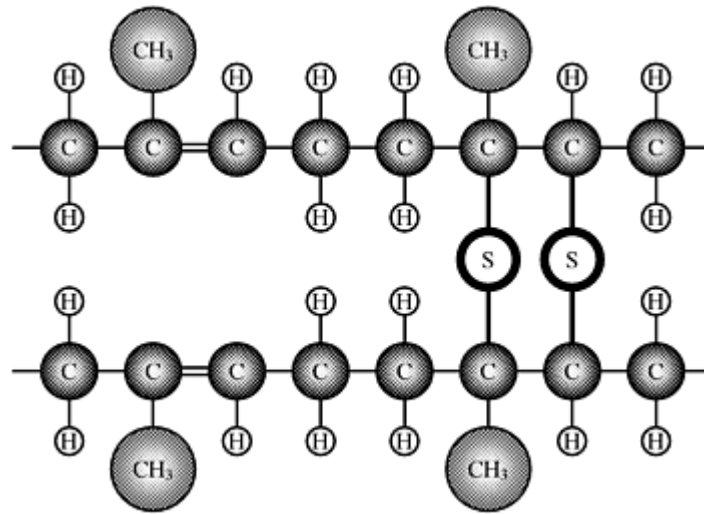


Fig. 16 Schematic representation of cross-linking in polyisoprene

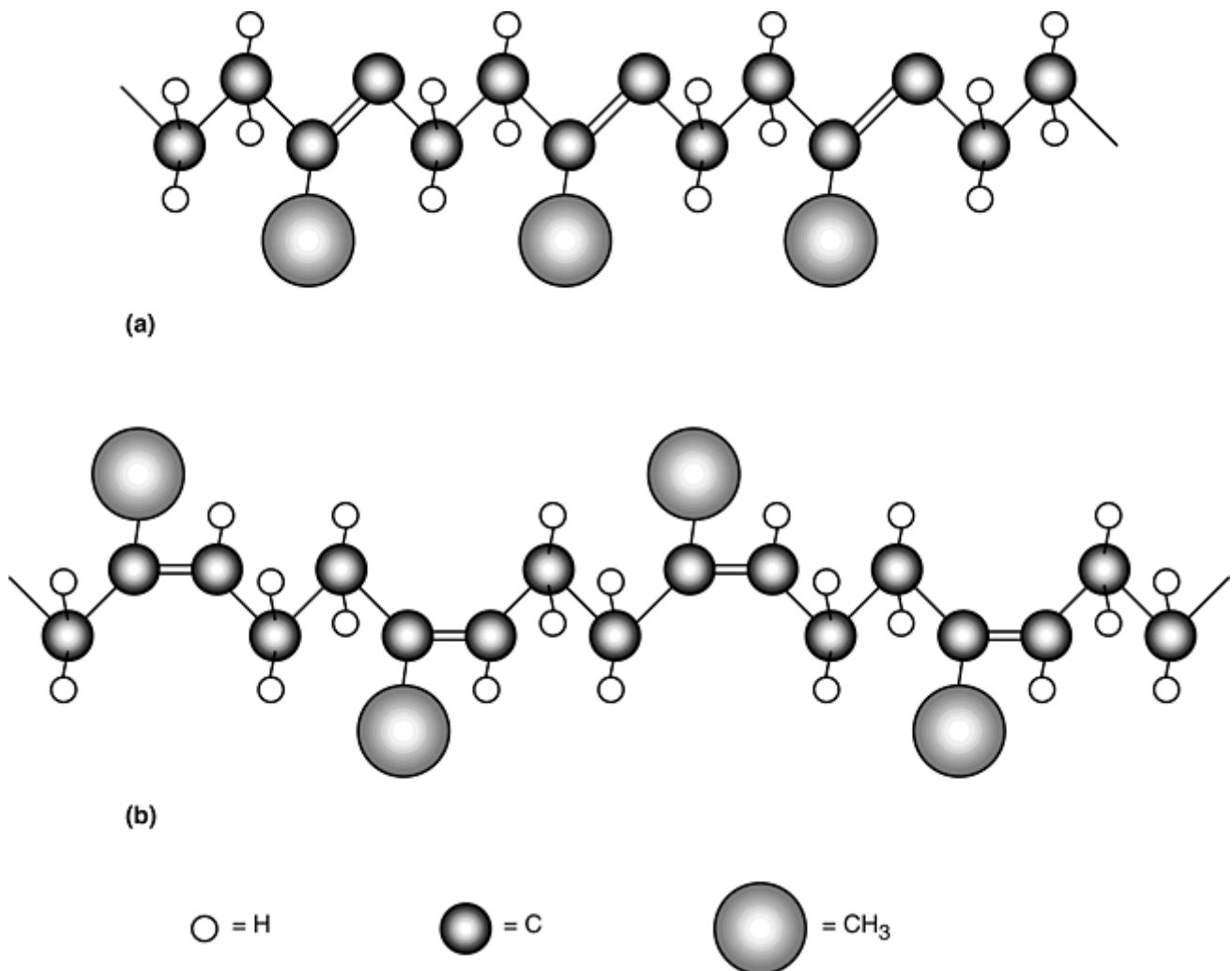


Fig. 17 Schematic representation of (a) cis and (b) trans structures in polyisoprene

References cited in this section

6. H. Baker, Structure and Properties of Metals, *Metals Handbook Desk Edition*, 2nd ed., ASM International, 1998, p 85–121

7. R.E. Reed-Hill and R. Abbaschian, *Physical Metallurgy Principles*, 3rd ed., PWS-Kent, Boston, 1992
8. R.H. Doremus, *Glass Science*, 2nd ed., John Wiley & Sons, 1994, p 109
9. W.G. Moffatt, G.W. Pearsall, and J. Wulff, *Structure*, Vol 1, *The Structure and Properties of Materials*, John Wiley & Sons, 1964, p 104
10. W.G. Moffatt, G.W. Pearsall, and J. Wulff, *Structure*, Vol 1, *The Structure and Properties of Materials*, John Wiley & Sons, 1964, p 106

Introduction to the Mechanical Behavior of Nonmetallic Materials

M.L. Weaver and M.E. Stevenson, The University of Alabama, Tuscaloosa

Deformation/Strengthening Mechanisms

Crystalline Solids

As noted in the previous article, metals generally deform via slip and/or twinning. Slip occurs via the motion of dislocations on close-packed planes and in close-packed directions, whereas twinning occurs via the cooperative movement of atoms producing a macroscopic shear. In slip, the combination of slip planes and directions are known as slip systems. The most common slip systems for disordered metals and alloys are schematically illustrated in Fig. 18. According to the von Mises criteria, at least five independent slip systems must be available in polycrystalline materials for the material to be capable of plastic deformation. Thus, the greater the number of independent slip systems, the greater is the possibility for plastic deformation. Most technically significant metals and alloys with cubic structures have five or more independent slip systems and thus exhibit substantial plasticity. For example, Ni and Cu, which are fcc metals, each have five independent slip systems and are extremely ductile at ambient temperatures. However, Co, which is an hcp metal, has less than five independent slip systems and is brittle at ambient temperatures. Metals with less than five slip systems can exhibit plasticity at ambient temperatures provided other deformation modes are available. A good example of this is Zn, which exhibits only three systems but also exhibits twinning.

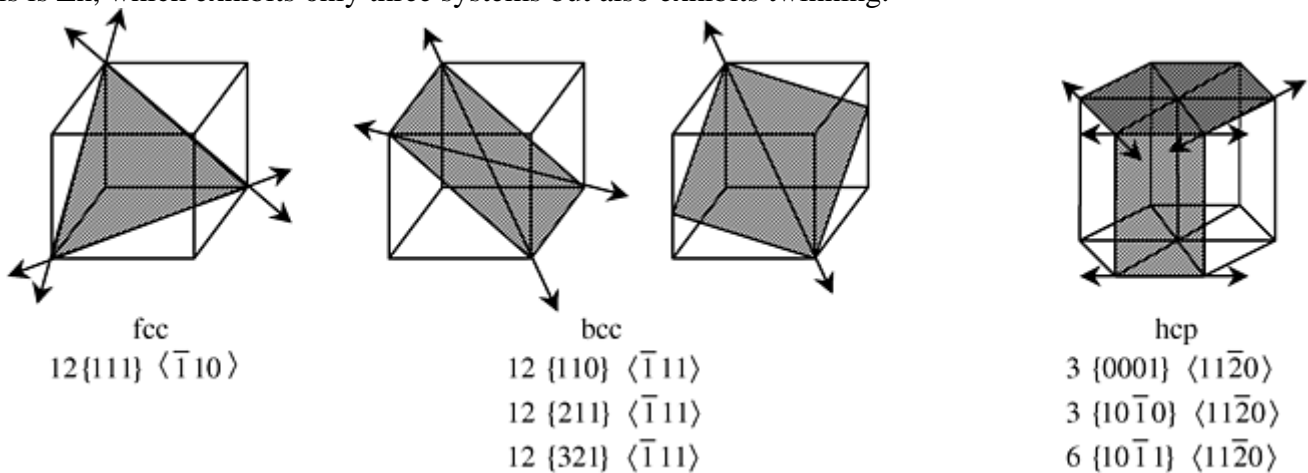


Fig. 18 Common slip systems observed for fcc, bcc, and hcp crystal structures

Twinning is a particularly important deformation mode in materials where slip is restricted. A schematic diagram of twinning is provided in Fig. 19. Twinning produces a reorientation of the lattice resulting in a region that is a mirror image of the parent lattice. The actual amount of strain that is gained from twinning is very small (typically less than 5%). The true benefit of twinning is that the lattice inside the twin is frequently

reoriented such that the slip systems are more favorably aligned with respect to the applied stress, which can allow some limited plastic deformation to occur.

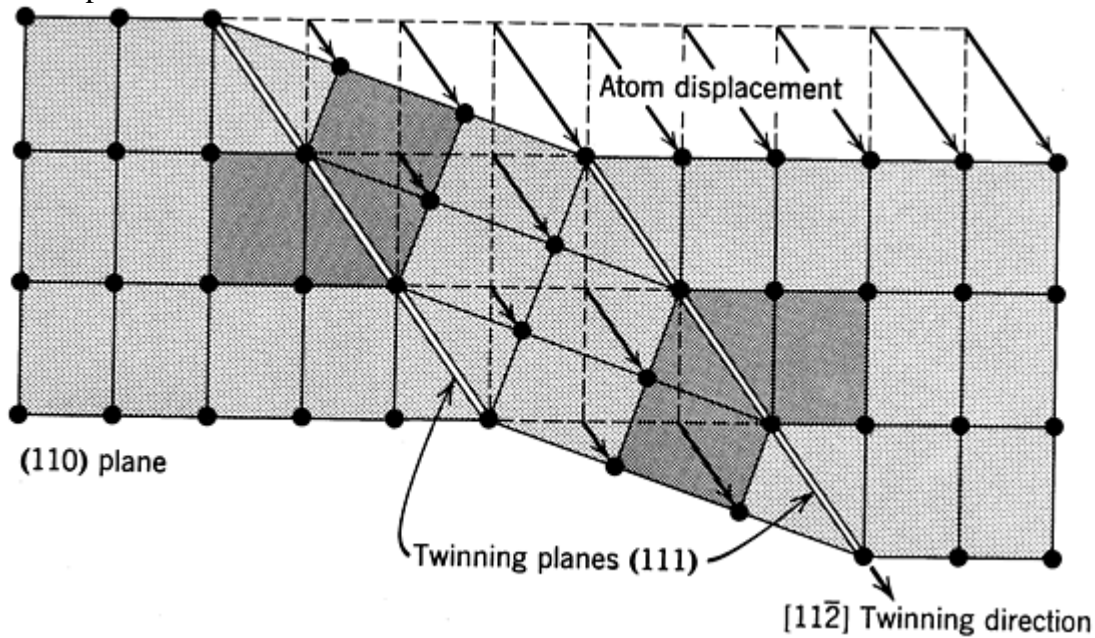


Fig. 19 Schematic of twinning as it occurs in an fcc lattice. Source: Ref 11

Plastic deformation in ceramic and intermetallics also occurs via slip and/or twinning. However, plastic deformation is typically more difficult in ceramics and intermetallics compared with metals, due, in part, to the strong and directional atomic bonds, ordered atomic distributions, and less symmetric lattice structures present in these materials. These features combine to restrict the motion of dislocations. In comparison with metals, ceramics are considered to be intrinsically hard and brittle. Intermetallics cannot be described as being intrinsically hard or soft; however, they are typically brittle. The different mechanical properties of these materials are related to bonding. The metallic bonds in metals make dislocation motion relatively easy, whereas the highly directional ionic, covalent, and mixed bonds observed in ceramics and intermetallics present large lattice resistance to dislocation motion.

In their polycrystalline form, most ceramics and intermetallics exhibit limited plasticity at ambient temperatures because they do not have enough independent slip systems for general deformation to occur. In many of these materials the lack of slip systems can be traced to the crystal structure, which is often so complex that the stress required to move a dislocation (the Peierls stress) becomes larger than the fracture stress. In NaCl, for example, slip occurs on $\{111\} \langle 1\bar{1}0 \rangle$ slip systems at ambient temperatures. This only yields two independent slip systems, which is not enough for polycrystalline ductility. In isostructural AgCl, slip occurs on both $\{111\}$ and $\{100\}$ planes, which provide enough independent slip systems for polycrystalline deformation.

In ionically bonded polycrystalline ceramics such as NaCl, deformation is further complicated because local charge neutrality must be maintained during deformation. In ionic ceramics, proper charge balance on either side of the slip plane is accomplished by introducing two extra half planes of atoms. The lines of ions at the bottoms of these half planes consist of alternating positive and negative ions. Dislocations can become charged, which can influence their mobility. The formation of a jog in a dislocation (20) can cause a localized charge imbalance, which must be compensated for by the formation of defects or the accumulation of atmospheres of oppositely charged impurities.

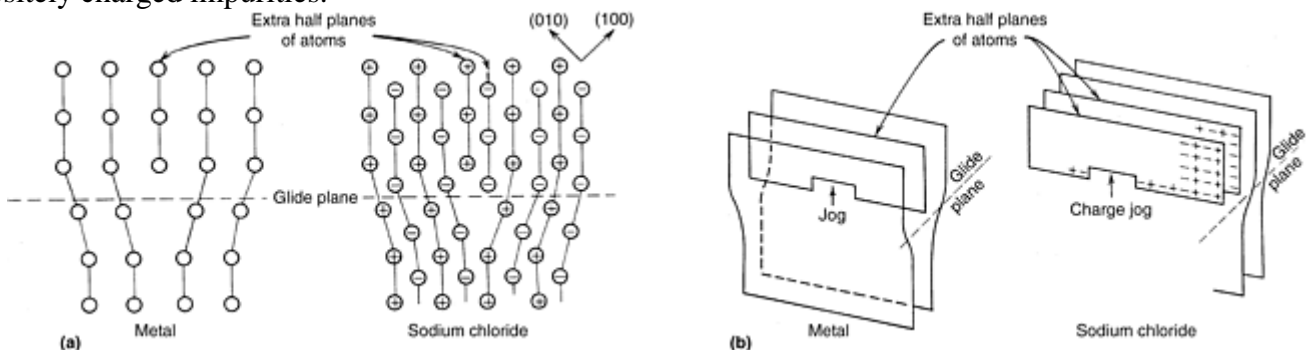


Fig. 20 (a) Schematic representation of an edge dislocation in NaCl. (b) Demonstration of how dislocation jogs in ionic crystals can have effective charges. Source: Ref 12

In more covalent ceramics and intermetallics, slip is complicated by the requirement that atomic order must be maintained. Perfect single dislocations, which do not influence the order of atoms, have longer Burgers vectors than dislocations in disordered alloys. Thus, these dislocations have higher strain energy. Such dislocations can assume lower energy configurations by dissociating into shorter dislocation segments, partial dislocations, which are separated by stacking faults and/or antiphase boundaries. These combinations of partial dislocations, stacking faults, and antiphase boundaries are known as superdislocations. When superdislocations move, the atomic order that is destroyed by passage of the leading partial dislocation is restored by passage of the trailing partial dislocation. Additional reasons for the lack of ductility in intermetallics include: difficulty transmitting slip across grain boundaries, intrinsic grain boundary weakness, segregation of deleterious solutes to grain boundaries, covalent bonding and high Peierls stress, and environmental susceptibility. Increased ductility can be obtained in some intermetallics by microalloying (e.g., NiAl with Fe, Mo, or Ga; Ni₃Al with B; or Ti₃Al with Nb). At higher temperatures, however, thermal activation permits additional slip activity to occur in all of these materials, which may allow them to be ductile.

Strengthening Mechanisms in Crystalline Solids (Ref 13, 14, 15)

As just discussed, ceramics and intermetallics generally deform via slip and/or twinning. As a result, anything that reduces the mobility of dislocations (i.e., anything that inhibits slip) will cause an increase in strength. The most common strengthening mechanisms, work hardening, solid-solution hardening, particle/precipitation hardening, and grain size hardening are described here.

Solid Solution Strengthening. Pure metals generally have low yield stresses compared with impure metals or single-phase alloys and compounds. The addition of substitutional or interstitial solute atoms to the lattice of a pure metal gives rise to local stress fields around each impurity atom. These local stress fields interact with those surrounding dislocations, which reduces the mobility of dislocations leading to increased strength. The amount of strengthening is related to the binding energy between the solute atoms and the dislocation, the concentration of the solute atoms, and the locations of the solute atoms within the lattice. For example, the magnitude of strengthening can be greater when solute atoms assume specific locations within the lattice (i.e., they order) as opposed to when they assume random positions. The same general principles apply in ceramics and intermetallics; however, the presence of long-range ordered crystal structures and charged ions within these materials makes it difficult to apply conventional models for solid solution hardening.

Solid solution strengthening can be considered by assuming that each foreign atom produces a restraining force, F , on the dislocation line. The magnitude of the restraining force (and thus the amount of strengthening obtained) depends on the nature of the interactions between foreign atoms and dislocations. The two most common interactions are elastic interactions and chemical interactions. Assuming that the atoms are spaced at an average distance, d , along the dislocation line, and that the dislocation glides a distance b on the slip plane, the ratio F/d gives the force per unit length of dislocation that must be overcome by the applied shear stress, τ . The increment in applied stress needed to overcome the restraining force per unit line length is $\Delta\tau b$ such that:

$$\Delta\tau = \frac{F}{bd} \quad (\text{Eq 2})$$

When the solute atoms have different sizes than the host atoms or different elastic moduli, they tend to alter the crystal lattice locally in the vicinity of the solute atom. This causes the moving dislocation to be either attracted to or repelled away from the solute. When the dislocation is attracted toward the solute, strengthening is caused because more force is required to pull the dislocation away from the solute. When the dislocation is repelled by the solute, strengthening is caused because more force is required to push the dislocation past the solute atom.

Solid solution strengthening can occur in ceramics and intermetallics just as it does in metals. Both substitutional and interstitial types are possible. In ceramics, interstitial solid-solution strengthening will occur if the ionic radius of the solute is small in comparison with the solvent (anion). In the case of substitutional solid-solution strengthening, because both anions and cations are present, a substitutional impurity will substitute for the host ion to which it is most similar in the electrical sense (i.e., if the impurity atom normally forms a cation in a ceramic material, then it will likely substitute for the host cation). In NaCl, for example,

Ca^{2+} and O^{2-} would probably substitute for Na^+ and Cl^- ions, respectively. To achieve appreciable solid solubility, the ionic size and charge of the substituting atoms must be nearly the same as those of the host ions. If impurity ions have different charges than the host ions, the crystal must compensate structurally such that charge neutrality is maintained. This can be accomplished by the formation of lattice defects, such as vacancies or interstitials (Schottky, Frenkel defects).

In ionic crystals, the presence of charged dislocations also plays a role. Solutes exhibiting different valence than the host atoms (i.e., aliovalent) are more effective in increasing the yield stress than ions with the same valence (isovalent). Aliovalent ions are more effective because they produce an asymmetric elastic distortion, which interacts strongly with dislocations. The stress increment caused by solid solution strengthening in ceramics is described by the equation:

$$\left(\frac{\Delta\tau}{\tau_0}\right)^{1/2} = 1 - \left(\frac{T}{T_0}\right)^{1/2} \quad (\text{Eq 3})$$

where T is the absolute temperature, $T_0 = G\Delta\epsilon b^3/(3.86\alpha k)$, $\tau_0 = G\Delta\epsilon c^{1/2}/(3.3)$, c is the concentration of defects, $\Delta\epsilon$ is the misfit strain, b is the Burgers vector, α is a constant, and k is Boltzmann's constant (Ref 14).

Work hardening, also known as strain hardening, is an important industrial process that is used to harden metals or alloys. The hardening or strengthening is a direct result of dislocation multiplication and dislocation-dislocation interactions. Work hardening is also an important phenomenon in some intermetallic systems but is not a viable process for ceramics and glasses. Polymers do not work harden; however, an analogous phenomenon, cold drawing, occurs in thermoplastics. Cold drawing is addressed in a subsequent section of this article.

When dislocations moving on intersecting slip systems collide some of them will become pinned. The more the material is plastically deformed, the higher the dislocation density becomes, resulting in more restricted dislocation motion. A high work hardening rate implies the obstruction of dislocations gliding on intersecting systems. Thus, techniques that increase dislocation density also increase strength. For a given dislocation distribution, the shear flow stress, τ , is related to the dislocation density, ρ , by an equation of the form:

$$\tau = \tau_0 + \alpha G b \rho^{1/2} \quad (\text{Eq 4})$$

where α is a materials specific constant that varies from 0.2 to 0.4 for different fcc and bcc metals, G is the material shear modulus, b is the Burgers vector, and τ_0 is the flow strength in absence of work hardening (Ref 6). At high strains, dislocations will tangle and form cell structures. The hardening then becomes more a function of cell size than of dislocation length.

Grain Size Strengthening. Internal boundaries also act as obstacles to dislocation motion. Boundaries impede dislocations over a large length, which often makes boundary strengthening a more potent strengthening mechanism than solid-solution strengthening or work hardening. At grain boundaries, there is a change in crystallographic orientation, which prevents or inhibits the passage of dislocations. For slip to continue across a grain boundary, yielding must occur within the adjacent grain. If the orientation of the adjacent grain is unfavorable, dislocations will pile up against the boundary leading to a stress concentration at the boundary. Under action of a stress concentration, slip can be initiated within the adjacent grain. The increase in stress associated with grain size can be represented by the Hall-Petch relation from which the stress increment can be written as:

$$\Delta\tau = \frac{k_y}{\sqrt{D}} \quad (\text{Eq 5})$$

where D is the grain diameter and k_y is a locking parameter that describes the relative strength of the boundary. This relationship shows that as the grain size increases, the stress concentration at the boundary decreases, resulting in reduced strengthening compared with fine-grained materials. Other boundaries such as subgrain boundaries and stacking faults can also form obstacles to dislocation motion; however, they are less potent strengtheners than grain boundaries.

Precipitation/Particle Hardening. Substantial strengthening can also be obtained by adding precipitates or dispersoids to the material. The extent of strengthening is determined by a number of factors including volume fraction, particle size, particle shape, and strength of the particle-matrix interface (Ref 14, 15). This is directly related to interactions between moving dislocations and the particles as the presence of particles inhibits dislocations by providing additional barriers to their motion.

To overcome the presence of particles, dislocations will either cut through (i.e., shear) them or will bow around them. If the particles are small and coherent, they are more likely to be shearable. Whether or not shearing occurs depends on a number of factors including particle misfit, particle modulus, and particle structure. In shearable particles, the presence of coherent particles with lattice parameters that are either larger or smaller than the matrix leads to internal stress fields that interact with dislocations. Similarly, particles exhibiting different shear moduli than the matrix will also alter or inhibit dislocation motion. Additional strengthening can also be achieved if the particles have low stacking fault energies or exhibit ordered crystal structures. An additional form of strengthening, chemical strengthening, is related to the energy required to create an additional area of particle-matrix *interface* when the particle is sheared. If the particles are large or incoherent, dislocations will bow around the particles until the bowing segments join. The dislocation can then proceed, leaving a dislocation loop around the particles. This is known as *Orowan looping*. As particle size increases, the bowing stress decreases. In precipitation-hardened systems, maximum strengthening (at a fixed volume) is achieved when the shearing stresses and the bowing stresses are equal.

The above descriptions refer to materials with a relatively low volume-fraction of particles. However, in metal-matrix composites, higher concentrations of particles have been used to strengthen materials. Usually in these dispersion-strengthened systems, high strength, high-modulus particles or fibers are artificially added to a low modulus substrate. The strengthening is believed to result in part from the modulus difference between the matrix and the dispersed particles. The high-modulus particles or fibers carry most of the stress, while the relatively ductile matrix accommodates most of the strain. There is also usually enhanced work hardening within the matrix near the particles, which leads to strengthening.

Deformation and Strengthening of Polymers (Ref 16, 17)

Mechanical properties of polymers are influenced by a variety of the structural parameters introduced previously. The strength of many polymers is directly related to the molecular weight and to the degree of crystallinity. Properties related to tension are often expressed in the form:

$$\text{Property} = a - \frac{b}{M_n} \quad (\text{Eq 6})$$

where \overline{M}_n is the number average molecular weight and a and b are experimental constants. The number average molecular weight is defined as:

$$\overline{M}_n = \frac{\sum[x_i M_i]}{\sum x_i} \quad (\text{Eq 7})$$

where x_i is the number of molecules in each size fraction and M_i is the molecular weight in each size fraction. Increased crystallinity can lead to increased tensile strength, stiffness, and yield strength. When polymers exhibit some crystallinity, stiffness and elastic modulus can change by more than an order of magnitude. Copolymerization of multiple monomers also can modify mechanical properties by decreasing crystallinity and, thus, lowering stiffness and yield point.

Many polymers exhibit viscoelastic behavior. When viscoelastic polymers are stressed, there is an immediate elastic response as indicated in Fig. 21 (Ref 17), followed by viscous flow, which decreases with increasing time until a steady state is achieved. If the material is then unloaded, the elastic strain is recovered followed by time dependent (delayed) recovery. Some permanent strain, denoted as permanent recovery in Fig. 21, remains.

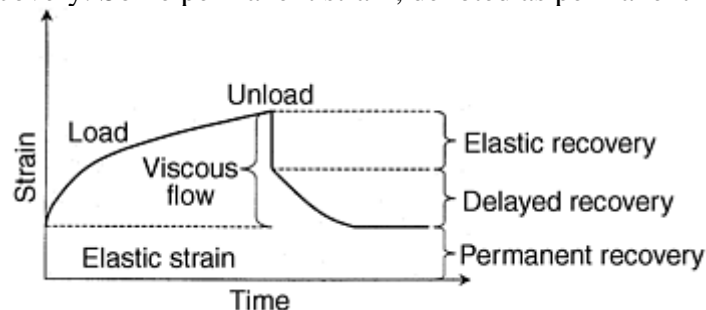


Fig. 21 Schematic representation of viscoelastic behavior of a polymer. Loading produces an immediate elastic strain followed by viscous flow. Unloading produces an immediate elastic recovery followed by additional recovery over a period of time. Source: Ref 17

In thermoplastic polymers, permanent deformation occurs via interchain sliding. Strengthening is accomplished by impeding chain sliding. One way to accomplish this is by adding “bulky” side groups to each polymer chain. This results in a geometric (steric) hindrance to chain sliding. For example, for a polymeric series based on the monomer C_2H_3R , where R represents a specific atom or side group, strength increases proportionally with the size of the side group. For example, polypropylene ($R = CH_3$) is stronger than polyethylene ($R = H$).

In general, crystalline polymers are much stronger than noncrystalline ones. Higher density in crystalline polymers can be correlated with the fact that the polymer chains are aligned closer together, which makes chain displacement more difficult. One good example of this is polyethylene where strengthening can be achieved by drawing, which effectively increases the amount of crystalline material. Most thermoplastic polymers are difficult to crystallize, however, due to their bulky side groups and greater viscosity (Ref 18).

Drawing is a technique used to strengthen thermoplastics. During drawing, the long axes of the polymer chains align along the drawing direction. In filament form, the strength of drawn polymers is related directly to the strength of the covalent bonds in the polymer backbone rather than the resistance to interchain sliding. This type of strengthening, which is truly realized only in filaments, forms the backbone of the textile industry.

Though different polymers can exhibit limited solubility between each other, polymers cannot really be solid-solution strengthened as metals, ceramics, and intermetallics can be. Exceptions occur when rigid rod molecules with very stiff backbones are added. These molecules reinforce the polymer when dispersed in it in the same way that fibers reinforce composite materials.

Deformation and Strengthening of Composite Materials

Composites are classified either by the type of matrix or the type of reinforcement. Common matrix classifications include polymer-matrix composite (PMC), metal-matrix composite (MMC), ceramic-matrix composite (CMC) and intermetallic-matrix composite (IMC). Reinforcement classification schemes include particulate-reinforced composite, fiber-reinforced composite, and laminate composite. Composites are designed to take advantage of the best characteristics of each component.

Microstructurally, composites consist of a matrix and a reinforcing phase. In fiber-reinforced composites, the matrix holds the fibers together, protects them from damage, and transmits load to the fibers. The reinforcing phases, which can be fibers, filaments, laminates, and so on, usually involves high strength, high modulus materials that are too fragile for use in a monolithic form. Ductile reinforcements can also be used to toughen brittle matrix materials.

Polymer-matrix composites are the commercially important composites. The polymer matrix is typically a thermoset, as opposed to a thermoplastic. Unlike thermoplastics, thermosets are relatively stable over a wide range of temperatures and are resistant to plastic deformation. Many common PMCs contain glass fibers embedded in epoxy resins. Stronger fiber, such as graphite fiber, is used as well.

Thermoset composites are made by adding a reinforcement to the thermoset during or prior to setting. The thermoset bonds the reinforcement together. The polymer matrix also protects glass-fiber interfaces from degradation. Glass is prone to react with water vapor in air, which induces corrosive surface flaws (crack initiation sites).

Basic composite mechanics can be addressed by considering Fig. 22. Consider a two-phase material consisting of N lamellae of α and β phases with thickness of l_α and l_β , respectively. The volume fractions of each phase are:

$$V_\alpha = \frac{l_\alpha}{(l_\alpha + l_\beta)} \quad \text{and} \quad V_\beta = \frac{l_\beta}{(l_\alpha + l_\beta)} \quad (\text{Eq 8})$$

The application of a force along the y -axis and the stresses experienced by each lamellae are equal (i.e., $\sigma_\alpha = \sigma_\beta = \sigma_c = F/L^2$); however, the strains differ from lamellae to lamellae. The composite strain is, thus, the weighted average of the individual strains or:

$$\epsilon_c = V_\alpha \epsilon_\alpha + V_\beta \epsilon_\beta \quad (\text{Eq 9})$$

From Hooke's Law, the composite modulus thus becomes:

$$E_c = \frac{E_\alpha E_\beta}{(V_\alpha E_\beta + V_\beta E_\alpha)} \quad (\text{Eq 10})$$

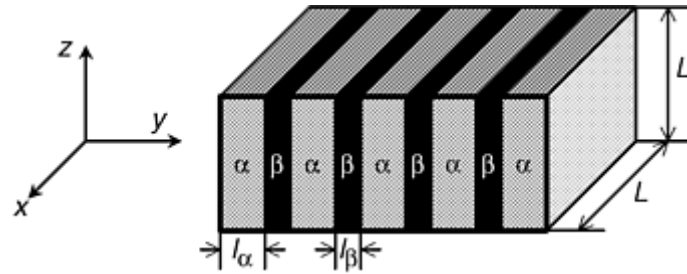


Fig. 22 Schematic representation of lamellar arrangement in a two-phase composite material. Source: Ref 19

When a force is applied along the z-direction, each lamellae experiences equal strains (i.e., $\epsilon_\alpha = \epsilon = \epsilon_\beta = \epsilon_c$); however, the stresses experienced differ. For example, the force carried by each α lamella can be approximated by assuming that the sum of the forces borne by the individual phases equals the total external force:

$$F = (F_\alpha + F_\beta) \quad (\text{Eq 11})$$

Because each lamellar carries a stress, the forces experienced by the respective α and β lamellae are:

$$F_\alpha = \sigma_\alpha N l_\alpha L \text{ and } F_\beta = \sigma_\beta N l_\beta L \quad (\text{Eq 12})$$

Substitution of these relationships into Eq 11 allows the respective volume fraction rules for composite stress and modulus to be calculated as:

$$\sigma_c = V_\alpha \sigma_\alpha + V_\beta \sigma_\beta \text{ and } E_c = V_\alpha E_\alpha + V_\beta E_\beta \quad (\text{Eq 13})$$

This volume fraction rule is the one most commonly followed by composites since the phase distributions in most composites are close to that for which the equal strain approximation is valid.

Using these relationships, it is useful to plot the influence of volume fraction upon the load carried by the reinforcement in the elastic regime. Such a plot is shown in Fig. 23 assuming that the α -phase is stronger than the β -phase. This plot effectively shows that the strengthening phase is much more effective in carrying load when forces are applied parallel to the axis of the reinforcing phase. Reinforcements can be dispersed in a variety of ways in composite materials.

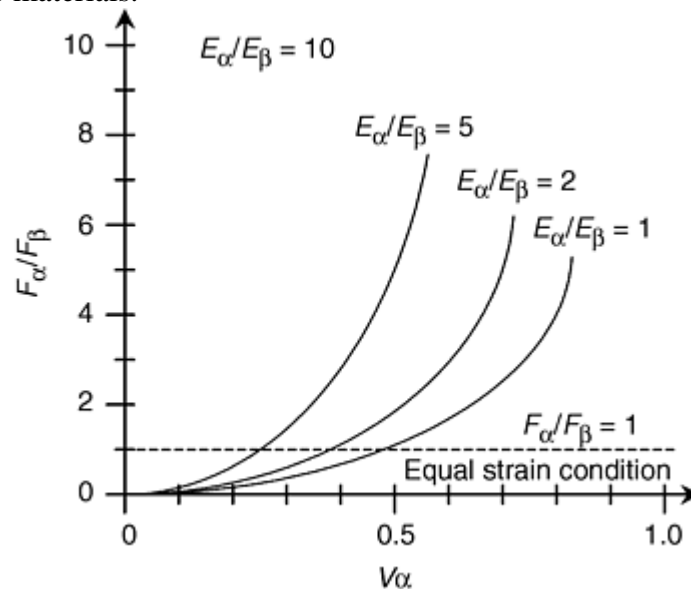


Fig. 23 Ratio of the force carried by the strong phase to that carried by the weak phase for deformation parallel and perpendicular to the lamellae. Source: Ref 19

Most composites are not as ideally arranged as those just described. Thus, variants of Eq 10 and 13 are used to describe the properties of materials possessing different types of reinforcements. For particle-reinforced materials, the composite stress and modulus can be expressed by:

$$\sigma_c = V_m \sigma_m + K_s V_p \sigma_p \text{ and} \quad (\text{Eq 14})$$

$$E_c = V_m E_m + K_c V_p E_p$$

where E_p and E_m represent the particle and matrix moduli, V_p and V_m represent the particle and matrix volume fractions, σ_m and σ_p represent the matrix and particle tensile strengths, and K_s and K_c represent constants.

One of the most common ways is to use reinforcements in the form of continuous fibers. A similar expression is valid for continuous fiber-reinforced composites; the volume fraction rule is similarly expressed as:

$$\sigma_c = V_f \sigma_f + V_m \sigma_m = V_f \sigma_f + (1 - V_f) \sigma_m \quad (\text{Eq 15})$$

where σ_c , σ_f , and σ_m represent the tensile strengths of the composite, fibers, and matrix, respectively, and V_f and V_m represent the respective fiber and matrix volume fractions in the composite. This equation applies when the long axis of the fibers is aligned parallel to the stress axis. Table 2 lists the properties of a number of continuous fibers. Nonmetallic fibers demonstrate high strengths and higher strength-to-density ratios, which make them attractive in applications such as aerospace where low weight is a premium. The volume fraction rule applies provided the long axis of the fibers remains aligned with the stress axis. Random distributions of fibers result in lower strengthening. In addition, strengthening is lower for particulates or when the fibers are not parallel to the stress axis. Expressions similar to the volume fraction rule derived here are used to estimate other composite properties like elastic modulus. Not all properties can be calculated using such a simple rule.

Table 2 Properties of selected fibers

Materials class	Material	Density mg/m ³ (ρ)	Tensile strength (TS)		TS/ρ, MNm/kg
			GPa	ksi	
Metals	Pearlitic steel (piano wire)	7.9	4.2	610	0.53
	Be	1.8	1.3	190	0.72
	Mo	10.3	2.1	310	0.2
	W	19.3	3.9	570	0.20
Ceramics and glasses	Al ₂ O ₃	3.96	2.0	290	0.51
	Graphite (Kevlar)	1.5	2.8	410	1.87
	S glass	2.5	6.0	870	2.4
	SiC	2.7	2.8	210	1.04
Polymers	Nylon 66	1.1	1.05	150	0.95
	Polyamide-hydrazide	1.47	2.4	350	1.63
	Copolyhydrazide	1.47	2.7	390	1.84
	Poly(P-phenylene) terephthalamide	1.44	2.8	410	1.94

Source: Ref 19

The use of metals to reinforce ceramics (or intermetallics) usually increases toughness but decreases strength. Increased toughness is the result of the blunting and/or arrest of cracks by the ductile reinforcement. Reinforcement geometry is also important. Fibers and laminates tend to improve toughness more than equiaxed particles. When cracks approach fibers or lamellae (plates), they are often deflected along the reinforcement-matrix interface. This increase in crack tortuosity provides additional work to fracture and, thus, an increase in fracture toughness. Additional information on structure-property relationships for composite materials can be found in Ref 20 and 21.

Deformation and Strengthening of Glasses

The mechanical behavior of glasses is similar to that of crystalline materials, in that increases in strain rate and decreases in temperature result in increased strength. The actual mechanisms that are responsible for deformation, however, differ from those exhibited by crystalline materials.

At low temperatures and low stresses, all glasses deform in a linear elastic manner. Linear elastic strains result from stretching of the chemical bonds making up the glass structure. Linear elastic deformation is followed by viscoelastic deformation at intermediate temperature, which is followed by Newtonian viscous flow at elevated temperatures (i.e., $T_g \leq T \leq T_{mp}$). Viscoelastic strains, which are time dependent and recoverable, result from conformal rearrangements of the basic structural units making up the glass structure (i.e., SiO₄ tetrahedra in silica-base glasses, individual atoms in metallic glasses, and long chain molecules in organic glasses). Newtonian viscous flow, which can be correlated with a linear dependence of the applied stress on the applied strain rate, results from localized slip processes, which result in the permanent displacement of basic structural units of the material with respect to each other. In glassy polymers, the units are long chain molecules whereas for metallic or inorganic glasses the basic units are single atoms or SiO₄ tetrahedra, respectively. Elevated temperature deformation of noncrystalline materials is distributed uniformly throughout the volume of the material. These facts are often exploited to form glassy materials into useful geometry. As temperature is decreased, the material becomes stronger, and an alteration in flow behavior occurs. In inorganic glasses, permanent deformation does not occur at low temperatures. On the other hand, in metallic and organic glasses, permanent deformation occurs in a heterogeneous fashion involving the cooperative displacement of atoms or molecules. This process is known as *shear banding*.

Metallic glasses become softer after shear band formation because the stress required to propagate the band is lower than the stress required to initiate it. Fracture usually occurs after the propagation of a single shear band. Conversely, in organic glasses, shear band formation is not followed by instability and fracture. More shear bands form until the density of bands is so high that they coalesce, resulting in a neck containing highly oriented molecules. Once the neck forms, it propagates up and down the gage length, leading to an increase in strength.

References cited in this section

6. H. Baker, Structure and Properties of Metals, *Metals Handbook Desk Edition*, 2nd ed., ASM International, 1998, p 85–121
11. H.W. Hayden, W.G. Moffatt, and J. Wulff, Mechanical Behavior, Vol 3, *The Structure and Properties of Materials*, John Wiley & sons, 1964, p 111
12. W.D. Kingery, H.K. Bowen, and D.R. Uhlmann, *Introduction to Ceramics*, 2nd ed., John Wiley & sons, 1976, p 172
13. J.D. Verhoeven, *Fundamentals of Physical Metallurgy*, John Wiley & Sons, 1975
14. D.J. Green, *An Introduction to the Mechanical Properties of Ceramics*, Cambridge University Press, Cambridge, 1998
15. D. Hull and D.J. Bacon, *Introduction to Dislocations*, Pergamon Press, Oxford, 1984
16. D.T. Grubb, Polymers, Mechanical Properties of, *Encyclopedia of Applied Physics*, Vol 14, VCH Publishers, Inc., 1996, p 531–548
17. R.M. Brick, A.W. Pense, and R.B. Gordon, *Structure and Properties of Engineering Materials*, 4th ed., McGraw-Hill, 1977
18. I.M. Ward, *Mechanical Properties of Solid Polymers*, John Wiley & Sons, 1971
19. T.H. Courtney, *Mechanical Behavior of Materials*, 2nd ed., McGraw-Hill, Inc., 2000

20. D. Hull, *An Introduction to Composite Materials*, Cambridge University Press, Cambridge, 1981

21. K.K. Chawla, *Composite Materials: Science and Engineering*, 2nd ed., Springer-Verlag, New York, 1999

Introduction to the Mechanical Behavior of Nonmetallic Materials

M.L. Weaver and M.E. Stevenson, The University of Alabama, Tuscaloosa

Fatigue and Fracture of Nonmetallic Materials (Ref 22, 23, 24)

Two important aspects of the mechanical behavior of any class of engineering material are the fatigue response and fracture resistance. Most engineering structures are subject, in some form, to fatigue. Therefore, the ability of a material to withstand the accumulation of damage from fatigue is very important in terms of the life span of the component. Additionally, the fracture behavior of a material is important in terms of preventing premature failure. Considering the importance of these properties, a brief overview of the response of ceramics and polymers is discussed here and comparison is made to many typical metallic materials.

Fatigue Response of Ceramics and Polymers

When discussing fatigue in terms of brittle solids, it is not necessarily assumed that the term *fatigue* refers to cyclic loading conditions. In most cases, fatigue in ceramics is limited to static loading conditions where the loss of strength with time is the underlying phenomenon. Until recently, it was a common misconception that cyclic fatigue damage was not observed in ceramics. More recently, the cyclic fatigue lives have been proven to be shorter than the static fatigue lives, which indicates that there is some effect, albeit an unclear one, that causes cyclic loading to vary from static loading.

In conventional metals, fatigue is commonly associated with some amount of plastic strain, which is not prevalent in ceramics and glasses. Since there is no dominance by plastic strains, application of the popular strain-life method is not possible for ceramic and glass materials at room temperature. For ceramics, the assumptions of linear elastic fracture mechanics (LEFM) are satisfied, and analysis using this method is more suitable.

In polymers, traditional fatigue analysis methods, such as those used in metals, can be applied. Polymers, however, involve a significant complication in the body of hysteresis heating and subsequent softening. This phenomenon significantly lowers the fatigue life and additionally induces the dominance of plastic flow as a deformation mechanism, whereas under isothermal conditions fatigue crack propagation dominates. In light of the additional heating and softening problem, polymers still exhibit a traditional fatigue limit, below which no cyclic deformation or resultant heating occurs significantly. Additionally, for polymer crystals, fatigue resistance increases as crystallinity increases (Ref 22, 23, 24).

Fracture Behavior of Ceramics and Polymers

The fracture behavior of materials is important in engineering design because of the high probability of flaws being present. As such, it is important to understand how a material will tolerate the presence under a flaw under operating conditions and how a material will resist the propagation of cracks from these flaws.

In ceramics, loading results in deformation in the elastic regime with little or no plastic deformation at fracture. Conversely, plastics exhibit little or no elastic deformation and a great degree of plastic deformation at final fracture. While the two materials do not share similar stress-strain curves, they do share low values for fracture toughness. The fracture toughness of a material is a measure of its ability to resist fracture propagation. Defined another way, it is the critical stress intensity at which final fracture occurs. In either case, both ceramics and polymers share low values of this parameter. Table 3 compares the approximate values of several classes of engineering materials in terms of their fracture toughness.

Table 3 Fracture toughness values for a variety of engineering materials

Material	Fracture toughness (K_{Ic}), MPa \sqrt{m}
Glasses	0.5–1
Most polymers	1–3
Ceramics	3–7
Intermetallics	1–20
Cast irons	10–40
Aluminum alloys	20–50
Titanium alloys	30–90
Steels (all types)	30–200

While polymers and ceramics do exhibit fracture toughness values that are of the same order of magnitude, the respective modes of fracture are not necessarily the same. In polymers, the fracture process is dominated in many cases by crazing, or the nucleation of small cracks and their subsequent growth. In ceramics and other ionic solids, cleavage on electrically neutral planes is often the dominant fracture mode. These two modes are distinctly different, even though the resistance to fracture for both classes of materials is similar. This brings up the point that, for most materials, no single parameter can quantify the behavior under a given set of conditions. In the example of fracture, K_{Ic} alone will not always provide sufficient data to understand the fracture process. Only an intimate knowledge of the materials structure and the fracture toughness will provide a completely accurate indicator. Besides the material aspects, the fracture process is also statistical in nature (weakest link theory). While fracture statistics can be complicated to understand fully, a good introduction can be found in Ref 24. A more detailed description of the fracture process of these classes of materials can be found by referring to the Selected References.

References cited in this section

22. S. Suresh, *Fatigue of Materials*, 2nd ed., Cambridge University Press, Cambridge, 1998, p 383–430
23. R.W. Hertzberg, *Deformation and Fracture Mechanics of Engineering Materials*, 4th ed., John Wiley & Sons, 1996, p 664–680
24. J.R. Wachtman, *Mechanical Properties of Ceramics*, John Wiley & Sons, 1996, p 235–246

Introduction to the Mechanical Behavior of Nonmetallic Materials

M.L. Weaver and M.E. Stevenson, The University of Alabama, Tuscaloosa

References

1. N.E. Dowling, *Mechanical Behavior of Materials: Engineering Methods for Deformation, Fracture, and Fatigue*, 2nd ed., Prentice Hall, 1999, p 23
2. T.H. Courtney, *Materials Selection and Design*, Vol 20, *ASM Handbook*, ASM International, 1997, p 336–356
3. N.E. Dowling, *Mechanical Behavior of Materials: Engineering Methods for Deformation, Fracture, and Fatigue*, 2nd ed., Prentice Hall, 1999, p 24
4. G. Sauthoff, *Intermetallics*, VCH Publishers, New York, 1995

5. W.D. Callister, *Materials Science and Engineering—An Introduction*, 4th ed., John Wiley & Sons, 1997, p 21
6. H. Baker, Structure and Properties of Metals, *Metals Handbook Desk Edition*, 2nd ed., ASM International, 1998, p 85–121
7. R.E. Reed-Hill and R. Abbaschian, *Physical Metallurgy Principles*, 3rd ed., PWS-Kent, Boston, 1992
8. R.H. Doremus, *Glass Science*, 2nd ed., John Wiley & Sons, 1994, p 109
9. W.G. Moffatt, G.W. Pearsall, and J. Wulff, *Structure*, Vol 1, *The Structure and Properties of Materials*, John Wiley & Sons, 1964, p 104
10. W.G. Moffatt, G.W. Pearsall, and J. Wulff, *Structure*, Vol 1, *The Structure and Properties of Materials*, John Wiley & Sons, 1964, p 106
11. H.W. Hayden, W.G. Moffatt, and J. Wulff, Mechanical Behavior, Vol 3, *The Structure and Properties of Materials*, John Wiley & sons, 1964, p 111
12. W.D. Kingery, H.K. Bowen, and D.R. Uhlmann, *Introduction to Ceramics*, 2nd ed., John Wiley & sons, 1976, p 172
13. J.D. Verhoeven, *Fundamentals of Physical Metallurgy*, John Wiley & Sons, 1975
14. D.J. Green, *An Introduction to the Mechanical Properties of Ceramics*, Cambridge University Press, Cambridge, 1998
15. D. Hull and D.J. Bacon, *Introduction to Dislocations*, Pergamon Press, Oxford, 1984
16. D.T. Grubb, Polymers, Mechanical Properties of, *Encyclopedia of Applied Physics*, Vol 14, VCH Publishers, Inc., 1996, p 531–548
17. R.M. Brick, A.W. Pense, and R.B. Gordon, *Structure and Properties of Engineering Materials*, 4th ed., McGraw-Hill, 1977
18. I.M. Ward, *Mechanical Properties of Solid Polymers*, John Wiley & Sons, 1971
19. T.H. Courtney, *Mechanical Behavior of Materials*, 2nd ed., McGraw-Hill, Inc., 2000
20. D. Hull, *An Introduction to Composite Materials*, Cambridge University Press, Cambridge, 1981
21. K.K. Chawla, *Composite Materials: Science and Engineering*, 2nd ed., Springer-Verlag, New York, 1999
22. S. Suresh, *Fatigue of Materials*, 2nd ed., Cambridge University Press, Cambridge, 1998, p 383–430
23. R.W. Hertzberg, *Deformation and Fracture Mechanics of Engineering Materials*, 4th ed., John Wiley & Sons, 1996, p 664–680
24. J.R. Wachtman, *Mechanical Properties of Ceramics*, John Wiley & Sons, 1996, p 235–246

Selected References

General

- M.F. Ashby and D.R.H. Jones, *Engineering Materials 1: An Introduction to Their Properties and Applications*, Pergamon Press, 1980
- M.F. Ashby and D.R.H. Jones, *Engineering Materials 2: An Introduction to Microstructures, Processing and Design*, Pergamon Press, 1986
- W.D. Callister, Jr., *Materials Science and Engineering: An Introduction*, 4th ed., 1997
- T.H. Courtney, *Mechanical Behavior of Materials*, 2nd ed., McGraw-Hill, 2000
- N.E. Dowling, *Mechanical Behavior of Materials*, 2nd ed., Prentice Hall, 1999
- W. Hayden, W.G. Moffatt, and J. Wulff, *Mechanical Behavior*, Vol III, *The Structure and Properties of Materials*, John Wiley & Sons, 1965
- W.G. Moffatt, G.W. Pearsall, and J. Wulff, *Structure*, Vol I, *The Structure and Properties of Materials*, John Wiley & Sons, 1965
- R.E. Smallman and R.J. Bishop, *Metals and Materials Science, Processes, Applications*, Butterworth Heinemann, 1995

Ceramics and Glasses

- R.H. Doremus, *Glass Science*, 2nd ed., John Wiley & Sons, 1994
- D.J. Green, *An Introduction to the Mechanical Properties of Ceramics*, Cambridge University Press, Cambridge, 1998
- V.A. Greenhut, Effect of Composition, Processing, and Structure on Properties of Ceramics and Glasses, *Materials Selection and Design*, Vol 20, *ASM Handbook*, ASM International, 1997
- W.D. Kingery, H.K. Bowen, and D.R. Uhlmann, *Introduction to Ceramics*, 2nd ed., John Wiley & Sons, 1976
- W.E. Lee and W.M. Rainforth, *Ceramic Microstructures*, Chapman & Hall, New York, 1994

Polymers

- N.G. McCrum, C.P. Buckley, and C.B. Bucknall, *Principles of Polymer Engineering*, 2nd ed., Oxford University Press, Oxford, 1997
- S.L. Rosen, *Fundamental Principles of Polymeric Materials*, John Wiley & Sons, 1982
- I.M. Ward, *Mechanical Properties of Solid Polymers*, John Wiley & Sons, 1971

Intermetallic Compounds

- R. Darolia, J.J. Lewandowski, C.T. Liu, P.L. Martin, D.B. Miracle, and M.V. Nathal, *Structural Intermetallics*, The Minerals, Metals and Materials Society, Warrendale, PA, 1993
- M.V. Nathal, R. Darolia, C.T. Liu, P.L. Martin, D.B. Miracle, R. Wagner, and M. Yamaguchi, *Structural Intermetallics 1997*, The Minerals, Metals and Materials Society, Warrendale, PA, 1997
- G. Sauthoff, *Intermetallics*, VCH Publishers, New York, 1995
- J.H. Westbrook, Guest Editor, *MRS Bulletin*, Vol 21 (No. 5), 1996

Composite Materials

- K.K. Chawla, *Composite Materials: Science and Engineering*, 2nd ed., Springer-Verlag, New York, 1999

- D. Hull, *An Introduction to Composite Materials*, Cambridge University Press, Cambridge, 1981

Mechanical Testing of Polymers and Ceramics

Introduction

THE MECHANICAL BEHAVIOR of polymers and ceramics differs from that of metallic materials due to some basic relationships between microstructure and mechanical properties, as described in the preceding article “Introduction to the Mechanical Behavior of Nonmetallic Materials” in this Volume. This article briefly reviews the general mechanical properties and test methods for polymers and ceramics. Additional coverage is also provided in other Sections of this Volume on hardness testing, high-strain-rate testing, fatigue testing, and fracture toughness. This article does not address the mechanical properties and testing of fiber-reinforced metal-matrix or polymer-matrix composites, which are a distinct product from that involves more specialized method for the testing and analysis of mechanical properties (see the article “Mechanical Testing of Fiber-Reinforced Composites” in this Volume).

Mechanical Testing of Polymers and Ceramics

Mechanical Testing of Polymers

Polymers are high-molecular-weight materials that may exhibit the mechanical behavior of a fiber, plastic, or elastomer (Fig. 1). The use of a polymer as an elastomer (rubber), a plastic, or a fiber depends on the relative strength of its intermolecular bonds and structural geometry. Noncrystalline polymers with weak intermolecular forces are usually elastomers or rubbers at temperatures above the glass transition temperature, T_g . In contrast, polymers with strong hydrogen bonds and the possibility of high crystallinity can be made into fibers. Polymers with moderate intermolecular forces are plastic at temperatures below T_g . Some polymers, such as nylon, can function both as a fiber and as a plastic. Other polymers, such as isotactic polypropylene, lack hydrogen bonds, but because of their good structural geometry, they can serve both as a plastic and as a fiber.

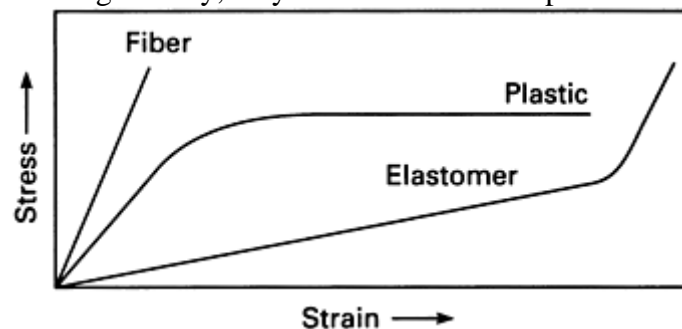


Fig. 1 Typical stress-strain curves for a fiber, a plastic, and an elastomer. Source: Ref 1

This section briefly reviews the mechanical properties and test methods commonly used for these three general categories of polymers, although most of the emphasis is placed on the mechanical properties of structural plastics. In terms of general structure, most polymers are amorphous (noncrystalline) materials with a hard glassy structure below the glass transition temperature (T_g), and either a viscous or rubbery structure above the glass transition temperature (Fig. 2a). This is in contrast to low-molecular-weight materials (such as metals) that typically have crystalline structures. However, the structure of some polymers is regular enough to promote some crystallization, which may result in a flexible crystalline structure above the glass transition temperature (Fig. 2b). For example, isotactic and syndiotactic polypropylenes can crystallize, but atactic polypropylene does

not (see the discussion with Fig. 14 in the preceding article “Introduction to the Mechanical Behavior of Nonmetallic Materials”). Generally, bulky side groups (as in polystyrene) hinder crystallization, while hydrogen bonding (as in nylons) promotes crystallization (Ref 2).

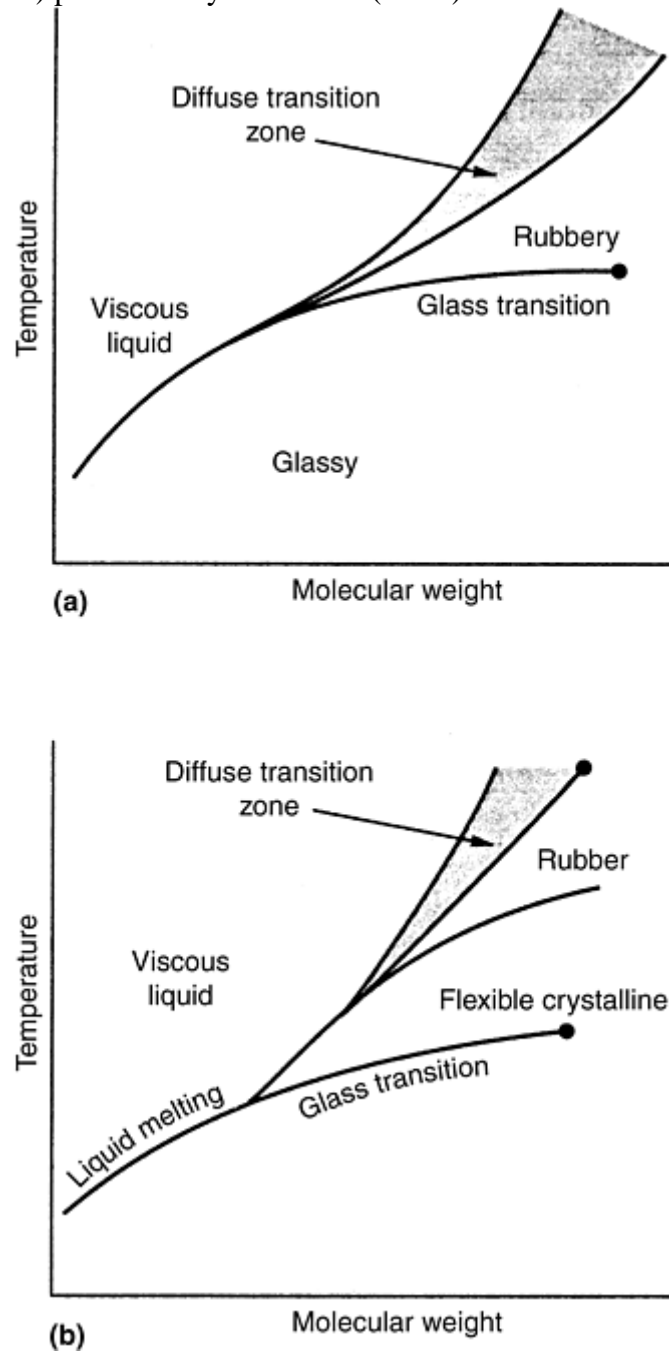


Fig. 2 Influence of molecular weight and temperature on the physical state of polymers. (a) Amorphous polymer. (b) Crystalline polymer. Source: Ref 2

Because of the partial or complete noncrystalline structure of polymers, they undergo a change in mechanical behavior that is not seen in fully crystalline materials. At temperatures well below T_g , plastics exhibit a high modulus and are only weakly viscoelastic. At temperatures above T_g , there is drastic reduction of modulus (Fig. 3), which may be as large as three orders of magnitude. Therefore, the glass transition temperature is the most important temperature that can be specified for most polymers because in all but highly crystalline polymers, it represents the temperature above which the polymer loses most of its stiffness and thus its dimensional stability.

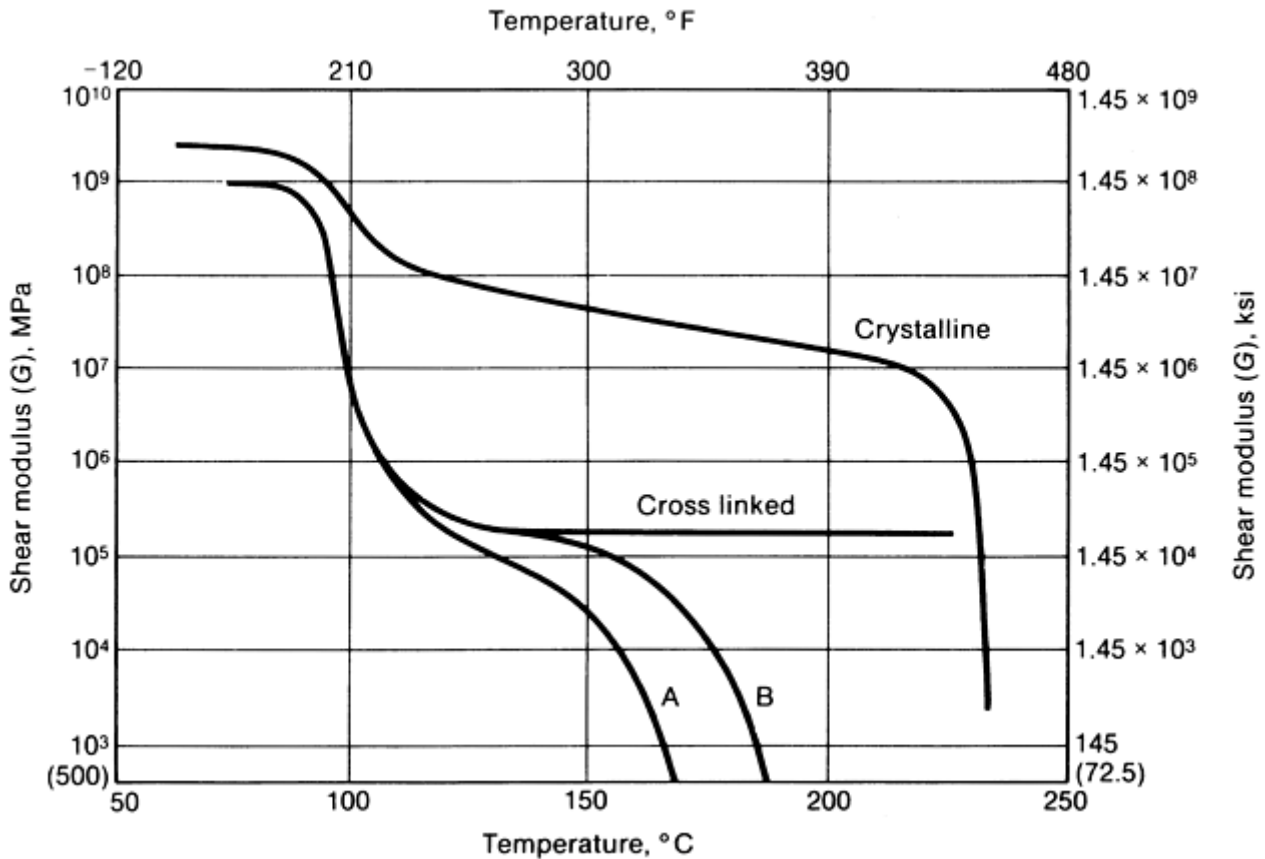


Fig. 3 Shear modulus versus temperature for crystalline isotactic polystyrene (PS), two linear atactic PS materials (A and B) with different molecular weights, and lightly cross-linked atactic PS

A typical modulus-temperature curve is shown in Fig. 3. At temperatures below T_g , most plastic materials have a tensile modulus of about 2 GPa (0.3×10^6 psi). If the material is crystalline, a small drop in modulus is generally observed at T_g , while a large drop is seen at the melting temperature, T_m . The T_g is primarily associated with amorphous, rather than crystalline, resins or cross-linked thermosets. Resins that are partially crystalline have at least a 50% amorphous region, which is the region that has a T_g . If a material is amorphous, a single decrease is usually seen at temperatures near T_g . At even higher temperatures, there is another similar drop in modulus, and the plastic flows easily as a high-viscosity liquid. At this condition, the plastic can be processed by extrusion or molding.

Mechanical properties are also affected by molecular weight. Most material manufacturers provide grades with different molecular weights. High-molecular-weight materials have high-melt viscosities and low-melt indexes. For a commercial product, a melt index is generally an inverse indicator of molecular weight.

When molecular weight is low, the applied mechanical stress tends to slide molecules over each other and separate them. The solid, with very little mechanical strength, has negligible structural value. With a continuing increase in molecular weight, the molecules become entangled, the attractive force between them becomes greater, and mechanical strength begins to improve.

It is generally desirable for material manufacturers to make plastics with sufficiently high-molecular weights to obtain good mechanical properties. For polystyrene, this molecular weight is 100,000 and for polyethylene this value is 20,000. It is not desirable to increase molecular weight further because melt viscosity will increase rapidly, although there are occasional exceptions to this rule. The yield strength of polypropylene decreases when molecular weight increases. High molecular weight and branching reduce crystallinity. Polymers with high intermolecular interaction, such as hydrogen bonding, do not require high molecular weight to achieve good mechanical properties. With low molecular weight, viscosity is very low, which is commonly observed for polyamides.

Typical T_g temperatures and some general thermal properties of selected plastics are listed in Tables 1, 2, and 3. It should also be understood that glass transition temperatures are not distinct transition temperatures like phase transformations, because the transition occurs over a range of temperatures. In a thermoplastic polymer such as polystyrene, the change that occurs gradually over the T_g region eventually leads to a complete loss of

dimensional stability. In a thermoset (network) polymer such as epoxy, the change is less severe, but nonetheless produces significant softening and loss of mechanical properties. The value of T_g may also depend upon the method of measuring viscoelastic transition. Thus, T_g for a polymer represents roughly the center of the transition region.

Table 1 Transition and continuous-use temperatures of general purpose plastics

Plastic	Glass transition temperature (T_g)		Melting temperature (T_m)		Continuous use temperature	
	°C	°F	°C	°F	°C	°F
Polystyrene (PS) Atactic (amorphous)	100–105	212–220	(a)	(a)	45	110
Isotactic (crystalline)	100–105	212–220	240	265	45	110
Polyvinyl chloride (PVC) Rigid PVC	75–105	170–220	212	415
Plasticized PVC	(b)	(b)
Chlorinated PVC	110	230	212	415
Polyethylene (PE) High-density	-90 or -20	-130 or -5	137	280	85	185
Low-density	-110 or -20	-165 or -5	115	240	85	185
Polypropylene (PP) Atactic (amorphous)	-6	21	165–175	330–350	105	220
Isotactic (crystalline)	-18	0	165–175	330–350	105	220
Syndiotactic	-4	25	165–175	330–350	105	220

(a) Amorphous.

(b) Varies with plasticizer content

Table 2 Transition and continuous-use temperatures of selected structural thermoplastics

Plastic	Glass transition temperature (T_g)		Melting temperature (T_m)		Continuous use temperature	
	°C	°F	°C	°F	°C	°F
Acetals (polyoxymethylene, POM)	-85	-120	163–175	325–345	90	195
Acrylics (polymethyl methacrylate, PMMA) Syndiotactic	3	35	105–220	220–250	90	195
Isotactic	3	35	45	115	90	195
Polyamides (PA) Nylon 6	50–70 ^(a)	120–160 ^(a)	225	440	95	200
Nylon 12	46	115	180	360
Nylon 6/6	57–80 ^(a)	135–175 ^(a)	265	510	105	220
Nylon 6/10	50	120	219	425
Nylon 6/I	142	290	210	410
Polycarbonate (PC)	150	300	265	510	120	250
Polyesters Polycaprolactone (PCL)	40	105	60–70	150–160
Polybutylene terephthalate (PBT)	60–70	140–160	225–235	440–455
Polyethylene terephthalate (PET)	78–80	170–175	260–265	500–510

(a) Varies with moisture content

Table 3 Glass transition and continuous-use temperatures for selected thermoset plastics

Plastic	Glass transition temperatures (T_g)		Continuous use temperature	
	°C	°F	°C	°F
Amino resins	None ^(a)		100	210
Polyurethane	135	275	90–120	190–250
Polyester	110	230	120–150	250–300
Epoxy	60–175	140–347	120–290	250–550
Phenolic	300	570	120–175	250–350
Polyimide	315–370^(a)	600–698^(a)	260–315	500–600

(a) Dry

Glass transition temperatures are also influenced by moisture absorption and the intentional addition of plasticizers. Absorbed moisture invariably lowers the T_g , and the more moisture is absorbed, the lower the transition temperature. This is consistent with the role of water as a plasticizer, which is why absorbed moisture can reduce the strength of plastics. Plasticizers are low-molecular-weight additives that lower strength and T_g . The lowering of transition temperatures by plasticizers can be quantitatively described by various mixing formulas (Ref 3, 4), which can be quite useful for predicting the loss of properties due to absorbed moisture.

References cited in this section

1. R. Seymour, Overview of Polymer Chemistry, *Engineering Plastics*, Vol 2, *Engineered Materials Handbook*, ASM International, 1988, p 64
2. A. Kumar and R. Gupta, *Fundamentals of Polymers*, McGraw-Hill, 1998, p 30, 337, 383
3. L.E. Nielson, *Mechanical Properties of Polymers*, Van Nostrand Reinhold, 1962
4. F.N. Kelly and F. Bueche, *J. Polym. Sci.*, Vol 50, 1961, p 549

Mechanical Testing of Polymers and Ceramics

Mechanical Testing of Plastics

Engineering plastics are either thermoplastic resins (which can be repeatedly reheated and remelted) or thermoset (network) resins (which are cured resins with cross links that depolymerize upon exposure to elevated temperatures above T_g). Typical mechanical properties of various thermoplastic and thermoset resins are briefly summarized in Tables 4 and 5. Engineering plastics are not as strong as metals, but due to the lower density of plastics, the specific strengths of structural plastics are higher than those of metallic materials. This is shown in Table 6, which compares the range of mechanical properties of plastics with those of other engineering materials. These data show that glass-filled plastics have strength-to-weight ratios that are twice those of steel and cast aluminum. In addition to glass fillers, other types of additives (such as plasticizers, flame retardants, stabilizers, and impact modifiers) can also modify the mechanical properties of plastics.

Table 4 Room-temperature mechanical properties of selected thermoplastics with glass filler

Thermoplastic	Glass fiber content, wt%	Tensile strength ^(a)		Tensile elongation at break ^(a) , %	Tensile modulus ^(a)		Flexural strength ^(b)		Flexural modulus ^(b)		Izod impact strength notched ^(c)		Compressive strength ^(d)	
		MPa	ksi		kPa	psi	MPa	ksi	GPa	10 ⁶ psi	J/m	ft · lbf/in.	MPa	ksi
Styrene	...	46	6.7	2.2	320	46	97	14.0	3	0.45	11	0.2	97	14.0
	20	76	11	1.0	760	110	107	15.5	7	0.96	53	1.0	111	16.1
	30	93	13.5	1.0	900	130	117	17.0	8	1.22	53	1.0	120	17.4
	40	103	15	1.0	1100	160	121	17.5	10	1.47	59	1.1	122	17.7
Styrene-acrylonitrile (SAN)	...	72	10.5	3.0	390	56	103	15.0	4	0.55	27	0.5	103	15.0
	20	90	13	2.0	860	125	129	18.7	8	1.10	53	1.0	134	19.5
	30	107	15.5	1.5	1000	145	155	22.5	10	1.52	53	1.0	141	20.5
	40	119	17.2	1.5	1240	180	161	23.4	12	1.80	53	1.0	148	21.5
Acrylonitrile-butadiene-styrene (ABS)	...	48	7	8.0	210	30	72	10.5	3	0.38	240	4.5	69	10.0
	20	90	13	3.0	620	90	117	17.0	6	0.80	80	1.5	86	12.5
	30	105	15.2	3.0	690	100	128	18.5	7	1.00	75	1.4	107	15.5
	40	110	16	2.0	1030	150	145	21.0	9	1.30	69	1.3	118	17.1
Flame-retardant ABS	...	40	5.8	5.1	240	35	83	12.0	2	0.33	213	4.0	52	7.5
	20	76	11	2.0	510	74	107	15.5	5	0.71	64	1.2	97	14.0
Polypropylene (PP)	...	32	4.7	15.0	130	19	41	6.0	2	0.30	27	0.5	34	5.0
	20	59	8.5	3.0	380	55	55	8.0	4	0.60	43	0.8	41	6.0
	30	62	9	3.0	450	65	59	8.5	6	0.80	59	1.1	45	6.5
	40	69	10	2.0	520	75	62	9.0	7	1.00	69	1.3	48	7.0
Glass-coupled PP	...	32	4.7	15.0	130	19	41	6.0	2	0.30	27	0.5	41	6.0
	20	76	11	3.0	410	60	83	12.0	4	0.60	75	1.4	69	10.0
	40	97	14	2.0	550	80	131	19.0	7	1.00	85	1.6	90	13.0
Polyethylene (PE)	...	30	4.3	9.0	100	15	38	5.5	2	0.22	69	1.3	28	4.0
	20	48	7	3.0	410	60	62	9.0	4	0.55	75	1.4	34	5.0
	30	69	10	2.0	590	85	76	11.0	6	0.80	91	1.7	48	7.0
	40	76	11	2.0	760	110	86	12.5	7	1.00	91	1.7	55	8.0
Acetal (AC)	...	61	8.8	60.0	280	41	90	13.0	3	0.37	69	1.3	36	5.2
	20	83	12	2.0	830	120	110	16.0	7	1.00	53	1.0	83	12.0
	30	90	13	1.8	930	135	114	16.5	8	1.20	43	0.8	83	12.0
Polyester	...	55	8	200.0	280	40	88	12.8	2	0.34	11	0.2	90	13.0
	20	117	17	5.0	690	100	152	22.0	6	0.85	80	1.5	110	16.0

	30	131	19	4.0	1030	150	179	26.0	8	1.20	96	1.8	124	18.0
	40	152	22	3.0	1380	200	207	30.0	10	1.50	107	2.0	138	20.0
Flame-retardant polyester	...	61	8.9	60.0	280	40	101	14.7	3	0.38	48	0.9	100	14.5
	30	131	19	3.0	1100	160	176	25.5	9	1.30	69	1.3	124	18.0
Nylon 6	...	81	11.8	200.0	280	40	103	15.0	3	0.40	53	1.0	90	13.0
	20	128	18.5	3.0	690	100	159	23.0	6	0.80	80	1.5	148	21.5
	30	155	22.5	3.0	900	130	186	27.0	8	1.10	117	2.2	159	23.0
	40	185	26.8	2.0	970	140	207	30.0	9	1.30	160	3.0	159	23.0
Flame-retardant Nylon 6	...	85	12.3	60.0	290	42	110	16.0	3	0.40	53	1.0	90	13.0
	30	152	22	3.0	900	130	228	33.0	9	1.35	91	1.7	16	2.3
Nylon 6/6	...	79	11.4	300.0	130	19	103	15.0	1	0.19	53	1.0	34	4.9
	20	138	20	3.0	830	120	193	28.0	6	0.85	64	1.2	159	23.0
	30	179	26	2.0	1030	150	259	37.5	9	1.30	107	2.0	165	24.0
	40	214	31	2.0	900	130	293	42.5	11	1.60	139	2.6	172	25.0
Flame-retardant Nylon 6/6	...	67	9.7	35.0	130	19	90	13.0	1	0.18	53	1.0	34	4.9
	30	148	21.5	2.0	830	120	172	25.0	7	1.00	85	1.6	159	23.0
Nylon 6/12	...	61	8.8	150.0	200	29	86	12.5	2	0.29	53	1.0	76	11.0
	20	124	18	4.0	690	100	193	28.0	6	0.90	59	1.1	131	19.0
	30	152	22	4.0	900	130	221	32.0	8	1.10	128	2.4	152	22.0
Polycarbonate (PC)	...	62	9	110.0	240	34.5	93	13.5	2	0.34	160	3.0	86	12.5
	10	90	13	5.0	480	70	110	16.0	4	0.60	107	2.0	124	18.0
	20	110	16	5.0	620	90	138	20.0	6	0.80	117	2.2	138	20.0
	30	131	19	4.0	900	130	165	24.0	8	1.20	128	2.4	145	21.0
	40	152	22	3.5	1170	170	193	28.0	10	1.40	144	2.7	148	21.5
Polysulfone (PSU)	...	70	10.2	75.0	250	36	106	15.4	3	0.39	32	0.6	97	14.0
	20	131	19	3.0	620	90	138	20.0	5	0.75	64	1.2	138	20.0
	30	148	21.5	3.0	830	120	155	22.5	7	1.00	75	1.4	155	22.5
	40	165	24	2.0	1240	180	172	25.0	9	1.25	107	2.0	172	25.0
Polyphenylene sulfide (PPS)	40	138	20	1.5	1410	205	234	34.0	12	1.80	80	1.5	172	25.0

(a) ASTM D 638 test method.

(b) ASTM D 790 test method.

(c) ASTM D 256 test method with 6.35 mm (1/4 in.) bar.

(d) ASTM D 695 test method

Table 5 Mechanical properties of fiberglass-reinforced thermoset resins

Resin	Tensile strength		Elongation, %	Compressive strength		Flexural strength		Izod impact strength, J/mm	Hardness, HRM
	MPa	ksi		MPa	ksi	MPa	ksi		
Polyester	173–206	25–30	0.5–5	103–206	15–30	69–276	10–40	0.1–0.5	70–120
Phenolic	35–69	5–10	0.02	117–179	17–26	69–415	10–60	0.5–2.5	95–100
Epoxy	97–206	14–30	4	206–262	30–38	138–180	20–26	0.4–0.75	100–108
Melamine	35–69	5–10	...	138–241	20–35	103–160	15–23	0.2–0.3	...
Polyurethane	31–55	4–8	10–650	138	20	48–62	7–9	No break	28 HRM-60 HRR

Table 6 Range of mechanical properties for common engineering materials

Material	Elastic modulus		Tensile strength		Maximum strength/density		Elongation at break, %
	GPa	10 ⁶ psi	MPa	ksi	(km/s) ²	(kft/s) ²	
Ductile steel	200	30	350–800	50–120	0.1	1	0.2–0.5
Cast aluminum alloys	65–72	9–10	130–300	19–45	0.1	1	0.01–0.14
Polymers	0.1–21	0.02–30	5–190	0.7–28	0.05	0.5	0–0.8
Glasses	40–140	6–20	10–140	1.5–21	0.05	0.5	0
Copper alloys	100–117	15–18	300–1400	45–200	0.17	1.8	0.02–0.65
Moldable glass-filled polymers	11–17	1.6–2.5	55–440	8–64	0.2	2	0.003–0.015
Graphite-epoxy	200	30	1000	150	0.65	1.3	0–0.02

The testing of plastics includes a wide variety of chemical, thermal, and mechanical tests (Table 7). The following sections briefly describe the test methods and comparative data for the mechanical property tests listed in Table 7. In addition, creep testing and dynamic mechanical analyses of viscoelastic plastics are also briefly described. For more detailed descriptions of these test methods and the other test methods listed in Table 7, readers are referred to Ref 5 and an extensive one-volume collection of ISO and European standards for plastic testing (Ref 6).

Table 7 ASTM and ISO mechanical test standards for plastics

ASTM standard	ISO standard	Topic area of standard
Specimen preparation		
D 618	291	Methods of specimen conditioning
D 955	294-4	Measuring shrinkage from mold dimensions of molded thermoplastics
D 3419	10724	In-line screw-injection molding of test specimens from thermosetting compounds
D 3641	294-1,2,3	Injection molding test specimens of thermoplastic molding and extrusion materials
D4703	293	Compression molding thermoplastic materials into test specimens, plaques, or sheets
D 524	95	Compression molding test specimens of thermosetting molding compounds
D 6289	2577	Measuring shrinkage from mold dimensions of molded thermosetting plastics
Mechanical properties		

D 256	180	Determining the pendulum impact resistance of notched specimens of plastics
D 638	527-1,2	Tensile properties of plastics
D 695	604	Compressive properties of rigid plastics
D 785	2039-2	Rockwell hardness of plastics and electrical insulating materials
D 790	178	Flexural properties of unreinforced and reinforced plastics and insulating materials
D 882	527-3	Tensile properties of thin plastic sheeting
D 1043	458-1	Stiffness properties of plastics as a function of temperature by means of a torsion test
D 1044	9352	Resistance of transparent plastics to surface abrasion
D 1708	6239	Tensile properties of plastics by use of microtensile specimens
D 1822	8256	Tensile-impact energy to break plastics and electrical insulating materials
D 1894	6601	Static and kinetic coefficients of friction of plastic film and sheeting
D 1922	6383-2	Propagation tear resistance of plastic film and thin sheeting by pendulum method
D 1938	6383-1	Tear propagation resistance of plastic film and thin sheeting by a single tear method
D 2990	899-1,2	Tensile, compressive, and flexural creep and creep-rupture of plastics
D 3763	6603-2	High-speed puncture properties of plastics using load and displacement sensors
D 4065	6721-1	Determining and reporting dynamic mechanical properties of plastics
D 4092	6721	Dynamic mechanical measurements on plastics
D 4440	6721-10	Rheological measurement of polymer melts using dynamic mechanical procedures
D 5023	6721-3	Measuring the dynamic mechanical properties of plastics using three-point bending
D 5026	6721-5	Measuring the dynamic mechanical properties of plastics in tension
D 5045	572	Plane-strain fracture toughness and strain energy release rate of plastic materials
D 5083	3268	Tensile properties of reinforced thermosetting plastics using straight-sided specimens
D 5279	6721	Measuring the dynamic mechanical properties of plastics in torsion

Source: Ref 5

Tensile Properties

The chemical composition and the long-chain nature of polymers lead to some important differences with metals. These differences include significantly lower stiffnesses, much higher elastic limits or recoverable strains, a wider range of Poisson's ratios, and time-dependent deformation from viscoelasticity. Thermoplastics also exhibit a unique variety of post-yield phenomena. For example, Fig. 4 is a typical stress-strain plot for aluminum and polyethylene. The aluminum sample necks and extends to 50% strain. The polyethylene sample necks and extends to 350% strain as a consequence of the long-chain nature of polymers. The polyethylene also shows a stiffening due to chain alignment at the highest strains. This postyield stiffening involves shear deformation as described in Ref 6.

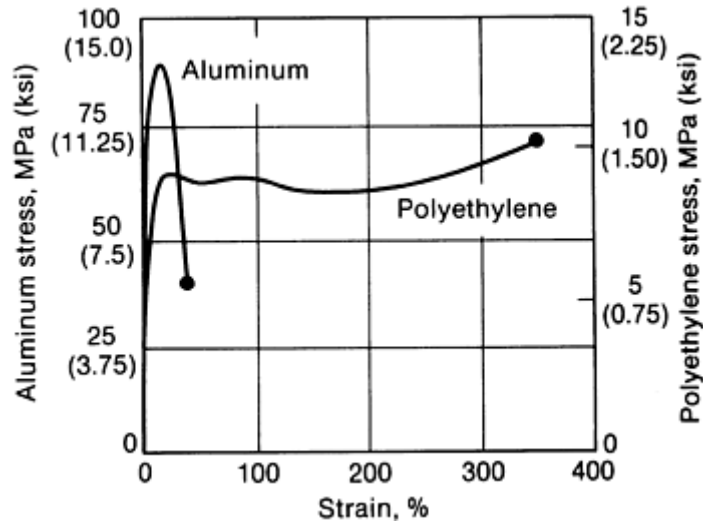


Fig. 4 Typical stress-strain curves for polycrystalline aluminum and semicrystalline polyethylene. Both materials neck. In polyethylene, chain alignment results in stiffening just before failure. Source: Ref 7

The ultimate tensile strengths of most unreinforced structural plastics range from 50 to 80 MPa (7–12 ksi) with elongation to final fracture much higher than metals (Fig. 5). It is very common to see large differences between metals and plastics in the amount of recoverable elastic strain. In metals, the amount of recoverable elastic strain is determined by the amount of strain that can be put into one of the metallic bonds before breaking. This amount of strain is typically less than 1%. In elastomers, the amount of recoverable strain can be 500% or more.

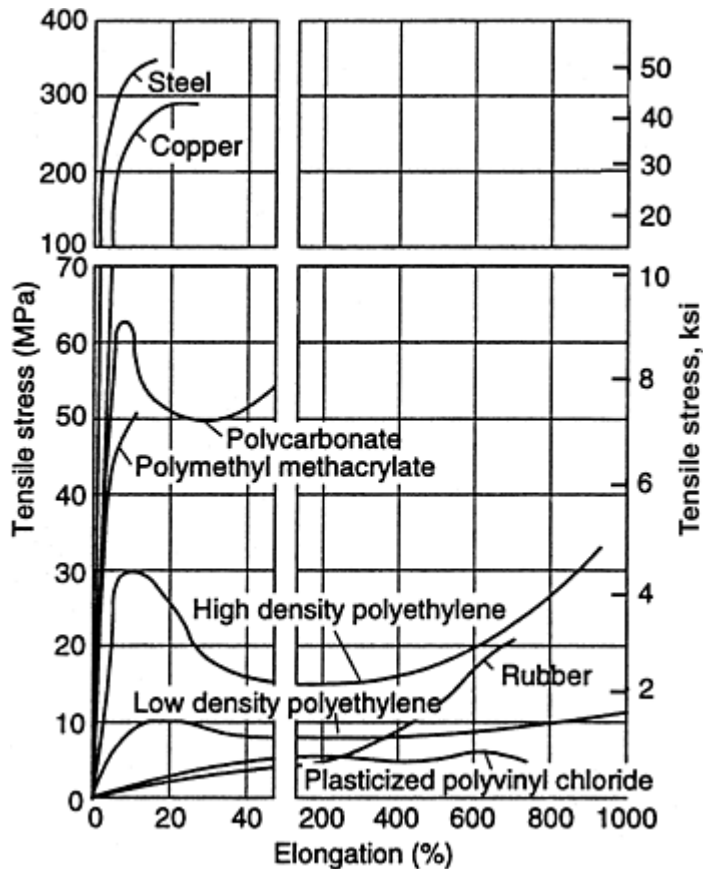


Fig. 5 Tensile stress-strain curves for copper, steel, and several thermoplastic resins. Source: Ref 8

When recoverable strain is this large, the individual polymer chains must be prevented from flowing past each other during deformation. This is easily accomplished by cross links tying the chains together (Ref 9). Even in glassy polymers, in which internal energy effects are evident in the elasticity, the recoverable strain is limited by the strain required to break the weaker and longer-range van der Waals bonds. Because these bonds can be

stretched farther than metallic bonds, it is possible to have a recoverable strain in glassy polymers of 5% or more. At such large strains, it is possible for the assumptions of small-strain elasticity to break down. Any standard test procedures based on small-strain elasticity may have to be modified to account for large elastic strains.

The mechanical behavior of polymers is also time dependent, or viscoelastic. Therefore, data based on short-term tests have the possibility of misrepresenting the tested polymer in a design application that involves long-term loading. The magnitude of the time dependence of polymers is very temperature dependent. Well below the T_g , glassy or semicrystalline polymers are only very weakly viscoelastic. For these polymers, test data based on a time-independent analysis will probably be adequate. As the temperature is increased, either by the environment or by heat given off during deformation, the time dependence of the mechanical response will increase.

Under viscoelastic conditions, one method useful for obtaining long-term design data is the time-temperature superposition principle. This principle states that the mechanical response at long times at some particular temperature is equivalent to the mechanical response at short times but at some higher temperature (Ref 8). By determining shift factors, it is possible to determine which temperature to use in obtaining long-term data from short-term tests. This is essentially true for linear viscoelastic behavior in the absence of a phase change.

The short-term tensile test (ASTM D 638 and ISO 517) is one of the most widely used mechanical tests of plastics for determining mechanical properties such as tensile strength, yield strength, yield point, and elongation. The stress-strain curve from tension testing is also a convenient way to classify plastics (Fig. 6). A soft and weak material, such as PTFE, is characterized by low modulus, low yield stress, and moderate elongation at break point. A soft but tough material such as polyethylene shows low modulus and low yield stress but very high elongation at break. A hard and brittle material such as general-purpose phenolic is characterized by high modulus and low elongation. It may or may not yield before break. A hard and strong material such as polyacetal has high modulus, high yield stress, high ultimate strength (usually), and low elongation. A hard and tough material such as polycarbonate is characterized by high modulus, high yield stress, high elongation at break, and high ultimate strength.

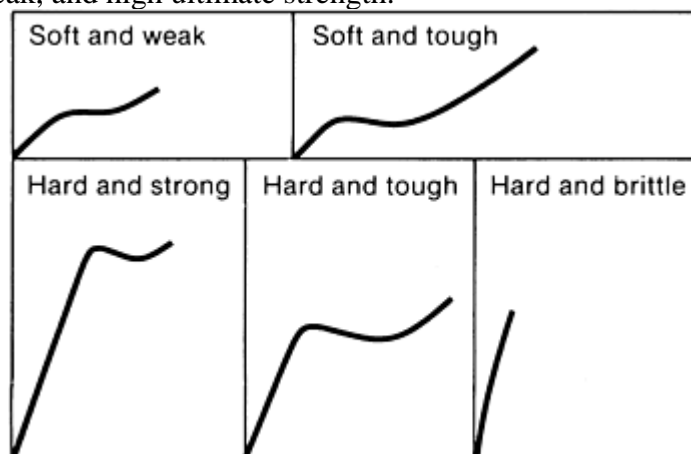


Fig. 6 Tensile stress-strain curves for several categories of plastic materials

Because of the diversity of mechanical behavior, the tension testing of plastics is subject to potential misapplication or misinterpretation of test results. This is particularly true for thermoplastics, which have some important differences with thermoset plastics. Compared to thermoset resins, thermoplastics exhibit more disruption or changes in the secondary bonding between the molecular chains during tension testing. This leads to a variety of postyield phenomena, such as the stiffening observed in polyethylene (Fig. 4). Another example is shown in Fig. 7. At the yield point the average axis of molecular orientation in thermoplastics may begin to conform increasingly with the direction of the stress. The term *draw* is sometimes used to describe this behavior. There is usually a break in the stress-strain curve as it begins to flatten out, and more strain is observed with a given increased stress. The result is that the giant molecules begin to align and team up in their resistance to the implied stress. Frequently, there is a final increase in the slope of the curve just before ultimate failure (Fig. 7). The extent to which this orientation takes place varies from one linear thermoplastic to the next, but the effect can be quite significant. Even the smallest amount of the teaming-up effect imparts greatly improved impact resistance and damage tolerance. In thermoplastics, there is much more area under the stress-

strain curve than in conventional thermosets, which are more rigid networks with much less area under the stress-strain curve.

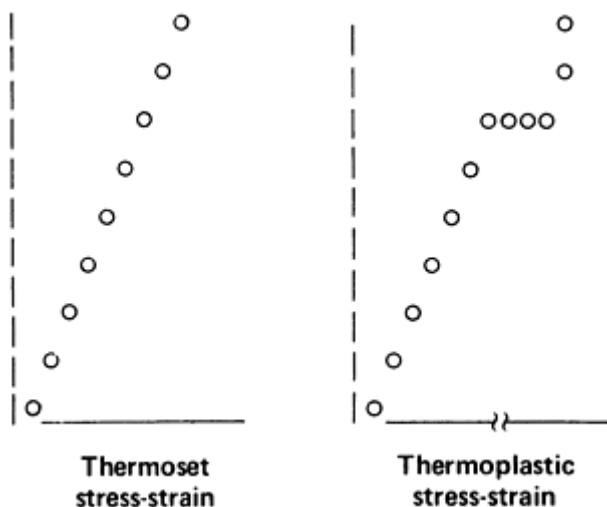


Fig. 7 Thermoset versus thermoplastic stress-strain behavior

Because the deformation of thermoplastics is time-dependent, careful control of test duration and strain rate is important. A slower test (i.e., one at a low strain rate) allows more time for deformation and thus alters the stress-strain curve and lowers the tensile strength. This effect is shown in Fig. 8 for polycarbonate.

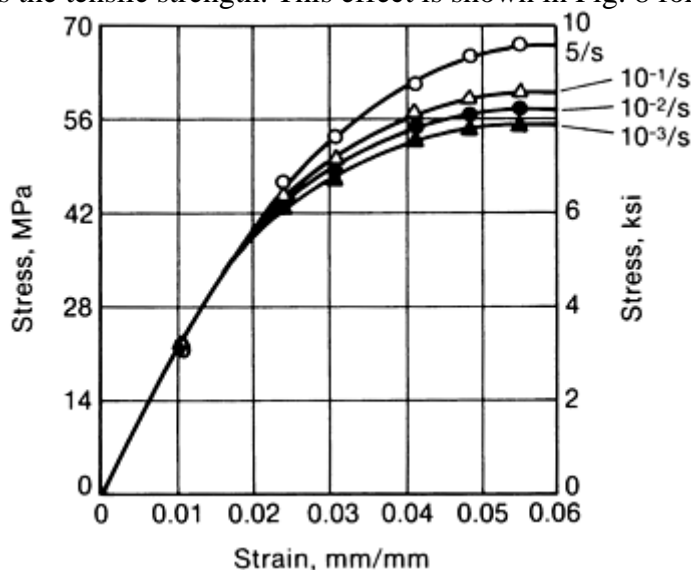


Fig. 8 Stress-strain curves for rubber-modified polycarbonate at room temperature as a function of strain rate

Short-term tensile properties are usually measured at a constant rate of 0.5 cm/min (0.2 in./min). It is recommended by the American Society for Testing and Materials (ASTM) that the speed of testing be such that rupture occurs in 0.5 to 5 min. Test coupons are either injection molded or compression molded and cut into a standard shape. In practice, injection-molded coupons are usually used.

The history of the plastic sample has some influence on tensile properties. A tensile bar prepared by injection molding with a high pressure tends to have higher tensile strength. A material that has been oriented in one direction tends to have a higher tensile strength and a lower elongation at break in the direction of orientation. In the direction perpendicular to the orientation, tensile strength is consistently lower. In a crystallizable material, stretching usually increases crystallinity.

Because the mechanical properties are sensitive to temperature and absorbed moisture, conditioning procedures for test specimens have been developed. These procedures are defined in ASTM D 618 and ISO 291.

Tensile Modulus. Because plastics are viscoelastic materials, stress-strain relationships are nonlinear and curved (usually convex upward). The curvature arises from two causes. First, the deflection axis is

simultaneously a time axis, and during the test, molecular relaxation processes continuously reduce the stress required to maintain any particular strain. Second, as the strain increases, the molecular resistance to further deformation decreases; that is, the effective modulus falls.

The degree of curvature depends on the material and the test conditions. At high strain rates and/or low temperatures, the stress-strain relationship usually approximates to a straight line. However, if the curvature is pronounced, the stress-strain ratio must be either a tangent modulus or a secant modulus. The tangent modulus is the instantaneous slope at any point on the stress-strain curve, while the secant modulus is the slope of a line drawn from the origin to any point on a nonlinear stress-strain curve. These moduli may be conservative or nonconservative, relative to one another and depending on the location on the curve.

The accuracy of modulus data derivable from a stress-strain test may be limited, mainly because axially loading is difficult to achieve and because the specimen bends initially rather than stretches. In addition, the origin of the force-deflection curve is often ill defined, and the curvature there is erroneous, to the particular detriment of the accuracy of the tangent modulus at the origin and, to a lesser degree, that of the secant moduli. Under the very best experimental conditions, the coefficient of variation for the modulus data derivable from tensile tests can be 0.03 or lower, but more typically it is 0.10 (Ref 10). If the strain is derived from the relative movement of the clamps rather than from an extensometer, the error in the calculated value of the tangent modulus at the origin can be 100% (Ref 9).

Yield stresses of plastics depend on a variety of molecular mechanisms, which vary among polymer classes and may not be strictly comparable. However, regardless of the underlying mechanisms, yield stress data have a low coefficient of variation, typically 0.03 (Ref 10). Brittle fracture strengths are much more variable, reflecting the distributions of defects that one might expect. The scatter due to the inherent defects in the materials is exacerbated when elongations at fracture are small because poor and variable alignment of the specimens induces apparently low strengths if the theoretical stresses are not corrected for the extraneous bending in the specimens (Ref 10).

Long-term uniaxial tensile creep testing of plastics is covered in ASTM D 2990 and ISO 899. ASTM D 2990 also addresses flexural and compressive creep testing. For the uniaxial tensile creep test in D 2990, the test specimen is either a standard type I or II bar, per ASTM D 638, that is preconditioned to ASTM D 618 specifications. The test apparatus is designed to ensure that the applied load does not vary with time and is uniaxial to the specimen. As with other tests, the test specimen must not slip in or creep from the grips. The load must be applied to the specimen in a smooth, rapid fashion in 1 to 5 s. If the test is run to specimen failure, the individual test cells must be isolated to eliminate shock loading from failure in adjacent test cells. Several types of tensile creep test systems are shown in Fig. 9.

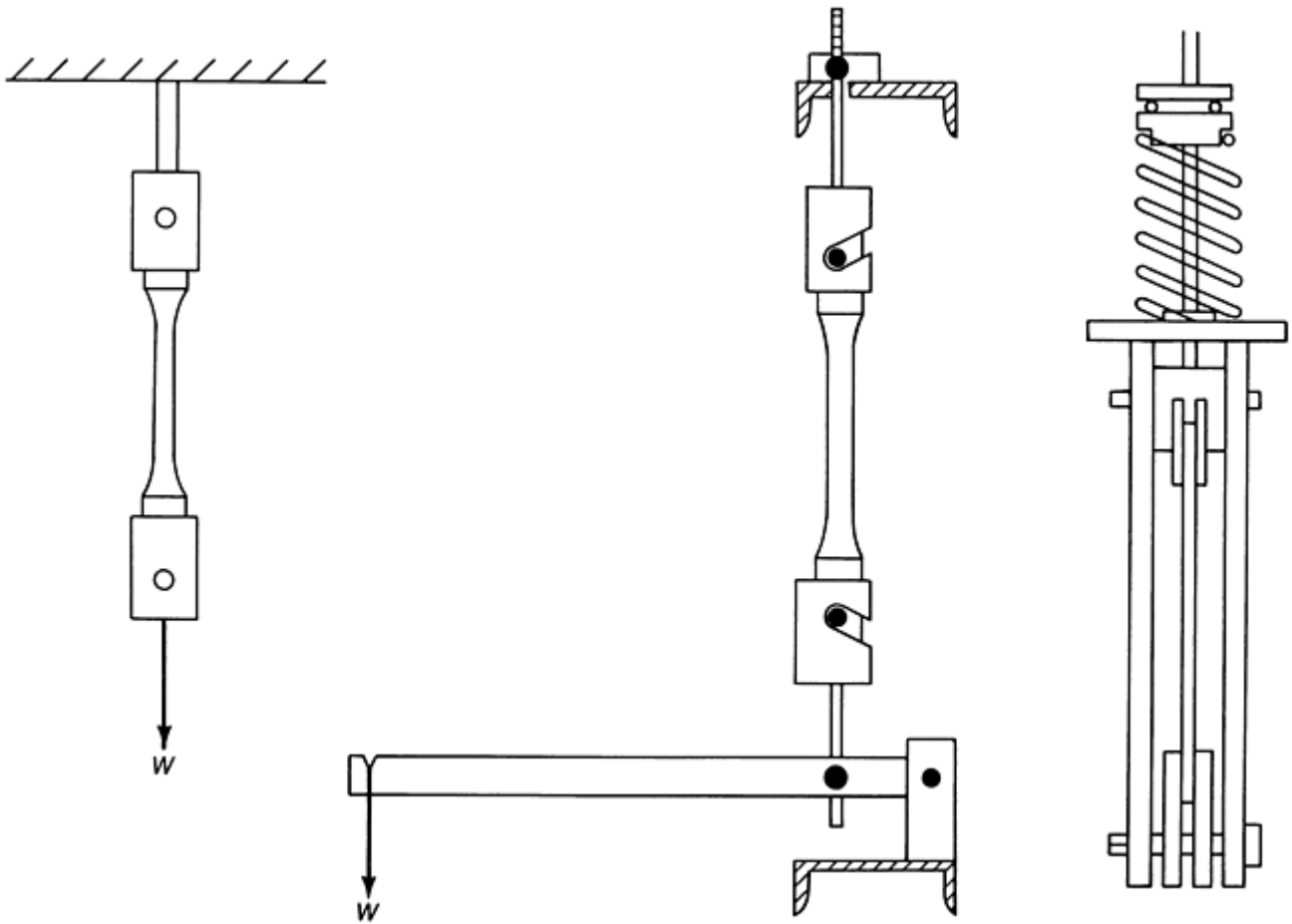


Fig. 9 Various equipment designs for the measurement of tensile creep in plastics

Creep curves generally exhibit three distinct phases. First-stage creep deformation is characterized by a rapid deformation rate that decreases slowly to a constant value. The four-parameter model was proposed to describe long-term creep. In this model, the first-stage creep deformation was called retarded elastic strain. Second-stage creep deformation is characterized by a relative constant, low-deformation rate. In the four-parameter model, this was called equilibrium viscous flow. The final or third-stage creep deformation is creep rupture, fracture, or breakage.

The generalized uniaxial tensile creep behavior of plastics under constant load, isothermal temperature, and a given environment can be illustrated as ductile creep behavior (Fig. 10a) or as brittle creep behavior (Fig. 10b). At very low stress levels, both types of plastics exhibit similar first-stage and second-stage creep deformation. The onset of creep rupture may not occur within the service life of the product (let alone the test). As the stress level increases, first-stage and second-stage creep deformation rates remain relatively the same for these types, but the time of failure is of course considerably reduced. In addition, third-stage creep deformation characteristics now differ considerably. The ductile plastic exhibits typical ductile yielding or irreversible plastic deformation prior to fracture. The brittle plastic, on the other hand, exhibits no observable gross plastic deformation and only abrupt failure.

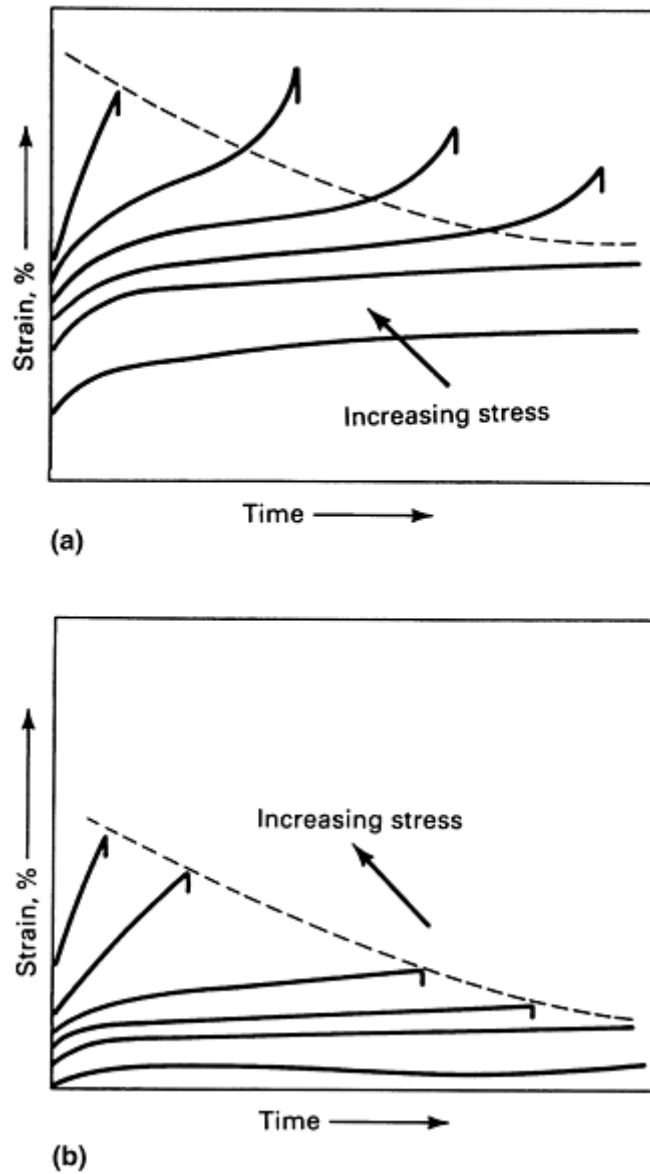


Fig. 10 Typical creep and creep rupture curves for polymers. (a) Ductile polymers. (b) Brittle polymers

Macroscopic yielding and fracture may not always be appropriate criteria for longtime duration material failure. For some plastics, stress crazing, stress cracking, or stress whitening may signal product failure and may therefore become a design limitation.

Creep strain is usually plotted against time on either semilog plots or log-log plots (Fig. 11). Extrapolation to times beyond the data can be difficult on the semilog plot (Fig. 11a). Replotting on log-log paper may allow easier extrapolation under one decade. Creep curves should not be extrapolated more than one decade, because some curvature still remains in the log-log plot. For small strains, the curves can be considered linear. These curves can usually be used to compare polymers at the same loading levels. Creep test data are also analyzed in various forms, as described further in the section “Creep Data Analysis” in this article.

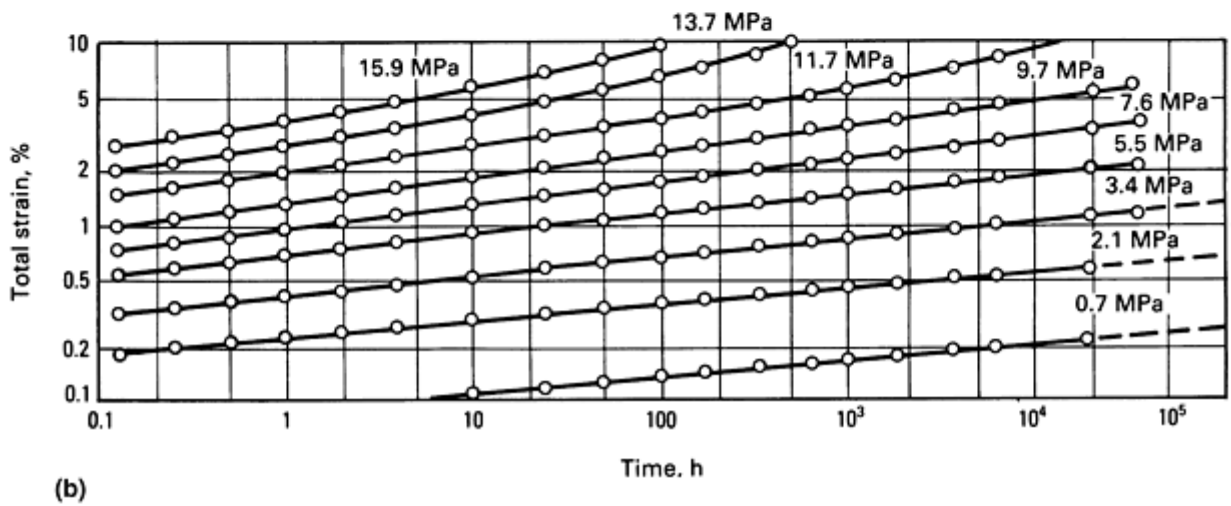
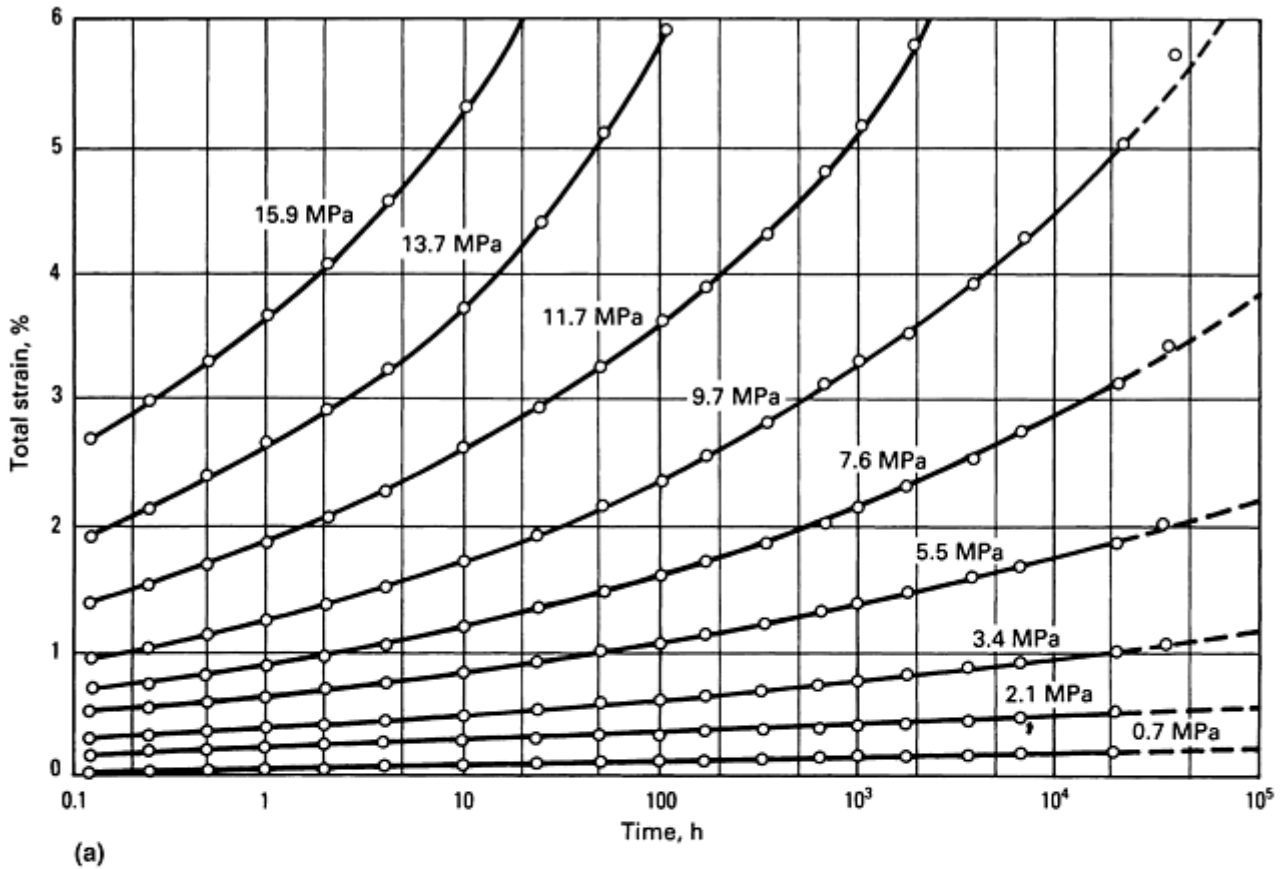


Fig. 11 Tensile creep strain of polypropylene copolymer. (a) Semilog plot. (b) Log-log plot

Other Strength/Modulus Tests

Compressive Strength Test (ASTM D 695 and ISO 604). Stress-strain properties are also measured for the behavior of a material under a uniform compressive load. The procedure and nomenclature for compression tests are similar to those for the tensile test. Universal testing machines can be used, and, like tension testing, specimens should be preconditioned according to ASTM D 618 or ISO 291.

The standard test specimen in ASTM D 695 is a cylinder 12.7 mm (1/2 in.) in diameter and 25.4 mm (1 in.) in height. The force of the compressive tool is increased by the downward thrust of the tool at a rate of 1.3 mm/min (0.05 in./min). The compressive strength is calculated by dividing the maximum compressive load by the original cross section of the test specimen.

For plastics that do not fail by shattering fracture, the compressive strength is an arbitrary value and not a fundamental property of the material tested. When there is no brittle failure, compressive strength is reported at

a particular deformation level such as 1 or 10%. Compressive strength of plastics may be useful in comparing materials, but it is especially significant in the evaluation of cellular or foamed plastics. Compression testing of cellular plastics is addressed in ISO Standards 1856 and 3386-1.

Typical compressive strengths for various plastics are compared in Fig. 12. Generally, the compressive modulus and strength are higher than the corresponding tensile values for a given material.

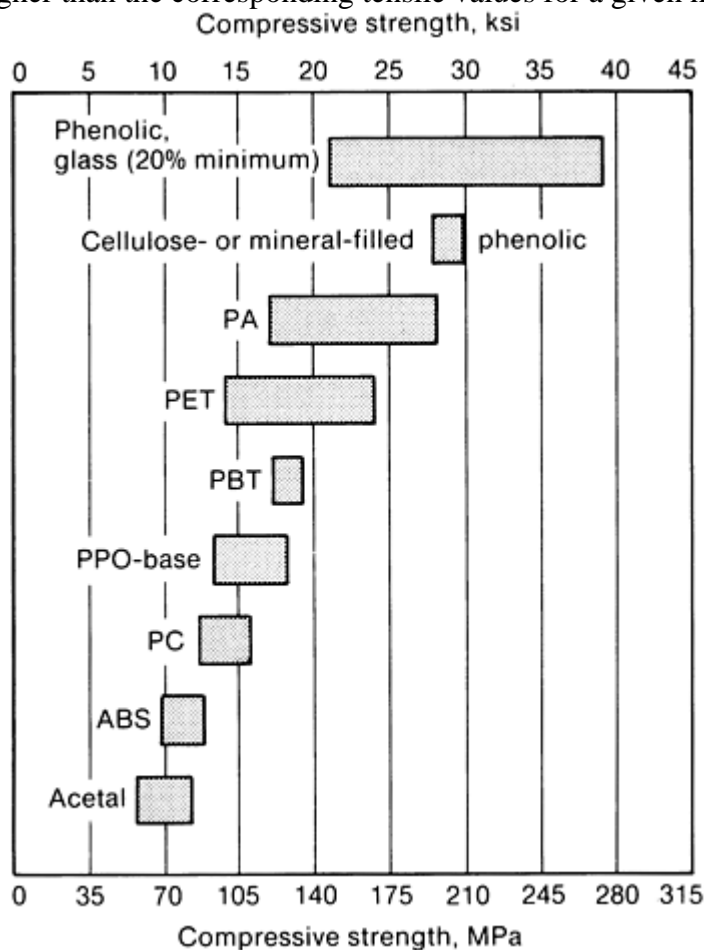


Fig. 12 **Compressive strength of engineering plastics. PA, polyamide; PET, polyethylene terephthalate; PBT, polybutylene terephthalate; PPO, polyphenylene oxide; PC, polycarbonate; ABS, acrylonitrile-butadiene-styrene**

Compressive creep testing of plastic is addressed in ASTM D 2990. Normally creep information is given for tension loading.

Flexural Strength Test (ASTM D 790 and ISO 178). Flexural strength or cross-breaking strength is the maximum stress developed when a bar-shaped test piece, acting as a simple beam, is subjected to a bending force. Two methods are used: three-point bending (Fig. 13) and four-point bending (Fig. 14). Four-point bending is useful in testing materials that do not fail at the point of maximum stress in three-point bending (Ref 12).

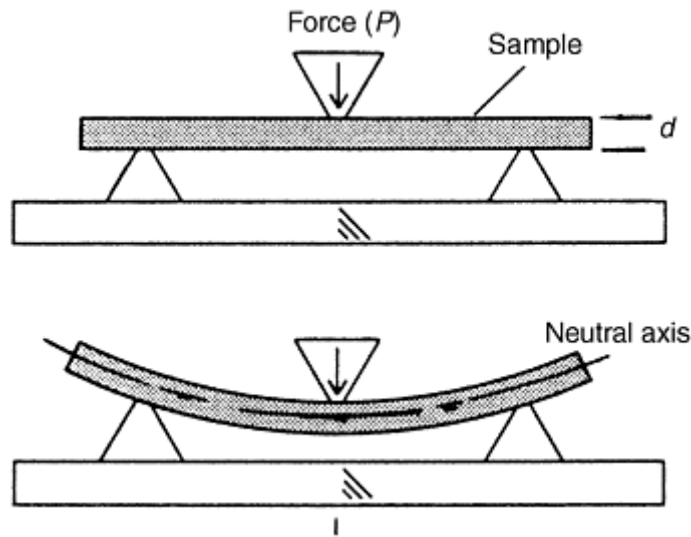


Fig. 13 Flexural test with three-point loading. Source: Ref 11

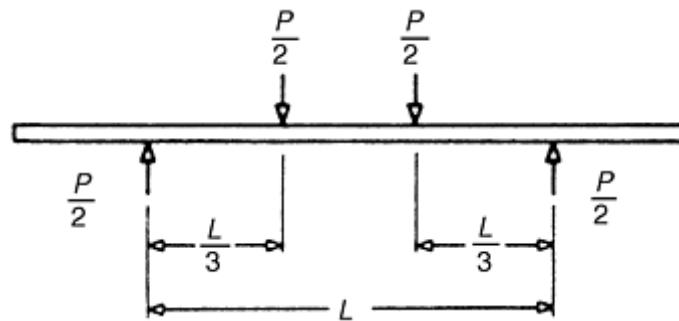


Fig. 14 Flexural test with four-point loading

For three-point bending, an acceptable test specimen is one at least 3.2 mm (0.125 in.) thick, 12.7 mm (0.5 in.) wide, and long enough to overhang the supports (but with overhang less than 6.4 mm (0.25 in.) on each end). The load should be applied at a specified crosshead rate, and the test should be terminated when the specimen bends or is deflected by 0.05 mm/min (0.002 in./min). The flexural stress (S) at the outer fibers at mid-span in three-point bending is calculated from the following expression:

$$S = 3PL/2bd^2$$

in which P is the force at a given point on the deflection curve, L is the support span, b is the width of the bar, and d is the depth of the beam.

Because most plastics do not break from deflection, the flexural strength is measured when 5% strain occurs for most thermoplastics and elastomers. Fracture strength under flexural load may be more suitable for thermosets. To obtain the strain, r , of the specimen under three-point test, the following expression applies:

$$r = 6Dd/L^2$$

in which D is the deflection to obtain the maximum strain (r) of the specimen under test. To obtain data for flexural modulus, which is a measure of stiffness, flexural stress is plotted versus strain, r , during the test; the slope of the curve obtained is the flexural modulus. Flexural moduli for various plastics are compared in Fig. 15.

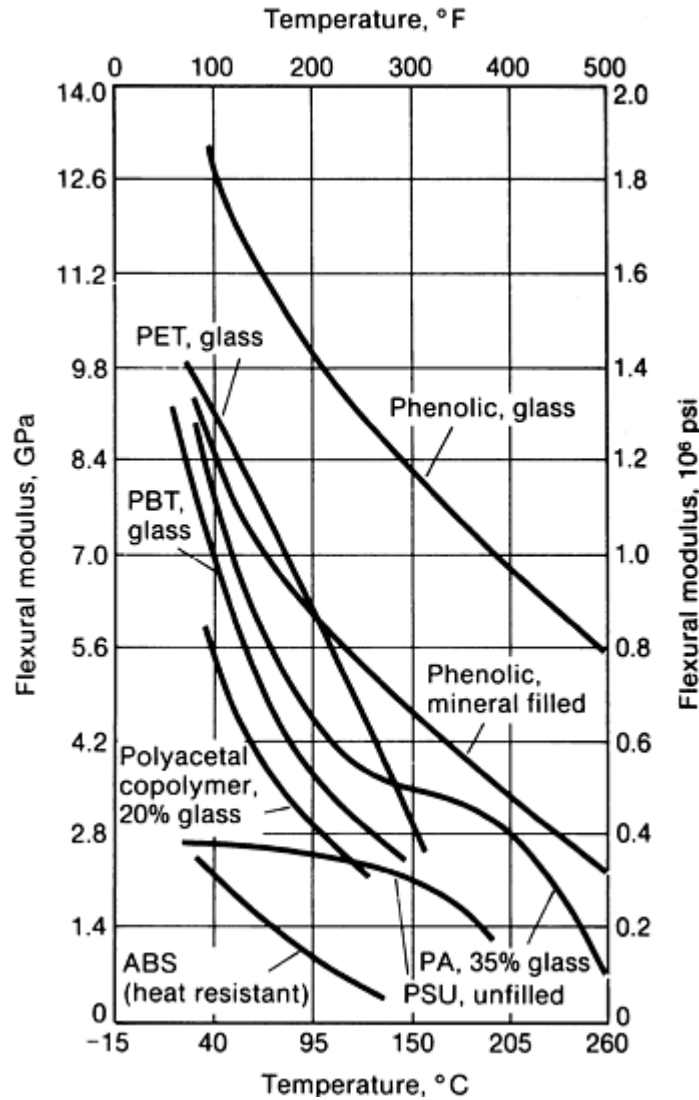


Fig. 15 Flexural modulus retention of engineering plastics at elevated temperatures. PET, polyethylene terephthalate; PBT, polybutylene terephthalate; ABS, acrylonitrile-butadiene-styrene; PA, polyamide; PSU, polysulfone

Flexural creep tests (ISO 899-2) are done with standard flexural test methods where the deflection is measured as a function of time. The flexural creep modulus at time, t , (E_t) for three-point bending (Fig. 13) is calculated as:

$$E_t = \frac{L^3 \cdot P}{4b \cdot d^3 \cdot s_t}$$

where s_t is the deflection at time, t .

Deflection Temperature under Load (ASTM D 648). Another measure of plastic rigidity under load is the deflection temperature under load (DTUL) test, also known as the heat deflection temperature (HDT) test. In the standard ASTM test (D 648), the heat deflection temperature is the temperature at which a 125 mm (5 in.) bar deflects 0.25 mm (0.010 in.) when a load is placed in the center. It is typically reported at both 460 and 1820 kPa (65 and 265 psi) stresses. The specimen is placed in an oil bath under a load of 460 or 1820 kPa (65 or 265 psi) in the apparatus shown in Fig. 16, and the temperature is raised at a rate of 2 °C/min. The temperature is recorded when the specimen deflects by 0.25 mm (0.01 in.). Because crystalline polymers, such as nylon 6/6, have a low heat deflection temperature value when measured under a load of 1820 kPa (265 psi), this test is often run at 460 kPa (65 psi).

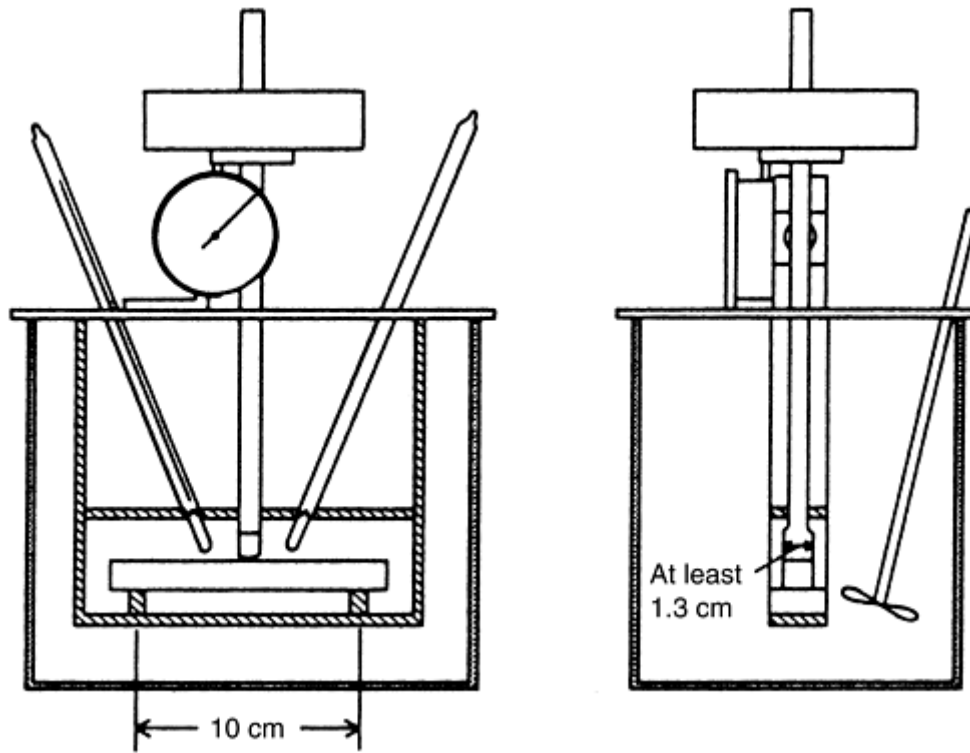


Fig. 16 Apparatus used in test for heat deflection temperature under load (460 or 1820 kPa, or 65 or 265 psi)

The heat deflection temperature is an often misused characteristic and must be used with caution. The established deflection is extremely small, and in some instances may be, at least in part, a measure of warpage or stress relief. The maximum resistance to continuous heat is an arbitrary value for useful temperatures, which are always below the DTUL value. The DTUL value is also influenced by glass reinforcement.

The heat deflection temperature is more an indicator of general short-term temperature resistance. For long-term temperature resistance, one of the most common measures is the thermal index determined by the Underwriters' Laboratory (UL) (Ref 13). In this test, standard test specimens are exposed to different temperatures and tested at varying intervals. Failure is said to occur when property values drop to 50% of their initial value. The property criterion for determining the long-term use temperature depends on the application. Table 8 lists typical HDT values and the UL temperature index for various plastics.

Table 8 Heat-deflection and Underwriters' Laboratories index temperatures for selected plastics

Material	Heat-deflection temperature at 1.82 MPa (0.264 ksi)		UL index	
	°C	°F	°C	°F
Acrylonitrile-butadiene-styrene (ABS)	99	210	60	140
ABS-polycarbonate alloy (ABS-PC)	115	240	60	140
Diallyl phthalate (DAP)	285	545	130	265
Polyoxymethylene (POM)	136	275	85	185
Polymethyl methacrylate (PMMA)	92	200	90	195
Polyarylate (PAR)	155	310
Liquid crystal polymer (LCP)	311	590	220	430
Melamine-formaldehyde (MF)	183	360	130	265
Nylon 6	65	150	75	165
Nylon 6/6	90	195	75	165
Amorphous nylon 12	140	285	65	150
Polyarylether (PAE)	160	320	160	320
Polybutylene terephthalate (PBT)	120	250

Polycarbonate (PC)	129	265	115	240
PBT-PC	129	265	105	220
Polyetheretherketone (PEEK)	250	480
Polyether-imide (PEI)	210	410	170	340
Polyether sulfone (PESV)	203	395	170	340
Polyethylene terephthalate (PET)	224	435	140	285
Phenol-formaldehyde (PF)	163	325	150	300
Unsaturated polyester (UP)	279	535	130	265
Modified polyphenylene oxide alloy (PPO)(mod)	100	212	80	175
Polyphenylene sulfide (PPS)	260	500	200	390
Polysulfone (PSU)	174	345	140	285
Styrene-maleic anhydride terpolymer (SMA)	103	215	80	175

Shear Strength Test (ASTM D 732). The specimen proscribed in ASTM D 732 is a disc or a plate with an 11 mm ($\frac{7}{16}$ in.) hole drilled through the center of the specimen. Testing can be done with a special fixture like the one shown in Fig. 17. Shear strength is defined as the force for separation during loading divided by the area of the sheared edge. Shear strength is often estimated as $\frac{1}{2}$ the tensile strength of a material. When a value for creep shear modulus is needed, it is reasonable to divide the creep tensile modulus by 2.8.

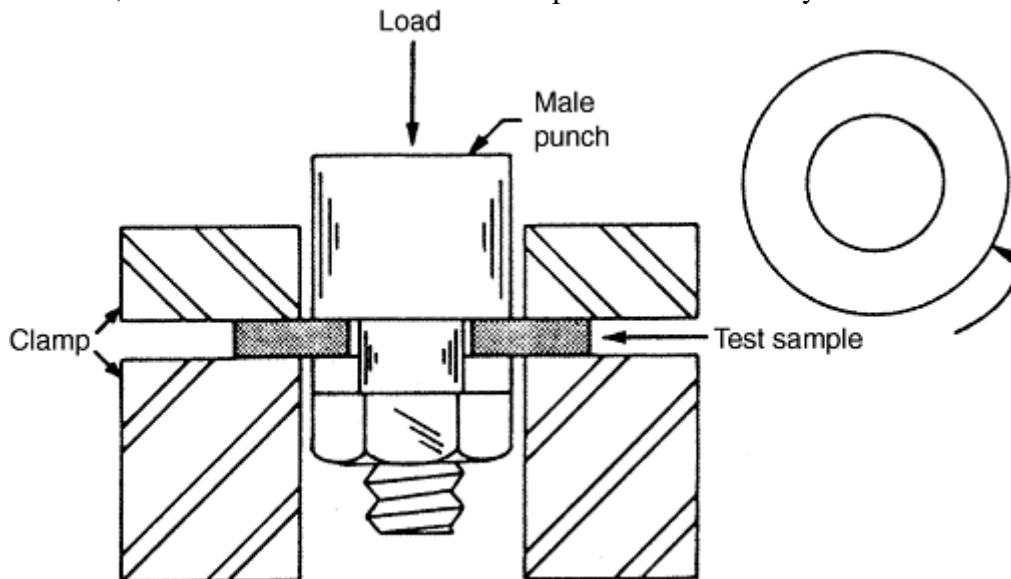


Fig. 17 Example of set for shear-strength testing of plastics

Creep Data Analysis

Mechanical tests under tensile, compressive, flexural, and shear loading can be performed as either short-term tests or long-term tests of creep deformation. Data for the long-term tests are typically recorded as time dependent displacement values at various levels of constant stress (Fig. 18a). This type of data, however, can be displayed and analyzed in several forms as shown in Fig. 18. There is no universal method of graphically displaying tensile creep or, in fact, creep for compressive, shear, or flexural loading.

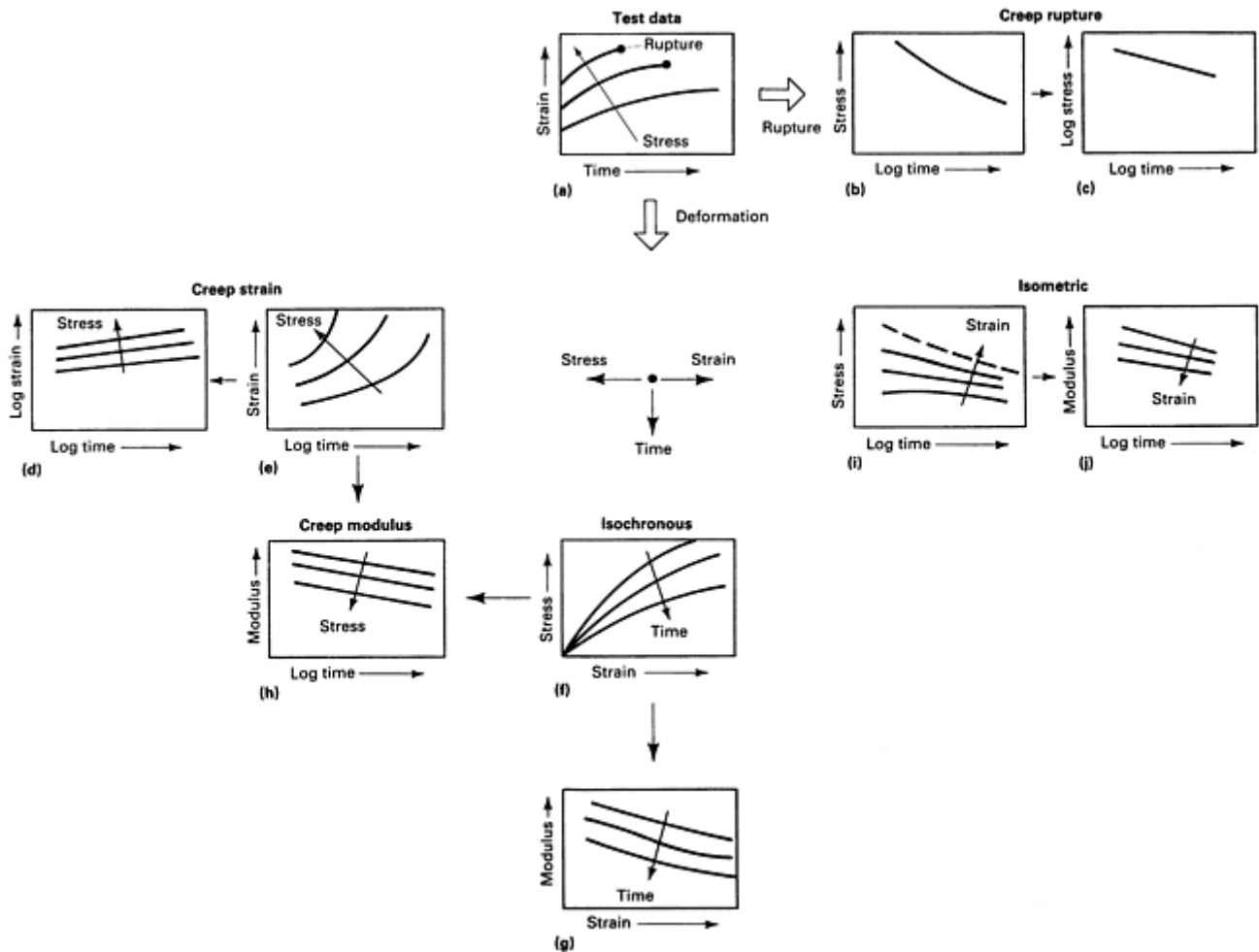


Fig. 18 Graphic representation of creep data showing various ways to plot time-dependent strain in response to time-dependent stress. See text for discussion.

Creep Modulus. In addition to stress-strain plots versus time, creep behavior is also expressed as a creep modulus, $E(t)$, where

$$E(t) = \sigma/\epsilon(t)$$

where σ is the applied stress and $\epsilon(t)$ is the creep strain as a function of time. The creep modulus is a measure of rigidity that can be applied for tensile, shear, compressive, or flexural load conditions. However, the creep modulus $E(t)$ is neither a design property nor a material constant. It is a time-dependent variable that is also a function of temperature and environment. The use of creep modulus data requires definition of intended design life and test conditions that accurately reflect the intended application.

Creep Rupture. Like the creep modulus, creep rupture data depend strongly on temperature. Creep rupture, in many respects, is a more important parameter because it represents the ultimate lifetime of a given material. Two types of graphic representation can be constructed for the creep rupture envelope, as shown in Fig. 18(b) and 18(c). Figure 18(b) shows a semilog plot of creep rupture stress as a function of failure time. For most plastic candidates for long-term performance, the design life can be quite long—months or years. As a result, the log-log coordinate system (Fig. 18c) has greater utility. Furthermore, creep rupture data tend to display linearly on this coordinate scheme.

Creep strain data plots can be done in various forms. Figure 18 shows three methods of analyzing these data. Each method holds one variable (stress, strain, or time) to be constant. For constant stress, Fig. 18(d) and 18(e) apply. The data can be displayed either as a set of (usually near-linear) linear lines on log-log paper (Fig. 18d) or as curvilinear lines on semilog paper (Fig. 18e). The parallel straight lines on log-log coordinates are called a creep strain plot (Fig. 18d).

Isochronous Creep Data. If the time parameter is held constant, a set of isochronous (or constant time) stress-strain curves results (Fig. 18f). A linear coordinate system is used to display these results. The slopes of these isochronous creep curves produce the isochronous modulus graph (Fig. 18g). If the slopes of the semilog curves

Polysulfone	B	B	B	B	B	B	B	B
High-density polyethylene	B	B	B	B	B	B	B	B
Rigid polyvinyl chloride	B	B	B	B	B	B	C	C
Polyphenylene oxide	B	B	B	B	B	B	C	C
Acrylonitrile-butadiene-styrene	B	B	B	B	B	B	C	C
Polycarbonate	B	B	B	B	C	C	C	C
Nylon (wet)	B	B	B	C	C	C	C	C
Polytetrafluoroethylene	B	C	C	C	C	C	C	C
Low-density polyethylene	C	C	C	C	C	C	C	C

(a) A, brittle even when unnotched; B, brittle, in the presence of a notch; C, tough

Although a number of standard impact tests are used to survey the performance of plastics exposed to different environmental and loading conditions, none of these tests provides real, geometry-independent material data that can be applied in design. Instead, they are only useful in application to quality control and initial material comparisons. Even in this latter role, different tests will often rank materials in a different order. As a result, proper test choice and interpretation require that the engineer have a very clear understanding of the test and its relationship to specific design requirements.

Because of differing engineering requirements, a wide variety of impact test methods have been developed. There is no one ideal method. The general classes of impact tests are shown in Fig. 19. However, this section briefly describes three of the most commonly used tests for impact performance: the Izod notched-beam test, the Charpy notched-beam test, and the dart penetration test.

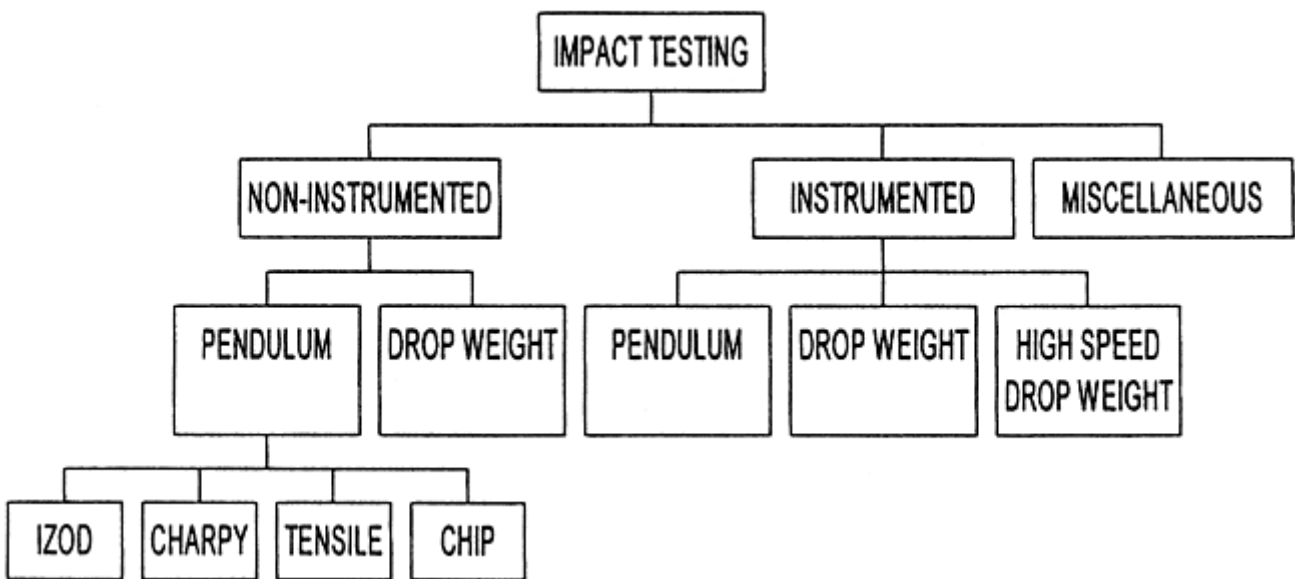


Fig. 19 Categories of impact test methods used in testing of plastics. Source: Ref 4

Charpy Impact Test (ASTM D 256 and ISO 179). The Charpy geometry consists of a simply supported beam with a centrally applied load on the reverse side of the beam from the notch (Fig. 20a). The notch serves to create a stress concentration and to produce a constrained multiaxial state of tension a small distance below the bottom of the notch. The load is applied dynamically by a free-falling pendulum of known initial potential energy. The important dimensions of interest for these tests include the notch angle, the notch depth, the notch tip radius, the depth of the beam, and the width of the beam. All these quantities, as well as more detailed information specifying loading geometry and conditions, are described in ASTM D 256 and ISO 179.

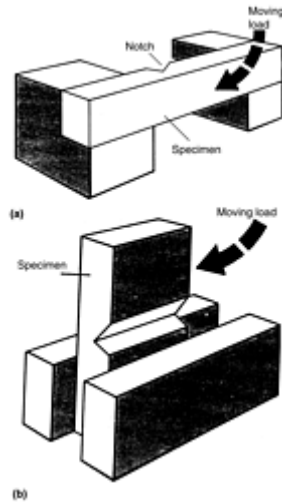


Fig. 20 Specimen types and test configurations for pendulum impact toughness tests. (a) Charpy method. (b) Izod method

Izod Impact Test (ASTM D 256 and ISO 180). Like the Charpy test, the Izod test involves a pendulum impact, but the Izod geometry consists of a cantilever beam with the notch located on the same side as the impact point (Fig. 20b). Because the pendulum hits the unnotched side of the sample in the Charpy test, Charpy values may be much higher impact strength values than Izod test values. However, the two measurements can be correlated (Ref 14). The Izod test is usually done on 3.2 mm ($\frac{1}{8}$ in.) thick samples. Materials such as polycarbonate exhibit thickness-dependent impact properties. Below 6.4 mm ($\frac{1}{4}$ in.), this material is ductile with a very high value, but above this thickness, the material has a much lower value.

Unnotched impact toughness tests in ASTM D 4812 and D 3029 (dart penetration test) have been replaced by ASTM D 5420. Impact values with unnotched samples are often considered a more definitive measure of impact strength, while the Izod test indicates notch sensitivity.

Dart Penetration (Puncture) Test. Another impact test that is often reported is the dart penetration (puncture) test. This test (Fig. 21) is different from the Izod and Charpy tests in a number of aspects. First, the stress state is two-dimensional in nature because the specimen is a plate rather than a beam. Second, the thin, platelike specimen does not contain any notches or other stress concentrations.

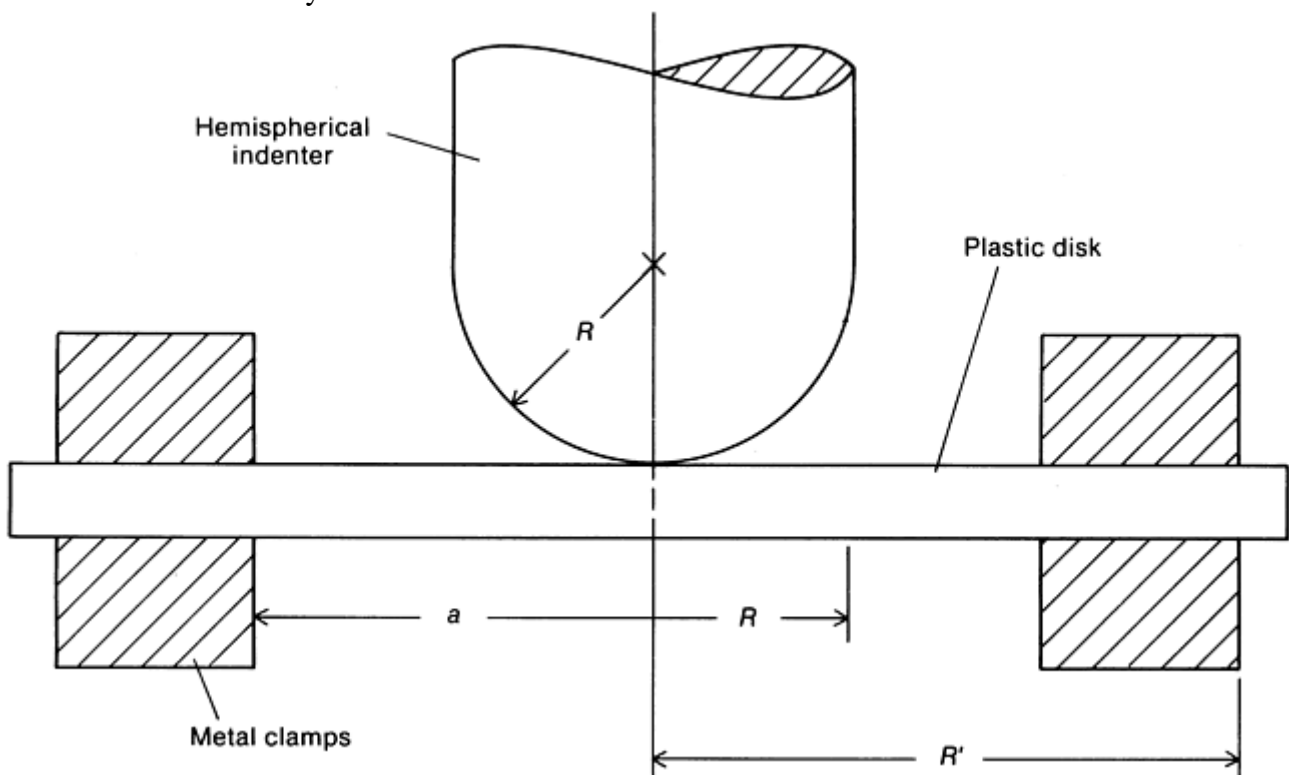


Fig. 21 Schematic puncture test geometry

The geometry and test conditions often applied using this specimen were described in ASTM D 3029 (now replaced by ASTM D 5420). The quantity most often quoted with respect to this test is the energy required for failure. Of course, these energy levels are very different from the notched beam energies-to-failure, but they also do not represent any fundamental material property. A marked transition in mode of failure can also be observed with this specimen as the rate is increased or the temperature is decreased. However, this transition temperature is quite different from that measured in the notched beam tests. Usually it displays a transition from ductile to brittle behavior at much lower temperatures than the notched specimens.

The dart penetration test is often performed with different specimens and indenter geometries. Linear elastic, small-displacement, thin-plate theory has occasionally been used to analyze test results in an effort to compare the performance of different materials tested with different specimen geometries. In all but the most brittle materials, this is an inappropriate simplification of the test. A number of very nonlinear events can take place during this test, including a growing indenter contact area, yielding, and large-displacement and large-strain deformation. References 15, 16, 17 provide more details on these events and their effects on the test data.

Fracture Mechanics. Another way to evaluate the toughness of materials is by fracture toughness testing, where the value of the critical stress-intensity factor for a material can be measured by testing standard cracked specimens, such as the compact-tension specimen. Standard test methods and specimen geometries are defined for measuring the critical stress-intensity factors for metals (ASTM E 399), but similar standards have yet to be officially defined for plastics. It appears that many of the recommendations of the ASTM E 399 test procedure for metals are equally worthwhile for plastics, although the ductile nature and low yield strength of plastics pose problems of specimen size.

In fracture toughness testing, the sample size can be reduced as long as all dimensions of the laboratory specimen are much larger than the plastic zone size. In fracture testing, according to ASTM E 399, the thickness, B , must be:

$$B \geq 2.5 \left(\frac{K_{Ic}}{\sigma_y} \right)^2 \approx 16r_p$$

where K_{Ic} is the plane-strain fracture toughness, σ_y is the yield stress, and r_p is the radius of the plastic zone, which is given by:

$$r_p = \frac{1}{2\pi} \left(\frac{K_{Ic}}{\sigma_y} \right)^2$$

By ensuring that the thickness is much larger than the yield zone size (at least 16 times larger), the laboratory specimen will be in the state of plane strain. Because of the hydrostatic stresses that develop at crack tips under plane-strain conditions, yielding is suppressed, and a minimum value for fracture toughness is obtained. The plane-strain fracture toughness can be used with confidence in designing large components.

Similar arguments hold for polymer fracture testing. To design large polymer components or to design for polymer applications in which yielding is suppressed, it is important to measure fracture properties under conditions of plane strain. However, typical engineering plastics have fracture toughnesses in the range of 2 to 4 MPa \sqrt{m} (1.8–3.6 ksi $\sqrt{in.}$) and yield strengths in the range of 50 to 80 MPa (7.3–11.6 ksi) (Ref 18). Plane-strain testing conditions would require sample thicknesses in the range of 1.6 to 16 mm (0.06–0.63 in.). The low-end range is a common size range, but the high end is more questionable. Engineering components designed with polymers almost never use polymers as thick as 16 mm (0.63 in.). Therefore, it is not clear that the plane-strain fracture toughness is the appropriate design data for engineering components in which the polymers will experience only plane-stress conditions. More importantly, fabricating thick polymer samples for plane-strain testing presents significant difficulties. Engineering plastics with fracture toughnesses in the range of 2 to 4 MPa \sqrt{m} (1.8–3.6 ksi $\sqrt{in.}$) are not particularly tough. Rubber-toughened polymers can have much higher toughness. Also, because the yield strength of rubber-toughened polymers is usually lower, the thickness requirements for plane-strain fracture testing are such that potential laboratory specimens cannot be prepared. Some of these toughened polymers can be tested with J integral techniques adapted from the J integral metals standard (Ref 19, 20). Another technique known as the essential work of fracture technique has been

considered. It has the potential to provide both plane-stress and plane-strain fracture toughness results for polymers. The essential work of fracture data can be obtained on thin polymers having thicknesses similar to those of typical polymer components (Ref 21).

Hardness Tests

Typical hardness values of common plastics are listed in Table 10. Rockwell testing and the durometer test method are the most common, although another type of hardness test for plastics is the Barcol method. A rough comparison of hardness scales for these methods is in Fig. 22, but it must be understood that any conversions from Fig. 22 are only rough estimates that vary depending on the materials. Hardness conversions are complicated by several material factors such as elastic recovery and, for plastics, the time-dependent effects from creep behavior. More information on the hardness testing of plastics is also given in the article “Selection and Industrial Applications of Hardness Tests” in this Volume.

Table 10 Typical hardness values of selected plastics

Plastic material	Rockwell		Durometer, Shore D	Barcol
	HRM	HRR		
Thermoplastic				
Acrylonitrile-butadiene-styrene	...	75–115
Acetal	94	120
Acrylic	85–105
Cellulosics	...	30–125
Polyphenylene oxide	80	120
Nylon	...	108–120
Polycarbonate	72	118
High-density polyethylene	60–70	...
Low-density polyethylene	40–50	...
Polypropylene	75–85	...
Polystyrene	68–70
Polyvinyl chloride (PVC)(rigid)	...	115
Polysulfone	70	120
Thermosets				
Phenolic (with cellulose)	100–110
Phenolic (mineral filler)	105–115
Unsaturated polyester (clear cast)	34–40
Polyurethane (high-density integral skin foam)	36–63	...
Polyurethane (solid reaction injection molded elastomer)	39–83	...
Epoxy (fiberglass reinforced)	106–108

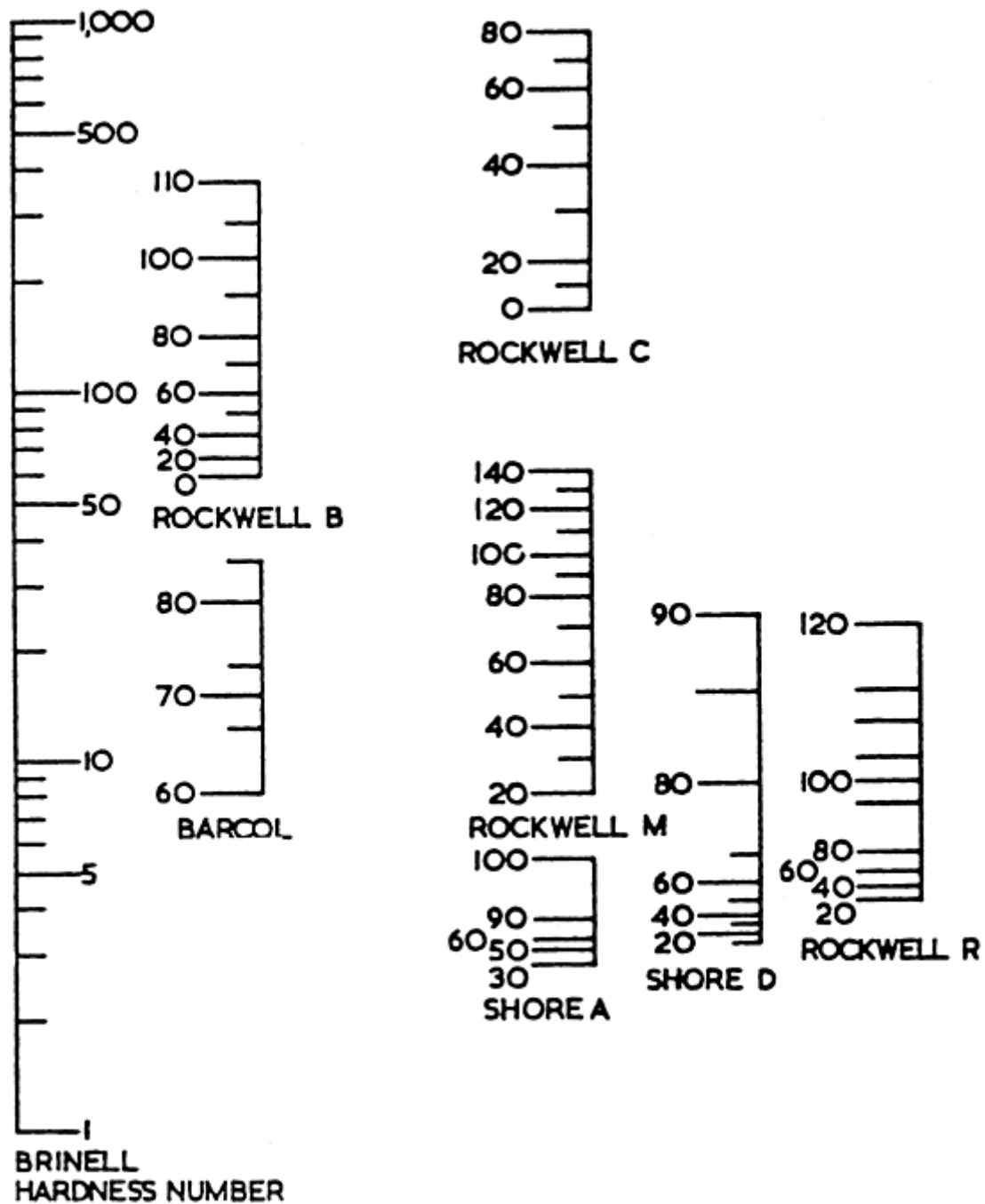


Fig. 22 Approximate relations among hardness scale for plastics

Rockwell hardness tests of plastics (ASTM D 785 and ISO 2039) are ball-indentation methods, where hardness is related to the net increase in the depth of an indentation after application of a minor load and a major load. The ball diameter and the loads are specified for each of the Rockwell scales, which are R, L, M, E, and K in order of increasing hardness. The Rockwell test is used for relatively hard plastics such as thermosets and structural thermoplastics such as nylons, polystyrene, acetals, and acrylics. Typical Rockwell values are shown in Fig. 23.

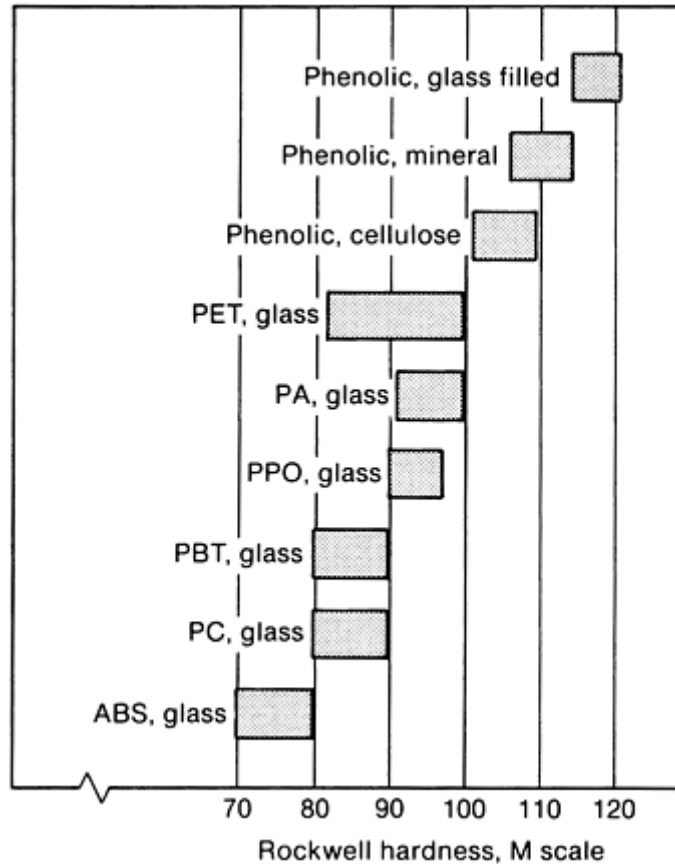


Fig. 23 Rockwell hardness of engineering plastics. PET, polyethylene terephthalate; PA, polyamide; PPO, polyphenylene oxide; PBT, polybutylene terephthalate; PC, polycarbonate; ABS, acrylonitrile-butadienestyrene

The durometer (or Shore hardness) method (ASTM D 2240 and ISO 868) registers the amount of indentation caused by a spring-loaded pointed indenter. This method is used for softer plastics and rubbers, and 100 is the highest hardness rating of this scale. Two types of durometers are used: type A and type D, as described further in the article “Selection and Industrial Applications of Hardness Tests” in this Volume.

The Barcol hardness test (ASTM D 2583) is mainly used for measuring the hardness of reinforced and unreinforced rigid plastics. A hardness value is obtained by measuring the resistance to penetration of a sharp steel point under a spring load. The instrument, called the Barcol impressor, gives a direct reading on a 0 to 100 scale. The hardness value is often used as a measure of the degree of cure of a plastic.

International Rubber Hardness Degrees (IRHD) Testing. The IRHD hardness test is very similar to durometer testing with some important differences. Durometer testers apply a load to the sample using a calibrated spring and a pointed or blunt shaped indenter. The load therefore will vary according to the depth of the indentation, because of the spring gradient. The IRHD tester uses a minor-major load system of constant load and a ball indenter to determine the hardness of the sample. This method is described further in the article “Miscellaneous Hardness Tests” in this Volume.

Fatigue Testing

Compared to testing of metals, the testing of plastics is a relatively recent pursuit. Because engineers and designers always use knowledge gained from previous experience, the methods used to test plastics in fatigue are largely based on methods developed for metals, with accommodations to account for the more obvious differences between the two materials.

For example, as previously noted in the section “Dynamic Mechanical Properties,” the role of high hysteresis losses in the repeated stressing of plastics is very important. Unlike metals, plastics deform in a largely nonelastic manner, resulting in part of the mechanical energy being converted into heat within the material. The gradual buildup of heat may be sufficient to cause a loss in strength and rigidity. This effect is further aggravated by the low thermal conductivity of plastics and a general increase in hysteresis losses with an

increase in temperature. Hysteresis losses are also a function of the loading rate (frequency), the type of load (bending, tension, or torsion), and the volume of material under stress. The hysteresis losses increase with loading rate and the volume of material under stress.

This also can be further extended to include the effects of different loading waveforms (sinusoid, saw tooth, or square) on the fatigue strength of viscoelastic materials. In addition, absorbed water and environmental variables also influence the fatigue strength of plastics. These and other factors are described in more detail in the article “Fatigue Testing and Behavior of Plastics” in this Volume.

References cited in this section

4. F.N. Kelly and F. Bueche, *J. Polym. Sci.*, Vol 50, 1961, p 549
5. V. Shah, *Handbook of Plastics Testing Technology*, 2nd ed., John Wiley & Sons, 1998
- *ISO/IEC Selected Standards for Testing Plastics*, 2nd ed., ASTM, 1999
12. J. Nairn and R. Farris, Important Properties Divergences, *Engineering Plastics*, Vol 2, *Engineered Materials Handbook*, ASM International, 1988, p 655–658
13. T. Osswald, *Polymer Processing Fundamentals*, Hanser/Gardner Publications Inc., 1998, p 19–43
14. K.M. Ralls, T.H. Courtney, and J. Wulff, *Introduction to Materials Science and Engineering*, John Wiley & Sons, 1976
15. S. Turner, Mechanical Testing, *Engineering Plastics*, Vol 2, *Engineered Materials Handbook*, ASM International, 1988, p 547
16. R.B. Seymour, *Polymers for Engineering Applications*, ASM International, 1987, p 155
17. V. Shah, *Handbook of Plastics Testing Technology*, 2nd ed., John Wiley & Sons, 1998
18. Recognized Components Directories, Underwriters Laboratories
19. R.D. Deanin, *Polymer Structure, Properties and Applications*, Cahnners, 1982
26. R.P. Nimmer, Analysis of the Puncture of a Polycarbonate Disc, *Polym. Eng. Sci.*, Vol 23, 1983, p 155
27. R.P. Nimmer, An Analytical Study of Tensile and Puncture Test Behavior as a Function of Large-Strain Properties, *Polym. Eng. Sci.*, Vol 27, 1987, p 263
28. L.M. Carapelucci, A.F. Yee, and R.P. Nimmer, Some Problems Associated with the Puncture Testing of Plastics, *J. Polym. Eng.*, June 1987
29. J.G. Williams, *Fracture Mechanics of Polymers*, Ellis Horwood, 1984
30. D.D. Huang and J.G. Williams, *J. Mater. Sci.*, Vol 22, 1987, p 2503
31. M.K.V. Chan and J.G. Williams, *Int. J. Fract.*, Vol 19, 1983, p 145
32. Y.W. Mai and B. Cotterell, *Int. J. Fract.*, Vol 32, 1986, p 105

Mechanical Testing of Polymers and Ceramics

Elastomers and Fibers

As previously noted, polymers can exhibit a range of mechanical behaviors that characterize their various classifications as elastomers, plastics, and fibers (Fig. 1). The following discussions briefly describe tension testing of elastomers and fibers.

Tension Testing of Elastomers

Elastomers have the ability to undergo high levels of reversible elongation that, in some cases, can reach up to 1000%. This high degree of reversible elongation allows stretching and recovery like that of a rubber band. Over 20 different types of polymers can be used as bases for elastomeric compounds, and each type can have a significant number of contrasting subtypes within it. Properties of different polymers can be markedly different: for instance, urethanes seldom have tensile strengths below 20.7 MPa (3.0 ksi), whereas silicones rarely exceed

8.3 MPa (1.2 ksi). Natural rubber is known for high elongation, 500 to 800%, whereas fluoroelastomers typically have elongation values ranging from 100 to 250%.

Literally hundreds of compounding ingredients are also available, including major classes such as powders (carbon black, clays, silicas), plasticizers (petroleum-base, vegetable, synthetic), and curatives (reactive chemicals that change the gummy mixture into a firm, stable elastomer). A rubber formulation can contain from four or five ingredients to 20 or more. The number, type, and level of ingredients can be used to change dramatically the properties of the resulting compound, even if the polymer base remains exactly the same.

ASTM D 412 is the U.S. Standard for tension testing of elastomers. It specifies two principal varieties of specimens: the more commonly used dumbbell-type, die cut from a standard test slab 150 mm by 150 mm by 20 mm (6 in. by 6 in. by 0.8 in.), and actual molded rings of rubber. The second type was standardized for use by the O-ring industry. For both varieties, several possible sizes are permitted, although, again, more tests are run on one of the dumbbell specimens (cut using the Die C shape) than on all other types combined. Straight specimens are also permitted, but their use is discouraged because of a pronounced tendency to break at the grip points, which makes the results less reliable.

The power-driven equipment used for testing is described, including details such as the jaws used to grip the specimen, temperature-controlled test chambers when needed, and the crosshead speed of 500 mm/min (20 in./min). The testing machine must be capable of measuring the applied force within 2%, and a calibration procedure is described. Various other details, such as die-cutting procedures and descriptions of fixtures, are also provided.

The method for determining actual elongation can be visual, mechanical, or optical, but the method must be accurate within 10% increments. In the original visual technique, the machine operator simply held a scale behind or alongside the specimen as it was being stretched and noted the progressive change in the distance between two lines marked on the center length of the dogbone shape. The degree of precision that could be attained using a handheld ruler behind a piece of rubber being stretched at a rate of over 75 mm/s (3 in./s) was always open to question, with 10% being an optimistic estimate.

More recent technology employs extensometers, which are comprised of pairs of very light grips that are clamped onto the specimen and whose motion is then measured to determine actual material elongation. The newest technology involves optical methods, in which highly contrasting marks on the specimen are tracked by scanning devices, with the material elongation again being determined by the relative changes in the reference marks.

Normal procedure calls for three specimens to be tested from each compound, with the median figure being reported. Provision is also made for use of five specimens on some occasions, with the median again being used.

Techniques for calculating the tensile stress, tensile strength, and elongation are described for the different types of test specimens. The common practice of using the unstressed cross-sectional area for calculation of tensile strength is used for elastomers, as it is for many other materials. It is interesting to note that if the actual cross-sectional area at fracture is used to calculate true tensile strength of an elastomer, values that are higher by orders of magnitude are obtained.

In recent years, attention has been given to estimating the precision and reproducibility of the data generated in this type of testing. Interlaboratory test comparisons involving up to ten different facilities have been run, and the later versions of ASTM D 412 contain the information gathered.

Variability of the data for any given compound is to some degree related to that particular formulation. When testing was performed on three different compounds of very divergent types and property levels, the pooled value for repeatability of tensile-strength determinations within labs was about 6%, whereas reproducibility between labs was much less precise, at about 18%. Comparable figures for ultimate elongation were approximately 9% (intralab) and 14% (interlab).

Similar comparisons of the 100% modulus (defined in "Modulus of the Compound" later in this section) have shown even less precision, with intralab variation of almost 20% and interlab variation of over 31%. This runs counter to the premise that modulus should be more narrowly distributed than tensile strength, because tensile strength and ultimate elongation are failure properties, and as such are profoundly affected by details of specimen preparation. Because the data do not support such a premise, some other factor must be at work. Possibly that factor is the lack of precision with which the 100% strain point is observed, but, in any case, it is important to determine the actual relationship between the precision levels of the different property measurements.

Significance and Use of Tensile-Testing Data for Elastomers. It is important to note that the tensile properties of elastomers are determined by a single application of progressive strain to a previously unstressed specimen to the point of rupture, which results in a stress-strain curve of some particular shape. The degree of nonlinearity and in fact complexity of that curve will vary substantially from compound to compound. Tensile properties of elastomers also have different significance than those of structural materials.

Tensile Strength of Elastomers. Because elastomers as a class of materials contain a substantial number of different polymers, the tensile strength of elastomers can range from as low as 3.5 MPa (500 psi) to as high as 55.2 MPa (8.0 ksi); however, the tensile strengths of the great majority of common elastomers tend to fall in the range from 6.9 to 20.7 MPa (1.0–3.0 ksi).

It should also be noted that successive strains to points just short of rupture for any given compound will yield a series of progressively different stress-strain curves; therefore, the tensile-strength rating of a compound would certainly change depending on how it was flexed prior to final fracture. Thus, the real meaning of elastomer tensile strength may be open to some question. However, some minimum level of tensile strength is often used as a criterion of basic compound quality, because the excessive use of inexpensive ingredients to fill out a formulation and lower the cost of the compound will dilute the polymer to the point that tensile strength decreases noticeably.

The meaning of tensile strength of elastomers must not be confused with the meaning of tensile strength of other materials, such as metals. Whereas tensile strength of a metal may be validly and directly used for a variety of design purposes, this is not true for tensile strength of elastomers. As stated early in ASTM D 412, “Tensile properties may or may not be directly related to the end-use performance of the product because of the wide range of performance requirements in actual use.” In fact, very seldom if ever can a given high level of tensile strength of a compound be used as evidence that the compound is fit for some particular application.

Elongation of Elastomers. Ultimate elongation is the property that defines elastomeric materials. Any material that can be reversibly elongated to twice its unstressed length falls within the formal ASTM definition of an elastomer. The upper end of the range for rubber compounds is about 800%, and although the lower end is supposed to be 100% (a 100% increase of the unstressed reference dimension), some special compounds with limits that fall slightly below 100% elongation still are accepted as elastomers.

Just as with tensile strength, certain minimum levels of ultimate elongation are often called out in specifications for elastomers. The particular elongation required will relate to the type of polymer being used and the stiffness of the compound. For example, a comparatively hard (80 durometer) fluoroelastomer might have a requirement of only 125% elongation, whereas a soft (30 durometer) natural rubber might have a minimum required elongation of at least 400%.

However, ultimate elongation still does not provide a precise indication of serviceability, because service conditions normally do not require the rubber to stretch to any significant fraction of its ultimate elongative capacity. Nonetheless, elongation is a key material selection factor that is more applicable as an end-use criterion for elastomers than is tensile strength.

Modulus of the Compound. Another characteristic of interest is referred to in the rubber industry as the modulus of the compound. Specific designations such as 100% modulus or 300% modulus are used. This is due to the fact that the number generated is not an engineering modulus in the normal sense of the term, but, rather, is the stress required to obtain a given strain. Therefore, the *100% modulus*, also referred to as M-100, is simply the stress required to elongate the rubber to twice its reference length.

Tensile modulus, better described as the stress required to achieve a defined strain, is a measurement of the stiffness of a compound. When the stress-strain curve of an elastomer is drawn, it can be seen that the tensile modulus is actually a secant modulus—that is, a line drawn from the origin of the graph straight to the point of the specific strain. However, an engineer needing to understand the forces that will be required to deform the elastomer in a small region about that strain would be better off drawing a line tangent to the curve at the specific level of strain and using the slope of that line to determine the approximate ratio of stress to strain in that region. This technique can be utilized in regard to actual elastomeric components as well as lab specimens.

Tension Set. A final characteristic that can be measured but that is used less often than the other three is called *tension set*. Often, when an elastomer or rubber is stretched to final rupture, the recovery in length of the two sections resulting from the break is less than complete. It is possible to measure the total length of the original reference dimension and calculate how much longer the total length of the two separate sections is. This is expressed as a percentage. Some elastomers will exhibit almost total recovery, whereas others may display

tension set as high as 10% or more. Tension set may also be measured on specimens stretched to less than breaking elongation.

The property of tension set is used as a rough measurement of the tolerance of high strain of the compound. This property is not tested very often, but, for some particular applications, such a test is considered useful. It could also be used as a quality-control measure or compound development tool, but most of the types of changes it will detect in a compound will also show up in tests of tensile strength, elongation, and other properties, and so its use remains infrequent.

Tensile-Test Curves. Figure 24 is a plot of tensile-test curves from five very different compounds, covering a range of base polymer types and hardnesses. The contrasts in properties are clearly visible, such as the high elongation (>700%) of the soft natural rubber compound compared with the much lower (about 275%) elongation of a soft fluorosilicone compound. Tensile strengths as low as 2.4 MPa (350 psi) and as high as 15.5 MPa (2.25 ksi) are observed. Different shapes in the curves can be seen, most noticeably in the pronounced curvature of the natural rubber compound.

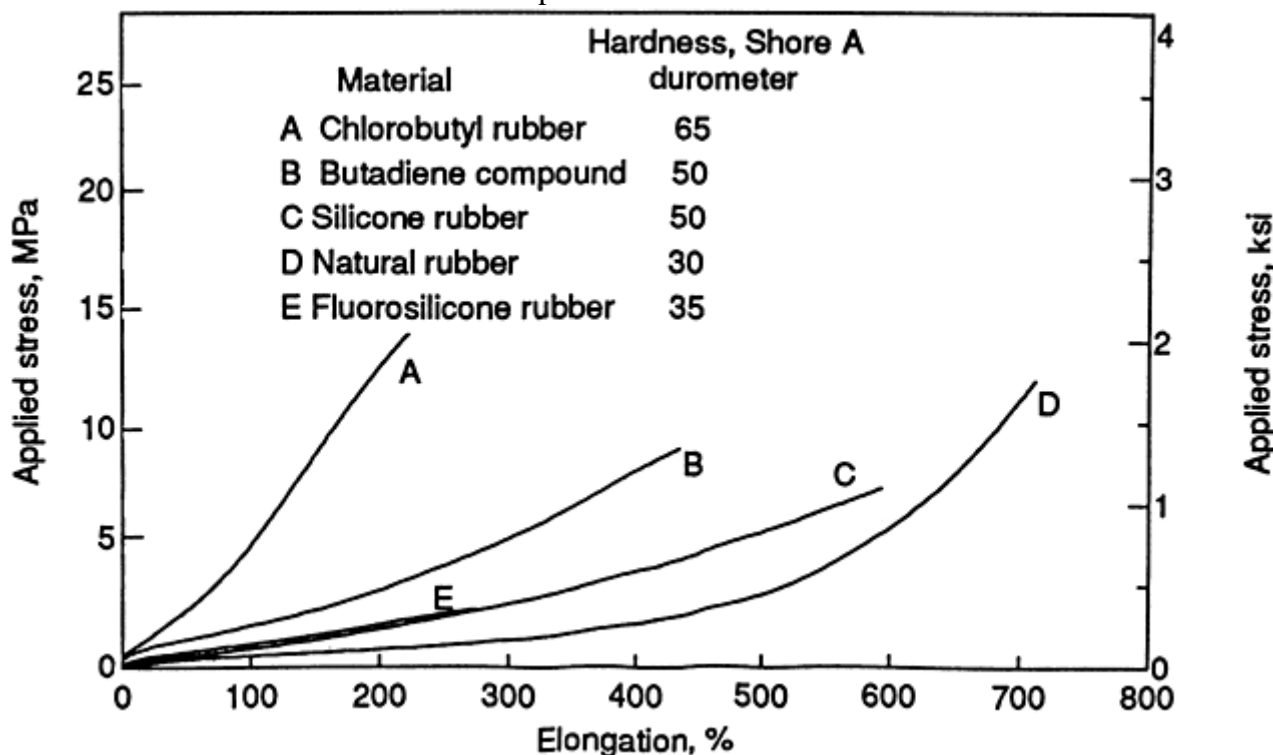


Fig. 24 Tensile-test curves for five different elastomer compounds

Figure 25 demonstrates that, even within a single elastomer type, contrasting tensile-property responses will exist. All four of the compounds tested were based on polychloroprene, covering a reasonably broad range of hardnesses, 40 to 70 Shore A durometer. Contrasts are again seen, but more in elongation levels than in final tensile strength. Two of the compounds are at the same durometer level and still display a noticeable difference between their respective stress-strain curves. This shows how the use of differing ingredients in similar formulas can result in some properties being the same or nearly the same whereas others vary substantially.

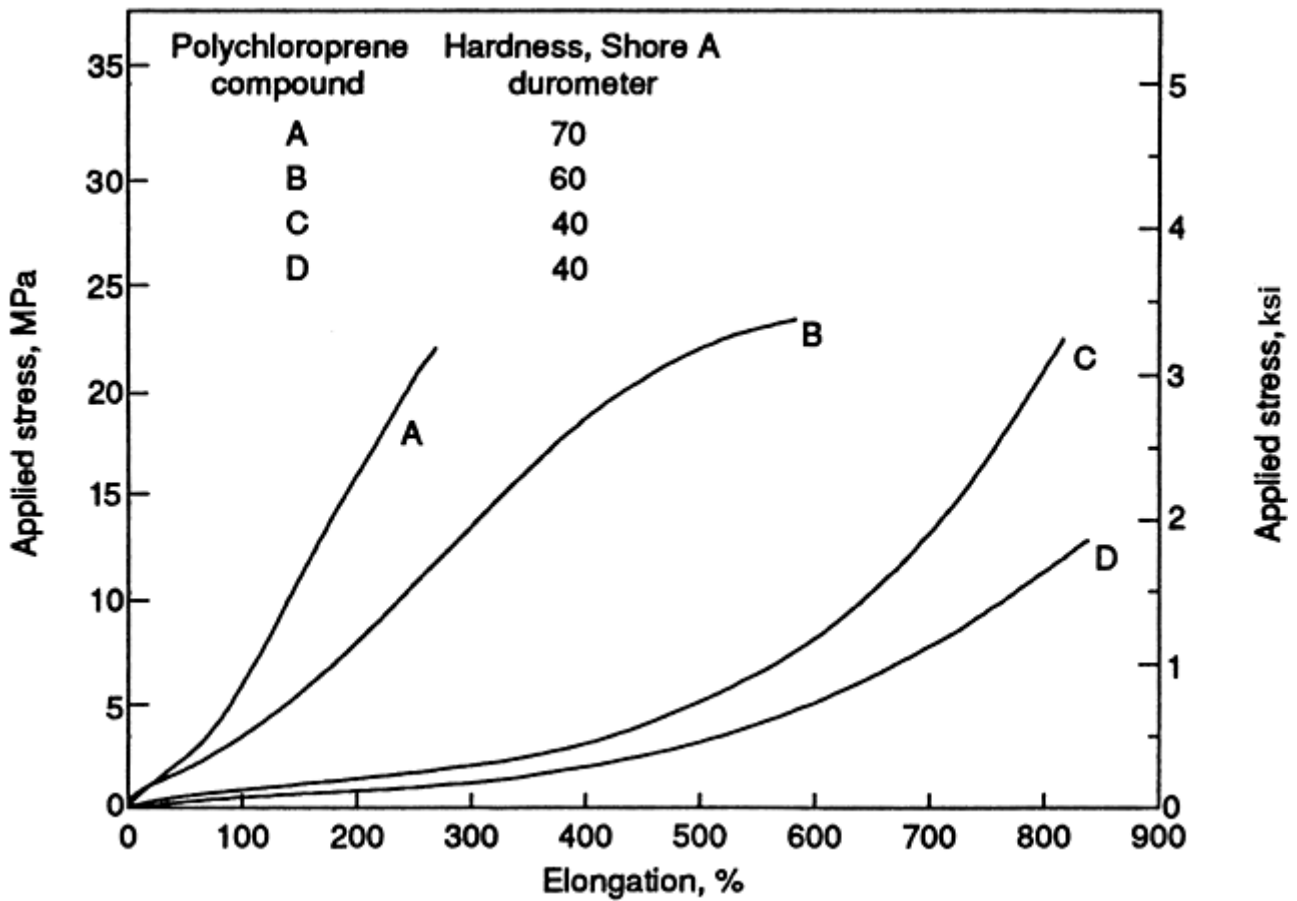


Fig. 25 Tensile-test curves for four polychloroprene compounds

Tests for Determining the Tensile Strength of Fibers

Mechanical properties of fibers are very dependent on test method. Two basic methods are the single-filament tension test and the tow tensile test of a group or strand of fibers.

Single-filament tensile strength (ASTM D 3379) is determined using a random selection of single filaments made from the material to be tested. Filaments are centerline-mounted on special slotted tabs. The tabs are gripped so that the test specimen is aligned axially in the jaws of a constant-speed movable-crosshead test machine. The filaments are then stressed to failure at a constant strain rate. For this test method, filament cross-sectional areas are determined by planimeter measurements of a representative number of filament cross sections as displayed on highly magnified micrographs. Alternative methods of area determination use optical gages, an image-splitting microscope, a linear weight-density method, and others.

Tensile strength and Young's modulus of elasticity are calculated from the load elongation records and the cross-sectional area measurements.

The specimen setup is shown in Fig. 26. Note that a system compliance adjustment may be necessary for single-filament tensile modulus.

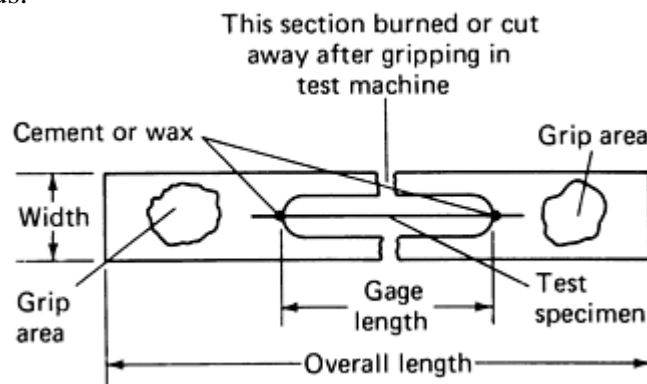


Fig. 26 Schematic showing typical specimen-mounting method for the single-filament fiber tension test (ASTM D 3379)

Tow Tensile Test (ASTM D 4018). The strength of fibers is rarely determined by testing single filaments and obtaining a numerical average of their strength values. Usually, a bundle or yarn of such fibers is impregnated with a polymer and loaded to failure. The average fiber strength is then defined by the maximum load divided by the cross-sectional area of the fibers alone.

Using ASTM D 4018 or an equivalent is recommended. This is summarized as finding the tensile properties of continuous filament carbon and graphite yarns, strands, rovings, and tows by the tensile loading to failure of the resin-impregnated fiber forms. This technique loses accuracy as the filament count increases. Strain and Young's modulus are measured by extensometer.

The purpose of using impregnating resin is to provide the fiber forms, when cured, with enough mechanical strength to produce a rigid test specimen capable of sustaining uniform loading of the individual filaments in the specimen.

To minimize the effect of the impregnating resin on the tensile properties of the fiber forms, the resin should be compatible with the fiber, the resin content in the cured specimen should be limited to the minimum amount required to produce a useful test specimen, the individual filaments of the fiber forms should be well collimated, and the strain capability of the resin should be significantly greater than the strain capability of the filaments.

ASTM D 4018 Method I test specimens require a special cast-resin end tab and grip design to prevent grip slippage under high loads. Alternative methods of specimen mounting to end tabs are acceptable, provided that test specimens maintain axial alignment on the test machine centerline and that they do not slip in the grips at high loads. ASTM D 4018 Method II test specimens require no special gripping mechanisms. Standard rubber-faced jaws should be adequate.

Mechanical Testing of Polymers and Ceramics

Mechanical Testing of Ceramics

Ceramic materials have been used in a variety of engineering applications that utilize their wear resistance, refractoriness, hardness, and high compression strength. Traditionally, they have not been used in tensile-loaded structures because they are brittle and experience catastrophic failure before permanent deformation. Nevertheless, their extreme refractoriness, chemical inertness, and favorable optical, electrical, and thermal properties are inducements to use ceramics in certain tensile load-bearing applications. Typical mechanical properties of common ceramics are listed in Table 11, and applicable ASTM standards for mechanical testing are listed in Table 12. More current information on mechanical testing of ceramics is provided in Ref 22.

Table 11 Typical mechanical properties of common ceramic materials

Material	Young's modulus		Flexural strength		Compressive strength	
	GPa	10 ⁶ psi	MPa	ksi	MPa	ksi
Brick	5–20	0.7–2.9	5–10	0.7–1.5	10–25	1.5–3.6
Roof tile	5–20	0.7–2.9	8–15	1.2–2.2	10–25	1.5–3.6
Steatite	1–3	0.1–0.4	140–160	20–23	850–1000	123–145
Silica refractories, 96–97% SiO ₂	8–14	1.2–2.0	30–80	4.4–11.6
Fireclay refractories, 10–44% Al ₂ O ₃	20–45	2.9–6.5	5–15	0.7–2.2	10–80	1.5–11.6
Corundum refractories, 75–90% Al ₂ O ₃	30–120	4.4–17.4	10–150	1.5–22	40–200	5.8–30.7
Forsterite refractories	25–30	3.6–4.4	5–10	0.7–1.5	20–40	2.9–5.8
Magnesia refractories	30–35	4.4–5.1	8–200	1.2–29	40–100	5.8–14.5
Zircon refractories	35–40	5.1–5.8	80–200	12–29	30–60	4.4–8.7

Whiteware	10–20	1.5–2.9	20–25	2.9–3.6	30–40	4.4–5.8
Stoneware	30–70	4.4–10.2	20–40	2.9–5.8	40–100	5.8–14.5
Electrical porcelain	55–100	8.0–14.5	90–145	13–21	55–100	8.0–14.5
Capacitor ceramics	90–160	13–23	300–1000	44–145

Source: Ref 21

Table 12 ASTM standards related to mechanical testing of ceramics

Terminology	
C 1145	Standard Definition of Terms Relating to Advanced Ceramics
C 1286	Standard System for Classification of Advanced Ceramics
Properties and performance (monolithic)	
C 1161	Standard Test Method for Flexural Strength of Advanced Ceramics at Ambient Temperature
C 1211	Standard Test Method for Flexural Strength of Advanced Ceramics at Elevated Temperatures
C 1259	Standard Test Method for Dynamic Young's Modulus
C 1273	Standard Practice for Tensile Strength of Monolithic Advanced Ceramics at Ambient Temperature
Design and evaluation	
C 1175	Standard Guide to Test Methods for Nondestructive Testing of Advanced Ceramics
C 1198	Standard Test Method for Dynamic Young's Modulus
C 1212	Standard Practice for Fabricating Ceramic Reference Specimens Containing Seeded Voids
C 1239	Standard Practice for Reporting Uniaxial Strength Data and Estimating Weibull Distribution Parameters for Advanced Ceramics
Characterization and processing	
C 1251	Standard Guide for Determination of Specific Surface Area of Advanced Ceramics by Gas Adsorption
C 1274	Standard Test Method for Advanced Ceramic Specific Surface Area by Physical Adsorption
C 1282	Standard Test Method for Determination of the Particle Size Distribution of Advanced Ceramics by Centrifugal Photosedimentation
Ceramic composites	
C 1275	Standard Practice for Monotonic Tensile Strength Testing of Continuous Fiber-Reinforced Advanced Ceramics with Solid Rectangular Cross Section at Ambient Temperatures

Source: Ref 21

References cited in this section

21. Y.W. Mai and B. Cotterell, *Int. J. Fract.*, Vol 32, 1986, p 105
22. C.R. Brinkman and G.D. Quinn, Standardization of Mechanical Properties Tests for Advanced Ceramics, *Mechanical Testing Methodology for Ceramic Design and Reliability*, Marcel Dekker, 1998, p 353–386

Room-Temperature Strength Tests

Uniaxial Tensile Strength. The nonductile nature of monolithic ceramics and their high sensitivity to stress concentrators has meant that conventional direct tensile testing is difficult and expensive. Gripping with jaws, screw threads, or other conventional devices causes invalid test results because of specimen breakage at the grips. The high stiffness (elastic modulus) of many ceramics means that a misalignment of only a few thousandths of a centimeter can lead to bending stresses with errors of 10% or more. Specimen preparation to exacting tolerances with minimal machining damage and careful tapers to avoid stress concentrators has been an expensive proposition. Considerable work has focused on improving tensile test methods for ceramics, with the result that tensile testing is becoming more routine. Commercial equipment is readily available, and specimen costs are falling. It will, however, always be more difficult to conduct direct tensile tests for ceramics than for metals.

The experimental difficulties, coupled with the problems of fabricating sufficiently large specimens, have prompted ceramists to use alternative test methods. The most common is flexure testing, in either the so-called three-point or four-point configuration. The latter is usually further specified by a description of the distance from the outer support points and the inner points, such as $\frac{1}{4}$ or $\frac{1}{3}$ four-point loading. The small size, low cost, and easy preparation of a flexure specimen account for its popularity, but there are distinct drawbacks. The bending creates a stress gradient in the specimen, and only a small volume is exposed to high tensile stress. The specimens are very sensitive to edge or surface machining damage. The test appears easy to set up and conduct, but misalignments and experimental errors can easily ruin it. Standard test methods are now available that permit accurate strength measurements for standard sizes and shapes, as shown in Fig. 27.

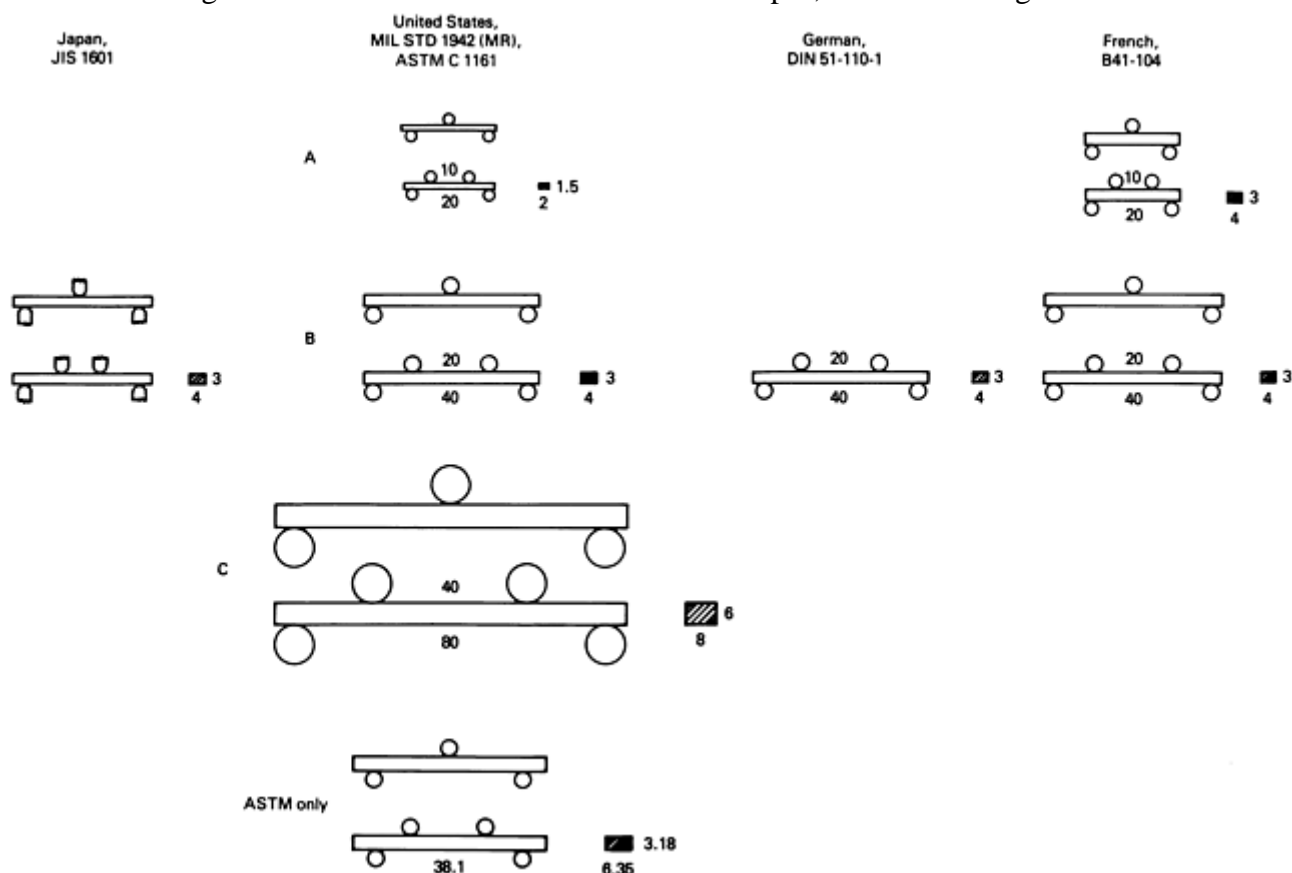


Fig. 27 Flexure strength standard test methods; all dimensions in mm

Nevertheless, it is still preferable to perform direct tension testing. Current testing systems are designed with self-aligning features that limit the imposed bending stresses to approximately 1%. There is usually less

extrapolation of the strength data from test specimen to component size. Tensile specimens are still expensive, however, because of costly fabrication and machining. They are inconveniently large, as well, because most systems are designed for high-temperature test rigs that use cold grips. Until recently, only a few laboratories had the ability to test or to even afford direct tensile experiments. A new emphasis on attaining accurate, quality data in support of ceramics in heat engine programs has led to rapid improvements in the field, and commercial test systems are now readily available. Different tensile specimen geometries that are being used are shown in Fig. 28 (Ref 23, 24, 25, 26, 27, 28).

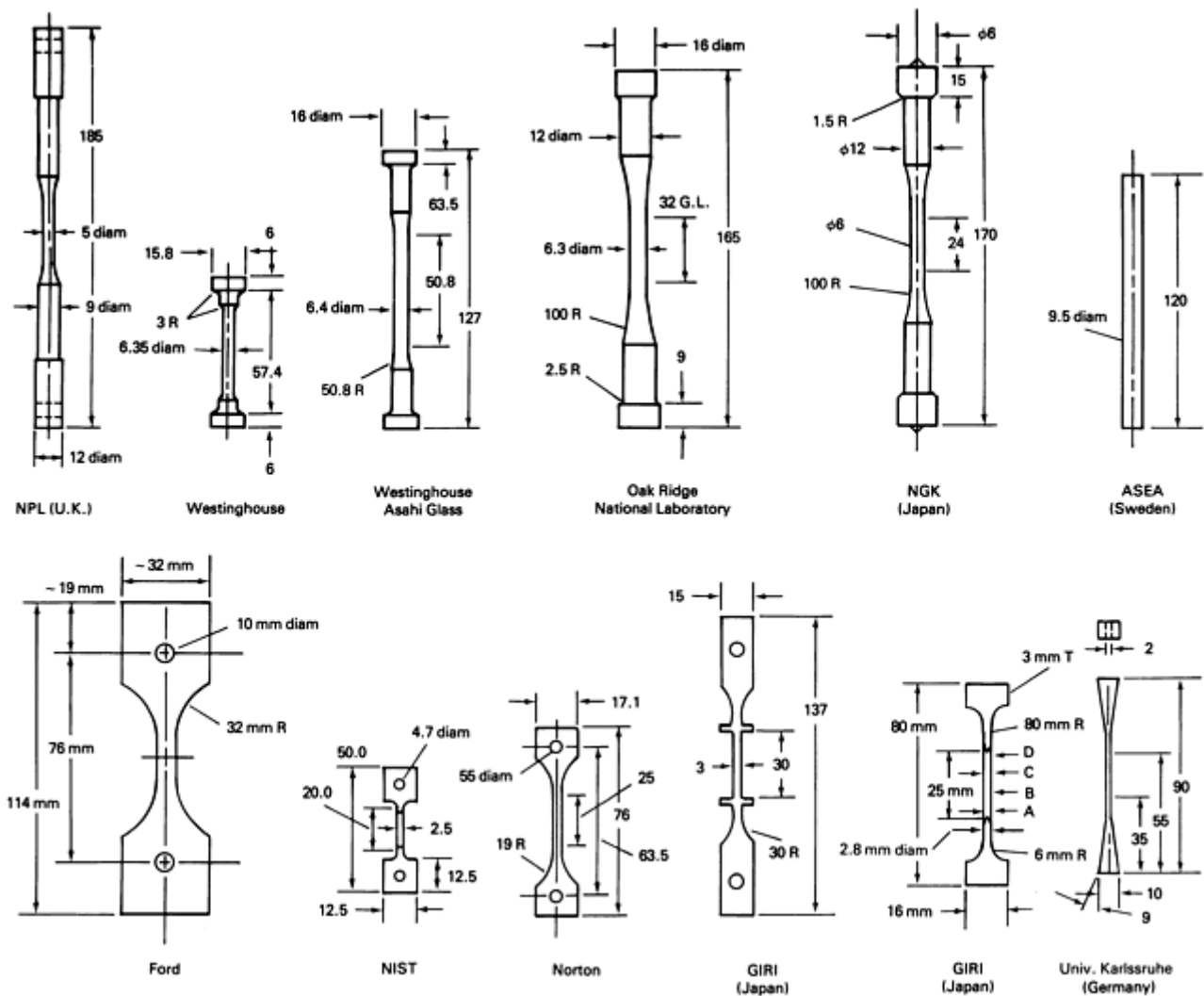


Fig. 28 Tension specimens used for monolithic ceramics (each is in correct proportion to the others); all dimensions in mm. Upper row for round specimens; lower row for flat specimens. Adapted from Ref 26

Another occasionally cited test for engineering ceramics is the so-called diametral compression test, or Brazilian disk test, wherein a circular cylinder is loaded at its ends (Ref 29, 30). The test is actually biaxial, because in addition to the tensile stresses that tend to laterally split the specimen, compressive stresses that are three times as great act axially through the specimen. However, compressive stresses of this magnitude are not likely to affect uniaxial strength, an effect peculiar to monolithic ceramics. The specimen loading is between two platens with pads of compliant material (such as a metallic shim or paper) to avoid high shearing stresses. Careful machining of the end faces of the specimen is essential, once again to avoid damage that compromises the test. This point is often overlooked. This test is occasionally employed by ceramics processors for ceramics fabricated in cylindrical shapes.

Many ceramic materials have strengths that are specific to the shaping process being used, such as injection-molded turbocharger rotors or extruded heat-exchanger tubes. In such cases, it is not practical to cut tensile specimens from the part, but separately cast tensile specimens may not have the same microstructure or defects as the component and, therefore, are irrelevant (Ref 31, 32, 33). It is optimal to test components in as close a configuration to the final component shape as possible. Thus, in the case of a tube, a ring can be cut from the

tube and pressurized to obtain a uniaxial hoop-stress-testing configuration (Ref 34, 35). Contrary to expectations, such a test can be conducted at high temperatures. Indeed, one of the highest recorded strength test temperatures for a ceramic (2180 °C, or 3955 °F) was on a pressurized tube (Ref 36). Extreme care must be taken to ensure that the edges are not chipped and do not have excessive machining damage, lest the test merely become a measure of machining damage.

There is no simple answer to the question of what specimen is best for measuring strength data. The best practice is to test a configuration that most resembles the actual component in its service conditions and to ensure that the test material accurately represents the component material. It is likely that the first available data will be flexure-strength data, which are typically higher (10–50%) than tensile specimen data because of the dependency of strength on test specimen size. Nevertheless, considering the tradeoffs in cost, quantity of results, and difficulty in testing, it is likely that future engineering databases will feature complementary flexure and tensile data. Indeed, it will be beneficial to have strength data from different sizes and shapes to permit an assessment of material consistency, flaw uniformity, and the veracity of strength-size scaling models.

Elastic Modulus. Several methods are used to evaluate the elastic moduli of monolithic or fine-scaled, isotropic composites. The most common are deflection measurements in flexural strength tests (with proper consideration of the test machine compliance) or strain gage experiments in flexure or direct tension. Dynamic measurements are also quite common, with either sonic excitation of prismatic specimens at their resonant frequency or time-of-flight measurements of ultrasonic waves.

Interpretation of Uniaxial Strength. The scatter in uniaxial strengths is well modeled by Weibull statistics. Weibull observed that the strength of brittle materials is controlled by the presence of randomly distributed defects and that failure is controlled by the largest, most severely stressed defect. Fracture occurs when a defect in one particular element of the body reaches a critical loading. This analysis is colloquially known as the weakest-link model, in direct analogy to the strength of a chain.

The Weibull modulus, m , has no units and is the factor that determines the scatter in strength. High values are optimum. Traditional ceramics, such as whitewares and brick, may have values from 3 to 5. A good material has a value that exceeds 10. A ceramic with an m value ≥ 30 has very consistent strengths and could be practically considered to have a deterministic value of strength over a range of several orders of magnitude volume.

Not only does strength scale with specimen size, but the magnitude of the change strongly depends on whether the defects are surface or volume. Obviously, it is essential to know whether flaws are of one or the other category if the laboratory strength data are going to be size-scaled to predict component performance.

A Weibull graph is a convenient means to report strength data. The graph usually has special axes chosen to linearize the data. This is done in the same fashion that probability paper can be used to linearize data for a Gaussian distribution.

The Weibull analysis is adequate for multiaxially, tensilely loaded ceramics, provided that the second or third principal stresses are significantly less than the principal tensile stress. If this is not the case, then it is appropriate to use more sophisticated analyses that take into account the effect of multiaxial tensile stresses on defects. The Weibull analysis also has limitations if the defects are likely to grow subcritically during a test. A newly recognized phenomenon that could occasionally pose problems in strength analysis is *latent* defect caused by localized surface impact or contact stresses. Concentrated microdamage can occur that can lead to a larger microcrack popping in after an incubation period (Ref 37, 38).

Strength values by themselves are only half the picture. The types of defects are equally important because each flaw type has its own Weibull distribution, and because multiple flaw populations are common in ceramics. Therefore, it is essential that the defects be as clearly associated with the strength values as possible.

Uniaxial Compression Strength. The high compressive strength of ceramics is a consequence of the resistance of the material to plastic flow and the insensitivity of defects to compressive stress. Ancient structural applications of ceramics were columns and walls that capitalized on high compressive strength. The fact that ceramics fail at all in compression is a result of the distortion of the stress field in the immediate vicinity of the tip of a defect. This distortion causes a localized tensile stress concentration that, for defects at the worst orientation (-30° to the axial stress) is about $\frac{1}{8}$ of the concentration if the specimen is loaded in tension. Thus, a Griffith-type criterion for failure would predict that the compression specimen will fail at about 30° to the specimen axial direction when the compressive stress is eight times the tension strength, but this is an oversimplification.

The tensile stresses in the immediate vicinity of a defect will cause a crack to propagate stably for a slight distance (Ref 39, 40). The crack then aligns itself with the compression stress and is arrested. Progressively more defects grow until the damage that has accumulated in the specimen reaches some limit, and the specimen virulently disintegrates into powder (often with a triboluminescent emission) (Ref 41, 42). Compression strength thus depends not on the largest, worst-oriented, highest-stressed defect, but on the entire defect population. The high compressive stresses can nucleate cracks due to twinning or dislocation activity, as well (Ref 43, 44). Compression strength may have a dependence on the square root of grain size, because the size of defects may scale with the average grain size or because of microplasticity in the grains. Weibull statistics are irrelevant, and compression strengths often have very low scatter (Ref 41, 42).

The compression test appears deceptively easy to conduct. However, it is extremely difficult to accurately measure compression strength, because slight misalignments can create bending stresses, and end loading effects can cause parasitic tensile stresses that cause fracture. Mismatches of the elastic properties of the platens and test specimen can cause tensile stresses or frictional constraints. Buckling can occur if specimens are too long. Because the stresses being applied to a compression specimen are extremely high, the alignment errors may be greater than they would be for an equivalent tensile test specimen. True compression tests may be as difficult to conduct as direct tensile tests. Refined compression strength tests have been developed, as shown in Fig. 29.

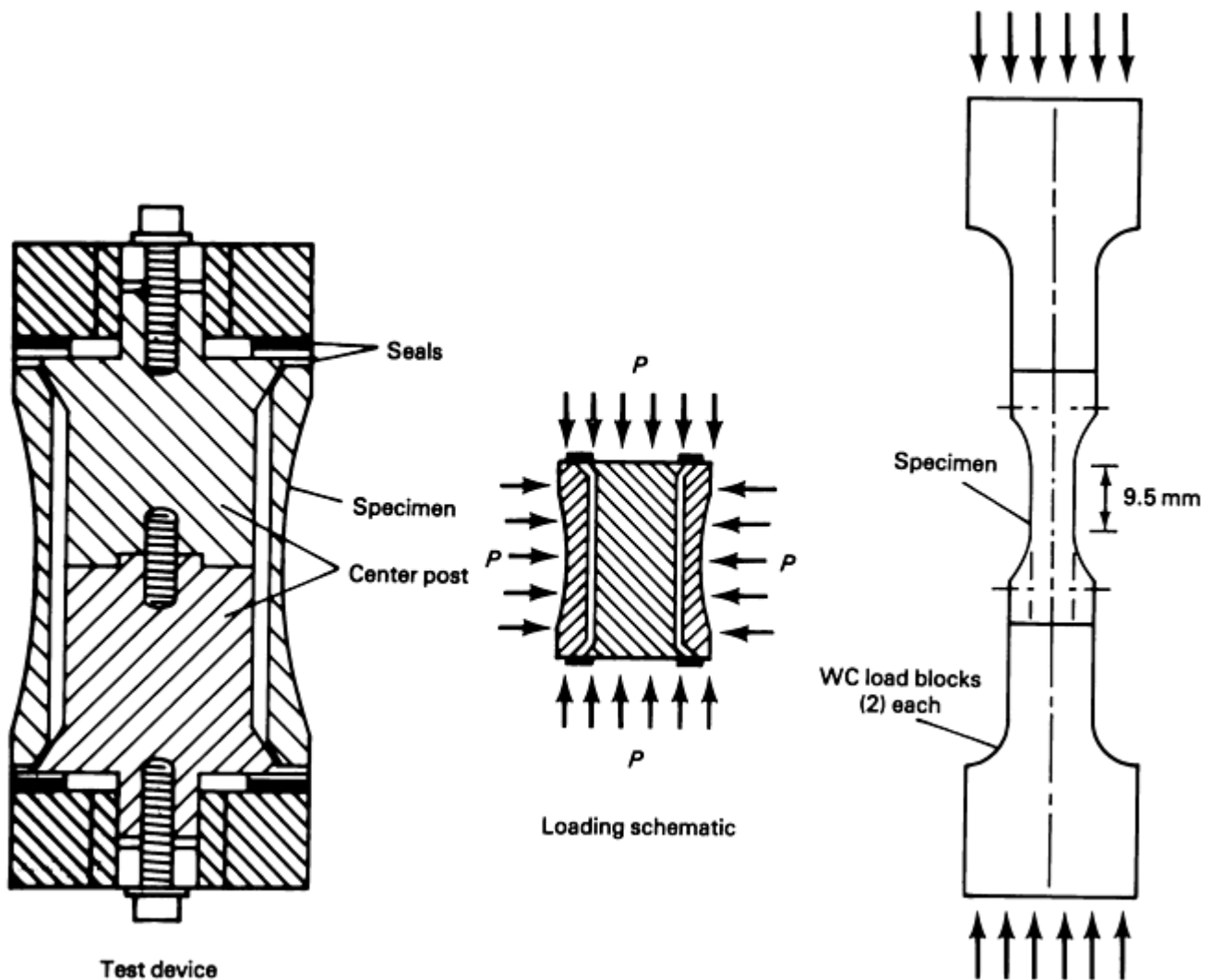


Fig. 29 Compression test specimens. P , applied load. Source: Ref 41 and 45

Fiber-Reinforced Ceramic Composites. Test methods for ceramic-matrix composites are typically quite different than for monolithics, and they borrow heavily from organic-matrix and carbon-carbon test procedures. Uniaxial tensile strength testing is most commonly done in direct tension or flexure loadings. Flexure testing is not preferred, because the failure mechanism can be tensile, compressive, or interlaminar shear, depending on the composite components, the reinforcement architecture, and the loading geometry. Flexure testing is acceptable for measuring the matrix microcracking stress, the shear strength of one-dimensionally reinforced

composites (with the fibers perpendicular to the maximum stress), the effects of exposure or heat treatments, or certain high-temperature properties.

Direct tensile loading is much easier to conduct for composites than for monolithics, because the former are more tolerant of slight misalignments. Flat specimens with glued tabs (to avoid gripping damage) are quite adequate with commercial test machine grips. Ordinary clip extensometers or strain gages are suitable for measuring strain. At high temperatures, glued tabs are not adequate, and specimens with holes or tapered-wedge shoulders are necessary. However, the low shear strength of unidirectionally reinforced composites can make testing of pin-loaded specimens difficult or impossible, because the pins shear through the specimen. It is actually easier to test two-dimensionally fiber-reinforced composites for this reason.

References cited in this section

23. D.F. Carroll, S.M. Wiederhorn, and D.E. Roberts, Technique for Tensile Creep Testing of Ceramics, *J. Am. Ceram. Soc.*, Vol 72 (No. 9), 1989, p 1610–1614
24. T. Soma, M. Matsui, and I. Oda, Tensile Strength of a Sintered Silicon Nitride, *Nonoxide Technical and Engineering Ceramics, Proc. of the International Conf.*, (Limerick, Ireland), S. Hampshire, Ed., 1985, p 361–374
25. T. Ohji, Towards Routine Tensile Testing, *Int. J. High Technol. Ceram.*, Vol 4, 1988, p 211–225
26. G. Grathwohl, Current Testing Methods—A Critical Assessment, *Int. J. High Technol. Ceram.*, Vol 4, 1988, p 123–142
27. K.C. Liu, H. Pih, and D.W. Voorhes, Uniaxial Tensile Strain Measurement for Ceramic Testing at Elevated Temperatures: Requirements, Problems, and Solutions, *Int. J. High Technol. Ceram.*, Vol 4, 1988, p 69–87
28. J. Nilsson and B. Mattsson, A New Tensile Test Method for Ceramic Materials, *Ceramic Materials and Components for Engines*, W. Bunk and H. Hausner, Ed., German Ceramic Society, Berlin, 1986, p 651–656
29. A. Rudnick, C.W. Marschall, W.H. Duckworth, and B.R. Emrich, “The Evaluation and Interpretation of Mechanical Properties of Brittle Materials,” U.S. Air Force Technical Report TR 67-316, Air Force Materials Laboratory, April 1968
30. J.E.O. Ovri and T.J. Davies, Diametral Compression of Silicon Nitride, *Mater. Sci. Eng.*, Vol 96, 1987, p 109–116
31. R. Morrell, Mechanical Properties of Engineering Ceramics: Test Bars versus Components, *Mater. Sci. Eng.*, Vol A109, 1989, p 131–137
32. G.D. Quinn and R. Morrell, Flexure Testing for Design of Engineering Ceramics: A Review, *J. Am. Ceram. Soc.*, Vol 74 (No. 9), 1991, p 2037–2066
33. S. Thrasher, Ceramic Applications in Turbine Engines (CATE) Program Summary, *Proc. of the 21st Contractors Coordination Meeting*, Report P138, Society of Automotive Engineers, March 1984, p 255–267
34. R. Sedlacek and F.A. Halden, Method for Tensile Testing Brittle Materials, *Rev. Sci. Instr.*, Vol 33 (No. 3), 1962, p 298–300
35. R. Jones and D.J. Rowcliffe, Tensile-Strength Distributions for Silicon Nitride and Silicon Carbide Ceramics, *J. Am. Ceram. Soc.*, Vol 58 (No. 9), 1979, p 836–844

36. R. Charles and S. Prochazka, "Stress Rupture Testing of Silicon Carbide at Very High Temperatures," Technical Report 77CRD035, General Electric Co., March 1977
37. T.P. Dabbs, C.J. Fairbanks, and B.R. Lawn, Subthreshold Indentation Flaws in the Study of Fatigue Properties of Ultrahigh-Strength Glass, *Methods for Assessing the Structural Reliability of Brittle Materials*, STP 844, S.W. Freiman and C.M. Hudson, Ed., ASTM, 1984, p 142–153
38. S.R. Choi, J.E. Ritter, and K. Jakus, Failure of Glass with Subthreshold Flaws, *J. Am. Ceram. Soc.*, Vol 72 (No. 2), 1990, p 268–274
39. M. Adams and G. Sines, A Statistical, Micromechanical Theory of the Compressive Strength of Brittle Materials, *J. Am. Ceram. Soc.*, Vol 61 (No. 3–4), 1978, p 126–131
40. M. Adams and G. Sines, Crack Extension from Flaws in a Brittle Material Subjected to Compression, *Technophysics*, Vol 49, 1978, p 97–118
41. C.A. Tracy, A Compression Test for High Strength Ceramics, *J. Test. Eval.*, Vol 15 (No. 1), 1987, p 14–19
42. C.A. Tracy, M. Slavin, and D. Viechnicki, Ceramic Fracture during Ballistic Impact, *Advances in Ceramics*, Vol 22, *Fractography of Glasses and Ceramics*, 1988, p 319–333
43. J. Lankford, Compressive Strength and Microplasticity in Polycrystalline Alumina, *J. Mater. Sci.*, Vol 12, 1977, p 791–796
44. J. Lankford, Uniaxial Compressive Damage in α -SiC at Low Homologous Temperatures, *J. Am. Ceram. Soc.*, Vol 62 (No. 5–6), 1979, p 310–312
45. M. Adams and G. Sines, Methods for Determining the Strength of Brittle Materials in Compressive Stress States, *J. Test. Eval.*, Vol 4 (No. 6), 1976, p 383–396

Mechanical Testing of Polymers and Ceramics

High-Temperature Strength Tests

Fast Fracture. The overwhelming majority of high-temperature strength tests of isotropic ceramics have been done in four-point loading. Standards are being developed that are extensions of the low-temperature procedures. A variety of furnaces and environments can be used, with temperatures typically up to 1600 °C (2910 °F) in air and with some vacuum and inert gas systems at temperatures up to 2000 °C (3630 °F). The test fixtures themselves must be dense ceramics, usually fairly pure forms of silicon carbide, although occasionally alumina fixtures are used at lower temperatures, and graphite fixtures are used in inert atmospheres.

The upsurge in tensile testing has been driven in large part by new programs to use ceramics at high temperatures in heat engines. As a result, most tensile test systems have been designed with high temperatures in mind (Ref 23, 24, 25, 26). The gripping schemes must be not only elaborate enough to avoid stress concentrators and to align very precisely, but also capable of being used in conjunction with furnaces. Most tension systems use cold grips with relatively long (for ceramics) specimens of 150 mm (6 in.). Such systems are commercially available, and extensive testing is underway in the United States, Japan, and Germany.

Multiaxial strength tests are extremely rare at high temperatures and usually based on ring-on-ring loaded disks. The limited results for these experiments suggest that the high-temperature equibiaxial strength is 15 to 30% less than uniaxial strengths (Ref 46, 47).

Creep and Stress Rupture. Direct tension tests of long duration are becoming more common, but most test systems are complicated and expensive. They typically are derivatives of the fast-fracture systems, using cold grips and long specimens (Ref 24, 25, 26, 27). Most experiments are limited to a 1000 h duration. An economical alternative test system with hot grips and a “flat dog bone” specimen configuration has been developed and is optimized for long-duration, low-stress creep experiments (Ref 23). A short tapered specimen for similar experiments has been successfully used (Ref 26).

Strains must be measured with specialized extensometers, because ceramic strains are extremely small and resolutions of 1 μm (0.04 mil) must be recorded over the course of hours. The extensometers in use today are either delicate mechanical units (Ref 26) or lasers that monitor distance between flags (Ref 23) or diffract when passed through a narrow slit between two flags (Ref 27).

Most investigators have at some time resorted to using flexure testing, which is much less expensive and allows strains to be readily measured from the curvature in the specimen. In a sense, the bend specimen acts as a deflection magnifier, because the deflection associated with the integrated curvature is larger and easier to measure than the extension of a tension specimen. The drawback of the method is that a stress gradient in the specimen changes dramatically as the material creeps. Flexural creep testing is not a constant stress test. The strain is measured from the curvature, but this too must be adjusted for the proper constitutive equation.

In recent years, it has become painfully evident that flexural creep data can be misleading or even erroneous, a consequence of the stress gradient, the relaxation of such gradient, and the complicated constitutive equations that apply to ceramics. Analytical attempts to deconvolute the tensile and compressive creep behavior are usually tainted or compromised by the assumptions that have to be made about the constitutive equations. It is far more rational to conduct direct tension or compression experiments for careful creep work. Flexure tests can be used for qualitative assessments of conditions for the onset of creep.

Stress-rupture data require extremely long-duration experiments. Some static-fatigue phenomena occur in the absence of bulk creep deformation, and flexure testing may be eminently suitable in these cases.

References cited in this section

23. D.F. Carroll, S.M. Wiederhorn, and D.E. Roberts, Technique for Tensile Creep Testing of Ceramics, *J. Am. Ceram. Soc.*, Vol 72 (No. 9), 1989, p 1610–1614
24. T. Soma, M. Matsui, and I. Oda, Tensile Strength of a Sintered Silicon Nitride, *Nonoxide Technical and Engineering Ceramics, Proc. of the International Conf.*, (Limerick, Ireland), S. Hampshire, Ed., 1985, p 361–374
25. T. Ohji, Towards Routine Tensile Testing, *Int. J. High Technol. Ceram.*, Vol 4, 1988, p 211–225
26. G. Grathwohl, Current Testing Methods—A Critical Assessment, *Int. J. High Technol. Ceram.*, Vol 4, 1988, p 123–142
27. K.C. Liu, H. Pih, and D.W. Voorhes, Uniaxial Tensile Strain Measurement for Ceramic Testing at Elevated Temperatures: Requirements, Problems, and Solutions, *Int. J. High Technol. Ceram.*, Vol 4, 1988, p 69–87
46. M.N. Giovan and G. Sines, Strength of a Ceramic at High Temperatures under Biaxial and Uniaxial Tension, *J. Am. Ceram. Soc.*, Vol 64 (No. 2), 1981, p 68–73
47. G.D. Quinn and G. Wirth, Multiaxial Strength and Stress Rupture of Hot Pressed Silicon Nitride, *J. Eur. Ceram. Soc.*, Vol 6 (No. 3), 1990, p 169–178

Proof Testing

Ceramic users ultimately must have confidence that components will have a reliable minimum strength or performance level. The object of using nondestructive evaluation methods is to be able to discern defects to permit the culling of unacceptable components, but the state of the art is inadequate at the moment. Proof testing is a viable means of weeding out unacceptable parts in monolithic, brittle ceramics (Ref 48, 49, 50).

Proof testing entails stressing all components to a proof stress, σ_p , in order to cause fracture in the parts that are weaker than σ_p .

There are, however, severe restrictions on the utility of this method. Proof testing is only effective if the test precisely simulates the actual service conditions. Any deviation incurs risk. A further problem occurs if the material is susceptible to slow crack growth during the proof test. For a proof test to be effective in narrowing a strength distribution, it can be shown that the slow-crack-growth exponent n must meet the criterion $(n - 2)/m > 1.0$ (Ref 50). Ideally, n should be high under the conditions of the proof test. In the worst case, if unloading rates are low, it is even possible for some specimens to be weaker than σ_p after the test.

Proof tests are typically done to stress levels commensurate with or somewhat higher than the stresses expected in service. If slow crack growth is anticipated in the service conditions, it may be necessary to apply proof stresses much higher than the service levels. Analytical procedures exist that permit integration of the slow crack growth and statistical analyses, which allow the estimation of minimum lifetimes (Ref 48, 51), usually in the form of strength-probability-time diagrams (Ref 51).

The proof test only culls out specimens with defects at the time of the proof test. If new flaws subsequently develop (e.g., during high-temperature exposure or service loadings), the proof test may be negated.

References cited in this section

48. S.M. Wiederhorn, Reliability, Life Prediction and Proof Testing of Ceramics, *Ceramics for High Performance Applications*, J. Burke, A. Gorum, and R. Katz, Ed., Brook Hill Publishing, 1974, p 635–664
49. D.W. Richerson, *Modern Ceramic Engineering*, Marcel Dekker, 1982
50. J.E. Ritter, Jr., P.B. Oates, E.R. Fuller, and S.M. Wiederhorn, Proof Testing of Ceramics, Part I: Experiment, *J. Mater. Sci.*, Vol 15, 1980, p 2275–2281
51. R.W. Davidge, *Mechanical Behavior of Ceramics*, Cambridge University Press, 1979

Fracture Toughness

Fracture toughness values are used extensively to characterize the fracture resistance of ceramics and other brittle materials. Numerous techniques are available, and the choice of technique is determined by the type of information needed and type of flaws.

Fracture toughness values obtained through different techniques cannot be directly compared. Although much effort has been focused on this subject, it appears that a complementary number of techniques may have to be used to generate K_{Ic} values under different testing conditions.

To successfully standardize test measurements, careful attention and consideration must be given to testing details (both operators and machine), sample preparation, and prehistory in terms of microstructure, thermomechanical processing, and composition.

Both indentation crack length (fracture) and indentation strength methods can be successfully used to measure K_{Ic} only at ambient temperature in ceramic materials where neither significant slow crack growth nor R -curve behavior is observed. Simple sample preparation and small sample size are needed for such techniques.

Double torsion is applicable at high temperatures when enough material is available and under conditions where notch/crack geometry is established to allow for nearly uniform K_I value at the crack front.

Various double-cantilever techniques are advantageous because they use a small amount of material. Analytical solutions are available for accurately computing K_I values from double-cantilever configurations. However, loading fixtures and details are difficult and cumbersome, especially for high-temperature use. In ceramic multilayer electronic capacitors, miniaturization of the double-cantilever beam has proven to be useful.

The Japanese Industrial Standards (JIS) Association committee on the standardization of fine ceramics adopted the use of both indentation crack length/fracture and single-edge precracked beam techniques as standards in JIS R 1607 in 1989. However, these and other techniques still need to resolve the meaning of average resistance to crack growth and the undesirably high cost of machining, sample preparation, and fixturing.

The following sections briefly describe some common methods of fracture toughness testing. More information is also provided in the article "Fracture Resistance Testing of Brittle Solids" in this Volume.

Double Torsion Technique. This type of specimen test is popular and allows the use of a variety of specimen geometries. Basically, the specimen is a thin plate of about 75 mm by 25 mm by 2 mm (3 in. by 1 in. by 0.08 in.). A variety of specimen width-to-length ratios can be used. The specimen sometimes has a side groove, which is usually cut along its length to guide the crack. Best results are obtained without a groove, provided that there is good alignment. The specimen is best loaded and supported by ball bearings. It can be studied in terms of crack-growth behavior as well as fast fracture toughness measurements.

The double torsion technique requires a large amount (volume) of material, which may not always be available. The technique also suffers from the fact that the crack front is curved, which means that it is not under a uniform stress intensity. However, the technique is useful at high temperatures and severe environments and requires no particular fixtures (simple loading conditions).

A rigid machine is essential to conduct either precracking work or experiments where crack velocity is related to specimen compliance (during constant deflection or deflection rate trials). Some strain energy is stored in the test machine because of its finite compliance.

Indentation Fracture. Interest in this technique stems from its simplicity and the small volume of material required to conduct K_{Ic} measurements. A Vickers indentation is implanted onto a flat ceramic surface, and cracks develop around the indentation in inverse proportion to the toughness of the material. By measuring crack lengths, it is possible to estimate K_{Ic} . The crack morphology formed during the elastic-plastic contact between a sharp indenter and a brittle medium consists of both median and lateral vent cracks. It must be noted that under small indentation loads, only small, shallow cracks form. The median vent cracks are used for fracture toughness computations.

Crack dependence on sample preparation is well known for shallow cracks. The preparation of the sample surface, using effective polishing to achieve a stress state representative of the bulk, is recommended in order to achieve maximum crack length. Annealing also can be used. Ratios of crack length to indent radius of about 23 or more are recommended in order to achieve consistent results. In addition, the crack length must be measured immediately after the indentation to minimize possible post-indentation slow crack growth, especially in glasses, glass-ceramics, and ceramics that have a glassy grain boundary.

Chevron Notch Method. This method is gaining popularity because it uses a relatively small amount of material. The fracture toughness calculations are dependent on the maximum load and on both specimen and loading geometries. No material constants are needed for the calculations. The technique is also suitable for high-temperature testing, because flaw healing is not a concern. However, it requires a complex specimen shape that has an extra machining cost. A sawed notch is induced in a test bar that is usually 3 mm by 4 mm by 50 mm (0.12 in. by 0.16 in. by 2 in.). The notch angle varies from 30 to 50°. On subsequent testing of the specimen, a crack will develop at the chevron tip and extend stably as the load is increased, and later there is catastrophic fracture.

Double-Cantilever Beam Method. In this method, one of three different loading configurations can be applied (wedge load, applied load, or applied moment). A tapered double-cantilever double beam has also been suggested. Fracture toughness is derived from the notch length, specimen dimensions, and normal tensile load. This technique has a number of advantages over other fracture toughness tests. Stress intensity is independent of the crack length, in the case of the constant applied moment loading, and sample preparation and the testing procedure are both relatively simple. The specimen must be precracked (sharp cracks emanating from a blunt notch) to ensure that failure initiates from a sharp flaw of the correct geometry. Most of the time, a number of very small cracks emanate from a blunt notch with a tip radius of about 15 nm (0.6 $\mu\text{in.}$) or more. This usually results in crack growth away from the notch tip (uncontrolled geometry) and produces anomalously higher fracture toughness values than those obtained from specimens that have sharp cracks with the appropriate geometry.

Single-Edge Notched Beam. This method has been commonly used because of its simplicity (Fig. 30). The sharp crack requirement is replaced by a narrow notch, which is easier to introduce and can be measured more accurately. Fracture-toughness measurements are usually conducted using four-point bending apparatus. Unfortunately, it has been reported that the results of this test are very sensitive to the notch width and depth, and either a precracked single-edge notched beam or a single-edge precracked beam is preferred.

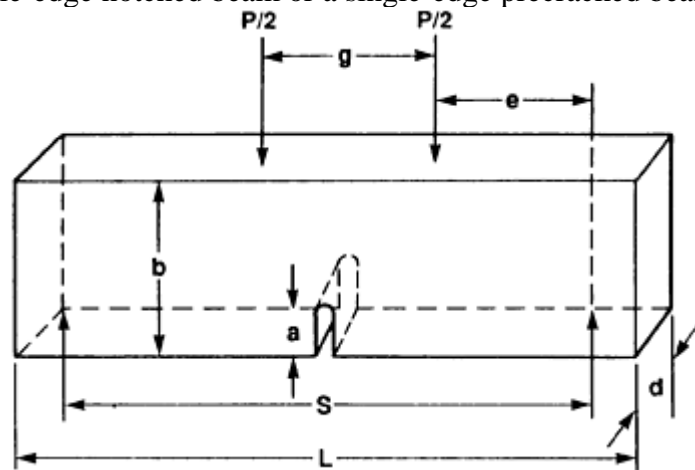


Fig. 30 Single-edge notched beam specimen

Single-Edge Precracked Beam. The main feature of the method is the loading fixture for precracking (Fig. 31), in which a beam-shaped specimen (flexure bend bar was also suggested) is compressively loaded against a centrally located groove in an anvil (Fig. 32). This generates a local tensile field of a Vickers indentation (or a straight notch), which is placed in the center of the tensile surface of the specimen. Then, on gradual loading, pop-in sound is detected, and a median crack is induced from the indent, extending both inward and sideways. Eventually, the crack front is arrested as a straight line through the thickness of the specimen.

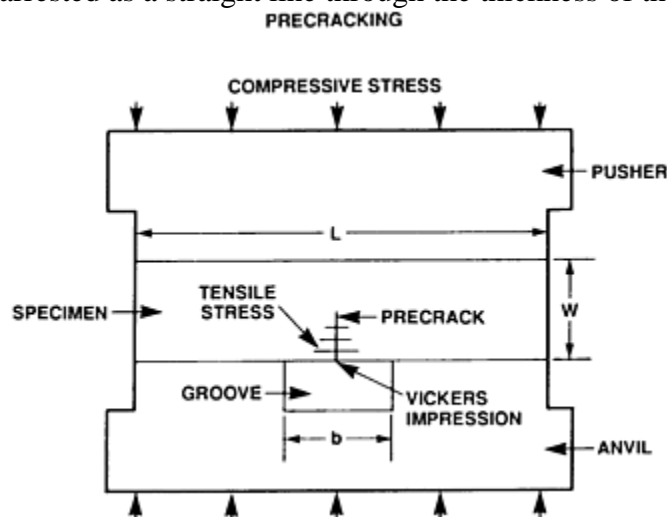


Fig. 31 Loading fixture for precracking of the single-edge precracked beam specimen

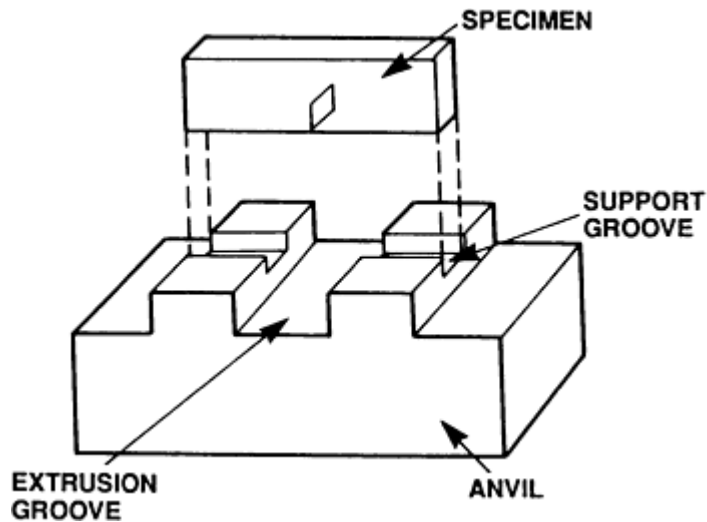


Fig. 32 Loading anvil technique for generating a precrack in the single-edge precracked beam method

This technique is a refinement of the single-edge notched beam technique for introducing a precrack. It is necessary to carefully prepare (grind/polish) the beam surfaces and edges 0.08 μm (3 mils) or better to help eliminate undesirable crack starters. Careful parallelism and squareness of sample surfaces is essential for the success of precracking. The specimen is then loaded to failure in bend fixtures in the same fashion as a single-edge notched beam.

Compression Precracking. Suresh et al. (Ref 52) developed this procedure for measuring fracture toughness in either bending or tension after precracking notched specimens in uniaxial cyclic compression to produce a controlled and through-thickness fatigue flaw. After precracking, the specimen can be loaded in flexure in the single-edge notched beam configuration.

Reference cited in this section

52. S. Suresh, L. Ewart, M. Maden, W.S. Slaughter, and M. Nguyen, Fracture Toughness Measurements in Ceramics: Precracking in Cyclic Compression, *J. Mater. Sci.*, Vol 22, 1987, p 1271

Mechanical Testing of Polymers and Ceramics

Hardness Testing

Hardness is defined in the conventional sense as a means of specifying the resistance of a material to deformation, scratching, and erosion. It is an important property for engineering applications that require good tribological resistance, such as seals, slurry pumps, rollers, and guides. Hardness tests are based on indenting the sample with a hard indenter, which may be spherical, conical, or pyramidal. There is a lack of experimental evidence to support the use of hardness for ceramics evaluation, because a combination of plastic flow, fragmentation, and cross-cracking leads to considerable scatter between indentations and to differences between observers.

Common techniques for measuring hardness in ceramics are Vickers (HV), Knoop (HK), and Rockwell superficial (HR). More detailed information is given in the article "Indentation Hardness Testing of Ceramics" in this Volume. The following guidelines should also be considered when conducting hardness measurements:

- Hardness tests can be used for engineering ceramics if it is recognized that errors (as high as 15%) and biases lead to high levels of uncertainty and increase with increasing hardness level.

- The indentation must be larger than the microstructural features. An adequate number of indentations must be used, preferably ten or more of good geometry.
- Badly damaged indentations must be ignored. Cracking from corners has to be accepted, but the impression of the corners must be undamaged.
- The machine-observer combination must have a means of calibration, preferably a high hardness test block.
- The geometry of the diamond indenter must be checked at intervals, especially in high-load tests.
- Hardness can vary with indentation load for small loads. Indentation loads greater than or equal to 9.8 N (2.2 lbf) are recommended for Knoop and Vickers indentations.

Mechanical Testing of Polymers and Ceramics

Acknowledgments

The information in this article is largely taken from:

- K.E. Amin, Toughness, Hardness, and Wear, *Ceramics and Glasses*, Vol 4, *Engineered Materials Handbook*, ASM International, 1991, p 599–609
- R.J. Del Vecchio, Tensile Testing of Elastomers, *Tensile Testing*, P. Han, Ed., ASM International, 1992, p 135–146
- J.-C. Huang, Mechanical Properties, *Engineering Plastics*, Vol 2, *Engineered Materials Handbook*, ASM International, 1988, p 433–438
- J.A. Nairn and R.J. Farris, Important Properties Divergences, *Engineering Plastics*, Vol 2, *Engineered Materials Handbook*, ASM International, 1988, p 655–658
- R. Nimmer, Impact Loading, *Engineering Plastics*, Vol 2, *Engineered Materials Handbook*, ASM International, 1988, p 679–700
- G.D. Quinn, Strength and Proof Testing, *Ceramics and Glasses*, Vol 4, *Engineered Materials Handbook*, ASM International, 1991, p 599–609
- R.B. Seymour, *Polymers for Engineering Applications*, ASM International, 1987, p 17–31, 151–157
- R.B. Seymour, Overview of Polymer Chemistry, *Engineering Plastics*, Vol 2, *Engineered Materials Handbook*, ASM International, 1988, p 63–67
- J.L. Throne and R.C. Progelhof, Creep and Stress Relaxation, *Engineering Plastics*, Vol 2, *Engineered Materials Handbook*, ASM International, 1988, p 659–678

Mechanical Testing of Polymers and Ceramics

References

1. R. Seymour, Overview of Polymer Chemistry, *Engineering Plastics*, Vol 2, *Engineered Materials Handbook*, ASM International, 1988, p 64
2. A. Kumar and R. Gupta, *Fundamentals of Polymers*, McGraw-Hill, 1998, p 30, 337, 383
3. L.E. Nielson, *Mechanical Properties of Polymers*, Van Nostrand Reinhold, 1962
4. F.N. Kelly and F. Bueche, *J. Polym. Sci.*, Vol 50, 1961, p 549

5. V. Shah, *Handbook of Plastics Testing Technology*, 2nd ed., John Wiley & Sons, 1998
6. *ISO/IEC Selected Standards for Testing Plastics*, 2nd ed., ASTM, 1999
7. J. Nairn and R. Farris, Important Properties Divergences, *Engineering Plastics*, Vol 2, *Engineered Materials Handbook*, ASM International, 1988, p 655–658
8. T. Osswald, *Polymer Processing Fundamentals*, Hanser/Gardner Publications Inc., 1998, p 19–43
9. K.M. Ralls, T.H. Courtney, and J. Wulff, *Introduction to Materials Science and Engineering*, John Wiley & Sons, 1976
10. S. Turner, Mechanical Testing, *Engineering Plastics*, Vol 2, *Engineered Materials Handbook*, ASM International, 1988, p 547
11. R.B. Seymour, *Polymers for Engineering Applications*, ASM International, 1987, p 155
12. V. Shah, *Handbook of Plastics Testing Technology*, 2nd ed., John Wiley & Sons, 1998
13. Recognized Components Directories, Underwriters Laboratories
14. R.D. Deanin, *Polymer Structure, Properties and Applications*, Cahners, 1982
15. R.P. Nimmer, Analysis of the Puncture of a Polycarbonate Disc, *Polym. Eng. Sci.*, Vol 23, 1983, p 155
16. R.P. Nimmer, An Analytical Study of Tensile and Puncture Test Behavior as a Function of Large-Strain Properties, *Polym. Eng. Sci.*, Vol 27, 1987, p 263
17. L.M. Carapelucci, A.F. Yee, and R.P. Nimmer, Some Problems Associated with the Puncture Testing of Plastics, *J. Polym. Eng.*, June 1987
18. J.G. Williams, *Fracture Mechanics of Polymers*, Ellis Horwood, 1984
19. D.D. Huang and J.G. Williams, *J. Mater. Sci.*, Vol 22, 1987, p 2503
20. M.K.V. Chan and J.G. Williams, *Int. J. Fract.*, Vol 19, 1983, p 145
21. Y.W. Mai and B. Cotterell, *Int. J. Fract.*, Vol 32, 1986, p 105
22. C.R. Brinkman and G.D. Quinn, Standardization of Mechanical Properties Tests for Advanced Ceramics, *Mechanical Testing Methodology for Ceramic Design and Reliability*, Marcel Dekker, 1998, p 353–386
23. D.F. Carroll, S.M. Wiederhorn, and D.E. Roberts, Technique for Tensile Creep Testing of Ceramics, *J. Am. Ceram. Soc.*, Vol 72 (No. 9), 1989, p 1610–1614
24. T. Soma, M. Matsui, and I. Oda, Tensile Strength of a Sintered Silicon Nitride, *Nonoxide Technical and Engineering Ceramics, Proc. of the International Conf.*, (Limerick, Ireland), S. Hampshire, Ed., 1985, p 361–374
25. T. Ohji, Towards Routine Tensile Testing, *Int. J. High Technol. Ceram.*, Vol 4, 1988, p 211–225
26. G. Grathwohl, Current Testing Methods—A Critical Assessment, *Int. J. High Technol. Ceram.*, Vol 4, 1988, p 123–142

27. K.C. Liu, H. Pih, and D.W. Voorhes, Uniaxial Tensile Strain Measurement for Ceramic Testing at Elevated Temperatures: Requirements, Problems, and Solutions, *Int. J. High Technol. Ceram.*, Vol 4, 1988, p 69–87
28. J. Nilsson and B. Mattsson, A New Tensile Test Method for Ceramic Materials, *Ceramic Materials and Components for Engines*, W. Bunk and H. Hausner, Ed., German Ceramic Society, Berlin, 1986, p 651–656
29. A. Rudnick, C.W. Marschall, W.H. Duckworth, and B.R. Emrich, “The Evaluation and Interpretation of Mechanical Properties of Brittle Materials,” U.S. Air Force Technical Report TR 67-316, Air Force Materials Laboratory, April 1968
30. J.E.O. Ovari and T.J. Davies, Diametral Compression of Silicon Nitride, *Mater. Sci. Eng.*, Vol 96, 1987, p 109–116
31. R. Morrell, Mechanical Properties of Engineering Ceramics: Test Bars versus Components, *Mater. Sci. Eng.*, Vol A109, 1989, p 131–137
32. G.D. Quinn and R. Morrell, Flexure Testing for Design of Engineering Ceramics: A Review, *J. Am. Ceram. Soc.*, Vol 74 (No. 9), 1991, p 2037–2066
33. S. Thrasher, Ceramic Applications in Turbine Engines (CATE) Program Summary, *Proc. of the 21st Contractors Coordination Meeting*, Report P138, Society of Automotive Engineers, March 1984, p 255–267
34. R. Sedlacek and F.A. Halden, Method for Tensile Testing Brittle Materials, *Rev. Sci. Instr.*, Vol 33 (No. 3), 1962, p 298–300
35. R. Jones and D.J. Rowcliffe, Tensile-Strength Distributions for Silicon Nitride and Silicon Carbide Ceramics, *J. Am. Ceram. Soc.*, Vol 58 (No. 9), 1979, p 836–844
36. R. Charles and S. Prochazka, “Stress Rupture Testing of Silicon Carbide at Very High Temperatures,” Technical Report 77CRD035, General Electric Co., March 1977
37. T.P. Dabbs, C.J. Fairbanks, and B.R. Lawn, Subthreshold Indentation Flaws in the Study of Fatigue Properties of Ultrahigh-Strength Glass, *Methods for Assessing the Structural Reliability of Brittle Materials*, STP 844, S.W. Freiman and C.M. Hudson, Ed., ASTM, 1984, p 142–153
38. S.R. Choi, J.E. Ritter, and K. Jakus, Failure of Glass with Subthreshold Flaws, *J. Am. Ceram. Soc.*, Vol 72 (No. 2), 1990, p 268–274
39. M. Adams and G. Sines, A Statistical, Micromechanical Theory of the Compressive Strength of Brittle Materials, *J. Am. Ceram. Soc.*, Vol 61 (No. 3–4), 1978, p 126–131
40. M. Adams and G. Sines, Crack Extension from Flaws in a Brittle Material Subjected to Compression, *Technophysics*, Vol 49, 1978, p 97–118
41. C.A. Tracy, A Compression Test for High Strength Ceramics, *J. Test. Eval.*, Vol 15 (No. 1), 1987, p 14–19
42. C.A. Tracy, M. Slavin, and D. Viechnicki, Ceramic Fracture during Ballistic Impact, *Advances in Ceramics*, Vol 22, *Fractography of Glasses and Ceramics*, 1988, p 319–333

43. J. Lankford, Compressive Strength and Microplasticity in Polycrystalline Alumina, *J. Mater. Sci.*, Vol 12, 1977, p 791–796
44. J. Lankford, Uniaxial Compressive Damage in α -SiC at Low Homologous Temperatures, *J. Am. Ceram. Soc.*, Vol 62 (No. 5–6), 1979, p 310–312
45. M. Adams and G. Sines, Methods for Determining the Strength of Brittle Materials in Compressive Stress States, *J. Test. Eval.*, Vol 4 (No. 6), 1976, p 383–396
46. M.N. Giovan and G. Sines, Strength of a Ceramic at High Temperatures under Biaxial and Uniaxial Tension, *J. Am. Ceram. Soc.*, Vol 64 (No. 2), 1981, p 68–73
47. G.D. Quinn and G. Wirth, Multiaxial Strength and Stress Rupture of Hot Pressed Silicon Nitride, *J. Eur. Ceram. Soc.*, Vol 6 (No. 3), 1990, p 169–178
48. S.M. Wiederhorn, Reliability, Life Prediction and Proof Testing of Ceramics, *Ceramics for High Performance Applications*, J. Burke, A. Gorum, and R. Katz, Ed., Brook Hill Publishing, 1974, p 635–664
49. D.W. Richerson, *Modern Ceramic Engineering*, Marcel Dekker, 1982
50. J.E. Ritter, Jr., P.B. Oates, E.R. Fuller, and S.M. Wiederhorn, Proof Testing of Ceramics, Part I: Experiment, *J. Mater. Sci.*, Vol 15, 1980, p 2275–2281
51. R.W. Davidge, *Mechanical Behavior of Ceramics*, Cambridge University Press, 1979
52. S. Suresh, L. Ewart, M. Maden, W.S. Slaughter, and M. Nguyen, Fracture Toughness Measurements in Ceramics: Precracking in Cyclic Compression, *J. Mater. Sci.*, Vol 22, 1987, p 1271

Overview of Mechanical Properties and Testing for Design

Howard A. Kuhn, Concurrent Technologies Corporation

Introduction

DESIGN is the ultimate function of engineering in the development of products and processes, and an integral aspect of design is the use of mechanical properties derived from mechanical testing. The basic objective of product design is to specify the materials and geometric details of a part, component, and assembly so that a system meets its performance requirements. For example, minimum performance of a mechanical system involves transmission of the required loads without failure for the prescribed product lifetime under anticipated environmental (thermal, chemical, electromagnetic, radiation, etc.) conditions. Optimum performance requirements may also include additional criteria such as minimum weight, minimum life cycle cost, environmental responsibility, human factors, and product safety and reliability.

This article introduces the basic concepts of mechanical design and its general relation with the properties derived from mechanical testing. Product design and the selection of materials are key applications of mechanical property data derived from testing. Although existing and feasible product shapes are of infinite variety and these shapes may be subjected to an endless array of complex load configurations, a few basic stress conditions describe the essential mechanical behavior features of each segment or component of the product. These stress conditions include the following:

- Axial tension or compression
- Bending, shear, and torsion
- Internal or external pressure
- Stress concentrations and localized contact loads

Mechanical testing under these basic stress conditions using the expected product load/time profile (static, impact, cyclic) and within the expected product environment (thermal, chemical, electromagnetic, radiation, etc.) provides the design data required for most applications.

In conducting mechanical tests, it is also very important to recognize that the material may contain flaws and that its microstructure (and properties) may be directional (as in composites) and heterogeneous or dependent on location (as in carburized steel). To provide accurate material characteristics for design, one must take care to ensure that the geometric relationships between the microstructure and the stresses in the test specimens are the same as those in the product to be designed.

It is also important to consider the complexity of materials selection for a combination of properties such as strength, toughness, weight, cost, and so on. This article briefly describes design criteria for some basic property combinations such as strength, weight, and costs. More detailed information on various performance indices in design, based on the methodology of Ashby, can be found in the article “Material Property Charts” in *Materials Selection and Design*, Volume 20 of *ASM Handbook*. The materials selection method developed by Ashby is also available as an interactive electronic product (Ref 1).

Reference cited in this section

1. Cambridge Engineering Selector, Granta Design Ltd., Cambridge, UK, 1998

Overview of Mechanical Properties and Testing for Design

Howard A. Kuhn, Concurrent Technologies Corporation

Product Design

Design involves the application of physical principles and experience-based knowledge to develop a predictive model of the product. The model may be a prototype, a simplified mathematical model, or a complex finite element model. Regardless of the level of sophistication of the model, reaching the product design objectives of material and geometry specifications for successful product performance requires accurate material parameters (Ref 2).

Modern design methods help manage the complex interactions between product geometry, material microstructure, loading, and environment. In particular, engineering mechanics (from simple equilibrium equations to complex finite element methods) extrapolates the results of basic mechanical testing of simple shapes under representative environments to predict the behavior of actual product geometries under real service environments.

In the following sections, a simple tie bar is used to illustrate the application of mechanical property data to material selection and design and to highlight the general implications for mechanical testing. Material subjected to the basic stress conditions is considered in order to establish design approaches and mechanical test methods, first in static loading and then in dynamic loading and aggressive environments. More detailed reference books on mechanical design and engineering methods are also listed in the “Selected References” at the end of this article.

Reference cited in this section

2. G.E. Dieter, *Engineering Design: A Materials and Processing Approach*, McGraw Hill, 1991, p 1–51, p 231–271

Tensile Loading

Design for Strength in Tension. Figure 1 shows an axial tensile load applied to a tie bar representing, for example, a boom crane support, cable, or bolt. For this elementary case, the stress in the bar is uniformly distributed over the cross section of the tie bar and is given by:

$$\sigma = F/A \quad (\text{Eq 1})$$

where F is the applied force and A is the cross-sectional area of the bar. To avoid failure of the bar, this stress must be less than the failure stress, or strength, of the material:

$$\sigma = F/A < \sigma_f \quad (\text{Eq 2})$$

where σ_f is the stress at failure. The failure stress, σ_f , can be the yield strength, σ_o , if permanent deformation is the criterion for failure, or the ultimate tensile strength, σ_u , if fracture is the criterion for failure. In a ductile metal or polymer, the ultimate tensile strength is defined as the stress at which necking begins, leading to fracture. In a brittle material, the ultimate strength is simply the stress at fracture. Typical values of yield and ultimate tensile strength for various materials are summarized in Tables 1, 2, and 3. These typical values are intended only for general comparisons; design values should be based on statistically based minimum values or on minimum values published in the purchase specifications of materials (such as ASTM standards).

Table 1 Typical room-temperature mechanical properties of ferrous alloys and superalloys

Material	Strength in tension, MPa (ksi)		0.2% offset compressive yield strength, MPa (ksi)	Strength in torsional shear, MPa (ksi)		Modulus of elasticity, GPa (10 ⁶ psi)		Elongation in 50 mm (2 in.), %	Hardness, HB
	0.2% offset yield strength	Ultimate		0.2% offset yield strength	Ultimate	Tension	Shear		
Cast irons									
Gray cast iron	...	140 (20)	240 (35)	...	255 (37)	105 (15)	40 (6)	1	130
White cast iron	...	415 (60)	690 (100)	...	415 (60)	140 (20)	55 (8)	...	400
Nickel cast iron, 1.5% nickel	...	310 (45)	415 (60)	140 (20)	55 (8)	1	200
Malleable iron	230 (33)	345 (50)	230 (33)	130 (19)	330 (48)	170 (25)	70 (10)	14	120
Ingot iron, annealed 0.02% carbon	165 (24)	290 (42)	145 (21)	105 (15)	205 (30)	205 (30)	85 (12)	45	70
Wrought iron, 0.10% carbon	205 (30)	345 (50)	205 (30)	125 (18)	240 (35)	185 (27)	70 (10)	30	100
Steels									
Wrought iron, 0.10% carbon	205 (30)	345 (50)	205 (30)	125 (18)	240 (35)	185 (27)	70(10)	30	100
Steel, 0.20% carbon Hot-rolled	275 (40)	415 (60)	275 (40)	165 (24)	310 (45)	200 (29)	85 (12)	35	120
Cold-rolled	415 (60)	550 (80)	415 (60)	250 (36)	415 (60)	200 (29)	85 (12)	15	160
Annealed castings	240 (35)	415 (60)	240 (35)	145 (21)	310 (45)	200 (29)	85 (12)	25	130
Steel, 0.40% carbon Hot-rolled	290 (42)	485 (70)	290 (42)	170 (25)	380 (55)	200 (29)	85 (12)	25	135
Heat-treated for fine grain	415 (60)	620 (90)	415 (60)	250 (36)	515 (75)	200 (29)	85 (12)	25	190
Annealed castings	240 (35)	450 (65)	240 (35)	145 (21)	380 (55)	200 (29)	85 (12)	15	130
Steel, 0.60% carbon Hot-rolled	435 (63)	690 (100)	435 (63)	255 (37)	550 (79.8)	200 (29)	85 (12)	15	200
Heat-treated for fine grain	540 (78)	825 (120)	540 (78)	325 (47)	690 (100)	200 (29)	85 (12)	15	235
Steel, 0.80% carbon Hot-rolled	505 (73)	825 (120)	505 (73)	305 (44)	725 (103)	200 (29)	85(12)	10	240
Oil-quenched, not drawn	860 (125)	1240 (180)	860 (125)	515 (75)	1035 (150)	200 (29)	85 (12)	2	360
Steel, 1.00% carbon Hot-rolled	570 (83)	930 (135)	570 (83)	345 (50)	795 (115)	200 (29)	85 (12)	10	260
Oil-quenched, not drawn	965 (140)	1515	965 (140)	580 (84)	1275	200 (29)	85 (12)	1	430

		(220)			(185)				
Nickel steel, 3.5% nickel, 0.40% carbon, max. hardness for machinability	1035 (150)	1170 (170)	1035 (150)	620 (90)	965 (140)	200 (29)	85 (12)	12	350
Silicomanganese steel, 1.95% Si, 0.70% Mn, spring tempered	895 (130)	1200 (174)	895 (130)	540 (78)	795 (115)	200 (29)	85 (12)	1	380
Superalloys (wrought)									
A286 (bar)	760 (110)	1080 (157)	180 (26)	...	28	...
Inconel 600 (bar)	250 (36)	620 (90)	47	...
IN-100 (60 Ni-10Cr-15Co, 3Mo, 5.5Al, 4.7Ti)	850 (123)	1010 (147)	215 (31)	...	9	...
IN-738	915 (133)	1100 (159)	200 (29)	...	5	...

Source: Ref 3, 4

Table 2 Typical room-temperature mechanical properties of nonferrous alloys

Metal or alloy	Approximate composition, %	Condition	0.2% offset tensile yield strength, MPa (ksi)	Tensile strength, MPa (ksi)	Tensile modulus of elasticity, GPa (10 ⁶ psi)	Elongation in 50 mm (2 in.), %	Ultimate shear strength, MPa (ksi)	Hardness
Heavy nonferrous alloys (~8–9 g/cm ³)								
Copper	Cu	Annealed	33 (4.8)	209 (30)	125 (18)	60
		Cold drawn	333 (48)	344 (50)	112 (16)	14	...	337 HRB
Free-cutting brass	61.5 Cu, 35.5 Zn, 3 Pb	Annealed	125 (18)	340 (49)	85 (12)	53	205 (30)	68 HRF
		Quarter hard, 15% reduction	310 (45)	385 (56)	85 (12)	20	230 (33)	62 HRB
		Half hard, 25% reduction	360 (52)	470 (68)	95 (14)	18	260 (38)	80 HRB
High-leaded brass (1 mm thick)	65 Cu, 33 Zn, 2 Pb	Annealed, 0.050 mm grain	105 (15)	325 (47)	85 (12)	55	230 (33)	66 HRF
		Extra hard	425 (62)	585 (85)	105 (15)	5	310 (45)	87 HRB
Red brass (1 mm thick)	85 Cu, 15 Zn	Annealed, 0.070 mm grain	70 (10)	270 (39)	85 (12)	48	215 (31)	66 HRF
		Extra hard	420 (61)	540 (78)	105 (15)	4	305 (44)	83 HRB
Aluminum bronze	89 Cu, 8 Al, 3 Fe	Sand cast	195 (28)	515 (75)	...	40
		Extruded	260 (38)	565 (82)	125 (18)	25
Beryllium copper	97.9 Cu, 1.9 Be, 0.2 Ni	A (solution annealed)	...	500 (73)	125 (18)	35	...	60 HRB
		HT (hardened)	1035 (150)	1380 (200)	125 (18)	2	...	42 HRC
Manganese bronze (A)	58.5 Cu, 39 Zn, 1.4 Fe, 1 Sn, 0.1 Mn	Soft annealed	205 (30)	450 (65)	90 (13)	35	290 (42)	65 HRB
		Hard, 15% reduction	415 (60)	565 (82)	105 (15)	25	325 (47)	90 HRB
Phosphor bronze, 5% (A)	95 Cu, 5 Sn	Annealed, 0.035 mm grain	150 (22)	340 (49)	90 (13)	57	...	33 HRB
		Extra hard, 0.015 mm grain	635 (92)	650 (94)	115 (17)	5	...	94 HRB
Cupronickel, 30%	70 Cu, 30 Ni	Annealed at 760 °C	140 (20)	380 (55)	150 (22)	45	...	37 HRB
		Cold drawn, 50% reduction	540 (78)	585 (85)	150 (22)	15	...	81 HRB
Light nonferrous alloys (~2.7 g/cm ³ for Al alloys; ~1.8 g/cm ³ for Mg alloys)								

Aluminum	Al	Sand cast, 1100-F	40 (5.8 or 6)	75 (11)	60 (9)	22
		Annealed sheet, 1100-O	35 (5.075)	90 (13)	70 (10)	35
		Hard sheet, 1100-H18	145 (21)	165 (24)	70 (10)	5
Aluminum alloy 2024	93 Al, 4.5 Cu, 1.5 Mg, 0.6 Mn	Temper O	75 (11)	185 (27)	73 (11)	20	125 (18)	90 HRH
		Temper T36	395 (57)	495 (72)	73 (11)	13	290 (42)	80 HRB
Aluminum alloy 2014	93 Al, 4.4 Cu, 0.8 Si, 0.8 Mn, 0.4 Mg	Temper O	95 (14)	185 (27)	73 (11)	18	125 (18)	192 HRH
		Temper T6	415 (60)	485 (70)	73 (11)	13	290 (42)	83 HRB
Aluminum alloy 5052	97 Al, 2.5 Mg, 0.25 Cr	Temper O	90 (13)	195 (28)	69 (10)	30	125 (18)	82 HRH
		Temper H38	255 (37)	290 (42)	69 (10)	8	164 (24)	85 HRE
Aluminum alloy 5456	94 Al, 5.0 Mg, 0.7 Mn, 0.15 Cu, 0.15 Cr	Temper O	160 (23)	310 (45)	...	24	195 (28)	...
		Temper H321	255 (37)	350 (51)	...	16	205 (30)	...
Aluminum alloy 7075	90 Al, 5.5 Zn, 1.5 Cu, 2.5 Mg, 0.3 Cr	Temper O	105 (15)	230 (33)	...	17	150 (22)	65 HRE
		Temper T6	505 (73)	570 (83)	...	11	330 (48)	90 HRB
Magnesium	Mg	Cast	21 (3)	90 (13)	40 (6)	2–6	...	16 HRE
		Extruded	69–105 (10–15)	195 (28)	40 (6)	5–8	...	26 HRE
		Rolled	115–140 (17–20)	200 (29)	40 (6)	2–10	...	51 HRE
Magnesium alloy AM100A	90 Mg, 10 Al, 0.1 Mn	Cast, condition F	85 (12)	150 (22)	45 (7)	2	125 (18)	64 HRE
		Cast, condition T61	150 (22)	275 (40)	45 (7)	1	145 (21)	80 HRE
Magnesium alloy AZ63A	91 Mg, 6 Al, 3 Zn, 0.2 Mn	Cast, condition F	95 (14)	200 (29)	45 (7)	6	125 (18)	59 HRE
		Cast, condition T6	130 (19)	275 (40)	45 (7)	5	140 (20)	83 HRE
Titanium alloys (~4.5 g/cm ³)								
Commercial ASTM grade 2 Ti	98 Ti	...	275 (40)	345 (50)	103 (15)	20	...	80 HRB
Ti-5Al-2.5Sn	92 Ti, 5 Al, 2.5 Sn	...	825 (120)	860 (125)	110 (16)	8–10	...	36 HRC
Ti-3Al-2.5V	94 Ti, 3 Al, 2.5 V	Annealed	560 (81)	655 (95)	103 (15)	29	...	15–25 HRC
		Cold worked and stress relieved	760 (110)	895 (130)	103 (15)	19	...	24–27 HRC
Ti-6Al-4V	90 Ti, 6 Al, 4 V	Solution treated and aged bar (1–2 in.)	965 (140)	1035 (150)	110 (16)	8	620 (90)	36–39 HRC
		Annealed bar	825 (120)	895 (130)	110 (16)	10
		Mill annealed	...	925 (134)	545 (79)	...

Table 3 Typical room-temperature mechanical properties of plastics

Material	Tensile strength, MPa (ksi)	Elongation, %	Modulus of elasticity GPa (10 ⁶ psi)	Compressive strength, MPa (ksi)	Modulus of rupture, MPa (ksi)	Hardness
Thermosets						
EP, reinforced with glass cloth	350 (51)	...	175 (25)	410 (59)	485 (70)	
MF, alpha-cellulose filler	50–90 (7–13)	0.6–0.9	9 (1)	170–300 (25–44)	70–110 (10–16)	110–125 HRM
PF, no filler	50–55 (7–9)	1.0–1.5	5–7 (0.7–1)	70–200 (10–29)	80–100 (12–15)	124–128 HRM
PF, wood flour filler	45–60 (7–9)	0.4–0.8	6–8 (0.87–1.16)	160–250 (23–36)	60–85 (9–12)	100–120 HRM
PF, macerated fabric filler	25–65 (4–9)	0.4–0.6	6–9 (0.87–1)	100–160 (15–24)	60–100 (9–15)	95–120 HRM
PF, cast, no filler	40–65 (6–9)	1.5–2.0	3 (0.43)	85–115 (12–17)	75–115 (11–17)	93–120 HRM
Polyester, glass-fiber filler	35–65 (5–9)	...	11–14 (1.6–2.0)	140–175 (20–25)	95–115 (14–17)	...
UF, alpha-cellulose filler	55–90 (8–13)	0.5–1.0	10 (1.5)	175–240 (25–35)	70–100 (10–15)	115–120 HRM
Thermoplastics						
ABS	35–45 (5–7)	15–60	1.7–2.2 (0.25–0.32)	25–50 (4–7)	...	95–105 HRR
CA	15–60 (2–9)	6–50	0.6–3.0 (0.1–0.4)	90–250 (13–36)	15–110 (2–16)	50–125 HRR
CN	50–55 (7–9)	40–45	1.3–15.0 (0.18–2)	150–240 (22–35)	60–75 (9–11)	95–115 HRR
PA	80 (12)	90	3.0 (0.43)	85 (12)	...	79 HRM, 118 HRR
PMMA	50–70 (7–10)	2–10	...	80–115 (12–17)	90–115 (13–17)	85–105 HRM
PS	35–60 (5–9)	1–4	3.0–4.0 (0.4–0.6)	80–110 (12–16)	55–110 (8–16)	65–90 HRM
PVC, rigid	40–60 (6–9)	5	2.4–2.7 (0.3–0.4)	60 (9)	...	110–120 HRR
PVCAc, rigid	50–60 (7–9)	...	2.0–3.0 (0.3–0.4)	70–80 (10–12)	85–100 (12–15)	...

ABS, acrylonitrile-butadiene-styrene; CA, cellulose acetate; CN, cellulose nitrate; EP, epoxy; MF, melamine formaldehyde; PA, polyamide (nylon); PF, phenol formaldehyde; PMMA, polymethyl methacrylate; PS, polystyrene; PVC, polyvinyl chloride; PVCAc, polyvinyl chloride acetate; UF, urea formaldehyde.

Source: Ref 6

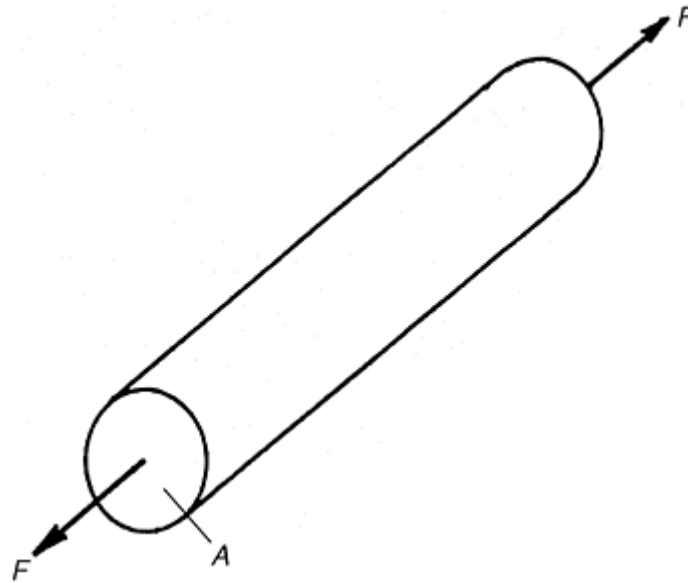


Fig. 1 Bar under axial tension

Equation 2 combines the performance of the part (load F) with the part geometry (cross-sectional area A) and the material characteristics (strength σ_f). The equation can be used several ways for design and material selection. If the material and its strength are specified, then, for a given load, the minimum cross-sectional area can be calculated; or, for a given cross-sectional area, the maximum load can be calculated. Conversely, if the force and area are specified, then materials with strengths satisfying Eq 2 can be selected.

Factor of Safety. Normally, designs involve the use of some type of a factor of safety. This factor, which is always greater than unity, is used in the design of components to ensure that the component can satisfactorily perform its intended purpose. The factor of safety is used to account for the uncertainties that exist in the real-world use of any component. Two main classifications of factors affect the factor of safety in a design, and they are these:

- Uncertainties associated with the material properties of the component itself, including the expected properties of the materials used to fabricate the component, as well as any uncertainties introduced by manufacturing and fabrication processing.
- Uncertainties associated with the level and type of loading the component will see, as well as the actual service conditions and any environmental conditions the component may experience.

The factor of safety is used to establish a target stress level for the design. This is sometimes referred to as the allowable stress, the maximum allowable stress, or simply, the design stress. In order to determine this allowable stress condition, the failure stress is simply divided by the safety factor. Safety factors ranging from 1.5 to 10 are typical. The lower the uncertainty is, the lower the safety factor.

Design for Strength, Weight, and Cost. If minimum weight or minimum cost criteria must also be satisfied, Eq 2 can be modified by introducing other material parameters. To illustrate, the area A in Eq 2 is related to density and mass by $A = M/\rho L$, where M is the mass of the bar, L is the length of the bar, and ρ is the material density. Solving Eq 2 for F and substituting for A :

$$F < \sigma_f A = (\sigma_f/\rho)(M/L) \quad (\text{Eq 3})$$

From Eq 3 it is clear that, to transmit a given load, F , the material mass will be minimized if the property ratio (σ_f/ρ) is maximized. The strength-to-weight ratio of a material is an important design and performance index; Fig. 2 is a plot developed by Ashby for comparison of materials by this design criterion. Similarly, material selection for minimum material cost can be obtained by maximizing the parameter $(\sigma_f/\rho c)$, or strength-to-cost ratio, where c represents the material cost per unit weight. These types of performance indices for design and the use of materials property charts like Fig. 2 are described in more detail in Ref 7 and in the articles “Material Property Charts” and “Performance Indices” in *Materials Selection and Design*, Volume 20 of *ASM Handbook*.

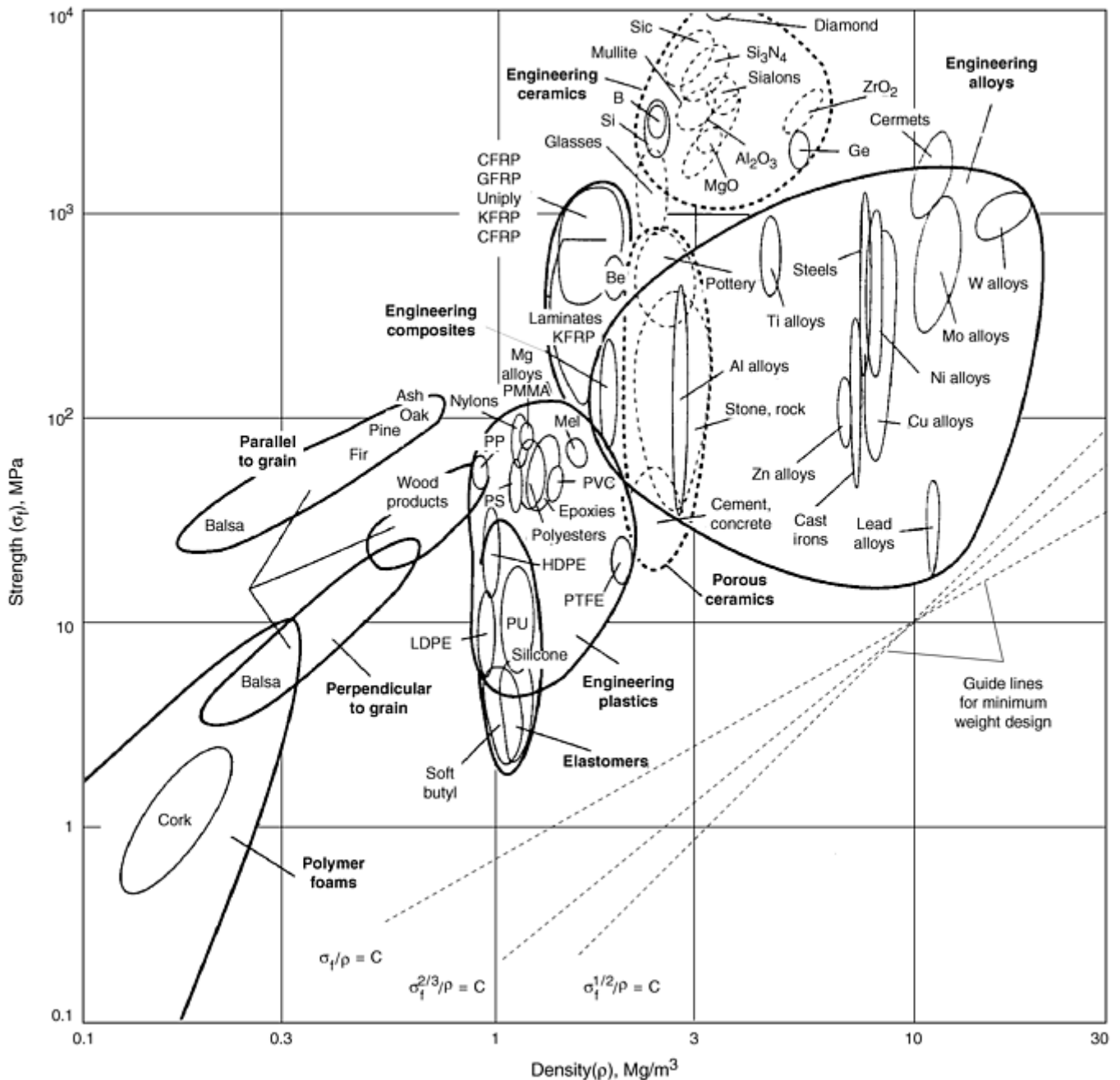


Fig. 2 Strength, σ_t , plotted against density, ρ , for various engineered materials. Strength is yield strength for metals and polymers, compressive strength for ceramic, tear strength for elastomers, and tensile strength for composites. Superimposing a line of constant σ_t/ρ enables identification of the optimum class of materials for strength at minimum weight.

Design for Stiffness in Tension. In addition to designing for strength, another important design criterion is often the stiffness or rigidity of a material. The elastic deflection of a component under load is governed by the stiffness of the material. For example, if a bridge or building is designed to avoid failure, it may still undergo motion under applied loads if it is not sufficiently rigid. As another example, if the tie bar in Fig. 1 were a bolt clamping a cap to a pressure vessel, excessive elastic change in length of the bolt under load might allow leakage through a gasket between the cap and vessel.

Elastic change in length occurs when an axial load is applied to the bar and is given by:

$$\Delta L = \epsilon L \quad (\text{Eq 4})$$

where ΔL is the change in length and ϵ is the strain in the bar. In the elastic range of deformation, axial stress is proportional to the strain:

$$\sigma = E\epsilon \quad (\text{Eq 5})$$

where the proportionality factor is E , the elastic modulus of the bar material.

The elastic modulus can be considered a physical property, because it is fundamentally related to the bond strength between the atoms or molecules in the material; that is, the stronger the bond, the higher the elastic modulus. Thus, the elastic modulus does not vary much in material with a given type of crystal structure or microstructure. For example, the elastic modulus of most steels is typically about 200 GPa (29×10^6 psi) for steels of various composition and strength levels (Fig. 3). However, the modulus can vary with direction if the material has an anisotropic structure. For example, Fig. 4 is a plot of the tensile and compressive modulus for type 301 austenitic stainless steel. Transverse and longitudinal values vary, as do values for tensile and compressive loads. At low stresses, the tension and compressive moduli are, by theory and experiment, identical. At higher stresses, however, differences in the compressive and tensile moduli can be observed due to the effects of deformation (e.g., elongation in tension). Typical values of elastic moduli are given in Table 4 for various alloys and metals.

Table 4 Elastic constants for polycrystalline metals at 20 °C

Metal	Elastic modulus (E)		Bulk modulus (K)		Shear modulus (G)		Poisson's ratio, ν
	GPa	10^6 psi	GPa	10^6 psi	GPa	10^6 psi	
Aluminum	70	10.2	75	10.9	26	3.80	0.345
Brass, 30 Zn	101	14.6	112	16.2	37	5.41	0.350
Chromium	279	40.5	160	23.2	115	16.7	0.210
Copper	130	18.8	138	20.0	48	7.01	0.343
Iron, soft	211	30.7	170	24.6	81	11.8	0.293
Iron, cast	152	22.1	110	15.9	60	8.7	0.27
Lead	16	2.34	46	6.64	6	0.811	0.44
Magnesium	45	6.48	36	5.16	17	2.51	0.291
Molybdenum	324	47.1	261	37.9	125	18.2	0.293
Nickel, soft	199	28.9	177	25.7	76	11.0	0.312
Nickel, hard	219	31.8	188	27.2	84	12.2	0.306
Nickel-silver, 55Cu-18Ni-27Zn	132	19.2	132	19.1	34	4.97	0.333
Niobium	104	15.2	170	24.7	38	5.44	0.397
Silver	83	12.0	103	15.0	30	4.39	0.367
Steel, mild	211	30.7	169	24.5	82	11.9	0.291
Steel, 0.75 C	210	30.5	169	24.5	81	11.8	0.293
Steel, 0.75 C, hardened	201	29.2	165	23.9	78	11.3	0.296
Steel, tool steel	211	30.7	165	24.0	82	11.9	0.287
Steel, tool steel, hardened	203	29.5	165	24.0	79	11.4	0.295
Steel, stainless, 2Ni-18Cr	215	31.2	166	24.1	84	12.2	0.283
Tantalum	185	26.9	197	28.5	69	10.0	0.342
Tin	50	7.24	58	8.44	18	2.67	0.357
Titanium	120	17.4	108	15.7	46	6.61	0.361
Tungsten	411	59.6	311	45.1	161	23.3	0.280
Vanadium	128	18.5	158	22.9	46.7	6.77	0.365
Zinc	105	15.2	70	10.1	42	6.08	0.249

Source: Ref 9

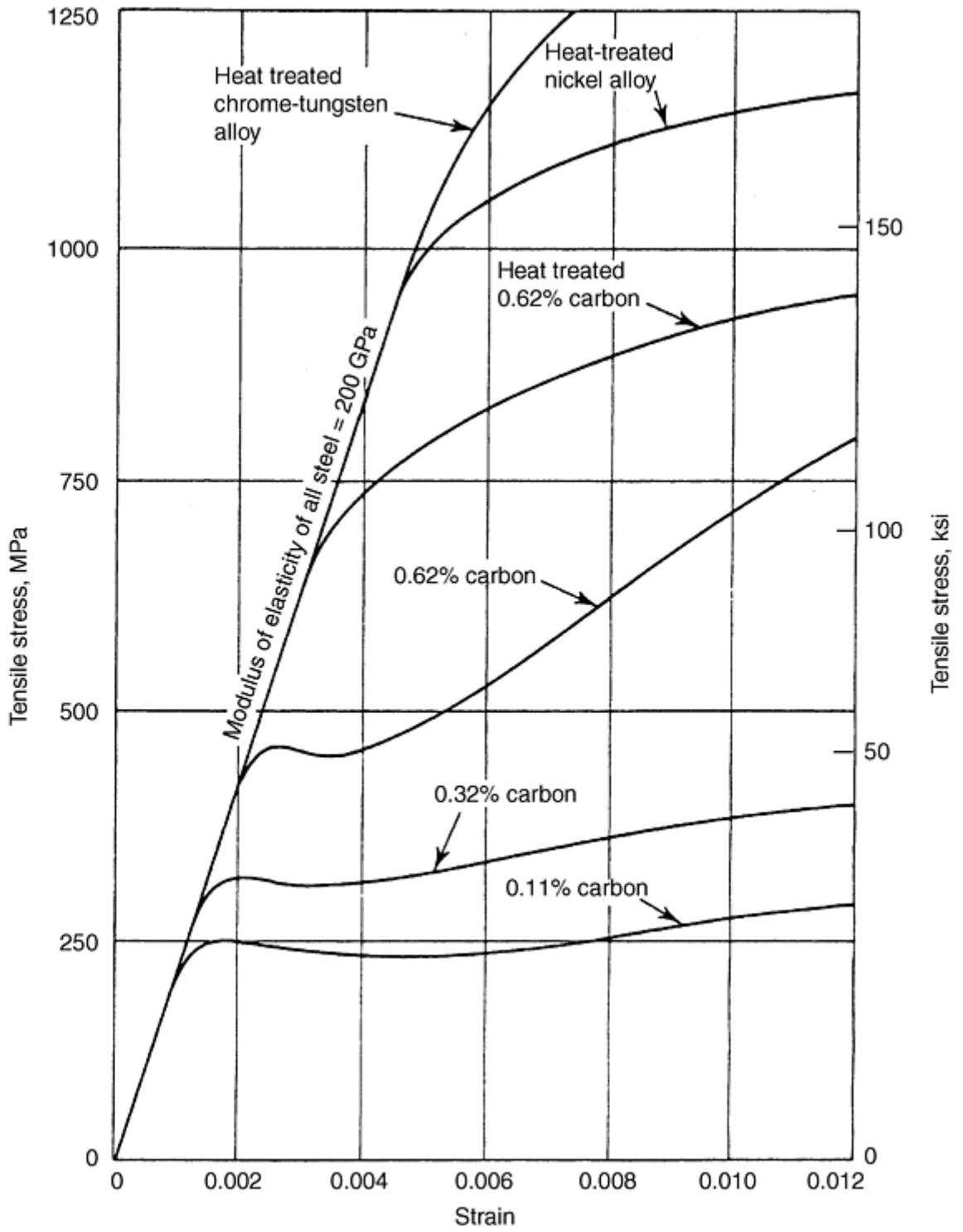


Fig. 3 Stress-strain diagram for various steels. Source: Ref 8

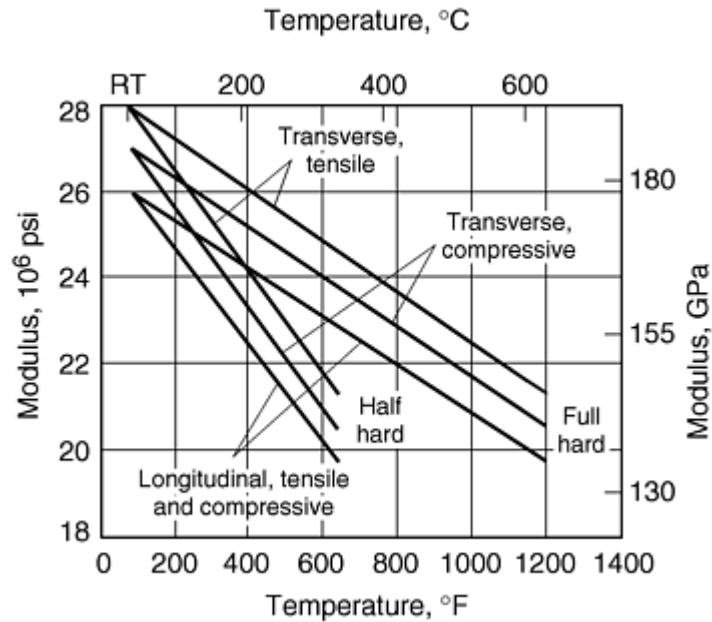


Fig. 4 Tensile and compressive modulus at half-hard and full-hard type 301 stainless steel in the transverse and longitudinal directions. Source: Ref 5

Equations 1 and 5 can be combined with Eq 4 to give the design equation:

$$\Delta L = FL/AE < \delta \quad (\text{Eq 6})$$

where δ is the design limit on change in length of the bar. Just as the strength, or load-carrying capacity, of the tie bar is related to geometry and material strength (Eq 2), the stiffness of the bar is related to geometry and the elastic modulus of the material. Again, part performance (force, F , and deflection, δ) is combined with part geometry (length, L , and cross-sectional area, A) and material characteristics (elastic modulus, E) in this design equation. To assure that the change in length is less than the allowable limit for a given force and material, the geometry parameters L and A can be calculated; or, for given dimensions, the maximum load can be calculated. Alternatively, for a given force and geometric parameters, materials can be selected whose elastic modulus, E , meets the design criterion given in Eq 6.

Similar to design for strength, additional criteria involving minimum weight or cost can be incorporated into design for stiffness. These criteria lead to the material selection parameters modulus-to-weight ratio (E/ρ) and modulus-to-cost ratio ($E/\rho c$), values that can be found in Ref 7 and *ASM Handbook*, Volume 20.

Mechanical Testing for Stress at Failure and Elastic Modulus. In Eq 2 and 6, the material properties σ_f and E play critical roles in design of the tie bar. These properties are determined from a simple tension test described in detail in the article “Uniaxial Tension Testing” in this Volume. The elastic modulus E is determined from the slope of the elastic part of the tensile stress strain curve, and the failure stress, σ_f , is determined from the tensile yield strength, σ_o , or the ultimate tensile strength, σ_u .

Tension-test specimens are cut from representative samples, as described in more detail in the article “Uniaxial Tension Testing.” in the example of the tie bar, test pieces would be cut from bar stock that has been processed similarly to the tie bar to be used in the product. In addition, the test piece should be machined such that its gage length is parallel to the axis of the bar. This ensures that any anisotropy of the microstructural features will affect performance of the tie bar in the same way that they influence the measurements in the tension test. For example, test pieces cut longitudinally and transverse to the rolling direction of hot rolled steel plates will exhibit the same elastic modulus and yield strength, but the tensile strength and ductility will be lower in the transverse direction because the stresses will be perpendicular to the alignment of inclusions caused by hot rolling (Ref 10).

During tension testing of a material to measure E and σ_f , in addition to the change in length due to the applied axial tensile loads, the material will undergo a decrease in diameter. This reflects another elastic property of materials, the Poisson ratio, given by:

$$\nu = -\epsilon_t/\epsilon_l \quad (\text{Eq 7})$$

where ε_t is the transverse strain and ε_l is the longitudinal strain measured during the elastic part of the tension test. Typical values of ν range from 0.25 to 0.40 for most structural materials, but ν approaches zero for structural foams and approaches 0.5 for materials undergoing plastic deformation. While the Poisson effect is of no consequence in the overall behavior of the tie bar (since the decrease in diameter has a negligible effect on the stress in the bar), the Poisson ratio is a very important material parameter in parts subjected to multiple stresses. The stress in one direction affects the stress in another direction via ν . Therefore, accurate measurements of the Poisson ratio are essential for reliable design analyses of the complex stresses in actual part geometries, as described later. Typical values of Poisson's ratio are given in Table 4.

Sonic methods also offer an alternative and more accurate measurement of elastic properties, because the velocity of an extensional sound wave (i.e., longitudinal wave speed, V_L) is directly related to the square root of the ratio of elastic modulus and density as follows:

$$V_L = (E/\rho)^{1/2} \quad (\text{Eq 8})$$

By striking a sample of material on one end and measuring the time for the pulse to travel to the other end, the velocity can be calculated. Combining this with independent measurement of the density, Eq 8 can be used to calculate the elastic modulus (Ref 8).

References cited in this section

3. *Metals Handbook*, American Society for Metals, 1948
4. F.B. Seely, *Resistance of Materials*, John Wiley & Sons, 1947
5. *Properties and Selection of Metals*, Vol 1, *Metals Handbook*, 8th ed., American Society for Metals, 1961, p 503
6. *Modern Plastics Encyclopedia*, McGraw Hill, 2000
7. M.F. Ashby, *Materials Selection for Mechanical Design*, 2nd ed., Butterworth-Heinemann, 1999
8. H. Davis, G. Troxell, and G. Hauck, *The Testing of Engineering Materials*, 4th ed., McGraw Hill, 1982, p 314
9. G. Carter, *Principles of Physical and Chemical Metallurgy*, American Society for Metals, 1979, p 87
10. M.A. Meyers and K.K. Chawla, *Mechanical Metallurgy*, Prentice-Hall, Edgewood Cliffs, NJ, 1984, p 626–627

Overview of Mechanical Properties and Testing for Design

Howard A. Kuhn, Concurrent Technologies Corporation

Compressive Loading

If the bar in Fig. 1 were subjected to a compressive axial load, the same design criteria, Eq 2 and 7, would apply with appropriate material parameters. Measurement of the material parameters could be performed through compression tests; however, in anisotropic materials, the yield strength, σ_o , will be the same in compression and tension. The material ultimate strength, σ_u , will generally be different, however, because the fracture behavior of a material in compression is different from that in tension. Tests for failure in compression are covered in the article “Uniaxial Compression Testing” in this volume. In carrying out compression tests, the same precautions used in tension testing must be applied regarding orientation of the specimen and load relative to the material microstructure.

In compressive loading of materials, buckling may precede other forms of failure, particularly in long thin bars. The critical compressive stress for buckling of bars with simple pin-end supports is given by:

$$\sigma_b = F/A = \pi^2 EI/L^2A \quad (\text{Eq 9})$$

where I is the moment of inertia of the bar cross section. The only material parameter in Eq 9 is the elastic modulus, which is the same in tension and compression for most materials. Any convenient test for E , then, can be used to provide the material parameter required for buckling predictions.

Overview of Mechanical Properties and Testing for Design

Howard A. Kuhn, Concurrent Technologies Corporation

Hardness Testing

When suitable samples for tension or compression test pieces are too difficult, costly, or time consuming to obtain, hardness testing can be a useful way to estimate the mechanical strength and characteristics of some materials. Hardness testing, therefore, is an indispensable tool for evaluating materials and estimating other mechanical properties from hardness (Ref 11, 12).

Correlation of hardness and strength has been examined for several materials as summarized in Ref 12. In hardness testing, a simple flat, spherical, or diamond-shaped indenter is forced under load into the surface of the material to be tested, causing plastic flow of material beneath the indenter as illustrated in Fig. 5. It would be expected, then, that the resistance to indentation or hardness is proportional to the yield strength of the material. Plasticity analysis (Ref 13) and empirical evidence (summarized in Ref 12) show that the pressure on the indenter is approximately three times the tensile yield strength of the material. However, correlation of hardness and yield strength is only straightforward when the strain-hardening coefficient varies directly with hardness. For carbon steels, the following relation has been developed to relate yield strength (YS) to Vickers hardness (HV) data (Ref 12):

$$\text{YS (in kgf/mm}^2\text{)} = \frac{1}{3}\text{HV (0.1)}^{m-2}$$

where m is Meyer's strain-hardening coefficient (see the article "Introduction to Hardness Testing" in this Volume). To convert kgf/mm^2 values to units of lb/in.^2 , multiply the former by 1422. This relation applies only to carbon steels. Correlation of yield strength and hardness depends on the strengthening mechanism of the material. With aluminum alloys, for example, aged alloys exhibit higher strain-hardening coefficients and lower yield strengths than cold worked alloys (Ref 12).

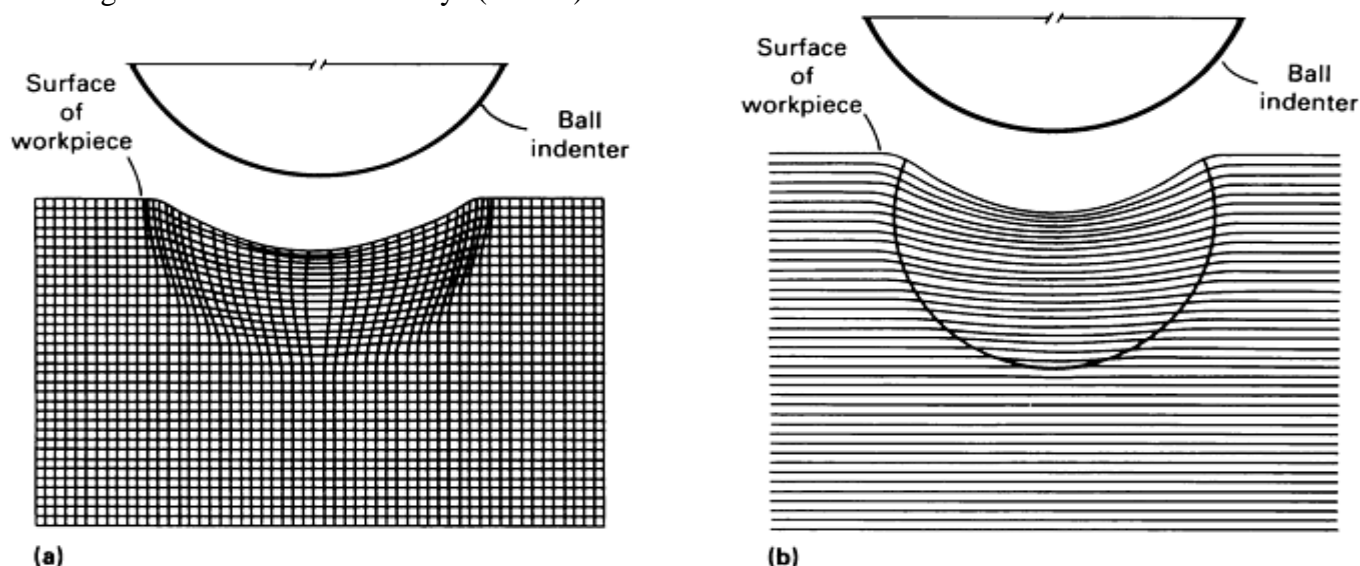


Fig. 5 Deformation beneath a hardness indenter. (a) Modeling clay. (b) Low-carbon steel

For many metals and alloys, there has been found to be a reasonably accurate correlation between hardness and tensile strength, σ_u (Ref 12). Several studies are cited and described in Ref 12, and Tables 5 and 6 summarize hardness-tensile strength multiplying factors for various materials. It must be emphasized, however, that these are empirically based relationships, and so testing may still be warranted to confirm a correlation of tensile strength and hardness for a particular material (and/or material condition). A correlation with hardness may not be evident. For example, magnesium alloy castings did not exhibit a hardness-strength correlation in a study by Taylor (Ref 11).

Table 5 Hardness-tensile strength conversions for steel

Material	Multiplying factor^(a)
Heat-treated alloy steel (250–400 HB)	470 HB
Heat-treated carbon and alloy steel (<250 HB)	482 HB
Medium carbon steel (as-rolled, normalized, or annealed)	493 HB

(a) Tensile strength (in psi) = multiplying factor \times HB.

Source: Ref 12

Table 6 Multiplying factors for obtaining tensile strength from hardness

Material	Multiplying factor range^(a)
Heat treated carbon and alloy steel	470–515 HB
Annealed carbon steel	515–560 HB
All steels	448–515 HV
Ni-Cr austenitic steels	448–482 HV
Steel; sheet, strip, and tube	414–538 HV
Aluminum alloys; bar and extrusions	426–650 HB
Aluminum alloys; bar and extrusions	414–605 HV
Aluminum alloys; sheet, strip, and tube	470–582 HV
Al-Cu castings	246–426 HB
Al-Si-Ni castings	336–426 HB
Al-Si castings	381–538 HB
Phosphor bronze castings	336–470 HB
Brass castings	470–672 HB

(a) Tensile strength (in psi) = multiplying factor \times hardness.

Source: Ref 11, 12

More information on hardness tests and the estimation of mechanical properties is in the article “Selection and Industrial Application of Hardness Tests” in this Volume. References 12 and 14 also contain information on the application of hardness testing.

References cited in this section

11. W.J. Taylor, The Hardness Test as a Means of Estimating the Tensile Strength of Metals, *J.R. Aeronaut. Soc.*, Vol 46 (No. 380), 1942, p 198–202
12. George Vander Voort, *Metallography: Principles and Practices*, ASM International, 1999, p 383–385 and 391–393
13. R.T. Shield, On the Plastic Flow of Metals under Conditions of Axial Symmetry, *Proc. R. Soc.*, Vol A233, 1955, p 267
14. H. Chandler, Ed., *Hardness Testing*, 2nd ed., ASM International, 1999

Torsion and Bending

Instead of axial loads, the tie bar in Fig. 1 may be subjected to torsion moments about its axis on each end, as shown in Fig. 6. This represents the loading in drive shafts or torsion bar suspensions, for example. In other applications, the bar may be subjected to loads perpendicular to its axis resulting in a bending moment, as shown in Fig. 7. Typical examples include leaf springs and structural beams.

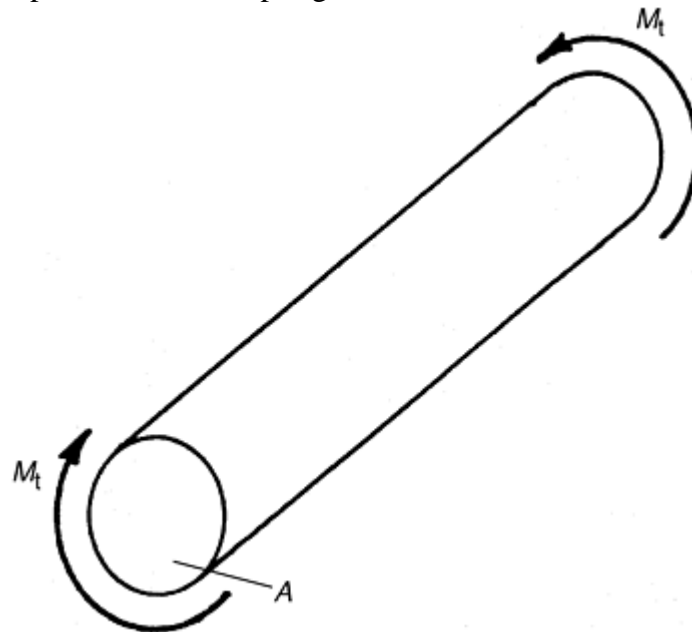


Fig. 6 Bar under torsion. M_t , applied torque. A , cross sectional area of the bar

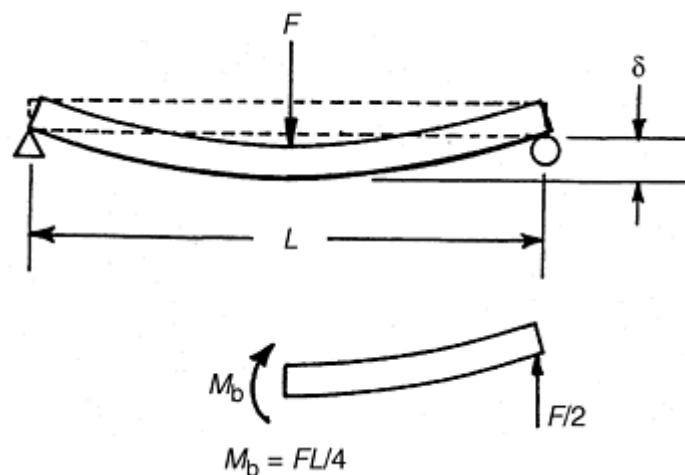


Fig. 7 Bar under bending by a transverse load. F , applied force; L , length of the bar; M_b , bending moment

Shear Stress Distributions. In both torsion and bending, the shear strain (in torsion) and the longitudinal strain (in bending) are zero at the centerline, or neutral axis, and increase linearly to maximum values at the outer surfaces. As a result, the stress distributions are linear, as shown in Fig. 8 for torsion and Fig. 9 for bending. Note that, in bending, the stress is tensile on the convex side of the bar and compressive on the concave side.

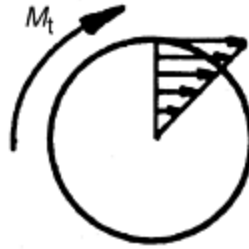


Fig. 8 Linear distribution of shear stress in torsion of a round bar. M_t , applied torque

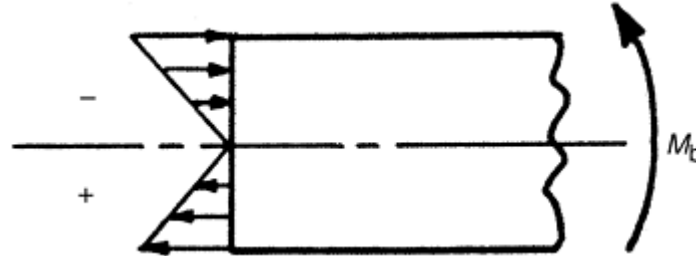


Fig. 9 Linear distribution of normal stress in bending. M_b , bending moment

The shear stress distribution in torsion is given by (Ref 15):

$$\tau = M_t r/J \quad (\text{Eq 10})$$

where τ is the shear stress, M_t is the applied torque, r is measured from the axis, and J is the polar moment of inertia (second moment about the axis of rotation) of the bar cross section. The influence of J in design is discussed later in “Shape Design” in this article. More detailed descriptions of rotational shear (i.e., torsion) are provided in the article “Fundamental Aspects of Torsional Loading” in this Volume.

The normal stress distribution in bending is given by (Ref 16):

$$\sigma = M_b z/I \quad (\text{Eq 11})$$

where σ is the longitudinal stress in the bar, M_b is the bending moment, z is measured from the neutral axis, and I is the moment of inertia (second moment about the bending axis) of the bar cross section. The role of I in design is also discussed later in “Shape Design.” More detailed descriptions of bending stress and strain behavior are provided in the article “Stress-Strain Behavior in Bending” in this Volume.

Design for Strength in Torsion or Bending. Design of bars under torsional or bending moments is based on preventing the maximum surface stresses from exceeding the failure limit of the material. For example, in torsion of a round bar, τ_{\max} occurs at $r = D/2$ (where D is the bar diameter) and must satisfy the design condition:

$$\tau_{\max} = M_t D/2J < \tau_f \quad (\text{Eq 12})$$

where τ_f is the failure shear strength of the material at failure. This value may be the shear yield strength, τ_o , or the ultimate shear strength, τ_u . Similarly, in bending, the maximum normal stress, σ_{\max} , occurs at $z = H/2$ (where H is the thickness of a symmetrical beam) and must satisfy the design condition:

$$\sigma_{\max} = M_b H/2I < \sigma_f \quad (\text{Eq 13})$$

where σ_f may be the tensile yield strength, σ_o , or the ultimate tensile strength, σ_u , for failure on the convex side of the bar. Compressive strengths apply to failure on the concave side of the bar.

In the same way that Eq 2 is used for design of bars under tensile loading, Eq 12 and 13 can be used to determine the maximum torque, M_t , or bending moment, M_b , that can be transmitted by a specific bar geometry (D and J , or H and I) and material (τ_f or σ_f). These equations can also be used to determine the geometric parameters required to transmit a specified torque or bending moment with a given bar material. Alternatively, Eq 12 and 13 can be used to select materials having the proper values of τ_f or σ_f to transmit a specified torque or bending moment in a bar of given geometry.

As with the case of simple tension, the design equations for torsion and bending can be modified to include the additional criteria of minimum weight or minimum cost. The material parameters for minimum weight or

minimum cost in this case depend on the geometric parameters that are fixed and those that are variable. For a beam with the width undefined, the design parameters are (σ_f/ρ) and $(\sigma_f/\rho c)$, while for beams in which the height is undefined, the design parameters are $(\sigma_f^{1/2}/\rho)$ and $(\sigma_f^{1/2}/c\rho)$ (Ref 1, 7).

Design for Stiffness in Torsion or Bending. Elastic deflection of a bar under bending moments and elastic twisting of the bar under torsion may lead to additional design limits. For example, in bending a simply supported beam (Fig. 7), the deflection at the center point is (Ref 16):

$$\delta = FL^3/48EI \quad (\text{Eq 14})$$

The beam stiffness is determined by the material parameter, E , and the geometry parameters, L and I . Beam design to meet deflection limitations can be accomplished by proper material specification or by geometric specifications.

Similarly, torsional rotation of a round bar is given by (Ref 15):

$$\theta = M_t L/GJ \quad (\text{Eq 15})$$

where M_t is the applied torque, L is the length of the bar, J is the polar moment of inertia, and G is the shear modulus of elasticity. Design for torsional stiffness involves selection of the bar dimensions as well as the material via its elastic property, G , which is related to other elastic properties by (Ref 15):

$$G = E/2(1 + \nu) \quad (\text{Eq 16})$$

Shape Design. Of particular interest in design of bars under torsion or beams under bending are the moments of inertia, J and I . Since the stress distributions in each case are linear and reach a maximum at the surface, as shown in Fig. 8 and 9, the best use of material is accomplished by distributing it near the surfaces rather than at the center. For example, the value of J for a solid circular cross section is:

$$J = \pi D^4/32 \quad (\text{Eq 17})$$

By removing material from the central region of the bar, which is under little stress, the torsional load carrying capacity is reduced slightly, but the area (and therefore weight) is reduced more significantly. Referring to Fig. 10, if one-half of the inner material is removed (i.e., inside diameter $D_i = D/\sqrt{2}$), the weight is reduced by 50%, but the value of J is reduced by just 25%.

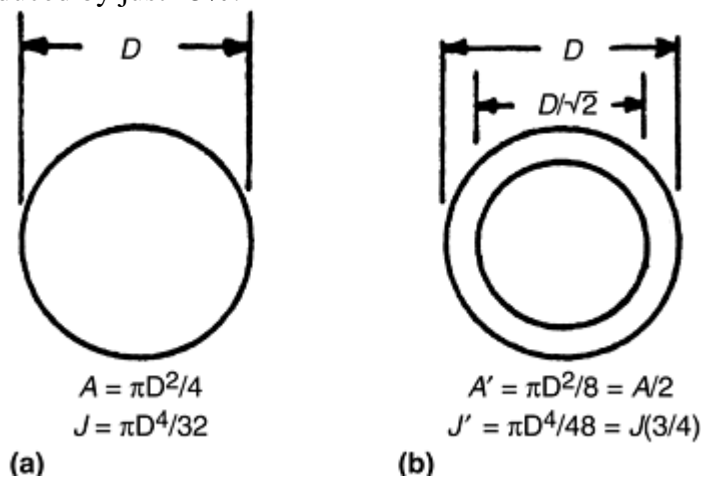


Fig. 10 Comparison of polar moment of inertia, J , for (a) solid and (b) hollow round bars. A , cross-sectional area; D , diameter

Similarly, in bending, efficient material use is accomplished by placing material at the upper and lower surfaces, as in the shape of an I-beam. To illustrate this, consider that the moment of inertia for a rectangle is given by:

$$I = bH^3/12 \quad (\text{Eq 18})$$

where b is the width and H is the height of the rectangle. Obviously, increasing H has a much larger effect on I than increasing b . For example, as shown in Fig. 11, a rectangle that is 3 units thick and 9 units long has a value of I that is 9 times larger in the vertical orientation compared to the horizontal orientation. However, if the same amount of material is rearranged into an I-beam configuration, the value of I increases further by a factor of nearly 3. Thus, weight savings in design for torsion and bending can be accomplished not only by selecting

materials having high strength-to-weight ratios, but also by careful attention to the distribution of material in the component.

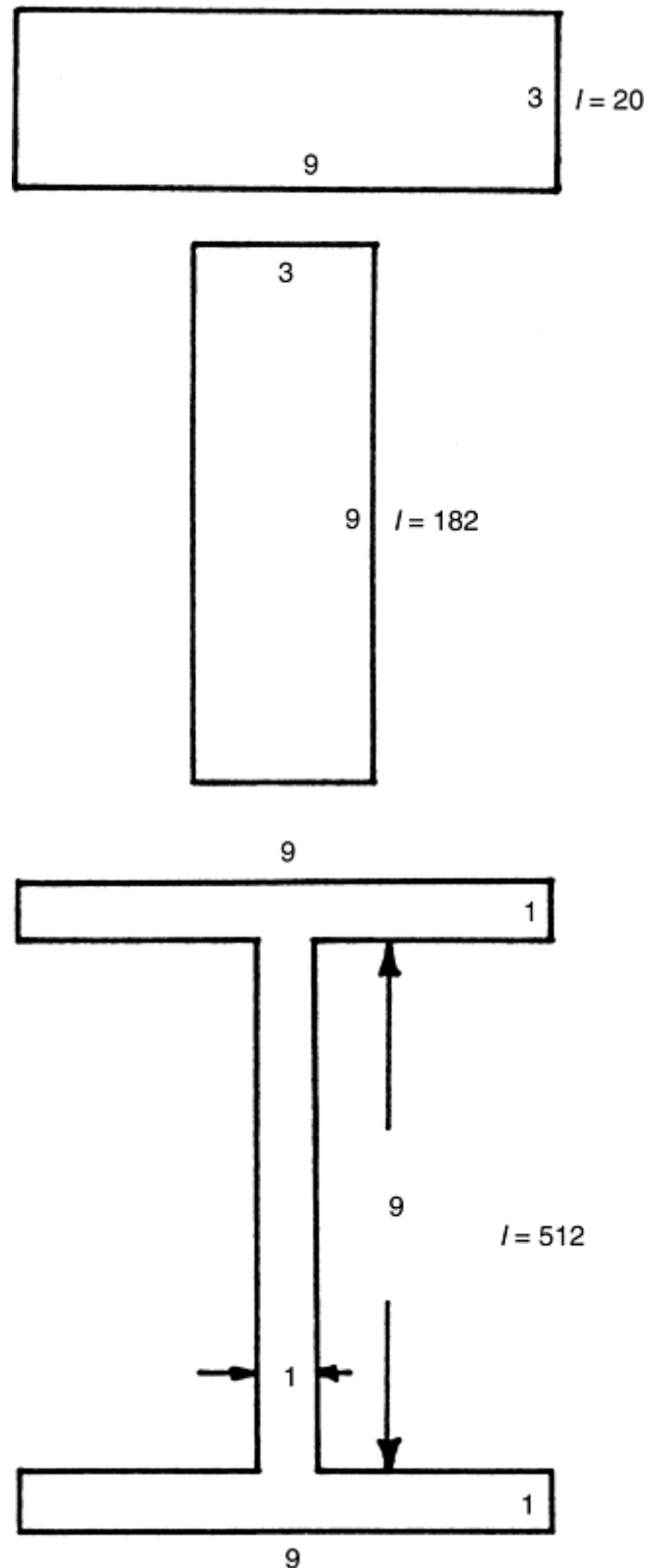


Fig. 11 Comparison of moment of inertia, I , for three different arrangements of the same amount of material

Mechanical Testing. Testing of materials for shear yield strength, τ_0 , to be used in Eq 12, or for tensile yield strength, σ_0 , for use in Eq 13, can be accomplished through a tension test. If the material is isotropic and homogeneous, the *shear yield strength* can also be calculated from the tensile yield strength (Ref 15):

$$\tau_0 = \sigma_0 / \sqrt{3} \quad (\text{Eq 19})$$

Fracture strengths, however, must be measured in torsion and bend tests because the mechanisms or modes of fracture may be different from those in tension testing.

Tensile yield strength, σ_o , and shear yield strength, τ_o , can also be derived directly from bending and torsion tests using Eq 12 and 13. Accuracy will be limited, however, because in both cases yielding occurs initially at the outside surfaces, so the effect on the measured loads is not as easily detectable as in the tension test, where yielding occurs simultaneously across the entire section.

Torsion and bend tests are particularly useful in evaluating materials that have been given surface treatments such as carburizing or shot peening to increase the strength of the surfaces and improve their resistance to the high stresses at the surface generated by torsional or bending moments. Generally, the metallurgical structures of such surfaces occur in a thin layer and cannot be produced easily in bulk form for measurement by tension testing. Then, Eq 12 can be used to determine the strength, τ_f , of the surface material in torsion, and Eq 13 can be used to determine the strength, σ_f , of surface material in bending. This approach is particularly useful for determining fracture strengths of the surface materials.

During bend or torsion testing of surface treated materials, however, certain precautions must be taken. First, the orientation of the bending and shear stresses in the test specimens must be in the same orientation with respect to the material microstructure as occurs in the actual components. Second, variations in material strength beneath the surface must be considered in comparison with the linear distributions of stress in bending and torsion shown in Fig. 8 and 9. Even though the surface material strength may be greater than the stress at the surface (such as in a case hardened part), away from the surface at the neutral axis of the bar the strength may decrease more rapidly than the applied stress, as illustrated in Fig. 12 (Ref 17). Then failure will occur beneath the surface where the stress exceeds the local strength of the material. Clearly, it is important to understand the strength distribution in a material in relation to the stress distribution acting on the material to ensure that the product design prevents such insidious failures. Details on torsion and bend testing are covered in separate articles in this Volume.

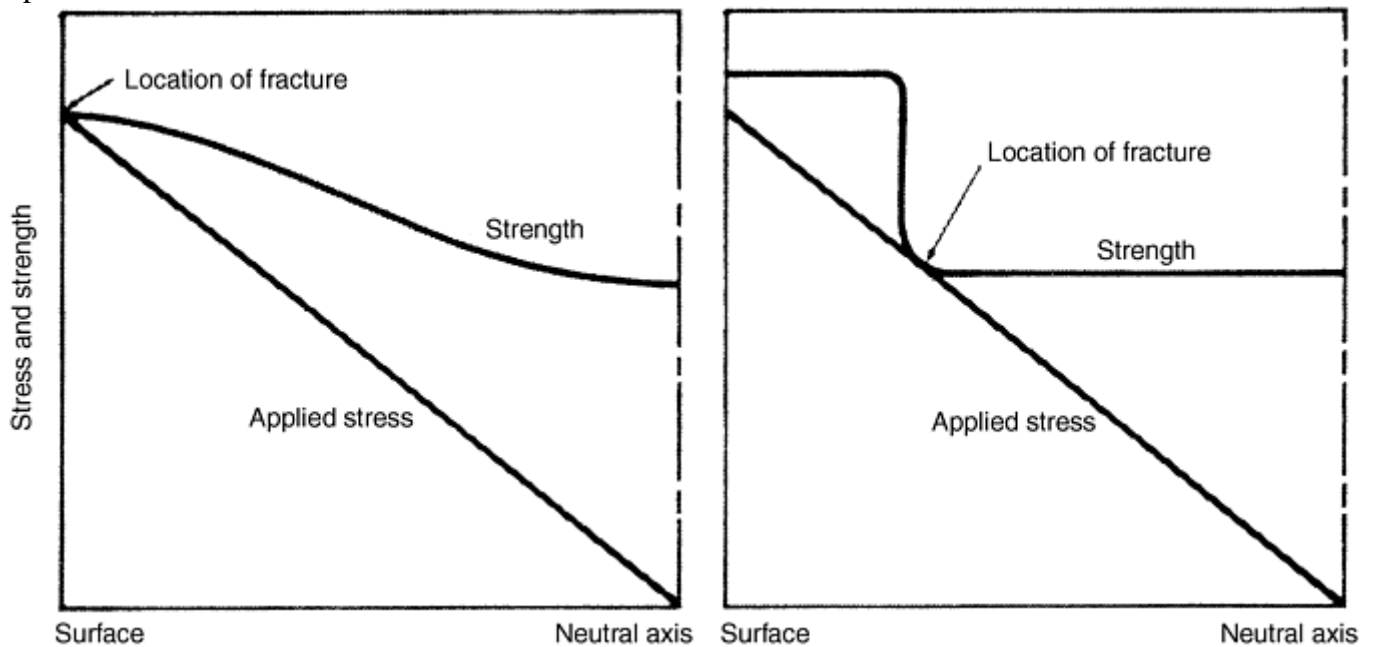


Fig. 12 Stress and strength distributions in a bar under torsion or bending. Failure occurs beneath the surface if the material strength decreases more rapidly than the stress in the material. Source: Ref 17

Equation 14 for deflection of a beam also suggests an alternative method for measuring the elastic modulus, E , of a material. For given geometry parameters, measured data pairs for force, F , and deflection, δ , lead to a calculation of E . Alternatively, resonant frequency methods can be used to measure E in the beam geometry shown in Fig. 7. The natural frequency of vibration of a beam is related to its geometry, density, and elastic modulus. To carry out the measurement, the beam is vibrated by a transducer connected to a frequency generator producing sinusoidal waves. By varying the frequency of the generator, the natural frequency is determined when resonance occurs. Then the elastic modulus can be calculated from (Ref 18):

$$E = Cf^2 \rho L^4 / H^2 \quad (\text{Eq 20})$$

where f is the resonant frequency, ρ is the material density, L is the beam length, H is the beam thickness, and C is a constant. The shear modulus, G , can also be measured by sonic and resonant frequency methods in torsion. Generally, resonant and sonic methods of measuring elastic properties are more accurate and easier to perform than direct measurement of stress and strain in a tension or torsion test.

References cited in this section

1. Cambridge Engineering Selector, Granta Design Ltd., Cambridge, UK, 1998
7. M.F. Ashby, *Materials Selection for Mechanical Design*, 2nd ed., Butterworth-Heinemann, 1999
15. G.E. Dieter, *Mechanical Metallurgy*, 2nd ed., McGraw Hill, 1976, p 49–50, 79–80, 379, 381, 385
16. J.H. Faupel and F.E. Fisher, *Engineering Design*, John Wiley & Sons, 1981, p 102, 113, 230–235, 802
17. D.J. Wulpi, *Understanding How Components Fail*, ASM International, 1966, p 27
18. T. Baumeistes, Ed., *Marks' Mechanical Engineers' Handbook*, 6th ed., McGraw-Hill, 1958, p 5–106

Overview of Mechanical Properties and Testing for Design

Howard A. Kuhn, Concurrent Technologies Corporation

Shear Loading

The torsion test described above subjects material to shear stress in a rotational mode, but shear stresses also occur in a translational mode. Such modes can be found, for example, in the end connectors of tie bars.

Design Examples. In an actual tie bar, the loads at each end of the bar in Fig. 1 would be applied through a pin connector or a threaded coupling, for example, as shown in Fig. 13(a). If the tie bar were a composite material (which cannot be threaded or drilled), the loads would most likely be applied through an adhesive lap joint, as shown in Fig. 13(b).

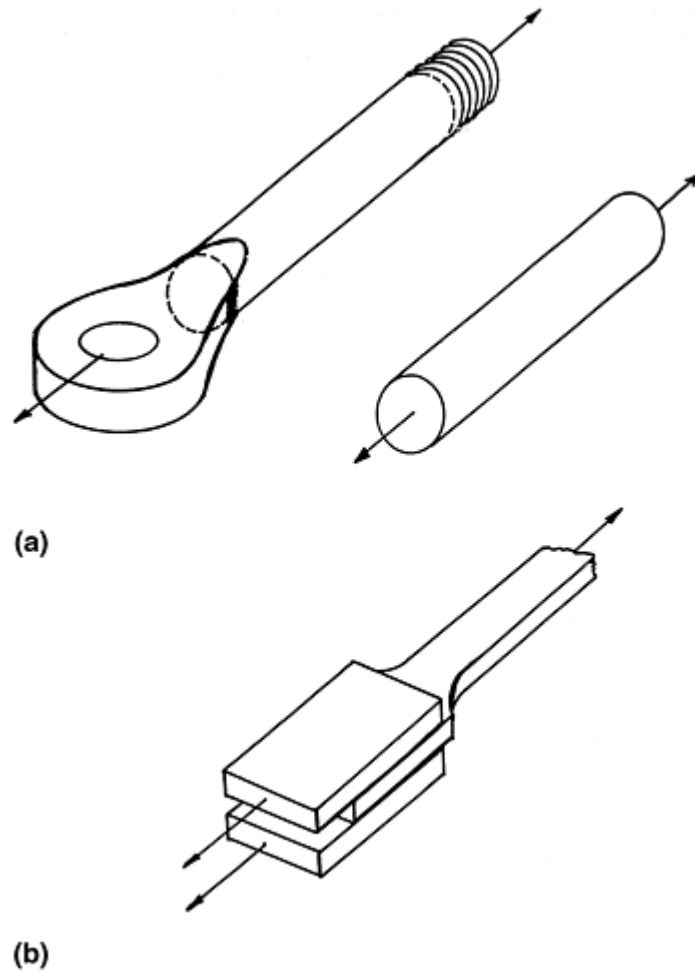


Fig. 13 Methods of connecting loads. (a) A load is applied to the tie bar in Fig. 1 by a pin/eye connector and a threaded connector. (b) End loads are applied to a composite bar by adhesives.

In these and all other types of connectors, shear stresses occur in the transition from the connection to the straight section of the bar. For example, Fig. 14(a) shows a pin through the eye of the tie bar and the forces applied to the tie bar through a clevis. The pin, Fig. 14(b), is subjected to shear stresses along the dotted planes between the eye of the tie bar and the clevis. Shear failure may occur along these planes. On the face view of the eye on the tie bar, Fig. 14(c), shear also acts along the dotted planes from the hole to the end of the bar, potentially leading to tear out of the end of the conductor. On the threaded end of Fig. 13(a), transmission of load from a threaded connector to the tie bar also is carried by shear stresses at the root of the threads, shown by the dotted lines in Fig. 15. In the lap joint shown in Fig. 13(b), shear would occur along the adhesive interfaces. Concentrated shear stresses, similar to those shown in Fig. 14(b) and 14(c), also occur in many machine elements, such as keys and keyways in drive shafts, shear pins, and splined couplings. These applications are critical to the safe operation of machinery and require robust design methods using accurate material properties.

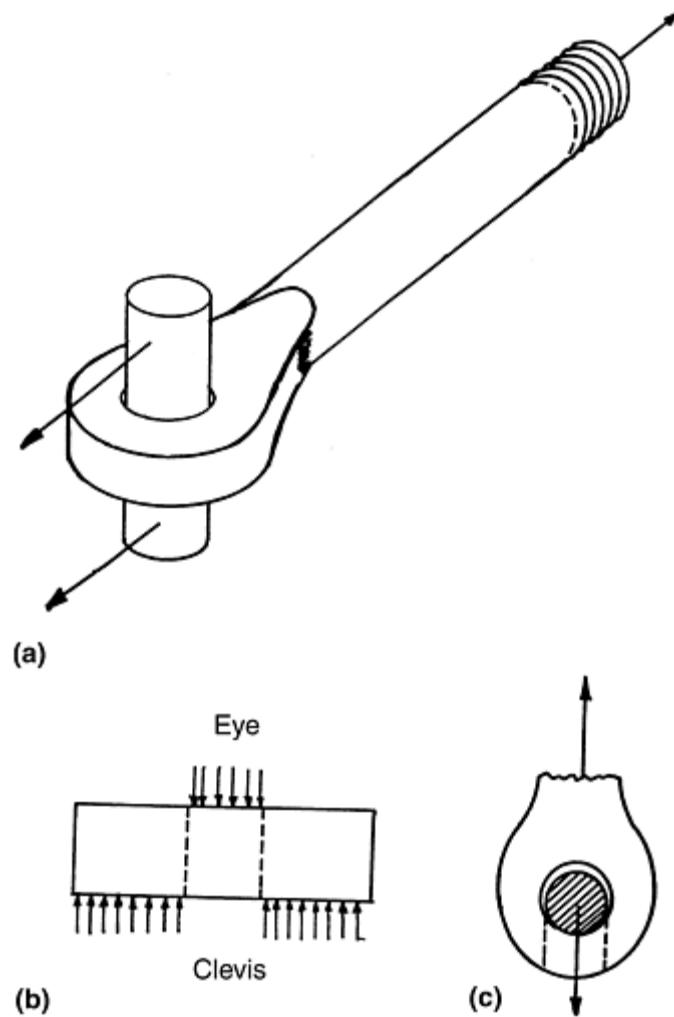


Fig. 14 Shear stresses in load end connectors. (a) A clevis and pin connected to the eye in Fig. 13(a). (b) Shear planes in the pin. (c) Shear planes in the eye

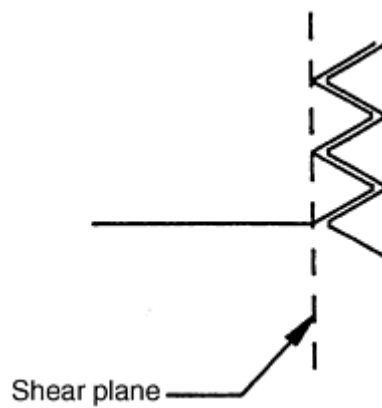


Fig. 15 Shear planes in a threaded end connector

In all of these examples, the average shear stress acting on the shear planes is:

$$\tau = F/A_s \quad (\text{Eq 21})$$

where F is the load transmitted and A_s is the total area of the shear planes. For design against failure, this shear stress must be less than the shear strength of the material.

Mechanical Testing. Measurement of the shear yield strength of the material can be extracted from a tension test by using Eq 19 if the material has an isotropic and homogeneous microstructure. The torsion test described previously also can be used to determine the shear strength of the material. However, the torsion test measures the shear strength of the material in rotational shear, but the applications shown in Fig. 13, 14, and 15 involve

linear shear along a plane through the material or along an interface. Linear shear behavior is affected significantly by anisotropy of the microstructure of the material, and specialized tests have been developed to determine the linear shear yield and fracture strength of materials. More details on torsion loading are in the article “Shear, Torsion, and Multiaxial Testing” in this Volume.

Overview of Mechanical Properties and Testing for Design

Howard A. Kuhn, Concurrent Technologies Corporation

Complex Stresses

The previous sections describe the relatively simple uniform and linear stress distributions occurring during tension, compression, torsion, bending, and shear. In all of these cases, one primary stress occurred. Nonelementary shapes, however, lead to nonuniform, nonlinear, and multiaxial stresses, and these complex stress states must be considered in a complete analysis for product design.

Constitutive Relations. To consider the effects of combined stresses in design, constitutive equations are required that give the relationships between multiple stresses and strains. A one-dimensional example of a constitutive relation is the combination of Eq 5 and 7, describing the elastic connection between uniaxial stress and strain. Extending this behavior to three dimensions, if σ_x is applied in the x -direction, the strain $\epsilon_x = \sigma_x/E$ occurs, and that same stress will generate transverse strains:

$$\epsilon_y = \epsilon_z = -\nu\epsilon_x = -\nu\sigma_x / E \quad (\text{Eq 22})$$

This leads to the complete three-dimensional expressions relating elastic stresses and strains (Ref 15):

$$\epsilon_x = (\sigma_x - \nu\sigma_y - \nu\sigma_z)/E \quad (\text{Eq 23a})$$

$$\epsilon_y = (\sigma_y - \nu\sigma_z - \nu\sigma_x)/E \quad (\text{Eq 23b})$$

$$\epsilon_z = (\sigma_z - \nu\sigma_x - \nu\sigma_y)/E \quad (\text{Eq 23c})$$

A complete description of material behavior requires a description of yielding under multiaxial stresses. Equations 2, 12, 13, and 21 express the conditions for yielding under the action of a single tensile or shear stress. For three-dimensional stresses, a commonly used criterion that includes the effect of all stresses acting at a point in a material is:

$$\begin{aligned} & [(\sigma_x - \sigma_y)^2 + (\sigma_y - \sigma_z)^2 + (\sigma_z - \sigma_x)^2 + 6\tau_{xy}^2 \\ & + 6\tau_{yz}^2 + 6\tau_{zx}^2]^{1/2} / \sqrt{2} = \sigma_o \end{aligned} \quad (\text{Eq 24})$$

where σ_o is the yield strength of the material in simple tension. Equation 24, known as the von Mises yield criterion (Ref 19), relates all of the stresses acting in a material to its yield strength. Note that, in a torsion test where normal stresses are zero and only one shear stress is applied, Eq 24 reduces to Eq 19, which enables shear yield strength values for design to be determined from a simple tension test.

Equations 23a, 23b, 23c, and 24 are the constitutive relations for elastic deformation and yielding of an isotropic material. More complex constitutive relations have been developed for anisotropic materials, composites, and rate dependent materials. For failure by fracture, no simple criterion, such as Eq 24, exists to express the effects of multiaxial stresses on failure.

Qualitative results from Eq 23a, 23b, 23c, and 24 lead to insights on the relationships between combined stresses and strains. For example, in a plane-strain tension test (Fig. 16), a groove across the face of the specimen will lead to stress $\sigma_x = F/tW$ where F is the applied load, t is the groove thickness, and W is the specimen width. Under the action of this stress, the material in the groove will tend to contract in the thickness direction, z , and in the width direction, y . There is no constraint preventing the material from contracting in the thickness, so $\sigma_z = 0$. In the width direction, however, the bulk material (thickness, T , much greater than t) on each side of the reduced section prevents material from contracting. That is, $\epsilon_y = 0$. Then, from Eq 23a, 23b, and 23c:

$$\epsilon_y = 0 = (\sigma_y - \nu\sigma_x)/E \quad (\text{Eq 25a})$$

or

$$\sigma_y = \nu\sigma_x \quad (\text{Eq 25b})$$

That is, a stress is generated in the y-direction because the natural tendency for the material to contract is constrained. The strain in the thickness direction will be:

$$\epsilon_z = -\nu(\sigma_x + \sigma_y)/E = -\nu(1 + \nu)\sigma_x/E \quad (\text{Eq 26})$$

which is slightly larger than the strain that would have occurred with no constraint in the y-direction. More complex interactions occur between three-dimensional stresses and strains in more complex geometries, and these interactions are influenced strongly by the Poisson ratio, ν .

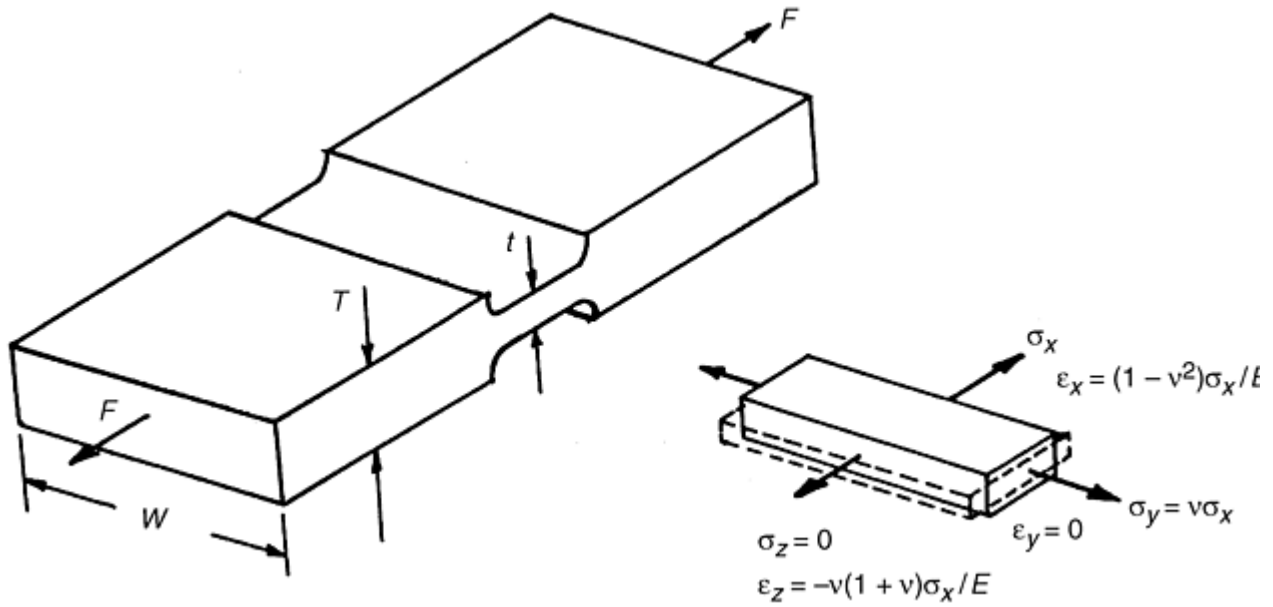


Fig. 16 Plane strain tension test specimen, showing the strains and stresses in the gage section

The multiaxial stresses in this example have an effect on yielding. The applied stress, σ_x , combined with the constraint of transverse strain in the y-direction, generates a stress in the y-direction given by Eq 25a and 25b. The applied stress σ_x required to cause failure by yielding can be found by substituting the stresses $\sigma_y = \nu\sigma_x$ and $\sigma_z = 0$ into Eq 24, giving:

$$(\sigma_x - \nu\sigma_x)^2 + (\nu\sigma_x)^2 + (-\sigma_x)^2 = 2\sigma_o^2 \quad (\text{Eq 27a})$$

or

$$\sigma_x = \sigma_o/(1 - \nu + \nu^2)^{1/2} \quad (\text{Eq 27b})$$

Substituting the value of $\nu = 0.5$ for material undergoing plastic deformation, $\sigma_x = 1.15 \sigma_o$; that is, because of the constraint to contraction in the y-direction of the geometry shown in Fig. 16, the stress required to yield the material is 15% higher than the axial stress required to yield the material if it were in simple tension.

Following are further examples of basic design stress conditions that involve nonlinear stress distributions and multiaxial stresses.

Stress Concentrations. In the transition from the pin connector to the uniform cylindrical part of the tie bar (Fig. 13a), the irregular geometry leads to concentrations of stress around the hole in the tie bar. The load applied by the pin is distributed as a nonuniform stress across the eye cross section, as shown in Fig. 17. Although the average stress on the cross section equals the load divided by the area, peak values of the stress occur at the inside of the eye.

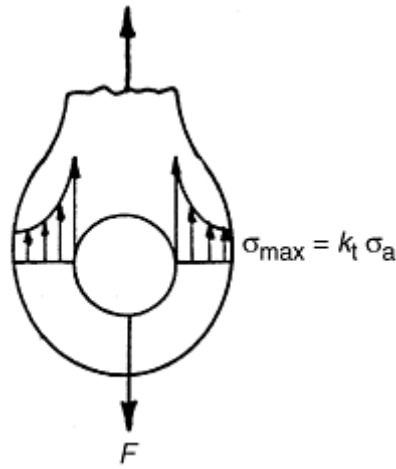


Fig. 17 Stress distribution on a cross section through the eye shown in Fig. 13(a)

Such concentrations of stress occur in all geometric irregularities such as fillet radii, notches, and holes. A simplistic but useful expression for the stress concentration is given by (Ref 19):

$$\sigma_{\max} = k_t \sigma_a \approx (1 + 2a/b) \sigma_a \quad (\text{Eq 28})$$

where k_t is the stress concentration factor, σ_a is the average stress, a is the dimension of the geometric irregularity perpendicular to the applied load, and b is the dimension parallel to the load (Fig. 18). In Fig. 17, for example, $a = b$, so the stress concentration factor is 3. For very small cracks perpendicular to the load, a is much greater than b so the stress concentration becomes $2 a/b$. Stress concentration factors for a wide range of practical geometries have been developed through extensive experimentation and analysis (Ref 16, 20). Failures usually initiate at these points of stress concentration and must be considered in all product designs.

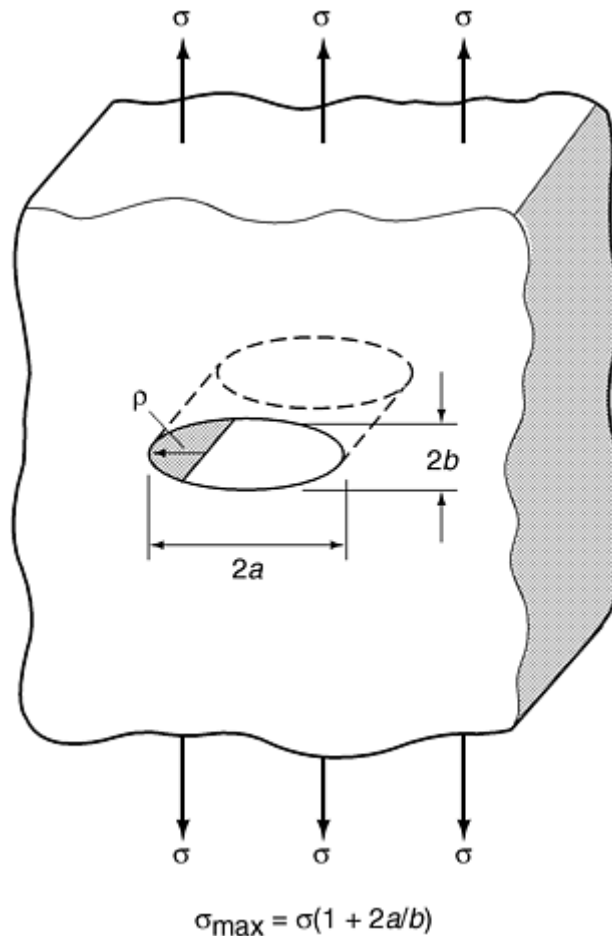


Fig. 18 Stress concentration around a flaw. Source: Ref 19

Pressure Vessels. Multiaxial stresses occur in shells subjected to internal or external pressure. Examples include tanks containing fluids, vessels containing a high-pressure and high-temperature chemical reaction (such as in petroleum refining), dirigibles, and submarine pressure hulls. Proper design of such pressure vessels must account for the multiaxial stresses.

A spherical shell containing pressure, for example, has equal stresses in any two perpendicular directions tangent to the sphere (Fig. 19), given by (Ref 22):

$$\sigma_{\theta} = \sigma_{\phi} = pD/4t \quad (\text{Eq 29})$$

where p is the internal pressure, D is the spherical diameter, and t is the wall thickness. Note that for D much greater than t , these stresses are much larger than the pressure, and stress through the thickness $\sigma_t \approx 0$.

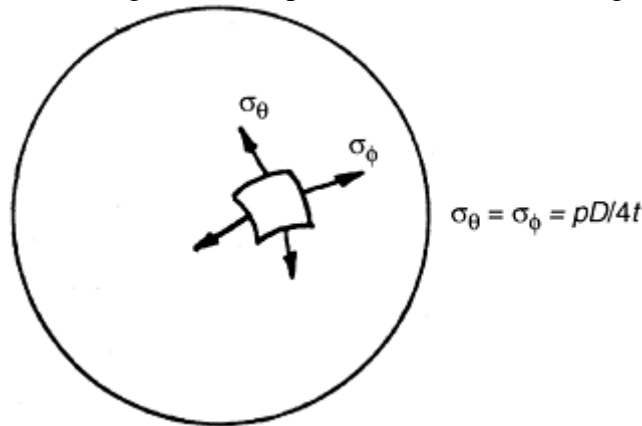


Fig. 19 Stresses in the wall of a spherical pressure vessel

A cylindrical pressure vessel wall will have a stress in the circumferential, or hoop, direction (Fig. 20), given by (Ref 16):

$$\sigma_{\theta} = pD/2t \quad (\text{Eq 30a})$$

and a stress in the axial direction given by:

$$\sigma_z = pD/4t \quad (\text{Eq 30b})$$

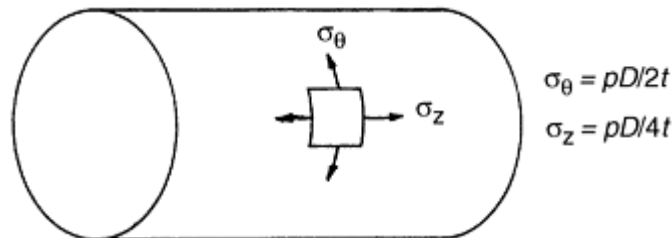


Fig. 20 Stresses in the wall of a cylindrical pressure vessel

Failure by yielding of a spherical pressure vessel can be found by substituting Eq 29 into Eq 24, giving:

$$p_{\max} = 4\sigma_o t/D \quad (\text{Eq 31})$$

For the cylindrical pressure vessel, substituting Eq 30a and 30b into Eq 24 gives:

$$p_{\max} = (4 / \sqrt{3})\sigma_o t/D \quad (\text{Eq 32})$$

In all pressure vessel applications, the stresses in the wall, given by Eq 29, 30a, and 30b, may be further complicated by stress concentrations due to holes for inlet and outlet piping.

In cases where the wall thickness is much less than the diameter, the stresses given by Eq 29, 30a, and 30b are nearly uniform through the thickness. For pressure containment where the wall thickness is a significant fraction of the diameter, such as in metalworking dies, the stress distribution is nonuniform with peak values at the inner surface (Ref 16). In these cases as well, Eq 24 is used to evaluate the initiation of failure by yielding.

Bearing Loads. Close examination of the pin end connector in Fig. 13(a) shows that the pin rests in a circular hole at the end of the tie bar. For ease of attachment to the connector, the pin diameter is smaller than the hole

diameter. As a result, the load transmitted from the pin to the inside surface of the hole occurs over a small area of contact, leading to high local pressures, as shown in Fig. 21. The pressure distribution in bearing contacts of this type is generally elliptical because the greatest elastic deformation occurs at the center of the contact zone. Figure 22 shows this more clearly in the contact pressure between a flat plate and a cylinder. Similar types of bearing loads and the accompanying elliptical pressure distributions occur in journal bearings, ball and roller bearings, gear tooth contacts, and railroad wheel/rail contacts. The nature of the contact pressure distributions and the internal distribution of stresses resulting from these loads have special implications regarding material testing and selection.

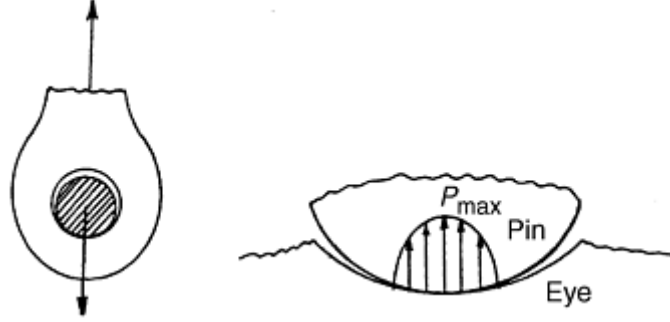


Fig. 21 Contact stresses between a pin and eye

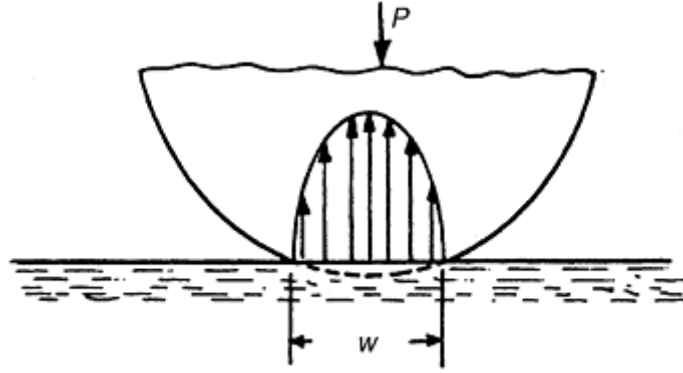


Fig. 22 Flattening and contact pressure distribution between a roller and flat plate

In roller-on-roller contacts, the elliptical pressure distributions in Fig. 21 and 22 have peak pressures given by (Ref 21):

$$p_{\max} = \sqrt{2P/\pi\Delta} \quad (\text{Eq 33a})$$

where P is the load per unit length of contact and

$$\Delta \equiv [1/(1/D_1 + 1/D_2)] [(1 - \nu_1^2)/E_1 + (1 - \nu_2^2)/E_2] \quad (\text{Eq 33b})$$

where D_1 and D_2 are the diameters of the rollers, and ν and E are the elastic properties of the materials in contact. The width, w , of the contact zone between the rollers is given by:

$$w = \sqrt{8P\Delta/\pi} \quad (\text{Eq 34})$$

In addition to the normal contact pressure shown as σ_z in Fig. 22, elastic deformation in the contact zone also generates σ_x parallel to the surface and σ_y parallel to the axes of the rollers (perpendicular to the view in Fig. 21). In this case, σ_x has the same magnitude and elliptical distribution as σ_z . Beneath the surface in Fig. 22, all of the stresses decrease because the contact load is spread over a larger area. Stress analysis leads to the stress distributions (Ref 21):

$$\sigma_z = -w/2\Delta\zeta \quad (\text{Eq 35a})$$

$$\sigma_x = -(\zeta - z')^2 w/2\Delta\zeta \quad (\text{Eq 35b})$$

$$\sigma_y = -\nu(\zeta - z') w/\Delta\zeta \quad (\text{Eq 35c})$$

where z is the distance beneath the contact surface, $z' = 2z/w$, and $\zeta = \sqrt{1+z'^2}$. These stresses are plotted in Fig. 23, which shows that σ_x decreases more rapidly than σ_z . The von Mises stress σ_{vm} is also plotted, which shows a maximum at a distance $0.4w$ beneath the surface (where w is the contact width calculated from Eq 34). Subsurface failure as a result of these stresses is common in rolling contact configurations such as Fig. 22.

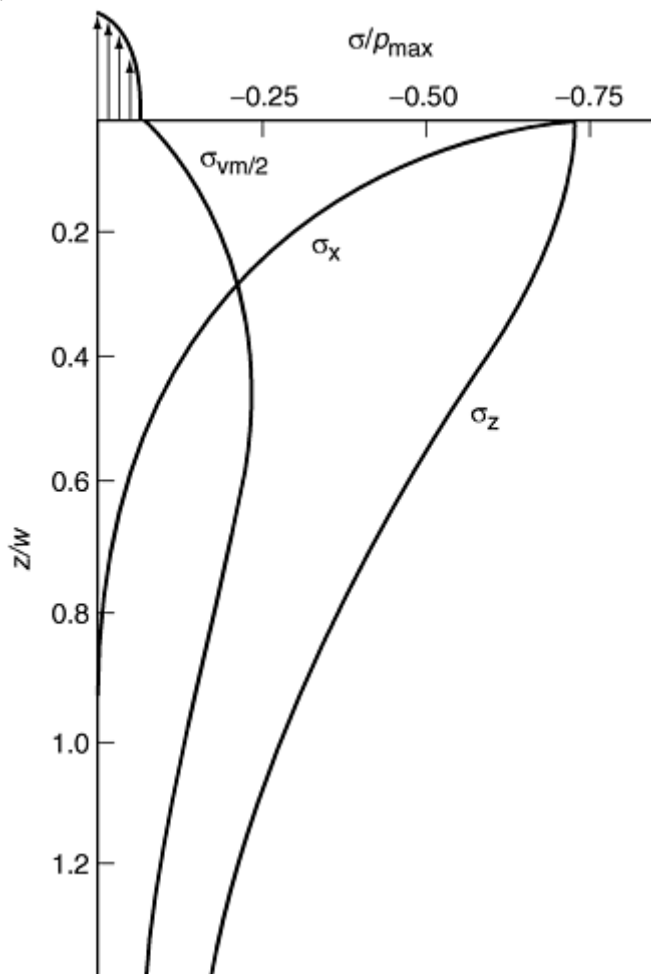


Fig. 23 Stresses beneath the contact zone in Fig. 22

Finite Element Analysis. For complex stress problems that are not easily solved using the basic loading situations (or their combinations) described previously, finite element analysis is commonly used. Over the past four decades, the finite element method has evolved from a structural analysis tool to a set of refined commercial programs that are invaluable aids in modern design. Much of this utility is a result of the availability of more rapid and powerful computers, improved numerical methods for solving the equations, and enhanced computer graphics for display of the results.

Finite element analysis reduces the infinite number of points in a prescribed product geometry to a finite number of elements bound by a finite number of points. The behavior of each element in a finite-element grid is governed by the same principles of equilibrium as in the tensile, compressive, torsional, and bend loadings described previously in this article, and by the material behavior described through constitutive equations (Eq 23a, 23b, 23c, and 24).

The beauty of finite element analysis for design is that it allows consideration of complicated geometries and any type of material for which the properties are known. Finite element analysis methods thus assist in the specification of geometry and material, which are the two primary objectives of design for mechanical applications. Evaluating small changes in geometry or variations in material properties via finite element modeling permits design optimization.

In the application of finite element analysis (Ref 22, 23), first the product geometry is described by a collection of two-dimensional or three-dimensional elements, such as those shown in Fig. 24. The choice of element type depends on the problem geometry and loading. From displacements of the nodal points in each element, the deformations and strains in the element are defined. Then the material constitutive equations (e.g., Eq 23a, 23b,

and 23c) relate these strains to the stresses in each element. Each node is connected to two or more elements, so there is interdependence between neighboring elements.

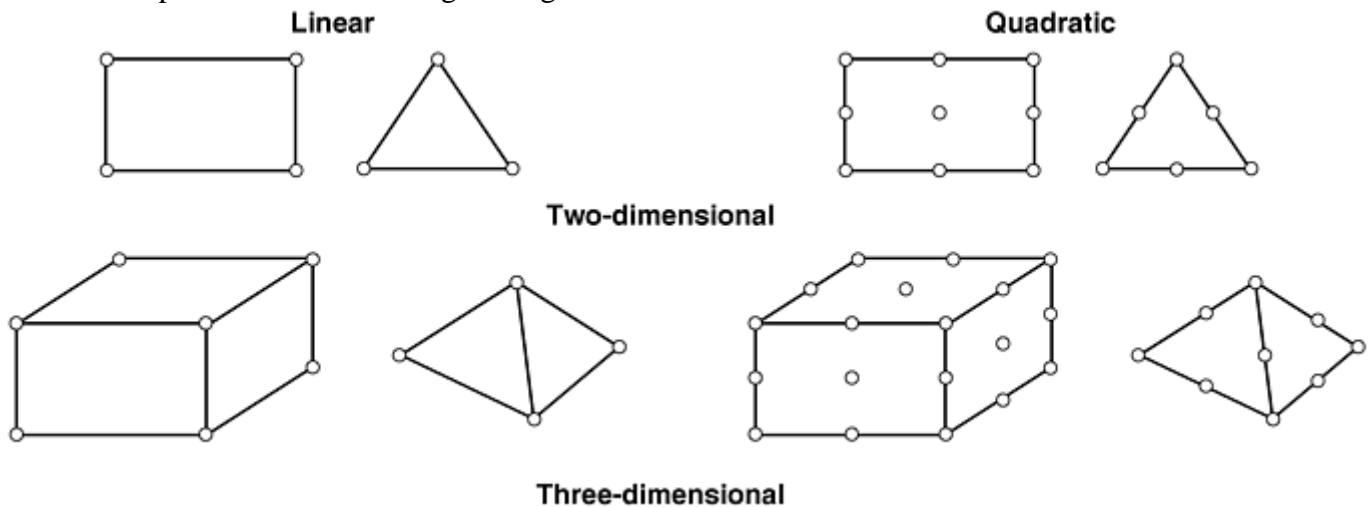


Fig. 24 Examples of element geometries used for finite element models

The next step is to define the boundary conditions (externally applied loads at the appropriate nodes) and constraints (identification of the nodes that are constrained from moving in at least one direction). This is a very important key to development of an accurate model and is based on mechanical insight of the person doing the modeling.

Energy methods are used to determine the interdependent nodal displacements (and stresses and strains) that minimize the total energy of the system. The resulting myriad of linear algebraic equations are then solved for all of the nodal displacements such that the stresses and deformations are compatible from element to element and are consistent with the externally applied loads and nodal constraints.

As an example, Fig. 25 shows a strip under tension and containing a hole, which was shown previously to cause a concentration of stress. The elements used for the analysis are quadrilateral to conform to the overall geometry of the part (Ref 24). In the vicinity of the hole, the elements are distorted to conform to the shape of the hole. In addition, the number of elements per unit area is increased in the vicinity of the hole because the stresses change rapidly. Taking advantage of symmetry, one-quarter of the geometry is considered to reduce the number of elements, nodes, and equations to be solved.

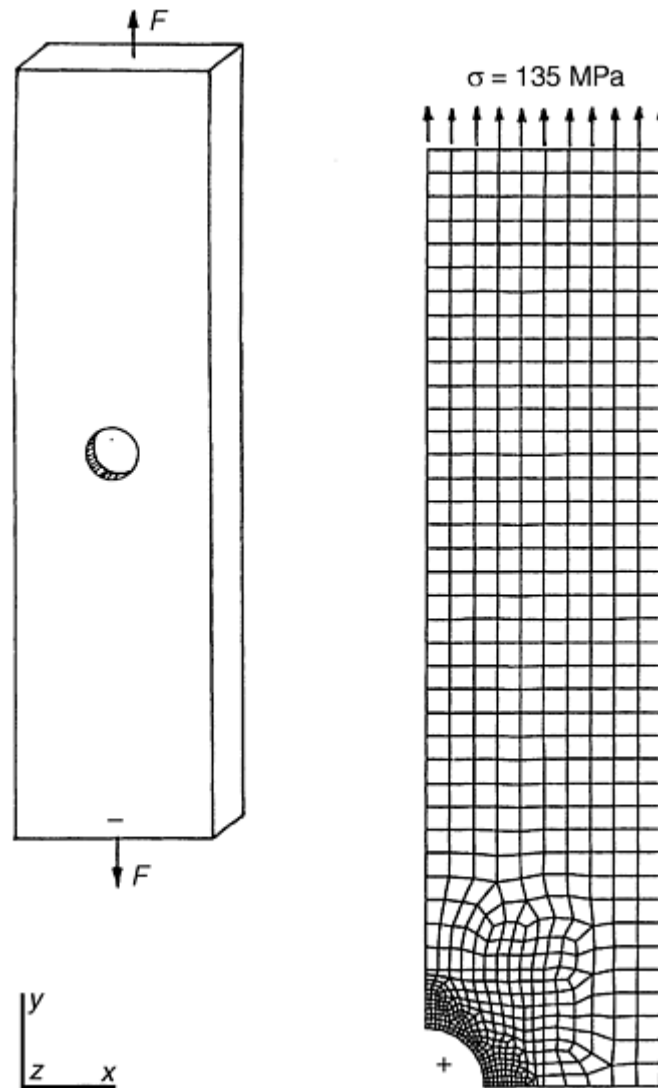


Fig. 25 Finite element model of a strip under tension and containing a hole. Source: Ref 24

Along the vertical line of symmetry, each nodal point is permitted to move vertically but not laterally. Along the horizontal line of symmetry, each node is permitted to move laterally but not vertically. These constitute the constraints on the problem.

At each of the nodal points along the upper surface, equal loads are applied that add up to the total applied load. Alternatively, uniform small displacements in the vertical direction can be applied to each node along the upper surface. This constitutes the loading for the problem. The material behavior is represented by elastic modulus, E , and Poisson ratio, ν , in the constitutive equations, Eq 23a, 23b, and 23c.

Results of solution of the simultaneous equations for all elements are shown in Fig. 26. Note that the axial stress, σ_y , along the horizontal plane through the hole has a peak value at the edge of the hole. Also, a small lateral stress distribution, σ_x , occurs along the horizontal plane of symmetry. Note that, along the vertical centerline, the axial stress is zero at the hole and then increases to the applied stress, while the lateral stress is compressive.

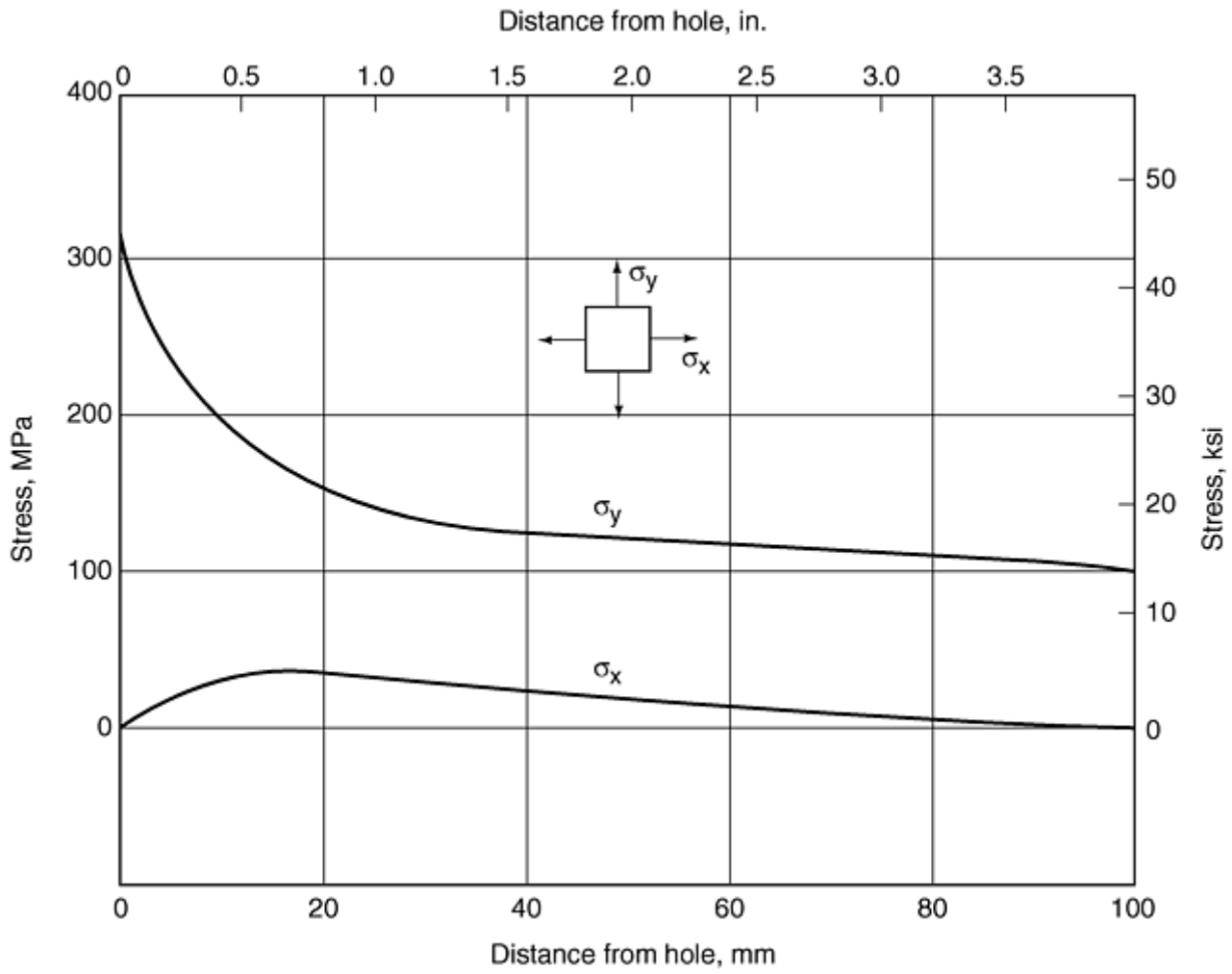


Fig. 26 Stress distributions calculated for the model shown in Fig. 25. Source: Ref 24

To evaluate failure by yielding, the stresses in each element of the model can be substituted into Eq 24. The resulting stress magnitude is called the von Mises stress and can be compared to the material yield strength, σ_o , to determine if yielding will occur. For example, Fig. 27 shows a contour plot of the von Mises stress for the problem shown in Fig. 25. Note that yielding would occur first at the inside of the hole and propagate along a 45° plane, illustrated by the band of high von Mises stress.

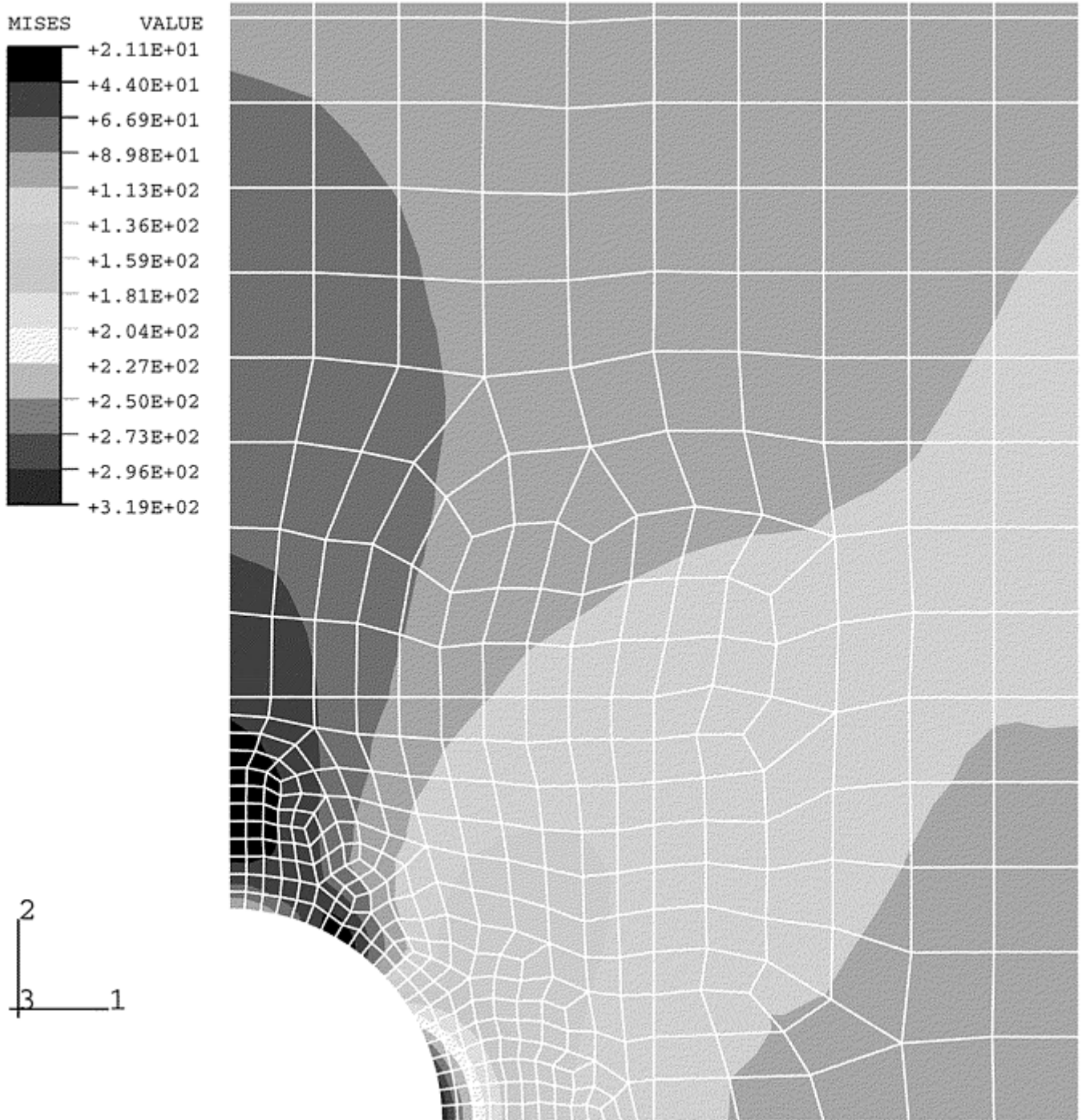


Fig. 27 Contour plot of von Mises stress for the model in Fig. 25. Source: Ref 24

As another example, a finite element analysis of the contact bearing load, described previously in Fig. 22, is shown in Fig. 28 (Ref 24). A contour plot of the calculated von Mises stress (Fig. 29) shows a potential subsurface failure point, as described previously by classical stress analysis (Fig. 22).

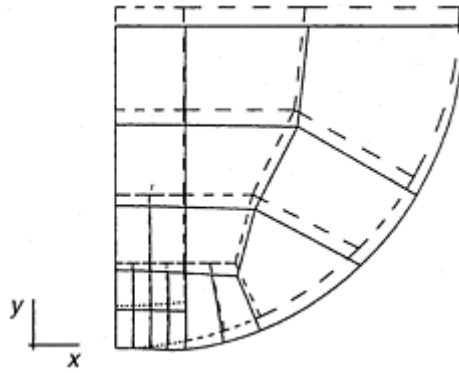


Fig. 28 Finite element model for contact stresses between a roller and flat plate, as in Fig. 22. Source: Ref 24

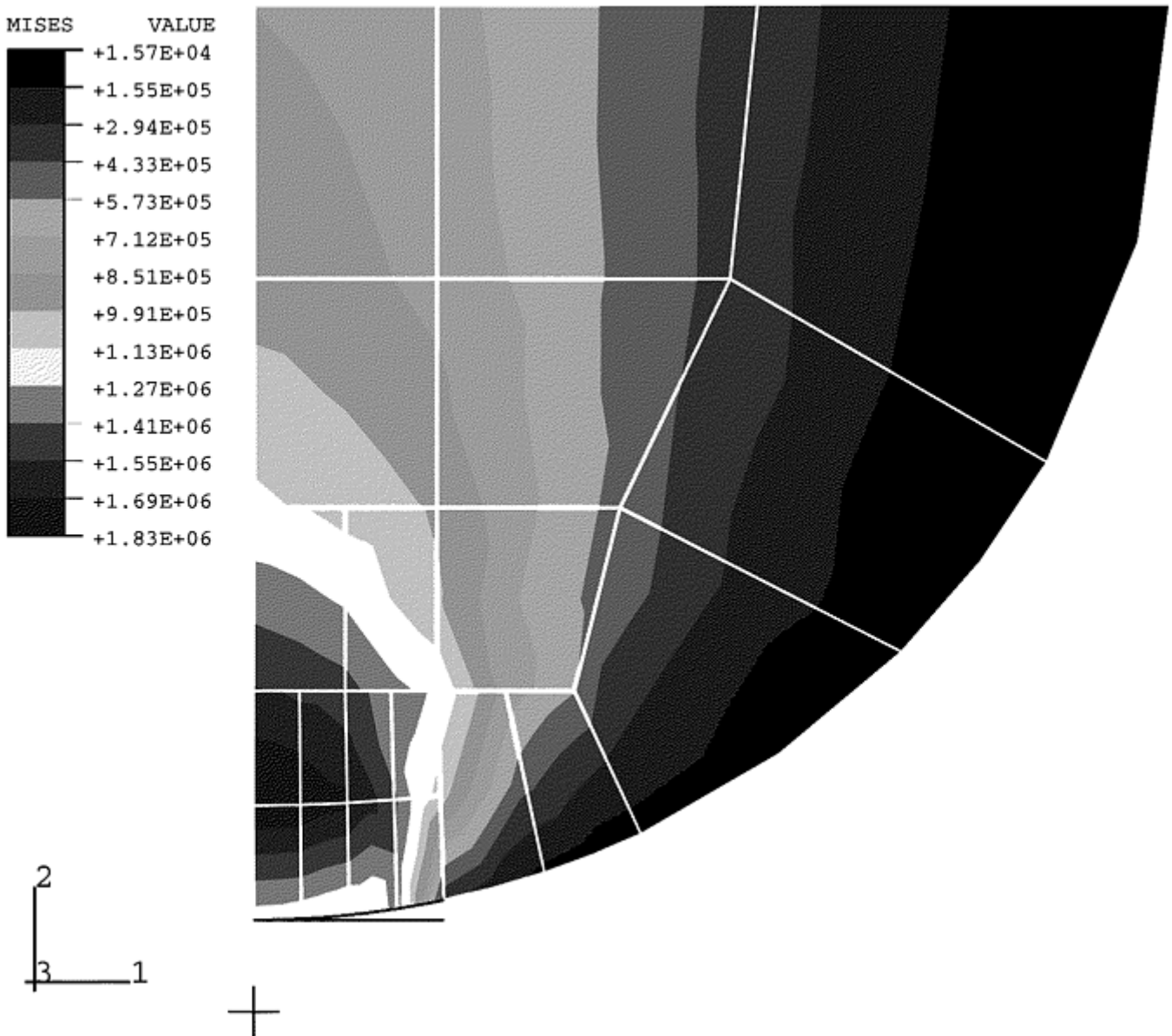


Fig. 29 Contour plot of von Mises stress beneath the zone of contact

These examples illustrate that finite element analysis tools provide deep insight into the mechanical behavior of materials for product design, but physical validity of the analytical results is a prime concern for designers who make decisions based on these results. Valid results depend on proper definition of the problem in terms of the meshing (element shape and size), loading (boundary conditions and constraints), and material characteristics

(constitutive relations). Setting up a valid problem and evaluating the results are greatly enhanced by knowledge of the stress, strain, and mechanical behavior of materials under the basic loading conditions presented in the previous paragraphs. Often, the cost and time for finite element analysis can be precluded by learned application of the knowledge of the basic modes of loading. This is the basis for the Cambridge Engineering Selector (Ref 1). On the other hand, some problems are so complex that only finite element analysis can provide the necessary information for design decisions. Analysts' and designers' skill and experience are the bases for judgment on the level of sophistication required for a given design problem.

Additional information on finite element methods is provided in the article, "Finite Element Analysis" in *Materials Selection and Design* Volume 20 of *ASM Handbook*.

Material Testing for Complex Stresses. In all of the cases given above for complex stresses, the tensile yield strength and the elastic properties, E and ν , are the key material parameters required for accurate design analyses. The yield criterion, using the tensile yield strength, σ_0 , is used to predict failure by yielding. All of these material parameters can be determined by tension testing.

The prediction of failure by yielding is also useful for prediction of the sites for fracture since localized yielding usually precedes fracture. Final failure by fracture, however, cannot be related to any single criterion or simple test. The following paragraphs describe approaches to material evaluation for various forms of failure by fracture.

References cited in this section

1. Cambridge Engineering Selector, Granta Design Ltd., Cambridge, UK, 1998
15. G.E. Dieter, *Mechanical Metallurgy*, 2nd ed., McGraw Hill, 1976, p 49–50, 79–80, 379, 381, 385
16. J.H. Faupel and F.E. Fisher, *Engineering Design*, John Wiley & Sons, 1981, p 102, 113, 230–235, 802
19. R.W. Hertzberg, *Deformation and Fracture Mechanics of Engineering Materials*, 2nd ed., John Wiley & Sons, 1983, p 240, 287, 288, 436–477
20. W.C. Young, *Formulas for Stress and Strain*, 5th ed., McGraw-Hill, 1975
21. S.P. Timoshenko and J. Goodier, *Theory of Elasticity*, 3rd ed., McGraw Hill, 1970, p 418–419
22. O.C. Zienkiewicz, *The Finite Element Method in Engineering Science*, 4th ed., McGraw Hill, 1987
23. K.H. Heubner, et al., *The Finite Element Method for Engineers*, 3rd ed., John Wiley & Sons, 1995
24. ABAQUS/Standard, Example Problems Manual, Vol 1, Version 5.7, 1997

Overview of Mechanical Properties and Testing for Design

Howard A. Kuhn, Concurrent Technologies Corporation

Fracture

The design approaches given in preceding sections of this article were based on prevention of failure by yielding or excessive elastic deflection. While the yield strength for ductile materials is below their tensile strength, it is well known that failure by fracture can occur even when the applied global stresses are less than the yield strength. Fractures initiate at localized inhomogenities, or defects, in the material, such as inclusions, microcracks, and voids. Previously it was shown that geometric inhomogenities in a part lead to

concentrations of stress (Fig. 18 and Eq 28). Material defects, generally having a sharp geometry (a much greater than b) lead to very high localized stresses.

Considering such defects in design against fracture requires looking beyond stress and elastic deformation to the combination of stress and strain, or energy per unit volume. Defects are commonplace in the microstructures of real materials and are generated both by materials processing and by service loads and environments. Under certain conditions, these defects can grow, unsteadily, leading to rapid and catastrophic fracture. This condition was first described by Griffith (Ref 25), who noted that a defect would grow when the elastic energy released by the growth of the defect exceeded the energy required to form the crack surfaces. The excess energy in the system, then, continuously feeds the fracture phenomenon, leading to unstable propagation. The driving energy from defect growth is a function of the applied stresses (loading, part, and defect size geometry), and the energy for crack surface formation is a function of the material microstructure. Details of the development can be found in Ref 19 and 27 and the Section “Impact Toughness Testing and Fracture Mechanics” in this Volume.

Design Approach. For design and materials selection to avoid fast fracture, the net result of these considerations is the basic design equation for stable crack growth (Ref 19):

$$K = Y\sigma\sqrt{\pi a} < K_c \quad (\text{Eq 36})$$

where K is the stress intensity factor, Y is a factor depending on the geometry of the crack relative to the geometry of the part, σ is the applied stress, a is the defect size or crack length, and K_c is a critical value of stress intensity. K must be less than K_c for stable crack growth.

The stress intensity K represents the effect of the stress field ahead of the crack tip and is related to the energy released as the crack grows. For example, Fig. 30 shows the results of finite element analysis of the stresses in the vicinity of a crack growing from a hole. The high level and distribution of stresses ahead of the crack tip all contribute to the stress intensity factor. When the stress intensity exceeds a critical value, K_c , the energy released exceeds the ability of the material to absorb that energy in forming new fracture surfaces, and crack growth becomes unstable. This critical value of the stress intensity is known as the fracture toughness of the material.

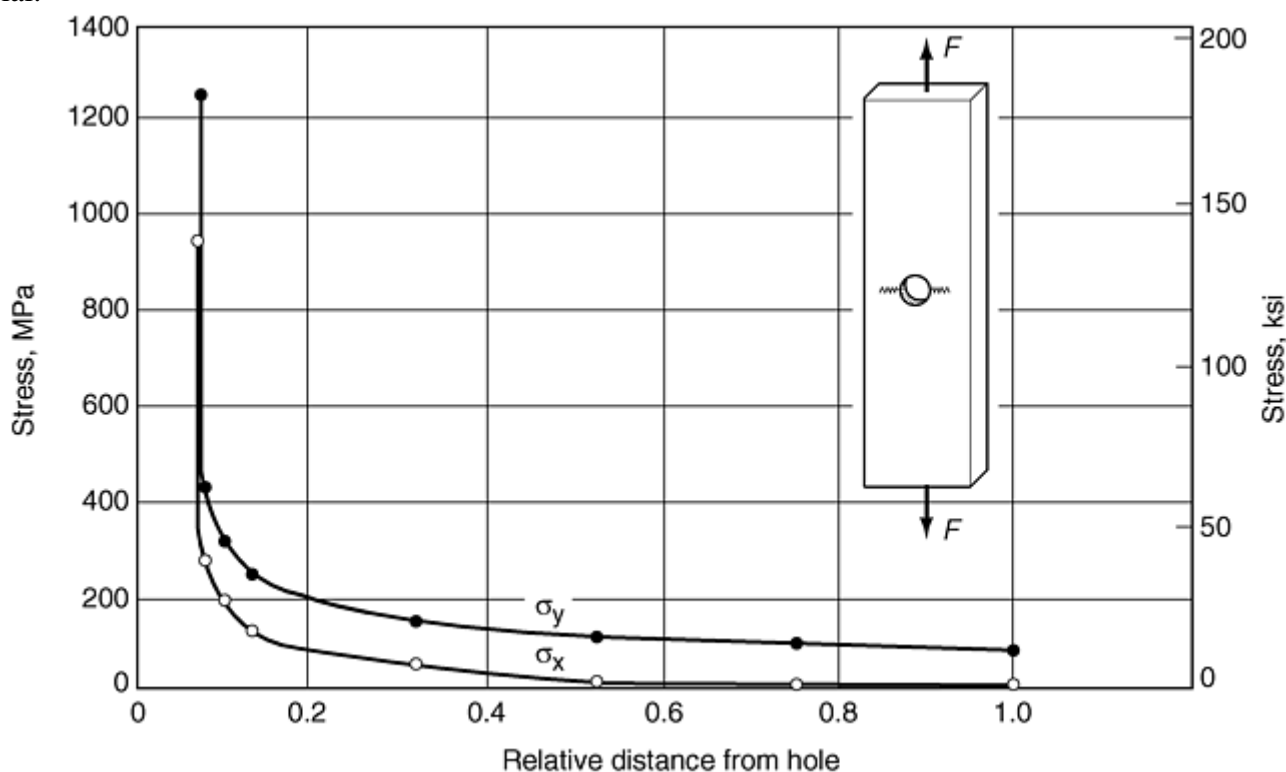


Fig. 30 Finite element calculation of stresses in the vicinity of a crack at the edge of a hole in a strip under axial tension

Equation 36 can be viewed in the same way as Eq 2 for tensile loading and Eq 12 and 13 for bending and torsion. The stress intensity factor, K , in Eq 36 is equivalent to stress, σ in Eq 2, 12, or 13. While the stress is

defined for each case by the applied load and geometry of the part, stress intensity is defined by the applied stress (load and part geometry) and the geometry of the crack relative to the geometry of the part, which is expressed by the factor Y . The important difference is that more information is given in the stress intensity factor since it involves the defect or crack size, which becomes an additional design parameter. Values of Y can be found in Ref 19 and 26, among others, for some common part geometries and crack configurations. Alternatively, finite element analysis can be used to determine K . The fracture toughness of the material, K_c , on the right side of Eq 36 is equivalent from a design perspective to the material strength, σ_f , in Eq 2, 12, and 13. In applying Eq 36, if the material is specified and the stress is known from the loading requirements, then the maximum flaw size that can be tolerated is $a_{\max} = K_c^2 / \sigma^2 \pi f^2$ (or $a_{\max} = Y^2 K_c^2 / \sigma^2 \pi$). This gives a clear objective for nondestructive inspection of flaws in the product. Alternatively, if the material is specified and a maximum flaw size is specified that can be easily seen by visual inspection, then the maximum stress that can be applied is $\sigma_{\max} = Y K_c / \sqrt{\pi a}$. On the other hand, if the stress and maximum flaw size are known, Eq 36 defines the value of K_c required to prevent fracture and is used for material selection from tables of fracture toughness. One application of the fracture criterion in Eq 36 is the design of pressure vessels, using a leak-before-break philosophy. If the pressure vessel contains a flaw that grows to extend through the pressure vessel wall without causing unstable fracture, then the internal pressurized fluid will leak out. On the other hand, if the flaw size in the pressure vessel is above the critical flaw size yet less than the wall thickness of the vessel, fracture will occur catastrophically. In Fig. 31, a flaw is shown having grown through the pressure vessel wall (Ref 19). If the critical flaw size is taken as the thickness of the pressure vessel wall, then Eq 36 gives $\sigma_{\max} = Y K_c / \sqrt{\pi t}$, where t is the thickness of the wall. Equations 29, 30a, and 30b can be used to define the applied stress in the pressure vessel wall and its relation to the internal pressure. Then, for a given material and its fracture toughness, K_c , the maximum stress and internal pressure is determined. Conversely, for a given pressure (and stress in the wall), the required value of fracture toughness is given by $K_c = \sigma \sqrt{\pi t} / Y$.

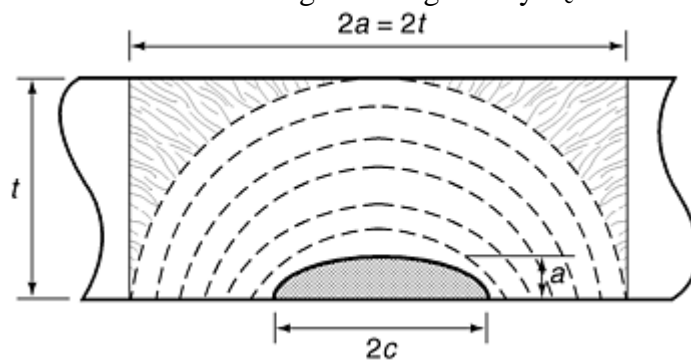


Fig. 31 Flaw in a pressure vessel wall. Source: Ref 19

Mechanical Testing. The crack opening mode described in this example is known as mode I, or crack opening perpendicular to a tensile stress (Fig. 32), which is the most common mode of fracture. Mode I cracking occurs, for example, in the tensile loading of the tie bar shown in Fig. 1, in the stress concentration around the eye in the end connector (Fig. 16) and in bending (Fig. 7 and 9). In this case, the critical stress intensity of the material, or fracture toughness, is designated K_{Ic} . However, two other crack opening modes are possible, as shown in Fig. 32. Mode II occurs in linear shear, as depicted in Fig. 14 and 15, while mode III occurs in torsional shear (Fig. 6 and 8). The critical stress intensity for these modes are denoted by K_{IIc} and K_{IIIc} . The mode of potential fracture prescribes the test and approach used for measurement of the respective fracture toughness values.

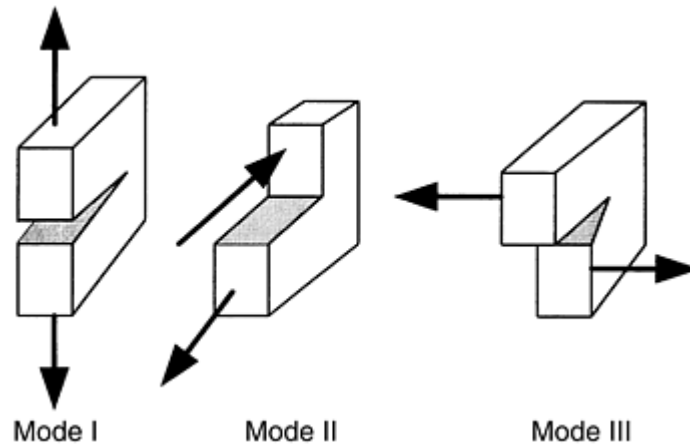


Fig. 32 Three crack opening modes

The material property to be determined for design against fracture is the fracture toughness, K_{Ic} , to be used in Eq 36. The critical stress intensity, K_{Ic} , or fracture toughness in mode I, for example, can be measured by a compact tension test as well as other standardized test specimens and procedures, as described in the Section “Impact Toughness Testing and Fracture Mechanics” in this Volume. In addition, fracture toughness values can be correlated with Charpy test measurements of toughness for certain steel alloys (Ref 27).

References cited in this section

19. R.W. Hertzberg, *Deformation and Fracture Mechanics of Engineering Materials*, 2nd ed., John Wiley & Sons, 1983, p 240, 287, 288, 436–477
25. A.A. Griffith, *Trans. ASM*, Vol 61, 1968, p 871
26. A.F. Liu, *Structural Life Assessment Methods*, ASM International, 1998
27. J.M. Barsom, *Engineering Fracture Mechanics*, Vol 7, 1975, p 605

Overview of Mechanical Properties and Testing for Design

Howard A. Kuhn, Concurrent Technologies Corporation

Fatigue

In the previous discussion, the various loads and the resulting stress distributions are defined for static conditions. In most design applications, however, parts and components are subjected to cyclic loads. In this case, the peak amplitude of a load cycle (σ_{max} in Fig. 33) is the maximum value of applied stress, which can be analyzed by the equations for static stress distributions (for example, from Eq 1, 12, 13, 21, and 27a 27b). However, materials under cyclic stress also undergo progressive damage, which lowers their resistance to fracture (even at stresses below the yield strength).

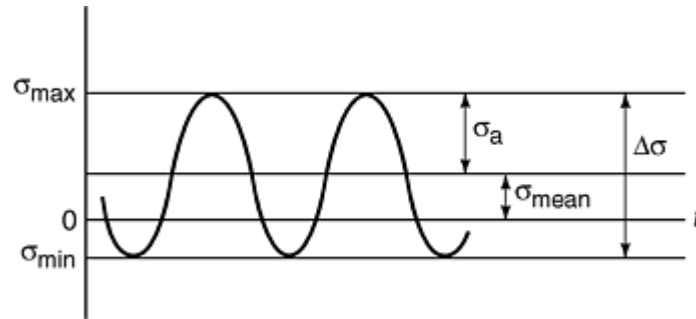


Fig. 33 Cyclic stress that may lead to fatigue failure

The occurrence of fatigue (paraphrasing from Ref 28) can be generally defined as the progressive, localized, and permanent structural change that occurs in a material subjected to repeated or fluctuating strains at nominal stresses that have maximum values less than (and often much less than) the static yield strength of the material. Fatigue damage is caused by the simultaneous action of cyclic stress, tensile stress, and plastic strain. If any one of these three is not present, a fatigue crack will not initiate and propagate. The plastic strain resulting from cyclic stress initiates the crack; the tensile stress promotes crack growth (propagation). Compressive stresses (typically) will not cause fatigue, although compressive loads may result in local tensile stresses.

During fatigue failure in a metal free of cracklike flaws, microcracks form, coalesce, or grow to macrocracks that propagate until the fracture toughness of the material is exceeded and final fracture occurs. Under usual loading conditions, fatigue cracks initiate near or at singularities that lie on or just below the surface, such as scratches, sharp changes in cross section, pits, inclusions, or embrittled grain boundaries (Ref 32).

The three major approaches of fatigue analysis and testing in current use are the stress-based (*S-N* curve) approach, the strain-based approach, and the fracture mechanics approach. Both the stress-based and strain-based approaches are based on cyclic loading of test coupons at a progressively larger number of cycles until the test piece fractures. In stress-based fatigue testing, steels and some other alloys may exhibit a fatigue endurance limit, which is the lower stress limit of the *S-N* curve for which fatigue fracture is not observed at testing above $\sim 10^7$ cycles (Fig. 34). The observation of a fatigue endurance limit does not occur for all alloys (e.g., aluminum alloy 7075 in Fig. 34), and the endurance limit can be reduced or eliminated by a number of environmental and material factors that introduce sites for initiation of fatigue cracks. For example, Fig. 35 shows the effect of different surface conditions on the fatigue endurance limit of steels, which in this case is approximately one-half of the tensile strength. Under these conditions, when the designs of components subjected to cyclic loading are expected to perform under $\sim 10^7$ cycles, design equations such as Eq 2 and 13 would be applicable where the fatigue limit, σ_e , of the material represents the failure stress, σ_f . For alloys without a fatigue endurance limit (such as aluminum alloy 7075 in Fig. 34), design stresses must be specified in terms of the specific number of cycles expected in the lifetime of the part.

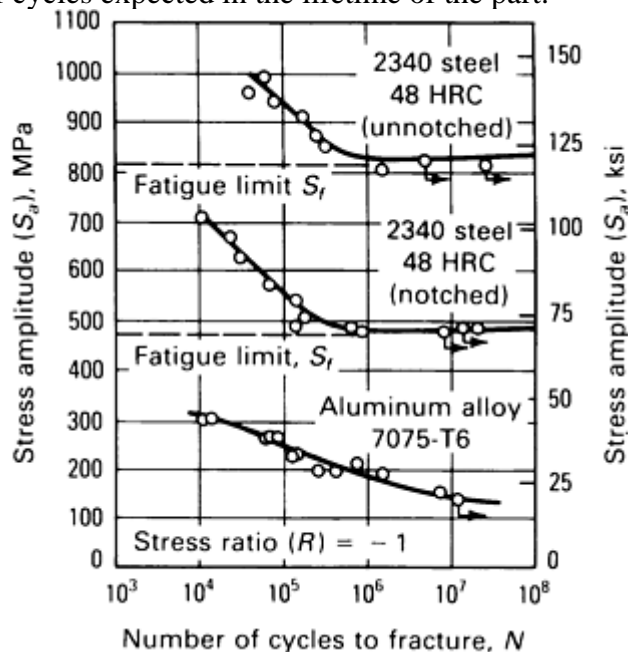


Fig. 34 Fatigue curves for ferrous and nonferrous alloys

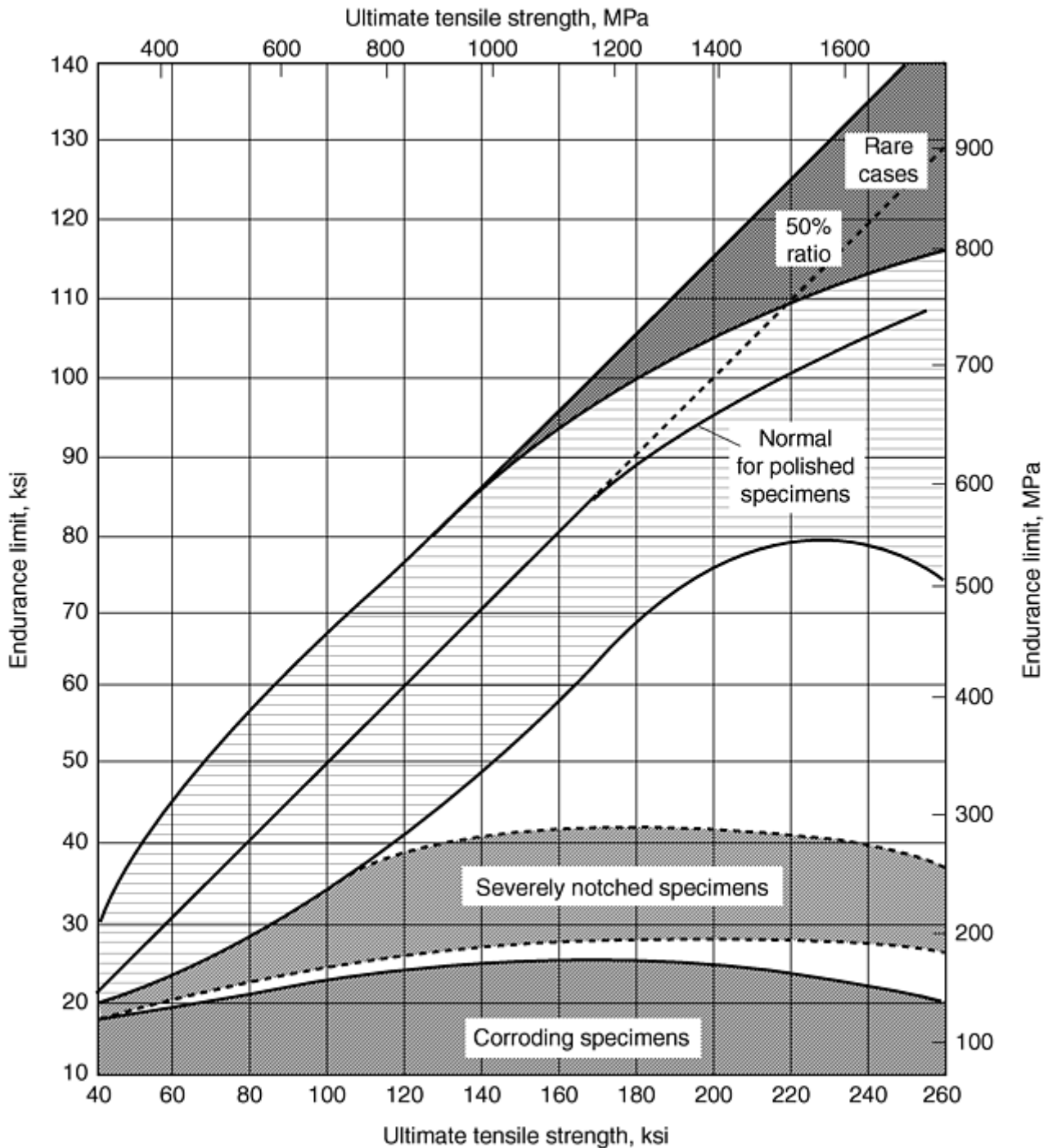


Fig. 35 Correlation between fatigue endurance limit and tensile strength for specimens tested under various environments

Strain-based fatigue is similar to stress-based fatigue, except that cycles to failure are measured and plotted versus strain instead of applied stress. This type of testing and analysis is extremely useful in determining conditions for initiation fatigue. Strain-based fatigue is used in many design cases when a major portion of total life is exhausted in the crack initiation phase of fatigue. Fundamental design methods for this type of fatigue analysis are described in more detail in Ref 29. Design aspects for variable amplitude and multiaxial conditions are also described in Ref 30 and 31. Testing methods for stress-based and strain-based fatigue are described in more detail in the article “Fatigue, Creep Fatigue, and Thermomechanical Fatigue Life Testing” in this Volume. Although design and analysis methods based on fatigue crack initiation are important, most parts have material flaws or geometric features that serve as sites for crack initiation. Therefore, fatigue crack growth is an integral part of fatigue life prediction analysis. This method is based on the concepts of fracture mechanics, where

fatigue crack growth rates are measured under conditions of a cyclic stress intensity (ΔK) at subcritical levels ($K < K_c$). Fatigue failures start at points of stress concentration and can be considered as flaws in the material. As these flaws grow during the fatigue process, they can reach the critical size and lead to catastrophic failure by rapid fracture. For this purpose, fatigue crack growth testing and analysis are used to determine the number of cycles to reach the critical flaw size for a given material (with a fracture toughness, K_c). These tests are described in more detail in the article “Fatigue Crack Growth Testing” in this Volume.

References cited in this section

28. M.E. Fine and Y.-W. Chung, Fatigue Failure in Metals, *Fatigue and Fracture*, Vol 19, *ASM Handbook*, ASM International, 1996, p 63
29. M.R. Mitchell, Fundamentals of Modern Fatigue Analysis for Design, *Fatigue and Fracture*, Vol 19, *ASM Handbook*, ASM International, 1996, p 227–249
30. N.E. Dowling, Estimating Fatigue Life, *Fatigue and Fracture*, Vol 19, *ASM Handbook*, ASM International, 1996, p 250–262
31. D.L. McDowell, Multiaxial Fatigue Strength, *Fatigue and Fracture*, Vol 19, *ASM Handbook*, ASM International, 1996, p 263–273
32. D. Woodford, Design for High-Temperature Applications, *Materials Selection and Design*, Vol 20, *ASM Handbook*, ASM International, 1998, p 580

Overview of Mechanical Properties and Testing for Design

Howard A. Kuhn, Concurrent Technologies Corporation

Creep

Many design applications involve materials and components that are subjected for extended periods of time to high-temperature environments. For example, the tie bar shown in Fig. 1 could be part of a hanger supporting steel parts in a furnace for heat treatment. Other examples include turbine blades in jet engines and pressure vessels in high-temperature refinery operations. In these cases, failure of the material occurs by complex diffusion-controlled phenomena leading to cavitation, creep elongation, and eventual rupture of the material. Testing of materials in its simplest forms involves subjecting a tensile specimen to constant load or constant stress within a high-temperature environment and measuring the elongation with time. A typical curve of creep elongation versus time is shown in Fig. 36. After initial rapid growth in creep strain, the rate of creep strain reaches a steady state, followed again by rapid growth to rupture. Increasing stress on temperature increases the rate of creep strain and decreases the time to creep rupture. Figure 37(a) shows the influence of temperature and stress on the time to rupture. Figure 37(b) shows the temperature dependence of yield strength, tensile strength, and stress for creep rupture at 1,000 h and 100,000 h. Typically, the stresses for creep rupture are less than the yield strength of the material, even for relatively short rupture times.

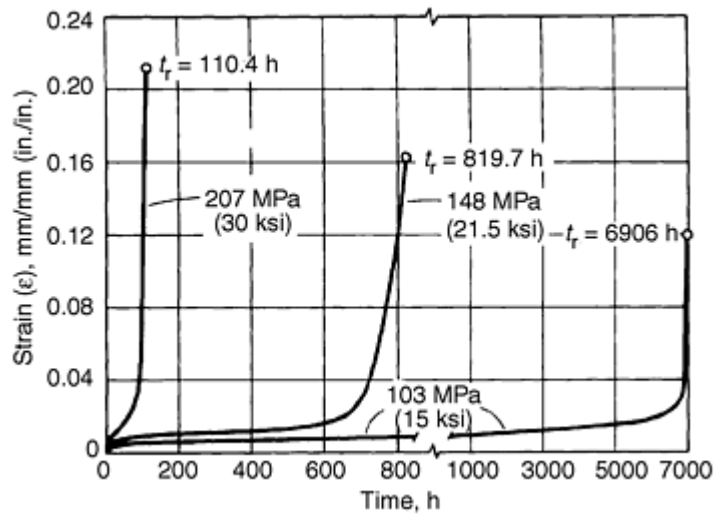
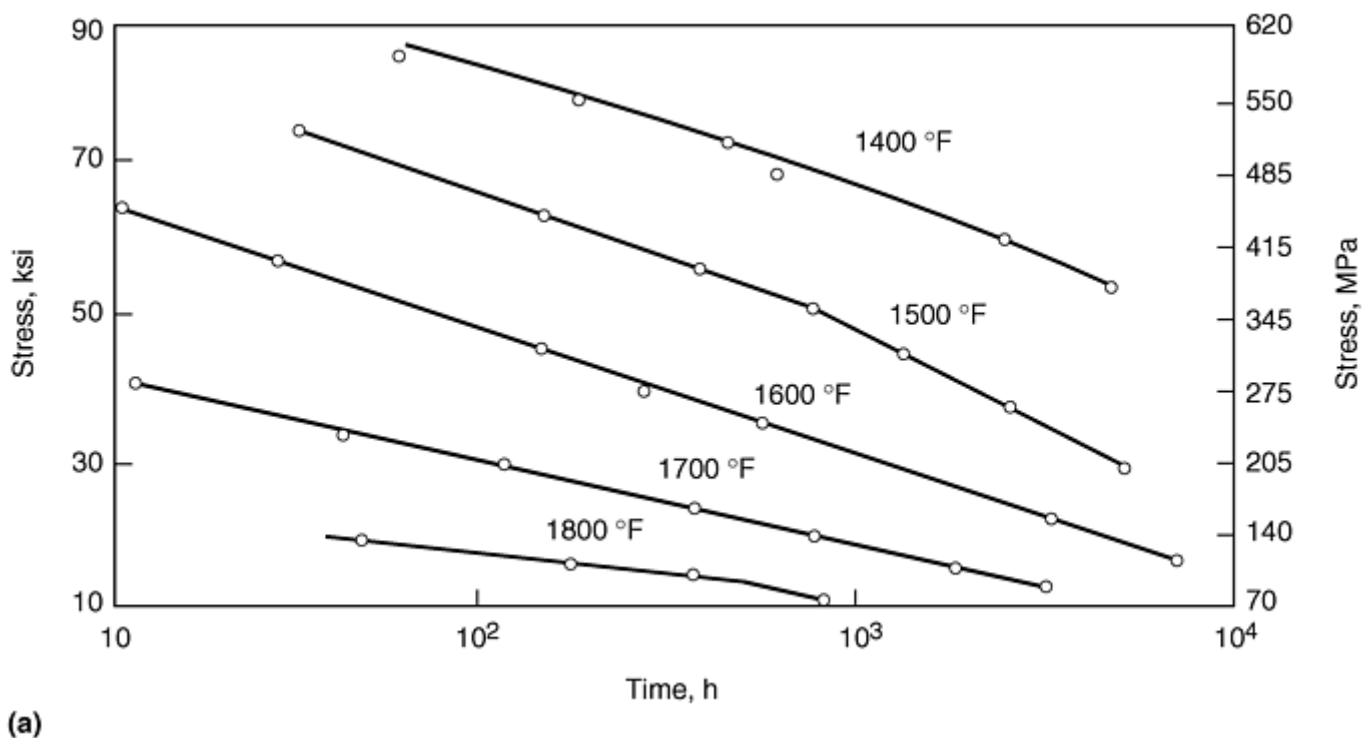
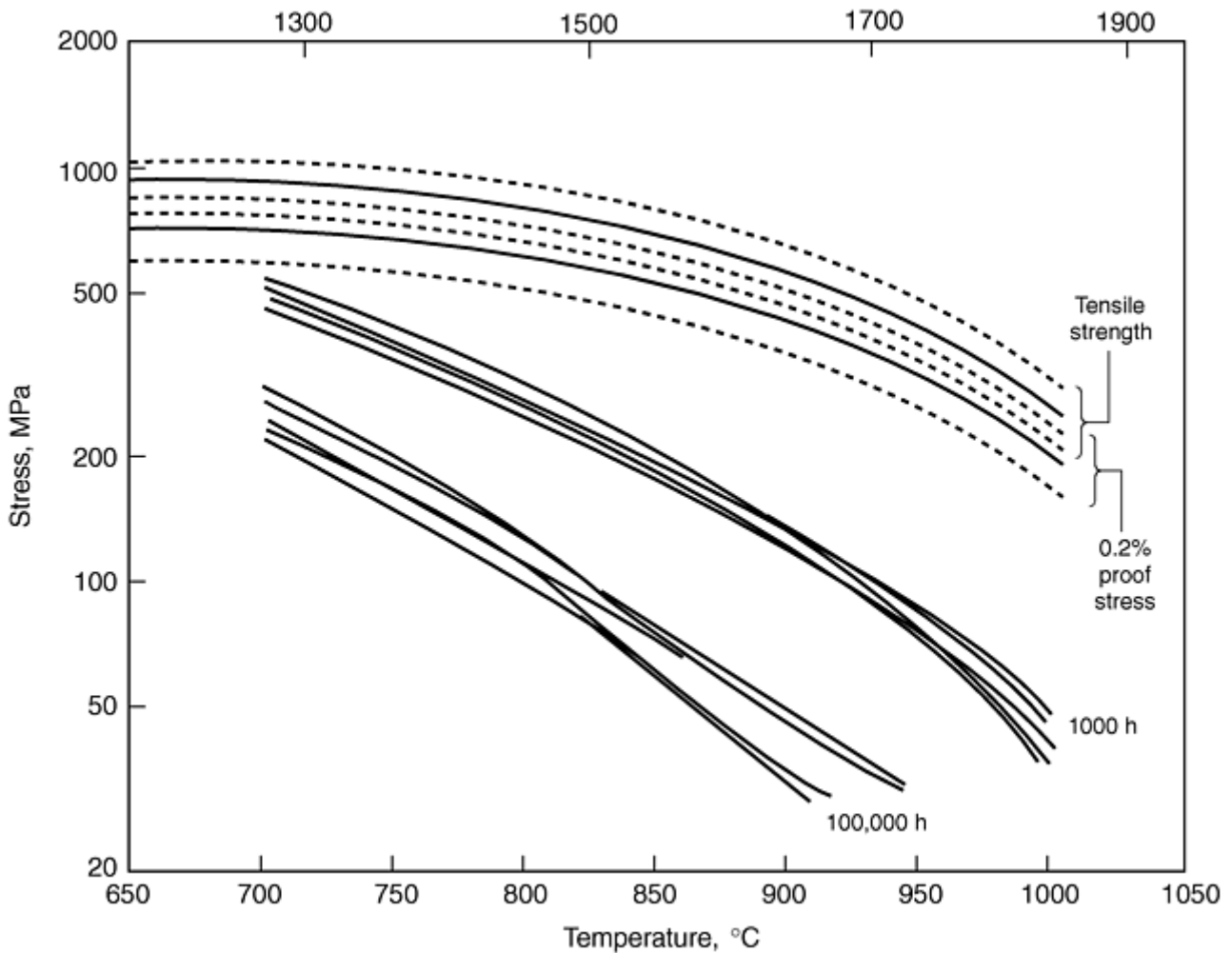


Fig. 36 Typical result for creep strain as a function of time



(a)

Fig. 37(a)



(b)

Fig. 37(b)

Typical data used for designs where materials are exposed to high temperatures for extended periods. (a) Creep stress versus time to rupture for Astroloy. (b) Temperature dependence of yield strength, tensile strength, and creep rupture strength at two different times for a nickel-based superalloy

In design applications to avoid creep rupture, the stresses on the material can be calculated as in the case of static loads such as Eq 2, 12, and 13. The failure stress, σ_f , used in these equations, however, would be the rupture strength of the material determined from curves such as Fig. 37(a) at the operating temperature of the components in the design application. Depending on the expected life of the part, then, the operating temperature will determine the maximum stress that can be applied. Alternatively, for a given operating stress and expected lifetime, the maximum operating temperature can be determined from data such as Fig. 37(a) (Ref 32).

In design applications where creep occurs, elongation of the material often becomes the limiting failure parameter rather than creep rupture strength. A major example is the elongation of turbine blades during turbine engine operation. If the blades elongate too much, they contact the internal parts of the engine leading to catastrophic failure. In this case, elongation would be described by the creep strain profile in Fig. 36, for example, rather than the elastic deflection calculated in Eq 4. Thus, for a given operating temperature and load, the lifetime for successful operation of a component would be obtained from data such as that provided in Fig. 36 for the specified limit on elongation.

Because of the importance of creep failure in many applications, refined test procedures have been developed for accurate measurement of creep behavior under complex thermal and stress histories, as well as various corrosive environments as described in the Section "Creep and Stress-Relaxation Testing" in this Volume.

Reference cited in this section

Overview of Mechanical Properties and Testing for Design

Howard A. Kuhn, Concurrent Technologies Corporation

Environmental Effects on Mechanical Properties

The mechanical properties of metals can be adversely affected when the metal is exposed to a corrosive environment while being simultaneously stressed. Even in only mildly corrosive environments, the consequences can be unexpected and serious. These mechanisms that cause adverse affects are collectively known as environmentally assisted cracking and include some of the more common mechanisms by which metals actually fail in service. The most important of the phenomena are *stress corrosion*, *hydrogen embrittlement*, and *corrosion fatigue*.

Stress-corrosion cracking (SCC) of metals occurs in certain environments when cracks initiate and propagate under conditions where neither the stress nor the environment acting alone would have caused cracking. The propagation of SCC may eventually lead to structural failure or at least to ineffective performance of a component (due to problems such as leaks and distortion). Stress-corrosion cracks initiate only at a surface—and only at a surface that is exposed to the damaging environment. Once initiated, they propagate laterally into the section thickness, by either transgranular cracking (across grains, Fig. 38) or intergranular cracking (along grain boundaries, Fig. 39). Most of the surface of a stress-cracked metal is essentially unattacked. Stress cracking may occur at relatively low stress levels compared with stress needed for failure (tensile strength) and at relatively low concentrations of chemicals (such as Cl⁻ for austenitic stainless steels).

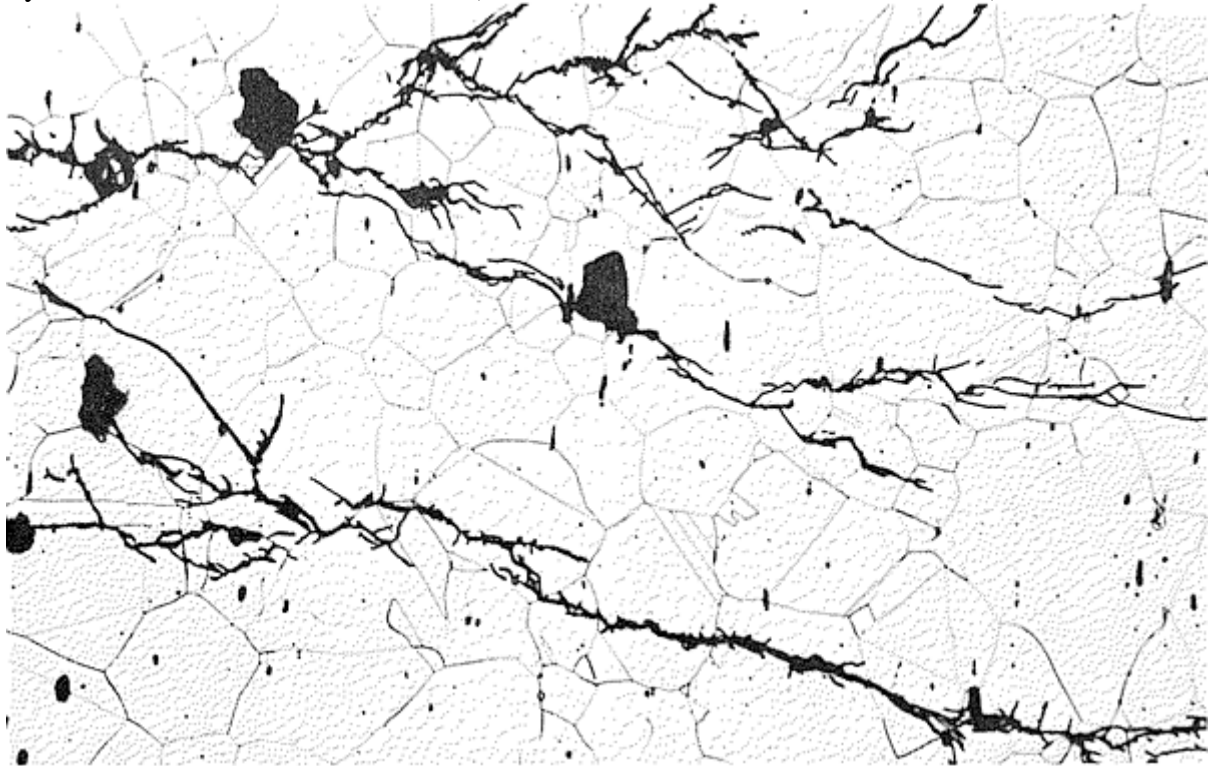


Fig. 38 Transgranular stress-corrosion cracking (SCC) in annealed 310 stainless steel after prolonged exposure in a chloride-containing environment. Electrolytic: 10% chromic acid etch. 150×

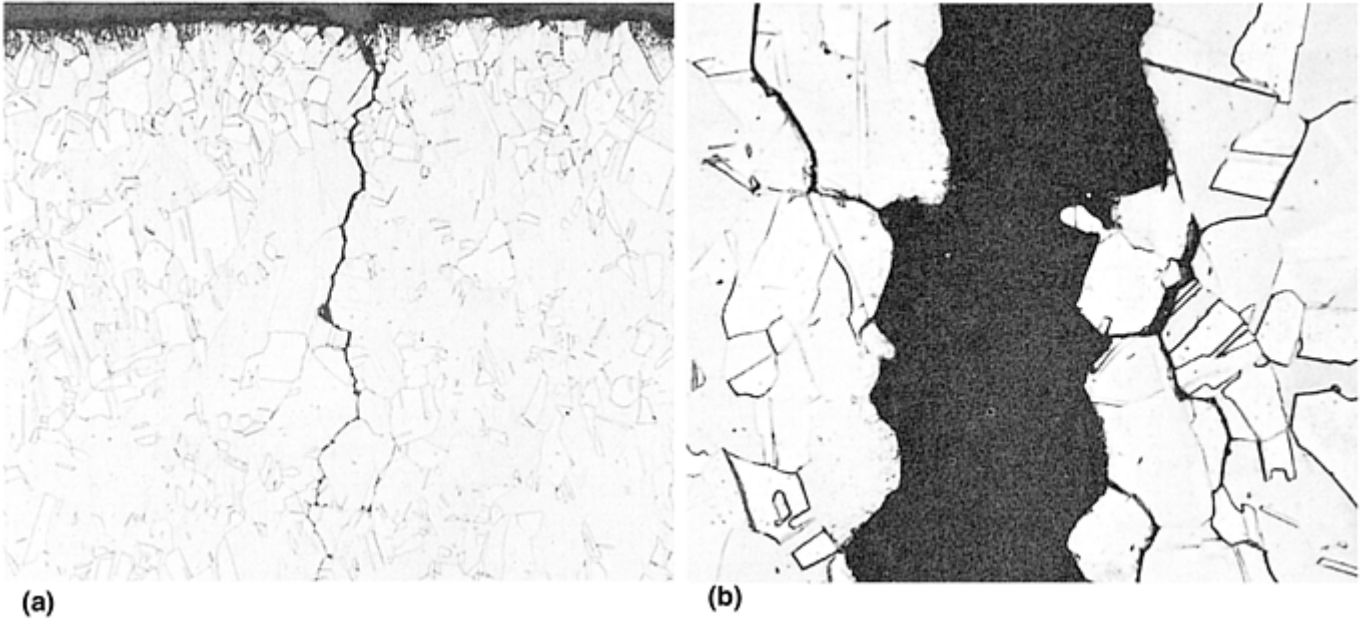
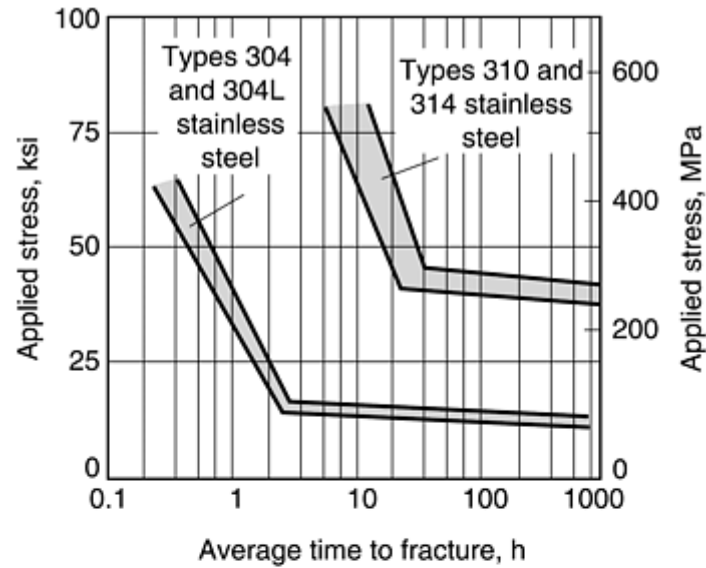
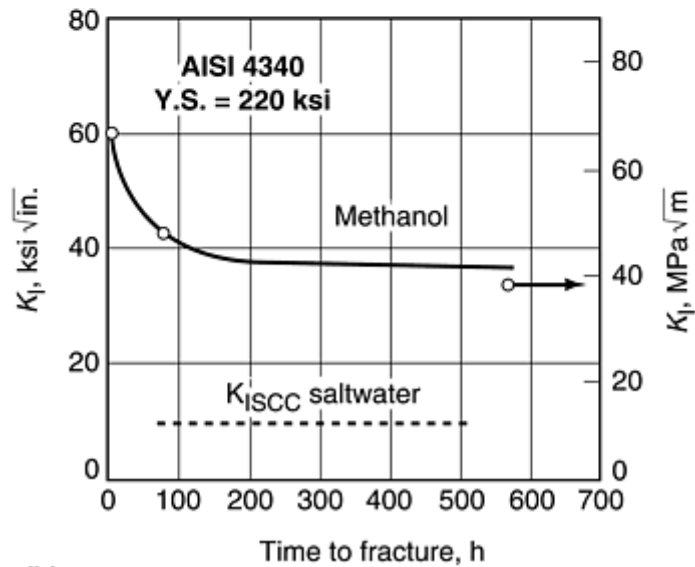


Fig. 39 Branched intergranular SCC in a lightly drawn tube of 12200 copper after exposure to an amine boiler-treatment compound. Potassium dichromate etch. (a) 100 \times . (b) 500 \times

Although the mechanism of stress corrosion is not completely understood, SCC appears to develop only when the stress (applied or residual) is tensile in nature and when its magnitude exceeds a threshold value (Fig. 40), a value that is near the yield strength of the metal. The rate of crack propagation thereafter increases rapidly with increasing stress. Once initiated, stress-corrosion cracks extend laterally and grow into the underlying section in a plane that is normal to the principal tensile stress. They tend to branch extensively in the process (Fig. 38 and 39), but there are occasional exceptions to this. Only a limited number of separate cracks are likely to initiate and then tend to be confined to a limited area of a component. This is in contrast to the more widespread and random nature of intercrystalline corrosion.



(a)



(b)

Fig. 40 Stress corrosion cracking threshold examples. (a) Stainless steels in boiling 42% magnesium chloride solution. (b) Comparison of K_{ISCC} of AISI 4340 steel (tensile yield strength, 1515 MPa, or 220 ksi) in methanol and salt water at room temperature

The environments that induce SCC are specific to particular metals, and only a limited range of environments can cause cracking in any one metal. Some examples of cracking environments are listed in Table 7, most of them being at worst only mildly corrosive in a general sense. The presence of oxygen is important in most of them. Many of these environments are also likely to be encountered in everyday usage, and some are virtually impossible to avoid. Moisture containing chlorides that will cause cracking of aluminum alloys is a case in point, because moisture and traces of chlorides are ubiquitous. Traces of ammonia that can cause cracking of brasses are also frequently present in the atmosphere due to the decomposition of organic matter and the presence of animal waste products (Ref 33).

Table 7 Alloy/environment systems exhibiting stress-corrosion cracking

Alloy	Environment
Carbon steel	Hot nitrate, hydroxide, anhydrous ammonia, and carbonate/bicarbonate solutions
High-strength steels	Aqueous electrolytes, particularly when containing H_2S
Austenitic stainless	Hot, concentrated chloride solutions; caustics, saline solution, and chloride-

steels	contaminated steam
High-nickel alloys	High-purity steam, hot caustics
Aluminum alloys	Aqueous Cl⁻, Br⁻, and I⁻ solutions, including contaminated water vapor
Titanium alloys	Aqueous Cl⁻, Br⁻, and I⁻ solutions; methanol organic liquids; N₂O₄; hydrochloric acid
Magnesium alloys	Aqueous Cl⁻ solutions
Zirconium alloys	Aqueous Cl⁻ solutions; organic liquids; I₂ at 350 °C (660 °F)
Copper alloys	Ammonia and amines for high-zinc brasses; ammoniacal solutions for α brass; range of solutions for other specific alloys
Gold alloys^(a)	Chlorides, particularly ferric chloride; ammonium hydroxide; nitric acid

(a) Alloys containing less than 67% gold

Prevention of SCC. Stress cracking may be reduced or prevented by the following practices:

- Decreasing the stress level by annealing, design, and so forth
- Avoiding the environment that leads to stress cracking
- Changing the metal if the environment cannot be changed
- Adding inhibitors or applying cathodic protection to reduce the rate of corrosion

In principal, the easiest way to prevent SCC is to specify the load and geometry for a given measured or assumed initial flaw size such that $K < K_{ISCC}$ (where K_{ISCC} is the critical stress intensity for stress-corrosion cracking). For some alloys, however, the value of K_{ISCC} may be so low that impossible initial flaw sizes or impractically low stresses must be specified. Alternatively, attention may be focused on the use of coatings, alternate materials, or other means of corrosion protection. It is also important to understand the nature of crack growth and avoid the conditions leading to fast fracture; that is, the stress intensity factor due to flaws developed by corrosion must be kept below K_c , the fracture toughness of the material, by limiting the stress or time of exposure so that cracks do not grow to the critical size.

Measuring and testing of SCC behavior is a complex subject, but one approach is to subject a material specimen containing a prescribed defect to stress in the chemical environment (Fig. 41) (Ref 19). The increase in K (usually resulting from increase in crack length a) is then measured as a function of time. As a increases, the applied stress, σ , may change, and the factor Y in Eq 37 may also change. Their combined effects contribute to the increase in K . Figure 42 shows a typical result (Ref 19). For each initial stress intensity value, K_i , the stress intensity increases until it reaches K_I , and fast fracture occurs. Below a certain value of K_i , crack growth does not occur; this level of K_i is denoted K_{ISCC} , or the critical stress intensity for stress corrosion cracking in the environment under which the test was conducted. For example, in saltwater, K_{ISCC} for heat treated 2000 and 7000 series aluminum alloys are approximately 80% of their K_I values. For heat treated 4340 and 300M steels, K_{ISCC} is about one-third of the K_I values, and for titanium alloys, K_{ISCC} varies widely from 25 to 40% of their K_I values (Ref 19).

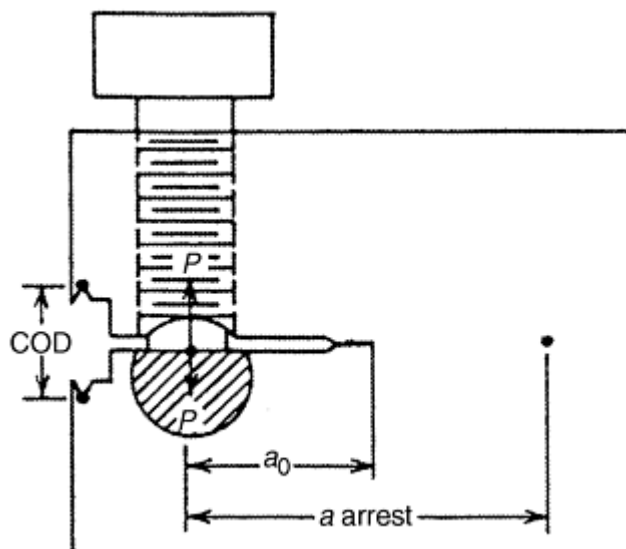


Fig. 41 Modified compact tension specimen for environmentally assisted cracking measurement.

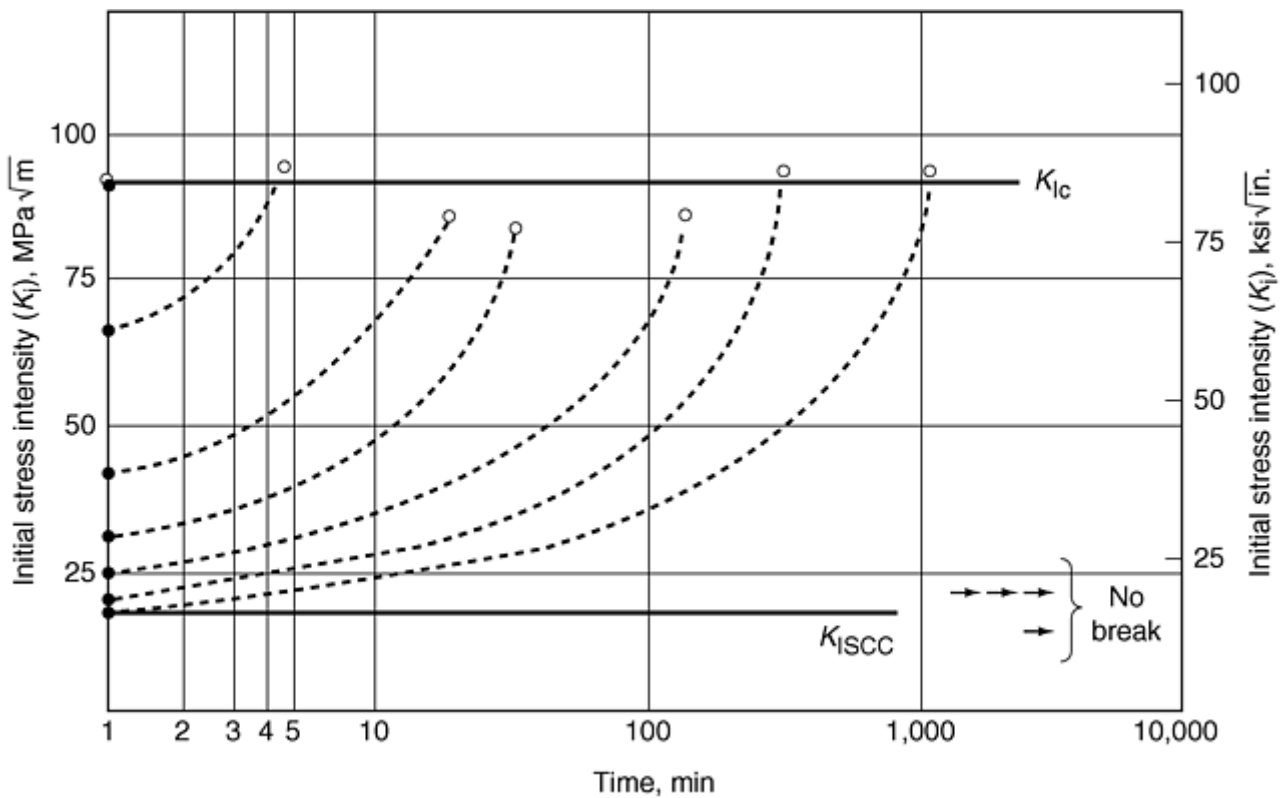
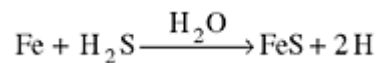


Fig. 42 Stress intensity growth with time in a corrosive environment

Hydrogen Embrittlement and Cracking. Hydrogen embrittlement is another form of environmentally assisted crack growth. Only a comparatively few metals are susceptible to this phenomenon, but prominent among them are the high-strength steels, that is, steels having tensile strengths above about 1000 MPa (145 ksi). In some aspects, hydrogen embrittlement is similar to stress-corrosion cracking. Hydrogen-induced cracking (HIC) has been proposed as the SCC mechanism for carbon and high-strength ferritic steels, nickel-base alloys, titanium alloys, and aluminum alloys (Ref 34).

Cracking resistance of steels is a major concern in refining and petrochemical industries where aqueous H₂S is present. The generally accepted theory of the mechanism for hydrogen damage in wet H₂S environments is that monatomic hydrogen is charged into steel as a result of sulfide corrosion reactions that take place on the material surface. The primary source of atomic hydrogen available at internal surfaces of pipeline and vessel steels is generally the oxygen-accelerated dissociation of the H₂S gas molecule in the presence of water. The basic reaction is:



The FeS formed on the surface of the steel is readily permeated by atomic hydrogen, which diffuses further into the steel.

This diffusion of atomic hydrogen into steel is associated with three distinct forms of cracking:

- Hydrogen-induced cracking
- Stress-oriented hydrogen-induced cracking
- Hydrogen stress cracking (also known as sulfide stress cracking and sulfide stress-corrosion cracking)

Hydrogen-induced cracking (HIC) and stress oriented hydrogen-induced cracking (SOHIC) are both caused by the formation of hydrogen gas (H₂) blisters in steel. Hydrogen-induced cracking, also called stepwise cracking or blister cracking, is primarily found in lower-strength steels, typically with tensile strengths less than about 550 MPa (80 ksi). It is primarily found in line pipe steels.

In contrast, hydrogen stress cracking does not involve blister formation, but it does involve cracking from the simultaneous presence of high stress and hydrogen embrittlement of the steel. Hydrogen stress cracking occurs in higher-strength steels or at localized hard spots associated with welds or steel treatment. As a general rule of thumb, hydrogen stress cracking can be expected to occur in process streams containing in excess of 50 ppm H₂S (although cracking has been found to occur at lower concentrations).

The basic factors of these cracking modes include temperature, pH, pressure, chemical species and their concentration, steel composition and condition, and welding or the condition of the weld heat-affect zone. These types of cracking and important variables for failure control are described in more detail in Ref 35 and 36.

Corrosion Fatigue. As previously noted and shown in Fig. 35, fatigue is affected seriously in the presence of a corrosive environment. Another consequence is that even those alloys that have definite fatigue endurance limits no longer do so. The presence of a particular environment is not required for the deterioration in properties, as it is for SCC. The sole requirement is that the environment be sufficiently corrosive, although there is not necessarily a direct correlation between general corrosiveness and effect on corrosion fatigue.

For steels, the corrosion endurance limit ranges from about 50 to 10% of the limit in air. The corrosion endurance limit also is independent of metallurgical structure and thus shows little correlation with strength. Therefore, the endurance limit of steels, even under mildly corrosive conditions, is much less than that in air and does not increase with an increase in the tensile strength of the steel (Ref 33). The combination of corrosion with a cycling stress eliminates the benefits of all efforts made to improve the strength of steels as assessed by static mechanical tests.

References cited in this section

19. R.W. Hertzberg, *Deformation and Fracture Mechanics of Engineering Materials*, 2nd ed., John Wiley & Sons, 1983, p 240, 287, 288, 436–477
33. L. Samuels, *Metals Engineering: A Technical Guide*, ASM International, 1988, p 161, 168
34. G. Koch, Stress-Corrosion Cracking and Hydrogen Embrittlement, *Fatigue and Fracture*, Vol 19, *ASM Handbook*, 1996, p 486
35. P. Timmins, Failure Control in Process Operations, *Fatigue and Fracture*, Vol 19, *ASM Handbook*, 1996, p 479
36. P. Timmins, *Solutions to Hydrogen Attack in Steels*, ASM International, 1997

Overview of Mechanical Properties and Testing for Design

Howard A. Kuhn, Concurrent Technologies Corporation

Shock Loading

Another nonstatic loading condition often found in machine parts involves shock, or impact forces. This condition occurs if the time duration of the load is less than the natural period of vibration of the part or structure. Failure of a part under shock loading, as with other types of loading, depends on material parameters and geometric factors.

To illustrate this condition, consider the tie bar (Fig. 1) under *impact* tensile loading. If the bar is used to stop the motion of another part, then the kinetic energy of the moving part is absorbed by elongation of the tie bar and converted into elastic strain energy in the bar. Then, the maximum stress in the bar will be:

$$\sigma = V\sqrt{Em/AL} \quad (\text{Eq 37})$$

where V is the velocity of the mass, m , when it impacts the bar; A and L are the cross-sectional area and length of the bar, respectively; and E is the elastic modulus of the bar material.

To prevent failure under a shock load, the stress in Eq 37 must be less than the strength of the material, σ_f . Then, the parameters in Eq 37 can be regrouped into:

$$V\sqrt{m} < (\sigma_f / \sqrt{E})(\sqrt{AL}) \quad (\text{Eq 38})$$

which shows that the combination of impact velocity and mass that can be tolerated depends not only on the material strength but also on its elastic modulus. In other words, selecting a material that maximizes the parameter σ_f^2/E will maximize the impact energy that can be absorbed. Equation 38 also shows that increasing the volume of material in the bar, AL , increases its shock resistance. For example, increasing the length of the bar does not affect its ability to carry static axial load but does increase its ability to resist an impact load.

The description of shock resistance of a tie bar can be extended to other forms of loading, such as bending. For example, for a beam subjected to a lateral impact load (Fig. 6), the kinetic energy of a mass that is stopped by the beam is converted into strain energy in the beam. Then, the maximum stress that is in the beam is given by:

$$\sigma = V\sqrt{3mE/LI_H} \quad (\text{Eq 39})$$

where V is the velocity of mass m when it impacts the beam; L and H are the beam length and height, respectively; I is the moment of inertia of the beam cross section; and E is the elastic modulus of the beam material. Again, σ must be less than the strength of the material, σ_f , and Eq 39 can be rearranged to:

$$V\sqrt{m} < (\sigma_f/\sqrt{E})(\sqrt{LI/3H^2}) \quad (\text{Eq 40})$$

As with the bar under axial impact loading, the material parameter that maximizes shock resistance is σ_f^2/E , but the geometry parameter is now LI/H^2 . In the case of rectangular beam, from Eq 18, $I = bH^3/12$. Then, the geometry parameter becomes $LbH/12$. Since bH is the cross-sectional area of the beam, the geometry parameter becomes $AL/12$, so the impact resistance of the beam is increased by increasing the beam volume, similar to the case of the bar under tensile impact. A longer beam, for example, will not carry as much static load as a shorter beam, but the longer beam will be more resistant to failure by impact loading.

More complicated geometries can be analyzed through finite element models, which give the distribution of stresses due to impact loads throughout the part. In these cases the same general effects of the material parameter (σ_f^2/E) and geometry parameter (volume) on shock resistance apply.

Overview of Mechanical Properties and Testing for Design

Howard A. Kuhn, Concurrent Technologies Corporation

Acknowledgments

Portions of the section “Environmental Effects on Mechanical Properties” were adapted from L.E. Samuels, *Metals Engineering: A Technical Guide*, ASM International, 1988.

References

1. Cambridge Engineering Selector, Granta Design Ltd., Cambridge, UK, 1998
2. G.E. Dieter, *Engineering Design: A Materials and Processing Approach*, McGraw Hill, 1991, p 1–51, p 231–271
3. *Metals Handbook*, American Society for Metals, 1948
4. F.B. Seely, *Resistance of Materials*, John Wiley & Sons, 1947
5. *Properties and Selection of Metals*, Vol 1, *Metals Handbook*, 8th ed., American Society for Metals, 1961, p 503
6. *Modern Plastics Encyclopedia*, McGraw Hill, 2000
7. M.F. Ashby, *Materials Selection for Mechanical Design*, 2nd ed., Butterworth-Heinemann, 1999
8. H. Davis, G. Troxell, and G. Hauck, *The Testing of Engineering Materials*, 4th ed., McGraw Hill, 1982, p 314
9. G. Carter, *Principles of Physical and Chemical Metallurgy*, American Society for Metals, 1979, p 87
10. M.A. Meyers and K.K. Chawla, *Mechanical Metallurgy*, Prentice-Hall, Edgewood Cliffs, NJ, 1984, p 626–627
11. W.J. Taylor, The Hardness Test as a Means of Estimating the Tensile Strength of Metals, *J.R. Aeronaut. Soc.*, Vol 46 (No. 380), 1942, p 198–202
12. George Vander Voort, *Metallography: Principles and Practices*, ASM International, 1999, p 383–385 and 391–393
13. R.T. Shield, On the Plastic Flow of Metals under Conditions of Axial Symmetry, *Proc. R. Soc.*, Vol A233, 1955, p 267
14. H. Chandler, Ed., *Hardness Testing*, 2nd ed., ASM International, 1999
15. G.E. Dieter, *Mechanical Metallurgy*, 2nd ed., McGraw Hill, 1976, p 49–50, 79–80, 379, 381, 385
16. J.H. Faupel and F.E. Fisher, *Engineering Design*, John Wiley & Sons, 1981, p 102, 113, 230–235, 802
17. D.J. Wulpi, *Understanding How Components Fail*, ASM International, 1966, p 27
18. T. Baumeistes, Ed., *Marks' Mechanical Engineers' Handbook*, 6th ed., McGraw-Hill, 1958, p 5–106
19. R.W. Hertzberg, *Deformation and Fracture Mechanics of Engineering Materials*, 2nd ed., John Wiley & Sons, 1983, p 240, 287, 288, 436–477

20. W.C. Young, *Formulas for Stress and Strain*, 5th ed., McGraw-Hill, 1975
21. S.P. Timoshenko and J. Goodier, *Theory of Elasticity*, 3rd ed., McGraw Hill, 1970, p 418–419
22. O.C. Zienkiewicz, *The Finite Element Method in Engineering Science*, 4th ed., McGraw Hill, 1987
23. K.H. Heubner, et al., *The Finite Element Method for Engineers*, 3rd ed., John Wiley & Sons, 1995
24. ABAQUS/Standard, Example Problems Manual, Vol 1, Version 5.7, 1997
25. A.A. Griffith, *Trans. ASM*, Vol 61, 1968, p 871
26. A.F. Liu, *Structural Life Assessment Methods*, ASM International, 1998
27. J.M. Barsom, *Engineering Fracture Mechanics*, Vol 7, 1975, p 605
28. M.E. Fine and Y.-W. Chung, Fatigue Failure in Metals, *Fatigue and Fracture*, Vol 19, *ASM Handbook*, ASM International, 1996, p 63
29. M.R. Mitchell, Fundamentals of Modern Fatigue Analysis for Design, *Fatigue and Fracture*, Vol 19, *ASM Handbook*, ASM International, 1996, p 227–249
30. N.E. Dowling, Estimating Fatigue Life, *Fatigue and Fracture*, Vol 19, *ASM Handbook*, ASM International, 1996, p 250–262
31. D.L. McDowell, Multiaxial Fatigue Strength, *Fatigue and Fracture*, Vol 19, *ASM Handbook*, ASM International, 1996, p 263–273
32. D. Woodford, Design for High-Temperature Applications, *Materials Selection and Design*, Vol 20, *ASM Handbook*, ASM International, 1998, p 580
33. L. Samuels, *Metals Engineering: A Technical Guide*, ASM International, 1988, p 161, 168
34. G. Koch, Stress-Corrosion Cracking and Hydrogen Embrittlement, *Fatigue and Fracture*, Vol 19, *ASM Handbook*, 1996, p 486
35. P. Timmins, Failure Control in Process Operations, *Fatigue and Fracture*, Vol 19, *ASM Handbook*, 1996, p 479
36. P. Timmins, *Solutions to Hydrogen Attack in Steels*, ASM International, 1997

Overview of Mechanical Properties and Testing for Design

Howard A. Kuhn, Concurrent Technologies Corporation

Selected References

- M. Ashby, *Materials Selection for Mechanical Design*, 2nd ed., Butterworth-Heinemann, 1999
- N. Dowling, *Mechanical Behavior of Materials: Engineering Methods for Deformation, Fracture, and Fatigue*, Prentice Hall, 1999
- R.C. Juvinall and K.M. Marshek, *Fundamentals of Machine Component Design*, 2nd ed., John Wiley & Sons, 1991

- J.E. Shigley and L.D. Mitchell, *Mechanical Engineering Design*, 4th ed., McGraw-Hill, 1983

Mechanical Testing for Metalworking Processes

Serope Kalpakjian, Illinois Institute of Technology

Introduction

AN IMPORTANT ACTIVITY in metalworking facilities is the testing of incoming raw materials for characteristics that ensure the integrity and quality of the products made. Several traditional as well as specialized tests are now available to assess the quality of materials, in bulk or sheet form, in order to predict their behavior in metalworking operations.

Because of the generally complex nature of the processes involved, the identification and quantification of appropriate parameters to predict performance and failure during processing continue to be challenging tasks. The metalworking industry has, by and large, depended on cumulative and long practical experience rather than on the continuous reporting of research findings in the technical literature. A notable exception is the automotive industry, particularly in sheet metal forming.

While such practical experience has been indispensable to the successful production of quality products, major efforts and investigations continue to be made to arrive at a comprehensive understanding of the underlying principles of the behavior of metals in deformation processing. The necessity for such an approach is self-evident, even though it is clear that there are, as yet, no simple criteria fully responsive to all metals and alloys, operations, and processing conditions.

This article generally reviews the state of knowledge in this subject. A more detailed discussion of various aspects related to specific topics and processes are given in *ASM Handbook*, Volume 14, *Forming and Forging*, and the other references cited in this article.

Mechanical Testing for Metalworking Processes

Serope Kalpakjian, Illinois Institute of Technology

Workability and Formability

A simple definition of *workability* is “the maximum amount of deformation a metal can withstand in a particular process without failure” (Ref 1). The term is generally applied to bulk deformation processes, such as forging, rolling, extrusion, and drawing, in which the forces applied are predominantly compressive in nature. In contrast, *formability* is usually applied to sheet-metal forming processes, in which the forces applied are primarily tensile. These definitions can also include undesirable conditions such as poor surface finish, sheet wrinkling, or lack of die fill in forging.

Although some definitions include the relative ease with which a metal can be shaped, the general definition of workability does not include forces or energies involved in processing. The reason is that forces and energies are related primarily to the strength of the workpiece material, tribological factors (friction, lubrication, and wear), and the size and capacity of the metalworking equipment.

The maximum amount of deformation has a different meaning depending on the particular metalworking process. For example, in bending, it is the minimum bend radius; in deep drawing, it is the maximum ratio of blank-to-punch diameters. In power spinning of tubular or curvilinear shapes, maximum deformation is the reduction in thickness per pass.

It is generally recognized that there are two basic types of failure in metalworking processes:

- Local or total separation of the metal: Surface cracking in upsetting or open-die forging, internal cracking in extrusion or drawing, and necking and subsequent tearing of sheet metals during forming
- Buckling: Upsetting of slender workpieces and wrinkling in sheet-metal forming operations

As a general guide to workability, some suppliers of metals have prepared tables or charts showing the relative workability or formability ratings (using letters, numbers, or terms such as excellent, good, fair, and poor). While such ratings are based on cumulative and proven experience on the plant floor and can indeed be useful, their application is somewhat limited due to the fact that ratings generally do not apply to specific processes and conditions and are not quantitative.

The behavior of a metal in an actual forming operation may be predicted from mechanical test results. Test specimens are cut from the same blank and, as much as possible, subjected to the same conditions (such as state of stress, temperature, and strain rate) as in the particular metalworking operation. Few metalworking processes can be simulated by such simple testing, however. Consequently, much effort has been expended toward the design of new test methods to simulate actual processing conditions. The alternative is, of course, to perform the actual process itself at a smaller scale, in a laboratory environment.

Reference cited in this section

1. G.E. Dieter, Ed., *Workability Testing Techniques*, ASM International, 1984, p 16, 33, 49, 61, 63, 163, 202, 206

Mechanical Testing for Metalworking Processes

Serope Kalpakjian, Illinois Institute of Technology

Mechanical Behavior of Metals Influencing Workability

This section presents a brief review of the common material parameters that can have a direct or indirect influence on workability and product quality. The parameters described in this section are most commonly obtained in tension tests (Ref 2, 3, 4). All discussions pertain to metals and their alloys.

Strength. The strength of a metal is defined in terms of quantities such as yield stress, ultimate tensile strength, and breaking stress. Although easily determined from normal stress-normal strain curves (including shear stress-shear strain curves) or obtained from published literature and handbooks, these quantities basically influence the stresses, forces, energies, and temperature rise during processing.

Although strength is not directly relevant to workability, it can indirectly indicate some measure of workability. For ductile metals, for example, observing the difference between the yield and tensile strengths can indirectly indicate a measure of workability. The closer the magnitude of these two stresses, the more work hardened the metal is, and, hence, the lower its ductility, that is, the narrower the stress-strain curve. The dependence of strength on orientation in a bulk workpiece or sheet metal can, of course, also influence material behavior (as discussed in subsequent sections). A common example is the formation of ears in deep-drawn cups due to the planar anisotropy of the sheet.

Ductility. Two traditional and common measures of ductility have been the tensile elongation and the tensile reduction of area, quantities that are readily available in handbooks and from material suppliers. However, these quantities depend on gage length and cross-sectional area of the specimen. Total elongation and tensile reduction of area both increase with increasing cross-sectional area of the specimen. Also, because necking is a local phenomenon, total percent elongation depends on gage length; as expected, percent elongation decreases with increasing gage length.

Relationships between specimen length and cross section have been established and standardized in different countries. In the United States and according to ASTM standards, for example, the gage length-to-diameter ratio is 4.0 for round and 4.5 for sheet specimens.

Hardness can be defined as resistance to permanent indentation. The influence of hardness may be summarized as follows:

- It can be related to the strength of the metal and, thus, indirectly, to its ductility (i.e., the higher the hardness, the stronger the metal is and, generally, the lower its ductility is).
- The type of indentation profile is a measure of strain hardening, (i.e., the sharper the profile and its raised ridge around the indentation, the more strain hardened the metal is). Hardness is, thus, an indirect measure of the capacity of the metal for plastic deformation in metalworking.
- It affects the frictional and wear characteristics in forming operations.

The strain-hardening exponent, also called the work-hardening exponent, is a measure of how rapidly the metal becomes stronger and harder as it is strained (worked). This exponent is typically obtained from the true stress-true strain curve of the metal (often derived from engineering stress-engineering strain curves) and is expressed as a power law:

$$\sigma = K\varepsilon^n \quad (\text{Eq 1})$$

where σ is the true stress, K is the strength coefficient, ε is the true strain, and n is the strain-hardening exponent.

At room temperature, for magnitude of K typically ranges from about 200 MPa for soft aluminum to about 2000 MPa for superalloys; it decreases as the temperature increases. Depending on the metal and its condition, the values of n typically range from 0.05 to 0.5 (Table 1).

Table 1 Typical values for strength coefficient, K , and strain-hardening exponent, n , (Eq 1) at room temperature

Material	K		n
	MPa	ksi	
Aluminum 1100-O	180	26	0.20
2024-T4	690	100	0.16
5052-O	210	30	0.13
6061-O	205	30	0.20
6061-T6	410	59	0.05
7075-O	400	58	0.17
Brass 60-39-1 Pb, annealed	800	116	0.33
70-30, annealed	895	130	0.49
85-15, cold rolled	580	84	0.34
Bronze (phosphor), annealed	720	104	0.46
Cobalt-base alloy, heat treated	2070	300	0.50
Copper, annealed	315	46	0.54
Molybdenum, annealed	725	105	0.13
Steel Low-carbon annealed	530	77	0.26
1045, hot rolled	965	140	0.14
1112, annealed	760	110	0.19
1112, cold rolled	760	110	0.08
4135, annealed	1015	147	0.17
4135, cold rolled	1100	160	0.14
4340, annealed	640	93	0.15

17-4 P-H, annealed	1200	174	0.05
52100, annealed	1450	210	0.07
302 stainless, annealed	1300	188	0.30
304 stainless, annealed	1275	185	0.45
410 stainless, annealed	960	139	0.10

Source: Ref 3

It can be shown that the exponent n also gives a direct indication of the uniform elongation of the metal; that is, the extent to which the metal can be stretched before it begins to neck (plastic instability). The relationship is given by the following:

$$\epsilon_{\text{necking}} = n \quad (\text{Eq 2})$$

for simple tension. For example, in sheet-metal stretching, if the sheet is 1 m long and $n = 0.2$, the sheet, thus, can be stretched uniaxially to a true strain of 0.2 (to 1.22 m) before it begins to neck.

The magnitude of the strain-hardening exponent also has an effect on the maximum reduction per pass in rod and wire drawing. The higher the value of n is, the higher the strength of the metal exiting the die and, hence, the smaller is the final cross-sectional area to which the metal can be reduced by drawing.

Strain-Rate Effects. The strength exhibited by a metal also depends on the rate at which it is being deformed. For simple tension, this relationship is given by the following:

$$\sigma = C\dot{\epsilon}^m \quad (\text{Eq 3})$$

where C is the strength coefficient, $\dot{\epsilon}$ is the true strain rate, and m is the strain-rate sensitivity exponent. The magnitude of C at room temperature typically ranges from as low as approximately 10 MPa for aluminum to about 1000 MPa for titanium (Table 2); it decreases with increasing temperature.

Table 2 Approximate range of values for the strength coefficient, C , and strain-rate sensitivity exponent, m (Eq 3)

Material	Temperature, °C	C		m
		MPa	ksi	
Aluminum	200–500	82–14	12–2	0.07–0.23
Aluminum alloys	200–500	310–35	45–5	0–0.20
Copper	300–900	240–20	35–3	0.06–0.17
Copper alloys (brasses)	200–800	415–14	60–2	0.02–0.3
Lead	100–300	11–2	1.6–0.3	0.1–0.2
Magnesium	200–400	140–14	20–2	0.07–0.43
Steel	900–1200	165–48	24–7	0.08–0.22
Low-carbon				
Medium-carbon	900–1200	160–48	23–7	0.07–0.24
Stainless	600–1200	415–35	60–5	0.02–0.4
Titanium	200–1000	930–14	135–2	0.04–0.3
Titanium alloys	200–1000	900–35	130–5	0.02–0.3
Ti-6Al-4V ^(a)	815–930	65–11	9.5–1.6	0.05–0.80
Zirconium	200–1000	830–27	120–4	0.04–0.4

As temperature increases, C decreases and m increases. As strain increases, C increases, and m may increase or decrease. Also, m may become negative within certain ranges of temperature and strain.

(a) At a strain rate of $2 \times 10^{-4} \text{ s}^{-1}$.

Source: Ref 3

The magnitude of the exponent m depends not only on the particular material but depends also with great sensitivity on temperature. The higher the temperature, the higher the magnitude of the exponent m is. At room temperature, m can approach zero, and at elevated temperatures, it can approach unity. Consequently, strain-rate and temperature effects in metals are generally studied and reported simultaneously.

Strain-rate sensitivity is an important parameter in the elongation and ductility of metals. As m increases, total elongation increases and the post-uniform elongation (elongation after the onset of necking) also increases (Fig. 1 and 2). This behavior is typically exhibited by certain very fine grained alloys (10 to 15 μm) where total

elongations up to 2000% at strain rates on the order of 10^{-4} to 10^{-2} s^{-1} are obtained at certain temperature ranges. This phenomenon is known as superplasticity.

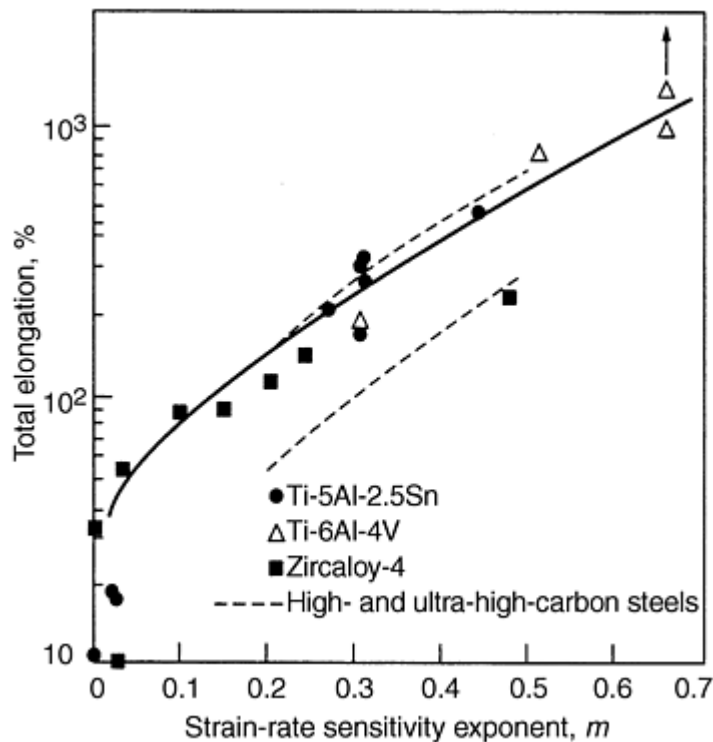


Fig. 1 The effect of the strain-rate sensitivity exponent, m , on the total elongation for various metals and alloys. Source: Ref 3

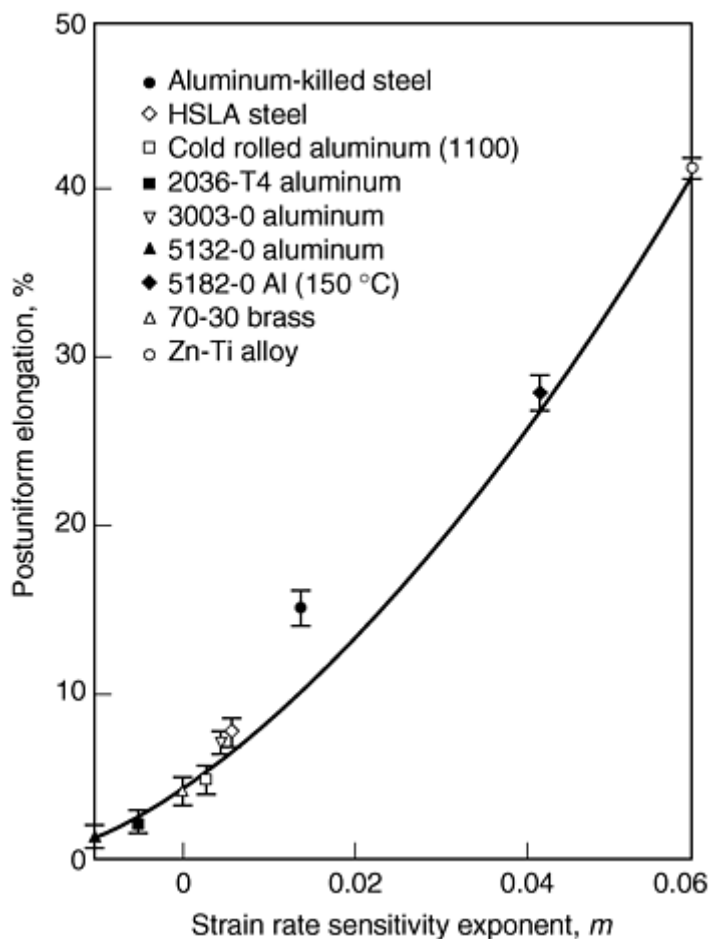


Fig. 2 The effect of strain-rate sensitivity exponent, m , on the post-uniform elongation for various metals and alloys. Source: Ref 3

Typical superplastic metals are zinc-aluminum, titanium, some aluminum alloys, nickel alloys, and iron-base superalloys. Superplastic forming has become important in fabricating sheet metal structures and various other components, particularly for aerospace applications.

Temperature effects generally are to decrease strength and increase workability. However, due to factors such as weakening of the grain boundaries (hot shortness), increased temperature can adversely influence workability and product quality.

Other related effects of temperature include (a) the blue brittleness range in steels, (b) surface oxidation, and (c) lubricant behavior, which, because it affects the tribological behavior at die-workpiece interfaces, can influence metal flow in dies (die filling, laps, defect formation).

State of stress in plastic deformation can have a major influence on workability. For example, even a very ductile metal can behave in a brittle manner when subjected to high levels of triaxial (hydrostatic) tensile stresses. Center-burst (chevron) cracking of solid rods in drawing and extrusion, plane-strain drawing of sheet or plate, and tube drawing or spinning are due to the high hydrostatic tensile stress component at the centerline of the workpiece during plastic deformation.

Another example of the importance of the state of stress is the favorable influence that normal compressive stress has on the maximum shear strain before fracture. Note (Fig. 3) that for torsion testing on steels, the shear strain to fracture rapidly increases as the compressive stress (normal to the cross section of the specimen) increases.

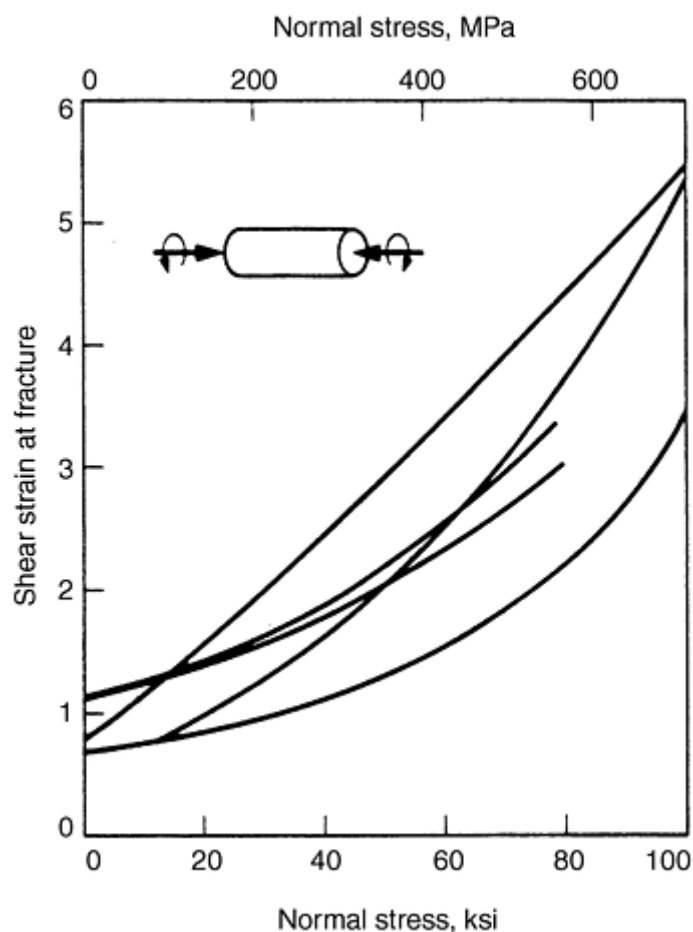


Fig. 3 The effect of axial compressive stress on the shear strain at fracture in torsion for various steels. Source: Ref 3

Effects of Hydrostatic Pressure. A highly beneficial state of stress is the environmental hydrostatic pressure; it has a major influence on the ductility of metals in metalworking operations. An otherwise brittle material can become ductile when plastically deformed under a state of high hydrostatic pressure, as has been observed in tension tests performed in highly pressurized chambers (Fig. 4).

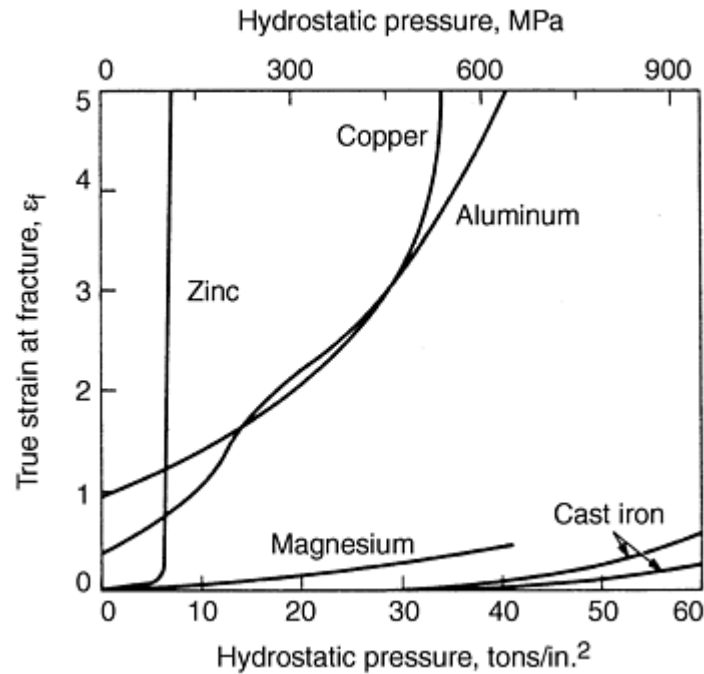


Fig. 4 The effect of hydrostatic pressure on the tensile ductility for various metals. Source: Ref 3

While with most metals ductility increases gradually with hydrostatic pressure, in others, such as zinc and its alloys (hcp structure) very ductile behavior occurs abruptly with a rapid transition from brittle behavior over a narrow pressure range. Hydrostatic extrusion is the most common example of the beneficial use of hydrostatic pressure.

References cited in this section

2. G.E. Dieter, *Mechanical Metallurgy*, 3rd ed., McGraw-Hill, 1986
3. S. Kalpakjian, *Manufacturing Processes for Engineering Materials*, 3rd ed., Addison-Wesley, 1997, p 44, 45, 50, 398, 399, 409, 416, 438
4. J.S. Schey, *Introduction to Manufacturing Processes*, 3rd ed, McGraw-Hill, 1999

Mechanical Testing for Metalworking Processes

Serope Kalpakjian, Illinois Institute of Technology

Mechanical Testing Methods and Sample Preparation

The material behavior characteristics already outlined in this article are typically determined by mechanical testing methods that are described in detail in other Sections of this Volume. Those aspects of testing that are particularly relevant to workability and quality control for metalworking processes are described later in this article (Ref 1, 2, 4, 5, 6).

Tension Test. Partly because of its relative simplicity, the tension test has been and continues to be the most common mechanical testing method. From the test results, true stress-true strain curves are constructed, with a correction made for necking of the specimen (Bridgman correction factor due to triaxial tensile state of stress in the necked region) (Ref 2, 3, 4). From these curves most of the material behavior characteristics can be determined easily.

The shape of the specimens may be round, sheet, or plate, and they are prepared and tested according to various international and national standards specifications (such as ASTM, ISO, JIS, and DIN). As described earlier, reporting of test results must specify specimen shape and dimensions, as well as parameters such as strain rate and temperature.

Plane-Strain Tension Test. A modification of the simple uniaxial tension test is the plane-strain tension test, in which the specimen has two deep grooves across its width (Fig. 5). This geometry restricts the deformation to length and thickness of the specimen, but not to its width (hence the term plane strain).

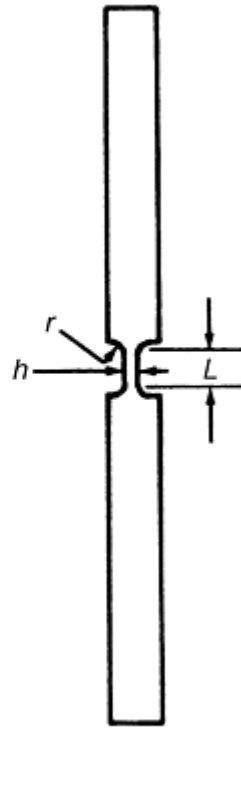


Fig. 5 Schematic of a plane-strain tension test specimen. Source: Ref 1

Compared to the simple tension test, in the plane-strain tension test the same metal exhibits a lower fracture strain. The plane-strain tension test attempts to simulate metalworking processes in which the workpiece (in whole or in part) is subjected to plane-strain conditions, typically in sheet metal forming operations. (See the section “Plane-Strain Compression Test” that follows.)

Compression Test. Unlike tension tests, the compression (upsetting) test has significant difficulties because of the friction at the platen-specimen interfaces, the surface characteristics of the contacting bodies, and the nature of lubrication. When conducted with care, reliable true stress-true strain curves can be obtained. It has been shown that for ductile metals, the true stress-true strain curves in tension and compression are the same (Ref 3). Barreling is an inevitable phenomenon in compression tests, although it can be minimized by effective lubrication and use of ultrasonic vibration of the platens. For specimens with high length-to-diameter ratio, there is a tendency for double barreling, near each end of the specimen.

The extent of deformation of the workpiece in compression tests (using either round or square specimens) indicates some measure of ductility in bulk deformation processes, particularly in forging and for metals with limited ductility. A crack usually develops on the cylindrical surface of the specimen, due to what are known as secondary tensile stresses. Depending on the state of stress and lubrication conditions, the direction of the crack may be at 45° to the long axis of the specimen, but it can be longitudinal as well, particularly if seams (a defect developed during prior processing) are present on the cylindrical surfaces of the specimen.

Compression tests at elevated temperature can be difficult to perform because of the heat loss to the dies. However, compression testing is commonly used as a simple measure of workability of metal, particularly in forging and similar bulk deformation processes.

Although test specimens for compression are typically prepared with relatively smooth surfaces, longitudinal notches are sometimes machined on the cylindrical or square surfaces (notched bar upsetting test). The purpose

of these notches is to cause regions of stress concentrations and, thus, to better simulate actual processing conditions, particularly for metals with limited forgeability.

Plane-Strain Compression Test. The purpose of this test is basically to determine the yield stress of the material under plane-strain conditions. The results are used to calculate the forces required in processes such as rolling of wide sheet and some regions of the workpiece in forging operations.

Partial-width indentation tests (Fig. 6) involve partial indentation of a simple wrought or as-cast rectangular slab. As a result, the overhangs (ribs) are subjected to secondary tensile stresses. The reduction in rib height (h_f) is a measure of the ductility of the metal. This test can be performed cold or hot.

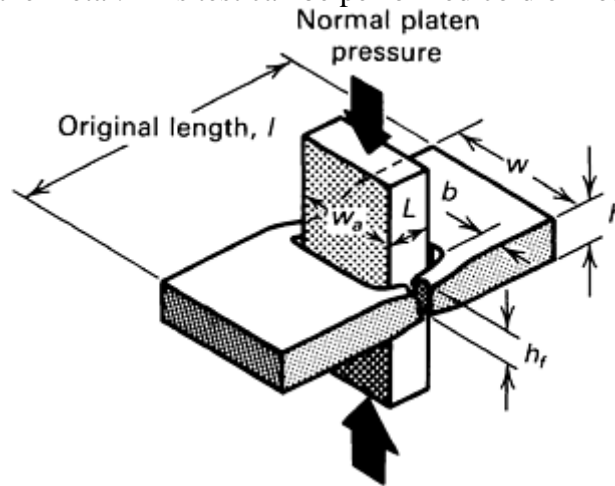


Fig. 6 Schematic of the partial-width-indentation test. $L \approx h$; $b = h/2$; $w_a = 2L$; $l = 4L$. Source: Ref 1

Torsion tests are generally performed on tubular specimens with reduced midsections in order to localize and control strains. Unlike in tension testing the specimen does not undergo necking (there is no plastic instability), and unlike in compression testing, there is no friction.

From test results, shear stress-shear strain curves are constructed. However, these curves are applicable to a limited number of processes, such as shearing (cropping) and power spinning of conical workpieces. Torsion tests at elevated temperatures (hot-twist tests) have long been found to be somewhat more suitable (as a measure of forgeability) than upsetting tests, particularly for alloy steels.

Sample Size and Aspect Ratio. As stated earlier, it has long been established that sample size and aspect ratio (length-to-cross section) have significant effects on mechanical test results, particularly ductility. These effects can be summarized as follows. In tension tests, the total percent elongation increases with increasing cross-sectional area and decreases with increasing gage length. For compression tests, the higher the aspect ratio, the higher is the tendency for buckling of the specimen and for double barreling.

Sample Location. Sample location as well as sample size can be important in applications where there are significant variations or gradients in the chemistry and defects present. Variations are, hence, present also in the mechanical properties of the workpiece material.

Even in seemingly simple metalworking operations (such as open-die forging, direct extrusion, and bending of thick plates), deformation of the metal is usually complex. There can be severe localized plastic deformation, therefore, property gradients within the workpiece. One example is the presence of shear bands (Fig. 7), developed during high deformation-rate processes and with metals whose strength decreases rapidly within a narrow temperature range. This phenomenon is similar to the formation of segmented or serrated chips in metal cutting, particularly in machining titanium.

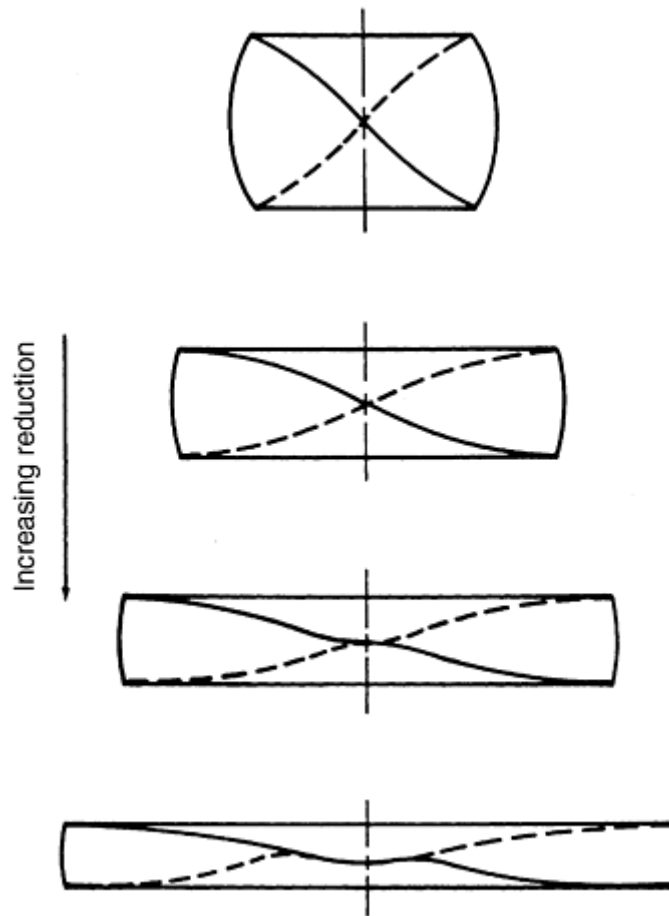


Fig. 7 Schematic of the mechanism of shear-band formation in upsetting. Source: Ref 1

Sample Orientation. Few metalworking processes involve simple, uniaxial deformation of the workpiece. Depending on the nature of the process, the metal is usually deformed in various directions. For example, in extrusion and rod drawing, the deformation is usually axisymmetric. Most forgings are typically multidirectional, and rolling of sheet is usually under plane-strain conditions, with the deformation principally in the direction of rolling. Because of the resulting anisotropy of the cold rolled metal, sample orientation can therefore be very significant, particularly in regard to subsequent processing such as bending or stamping.

In sheet metals, anisotropy is also important in springback behavior; this is because the amount of springback depends on the yield stress. All other variables being the same, the springback increases with increasing yield stress. (Note, for example, how helical or leaf springs are heat treated to increase their yield stress and, thus, attain full springback.) Control of springback is an important consideration in most sheet forming operations.

There are two basic types of anisotropy: preferred orientation and mechanical fibering. Preferred orientation (also called crystallographic anisotropy) arises from the alignment of grains in the general direction of material flow during deformation. (This type of anisotropy can be eliminated or minimized by annealing.) Mechanical fibering is due to the alignment of impurities, inclusions (stringers), and voids in the material during deformation processing. This phenomenon is typically observed in metals and alloys with poor quality.

An important beneficial effect of anisotropy is in deep drawing of sheet metals whereby the deep drawability increases with increasing normal anisotropy. On the other hand, planar anisotropy causes earing of the drawn cup (discussed in the section "Deep Drawing" in "Factors Influencing Formability in Sheet Metal Forming" in this article).

References cited in this section

1. G.E. Dieter, Ed., *Workability Testing Techniques*, ASM International, 1984, p 16, 33, 49, 61, 63, 163, 202, 206
2. G.E. Dieter, *Mechanical Metallurgy*, 3rd ed., McGraw-Hill, 1986

3. S. Kalpakjian, *Manufacturing Processes for Engineering Materials*, 3rd ed., Addison-Wesley, 1997, p 44, 45, 50, 398, 399, 409, 416, 438
4. J.S. Schey, *Introduction to Manufacturing Processes*, 3rd ed, McGraw-Hill, 1999
5. G.E. Dieter, *Engineering Design: A Materials and Processing Approach*, 2nd ed., McGraw-Hill, 1994
6. K. Lange, Ed., *Handbook of Metal Forming*, McGraw-Hill, 1985

Mechanical Testing for Metalworking Processes

Serope Kalpakjian, Illinois Institute of Technology

Quality Control

In addition to the various factors and parameters described so far, other considerations outlined in this section can have a direct and significant influence on workpiece quality.

Surface integrity includes both purely geometric features of a surface (such as roughness and lay) and its properties (such as the presence of cracks, discontinuities, and surface and subsurface defects). Because of the often large strains to which workpiece surfaces are subjected during processing, surface integrity can be of major importance.

For example, workpiece materials that are sensitive to surface scratches (notch sensitivity and lack of fracture toughness) can develop major flaws in the product, either in bulk or sheet form. Likewise, sheet blanks with poor edge conditions (roughness and severe strain and hardness gradients) have poor bendability due to premature cracking.

Structural Integrity. Depending on its processing history, a workpiece to be subjected to further metalworking operations may contain significant structural defects such as voids (microporosity), impurities, inclusions, inhomogeneities, internal cracks (chevron), and second-phase particles. These defects can have a major adverse effect on the ductility and workability of the metal (Fig. 8). Furthermore, the defects may or may not be distributed uniformly throughout the workpiece.

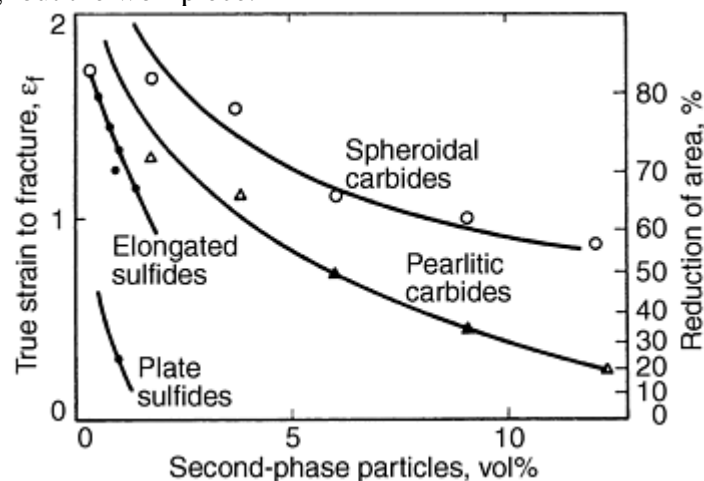


Fig. 8 The effect of volume fraction of second-phase particles on tensile ductility of steels. Source: Ref 1

Depending on the state of stress during deformation, these flaws can lead to major defects in the final product. For example, voids can form, coalesce, and open; external or internal cracks can propagate throughout the material. High shear bands can develop in certain regions, possibly leading to failure during the service life of the product.

In elevated temperature metalworking, minute amounts of impurities, small changes in composition, and phase changes throughout the workpiece (such as in bulk deformation of titanium alloys) can cause a major reduction in ductility. Embrittlement of grain boundaries (hot shortness) due to the presence of low-melting-point impurities can be a severe problem (liquid-metal or solid-metal embrittlement).

Residual Stresses. These internal stresses result typically from nonuniform deformation of the metal during metalworking and heat treatment and from thermal gradients. Residual stresses can have beneficial effects (improved fatigue life, if compressive on the surface) as well as adverse effects, such as stress cracking and distortion after subsequent processing (removing a layer of material, drilling a hole, or blanking). Stress relieving is commonly used to reduce the adverse effects.

Tribological Considerations. Equally important in product quality are tribological factors, namely friction, lubrication, and wear (Ref 3, 4, 6). Friction at tool, die, and workpiece interfaces can have a major effect on material flow (e.g., die filling in forging or the distribution of stresses in sheet forming), external and internal defect formation (e.g., poor surface finish, severe surface shear stresses, or excessive temperature rise during processing), and force and energy requirements in processing, because of the frictional energy involved.

Consequently, proper lubrication to control friction as well as to reduce tool and die wear are major concerns. These considerations are, in themselves, complex phenomena, and it is essential to select and apply appropriate lubricants, which are now largely water-based for environmental concerns.

Because the wear of tools and dies is inevitable, identification of the specific mechanisms of wear (adhesive, abrasive, corrosive, fatigue, and impact) is important. This helps determine the proper action to take in order to minimize or reduce the rate of wear, thereby improving the dimensional accuracy and surface finish of the products, as well as the overall economy of production.

References cited in this section

1. G.E. Dieter, Ed., *Workability Testing Techniques*, ASM International, 1984, p 16, 33, 49, 61, 63, 163, 202, 206
3. S. Kalpakjian, *Manufacturing Processes for Engineering Materials*, 3rd ed., Addison-Wesley, 1997, p 44, 45, 50, 398, 399, 409, 416, 438
4. J.S. Schey, *Introduction to Manufacturing Processes*, 3rd ed, McGraw-Hill, 1999
6. K. Lange, Ed., *Handbook of Metal Forming*, McGraw-Hill, 1985

Mechanical Testing for Metalworking Processes

Serope Kalpakjian, Illinois Institute of Technology

Factors Influencing Workability in Bulk Deformation Processes

Forging is a basic bulk deformation process typically involving a variety of processes such as open-die, impression-die, and closed-die forging (Ref 1, 3, 4, 6, 7, 8, 9, 10, 11). It is generally agreed that forgeability involves three basic parameters: flow stress, ductility, and the coefficient of friction, with temperature and speed being additional variables. Although no standard forgeability test has yet been devised, nearly all conventional mechanical tests have been utilized such as compression, tension, bend, torsion (twist), and impact tests.

Upsetting a solid cylindrical blank (pancaking) has been studied most extensively since it incorporates all the major factors involved. Typically, a solid cylindrical specimen is upset between flat dies (platens), and the cylindrical surfaces are inspected for the initiation of cracks. The original surface condition of the specimen is important in that the presence of defects (such as seams) can cause premature crack initiation.

In cold upsetting tests, linear relationships have been observed between the total surface strains at fracture, and the fracture loci have been established (Fig. 9). These plots consist of tensile strains versus compressive strains on the surface of the specimen (typically with a slope of -0.5), and they represent material limits to plastic deformation.

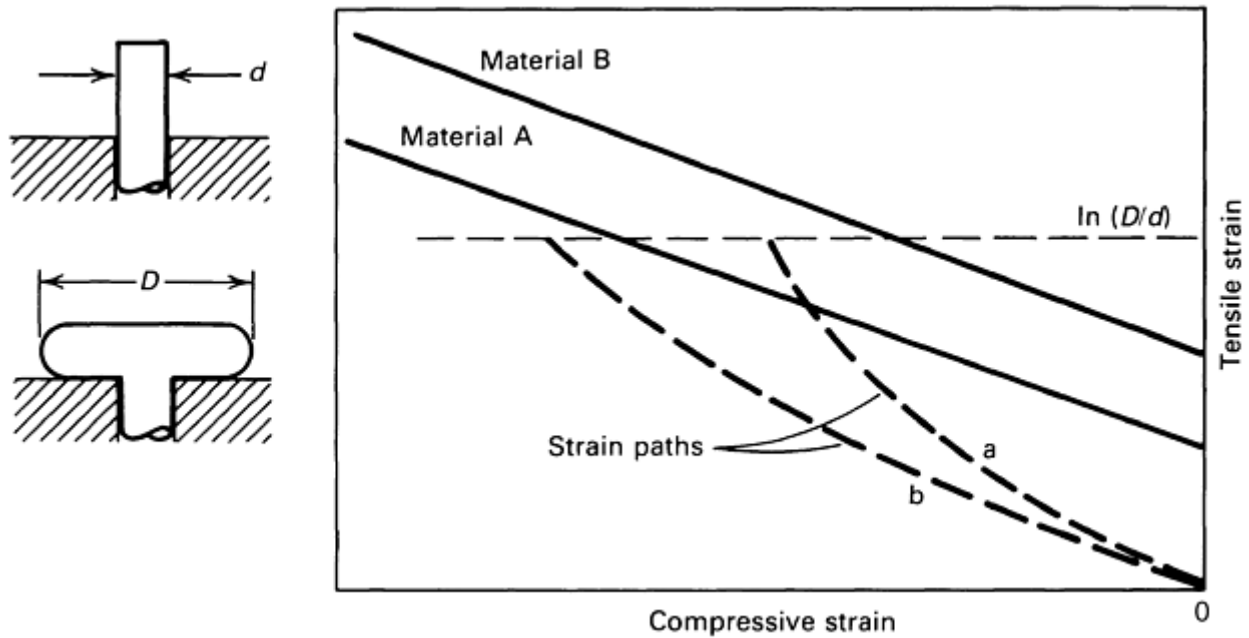


Fig. 9 Comparison of strain paths and fracture locus lines in cold upsetting. Source: Ref 1

A tapered, wedge-shaped test specimen has also been used (Fig. 10) whereby, as the upper flat die descends, the specimen undergoes varying degrees of deformation throughout its length. The onset of surface cracking can then be observed and related to the reduction in height at that particular location.

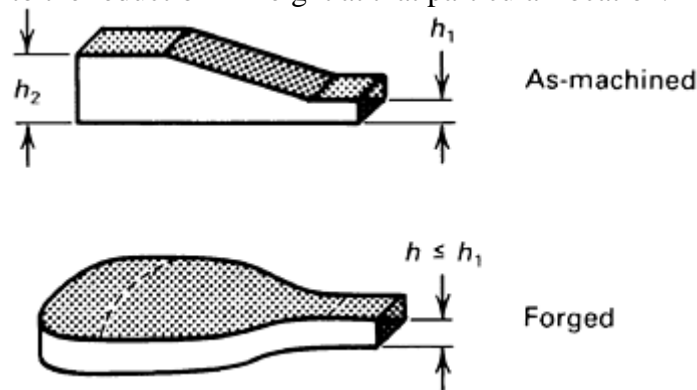


Fig. 10 Schematic illustration of a wedge-test specimen showing deformation after upsetting. Source: Ref 1

Forging of solid round blanks in the diametral direction in a manner similar to the disk test has also been investigated. In upsetting a round blank with flat dies, an internal lateral tensile stress develops at the center of the blank, leading to a vertical crack (Fig. 11). Although such a crack would normally be considered a defect, this phenomenon is the principle of the Mannesmann process for the production of seamless tubing and pipe.

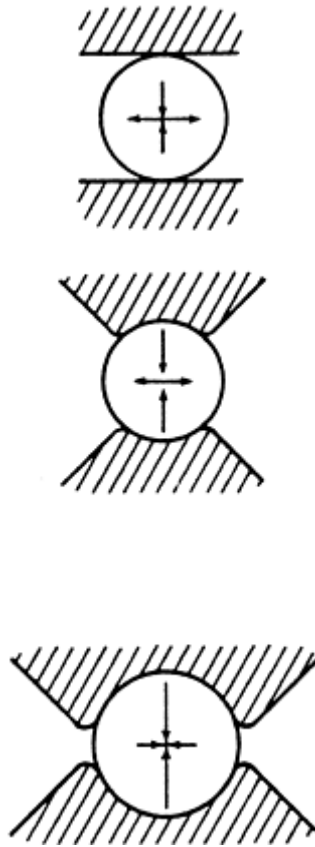


Fig. 11 Effect of contact area between dies and workpiece in forging a solid round billet. Source: Ref 1

Note in Fig. 11 that as the contact area between the dies and the billet surface increases, the lateral tensile stress decreases and becomes compressive. Consequently, the tendency for internal crack formation is eliminated with increasing contact area.

Another test (hot twist) has been shown to be a good indicator of forgeability. A solid round bar with specific length (typically 10 to 50 mm) and diameter (typically 8 to 25 mm) is heated and twisted continuously until it fractures. Round tubular specimens can also be used for this test. In addition to temperature as a parameter, rotational (twisting) speeds are varied, particularly because of the greater sensitivity of the metal to higher strain rates at elevated temperatures. The torque and shear strains (which can then be converted to normal strains and effective strains) are monitored as an indication of the strength and ductility of the metal at various temperatures.

Rolling. One of the most important primary metalworking processes (performed either hot or cold), rolling involves several parameters. Control of these parameters is essential to avoiding defects such as alligating, edge cracking, and surface damage (Ref 1, 2, 3, 4, 6). In cold rolling, the quality and surface condition of the billet, slab, or plate to be rolled is as important as they are in all metalworking operations.

Deformation of the metal in the roll gap can be complex, because inhomogeneities usually exist throughout the thickness of the stock being rolled, depending primarily on the interrelationship between roll radius, R , and roll-strip contact length, L . These inhomogeneities also lead to residual stresses in cold rolled products. These stresses can be important because of the possibility of distortion and warping in subsequent processing of the rolled product (when it is cut into individual blanks), as well as the possibility of affecting springback and stress-corrosion cracking.

Alligating has been attributed to inhomogeneous deformation during rolling and the presence of defects such as piping in the original ingot. Barreling (or double barreling) in rolling can cause edge cracking. This tendency can be minimized by using edge-restraint rolling (Ref 4) and controlling the quality of the original edges of the sheet or plate. Surface damage in rolling can be controlled primarily by effective lubrication.

Extrusion. Although the extrusion process has been studied extensively, there is as yet no criterion or coined term (like *forgeability* or *machinability*) for establishing the capability of a material to be extruded (Ref 2, 3, 4, 6, 8, 11, 12).

Internal defects in extrusion, known variously as chevron or centerburst cracking, have been studied extensively. It has been established that these internal cracks are due to a high hydrostatic tensile stress component at the centerline in the deformation zone during extrusion.

These stresses can be reduced or eliminated by (a) increasing the extrusion ratio (i.e., the ratio of billet-to-extrusion cross-sectional areas), (b) decreasing the die angle, and (c) ensuring that the billet does not contain significant amounts of inclusions, voids, or impurities, which otherwise act as stress raisers, particularly if they are concentrated along the center-line of the billet.

Although not commercially practiced to a significant extent, hydrostatic extrusion can be employed to enhance the ductility of the metal. Further increase in ductility can be obtained by extruding the material into a second chamber of pressurized fluid (fluid-to-fluid extrusion).

Rod and wire drawing is a process in which the force and energy required for deformation is applied through the product (rod or wire) itself. Drawability is usually defined in terms of the maximum reduction in cross-sectional area per pass. The analysis is based on the condition that it is the tensile stress that causes failure (breakage of rod or wire), and that this stress must be below the flow stress of the metal at the die exit. Thus, strain hardening, die angle, and friction are important parameters (Ref 2, 3, 4, 6, 11, 12).

In the analysis of maximum reduction per pass, there are the underlying assumptions that the metal is sufficiently ductile to undergo the strains involved in this process without fracture, and that the magnitude of the tensile stress in the exiting material causes failure. For round bars or wire, the maximum reduction per pass is shown theoretically to be 63% in the absence of friction, redundant work, and strain hardening. As expected, friction and redundant work decrease this reduction. For plane-strain drawing of sheet and plate under the same conditions, the maximum reduction per pass is 57%.

The effect of strain hardening of the material is to increase the maximum reduction per pass from the theoretical limits. This is because of the higher strength of the exiting rod or wire as compared to the average strength that the material exhibits in the die gap. In practice, however, reductions per pass are much lower than these theoretical limits, typically being on the order of 10 to 45% to ensure successful drawing.

The possibility of chevron or centerburst cracking also exists in rod and wire drawing. The relevant parameters are the same as in extrusion, namely reduction per pass, die angle, and the quality of the material entering the die, particularly along its centerline where the hydrostatic tensile stress component is highest. As in forgeability, hot-twist tests have been shown to give some qualitative measure of the workability of metals in drawing.

In addition to internal defects, external defects such as circumferential surface cracks (fir-tree cracking and bamboo defects), crow's feet cracking (approximately at 45°), and splitting of the product in the longitudinal direction may also develop in drawing. In addition to the inherent ductility of the metal, other important parameters are the states of stress and strain and frictional behavior.

Spinning. Power spinning studies have been conducted to predict spinnability (maximum reduction in thickness per pass before failure) from the mechanical properties of the material. It has been shown, both experimentally and analytically, that the maximum reduction per pass can be predicted from the tensile reduction of area of the material, both for conical and tube spinning (Ref 3).

From the experimental data shown (Fig. 12), a maximum spinning reduction per pass of about 80% is possible when the metal possesses a tensile reduction of area of about 50%. Beyond this tensile reduction, there is no further increase in spinnability. Increased ductility beyond 50% thus, has no additional benefit. For metals with a reduction in area of less than this critical value, spinnability depends on the ductility. It is interesting to note that in bending of sheet metal, maximum bendability is achieved again at a tensile reduction of area of about 50%.

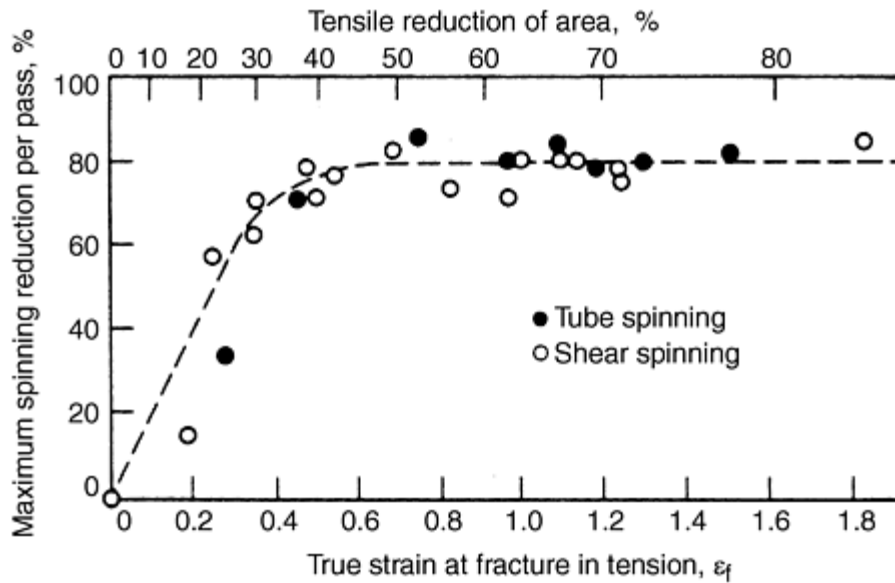


Fig. 12 Experimental data showing the relationship between maximum spinning reduction per pass and the tensile reduction of area of the material. Source: Ref 3

References cited in this section

1. G.E. Dieter, Ed., *Workability Testing Techniques*, ASM International, 1984, p 16, 33, 49, 61, 63, 163, 202, 206
2. G.E. Dieter, *Mechanical Metallurgy*, 3rd ed., McGraw-Hill, 1986
3. S. Kalpakjian, *Manufacturing Processes for Engineering Materials*, 3rd ed., Addison-Wesley, 1997, p 44, 45, 50, 398, 399, 409, 416, 438
4. J.S. Schey, *Introduction to Manufacturing Processes*, 3rd ed, McGraw-Hill, 1999
6. K. Lange, Ed., *Handbook of Metal Forming*, McGraw-Hill, 1985
7. T. Altan, S.I. Oh, and H.C. Gegel, *Metal Forming—Fundamentals and Applications*, ASM International, 1983
8. *Forming and Forging*, Vol 14, *ASM Handbook*, ASM International, 1988
9. T.G. Byrer, Ed., *Forging Handbook*, ASM International, 1985
10. H.A. Kuhn and B.L. Ferguson, *Powder Forging*, Metal Powder Industries Federation, 1990
11. *Forming*, Vol 2, *Tool and Manufacturing Engineers Handbook*, 4th ed., Society of Manufacturing Engineers, 1984
12. H.F. Hosford and R.M. Caddell, *Metal Forming: Mechanics and Metallurgy*, 2nd ed., Prentice Hall, 1993

Factors Influencing Formability in Sheet-Metal Forming

Sheet-metal forming operations consist of a large family of processes, ranging from simple bending to stamping and deep drawing of complex shapes (Ref 2, 3, 4, 5, 6, 8, 11, 12). Formability of a sheet metal depends greatly on the nature of the forming operation. In simple stretching operations, for example, the forming limit is determined by the uniform elongation of the metal as it is related to the strain-hardening exponent, n .

Because most sheet forming operations usually involve stretching and some shallow drawing (see the “Deep Drawing” section in this article), the product of the strain hardening exponent, n , and the normal anisotropy, R , of the sheet has been shown to be a significant parameter. Normal anisotropy is the ratio of width to thickness strains in a simple tension test (also called strain ratio or plastic anisotropy).

The factors influencing formability for major classes of sheet forming are reviewed in the following sections.

Bending. Bending is a common metalworking operation in which bendability is defined as the minimum bend radius, R (measured to the inner surface of the bent part), to which a sheet metal can be bent without cracking of its outer surface. It is usually given as the minimum R/T ratio, where T is the sheet thickness.

The most consistent indication of bendability has been shown to be the tensile reduction of the area of the sheet metal, as obtained from a tension test specimen and cut in the direction of bending. Because of planar anisotropy of cold rolled sheets (with higher ductility in the rolling direction than in the transverse direction), it is important to prepare the specimens accordingly.

A theoretical relationship for bendability has been obtained:

$$\text{Minimum } R/T = (50/RA) - 1 \tag{Eq 4}$$

where RA is the tensile reduction of area of the sheet. This equation has been derived by equating the true strain at which the outer fiber in bending begins to crack to the true fracture strain of the sheet specimen in simple tension.

Experimental results are in reasonably good agreement with this expression, with a curve-fitting modification made by increasing the numerator in the equation from 50 to 60 (Fig. 13). Thus, a sheet with a tensile reduction of area of 60% can be bent completely over itself (hemming) without cracking, much like folding a piece of paper. Note that in the preceding section, “Spinning,” it was indicated that maximum spinnability is also obtained at a tensile reduction of area of about 50%.

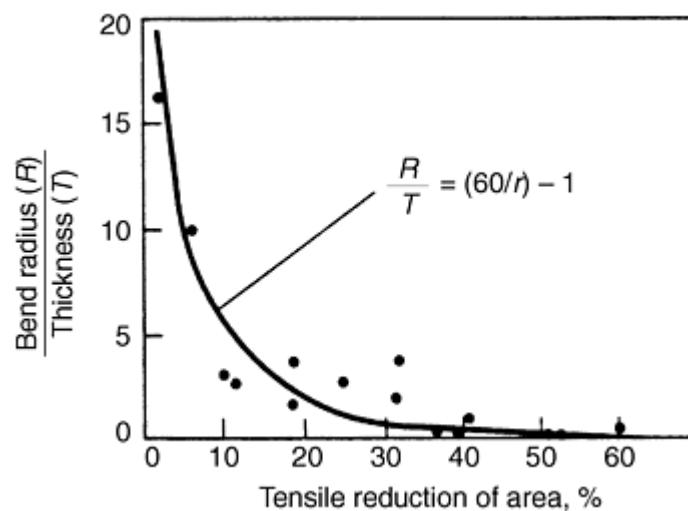


Fig. 13 Experimental data showing the relationship between bend radius-to-sheet thickness ratio and the tensile reduction of area for various sheet metals. Source: Ref 3

It has also been shown that as the sheet width-to-thickness ratio increases (thus changing the deformation condition from one of plane stress to plane strain), bendability decreases (Fig. 14). Edge condition of the sheet

is also significant; the rougher the edge, the greater is the tendency for edge cracking. Bendability, thus, decreases.

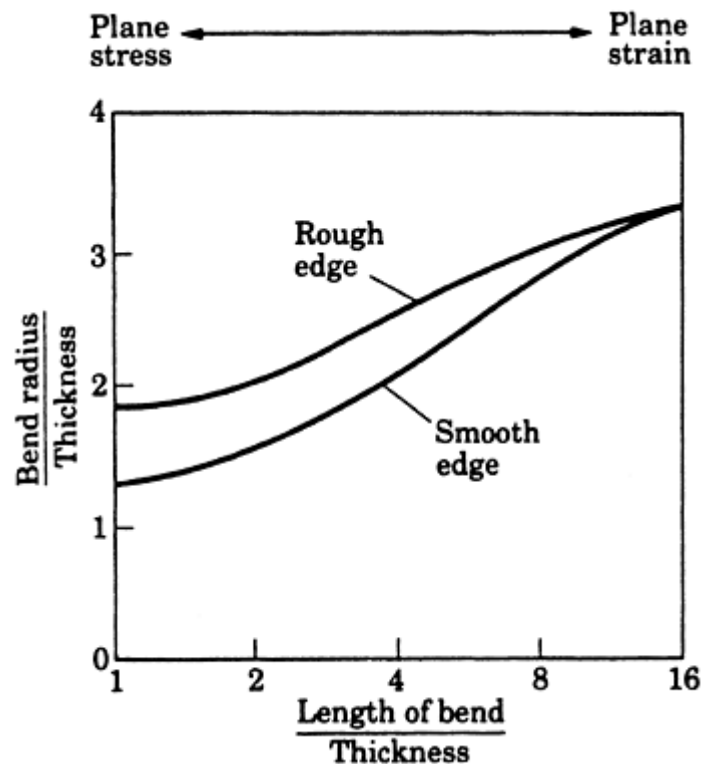


Fig. 14 The effect of length of bend (strip width) and sheared-edge condition on bend radius-to-sheet thickness ratio for 7075 aluminum. Source: Ref 3

The effects of notch sensitivity, surface finish of the sheet metal and its lay, and rate of deformation are factors that should be taken into consideration. Note that bending is one of the metalworking processes in which formability depends not only on the property of the metal but also on the state of stress (geometric factors) and edge quality.

The beneficial effect of hydrostatic pressure has also been observed in bending. Although specimen size is limited, bending of metals with limited ductility has been carried out successfully in a pressurized chamber, and major increases in bendability have been observed.

Forming-Limit Diagrams (FLD). Cupping tests commonly used in the past have been Erichsen and Olsen tests (which involve stretching of the sheet by a steel ball) and Swift and Fukui tests (which principally involve the drawing of the sheet into a cavity and some stretching). Although easy to perform and providing some general and relative indication of formability, these tests rarely represent the biaxial state of stress typically encountered by the sheet metal during actual forming operations.

A major development in establishing sheet metal formability under biaxial stresses is the construction of forming limit diagrams (Ref 1, 2, 3, 4, 5, 12). In this test, sheets of different widths are marked with a grid pattern of circles, using chemical etching or photoprinting techniques. The specimens are then clamped over a fixture using draw beads (to prevent the sheet from being drawn in) and are stretched with a punch until fracture (tearing) is observed.

The narrower the specimen is, the closer the state of stress becomes to one of simple stretching. In contrast, a square specimen undergoes biaxial stretching. By observing and recording the deformation of the original grid patterns (along the cracked or torn region) from circular to elliptical (Fig. 15), the major and minor strains (generally engineering strains) can be calculated as percentages. For improved accuracy, the circle diameters and the thickness of the lines should be as small and thin as practicable in order to locate more accurately the region of maximum deformation (which would eventually lead to thinning and tearing).

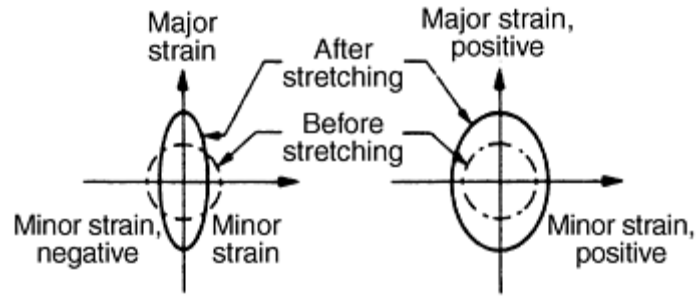


Fig. 15 Deformation of circles into ellipses, showing major and minor strains in forming-limit diagrams

The major and minor strains observed are then plotted as shown in Fig. 16, in which the regions above the boundaries indicate the failure zone and the regions below the boundaries indicate the safe zone. The measurement of the grid distortions and the continuous plotting of data are now automated, using computer software and controls. It can be seen in Fig. 16 that the minor strains may be positive or negative, but the major strains are always positive. This is because a sheet forming operation always involves stretching the sheet (hence positive strain) in at least one direction.

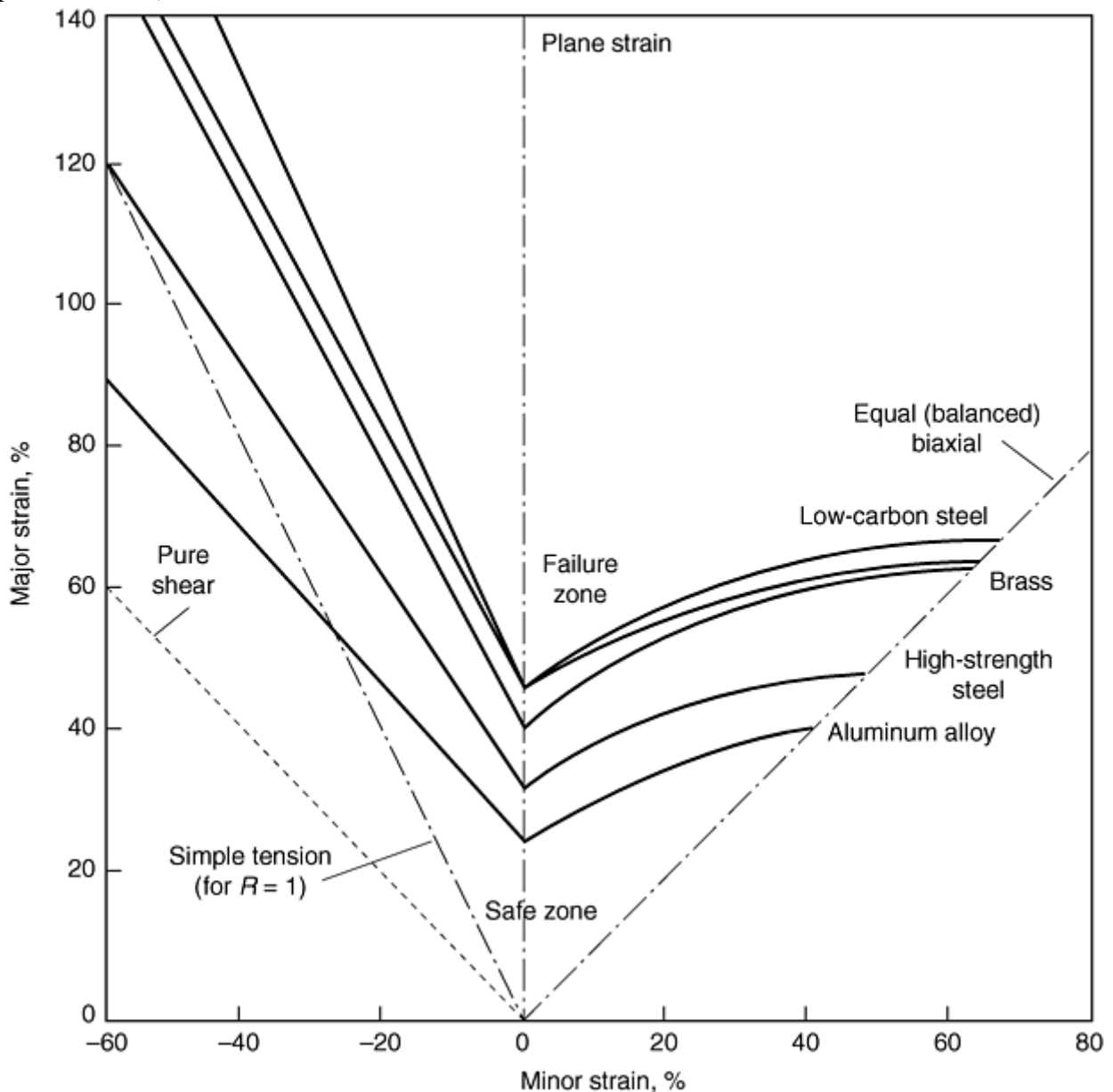


Fig. 16 Forming-limit diagram for various sheet metals. Source: Ref 3

Note that the broken straight lines show the states of strain (Fig. 16). The pure shear line indicates that the tensile and compressive strains on the sheet are equal (therefore, the negative 45° slope). The simple tension line indicates a slope which relates to Poisson's ratio in plastic deformation (i.e., 0.5). The vertical line shows the plane-strain condition, where there is no width change (minor strain is zero) as the sheet is stretched over the punch. Finally, the 45° line on the right-hand side of the diagram indicates equal biaxial tension, meaning the major and the minor strains are both tensile and equal.

Because of volume constancy in plastic deformation, the thickness change in a particular location can also be calculated by comparing the surface areas of the original and distorted circles. If the area of the ellipse is larger than the area of the original circle, the sheet has undergone thinning. If the areas are the same, there is no thickness change. It is thus possible to predict thinning and tearing of the sheet by observing the shape changes of the original circles during forming.

As expected, friction between the punch and the sheet affects the test results; hence, lubrication of the punch-sheet interface is an important parameter. As for the effect of sheet thickness, experimental results indicate that the boundaries in Fig. 16 rise with increasing sheet thickness; that is, the safe zone is expanded.

Also note that the left-hand side of the FLD has a larger safe zone than the right-hand side, indicating the desirability of encouraging the development of a compressive strain during the forming of the sheet. This phenomenon has been utilized successfully in practice, such as in bulging of tubular workpieces or bending of tubes by applying a compressive force through the axis of the tube (Fig. 17).

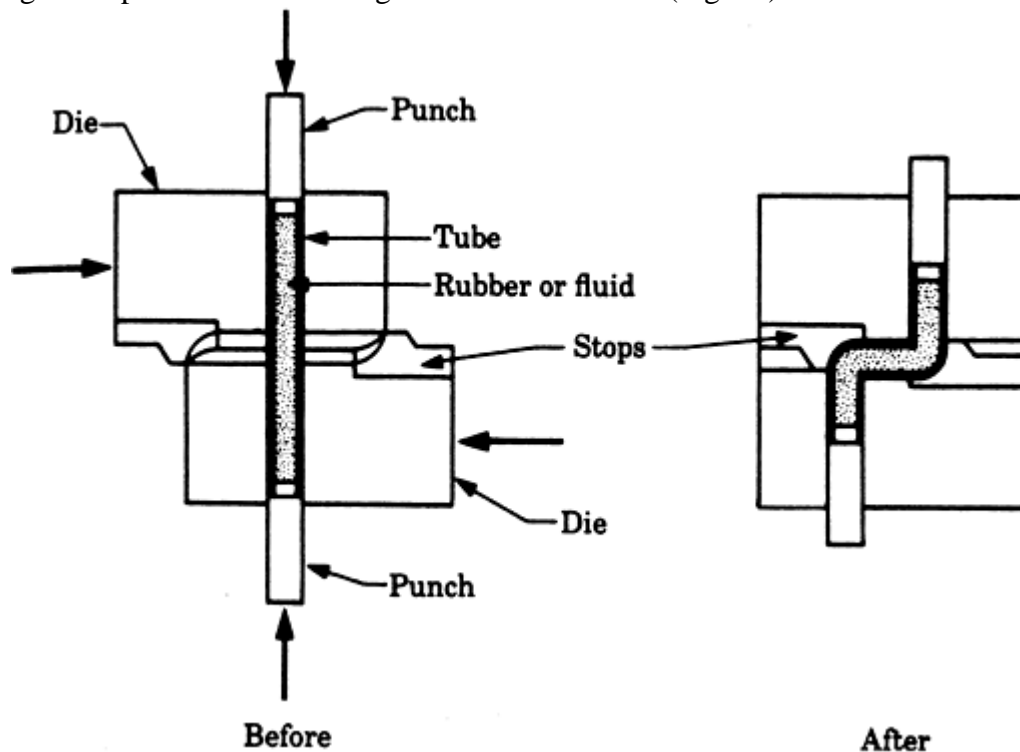


Fig. 17 A method of forming a tube with sharp bends, using axial compressive forces. Source: Ref 3

A similar observation can be made with regard to bending, a process that is usually carried out in V-dies or by air bending with punch between two supports. It can be seen readily that the bending of less ductile metals can be performed by applying through-thickness compressive forces and pushing the piece into, for example, a 90° inner corner. In this way, the tensile stresses on the outer fibers, hence the tendency for fracture, are reduced or eliminated.

Limiting Dome Height (LDH). In this test, the sheet specimens with varying widths are prepared in a manner similar to that for the FLD test, but instead of measuring the strains on the distorted grid patterns, the height of the dome at the onset of failure is measured (or when the punch force reaches a maximum). Thus, the test result is a measure of the stretchability of the sheet, and the test can be used as a tool for quality control.

The data are plotted in a manner similar to FLDs, except that the ordinate is the ratio of LDH/punch radius. It has been shown that high LDH values for a sheet metal are related to such properties as high n and high m values, as well as high total elongation of the sheet metal in uniaxial tension.

Deep drawing of sheet metals has been studied extensively, and the term limiting drawing ratio (LDR, the ratio of maximum blank diameter to punch diameter) is used to define deep drawability. Several parameters are involved in deep drawing, and their control is important in avoiding tearing of the cup being drawn, wrinkling of the flange, or other defects.

After numerous investigations attempting to establish a relationship between the LDR and some mechanical property of the sheet metal, it has been shown that for pure drawing (as contrasted to pure stretching as in the FLD or LDH tests), the important parameter in deep drawability is the normal anisotropy of the sheet, R . This parameter is the ratio of width strain to longitudinal strain in simple tension, and it is generally measured at an elongation of 15 to 20% of the sheet specimen.

Because cold rolled sheet metals generally develop planar anisotropy (which causes earing during drawing), the tension-test specimens are cut at 0° , 45° , and 90° , respectively, to the rolling direction. The average normal anisotropy (or strain ratio), \bar{R} , is then given by the expression:

$$\bar{R} = (R_0 + 2R_{45} + R_{90})/4 \quad (\text{Eq 5})$$

When the results of LDR and \bar{R} are plotted on a log-log paper, it can be seen that there is a straight linear relationship between the two parameters (Fig. 18). Consequently, \bar{R} is a reliable and consistent indicator of deep drawability. In addition to the type of sheet metal and its processing history, the magnitude of the average normal anisotropy also depends on grain size. It increases as grain size increases (or as the ASTM number decreases).

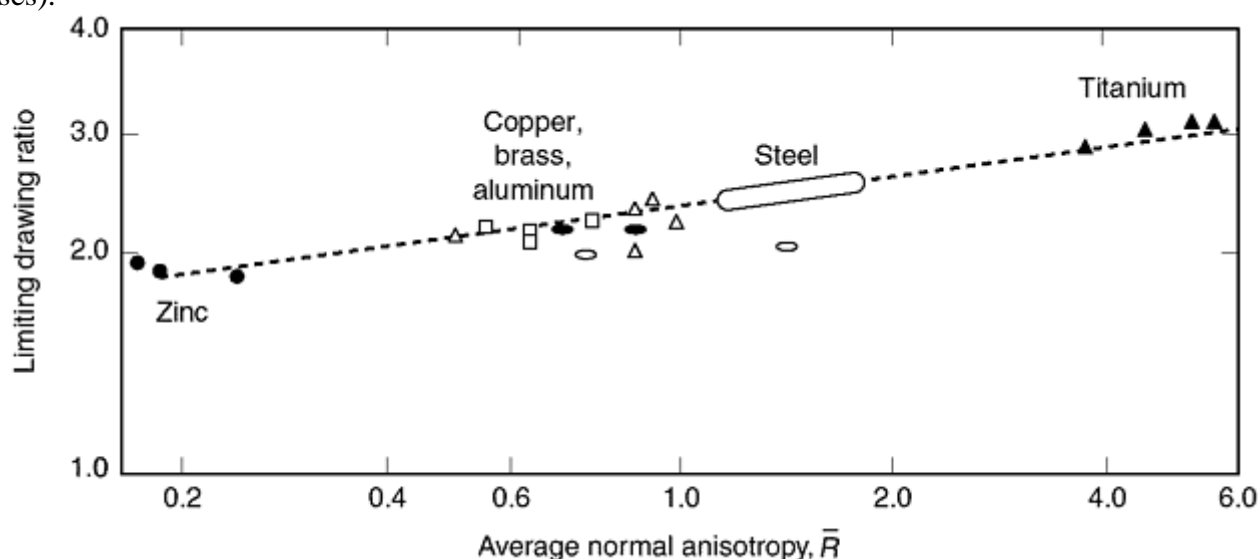


Fig. 18 Relationship between limiting drawing ratio, LDR, and the average normal anisotropy (or strain ratio), \bar{R} , for a variety of sheet metals. Source: Ref 1

Earing can also be predicted from the expression for planar anisotropy, ΔR :

$$\Delta R = (R_0 - 2R_{45} + R_{90})/2 \quad (\text{Eq 6})$$

When ΔR is zero, there is no earing. Deep drawability is thus enhanced by high values and low ΔR values.

Although \bar{R} can be obtained from tensile tests on the sheet metal, another method is based on the observation that, especially for steels, there is a relationship between the modulus of elasticity, E , and the \bar{R} value of the sheet. The modulus of elasticity can be determined from the natural frequency of a vibrating beam (which is directly proportional to E). Based on this relationship, the modul-r drawability system (developed at U.S. Steel and licensed to different manufacturers such as Control Products, NASH International, Inc., and Tinius Olsen) is available that directly gives the R value when a simple strip of metal is inserted in the unit and vibrated automatically; results are displayed digitally.

References cited in this section

1. G.E. Dieter, Ed., *Workability Testing Techniques*, ASM International, 1984, p 16, 33, 49, 61, 63, 163, 202, 206

2. G.E. Dieter, *Mechanical Metallurgy*, 3rd ed., McGraw-Hill, 1986
3. S. Kalpakjian, *Manufacturing Processes for Engineering Materials*, 3rd ed., Addison-Wesley, 1997, p 44, 45, 50, 398, 399, 409, 416, 438
4. J.S. Schey, *Introduction to Manufacturing Processes*, 3rd ed, McGraw-Hill, 1999
5. G.E. Dieter, *Engineering Design: A Materials and Processing Approach*, 2nd ed., McGraw-Hill, 1994
6. K. Lange, Ed., *Handbook of Metal Forming*, McGraw-Hill, 1985
8. *Forming and Forging*, Vol 14, *ASM Handbook*, ASM International, 1988
11. *Forming*, Vol 2, *Tool and Manufacturing Engineers Handbook*, 4th ed., Society of Manufacturing Engineers, 1984
12. H.F. Hosford and R.M. Caddell, *Metal Forming: Mechanics and Metallurgy*, 2nd ed., Prentice Hall, 1993

Mechanical Testing for Metalworking Processes

Serope Kalpakjian, Illinois Institute of Technology

Conclusions

This brief review shows that product quality and control in metalworking facilities depend on a large number of material and process variables. Important parameters are the material properties, such as the inherent ductility of the material and its prior history, the state of stress and strain, the presence and location of external and internal defects in the original material, the strain hardening exponent and strain-rate sensitivity exponent, planar and normal anisotropy, temperature, surface roughness and integrity, workpiece-die contact geometry, and tribological factors.

Considerable success has been obtained in specific metalworking processes, particularly in sheet metal forming operations. Even then, such factors as workpiece size, shape, complexity, temperature, deformation rate, and tribological behavior encountered in actual practice continue to be difficult to simulate accurately in laboratory environments. The establishment of reliable quantitative relationships among the wide range of parameters involved (that are also applicable to a wide variety of processes and conditions) remains a challenging task.

Mechanical Testing for Metalworking Processes

Serope Kalpakjian, Illinois Institute of Technology

References

1. G.E. Dieter, Ed., *Workability Testing Techniques*, ASM International, 1984, p 16, 33, 49, 61, 63, 163, 202, 206
2. G.E. Dieter, *Mechanical Metallurgy*, 3rd ed., McGraw-Hill, 1986

3. S. Kalpakjian, *Manufacturing Processes for Engineering Materials*, 3rd ed., Addison-Wesley, 1997, p 44, 45, 50, 398, 399, 409, 416, 438
4. J.S. Schey, *Introduction to Manufacturing Processes*, 3rd ed, McGraw-Hill, 1999
5. G.E. Dieter, *Engineering Design: A Materials and Processing Approach*, 2nd ed., McGraw-Hill, 1994
6. K. Lange, Ed., *Handbook of Metal Forming*, McGraw-Hill, 1985
7. T. Altan, S.I. Oh, and H.C. Gegel, *Metal Forming—Fundamentals and Applications*, ASM International, 1983
8. *Forming and Forging*, Vol 14, *ASM Handbook*, ASM International, 1988
9. T.G. Byrer, Ed., *Forging Handbook*, ASM International, 1985
10. H.A. Kuhn and B.L. Ferguson, *Powder Forging*, Metal Powder Industries Federation, 1990
11. *Forming*, Vol 2, *Tool and Manufacturing Engineers Handbook*, 4th ed., Society of Manufacturing Engineers, 1984
12. H.F. Hosford and R.M. Caddell, *Metal Forming: Mechanics and Metallurgy*, 2nd ed., Prentice Hall, 1993

Testing Machines and Strain Sensors

Joel W. House, Air Force Research Laboratory; Peter P. Gillis, University of Kentucky

Introduction

MECHANICAL TESTING MACHINES have been commercially available since 1886 (Ref 1) and have evolved from purely mechanical machines (like the popular “Little Giant” hand-cranked tensile tester of Tinius Olsen, circa 1900, shown in Fig. 1) to more sophisticated electromechanical and servohydraulic machines with advanced electronics and microcomputers. Electronic circuitry and microprocessors have increased the reliability of experimental data, while reducing the time to analyze information. This transition has made it possible to determine rapidly and with great precision ultimate tensile strength and elongation, yield strength, modulus of elasticity, and other mechanical properties. Current equipment manufacturers also offer workstation configurations that automate mechanical testing.

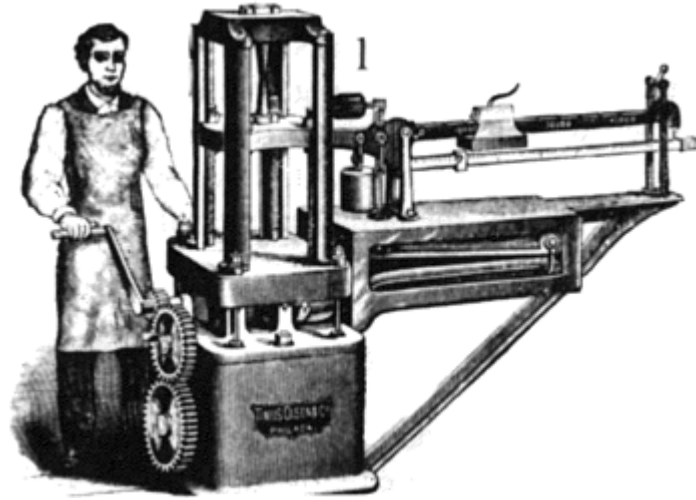


Fig. 1 “Little-Giant” hand-cranked tensile tester of Tinius Olsen, circa 1900

Conventional test machines for measuring mechanical properties include tension testers, compression testers, or the more versatile universal testing machine (UTM) (Ref 2). UTMs have the capability to test material in tension, compression, or bending. The word *universal* refers to the variety of stress states that can be studied. UTMs can load material with a single, continuous (monotonic) pulse or in a cyclic manner. Other conventional test machines may be limited to either tensile loading or compressive loading, but not both. These machines have less versatility than UTM equipment, but are less expensive to purchase and maintain. The basic aspects of UTM equipment and testing generally apply to tension or compression testing machines as well.

This article reviews the current technology and examines force application systems, force measurement, strain measurement, important instrument considerations, gripping of test specimens, test diagnostics, and the use of computers for gathering and reducing data. Emphasis is placed on UTMs with some separate discussions of equipment factors for tensile testing and compression testing. The influence of the machine stiffness on the test results is also described, along with a general assessment of test accuracy, precision, and repeatability of modern equipment.

References cited in this section

1. R.C. Anderson, *Inspection of Metals: Destructive Testing*, ASM International, 1988, p 83–119
2. H.E. Davis, G.E. Troxell, and G.F.W. Hauck, *The Testing of Engineering Materials*, 4th ed., McGraw-Hill, 1982, p 80–124

Testing Machines and Strain Sensors

Joel W. House, Air Force Research Laboratory; Peter P. Gillis, University of Kentucky

Testing Machines

Although there are many types of test systems in current use, the most common are universal testing machines, which are designed to test specimens in tension, compression, or bending. The testing machines are designed to apply a force to a material to determine its strength and resistance to deformation. Regardless of the method of force application, testing machines are designed to drive a crosshead or platen at a controlled rate, thus applying a tensile or compressive load to a specimen. Such testing machines measure and indicate the applied force in pound-force (lbf), kilogram-force (kgf), or newtons (N). These customary force units are related by the

following: 1 lbf = 4.448222 N; 1 kgf = 9.80665 N. All current testing machines are capable of indicating the applied force in either lbf or N (the use of kgf is not recommended).

The load-applying mechanism may be a hydraulic piston and cylinder with an associated hydraulic power supply, or the load may be administered via precision-cut machine screws driven by the necessary gears, reducers, and motor to provide a suitable travel speed. In some light-capacity machines (only a few hundred pounds maximum), the force is applied by an air piston and cylinder. Gear-driven systems obtain load capacities up to approximately 600 kN (1.35×10^5 lbf), while hydraulic systems can obtain forces up to approximately 4500 kN (1×10^6 lbf).

Whether the machine is a gear-driven system or hydraulic system, at some point the test machine reaches a maximum speed for loading the specimen. Gear driven test machines have a maximum crosshead speed limited by the speed of the electric motor in combination with the design of the gear box transmission. Crosshead speed of hydraulic machines is limited to the capacity of the hydraulic pump to deliver a steady pressure on the piston of the actuator or crosshead. Servohydraulic test machines offer a wider range of crosshead speeds; however, there are continuing advances in the speed control of screw-driven machines, which can be just as versatile as, or perhaps more versatile than, servohydraulic machines.

Conventional gear-driven systems are generally designed for speeds of about 0.001 to 500 mm/min (4×10^{-6} to 20 in./min), which is suitable for quasi-static testing. Servohydraulic systems are generally designed over a wider range of test speeds, such as:

- 1 $\mu\text{m}/\text{h}$ test speeds for creep-fatigue, stress-corrosion, and stress-rupture testing
- 1 $\mu\text{m}/\text{min}$ test speeds for fracture testing of brittle materials
- 10 m/s (400 in./s) test speeds for dynamic testing of components like bumpers or seat belts

Servohydraulic UTM systems may also be designed for cycle rates from 1 cycle/day to over 200 cycles/s. Gear-driven systems typically allow cycle rates between 1 cycle/h and 1 cycle/s.

Gear-driven (or screw-driven) machines are electromechanical devices that use a large actuator screw threaded through a moving crosshead (Fig. 2). The screw is turned in either direction by an electric motor through a gear reduction system. The screws are rotated by a variable-control motor and drive the moveable crosshead up or down. This motion can load the specimen in either tension or compression, depending on how the specimen is to be held and tested.

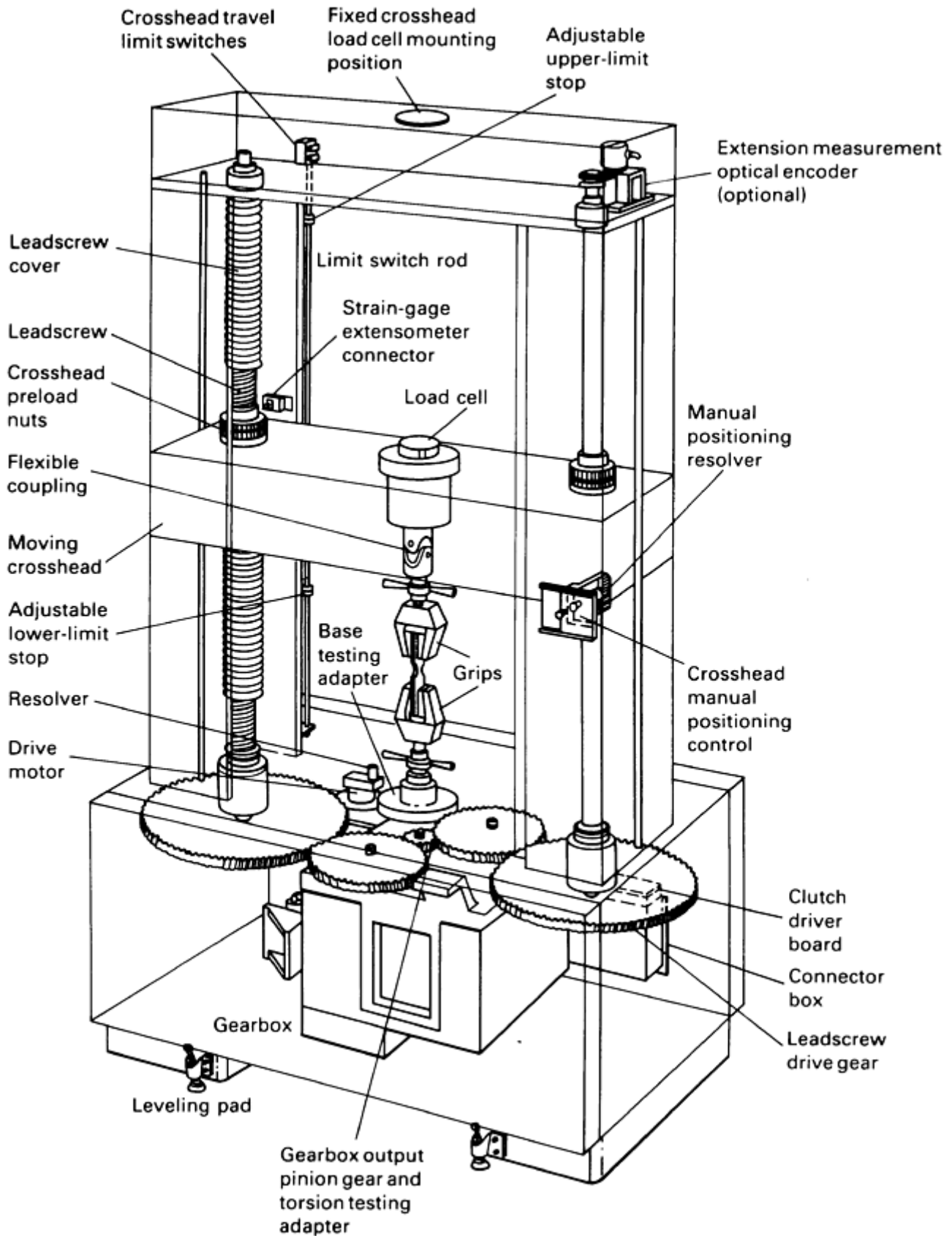


Fig. 2 Components of an electromechanical (screw-driven) testing machine. For the configuration shown, moving the lower (intermediate) head upward produces tension in the lower space between the crosshead and the base

Screw-driven testing machines currently used are of either a one-, two-, or four-screw design. To eliminate twist in the specimen from the rotation of the screws in multiple-screw systems, one screw has a right-hand thread, and the other has a left-hand thread. For alignment and lateral stability, the screws are supported in

bearings on each end. In some machines, loading crossheads are guided by columns or guideways to achieve alignment.

A range of crosshead speeds can be achieved by varying the speed of the electric motor and by changing the gear ratio. A closed-loop servodrive system ensures that the crosshead moves at a constant speed. The desired or user-selected speed and direction information is compared with a known reference signal, and the servomechanism provides positional control of the moving crosshead to reduce any error or difference. State-of-the-art systems use precision optical encoders mounted directly on preloaded twin ball screws. These types of systems are capable of measuring crosshead displacement to an accuracy of 0.125% or better with a resolution of 0.6 μm .

As noted above, typical screw-driven machines are designed for speeds of 1 to 20 mm/min (0.0394–0.788 in./min) for quasi-static test applications; however, machines can be designed to obtain higher speeds, although the useful force available for application to the specimen decreases as the speed of the cross-head motion increases. Modern high-speed systems generally are useful in ranges up to 500 mm/min (20 in./min) (Ref 3). Nonetheless, top crosshead speeds of 1250 mm/min (50 in./min) can be attained in screw-driven machines, and servohydraulic machines can be driven up to 2.5×10^5 mm/min (10^4 in./min) or higher.

Due to the high forces involved, bearings and gears require particular attention to reduce friction and wear. Backlash, which is the free movement between the mechanical drive components, is particularly undesirable. Many instruments incorporate antibacklash preloading so that forces are translated evenly through the lead screw and crosshead. However, when the crosshead direction is constantly in one direction, antibacklash devices may be unnecessary.

Servohydraulic machines use a hydraulic pump and servohydraulic valves that move an actuator piston (Fig. 3). The actuator piston is attached to one end of the specimen. The motion of the actuator piston can be controlled in both directions to conduct tension, compression, or cyclic loading tests.

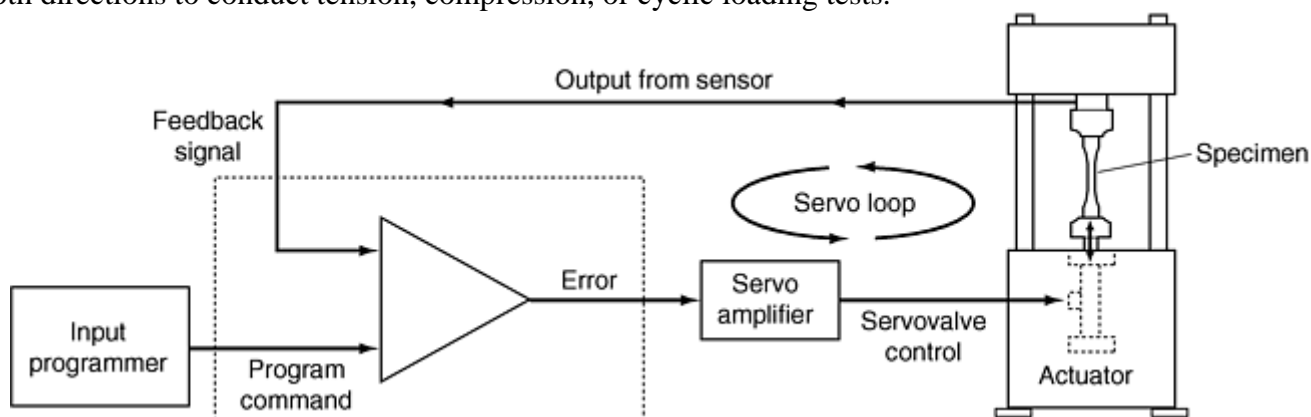


Fig. 3 Schematic of a basic servohydraulic, closed-loop testing machine

Servohydraulic test systems have the capability of testing at rates from as low as 45×10^{-11} m/s (1.8×10^{-9} in./s) to 30 m/s (1200 in./s) or more. The actual useful rate for any particular system depends on the size of the actuator, the flow rating of the servovalve, and the noise level present in the system electronics. A typical servohydraulic UTM system is shown in Fig. 4.

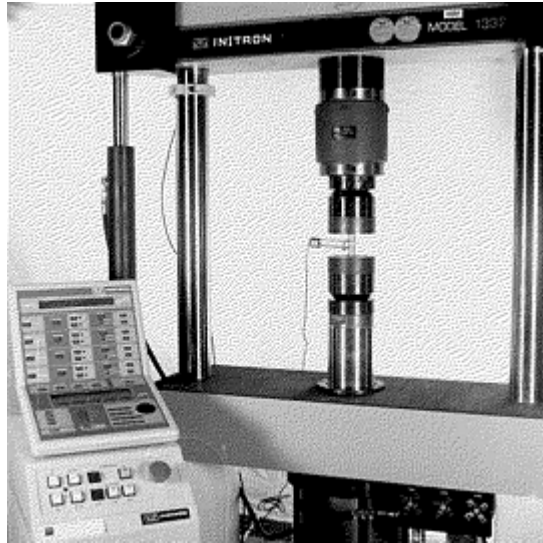


Fig. 4 Servohydraulic testing machine and load frame with a dedicated microprocessor-based controller

Hydraulic actuators are available in a wide variety of force ranges. They are unique in their ability to economically provide forces of 4450 kN (1,000,000 lbf) or more. Screw-driven machines are limited in their ability to provide high forces due to problems associated with low machine stiffness and large and expensive loading screws, which are increasingly more difficult to produce as the force rating goes up.

Microprocessors for Testing and Data Reduction. Contemporary UTMs are controlled by microprocessor-based electronics. One class of controller is based on dedicated microprocessors for test machines (Fig. 4). Dedicated microprocessors are designed to perform specific tasks and have displays and input functions that are limited to those tasks. The dedicated microprocessor sends signals to the experimental apparatus and receives information from various sensors. The data received from sensors can be passed to oscilloscopes or computers for display and storage. The experimental results consist of time and voltage information that must be further reduced to analyze material behavior. Analysis of the data requires the conversion of test results, such as voltage, to specific quantities, such as displacement and load, based on known conversion factors.

The second class of controller is the personal computer (PC) designed with an electronic interface to the experimental apparatus, and the appropriate application software. The software takes the description of the test to be performed, including specimen geometry data, and establishes the requisite electronic signals. Once the test is underway, the computer controls the tests and collects, reduces, displays, and stores the data. The obvious advantage of the PC-based controller is reduced time to generate graphic results, or reports. The other advantage is the elimination of some procedural errors, or the reduction of the interfacing details between the operator and the experimental apparatus. Some systems are designed with both types of controllers. Having both types of controllers provides maximum flexibility in data gathering with a minimal amount of time required for reducing data when conducting standard experiments.

Reference cited in this section

3. P. Han, Ed., *Tensile Testing*, ASM International, 1992, p 28

Testing Machines and Strain Sensors

Joel W. House, Air Force Research Laboratory; Peter P. Gillis, University of Kentucky

Principles of Operation

The operation of a universal testing machine can be understood in terms of the main elements for any stress analysis, which include material response, specimen geometry, and load or boundary condition.

Material response, or material characterization, is studied by adopting standards for the other two elements. Specimen geometries, which are specific for tension, compression, or bending tests, are described in separate sections at the end of this article. This section briefly describes load condition factors, such as strain rate, machine rigidity, and various testing modes by load control, speed control, strain control, and strain-rate control.

Strain rate, or the rate at which a specimen is deformed, is a key test variable that is controlled within prescribed limits, depending on the type of test being performed. Table 1 summarizes the general strain-rate ranges that are required for various types of property tests. Creep tests require low strain rates, while conventional (quasi-static) tension and compression tests require strain rates between 10^{-5} and 10^{-1} s^{-1} .

Table 1 Strain rate ranges for different tests

Type of test	Strain rate range, s^{-1}
Creep tests	10^{-8} to 10^{-5}
Pseudostatic tension or compression tests	10^{-5} to 10^{-1}
Dynamic tension or compression tests	10^{-1} to 10^2
Impact bar tests involving wave propagation effects	10^2 to 10^4

Source: Ref 4

A typical mechanical test on metallic materials is performed at a strain rate of approximately 10^{-3} s^{-1} , which yields a strain of 0.5 in 500 s. Conventional equipment and techniques generally can be extended to strain rates as high as 0.1 s^{-1} without difficulty. Tests at higher strain rates necessitate additional considerations of machine stiffness and strain measurement techniques. In terms of machine capability, servohydraulic load frames equipped with high-capacity valves can be used to generate strain rates as high as 200 s^{-1} . These tests are complicated by load and strain measurement and data acquisition.

If the crosshead speed is too high, inertia effects can become important in the analysis of the specimen stress state. Under conditions of high crosshead speed, errors in the load cell output and crosshead position data may become unacceptably large. A potential exists to damage load cells and extensometers under rapid loading. The damage occurs when the specimen fractures and the load is instantaneously removed from the specimen and the load frame.

At strain rates greater than 200 s^{-1} , the required crosshead speeds exceed the speeds easily obtained with screw-driven or hydraulic machines. Specialized high strain rate methods are discussed in more detail in the Section “High Strain Rate Testing” in this Volume.

Determination of Strain Rates for Quasi-Static Tension Tests. Strength properties for most materials tend to increase at higher rates of deformation. In order to quantify the effect of deformation rate on strength and other properties, a specific definition of strain rate is required. During a conventional (quasi-static) tension test, for example, ASTM E 8 “Tension Testing of Metallic Materials” prescribes an upper limit of deformation rate as determined quantitatively during the test by one of the following methods (listed in decreasing order of precision):

- Rate of straining
- Rate of stressing (when loading is below the proportional limit)
- Rate of crosshead separation during the tests
- Elapsed time
- Free-running crosshead speed

For some materials, the free-running crosshead speed, which is the least accurate, may be adequate, while for other materials, one of the remaining methods with higher precision may be necessary in order to obtain test values within acceptable limits. When loading is below the proportional limit, the deformation rate can be specified by the “loading rate” units of stress per unit of time such that:

$$\dot{\sigma} = E\dot{\epsilon}$$

where, according to Hooke's law, $\dot{\sigma}$ is stress, E is the modulus of elasticity, $\dot{\epsilon}$ is strain, and the superposed dots denote time derivatives.

ASTM E 8 specifies that the test speed must be low enough to permit accurate determination of loads and strains. When the rate of stressing is stipulated, ASTM E 8 requires that it not exceed 690 MPa/min (100 ksi/min). This corresponds to an elastic strain rate of about $5 \times 10^{-5} \text{ s}^{-1}$ for steel or $15 \times 10^{-5} \text{ s}^{-1}$ for aluminum. When the rate of straining is stipulated, ASTM E 8 prescribes that after the yield point has been passed, the rate can be increased to about $1000 \times 10^{-5} \text{ s}^{-1}$; presumably, the stress rate limitation must be applied until the yield point is passed. Lower limits are also given in ASTM E 8.

In ASTM standard E 345, "Tension Testing of Metallic Foil," the same upper limit on the rate of stressing is recommended. In addition, a lower limit of 7 MPa/min (1 ksi/min) is given. ASTM E 345 further specifies that when the yield strength is to be determined, the strain rate must be in the range from approximately 3×10^{-5} to $15 \times 10^{-5} \text{ s}^{-1}$.

Inertia Effects. A fundamental difference between a high strain rate tension test and a quasi-static tension test is that inertia and wave propagation effects are present at high rates. An analysis of results from a high strain rate test thus requires consideration of the effect of stress wave propagation along the length of the test specimen in order to determine how fast a uniaxial test can be run to obtain valid stress-strain data.

For high loading rates, the strain in the specimen may not be uniform. Figure 5 illustrates an elemental length dx_0 of a tension test specimen whose initial cross-sectional area is A_0 and whose initial location is prescribed by the coordinate x . Neglecting gravity, no forces act on this element in its initial configuration. After the test has begun, the element is shown displaced by a distance u , deformed to new dimensions dx and A , and subjected to forces F and $F + dF$. The difference, dF , between these end-face forces causes the motion of the element that is manifested by the displacement, u . This motion is governed by Newton's second law, force equals mass times acceleration:

$$dF = \rho_0 A_0 dx_0 \left(\frac{d^2 u}{dt^2} \right) \quad (\text{Eq 1})$$

where $\rho_0 A_0 dx_0$ is the mass of the element, $A_0 dx_0$ is the volume, ρ is the density of the material, and $(d^2 u/dt^2)$ is its acceleration. Tests that are conducted very slowly involve extremely small accelerations. Thus, Eq 1 shows that the variation of force dF along the specimen length is negligible.

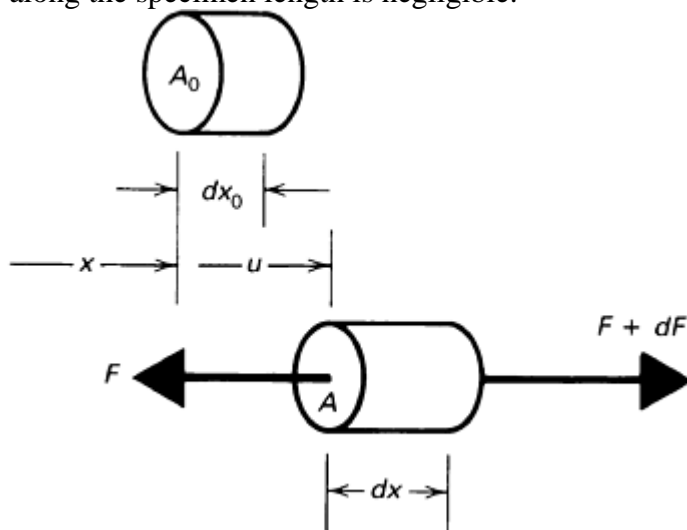


Fig. 5 The deformation of an elemental length, dx_0 , of a tension test specimen of initial cross-sectional area, A_0 , by a stress wave. The displacement of the element is u ; the differential length of the element as a function of time is dx ; the forces acting on the faces of the element are given by F and $F + dF$.

However, for tests of increasingly shorter durations, the acceleration term on the right side of Eq 1 becomes increasingly significant. This produces an increasing variation of axial force along the length of the specimen. As the force becomes more nonuniform, so must the stress. Consequently, the strain and strain rate will also vary with axial position in the specimen. When these effects become pronounced, the concept of average values of stress, strain, and strain rate become meaningless, and the test results must be analyzed in terms of the propagation of waves through the specimen. This is shown in Table 1 as beginning near strain rates of 10^2 s^{-1} . In an intermediate range of strain rates (denoted as dynamic tests in Table 1), an effect known as "ringing" of the load-measuring device obscures the interpretation of test data. An example of this condition is shown in Fig.

6, which is a tracing of load cell force versus time during a dynamic tension test of a 2024-T4 aluminum specimen. Calculation showed that the oscillations apparent in the figure are consistent with vibrations at the approximate natural frequency of the load cell used for this test (Ref 5, 6).

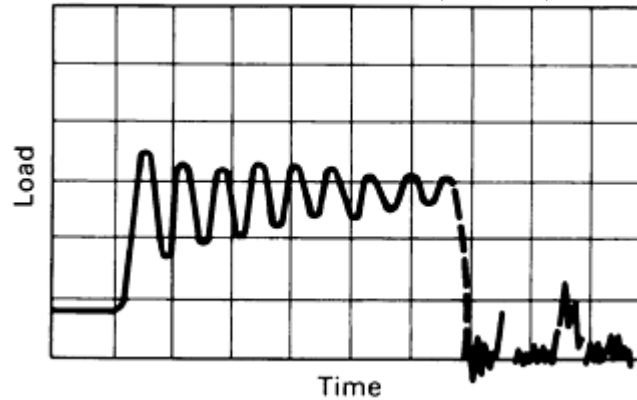


Fig. 6 Oscilloscope record of load cell force versus time during a dynamic tension test depicting the phenomenon of ringing. The uncontrolled oscillations result when the loading rate is near the resonant frequency of the load cell. The scales are arbitrary. Source: Ref 5

In many machines currently available for dynamic testing, electronic signal processing is used to filter out such vibrations, thus making the instrumentation records appear much smoother than the actual load cell signal. However, there is still a great deal of uncertainty in the interpretation of dynamic test data. Consequently, the average value of the high-frequency vibrations associated with the load cell can be expected to differ from the force in the specimen. This difference is caused by vibrations near the natural frequency of the testing machine, which are so low that the entire test can occur in less than $\frac{1}{10}$ of a cycle. Hence, these low-frequency vibrations usually are impossible to detect in a test record, but can produce significant errors in the analysis of test results. The ringing frequency for typical load cells ranges from 2400 to 3600 Hz.

Machine Stiffness. The most common misconception relating to strain rate effects is that the testing machine is much stiffer than the specimen. Such an assumption leads to the concept of deformation of the specimen by an essentially rigid machine. However, for most tests the opposite is true: the conventional tensile specimen is much stiffer than most testing machines. As shown in Fig. 7, for example, if crosshead displacement is defined as the relative displacement, Δ , that would occur under conditions of zero load, then with a specimen gripped in a testing machine and the driving mechanism engaged, the crosshead displacement equals the deformation in the gage length of the specimen plus elastic deflections in components such as the machine frame, load cell, grips, and specimen ends. Before yielding, the gage length deformation is a small fraction of the crosshead displacement.

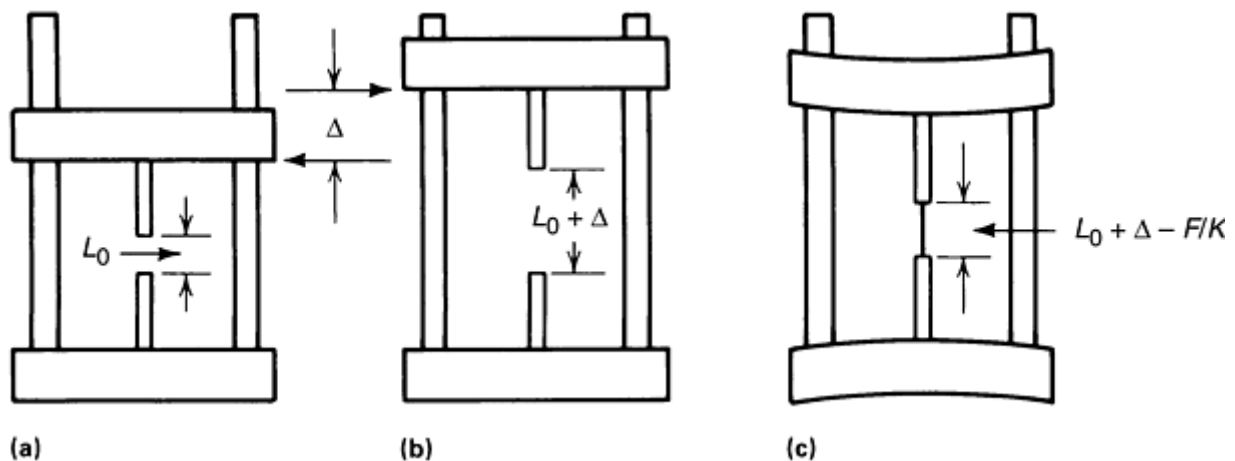


Fig. 7 Schematic illustrating crosshead displacement and elastic deflection in a tension testing machine. Δ is the displacement of the crosshead relative to the zero load displacement; L_0 is the initial gage length of the specimen; K is the composite stiffness of the grips, loading frame, load cell, specimen ends, etc.; F is the force acting on the specimen. The development of Eq 2, 3, 4, 5, 6, 7, 8, 9, 10, 11, and 12 describes the effects of testing machine stiffness on tensile properties. Source: Ref 7

After the onset of gross plastic yielding of the specimen, conditions change. During this phase of deformation, the load varies slowly as the material strain hardens. Thus, the elastic deflections in the machine change slowly, and most of the relative crosshead displacement produces plastic deformation in the specimen. Qualitatively, in a test at approximately constant crosshead speed, the initial elastic strain rate in the specimen will be small, but the specimen strain rate will increase when plastic flow occurs.

Quantitatively, this effect can be estimated as follows. Consider a specimen having an initial cross-sectional area A_0 and modulus of elasticity E gripped in a testing machine so that its axially stressed gage length initially is L_0 . (This discussion is limited to the range of testing speeds where wave propagation effects are negligible. This restriction implies that the load is uniform throughout the gage length of the specimen.) Denote the stiffness of the machine, grips, and so on, by K and the crosshead displacement rate (nominal crosshead speed) by S . The ratio S/L_0 is sometimes called the nominal rate of strain, but because it is often substantially different from the rate of strain in the specimen, the term specific crosshead rate is preferred (Ref 8).

Let loading begin at time t equal to zero. At any moment thereafter, the displacement of the crosshead must equal the elastic deflection of the machine plus the elastic and plastic deflections of the specimen. Letting s denote the engineering stress in the specimen, the machine deflection is then sA_0/K . It is reasonable to assume that Hooke's law adequately describes the elastic deformation of the specimen at ordinary stress levels. Thus, the elastic strain e_e is s/E .

Denoting the average plastic strain in the specimen by e_p , the above displacement balance can be expressed as:

$$\int_0^t S dt = s \left(\frac{A_0}{K} + \frac{L_0}{E} \right) + e_p L_0 \quad (\text{Eq 2})$$

Differentiating Eq 2 with respect to time and dividing by L_0 gives:

$$\frac{S}{L_0} = \left(\frac{\dot{s}}{E} \right) \left(\frac{A_0 E}{K L_0} + 1 \right) + \dot{e}_p \quad (\text{Eq 3})$$

The strain rate in the specimen is the sum of the elastic and plastic strain rates:

$$\dot{e} = \dot{e}_e + \dot{e}_p = \left(\frac{\dot{s}}{E} \right) + \dot{e}_p \quad (\text{Eq 4})$$

Using Eq 3 to eliminate the stress rate from Eq 4 yields:

$$\dot{e} = \frac{\left(\frac{SK}{A_0 E} + \dot{e}_p \right)}{\left(\frac{K L_0}{A_0 E} + 1 \right)} \quad (\text{Eq 5})$$

Thus, it is seen that the specimen strain rate usually will differ from the specific crosshead rate by an amount dependent on the rate of plastic deformation and the relative stiffnesses of the specimen ($A_0 E/L_0$) and the machine, K .

Accounting for Testing Machine Stiffness. Machine stiffness is the amount of deflection in the load frame and the grips for each unit of load applied to the specimen. This deflection not only encompasses elastic deflection of the load frame, but includes any motion in the grip mechanism, or at any interface (threads, etc.) in the system. These deflections are substantial during the initial loading of the specimen, that is, through the elastic regime. This means that the initial crosshead speed (specified by the operator) is not an accurate measure of specimen displacement (strain). If the strain in the elastic regime is not accurately known, then extremely large errors may result in the calculation of Young's modulus (E , the ratio of stress versus strain in the elastic regime). In the analysis by Hockett and Gillis (Ref 9), the machine stiffness K is accounted for in the following equation:

$$K = \left(\frac{S}{\dot{P}_0} - \frac{L_0}{A_0 E} \right)^{-1} \quad (\text{Eq 6})$$

where L_0 is initial specimen gage length, S is crosshead speed of the testing machine, A_0 is initial cross-sectional area of the specimen, \dot{P}_0 is specimen load rate ($dF/dt = A_0\dot{S}$), and E is Young's modulus of the specimen material.

Research in this area showed that a significant amount of scatter was found in the measurement of machine stiffness. This variability can be attributed to relatively small differences in test conditions. For characterization of the elastic response of a material and for a precise measure of yield point, the influence of machine stiffness requires that an extensometer, or a bonded strain gage, be used. After yielding of the specimen material, the change of machine deflection is very small because the load changes slowly. If the purpose of the experiment is to study large strain behavior, then the error associated with the use of the crosshead displacement is small relative to other forms of experimental uncertainties.

Control Modes. During a test, control circuits and servomechanisms monitor and control the key experimental conditions, such as force, specimen deformation, and the position of the moveable crosshead. These are the key boundary conditions, which are analyzed to provide mechanical property data. These boundary conditions on the specimen can also be controlled in different ways, such as constant load control, constant strain control, and constant crosshead speed control. Constant crosshead speed is the most common method for tension tests.

Constant Load Rate Testing. With appropriate modules on a UTM system, a constant load rate test can be accomplished easily. In this configuration, a load-control module allows the machine with the constant rate of extension to function as a constant load rate device. This is accomplished by a feedback signal from a load cell, which generates a signal that automatically adjusts to the motion controller of the crosshead. Usually, the servomechanism system response is particularly critical when materials are loaded through the yield point.

Constant Strain Rate Testing. Commercial systems have been developed to control the experiment based on a constant rate of straining in the specimen. These systems rely on extensometers measuring the change in gage length to provide data on strain as a function of time. The resulting signal is processed to determine the current strain rate and is used to adjust the crosshead displacement rate throughout the test. Again, servomechanism response time is particularly critical when materials are taken through yield.

To maintain a constant average strain rate during a test, the crosshead speed must be adjusted as plastic flow occurs so that the sum $(SK/A_0E + e_p)$ remains constant. For most metallic materials at the beginning of a test, the plastic strain rate is ostensibly zero, and from Eq 5 the initial strain rate is:

$$\dot{e}_0 = \frac{\left(\frac{S_0}{L_0}\right)}{1 + \left(\frac{A_0E}{KL_0}\right)} \quad (\text{Eq 7})$$

where S_0 is the crosshead speed at the beginning of the test. For materials that have a definite yield, $\dot{S} = 0$ at the yield point. Therefore, from Eq 3 and 4, the yield point strain rate is:

$$\dot{e}_1 = \left(\frac{S_1}{L_0}\right) \quad (\text{Eq 8})$$

where S_1 is the crosshead speed at the yield point. Equating these two values of strain rate shows that the crosshead speed must be reduced from its initial value to its yield-point value by a factor of:

$$\frac{S_0}{S_1} = \left(1 + \frac{A_0E}{KL_0}\right) \quad (\text{Eq 9})$$

For particular measured values of machine stiffness given in Table 2, this factor for a standard 12.8 mm (0.505 in.) diameter steel specimen is typically greater than 20 and can be as high as 100. Only for specially designed machines will the relative stiffness of the machine exceed that of the specimen. Even for wire-like specimens, the correspondingly delicate gripping arrangement will ensure that the machine stiffness is less than that of the specimen. Thus, large changes in crosshead speed usually are required to maintain a constant strain rate from the beginning of the test through the yield point.

Table 2 Experimental values of testing machine stiffness

Machine stiffness		Source
kg/mm	lb/in.	
740	41,500	Ref 10
460	26,000	Ref 11
1800	100,000	Ref 12
1390–2970	77,900–166,500	Ref 13

Furthermore, for many materials, the onset of yielding is quite rapid, so that this large change in speed must be accomplished quickly. Making the necessary changes in speed generally requires not only special strain-sensing equipment, but also a driving unit that is capable of extremely fast response. The need for fast response in the driving system eliminates the use of screw-driven machines for constant strain-rate testing. Servohydraulic machines may be capable of conducting tests at constant strain rate through the yield point of a material.

Equation 9 indicates the magnitude of speed changes required only for tests in which there is no yield drop. For materials having upper and lower yield points, the direction of crosshead motion may have to be reversed after initial yielding to maintain a constant strain rate. This reversal may be necessary, because plastic strains beyond the upper yield point can be imposed at a strain rate greater than the desired rate by recovery of elastic deflections of the machine as the load decreases. For a description of yield point phenomena, see the article “Mechanical Behavior under Tensile and Compressive Loads” in this Volume.

Another important test feature related to the speed change capability of the testing machine is the rate at which the crosshead can accelerate from zero to the prescribed test speed at the beginning of the test. For a slow test this may not be critical, but for a high-speed test, the yield point could be passed before the crosshead achieves full testing speed. Thus, the crosshead may still be accelerating when it should be decelerating, and accurate information concerning the strain rate will not be obtained. With the advent of closed-loop servohydraulic machines and electromagnetic shakers, the speed at which the ram (crosshead) responds is two orders of magnitude greater than for screw-driven machines.

Tests at Constant Crosshead Speeds. Machines with a constant rate of extension are the most common type of screw-driven testers and are characterized by a constant rate of crosshead travel regardless of applied loads. They permit testing without speed variations that might alter test results; this is particularly important when testing rate-sensitive materials such as polymers, which exhibit different ultimate strengths and elongations when tested at different speeds.

For a gear-driven system, applying the boundary condition is as simple as engaging the electric motor with a gear box transmission. At this point, the crosshead displacement will be whatever speed and direction was selected. More sophisticated systems use a command signal that is compared with a feedback signal from a transducer monitoring the position of the crosshead. Using this feedback circuit, the desired boundary condition can be achieved.

Tension tests usually can be carried out at a constant crosshead speed on a conventional testing machine, provided the machine has an adequate speed controller and the driving mechanism is sufficiently powerful to be insensitive to changes in the loading rate. Because special accessory equipment is not required, such tests are relatively simple to perform. Also, constant crosshead speed tests typically provide as good a comparison among materials and as adequate a measure of strain-rate sensitivity as constant strain-rate tests.

Two of the most significant test quantities—yield strength and ultimate tensile strength—frequently can be correlated with initial strain rate and specific crosshead rate, respectively. The strain rate up to the proportional limit equals the initial strain rate. Thus, for materials that yield sharply, the time-average strain rate from the beginning of the test to yield is only slightly greater than the initial strain rate:

$$\dot{\epsilon}_0 = \left(\frac{\frac{S}{L_0}}{1 + \frac{A_0 E}{KL_0}} \right) \quad (\text{Eq 10})$$

even though the instantaneous strain rate at yield is the specific crosshead rate:

$$\dot{\epsilon}_1 = \left(\frac{S}{L_0} \right) \quad (\text{Eq 11})$$

However, beyond the yield point, the stress rate is small so that the strain rate remains close to the specific crosshead rate (Eq 11). Thus, ductile materials, for which a rather long time will elapse before reaching ultimate strength, have a time-average strain rate from the beginning of the test to ultimate that is only slightly less than the specific crosshead rate. Also, because the load rate is zero at ultimate as well as at yield, the instantaneous strain rate at ultimate equals the specific crosshead rate.

During a test at constant crosshead speed, the variation of strain rate from initial to yield-point values is precisely the inverse of the crosshead speed change required to maintain a constant strain rate (Eq 9):

$$\frac{\dot{\epsilon}_1}{\dot{\epsilon}_0} = \left(1 + \frac{A_0 E}{KL_0} \right) \quad (\text{Eq 12})$$

Consequently, in an ordinary tension test, the yield strength and ultimate tensile strength may be determined at two different strain rates, which can vary by a factor of 20 to 100, depending on machine stiffness. If a yield drop occurs, elastic recovery of machine deflections will impose a strain rate even greater than the specific crosshead rate given by Eq 12.

A point of interest from the analysis involves testing of different sized specimens at about the same initial strain rate. Assuming that these tests are to be made on one machine under conditions for which K remains substantially constant, the crosshead speed must be adjusted to ensure that specimens of different lengths, diameters, or materials will experience the same initial strain rate. In the typical case where the specimen is much stiffer than the machine, $(1 + A_0 E / KL_0)$ in Eq 10 can be approximated simply by $(A_0 E / KL_0)$, so that the initial strain rate is approximately $\dot{\epsilon}_0 = SK / A_0 E$. Thus, specimens of various lengths, tested at the same crosshead speed, will generally experience nearly the same initial strain rate. However, changing either the specimen cross section or material necessitates a corresponding change in crosshead speed to obtain the same initial rate.

A change in specimen length has substantially the same effect on both the specific crosshead rate (S/L_0) and the stiffness ratio of specimen to machine ($A_0 E / KL_0$) and, therefore, has no net effect. For example, an increase in specimen length tends to decrease the strain rate by distributing the crosshead displacement over the longer length; however, at the same time, the increase in length reduces the stiffness of the specimen so that more of the crosshead displacement goes into deformation of the specimen and less into deflection of the machine. These two effects are almost exactly equal in magnitude. Thus, no change in initial strain rate is expected for specimens of different lengths tested at the same crosshead speed.

References cited in this section

4. G.E. Dieter, *Mechanical Metallurgy*, McGraw-Hill, 2nd ed., 1976, p 349
5. D.J. Shippy, P.P. Gillis, and K.G. Hoge, Computer Simulation of a High Speed Tension Test, *J. Appl. Polym. Sci.*, Applied Polymer Symposia (No. 5), 1967, p 311–325
6. P.P. Gillis and D.J. Shippy, Vibration Analysis of a High Speed Tension Test, *J. Appl. Polym. Sci.*, Applied Polymer Symposia (No. 12), 1969, p 165–179
7. M.A. Hamstad and P.P. Gillis, Effective Strain Rates in Low-Speed Uniaxial Tension Tests, *Mater. Res. Stand.*, Vol 6 (No. 11), 1966, p 569–573
8. P. Gillis and J.J. Gilman, Dynamical Dislocation Theories of Crystal Plasticity, *J. Appl. Phys.*, Vol 36, 1965, p 3375–3386
9. J.E. Hockett and P.P. Gillis, Mechanical Testing Machine Stiffness, Parts I and II, *Int. J. Mech. Sci.*, Vol 13, 1971, p 251–275
10. W.G. Johnston, Yield Points and Delay Times in Single Crystals, *J. Appl. Phys.*, Vol 33, 1962, p 2716
11. H.G. Baron, Stress-Strain Curves of Some Metals and Alloys at Low Temperatures and High Rates of Strain, *J. Iron Steel Inst. (Brit.)*, Vol 182, 1956, p 354

12. J. Miklowitz, The Initiation and Propagation of the Plastic Zone in a Tension Bar of Mild Steel as Influenced by the Speed of Stretching and Rigidity of the Testing Machine, *J. Appl. Mech. (Trans. ASME)*, Vol 14, 1947, p A-31
13. M.A. Hamstead, "The Effect of Strain Rate and Specimen Dimensions on the Yield Point of Mild Steel," Lawrence Radiation Laboratory Report UCRL-14619, April 1966

Testing Machines and Strain Sensors

Joel W. House, Air Force Research Laboratory; Peter P. Gillis, University of Kentucky

Measuring Load

Prior to the development of load cells, testing machine manufacturers used several types of devices for the measurement of force. Early systems, some of which are still in use, employ a graduated balanced beam similar to platform-scale weighing systems. Subsequent systems have used Bourdon tube hydraulic test gages, Bourdon tubes with various support and assist devices, and load cells of several types. One of the most common load-measuring systems, prior to the development of load cells, was the displacement pendulum, which measured load by the movement of the balance displacement pendulum. The pendulum measuring system was used widely, because it is applicable to both hydraulic and screw-driven machines and has a high degree of reliability and stability. Many machines of this design are still in use, and they are still manufactured in Europe, India, South America, and Asia. Another widely used testing system was the Emery-Tate oil-pneumatic system, which accurately senses the hydraulic pressure in a closed, flat capsule.

Load Cells. Current testing machines use strain-gage load cells and pressure transducers. In a load cell, strain gages are mounted on precision-machined alloy-steel elements, hermetically sealed in a case with the necessary electrical outlets, and arranged for tensile and/or compressive loading. The load cell can be mounted so that the specimen is in direct contact, or the cell can be indirectly loaded through the machine crosshead, table, or columns of the load frame. The load cell and the load cell circuit are calibrated to provide a specific voltage as an output signal when a certain force is detected. In pressure transducers, which are variations of strain-gage load cells, the strain-gaged member is activated by the hydraulic pressure of the system.

Strain gages, strain-gage load cells, and pressure transducers are manufactured to several degrees of accuracy; however, when used as the load-measuring mechanism of a testing machine, the mechanisms must conform to ASTM E 4, as well as to the manufacturer's quality standards. Load cells are rated by the maximum force in their operating range, and the deflection of the load cell must be maintained within the elastic regime of the material from which the load cell was constructed. Because the load cell operates within its elastic range, both tensile and compressive forces can be monitored.

Electronics provide a wide range of signal processing capability to optimize the resolution of the output signal from the load cell. Temperature-compensating gages reduce measurement errors from changes in ambient temperature. A prior knowledge of the mechanical properties of the material being studied is also useful to obtain full optimization of these signals.

Within individual load cells, mechanical stops can be incorporated to minimize possible damage that could be caused by accidental overloads. Also, guidance and supports can be included to prevent the deleterious effects of side loading and to give desired rigidity and ruggedness. This is important in tension testing of metals because of the elastic recoil that can occur when a stiff specimen fails.

Calibration of Load-Measuring Devices. Calibration of load-measuring devices refers to the procedure of determining the magnitude of error in the indicated loads. Only load-indicating mechanisms that comply with standard calibration methods (e.g., ASTM E 74) should be used for the load calibration and verification of universal testing machines (see the section "Force Verification of Universal Testing Machines" in this article).

Calibration of load-measuring devices for mechanical test machines is covered in specifications of several standards organizations such as:

Specification number	Specification title
ASTM E 74	Standard Practice for Calibration of Force-Measuring Instruments for Verifying the Force Indication of Testing Machines
EN 10002-3	Part 3: Calibration of Force-Proving Instruments Used for the Verification of Testing Machines
ISO 376	Metallic Materials—Calibration of Force-Proving Instruments Used for the Verification of Testing Machines
BS EN 10002-3	Calibration of Force-Proving Instruments Used for the Verification of Uniaxial Testing Machines

To ensure valid load verification, calibration procedures should be performed by skilled personnel who are knowledgeable about testing machines and related instruments and the proper use of calibration standards. Load verification of load-weighing systems can be accomplished using methods based on the use of standard weights, standard weights and lever balances, and elastic calibration devices. Of these calibration methods, elastic calibration devices have the fewest inherent problems and are widely used. The two main types of elastic load-calibration devices are elastic proving rings and strain-gage load cells, as briefly described below. The elastic proving ring (Fig. 8a, b) is a flawless forged steel ring that is precisely machined to a fine finish and closely maintained tolerances. This device has a uniform and repeatable deflection throughout its loaded range. Elastic proving rings usually are designed to be used only in compression, but special rings are designed to be used in tension or compression.

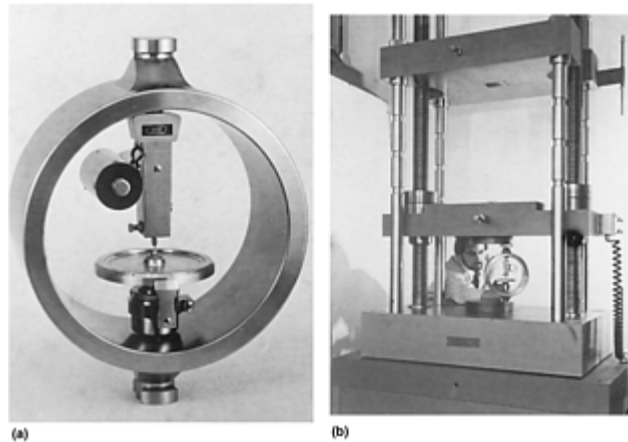


Fig. 8 Proving rings. (a) Elastic proving ring with precision micrometer for deflection/load readout. (b) Load calibration of 120,000 lbf screw-driven testing machine with a proving ring

As the term “elastic device” implies, the ring is used well within its elastic range, and the deflection is read by a precise micrometer. Proving rings are available with capacities ranging from 4.5 to over 5000 kN (1000 to 1.2×10^6 lbf). Their usable range is from 10 to 100% of load capacity, based on compliance with the ASTM E 74 verification procedure.

Proving rings vary in weight from about 2 kg (5 lb) to hundreds of kilograms (or several hundred pounds). They are portable and easy to use. After initial certification, they should be recalibrated and recertified at intervals not exceeding 2 years.

Proving rings are not load rings. Although the two devices are of similar design and construction, only proving rings that use a precise micrometer for measuring deflection can be used for calibration. Load rings employ a dial indicator to measure deflection and usually do not comply with the requirements of ASTM E 74.

Calibration strain-gage load cells are precisely machined high-alloy steel elements designed to have a positive and predetermined uniform deflection under load. The steel load cell element contains one or more reduced sections, onto which wire or foil strain gages are attached to form a balanced circuit containing a temperature-compensating element.

Strain-gage load cells used for calibration purposes are either compression or tension-compression types and have built-in capacities ranging from about 0.4 to 4000 kN (100 to 1,000,000 lbf). Their usable range is typically from 5 to 100% of capacity load, and their accuracy is $\pm 0.05\%$, based on compliance with applicable

calibration procedures, such as ASTM E 74. Figure 9 illustrates a load cell system used to calibrate a UTM. This particular system incorporates a digital load indicator unit.

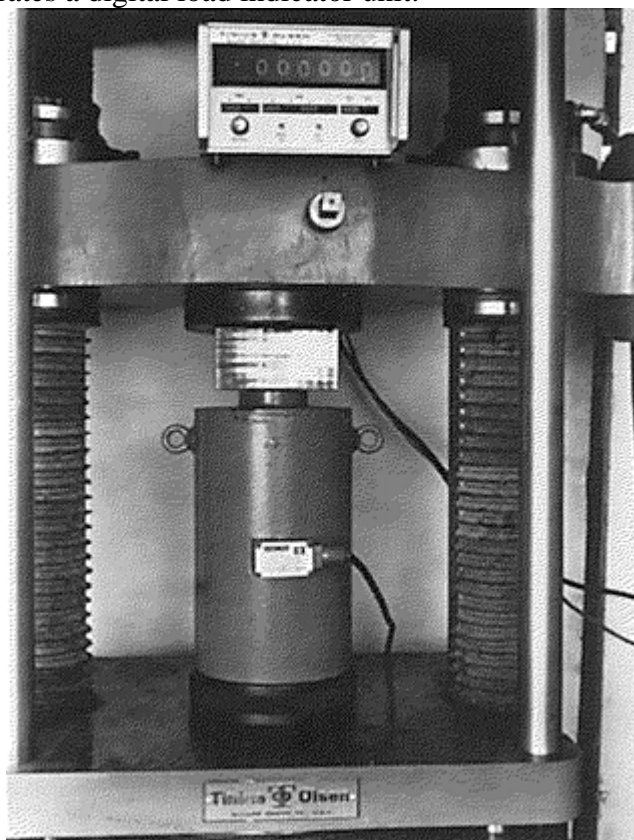


Fig. 9 Load cell and digital load indicator used to calibrate a 200,000 lbf hydraulic testing machine

Comparison of Elastic Calibration Devices. The deflection of a proving ring is measured in divisions that are assigned a value in lbf, kgf, or N. The force is then calculated in the desired units. Although the deflection of a load cell is given numerically and a force value can be assigned with a load cell reading, electric circuits can provide direct readout in lbf, kgf, or N. Thus, certified load cells are more practical and convenient to use and minimize errors in calculation.

In small capacities (5 to 20 kN, or 1000 to 5000 lbf), proving rings and load cells are of similar size and weight (2 to 5 kg, or 4 to 10 lb). In large capacities (2000 to 2700 kN, or 400,000 to 600,000 lbf), load cells are about one half the size and weight of proving rings. Proving rings are a single-piece, self-contained unit. A load cell calibration kit consists of two parts: the load cell and the display indicator (Fig. 9). Although the display indicator is designed to be used with a load cell of any capacity, it can only be used with load cells that have been verified with it as a system.

Although both proving rings and load cells are portable, the lighter weight and smaller size of high-capacity load cells enhance their suitability for general use. Load cells and their display indicators require a longer setup time; however, their direct readout feature reduces the overall calibration and reporting time. After initial certification, the load cell should be recalibrated after one year and thereafter at intervals not exceeding two years.

Both types of calibration devices are certified in accordance with the provisions of calibration standards. In the United States, devices are certified in accordance with ASTM E 74 and the verification values determined by the National Institute of Standards and Technology (NIST). NIST maintains a 1,000,000 lbf deadweight calibrator that is kept in a temperature- and humidity-controlled environment. This force-calibrating machine incorporates twenty 50,000 lb stainless steel weights, each accurate to within ± 0.25 lb. This machine, and six others of smaller capacities, are used to calibrate elastic calibrating devices, which in turn are employed to accurately calibrate other testing equipment.

Elastic calibrating devices for verification of testing machines are calibrated to primary standards, which are weights. The masses of the weights used are determined to 0.005% of their values.

Strain Measurement

Deformation of the specimen can be measured in several ways, depending on the size of specimen, environmental conditions, and measurement requirements for accuracy and precision of anticipated strain levels. A simple method is to use the velocity of the crosshead while tracking the load as a function of time. For the load and time data pair, the stress in the specimen and the amount of deformation, or strain, can be calculated. When the displacement of the platen is assumed to be equal to the specimen displacement, an error is introduced by the fact that the entire load frame has been deflected under the stress state. This effect is related to the concept of machine stiffness, as previously discussed.

Extensometry. The elongation of a specimen during load application can be measured directly with various types of devices, such as clip-on extensometers (Fig. 10), directly-mounted strain gages (Fig. 11), and various optical devices. These devices are used extensively and can provide a high degree of deformation- (strain-) measurement accuracy. Other more advanced instrumentations, such as laser interferometry and video extensometers, are also available.



Fig. 10 Test specimen with an extensometer attached to measure specimen deformation. Courtesy of Epsilon Technology Corporation

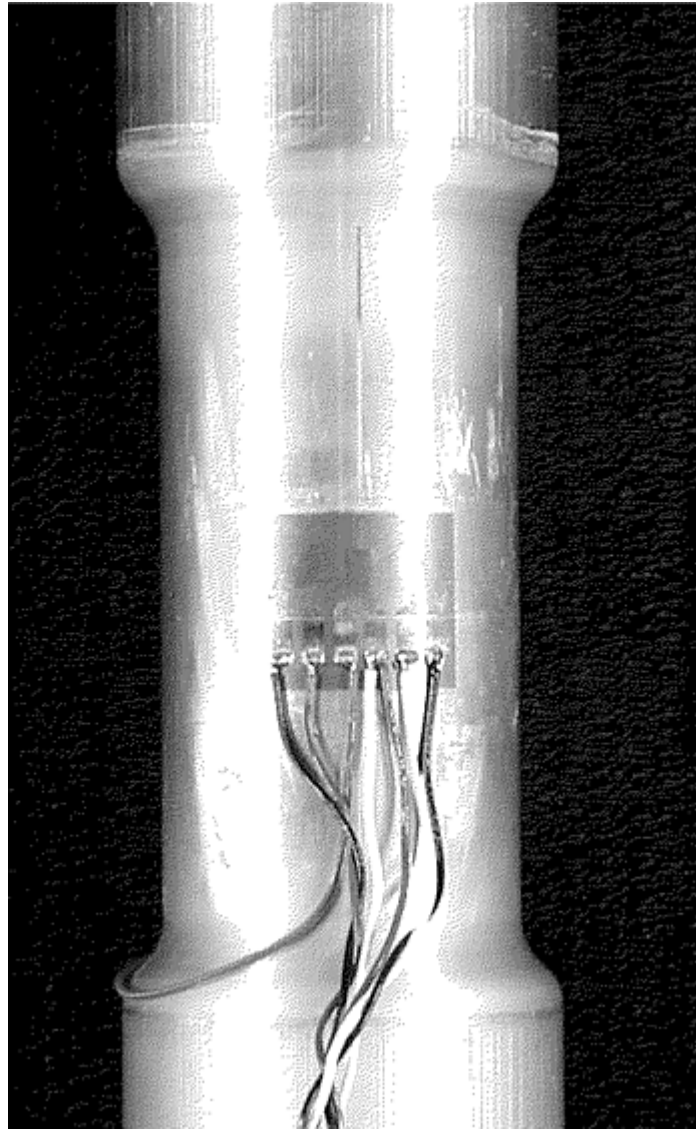


Fig. 11 Strain gages mounted directly to a specimen

Various types of extensometers and strain gages are described below. Selection of a device for strain measurement depends on various factors:

- The useable range and accuracy of the gage
- Techniques for mounting the gage
- Specimen size
- Environmental test conditions
- Electronic circuit configuration and analysis for signal processing

The last item should include the calibration of the extensometer device over its full operating range. In addition, one challenge of working with clip-on extensometers is to ensure proper attachment to the specimen. If the extensometer slips as the specimen deforms, the resulting signal will give a false reading.

Clip-on extensometers can be attached to a test specimen to measure elongation or strain as the load is applied. This is particularly important for metals and similar materials that exhibit high stiffness. Typical extensometers have fixed gage lengths such as 25 or 50 mm (1 or 2 in.). They are also classified by maximum percent elongation so that a typical 25 mm (1 in.) gage length unit would have different models for 10, 50, or 100% maximum strain. Extensometers are used to measure axial strain in specimens. There also are transverse strain-measuring devices that indicate the reduction in width or diameter as the specimen is tested.

The two basic types of clip-on extensometers are linear variable differential transformer (LVDT) devices and strain-gage devices. These two types are described along with a description of earlier dial-type extensometers.

Early extensometers were held to the specimen with center points matching the specimen gage-length punch marks, and elongation was indicated between the points by a dial indicator. Because of mechanical problems associated with these early devices, most dial extensometers use knife edges and leaf-spring pressure for specimen attachment. An extensometer using a dial indicator to measure elongation is shown in Fig. 12. The dial indicator usually is marked off in 0.0025 mm (0.0001 in.) increments and measures the total extension between the gage points. This value divided by the gage length gives strain in mm/mm, or in./in.

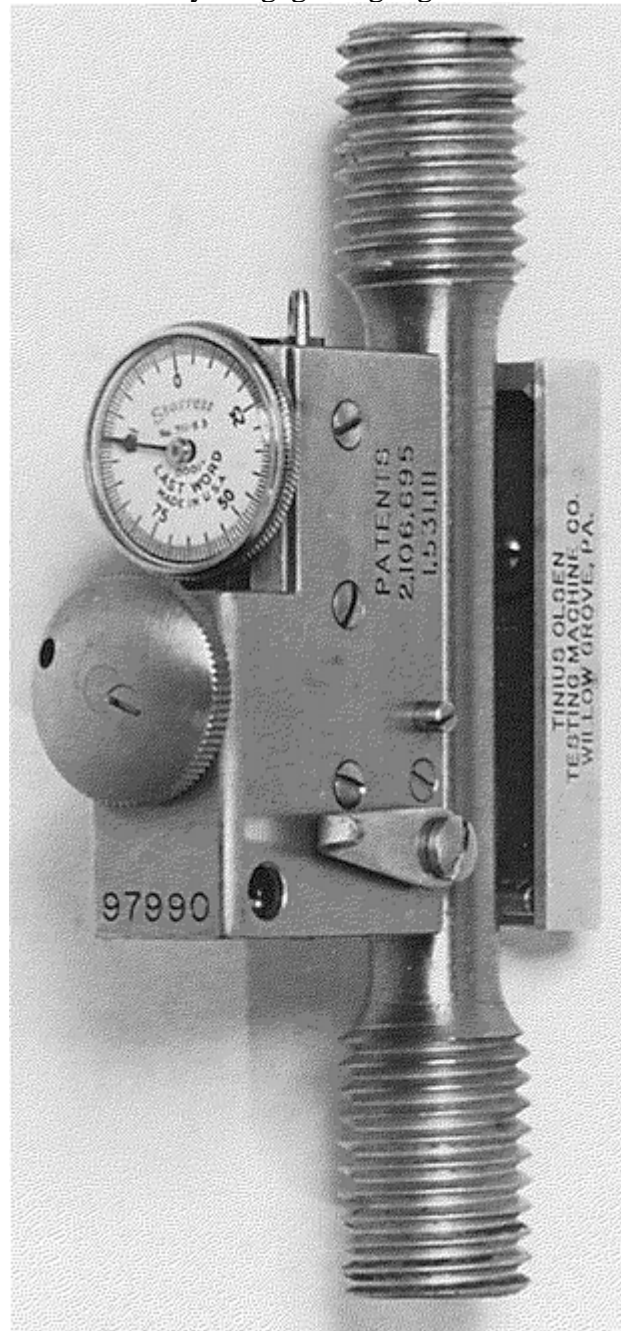


Fig. 12 Dial-type extensometer, 50 mm (2 in.) gage length

LVDT extensometers employ an LVDT with a core, which moves from specimen deformation and produces an electrical signal proportional to amount of core movement (Fig. 13). LVDT extensometers are small, light weight, and easy to use. Knife edges provide an exact point of contact and are mechanically set to the exact gage length. Unless the test report specifies total elongation, center punch marks or scribed lines are not required to define the gage length. They are available with gage lengths ranging from 10 to 2500 mm (0.4 to 100 in.) and can be fitted with breakaway features (Fig. 14), sheet metal clamps, low-pressure clamping arrangements (film clamps, as shown in Fig. 15), and other devices. Thus, they can be used on small specimens—such as thread, yarn, and foil—and on large test specimens—such as reinforcing bars, heavy steel plate, and tubing up to 75 mm (3 in.) in diameter.

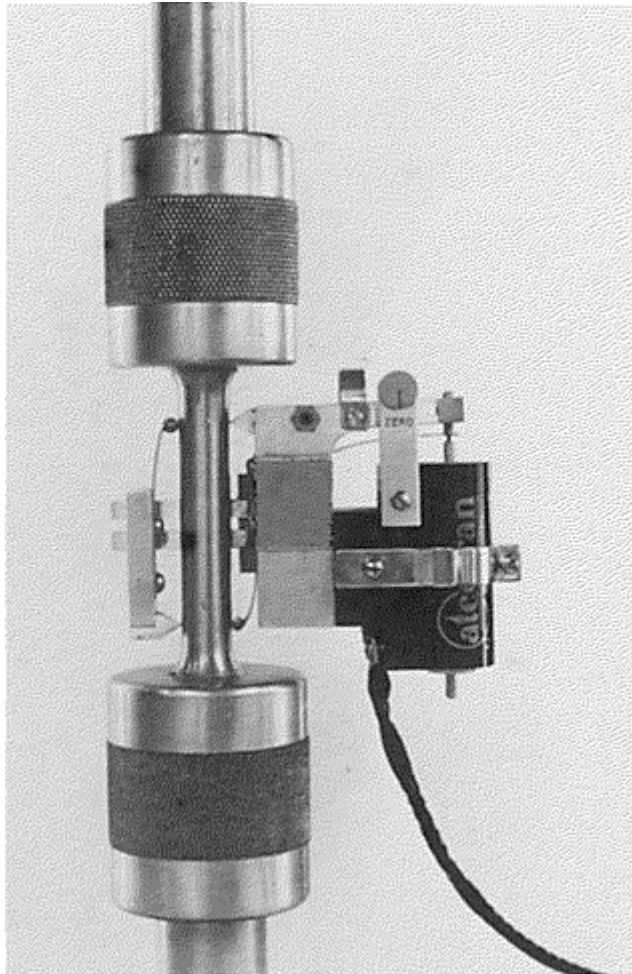


Fig. 13 Averaging LVDT extensometer (50 mm, or 2 in. gage length) mounted on a threaded tension specimen

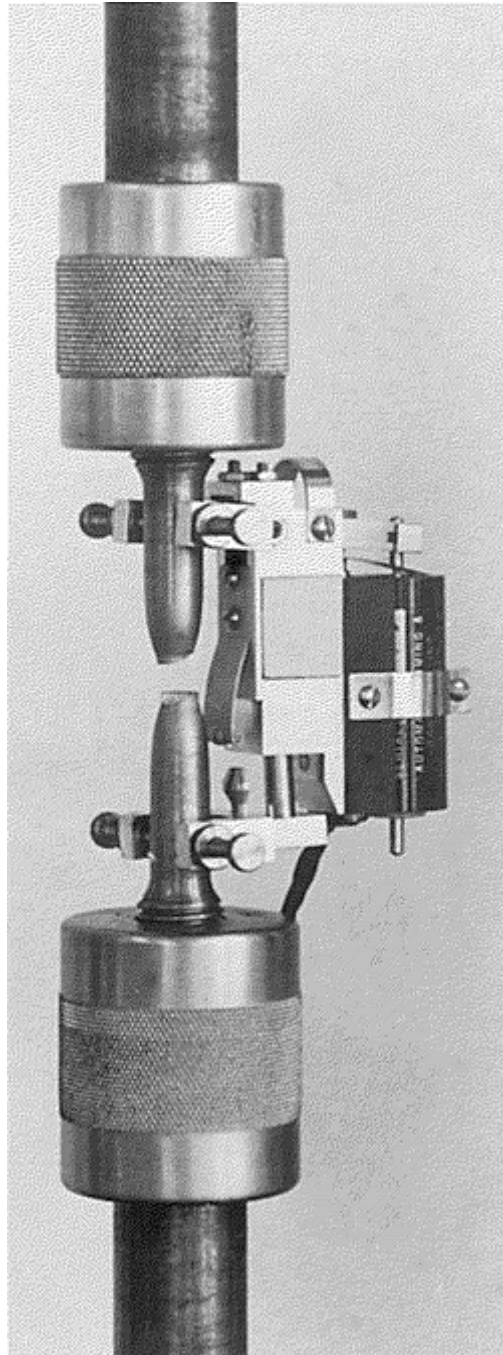


Fig. 14 Breakaway-type LVDT extensometer (50 mm, or 2 in. gage length) that can remain on the specimen through rupture

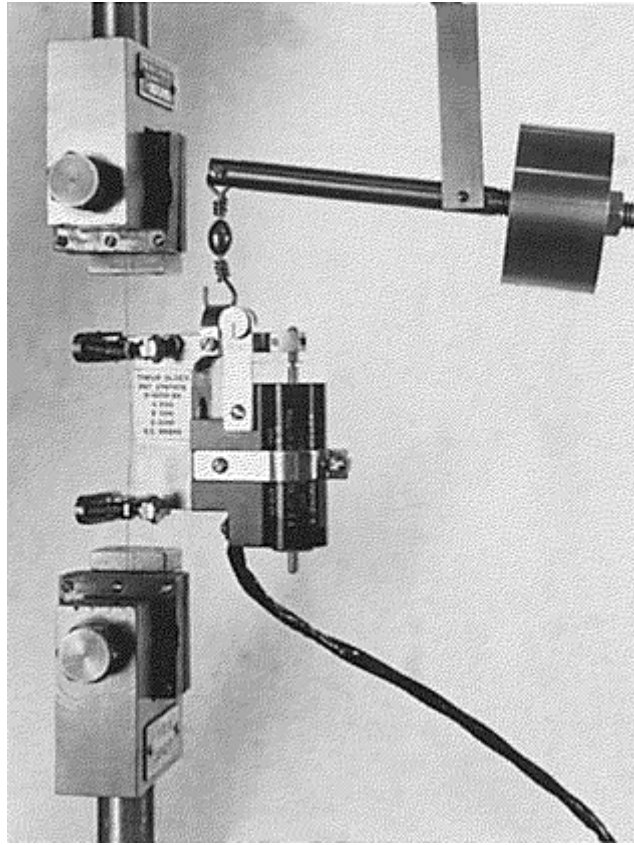


Fig. 15 Averaging LVDT extensometer (50 mm, or 2 in. gage length) mounted on a 0.127 mm (0.005 in.) wire specimen. The extensometer is fitted with a low-pressure clamping arrangement (film clamps) and is supported by a counterbalance device.

Modifications of the LVDT extensometer also permit linear measurements at temperatures ranging from -75 to 1205 °C (-75 to 2200 °F). Accurate measurements can also be made in a vacuum. For standard instruments, the working temperature range is approximately -75 to 120 °C (-100 to 250 °F). However, by substituting an elevated-temperature transformer coil, the usable range of the instrument can be extended to -130 to 260 °C (-200 to 500 °F).

Strain-gage extensometers, which use strain gages rather than LVDTs, are also common and are lighter in weight and smaller in size, but strain gages are somewhat more fragile than LVDTs. The strain gage usually is mounted on a pivoting beam, which is an integral part of the extensometer. The beam is deflected by the movement of the extensometer knife edge when the specimen is stressed. The strain gage attached to the beam is an electrically conductive small-sized grid that changes its resistance when deformed in tension, compression, bending, or torsion. Thus, strain gages can be used to supply the information necessary to calculate strain, stress, angular torsion, and pressure.

Strain gages have been improved and refined, and their use has become widespread. Basic types include wire gages, foil gages, and capacitive gages. Wire and foil bonded resistance strain gages are used for measuring stress and strain and for calibration of load cells, pressure transducers, and extensometers. These gages typically measure 9.5 to 13 mm ($\frac{3}{8}$ to $\frac{1}{2}$ in.) in width and 13 to 19 mm ($\frac{1}{2}$ to $\frac{3}{4}$ in.) in length and are adhesively bonded to a metal element (Fig. 16).

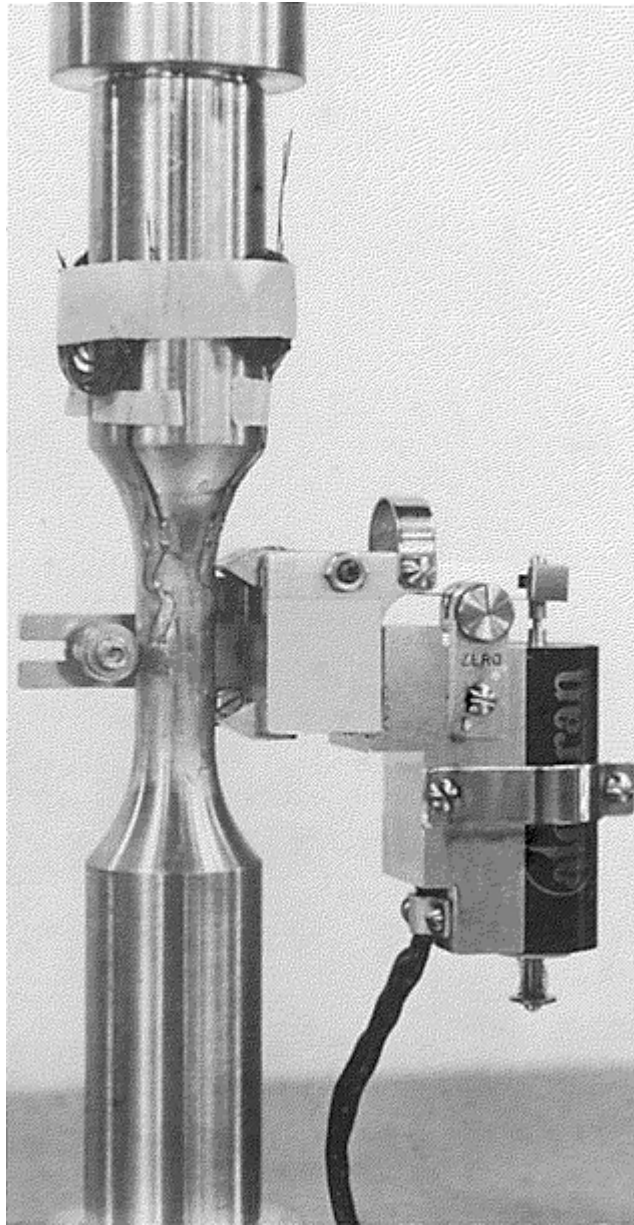


Fig. 16 Fatigue test specimen with bonded resistance strain gages and a 25 mm (1 in.) gage length extensometer mounted on the reduced section

Operation of strain-gage extensometers is based on gages that are bonded to a metallic element and connected to a bridge circuit. Deflection of the element, due to specimen strain, changes the gage's resistance that produces an output signal from a bridge circuit. This signal is amplified and processed by signal conditioners before being displayed on a digital readout, chart recorder, or computer. The circuitry in the strain-measuring system allows multiple ranges of sensitivity, so one transducer can be used over broad ranges. The magnification ratio, which is the ratio of output to extensometer deflection, can be as high as 10,000 to 1.

Strain Gages Mounted Directly to the Test Specimen. For some strain measurements, strain gages are mounted on the part being tested (Fig. 11). When used in this manner, they differ from extensometers in that they measure average unit elongation over nominal gage length rather than total elongation between definite gage points. For some testing applications, strain gages are used in conjunction with extensometers (Fig. 16).

In conventional use, wire or foil strain gages, when mounted on structures and parts for stress analysis, are discarded with the tested item. Thus, strain gages are seldom used in production testing of standard tension specimens. Foil strain gages currently are the most widely used, due to the ease of their attachment.

Averaging Extensometers. Typically extensometers are either nonaveraging or averaging types. A nonaveraging extensometer has one fixed nonmovable knife edge or center point and one movable knife edge or center point on the same side of the specimen. This arrangement results in extension measurements that are

taken on one side of the specimen only; such measurements do not take into account that elongation may be slightly different on the other side.

For most specimens, notably those with machined rounds or reduced gage length flats, there is no significant difference in elongation between the two sides. However, for as-cast specimens, high-modulus materials, some forged parts, and specimens made from tubing, a difference in elongation sometimes exists on opposite sides of the specimen when subjected to a tensile load. This is due to part configuration and/or internal stress. Misalignment of grips also contributes to elongation measurement variations in the specimen. For these situations, averaging extensometers are used. Averaging extensometers use dual-measuring elements that measure elongation on both sides of a sample; the measurements are then averaged to obtain a mean strain.

Optical Systems. Lasers and other systems can also be used to obtain linear strain measurements. Optical extensometers are particularly useful with materials such as rubber, thin films, plastics, and other materials where the weight of a conventional extensometer would distort the workpiece and affect the readings obtained. In the past, such strain-measuring systems were expensive, and their principal use has been primarily in research and development work. However, these optical techniques are becoming more accessible for commercial testing machines. For example, bench-top UTM systems with a laser extensometer are available (Fig. 17). This laser extensometer allows accurate measurement of strain in thin films, which would not otherwise be practical by mechanical attachment of extensometer devices. Optical systems also allow non-contact measurement from environmental test chambers.

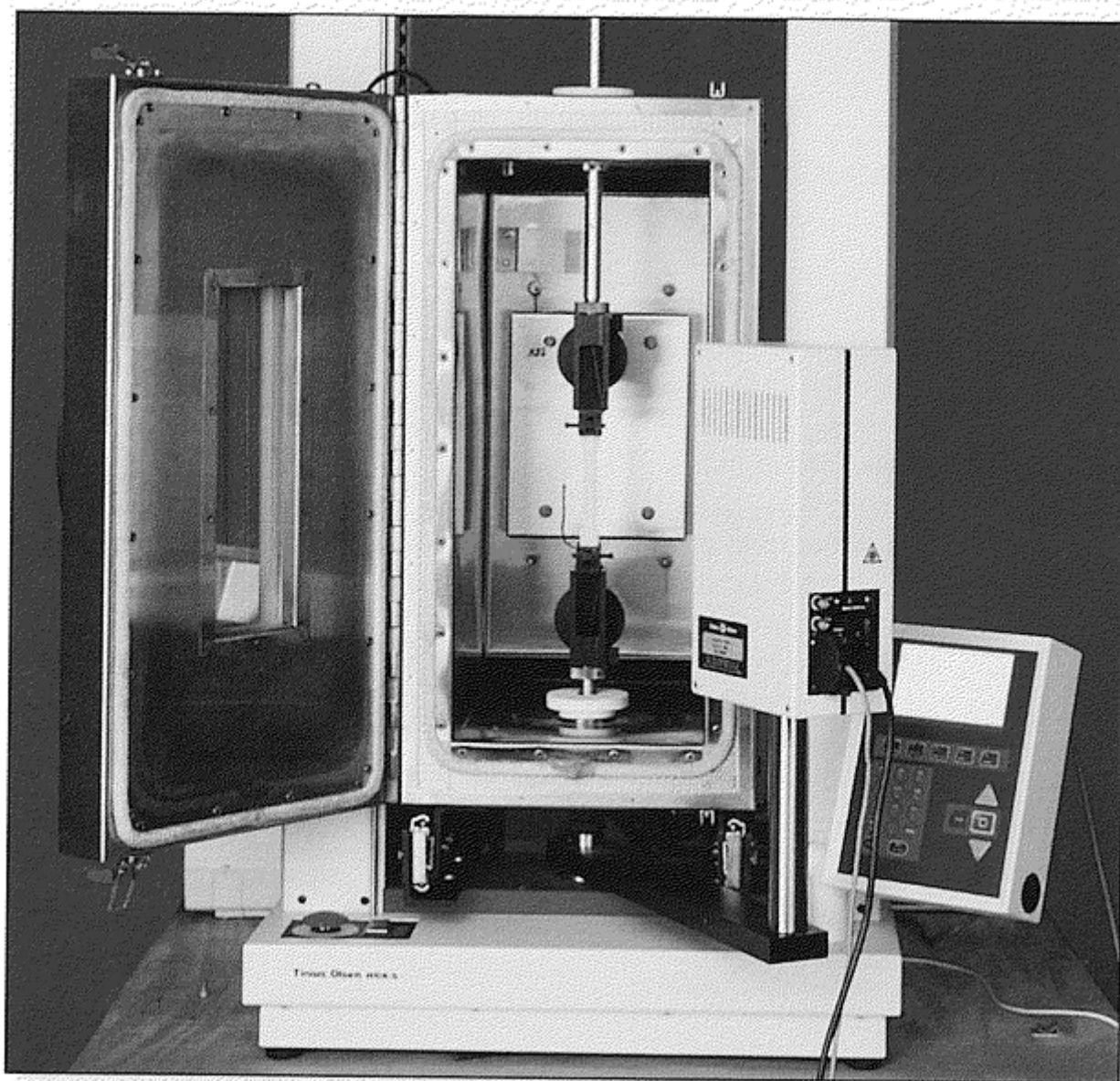


Fig. 17 Bench-top UTM with laser extensometer. Courtesy of Tinius Olsen Testing Machine Company, Inc.

Calibration, Classification, and Verification of Extensometers. All types of extensometers for materials testing must be verified, classified, and calibrated in accordance with applicable standards. Calibration of extensometers refers to the procedure of determining the magnitude of error in strain measurements. Verification is a calibration to ascertain whether the errors are within a predetermined range. Verification also implies certification that an extensometer meets stated accuracy requirements, which are defined by classifications such as those in ASTM E 83 (Table 3).

Table 3 Classification of extensometer systems

Error of strain not to exceed the greater of ^(a) :			Error of gage length not to exceed the greater of:	
Classification	Fixed error, in./in.	Variable error, % of strain	Fixed error, in.	Variable error, % of gage length
Class A	0.00002	±0.1	±0.001	±0.01
Class B-1	0.0001	±0.5	±0.0025	±0.25
Class B-2	0.0002	±0.5	±0.005	±0.5
Class C	0.001	±1	±0.01	±1
Class D	0.01	±1	±0.01	±1
Class E	0.1	±1	±0.01	±1

(a) Strain of extensometer system—ratio of applied extension to the gage length.

Source: ASTM E 83

Several calibration devices can be used, including an interferometer, calibrated standard gage blocks and an indicator, and a micrometer screw. Applicable standards for extensometer calibration or verification include:

Specification number	Specification title
DIN EN 10002-4	Part 4: Verification of Extensometers Used in Uniaxial Testing, Tensile
ISO 9513	Metallic Materials—Verification of Extensometers Used in Uniaxial Testing
BS EN 10002-4	Verification of Extensometers Used in Uniaxial Testing
ASTM E 83	Standard Practice for Verification and Classification of Extensometers
BS 3846	Methods for Calibration and Grading of Extensometers for Testing of Materials

Verification and classification of extensometers are applicable to instruments of both the averaging and nonaveraging type.

Procedures for the verification and classification of extensometers can be found in ASTM E 83. It establishes six classes of extensometers (Table 3), which are based on allowable error deviations, as discussed later in this article. This standard also establishes a verification procedure to ascertain compliance of an instrument to a particular classification. In addition, it stipulates that a certified calibration apparatus must be used for all applied displacements and that the accuracy of the apparatus must be five times more precise than allowable classification errors. Ten displacement readings are required for verification of a classification.

Class A extensometers, if available, would be used for determining precise values of the modulus of elasticity and for precise measurements of permanent set or very slight deviations from Hooke's law. Currently, however, there are no commercially available extensometers manufactured that are certified to comply with class A requirements.

Class B-1 extensometers are frequently used to determine values of the modulus of elasticity and to measure permanent set or deviations from Hooke's law. They are also used for determining values such as the yield strength of metallic materials.

Class B-2 extensometers are used for determining the yield strength of metallic materials.

All LVDT and strain-gage extensometers can comply with class B-1 or class B-2 requirements if their measuring ranges do not exceed 0.5 mm (0.02 in.). Instruments with measuring ranges of over 0.5 mm (0.02 in.) can be class C instruments.

Most electrical differential transformer extensometers of 500-strain magnification and higher can conform to class B-1 requirements throughout their measuring range. Extensometers of less than 500-strain magnification can comply only with class B-1 requirements in their lower (40%) measuring range and are basically class B-2 instruments.

Dial Extensometers. Although all dial instruments usually are considered class C instruments, the majority (up to a gage length of 200 mm, or 8 in.) are class B-1 and class B-2 in their initial 40% measuring range, and class C throughout the remainder of the range. Dial instruments are used universally for determining yield strength by the extension-under-load method and yield strength of 0.1% offset and greater.

Class C and D Extensometers. Extensometers with a gage length of 610 mm (24 in.) begin in class C, although their overall measuring range must be considered as class D.

Testing Machines and Strain Sensors

Joel W. House, Air Force Research Laboratory; Peter P. Gillis, University of Kentucky

Gripping Techniques

The use of proper grips and faces for testing materials in tension is critical in obtaining meaningful results. Trial and error often will solve a particular gripping problem. Tension testing of most flat or round specimens can be accommodated with wedge-type grips (Fig. 18). Wire and other forms may require different grips, such as capstan or snubber types. The load capacities of grips range from under 4.5 kgf (10 lbf) to 45,000 kgf (100,000 lbf) or more. ASTM E 8 describes the various types of gripping devices used to transmit the measured load applied by the test machine to the tension test specimen.

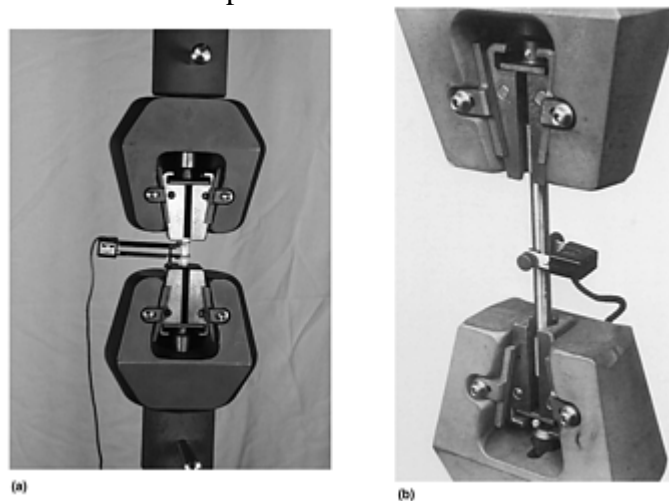


Fig. 18 Test setup using wedge grips on (a) a flat specimen with axial extensometer and (b) a round specimen with diametral extensometer

Screw-action grips, or mechanical grips, are low in cost and are available with load capacities of up to 450 kgf (1000 lbf). This type of grip, which is normally used for testing flat specimens, can be equipped with interchangeable grip faces that have a variety of surfaces. Faces are adjustable to compensate for different specimen thicknesses.

Wedge-type grips (Fig. 18) are self-tightening and are built with capacities of up to 45,000 kgf (100,000 lbf) or more. Some units can be tightened without altering the vertical position of the faces, making it possible to preselect the exact point at which the specimen will be held. The wedge-action design works well on hard-to-hold specimens and prevents the introduction of large compressive forces that cause specimen buckling.

Pneumatic-action grips are available in various designs with capacities of up to 90 kgf (200 lbf). This type of grip clamps the specimen by lever arms that are actuated by compressed air cylinders built into the grip bodies. A constant force maintained on the specimen compensates for decrease of force due to creep of the specimen in the grip. Another advantage of this design is the ability to optimize gripping force by adjusting the air pressure, which makes it possible to minimize specimen breaks at the grip faces.

Buttonhead grips enable the rapid insertion of threaded-end or mechanical-end specimens. They can be manually or pneumatically operated, as required by the type of material or test conditions.

Alignment. Whether the specimen is threaded into the crossheads, held by grips, or is in direct contact with platens, the specimen must be well aligned with the load cell. Any misalignment will cause a deviation from uniaxial stress in the material studied.

Testing Machines and Strain Sensors

Joel W. House, Air Force Research Laboratory; Peter P. Gillis, University of Kentucky

Force Verification of Universal Testing Machines

The calibration and verification of UTM systems refer to two different methods that are not synonymous. Calibration of testing machines refers to the procedure of determining the magnitude of error in the indicated loads. Verification is a calibration to ascertain whether the errors are within a predetermined range. Verification also implies certification that a machine meets stated accuracy requirements. Valid verification requires device calibration by skilled personnel who are knowledgeable about testing machines, related instruments, and the proper use of device calibration standards (such as ASTM E 74 for load indicators and ASTM E 83 for extensometer devices). After verification is performed, the calibrator or agency must issue reports and certificates attesting to compliance of the equipment with the verification requirements, including the loading range(s) for which the system may be used.

Force Verification. For the load verification to be valid, the weighing system(s) and associated instrumentation and data systems must be verified annually. In no case should the time interval between verifications exceed 18 months. Testing systems and their loading ranges should be verified immediately after relocation of equipment, after repairs or parts replacement (mechanical or electric/electronic) that could affect the accuracy of the load-measuring system(s), or whenever the accuracy of indicated loads is suspect, regardless of when the last verification was made.

Force verification standards for mechanical testing machines include specifications from various standards organizations such as:

Specification number	Specification title
EN 10002-2	Metallic Materials—Tensile Testing—Part 2: Verification of the Force Measurements
DIN EN 10002-2	Part 2: Verification of the Force-Measuring System of Tensile Testing Machines
BS 1610	Materials Testing Machines and Force Verification Equipment
BS EN 10002-2	Verification of the Force Measuring System of the Tensile Testing Machine
ASTM E 4	Standard Practices for Force Verification of Testing Machines

To comply with ASTM E 4, one or a combination of the three allowable verification methods must be used in the determination of the loading range or multiple loading ranges of the testing system. These methods are based on the use of:

- Standard weights
- Standard weights and lever balances
- Elastic calibration devices

For each loading range, at least five (preferably more) verification load levels must be selected. The difference between any two successive test loads must not be larger than one third of the difference between the maximum and minimum test loads. The maximum can be the full capacity of an individual range. For example, acceptable test load levels could be 10, 25, 50, 75, and 100%, or 10, 20, 40, 70, and 100%, of the stated machine range.

Regardless of the load verification method used at each of the test levels, the values indicated by the load-measuring system(s) of the testing machine must be accurate to within $\pm 1\%$ of the loads indicated by the calibration standard. If all five or more of the successive test load deviations are within the $\pm 1\%$ required in ASTM E 4, the loading ranges may be established and reported to include all of the values. If any deviations are

larger than $\pm 1\%$, the system should be corrected or repaired immediately. For determining accuracy of values at various test loads (or the deviation from the indicated load of the standard), ASTM E 74 specifies the required calibration accuracy tolerances of the three allowable types of verification methods.

For determining material properties, the testing machine loads should be as accurate as possible. In addition, deformations resulting from load applications should be measured as precisely as possible. This is particularly important because the relationship of load to deformation, which may be, for example, extension or compression, is the main factor in determining material properties.

As described previously, load accuracy may be ensured by following the ASTM E 4 procedure. In a similar manner, the methods contained in ASTM E 83, if followed precisely, will ensure that the devices or instruments used for deformation (strain) measurements will operate satisfactorily.

Manufacturers of testing machines calibrate before shipping and certify conformation to the manufacturer's guarantee of accuracy and any applicable standards, such as ASTM E 4. Subsequent calibrations can be made by the manufacturer or another organization with recognized equipment that is properly maintained and recertified periodically.

Example: Calibrating a 60,000 lbf Capacity Testing Machine. A 60,000 lbf capacity dial-type UTM of either hydraulic or screw-driven design will have the following typical scale ranges:

- 0 to 60,000 lbf reading by 50 lbf divisions
- 0 to 30,000 lbf reading by 25 lbf divisions
- 0 to 12,000 lbf reading by 10 lbf divisions
- 0 to 1200 lbf reading by 1 lbf divisions

As discussed previously, the ASTM required accuracy is $\pm 1\%$ of the indicated load above 10% of each scale range. Most manufacturers produce equipment to an accuracy of $\pm 0.5\%$ of the indicated load or \pm one division, whichever is greater.

According to ASTM specifications, the 60,000 lbf scale range must be within 1% at 60,000 lbf (± 600 lbf) and at 6000 lbf (± 60 lbf). In both cases, the increment division is 50 lbf. Although the initial calibration by the manufacturer is to closer tolerance than ASTM E 4, subsequent recalibrations are usually to the $\pm 1\%$ requirement. In the low range, the machine must be accurate ($\pm 1\%$) from 120 to 1200 lbf. Thus, the machine must be verified from 120 to 60,000 lbf.

If proving rings are used in calibration, a 60,000 lbf capacity proving ring is usable down to a 6000 lbf load level. A 6000 lbf capacity proving ring is usable down to a 600 lbf load level, and a 1000 lbf capacity proving ring is usable down to a 100 lbf load level.

If calibrating load cells are used, a 60,000 lbf capacity load cell is usable down to a 3000 lbf load level, a 6000 lbf capacity load cell is usable to a 300 lbf load level, and a 600 lbf capacity load cell is usable down to a 120 lbf load level.

Before use, proving rings and load cells must be removed from their cases and allowed to stabilize to ambient (surrounding) temperature. Upon stabilization, either type of unit is placed on the table of the testing machine. At this stage, proving rings are ready to operate, but load cells must be connected to an appropriate power source and again be allowed to stabilize, generally for 5 to 15 min.

Each system is set to zero, loaded to the full capacity of the machine or elastic device, then unloaded to zero for checking. Loading to full capacity and unloading must be repeated until a stable zero is obtained, after which the load verification readings are made at the selected test load levels.

For the highest load range of 60,000 lbf, loads are applied to the calibrating device from its minimum lower limit (6000 lbf for proving rings and 3000 lbf for load cells) to its maximum 60,000 lbf in a minimum of five steps, or test load levels, as discussed in the section "Force Verification" in this article. In the verification loading procedure for proving rings, a "set-the-load" method usually is used. The test load is determined, and the nominal load is preset on the proving ring. The machine load readout is read when the nominal load on the proving ring is achieved. For load cells, a "follow-the-load" method can be used, wherein the load on the display indicator is followed until the load reaches the nominal load, which is the preselected load level on the readout of the testing machine.

In both methods, the load of the testing machine and the load of the calibration device are recorded. The error, E , and the percent error, E_p , can be calculated as:

$$E = A - B$$

$$E_p = \frac{(A - B)}{B} \times 100$$

(Eq 13)

where A is the load indicated by the machine being verified in lbf, kgf, or N, and B is the correct value of the applied load (lbf, kgf, or N), as determined by the calibration device.

This procedure is repeated until each scale range of the testing machine has been calibrated from minimum to maximum capacity. The necessary reports and certificates are then prepared, with the loading range(s) indicated clearly as required by ASTM E 4. Figures 8(b) and 9 illustrate UTMs being calibrated with elastic proving rings and calibration load cells.

Testing Machines and Strain Sensors

Joel W. House, Air Force Research Laboratory; Peter P. Gillis, University of Kentucky

Tensile Testing

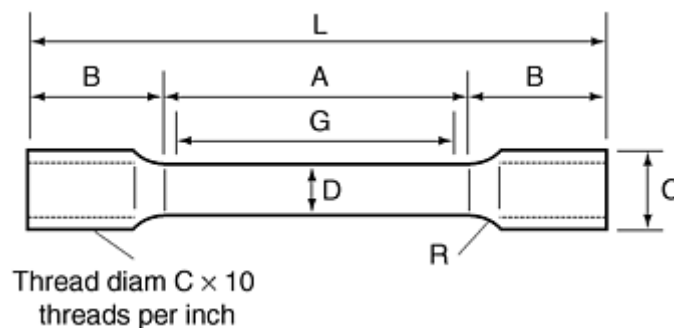
Tensile testing requirements are specified in various standards for a wide variety of different materials and products. Table 4 lists various tensile testing specifications from several standards organizations. These specifications define requirements for the test apparatus, test specimens, and test procedures.

Table 4 Tension testing standards for various materials and product forms

Specification number	Specification title
ASTM A 770	Standard Specification for Through-Thickness Tension Testing of Steel Plates for Special Applications
ASTM A 931	Standard Test Method for Tension of Wire Ropes and Strand
ASTM B 557	Standard Test Methods of Tension Testing Wrought and Cast Aluminum- and Magnesium-Alloy Products
ASTM B 557M	Standard Test Methods of Tension Testing Wrought and Cast Aluminum- and Magnesium-Alloy products [Metric]
ASTM C 565	Standard Test Methods for Tension Testing of Carbon and Graphite Mechanical Materials
ASTM C 1275	Standard Test Method for Monotonic Tensile Strength Testing of Continuous Fiber-Reinforced Advanced Ceramics with Solid Rectangular Cross-Section Specimens at Ambient Temperature
ASTM C 1359	Standard Test Method for Monotonic Tensile Strength Testing of Continuous Fiber-Reinforced Advance Ceramics with Solid Rectangular Cross-Section Specimens at Elevated Temperatures
ASTM D 76	Standard Specification for Tensile Testing Machines for Textiles
ASTM E 8	Standard Test Methods for Tension Testing of Metallic Materials
ASTM E 8M	Standard Test Methods for Tension Testing of Metallic Materials [Metric]
ASTM E 338	Standard Test Method of Sharp-Notch Tension Testing of High-Strength Sheet Materials
ASTM E 345	Standard Test Methods of Tension Testing of Metallic Foil
ASTM E 602	Standard Method for Sharp-Notch Tension Testing with Cylindrical Specimens
ASTM E 740	Standard Practice for Fracture Testing with Surface-Crack Tension Specimens
ASTM E 1450	Standard Test Method for Tension Testing of Structural Alloys in Liquid Helium
ASTM F 1501	Standard Test Method for Tension Testing of Calcium Phosphate Coatings

ASTM F 152	Standard Test Methods for Tension Testing of Nonmetallic Gasket Materials
ASTM F 19	Standard Test Method for Tension and Vacuum Testing Metallized Ceramic Seals
ASTM F 1147	Standard Test Method for Tension Testing of Porous Metal Coatings
BS EN 10002	Tensile Testing of Metallic Materials
BS 18	Method for Tensile Testing of Materials (Including Aerospace Materials)
BS 4759	Method for Determination of K-Values of a Tensile Testing System
BS 3688-1	Tensile Testing
BS 3500-6	Tensile Stress Relaxation Testing
BS 3500-3	Tensile Creep Testing
BS 3500-1	Tensile Rupture Testing
BS 1687	Medium-Sensitivity Tensile Creep Testing
BS 1686	Long-Period, High-Sensitivity, Tensile Creep Testing
DIN 53455	Tensile Testing: Testing of Plastics
DIN 53328	Testing of Leather, Tensile Test
DIN 50149	Tensile Test, Testing of Malleable Cast Iron
EN 10002-1	Metallic Materials—Tensile Testing—Part 1: Method of test at Ambient Temperature
ISO 204	Metallic Materials—Uninterrupted Uniaxial Creep Testing Intension—Method of Test
ISO 783	Metallic Materials—Tensile Testing at Elevated Temperature
ISO 6892	Metallic Materials—Tensile Testing at Ambient Temperature
JIS B 7721	Tensile Testing Machines
JIS K 7113	Testing Methods for Tensile Properties of Plastics (English Version)

Standard tensile tests are conducted using a threaded tensile specimen geometry, like the standard ASTM geometry (Fig. 19) of ASTM E 8. To load the specimen in tension, the threaded specimen is screwed into grips attached to each crosshead. The boundary condition, or load, is applied by moving the crossheads away from one another.



Abbreviation	Dimension	Measurement	
		in.	mm
G	Gage length	2.4606	62.5 ±0.1
D	Diameter	0.4920 ±0.2	12.5 ± 0.2
R	Radius of fillet	0.3937	10.0
A	Length of reduced section	2.953	75
L	Approximate overall length	5.7086	145.0
B	Length of end section	1.378	35.0
C	Diameter of end section	0.787	20

Fig. 19 Standard ASTM geometry for threaded tensile specimens. Dimensions for the specimen are taken from ASTM 8M (metric units), or ASTM E 8 (English units).

For a variety of reasons, it is not always possible to fabricate a specimen as shown in Fig. 19. For thin plate or sheet materials, a flat, or dog-bone, specimen geometry is used. The dog-bone specimen is held in place by wedge shaped grips. The holding capacity of the grips provides a practical limit to the strength of material that a machine can test. Other specimen geometries can be tested, with certain cautions, and formulas for critical dimensions are given in ASTM E 8.

Accuracy, Repeatability, and Precision of Tension Tests. Accuracy and precision of test results can only be quantified when known quantities are measured. One difficulty of assessing data is that no agreed-upon “material standard” exists as reference material with known properties for strength and elongation. Tests of the “standard material” would reveal the system accuracy, and repeated experiments would quantify its precision and repeatability.

A variety of factors influence accuracy, precision, and repeatability of test results. Sources for errors in tension testing are mentioned in the appendix of ASTM E 8. Errors can be grouped into three broad categories:

- *Instrumental errors:* These can involve machine stiffness, accuracy and resolution of the load cell output, alignment of the specimen, gripping of the specimen, and accuracy of the extensometer.
- *Testing errors:* These can involve initial measurement of specimen geometry, electronic zeroing, and establishing a preload stress level in the specimen.
- *Material factors:* These describe the relationship between the material intended to be studied and that being tested. For example, does the material in the specimen represent the parent material, and is it homogenous? Other material factors would include specimen preparation, specimen geometry, and material strain-rate sensitivity.

The ASTM committee for tensile testing reported on a round robin set of experiments to assess repeatability and to judge precision of standard quantities. In this series (see appendix of ASTM E 8) six specimens of six materials were tested at six different laboratories. The comparison of measurements within a laboratory and between laboratories is given in Table 5. The data show the highest level of reproducibility in the strength measurements; the lowest reproducibility is found in elongation and reduction of area. Within-laboratory results were always more reproducible than those between laboratories.

Table 5 Results of round-robin testing

Property	Coefficient of variation, %	
	Within laboratory	Between laboratory
Tensile strength	0.91	1.30
0.02% yield strength	2.67	4.46
0.2% yield strength	1.35	2.32
Elongation in <i>5D</i>	2.97	6.36
Reduction in area	2.80	4.59

Source: ASTM E 8

Testing Machines and Strain Sensors

Joel W. House, Air Force Research Laboratory; Peter P. Gillis, University of Kentucky

Compression Testing

Compression tests are conducted to provide engineering data on compressive strength and compressive failure. These data can differ substantially from tensile properties. Data on the response of materials to compression are needed for engineering design, such as loading concrete structures, or in metal fabrication, such as forging and rolling. One advantage of compression testing is the elimination of necking instability found in tensile testing of ductile metals. However, the geometry of compression specimens can cause buckling instabilities and failure, and frictional effects between the specimen and the platens can cause barreling. From a practical point of view, compression testing can reach the capacity of some machines because the force requirement increases with material hardening and with the increase in cross-sectional area of the specimen. This increase in area contributes to the frictional effects as well.

When testing high-strength brittle materials to failure, there exists a potential hazard from fragments of the specimen being ejected at high velocity. Personnel and equipment should be appropriately shielded. General Procedures. Various standards for compression testing are listed in Table 6 along with ASTM E 9. The most common specimen geometry for compression testing is a right circular cylinder with flat planar ends. ASTM E 9 identifies three sizes of specimens grouped as small, medium, and long. These samples differ in the ratio of length to diameter. Other shapes can be tested, but to avoid geometric buckling, special fixtures are required.

Table 6 Compression testing standards for various materials and products forms

Specification number	Specification title
ASTM A 256	Standard Method of Compression Testing of Cast Iron (discontinued)
ASTM B 485	Standard Method for Diametral Compression Testing of Cemented Carbides (discontinued)
ASTM C 1358	Standard Test Method for Monotonic Compressive Strength Testing of Continuous Fiber-Reinforced Advanced Ceramics with Solid Rectangular Cross-Section Specimens at Ambient Temperature
ASTM E 9	Standard Test Methods of Compression Testing of Metallic Materials at Room Temperature
BS 1881-115	Specification for Compression Testing Machines for Concrete
DIN 18554-1	Testing of Masonry, Determination of Compressive Strength and of Elastic Modulus
DIN 52185	Testing of Wood; Compression Test Parallel to Grain
DIN 52192	Testing of Wood; Compression Test Perpendicular to Grain
DIN 53517	Testing of Rubber and Elastomers
ISO 3132	Wood—Testing in Compression Perpendicular to Grain
ISO 4385	Plain Bearings—Compression Testing of Metallic Bearing Materials
JIS Z 0234	Testing Methods of Static Compression for Package Cushioning Materials
JIS Z 0235	Testing Methods of Dynamic Compression for Package Cushioning Materials

To load the standard specimen (right circular cylinder) a pair of platens attached to the crossheads make contact with the specimen. These platens must be flat, smooth, and parallel to one another. To avoid frictional effects, the specimen and platen interface is lubricated with silicon grease. In the case of compression testing, the crossheads move toward one another.

Compression tests can be performed using UTM equipment with or without a subpress, or with a unit specifically designed for compression testing. The unit specifically designed for compression testing may be portable for such purposes as in-the-field measurement of concrete compressive-failure strength. Figure 20 shows a diagram of a subpress. This unit is inserted between the crosshead platens of a conventional UTM machine. The subpress eliminates any lateral loads when aligned in the UTM.

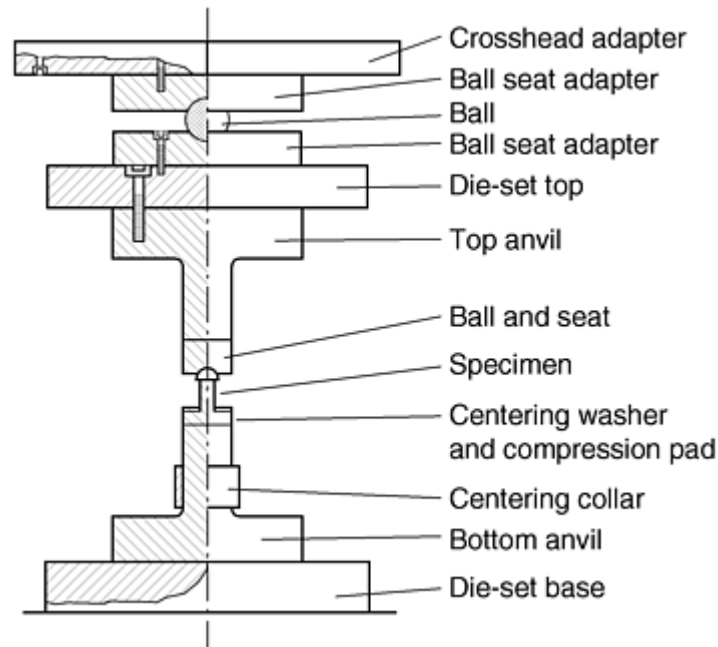


Fig. 20 Subpress used during compression testing. Source: ASTM E 9

The boundary condition for compression testing can be established by load rate or with crosshead speed, such that the specimen deforms at a strain rate of 0.005/min as given in ASTM E 9. The analysis of deformation should be limited to the region of the test where deformation occurs homogeneously. The test should also be halted if the load reaches the capacity of the load cell as a result of increased cross-sectional area of the specimen.

Specimen Geometry. As previously noted, a right circular cylinder is the standard specimen defined in ASTM E 9. Most common in compression testing is a right circular cylinder with a length-to-diameter ratio in the range of 1 to 3. Longer specimens can be tested but failure from buckling instability will occur.

Measuring loads that cause a column of material to buckle can be the purpose of the experiment. Sheet or thin plate material can be tested to some extent. Specimens must be held in fixtures that constrain the material motion to the load plane, preventing buckling. This type of test configuration can provide useful engineering data for in-service conditions; it cannot measure material properties beyond a few percent strain.

Specimens of cylindrical shape will barrel as the deformation becomes large. Barreling is the influence of frictional effects, between the platens and the specimen, that changes the stress state in the material. When barreling occurs, the assumption of homogenous stress state throughout the sample is no longer valid. Lubricants and Teflon sheet material placed at the interfaces have been found to reduce this effect. At large strains, the stress at the interface will squeeze the lubrication from between the platens and the specimen.

Short specimen length makes it difficult to use an extensometer on the sample. The short specimen length means the gap between the platen faces (through which the arms of an extensometer must extend) is narrow at the beginning of the test and will decrease throughout the experiment. Unless the specimen has a length-to-diameter ratio of 3 to 1 or higher, most of the deformation data is taken indirectly from the actuator position. As mentioned above, machine stiffness effects can produce errors in such data.

Testing Machines and Strain Sensors

Joel W. House, Air Force Research Laboratory; Peter P. Gillis, University of Kentucky

Bending Tests

Bending tests require a different specimen geometry and a different configuration for applying the load. The typical specimen geometry is a beam with uniform cross section. In three-point bending, the load is applied at

the mid-span of a simply supported beam. In four-point bending, equal loads are applied at equal distances from the simple supports to create a shear-free central region. Various specifications are listed in Table 7.

Table 7 Bend testing standards for various materials and product forms

Specification number	Specification title
ASTM B 593	Standard Test Method for Bending Fatigue Testing for Copper-Alloy Spring Materials
ASTM E 290	Standard Test Method for Semi-Guided Bend Test for Ductility of Metallic Materials
ASTM E 855	Standard Test Methods for Bend Testing of Metallic Flat Materials for Spring Applications Involving Static Loading
ASTM F 1659	Bending and Shear Fatigue Testing of Calcium Phosphate Coatings on Solid Metallic Substrates
ASTM F 383	Standard Test Method for Static Bend and Torsion Testing of Intramedullary Rods, Standard Recommended Practice
ASTM F 384	Standard Practice for Static Bend Testing of Nail Plates
BS 1639	Methods for Bend Testing of Metals
DD 87	Method for Testing Bending Strength and Stiffness of Bone Plates for Use in Orthopedic
DIN 50153	Reverse Bending Test of Sheets or Strips Less Than 3 mm Thick, Testing of Metallic
DIN 51211	Testing of Metallic Materials, Reverse Bend Test of Wires
DIN 53457	Determination of the Elastic Modulus by Tensile, Compression and Bend Testing
DIN EN 910	Bend Testing of Welds in Metallic Materials, English Version
ISO 1143	Metals—Rotating Bar Bending Fatigue Testing
ISO 144	Steel—Reverse Bend Testing of Wire

Testing Machines and Strain Sensors

Joel W. House, Air Force Research Laboratory; Peter P. Gillis, University of Kentucky

References

1. R.C. Anderson, *Inspection of Metals: Destructive Testing*, ASM International, 1988, p 83–119
2. H.E. Davis, G.E. Troxell, and G.F.W. Hauck, *The Testing of Engineering Materials*, 4th ed., McGraw-Hill, 1982, p 80–124
3. P. Han, Ed., *Tensile Testing*, ASM International, 1992, p 28
4. G.E. Dieter, *Mechanical Metallurgy*, McGraw-Hill, 2nd ed., 1976, p 349
5. D.J. Shippy, P.P. Gillis, and K.G. Hoge, Computer Simulation of a High Speed Tension Test, *J. Appl. Polym. Sci.*, Applied Polymer Symposia (No. 5), 1967, p 311–325
6. P.P. Gillis and D.J. Shippy, Vibration Analysis of a High Speed Tension Test, *J. Appl. Polym. Sci.*, Applied Polymer Symposia (No. 12), 1969, p 165–179

7. M.A. Hamstad and P.P. Gillis, Effective Strain Rates in Low-Speed Uniaxial Tension Tests, *Mater. Res. Stand.*, Vol 6 (No. 11), 1966, p 569–573
8. P. Gillis and J.J. Gilman, Dynamical Dislocation Theories of Crystal Plasticity, *J. Appl. Phys.*, Vol 36, 1965, p 3375–3386
9. J.E. Hockett and P.P. Gillis, Mechanical Testing Machine Stiffness, Parts I and II, *Int. J. Mech. Sci.*, Vol 13, 1971, p 251–275
10. W.G. Johnston, Yield Points and Delay Times in Single Crystals, *J. Appl. Phys.*, Vol 33, 1962, p 2716
11. H.G. Baron, Stress-Strain Curves of Some Metals and Alloys at Low Temperatures and High Rates of Strain, *J. Iron Steel Inst. (Brit.)*, Vol 182, 1956, p 354
12. J. Miklowitz, The Initiation and Propagation of the Plastic Zone in a Tension Bar of Mild Steel as Influenced by the Speed of Stretching and Rigidity of the Testing Machine, *J. Appl. Mech. (Trans. ASME)*, Vol 14, 1947, p A-31
13. M.A. Hamstead, “The Effect of Strain Rate and Specimen Dimensions on the Yield Point of Mild Steel,” Lawrence Radiation Laboratory Report UCRL-14619, April 1966

Accreditation of Mechanical Testing Laboratories

Roxanne M. Robinson, American Association for Laboratory Accreditation

Introduction

ACCREDITATION is a “procedure by which an authoritative body gives formal recognition that a body or person is competent to carry out specific tasks” (Ref 1). The basic purpose of accreditation is to have the means to evaluate and assure high-quality results from suppliers of products or services without incurring the costs associated with auditing each supplier. This also applies to the accreditation of testing laboratories. The final product of a laboratory is test data, and confidence in test data is paramount to product acceptance. Laboratory accreditation, therefore, is gaining favor as an effective means to evaluate and improve product quality.

This article describes laboratory accreditation based on the general requirements of International Organization for Standardization/International Electrotechnical Commission (ISO/IEC) Guide 25, “General Requirements for the Competence of Calibration and Testing Laboratories” (Ref 2). The ISO/IEC Guide 25 is an international standard that is generally recognized as the criteria for laboratory accreditation. This standard not only requires a quality system and manual in the laboratory but also requires that the laboratory be found competent to perform specific tests and types of tests. In 1990, Guide 25 was revised to reflect the content of ISO 9002, “Quality Systems—Model for Quality Assurance in Production, Installation, and Servicing.” Guide 25 is also presently undergoing another revision. When the latest revision is finalized, it will be published as standard, ISO/IEC 17025.

This article is also written to describe an accreditation process that would enhance the international acceptance of test data for mechanical testing laboratories. Laboratory accreditation is a valuable tool to enhance the international acceptance of test data in a more global economy. It also eliminates the need for multiple assessments. Thus, laboratory accreditation allows manufacturers to test products once with the results accepted in multiple markets on an international scale.

References cited in this section

1. "General Terms and Their Definitions Concerning Standardization and Related Activities," ISO/IEC Guide 2, 1993
2. "General Requirements for the Competence of Calibration and Testing Laboratories," ISO/IEC Guide 25, 1990

Accreditation of Mechanical Testing Laboratories

Roxanne M. Robinson, American Association for Laboratory Accreditation

Accreditation Bodies

The accreditation process is typically carried out by third-party entities, which are capable of acting as an authoritative body to perform ISO/IEC Guide 25 assessments. These third-party entities gain the status as an authoritative body with peer accrediting organizations through a mutual recognition agreement (MRA) process. The MRA process allows accreditation to be recognized by international parties and allows testing of products once with the results accepted in other countries. In the United States, for example, the American Association for Laboratory Accreditation (A2LA) and the National Voluntary Laboratory Accreditation Program (NVLAP) have well-established programs that have been recognized through the MRA process to accredit mechanical testing laboratories. The goal is to provide a comprehensive national laboratory accreditation system that establishes widespread recognition of the competence of accredited laboratories. Elimination of the unnecessary multiple assessment of laboratories is also a goal.

The operations of an accreditation body must be designed to meet the requirements of ISO/IEC Guide 58 (Ref 3). Accrediting bodies may offer accreditation for a very narrow area of testing specific to a certain industry group or may offer a very broad-based program to meet needs across different materials, products, and testing procedures. For the purposes of this article, the accreditation process is described for mechanical testing laboratories.

Assessors may be employees or persons contracted on an as-needed basis to perform the laboratory assessments. They may be drawn from the ranks of the recently retired, consultants, industry, academia, government agencies, and the laboratory community. Candidates must have several years of direct laboratory experience in order to qualify as assessors. Auditing experience is a plus. They must be technically very knowledgeable in the mechanical testing area in which they assess. They must also be knowledgeable about the accreditation criteria and the policies and processes of the accrediting body.

Most accrediting bodies follow a similar process for qualifying assessor candidates to work for them. A background check is performed, and then new assessors may be evaluated as technical assessors on a team assessment and/or as the leader of an assessment team. Criteria based on Part 2 of ISO 10011-2 (Ref 4) are used to evaluate assessors. All new assessors and those needing refresher training should participate in available training courses, and approved assessors must be reevaluated at appropriate intervals. The assessors are also evaluated through their written reports, and laboratories may be given the opportunity to evaluate the assessor(s) who assessed the laboratory. Assessors are sometimes paid; other accrediting bodies use volunteer assessors.

Advisory Committees. Often accrediting bodies set up advisory committees for certain fields of testing or program areas if advice is needed beyond that which can be obtained from existing consensus standards writing organizations or industry committees, such as ASTM. Each advisory committee provides advice on the development of program requirements and the interpretation and/or amplification of ISO/IEC Guide 25 requirements for a particular field of testing.

References cited in this section

3. "Calibration and Testing Laboratory Accreditation Systems—General Requirements for Operation and Recognition," ISO/IEC Guide 58, 1993
4. "Guidelines for Auditing Quality Systems, Part 1: Auditing; Part 2: Qualification Criteria for Auditors," ISO 10011, 1992

Accreditation of Mechanical Testing Laboratories

Roxanne M. Robinson, American Association for Laboratory Accreditation

Accreditation versus ISO 9000 Certification

The purposes of laboratory accreditation as stated in ISO/IEC Guide 25 (Ref 2) and quality system certifications such as ISO 9002 (Ref 5) are different, and, thus, examination against them gives different levels of assurance. The ISO 9000 series of standards provides a generic system for quality management of an organization, irrespective of the product or service it provides. In contrast, the ISO/IEC Guide 25 is a document developed specifically to provide minimum requirements to laboratories on both quality management in a laboratory environment and technical requirements for the proper operation of a laboratory. To the extent that both documents address quality management, Guide 25 can be considered as a complementary document to ISO 9002, which is written in terms most understandable by laboratory managers.

Some have expressed the view that the application of ISO 9002 alone is sufficient to ensure the effective operation of a laboratory and the validity of test data. Several significant differences, however, exist between laboratory accreditation using ISO/IEC Guide 25 and quality system certifications such as ISO 9002 (Ref 5). One key difference is that ISO/IEC Guide 25 is intended to ensure the validity of test data, while technical credibility is not addressed in quality management requirements of standards such as ISO 9002. From the point of view of the user of test data, quality management systems (ISO 9000) are deficient in that they do not necessarily provide any assessment of the technical competence of personnel engaged in what can only be described as a very technical activity, nor do quality management systems necessarily address the specific requirements of particular products or measurements. The better method of achieving these two objectives is through laboratory accreditation bodies operating according to an international practice, where laboratories adopt best practices by working with assessors who are expert in the specific tests in which the customer is interested.

It is also important to examine the differences in skill and emphasis of assessors involved in quality system certification and laboratory accreditation assessments. For quality system certification, emphasis is traditionally placed on the qualifications of the assessor to perform assessment against the systems standard. The systems assessor (often referred to as the lead assessor) is expected to have a thorough knowledge of the requirements of the standard. In current practice internationally, a quality system assessment team may or may not include personnel who have specific technical backgrounds or process familiarity relevant to the organizations being assessed.

For laboratory accreditation, the assessment team always involves a combination of personnel who have expert technical knowledge of the test or measurement methodology being evaluated for recognition in a specific laboratory, together with personnel who have specific knowledge of the policies and practices of the accreditation body and the general systems applicable to all accredited laboratories. The laboratory accreditation assessment, thus, includes a technical peer review component plus a systems compliance component.

Unlike quality system assessment, laboratory accreditation involves appraisal of the competence of personnel as well as systems. Part of the evaluation of a laboratory includes evaluation of supervisory personnel, in many cases leading to recognition of specific individuals as part of the laboratory accreditation. The technical competence and performance of laboratory operators may also be witnessed as part of the assessment process. The loss of key personnel may affect the continuing accreditation of the laboratory by the accrediting body; for

example, loss of key staff whose absence reduces the technical competence of the laboratory may prompt a reassessment before it would be normally scheduled.

Quality system certification, on the other hand, is not normally linked to nominated key personnel. The technical competence of managers and process operators is not a defined activity for quality system assessment teams. It is through the documented policies, job descriptions, procedures, work instructions, and training requirements of organizations and through objective evidence of their implementation that quality system certifiers appraise the personnel component of a system. Staff turnover is not an issue in maintaining certification.

The final product of a laboratory is test data. In many cases, laboratory accreditation assessments also include some practical testing of the laboratory through various forms of proficiency testing (interlaboratory comparisons or reference materials testing). This is another way that accreditation differs from quality system certification.

References cited in this section

2. “General Requirements for the Competence of Calibration and Testing Laboratories,” ISO/IEC Guide 25, 1990
5. ISO 9002, Quality Systems—Model for Quality Assurance in Production and Installation, 1994

Accreditation of Mechanical Testing Laboratories

Roxanne M. Robinson, American Association for Laboratory Accreditation

Requirements of ISO/IEC Guide 25 (1990)

For international acceptance, accredited laboratories are required to comply with ISO/IEC Guide 25 (Ref 2). In this guide, attention is paid to the activities of both calibration and testing laboratories, and account is taken of other requirements for laboratory competence such as those of the Organization of Economic Cooperation and Development (OECD) *Code of Good Laboratory Practice* (GLP) (Ref 6) and the ISO 9000 series of quality assurance standards. Additional program requirements (specific criteria) for specific fields of testing (e.g., mechanical) or product requirements (e.g., fastener quality) (Ref 7) may also complement general requirements in particular areas.

ISO Guide 25 is recognized on an international level as the appropriate standard for determining the competency of a laboratory to perform specific tests or types of tests, or calibrations. Guide 25 is a balanced standard that addresses quality system requirements of ISO 9000 and the technical requirements needed to perform testing or calibration. The following criteria are included in ISO Guide 25:

- Organization and management
- Quality system, audit, and review
- Personnel
- Accommodation and environment
- Equipment and reference materials
- Measurement traceability and calibration
- Calibration and test methods
- Handling calibration and test items
- Records
- Certificates and reports
- Subcontracting calibration or testing
- Outside support and services

- Complaints

The mechanical testing accreditation program offered by accrediting bodies may differ in the breadth of testing each program covers. By the same token, a mechanical testing laboratory can request to be accredited for only a portion of, or the entire, testing capability of the laboratory. The scope of accreditation is based on the information provided by the laboratory to describe in detail the kinds of products tested, the test technologies used, and the specific test methods performed.

References cited in this section

2. “General Requirements for the Competence of Calibration and Testing Laboratories,” ISO/IEC Guide 25, 1990
6. “Good Laboratory Practice Principles,” Organization for Economic Cooperation and Development (OECD), 1998
7. *Fastener Quality Act*, H. R. 3000 or PL 101–592, *Federal Register*, 26 Sept 1996

Accreditation of Mechanical Testing Laboratories

Roxanne M. Robinson, American Association for Laboratory Accreditation

Accreditation Process

Application. A laboratory applies for accreditation by obtaining the application package from the accrediting body headquarters and completing appropriate application sheets. All applicants may have to agree to the set of conditions for accreditation, pay the appropriate fees, and provide detailed supporting information on the following:

- Scope of testing in terms of field(s) of testing, testing technologies, test methods, and relevant standards (Table 1)
- Organization structure
- Proficiency testing

Table 1 Examples of items that can be specified in the scope of accreditation for a mechanical testing laboratory

Category	Examples
Products tested	Abrasives; adhesives and sealants; aircraft and automotive components; ceramics; coatings; fasteners; films; packaging; furniture; gaskets; glass and glass products; gypsum and gypsum products; leather; metals and alloys; packaging and containers; paper, paperboard, and pulp; plastic and polymers; pipes, hoses, valves, and fittings; pressure vessels; rubber and rubber products; safety tests on motor vehicles, toys, helmets; textiles; tools; windows and doors; and wood and wood products
Testing technologies used	Mechanical testing, including tensile, compression, hardness, shear, torsion, ductility, stress rupture; fracture (Charpy, Izod, etc.) and fatigue testing
	Metallography, including preparation, microstructure, inclusion content, grain size, hydrogen embrittlement, macroetching and microetching, depth of decarburization, and case depth
	Environmental simulation, including acceleration, altitude, durability, explosion,

	fungus, high/low temperature, high pressure, humidity, radioactivity, salt spray, sea water immersion, shock, and sun exposure simulation
	Dimensional inspection^(a)
Applicable standards or test methods	Consensus methods such as those issued by standards organizations such as ASTM, SAE^(b), and ISO^(c), or by companies such as General Motors Corp. and Ford Motor Co.^(d)
	In-house test methods^(e)

(a) Additional information concerning the range of measurement for each parameter and best measurement capability may have to be determined and included in the scope of accreditation.

(b) SAE, Society of Automotive Engineers.

(c) ISO, International Organization for Standardization.

(d) Usually, the laboratory must identify standard methods by designation and short title (e.g., ASTM B 117 Salt Spray).

(e) Accredited in-house methods are nonproprietary and must be made available to public persons with a valid reason to make such a request.

Applicants may also need to provide their quality manual or quality manual references, which address the documentation requirements of ISO/IEC Guide 25 and provide a matrix of the technical training of their laboratory personnel.

On-Site Assessment. Once the application information is completed and the appropriate fees are paid, headquarters staff identifies and tentatively assigns one or more assessors to conduct an on-site assessment. The laboratory has the right to ask for another assessor if it objects to the original assignment. Assessments may last from one to several days.

Assessors are given an assessor guide and checklists to follow in performing an assessment. These documents are intended to ensure that assessments are conducted as uniformly and completely as possible among the assessors and from laboratory to laboratory.

Before the assessment is conducted, the assessor team requests copies of the quality manual and related documentation (i.e., standard operating procedures related to Guide 25 requirements) in order to prepare for the assessment. The quality manual and related documentation must be reviewed by the assessor team before the on-site assessment can begin. Ideally, this review is done before the assessment is scheduled. Upon review of submitted documentation, the assessor(s) may ask the laboratory to implement corrective action to fill any documentation gaps required by Guide 25 before scheduling the assessment. A preassessment visit may be requested by the laboratory as an option at this point to enhance the success of the full assessment. Prior to scheduling the full assessment, the assessor reviews the scope of the draft to determine the tests to possibly witness and checks on the availability of the technical personnel who perform the tests. The assessor provides an assessment agenda.

The full assessment generally involves the following activities:

- An entry briefing with laboratory management
- Audit of the quality system to verify that it is fully operational and that it conforms to all sections of ISO/IEC Guide 25, including documentation
- Interviews with technical staff
- Demonstration of selected tests including, as applicable, tests done at representative field locations
- Examination of equipment and calibration records
- A written report of assessor findings
- An exit briefing including the specific written identification of any deficiencies

The objective of an assessment is to establish whether or not a laboratory complies with the requirements for accreditation and can competently perform the types of mechanical tests for which accreditation is sought. However, when accreditation is required to demonstrate compliance with additional criteria that may be imposed by other authorities, such as in the case of the *Fastener Quality Act*, the assessment will include such additional criteria. Assessors may also provide advice, based on observations or in response to questions, in order to help the laboratory improve its performance.

Deficiencies. During the assessment, assessors may observe deficiencies. A deficiency is any nonconformity to accreditation requirements including the following:

- The inability of a laboratory to perform a test or type of test for which the laboratory seeks accreditation.
- The nonconformance of a laboratory quality system to a clause or section of ISO/IEC Guide 25, inadequate documentation of a quality system, or a quality system that is not completely operational
- The nonconformance of a laboratory to any additional requirements of the accrediting body or specific fields of testing or programs necessary to meet particular needs

At the conclusion of an assessment, the assessor prepares a report of findings identifying deficiencies that, in the assessor's judgment, the laboratory must resolve in order to be accredited. The assessor holds an exit briefing with top management of the laboratory. The assessor goes over the findings and presents the list of deficiencies (deficiency report). The authorized representative of the laboratory (or designee) is asked to sign the deficiency report to attest that the deficiency report has been reviewed with the assessor. The signature does not imply that the laboratory representative concurs that the individual item(s) constitute a deficiency. The laboratory is requested to respond promptly after the date of the exit briefing, detailing either its corrective action or why it does not believe that a deficiency exists. The corrective action response should include a copy of any objective evidence (e.g., calibration certificates, lab procedures, paid invoices, packaging slips, and training records) to indicate that the corrective actions have been implemented/completed.

It is entirely possible that the laboratory will disagree with the findings that one or more items are deficiencies. In that case, the laboratory is requested to explain in its response why it disagrees with the assessor.

If the laboratory fails to respond in the agreed time frame, it may be treated as a new applicant subject to new fees and reassessment should it wish to pursue accreditation after that time.

Proficiency testing is a process for checking actual laboratory testing performance, usually by means of interlaboratory test data comparisons. For many test methods, results from proficiency testing are very good indicators of testing competence. Proficiency testing programs may take many forms, and standards for satisfactory performance can vary depending on the field. An accredited laboratory must participate in method-specific proficiency testing related to its field(s) of accreditation if such programs are available. There are commercially available proficiency testing programs that cover a wide array of mechanical testing procedures. Proficiency testing is available for plastics, rubber, textiles, paper, metals, and fasteners. Where proficiency testing programs are not available or suitable to the accredited testing, the laboratories often devise their own round-robin testing with a limited number of similar laboratories. Data from these round-robin studies are acceptable alternatives to proficiency testing program participation. When neither proficiency testing nor round-robin testing is available, internal performance-based data can substitute.

Accreditation Decisions. Before an accreditation decision ballot is sent to the person or group making the accreditation decision, the laboratory staff may review the deficiency response, including objective evidence of completed corrective action, for adequacy and completeness. If there is any doubt about the adequacy or completeness of any part of the deficiency response, the response may be submitted to the assessor(s) for additional review. The laboratory may then be asked to respond further to ensure a successful accreditation decision. The accreditation body then reviews the assessment record and any corrective action response to render a decision. Any concerns or negative decisions are relayed back to the laboratory for further response until the issue is resolved in a satisfactory way for final accreditation of the laboratory.

When accreditation is granted, the laboratory is issued a certificate and scope of accreditation for the mechanical field of testing and any special testing program. The laboratory should keep its scope of accreditation available to show clients or potential clients the testing technologies and test methods for which it is accredited. The scopes of accreditation are also used by the accrediting body to respond to inquiries and to prepare the directory of accredited laboratories.

Annual Review. Accreditation is generally established for a certain period of time before a reassessment is required. However, at set intervals between this established accreditation period, each laboratory would likely pay annual fees and undergo some type of surveillance activity that could include a one-day surveillance visit by an assessor. This surveillance visit is performed to confirm that the quality system of a laboratory and technical capabilities remain in compliance with the accreditation requirements. Other possible surveillance activities may include submission of updating information by the laboratory on its organization, facilities, and key personnel, and the results of any proficiency testing. Objective evidence of completion of the internal audit and management review may also be required. If the laboratory does not promptly provide complete annual

review documentation, or significant changes to the facility or organization have occurred, a one-day surveillance visit and payment of the associated assessor fees may be required.

Reassessment and Renewal of Accreditation. Full on-site reassessments of all accredited laboratories are conducted at intervals determined by the period of accreditation. Reassessments are also conducted when evaluations and submissions from the laboratory or its clients indicate significant technical changes in the capability of the laboratory have occurred.

The accredited laboratory is sent some type of renewal prompt, well in advance of the expiration date of its accreditation, to allow sufficient time to complete the renewal process. A successful on-site reassessment must be completed before accreditation is extended.

If deficiencies are noted during the renewal assessment, the laboratory is asked to respond in a timely fashion with a corrective action. All deficiencies must be resolved before accreditation is renewed.

Accreditation of Mechanical Testing Laboratories

Roxanne M. Robinson, American Association for Laboratory Accreditation

References

1. "General Terms and Their Definitions Concerning Standardization and Related Activities," ISO/IEC Guide 2, 1993
2. "General Requirements for the Competence of Calibration and Testing Laboratories," ISO/IEC Guide 25, 1990
3. "Calibration and Testing Laboratory Accreditation Systems—General Requirements for Operation and Recognition," ISO/IEC Guide 58, 1993
4. "Guidelines for Auditing Quality Systems, Part 1: Auditing; Part 2: Qualification Criteria for Auditors," ISO 10011, 1992
5. ISO 9002, Quality Systems—Model for Quality Assurance in Production and Installation, 1994
6. "Good Laboratory Practice Principles," Organization for Economic Cooperation and Development (OECD), 1998
7. *Fastener Quality Act*, H. R. 3000 or PL 101–592, *Federal Register*, 26 Sept 1996

Mechanical Behavior Under Tensile and Compressive Loads*

George E. Dieter, University of Maryland

Introduction

THE MECHANICAL BEHAVIOR OF MATERIALS is described by their deformation and fracture characteristics under applied tensile, compressive, or multiaxial stresses. Determination of this mechanical behavior is influenced by several factors that include metallurgical/material variables, test methods, and the nature of the applied stresses.

This article focuses on mechanical behavior under conditions of uniaxial tension and compression. The main emphasis is on mechanical behavior during the engineering tension test, which is widely used to provide basic design information on the strength of materials and as an acceptance test for the specification of materials. In this test procedure, a specimen is subjected to a continually increasing uniaxial load (force), while simultaneous observations are made of the elongation of the specimen. In this article, emphasis is placed on the interpretation of these observations rather than on the procedures for conducting the tests. The article “Uniaxial Tensile Testing” in this Volume discusses the influence of test procedure variables.

Footnote

* Reprinted in part from *Mechanical Metallurgy*, 3rd ed., McGraw-Hill, New York, 1986, p 275–295, with permission

Mechanical Behavior Under Tensile and Compressive Loads*

George E. Dieter, University of Maryland

Engineering Stress-Strain Curve

In the conventional engineering tension test, an engineering stress-strain curve is constructed from the load-elongation measurements made on the test specimen (Fig. 1). The engineering stress (s) used in this stress-strain curve is the average longitudinal stress in the tensile specimen. It is obtained by dividing the load (P) by the original area of the cross section of the specimen (A_0):

$$s = \frac{P}{A_0} \quad (\text{Eq 1})$$

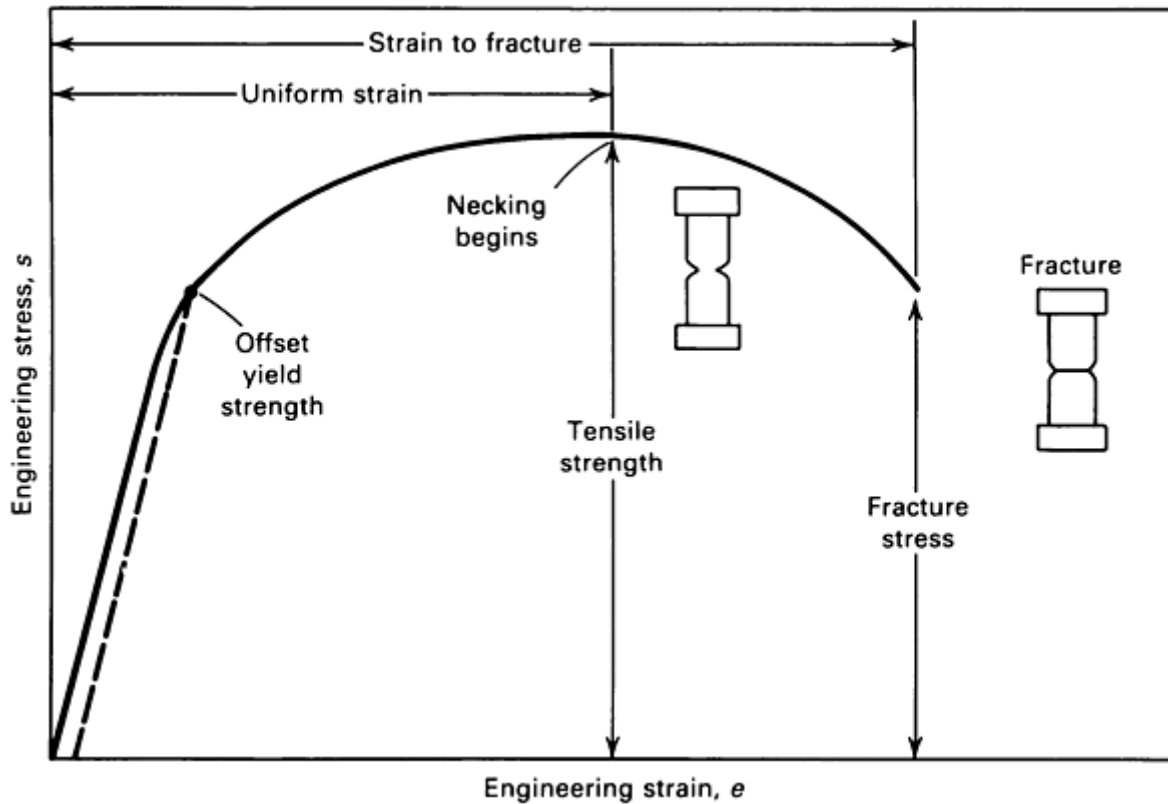


Fig. 1 Engineering stress-strain curve. Intersection of the dashed line with the curve determines the offset yield strength. See also Fig. 2 and corresponding text.

The strain, e , used for the engineering stress-strain curve is the average linear strain, which is obtained by dividing the elongation of the gage length of the specimen (δ) by its original length (L_0):

$$e = \frac{\delta}{L_0} = \frac{\Delta L}{L_0} = \frac{L - L_0}{L_0} \quad (\text{Eq 2})$$

Because both the stress and the strain are obtained by dividing the load and elongation by constant factors, the load-elongation curve has the same shape as the engineering stress-strain curve. The two curves frequently are used interchangeably.

The shape and magnitude of the stress-strain curve of a metal depend on its composition, heat treatment, prior history of plastic deformation, and the strain rate, temperature, and state of stress imposed during the testing. The parameters that are used to describe the stress-strain curve of a metal are the tensile strength, yield strength or yield point, percent elongation, and reduction in area. The first two are strength parameters; the last two indicate ductility.

The general shape of the engineering stress-strain curve (Fig. 1) requires further explanation. In the elastic region, stress is linearly proportional to strain. When the stress exceeds a value corresponding to the yield strength, the specimen undergoes gross plastic deformation. If the load is subsequently reduced to zero, the specimen will remain permanently deformed. The stress required to produce continued plastic deformation increases with increasing plastic strain; that is, the metal strain hardens. The volume of the specimen (area \times length) remains constant during plastic deformation, $AL = A_0L_0$, and as the specimen elongates, its cross-sectional area decreases uniformly along the gage length.

Initially, the strain hardening more than compensates for this decrease in area, and the engineering stress (proportional to load P) continues to rise with increasing strain. Eventually, a point is reached where the decrease in specimen cross-sectional area is greater than the increase in deformation load arising from strain hardening. This condition will be reached first at some point in the specimen that is slightly weaker than the rest. All further plastic deformation is concentrated in this region, and the specimen begins to neck or thin down locally. Because the cross-sectional area now is decreasing far more rapidly than the deformation load is increased by strain hardening, the actual load required to deform the specimen falls off, and the engineering stress defined in Eq 1 continues to decrease until fracture occurs.

The tensile strength, or ultimate tensile strength (s_u) is the maximum load divided by the original cross-sectional area of the specimen:

$$s_u = \frac{P_{\max}}{A_0} \quad (\text{Eq 3})$$

The tensile strength is the value most frequently quoted from the results of a tension test. Actually, however, it is a value of little fundamental significance with regard to the strength of a metal. For ductile metals, the tensile strength should be regarded as a measure of the maximum load that a metal can withstand under the very restrictive conditions of uniaxial loading. This value bears little relation to the useful strength of the metal under the more complex conditions of stress that usually are encountered.

For many years, it was customary to base the strength of members on the tensile strength, suitably reduced by a factor of safety. The current trend is to use the more rational approach of basing the static design of ductile metals on the yield strength. However, due to the long practice of using the tensile strength to describe the strength of materials, it has become a familiar property, and as such, it is a useful identification of a material in the same sense that the chemical composition serves to identify a metal or alloy. Furthermore, because the tensile strength is easy to determine and is a reproducible property, it is useful for the purposes of specification and for quality control of a product. Extensive empirical correlations between tensile strength and properties such as hardness and fatigue strength are often useful. For brittle materials, the tensile strength is a valid design criterion.

Measures of Yielding. The stress at which plastic deformation or yielding is observed to begin depends on the sensitivity of the strain measurements. With most materials, there is a gradual transition from elastic to plastic behavior, and the point at which plastic deformation begins is difficult to define with precision. In tests of materials under uniaxial loading, three criteria for the initiation of yielding have been used: the elastic limit, the proportional limit, and the yield strength.

Elastic limit, shown at point A in Fig. 2, is the greatest stress the material can withstand without any measurable permanent strain remaining after the complete release of load. With increasing sensitivity of strain measurement, the value of the elastic limit is decreased until it equals the true elastic limit determined from microstrain measurements. With the sensitivity of strain typically used in engineering studies (10^{-4} in./in.), the elastic limit is greater than the proportional limit. Determination of the elastic limit requires a tedious incremental loading-unloading test procedure. For this reason, it is often replaced by the proportional limit.

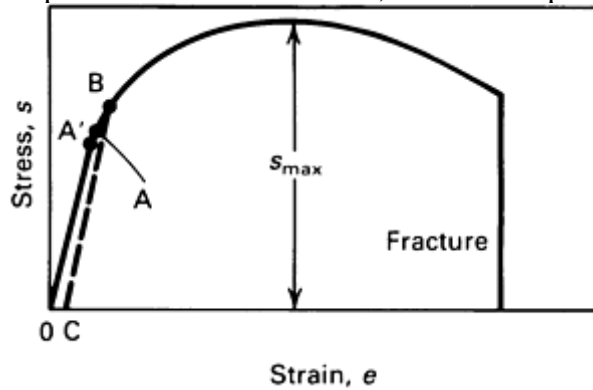


Fig. 2 Typical tension stress-strain curve for ductile metal indicating yielding criteria. Point A, elastic limit; point A', proportional limits; point B, yield strength or offset (0 to C) yield strength; 0, intersection of the stress-strain curve with the strain axis

Proportional limit, shown at point A' in Fig. 2, is the highest stress at which stress is directly proportional to strain. It is obtained by observing the deviation from the straight-line portion of the stress-strain curve.

The yield strength, shown at point B in Fig. 2, is the stress required to produce a small specified amount of plastic deformation. The usual definition of this property is the offset yield strength determined by the stress corresponding to the intersection of the stress-strain curve offset by a specified strain (see Fig. 1 and 2). In the United States, the offset is usually specified as a strain of 0.2 or 0.1% ($e = 0.002$ or 0.001):

$$s_0 = \frac{P_{(\text{strain offset}=0.002)}}{A_0} \quad (\text{Eq 4})$$

Offset yield strength determination requires a specimen that has been loaded to its 0.2% offset yield strength and unloaded so that it is 0.2% longer than before the test. The offset yield strength is often referred to in Great Britain as the proof stress, where offset values are either 0.1 or 0.5%. The yield strength obtained by an offset method is commonly used for design and specification purposes, because it avoids the practical difficulties of measuring the elastic limit or proportional limit.

Some materials have essentially no linear portion to their stress-strain curve, for example, soft copper, gray cast iron, and many polymers. For these materials, the offset method cannot be used, and the usual practice is to define the yield strength as the stress to produce some total strain, for example, $e = 0.005$.

Some metals, particularly annealed low-carbon steel, show a localized, heterogeneous type of transition from elastic to plastic deformation that produces a yield point in the stress-strain curve. Rather than having a flow curve with a gradual transition from elastic to plastic behavior, such as Fig. 1 and 2, metals with a yield point produce a flow curve or a load-elongation diagram similar to Fig. 3. The load increases steadily with elastic strain, drops suddenly, fluctuates about some approximately constant value of load, and then rises with further strain.

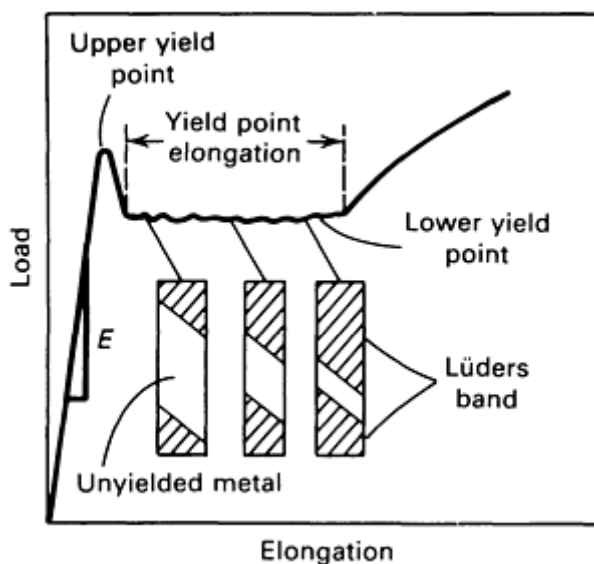


Fig. 3 Typical yield-point behavior of low-carbon steel. The slope of the initial linear portion of the stress-strain curve, designated by E , is the modulus of elasticity.

The load at which the sudden drop occurs is called the upper yield point. The constant load is called the lower yield point, and the elongation that occurs at constant load is called the yield-point elongation. The deformation occurring throughout the yield-point elongation is heterogeneous. At the upper yield point, a discrete band of deformed metal, often readily visible, appears at a stress concentration, such as a fillet. Coincident with the formation of the band, the load drops to the lower yield point. The band then propagates along the length of the specimen, causing the yield-point elongation. A similar behavior occurs with some polymers and superplastic metal alloys, where a neck forms but grows in a stable manner, with material being fed into the necked region from the thicker adjacent regions. This type of deformation in polymers is called “drawing”.

In typical cases, several bands form at several points of stress concentration. These bands are generally at approximately 45° to the tensile axis. They are usually called Lüders bands or stretcher strains, and this type of deformation is sometimes referred to as the Piobert effect. When several Lüders bands are formed, the flow curve during the yield-point elongation is irregular, each jog corresponding to the formation of a new Lüders band. After the Lüders bands have propagated to cover the entire length of the specimen test section, the flow will increase with strain in the typical manner. This marks the end of the yield-point elongation. Lüders bands formed on a rimmed 1008 steel are shown in Fig. 4.



Fig. 4 Rimmed 1008 steel with Lüders bands on the surface as a result of stretching the sheet just beyond the yield point during forming

Measures of Ductility. Currently, ductility is considered a qualitative, subjective property of a material. In general, measurements of ductility are of interest in three respects (Ref 1):

- To indicate the extent to which a metal can be deformed without fracture in metalworking operations, such as rolling and extrusion
- To indicate to the designer the ability of the metal to flow plastically before fracture. A high ductility indicates that the material is “forgiving” and likely to deform locally without fracture should the designer err in the stress calculation or the prediction of severe loads.
- To serve as an indicator of changes in impurity level or processing conditions. Ductility measurements may be specified to assess material quality, even though no direct relationship exists between the ductility measurement and performance in service.

The conventional measures of ductility that are obtained from the tension test are the engineering strain at fracture (e_f) (usually called the elongation) and the reduction in area at fracture (q). Elongation and reduction in area usually are expressed as a percentage. Both of these properties are obtained after fracture by putting the specimen back together and taking measurements of the final length, L_f , and final specimen cross section, A_f :

$$e_f = \frac{L_f - L_0}{L_0} \quad (\text{Eq 5})$$

$$q = \frac{A_0 - A_f}{A_0} \quad (\text{Eq 6})$$

Because an appreciable fraction of the plastic deformation will be concentrated in the necked region of the tension specimen, the value of e_f will depend on the gage length (L_0) over which the measurement was taken (see the section of this article on ductility measurement in tension testing). The smaller the gage length, the greater the contribution to the overall elongation from the necked region and the higher the value of e_f . Therefore, when reporting values of percentage elongation, the gage length should always be given.

Reduction in area does not suffer from this difficulty. These values can be converted into an equivalent zero-gage-length elongation (e_0). From the constancy of volume relationship for plastic deformation, $AL = A_0L_0$:

$$\frac{L}{L_0} = \frac{A_0}{A} = \frac{1}{1-q}$$

(Eq 7)

$$e_0 = \frac{L - L_0}{L_0} = \frac{A_0}{A} - 1 = \frac{1}{1-q} - 1 = \frac{q}{1-q}$$

This represents the elongation based on a very short gage length near the fracture.

Another way to avoid the complications resulting from necking is to base the percentage elongation on the uniform strain out to the point at which necking begins. The uniform elongation (e_u), correlates well with stretch-forming operations. Because the engineering stress-strain curve often is quite flat in the vicinity of necking, it may be difficult to establish the strain at maximum load without ambiguity. In this case, the method suggested in Ref 2 is useful.

Modulus of Elasticity. The slope of the initial linear portion of the stress-strain curve is the modulus of elasticity, or Young's modulus, as shown in Fig. 3. The modulus of elasticity (E) is a measure of the stiffness of the material. The greater the modulus, the smaller the elastic strain resulting from the application of a given stress. Because the modulus of elasticity is needed for computing deflections of beams and other members, it is an important design value.

The modulus of elasticity is determined by the binding forces between atoms. Because these forces cannot be changed without changing the basic nature of the material, the modulus of elasticity is one of the most structure-insensitive of the mechanical properties. Generally, it is only slightly affected by alloying additions, heat treatment, or cold work (Ref 3). However, increasing the temperature decreases the modulus of elasticity. At elevated temperatures, the modulus is often measured by a dynamic method (Ref 4). Typical values of the modulus of elasticity for common engineering metals at different temperatures are given in Table 1.

Table 1 Typical values of modulus of elasticity at different temperature

Material	Modulus of elasticity GPa (10^6 psi), at:				
	Room temperature	250 °C (400 °F)	425 °C (800 °F)	540 °C (1000 °F)	650 °C (1200 °F)
Carbon steel	207 (30.0)	186 (27.0)	155 (22.5)	134 (19.5)	124 (18.0)
Austenitic stainless steel	193 (28.0)	176 (25.5)	159 (23.0)	155 (22.5)	145 (21.0)
Titanium alloys	114 (16.5)	96.5 (14.0)	74 (10.7)	70 (10.0)	...
Aluminum alloys	72 (10.5)	65.5 (9.5)	54 (7.8)

Resilience. The ability of a material to absorb energy when deformed elastically and to return it when unloaded is called resilience. This property usually is measured by the modulus of resilience, which is the strain energy per unit volume (U_0) required to stress the material from zero stress to the yield stress (σ_0). The strain energy per unit volume for uniaxial tension is:

$$U_0 = \frac{1}{2} \sigma_x e_x \quad (\text{Eq 8})$$

From the above definition, the modulus of resilience (U_R) is:

$$U_R = \frac{1}{2} s_0 e_0 = \frac{1}{2} s_0 \frac{s_0}{E} = \frac{s_0^2}{2E} \quad (\text{Eq 9})$$

This equation indicates that the ideal material for resisting energy loads in applications where the material must not undergo permanent distortion, such as in mechanical springs, is one having a high yield stress and a low modulus of elasticity.

For various grades of steel, the modulus of resilience ranges from 100 to 4500 kJ/m³ (14.5–650 lbf · in./in.³), with the higher values representing steels with higher carbon or alloy contents (Ref 5). The cross-hatched regions in Fig. 5 indicate the modulus of resilience for two steels. Due to its higher yield strength, the high-carbon spring steel has the greater resilience.

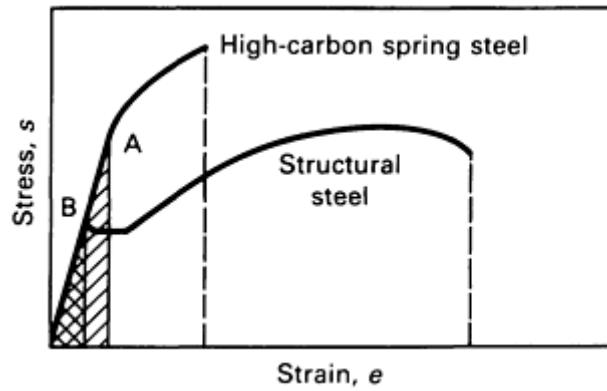


Fig. 5 Comparison of stress-strain curves for high- and low-toughness steels. Cross-hatched regions in this curve represent the modulus of resilience (U_R) of the two materials. The U_R is determined by measuring the area under the stress-strain curve up to the elastic limit of the material. Point A represents the elastic limit of the spring steel; point B represents that of the structural steel.

The toughness of a material is its ability to absorb energy in the plastic range. The ability to withstand occasional stresses above the yield stress without fracturing is particularly desirable in parts such as freight-car couplings, gears, chains, and crane hooks. Toughness is a commonly used concept that is difficult to precisely define. Toughness may be considered to be the total area under the stress-strain curve. This area, which is referred to as the modulus of toughness (U_T) is an indication of the amount of work per unit volume that can be done on the material without causing it to rupture.

Figure 5 shows the stress-strain curves for high- and low-toughness materials. The high-carbon spring steel has a higher yield strength and tensile strength than the medium-carbon structural steel. However, the structural steel is more ductile and has a greater total elongation. The total area under the stress-strain curve is greater for the structural steel; therefore, it is a tougher material. This illustrates that toughness is a parameter that comprises both strength and ductility.

Several mathematical approximations for the area under the stress-strain curve have been suggested. For ductile metals that have a stress-strain curve like that of the structural steel, the area under the curve can be approximated by:

$$U_T \approx s_u e_f \quad (\text{Eq 10})$$

or

$$U_T \approx \frac{s_0 + s_u}{2} e_f \quad (\text{Eq 11})$$

For brittle materials, the stress-strain curve is sometimes assumed to be a parabola, and the area under the curve is given by:

$$U_T \approx \frac{2}{3} s_u e_f \quad (\text{Eq 12})$$

Typical Stress-Strain Curves. Figure 6 compares the engineering stress-strain curves in tension for three materials. The 0.8% carbon eutectoid steel is representative of a material with low ductility. The annealed 0.2% carbon mild steel shows a pronounced upper and lower yield point. The polycarbonate engineered polymer has no well-defined linear modulus, and a large strain to fracture. Note the pronounced difference in stress level at which yielding is defined, as well as the quite different shape of the stress-strain curves.

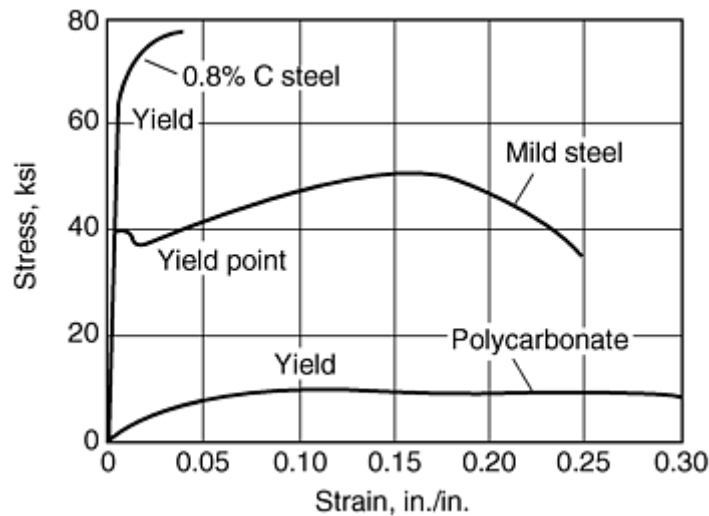


Fig. 6 Typical engineering stress-strain curves

Footnote

* Reprinted in part from *Mechanical Metallurgy*, 3rd ed., McGraw-Hill, New York, 1986, p 275–295, with permission

References cited in this section

1. G.E. Dieter, Introduction to Ductility, in *Ductility*, American Society for Metals, 1968
2. P.G. Nelson and J. Winlock, *ASTM Bull.*, Vol 156, Jan 1949, p 53
3. D.J. Mack, *Trans. AIME*, Vol 166, 1946, p 68–85
4. P.E. Armstrong, Measurement of Elastic Constants, in *Techniques of Metals Research*, Vol V, R.F. Brunshaw, Ed., Interscience, New York, 1971
5. H.E. Davis, G.E. Troxell, and G.F.W. Hauck, *The Testing of Engineering Materials*, McGraw-Hill, New York, 1964, p 33

Mechanical Behavior Under Tensile and Compressive Loads*

George E. Dieter, University of Maryland

True Stress-True Strain Curve

The engineering stress-strain curve does not give a true indication of the deformation characteristics of a metal because it is based entirely on the original dimensions of the specimen, and these dimensions change continuously during the test. Also, ductile metal that is pulled in tension becomes unstable and necks down during the course of the test. Because the cross-sectional area of the specimen is decreasing rapidly at this stage in the test, the load required to continue deformation falls off.

The average stress based on the original area likewise decreases, and this produces the fall-off in the engineering stress-strain curve beyond the point of maximum load. Actually, the metal continues to strain harden to fracture, so that the stress required to produce further deformation should also increase. If the true

stress, based on the actual cross-sectional area of the specimen, is used, the stress-strain curve increases continuously to fracture. If the strain measurement is also based on instantaneous measurement, the curve that is obtained is known as true stress-true strain curve. This is also known as a flow curve because it represents the basic plastic-flow characteristics of the material.

Any point on the flow curve can be considered the yield stress for a metal strained in tension by the amount shown on the curve. Thus, if the load is removed at this point and then reapplied, the material will behave elastically throughout the entire range of reloading.

The true stress (σ) is expressed in terms of engineering stress (s) by:

$$\sigma = \frac{P}{A_0}(e + 1) = s(e + 1) \quad (\text{Eq 13})$$

The derivation of Eq 13 assumes both constancy of volume and a homogeneous distribution of strain along the gage length of the tension specimen. Thus, Eq 13 should be used only until the onset of necking. Beyond the maximum load, the true stress should be determined from actual measurements of load and cross-sectional area.

$$\sigma = \frac{P}{A} \quad (\text{Eq 14})$$

The true strain, ϵ , may be determined from the engineering or conventional strain (e) by:

$$\epsilon = \ln(e + 1) = \ln \frac{L}{L_0} \quad (\text{Eq 15})$$

This equation is applicable only to the onset of necking for the reasons discussed above. Beyond maximum load, the true strain should be based on actual area or diameter (D) measurements:

$$\epsilon = \ln \frac{A_0}{A} = \ln \frac{\left(\frac{\pi}{4}\right)D_0^2}{\left(\frac{\pi}{4}\right)D^2} = 2 \ln \frac{D_0}{D} \quad (\text{Eq 16})$$

Figure 7 compares the true stress-true strain curve with its corresponding engineering stress-strain curve. Note that because of the relatively large plastic strains, the elastic region has been compressed into the y-axis. In agreement with Eq 13 and 15, the true stress-true strain curve is always to the left of the engineering curve until the maximum load is reached.

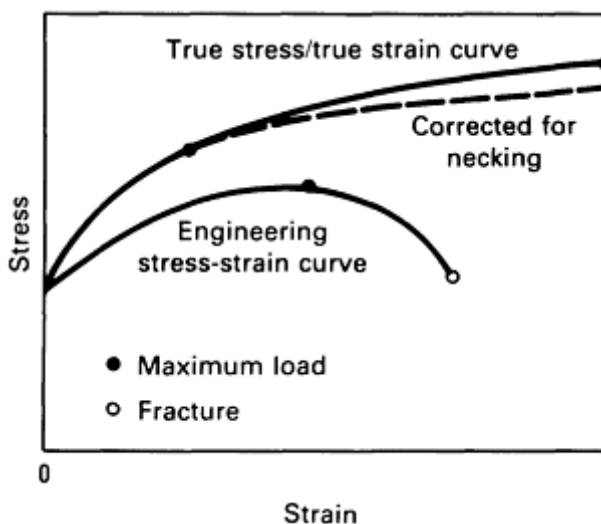


Fig. 7 Comparison of engineering and true stress-true strain curves

However, beyond maximum load, the high, localized strains in the necked region that are used in Eq 16 far exceed the engineering strain calculated from Eq 2. Frequently, the flow curve is linear from maximum load to fracture, while in other cases its slope continuously decreases to fracture. The formation of a necked region or mild notch introduces triaxial stresses that make it difficult to determine accurately the longitudinal tensile stress from the onset of necking until fracture occurs. This concept is discussed in greater detail in the section of

this article on instability in tension. The following parameters usually are determined from the true stress-true strain curve.

The true stress at maximum load corresponds to the true tensile strength. For most materials, necking begins at maximum load at a value of strain where the true stress equals the slope of the flow curve. Let σ_u and ϵ_u denote the true stress and true strain at maximum load when the cross-sectional area of the specimen is A_u . The ultimate tensile strength can be defined as:

$$s_u = \frac{P_{\max}}{A_0} \quad (\text{Eq 17})$$

and

$$\sigma_u = \frac{P_{\max}}{A_u} \quad (\text{Eq 18})$$

Eliminating P_{\max} yields:

$$\sigma_u = s_u \frac{A_0}{A_u} \quad (\text{Eq 19})$$

and

$$\sigma_u = s_u e^{\epsilon} \quad (\text{Eq 20})$$

The true fracture stress is the load at fracture divided by the cross-sectional area at fracture. This stress should be corrected for the triaxial state of stress existing in the tensile specimen at fracture. Because the data required for this correction frequently are not available, true fracture stress values are frequently in error.

The true fracture strain, ϵ_f , is the true strain based on the original area (A_0) and the area after fracture (A_f):

$$\epsilon_f = \ln \frac{A_0}{A_f} \quad (\text{Eq 21})$$

This parameter represents the maximum true strain that the material can withstand before fracture and is analogous to the total strain to fracture of the engineering stress-strain curve. Because Eq 15 is not valid beyond the onset of necking, it is not possible to calculate ϵ_f from measured values of e_f . However, for cylindrical tensile specimens, the reduction in area (q) is related to the true fracture strain by:

$$\epsilon_f = \ln \frac{1}{1 - q} \quad (\text{Eq 22})$$

The true uniform strain ϵ_u , is the true strain based only on the strain up to maximum load. It may be calculated from either the specimen cross-sectional area (A_u) or the gage length (L_u) at maximum load. Equation 15 may be used to convert conventional uniform strain to true uniform strain. The uniform strain frequently is useful in estimating the formability of metals from the results of a tension test:

$$\epsilon_u = \ln \frac{A_0}{A_u} \quad (\text{Eq 23})$$

The true local necking strain (ϵ_n) is the strain required to deform the specimen from maximum load to fracture:

$$\epsilon_n = \ln \frac{A_u}{A_f} \quad (\text{Eq 24})$$

Footnote

* Reprinted in part from *Mechanical Metallurgy*, 3rd ed., McGraw-Hill, New York, 1986, p 275–295, with permission

Mathematical Expressions for the Flow Curve

The flow curve of many metals in the region of uniform plastic deformation can be expressed by the simple power curve relation:

$$\sigma = K\epsilon^n \tag{Eq 25}$$

where n is the strain-hardening exponent, and K is the strength coefficient. A log-log plot of true stress and true strain up to maximum load will result in a straight line if Eq 25 is satisfied by the data (Fig. 8).

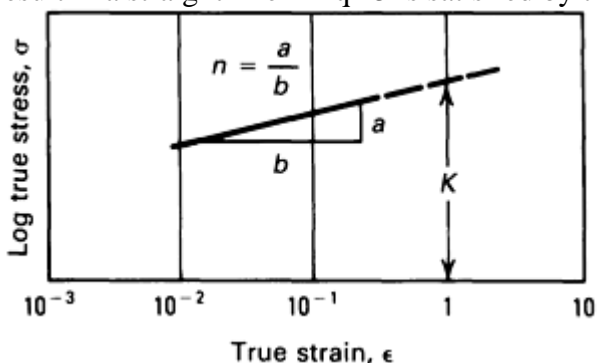


Fig. 8 Log-log plot of true stress-true strain curve n is the strain-hardening exponent; K is the strength coefficient.

The linear slope of this line is n , and K is the true stress at $\epsilon = 1.0$ (corresponds to $q = 0.63$). As shown in Fig. 9, the strain-hardening exponent may have values from $n = 0$ (perfectly plastic solid) to $n = 1$ (elastic solid). For most metals, n has values between 0.10 and 0.50 (see Table 2).

Table 2 Values for n and K for metals at room temperature

Metals	Condition	n	K		Ref
			MPa	ksi	
0.05% carbon steel	Annealed	0.26	530	77	6
SAE 4340 steel	Annealed	0.15	641	93	6
0.6% carbon steel	Quenched and tempered at 540 °C (1000 °F)	0.10	1572	228	7
0.6% carbon steel	Quenched and tempered at 705 °C (1300 °F)	0.19	1227	178	7
Copper	Annealed	0.54	320	46.4	6
70/30 brass	Annealed	0.49	896	130	7

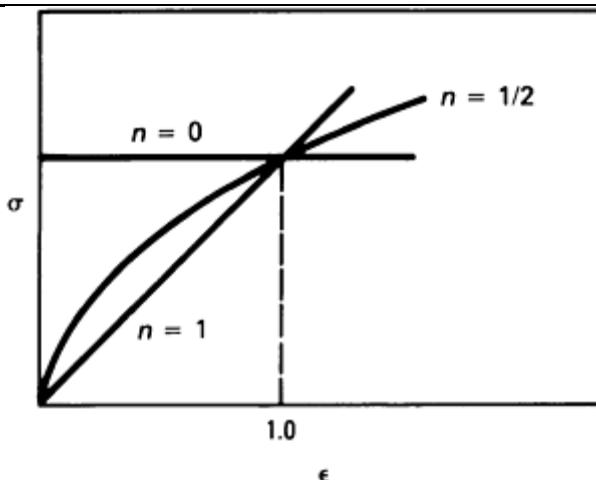


Fig. 9 Various forms of power curve $\sigma = K\varepsilon^n$

The rate of strain hardening $d\sigma/d\varepsilon$ is not identical to the strain-hardening exponent. From the definition of n :

$$n = \frac{d(\log \sigma)}{d(\log \varepsilon)} = \frac{d(\ln \sigma)}{d(\ln \varepsilon)} = \frac{\varepsilon}{\sigma} \frac{d\sigma}{d\varepsilon}$$

or

$$\frac{d\sigma}{d\varepsilon} = n \frac{\sigma}{\varepsilon} \quad (\text{Eq 26})$$

Deviations from Eq 25 frequently are observed, often at low strains (10^{-3}) or high strains ($\varepsilon \approx 1.0$). One common type of deviation is for a log-log plot of Eq 25 to result in two straight lines with different slopes. Sometimes data that do not plot according to Eq 25 will yield a straight line according to the relationship:

$$\sigma = K(\varepsilon_0 + \varepsilon)^n \quad (\text{Eq 27})$$

ε_0 can be considered to be the amount of strain that the material received prior to the tension test (Ref 8). Another common variation on Eq 25 is the Ludwik equation:

$$\sigma = \sigma_0 + K\varepsilon^n \quad (\text{Eq 28})$$

where σ_0 is the yield stress, and K and n are the same constants as in Eq 25. This equation may be more satisfying than Eq 25, because the latter implies that at zero true strain the stress is zero. It has been shown that σ_0 can be obtained from the intercept of the strain-hardening portion of the stress-strain curve and the elastic modulus line by (Ref 9):

$$\sigma_0 = \left(\frac{K}{E^n} \right)^{\frac{1}{1-n}} \quad (\text{Eq 29})$$

The true stress-true strain curve of metals such as austenitic stainless steel, which deviate markedly from Eq 25 at low strains (Ref 10), can be expressed by:

$$\sigma = K\varepsilon^n + e^{K_1} + e^{K_1} e^{n_1 \varepsilon} \quad (\text{Eq 30})$$

where e^{K_1} is approximately equal to the proportional limit, and n_1 is the slope of the deviation of stress from Eq 25 plotted against ε . Other expressions for the flow curve are available (Ref 11, 12). The true strain term in Eq 25 26 27 28 properly should be the plastic strain, $\varepsilon_p = \varepsilon_{\text{total}} - \varepsilon_E = \varepsilon_{\text{total}} - \sigma/E$, where ε_E represents elastic strain.

Footnote

* Reprinted in part from *Mechanical Metallurgy*, 3rd ed., McGraw-Hill, New York, 1986, p 275–295, with permission

References cited in this section

6. J.R. Low and F. Garofalo, *Proc. Soc. Exp. Stress Anal.*, Vol 4 (No. 2), 1947, p 16–25
7. J.R. Low, *Properties of Metals in Materials Engineering*, American Society for Metals, 1949
8. J. Datsko, *Material Properties and Manufacturing Processes*, John Wiley & Sons, New York, 1966, p 18–20
9. W.B. Morrison, *Trans. ASM*, Vol 59, 1966, p 824
10. D.C. Ludwigson, *Metall. Trans.*, Vol 2, 1971, p 2825–2828
11. H.J. Kleemola and M.A. Nieminen, *Metall. Trans.*, Vol 5, 1974, p 1863–1866

Mechanical Behavior Under Tensile and Compressive Loads*

George E. Dieter, University of Maryland

Effect of Strain Rate and Temperature

The rate at which strain is applied to the tension specimen has an important influence on the stress-strain curve. Strain rate is defined as $\dot{\epsilon} = d\epsilon/dt$. It is expressed in units of s^{-1} . The range of strain rates encompassed by various tests is shown in Table 3.

Table 3 Range of strain rates in common mechanical property tests

Range of strain rate	Type of test
10^{-8} to $10^{-5} s^{-1}$	Creep test at constant load or stress
10^{-5} to $10^{-1} s^{-1}$	Tension test with hydraulic or screw driven machines
10^{-1} to $10^2 s^{-1}$	Dynamic tension or compression tests
10^2 to $10^4 s^{-1}$	High-speed testing using impact bars
10^4 to $10^8 s^{-1}$	Hypervelocity impact using gas guns or explosively driven projectiles

Increasing strain rate increases the flow stress. Moreover, the strain-rate dependence of strength increases with increasing temperature. The yield stress and the flow stress at lower values of plastic strain are more affected by strain rate than the tensile strength.

If the crosshead velocity of the testing machine is $v = dL/dt$, then the strain rate expressed in terms of conventional engineering strain is:

$$\dot{\epsilon} = \frac{de}{dt} = \frac{d(L - L_0) / L_0}{dt} = \frac{1}{L_0} \frac{dL}{dt} = \frac{v}{L_0} \tag{Eq 31}$$

The engineering strain rate is proportional to the crosshead velocity. In a modern testing machine, in which the crosshead velocity can be set accurately and controlled, it is a simple matter to carry out tension tests at a constant engineering strain rate.

The true strain rate is given by:

$$\dot{\epsilon} = \frac{d\epsilon}{dt} = \frac{d[\ln(L / L_0)]}{dt} = \frac{1}{L} \frac{dL}{dt} = \frac{v}{L} \tag{Eq 32}$$

Equation 32 shows that for a constant crosshead velocity the true strain rate will decrease as the specimen elongates or cross-sectional area shrinks. To run tension tests at a constant true strain rate requires monitoring the instantaneous cross section of the deforming region, with closed-loop control feed back to increase the crosshead velocity as the area decreases. The true strain rate is related to the engineering strain rate by the following equation:

$$\dot{\epsilon} = \frac{v}{L} = \frac{L_0}{L} \frac{de}{dt} = \frac{1}{1 + e} \frac{de}{dt} = \frac{\dot{\epsilon}}{1 + e} \tag{Eq 33}$$

The strain-rate dependence of flow stress at constant strain and temperature is given by:

$$\sigma = C (\dot{\epsilon})^m |_{\epsilon, T} \tag{Eq 34}$$

The exponent in Eq 34, m , is known as the strain-rate sensitivity, and C is the strain hardening coefficient. It can be obtained from the slope of a plot of $\log \sigma$ versus $\log \dot{\epsilon}$. However, a more sensitive way to determine m is with a rate-change test (Fig. 10). A tensile test is carried out at strain rate $\dot{\epsilon}_1$ and at a certain flow stress, σ_1 , the strain rate is suddenly increased to $\dot{\epsilon}_2$. The flow stress quickly increases to σ_2 . The strain-rate sensitivity, at constant strain and temperature, can be determined from:

$$m = \left(\frac{\partial \ln \sigma}{\partial \ln \dot{\epsilon}} \right)_{\epsilon, T} = \frac{\dot{\epsilon}}{\sigma} \left(\frac{\partial \sigma}{\partial \dot{\epsilon}} \right) = \frac{\Delta \log \sigma}{\Delta \log \dot{\epsilon}} \quad (\text{Eq 35})$$

$$= \frac{\log \sigma_2 - \log \sigma_1}{\log \dot{\epsilon}_2 - \log \dot{\epsilon}_1} = \frac{\log(\sigma_2 / \sigma_1)}{\log(\dot{\epsilon}_2 / \dot{\epsilon}_1)}$$

The strain-rate sensitivity of metals is quite low (<0.1) at room temperature, but m increases with temperature. At hot-working temperatures, $T/T_m > 0.5$, m values of 0.1 to 0.2 are common in metals. Polymers have much higher values of m , and may approach $m = 1$ in room-temperature tests for some polymers.

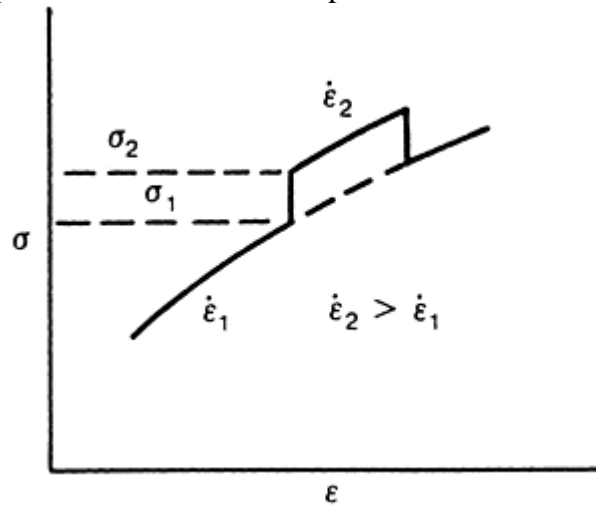


Fig. 10 Strain-rate change test, used to determine strain-rate sensitivity, m . See text for discussion

The temperature dependence of flow stress can be represented by:

$$\sigma = C_2 e^{Q/RT} \Big|_{\epsilon, \dot{\epsilon}} \quad (\text{Eq 36})$$

where Q is an activation energy for plastic flow, cal/g · mol; R is universal gas constant, 1.987 cal/K · mol; and T is testing temperature in kelvin. From Eq 36, a plot of $\ln \sigma$ versus $1/T$ will give a straight line with a slope Q/R .

Footnote

* Reprinted in part from *Mechanical Metallurgy*, 3rd ed., McGraw-Hill, New York, 1986, p 275–295, with permission

Mechanical Behavior Under Tensile and Compressive Loads*

George E. Dieter, University of Maryland

Instability in Tension

Necking generally begins at maximum load during the tensile deformation of a ductile metal. An exception to this is the behavior of cold-rolled zirconium tested at 200 to 370 °C (390–700 °F), where necking occurs at a strain of twice the strain at maximum load (Ref 13). An ideal plastic material in which no strain hardening occurs would become unstable in tension and begin to neck as soon as yielding occurred. However, an actual metal undergoes strain hardening, which tends to increase the load-carrying capacity of the specimen as deformation increases.

This effect is opposed by the gradual decrease in the cross-sectional area of the specimen as it elongates. Necking or localized deformation begins at maximum load, where the increase in stress due to decrease in the cross-sectional area of the specimen becomes greater than the increase in the load-carrying ability of the metal due to strain hardening. This condition of instability leading to localized deformation is defined by the condition $dP = 0$:

$$P = \sigma A \quad (\text{Eq 37})$$

$$dP = \sigma dA + A d\sigma = 0 \quad (\text{Eq 38})$$

From the constancy-of-volume relationship:

$$\frac{dL}{L} = -\frac{dA}{A} = d\epsilon \quad (\text{Eq 39})$$

and from the instability condition, Eq 38:

$$-\frac{dA}{A} = \frac{d\sigma}{\sigma} \quad (\text{Eq 40})$$

so that at a point of tensile instability:

$$\frac{d\sigma}{d\epsilon} = \sigma \quad (\text{Eq 41})$$

Therefore, the point of necking at maximum load can be obtained from the true stress-true strain curve by finding the point on the curve having a subtangent of unity (Fig. 11a), or the point where the rate of strain hardening equals the stress (Fig. 11b). The necking criterion can be expressed more explicitly if engineering strain is used. Starting with Eq 41:

$$\frac{d\sigma}{de} = \frac{d\sigma}{d\epsilon} \frac{de}{d\epsilon} = \frac{d\sigma}{d\epsilon} \frac{L_0}{L} = \frac{d\sigma}{d\epsilon} \frac{L}{L_0} = \frac{d\sigma}{d\epsilon} (1 + e) = \sigma \quad (\text{Eq 42})$$

$$\frac{d\sigma}{de} = \frac{\sigma}{1 + e}$$

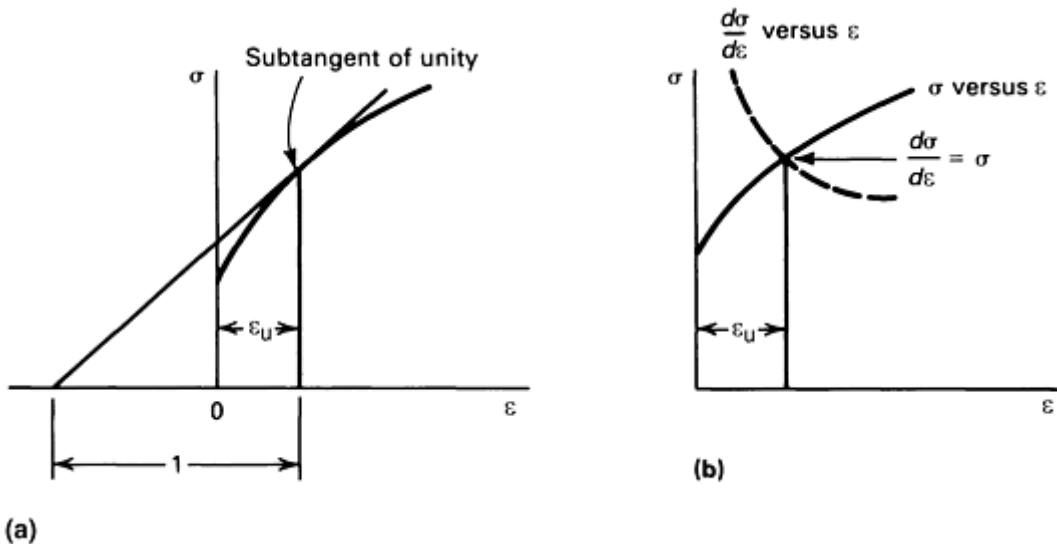


Fig. 11 Graphical interpretation of necking criterion. The point of necking at maximum load can be obtained from the true stress-true strain curve by finding (a) the point on the curve having a subtangent of unity or (b) the point where $d\sigma/d\epsilon = \sigma$.

Equation 42 permits an interesting geometrical construction for the determination of the point of maximum load (Ref 14). In Fig. 12, the stress-strain curve is plotted in terms of true stress against engineering strain. Let point A represent a negative strain of 1.0. A line drawn from point A, which is tangent to the stress-strain curve, will establish the point of maximum load because, according to Eq 42, the slope at this point is $\sigma/(1 + e)$.

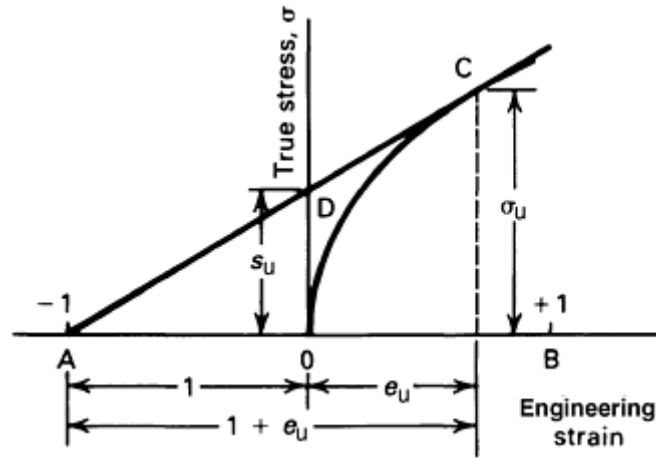


Fig. 12 Considérés construction for the determination of the point of maximum load.
Source: Ref 14

By substituting the necking criterion given in Eq 41 into Eq 26, a simple relationship for the strain at which necking occurs is obtained:

$$\epsilon_u = n \quad (\text{Eq 43})$$

Although Eq 26 is based on the assumption that the flow curve is given by Eq 25, it has been shown that $\epsilon_u = n$ does not depend on this power law behavior (Ref 15).

Footnote

* Reprinted in part from *Mechanical Metallurgy*, 3rd ed., McGraw-Hill, New York, 1986, p 275–295, with permission

References cited in this section

13. J.H. Keeler, *Trans. ASM*, Vol 47, 1955, p 157–192
14. A. Considère, *Ann. Ponts Chaussées*, Vol 9, 1885, p 574–775
15. G.W. Geil and N.L. Carwile, *J. Res. Natl. Bur. Stand.*, Vol 45, 1950, p 129

Mechanical Behavior Under Tensile and Compressive Loads*

George E. Dieter, University of Maryland

Stress Distribution at the Neck

The formation of a neck in the tensile specimen introduces a complex triaxial state of stress in that region. The necked region is in effect a mild notch. A notch under tension produces radial stress (σ_r) and transverse stress (σ_t) which raise the value of longitudinal stress required to cause the plastic flow. Therefore, the average true stress at the neck, which is determined by dividing the axial tensile load by the minimum cross-sectional area of the specimen at the neck, is higher than the stress that would be required to cause flow if simple tension prevailed.

Figure 13 illustrates the geometry at the necked region and the stresses developed by this localized deformation. R is the radius of curvature of the neck, which can be measured either by projecting the contour of the necked region on a screen or by using a tapered, conical radius gage.

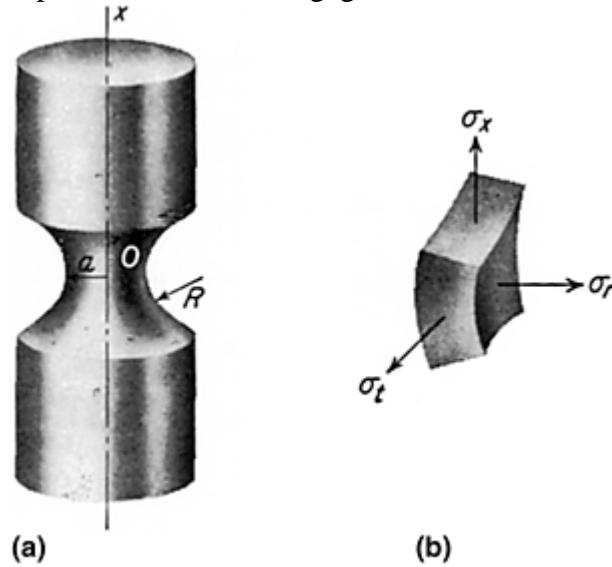


Fig. 13 Stress distribution at the neck of a tensile specimen. (a) Geometry of necked region. R is the radius of curvature of the neck; a is the minimum radius at the neck. (b) Stresses acting on element at point O. σ_x is the stress in the axial direction; σ_r is the radial stress; σ_t is the transverse stress.

Bridgman made a mathematical analysis that provides a correction to the average axial stress to compensate for the introduction of transverse stresses (Ref 16). This analysis was based on the following assumptions:

- The contour of the neck is approximated by the arc of a circle.
- The cross section of the necked region remains circular throughout the test.
- The von Mises criterion for yielding applies.
- The strains are constant over the cross section of the neck.

According to this analysis, the uniaxial flow stress corresponding to that which would exist in the tension test if necking had not introduced triaxial stresses is:

$$\sigma = \frac{(\sigma_x)_{\text{avg}}}{\left(\frac{1+2R}{a}\right) \left[\ln \left(1 + \frac{a}{2R} \right) \right]} \quad (\text{Eq 44})$$

where $(\sigma_x)_{\text{avg}}$ is the measured stress in the axial direction (load divided by minimum cross section) and a is the minimum radius at the neck. Figure 7 shows how the application of the Bridgman correction changes the true stress-true strain curve. A correction for the triaxial stresses in the neck of a flat tensile specimen has been considered (Ref 17). The values of a/R needed for the analysis can be obtained either by straining a specimen a given amount beyond necking and unloading to measure a and R directly, or by measuring these parameters continuously past necking using photography or a tapered ring gage (Ref 18).

To avoid these measurements, Bridgman presented an empirical relation between a/R and the true strain in the neck. Figure 14 shows that this gives close agreement for steel specimens, but not for other metals with widely different necking strains. A much better correlation is obtained between the Bridgman correction and the true strain in the neck minus the true strain at necking, ϵ_u (Ref 20).

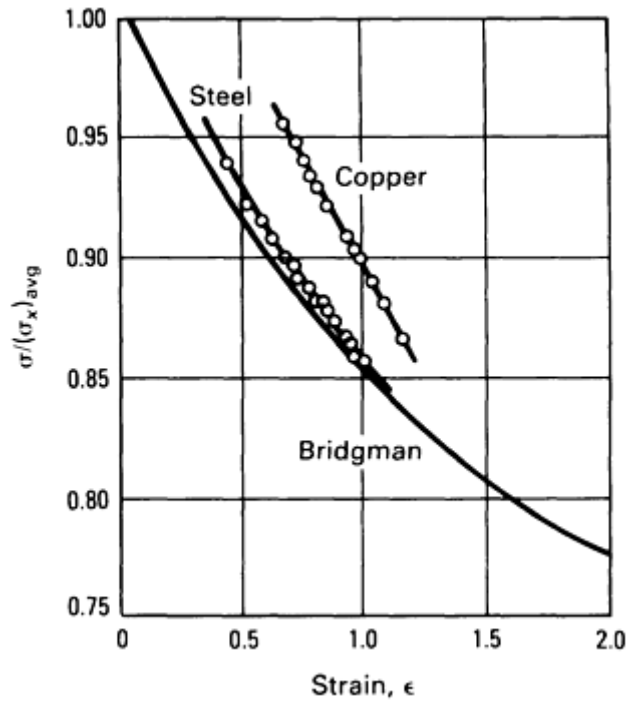


Fig. 14 Relationship between Bridgman correction factor $\sigma/(\sigma_x)_{avg}$ and true tensile strain.
Source: Ref 19

Dowling (Ref 21) has shown that the Bridgman correction factor B can be estimated from:

$$B = 0.83 - 0.186 \log \epsilon \quad (0.15 \leq \epsilon \leq 3) \quad (\text{Eq 45})$$

where $B = \sigma/(\sigma_x)_{avg}$.

Footnote

* Reprinted in part from *Mechanical Metallurgy*, 3rd ed., McGraw-Hill, New York, 1986, p 275–295, with permission

References cited in this section

16. P.W. Bridgman, *Trans. ASM*, Vol 32, 1944, p 553
17. J. Aronofsky, *J. Appl. Mech.*, Vol 18, 1951, p 75–84
18. T.A. Trozera, *Trans. ASM*, Vol 56, 1963, p 280–282
19. E.R. Marshall and M.C. Shaw, *Trans. ASM*, Vol 44, 1952, p 716
20. W.J. McG. Tegart, *Elements of Mechanical Metallurgy*, Macmillan, New York, 1966, p 22
21. N.E. Dowling, *Mechanical Behavior of Materials*, Prentice-Hall, Englewood Cliffs, NJ, 1993, p 165

Ductility Measurement in Tension Testing

The measured elongation from a tension specimen depends on the gage length of the specimen, or the dimensions of its cross section. This is because the total extension consists of two components: the uniform extension up to necking and the localized extension once necking begins. The extent of uniform extension depends on the metallurgical condition of the material (through n) and the effect of specimen size and shape on the development of the neck.

Figure 15 illustrates the variation of the local elongation, as defined in Eq 7, along the gage length of a prominently necked tensile specimen. The shorter the gage length, the greater the influence of localized deformation at the neck on the total elongation of the gage length. The extension of a specimen at fracture can be expressed by:

$$L_f - L_0 = \alpha + e_u L_0 \quad (\text{Eq 46})$$

where α is the local necking extension, and $e_u L_0$ is the uniform extension. The tensile elongation is then:

$$e_f = \frac{L_f - L_0}{L_0} = \frac{\alpha}{L_0} + e_u \quad (\text{Eq 47})$$

This clearly indicates that the total elongation is a function of the specimen gage length. The shorter the gage length, the greater the percent elongation.

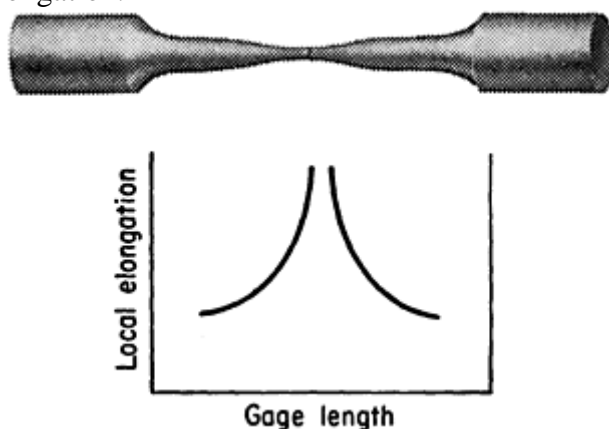


Fig. 15 Variation of local elongation with position along gage length of tensile specimen

Numerous attempts have been made to rationalize the strain distribution in the tension test. Perhaps the most general conclusion that can be drawn is that geometrically similar specimens develop geometrically similar necked regions. According to Barba's law (Ref 22), $\alpha = \beta \sqrt{A_0}$, and the elongation equation becomes:

$$e_f = \beta \frac{\sqrt{A_0}}{L_0} + e_u \quad (\text{Eq 48})$$

where β is a coefficient of proportionality.

To compare elongation measurements of different sized specimens, the specimens must be geometrically similar. Equation 48 shows that the critical geometrical factor for which similitude must be maintained is $L_0/\sqrt{A_0}$ for sheet specimens, or L_0/D_0 for round bars. In the United States, the standard round tensile specimen has a 12.8 mm (0.505 in.) diameter and a 50 mm (2 in.) gage length. Subsize specimens have the following respective diameter and gage length: 9.06 and 35.6 mm (0.357 and 1.4 in.), 6.4 and 25 mm (0.252 and 1.0 in.), and 4.06 and 16.1 mm (0.160 and 0.634 in.). Different values of $L_0/\sqrt{A_0}$ are specified for sheet specimens by the standardizing agencies in different countries. In the United States, ASTM recommends a $L_0/\sqrt{A_0}$ value of 4.5 for sheet specimens and a L_0/D_0 value of 4.0 for round specimens.

Generally, a given elongation will be produced in a material if $\sqrt{A_0}/L_0$ is maintained constant as predicted by Eq 48. Thus, at a constant value of elongation $\sqrt{A_1}/L_1 = \sqrt{A_2}/L_2$, where A and L are the areas and gage lengths of two different specimens, 1 and 2, of the same metal. To predict elongation using gage length L_2 on a specimen with area A_2 by means of measurements on a specimen with area A_1 , it only is necessary to adjust the

gage length of specimen 1 to conform with $L_1 = L_2 \sqrt{A_1/A_2}$. For example, suppose that a 3.2 mm (0.125 in.) thick sheet is available, and one wishes to predict the elongation with a 50 mm (2 in.) gage length for the identical material but in 2.0 mm (0.080 in.) thickness. Using 12.7 mm (0.5 in.) wide sheet specimens, a test specimen with a gage length $L = 50 \text{ mm} (3.2 \text{ mm}/2.0 \text{ mm})^{1/2} = 63 \text{ mm}$, or 2 in. $(0.125 \text{ in.}/0.080 \text{ in.})^{1/2} = 2.5 \text{ in.}$, made from the 3.2 mm (0.125 in.) sheet would be predicted to give the same elongation as a 50 mm (2 in.) gage length in 2.0 mm (0.080 in.) thick sheet. Experimental verification for this procedure has been shown in Ref 23.

The occurrence of necking in the tension test, however, makes any quantitative conversion between elongation and reduction in area impossible. Although elongation and reduction in area usually vary in the same way—for example, as a function of test temperature, tempering temperature, or alloy content—this is not always the case. Generally, elongation and reduction in area measure different types of material behavior. Provided the gage length is not too short, percent elongation is primarily influenced by uniform elongation, and thus it is dependent on the strain-hardening capacity of the material.

Reduction in area is more a measure of the deformation required to produce fracture, and its chief contribution results from the necking process. Because of the complicated stress state in the neck, values of reduction in area are dependent on specimen geometry and deformation behavior, and they should not be taken as true material properties. However, reduction in area is the most structure-sensitive ductility parameter, and as such, it is useful in detecting quality changes in the material.

Footnote

* Reprinted in part from *Mechanical Metallurgy*, 3rd ed., McGraw-Hill, New York, 1986, p 275–295, with permission

References cited in this section

22. M.J. Barba, *Mem. Soc. Ing. Civils*, Part 1, 1880, p 682

23. E.G. Kula and N.N. Fahey, *Mater. Res. Stand.*, Vol 1, 1961, p 631

Mechanical Behavior Under Tensile and Compressive Loads*

George E. Dieter, University of Maryland

Notch Tensile Test

Ductility measurements on standard smooth tensile specimens do not always reveal metallurgical or environmental changes that lead to reduced local ductility. The tendency for reduced ductility in the presence of a triaxial stress field and steep stress gradients (such as occur at a notch) is called notch sensitivity. A common way of evaluating notch sensitivity is a tension test using a notched specimen.

The notch tensile test has been used extensively for investigating the properties of high-strength steels, for studying hydrogen embrittlement in steels and titanium, and for investigating the notch sensitivity of high-temperature alloys. More recently, notched tension specimens have been used for fracture mechanics measurements (see the Section “Impact Toughness Testing and Fracture Mechanics” in this Volume). Notch sensitivity can also be investigated with the notched-impact test.

The most common notch tensile specimen uses a 60° notch with a root radius 0.025 mm (0.001 in.) or less introduced into a round (circumferential notch) or flat (double-edge notch) tensile specimen. Usually, the depth of the notch is such that the cross-sectional area at the root of the notch is one half of the area in the unnotched section. The specimen is aligned carefully and loaded in tension until fracture occurs. The notch strength is

defined as the maximum load divided by the original cross-sectional area at the notch. Because of the plastic constraint at the notch, this value will be higher than the tensile strength of an unnotched specimen if the material possesses some ductility. Therefore, the common way of detecting notch brittleness (or high notch sensitivity) is by determining the notch-strength ratio, NSR:

$$NSR = \frac{s_{net}(\text{for notched specimen at maximum load})}{s_u(\text{tensile strength for unnotched specimen})} \quad (\text{Eq 49})$$

If the NSR is less than unity, the material is notch brittle. The other property that is measured in the notch tensile test is the reduction in area at the notch.

As strength, hardness, or some metallurgical variable restricting plastic flow increases, the metal at the root of the notch is less able to flow, and fracture becomes more likely. Notch brittleness may be considered to begin at the strength level where the notch strength begins to fall or, more conventionally, at the strength level where the NSR becomes less than unity.

The sensitivity of notch strength for detecting metallurgical embrittlement is illustrated in Fig. 16. Note that the conventional elongation measured on a smooth specimen was unable to detect the fall in notch strength produced by tempering in the 330 to 480 °C (600–900 °F) range. For a more detailed review of notch tensile testing, see Ref 25.

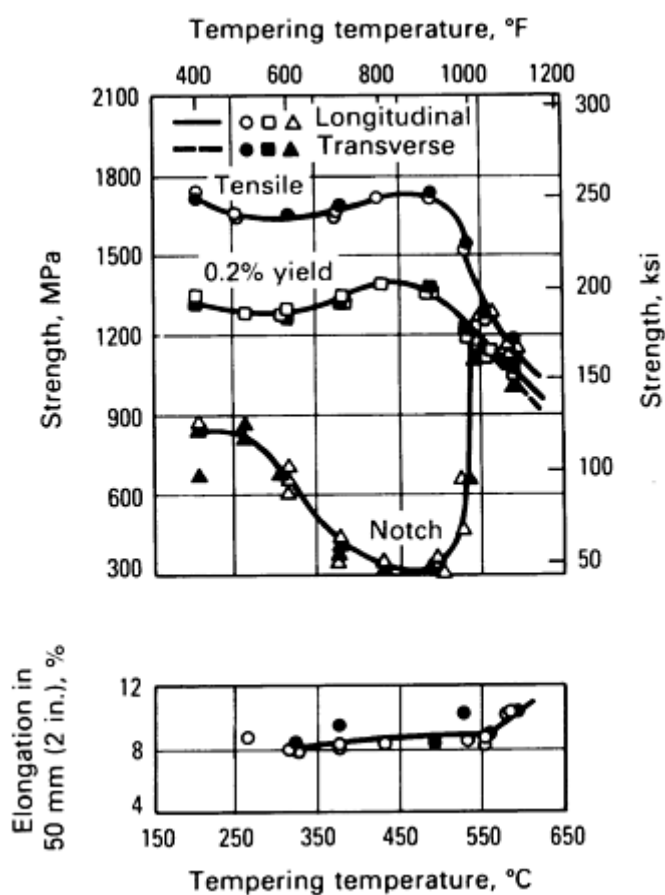


Fig. 16 Notched and unnotched tensile properties of an alloy steel as a function of tempering temperature. Source: Ref 24

Footnote

* Reprinted in part from *Mechanical Metallurgy*, 3rd ed., McGraw-Hill, New York, 1986, p 275–295, with permission

References cited in this section

24. G.B. Espey, M.H. Jones, and W.F. Brown, Jr., *ASTM Proc.*, Vol 59, 1959, p 837

Mechanical Behavior Under Tensile and Compressive Loads*

George E. Dieter, University of Maryland

Compression Test

The compression test consists of deforming a cylindrical specimen to produce a thinner cylinder of larger diameter (upsetting). The compression test is a convenient method for determining the stress-strain response of materials at large strains ($\epsilon > 0.5$) because the test is not subject to the instability of necking that occurs in a tension test. Also, it may be convenient to use the compression test because the specimen is relatively easy to make, and it does not require a large amount of material. The compression test is frequently used in conjunction with evaluating the workability of materials, especially at elevated temperature, because most deformation processes, like forging, have a high component of compressive stress. The test is also used with brittle materials, for which it is extremely difficult to machine a specimen and tensile test it in perfect alignment.

There are two inherent difficulties with the compression test that must be overcome by the test technique: buckling of the specimen and barreling of the specimen. Both conditions cause nonuniform stress and strain distributions in the specimen that make it difficult to analyze the results.

Buckling is a mode of failure characterized by an unstable lateral material deflection caused by compressive stresses. Buckling is controlled by selecting a specimen geometry with a low length-to-diameter ratio. L/D should be less than 2, and a compression specimen with $L/D = 1$ is often used. It also is important to have a very well aligned load train and to ensure that the end faces of the specimen are parallel and perpendicular to the load axis (Ref 26). Often a special alignment fixture is used with the testing machine to ensure an accurate load path (Ref 27).

Barreling is the generation of a convex surface on the exterior of a cylinder that is deformed in compression. The cross section of such a specimen is barrel shaped. Barreling is caused by the friction between the end faces of the compression specimen and the anvils that apply the load. As the cylinder decreases in height (h) it wants to increase in diameter (D) because of the volume of an incompressible material must remain constant. As

$$\frac{\pi}{4} D_1^2 h_1 = \frac{\pi}{4} D_2^2 h_2 \tag{Eq 50}$$

As the material spreads outward over the anvils, it is restrained by the friction at this interface. The material near the mid-height position is less restrained by friction and spreads laterally to the greatest extent. The material next to the anvil surfaces is restrained from spreading the most; hence, the creation of a barreled profile. This deformation pattern also leads to the development of a region of relatively undeformed materials under the anvil surfaces.

This deformation behavior clearly means that the stress state is not uniform axial compression. In addition to the axial compressive stress, a circumferential tensile stress develops as the specimen barrels (Ref 28). Because barreling increases with the specimen ratio D/h , the force to deform a compression cylinder increases with D/h (Fig. 17).

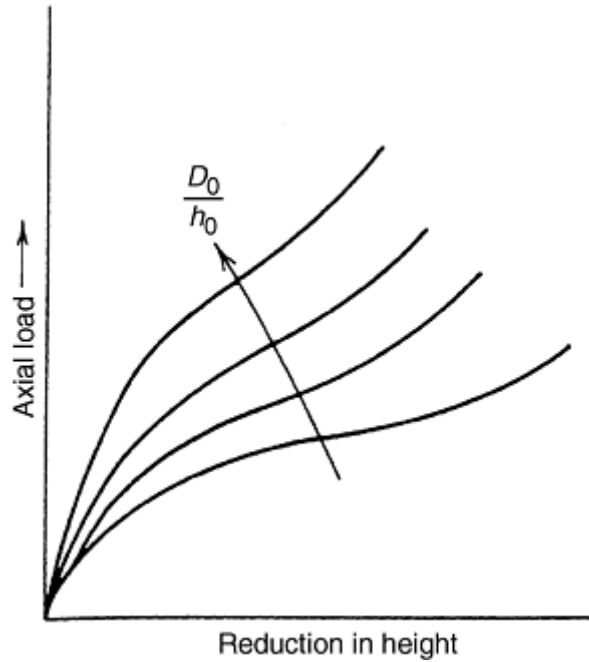


Fig. 17 Load-deformation curves for compression tests with specimens having different initial values of D/h

Calculation of Stress and Strain. The calculation of stress and strain for the compression test is based on developing a test condition that minimizes friction (and barreling) and assumes the stress state is axial compression. When friction can be neglected, the uniaxial compressive stress (flow stress) is related to the deformation force P by:

$$\sigma_f = \frac{P}{A} = \frac{4P}{\pi D^2} = \frac{4Ph_2}{\pi D_1^2 h_1} \quad (\text{Eq 51})$$

where the last term is obtained by substituting from Eq 50. In Eq 51 state 1 refers to the initial values of D and h , while state 2 refers to conditions at some subsequent value of specimen height, h . Equation 51 shows that the flow stress can be obtained directly from the load P and the instantaneous height (h_2), provided that friction can be neglected.

The true strain in the compression test is given by:

$$\epsilon = \ln\left(\frac{h_1}{h_2}\right) = 2 \ln\left(\frac{D_2}{D_1}\right) \quad (\text{Eq 52})$$

where either the displacement of the anvil or the diameter of the specimen can be used, whichever is more convenient.

Minimizing barreling of the compression specimen means minimizing friction on the ends of the specimen that are in contact with the anvils. This is done by using an effective lubricant and machining concentric rings on the end of the specimen to retain the lubricant and keep it from being squeezed out. An extensive series of tests have shown what works best (Ref 29).

Figure 18 shows the true stress-true strain curve (flow curve) for an annealed Al-2%Mg alloy. Stress and strain were calculated as described in the previous section. Note how the flow curve in compression agrees with that determined in a tensile test, and how the compressive curves extend to much larger strains because there is no specimen necking. Figure 19 extends the strain over double the range of Fig. 18. Note that once beyond $\epsilon > 0.5$ the curves begin to diverge depending on the effectiveness of the lubrication. The highest curve (greatest deviation from uniaxial stress) is for grooved anvils (platens) that dig in and prevent sidewise flow. The least friction is for the condition where a Teflon (E.I. Du Pont de Nemours & Co., Inc., Wilmington, DE) film sprayed with Molykote (Dow Corning Corporation, Midland, MI) is placed between the anvil and the specimen.

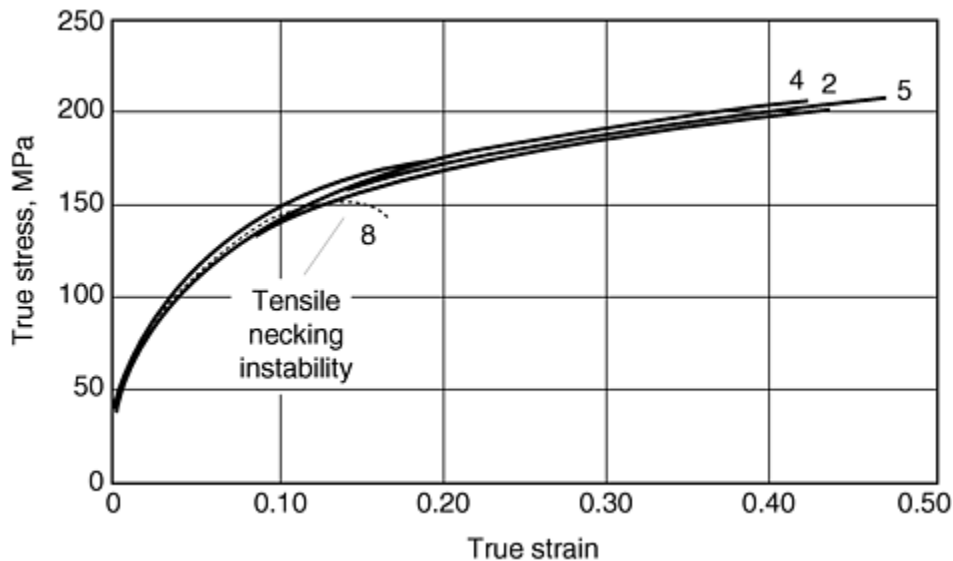


Fig. 18 Comparison of true stress-true strain curves in tension and compression (various lubricant conditions) for Al-2%Mg alloy. Curve 2, Molykote spray; curve 4, boron nitride + alcohol; curve 5, Teflon + Molykote spray; curve 8, tensile test. Source: Ref 29

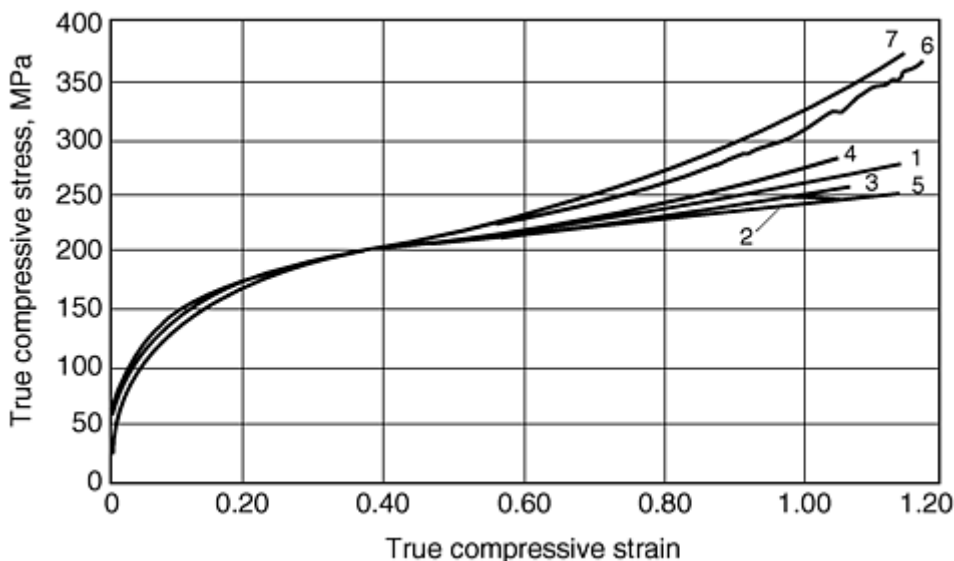


Fig. 19 Flow curves for Al-2%Mg alloy tested in compression for various lubricant conditions out to $\epsilon \approx 1.0$. Curve 1, molygrease; curve 2, Molykote spray; curve 3, boron-nitride spray; curve 4, boron-nitride and alcohol; curve 5, Teflon and Molykote spray; curve 6, polished dry anvils; curve 7, grooved anvils. Source: Ref 29

Essentially no barreling occurs in room-temperature compression tests when Teflon film is placed between the anvil and the end of the specimen. Because the film will eventually tear, it is necessary to run the test incrementally, and replace the film when an electrical signal indicates that there is no longer a continuous film. Obviously, the need to run the test incrementally is inconvenient. A series of single-increment compression tests on a range of materials with strain-hardening exponents from $n = 0.08$ to 0.49 showed that lubricant conditions do not become significant until $\epsilon > 0.5$ so long as $n > 0.15$. For strains out to $\epsilon = 1.0$, a grooved specimen with molybdenum disulfide (MoS_2) grease lubricant gave consistently good results. Nearly as good results are achieved with smooth anvils and a spray coat of MoS_2 (Ref 29).

For additional details on compression testing, see the article “Uniaxial Compression Testing” in this Volume. For information on hot compression testing and other forms of the compression test, see the article “Hot Tension and Compression Testing” in this Volume.

Footnote

* Reprinted in part from *Mechanical Metallurgy*, 3rd ed., McGraw-Hill, New York, 1986, p 275–295, with permission

References cited in this section

26. “Standard Methods of Compression Testing of Metallic Materials at Room Temperature,” E-9, *Annual Book of ASTM Standards*, ASTM, Philadelphia, PA
27. G. Sines, T. Okada, and S. Mack, Fixture for Accurate Load Path in Axial Compression, *Compression Testing of Homogeneous Materials and Composites*, R. Chait and R. Papirno, Ed., STP 808, ASTM, Philadelphia, PA, 1983, p 97–108
28. P. Dadras and J.F. Thomas, Deformation Inhomogeneities in Upset Forging, *Compression Testing of Homogeneous Materials and Composites*, R. Chait and R. Papirno, Ed., STP 808, ASTM, Philadelphia, PA, 1983, p 24–39
29. M.L. Lovato and M.G. Stout, *Met. Trans. A*, Vol 23, 1992, p 935–951

Mechanical Behavior Under Tensile and Compressive Loads*

George E. Dieter, University of Maryland

References

1. G.E. Dieter, Introduction to Ductility, in *Ductility*, American Society for Metals, 1968
2. P.G. Nelson and J. Winlock, *ASTM Bull.*, Vol 156, Jan 1949, p 53
3. D.J. Mack, *Trans. AIME*, Vol 166, 1946, p 68–85
4. P.E. Armstrong, Measurement of Elastic Constants, in *Techniques of Metals Research*, Vol V, R.F. Brunshaw, Ed., Interscience, New York, 1971
5. H.E. Davis, G.E. Troxell, and G.F.W. Hauck, *The Testing of Engineering Materials*, McGraw-Hill, New York, 1964, p 33
6. J.R. Low and F. Garofalo, *Proc. Soc. Exp. Stress Anal.*, Vol 4 (No. 2), 1947, p 16–25
7. J.R. Low, *Properties of Metals in Materials Engineering*, American Society for Metals, 1949
8. J. Datsko, *Material Properties and Manufacturing Processes*, John Wiley & Sons, New York, 1966, p 18–20
9. W.B. Morrison, *Trans. ASM*, Vol 59, 1966, p 824
10. D.C. Ludwigson, *Metall. Trans.*, Vol 2, 1971, p 2825–2828
11. H.J. Kleemola and M.A. Nieminen, *Metall. Trans.*, Vol 5, 1974, p 1863–1866
12. C. Adams and J.G. Beese, *Trans. ASME*, Series H, Vol 96, 1974, p 123–126

13. J.H. Keeler, *Trans. ASM*, Vol 47, 1955, p 157–192
14. A. Considère, *Ann. Ponts Chaussées*, Vol 9, 1885, p 574–775
15. G.W. Geil and N.L. Carwile, *J. Res. Natl. Bur. Stand.*, Vol 45, 1950, p 129
16. P.W. Bridgman, *Trans. ASM*, Vol 32, 1944, p 553
17. J. Aronofsky, *J. Appl. Mech.*, Vol 18, 1951, p 75–84
18. T.A. Trozera, *Trans. ASM*, Vol 56, 1963, p 280–282
19. E.R. Marshall and M.C. Shaw, *Trans. ASM*, Vol 44, 1952, p 716
20. W.J. McG. Tegart, *Elements of Mechanical Metallurgy*, Macmillan, New York, 1966, p 22
21. N.E. Dowling, *Mechanical Behavior of Materials*, Prentice-Hall, Englewood Cliffs, NJ, 1993, p 165
22. M.J. Barba, *Mem. Soc. Ing. Civils*, Part 1, 1880, p 682
23. E.G. Kula and N.N. Fahey, *Mater. Res. Stand.*, Vol 1, 1961, p 631
24. G.B. Espey, M.H. Jones, and W.F. Brown, Jr., *ASTM Proc.*, Vol 59, 1959, p 837
25. J.D. Lubahn, *Trans. ASME*, Vol 79, 1957, p 111–115
26. “Standard Methods of Compression Testing of Metallic Materials at Room Temperature,” E-9, *Annual Book of ASTM Standards*, ASTM, Philadelphia, PA
27. G. Sines, T. Okada, and S. Mack, Fixture for Accurate Load Path in Axial Compression, *Compression Testing of Homogeneous Materials and Composites*, R. Chait and R. Papirno, Ed., STP 808, ASTM, Philadelphia, PA, 1983, p 97–108
28. P. Dadras and J.F. Thomas, Deformation Inhomogeneities in Upset Forging, *Compression Testing of Homogeneous Materials and Composites*, R. Chait and R. Papirno, Ed., STP 808, ASTM, Philadelphia, PA, 1983, p 24–39
29. M.L. Lovato and M.G. Stout, *Met. Trans. A*, Vol 23, 1992, p 935–951

Footnote

* Reprinted in part from *Mechanical Metallurgy*, 3rd ed., McGraw-Hill, New York, 1986, p 275–295, with permission

Stress-Strain Behavior in Bending

P. Dadras, Wright State University (retired)

Introduction

A CHARACTERISTIC FEATURE of bending is the inhomogeneous (nonuniform) nature of the deformation. Therefore, in a bent specimen the strain and stress at a given point are dependent on the location of the point with respect to the neutral axis of the cross-sectional area of the specimen. In cases where the applied bending moment varies along the length of the specimen (as in three-point bending), the strains and stresses become dependent on axial location as well. Because of these inhomogeneities, a full appreciation of stress and strain distributions is of utmost importance in bending analyses and computations. Stress-strain relationships, strain curvature, and stress-moment equations are discussed in this article. The formulations are for elastic, elastic-plastic, and fully plastic bending conditions.

Stress-Strain Behavior in Bending

P. Dadras, Wright State University (retired)

Elastic Bending

Elastic analysis of bending deformation can be performed by simple-beam theory (Ref 1), elasticity solutions, and numerical methods such as the finite-difference and finite-element methods (Ref 2). Generally, numerical methods are suitable for bending of specimens that are subjected to complex loading patterns and that have irregular and/or varying cross-sectional areas. Elasticity solutions are useful when accuracies better than ~5% are desired. Simple-beam theory is used in most testing applications in which plates, strips, bars, and rods are bent in three-point or four-point bending modes. The basic assumptions of the simple-beam theory for pure elastic bending (shear force = 0) are: (a) all sections that are initially plane and perpendicular to the axis of the beam remain plane and perpendicular to it after bending; (b) all longitudinal elements (fibers) bend into concentric circular arcs (hence, cylindrical bending); and (c) a one-dimensional stress state is assumed, and the same stress-strain relationship is used for tension and compression.

The first assumption implies a linear distribution for fiber elongations and contractions, as shown in Fig. 1(a). The resulting strain distributions (Fig. 1b, c) are given by (engineering bending strain):

$$\epsilon_x = -\frac{y}{R_n} \quad (\text{Eq 1})$$

and (true bending strain):

$$\epsilon_x = \ln\left(1 - \frac{y}{R_n}\right) \quad (\text{Eq 2})$$

where R_n is the radius of curvature of the neutral axis. For $\epsilon_x \leq 0.1$, the difference between these two strain definitions is $\leq 5\%$. Therefore, for most elastic bendings, the engineering strain definition is sufficiently accurate and more convenient. As shown in Fig. 1, the true strain description indicates a nonlinear strain distribution and a maximum compressive strain in the concave inner fiber that is greater than the maximum tensile strain in the outermost fiber.

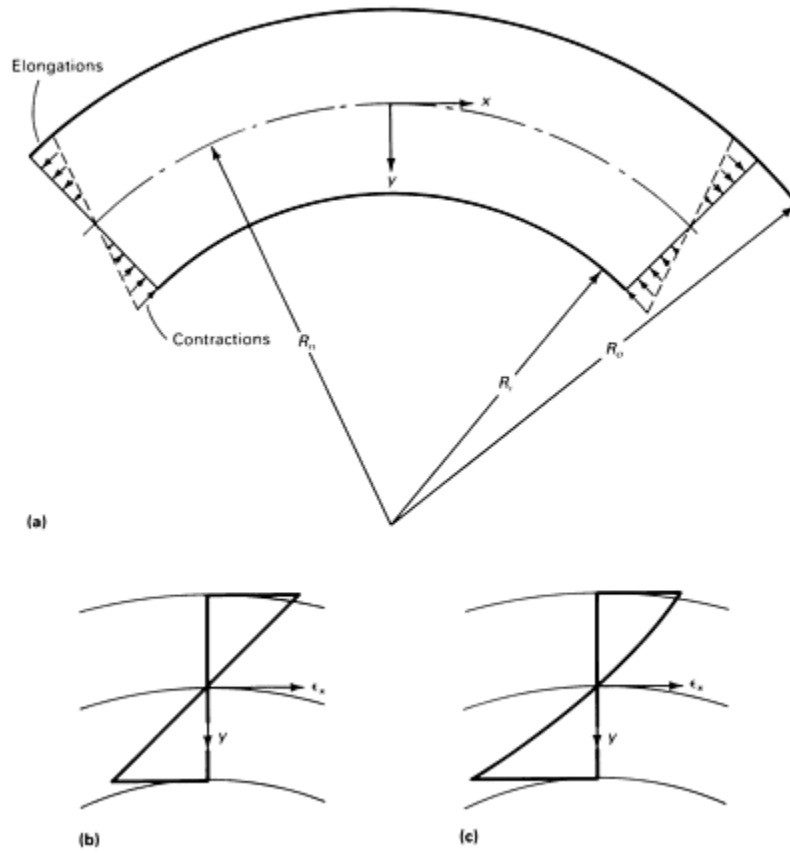


Fig. 1 Distribution of strain determined by the simple-beam theory. (a) Linear distribution for fiber elongations and contractions. (b) Distribution of engineering strain. (c) Distribution of true strain. R_n = radius of neutral axis; R_i = inner radius; R_o = outer radius

For a linear elastic material:

$$\epsilon_x = \frac{1}{E}[\sigma_x - \nu(\sigma_y + \sigma_z)] \quad (\text{Eq 3})$$

where E is the modulus of elasticity for axial loading (Young's modulus), and ν is Poisson's ratio. From the third assumption, $\sigma_y = \sigma_z = 0$. Therefore:

$$\sigma_x = -E \frac{y}{R_n} \quad (\text{Eq 4})$$

When expressions similar to Eq 3 are written for ϵ_z and ϵ_y , the following results are obtained:

$$\epsilon_z = \epsilon_y = \nu \frac{y}{R_n} \quad (\text{Eq 5})$$

Also:

$$\epsilon_{xy} = \epsilon_{yz} = \epsilon_{xz} = 0 \quad (\text{Eq 6})$$

Figure 2 illustrates grid deformations in the longitudinal and cross directions. A transverse curvature, called anticlastic curvature (Ref 3) develops with a radius of curvature equal to (R_n/ν) . Experimental evidence indicates that the actual radius of anticlastic curvature depends on $(b^2/2R_nh)$, where b is the width and $2h$ is the thickness of the beam. For $(b^2/2R_nh) \leq 1$ (i.e., narrow beams), the R_n/ν estimate is sufficiently accurate. For plates and wide beams ($b^2/2R_nh > 20$), the anticlastic deformation is primarily concentrated at the edges.

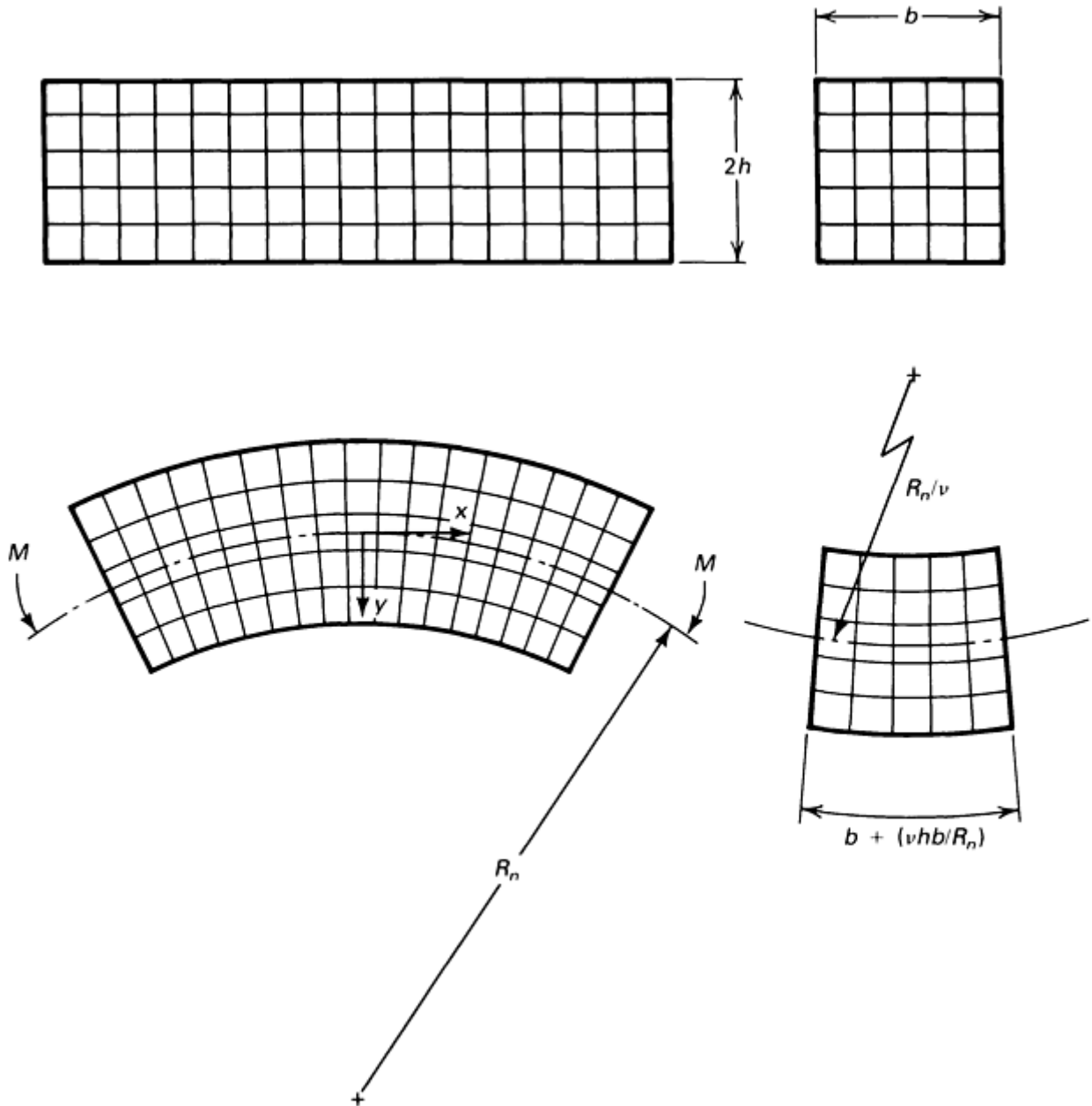


Fig. 2 Grid deformations in the longitudinal and cross directions of a beam

The location of the neutral axis, which is the line of zero fiber stress in any given section of a member subject to bending, is determined from the condition of zero axial forces acting on the beam. Therefore:

$$\int_A \sigma_x dA = -\frac{E}{R_n} \int_A y dA = 0 \quad (\text{Eq 7})$$

where A is the cross-sectional area. This equation indicates that the first moment of the cross-sectional area about the neutral axis is zero, which implies that the neutral and the central (centroidal) axes are coincident.

The moment-curvature and moment-stress relationships are found by equating the externally applied bending moment to the internal bending moment at any cross section:

$$M = -\int_A (\sigma_x dA) y \quad (\text{Eq 8})$$

where M is the bending moment.

For the linear stress distribution shown in Fig. 3, the results are:

$$R_n = \frac{E}{M} I_z \quad (\text{Eq 9})$$

and

$$\sigma_x = -\frac{My}{I_z} \quad (\text{Eq 10})$$

where I_z is the area moment of inertia of the cross section about the z axis, which is coincident on the centroidal axis.

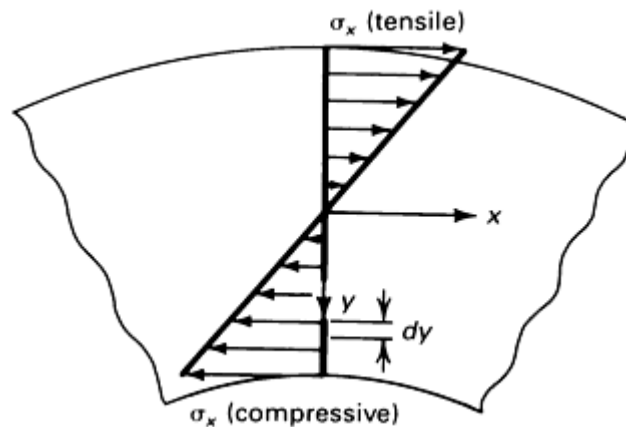


Fig. 3 Linear stress distributions in a beam

The sign (positive or negative) of the bending moment is found from the following relationship: (sign of the bending moment) = (sign of the moment vector) \times (sign of the outward normal to the section). For example, the bending moment acting on section $ABCD$ in Fig. 4 is positive, because the moment vector, \vec{M} , is in the positive z -direction (right-hand rule) and outward normal of the plane, \vec{n} , is also in the positive x -direction.

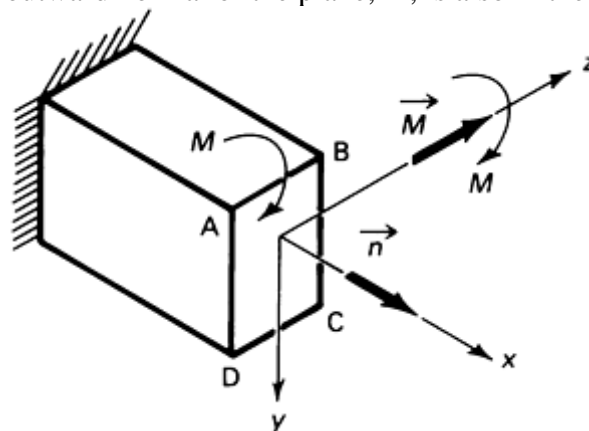


Fig. 4 Sign convention for the bending moment

References cited in this section

1. J.M. Gere and S.P. Timoshenko, *Mechanics of Materials*, 4th ed., PWS Publishing Co., 1997
2. A.C. Ugural and S.K. Fenster, *Advanced Strength and Applied Elasticity*, 3rd ed., Prentice Hall, 1995
3. D. Horrocks and W. Johnson, On Anticlastic Curvature with Special Reference to Plastic Bending: A Literature Survey and Some Experimental Investigations, *Int. J. Mech. Sci.*, Vol 9, 1967, p 835–861

Stress-Strain Behavior in Bending

P. Dadras, Wright State University (retired)

Noncylindrical Bending

In the previous section it was stated that the simple beam theory considers the effect of bending moments alone (shear force = 0) and assumes a bent configuration consisting of concentric circular arcs (cylindrical bending). For cylindrical bending to occur, these conditions must be met:

- Bending must occur under the action of bending moments alone, which implies zero applied shear force.
- The cross-sectional area of the beam must possess at least one axis of symmetry.
- The vector of the applied bending moment must be in the direction of an axis of symmetry.

For asymmetrical beams such as Z-sections and unequal L-sections, the second and third conditions for cylindrical bending are not satisfied; for unsymmetrical bending of symmetrical beams, the third condition is not met. These cases are significant in structural design and will not be considered here. Information on unsymmetrical loading of straight beams can be found in Ref 2.

In a majority of testing applications such as three-point bending, roll bending, and press-brake forming, the applied bending moment varies along the length of the specimen. Because shear force $V = (dM/dx)$, such variations in the bending moment imply a nonzero shear force. Therefore, condition 1 for cylindrical bending is not met. The resulting shear-stress, τ_{xy} , which is determined from the equilibrium considerations at a typical section $m-n$ (Fig. 5a), is:

$$\text{(Eq 11)}$$

where

$$Q = \int_{A_s} y dA \quad \text{(Eq 12)}$$

is the first moment of the shaded area (A_s) with respect to the neutral axis (Fig. 5b). The first moment of the unshaded area with respect to the neutral axis gives the same Q . The distribution of τ_{xy} for a rectangular cross section is shown in Fig. 5(c).

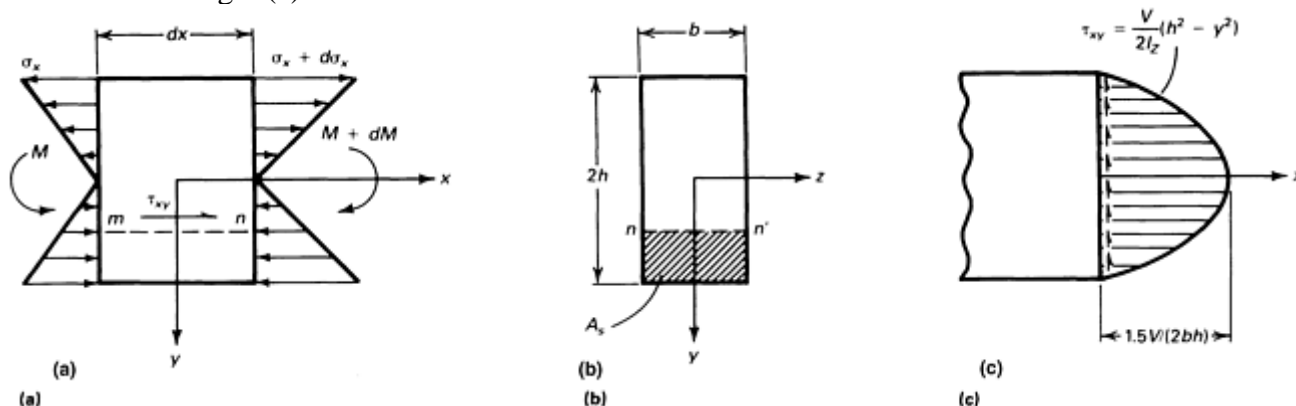


Fig. 5 Distribution of shear stress, τ_{xy} , for a rectangular specimen. See text for details.

Reference cited in this section

2. A.C. Ugural and S.K. Fenster, *Advanced Strength and Applied Elasticity*, 3rd ed., Prentice Hall, 1995

Stress-Strain Behavior in Bending

P. Dadras, Wright State University (retired)

Elastic-Plastic Bending

The limit for elastic bending, which is the onset of elastic-plastic bending, is reached when the maximum fiber strain $(\epsilon_x)_{\max} = (h/R_n)$ becomes equal to $9 (\sigma_y/E)$, where σ_y is the yield strength and E is Young's modulus of the material. For bending beyond this limit, the beam consists of a central elastic core and two plastically deforming zones remote from the neutral axis. For accurate analysis of elastic-plastic bending, factors such as the shift of the neutral axis from the centroidal axis and the effect of radial (transverse) stresses must be considered. Elastic-perfect plastic (Ref 4) and elastic-linear hardening (Ref 5) analyses are available. However, in view of analytical and computational difficulties, an approximate method, which is an extension of the simple-beam theory, is commonly employed. Therefore, the three assumptions stated for elastic bending will be enforced. The location of the neutral axis is assumed to be fixed at the centroidal axis, as it is for elastic bending.

For a beam with the stress-strain curve shown in Fig. 6(a), the development of longitudinal strain and stress at different stages of deformation is shown in Fig. 6(b) and 6(c), respectively. In Fig. 6(b), a linear strain distribution given by $\epsilon_x = (-y/R_n)$ was used. When the strain at the outermost fiber exceeds 0.1, it is suggested that the true strain distribution (Eq 2) be used. For bending to a radius of curvature equal to R_n , the strain distribution and the subsequent stress distribution (from the $\sigma - \epsilon$ curve or from a known constitutive equation for the $\sigma - \epsilon$ dependence) can be found. The moment, M , required to produce R_n is:

$$M = - \int_A (\sigma_x dA) y \quad (\text{Eq 13})$$

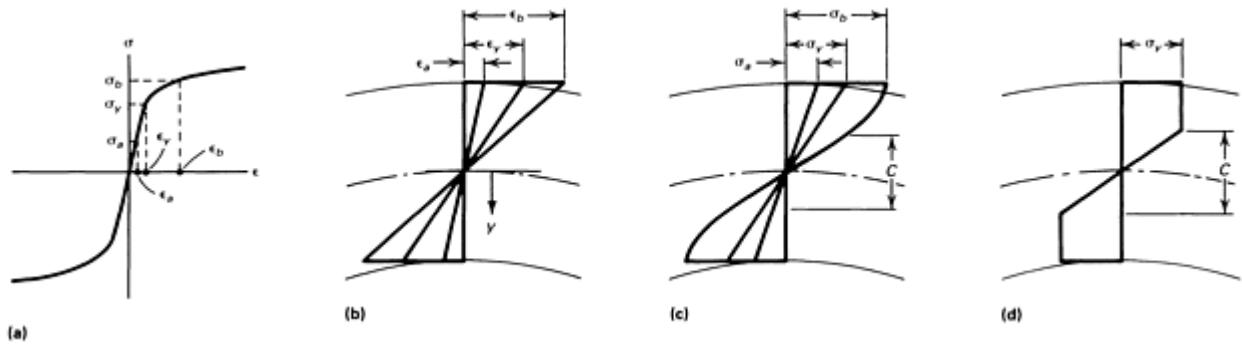


Fig. 6 Stress-strain distributions in a beam. (a) Stress-strain curve. (b) Strain distribution. (c) Stress distribution. (d) Stress distribution for elastic-perfect plastic material

The thickness of the elastic core, C (Fig. 6c), is:

$$C = 2R_n \left(\frac{\sigma_y}{E} \right) \quad (\text{Eq 14})$$

Therefore, in bending plates of the same material to the same radius of curvature R_n , the fractional thickness of the elastic core $C/2h$ becomes smaller as the thickness increases.

For elastic-plastic bending, a general equation for the relationship between R_n and M (analogous to Eq 9 for the elastic case) does not exist. For the simple case of an elastic-perfect plastic material (Fig. 6d), the following equation is obtained:

$$R_n = \frac{E}{\sigma_y} \left[3 \left(\frac{\sigma_y b h^2 - M}{b \sigma_y} \right) \right]^{1/2} \quad (\text{Eq 15})$$

The predictions of this equation at large plastic deformations ($C/2h \leq 0.02$) are not reliable.

References cited in this section

4. J. Chakrabarty, *Theory of Plasticity*, McGraw-Hill, 1987
5. P. Dadras, Plane Strain Elastic-Plastic Bending of a Strain-Hardening Curved Beam, *Int. J. Mech. Sci.*, in press Nov 2000

Pure Plastic Bending

The fractional thickness of the elastic core decreases as the ratio $R_n/2h$ decreases. For $R_n/2h \leq 10$, the thickness of the elastic core in a hot rolled strip of AISI 1020 steel is $\leq 3.2\%$. In such cases it is possible to ignore the elastic core altogether and use the analysis for pure plastic bending.

Most plastic bending analyses are for sheet-type specimens in which b is much greater than $2h$. The width strain is small for such a geometry and plane-strain bending deformation ($\epsilon_z = 0$) is commonly assumed. Also, the first two assumptions of the simple-beam theory are still applied. However, the radial (transverse) stresses and strains induced by higher curvatures are considered, and a plane-in state, rather than a one-dimensional stress state (the third assumption of the simple-beam theory), is assumed. Also, the neutral axis is not fixed at the centroid, and thickness variations due to bending sometimes are incorporated into the solution. Figure 7 shows the geometry of deformation and the strain and stress states at different zones.

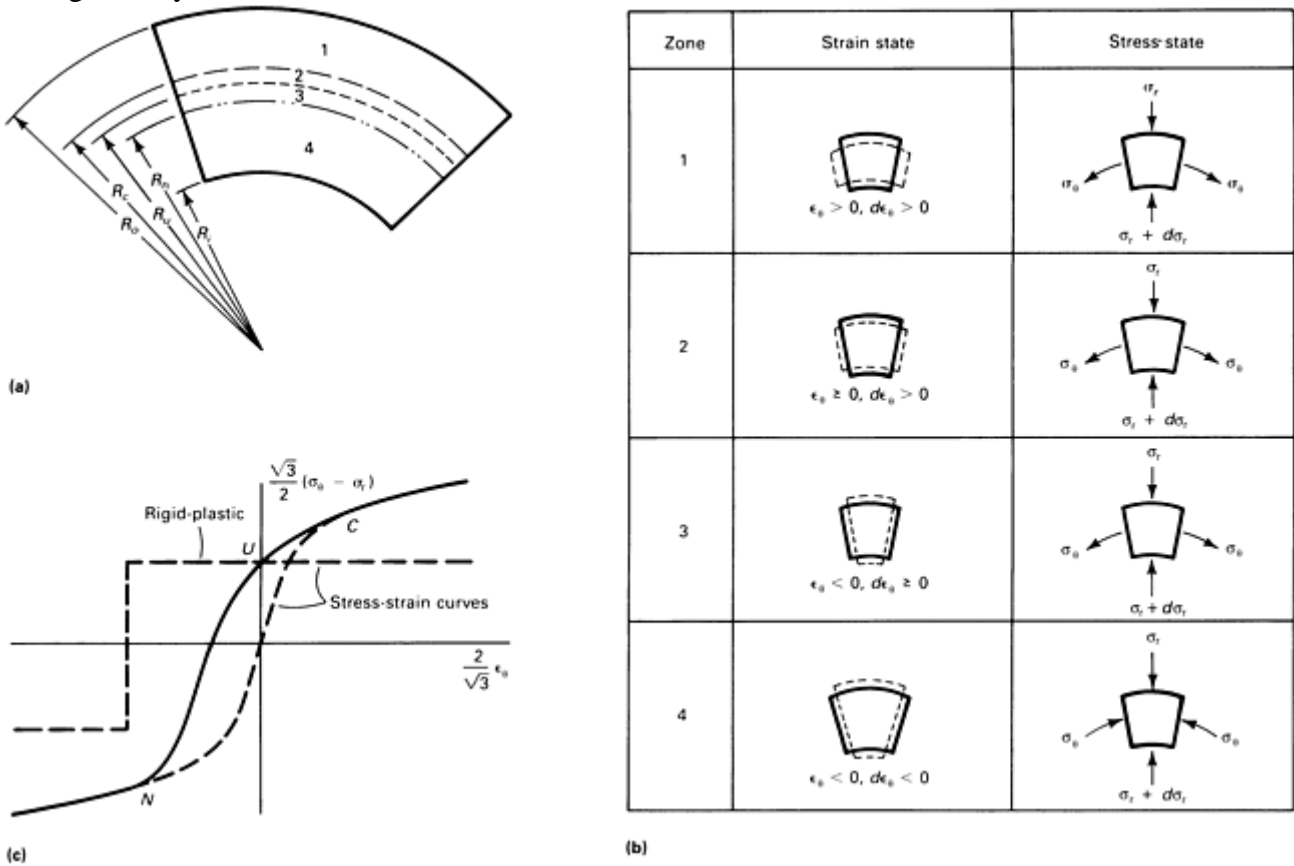


Fig. 7 Pure plastic bending of strip specimen. (a) Geometry of deformation. R_i = inner radius of curvature; R_o = outer radius of curvature; R_n = radius of curvature of the neutral axis; R_u = radius of currently unstretched fiber; R_c = current radius of curvature of original center fiber. (b) Strain and stress states in different zones.---, deformed state. $\epsilon_\theta = \ln r/R_n$ is the circumferential strain. (c) Stress-strain curves and stress-strain states at various locations. N = stress-strain state at R_n ; U = stress-strain state at R_u ; C = stress-strain state at R_c .

At the onset of the assumed full plastic condition, $R_c = R_n = R_u$. In the current state, the fiber with radius of curvature equal to R_n is being overtaken by the neutral axis and is experiencing unloading from a compressive tangential stress field. Accordingly, all fibers below the neutral axis $r \leq R_n$ have been progressively compressed, while those situated above R_c have been consistently stretched during deformation. All fibers in the interval R_n

$\leq r < R_c$ have been overtaken by the neutral axis. Fibers between $R_u < r < R_c$ have now been stretched beyond their original length due to reverse loading, while those located in $R_n \leq r \leq R_u$ have yet to recover their original undeformed length.

As expected, a comprehensive analysis accounting for the described fiber movements is very complicated (Ref 6). A compromise solution (Ref 7), which ignores thickness variations and assumes rigid-perfect plastic material behavior, provides useful approximations for the stress-strain distributions in plastic bending.

When a rigid-perfect plastic material model is used (Fig. 7c), the same stress-strain relationship applies to all fibers with $r \geq R_n$. As a result, the distinction among R_n , R_u , and R_c becomes inconsequential. This eliminates the complicated task of describing the behavior of fibers in reversed loading and the Bauschinger effect.

The state of stress acting on a typical element is shown in Fig. 8, where σ_θ is the circumferential (tangential) stress, and σ_r is the radial (transverse) stress. The equilibrium equation for plane strain deformation is:

$$\frac{d\sigma_r}{dr} = \frac{\sigma_\theta - \sigma_r}{r} \quad (\text{Eq 16})$$

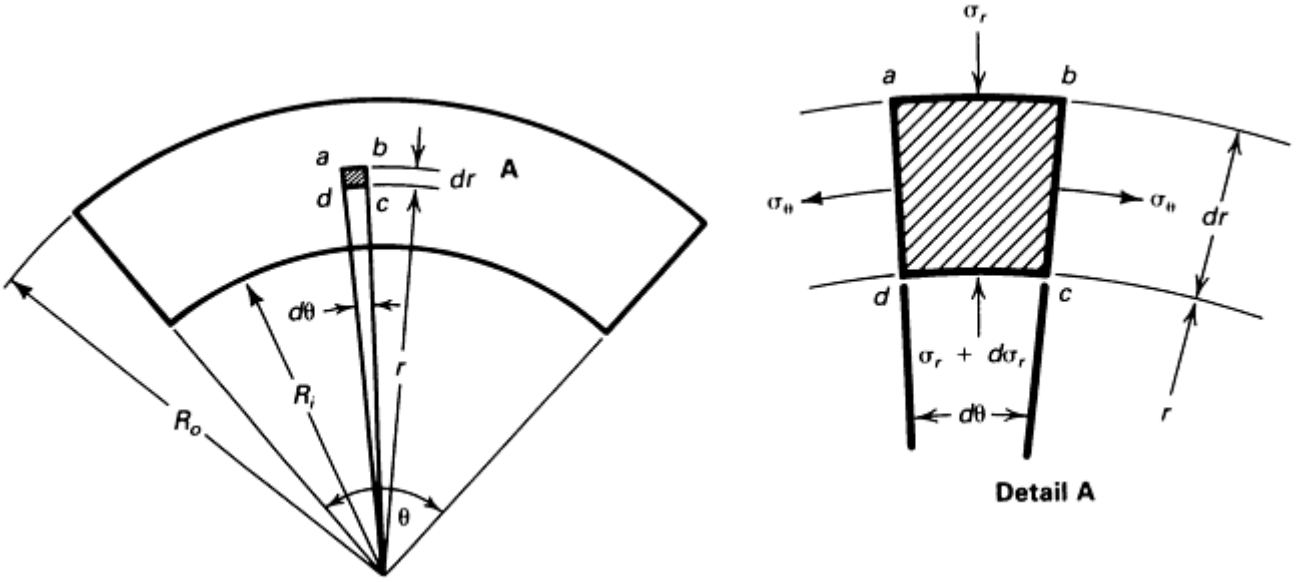


Fig. 8 State of stress acting on a typical element in plane-strain bending

The effective or significant stress, $\bar{\sigma}$, and strain, $\bar{\epsilon}$, for plane strain deformation, using von Mises criterion, are, respectively:

$$\bar{\sigma} = \pm \frac{\sqrt{3}}{2} (\sigma_\theta - \sigma_r) \quad \begin{array}{l} (+) \text{ for } R_o \geq r \geq R_n \\ (-) \text{ for } R_n > r > R_i \end{array} \quad (\text{Eq 17})$$

and

$$\bar{\epsilon} = \frac{2}{\sqrt{3}} |\epsilon_\theta| \quad (\text{Eq 18})$$

where $\epsilon_\theta = \ln r/R_n$. Substituting $(\sigma_\theta - \sigma_r)$ from Eq 16 into Eq 15 and putting $\sigma_r = 0$ at $r = R_o$ and $r = R_i$, these equations for the distribution of σ_r are obtained:

$$\sigma_r = - \left(\frac{2\bar{\sigma}}{\sqrt{3}} \right) \ln \left(\frac{R_o}{r} \right) \quad \text{for } R_n \leq r \leq R_o \quad (\text{Eq 19})$$

$$\sigma_r = - \left(\frac{2\bar{\sigma}}{\sqrt{3}} \right) \ln \left(\frac{r}{R_i} \right) \quad \text{for } R_i \leq r \leq R_n \quad (\text{Eq 20})$$

From the expressions for σ_r and Eq 16, the following expressions for σ_θ are determined:

$$\sigma_\theta = - \left(\frac{2\bar{\sigma}}{\sqrt{3}} \right) \left[1 - \ln \left(\frac{R_o}{r} \right) \right] \quad \text{for } R_n \leq r \leq R_o \quad (\text{Eq 21})$$

$$\sigma_{\theta} = -\left(\frac{2\bar{\sigma}}{\sqrt{3}}\right)\left[1 + \ln\left(\frac{r}{R_i}\right)\right] \quad \text{for } R_i \leq r \leq R_n \quad (\text{Eq 22})$$

Because of equilibrium considerations, the radial stress must be continuous at $r = R_n$. Applying this condition to Eq 19 and 20, the location of the neutral axis can be found:

$$R_n = \sqrt{R_i R_o} \quad (\text{Eq 23})$$

Figure 9 is a schematic of the distributions of σ_r and σ_{θ} . In the figure, σ_r is continuous and compressive throughout the plate thickness, while σ_{θ} changes from tension to compression at the neutral axis. The bending moment, which according to this solution is independent of R_n , becomes:

$$M = \int_{R_i}^{R_o} (\sigma_{\theta} b dr) r = \left(\frac{2}{\sqrt{3}}\right) \bar{\sigma} b h^2 \quad (\text{Eq 24})$$

where h is half thickness, and b is the plate width.

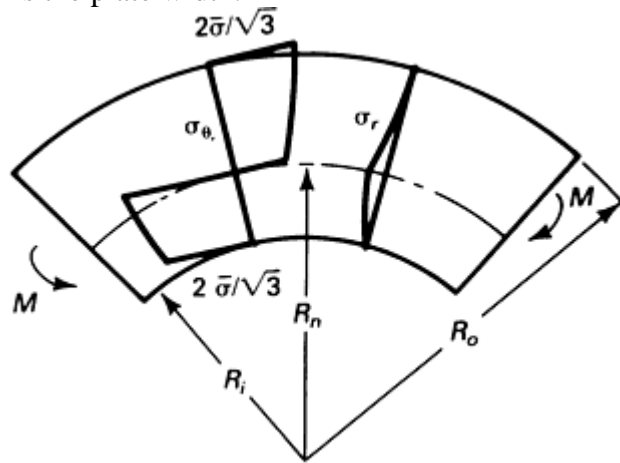


Fig. 9 Schematic of circumferential, σ_{θ} , and radial, σ_r , stresses in a plate during bending. Source: Ref 7

The maximum radial stress occurs at the neutral axis. Its magnitude from Eq 19 and 23 is:

$$(\sigma_r)_{\max} = -\left(\frac{\bar{\sigma}}{\sqrt{3}}\right) \ln\left(\frac{R_o}{R_i}\right) \quad (\text{Eq 25})$$

The ratio between $(\sigma_r)_{\max}$ and the tangential stress at $r = R_o$ for four plates of different thicknesses, all bent to an inside radius of $R_i = 25$ mm (1 in.), is given in Table 1. This table shows that for plastic bending to $(R_n/2h) > 10$, the magnitude of $(\sigma_r)_{\max}$ becomes very small. In such cases, the effect of σ_r can be neglected in the analysis and the elastic-plastic bending solution based on the simple-beam theory can be used.

Table 1 Ratio between maximum radial stress and tangential stress for plate of various thicknesses

R_i	Thickness		$R_n / 2h$	$\sigma_r \max /$	
mm	in.	mm	in.	$(\sigma_{\theta} \text{ at } r = R_n)$	
25	1	1.59	0.0625	16.49	0.030
25	1	3.17	0.125	8.48	0.059
25	1	6.35	0.25	4.47	0.112
25	1	12.7	0.5	2.45	0.203

See text for explanation of symbols

More elaborate analyses of plastic bending (Ref 6 and 8) commonly involve complicated numerical computations. Hence, no equations can be given. A comparison between the results of the analysis in Ref 7 and a solution for rigid work-hardening material behavior (Ref 6) is shown in Fig. 10. In this case, the result from Ref 6 is for a model material with a high rate of strain hardening.

$$\bar{\sigma} = 70 + 300\bar{\epsilon}^{0.5} \text{ MPa} \quad (\text{Eq 26})$$

In using the analysis from Ref 6, $\bar{\sigma} = 120 \text{ MPa}$ (17.4 ksi), which is the approximate average flow stress for bending to $\bar{\epsilon} = 0.11$, and $\bar{\sigma} = 169.5 \text{ MPa}$ (24.6 ksi), as shown in Fig. 10(b), have been assumed. As expected, some differences in the predicted stress distributions are observed.

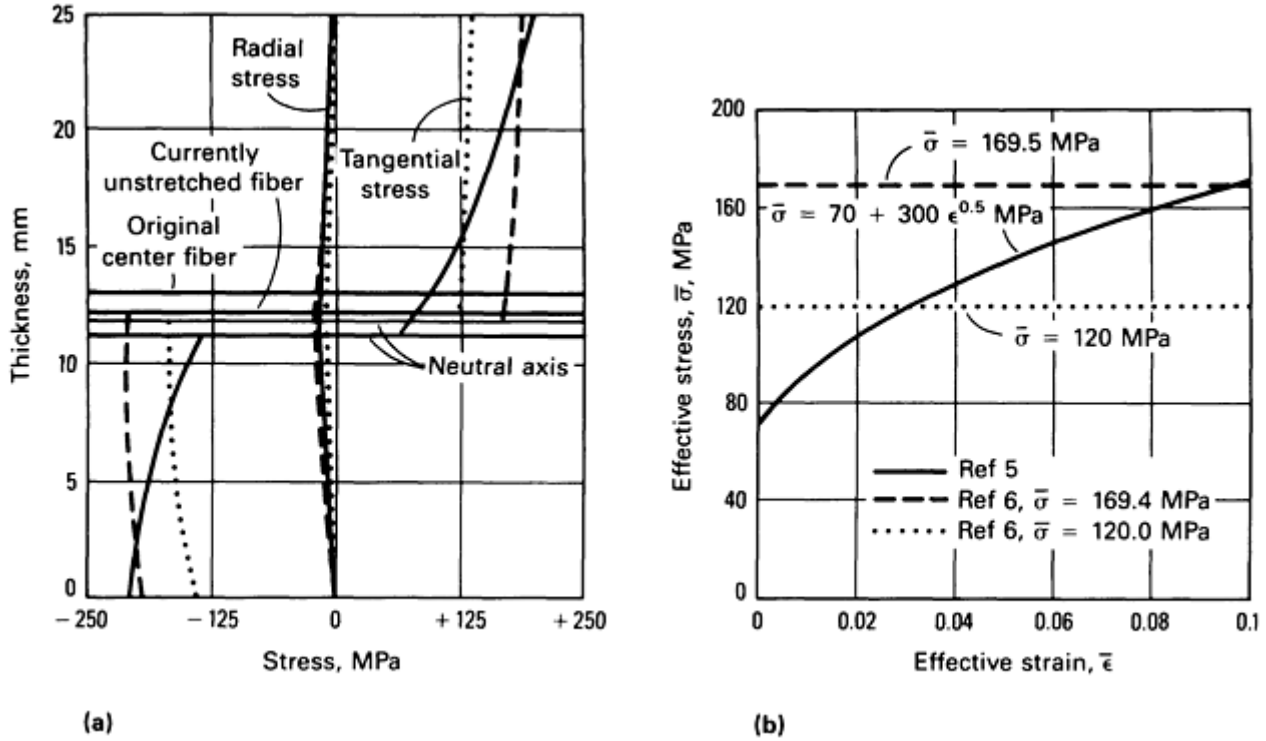


Fig. 10 Comparison of results for determining plastic bending in a plate. (a) Distribution of tangential and radial stresses for a 25 mm (1 in.) thick plate bent to $R_i = 100 \text{ mm}$ (4 in.). (b) Stress-strain diagrams used in the analyses for (a)

However, by using $\bar{\sigma} = 169.5 \text{ MPa}$ (24.6 ksi) in the solution from Ref 6, a close agreement (percent different < 6) between the estimates for the fiber stresses at $r = R_i$ and $r = R_o$ is obtained. Because the prediction of maximum fiber stress and strain is of special interest, the following procedure based on the solution in Ref 6 is suggested. First, find the maximum fiber strain:

$$\epsilon_o = -\epsilon_i = \ln \sqrt{\frac{R_o}{R_i}} \quad (\text{Eq 27})$$

where ϵ_o and ϵ_i represent the maximum fiber strain at the outer and inner radii, respectively. Using the stress-strain equation or stress-strain curve for the material, determine $\bar{\sigma}$ as the flow stress at ϵ_o . The maximum fiber stress is $2\bar{\sigma}/\sqrt{3}$.

References cited in this section

6. P. Dadras and S.A. Majlessi, Plastic Bending of Work Hardening Materials, *ASME Trans. J. Eng. Ind.*, Vol 104, 1982, p 224–230
7. R. Hill, *The Mathematical Theory of Plasticity*, Oxford University Press, London, 1950
8. H. Verguts and R. Sowerby, The Pure Plastic Bending of Laminated Sheet Metals, *Int. J. Mech. Sci.*, Vol 17, 1975, p 31

Residual Stress and Springback

When a specimen that has been bent beyond the elastic limit is unloaded, the applied moment M becomes zero, and the radius of curvature increases from R_n to R'_n . For a fiber at distance y from the neutral axis, this produces a strain difference:

$$\Delta\varepsilon_x = y\left(\frac{1}{R_n} - \frac{1}{R'_n}\right) \quad (\text{Eq 28})$$

The removal of the bending moment, which is an unloading event, is assumed to be elastic. Therefore:

$$\Delta\sigma_x = E\Delta\varepsilon_x = Ey\left(\frac{1}{R_n} - \frac{1}{R'_n}\right) \quad (\text{Eq 29})$$

The change in bending moment for complete unloading is $\Delta M = M$, where M is the applied bending moment prior to unloading. Therefore:

$$\int_A \left[Ey\left(\frac{1}{R_n} - \frac{1}{R'_n}\right) dA \right] y = - \int_A (\sigma_x dA) y \quad (\text{Eq 30})$$

which reduces to

$$\frac{1}{R_n} - \frac{1}{R'_n} = - \frac{\int_A \sigma_x y dA}{EI_z} \quad (\text{Eq 31})$$

The distribution of the residual stresses can be found from either of the following equations:

$$\sigma'_x = \sigma_x + \Delta\sigma_x = \sigma_x - \left(\frac{y}{I_z}\right) \int_A \sigma_x y dA \quad (\text{Eq 32})$$

$$\sigma'_x = \sigma_x + yE\left(\frac{1}{R_n} - \frac{1}{R'_n}\right) \quad (\text{Eq 32a})$$

It is important that the correct signs for σ_x and y be used when applying these equations.

As an example, the springback and the residual stress distribution of a strip of annealed 1095 steel was examined (Ref 9). For this material, yield strength is $\sigma_y = 308$ MPa (44.7 ksi), Poisson's ratio is $\nu = 0.28$, and the approximate constitutive equation for σ in metric units of measure is:

$$\bar{\sigma} = (2 \times 10^5 \text{ MPa})\varepsilon \text{ for } \varepsilon \leq 0.00154 \quad (\text{Eq 33})$$

$$\bar{\sigma} = (896 \text{ MPa})\varepsilon^{0.16} \text{ for } \varepsilon \geq 0.00154 \quad (\text{Eq 34})$$

In English units of measure, σ is:

$$\bar{\sigma} = (29 \times 10^6 \text{ psi})\varepsilon \text{ for } \varepsilon \leq 0.00154$$

$$\bar{\sigma} = (126 \text{ ksi})\varepsilon^{0.16} \text{ for } \varepsilon \geq 0.00154$$

The width of the strip, b , is 50 mm (2 in.), and its thickness, $2h$, is 5 mm (0.2 in.). It is assumed that the strip is bent to $R_n = 100$ mm (4 in.). Because $(b/2h) = 10$, plane-strain deformation prevails. Because of this, the elastic modulus in plane-strain

$$E' = \frac{E}{1 - \nu^2} \quad (\text{Eq 35})$$

is employed, and the plastic flow stresses (Eq 34) are multiplied by $(2 / \sqrt{3})$. These approximate plane-strain adjustments are considered adequate when the simplified elastic-plastic analysis, which was discussed earlier in this article, is used. The thickness of the elastic core in metric units of measure is:

$$C = \frac{2R_n\sigma_y}{E'} = 2(100) \frac{(2 \times 308)/\sqrt{3}}{2.17 \times 10^5} \quad (\text{Eq 36})$$

$$C = 0.33 \text{ mm}$$

In English units of measure, the thickness of the elastic core is:

$$C = \frac{2R_n\sigma_y}{E'} = \frac{2(3.937) \left(2 \times \frac{44.7}{\sqrt{3}} \right)}{(31465)}$$

$$C = 0.013 \text{ in.}$$

which is 6.6% of the total plate thickness. The final radius of curvature in metric units of measure after springback is found from Eq 31:

$$\begin{aligned} \frac{1}{100} - \frac{1}{R'_n} = & - \frac{2}{El_z} \\ & \times \left[\int_0^{C/2} -2.17 \times 10^5 \left(\frac{y}{100} \right) b \, dy \right. \\ & \left. + \int_{C/2}^h - \left(\frac{2}{\sqrt{3}} \right) 869 \left(\frac{y}{100} \right)^{0.16} b y \, dy \right] \end{aligned} \quad (\text{Eq 37})$$

which results in $R'_n = 116.9 \text{ mm}$ (4.60 in.). A more elaborate analysis of springback (Ref 9) for this case predicts $R'_n/2h = 23.41$ (or $R'_n = 117.05 \text{ mm}$, or 4.608 in.). Also, for bending the same strip to $R_n = 40 \text{ mm}$ (1.6 in.) and $R_n = 500 \text{ mm}$ (19.7 in.), the final radii of curvature from Eq 31 are 42.8 mm (1.68 in.) and 1150 mm (45.3 in.), respectively. The corresponding results from Ref 9 are 42.9 mm (1.69 in.) and 1075 mm (42.3 in.). The distribution of residual stresses after bending to $R_n = 100 \text{ mm}$ (3.937 in.) is obtained from Eq 32a(a). Therefore, in this case, in metric units:

$$\sigma'_x = \sigma_x + yE(0.0014457) \quad (\text{Eq 38})$$

In English units:

$$\sigma'_x = \sigma_x + yE(0.03672)$$

At $R = R_i$, $y = h = 2.5 \text{ mm}$ (0.098 in.):

$$\varepsilon_x = -0.025$$

and

$$\sigma_x = - \left(\frac{2}{\sqrt{3}} \right) (869) (0.025)^{0.16} = -556 \text{ MPa}$$

or

$$\sigma_x = - \left(\frac{2}{\sqrt{3}} \right) (126) (0.025)^{0.16} = -80.63 \text{ ksi}$$

For this location:

$$\begin{aligned} \sigma'_x = & -556 + 2.5(2.17 \times 10^5) \\ & \times (0.0014457) = +228 \text{ MPa} \end{aligned}$$

or

$$\sigma'_x = -80.63 + 0.098 (31465)(0.03672) = +32.6 \text{ ksi}$$

Similarly, the magnitude of σ_x for other values of y can be determined. Figure 11 shows the distribution of applied and residual stresses.

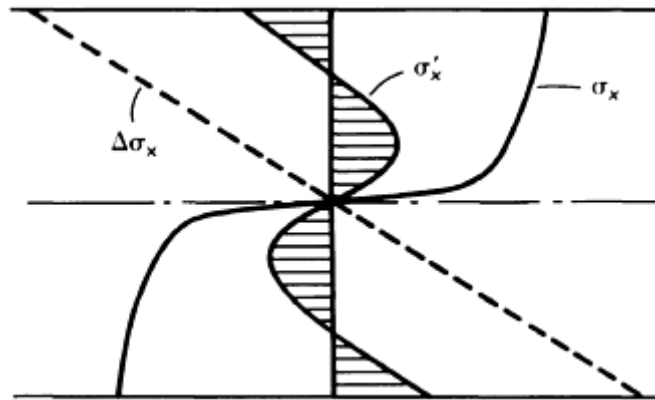


Fig. 11 Distribution of applied and residual stresses

Reference cited in this section

9. O.M. Sidebottom and C.F. Gebhardt, Elastic Springback in Plates and Beams Formed by Bending, *Exp. Mech.*, Vol 19, 1979, p 371–377

Stress-Strain Behavior in Bending

P. Dadras, Wright State University (retired)

References

1. J.M. Gere and S.P. Timoshenko, *Mechanics of Materials*, 4th ed., PWS Publishing Co., 1997
2. A.C. Ugural and S.K. Fenster, *Advanced Strength and Applied Elasticity*, 3rd ed., Prentice Hall, 1995
3. D. Horrocks and W. Johnson, On Anticlastic Curvature with Special Reference to Plastic Bending: A Literature Survey and Some Experimental Investigations, *Int. J. Mech. Sci.*, Vol 9, 1967, p 835–861
4. J. Chakrabarty, *Theory of Plasticity*, McGraw-Hill, 1987
5. P. Dadras, Plane Strain Elastic-Plastic Bending of a Strain-Hardening Curved Beam, *Int. J. Mech. Sci.*, in press Nov 2000
6. P. Dadras and S.A. Majlessi, Plastic Bending of Work Hardening Materials, *ASME Trans. J. Eng. Ind.*, Vol 104, 1982, p 224–230
7. R. Hill, *The Mathematical Theory of Plasticity*, Oxford University Press, London, 1950
8. H. Verguts and R. Sowerby, The Pure Plastic Bending of Laminated Sheet Metals, *Int. J. Mech. Sci.*, Vol 17, 1975, p 31
9. O.M. Sidebottom and C.F. Gebhardt, Elastic Springback in Plates and Beams Formed by Bending, *Exp. Mech.*, Vol 19, 1979, p 371–377

Fundamental Aspects of Torsional Loading

John A. Bailey, North Carolina State University; Jamal Y. Sheikh-Ahmad, Wichita State University

Introduction

TORSION TESTS can be carried out on most materials, using standards specimens, to determine mechanical properties such as modulus of elasticity in shear, yield shear strength, ultimate shear strength, modulus of rupture in shear, and ductility. Torsion tests can also be carried out on full-size parts (shafts, axles, and twist drills) and structures (beams and frames) to determine their response to torsional loading. In torsion testing, unlike tension testing and compression testing, large strains can be applied before plastic instability occurs, and complications due to friction between the test specimen and dies do not arise.

Torsion tests are most frequently carried out on prismatic bars of circular cross section by applying a torsional moment about the longitudinal axis. The shear stress versus shear strain curve can be determined from simultaneous measurements of the torque and angle of twist of the test specimen over a predetermined gage length.

Certain shear properties of materials can also be determined by single or double direct shear tests. In these types, of tests loads are applied to bars, usually of circular section, in such a way as to produce failure (shear) on either one (single) or two (double) transverse planes perpendicular to the axis of the bar. The shear strength of the bar is determined by dividing the shear load by the cross-sectional area of the bar. Such tests provide little fundamental information on the shear properties of materials and are primarily used in the design of rivets, bolts keyway systems, and so forth, that are subjected to shearing loads in service (Ref 1) (see also the article "Shear, Torsion, and Multiaxial Testing" in this Volume).

The following sections discuss the torsional deformation of prismatic bars of circular cross section. Discussion of the torsional response of prismatic bars of noncircular cross section (rectangular, elliptical, triangular) in the elastic range can be found in Ref 2.

References cited in this section

1. C.L. Harmsworth, *Mechanical Testing*, Vol 8, *ASM Handbook*, American Society for Metals, 1985, p 62
2. S.P. Timoshenko and J.N. Goodier, *Theory of Elasticity*, 3rd ed., McGraw-Hill, 1970, p 291

Fundamental Aspects of Torsional Loading

John A. Bailey, North Carolina State University; Jamal Y. Sheikh-Ahmad, Wichita State University

Prismatic Bars of Circular Cross Section

Elastic Deformation (Solid Bars). In torsional testing of prismatic bars of circular cross section it is assumed that:

- Bar material is homogeneous and isotropic.
- Twist per unit length along the bar is constant.
- Sections that are originally plane to the torsional axis remain plane after deformation.

- Initially straight radii remain straight after deformation.

Figure 1 shows the torsional deformation of a long, straight, isotropic prismatic bar of circular section. Assuming the above-mentioned constraints, the displacements are given by:

$$\begin{aligned} u_r &= 0 \\ u_z &= 0 \\ u_\theta &= rz \left(\frac{d\theta}{dz} \right) \end{aligned} \quad (\text{Eq 1})$$

where $d\theta/dz$ is the angle of twist per unit length (θ/L) and L is the gage length of the test specimen. The strains are given by:

$$\begin{aligned} \epsilon_{zz} &= 0 \\ \epsilon_{rr} &= 0 \\ \epsilon_{\theta\theta} &= 0 \\ \gamma_{zr} &= 0 \\ \gamma_{r\theta} &= 0 \\ \gamma_{z\theta} &= \frac{rd\theta}{dz} \end{aligned} \quad (\text{Eq 2})$$

For an isotropic material that obeys Hooke's law, the corresponding stress state is given by:

$$\begin{aligned} \sigma_{zz} &= 0 \\ \sigma_{rr} &= 0 \\ \sigma_{\theta\theta} &= 0 \\ \tau_{zr} &= 0 \\ \tau_{r\theta} &= 0 \\ \tau_{z\theta} &= G\gamma_{z\theta} \end{aligned} \quad (\text{Eq 3})$$

where G is the shear modulus that is related to Young's modulus (E) and Poisson's ratio (ν) by:

$$G = \frac{E}{2(1 + \nu)} \quad (\text{Eq 4})$$

The stress distribution across a prismatic bar of circular cross section is given by:

$$\tau_{z\theta} = \frac{Gr\theta}{L} \quad (\text{Eq 5})$$

Thus, the shear stress is zero at the center of the bar ($r = 0$) and increases linearly with radius. The maximum value of the shear stress occurs at the surface of the bar ($r = a$) and is given by:

$$\tau_{z\theta \text{ max}} = \frac{Ga\theta}{L} \quad (\text{Eq 6})$$

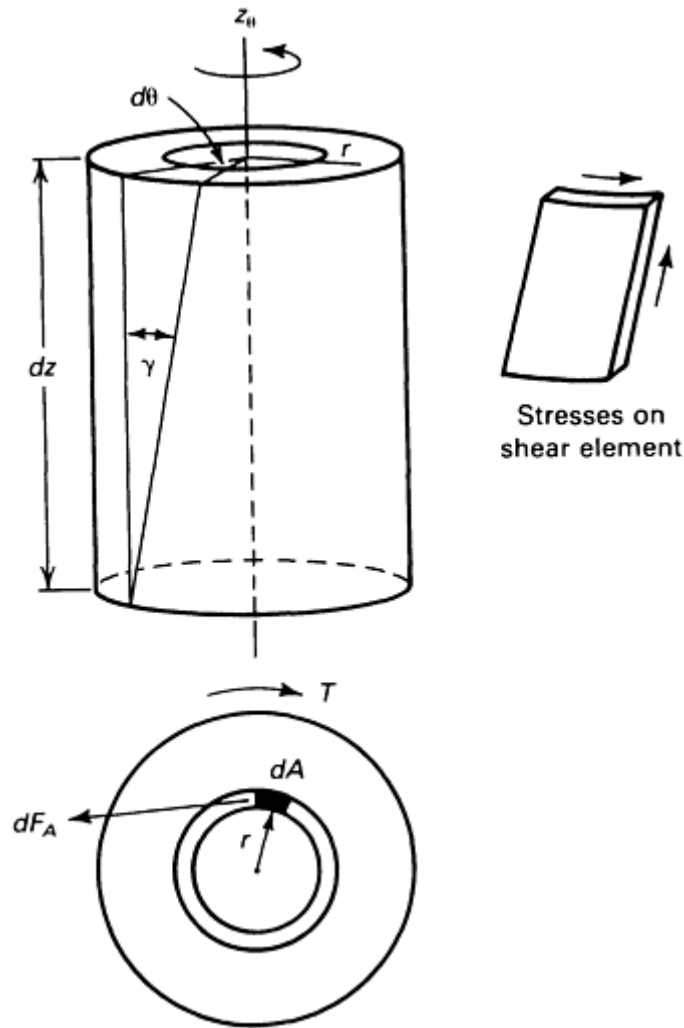


Fig. 1 Torsion of a solid circular prismatic section

The torque (T) transmitted by the elemental section shown in Fig. 1 is given by:

$$dT = (\tau_{z\theta} r) dA \quad (\text{Eq 7})$$

or

$$T = \int_0^a \tau_{z\theta} 2\pi r^2 dr \quad (\text{Eq 8})$$

Combining Eq 5 and 8 gives:

$$T = \frac{G\theta}{L} \int_0^a 2\pi r^3 dr \quad (\text{Eq 9})$$

Integration gives:

$$T = \frac{\pi a^4 G\theta}{2L} \quad (\text{Eq 10})$$

or on rearrangement:

$$\theta = \frac{TL}{GJ} \quad (\text{Eq 11})$$

where $J = \pi a^4/2$ is the polar moment of inertia of a prismatic bar of circular section about its axis of symmetry. Thus, the angle of twist can be calculated from knowledge of the applied torsional load, shear modulus, and bar geometry. Combining Eq 6 and 10 gives:

$$(\tau_{z\theta})_{\max} = \frac{2T}{\pi a^3} \quad (\text{Eq 12})$$

or

$$(\tau_{z\theta})_{\max} = \frac{Ta}{J} \quad (\text{Eq 13})$$

Thus, the maximum shear stress can be calculated from knowledge of the torsional loading and bar geometry. Plastic Deformation (Solid Bars) of Non-Work-Hardening Material. When the surface shear stress $(\tau_{z\theta})_{\max}$ of a solid bar during torsional loading reaches the yield shear stress (k) of the test material, plastic deformation (flow) occurs. The deformation zone begins at the surface of the bar and advances inward as an annulus surrounding an elastic core. The stress distributions are shown schematically in Fig. 2 for a non-work-hardening and a work-hardening material.

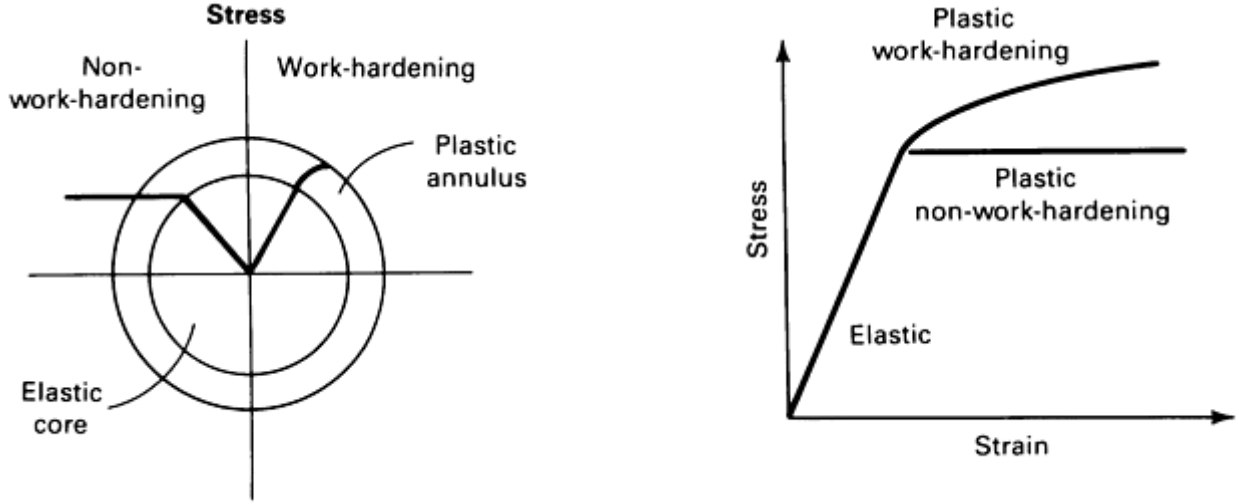


Fig. 2 Section through prismatic bar of circular section

For a non-work-hardening material, the total torque transmitted by the bar, according to Ref 3, is given by:

$$T = \int_{r=0}^{r=r_p} \tau_{z\theta} 2\pi r^2 dr + \int_{r=r_p}^{r=a} k 2\pi r^2 dr \quad (\text{Eq 14})$$

The first term on the right side of Eq 14 is the torque transmitted by the elastic core, where the shear stress varies linearly with r . The second term on the right side of Eq 14 is the torque transmitted by the plastic annulus, where the shear stress is constant and independent of r . The elastic-plastic boundary occurs at $r = r_p$. Integration of Eq 14 gives:

$$T = \frac{\pi r_p^4 G\theta}{2L} + \frac{2\pi a^3 k}{3} - \frac{2\pi r_p^3 k}{3} \quad (\text{Eq 15})$$

Compatibility at the elastic-plastic boundary requires that:

$$k = \frac{G\theta r_p}{L} \quad (\text{Eq 16})$$

Combining Eq 15 and 16 and rearranging gives:

$$T = \frac{2\pi a^3 k}{3} \left\{ 1 - \frac{1}{4} \left(\frac{r_p}{a} \right)^3 \right\} \quad (\text{Eq 17})$$

or

$$T = \frac{2\pi a^3 k}{3} \left\{ 1 - \frac{1}{4} \left(\frac{\theta_y}{\theta} \right)^3 \right\} \quad (\text{Eq 18})$$

where θ_y is the angle of twist at which yielding begins. When θ is very large compared to θ_y , then:

$$T_p = \frac{2\pi a^3 k}{3} \quad (\text{Eq 19})$$

where T_p is the torque required for fully plastic flow. Equation 18 can now be rewritten as:

$$T = T_p \left\{ 1 - \frac{1}{4} \left(\frac{\theta_y}{\theta} \right)^3 \right\} \quad (\text{Eq 20})$$

When the bar becomes fully plastic, the torque becomes independent of the angle of twist. In the elastic regime, the shear stress at the surface of the bar is given by Eq 6. In the elastic-plastic and fully plastic regimes, the shear stress at the surface of the bar is k . The shear strain at the surface of the bar is:

$$\gamma = \frac{a\theta}{L} \quad (\text{Eq 21})$$

for all regimes.

Plastic Deformation (Solid Bars) of Work-Hardening Material. In practice, most materials work harden when tested at temperatures below $0.5 T_H$, where T_H is the homologous temperature and is given by $T_H = T_T/T_M$ (where T_T is the testing temperature and T_M is the melting point temperature of the material). The result is that the torque continues to increase up to fracture.

The shear stress versus shear strain curve in the plastic range can be computed from the torque-twist curve using the procedure given below. It is important to note that the computed values of stress and strain are those that occur at the surface of the bar and that the material is insensitive to the rate of deformation.

The torque, according to Ref 3 and 4, is given by:

$$T = \int_0^a \tau 2\pi r^2 dr \quad (\text{Eq 22})$$

where the subscripts on the shear stress are dropped. Changing the variable from r to γ gives:

$$T = \int_0^{\gamma_a} \frac{\tau 2\pi\gamma^2 d\gamma}{\theta_1^3} \quad (\text{Eq 23})$$

where θ_1 is the twist per unit length. In general, the shear stress versus shear strain curve can be written as:

$$\tau = f(\gamma) \quad (\text{Eq 24})$$

Thus, Eq 24 becomes:

$$T = \int_0^{\gamma_a} \frac{2\pi f(\gamma)\gamma^2 d\gamma}{\theta_1^3} \quad (\text{Eq 25})$$

Differentiating Eq 25 with respect to θ_1 gives:

$$d(T\theta_1^3) = 2\pi f(\gamma_a) \gamma_a^2 d\gamma_a \quad (\text{Eq 26})$$

At the specimen surface:

$$\tau_a = f(\gamma_a) \quad (\text{Eq 27})$$

and

$$\gamma_a = a\theta_1 \quad (\text{Eq 28})$$

Substituting Eq 27 and 28 into Eq 26 gives:

$$d(T\theta_1^3) = 2\pi\tau_a a^3 \theta_1^2 d\theta_1$$

or

$$\frac{d(T\theta_1^3)}{d\theta_1} = 2\pi\tau_a^3 \theta_1^2 a^3 \quad (\text{Eq 29})$$

Expanding Eq 29 gives:

$$\frac{dT}{d\theta_1} \theta_1^3 + 3T\theta_1^2 = 2\pi\tau_a a^3 \theta_1^2$$

or

$$\tau_a = \frac{1}{2 \pi a^3} \left[3T + \theta_1 \frac{dT}{d\theta_1} \right] \quad (\text{Eq 30})$$

The first term on the right side of Eq 30 is the torque due to the maximum yield shear stress of τ_a in a fully plastic non-strain-hardening material, whereas the second term is a correction for strain hardening. These terms can be readily derived from the torque-twist curve shown in Fig. 3, where:

$$\begin{aligned} \frac{dT}{d\theta_1} &= \frac{BC}{CD} \\ \theta_1 &= CD \\ \theta_1 \frac{dT}{d\theta_1} &= BC \end{aligned}$$

so that:

$$\tau_a = \frac{1}{2 \pi a^3} \{ 3BA + BC \} \quad (\text{Eq 31})$$

The shear strain at the surface is given by Eq 28. Thus, the shear stress versus shear strain curve can be deduced by drawing tangents to the torque versus the angle of twist per unit length curve.

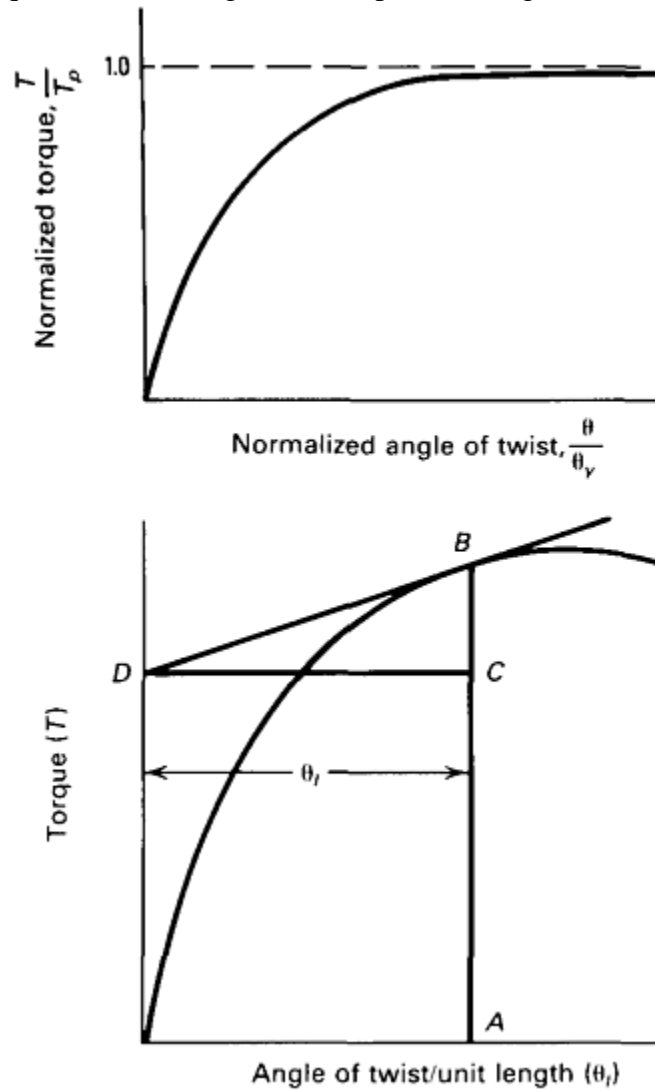


Fig. 3 Torque-twist curves

In experimental work, it has often been found that the torque (T) is related to the angle of twist per unit length by the expression:

$$T = T_0 \theta_1^n \quad (\text{Eq 32})$$

where T_0 is the torque at unit angle of twist, and n is the exponent. A graph of the logarithm of the torque (T) versus the logarithm of the angle of twist per unit length (θ_1) at constant rate of twist ($\dot{\theta}_1$) is linear and of slope n . Differentiating Eq 32 gives:

$$\left(\frac{dT}{d\theta_1} \right)_{\dot{\theta}_1} = \frac{nT}{\theta_1} \quad (\text{Eq 33})$$

Combining Eq 30 and 33 gives:

$$\tau_a = \frac{T}{2\pi a^3} [3 + n] \quad (\text{Eq 34})$$

This expression has been derived in Ref 3.

Shear stress versus shear strain curves may also be derived by the method of differential testing, where tests are carried out on two specimens of slightly different radii, a_1 and a_2 . The shear stress and shear strain are given by:

$$\tau = \frac{3(T_1 - T_2)}{2\pi(a_1^3 - a_2^3)} \quad (\text{Eq 35})$$

and

$$\gamma = \frac{(a_1 + a_2)\theta_1}{2} \quad (\text{Eq 36})$$

respectively. An excellent critical review of existing methods for converting torque to shear stress is given in Ref 5.

The stress gradient across the diameter of a solid bar allows the less highly stressed inner fibers to restrain the surface fibers from yielding. Thus, the onset of yielding is generally not apparent. This effect can be minimized by the use of thin-walled tubes, in which the stress across the tube wall can be assumed to be constant. For a thin-walled tube, the shear stress and shear strain are given by:

$$\tau = \frac{T}{2\pi a^2 t} \quad (\text{Eq 37})$$

and

$$\gamma = \frac{a\theta}{L} \quad (\text{Eq 38})$$

respectively, where a is now the mean radius of the tube, t is the thickness of the tube wall, θ is the angle of twist, and L is the specimen gage length. Thus, from measurements of the torque (T) and angle of twist (θ), it is possible to construct the shear stress (τ) versus shear strain (γ) curve directly. The dimensions of the tube must be chosen carefully to avoid buckling.

Effect of Strain Rate on Plastic Deformation. In the analysis presented in the previous section, it is inherently assumed that the shear stress is independent of strain rate. The assumption is approximately valid at low homologous temperatures, but is not valid at high homologous temperatures, where the strain-rate sensitivity of materials is usually large. A graphical procedure for accounting for strain-rate effects is presented in Ref 3 and 6.

If it is assumed that the torque is a function of both the angle of twist and the twisting rate, that is, $T = f(\theta, \dot{\theta})$, then the change in torque with respect to a change in the angle of twist is given by:

$$\frac{dT}{d\theta_1} = \left(\frac{dT}{d\theta_1} \right)_{\dot{\theta}_1} + \left(\frac{dT}{d\dot{\theta}_1} \right)_{\theta_1} \frac{\dot{\theta}_1}{\theta_1} \quad (\text{Eq 39})$$

The first term on the right-hand side of this equation has been evaluated (Eq 33). The second term can be evaluated from the experimental observation that a logarithmic graph of torque (T) versus the rate of twist ($\dot{\theta}_1$) at a constant angle of twist per unit length (θ_1) is often linear. The slope of the graph corresponds to the twist-rate sensitivity (m). Strain hardening predominates at low temperatures, whereas twist-rate sensitivity predominates at elevated temperatures.

If the effect of twist rate on torque can be expressed by:

$$T = T_1 \dot{\theta}_1^m \quad (\text{Eq 40})$$

then, at constant strain:

$$\left(\frac{dT}{d\dot{\theta}_1} \right)_{\theta_1} = \frac{mT}{\dot{\theta}_1} \quad (\text{Eq 41})$$

Substitution of Eq 33 and 41 into Eq 39 gives:

$$\frac{dT}{d\dot{\theta}_1} = \frac{T}{\theta_1} (m + n) \quad (\text{Eq 42})$$

Combining Eq 30 and 42 gives:

$$\tau_a = \frac{T}{2\pi a^3} (3 + m + n) \quad (\text{Eq 43})$$

The shear strain is again given by:

$$\gamma = a\theta_1 \quad (\text{Eq 44})$$

Equations 43 and 44 can be used to plot graphs of shear stress versus shear strain for all temperatures and strain rates up to the point of torsional instability.

A new method of converting torque to surface shear stress (Ref 5) is based on the assumption that the shear stress at radius r is affected only by the history of this particular location. The torque is given by:

$$T = \int_0^a 2\pi r \tau r^2 dr \quad (\text{Eq 45})$$

The derivative of this integral at a given angle of twist and strain rate is:

$$\frac{dT}{dr} = 2\pi \tau_a r_a^2 \quad (\text{Eq 46})$$

In this method, torque versus angle of twist curves are determined on specimens of increasing radii from which the torque versus radii relationship can be determined at a given strain (twist) and strain rate (twist rate). The slope of this curve at any given radius can be substituted into Eq 46 to determine the current shear stress at this radius. This method appears to reduce significantly the errors inherent in previous methods.

References cited in this section

3. W.J.McG. Tegart, *Elements of Mechanical Metallurgy*, Macmillan, 1967, p 64
4. A. Nadai, *Theory of Flow and Fracture of Solids*, Vol 1, McGraw-Hill, 1950, p 349
5. G.R. Canova, et al., *Formability of Metallic Materials—2000 A.D.*, STP 753, J.R. Newby and B.A. Niemeier, Ed., ASTM, 1982, p 189
6. D.S. Fields and W.A. Backofen, *Proc. ASTM*, Vol 57, 1957, p 1259

Fundamental Aspects of Torsional Loading

John A. Bailey, North Carolina State University; Jamal Y. Sheikh-Ahmad, Wichita State University

Effective Stresses and Strains

It is often helpful to convert data derived under one state of stress to another state of stress. This can be accomplished by the use of so-called effective or tensile equivalent stresses and strains. The form of the relationships from shear stresses and strains to effective stresses and strains depends on the particular yield criterion used (Ref 7).

For the distortional energy (von Mises) criterion, the effective stress and strain are given by:

$$\bar{\sigma} = C_1 [(\sigma_1 - \sigma_2)^2 + (\sigma_2 - \sigma_3)^2 + (\sigma_3 - \sigma_1)^2]^{1/2} \quad (\text{Eq 47})$$

and

$$d\bar{\epsilon} = C_2 [(d\epsilon_1 - d\epsilon_2)^2 + (d\epsilon_2 - d\epsilon_3)^2 + (d\epsilon_3 - d\epsilon_1)^2]^{1/2} \quad (\text{Eq 48})$$

respectively, where the variables have their usual significance (Ref 7). The constants C_1 and C_2 are now chosen so that the effective stresses and strains are identical to the stresses and strains in uniaxial tension (or compression). For uniaxial tension:

$$\begin{aligned} \sigma_1 &= \sigma_0 & d\epsilon_1 &= d\epsilon_1 \\ \sigma_2 &= 0 & d\epsilon_2 &= \frac{-d\epsilon_1}{2} \\ \sigma_3 &= 0 & d\epsilon_3 &= \frac{-d\epsilon_1}{2} \end{aligned} \quad (\text{Eq 49})$$

Substituting Eq 49 into Eq 47 and 48 gives:

$$C_1 = \frac{1}{\sqrt{2}}$$

and

$$C_2 = \frac{\sqrt{2}}{3}$$

Thus, the effective stresses and strains become:

$$\bar{\sigma} = \frac{1}{\sqrt{2}} [(\sigma_1 - \sigma_2)^2 + (\sigma_2 - \sigma_3)^2 + (\sigma_3 - \sigma_1)^2]^{1/2} \quad (\text{Eq 50})$$

and

$$d\bar{\epsilon} = \frac{\sqrt{2}}{3} [(d\epsilon_1 - d\epsilon_2)^2 + (d\epsilon_2 - d\epsilon_1)^2 + (d\epsilon_3 - d\epsilon_1)^2]^{1/2} \quad (\text{Eq 51})$$

respectively. For the state of pure shear (torsion):

$$\begin{aligned} \sigma_1 &= k & d\epsilon_1 &= \frac{d\gamma}{2} \\ \sigma_2 &= 0 & d\epsilon_2 &= 0 \\ \sigma_3 &= -k & d\epsilon_3 &= -\frac{d\gamma}{2} \end{aligned} \quad (\text{Eq 52})$$

Substitution of Eq 52 into 50 and 51 gives:

$$\bar{\sigma} = \sqrt{3}k$$

$$d\bar{\epsilon} = \frac{2}{\sqrt{3}} d\epsilon_1$$

or

$$d\bar{\epsilon} = \frac{1}{\sqrt{3}} d\gamma$$

Thus, the effective stresses and strains are related to the shear stresses and strains by the factors $\sqrt{3}$ and $1/\sqrt{3}$, respectively; that is, the shear stress versus shear strain curve can be converted to a true (tensile) stress versus strain curve by using:

$$\bar{\sigma} = \sqrt{3}\tau$$

$$\bar{\epsilon} = \frac{\gamma}{\sqrt{3}}$$

For the Tresca (maximum shear stress) criterion, the effective stresses and strains are given by:

$$\bar{\sigma} = C_3(\sigma_1 - \sigma_3) \quad (\text{Eq 53})$$

and

$$d\bar{\epsilon} = C_4(d\epsilon_1 - d\epsilon_3) \quad (\text{Eq 54})$$

respectively (Ref 7). The constants C_3 and C_4 are again chosen so that the effective stresses and strains are identical to the stresses and strains in uniaxial tension (or compression). Using the conditions defined by Eq 49 gives:

$$C_3 = 1$$

and

$$C_4 = \frac{2}{3}$$

Thus, the effective stresses and strains become:

$$\bar{\sigma} = (\sigma_1 - \sigma_3) \quad (\text{Eq 55})$$

and

$$d\bar{\epsilon} = \frac{2}{3}(d\epsilon_1 - d\epsilon_3) \quad (\text{Eq 56})$$

Substitution of Eq 52 into Eq 55 and 56 gives:

$$\bar{\sigma} = 2k$$

and

$$d\bar{\epsilon} = \frac{4}{3} d\epsilon_1$$

or

$$d\bar{\epsilon} = \frac{2}{3} d\gamma$$

Thus, the effective stresses and strains are related to the shear stresses and shear strains by the factors 2 and $\frac{2}{3}$, respectively; that is, the shear stress versus shear strain curve can be converted to a true (tensile) stress versus strain curve by using:

$$\sigma = 2\tau \quad (\text{Eq 57})$$

and

$$\bar{\epsilon} = \frac{2}{3} \gamma \quad (\text{Eq 58})$$

The work of deformation per unit volume in terms of the effective stresses is given by:

$$u = \int \bar{\sigma} d\bar{\epsilon} \quad (\text{Eq 59})$$

The work of deformation in torsion can be calculated from the expressions:

$$\bar{\sigma} = 2\tau \quad (\text{Eq 60})$$

$$d\bar{\epsilon} = \frac{2}{3} d\gamma$$

and

$$\bar{\sigma} = \sqrt{3}\tau \quad (\text{Eq 61})$$

$$d\bar{\epsilon} = \frac{d\gamma}{\sqrt{3}}$$

for the Tresca (maximum shear stress) criterion and distortional energy criterion, respectively. For the Tresca criterion, substitution of Eq 60 into Eq 59 gives:

$$u = \int 2\tau \cdot \frac{2}{3} d\gamma \quad (\text{Eq 62})$$

$$u = \int \frac{4}{3} \tau d\gamma$$

For the distortional energy criterion, substitution of Eq 61 into Eq 59 gives:

$$u = \int \sqrt{3} \tau \cdot \frac{1}{\sqrt{3}} d\gamma \quad (\text{Eq 63})$$

$$u = \int \tau d\gamma$$

It is evident that the work obtained by the Tresca criterion is too high and that the distortional energy criterion gives the correct result.

Reference cited in this section

7. S. Kalpakjian, *Mechanical Processing of Materials*, D. Van Nostrand, 1967, p 31

Fundamental Aspects of Torsional Loading

John A. Bailey, North Carolina State University; Jamal Y. Sheikh-Ahmad, Wichita State University

Constitutive Relationships

Application to Metalworking Analyses. In the past, numerous techniques were developed for the analysis of metalworking processes including slip-line field theory, upper and lower bound approaches, slab/disk/tube approaches, viscoplasticity theory, and the method of weighted residuals (Ref 8). These techniques are usually based on various simplifying assumptions that often severely restrict their usefulness. However, recent advances in the development of numerical methods (e.g., finite element analysis) and computational techniques have led to the evolution of new tools for the analysis and design of metalworking processes. A key feature of such tools should be their ability to calculate the influence of processing variables on forming loads, torques,

and power requirement as well as capturing a quantitative description of workpiece deformation. Inherent in performing such calculations is knowledge of the effects of strain, strain rate, and temperature on the flow stress of the work material. Such effects are described by a constitutive model that represents material behavior. Effects of Strain, Strain Rate, and Temperature on Flow Stress. There is much evidence suggesting that the torsion of hollow tubes of the appropriate dimensions (Ref 9) may be one of the better ways to obtain information on the effect of strain, strain rate, and temperature on the flow stress of materials over the range of these variables usually encountered in metalworking processes. Tests can be carried out to large strains over a wide range of temperature and at constant true strain rates. In addition, the occurrence of frictional effects (compression) and instability (tension) are absent.

The preceding sections present methods for obtaining the shear stress and shear strain from measures of the torque and angle of twist. It is also shown that the shear stresses and shear strains could be readily converted into effective stresses and strains. This section includes some simple relationships that relate the effective stress to the effective strain, effective strain rate, and temperature.

The effective stress is often related to the effective strain by the expression:

$$\bar{\sigma} = K(\bar{\epsilon})^n \quad (\text{Eq 64})$$

at constant strain rate and temperature, where K is a strength coefficient and n is the strain-hardening exponent. A plot of $\log \bar{\sigma}$ against $\log \bar{\epsilon}$ is usually linear and of slope n . The strength coefficient K is the value of the effective stress at an effective strain of unity.

The effective stress is often related to the effective strain rate by the expression:

$$\bar{\sigma} = C_1 (\dot{\bar{\epsilon}})^m \quad (\text{Eq 65})$$

at constant strain and temperature where C_1 is a strength coefficient and m is the strain-rate sensitivity. A plot of $\log \bar{\sigma}$ against $\log \dot{\bar{\epsilon}}$ is usually linear and of slope m . The strength coefficient is the value of the effective stress at an effective strain rate of unity. The combined effect of strain and strain rate on the effective stress can often be described by the expression:

$$\bar{\sigma} = A(\bar{\epsilon})^n (\dot{\bar{\epsilon}})^m \quad (\text{Eq 66})$$

at constant temperature where A is a strength coefficient. Graphical procedures based on experimental results can be used to solve for the unknown constants.

The effective stress is often related to temperature by the expression:

$$\bar{\sigma} = C_2 \exp(Q/RT) \quad (\text{Eq 67})$$

at constant strain and strain rate where C_2 is a strength coefficient, Q is the activation energy for plastic deformation, and R is the universal gas constant. A plot of $\log \bar{\sigma}$ against $1/T$ is often linear and of slope Q/R , from which Q can be calculated. The value of the flow stress depends on the dislocation structure at the time at which the flow stress is measured. However, dislocation structure may change with strain, strain rate, and temperature. One way to minimize this effect is to evaluate Q using a temperature change test. Such tests are carried out at constant strain rate and at a desired value of the plastic strain the temperature is changed from, say, T_1 to T_2 , and the new stress ($\bar{\sigma}_2$) is measured (Ref 10).

The activation energy is then given by the expression:

$$Q = R \log \left(\frac{\bar{\sigma}_1}{\bar{\sigma}_2} \right) \cdot \frac{T_1 T_2}{T_2 - T_1} \quad (\text{Eq 68})$$

The combined effect of strain rate and temperature on flow stress can often be described by the expression:

$$\bar{\sigma} = f(Z) \quad (\text{Eq 69})$$

at constant strain where Z is the Zener-Hollomon parameter and is given by the expression:

$$Z = \dot{\bar{\epsilon}} \exp(\Delta H/RT) \quad (\text{Eq 70})$$

where ΔH is an activation energy that is related to Q by the expression:

$$Q = m \Delta H \quad (\text{Eq 71})$$

In the past, Eq 69 was considered to be a mechanical equation of state. However, this is no longer regarded as being valid (Ref 10).

In torsion tests and plane strain compression tests that are carried out to large strains, it is often found that deformation occurs under steady-state conditions, and the flow stress attains a constant value, independent of further straining. Such a condition is often encountered in many hot metalworking processes. It is then found that stress, strain rate, and temperature are related by the well-known creep equation (Ref 11 and 12) that also applies to steady-state deformation:

$$\dot{\bar{\epsilon}} = A(\sinh \alpha \bar{\sigma})^{n'} \exp(-Q/RT) \quad (\text{Eq 72})$$

where α , n' , and A are constants and the remaining symbols have their usual significance. At low stress (high temperature) and high stress (low temperature), Eq 72 reduces to a power law:

$$\dot{\bar{\epsilon}} = A_1 \bar{\sigma}^{n'} \exp(-Q/RT) \quad (\text{Eq 73})$$

and an exponential law:

$$\dot{\bar{\epsilon}} = A_2 \exp(\beta \bar{\sigma}) \exp(-Q/RT) \quad (\text{Eq 74})$$

respectively. It is found for many materials that linear relationships exist between $\log_e \dot{\bar{\epsilon}}$ and $\log_e [\sinh \alpha \bar{\sigma}]$ at constant temperature and between $\log_e \dot{\bar{\epsilon}}$ and $1/T$ at constant $\sinh \alpha \bar{\sigma}$. The latter relationship enables the value of Q to be determined. An alternative and simpler method for calculating Q is to recognize that Eq 72 can be written in the form:

$$Q = 2.3R \left(\frac{\partial \log \dot{\bar{\epsilon}}}{\partial \log [\sinh \alpha \bar{\sigma}]} \right)_T \times \left(\frac{\partial \log [\sinh \alpha \bar{\sigma}]}{\partial 1/T} \right)_{\dot{\bar{\epsilon}}} \quad (\text{Eq 75})$$

or

$$Q = 2.3R(n')_T(n'')_{\dot{\bar{\epsilon}}} \quad (\text{Eq 76})$$

Linear relationships usually exist between $\log_e \dot{\bar{\epsilon}}$ and $\log_e [\sinh \alpha \bar{\sigma}]$ and between $\log_e [\sinh \alpha \bar{\sigma}]$ and $1/T$ at constant temperature and strain rate, respectively. Data over a wide range of temperature in the hot-working regime can be reduced to a single linear relationship by plotting $\log_e [\dot{\bar{\epsilon}} \exp Q/RT]$ versus $\log_e [\sinh \alpha \bar{\sigma}]$ (Ref 13).

In some practical metalworking operations, steady-state deformation may not be achieved because temperatures and plastic strains may be too low. Flow stress then depends upon strain, strain rate, and temperature. In these situations, a general constitutive relation of the form:

$$\bar{\sigma} [B \bar{\epsilon}^n] [1 + C \log_c \dot{\bar{\epsilon}} / \dot{\bar{\epsilon}}_0] f(\bar{T}) \quad (\text{Eq 77})$$

where B , n , and C are material constants has been found to be very useful (Ref 14, 15, 16). The quantity \bar{T} (dimensionless temperature) is given by the expression:

$$\bar{T} = (T_m - T) / (T_m - T_0) \quad (\text{Eq 78})$$

where T_m is the melting point temperature of the material, and $\dot{\bar{\epsilon}}_0$ and T_0 are reference strain rates and temperatures, respectively.

The first term in Eq 77 accounts for strain-hardening effects, the second term accounts for strain-rate effects, and the third term accounts for temperature effects. Linear, bilinear, and exponential forms (Ref 16) of the term $f(\bar{T})$ have been used by many investigators. The advantage of the above constitutive relationship (model) is that the effects of strain, strain rate, and temperature are uncoupled, which greatly simplifies the evaluation of the constants from experimental data.

References cited in this section

8. E.M. Mielnik, *Metal Working Science and Engineering*, McGraw-Hill, 1991, p 220
9. J.A. Bailey, S.L. Haas, and M.K. Shah, *Int. J. Mech. Sci.*, Vol 14, 1972, p 735

10. G. Dieter, *Mechanical Metallurgy*, 2nd ed., McGraw-Hill, 1976, p 353
11. F. Garafalo, *Fundamentals of Creep and Creep Rupture of Metals*, Macmillan, 1965
12. C.M. Sellars and W.J.McG. Tegart, *Int. Met. Rev.*, Vol 7, 1972, p 1
13. J.J. Jonas, C.M. Sellars, and W.J.McG. Tegart, *Met. Rev.*, Vol 130, 1969, p 14
14. G.R. Johnson and W.H. Cook, *Proc. Seventh Int. Symp. Ballistics*, 1983, p 541
15. G.R. Johnson, J.M. Hoegfeldt, U.S. Lindholm, and A. Nagy, *J. Eng. Mater. Technol. (Trans. ASME)*, Vol 105, 1983, p 42
16. G.R. Johnson, J.M. Hoegfeldt, U.S. Lindholm, and A. Nagy, *J. Eng. Mater. Technol. (Trans. ASME)*, Vol 105, 1983, p 48

Fundamental Aspects of Torsional Loading

John A. Bailey, North Carolina State University; Jamal Y. Sheikh-Ahmad, Wichita State University

Anisotropy in Plastic Torsion

Marked dimensional changes can occur during the torsional straining of solid bars and hollow cylinders of circular cross section (Ref 7, 9, and 17). These changes may produce either an increase or a decrease in the length of test specimens. Changes in length produced in hollow cylinders are considerably greater than those produced in solid bars because of the constraining effect of the solid core with the latter geometry. If changes in length are suppressed, then large axial stresses may be produced.

Dimensional changes have been attributed to the development of crystallographic anisotropy that arises because of a continuous change in the orientation of individual grains. This produces preferred orientation, where the yield stresses and macroscopic stress versus strain relationships vary with direction. The general observation is that the torsional deformation of solid bars and tubes produces axial extension at ambient temperatures and contraction that is often preceded by an initial period of lengthening, at elevated temperatures. Specific results, however, depend on the initial state (anisotropy) of the test material.

Theory of Anisotropy. A general phenomenological theory of anisotropy (Ref 17) proposes that the criterion describing the yield direction for anisotropic and orthotropic materials be quadratic in stress components and of the form:

$$\begin{aligned}
 2f(\sigma_{ij}) = & F(\sigma_y - \sigma_z)^2 + G(\sigma_z - \sigma_x)^2 \\
 & + H(\sigma_x - \sigma_y)^2 + 2L\tau_{yz} + 2M\tau_{zx} \\
 & + 2N\tau_{xy}
 \end{aligned}
 \tag{Eq 79}$$

where F , G , H , L , M , and N are six parameters describing the current state of anisotropy, $f(\sigma)_{ij}$ is the plastic potential, and the remaining symbols have their usual significance. The set of axes used in this criterion is assumed to be coincident with the principal axes of anisotropy. For an orthotropic material, the plastic properties at a given point are symmetric with respect to three orthogonal planes whose intersection defines the principal axes of anisotropy. It is clear that any practical application of this criterion requires prior knowledge of the principal axes of anisotropy and the numerical values of F , G , H , L , M , and N .

The basic theory of anisotropy (Ref 17) has been applied to the torsional straining of a thin-walled cylinder in an attempt to describe the changes in dimensions that occur. For a thin-walled cylinder, the radius is large compared with the wall thickness, and thus anisotropy can be considered to be uniformly distributed throughout

the volume of the material deformed. It was also assumed that the axes of anisotropy along the surface of an initially anisotropic cylinder were coincident with the directions of greatest accumulated tensile and compressive strain. These axes were also assumed to be mutually perpendicular and oriented at an angle ϕ to the transverse axis of the cylinder. This geometry is shown in Fig. 4. For an initially isotropic cylinder, the angle ϕ is a function of the shear strain (γ) and increases from $\pi/4$, approaching $\pi/2$ at large strains. This rotation is confined to the (x,y) plane about the z -axis that is perpendicular to the surface of the cylinder.

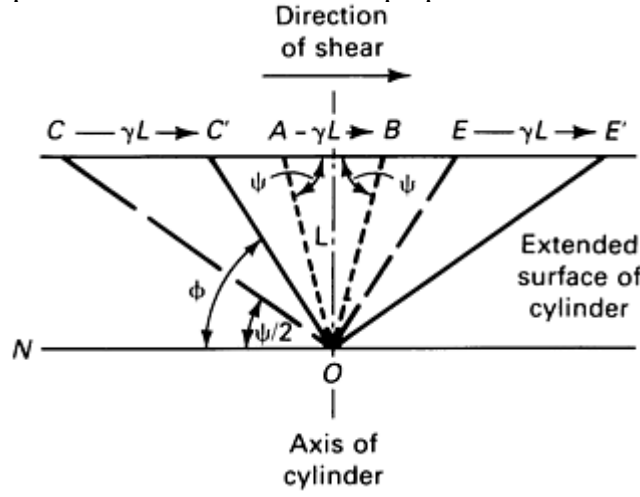


Fig. 4 Geometry of deformation for the plastic straining of a hollow cylinder. γ , shear strain; L , initial length of cylinder; OC , initial direction of greatest compression; OC' , final direction of greatest compression; OE , initial direction of greatest extension; OE' , final direction of greatest extension

From an analysis of the deformation, it was shown that the change in axial strain with shear strain is given by:

$$\frac{d\epsilon_a}{d\gamma} = \frac{(N - G - 2H) \sin \phi \sin 2\phi}{2N + (F + G + 4H - 2N) \sin^2 2\phi} - \frac{(N - F - 2H) \cos^2 \phi \sin 2\phi}{2N + (F + G + 4H - 2N) \sin^2 2\phi} \quad (\text{Eq 80})$$

It is clear from Eq 80 that measurement of the change in axial strain with shear strain is insufficient to determine the anisotropic parameters and yield stresses along the anisotropic axes and thereby insufficient to describe quantitatively the state of anisotropy. Simple expressions for the variation of the anisotropic parameters and yield stresses along the anisotropic axes with shear strain have been developed in terms of the changes in axial strain, tangential strain, principal yield shear stress, and through thickness yield stress of the hollow cylinder (Ref 18), all of which can be determined easily by experiment. It was found that the anisotropic parameters decrease and that the yield stresses along the anisotropic axes increase with an increase in strain, eventually becoming independent of strain when the test material is fully work hardened.

Montheillet and his coworkers (Ref 19, 20) modified Hill's theory of anisotropy by aligning the principal axes of anisotropy with the $\langle 100 \rangle$ directions of the ideal orientation prevailing in a polycrystal. Following the alignment, an optimization process was carried out such that the modified yield surface gives a good fit to the crystallographic yield surface of the single crystal representing the ideal orientation. The anisotropic parameters can then be determined. A direct relationship between the axial forces generated (positive, negative, zero) and the crystallographic texture developed for several materials was proposed. The sign and approximate magnitude of the effects was predicted from knowledge of the ideal orientation.

Utilizing the rate-sensitive theory of crystal plasticity based on glide modeling, a number of researchers have succeeded in developing computer models that are capable of predicting and explaining the evolution of texture and the subsequent lengthening and axial compressive stresses that develop during free-end and fixed-end twisting, respectively. A brief review of this work is given in Ref 21. Glide-modeling methods alone, however, are not capable of predicting and explaining the shortening behavior noted at elevated temperatures. A more plausible explanation of this phenomenon was provided by taking into account the occurrence of dynamic recrystallization (DRX) at elevated temperatures. In a series of recent studies (Ref 22, 23, and 24), Toth, Jonas, and coworkers were able to characterize and model the texture developed during the free-end hot torsion of

copper bars under DRX conditions. A computational method based on both glide and DRX modeling was developed. In this method, the texture is first determined by glide modeling until a critical strain is reached, at which DRX sets in. It was shown that the principal effects of DRX on texture development and the resulting free-end effect (shortening) can be predicted reasonably accurately.

The changes in length of a twisted bar during straining result in a continuous change in the specimen cross-sectional area. Thus, if the true shear stress versus shear strain curve is required, then instantaneous values of specimen dimensions must be used in computing shear stress and shear strain from the measured torque and angle of twist. Since the shear stress is proportional to r^{-3} and the shear strain is proportional to r/ℓ (Eq 12, 21), the use of initial values of r and ℓ in calculating the shear stress and shear strain curve will generate an error of 15 and 6%, respectively, if a length change of 10% took place (Ref 25). On the other hand, if the length of the specimen is held constant the developed axial stresses will range from 2 to 20% of the developed shear stress. In this case, the ratio ($\bar{\sigma}_{fx}/\bar{\sigma}$) of the effective stress in the fixed-end condition to that in the free-end condition is in the range from 1.0 to 1.01 for face-centered cubic metals, and in the range from 1.0 to 1.08 for body-centered cubic metals (Ref 19, 20).

References cited in this section

7. S. Kalpakjian, *Mechanical Processing of Materials*, D. Van Nostrand, 1967, p 31
9. J.A. Bailey, S.L. Haas, and M.K. Shah, *Int. J. Mech. Sci.*, Vol 14, 1972, p 735
17. R.R. Hill, *The Mathematical Theory of Plasticity*, Clarendon Press, Oxford, 1950, p 317
18. J.A. Bailey, S.L. Haas, and K.C. Nawareb, *J. Basic Eng. (Trans. ASME)*, March 1972, p 231
19. F. Montheillet, M. Cohen, and J.J. Jonas, *Acta Metall.*, Vol 32, 1984, p 2077–2089
20. F. Montheillet, P. Gilormini, and J. J. Jonas, *Acta Metall.*, Vol. 33, 1985, p 2126–2136
21. J.J. Jonas, *Int. J. Mech. Sci.*, Vol 35, 1993, p 1065–1077
22. L.S. Toth and J.J. Jonas, *Scr. Metall.*, Vol 27, 1992, p 359–363
23. L.S. Toth, J.J. Jonas, D. Daniel, and J.A. Bailey, *Textures and Microstructures*, Vol 19, 1992, p 245–262
24. J.J. Jonas and L.S. Toth, *Scr. Metall.*, Vol 27, 1992, p 1575–1580
25. S.L. Semiatin, G.D. Lahoti, and J.J. Jonas, *Mechanical Testing*, Vol 8, *ASM Handbook*, American Society for Metals, 1985, p 154

Fundamental Aspects of Torsional Loading

John A. Bailey, North Carolina State University; Jamal Y. Sheikh-Ahmad, Wichita State University

Testing Equipment

A typical torsion testing machine consists of a drive system, a test section, torque and rotational displacement transducers, and a rigid frame. A rigid frame that is capable of allowing accurate alignment of the various torsion machine components is necessary for twisting the torsion specimen accurately around its axis with no

superimposed flexural loading. For this purpose, Culver (Ref 26) and Kobayashi (Ref 27), among others, used a lathe bed for constructing their torsion testing machine because of its high rigidity and precision-machined slides. In addition to the components mentioned above, a heating chamber with vacuum or inert gas environment is required when tests are conducted at high temperatures. A variety of torsion testing machines have been designed and built, and an excellent review of some of these machines is given in Ref 27 and 28. More information on torsion testing is also provided in the article “Shear, Torsion, and Multiaxial Testing” in this Volume.

Drive Systems. Most of the differences between existing torsion testing machines lie in the type of drive system used. The drive system is required to provide sufficient power to twist the test specimen at a constant rotational speed. Electric drive systems were used in most of the early torsion testing machines, such as the one shown in Fig. 5 (Ref 9). The electric drive system consists of an electric motor, gearbox or hydraulic reducers, a flywheel, and a clutch and brake system. The torsion machine shown here uses a 2.2 kW induction motor and a drive train consisting of two planetary gear reducers and three gear pairs and is capable of providing 24 different rotational speeds in the range from 0.0115 to 1745 rpm. A flywheel is required in this system in order to maintain approximately constant rotational speed at clutch engagement and during specimen twisting. A pneumatic disk clutch that is activated by a three-way solenoid provides quick transmission of torque from the flywheel to the test section. An inherent problem in this type of drive system is the lack of positive engagement between the drive system and the test section, which causes loss of rotational speed because of slippage, especially at high rates of twisting. This problem can be avoided to some extent by using a positive engagement mechanical “dog or ramp” clutch (Ref 26, 27) or an electromagnetic clutch (Ref 29) that allows shear strain rates of the order to 300 and 1000 s^{-1} , respectively, to be achieved.

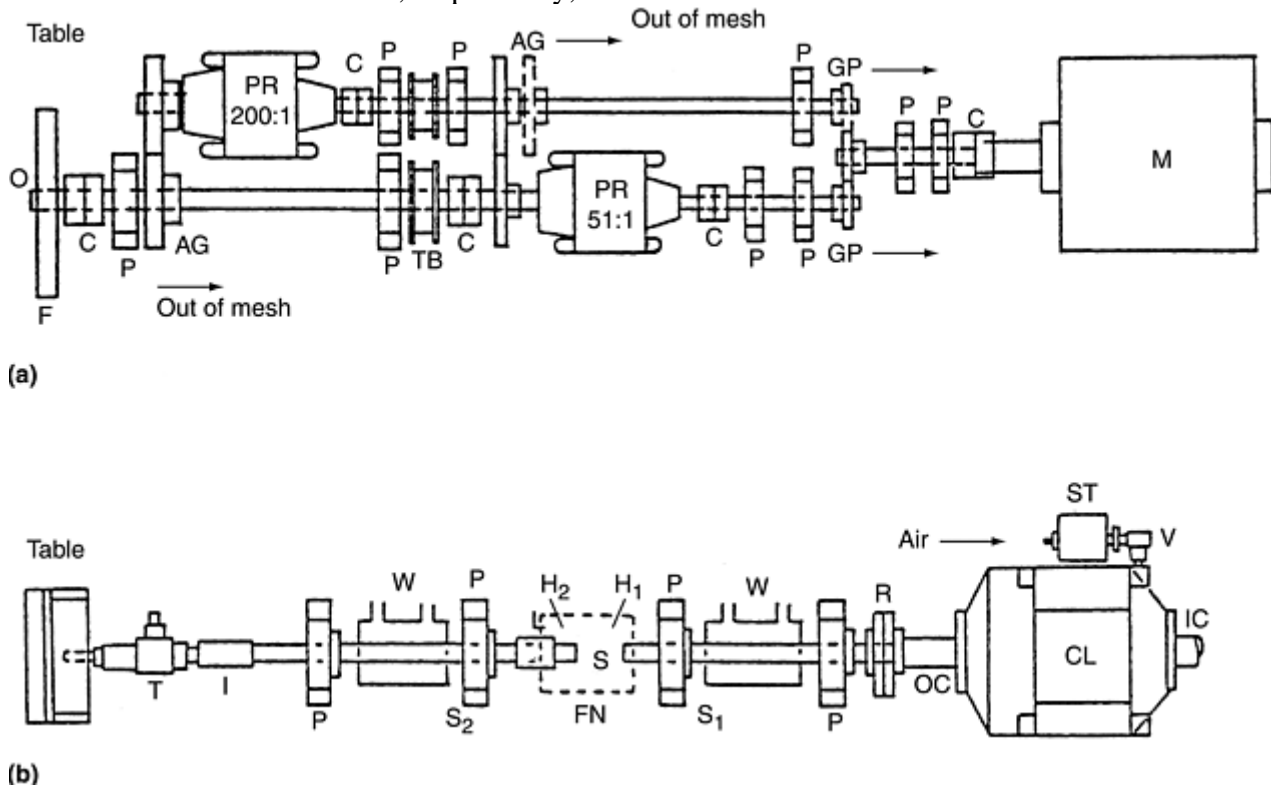


Fig. 5 Torsion testing machine. (a) Drive section. C, coupling; F, flywheel; M electric motor; O, output shaft; P, pillow block; AG, gear pair; GP, interchangeable gear pair; PR, planetary reducer; TB, timing belt drive. (b) Test section. H1, H2, specimen holders; I, low inertia coupling; L, linear bearing; P, pillow block; S, specimen; S1, S2, shafts; T, transducer; V, solenoid valve; W, water jacket; CL, clutch; FN, furnace; IC, input shaft; OC, output shaft; ST, surge tank

The use of a hydraulic drive system abolishes the need for a drive train and clutch and brake system, thus eliminating the inherent problems associated with these components. A typical hydraulic drive system consists of a hydraulic motor (Ref 30) or a hydraulic rotary actuator (Ref 31), a source of hydraulic power in the form of pressurized oil, and servocontrollers for controlling the flow of oil by means of servovalves. The torque in the

hydraulic drive system is provided by the pressurized oil as it pushes against a set of rotary vanes. The advantage of this system is that it can be accurately controlled in a closed-loop arrangement so that the prescribed loading history can be obtained. Because angular displacement in a rotary actuator system is limited to a fraction of a revolution, special torsion specimen designs with a short gage length and a large gage diameter are required to achieve high values of shear strain and strain rate.

The test section in most torsion testing machines consists of a pair of grips for attaching both ends of the specimen to the torsion machine and a furnace for heating the specimen. One end of the test specimen is attached to the output side of the loading train. The other end of the specimen is rigidly mounted to the torque and axial force transducers. Grips are usually designed in such a way as to eliminate the relative motion between the test specimen and the testing machine. The grips shown in Fig. 6 utilize a chuck-type design with three moving jaws. When the test is conducted at elevated temperatures, special care must be taken to reduce the conduction of heat from the specimen to the drive train and the load cells. This is usually done by constructing a cooling water jacket around the grips. In addition, the grip design shown in Fig. 6 uses a thick ceramic disk as a thermal insulator.

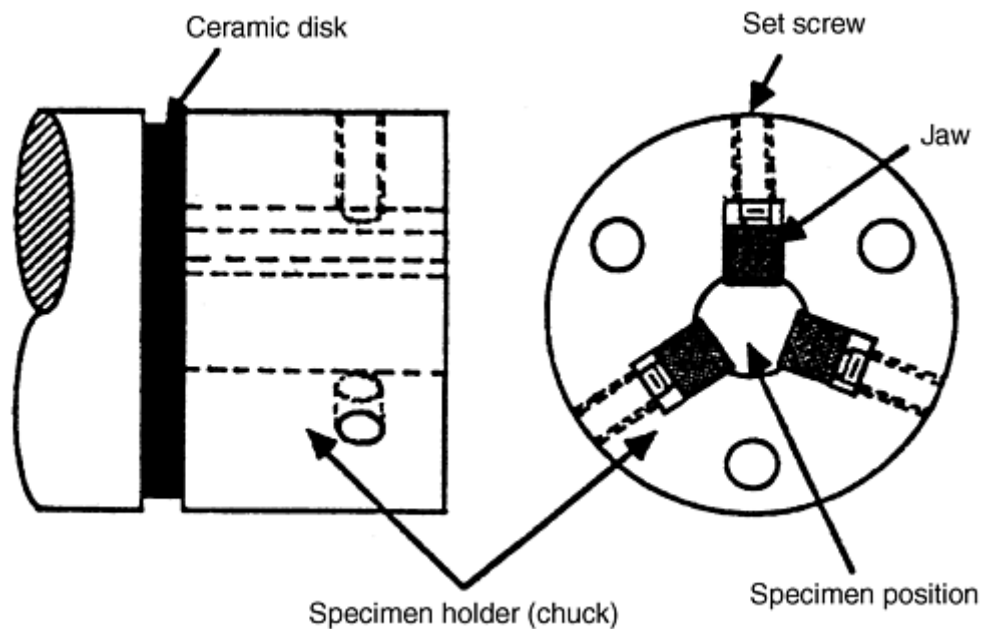


Fig. 6 Detailed view of a torsion test specimen holder with a three-jaw chuck

It is known that torsional straining of metals induces axial stresses when the testing is conducted under fixed-end conditions (i.e., specimen ends are constrained axially). Similarly, when testing is conducted under free-end conditions (i.e., one end of the specimen is allowed to move axially), the specimen undergoes lengthening or shortening depending on the workpiece material and testing temperature. These axial effects are inherent in torsion testing because they are associated with texture development and evolution in the workpiece material, as discussed in the previous section. Therefore, it is necessary when conducting a torsion test to monitor these changes and account for their effects when determining the effective stress-strain relationships from experimental data. Conducting a test under free-end conditions is more difficult than under fixed-end conditions because of the difficulties in designing grips or fixtures that allow both a rigid reaction to the torsional load applied and a true free movement axially. In the torsion machine discussed previously, a linear bearing mechanism was used to ensure free-end movement of the specimen. This mechanism is shown in Fig. 7. It consists of three case-hardened steel shafts press fitted 120° apart in the free end of the specimen holder. The three shafts slide freely inside three pairs of linear bearings press fitted 120° apart in the fixed end of the holder. A linear differential transformer is used to continuously monitor the relative motion between the free end and fixed end of the linear bearing mechanism.

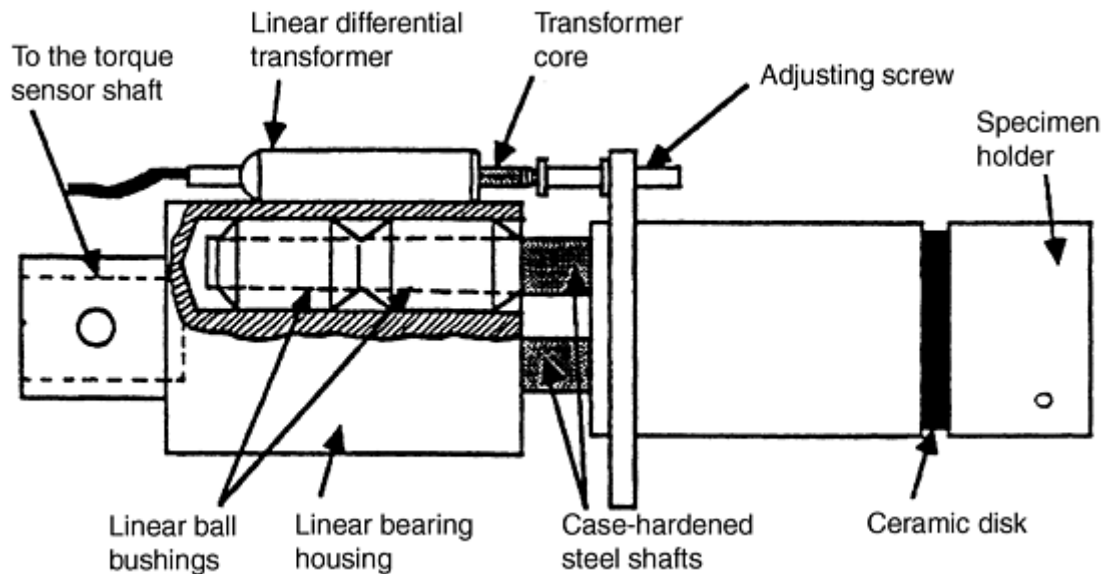


Fig. 7 Detailed view of a linear bearing mechanism used to ensure free-end movement of the specimen in torsion testing

Load and Displacement Transducers. It was shown previously that knowledge of the applied torque and rotational displacement are sufficient to calculate the state of shear stress and shear strain based on specimen geometry. It is of interest, therefore, to measure both the applied torque and rotation continuously during the torsion test. It is also necessary to monitor the axial force induced by fixed-end testing or the change in specimen length induced in free-end testing. The measurement of axial and torsional loads are performed using various types of reaction-load transducers that utilize foil strain gages as the load-sensing element. These load cells are conveniently mounted at the fixed end of the torsion machine. Rotational displacement is measured electrically using a variable resistor or a differential capacitor or optically using photoelectric devices in combination with a perforated disk or an optically encoded shaft. The torsion machine uses a perforated disk with 120 holes equally spaced around its circumference. A photo transistor detects the holes and sends an electric pulse to the control panel for conditioning and amplification. The output signal is recorded simultaneously with the torque signal generated by the load cell using a chart recorder or a storage oscilloscope.

Torsion Specimens. A wide range of specimen sizes and geometries have been used in the past, and a standard size or geometry has not been agreed upon. A good survey of various specimen designs used in torsion testing is given in Ref 27. A typical torsion specimen is composed of a uniform cylindrical gage section, two shoulders for clamping into the machine grips, and two fillets to connect the gage section to the shoulders. Solid and hollow gage sections have been used. Thin-walled specimens that have a hollow gage section and a wall thickness that is a small fraction of the radius of the section offer the possibility of homogeneous stress and strain states in the gage section. However, because of their tendency toward torsional buckling, solid specimens are preferred over hollow specimens for large deformation studies. The problem of torsional buckling in thin-walled specimens can be suppressed, to some extent, by shortening the gage length. The range of ratios of gage length to gage radius (l/r) for specimens reported in the literature varies from 0.67 to 8 (Ref 28). A small length-to-radius ratio is preferred because it provides an increase in the maximum shear strain and shear strain rate for a given rotational displacement and rotational speed, respectively.

In torsion specimen design, care must be taken to maintain uniform plastic deformation throughout the gage section. This can be achieved by maintaining a truly uniform cross section, proper polishing of the outside surface to eliminate stress raisers such as scratches, and by providing properly sized fillets. In addition, bulky shoulders as compared with the gage section will help to constrain the plastic deformation in the gage section. White (Ref 32) performed an analysis of the plastic deformation in a thin-walled specimen using the finite element method. He reported that plastic deformation extends into the transition region between the gage section and the grips. The fraction of the total torsional displacement that is experienced by the gage section was determined. Knowledge of this factor allows for the correct evaluation of shear strain in the gage section. Khoddam and coworkers (Ref 33) studied the effect of plastic deformation outside the gage section on the analysis of shear stress and shear strain. They suggested that an effective gage length be used in the calculation

of stress and strain, instead of the actual length. For a power law constitutive equation, the effective length was found to be a function of specimen geometry and the coefficients in the constitutive equation.

Another factor that may affect the uniformity of deformation during twisting is the temperature rise in the gage section that is caused by plastic deformation. At high rates of deformation, and especially for materials with low thermal conductivity, the temperature rise may lead to localized flow and shear banding (Ref 34, 35, and 36). The temperature distribution in torsion specimens can be determined numerically as described in previous work. Once the temperature distribution in the gage section is known, the effect of temperature on flow stress can be determined (Ref 36). Zhou and Clode (Ref 37) used the finite element method to study the effect of specimen design on temperature rise in the gage section of an aluminum specimen. Their work showed the effect of temperature rise can be minimized by proper specimen design, but it cannot be totally eliminated.

References cited in this section

9. J.A. Bailey, S.L. Haas, and M.K. Shah, *Int. J. Mech. Sci.*, Vol 14, 1972, p 735
26. R.S. Culver, *Exp. Mech.*, Vol 12, 1972, p 398–405
27. H. Kobayashi, “Shear Localization and Fracture in Torsion of Metals,” Ph.D. thesis, University of Reading, Reading, U.K., 1987
28. M.J. Luton, *Workability Testing Techniques*, G.E. Dieter, Ed., American Society for Metals, 1984, p 95
29. T. Vinh, M. Afzali, and A. Roche, *Third Int. Conf. Mechanical Behavior of Materials (ICM 3)*, Vol 2, K.J. Miller and R.F. Smith, Ed., Pergamon Press, 1979, p 633–642
30. H. Weiss, D.H. Skinner, and J.R. Everett, *J. Phys. E, Sci. Instr.*, Vol 6, 1973, p 709–714
31. U.S. Lindholm, A. Nagy, G.R. Johnson, and J.M. Hoegfeldt, *J. Eng. Mater. Technol.*, Vol 102, 1980, p 376–381
32. C.S. White, *J. Eng. Mater. Technol.*, Vol 114, 1992, p 384–389
33. I. Khoddam, Y.C. Lam, and P.F. Thomson, *J. Test. Eval.*, Vol 26, 1998, p 157–167
34. G.R. Johnson, *J. Eng. Mater. Technol.*, Vol 103, 1981, p 201–206
35. H. Kobayashi and B. Dodd, *Int. J. Impact Eng.*, Vol 8, 1989, p 1–13
36. J.Y. Sheikh-Ahmad and J.A. Bailey, *J. Eng. Mater. Technol.*, Vol 117, 1995, p 255–259
37. M. Zhou and M.P. Clode, *Mater. Des.*, Vol 17, 1996, p 275–281

Fundamental Aspects of Torsional Loading

John A. Bailey, North Carolina State University; Jamal Y. Sheikh-Ahmad, Wichita State University

References

1. C.L. Harmsworth, *Mechanical Testing*, Vol 8, *ASM Handbook*, American Society for Metals, 1985, p 62

2. S.P. Timoshenko and J.N. Goodier, *Theory of Elasticity*, 3rd ed., McGraw-Hill, 1970, p 291
3. W.J.McG. Tegart, *Elements of Mechanical Metallurgy*, Macmillan, 1967, p 64
4. A. Nadai, *Theory of Flow and Fracture of Solids*, Vol 1, McGraw-Hill, 1950, p 349
5. G.R. Canova, et al., *Formability of Metallic Materials—2000 A.D.*, STP 753, J.R. Newby and B.A. Niemeier, Ed., ASTM, 1982, p 189
6. D.S. Fields and W.A. Backofen, *Proc. ASTM*, Vol 57, 1957, p 1259
7. S. Kalpakjian, *Mechanical Processing of Materials*, D. Van Nostrand, 1967, p 31
8. E.M. Mielnik, *Metal Working Science and Engineering*, McGraw-Hill, 1991, p 220
9. J.A. Bailey, S.L. Haas, and M.K. Shah, *Int. J. Mech. Sci.*, Vol 14, 1972, p 735
10. G. Dieter, *Mechanical Metallurgy*, 2nd ed., McGraw-Hill, 1976, p 353
11. F. Garafalo, *Fundamentals of Creep and Creep Rupture of Metals*, Macmillan, 1965
12. C.M. Sellars and W.J.McG. Tegart, *Int. Met. Rev.*, Vol 7, 1972, p 1
13. J.J. Jonas, C.M. Sellars, and W.J.McG. Tegart, *Met. Rev.*, Vol 130, 1969, p 14
14. G.R. Johnson and W.H. Cook, *Proc. Seventh Int. Symp. Ballistics*, 1983, p 541
15. G.R. Johnson, J.M. Hoegfeldt, U.S. Lindholm, and A. Nagy, *J. Eng. Mater. Technol. (Trans. ASME)*, Vol 105, 1983, p 42
16. G.R. Johnson, J.M. Hoegfeldt, U.S. Lindholm, and A. Nagy, *J. Eng. Mater. Technol. (Trans. ASME)*, Vol 105, 1983, p 48
17. R.R. Hill, *The Mathematical Theory of Plasticity*, Clarendon Press, Oxford, 1950, p 317
18. J.A. Bailey, S.L. Haas, and K.C. Naweib, *J. Basic Eng. (Trans. ASME)*, March 1972, p 231
19. F. Montheillet, M. Cohen, and J.J. Jonas, *Acta Metall.*, Vol 32, 1984, p 2077–2089
20. F. Montheillet, P. Gilormini, and J. J. Jonas, *Acta Metall.*, Vol. 33, 1985, p 2126–2136
21. J.J. Jonas, *Int. J. Mech. Sci.*, Vol 35, 1993, p 1065–1077
22. L.S. Toth and J.J. Jonas, *Scr. Metall.*, Vol 27, 1992, p 359–363
23. L.S. Toth, J.J. Jonas, D. Daniel, and J.A. Bailey, *Textures and Microstructures*, Vol 19, 1992, p 245–262
24. J.J. Jonas and L.S. Toth, *Scr. Metall.*, Vol 27, 1992, p 1575–1580
25. S.L. Semiatin, G.D. Lahoti, and J.J. Jonas, *Mechanical Testing*, Vol 8, *ASM Handbook*, American Society for Metals, 1985, p 154
26. R.S. Culver, *Exp. Mech.*, Vol 12, 1972, p 398–405

27. H. Kobayashi, "Shear Localization and Fracture in Torsion of Metals," Ph.D. thesis, University of Reading, Reading, U.K., 1987
28. M.J. Luton, *Workability Testing Techniques*, G.E. Dieter, Ed., American Society for Metals, 1984, p 95
29. T. Vinh, M. Afzali, and A. Roche, *Third Int. Conf. Mechanical Behavior of Materials (ICM 3)*, Vol 2, K.J. Miller and R.F. Smith, Ed., Pergamon Press, 1979, p 633–642
30. H. Weiss, D.H. Skinner, and J.R. Everett, *J. Phys. E, Sci. Instr.*, Vol 6, 1973, p 709–714
31. U.S. Lindholm, A. Nagy, G.R. Johnson, and J.M. Hoegfeldt, *J. Eng. Mater. Technol.*, Vol 102, 1980, p 376–381
32. C.S. White, *J. Eng. Mater. Technol.*, Vol 114, 1992, p 384–389
33. I. Khoddam, Y.C. Lam, and P.F. Thomson, *J. Test. Eval.*, Vol 26, 1998, p 157–167
34. G.R. Johnson, *J. Eng. Mater. Technol.*, Vol 103, 1981, p 201–206
35. H. Kobayashi and B. Dodd, *Int. J. Impact Eng.*, Vol 8, 1989, p 1–13
36. J.Y. Sheikh-Ahmad and J.A. Bailey, *J. Eng. Mater. Technol.*, Vol 117, 1995, p 255–259
37. M. Zhou and M.P. Clode, *Mater. Des.*, Vol 17, 1996, p 275–281

Uniaxial Tension Testing

John M. (Tim) Holt, Alpha Consultants and Engineering

Introduction

THE TENSION TEST is one of the most commonly used tests for evaluating materials. In its simplest form, the tension test is accomplished by gripping opposite ends of a test item within the load frame of a test machine. A tensile force is applied by the machine, resulting in the gradual elongation and eventual fracture of the test item. During this process, force-extension data, a quantitative measure of how the test item deforms under the applied tensile force, usually are monitored and recorded. When properly conducted, the tension test provides force-extension data that can quantify several important mechanical properties of a material. These mechanical properties determined from tension tests include, but are not limited to, the following:

- Elastic deformation properties, such as the modulus of elasticity (Young's modulus) and Poisson's ratio
- Yield strength and ultimate tensile strength
- Ductility properties, such as elongation and reduction in area
- Strain-hardening characteristics

These material characteristics from tension tests are used for quality control in production, for ranking performance of structural materials, for evaluation of newly developed alloys, and for dealing with the static-strength requirements of design.

The basic principle of the tension test is quite simple, but numerous variables affect results. General sources of variation in mechanical-test results include several factors involving materials, namely, methodology, human factors, equipment, and ambient conditions, as shown in the "fish-bone" diagram in Fig. 1. This article

discusses the methodology of the tension test and the effect of some of the variables on the tensile properties determined. The following methodology and variables are discussed:

- Shape of the item being tested
- Method of gripping the item
- Method of applying the force
- Determination of strength properties other than the maximum force required to fracture the test item
- Ductility properties to be determined
- Speed of force application or speed of elongation (e.g., control of stress rate or strain rate)
- Test temperature

The main focus of this article is on the methodology of tension tests as it applies to metallic materials. Factors associated with test machines and their method of force application are described in more detail in the article “Testing Machines and Strain Sensors” in this Volume.

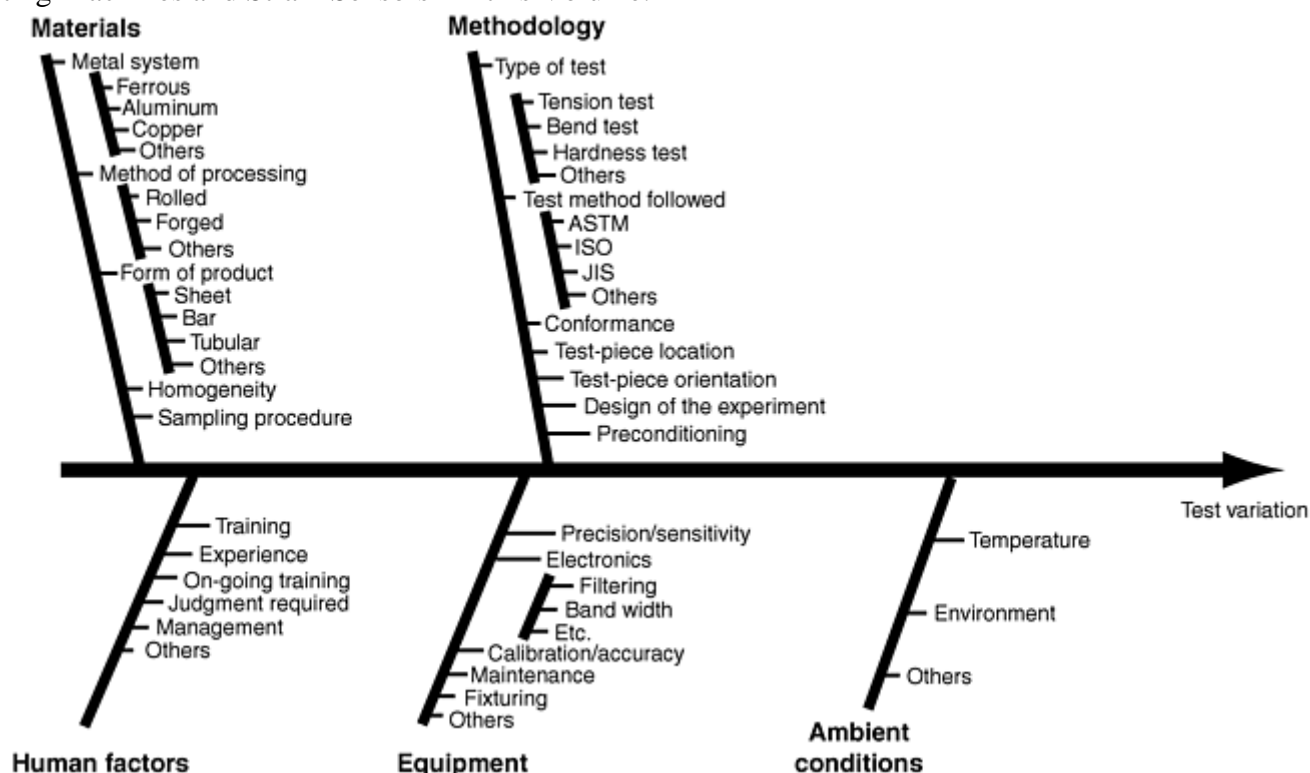


Fig. 1 “Fish-bone” diagram of sources of variability in mechanical-test results

This article does not address the tension testing of nonmetallic materials, such as plastics, elastomers, or ceramics. Although uniaxial tension testing is used in the mechanical evaluation of these materials, other test methods often are used for mechanical-property evaluation. The general concept of tensile properties is very similar for these nonmetallic materials, but there are also some very important differences in their behavior and the required test procedures for these materials:

- *Tension-test results for plastics* depend more strongly on the strain rate because plastics are viscoelastic materials that exhibit time-dependent deformation (i.e., creep) during force application. Plastics are also more sensitive to temperature than metals. Thus, control of strain rates and temperature are more critical with plastics, and sometimes tension tests are run at more than one strain and/or temperature. The ASTM standard for tension testing of plastics is D 638.
- *Tension testing of ceramics* requires more attention to alignment and gripping of the test piece* in the test machine because ceramics are brittle materials that are extremely sensitive to bending strains and because the hard surface of ceramics reduces the effectiveness of frictional gripping devices. The need for a large gripping areas thus requires the use of larger test pieces (Ref 1). The ASTM standard for tension testing of monolithic ceramics at room temperature is C 1275. The standard for continuous fiber-reinforced advanced ceramics at ambient temperatures is C 1273.

- *Tension testing of elastomers* is described in ASTM D 412 with specific instructions about test-piece preparation, equipment, and test conditions. Tensile properties of elastomers vary widely, depending on the particular formulation, and scatter both within and between laboratories is appreciable compared with the scatter of tensile-test results of metals (Ref 2). The use of tensile-test results of elastomers is limited principally to comparison of compound formulations.

Footnote

* The term “test piece” is used in this article for what is often called a “specimen” (see “The Test Piece” in this article).

References cited in this section

1. D. Lewis, Tensile Testing of Ceramics and Ceramic-Matrix Composites, *Tensile Testing*, P. Han, Ed., ASM International, 1992, p 147–182
2. R.J. Del Vecchio, Tensile Testing of Elastomers, *Tensile Testing*, P. Han, Ed., ASM International, 1992, p 135–146

Uniaxial Tension Testing

John M. (Tim) Holt, Alpha Consultants and Engineering

Definitions and Terminology

The basic results of a tension test and other mechanical tests are quantities of stress and strain that are measured. These basic terms and their units are briefly defined here, along with discussions of basic stress-strain behavior and the differences between related terms, such as stress and force and strain and elongation.

Load (or force) typically refers to the force acting on a body. However, there is currently an effort within the technical community to replace the word load with the more precise term *force*, which has a distinct meaning for any type of force applied to a body. Load applies, in a strict sense, only to the gravitational force that acts on a mass. Nonetheless, the two terms are often used interchangeably.

Force is usually expressed in units of pounds-force, lbf, in the English system. In the metric system, force is expressed in units of newtons (N), where one newton is the force required to give a 1 kg mass an acceleration of 1 m/s^2 ($1 \text{ N} = 1 \text{ kgm/s}^2$). Although newtons are the preferred metric unit, force is also expressed as kilogram force, kgf, which is the gravitational force on a 1 kg mass on the surface of the earth. The numerical conversions between the various units of force are as follows:

- $1 \text{ lbf} = 4.448222 \text{ N}$ or $1 \text{ N} = 0.2248089 \text{ lbf}$
- $1 \text{ kgf} = 9.80665 \text{ N}$

In some engineering disciplines, such as civil engineering, the quantity of 1000 lbf is also expressed in units of kip, such that $1 \text{ kip} = 1000 \text{ lbf}$.

Stress is simply the amount of force that acts over a given cross-sectional area. Thus, stress is expressed in units of force per area units and is obtained by dividing the applied force by the cross-sectional area over which it acts. Stress is an important quantity because it allows strength comparison between tests conducted using test pieces of different sizes and/or shapes. When discussing strength values in terms of force, the load (force) carrying capacity of a test piece is a function of the size of the test piece. However, when material strength is defined in terms of stress, the size or shape of the test piece has little or no influence on stress measurements of strength (provided the cross section contains at least 10 to 15 metallurgical grains).

Stress is typically denoted by either the Greek symbol sigma, σ , or by s , unless a distinction is being made between true stress and nominal (engineering) stress as discussed in this article. The units of stress are typically lbf/in.² (psi) or thousands of psi (ksi) in the English system and a pascal (Pa) in the metric system. Engineering stresses in metric units are also expressed in terms of newtons per area (i.e., N/m² or N/mm²) or as kilopascals (kPa) and megapascals (MPa). Conversions between these various units of stress are as follows:

- 1 Pa = 1.45×10^{-4} psi
- 1 Pa = 1 N/m²
- 1 kPa = 10³ Pa or 1 kPa = 0.145 psi
- 1 MPa = 10⁶ Pa or 1 MPa = 0.145 ksi
- 1 N/mm² = 1 MPa

Strain and elongation are similar terms that define the amount of deformation from a given amount of applied stress. In general terms, strain is defined (by ASTM E 28) as “the change per unit length due to force in an original linear dimension.” The phrase *change per unit length* means that a change in length, ΔL , is expressed as a ratio of the original length, L_0 . This change in length can be expressed in general terms as a strain or as elongation of gage length, as described subsequently in the context of a tension test.

Strain is a general term that can be expressed mathematically, either as engineering strain or as true strain. Nominal (or engineering) strain is often represented by the letter e , and logarithmic (or true) strain is often represented by the Greek letter ε . The equation for engineering strain, e , is based on the nominal change in length, (ΔL) where:

$$e = \Delta L/L_0 = (L - L_0)/L_0$$

The equation for true strain, ε , is based on the instantaneous change in length (dl) where:

$$\varepsilon = \int_{L_0}^L \frac{dl}{l} = \ln\left(\frac{L}{L_0}\right)$$

These two basic expressions for strain are interrelated, such that:

$$\varepsilon = \ln(1 + e)$$

In a tension test, the typical measure of strain is engineering strain, e , and the units are inches per inch (or millimeter per millimeter and so on). Often, however, no units are shown because strain is the ratio of length in a given measuring system.

This article refers to only engineering strain unless otherwise specified. In a tension test, true strain is based on the change in the cross-sectional area of the test piece as it is loaded. It is not further discussed herein, but a detailed discussion is found in the article “Mechanical Behavior under Tensile and Compressive Loads” in this Volume.

Elongation is a term that describes the amount that the test-piece stretches during a tension test. This stretching or elongation can be defined either as the total amount of stretch, ΔL , that a part undergoes or the increase in gage length per the initial gage length, L_0 .

The latter definition is synonymous with the meaning of engineering strain, $\Delta L/L_0$, while the first definition is the total amount of extension. Because two definitions are possible, it is imperative that the exact meaning of elongation be understood each time it is used.

This article uses the term elongation, e , to mean nominal or engineering strain (i.e., $e = \Delta L/L_0$). The amount of stretch is expressed as extension, or the symbol ΔL . In many cases, elongation, e , is also reported as a percentage change in gage length as a measure of ductility (i.e., percent elongation), $(\Delta L/L_0) \times 100$.

Engineering Stress and True Stress. Along with the previous descriptions of engineering strain and true strain, it is also possible to define stress in two different ways as engineering stress and true stress. As is intuitive, when a tensile force stretches a test piece, the cross-sectional area must decrease (because the overall volume of the test piece remains essentially constant). Hence, because the cross section of the test piece becomes smaller during a test, the value of stress depends on whether it is calculated based on the area of the unloaded test piece (the initial area) or on the area resulting from that applied force (the instantaneous area). Thus, in this context, there are two ways to define stress:

- *Engineering stress, s* : The force at any time during the test divided by the initial area of the test piece; $s = F/A_0$ where F is the force, and A_0 is the initial cross section of a test piece.
- *True stress, σ* : The force at any time divided by the instantaneous area of the test piece; $\sigma = F/A_i$ where F is the force, and A_i is the instantaneous cross section of a test piece.

Because an increasing force stretches a test piece, thus decreasing its cross-sectional area, the value of true stress will always be greater than the nominal, or engineering, stress.

These two definitions of stress are further related to one another in terms of the strain that occurs when the deformation is assumed to occur at a constant volume (as it frequently is). As previously noted, strain can be expressed as either engineering strain (e) or true strain, where the two expressions of strain are related as $\epsilon = \ln(1 + e)$. When the test-piece volume is constant during deformation (i.e., $A_i L_i = A_0 L_0$), then the instantaneous cross section, A_i , is related to the initial cross section, A_0 , where

$$A = A_0 \exp \{-\epsilon\}$$

$$= A_0 / (1 + e)$$

If these expressions for instantaneous and initial cross sections are divided into the applied force to obtain values of true stress (at the instantaneous cross section, A_i) and engineering stress (at the initial cross section, A_0), then:

$$\sigma = s \exp \{\epsilon\} = s (1 + e)$$

Typically, engineering stress is more commonly considered during uniaxial tension tests. All discussions in this article are based on nominal engineering stress and strain unless otherwise noted. More detailed discussions on true stress and true strain are in the article “Mechanical Behavior under Tensile and Compressive Loads” in this Volume.

Uniaxial Tension Testing

John M. (Tim) Holt, Alpha Consultants and Engineering

Stress-Strain Behavior

During a tension test, the force applied to the test piece and the amount of elongation of the test piece are measured simultaneously. The applied force is measured by the test machine or by accessory force-measuring devices. The amount of stretching (or extension) can be measured with an extensometer. An extensometer is a device used to measure the amount of stretch that occurs in a test piece. Because the amount of elastic stretch is quite small at or around the onset of yielding (in the order of 0.5% or less for steels), some manner of magnifying the stretch is required. An extensometer may be a mechanical device, in which case the magnification occurs by mechanical means. An extensometer may also be an electrical device, in which case the magnification may occur by mechanical means, electrical means, or by a combination of both. Extensometers generally have fixed gage lengths. If an extensometer is used only to obtain a portion of the stress-strain curve sufficient to determine the yield properties, the gage length of the extensometer may be shorter than the gage length required for the elongation-at-fracture measurement. It may also be longer, but in general, the extensometer gage length should not exceed approximately 85 to 90% of the length of the reduced section or of the distance between the grips for test pieces without reduced sections. This ratio for some of the most common test configurations with a 2 in. gage length and $2\frac{1}{4}$ in. reduced section is 0.875%.

The applied force, F , and the extension, ΔL , are measured and recorded simultaneously at regular intervals, and the data pairs can be converted into a stress-strain diagram as shown in Fig. 2. The conversion from force-extension data to stress-strain properties is shown schematically in Fig. 2(a). Engineering stress, s , is obtained by dividing the applied force by the original cross-sectional area, A_0 , of the test piece, and strain, e , is obtained by dividing the amount of extension, ΔL , by the original gage length, L . The basic result is a stress-strain curve

(Fig. 2b) with regions of elastic deformation and permanent (plastic) deformation at stresses greater than those of the elastic limit (EL in Fig. 2b).

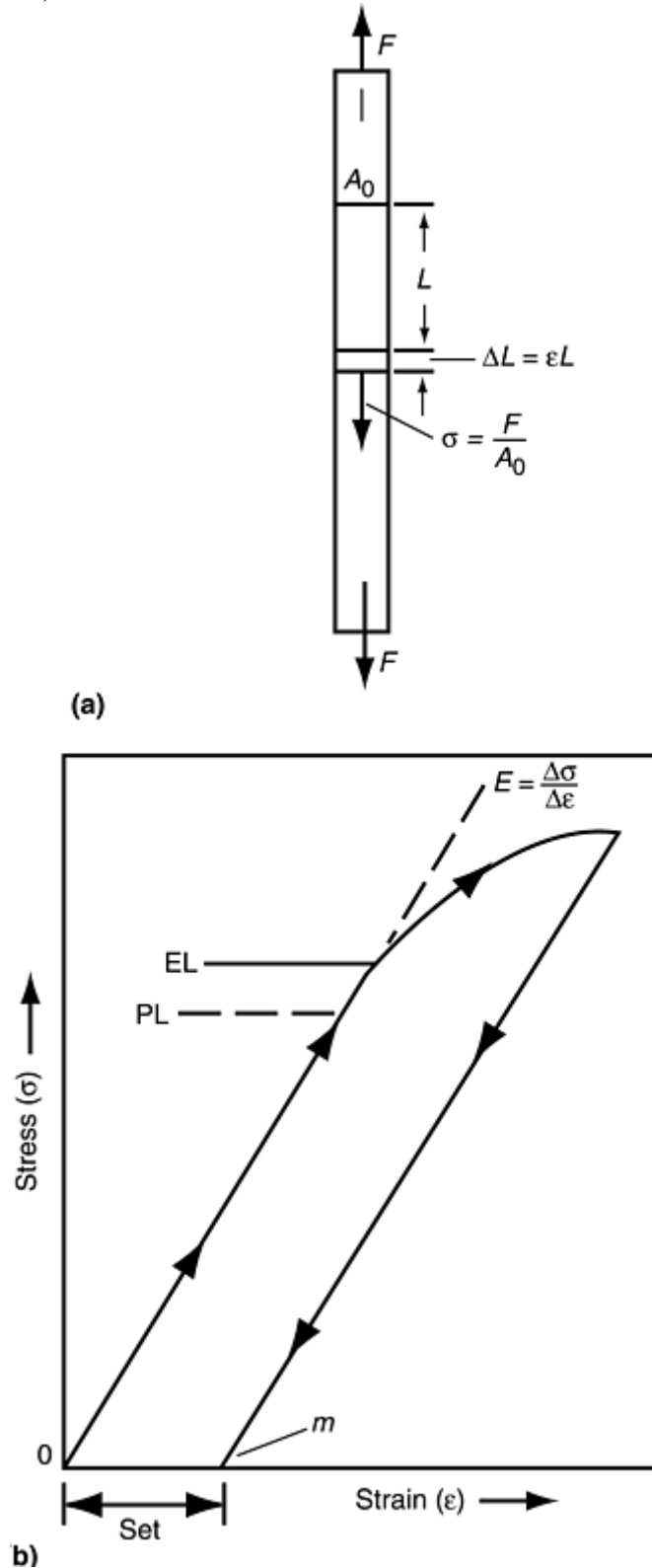


Fig. 2 Stress-strain behavior in the region of the elastic limit. (a) Definition of σ and ϵ in terms of initial test piece length, L , and cross-sectional area, A_0 , before application of a tensile force, F . (b) Stress-strain curve for small strains near the elastic limit (EL)

Typical stress-strain curves for three types of steels, aluminum alloys, and plastics are shown in Fig. 3 (Ref 3). Stress-strain curves for some structural steels are shown in Fig. 4(a) (Ref 4) for elastic conditions and for small amounts of plastic deformation. The general shape of the stress-strain curves can be described for deformation in this region. However, as plastic deformation occurs, it is more difficult to generalize about the shape of the stress-strain curve. Figure 4(b) shows the curves of Fig. 4(a) continued to fracture.

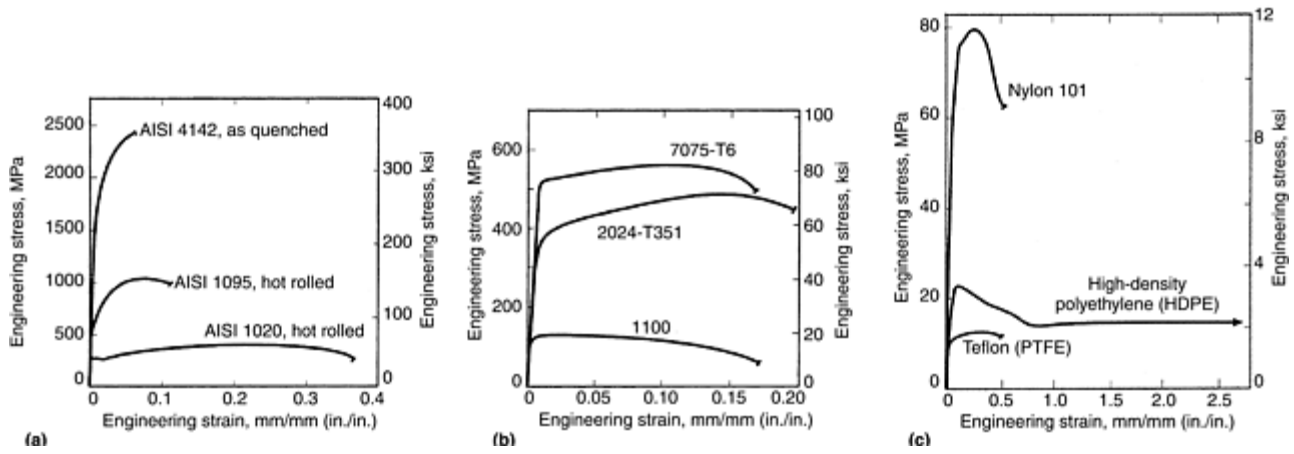


Fig. 3 Typical engineering stress-strain curves from tension tests on (a) three steels, (b) three aluminum alloys, and (c) three plastics. PTFE, polytetrafluoroethylene. Source: Ref 3

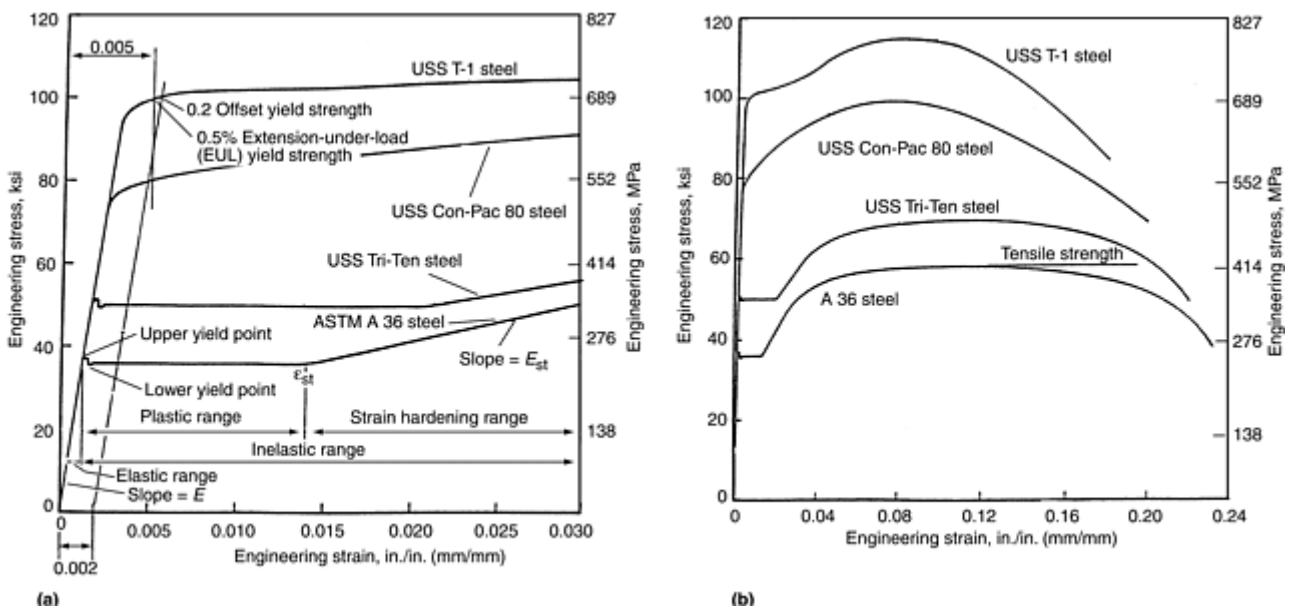


Fig. 4 Typical stress-strain curves for structural steels having specified minimum tensile properties. (a) Portions of the stress-strain curves in the yield-strength region. (b) Stress-strain curves extended through failure. Source: Ref 4

Elastic deformation occurs in the initial portion of a stress-strain curve, where the stress-strain relationship is initially linear. In this region, the stress is proportional to strain. Mechanical behavior in this region of stress-strain curve is defined by a basic physical property called the modulus of elasticity (often abbreviated as E). The modulus of elasticity is the slope of the stress-strain line in this linear region, and it is a basic physical property of all materials. It essentially represents the spring constant of a material.

The modulus of elasticity is also called Hooke's modulus or Young's modulus after the scientists who discovered and extensively studied the elastic behavior of materials. The behavior was first discovered in the late 1600s by the English scientist Robert Hooke. He observed that a given force would always cause a repeatable, elastic deformation in all materials. He further discovered that there was a force above which the deformation was no longer elastic; that is, the material would not return to its original length after release of the force. This limiting force is called the elastic limit (EL in Fig. 2b). Later, in the early 1800s, Thomas Young, an English physicist, further investigated and described this elastic phenomenon, and so his name is associated with it.

The proportional limit (PL) is a point in the elastic region where the linear relationship between stress and strain begins to break down. At some point in the stress-strain curve (PL in Fig. 2b), linearity ceases, and small increase in stress causes a proportionally larger increase in strain. This point is referred to as the proportional limit (PL) because up to this point, the stress and strain are proportional. If an applied force below the PL point

is removed, the trace of the stress and strain points returns along the original line. If the force is reapplied, the trace of the stress and strain points increases along the original line. (When an exception to this linearity is observed, it usually is due to mechanical hysteresis in the extensometer, the force indicating system, the recording system, or a combination of all three.)

The elastic limit (EL) is a very important property when performing a tension test. If the applied stresses are below the elastic limit, then the test can be stopped, the test piece unloaded, and the test restarted without damaging the test piece or adversely affecting the test results. For example, if it is observed that the extensometer is not recording, the force-elongation curve shows an increasing force, but no elongation. If the force has not exceeded the elastic limit, the test piece can be unloaded, adjustments made, and the test restarted without affecting the results of the test. However, if the test piece has been stressed above the EL, plastic deformation (set) will have occurred (Fig. 2b), and there will be a permanent change in the stress-strain behavior of the test piece in subsequent tension (or compression) tests.

The PL and the EL are considered identical in most practical instances. In theory, however, the EL is considered to be slightly higher than the PL, as illustrated in Fig. 2b. The measured values of EL or PL are highly dependent on the magnification and sensitivity of the extensometer used to measure the extension of the test piece. In addition, the measurement of PL and EL also highly depends on the care with which a test is performed.

Plastic Deformation (Set) from Stresses above the Elastic Limit. If a test piece is stressed (or loaded) and then unloaded, any retest proceeds along the unloading path whether or not the elastic limit was exceeded. For example, if the initial stress is less than the elastic limit, the load-unload-reload paths are identical. However, if a test piece is stressed in tension beyond the elastic limit, then the unload path is offset and parallel to the original loading path (Fig. 2b). Moreover, any subsequent tension measurements will follow the previous unload path parallel to the original stress-strain line. Thus, the application and removal of stresses above the elastic limit affect all subsequent stress-strain measurements.

The term *set* refers to the permanent deformation that occurs when stresses exceed the elastic limit (Fig. 2b). ASTM E 6 defines set as the strain remaining after the complete release of a load-producing deformation. Because set is permanent deformation, it affects subsequent stress-strain measurements whether the reloading occurs in tension or compression. Likewise, permanent set also affects all subsequent tests if the initial loading exceeds the elastic limit in compression. Discussions of these two situations follow.

Reloading after Exceeding the Elastic Limit in Tension. If a test piece is initially loaded in tension beyond the elastic limit and then unloaded, the unload path is parallel to the initial load path but offset by the set; on reloading in tension, the unloading path will be followed. Figure 5 illustrates a series of stress-strain curves obtained using a machined round test piece of steel. (The strain axis is not to scale.) In this figure, the test piece was loaded first to Point A and unloaded. The area of the test piece was again determined (A_2) and reloaded to Point B and unloaded. The area of the test piece was determined for a third time (A_3) and reloaded until fracture occurred. Because during each loading the stresses at Points A and B were in excess of the elastic limit, plastic deformation occurred. As the test piece is elongated in this series of tests, the cross-sectional area must decrease because the volume of the test piece must remain constant. Therefore, $A_1 > A_2 > A_3$.

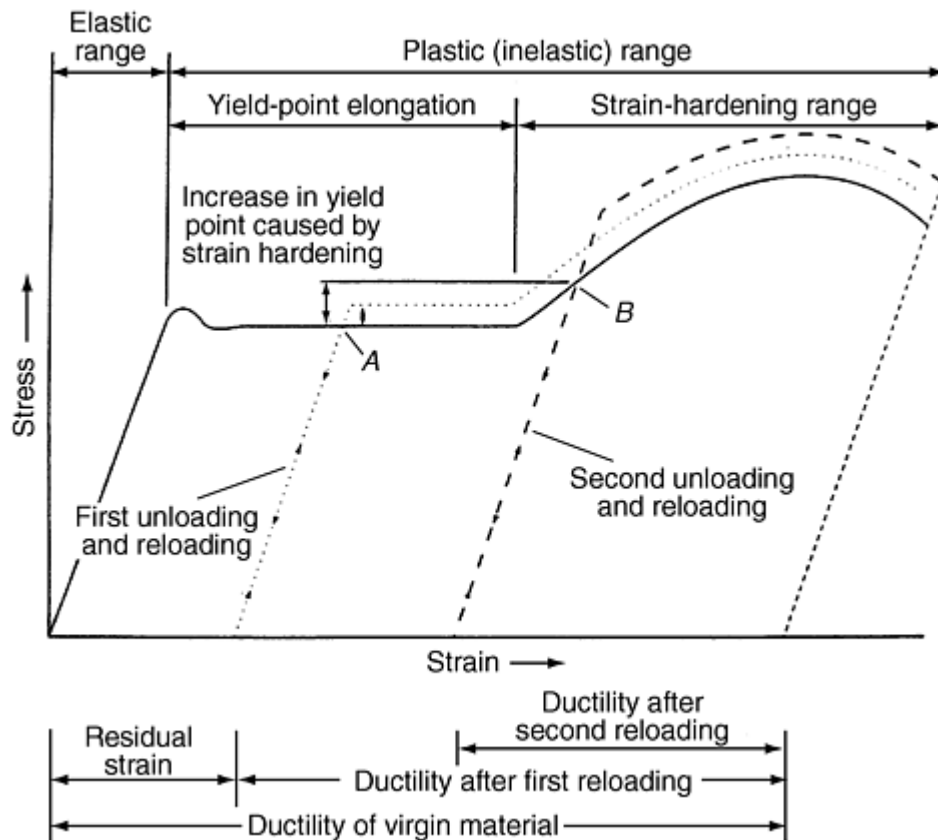


Fig. 5 Effects of prior tensile loading on tensile stress-strain behavior. Solid line, stress-strain curve based on dimensions of unstrained test piece (unloaded and reloaded twice); dotted line, stress-strain curve based on dimensions of test piece after first unloading; dashed line, stress-strain curve based on dimensions of test piece after second unloading. Note: Graph is not to scale.

The curve with a solid line in Fig. 5 is obtained for engineering stresses calculated using the applied forces divided by the original cross-sectional area. The curve with a dotted line is obtained from stresses calculated using the applied forces divided by the cross-sectional area, A_2 , with the origin of this stress-strain curve located on the abscissa at the end point of the first unloading line. The curve represented by the dashed line is obtained from the stresses calculated using the applied forces divided by the cross-sectional area, A_3 , with the origin of this stress-strain curve located on the abscissa at the end point of the second unloading line. This figure illustrates what happens if a test is stopped, unloaded, and restarted. It also illustrates one of the problems that can occur when testing pieces from material that has been formed into a part (or otherwise plastically strained before testing). An example is a test piece that was machined from a failed structure to determine the tensile properties. If the test piece is from a location that was subjected to tensile deformation during the failure, the properties obtained are probably not representative of the original properties of the material.

Bauschinger Effect. The other loading condition occurs when the test piece is initially loaded in compression beyond the elastic limit and then unloaded. The unload path is parallel to the initial load path but offset by the set; on reloading in tension, the elastic limit is much lower, and the shape of the stress-strain curve is significantly different. The same phenomenon occurs if the initial loading is in tension and the subsequent loading is in compression. This condition is called the Bauschinger effect, named for the German scientist who first described it around 1860. Again, the significance of this phenomenon is that if a test piece is machined from a location that has been subjected to plastic deformation, the stress-strain properties will be significantly different than if the material had not been so strained. This occurrence is illustrated in Fig. 6, where a machined round steel test piece was first loaded in tension to about 1% strain, unloaded, loaded in compression to about 1% strain, unloaded, and reloaded in tension. For this steel, the initial portion of tension and compression stress-strain curves are essentially identical.

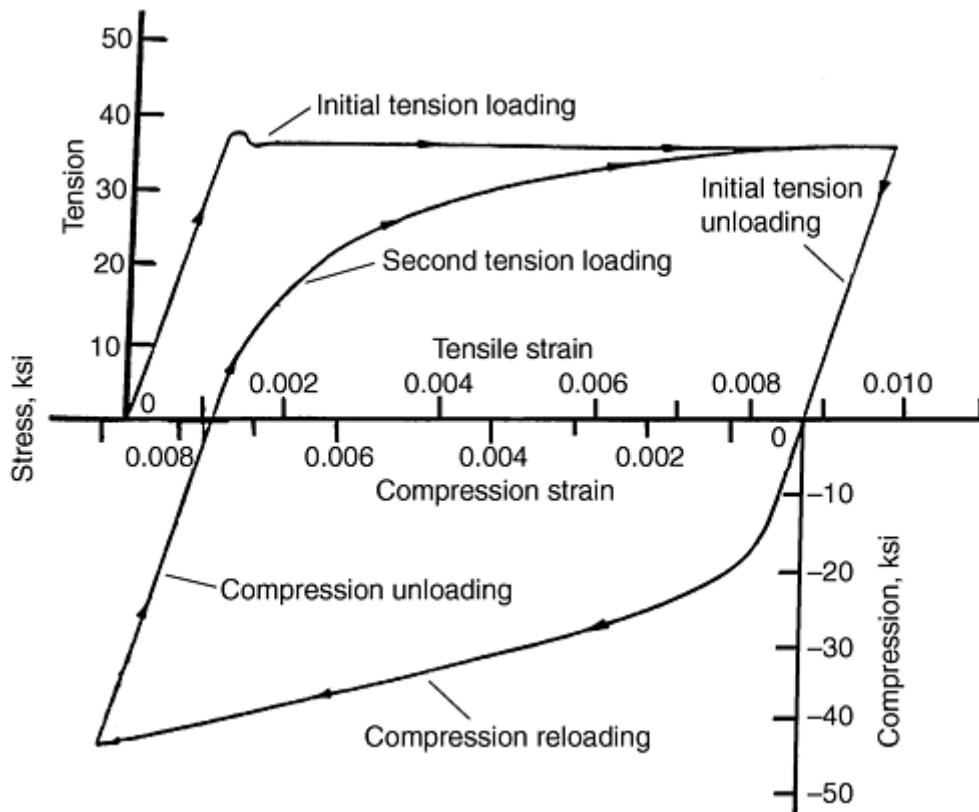


Fig. 6 Example of the Bauschinger effect and hysteresis loop in tension-compression-tension loading. This example shows initial tension loading to 1% strain, followed by compression loading to 1% strain, and then a second tension loading to 1% strain.

References cited in this section

3. N.E. Dowling, *Mechanical Behavior of Materials—Engineering Methods for Deformation, Fracture, and Fatigue*, 2nd ed., Prentice Hall, 1999, p 123
4. R.L. Brockenbough and B.G. Johnson, “Steel Design Manual,” United States Steel Corporation, ADUSS 27 3400 03, 1974, p 2–3

Uniaxial Tension Testing

John M. (Tim) Holt, Alpha Consultants and Engineering

Properties from Test Results

A number of tensile properties can be determined from the stress-strain diagram. Two of these properties, the tensile strength and the yield strength, are described in the next section of this article, “Strength Properties.” In addition, total elongation (ASTM E 6), yield-point elongation (ASTM E 6), Young's modulus (ASTM E 111), and the strain-hardening exponent (ASTM E 646) are sometimes determined from the stress-strain diagram. Other tensile properties include the following:

- Poisson's ratio (ASTM E 132)
- Plastic-strain ratio (ASTM E 517)
- Elongation by manual methods (ASTM E 8)

- Reduction of area

These properties require more information than just the data pairs generating a stress-strain curve. None of these four properties can be determined from a stress-strain diagram.

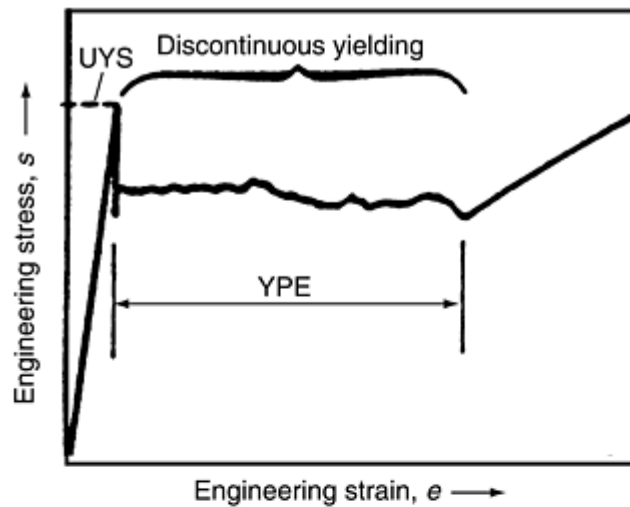
Strength Properties

Tensile strength and yield strength are the most common strength properties determined in a tension test. According to ASTM E 6, tensile strength is calculated from the maximum force during a tension test that is carried to rupture divided by the original cross-sectional area of the test piece. By this definition, it is a stress value, although some product specifications define the tensile strength as the force (load) sustaining ability of the product without consideration of the cross-sectional area. Fastener specifications, for example, often refer to tensile strength as the applied force (load-carrying) capacity of a part with specific dimensions.

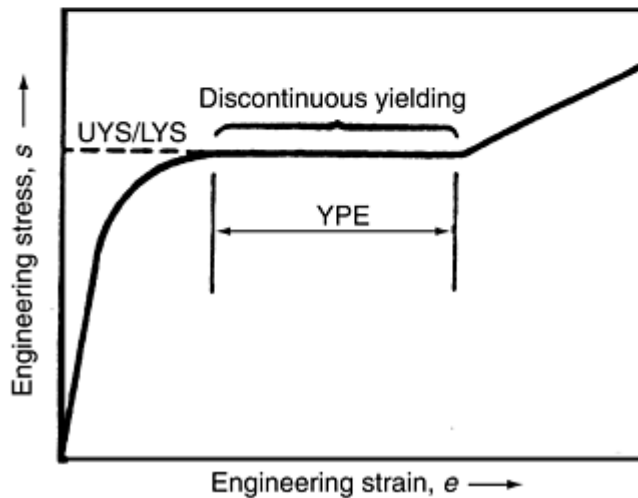
The yield strength refers to the stress at which a small, but measurable, amount of inelastic or plastic deformation occurs. There are three common definitions of yield strength:

- Offset yield strength
- Extension-under-load (EUL) yield strength
- Upper yield strength (or upper yield point)

An upper yield strength (upper yield point) (Fig. 7a) usually occurs with low-carbon steels and some other metal systems to a limited degree. Often, the pronounced peak of the upper yield is suppressed due to slow testing speed or nonaxial loading (i.e., bending of the test piece), metallurgical factors, or a combination of these; in this case, a curve of the type shown in Fig. 7(b) is obtained. The other two definitions of yield strength, EUL and offset, were developed for materials that do not exhibit the yield-point behavior shown in Fig. 7. Stress-strain curves without a yield point are illustrated in Fig. 4(a) for USS Con-Pac 80 and USS T-1 steels. To determine either the EUL or the offset yield strength, the stress-strain curve must be determined during the test. In computer-controlled testing systems, this curve is often stored in memory and may not be charted or displayed.



(a)



(b)

Fig. 7 Examples of stress-strain curves exhibiting pronounced yield-point behavior. Pronounced yielding, of the type shown, is usually called yield-point elongation (YPE). (a) Classic example of upper-yield-strength (UYS) behavior typically observed in low-carbon steels with a very pronounced upper yield strength. (b) General example of pronounced yielding without an upper yield strength. LYS, lower yield strength

Upper yield strength (or upper yield point) can be defined as the stress at which measurable strain occurs without an increase in the stress; that is, there is a horizontal region of the stress-strain curve (Fig. 7) where discontinuous yielding occurs. Before the onset of discontinuous yielding, a peak of maximum stress for yielding is typically observed (Fig. 7a). This pronounced yielding, of the type shown, is usually called yield-point elongation (YPE). This elongation is a diffusion-related phenomenon, where under certain combinations of strain rate and temperature as the material deforms, interstitial atoms are dragged along with dislocations, or dislocations can alternately break away and be repinned, with little or no increase in stress. Either or both of these actions cause serrations or discontinuous changes in a stress-strain curve, which are usually limited to the onset of yielding. This type of yield point is sometimes referred to as the upper yield strength or upper yield point. This type of yield point is usually associated with low-carbon steels, although other metal systems may exhibit yield points to some degree. For example, the stress-strain curves for A36 and USS Tri-Ten steels shown in Fig. 4(a) exhibit this behavior.

The yield point is easy to measure because the increase in strain that occurs without an increase in stress is visually apparent during the conduct of the test by observing the force-indicating system. As shown in Fig. 7,

the yield point is usually quite obvious and thus can easily be determined by observation during a tension test. It can be determined from a stress-strain curve or by the halt of the dial when the test is performed on machines that use a dial to indicate the applied force. However, when watching the movement of the dial, sometimes a minimum value, recorded during discontinuous yielding, is noted. This value is sometimes referred to as the lower yield point. When the value is ascertained without instrumentation readouts, it is often referred to as the halt-of-dial or the drop-of-beam yield point (as an average usually results from eye readings). It is almost always the upper yield point that is determined from instrument readouts.

Extension-under-load (EUL) yield strength is the stress at which a specified amount of stretch has taken place in the test piece. The EUL is determined by the use of one of the following types of apparatus:

- Autographic devices that secure stress-strain data, followed by an analysis of this data (graphically or using automated methods) to determine the stress at the specified value of extension
- Devices that indicate when the specified extension occurs so that the stress at that point may be ascertained

Graphical determination is illustrated in Fig. 8. On the stress-strain curve, the specified amount of extension, $0-m$, is measured along the strain axis from the origin of the curve and a vertical line, $m-n$, is raised to intersect the stress-strain curve. The point of intersection, r , is the EUL yield strength, and the value R is read from the stress axis. Typically, for many materials, the extension specified is 0.5%; however, other values may be specified. Therefore, when reporting the EUL, the extension also must be reported. For example, yield strength (EUL = 0.5%) = 52,500 psi is a correct way to report an EUL yield strength. The value determined by the EUL method may also be termed a yield point.

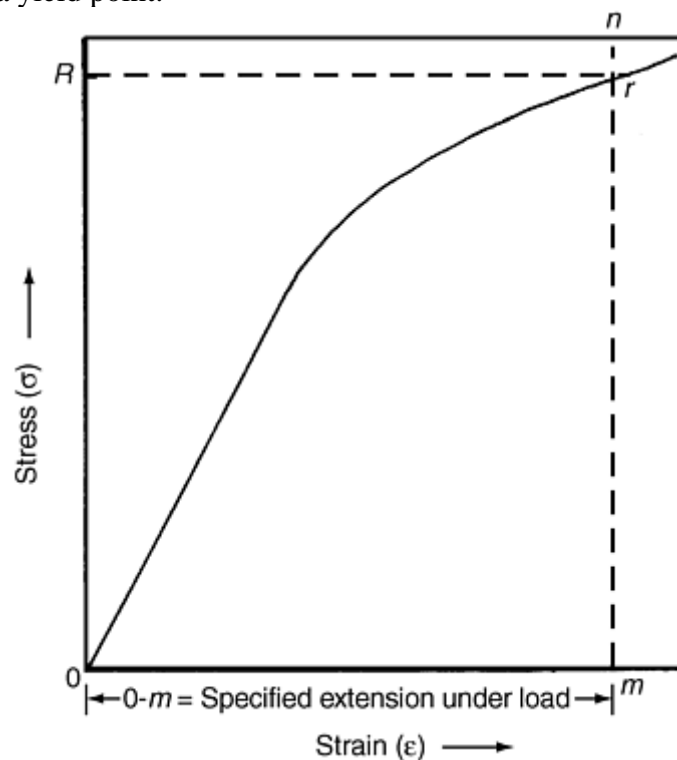


Fig. 8 Method of determining yield strength by the extension-under-load method (EUL) (adaptation of Fig. 22 in ASTM E 8)

Offset yield strength is the stress that causes a specified amount of set to occur; that is, at this stress, the test piece exhibits plastic deformation (set) equal to a specific amount. To determine the offset yield strength, it is necessary to secure data (autographic or numerical) from which a stress-strain diagram may be constructed graphically or in computer memory. Figure 9 shows how to use these data; the amount of the specified offset $0-m$ is laid out on the strain axis. A line, $m-n$, parallel to the modulus of elasticity line, $0-A$, is drawn to intersect the stress-strain curve. The point of intersection, r , is the offset yield strength, and the value, R , is read from the stress axis. Typically, for many materials, the offset specified is 0.2%; however, other values may be specified. Therefore, when reporting the offset yield strength, the amount of the offset also must be reported; for example,

“0.2 % offset yield strength = 52.8 ksi” or “yield strength (0.2% offset) = 52.8 ksi” are common formats used in reporting this information.

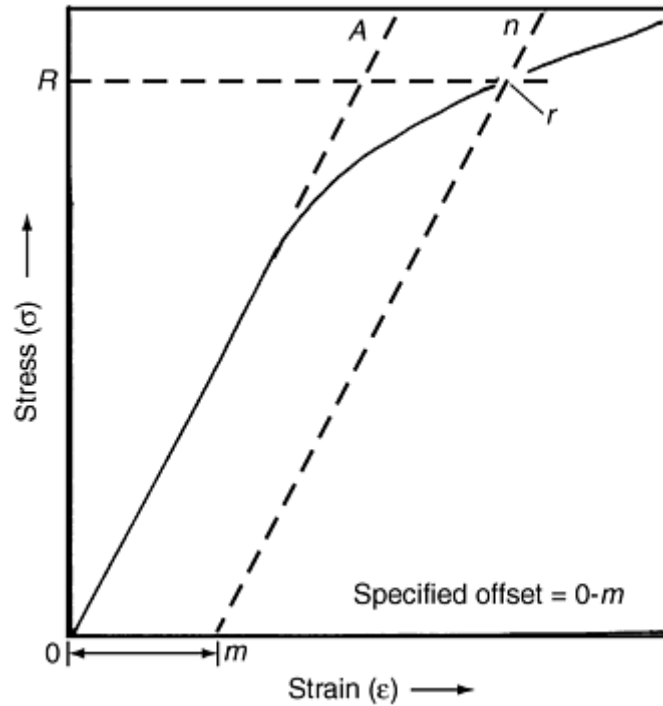


Fig. 9 Method of determining yield strength by the offset method (adaptation of Fig. 21 in ASTM E 8)

In Fig. 8 and 9, the initial portion of the stress-strain curve is shown in ideal terms as a straight line. Unfortunately, the initial portion of the stress-strain curve sometimes does not begin as a straight line but rather has either a concave or a convex foot (Fig. 10) (Ref 5). The shape of the initial portion of a stress-strain curve may be influenced by numerous factors such as, but not limited to, the following:

- Seating of the test piece in the grips
- Straightening of a test piece that is initially bent by residual stresses or bent by coil set
- Initial speed of testing

Generally, the aberrations in this portion of the curve should be ignored when fitting a modulus line, such as that used to determine the origin of the curve. As shown in Fig. 10, a “foot correction” may be determined by fitting a line, whether by eye or by using a computer program, to the linear portion and then extending this line back to the abscissa, which becomes point 0 in Fig. 8 and 9. As a rule of thumb, Point *D* in Fig. 10 should be less than one-half the specified yield point or yield strength.

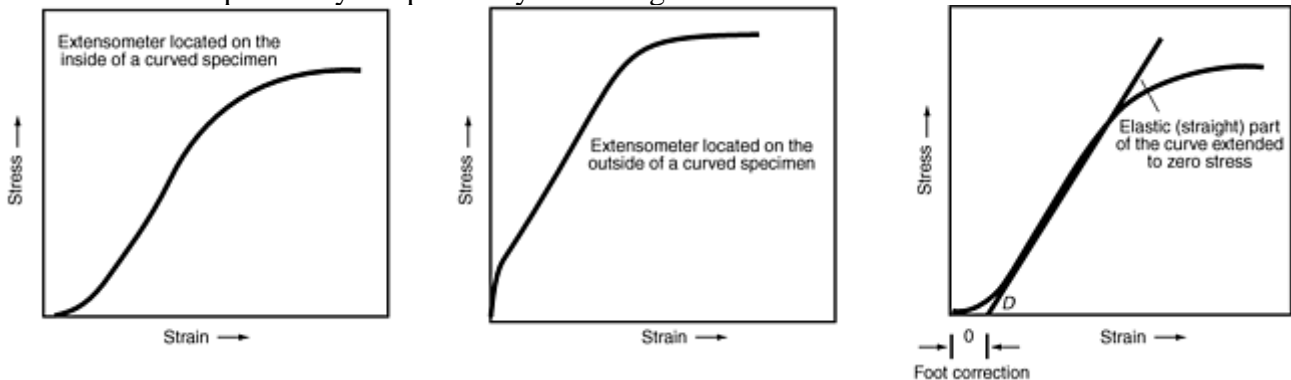


Fig. 10 Examples of stress-strain curves requiring foot correction. Point *D* is the point where the extension of the straight (elastic) part diverges from the stress-strain curve. Source: Ref 5

Tangent or Chord Moduli. For materials that do not have a linear relationship between stress and strain, even at very low stresses, the offset yield is meaningless without defining how to determine the modulus of elasticity. Often, a chord modulus or a tangent modulus is specified. A chord modulus is the slope of a chord between any two specified points on the stress-strain curve, usually below the elastic limit. A tangent modulus is the slope of the stress-strain curve at a specified value of stress or of strain. Chord and tangent moduli are illustrated in Fig. 11. Another technique that has been used is sketched in Fig. 12. The test piece is stressed to approximately the yield strength, unloaded to about 10% of this value, and reloaded. As previously discussed, the unloading line will be parallel to what would have been the initial modulus line, and the reloading line will coincide with the unloading line (assuming no hysteresis in any of the system components). The slope of this line is transferred to the initial loading line, and the offset is determined as before. The stress or strain at which the test piece is unloaded usually is not important. This technique is specified in the ISO standard for the tension test of metallic materials, ISO 6892.

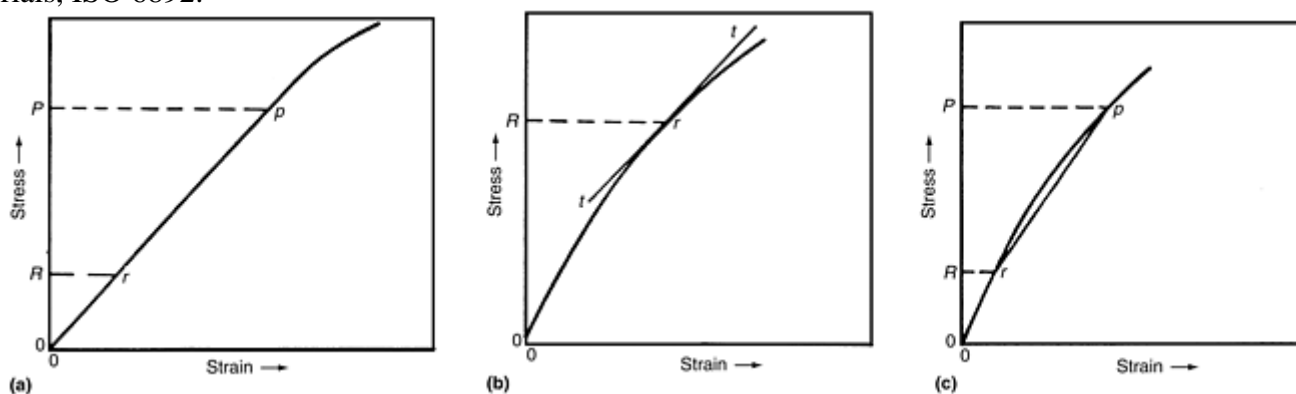


Fig. 11 Stress-strain curves showing straight lines corresponding to (a) Young's modulus between stress, *P*, below proportional limit and *R*, or preload; (b) tangent modulus at any stress, *R*; and (c) chord modulus between any two stresses, *P* and *R*. Source: Ref 6

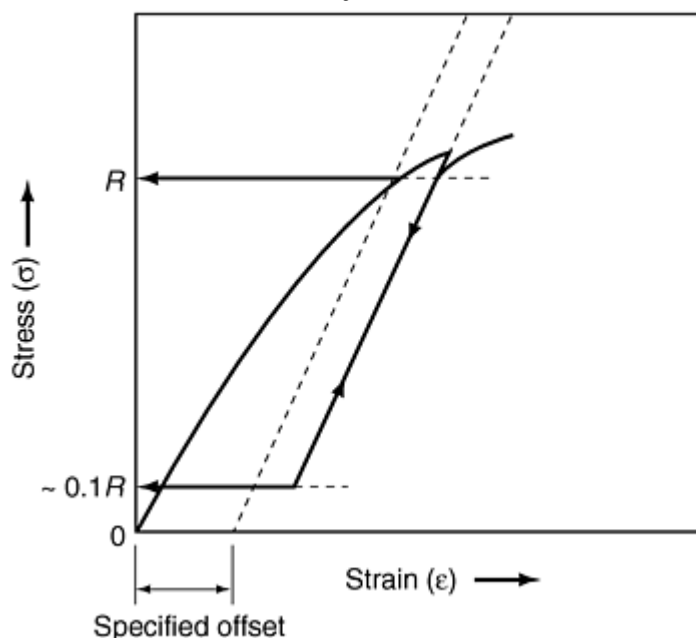


Fig. 12 Alternate technique for establishing Young's modulus for a material without an initial linear portion

Yield-strength-property values generally depend on the definition being used. As shown in Fig. 4(a) for the USS Con-Pac steel, the EUL yield is greater than the offset yield, but for the USS T-1 steel (Fig. 4a), the opposite is true. The amount of the difference between the two values is dependent upon the slope of the stress-

strain curve between the two intersections. When the stress-strain data pairs are sampled by a computer, and a yield spike or peak of the type shown in Fig. 7(a) occurs, the EUL and the offset yield strength will probably be less than the upper yield point and will probably differ because the m - n lines of Fig. 8 and 9 will intersect at different points in the region of discontinuous yielding.

Ductility

Ductility is the ability of a material to deform plastically without fracturing. Figure 13 is a sketch of a test piece with a circular cross section that has been pulled to fracture. As indicated in this sketch, the test piece elongates during the tension test and correspondingly reduces in cross-sectional area. The two measures of the ductility of a material are the amount of elongation and reduction in area that occurs during a tension test.

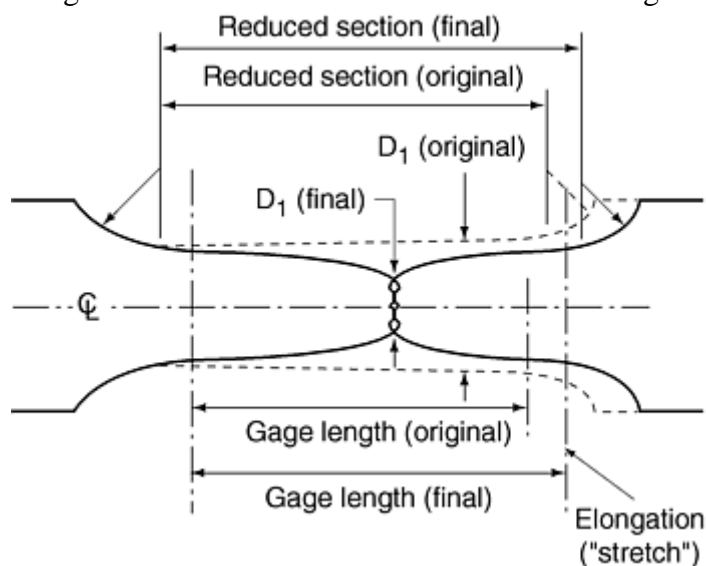


Fig. 13 Sketch of fractured, round tension test piece. Dashed lines show original shape. Strain = elongation/gage length

Elongation, as previously noted, is defined in ASTM E 6 as the increase in the gage length of a test piece subjected to a tension force, divided by the original gage length on the test piece. Elongation usually is expressed as a percentage of the original gage length. ASTM E 6 further indicates the following:

- The increase in gage length may be determined either at or after fracture, as specified for the material under test.
- The gage length shall be stated when reporting values of elongation.
- Elongation is affected by test-piece geometry (gage length, width, and thickness of the gage section and of adjacent regions) and test procedure variables, such as alignment and speed of pulling.

The manual measurement of elongation on a tension test piece can be done with the aid of gage marks applied to the unstrained reduced section. After the test, the amount of stretch between gage marks is measured with an appropriate device. The use of the term elongation in this instance refers to the total amount of stretch or extension. Elongation, in the sense of nominal engineering strain, e , is the value of gage extension divided by the original distance between the gage marks. Strain elongation is usually expressed as a percentage, where the nominal engineering strain is multiplied by 100 to obtain a percent value; that is:

$$e, \% = \left[\frac{(\text{final gage length} - \text{original gage length})}{\text{original gage length}} \right] \times 100$$

The final gage length at the completion of the test may be determined in two ways. Historically, it was determined manually by carefully fitting the two ends of the fractured test piece together (Fig. 13) and measuring the distance between the gage marks. However, some modern computer-controlled testing systems obtain data from an extensometer that is left on the test piece through fracture. In this case, the computer may

be programmed to report the elongation as the last strain value obtained prior to some event, perhaps the point at which the applied force drops to 90% of the maximum value recorded. There has been no general agreement about what event should be the trigger, and users and machine manufacturers find that different events may be appropriate for different materials (although some consensus has been reached, see ASTM E 8-99). The elongation values determined by these two methods are not the same; in general, the result obtained by the manual method is a couple of percent larger and is more variable because the test-piece ends do not fit together perfectly. It is strongly recommended that when disagreements arise about elongation results, agreement should be reached on which method will be used prior to any further testing.

Test methods often specify special conditions that must be followed when a product specification specifies elongation values that are small, or when the expected elongation values are small. For example, ASTM E 8 defines small as 3% or less.

Effect of Gage Length and Necking. Figure 14 (Ref 7) shows the effect of gage length on elongation values. Gage length is very important; however, as the gage length becomes quite large, the elongation tends to be independent of the gage length. The gage length must be specified prior to the test, and it must be shown in the data record for the test.

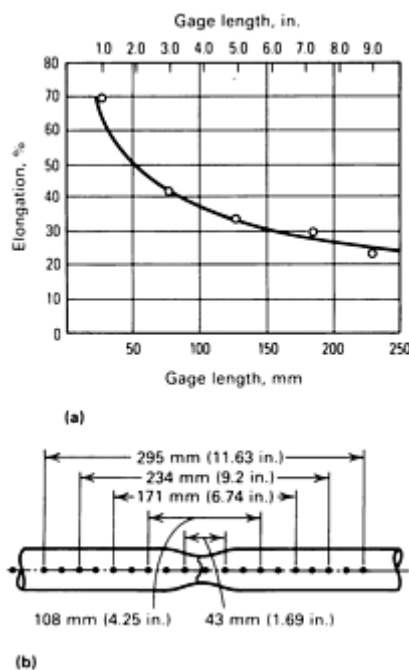


Fig. 14 Effect of gage length on the percent elongation. (a) Elongation, %, as a function of gage length for a fractured tension test piece. (b) Distribution of elongation along a fractured tension test piece. Original spacing between gage marks, 12.5 mm (0.5 in.). Source: Ref 7

Figures 13 and 14 also illustrate considerable localized deformation in the vicinity of the fracture. This region of local deformation is often called a neck, and the occurrence of this deformation is termed necking. Necking occurs as the force begins to drop after the maximum force has been reached on the stress-strain curve. Up to the point at which the maximum force occurs, the strain is uniform along the gage length; that is, the strain is independent of the gage length. However, once necking begins, the gage length becomes very important. When the gage length is short, this localized deformation becomes the principal portion of measured elongation. For long gage lengths, the localized deformation is a much smaller portion of the total. For this reason, when elongation values are reported, the gage length must also be reported, for example, elongation = 25% (50 mm, or 2.00 in., gage length).

Effect of Test-Piece Dimensions. Test-piece dimensions also have a significant effect on elongation measurements. Experimental work has verified the general applicability of the following equation:

$$e = e_0(L/A)^{1/2} - a$$

where e_0 is the specific elongation constant; $L/A^{1/2}$ the slimmness ratio, K , of gage length, L , and cross-sectional areas, A ; and a is another material constant. This equation is known as the Bertella-Oliver equation, and it may be transformed into logarithmic form and plotted as shown in Fig. 15. In one study, quadruplet sets of machined

circular test pieces (four different diameters ranging from 0.125 to 0.750 in.) and rectangular test pieces ($\frac{1}{2}$ in. wide with three thicknesses and $1\frac{1}{2}$ in. wide with three thicknesses) were machined from a single plate. Multiple gage lengths were scribed on each test piece to produce a total of 40 slinness ratios. The results of this study, for one of the grades of steel tested, are shown in Fig. 16.

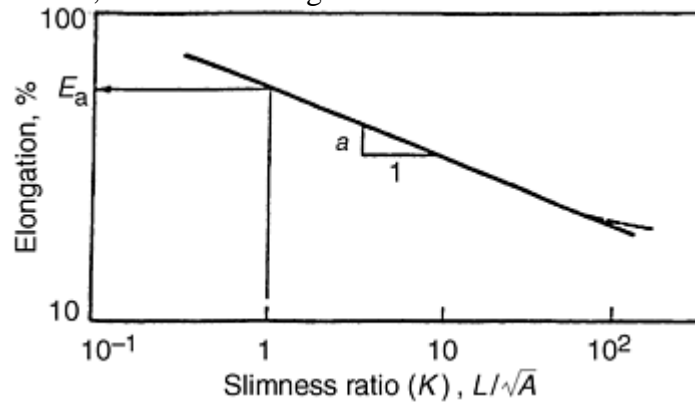


Fig. 15 Graphical form of the Bertella-Oliver equation.

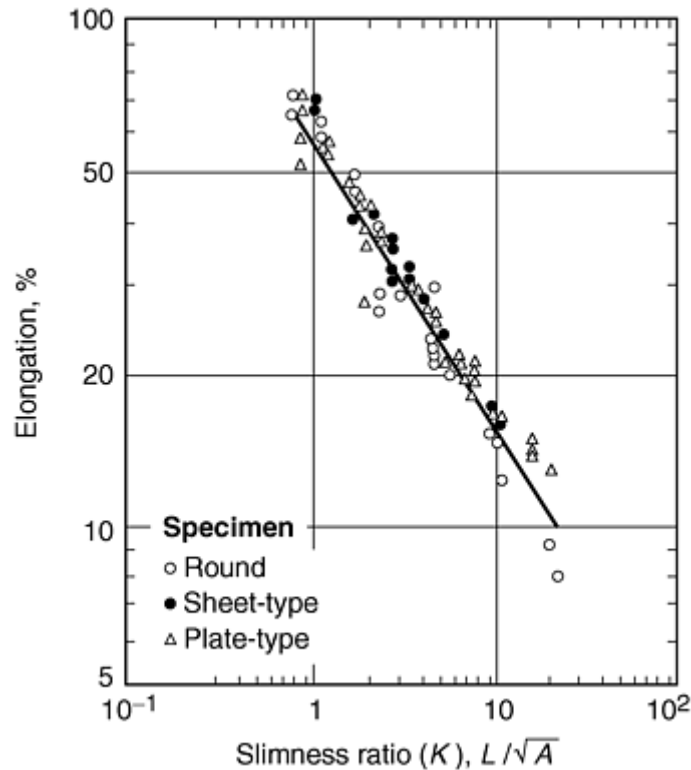


Fig. 16 Graphical form of the Bertella-Oliver equation showing actual data

In order to compare elongation values of test pieces with different slinness ratios, it is necessary only to determine the value of the material constant, a . This calculation can be made by testing the same material with two different geometries (or the same geometry with different gage lengths) with different slinness ratios, K_1 and K_2 , where

$$e_0 = e_1 / K_1^{-a} = e_2 / K_2^{-a}$$

solving for a , then:

$$(K_2/K_1)^{-a} = e_2/e_1$$

or:

$$-a = \frac{\ln(e_2/e_1)}{\ln(K_2/K_1)} \tag{Eq 1}$$

$$-a = \frac{\ln(e_2) - \ln(e_1)}{\ln(K_2) - \ln(K_1)} \quad (\text{Eq 2})$$

The values of the e_0 and a parameters depend on the material composition, the strength, and the material condition and are determined empirically with a best-fit line plot around data points. Reference 8 specifies “value $a = 0.4$ for carbon, carbon-manganese, molybdenum, and chromium-molybdenum steels within the tensile strength range of 275 to 585 MPa (40 to 85 ksi) and in the hot-rolled, in the hot-rolled and normalized, or in the annealed condition, with or without tempering. Materials that have been cold reduced require the use of a different value for a , and an appropriate value is not suggested.” Reference 8 uses a value of $a = 0.127$ for annealed, austenitic stainless steels. However, Ref 8 states that “these conversions shall not be used where the width-to-thickness ratio, w/t , of the test piece exceeds 20.” ISO 2566/1 (Ref 9) contains similar statements. In addition to the limit of $(w/t) < 20$, Ref 9 also specifies that the slimmness ratio shall be less than 25.

Some tension-test specifications do not contain standard test-piece geometries but require that the slimmness ratio be either 5.65 or 11.3. For a round test piece, a slimmness ratio of 5.65 produces a 5-to-1 relation between the diameter and the gage length, and a slimmness ratio of 4.51 produces a 4-to-1 relation between the diameter and gage length (which is that of the test piece in ASTM E 8).

Reduction of area is another measure of the ductility of metal. As a test piece is stretched, the cross-sectional area decreases, and as long as the stretch is uniform, the reduction of area is proportional to the amount of stretch or extension. However, once necking begins to occur, proportionality is no longer valid.

According to ASTM E 6, reduction of area is defined as “the difference between the original cross-sectional area of a tension test piece and the area of its smallest cross section.” Reduction of area is usually expressed as a percentage of the original cross-sectional area of the test piece. The smallest final cross section may be measured at or after fracture as specified for the material under test. The reduction of area (RA) is almost always expressed as a percentage:

$$\text{Ra, \%} = \left[\frac{(\text{original area} - \text{final area})}{\text{original area}} \right] \times 100$$

Reduction of area is customarily measured only on test pieces with an initial circular cross section because the shape of the reduced area remains circular or nearly circular throughout the test for such test pieces. With rectangular test pieces, in contrast, the corners prevent uniform flow from occurring, and consequently, after fracture, the shape of the reduced area is not rectangular (Fig. 17). Although a number of expressions have been used in an attempt to describe the way to determine the reduced area, none has received general agreement. Thus, if a test specification requires the measurement of the reduction of area of a test piece that is not circular, the method of determining the reduced area should be agreed prior to performing the test.

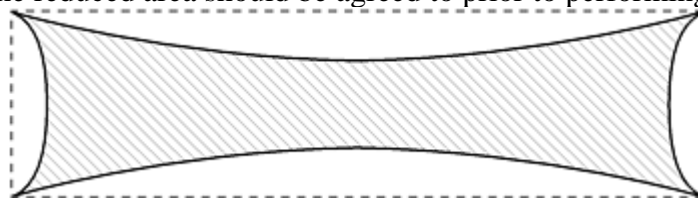


Fig. 17 Sketch of end view of rectangular test piece after fracture showing constraint at corners indicating the difficulty of determining reduced area

References cited in this section

5. P.M. Mumford, Test Methodology and Data Analysis, *Tensile Testing*, P. Han, Ed., ASM International, 1992, p 55
6. “Standard Test Method for Young's Modulus, Tangent Modulus, and Chord Modulus,” E 111, ASTM
7. *Making, Shaping, and Treating of Steel*, 10th ed., U.S. Steel, 1985, Fig. 50-12 and 50-13
8. “Standard Test Methods and Definitions for Mechanical Testing of Steel Products,” A 370, Annex 6, *Annual Book of ASTM Standards*, ASTM, Vol 1.03

9. "Conversion of Elongation Values, Part 1: Carbon and Low-Alloy Steels," 2566/1, International Organization for Standardization, revised 1984

Uniaxial Tension Testing

John M. (Tim) Holt, Alpha Consultants and Engineering

General Procedures

Numerous groups have developed standard methods for conducting the tension test. In the United States, standards published by ASTM are commonly used to define tension-test procedures and parameters. Of the various ASTM standards related to tension tests (for example, those listed in "Selected References" at the end of this article), the most common method for tension testing of metallic materials is ASTM E 8 "Standard Test Methods for Tension Testing of Metallic Materials" (or the version using metric units, ASTM E 8M). Standard methods for conducting the tension test are also available from other standards organizations, such as the Japanese Industrial Standards (JIS), the Deutsche Institut für Normung (DIN), and the International Organization for Standardization (ISO). Other domestic technical groups in the United States have developed standards, but in general, these are based on ASTM E 8.

With the increasing internationalization of trade, methods developed by other national standards organizations (such as JIS, DIN, or ISO standards) are increasingly being used in the United States. Although most tension-test standards address the same concerns, they differ in the values assigned to variables. Thus, a tension test performed in accordance with ASTM E 8 will not necessarily have been conducted in accordance with ISO 6892 or JIS Z2241, and so on, and vice versa. Therefore, it is necessary to specify the applicable testing standard for any test results or mechanical property data.

Unless specifically indicated otherwise, the values of all variables discussed hereafter are those related to ASTM E 8 "Standard Test Methods for Tension Testing of Metallic Materials." A flow diagram of the steps involved when a tension test is conducted in accordance with ASTM E 8 is shown in Fig. 18. The test consists of three distinct parts:

- Test-piece preparation, geometry, and material condition
- Test setup and equipment
- Test

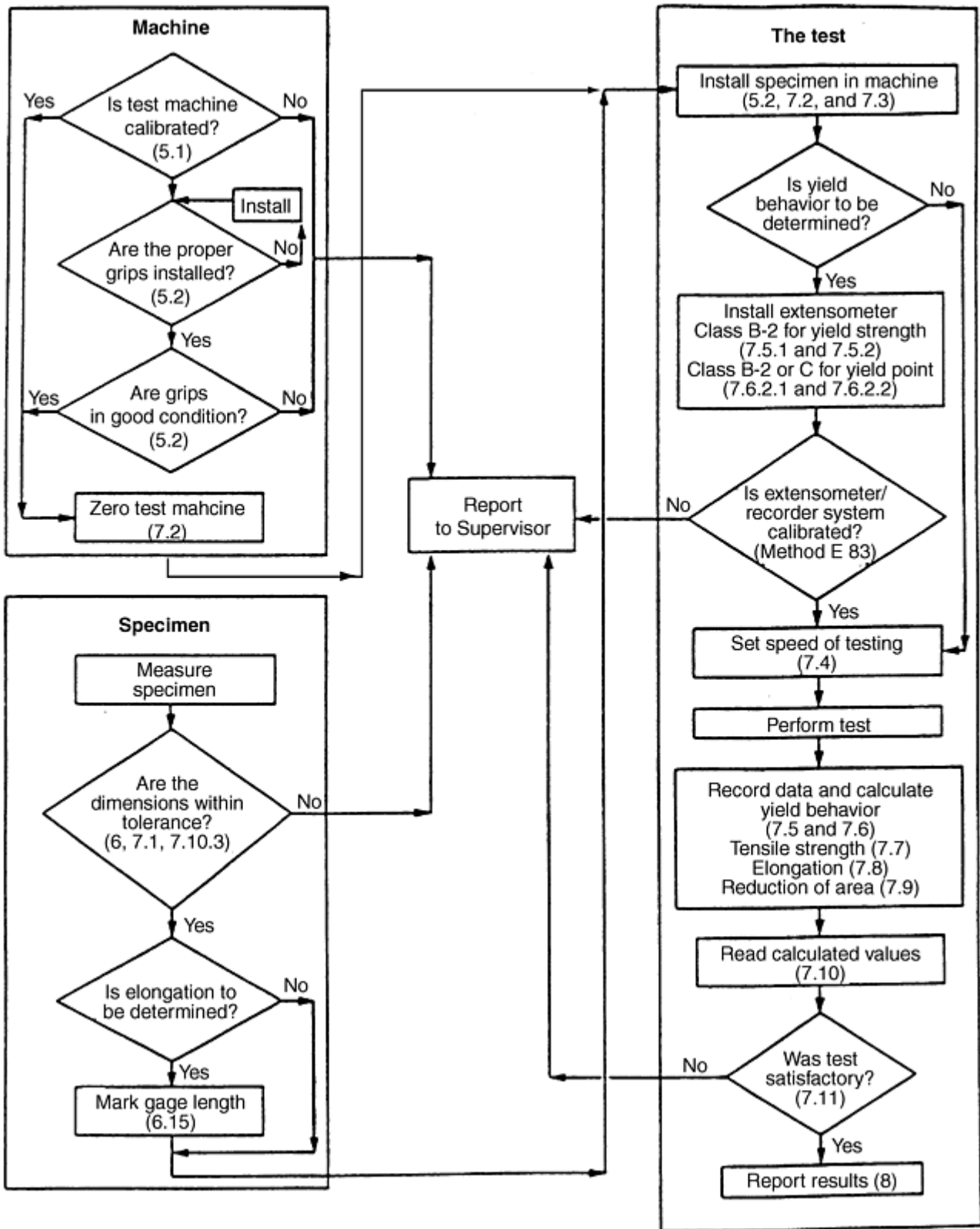


Fig. 18 General flow chart of the tension test per procedures in ASTM E 8. Relevant paragraph numbers from ASTM E 8 are shown in parentheses.

The Test Piece

The test piece is one of two basic types. Either it is a full cross section of the product form, or it is a small portion that has been machined to specific dimensions. Full-section test pieces consist of a part of the test unit as it is fabricated. Examples of full-section test pieces include bars, wires, and hot-rolled or extruded angles cut to a suitable length and then gripped at the ends and tested. In contrast, a machined test piece is a representative sample, such as one of the following:

- Test piece machined from a rough specimen taken from a coil or plate
- Test piece machined from a bar with dimensions that preclude testing a full-section test piece because a full-section test piece exceeds the capacity of the grips or the force capacity of the available testing machine or both
- Test piece machined from material of great monetary or technical value

In these cases, representative samples of the material must be obtained for testing. The descriptions of the tension test in this article proceed from the point that a rough specimen (Fig. 19) has been obtained. That is, the rough specimen has been selected based on some criteria, usually a material specification or a test order issued for a specific reason.

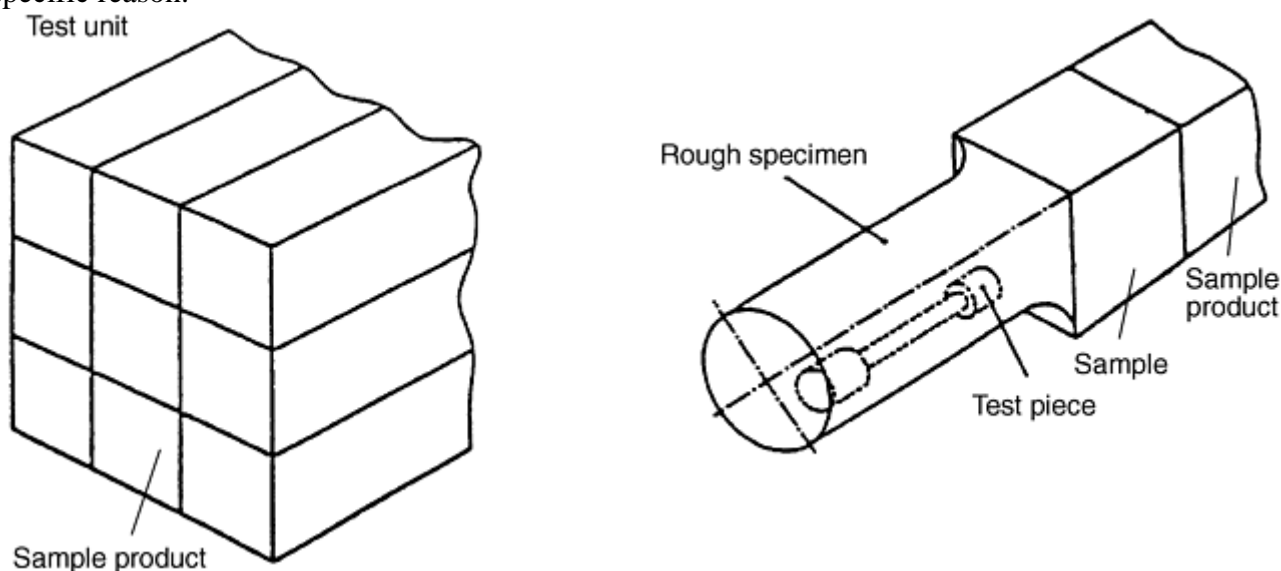


Fig. 19 Illustration of ISO terminology used to differentiate between sample, specimen, and test piece (see text for definitions of test unit, sample product, sample, rough specimen, and test piece). As an example, a test unit may be a 250-ton heat of steel that has been rolled into a single thickness of plate. The sample product is thus one plate from which a single test piece is obtained.

In this article, the term *test piece* is used for what is often called a specimen. This terminology is based on the convention established by ISO Technical Committee 17, Steel in ISO 377-1, “Selection and Preparation of Samples and Test Pieces of Wrought Steel,” where terms for a test unit, a sample product, sample, rough specimen, and test piece are defined as follows:

- *Test unit*: The quantity specified in an order that requires testing (for example, 10 tons of $\frac{3}{4}$ in. bars in random lengths)

- *Sample product*: Item (in the previous example, a single bar) selected from a test unit for the purpose of obtaining the test pieces
- *Sample*: A sufficient quantity of material taken from the sample product for the purpose of producing one or more test pieces. In some cases, the sample may be the sample product itself (i.e., a 2 ft length of the sample product).
- *Rough specimen*: Part of the sample having undergone mechanical treatment, followed by heat treatment where appropriate, for the purpose of producing test pieces; in the example, the sample is the rough specimen.
- *Test piece*: Part of the sample or rough specimen, with specified dimensions, machined or unmachined, brought to the required condition for submission to a given test. If a testing machine with sufficient force capacity is available, the test piece may be the rough specimen; if sufficient capacity is not available, or for another reason, the test piece may be machined from the rough specimen to dimensions specified by a standard.

These terms are shown graphically in Fig. 19. As can be seen, the test piece, or what is commonly called a specimen, is a very small part of the entire test unit.

Description of Test Material

Test-Piece Orientation . Orientation and location of a test material from a product can influence measured tensile properties. Although modern metal-working practices, such as cross rolling, have tended to reduce the magnitude of the variations in the tensile properties, it must not be neglected when locating the test piece within the specimen or the sample.

Because most materials are not isotropic, test-piece orientation is defined with respect to a set of axes as shown in Fig. 20. These terms for the orientation of the test-piece axes in Fig. 20 are based on the convention used by ASTM E 8 "Fatigue and Fracture." This scheme is identical to that used by the ISO Technical Committee 164 "Mechanical Testing," although the *L*, *T*, and *S* axes are referred to as the *X*, *Y*, and *Z* axes, respectively, in the ISO documents.

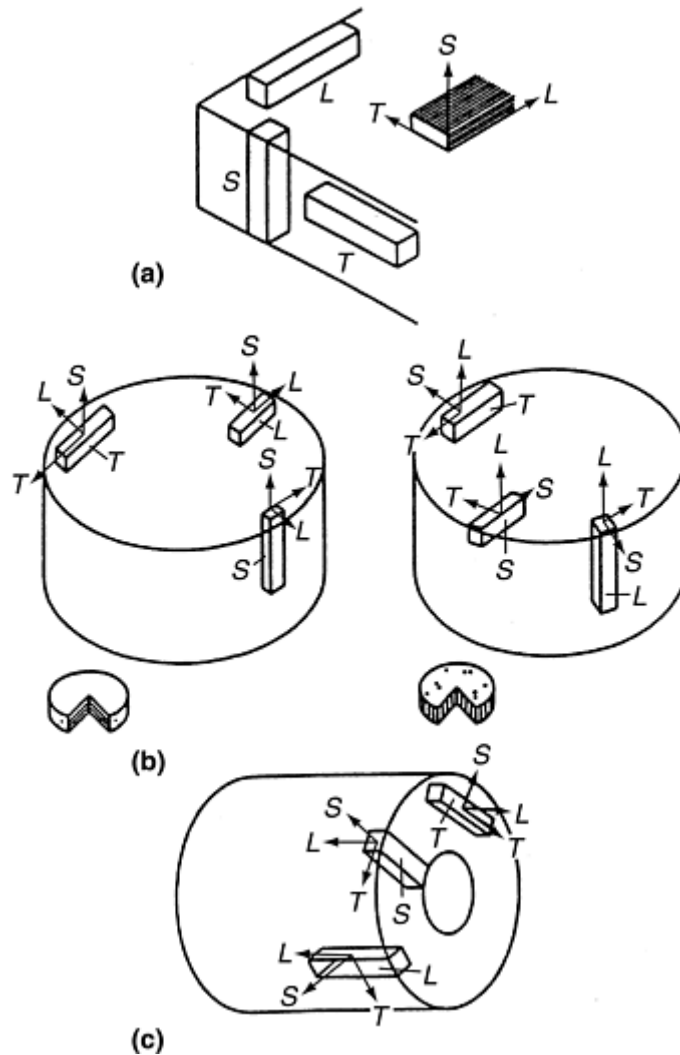


Fig. 20 System for identifying the axes of test-piece orientation in various product forms. (a) Flat-rolled products. (b) Cylindrical sections. (c) Tubular products

When a test is being performed to determine conformance to a product standard, the product standard must state the proper orientation of the test piece with regard to the axis of prior working, (e.g., the rolling direction of a flat product). Because alloy systems behave differently, no general rule of thumb can be stated on how prior working may affect the directionality of properties. As can be seen in Table 1, the longitudinal strengths of steel are generally somewhat less than the transverse strength. However, for aluminum alloys, the opposite is generally true.

Table 1 Effect of test-piece orientation on tensile properties

Orientation	Yield strength, ksi	Tensile strength, ksi	Elongation in 50 mm (2 in.), %	Reduction of area, %
ASTM A 572, Grade 50 (3/4in. thick plate, low sulfur level)				
Longitudinal	58.8	84.0	27.0	70.2
Transverse	59.8	85.2	28.0	69.0
ASTM A 656, Grade 80 (3/4in. thick plate, low sulfur level + controlled rolled)				
Longitudinal	81.0	102.3	25.8	71.2
Transverse	86.9	107.9	24.5	67.1
ASTM A 5414 (3/4in. thick plate, low sulfur level)				
Longitudinal	114.6	121.1	19.8	70.6
Transverse	116.3	122.2	19.5	69.9

Source: Courtesy of Francis J. Marsh

Many standards, such as ASTM A 370, E 8, and B 557, provide guidance in the selection of test-piece orientation relative to the rolling direction of the plate or the major forming axes of other types of products and in the selection of specimen and test-piece location relative to the surface of the product. Orientation is also important when characterizing the directionality of properties that often develops in the microstructure of materials during processing. For example, some causes of directionality include the fibering of inclusions in steels, the formation of crystallographic textures in most metals and alloys, and the alignment of molecular chains in polymers.

The location from which a test material is taken from the initial product form is important because the manner in which a material is processed influences the uniformity of microstructure along the length of the product as well as through its thickness properties. For example, the properties of metal cut from castings are influenced by the rate of cooling and by shrinkage stresses at changes in section. Generally, test pieces taken from near the surface of iron castings are stronger. To standardize test results relative to location, ASTM A 370 recommends that tension test pieces be taken from midway between the surface and the center of round, square, hexagon, or octagonal bars. ASTM E 8 recommends that test pieces be taken from the thickest part of a forging from which a test coupon can be obtained, from a prolongation of the forging, or in some cases, from separately forged coupons representative of the forging.

Test-Piece Geometry

As previously noted, the item being tested may be either the full cross section of the item or a portion of the item that has been machined to specific dimensions. This article focuses on tension testing with test pieces that are machined from rough samples. Component testing is discussed in more detail in the article “Mechanical Testing of Fiber Reinforced Composites” in this Volume.

Test-piece geometry is often influenced by product form. For example, only test pieces with rectangular cross sections can be obtained from sheet products. Test pieces taken from thick plate may have either flat (plate-type) or round cross sections. Most tension-test specifications show machined test pieces with either circular cross sections or rectangular cross sections. Nomenclature for the various sections of a machined test piece are shown in Fig. 21. Most tension-test specifications present a set of dimensions, for each cross-section type, that are standard, as well as additional sets of dimensions for alternative test pieces. In general, the standard dimensions published by ASTM, ISO, JIS, and DIN are similar, but they are not identical.

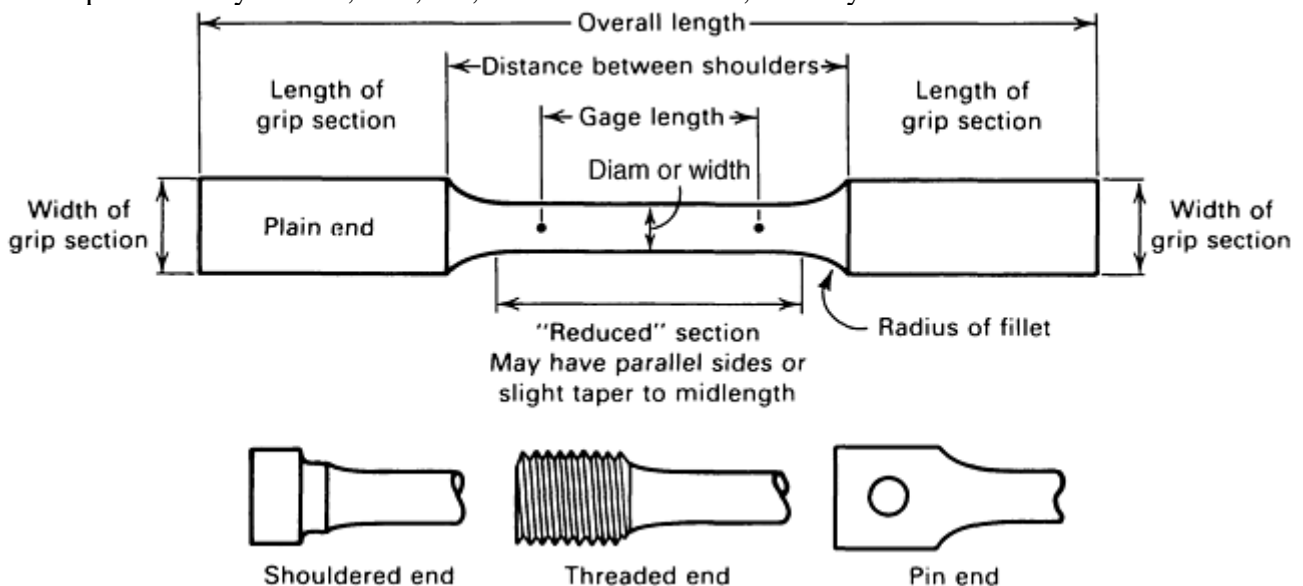
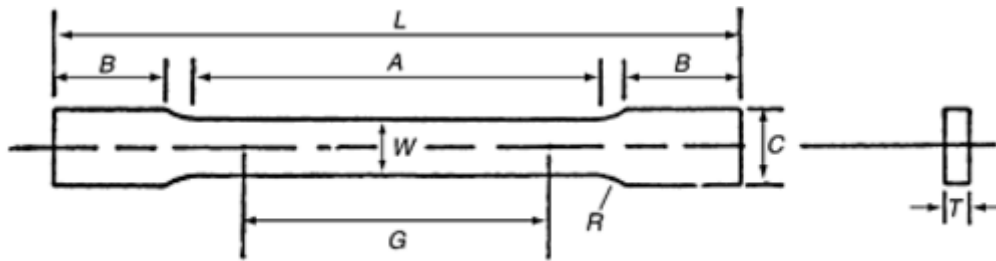


Fig. 21 Nomenclature for a typical tension test piece

Gage lengths and standard dimensions for machined test pieces specified in ASTM E 8 are shown in Fig. 22 for rectangular and round test pieces. From this figure, it can be seen that the gage length is proportionally four times (4 to 1) the diameter (or width) of the test piece for the standard machined round test pieces and the sheet-type, rectangular test pieces. The length of the reduced section is also a *minimum* of $4\frac{1}{2}$ times the diameter (or width) of these test-piece types. These relationships do not apply to plate-type rectangular test pieces.



(a)

	Standard specimens, in.		Subsize specimen, 1/4 in. wide, in.
	Plate type, 1 1/2 in. wide	Sheet type, 1/2 in. wide	
G, gage length^{(a)(b)}	8.00 ± 0.01	2.00 ± 0.005	1.000 ± 0.003
W, width^{(c)(d)}	1 1/2 + 1/8 - 1/4	0.500 ± 0.010	0.250 ± 0.005
T, thickness^(e)	3/16	0.005 ≤ T ≤ 3/4	0.005 ≤ T ≤ 1/4
R, radius of fillet, min^(f)	1	1/2	1/4
L, overall length, min^{(b)(g)}	18	8	4
A, length of reduced section, min	9	2 1/4	1 1/4
B, length of grip section, min^(h)	3	2	1 1/4
C, width of grip section, approximate^{(d)(i)}	2	3/4	3/8

Note:

(a) For the 1 1/2 in. wide specimen, punch marks for measuring elongation after fracture shall be made on the flat or on the edge of the specimen and within the reduced section. Either a set of nine or more punch marks 1 in. apart or one or more pairs of punch marks 8 in. apart may be used.

(b) When elongation measurements of 1 1/2 in. wide specimens are not required, a minimum length of reduced section (A) of 2 1/4 in. may be used with all other dimensions similar to those of the plate-type specimen.

(c) For the three sizes of specimens, the ends of the reduced section shall not differ in width by more than 0.004, 0.002, or 0.001 in., respectively. Also, there may be a gradual decrease in width from the ends to the center, but the width at each end shall not be more than 0.015, 0.005, or 0.003 in., respectively, larger than the width at the center.

(d) For each of the three sizes of specimens, narrower widths (W and C) may be used when necessary. In such cases the width of the reduced section should be as large as the width of the material being tested permits; however, unless stated specifically, the requirements for elongation in a product specification shall not apply when these narrower specimens are used.

(e) The dimension T is the thickness of the test specimen as provided for in the applicable material specifications. Minimum thickness of 1 1/2 in. wide specimens shall be 3/16 in. Maximum thickness of 1/2 in. and 1/4 in. wide specimens shall be 3/4 in. and 1/4 in., respectively.

(f) For the 1 1/2 in. wide specimen, a 1/2 in. minimum radius at the ends of the reduced section is permitted for steel specimens under 100,000 psi in tensile strength when a profile cutter is used to machine the reduced section.

(g) To aid in obtaining axial force application during testing of 1/4 in. wide specimens, the overall length should be as large as the material will permit, up to 8.00 in.

(h) It is desirable, if possible, to make the length of the grip section large enough to allow the specimen to extend into the grips a distance equal to two-thirds or more of the length of the grips. If the thickness of 1/2 in. wide specimens is over 3/8 in., longer grips and correspondingly longer grip sections of the specimen may be necessary to prevent failure in the grip section.

(i) For the three sizes of specimens, the ends of the specimen shall be symmetrical in width with the center line of the reduced section within 0.10, 0.05, and 0.005 in., respectively. However, for referee testing and when required by product specifications, the ends of the 1/2 in. wide specimen shall be symmetrical within 0.01 in.

Fig. 22 Examples of tension test pieces per ASTM E 8. (a) Rectangular (flat) test pieces. (b) Round test-piece

	Standard specimen, in., at nominal diameter:		Small-size specimens proportional to standard, in., at nominal diameter:				
	0.500	0.350	0.250	0.160	0.113		
G, gage length	2.000	± 1.400	± 1.000	± 0.640	± 0.450	±	±
	0.005	0.005	0.005	0.005	0.005		
D, diameter^(a)	0.500	± 0.350	± 0.250	± 0.160	± 0.113	±	±
	0.010	0.007	0.005	0.003	0.002		
R, radius of fillet, min	$\frac{3}{8}$	$\frac{1}{4}$	$\frac{3}{16}$	$\frac{5}{32}$	$\frac{3}{32}$		
A, length of reduced section, min^(b)	$2\frac{1}{4}$	$1\frac{3}{4}$	$1\frac{1}{4}$	$\frac{3}{4}$	$\frac{5}{8}$		

Note:
 (a) The reduced section may have a gradual taper from the ends toward the center, with the ends not more than 1% larger in diameter than the center (controlling dimension).
 (b) If desired, the length of the reduced section may be increased to accommodate an extensometer of any convenient gage length. Reference marks for the measurement of elongation should, nevertheless, be spaced at the indicated gage length.

Fig. 22

Many specifications outside the United States require that the gage length of a test piece be a fixed ratio of the square root of the cross-sectional area, that is:

$$\text{Gage length} = \text{constant} \times (\text{cross-sectional area})^{1/2}$$

The value of this constant is often specified as 5.65 or 11.3 and applies to both round and rectangular test pieces. For machined round test pieces, a value of 5.65 results in a 5-to-1 relationship between the gage length and the diameter.

Many tension-test specifications permit a slight taper toward the center of the reduced section of machined test pieces so that the minimum cross section occurs at the center of the gage length and thereby tends to cause fracture to occur at the middle of the gage length. ASTM E 8-99 specifies that this taper cannot exceed 1% and requires that the taper is the same on both sides of the midlength.

When test pieces are machined, it is important that the longitudinal centerline of the reduced section be coincident with the longitudinal centerlines of the grip ends. In addition, for the rectangular test pieces, it is essential that the centers of the transition radii at each end of the reduced section are on common lines that are perpendicular to the longitudinal centerline. If any of these requirements is violated, bending will occur, which may affect test results.

The transition radii between the reduced section and the grip ends can be critical for test pieces from materials with very high strength or with very little ductility or both. This is discussed more fully in the section “Effect of Strain Concentrations” in this article.

Measurement of Initial Test-Piece Dimensions. Machined test pieces are expected to meet size specifications, but to ensure dimensional accuracy, each test piece should be measured prior to testing. Gage length, fillet radius, and cross-sectional dimensions are measured easily. Cylindrical test pieces should be measured for concentricity. Maintaining acceptable concentricity is extremely important in minimizing unintended bending stresses on materials in a brittle state.

Measurement of Cross-Sectional Dimensions. The test pieces must be measured to determine whether they meet the requirements of the test method. Test-piece measurements must also determine the initial cross-sectional area when it is compared against the final cross section after testing as a measure of ductility.

The precision with which these measurements are made is based on the requirements of the test method, or if none are given, on good engineering judgment. Specified requirements of ASTM E 8 are summarized as follows:

- For referee testing of test pieces under $\frac{3}{16}$ in. in their least dimension, the dimensions should be measured where the least cross-sectional area is found.

- For cross sectional dimensions of 0.200 in. or more, cross-sectional dimensions should be measured and recorded to the nearest 0.001 in.
- For cross sectional dimensions from 0.100 in. but less than 0.200 in., cross-sectional dimensions should be measured and recorded to the nearest 0.0005 in.
- For cross sectional dimensions from 0.020 in. but less than 0.100 in., cross-sectional dimensions should be measured and recorded to the nearest 0.0001 in.
- When practical, for cross-sectional dimensions less than 0.020 in., cross-sectional dimensions should be measured to the nearest 1%, but in all cases, to at least the nearest 0.0001 in.

ASTM E 8 goes on to state how to determine the cross-sectional area of a test piece that has a nonsymmetrical cross section using the weight and density. When measuring dimensions of the test piece, ASTM E 8 makes no distinction between the shape of the cross section for standard test pieces.

Measurement of the Initial Gage Length. ASTM E 8 assumes that the initial gage length is within specified tolerance; therefore, it is necessary only to verify that the gage length of the test piece is within the tolerance.

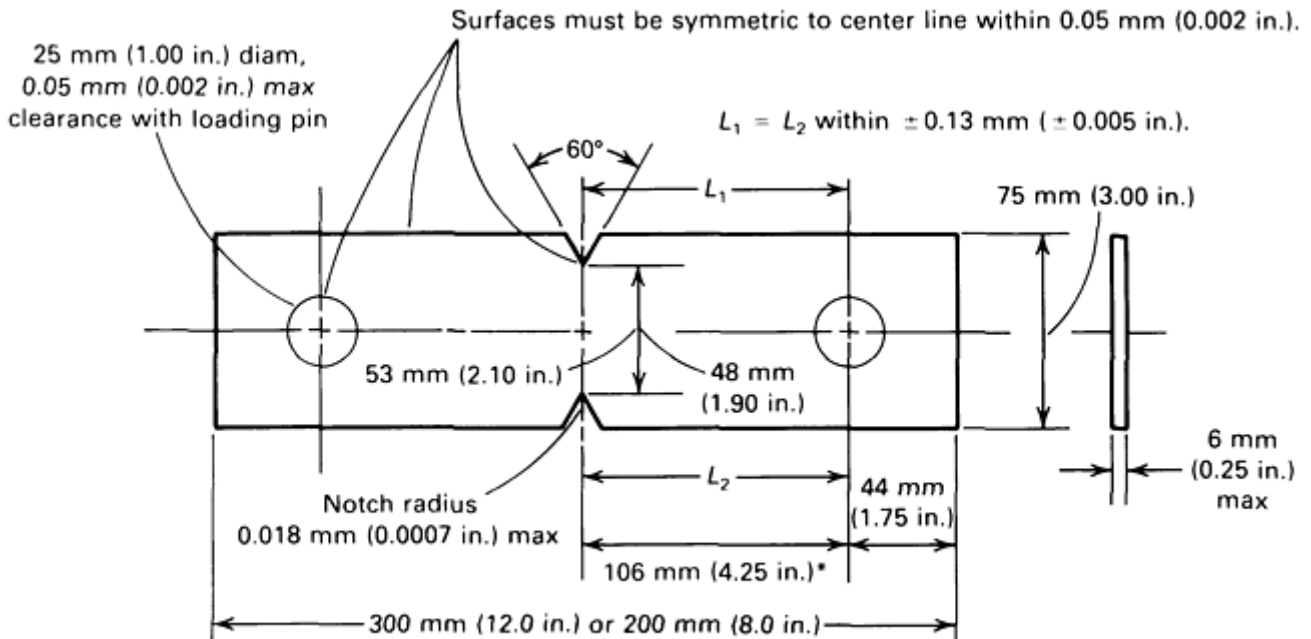
Marking Gage Length. As shown in the flow diagram in Fig. 18, measurement of elongation requires marking the gage length of the test piece. The gage marks should be placed on the test piece in a manner so that when fracture occurs, the fracture will be located within the center one-third of the gage length (or within the center one-third of one of several sets of gage-length marks). For a test piece machined with a reduced-section length that is the minimum specified by ASTM E 8 and with a gage length equal to the maximum allowed for that geometry, a single set of marks is usually sufficient. However, multiple sets of gage lengths must be applied to the test piece to ensure that one set spans the fracture under any of the following conditions:

- Testing full-section test pieces
- Testing pieces with reduced sections significantly longer than the minimum
- Test requirements specify a gage length that is significantly shorter than the reduced section

For example, some product specifications require that the elongation be measured over a 2 in. gage length using the machined plate-type test piece with a 9 in. reduced section (Fig. 22a). In this case, it is recommended that a staggered series of marks (either in increments of 1 in. when testing to ASTM E 8 or in increments of 25.0 mm when testing to ASTM E 8M) be placed on the test piece such that, after fracture, the elongation can be measured using the set that best meets the center-third criteria. Many tension-test methods permit a retest when the elongation is less than the minimum specified by a product specification if the fracture occurred outside the center third of the gage length. When testing full-section test pieces and determining elongation, it is important that the distance between the grips be greater than the specified gage length unless otherwise specified. As a rule of thumb, the distance between grips should be equal to at least the gage length plus twice the minimum dimension of the cross section.

The gage marks may be marks made with a center punch, or may be lines scribed using a sharp, pointed tool, such as a machinist's scribe (or any other means that will establish the gage length within the tolerance permitted by the test method). If scribed lines are used, a broad line or band may first be drawn along the length of the test piece using machinist's layout ink (or a similar substance), and the gage marks are made on this line. This practice is especially helpful to improve visibility of scribed gage marks after fracture. If punched marks are used, a circle around each mark or other indication made by ink may help improve visibility after fracture. Care must be taken to ensure that the gage marks, especially those made using a punch, are not deep enough to become stress raisers, which could cause the fracture to occur through them. This precaution is especially important when testing materials with high strength and low ductility.

Notched Test Pieces. Tension test pieces are sometimes intentionally notched in the center of the gage length (Fig. 23). ASTM E 338 and E 602 describe procedures for testing notched test pieces. Results obtained using notched test pieces are useful for evaluating the response of a material to a localized stress concentration. Detailed information on the notch tensile test and a discussion of the related material characteristics (notch sensitivity and notch strength) can be found in the article "Mechanical Behavior Under Tensile and Compressive Loads" in this Volume. The effect of stress (or strain) concentrations is also discussed in the section "Effect of Strain Concentrations" in this article.



*This dimension is 56 mm (2.25 in.) for the substandard length specimen.

Fig. 23 Example of notched tension-test test piece per ASTM E 338 “Standard Test Method of Sharp-Notch Tension Testing of High-Strength Sheet Materials”

Surface Finish and Condition. The finish of machined surfaces usually is not specified in generic test methods (that is, a method that is not written for a specific item or material) because the effect of finish differs for different materials. For example, test pieces from materials that are not high strength or that are ductile are usually insensitive to surface finish effects. However, if surface finish in the gage length of a tensile test piece is extremely poor (with machine tool marks deep enough to act as stress-concentrating notches, for example), test results may exhibit a tendency toward decreased and variable strength and ductility.

It is good practice to examine the test piece surface for deep scratches, gouges, edge tears, or shear burrs. These discontinuities may sometimes be minimized or removed by polishing or, if necessary, by further machining; however, dimensional requirements often may no longer be met after additional machining or polishing. In all cases, the reduced sections of machined test pieces must be free of detrimental characteristics, such as cold work, chatter marks, grooves, gouges, burrs, and so on. Unless one or more of these characteristics is typical of the product being tested, an unmachined test piece must also be free of these characteristics in the portion of the test piece that is between the gripping devices. When rectangular test pieces are prepared from thin-gage sheet material by shearing (punching) using a die the shape of the test piece, ASTM E 8 states that the sides of the reduced section may need to be further machined to remove the cold work and shear burrs that occur when the test piece is sheared from the rough specimen. This method is impractical for material less than 0.38 mm (0.015 in.) thick. Burrs on test pieces can be virtually eliminated if punch-to-die clearances are minimized.

Uniaxial Tension Testing

John M. (Tim) Holt, Alpha Consultants and Engineering

Test Setup

The setup of a tensile test involves the installation of a test piece in the load frame of a suitable test machine. Force capacity is the most important factor of a test machine. Other test machine factors, such as calibration and load-frame rigidity, are discussed in more detail in the article “Testing Machines and Strain Sensors” in this Volume. The other aspects of the test setup include proper gripping and alignment of the test piece, and the

installation of extensometers or strain sensors when plastic deformation (yield behavior) of the piece is being measured, as described below.

Gripping Devices. The grips must furnish an axial connection between the test piece and the testing machine; that is, the grips must not cause bending in the test piece during loading. The choice of grip is primarily dependent on the geometry of the test piece and, to a lesser degree, on the preference of the test laboratory. That is, rarely do tension-test methods or requirements specify the method of gripping the test pieces.

Figure 24 shows several of the many grips that are in common use, but many other designs are also used. As can be seen, the gripping devices can be classified into several distinct types, wedges, threaded, button, and snubbing. Wedge grips can be used for almost any test-piece geometry; however, the wedge blocks must be designed and installed in the machine to ensure axial loading. Threaded grips and button grips are used only for machined round test pieces. Snubbing grips are used for wire (as shown) or for thin, rectangular test pieces, such as those made from foil.

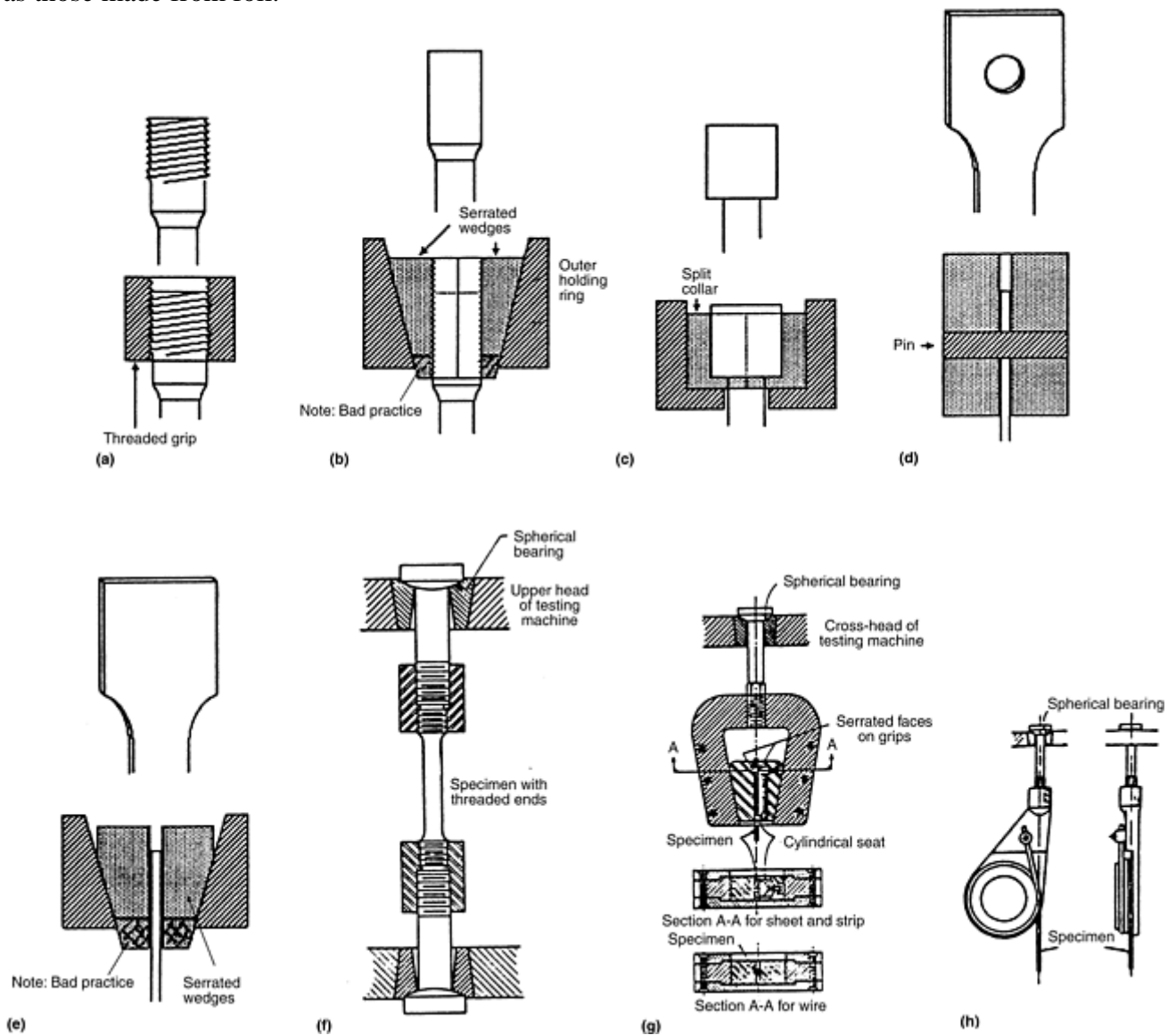


Fig. 24 Examples of gripping methods for tension test pieces. (a) Round specimen with threaded grips. (b) Gripping with serrated wedges with hatched region showing bad practice of wedges extending below the outer holding ring. (c) Butt-end specimen constrained by a split collar. (d) Sheet specimen with pin constraints. (e) Sheet specimen with serrated-wedge grip with hatched region showing the bad practice of wedges extended below the outer holding ring. (f) Gripping device for threaded-end specimen. (g) Gripping device for sheet and wire. (h) Snubbing device for testing wire. Sources: Adapted from Ref 1 and ASTM E 8

As shown in Fig. 22, the dimensions of the grip ends for machined round test pieces are usually not specified, and only approximate dimensions are given for the rectangular test pieces. Thus, each test lab must prepare/machine grip ends appropriate for its testing machine. For machined-round test pieces, the grip end is often threaded, but many laboratories prefer either a plain end, which is gripped with the wedges in the same manner as a rectangular test piece, or with a button end that is gripped in a mating female grip. Because the principal disadvantage of a threaded grip is that the pitch of the threads tend to cause a bending moment, a fine-series thread is often used.

Bending stresses are normally not critical with test pieces from ductile materials. However, for test pieces from materials with limited ductility, bending stresses can be important, better alignment may be required. Button grips are often used, but adequate alignment is usually achieved with threaded test pieces. ASTM E 8 also recommends threaded gripping for brittle materials. The principal disadvantage of the button-end grip is that the diameter of the button or the base of the cone is usually at least twice the diameter of the reduced section, which necessitates a larger, rough specimen and more metal removal during machining.

Alignment of the Test Piece. The force-application axis of the gripping device must coincide with the longitudinal axis of symmetry of the test piece. If these axes do not coincide, the test piece will be subjected to a combination of axial loading and bending. The stress acting on the different locations in the cross section of the test piece then varies, from the sum of the axial and bending stresses on one side of the test piece, to the difference between the two stresses on the other side. Obviously, yielding will begin on the side where the stresses are additive and at a lower apparent stress than would be the case if only the axial stress were present. For this reason, the yield stress may be lowered, and the upper yield stress would appear suppressed in test pieces that normally exhibit an upper yield point. For ductile materials, the effect of bending is minimal, other than the suppression of the upper yield stress. However, if the material has little ductility, the increased strain due to bending may cause fracture to occur at a lower stress than if there were no bending.

Similarly, if the test piece is initially bent, for example, coil set in a machined-rectangular cross section or a piece of rod being tested in a full section, bending will occur as the test piece straightens, and the problems exist.

Methods for verification of alignment are described in ASTM E 1012.

Extensometers. When the tension test requires the measurement of strain behavior (i.e., the amount of elastic and/or plastic deformation occurring during loading), extensometers must be attached to the test piece. The amount of strain can be quite small (e.g., approximately 0.5% or less for elastic strain in steels), and extensometers and other strain-sensing systems are designed to magnify strain measurement into a meaningful signal for data processing.

Several types of extensometers are available, as described in more detail in the article “Testing Machines and Strain Sensors” in this Volume. Extensometers generally have fixed gage lengths. If an extensometer is used only to obtain a portion of the stress-strain curve sufficient to determine the yield properties, the gage length of the extensometer may be shorter than the gage length required for the elongation-at-fracture measurement. It may also be longer, but in general, the extensometer gage length should not exceed approximately 85% of the length of the reduced section or the distance between the grips for test pieces without reduced sections. National and international standardization groups have prepared practices for the classification of extensometers, as described in the article “Testing Machines and Strain Sensors” extensometer classifications usually are based on error limits of a device, as in ASTM E 83 “Standard Practice for Verification and Classification of Extensometers.”

Temperature Control. Tension testing is sometimes performed at temperatures other than room temperature. ASTM E 21 describes standard procedures for elevated-temperature tension testing of metallic materials, which is described further in the article “Hot Tension and Compression Testing” in this Volume. Currently, there is no

ASTM standard procedure for cryogenic testing; further information is contained in the article “Tension and Compression Testing at Low Temperatures” in this Volume.

Temperature gradients may occur in temperature-controlled systems, and gradients must be kept within tolerable limits. It is not uncommon to use more than one temperature-sensing device (e.g., thermocouples) when testing at other than room temperature. Besides the temperature-sensing device used in the control loop, auxiliary sensing devices may be used to determine whether temperature gradients are present along the gage length of the test piece.

Temperature control is also a factor during room-temperature tests because deformation of the test piece causes generation of heat within it. Test results have shown that the heating that occurs during the straining of a test piece can be sufficient to significantly change the properties that are determined because material strength typically decreases with an increase in the test temperature. When performing a test to duplicate the results of others, it is important to know the test speed and whether any special procedures were taken to remove the heat generated by straining the test piece.

Reference cited in this section

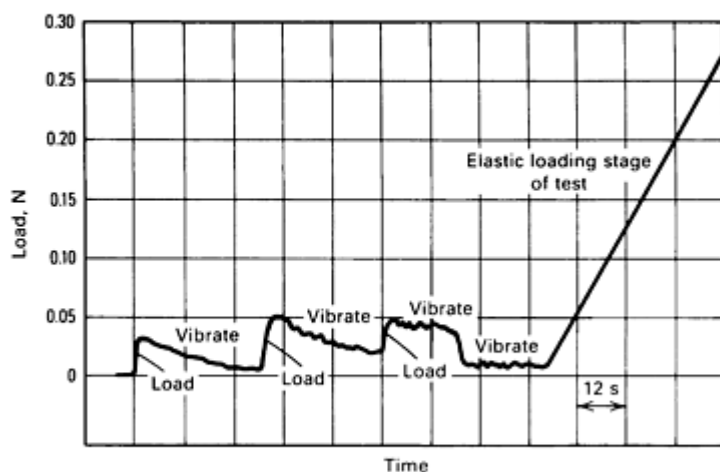
1. D. Lewis, Tensile Testing of Ceramics and Ceramic-Matrix Composites, *Tensile Testing*, P. Han, Ed., ASM International, 1992, p 147–182

Uniaxial Tension Testing

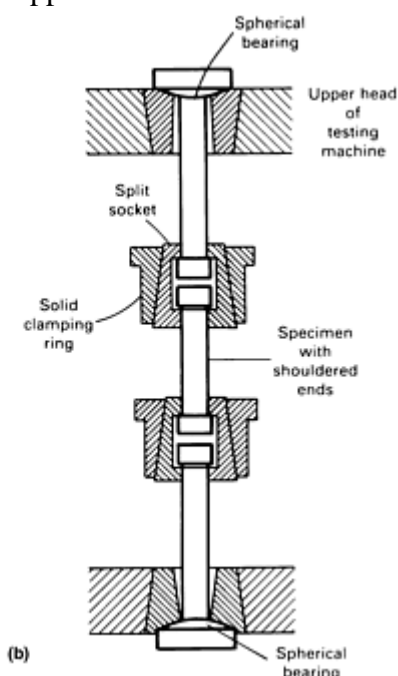
John M. (Tim) Holt, Alpha Consultants and Engineering

Test Procedures

After the test piece has been properly prepared and measured and the test setup established, conducting the test is fairly routine. The test piece is installed properly in the grips, and if required, extensometers or other strain-measuring devices are fastened to the test piece for measurement and recording of extension data. Data acquisition systems also should be checked. In addition, it is sometimes useful to repetitively apply small initial loads and vibrate the load train (a metallographic engraving tool is a suitable vibrator) to overcome friction in various couplings, as shown in Fig. 25(a). A check can also be run to ensure that the test will run at the proper testing speed and temperature. The test is then begun by initiating force application.



(a)



(b)

Fig. 25(a) Effectiveness of vibrating the load train to overcome friction in the spherical ball and seat couplings shown in (b). (b) Spherically seated gripping device for shouldered tension test piece.

Speed of Testing

The speed of testing is extremely important because mechanical properties are a function of strain rate, as discussed in the section “Effect of Strain Rate” in this article. It is, therefore, imperative that the speed of testing be specified in either the tension-test method or the product specification.

In general, a slow speed results in lower strength values and larger ductility values than a fast speed; this tendency is more pronounced for lower-strength materials than for higher-strength materials and is the reason that a tension test must be conducted within a narrow test-speed range.

In order to quantify the effect of deformation rate on strength and other properties, a specific definition of testing speed is required. A conventional (quasi-static) tension test, for example, ASTM E 8, prescribes upper and lower limits on the deformation rate, as determined by one of the following methods during the test:

- Strain rate
- Stress rate (when loading is below the proportional limit)
- Cross-head separation rate (or free-running cross-head speed) during the test
- Elapsed time

These methods are listed in order of decreasing precision, except during the occurrence of upper-yield-strength behavior and yield point elongation (YPE) (where the strain rate may not necessarily be the most precise method). For some materials, elapsed time may be adequate, while for other materials, one of the remaining methods with higher precision may be necessary in order to obtain test values within acceptable limits. ASTM E 8 specifies that the test speed must be slow enough to permit accurate determination of forces and strains. Although the speeds specified by various test methods may differ somewhat, the test speeds for these methods are roughly equivalent in commercial testing.

Strain rate is expressed as the change in strain per unit time, typically expressed in units of min^{-1} or s^{-1} because strain is a dimension-less value expressed as a ratio of change in length per unit length. The strain rate can usually be dialed, or programmed, into the control settings of a computer-controlled system or paced or timed for other systems.

Stress rate is expressed as the change in stress per unit of time. When the stress rate is stipulated, ASTM E 8 requires that it not exceed 100 ksi/ min. This number corresponds to an elastic strain rate of about $5 \times 10^{-5} \text{ s}^{-1}$ for steel or $15 \times 10^{-5} \text{ s}^{-1}$ for aluminum. As with strain rate, stress rate usually can be dialed or programmed into the control settings of computer-controlled test systems. However, because most older systems indicate force being applied, and not stress, the operator must convert stress to force and control this quantity. Many machines are equipped with pacing or indicating devices for the measurement and control of the stress rate, but in the absence of such a device, the average stress rate can be determined with a timing device by observing the time required to apply a known increment of stress. For example, for a test piece with a cross section of 0.500 in. by 0.250 in. and a specified stress rate of 100,000 psi/min, the maximum force application rate would be 12,500 lbf/min (force = stress rate \times area = 100,000 psi/min \times (0.500 in. \times 0.250 in.)). A minimum rate of $\frac{1}{10}$ of the maximum rate is usually specified.

Comparison between Strain-Rate and Stress-Rate Methods. Figure 26 compares strain-rate control with stress-rate control for describing the speed of testing. Below the elastic limit, the two methods are identical. However, as shown in Fig. 26, once the elastic limit is exceeded, the strain rate increases when a constant stress rate is applied. Alternatively, the stress rate decreases when a constant strain rate is specified. For a material with discontinuous yielding and a pronounced upper yield spike (Fig. 7a), it is a physical impossibility for the stress rate to be maintained in that region because, by definition, there is not a sustained increase in stress in this region. For these reasons, the test methods usually specify that the rate (whether stress rate or strain rate) is set prior to the elastic limit (EL), and the crosshead speed is not adjusted thereafter. Stress rate is not applicable beyond the elastic limit of the material. Test methods that specify rate of straining expect the rate to be controlled during yield; this minimizes effects on the test due to testing machine stiffness.

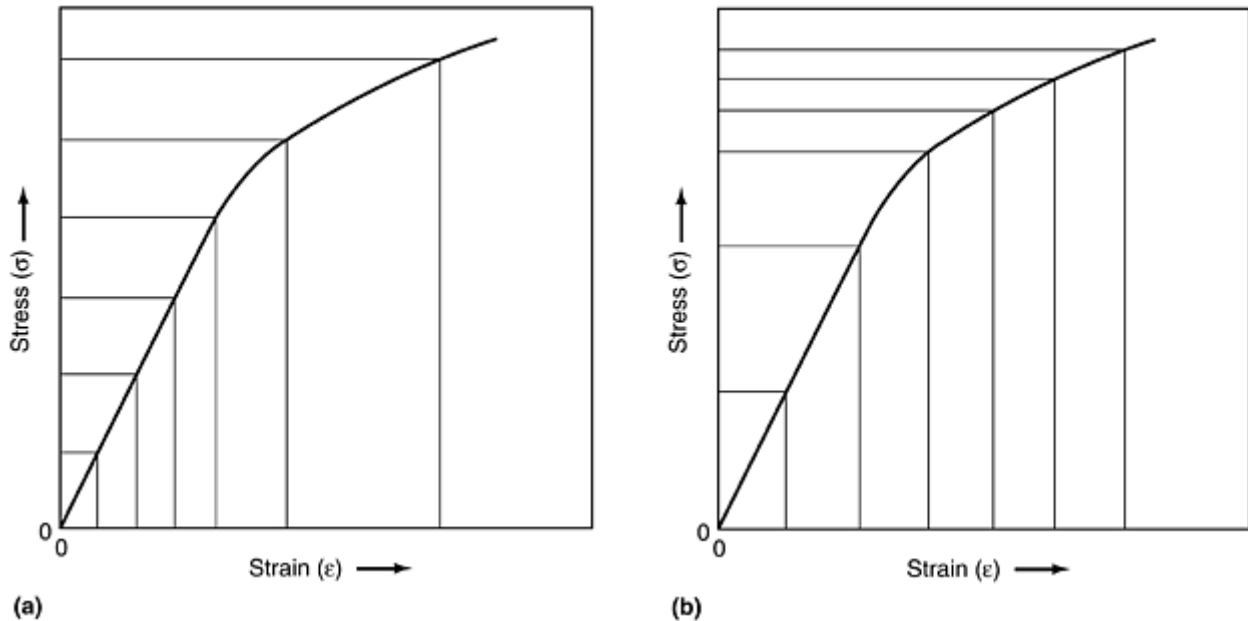


Fig. 26 Illustration of the differences between constant stress increments and constant strain increments. (a) Equal stress increments (increasing strain increments). (b) Equal strain increments (decreasing stress increments)

The rate of separation of the grips (or rate of separation of the cross heads or the cross-head speed) is a commonly used method of specifying the speed of testing. In ASTM A 370, for example, the specification of test speed is that “through the yield, the maximum speed shall not exceed $\frac{1}{16}$ in. per inch of reduced section per minute; beyond yield or when determining tensile strength alone, the maximum speed shall not exceed $\frac{1}{2}$ in. per inch of reduced section per minute. For both cases, the minimum speed shall be greater than $\frac{1}{10}$ of this amount.” This means that for a machined round test piece with a $2\frac{1}{4}$ in. reduced section, the rate prior to yielding can range from a maximum of $\frac{9}{64}$ in./min (i.e., $2\frac{1}{4}$ in. reduced-section length $\times \frac{1}{16}$ in./min) down to $\frac{9}{640}$ in./min (i.e., $2\frac{1}{4}$ in. reduced-section length $\times \frac{1}{160}$ in./min).

The elapsed time to reach some event, such as the onset of yielding or the tensile strength, or the elapsed time to complete the test, is sometimes specified. In this case, multiple test pieces are usually required so that the correct test speed can be determined by trial and error.

Many test methods permit any speed of testing below some percentage of the specified yield or tensile strength to allow time to adjust the force application mechanism, ensure that the extensometer is working, and so on. Values of 50 and 25%, respectively, are often used.

Uniaxial Tension Testing

John M. (Tim) Holt, Alpha Consultants and Engineering

Post-Test Measurements

After the test has been completed, it is often required that the cross-sectional dimensions again be measured to obtain measures of ductility. ASTM E 8 states that measurements made after the test shall be to the same accuracy as the initial measurements.

Method E 8 also states that upon completion of the test, gage lengths 2 in. and under are to be measured to the nearest 0.01 in., and gage lengths over 2 in. are to be measured to the nearest 0.5%. The document goes on to state that a percentage scale reading to 0.5 % of the gage length may be used. However, if the tension test is

being performed as part of a product specification, and the elongation is specified to meet a value of 3% or less, special techniques, which are described, are to be used to measure the final gage length. These measurements are discussed in a previous section, "Elongation," in this article.

Uniaxial Tension Testing

John M. (Tim) Holt, Alpha Consultants and Engineering

Variability of Tensile Properties

Even carefully performed tests will exhibit variability because of the nonhomogenous nature of metallic materials. Figure 27 (Ref 10) shows the three-sigma distribution of the offset yield strength and tensile strength values that were obtained from multiple tests on a single aluminum alloy. Distribution curves are presented for the results from multiple tests of a single sheet and for the results from tests on a number of sheets from a number of lots of the same alloy. Because these data are plotted with the minus three-sigma value as zero, it appears there is a difference between the mean values; however, this appearance is due only to the way the data are presented. Figures 28(a) and (b) show lines of constant offset yield strength and constant tensile strength, respectively, for a 1 in. thick, quenched and tempered plate of an alloy steel. In this case, rectangular test pieces 1½ in. wide were taken along the transverse direction (*T* orientation in Fig. 20) every 3 in. along each of the four test-piece centerlines shown. These data indicate that the yield and tensile strengths vary greatly within this relatively small sample and that the shape and location of the yield strength contour lines are not the same as the shape and location of the tensile strength lines.

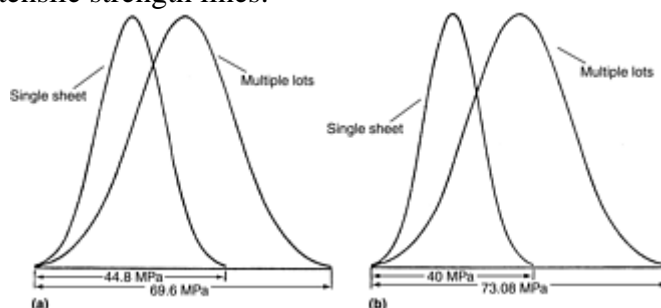


Fig. 27 Distribution of (a) yield and (b) tensile strengths for multiple tests on single sheet and on multiple lots of aluminum alloy 7075-T6. Source: Ref 10

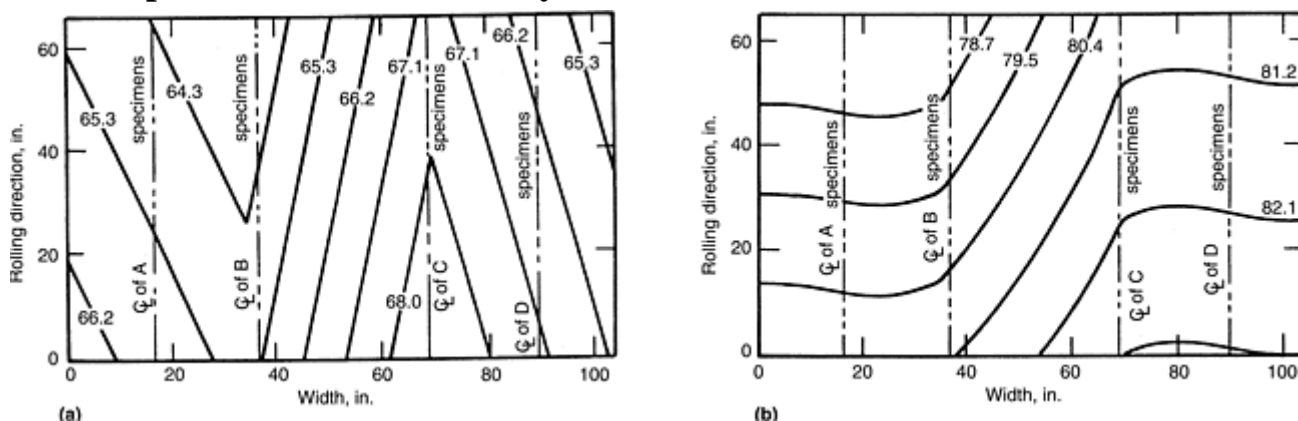


Fig. 28 Contour maps of (a) constant yield strength (0.5% elongation under load, ksi) and (b) constant tensile strength (ksi) for a plate of alloy steel

Effect of Strain Concentrations. During testing, strain concentrations (often called stress concentrations) occur in the test piece where there is a change in the geometry. In particular, the transition radii between the reduced section and the grip ends are important, as previously noted in the section on test-piece geometry. Most test

methods specify a minimum value for these radii. However, because there is a change in geometry, there is still a strain concentration at the point of tangency between the radii and the reduced section. Figure 29(a) (Ref 11) shows a test piece of rubber with an abrupt change of section, which is a model of a tension test piece in the transition region. Prior to applying the force at the ends of the model, a rectangular grid was placed on the test piece. When force is applied, it can be seen that the grid is severely distorted at the point of tangency but to a much lesser degree at the center of the model. The distortion is a visual measure of strain. The strain distribution across section $n-n$ is plotted in Fig. 29(b). From the stress-strain curve for the material (Fig. 29c), the stresses on this section can be determined. It is apparent that the test piece will yield at the point of tangency prior to general yielding in the reduced section. The ratio between the nominal strain and actual, maximum strain is often referred to as the strain-concentration factor, or the stress-concentration factor if the actual stress is less than the elastic limit. This ratio is often abbreviated as k_t . Studies have shown that k_t is about 1.25 when the radii are $\frac{1}{2}$ in., the width (or diameter) of the reduced section is 0.500 in., and the width (or diameter) of the grip end is $\frac{3}{4}$ in. That is, the actual strain or the actual elastic stress at the transition (if less than the yield of the material) is 25% greater than would be expected without consideration of the strain or stress concentration. The value of k_t decreases as the radii increase such that, for the above example, if the radii are 1.0 in., and k_t decreases to about 1.15.

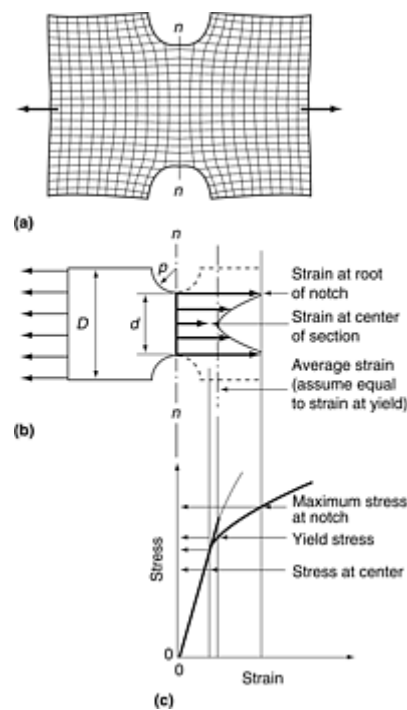


Fig. 29 Effect of strain concentrations on section $n-n$. (a) Strain distribution caused by an abrupt change in cross section (grid on sheet of rubber) (Ref 11). (b) Schematic of strain distribution on cross section (Ref 11). (c) Calculation of stresses at abrupt change in cross section $n-n$ by graphical means

Various techniques have been tried to minimize k_t , including the use of spirals instead of radii, but there will always be strain concentration in the transition region. This indicates that the yielding of the test piece will always initiate at this point of tangency and proceed toward midlength. For these reasons, it is extremely important that the radii be as large as feasible when testing materials with low ductility.

Strain concentrations can be caused by notches deliberately machined in the test piece, nicks from accidental causes, or shear burrs, machining marks, or gouges that occur during the preparation of the test piece or from many other causes.

Effect of Strain Rate. Although the mechanical response of different materials varies, the strength properties of most materials tend to increase at higher strain rates. For example, the variability in yield strength of ASTM A 36 structural steel over a limited range of strain rates is shown in Fig. 30 (Ref 12). A “zero-strain-rate” stress-strain curve (Fig. 31) is generated by applying forces to a test piece to obtain a small plastic strain and then maintaining that strain until the force ceases to decrease (Point A). Force is reapplied to the test piece to obtain another increment of plastic strain, which is maintained until the force ceases to decrease (Point B). This

procedure is continued for several more cycles. The smooth curve fitted through Points A, B, and so on is the “zero-strain-rate” stress-strain curve, and the yield value is determined from this curve.

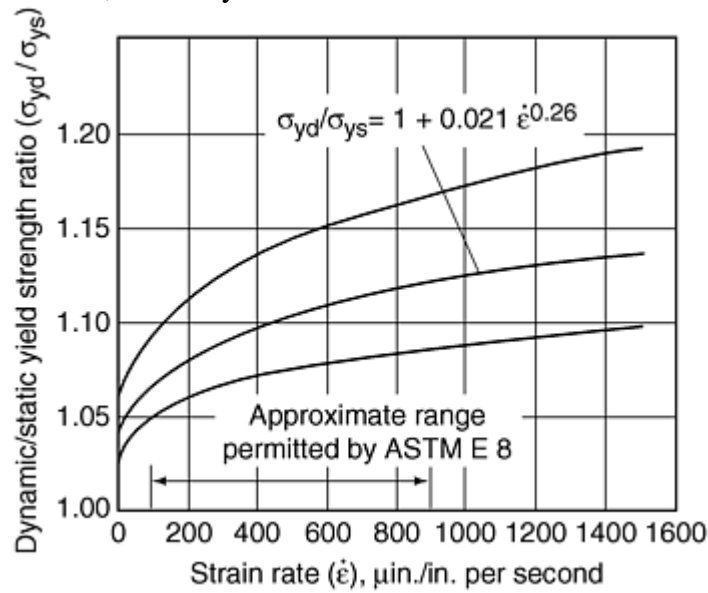


Fig. 30 Effect of strain rate on the ratio of dynamic yield-stress and static yield-stress level of A36 structural steel. Source: Ref 12

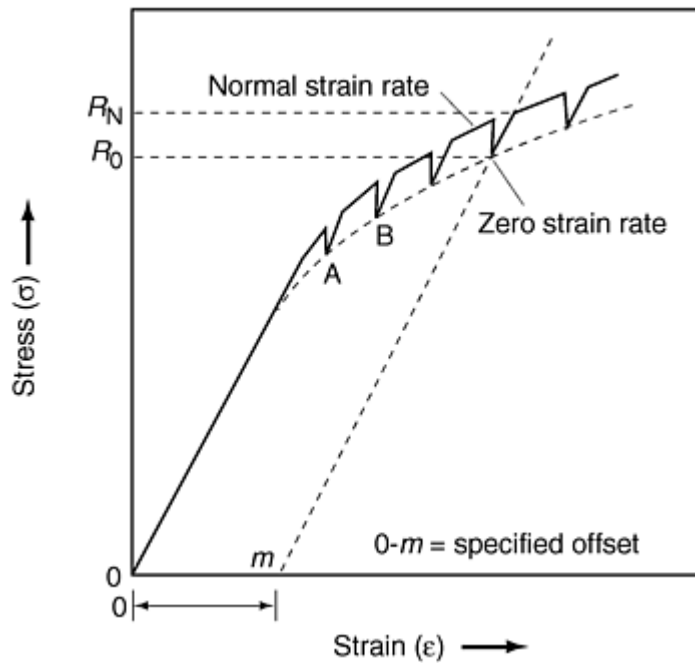


Fig. 31 Stress-strain curves for tests conducted at “normal” and “zero” strain rates

The effect of strain rate on strength depends on the material and the test temperature. Figure 32 (Ref 13) shows graphs of tensile strength and yield strength for a common heat-resistant low-alloy steel ($\frac{1}{4}$ Cr-1 Mo) over a wide range of temperatures and strain rates. In this figure, the strain rates were generally faster than those prescribed in ASTM E 8.

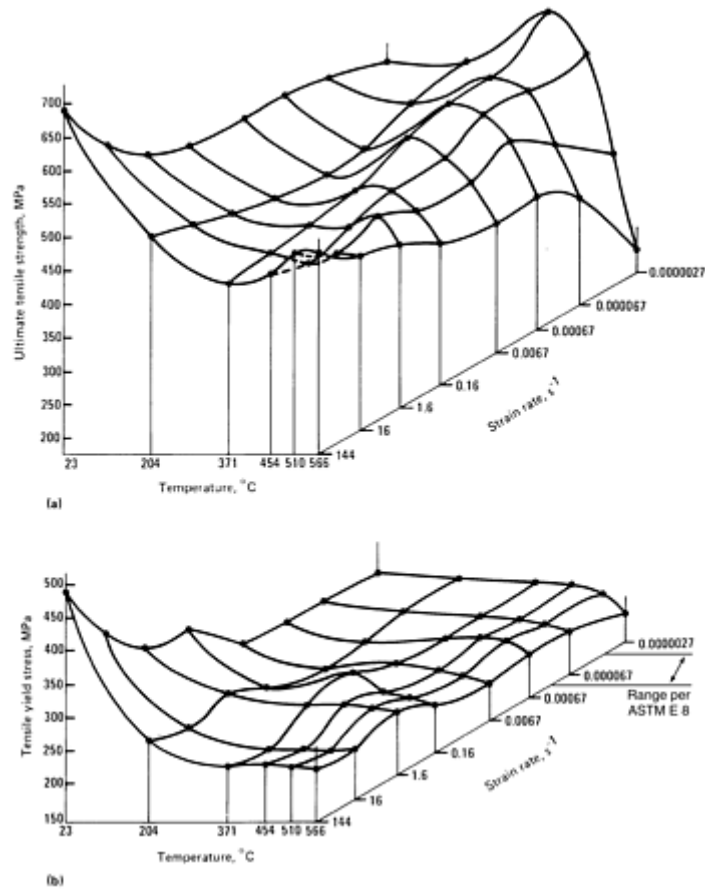


Fig. 32 Effect of temperature and strain rate on (a) tensile strength and yield strength of $2\frac{1}{4}$ Cr-1 Mo Steel. Note: Stain-rate range permitted by ASTM Method E8 when determining yield strength at room temperature is indicated. Source: Ref 13

Another example of strain effects on strength is shown in Fig. 33 (Ref 14). This figure illustrates true yield stress at various strains for a low-carbon steel at room temperature. Between strain rates of 10^{-6} s^{-1} and 10^{-3} s^{-1} (a thousandfold increase), yield stress increases only by 10%. Above 1 s^{-1} , however, an equivalent rate increase doubles the yield stress. For the data in Fig. 33, at every level of strain the yield stress increases with increasing strain rate. However, a decrease in strain-hardening rate is exhibited at the higher deformation rates. For a low-carbon steel tested at elevated temperatures, the effects of strain rate on strength can become more complicated by various metallurgical factors such as dynamic strain aging in the “blue brittleness” region of some mild steels (Ref 14).

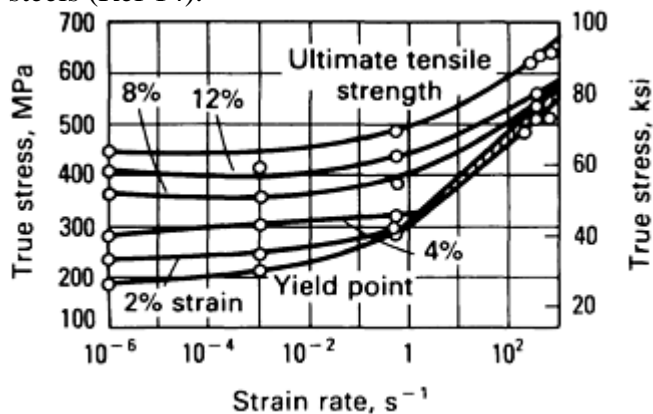


Fig. 33 True stresses at various strains vs. strain rate for a low-carbon steel at room temperature. The top line in the graph is tensile strength, and the other lines are yield points for the indicated level of strain. Source: Ref 14

Structural aluminum is less strain-rate sensitive than steels. Figure 34 (Ref 15) shows data obtained for 1060-O aluminum. Between strain rates of 10^{-3} s^{-1} and 10^3 s^{-1} (a millionfold increase), the stress at 2% plastic strain increases by less than 20%.

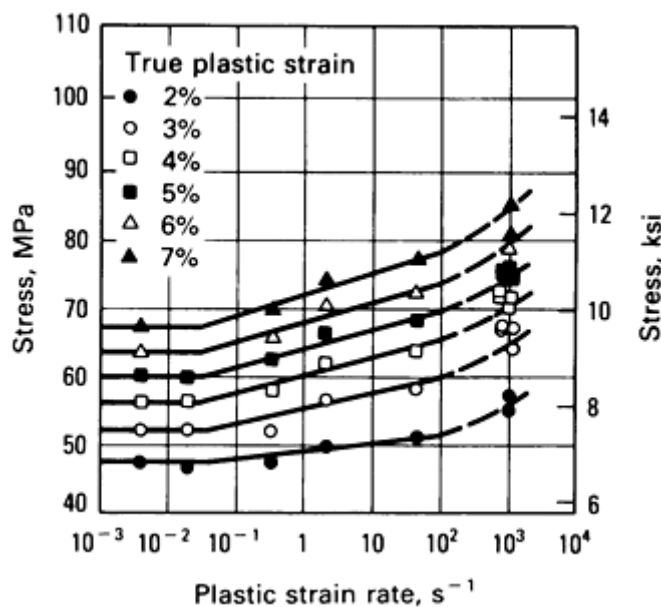


Fig. 34 Uniaxial stress/strain/strain rate data for aluminum 1060-O. Source: Ref 1

References cited in this section

10. W.P. Goepfert, Statistical Aspects of Mechanical Property Assurance, *Reproducibility and Accuracy of Mechanical Tests*, STP 626, ASTM, 1977, p 136–144
11. F.B. Seely and J.O. Smith, *Resistance of Materials*, 4th ed., John Wiley & Sons, p 45
12. N.R.N. Rao et al., “Effect of Strain Rate on the Yield Stress of Structural Steel,” Fritz Engineering Laboratory Report 249.23, 1964
13. R.L. Klueh and R.E. Oakes, Jr., High Strain-Rate Tensile Properties of 2¼ Cr-1 Mo Steel, *J. Eng. Mater. Technol.*, Oct 1976, p 361–367
14. M.J. Manjoine, Influence of Rate of Strain and Temperature on Yield Stresses of Mild Steel, *J. Appl. Mech.*, Vol 2, 1944, p A-211 to A-218
15. A.H. Jones, C.J. Maiden, S.J. Green, and H. Chin, Prediction of Elastic-Plastic Wave Profiles in Aluminum 1060-O under Uniaxial Strain Loading, *Mechanical Behavior of Materials under Dynamic Loads*, U.S. Lindholm, Ed., Springer-Verlag, 1968, p 254–269
16. “Standard Method of Sharp-Notch Tension Testing of High-Strength Sheet Materials,” E 338, ASTM

Uniaxial Tension Testing

John M. (Tim) Holt, Alpha Consultants and Engineering

References

1. D. Lewis, Tensile Testing of Ceramics and Ceramic-Matrix Composites, *Tensile Testing*, P. Han, Ed., ASM International, 1992, p 147–182
2. R.J. Del Vecchio, Tensile Testing of Elastomers, *Tensile Testing*, P. Han, Ed., ASM International, 1992, p 135–146
3. N.E. Dowling, *Mechanical Behavior of Materials—Engineering Methods for Deformation, Fracture, and Fatigue*, 2nd ed., Prentice Hall, 1999, p 123
4. R.L. Brockenbough and B.G. Johnson, “Steel Design Manual,” United States Steel Corporation, ADUSS 27 3400 03, 1974, p 2–3
5. P.M. Mumford, Test Methodology and Data Analysis, *Tensile Testing*, P. Han, Ed., ASM International, 1992, p 55
6. “Standard Test Method for Young's Modulus, Tangent Modulus, and Chord Modulus,” E 111, ASTM
7. *Making, Shaping, and Treating of Steel*, 10th ed., U.S. Steel, 1985, Fig. 50-12 and 50-13
8. “Standard Test Methods and Definitions for Mechanical Testing of Steel Products,” A 370, Annex 6, *Annual Book of ASTM Standards*, ASTM, Vol 1.03
9. “Conversion of Elongation Values, Part 1: Carbon and Low-Alloy Steels,” 2566/1, International Organization for Standardization, revised 1984
10. W.P. Goepfert, Statistical Aspects of Mechanical Property Assurance, *Reproducibility and Accuracy of Mechanical Tests*, STP 626, ASTM, 1977, p 136–144
11. F.B. Seely and J.O. Smith, *Resistance of Materials*, 4th ed., John Wiley & Sons, p 45
12. N.R.N. Rao et al., “Effect of Strain Rate on the Yield Stress of Structural Steel,” Fritz Engineering Laboratory Report 249.23, 1964
13. R.L. Klueh and R.E. Oakes, Jr., High Strain-Rate Tensile Properties of 2¼ Cr-1 Mo Steel, *J. Eng. Mater. Technol.*, Oct 1976, p 361–367
14. M.J. Manjoine, Influence of Rate of Strain and Temperature on Yield Stresses of Mild Steel, *J. Appl. Mech.*, Vol 2, 1944, p A-211 to A-218
15. A.H. Jones, C.J. Maiden, S.J. Green, and H. Chin, Prediction of Elastic-Plastic Wave Profiles in Aluminum 1060-O under Uniaxial Strain Loading, *Mechanical Behavior of Materials under Dynamic Loads*, U.S. Lindholm, Ed., Springer-Verlag, 1968, p 254–269

Uniaxial Tension Testing

John M. (Tim) Holt, Alpha Consultants and Engineering

Selected References

- “Standard Method of Sharp-Notch Tension Testing of High-Strength Sheet Materials,” E 338, ASTM

- “Standard Method of Sharp-Notch Tension Testing with Cylindrical Specimens,” E 602, ASTM
- “Standard Methods and Definitions for Mechanical Testing of Steel Products,” A 370, ASTM
- “Standard Methods of Tension Testing of Metallic Foil,” E 345, ASTM
- “Standard Test Methods for Poisson's Ratio at Room Temperature,” E 132, ASTM
- “Standard Test Methods for Static Determination of Young's Modulus of Metals at Low and Elevated Temperatures,” E 231, ASTM
- “Standard Test Methods for Young's Modulus, Tangent Modulus, and Chord Modulus,” E 111, ASTM
- “Standard Methods of Tension Testing of Metallic Materials,” E 8, ASTM
- “Standard Methods of Tension Testing Wrought and Cast Aluminum- and Magnesium-Alloy Products,” B 557, ASTM
- “Standard Recommended Practice for Elevated Temperature Tension Tests of Metallic Materials,” E 21, ASTM
- “Standard Recommended Practice for Verification of Specimen Alignment Under Tensile Loading,” E 1012, ASTM

Uniaxial Compression Testing

Howard A. Kuhn, Concurrent Technologies Corporation

Introduction

COMPRESSION LOADS occur in a wide variety of material applications, such as steel building structures and concrete bridge supports, as well as in material processing, such as during the rolling and forging of a billet. Characterizing the material response to these loads requires tests that measure the compressive behavior of the materials. Results of these tests provide accurate input parameters for product-or process-design computations. Under certain circumstances, compression testing may also have advantages over other testing methods. Tension testing is by far the most extensively developed and widely used test for material behavior, and it can be used to determine all aspects of the mechanical behavior of a material under tensile loads, including its elastic, yield, and plastic deformation and its fracture properties. However, the extent of deformation in tension testing is limited by necking. To understand the behavior of materials under the large plastic strains during deformation processing, measurements must be made beyond the tensile necking limit. Compression tests and torsion tests are alternative approaches that overcome this limitation.

Furthermore, compression-test specimens are simpler in shape, do not require threads or enlarged ends for gripping, and use less material than tension-test specimens. Therefore, compression tests are often useful for subscale testing and for component testing where tension-test specimens would be difficult to produce. Examples of these applications include through-thickness property measurements in plates and forgings (Ref 1), weld heat-affected zones, and precious metals (Ref 2) where small amounts of material are available.

In addition, characterizing the mechanical behavior of anisotropic materials often requires compression testing. For isotropic polycrystalline materials, compressive behavior is correctly assumed to be identical to tensile behavior in terms of elastic and plastic deformation. However, in highly textured materials that deform by twinning, as opposed to dislocation slip, compressive and tensile deformation characteristics differ widely (Ref 3). Likewise, the failure of unidirectionally reinforced composite materials, particularly along the direction of reinforcement, is much different in compression than in tension.

In this article, the characteristics of deformation during axial compression testing are described, including the deformation modes, compressive properties, and compression-test deformation mechanics. Procedures are described for the use of compression testing for measurement of the deformation properties and fracture properties of materials.

References cited in this section

1. T. Erturk, W.L. Otto, and H.A. Kuhn, Anisotropy of Ductile Fracture—An Application of the Upset Test, *Metall. Trans.*, Vol 5, 1974, p 1883
2. W.A. Kawahara, Tensile and Compressive Materials Testing with Sub-Sized Specimens, *Exp. Tech.*, Nov/Dec, 1990, p 27–29
3. W.A. Backofen, *Deformation Processing*, Addison-Wesley, Reading, MA, p 53

Uniaxial Compression Testing

Howard A. Kuhn, Concurrent Technologies Corporation

Deformation Modes in Axial Compression

Compression tests can provide considerable useful information on plastic deformation and failure, but certain precautions must be taken to assure a valid test of material behavior. Figure 1 illustrates the modes of deformation that can occur in compression testing. The buckling mode shown in Fig. 1(a) occurs when the length-to-width ratio of the test specimen is very large, and can be treated by classical analyses of elastic and plastic buckling (Ref 4). These analyses predict that cylindrical specimens having length-to-diameter ratios, L/D , less than 5.0 are safe from buckling and can be used for compression testing of brittle and ductile materials. Practical experience with ductile materials, on the other hand, shows that even L/D ratios as low as 2.5 lead to unsatisfactory deformation responses. For these geometries, even slightly eccentric loading or nonparallel compression plates will lead to shear distortion, as shown in Fig. 1(b). Therefore, L/D ratios less than 2.0 are normally used to avoid buckling and provide accurate measurements of the plastic deformation behavior of materials in compression.

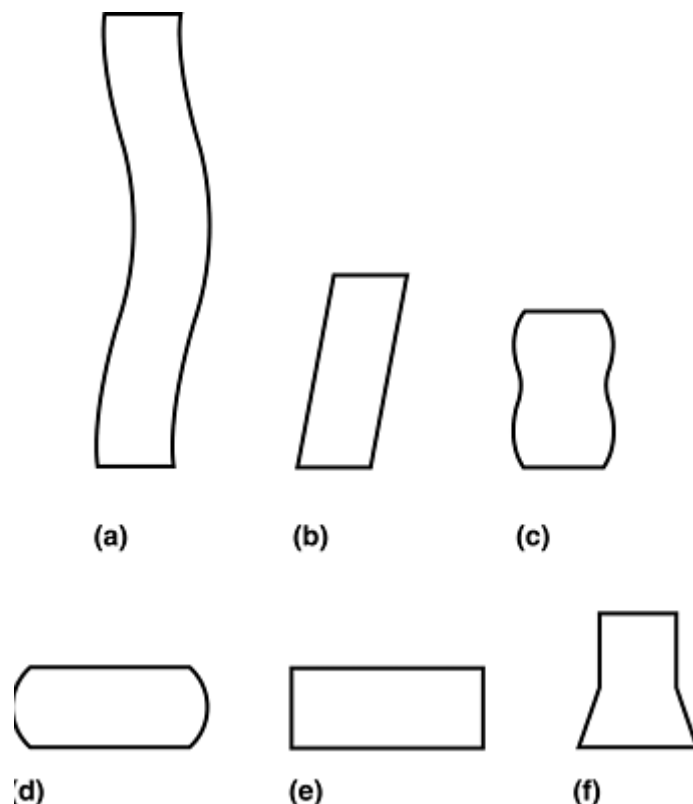


Fig. 1 Modes of deformation in compression. (a) Buckling, when $L/D > 5$. (b) Shearing, when $L/D > 2.5$. (c) Double barreling, when $L/D > 2.0$ and friction is present at the contact surfaces. (d) Barreling, when $L/D < 2.0$ and friction is present at the contact surfaces. (e) Homogenous compression, when $L/D < 2.0$ and no friction is present at the contact surfaces. (f) Compressive instability due to work-softening material

Friction is another source of anomalous deformation in compression testing of ductile materials. Friction between the ends of the test specimen and the compression platens constrains lateral flow at the contact surfaces, which leads to barreling or bulging of the cylindrical surface. Under these circumstances, for L/D ratios on the order of 2.0, a double barrel forms, as shown in Fig. 1(c), smaller L/D ratios lead to a single barrel, as in Fig. 1(d). Barreling indicates that the deformation is nonuniform (i.e., the stress and strain vary throughout the test specimen), and such tests are not valid for measurement of the bulk elastic and plastic properties of a material. Barreling, however, can be beneficial for the measurement of the localized fracture properties of a material, as described in the section “Instability in Compression” of this article.

If the compression test can be carried out without friction between the specimen and compression platens, barreling does not occur, as shown in Fig. 1(e), and the deformation is uniform (homogenous). For measurement of the bulk deformation properties of materials in compression, this configuration must be achieved.

A final form of irregular deformation in axial compression is an instability that is the antithesis of necking in tension. In this case, the instability occurs due to work softening of the material and takes the form of rapid, localized expansion, as shown in Fig. 1(f).

Reference cited in this section

4. J.H. Faupel and F.E. Fisher, *Engineering Design*, John Wiley & Sons, 1981, p 566–592

Uniaxial Compression Testing

Howard A. Kuhn, Concurrent Technologies Corporation

Compressive Properties

The bulk elastic and plastic deformation characteristics of polycrystalline materials are generally the same in compression and tension. As a result, the elastic-modulus, yield-strength, and work-hardening curves will be the same in compression and tension tests. Fracture strength, ultimate strength, and ductility, on the other hand, depend on localized mechanisms of deformation and fracture, and are generally different in tension and compression testing. Anisotropic materials, such as composite materials and highly textured polycrystalline materials, also exhibit considerable differences between tensile and compressive behaviors beyond initial elastic response.

Measurements of bulk elastic modulus and yield strength require accurate measurements of the axial strain of the material under compression testing. This is accomplished by attaching to the specimen an extensometer, which uses a differential transformer or strain gages to provide an electronic signal that is proportional to the displacement of gage marks on the specimen. Extensometers are most easily used in tension testing because tension test specimens are long and provide ample space for attachment of the extensometer clips. Due to the limitations noted in the previous section (Fig. 1a and b), compression-test specimens are considerably smaller in length and make attachment of the extensometer clips difficult. Alternatively, a differential transformer can be used to measure the displacement between the compression platen surfaces. Because the measurement is not made directly on the specimen, however, elastic distortion and slight rotations of the platens during testing will give false displacement readings.

Measurement of the work-hardening, or plastic-flow, curve of a material is best carried out by compression testing, particularly if the application, such as bulk metalworking, requires knowledge of the flow behavior at large plastic strains beyond the necking limit in tension testing. In this case, the strains are many orders of magnitude larger than the elastic strains, and indirect measurement of the axial strain by monitoring the motion of the compression platens is sufficiently accurate. Any systematic errors caused by elastic deformation of the platens or test equipment are insignificant compared to the large plastic displacements of the compression specimen.

The fracture strength of a material is much different in tension and compression. In tension, the fracture strength of a ductile material is determined by its necking behavior, which concentrates the plastic deformation in a small region, generates a triaxial stress state in the neck region, and propagates ductile fracture from voids that initiate at the center of the neck region. The fracture strength of a brittle material in tension, on the other hand, is limited by its cleavage stress.

In compression of a ductile material, necking does not occur, so the void generation and growth mechanism that leads to complete separation in the tension test does not terminate the compression test. Ductile fractures can form, however, on the barreled surface of a compression specimen with friction. These fractures generally grow slowly and do not lead to complete separation of the specimen, so the load-carrying capacity of the material is not limited. As a result, there is no definition of fracture strength in compression of ductile materials. Surface cracks that may form on the barreled surface of compression tests with friction depend not only on the material,

but also on the amount of friction and the L/D ratios of the specimen, as described in the section “Compression Testing for Ductile Fracture” in this article.

In compression of a brittle or low-ductility material, however, fracture occurs catastrophically by shear. The failure either occurs along one large shear plane, leading to complete separation, or at several sites around the specimen, leading to crushing of the material. In either case, the load-carrying capacity of the material comes to an abrupt halt, and the fracture strength of the material is easily defined as the load at that point divided by the cross-sectional area.

The ultimate strength of a material in tension is easily defined as the maximum load-bearing capacity. In a ductile material, this occurs at the initiation of necking. In a brittle material, it occurs at fracture. Because necking does not occur in compression testing, there is no ultimate compressive strength in ductile materials, and in brittle materials the ultimate compressive strength occurs at fracture. The only exception to this is in materials that exhibit severe work softening, in which case, plastic instability (Fig. 1f) leads to an upper limit in load-carrying capacity, which defines the ultimate strength of the material, as described in the section "Instability in Compression" in this article.

Uniaxial Compression Testing

Howard A. Kuhn, Concurrent Technologies Corporation

Plasticity Mechanics

Further understanding of the axial compression test can be obtained by examining the interactions between the plastic flow and forces acting during the test. The essential features of this interaction can be developed by considering a thin, vertical slab of material in a compression-test specimen (Fig. 2a). Pressure, P , from the compression platens acts on the top and bottom of the slab. Because this slab is to the right of the centerline, the slab moves to the right as the compression test progresses. Motion of the slab to the right, coupled with the pressure from the platens, causes friction, f , on the top and bottom surfaces of the slab. The direction of friction on the slab is to the left, opposing the motion of the slab.

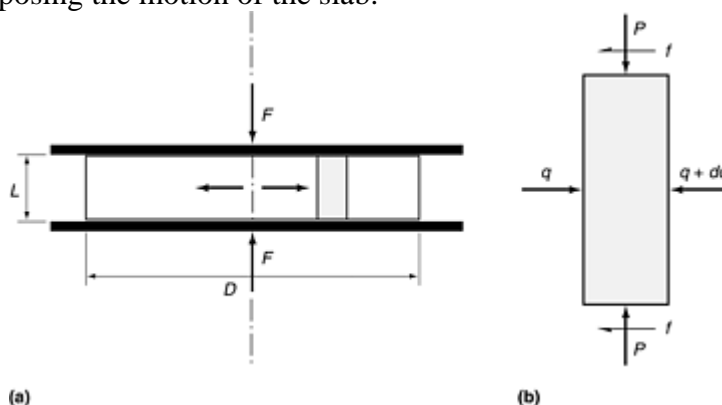


Fig. 2 Interactions between plastic flow and forces acting during compression testing. (a) Schematic of a compression test showing applied force F , radial expansion away from the centerline, and a slab element of material in a compression test. (b) Forces acting on the slab. P , pressure from the compression platens; f , friction at the contact surfaces, acting opposite to motion of the slab; q , internal radial pressure in the test specimen

Extracting the slab from the compression test, shown in Fig. 2(b), it is clear that the friction forces on the top and bottom of the slab cause an imbalance of forces in the horizontal direction. This implies that there must be internal horizontal forces acting on the vertical faces of the slab to maintain force equilibrium (forces due to acceleration are negligible). As shown in Fig. 2(b), the resulting horizontal pressure, q , acting on opposite sides of the slab must differ by some amount, dq , to achieve equilibrium.

Applying the principle of equilibrium to the slab in the horizontal direction gives a simple differential equation for the horizontal pressure q :

$$dq/dr = -2f/L \quad (\text{Eq 1})$$

where L is the thickness of the compression-test specimen. At the outside edge of the test specimen ($r = D/2$), the horizontal pressure must be zero (free surface); therefore, Eq 1 shows that q increases from zero at the edge to positive values inside the test specimen. Furthermore, Eq 1 shows that the rate of increase of q toward the centerline is larger for high values of friction and low values of specimen thickness. If f is constant, the internal pressure distribution is:

$$q = f(D/L)(1 - 2r/D) \quad (\text{Eq 2})$$

which has a peak value at $r = 0$.

Finally, the vertical pressure, P , is related to the internal pressure, q , by the yield criterion for plastic deformation:

$$P = q + \sigma_0 \quad (\text{Eq 3})$$

where σ_0 is the yield strength of the material. Therefore, P has the same distribution as the radial stress, q , plus the material yield strength. Integrating this pressure distribution over the contact area gives the total force, F .

Schematic plots of the pressure distribution, P , in axial compression are given in Fig. 3. Note that even though the deformation is uniform at every point, the compressive stress is not uniform, but reaches peak values at the centerline. The values of this peak pressure increase as friction increases and as the test specimen aspect ratio, L/D , decreases. More importantly, if friction is zero, Eq 2 shows that internal pressure, q , is zero throughout the test specimen. Then, from Eq 3, P is uniform and equal to σ_0 . Frictionless conditions, therefore, must be used to measure the plastic deformation response of a material, as described in the next section. More detailed analysis of the plasticity mechanics of axial compression are given in Ref 5.

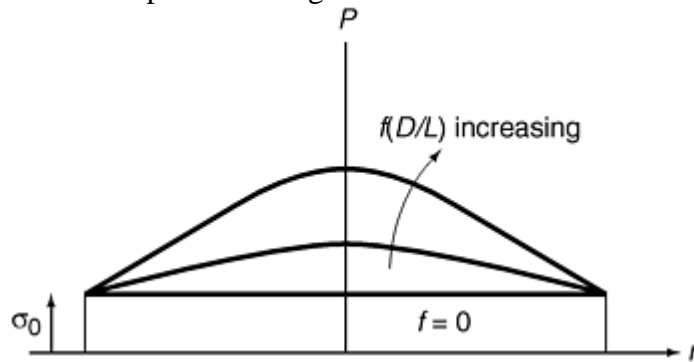


Fig. 3 Schematic of pressure distributions, P , in a compression test. When friction is zero, P is uniform and equal to the material flow stress, σ_0 , but increasing friction and decreasing L/D with friction lead to increasingly nonuniform pressure distributions with peak values at the centerline.

The analysis given above is strictly valid only for specimens having very low aspect ratios. However, the essential roles of friction and geometry are valid qualitatively for test specimens having large aspect ratios; for these test specimens, the deformation patterns are very complex and vary in the thickness direction, as well as in the lateral direction. A macrograph of a compression test cross section, shown in Fig. 4(a), reveals the nonuniformity of internal deformation patterns due to friction at the contact surfaces. In general, the internal deformation depicted in Fig. 4(b) can be described as three zones (Ref 6): (a) nearly undeformed wedges at the top and bottom (referred to as dead-metal zones), (b) crisscrossing regions of intense shear deformation, and (c) moderately deformed regions near the barrel surfaces. The severity of barreling and the differences in degree of deformation between the three regions increase as friction at the contact surfaces increases.

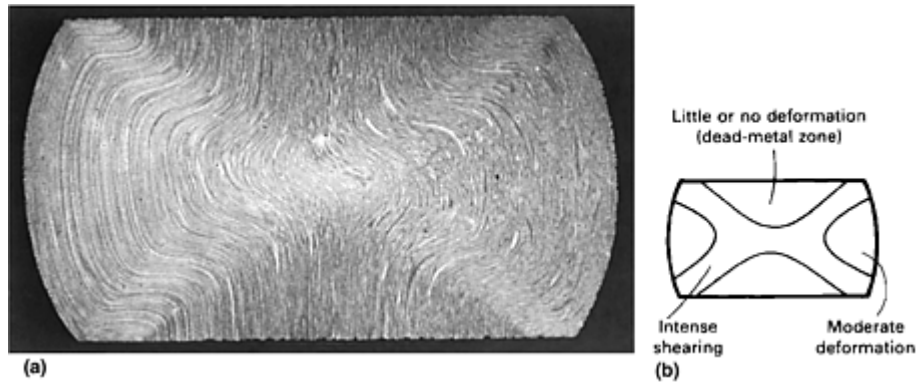


Fig. 4 Internal deformation in compression testing. (a) Macrograph of the internal deformation in a compression-test specimen with high-contact surface friction. Source: Ref 5. (b) Schematic representation of the internal deformation into three zones. I, nearly undeformed wedges at the contact surfaces (dead-metal zones); II, criss-crossing regions of intense shear deformation; III, moderately deformed regions near the bulge surface. Source: Ref 6

References cited in this section

5. G.E. Dieter, *Mechanical Metallurgy*, 2nd ed., McGraw-Hill, 1976, p 561–565
6. G.E. Dieter, Evaluation of Workability: Introduction, *Forming and Forging*, Vol 14, *ASM Handbook*, ASM International, 1988, p 365

Uniaxial Compression Testing

Howard A. Kuhn, Concurrent Technologies Corporation

Homogenous Compression for Plastic Deformation Behavior

Under homogenous-compression conditions (frictionless compression), height reduction and the resulting radial and circumferential expansion are uniform throughout the test specimen. Furthermore, under these conditions, radial and circumferential stresses are zero, and the only stress acting is the uniform compressive stress in the axial direction, as described in the previous section.

Homogenous compression is accomplished by eliminating friction at the contact surfaces, which obviously requires the use of lubricants. Polishing the ends of the compression-test specimens as well as the die platens provides smooth surfaces, and lubricants applied to the contact surfaces form a low-friction layer between these surfaces. However, during compression of high-strength materials, the interface pressure between the test specimen and die platens becomes extremely high, and the lubricant squeezes out, leaving metal-on-metal contact, resulting in high friction.

One approach to retaining lubricants at the contact surface involves machining concentric circular grooves into the end faces of the test specimen (Fig. 5a) (Ref 7). Another approach was pioneered by Rastegaev and refined by Herberthz and Wiegels (Ref 8), in which the entire end face is machined away except for a small rim, as shown in Fig. 5(b). This traps a small volume of lubricant in the cavity, forming a hydrostatic cushion with nearly zero friction. This approach was modified by machining a tapered recess, as shown in Fig. 5(c), which reduces the amount of material removed and diminishes the strain measurement error. Furthermore this lubricant recess provides greater lubrication at the rim where material movement is greatest. During compression testing, radial displacement of the test material is zero at the center and increases linearly to the

outer rim. Evaluations of lubrication practice for high-temperature testing have shown that the tapered lubricant reservoir shown in Fig. 5(c) leads to the greatest reproducibility (Ref 9).

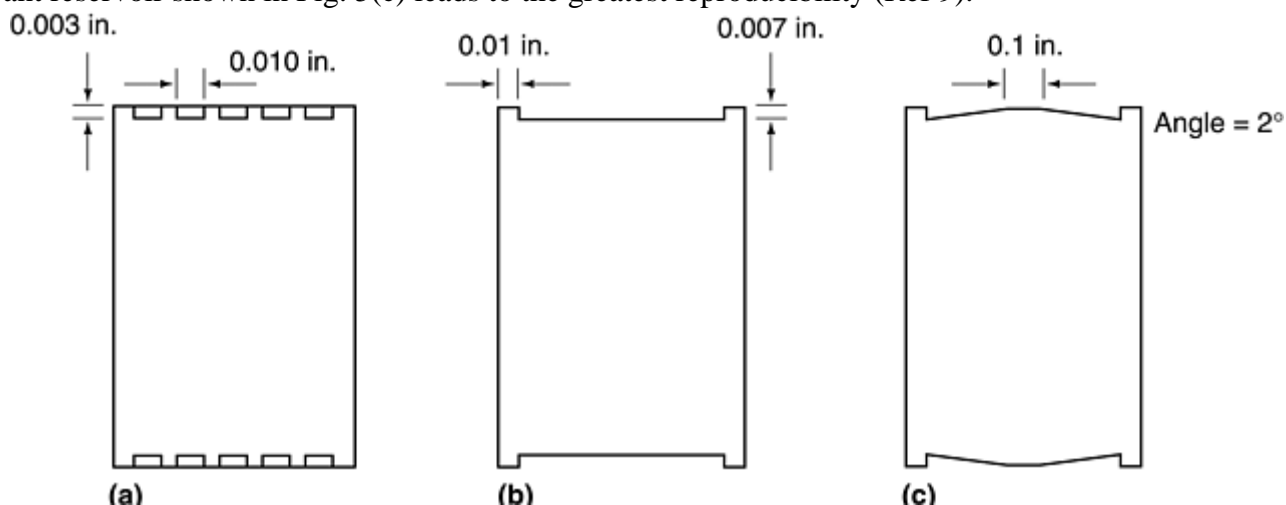


Fig. 5 Compression-test end profiles for lubricant entrapment. (a) Concentric grooves. Source: Ref 7. (b) Rastegaev reservoir. Source: Ref 8. (c) Modified Rastegaev reservoir. Source: Ref 9

Several high-pressure lubricants are available for room-temperature compression tests, including mineral oil, palm oil, stearates, and molybdenum disulfide. Teflon (E.I. DuPont de Nemours & Co., Inc., Wilmington, DE) in the form of spray or sheet is also widely used at room temperature and can be used at temperatures up to 500 °C (930 °F). For high-temperature testing of steels, titanium, and superalloys, one can use emulsions of graphite, molybdenum disulfide, and various glasses. It is important to match the grade of glass and resulting viscosity with the test temperature.

In homogenous compression tests, the plastic stress-strain curve can be easily calculated by measurement of the load, cross-sectional area, and height of the specimen throughout the test. The test can be conducted incrementally at room temperature wherein the specimen height and lateral dimensions are measured after each increment of deformation. For high-temperature deformation or continuous testing, the test-equipment load cell and crosshead displacement can be used to determine the load and dimensional changes of the specimen. In the latter measurement, it is necessary to remove systematic errors by first carrying out the compression test with no test specimen in place. This provides a load-stroke curve for the test-machine load train and measures the compliance of the various elements in the loaded column. Subtracting this compliance from the measured crosshead stroke during a compression test then provides a more accurate measurement of the specimen deformation. In any event, if constancy of volume can be assumed for the material being tested, then the cross-sectional area can be readily calculated from the specimen height at any point throughout the test.

References cited in this section

7. J.E. Hockett, The Cam Plastometer, in *Mechanical Testing*, Vol 8, *ASM Handbook*, ASM International, 1985, p 197
 8. R. Herbertz and H. Wiegels, Ein Verfahren Zur Verwirklichung des Reibungsfreien Zylinderstanch versuchs für die Ermittlung von Fließcurven, *Stahl Eisen*, Vol 101, 1981, p 89–92
 9. K. Lintermanns Fander, “The Flow and Fracture of Al-High Mg-Mn Alloys at High Temperatures and Strain Rates,” Ph.D. dissertation, University of Pittsburgh, 1984, p 258
-

Compression Testing for Ductile Fracture

When friction exists at the die contact surfaces, material at the contact surfaces is retarded from moving outward while the material at the midplane is not constrained. As a result, barreling occurs, as shown in Fig. 1(c) and 1(d). Under these conditions, for a given axial compressive strain, the bulge profile provides circumferential strain at the equator that is greater than the strain that occurs during homogenous compression. At the same time, due to the bulge profile, the local compressive strain at the equator is less than the strain that would have occurred during homogenous compression for the same overall height strain. These surface strain deviations from homogenous compression increase as bulging increases; the severity of the bulge, in turn, is controlled by the magnitude of friction and the L/D ratio of the specimen. Figure 6 illustrates the progressive change in strain at the bulge surface for different lubrication and L/D ratios (Ref 10).

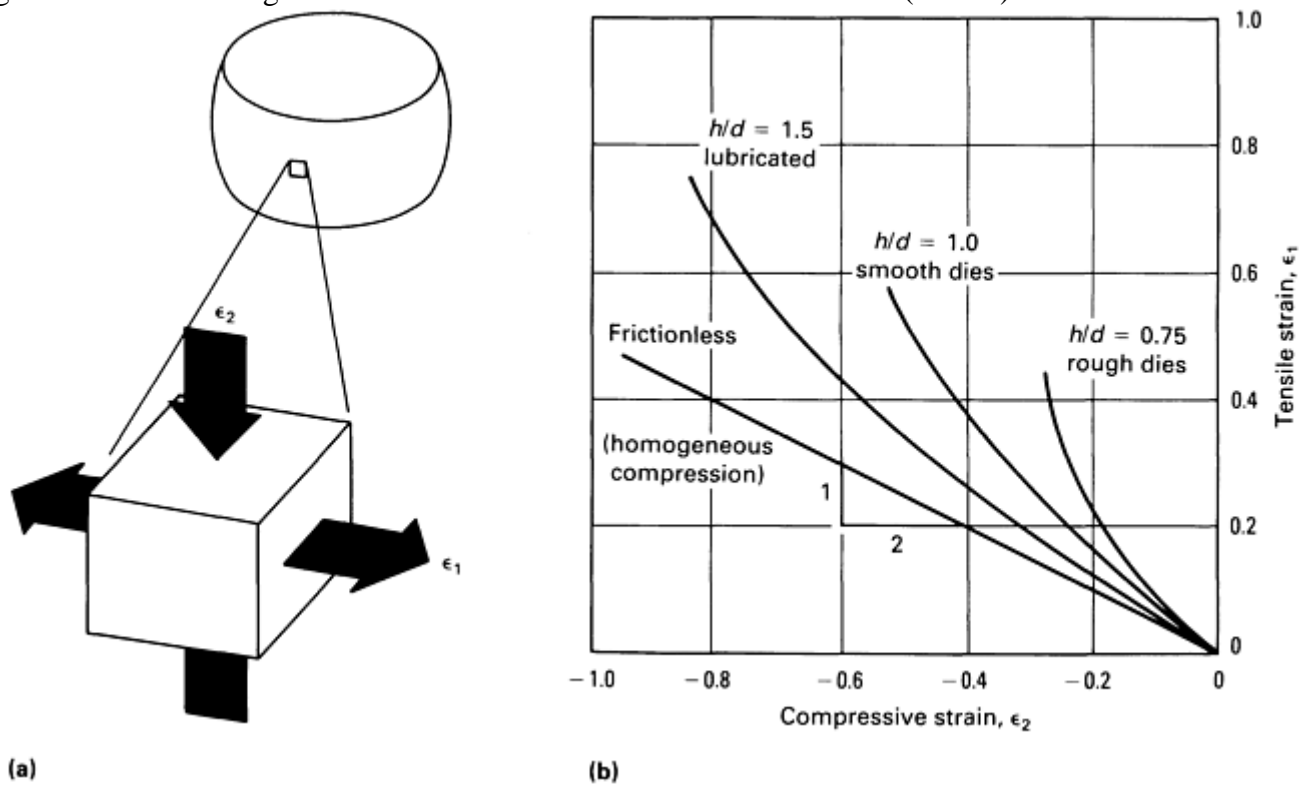


Fig. 6 Progressive change in strain at the bulge surface in compression testing. (a) Strains at the bulge surface of a compression test. (b) Variation of the strains during a compression test without friction (homogenous compression) and with progressively higher levels of friction and decreasing aspect ratio L/D (shown as h/d)

These strain combinations lead to tensile stress around the circumference and reduced compressive stress at the bulge equator. Therefore, compression tests with friction, and consequent bulging, can be used as tests for fracture. Figure 7 shows compression-test specimens with and without friction. Note that the compression test with the bulge surface, that is, with friction at the contact surfaces, has a crack caused by the tensile stress in the circumferential direction at the bulge surface. The homogenous compression specimen, even after greater height compression, has not bulged; therefore, there is no tensile stress in the circumferential direction, and the specimen has not cracked.

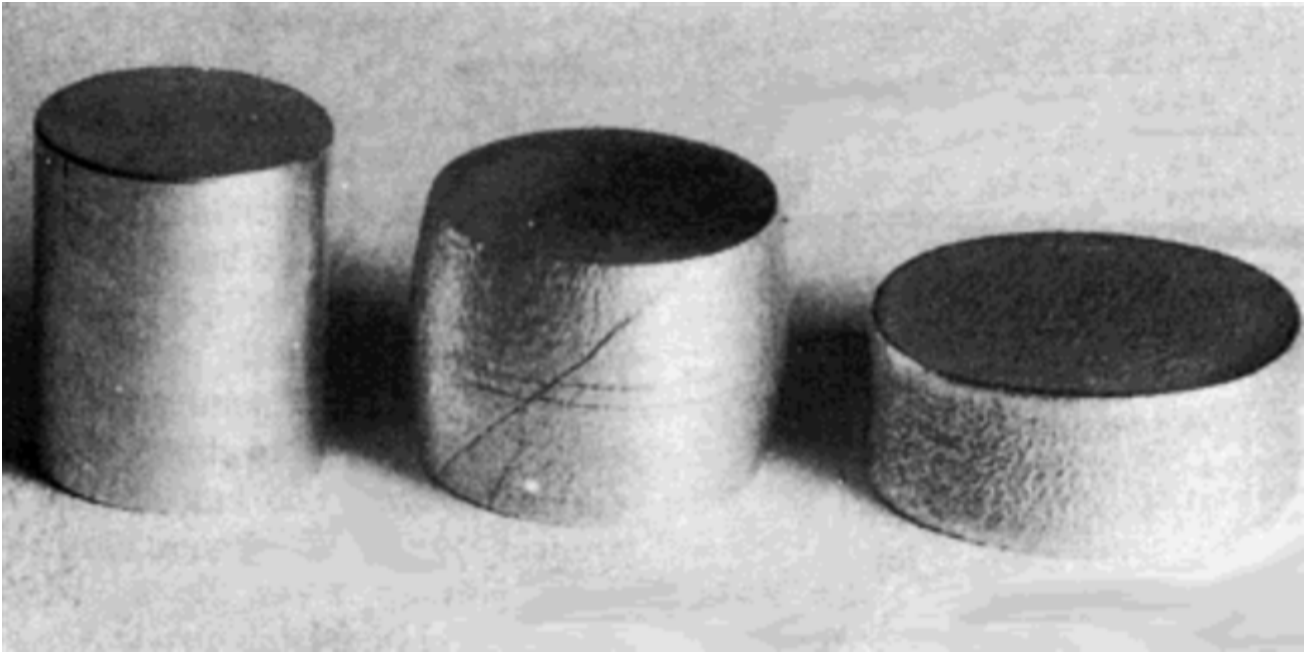


Fig. 7 Compression tests on 2024-T35 aluminum alloy. Left, undeformed specimen; center, compression with friction (cracked); right, compression without friction (no cracks)

The stress and strain environment at the bulge surface of upset cylinders suggests that axial compression tests can be used for workability measurements by carrying out the tests under a variety of conditions regarding interface friction and L/D ratios. By plotting the surface strains at fracture for each condition, a fracture strain locus can be generated representing the workability of the material. Figure 8 illustrates such a fracture locus. Modifications of the cylindrical compression-test specimen geometry have been used to enhance the range of strains over which fracture can be measured (Ref 11).

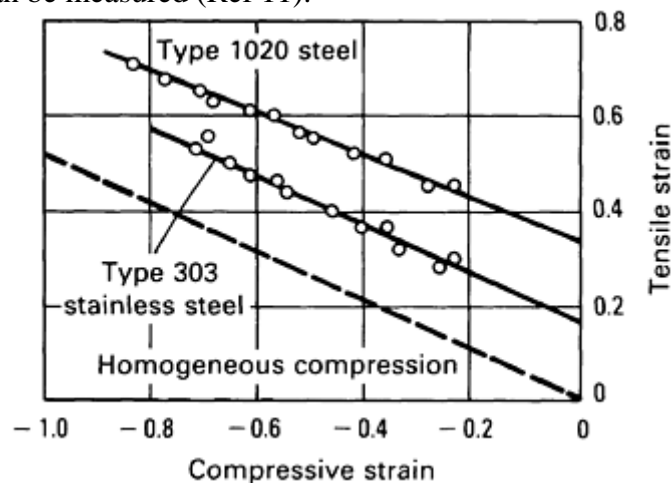


Fig. 8 Locus of fracture strains (workability) determined from compression test with friction. Source: Ref 10

References cited in this section

10. H.A. Kuhn, P.W. Lee, and T. Erturk, A Fracture Criterion for Cold Forging, *J. Eng. Mater. Technol. (Trans. ASME)*, Vol 95, 1973, p 213–218
11. H.A. Kuhn, Workability Theory and Application in Bulk Forming Processes, *Forming and Forging*, Vol 14, *ASM Handbook*, ASM International, 1988, p 389–391

Instability in Compression

In tension testing, the onset of necking indicates unstable flow, characterized by a rapid decrease in diameter localized to the neck region. Up to this point, as the test specimen elongates, work hardening of the material compensates for the decrease in cross-sectional area; therefore, the material is able to carry an increasing load. However, as the work-hardening rate decreases, the flow stress acting across the decreasing cross-sectional area is no longer able to support the applied axial load. At this point, necking begins and the rate of decrease of cross-sectional area exceeds the rate of increase of work hardening, leading to instability and a rapidly falling tensile load as the neck progresses toward fracture.

In compression testing, a similar phenomenon occurs when work softening is prevalent (Ref 12). That is, during compression, the cross-sectional area of the specimen increases, which increases the load-carrying capability of the material. However, if work softening occurs, its load-carrying capability is decreased. When the rate of decrease in strength of the material due to work softening exceeds the rate of increase in the area of the specimen, an unstable mode of deformation occurs in which the material rapidly spreads in a localized region, as shown in Fig. 1(f).

Instability in tension and compression can be described through the Considère construction. Instability occurs when the slope of the load-elongation curve becomes zero, that is:

$$dF = d(\sigma A) = \sigma dA + Ad\sigma = 0$$

or

$$d\sigma/\sigma = -dA/A = d\varepsilon = de/(1 + e)$$

and

$$d\sigma/de = \sigma/(1 + e) \tag{Eq 4}$$

where σ is true stress, ε is true strain, e is engineering strain, F is force, and A is area.

Equation 4 indicates that instability occurs when the slope of the true stress-engineering strain curve equals the ratio of true stress to one plus the engineering strain. This leads to the Considère construction for instability (Fig. 9). The upper part of Fig. 9 shows the Considère construction for a tension test. When the work hardening stress-strain curve reaches point C , necking begins and unstable deformation continues through to complete separation or fracture. This defines the ultimate strength of the material in tension. In the lower part of Fig. 9, the Considère construction for the compression test shows that, for a work softening material, unstable flow commences at point C' , leading to a configuration as shown in Fig. 1(f). Thus, the ultimate strength of the material in compression in this case can be defined as the stress at this point.

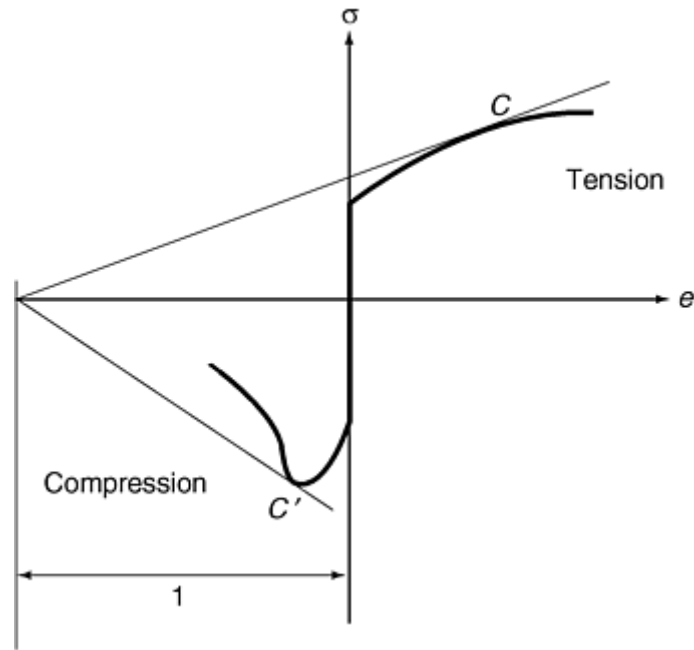


Fig. 9 Considère construction showing instability conditions in tension testing (due to decreasing work-hardening rate) and in compression testing (due to work softening)

Materials that undergo severe work softening are prone to compressive instabilities. While useful in itself, this precludes measurement of the bulk plastic deformation behavior of the material, just as the necking instability in tension testing prevents measurement of plastic deformation behavior at large strains. Several metallurgical conditions can lead to such work softening. These include dynamic recovery and dynamic recrystallization where substructure rearrangements and dislocation reductions lead to a rapid decrease in flow stress. Morphological changes in second phases, such as the rapid spheroidization of pearlite at elevated temperatures, the coarsening of small spherical precipitates, and the coarsening of martensitic substructures, are another source of work softening. Further examples of work softening include incipient melting of eutectic phases and localized shear-band formation, seen commonly in titanium alloys.

Reference cited in this section

12. J.J. Jonas and M.J. Luton, Flow Softening at Elevated Temperatures, *Advances in Deformation Processing*, J.J. Burke and V. Weiss, Ed., Plenum, 1978, p 238

Uniaxial Compression Testing

Howard A. Kuhn, Concurrent Technologies Corporation

Test Methods

Axial compression testing is a useful procedure for measuring the plastic flow behavior and ductile fracture limits of a material. Measuring the plastic flow behavior requires frictionless (homogenous compression) test conditions, while measuring ductile fracture limits takes advantage of the barrel formation and controlled stress and strain conditions at the equator of the barreled surface when compression is carried out with friction. Axial compression testing is also useful for measurement of elastic and compressive fracture properties of brittle materials or low-ductility materials. In any case, the use of specimens having large L/D ratios should be avoided to prevent buckling and shearing modes of deformation.

Axial compression tests for determining the stress-strain behavior of metallic materials are conducted by techniques described in test standards, such as:

- ASTM E 9, “Compression Testing of Metallic Materials at Room Temperature”
- DIN 50106, “Compression Test, Testing of Metallic Materials”
- ASTM E 209, “Compression Tests of Metallic Materials at Elevated Temperatures with Conventional or Rapid Heating Rates and Strain Rates”

This section briefly reviews the factors that influence the generation of valid test data for tests conducted in accordance with ASTM E 9 and the capabilities of conventional universal testing machines (UTMs) for compression testing.

Specimen Buckling

As previously noted, errors in compressive stress-strain data can occur by the nonuniform stress and strain distributions from specimen buckling and barreling. Buckling can be prevented by avoiding the use of specimens with large length-to-diameter ratios, L/D . In addition, the risk of specimen buckling can be reduced by careful attention to alignment of the loading train and by careful manufacture of the specimen according to the specifications of flatness, parallelism, and perpendicularity given in ASTM E 9. However, even with well-made specimens tested in a carefully aligned loading train, buckling may still occur. Conditions that typically induce buckling are discussed in the following sections.

Alignment. The loading train, including the loading faces, must maintain initial alignment throughout the entire loading process. Alignment, parallelism, and perpendicularity tests should be conducted at maximum load conditions of the testing apparatus.

Specimen Tolerances. The tolerances given in ASTM E 9 for specimen end-flatness, end-parallelism, and end-perpendicularity should be considered as upper limits. This is also true for concentricity of outer surfaces in cylindrical specimens and uniformity of dimensions in rectangular sheet specimens. If tolerances are reduced from these values, the risk of premature buckling is also reduced.

Inelastic Buckling. Only elastic buckling is discussed in ASTM E 9. This may be somewhat unrealistic, because for the most slender specimen recommended, the calculated elastic buckling stresses are higher than can be achieved in a test. This specimen has a length-to-diameter ratio of 10. An approximate calculation using the elastic Euler equation for a steel specimen with flat ends on a flat surface (assumed value of end-fixity coefficient is 3.5) yields a buckling stress in excess of 4100 MPa (600 ksi); the comparable value for an aluminum specimen would be 1380 MPa (200 ksi). These values, however, are not realistic.

Buckling stress in the above example should not be calculated by an elastic formula but by an inelastic buckling relation. In terms of inelastic buckling it has been concluded that the following relation appropriately calculates inelastic buckling stresses (Ref 13):

$$S_{cr} = C\pi^2 \left[\frac{E_t}{(L/\rho)^2} \right] \quad (\text{Eq 5})$$

where S_{cr} is the buckling stress in MPa (ksi); C is the end-fixity coefficient; E_t is the tangent modulus of the stress-strain curve in MPa (ksi); L is the specimen length in mm (in.); and r is the radius of gyration of specimen cross section in mm (in.). Equation 1 reduces to the Euler equation if E , the modulus of elasticity, is substituted for E_t .

Rearranging Eq 5 to combine the stress-related factors results in:

$$\left(\frac{1}{C\pi^2} \right) \left(\frac{L}{\rho} \right)^2 = \frac{E_t}{S_{cr}} \quad (\text{Eq 6})$$

Note that the value of the right side of Eq 6 decreases as stress increases in a stress-strain curve. In a material with an elastic-pure-plastic response, the right side of Eq 6 vanishes, because E_t becomes zero, and buckling will always occur at the yield stress. When the material exhibits strain hardening, calculations using Eq 6 will yield the appropriate specimen dimensions to resist buckling for given values of stress.

Side Slip. Figure 10 illustrates one form of buckling of cylindrical specimens that can result from misalignment of the loading train under load or from loose tolerances on specimen dimensions. The ends of the specimen undergo sideslip, resulting in a sigmoidal central axis. This form of buckling could be described by Eq 5 and 6, provided an appropriate value of the end-fixity coefficient can be assigned.

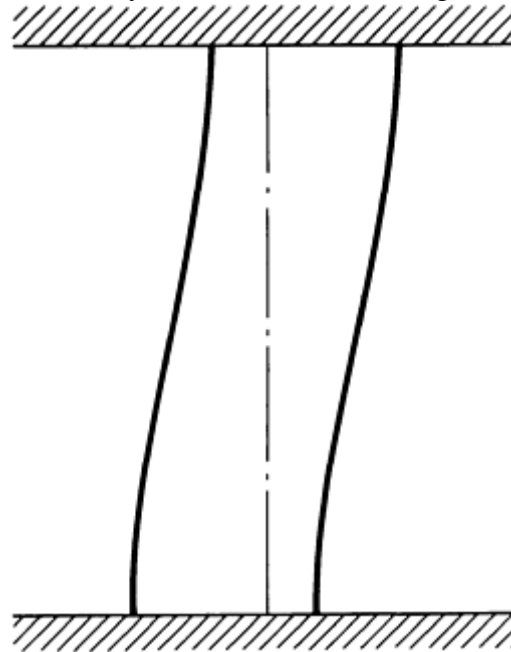


Fig. 10 Schematic diagram of side-slip buckling. The original position of the specimen centerline is indicated by the dashed line.

Thin-Sheet Specimens. In testing thin sheet in a compression jig, approximately 2% of the specimen length protrudes from the jig. Buckling of this unsupported length can occur if there is misalignment of the loading train such that it does not remain coaxial with the specimen throughout the test (Ref 14). A typical compression jig and contact-point compressometer are shown in Fig. 11(a) and (b) respectively.

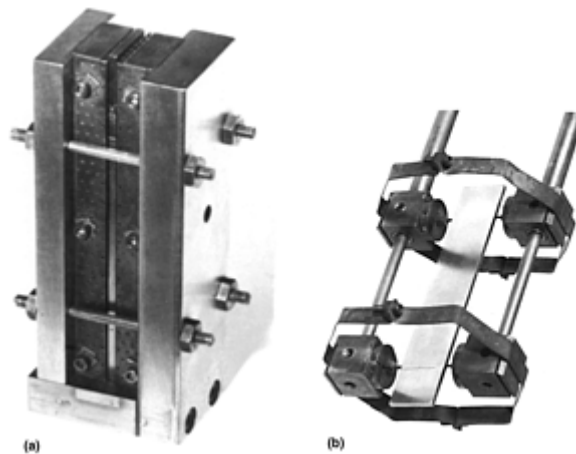


Fig. 11 Compression testing of thin-sheet specimens. (a) Sheet compression jig suitable for room-temperature or elevated-temperature testing. (b) Contact-point compressometer installed on specimen removed from jig. Contact points fit in predrilled shallow holes in the edge of the specimen.

Barreling of Cylindrical Specimens

When a cylindrical specimen is compressed, Poisson expansion occurs. If this expansion is restrained by friction at the loading faces of the specimen, nonuniform states of stress and strain occur as the specimen acquires a barreled shape (Fig. 12). The effect on the stress and strain distributions is of consequence only when the deformations are on the order of 10% or more.

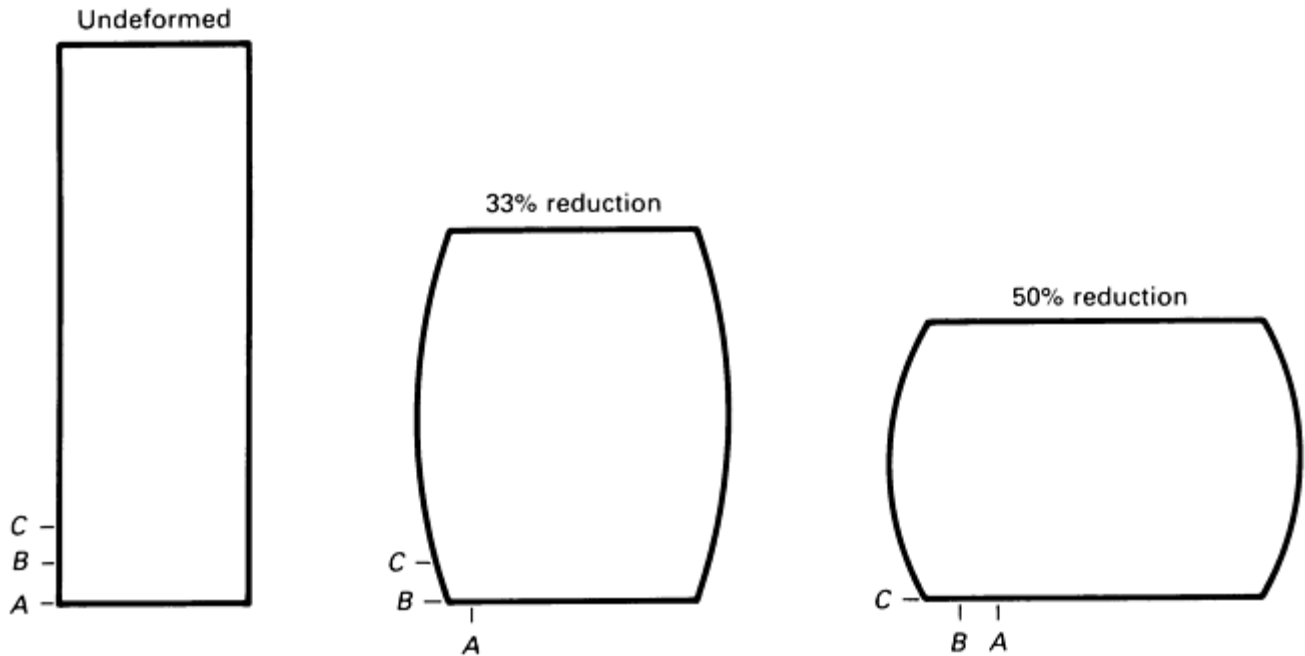


Fig. 12 Barreling during a test when the friction coefficient is 1.00 at the specimen loading face. Note that as the deformation increase, points *A*, *B*, and *C* originally on the specimen sides, move to the loading face.

Friction on the loading face causes rollover. As shown in Fig. 12, points originally on the sides of the specimen are ultimately located on the specimen end face. Use of a high-pressure lubricant at the loading surface of the specimen reduces friction. One such material commonly used is 0.1 mm (0.004 in.) thick Teflon sheet. The action of the lubricant may be enhanced if the bearing surfaces that apply the load are hard and highly polished. The use of tungsten-carbide bearing blocks is recommended for all materials undergoing compression testing. Other techniques have been used to reduce nonuniformity of stress and strain distributions along the gage length (Ref 15, 16).

The contact area between the lateral faces of the specimen and the lateral support guides of the testing jig must be well lubricated. Personnel engaged in sheet compression testing should become familiar with the literature on the subject. A selected bibliography on this subject is given in ASTM E 9.

Testing Machine Capacity

In a compression test performed to large strains (e.g., to obtain fracture data), a large load capacity may be required. For example, consider four medium-length cylindrical specimens suggested in ASTM E 9, where specimens are specified with diameters that range from 12.7 to 28.4 mm (0.50 to 1.12 in.) and with length-to-diameter ratios of 3. Using these specimen sizes, consider the testing of a material with a yield stress of 1380 MPa (200 ksi) and a compression strain-hardening exponent of 0.05. Figure 13 illustrates the load-capacity requirements to reach a height reduction of 60% for each of the four cylinders recommended in ASTM E 9. The maximum required load is approximately 3.5 times the load at yield. The required capacity for testing the same specimens to failure at 60% strain in tension would be no more than 1.5 times the yield loads.

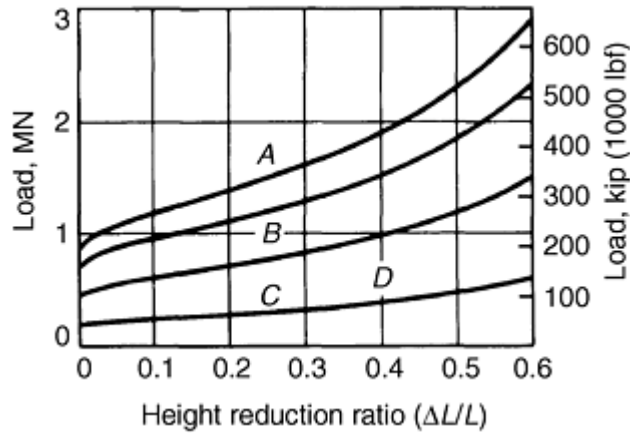


Fig. 13 Load requirements for compressing specimens of various diameters made of a material with a yield stress of 1380 MPa (200 ksi) and a strain-hardening exponent of 0.05. Diameters: A = 28.4 mm (1.12 in.), B = 25.4 mm (1.00 in.), C = 20.3 mm (0.80 in.), D = 12.7 mm (0.50 in.). Length-to-diameter ratio (L/D) = 3

Medium-Strain-Rate Testing

Medium-strain-rate compression testing with conventional load frames is very similar to low-strain-rate compression testing. For medium-rate testing, the load frames require the capability to generate higher crosshead or ram velocities. An important consideration is the stiffness of the machine, as discussed in more detail in the article “Testing Machines and Strain Sensors” in this Volume. For tests at a uniform strain rate, a high machine stiffness is desired; techniques to increase the stiffness of a hydraulic machine are described in Ref 17. This section describes some of the techniques used to obtain medium strain rates with conventional test frames and additional experimental factors for measurement of load and strain at medium rates.

Grip design for compression testing at medium strain rates requires the same considerations that apply to grip design for low strain rates. The compression specimen typically is sandwiched between two hard, polished platens that are placed in a subpress designed to maintain parallel faces during deformation. A typical grip assembly is shown in Fig. 14, in which a compression specimen (5.1 mm, or 0.2 in., long by 5.1 mm, or 0.2 in., diam) is in place and ready for testing. The ram is shown in position and is separated from the subpress by approximately 20 mm (0.8 in.). This gap allows time (approximately 2 ms at the highest ram velocity) for the ram to accelerate to the specified velocity. In this test, the stroke of the ram must be set accurately to ensure the desired deformation.

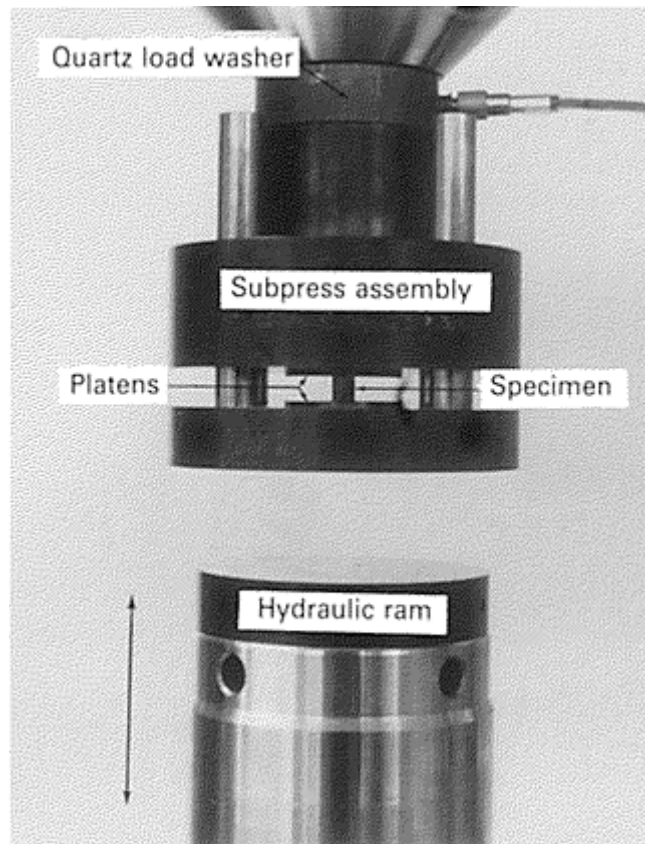


Fig. 14 Subpress assembly for medium strain-rate testing with conventional load frame. The specimen, which is 5.1 mm (0.2 in.) diam by 5.1 mm (0.2 in.) long, is sandwiched between two highly polished platens. A quartz load washer is shown positioned above the subpress assembly.

Measurement of Load and Displacement. As the strain rate increases, the measurement of load and displacement becomes increasingly more difficult. The requirement for adequate frequency response in the signal conditioners and the problems associated with load-cell ringing were discussed in the introduction to this article. In this section, the measurement of load and displacement at medium strain rates is described in more detail.

Measurement of Load. A typical load cell determines load by measuring displacement in an elastic member, such as a diaphragm or cylinder. The displacements are measured with bonded strain gages; this gives the load cell sufficient intrinsic frequency response for testing at medium strain rates. However, a problem often arises due to ringing in the load cell. The load cell has a natural frequency of vibration determined by geometry and physical properties, such as density and elastic modulus. Typical load cells have a natural frequency in the range of 500 to 5000 Hz. In effect, the natural frequency of vibration sets the bandwidth of the load-measuring system.

By this criterion alone, load cells should be sufficient for compression testing at strain rates as high as 100 s^{-1} . However, the transient response of the load cell in practice limits the measurement to much lower strain rates. When a constant-strain-rate test is desired, deformation must be initiated by an impact due to the acceleration time required by the ram. This impact can excite the natural vibrational mode of the load cell, which will produce oscillations in the output signal that can mask the actual load measurement. Unless the impact is dampened by some means, load measurement at strain rates greater than about 1 s^{-1} can be subject to load-cell ringing.

Ringing of the load cell can be minimized by selecting a load cell with a high vibrational frequency. If the natural frequency is sufficiently high, the vibrational mode may not be excited by the impact, or if excited, it may be possible to remove it from the signal with a low pass filter. Another method to reduce ringing is to dampen the impact that initiates deformation within the specimen. Often, a thin layer of deformable material placed between the impacting surfaces is sufficient to remove the higher frequencies generated by the impact that can excite the natural frequency of the load cell. For example, in the configuration shown in Fig. 14, a single loop, approximately 50 mm (2 in.) in diameter, of 0.51 mm (0.02 in.) diameter lead-tin solder wire

placed on the impacting face of the hydraulic ram was found to be effective in minimizing load-cell ringing. Such layers, however, may complicate measurement of displacement within the specimen.

At strain rates close to 100 s^{-1} , the standard load cell either may not possess the necessary frequency response, or it may ring excessively. These characteristics can make the load cell inadequate for load measurement. Under these conditions, a quartz piezoelectric device, such as a load washer (Fig. 14), is useful. The load washer is convenient because it is easily adapted to a compression test; it also has excellent intrinsic frequency response and a high fundamental vibrational frequency. However, these devices require special signal conditioning and low-capacitance cables.

Measurement of Strain. The direct measurement of strain at medium strain rates presents a challenge. Many of the devices typically used for low-strain-rate testing are inappropriate at medium strain rates. Extensometers, for example, may have the necessary response characteristics for medium-strain-rate testing. However, it is difficult to ensure that the rapid and large displacement in small compression specimens will not damage the fragile extensometer.

Many hydraulic test frames use a linear variable differential transformer (LVDT) to control the motion of the hydraulic ram. This LVDT signal is comprised of displacements within the specimen as well as elastic displacements throughout the test frame. To relate this signal to displacements within the specimen, the latter contribution must be subtracted; this problem also is encountered at low strain rates. If a deformable material is placed between the impact surfaces to dampen the impact, the displacements within this layer also must be subtracted from the LVDT signal.

A common practice is to mount the LVDT at an off-axis position adjacent to the specimen. The benefit of this configuration is that a displacement measurement is possible between two points that are quite close to the specimen; this measurement includes less of the elastic deformation in the load frame. When a measurement is made at an off-axis position, it is important to verify that the measurement truly represents displacements within the sample. Often, two LVDT units are mounted at diametrically opposite positions, and their outputs are processed to eliminate the effects of nonplanar motion. The LVDT suffers from an intrinsic frequency-response limitation determined by the excitation frequency. Standard excitation frequencies are in the range of 1 to 5 kHz, which limits the frequency response to around 100 to 500 Hz.

Velocity transducers, which have good intrinsic frequency response, have been used to measure the motion of the specimen and grip assembly (Ref 17). Their output can be integrated electronically or by computer to obtain the displacement. Generally, these also require mounting at off-axis locations.

Strain measurement by noncontact methods is becoming more common with optical extensometers or laser interferometers. Laser interferometers, which are capable of operating at high sampling rates, can be used to measure strain at strain rates exceeding 10^3 s^{-1} .

Types of Compressive Fracture

For all but the most ductile materials, cylindrical specimens develop cracks when they are compressed. The cracks generally initiate on the outer surface of the compressed specimen. As the specimen is further deformed, the initiated cracks propagate, and new cracks form. Some different modes of compression fracture are described in Ref 18 and some examples are described in the following sections.

Orange Peel Cracking. In many materials, roughening or wrinkling of the surface (orange peel effect) occurs prior to compressive cracking. This effect is particularly prominent in some aluminum alloys. An extreme example is illustrated for an aluminum alloy 7075-T6 specimen in Fig. 15. The specimen is shown after 72% deformation. Wrinkling first appeared at 10 to 15% compressive deformation, and macrocracking occurred after 50 to 60% deformation. Microscopic examination revealed many microcracks in the valleys of the wrinkles, with greatest concentration in the equatorial region of the specimen. Defining a compression strength or a strain criterion of fracture would be difficult for this material.

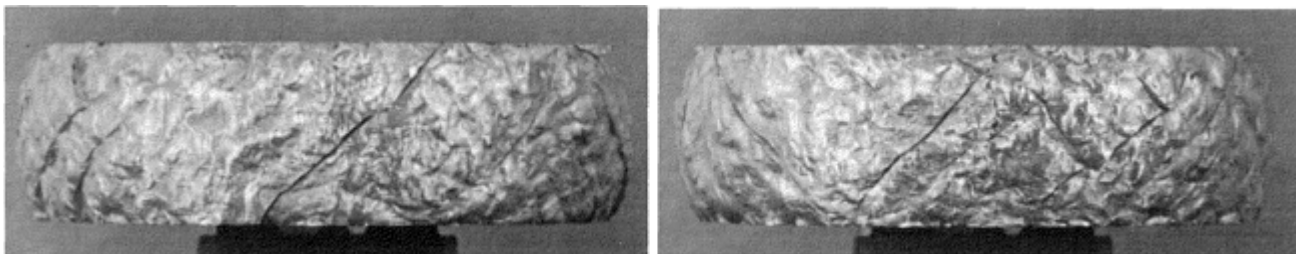


Fig. 15 Two views of a 72% compressed specimen of aluminum alloy 7075-T6 displaying orange peel effect. The loading axis is vertical. Extensive macrocracking is evident in the severely wrinkled surface. Microscopic examination of the surface revealed extensive microcracking in the valleys of the wrinkles. Source: Ref 16

Macrocracks in Steel. A case in which macrocracks form without apparent precursor microcracks is shown in Fig. 16. The material is AISI-SAE 4340 steel tempered at 204 °C (400 °F), yielding a hardness of 52 HRC. The cracks initiated one at a time and extended across the surface of the specimen almost instantaneously. The first cracks appeared when the compressive deformation reached 30%, and other cracks continued to initiate until the test was concluded at 72% deformation, which is the condition shown in Fig. 16. The specimen was still intact, and subsequent sectioning revealed that the cracks penetrated inward a distance of diameter.

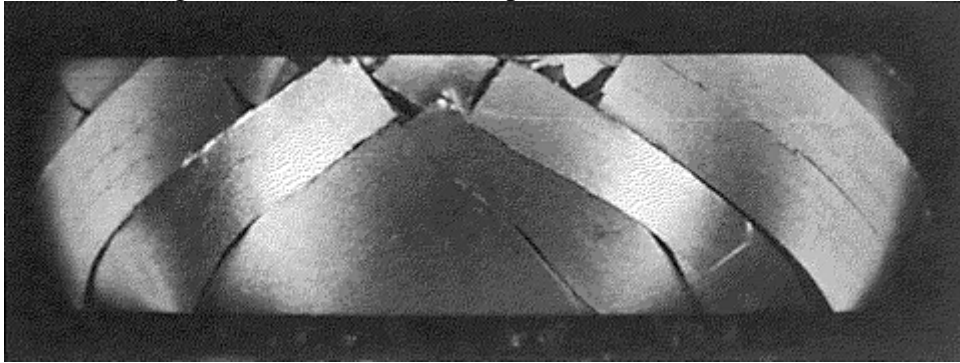


Fig. 16 Shear cracks in a 72% compressed specimen of AISI-SAE 4340 steel. The cracks initiated one at a time, starting when the deformation was 30%. Source: Ref 16

Microcrack to Macrocrack Coalescence. In some tungsten alloys, the first visible evidence of fracture is a shear macrocrack that appears at the equator of the specimen after 45 to 50% compressive deformation. However, using fluorescent-dye penetrant methods, microcrack initiation was detected at 25% deformation (Ref 18). For this material, if crack initiation is the criterion of failure, it is necessary to state the method of crack detection with the selected parameter for strength.

References cited in this section

13. G. Gerard, *Introduction to Structural Stability Theory*, McGraw-Hill, 1962, p 19–29
14. R. Papirno and G. Gerard, “Compression Testing of Sheet Materials at Elevated Temperatures,” *Elevated Compression Testing of Sheet Materials*, STP 303, ASTM, 1962, p 12–31
15. T.C. Hsu, A Study of the Compression Test for Ductile Materials, *Mater. Res. Stand.*, Vol 9 (No. 12), Dec 1969, p 20
16. R. Chait and C.H. Curll, “Evaluating Engineering Alloys in Compression,” *Recent Developments in Mechanical Testing*, STP 608, ASTM, 1976, p 3–19
17. R.H. Cooper and J.D. Campbell, Testing of Materials at Medium Rates of Strain, *J. Mech. Eng. Sci.*, Vol 9, 1967, p 278
18. R. Papirno, J.F. Mescall, and A.M. Hansen, “Fracture in Axial Compression of Cylinders,” *Compression Testing of Homogeneous Materials and Composites*, R. Chait and R. Papirno, Ed., STP 808, ASTM, 1983, p 40–63

Uniaxial Compression Testing

Howard A. Kuhn, Concurrent Technologies Corporation

Acknowledgments

Portions of this article were adapted from R. Papirno, Axial Compression Testing (p 55–58) and P.S. Follansbee and P.E. Armstrong, Compression Testing by Conventional Load Frames at Medium Strain Rates (p 192–193) in *Mechanical Testing*, Vol 8, *ASM Handbook*, ASM International, 1985.

Uniaxial Compression Testing

Howard A. Kuhn, Concurrent Technologies Corporation

References

1. T. Erturk, W.L. Otto, and H.A. Kuhn, Anisotropy of Ductile Fracture—An Application of the Upset Test, *Metall. Trans.*, Vol 5, 1974, p 1883
2. W.A. Kawahara, Tensile and Compressive Materials Testing with Sub-Sized Specimens, *Exp. Tech.*, Nov/Dec, 1990, p 27–29
3. W.A. Backofen, *Deformation Processing*, Addison-Wesley, Reading, MA, p 53
4. J.H. Faupel and F.E. Fisher, *Engineering Design*, John Wiley & Sons, 1981, p 566–592
5. G.E. Dieter, *Mechanical Metallurgy*, 2nd ed., McGraw-Hill, 1976, p 561–565
6. G.E. Dieter, Evaluation of Workability: Introduction, *Forming and Forging*, Vol 14, *ASM Handbook*, ASM International, 1988, p 365
7. J.E. Hockett, The Cam Plastometer, in *Mechanical Testing*, Vol 8, *ASM Handbook*, ASM International, 1985, p 197
8. R. Herbertz and H. Wiegels, Ein Verfahren Zur Verwirklichung des Reibungsfreien Zylinderstanch versuchs für die Ermittlung von Fließcurven, *Stahl Eisen*, Vol 101, 1981, p 89–92
9. K. Lintermanns Fander, “The Flow and Fracture of Al-High Mg-Mn Alloys at High Temperatures and Strain Rates,” Ph.D. dissertation, University of Pittsburgh, 1984, p 258
10. H.A. Kuhn, P.W. Lee, and T. Erturk, A Fracture Criterion for Cold Forging, *J. Eng. Mater. Technol. (Trans. ASME)*, Vol 95, 1973, p 213–218
11. H.A. Kuhn, Workability Theory and Application in Bulk Forming Processes, *Forming and Forging*, Vol 14, *ASM Handbook*, ASM International, 1988, p 389–391
12. J.J. Jonas and M.J. Luton, Flow Softening at Elevated Temperatures, *Advances in Deformation Processing*, J.J. Burke and V. Weiss, Ed., Plenum, 1978, p 238

13. G. Gerard, *Introduction to Structural Stability Theory*, McGraw-Hill, 1962, p 19–29
14. R. Papirno and G. Gerard, “Compression Testing of Sheet Materials at Elevated Temperatures,” *Elevated Compression Testing of Sheet Materials*, STP 303, ASTM, 1962, p 12–31
15. T.C. Hsu, A Study of the Compression Test for Ductile Materials, *Mater. Res. Stand.*, Vol 9 (No. 12), Dec 1969, p 20
16. R. Chait and C.H. Curll, “Evaluating Engineering Alloys in Compression,” *Recent Developments in Mechanical Testing*, STP 608, ASTM, 1976, p 3–19
17. R.H. Cooper and J.D. Campbell, Testing of Materials at Medium Rates of Strain, *J. Mech. Eng. Sci.*, Vol 9, 1967, p 278
18. R. Papirno, J.F. Mescall, and A.M. Hansen, “Fracture in Axial Compression of Cylinders,” *Compression Testing of Homogeneous Materials and Composites*, R. Chait and R. Papirno, Ed., STP 808, ASTM, 1983, p 40–63

Hot Tension and Compression Testing

Dan Zhao, Johnson Controls, Inc.; Steve Lampman, ASM International

Introduction

HIGH-TEMPERATURE MECHANICAL PROPERTIES of metals are determined by three basic methods:

- Short-term tests at elevated temperatures
- Long-term tests of creep deformation at elevated temperatures
- Short-term and long-term tests following long-term exposure to elevated temperatures

This article focuses on short-term tension and compression testing at high temperatures. The basic methods and specimens are similar to room-temperature testing, although the specimen heating, test setup, and material behavior at higher temperatures do introduce some additional complexities and special issues for high-temperature testing.

Two types of long-term testing for high-temperature applications are not discussed in this article. The first type is long-term exposure testing, where materials are exposed to high temperatures prior to mechanical testing at either ambient or elevated temperatures. This type of testing is needed for the evaluation of metallurgical changes that can occur during exposure to high temperatures. The second type of long-term test for many high-temperature structural applications is the creep test. When the application temperature, T , of a stressed metallic or ceramic material is in the range of about $0.3 T_M < T < 0.6 T_M$ (where T_M is the melting point of the material in Kelvin), the stressed material undergoes a continuous accumulation of plastic strain (i.e., creep) over time. The continuous accumulation of creep strain can occur even when the material is stressed below its elastic limit; therefore many high-temperature structural applications require creep testing. This type of testing is discussed in more detail in the Section “Creep and Stress-Relaxation Testing” in this Volume. For metals and ceramics, creep occurs in the temperature range of about $0.3 T_M$ to $0.6 T_M$. For polymers, creep deformation is a factor at temperatures above the glass transition temperature, T_g , of a polymer.

Hot Tension and Compression Testing

Dan Zhao, Johnson Controls, Inc.; Steve Lampman, ASM International

Effects of Temperature

In general terms, the effects of temperature on the mechanical behavior of metals can be classified into three basic ranges based on the application temperature, T , relative to the melting point, T_M , of a metal as follows:

- Cold working applications, $T < 0.3 T_M$
- Warm working applications, $0.3 T_M < T < 0.6 T_M$
- Hot working applications, $T > 0.6 T_M$

These general temperature ranges are based on the underlying physical processes that influence mechanical behavior at different temperatures. For example, the warm working temperature range ($0.3 T_M < T < 0.6 T_M$) is the region of creep deformation. It is also the region of recovery and recrystallization. This includes high-temperature applications of structural materials (such as those listed in Table 1) and room-temperature testing of metals with low melting points.

Table 1 Typical elevated temperatures in engineering applications

Application	Typical materials	Typical temperatures , K	Homologous temperatures , T/T_{ME}
Rotors and piping for steam turbines	Cr-Mo-V steels	825–975	0.45–0.50
Pressure vessels and piping in nuclear reactors	316 stainless steel	650–750	0.35–0.40
Reactor skirts in nuclear reactors	316 stainless steel	850–950	0.45–0.55
Gas turbine blades	Nickel-base superalloys	775–925	0.45–0.60
Burner cans for gas turbine engines	Oxide dispersion-strengthened nickel-base alloys	1350–1400	0.55–0.65

Source: Ref 1

In general, strength is reduced at high temperatures, and materials become softer and more ductile as temperature increases. However, the rate and direction of property changes can vary widely for the yield strength and elongation of various alloys as function of temperature, as shown in Fig. 1. These changes are due to various metallurgical factors. For example, there is a significant drop in the ductility of 304 stainless steel in the temperature range of 425 to 870 °C (800–1000 °F). This ductility drop is from the embrittling effect of carbide precipitation in the grain boundaries.

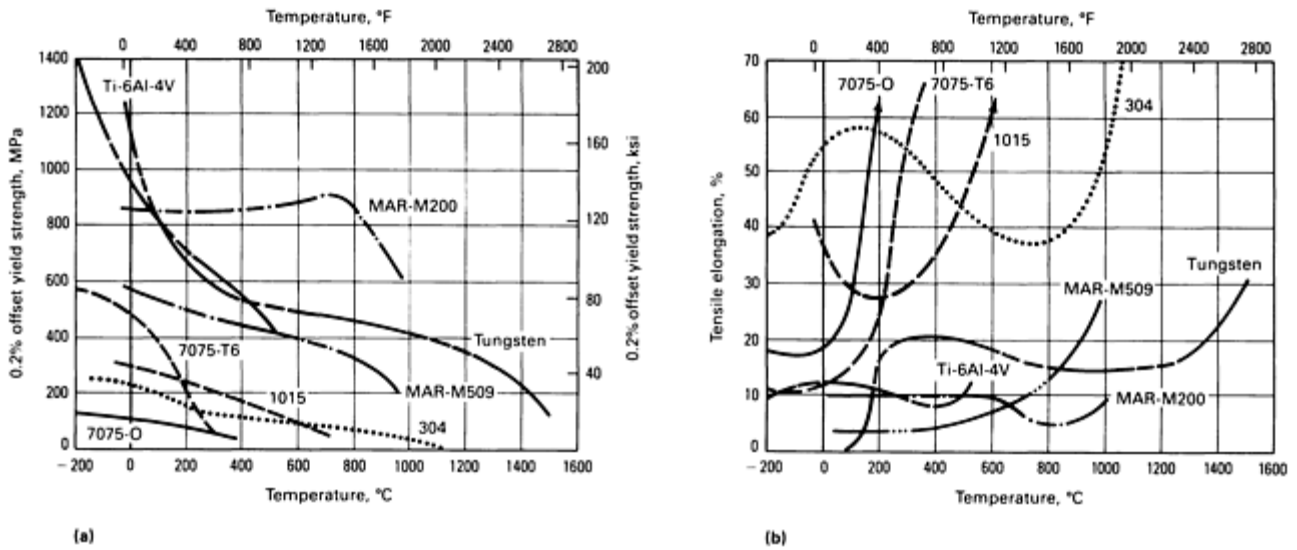


Fig. 1 Effect of temperature on strength and ductility of various materials. (a) 0.2 offset yield strength. (b) Tensile elongation. Source: Ref 2

Other factors, which often cannot be easily predicted, can also affect mechanical behavior at high temperatures. For example, resolutioning, precipitation, and aging (diffusion-controlled particle growth) can occur in two-phase alloys, both during heating prior to testing and during testing itself. These processes can produce a wide variety of responses in mechanical behavior depending on the material. For example, Fig. 2 shows the effect of exposure time on the high-temperature yield strength and elongation of a precipitation-hardening aluminum alloy.

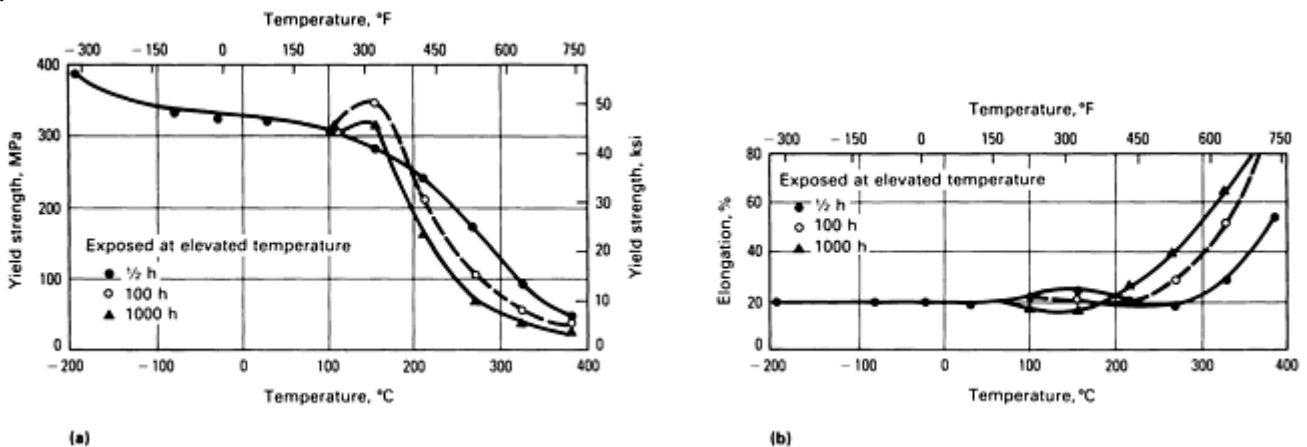
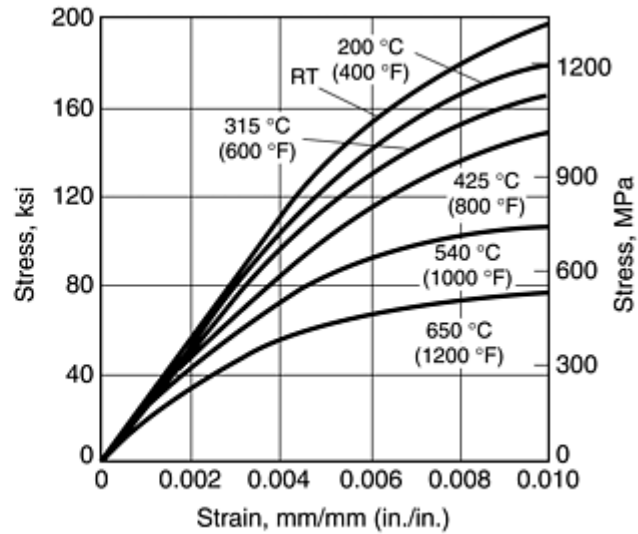
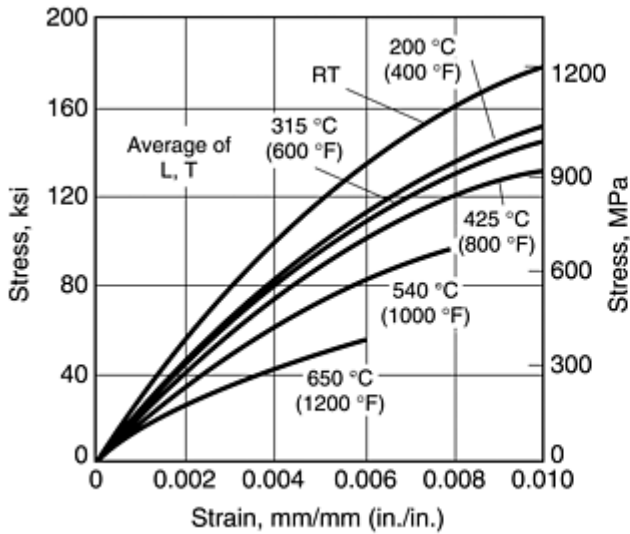


Fig. 2 Effect of exposure time on (a) yield strength and (b) elongation at testing temperature for an aluminum alloy 2024. Source: Ref 2

Effect of Temperature on Deformation and Strain Hardening. As temperature increases, the strength of a material usually decreases and the ductility increases. The general reduction in strength and increase in ductility of metals at high temperatures can be related to the effect of temperature on deformation of the material. At room temperature, plastic deformation occurs when dislocations in the material slip. The dislocations also intersect and build up in the material as they slip. This build-up of dislocations restricts the slip, and, thus, increases the forces necessary for continued deformation. This process is known as strain hardening or work hardening.

At elevated temperatures, dislocation climb comes into play as another deformation mechanism. Further, the build-up of strain energy from strain hardening can be relieved at high temperatures when crystal imperfections are rearranged or eliminated into new configurations. This process is known as recovery. A much more rapid restoration process is recrystallization, in which new, dislocation-free crystals nucleate and grow at the expense of original grains. The restoration processes can be greatly enhanced by the increase in the thermal activity and mobility of atoms at higher temperatures. As a result, lower stress is required for deformation, as shown in the stress-strain diagrams of several materials at elevated temperatures (Fig. 3 4 5 6 7).



(a)

(b)

Fig. 3 Elevated-temperature stress-strain curves in tension for Fe-18Cr-8Ni (Type 301) stainless steel. (a) 0.508 mm (0.020 in.) sheet full hard from 40% reduction (data average of longitudinal and transverse). (b) 0.813 mm (0.032 in.) sheet full hard with stress relief at 425 °C (800 °F) for 8 h. Source: Ref 3

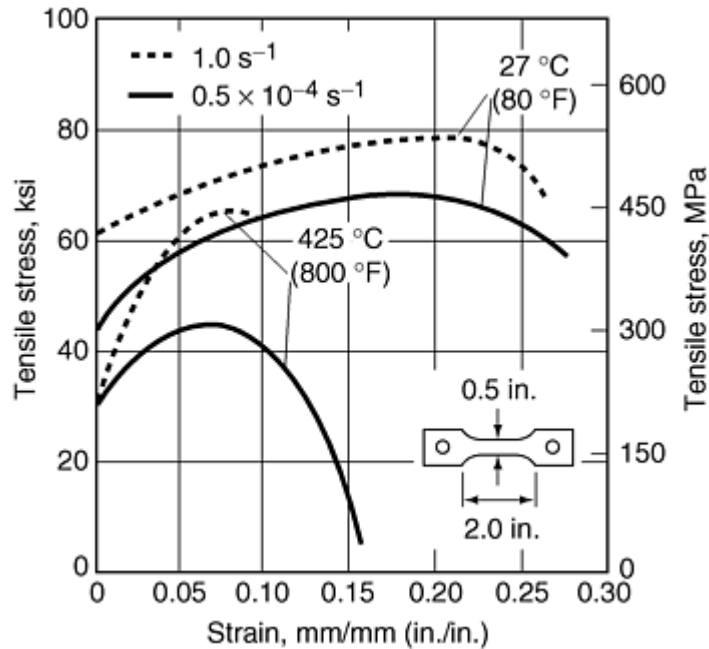


Fig. 4 Effect of high (1.0 s^{-1}) and low ($0.05 \times 10^{-4} \text{ s}^{-1}$) strain rates and temperature on stress-strain curves of 1020 hot-rolled carbon steel sheet (1.644 mm, or 0.064 in.). Source: Ref 4

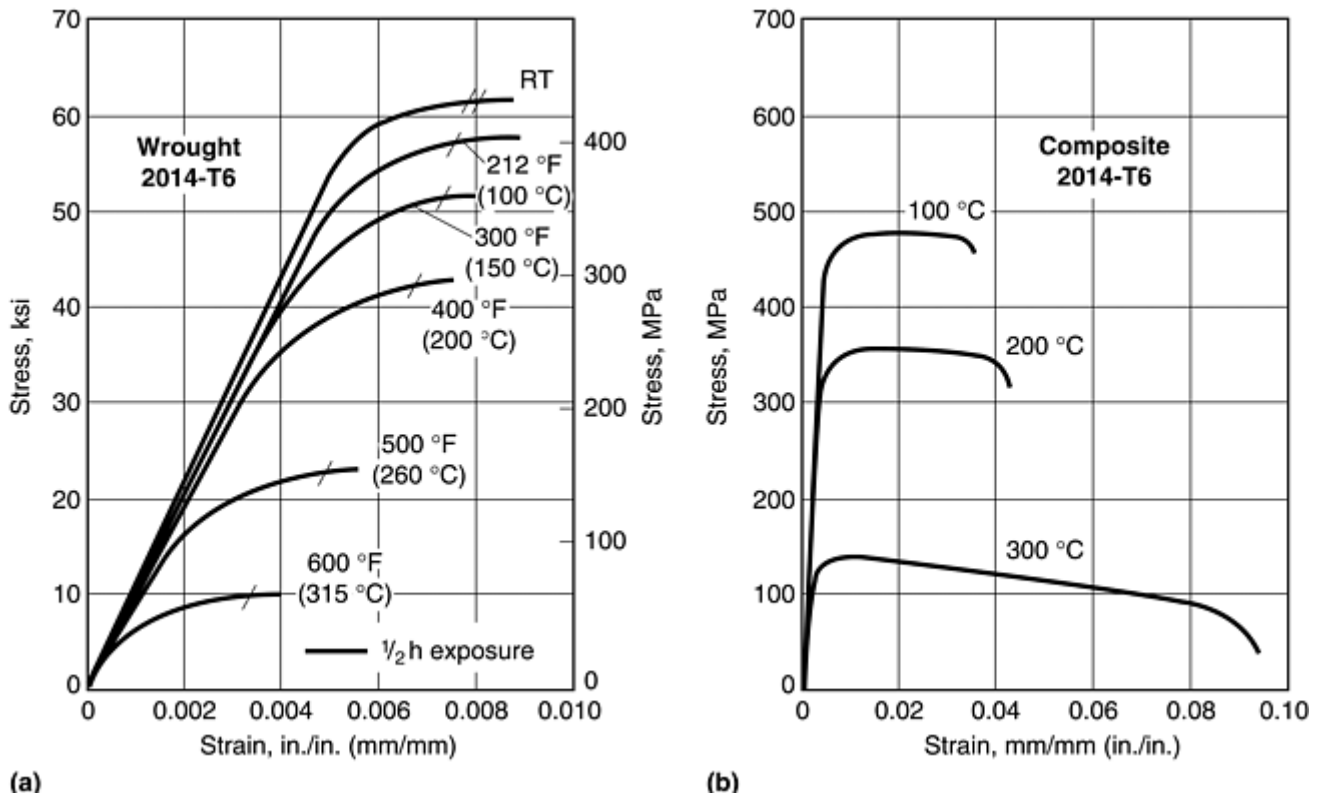


Fig. 5 Stress-strain curves in tension at elevated temperature of wrought and composite 2014 aluminum alloy. (a) Wrought 2014-T6, 19.05 mm ($\frac{3}{4}$ in.) bar. (b) Discontinuously reinforced 2014 composite (15 vol% Al_2O_3 , 0.5 h after T6). Source: Ref 4, 5

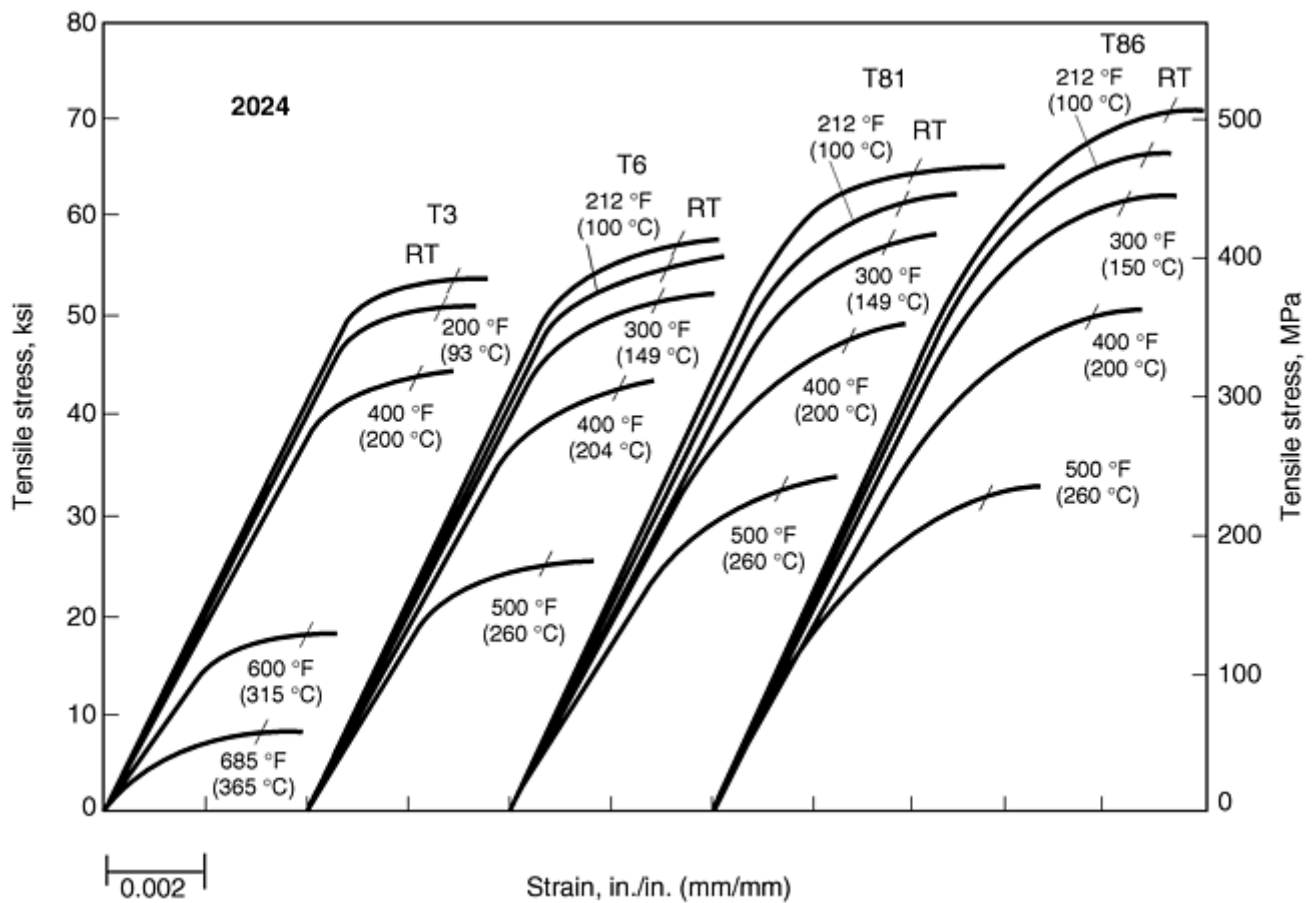


Fig. 6 Stress-strain curves in tension at various temperatures (30 min exposure) for 2024 aluminum sheet and plate in T3, T6, T81, and T86 conditions. Source: Ref 4

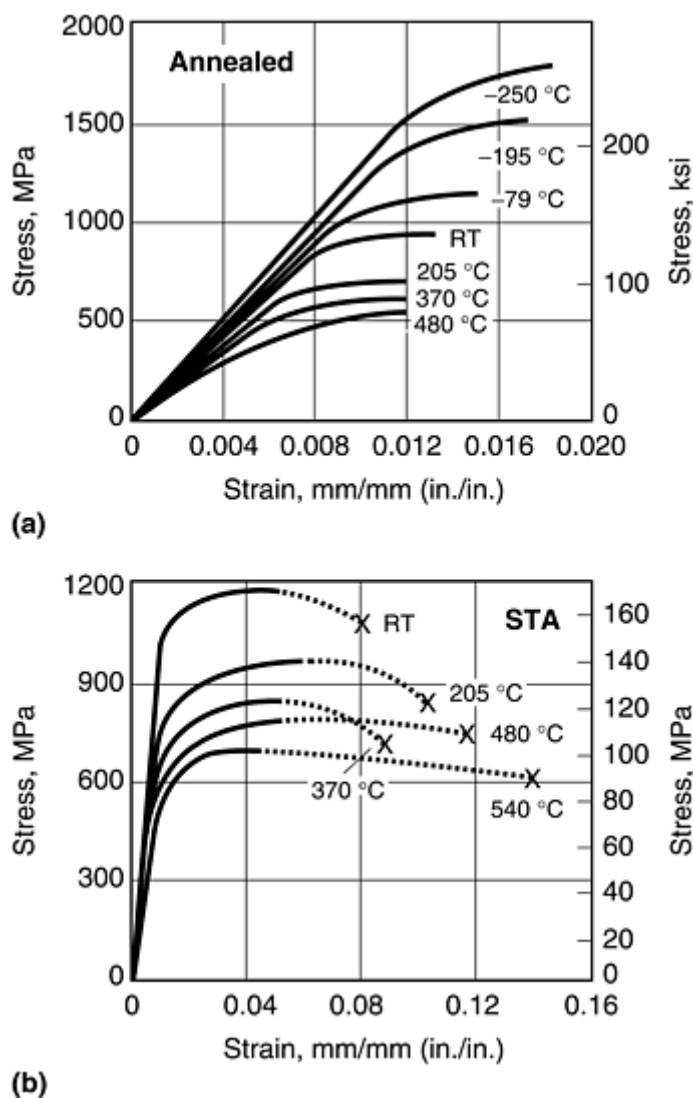


Fig. 7 Typical stress-strain curves in tension for wrought Ti-6Al-4V. (a) Annealed extrusions. Static strain rate, after 1/2h exposure. (b) All product forms, solution treated and aged (STA), longitudinal direction, after 1/2h exposure. Source: Ref 6

Deformation under tensile conditions is also governed to some extent by crystal structure. Face-centered cubic (fcc) materials generally exhibit a gradual change in strength and ductility as a function of temperature. Such a change in the strength of 304 austenitic stainless steel is illustrated in Fig. 1. Some body-centered cubic (bcc) alloys, however, exhibit an abrupt change at the ductile-to-brittle transition temperature (~ 200 °C, or 390 °F, for tungsten in Fig. 1), below which there is little plastic flow. In hexagonal close-packed (hcp) and bcc materials, mechanical twinning can also occur during testing. However, twinning by itself contributes little to the overall elongation; its primary role is to reorient previously unfavorable slip systems to positions in which they can be activated.

There are exceptions to these generalizations, particularly at elevated temperatures. For example, at sufficiently high temperatures, the grain boundaries in polycrystalline materials are weaker than the grain interiors, and intergranular fracture occurs at relatively low elongation. In complex alloys, hot shortness, in which a liquid phase forms at grain boundaries, or grain boundary precipitation can lead to low strength and/or ductility.

Diffusion processes are also involved in yield-point and strain-aging phenomena. Under certain combinations of strain rate and temperature, interstitial atoms can be dragged along with dislocations, or dislocations can alternately break away and be repinned, producing serrations in the stress-strain curves. This produces effects such as discontinuous yielding and upper yield-strength behavior, which are a common occurrence in the tension testing of low-carbon steels (see the article "Uniaxial Tension Testing" in this Volume).

Another effect that can be accelerated during high-temperature testing is strain aging. In strain aging, cold-worked steels (especially rimmed or capped steels) undergo a loss in ductility while stored at room temperature. This loss in ductility is typically attributed to precipitation and diffusion-controlled particle growth along the slip planes. The precipitation occurs along slip lines because plastic deformation presumably causes local areas of supersaturation along the slip lines (Ref 7). Strain aging is more pronounced in rimmed and capped steels than in killed steels. Steels that are drastically deoxidized with aluminum or aluminum and titanium are essentially nonaging (Ref 8).

Strain aging also causes a ductility drop (and a corresponding increase in hardness and strength) during high-temperature tension testing of some steels. This effect on tensile strength is shown in Fig. 8 for a mild steel and a stabilized (nonaging) steel. The increase in strength at elevated temperature is attributed to the acceleration of precipitation in the grain boundaries, and at high temperature, the influence of strain on precipitation can be the actual deformation occurring during the hot tension test (Ref 4). This effect is known as strain-age embrittlement.

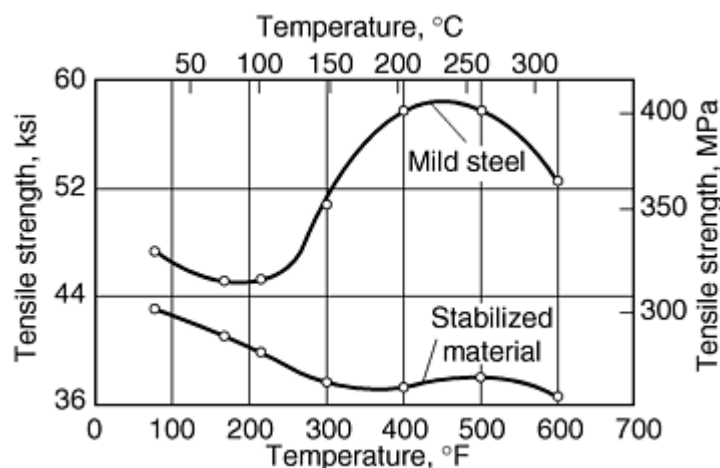


Fig. 8 Effect of testing temperature on tensile strength of ordinary mild steel and of nonaging steel. The nonaging steel gives almost no indication of the “blue heat” phenomenon. The ductility in a tension test of the nonaging steel in the “blue heat” region is considerably higher than the ductility of ordinary aging mild steel sheet. Source: Ref 7

Hot tension testing is one of the simplest ways to distinguish aging steels from nonaging steels. This is shown in Fig. 8 and 9. Aging steels develop an increase in strength and a decrease in ductility within the temperature range of about 230 to 370 °C (450–700 °F). This strain-aging effect is also known as blue brittleness, because the effect occurs in the blue-heat region. Tension testing in the blue-heat region is thus one way to identify aging steels. Blue brittleness affects tensile strength and elongation values (Fig. 10a and b) but not yield strength (Fig. 10c). Although the effect is more pronounced in rimmed or capped steels, strain aging is also observed in killed steels (Fig. 11). Drastically killed steels are nonaging.

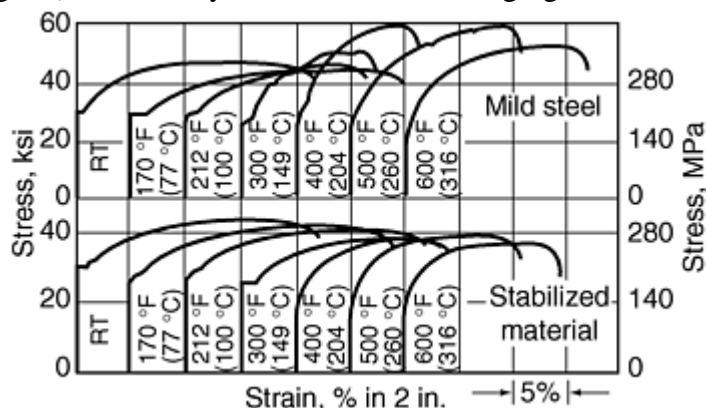


Fig. 9 Stress-strain curves of ordinary mild steel sheet and nonaging sheet tested at various temperatures. The higher tensile strength and the “stepped” or “saw-toothed”

stress-strain curve of the ordinary sheet in the “blue heat” region are characteristic. These features are absent in the nonaging sheet. Source: Ref 7

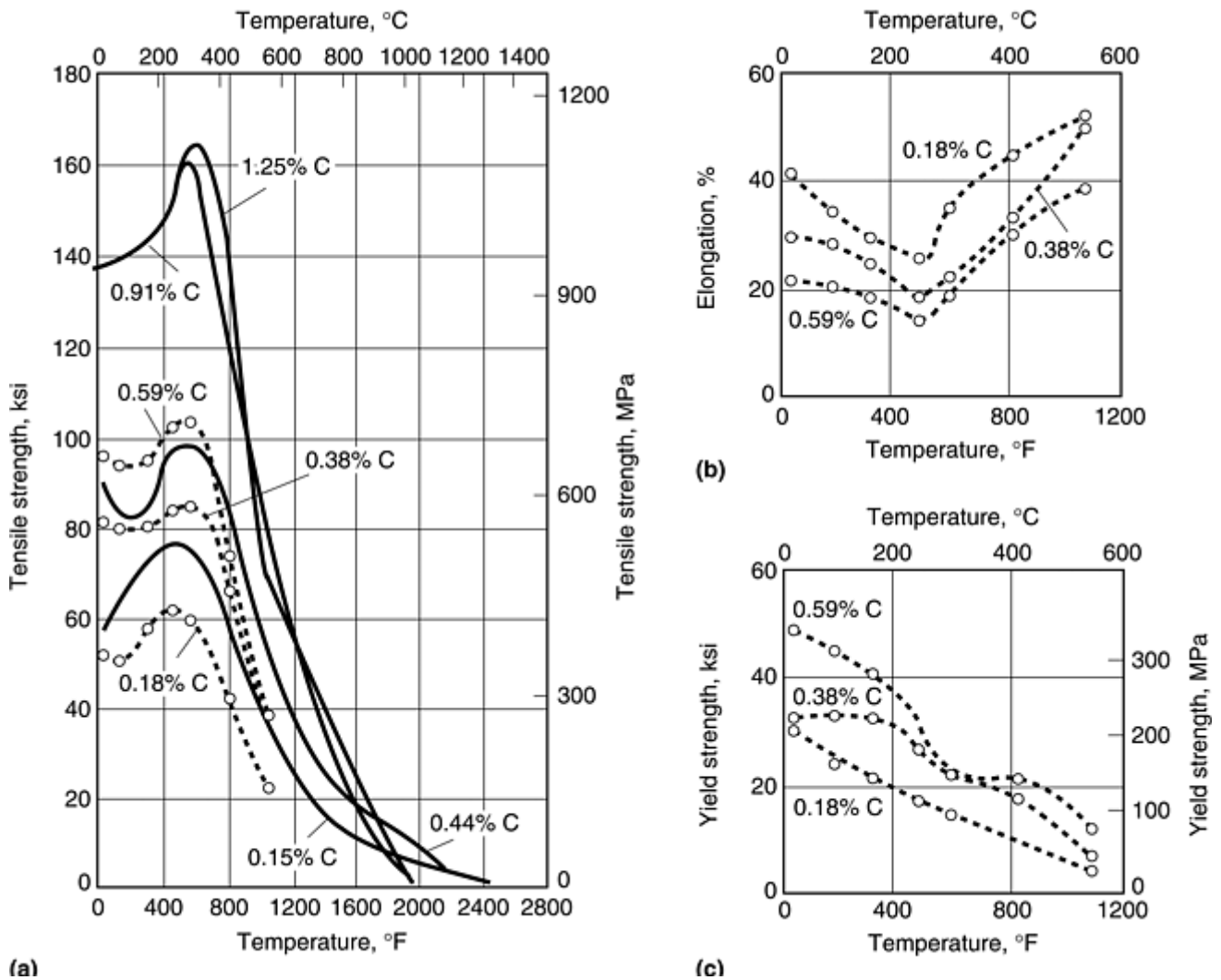
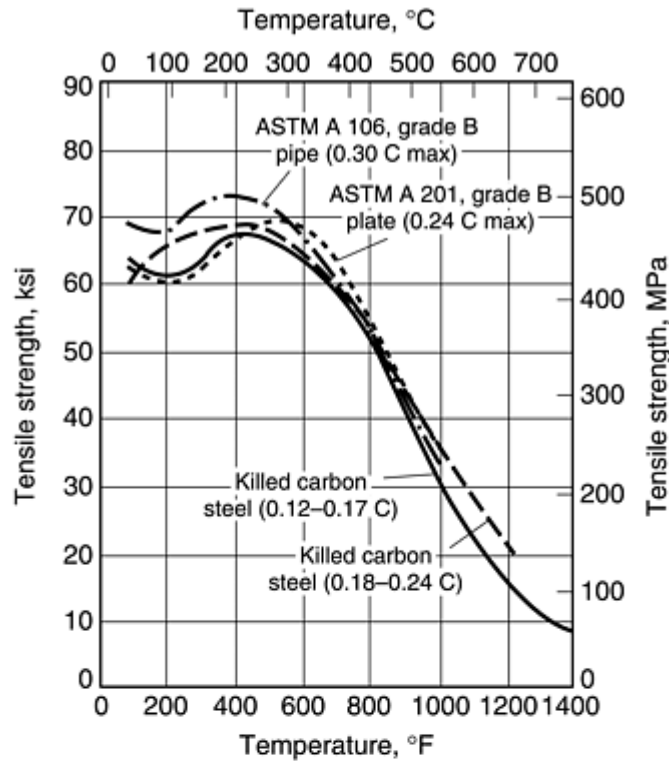
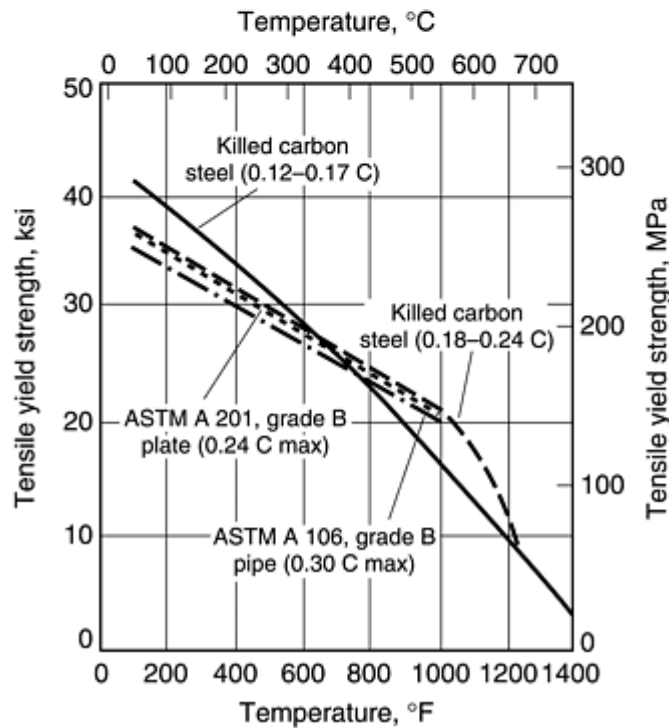


Fig. 10 Short-term elevated-temperature tensile properties of various normalized carbon steels. (a) Tensile strength. (b) Elongation. (c) Yield strength. Source: Ref 9



(a)



(b)

Fig. 11 Effect of temperature on tensile strength and yield strength of structural carbon steels. (a) Tensile strength. (b) Yield strength. Source: Ref 4

High-Temperature Creep in Structural Alloys. At higher temperatures (between $0.3 T_M$ and $0.6 T_M$), metals and ceramics are subject to thermally activated processes that can produce continuous plastic deformation (creep) with the application of a constant stress. For metals, various mechanisms are used to explain creep deformation, but all the mechanisms can fall into two basic categories: diffusional creep and dislocation creep (Ref 10).

In diffusional creep, diffusion of single atoms or ions, either by bulk transport (Nabarro-Herring creep) or by grain-boundary transport (Coble creep) leads to Newtonian viscous flow. In this type of creep, steady-state creep rates vary linearly. At low stresses, diffusional creep is seen only at very high temperatures in the hot working region ($T > 0.6 T_M$) and, thus, is not a factor in typical high-temperature structural applications.

For high-temperature structural applications (such as the examples in Table 1), dislocation creep mechanisms are operative at intermediate and high stresses. These mechanisms include thermally activated processes, such as multiple slip and cross slip, allowing stress relaxation and reductions in strength. In this temperature region, creep rates are typically a nonlinear function of stress. They are either a power function or an exponential function of stress (Ref 7).

Mechanical Testing for High-Temperature Structural Alloys. Maximum-use temperatures of structural materials can depend on different design criteria, such as strength or graphitization/oxidation in steels (Table 2) or creep rate and rupture strength (Table 3). When mechanical testing is performed for high-temperature structural applications, the testing generally includes a combination of both short-term testing for tensile properties and long-term testing of creep rate and rupture strength.

Table 2 Temperature limits of superheater tube materials covered in ASME Boiler Codes

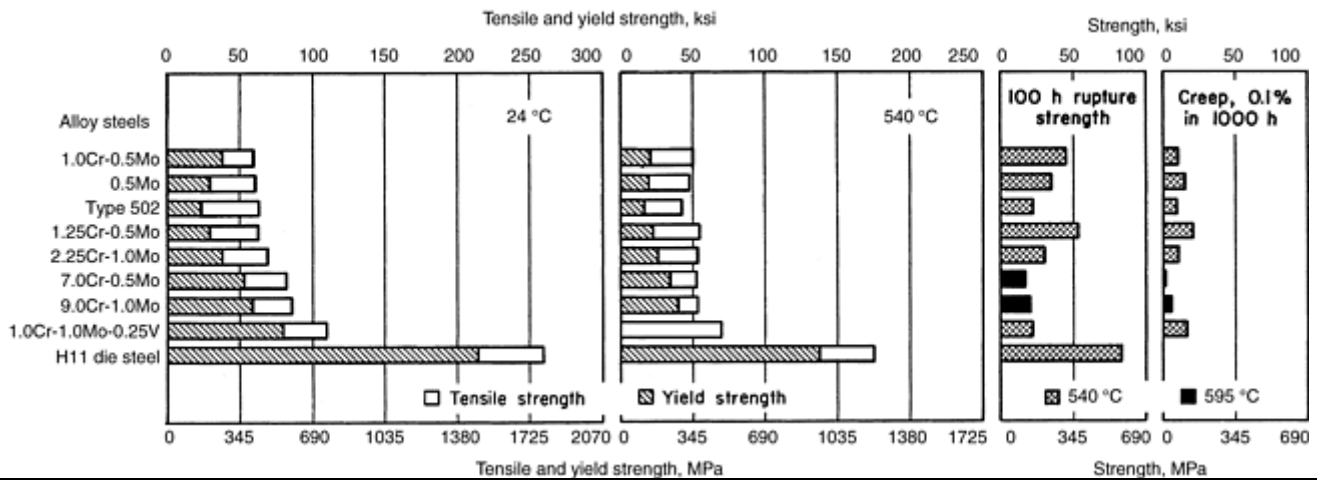
Material	Maximum-use temperature			
	Oxidation/graphitization criteria, metal surface ^(a)		Strength criteria, metal midsection	
	°C	°F	°C	°F
SA-106 carbon steel	400–500	750–930	425	795
Ferritic alloy steels	550	1020	510	950
0.5Cr-0.5Mo				
1.2Cr-0.5Mo	565	1050	560	1040
2.25Cr-1Mo	580	1075	595	1105
9Cr-1Mo	650	1200	650	1200
Austenitic stainless steel, Type 304H	760	1400	815	1500

(a) In the fired section, tube surface temperatures are typically 20–30 °C (35–55 °F) higher than the tube midwall temperature. In a typical U.S. utility boiler, the maximum metal surface temperature is approximately 625 °C (1155 °F).

Table 3 Suggested maximum temperatures in petrochemical operations for continuous service based on creep or rupture data

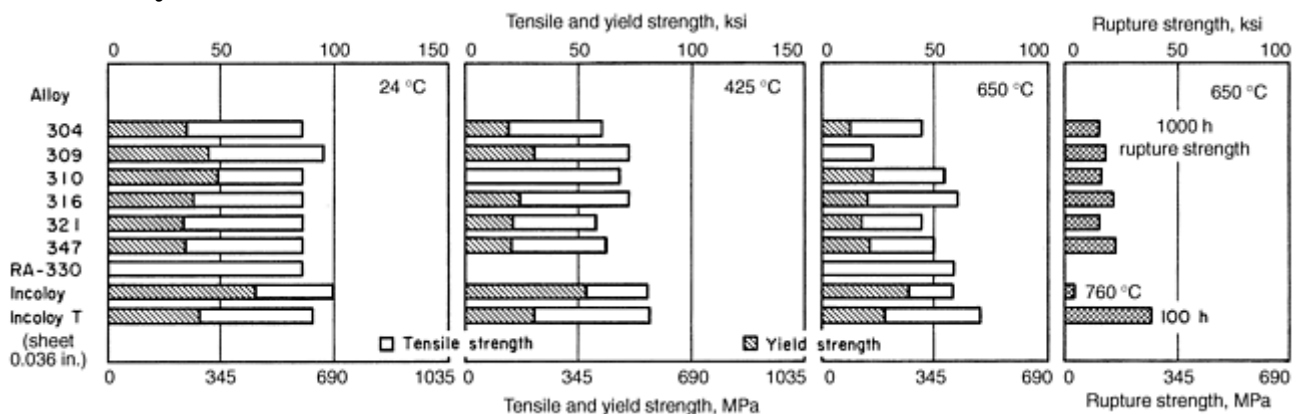
Material	Maximum temperature based on creep rate		Maximum temperature based on rupture	
	°C	°F	°C	°F
Carbon steel	450	850	540	1000
C-0.5Mo steel	510	950	595	1100
2¼Cr-1Mo steel	540	1000	650	1200
Type 304 stainless steel	595	1100	815	1500
Alloy-C-276 nickel-base alloy	650	1200	1040	1900

The test temperatures for short-term properties depend on the alloy and its typical maximum-use temperature for application. For example, Fig. 12 is a summary of short-term and long-term properties of various low-alloy steels with short-term properties up to about 540 °C (1000 °F). In contrast, short-term strength for austenitic stainless steels (Fig. 13), martensitic stainless steels (Fig. 14), and superalloys (Fig. 15) are tested at higher temperatures. Other examples of short-term strength at high temperatures are shown for nonferrous alloys (Fig. 16) and precipitation-hardening (PH) stainless steels (Fig. 17). The PH stainless steels have lower maximum-use temperatures than other stainless steels due to a rapid drop in strength at about 425 °C (800 °F) (Fig. 18).



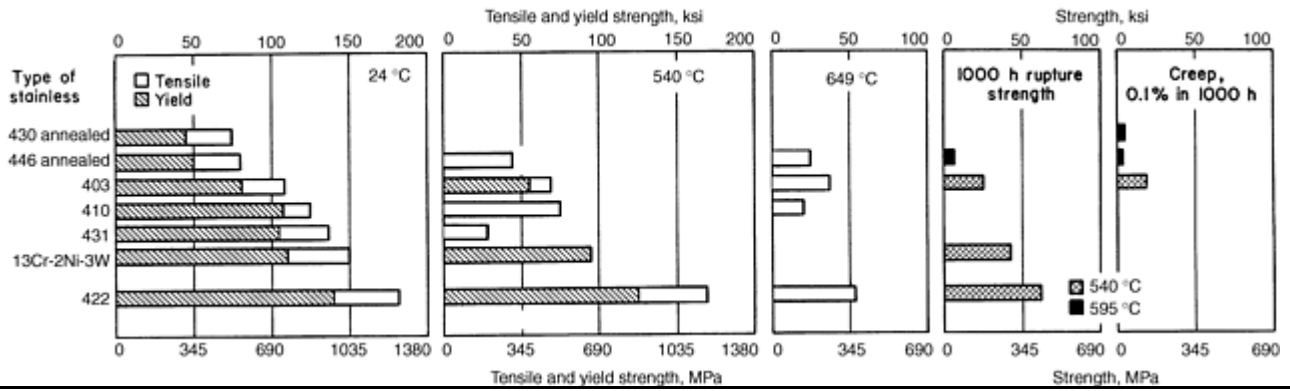
Alloy	Heat treatment
1.0%Cr-0.5%Mo	Annealed at 845 °C (1550 °F)
0.5%Mo	Annealed at 845 °C (1550 °F)
Type 502	Annealed at 845 °C (1550 °F)
2.25%Cr-1.0%Mo	Annealed at 845 °C (1550 °F)
1.25%Cr-1.5%Mo	Annealed at 815 °C (1500 °F)
7.0%Cr-0.5%Mo	Annealed at 900 °C (1650 °F)
9.0%Cr-1.0%Mo	Annealed at 900 °C (1650 °F)
1.0%Cr-1.0%Mo-0.25%V	Normalized at 955 °C (1750 °F), tempered at 649 °C (1200 °F)
H11	Hardened at 1010 °C (1850 °F), tempered at 565 °C (1050 °F)

Fig. 12 Tensile, yield, rupture, and creep strengths of wrought alloy steels containing less than 10% alloy



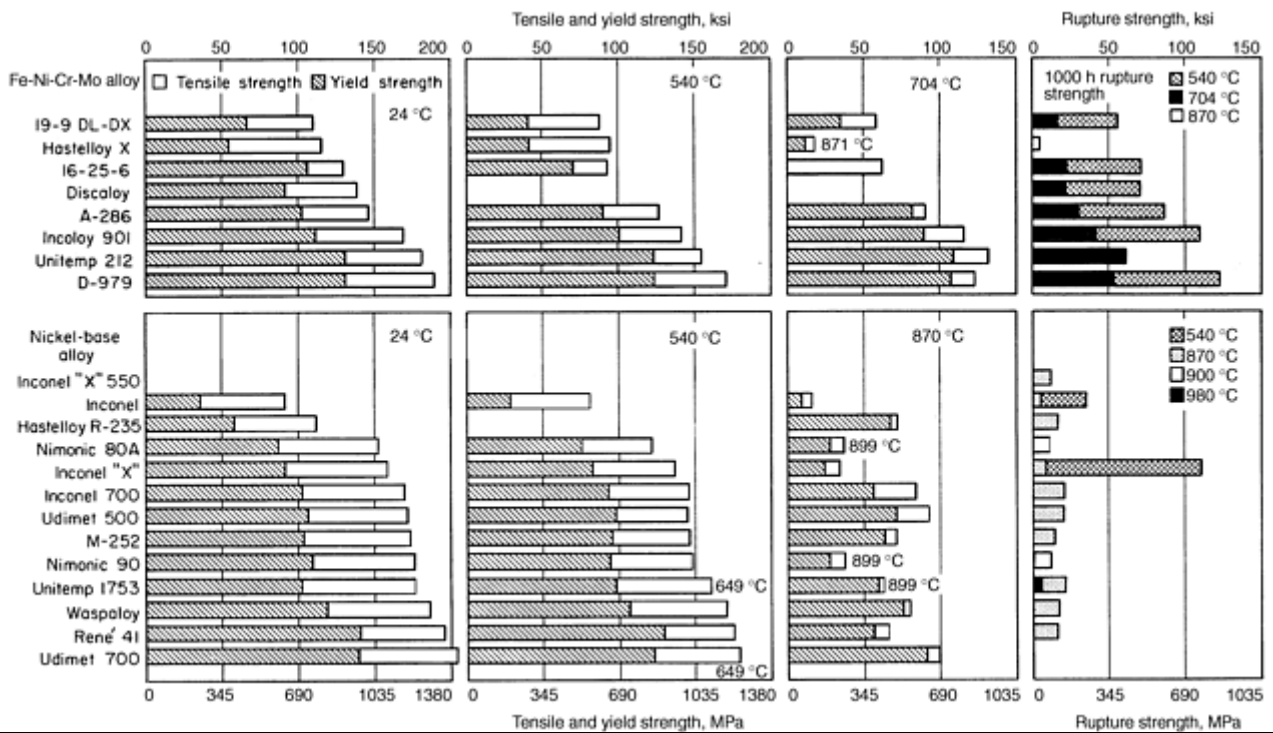
Alloy	Annealed by rapid cooling from
304	1065 °C (1950 °F)
316	1065 °C (1950 °F)
347	1065 °C (1950 °F)
309	1095 °C (2000 °F)
310	1095 °C (2000 °F)
321 (stainless)	1010 °C (1850 °F)

Fig. 13 Tensile, yield, and rupture strengths of several stainless steels and higher-nickel austenitic alloys



Alloy	Heat treatment
430	Annealed
446	Annealed
403	Quenched from 870 °C (1600 °F), tempered at 621 °C (1150 °F)
410	Quenched from 955 °C (1750 °F), tempered at 593 °C (1100 °F)
431	Quenched from 1025 °C (1875 °F), tempered at 593 °C (1100 °F)
13%Cr-2% Ni-3%W (Greek Ascoloy)	Quenched from 955 °C (1750 °F), tempered at 593 °C (1100 °F)
422	Quenched from 1040 °C (1900 °F), tempered at 593 °C (1100 °F)

Fig. 14 Tensile, yield, rupture, and creep strengths for seven ferritic and martensitic stainless steels



Alloy	Heat treatment
19-9 DL-DX	Air cooled from 1010 °C (1850 °F), hot worked at 650 °C (1200 °F), air cooled
Hastelloy X	Water quenched from 1175 °C (2150 °F), air cooled
16-25-6	Water quenched from 1175 °C (2150 °F), hot worked at 790 °C (1450 °F), air cooled from 649 °C (1200 °F)
Discaloy	Oil quenched from 980 °C (1800 °F), reheated to 720 °C (1325 °F), air cooled, reheated to 650 °C (1200 °F), air cooled
A-286	Oil quenched from 900 °C (1650 °F), reheated to 720 °C (1325 °F), air cooled
Incoloy 901	Oil quenched from 1120 °C (2050 °F), reheated to 705 °C (1300 °F), air cooled
Unitemp 212	Rolled at 1010 °C (1850 °F), air cooled, reheated to 720 °C (1325 °F), air cooled
D-979 (vacuum melted)	Oil quenched from 1010 °C (1850 °F), reheated to 843 °C (1550 °F), air cooled, reheated to 705 °C (1300 °F), air cooled

Inconel "X" 550	Air cooled from 1177 °C (2150 °F), reheated to 871 °C (1600 °F), air cooled, reheated to 730 °C (1350 °F), air cooled
Inconel	Annealed at 900 °C (1650 °F)
Hastelloy R-235	Water quenched from 1205 °C (2200 °F)
Nimonic 80A	Air cooled from 1080 °C (1975 °F), reheated to 704 °C (1300 °F), air cooled
Inconel "X"	Air cooled from 1150 °C (2100 °F), reheated to 845 °C (1550 °F), air cooled, reheated to 704 °C (1300 °F), air cooled
Inconel 700	Air cooled from 1180 °C (2160 °F), reheated to 871 °C (1600 °F), air cooled
Udimet 500	Air cooled from 1080 °C (1975 °F), reheated to 845 °C (1550 °F), air cooled, reheated to 760 °C (1400 °F), air cooled
Nimonic 90	Air cooled from 1080 °C (1975 °F), reheated to 705 °C (1300 °F), air cooled
Unitemp 1753	Air cooled from 1175 °C (2150 °F), reheated to 900 °C (1650 °F), air cooled
Waspaloy	Air cooled from 1080 °C (1975 °F), reheated to 845 °C (1550 °F), air cooled, reheated to 760 °C (1400 °F), air cooled
René 41	Air cooled from 1177 °C (2150 °F), reheated to 900 °C (1650 °F), air cooled
Udimet 700 (vacuum melted)	Annealed at 1150 °C (2100 °F), air cooled, solution treated at 1080 °C (1975 °F), air cooled, reheated to 815 °C (1500 °F), air cooled, reheated to 760 °C (1400 °F), air cooled

Fig. 15 Temperature versus tensile, yield, and rupture strengths of iron-nickel-chromium-molybdenum and nickel-base alloys

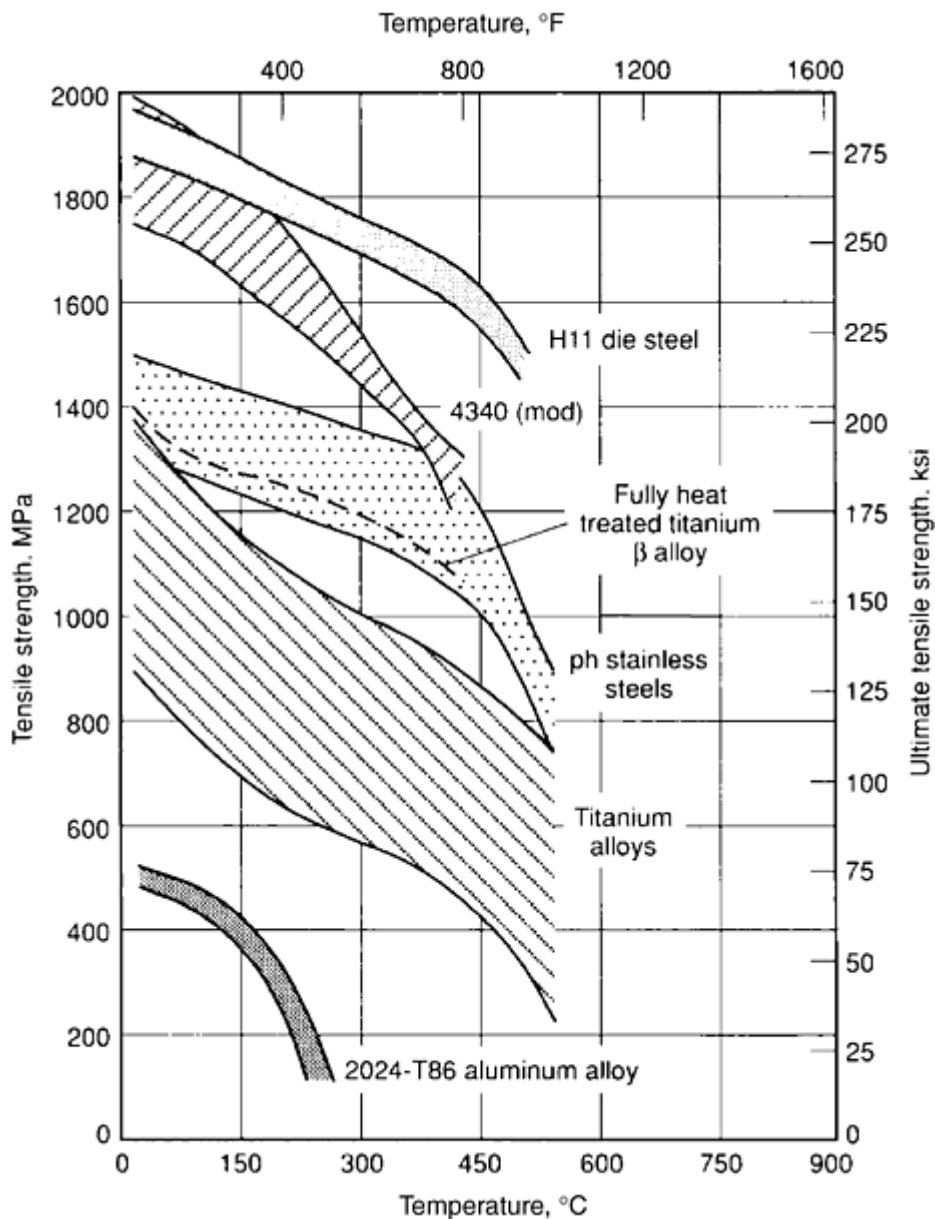
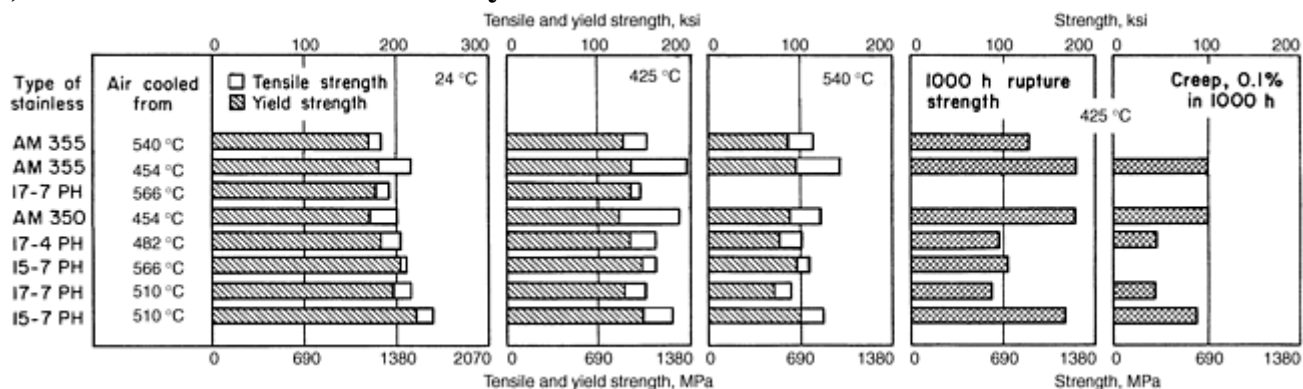


Fig. 16 Comparison of short-time tensile strength for titanium alloys, three classes of steel, and 2024-T86 aluminum alloy



Alloy	Heat treatment
AM 355	Finish hot worked from a maximum temperature of 980 °C (1800 °F), reheated to 932–954 °C (1710–1750 °F), water quenched, treated at -73 °C (-100 °F), and aged at 538 °C (1000 °F)
	Finish hot worked from a maximum temperature or 980 °C (1800 °F), reheated to 932–954 °C (1710–1750 °F), water quenched, treated at -73 °C (-100 °F), aged at 455 °C (850 °F)
17-7 (TH1050) PH	Reheated to 760 °C (1400 °F), air cooled to 16 °C (60 °F) within 1 h, aged at 565 °C (1050 °F) for 90 min
15-7 (TH1050) PH Mo	Reheated to 760 °C (1400 °F), air cooled to 16 °C (60 °F) within 1 h, aged at 565 °C (1050 °F) for 90 min
17-7 (RH950) PH	Reheated to 954 °C (1750 °F) after solution annealing, cold treated at -73 °C (-100 °F), aged at 510 °C (950 °F)
15-7 (RH950) PH Mo	Reheated to 955 °C (1750 °F) after solution annealing, cold treated at -73 °C (-100 °F), aged at 510 °C (950 °F)
17-4 PH	Aged at 480 °C (900 °F) after the solution anneal
AM 350	Solution annealed at 1038–1066 °C (1900–1950 °F), reheated to 932 °C (1710 °F), cooled in air, treated at -73 °C (-100 °F), aged at 454 °C (850 °F)

Fig. 17 Short-time tensile, rupture, and creep properties of precipitation-hardening stainless steels

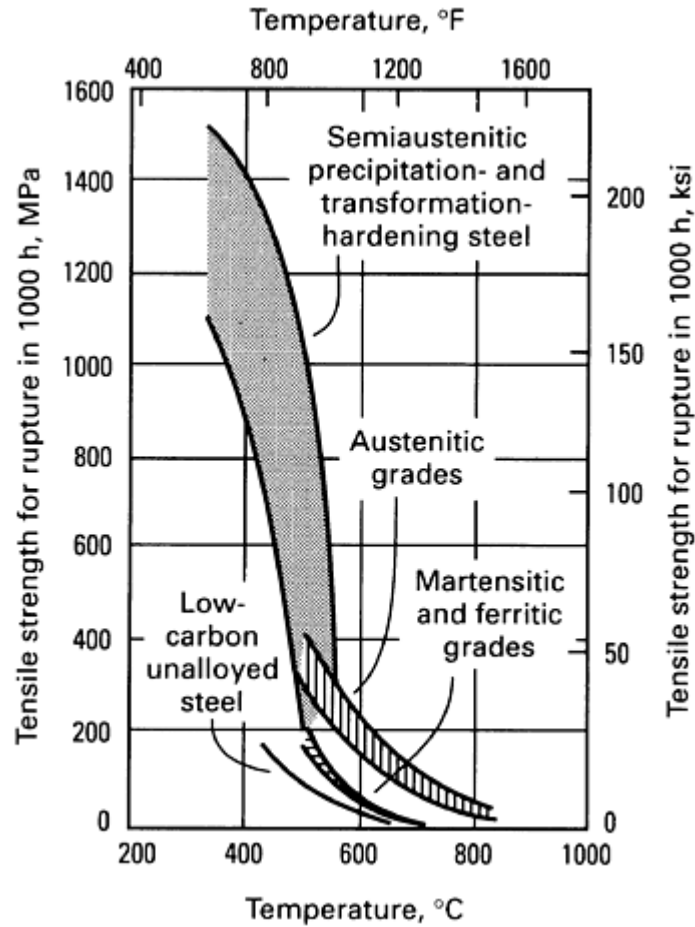


Fig. 18 General comparison of the hot-strength characteristics of austenitic, martensitic, and ferritic stainless steels with those of low-carbon unalloyed steel and semiaustenitic precipitation and transformation-hardening steels

When short-term tests are considered at high-temperature, the effect of testing time must be considered. Because creep occurs continuously over time, a longer test in the creep region results in lower strength values. This is shown in Fig. 19 for various mechanical properties of H11 die steel. Testing at higher temperatures also increases strain-rate effects because slower strain rates allow more time for creep to occur (Fig. 4).

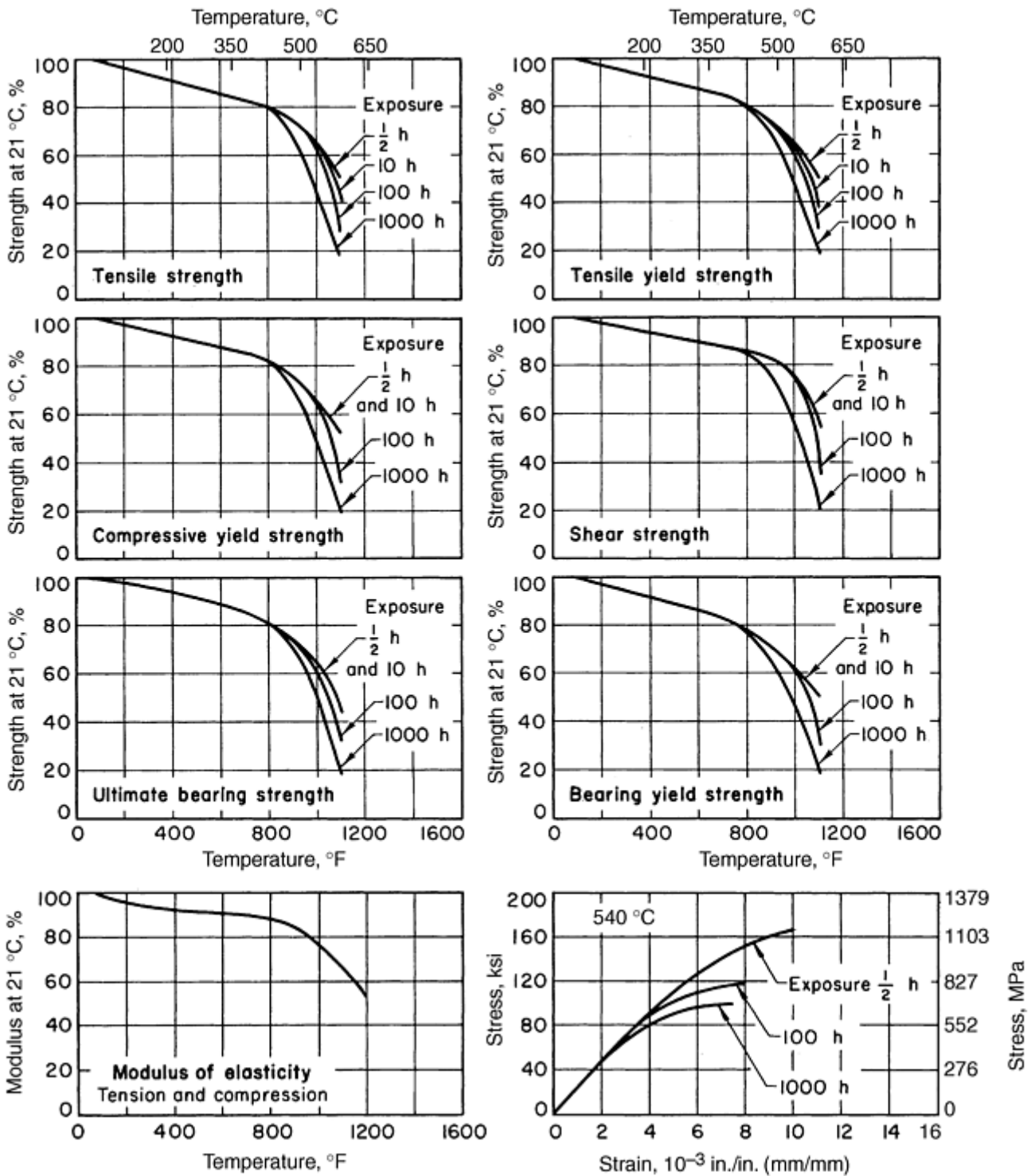


Fig. 19 Effect of time on high-temperature mechanical properties of H11 die steel

The time-dependent properties of high-temperature structural alloys are determined by a variety of methods, as discussed in more detail in the Section “Creep and Stress-Relaxation Testing” in this Volume. Many of these test methods in the creep region involve long-term testing. However, short-term tension tests on universal testing machines (UTMs) can also be used in the evaluation of creep deformation or stress relaxation. (See the article “Stress-Relaxation Testing” in this Volume.)

Hot Working Range. At higher temperatures in the hot working range ($T > 0.6 T_M$), mechanical behavior is different from plastic deformation at cold and warm working temperatures (where the change in microstructure is largely a distortion in the grains). In the hot working regime, creep and work softening can occur from self-diffusion (diffusion creep), dynamic recovery, and dynamic recrystallization. These high-temperature mechanisms are only briefly described here as a general reference on the overall effects of temperature on mechanical properties. More detailed coverage appears in the Section “Testing for Deformation Processes” in this Volume.

Static Recrystallization. When work-hardened alloys are heated, at some point a temperature level is reached where the atoms rearrange to form an entirely new set of crystals. This process, where the stored energy (produced by previous working at cold or warm temperatures) is released by migration of the grain boundaries, is known as recrystallization. The process is distinct from recovery, and the starting temperature for recrystallization depends on the amount of prior plastic deformation. At higher levels of working, more strain energy is stored in the crystal structure; therefore, a lower temperature initiates recrystallization.

Dynamic Recovery. In some cases, increased plastic strain results in a decrease in the necessary stress for continued deformation. This effect, known as work softening, occurs in the hot working range, as shown schematically in Fig. 20. The two main mechanisms of work softening in the hot working regime are dynamic recovery and dynamic recrystallization.

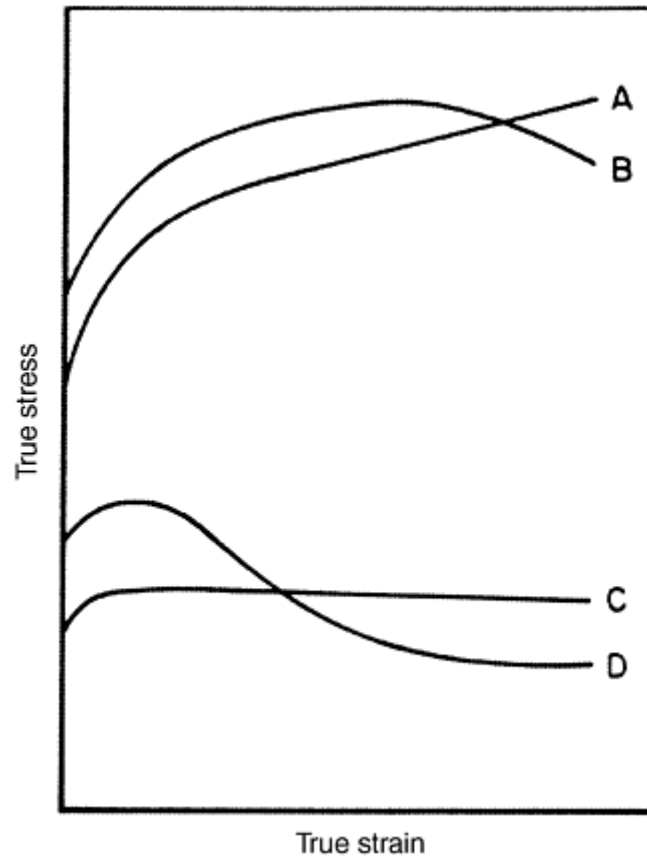


Fig. 20 Typical flow curves for metals deformed at cold working temperatures (A, low strain rate; B, high strain rate) and at hot working temperatures (C, D). Strain hardening persists to large strains for curve A. The flow stress maximum and flow softening in curve B arise from deformation heating. The steady-state flow stress exhibited by curve C is typical of metals that dynamically recover. The flow stress maximum and flow softening in curve D may result from a number of metallurgical processes. Source: Ref 11

In dynamic recovery, the dislocations obtained during previous working become unstable upon further working. The relative amount of softening depends on the ratio of the yield strength to the applied stress and the ratio of strength from previous work hardening to the yield strength (Ref 11). For example, as noted in Ref 11, the bcc and hcp metals have relatively high yield strengths in the annealed condition, so the amount of strain hardening is typically a smaller percentage of overall strength than for fcc metals. Thus, the amount of strain softening for fcc metals tends to be greater than that for hcp or bcc metals (Ref 11).

Dynamic Recrystallization. In contrast to dynamic recovery, dynamic recrystallization involves the motion of grain boundaries and annihilation of large numbers of dislocations in a single event, thereby producing new strain-free grains. Dynamic recrystallization is also distinct from static recrystallization (Ref 12). In dynamic recrystallization, the process occurs during the deformation process, thus facilitating working. In contrast, static recrystallization is a purely kinetic process where a fixed amount of stored energy (dependent on cold work) is released by thermally activated dislocation recovery and migration of the grain boundaries.

Dynamic recrystallization is largely limited to the fcc metals (Ref 11). For example, Fig. 21 shows true stress-strain curves for HY-100 steel tested in compression at 1000 °C (1832 °F) and different strain rates (Ref 13). There is a peak on the curves at strain rates of 0.01 s⁻¹ and above, which is usually an indication of dynamic recrystallization. The amount of strain required to trigger recrystallization during deformation varies with temperatures and strain rates.

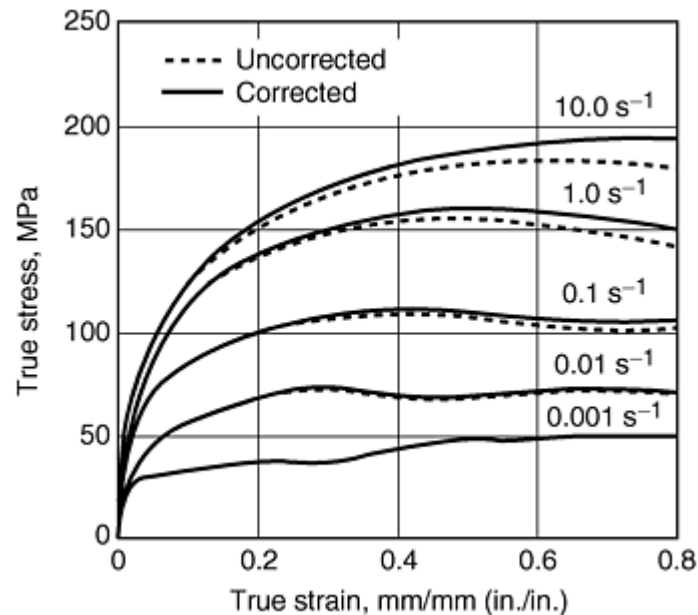


Fig. 21 True stress-strain curves for HY-100 steel tested in compression of 1000 °C (1832 °F) and various strain rates. Source: Ref 13

References cited in this section

1. W.D. Nix and J.C. Gibeling, Mechanisms of Time-Dependent Flow and Fracture of Metals, *Flow and Fracture at Elevated Temperatures*, R. Raj, Ed., American Society for Metals, 1985, p 2
2. J.D. Wittenberger and M.V. Nathal, Elevated/Low Temperature Tension Testing, *Mechanical Testing*, Vol 8, *Metals Handbook*, ASM International, 1985, p 36
3. W.F. Brown, Jr., Ed., *Aerospace Structural Metals Handbook*, Metals and Ceramic Information Center, Columbus, OH, 1982
4. *Structural Alloys Handbook*, Metals and Ceramic Information Center, Columbus, OH, 1973
5. D. Zhao, "Deformation and Fracture in Al₂O₃ Particle-Reinforced Aluminum Alloy 2014," Ph.D. thesis, Worcester Polytechnic Institute, 1990
6. *MIL-HDBK 5*, 1991
7. *Metals Handbook*, American Society for Metals, 1948, p 441
8. *The Making, Shaping, and Treating of Steel*, United States Steel, 1957, p 822–823
9. F.T. Sisco, *Properties*, Vol 2, *The Alloys of Iron and Carbon*, McGraw-Hill, 1937, p 431
10. R. Viswanathan, Damage Mechanisms and Life Assessment of High Temperature Components, ASM International, 1989, p 62

11. S.L. Semiatin and J.J. Jonas, *Formability and Workability of Metals: Plastic Instability and Flow Localization*, American Society for Metals, 1984, p 1–5, 93–97
12. Y.V.R.K. Prasad and S. Sasidhara, *Hot Working Guide: A Compendium of Processing Maps*, ASM International, 1997, p 9
13. M. Thirukkonda, D. Zhao, and A.T. Male, Materials Modeling Effort for HY-100 Steel, *NCEMT Technical Report*, TR No. 96–027, Johnstown, PA, March, 1996

Hot Tension and Compression Testing

Dan Zhao, Johnson Controls, Inc.; Steve Lampman, ASM International

Hot Tension Testing

Tension testing is a very common mechanical test for the evaluation of service properties. Most materials laboratories have tensile-testing machines. When compression-testing equipment is not available, or when a metalworking process involves mainly tensile stresses, the tension test can also be used for processing properties. More information on typical tension testing at room temperature is provided in the article “Uniaxial Tension Testing” in this Volume.

At high temperatures, the procedures and specimens of the tension test are basically the same as room-temperature testing. The key differences are the heating apparatus, accurate measurement of specimen temperature, and suitable instruments for measuring strain at high temperature. ASTM E 21 is the prevailing U.S. standard for high-temperature tensile testing (Ref 14).

General Characteristics. A typical high-temperature mechanical test setup is shown in Fig. 22. The system is the same as that used at room temperature, except for the high-temperature capabilities, including the furnace, cooling system, grips, and extensometer. In this system, the grips are inside the chamber but partly protected by refractory from heating elements. Heating elements are positioned around a tensile specimen. Thermocouple and extensometer edges touch the specimen.

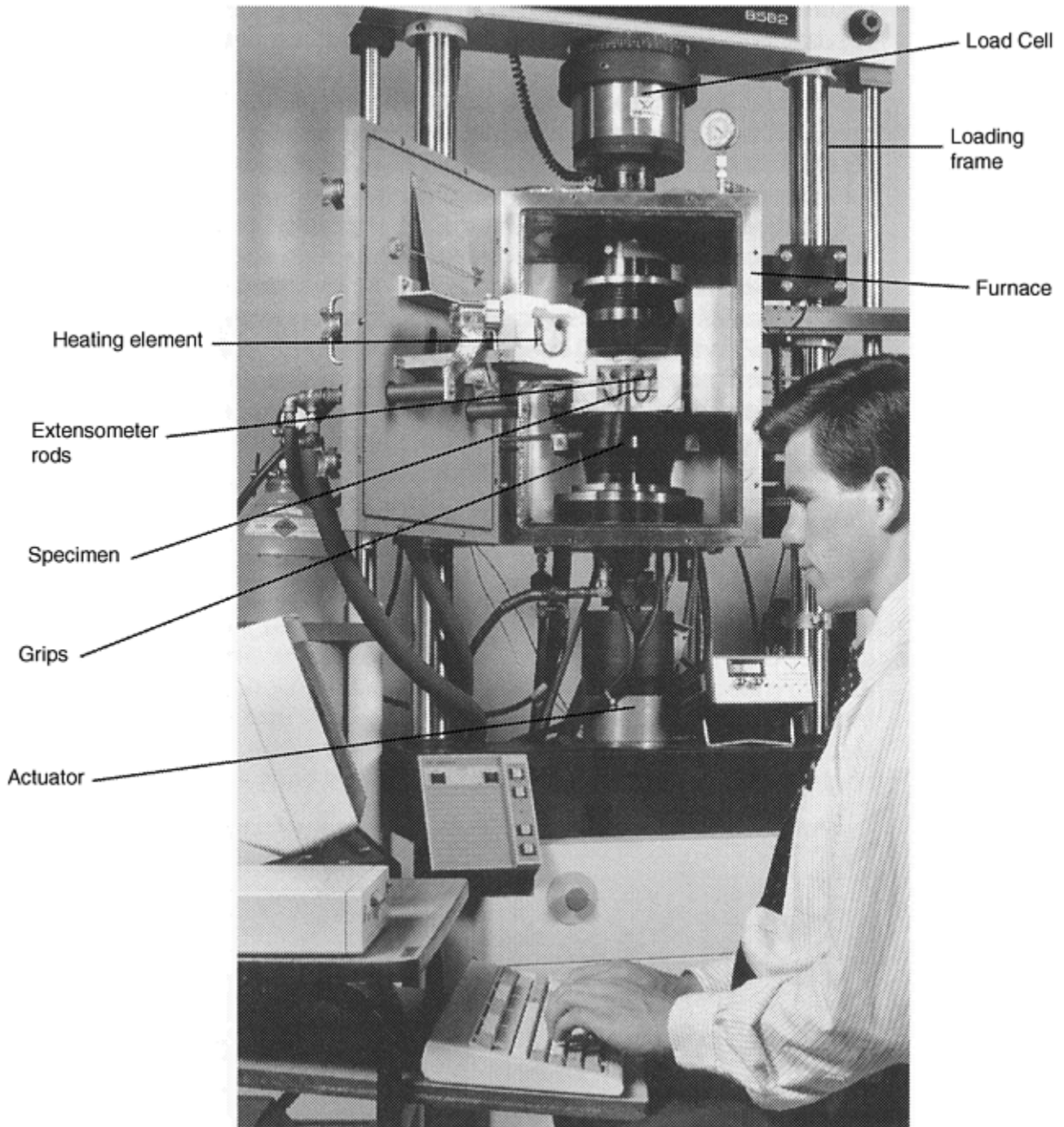


Fig. 22 A typical high-temperature mechanical testing system

Most tensile specimens are cylindrical. Specimens with rectangular cross sections can also be used. The specimen ends can be machined into smooth cylindrical or screw heads. The cylindrical head is usually used with split-ring types of grips, which provide for quick removal of the specimen if quenching outside the furnace immediately after testing is specified.

Universal joints are necessary to align the loading train. In any case, the maximum bending strain should not exceed 10% of the axial strain. Strain gages can be used to examine bending strains of the gage length. If the maximum (or minimum) bending strain is within the limit at room temperature, the alignment should be fine at elevated temperatures. Care must be taken to ensure that the alignment of the loading train is maintained when attaching the furnace and its accessories. The alignment needs to be tested periodically.

Heating methods for high-temperature mechanical testing include vacuum or environmental furnaces, induction heating, and resistance heating of the specimen. Vacuum furnaces are expensive and have high maintenance costs. The furnace has to be mounted on the machine permanently, making it inconvenient if another type of heating device is to be used. The heating element is expensive and oxidizes easily. The furnace can only be

opened at relatively lower temperatures to avoid oxidation. Quenching has to be performed with an inert gas, such as helium.

Environmental chambers are less expensive (Fig. 23). An environmental chamber has a circulation system to maintain uniform temperature inside the furnace. Inert gas can flow through the chamber to keep the specimen from oxidizing. Temperature inside the chamber can be kept to ± 1 °C (2 °F), about the nominal testing temperature. However, the maximum temperature of an environmental chamber is usually 550 °C (1000 °F), while that of a vacuum furnace can be as high as 2500 °C (4500 °F). The chamber can either be mounted on the machine or rolled in and out on a cart.



Fig. 23 Environmental chamber for elevated-temperature mechanical testing

A split furnace is also cost effective and easy to use (Fig. 24). When not in use, it can be swung to the side. The split furnace shown in Fig. 24 has only one heating zone. More sophisticated split furnance have three heating zones for better temperature control. Heating rate is also programmable.

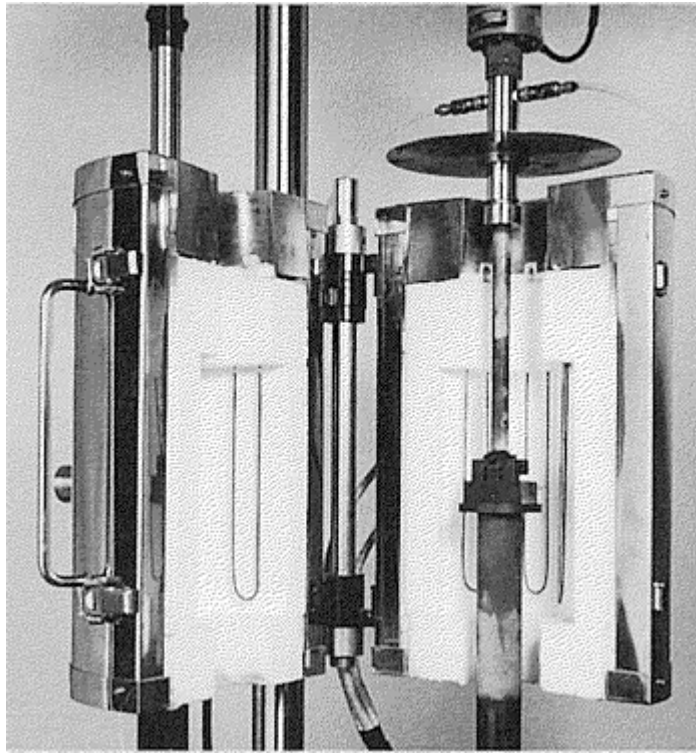


Fig. 24 Split furnace for high-temperature mechanical testing

Induction-heating systems allow fast heating rates (Fig. 25). Specimens can reach testing temperatures within seconds. Induction heating heats up the outer layer of the specimen first. Furnaces with a lower frequency have better penetration capability. Coupling of the heating coil and the specimen also plays an important role in heating efficiency. The interior of the specimen is heated through conduction. With the rapid heating rate, the temperature is often overshoot and nonuniform heating often occurs.

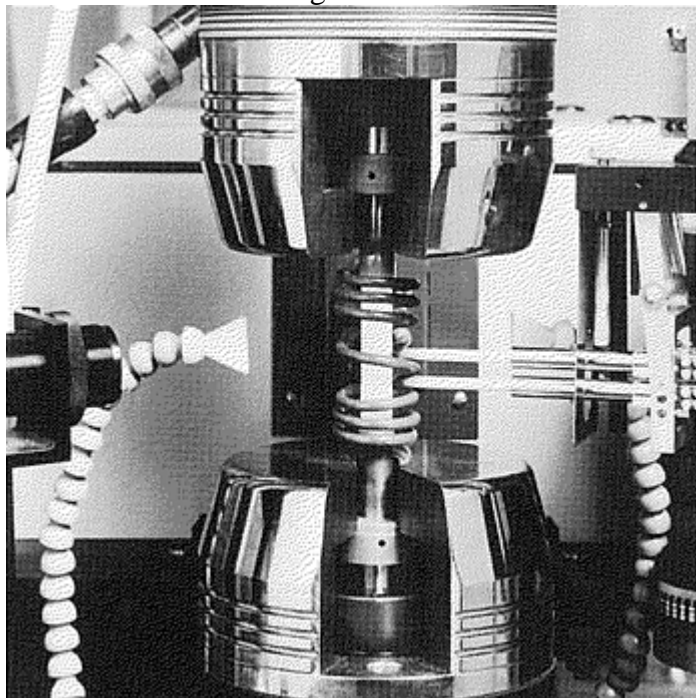


Fig. 25 Induction-heating furnace for high-temperature mechanical testing

Direct resistant heating is used in Gleeble machines with electric current going through the specimen (Ref 15). Advanced Gleeble testing systems, as shown in Fig. 26, are capable of rapid heating rates up to 10,000 °C/s (20,000 °F/s) (Ref 16). Grips with high thermal conductivity also allow rapid cooling rates up to 10,000°C/s (20,000°F/s) at the specimen surface.



Fig. 26 A Gleeble 3800 testing system. Source: Ref 12

Temperature Measurement. Thermocouples are the most common method for temperature measurement in hot tension tests. Because tensile specimens usually have longer gage length than compression specimens, more than one thermocouple may be needed to monitor the temperature along the gage length of the specimen. It is necessary to shield the thermocouple unless the difference in indicated temperature from an unshielded bead and a bead inserted in a hole in the specimen has been shown to be less than one half the variation listed below (Ref 14):

Temperature	Variation
Up to including 1800 °F (1000 °C)	± 5 °F (3 °C)
Above 1800 °F (1000 °C)	± 10 °F (6 °C)

Thermocouples need to be calibrated as specified in Ref 10. Thermocouple wire exposed to a hot zone should be cut off after each test, and a new bead should be formed for subsequent tests. During the entire test, temperature variation should not exceed the ranges indicated previously for the entire test, temperature variation should not exceed the ranges indicated previously for the entire gage length.

When testing with high heating rates, a thermocouple welded on the test specimen can provide a more accurate temperature reading (Ref 15). A thermocouple touching the specimen surface usually takes more time to reach the same reading as a thermocouple welded on the specimen. However, welding produces a heating affected zone and must be conducted carefully to minimize this effect. Drilling a hole in the gage length of a specimen for insertion of a thermocouple is not recommended, especially for specimens with small diameters. The hole may cause premature necking and failure, and lower the ultimate tensile strength.

Strain-Measurement. The simplest method for strain measurement is to take the crosshead displacement as the deformation of the specimen reduced section. However, this assumes that the rest of the loading train does not deform during testing and introduce error only at large plastic strains. Young's modulus cannot be determined in this way, and 0.2% offset yield strength would not be accurate. To accurately measure strains, strain gages or extensometers must be employed.

Strain gages can be used up to 600 °C (1112 °F) (Ref 2). Several extensometers are commercially available for strain measurement at high temperature: clip-on, water cooled, air cooled, and noncontact extensometers. Clip-on extensometers can be used up to 200 °C (392 °F); they are simple easy to use, and provide accurate readings. Water-cooled (Fig. 27) and air-cooled (Fig. 28) extensometers can be used at higher temperatures, up to 500 °C (930 °F) and 2500 °C (4500 °F), respectively.

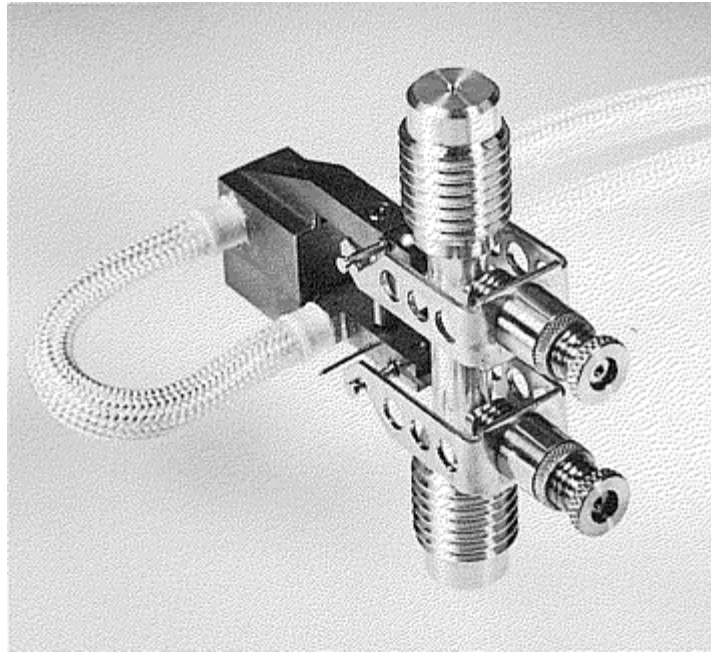


Fig. 27 Water-cooled extensometer used up to 500 °C (932 °F)

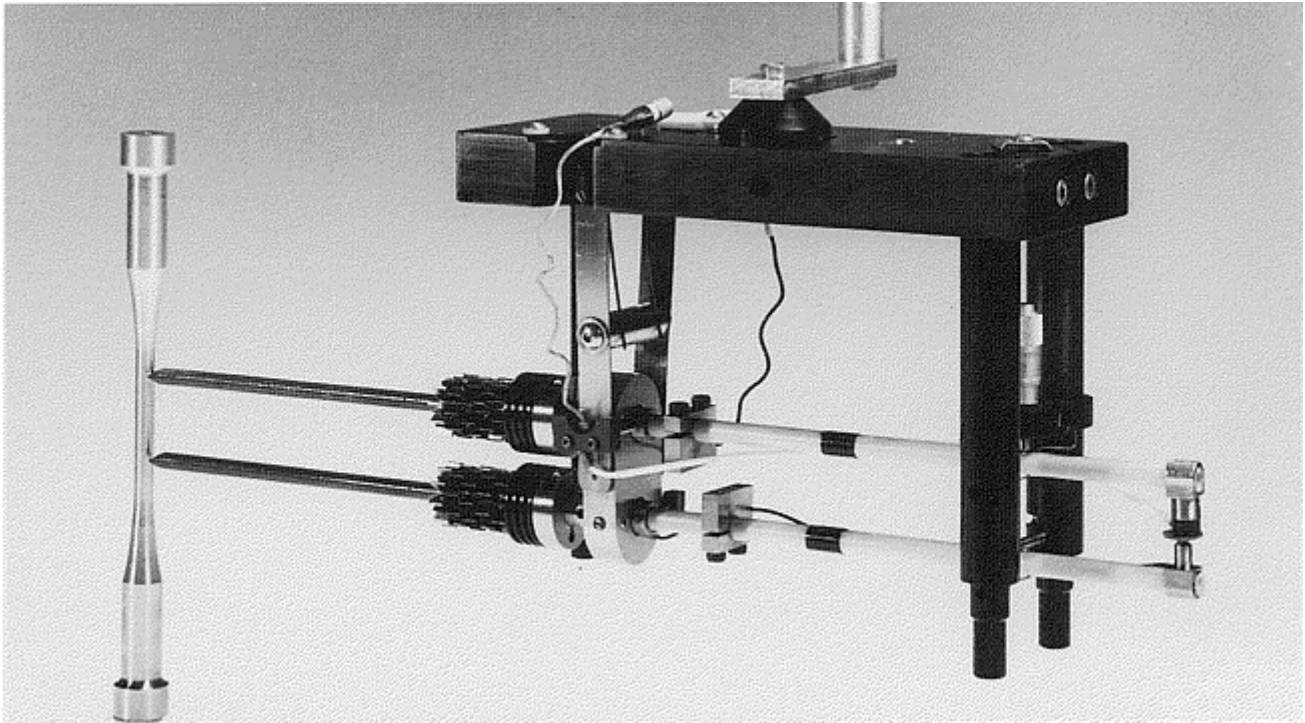


Fig. 28 Air-cooled extensometer used at temperatures up to 2500 °C (4532 °F)

Water- and air-cooled extensometers are contact extensometers that use rods touching the specimen; the rods transmit the relative motion of the specimen to a sensing device, usually a linear variable differential transformer (LVDT). Some capacitive extensometers have high resolution and extremely low contact force. The contact rods are made of various materials, ranging from nickel-base superalloys to ceramics, for different temperature ranges.

The extensometer should be attached very carefully because it may affect alignment (Ref 17). Attaching extensometers on opposite sides and averaging the reading may reduce the error. Some of the commercial extensometers are designed to attach to both sides of the specimen. Whenever feasible, extensometers should be attached directly to the reduced section (Ref 14). Stress-strain data may not be useful beyond the maximum-load point due to necking.

Noncontact extensometers include laser interferometers, optical extensometers, and video extensometers. These methods use more sophisticated instrumentation and are more expensive, but they are becoming more common. Laser extensometers, which allow faster sampling rates than optical extensometers, are used for measuring

strain rates in excess of 10^3 s^{-1} . Video extensometers, where a camera records the displacement of marks on a specimen through a glass window, can also be used with temperature chambers.

References cited in this section

2. J.D. Wittenberger and M.V. Nathal, Elevated/Low Temperature Tension Testing, *Mechanical Testing*, Vol 8, *Metals Handbook*, ASM International, 1985, p 36
10. R. Viswanathan, Damage Mechanisms and Life Assessment of High Temperature Components, ASM International, 1989, p 62
12. Y.V.R.K. Prasad and S. Sasidhara, *Hot Working Guide: A Compendium of Processing Maps*, ASM International, 1997, p 9
14. "Standard Test Methods for Elevated Temperature Tension Tests of Metallic Materials," ASTM E 21-92, *Annual Book of ASTM Standards*, 1994
15. R.E. Bailey, R.R. Shiring, and H.L. Black, Hot Tension Testing, *Workability Testing Techniques*, G.E. Dieter, Ed., American Society for Metals, 1984, p 73–94
16. *Gleeble[®] 3800 System*, Dynamic Systems Inc., Poestenkill, NY, May 1997
17. D.N. Tishler and C.H. Wells, An Improved High-Temperature Extensometer, *Mat. Res. Stand.*, ASTM, MTRSA, Vol 6 (No. 1), Jan 1966, p 20–22

Hot Tension and Compression Testing

Dan Zhao, Johnson Controls, Inc.; Steve Lampman, ASM International

Hot Compression Testing

Hot compression testing is also relatively easy to perform because of its simple specimen geometry (e.g., a cylinder). Testing machines and accessories are similar to those for hot tensile testing except the pull bars and grips are replaced by pushing anvils and platens. The anvils and platens can be made of stainless steel, tungsten carbide, TZM (Ti-Zr-Mo alloy), ceramics, or carbon.

Details on the applicable temperature ranges of anvils and platens are provided in the article "Testing for Deformation Modeling" in this Volume. The flat and parallel of platens should be within 0.0051 mm (0.0002 in.) (Ref 18). To improve parallelism, adjustable platens (bearing blocks) can be used. A drawing of such blocks can be found in Ref 19. Using a subpress, as suggested in the ASTM standards (Ref 18, 20), is very difficult with the limited space inside the furnace.

Specimen. The simplest specimen geometry is a cylinder. The aspect ratio (height to diameter) is usually between 1 and 2. An aspect ratio that is too high can cause the specimen to buckle, while one that is too low can increase friction even if lubricant is applied (see the article "Uniaxial Compression Testing" in this Volume). Typical specimen diameter is 10 to 15 mm (0.394–0.591 in.), depending on microstructure. For a cast alloy with coarse grains, large specimens are necessary. Subscale specimens can also be used for fine grain structure. In general, the specimen size must be representative of the material being tested. Other types of specimens, such as those with square or rectangular cross sections, can also be used, depending on the purpose of the tests. For example, a plane-strain compression specimen can have a rectangular cross section (Ref 19).

Lubrication. For testing at elevated temperatures, water-base graphite, graphite sheet, boron nitride solution, glass-base lubricant, and molybdenum disulfide may be used (Ref 13, 21). The lubricants can be applied to the

top and bottom ends of the specimen. They can also be applied to the platens at the same time to increase the effectiveness of lubrication. To retain the lubricant, grooves can be machined into the ends. Detailed specimen and groove dimensions can be found in the article “Testing for Deformation Modeling” in this Volume.

Temperature Control. As mentioned for hot tensile testing, a thermocouple that just touches the specimen does not provide an accurate temperature measurement unless the specimen is soaked at the nominal testing temperature for some time. To accurately measure the temperature of a specimen, thermocouples can either be welded to the specimen or inserted into a small hole drilled into the specimen. Compression-testing specimens are usually larger in diameter than tensile specimens, so a small hole drilled into the specimen to insert thermocouples may have little impact on the stress-strain curves. However, a hole may induce false cracking in a workability test, especially for brittle materials such as intermetallic compounds.

To determine the uniformity of temperature within the specimen, three thermocouples may be used to measure the top, bottom, and center temperatures of a dummy specimen as a function of time. If the temperatures are identical, only one thermocouple is necessary during testing. If it takes some time for the entire specimen to reach the set temperature, this procedure can also be used to determine the necessary soaking time.

To ensure the correct microstructure or specimen condition right before the compression testing commences, a specimen soaked at the testing temperature for the specified soaking time should be quenched and examined to determine the starting microstructure. It is essential that the platens be at the same temperature as the specimen. A temperature difference between the platens and the specimen results in a deformation gradient and, therefore, barreling of the deformed specimen (Ref 22).

Data Reduction and Temperature Correction. Load and displacement data are acquired from testing. To reduce the data into true stress and true strain, deformation is assumed homogeneous. Correction for the elastic deflection of the machine needs to be taken into account. True stress is simply the load divided by instantaneous cross-sectional area, which can be calculated by assuming constant volume in the specimen. For a cylindrical specimen, true stress, σ , is calculated as (Ref 19):

$$\sigma = \frac{P}{A} = \frac{4P}{\pi D^2} = \frac{4Ph}{\pi D_0^2 h_0} \quad (\text{Eq 1})$$

where P is load, A is cross-sectional area, D and D_0 are the instantaneous and initial diameter of the specimen, respectively, and h and h_0 are the instantaneous and initial height of the specimen, respectively. If friction is significant, the average pressure, \bar{P} , required to deform the specimen is greater than the flow stress of the material, σ :

$$\frac{\bar{P}}{\sigma} = \left(\frac{h}{2\mu D} \right)^2 \left[\exp\left(\frac{\mu}{h} \right) - \frac{\mu}{h} - 1 \right] \quad (\text{Eq 2})$$

where μ is the Coulomb coefficient of friction. The true strain, ϵ is given by:

$$\epsilon = \ln \frac{h_0}{h} \quad (\text{Eq 3})$$

Deformation heating occurs inevitably during testing, especially at high strain rates. Because isothermal stress-strain curves are desired for analysis, correction for deformation heating is necessary. The procedure for the correction can be found in the article “Testing for Deformation Modeling” in this Volume.

References cited in this section

13. M. Thirukkonda, D. Zhao, and A.T. Male, Materials Modeling Effort for HY-100 Steel, *NCEMT Technical Report*, TR No. 96-027, Johnstown, PA, March, 1996
18. “Standard Methods of Compression Testing of Metallic Materials at Room Temperature,” ASTM E 9-89a, *Annual Book of ASTM Standards*, 1994
19. A.T. Male and G.E. Dieter, Hot Compression Testing, *Workability Testing Techniques*, G.E. Dieter, Ed., American Society for Metals, 1984, p 51-72

20. "Standard Practice for Compression Tests of Metallic Materials at Elevated Temperatures with Conventional or Rapid Heating Rates and Strain Rates," ASTM E 209-65, *Annual Book of ASTM Standards*, 1994
21. M.L. Lovato and M.G. Stout, Compression Testing Techniques to Determine the Stress/Strain Behavior of Metals Subject to Finite Deformation, *Metall. Trans. A*, Vol 23, 1992, p 935–951
22. M.C. Mataya, Simulating Microstructural Evolution during the Hot Working of Alloy 718, *JOM*, Jan 1999, p 18–26

Hot Tension and Compression Testing

Dan Zhao, Johnson Controls, Inc.; Steve Lampman, ASM International

References

1. W.D. Nix and J.C. Gibeling, Mechanisms of Time-Dependent Flow and Fracture of Metals, *Flow and Fracture at Elevated Temperatures*, R. Raj, Ed., American Society for Metals, 1985, p 2
2. J.D. Wittenberger and M.V. Nathal, Elevated/Low Temperature Tension Testing, *Mechanical Testing*, Vol 8, *Metals Handbook*, ASM International, 1985, p 36
3. W.F. Brown, Jr., Ed., *Aerospace Structural Metals Handbook*, Metals and Ceramic Information Center, Columbus, OH, 1982
4. *Structural Alloys Handbook*, Metals and Ceramic Information Center, Columbus, OH, 1973
5. D. Zhao, "Deformation and Fracture in Al₂O₃ Particle-Reinforced Aluminum Alloy 2024," Ph.D. thesis, Worcester Polytechnic Institute, 1990
6. *MIL-HDBK 5*, 1991
7. *Metals Handbook*, American Society for Metals, 1948, p 441
8. *The Making, Shaping, and Treating of Steel*, United States Steel, 1957, p 822–823
9. F.T. Sisco, *Properties*, Vol 2, *The Alloys of Iron and Carbon*, McGraw-Hill, 1937, p 431
10. R. Viswanathan, Damage Mechanisms and Life Assessment of High Temperature Components, ASM International, 1989, p 62
11. S.L. Semiatin and J.J. Jonas, *Formability and Workability of Metals: Plastic Instability and Flow Localization*, American Society for Metals, 1984, p 1–5, 93–97
12. Y.V.R.K. Prasad and S. Sasidhara, *Hot Working Guide: A Compendium of Processing Maps*, ASM International, 1997, p 9
13. M. Thirukkonda, D. Zhao, and A.T. Male, Materials Modeling Effort for HY-100 Steel, *NCEMT Technical Report*, TR No. 96–027, Johnstown, PA, March, 1996

14. "Standard Test Methods for Elevated Temperature Tension Tests of Metallic Materials," ASTM E 21-92, *Annual Book of ASTM Standards*, 1994
15. R.E. Bailey, R.R. Shiring, and H.L. Black, Hot Tension Testing, *Workability Testing Techniques*, G.E. Dieter, Ed., American Society for Metals, 1984, p 73–94
16. *Gleeble[®] 3800 System*, Dynamic Systems Inc., Poestenkill, NY, May 1997
17. D.N. Tishler and C.H. Wells, An Improved High-Temperature Extensometer, *Mat. Res. Stand.*, ASTM, MTRSA, Vol 6 (No. 1), Jan 1966, p 20–22
18. "Standard Methods of Compression Testing of Metallic Materials at Room Temperature," ASTM E 9-89a, *Annual Book of ASTM Standards*, 1994
19. A.T. Male and G.E. Dieter, Hot Compression Testing, *Workability Testing Techniques*, G.E. Dieter, Ed., American Society for Metals, 1984, p 51–72
20. "Standard Practice for Compression Tests of Metallic Materials at Elevated Temperatures with Conventional or Rapid Heating Rates and Strain Rates," ASTM E 209-65, *Annual Book of ASTM Standards*, 1994
21. M.L. Lovato and M.G. Stout, Compression Testing Techniques to Determine the Stress/Strain Behavior of Metals Subject to Finite Deformation, *Metall. Trans. A*, Vol 23, 1992, p 935–951
22. M.C. Mataya, Simulating Microstructural Evolution during the Hot Working of Alloy 718, *JOM*, Jan 1999, p 18–26

Tension and Compression Testing at Low Temperatures

Robert P. Walsh, National High Magnetic Field Laboratory, Florida State University

Introduction

THE SUCCESSFUL USE of engineering materials at low temperatures requires that knowledge of material properties be available. Numerous applications exist where the service temperature changes or is extreme. Therefore, the engineer must be concerned with materials properties at different temperatures. Some of the typical materials properties of concern are strength, elastic modulus, ductility, fracture toughness, thermal conductivity, and thermal expansion. The lack of low temperature engineering data, as well as the use of less common engineering materials at low temperatures, results in the need for low-temperature testing.

The terms "high temperature" and "low temperature" are typically defined in terms of the homologous temperature (T/T_M), (where T is the exposure temperature, and T_M is the melting point of a material (both given on the absolute temperature scale, K). The homologous temperature is used to define the range of application temperatures in terms of the thermally activated metallurgical processes that influence mechanical behavior.

The term "low temperature" is typically defined in terms of boundaries where metallurgical processes change. One general definition of "low-temperature" is $T < 0.5 T_M$. For many structural metals, another definition of low temperature is $T < 0.3 T_M$, where recovery processes are not possible in metals and where the number of slip systems is restricted. For these definitions, room temperature (293 K) is almost always considered a low

temperature for a metal with a few exceptions, such as metals that have melting temperatures below 700 °C (indium and mercury). In a structural engineering sense, low temperature may be one caused by extreme cold weather. A well-known example of this is the brittle fracture of ship hulls during WWII that occurred in the cold seas of the North Atlantic (Ref 1). For many applications, low temperature refers to the cryogenic temperatures associated with liquid gases. Gas liquefaction, aerospace applications, and superconducting machinery are examples of areas in engineering that require the use of materials at very low temperatures. The term cryogenic typically refers to temperatures below 150 K. Service conditions in superconducting magnets that use liquid helium for cooling are in the 1.8 to 10 K range.

The mechanical properties of materials are usually temperature dependent. The most common way to characterize the temperature dependence of mechanical properties is to conduct tensile or compressive tests at low temperatures. Depending on the data needed, a test program can range from a full characterization of the response of a material over a temperature range, to a few specific tests at one temperature to verify a material performance. Many of the rules for conducting low temperature tests are the same as for room temperature tests. Low-temperature test procedures and equipment are detailed in this article. The role that temperature plays on the properties of typical engineering materials is discussed also. Important safety concerns associated with low-temperature testing are reviewed.

Reference cited in this section

1. E.R. Parker, *Brittle Behavior of Engineering Structures*, John Wiley & Sons, 1957

Tension and Compression Testing at Low Temperatures

Robert P. Walsh, National High Magnetic Field Laboratory, Florida State University

Mechanical Properties at Low Temperatures

In general, lowering the temperature of a solid increases its flow strength and fracture strength. The effect that lowering the temperature of a solid has on the mechanical properties of a material is summarized below for three principal groups of engineering materials: metals, ceramics, and polymers (including fiber-reinforced polymer, or FRP composites). An excellent source for an in-depth coverage of material properties at low temperatures is Ref 2.

Metals. Most metals are polycrystalline and have one of three relatively simple structures: face-centered cubic (fcc), body-centered cubic (bcc), and close-packed hexagonal (hcp). The temperature dependence of the mechanical properties of the fcc materials are quite distinct from those of the bcc materials. The properties of hcp materials are usually somewhere in between fcc and bcc materials. The general aspects of temperature-dependent mechanical behavior may be discussed using the deformation behavior maps shown in Fig. 1(a) and 1(b). The axes of these graphs are normalized for temperature and stress. Temperature is normalized to the melting temperature, while stress is normalized to the room temperature shear modulus, G (Ref 2).

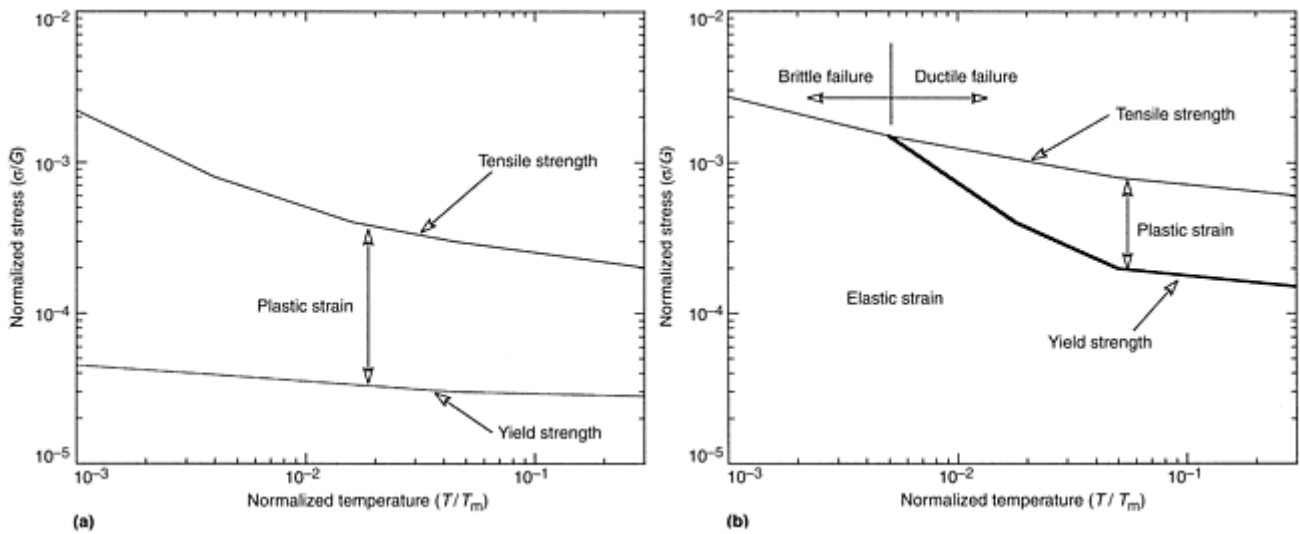


Fig. 1 Simplified deformation behavior (Ashby) maps (a) for face-centered cubic metals and (b) for body-centered cubic metals. Source: Ref 2

The behavior characteristic of a pure, annealed fcc material is shown in Fig. 1(a). The small increase of yield strength that occurs upon cooling is characteristic of the fcc behavior. The ultimate strength, which is shown as the ductile failure line, increases much more than the yield strength on cooling. The large increase in ultimate strength coupled with the relatively small increase in yield strength in fcc materials results from ductile, rather than brittle, failure (Ref 2).

Figure 1(b) illustrates the classic bcc behavior. The large temperature dependence of the yield strength, the smaller temperature dependence of the ultimate strength, and a region where the specimen fails before any significant plastic deformation occurs should be noted (Ref 2).

The previous discussion is for pure annealed metals. Engineering alloys may behave somewhat differently, but the trends are relatively consistent. Solid solution strengthening typically increases yield and ultimate strengths of the fcc alloys while giving the yield strength an increased temperature dependence. The temperature dependence of the ultimate strength is still greater than that of the yield strength, allowing the alloy to maintain its ductile behavior. The ultimate tensile strengths of the fcc metals have stronger temperature dependence than those of bcc metals. Austenitic stainless steels have fcc structures and are used extensively at cryogenic temperatures because of their ductility, toughness, and other attractive properties. Some austenitic steels are susceptible to martensitic transformation (bcc structure) and low-temperature embrittlement. Plain carbon and low alloy steels having bcc structures are almost never used at cryogenic temperatures because of their extreme brittleness. Cases of anomalous strength behavior have been reported where a maximum strength is reached at temperatures above 0 K. These cases are unique and usually involve single crystal research materials or very soft materials, although yield strengths of commercial brass alloys are reported to be higher at 20 K than at 4 K (Ref 2).

Ceramics. Ceramics are inorganic materials held together by strong covalent or ionic bonds. The strong bonds give them the desirable properties of good thermal and electrical resistance and high strength but also make them very brittle. Graphite, glass, and alumina are ceramics used at low temperature usually in the form of fibers that reinforce polymer-matrix composite materials. The high temperature (~77 K) superconducting compounds are ceramics that pose challenging problems with respect to using brittle materials at low temperatures.

Polymers and Fiber-Reinforced Polymer (FRP) Composites. Polymers are rather complex materials having many classifications and a wide range of properties. Two important properties of polymers are the melting temperature, T_m , and the glass transition temperature, T_g , both of which indicate the occurrence of a phase change. The glass transition temperature, the most important material characteristic related to the mechanical properties of polymer, is influenced by degree of polymerization. The T_g is the temperature, upon cooling, at which the amorphous or crystalline polymer changes phase to a glassy polymer. For most polymers at temperatures below T_g , the stress-strain relationship becomes linear-elastic, and brittle behavior is common. Some ductile or tough polymers exhibit plastic yielding at temperatures below T_g . The T_g represents the temperature below which mass molecular motion (such as chain sliding) ceases to exist, and ductility is

primarily due to localized strains. Suppression of T_g helps to produce tougher polymers. The strong temperature dependence of the modulus is a distinguishing feature of polymers compared to metals or ceramics.

Fiber-reinforced polymer composites are used extensively at low temperatures because of their high strength-to-weight ratio and their thermal and electrical insulating characteristics. The FRPs tend to have excellent tensile and compression strength that increases with decreasing temperature. Reinforcing fibers commonly used in high-performance composites for low-temperature applications are alumina, aramid, carbon, and glass. Typical product forms are high-pressure molded laminates (such as cotton/ phenolics and G-10) and filament-wound or pultruded tubes, straps, and structures. Although the FRP composites have desirable tensile and compressive strengths, other mechanical properties such as fatigue and interlaminar shear strength are sometimes questionable. Two good sources of properties of structural composites at low temperature are Ref 4 and 5.

References cited in this section

2. R.P. Reed and A.F. Clark, Ed., *Materials at Low Temperatures*, ASM, 1983
4. M.B. Kasen et al., Mechanical, Electrical, and Thermal Characterization of G-10CR and G-11CR Glass-Cloth/Epoxy Laminates Between Room Temperature and 4 K, *Advances in Cryogenic Engineering*, Vol 28, 1980, p 235–244
5. R.P. Reed and M. Golda, Cryogenic Properties of Unidirectional Composites, *Cryogenics*, Vol 34 (No. 11), 1994, p 909–928

Tension and Compression Testing at Low Temperatures

Robert P. Walsh, National High Magnetic Field Laboratory, Florida State University

Test Selection Factors

Tensile and compression tests produce engineering data but also facilitate study of fundamental mechanical-metallurgical behavior of a material, such as deformation and fracture processes. If obtaining engineering data is the objective and the materials application is at low temperature, the designer must be sure that mechanical properties are stable at the desired temperatures. One important factor related to low-temperature testing is that the low temperature may cause unstable brittle fracture behavior that tensile or compression tests may fail to reveal. The cooling of materials, especially bcc metals and polymers, can cause the materials to undergo a ductile-to-brittle transition. This behavior is not unique to steel but has its counterpart in many other materials. Brittle fracture occurs in the presence of a triaxial stress state to which a simple tensile or compression test will not subject the material. Brittle fracture is caused by high tensile stress, while ductile behavior is related to shear stress. A metal that flows at low stress and fractures at high stress will always be ductile. If, however, the same material is retreated so that its yield strength approaches its fracture strength, its behavior may become altered, and brittleness may ensue (Ref 1). If the materials application is at low temperature, the designer must be sure that mechanical properties are stable, because the possibility of brittle fracture requires modification of the design approach.

If the material in question is a new material or a material for which little or no low-temperature data exist, screening tests that can assess susceptibility to brittle fracture are advisable. Two such screening tests are Charpy impact tests and notch tensile tests. Conducting Charpy or notch tensile tests at various temperatures can detect a ductile-to-brittle transition over a temperature range. Ultimately, if the fracture toughness of the material is an issue, fracture toughness testing should be performed.

The intended service condition for the material should influence the test temperature and the decision to perform tensile or compressive tests. It is good practice to determine the properties while simulating the service

conditions. Of course, life is not always this simple, and actual service conditions may not be easily achieved with an axial stress test at a given temperature.

Tensile testing is the most common test of mechanical properties and is usually easier than compression testing to conduct properly at any temperature. The compressive and tensile Young's moduli of most materials are identical. Fracture of a material is caused by tensile stress that causes crack propagation. Tensile tests lend themselves well to low-temperature test methods because the use of environmental chambers necessitates longer than normal load trains. Pin connections and spherical alignment nuts can be used to take advantage of the increased length for self-alignment purposes. For most homogeneous materials, stress-strain curves obtained in tension are almost identical to those obtained in compression (Ref 6). Exceptions exist where there is disagreement between the stress-strain curves in tension and compression. This effect, termed "strength differential effect," is especially noticeable in high-strength steels (Ref 7).

There are times when compression testing is required such as when the service-condition stress is compressive or when the strength of an extremely brittle material is required. The second case is true for almost all polymers at cryogenic temperatures as they become extremely brittle, glassy materials. The fillet radius of a reduced-section tensile-test sample can create enough of a stress riser that the material fails prematurely. Stress concentrations, flaws, and submicroscopic cracks largely determine the tensile properties of brittle materials. Flaws and cracks do not play such an important role in compression tests because the stress tends to close the cracks rather than open them. The compression tests are probably a better measure of the bulk material behavior because they are not as sensitive to factors that influence brittle fracture (Ref 3). A brittle material will be nearly linear-elastic to failure, providing a well-defined ultimate compressive strength. The following table lists competing factors that influence the test method choice, many of which are generic while some are specific to conditions associated with low-temperature testing.

The temperature at which to run the test can be a simple determination such as when mechanical properties data for a material at the

Tension	Compression
Advantages	
Common	Good for modulus and yield strength
Self-aligning	
Well-defined gage section	No grips
Good for modulus, yield, ultimate, and ductility parameters	No stress concentration in sample design
	Good for ultimate strength of brittle materials
	Easy sample installation
	Inexpensive sample cost
Disadvantages	
Sensitive to specimen design	End effects (friction/constraint)
Difficult to test brittle materials and composites where machining reduced section is not plausible	Sensitive to alignment
	Not always good for ultimate strength
	Need containment for fractured material

proposed service temperature are not available. Other cases are not so straightforward, and the temperature choice should be based on cost and the ability to provide conservative results. Sometimes, a material is to be used at a cold temperature, but testing it at room temperature will yield conservative data that are sufficient for the application. For many 4 K applications, conservative properties can be measured at 77 K in a simpler, more economical test. The degree of strengthening that will occur upon cooling from 77 to 4 K is much less than that which occurs from 295 to 77 K. When there is doubt about the applicability of data from tests at a temperature other than the service temperature, testing should be done at the service temperature. Good practice is to test above, below, and at the service temperature for a more complete understanding of the material behavior.

The relative costs and difficulty of the tests are important. Tests conducted in liquid media are simpler to perform, in general, than intermediate temperature tests that require temperature control. Below is a list of testing media and their associated temperatures (Ref 2).

Substance	Temperature, K	Bath type
Ice water	273	Slush
Isobutane	263	Liquid at BP
Carbon tetrachloride	250	Slush
Propane	231	Liquid at BP
Trichloroethylene	200	Slush
Carbon dioxide	195	Solid
Methanol	175	Slush
n-pentane	142	Slush
Iso-pentane	113	Slush
Methane	112	Liquid at BP
Oxygen	90.1	Liquid at BP
Nitrogen	77.3	Liquid at BP
Neon	27.2	Liquid at BP
Hydrogen	20.4	Liquid at BP
Helium (He₄)	4.2	Liquid at BP
Helium (He₃)	3.2	Liquid at BP

All temperatures given at 0.1 MPa (1 atm). BP, boiling point

Some of these substances are more common, cheaper, or easier to handle than others. The most commonly used substances in mechanical tests are ice water, CO₂/methanol slush, liquid-nitrogen (LN₂) cooled methanol, LN₂, and liquid helium (LHe). Obvious hazards are associated with the use of oxygen and hydrogen, and they should be avoided if possible. Safety issues concerning the use of cooled methanol, LN₂, and LHe are discussed subsequently in this section. Cost of the cryogenic medium is also an issue. Since LN₂ is common and readily available, its cost is relatively low. LHe, on the other hand, is about a factor of ten times as expensive as LN₂. Liquid neon is sometimes used because it is easy to handle and its liquid boiling point temperature is relatively close to that of liquid hydrogen, but it can be 20 to 40 times as expensive as LHe. The sublimation temperature of dry ice (CO₂) is 195 K, and it can be used to cool a methanol or propanol bath with relative ease. Many of these bath cooling techniques are tried and true methods that require some practice to perfect but are usually inexpensive and simple ways to control test sample temperature. Low-temperature control can also be accomplished with electronic temperature control systems that utilize heaters and a cooling medium. Electronic temperature control systems are described in the following section.

References cited in this section

1. E.R. Parker, *Brittle Behavior of Engineering Structures*, John Wiley & Sons, 1957
2. R.P. Reed and A.F. Clark, Ed., *Materials at Low Temperatures*, ASM, 1983
3. L.E. Neilsen and R.F. Landel, *Mechanical Properties of Polymers and Composites*, Marcel Dekker, NY, 1994, p 249–263
6. E.P. Popov, *Mechanics of Materials*, 2nd ed., Prentice-Hall, NJ, 1976
7. J.P Hirth and M. Cohen, *Metall. Trans.*, Vol 1, Jan 1970, p 3

Equipment

Low-temperature tensile and compression tests can be performed on electromechanical or servo-hydraulic test machines with capacities of approximately 50 to 100 kN. The 100 kN machine is preferable for high strength materials such as steels or composites but of course larger or smaller capacities can be used as necessary. Direct tension and compression tests usually require a simple ramp function that is possible on the more economical electromechanical (screw-drive) test machine. Computer controlled servo-hydraulic test systems are versatile and can perform a variety of tasks as well as direct tension and compression tests.

To facilitate the low-temperature requirement, the test machine must be equipped with a temperature-controlled environmental chamber. One consideration for the suitability of the machine for low-temperature tests is the ease with which a low-temperature environmental chamber can be implemented. The physical characteristics of the test machine come into play, such as the maximum distance between crossheads and load columns.

A major factor to consider for cryogenic tests is the cryostat. "Cryostat" is a general term for an environmental chamber designed for cryogenic temperatures and can be as simple as a container (dewar) to hold a liquid cryogen. Cryostats designed for mechanical testing have the added requirement of providing structural support to react to tensile or compressive forces that are applied to the test material. Typically, a load frame is designed as an insert to a dewar. Since a dewar is a vacuum-insulated bucket to hold liquid, it is not advisable to have a hole in the bottom for pull-rod penetration because it introduces a leak potential for liquid, vacuum, and heat. The closed-bottom feature of a cryostat necessitates that the applied load and reacted load be introduced from the top. Cryostats are described further in the section "Environmental Chambers" below.

The simplest method to introduce the load path from the top on a servo-hydraulic machine is to use a machine that has the hydraulic actuator mounted on top of the upper crosshead. Hydraulic machines with this configuration are available, and the arrangement does not restrict normal use of the machine. Figure 2 shows a servo-hydraulic test machine equipped with a mechanical test cryostat. The screw-drive type test machine is usually accommodating and should have a movable lower crosshead with a through hole for the load train. References 8 and 9 give details of the design of cryostats for mechanical test machines.



Fig. 2 A 100 kN capacity test machine equipped with cryostat for low-temperature testing

If the machine is not configured as described in the preceding paragraphs, the machine is relatively incompatible for cryogenic tests. Cryogenic tests on an incompatible machine require specially designed cryostats or an external frame system both of which are usually expensive and cumbersome alternatives. Figure 3 shows a schematic of a simple test chamber (canister) for immersion bath tests above liquid nitrogen temperature. This fixture provides an inexpensive method for conducting tests on conventional machines down to approximately 100 K.

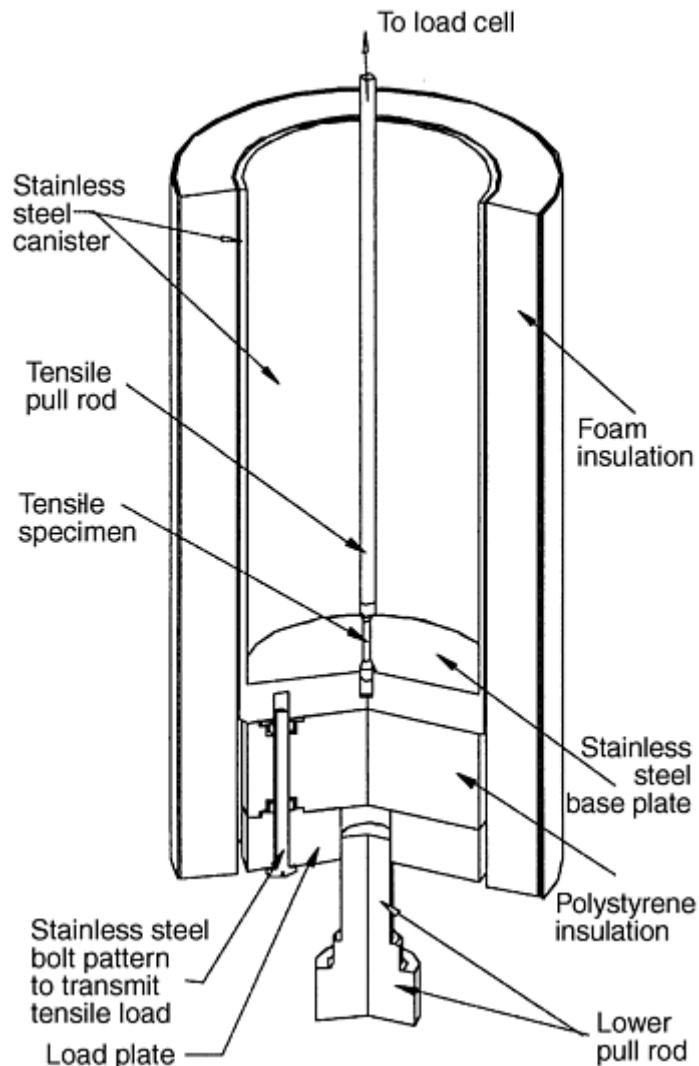


Fig. 3 Schematic of simple tensile canister from a standard-configuration machine for low-temperature testing

Environmental Chambers. For low temperature tests, an environmental chamber is a thermal chamber that contains a gaseous or liquid bath media used to control the low temperature of a test. Sub-room-temperature environments are obtained with three basic chamber designs: a conventional refrigeration chamber; a thermally insulated box-container, or a cryostat designed for cryogenic temperatures with vacuum insulation; and thermal radiation shielding.

Conventional refrigeration covers the temperature range from +10 to -100 °C and could be employed for tests in this range, much the same as furnaces are used on test machines to achieve elevated temperatures. Although mechanical refrigeration seems like a logical choice to cool environmental chambers, it is rarely used. This is probably because of the capital expense and the relative simplicity of other methods.

Commercial environmental chambers designed for use with test machines are available for controlling temperatures from approximately 800 K down to 80 K. Such chambers use electrical heaters for elevated temperatures and cold nitrogen gas cooling for sub-room-temperature. The cold nitrogen gas is supplied from a liquid nitrogen storage dewar. The flow of cold gas determines the cooling power and is controlled at the inlet with a variable flow valve that is regulated by the temperature controller. These systems are versatile in that a wide range of test temperature is possible with a single system. Some of the disadvantages are bulkiness, which can make setup difficult, and that the tests can be time consuming with respect to attaining equilibrated test temperatures.

Cryogenic temperature tests are conducted in an environmental chamber called a cryostat. Cryostat is a general description of a low-temperature environmental chamber and can be as simple as a container (dewar) to hold a liquid cryogen. Reference 10 is an excellent historical perspective on low-temperature mechanical tests that details a number of cryostat designs, many of which use conventional machines with standard load path configurations. As mentioned previously, pull-rod penetration through the bottom of a cryostat introduces a

leak potential for liquid, vacuum, and heat and is not recommended for liquid bath-cooled tests. Modern mechanical test cryostats are typically a combination of a custom designed structural load frame fit into a commercial open-mouth bucket dewar. Some of the design details of a tensile test cryostat are shown in the schematic in Fig. 4 and photograph in Fig. 5. The design of the cryostat load frame is driven by engineering design factors such as cost, strength, stiffness, thermal efficiency, and ease of use. A good design philosophy is to produce a versatile fixture that can test a variety of specimens over a range of temperatures. The effect of lowering the temperature on the properties of a material can be evaluated by comparing the baseline room temperature properties. It is advisable to have the test apparatus capable of testing the material at both room temperature and cold temperatures. Construction materials used are austenitic stainless steels, titanium alloys, maraging steels, and FRP composites. For tensile tests, the cryostat frame reacts to the load in compression. The frame can be thermally isolated with low-thermal conductivity, FRP composite standoffs. For compression tests, the reaction frame is in tension and is not as easily thermally isolated. The cryostat shown here is easily converted between the more thermally efficient tensile cryostat and the more robust compressive cryostat (Fig. 6).

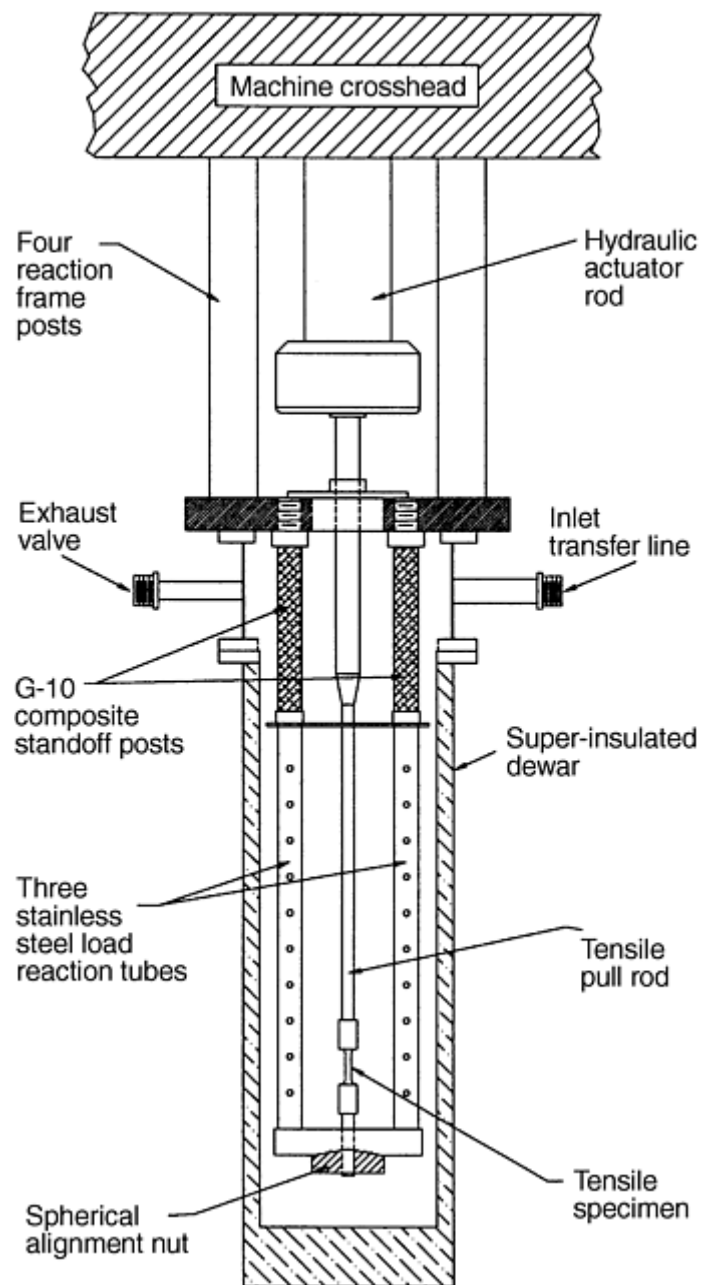


Fig. 4 Schematic of a tensile test cryostat

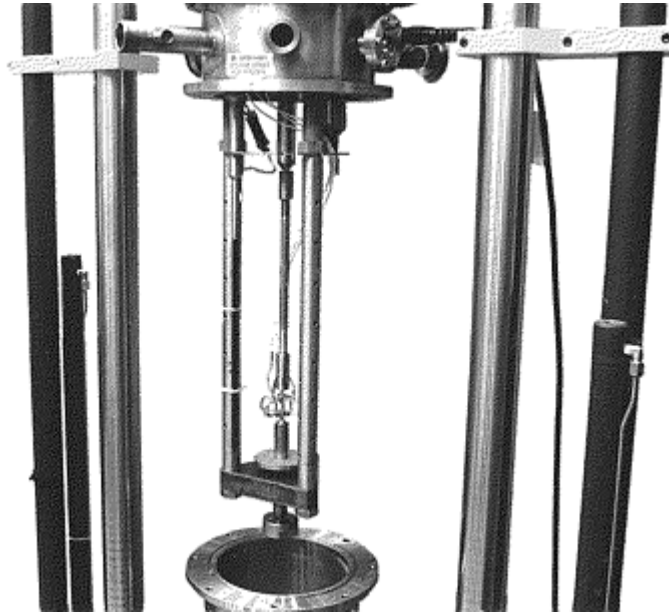


Fig. 5 Tensile test cryostat. The force-reaction posts have fiber-reinforced polymer composite stand-offs.

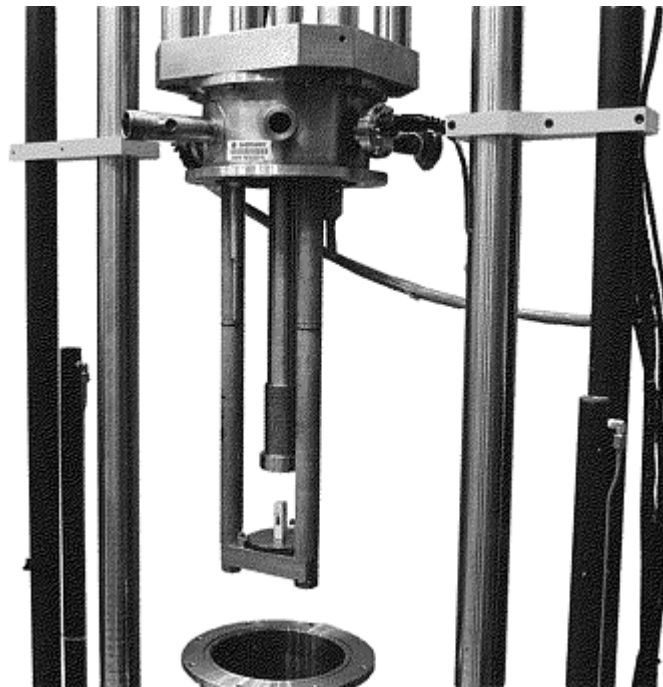


Fig. 6 Compression test cryostat, including heavier force-reaction posts and a tubular push rod designed to withstand buckling

Cryogen Liquid Transfer Equipment. The supply and delivery of cryogenic fluids require special equipment. The equipment described here pertains to the use of the two most common cryogen test media, liquid nitrogen and liquid helium. Both liquid helium and nitrogen can be purchased from suppliers (usually welding supply distributors) in various quantities that are delivered in roll-around storage dewars. Liquid nitrogen can be transferred out of the storage dewar into the test dewar with simple or common tubing materials. Its thermal properties and inexpensive price allow its flow through uninsulated tubes. For example, butyl rubber hose can be attached to the storage dewar, and the hose will freeze as the liquid passes through. Liquid helium, on the other hand, is more difficult to handle, and it requires special vacuum-insulated transfer lines. Liquid helium transfer lines are usually flexible stainless steel lines with end fittings to match the inlet ports of the test cryostat and the supply cryostat. For both liquid nitrogen and helium, the storage tank is pressurized to enable transfer of the liquid.

Instrumentation. The minimum instrumentation requirement in any tensile or compression test is that for force measurement. Typically, forces are measured with the test machine force transducer (load cell) in the same manner as for forces measured in room temperature tests. During low-temperature tests, precautions should be taken to ensure the load cell remains at ambient room temperature.

Strain measurements may require temperature dependent calibration. Common strain measurement methods used are test machine displacement, bondable resistance strain gages, and clip-on extensometers or compressometers. Also applicable to low-temperature strain measurements but less commonly used are capacitive transducer methods (Ref 11), noncontact laser extensometers, and linear variable differential transformers (LVDT) with extension rods to transmit displacements outside of the environmental chamber to the LVDT-sensing device.

Test machine displacement (stroke or crosshead movement) is a simple, low-accuracy method of estimating specimen strain. The inaccuracy comes because the displacement includes deflection of the test fixturing plus the test specimen gage section. Compensating for test fixturing compliance improves accuracy.

Bondable resistance strain gages are for sensitive measurements such as modulus and yield strength determination. The strain gage manufacturer supplies strain gage bonding procedures for use at cryogenic temperatures. The overall range of strain gages at cryogenic temperatures is limited to about 2% strain. Applicable strain gages recommended by strain gage manufacturers have temperature dependent calibration data down to 77 K. Interest in their use down to 4 K has resulted in strain gage research verifying their performance to 4 K (Ref 12). A typical gage factor (GF) is 2 for NiCr alloy foil gages and it increases approximately 2 to 3% on cooling from 295 to 4 K. Thermal output strain signals are a large source of error that must be compensated for. Compensation is usually accomplished using the bridge balance of the strain circuit where zero strain can be adjusted to coincide with zero stress. If this is not possible, other steps must be taken to electrically or mathematically correct the thermal output strain.

Extensometers and compressometers applicable to low-temperature tests utilize strain gages mounted to a bending beam element. The temperature sensitivity can be determined by calibrating with a precision calibration fixture that enables calibration at various temperatures. Depending on the accuracy desired, it is possible to use one or two calibration factors over a large temperature range. A typical strain-gage extensometer-calibration factor changes about $\pm 1\%$ over the temperature range from 295 to 4 K.

Temperature measurement is done with an assortment of temperature sensors. Reference 2 has a section devoted to temperature measurement at low temperatures. The most common method of temperature measurement is to use a thermocouple. Type E thermocouples (Chromel versus Constantan) and Type K (Chromel versus Alumel) cover a wide range of temperature and can be used at 4 K when carefully calibrated. A better choice of thermocouple, designed to have higher sensitivity at cryogenic temperatures, is a AuFe alloy versus Chromel thermocouple. Electronic temperature sensors (diodes and resistance devices) are available with readout devices that have higher precision than thermocouples. Silicon diodes, gallium-aluminum-arsenide diode, carbon glass resistor, platinum resistor, and germanium resistor are some of the more commonly used types of sensors.

Cryogenic temperature controllers that work with the types of temperature sensors named above are available. The majority of temperature controllers vary heating power and require that the test chamber environment is slightly cooler than the set-point temperature. The test engineer is responsible for the environmental chamber and cooling medium of the system. The controllers use the temperature sensors as the feedback sensor to operate a control loop and supply power for resistive heaters.

Additional Equipment Considerations. Teflon-insulated (E.I. DuPont de Nemours & Co., Inc., Wilmington, DE) lead wires are advisable at very low temperatures because the insulation will be less likely to crack and cause problems. Electronic noise reduction can be an issue in low-temperature tests because lead wires tend to be long. Standard methods of noise-reduction are shielding and grounding. Self-heating and thermocouple effects are important issues at low temperatures. Precautions should be taken to ensure that thermal effects do not mask the test data. Strain gage excitation voltages should be kept low. Reference 10 gives the parameters in terms of power density for calculating excitation voltage to be used for strain gages at 4 K.

References cited in this section

2. R.P. Reed and A.F. Clark, Ed., *Materials at Low Temperatures*, ASM, 1983

8. G. Hartwig and F. Wuchner, Low Temperature Mechanical Testing Machine, *Rev. Sci. Instrum.*, Vol 46, 1975, p 481–485
9. R.P. Reed, A Cryostat for Tensile Test in the Temperature Range 300 to 4 K, *Advances in Cryogenic Engineering*, Vol 7, Plenum Press, NY, 1961, p 448–454
10. J.H. Lieb and R.E. Mowers, Testing of Polymers at Cryogenic Temperatures, *Testing of Polymers*, J.V.Schmitz, Ed., Vol 2, John Wiley & Sons, 1965, p 84–108
11. R.P. Reed and R.L. Durcholz, Cryostat and Strain Measurement for Tensile Tests to 1.5 K, *Advances in Cryogenic Engineering*, Vol 15, Plenum Press, NY, 1970, p 109–116
12. C. Ferrero, Stress Analysis Down to Liquid Helium Temperature, *Cryogenics*, Vol 30, March 1990, p 249–254

Tension and Compression Testing at Low Temperatures

Robert P. Walsh, National High Magnetic Field Laboratory, Florida State University

Tension Testing

As at room temperature, tensile tests at low temperature are for determining engineering design data as well as for studying fundamental mechanical-metallurgical behaviors of a material such as deformation and fracture processes. The usual engineering data from tensile tests are yield strength, ultimate tensile strength, elastic modulus, elongation to failure, and reduction of area. The effects of material flaws (inclusions, voids, scratches, etc.) are amplified in low-temperature testing, as materials become more brittle and sensitive to stress concentrations. Data scatter tends to increase, and the quantity of tests to characterize a material is usually greater than that used for room temperature testing. The test engineer must judge when sufficient testing has been done to provide representative data on a material.

Test fixture alignment is important at low temperatures because of necessarily long load trains. Self-alignment in tensile tests can be accomplished through the use of universal joints, spherical bearings, and pin connections. The alignment should meet specifications detailed in ASTM E 1012, “Standard Practice for Verification of Specimen Alignment Under Tensile Loading.” Strain measurement should be done using an averaging technique that can reduce errors associated with misalignment or bending stress. Strain measurement equipment is detailed above in the instrumentation section.

Metals. The standard tensile test method for metals, ASTM E 8, covers the temperature range from 50 to 100 °F and is used as a guideline for lower temperature tests. The need for engineering data in the design of superconducting magnets has resulted in the adoption of the tensile test standard ASTM E 1450 for tests of structural alloys in liquid helium at 4.2 K.

The strain rate sensitivity of the flow stress in metals decreases as temperature is reduced. Typical strain rates in standard tensile tests are on the order of 10^{-5} s^{-1} to 10^{-2} s^{-1} and do not have a pronounced effect on the material flow stress. The strain rate becomes important in cryogenic temperature tests because of a tendency for specimen heating causing discontinuous yielding in displacement control tests. Discontinuous yielding is a subject of low-temperature research of alloys, well described in ASTM E 1450. The localized strain/heating phenomenon typically initiates after the onset of plastic strain and results in a serrated stress-strain curve. ASTM test standard E 1450 prescribes a maximum strain rate of 10^{-3} s^{-1} and notes that lower rates may be necessary. The strain required to initiate discontinuous yielding increases with decreasing strain rate. If discontinuous yielding starts before the 0.2% offset yield strength is reached, the associated load drop affects the estimation of the yield strength. It may be possible to slow the strain rate to postpone the serrated curve

until after the 0.2% offset yield strength is reached and then to increase the rate, not to exceed 10^{-3} s^{-1} . Reference 13 reports research on the effect of strain rate in tensile tests at 4 K.

Test specimen sizes are preferably small for low-temperature tests. The common 0.5 in. round, ASTM-standard tensile specimen is rarely used at low temperature. Tensile specimens should be small due to size constraints placed by the environmental test chamber, which is designed for thermal efficiency. Standard capacity test machines (100 and 50 kN) favor small specimens due to high tensile strengths encountered at low temperatures. A subscale version of the 0.5 in. round that meets ASTM specifications and works well at cryogenic temperature is shown in Fig. 7(a). A 100 kN force capacity test machine can generate about 3.5 GPa stress on a 6 mm diameter gage section. Figure 7(b) shows a flat, subscale tensile specimen that is also commonly used at cryogenic temperatures.

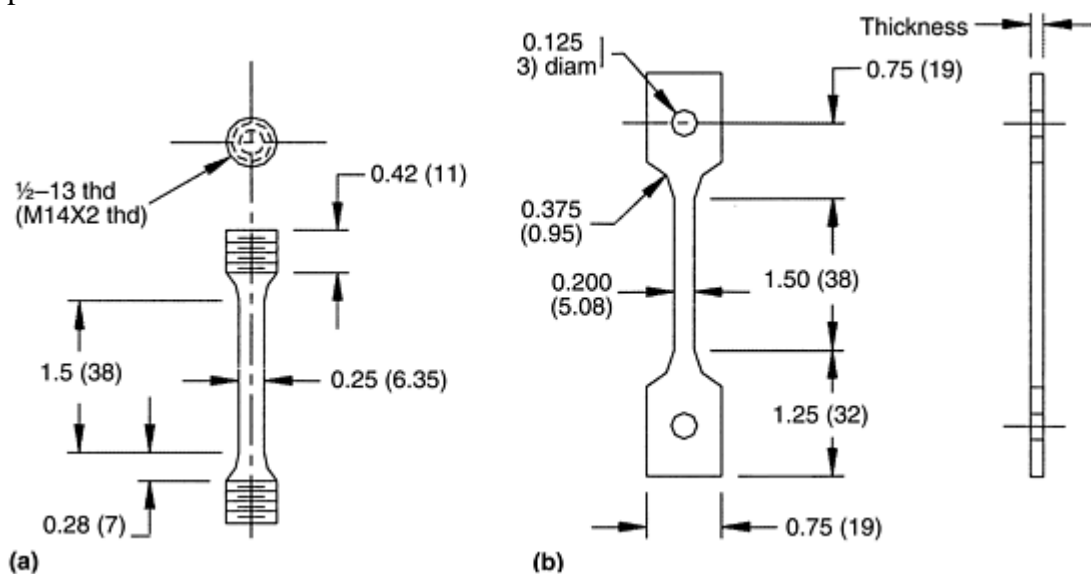


Fig. 7 Schematics of tensile specimen commonly used at low temperature. (a) Round. (b) Flat. Dimensions are in inches (millimeters.) thd, threaded

Polymers and Fiber-Reinforced Polymer (FRP) Composites. Tension tests of FRP composites are governed in test procedure ASTM D 3039, while polymers and low modulus ($<20 \text{ GPa}$) composites are tested using the guidelines established in ASTM D 638. Neither have specific temperature ranges or limitations.

The problem with testing polymers at low temperatures is the tendency for polymers to be extremely brittle materials. Test temperatures below room temperature are usually well below the glass transition temperature, T_g , of the polymer. The test specimen designs in ASTM D 638 are susceptible to grip failures once the material is brittle. Traditional strain measurement techniques must be performed carefully. Clip-on extensometers must mechanically attach to the material, usually producing some sort of stress concentration that may initiate failure. Strain gages locally reinforce low-modulus material, and the associated error and correction method is explained in Ref 14. Most tensile tests of polymers show an increase in tensile strength upon cooling from 295 to 77 K and a decrease or constant level of strength with continued cooling to 4 K (Ref 15). One would expect the strength to continue to increase with decreasing temperature. This anomalous behavior is probably an artifact of the tensile testing of an extremely brittle material.

Tensile tests of FRP composites at low temperatures are simpler than tests of neat polymers because of the more rugged sample. One challenge is the gripping of high-strength, unidirectionally reinforced composites. The convenience of hydraulic wedge grips is not usually an option in low-temperature tests. An example of a low-temperature tension and compression test program to characterize a unidirectionally reinforced epoxy composite from 295 to 4 K is described in Ref 16.

References cited in this section

13. R.P. Reed and R.P. Walsh, Tensile Strain Effects in Liquid Helium, *Advances in Cryogenic Engineering*, Vol 34, Plenum Press, 1988, p 199–208

14. C.C. Perry, Strain Gage Reinforcement Effects on Low Modulus Materials, *Manual on Experimental Methods for Mechanical Testing of Composites*, R.L. Pendelton and M.E. Tuttle, Ed., Society for Experimental Mechanics, 1989, p 35–38
15. R.P. Reed and R.P. Walsh, Tensile Properties of Resins at Low Temperatures, *Advances in Cryogenic Engineering*, Vol 40, Plenum Press, NY, 1994, p 1129–1136
16. R.P. Walsh, J.D. McColskey, and R.P. Reed, Low Temperature Properties of a Unidirectionally Reinforced Epoxy Fibreglass Composite, *Cryogenics*, Vol 35 (No. 11), 1995, p 723–725

Tension and Compression Testing at Low Temperatures

Robert P. Walsh, National High Magnetic Field Laboratory, Florida State University

Compression Testing

Compressive properties are of interest to the design and analysis of structures subjected to compressive or bending stress. Compressive properties include modulus of elasticity, yield stress, deformation beyond yield point, and compressive strength (assuming that the material does not just flatten).

Compression testing of metals is conducted using the guidelines established in test procedure ASTM E 9, “Standard Test Methods of Compression Testing of Metallic Materials at Room Temperature.” An application of low-temperature compression tests is to determine if there is a strength differential effect for a particular metal. Another case for compression tests is to measure the yield strength of a brittle metal that tends to fail in tension before the 0.2% offset yield strength is reached.

Polymers are compression tested at low temperatures using ASTM D 695, “Standard Test Method for Compressive Properties of Rigid Plastics” for guidance. This standard states that it is applicable to tests of unreinforced and reinforced rigid plastics, including high-modulus composites. Research comparing results for different compressive test methods on high-modulus composites has shown that ASTM D 695 is acceptable for modulus determination but not a good method for strength measurement (Ref 17). This direct compression test method is excellent for determining the strength and modulus of brittle polymers at low temperatures. A compressive test fixture used for testing polymers and composites at low temperatures is shown in Fig. 6. The fixture uses a spherical bearing seat on the lower stationary compression platen (dry graphite powder is used as a lubricant) to adjust platen parallelism. Applying a nominal load with the upper platen aligns the lower platen, which is then locked into place with three clamps. Figure 8 shows some data from recent low-temperature tests on a high-strength polymer (Ref 18). The results graphically show the difference between the tension (ASTM D 638) and compression (ASTM D 695) tests of these relatively brittle materials.

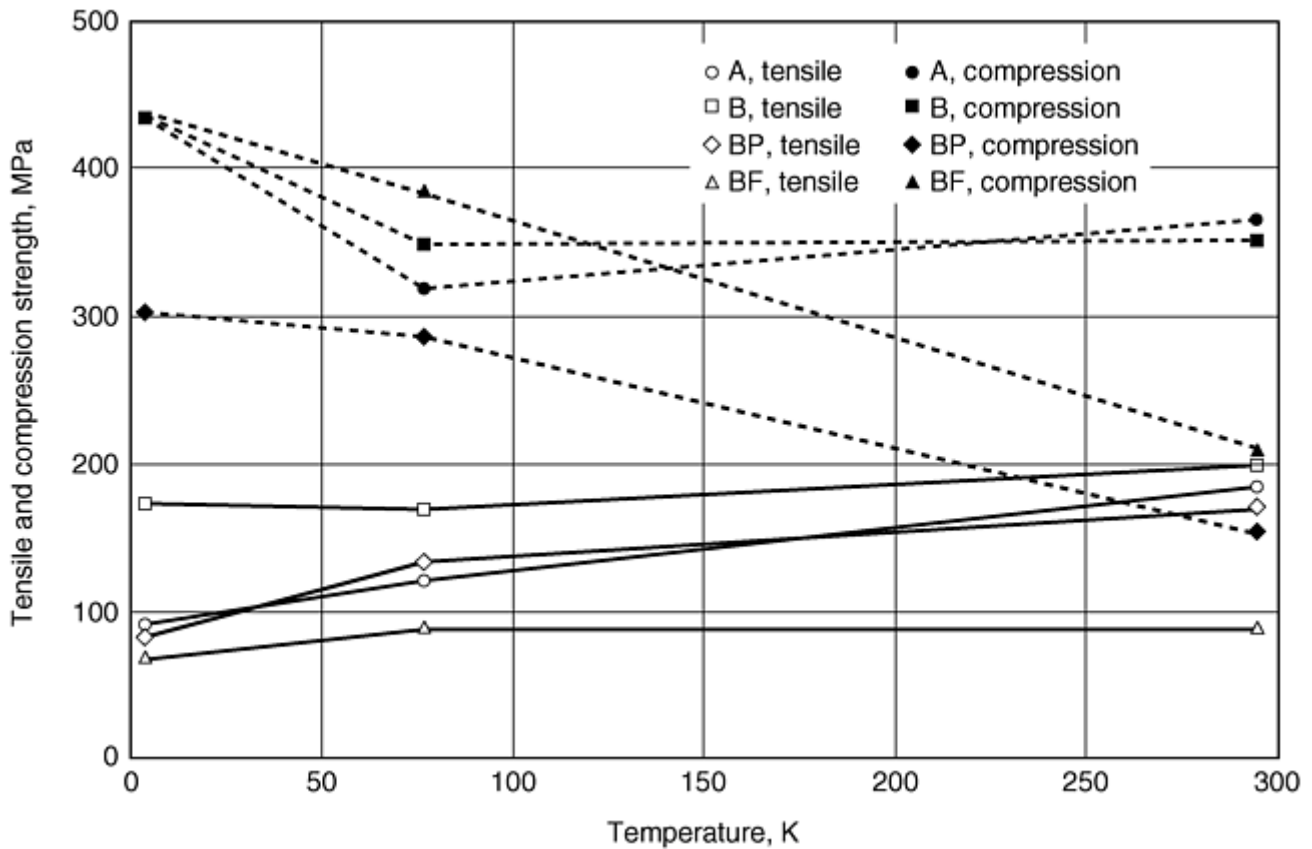


Fig. 8 A comparison of the effect of temperature on tensile and compressive properties of some high strength polymers. A, polyphenylene; B, modified polyphenylene; BF, chopped fiber-reinforced polyphenylene; and BP, polyphenylene with plasticizer

Compression tests of FRP composites are governed by ASTM D 3410, “Standard Test Method for Compressive Properties of Polymer Matrix Composite Materials with Unsupported Gage Section by Shear Loading.” This standard is for high-modulus composites where the elastic modulus of the composite is greater than 21 GPa. The test standard has three test procedures within it. Procedure A uses a compression test fixture commonly called the Celanese compression fixture. This test fixture has been applied to low-temperature tests described in Ref 16. Test procedure B is similar but uses a different test fixture, commonly called the IITRI (Illinois Institute of Technology Research Institute) fixture. Test procedure C is a sandwich beam test where the beam is loaded in four-point bending. All three-test procedures are rather compact and well suited for low-temperature testing. The Celanese and IITRI fixtures are rather heavy and take some time to heat and cool. This is a consideration when repetitive testing is to be done at low temperature. These two fixtures also have alignment sleeves or pins that may have a tendency to freeze at low temperatures due to differential thermal contractions and/or due to ice. The sandwich beam test specimen is rather small and may be well suited for low-temperature tests.

References cited in this section

16. R.P. Walsh, J.D. McColskey, and R.P. Reed, Low Temperature Properties of a Unidirectionally Reinforced Epoxy Fibreglass Composite, *Cryogenics*, Vol 35 (No. 11), 1995, p 723–725
17. N.R. Adsit, Compression Testing of Graphite Epoxy, *Compression Testing of Homogeneous Materials and Composites*, STP 808, R. Chait and R. Papirno, Ed., ASTM, 1983, p 175–186
18. V.J. Toplosky, R.P. Walsh, S.W. Tozer, and F. Motamedi, Mechanical and Thermal Properties of Unreinforced and Reinforced Polyphenylenes at Cryogenic Temperatures, *Advances in Cryogenic Engineering*, Vol 46, Plenum Press, NY, 1999

Tension and Compression Testing at Low Temperatures

Robert P. Walsh, National High Magnetic Field Laboratory, Florida State University

Temperature Control

Test temperature is controlled by a bath temperature or by controlling the temperature of a gaseous environment. The temperature of the test specimen should be maintained ± 1 K for the duration of the test. For bath-cooled tests, the temperature of the bath and the specimen should be the same. A potential source for error is the conduction path or heat sink that the load train provides, possibly causing the specimen to be warmer than the bath. For tests at temperatures below 77 K (typically 4 K tests), the test cryostat is precooled with liquid nitrogen as an economical time-saving step.

The temperature of the specimen is usually monitored for tests using gaseous environment temperature control. The temperature should be measured at the gage section and at the gripped ends to ensure that the temperature across the length of the specimen is constant. For temperatures above 80 K, the cooling can be a static method, such as a pool of liquid nitrogen in the dewar below the test fixturing. Test temperatures below the liquid nitrogen bath temperature are best accomplished through the use of cold helium gas for cooling power. This can be accomplished with a flow cryostat, where cooling power is regulated by throttling the flow of the cold gas or liquid. Between the manual regulation of the cooling medium and the regulated heater power, one can obtain constant test temperatures between 77 and 4 K. Variations of cryogenic temperature control exist such as cryogenic refrigerators, which can be applied to the temperature control of mechanical tests. Cryocoolers and other mechanical refrigeration techniques are not commonly used in mechanical tests, due to the initial capital expense and the relative simplicity of other cooling methods.

Tension and Compression Testing at Low Temperatures

Robert P. Walsh, National High Magnetic Field Laboratory, Florida State University

Safety

Safety in a laboratory or industrial setting is always a concern. Some of the safety issues with respect to low-temperature testing are common sense issues, while some others are not so obvious. Table 1 describes the most common safety issues and appropriate solutions for each. Safety issues associated with the use of liquid hydrogen or liquid oxygen are not dealt with in this article and can be found in Ref 10. In addition to the issues listed in Table 1, personnel should consider general safety issues related to tension and compression testing at all temperature ranges.

Table 1 Safety issues associated with the use of liquid cryogens for low-temperature testing

Safety issue	Solution
Liquid cryogens can spill or splash onto the body and cause freezing of human tissue.	Personnel should wear appropriate clothing and avoid direct contact with cold parts.
Helium, nitrogen, or carbon dioxide can displace air in a confined area.	Cryogens should be used only in well-ventilated areas.
Volumetric expansion is extremely high (typically 700–1000 times) when a liquid cryogen vaporizes. Such expansion is dangerous when it occurs in closed containers or fixture components with potential for trapped gas/liquid volumes.	Cryostats must include safety pressure-relief capabilities; redundancy is necessary because mechanical relief valves may freeze or malfunction. Component parts such as tubes or threaded connections that can trap liquids or gases should be identified, and

	solutions (such as weep holes) included in the design. If there is potential for liquid to get into a space, provide exit relief rather than trying to seal the liquid out.
Oxygen-rich (flammable) condensation can form on chilled surfaces (surfaces that are chilled to temperatures below 90 K and then exposed to air; common on uninsulated liquid nitrogen transfer lines and inside open-mouth dewars containing liquid nitrogen or helium residue).	Inform personnel of potential fire hazard, and take appropriate precautions.
Low temperatures may cause embrittlement of the material, causing it to fail at lower-than-expected loads.	Test personnel must be aware of the potential and prepare for brittle fracture of structural components.

Reference cited in this section

10. J.H. Lieb and R.E. Mowers, Testing of Polymers at Cryogenic Temperatures, *Testing of Polymers*, J.V.Schmitz, Ed., Vol 2, John Wiley & Sons, 1965, p 84–108

Tension and Compression Testing at Low Temperatures

Robert P. Walsh, National High Magnetic Field Laboratory, Florida State University

References

1. E.R. Parker, *Brittle Behavior of Engineering Structures*, John Wiley & Sons, 1957
2. R.P. Reed and A.F. Clark, Ed., *Materials at Low Temperatures*, ASM, 1983
3. L.E. Neilsen and R.F. Landel, Mechanical Properties of Polymers and Composites, Marcel Dekker, NY, 1994, p 249–263
4. M.B. Kasen et al., Mechanical, Electrical, and Thermal Characterization of G-10CR and G-11CR Glass-Cloth/Epoxy Laminates Between Room Temperature and 4 K, *Advances in Cryogenic Engineering*, Vol 28, 1980, p 235–244
5. R.P. Reed and M. Golda, Cryogenic Properties of Unidirectional Composites, *Cryogenics*, Vol 34 (No. 11), 1994, p 909–928
6. E.P. Popov, *Mechanics of Materials*, 2nd ed., Prentice-Hall, NJ, 1976
7. J.P Hirth and M. Cohen, *Metall. Trans.*, Vol 1, Jan 1970, p 3
8. G. Hartwig and F. Wuchner, Low Temperature Mechanical Testing Machine, *Rev. Sci. Instrum.*, Vol 46, 1975, p 481–485
9. R.P. Reed, A Cryostat for Tensile Test in the Temperature Range 300 to 4 K, *Advances in Cryogenic Engineering*, Vol 7, Plenum Press, NY, 1961, p 448–454
10. J.H. Lieb and R.E. Mowers, Testing of Polymers at Cryogenic Temperatures, *Testing of Polymers*, J.V.Schmitz, Ed., Vol 2, John Wiley & Sons, 1965, p 84–108

11. R.P. Reed and R.L. Durcholz, Cryostat and Strain Measurement for Tensile Tests to 1.5 K, *Advances in Cryogenic Engineering*, Vol 15, Plenum Press, NY, 1970, p 109–116
12. C. Ferrero, Stress Analysis Down to Liquid Helium Temperature, *Cryogenics*, Vol 30, March 1990, p 249–254
13. R.P. Reed and R.P. Walsh, Tensile Strain Effects in Liquid Helium, *Advances in Cryogenic Engineering*, Vol 34, Plenum Press, 1988, p 199–208
14. C.C. Perry, Strain Gage Reinforcement Effects on Low Modulus Materials, *Manual on Experimental Methods for Mechanical Testing of Composites*, R.L. Pendelton and M.E. Tuttle, Ed., Society for Experimental Mechanics, 1989, p 35–38
15. R.P. Reed and R.P. Walsh, Tensile Properties of Resins at Low Temperatures, *Advances in Cryogenic Engineering*, Vol 40, Plenum Press, NY, 1994, p 1129–1136
16. R.P. Walsh, J.D. McColskey, and R.P. Reed, Low Temperature Properties of a Unidirectionally Reinforced Epoxy Fibreglass Composite, *Cryogenics*, Vol 35 (No. 11), 1995, p 723–725
17. N.R. Adsit, Compression Testing of Graphite Epoxy, *Compression Testing of Homogeneous Materials and Composites*, STP 808, R. Chait and R. Papirno, Ed., ASTM, 1983, p 175–186
18. V.J. Toplosky, R.P. Walsh, S.W. Tozer, and F. Motamedi, Mechanical and Thermal Properties of Unreinforced and Reinforced Polyphenylenes at Cryogenic Temperatures, *Advances in Cryogenic Engineering*, Vol 46, Plenum Press, NY, 1999

Bend Testing

Eugene Shapiro, Olin Corporation

Introduction

BEND TESTS are conducted to determine the ductility or strength of a material. The tests typically used are discussed in this article with details on test methods, apparatuses, procedures, specimen preparation, and interpretation and reporting of results. The section “Bending Ductility Tests” also includes representative test data for many metals.

Bend tests for ductility differ fundamentally from other mechanical tests in that most mechanical tests are designed to give a quantitative result and have an objective endpoint. In contrast, bending ductility tests give a pass/fail result with a subjective endpoint; the test operator judges whether a surface has undergone cracking.

The bending ductility test developed as a shop-floor material inspection test because of its pass/fail qualities and the simplicity and low cost of the required tooling. As a consequence, the development of bending ductility test methods and apparatuses has been carried out by users rather than by mechanical-test equipment manufacturers.

Test procedures and specimen preparation methods have evolved without close attention to detail. Therefore, despite the value of the test and its long history of use, there has been minimal standardization. There are, however, two ASTM standards—ASTM E 190, “Standard Test Method for Guided Bend Test for Ductility of Welds” (Ref 1), and ASTM E 290, “Standard Test Method for Semi-Guided Bend Test for Ductility of Metallic Materials” (Ref 2)—which provide guidelines for testing strip, sheet, plate, and weldments.

Tests for determining the bending strength of metals have not been used widely, although the information from such tests is clearly useful. ASTM E 855, “Standard Methods of Bend Testing of Metallic Flat Materials for Spring Applications” (Ref 3), discusses the techniques for determining the bending strength of metal. These testing methodologies are described extensively in this article with greater emphasis on interpretation and analysis. Also included are descriptions of methods used in Europe and Japan. Finally, a section on computerized testing is included.

Bending tests that have been developed for brittle materials, coatings, construction (girder and beam) sections, and other specific product forms are not covered in this article. However, descriptions of these test methods can be found in the ASTM standards.

References cited in this section

1. “Standard Test Method for Guided Bend Test for Ductility of Welds,” ASTM E 190, *Annual Book of ASTM Standards*, Vol 03.01, ASTM, 1984, p 336–339
2. “Standard Test Method for Semi-Guided Bend Test for Ductility of Metallic Materials,” ASTM E 290, *Annual Book of ASTM Standards*, Vol 03.01, ASTM, 1984, p 430–434
3. “Standard Test Methods of Bend Testing of Metallic Flat Materials for Spring Applications Involving Static Loading,” ASTM E 855, *Annual Book of ASTM Standards*, Vol 03.01, ASTM, 1998, p 640–647

Bend Testing

Eugene Shapiro, Olin Corporation

Bending Ductility Tests

Frank N. Mandigo, Olin Corporation

Bending ductility tests determine the smallest radius around which a specimen can be bent without cracks being observed in the outer fiber (tension) surface. This forming limit commonly is called the minimum bend radius and is expressed in multiples of specimen thickness, t . A material with a minimum bend radius of $3t$ can be bent without cracking through a radius equal to three times the specimen thickness. It thus follows that a material with a minimum bend radius of $1t$ has greater ductility than a material with minimum bend radius of $5t$. Alternatively, the bend radius can be fixed, and the angle of bend at which fracture occurs noted. Figure 1 illustrates bend radius, angle of bend, and other concepts associated with bending tests.

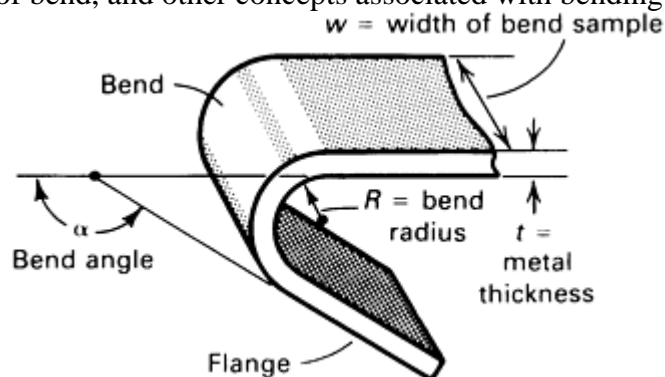


Fig. 1 Terms used in bend testing

This article describes apparatuses, specimen, preparation, and test procedures used in bending ductility testing. Bending tests are usually performed on strip, sheet, or plate; however, the same methods and apparatuses can be

used to evaluate the bending ductility of other product forms (drawn or extruded rounds, squares, or polygonal shapes) and of weldments.

Evaluating and reporting results of bending tests are also discussed. This discussion includes a description of failure criteria, strain distribution, directionality, and factors that affect bend ductility. Finally, a compilation of bend data for select engineering materials is presented.

Bend Testing

Eugene Shapiro, Olin Corporation

Apparatuses

Bending test apparatuses include wrap, wipe, V-block, and soft tooling devices that may have interchangeable die radii and are able to bend test specimens to several preset angles. The pins, mandrels, rollers, radiused flats, and clamping devices must be longer than the specimen width, and they must be strong and rigid enough to resist deformation and wear. Descriptions of basic types of bending devices follow.

Wrap bending devices (Fig. 2) grip the test specimen at one end; a mandrel, reaction pin, or block with the desired bend radius is positioned at midlength. A roller that sweeps concentrically around the bend radius applies the bending force. The distance from the mandrel to the loading roller generally is equal to the thickness or diameter of the test piece, plus clearance. The clearance is adjusted to allow the test specimen to bend to the desired radius or angle without scuffing, smearing, or galling of strip and die surfaces.

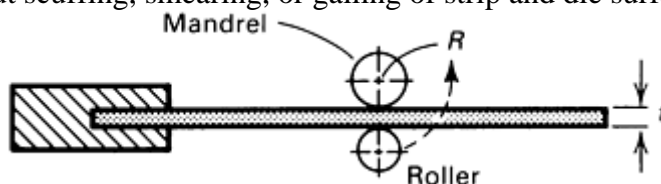


Fig. 2 Wrap bending device. Bending force is applied by a roller that sweeps concentrically around the bend radius.

Wipe bending devices (Fig. 3) are similar to wrap bending devices, except that the bending force is applied by a mandrel or roller that moves perpendicular to the clamped specimen.

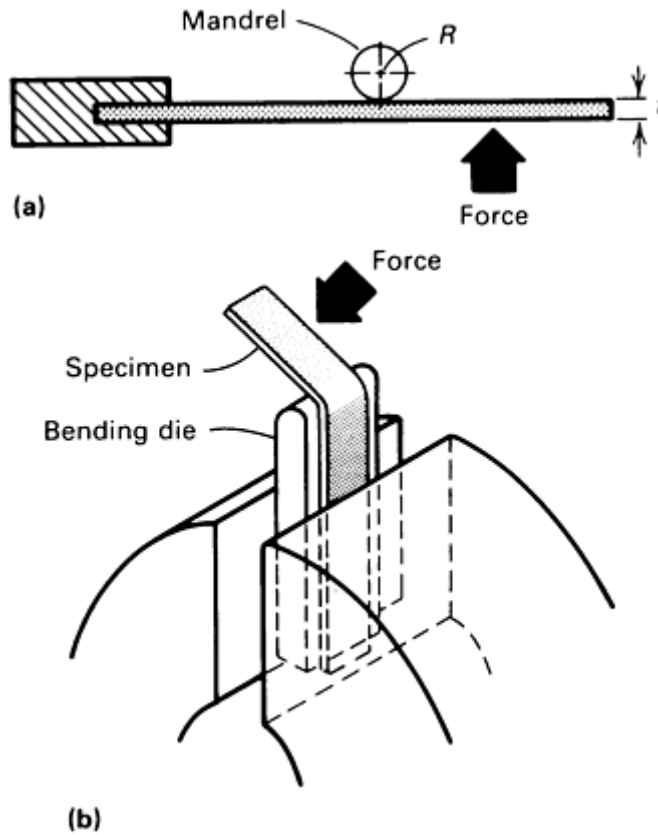


Fig. 3 Wipe bending devices. (a) Mandrel type with force applied near free end. (b) Die type with force applied near free end

V-block bending devices consist of a mandrel and a bottom block (Fig. 4a) or specimen supports (Fig. 4b). The sample rests on supports or on the bottom block and is not clamped during the test. The distance between supports is selected to force the specimen to conform to the mandrel radius without excessive interference. This clearance is often the mandrel diameter, d , plus three times the specimen thickness, t . Bending force is applied at the center of the specimen. The bottom block normally is a V or U shape. Bends made with conforming bottom block radii are bottoming or closed-die bends (Fig. 4a); those without conforming bottom block radii are air or free bends (Fig. 4b).

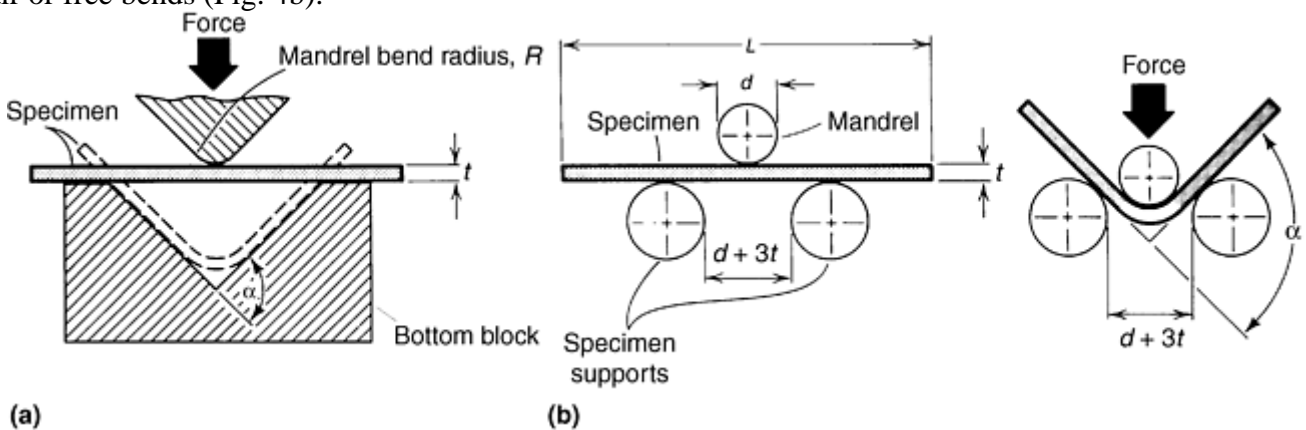


Fig. 4 V-block bending devices. (a) Closed V-block. (b) Open V-block

Soft tool bending, or rubber pad bending, is similar to V-block bending, except that the bottom block is replaced by highly compressible materials such as polyurethane. Figure 5 illustrates various setups for soft tool bending.

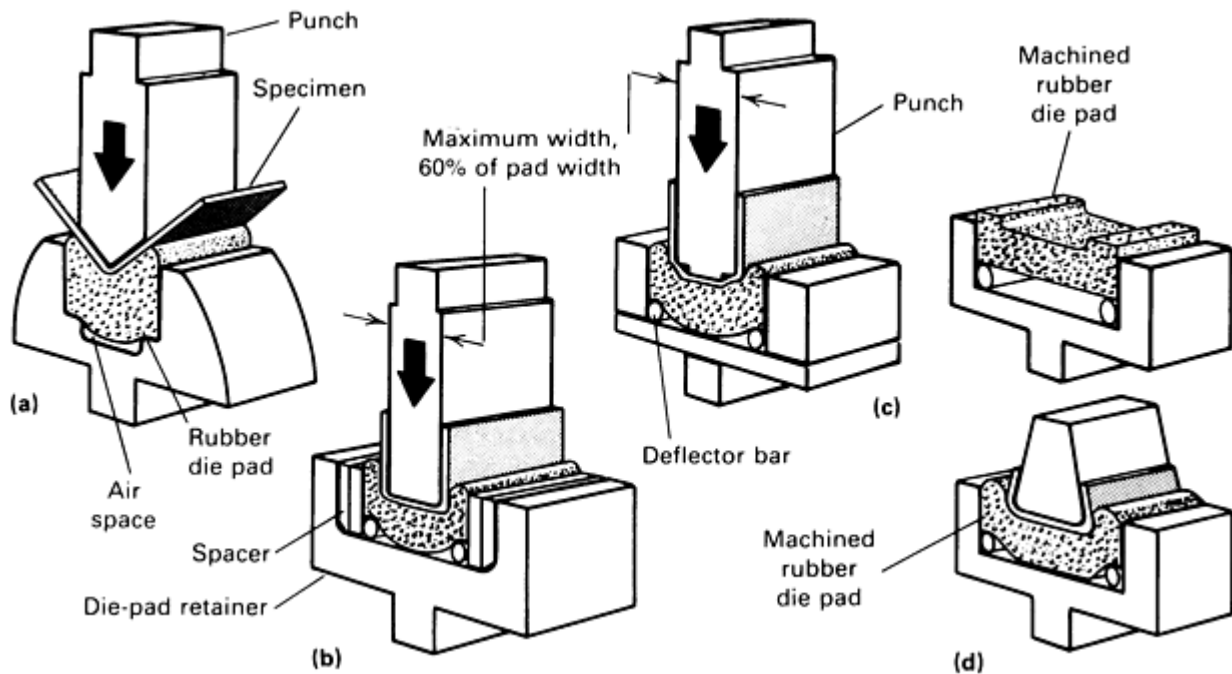


Fig. 5 Setups for soft tool (rubber pad) bending of sheet metal. (a) Simple 90° V-bend. Air space below die pad permits deep penetration. (b) Simple U-bend or channel. Spacers enable U-bends of varying widths to be formed in the same die-pad retainer. Deflector bars help provide uniform distribution of punch pressure. (c) Modified U-bend with partial air bending. (d) Acute-angle U-bend. High side pressures are obtained by using a conforming rubber die pad and deflector bars.

Bend Testing

Eugene Shapiro, Olin Corporation

Specimen Preparation

Sheet and plate specimens normally are full thickness and are prepared by shearing or sawing. Narrow strip and bar sections can be tested with specimens cut to length. For polygonal shapes, it is sometimes necessary to machine or grind a flat, with the unmachined surface to be placed on the tension side of the bend. The rough edges of cut samples can be removed by processes such as belt sanding and filing. The edges of rectangular-section test pieces can be rounded to a radius up to one tenth of the sample thickness. Edge preparation is not required for specimens with width-to-thickness ratios (w/t) greater than 8 to 1, unless cracking initiates from the edge during bending.

A specimen can be machined to fit if it is too thick for the bending device or if the required bending forces exceed the capacity of the bending device. The unmachined surface is placed on the tension side. If reduced thickness samples are used, the specimen dimensions must be held constant during testing and noted in the test report.

Specimens must be long enough to be clamped securely to prevent slippage in wrap and wipe tests. Specimens for V-block and soft tool bending can be of any length greater than the distance between specimen supports (Fig. 4b).

Test specimens usually are cut parallel or perpendicular to the direction of rolling, drawing, or extrusion. However, any orientation in the plane of the product width and length can be tested. Specimen dimensions should be the same for any test orientation. Figure 6 shows the orientation of a bending test specimen with the rolling direction for a longitudinal orientation and a transverse orientation. The transverse orientation generally

produces lower ductility because the tensile bending stresses are oriented perpendicular to the fiber structure developed by the rolling procedure used to produce sheet and plate products.

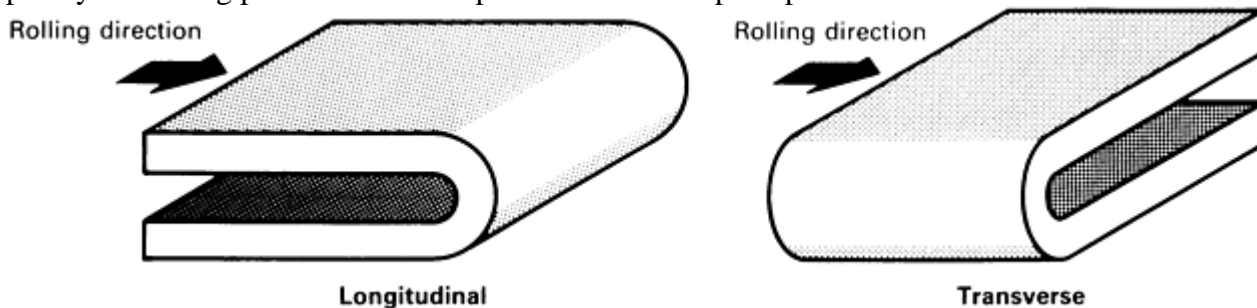


Fig. 6 Relative orientation of longitudinal and transverse bending tests

Cold rolling oils or other protective coatings usually are left on specimens to serve as a lubricating film during bending tests. Other lubricants can be used if they reflect field conditions.

The principal stress and strain directions developed during bending are defined in Fig. 7(a). The specimen width-to-thickness ratio (w/t) determines the respective stress and strain states. At $w/t > 8$, bending occurs under plane-strain conditions ($\epsilon_2 = 0$ and $\sigma_2/\sigma_1 = 0.5$) and bend ductility is independent of the exact width-to-thickness ratio (Fig. 7b). At $w/t < 8$, bending occurs under plane-stress conditions ($\sigma_2/\sigma_1 < 0.5$) with plastic deformation in all principal strain directions, and the measured bend ductility is strongly dependent on the width-to-thickness ratio (Fig. 7b). Therefore, bending tests are conducted at width-to-thickness ratios greater than 8 to 1 whenever possible to eliminate geometric effects on the test results. Although specimens with width-to-thickness ratios less than 8 to 1 can be tested, the entire test lot must have the same width-to-thickness ratio.

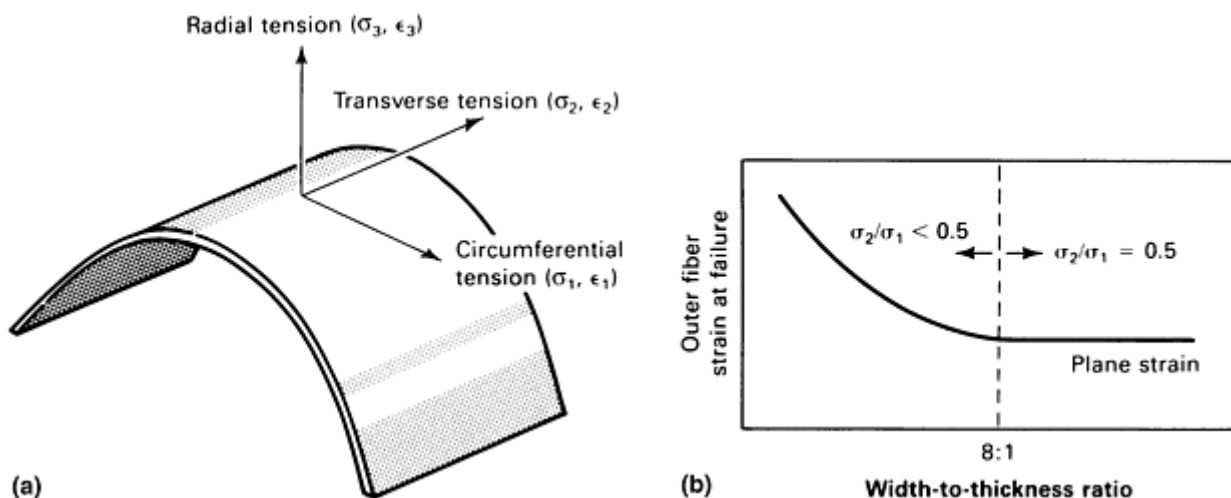


Fig. 7 Stress and strain in bending. (a) Schematic of the bend region defining the direction of principal stresses and strains. (b) Outer fiber strain at fracture versus width-to-thickness ratio

Bend Testing

Eugene Shapiro, Olin Corporation

Test Method

Specimens and apparatuses should be carefully inspected. Specimens with scuff marks, scratches, excessive curvature, twisting, or other surface defects should be discarded. Bend radii, mandrels, and support blocks must be free of scuff marks or other visible damage.

In bending tests, specimens are bent around progressively tighter radii, or to large bend angles, until failure or cracking occurs on the convex surface. If wipe or wrap bending apparatus is used, the clearance must be adjusted for each radius. Any method can be used to force the specimen to obtain the desired radius or angle; however, it must be applied slowly and steadily without significant lateral motion. Bend angles of 180° are obtained by pressing bent specimens between platens (Fig. 8), maintaining the bend radius with a spacer block twice as thick as the radius between the legs of the specimen.

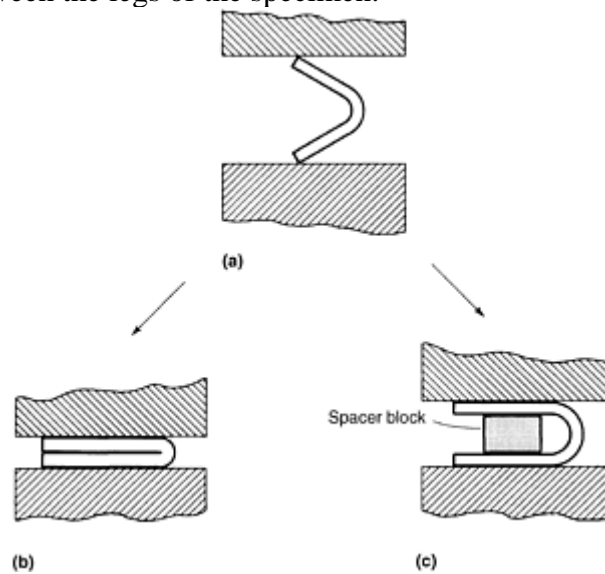


Fig. 8 Methods used to develop 180° bend angles. (a) Bend sample from wipe or V-block placed between platens. (b) Sharp (180°) bend. (c) Bend with radius equal to one-half the spacer-block thickness

During bending, the specimen can be removed to inspect the convex surface for cracks. The test is complete when product specifications have been achieved.

Bend Testing

Eugene Shapiro, Olin Corporation

Interpretation

Specimens are examined for cracking at the apex of the bend with magnifications of up to $20\times$. A specimen is acceptable if there are no visible cracks on its outside surface. Surface rumples and orange peeling are not considered fracture sites. If cracking occurs at the edges of the bent sample when the specimen width-to-thickness ratio is 8 to 1 or greater, the edges of the sample should be polished or ground and the specimen retested. At width-to-thickness ratios less than 8 to 1, edge preparation may be required to obtain reproducible measurements of minimum bend radii.

The bending method can influence the strain distribution on the surface of the specimen (Fig. 9). V-block bending (Fig. 9b) develops a nonuniform strain distribution, while wrap or wipe bending produces strain that increases progressively with the bend angle until saturation. Circumferential strain becomes uniform only after the bend angle exceeds certain minimum values (Fig. 10 and 11). For wipe or wrap bending, these values are a 90° bend angle and a $1t$ radius.

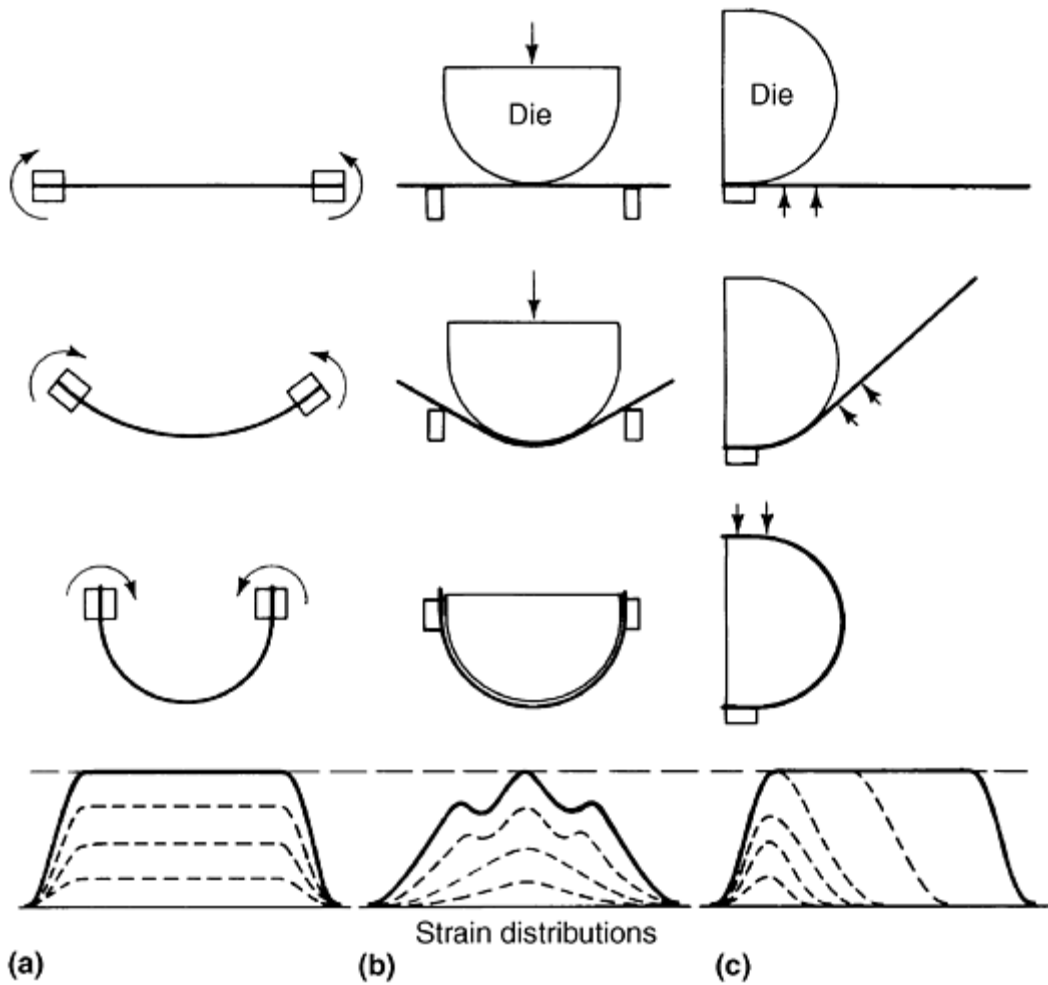


Fig. 9 Comparison of strain distributions produced by different bending methods. (a) Application of a pure bending moment (not achievable in commercial bending devices). (b) V-block bending. (c) Wipe bending

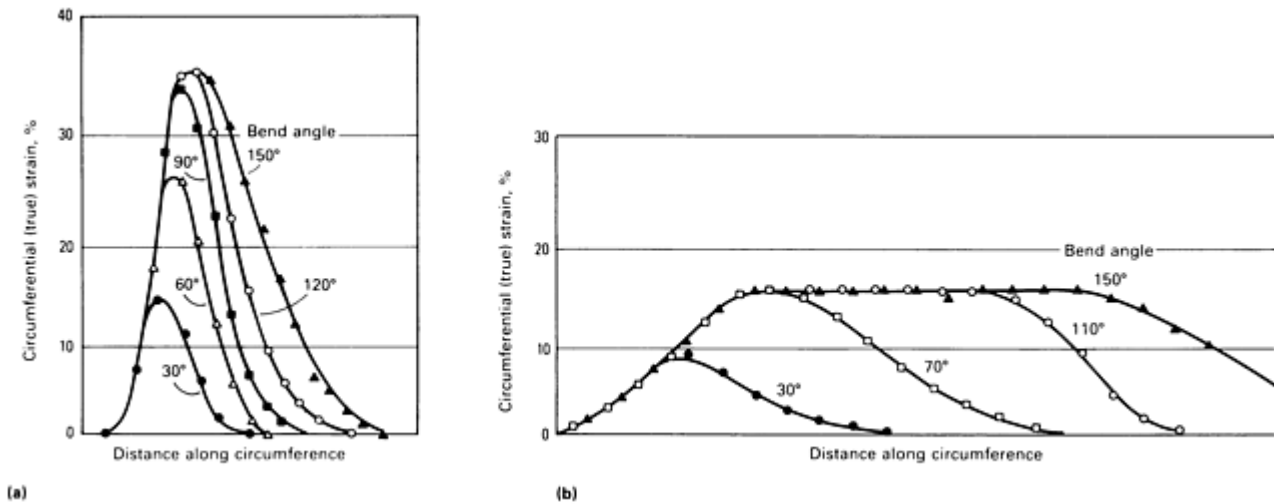


Fig. 10 Effect of bend angle on strain distribution along the circumference of bends for tempered aluminum alloy 2024 sheet. (a) 3.2 mm (0.125 in.) thick sheet, $R/t = 0.7$. (b) 6.4 mm (0.25 in.) thick sheet, $R/t = 2.5$

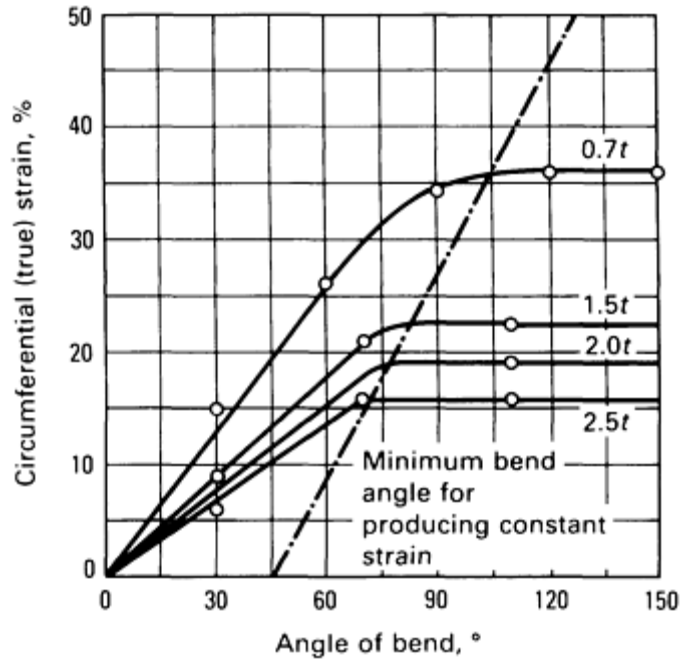


Fig. 11 Dependence of measured circumferential strain on bend angle for tempered aluminum alloy 2024 sheet. Radius expressed in terms of thickness, t

Minimum bend radii reported are subjective measurements, not intrinsic material properties. This subjectivity is due to visual assessment of pass/fail criteria and the incremental steps of the available bend radii. The problems associated with visual assessment include reproducibility by one tester over time and the difficulty of two or more testers agreeing on the definition of a visible crack. The problems associated with the incremental steps of the bend radii can be minimized by using closely spaced bend radii.

A number of characteristics can be expected when performing bending tests on metallic materials. The minimum bend radius is dependent on alloy composition. The minimum bend radius increases as strip or bar temper increases. Annealed strips generally have isotropic bend characteristics in the plane of the sheet (the minimum bend radii are similar both parallel or perpendicular to the process direction). Strips in highly cold-rolled tempers usually have better bend properties when bends are made perpendicular to the rolling direction. For a given alloy and temper, the minimum bend radius usually is directly proportional to strip thickness, as indicated in the following equation:

$$\frac{\text{Minimum bend radius}}{\text{Strip thickness}} = \text{Constant}$$

Because of these characteristics, caution should be used in choosing a bending test method or using tabulated data. The best practice is to use the same test method, specimen dimensions, bend angle, and bend radii that are used during part fabrication. Representative data for aluminum and ferrous sheet are provided in Tables 1, 2, 3, and 4.

Table 1 Recommended minimum bend radii for 90° cold forming of aluminum alloy sheet and plate

Alloy	Temper	Radii for various thicknesses expressed in terms of thickness, t							
		0.4 mm $\frac{1}{64}$ in.)	0.8 mm $\frac{1}{32}$ in.)	1.6 mm $\frac{1}{16}$ in.)	3.2 mm $\frac{1}{8}$ in.)	4.8 mm $\frac{3}{16}$ in.)	6.4 mm $\frac{1}{4}$ in.)	9.5 mm $\frac{3}{8}$ in.)	12.7 mm $\frac{1}{2}$ in.)
1100	O	0	0	0	0	$\frac{1}{2}t$	$1t$	$1t$	$\frac{1}{12}t$
	H12	0	0	0	$\frac{1}{2}t$	$1t$	$1t$	$\frac{1}{12}t$	$2t$
	H14	0	0	0	$1t$	$1t$	$\frac{1}{12}t$	$2t$	$\frac{1}{2}t$
	H16	0	$\frac{1}{2}t$	$1t$	$\frac{1}{12}t$	$\frac{1}{12}t$	$\frac{1}{22}t$	$3t$	$4t$

	H18	$1t$	$1t$	$\frac{1}{12t}$	$\frac{1}{22t}$	$3t$	$\frac{1}{2t}$	$4t$	$\frac{1}{42t}$
2014	O	0	0	0	$\frac{1}{2t}$	$1t$	$1t$	$\frac{1}{22t}$	$4t$
	T3	$\frac{1}{12t}$	$\frac{1}{22t}$	$3t$	$4t$	$5t$	$5t$	$6t$	$7t$
	T4	$\frac{1}{12t}$	$\frac{1}{22t}$	$3t$	$4t$	$5t$	$5t$	$6t$	$7t$
	T6	$3t$	$4t$	$4t$	$5t$	$6t$	$8t$	$8\frac{1}{2}t$	$9\frac{1}{2}t$
2024	O	0	0	0	$\frac{1}{2t}$	$1t$	$1t$	$\frac{1}{22t}$	$4t$
	T3	$\frac{1}{22t}$	$3t$	$4t$	$5t$	$5t$	$6t$	$7t$	$7\frac{1}{2}t$
	T361 ^(a)	$3t$	$4t$	$5t$	$6t$	$6t$	$8t$	$8\frac{1}{2}t$	$9\frac{1}{2}t$
	T4	$\frac{1}{22t}$	$3t$	$4t$	$5t$	$5t$	$6t$	$7t$	$7\frac{1}{2}t$
	T81	$\frac{1}{42t}$	$\frac{1}{52t}$	$6t$	$7\frac{1}{2}t$	$8t$	$9t$	$10t$	$10\frac{1}{2}t$
	T861 ^(a)	$5t$	$6t$	$7t$	$8\frac{1}{2}t$	$9\frac{1}{2}t$	$10t$	$11\frac{1}{2}t$	$11\frac{1}{2}t$
2036	T4	...	$1t$	$1t$
3003	O	0	0	0	0	$\frac{1}{2t}$	$1t$	$1t$	$\frac{1}{12t}$
	H12	0	0	0	$\frac{1}{2t}$	$1t$	$1t$	$\frac{1}{12t}$	$2t$
	H14	0	0	0	$1t$	$1t$	$\frac{1}{12t}$	$2t$	$\frac{1}{22t}$
	H16	$\frac{1}{2t}$	$1t$	$1t$	$\frac{1}{12t}$	$\frac{1}{22t}$	$3t$	$3\frac{1}{2}t$	$4t$
	H18	$1t$	$\frac{1}{12t}$	$2t$	$\frac{1}{22t}$	$3\frac{1}{2}t$	$4\frac{1}{2}t$	$5\frac{1}{2}t$	$6\frac{1}{2}t$
	3004	O	0	0	0	$\frac{1}{2t}$	$1t$	$1t$	$1t$
	H32	0	0	$\frac{1}{2t}$	$1t$	$1t$	$\frac{1}{12t}$	$\frac{1}{12t}$	$2t$
	H34	0	$1t$	$1t$	$\frac{1}{12t}$	$\frac{1}{12t}$	$\frac{1}{22t}$	$\frac{1}{22t}$	$3t$
	H36	$1t$	$1t$	$\frac{1}{12t}$	$\frac{1}{22t}$	$3t$	$\frac{1}{2t}$	$4t$	$\frac{1}{42t}$
	H38	$1t$	$\frac{1}{12t}$	$\frac{1}{22t}$	$3t$	$4t$	$5t$	$5\frac{1}{2}t$	$\frac{1}{62t}$
3105	H25	...	$\frac{1}{2t}$	$\frac{1}{2t}$
5005	O	0	0	0	0	$\frac{1}{2t}$	$1t$	$1t$	$\frac{1}{12t}$
	H12	0	0	0	$\frac{1}{2t}$	$1t$	$1t$	$\frac{1}{12t}$	$2t$
	H14	0	0	0	$1t$	$\frac{1}{12t}$	$\frac{1}{2t}$	$2t$	$\frac{1}{22t}$
	H16	$\frac{1}{2t}$	$1t$	$1t$	$\frac{1}{12t}$	$\frac{1}{22t}$	$3t$	$3\frac{1}{2}t$	$4t$
	H18	$1t$	$\frac{1}{12t}$	$2t$	$\frac{1}{22t}$	$3\frac{1}{2}t$	$4\frac{1}{2}t$	$5\frac{1}{2}t$	$6\frac{1}{2}t$
	H32	0	0	0	$\frac{1}{2t}$	$1t$	$1t$	$\frac{1}{12t}$	$2t$
	H34	0	0	0	$1t$	$\frac{1}{12t}$	$\frac{1}{12t}$	$\frac{1}{22t}$	$\frac{1}{22t}$
	H36	$\frac{1}{2t}$	$1t$	$1t$	$\frac{1}{12t}$	$\frac{1}{22t}$	$3t$	$3\frac{1}{2}t$	$4t$
	H38	$1t$	$\frac{1}{12t}$	$2t$	$\frac{1}{22t}$	$3\frac{1}{2}t$	$4\frac{1}{2}t$	$5\frac{1}{2}t$	$6\frac{1}{2}t$
	5050	O	0	0	0	$\frac{1}{2t}$	$1t$	$1t$...
	H32	0	0	0	$1t$	$1t$	$\frac{1}{12t}$
	H34	0	0	$1t$	$\frac{1}{12t}$	$\frac{1}{12t}$	$2t$

	H36	$1t$	$1t$	$\frac{1}{12t}$	$2t$	$\frac{1}{22t}$	$3t$
	H38	$1t$	$\frac{1}{12t}$	$\frac{1}{22t}$	$3t$	$4t$	$5t$
5052	O	0	0	0	$\frac{1}{2t}$	$1t$	$1t$	$\frac{1}{12t}$	$\frac{1}{12t}$
	H32	0	0	$1t$	$\frac{1}{12t}$	$\frac{1}{12t}$	$\frac{1}{12t}$	$\frac{1}{12t}$	$2t$
	H34	0	$1t$	$\frac{1}{12t}$	$2t$	$2t$	$\frac{1}{22t}$	$\frac{1}{22t}$	$3t$
	H36	$1t$	$1t$	$\frac{1}{12t}$	$\frac{1}{22t}$	$3t$	$\frac{1}{32t}$	$4t$	$\frac{1}{42t}$
	H38	$1t$	$\frac{1}{12t}$	$\frac{1}{22t}$	$3t$	$4t$	$5t$	$\frac{1}{52t}$	$\frac{1}{62t}$
5083	O	$\frac{1}{2t}$	$1t$	$1t$	$1t$	$\frac{1}{12t}$	$\frac{1}{12t}$
	H321	$1t$	$\frac{1}{12t}$	$\frac{1}{12t}$	$\frac{1}{12t}$	$2t$	$\frac{1}{22t}$
5086	O	0	0	$\frac{1}{2t}$	$1t$	$1t$	$1t$	$\frac{1}{12t}$	$\frac{1}{12t}$
	H32	0	$\frac{1}{2t}$	$1t$	$\frac{1}{12t}$	$\frac{1}{12t}$	$2t$	$\frac{1}{22t}$	$3t$
	H34	$\frac{1}{2t}$	$1t$	$\frac{1}{12t}$	$2t$	$\frac{1}{22t}$	$3t$	$\frac{1}{32t}$	$4t$
	H36	$3t$	$\frac{1}{32t}$	$4t$	$\frac{1}{42t}$	$5t$
5154	O	0	0	$\frac{1}{2t}$	$1t$	$1t$	$1t$	$\frac{1}{12t}$	$\frac{1}{12t}$
	H32	0	$\frac{1}{2t}$	$1t$	$\frac{1}{12t}$	$\frac{1}{12t}$	$2t$	$\frac{1}{22t}$	$\frac{1}{32t}$
	H34	$\frac{1}{2t}$	$1t$	$\frac{1}{12t}$	$2t$	$\frac{1}{22t}$	$3t$	$\frac{1}{32t}$	$4t$
	H36	$1t$	$\frac{1}{12t}$	$2t$	$3t$	$\frac{1}{32t}$	$4t$	$\frac{1}{42t}$	$5t$
	H38	$\frac{1}{12t}$	$\frac{1}{22t}$	$3t$	$4t$	$5t$	$5t$	$\frac{1}{62t}$	$\frac{1}{62t}$
5252	H25	0	0	$1t$	$2t$
	H28	$1t$	$\frac{1}{12t}$	$\frac{1}{22t}$	$3t$
5254	O	0	0	$\frac{1}{2t}$	$1t$	$1t$	$1t$	$\frac{1}{12t}$	$\frac{1}{12t}$
	H32	0	$\frac{1}{2t}$	$1t$	$\frac{1}{12t}$	$\frac{1}{12t}$	$2t$	$\frac{1}{22t}$	$\frac{1}{32t}$
	H34	$\frac{1}{2t}$	$1t$	$\frac{1}{12t}$	$2t$	$\frac{1}{22t}$	$3t$	$\frac{1}{32t}$	$4t$
	H36	$1t$	$\frac{1}{12t}$	$2t$	$3t$	$\frac{1}{32t}$	$4t$	$\frac{1}{42t}$	$5t$
	H38	$\frac{1}{12t}$	$\frac{1}{22t}$	$3t$	$4t$	$5t$	$5t$	$\frac{1}{62t}$	$\frac{1}{62t}$
5454	O	0	$\frac{1}{2t}$	$1t$	$1t$	$1t$	$\frac{1}{12t}$	$\frac{1}{12t}$	$2t$
	H32	$\frac{1}{2t}$	$\frac{1}{2t}$	$1t$	$2t$	$2t$	$\frac{1}{22t}$	$3t$	$4t$
	H34	$\frac{1}{2t}$	$1t$	$\frac{1}{12t}$	$2t$	$\frac{1}{22t}$	$3t$	$\frac{1}{32t}$	$4t$
5456	O	$1t$	$\frac{1}{12t}$	$\frac{1}{12t}$	$2t$	$2t$
	H321	$2t$	$2t$	$\frac{1}{22t}$	$3t$	$\frac{1}{32t}$
5457	O	0	0	0	$\frac{1}{2t}$	$1t$	$1t$	$1t$	$\frac{1}{12t}$
5652	O	0	0	0	$\frac{1}{2t}$	$1t$	$1t$	$\frac{1}{12t}$	$\frac{1}{12t}$
	H32	0	0	1	$\frac{1}{12t}$	$\frac{1}{12t}$	$\frac{1}{12t}$	$\frac{1}{12t}$	$2t$
	H34	0	$1t$	$\frac{1}{12t}$	$2t$	$2t$	$\frac{1}{22t}$	$\frac{1}{22t}$	$3t$
	H36	$1t$	$1t$	$\frac{1}{12t}$	$\frac{1}{22t}$	$3t$	$\frac{1}{32t}$	$4t$	$\frac{1}{42t}$

	H38	$1t$	$\frac{1}{12}t$	$\frac{1}{22}t$	$3t$	$4t$	$5t$	$\frac{1}{52}t$	$\frac{1}{62}t$
5657	H25	0	0	0	$1t$
	H28	$1t$	$\frac{1}{12}t$	$\frac{1}{22}t$	$3t$
6061^(b)	O	0	0	0	$1t$	$1t$	$1t$	$\frac{1}{12}t$	$2t$
	T4	0	0	$1t$	$\frac{1}{12}t, \frac{1}{22}t$	$\frac{1}{22}t$	$3t$	$\frac{1}{32}t$	$4t$
	T6	$1t$	$1t$	$\frac{1}{12}t$	$\frac{1}{22}t$	$3t$	$\frac{1}{32}t$	$\frac{1}{42}t$	$5t$
7072	O	0	0
	H12	0	0
	H14	0	0
	H16	0	$\frac{1}{2}t$
	H18	$1t$	$1t$
7075^(b)	O	0	0	$1t$	$1t$	$\frac{1}{12}t$	$\frac{1}{22}t$	$\frac{1}{32}t$	$4t$
	T6	$3t$	$4t$	$5t$	$6t$	$6t$	$8t$	$9t$	$\frac{1}{92}t$
7178^(b)	O	0	0	$1t$	$\frac{1}{12}t$	$\frac{1}{12}t$	$\frac{1}{22}t$	$\frac{1}{32}t$	$4t$
	T6	$3t$	$4t$	$5t$	$6t$	$6t$	$8t$	$9t$	$\frac{1}{92}t$

(a) The radii listed are the minimum recommended for bending sheets and plates without fracturing in a standard press brake with air bend dies. Other bending operations may require larger radii or permit smaller radii. The minimum permissible radii also vary with the design and condition of the tooling.

(b) Tempers T361 and T861 formerly designated T36 and T86, respectively.

(c) Alclad sheet in the heat treatable alloys can be bent over slightly smaller radii than the corresponding tempers of the bare alloy.

Table 2 Maximum thicknesses of aluminum alloy sheet that can be cold bent 180° over zero radius

Alloy	Temper	Maximum sheet thickness	
		mm	in.
1100	O	3.2	$\frac{1}{8}$
	H12	1.6	$\frac{1}{16}$
	H14	1.6	$\frac{1}{16}$
	H16	0.4	$\frac{1}{64}$
Alclad 2014	O	1.6	$\frac{1}{16}$
2024	O	1.6	$\frac{1}{16}$
3003	O	3.2	$\frac{1}{8}$
	H12	1.6	$\frac{1}{16}$
	H14	1.6	$\frac{1}{16}$
3004	O	3.2	$\frac{1}{8}$
	H32	0.8	$\frac{1}{32}$
	H34	0.4	$\frac{1}{64}$
5005	O	3.2	$\frac{1}{8}$
	H12	1.6	$\frac{1}{16}$
	H14	1.6	$\frac{1}{16}$
	H32	3.2	$\frac{1}{8}$

	H34	0.8	$\frac{1}{32}$
5050	O	3.2	$\frac{1}{8}$
	H32	1.6	$\frac{1}{16}$
	H34	0.8	$\frac{1}{32}$
5052	O	3.2	$\frac{1}{8}$
	H32	0.8	$\frac{1}{32}$
	H34	0.4	$\frac{1}{64}$
5086	O	3.2	$\frac{1}{8}$
5154	O	1.6	$\frac{1}{16}$
	H32	0.8	$\frac{1}{32}$
5457	O	3.2	$\frac{1}{8}$
	H25	0.8	$\frac{1}{32}$
6061	O	1.6	$\frac{1}{16}$
	T4	0.8	$\frac{1}{32}$
7075	O	0.8	$\frac{1}{32}$

Table 3 Minimum bend radii for 1008 or 1010 steel sheet

Quality or temper	Minimum bend radius	
	Parallel to rolling direction	Across rolling direction
Cold rolled		
Commercial	0.25 mm (0.01 in.)	0.25 mm (0.01 in.)
Drawing, rimmed	0.25 mm (0.01 in.)	0.25 mm (0.01 in.)
Drawing, killed	0.25 mm (0.01 in.)	0.25 mm (0.01 in.)
Enameling	0.25 mm (0.01 in.)	0.25 mm (0.01 in.)
Cold rolled, special properties		
Quarter hard ^(a)	1t	$\frac{1}{2}$
Half hard ^(b)	NR	1t
Full hard ^(c)	NR	NR
Hot rolled		
Commercial	$\frac{3}{4}t$	$\frac{1}{2}t$
Up to 2.3 mm (0.090 in.)		
More than 2.3 mm (0.090 in.)	$1-\frac{1}{2}t$	1t
Drawing	$\frac{1}{2}t$	$\frac{1}{4}t$
Up to 2.3 mm (0.090 in.)		
More than 2.3 mm (0.090 in.)	$\frac{3}{4}t$	$\frac{1}{2}t$

(a) Note: t , sheet thickness; NR, not recommended.

(b) 60–75 HRB.

(c) 70–85 HRB.

(d) 84 HRB min

Table 4 Typical bending limits for six commonly formed stainless steels

Type	Minimum bend radius		
	Annealed to 4.7 mm (0.187 in.) thick (180° bend)	To 1.27 mm (0.050 in.) thick (180° bend)	Quarter hard, cold rolled 1.3 to 4.7 mm (0.051 to 0.187 in.) thick (90° bend)
301, 302, 304	$\frac{1}{2}t$	$\frac{1}{2}t$	$1t$
316	$\frac{1}{2}t$	$1t$	$1t$
410, 430	$1t$

Note: t , stock thickness

Introduction to Hardness Testing

Gopal Revankar, Deere & Company

Introduction

THE TERM HARDNESS, as it is used in industry, may be defined as the ability of a material to resist permanent indentation or deformation when in contact with an indenter under load. Generally a hardness test consists of pressing an indenter of known geometry and mechanical properties into the test material. The hardness of the material is quantified using one of a variety of scales that directly or indirectly indicate the contact pressure involved in deforming the test surface. Since the indenter is pressed into the material during testing, hardness is also viewed as the ability of a material to resist compressive loads. The indenter may be spherical (Brinell test), pyramidal (Vickers and Knoop tests), or conical (Rockwell test). In the Brinell, Vickers, and Knoop tests, hardness value is the load supported by unit area of the indentation, expressed in kilograms per square millimeter (kgf/mm^2). In the Rockwell tests, the depth of indentation at a prescribed load is determined and converted to a hardness number (without measurement units), which is inversely related to the depth.

Hardness tests are no longer limited to metals, and the currently available tools and procedures cover a vast range of materials including polymers, elastomers, thin films, semiconductors, and ceramics. Hardness measurements as applied to specific classes of materials convey different fundamental aspects of the material. Thus, for metals, hardness is directly proportional to the uniaxial yield stress at the strain imposed by the indentation. This statement, however, may not apply in the case of polymers, since their yield stress is ill defined. Yet hardness measurement may be a useful characterization technique for different properties of polymers, such as storage and loss modulus. Similarly, the measured hardness of ceramics and glasses may relate to their fracture toughness, and there appears to be some correlation between microhardness and compressive strength (Ref 1).

The consequence of material hardness also depends on its application in industry. For example, a fracture mechanics engineer may consider a hard material as brittle and less reliable under impact loads; a tribologist may consider high hardness as desirable to reduce plastic deformation and wear in bearing applications. A metallurgist would like to have lower hardness for cold rolling of metals, and a manufacturing engineer would prefer less hard materials for easy and faster machining and increased production. These considerations lead, during component design, to the selection of different types of materials and manufacturing processes to obtain the required material properties of the final product, which are, in many cases, estimated by measuring the hardness of the material.

Hardness, though apparently simple in concept, is a property that represents an effect of complex elastic and plastic stress fields set up in the material being tested. The microscopic events such as dislocation movements and phase transformations that may occur in a material under the indenter should not be expected to exactly repeat themselves for every indentation, even under identical test conditions. Yet experience has shown that the indentations produced under the same test conditions are macroscopically nearly identical, and measurements of their dimensions yield fairly repeatable hardness numbers for a given material. This observation by James A. Brinell in the case of a spherical indenter led to the introduction of the Brinell hardness test (Ref 2). This was followed by other tests (already mentioned) with unique advantages over the Brinell indenter, as described in the various articles of this Section.

Hardness testing is perhaps the simplest and the least expensive method of mechanically characterizing a material since it does not require an elaborate specimen preparation, involves rather inexpensive testing equipment, and is relatively quick. The theoretical and empirical investigations have resulted in fairly accurate quantitative relationships between hardness and other mechanical properties of materials such as ultimate tensile strength, yield strength and strain hardening coefficient (Ref 3, 4), and fatigue strength and creep (Ref 5). These relationships help measure these properties with an accuracy sufficient for quality control during the intermediate and final stages of manufacturing. Many times hardness testing is the only nondestructive test alternative available to qualify and release finished components for end application.

References cited in this section

1. R.W. Rice, *The Compressive Strength of Ceramics in Materials Science Research*, Vol 5, Ceramics in Severe Environments, W.W. Kriegel and H. Palmour III, Ed., Plenum, 1971, p 195–229
2. J.A. Brinell, *II Cong. Int. Méthodes d' Essai (Paris)*, 1900
3. M.O. Lai and K.B. Lim, *J. of Mater. Sci.*, Vol 26 (1991), p 2031–2036
4. S.C. Chang, M.T. Jahn, C.M. Wan, J.Y.M. Wan, and T.K. Hsu, *J. Mater. Sci.*, Vol 11, 1976, p 623
5. W. Kohlhöfer and R.K. Penny, *Int. J. Pressure Vessels Piping*, Vol 61, 1995, p 65–75

Introduction to Hardness Testing

Gopal Revankar, Deere & Company

Principles of Hardness Testing (Ref 6)

Brinell versus Meyer Hardness. In the Brinell hardness test, a hard spherical indenter is pressed under a fixed normal load onto the smooth surface of a material. When the equilibrium is reached, the load and the indenter are withdrawn, and the diameter of the indentation formed on the surface is measured using a microscope with a built-in millimeter scale. The Brinell hardness is expressed as the ratio of the indenter load W to the area of the concave (i.e., contact) surface of the spherical indentation that is assumed to support the load and is given as Brinell hardness number (BHN) denoted by HB. Thus:

$$HB = 2W / \pi D^2 \left[1 - \sqrt{1 - (d / D)^2} \right] \quad (\text{Eq 1})$$

where W is the load in kilograms, and d and D are the diameters of the indentation and the indenter, respectively, in millimeters.

However, BHN, though widely and universally accepted in manufacturing practice, is not considered a satisfactory concept, since it does not represent the mean pressure over the curved area (see the following discussion). Consideration of equilibrium of the indenter (sphere) under load would show (Ref 6) that the mean pressure over the indentation spherical area is given by load *divided* by the projected area of indentation, or:

$$P = W / (\pi d^2 / 4) \quad (\text{Eq 2})$$

where P is the Meyer hardness (Ref 7), also expressed in kilograms per square millimeter (kgf/mm^2). A more fundamental relationship between the load and the indentation diameter is given by Meyer's law, which states that:

$$W = cd^n \quad (\text{Eq 3})$$

where c and n are constants for a given material. The value of n generally varies between 2 and 2.5; it is approximately 2.6 for fully annealed metals and approximately 2.0 for fully cold worked metals. It may be mentioned here that fully annealed metals tend to work harden whereas the highly cold worked metals have a near ideal plastic behavior; that is, they do not work harden.

If D_1, D_2, D_3, \dots are the diameters of the indenters producing indentations of diameters d_1, d_2, d_3, \dots produced by the same load, then Meyer's law states that:

$$W = c_1 d_1^{n_1} = c_2 d_2^{n_2} = c_3 d_3^{n_3} = \dots \quad (\text{Eq 4})$$

Meyer determined experimentally that, for a given material, the value of n is almost independent of D , and that c and D are inversely related such that:

$$A = c_1 D_1^{n-2} = c_2 D_2^{n-2} = c_3 D_3^{n-2} \dots = \text{constant}$$

Equation 4 then becomes:

$$W = Ad_1^n/D_1^n = Ad_2^n/D_2^n \quad (\text{Eq 5})$$

$$= Ad_3^n/D_3^n \dots$$

This relationship may be expressed in two useful forms:

$$W/d^2 = A(d/D)^{n-2} \quad (\text{Eq 6})$$

and

$$W/D^2 = A (d/D)^n \quad (\text{Eq 7})$$

where A is a constant.

Equation 6 shows that, for geometrically similar indentations (see Fig. 1) for which d/D is fixed, the ratio W/d^2 , and, hence, Meyer hardness, which is proportional to this ratio, will be constant. Similarly, the Brinell hardness values, which are related to Meyer hardness through a constant, will also be constant. According to Eq 7, the indentations produced by using different values of W and D will be geometrically similar (i.e., $d/D = \text{a constant}$) and will give the same hardness values if the ratio W/D^2 is held constant. This concept is used in practical hardness measurements when the load, and, hence, D , need to be varied depending on the type of material and the shape and size of the component. Thus hardness values obtained using a 3000 kg load and 10 mm diameter ball would be practically the same as when a 750 kg load and a 5 mm diameter ball are used, since $W/D^2 = 30$ in both cases.

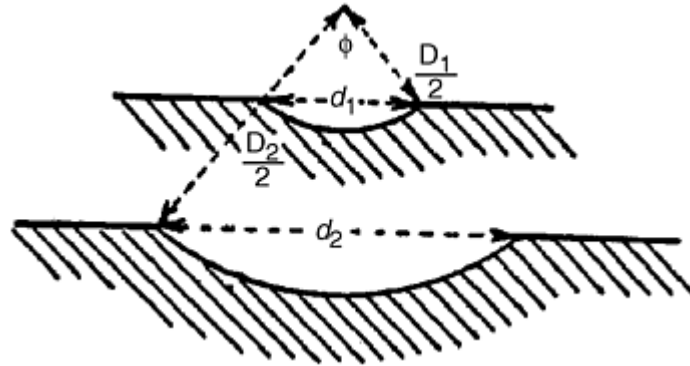


Fig. 1 Geometrically similar indentations produced by spherical indenters of different diameters. Note that the solid angle ϕ and the ratio d/D are the same for both the indentations

In the case of highly cold worked metals, it is experimentally observed that Meyer hardness is independent of the applied load; that is, the mean pressure resisting deformation is approximately constant. Brinell hardness, however, is nearly constant at smaller loads but decreases as the load is increased, indicating incorrectly that the materials soften at higher indentation loads. Similarly, for fully annealed metals (which undergo work hardening during the indentation process), Meyer hardness is found to increase steadily with load, suggesting the presence of work hardening. Brinell hardness would, however, rise at first and then fall as the load increases, again suggesting material softening. Meyer hardness, which is an expression of the mean yield pressure, is therefore considered a more appropriate and satisfactory measure of resistance to indentation (see also further discussion that follows and “Summary” in this article).

Plastic Deformation of Ideal Plastic Metals under an Indenter. The complex stresses set up in a material due to indentation and immediately next to the indenter can be resolved into three principal stresses, p_1 , p_2 , and p_3 , and it has been shown empirically that, for the onset of plastic deformation:

$$\frac{1}{3}[(p_1 - p_2)^2 + (p_2 - p_3)^2 + (p_3 - p_1)^2] = \text{constant} \quad (\text{Eq 8})$$

For uniaxial stresses as in a tensile test, $p_2 = p_3 = 0$ and $p_1 = Y$ at the onset of yielding, where Y is the yield stress. Equation 8 gives:

$$\frac{1}{3}(2 Y^2) = \frac{1}{3}(2 Y^2) = \text{constant}$$

This leads to the equation:

$$(p_1 - p_2)^2 + (p_2 - p_3)^2 + (p_3 - p_1)^2 = 2Y^2 \quad (\text{Eq 9})$$

which is the Huber-Mises criterion for the onset of plasticity.

An alternative criterion, due to Tresca and Mohr, is based on the assumption that plastic deformation occurs under the action of three principle stresses, $p_1 > p_2 > p_3$, when the maximum shear stress, $\frac{1}{2}(p_1 - p_3)$, exceeds a critical value. The value of this stress can be obtained, again, by considering uniaxial loading with $p_2 = p_3 = 0$, when the maximum shear stress is $\frac{1}{2}p_1$. Since $p_1 = Y$ at yielding:

$$\frac{1}{2}(p_1 - p_3) = \frac{1}{2}Y \text{ or}$$

$$p_1 - p_3 = Y, \text{ when } p_1 > p_2 > p_3 \quad (\text{Eq 10})$$

It may be shown for a two dimensional plastic flow, that is, under plane strain conditions of deformation, that $p_2 = \frac{1}{2}(p_1 + p_3)$, with zero strain in the direction of p_2 . Substituting this in Eq 9 yields:

$$p_1 - p_3 = (2/\sqrt{3})Y \quad (\text{Eq 11})$$

Thus, according to the Huber-Mises criterion, the plasticity under the indenter occurs when $(p_1 - p_3)$ reaches the value $(2/\sqrt{3})Y$ (or $1.15 Y$), which is 15% higher than that for Tresca or Mohr criterion.

When plastic strain occurs in a plane (plane strain), the system of stresses can be represented by the sum of a hydrostatic pressure, p , and a maximum shear stress, k , where $2k = 1.15 Y$ or Y (depending on the criterion chosen) at every point in the plastically deformed region of the material. Since the hydrostatic component does not produce deformation, only the shear stress may be considered responsible for the plastic strain. The stress field in the deformed material volume may therefore be represented by the maximum shear stresses in the form of slip lines (see Fig. 2). These lines should not be confused with the slip lines associated with dislocation movements under the action of stresses, which appear on the metal surface, or the dislocation images observed as lines in transmission electron microscopy.

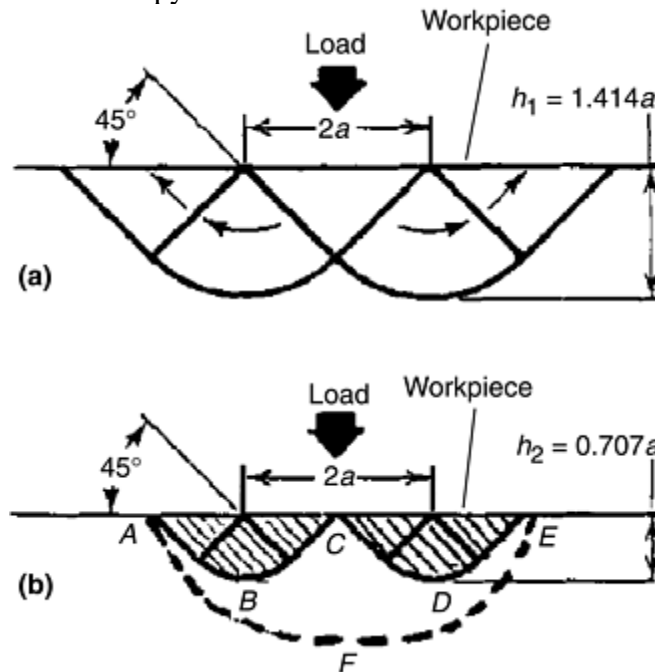


Fig. 2 Slip-line field solutions for a flat-ended, two-dimensional punch having a width $2a$. (a) Prandtl's flow pattern. Flow in the center area is downward and to the left and right, as indicated by arrows in the adjoining areas. (b) Hill's flow pattern. Flow is to left and right in directions indicated by arrows in (a), but is separated. The dashed line AFE has been added to 3(a) to approximately suggest areas of elastic-plastic and elastic strain regions. Strain between ABCDE and AFE is partly plastic and partly elastic, and that below AFE is mostly elastic. Source: Ref 6

Deformation of an Ideal Plastic Metal by a Flat Punch (Two Dimensional Deformation). The rigorous solutions for the problem of plastic indentation have been possible only for the case of a two-dimensional deformation. When a load is first applied to an infinitely long and rigid punch with uniform width and negligible thickness, the shear stresses in an ideal plastic metal at the punch edges *A* and *B* (Fig. 3) will be very high, and these points will reach a plasticity state much earlier than the rest of the contact length. As the load is increased, the plasticity region expands outward from these edges until it covers the whole width of the punch. The pressure on the punch face at this state of plastic deformation was first derived by Prandtl (Ref 8) and later by Hill (Ref 9) through the slip line analysis already mentioned, and the corresponding slip line patterns are shown in Fig. 2.

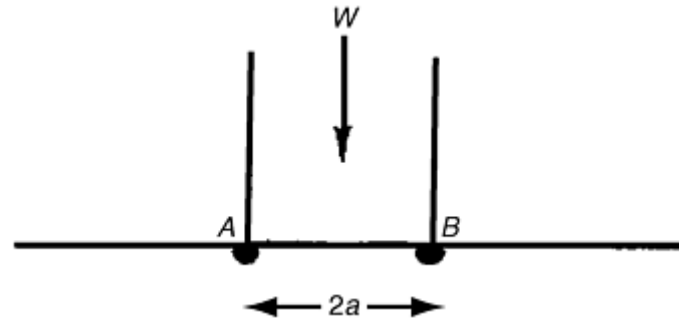


Fig. 3 Two-dimensional deformation (plain strain) of an ideal plastic semi-infinite metal by a rigid flat punch of width $2a$. The onset of plasticity occurs at the edges *A* and *B*. Source: Ref 6

The slip line analysis of plastic deformation shows that the mean normal pressure, P_m , on the punch is given by:

$$P_m = 2k(1 + \frac{1}{2}\pi) \quad (\text{Eq 12})$$

where k is the magnitude of maximum shear stress, equal to $Y/2$ if Tresca or Mohr criterion is used and $(1.15Y)/2$ if Huber-Mises criterion is used. The Tresca or Mohr criterion holds for fully annealed mild steel, whereas the Huber-Mises criterion is applicable to most other metals. The mean pressure on the punch, therefore, would be between $2.6Y$ and $3.0Y$. The shaded region in Fig. 2(b) represents the volume of plastic deformation where elastic strains may be neglected, and the region between *ABCDE* and *AFE* may be considered to have both plastic and elastic deformation. The volume below *AFE* may be considered a region of totally elastic strain.

An approximate extension of the above analysis for a two-dimensional flat punch to the case of a three-dimensional circular punch has shown that the pressure is not uniform over the area of the circular punch (as it is slightly higher at the center than at the edges) and that the mean pressure, P_m , over the face of the punch when the material under the punch is plastically deformed is still given by the same relationship, $P_m \approx 3Y$. Note that P_m is a quantity similar to Meyer hardness discussed previously.

Deformation of Ideal Plastic Metal by Spherical Indenters. The preceding analysis of plastic deformation under the flat and circular punches may now be used to understand the stress field under a spherical indenter pressed into the surface of an ideal plastic metal.

Based on Tresca or Huber-Mises criterion, Timoshenko (Ref 10) showed that when a sphere is pressed into a metal under load, the maximum shear stress and, hence, the plastic deformation starts at a depth equal to $0.5a$ where $2a$ is the indentation diameter, as at *X* in Fig. 4. The maximum shear stress at this point has been shown to be $0.47 P_m$ where P_m is the mean pressure on the indenter. From Tresca-Mohr criterion, it is obvious, the plastic transformation would start at *X* when $0.47 P_m = \frac{1}{2}Y$, or $P_m = 1.1Y$. Figure 4 also shows contours (Ref 11) of shear stress expressed in terms of P_m as a function of the distance from *X*.

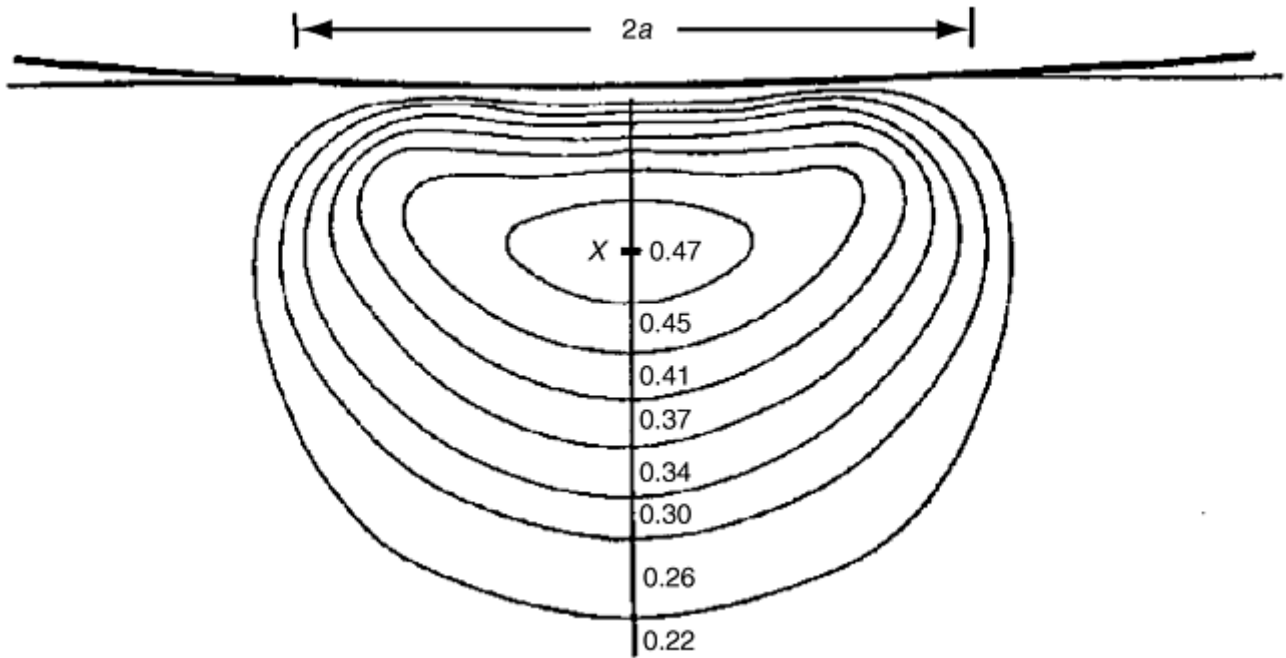


Fig. 4 Elastic deformation of a flat surface on an elastic semi-finite body under a frictionless load, by a rigid sphere of a large radius, showing the location of maximum shear stress in the bulk material below the deformed surface. The maximum shear stress occurs at X , $0.5a$ below the center of the circle of contact and has a value of about $0.47 P_m$ where P_m is the mean pressure. The contours represent lines of constant shear stress in the deformed material. Source: Ref 6

If the load is reduced or removed before P_m reaches the value $1.1Y$ at X , there will be no permanent deformation or indentation; that is, there will be a complete elastic recovery. If, however, P_m exceeds the value $1.1Y$, plastic deformation begins at X , and the plastic region would grow in size at the expense of the elastic-plastic and elastic regions underlying the indenter. This process will continue until the mean pressure in the plastic volume reaches a value $\approx 3Y$. If the load is now increased, the indenter penetrates the metal further, and the plastic zone would expand until the value of P_m in the newly formed plastic volume again equals $\approx 3Y$. When the equilibrium is reached between the indenter and the material during indentation, and the plastic flow has stopped, the indenter load is supported by the elastic stresses in the material. If the load is removed, therefore, there will be an elastic recovery with a corresponding change in shape of the plastically deformed volume and, hence, that of the indentation.

The spherical indentation process may be visualized through an experimental trace of pressure-load for indentations formed in work hardened mild steel by a spherical indenter. In Fig. 5, point L represents the onset of plastic deformation at a mean pressure corresponding to $1.1Y$. The interval $L-M$ represents a gradual increase in the plastic stress, which ultimately reaches a value $\approx 3Y$ corresponding to $M-N$ section of the curve when full plasticity is attained.

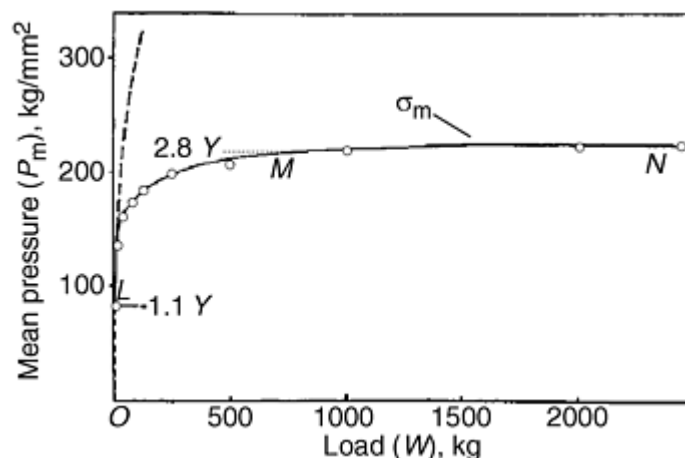


Fig. 5 Experimental pressure-load characteristic of indentations formed in work-hardened mild steel by a hard spherical indenter. Yield stress of steel, $Y = 77 \text{ kg/mm}^2$. Ball diameter is 10 mm. The broken line is the theoretical result for elastic deformation. OL, elastic region; LM, elastic-plastic region; and MN, fully plastic region. Source: Ref 6

Fully Cold Worked versus Fully Annealed Metals. The above discussion has considered ideal plastic metals, which, by definition, do not work harden during deformation and show a constant yield stress when the linear strain is increased as in a tensile or compressive test. Metals that have been sufficiently cold worked would behave in approximately this manner. However, fully annealed, and, in reality, most metals will have a tendency to work harden during deformation and will be characterized by a continuously increasing yield stress with increasing strain. The relation $P_m = CY$ ($C \approx 3$), which applies to fully cold worked metals, also holds for fully annealed metals provided Y denotes the yield stress corresponding to the strain produced during testing, which is higher than the initial yield stress. The value of C has the same approximate value of 3 as for ideal plastic metals. Also, P_m is found to be a function of d/D for fully annealed metals, and therefore, geometrically similar indentations would give identical hardness values, as for ideal plastic metals. It may be noted here that the value of $C \approx 3$ obtained through slip line analysis as already mentioned has also been recently confirmed through finite element analysis (Ref 12, 13).

Tabor (Ref 6) showed that the strain, ϵ , in the plastic region of an indentation is proportional to the ratio d/D and empirically determined the proportionality constant to be approximately 20 for many metals, thus arriving at the relation, $\epsilon = 20d/D$. Combining this equation with the relationship $Y = b\epsilon^x$, where b and x are constants for a given metal and x is the strain hardening coefficient, Tabor has shown that $W = c_1d_1^n = c_2d_2^n = c_3d_3^n$ and so on for indentations made with indenters of different diameters $D_1, D_2, D_3 \dots$. This is Meyer's law, mentioned earlier and first derived by Meyer empirically. This relation has been shown to hold fairly well for many materials. The value of n in the Meyer equation is roughly related to the strain hardening coefficient x by the relation $n = x + 2$.

Conical and Pyramidal Indenters (Ref 6). Shortly after the introduction of Brinell hardness testing, Ludwik (Ref 14) proposed hardness testing using a conical indenter and defined the hardness as the mean pressure over the surface of the indentation. Thus, for an indent with an included angle of 90° , the Ludwik hardness number is given by:

$$HL = 4W / \sqrt{2\pi d^2} \quad (\text{Eq 13})$$

where d is the diameter of the impression. This concept is similar to that of Brinell and therefore has no real physical significance. The true pressure, P , between the indenter and the indentation is given by the ratio of load to projected area, that is, $4W/\pi d^2$ (similar to Meyer's concept for a spherical indenter), which means that the Ludwik hardness number is $1/\sqrt{2}$ times the mean yield pressure P . Experiments have shown that Ludwik hardness is practically independent of the load for a given indenter, though it depends on the cone angle. It is observed that the yield pressure increases as the cone semi-angle decreases, and the effect may be partially explained as due to friction between the indenter and the indentation (Ref 15).

The diamond pyramidal indenter was first introduced by Smith and Sandland (Ref 16) and was later developed by Vickers-Armstrong, Ltd. The indenter is in the form of a square pyramid with opposite faces making an included angle of 136° with each other. The origin of this value of the angle is traced to the Brinell hardness testing practice. It is customary in Brinell hardness testing to select loads so that the indentation diameter lies between $0.25D$ and $0.5D$ where D is the indenter diameter. Thus, an average of the two diameters, $0.375D$, was chosen for the indentation diameter as shown in Fig. 6, which also shows the origin of the included angle 136° of the Vickers indenter. The geometry of the indenter is such that projected area of the indentation is 0.927 times the area of the contact surface. Since Vickers hardness, HV, is defined as the load divided by the surface area of the indentation, the yield pressure, P , is related to the Vickers hardness number by the relation $HV = 0.927P$.

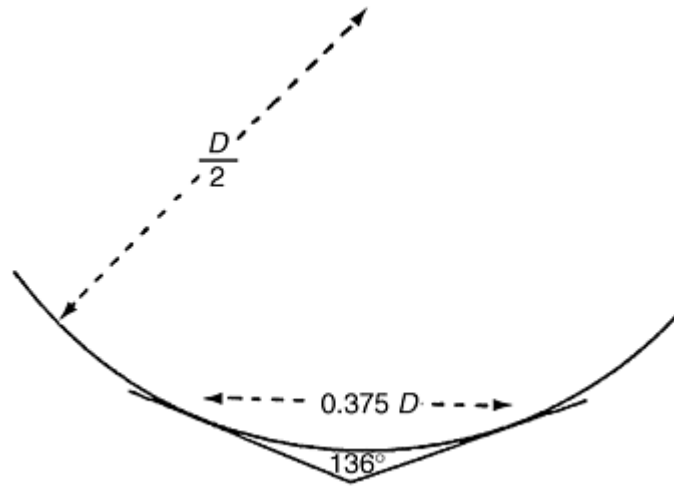


Fig. 6 Relationship between the 136° included angle between the opposite faces of a Vickers indenter and the spherical Brinell indenter of diameter D

During Vickers hardness tests, the lengths of the two diagonals of the indentation are measured, and their mean value, d , is calculated. If the indentation is square, the projected area of the indentation is $d^2/2$, so that the yield pressure is $2W/d^2$ and $HV = 0.927 (2W/d^2)$. As in the case of the conical indenter, experiments have shown that the Vickers hardness number is independent of the size of the indentation, and hence, of the load. It is interesting to note that the Brinell hardness values, obtained by using a 10 mm steel ball loaded to give an indentation diameter equal to $0.375D$, have been shown to closely match the Vickers hardness numbers (Ref 17), thus giving some justification to the selection of 136° as the included angle.

The Knoop diamond indenter is a variation of the Vickers indenter. It is a pyramid in which the included angles are 172° 30' and 130°, and the indentation has the shape of a parallelogram with the longer diagonal about seven times as long as the shorter diagonal. The Knoop hardness is defined as the load, W , divided by the *projected* area A of the indentation. Thus $HK = W/A$, which gives the yield pressure. The hardness values obtained by the Knoop method are, as would be expected, nearly independent of the load and are almost identical with HV numbers.

The elastic and plastic deformation processes that occur in the case of conical and pyramidal indenters are similar to those described for a spherical indenter.

Again, as in the case of a flat punch already described, slip line analysis has been done (Ref 18) for the plastic deformation under a two-dimensional conical and pyramidal indenter in the form of a wedge. The slip line pattern in Fig. 7 shows that the analysis allows for metal flow past the indenter surface to form a ridge. The pressure normal to the indenter surface is given by (Ref 6):

$$P = 2k(1 + \theta) \quad (\text{Eq 14})$$

where θ is the angle as shown in Fig. 6, and is related to α , the semi-angle of the wedge, by the equation:

$$\text{Cos}(2\alpha - \theta) = \text{cos}\theta / (1 + \sin\theta) \quad (\text{Eq 15})$$

Since $2k = 1.15Y$ for Huber-Mises criterion:

$$P = 1.15Y(1 + \theta) \quad (\text{Eq 16})$$

As seen from Fig. 7, when the semi-angle $\alpha = 90^\circ$, $\theta = 90^\circ$. The wedge forms flat punch, as discussed. Equation 15 becomes:

$$P = 1.15Y(1 + \frac{1}{2}\pi) \quad (\text{Eq 17a})$$

or

$$P = 2.96Y \quad (\text{Eq 17b})$$

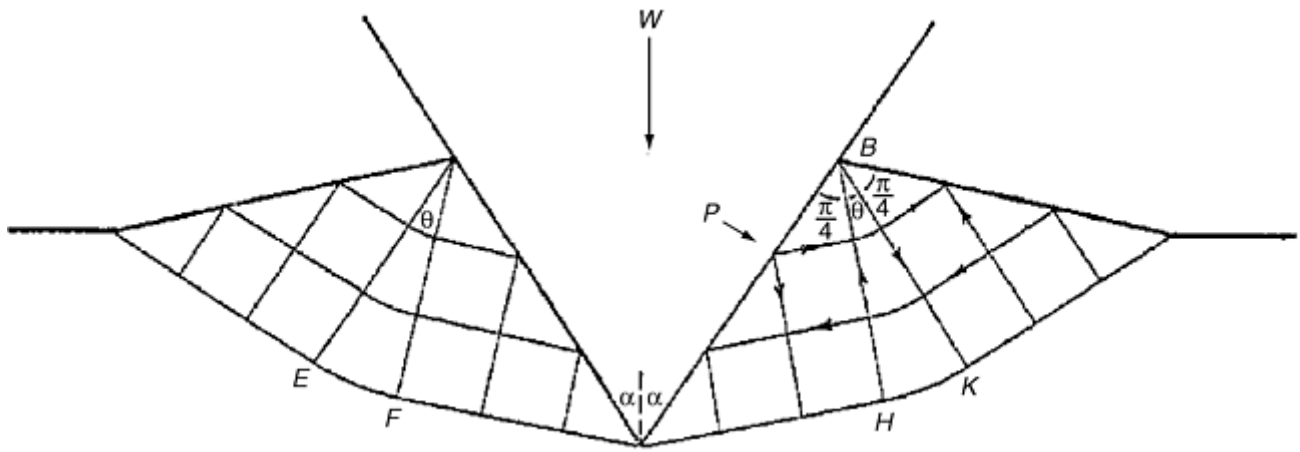


Fig. 7 Slip-line pattern for a two-dimensional wedge penetrating an ideally plastic material (Ref 18). The pressure across the face of the indenter is uniform and has the value $P = 2k(1 + \theta)$, where θ is the angle HBK in radians. This analysis allows for the displacement of the deformed material as can be seen in the figure. Source: Ref 6

Equation 17a 17b is the same as Eq 12 derived for a flat punch and shows the yield pressure is again about three times the yield stress. The two-dimensional analysis and the expression for yield pressure ($P = CY$) for a wedge are expected to apply to the case of solid pyramidal and conical indenters just as the flat punch analysis was found to hold fairly well for a flat circular punch. In fact, it has been shown experimentally that it is true. However, the value of C for these solid indenters is found in practice to be slightly higher than for a spherical indenter (3.2 versus 3.0), and this is considered to be probably due to the higher friction between the indenter and the material.

The pyramidal and conical indenters may be considered to have a spherical indentation point with an extremely small radius. The plastic deformation therefore starts immediately after the indenter comes in contact with the material surface, even at very small loads. As the load is increased, the indentation increases in size and depth, but its shape and the flow pattern remain unchanged whatever its depth. This implies that the indentations produced by these indenters are geometrically similar for all indentation loads, and hence, the hardness values measured by these indenters are, for all practical purposes, independent of the indentation load (compare this with the case of the Brinell test where the requirement is that the d/D ratio should be constant to obtain identical hardness values).

The preceding discussion is true for the commonly used microhardness and macrohardness tests with indentations above a certain size where the hardness is independent of their depth. However, recent investigations have shown that for indentations of extremely small depths (50 nm), the hardness can vary inversely with depth due to the probable influence of several surface factors such as dislocation image forces, contamination layers, and electric fields (Ref 19).

Rockwell Hardness Test with a Conical Indenter. In the Rockwell test, a load of 10 kg is first applied to the material surface, and the depth of penetration is considered as zero for further depth measurements. A load of 90 or 140 kg is then applied and removed, leaving the minor load in place, and the additional depth of penetration is measured directly on a dial gage, which gives the hardness value that may be correlated with Vickers or Brinell values. In the Rockwell test, a spherical indenter is used for softer materials (Rockwell B scale), and a conical indenter is used for hard materials (Rockwell C scale). Other scales of Rockwell test are omitted from this discussion but are described in the article "Indentation Hardness Testing of Metals and Alloys" in this Section.

Rockwell testing has two important advantages as compared to other tests previously discussed:

- Application and retention of the minor load during the test prepares the surface upon which the incremental penetration depth due to the major load is measured.
- The hardness value is read directly on the dial gage without the necessity for measuring the indentation dimensions, as in other hardness testing methods. This expedites the testing process—an important advantage in manufacturing and quality control.

However, there may be appreciable elastic recovery of the material when the major load is removed, and the recovered indentation depth will be less than the depth before removing the load. The hardness value deduced from the depth of recovered indentation may, therefore, be in error. This error may not be serious if the instrument is calibrated for materials having approximately the same elastic modulus, a requirement that is generally satisfied in industry where the most common materials used in manufacturing are ferrous and have approximately the same elastic modulus.

If the above effect is neglected and the plastic deformation is large compared to the elastic recovery, then it is relatively simple to obtain a relationship between the hardness values obtained from depth measurements and those from diameter measurements of the spherical indentation. Thus, assuming that the penetration depth, t , is small as compared to the ball diameter, D , one can obtain from simple geometry considerations that $t = d^2/4D$ where d is the diameter of the indentation. Since the mean pressure P across the indentation, which is equivalent to the Meyer hardness, is given by $P = 4W/\pi d^2$:

$$t = (W/P)(1/\pi D) \quad (\text{Eq 18})$$

Thus, if the load is kept constant as in a Rockwell test, Eq 18 shows depth of penetration t is inversely proportional to P ; that is, the depth of penetration increases with decreasing hardness. This fact is reflected in the dial gage readings, which do not give the actual depth of penetration but, rather, give a quantity, R , given by 100 scale divisions minus the depth penetrated. Thus:

$$R = \text{constant} - t$$

or

$$R = C_1 - C_2 / P \quad (\text{Eq 19})$$

where C_1 and C_2 are constants.

This type of relation is approximately obeyed if a spherical indenter is employed. However, a different relation is obtained if a conical indenter is used. Thus if α is the semi-angle of the cone and the depth of penetration is $t = a \cot \alpha$ where $2a$ is the indentation diameter, then:

$$t = \sqrt{(W/\pi P)} \cot \alpha \quad (\text{Eq 20})$$

where P , the mean pressure, is again given by $P = W/\pi a^2$. Since t is inversely proportional to P for a given value of α , the Rockwell number may be expressed by the relationship:

$$R = C_3 - C_4 / \sqrt{P} \quad (\text{Eq 21})$$

where C_3 and C_4 are constants. If Rockwell hardness values R_c , obtained using a spherically tipped conical indenter, are plotted against Brinell hardness numbers, B , it is found that the curve can be approximately represented by the relationship:

$$R_c = C_5 - C_6 / \sqrt{B} \quad (\text{Eq 22})$$

where C_5 and C_6 are constants.

Equation 22 is similar to Eq 21 with P replaced by B . Since it is reasonable to assume Meyer hardness P is not widely different from B , it may be concluded that the theoretical relation between R_c and B (Eq 21) is substantiated by the empirical observations (Eq 22), and this provides a degree of validity to the concept of measurement of hardness from depth measurements.

Summary. The indentation hardness values are essentially a measure of the elastic limit or yield stress of the material being tested. For most types of indenters in use, the yield pressure under conditions of appreciable plastic flow is approximately three times the yield stress of the material. The elastic recovery of the indentation when the load and the indenter are removed seems to affect mostly the depth of the indentation rather than the projected area of the indentation. Consequently the yield pressure or the hardness as measured from the indentation dimensions are nearly the same as would be obtained if measurements were made before the load and the indenter were removed.

The yield pressure is mostly dependent on the plastic properties of the material and only to a secondary extent on the elastic properties. If the hardness measurements are made based on the depth measurements, then the elastic recovery may affect the calculated yield pressure, which may be in error when compared with the actual values that may be obtained during indentation. However, this error may be small when the instrument is calibrated for materials with similar elastic moduli.

With conical and pyramidal indenters, the indentations are geometrically similar (whatever the indentation size), and, therefore, the mean pressure to produce the plastic flow is almost independent of the indentation size. Consequently the hardness value is fairly constant over a wide range of loads. This means it is not necessary in practice to specify the load.

With spherical indenters, the shape of the indentation varies with its size so that the amount of work hardening, the elastic limit, and, as a result, the yield pressure in general increase with the size of the indentation and hence with the load. It is therefore necessary in Brinell hardness measurements to specify the load and the diameter of the indenter. With spherical indenters the ratio W/D^2 must be maintained constant to produce geometrically similar indentations and nearly identical hardness numbers.

In Brinell testing, the increase in the yield pressure with the size of indentation provides useful information about the yield stress of the material and about the way in which the yield stress increases with the amount of deformation. In fact, the hardness measurements made using a spherical indenter can be used in conjunction with the Meyer analysis and Meyer's index, n , to determine the work hardening coefficient, x , using the relationship $n = x + 2$.

References cited in this section

6. D. Tabor, *The Hardness of Metals*, Clarendon Press, Oxford, 1951
7. E. Meyer, *Zeits. D. Vereines Deutsch. Ingenieure*, Vol 52, 1908, p 645
8. L. Prandtl, *Nachr. d. Gesellschaft d. Wissensch, zu Göttingen, Math.-Phys.Klasse*, 1920, p 74
9. R. Hill, *The Mathematical Theory of Plasticity*, Oxford, 1950, p 254
10. S. Timoshenko, *Theory of Elasticity*, McGraw-Hill, 1934
11. R.M. Davies, *Proc. R. Soc. (London) A*, Vol 197, 1949, p 416
12. Y.-T. Cheng and C.-M. Cheng, *Philos. Mag. Lett.*, Vol 77 (No. 1), 1998, p 39–47
13. A. Bolshakov and G.M. Pharr, *J. Mater. Res.*, Vol 13 (No. 4), April 1998, p 1049–1058
14. P. Ludwik, *Die Kegelprobe*, J. Springer (Berlin), 1908
15. G.A. Hankins, *Proc. Inst. Mech. Eng. D*, 1925
16. R. Smith and G. Sandland, *Proc. Inst. Mech. Eng.*, Vol 1, 1922, p 623
17. S.R. Williams, *Hardness and Hardness Measurements*, American Society for Metals, 1942
18. R. Hill, E.H. Lee, and S.J. Tupper, *Proc. R. Soc. (London) A*, 1947, Vol 188, p 273
19. W.C. Oliver, R. Hutchings, and J.B. Pethica, STP 889, ASTM, 1995, p 90–108

Introduction to Hardness Testing

Gopal Revankar, Deere & Company

Classification of Hardness Tests

The hardness tests may be classified using various criteria, including type of measurement, magnitude of indentation load, and nature of the test (i.e., static, dynamic, or scratch).

Type of Measurement. Hardness tests may be classified into two types: one, involving measurement of dimensions of the indentation (Brinell, Vickers, Knoop) and the other, measuring the depth of indentation (Rockwell, nanoindentation). They may also be classified as the traditional tests, which measure one contact area or penetration depth at a prescribed load (Brinell, Vickers, Knoop, Rockwell), and the recent instrumented-indentation tests, which allow for a continuous measurement of load and displacement.

Magnitude of Indentation Load. Hardness tests may be classified based on the magnitudes of indentation loads. There are, thus, macrohardness, microhardness, and the relatively new nanohardness tests. For macrohardness tests, indentation loads are 1 kgf or greater: Vickers testing may use loads from 1 to 120 kgf. Rockwell test loads vary from 15 to 150 kgf, depending on the type of indenter and the Rockwell scale of measurement. Brinell tests involve 500 and 3000 kgf loads though intermediate loads. Loads as low as 6.25 kgf are occasionally used.

The microhardness tests (Vickers and Knoop) use smaller loads ranging from 1 gf to 1 kgf, the most common being 100 to 500 gf and suited for material layers that are thicker than about 3 μm . The nanoindentation test, also called the instrumented indentation test, depends on the simultaneous measurement of the load and depth of indentation produced by loads that may be as small as 0.1 mN, with depth measurements in the 20 nm range.

Static, Dynamic, or Scratch Types. All of the above mentioned tests are of the static type. In the dynamic tests, the indenter, usually spherical or conical, is allowed to bounce off the surface of the material to be tested, and the rebound height of the indenter is used as a measure of hardness. The scleroscope is the most popular test of this type. In the scratch test, a material of known hardness is used to scratch the surface of material of unknown hardness to determine if the latter is more or less hard than the reference material.

Eddy current hardness testing, which does not fall into any of the above categories, is a noncontact method and does not use an indenter. The method depends on the measurement of eddy current permeability of the material surface layer, which is determined by its microstructure and hence hardness.

These and various other test methods are discussed in greater detail in the subsequent articles of this Section.

Introduction to Hardness Testing

Gopal Revankar, Deere & Company

Acknowledgments

Substantial portions of this brief review are adaptations from the classic work of Tabor on hardness (Ref 6). The author is indebted to the continued usefulness of that book.

Reference cited in this section

6. D. Tabor, *The Hardness of Metals*, Clarendon Press, Oxford, 1951

Introduction to Hardness Testing

Gopal Revankar, Deere & Company

References

1. R.W. Rice, *The Compressive Strength of Ceramics in Materials Science Research*, Vol 5, Ceramics in Severe Environments, W.W. Kriegel and H. Palmour III, Ed., Plenum, 1971, p 195–229

2. J.A. Brinell, *II Cong. Int. Méthodes d' Essai (Paris)*, 1900
3. M.O. Lai and K.B. Lim, *J. of Mater. Sci.*, Vol 26 (1991), p 2031–2036
4. S.C. Chang, M.T. Jahn, C.M. Wan, J.Y.M. Wan, and T.K. Hsu, *J. Mater. Sci.*, Vol 11, 1976, p 623
5. W. Kohlhöfer and R.K. Penny, *Int. J. Pressure Vessels Piping*, Vol 61, 1995, p 65–75
6. D. Tabor, *The Hardness of Metals*, Clarendon Press, Oxford, 1951
7. E. Meyer, *Zeits. D. Vereines Deutsch. Ingenieure*, Vol 52, 1908, p 645
8. L. Prandtl, *Nachr. d. Gesellschaft d. Wissensch, zu Göttingen, Math.-Phys.Klasse*, 1920, p 74
9. R. Hill, *The Mathematical Theory of Plasticity*, Oxford, 1950, p 254
10. S. Timoshenko, *Theory of Elasticity*, McGraw-Hill, 1934
11. R.M. Davies, *Proc. R. Soc. (London) A*, Vol 197, 1949, p 416
12. Y.-T. Cheng and C.-M. Cheng, *Philos. Mag. Lett.*, Vol 77 (No. 1), 1998, p 39–47
13. A. Bolshakov and G.M. Pharr, *J. Mater. Res.*, Vol 13 (No. 4), April 1998, p 1049–1058
14. P. Ludwik, *Die Kegelprobe*, J. Springer (Berlin), 1908
15. G.A. Hankins, *Proc. Inst. Mech. Eng. D*, 1925
16. R. Smith and G. Sandland, *Proc. Inst. Mech. Eng.*, Vol 1, 1922, p 623
17. S.R. Williams, *Hardness and Hardness Measurements*, American Society for Metals, 1942
18. R. Hill, E.H. Lee, and S.J. Tupper, *Proc. R. Soc. (London) A*, 1947, Vol 188, p 273
19. W.C. Oliver, R. Hutchings, and J.B. Pethica, STP 889, ASTM, 1995, p 90–108

Macroindentation Hardness Testing

Edward L. Tobolski, Wilson Instruments Division, Instron Corporation; Andrew Fee, Consultant

Introduction

ALMOST ALL indentation hardness testing is done with Brinell, Rockwell, Vickers, and Knoop indenters. These modern methods of indentation testing began with the Brinell test, which was developed around 1900 when the manufacturing of ball bearings prompted J.A. Brinell in Sweden to use them as indenters. The Brinell test was quickly adopted as an industrial test method soon after its introduction, but several limitations also became apparent. Basic limitations included test duration, the large size of the impressions from the indent, and the fact that high-hardness steels could not be tested with the Brinell method of the early 1900s.

The limitations of the indentation test developed by Brinell prompted the development of other macroindentation hardness tests, such as the Vickers test introduced by R. Smith and G. Sandland in 1925, and the Rockwell test invented by Stanley P. Rockwell in 1919. The Vickers hardness test follows the same

principle of the Brinell test—that is, an indenter of definite shape is pressed into the material to be tested, the load removed, the diagonals of the resulting indentation measured, and the hardness number calculated by dividing the load by the surface area of indentation. The principal difference is that the Vickers test uses a pyramid-shaped diamond indenter that allows testing of harder materials, such as high-strength steels.

The Rockwell hardness test differs from Brinell hardness testing in that the hardness is determined by the depth of indentation made by a constant load impressed upon an indenter. Rockwell hardness testing is the most widely used method for determining hardness, primarily because the Rockwell test is fast, simple to perform, and does not require highly skilled operators. By use of different loads (force) and indenters, Rockwell hardness testing can determine the hardness of most metals and alloys, ranging from the softest bearing materials to the hardest steels.

This article describes the principal methods for macroindentation hardness testings by the Brinell, Vickers, and Rockwell methods. Microindentation hardness tests with the Knoop and Vickers indenters are described further in the next article “Microindentation Hardness Testing.” An overall discussion on the applications and selection of these test methods is provided in the article “Selection and Industrial Applications of Hardness Tests” in this Volume.

Macroindentation Hardness Testing

Edward L. Tobolski, Wilson Instruments Division, Instron Corporation; Andrew Fee, Consultant

Rockwell Hardness Testing

The Rockwell hardness test is defined in ASTM E 18 and several other standards (Table 1). Rockwell hardness testing differs from Brinell testing in that the Rockwell hardness number is based on the difference of indenter depth from two load applications (Fig. 1). Initially a minor load is applied, and a zero datum is established. A major load is then applied for a specified period of time, causing an additional penetration depth beyond the zero datum point previously established by the minor load. After the specified dwell time for the major load, it is removed while still keeping the minor load applied. The resulting Rockwell number represents the difference in depth from the zero datum position as a result of the application of the major load. The entire procedure requires only 5 to 10 s.

Table 1 Selected Rockwell hardness test standards for metals and hardmetals

Standard No.	Title
ASTM B 294	Standard Test Method for Hardness Testing of Cemented Carbides
ASTM E 18	Test Methods for Hardness and Rockwell Superficial Hardness of Metallic Materials
ASTM E 1842	Test Method for Macro-Rockwell Hardness Testing of Metallic Materials
BS 5600-4.5	Powder Metallurgical Materials and Products—Methods of Testing and Chemical Analysis of Hardmetals—Rockwell Hardness Test (Scale A)
BS EN ISO 6508-1	Metallic Materials—Rockwell Hardness Test—Part 1: Test Method (Scales A, B, C, D, E, F, G, H, K, N, T)
BS EN ISO 6508-2	Metallic Materials—Rockwell Hardness Test—Part 2: Verification and Calibration of Testing Machines (Scales A, B, C, D, E, F, G, H, K, N, T)
BS EN ISO 6508-3	Metallic Materials—Rockwell Hardness Test—Part 3: Calibration of Reference Blocks (Scales A, B, C, D, E, F, G, H, K, N, T)
ISO 3738-1	Hardmetals—Rockwell Hardness Test (Scale A)—Part 1: Test Method
ISO 3738-2	Hardmetals—Rockwell Hardness Test (Scale A)—Part 2: Preparation and Calibration of Standard Test Blocks
JIS B 7726	Rockwell Hardness Test—Verification of Testing Machines
JIS B 7730	Rockwell Hardness Test—Calibration of Reference Blocks

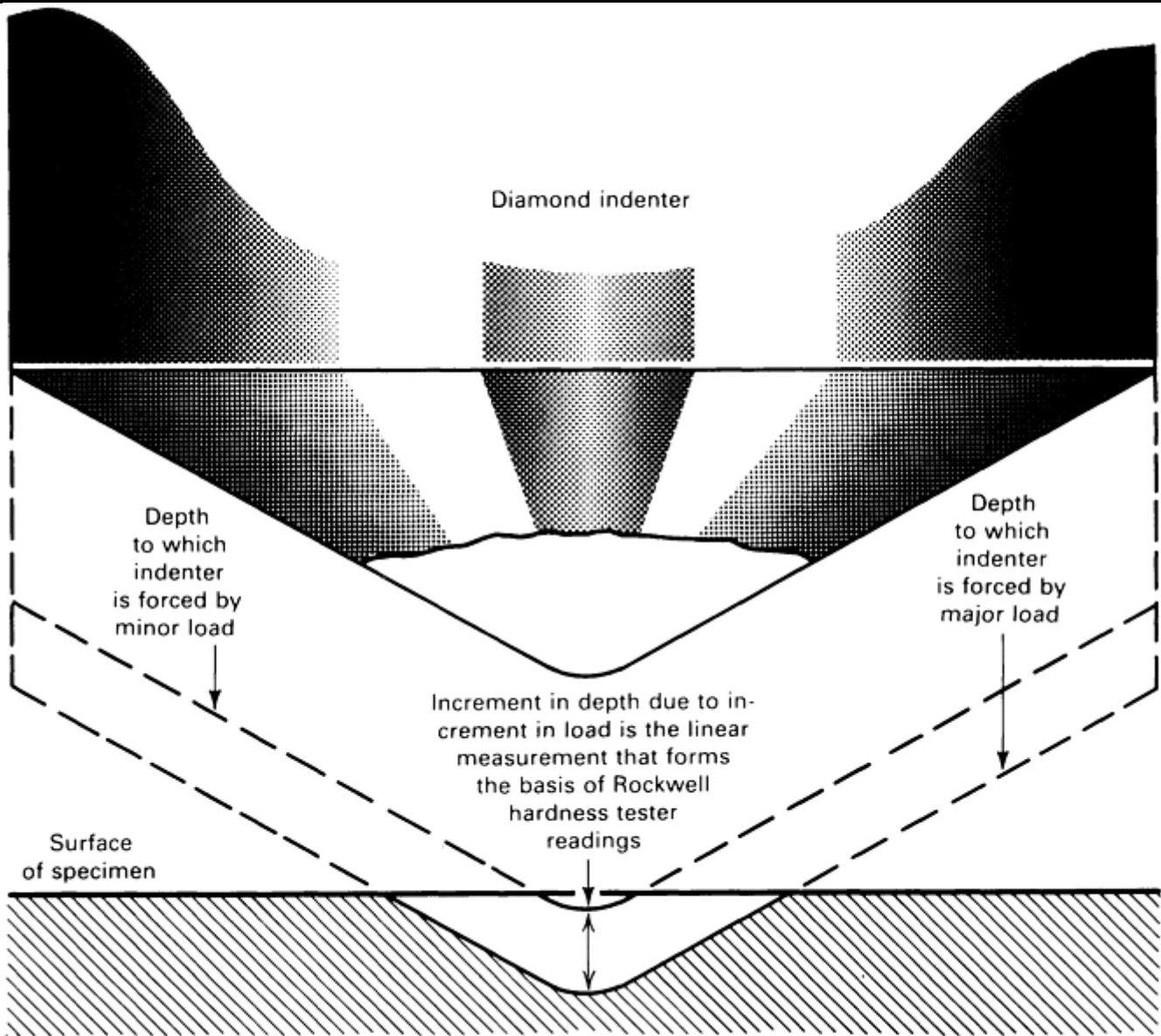


Fig. 1 Principle of the Rockwell test. Although a diamond indenter is illustrated, the same principle applies for steel ball indenters and other loads.

Use of a minor load greatly increases the accuracy of this type of test, because it eliminates the effect of backlash in the measuring system and causes the indenter to break through slight surface roughness. The basic principle involving minor and major loads is shown in Fig. 1. Although the principle is illustrated with a diamond indenter, the same principle applies for hardened steel ball indenters and other loads.

Test Types and Indenters

There are two types of Rockwell tests: Rockwell and superficial Rockwell. In Rockwell testing, the minor load is 10 kgf, and the major load is 60, 100, or 150 kgf. In superficial Rockwell testing, the minor load is 3 kgf, and major loads are 15, 30, or 45 kgf. In both tests, the indenter may be either a diamond cone or a hardened ball depending principally on the characteristics of the material being tested.

Hardened ball indenters with diameters of $\frac{1}{16}$, $\frac{1}{8}$, $\frac{1}{4}$ and, $\frac{1}{2}$ in. (1.588, 3.175, 6.35, and 12.7 mm) are used for testing softer materials such as fully annealed steels, softer grades of cast irons, and a wide variety of nonferrous metals. Hardened steel balls have traditionally been used for Rockwell testing. However, a changeover to tungsten carbide is in process. All future testing will be done with carbide balls. This will improve the durability of the balls significantly, but a slight change in hardness results may occur.

Rockwell diamond indenters are used mainly for testing hard materials such as hardened steels and cemented carbides. “Hard materials” are those with hardness greater than 100 HRB and greater than 83.1 HR30T (see the section “Rockwell Scales” in this article for further explanation).

The Rockwell diamond indenter is a spheroconical shape with a 120° cone and a spherical tip radius of 200 μm (Fig. 2a). Older standard indenters in the United States had a nominal radius closer to 192 μm, which was within ASTM specifications ($200 \pm 10 \mu\text{m}$); standard indenters in the rest of the world have been closer to 200 μm. While not out of tolerance, the old U.S. standard indenter is at the low end of the specification. This led to a change in tip radius closer to 200 μm used in the rest of the world.

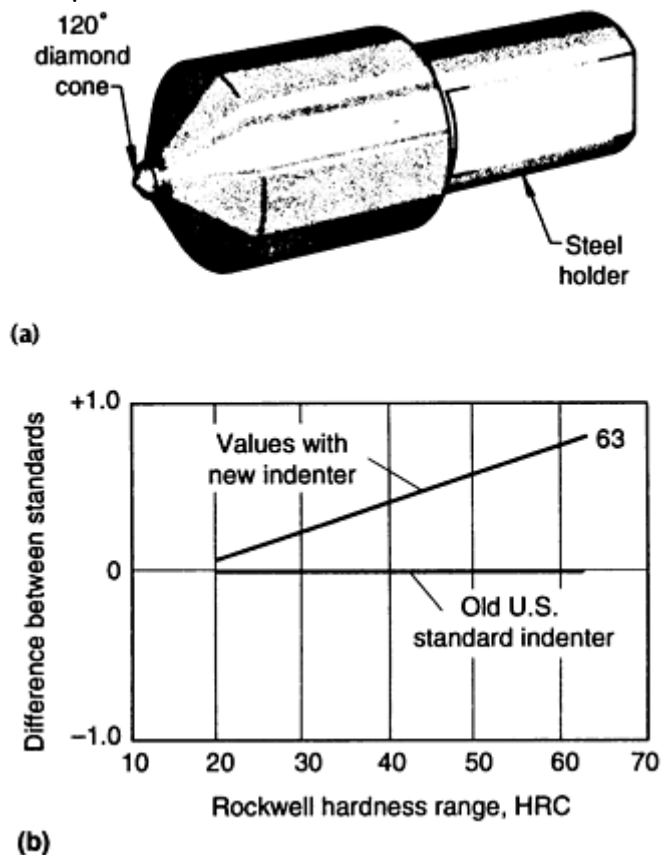


Fig. 2 Rockwell indenter. (a) Diamond-cone Brale indenter (shown at about 2×). (b) Comparison of old and new U.S. diamond indenters. The angle of the new indenter remains at 120°, but has a larger radius closer to the average ASTM specified value of 200 μm; the old indenter has a radius of 192 μm. The indenter with the larger radius has a greater resistance to penetration of the surface.

A comparison of the old (192 μm) U.S. standard diamond indenter and the current (200 μm tip) U.S. indenter is shown in Fig. 2(b). The larger radius increases the resistance of the indenter to penetration into the surface of the testpiece. At higher Rockwell C hardness, most of the indenter travel is along the radius; whereas at the lower hardnesses, more indenter travel is along the angle. This is why the hardness shift from old to new has been most significant in the 63 HRC range and not the 25 HRC range.

Rockwell Scales

Rockwell hardness values are expressed as a combination of hardness number and a scale symbol representing the indenter and the minor and major loads. The Rockwell hardness is expressed by the symbol HR and the scale designation. For example, 64.0 HRC represents the Rockwell hardness number of 64.0 on the Rockwell C scale; 81.3 HR30N represents the Rockwell superficial hardness number of 81.3 on the Rockwell 30N scale. Because of the changeover to carbide balls, the designation for the ball scales will require the use of an S or W to indicate the ball used. For example, a HRB scale reading of 80.0 obtained using a steel ball would be labeled 80.0 HRBS, while the same result using a carbide ball would be designated 80.0 HRBW.

There are 30 different scales, defined by the combination of the indenter and the minor and major loads (Tables 2 and 3). In many instances, Rockwell hardness tolerances are specified or are indicated on drawings. At times, however, the Rockwell scale must be selected to suit a given set of circumstances.

Table 2 Rockwell standard hardness

Scale symbol	Indenter	Major load, kgf	Typical applications
A	Diamond (two scales—carbide and steel)	60	Cemented carbides, thin steel, and shallow case-hardened steel
B	$\frac{1}{16}$ in. (1.588 mm) ball	100	Copper alloys, soft steels, aluminum alloys, malleable iron
C	Diamond	150	Steel, hard cast irons, pearlitic malleable iron, titanium, deep case-hardened steel, and other materials harder than 100 HRB
D	Diamond	100	Thin steel and medium case-hardened steel and pearlitic malleable iron
E	$\frac{1}{8}$ in. (3.175 mm) ball	100	Cast iron, aluminum and magnesium alloys, bearing metals
F	$\frac{1}{16}$ in. (1.588 mm) ball	60	Annealed copper alloys, thin soft sheet metals
G	$\frac{1}{16}$ in. (1.588 mm) ball	150	Phosphor bronze, beryllium copper, malleable irons. Upper limit 92 HRG to avoid possible flattening of ball
H	$\frac{1}{8}$ in. (3.175 mm) ball	60	Aluminum, zinc, lead
K	$\frac{1}{8}$ in. (3.175 mm) ball	150	Bearing metals and other very soft or thin materials. Use smallest ball and heaviest load that do not produce anvil effect.
L	$\frac{1}{4}$ in. (6.350 mm) ball	60	Bearing metals and other very soft or thin materials. Use smallest ball and heaviest load that do not produce anvil effect.
M	$\frac{1}{4}$ in. (6.350 mm) ball	100	Bearing metals and other very soft or thin materials. Use smallest ball and heaviest load that do not produce anvil effect.
P	$\frac{1}{4}$ in. (6.350 mm) ball	150	Bearing metals and other very soft or thin materials. Use smallest ball and heaviest load that do not produce anvil effect.
R	$\frac{1}{2}$ in. (12.70 mm) ball	60	Bearing metals and other very soft or thin materials. Use smallest ball and heaviest load that do not produce anvil effect.
S	$\frac{1}{2}$ in. (12.70 mm) ball	100	Bearing metals and other very soft or thin materials. Use smallest ball and heaviest load that do not produce anvil effect.
V	$\frac{1}{2}$ in. (12.70 mm) ball	150	Bearing metals and other very soft or thin materials. Use smallest ball and heaviest load that do not produce anvil effect.

Source: ASTM E 18

Table 3 Rockwell superficial hardness scales

Scale symbol	Indenter	Major load, kgf
15N	Diamond	15
30N	Diamond	30
45N	Diamond	45
15T	$\frac{1}{16}$ in. (1.588 mm) ball	15
30T	$\frac{1}{16}$ in. (1.588 mm) ball	30
45T	$\frac{1}{16}$ in. (1.588 mm) ball	45
15W	$\frac{1}{8}$ in. (3.175 mm) ball	15
30W	$\frac{1}{8}$ in. (3.175 mm) ball	30
45W	$\frac{1}{8}$ in. (3.175 mm) ball	45
15X	$\frac{1}{4}$ in. (6.350 mm) ball	15
30X	$\frac{1}{4}$ in. (6.350 mm) ball	30
45X	$\frac{1}{4}$ in. (6.350 mm) ball	45
15Y	$\frac{1}{2}$ in. (12.70 mm) ball	15
30Y	$\frac{1}{2}$ in. (12.70 mm) ball	30
45Y	$\frac{1}{2}$ in. (12.70 mm) ball	45

Note: The Rockwell N scales of a superficial hardness tester are used for materials similar to those tested on the Rockwell C, A, and D scales, but of thinner gage or case depth. The Rockwell T scales are used for materials similar to those tested on the Rockwell B, F, and G scales, but of thinner gage. When minute indentations are required, a superficial hardness tester should be used. The Rockwell W, X, and Y scales are used for very soft materials. The letter N designates the use of the diamond indenter; the letters T, W, X, and Y designate steel ball indenters. Superficial Rockwell hardness values are always expressed by the number suffixed by a number and a letter that show the load and indenter combination. For example, 80 HR30N indicates a reading of 80 on the superficial Rockwell scale using a diamond indenter and a major load of 30 kgf

The majority of applications for testing steel, brass, and other materials are covered by the Rockwell C and B scales. However, the increasing use of materials other than steel and brass as well as thin materials necessitates a basic knowledge of the factors that must be considered in choosing the correct scale to ensure an accurate Rockwell test. The choice is not only between the regular hardness test and superficial hardness test, with three different major loads for each, but also between the diamond indenter and the $\frac{1}{16}$, $\frac{1}{8}$, $\frac{1}{4}$, and $\frac{1}{2}$ in. (1.588, 3.175, 6.35, and 12.7 mm) diam ball indenters.

If no specification exists or there is doubt about the suitability of the specified scale, an analysis should be made of the following factors that control scale selection:

- Type of material
- Specimen thickness or the thickness of a hardened layer on the surface of the part
- Test location
- Scale limitations

In general, the best results are obtained using the highest loads that the specimen will allow.

Selection of Scale Based on Material Type. Standard Rockwell scales and typical materials for which these scales are applicable are listed in Table 2. For example, when a hard material such as steel or tungsten carbide is tested, a diamond indenter would be used. This automatically limits the choice of scale to one of six: Rockwell C, A, D, 45N, 30N, or 15N. The next step is to determine which scale will provide the best accuracy, sensitivity, and repeatability. Typically, as the thickness of the sample decreases the major load should also decrease.

Effect of Specimen Thickness. The material immediately surrounding a Rockwell indentation is cold worked. The extent of the cold-worked area depends on the type of material and previous work hardening of the test specimen. The depth of material affected has been found by extensive experimentation to be on the order of 10 to 15 times the depth of the indentation. Therefore, unless the thickness of the material being tested is at least

10 times the depth of the indentation, an accurate Rockwell test cannot be ensured. This “minimum thickness ratio” of 10 to 1 should be regarded only as an approximation.

The depth of the indentation can be determined as follows. One Rockwell number is equal to 0.002 mm (0.00008 in.). When the reading is taken with a diamond indenter, the Rockwell hardness number obtained on the sample is subtracted from 100, and the result multiplied by 0.002 mm. Therefore, a reading of 60 HRC indicates an indentation depth from minor to major load of:

$$(100 - 60) \times 0.002 \text{ mm} = 0.08 \text{ mm}$$

$$\text{Depth} = 0.08 \text{ mm (0.003 in.)}$$

When a ball indenter is used, the hardness number is subtracted from 130; therefore, for a dial reading of 90 HRB, the depth is determined by:

$$(130 - 80) \times 0.002 \text{ mm} = 0.10 \text{ mm}$$

$$\text{Depth} = 0.10 \text{ mm (0.004 in.)}$$

In Rockwell superficial tests, regardless of the type of indenter used, one number represents an indentation of 0.001 mm (0.00004 in.). Therefore, a reading of 80 HR30N indicates a depth of indentation from minor to major load of:

$$(100 - 80) \times 0.001 \text{ mm} = 0.02 \text{ mm}$$

$$\text{Depth} = 0.02 \text{ mm (0.0008 in.)}$$

As indicated above, computation of the depth of penetration for any Rockwell test requires only simple arithmetic. However, in actual practice, computation is not necessary because minimum thickness values have been established (Table 4). These minimum thickness values generally follow the 10-to-1 ratio, but they are based on experimental data accumulated for varying thickness of low-carbon steels and of hardened-and-tempered strip steel.

Table 4 Minimum work metal hardness values for testing various thicknesses of metals with standard and superficial Rockwell hardness testers

Metal thickness		Minimum hardness for standard hardness testing						Minimum hardness for superficial hardness testing					
		Diamond indenter			Ball indenter, $\frac{1}{16}$ in. (1.588 mm)			Diamond indenter			Ball indenter, $\frac{1}{16}$ in. (1.588 mm)		
mm	in.	A (60 kgf)	D (100 kgf)	C (150 kgf)	F (60 kgf)	B (100 kgf)	G (150 kgf)	15 N (15 kgf)	30 N (30 kgf)	45 N (45 kgf)	15 T (15 kgf)	30 T (30 kgf)	45 T (45 kgf)
0.127	0.005	93
0.152	0.006	92
0.203	0.008	90
0.254	0.010	88	91
0.305	0.012	83	82	77	86
0.356	0.014	76	78.5	74	81	80	...
0.381	0.015
0.406	0.016	86	68	74	72	75	72	71
0.457	0.018	84	^(a)	66	68	68	64	62
0.508	0.020	82	77	...	100	^(a)	57	63	^(a)	55	53
0.559	0.022	78	75	69	^(a)	47	58	...	45	43
0.610	0.024	76	72	67	98	94	94	^(a)	^(a)	51	...	34	31
0.635	0.025	^(a)	^(a)	...	^(a)	^(a)	...
0.660	0.026	71	68	65	91	87	87	^(a)	^(a)	37	18

0.711	0.028	67	63	62	85	...	76	(a)	(a)	20	4
0.762	0.030	60	58	57	77	71	68	(a)	(a)	(a)	(a)	(a)	(a)
0.813	0.032	(a)	51	52	69	62	59	(a)	(a)	(a)
0.864	0.034	(a)	43	45	...	52	50	(a)	(a)	(a)
0.889	0.035	(a)	(a)	(a)	(a)	(a)	(a)	(a)
0.914	0.036	(a)	(a)	37	...	40	42	(a)	(a)	(a)
0.965	0.038	(a)	(a)	28	...	28	31	(a)	(a)	(a)
1.016	0.040	(a)	(a)	20	(a)	...	22	(a)	(a)	(a)	(a)	(a)	(a)

Note: These values are approximate only and are intended primarily as a guide; see text for example of use. Material thinner than shown should be tested with a microhardness tester. The thickness of the workpiece should be at least 1.5 times the diagonal of the indentation when using a Vickers indenter, and at least one-half times the long diagonal when using a Knoop indenter.

(a) No minimum hardness for metal of equal or greater thickness.

Consider a requirement to check the hardness of a strip of steel 0.36 mm (0.014 in.) thick with an approximate hardness of 63 HRC. According to the established minimum thickness values, material in the 63 HRC range must be approximately 0.71 mm (0.028 in.) thick for an accurate Rockwell C scale test. Therefore, 63 HRC must be converted to an approximate equivalent hardness on other Rockwell scales. These values, taken from a conversion table, are 73 HRD, 82.8 HRA, 69.9 HR45N, 80.1 HR30N, and 91.4 HR15N. Hardness conversion tables are provided in the article “Hardness Conversions for Steels” in this Volume.

Referring to Table 4, there are only three appropriate Rockwell scales—45N, 30N, and 15N—for hardened 0.356 mm (0.014 in.) thick material. The 45N scale is not suitable because the material should be at least 74 HR45N. The 30N scale requires the material to be at least 80 HR30N; on the 15N scale, the material must be at least 76 HR15N. Therefore, either the 30N or 15N scale can be used.

If a choice remains after all criteria have been applied, then the scale applying the heavier load should be used. A heavier load produces a larger indentation covering a greater portion of the material, as well as a Rockwell hardness number more representative of the material as a whole. In addition, the heavier the load, the greater the sensitivity of the scale.

In the example under consideration, a conversion chart will indicate that, in the hard steel range, a difference in hardness of one point on the Rockwell 30N scale represents a difference of only 0.5 points on the Rockwell 15N scale. Therefore, smaller differences in hardness can be detected when using the 30N scale. This approach also applies when selecting a scale to accurately measure hardness when approximate case depth and hardness are known.

Minimum thickness charts and the 10-to-1 ratio serve only as guides. After determining which Rockwell scale should be used based on minimum thickness values, an actual test should be performed, and the side directly beneath the indentation should be examined to determine whether the material was disturbed or a bulge exists. If so, the material is not sufficiently thick for the applied load. This results in a condition known as “anvil effect.” When anvil effect or flow exists, the Rockwell hardness number obtained may not be a true value. The Rockwell scale applying the next lighter load should then be used.

Use of several specimens, one on top of the other, is not allowed. Slippage between the contact surfaces of the specimens makes a true value impossible to obtain. The only exception is in the testing of plastics; use of several thicknesses for elastomeric materials when anvil effect is present is recommended in ASTM D 785, “Standard Test Method for Rockwell Hardness of Plastics and Electrical Insulating Materials.” Testing performed on soft plastics may not have an adverse effect when the test specimen is composed of a stack of several pieces of the same thickness, provided that the surfaces of the pieces are in total contact and not held apart by sink marks, buffs from saw cuts, or other protrusions.

When testing specimens for which the anvil effect results, the condition of the supporting surface of the anvil must be observed carefully. After several tests, this surface may become marred, or a small indentation may be produced. Either condition affects the Rockwell test, because under the major load the test material will sink into the indentation in the anvil and a lower reading will result. If a specimen is found to have been too thin during testing, the anvil surface should be inspected; if damaged, it should be relapped or replaced.

When using a ball indenter and a superficial scale load of 15 kgf on a specimen in which anvil effect or material flow is present, a diamond spot anvil can be used in place of the standard steel anvil. Under these conditions, the hard diamond surface is not likely to be damaged when testing thin materials. Furthermore, with materials

that flow under load, the hard polished diamond provides a somewhat standardized frictional condition with the underside of the specimen, which improves repeatability of readings.

Additional information is provided in the section “Anvil Effect” in the article “Selection and Industrial Application of Hardness Tests” in this Volume.

Test Location

If an indentation is placed too close to the edge of a specimen, the workpiece edge may bulge, causing the Rockwell hardness number to decrease accordingly. To ensure an accurate test, the distance from the center of the indentation to the edge of the specimen must be at least 2.5 times the diameter of the indent. Therefore, when testing in a narrow area, the width of this area must be at least five diameters when the indentation is placed in the center. The appropriate scale must be selected for this minimum width. Although the diameter of the indentation can be calculated, for practical purposes the minimum distance can be determined visually.

An indentation hardness test cold works the surrounding material. If another indentation is placed within this cold-worked area, the reading usually will be higher than that obtained had it been placed outside this area. Generally, the softer the material, the more critical the spacing of indentations. However, a distance three diameters from the center of one indentation to another is sufficient for most materials.

Scale Limitations

Because diamond indenters are not calibrated below values of 20, they should not be used when readings fall below this level. If used on softer materials, results may not agree when the indenters are replaced, and another scale—for example, the Rockwell B scale—should be used.

There is no upper limit to the hardness of a material that can be tested with a diamond indenter. However, the Rockwell C scale should not be used on tungsten carbide because the material will fracture or the diamond life will be reduced considerably. The Rockwell A scale is the accepted scale in the carbide products industry. Due to the unique requirements for the Rockwell testing of carbide materials, a separate ASTM test method has been developed. That test method, ASTM B 294, defines the tighter requirements necessary when testing carbide. The carbide hardness levels have been established and are maintained by the Cemented Carbide Producers Association (CCPA). Standard test blocks and indenters traceable to the CCPA standards are available. The user should note that diamond indenters for carbide testing are different than normal HRA scale testing indenters and should not be mixed. Because of the high stress on the tip of the indenter, the life of carbide indenters is normally much shorter than other Rockwell indenters.

Although scales that use a ball indenter (for example, the Rockwell B scale) range to 130, readings above 100 are not recommended, except under special circumstances. Between approximately 100 and 130, only the tip of the ball is used. Because of the relatively blunt shape in that part of the indenter, the sensitivity of most scales is poor in this region.

Also, with smaller diameter indenters, flattening of the ball is possible because of the high stress developed at the tip. However, because there is a loss of sensitivity as the size of the ball increases, the smallest possible ball should be used. If values above 100 are obtained, the next heavier load, or next smaller indenter, should be used. If readings below 0 are obtained, the next lighter load, or next larger indenter, should be used. Readings below 0 are not recommended on any Rockwell scale, because misinterpretation may result when negative values are used. On nonhomogeneous materials, a scale should be selected that gives relatively consistent readings. If the ball indenter is too small in diameter or the load is too light, the resulting indentation will not cover an area sufficiently representative of the material to yield consistent hardness readings.

Rockwell Testing Machines

Many different types of Rockwell testers are currently produced. Test loads can be applied in a number of ways; most utilize deadweight, springs, or closed-loop load-cell systems. Many testers use a dial (analog) measuring device. However, digital-readout testers are becoming the norm because of improved readability and accuracy. Some testers use microprocessors to control the test process, and such testers can be used to interface with computers. These testers can have significantly greater capabilities such as automatic conversions,

correction factors, and tolerance limits. Most digital units now have outputs to interface with a host computer or printer.

Various methods for performing the function of a Rockwell test have been developed by manufacturers. Generally, different machines are used to make standard Rockwell and superficial Rockwell tests. However, there are combination (twin) machines available that can perform both types of tests. The principal components of a deadweight type Rockwell tester are shown in Fig. 3.

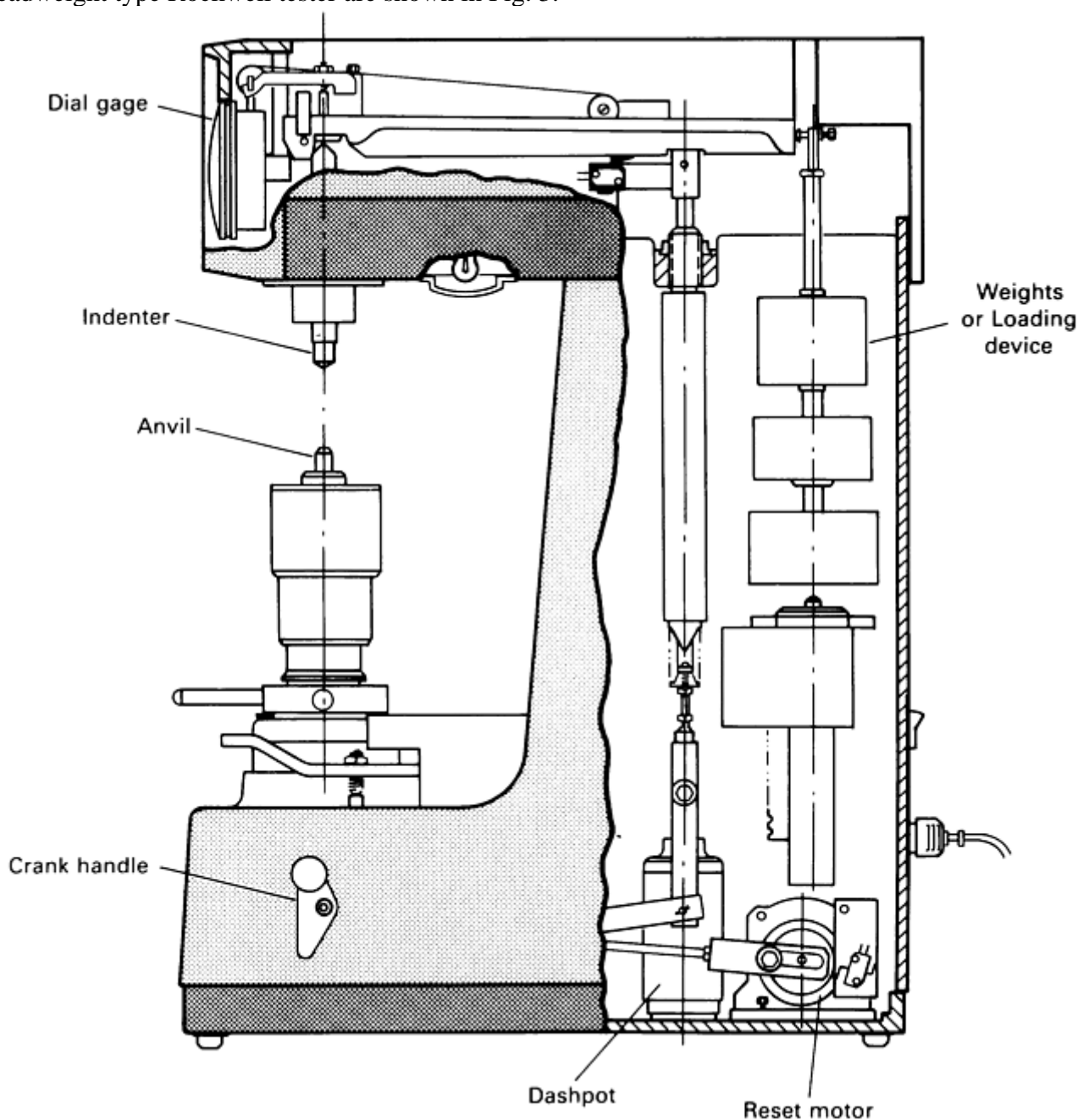


Fig. 3 Schematic of Rockwell testing machine

Bench-Type Testing Machines. Routine testing is commonly performed with bench-type machines (Fig. 4), which are available with vertical capacities of up to 400 mm (16 in.). A machine of this type can accommodate a wide variety of part shapes by capitalizing on standard as well as special anvil designs. The usefulness of this standard type of machine can be greatly extended by the use of various accessories, such as:

- Outboard or counterweighted anvil adapters for testing unwieldy workpieces such as long shafts
- Clamps that apply pressure on the part, which are particularly suited for testing parts that have a large overhang or long parts such as shafts
- Gooseneck anvil adapters for testing inner and outer surfaces of cylindrical objects



Fig. 4 Bench-type Rockwell tester

Production Testing Machines. When large quantities of similar workpieces must be tested, conventional manually operated machines may not be adequate. With a motorized tester, hourly production can be increased by up to 30%.

To achieve still greater production rates, high-speed testers (5) are used. High-speed testers can be automated to include automatic feeding, testing, and tolerance sorting. Upper and lower tolerance limits can be set from an operator control panel. These testers allow test loads to be applied at high speed with short dwell times. Up to 1000 parts per hour can be tested. These testers are normally dedicated to specific hardness ranges.

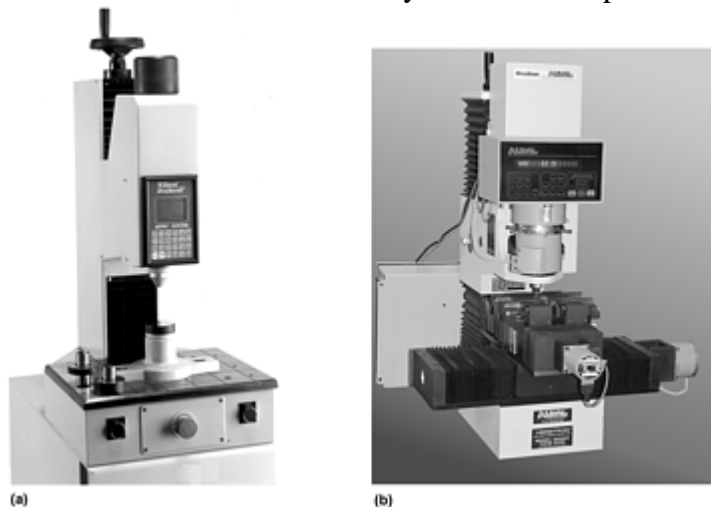


Fig. 5 Production Rockwell testers. (a) High-speed Rockwell tester. (b) Automated Rockwell tester for high-rate testing, such as the setup shown for Jominy end-quench hardenability testing

Computerized Testing Systems. With the use of microprocessors in digital testers, the ability to add computer control is possible. The computer can be programmed to perform a series of tests such as a case-depth study or a Jominy test. Using a motorized stage, any combination of test patterns can be performed with little operator effort. Automatic test reports and data storage are normally part of the program.

Portable Testing Machines. For hardness testing of large workpieces that cannot be moved, portable units are available in most regular and superficial scales and in a wide range of capacities (up to about a 355 mm, or 14 in., opening between anvil and indenter). Most portable hardness testers follow the Rockwell principle of minor and major loads, with the Rockwell hardness number indicated directly on the measuring device. Both digital and analog models are available. In Fig. 6(a), the workpiece is clamped in a C-clamp arrangement, and the indenter is recessed into a ring-type holder that is part of the clamp. The test principle is identical to that of bench-type models. The workpiece is held by the clamp between what is normally the anvil and the holder (which, in effect, serves as an upper anvil). The indenter is lowered to the workpiece through the holder. Other types of portable units (Fig. 6b) use the near-Rockwell method, where the diamond indenter is a truncated cone.

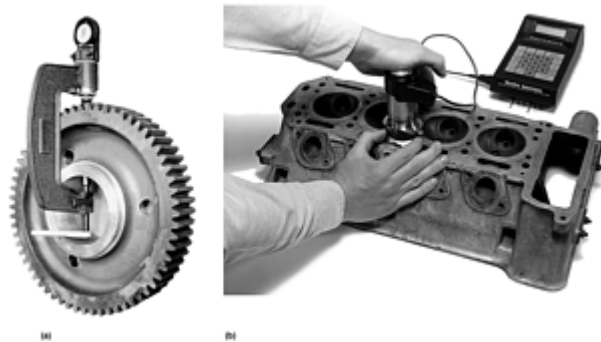


Fig. 6 Portable Rockwell testers. (a) C-clamp setup with a portable tester. (b) Portable near-Rockwell hardness tester

Calibration

If a Rockwell testing system is in constant use, a calibration check should be performed daily. Testers not used regularly should be checked before use. This check uses standardized test blocks to determine whether the tester and its indenter are in calibration.

Rockwell test blocks are made from high-quality materials for uniformity of test results. To maintain the integrity of the test block, only the calibrated surface can be used. Regrinding of this surface is not recommended due to the high possibility of hardness variations between the new and original surfaces.

If a tester is used throughout a given hardness scale, the recommended practice is to check it at the high, middle, and low ranges of the scale. For example, to check the complete Rockwell C scale, the tester should be checked at values such as 63, 45, and 25 HRC. On the other hand, if only one or two ranges are used, test blocks should be chosen that fall within 5 hardness numbers of the testing range on any scale using a diamond indenter and within 10 numbers on any scale using a ball indenter.

A minimum of five tests should be made on the standardized surface of the block. The tester is in calibration if the average of these tests falls within the tolerances indicated on the side of the test block. For best results, a pedestal spot anvil should be used for all calibration work.

If the average of the five readings falls outside the Rockwell test block limits, the ball in the ball indenter should be inspected visually; in the case of a diamond indenter, the point should be examined using at least a 10× magnifier. If there is any indication of damage, the damaged component must be replaced.

Rockwell Hardness Level National Standards. For more than 75 years, the producers of test blocks held the Rockwell hardness standards. While this worked well when there was only one manufacturer, the situation changed as more and more companies produced test blocks. To make matters worse, the U.S. standard did not match that used in the rest of the world and could not be traced to a government agency. In general, HRC hardness results with the old U.S. indenter appeared slightly softer (Fig. 2).

With involvement of the National Institute of Standards and Technology (NIST), a new U.S. Rockwell hardness standard was created. As expected, the level is very close to the other standardizing laboratories around the world. As soon as NIST released the new standard, many of the manufacturers started to calibrate their test blocks to the new standard. At the same time, ASTM Subcommittee E-28.06 started working on revisions to

ASTM E 18 to require the use of NIST traceable test blocks in the calibration of the blocks and testers. NIST initially released the Rockwell C scale, but they will eventually maintain standards for most of the commonly used scales (HRB, HRA, HR30N, HR30T, HR15N, and HR15T).

The impact of the new Rockwell C scale standards is that scales are shifted up slightly. The shift is greater in the high ranges (Fig. 2). For example, a piece of hardened steel that was determined to be 63.0 HRC under the old standard is now 63.6 HRC. This shift will impact some users more than others. The shift at the low end of the C scale is much less and will not be a problem to most users. The benefit to the new standard is that testers in the United States now have traceability, and results are comparable to those in the rest of the world.

Gage Repeatability and Reproducibility (GRR) Studies. Computerized statistical process control (SPC) techniques are used more and more by industry to control the manufacturing process. Gage repeatability and reproducibility studies are commonly used to evaluate the performance of gages.

Because hardness testers can be considered as gages, there have been some efforts by manufacturers and users of hardness testers to use GRR studies to determine what percent of the part tolerance is being used up by tester variations (see the article “Gage Repeatability and Reproducibility in Hardness Testing” in this Volume). The major problem associated with doing this type of study on any material testing instrument is that the material being tested can contribute significantly to the final results. This is due to unavoidable variations inherent in the material being tested. It is also not possible to test the exact same spot, and no material has completely uniform hardness. To obtain reasonable GRR results of hardness testing, material variability must be addressed. Test blocks that have known good uniformity should be used. Normally, blocks in the 63 HRC range with a reasonable tolerance will work. Using 63 HRC test blocks with low variations and a tolerance of ± 3 HRC points, it is possible to achieve GRR results in the 10% range or better. Good basic techniques must also be used to eliminate any other factors that could affect the results.

Testing Methodology

Although the Rockwell test is simple to perform, accurate results depend greatly on proper testing methods.

Indenters. The mating surfaces of the indenter and plunger rod should be clean and free of dirt, machined chips, and oil, which prevent proper seating and can cause erroneous test results. After replacing an indenter, a ball in a steel ball indenter, or an anvil, several tests should be performed to seat these parts before a hardness reading is taken. Indenters should be visually inspected to determine whether any obvious physical damage is present that may affect results.

Anvils should be selected to minimize contact area of the workpiece while maintaining stability. Figure 7 illustrates several common types of anvils that can accommodate a broad range of workpiece shapes. An anvil with a large flat surface (Fig. 7b) should be used to support flat-bottom workpieces of thick section. Anvils with a surface diameter greater than about 75 mm (3 in.) should be attached to the elevating screw by a threaded section, rather than inserted in the anvil hole in the elevating screw.



Fig. 7 Typical anvils for Rockwell hardness testing. (a) Standard spot, flat, and V anvils. (b) Testing table for large workpieces. (c) Cylinder anvil. (d) Diamond spot anvil. (e) Eyeball anvil

Sheet metal and small workpieces that have flat undersurfaces are best tested on a spot anvil with a small, elevated, flat bearing surface (Fig. 7a). Workpieces that are not flat should have the convex side down on the bearing surface. Round workpieces should be supported in a V-slot anvil (Fig. 7a and c). Diamond spot anvils (Fig. 7d) are used only for testing very thin sheet metal samples in the HR15T and HR30T scales.

Other anvil designs are available for a wide range of odd-shaped parts, such as the eyeball anvil (Fig. 7e) that is used for tapered parts. Special anvils to accommodate specific workpiece configurations can be fabricated. Regardless of anvil design, rigidity of the part to prevent movement during the test is absolutely essential for accurate results, as is cleanliness of the mating faces of the anvil and its supporting surface.

Specimen Surface Preparation. The degree of workpiece surface roughness that can be tolerated depends on the Rockwell scale being used. As a rule, for a load of 150 kgf on a diamond indenter, or 100 kgf on a ball indenter, a finish ground surface is sufficient to provide accurate readings. As loads become lighter, surface requirements become more rigorous. For a 15 kgf load, a polished or lapped surface usually is required.

Surfaces that are visibly ridged due to rough grinding or coarse machining offer unequal support to the indenter. Loose or flaking scale on the specimen at the point of indenter contact may chip and cause a false test. Scale should be removed by grinding or filing. Decarburized surface metal must also be removed to permit the indenter to test the true metal beneath.

Workpiece Mounting. An anvil must solidly support the test specimen. The movement of the plunger rod holding the indenter measures the depth of indentation when the major load is applied; any slippage or movement of the workpiece will be followed by the plunger rod. The motion will be transferred to the measuring system. Errors of this type always produce softer hardness values. Because one point of hardness represents a depth of only 0.002 mm (0.00008 in.), a movement of only 0.025 mm (0.001 in.) could cause an error of more than 10 Rockwell points.

Integral Clamping Systems. Some testers are designed with a clamping surface that surrounds the indenter either built into the test head or as a removable assembly (Fig. 8). These clamps can be helpful if a rapid test cycle is desired or the test point is on the end of a long overhung part. The anviling surface on the part is less critical; however, any movement of the part during the test will cause errors in the test results.



Fig. 8 Rockwell tester with removable clamping assembly

Angle of Test Surface. The test surface should be perpendicular to the indenter axis. Extensive experimentation has found errors of 0.1 to 1.5 HRC, depending on the hardness range being tested, with a 3° angle deviation. Such errors produce softer hardness values.

Load Application. The minor load should be applied to the test specimen in a controlled manner, without inducing impact or vibration. With manually operated testing machines, the measuring device must then be set to zero datum, or set point, position. The major load is then applied in a controlled fashion.

During the test cycle on a manually operated tester, the operator should not force the crank handle because inaccuracies and damage to the tester may result. When the large pointer comes to rest or slows appreciably, the full major load has been applied and should dwell for up to 2 s. The load is then removed by returning the crank handle to the latched position. The hardness value can then be read directly from the measuring device. Semiautomatic digital testers perform most of these steps automatically.

Homogeneity. A Rockwell tester measures the hardness of a specimen at the point of indentation, but the reading is also influenced by the hardness of the material under and around the indentation. The effects of indentation extend about 10 times the depth of the indentation. If a softer layer is located in this depth, the impression will be deeper, and the apparent hardness will be less.

The factor must be taken into account when testing material with a superficial hardness such as case-hardened work. To obtain the average hardness of materials such as cast iron with relatively large graphite particles, or nonferrous metals with crystalline aggregates that are greater than the area of the indenter, a larger indenter must be used. In many instances, a Brinell test may be more valid for this type of material.

Spacing of indentations is very important. The distance from the center of one indentation to another must be at least three indentation diameters, and the distance to the edge should be a minimum of 2.5 diameters. Readings from any indentation spaced closer should be disregarded. These guidelines apply for all materials.

Configuration Adjustments

When performing a Rockwell test, specimen size and configuration may require that modifications in the test setup be made. For example, large specimens and thin-wall rings and tubing may need additional support equipment, and test results obtained from curved surfaces may require a correction factor.

Large Specimens. Many specially designed Rockwell hardness testers that have been developed to accommodate the testing of large specimens cannot conveniently be brought to or placed in a bench-type tester. For large and heavy workpieces, or workpieces of peculiar shape that must rest in cradles or on blocks, use of a large testing table is recommended.

Long Specimens. Work supports are available for long workpieces that cannot be firmly held on an anvil by the minor load. Because manual support is not practical, a jack-rest should be provided at the overhang end to prevent pressure between the specimen and the penetrator. Figure 9 illustrates methods for testing long, heavy workpieces.



Fig. 9 Rockwell test setups for long testpieces. (a) Jack setup. (b) Variable rest setup

Workpieces with Curved Surfaces. When an indenter is forced into a convex surface, there is less lateral support supplied for the indenting force; consequently, the indenter will sink farther into the metal than it would into a flat surface of the same hardness. Therefore, for convex surfaces, low readings will result. On the other hand, when testing a concave surface, opposite conditions prevail; that is, additional lateral support is provided, and the readings will be higher than when testing the same metal with a flat surface.

Results from tests on a curved surface may be in error and should not be reported without stating the radius of curvature. For diameters of more than 25 mm (1 in.), the difference is negligible. For diameters of less than 25 mm (1 in.), particularly for softer materials that involve larger indentation, the curvature, whether concave or convex, must be taken into account if a comparison is to be made with different diameters or with a flat surface. Correction factors should be applied when workpieces are expected to meet a specified value. Typical correction factors for regular and superficial hardness values are presented in the article "Selection and Industrial Applications of Hardness Tests" in this Volume (see Table 4 in that article). The corrections are added to the hardness value when testing on convex surfaces and subtracted when testing on concave surfaces.

On cylinders with diameters as small as 6.35 mm (0.25 in.), standard Rockwell scales can be used; for the superficial Rockwell test, correction factors for diameters as small as 3.175 mm (0.125 in.) are given in the article "Selection and Industrial Applications of Hardness Tests" in this Volume (see Table 4 in that article). Diameters smaller than 3.175 mm (0.125 in.) should be tested by microindentation methods (see the article "Microindentation Hardness Testing" in this Section).

When testing cylindrical pieces such as rods, the shallow V or standard V anvil should be used, and the indenter should be applied over the axis of the rod. Care should be taken that the specimen lies flat, supported by the sides of the V. 10 Figure 10 illustrates correct and incorrect methods of supporting cylindrical work while testing.

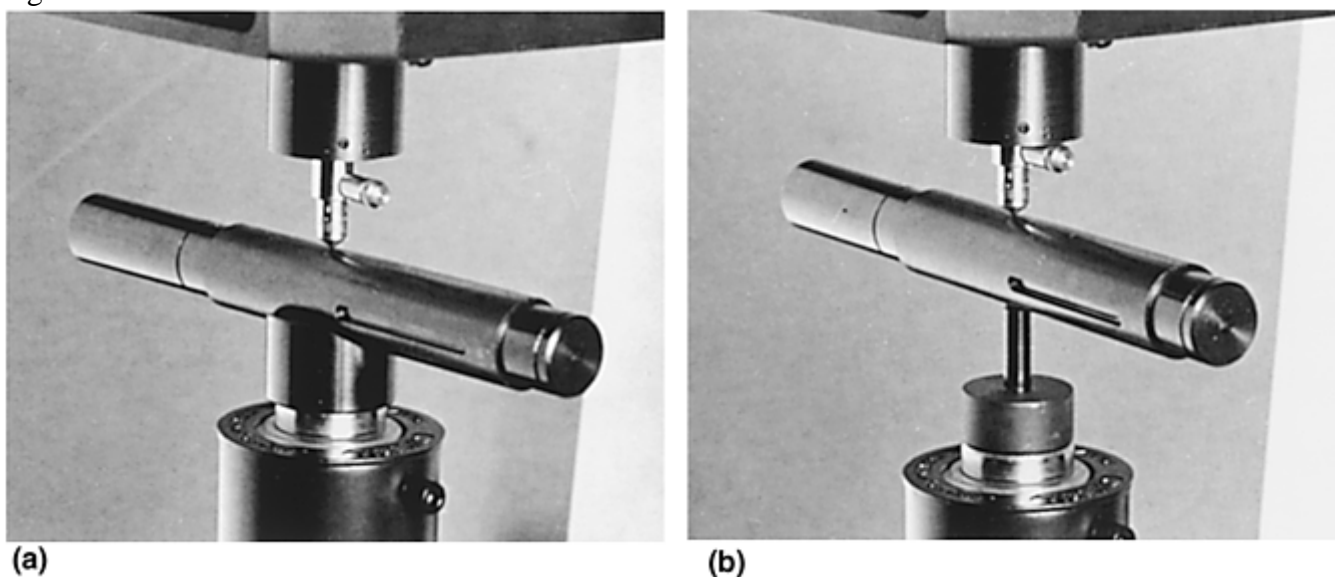


Fig. 10 Anvil support for cylindrical workpieces. (a) Correct method places the specimen centrally under indenter and prevents movement of the specimen under testing loads. (b) Incorrect method of supporting cylindrical work on spot anvil. The testpiece is not firmly secured, and rolling of the specimen can cause damage to the indenter or erroneous readings.

Inner Surfaces. The most basic approach to Rockwell hardness testing of inner surfaces is to use a gooseneck adapter for the indenter, as illustrated in Fig. 12. This adapter can be used for testing in holes or recesses as small as 11.11 mm (0.4375 in.) in diameter or height. Some testers are designed with an extended indenter holder to allow easier internal testing.

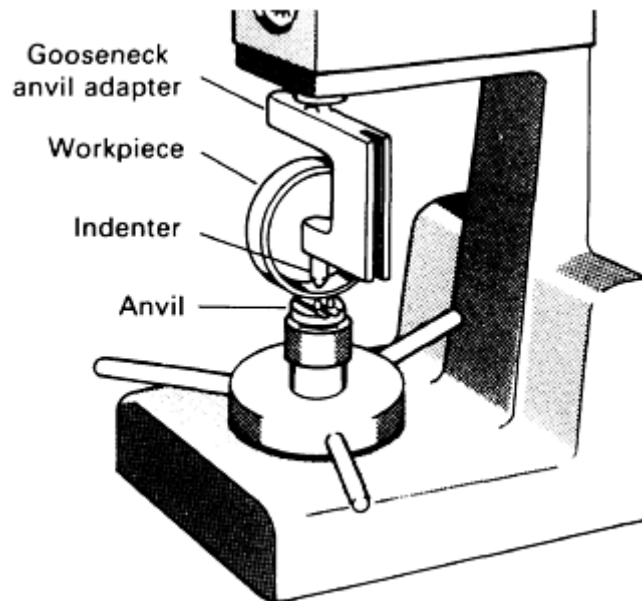


Fig. 11 Setup for Rockwell hardness testing of inner surfaces of cylindrical workpieces, using a gooseneck adapter

Thin-Wall Rings and Tubes. When testing pieces such as thin-wall rings and tubing that may deform permanently under load, a test should be conducted in the usual manner to see if the specimen becomes permanently deformed. If it has been permanently deformed either an internal mandrel on a gooseneck anvil or a lighter test load should be used.

Excessive deformation of tubing (either permanent or temporary) can also affect the application of the major load. If through deformation the indenter travels to its full extent, complete application of the major load will be prevented, and inaccurately high readings will result.

Gears and other complex shapes often require the use of relatively complex anvils in conjunction with holding fixtures. When hardness testing workpieces that have complex shapes—for example, the pitch lines of gear teeth—it is sometimes necessary to design and manufacture special anvils and fixtures; specially designed hardness testers may be required to accommodate these special fixtures.

Testing at Elevated Temperatures

Several methods have been devised to determine hardness at elevated temperatures, but a modified Rockwell test is used most often. Elevated-temperature testing typically consists of a Rockwell tester with a small furnace mounted on it. The furnace has a controlled atmosphere, usually argon, although a vacuum furnace may be used. Testing up to 760°C (1400°F) is possible; however, diamond indenters have a very limited life at high temperatures.

High-temperature test setups may also feature an indexing fixture that makes it possible to bring any area of the specimen under the indenter without contaminating the atmosphere or disturbing the temperature equilibrium. This arrangement permits several tests to be made on a single specimen while maintaining temperature and atmosphere.

In addition to modified Rockwell testers, hot hardness testers using a Vickers sapphire indenter with provisions for testing in either vacuum or inert atmospheres have also been described (Ref 1, 2). An extensive review of hardness data at elevated temperatures is presented in Ref 3. The development and design of hot hardness testing furnaces is described in Ref 4.

Rockwell Testing of Specific Materials

Most homogeneous metals or alloys, including steels of all product forms and heat treatment conditions and the various wrought and cast nonferrous alloys, can be accurately tested by one or more of the 30 indenter-load combinations listed in Tables 2 and 3. However, some nonhomogeneous materials and case-hardened materials present problems and therefore require special consideration.

Cast irons, because of graphite inclusions, usually show indentation values that are below the matrix value. For small castings or restricted areas in which a Brinell test is not feasible, tests may be made with either the Rockwell B or C scale. If the hardness range permits, however, the Rockwell E or K scale is preferred, because the 3.175 mm ($\frac{1}{8}$ in.) diam ball provides a better average reading.

Powder metallurgy (P/M) parts usually are tested on the Rockwell F, H, or B scale. Where possible, the Rockwell B scale should be used. In all instances, the result is apparent hardness because of the voids present in the P/M parts. Therefore, indentation testing does not provide accurate results of matrix hardness, although it serves well as a quality-control tool.

Cemented carbides are usually tested with the Rockwell A scale. If voids exist, the result is apparent hardness, and matrix evaluations are possible only by microhardness testing.

Case-Hardened Parts. For accuracy in testing case-hardened workpieces, the effective case depth should be at least 10 times the indentation depth. Generally, cases are quite hard and require the use of a diamond indenter; thus, a choice of six scales exists, and the scale should be selected in accordance with the case depth.

If the case depth is not known, a skilled operator can, by using several different (sometimes only two) scales and making comparisons on a conversion table, determine certain case characteristics. For example, if a part shows a reading of 91 HR15N and 62 HRC, this indicates a case that is hard at the surface, as well as at an appreciable depth, because the equivalent of 62 HRC is 91 HR15N. However, if the reading shows 91 HR15N and only 55 HRC, this indicates that the indenter has broken through a relatively thin case.

Decarburization can be detected by the indentation hardness test, essentially by reversing the technique described above for obtaining an indication of case depth. Two indentation tests—one with the Rockwell 15N scale and another with the Rockwell C scale—should be performed. If the equivalent hardness is not obtained in converting from the Rockwell 15N to the Rockwell C scale, a decarburized layer is indicated. This technique is most effective for determining very thick layers of decarburization, 0.1 mm (0.004 in.) or less. When decarburization is present, other methods such as microindentation hardness testing should be used to determine the extent.

References cited in this section

1. F. Garofalo, P.R. Malenock, and G.V. Smith, Hardness of Various Steels at Elevated Temperatures, *Trans. ASM*, Vol 45, 1953, p 377–396
2. M. Semchyshen and C.S. Torgerson, Apparatus for Determining the Hardness of Metals at Temperatures up to 3000 °F, *Trans. ASM*, Vol 50, 1958, p 830–837
3. J.H. Westbrook, Temperature Dependence of the Hardness of Pure Metals, *Trans. ASM*, Vol 45, 1953, p 221–248
4. L. Small, “Hardness—Theory and Practice,” Service Diamond Tool Company, Ferndale, MI, 1960, p 363–390

Macroindentation Hardness Testing

Edward L. Tobolski, Wilson Instruments Division, Instron Corporation; Andrew Fee, Consultant

Brinell Hardness Testing

The Brinell test is a simple indentation test for determining the hardness of a wide variety of materials. The test consists of applying a constant load (force), usually between 500 and 3000 kgf, for a specified time (10 to 30 s) using a 5 or 10 mm (0.2 or 0.4 in.) diam tungsten carbide ball on the flat surface of a workpiece (Fig. 12a). The

load time period is required to ensure that plastic flow of the metal has ceased. After removal of the load, the resultant recovered round impression is measured in millimeters using a low-power microscope (Fig. 12b).

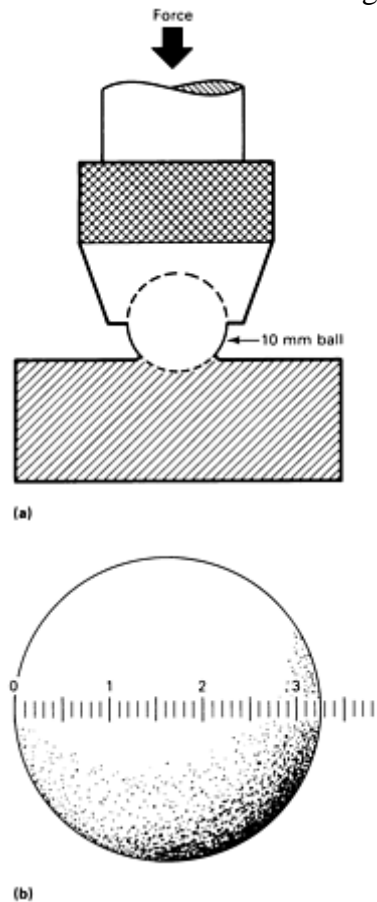


Fig. 12 Brinell indentation process. (a) Schematic of the principle of the Brinell indentation process. (b) Brinell indentation with measuring scale in millimeters

Hardness is determined by taking the mean diameter of the indentation (two readings at right angles to each other) and calculating the Brinell hardness number (HB) by dividing the applied load by the surface area of the indentation according to the following formula:

$$HB = \frac{2P}{\pi D (D - \sqrt{D^2 - d^2})}$$

where P is load (in kgf), D is ball diameter (in mm), and d is diameter of the indentation (in mm).

It is not necessary to make the above calculation for each test. Calculations have already been made and are available in tabular form for various combinations of diameters of impressions and load. Table 5 lists Brinell hardness numbers for indentation diameters of 2.00 to 6.45 mm for 500, 1000, 1500, 2000, 2500, and 3000 kgf loads.

Table 5 Brinell hardness numbers

Ball diameter, 10 mm

Ball impression, diam, mm	Brinell hardness number at load, kgf					
	500	1000	1500	2000	2500	3000
2.00	158	316	473	632	788	945
2.05	150	300	450	600	750	899
2.10	143	286	428	572	714	856
2.15	136	272	408	544	681	817
2.20	130	260	390	520	650	780
2.25	124	248	372	496	621	745

2.30	119	238	356	476	593	712
2.35	114	228	341	456	568	682
2.40	109	218	327	436	545	653
2.45	104	208	313	416	522	627
2.50	100	200	301	400	500	601
2.55	96.3	193	289	385	482	578
2.60	92.6	185	278	370	462	555
2.65	89.0	178	267	356	445	534
2.70	85.7	171	257	343	429	514
2.75	82.6	165	248	330	413	495
2.80	79.6	159	239	318	398	477
2.85	76.8	154	230	307	384	461
2.90	74.1	148	222	296	371	444
2.95	71.5	143	215	286	358	429
3.00	69.1	138	207	276	346	415
3.05	66.8	134	200	267	334	401
3.10	64.6	129	194	258	324	388
3.15	62.5	125	188	250	313	375
3.20	60.5	121	182	242	303	363
3.25	58.6	117	176	234	293	352
3.30	56.8	114	170	227	284	341
3.35	55.1	110	165	220	276	331
3.40	53.4	107	160	214	267	321
3.45	51.8	104	156	207	259	311
3.50	50.3	101	151	201	252	302
3.55	48.9	97.8	147	196	244	293
3.60	47.5	95.0	142	190	238	285
3.65	46.1	92.2	138	184	231	277
3.70	44.9	89.8	135	180	225	269
3.75	43.6	87.2	131	174	218	262
3.80	42.4	84.8	127	170	212	255
3.85	41.3	82.6	124	165	207	248
3.90	40.2	80.4	121	161	201	241
3.95	39.1	78.2	117	156	196	235
4.00	38.1	76.2	114	152	191	229
4.05	37.1	74.2	111	148	186	223
4.10	36.2	72.4	109	145	181	217
4.15	35.3	70.6	106	141	177	212
4.20	34.4	68.8	103	138	172	207
4.25	33.6	67.2	101	134	167	201
4.30	32.8	65.6	98.3	131	164	197
4.35	32.0	64.0	95.9	128	160	192
4.40	31.2	62.4	93.6	125	156	187
4.45	30.5	61.0	91.4	122	153	183
4.50	29.8	59.6	89.3	119	149	179
4.55	29.1	58.2	87.2	116	145	174
4.60	28.4	56.8	85.2	114	142	170
4.65	27.8	55.6	83.3	111	139	167
4.70	27.1	54.2	81.4	108	136	163
4.75	26.5	53.0	79.6	106	133	159
4.80	25.9	51.8	77.8	104	130	156

4.85	25.4	50.8	76.1	102	127	152
4.90	24.8	49.6	74.4	99.2	124	149
4.95	24.3	48.6	72.8	97.2	122	146
5.00	23.8	47.6	71.3	95.2	119	143
5.05	23.3	46.6	69.8	93.2	117	140
5.10	22.8	45.6	68.3	91.2	114	137
5.15	22.3	44.6	66.9	89.2	112	134
5.20	21.8	43.6	65.5	87.2	109	131
5.25	21.4	42.8	64.1	85.6	107	128
5.30	20.9	41.8	62.8	83.6	105	126
5.35	20.5	41.0	61.5	82.0	103	123
5.40	20.1	40.2	60.3	80.4	101	121
5.45	19.7	39.4	59.1	78.8	98.5	118
5.50	19.3	38.6	57.9	77.2	96.5	116
5.55	18.9	37.8	56.8	75.6	95.0	114
5.60	18.6	37.2	55.7	74.4	92.5	111
5.65	18.2	36.4	54.6	72.8	90.8	109
5.70	17.8	35.6	53.5	71.2	89.2	107
5.75	17.5	35.0	52.5	70.0	87.5	105
5.80	17.2	34.4	51.5	68.8	85.8	103
5.85	16.8	33.6	50.5	67.2	84.2	101
5.90	16.5	33.0	49.6	66.0	82.5	99.2
5.95	16.2	32.4	48.7	64.8	81.2	97.3
6.00	15.9	31.8	47.7	63.6	79.5	95.5
6.05	15.6	31.2	46.8	62.4	78.0	93.7
6.10	15.3	30.6	46.0	61.2	76.7	92.0
6.15	15.1	30.2	45.2	60.4	75.3	90.3
6.20	14.8	29.6	44.3	59.2	73.8	88.7
6.25	14.5	29.0	43.5	58.0	72.6	87.1
6.30	14.2	28.4	42.7	56.8	71.3	85.5
6.35	14.0	28.0	42.0	56.0	70.0	84.0
6.40	13.7	27.4	41.2	54.8	68.8	82.5
6.45	13.5	27.0	40.5	54.0	67.5	81.0

Before using the Brinell test, several points must be considered. The size and shape of the workpiece must be capable of accommodating the relatively large indentation and heavy test loads. Because of the large indentation, some workpieces may not be usable after testing and others may require further machining. In addition, the maximum range of Brinell hardness values is 16 HB for very soft aluminum to 627 HB for hardened steels (approximately 60 HRC).

Several standards specify requirements for Brinell hardness testing. Table 6 is a partial list of several Brinell standards, which should be compared in detail if equivalency is being considered.

Table 6 Selected Brinell hardness test standards

Standard No.	Title
ASTM E 10	Standard Test Method for Brinell Hardness of Metallic Materials
BS EN ISO 6506-1	Metallic Materials—Brinell Hardness Test—Test Method
BS EN ISO 6506-2	Metallic Materials—Brinell Hardness Test—Verification and Calibration of Brinell Hardness Testing Machines
BS EN ISO 6506-3	Metallic Materials—Brinell Hardness Test—Calibration of Reference Blocks
DIN EN	Brinell Hardness Test—Test Method

10003-1	
DIN EN 10003-2	Metallic Materials—Brinell Hardness Test—Verification of Brinell Hardness Testing Machines
DIN EN 10003-3	Metallic Materials—Brinell Hardness Test—Calibration of Standardized Blocks to be Used for Brinell Hardness Testing Machines
JIS B 7724	Brinell Hardness Testing Machines
JIS B 7736	Standardized Blocks of Brinell Hardness
JIS Z 2243	Method of Brinell Hardness Test

Indenter Selection and Geometry

The standard ball for Brinell hardness testing is 10.0 mm (0.39 in) in diameter. ASTM E 10, “Standard Test Method for Brinell Hardness of Metallic Materials,” specifies that the 10 mm ball indenter shall not deviate more than ± 0.005 mm in any diameter. When balls smaller than 10 mm in diameter are used, both the test load and ball size should be specifically stated in the test report. The tolerance for balls differing in size from the standard 10 mm ball should conform to standard limits, such as those in Table 7 from ASTM E 10. When using a different size ball, more comparable results can be obtained if the load to diameter squared ratios are similar.

Table 7 Tolerances for Brinell indenter balls other than standard

Ball diameter, mm	Tolerance^(a), mm
1–3, inclusive	± 0.0035
More than 3–6, inclusive	± 0.004
More than 6–10, inclusive	± 0.0045

(a) Balls for ball bearings normally satisfy these tolerances.

Source: ASTM E 10

Hardened steel balls have been used in the past for testing material up to 444 HB (2.90 mm diam indentation). Testing at higher hardness with steel balls may cause appreciable error due to the possible flattening and permanent deformation of the ball. Therefore, the latest ASTM standards require the use of only tungsten carbide balls with a minimum hardness of 1500 HV10. Tungsten carbide ball indenters are usable up to 627 HB (2.40 mm diam indentation). The user is cautioned that slightly higher hardness values result when using carbide balls instead of steel balls because of the difference in elastic properties between these materials. To avoid any confusion, whenever a steel ball is used, the hardness is reported as HBS, and when a carbide ball is used the HBW designation is required.

Load Selection and Impression Size

While theoretically any load can be used, the loads considered standard are 500, 1000, 1500, 2000, 2500, and 3000 kgf. The test load used is dependent mainly on size of impression, specimen thickness, and test surface. The 500 kgf load is usually used for testing relatively soft metals such as copper and aluminum alloys. The 3000 kgf load is most often used for testing harder materials such as steels and cast irons.

It is recommended that the test load be of such magnitude that the diameter of the impression be in the range 2.40 to 6.00 mm (24.0–60.0% of ball diameter). Upper and lower limits of impression diameters are necessary because the sensitivity of the test is reduced as impression size exceeds the limits specified above. In addition, the upper limit may be influenced by limitations of the travel of the indenter in certain types of testers. Other nonstandard lighter loads can be used as required on softer or thinner materials.

Indentation Measurement

The diameter of the indentation is frequently measured to the nearest 0.01 mm by means of a specially designed microscope having a built-in millimeter scale. To eliminate error in the measurements due to slightly out-of-round impressions, two diameter measurements should be taken at 90° to each other. The Brinell hardness

number is based on the average of these two measurements. Table 5 provides a simple way to convert the indentation diameter to the Brinell hardness number.

The indentations produced in Brinell hardness tests may exhibit different surface characteristics. In some instances there is a ridge around the indentation that extends above the surface of the workpiece. In other instances the edge of the indentation is below the original surface. Sometimes there is no difference at all. The first phenomenon, called “ridging,” is illustrated in Fig. 13(a). The second phenomenon, called “sinking,” is illustrated in Fig. 13(b). An example of no difference is shown in Fig. 13(c). Cold-worked metals and decarburized steels are those most likely to exhibit ridging. Fully annealed metals and light case-hardened steels more often show sinking around the indentation.

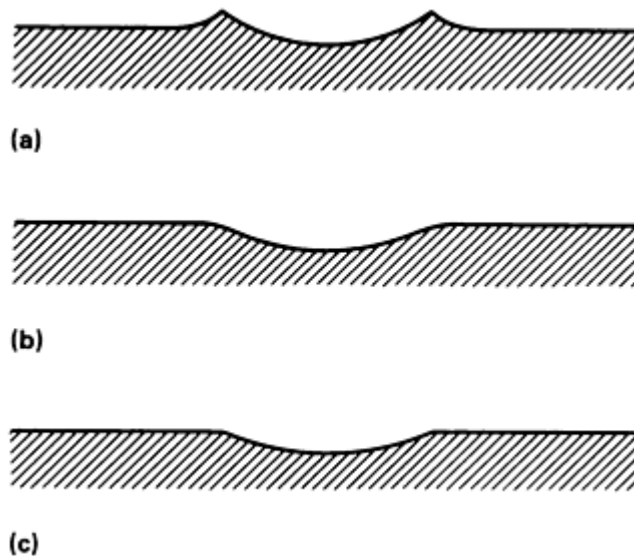


Fig. 13 Sectional views of Brinell indentations. (a) Ridging-type Brinell impression. (b) Sinking-type Brinell impression. (c) Flat-type Brinell impression

The Brinell hardness number is related to the surface area of the indentation. This is obtained by measuring the diameter of the indentation, based on the assumption that it is the diameter with which the indenter was in actual contact. However, when either ridging or sinking is encountered there is always some doubt as to the exact part of the visible indentation with which the actual contact was made. When ridging is present, the apparent diameter of the indentation is greater than the true value, whereas the reverse is true when sinking occurs.

Because of the above conditions, measurements of indentation diameters require experience and some judgment on the part of the operator. Experience can be gained by measuring calibration indents in the standardized test block.

Even when all precautions and limitations are observed, the Brinell indentations for some materials vary in shape. For example, materials that have been subjected to unidirectional cold working often exhibit extreme elliptical indentations. In such cases, where best possible accuracy is required, the indentation is measured in four directions approximately 45° apart, and the average of these four readings is used to determine the Brinell hardness number. Other techniques such as Rockwell-type depth measurements are often used with high-production equipment.

Semiautomatic Indent Measurements. In an effort to reduce measurement errors, image analysis systems are available for the measurement of the indent area. The systems normally consist of a solid-state camera mounted on a flexible probe, which is typically manually placed over the indent (Fig. 14). A computer program then analyzes the indent and calculates the size and Brinell number. The advantage of these systems is that they can reduce the errors associated with the optical measurements done by an operator. The surface finish requirements are frequently higher as the computer can have difficulty measuring noncircular indents or jagged edges for which an experienced operator could make judgments and correct as needed.



Fig. 14 Computerized Brinell hardness testing optical scanning system

General Precautions and Limitations

To avoid misapplication and errors in Brinell hardness testing, the fundamentals and limitations of the test must be thoroughly understood. The following precautions should be observed before testing.

Thickness of the testpiece should be such that no bulge or other marking showing the effect of the load appears on the side of the piece opposite the impression. The thickness of the specimen should be at least ten times the depth of the indentation. Depth of indentation may be calculated from the formula:

$$\text{Depth (mm)} = \frac{P}{\pi D \times (\text{HB})}$$

where P is load in kgf, D is ball diameter in mm, and HB is Brinell hardness number. For example, a reading of 300 HB indicates:

$$\begin{aligned} \text{Depth} &= \frac{3000}{\pi D \times 300} \\ \text{Depth} &= \frac{1}{\pi} = 0.32 \text{ mm} \end{aligned}$$

Therefore, the minimum thickness of the workpiece is 10×0.32 or 3.2 mm (0.125 in.). Table 8 gives minimum thickness requirements.

Table 8 Minimum thickness requirements for Brinell hardness tests

Minimum thickness of specimen		Minimum hardness for which the Brinell test may be made safely		
mm	in.	3000 kgf load	1500 kgf load	500 kgf load
1.6	0.0625	602	301	100
3.2	0.125	301	150	50

4.8	0.1875	201	100	33
6.4	0.250	150	75	25
8.0	0.3125	120	60	20
9.6	0.375	100	50	17

Test surfaces that are flat give best results. Curved test surfaces of less than 25 mm (1 in.) radius should not be tested.

Spacing of Indentations. For accurate results, indentations must not be made near the edge of the workpiece. Lack of sufficient supporting material on one side will result in abnormally large, unsymmetrical indentations. In most instances the error in Brinell hardness number will not be significant if the distance from the center of the indentation to any edge of the workpiece is more than three times the diameter of the indentation.

Similarly, Brinell indentations must not be made too close to one another. The first indentation may cause cold working of the surrounding area that could affect the subsequent test if made within this affected region. It is generally agreed that the distance between centers of adjacent indentations should be at least three times the diameter of the indentation to eliminate significant errors.

Anvilting. The part must be anvilged properly to minimize workpiece movement during the test and to position the test surface perpendicular to the test force within 2°.

Surface Finish. The degree of accuracy attainable by the Brinell test can be greatly influenced by the surface finish of the workpiece. The surface of the workpiece should be milled, ground, or polished so that the indentation is defined clearly enough to permit accurate measurement. Care should be taken to avoid overheating or cold working the surface, as that may affect the hardness of the material. In addition, for accurate results, the workpiece surface must be representative of the material. Decarburization or any form of surface hardening must be removed prior to testing.

Testing Machines

Various kinds of Brinell testers are available for laboratory, production, automatic, and portable testing. These testers commonly use deadweight, hydraulic, pneumatic, elastic members (i.e., springs), or a closed-loop load-cell system to apply the test loads. All testers must have a rigid frame to maintain the load and a means of controlling the rate of load application to avoid errors due to impact (500 kgf/s maximum). The loads must be consistently applied within 1.0% as indicated in ASTM E 10. In addition, the load must be applied so that the direction of load is perpendicular to the workpiece surface within 2° for best results.

Bench units for laboratory testing are available with deadweight loading and/or pneumatic loading. Because of their high degree of accuracy, deadweight testers are most commonly used in laboratories and shops that do low- to medium-rate production. These units are constructed with weights connected mechanically to the Brinell ball indenter. Minimum maintenance is required because there are few moving parts. Figure 15(a) is an example of a motorized deadweight tester.



Fig. 15 Bench-type Brinell testers. (a) Motorized tester with deadweight loading. Courtesy of Wilson Instruments. (b) Brinell tester with combined deadweight loading and pneumatic operation. Courtesy of NewAge Industries

Bench units are also available with pneumatic load application or a combination of deadweight/pneumatic loading. Figure 15(b) shows an example of the latter, where the load can be applied by release of deadweights or by pneumatic actuation.

In both deadweight and pneumatic bench units, the testpiece is placed on the anvil, which is raised by an elevating screw until the testpiece nearly touches the indenter ball. Operator controls initiate the load, which is applied at a controlled rate and time duration by the test machine. The testpiece is then removed from the anvil, and the indentation width is measured with a Brinell scope, typically at 20× power. Testing with this type of apparatus is relatively slow and prone to operator influence on the test results.

Machines for Production Testing. Hydraulic testers were developed to reduce testing time and operator fatigue in production operations. Advantages of hydraulic testers include operating economy, simplicity of controls, and dependable accuracy. The controls prevent the operator from applying the load too quickly and thus overloading. The load is applied by a hydraulic cylinder and monitored by a pressure gage. Normally the pressure can be adjusted to apply any load between 500 and 3000 kgf. Hydraulic machines for production are available as bench-top or floor units (Fig. 16).

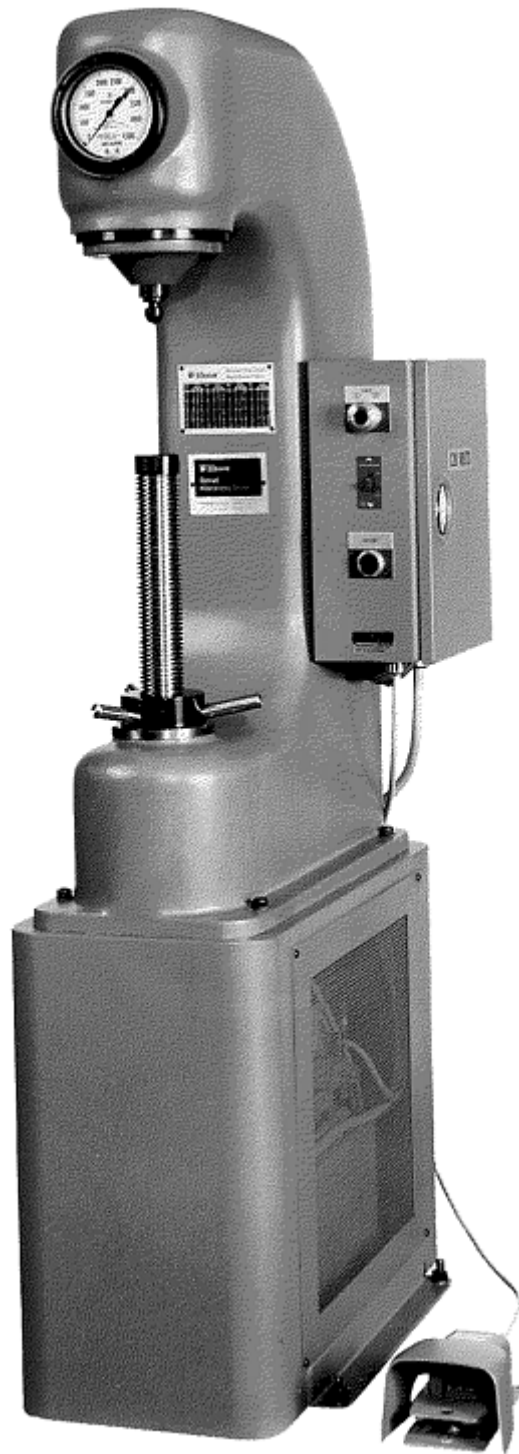


Fig. 16 Hydraulic Brinell tester. Courtesy of Wilson Instruments

Automatic Testers. Many types of automatic Brinell testers are currently available. Most of these testers (such as the one shown in Fig. 17) use a depth-measurement system to eliminate the time-consuming and operator-biased measurement of the diameters. All of these testers use a preliminary load (similar to the Rockwell principle) in conjunction with the standard Brinell loads. Simple versions of this technique provide only comparative “go/no-go” hardness indications; more sophisticated models offer a microprocessor-controlled digital readout to convert the depth measurement to Brinell numbers. Conversion from depth to diameter frequently varies for different materials and may require correlation studies to establish the proper relationship.



Fig. 17 Automatic Brinell hardness tester with digital readout. Courtesy of NewAge Industries

These units can be fully automated to obtain production rates up to 600 tests per hour and can be incorporated into in-line production equipment. The high-speed automatic testers typically comply with ASTM E 103, “Standard Method of Rapid Indentation Hardness Testing of Metallic Materials.”

Portable Testing Machines. The use of conventional hardness testers may occasionally be limited because the work must be brought to the machine and because the workpieces must be placed between the anvil and the indenter. Portable Brinell testers that circumvent these limitations are available. A typical portable instrument is shown in Fig. 18. This type of tester weighs only about 11.4 kg (25 lb), so it can be easily transported to the workpieces. Portable testers can accommodate a wider variety of workpieces than can the stationary types. The tester attaches to the workpiece as would a C-clamp with the anvil on one side of the workpiece and the indenter on the other. For very large parts, an encircling chain is used to hold the tester in place as pressure is applied.

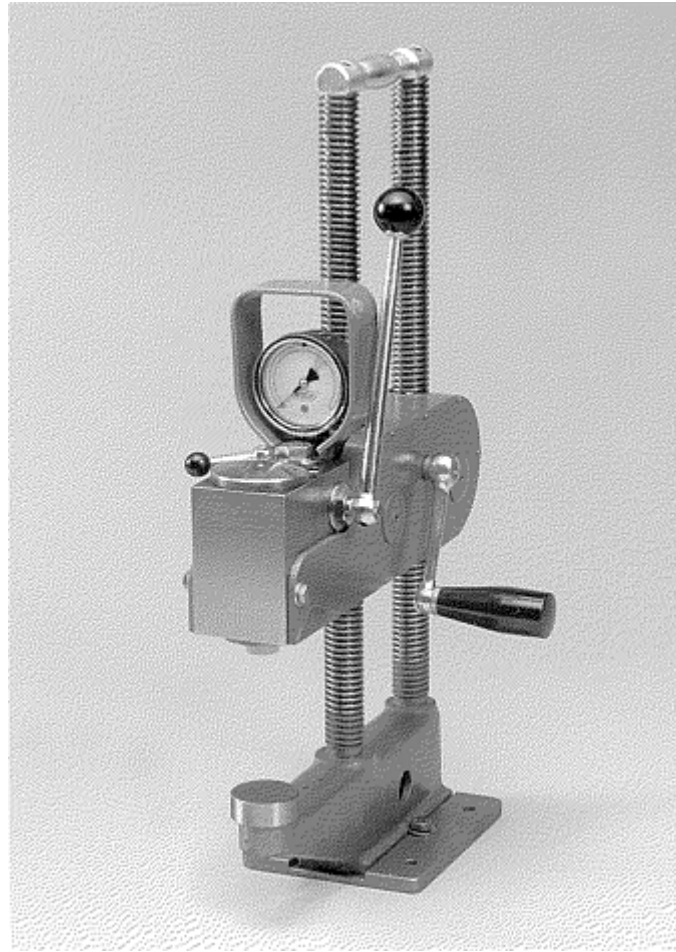


Fig. 18 Hydraulic, manually operated portable Brinell hardness tester

Portable testers generally apply the load hydraulically, employing a spring-loaded relief valve. The load is applied by operating the hydraulic pump until the relief valve opens momentarily. With this type of tester, the hydraulic pressure should be applied three times when testing steel with a 3000 kgf load. This is equivalent to a holding time of 15 s, as required by the more conventional method. For other materials and loads, comparison tests should be made to determine the number of load applications required to give results equivalent to the conventional method.

A comparison-type tester that uses a calibrated shear pin is shown in 19Fig. 19. In this method, a small pin of a known shear load is placed in the indenter assembly against the indenter (Fig. 19b). Through hammer impact or static clamping load, the indenter is forced into the material only as far as it takes to shear the pin. Excessive force is absorbed after shear by upward movement of the indenter into an empty cavity. The resulting impression is measured by the conventional Brinell method. This method does not comply with ASTM E 10.

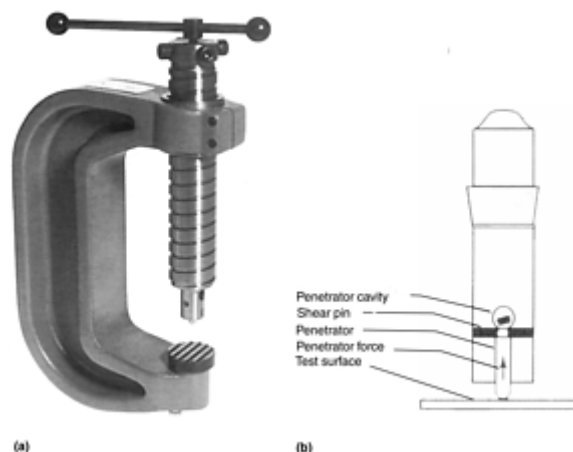


Fig. 19 Pin Brinell hardness tester. (a) Clamp loading tester. (b) Schematic of pin Brinell principle

Equipment Maintenance. To maintain accurate results from Brinell testing, equipment must be calibrated and serviced regularly, especially when machines are exposed to shop environments. The frequency of servicing depends on whether the testers are used in a production line or for making an occasional test. However, it is important that they be serviced and calibrated on a regular basis. Regular checking of the ball indenter for deformation is particularly important. Indenters are susceptible to wear as well as to damage. When an indenter becomes worn or damaged so that indentations no longer meet the standards, it must be replaced. Under no circumstances should attempts be made to compensate for a worn or damaged indenter.

Verification of Loads, Indenters, and Microscopes. As with any procedure that is dependent on several components, the accuracy of each must be verified to determine the accuracy of the result. In the case of Brinell hardness testing, load, indenter, and microscope accuracies must lie within a specified tolerance to ensure accurate results.

Load Verification. ASTM E 10 specifies that a Brinell hardness tester is acceptable for use over a load range within which the load error does not exceed $\pm 1\%$. Test loads should be checked by periodic calibration with a proving ring or load cell, the accuracy of which is traceable to the National Institute of Standards and Technology (NIST). Proving rings (see Fig. 20) are an elastic calibration device that is placed on the anvil of the tester. The deflection of the ring under the applied load is measured either by a micrometer screw and a vibrating reed or a reading dial gage. The amount of elastic deflection is then converted into load in kilograms and compared with required accuracies.

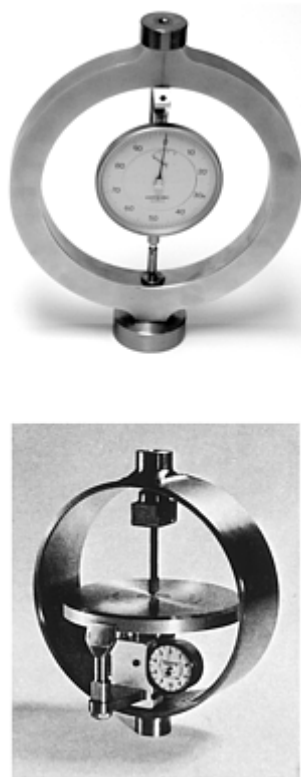


Fig. 20 Proving rings used for calibrating Brinell hardness testers

Ball Indenter Verification. The ball indenter must be accurate within ± 0.0005 mm of its nominal diameter. It is very difficult for the user to measure the ball in enough locations to guarantee the correct shape. Therefore, a close visual inspection is normally done, and any sign of damage will require replacement. A performance test (indirect verification) using test blocks is the best way to verify the ball. When in doubt, the ball should be replaced with a new ball certified by the manufacturer to meet all of the requirements in ASTM E 10.

Microscope Verification. The measuring microscope or other device used for measuring the diameter of the impression should be verified at five intervals over the working range by the use of a scale of known accuracy such as a stage micrometer. The adjustment of the micrometer microscope should be such that, throughout the range covered, the difference between the scale divisions of the microscope and of the calibrating scale does not exceed 0.01 mm.

Verification by Test Block (Indirect Verification). Standardized Brinell test blocks are available so that the accuracy of the Brinell hardness tester can be indirectly verified at the hardness level of the work being tested. Commonly available hardnesses are:

Test block material	Hardness, HB
Steel	500, 400, 350, 300, 250, 200
Brass	90
Aluminum	140

Good practice is to verify the tester throughout the hardness range encountered. This ensures that all test parameters are within tolerance.

Application for Specific Materials

As is true for other indentation methods of testing hardness, the most accurate results are obtained when testing homogeneous materials, regardless of the hardness range.

Steels. Virtually all hardened-and-tempered or annealed steels within the range of hardness mentioned provide accurate results with the Brinell test. However, as a rule, case-hardened steels are totally unsuitable for Brinell testing. In most instances, the surface hardness is above the practical range and is rarely thick enough to provide the required support for a Brinell test. Thus, “cave in” results, and grossly inaccurate readings are obtained.

Cast Irons. The large area of the test serves to average out the hardness difference between the iron and graphite particles present in most cast iron. This averaging effect allows the Brinell test to serve as an excellent quality-control tool.

Nonferrous metals (especially the wrought types) are generally amenable to Brinell testing, usually with the 500 kgf load, but occasionally with the 1500 kgf load. Some high-strength alloys such as titanium- and nickel-base alloys that are phase-transformation- or age-hardened can utilize the 3000 kgf load. In this situation, practical limits must be observed and some testing may be required to establish the optimal technique for testing a specific metal or alloy.

There are certain multiphase cast nonferrous alloys that are simply too soft for accurate Brinell testing. Microhardness testing is then employed. The lower limit of 16 HB with a 500 kgf load must always be observed.

Powder Metallurgy Parts. Testing of P/M parts with a Brinell tester (or any sort of macro-hardness tester) involves the same problem as encountered with cast iron. Instead of a soft graphite phase (some P/M parts also contain free graphite), P/M parts contain voids that may vary widely in size and number. Light-load Brinell testing is sometimes used successfully for testing of P/M parts, but its only real value is as a quality-control tool in measuring the apparent hardness of P/M parts (see the article “Selection and Industrial Applications of Hardness Tests” for more information on P/M hardness testing.)

Macroindentation Hardness Testing

Edward L. Tobolski, Wilson Instruments Division, Instron Corporation; Andrew Fee, Consultant

Vickers Hardness Testing

The Vickers hardness was first introduced in England in 1925 by R. Smith and G. Sandland (Ref 5). It was originally known as the 136° diamond pyramid hardness test because of the shape of the indenter. The manufacture of the first tester was a company known as Vickers-Armstrong Limited, of Crayford, Kent, England. As the test and the tester gained popularity, the name Vickers became the recognized designation for the test.

The Vickers test method is similar to the Brinell principle in that a defined shaped indenter is pressed into a material, the indenting force is removed, the resulting indentation diagonals are measured, and the hardness number is calculated by dividing the force by the surface area of the indentation. Vickers testing is divided into two distinct types of hardness tests: macroindentation and microindentation tests. These two types of tests are

defined by the forces. Microindentation Vickers (ASTM E 384) is from 1 to 1000 gf and is covered in detail in the article “Microindentation Hardness Testing.” this section focuses on the macroindentation range with test forces from 1 to 120 kgf as defined in ASTM E 92. Selected international standards for Vickers hardness testing are listed in Table 9.

Table 9 Selected Vickers hardness testing standards

Standard No.	Title
ASTM E 92	Standard Test Method for Vickers Hardness of Metallic Materials
BS EN ISO 6507-1	Metallic Materials—Vickers Hardness Test—Part 1: Test Method
BS EN ISO 6507-2	Metallic Materials—Vickers Hardness Test—Part 2: Verification of Testing Machines
BS EN ISO 6507-3	Metallic Materials—Vickers Hardness Test—Part 3: Calibration of Reference Blocks
EN 23878	Hardmetals—Vickers Hardness Test
JIS B 7725	Vickers Hardness—Verification of Testing Machines
JIS B 7735	Vickers Hardness Test—Calibration of the Reference Blocks
JIS Z 2244	Vickers Hardness Test—Test Method
JIS Z 2252	Test Methods for Vickers Hardness at Elevated Temperatures

Test Method

As mentioned previously, the principle of the Vickers test is similar to the Brinell test, but the Vickers test is performed with different forces and indenters. The square-base pyramidal diamond indenter is forced under a predetermined load ranging from 1 to 120 kgf into the material to be tested. After the forces have reached a static or equilibrium condition and further penetration ceases, the force remains applied for a specific time (10 to 15 s for normal test times) and is then removed. The resulting unrecovered indentation diagonals are measured and averaged to give a value in millimeters. These length measurements are used to calculate the Vickers hardness number (HV).

The Vickers hardness number (formerly known as DPH for diamond pyramid hardness) is a number related to the applied force and the surface area of the measured unrecovered indentation produced by a square-base pyramidal diamond indenter. The Vickers indenter has included face angles of 136° (Fig. 21), and the Vickers hardness number (HV) is computer from the following equation:

$$HV = \frac{2P \sin(136/2)}{d^2} = \frac{1.8544P}{d^2}$$

where P is the indentation load in kgf, and d is the mean diagonal of indentation, in mm. This calculation of Vickers hardness can be done directly from this formula or from Table 10 (lookup table in ASTM E 92). This table contains calculated Vickers numbers for a 1 kgf load, so that it is not necessary to calculate every test result. For example, if the average measured diagonal length, d , is 0.0753 mm with a 1 kgf load, then the Vickers number is:

$$HV = \frac{1.8544 (1 \text{ kgf})}{(0.0753)^2}$$

$$HV = 327$$

This value can be obtained directly from the lookup table. For obtaining hardness numbers when other loads are used, simply multiply the number from the lookup table by the test load.

Table 10 Vickers hardness numbers

Diamond indenter, 136° face angle, load of 1 kgf

Diagonal of impression, nm	Vickers hardness number for diagonal measured to 0.0001 mm									
	0.0000	0.0001	0.0002	0.0003	0.0004	0.0005	0.0006	0.0007	0.0008	0.0009
0.005	74,170	71,290	68,580	66,020	63,590	61,300	59,130	57,080	55,120	53,270
0.006	51,510	49,840	48,240	46,720	45,270	43,890	42,570	41,310	40,100	38,950
0.007	37,840	36,790	35,770	34,800	33,860	32,970	32,100	31,280	30,480	29,710
0.008	28,970	28,260	27,580	26,920	26,280	25,670	25,070	24,500	23,950	23,410
0.009	22,890	22,390	21,910	21,440	20,990	20,550	20,120	19,710	19,310	18,920
0.010	18,540	18,180	17,820	17,480	17,140	16,820	16,500	16,200	15,900	15,610
0.011	15,330	15,050	14,780	14,520	14,270	14,020	13,780	13,550	13,320	13,090
0.012	12,880	12,670	12,460	12,260	12,060	11,870	11,680	11,500	11,320	11,140
0.013	10,970	10,810	10,640	10,480	10,330	10,170	10,030	9,880	9,737	9,598
0.014	9,461	9,327	9,196	9,068	8,943	8,820	8,699	8,581	8,466	8,353
0.015	8,242	8,133	8,026	7,922	7,819	7,718	7,620	7,523	7,428	7,335
0.016	7,244	7,154	7,066	6,979	6,895	6,811	6,729	6,649	6,570	6,493
0.017	6,416	6,342	6,268	6,196	6,125	6,055	5,986	5,919	5,853	5,787
0.018	5,723	5,660	5,598	5,537	5,477	5,418	5,360	5,303	5,247	5,191
0.019	5,137	5,083	5,030	4,978	4,927	4,877	4,827	4,778	4,730	4,683
0.020	4,636	4,590	4,545	4,500	4,456	4,413	4,370	4,328	4,286	4,245
0.021	4,205	4,165	4,126	4,087	4,049	4,012	3,975	3,938	3,902	3,866
0.022	3,831	3,797	3,763	3,729	3,696	3,663	3,631	3,599	3,567	3,536
0.023	3,505	3,475	3,445	3,416	3,387	3,358	3,329	3,301	3,274	3,246
0.024	3,219	3,193	3,166	3,140	3,115	3,089	3,064	3,039	3,015	2,991
0.025	2,967	2,943	2,920	2,897	2,874	2,852	2,830	2,808	2,786	2,764
0.026	2,743	2,722	2,701	2,681	2,661	2,641	2,621	2,601	2,582	2,563
0.027	2,544	2,525	2,506	2,488	2,470	2,452	2,434	2,417	2,399	2,382
0.028	2,365	2,348	2,332	2,315	2,299	2,283	2,267	2,251	2,236	2,220
0.029	2,205	2,190	2,175	2,160	2,145	2,131	2,116	2,102	2,088	2,074
0.030	2,060	2,047	2,033	2,020	2,007	1,993	1,980	1,968	1,955	1,942
0.031	1,930	1,917	1,905	1,893	1,881	1,869	1,857	1,845	1,834	1,822
0.032	1,811	1,800	1,788	1,777	1,766	1,756	1,745	1,734	1,724	1,713
0.033	1,703	1,693	1,682	1,672	1,662	1,652	1,643	1,633	1,623	1,614
0.034	1,604	1,595	1,585	1,576	1,567	1,558	1,549	1,540	1,531	1,522
0.035	1,514	1,505	1,497	1,488	1,480	1,471	1,463	1,455	1,447	1,439
0.036	1,431	1,423	1,415	1,407	1,400	1,392	1,384	1,377	1,369	1,362
0.037	1,355	1,347	1,340	1,333	1,326	1,319	1,312	1,305	1,298	1,291
0.038	1,284	1,277	1,271	1,264	1,258	1,251	1,245	1,238	1,232	1,225
0.039	1,219	1,213	1,207	1,201	1,195	1,189	1,183	1,177	1,171	1,165
0.040	1,159	1,153	1,147	1,142	1,136	1,131	1,125	1,119	1,114	1,109
0.041	1,103	1,098	1,092	1,087	1,082	1,077	1,072	1,066	1,061	1,056
0.042	1,051	1,046	1,041	1,036	1,031	1,027	1,022	1,017	1,012	1,008
0.043	1,003	998	994	989	985	980	975	971	967	962
0.044	958	953	949	945	941	936	932	928	924	920
0.045	916	912	908	904	900	896	892	888	884	880
0.046	876	873	869	865	861	858	854	850	847	843
0.047	839	836	832	829	825	822	818	815	812	808
0.048	805	802	798	795	792	788	785	782	779	775
0.049	772	769	766	763	760	757	754	751	748	745
0.050	742	739	736	733	730	727	724	721	719	716

0.051	713	710	707	705	702	699	696	694	691	688
0.052	686	683	681	678	675	673	670	668	665	663
0.053	660	658	655	653	650	648	645	643	641	638
0.054	636	634	631	629	627	624	622	620	617	615
0.055	613	611	609	606	604	602	600	598	596	593
0.056	591	589	587	585	583	581	579	577	575	573
0.057	571	569	567	565	563	561	559	557	555	553
0.058	551	549	547	546	544	542	540	538	536	535
0.059	533	531	529	527	526	524	522	520	519	516.8
0.060	515.1	513.4	511.7	510.0	508.3	506.6	505.0	503.0	501.6	500.0
0.061	498.4	496.7	495.1	493.5	491.9	490.3	488.7	487.1	485.5	484.0
0.062	482.4	480.9	479.3	477.8	476.2	474.7	473.2	471.7	470.2	468.7
0.063	467.2	465.7	464.3	462.8	461.3	459.9	458.4	457.0	455.6	454.1
0.064	452.7	451.3	449.9	448.5	447.1	445.7	444.4	443.0	441.6	440.3
0.065	438.9	437.6	436.2	434.9	433.6	432.2	430.9	429.6	428.3	427.0
0.066	425.7	424.4	423.1	421.9	420.6	419.3	418.1	416.8	415.6	414.3
0.067	413.1	411.9	410.6	409.4	408.2	407.0	405.8	404.6	403.4	402.2
0.068	401.0	399.9	398.7	397.5	396.6	395.2	394.0	392.9	391.8	390.6
0.069	389.5	388.4	387.2	386.1	385.0	383.9	382.8	381.7	380.6	379.5
0.070	378.4	377.4	376.3	375.2	374.2	373.1	372.0	371.0	369.9	368.9
0.071	367.9	366.8	365.8	364.8	363.7	362.7	361.7	360.7	359.7	358.7
0.071	367.9	366.8	365.8	364.8	363.7	362.7	361.7	360.7	359.7	358.7
0.072	357.7	356.7	355.7	354.7	353.8	352.8	351.8	350.9	349.9	348.9
0.073	348.0	347.0	346.1	345.1	344.2	343.3	342.3	341.4	340.5	339.6
0.074	338.6	337.7	336.8	335.9	335.0	334.1	333.2	332.3	331.4	330.5
0.075	329.7	328.8	327.9	327.0	326.2	325.3	324.5	323.6	322.7	321.9
0.076	321.0	320.2	319.4	318.5	317.7	316.9	316.0	315.2	314.4	313.6
0.077	312.8	312.0	311.1	310.3	309.5	308.7	307.9	307.2	306.4	305.6
0.078	304.8	304.0	303.2	302.5	301.7	300.9	300.2	299.4	298.6	297.9
0.079	297.1	296.4	295.6	294.9	294.1	293.4	292.7	291.9	291.2	290.5
0.080	289.7	289.0	288.3	287.6	286.9	286.2	285.4	284.7	284.0	283.3
0.081	282.6	281.9	281.2	280.6	279.9	279.2	278.5	277.8	277.1	276.5
0.082	275.8	275.1	274.4	273.8	273.1	272.4	271.8	271.1	270.5	269.8
0.083	269.2	268.5	267.9	267.2	266.6	266.0	265.3	264.7	264.1	263.4
0.084	262.8	262.2	261.6	260.9	260.3	259.7	259.1	258.5	257.9	257.3
0.085	256.7	256.1	255.5	254.9	254.3	253.7	253.1	252.5	251.9	251.3
0.086	250.7	250.1	249.6	249.0	248.4	247.8	247.3	246.7	246.1	245.6
0.087	245.0	244.4	243.9	243.3	242.8	242.2	241.6	241.1	240.6	240.0
0.088	239.5	238.9	238.4	237.8	237.3	236.8	236.2	235.7	235.2	234.6
0.089	234.1	233.6	233.1	232.5	232.0	231.5	231.0	230.5	230.0	229.4
0.090	228.9	228.4	227.9	227.4	226.9	226.4	225.9	225.4	224.9	224.4
0.091	223.9	223.4	222.9	222.5	222.0	221.5	221.0	220.5	220.0	219.6
0.092	219.1	218.6	218.1	217.7	217.1	216.7	216.3	215.8	215.3	214.9
0.093	214.4	213.9	213.5	213.0	212.6	212.1	211.7	211.2	210.8	210.3
0.094	209.9	209.4	209.0	208.5	208.1	207.6	207.2	206.8	206.3	205.9
0.095	205.5	205.0	204.6	204.2	203.8	203.3	202.9	202.5	202.1	201.6
0.096	201.2	200.8	200.4	200.0	199.5	199.1	198.7	198.3	197.9	197.5
0.097	197.1	196.7	196.3	195.9	195.5	195.1	194.7	194.3	193.9	193.5
0.098	193.1	192.7	192.3	191.9	191.5	191.1	190.7	190.4	190.0	189.6
0.099	189.2	188.8	188.4	188.1	187.7	187.3	186.9	186.6	186.2	185.5

Source: ASTM E 92

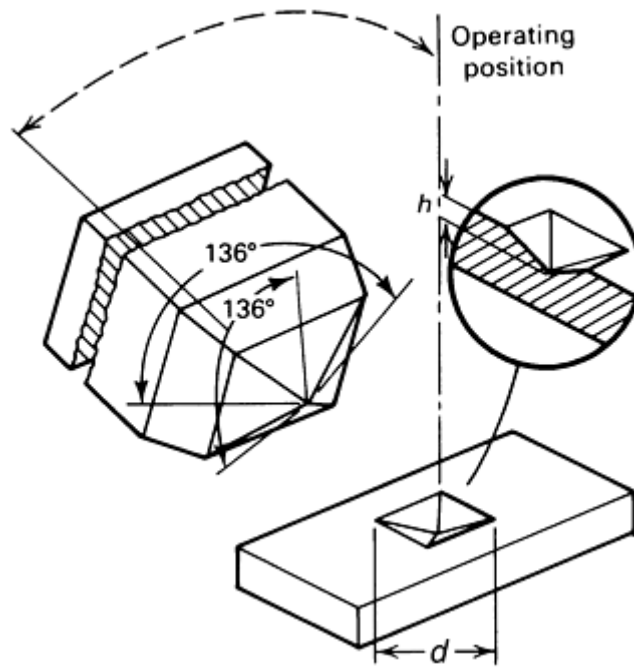


Fig. 21 **Diamond pyramid indenter used for the Vickers test and resulting indentation in the workpiece. d , mean diagonal of the indentation in millimeters**

Quite often the length of indentations are larger than the values given in most lookup tables. Calculation of larger indentations is best shown by the following example: with a test load of 50 kgf, the averaged diagonal length is measured at 0.753 mm. This length is beyond the range of the lookup table; however, the table can be extended by looking up the hardness number for a 0.0753 mm indent diagonal, which has a Vickers hardness of 327 for a 1 kgf load (Table 10). Therefore, for a 0.753 mm diagonal, the table (if extended) would read 3.27 HV at 1 kgf. With a 50 kgf load, then:

$$\text{HV} = 3.27 \times 50 = 163.5$$

The Vickers hardness number is followed by the symbol “HV” with a suffix number denoting the force and a second suffix number indicating the dwell time, if different from 10 to 15 s, which is normal dwell time. For example:

6. A value of 440 HV30 represents Vickers hardness of 440 made with a force of 30 kgf applied for 10 to 15 s.
7. 440 HV30/20 represents Vickers hardness of 440 made with a force of 30 kgf applied for 20 s.

Macroindentation Vickers Test Loads. The forces of 5, 10, 20, 30, 50, 100, and 120 kgf are the most commonly used in industry today for Vickers macroindentation hardness testing. The 30 kgf force seems to be the most desirable and is used for most standardizing and calibration work. This is not to imply that the other forces cannot be used for calibrating the testers by the indirect or test block method. The applied forces normally are checked by using a calibrated electronic load cell. A Vickers hardness tester should be verified at a minimum of three forces including the forces specified for testing. The tester is considered force calibrated if the error is not greater than 1%. These forces should be applied in a smooth and gradual manner so that impact or overloading is avoided. The loading should be such that it does not cause any movement of the specimen while under test.

The Vickers indenter is a highly polished, pointed square-base pyramidal diamond (Fig. 21) with opposite face angles of $136 \pm 5^\circ$ that produces edge angles of $148^\circ 06' 43''$. All four faces are equally inclined to the vertical axis of the indenter to within $\pm 30'$ and meet at a common point so as not to produce an offset greater than 0.001 mm in length. The indenter should be periodically examined by making an indentation in a polished steel block and observing the indent formed under high magnification (500 \times). The indentation edges and point should be examined for rounding and chipping or other damage to the diamond. A wider and brighter image at the point or diagonal edges will indicate excessive wear. If chipping occurs, it will be indicated by a bright spot that usually occurs on the angle edges (diagonals). Any noticeable damage or wear would indicate that the indenter should be replaced.

The measuring microscope or measuring device must be capable of determining the length of the indentation diagonals to ± 0.0005 mm ($0.5 \mu\text{m}$) or $\pm 0.5\%$ of length, whichever is larger, in accordance to ASTM E 92, "Standard Test Method for Vickers Hardness of Metallic Materials." The most common measuring system is either a basic vertical light microscope or an optical projection screen (Fig. 22). The magnification range is usually from 4 to 500 \times , depending on the size of the indentation to be measured. The optical measuring device generally uses a Fililar micrometer eyepiece, a graduated incremental scale, or a sliding vernier attachment. The measuring microscope or other device for measuring the diagonals of the indentation is calibrated with a precision stage micrometer. As per ASTM E 92 the error of the spacing of the lines of the stage micrometer shall not exceed $0.05 \mu\text{m}$ or 0.05% of any interval. The measuring device is calibrated throughout its range of use, and a calibration factor is utilized so that an error shall not exceed $\pm 0.5\%$.

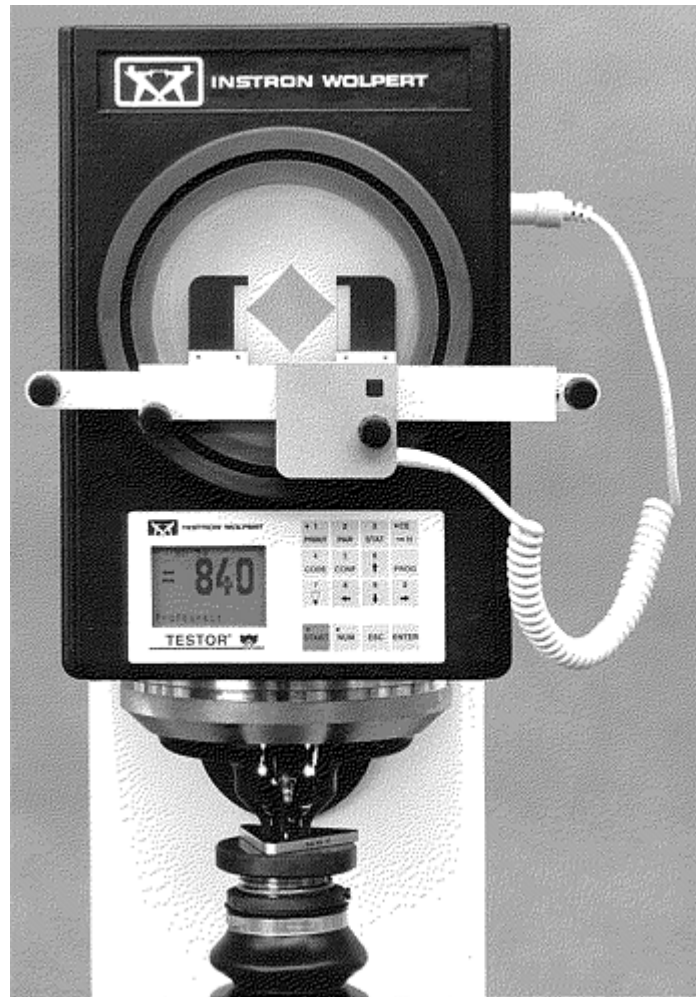


Fig. 22 **Optical projection screen and caliper for diagonal measurement in Vickers hardness testing**

Determining the calibration factor is critical for accurate diagonal measurements and should be done with care and precision. Multiple verifications should be made at several micron lengths representing the full range of measurements normally used. The averaged values should be used to calculate the calibration factor.

Video Measuring Systems and Image Processors. Newer measurement techniques successfully use image processing and analysis. This technique utilizes a scanning device, usually a microscope equipped with a solid-state video camera with a photodiode array lens that is sensitized to gray shading of the field of view. The digital image is sent to a computer that processes the photo-array output and sends a signal that projects an image on a television screen. This technique, due to the limitations of the pixel arrays in the cameras, does not have the accuracy of a trained operator using a high-quality conventional microscope. However, the method can improve the level of repeatability, especially when multiple operators are involved. The accuracy is being improved as the pixel arrays are reduced in size; however, measurements below $0.05\mu\text{m}$ are not possible with existing equipment. Another use of a solid-state video camera is commonly called a video Fililar, or Vilar, system (Fig. 23). With this type of system the operator still has to locate the indent diagonals using a joystick or

mouse; however, observing the image on the television screen is easier and less tiring than a microscope, resulting in more consistent results.



Fig. 23 Vilar system for digital image processing of Vickers indents

Application Factors

Test Specimen. The Vickers hardness test is adaptable to most test specimens ranging from large bars and rolled stock to small pieces in metallographic mounts. The surface should be flat, polished, and supported rigidly normal to the axis of the indenter. The distance from the center of the indentation to other indents or from the specimen edge should be at least 2.5 times the diagonal length. The thickness of the test specimen should be such that no bulge or marking appear on the underside surface directly opposite the indentation, and it is recommended that the thickness of the testpiece be equal to 1.5 times the length of the diagonal of the indentation. As the depth of the Vickers test is approximately $\frac{1}{7}$ of the diagonal, the rule of thumb is that the thickness of the testpiece should be 10 times the depth of the indentation.

The finish of the specimen must be smooth enough to permit the ends of the diagonals to be clearly defined so the length can be measured with a precision of 0.0005 mm or 0.5% of the length of the diagonals, whichever is larger. It is necessary that sample preparation be carefully controlled to ensure that changes to the hardness of the material are avoided. The test surface of the specimen should be presented normal to the axis of the indenter within $\pm 1^\circ$.

Testing of Cylindrical and Spherical Rounds. When testing specimens with radius of curvature, a factor is required to correct the readings as though the testing was done on a flat surface. A method for correcting Vickers hardness values taken on spherical and cylindrical surfaces has been standardized as ISO 6507-1. The correction factors are tabulated in terms of the ratio of the mean diagonal d of the indentation to the diameter D of the sphere or cylinder. Tables listing correction factors for convex and concave spherical surfaces and for cylindrical surfaces are provided in the article "Selection and Industrial Applications of Hardness Tests" in this Volume.

The rationale for this manner of correcting Vickers values on spheres and cylinders is that when testing a convex cylinder the indentation will have shorter diagonals in the curve region (90° to the longitudinal axis) compared to diagonals parallel to the long axis. This results in a shorter mean diagonal length (and a higher hardness number) than if tested on a flat surface. The correction for a convex surface therefore must be less than 1.0 to reduce the higher hardness value caused by the convex surface. The reverse is true for concave radii; the correction ratios are greater than 1.0, which increases the hardness value. The corrections for similar d/D ratios are the largest for the spherical surfaces.

Following is an example of hardness correction for a spherical surface. Similar examples for cylindrical surfaces are given in the article “Selection and Industrial Applications of Hardness Tests” in this Volume. For cylinders, correction factors depend on whether the diagonal is parallel or perpendicular to the longitudinal axis of the cylinder. In general, correction factors for cylinders are smallest when the measured diagonal is parallel to the longitudinal axis of a cylinder.

Example 1: Hardness Correction for a Convex Sphere. The test conditions are:

Force, kgf	10
Diameter of sphere (D), mm	10
Mean diagonal of indentation (d), mm	0.150
d/D	$0.150/10 = 0.015$

From the Vickers hardness table (Table 10) and adjusted for 10 kgf load, hardness for a flat surface would be 824 HV10. From the correction table (see Table 5 in the article “Selection and Industrial Application of Hardness Tests” in this Volume), the correction factor (by interpolation) is 0.983. Thus, the corrected hardness of the sphere is $824 \times 0.983 = 810$ HV 10.

Advantages and Disadvantages. One advantage of the Vickers test is that in theory constant hardness values can be obtained from homogeneous material irrespective of the test force. This generally works for force levels above 5 kg. The other advantage is that one hardness scale can be used from the softest to the hardest metals including carbides. As a result of these advantages and the relative simplicity of the test process, the Vickers scale may be useful for maintaining stable hardness standards.

In summary, advantages of the Vickers test are:

8. Vickers hardness, in general, is independent of force when determined on homogeneous material, except possibly at forces below 5 kgf.
9. The edge or ends of the diagonals are usually well defined for measurement.
10. The indentations are geometrically similar, irrespective of size.
11. One continuous scale is used for a given force, from lowest to highest values.
12. Indenter deformation is negligible on hard material.

Disadvantages of the Vickers test are:

13. Test is slow and not well adapted for routine testing. Typical test and measurement times are in the one-minute range.
14. Careful surface preparation of the specimen is necessary, especially for shallow indentations.
15. Measurement of diagonals is operator dependent, with possible eyestrain and fatigue adding to test errors.

Comparison with Brinell Testing. Because of the geometric similarity of the indentations, Vickers hardness values are independent of the applied force. That is to say that on homogeneous material the hardness value obtained with a 10 kgf load should be the same as that obtained with a 50 kgf load. When the Vickers test was first introduced, Vickers hardness values were practically constant under different forces for different materials, whereas values from Brinell testing were not. The angle of 136° was chosen by Smith and Sandland (Ref 5) to represent the most desirable ratio of indentation diameter to the ball diameter in the Brinell test.

Due to the fact that the Brinell test does not always yield constant hardness values with varying forces, and in order to minimize this variable, it is generally advisable to restrict the indentations to 25 to 50% of the diameter of the ball. Therefore the ideal size of the ball indentation lies midway between these ratios or at $0.375D$. This was the reasoning of Smith and Sandland so that some method of comparison between their test and Brinell testing could be done. The tangential angle of indentation corresponding with 0.375 times the ball diameter is 136° .

Studies have shown that hardness values obtained with Vickers testing are almost identical to those done with the Brinell test when the force has been such to produce an indentation in the range of 0.375 times the ball diameter. This similarity only holds true in the softer hardness ranges from approximately 100 to 300 HB. At approximately 350 HB the Brinell test has a slight tendency to yield lower readings than does the Vickers test, and this tendency becomes more pronounced as the hardness increases. It should be noted that some studies

have indicated a decrease in hardness values as the forces are increased when testing mild steels and soft coppers.

Effect of Elastic Recovery. As noted in the article “Selection and Industrial Applications of Hardness Tests,” the elastic response of a material can cause a change in the indent shape after unloading. A perfect pyramid indentation (area A_2 in Fig. 24) does not always remain after unloading. This is caused by “ridging” and “sinking” at the surface of the material being tested. Ridging during Vickers does not occur in a concentric ridge, as found in the Brinell test, but rather the material extrudes upward along the face of the diamond leaving the material at the corners of the indentation near the original level. This bulging effect on the sides of the indentation (A_3 in Fig. 24) is called “convexity” and indicates the material has been cold worked. Indents with a sinking-in appearance (A_1 in Fig. 24) show a downward curvature of the material along the face of the diamond called “concavity.”

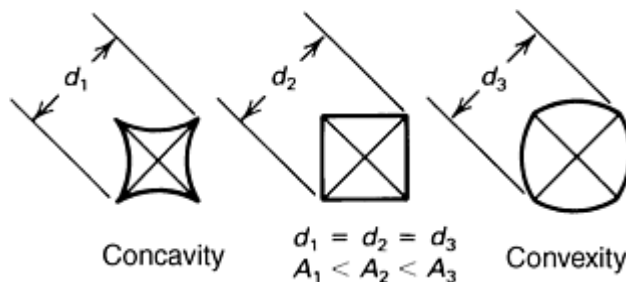


Fig. 24 Vickers indentations with equal diameters but different areas

Because Vickers hardness is related to the surface area of the indentation, these effects influence hardness readings. When ridging occurs, the diagonal measurement gives a low value for the true contact area and therefore a higher hardness value ($A_2 < A_3$ in Fig. 24). The exact opposite occurs with the sinking type and causes high values of the area and low hardness numbers ($A_1 < A_2$ in Fig. 24). It has been shown that errors as high as 10% in hardness numbers using the conventional formula may occur on different metals due to these effects. Generally, cold-worked alloys and decarburized steels will demonstrate the ridging type, while annealed and softer metals are prone to the sinking type.

Anisotropy. When testing anisotropic or heavily rolled materials, it is recommended that the test specimen be oriented to have both diagonals approximately the same length. This would necessitate reorienting the testpiece so that its direction of rolling is at a 45° angle to the diagonals direction, thus equalizing the lengths. Distortion of the indentation, due to crystallographic or microstructural texture, influences diagonal lengths and the validity of the hardness value. A Vickers indentation that has one-half of either diagonal 5% longer than the other half of the diagonal will produce an error of approximately 2.5% in hardness values. Therefore it is recommended, whenever possible, that only symmetrical indentations be used to obtain hardness values.

If the diagonal legs are unequal, the specimen should be rotated 90° and another indent made. If the nonsymmetrical aspect of the indent has rotated, this indicates that the specimen surface is not perpendicular to the indenter axis. If the nonsymmetrical nature remains in the same orientation, the indenter is misaligned or damaged.

Vickers testers should be designed to apply the force smoothly and friction free without impact. The error of the indenting force must not exceed 1%, and the measuring device shall be capable of measuring accuracies within ± 0.0005 mm or $\pm 0.5\%$, whichever is larger. Many of the testers available today apply force by means of deadweights and lever combinations, usually with a dashpot control to impede overshoot.

Recently, motorized closed-loop, load-cell force application testers (Fig. 25) have been developed. They have the advantage of allowing a nearly limitless selection of test forces. Manual measuring devices that require operator calculation of the Vickers number are still produced; however, most testers have full digital systems that automatically do the calculations. Digital testers also have the ability to download test results to a printer or host computer.

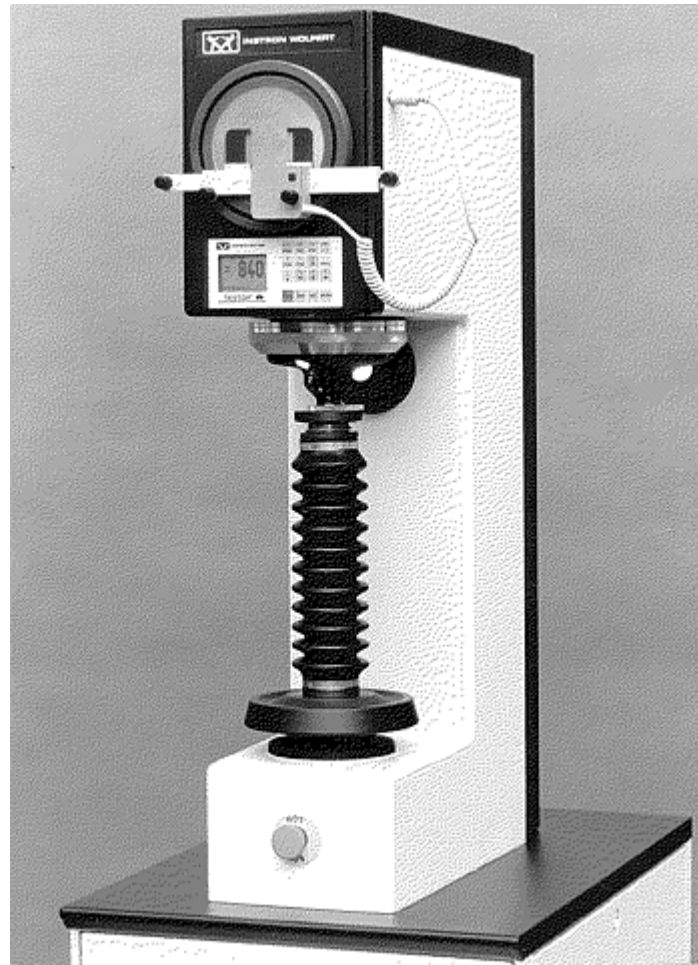


Fig. 25 Closed-loop servo controlled Vickers hardness testing unit

Calibrations. Vickers testers are typically indirectly verified for performance by doing periodic tests on certified test blocks. A wide variety of test blocks are available in different hardness ranges calibrated with different test forces. It is recommended that each test force used be verified using at least two test blocks of different hardnesses.

Reference cited in this section

16. R.L. Smith and G.E. Sandland, Some Notes on the Use of a Diamond Pyramid for Hardness Testing, *J. Iron Steel Inst. (London)*, 1925

Macroindentation Hardness Testing

Edward L. Tobolski, Wilson Instruments Division, Instron Corporation; Andrew Fee, Consultant

References

17. F. Garofalo, P.R. Malenock, and G.V. Smith, Hardness of Various Steels at Elevated Temperatures, *Trans. ASM*, Vol 45, 1953, p 377–396
18. M. Semchyshen and C.S. Torgerson, Apparatus for Determining the Hardness of Metals at Temperatures up to 3000 °F, *Trans. ASM*, Vol 50, 1958, p 830–837
19. J.H. Westbrook, Temperature Dependence of the Hardness of Pure Metals, *Trans. ASM*, Vol 45, 1953, p 221–248

20. L. Small, "Hardness—Theory and Practice," Service Diamond Tool Company, Ferndale, MI, 1960, p 363–390
21. R.L. Smith and G.E. Sandland, Some Notes on the Use of a Diamond Pyramid for Hardness Testing, *J. Iron Steel Inst. (London)*, 1925

Microindentation Hardness Testing

George F. Vander Voort, Buehler Ltd.

Introduction

IN MICROINDENTATION HARDNESS TESTING (MHT), a diamond indenter of specific geometry is impressed into the surface of the test specimen using a known applied force (commonly called a "load" or "test load") of 1 to 1000 gf. Historically, the term "microhardness" has been used to describe such tests. This term, taken at face value, suggests that measurements of very low hardness values are being made, rather than measurements of very small indents. Although the term "microhardness" is well established and is generally interpreted properly by test users, it is best to use the more correct term, microindentation hardness testing.

There is some disagreement over the applied force range for MHT. ASTM E 384 states that the range is 1 to 1000 gf, and this is the commonly accepted range in the United States. Europeans tend to call the range of 200 to 3000 gf the "low-load" range. They do this because forces smaller than 200 gf generally produce hardness numbers that are different from those determined from tests conducted with forces ≥ 200 gf. This problem is discussed later in this article.

The hardness number is based on measurements made of the indent formed in the surface of the test specimen. It is assumed that recovery does not occur upon removal of the test force and indenter, but this is rarely the case. The Knoop test is claimed to eliminate recovery, but again, this is not true for tests of metallic materials. For the Vickers test, both diagonals are measured and the average value is used to compute the Vickers hardness (HV). The hardness number is actually based on the surface area of the indent itself divided by the applied force, giving hardness units of kgf/mm^2 . In the Knoop test, only the long diagonal is measured, and the Knoop hardness (HK) is calculated based on the projected area of the indent divided by the applied force, also giving test units of kgf/mm^2 . In practice, the test units kgf/mm^2 (or $\text{gf}/\mu\text{m}^2$) are not reported with the hardness value.

Microindentation Hardness Testing

George F. Vander Voort, Buehler Ltd.

Vickers Hardness Test

In 1925, Smith and Sandland of the United Kingdom developed an indentation test that employs a square-based pyramidal-shaped indenter made from diamond (Fig. 1a). Figure 1(b) shows examples of Vickers indents to illustrate the influence of test force on indent size. The test was developed because the Brinell test, using a spherical hardened steel indenter, could not test hard steels. They chose the pyramidal shape with an angle of 136° between opposite faces in order to obtain hardness numbers that would be as close as possible to Brinell hardness numbers for the same specimens. This made the Vickers test easy to adopt, and it rapidly gained acceptance. Unlike Rockwell tests, the Vickers test has the great advantage of using one hardness scale to test all materials.

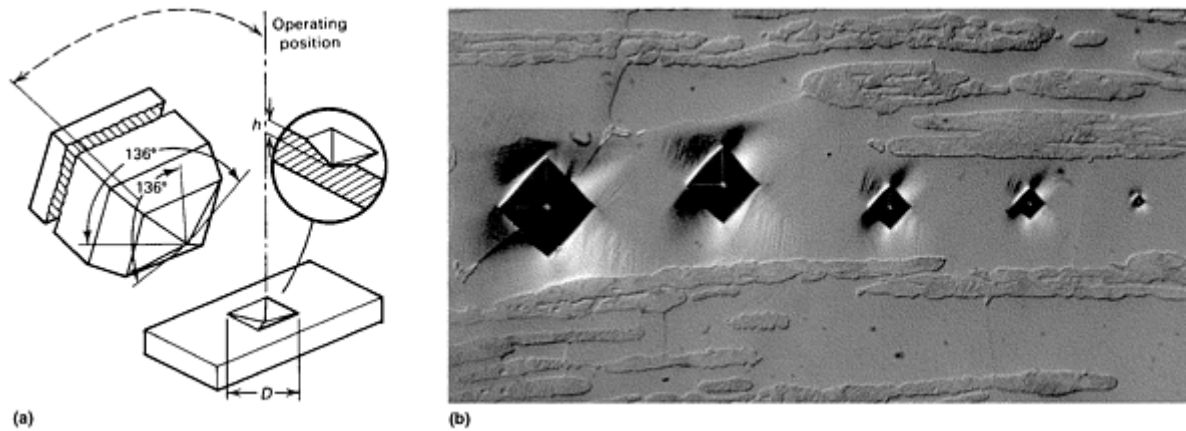


Fig. 1 Vickers hardness test. (a) Schematic of the square-based diamond pyramidal indenter used for the Vickers test and an example of the indentation it produces. (b) Vickers indents made in ferrite in a ferritic-martensitic high-carbon version of 430 stainless steel using (left to right) 500, 300, 100, 50, and 10 gf test forces (differential interference contrast illumination, aqueous 60% nitric acid, 1.5 V dc). 250×

In this test, the force is applied smoothly, without impact, and held in contact for 10 to 15 s. The force must be known precisely (refer to ASTM E 384 for tolerances). After the force is removed, both diagonals are measured and the average is used to calculate the HV according to:

$$HV = \frac{2000P \sin(\alpha/2)}{d^2} = \frac{1854.4P}{d^2} \quad (\text{Eq 1})$$

where d is the mean diagonal in μm , P is the applied load in gf, and α is the face angle (136°).

The hardness can be computed with the formula and a pocket calculator, or using a spreadsheet program. Most modern MHT units have the calculation capability built in and display the hardness value along with the measured diagonals. A book of tables of HV as a function of d and P also accompanies most testers, and ASTM E 384 includes such tables.

The macro-Vickers test (ASTM E 92) operates over a range of applied forces from 1 to 120 kgf, although many testers cover a range of only 1 to 50 kgf, which is usually adequate. The use of forces below 1 kgf with the Vickers test was first evaluated in 1932 at the National Physical Laboratory in the United Kingdom. Four years later, Lips and Sack constructed the first Vickers tester designed for low applied forces.

Microindentation Hardness Testing

George F. Vander Voort, Buehler Ltd.

Knoop Hardness Test

In 1939, Frederick Knoop and his associates at the former National Bureau of Standards developed an alternate indenter based on a rhombohedral-shaped diamond with the long diagonal approximately seven times as long as the short diagonal (Fig. 2a). Figure 2(b) shows examples of Knoop indents to illustrate the influence of applied load on indent size. The Knoop indenter is used in the same machine as the Vickers indenter, and the test is conducted in exactly the same manner, except that the Knoop hardness (HK) is calculated based on the measurement of the long diagonal only and calculation of the projected area of the indent rather than the surface area of the indent:

$$HK = \frac{1000P}{C_p d^2} = \frac{14229P}{d^2} \quad (\text{Eq 2})$$

where C_p is the indenter constant, which permits calculation of the projected area of the indent from the long diagonal squared.

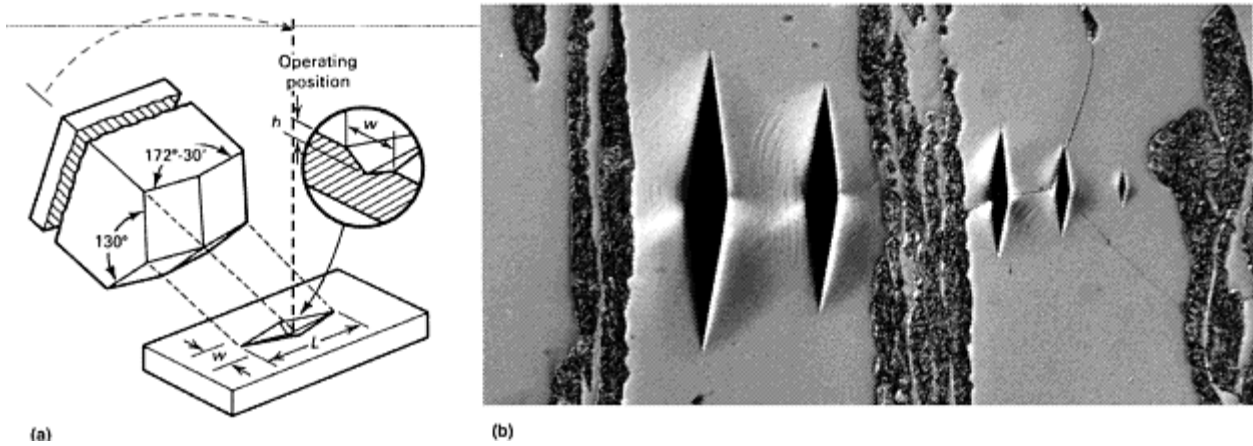


Fig. 2 Knoop hardness test. (a) Schematic of the rhombohedral-shaped diamond indenter used for the Knoop test and an example of the indentation it produces. (b) Knoop indents made in ferrite in a ferritic-martensitic high-carbon version of 430 stainless steel using (left to right) 500, 300, 100, 50, and 10 gf test forces (differential interference contrast illumination, aqueous 60% nitric acid, 1.5 V dc). 300×

The Knoop indenter has a polished rhombohedral shape with an included longitudinal angle of $172^{\circ} 30'$ and an included transverse angle of $130^{\circ} 0'$. The narrowness of the indenter makes it ideal for testing specimens with steep hardness gradients. In such specimens, it may be impossible to get valid Vickers indents as the change in hardness may produce a substantial difference in length of the two halves of the indent parallel to the hardness gradient. With the Knoop test, the long diagonal is set perpendicular to the hardness gradient and the short diagonal is in the direction of the hardness gradient.

For the same test force, Knoop indents can be more closely spaced than Vickers indents, making hardness traverses easier to perform. The Knoop indenter is a better choice for hard brittle materials where indentation cracking would be more extensive using the Vickers indenter at the same load. The Knoop indent is shallower (depth is approximately $\frac{1}{30}$ the long diagonal) than the Vickers indent (depth is approximately $\frac{1}{7}$ the average diagonal). Hence, the Knoop test is better suited for testing thin coatings. On the negative side, the Knoop hardness varies with test load and results are more difficult to convert to other test scales.

Microindentation Hardness Testing

George F. Vander Voort, Buehler Ltd.

Expression of Test Results

Historically, the official way in which Vickers and Knoop hardness numbers have been presented has varied with time, although many users seem to be unaware of the preferred style. The acronyms VHN and KHN were introduced many years ago and stand for Vickers hardness number and Knoop hardness number. DPN, for diamond-pyramid hardness number, was introduced at approximately the same time. While some have claimed the DPN and VHN are not the same, this is not true. In the early 1960s, ASTM initiated a more modern, systematic approach for all hardness tests and adopted the acronyms HV and HK for the two tests, yet the former acronyms are still widely used (as are many other obsolete acronyms, like BHN and R_C instead of HB and HRC). Style guides for many publications do not seem to track these changes carefully.

For stating the actual hardness results, ASTM advocates the following approach. ASTM E 384 recommends expressing a mean hardness of 425 in the Vickers test using a 100 gf applied force as 425 HV₁₀₀, while by ISO rules, it would be expressed as 425 HV_{0.1} (because 100 gf would be expressed as 0.1 kgf). ASTM Committee E-4 is currently recommending adoption of a slightly different approach: 425 HV 100 gf. While it has proven difficult to get people to adopt a unified expression style, it is important that the stated results indicate the mean value, the test used, and the test force as a minimum.

Microindentation Hardness-Testing Equipment

A variety of microindentation test machines are produced, ranging from relatively simple, low-priced units (Fig. 3) to semiautomated systems (Fig. 4a) and fully automated systems (Fig. 4b). In most cases, either a Knoop or a Vickers indenter can be used with the same machine, and it is a relatively simple matter to exchange indenters. The force is applied either directly as a dead weight or indirectly by a lever and lighter weights. New testers using a closed-loop load-cell system (Fig. 5) are also available. The magnitude of the weights and force application must be controlled precisely (refer to ASTM E 384).

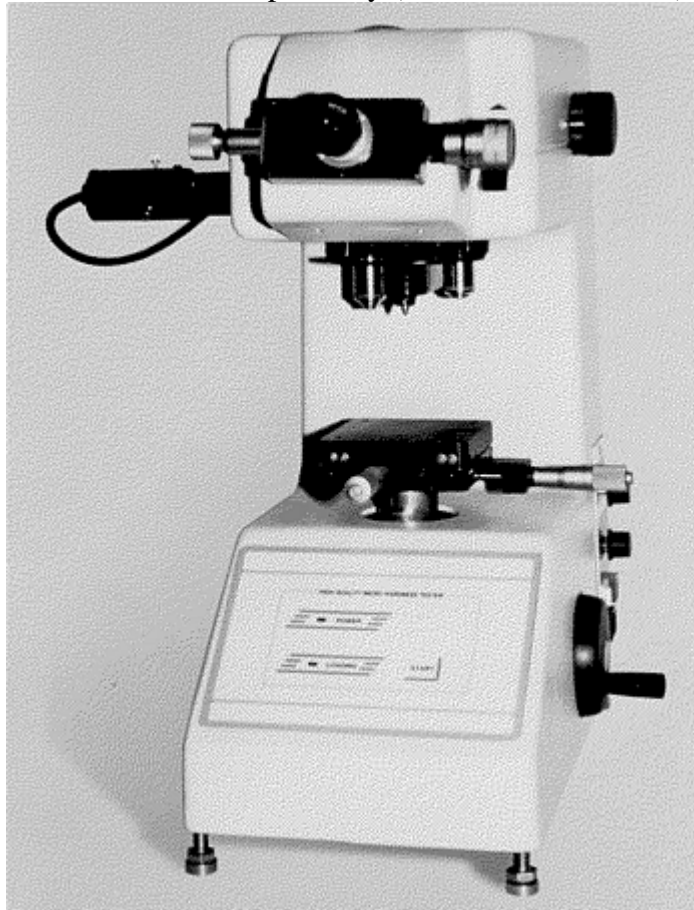


Fig. 3 Example of a simple, low-cost manual microindentation hardness-testing unit with a Filar micrometer for measurements but no automation

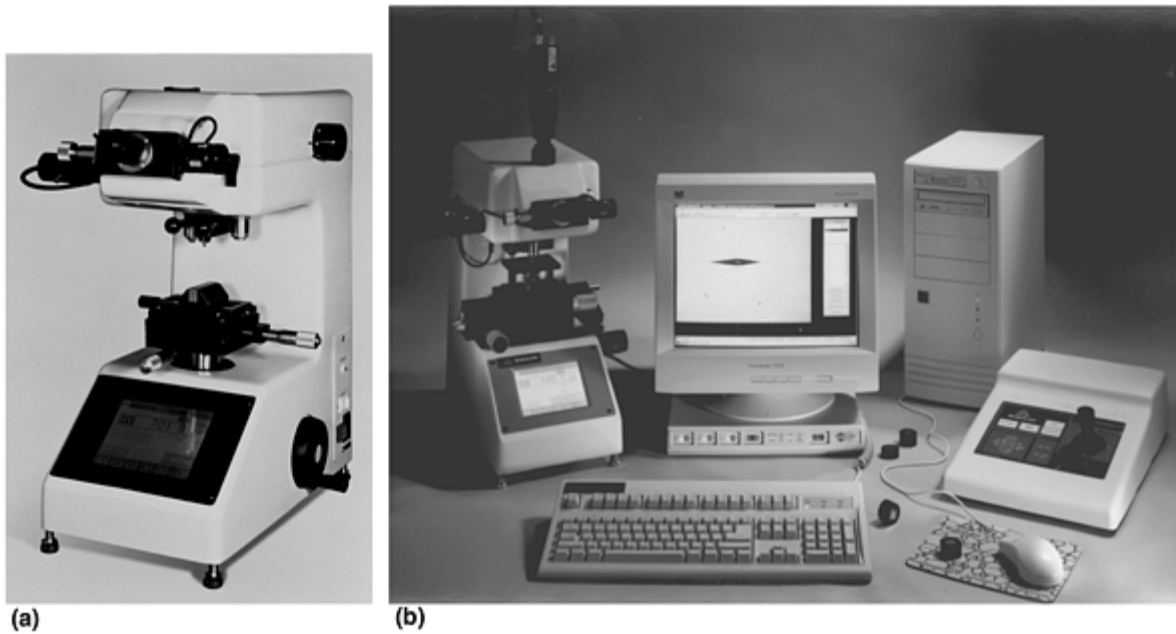


Fig. 4 Semiautomated and fully automated microindentation hardness testers. (a) Semiautomated tester with a Filar micrometer for measurements, automated readout of the test results with its equivalent hardness in another selected scale. (b) Fully automated tester interfaced to an image analyzer to control indenting, measurement, and data manipulation



Fig. 5 Closed-loop load-cell microindentation hardness tester

Most tester systems use an automated test cycle of loading, applying the load for the desired time, and unloading to ensure reproducibility in the test. Vibrations must be carefully controlled, and this becomes even more important as the applied force decreases. Manual application and removal of the applied force is not recommended due to the difficulty in preventing vibrations that will enlarge the indent size.

The indenter must be perpendicular to the test piece. An error of as little as 2° from perpendicular will distort the indentation shape and introduce errors. A larger tilt angle may cause the specimen to move under the applied force. To aid in controlling this problem, most testers come with a device that can be firmly attached to

the stage (Fig. 6). The mounted specimen, or a bulk unmounted specimen of the proper size, can be placed within this device and the plane-of-polish is automatically indexed perpendicularly to the indenter. Historically, it has been a common practice to simply place a specimen on the stage and proceed with indentation, but if the plane-of-polish is not parallel to the back side of the specimen, it will not be perpendicular to the indenter, introducing tilt errors.

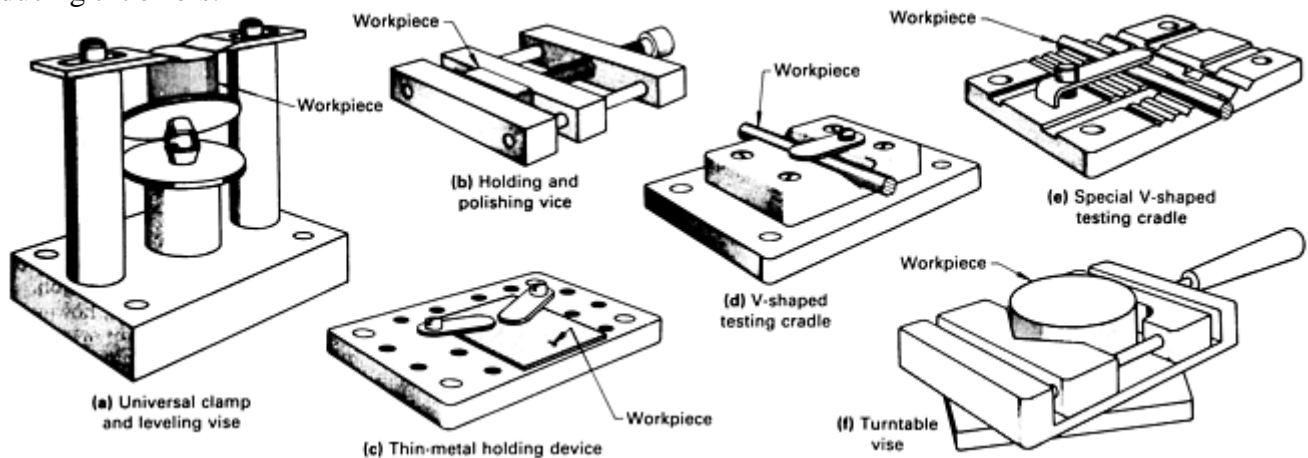


Fig. 6 Examples of fixtures for holding test pieces for microindentation hardness testing

The stage is an important part of the tester. The stage must be movable and movement is usually controlled in the x and y directions by micrometers. Once the specimen is placed in the top-indexed holder, the operator must move the stage micrometers to select the desired location for indenting. If a traverse of several hardness readings is desired at inward intervals from a side surface of the specimen (as in case-depth measurements), then the surface of interest should be oriented in the holder so that it is perpendicular to either the x or y direction of the traverse. If the Knoop indenter is chosen, its long diagonal must also be parallel to the surface of interest. For example, if the Knoop long axis is in the direction going from the front to the back of the tester, then the surface of interest must also be aligned in the same direction. Accordingly, the x -axis (left to right) micrometer is used to select the desired indentation positions. The micrometers are ruled in either inches or millimeters and are capable of making very precise movement control.

Because the diagonals must be measured after the force has been removed, the tester is equipped with at least two metallurgical objectives (i.e., reflected light), usually $10\times$ and $40\times$. Some systems may have a third or fourth objective on the turret. For measurement of small indents ($<20\ \mu\text{m}$ in diagonal length), a higher-power objective ($60\times$, $80\times$, or $100\times$) can be used in place of the $40\times$ objective if the tester has places for only two objectives. The objectives should have a reasonably high numerical aperture for their magnifications to give the best resolution. The $10\times$ objective is usually used as a spotter, that is, simply to find the desired test location. The measuring eyepiece is generally $10\times$. Naturally, the optical system must be carefully calibrated using a stage micrometer. In general, indents are measured to the nearest $0.1\ \mu\text{m}$ with an accuracy of no more than $\pm 0.5\ \mu\text{m}$ in length. A proper Köhler illumination system is necessary to fully illuminate the specimen. In general, a magnification that makes the diagonal between 25% and less than 75% of the field width is ideal; however, it is not always possible to follow this rule.

Calculation of the hardness is based on the length of the diagonals. The major problem is defining where the indent tips are located. This requires proper illumination, adjustment of the optics for best resolution and contrast, and careful focusing. Every laboratory should have a regular schedule for cleaning the optical components of their MHT apparatuses, as well as for verifying their calibration. A Filar micrometer is used for the diagonal measurement. The micrometer lines have a finite thickness, which requires use of a systematic measurement scheme. Several indent measurement approaches can be used. One popular approach is to bring the two Filar lines just into contact and then zero the micrometer. The interior sides of the Filar lines are then adjusted so that the indent tips just touch the inside of each line.

In recent years, the MHT system has been automated by coupling it to an image analyzer (Fig. 4b). The image-analysis system software is used to control all of the functions regarding indent location, indent spacing, number of indents, indenting, measurement of the indents, calculation of hardness values, and data plotting. For those who perform a substantial number of hardness traverses, this equipment is very useful because the test work is automated, allowing the metallographer to do other tasks.

Hardness Conversions

Sometimes it is desirable to know the equivalent hardness in a scale other than the Vickers or Knoop. It is not uncommon for product specifications to define the hardness for a case depth in the Rockwell C scale, which, of course, is a bulk test scale unsuitable for case depth determination. Although this seems (and is) illogical, it is widely practiced, probably because designers are not familiar with the Vickers or Knoop scales. Hardness conversions are developed empirically, and there is a degree of error associated with all conversions. The primary source for hardness conversions is ASTM E 140, which lists the conversions in tabular form and also contains equations based on the tabular data. Some MHT units have these tables or the equations built in and will list an equivalent hardness of your choice with each measurement. The most common conversion is from a Vickers or Knoop scale to a Rockwell C scale. In general, these conversions are most commonly available for steels, aluminum alloys, and nickel alloys. Conversions between various scales may be material sensitive.

Conversion of Vickers data to other scales is more straightforward than converting Knoop data to other scales. Basically, the ASTM E 140 conversions between Vickers and other scales can be used for any test force greater than 100 gf. Conversions of Knoop to other scales are problematic because Knoop hardness varies more with load. If the published conversion is for a 500 gf applied load, then this conversion is best for that load and reasonably accurate for loads slightly lower and generally adequate for greater loads, as the Knoop hardness is reasonably constant for loads of 500 gf and above. Aside from the E 140 conversions, two published conversion charts are worth noting. First, Emond (Ref 1) published a correlation chart of Vickers hardness (10 kgf load) to Knoop hardness at loads of 10, 25, 50, 100, 200, and 500 gf (Fig. 7). Second, Batchelder (Ref 2) published conversions from Knoop hardness, with loads of 15, 25, 50, 100, 200, 300, 500, and 1000 gf, to Rockwell C (Fig. 8). Before using these conversions, it is a good practice to test your material with both scales to see how well the conversion chart agrees with your bulk test specimens before utilizing the conversions.

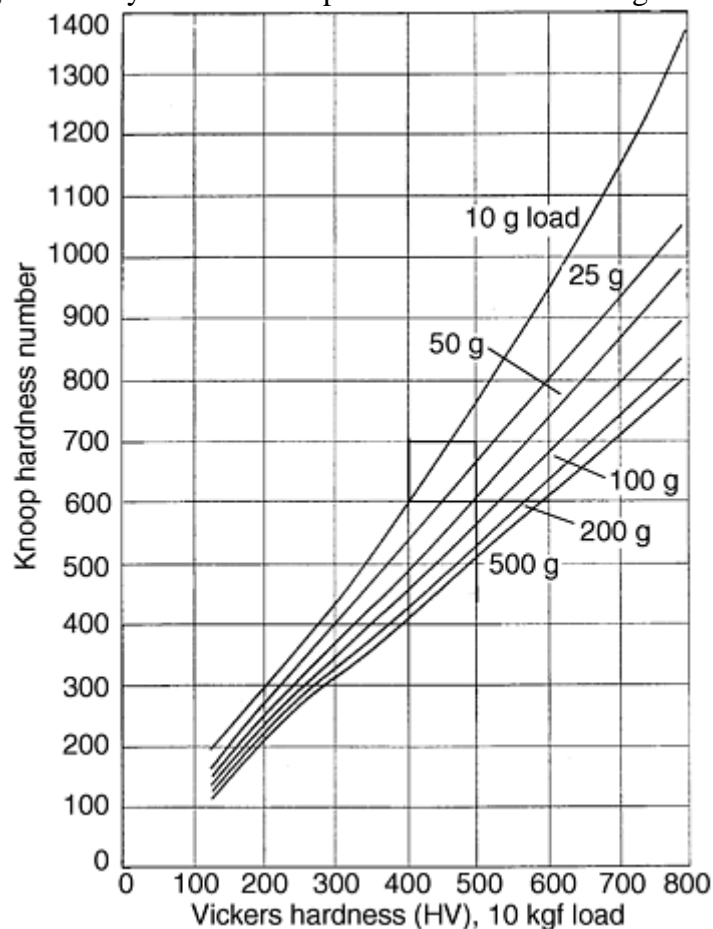


Fig. 7 Correlations between Vickers hardness determined with a 10 kgf load and Knoop hardness determined with loads from 10-500 gf. Source: Ref 1

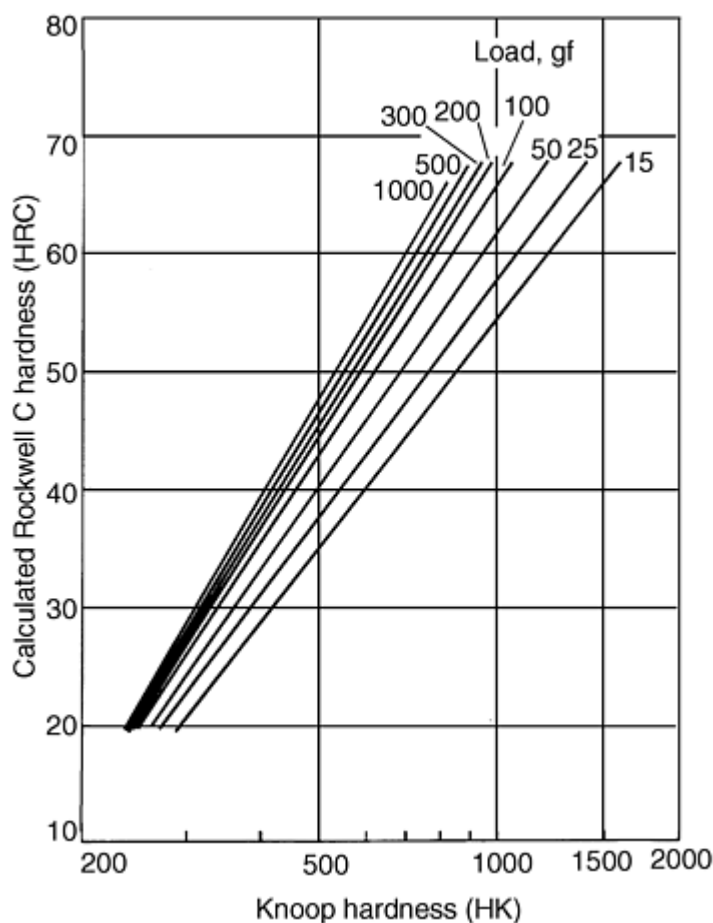


Fig. 8 Correlations between Knoop hardness at loads form 15-1000 gf and Rockwell C hardness. Source: Ref 2

References cited in this section

1. L. Emond, Vickers-Knoop Hardness Conversion, *Met. Prog.*, Vol 74, Sep 1958, p 97, 96B; Vol 76, Aug 1959, p 114, 116, 118
2. G.M. Batchelder, The Nonlinear Disparity in Converting Knoop to Rockwell C Hardness, *ASTM Mater. Res. Stand.*, Vol 9, Nov 1969, p 27-30

Microindentation Hardness Testing

George F. Vander Voort, Buehler Ltd.

Specimen Preparation

Specimen preparation for microindentation hardness testing is not a trivial matter and becomes more critical as the applied force decreases. Further, if testing is to be done near an edge, then edge preservation (i.e., flatness out to the edge) is also required. For relatively high test forces, for example, 300 to 1000 gf, a perfectly prepared specimen is not required. However, this does not mean that sectioning and grinding damage need not be removed. Rather, the normal preparation procedure could be stopped after grinding and polishing down to a 6, 3, or 1 μm diamond finish. For lower loads, it is advisable to completely prepare the specimen to a damage-

free condition. Excessive residual damage from sectioning and grinding will influence test results and produce erroneous hardness values. Depending on the nature of the specimen, preparation damage can cause either an increase or a decrease in the apparent hardness relative to the true hardness. Guidelines for preparing metallographic test specimens are given in ASTM E 3 and in standard textbooks (Ref 3) and handbooks (Ref 4, 5).

Microindentation hardness testing near the edge of a specimen is used frequently to determine the hardness of coatings or to evaluate the extent of the increase in surface hardness due to treatments such as induction hardening, carburizing, or nitriding, or due to the loss in hardness because of decarburization. A variety of procedures have been developed to provide good edge retention. Today, with a good thermosetting epoxy resin (for best results, cool back to ambient temperature under pressure during mounting), automated preparation equipment, and modern consumable products (use napless cloths for best results), adequate edge retention is readily achievable without requiring protective surface platings (e.g., electroless nickel). It is also possible to prepare unmounted bulk specimens with adequate edge retention using automated equipment and consumables.

References cited in this section

3. G. F. Vander Voort, *Metallography: Principles and Practice*, McGraw-Hill, 1984; reprinted by ASM International, 1999, p 356, 381
4. *Metallography and Microstructures*, Vol 9, *ASM Handbook*, ASM International, 1985
5. G.F. Vander Voort, Ed., *Metallography, Metals Handbook Desk Edition*, 2nd ed., ASM International, p 1356–1409

Microindentation Hardness Testing

George F. Vander Voort, Buehler Ltd.

Important Test Considerations

All tests require both properly operating equipment and knowledge of how to use it. To obtain precise, unbiased hardness data, a properly prepared specimen must be tested in the correct manner using a properly operating, calibrated tester. ASTM E 384 provides guidance on operating variables developed both theoretically and empirically over a long period of time. Conservative application of these rules is advisable.

Indent Size. In general, the larger the indent is, the better the precision will be. Due to the mathematical approach to defining the Vickers and Knoop hardnesses (Eq 1 and 2, where the denominator is d^2), the curves of diagonal length versus HV or HK get steeper as the test force decreases, as shown in Fig. 9 and 10. Note that as the test force decreases, smaller and smaller variations in diagonal length correlate to larger and larger variations in hardness.

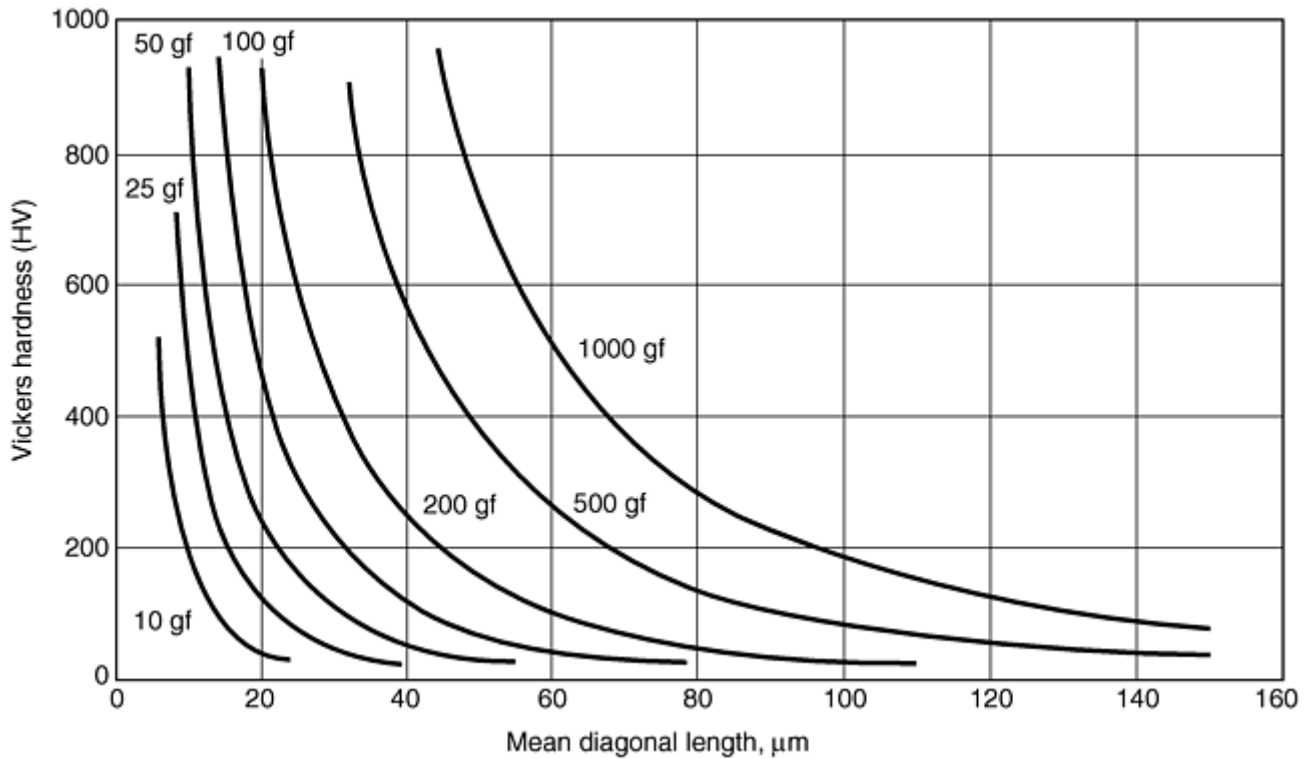


Fig. 9 Relationships between the mean diagonal length and the Vickers hardness for loads of 10-1000 gf

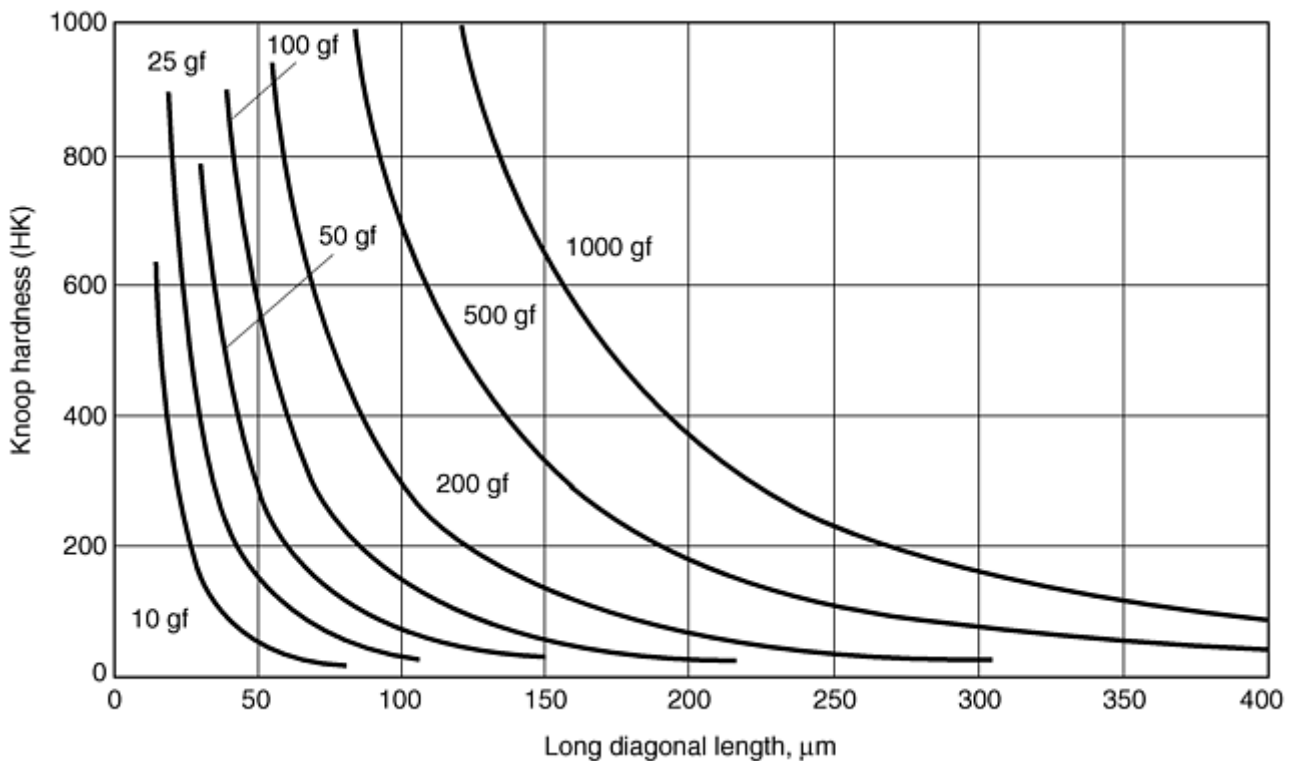


Fig. 10 Relationships between the long diagonal length and the Knoop hardness for loads of 10-1000 gf

Experience has shown that a single operator typically exhibits a $\pm 0.5 \mu\text{m}$ variation when measuring the same indent over a period of time, while multiple operators exhibit approximately a $\pm 1.0 \mu\text{m}$ variation over time. Larger variations have also been observed (Ref 6, 7). A $\pm 0.5 \mu\text{m}$ variation in the measured diagonal has a greater influence on hardness as the test load decreases, that is, as the diagonal size decreases.

As an example, Fig. 11 shows the change in Vickers hardness when $0.5 \mu\text{m}$ is either added to, or subtracted from, the diagonal measurement for diagonals $\leq 40 \mu\text{m}$ in length. Note that subtracting $0.5 \mu\text{m}$ has a greater effect on the calculated HV than adding $0.5 \mu\text{m}$. This is again due to the d^2 divisor in Eq 1. The graph shows

that for a Vickers indent with a 10 μm average diagonal, a $\pm 0.5 \mu\text{m}$ measurement variation can produce approximately a 10% rise or drop in the hardness. If the hardness is low, this is not too much of a problem, but for high-hardness specimens, a $\pm 10\%$ variation is substantial.

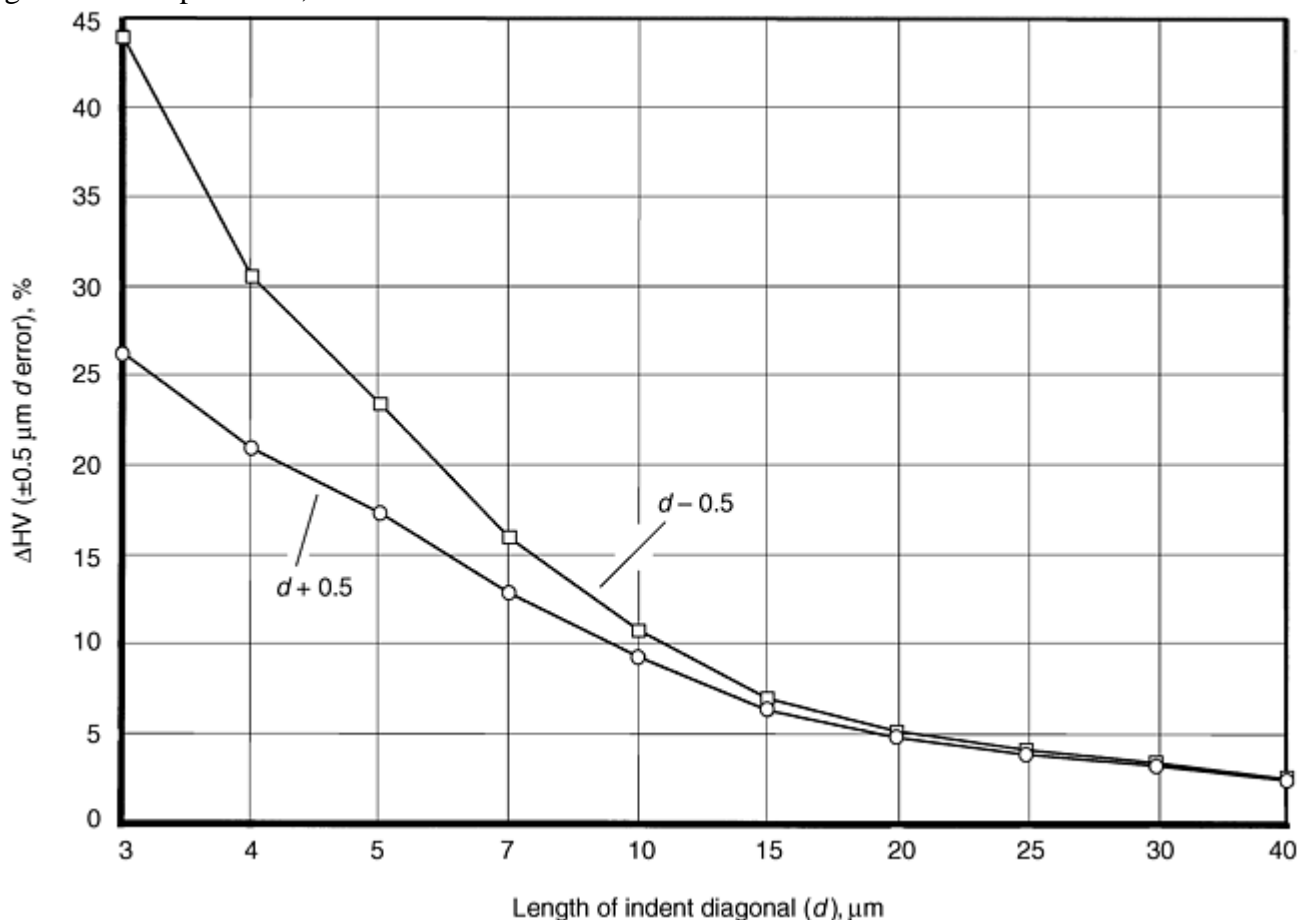


Fig. 11 Influence of a measurement error of $\pm 0.5 \mu\text{m}$ on the calculated Vickers hardness as a function of diagonal length

ASTM E 384 recommends that the operator should try to keep indents larger than 20 μm in d . Figure 11 demonstrates the reason for this recommendation. A similar graph could be constructed for the Knoop test. In general, determining the location of the tips of the Knoop indent to measure the long diagonal is more difficult than with a Vickers indent because the contrast at the Knoop indent tips is not as strong. The $\pm 0.5 \mu\text{m}$ measurement variability for the same person as a function of time may be a bit conservative for the Knoop test. If the operator has a rough idea of the hardness of the test piece, then a good estimate can be made of the appropriate test load to choose. The harder the specimen, the greater the test load needed to keep d greater than 20 μm . Figures 9 and 10 can be used as a guide. For example, assume that a hardness traverse is to be made on an induction-hardened specimen that is expected to vary in hardness from approximately 750 HV at the surface to 250 HV in the core. Figure 9 says that an applied force of 200 gf will produce approximately a 22 μm diagonal indent for a 750 HV steel and close to a 40 μm diagonal indent for a 250 HV steel. For a 100 gf applied force, the diagonal for 750 HV is less than 16 μm , so it would be best to use a higher load. A 300 gf applied force produces approximately a 27 μm diagonal for 750 HV and approximately a 47 μm diagonal at 250 HV, and it may be a better choice than a 200 gf or 100 gf load. If the hardened case is rather shallow, it may be necessary to space indents along several different parallel traces at different depths so that the gradient can be assessed satisfactorily without tight indent spacing adversely influencing the test data.

The opposite problem, that of an excessively large ($d > 75\%$ of the field width) indent is less common, but may arise depending on test conditions. In general, MHT is performed in an effort to measure spatial variations in hardness or the hardness of small regions. But sometimes it is used as a convenient substitute for a bulk hardness test on a small specimen of homogenous nature at the same time as the structure is examined. In that case, the indent size is not too critical as long as a $\pm 0.5 \mu\text{m}$ measurement variation has only a small influence on

the calculated HV. With a very soft material, the indent should be small enough that it can be kept entirely in the field of view of the optics.

Indent Spacing. In general, the same guidelines used in bulk hardness tests are used for MHT. Indenting creates both elastic and plastic deformation and a substantial strain field around the indent. If a second indent is made too close to a prior indent, its shape will be distorted on the side toward the first indent. This produces erroneous test results.

In general, the spacing between indents should be at least 2.5 times the d length for the Vickers test and at least twice the length of the short diagonal for the Knoop test. The minimum spacing between the edge of a specimen and the center of an indent should be $2.5d$, although values as low as $1.8d$ have been demonstrated to be acceptable.

References cited in this section

6. G.F. Vander Voort, "Results of an ASTM E-4 Round-Robin on the Precision and Bias of Measurements of Microindentation Hardness Impressions," ASTM STP 1025, "Factors that Affect the Precision of Mechanical Tests," ASTM, 1989, p 3–39
7. G.F. Vander Voort, "Operator Errors in the Measurement of Microindentation Hardness," ASTM STP 1057, "Accreditation Practices for Inspections, Tests and Laboratories," ASTM, 1989, p 47–77

Microindentation Hardness Testing

George F. Vander Voort, Buehler Ltd.

Hardness versus Applied Test Force

For the Vickers test, especially in the macro applied force range, it is commonly stated that the hardness is constant as the load is changed. For microindentation tests, the Vickers hardness is not constant over the entire range of test forces. For Vickers tests with an applied force of 100 to 1000 gf, the measured hardnesses are usually equivalent within statistical precision. The Vickers indent produces a geometrically similar indent shape at all loads, and a log-log plot of applied force (load) versus diagonal length should exhibit a constant slope, n , of 2 for the full range of applied force (Kick's Law); however, this usually does not occur at forces under 100 gf.

Reference 6 shows four trends for force (load) and Vickers MHT data:

- *Trend 1:* HV increases as force decreases ($n < 2.0$).
- *Trend 2:* HV decreases as force decreases ($n > 2.0$).
- *Trend 3:* HV essentially constant as force varies ($n = 2.0$).
- *Trend 4:* HV increases, then decreases with decreasing force.

Trends 1, 2, and 4 are more easily detected in hard specimens than on soft specimens where trend 3 is observed. Many publications, particularly those reporting trends 1 and 2, have attributed these trends to material characteristics.

The Knoop indenter does not produce geometrically similar indents, so the hardness should increase with decreasing test force. Due to the poor image contrast at the Knoop indent tips (long diagonal), it is far more likely that d will be undersized, leading to a higher hardness number. Consequently, the Knoop hardness increases with decreasing test force, and the magnitude of the increase rises with increasing hardness. However, a few studies reported a variation in this trend: HK increased with decreasing force and then decreased at the lowest applied force.

It is widely claimed in the literature that the Vickers hardness is constant with test force in the macro force range (≥ 1 kgf). However, a search in the literature for data to prove this point yielded very little evidence. Reference 3 gives measurements made on five polished HRC test blocks, with hardnesses ranging from 22.9 to 63.2 HRC, using six test forces from 1 to 50 kgf. At each force, six impressions were made, and the mean results are in Fig. 12. The Filar micrometer used a magnification of 100 \times . Note that the HV is essentially constant for forces of 10 kgf and greater. For each test block, the hardness decreased for test forces less than 10 kgf. The degree of decrease increased with increasing hardness. Thus, for this macro Vickers tester, HV was not constant but exhibited trend 2, the most commonly observed trend for studies of MHT and HV force.

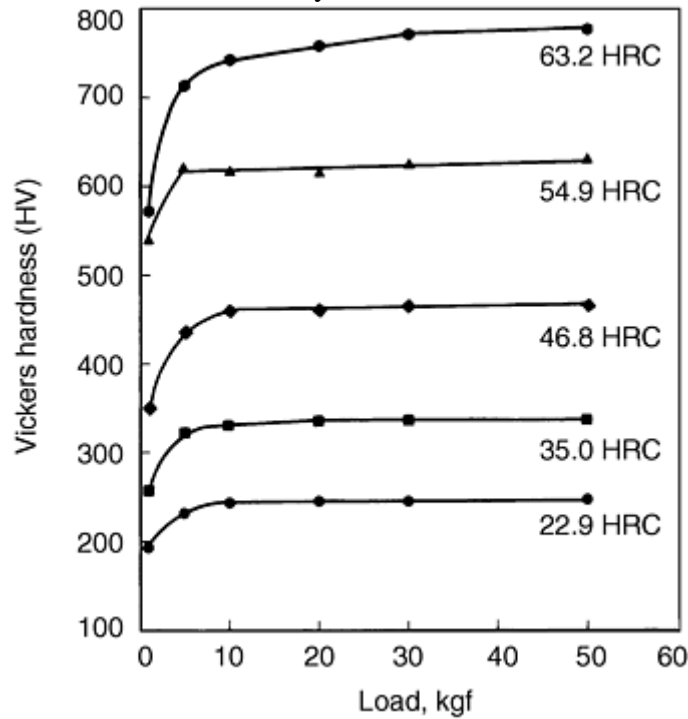


Fig. 12 Measured Vickers macrohardness for five steel test blocks using test forces from 1-50 kgf. Source: Ref 3

The exact same steel test blocks were also subjected to Vickers microindentation hardness tests using nine different forces from 5 to 500 gf (Ref 3). Again, six impressions were made at each test force, and the mean values are plotted in Fig. 13. These impressions were measured at 500 \times . Again, the same basic trend is observed. In most cases, HV is essentially constant at forces down to 100 gf, then the hardness decreases. The magnitude of this decrease again increases with increasing specimen hardness. For several of the data, the hardness appears to rise slightly as the force drops below 100 gf, and then it decreases (trend 4). Thus, for the work detailing MHT in HV versus the test forces, both trends 2 and 4 were obtained.

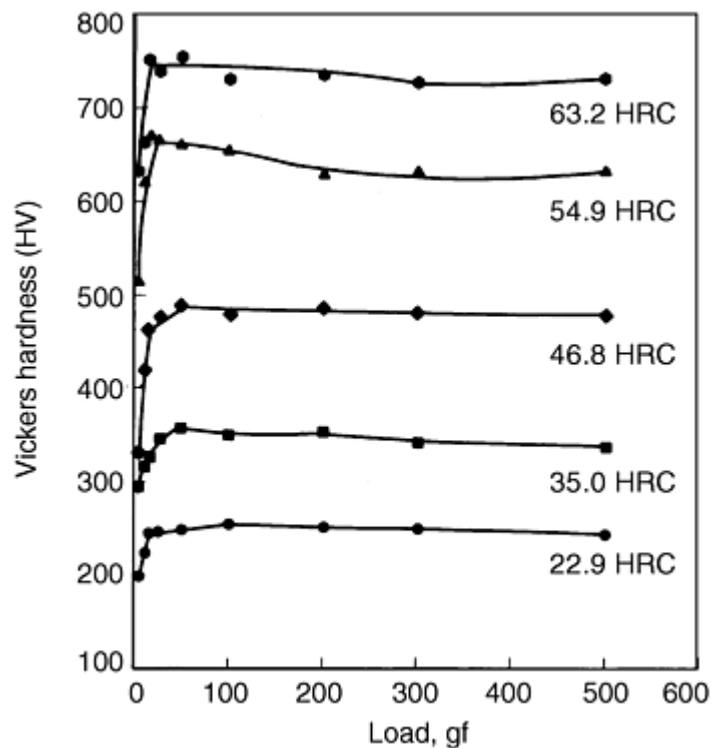


Fig. 13 Measured Vickers microindentation hardness for five steel test blocks using test forces from 5-500 gf. Source: Ref 3

These results, using the same set of five specimens with a wide range of hardnesses and tests with both micro- and macro-Vickers units, revealed basically the same trend. At small indent sizes for both testers, measurements yielded lower hardness (indents being oversized) than they should. This can only be due to visual perception problems in sizing small indents at the tester magnifications employed (100× for the macro system and 500× for the micro system). No material characteristic can possibly explain this problem.

To further demonstrate that the observed trends of HV versus test force (load) are due to measurement difficulties, the results of an ASTM Committee E-4 interlaboratory round-robin test program is cited (Ref 6, 7). In this study, one person indented three ferrous and four nonferrous specimens at test forces of 25, 50, 100, 200, 500, and 1000 gf (five times at each force). Then, twenty-four people measured the indents: thirteen measured all of the Knoop and Vickers indents in the ferrous specimens (fourteen actually measured specimen F1), and eleven measured the Knoop and Vickers indents in the nonferrous specimens. Agreement was best for the low hardness specimens, as would be expected, because they had the largest indents and the effect of small measurement errors is minimal. The Vickers hardness, in most cases, decreased with forces below 100 gf, but all four possible trends reported in the literature can be seen in the measurement data for the same indents.

As an example, Fig. 14 shows the data for nine of the fourteen people who measured the Vickers indents in the hardest ferrous specimen (specimen F1). The overall trend for the data is trend 2. However, examination of the data shows that test lab 8 followed trend number 1, lab 1 followed trend 3, and lab 3 followed trend 4. Statistical analysis of all of the test data suggested that these nine people obtained essentially the same test results while some or all of the data from the other five people represented “outlier” conditions. Figure 15 shows the data for the five outlier labs for the F1 specimen (where lab F was defined as an outlier lab based on results for other specimens—their results for specimen F1 were marginal). The “good max” and “good min” lines in Fig. 15 encompass the range of “good” data shown in Fig. 14. Again, several HV-versus-force trends are observed: labs E, H, and J follow trend 1, and labs F and M follow trend 2. Because exactly the same indents were measured, these variations in test results come only from measurement inconsistencies. This study reveals that the most commonly obtained trend was trend 2, decreasing HV with decreasing test force, and this is the most commonly reported trend in the literature. Thus, it is more likely for an operator to oversize small Vickers indents than to undersize them or to measure their true size.

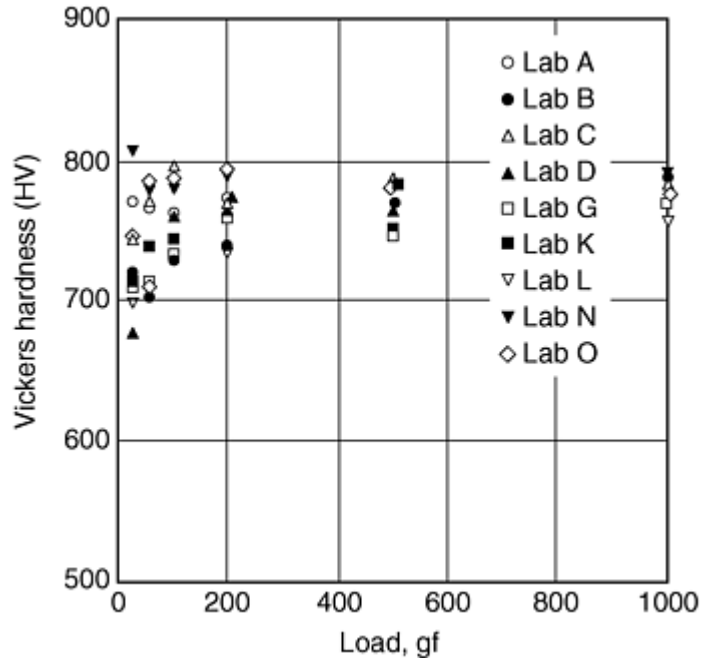


Fig. 14 ASTM E-4 round-robin interlaboratory Vickers microindentation hardness-testing data for the hardest (F1) test specimen and nine people (measuring the same indents) who produced “good” data for test loads from 25-1000 gf. Source: Ref 6, 7

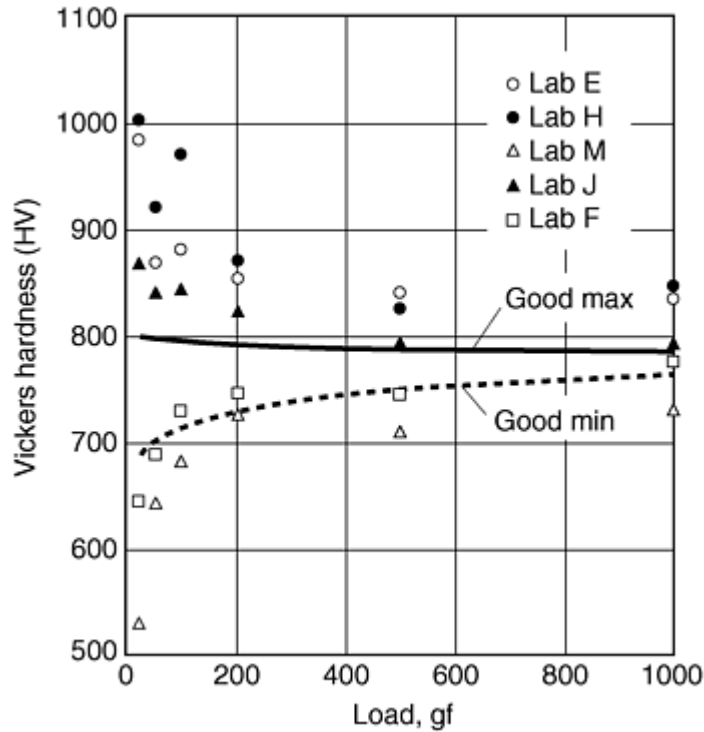


Fig. 15 Data shown in Fig. 14 (all points fall within the two lines) plus the individual data from four “outlier” raters. Source: Ref 6, 7

Measurements of the Knoop indents also reveal substantial variations in the data. In most cases, the HK rose as the test force decreased, with most of the increase occurring at forces less than 200 gf. In general, HK results were statistically identical for each specimen at forces from 200 to 1000 gf. For the nonferrous specimens, one rater consistently obtained the very unusual trend of decreasing HK with forces less than 200 gf. One other rater obtained a similar, but less pronounced, decrease in HK with decreasing test forces; but this was only for the hardest nonferrous specimen (mean hardness, approximately 330 HK).

The visibility of the tips of the long diagonal on the Knoop indent is poorer than for Vickers indents. Thus, for Knoop indents, undersizing the indent is far more likely than oversizing. However, it is clear that one of the eleven people who measured the Knoop indents in this study consistently oversized the Knoop indents. At test forces above 200 gf, this person's results agreed with the mean results in two cases, were below the mean in one case, and were above the mean in another case. A calibration error would produce a consistent bias in all of the data; however, this could not be the case for this person's test results. Interestingly, this person was an experienced metallographer, not a novice.

There are times when the hardness tester can be the source of a variation in the load-hardness relationship. Before using a new MHT unit, it is a good practice to select a specimen with a homogeneous microstructure and a known hardness and then perform a series of tests using the full range of applied test forces available for the unit. To obtain good statistics, make a number of impressions at each load. As an illustration of this problem, two testers were evaluated over their full ranges using a hardened specimen of type 440C martensitic stainless steel. For tester A, six indents were made at each available test load, while for tester B, only three indents were made at each load due to time limitations with the unit. The mean results are plotted in Fig. 16. While tester A produced virtually identical results over the full load range, it is clear that tester B was applying excessively high test forces at all loads under 1000 gf. Clearly this was a machine problem because the same person performed both sets of measurements on the same specimen. Verification of the instrument using properly calibrated test blocks should help identify this type of problem.

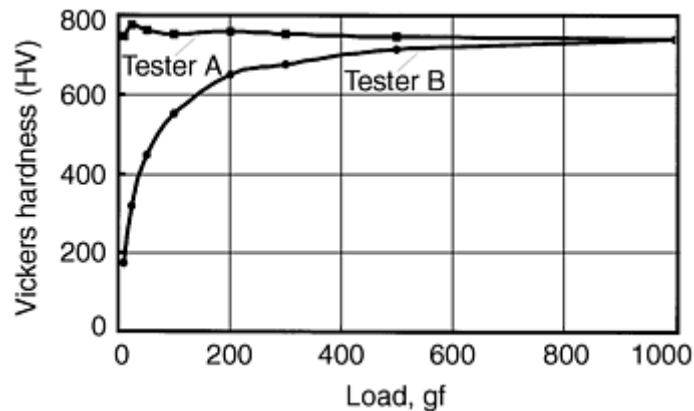


Fig. 16 Curves showing load versus Vickers hardness for two testers (with the same operator) evaluating the hardness of the same type 440C martensitic stainless steel specimen (62.7 HRC)

References cited in this section

3. G. F. Vander Voort, *Metallography: Principles and Practice*, McGraw-Hill, 1984; reprinted by ASM International, 1999, p 356, 381
6. G.F. Vander Voort, "Results of an ASTM E-4 Round-Robin on the Precision and Bias of Measurements of Microindentation Hardness Impressions," ASTM STP 1025, "Factors that Affect the Precision of Mechanical Tests," ASTM, 1989, p 3-39
7. G.F. Vander Voort, "Operator Errors in the Measurement of Microindentation Hardness," ASTM STP 1057, "Accreditation Practices for Inspections, Tests and Laboratories," ASTM, 1989, p 47-77

Microindentation Hardness Testing

George F. Vander Voort, Buehler Ltd.

Repeatability and Reproducibility

Appendix X2 of ASTM E 384, along with Ref 6 and 7, describes the results of an ASTM interlaboratory round-robin program used to determine the precision of measuring Knoop and Vickers indents and the repeatability and reproducibility of such measurements. Repeatability is a measure of how well an individual operator can replicate results on different days with the same specimen and the same equipment. Reproducibility measures the ability of different operators, in different laboratories, to obtain the same results, within statistical limits. Repeatability and reproducibility were best for low-hardness specimens and got poorer as the hardness increased; that is, as the indent size decreased. Repeatability was always somewhat better than reproducibility, as might be expected. For a material with a hardness of 900 HV, repeatability for a 25 gf load was approximately ± 170 HV, and for a 1000 gf load it was approximately ± 25 HV, while reproducibility for a 25 gf load was approximately ± 220 HV, and for a 1000 gf load it was approximately ± 40 HV. For a material with a hardness of 900 HK, repeatability for a 25 gf load was approximately ± 75 HK, and for a 1000 gf load it was approximately ± 25 HK, while reproducibility for a 25 gf load was approximately ± 105 HK, and for a 1000 gf load it was approximately ± 40 HK. This shows that the repeatability and reproducibility values at the highest loads were similar for both types of indents, but as the test load decreased, the longer Knoop indent (at each load) yielded better repeatability and reproducibility than the smaller Vickers indent at the same load. These trends again highlight the importance of trying to use the greatest possible load for any test.

References cited in this section

6. G.F. Vander Voort, "Results of an ASTM E-4 Round-Robin on the Precision and Bias of Measurements of Microindentation Hardness Impressions," ASTM STP 1025, "Factors that Affect the Precision of Mechanical Tests," ASTM, 1989, p 3–39
7. G.F. Vander Voort, "Operator Errors in the Measurement of Microindentation Hardness," ASTM STP 1057, "Accreditation Practices for Inspections, Tests and Laboratories," ASTM, 1989, p 47–77

Microindentation Hardness Testing

George F. Vander Voort, Buehler Ltd.

Applications

Because hardness tests are a quick and convenient way to evaluate the quality or characteristics of a material, hardness testing is widely used in quality-control studies of heat treatment, fabrication, and materials processing. It is also a key test used in failure analysis work.

Microindentation hardness testing provides the same benefit as bulk hardness testing, but with a much smaller indent. Because the indents are small, MHT can be used for many parts or material forms that are too small or too thin to test with bulk test procedures. Likewise, MHT allows hardness measurements of microstructural constituents. For example, the determination of hardness of specific types of carbides, nitrides, borides, sulfides, or oxides in metals has been widely performed, particularly in wear and in machinability research.

There is a long list of applications where MHT is indispensable. A few examples are described in this section. The examples are just a few of the many that could be chosen to demonstrate the value of MHT. To a large extent, MHT can be considered as simply an extension of bulk hardness testing, in that it can be used for all the same purposes as bulk hardness tests. However, due to the very small size of the indent, MHT has a host of applications that cannot be performed with bulk tests. It can also be considered as a strength microprobe and, thus, an extension of tensile testing. When properly used, MHT is a great asset in any laboratory.

Hardness Testing of Thin Products

Foil or wire product forms depend on MHT in quality-control programs. In general, the indent depth should be no more than 10% of the thickness or diameter of the products. Figure 17 shows the relationship among the minimum foil thickness that can be tested, the applied force, and the Knoop hardness. As this figure shows, for thicknesses less than 0.010 in. (254 μm), test-force selection becomes more critical as the thickness decreases and the hardness decreases. For example, for a foil 0.002 in. thick (51 μm) with high hardness (e.g., greater than 500 HK), test forces up to 800 gf can be used. However, if the hardness is not known, and a 500 gf load indicates a hardness of approximately 200 HK, then it would be advisable to retest the foil using a force of, at most, 300 gf because the test at 500 gf may not be valid.

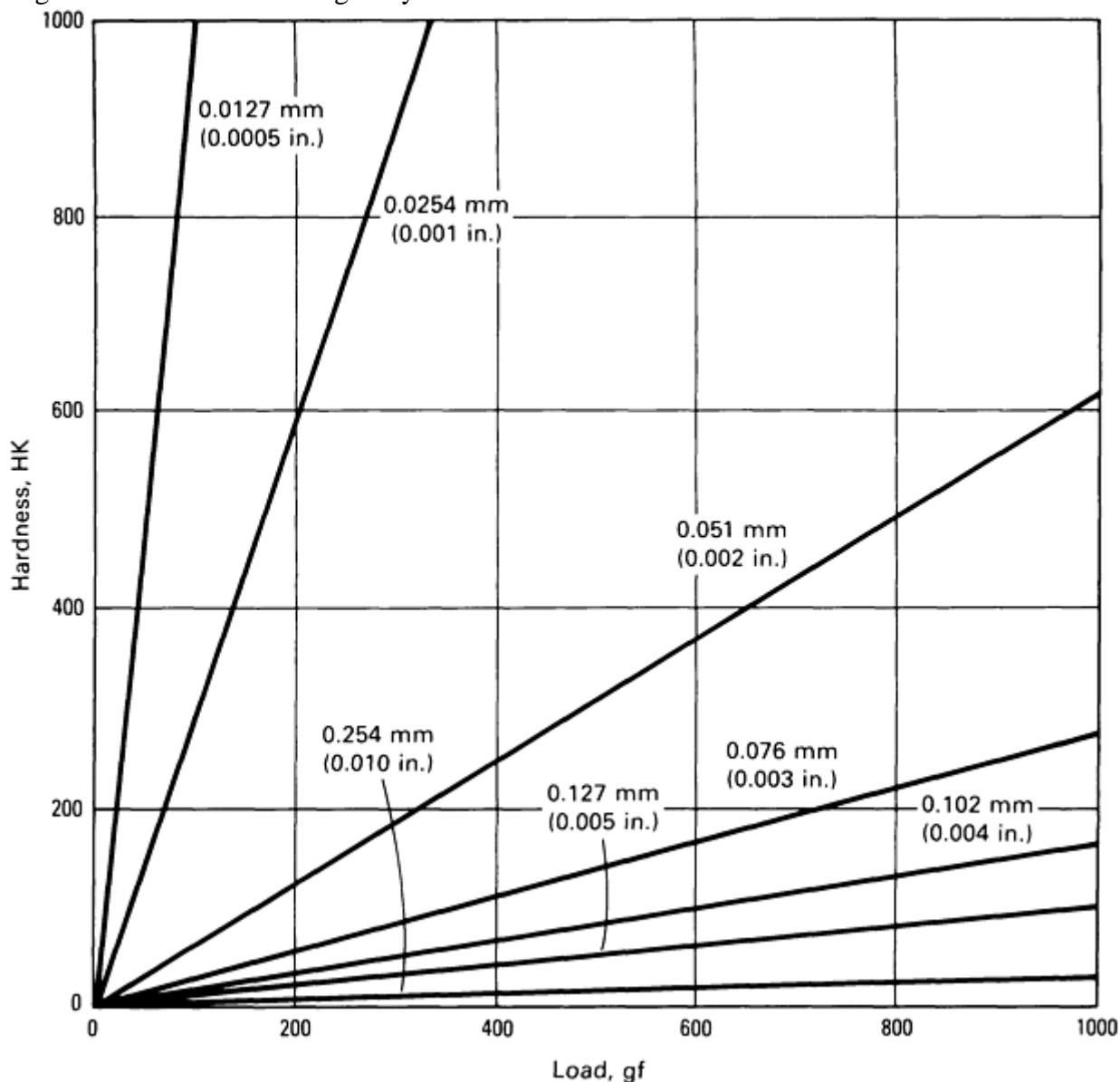


Fig. 17 Minimum thickness of test specimens for the Knoop test as a function of applied force (load) and Knoop hardness

Hardness tests of thin materials and thin coatings often require very low applied forces (loads). As already demonstrated, it is quite difficult to measure very small indents. MHT units are readily available for making impressions at forces down to 1 gf, and special testers are available that can indent at even lower forces. (These devices are not discussed in this article, however.) In the case of MHT systems using indenting forces less than 25 gf and indents between 1 and 25 μm , it may be advisable to place the tester on an antivibration platform and to use at least 60 \times objectives with a high numerical aperture for measurements. Oil-immersion objectives may be required, particularly for materials with poor light reflectivity.

Case Hardness Measurement

Perhaps the classic application of MHT is the assessment of changes in surface hardness: usually increases due to surface treatments, such as carburizing, nitriding, or localized surface-hardening processes, are analyzed, but decreases in hardness due to local chemistry changes (decarburization) or localized heating are also examined. While these changes are usually detectable by eye on a properly prepared metallographic cross-section, hardness traverses define the magnitude and extent of such changes with greater precision and detail. It is not uncommon for quality-control tests to require determination of the depth to a specific hardness for a carburized or nitrided part.

Figure 18 demonstrates the measurement of case depth by a series of indentations that traverse a cross-section from a flame-hardened SAE 8660 specimen. The hardness traverses used a Vickers tester with the fully automated device (Fig. 4b) and a 300 gf load. The surface hardness is approximately 830 HV, and the hardness drops steadily until, at 2.5 mm depth, the core hardness (~200 HV) is reached. The effective case depth (the depth to 550 HV) occurs at a depth of 1.95 mm.

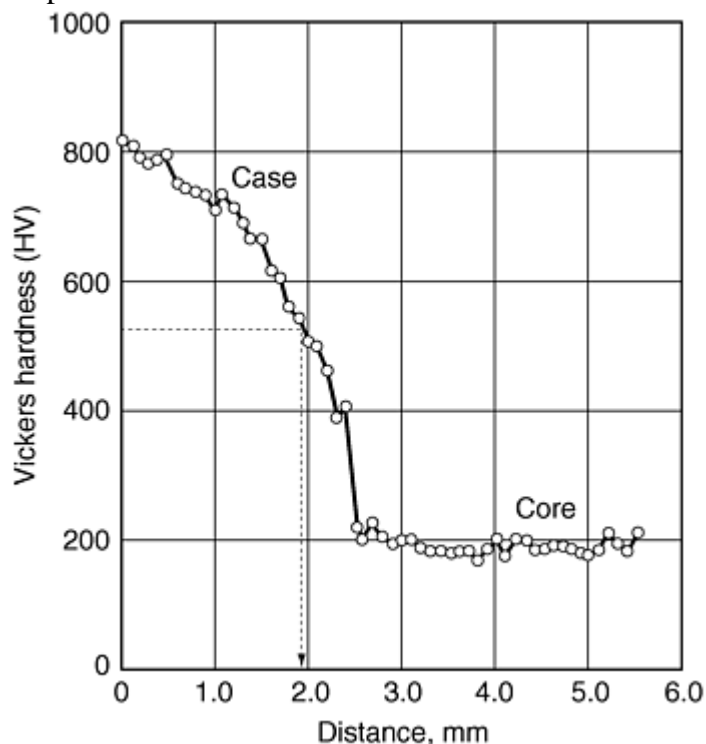


Fig. 18 Vickers traverse showing the hardness profile results from a flame-hardened SAE 8660 gear using a fully automated microindentation hardness-testing system

Figure 19 shows the hardness profile for an induction-hardened SAE 1053 carbon-steel gear using the fully automated system and a 300 gf load. Note that the surface hardness increased slowly from the surface to a depth of 4.1 mm. In this specimen, the microstructure contained at the surface substantial retained austenite, which decreased until it was undetectable at a depth of approximately 3 mm. The prior-austenitic grain size was coarse at the surface and decreased in size through the hardened case. These trends are caused by the temperature profile from induction heating. The hardness drops rapidly in the depth range of 4 to 4.6 mm, and the microstructure changes from predominantly martensite to ferrite and pearlite with a hardness of approximately 230 HV.

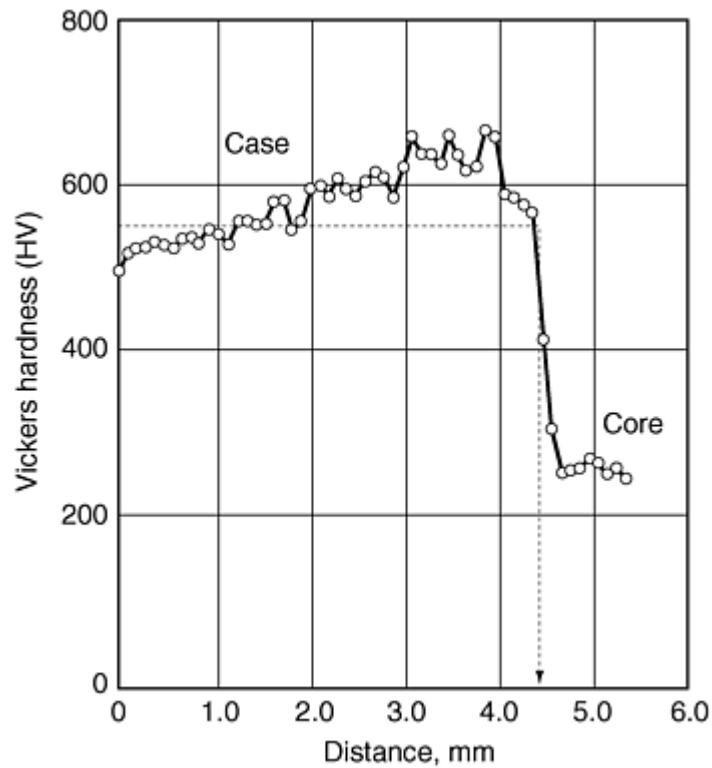


Fig. 19 Vickers traverse showing the hardness profile results from an induction-hardened SAE 1053 gear using a fully automated microindentation hardness-testing system

When manual MHT systems are used to determine the effective case depth, it is quite common to etch the specimen and find the depth where the microstructure changes from hardened to unhardened. Then, the operator places a few indents in this region and interpolates the depth to the desired hardness, most often 500 or 550 HV, depending on the carbon content. Of course, the very interesting rise in hardness (Fig. 19) from the surface to 4.1 mm would not be detected. This may have an adverse effect on the wear behavior and presents a dilemma for the analyst because the surface hardness is less than the hardness criteria for the effective case depth. Note that the surface does not exceed 550 HV until a depth of approximately 1.5 mm. Then, the hardness raises to approximately 680 HV at approximately 4 mm depth. The hardness falls again to 550 HV at approximately 4.5 mm depth. The detailed variation of hardness with depth can be observed more easily with automated traverse hardness tests.

Figure 20 shows a hardness traverse for a carburized SAE 8620 mold that exhibited substantial retained austenite in the hardened case. Again, the specimen was evaluated with the fully automated system in Fig. 5 with a 300 gf load. Note that the hardness is somewhat erratic in the fully hardened surface layer (surface to approximately 1.8 mm depth). This is due to the presence of retained austenite in this zone, which is substantially lower in hardness than plate martensite. If a lower test force were used, the scatter would be greater. Very low test forces, producing very small indents, might produce a hardness variation of several hundred HV in the case. The effective case depth (depth to 550 HV) is at 2.1 mm, and the core is reached at approximately 2.5 mm (~400 HV). Again, if testing were performed manually and only in the transition zone, the metallographer would not have observed the variability in hardness in the fully hardened zone.

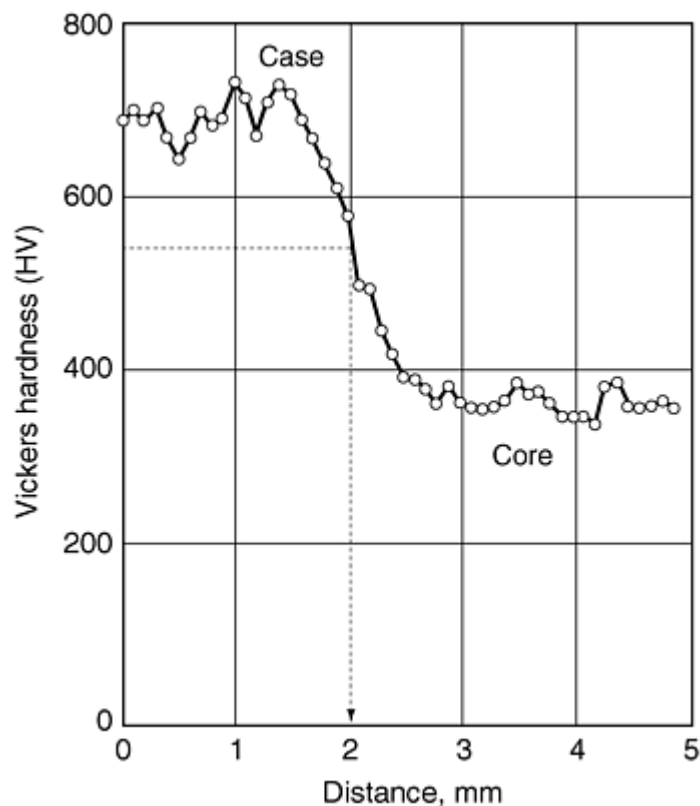


Fig. 20 Vickers traverse showing the hardness profile results from a carburized and hardened SAE 8620 mold using a fully automated microindentation hardness-testing system

Alloy Phase Hardness Measurements

Microindentation hardness testing has been widely used in alloy development research, particularly in multiphase alloy studies. Because hardness can be correlated to strength, MHT can be used to determine the properties of phases or constituents. Some such examples are described here.

Example 1: Hardness Measurement on Ferrite and Austenite Grains in Dual Phase Steel. Microindentation testing was performed on the ferrite and austenite grains in a specimen of hot-rolled dual-phase stainless steel. The specimen was prepared so that a plane parallel to the hot-working direction could be observed. Because the phases were elongated rather than equiaxed, the Knoop indenter was used (with a 50 gf load). The specimen was lightly etched electrolytically with 20% nitric acid, which colors the ferrite grains. Indents were made in a number of grains (six or more indents per constituent type, as a rule) to calculate the mean, standard deviation, and the 95% confidence interval. The ferrite had a hardness of $263.5 \pm 5 \text{ HK}_{50}$ (mean $\pm 95\%$ confidence interval), while the austenite had a hardness of $361.8 \pm 18.6 \text{ HK}_{50}$. This difference was significant at the 99.9% confidence level. Figure 21 shows the microstructure of this specimen along with a number of Knoop indents.

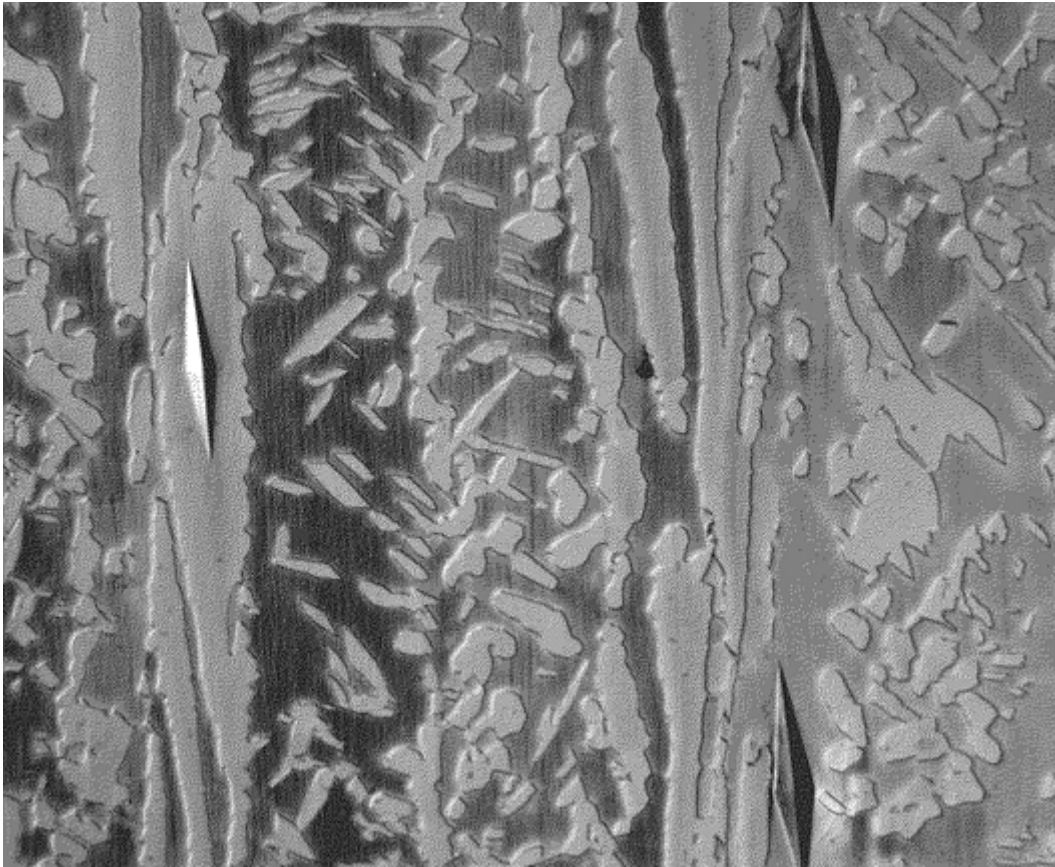


Fig. 21 Knoop indents in ferrite (dark) and austenite (white) grains in a dual-phase stainless steel (differential interference contrast illumination, aqueous 20% nitric acid, 3 V dc). 500×

Example 2: Hardness Measurement on Alpha and Beta Phases in Naval Brass. Microindentation testing with a Knoop indenter was performed on the alpha and beta phases in a specimen of naval brass (C 46400). A longitudinally oriented test plane was evaluated, and the Knoop indenter was used due to the elongated shape of the grains. A test load of 50 gf was used to keep the indents within the grains. The specimen was tint etched with Klemm's I, which colors the beta phase. Again, indents were made on a number of grains of each phase. The alpha phase had a hardness of $178.1 \pm 8.8 \text{ HK}_{50}$, while the beta phase had a hardness of $185.4 \pm 13.7 \text{ HK}_{50}$. The difference in hardness between alpha and beta phases was not statistically significant. Figure 22 shows the microstructure of this specimen and several of the Knoop indents.

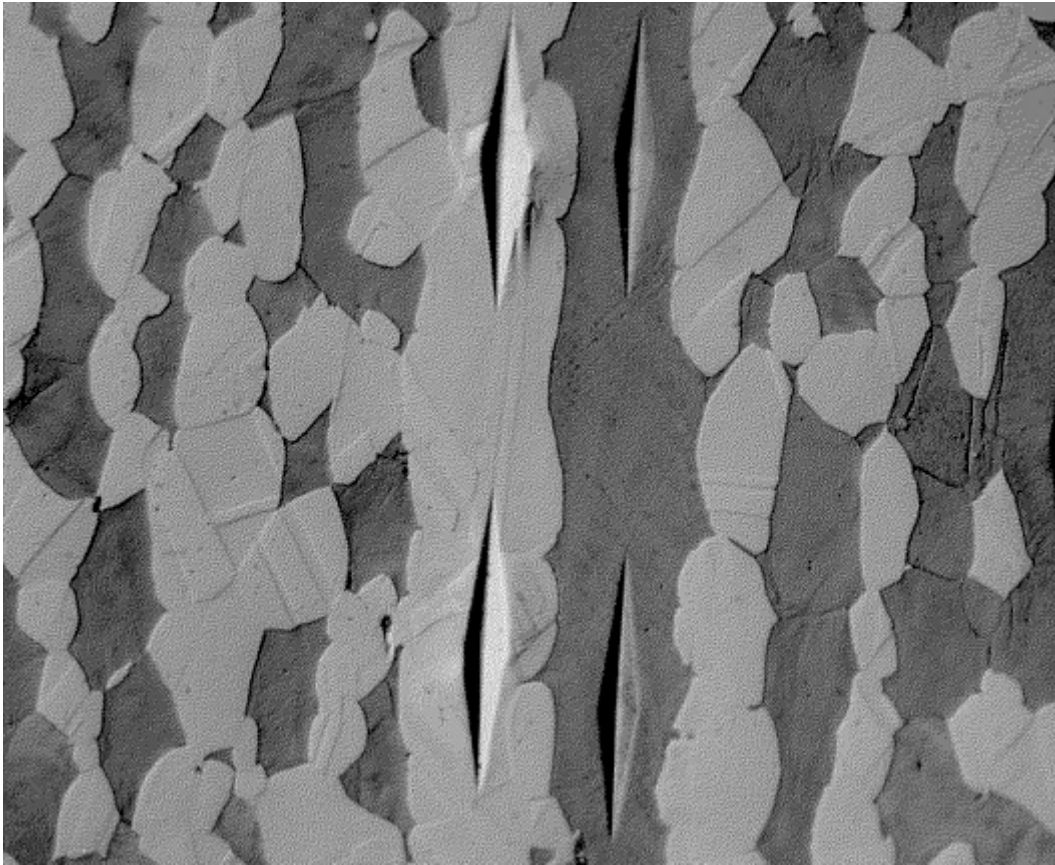


Fig. 22 Knoop indents (50 gf) in alpha (white) and beta (dark) grains in naval brass (C 46400) (differential interference contrast illumination, Klemm's I reagent). 500×

Example 3: Microindentation Hardness of Phases in 430 Stainless Steel. Similar tests were performed on a dual-phase, ferrite and martensite, high-carbon, type 430 stainless-steel specimen. It was possible to test with a 100 gf load using the Vickers indenter. The ferrite had an average hardness of $152.3 \pm 5.7 \text{ HV}_{100}$ while the martensite had a mean hardness of $473 \pm 41.5 \text{ HV}_{100}$. Again, at least six impressions were made in each constituent. The specimen, shown in Fig. 23, was electrolytically etched with aqueous 60% nitric acid at 1.5 V dc. The difference in hardness between the alpha phase and martensite was statistically significant at the 99.9% confidence level.

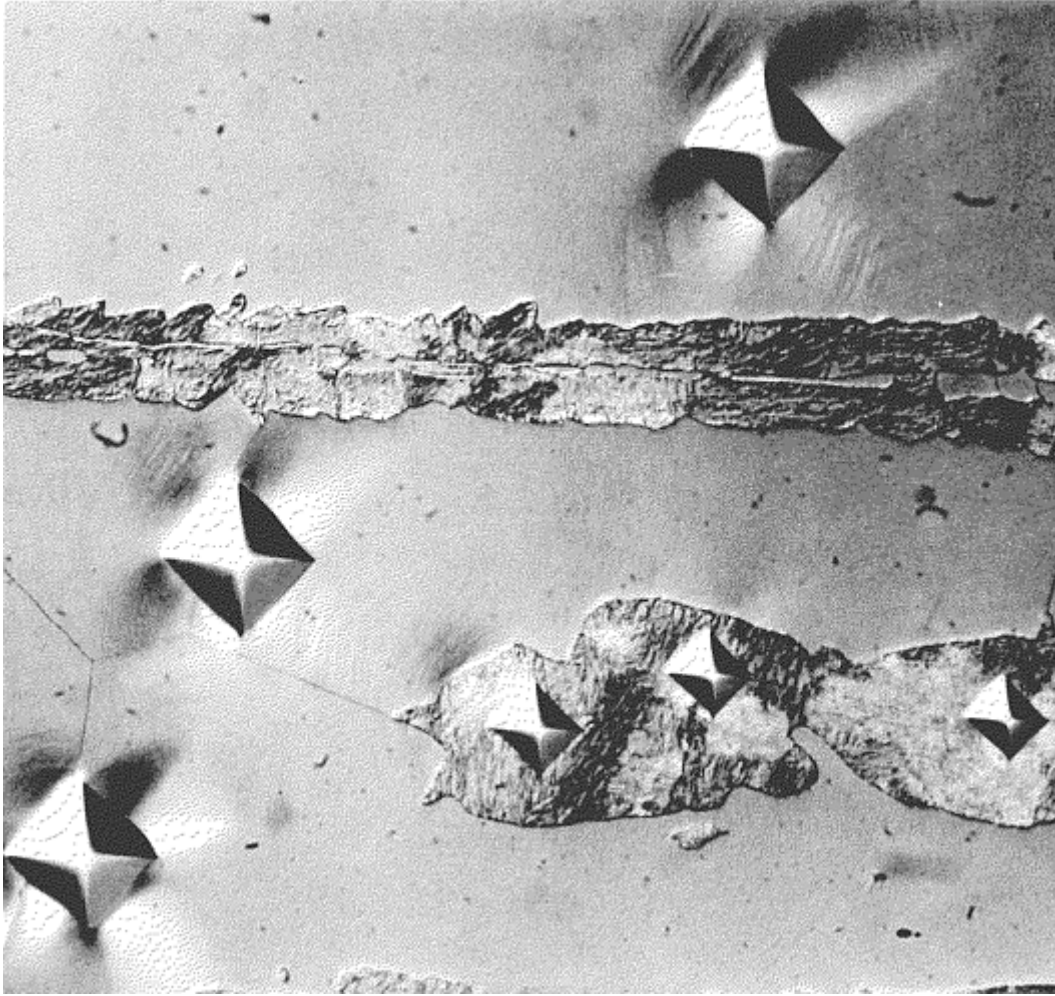


Fig. 23 Vickers indents (100 gf) in alpha (white) and martensite (dark) grains in a high-carbon version of 430 stainless steel (differential interference contrast illumination, aqueous 60% nitric acid, 1.5 V dc). 500×

Example 4: Hardness of Phases in As-Cast Beryllium Copper. MHT can be used to study effects of heat treatment and segregation on the hardness of the phases in as-cast beryllium copper (C 82500) that has been solution treated at 871 °C, hot enough to cause incipient melting. One specimen was age hardened and one was not. Because the phases were essentially equiaxed in shape, the Vickers indenter was used. In the unaged specimen, a 50 gf test force was used, while in the harder, aged specimen, 100 gf could be used. Again, a number of indents, at least six, were made in each phase. For the unaged specimen, shown in Fig. 24, the alpha matrix had a hardness of $107.6 \pm 4.8 \text{ HV}_{50}$, while the intergranular beta had a hardness of $401.0 \pm 63.0 \text{ HV}_{50}$. For the aged specimen, shown in Fig. 25, the alpha matrix exhibited light and dark crosshatched etched areas suggesting chemical segregation. The light etching alpha had a hardness of $316.1 \pm 38.3 \text{ HV}_{100}$, while the dark etching alpha had a hardness of $416.6 \pm 8.6 \text{ HV}_{100}$. This difference in hardness was statistically significant at the 99.9% confidence level. The intergranular beta phase also exhibited a crosshatched etched appearance and had a hardness of $521.6 \pm 31.9 \text{ HV}_{100}$. The difference in hardness of the intergranular beta phase in the aged versus unaged condition was statistically significant at the 99.9% confidence level. The specimens were etched with aqueous 3% ammonium persulfate-1% ammonium hydroxide. It is best to use the same applied force for each phase or constituent when doing such comparisons, rather than the highest possible applied force in each phase or constituent.

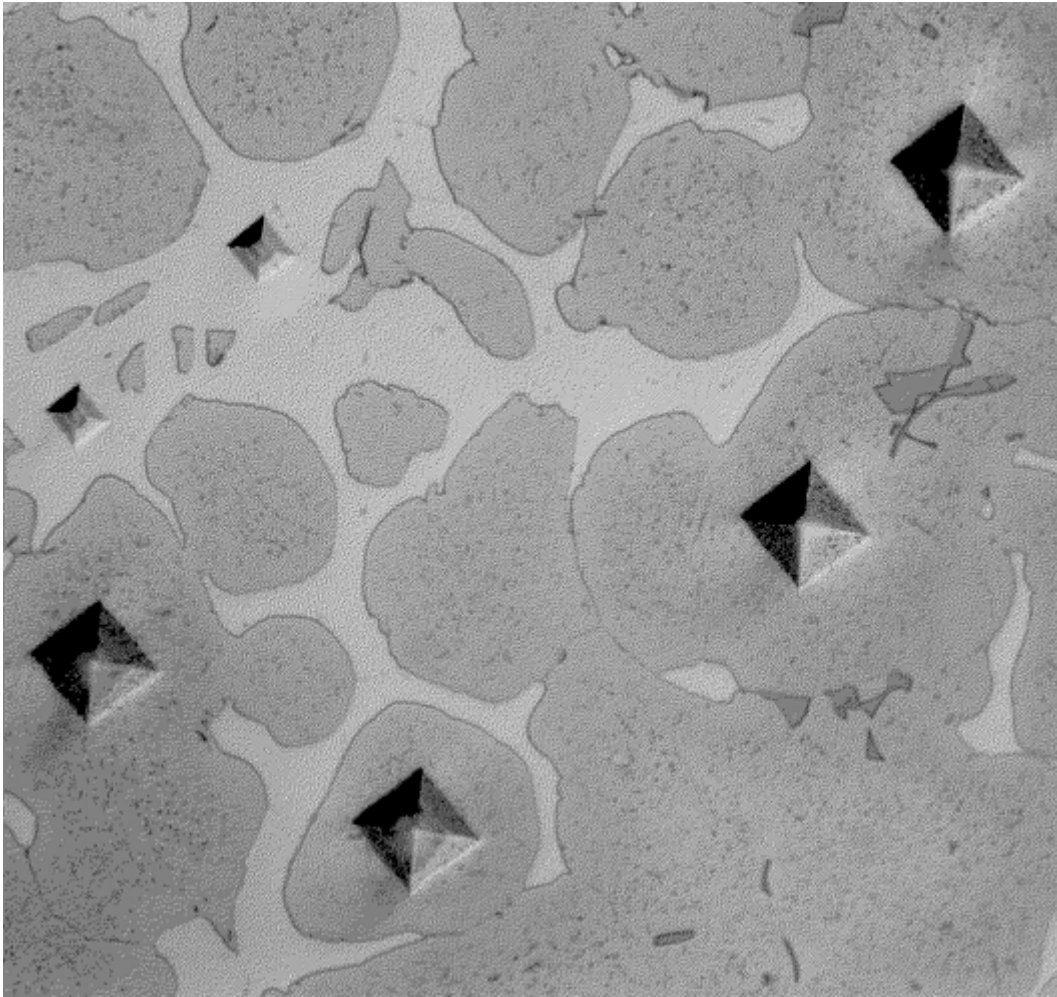


Fig. 24 Vickers indents (50 gf) in the matrix (dark) and in the intergranular beta (white) phase in as-cast beryllium copper (C 82500) that was burnt in solution annealing (differential interference contrast illumination, aqueous 3% ammonium persulfate and 1% ammonium hydroxide). 500×



Fig. 25 Vickers indents (100 gf) in the matrix (dark) and in the intergranular beta (white) phase in an age-hardened as-cast beryllium copper (C 82500) that was burnt in solution annealing (differential interference contrast illumination, aqueous 3% ammonium persulfate and 1% ammonium hydroxide). 500×

Microindentation Hardness Testing

George F. Vander Voort, Buehler Ltd.

References

1. L. Emond, Vickers-Knoop Hardness Conversion, *Met. Prog.*, Vol 74, Sep 1958, p 97, 96B; Vol 76, Aug 1959, p 114, 116, 118
2. G.M. Batchelder, The Nonlinear Disparity in Converting Knoop to Rockwell C Hardness, *ASTM Mater. Res. Stand.*, Vol 9, Nov 1969, p 27–30
3. G. F. Vander Voort, *Metallography: Principles and Practice*, McGraw-Hill, 1984; reprinted by ASM International, 1999, p 356, 381
4. *Metallography and Microstructures*, Vol 9, *ASM Handbook*, ASM International, 1985
5. G.F. Vander Voort, Ed., *Metallography, Metals Handbook Desk Edition*, 2nd ed., ASM International, p 1356–1409
6. G.F. Vander Voort, “Results of an ASTM E-4 Round-Robin on the Precision and Bias of Measurements of Microindentation Hardness Impressions,” ASTM STP 1025, “Factors that Affect the Precision of Mechanical Tests,” ASTM, 1989, p 3–39

7. G.F. Vander Voort, "Operator Errors in the Measurement of Microindentation Hardness," ASTM STP 1057, "Accreditation Practices for Inspections, Tests and Laboratories," ASTM, 1989, p 47–77

Instrumented Indentation Testing

J.L. Hay, MTS Systems Corporation; G.M. Pharr, The University of Tennessee and Oak Ridge National Laboratory

Introduction

INSTRUMENTED INDENTATION TESTING (IIT), also known as depth-sensing indentation, continuous-recording indentation, ultra-low-load indentation, and nanoindentation, is a relatively new form of mechanical testing that significantly expands on the capabilities of traditional hardness testing. Developed largely over the past two decades, IIT employs high-resolution instrumentation to continuously control and monitor the loads and displacements of an indenter as it is driven into and withdrawn from a material (Ref 1, 2, 3, 4, 5, 6, 7, 8, 9, 10, 11, 12, 13). Depending on the details of the specific testing system, loads as small as 1 nN can be applied, and displacements of 0.1 nm (1 Å) can be measured. Mechanical properties are derived from the indentation load-displacement data obtained in simple tests.

The advantages of IIT are numerous, as indentation load-displacement data contain a wealth of information, and techniques have been developed for characterizing a variety of mechanical properties. The technique most frequently employed measures the hardness, but it also gives the elastic modulus (Young's modulus) from the same data (Ref 8, 11). Although not as well-developed, methods have also been devised for evaluating the yield stress and strain-hardening characteristic of metals (Ref 14, 15, 16); parameters characteristic of damping and internal friction in polymers, such as the storage and loss modulus (Ref 17, 18); and the activation energy and stress exponent for creep (Ref 19, 20, 21, 22, 23, 24, 25). IIT has even been used to estimate the fracture toughness of brittle materials using optical measurement of the lengths of cracks that have formed at the corners of hardness impressions made with special sharp indenters (Ref 13, 26, 27). In fact, almost any material property that can be measured in a uniaxial tension or compression test can conceivably be measured, or at least estimated, using IIT.

An equally important advantage of IIT results because load-displacement data can be used to determine mechanical properties without having to image the hardness impressions. This facilitates property measurement at very small scales. Mechanical properties are routinely measured from submicron indentations, and with careful technique, properties have even been determined from indentations only a few nanometers deep. Because of this, IIT has become a primary tool for examining thin films, coatings, and materials with surfaces modified by techniques such as ion implantation and laser heat treatment.

Many IIT testing systems are equipped with automated specimen manipulation stages. In these systems, the spatial distribution of the near-surface mechanical properties can be mapped on a point-to-point basis along the surface in a fully automated way. Lateral spatial resolutions of about a micron have been achieved. An example of small indentations located at specific points in an electronic microcircuit is shown in Fig. 1.

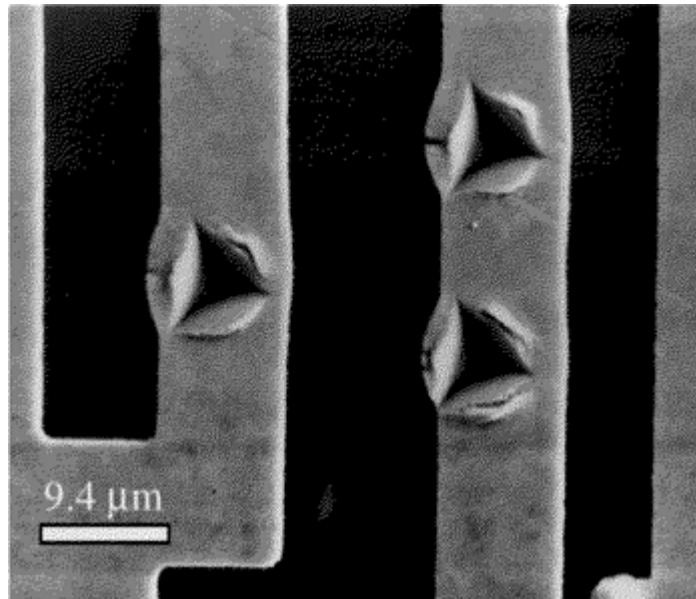


Fig. 1 Small Berkovich indentations located at specific positions in an electronic microcircuit

The purpose of this article is to provide a practical reference guide for instrumented indentation testing. Emphasis is placed on the better-developed measurement techniques and the procedures and calibrations required to obtain accurate and meaningful measurements.

References cited in this section

1. S.I. Bulychev, V.P. Alekhin, M.Kh. Shorshorov, A.P. Ternovskii, and G.D. Shnyrev, Determining Young's Modulus from the Indenter Penetration Diagram, *Zavod. Lab.*, Vol 41 (No. 9), 1975, p 1137–1140
2. F. Frohlich, P. Grau, and W. Grellmann, Performance and Analysis of Recording Microhardness Tests, *Phys. Status Solidi (a)*, Vol 42, 1977, p 79–89
3. M. Kh. Shorshorov, S.I. Bulychev, and V.P. Alekhin, Work of Plastic Deformation during Indenter Indentation, *Sov. Phys. Dokl.*, Vol 26 (No. 8), 1982, p 769–771
4. D. Newey, M.A. Wilkens, and H.M. Pollock, An Ultra-Low-Load Penetration Hardness Tester, *J. Phys. E, Sci. Instrum.*, Vol 15, p 119–122
5. J.B. Pethica, R. Hutchings, and W.C. Oliver, Hardness Measurements at Penetration Depths as Small as 20 nm, *Philos. Mag. A*, Vol 48 (No. 4), 1983, p 593–606
6. W.C. Oliver, Progress in the Development of a Mechanical Properties Microprobe, *MRS Bull.*, Vol 11 (No. 5), 1986, p 15–19
7. J.L. Loubet, J.M. Georges, O. Marchesini, and G. Meille, Vickers Indentation Curves of MgO, *J. Tribology (Trans. ASME)*, Vol 106, 1984, p 43–48
8. M.F. Doerner and W.D. Nix, A Method for Interpreting the Data from Depth-Sensing Indentation Instruments, *J. Mater. Res.*, Vol 1, 1986, p 601–609
9. H.M. Pollock, D. Maugis, and M. Barquins, "Characterization of Sub-Micrometer Layers by Indentation," ASTM STP 889, *Microindentation Techniques in Materials Science and Engineering*, P.J. Blau and B.R. Lawn, Ed., ASTM, 1986, p 47–71

10. W.D. Nix, Mechanical Properties of Thin Films, *Metall. Trans. A*, Vol 20, 1989, p 2217–2245
11. W.C. Oliver and G.M. Pharr, An Improved Technique for Determining Hardness and Elastic Modulus Using Load and Displacement Sensing Indentation Experiments, *J. Mater. Res.*, Vol 7 (No. 6), 1992, p 1564–1583
12. G.M. Pharr and W.C. Oliver, Measurement of Thin Film Mechanical Properties Using Nanoindentation, *MRS Bull.*, Vol 17, 1992, p 28–33
13. G.M. Pharr, Measurement of Mechanical Properties by Ultra-low Load Indentation, *Mater. Sci. Eng. A*, Vol 253, 1998, p 151–159
14. J.S. Field and M.V. Swain, A Simple Predictive Model for Spherical Indentation, *J. Mater. Res.*, Vol 8 (No. 2), 1993, p 297–306
15. J.S. Field and M.V. Swain, Determining the Mechanical Properties of Small Volumes of Material from Submicron Spherical Indentations, *J. Mater. Res.*, Vol 10 (No. 1), 1995, p 101–112
16. M.V. Swain, Mechanical Property Characterization of Small Volumes of Brittle Materials with Spherical Tipped Indenters, *Mater. Sci. Eng. A*, Vol 253, 1998, p 160–166
17. J.-L. Loubet, B.N. Lucas, and W.C. Oliver, Some Measurements of Viscoelastic Properties with the Help of Nanoindentation, *NIST Special Publication 896: International Workshop on Instrumented Indentation*, 1995, p 31–34
18. B.N. Lucas, C.T. Rosenmayer, and W.C. Oliver, Mechanical Characterization of Sub-Micron Polytetrafluoroethylene (PTFE) Thin Films, in *Thin Films—Stresses and Mechanical Properties VII, MRS Symposium Proc.*, Vol 505, Materials Research Society, 1998, p 97–102
19. M.J. Mayo and W.D. Nix, A Microindentation Study of Superplasticity in Pb, Sn, and Sn-38wt%Pb, *Acta Metall.*, Vol 36 (No. 8), 1988, p 2183–2192
20. M.J. Mayo, R.W. Siegel, A. Narayanasamy, and W.D. Nix, Mechanical Properties of Nanophase TiO₂ as Determined by Nanoindentation, *J. Mater. Res.*, Vol 5 (No. 5), 1990, p 1073–1082
21. V. Raman and R. Berriche, An Investigation of Creep Processes in Tin and Aluminum Using Depth-Sensing Indentation Technique, *J. Mater. Res.*, Vol 7 (No. 3), 1992, p 627–638
22. M.J. Mayo and W.D. Nix, in *Proc. of the 8th Int. Conf. on the Strength of Metals and Alloys*, Pergamon Press, 1988, p 1415
23. W.H. Poisl, W.C. Oliver, and B.D. Fabes, The Relation between Indentation and Uniaxial Creep in Amorphous Selenium, *J. Mater. Res.*, Vol 10 (No. 8), 1995, p 2024–2032
24. B.N. Lucas, W.C. Oliver, J.-L. Loubet, and G.M. Pharr, Understanding Time Dependent Deformation During Indentation Testing, in *Thin Films—Stresses and Mechanical Properties VI, MRS Symposium Proc.*, Vol 436, Materials Research Society, 1997, p 233–238
25. B.N. Lucas and W.C. Oliver, Indentation Power-Law Creep of High-Purity Indium, *Metall. Mater. Trans. A*, Vol 30, 1999, p 601–610
26. G.M. Pharr, D.S. Harding, and W.C. Oliver, Measurement of Fracture Toughness in Thin Films and Small Volumes Using Nanoindentation Methods, *Mechanical Properties and Deformation Behavior of Materials Having Ultra-Fine Microstructures*, Kluwer Academic Publishers, 1993, p 449–461

Instrumented Indentation Testing

J.L. Hay, MTS Systems Corporation; G.M. Pharr, The University of Tennessee and Oak Ridge National Laboratory

Testing Equipment

As shown schematically in Fig. 2, equipment for performing instrumented indentation tests consists of three basic components: (a) an indenter of specific geometry usually mounted to a rigid column through which the force is transmitted, (b) an actuator for applying the force, and (c) a sensor for measuring the indenter displacements. Because these are also the basic components used in tensile testing, a standard commercial tensile-testing machine can be adapted for IIT testing. However, to date, most IIT development has been performed using instruments specifically designed for small-scale work. Advances in instrumentation have been driven by technologies that demand accurate mechanical properties at the micron and submicron levels, such as the microelectronic and magnetic storage industries. Thus, while the principles and techniques described in this article were developed primarily using instruments designed for small-scale work, there is no inherent reason that they could not be applied at larger scales using equipment available in most mechanical-testing laboratories.

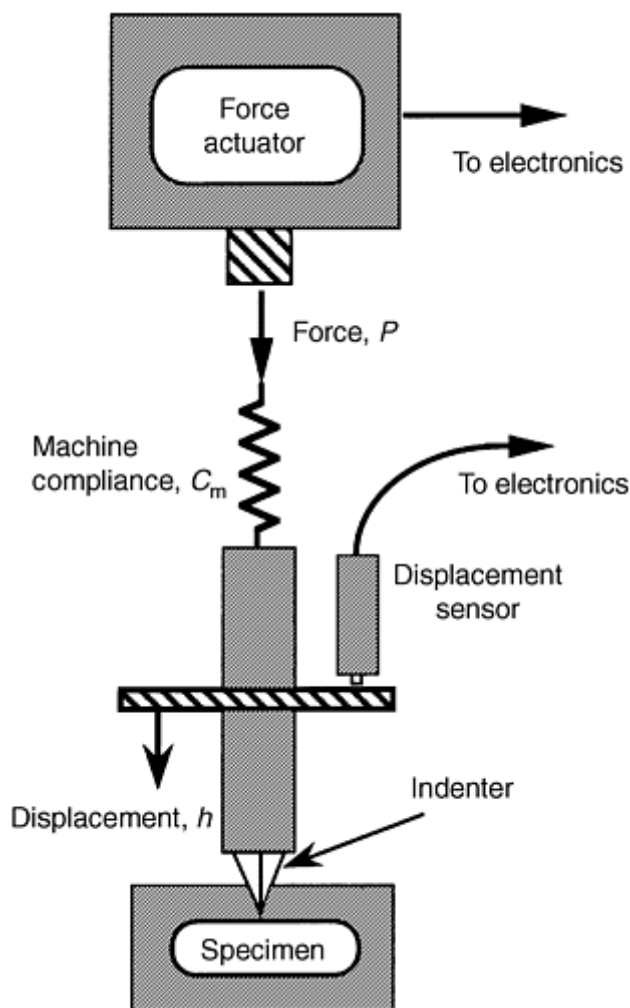


Fig. 2 Schematic representation of the basic components of an instrumented indentation testing system

Several small-scale IIT testing systems are commercially available. They differ primarily in the ways the force is applied and the displacement is measured. Small forces can be conveniently generated (a) electromagnetically with a coil and magnet assembly, (b) electrostatically using a capacitor with fixed and moving plates, and (c) with piezoelectric actuators. The magnitudes of the forces are usually inferred from the voltages or currents applied to the actuator, although in piezoelectrically driven instruments, a separate load cell is often included to provide a direct measurement of the force. Displacements are measured by a variety of means, including capacitive sensors, linear variable differential transformers (LVDTs), and laser interferometers. The range and resolution of the instrument are determined by the specific devices employed.

It is important to realize that as in a commercial tensile-testing machine, the displacements measured in an IIT system include a component from the compliance of the machine itself. Under certain circumstances, the machine compliance can contribute significantly to the total measured displacement, so it must be carefully calibrated and removed from the load-displacement data in a manner analogous to tension and compression testing. Specific procedures for determining the machine compliance in IIT testing are outlined in this article.

A variety of indenters made from a variety of materials are used in IIT testing. Diamond is probably the most frequently used material because its high hardness and elastic modulus minimize the contribution to the measured displacement from the indenter itself. Indenters can be made of other less-stiff materials, such as sapphire, tungsten carbide, or hardened steel, but as in the case of the machine compliance, the elastic displacements of the indenter must be accounted for when analyzing the load-displacement data.

Pyramidal Indenters. The most frequently used indenter in IIT testing is the Berkovich indenter, a three-sided pyramid with the same depth-to-area relation as the four-sided Vickers pyramid used commonly in microhardness work. The Berkovich geometry is preferred to the Vickers because a three-sided pyramid can be ground to a point, thus maintaining its self-similar geometry to very small scales. A four-sided pyramid, on the other hand, terminates at a “chisel edge” rather than at a point, causing its small-scale geometry to differ from that at larger scales; even for the best Vickers indenters, the chisel-edge defect has a length of about a micron. Although Vickers indenters could conceivably be used at larger scales, their use in IIT has been limited because most work has focused on small-scale testing.

Spherical Indenters. Another important indenter geometry in IIT testing is the sphere. Spherical contact differs from the “sharp” contact of the Berkovich or Vickers indenters in the way in which the stresses develop during indentation. For spherical indenters, the contact stresses are initially small and produce only elastic deformation. As the spherical indenter is driven into the surface, a transition from elastic to plastic deformation occurs, which can theoretically be used to examine yielding and work hardening, and to recreate the entire uniaxial stress-strain curve from data obtained in a single test (Ref 14, 15). IIT with spheres has been most successfully employed with larger-diameter indenters. At the micron scale, the use of spherical indenters has been impeded by difficulties in obtaining high-quality spheres made from hard, rigid materials. This is one reason the Berkovich indenter has been the indenter of choice for most small-scale testing, even though it cannot be used to investigate the elastic-plastic transition.

Cube-Corner Indenters. Another indenter used occasionally in IIT testing is the cube—corner indenter, a three-sided pyramid with mutually perpendicular faces arranged in a geometry like the corner of a cube. The centerline-to-face angle for this indenter is 34.3° , whereas for the Berkovich indenter it is 65.3° . The sharper cube corner produces much higher stresses and strains in the vicinity of the contact, which is useful, for example, in producing very small, well-defined cracks around hardness impressions in brittle materials; such cracks can be used to estimate the fracture toughness at relatively small scales (Ref 13, 26, 27).

Conical Indenters. A final indenter geometry worth mentioning is the cone. Like the Berkovich, the cone has a sharp, self-similar geometry, but its simple cylindrical symmetry makes it attractive from a modeling standpoint. In fact, many modeling efforts used to support IIT are based on conical indentation contact (Ref 28, 29, 30, 31, 32, 33, 34, and 35). The cone is also attractive because the complications associated with the stress concentrations at the sharp edges of the indenter are absent. Curiously, however, very little IIT testing has been conducted with cones. The primary reason is that it is difficult to manufacture conical diamonds with sharp tips, making them of little use in the small-scale work around which most of IIT has developed (Ref 36). This problem does not apply at larger scales, where much could be learned by using conical indenters in IIT experimentation.

A summary of the indenters used in IIT testing and parameters describing their geometries is given in Table 1.

Table 1 Summary of nominal geometric relationships for several indenters used in IIT

Parameter	Vickers	Berkovich	Cube-corner	Cone (angle ψ)	Sphere (radius R)
Centerline-to-face angle, α	68°	65.3°	35.2644°
Area (projected), $A(d)$	24.504 d^2	24.56 d^2	2.5981 d^2	πa^2	πa^2
Volume-depth relation, $V(d)$	8.1681 d^3	8.1873 d^3	0.8657 d^3
Projected area/face area, A/A_f	0.927	0.908	0.5774
Equivalent cone angle, ψ	70.2996°	70.32°	42.28°	ψ	...
Contact radius, a	$d \tan \psi$	$(2Rd - d^2)^{1/2}$

References cited in this section

13. G.M. Pharr, Measurement of Mechanical Properties by Ultra-low Load Indentation, *Mater. Sci. Eng. A*, Vol 253, 1998, p 151–159
14. J.S. Field and M.V. Swain, A Simple Predictive Model for Spherical Indentation, *J. Mater. Res.*, Vol 8 (No. 2), 1993, p 297–306
15. J.S. Field and M.V. Swain, Determining the Mechanical Properties of Small Volumes of Material from Submicron Spherical Indentations, *J. Mater. Res.*, Vol 10 (No. 1), 1995, p 101–112
26. G.M. Pharr, D.S. Harding, and W.C. Oliver, Measurement of Fracture Toughness in Thin Films and Small Volumes Using Nanoindentation Methods, *Mechanical Properties and Deformation Behavior of Materials Having Ultra-Fine Microstructures*, Kluwer Academic Publishers, 1993, p 449–461
27. D.S. Harding, W.C. Oliver, and G.M. Pharr, Cracking During Nanoindentation and Its Use in the Measurement of Fracture Toughness, in *Thin Films—Stresses and Mechanical Properties V*, MRS Symposium Proc., Vol 356, Materials Research Society, 1995, p 663–668
28. A.E.H. Love, Boussinesq's Problem for a Rigid Cone, *Q. J. Math.*, Vol 10, 1939, p 161–175
29. I.N. Sneddon, The Relation Between Load and Penetration in the Axisymmetric Boussinesq Problem for a Punch of Arbitrary Profile, *Int. J. Eng. Sci.*, Vol 3, 1965, p 47–56
30. Y.-T. Cheng and C.-M. Cheng, Scaling Approach to Conical Indentation in Elastic-Plastic Solids with Work Hardening, *J. Appl. Phys.*, Vol 84, 1998, p 1284–1291
31. A. Bolshakov and G.M. Pharr, Influences of Pile-Up on the Measurement of Mechanical Properties by Load and Depth Sensing Indentation Techniques, *J. Mater. Res.*, Vol 13, 1998, p 1049–1058
32. A.K. Bhattacharya and W.D. Nix, Finite Element Simulation of Indentation Experiments, *Int. J. Solids Struct.*, Vol 24 (No. 9), 1988, p 881–891
33. A.K. Bhattacharya and W.D. Nix, Analysis of Elastic and Plastic Deformation Associated with Indentation Testing of thin Films on Substrates, *Int. J. Solids Struct.*, Vol 24 (No. 12), 1988, p 1287–1298
34. T.A. Laursen and J.C. Simo, A Study of the Mechanics of Microindentation Using Finite Elements, *J. Mater. Res.*, Vol 7, 1992, p 618–626
35. J.A. Knapp, D.M. Follstaedt, S.M. Myers, J.C. Barbour, and T.A. Friedman, Finite-Element Modeling of Nanoindentation, *J. Appl. Phys.*, Vol 85 (No. 3), 1999, p 1460–1474

Instrumented Indentation Testing

J.L. Hay, MTS Systems Corporation; G.M. Pharr, The University of Tennessee and Oak Ridge National Laboratory

Testing Equipment

As shown schematically in Fig. 2, equipment for performing instrumented indentation tests consists of three basic components: (a) an indenter of specific geometry usually mounted to a rigid column through which the force is transmitted, (b) an actuator for applying the force, and (c) a sensor for measuring the indenter displacements. Because these are also the basic components used in tensile testing, a standard commercial tensile-testing machine can be adapted for IIT testing. However, to date, most IIT development has been performed using instruments specifically designed for small-scale work. Advances in instrumentation have been driven by technologies that demand accurate mechanical properties at the micron and submicron levels, such as the microelectronic and magnetic storage industries. Thus, while the principles and techniques described in this article were developed primarily using instruments designed for small-scale work, there is no inherent reason that they could not be applied at larger scales using equipment available in most mechanical-testing laboratories.

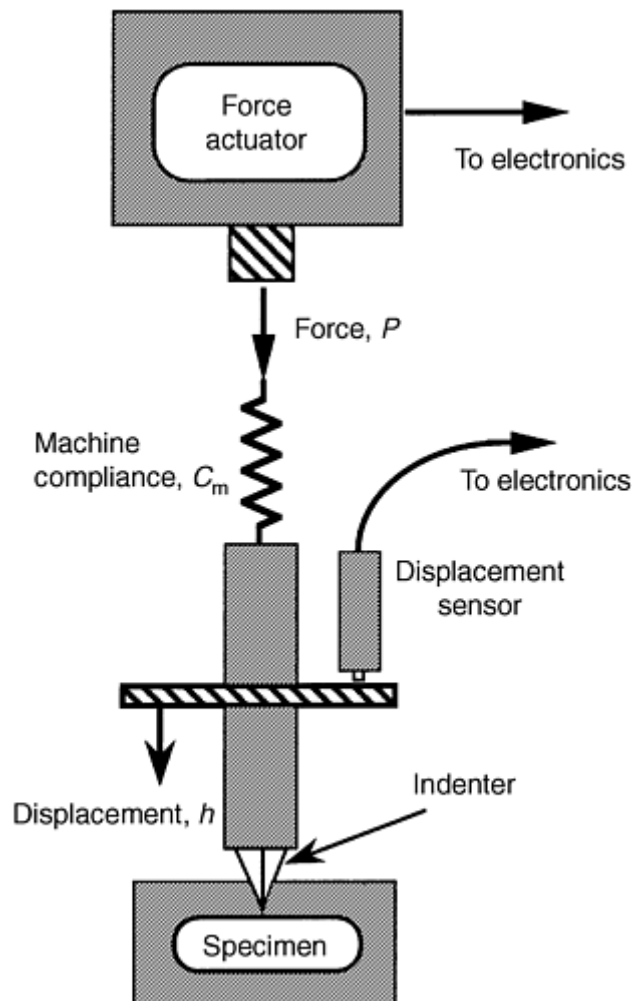


Fig. 2 Schematic representation of the basic components of an instrumented indentation testing system

Several small-scale IIT testing systems are commercially available. They differ primarily in the ways the force is applied and the displacement is measured. Small forces can be conveniently generated (a) electromagnetically with a coil and magnet assembly, (b) electrostatically using a capacitor with fixed and moving plates, and (c) with piezoelectric actuators. The magnitudes of the forces are usually inferred from the voltages or currents applied to the actuator, although in piezoelectrically driven instruments, a separate load cell is often included to provide a direct measurement of the force. Displacements are measured by a variety of means, including capacitive sensors, linear variable differential transformers (LVDTs), and laser interferometers. The range and resolution of the instrument are determined by the specific devices employed.

It is important to realize that as in a commercial tensile-testing machine, the displacements measured in an IIT system include a component from the compliance of the machine itself. Under certain circumstances, the machine compliance can contribute significantly to the total measured displacement, so it must be carefully calibrated and removed from the load-displacement data in a manner analogous to tension and compression testing. Specific procedures for determining the machine compliance in IIT testing are outlined in this article.

A variety of indenters made from a variety of materials are used in IIT testing. Diamond is probably the most frequently used material because its high hardness and elastic modulus minimize the contribution to the measured displacement from the indenter itself. Indenters can be made of other less-stiff materials, such as sapphire, tungsten carbide, or hardened steel, but as in the case of the machine compliance, the elastic displacements of the indenter must be accounted for when analyzing the load-displacement data.

Pyramidal Indenters. The most frequently used indenter in IIT testing is the Berkovich indenter, a three-sided pyramid with the same depth-to-area relation as the four-sided Vickers pyramid used commonly in microhardness work. The Berkovich geometry is preferred to the Vickers because a three-sided pyramid can be ground to a point, thus maintaining its self-similar geometry to very small scales. A four-sided pyramid, on the other hand, terminates at a “chisel edge” rather than at a point, causing its small-scale geometry to differ from that at larger scales; even for the best Vickers indenters, the chisel-edge defect has a length of about a micron. Although Vickers indenters could conceivably be used at larger scales, their use in IIT has been limited because most work has focused on small-scale testing.

Spherical Indenters. Another important indenter geometry in IIT testing is the sphere. Spherical contact differs from the “sharp” contact of the Berkovich or Vickers indenters in the way in which the stresses develop during indentation. For spherical indenters, the contact stresses are initially small and produce only elastic deformation. As the spherical indenter is driven into the surface, a transition from elastic to plastic deformation occurs, which can theoretically be used to examine yielding and work hardening, and to recreate the entire uniaxial stress-strain curve from data obtained in a single test (Ref 14, 15). IIT with spheres has been most successfully employed with larger-diameter indenters. At the micron scale, the use of spherical indenters has been impeded by difficulties in obtaining high-quality spheres made from hard, rigid materials. This is one reason the Berkovich indenter has been the indenter of choice for most small-scale testing, even though it cannot be used to investigate the elastic-plastic transition.

Cube-Corner Indenters. Another indenter used occasionally in IIT testing is the cube—corner indenter, a three-sided pyramid with mutually perpendicular faces arranged in a geometry like the corner of a cube. The centerline-to-face angle for this indenter is 34.3° , whereas for the Berkovich indenter it is 65.3° . The sharper cube corner produces much higher stresses and strains in the vicinity of the contact, which is useful, for example, in producing very small, well-defined cracks around hardness impressions in brittle materials; such cracks can be used to estimate the fracture toughness at relatively small scales (Ref 13, 26, 27).

Conical Indenters. A final indenter geometry worth mentioning is the cone. Like the Berkovich, the cone has a sharp, self-similar geometry, but its simple cylindrical symmetry makes it attractive from a modeling standpoint. In fact, many modeling efforts used to support IIT are based on conical indentation contact (Ref 28, 29, 30, 31, 32, 33, 34, and 35). The cone is also attractive because the complications associated with the stress concentrations at the sharp edges of the indenter are absent. Curiously, however, very little IIT testing has been conducted with cones. The primary reason is that it is difficult to manufacture conical diamonds with sharp tips, making them of little use in the small-scale work around which most of IIT has developed (Ref 36). This problem does not apply at larger scales, where much could be learned by using conical indenters in IIT experimentation.

A summary of the indenters used in IIT testing and parameters describing their geometries is given in Table 1.

Table 1 Summary of nominal geometric relationships for several indenters used in IIT

Parameter	Vickers	Berkovich	Cube-corner	Cone (angle ψ)	Sphere (radius R)
Centerline-to-face angle, α	68°	65.3°	35.2644°
Area (projected), $A(d)$	24.504 d^2	24.56 d^2	2.5981 d^2	πa^2	πa^2
Volume-depth relation, $V(d)$	8.1681 d^3	8.1873 d^3	0.8657 d^3
Projected area/face area, A/A_f	0.927	0.908	0.5774
Equivalent cone angle, ψ	70.2996°	70.32°	42.28°	ψ	...
Contact radius, a	$d \tan \psi$	$(2Rd - d^2)^{1/2}$

References cited in this section

13. G.M. Pharr, Measurement of Mechanical Properties by Ultra-low Load Indentation, *Mater. Sci. Eng. A*, Vol 253, 1998, p 151–159
14. J.S. Field and M.V. Swain, A Simple Predictive Model for Spherical Indentation, *J. Mater. Res.*, Vol 8 (No. 2), 1993, p 297–306
15. J.S. Field and M.V. Swain, Determining the Mechanical Properties of Small Volumes of Material from Submicron Spherical Indentations, *J. Mater. Res.*, Vol 10 (No. 1), 1995, p 101–112
26. G.M. Pharr, D.S. Harding, and W.C. Oliver, Measurement of Fracture Toughness in Thin Films and Small Volumes Using Nanoindentation Methods, *Mechanical Properties and Deformation Behavior of Materials Having Ultra-Fine Microstructures*, Kluwer Academic Publishers, 1993, p 449–461
27. D.S. Harding, W.C. Oliver, and G.M. Pharr, Cracking During Nanoindentation and Its Use in the Measurement of Fracture Toughness, in *Thin Films—Stresses and Mechanical Properties V*, MRS Symposium Proc., Vol 356, Materials Research Society, 1995, p 663–668
28. A.E.H. Love, Boussinesq's Problem for a Rigid Cone, *Q. J. Math.*, Vol 10, 1939, p 161–175
29. I.N. Sneddon, The Relation Between Load and Penetration in the Axisymmetric Boussinesq Problem for a Punch of Arbitrary Profile, *Int. J. Eng. Sci.*, Vol 3, 1965, p 47–56
30. Y.-T. Cheng and C.-M. Cheng, Scaling Approach to Conical Indentation in Elastic-Plastic Solids with Work Hardening, *J. Appl. Phys.*, Vol 84, 1998, p 1284–1291
31. A. Bolshakov and G.M. Pharr, Influences of Pile-Up on the Measurement of Mechanical Properties by Load and Depth Sensing Indentation Techniques, *J. Mater. Res.*, Vol 13, 1998, p 1049–1058
32. A.K. Bhattacharya and W.D. Nix, Finite Element Simulation of Indentation Experiments, *Int. J. Solids Struct.*, Vol 24 (No. 9), 1988, p 881–891
33. A.K. Bhattacharya and W.D. Nix, Analysis of Elastic and Plastic Deformation Associated with Indentation Testing of thin Films on Substrates, *Int. J. Solids Struct.*, Vol 24 (No. 12), 1988, p 1287–1298
34. T.A. Laursen and J.C. Simo, A Study of the Mechanics of Microindentation Using Finite Elements, *J. Mater. Res.*, Vol 7, 1992, p 618–626
35. J.A. Knapp, D.M. Follstaedt, S.M. Myers, J.C. Barbour, and T.A. Friedman, Finite-Element Modeling of Nanoindentation, *J. Appl. Phys.*, Vol 85 (No. 3), 1999, p 1460–1474

36. T.Y. Tsui, W.C. Oliver, and G.M. Pharr, Indenter Geometry Effects on the Measurement of Mechanical Properties by Nanoindentation with Sharp Indenters, in *Thin Films—Stresses and Mechanical Properties VI, MRS Symposium Proc.*, Vol 436, Materials Research Society, 1997, p 147–152

Instrumented Indentation Testing

J.L. Hay, MTS Systems Corporation; G.M. Pharr, The University of Tennessee and Oak Ridge National Laboratory

Time-Dependent Materials and Properties

All of the discussion so far has assumed that the material response to indentation contact is instantaneous, or nearly so, as is the case for most metals and ceramics tested at room temperature. In general, however, indentation deformation can be time-dependent, with the extent and nature of the time dependence strongly influenced by temperature. Time dependence is the rule rather than the exception in polymers—the viscoelastic behavior of polymers at room temperature is well known—and time-dependent creep is an important phenomenon in metals and ceramics at elevated temperatures. Methods for probing and characterizing the time-dependent phenomena, although not nearly as well developed as methods for measuring H and E , are now examined.

Influences on the Measurement of H and E . One important aspect of time-dependent behavior is an experimental complication arising in the measurements of hardness and modulus. Time-dependent creep and/or viscoelastic deformation can cause the indentation displacement to increase even as the indenter is unloaded, giving abnormally high contact stiffnesses that adversely affect the measurement of hardness and modulus. This is commonly encountered, for example, when testing soft metals, such as aluminum, with sharp indenters like the Berkovich. In some cases, the time-dependent portion of the displacement can be large enough to produce an unloading curve with a negative slope. When creep is observed or suspected, holding the load constant for a period of time prior to unloading, which allows the creep displacements to dissipate, can help alleviate the problem, at least in materials with short-lived creep responses.

Measurement of Creep Parameters. For materials in which the creep response is dominant, IIT can be used to characterize and quantify important creep parameters. For conventional creep tests conducted in uniaxial tension, the temperature and stress dependence of the steady state creep rate ($\dot{\epsilon}$) are often described by the relation:

$$\dot{\epsilon} = \alpha \sigma^n \exp(-Q_c/RT) \quad (\text{Eq 10})$$

where α is a material constant, σ is stress, n is the stress exponent for creep, Q_c is the activation energy, R is the gas constant, and T is temperature. Values of n ranging from 3 to 5 are typical for many metals. By analogy, an equivalent expression can be developed for indentation creep conducted, for example, by applying a constant load to the indenter and monitoring its displacement as a function of time. The expression follows by defining an indentation strain rate as $\dot{\epsilon}_i = h/\dot{h}$, that is, the normalized rate of indentation displacement (Ref 19, 24, 25). This definition is appropriate for cones and pyramids (Ref 9, 68). Noting that the equivalent of stress in an indentation test is the mean contact pressure $H = P/A$, the analog of Eq 10 for an indentation creep test is:

$$\dot{\epsilon}_i = \alpha_i H^n \exp(-Q_c/RT) \quad (\text{Eq 11})$$

where α_i is a material constant.

Equation 11 has been found to adequately describe creep behavior of some but not all materials (Ref 19, 21, 22, 23, 24, 25, 68, 69). When it does, a log-log plot of the indentation strain rate versus hardness produces a straight line with a slope that gives the stress exponent, n . Interestingly, such a plot can often be constructed from data obtained in a single indentation test. As an example, consider the indentation creep data in Fig. 9 for indium, a material that creeps at room temperature by virtue of its relatively low melting point (Ref 25). The data were obtained by loading a Berkovich indenter at a fixed rate of loading and then holding at a maximum load while monitoring the indenter displacement as a function of time. As the indenter penetrates, the contact area increases (thereby reducing the contact pressure), and the rate of displacement decreases correspondingly. In a

test like this, it is not unusual to obtain creep data over several orders of magnitude in $\dot{\epsilon}_i$. The stress exponent deduced from the data, $n = 6$, is very close to the value derived using conventional creep testing techniques.

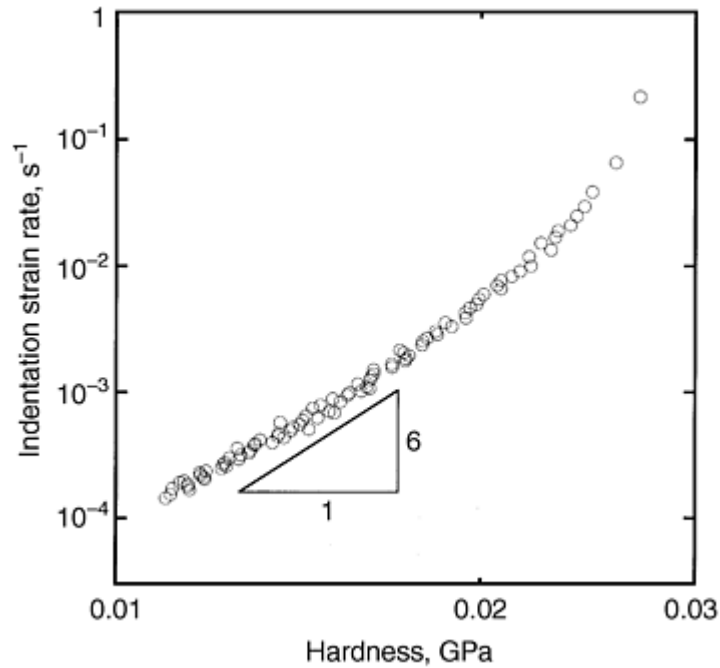


Fig. 9 Room-temperature indentation creep data for indium obtained by loading the indenter at a constant rate (10 mN/s) to a peak load and holding for an extended period of time. Source: Ref 25

To date, indentation creep tests have been limited largely to the low-melting metals that exhibit creep at room temperature. In some cases, the stress exponent measured by indentation techniques has been close to that determined in conventional tests, but in others it has not. One important reason for the difference concerns the influence of transients on the creep response. For an indentation creep test, the stresses in the vicinity of the contact vary with time and position as the indenter penetrates the specimen. Thus, transient effects (primary creep) and stress-induced changes in microstructure can influence the behavior in a manner that is not observed in uniaxial creep testing, for which the stress is relatively uniform and invariant with time. Carefully conducted indentation creep tests have shown that when $\dot{\epsilon}_i$ varies significantly during the test, transient effects do indeed affect the results and are particularly important at high strain rates (Ref 25). It has been suggested that better results can be obtained by performing a series of tests over a range of $\dot{\epsilon}_i$ in which the indentation strain rate in any one test is held constant. This is easily achieved in a displacement-controlled machine by maintaining \dot{h}/h constant. Under conditions for which the deformation is predominantly steady state, a constant indentation strain rate can be obtained in a load-controlled system by holding the normalized loading rate (\dot{P}/P) constant (Ref 25).

The effect of temperature on creep, as quantified by the activation energy (Q_c) has been investigated only to a very limited extent (Ref 23, 25, 68, 69). Such tests are challenging due to inherent difficulties in measuring small displacements at elevated temperatures. When the specimen and/or testing apparatus are heated, the measured displacements are often dominated by thermal expansions and contractions of the machine, which are difficult to separate from the data.

Viscoelasticity. In addition to creep, indentation techniques have also been developed to characterize the time-dependent properties of viscoelastic materials like polymers. Dynamic stiffness measurement techniques offer distinct advantages here. Using the amplitude and phase of the force and displacement oscillations, the storage modulus (E'), characteristic of elasticity, and the loss modulus (E''), characteristic of internal friction and damping, can both be measured (Ref 17, 18). In its simplest form, the analysis follows by modeling the contact as a spring of stiffness S in parallel with a dashpot with damping coefficient $C\omega$, where ω is the angular frequency of the dynamic oscillation. Provided the dynamic response of the testing system is well known, S and $C\omega$ can be measured from the amplitude and phase of the load and displacement oscillations. The storage modulus is related to S by Eq 2; that is:

$$E' = \frac{\sqrt{\pi} S}{2\beta \sqrt{A}} \quad (\text{Eq 12})$$

and by analogy to this equation, it has been suggested that the loss modulus is related to $C\omega$ through:

$$E'' = \frac{\sqrt{\pi} C\omega}{2\beta \sqrt{A}} \quad (\text{Eq 13})$$

Other models for the dynamic response of the specimen-indenter contact can be used to give similar results. Although quite promising, the technique has yet to be rigorously tested on a variety of materials. Thus far, only materials with exceptionally high damping, like natural rubber, have been examined.

References cited in this section

9. H.M. Pollock, D. Maugis, and M. Barquins, "Characterization of Sub-Micrometer Layers by Indentation," ASTM STP 889, *Microindentation Techniques in Materials Science and Engineering*, P.J. Blau and B.R. Lawn, Ed., ASTM, 1986, p 47–71
17. J.-L. Loubet, B.N. Lucas, and W.C. Oliver, Some Measurements of Viscoelastic Properties with the Help of Nanoindentation, *NIST Special Publication 896: International Workshop on Instrumented Indentation*, 1995, p 31–34
18. B.N. Lucas, C.T. Rosenmayer, and W.C. Oliver, Mechanical Characterization of Sub-Micron Polytetrafluoroethylene (PTFE) Thin Films, in *Thin Films—Stresses and Mechanical Properties VII, MRS Symposium Proc.*, Vol 505, Materials Research Society, 1998, p 97–102
19. M.J. Mayo and W.D. Nix, A Microindentation Study of Superplasticity in Pb, Sn, and Sn-38wt%Pb, *Acta Metall.*, Vol 36 (No. 8), 1988, p 2183–2192
21. V. Raman and R. Berriche, An Investigation of Creep Processes in Tin and Aluminum Using Depth-Sensing Indentation Technique, *J. Mater. Res.*, Vol 7 (No. 3), 1992, p 627–638
22. M.J. Mayo and W.D. Nix, in *Proc. of the 8th Int. Conf. on the Strength of Metals and Alloys*, Pergamon Press, 1988, p 1415
23. W.H. Poisl, W.C. Oliver, and B.D. Fabes, The Relation between Indentation and Uniaxial Creep in Amorphous Selenium, *J. Mater. Res.*, Vol 10 (No. 8), 1995, p 2024–2032
24. B.N. Lucas, W.C. Oliver, J.-L. Loubet, and G.M. Pharr, Understanding Time Dependent Deformation During Indentation Testing, in *Thin Films—Stresses and Mechanical Properties VI, MRS Symposium Proc.*, Vol 436, Materials Research Society, 1997, p 233–238
25. B.N. Lucas and W.C. Oliver, Indentation Power-Law Creep of High-Purity Indium, *Metall. Mater. Trans. A*, Vol 30, 1999, p 601–610
68. A.G. Atkins, A. Silverio, and D. Tabor, Indentation Creep, *J. Inst. Metals*, Vol 94, 1966, p 369–378
69. D.S. Stone and K.B. Yoder, Division of the Hardness of Molybdenum into Rate-Dependent and Rate-Independent Components, *J. Mater. Res.*, Vol 9 (No. 10), 1994, p 2524–2533

Good Experimental Practice

As in any experimental work, accurate measurements can be obtained only with good experimental technique and practice. A discussion of some of the factors that should be considered in making high-quality measurements follows. Emphasis is placed on those that are common to many measurement procedures and independent of the specific apparatus used to make them.

Choosing an appropriate indenter requires consideration of a number of factors. One consideration is the strain the tip imposes on the test material. Although the indentation process produces a complex strain field beneath the indenter, it has proven useful to quantify the field with a single quantity, often termed the characteristic strain (ϵ) (Ref 70, 71). Empirical studies in metals have shown that the characteristic strain can be used to correlate the hardness to the flow stress in a uniaxial compression test (Ref 70). For sharp indenters, such as self-similar cones and pyramids, the characteristic strain is constant regardless of the load or displacement, and is given by:

$$\epsilon = 0.2 \cot(\psi) \quad (\text{Eq 14})$$

where ψ is the half-included angle of the indenter for cones; for pyramids, ψ is the half-included angle of the cone having the same area-to-depth relationship (Ref 70, 71). Thus, the sharper the cone or pyramid, the larger the characteristic strain. For the two most commonly used pyramidal indenters, the Berkovich and Vickers, the characteristic strain is about 8%, and the measured hardness is about 2.8 times the stress measured at 8% strain in a uniaxial compression test.

The use of sharper pyramidal indenters (smaller centerline-to-face angles), such as the cube-corner, is required when one wishes to produce larger strains. For example, cube-corner indenters are preferred to Berkovich indenters when investigating fracture toughness at small scales by indentation-cracking methods because the larger strain induces cracking at much smaller loads (Ref 13, 26, 27). There are problems, however, in obtaining accurate measurements of hardness and elastic modulus with cube-corner indenters (Ref 43, 44, 45). Although not entirely understood, the problems appear to have two separate origins. First, as the angle of the indenter decreases, friction in the specimen-indenter interface and its influence on the contact mechanics becomes increasingly important. Second, as mentioned earlier, recent analytical work has shown that Eq 2 is not an entirely adequate description of the relation among the contact stiffness, contact area, and reduced elastic modulus (Ref 42, 43, 44, 45). Corrections are required, and the magnitude of the correction factor depends on angle of the indenter. The correction is relatively small for the Berkovich indenter, but much greater for the cube-corner indenter. Future measurement of H and E with cube-corner indenters will require methods for dealing with these complications (Ref 45).

For spherical indenters, the characteristic strain changes continuously as the indenter penetrates the material, as given by:

$$\epsilon = 0.2a/R \quad (\text{Eq 15})$$

where a is the radius of contact and R is the radius of the indenter (Ref 71). Thus, spheres can be used when one wishes to take advantage of the continuously changing strain. In principle, one can determine the elastic modulus, yield stress, and strain-hardening behavior of a material all in one test. However, because plasticity commences well below the surface (Ref 70, 71, 72, 73), the point of initial yielding can be difficult to detect experimentally. Specific methods for exploring the stress-strain curve with spherical indenters are described elsewhere (Ref 14, 15, 16, 70).

It is important to note that in order to measure a value for the hardness that is consistent with the traditional definition—that is, the indentation load normalized by the area of the *residual* hardness impression—the contact must be fully plastic. For spherical indenters, full plasticity is achieved in elastic-perfectly-plastic materials when $E_r a / \sigma_y R > 30$ (Ref 71). Thus, the contact radius (a) and, therefore, the penetration depth at which full plasticity is achieved are smaller for spherical indenters with smaller radii (R). This is one important reason that sharp pyramids, such as the Berkovich, are often preferred to spheres for small depth testing. The tip

radii on precision-ground Berkovich indenters are usually no greater than 100 nm—often better—implying that fully plastic contact is achieved at very small depths. Table 1 provides useful information on indenter geometries commonly used in IIT testing.

Environmental Control. To take full advantage of the fine displacement resolution available in most IIT testing systems, several precautions must be taken in choosing and preparing the testing environment. Uncertainties and errors in measured displacements arise from two separate environmental sources: vibration and variations in temperature that cause thermal expansion and contraction of the sample and testing system.

To minimize vibration, testing systems should be located on quiet, solid foundations (ground floors) and mounted on vibration-isolation systems. Thermal stability can be provided by enclosing the testing apparatus in an insulated cabinet to thermally buffer it from its surroundings and by controlling room temperature to within ± 0.5 °C. If the material is thermally stable (i.e., not time dependent), one can account for small thermal displacements using procedures described later. However, for time-dependent materials, extra care must be taken in providing thermal stability, because separation of the thermal displacements from the specimen displacements is virtually impossible and, therefore, introduces large uncertainties into the displacement data.

Surface Preparation. Surface roughness is extremely important in instrumented indentation testing because the contact areas from which mechanical properties are deduced (for instance, using Eq 5, 6, and 7) are calculated from the contact depth and area function *on the presumption that the surface is flat*. Thus, the allowable surface roughness depends on the anticipated magnitude of the measured displacements and the tolerance for uncertainty in the contact area. The greatest problems are encountered when the characteristic wavelength of the roughness is comparable to the contact diameter. In this case, the contact area determined from the load-displacement data underestimates the true contact area for indentations residing in “valleys” and overestimates it for indentations on “peaks.” The magnitude of the error depends on the wavelength and amplitude of the roughness relative to the contact dimensions. Thus, one should strive to prepare the specimen so that the amplitude of the roughness at wavelengths near the contact dimension is minimized. For metallographic specimens, a good guide for surface preparation is ASTM E 380 (Ref 74). One can normally determine whether roughness is an issue by performing multiple tests in an area and examining the scatter in measured properties. For a homogeneous material with minimal roughness, scatter of less than a few percent can be expected with a good testing system and technique.

Testing Procedure. To avoid interference, successive indentations should be separated by at least 20 to 30 times the maximum depth when using a Berkovich or Vickers indenter. For other geometries, the rule is 7 to 10 times the maximum contact radius. The importance of frequently testing a standard material cannot be overemphasized. For reasons explained in the calibration section, fused quartz is a good choice for such a standard. It is good practice to routinely perform 5 to 10 indents on the standard; when the measured properties of the standard appear to change, the user is immediately alerted to problems in the testing equipment and/or procedures.

Detecting the Surface. One very important part of any good IIT testing procedure is accurate identification of the location of the surface of the specimen. This is especially important for very small contacts, for which small errors in surface location can produce relatively large errors in penetration depth that percolate through the calculation procedures to all those properties derived from the load-displacement data (Ref 75). Schemes for detecting the surface are frequently based on the change in a contact-sensitive parameter that is measured continuously as the indenter approaches the surface. For hard and stiff materials, such as hardened metals and ceramics, the load and/or contact stiffness, both of which increase upon contact, are often used. However, for soft, compliant materials, like polymers and biological tissues, the rate of increase in load and contact stiffness is often too small to allow for accurate surface identification. In these situations, a better method is sometimes offered by dynamic stiffness measurement, for which the phase shift between the load and displacement oscillations can potentially provide a more sensitive indication of contact, depending on the dynamics of the testing apparatus and the properties of the material (Ref 48, 49).

References cited in this section

13. G.M. Pharr, Measurement of Mechanical Properties by Ultra-low Load Indentation, *Mater. Sci. Eng. A*, Vol 253, 1998, p 151–159

14. J.S. Field and M.V. Swain, A Simple Predictive Model for Spherical Indentation, *J. Mater. Res.*, Vol 8 (No. 2), 1993, p 297–306
15. J.S. Field and M.V. Swain, Determining the Mechanical Properties of Small Volumes of Material from Submicron Spherical Indentations, *J. Mater. Res.*, Vol 10 (No. 1), 1995, p 101–112
16. M.V. Swain, Mechanical Property Characterization of Small Volumes of Brittle Materials with Spherical Tipped Indenters, *Mater. Sci. Eng. A*, Vol 253, 1998, p 160–166
26. G.M. Pharr, D.S. Harding, and W.C. Oliver, Measurement of Fracture Toughness in Thin Films and Small Volumes Using Nanoindentation Methods, *Mechanical Properties and Deformation Behavior of Materials Having Ultra-Fine Microstructures*, Kluwer Academic Publishers, 1993, p 449–461
27. D.S. Harding, W.C. Oliver, and G.M. Pharr, Cracking During Nanoindentation and Its Use in the Measurement of Fracture Toughness, in *Thin Films—Stresses and Mechanical Properties V*, *MRS Symposium Proc.*, Vol 356, Materials Research Society, 1995, p 663–668
42. A. Bolshakov and G.M. Pharr, Inaccuracies in Sneddon's Solution for Elastic Indentation by a Rigid Cone and Their Implications for Nanoindentation Data Analysis, in *Thin Films—Stresses and Mechanical Properties VI*, *MRS Symposium Proc.*, Vol 436, Materials Research Society, 1997, p 189–194
43. J.C. Hay, A. Bolshakov, and G.M. Pharr, A Critical Examination of the Fundamental Relations in the Analysis of Nanoindentation Data, *J. Mater. Res.*, Vol 14 (No. 6), 1999, p 2296–2305
44. J.C. Hay, A. Bolshakov, and G.M. Pharr, Applicability of Sneddon Relationships to the Real Case of a Rigid Cone Penetrating an Infinite Half Space, in *Fundamentals of Nanoindentation and Nanotribology*, *MRS Symposium Proc.*, Vol 522, Materials Research Society, 1998, p 263–268
45. J.C. Hay and G.M. Pharr, Experimental Investigations of the Sneddon Solution and an Improved Solution for the Analysis of Nanoindentation Data, in *Fundamentals of Nanoindentation and Nanotribology*, *MRS Symposium Proc.*, Vol 522, Materials Research Society, 1998, p 39–44
48. J.B. Pethica and W.C. Oliver, Mechanical Properties of Nanometer Volumes of Material: Use of the Elastic Response of Small Area Indentations, in *Thin Films—Stresses and Mechanical Properties*, *MRS Symposium Proc.*, Vol 130, Materials Research Society, 1989, p 13–23
49. B.N. Lucas, W.C. Oliver, and J.E. Swindeman, The Dynamics of Frequency-Specific, Depth-Sensing Indentation Testing, *Fundamentals of Nanoindentation and Nanotribology*, *MRS Symposium Proc.*, Vol 522, Materials Research Society, 1998, p 3–14
70. D. Tabor, *Hardness of Metals*, Oxford University Press, 1951, p 46, 67–83, 105–106
71. K.L. Johnson, *Contact Mechanics*, Cambridge University Press, 1985, p 94, 176
72. W.B. Morton and L.J. Close, Notes on Hertz' Theory of Contact Problems, *Philos. Mag.*, Vol 43, 1922, p 320
73. R.M. Davies, The Determination of Static and Dynamic Yield Stresses Using a Steel Ball, *Proc. R. Soc. (London) A*, Vol 197, 1949, p 416
74. “Standard Methods of Preparation of Metallographic Specimens,” E 380, *Annual Book of ASTM Standards*, ASTM, reapproved 1993

Instrumented Indentation Testing

J.L. Hay, MTS Systems Corporation; G.M. Pharr, The University of Tennessee and Oak Ridge National Laboratory

Calibrations

The accurate measurement of mechanical properties by IIT requires well-calibrated testing equipment. While load and displacement calibrations are usually provided by the manufacturer using procedures specific to the machine, a number of calibrations must be routinely performed by the user. These calibrations are discussed in an order that roughly reflects the frequency of their necessity; that is, thermal-drift calibration is performed most often. With minor modifications, the procedures are essentially those developed by Oliver and Pharr (Ref 11).

Many of the calibrations require that a calibration material be indented during the procedure. One material commonly used for this purpose is fused quartz. This relatively inexpensive material is readily available in a highly polished form that gives repeatable results with very little scatter. Due to its amorphous nature, it is highly isotropic, and its relatively low elastic modulus, ($E = 72$ GPa) and high hardness ($H = 9$ GPa), facilitate calibrations that are best served by a large elastic recovery during unloading, such as area-function calibrations. Pile-up is not observed in fused quartz, and because it is not subject to oxidation, its near-surface properties are similar to those of the bulk and do not depend to a large degree on the depth of penetration. Fused quartz also exhibits essentially no time dependence when indented at room temperature, so there are no complications in separating thermal drift from time-dependent deformation effects.

Thermal-Drift Calibration. Thermal drift calibration seeks to adjust the measured displacements to account for small amounts of thermal expansion or contraction in the test material and/or indentation equipment. Good technique requires that it be performed individually for each indentation because the drift rate can vary in relatively short time spans. In fact, the calibration is best achieved by incorporation directly into the indentation test procedure itself. A procedure that works well for materials exhibiting little or no time-dependent deformation behavior (metals and ceramics tested at room temperature) is based on the notion that displacements observed when the indenter is pressed against the sample surface at a small, fixed load must arise from thermal drift. This can be implemented in an indentation experiment by including a period near the end of the test during which the load is held constant for a fixed period of time (about 100 seconds is usually sufficient) while the displacements are monitored to measure the thermal-drift rate. A small load is preferred to minimize the possibility of creep in the specimen; a good guideline for this load is 10% of the maximum indentation load. Displacement changes measured during this period are attributed to thermal expansion or contraction in the test material and/or indentation equipment, and a drift rate is calculated from the data. All displacements measured during the indentation test are then corrected according to the time at which they were acquired. For example, if the measured thermal drift rate is $+0.05$ nm/s, then a displacement acquired 10 s into the experiment must be corrected by -0.5 nm.

Figure 10 shows displacement-versus-time data acquired during a constant load period near the end of a test in fused quartz. In this case, the drift rate was fairly high, about 0.31 nm/s. Figure 11 shows the effect of applying this correction to the indentation load-displacement data. The shift in the corrected load-displacement curves has important consequences for the calculated contact area by affecting the maximum depth of penetration and the contact depth. Although not quite as obvious, the thermal drift also affects the contact stiffness determined from the slope of the unloading curve.

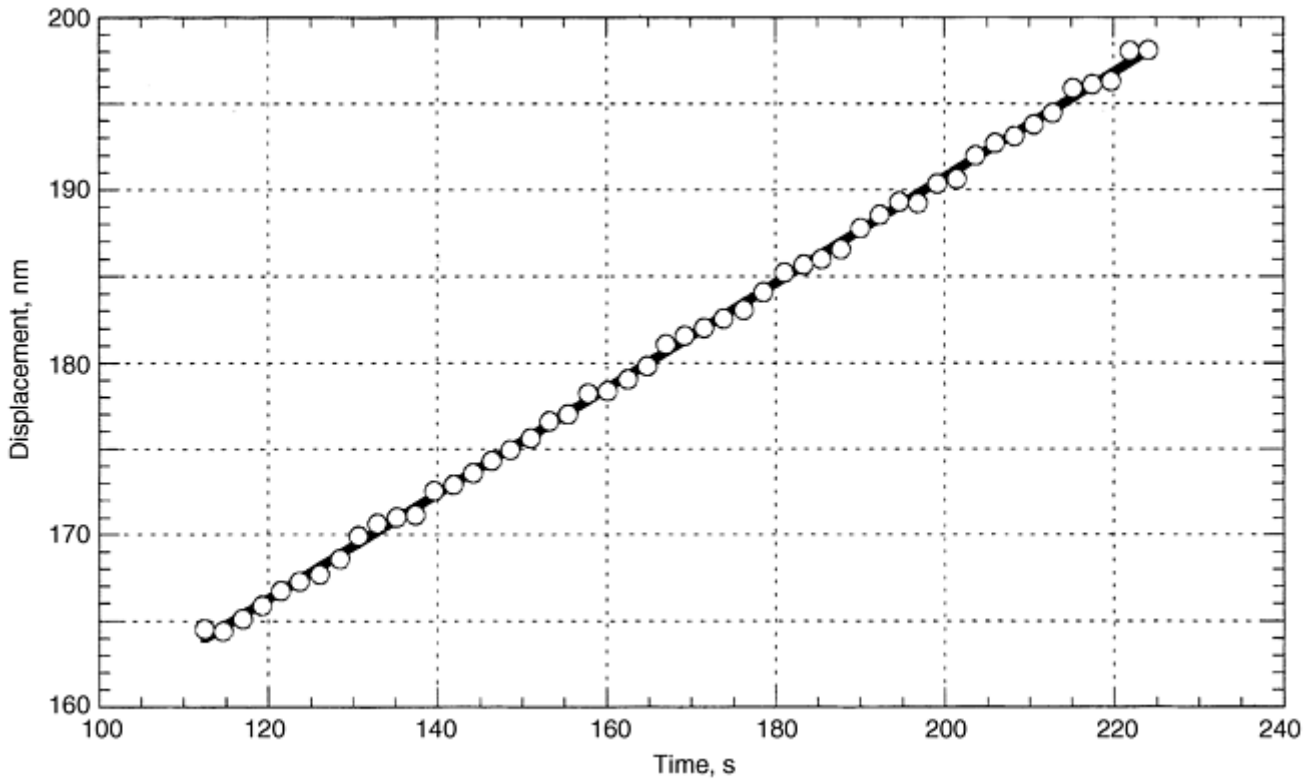


Fig. 10 Indenter displacement versus time during a period of constant load showing thermal drift in a fused quartz specimen. The measured drift rate, 0.31 nm/s, is used to correct the load-displacement data shown in Fig. 11.

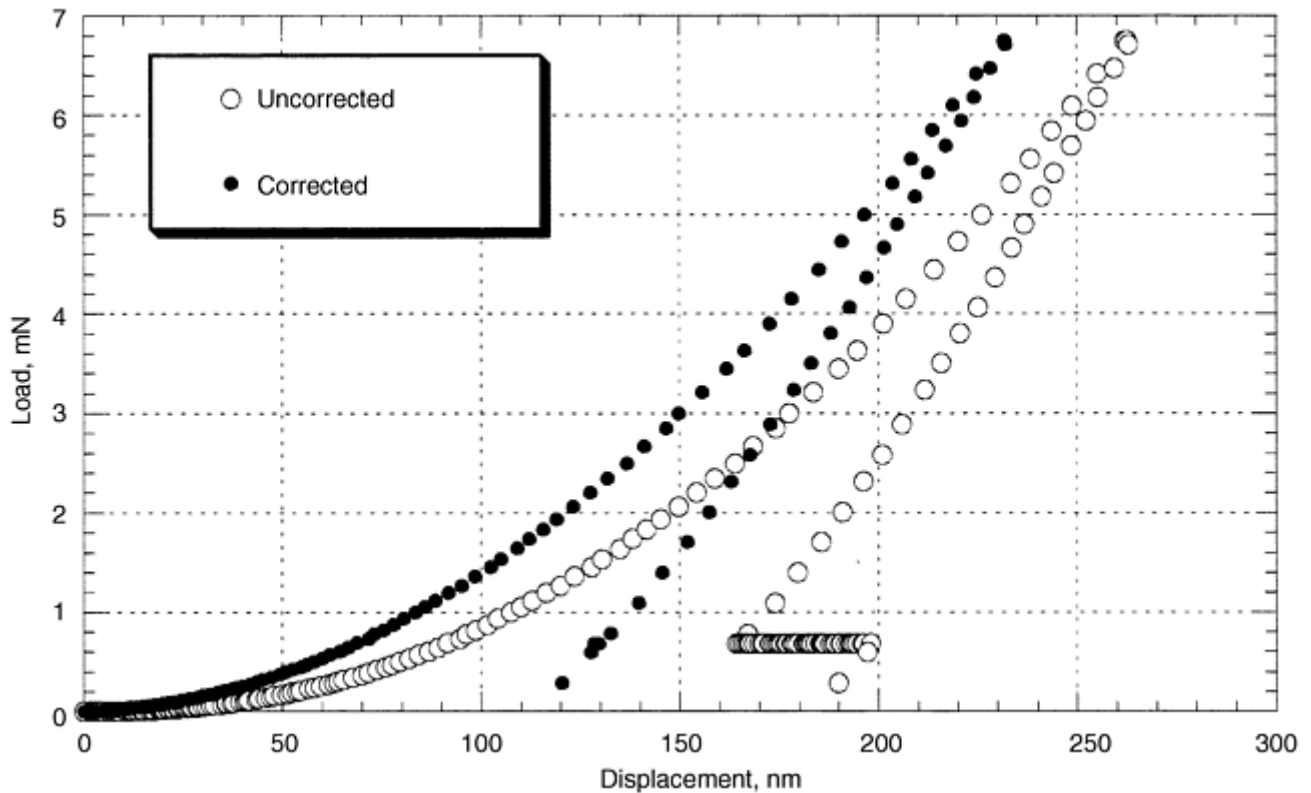


Fig. 11 Load-displacement data for fused quartz showing correction for thermal drift

If the test material exhibits significant time-dependent deformation, as might be the case for polymers or metals tested at a significant fraction of their melting point, thermal drift correction should not be used because it is not possible to distinguish the thermal displacements from time-dependent deformation in the specimen. Under

such circumstances, thermal drift should be minimized by precisely controlling the temperature of the testing environment and allowing samples to thermally equilibrate for long periods of time prior to testing.

Machine Compliance (Stiffness) Calibration. Determination of the machine compliance (C_m) or equivalently, the machine stiffness ($K_m = 1/C_m$) allows one to determine that part of the total measured displacement (h_t) that occurs in the test equipment and correct the indentation data for it. If C_m or K_m is known, then the displacement in the machine at any load (P) is simply $h_m = C_m P = P/K_m$, and the true displacement in the specimen is given by:

$$h = h_t - C_m P = h_t - P/K_m \quad (\text{Eq 16})$$

To determine C_m or K_m , the machine and contact are modeled as springs in series whose compliances are additive. Thus, the total measured compliance (C_t) is given by:

$$C_t = C_s + C_m \quad (\text{Eq 17})$$

where C_s is the elastic compliance of the indenter-specimen contact. Because C_t is just the inverse of the total measured stiffness (S_t), and C_s is the inverse of the elastic contact stiffness (S), Eq 2 and 17 combine to yield:

$$C_t = \frac{\sqrt{\pi}}{2\beta E_r \sqrt{A}} + C_m \quad (\text{Eq 18})$$

Thus, the intercept of a plot of C_t versus $A^{-1/2}$ gives the machine compliance (C_m) and the slope of the plot is related to the reduced modulus (E_r). Because extrapolation of the data to $A^{-1/2} = 0$ is required, the best measures of C_m are obtained when the first term on the right is small, that is, for large contacts.

A convenient procedure for determining C_m is based on the assumption that the area function of the indenter at large depths is well described by the ideal area function, that is, the area function under the assumption that the indenter has no deviations from its perfect geometric shape. For pyramidal and conical indenters, the ideal area function is given by:

$$A = F_1 d^2 \quad (\text{Eq 19})$$

where the constant F_1 follows from geometry. Values of F_1 for several important indenters are included in Table 1. For spherical indenters, the ideal area function depends on the diameter of the sphere (D) through:

$$A = \pi d(D - d) = -\pi d^2 + \pi Dd \quad (\text{Eq 20})$$

which, for small penetration depths relative to the sphere diameter ($d < D$), simplifies to:

$$A = \pi Dd = F_2 d \quad (\text{Eq 21})$$

where $F_2 = \pi D$.

The specific calibration procedure used to determine the machine compliance is an iterative one that uses data from a calibration material such as fused quartz. Indentations are made at several large depths for which the ideal area function is expected to apply. Assuming first that $C_m = 0$, the load-displacement data are corrected for the machine compliance according to Eq 16 and analyzed according to Eq 4, 5, 6, and 7 to determine the contact area at each depth. The intercept of a plot of C_t versus $A^{-1/2}$ then gives a new estimate of C_m . After correcting the load-displacement data for the new C_m , which affects the values of $A^{-1/2}$, the procedure is iteratively repeated until adequate convergence in C_m is obtained. As a check on the procedure, the slope of the final C_t versus $A^{-1/2}$ plot should be within a few percent of $\sqrt{\pi}/(2\beta E_r)$, as indicated in Eq 18. If not, one must question whether the assumed ideal geometry is correct and carefully inspect the indenter to check on it.

Accurately knowing C_m and K_m becomes increasingly important as the contact stiffness (S) approaches the machine stiffness (K_m). Because S increases with \sqrt{A} , machine stiffness corrections are most important for larger contacts. For example, Fig. 12 shows the effect of K_m on load-displacement data for relatively small and large indentations in fused quartz obtained with a Berkovich indenter. In each plot, the data have been reduced in two ways: (a) using $K_m = 1 \times 10^{30}$ N/m, that is, an essentially infinite machine stiffness; (b) using the correct value, $K_m = 6.8 \times 10^6$ N/m. The data in Fig. 12(a) are largely unaffected by the machine stiffness correction because the small load ($P_{\max} = 7$ mN) is associated with a small contact stiffness; in this case, the contact stiffness is less than 1% of K_m . In Fig. 12(b), however, the machine stiffness correction is much more important because the contact stiffness at the larger peak load, 600 mN, is approximately 10% of the machine stiffness. One sure symptom of an incorrect K_m is a steady change in E with depth in a sample that should have depth-

independent properties. Assuming all else is correct, if one uses a value of K_m that is too large, E will be correct at small depths, but will steadily decrease at larger depths; the converse is also true.

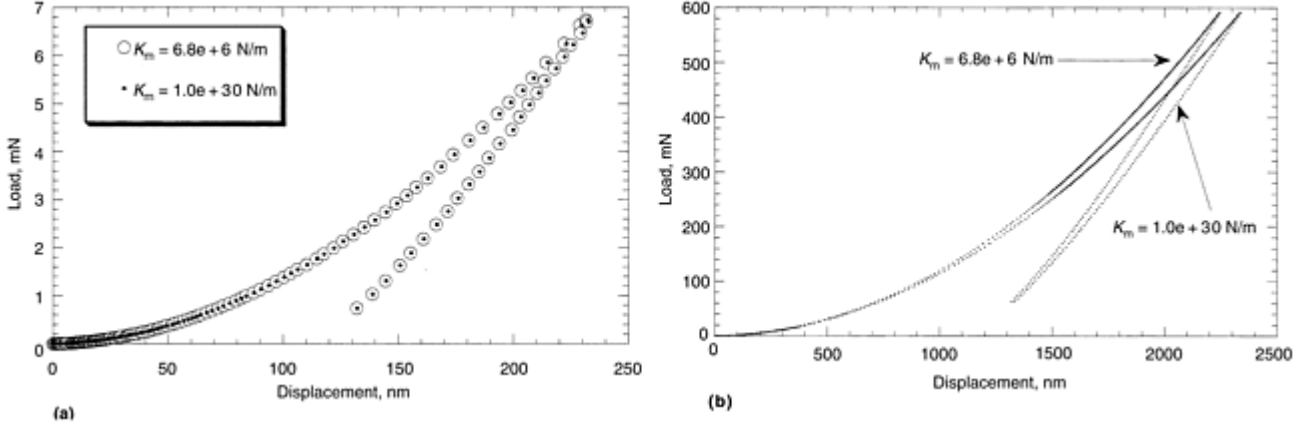


Fig. 12 Load-displacement data for fused quartz showing machine stiffness corrections at two peak loads: (a) 7 mN and (b) 600 mN. The correct machine stiffness is 6.8×10^6 N/m, while the value $K_m = 1 \times 10^{30}$ is used to represent an infinite stiffness. The plots illustrate the insensitivity of the load-displacement data to machine stiffness corrections for small contacts, but the stiffness correction is more important when the contact is large.

Area-Function Calibration. Although the ideal area function sometimes provides an accurate description of the contact geometry, especially at larger contact depths, deviations from geometrical perfection near the indenter tip, even when subtle, must be properly taken into account when measurements are to be made at small scales. For pyramidal indenters and cones, variations from the ideal self-similar geometry are produced by tip blunting. For spherical indenters, knowledge of the precise tip shape is important because small deviations from perfect spherical geometry can have large effects on the measured contact area. There may also be circumstances for which the ideal area function is not known, as in the case of a pyramidal indenter not ground precisely to the appropriate face angles. In each of these situations, the area function must be determined by an independent method. A general procedure for calibrating area functions without having to image the indenter or contact impressions follows.

The area function is determined by making a series of indentations at various depths in a calibration material of well-known elastic properties. The data can also be acquired using dynamic stiffness measurement, which has the advantage of being able to obtain all the necessary data in a few tests. The basic assumption is that the elastic modulus is independent of depth, so it is imperative that a calibration material be chosen that is free of oxides and other surface contaminants that may alter the near-surface elastic properties. It is also imperative that there be no pile-up, because the procedure is based on Eq 4, 5, 6, and 7, which do not account for the influences of pile-up on the contact depth. For these reasons, fused quartz is a good choice, although because of its relatively high hardness ($H = 9$ GPa), the upper limit on the achievable depth is somewhat restricted. For the specific procedure outlined here, the machine compliance must also be known from the procedures outlined in the previous section. In cases for which this is not possible, as when the ideal area function is not known or suspected to be inaccurate, an alternative procedure must be adopted in which the machine compliance and the area function are determined simultaneously in a coupled, iterative process. This procedure, which is considerably more complex, is described in detail elsewhere (Ref 11).

To implement the area-function calibration, a series of indentations is made at depths spanning the range of interest, usually from as small as possible to as large as possible, so that the area function is established over a wide range. Correcting for machine compliance, the load-displacement data are reduced and used to obtain the contact stiffnesses (S) and the contact depths (h_c) by means of Eq 5 and 6. From these quantities and the known elastic properties of the calibration material, the contact areas are determined by rewriting Eq 2 as:

$$A = \frac{\pi}{4} \left(\frac{S}{\beta E_r} \right)^2 \quad (\text{Eq 22})$$

When fused quartz is used as the calibration material ($E = 72$ GPa; $\nu = 0.17$) and the indenter is diamond ($E = 1141$ GPa; $\nu = 0.07$), the reduced modulus in the above expression is $E_r = 69.6$ GPa. A plot of A versus h_c then

gives a graphical representation of the area function, which can be curve fit according to any of a number of functional forms. A general form that is often used is:

$$A = C_1d^2 + C_2d + C_3d^{1/2} + C_4d^{1/4} + C_5d^{1/8} + \dots \quad (\text{Eq 23})$$

where the number of terms is chosen to provide a good fit over the entire range of depths as assessed by comparing a log-log plot of the fit with the data. Because data are often obtained over more than one order of magnitude in depth, a weighted fitting procedure should be used to assure that data from all depths have equal importance. Note that the first term in the expression represents the ideal area function for a pyramidal or conical indenter provided $C_1 = F_1$ in Eq 19. Thus, for pyramidal and conical indenters for which the ideal area function is known, it is often convenient to fix $C_1 = F_1$. Similarly, inspection of Eq 20 shows that for spherical indenters of known diameter D , one may wish to set $C_1 = -\pi$ and $C_2 = \pi D$. Fixing the values of these constants is particularly important when areas greater than those achievable in the calibration material are to be determined by extrapolating the area function to larger depths. Such extrapolations should be used with caution and only when there is confidence that the ideal area function applies at large depths. At depths greater than those included in the calibration, it is usually best to use the ideal area function of the indenter.

Figure 13 shows area functions determined with these procedures for three separate diamond indenters: Berkovich, Vickers, and a 70.3° cone (Ref 36). All three have nominally the same ideal area function, $A = 24.5d^2$, and tend to this function at large depths. However, the data show that there is indeed tip blunting for all three indenters, the conical diamond having the most and the Berkovich the least. The data corroborate the claim that the sharpest diamonds are those with the Berkovich geometry.

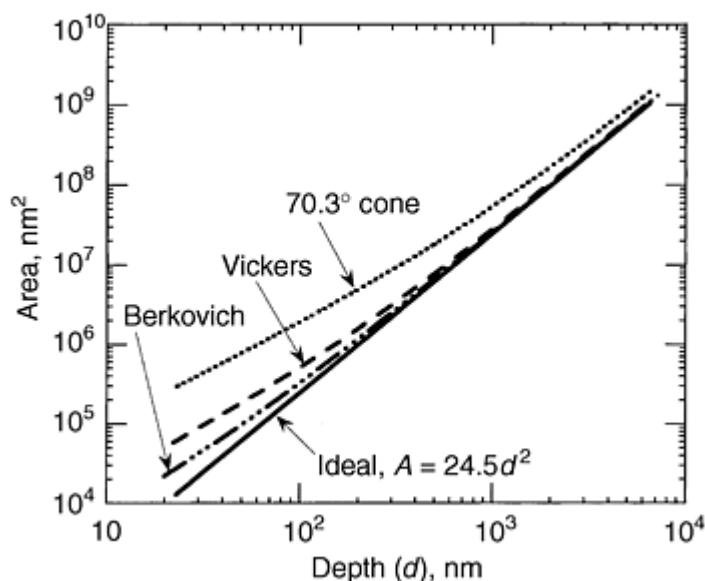


Fig. 13 Calibrated area functions for three indenters. Although the ideal area function, $A = 24.5d^2$, is nominally the same for each, the area functions differ due to different degrees of tip rounding. Source: Ref 36

References cited in this section

11. W.C. Oliver and G.M. Pharr, An Improved Technique for Determining Hardness and Elastic Modulus Using Load and Displacement Sensing Indentation Experiments, *J. Mater. Res.*, Vol 7 (No. 6), 1992, p 1564–1583
36. T.Y. Tsui, W.C. Oliver, and G.M. Pharr, Indenter Geometry Effects on the Measurement of Mechanical Properties by Nanoindentation with Sharp Indenters, in *Thin Films—Stresses and Mechanical Properties VI*, MRS Symposium Proc., Vol 436, Materials Research Society, 1997, p 147–152

Instrumented Indentation Testing

J.L. Hay, MTS Systems Corporation; G.M. Pharr, The University of Tennessee and Oak Ridge National Laboratory

Future Trends

Instrumented indentation testing is a dynamic, growing field for which many new developments can be expected in the near future. From an equipment standpoint, one can expect that conventional microhardness testing equipment will be adapted to expand its capabilities in the manners afforded by IIT. This will lead to a new generation of relatively inexpensive IIT testing systems that operate primarily in the microhardness regime. Integration of atomic force microscopy with IIT will become increasingly more commonplace, allowing one to obtain three-dimensional images of small indentations to confirm contact areas and to examine pile-up phenomena. New displacement measurement methods based on laser interferometry can be expected to improve displacement measurement resolution and reduce the influences of machine compliance and thermal drift on measured properties. Laser interferometry will also facilitate testing at nonambient temperatures.

One can also expect new developments in techniques for measurement and analysis. Finite-element simulation may become an integral part of property measurement, accounting for the influences of pile-up and aiding the separation of film properties from substrate influences. Finite-element techniques may also prove useful in establishing tensile stress-strain behavior from experimental data obtained with spherical indenters. New methods and analyses based on dynamic measurement techniques can be expected to expand the characterization of the viscoelastic behavior of polymers over a wide range of frequency.

One of the great challenges in IIT is to develop equipment and techniques for measuring the properties of ultra-thin films, such as the hard protective overcoats used in magnetic disk storage, some of which are only 5 nm thick. At these scales, surface contaminants and surface forces due to absorbed liquid films severely complicate contact phenomena and analyses. New methods for obtaining and analyzing such data will be required.

Instrumented Indentation Testing

J.L. Hay, MTS Systems Corporation; G.M. Pharr, The University of Tennessee and Oak Ridge National Laboratory

Acknowledgments

This work was sponsored in part by the Division of Materials Sciences, U.S. Department of Energy, under contract DE-AC05-96OR22464 with Lockheed Martin Energy Research Corp. and through the SHaRE Program under contract DE-AC05-76OR00033 with Oak Ridge Associated Universities.

Instrumented Indentation Testing

J.L. Hay, MTS Systems Corporation; G.M. Pharr, The University of Tennessee and Oak Ridge National Laboratory

References

1. S.I. Bulychev, V.P. Alekhin, M.Kh. Shorshorov, A.P. Ternovskii, and G.D. Shnyrev, Determining Young's Modulus from the Indenter Penetration Diagram, *Zavod. Lab.*, Vol 41 (No. 9), 1975, p 1137–1140

2. F. Frohlich, P. Grau, and W. Grellmann, Performance and Analysis of Recording Microhardness Tests, *Phys. Status Solidi (a)*, Vol 42, 1977, p 79–89
3. M. Kh. Shorshorov, S.I. Bulychev, and V.P. Alekhin, Work of Plastic Deformation during Indenter Indentation, *Sov. Phys. Dokl.*, Vol 26 (No. 8), 1982, p 769–771
4. D. Newey, M.A. Wilkens, and H.M. Pollock, An Ultra-Low-Load Penetration Hardness Tester, *J. Phys. E, Sci. Instrum.*, Vol 15, p 119–122
5. J.B. Pethica, R. Hutchings, and W.C. Oliver, Hardness Measurements at Penetration Depths as Small as 20 nm, *Philos. Mag. A*, Vol 48 (No. 4), 1983, p 593–606
6. W.C. Oliver, Progress in the Development of a Mechanical Properties Microprobe, *MRS Bull.*, Vol 11 (No. 5), 1986, p 15–19
7. J.L. Loubet, J.M. Georges, O. Marchesini, and G. Meille, Vickers Indentation Curves of MgO, *J. Tribology (Trans. ASME)*, Vol 106, 1984, p 43–48
8. M.F. Doerner and W.D. Nix, A Method for Interpreting the Data from Depth-Sensing Indentation Instruments, *J. Mater. Res.*, Vol 1, 1986, p 601–609
9. H.M. Pollock, D. Maugis, and M. Barquins, “Characterization of Sub-Micrometer Layers by Indentation,” ASTM STP 889, *Microindentation Techniques in Materials Science and Engineering*, P.J. Blau and B.R. Lawn, Ed., ASTM, 1986, p 47–71
10. W.D. Nix, Mechanical Properties of Thin Films, *Metall. Trans. A*, Vol 20, 1989, p 2217–2245
11. W.C. Oliver and G.M. Pharr, An Improved Technique for Determining Hardness and Elastic Modulus Using Load and Displacement Sensing Indentation Experiments, *J. Mater. Res.*, Vol 7 (No. 6), 1992, p 1564–1583
12. G.M. Pharr and W.C. Oliver, Measurement of Thin Film Mechanical Properties Using Nanoindentation, *MRS Bull.*, Vol 17, 1992, p 28–33
13. G.M. Pharr, Measurement of Mechanical Properties by Ultra-low Load Indentation, *Mater. Sci. Eng. A*, Vol 253, 1998, p 151–159
14. J.S. Field and M.V. Swain, A Simple Predictive Model for Spherical Indentation, *J. Mater. Res.*, Vol 8 (No. 2), 1993, p 297–306
15. J.S. Field and M.V. Swain, Determining the Mechanical Properties of Small Volumes of Material from Submicron Spherical Indentations, *J. Mater. Res.*, Vol 10 (No. 1), 1995, p 101–112
16. M.V. Swain, Mechanical Property Characterization of Small Volumes of Brittle Materials with Spherical Tipped Indenters, *Mater. Sci. Eng. A*, Vol 253, 1998, p 160–166
17. J.-L. Loubet, B.N. Lucas, and W.C. Oliver, Some Measurements of Viscoelastic Properties with the Help of Nanoindentation, *NIST Special Publication 896: International Workshop on Instrumented Indentation*, 1995, p 31–34
18. B.N. Lucas, C.T. Rosenmayer, and W.C. Oliver, Mechanical Characterization of Sub-Micron Polytetrafluoroethylene (PTFE) Thin Films, in *Thin Films—Stresses and Mechanical Properties VII, MRS Symposium Proc.*, Vol 505, Materials Research Society, 1998, p 97–102

19. M.J. Mayo and W.D. Nix, A Microindentation Study of Superplasticity in Pb, Sn, and Sn-38wt%Pb, *Acta Metall.*, Vol 36 (No. 8), 1988, p 2183–2192
20. M.J. Mayo, R.W. Siegel, A. Narayanasamy, and W.D. Nix, Mechanical Properties of Nanophase TiO₂ as Determined by Nanoindentation, *J. Mater. Res.*, Vol 5 (No. 5), 1990, p 1073–1082
21. V. Raman and R. Berriche, An Investigation of Creep Processes in Tin and Aluminum Using Depth-Sensing Indentation Technique, *J. Mater. Res.*, Vol 7 (No. 3), 1992, p 627–638
22. M.J. Mayo and W.D. Nix, in *Proc. of the 8th Int. Conf. on the Strength of Metals and Alloys*, Pergamon Press, 1988, p 1415
23. W.H. Poisl, W.C. Oliver, and B.D. Fabes, The Relation between Indentation and Uniaxial Creep in Amorphous Selenium, *J. Mater. Res.*, Vol 10 (No. 8), 1995, p 2024–2032
24. B.N. Lucas, W.C. Oliver, J.-L. Loubet, and G.M. Pharr, Understanding Time Dependent Deformation During Indentation Testing, in *Thin Films—Stresses and Mechanical Properties VI, MRS Symposium Proc.*, Vol 436, Materials Research Society, 1997, p 233–238
25. B.N. Lucas and W.C. Oliver, Indentation Power-Law Creep of High-Purity Indium, *Metall. Mater. Trans. A*, Vol 30, 1999, p 601–610
26. G.M. Pharr, D.S. Harding, and W.C. Oliver, Measurement of Fracture Toughness in Thin Films and Small Volumes Using Nanoindentation Methods, *Mechanical Properties and Deformation Behavior of Materials Having Ultra-Fine Microstructures*, Kluwer Academic Publishers, 1993, p 449–461
27. D.S. Harding, W.C. Oliver, and G.M. Pharr, Cracking During Nanoindentation and Its Use in the Measurement of Fracture Toughness, in *Thin Films—Stresses and Mechanical Properties V, MRS Symposium Proc.*, Vol 356, Materials Research Society, 1995, p 663–668
28. A.E.H. Love, Boussinesq's Problem for a Rigid Cone, *Q. J. Math.*, Vol 10, 1939, p 161–175
29. I.N. Sneddon, The Relation Between Load and Penetration in the Axisymmetric Boussinesq Problem for a Punch of Arbitrary Profile, *Int. J. Eng. Sci.*, Vol 3, 1965, p 47–56
30. Y.-T. Cheng and C.-M. Cheng, Scaling Approach to Conical Indentation in Elastic-Plastic Solids with Work Hardening, *J. Appl. Phys.*, Vol 84, 1998, p 1284–1291
31. A. Bolshakov and G.M. Pharr, Influences of Pile-Up on the Measurement of Mechanical Properties by Load and Depth Sensing Indentation Techniques, *J. Mater. Res.*, Vol 13, 1998, p 1049–1058
32. A.K. Bhattacharya and W.D. Nix, Finite Element Simulation of Indentation Experiments, *Int. J. Solids Struct.*, Vol 24 (No. 9), 1988, p 881–891
33. A.K. Bhattacharya and W.D. Nix, Analysis of Elastic and Plastic Deformation Associated with Indentation Testing of thin Films on Substrates, *Int. J. Solids Struct.*, Vol 24 (No. 12), 1988, p 1287–1298
34. T.A. Laursen and J.C. Simo, A Study of the Mechanics of Microindentation Using Finite Elements, *J. Mater. Res.*, Vol 7, 1992, p 618–626
35. J.A. Knapp, D.M. Follstaedt, S.M. Myers, J.C. Barbour, and T.A. Friedman, Finite-Element Modeling of Nanoindentation, *J. Appl. Phys.*, Vol 85 (No. 3), 1999, p 1460–1474

36. T.Y. Tsui, W.C. Oliver, and G.M. Pharr, Indenter Geometry Effects on the Measurement of Mechanical Properties by Nanoindentation with Sharp Indenters, in *Thin Films—Stresses and Mechanical Properties VI, MRS Symposium Proc.*, Vol 436, Materials Research Society, 1997, p 147–152
37. G. Simmons and H. Wang, *Single Crystal Elastic Constants and Calculated Aggregate Properties: A Handbook*, 2nd ed., The M.I.T. Press, 1971
38. G.M. Pharr, W.C. Oliver, and F.R. Brotzen, On the Generality of the Relationship among Contact Stiffness, Contact Area, and Elastic Modulus, *J. Mater. Res.*, Vol 7 (No. 3), 1992, p 613–617
39. R.B. King, Elastic Analysis of Some Punch Problems for a Layered Medium, *Int. J. Solids Struct.*, Vol 23, 1987, p 1657–1664
40. H.J. Gao and T.-W. Wu, *J. Mater. Res.*, Vol 8 (No. 12), 1993, p 3229–3232
41. B.C. Hendrix, The Use of Shape Correction Factors for Elastic Indentation Measurements. *J. Mater. Res.*, Vol 10 (No. 2), 1995, p 255–257
42. A. Bolshakov and G.M. Pharr, Inaccuracies in Sneddon's Solution for Elastic Indentation by a Rigid Cone and Their Implications for Nanoindentation Data Analysis, in *Thin Films—Stresses and Mechanical Properties VI, MRS Symposium Proc.*, Vol 436, Materials Research Society, 1997, p 189–194
43. J.C. Hay, A. Bolshakov, and G.M. Pharr, A Critical Examination of the Fundamental Relations in the Analysis of Nanoindentation Data, *J. Mater. Res.*, Vol 14 (No. 6), 1999, p 2296–2305
44. J.C. Hay, A. Bolshakov, and G.M. Pharr, Applicability of Sneddon Relationships to the Real Case of a Rigid Cone Penetrating an Infinite Half Space, in *Fundamentals of Nanoindentation and Nanotribology, MRS Symposium Proc.*, Vol 522, Materials Research Society, 1998, p 263–268
45. J.C. Hay and G.M. Pharr, Experimental Investigations of the Sneddon Solution and an Improved Solution for the Analysis of Nanoindentation Data, in *Fundamentals of Nanoindentation and Nanotribology, MRS Symposium Proc.*, Vol 522, Materials Research Society, 1998, p 39–44
46. A. Bolshakov, W.C. Oliver, and G.M. Pharr, An Explanation for the Shape of Nanoindentation Unloading Curves Based on Finite Element Simulation, in *Thin Films—Stresses and Mechanical Properties V, MRS Symposium Proc.*, Vol 356, Materials Research Society, 1995, p 675–680
47. J.B. Pethica and W.C. Oliver, Tip Surface Interactions in STM and AFM, *Phys. Scr. Vol. T*, Vol 19, 1987, p 61
48. J.B. Pethica and W.C. Oliver, Mechanical Properties of Nanometer Volumes of Material: Use of the Elastic Response of Small Area Indentations, in *Thin Films—Stresses and Mechanical Properties, MRS Symposium Proc.*, Vol 130, Materials Research Society, 1989, p 13–23
49. B.N. Lucas, W.C. Oliver, and J.E. Swindeman, The Dynamics of Frequency-Specific, Depth-Sensing Indentation Testing, *Fundamentals of Nanoindentation and Nanotribology, MRS Symposium Proc.*, Vol 522, Materials Research Society, 1998, p 3–14
50. T.F. Page, G.M. Pharr, J.C. Hay, W.C. Oliver, B.N. Lucas, E. Herbert, and L. Riester, Nanoindentation Characterization of Coated Systems: P:S²—A New Approach Using the Continuous Stiffness Technique, in *Fundamentals of Nanoindentation and Nanotribology, MRS Symposium Proc.*, Vol 522, Materials Research Society, 1998, p 53–64

51. K.W. McElhane, J.J. Vlassak, and W.D. Nix, Determination of Indenter Tip Geometry and Indentation Contact Area for Depth-Sensing Indentation Experiments, *J. Mater. Res.*, Vol 13 (No. 5), 1998, p 1300–1306
52. B. Taljat, T. Zacharia, and G.M. Pharr, Pile-Up Behavior of Spherical Indentations in Engineering Materials, in *Fundamentals of Nanoindentation and Nanotribology, MRS Symposium Proc.*, Vol 522, Materials Research Society, 1998, p 33–38
53. J.L. Hay, W.C. Oliver, A. Bolshakov, and G.M. Pharr, Using the Ratio of Loading Slope and Elastic Stiffness to Predict Pile-Up and Constraint Factor During Indentation, in *Fundamentals of Nanoindentation and Nanotribology, MRS Symposium Proc.*, Vol 522, Materials Research Society, 1998, p 101–106
54. Standard Test for Microhardness of Materials, “ASTM Standard Test Method E 384,” *Annual Book of Standards 3.01*, American Society for Testing and Materials, 1989, p 469
55. P.J. Burnett and D.S. Rickerby, The Mechanical Properties of Wear Resistant Coatings 1: Modeling of Hardness Behaviour, *Thin Solid Films*, Vol 148, 1987, p 41–50
56. P.J. Burnett and D.S. Rickerby, The Mechanical Properties of Wear Resistant Coatings 2, *Thin Solid Films*, Vol 148, 1987, p 51–65
57. B. Jonsson and S. Hogmark, *Thin Solid Films*, Vol 114, 1984, p 257
58. T.Y. Tsui, W.C. Oliver, and G.M. Pharr, Nanoindentation of Soft Films on Hard Substrates—The Importance of Pileup, in *Thin Films—Stresses and Mechanical Properties VI, MRS Symposium Proc.*, Vol 436, 1997, p 207–212
59. T.Y. Tsui, C.A. Ross, and G.M. Pharr, Nanoindentation Hardness of Soft Films on Hard Substrates: Effects of the Substrate, in *Materials Reliability in Microelectronics VII, MRS Symposium Proc.*, Vol 473, 1997, p 57–62
60. B.D. Fabes and W.C. Oliver, Mechanical Properties of Coating and Interfaces, in *Thin Films—Stresses and Mechanical Properties II, MRS Symposium Proc.*, Vol 188, 1990, p 127–132
61. H. Gao, C.-H. Chiu, and J. Lee, Elastic Contact Versus Indentation Modeling of Multi-Layered Materials, *Int. J. Solids Struct.*, Vol 29 (No. 20), 1992, p 2471–2492
62. D.S. Stone, *J. Electron. Packaging*, Vol 112, 1990, p 41
63. H.Y. Yu, S.C. Sanday, and B.B. Rath, The Effect of Substrate on the Elastic Properties of Films Determined by the Indentation Test—Axisymmetric Boussinesq Problem, *J. Mech. Phys. Solids*, Vol 38, 1990, p 745–764
64. J. Mencik, D. Munz, E. Quandt, E.R. Weppelmann, and M.V. Swain, Determination of Elastic Modulus of Thin Layers Using Nanoindentation, *J. Mater. Res.*, Vol 12 (No. 9), 1997, p 2475–2484
65. T.Y. Tsui and G.M. Pharr, Substrate Effects on Nanoindentation Mechanical Property Measurement of Soft Films on Hard Substrates, *J. Mater. Res.*, Vol 14, 1999, p 292–301
66. G.M. Pharr, A. Bolshakov, T.Y. Tsui, and J.C. Hay, Nanoindentation of Soft Films on Hard Substrates: Experiments and Finite Element Simulations, in *Thin Films—Stresses and Mechanical Properties VII, MRS Symposium Proc.*, Vol 505, 1998, p 109–120

67. J.C. Hay and G.M. Pharr, Critical Issues in Measuring the Mechanical Properties of Hard Films on Soft Substrates by Nanoindentation Techniques, in *Thin Films—Stresses and Mechanical Properties VII, MRS Symposium Proc.*, Vol 505, 1998, p 65–70
68. A.G. Atkins, A. Silverio, and D. Tabor, Indentation Creep, *J. Inst. Metals*, Vol 94, 1966, p 369–378
69. D.S. Stone and K.B. Yoder, Division of the Hardness of Molybdenum into Rate-Dependent and Rate-Independent Components, *J. Mater. Res.*, Vol 9 (No. 10), 1994, p 2524–2533
70. D. Tabor, *Hardness of Metals*, Oxford University Press, 1951, p 46, 67–83, 105–106
71. K.L. Johnson, *Contact Mechanics*, Cambridge University Press, 1985, p 94, 176
72. W.B. Morton and L.J. Close, Notes on Hertz' Theory of Contact Problems, *Philos. Mag.*, Vol 43, 1922, p 320
73. R.M. Davies, The Determination of Static and Dynamic Yield Stresses Using a Steel Ball, *Proc. R. Soc. (London) A*, Vol 197, 1949, p 416
74. “Standard Methods of Preparation of Metallographic Specimens,” E 380, *Annual Book of ASTM Standards*, ASTM, reapproved 1993
75. J. Mencik and M.V. Swain, Errors Associated with Depth-Sensing Microindentation Tests, *J. Mater. Res.*, Vol 10 (No. 6), 1995, p 1491–1501

Instrumented Indentation Testing

J.L. Hay, MTS Systems Corporation; G.M. Pharr, The University of Tennessee and Oak Ridge National Laboratory

References

1. S.I. Bulychev, V.P. Alekhin, M.Kh. Shorshorov, A.P. Ternovskii, and G.D. Shnyrev, Determining Young's Modulus from the Indenter Penetration Diagram, *Zavod. Lab.*, Vol 41 (No. 9), 1975, p 1137–1140
2. F. Frohlich, P. Grau, and W. Grellmann, Performance and Analysis of Recording Microhardness Tests, *Phys. Status Solidi (a)*, Vol 42, 1977, p 79–89
3. M. Kh. Shorshorov, S.I. Bulychev, and V.P. Alekhin, Work of Plastic Deformation during Indenter Indentation, *Sov. Phys. Dokl.*, Vol 26 (No. 8), 1982, p 769–771
4. D. Newey, M.A. Wilkens, and H.M. Pollock, An Ultra-Low-Load Penetration Hardness Tester, *J. Phys. E, Sci. Instrum.*, Vol 15, p 119–122
5. J.B. Pethica, R. Hutchings, and W.C. Oliver, Hardness Measurements at Penetration Depths as Small as 20 nm, *Philos. Mag. A*, Vol 48 (No. 4), 1983, p 593–606
6. W.C. Oliver, Progress in the Development of a Mechanical Properties Microprobe, *MRS Bull.*, Vol 11 (No. 5), 1986, p 15–19

7. J.L. Loubet, J.M. Georges, O. Marchesini, and G. Meille, Vickers Indentation Curves of MgO, *J. Tribology (Trans. ASME)*, Vol 106, 1984, p 43–48
8. M.F. Doerner and W.D. Nix, A Method for Interpreting the Data from Depth-Sensing Indentation Instruments, *J. Mater. Res.*, Vol 1, 1986, p 601–609
9. H.M. Pollock, D. Maugis, and M. Barquins, “Characterization of Sub-Micrometer Layers by Indentation,” ASTM STP 889, *Microindentation Techniques in Materials Science and Engineering*, P.J. Blau and B.R. Lawn, Ed., ASTM, 1986, p 47–71
10. W.D. Nix, Mechanical Properties of Thin Films, *Metall. Trans. A*, Vol 20, 1989, p 2217–2245
11. W.C. Oliver and G.M. Pharr, An Improved Technique for Determining Hardness and Elastic Modulus Using Load and Displacement Sensing Indentation Experiments, *J. Mater. Res.*, Vol 7 (No. 6), 1992, p 1564–1583
12. G.M. Pharr and W.C. Oliver, Measurement of Thin Film Mechanical Properties Using Nanoindentation, *MRS Bull.*, Vol 17, 1992, p 28–33
13. G.M. Pharr, Measurement of Mechanical Properties by Ultra-low Load Indentation, *Mater. Sci. Eng. A*, Vol 253, 1998, p 151–159
14. J.S. Field and M.V. Swain, A Simple Predictive Model for Spherical Indentation, *J. Mater. Res.*, Vol 8 (No. 2), 1993, p 297–306
15. J.S. Field and M.V. Swain, Determining the Mechanical Properties of Small Volumes of Material from Submicron Spherical Indentations, *J. Mater. Res.*, Vol 10 (No. 1), 1995, p 101–112
16. M.V. Swain, Mechanical Property Characterization of Small Volumes of Brittle Materials with Spherical Tipped Indenters, *Mater. Sci. Eng. A*, Vol 253, 1998, p 160–166
17. J.-L. Loubet, B.N. Lucas, and W.C. Oliver, Some Measurements of Viscoelastic Properties with the Help of Nanoindentation, *NIST Special Publication 896: International Workshop on Instrumented Indentation*, 1995, p 31–34
18. B.N. Lucas, C.T. Rosenmayer, and W.C. Oliver, Mechanical Characterization of Sub-Micron Polytetrafluoroethylene (PTFE) Thin Films, in *Thin Films—Stresses and Mechanical Properties VII*, *MRS Symposium Proc.*, Vol 505, Materials Research Society, 1998, p 97–102
19. M.J. Mayo and W.D. Nix, A Microindentation Study of Superplasticity in Pb, Sn, and Sn-38wt%Pb, *Acta Metall.*, Vol 36 (No. 8), 1988, p 2183–2192
20. M.J. Mayo, R.W. Siegel, A. Narayanasamy, and W.D. Nix, Mechanical Properties of Nanophase TiO₂ as Determined by Nanoindentation, *J. Mater. Res.*, Vol 5 (No. 5), 1990, p 1073–1082
21. V. Raman and R. Berriche, An Investigation of Creep Processes in Tin and Aluminum Using Depth-Sensing Indentation Technique, *J. Mater. Res.*, Vol 7 (No. 3), 1992, p 627–638
22. M.J. Mayo and W.D. Nix, in *Proc. of the 8th Int. Conf. on the Strength of Metals and Alloys*, Pergamon Press, 1988, p 1415
23. W.H. Poisl, W.C. Oliver, and B.D. Fabes, The Relation between Indentation and Uniaxial Creep in Amorphous Selenium, *J. Mater. Res.*, Vol 10 (No. 8), 1995, p 2024–2032

24. B.N. Lucas, W.C. Oliver, J.-L. Loubet, and G.M. Pharr, Understanding Time Dependent Deformation During Indentation Testing, in *Thin Films—Stresses and Mechanical Properties VI, MRS Symposium Proc.*, Vol 436, Materials Research Society, 1997, p 233–238
25. B.N. Lucas and W.C. Oliver, Indentation Power-Law Creep of High-Purity Indium, *Metall. Mater. Trans. A*, Vol 30, 1999, p 601–610
26. G.M. Pharr, D.S. Harding, and W.C. Oliver, Measurement of Fracture Toughness in Thin Films and Small Volumes Using Nanoindentation Methods, *Mechanical Properties and Deformation Behavior of Materials Having Ultra-Fine Microstructures*, Kluwer Academic Publishers, 1993, p 449–461
27. D.S. Harding, W.C. Oliver, and G.M. Pharr, Cracking During Nanoindentation and Its Use in the Measurement of Fracture Toughness, in *Thin Films—Stresses and Mechanical Properties V, MRS Symposium Proc.*, Vol 356, Materials Research Society, 1995, p 663–668
28. A.E.H. Love, Boussinesq's Problem for a Rigid Cone, *Q. J. Math.*, Vol 10, 1939, p 161–175
29. I.N. Sneddon, The Relation Between Load and Penetration in the Axisymmetric Boussinesq Problem for a Punch of Arbitrary Profile, *Int. J. Eng. Sci.*, Vol 3, 1965, p 47–56
30. Y.-T. Cheng and C.-M. Cheng, Scaling Approach to Conical Indentation in Elastic-Plastic Solids with Work Hardening, *J. Appl. Phys.*, Vol 84, 1998, p 1284–1291
31. A. Bolshakov and G.M. Pharr, Influences of Pile-Up on the Measurement of Mechanical Properties by Load and Depth Sensing Indentation Techniques, *J. Mater. Res.*, Vol 13, 1998, p 1049–1058
32. A.K. Bhattacharya and W.D. Nix, Finite Element Simulation of Indentation Experiments, *Int. J. Solids Struct.*, Vol 24 (No. 9), 1988, p 881–891
33. A.K. Bhattacharya and W.D. Nix, Analysis of Elastic and Plastic Deformation Associated with Indentation Testing of thin Films on Substrates, *Int. J. Solids Struct.*, Vol 24 (No. 12), 1988, p 1287–1298
34. T.A. Laursen and J.C. Simo, A Study of the Mechanics of Microindentation Using Finite Elements, *J. Mater. Res.*, Vol 7, 1992, p 618–626
35. J.A. Knapp, D.M. Follstaedt, S.M. Myers, J.C. Barbour, and T.A. Friedman, Finite-Element Modeling of Nanoindentation, *J. Appl. Phys.*, Vol 85 (No. 3), 1999, p 1460–1474
36. T.Y. Tsui, W.C. Oliver, and G.M. Pharr, Indenter Geometry Effects on the Measurement of Mechanical Properties by Nanoindentation with Sharp Indenters, in *Thin Films—Stresses and Mechanical Properties VI, MRS Symposium Proc.*, Vol 436, Materials Research Society, 1997, p 147–152
37. G. Simmons and H. Wang, *Single Crystal Elastic Constants and Calculated Aggregate Properties: A Handbook*, 2nd ed., The M.I.T. Press, 1971
38. G.M. Pharr, W.C. Oliver, and F.R. Brotzen, On the Generality of the Relationship among Contact Stiffness, Contact Area, and Elastic Modulus, *J. Mater. Res.*, Vol 7 (No. 3), 1992, p 613–617
39. R.B. King, Elastic Analysis of Some Punch Problems for a Layered Medium, *Int. J. Solids Struct.*, Vol 23, 1987, p 1657–1664
40. H.J. Gao and T.-W. Wu, *J. Mater. Res.*, Vol 8 (No. 12), 1993, p 3229–3232

41. B.C. Hendrix, The Use of Shape Correction Factors for Elastic Indentation Measurements. *J. Mater. Res.*, Vol 10 (No. 2), 1995, p 255–257
42. A. Bolshakov and G.M. Pharr, Inaccuracies in Sneddon's Solution for Elastic Indentation by a Rigid Cone and Their Implications for Nanoindentation Data Analysis, in *Thin Films—Stresses and Mechanical Properties VI, MRS Symposium Proc.*, Vol 436, Materials Research Society, 1997, p 189–194
43. J.C. Hay, A. Bolshakov, and G.M. Pharr, A Critical Examination of the Fundamental Relations in the Analysis of Nanoindentation Data, *J. Mater. Res.*, Vol 14 (No. 6), 1999, p 2296–2305
44. J.C. Hay, A. Bolshakov, and G.M. Pharr, Applicability of Sneddon Relationships to the Real Case of a Rigid Cone Penetrating an Infinite Half Space, in *Fundamentals of Nanoindentation and Nanotribology, MRS Symposium Proc.*, Vol 522, Materials Research Society, 1998, p 263–268
45. J.C. Hay and G.M. Pharr, Experimental Investigations of the Sneddon Solution and an Improved Solution for the Analysis of Nanoindentation Data, in *Fundamentals of Nanoindentation and Nanotribology, MRS Symposium Proc.*, Vol 522, Materials Research Society, 1998, p 39–44
46. A. Bolshakov, W.C. Oliver, and G.M. Pharr, An Explanation for the Shape of Nanoindentation Unloading Curves Based on Finite Element Simulation, in *Thin Films—Stresses and Mechanical Properties V, MRS Symposium Proc.*, Vol 356, Materials Research Society, 1995, p 675–680
47. J.B. Pethica and W.C. Oliver, Tip Surface Interactions in STM and AFM, *Phys. Scr. Vol. T*, Vol 19, 1987, p 61
48. J.B. Pethica and W.C. Oliver, Mechanical Properties of Nanometer Volumes of Material: Use of the Elastic Response of Small Area Indentations, in *Thin Films—Stresses and Mechanical Properties, MRS Symposium Proc.*, Vol 130, Materials Research Society, 1989, p 13–23
49. B.N. Lucas, W.C. Oliver, and J.E. Swindeman, The Dynamics of Frequency-Specific, Depth-Sensing Indentation Testing, *Fundamentals of Nanoindentation and Nanotribology, MRS Symposium Proc.*, Vol 522, Materials Research Society, 1998, p 3–14
50. T.F. Page, G.M. Pharr, J.C. Hay, W.C. Oliver, B.N. Lucas, E. Herbert, and L. Riester, Nanoindentation Characterization of Coated Systems: $P:S^2$ —A New Approach Using the Continuous Stiffness Technique, in *Fundamentals of Nanoindentation and Nanotribology, MRS Symposium Proc.*, Vol 522, Materials Research Society, 1998, p 53–64
51. K.W. McElhane, J.J. Vlassak, and W.D. Nix, Determination of Indenter Tip Geometry and Indentation Contact Area for Depth-Sensing Indentation Experiments, *J. Mater. Res.*, Vol 13 (No. 5), 1998, p 1300–1306
52. B. Taljat, T. Zacharia, and G.M. Pharr, Pile-Up Behavior of Spherical Indentations in Engineering Materials, in *Fundamentals of Nanoindentation and Nanotribology, MRS Symposium Proc.*, Vol 522, Materials Research Society, 1998, p 33–38
53. J.L. Hay, W.C. Oliver, A. Bolshakov, and G.M. Pharr, Using the Ratio of Loading Slope and Elastic Stiffness to Predict Pile-Up and Constraint Factor During Indentation, in *Fundamentals of Nanoindentation and Nanotribology, MRS Symposium Proc.*, Vol 522, Materials Research Society, 1998, p 101–106
54. Standard Test for Microhardness of Materials, “ASTM Standard Test Method E 384,” *Annual Book of Standards 3.01*, American Society for Testing and Materials, 1989, p 469

55. P.J. Burnett and D.S. Rickerby, The Mechanical Properties of Wear Resistant Coatings 1: Modeling of Hardness Behaviour, *Thin Solid Films*, Vol 148, 1987, p 41–50
56. P.J. Burnett and D.S. Rickerby, The Mechanical Properties of Wear Resistant Coatings 2, *Thin Solid Films*, Vol 148, 1987, p 51–65
57. B. Jonsson and S. Hogmark, *Thin Solid Films*, Vol 114, 1984, p 257
58. T.Y. Tsui, W.C. Oliver, and G.M. Pharr, Nanoindentation of Soft Films on Hard Substrates—The Importance of Pileup, in *Thin Films—Stresses and Mechanical Properties VI, MRS Symposium Proc.*, Vol 436, 1997, p 207–212
59. T.Y. Tsui, C.A. Ross, and G.M. Pharr, Nanoindentation Hardness of Soft Films on Hard Substrates: Effects of the Substrate, in *Materials Reliability in Microelectronics VII, MRS Symposium Proc.*, Vol 473, 1997, p 57–62
60. B.D. Fabes and W.C. Oliver, Mechanical Properties of Coating and Interfaces, in *Thin Films—Stresses and Mechanical Properties II, MRS Symposium Proc.*, Vol 188, 1990, p 127–132
61. H. Gao, C.-H. Chiu, and J. Lee, Elastic Contact Versus Indentation Modeling of Multi-Layered Materials, *Int. J. Solids Struct.*, Vol 29 (No. 20), 1992, p 2471–2492
62. D.S. Stone, *J. Electron. Packaging*, Vol 112, 1990, p 41
63. H.Y. Yu, S.C. Sanday, and B.B. Rath, The Effect of Substrate on the Elastic Properties of Films Determined by the Indentation Test—Axisymmetric Boussinesq Problem, *J. Mech. Phys. Solids*, Vol 38, 1990, p 745–764
64. J. Mencik, D. Munz, E. Quandt, E.R. Weppelmann, and M.V. Swain, Determination of Elastic Modulus of Thin Layers Using Nanoindentation, *J. Mater. Res.*, Vol 12 (No. 9), 1997, p 2475–2484
65. T.Y. Tsui and G.M. Pharr, Substrate Effects on Nanoindentation Mechanical Property Measurement of Soft Films on Hard Substrates, *J. Mater. Res.*, Vol 14, 1999, p 292–301
66. G.M. Pharr, A. Bolshakov, T.Y. Tsui, and J.C. Hay, Nanoindentation of Soft Films on Hard Substrates: Experiments and Finite Element Simulations, in *Thin Films—Stresses and Mechanical Properties VII, MRS Symposium Proc.*, Vol 505, 1998, p 109–120
67. J.C. Hay and G.M. Pharr, Critical Issues in Measuring the Mechanical Properties of Hard Films on Soft Substrates by Nanoindentation Techniques, in *Thin Films—Stresses and Mechanical Properties VII, MRS Symposium Proc.*, Vol 505, 1998, p 65–70
68. A.G. Atkins, A. Silverio, and D. Tabor, Indentation Creep, *J. Inst. Metals*, Vol 94, 1966, p 369–378
69. D.S. Stone and K.B. Yoder, Division of the Hardness of Molybdenum into Rate-Dependent and Rate-Independent Components, *J. Mater. Res.*, Vol 9 (No. 10), 1994, p 2524–2533
70. D. Tabor, *Hardness of Metals*, Oxford University Press, 1951, p 46, 67–83, 105–106
71. K.L. Johnson, *Contact Mechanics*, Cambridge University Press, 1985, p 94, 176
72. W.B. Morton and L.J. Close, Notes on Hertz' Theory of Contact Problems, *Philos. Mag.*, Vol 43, 1922, p 320

73. R.M. Davies, The Determination of Static and Dynamic Yield Stresses Using a Steel Ball, *Proc. R. Soc. (London) A*, Vol 197, 1949, p 416
74. "Standard Methods of Preparation of Metallographic Specimens," E 380, *Annual Book of ASTM Standards*, ASTM, reapproved 1993
75. J. Mencik and M.V. Swain, Errors Associated with Depth-Sensing Microindentation Tests, *J. Mater. Res.*, Vol 10 (No. 6), 1995, p 1491–1501

Indentation Hardness Testing of Ceramics

G.D. Quinn, Ceramics Division, National Institute of Standards and Technology

Introduction

HARDNESS is a key attribute of ceramics. One would suppose that measuring and interpreting ceramic hardness is routine, but there are pitfalls, controversies, new developments, and sometimes even surprises. Although commonly measured for a ceramic, hardness is usually evaluated for different purposes than for metallic materials. Ceramists are more concerned with evaluating the generic ceramic hardness rather than verifying that a correct heat treatment or surface treatment has been applied to a body. Hardness of ceramics is important for characterizing ceramic cutting tools, wear and abrasion resistant parts, prosthetic hip joint balls and sockets, optical lens glasses (for scratch resistance), ballistic armor, molds and dies, and valves and seals. Typically, ceramic material specifications may have minimum hardness requirements. For example, a zirconia specification for surgical implants, ASTM F 1873-98 (Ref 1), states that Vickers hardness (HV) shall be no less than 11.8 GPa (1200 kgf/mm²) at 9.8 N (1 kgf) load.

Hardness characterizes the resistance of the ceramic to deformation, densification, displacement, and fracture. Densification often is important because it relates to the microporosity that is often present in sintered ceramics. Densification may also occur in some glasses. Microfracture and shear fracture under an indentation are also important deformation components. The complexity of the deformation, displacement, and fracture processes is beautifully illustrated in Ref 2.

Hardness is usually measured with conventional microindentation hardness machines using Knoop or Vickers diamond indenters. Figures 1 and 2 show some typical well-formed indentations, whose diagonal length is measured with an attached optical microscope. For research purposes, Vickers, Knoop, and Berkovich (triangular pyramid) indenters are used. Rockwell and Brinell indenters are rarely used for ceramics research. In engineering and characterization applications, approximately 60% of worldwide published ceramic hardness values are Vickers, with loads typically in the range of a few Newtons to 9.8 N (>100 gf-1 kgf) with occasional data for soft or high toughness ceramics at loads as high as 98 N (10 kgf). About 35% are Knoop with loads from as low as 0.98 up to 19.6 N (0.10–2 kgf). Knoop hardness is more frequently cited in the United States than in the rest of the world, presumably due to the existence of ASTM standards C 730 for glass (Ref 3), C 849 for ceramic whitewares (Ref 4), and C 1326 for advanced ceramics (Ref 5). Knoop testing is frequently used to study the hardness of ceramic single crystals (Ref 6), because orientation effects may be studied by varying the diagonal axis orientation. Cracking problems are also less severe than with Vickers indentations.

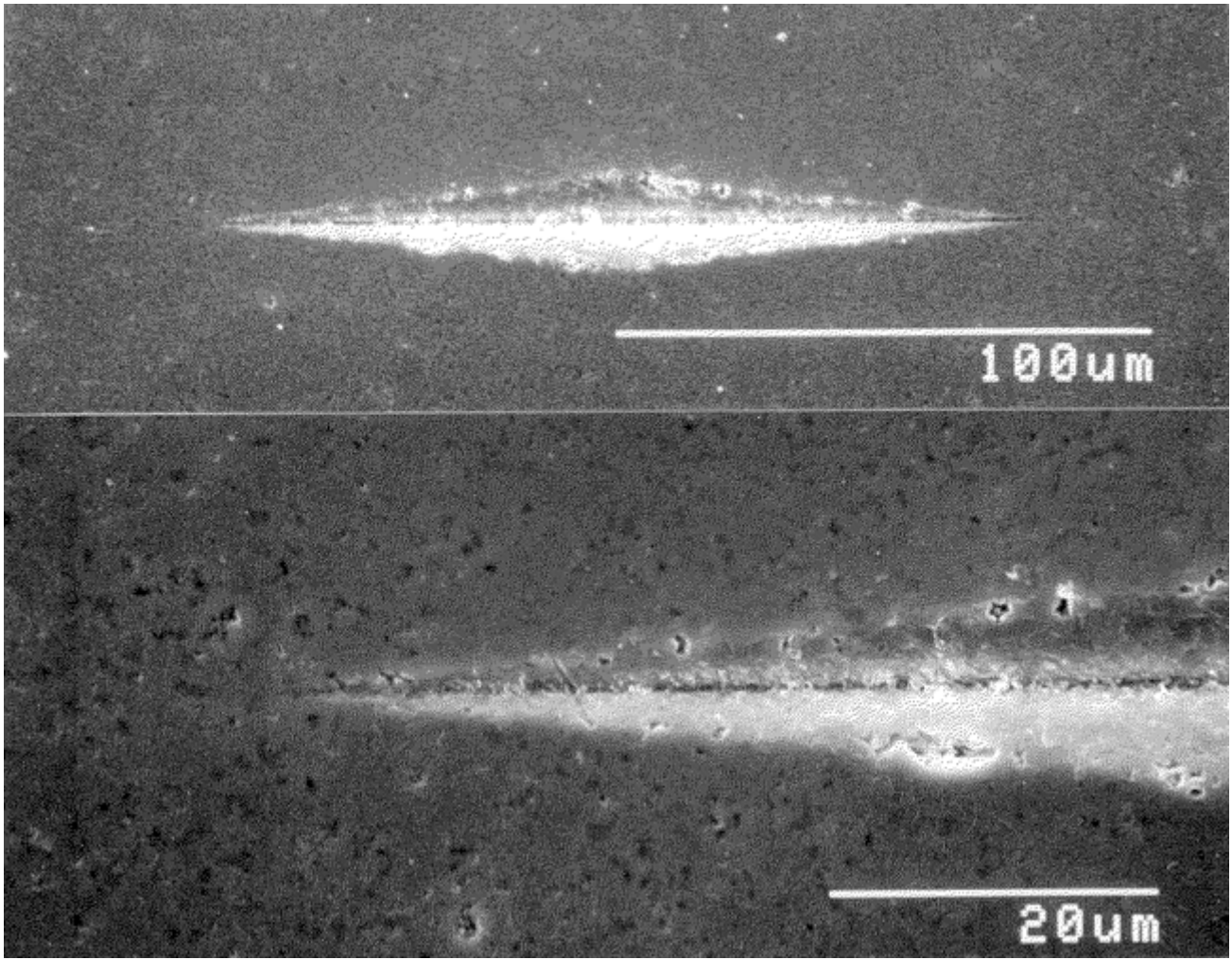


Fig. 1 Scanning electron micrographs, entire indentation and closeup of one tip, of Knoop indentation (19.6 N, or 2 kgf) in a silicon nitride.

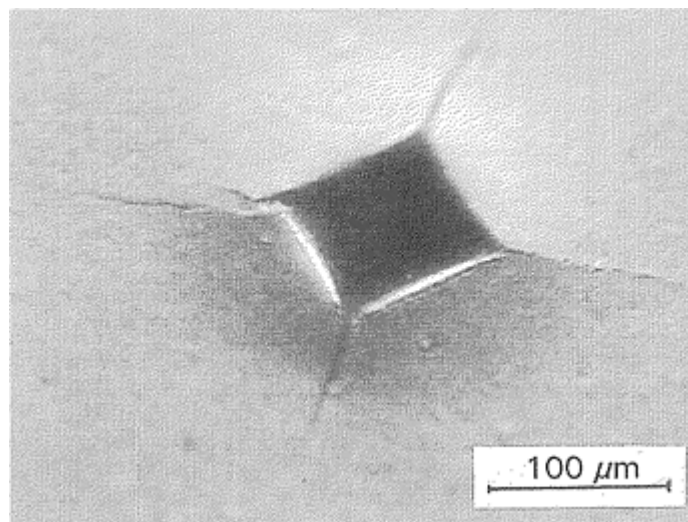


Fig. 2 Light micrograph of Vickers indentation (98 N, or 10 kgf) in a silicon nitride. Specimen is tilted to show the three-dimensional form of the indentation.

About another 5% of published hardness values are Rockwell, usually the HRA or superficial HR45N scales. Another scale for measuring ceramic hardness is the traditional Moh's scale from a scratch hardness test, which ranks various minerals from gypsum (hardness of 1) to corundum (9) and diamond (10). Although popular in mineralogy and geology, the Mohs scale is rarely used for engineering purposes.

The indentation size effect in ceramics wherein hardness decreases with increasing indentation load (Fig. 3) occurs for both conventional Knoop and Vickers hardness but with slightly different trends. The Meyer-law exponent, n (see Eq 6), is less than 2. A constant hardness is reached at loads from 5 to 100 N (0.5–10.2 kgf) depending on the ceramic. The Knoop hardness often is greater at small loads, but then decreases to a plateau load that is somewhat less (~10%) than the Vickers hardness at large loads. The differences in hardness are due to different relative amounts of deformation, densification, displacement, and fracture in the material beneath the Knoop and Vickers indenters.

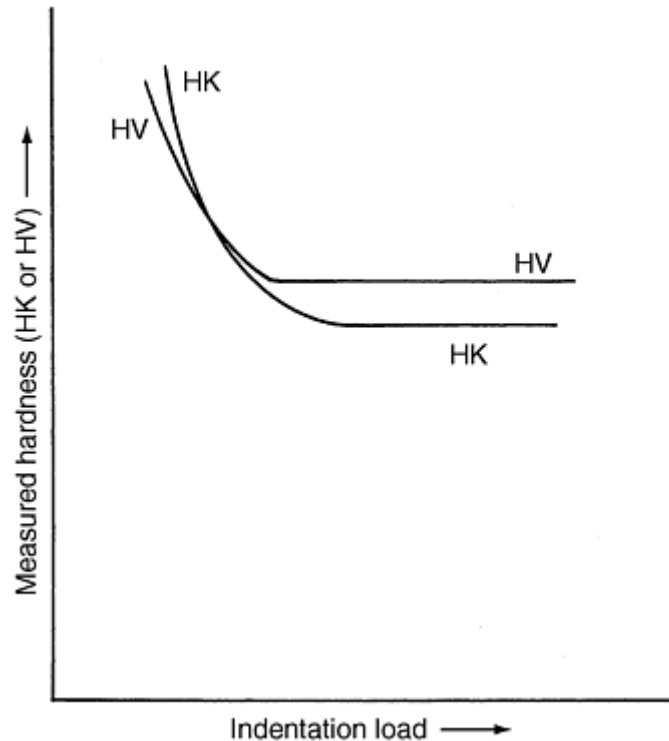


Fig. 3 Effect of indentation size on the measured hardness of ceramics

Ideally, one should measure the entire hardness-load curve, but in practice testers often chose one reference or standard load to allow comparisons between materials. It is preferable to make the indentations as large as possible to reduce measurement uncertainties, yet not so large as to induce excessive cracking that interferes with the measurement or destroys the indentation altogether. The preferred indentation loads that are specified in world standards are listed in the following sections. Indentation load should always be reported with the hardness outcome. Many contemporary structural ceramics have hardnesses in the 10 to 30 GPa (1020–3060 kgf/mm²) range. For the latter hardness, Vickers indentations made at 9.8 N (1 kgf) load are 25 μ m long and Knoop indentations are 68 μ m long.

The preponderance of published Vickers and Knoop hardness values in the ceramics technical literature and in many company product brochures are reported with *units of GPa*. Thus, the hardness of dense silicon nitride is of the order of 15 GPa. Some values are published either with older units of kgf/mm², or as dimensionless hardness with kgf/mm² implied (e.g., 1500 kgf/mm² or 1500). ISO 14705 for hardness of fine ceramics (advanced ceramics) (Ref 7) recommends the use of GPa, but allows the dimensionless values as an alternative.

References cited in this section

1. “Standard Specification for High-Purity Dense Yttria Tetragonal Zirconium Oxide Polycrystal (γ -TZP) for Surgical Implant Applications,” E 1873-98, *Annual Book of ASTM Standards*, Vol 13.01, ASTM, 1999
2. J.T. Hagan and M.V. Swain, The Origin of Median and Lateral Cracks around Plastic Indents in Brittle Materials, *J. Phys. D: Appl. Phys.*, Vol 11, 1978, p 2091–2102

3. "Standard Test Method for Knoop Indentation Hardness of Glass," C 730-98, *Annual Book of ASTM Standards*, Vol 15.02, ASTM, 1999
4. "Standard Test Method for Knoop Indentation Hardness of Ceramic Whitewares," C 849-88, *Annual Book of ASTM Standards*, Vol 15.02, ASTM, 1999
5. "Standard Test Method for Knoop Indentation Hardness of Advanced Ceramics," C 1326-99, *Annual Book of ASTM Standards*, Vol 15.01, ASTM, 1999
6. I.J. McHolm, *Ceramic Hardness*, Plenum, 1990
7. "Fine Ceramics (Advanced Ceramics, Advanced Technical Ceramics), Test Method for Hardness at Room Temperature," ISO 14705, International Organization for Standards, Geneva, Switzerland

Indentation Hardness Testing of Ceramics

G.D. Quinn, Ceramics Division, National Institute of Standards and Technology

Microindentation Hardness

Metrology Issues of Knoop and Vickers Hardness. At small indentation loads (<9.8 N, or 1 kgf) problems arise from the significant load dependence of hardness and measurement uncertainty due to the small indentation size. At higher loads (>49 N, or 5 kgf), cracking and spalling can be a problem and may make measurement impossible. The difficulties in obtaining accurate and precise hardness readings are not fully appreciated. Figure 4 shows some of the common, serious issues with hardness measurements in ceramics. The slightest bump to a hardness machine or the table on which it sits while the indenter is in contact with the specimen can create an appreciable error. Hardness is proportional to the square of the diagonal length of the indentation, and so any error in length measurement has the effect of doubling the error in hardness measurement. It is crucial that the diagonal length be measured carefully, especially for ceramics where the indentation size is small and the percentage error is larger. Many ceramics and glasses are often transparent or translucent and require careful microscopic examination. A Versailles Advanced Materials and Standards (VAMAS) round-robin project with two alumina ceramics showed that the reproducibility (between-laboratory) uncertainty in reported mean hardness was 10 to 15%, and in some instances, much greater (Ref 8, 9).

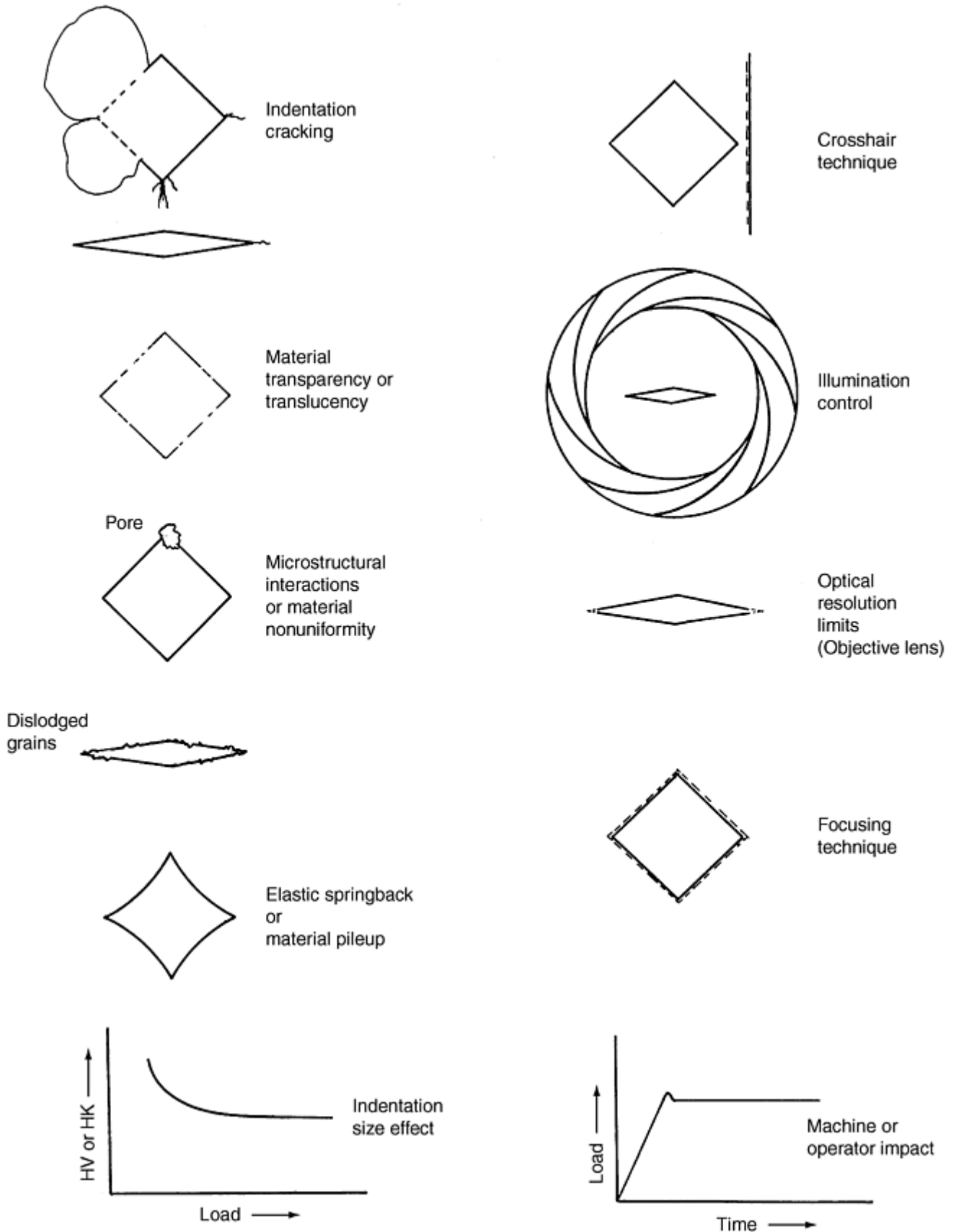


Fig. 4 Common problems in ceramic hardness testing

Indentations in ceramics and glasses are often very small, and microindentation hardness machines should have a microscope with a magnification capability of *no less than 400*×. Optical microscopy technique is crucial. Reasonable skill, experience, and careful experimental technique are necessary to accurately and precisely measure diagonal lengths. This skill level is readily achievable through practice and use of reference hardness blocks. The early microindentation hardness literature (e.g., Ref 10, 11, 12) has numerous discussions of

objective lens quality and design, optical resolution limits, crosshair technique, and information on the use of field and aperture diaphragms to control contrast and brightness. The latter are especially important for translucent or transparent ceramics and glasses. Much of the difference in interpretation of indentation tip location between observers can be traced to illumination and contrast control.

Although many machines have digital readouts to 0.1 μm (4 μm in.), users should recognize this is less than the wavelength of light and does not represent the true machine accuracy or machine precision, which are probably several times larger. In practice, the resolution of the indentation tips and the subjectivity of the viewer usually leads to a between-observer variability of 0.5 to 1.0 μm in diagonal size. In light of the importance of optical technique, it is amazing and regrettable that some contemporary commercial hardness machines have no aperture diaphragm. Some have neither an aperture nor a field diaphragm. Optimum indentation illumination on ceramics and glasses cannot be achieved with such equipment. The emphasis with some contemporary machines seems to be on capturing the indentation image with a video camera and projecting the image onto a monitor and interpreting results with a computer. Computer analysis and controls cannot overcome basic optical limitations of an instrument. In many instances, a single monitor pixel can represent as much as 0.5 μm and is a significant fraction of the size of a small ceramic indentation. Of course, whatever system is used to measure diagonal lengths, it should be verified by use of a calibrated stage micrometer or other magnification verification device. Ceramic hardness reference blocks with certified indentation sizes may be used to verify length measurements as well.

With some care and practice, an operator should be able to measure a well-formed $\sim 50 \mu\text{m}$ Vickers indentation diagonal size to within 0.5 μm and to within 1.0 μm for a 50 to 100 μm Knoop indentation with 400 to 500 \times optical magnification. As previously noted, different observers using the same equipment and viewing the same indentations typically agree within 0.5 and 1.0 μm (20 and 40 $\mu\text{in.}$) for Vickers and Knoop indentations, respectively. Practice with reference blocks can improve this precision considerably.

Knoop Hardness of Ceramics and Glasses. Frederick Knoop developed his elongated pyramidal indenter as an alternative to the square base pyramidal Vickers indenter, in large part to overcome the cracking observed in brittle materials (Ref 13, 14). Knoop indentations are far less apt to manifest severe cracking than Vickers indentations. Several key standards for Knoop hardness of ceramics or glasses are listed in Table 1. The European Community standard CEN ENV 843-4 has Knoop as well as Vickers and Rockwell A and N hardness methods. The new ISO 14705 standard from Technical Committee TC 206, Fine Ceramics, includes both Knoop and Vickers hardness.

Table 1 Knoop hardness standard test methods for ceramics and glasses

Standard	Materials covered	Preferred test load		Alternate test load		Ref
		N	kgf	N	kgf	
ASTM C 730	Glass	0.98	0.1	3
ASTM C 849	Ceramic whitewares	9.8	1	4
ASTM C 1326	Advanced ceramics	19.6	2	9.8	1	5
CEN 843-4	Advanced technical ceramics	9.8	1	16
DIN 52333	Glass and glass ceramics	0.98	0.1 ^(a)	17
ISO 14705	Fine (advanced, advanced technical) ceramics	19.6	2	9.8	1	7
ISO 9385	Glass and glass-ceramics	0.98	0.1 ^(a)	18

(a) At least two other test loads that are not likely to cause excessive fracture shall also be used.

The preferred loads for testing are all within the range of most microindentation hardness testing machines. The standards usually include provisions for alternative (usually smaller) loads if cracking is a problem. The three ASTM standards all refer back to the master standard E 384 (Ref 15), "Microindentation Hardness of Materials," but each have specific conditions and requirements for ceramics or glasses. For example, the indenter displacement rate is much slower in C 730 than for the other standards, which reflects some concern about loading rate effects. In addition, C 730 and C 849 include an important correction factor for optical resolution limitations. Figure 5 shows acceptable and unacceptable indentations according to ASTM C 1326 and ISO 14705. The glass standards all recommend 0.98 N (100 gf) as the standard test force. This small load is

used because glasses have low hardness, and so a small test load will produce a moderate-sized indentation. The small load also avoids cracking. The ceramic standards all prescribe 19.6 or 9.8 N (2 or 1 kgf). The larger 19.6 N (2 kgf) force is advantageous since the larger indentation produces more precise readings, as is discussed below. The 9.8 or 19.6 N forces may not be sufficiently large to ensure that hardness has reached the plateau, however. These forces were chosen because they are within the load capacity of most commercial microindentation hardness machines.

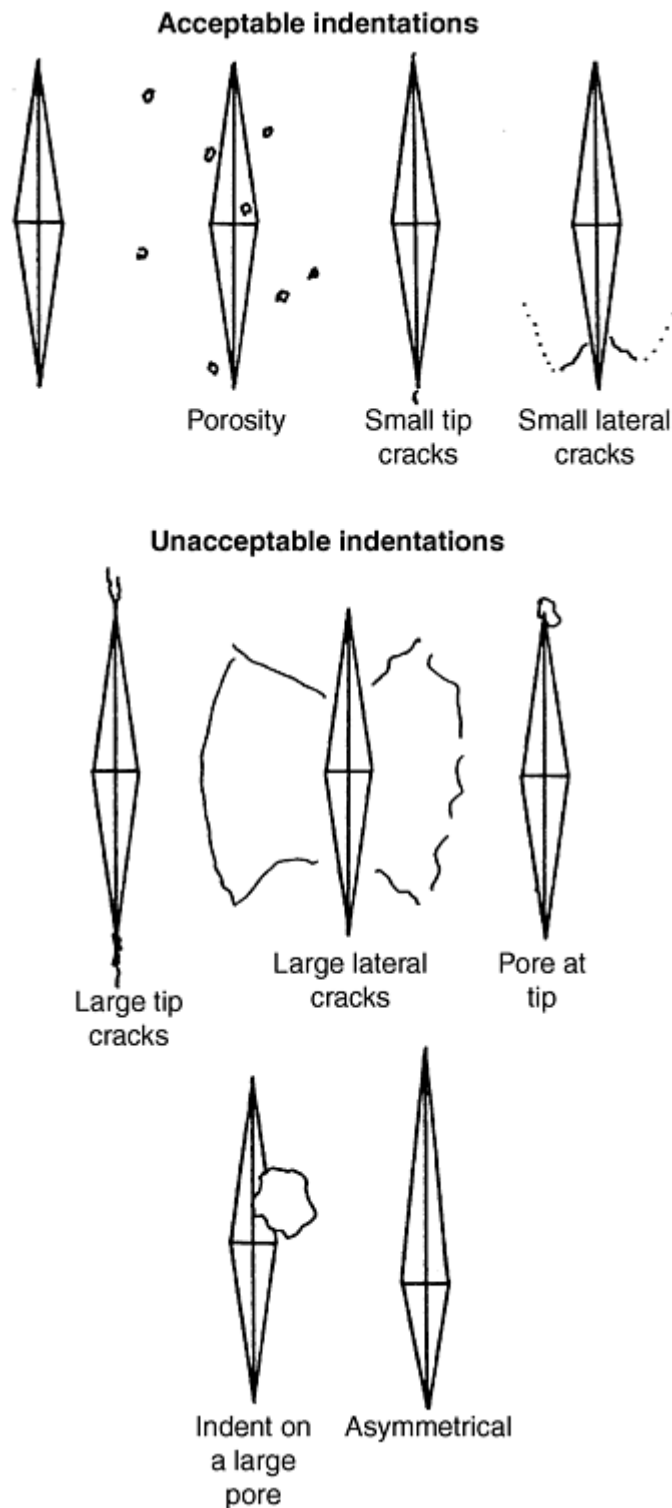


Fig. 5 Acceptable and unacceptable Knoop indentations in ceramics

As noted earlier, it is essential that the test force be reported along with any ceramic hardness number. ISO 14705 requires the use of one of two methods of reporting Knoop hardness. The preferred scheme is SI compatible and has the symbol HK preceded by the hardness value and supplemented by a number representing the test force:

15.0 GPa HK 9.807 N

which denotes a Knoop hardness of 15.0 GPa determined with a test force of 9.807 N (1 kgf). Alternately:

1500 HK 1

denotes a Knoop hardness of 1500 (dimensionless) determined with a test force of 9.807 N (1 kgf).

Fortunately, all world standards and the entire ceramics community use the traditional definition of Knoop hardness based upon test force divided by projected surface area:

$$HK = 14.229 \frac{W}{d^2} \quad (\text{Eq 1})$$

where W is the indenter force and d is the long diagonal length.

Knoop indentations are 2.8× longer than Vickers indentations made at the same load. The longer indentations in principle should make an easier-to-read indentation, but in practice the length advantage is offset by the greater difficulty in determining where the tapered tip ends. A major advantage of the Knoop indentation over Vickers for ceramics is that larger indentation loads may be used without cracking. Even if the sides of the indentation are displaced or cracked, a credible diagonal length reading and hardness estimate may be made. The tip uncertainty is often of the order of 0.5 to 1.0 μm, irrespective of the indentation size, and consequently the percentage error is minimized with long indentations. In addition, it is easier to measure hardness in the constant-hardness region of the indentation size effect curve. Knoop hardness is not fully utilized or appreciated by the ceramics community.

Optical microscope resolution limitations are a problem for Knoop indentations due to the slender tapered tip (Fig. 6). The error in underestimating the true tip location has been estimated as $7\lambda/2(\text{NA})$ where λ is the wavelength of light and NA is the objective lens numerical aperture (Ref 12). For a typical microscope having a 40×, 0.65 NA objective lens, the calculated correction for green light ($\lambda = 0.55 \mu\text{m}$) is thus 3.0 μm, a significant number. A correction for this is incorporated in the two older ASTM Knoop standards; C 730 for glass and C 849 for ceramic whitewares, but is not used either in the master microindentation hardness of materials standard E 384 or in the advanced ceramic standard, C 1326. The confusion about whether to add this correction factor reached the point where a major glass manufacturer at one time included both uncorrected and corrected numbers for Knoop hardness numbers in their product data handbook.

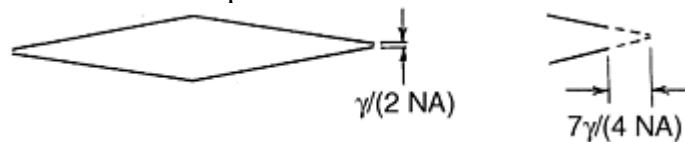


Fig. 6 Resolution limits of light microscopy when measuring the long, slender tips of Knoop indents. λ , wavelength of light; NA, numerical aperture of objective lens

To determine whether the $7\lambda/2(\text{NA})$ correction is appropriate, the National Institute of Standards and Technology (NIST) compared calibrated scanning electron microscope (SEM) diagonal length measurements to optical microscope measurements on a Knoop impression in a silicon nitride reference block (Ref 19, 20). The indentation was measured optically by four skilled operators. Three used the optical system on a conventional microindentation hardness machine, and the fourth used a metallograph used to certify metallic microindentation hardness standard reference materials (SRMs). The length was measured using several lenses with different numerical apertures, all calibrated using the same NIST-certified stage micrometer. Five or ten repetitions were made by each observer. The SEM measurements benefited from higher magnification photographs (1500×, 5000×), which aided the interpretation of the exact tip location. The mean SEM length measurement was 146.8 μm (standard deviation ±0.2 μm). The mean optical diagonal lengths were 0.4 to 2.1 μm shorter than the SEM readings. These differences are less than the full $7\lambda/2(\text{NA}) = 3.0 \mu\text{m}$ correction probably because the optical observers did discern the tip as a faint black line, albeit not as two distinguishable tip lines as shown in Fig. 6. Later, as part of an eleven-laboratory international round-robin, three certification laboratories using their normal optical microscopes obtained average diagonal length readings (10 indentations) that were within 0.4 to 1.2 μm of the NIST SEM readings. This is better than 1% agreement on 142 μm long indentations and underscores how the percentage error may be kept small by utilizing large Knoop indentation

sizes. In conclusion, with careful optical microscopy the diagonal length readings for this opaque reference material were close to the calibrated SEM values, and the $7\lambda/2(\text{NA})$ correction factor is excessive.

Knoop indenters sometimes are used to create a controlled surface microflaw in ceramic fracture specimens for fracture toughness determination by the surface crack in flexure method. The indentation and the residual stress damage zone underneath it are removed by polishing or hand grinding. The specimen is fractured and fracture toughness evaluated from the fracture load and the precrack dimensions. This approach has been adopted in ASTM and ISO standards. Indentation loads are usually 19.6 to 49.0 N (2–5 kgf), which cause no damage to the diamond indenter (see the article “Fracture Toughness of Ceramics and Ceramic Matrix Composites” in this Volume).

Vickers Hardness of Ceramics. The square pyramidal Vickers indenter creates smaller, deeper impressions than Knoop indentations at the same load. Vickers indentations are more apt to crack. There are no Vickers standard test methods for glasses, undoubtedly due to cracking problems. Table 2 shows some of the current key world standards and preferred test loads. All standards have settled on a reference test force of 9.8 N (1 kgf), which is within the capacity of nearly all microindentation hardness testing machines, but probably is not on the hardness plateau for a hardness versus load curve for many ceramics. Japanese Industrial Standard (JIS) R 1610 and ISO 14705 also allow 98.0 N (10 kgf), but these large loads cause extreme fracturing in ceramics such as silicon carbide and boron carbide.

Table 2 Vickers hardness standard test methods for ceramics

Standard	Materials covered	Preferred test load		Alternative test load		Ref
		N	kgf	N	kgf	
ASTM C 1327	Advanced ceramics	9.8	1	21
CEN 843-4	Advanced technical ceramics	9.8	1	16
JIS R 1610	Fine ceramics	9.8	1	98.0	10	22
ISO 14705	Fine (advanced, advanced technical) ceramics	9.8	1	98.0	10	7

The late 1970s and early 1980s saw the advent of indentation fracture studies wherein Vickers indentations were used to study fracture behavior and, in particular, to estimate fracture toughness. In this approach, a Vickers indentation is made into a polished surface, and the lengths of the four long cracks that emanate from the indentation corners are measured. Many workers began to try to measure hardness and fracture toughness at the same time on the same indentations. Indentation loads were varied in order to adjust the crack sizes. This frequently led to the use of very large indentation loads, much greater than the 9.8 N (1 kgf) or even the 98 N (10 kgf) forces recommended in the hardness standards. Often the hardness data were of poor quality. Mangled indentations and mangled diamond indenters often resulted. Diamond indenters may be damaged by edge cracking or loss of the meticulously prepared tips, rendering them useless for quality hardness measurements in the microhardness range.

The optical resolution limits are estimated to be only $1.0\lambda/2(\text{NA})$ or $\sim 0.4 \mu\text{m}$ for Vickers indentations (Ref 12) with a 40 \times , 0.65 NA objective lens. Correction factors are rarely applied to the length measurements and are not incorporated into any Vickers standard. Figure 2 shows a typical well-formed indentation in a silicon nitride specimen and illustrates the three-dimensional nature of the indentation as well as a modest amount of tip cracking. There is considerable uplift to the indentation sides. Although the indentation tips are “blunter” and easier to judge than the slender, tapered Knoop indentations, the Vickers indentation lengths are much shorter. Consequently, any error in measuring the diagonal size of a Vickers indentation is a larger fraction of the diagonal size. The hardness uncertainty is similar to or greater than that for Knoop hardness measurements at the same load. The cracks at the Vickers indentation corners typically are wider and more pronounced and may interfere with the interpretation of the tip location. In the limit, cracking can be so extensive that portions of the indentation spall off as shown in Fig. 7, making measurements imprudent or impossible. Figure 8 illustrates acceptable and unacceptable Vickers indentations according to ASTM C 1327 and ISO 14705.

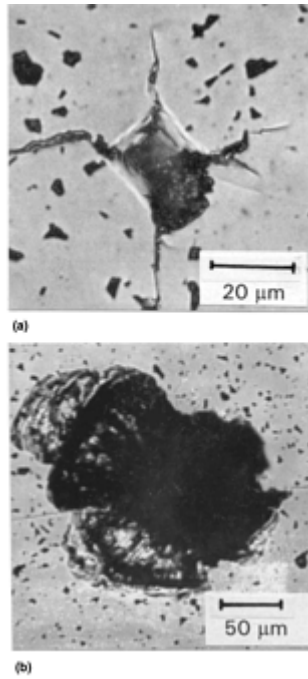


Fig. 7 Badly spalled and fractured Vickers indentation in boron carbide at indentation loads of (a) 9.8 N (1 kgf) and (b) 98.0 N (10 kgf)

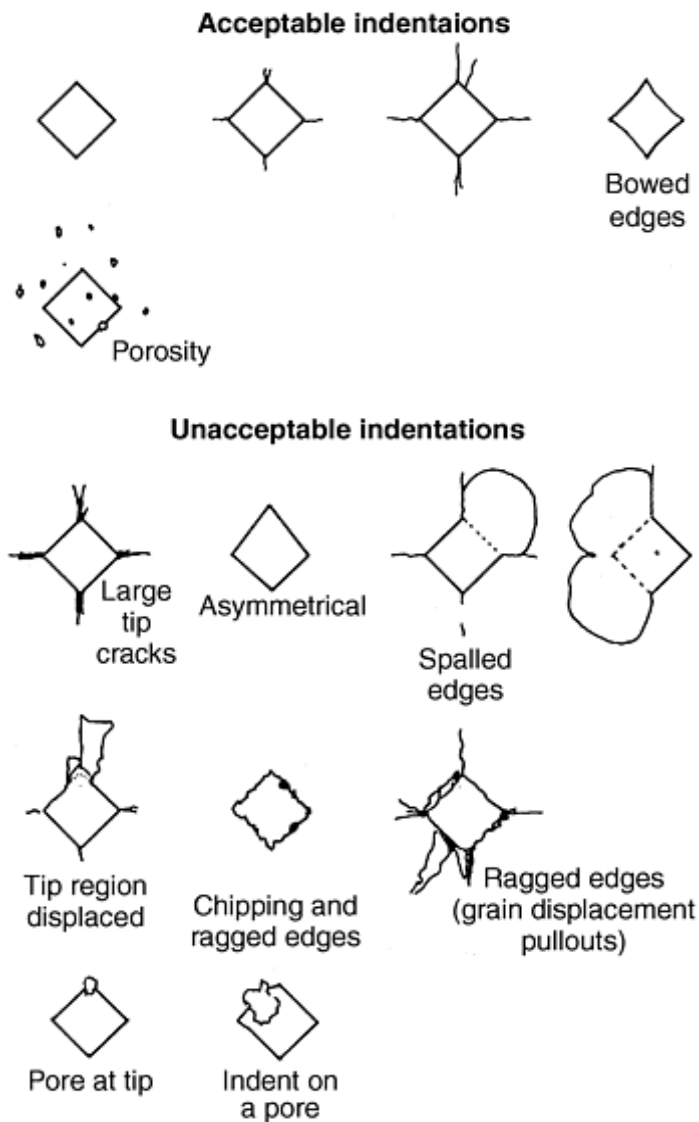


Fig. 8 Acceptable and unacceptable Vickers indentations in ceramics

It is essential that the test force be reported along with any ceramic hardness number. ISO 14705 requires the use of one of two methods of reporting Vickers hardness. The preferred scheme is to use the symbol HV preceded by the hardness value and supplemented by a number representing the test force:

$$15.0 \text{ GPa HV } 9.807 \text{ N}$$

which denotes a Vickers hardness of 15.0 GPa determined with a test force of 9.807 N (1 kgf). Alternately:

$$1500 \text{ HV } 1$$

denotes a Vickers hardness of 1500 (dimensionless) determined with a test force of 9.807 N (1 kgf).

All world standards and most of the ceramics community use the traditional definition of conventional Vickers hardness based upon test force divided by contact area:

$$\text{HV} = 1.8544 \frac{W}{d^2} \quad (\text{Eq 2})$$

where W is the indenter force and d is the long diagonal length. This is the preferred, consensus world standard formulation for conventional Vickers hardness. Unfortunately, some practitioners in the ceramics community (those who use Vickers indentations to study fracture, or those who use instrumented or load and depth-sensing methods) use a formula for hardness (H) based upon test force divided by *projected surface area*:

$$H = 2.0 \frac{W}{d^2} \quad (\text{Eq 3})$$

which is sometimes expressed alternately as

$$H = 2.0 \frac{W}{(2a)^2} = 0.5 \frac{W}{a^2} \quad (\text{Eq 4})$$

where a is the indentation half diagonal size. Many papers or reports do not state which equation was used to compute a conventional Vickers hardness value or even the indentation load. Hardness values in such cases should be discounted because they are almost worthless. If the symbol HV is used in reporting hardness, the odds are very good that the data were generated by a sound test method and hardness calculated by Eq 2.

References cited in this section

3. "Standard Test Method for Knoop Indentation Hardness of Glass," C 730-98, *Annual Book of ASTM Standards*, Vol 15.02, ASTM, 1999
4. "Standard Test Method for Knoop Indentation Hardness of Ceramic Whitewares," C 849-88, *Annual Book of ASTM Standards*, Vol 15.02, ASTM, 1999
5. "Standard Test Method for Knoop Indentation Hardness of Advanced Ceramics," C 1326-99, *Annual Book of ASTM Standards*, Vol 15.01, ASTM, 1999
7. "Fine Ceramics (Advanced Ceramics, Advanced Technical Ceramics), Test Method for Hardness at Room Temperature," ISO 14705, International Organization for Standards, Geneva, Switzerland
8. D.M. Butterfield, D.J. Clinton, and R. Morrell, "The VAMAS Hardness Tests Round-Robin on Ceramic Materials," Report No. 3, Versailles Advanced Materials and Standards/National Physical Laboratory, April 1989
9. R. Morrell, D.M. Butterworth, and D.J. Clinton, Results of the VAMAS Ceramics Hardness Round Robin, *Euroceramics*, Vol 3, *Engineering Ceramics*, G. de With, R.A. Terpstra, and R. Metselaar, Ed., Elsevier, London, 1989, p 339–345
10. N. Thibault and H. Nyquist, The Measured Knoop Hardness of Hard Substances and Factors Affecting Its Determination, *Trans. ASM*, Vol 38, 1947, p 271–330

11. L. Tarasov and N. Thibault, Determination of Knoop Hardness Numbers Independent of Load, *Trans. ASM*, Vol 38, 1947, p 331–353
12. B.W. Mott, *Micro-Indentation Hardness Testing*, Butterworth, London, 1955
13. F. Knoop, C. Peters, and W. Emerson, A Sensitive Pyramidal-Diamond Tool for Indentation Measurements, *J. Res. Nat. Bur. Std.*, Vol 23, July 1939, p 39–61
14. C.G. Peters and F. Knoop, Resistance of Glass to Indentation, *Glass Ind.*, Vol 20, May 1939, p 174–176
15. “Standard Test Method for Microhardness of Materials,” E 384-89 (1997)e2, *Annual Book of ASTM Standards*, Vol 3.01, ASTM, 1999
16. “Advanced Technical Ceramics, Monolithic Ceramics, Mechanical Properties at Room Temperature, Part 4. Vickers, Knoop and Rockwell Superficial Hardness Tests,” CEN EN 843-4, European Committee for Standardization, Brussels, 1994
17. “Knoop Hardness Testing, Glass and Glass Ceramic,” DIN 52333, Entwurf German Institute for Standards, Berlin, 1987
18. “Glass and Glass-Ceramics, Knoop Hardness,” ISO 9385, International Organization for Standards, Geneva, 1990
19. R.J. Gettings, G.D. Quinn, A.W. Ruff, and L.K. Ives, Development of Ceramic Hardness Reference Materials, *New Horizons for Materials*, P. Vincenzini, Ed., Proc. Eighth World Ceramic Congress, CIMTEC (Florence, Italy), July 1994, Techna, Florence, 1995, p 617–624
20. R.J. Gettings, G.D. Quinn, A.W. Ruff, and L.K. Ives Hardness Standard Reference Materials (SRMs) for Advanced Ceramics (No. 1194), *Proc. Ninth International Symposium on Hardness Testing in Theory and Practice*, (Dusseldorf), Nov 1995, VDI Berichte 1995, p 255–264
21. “Standard Test Method for Vickers Indentation Hardness of Advanced Ceramics,” C 1327–99, *Annual Book of ASTM Standards*, Vol 15.01, ASTM, 1999
22. “Testing Method for Vickers Hardness of High Performance Ceramics,” JIS R 1610, Japanese Standards Association, Tokyo, 1991

Indentation Hardness Testing of Ceramics

G.D. Quinn, Ceramics Division, National Institute of Standards and Technology

Hardness and Microstructure

Ceramic hardness is strongly dependent on the microstructure of the material. Grain size, grain morphology, porosity, and secondary phases (even in trace amounts), all affect measured hardnesses (Ref 6, 23). The porosity dependence of hardness may be expressed as:

$$H = H_0 \exp^{-bP} \quad (\text{Eq 5})$$

where H_0 is the hardness with zero porosity, P is the volume fraction of porosity, and b is a constant. Values for b , which range from 3 to 11 depending upon the ceramic, attest to the significant influence of porosity on hardness. Hardness usually increases with decreasing grain size in accordance with a Hall-Petch relationship,

wherein hardness varies with the inverse square root of grain size (Ref 23, 24, 25, 26). At very large grain sizes, the trend may change and hardness may increase with increasing grain size and approach single-crystal hardness values (Ref 23). Examples of the effect of grain size on Vickers hardness are shown by Rice et al. (Ref 23), Clinton and Morrell (Ref 24), and Krell and Blank (Ref 25), and for Knoop hardness by Skrovanek and Bradt (Ref 26). Just as one cannot generalize and attribute a value of hardness to “steel,” one should not generalize and assign a value to “alumina.” The more specific one can be about the ceramic (i.e., its code designation, grain size, and porosity) the better.

References cited in this section

6. I.J. McHolm, *Ceramic Hardness*, Plenum, 1990
23. R.W. Rice, C.C. Wu, and F. Borchelt, Hardness-Grain Size Relations in Ceramics, *J. Am. Ceram. Soc.*, Vol 77 (No. 10), 1994, p 2539–2553
24. D.J. Clinton and R. Morrell, Hardness Testing of Ceramic Materials, *Mater. Chem. Phys.*, Vol 17, 1989, p 461–473
25. A. Krell and P. Blank, Grain Size Dependence of Hardness in Dense Submicrometer Alumina, *J. Am. Ceram. Soc.*, Vol 78 (No. 4), 1995, p 1118–1120
26. S.D. Skrovanek and R.C. Bradt, Microhardness of a Fine-Grain-Size Al₂O₃, *J. Am. Ceram. Soc.*, Vol 62 (No. 3–4), 1979, p 215–216

Indentation Hardness Testing of Ceramics

G.D. Quinn, Ceramics Division, National Institute of Standards and Technology

Ceramic Hardness Reference Materials

The poor results from a 1988–1989 VAMAS round-robin study (Ref 8, 9) with Knoop, Vickers, and Rockwell tests on alumina ceramics underscored the need for standard reference materials (SRMs). In response to this need, NIST subsequently prepared for Knoop hardness NIST SRM 2830, which is a hot isopressed silicon nitride disk that was prepared from a ceramic bearing ball (Ref 19, 20). It has a high-quality polish with five well-defined indentations and has a nominal hardness of 14.0 GPa (1400 kgf/mm²). A typical 19.6 N (2 kgf) impression is shown in Fig. 1. The average diagonal length (~142.0 μm, or 5590 μin.) for each block is listed and certified to within 0.6 μm (24 μin.) (0.4%) at a 95% confidence interval. The 19.6 N (2 kgf) load is used to exploit the advantage that long Knoop indentations can reduce the percentage error to such remarkably small levels. Hardness is certified to within 0.9% or within 0.12 GPa (12 kgf/mm²). A calibrated scanning electron microscope was used to make all length measurements. An eleven-laboratory international round-robin verified that operators with conventional optical microscopes obtained readings in excellent agreement with the SEM readings. This was especially true for the three participating certification labs: NIST's Metallurgy Division, Wilson Division of Instron, and the Materials Testing Institute, Nordrhein-Westfalen, Germany. The Fraunhofer Institute for Ceramic Technologies and Sintered Material (IKTS), Dresden, also has prepared ceramic Knoop hardness reference blocks to support EN 843-4.

NIST SRM 2831 for Vickers hardness was still in preparation as of 2000. It is a tungsten carbide with cobalt binder with five indentations made at a load of 9.8 N (1 kgf) (Ref 19, 20). A tungsten carbide was chosen since it is an opaque ceramic (hardmetal) that does not crack at the tips.

References cited in this section

8. D.M. Butterfield, D.J. Clinton, and R. Morrell, "The VAMAS Hardness Tests Round-Robin on Ceramic Materials," Report No. 3, Versailles Advanced Materials and Standards/National Physical Laboratory, April 1989
9. R. Morrell, D.M. Butterworth, and D.J. Clinton, Results of the VAMAS Ceramics Hardness Round Robin, *Euroceramics*, Vol 3, *Engineering Ceramics*, G. de With, R.A. Terpstra, and R. Metselaar, Ed., Elsevier, London, 1989, p 339–345
19. R.J. Gettings, G.D. Quinn, A.W. Ruff, and L.K. Ives, Development of Ceramic Hardness Reference Materials, *New Horizons for Materials*, P. Vincenzini, Ed., Proc. Eighth World Ceramic Congress, CIMTEC (Florence, Italy), July 1994, Techna, Florence, 1995, p 617–624
20. R.J. Gettings, G.D. Quinn, A.W. Ruff, and L.K. Ives Hardness Standard Reference Materials (SRMs) for Advanced Ceramics (No. 1194), *Proc. Ninth International Symposium on Hardness Testing in Theory and Practice*, (Dusseldorf), Nov 1995, VDI Berichte 1995, p 255–264

Indentation Hardness Testing of Ceramics

G.D. Quinn, Ceramics Division, National Institute of Standards and Technology

Cracking from Vickers Indentations

Hardness testing usually seeks to avoid the cracking that interferes with the hardness measurement. On the other hand, the ceramics community has contrived a simple method to estimate fracture toughness (K_{Ic}) from Vickers indentation cracking. The indentation crack length or "indentation fracture" method is based on measurement of the crack lengths emanating from the corners of Vickers hardness indentations on polished surfaces (Ref 27, 28). The lengths of the cracks and the indentation half diagonal size are related to the hardness, elastic modulus, and fracture toughness of the material by a semiempirical analytical expression. The expression inevitably has a calibration constant with considerable uncertainty. The early work on this methodology claimed that K_{Ic} calculations were accurate to within 30 to 40%. Despite this uncertainty, the method is popular because of its seeming simplicity, the need for only one small piece, and the potential to make repeat measurements.

The mediocre success of the early equations prompted the ceramics community to spawn a plethora of alternative expressions, to the point that massive confusion now reigns in the ceramics community (Ref 6, 29) (see, for example, the chapter "Cracked Indents—Friend or Foe" in Ref 6). The failure of a single equation to apply and the large uncertainty in the calibration constants originate in the complicated, material-specific deformation-crack patterns and residual stress fields underneath a hardness indentation. The method also suffers from the drawback that toughness depends on the measured crack length raised to the 1.5 power. The substantial uncertainties in measuring the crack size (far worse than measuring indentation size) are thus magnified. Data consistency among laboratories is usually poor due to variations in the interpretation of the crack length arising from microscopy limitations as well as operator experience or subjectivity. A VAMAS round-robin demonstrated variability of almost a factor of 2 in reported toughness (Ref 30, 31). The requirement to obtain cracks lengths that are sufficiently long ($>2.0\times$ the half diagonal size) has led some to use enormous loads (sometimes up to 500 N, or 50 kgf) that cause severe shattering, prompting one skeptical group to remark that indentations in some materials might resemble "nuclear bomb craters" (Ref 32). This method may have some utility within a laboratory for research purposes, but experience belies its suitability for producing accurate fracture toughness results that can be compared between laboratories.

References cited in this section

6. I.J. McHolm, *Ceramic Hardness*, Plenum, 1990
27. A. Evans and E. Charles, Fracture Toughness Determination by Indentation, *J. Am. Ceram. Soc.*, Vol 59 (No. 7–8), 1976, p 371–372
28. G. Anstis, P. Chantikul, B. Lawn, and D. Marshall, A Critical Evaluation of Indentation Techniques for Measuring Fracture Toughness: I, Direct Crack Measurements, *J. Am. Ceram. Soc.*, Vol 64 (No. 9), 1981, p 533–538
29. C.B. Ponton and R.D. Rawlings, Dependence of the Vickers Indentation Fracture Toughness on the Surface Crack Length, *Br. Ceram. Trans. J.*, Vol 88, 1989, p 83–90
30. H. Awaji, T. Yamada, and H. Okuda, Results of the Fracture Toughness Test Round Robin on Ceramics, VAMAS Project, *J. Ceram. Soc. Jpn., Int. Ed.*, Vol 99 (No. 5), 1991, p 403–408
31. G. Quinn, J. Salem, I. Bar-on, K. Chu, M. Foley, and H. Fang, Fracture Toughness of Advanced Ceramics at Room Temperature, *J. Res. NIST*, Vol 97 (No. 5), Sept–Oct 1992, p 579–607
32. Z. Li, A. Ghosh, A. Kobayashi, and R. Bradt, Reply to Comment on Indentation Fracture Toughness of Sintered Silicon Carbide in the Palmqvist Crack Regime, *J. Am. Ceram. Soc.*, Vol 74 (No. 4), 1991, p 889–890

Indentation Hardness Testing of Ceramics

G.D. Quinn, Ceramics Division, National Institute of Standards and Technology

Instrumented Hardness Testing

Instrumented hardness testing, wherein displacement is monitored during load application, is an important emerging technology. Load displacements typically appear as shown in Fig. 9, but test cycles with partial unloading and reloading are often used. Vickers or Berkovich (triangular pyramid) indenters may be used. The Berkovich indenter avoids the flat, or “chisel tip” that inevitably exists in Vickers pyramids in which four surfaces or edges meet almost (but not quite) at a point. Tip shape is crucial in instrumented hardness tests at low loads. Various indices of hardness may be deduced from the load and depth of penetration of the indenter, and, if it is assumed that the diamond indenter does not change shape, it is even possible to compute a conventional HV hardness. An enormous advantage of this methodology is that it obviates the need for microscopy for measuring the indentation size, thereby eliminating operator skill or subjectivity and microscopy limitations. On the other hand, complications arise because of the need to make assumptions about the analytical form of the load-displacement curves. Unloading curves may be analyzed to determine the elastic modulus, but again assumptions about the indenter shape and penetration geometries must be made. There is no consensus on the interpretation of these curves. For example, one commercial apparatus that is widely used in Europe to measure a so-called “universal hardness” actually measures a hardness defined as the load divided by assumed contact area while the load is still applied. Consequently, this universal hardness includes both plastic and elastic deformation components. Another problem common to all instrumented hardness testers is the uncertainty associated with determining the exact initial contact point.

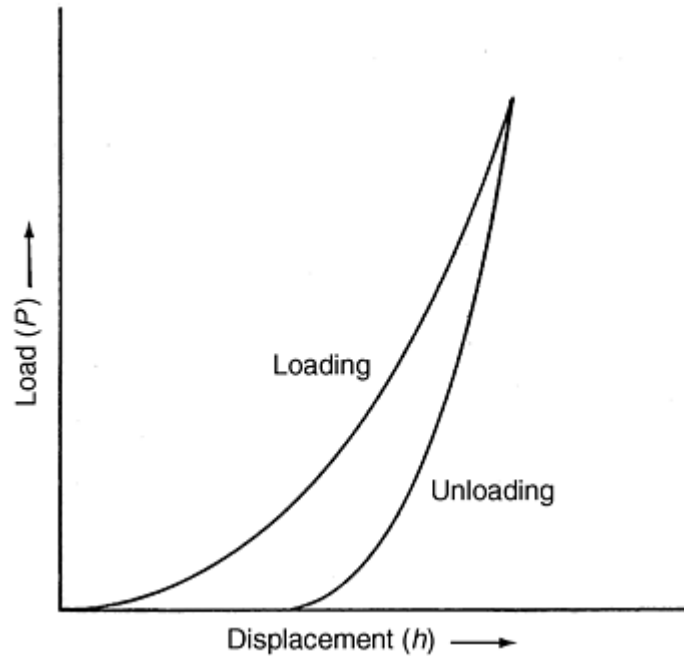


Fig. 9 A typical load-displacement trace for instrumented hardness testing

Sometimes ordinary microindentation hardness machines may be retrofitted with displacement transducers, but care must be taken to measure displacement as close to the indenter-specimen contact point as possible. Frame compliance is an important source of error with retrofitted machines. Severe variability (up to a factor of 2) in instrumented hardness results were recently demonstrated in a VAMAS round-robin exercise with a borosilicate crown glass and NIST SRM 2830 silicon nitride blocks (Ref 33, 34). Dedicated low-load instrumented hardness or even extremely low-load nanohardness machines are now commercially available. This emerging technology has great promise, but consensus on the analyses, standard procedures, and reference materials are sorely needed.

References cited in this section

33. C. Ullner and G. Quinn, "Round Robin on Recording Hardness," Report No. 33, VAMAS (Versailles Advanced Materials and Standards), BAM, Berlin/NIST, Feb 1998
34. C. Ullner and G. Quinn, Interlaboratory Study on Depth Sensing Hardness on Ceramics, to be presented at IMEKO XV Conference (Osaka, Japan) as Reference No. 269, June 1999

Indentation Hardness Testing of Ceramics

G.D. Quinn, Ceramics Division, National Institute of Standards and Technology

Hardness and Brittleness

Much of the ceramics literature has thus far emphasized the effect of load and hardness on fracture processes and fracture toughness. It has not considered in detail the reverse effect of fracture on hardness. This article notes that the hardness of a brittle material is a measure of the resistance of the material to deformation, densification, displacement, and fracture. Local fracture around and under an indentation can affect the impression size and can be considered an intrinsic part of the indentation process. The degree of fracture at

ceramic indentations is load dependent. Deformation is predominant at low loads, while fracture is more evident at high loads. The Meyer law is:

$$W = cd^n \quad (\text{Eq 6})$$

where W is the load, c is a constant, and n is the Meyer or logarithmic index. As noted previously, for ceramics and glasses, $n < 2$ and hardness decreases with increasing load. The hardness-load curves for many ceramics deviate somewhat from the empirical Meyer law. This has prompted alternative attempts to achieve improved curve fits to hardness-load or hardness-indentation size data. Bückle (Ref 35) and later Mitsche (Ref 36) suggested a power series expansion that was later simplified to only two terms:

$$W = a_1d + a_2d^2 \quad (\text{Eq 7})$$

where a_1 and a_2 are constants. This equation alternatively may be expressed as an energy balance by multiplying both sides by d :

$$Wd = a_1d^2 + a_2d^3 \quad (\text{Eq 8})$$

The term Wd is proportional to the external work done by the indenter, $W\ell$, where ℓ is the indenter penetration depth, which is proportional to d for self-similar indentations. A number of investigators have attempted to correlate surface energy processes to the a_1d^2 term (Ref 37, 38, 39, 40), while Li et al. (Ref 41, 42) have related this term to frictional and elastic contributions in their “proportional specimen resistance” model. The a_2d^3 term, on the other hand, is considered to be the “work of permanent deformation” (Ref 39) or the “volume energy of deformation” (Ref 42).

Close examination of experimental ceramic Vickers hardness-load curves (on either HV versus load or HV versus diagonal size graphs) suggests a discrete transition point may exist where hardness changes from being load dependent to load independent as shown in Fig. 10 (Ref 43). The Meyer relationship and energy models (Eq 2 3 4) do not predict a specific transition point to constant hardness. The transition point, which is usually overlooked, appears to be associated with the onset of extensive cracking around and underneath the indentation. Cracking, an integral response of the ceramic to indentation even at small loads, may either be localized or, at higher loads, massive to the extent that crushing occurs. Yurkov and Bradt (Ref 44) detected significant acoustic emission activity at the indentation load where the constant hardness plateaus were reached for five sialon ceramics. Knoop hardness does not exhibit an abrupt transition to a constant hardness plateau, presumably because there is less cracking. The Vickers hardness transition point is related to a new index of ceramic brittleness defined as (Ref 43):

$$B = \frac{HV_c \cdot E}{K_{Ic}^2} \quad (\text{Eq 9})$$

where HV_c is Vickers hardness at the plateau, E is the elastic modulus, and K_{Ic} is the fracture toughness.

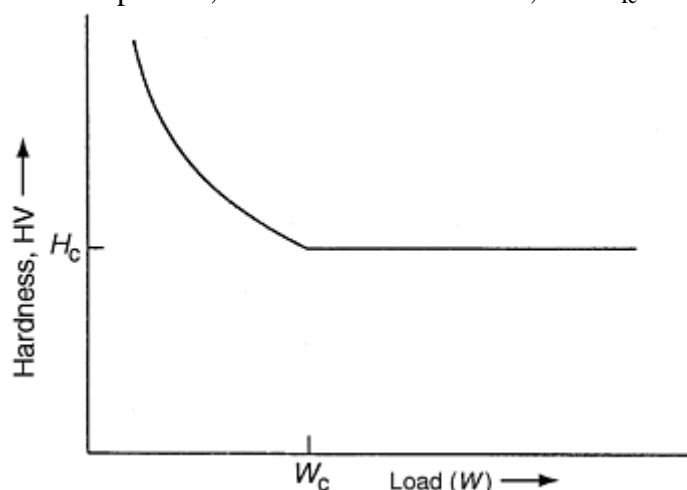


Fig. 10 Vickers hardness versus load (indentation size effect) curve for ceramics, showing a distinct transition to a plateau hardness, H_c , at W_c

B may also be expressed as:

$$B \propto \frac{HV_c}{2\gamma_f}$$

(Eq 10)

where γ_f is the fracture surface energy. B is the ratio of hardness to the fracture surface energy. Hardness has units of work per unit volume and may be considered the work to create unit deformed volume, whereas γ_f is the work to create unit surface area. In other words, B is a ratio of volume deformation energy to surface fracture energy. Figure 11 shows some hardness versus indentation load data for three ceramics of varying brittleness. The transition point is easy to detect in brittle ceramics such as silicon carbide but may require very careful measurements in less brittle materials.

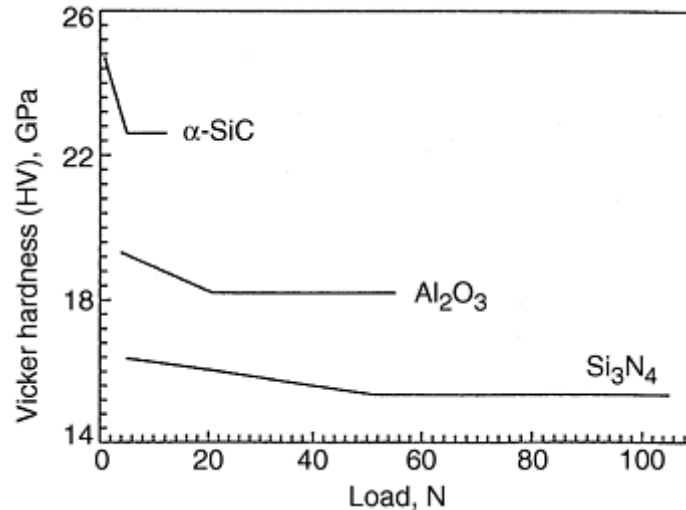


Fig. 11 Hardness versus load for three ceramics. The silicon carbide is the most brittle of the three.

References cited in this section

35. H. Bückle, *Mikrohärteprüfung*, Berliner Union Verlag, Stuttgart, 1965
36. R. Mitsche, Über die Eindringhärte Metallischer Fest und Lockerkörper, *Osterr. Chem. Z.*, Vol 49, 1948, p 186 (in German)
37. E.O. Bernhardt, On Microhardness of Solids at the Limit of Kick's Similarity Law, *Z. Metallkd.*, Vol 33, 1941, p 135–144
38. K. Hirao and M. Tomozawa, Microhardness of SiO_2 Glass in Various Environments, *J. Am. Ceram. Soc.*, Vol 70 (No. 7), 1987, p 497–502
39. F. Fröhlich, P. Grau, and W. Grellmann, Performance and Analysis of Recording Microhardness Tests, *Phys. Status Solidi (a)*, Vol 42, 1977, p 79–89
40. M. Swain and M. Wittling, The Indentation Size Effect for Brittle Materials: Is There a Simple Fracture Mechanics Explanation, *Fracture Mechanics of Ceramics*, Plenum, 1996, p 379–388
41. H. Li and R.C. Bradt, The Microhardness Indentation Load/Size Effect in Rutile and Cassiterite Single Crystals, *J. Mater. Sci.*, Vol 28, 1993, p 917–926
42. H. Li, A. Ghosh, Y.H. Han, and R.C. Bradt, The Frictional Component of the Indentation Size Effect in Low Hardness Testing, *J. Mater. Res.*, Vol 8 (No. 5), 1993, p 1028–1032
43. J. Quinn and G. Quinn, Indentation Brittleness of Ceramics: A Fresh Approach, *J. Mater. Sci.*, Vol 32, 1997, p 4331–4346

Indentation Hardness Testing of Ceramics

G.D. Quinn, Ceramics Division, National Institute of Standards and Technology

Summary

Hardness testing of ceramics, while conceptually simple, has many pitfalls. Sound metrological practices using quality equipment (microscopes and optical controls with aperture and diaphragm stops) coupled with the use of ceramic reference blocks will dramatically improve the quality of conventional test data. High-quality ceramic or glass standard test methods that have been backed by major international round-robins are on the books. New schemes for designating conventional hardness will rationalize the reporting of results. Hardness in SI units is widely used and is codified in several world standards. The indentation load should always be reported with the hardness data. New interpretations of conventional tests (such as brittleness, or fracture toughness) and emerging new instrumented hardness technologies hold great promise for the future.

Indentation Hardness Testing of Ceramics

G.D. Quinn, Ceramics Division, National Institute of Standards and Technology

References

1. “Standard Specification for High-Purity Dense Ytria Tetragonal Zirconium Oxide Polycrystal (γ -TZP) for Surgical Implant Applications,” E 1873-98, *Annual Book of ASTM Standards*, Vol 13.01, ASTM, 1999
2. J.T. Hagan and M.V. Swain, The Origin of Median and Lateral Cracks around Plastic Indents in Brittle Materials, *J. Phys. D: Appl. Phys.*, Vol 11, 1978, p 2091–2102
3. “Standard Test Method for Knoop Indentation Hardness of Glass,” C 730-98, *Annual Book of ASTM Standards*, Vol 15.02, ASTM, 1999
4. “Standard Test Method for Knoop Indentation Hardness of Ceramic Whitewares,” C 849-88, *Annual Book of ASTM Standards*, Vol 15.02, ASTM, 1999
5. “Standard Test Method for Knoop Indentation Hardness of Advanced Ceramics,” C 1326-99, *Annual Book of ASTM Standards*, Vol 15.01, ASTM, 1999
6. I.J. McHolm, *Ceramic Hardness*, Plenum, 1990
7. “Fine Ceramics (Advanced Ceramics, Advanced Technical Ceramics), Test Method for Hardness at Room Temperature,” ISO 14705, International Organization for Standards, Geneva, Switzerland
8. D.M. Butterfield, D.J. Clinton, and R. Morrell, “The VAMAS Hardness Tests Round-Robin on Ceramic Materials,” Report No. 3, Versailles Advanced Materials and Standards/National Physical Laboratory, April 1989

9. R. Morrell, D.M. Butterworth, and D.J. Clinton, Results of the VAMAS Ceramics Hardness Round Robin, *Euroceramics*, Vol 3, *Engineering Ceramics*, G. de With, R.A. Terpstra, and R. Metselaar, Ed., Elsevier, London, 1989, p 339–345
10. N. Thibault and H. Nyquist, The Measured Knoop Hardness of Hard Substances and Factors Affecting Its Determination, *Trans. ASM*, Vol 38, 1947, p 271–330
11. L. Tarasov and N. Thibault, Determination of Knoop Hardness Numbers Independent of Load, *Trans. ASM*, Vol 38, 1947, p 331–353
12. B.W. Mott, *Micro-Indentation Hardness Testing*, Butterworth, London, 1955
13. F. Knoop, C. Peters, and W. Emerson, A Sensitive Pyramidal-Diamond Tool for Indentation Measurements, *J. Res. Nat. Bur. Std.*, Vol 23, July 1939, p 39–61
14. C.G. Peters and F. Knoop, Resistance of Glass to Indentation, *Glass Ind.*, Vol 20, May 1939, p 174–176
15. “Standard Test Method for Microhardness of Materials,” E 384-89 (1997)e2, *Annual Book of ASTM Standards*, Vol 3.01, ASTM, 1999
16. “Advanced Technical Ceramics, Monolithic Ceramics, Mechanical Properties at Room Temperature, Part 4. Vickers, Knoop and Rockwell Superficial Hardness Tests,” CEN EN 843-4, European Committee for Standardization, Brussels, 1994
17. “Knoop Hardness Testing, Glass and Glass Ceramic,” DIN 52333, Entwurf German Institute for Standards, Berlin, 1987
18. “Glass and Glass-Ceramics, Knoop Hardness,” ISO 9385, International Organization for Standards, Geneva, 1990
19. R.J. Gettings, G.D. Quinn, A.W. Ruff, and L.K. Ives, Development of Ceramic Hardness Reference Materials, *New Horizons for Materials*, P. Vincenzini, Ed., Proc. Eighth World Ceramic Congress, CIMTEC (Florence, Italy), July 1994, Techna, Florence, 1995, p 617–624
20. R.J. Gettings, G.D. Quinn, A.W. Ruff, and L.K. Ives Hardness Standard Reference Materials (SRMs) for Advanced Ceramics (No. 1194), *Proc. Ninth International Symposium on Hardness Testing in Theory and Practice*, (Dusseldorf), Nov 1995, VDI Berichte 1995, p 255–264
21. “Standard Test Method for Vickers Indentation Hardness of Advanced Ceramics,” C 1327–99, *Annual Book of ASTM Standards*, Vol 15.01, ASTM, 1999
22. “Testing Method for Vickers Hardness of High Performance Ceramics,” JIS R 1610, Japanese Standards Association, Tokyo, 1991
23. R.W. Rice, C.C. Wu, and F. Borchelt, Hardness-Grain Size Relations in Ceramics, *J. Am. Ceram. Soc.*, Vol 77 (No. 10), 1994, p 2539–2553
24. D.J. Clinton and R. Morrell, Hardness Testing of Ceramic Materials, *Mater. Chem. Phys.*, Vol 17, 1989, p 461–473
25. A. Krell and P. Blank, Grain Size Dependence of Hardness in Dense Submicrometer Alumina, *J. Am. Ceram. Soc.*, Vol 78 (No. 4), 1995, p 1118–1120

26. S.D. Skrovanek and R.C. Bradt, Microhardness of a Fine-Grain-Size Al_2O_3 , *J. Am. Ceram. Soc.*, Vol 62 (No. 3–4), 1979, p 215–216
27. A. Evans and E. Charles, Fracture Toughness Determination by Indentation, *J. Am. Ceram. Soc.*, Vol 59 (No. 7–8), 1976, p 371–372
28. G. Anstis, P. Chantikul, B. Lawn, and D. Marshall, A Critical Evaluation of Indentation Techniques for Measuring Fracture Toughness: I, Direct Crack Measurements, *J. Am. Ceram. Soc.*, Vol 64 (No. 9), 1981, p 533–538
29. C.B. Ponton and R.D. Rawlings, Dependence of the Vickers Indentation Fracture Toughness on the Surface Crack Length, *Br. Ceram. Trans. J.*, Vol 88, 1989, p 83–90
30. H. Awaji, T. Yamada, and H. Okuda, Results of the Fracture Toughness Test Round Robin on Ceramics, VAMAS Project, *J. Ceram. Soc. Jpn., Int. Ed.*, Vol 99 (No. 5), 1991, p 403–408
31. G. Quinn, J. Salem, I. Bar-on, K. Chu, M. Foley, and H. Fang, Fracture Toughness of Advanced Ceramics at Room Temperature, *J. Res. NIST*, Vol 97 (No. 5), Sept–Oct 1992, p 579–607
32. Z. Li, A. Ghosh, A. Kobayashi, and R. Bradt, Reply to Comment on Indentation Fracture Toughness of Sintered Silicon Carbide in the Palmqvist Crack Regime, *J. Am. Ceram. Soc.*, Vol 74 (No. 4), 1991, p 889–890
33. C. Ullner and G. Quinn, “Round Robin on Recording Hardness,” Report No. 33, VAMAS (Versailles Advanced Materials and Standards), BAM, Berlin/NIST, Feb 1998
34. C. Ullner and G. Quinn, Interlaboratory Study on Depth Sensing Hardness on Ceramics, to be presented at IMEKO XV Conference (Osaka, Japan) as Reference No. 269, June 1999
35. H. Bückle, *Mikrohärteprüfung*, Berliner Union Verlag, Stuttgart, 1965
36. R. Mitsche, Über die Eindringhärte Metallischer Fest und Lockerkörper, *Osterr. Chem. Z.*, Vol 49, 1948, p 186 (in German)
37. E.O. Bernhardt, On Microhardness of Solids at the Limit of Kick's Similarity Law, *Z. Metallkd.*, Vol 33, 1941, p 135–144
38. K. Hirao and M. Tomozawa, Microhardness of SiO_2 Glass in Various Environments, *J. Am. Ceram. Soc.*, Vol 70 (No. 7), 1987, p 497–502
39. F. Fröhlich, P. Grau, and W. Grellmann, Performance and Analysis of Recording Microhardness Tests, *Phys. Status Solidi (a)*, Vol 42, 1977, p 79–89
40. M. Swain and M. Wittling, The Indentation Size Effect for Brittle Materials: Is There a Simple Fracture Mechanics Explanation, *Fracture Mechanics of Ceramics*, Plenum, 1996, p 379–388
41. H. Li and R.C. Bradt, The Microhardness Indentation Load/Size Effect in Rutile and Cassiterite Single Crystals, *J. Mater. Sci.*, Vol 28, 1993, p 917–926
42. H. Li, A. Ghosh, Y.H. Han, and R.C. Bradt, The Frictional Component of the Indentation Size Effect in Low Hardness Testing, *J. Mater. Res.*, Vol 8 (No. 5), 1993, p 1028–1032
43. J. Quinn and G. Quinn, Indentation Brittleness of Ceramics: A Fresh Approach, *J. Mater. Sci.*, Vol 32, 1997, p 4331–4346

Miscellaneous Hardness Tests

Edward L. Tobolski, Wilson Instrument Division, Instron Corporation

Introduction

MISCELLANEOUS HARDNESS TESTS encompass, for the purpose of this article, a number of test methods that have been developed for specific applications. These include dynamic, or “rebound,” hardness tests using a Leeb tester or a Scleroscope, static indentation tests on rubber or plastic products using the durometer or IRHD testers, scratch hardness tests, and ultrasonic microindentation testing. This article reviews the procedures, equipment, and applications associated with these alternate hardness test methods.

Miscellaneous Hardness Tests

Edward L. Tobolski, Wilson Instrument Division, Instron Corporation

Dynamic (Rebound) Test Methods

Hardness can be empirically related to either the elastic response of a material or the plastic deformation of a material. Indentation hardness tests determine hardness in terms of plastic behavior, while dynamic test methods relate hardness to the elastic response of a material.

A number of dynamic hardness test methods have been developed, but only a few have common use. The two most common methods of dynamic hardness testing are the Shore Scleroscope and the Leeb tester. These two methods are rebound-type tests and are described further here. Other dynamic hardness tests include a pendulum test method and dynamic indentation hardness testing using a Hopkinson-bar technique (the article “Dynamic Indentation Testing” in this Volume contains details).

Scleroscope Hardness Testing

The Scleroscope (Instron Corporation, Canton, MA) dynamic hardness tester was invented by Albert F. Shore in 1907 and was the first commercially available metallurgical hardness tester produced in the United States. While Scleroscopes are not currently manufactured in the United States, the unit is still used frequently for testing very large specimens such as forged steel or wrought alloy steel rolls. In this procedure, a diamond-tipped hammer is dropped from a fixed height onto the surface of the material being tested. The height of rebound of the hammer is a measure of the hardness of the metal.

The Scleroscope scale consists of units determined by dividing into 100 units the average rebound of a hammer from a quenched (to maximum hardness) and untempered water-hardened tool steel. The scale is continued above 100 units to permit testing of materials with hardnesses greater than that of fully hardened tool steel.

Testers. Two types of Scleroscope hardness testers were manufactured. The model C Scleroscope (Fig. 1) consists of vertically disposed barrel containing a precision-bore glass tube. A scale, graduated from 0 to 140, is set behind the tube and is visible through it. Hardness is read from the vertical scale, usually with the aid of a reading glass attached to the tester. A pneumatic actuating head, affixed to the top of the barrel, is manually operated by use of a rubber bulb and tube. The hammer drops and rebounds within the glass tube.

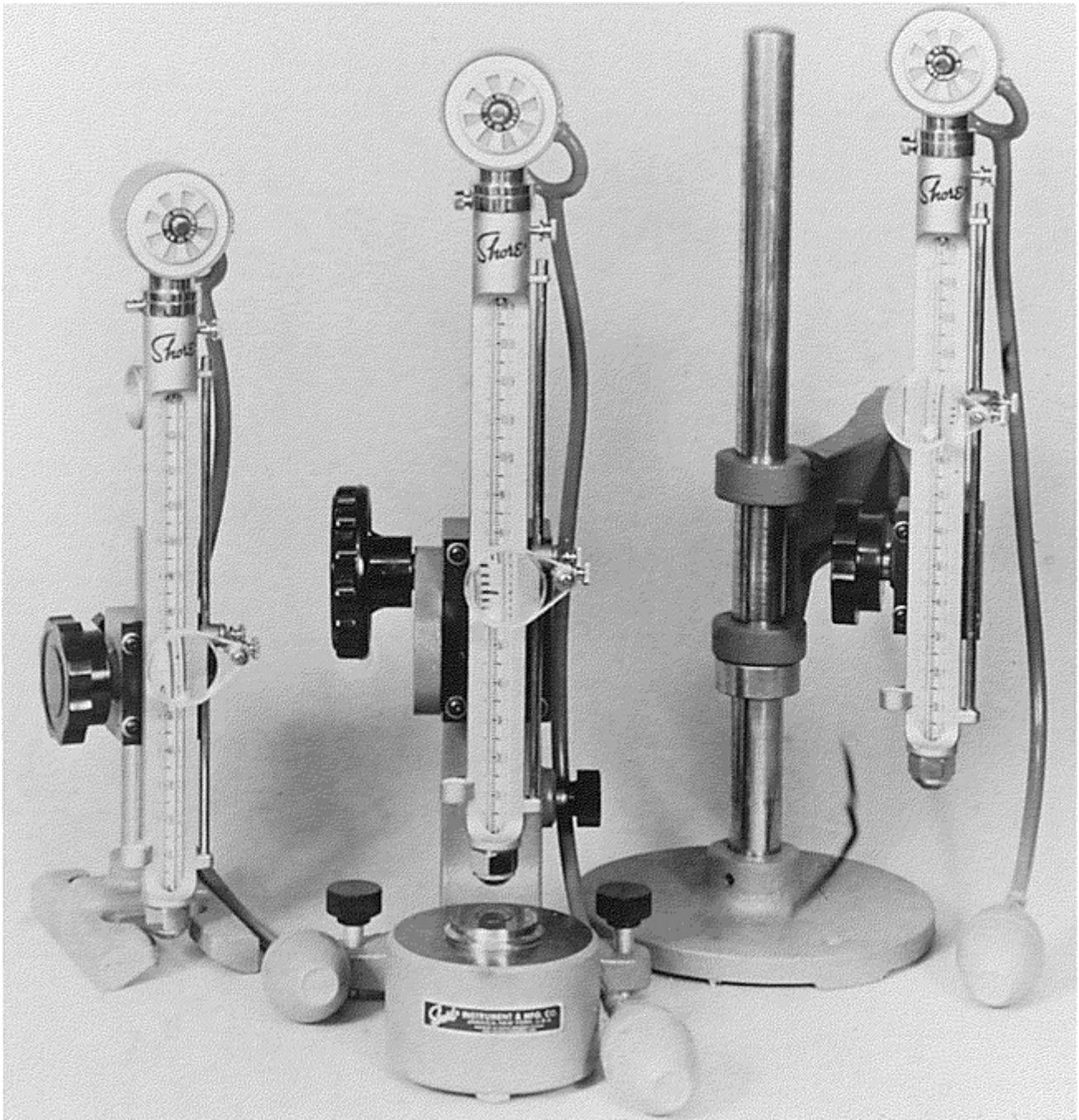


Fig. 1 Model C Scleroscope hardness testers mounted in stands

The model D Scleroscope hardness tester (Fig. 2) may have either analog (dial) or digital readouts. The tester consists of a vertically disposed barrel that contains a clutch to arrest the hammer at the maximum height of rebound. This is possible because of the short rebound height. The hammer is longer and heavier than the hammer used in the model C Scleroscope, developing the same striking energy even through dropping a shorter distance.

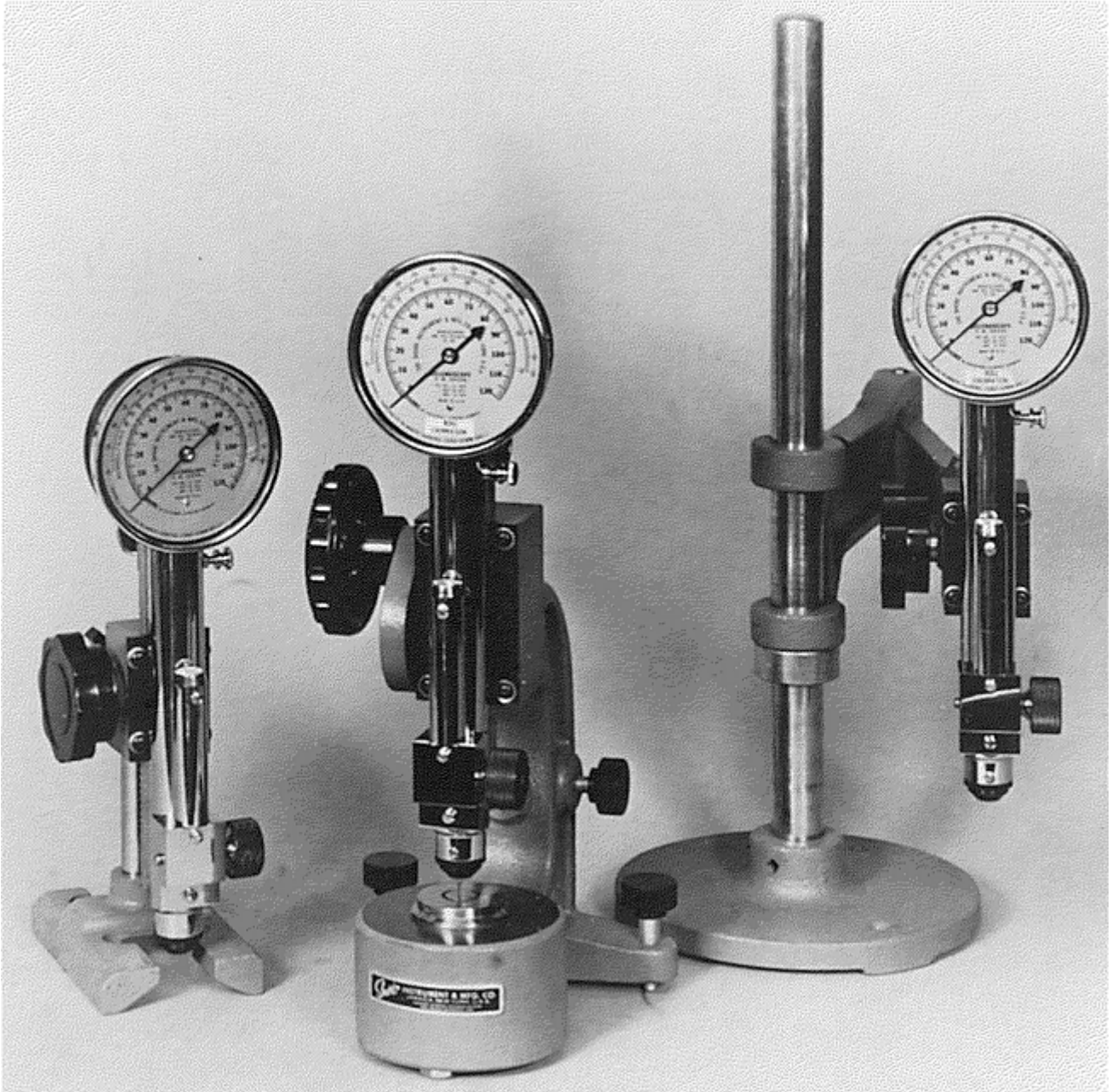


Fig. 2 Model D Scleroscope hardness testers mounted in stands

Models C, D, and D digital Scleroscopes were available in two calibrations: standard and roll. Standard calibration, which conforms to ASTM E-448, "Standard Practice for Scleroscope Hardness Testing of Metallic Materials," has a direct correlation to Rockwell C, Brinell, and Vickers hardness values (Table 1). Roll calibration conforms to ASTM A 427, "Standard Specification for Wrought Alloy Steel Rolls for Cold and Hot Reduction," and is used to determine hardness values of homogeneous wrought hardened alloy steel rolls for use in reduction of flat-rolled products. This calibration is symbolized by HFRSc or HFRSd. The model C Scleroscope can also be calibrated in accordance with ASTM C 886, "Standard Test Method for Scleroscope Hardness Testing of Fine-Grained Carbon and Graphite Materials." This is referred to as model C carbon calibration.

Table 1 Approximate hardness conversion numbers for nonaustenitic steels

Scleroscope hardness	Rockwell C hardness number, HRC	Vickers hardness number, HV	Brinell hardness number, HB	
			10 mm standard ball, 3000 kgf load	10 mm carbide ball, 3000 kgf load
97.3	68	940
95.0	67	900
92.7	66	865
90.6	65	832	...	739
88.5	64	800	...	722
86.5	63	772	...	705
84.5	62	746	...	688
82.6	61	720	...	670
80.8	60	697	...	654
79.0	59	674	...	634
77.3	58	653	...	615
75.6	57	633	...	595
74.0	56	613	...	577
72.4	55	595	...	560
70.9	54	577	...	543
69.4	53	560	...	525
67.9	52	544	500	512
66.5	51	528	487	496
65.1	50	513	475	481
63.7	49	498	464	469
62.4	48	484	451	455
61.1	47	471	442	443
59.8	46	458	432	432
58.5	45	446	421	421
57.3	44	434	409	409
56.1	43	423	400	400
54.9	42	412	390	390
53.7	41	402	381	381
52.6	40	392	371	371
51.5	39	382	362	362
50.4	38	372	353	353
49.3	37	363	344	344
48.2	36	354	336	336
47.1	35	345	327	327
46.1	34	336	319	319
45.1	33	327	311	311
44.1	32	318	301	301
43.1	31	310	294	294
42.2	30	302	286	286
41.3	29	294	279	279
40.4	28	286	271	271
39.5	27	279	264	264
38.7	26	272	258	258
37.8	25	266	253	253
37.0	24	260	247	247

Scleroscope hardness	Rockwell C hardness number, HRC	Vickers hardness number, HV	Brinell hardness number, HB	
			10 mm standard ball, 3000 kgf load	10 mm carbide ball, 3000 kgf load
36.3	23	254	243	243
35.5	22	248	237	237
34.8	21	243	231	231
34.2	20	238	226	226

Note: These Scleroscope hardness conversions are based on Vickers/Scleroscope hardness relationships developed from Vickers hardness data provided by the National Bureau of Standards for 13 steel reference blocks. Scleroscope hardness values obtained on these blocks by the Shore Instrument and Mfg. Co. Inc., the Roll Manufacturers Institute, and members of this institute, and also on hardness conversions previously published by the American Society for Metals and the Roll Manufacturers Institute.

Source: Ref 1

Both models of Scleroscopes can be mounted on various types of bases, although the model C Scleroscope is commonly used unmounted when testing large workpieces with a minimum weight of 2.3 kg (5 lb). Due to its critical vertical alignment, the model D Scleroscope should not be used unmounted, as erroneous readings may result.

Workpiece Surface Finish. In Scleroscope-hardness testing, certain workpiece surface finish requirements must be met in order to obtain accurate, consistent readings. An excessively coarse surface finish will yield erratic readings; when necessary, the surface of the workpiece should be filed, machined, ground, or polished.

Care should be taken to avoid overheating or excessively cold working the surface. The surface finish required to obtain reproducible results varies with the hardness of the workpiece. In proceeding from soft metals to hardened steel, the required surface finish ranges from a minimum finish, as produced by a No. 2 file, to a finely ground or polished finish.

Limitations on Workpiece and Case Thickness. Case-hardened steel with cases as thin as 0.25 mm (0.010 in.) can be accurately hardness tested provided the core hardness is no less than 30 Scleroscope. Softer cores require a minimum case thickness of 0.38 mm (0.015 in.) for accurate results.

Thin strip or sheet may be tested, with some limitations, but only when the Scleroscope hardness tester is mounted in a clamping stand. Ideally, the sheet should be flat and without undulation. If the sheet material is bowed, the concave side should be placed upwards to preclude any possibility of erroneous readings due to spring effect. The minimum thicknesses of sheet in various categories that may be hardness tested with a Scleroscope are as follows:

Metal	Minimum thickness	
	mm	in.
Hardened steel	0.13	(0.005)
Cold-finished steel strip	0.25	(0.010)
Annealed brass strip	0.38	(0.015)
Half-hard brass strip	0.25	(0.010)

Test Procedure. To perform a hardness test with either the model C or the model D Scleroscope, the tester should be held or set in a vertical position, with the bottom of the barrel in firm contact with the workpiece. The hammer is elevated and then allowed to fall and strike the surface of the workpiece. The height of rebound is then measured, which indicates the hardness.

When using the model C Scleroscope, the hammer is elevated by squeezing a pneumatic bulb. The hammer is released by again squeezing the bulb. When using the model D Scleroscope, the hammer is elevated by turning a knurled control knob clockwise until a definite stop is reached. The hammer strikes the workpiece when the control knob is released, and the reading is recorded on a dial. Hard steel tests about 100, medium-hard about 50, and soft metals 10 to 15.

Vertical Alignment. To minimize error, the hardness tester must be set or held in a vertical position, using the plumb rod or level on the machine to determine vertical alignment. The most accurate readings are obtained with the Scleroscope hardness tester mounted in a C-frame base that rests on three points, two of which are adjustable to facilitate leveling of the anvil and to ensure vertical alignment of the barrel. When using a

mounted tester, the opposite sides of the workpiece must be parallel to each other. Vibration impedes the free fall of the hammer, thereby producing low readings, and must be avoided.

Spacing of Indentations. Indentations should be singly spaced at least 0.50 mm (0.020 in.) apart. Flat workpieces with parallel surfaces may be hardness tested within 6 mm (0.25 in.) of the edge when properly clamped.

Taking the Readings. Experience is necessary to interpret readings accurately on a model C Scleroscope hardness tester. Thin materials, or those weighing less than 2.3 kg (5 lb), must be securely clamped to absorb the inertia of the hammer. The sound of the impact is an indication of the effectiveness of the clamping; a dull thud indicates that the workpiece has been clamped solidly, whereas a hollow ringing sound indicates that the workpiece is not tightly clamped or is warped and not properly supported. Five hardness determinations should be made, and their average taken as representative of the hardness of a particular workpiece.

Calibration. Scleroscope hardness testers are supplied with reference bars (or test blocks) of known hardness. The reference bars can be used correctly only with the Scleroscope mounted in a clamping stand, because they do not have sufficient mass to produce a full rebound of the hammer unless firmly clamped. If actual Scleroscope readings do not correspond to the values of the reference bars, the instrument should be returned to the manufacturer for service.

Advantages. The Scleroscope hardness test has several advantages. Tests can be made very rapidly; over 1000 tests per hour are possible. Operation is simple and does not require highly skilled technicians.

The model C Scleroscope is portable and can be used unmounted for testing workpieces of unlimited size (rolls and large dies). The Scleroscope hardness test is considered a nonmarring test; no obvious crater is left and only in the most unusual instances would the tiny hammer mark be objectionable on a finished workpiece. Additionally, a single scale covers the entire hardness range from the softest to the hardest metals.

Limitations of the Scleroscope hardness test include the necessity of keeping the test instrument in a vertical position so that the hammer can fall freely. Scleroscope hardness tests are more sensitive to variations in surface conditions than other hardness tests are. Because readings taken with the model C Scleroscope are indicated by the maximum rebound of the hammer on the first bounce, even the most experienced operators may disagree by one or two points. Also, the mass or configuration of the part can affect the accuracy of readings.

Leeb Scale (Equotip) Hardness Testing

Leeb testers (Fig. 3) are portable hardness testers that operate on a dynamic rebound principal similar to the Scleroscope. An impact device is propelled into the sample using a spring for the initial energy. The impact device travels a short distance until it contacts the sample. A small indent is formed, and the impact device rebounds away from the test surface according to the hardness and elasticity of the material. An electronic induction coil measures the velocity of the impact device before and after it contacts the sample. The Leeb hardness number is defined as the following:

$$L = \frac{\text{Rebound velocity}}{\text{Impact velocity}} \times 1000$$

The Leeb hardness number is followed by “HL,” with one or more suffix characters representing the impact device (Table 2). Leeb hardness is also known as Equotip hardness (for example, in ASTM A 956 “Standard Test Method for Equotip Hardness Testing of Steel Products”). (Equotip is the trademark of PROCEQ SA, Zurich, Switzerland.)

Table 2 Application guidelines for Leeb hardness testers

Impact device	Maximum hardness, HRC	Minimum sample size		Description and use guidelines
		kg	lb	
D	68	5	11	The basic impact device used for most testing of forged and cast steels, aluminum alloys, copper alloys, and cast irons
DC	68	5	11	A special impact device designed to make hardness measurements in very confined spaces such as bores. Material applications are the

				same as those for the D device.
D + 15	68	5	11	A special impact device, very slim with the measuring coil set back for access to small holes and grooves. Material applications are the same as those for the D device.
G	60	15	33	A special impact device, larger in size and impact energy than the other devices, for use on large, heavy test pieces. For testing of steel forgings, cast iron, and cast steel
C	68	1.5	3.3	A special impact device with low impact energy that can be used for testing of surface-hardened components, coatings, and thin-walled components of steel
E	70	5	11	A special impact device, with a synthetic diamond test tip that can be used for testing of steel forgings or castings with extremely high hardness

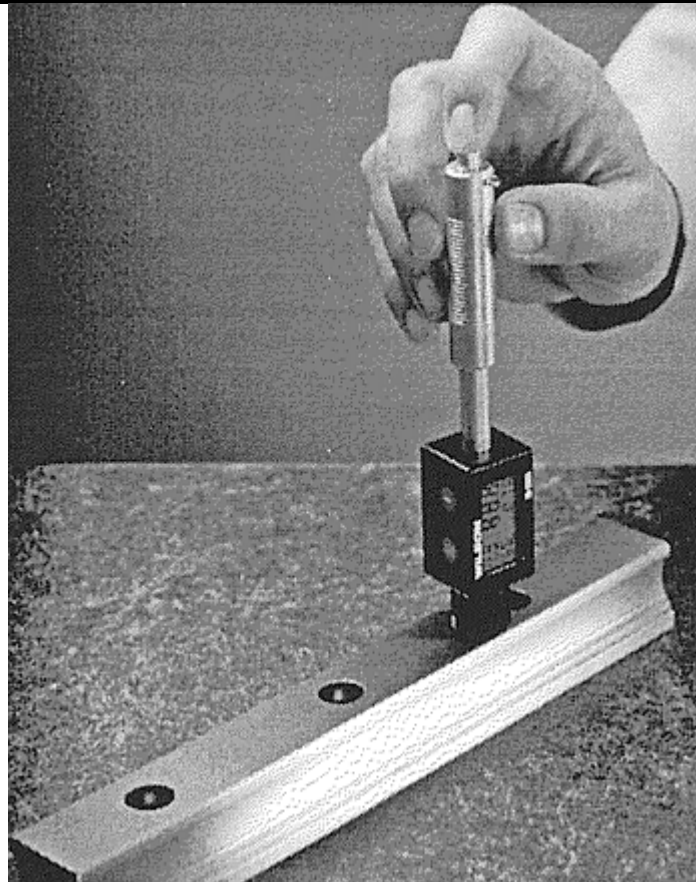


Fig. 3 Handheld Leeb hardness tester

Testers. By definition, all Leeb testers are electronic; therefore, they display the hardness result digitally. There are several different types available to test a variety of different size and shape samples (Table 2). The D model is the most common and suits a wide variety of materials. All models use either a tungsten carbide ball or diamond as the indenter part of the impact device. Since the Leeb hardness value is not recognized universally, most of the testers provide a built-in conversion to the other more common hardness scales (Rockwell, Brinell, Vickers, and Scleroscope). The problem with these conversions is that they are very material dependent, usually a function of the elastic modulus of the material. Therefore, most units include separate conversion data for several different classes of materials. Steels, cast iron, aluminum, and brass are some of the materials normally included internal to the tester.

Operation of the Tester. The Leeb testers are very simple to use. First, it is necessary to compress the impact device against the spring and lock it in place. Then the unit is positioned carefully over the test point, making sure that it is perpendicular to the surface. The release button is then pressed, allowing the impact device to be propelled into the sample. As soon as the impact is felt, the result is indicated on the digital display.

Applications. Table 2 shows the normal applications for the various types. Since the test uses a rebound principle, the mass of the sample is critical to the test result. Table 2 shows the desired minimum mass of the sample for the different types. Smaller masses can be tested by carefully coupling the sample to a larger mass. The Leeb testers also normally have the ability to test at various angles. Correction factors are frequently built into the tester or provided as a table. The table provides a value to be subtracted from the result to account for the effect of gravity on the velocity of the impact device when testing in any position other than vertical.

Like all hardness tests, the surface finish of the test point is important to the accuracy of the results. Rougher surfaces will normally give softer results. Concave or convex surfaces can be tested with a Leeb tester if the radius of curvature is greater than 30 mm (1.18 in.) for all units except the G type, which requires a radius of 50 mm (2 in.). Most testers can be purchased with a variety of adapters to facilitate the testing of various round and odd surfaces.

Calibration. The only method to verify the calibration of Leeb testers is by using standardized test blocks. The procedure is to make ten readings on the test surface of the blocks and average the readings. If the average is within 13 numbers of the calibration certificate, the unit is considered calibrated. A limited number of hardness ranges are available from the manufacturers.

Reference cited in this section

1. "Standard Hardness Conversion Tables for Metals," E 140, *Annual Book of ASTM Standards*, ASTM, 1997

Miscellaneous Hardness Tests

Edward L. Tobolski, Wilson Instrument Division, Instron Corporation

Durometer Hardness Testing

The durometer is a hand-sized instrument that measures the indentation hardness of rubber and plastic products. It is manually applied to the test specimen, and the reading is observed on a dial or digital indicator. Laboratory accuracy can also be obtained by mounting the durometer on one of several types of operating stands. Durometer hardness is the resistance of the material being tested to the penetration of the indenter as the result of a variable force applied to the indenter by a spring. An infinitely hard material would yield a durometer hardness of 100, because there would be zero penetration.

Durometer selection depends on the material being tested. Several types of durometers are available, as shown in Table 3. All of these conform to ASTM D 2240, "Standard Test Method for Rubber Property—Durometer Hardness."

Table 3 Specifications of durometers

Durometer type	Main spring	Indenter	Applications
A (conforms to ASTM D 2240)	822 g	Frustum cone	Soft vulcanized rubber and all elastomeric materials, natural rubber, GR-S, GR-I, neoprene, nitrile rubbers, Thiokol, flexible polyester cast resins, polyacrylic esters, wax, felt, leather, etc.
B	822 g	Sharp 30° included angle	Moderately hard rubber such as typewriter rollers, platens, etc.
C	4.54 kg (10 lb)	Frustum cone	Medium-hard rubber and plastics
D (conforms to)	4.54 kg	Sharp 30°	Hard rubber and the harder grades of plastics such as rigid

ASTM D 2240)	(10 lb)	included angle	thermoplastic sheet, Plexiglas (AtoHaas Americas, Inc., Philadelphia, PA), polystyrene, vinyl sheet, cellulose acetate and thermosetting laminates such as formica (Formica Corp., Cincinnati, OH), paper-filled calendar rolls, calendar bowls, etc.
D0	4.54 kg (10 lb)	2.38 mm ($\frac{3}{32}$ in.) sphere	Very dense textile windings, slasher beams, etc.
0	822 g	2.38 mm ($\frac{3}{32}$ in.) sphere	Soft printer rollers, Artgum, medium-density textile windings of rayon, orlon, nylon, etc.
00	113 g (4 oz)	2.38 mm ($\frac{3}{32}$ in.) sphere	Sponge rubber and plastics, low-density textile windings; not for use on foamed latex
000 (available with round dial only)	113 g (4 oz)	12.7 mm ($\frac{1}{2}$ in.) diam spherical	Ultrasoft sponge rubber and plastic
T	822 g	2.38 mm ($\frac{3}{32}$ in.) sphere	Medium-density textile windings on spools and bobbins with a maximum diameter of 100 mm (4 in.); types T and T-2 have a concave bottom plate to facilitate centering on cylindrical specimens

With the exceptions of types 00 and M, all durometer types are variations of the ASTM types A and D specifications by changing the indenters and/or load springs. Durometers are available with either a round or quadrant style face (Fig. 4) or with a digital display (Fig. 5). The M style is not available in the quadrant design. Pencil-style durometers are also available, but only in the A scale (Fig. 6).

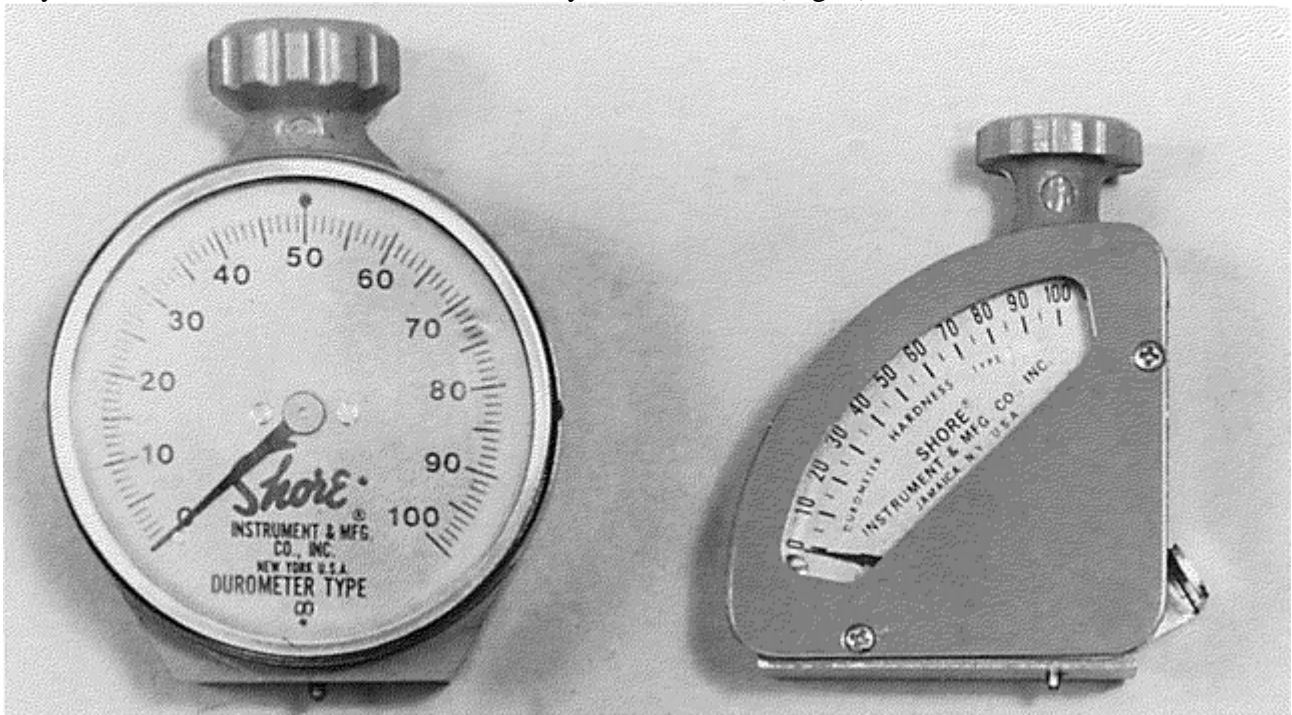


Fig. 4 Round- and quadrant-style durometer hardness testers

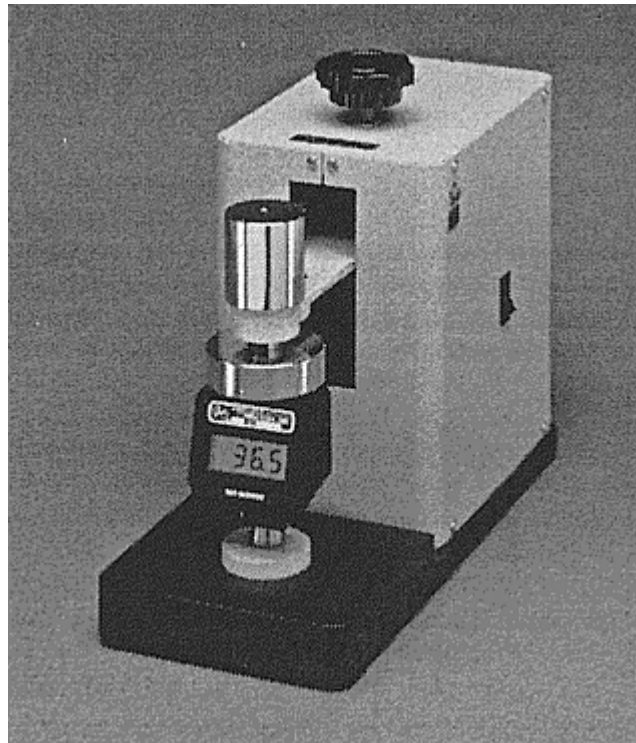


Fig. 5 Digital durometer with stand

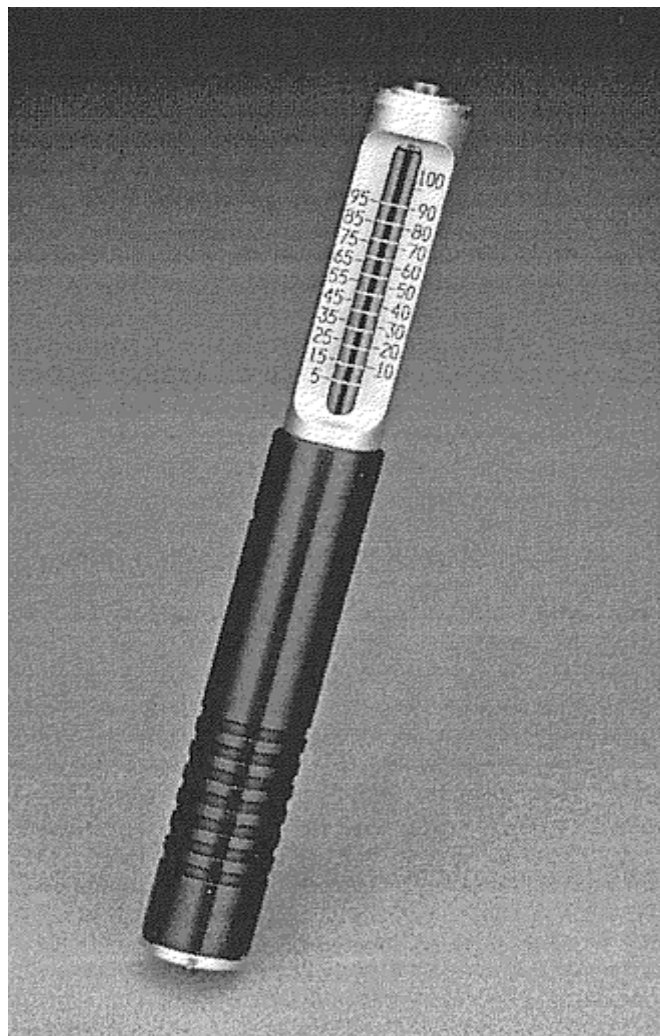


Fig. 6 Pencil durometer hardness tester

The total measurement range is from 0 to 100 points. This represents a total travel of the indenter of 2.5 mm (0.10 in.) for all scales except the M scale, which is 1.25 mm (0.05 in.). The hardness numbers are typically displayed in increments that vary from five points for the quadrant and pencil styles, to one point for the round, and in tenths of a point on digital units.

The M scale is relatively new and was developed to test O-rings. Testing small round sections down to 1.25 mm (0.05 in.) is possible with the M scale. This is possible because of a smaller spring load and shorter depth of penetration. Because of the increased sensitivity, M scale units can only be used in a stand. Normally, the stand is equipped with an alignment fixture to properly align the round samples with the indenter. Proper alignment is critical to obtain accurate results.

Testing Procedure. Test specimens should have a minimum thickness of at least 6 mm (0.2 in.) (1.25 mm, or 0.05 in., for the M scale), unless it is known that identical results are obtained on thinner specimens. Thinner specimens may be stacked to obtain an indicative reading.

Readings should not be taken on an uneven, irregular, or coarsely grained surface. Round or cylindrical surfaces, such as rubber rollers, can be tested by “rocking” the durometer on the convex surface and observing the maximum reading that is attained when the indenter is aligned with the axis of the roller.

Application pressure should be sufficient to ensure firm contact between the flat bottom of the durometer and the test specimen; the reading should be taken within 1 s after firm contact has been established. However, after attaining an initially high reading, the dial hand may gradually recede on specimens exhibiting cold flow or creep characteristics (such as nitrile rubber stock). In such instances, both the instantaneous, or maximum, reading and the reading after a specified time interval—for example, 10 or 15 s—should be recorded.

Testing Results. Durometer hardness numbers, although arbitrary, have an inverse relationship to indentation by the indenter. For example, a reading of 30 on the type A durometer on a soft rubber roller indicates an indenter indentation of 1.8 mm (0.07 in.). Similarly, a reading of 90 on a neoprene faucet washer indicates an indenter indentation of 0.25 mm (0.01 in.). The use of the durometer at the extreme ends of the scale (below 20 and above 90) is not recommended. Materials reading above 90 on the type A scale should be tested with the type D durometer. Materials reading below 20 on the type D scale should be tested with a type A durometer.

One of the most common causes of disagreement in readings among operators is variation in the speed with which the durometer is applied to the elastomer. For example, in testing a high-creep nitrile rubber, if the durometer is applied too rapidly to the test specimen, an erroneously high reading is initially attained, with the dial hand dropping as the durometer is held in contact. At the other extreme, the durometer may be applied too slowly, causing a significant percentage of indenter penetration to occur before the presser foot of the durometer is in flush contact with the test specimen, resulting in an inaccurately low reading.

Disagreement can also occur when an insufficient number of tests have been made. Reporting the average of five readings gives the best results. Tests on a particular material should all be run at the same temperature. Proper spacing must be allowed between the test point and the edge of the sample.

Scale Relationships. It should be noted that there is no fixed relationship between the test results from the different scales. A hardness reading of 50 on the A scale is not the same hardness as a 50 reading on the M or any other scale.

Durometer Calibration. Durometers frequently are equipped with a metal or rubber test block, which enables the user to ascertain whether the durometer is operating properly at one point on the scale (usually 60 durometer). The metal test block consists of a flat piece of metal with a blind hole on its top surface. When the presser foot is held against the top surface with the indenter in the blind hole, the durometer reading should agree with the hardness number stamped on the side of the block, within plus or minus one point. Rubber test blocks are simply tested like a sample and the result compared to the certificate.

A correct reading on the test block does not mean that the durometer is in calibration. The only way to accurately verify the durometer is to directly measure the loads applied over the full range for a given indicating device, indenter extension, and indenter shape. Calibrations of this type are recommended annually.

A durometer calibrating device is also available. This mechanism has limited capabilities and is recommended for end users who have several durometers to monitor. The durometer may be returned to the manufacturer for periodic inspection and calibration.

Auxiliary Equipment. The operating stand (Fig. 7) is designed to enable absolutely flush application of the durometer to the test specimen, thus eliminating errors in readings due to out-of-perpendicular contact. The stand is intended primarily for testing specimens with parallel opposite sides (except for the M-scale stands that provide a means to align O-rings). Additional weights are frequently applied to the top of the stands (see the

tester setup on the right side of Fig. 7). The higher load on the presser foot can greatly improve the repeatability of the results. Operating stands normally provide some means to ensure constant velocity and constant load applications. This helps to eliminate user error due to too rapid or too slow an application, as discussed earlier.

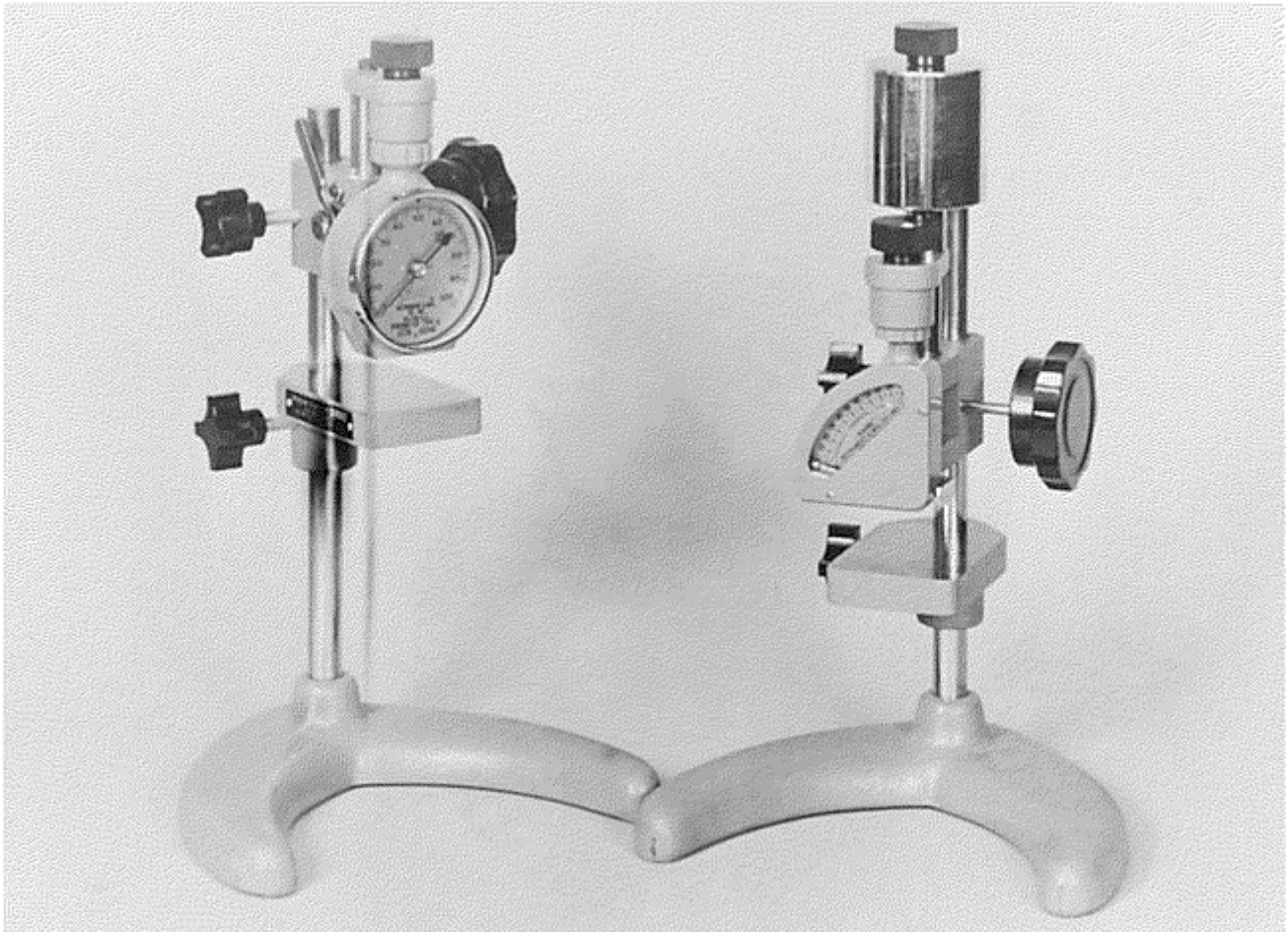


Fig. 7 Durometer hardness testers mounted in operating stands

Miscellaneous Hardness Tests

Edward L. Tobolski, Wilson Instrument Division, Instron Corporation

IRHD Rubber Hardness Testing

International rubber hardness degrees (IRHD) testing is very similar to durometer testing with some important differences. Durometer testers apply a load to the sample using a calibrated spring and a pointed or blunt-shaped indenter. The load, therefore, will vary according to the depth of the indentation because of the spring gradient. The IRHD tester uses a minor-major load system of constant load and a ball indenter to determine the hardness of the sample. In the procedure, the minor load is applied to the sample through the ball indenter. After 5 s, the depth-measuring system is set to zero. The higher major load is then applied. After 30 s, the IRHD hardness number is read from the depth-measuring indicator.

Testers. The instruments used for IRHD testing look very similar to the durometer testers described in the previous section. The IRHD tester cannot be used as a handheld instrument due to the requirements to apply the minor and major loads accurately. Therefore, all IRHD units have a built-in stand to hold the indicator and loading mechanism. The presser foot size and load applied to it during the test are critical to the final results.

Applications. IRHD testers come in two different versions, standard and micro (see Table 4) and are capable of testing a range of soft elastomers. The standard units are intended to test flat parallel samples thicker than 4 mm

(0.16 in.). Microtesters can test parts as thin as 1 mm (0.04 in.) and are used to test O-rings or other curved samples. A maximum of two layers of material may be used to reach the minimum thickness requirements. The test spacing and edge-clearance requirements for IRHD testing are similar to those of durometer testing.

Table 4 Comparison of standard and micro IRHD hardness testers

Parameter	Standard testers	Microtesters
Diam of ball, mm	2.50 ± 0.01	0.395 ± 0.005
Minor force on ball, N	0.29 ± 0.02	0.0083 ± 0.0005
Major force on ball, N	5.4 ± 0.01	0.1455 ± 0.0005
Total force on ball, N	5.7 ± 0.03	0.153 ± 0.001
Outside diam of foot, mm	6 ± 1	1.00 ± 0.15
Force on foot, N	8.3 ± 1.5	0.235 ± 0.03

Miscellaneous Hardness Tests

Edward L. Tobolski, Wilson Instrument Division, Instron Corporation

Scratch Hardness Tests

Scratch hardness tests represent the oldest type of hardness evaluation procedures. The two most common techniques for measuring scratch hardness are the Mohs scale, which is used for testing minerals, and the file hardness test, which is used for testing steels.

A third type of scratch hardness test sometimes referred to as the “plowing test” is not discussed in detail in this article. This test measures the width of a scratch made by drawing a diamond indenter across the surface under a definite load. Loads on the indenter of 1, 2, 5, 10, and 25 g are commonly used. This is a useful tool for studying the relative hardness of microconstituents, but it does not lend itself to high reproducibility or extreme accuracy. For more information, see the article “Scratch Testing” in this Volume.

The Mohs scale of hardness was devised in 1822 by German mineralogist Friedrich Mohs. The Mohs scale consists of ten minerals arranged in order from 1 (softest) to 10 (hardest). Each mineral in the scale will scratch all those below it:

Mineral	Hardness index
Diamond	10
Corundum	9
Topaz	8
Quartz	7
Orthoclase (feldspar)	6
Apatite	5
Fluorite	4
Calcite	3
Gypsum	2
Talc	1

The steps between numbers on the scale are not of equal value; for example, the difference in hardness between 9 and 10 is much greater than between 1 and 2. To determine the hardness of a mineral, it must be determined which of the standard materials the unknown will scratch. The hardness will lie between two points on the scale, the point between the mineral, which may be scratched, and the next one harder.

Materials engineers and metallurgists find little use for the Mohs scale due to its nonquantitative nature. However, the hardness of iron with 0.1% carbon maximum is between 3 and 4 on the Mohs scale, and copper is between 2 and 3. Fully hardened high-carbon tool steel is between 7 and 8.

The file hardness test was one of the first scratch tests used for evaluating the hardness of metallic materials. The file test is useful in estimating the hardness of steels in the high hardness ranges. It provides information on soft spots and decarburization quickly and easily and is readily adaptable to odd shapes and sizes that are difficult to test by other methods.

Standard test files are heat treated to approximately 67 to 70 HRC. The flat face of the file is pressed firmly against, and slowly drawn across, the surface to be tested. If the file does not bite, the material is designated as file hard. A number of factors, such as pressure, speed, angle of contact, and surface roughness, influence the results of the test. Consequently, its ability to give reproducible hardness values is rather limited, and reasonable accuracy is obtained only at the highest hardness levels.

Miscellaneous Hardness Tests

Edward L. Tobolski, Wilson Instrument Division, Instron Corporation

Ultrasonic Microhardness Testing

Ultrasonic microhardness testing offers an alternative to the more conventional methods based on visual (microscopic) evaluation of an indentation after the load has been removed. Ultrasonic testing uses a maximum indentation load of approximately 800 gf. Therefore, as in other microhardness techniques, the indentation depth is relatively small (from 4 to 18 μm). In the vast majority of instances, the workpiece surface is unharmed, thus classifying this test as nondestructive. Measured values in either the Vickers or Rockwell C scale are displayed on a digital readout display directly after penetration of the test piece. This feature renders the method suitable for automated on-line testing. Up to 1200 parts/h can be tested.

In ultrasonic microhardness testing, a Vickers diamond is attached to one end of a magnetostrictive metal rod. The diamond-tipped rod is excited to its natural frequency by a piezoelectric converter. The resonant frequency of the rod changes as the free end of the rod is brought into contact with the surface of a solid body. Once the device is calibrated for the known modulus of elasticity of the tested material, the area of contact between the diamond tip and the tested surface can be derived from the measured resonant frequency. The area of contact is inversely proportional to the hardness of the tested material, provided the force pressing the surface is constant. Consequently, the measured frequency value can be converted into the corresponding hardness number.

Components of an ultrasonic hardness tester are shown schematically in Fig. 8. The hardness number is displayed on a digital readout, while the oscillating rod is retracted to protect it until the next reading. The entire process generally takes less than 15 s. This type of instrument is quite small and can be battery powered for portability. The automatic probe allows hardness measurements to be made in any orientation, further enhancing its usefulness. By means of a probe and suitably designed fixtures for holding the probe, the possibilities are virtually unlimited. For example, Fig. 9 shows the test point, fixture, and actual testing of fillet radii on an engine crankshaft. In this instance, it was possible to take ten readings/min.

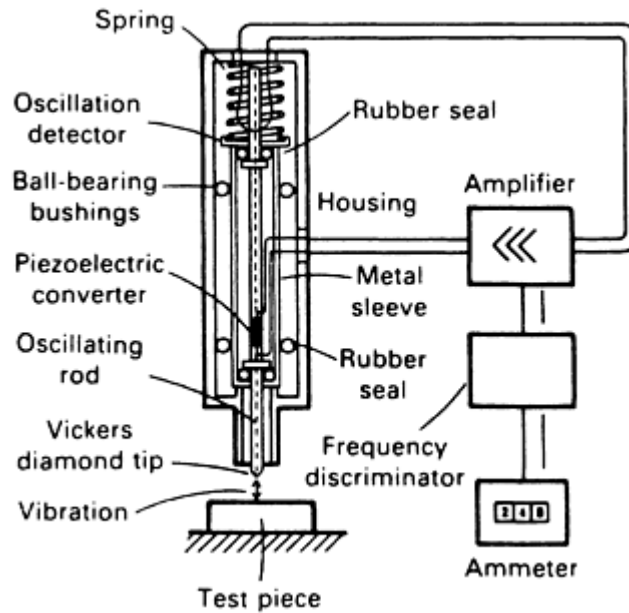
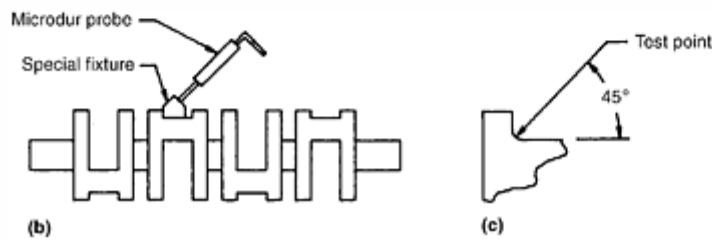


Fig. 8 Components of an ultrasonic hardness tester



(a)



(b)

(c)

Fig. 9 Ultrasonic hardness testing application. (a) Hardness testing of fillet radius on an engine crankshaft. (b) Probe and special fixture. (c) Test location. Courtesy of Krautkramer Branson

Various types of probes are available, but one popular type has a round, flat end and can be handheld. This type of instrument is most frequently used on flat workpieces. In one specific instance, a die casting plant was experiencing problems with heat checking dies. The dies were made from H13 tool steel, quenched and tempered. On-site hardness tests with an ultrasonic instrument proved that the superficial surface was quite soft as a result of decarburization, even though Rockwell C readings (actual) were acceptable. The decarburized layer was thus the cause of heat checking, and corrective measures were applied to the heat treating procedure.

Capabilities of Ultrasonic Microhardness Testing. There are several advantages of the ultrasonic hardness testing system. With ultrasonic hardness testing, one advantage is the ability to measure the area of indentation during loading. This differs from conventional microhardness tests, where the indent area is determined after loading. This conventional method can lead to erroneous hardness values due to elastic recovery on unloading (see Fig. 1 in the article "Selection and Industrial Applications of Hardness Tests" in this Volume).

As in conventional Vickers and Brinell hardness testing, a single loading force is used. Thus, in ultrasonic hardness testing, no time is lost in consecutive load application as in Rockwell testing. Because only one test load is used in ultrasonic testing, sensitive displacement-measuring instruments are not necessary, and rigid machine frames are not required. In many instances, it is possible to perform the hardness measurement with ultrasonic testing without clamping or rigidly supporting the test material, which simplifies design and handling.

Because the sensitivity and resolving power of the ultrasonic instrument can be increased to high levels, it is possible to measure even the smallest indentation. Hardness profile curves can be obtained by untrained personnel automatically in a fraction of the time previously required. The digital display virtually eliminates operator interpretation errors. A memory feature, which will hold the last reading displayed for up to 3 min or until another reading is taken, facilitates any manual recording of data that is necessary.

A one-point calibration procedure allows the instrument to be set up quickly and easily. The few controls and adjustments that are required, coupled with a motor-driven probe, facilitate repeatable test results. The portability of ultrasonic microhardness testers allows hardness evaluations to be taken not only in a laboratory environment but also on site, in the field, and in any specimen orientation. Inspection of large parts and on-line, in-process inspection hardness testing is possible.

Typical applications of ultrasonic microhardness testing are in the automotive, nuclear, petrochemical, aerospace, and machinery manufacturing industries, including finished goods with hardened surfaces, thin case-hardened parts, thin sheet, strip, coils, platings, and coatings. Often, 100% inspection is possible on critically stressed components. Small components and difficult-to-access parts can also be tested by the ultrasonic microhardness method, either in a handheld or a fixtured mode.

Portability is one of the important advantages of ultrasonic microhardness testers. The entire assembly fits into a convenient carrying case so that it can be easily hand carried. It is, by far, the most portable microhardness tester and exceeds the Scleroscope in degree of portability. While it is preferable to hold the element in a fixture and test on a flat surface, there are numerous other positions in which it can be used with a wide variety of fixtures, or by hand with the probe. Thus, this type of instrument is not only a laboratory instrument but can also be used as an on-site inspection tool.

Limitations of Ultrasonic Microhardness Testing. The principal disadvantage of the ultrasonic technique is the lack of an optical system, a characteristic that is, in many cases, an advantage. Reading the indentations by an optical system is slow and tedious, but it does permit precise location of the indenter in relation to locations on the test metal. With the ultrasonic system, obtaining readings on microconstituents becomes difficult, because there is no way to precisely spot the indenter.

This characteristic of ultrasonic testing is, in many instances, a drawback in making hardness traverses on case-hardened steels. With the conventional Vickers or Knoop systems, common practice is to position the test piece so that the first indentation is made at some prescribed distance from the edge, such as 0.05 or 0.10 mm (0.002 or 0.004 in.), for example, and then make a series of indentations at established intervals for the distance required to determine the depth of hard case. With ultrasonic instruments, however, positioning the indenter to obtain a near-the-edge reading is very difficult. This difficulty can be overcome by taking the first reading at an appreciable distance from the edge (beyond the point at which the case exists), then working outward at prescribed intervals toward the edge until a very soft reading occurs, thus indicating that the indenter has reached the softer mounting material.

Surface Finish Requirements. Regardless of other variations, ultrasonic testing actually constitutes microhardness testing, and as such, the surface finish of the test material must be taken into account. To accurately measure any Vickers (diamond pyramid) indentation, it must be clearly defined. Therefore, requirements for surface finish are stringent. These requirements become increasingly stringent as the load decreases. Therefore, to accommodate the force used in ultrasonic testing, a metallographic finish is required. When grinding or polishing, or when both operations are necessary for specimen preparation, care should be taken to minimize heating and distortion of the specimen surface. Polishing should be performed according to the procedures outlined in ASTM E 3, "Standard Practice for Preparation of Metallographic Specimens." When

the specimen to be tested for microhardness will also be used for metallographic examination, mounting (usually in plastic) and polishing are justified. In other instances, only polishing is required.

When mounting is not necessary, fixtures may be used for holding the specimens or workpieces. Most workpieces can be adapted to any one of the commonly used fixture types. The fixture must maintain a rigid surface perpendicular to the indenter. A holding and polishing vise can reduce preparation time because the specimen can be polished and tested without removing it from the vise. A turntable vise fixture is convenient for holding mounted specimens.

When ultrasonic readings are taken in the shop on actual workpieces, some means of obtaining a good surface finish must be used. This goal usually can be accomplished by metallographic emery papers. As a rule, it is desirable to avoid stock removal on actual parts that are scheduled to undergo hardness testing.

Miscellaneous Hardness Tests

Edward L. Tobolski, Wilson Instrument Division, Instron Corporation

Reference

1. "Standard Hardness Conversion Tables for Metals," E 140, *Annual Book of ASTM Standards*, ASTM, 1997

Miscellaneous Hardness Tests

Edward L. Tobolski, Wilson Instrument Division, Instron Corporation

Selected References

- H. Chandler, Ed., *Hardness Testing*, 2nd Ed., ASM International, 1999
- V.E. Lysaght, *Indentation Hardness Testing*, Reinhold Publishing, New York, 1949
- V.E. Lysaght and A. DeBellis, *Hardness Testing Handbook*, American Chain and Cable Co., Bridgeport, CT, 1969
- L. Small, *Hardness—Theory and Practice*, Service Diamond Tool Co., Ferndale, MI, 1960
- "Standard Test Method for Equotip Hardness Testing of Steel Products," A 956, *Annual Book of ASTM Standards*, ASTM, 1998
- "Standard Test Method for Rubber Property—Durometer Hardness," D 2240, *Annual Book of ASTM Standards*, ASTM, 1999
- "Standard Test Method for Rubber Property—International Hardness," D 1415, *Annual Book of ASTM Standards*, ASTM, 1998
- G.V. Vander Voort, *Hardness, Metallography: Principles and Practice*, McGraw-Hill, 1984 (reprinted by ASM International, 1999), p 334–409

Selection and Industrial Applications of Hardness Tests

Andrew Fee, Consultant

Introduction

HARDNESS TESTING includes a variety of techniques that can be generally classified into the following categories (Ref 1):

- Indentation tests (such as Brinell, Rockwell, Vickers, Knoop, and ultrasonic testing)
- Scratch tests (such as the Mohs test)
- Dynamic tests (such as the Shore test and Hopkinson pressure bar methods)
- Abrasion tests
- Erosion tests

The more common types of hardness tests are the indentation methods, described in previous articles in this Section. These tests use a variety of indentation loads ranging from 1 gf (microindentation) to 3000 kgf (Brinell). Low- and high-powered microscopes (Brinell, Vickers, and microindentation) also help measure the resulting indentation diagonals from which a hardness number is calculated using a formula. In the Rockwell test, the depth of indentation is measured and converted to a hardness number, which is inversely related to the depth. Another type of indentation test is ultrasonic hardness testing, which is described further in the article “Miscellaneous Hardness Tests” in this Volume.

A general comparison of indentation hardness testing methods, including ultrasonic, is given in Table 1. This article focuses principally on the selection and application of Brinell, Rockwell, Vickers, and Knoop methods. However, ultrasonic hardness testing is also an important method, because the area of indentation is measured *during* the application of load. This is an important feature that is not affected by elastic recovery. For example, a perfect indentation made with a perfect Vickers indenter would be a square (Fig. 1a). However, anomalies may be observed with a pyramid indenter. The pincushion indentation (Fig. 1b) can occur from the inward sinking of the metal around the flat faces of the pyramid. This condition is observed with annealed metals and results in an overestimate of the diagonal length. The barrel-shaped indentation in Fig. 1(c) is found in cold-worked metals. It results from ridging or piling up of the metal around the faces of the indenter. The diagonal measurement in this case produces a low value of the contact area so that the hardness numbers are erroneously high. These types of anomalies can be prevented in ultrasonic testing, which is based on measurement of the indentation area under load.

Table 1 Comparison of indentation hardness tests

The minimum material thickness for a test is usually taken to be 10 times the indentation depth.

Test	Indenter(s)	Indent		Load(s)	Method of measurement	Surface preparation	Tests per hour	Applications	Remarks
		Diagonal or diameter	Depth						
Brinell	Ball indenter, 10 mm (0.4 in.) or 2.5 mm (0.1 in.) in diameter	1–7 mm (0.04–0.28 in.)	Up to 0.3 mm (0.01 in.) and 1 mm (0.04 in.), respectively, with 2.5 mm (0.1 in.) and 10 mm (0.4 in.) diam balls	3000 kgf for ferrous materials down to 100 kgf for soft metals	Measure diameter of indentation under microscope; read hardness from tables	Specially ground area for measurements of diameter	50 with diameter measurements	Large forged and cast parts	Damage to specimen minimized by use of lightly loaded ball indenter. Indent then less than Rockwell
Rockwell	120° diamond cone, 1.6–13 mm ($\frac{1}{16}$ to $\frac{1}{2}$ in.) diam ball	0.1–1.5 mm (0.004–0.06 in.)	25–375 µm (0.1–1.48 µin.)	Major 60–150 kgf Minor 10 kgf	Read hardness directly from meter or digital display	No preparation necessary on many surfaces	300 manually 900 automatically	Forgings, castings, roughly machined parts	Measure depth of penetration, not diameter
Rockwell superficial	As for Rockwell	0.1–0.7 mm (0.004–0.03 in.)	10–110 µm (0.04–0.43 µin.)	Major 15–45 kgf Minor 3 kgf	As for Rockwell	Machined surface, ground	As for Rockwell	Critical surfaces of finished parts	A surface test of case hardening and annealing
Vickers	136° diamond pyramid	Measure diagonal, not diameter	30–100 µm (0.12–0.4 µin.)	1–120 kgf	Measure indent with low-power microscope; read hardness from tables	Smooth clean surface, symmetrical if not flat	Up to 180	Fine finished surfaces, thin specimens	Small indent but high local stresses
Microhardness	136° diamond	40 µm (0.16	1–4 µm (0.004–0.016	1 gf-1 kgf	Measure indentation	Polished surface	Up to 60	Surface layers, thin	Laboratory test used on brittle

	indenter or a Knoop indenter	μin.)	μin.)		with low-power microscope; read hardness from tables			stock, down to 200 μm	materials or microstructural constituents
Ultrasonic	136° diamond pyramid	15–50 μm (0.06–0.2 μin.)	4–18 μm (0.016–0.07 μin.)	800 gf	Direct readout onto meter or digital display	Surface better than 1.2 μm (0.004 μin.) for accurate work. Otherwise, up to 3 μm (0.012 μin.)	1200 (limited by speed at which operator can read display)	Thin stock and finished surfaces in any position	Calibration for Young's modulus necessary, 100% testing of finished parts. Completely nondestructive

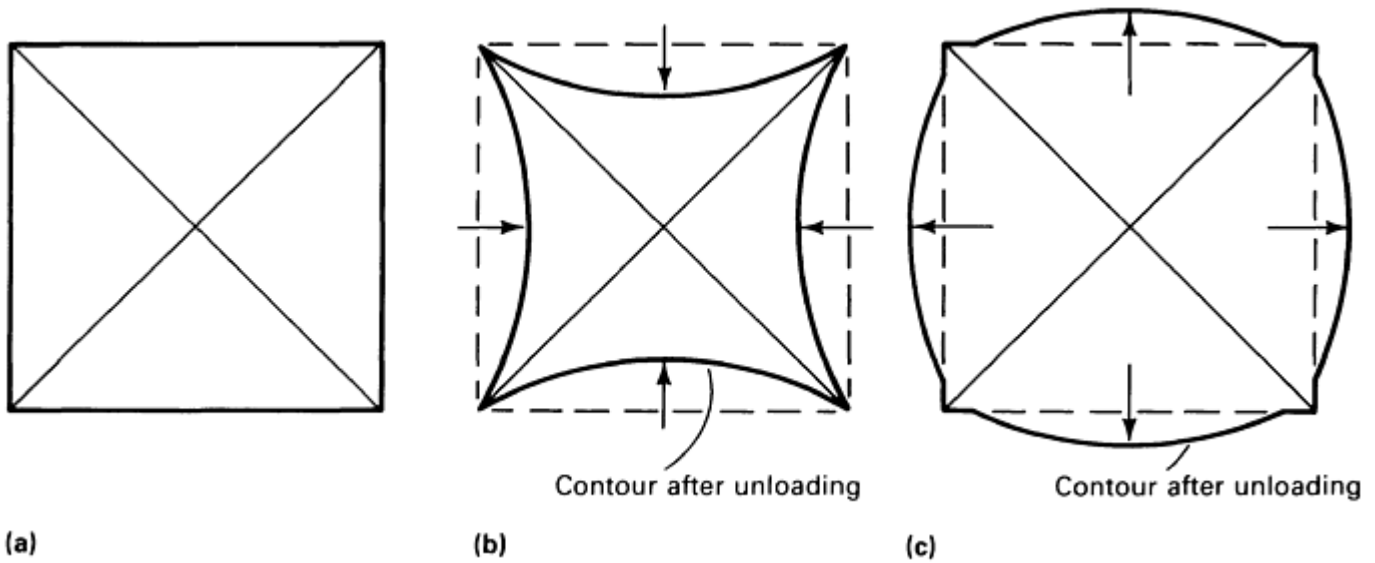


Fig. 1 Distortion of diamond pyramid indentations due to elastic effects. (a) Perfect indentation. (b) Pincushion indentation due to material sinking in and around the flat faces of the pyramid. (c) Barreled indentation due to ridging of the material around the faces of the indenter

Reference cited in this section

1. G. Vander Voort, *Metallography: Principles and Practice*, McGraw-Hill, 1984 (reprinted by ASM International, 1999), p 340 and 390–393

Selection and Industrial Applications of Hardness Tests

Andrew Fee, Consultant

General Factors

Selection of a hardness test is relatively straightforward if tests are conducted on simple, flat pieces with a minimum thickness of about 3 mm (0.125 in.) and a homogeneous composition or microstructure. However, in actual applications there are a number of factors that can have a significant effect on the method selected and the interpretation of test results. General factors (not necessarily in order of importance) that influence the selection of hardness include:

- Hardness level (and scale limitations)
- Specimen thickness
- Size and shape of the workpiece
- Specimen surface flatness and surface condition
- Indent location
- Production rates
- Type of material being tested

The first six factors in this list are reviewed in this section; the remaining sections focus on selection for specific types of materials and industrial applications of hardness tests.

Hardness Level and Scale Limitations

It is essential to select a suitable hardness scale for good repeatability of test results. Selection of an appropriate hardness scale depends on the expected hardness range of the material being tested (which can be determined from its general composition and processing history or some trial-and-error tests) and on the type of indenter.

Diamond Indenters. There is no upper hardness limit when using the diamond indenters for Rockwell, Vickers, and Knoop scales. The only limitations are:

- Because Rockwell diamond indenters are not calibrated below 20 HRC, they should not be used when readings fall below this level.
- When performing Vickers testing, hardness must be high enough so that only the diamond portion of the penetrator is in contact with the material and not the mounting material.

Brinell Ball Indenters. For hard test materials, the ball indenter of the Brinell tester may undergo deformation. The standard Brinell ball has been changed from steel to carbide to minimize permanent ball deformation when testing very hard materials. Even when using a tungsten carbide ball, some elastic or temporary deformation will occur, but the extent of this is small and will have only a negligible effect on the final results. For the Brinell test, it is recommended that the test force be of such magnitude that it produces an indentation of 25 to 60% of the ball diameter; that is, the ideal indentation for a 10 mm (0.4 in.) ball should range from 2.5 to 6.0 mm (0.10 to 0.24 in.) in diameter. The reading error of the small diameters becomes very critical and the test becomes supersensitive as small changes in hardness create large diameter changes. For indentation diameters greater than 6.0 mm (0.24 in.) the test becomes insensitive. Recommended hardness ranges for various forces to produce the above range of indentation diameters (using a 10 mm, or 0.4 in., diam ball) are:

Rockwell Ball Indenters. Rockwell scales using the ball indenters (e.g., Rockwell B) range from 0 to 130 points; however, readings above 100 should be avoided, except under special circumstances. The ball indenter can be easily damaged when testing material above 100; therefore it is necessary to change the ball

Load, kgf	Recommended hardness range, HB
3000	96–600
1500	48–300
500	16–100

frequently to avoid errors.

Between 100 and 130, the extreme tip of the ball is used. Because of the blunt shape of the ball at this location, the sensitivity of most scales is poor. It should be realized that as the diameter of the ball is increased the sensitivity of the test decreases. Therefore, it is recommended that the smallest diameter ball should always be used. On the other hand, if Rockwell B readings are below 50, the indenter may be sinking too deeply for accurate readings, and the load should be decreased or the size of the indenter should be increased. This also applies to the Rockwell E and F scales.

Specimen Thickness

The material immediately surrounding indentations is cold worked due to the flow of the material caused by the indenting process. The extent of this cold-work area depends on the material and any previous work hardening of the test specimen. The depth of material affected also extends down below the indentation. Studies and experiments indicate that the affected zone is approximately 10 times the indentation depth. Therefore, as a rule it is recommended that the thickness of the specimen be at least 10 times the depth of indentation with diamond indenters and 15 times with ball indenters. There should not be any deformation or mark visible on the opposite side of the test specimen after testing, although not all such markings are indicative of a bad test. Any bulging or marking on the underside of the specimen is commonly referred to as “anvil effect,” (see the section “Anvil Effect” in this article).

Depth of the Brinell indentation can be calculated from:

$$\text{Depth of indentation (in mm)} = \frac{F}{D \times (HB)(\pi)}$$

where F is the force (in kgf), D is the ball diameter (in mm), and (HB) is the Brinell hardness number. Table 2 is a summary of minimum thickness requirements for Brinell tests done at 500, 1500, and 3000 kgf with a 10 mm (0.4 in.) ball; other forces and ball sizes can be calculated using the above formula.

Table 2 Minimum thickness requirements for Brinell hardness tests using a 10 mm (0.4 in.) ball indenter

Minimum thickness of specimen		Minimum hardness for which the Brinell test may safely be made at indicated load		
mm	in.	3000 kgf	1500 kgf	500 kgf
1.6	$\frac{1}{16}$	602	301	100

Minimum thickness of specimen		Minimum hardness for which the Brinell test may safely be made at indicated load		
mm	in.	3000 kgf	1500 kgf	500 kgf
3.2	$\frac{1}{8}$	301	150	50
4.8	$\frac{3}{16}$	201	100	33
6.4	$\frac{1}{4}$	150	75	25
8.0	$\frac{5}{16}$	120	60	20
9.6	$\frac{3}{8}$	100	50	17

Microindentation hardness tests are routinely done on thin sheet metals and other small parts of 0.025 mm (0.001 in.) or less thickness. The Vickers indenter makes an indentation with a depth of one-seventh of the length of the mean diagonals. The Knoop indenter makes an indentation depth of one-thirtieth of the long diagonal. Generally, the same ratio (10:1) of depth of indent to thickness follows the same criteria as the other tests. The following examples show this calculation.

Because the depth of the Vickers test is one-seventh of the diagonal length, the depth calculation is simply as follows:

$$\text{Indentation depth} = \frac{\text{Mean diagonal length}}{7}$$

For example, if the Vickers indentation mean diagonal is measured at 0.074 mm, then the corresponding depth would be 0.0106 mm = 0.074 mm/7. The minimum thickness of the specimen thus should be 0.106 mm = 0.0106 mm × 10.

The depth of the Knoop indenter is one-thirtieth the longitudinal diagonal, and depth is calculated as follows: if the long diagonal of a Knoop indentation is measured at 136.4 μm, then the indentation depth is 4.55 μm = 136.4 μm/30. The minimum thickness of the specimen thus should be at minimum 46 μm = 4.55 μm × 10.

Depth of the Rockwell Test Indentations. When using the C, A, or D scales, the Rockwell number is subtracted from 100 and the result is multiplied by 0.002 mm. Therefore, a reading of 60 HRC indicates an indentation increase in depth from preliminary to total force:

$$\text{Depth} = (100 - 60) \times 0.002 \text{ mm} = 0.08 \text{ mm}$$

When the 1.59 mm ($\frac{1}{16}$ in.) ball indenter with the B, F, or G scale is used, the hardness number is subtracted from 130; therefore, for a reading of 80 HRB the depth is determined by:

$$\text{Depth} = (130 - 80) \times 0.002 \text{ mm} = 0.10 \text{ mm}$$

In Rockwell superficial testing, regardless of the type of indenter used, one number represents an indentation of 0.001 mm (0.00004 in.). Therefore, a reading of 80 HR30N indicates an increase in depth of indentation from preliminary to total force of:

$$\text{Depth} = (100 - 80) \times 0.001 = 0.02 \text{ mm}$$

Generally, depth computation is not necessary because minimum thickness values have been calculated (Table 3). These minimum thickness values follow the 10-to-1 ratio for scales using the diamond indenter and 15-to-1 using the ball indenters. It should also be noted that the initial indentation from the preliminary force is not included in these calculations.

Table 3 Minimum work metal hardness values for testing various thicknesses of metals with standard and superficial Rockwell hardness testers

Metal thickness		Minimum hardness for standard testers at indicated scale and load (in kgf)						Minimum hardness for superficial testers at indicated scale and load (in. kgf)					
		Diamond indenter			Ball indenter (1.59 mm, or $\frac{1}{16}$ in., diam)			Diamond indenter			Ball indenter (1.59 mm, or $\frac{1}{16}$ in., diam)		
mm	in.	A (60)	D (100)	C (150)	F (60)	B (100)	G (150)	15N (15)	30N (30)	45N (45)	15T (15)	30T (30)	45T (45)
0.152	0.006	92	92
0.203	0.008	90	90
0.254	0.010	88	91
0.305	0.012	83	82	77	86
0.356	0.014	76	78.5	74	81	80	...
0.406	0.016	86	68	74	72	75	72	71
0.457	0.018	84	66	68	68	64	62

Metal thickness		Minimum hardness for standard testers at indicated scale and load (in kgf)						Minimum hardness for superficial testers at indicated scale and load (in. kgf)					
		Diamond indenter			Ball indenter (1.59 mm, or $\frac{1}{16}$ in., diam)			Diamond indenter			Ball indenter (1.59 mm, or $\frac{1}{16}$ in., diam)		
mm	in.	A (60)	D (100)	C (150)	F (60)	B (100)	G (150)	15N (15)	30N (30)	45N (45)	15T (15)	30T (30)	45T (45)
2.032	0.080
2.083	0.082
2.134	0.084
2.184	0.086
2.235	0.088
2.286	0.090
2.337	0.092
2.388	0.094
2.438	0.096
2.489	0.098
2.540	0.100

Note: These values are approximate only and are intended primarily as a guide. Material thinner than shown should be tested with a microindentation hardness tester. The thickness of the workpiece should be at least 1.5 times the diagonal of the indentation when using a Vickers indenter, and at least 0.5 times the long diagonal when using a Knoop indenter.

(a) No minimum hardness for metal of equal or greater thickness

Example: Scale Selection for Thin Steel Strip. Consider a requirement to check the hardness of 0.36 mm (0.014 in.) thick steel strip with a suspected hardness of 63 HRC. According to Table 3, material in this hardness range must be approximately 0.71 mm (0.028 in.) thick for an accurate Rockwell C test. Therefore, 63 HRC must be converted to an approximate equivalent hardness on other Rockwell scales. These hardness values taken from a conversion table are 82.8 HRA, 73 HRD, 69.9 HR45N, 80.1 HR30N, and 91.4 HR15N. (See the article “Hardness Conversions for Steels” in this Volume.)

Referring to Table 3, only three Rockwell scales—45N, 30N, and 15N—are appropriate for testing this hardened 0.36 mm (0.014 in.) thick material. The 45N scale is unsuitable because the material should be at least 72 HR45N. The 30N scale requires the material to be 64 HR30N; on the 15N scale, the material must be at least 70 HR15N. Therefore, either the 30N or 15N scale should be used.

If a choice remains after all the criteria have been applied, then the scale applying the heaviest force should be used. A heavier force produces a larger indentation covering a greater portion of the material and a better representation of the material as a whole. In addition, the heavier the force, the greater the sensitivity of the scale. In this example, a conversion chart indicates that, in the hard steel range, a difference in hardness of one Rockwell number in the 30N scale represents just one-half of a point on the 15N scale. Therefore, smaller differences can be detected when using the 30N scale. This approach also applies when selecting a scale to accurately measure hardness when approximate case depth and hardness are known.

Anvil Effect. Minimum thickness charts and the 10-to-1 ratio serve only as guides. After determining which Rockwell scale should be used based on minimum thickness values, an actual test should be performed, and the specimen side opposite the indentation should be examined for any marking, bulging, or disturbed material; these indicate that the material is not thick enough for the applied force. This condition is known as “anvil effect.” When anvil effect or material flow restriction is encountered, the Rockwell value may not be correct and should be considered an invalid test. The Rockwell scale applying the lower force should be used.

Use of several specimens or stacking is not recommended. Slippage between the contact surfaces of the specimens makes a valid test impossible to obtain. The only exception is when testing plastics. The use of several thicknesses for elastomeric materials when anvil effect is present is considered in ASTM D 785 (Ref 2). Testing performed on soft plastics does not have an adverse effect when the test specimen is composed of a stack of several pieces of the same thickness, provided that the surfaces are in total contact and not held apart by sink marks, burrs from saw cuts, or any protrusions that would permit an air gap between the pieces.

When testing specimens from which the anvil effect results, the condition of the supporting surface of the anvil should be inspected. After several tests, this surface can become marred or indented. Either condition will have adverse results with Rockwell testing, because under the total force, the test material will sink into the indentation in the anvil and a lower reading will result. If the anvil surface shows any damage it should be replaced or relapped.

When using a ball indenter and a superficial scale of 15 kgf on a specimen in which anvil effect or material flow is present, a diamond spot anvil is used in place of the hardened steel anvil. Under these conditions, the diamond surface is not likely to be damaged when testing thin materials. Furthermore, with materials that flow under load, the hard polished diamond surface provides a more uniform frictional condition with the underside of the specimen, which improves repeatability of readings. These results should be used in a comparative manner inasmuch as they may not be the same as those obtained with a steel anvil.

Workpiece Size and Shape

Specimen size and configuration may require modification in the test setup for some indentation-type testing. For example, large specimens and thin-wall rings or tubing may need additional support equipment as well as correction factors for curved surfaces. A few examples and illustrations are provided here.

Workpiece Size. For large workpieces that are not easily transported to the stationary testers, the logical procedure is to take the testers to the workpiece. Portable machines often are used for onsite testing of workpieces that are too large and/or unwieldy to transport to the tester. In many applications where on-site testing is required, the Scleroscope can be a great advantage. Likewise, ultrasonic instruments can be used for on-site testing. When using either Scleroscope or ultrasonic testing, however, surface condition is critical to obtaining accurate results. Neither method is well suited for testing cast irons.

Many specially designed Rockwell hardness testers also have been developed to accommodate the testing of unusually large specimens, such as railroad car wheels and large turbine blades that cannot be conveniently brought to or placed in a bench-type tester. Figure 2 shows an example of a Rockwell tester for large parts. For large and heavy workpieces or workpieces of peculiar shape, a large support table may be required.

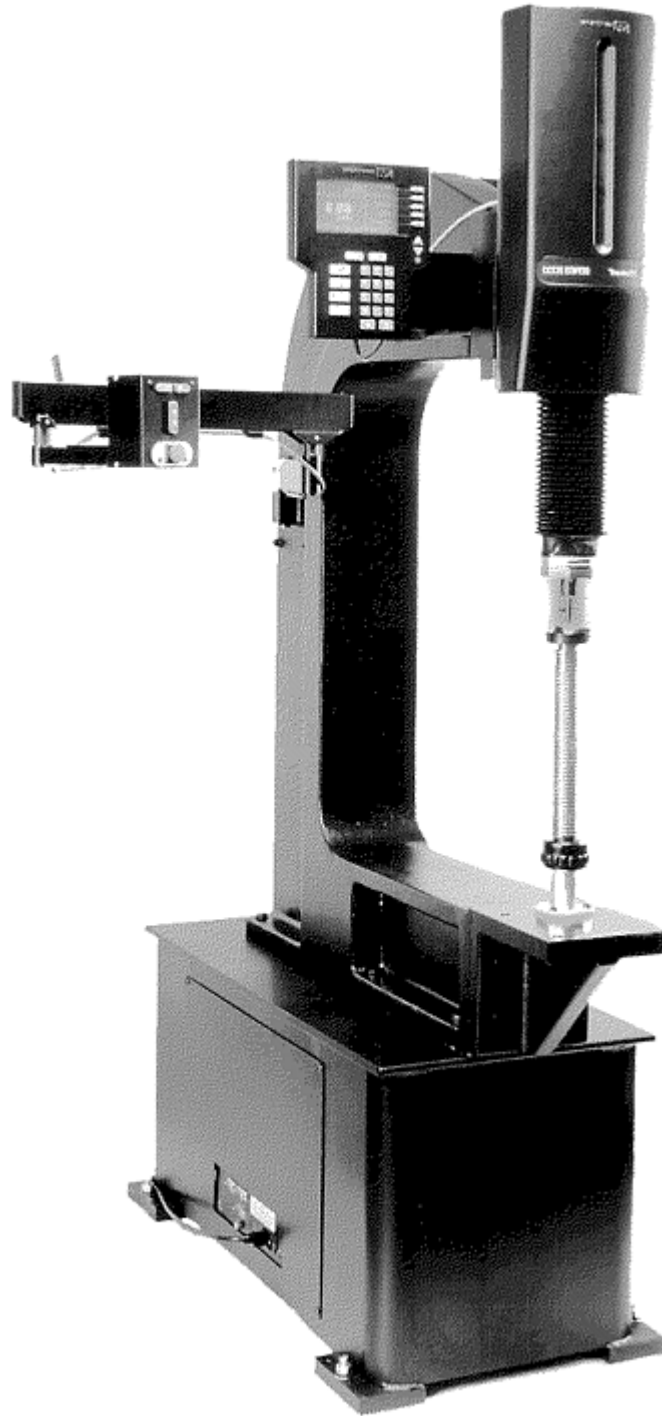


Fig. 2 Rockwell tester for large parts

Shape of the Workpiece. The ideal shape for hardness testing is a square block of sufficient size to permit making any kind of indentation required. Such ideal conditions seldom exist, and arrangements must be made to accommodate a variety of shapes.

The first step in dealing with different shapes is to have a variety of anvils for either Rockwell or Brinell testing. Several options exist for dealing with unwieldy parts (long shafts, for instance). The use of outboard supports or counter-weights are two possibilities. Another approach is to use a type of tester that firmly clamps the workpiece before the load is applied.

Cylindrical Shapes. Round ringlike parts often are tested by using special adapters or specially designed instruments. Cylindrical parts can be tested accurately by either the Brinell or Rockwell method with the use of correction factors. In Brinell testing of cylindrical surfaces an oval indentation results, but this can be corrected to a reasonable degree by obtaining the average of four optical readings taken at 45° apart.

When testing cylindrical pieces, such as rods, the shallow V or standard V anvil should be used, and the test should be applied over the axis of the rod. Care should be taken that the specimen lies flat, supported by the sides of the V anvil. Figure 3 illustrates correct and incorrect methods of supporting cylindrical work for testing.

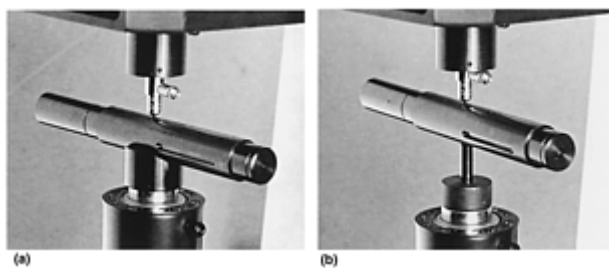


Fig. 3 Anvil support for cylindrical workpieces. (a) Correct method places the specimen centrally under indenter and prevents movement of the specimen under testing loads. (b) Incorrect method of supporting cylindrical work on spot anvil. The testpiece is not firmly secured, and rolling of the specimen can cause damage to the indenter or erroneous readings

Inner Surfaces. The most common approach to Rockwell testing of inner surfaces is to use a gooseneck adapter for the indenter (Fig. 4). This method can be used to test inner surfaces as small as 11.11 mm (0.4375 in.) in diameter or height. Many of the smaller gooseneck adapters can be used with any tester; larger units may require a special gooseneck tester.

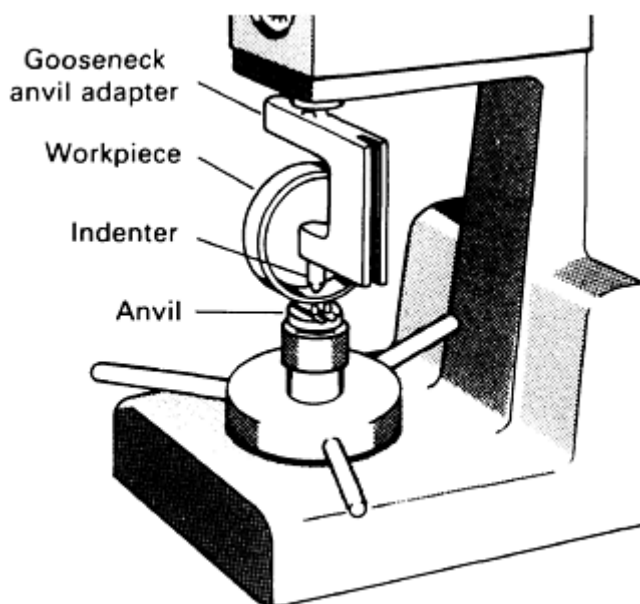


Fig. 4 Setup for hardness testing of inner surfaces of cylindrical workpieces using a gooseneck adapter

Thin-Wall Rings or Tubes. When testing thin-wall rings or tubing that may not support the applied force and therefore deform permanently, a test should be made to determine if this condition exists. If the specimen is permanently deformed, either an internal mandril on a gooseneck anvil and/or a lighter force should be used. Excessive deformation of tubing (either permanent or temporary) can affect the application of the total force. If through deformation the indenter travels to its full extent, complete application of the applied force may not be achieved and an inaccurately high reading will result.

Gears and other complex shapes often require the use of relatively complex anvils and related holding fixtures. When testing workpieces that have complex shapes, for example testing on the pitch line of gear teeth, a specially designed anvil or fixture usually is required. In some cases a specially designed tester may be required. Portable testers may work well for testing large, odd-shaped parts.

Long Specimens. When a workpiece has excessive overhang because of its configuration and cannot be firmly held by the application of the preliminary force, additional support must be used to ensure that the surface to be tested is perpendicular to the indenter axis and that the workpiece will not move during testing. Because manual support is not

practical, a jack-rest should be provided at the overhang end for adequate support. Figure 5 illustrates the correct and incorrect methods for testing long, heavy workpieces.

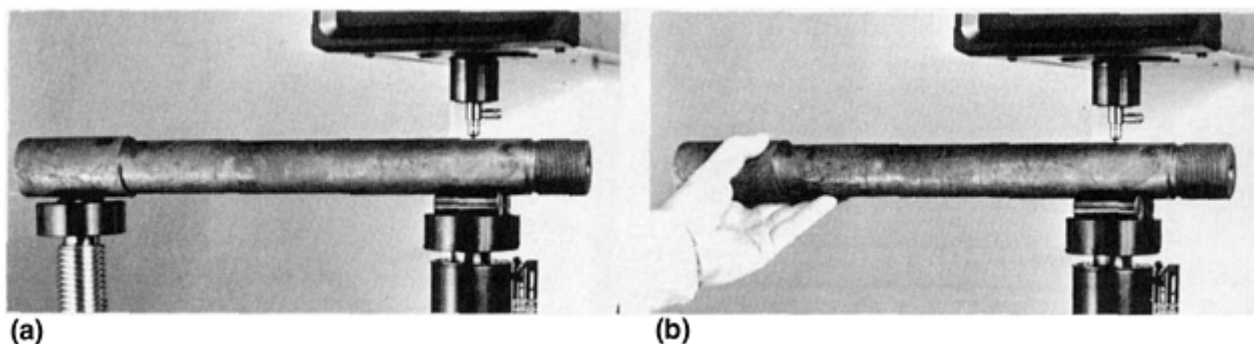


Fig. 5 Method for mounting and testing long, heavy workpieces. (a) Correct method requires a support of the extended end of the piece to prevent any pressure of specimen against indenter. The jack-rest support is available as an accessory. (b) Incorrect method causes damage to indenter and, through leverage action, causes drag and jamming of plunger rod, producing inaccurate readings. When testing, the specimen must be pressed rigidly on the anvil by the pressure of the minor load. Because of this, only short or lightweight material may be permitted much overhang.

Correction Factors for Workpieces with Curved Surfaces. When an indenter is forced into a convex surface, there is less lateral support supplied for the indenting force; consequently, the indenter will sink deeper into the material than it would into a flat surface of the same hardness. Therefore, for convex surfaces, lower hardness values will result. The opposite is true for concave surfaces because additional lateral support is provided, resulting in higher hardness values than when testing the same hardness material with a flat surface.

Results from tests made on a curved surface may be in error and should not be reported without stating the radius of curvature. For Brinell testing, the radius of curvature of the surface shall be greater than 2.5 times the diameter of the indenter. For Rockwell testing diameters of more than 25 mm (1 in.), the difference is negligible. For diameters less than 25 mm (1 in.), particularly for softer materials that involve larger indentations, the curvature, whether convex or concave, must be taken into account if a comparison is to be made with different diameters or with a flat surface.

Correction factors should be applied when workpieces are expected to meet specified values. Typical correction factors for regular and superficial Rockwell hardness values are given in Table 4. The correction values are added to the hardness value when testing convex surfaces and subtracted when testing concave surfaces. On cylinders with diameters as small as 6.35 mm (0.25 in.) regular Rockwell scales may be used; for superficial Rockwell testing, correction factors as small as 3.175 mm (0.125 in.) are given in Table 4.

Table 4 Correction factors for cylindrical workpieces tested with standard and superficial Rockwell hardness testers

Observed reading	Correction factor for workpiece with diameter of:							
	3.175 mm (0.125 in.)	6.350 mm (0.250 in.)	9.525 mm (0.375 in.)	12.700 mm (0.500 in.)	15.875 mm (0.625 in.)	19.050 mm (0.750 in.)	22.225 mm (0.875 in.)	25.400 mm (1.000 in.)
Standard hardness testing, $\frac{1}{16}$ in. (1.588 mm) ball indenter (Rockwell B, F, and G scales)								
100	...	3.5	2.5	1.5	1.5	1.0	1.0	0.5
90	...	4.0	3.0	2.0	1.5	1.5	1.5	1.0

Observed reading	Correction factor for workpiece with diameter of:							
	3.175 mm	6.350 mm	9.525 mm	12.700 mm	15.875 mm	19.050 mm	22.225 mm	25.400 mm
	(0.125 in.)	(0.250 in.)	(0.375 in.)	(0.500 in.)	(0.625 in.)	(0.750 in.)	(0.875 in.)	(1.000 in.)
80	...	5.0	3.5	2.5	2.0	1.5	1.5	1.5
70	...	6.0	4.0	3.0	2.5	2.0	2.0	1.5
60	...	7.0	5.0	3.5	3.0	2.5	2.0	2.0
50	...	8.0	5.5	4.0	3.5	3.0	2.5	2.0
40	...	9.0	6.0	4.5	4.0	3.0	2.5	2.5
30	...	10.0	6.5	5.0	4.5	3.5	3.0	2.5
20	...	11.0	7.5	5.5	4.5	4.0	3.5	3.0
10	...	12.0	8.0	6.0	5.0	4.0	3.5	3.0
0	...	12.5	8.5	6.5	5.5	4.5	3.5	3.0
Standard hardness testing, diamond indenter (Rockwell C, D, and A scales)								
80	...	0.5	0.5	0.5
70	...	1.0	1.0	0.5	0.5	0.5
60	...	1.5	1.0	1.0	0.5	0.5	0.5	0.5
50	...	2.5	2.0	1.5	1.0	1.0	0.5	0.5
40	...	3.5	2.5	2.0	1.5	1.0	1.0	1.0
30	...	5.0	3.5	2.5	2.0	1.5	1.5	1.0
20	...	6.0	4.5	3.5	2.5	2.0	1.5	1.5

Observed reading	Correction factor for workpiece with diameter of:							
	3.175 mm	6.350 mm	9.525 mm	12.700 mm	15.875 mm	19.050 mm	22.225 mm	25.400 mm
	(0.125 in.)	(0.250 in.)	(0.375 in.)	(0.500 in.)	(0.625 in.)	(0.750 in.)	(0.875 in.)	(1.000 in.)

Superficial hardness testing, $\frac{1}{16}$ in. (1.588 mm) ball indenter (Rockwell 15T, 30T, and 45T scales)

90	1.5	1.0	1.0	0.5	0.5	0.5	...	0.5
80	3.0	2.0	1.5	1.5	1.0	1.0	...	0.5
70	5.0	3.5	2.5	2.0	1.5	1.0	...	1.0
60	6.5	4.5	3.0	2.5	2.0	1.5	...	1.5
50	8.5	5.5	4.0	3.0	2.5	2.0	...	1.5
40	10.0	6.5	4.5	3.5	3.0	2.5	...	2.0
30	11.5	7.5	5.0	4.0	3.5	2.5	...	2.0
20	13.0	9.0	6.0	4.5	3.5	3.0	...	2.0

Superficial hardness testing, diamond indenter (Rockwell 15N, 30N, and 45N scales)

90	0.5	0.5
85	0.5	0.5	0.5
80	1.0	0.5	0.5	0.5
75	1.5	1.0	0.5	0.5	0.5	0.5
70	2.0	1.0	1.0	0.5	0.5	0.5	...	0.5
65	2.5	1.5	1.0	0.5	0.5	0.5	...	0.5
60	3.0	1.5	1.0	1.0	0.5	0.5	...	0.5

Observed reading	Correction factor for workpiece with diameter of:							
	3.175 mm	6.350 mm	9.525 mm	12.700 mm	15.875 mm	19.050 mm	22.225 mm	25.400 mm
	(0.125 in.)	(0.250 in.)	(0.375 in.)	(0.500 in.)	(0.625 in.)	(0.750 in.)	(0.875 in.)	(1.000 in.)
55	3.5	2.0	1.5	1.0	1.0	0.5	...	0.5
50	3.5	2.0	1.5	1.0	1.0	1.0	...	0.5
45	4.0	2.5	2.0	1.0	1.0	1.0	...	1.0
40	4.5	3.0	2.0	1.5	1.0	1.0	...	1.0

Note: These correction factors are added to the dial-gage reading when hardness testing on the outer (convex) surface and subtracted when testing on the inner (concave) surface. The values are approximate only and represent the averages, to the nearest half Rockwell number, of numerous actual observations by different investigators, as well as mathematical analyses of the same problem. The accuracy of tests on cylindrical workpieces will be seriously affected by alignment of elevating screw, V-anvil, and indenters, and by surface finish and straightness of the cylinders.

The method recommended by the International Organization for Standardization for correcting Vickers hardness values taken on spherical or cylindrical surfaces is given in Tables 5, 6, and 7. These tables give correction factors to be applied to Vickers hardness values when testing on curved surfaces. The correction factors are tabulated in terms of the ratio of the mean diagonal d of the indentation to the diameter D of the sphere or cylinder.

Table 5 Correction factors for use in Vickers hardness tests made on spherical surfaces

d/D	Correction factor
Convex surface	
0.004	0.995
0.009	0.990
0.013	0.985
0.018	0.980
0.023	0.975
0.028	0.970
0.033	0.965

<i>d/D</i>	Correction factor
0.038	0.960
0.043	0.955
0.049	0.950
0.055	0.945
0.061	0.940
0.067	0.935
0.073	0.930
0.079	0.925
0.086	0.920
0.093	0.915
0.100	0.910
0.107	0.905
0.114	0.900
0.122	0.895
0.130	0.890
0.139	0.885
0.147	0.880
0.156	0.875
0.165	0.870

<i>d/D</i>	Correction factor
0.175	0.865
0.185	0.860
0.195	0.855
0.206	0.850
Concave surface	
0.004	1.005
0.008	1.010
0.012	1.015
0.016	1.020
0.020	1.025
0.024	1.030
0.028	1.035
0.031	1.040
0.035	1.045
0.038	1.050
0.041	1.055
0.045	1.060
0.048	1.065
0.051	1.070

<i>d/D</i>	Correction factor
0.054	1.075
0.057	1.080
0.060	1.085
0.063	1.090
0.066	1.095
0.069	1.100
0.071	1.105
0.074	1.110
0.077	1.115
0.079	1.200
0.082	1.125
0.084	1.130
0.087	1.135
0.089	1.140
0.091	1.145
0.094	1.150

D, diameter of cylinder in millimeters; *d*, mean diagonal of impression in millimeters.

Source: ASTM E 92 (Ref 3)

Table 6 Correction factors for use in Vickers hardness tests made on cylindrical surfaces

Diagonals at 45° to the axis

<i>d/D</i>	Correction factor
Convex surface	
0.009	0.995
0.017	0.990
0.026	0.985
0.035	0.980
0.044	0.975
0.053	0.970
0.062	0.965
0.071	0.960
0.081	0.955
0.090	0.950
0.100	0.945
0.109	0.940
0.119	0.935
0.129	0.930
0.139	0.925
0.149	0.920
0.159	0.915

<i>d/D</i>	Correction factor
0.169	0.910
0.179	0.905
0.189	0.900
0.200	0.895
Concave surface	
0.009	1.005
0.017	1.020
0.025	1.015
0.034	1.020
0.042	1.025
0.050	1.030
0.058	1.035
0.066	1.040
0.074	1.045
0.082	1.050
0.089	1.055
0.097	1.060
0.104	1.065
0.112	1.070

<i>d/D</i>	Correction factor
0.119	1.075
0.127	1.080
0.134	1.085
0.141	1.090
0.148	1.095
0.155	1.100
0.162	1.105
0.169	1.110
0.176	1.115
0.183	1.120
0.189	1.125
0.196	1.130
0.203	1.135
0.209	1.140
0.216	1.140
0.222	1.150

D, diameter of sphere in millimeters; *d*, mean diagonal of impression in millimeters.

Source: ASTM E 92 (Ref 3)

Table 7 Correction factors for use in Vickers hardness tests made on cylindrical surfaces

One diagonal parallel to axis

<i>d/D</i>	Correction factor
Convex surface	
0.009	0.995
0.019	0.990
0.029	0.985
0.041	0.980
0.054	0.975
0.068	0.970
0.085	0.965
0.104	0.960
0.126	0.955
0.153	0.950
0.189	0.945
0.234	0.940
Concave surface	
0.008	1.005
0.016	1.020
0.023	1.015
0.030	1.020

<i>d/D</i>	Correction factor
0.036	1.025
0.042	1.030
0.048	1.035
0.053	1.040
0.058	1.045
0.063	1.050
0.067	1.055
0.071	1.060
0.076	1.065
0.079	1.070
0.083	1.075
0.087	1.080
0.090	1.085
0.093	1.090
0.097	1.095
0.100	1.100
0.103	1.105
0.105	1.110
0.108	1.115

<i>d/D</i>	Correction factor
0.111	1.120
0.113	1.125
0.116	1.130
0.118	1.135
0.120	1.140
0.123	1.145
0.125	1.150

D, diameter of cylinder in millimeters; *d*, mean diagonal of impression in millimeters.

Source: ASTM E 92 (Ref 3)

Example: Correction Factors for Vickers Hardness of a Convex Sphere. The test conditions are:

Diameter of sphere (<i>D</i>), mm	10
Vickers test load, kgf	10
Mean diagonal of indentation (<i>d</i>), mm	0.150
<i>d/D</i>	0.015 (i.e., 0.150/10)

With a mean diagonal of 150 μm and a test load of 10 kgf, the Vickers hardness number for a flat surface is 824 (per ASTM E 92, Ref 3). From Table 5, the correction factor (by interpolation) for a convex surface is 0.983. The corrected hardness of the sphere is thus $824 \times 0.983 = 810 \text{ HV10}$.

Example: Correction Factors for Vickers Hardness of a Concave Cylinder (One Diagonal Parallel to Axis). The test conditions are:

Diameter of cylinder (D), mm	5
Vickers test load, kgf	30
Mean diagonal of indentation (d), mm	0.415
d/D	0.083 (i.e., 0.415/5)

With a mean diagonal of 415 μm and a test load of 30 kgf, the Vickers hardness number for a flat surface is 323 (per ASTM E 92, Ref 3). From Table 7, the correction factor is 1.075 when $d/D = 0.083$. Thus, the hardness of the cylinder after correction is $323 \times 1.075 = 347 \text{ HV}_{30}$.

Degree of Flatness. An absolutely flat surface is the ideal condition for hardness testing, and some methods are more sensitive to this condition than are others. To obtain accurate readings from Brinell, Rockwell, Scleroscope, and conventional microhardness testers, the surface being tested should be at least within 2 or 3° of flatness—that is, close to 90° of the direction of travel of the indenter. For example, when odd-shaped workpieces do not have any surfaces parallel to the surface to be tested, it is often possible to provide adjustable fixtures, which can be tilted as required to allow a flat surface for testing. This accommodation often is made with either the Brinell or the Rockwell tester.

In microhardness testing, securing and holding devices are used to attain a test surface that is sufficiently flat. Similar approaches have been used for Brinell and Rockwell testing; frequently, devices are designed for specific workpieces. Ultrasonic microhardness tests can be performed on surfaces that are not flat, however, because different principles are involved.

Surface Condition

Surface condition is a term covering two different conditions, surface finish and surface composition, both of which can affect the selection of the optimal method and/or testing technique.

Surface Finish. In general, the degree of surface smoothness required for accurate results is related directly to the size of the indenter. Although the smoother finishes are highly desirable for any testing method, the Brinell test, which involves a large indenter, can be made and read with a reasonable degree of accuracy when the finish is comparable to finished-machined or rough-ground types. In Rockwell testing, a finished ground surface is generally the minimum requirement, but polished surfaces are preferred. In Vickers testing through microhardness testing (including Scleroscope), finish requirements are far more stringent. By comparison, in microhardness testing with very light loads (less than 100 gf), the workpiece or specimen requires a surface finish equal to that used for microscopic examination at high magnification. It is obvious that the degree of smoothness that can be obtained can have a profound effect on which test method is selected.

Surface Composition. The other surface condition that can affect the selection of the hardness test method is surface composition (generally unique to steels). Decarburization, retained austenite, carburization, or other composition changes that result in a hard case are likely to influence selection. In many instances, differences in surface conditions require the use of more than one method or scale.

Indent Location and Effects

Location. If an indentation is placed too close to the edge of a specimen the testpiece edge may bulge, causing a lower hardness value because of improper support in the test area. To ensure an accurate test, the distance from the center of the indentation to the edge of the testpiece shall be at least 2.5 times the diameter of the indentation. Therefore, when testing in a narrow area, the width of the test area must be at least five diameters when the indentation is made in the center. The appropriate scale or test force must be selected for this minimum width. Although the diameter of the indentation can be calculated, for practical purposes the minimum distance can be determined visually.

Effect of Indentation Marks. An indentation hardness test cold works and/or work hardens the surrounding area. If another indentation is made too close to this work-hardened area, the reading is usually higher in value than if placed outside the hardened area. Generally, the softer the material, the more critical the spacing of the indentations. A distance between the center of two adjacent indentations of at least three times the diameter of the indentations should be sufficient for most materials.

The presence (or absence) of test marks on a part can also be a factor in selecting a test procedure. In most instances, the presence of Brinell impressions on workpieces such as forgings and castings is not objectionable. On a finished part, however, a mark as large as a Brinell impression might be undesirable from an appearance standpoint, or in some instances, can interfere with its function. There are notable cases where analysis of a service failure proved that a fracture was nucleated by a Brinell impression.

Rockwell indentation marks also can have a deleterious effect, although because the indentations are much smaller, the likelihood of damage is usually less than that caused by Brinell marks. Generally, diamond indenter marks are not sufficient to impair the function of a part, except in the case of precision parts used for purposes such as in fuel control systems. Rarely are marks left by Scleroscope or microhardness testers objectionable.

Production Rates

The number of identical or similar parts being tested can also be a selection factor. The Scleroscope lends itself to very rapid testing, when specific conditions exist, and is used frequently for high-production testing. Likewise, under certain conditions, the ultrasonic hardness test can be used for microhardness testing of many identical parts.

As a rule, however, mass-production hardness testing is done with either the Brinell or the Rockwell tester. Either instrument is available in partly or completely automated setups in which rejects are automatically separated.

References cited in this section

2. "Standard Test Method for Rockwell Hardness of Plastics and Electrical Insulating Materials," D 785-98, *Annual Book of ASTM Standards*, ASTM
3. "Standard Test Method for Vickers Hardness of Metallic Materials," E 92-82(1997)e2, *Annual Book of ASTM Standards*, ASTM

Accuracy and Frequency of Calibration

Although the indentation-type test is a comparatively simple test to perform, reliable results depend a great deal on the accuracy of the equipment and the proper test method. It is recommended the tester be checked each day that hardness tests are to be made and whenever the indenter, anvil, or test force is changed.

Standardized test blocks should be used to monitor the performance of the tester daily. At least two test blocks should be used with hardness levels that bracket below and above the range of hardness levels that are normally tested. Prior to doing any testing, it is good practice to ensure that the tester is operating according to manufacturer requirements and that the anvil and indenter are seated properly. At least three hardness measurements should be made on any uniform specimen having a high hardness level in the scale to be verified. The measurements should be continued until there is no trend (increasing or decreasing hardness) in the measurement values. This technique implies that the tester's repeatability is consistent and that the indenter and anvil are seated adequately. These results need not be recorded.

After the trial tests, at least three uniformly spaced hardness measurements should be made on each of the standardized test blocks. If the average of the hardness measurements are within the tolerance marked on the blocks, the tester may be regarded as performing satisfactorily. If not, an indirect verification should be performed. In monitoring the tester in this manner it is recommended that these hardness measurements be recorded using acceptable statistical process control techniques, such as X-bar charts (measurement averages), *R*-charts (measurement ranges), gage repeatability and reproducibility (GRR) studies, and histograms (see the article “Gage Repeatability and Reproducibility in Hardness Testing” in this Volume).

Most indentation-type testing should be carried out at a temperature within the limits of 10 to 35 °C (50–95 °F). If there is a possibility of hardness variation within these test-temperature limits, users may choose to control temperatures within a tighter range. A range of 18 to 23 °C (64–81 °F) is recommended. Tests performed outside this temperature range should be considered suspect.

NIST-Traceable Test Blocks. Due to the empirical nature of hardness testing, the need for standardization of hardness values is an area of continued attention. In many countries of Europe and Asia, for example, nationally traceable hardness standards have been around for many years. Traceable standards can help resolve or reduce differences in test results between vendors and customers, who each rely on their test block for machine verification.

In 1990, after several meetings between the American Society for Testing and Materials (ASTM) and standards groups from Europe and Asia, the U.S. government agreed to provide hardness standards for U.S. manufacturers. The reason for the change is that hardness, though based on traceable parameters, has had no absolute numbers. For example, the loads on a tester can be verified with a traceable load cell, but the hardness values themselves are empirical; that is, hardness would not be directly traceable to any standard, national or otherwise.

In order to evaluate the magnitude of variation, commercially available test blocks were evaluated by the National Institute of Standards and Technology (NIST). A variation of 1.0 HRC was found to exist among test blocks supplied by domestic manufacturers. A shift of almost 1.0 HRC also was realized versus standards from other countries. This finding reinforced the need for standardization.

The hardness program at NIST involves traceable Standard Reference Material (SRM) blocks—or what industry refers to as “NIST-traceable test blocks.” The SRMs are calibrated at NIST by means of a dead-weight tester. Only two of these machines exist in the world. Other primary machines exist in other countries, but the only exact duplicate of the NIST machine is located at IMGIC, which is the NIST equivalent in Italy.

NIST-traceable test blocks are available for three nominal ranges in the Rockwell C scale:

- SRM 2810, “Rockwell C Scale Hardness—Low Range” (25 HRC nominal)
- SRM 2811, “Rockwell C Scale Hardness—Mid Range” (45 HRC nominal)
- SRM 2812, “Rockwell C Scale Hardness—High Range” (63 HRC nominal)

The new NIST-traceable blocks, at a nominal size of 60 mm (2.36 in.) diameter and 15 mm (0.6 in.) thick, are larger than the typical Rockwell hardness test blocks. They are made of steel in the appropriate Rockwell C range and have a polished mirrorlike surface. Although most ASTM-type Rockwell C test blocks are labeled ± 0.5 HRC on the high end (60 HRC range), the NIST blocks have much tighter tolerances (down to 0.1). Test locations are indicated on the block; associated hardness numbers and statistical information are listed on the certificate, enabling the user to find more than just the arithmetic mean of the hardness.

Secondary traceable standards are available from commercial test block manufacturers. NIST standardized test blocks are based on methods (especially on the diamond indenter) that are more closely aligned with those of the national laboratories of other nations than with the values that were being used in North America. The most dramatic change is tighter specification of indenter radius closer to the average ASTM-specified value of 200 μm . This is slightly larger than previous standard indenter radius of 192 μm . This change in indenter radius shifts values at the upper end of the Rockwell C scale (59–63 HRC), where values shifted upward by 0.5 to 0.8 points HRC. From 46 to 58 HRC the shift was from 0.2 to 0.49 points, while the shift was insignificant below 46 HRC.

Selection and Industrial Applications of Hardness Tests

Andrew Fee, Consultant

Hardness Test Selection for Specific Materials

Generally, the scale to be used for a specified material is indicated on engineering design drawings or in the test specifications. However, at times the scale must be determined and selected to suit a given set of circumstances. In general, the scale using a diamond indenter (Rockwell and Vickers) are used for testing hardened steels and alloys, while the ball indenters (Brinell and Rockwell) are used on more malleable materials.

Table 8 is a general guide relating materials and scales for regular Rockwell testing. As noted in Table 8, the Rockwell superficial scales (N and T) are used for testing similar material that may be too thin to accommodate the regular scales. In microindentation hardness testing, the Knoop and Vickers diamond indenters are used for all testing. Additional details about these indentation hardness test methods are given in separate articles in this Section of the Handbook.

Table 8 Typical applications of regular Rockwell hardness scales

Scale ^(a)	Typical applications
B	Copper alloys, soft steels, aluminum alloys, malleable iron
C	Steel, hard cast irons, pearlitic malleable iron, titanium, deep case-hardened steel, and other materials harder than 100 HRB
A	Cemented carbides, thin steel, and shallow case-hardened steel
D	Thin steel and medium case-hardened steel and pearlitic malleable iron
E	Cast iron, aluminum and magnesium alloys, bearing metals
F	Annealed copper alloys, thin soft sheet metals
G	Phosphor bronze, beryllium copper, malleable irons. Upper limit is 92 HRG to avoid flattening of ball.
H	Aluminum, zinc, lead
K, L, M, P, R, S, V	Bearing metals and other very soft or thin materials. Use smallest ball and heaviest load that do not give anvil effect.

(a) The N scales of a superficial hardness tester are used for materials similar to those tested on the Rockwell C, A, and D scales but of thinner gage or case depth. The T scales are used for materials similar to those tested on the Rockwell B, F, and G scales but of thinner gage. When minute indentations are required, a superficial hardness tester should be used. The W, X, and Y scales are used for very soft materials

Conversion from one hardness scale to another also depends on the material being tested. Therefore, this section provides some hardness conversion data for materials other than steel. Hardness conversion tables for steel are included in the article “Hardness Conversions for Steels.”

Steels

Forgings, Castings, and Plate Products. Annealed, hot-rolled, cold-finished, forged, or cast carbon and alloy steels usually are tested by the Brinell or Rockwell B method. Because of the nature of forgings and most iron and steel castings, the Brinell test is the preferred test method; the larger Brinell indentation gives a better average value of the local surface and thus a truer homogenic hardness than would be expected with the Rockwell test.

Rockwell testing is used on specimens with fine grain composition or those that lack sufficient area to accommodate a Brinell test. Although the Rockwell B scale (1.59 mm, or $\frac{1}{16}$ in., ball indenter) is used sometimes, the Rockwell E and K scales (3.175 mm, or $\frac{1}{8}$ in., ball indenter) are preferred because the larger indenter gives a better average reading. The surface that is to be tested should be prepared, if needed, to allow for a well-defined indentation for accurate measurement. Care should be taken to ensure that any surface preparation will not influence the condition of the surface by overheating and cold working. To better correlate between Rockwell and Brinell values, it is suggested that three to five Rockwell tests be made and averaged to give a more representative hardness value because of the possible variations within the cast part. Hard white iron castings and chilled rolls are usually tested using the Rockwell C and Vickers scales.

Hardened and Tempered Steels. The hardness of quenched-and-tempered carbon, alloy, tool, and stainless steels is typically tested with a diamond indenter by Rockwell, Vickers, or microindentation techniques. The Rockwell C test generally is used when conditions permit. Rockwell C readings of less than 20 (or its equivalent in other scales) should not be considered valid, and some inaccuracy can be expected as the value drops below 30 HRC. For hardenability testing, the Rockwell C scale is preferred (see the section “Hardenability Testing” in this article).

Steel Sheet. Depending on the thickness of the sheet, hardness specifications are usually given in the Rockwell B scale or a superficial Rockwell scale (HR30T or sometimes HR15T). Sheet metal is usually tested and controlled for its drawing and stamping capabilities with the Rockwell test.

A common industry description of the various sheet steel tempers is:

Temper	Hardness, HRB
No. 1 Hard	90 ± 5
No. 2 Half-hard	80 ± 5
No. 3 Quarter-hard	70 ± 5
No. 4 Soft	60 ± 5
No. 5 Dead-soft	45 ± 5

The verbal descriptions of the tempers involve wide tolerances, and a specification in the actual Rockwell hardness gives a more precise and defined tolerance for control of the end product.

Powder Metallurgy (P/M) Steels. Because the density of P/M steels may vary from less than 7 g/cm³ (0.25 lb/in.³) to a density approaching that of wrought steel (about 7.8 g/cm³, or 0.28 lb/in.³), the variation in hardness can vary widely. Besides porosity, sintered P/M steels may also have inhomogeneous microstructures from graphite. At least five consistent readings should be taken, in addition to any obviously high or low readings, which should be discarded. The remaining five readings should be averaged.

Because of the variety of compositions and densities encountered in P/M materials, the recommendation for suitable test methods may require preliminary trials. Generally, the Rockwell test, with its variety of scales, is the usual choice. The Rockwell F, H, B, and the superficial T scales are generally used for hardness testing of P/M materials. Heat treated P/M steels are sometimes tested in the Rockwell C scale (Table 9). Although not widely used, the Rockwell B scale may be combined with a carbide ball for testing hardened parts. Data scattering is minimized with a Rockwell B 1.59 mm ($\frac{1}{16}$ in.) diameter ball, and it is useful up to 120 HRB.

Table 9 Common hardness scales used for P/M parts

Material	Sintered hardness scale	Heat treated hardness scale
Iron	HRH, HRB	HRB, HRC
Iron-carbon	HRB	HRB, HRC
Iron-nickel-carbon	HRB	HRC
Prealloyed steel	HRB	HRC
Bronze	HRH	...
Brass	HRH	...

Apparent Hardness. In powder metallurgy there are generally two types of hardness specified—apparent hardness (macrohardness) and microhardness. The microhardness is the hardness of each particle of material, and the apparent hardness is the hardness of the surface—bridging across many particles and the porosity, too. Apparent hardness is typically measured according to Metal Powder Industries Federation (MPIF) Standard 43 (Ref 4). The procedure is relatively straightforward and quick. The basics are:

1. Obtain a sample part of adequate thickness and parallel configuration (or, for cylindrical parts, a correction factor may be used).
2. The sample must be large enough so that the indenter marks from the hardness tester are at least three indenter diameters from any edge or previous impression.
3. Sand each face of the sample so that no burrs are present (burrs will cause erroneous readings), or be sure to use a holding fixture that avoids the burrs.
4. Take readings with a properly calibrated hardness tester.
5. Reject obvious outliers and report the average of at least five nonoutliers.

Typically, the outliers are on the low side. The cause of these occasional low readings is a chance happening that the hardness indenter falls right into a pore.

Microhardness is usually measured according to MPIF Standard 51 (Ref 5). The determination of microhardness is significantly more difficult than measuring apparent hardness and requires specialized equipment that many P/M users do not have on-site. The procedure involves:

1. Sectioning the part and making a polished mount for the evaluation.
2. Placing the mount in a special microhardness testing machine.
3. Under magnification, orienting the mount and making a diamond indenter mark precisely over a particle of the material.
4. Measuring the length of the penetration on the particle and converting this length to a hardness reading.

Microindentation hardness tests of porous materials can best be measured with Knoop or diamond pyramid hardness indenters at loads of 100 gf or greater. In atomized irons, particles exhibit minimal porosity; consequently, the Knoop indenter is suitable because it makes a very shallow indentation and is not frequently disturbed by entering undisclosed pores. Care should be taken in preparing the sample surface. The diamond pyramid indenter is particularly well suited to irons that contain numerous fine internal pores. Because of its greater depth of penetration, the diamond pyramid indenter frequently encounters hidden pores. Microhardness testing and the measurement of effective case depth are covered by MPIF standard 51 (Ref 6).

Cast Irons

Accurate hardness values often are difficult to attain when the material has an inhomogeneous structure and composition. This applies to the complex metal-carbon structure of cast irons. Conventional hardness measurements of cast irons thus tend to be lower values than the hardness of the metal portion. This discrepancy, which is more pronounced in gray iron than in ductile and malleable irons, occurs because conventional hardness readings are composite values that reflect the hardnesses of both the matrix metal and

soft graphite. Greater variations in hardness results may also occur from the inhomogeneous structure. Therefore, a Brinell hardness test, by virtue of its indenter size, is preferred to provide more consistent average hardness values. However, sometimes other scales may be required. For example, when determining the hardness of small castings, it is often impossible to use a Brinell tester; a Rockwell tester must be used. Fine grain structure, hard white-iron castings, and chilled rolls may also require the use of other scales, as previously noted in the section “Forgings, Castings, and Plate Products” in this article.

Conversions between different hardness scales have been developed for some types of cast irons. For example, Fig. 6 shows conversions from Brinell to Rockwell B and G scales for malleable and pearlitic malleable irons, respectively. Figure 6(b) shows Rockwell C equivalents for Brinell values of pearlitic malleable iron. These conversions generally are accepted by producers of malleable iron. Reliable hardness conversion for other types of cast irons, especially gray irons, is more difficult due to the variations in metallurgical conditions. For example, Fig. 7 shows the relationship between observed Rockwell C readings and those converted from microhardness values for five gray irons of different carbon equivalents. The wide variation illustrates the need to know the carbon equivalent of the iron being tested before a conversion chart can be developed. For white iron, conversions are shown in Table 10.

Table 10 Approximate equivalent hardness numbers of alloyed white irons

Vickers hardness No., HV50	Brinell hardness No. ^(a) , HBW	Rockwell C hardness No., HRC
1000	(903)	70
980	(886)	69
960	(868)	68
940	(850)	68
920	(833)	67
900	(815)	66
880	(798)	66
860	(780)	65
840	(762)	64
820	(745)	63
800	(727)	62
780	(710)	62
760	(692)	61
740	(674)	60
720	(657)	59
700	(639)	58
680	621	57
660	604	56
640	586	55
620	569	54
600	551	53
580	533	52
560	516	51
540	498	50
520	481	48
500	463	47
480	445	45
460	428	44
440	410	42
420	393	40
400	375	38
380	357	35

Note: Brinell hardness numbers in parentheses are beyond the normal range and are presented for information only.

(a) 10 mm (0.4 in.) diam tungsten carbide ball; 3000 kgf load.

Source: ASTM E 140 (Ref 6)

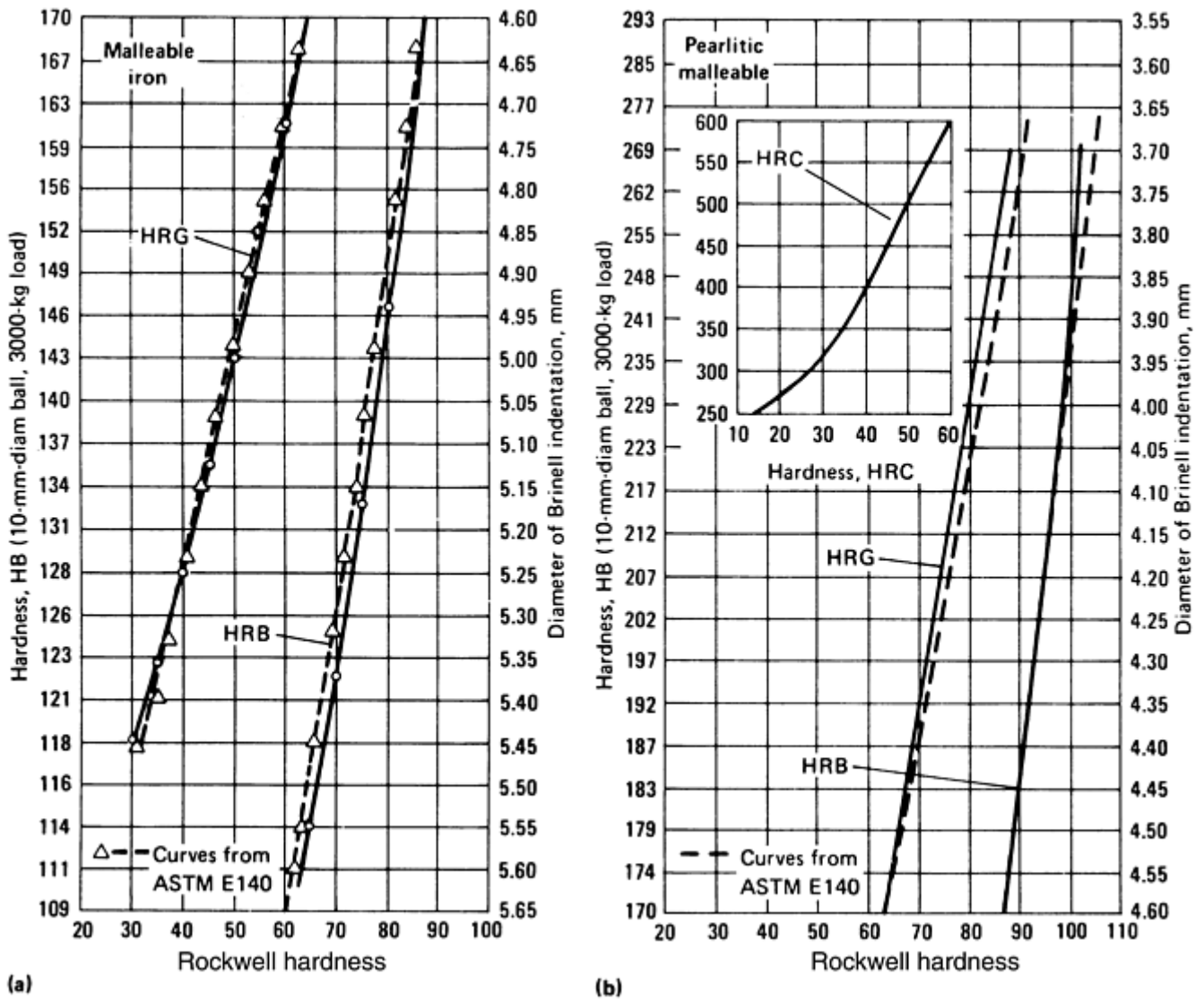


Fig. 6 Hardness conversions for malleable iron. (a) Conversion from Brinell to Rockwell G scales for malleable iron. (b) Conversion from Brinell to Rockwell B, C, and G scales for pearlitic malleable iron

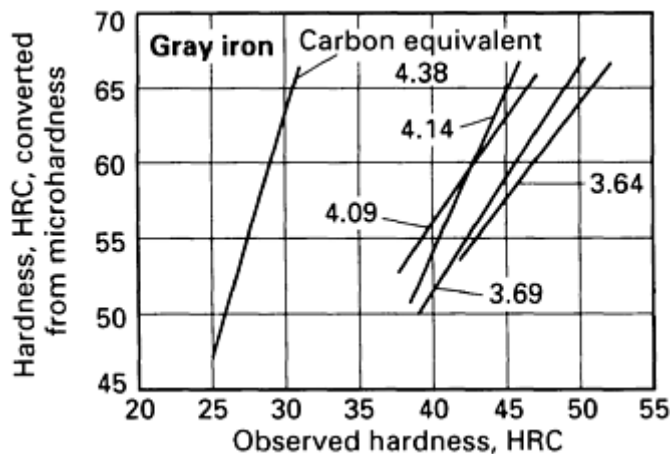


Fig. 7 Relationship between observed and converted hardness values, as influenced by carbon equivalent, for gray iron containing type 3 graphite

Nonferrous Alloys

To a great extent, the same general guidelines apply to both nonferrous and ferrous materials. Indentation spacing, proximity to edges, thickness of testing material, and the selection of indenter and load combinations are all factors that influence hardness readings.

With very few exceptions, nonferrous metals are generally softer than steels and cast irons. Brinell testing and Rockwell testing with ball indenters under a variety of test loads are most often used. Many of the higher strength or higher hardness nonferrous metals can be accurately tested with the Brinell test method when the workpiece is of sufficient thickness and size.

The Brinell test is the preferred test for wrought aluminum alloys and large nonferrous castings, which are usually tested with the 500 kgf load. Some high-strength alloys such as titanium-base alloys that are phase transformation or age hardened can be tested with the 3000 kgf load. Diamond indenters are sometimes used—notably, the Rockwell A scale. Some multiphased cast nonferrous alloys that are too soft for Brinell testing will require the Rockwell or Vickers test methods. Typical Rockwell scales used for a wide variety of nonferrous metals and other materials are listed in Table 8. Very small nonferrous metal parts made of extremely thin sheet, strip, or foil are tested by microindentation methods.

Aluminum and aluminum alloys are tested frequently for hardness to distinguish between annealed, cold-worked, and heat treated grades. The Rockwell B scale (100 kgf load with a 1.58 mm, or $\frac{1}{16}$ in., steel ball indenter) generally is suitable in testing grades that have been precipitation hardened to relatively high strength levels. For softer grades and commercially pure aluminum, hardness testing usually is done with the Rockwell F, E, and H scales. For hardness testing of thin gages of aluminum, the 15T and 30T scales of the Rockwell superficial tester are recommended. Approximate hardness conversions for wrought aluminum are listed in Table 11.

Table 11 Approximate equivalent hardness numbers for wrought aluminum products

Brinell hardness No., 500 kgf, 10 mm ball, HBS	Vickers hardness No., 15 kgf, HV	Rockwell hardness No.			Rockwell superficial hardness No.		
		B scale, 100 kgf, $\frac{1}{16}$ in. ball, HRB	E scale, 100 kgf, $\frac{1}{8}$ in. ball, HRE	H scale, 60 kgf, $\frac{1}{8}$ in. ball, HRH	15T scale, 15 kgf, $\frac{1}{16}$ in. ball, HR15T	30T scale, 30 kgf, $\frac{1}{16}$ in. ball, HR30T	15W scale, 15 kgf, $\frac{1}{8}$ in. ball, HR15W
160	189	91	89	77	95
155	183	90	89	76	95
150	177	89	89	75	94
145	171	87	88	74	94
140	165	86	88	73	94
135	159	84	87	71	93
130	153	81	87	70	93
125	147	79	86	68	92
120	141	76	101	...	86	67	92
115	135	72	100	...	86	65	91
110	129	69	99	...	85	63	91
105	123	65	98	...	84	61	91
100	117	60	83	59	90
95	111	56	96	...	82	57	90
90	105	51	94	108	81	54	89
85	98	46	91	107	80	52	89
80	92	40	88	106	78	50	88

75	86	34	84	104	76	47	87
70	80	28	80	102	74	44	86
65	74	...	75	100	72	...	85
60	68	...	70	97	70	...	83
55	62	...	65	94	67	...	82
50	56	...	59	91	64	...	80
45	50	...	53	87	62	...	79
40	44	...	46	83	59	...	77

Source: ASTM E 140 (Ref 6)

Copper and Copper Alloys. Because copper alloys vary so widely in hardness, a wide range of indenters and loads may apply to this family of alloys. Beginning at the top of the range, the precipitation-hardenable alloys (such as C17000, C17200, and C17300) may be regarded as essentially the same as steel in their hardened condition because they are generally within the range of 36 to 45 HRC. Therefore, these alloys can be tested satisfactorily with the Rockwell C scale. For thinner gages, the 15H or 30H scale is used. The Brinell test, using 1500 to 3000 kgf loads, is also appropriate for testing the harder copper alloys. When these alloys are in the annealed or cold-worked condition, the Rockwell B scale is recommended, or the 15T or 30T scale for very thin sections. When the indenter is penetrating the test material too deeply with the B scale, a lighter load or larger ball, such as that used for Rockwell E or F scale, must be used. Approximate hardness conversions for wrought copper alloys and cartridge brass are listed in Tables 12 and 13, respectively.

Table 12 Approximate equivalent hardness numbers for wrought coppers (>99% Cu, alloys C10200 through C14200)

Vickers hardness No.		Knoop hardness No.		Rockwell superficial hardness No.			Rockwell hardness No.	Rockwell superficial hardness No.			Brinell hardness No.		
100 kgf, HV	100 gf, HV	1 kgf, HK	500 gf, HK	15T scale, 15 kgf, $\frac{1}{16}$ in. (1.588 mm) ball, HR15T ^(a)	15T scale, 15 kgf, $\frac{1}{16}$ in. (1.588 mm) ball, HR15T ^(b)	30T scale, 30 kgf, $\frac{1}{16}$ in. (1.588 mm) ball, HR30T ^(b)	B scale, 100 kgf, $\frac{1}{16}$ in. (1.588 mm) ball, HRB ^(c)	F scale, 60 kgf, $\frac{1}{16}$ in. (1.588 mm) ball, HRF ^(c)	15T scale, 15 kgf, $\frac{1}{16}$ in. (1.588 mm) ball, HR15T ^(c)	30T scale, 30 kgf, $\frac{1}{16}$ in. (1.588 mm) ball, HR30T ^(c)	45T scale, 45 kgf, $\frac{1}{16}$ in. (1.588 mm) ball, HR45T ^(c)	500 kgf, 10 mm diam ball, HBS ^(d)	20 kgf, 2 mm diam ball, HBS ^(e)
130	127.0	138.7	133.8	...	85.0	...	67.0	99.0	...	69.5	49.0	...	119.0
128	125.2	136.8	132.1	83.0	84.5	...	66.0	98.0	87.0	68.5	48.0	...	117.5
126	123.6	134.9	130.4	...	84.0	...	65.0	97.0	...	67.5	46.5	120.0	115.0
124	121.9	133.0	128.7	82.5	83.5	...	64.0	96.0	86.0	66.5	45.0	117.5	113.0
122	121.1	131.0	127.0	...	83.0	...	62.5	95.5	85.5	66.0	44.0	115.0	111.0
120	118.5	129.0	125.2	82.0	82.5	...	61.0	95.0	...	65.0	42.5	112.0	109.0
118	116.8	127.1	123.5	81.5	59.5	94.0	85.0	64.0	41.0	110.0	107.5
116	115.0	125.1	121.7	...	82.0	...	58.5	93.0	...	63.0	40.0	107.0	105.5
114	113.5	123.2	119.9	81.0	81.5	...	57.0	92.5	84.5	62.0	38.5	105.0	103.5
112	111.8	121.4	118.1	80.5	81.0	...	55.0	91.5	...	61.0	37.0	102.0	102.0
110	109.9	119.5	116.3	80.0	53.5	91.0	84.0	60.0	36.0	99.5	100.0
108	108.3	117.5	114.5	...	80.5	...	52.0	90.5	83.5	59.0	34.5	97.0	98.0
106	106.6	115.6	112.6	79.5	80.0	...	50.0	89.5	...	58.0	33.0	94.5	96.0
104	104.9	113.5	110.1	79.0	79.5	...	48.0	88.5	83.0	57.0	32.0	92.0	94.0
102	103.2	111.5	108.0	78.5	79.0	...	46.5	87.5	82.5	56.0	30.0	89.5	92.0
100	101.5	109.4	106.0	78.0	78.0	...	44.5	87.0	82.0	55.0	28.5	87.0	90.0
98	99.8	107.3	104.0	77.5	77.5	...	42.0	85.5	81.0	53.5	26.5	84.5	88.0
96	98.0	105.3	102.1	77.0	77.0	...	40.0	84.5	80.5	52.0	25.5	82.0	86.5
94	96.4	103.2	100.0	76.5	76.5	...	38.0	83.0	80.0	51.0	23.0	79.5	85.0
92	94.7	101.0	98.0	76.0	75.5	...	35.5	82.0	79.0	49.0	21.0	77.0	83.0
90	93.0	98.9	96.0	75.5	75.0	...	33.0	81.0	78.0	47.5	19.0	74.5	81.0
88	91.2	96.9	94.0	75.0	74.5	...	30.5	79.5	77.0	46.0	16.5	...	79.0
86	89.7	95.5	92.0	74.5	73.5	...	28.0	78.0	76.0	44.0	14.0	...	77.0
84	87.9	92.3	90.0	74.0	73.0	...	25.5	76.5	75.0	43.0	12.0	...	75.0

82	86.1	90.1	87.9	73.5	72.0	...	23.0	74.5	74.5	41.0	9.5	...	73.0
80	84.5	87.9	86.0	72.5	71.0	...	20.0	73.0	73.5	39.5	7.0	...	71.5
78	82.8	85.7	84.0	72.0	70.0	...	17.0	71.0	72.5	37.5	5.0	...	69.5
76	81.0	83.5	81.9	71.5	69.5	...	14.5	69.0	71.5	36.0	2.0	...	67.5
74	79.2	81.1	79.9	71.0	68.5	...	11.5	67.5	70.0	34.0	66.0
72	77.6	78.9	78.7	70.0	67.5	...	8.5	66.0	69.0	32.0	64.0
70	75.8	76.8	76.6	69.5	66.5	...	5.0	64.0	67.5	30.0	62.0
68	74.3	74.1	74.4	69.0	65.5	...	2.0	62.0	66.0	28.0	60.5
66	72.6	71.9	71.9	68.0	64.5	60.0	64.5	25.5	58.5
64	70.9	69.5	70.0	67.5	63.5	58.0	63.5	23.5	57.0
62	69.1	67.0	67.9	66.5	62.0	56.0	61.0	21.0	55.0
60	67.5	64.6	65.9	66.0	61.0	54.0	59.0	18.0	53.0
58	65.8	62.0	63.8	65.0	60.0	51.5	57.0	15.5	51.5
56	64.0	59.8	61.8	64.5	58.5	49.0	55.0	13.0	49.5
54	62.3	57.4	59.5	63.5	57.5	47.0	53.0	10.0	48.0
52	60.7	55.0	57.2	63.0	56.0	44.0	51.5	7.5	46.5
50	58.9	52.8	55.0	62.0	55.0	41.5	49.5	4.5	44.5
48	57.3	50.3	52.7	61.0	53.5	39.0	47.5	1.5	42.0
46	55.8	48.0	50.2	60.5	52.0	36.0	45.0	41.0
44	53.9	45.9	47.8	59.5	51.0	33.5	43.0
42	52.2	43.7	45.2	58.5	49.5	30.5	41.0
40	51.3	40.2	42.8	57.5	48.0	28.0	38.5

(a) For 0.010 in. (0.25 mm) strip.

(b) For 0.020 in. (0.51 mm) strip.

(c) For 0.040 in. (1.02 mm) strip and greater.

(d) For 0.080 in. (2.03 mm) strip.

(e) For 0.040 in. (1.02 mm) strip.

Source: ASTM E 140 (Ref 6)

Table 13 Approximate equivalent hardness numbers for cartridge brass (70% Cu, 30% Zn)

Vickers hardness No., HV	Rockwell hardness No.		Rockwell superficial hardness No.			Brinell hardness No. 500 kgf, 10 mm ball, HBS
	B scale, 100 kgf, $\frac{1}{16}$ in. (1.588 mm) ball, HRF	F scale, 60 kgf, $\frac{1}{16}$ in. (1.588 mm) ball, HRF	15T scale, 15 kgf, $\frac{1}{16}$ in. (1.588 mm) ball, HR15T	30T scale, 30 kgf, $\frac{1}{16}$ in. (1.588 mm) ball, HR30T	45T scale, 45 kgf, $\frac{1}{16}$ in. (1.588 mm) ball, HR45T	
196	93.5	110.0	90.0	77.5	66.0	169
194	...	109.5	65.5	167
192	93.0	77.0	65.0	166
190	92.5	109.0	...	76.5	64.5	164
188	92.0	...	89.5	...	64.0	162
186	91.5	108.5	...	76.0	63.5	161
184	91.0	75.5	63.0	159
182	90.5	108.0	89.0	...	62.5	157
180	90.0	107.5	...	75.0	62.0	156
178	89.0	74.5	61.5	154
176	88.5	107.0	61.0	152
174	88.0	...	88.5	74.0	60.5	150
172	87.5	106.5	...	73.5	60.0	149
170	87.0	59.5	147
168	86.0	106.0	88.0	73.0	59.0	146
166	85.5	72.5	58.5	144
164	85.0	105.5	...	72.0	58.0	142
162	84.0	105.0	87.5	...	57.5	141
160	83.5	71.5	56.5	139
158	83.0	104.5	...	71.0	56.0	138
156	82.0	104.0	87.0	70.5	55.5	136
154	81.5	103.5	...	70.0	54.5	135
152	80.5	103.0	54.0	133
150	80.0	...	86.5	69.5	53.5	131
148	79.0	102.5	...	69.0	53.0	129
146	78.0	102.0	...	68.5	52.5	128
144	77.5	101.5	86.0	68.0	51.5	126
142	77.0	101.0	...	67.5	51.0	124
140	76.0	100.5	85.5	67.0	50.0	122
138	75.0	100.0	...	66.5	49.0	121
136	74.5	99.5	85.0	66.0	48.0	120
134	73.5	99.0	...	65.5	47.5	118
132	73.0	98.5	84.5	65.0	46.5	116
130	72.0	98.0	84.0	64.5	45.5	114
128	71.0	97.5	...	63.5	45.0	113
126	70.0	97.0	83.5	63.0	44.0	112
124	69.0	96.5	...	62.5	43.0	110
122	68.0	96.0	83.0	62.0	42.0	108
120	67.0	95.5	...	61.0	41.0	106
118	66.0	95.0	82.5	60.5	40.0	105
116	65.0	94.5	82.0	60.0	39.0	103
114	64.0	94.0	81.5	59.5	38.0	101

112	63.0	93.0	81.0	58.5	37.0	99
110	62.0	92.6	80.5	58.0	35.5	97
108	61.0	92.0	...	57.0	34.5	95
106	59.5	91.2	80.0	56.0	33.0	94
104	58.0	90.5	79.5	55.0	32.0	92
102	57.0	89.8	79.0	54.5	30.5	90
100	56.0	89.0	78.5	53.5	29.5	88
98	54.0	88.0	78.0	52.5	28.0	86
96	53.0	87.2	77.5	51.5	26.5	85
94	51.0	86.3	77.0	50.5	24.5	83
92	49.5	85.4	76.5	49.0	23.0	82
90	47.5	84.4	75.5	48.0	21.0	80
88	46.0	83.5	75.0	47.0	19.0	79
86	44.0	82.3	74.5	45.5	17.0	77
84	42.0	81.2	73.5	44.0	14.5	76
82	40.0	80.0	73.0	43.0	12.5	74
80	37.5	78.6	72.0	41.0	10.0	72
78	35.0	77.4	71.5	39.5	7.5	70
76	32.5	76.0	70.5	38.0	4.5	68
74	30.0	74.8	70.0	36.0	1.0	66
72	27.5	73.2	69.0	34.0	...	64
70	24.5	71.8	68.0	32.0	...	63
68	21.5	70.0	67.0	30.0	...	62
66	18.5	68.5	66.0	28.0	...	61
64	15.5	66.8	65.0	25.5	...	59
62	12.5	65.0	63.5	23.0	...	57
60	10.0	62.5	62.5	55
58	...	61.0	61.0	18.0	...	53
56	...	58.8	60.0	15.0	...	52
54	...	56.5	58.5	12.0	...	50
52	...	53.5	57.0	48
50	...	50.5	55.5	47
49	...	49.0	54.5	46
48	...	47.0	53.5	45
47	...	45.0	44
46	...	43.0	43
45	...	40.0	42

Source: ASTM E 140 (Ref 6)

Magnesium and magnesium alloys are tested by applying the Rockwell B scale, but when the alloys are softer (annealed), the indenter size is increased to 3.175 mm ($\frac{1}{8}$ in.) using the Rockwell E scale. As with other metals and alloys, thin sections of magnesium alloys must be tested with the 15T or 30T scale to avoid the anvil effect. Titanium. The Rockwell A scale is best suited for testing titanium. The 60 kgf load tends to increase the life of the diamond penetrator because there is an affinity between diamond and titanium, which usually shortens diamond life. Titanium tends to adhere to the tip of the diamond penetrator and can readily be removed with 3/0 grade emery paper when the penetrator is rotated in a lathe. Maintaining a clean diamond will give more reliable results.

Zinc and lead alloys are typically tested using the Rockwell method. They exhibit extensive time-dependent plasticity characteristics and therefore require longer dwell time of load application to obtain accurate and repeatable results. For materials that show some time-dependent plasticity, the dwell time of indent load should be 5 to 6 s using a diamond indenter. For materials that show considerable time-dependent plasticity, dwell time should be 20 to 25 s using any indenter. One method for determining the magnitude of time-dependent plasticity is to do a series of tests at progressively longer dwell times. As the dwell increases the hardness

values will decrease significantly. When the rate of change decreases significantly the proper dwell time has been reached.

Zinc. The Rockwell E scale is used for zinc sheets down to 3.2 mm (0.125 in.) and the Rockwell H scale for sheets down to 1.25 mm (0.050 in.) gage. These values are for zinc in the soft condition, thinner sheets may be tested if the zinc is relatively hard. For thinner sheet, the 15T or 30T scale of the Rockwell superficial tester should be used.

Lead. Most testing on lead is done on thicker specimens with the Rockwell E and H scales.

Tin plate is tested on the Rockwell superficial HR15T, HR30T, and HR45T scales along with a diamond spot anvil in accordance with the following criteria:

Thickness		Scale
mm	in.	
<0.212	<0.0083	HR15T
0.213–0.547	0.0084–0.0215	HR30T
0.548–0.770	0.0216–0.0303	HR45T

Since most results are reported in the HR30T scales, all test results in the other scales are converted using the standard conversion chart found in ASTM E 140 (Ref 6).

Cemented carbides are tested primarily with the Rockwell A scale as designated in ASTM B 294 (Ref 7). Using the Rockwell C scale has resulted in poor diamond longevity due to breakage. Because of the extremely high stress placed on the diamond point, only indenters designated for carbide testing should be used. It should be noted that the carbide Rockwell A scale hardness levels are not the same as the steel Rockwell A scale levels because of the use of diamond indenters. Interchanging indenters will give incorrect results. See the section on Rockwell hardness testing in the article “Macroindentation Hardness Testing” for more information about the differences.

Cemented carbides are P/M products produced by sintering and thus may also contain tiny voids. However, the amount of void area on the surface usually is not large enough to complicate hardness testing. Cemented carbides are also composite materials made of hard carbides with a cobalt binder. The soft cobalt binder occupies approximately 20% of the area, whereas the remaining 80% consists of hard carbide particles that have hardness values of 9 on Mohs scale (diamond is 10) or 1500 HV and above. Obviously, the macroindentation hardness is an average value for this composite material. The carbide content is the principal contributor to the hardness.

Hardness Testing of Plastics

Hardness testing of plastics presents many variables that do not relate to the testing of metals. For example, plastics are much more sensitive to humidity and temperature than metals. The deformation of plastics is also very time dependent, and plastics may exhibit excessive flow characteristics during force applications. Because of these extenuating factors special procedures are given in ASTM D 785 (Ref 2) for Rockwell testing of plastics. These include:

5. Conditioning of the test specimen at a controlled temperature and relative humidity level
6. Requirements for the application and dwell time of the preliminary force
7. Application of the additional force within 10 s of applying the preliminary force
8. Removing the additional force, after the extended dwell time (usually 15 s) or until further penetration has apparently stopped, as indicated with the depth indicator (gage)
9. Extending the read time to 15 s after the removal of the additional force

It should be noted that some of these same conditions also apply to Vickers or Knoop hardness testing of plastics.

In the Rockwell test (ASTM D 785) (Ref 2), penetrators generally are balls 3.18, 6.35, and 12.7 mm (0.125, 0.25, and 0.50 in.) diameter at major loads of 60, 100, and 150 kg. Because of the creep and recovery characteristics of plastics, dwell times are carefully controlled, and specimens should be conditioned for temperature and humidity. Hardness tests on plastics are an indication of cure of some thermosetting materials and an indication of punching quality of laminated sheet stock.

For metals, excluding shapes such as tubes, the movement of the dial gage caused by the elasticity of the metal being tested is small and not considered to be a problem. Elasticity may reach considerable proportions with plastics. In addition to the spring of the tester frame, elasticity may prevent full application of the major load because of limitations in the design of the tester.

The limitation of the standard model Rockwell tester is considered to be 150 dial gage divisions under a 150 kgf load. This figure represents the number of divisions of travel on the dial gage, when the major load is applied, due to penetration into the material under tests, spring of the frame, penetrator, plunger rod system, and elasticity of the material under test. Special Rockwell testers, designated as “PL” models, increase this limitation to 250 divisions under a load of 150 kgf.

To determine whether the machine limitation is being exceeded and the major load is being fully applied, the major load can be tested in the following manner. With the major load still applied, an additional load can be applied by manually exerting pressure on the weights on the machine; the dial gage needle then should indicate additional penetration. If not, the full major load might not be acting (due to reaching limit of depth of indentation), and faulty readings can result. In this instance, the manufacturer should be contacted.

Use of the Alpha Scale. A variation of the standard Rockwell test is often used for testing plastics. It is referred to as the alpha Rockwell hardness number in Procedure B of ASTM D 785 (Ref 2). The advantage of the alpha scale is that it covers the range of plastics.

The standard Rockwell tester is used with a major load of 60 kgf and 12.7 mm (½ in.) ball penetrator. The test is made by applying the minor load in the usual manner, setting the dial to “set,” and applying the 60 kgf major load for 15 s. With the major load applied, the number of divisions the penetrator has traveled from “set” is read on the dial gage. From this reading, the spring of the tester is subtracted, determined under the major load of 60 kgf, and the remainder is subtracted from 150.

The spring of the machine, known as the “spring constant,” is determined as follows:

- Place a soft copper block of sufficient thickness and with plane parallel surfaces on the anvil in the normal testing position.
- Raise the sample and the anvil by the capstan screw until the large pointer is at the set position.
- Apply the major load by tripping the load release lever.

The dial gage then will indicate the vertical distance of indentation, the spring of the machine frame, and any other elastic compressible deformation of the plunger rod system and penetrator. This operation should be repeated several times without moving the block. However, the dial must be reset after each test while under minor load until the deflection of the dial gage becomes constant—that is, until no further indentation takes place, and only the spring of the instrument remains. This value, in terms of dial divisions, is the spring constant.

Durometer Testing. The durometer is a well-known and widely used instrument for measuring hardness of virtually all types of plastics, rubbers, and various rubberlike materials. The durometer measures hardness by means of an indentation much like that used in hardness testing of metals. The indenters used in durometers, however, are spring loaded rather than forced by weights. Nonmetallic materials, similar to metals, vary greatly in hardness, thus requiring a variety of test instruments. Several types of durometers accommodate the full range of hardness, and special instruments are available for testing O-rings and extremely thin materials. The various types available are listed in the left column of Table 14; however, only two (A and D) are covered in ASTM D 2240 (Ref 8).

Table 14 Specifications of durometers

Durometer type	Main spring	Indenter	Applications
A (conforms to ASTM D 2240)	822 g	Frustum cone	Soft vulcanized rubber and all elastomeric materials, natural rubber, GR-S, GR-1, neoprene, nitrile rubbers, Thiokol, flexible polyester cast resins, polyacrylic esters, wax, felt, and leather
B	822 g	Sharp included angle	30° Moderately hard rubber such as typewriter rollers and platens
C	20 lb	Frustum cone	Medium-hard rubber and plastics
D (conforms to ASTM D 2240)	10 lb	Sharp included angle	30° Hard rubber and the harder grades of plastics such as rigid thermoplastic sheet. Plexiglas (AtoHaas Americas Inc.), polystyrene, vinyl sheet, cellulose acetate and thermosetting laminates such as Formica (Formica Corp., Cincinnati, OH), paper-filled calendar rolls, and calendar bowls
D0	10 lb	2.4 mm (3/32 in.) sphere	Very dense textile windings and slasher beams
0	822 g	2.4 mm (3/32 in.) sphere	Soft printer rollers, Artgum, medium-density textile windings of rayon, orlon, and nylon
00	4 oz	2.4 mm (3/32 in.) sphere	Sponge rubber and plastics, low-density textile windings; not for use on foamed latex
000 (available with round dial only)	4 oz	13 mm (1/2 in.) diam spherical	Ultrasoft sponge rubber and plastic
T	822 g	2.4 mm (3/32 in.) sphere	Medium-density textile windings on spools and bobbins with a maximum diam of 100 mm (4 in.); types T and T-2 have a concave bottom plate to facilitate centering on cylindrical specimens

Durometers are used for measuring hardness of plastics and rubbers ranging from ultrasoft sponge rubbers to hard plastics. A list of test materials correlated with the specific type of durometer, main spring data, and type of indenter is presented in Table 15. In some instances, durometer test results can be converted to another scale. A partial conversion chart is shown in Fig. 8. The types of durometers range from simple handheld devices (Fig. 9) to laboratory instruments with digital readout for accurate and reproducible readings. Materials that are too thin for hardness measurement by conventional instruments can be measured with durometers for thin and microthin samples.

Table 15 Taylor's equations for estimating the tensile strength from hardness data

Material	Tensile strength (MPa)	Tensile strength (ksi)
Heat treated carbon and alloy steels	(3.24–3.55) HB	(0.470–0.515) HB
Annealed carbon steels	(3.55–3.86) HB	(0.515–0.560) HB
All steels	(3.09–3.55) HB	(0.448–0.515) HV
Nickel-chromium austenitic stainless steels	(3.09–3.32) HV	(0.448–0.482) HV
Steel: sheet, strip, and tube	(2.85–3.71) HV	(0.414–0.538) HV
Aluminum alloys: bar and extrusions	(2.94–4.48) HB (2.85–4.17) HV	(0.426–0.650) HB (0.414–0.605) HV
Aluminum alloys: sheet, strip, and tube	(3.24–4.01) HV	(0.470–0.582) HV

Aluminum-copper castings	(1.70–2.94) HB	(0.246–0.426) HB
Al-Si-Ni castings	(2.32–2.94) HB	(0.336–0.426) HB
Aluminum-silicon castings	(2.63–3.71) HB	(0.381–0.538) HB
Phosphor bronze castings	(2.32–3.24) HB	(0.336–0.470) HB
Brass castings	(3.24–4.63) HB	(0.470–0.672) HB

Source: Ref 9

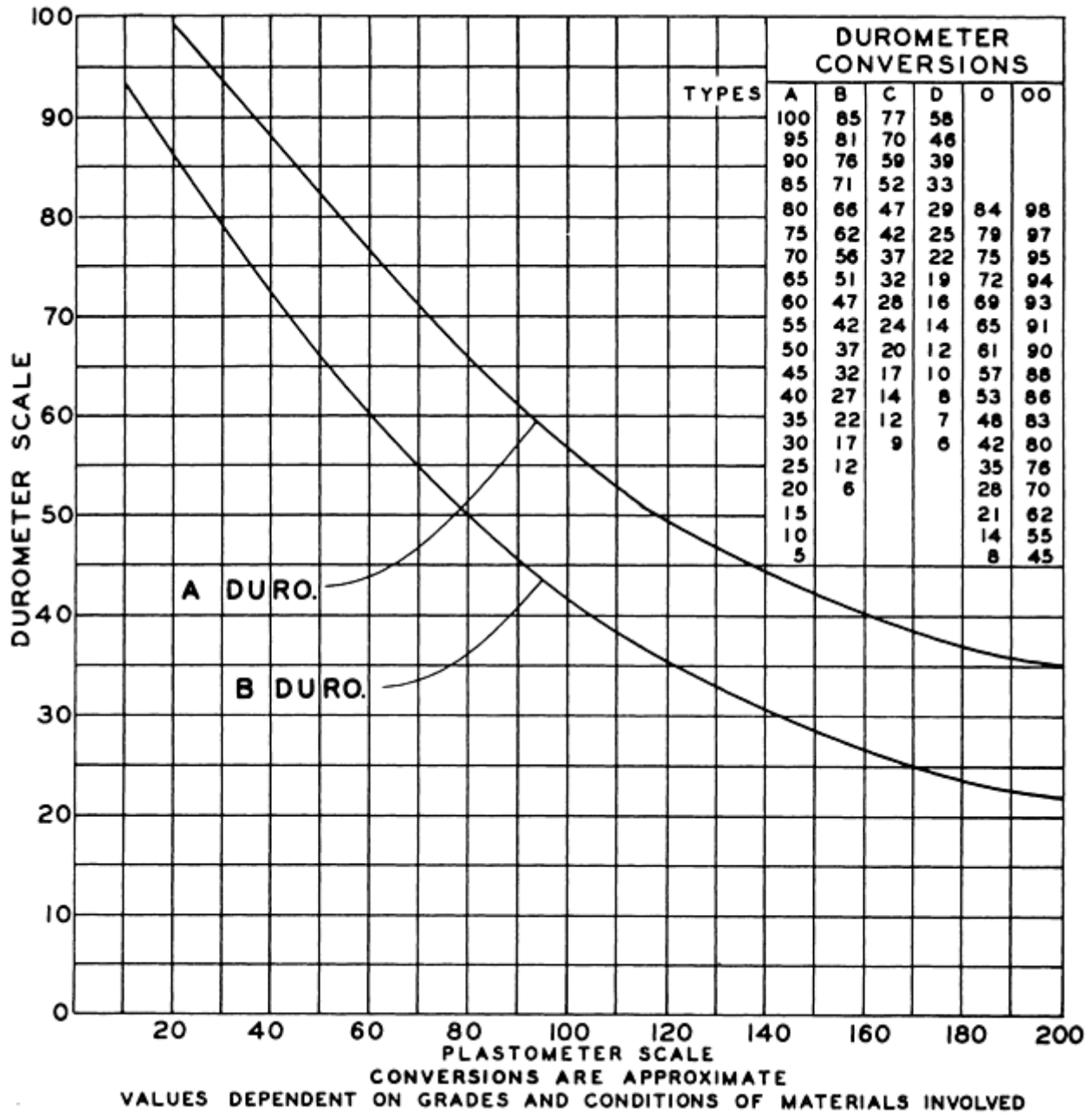


Fig. 8 Durometer-plastometer conversion chart. Courtesy of Shore Instruments, Division of Instron Corporation



Fig. 9 Handheld durometer for testing hardness of plastic and rubber materials. Courtesy of NewAge Industries

Additional information about durometer testing is provided in the article “Miscellaneous Hardness Tests” in this Volume.

References cited in this section

1. “Standard Test Method for Rockwell Hardness of Plastics and Electrical Insulating Materials,” D 785-98, *Annual Book of ASTM Standards*, ASTM
2. “Determination of Apparent Hardness of Powder Metallurgy Products,” MPIF 43 (1995), *Standard Test Methods for Metal Powders and Powder Metallurgy Products*, Metal Powder Industries Federation, 1999
4. “Determination of Microhardness of Powder Metallurgy Materials,” MPIF 51 (1994), *Standard Test Methods for Metal Powders and Powder Metallurgy Products*, Metal Powder Industries Federal, 1999
5. “Standard Hardness Conversion Tables for Metals (Relationship among Brinell Hardness, Vickers Hardness, Rockwell Hardness, Rockwell Superficial Hardness, Knoop Hardness, and Scleroscope Hardness),” E 140-97e1, *Annual Book of ASTM Standards*, ASTM
6. “Standard Test Method for Hardness Testing of Cemented Carbides,” B 294-92(1997), *Annual Book of ASTM Standards*, ASTM
7. “Standard Test Method for Rubber Property-Durometer Hardness,” D 2240-97e1, *Annual Book of ASTM Standards*, ASTM
8. W.J. Taylor, The Hardness Test as a Means of Estimating the Tensile Strength of Metals, *J. Royal Aeronaut. Soc.*, Vol 46 (No. 380), 1942, p 198–209

Selection and Industrial Applications of Hardness Tests

Andrew Fee, Consultant

Applications of Hardness Testing

Hardness testing has many applications in quality control, materials evaluation, and the prediction of properties. Because hardness testing is nondestructive and quick, it is a very useful tool for manufacturing and process control. For example, the most common application of the Rockwell test is testing steels that have been hardened and tempered. If a hardened-and-quenched steel piece is tempered by reheating at a controlled and relatively low temperature and then cooled at a control rate and time, it is possible to produce a wide range of desired hardness levels. By using a hardness test to monitor the end results, the operator is able to determine and control the ideal temperatures and times so that a specified hardness may be obtained.

Quality Control

Decarburization. In general, decarburization is an unwanted condition that results in a softer surface (or skin) on the metal. This is caused by the loss of carbon from the surface of the material during a heat treatment process. Unless it is removed, the part may not have the properties necessary to perform its function. A Rockwell test, because it is done on the surface of the part, will frequently indicate this soft condition. An example of the most commonly used method to determine if decarburization exists is to make Rockwell 15N and C scale tests in the same area of the part. When the converted values are compared, if the Rockwell 15N value, converted to C, is significantly lower than the unconverted Rockwell C value, a soft, decarburized layer is most likely present. Removing the layer and retesting will confirm the diagnosis.

Statistical Process Control (SPC). When large populations of materials make testing each workpiece impractical and a tighter control is demanded for a product, SPC is usually incorporated. This means of statistical control can enable continual product manufacturing with minimum testing and a high level of quality. Because many hardness tests are done rapidly, they are well suited for use with SPC techniques. Users are cautioned that the proper testing procedures must be followed to ensure the high degree of accuracy necessary when using SPC.

Measurement of Case Depth

The surface layer of case-hardened steels is generally characterized in terms of:

- Case hardness
- Effective case depth (typically defined as the depth where hardness has a value of 50 HRC, unless otherwise specified)
- Total case depth (which is the depth at which no difference in chemical or physical properties can be distinguished between the case and the core)

In testing case-hardened material it is essential that the depth of case be sufficient to support the test being conducted. The rule that the case be at least 10 times thicker than the depth of indentation should be followed. This 10-to-1 ratio is based on the flow characteristics of most steels; if, however, the material being tested has flow characteristics unlike most steels a greater ratio may be required.

The most accurate and repeatable method of determining effective or total case depth is by means of some type of hardness traverse. A hardness traverse indicates the precise hardness characteristics from the edge to the core. Hardness depths may be studied by either taper or step grinding as illustrated in Fig. 10. When the case is very thin, but quite hard, as usually found in materials that have been nitrided, a more qualitative method for determining case depth is done by making a microindentation hardness traverse on a cross section of a prepared specimen. Surface hardness can be determined on cases as thin as 10 μm (0.0005 in.) with this method. The cross-section method, while time consuming, is the most common process used to determine case depth.

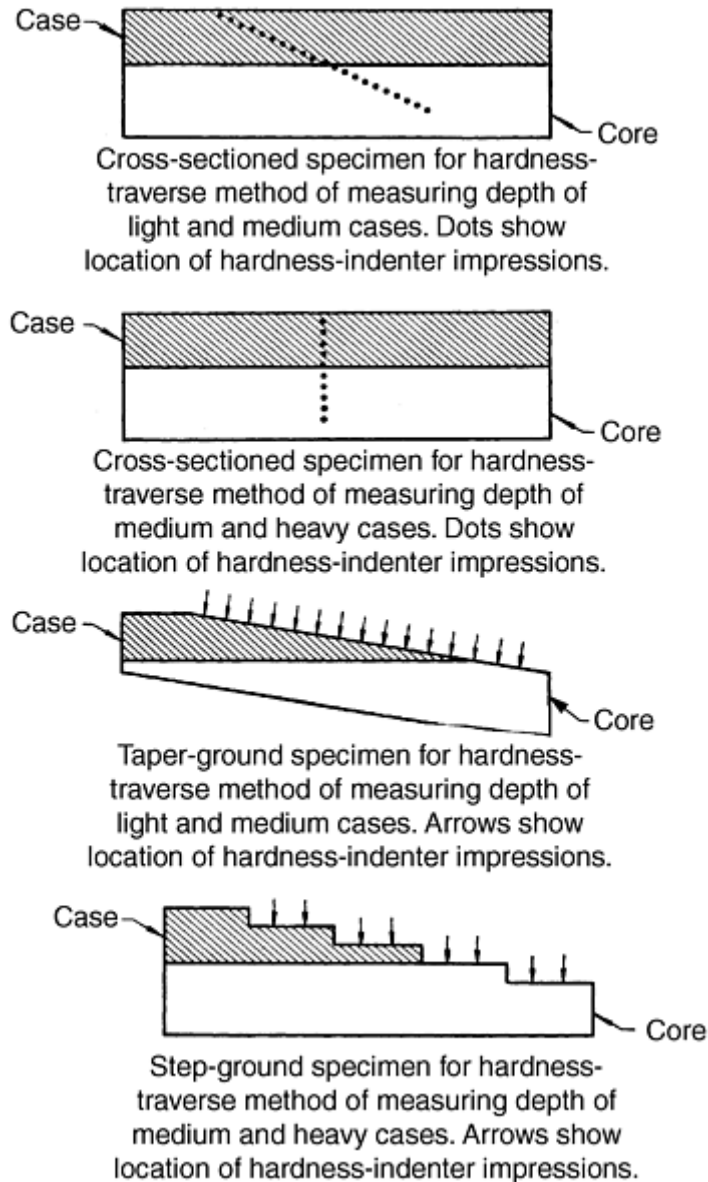


Fig. 10 Hardness traverse methods for case-hardness profiling

Hardenability Testing

One of the important properties of alloyed steels is their ability to be hardened to a much greater depth than plain-carbon steels. In many cases, they can be hardened throughout their entire thickness. The degree of depth hardening is not the same for all alloying elements. Therefore, hardenability testing is used to evaluate the hardening of steels.

A number of hardenability tests have been devised (principally by means of the Rockwell C scale), but the Jominy end-quenching hardness test has proved to be the method with the highest degree of reproducibility. It has been almost universally adopted in evaluating virtually all standard alloy steels and for some grades of carbon steels. The test is relatively simple to perform and can produce much useful information for the designer, as well as for the fabricator.

Jominy End-Quenching Hardness Test. Although variations are sometimes made to accommodate specific requirements, the test bars for the end-quench test are normally 25 mm (1 in.) in diameter by 100 mm (4 in.) long. The specimen has a collar on one end to hold it in a quenching jig (Fig. 11).

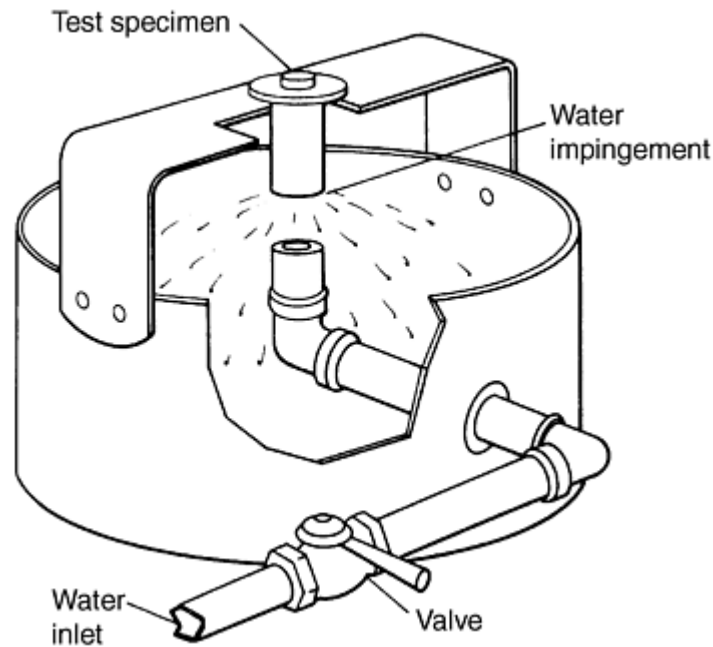


Fig. 11 Standard end-quench (Jominy) test specimen and method of quenching in quenching jig

In this test, the water flow is controlled by a suitable valve so that the amount striking the end of the specimen (Fig. 11) is constant in volume and velocity. The water impinges on the end of the specimen only and drains away. By this means, cooling rates vary from about the fastest possible on the quenched end to very slow, essentially equal to cooling in still air, on the opposite end. This results in a wide range of hardnesses along the length of the bar.

After the test bar has been quenched, two opposite and flat parallel surfaces are ground along the length of the bar to a depth of 0.381 mm (0.015 in.). Rockwell C hardness determinations then are made every 1.59 mm (0.0625 in.). A specimen-holding indexing fixture is helpful for this operation for convenience, as well as for accuracy. Such fixtures are available as accessory attachments for conventional Rockwell testers.

The next step is to record the readings and plot them on graph paper to develop a curve (Fig. 12). By comparing the curves resulting from end-quench tests of different grades of steel (Fig. 13), relative hardenability can be established. Steels with higher hardenability will be harder at a given distance from the quenched end of the specimen than steels with lower hardenability. Thus, the flatter the curve is, the greater the hardenability will be. On the end-quench curves, hardness usually is not measured beyond approximately 50 mm (2 in.) because hardness measurements beyond this distance are seldom of any significance. At approximately 50 mm (2 in.) from the quenched end, the effect of water on the quenched end has deteriorated, and the effect of cooling from the surrounding air has become significant. An absolutely flat curve demonstrates conditions of very high hardenability, which characterize an air-hardening steel, such as some highly alloyed steels.

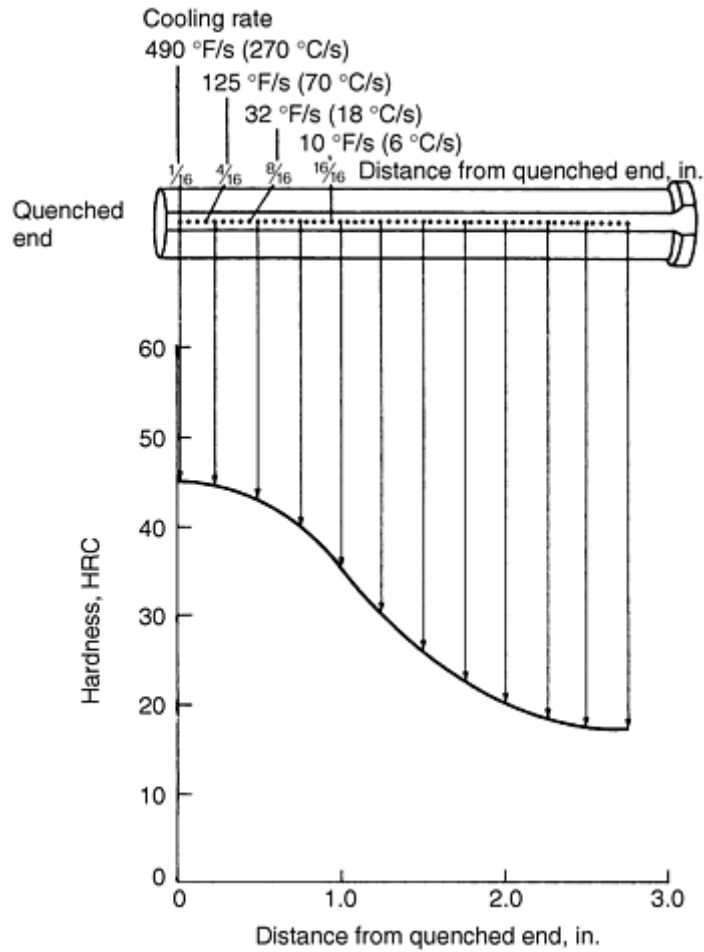


Fig. 12 Method of developing end-quench curve by plotting hardness versus distance from quenched end. Hardness plotted every 6.4 mm ($\frac{1}{4}$ in.), although Rockwell C readings were taken in increments of 1.59 mm ($\frac{1}{16}$ in.), as shown on top of illustration.

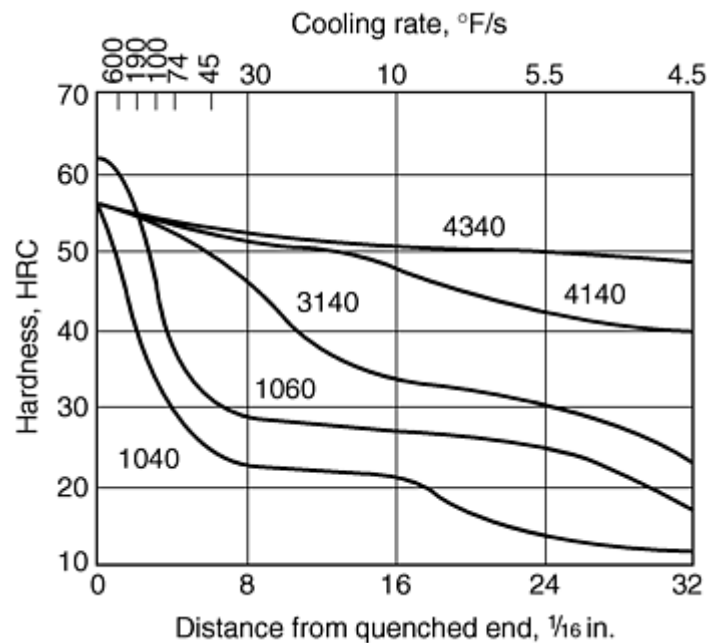


Fig. 13 Plot of end-quench test results for five different steels

Additional information about Jominy end-quench hardenability is provided in the article “Quantitative Prediction of Transformation Hardening in Steels” in *Heat Treating*, Volume 4 of *ASM Handbook*.

Introduction to Adhesion, Friction, and Wear Testing

Peter J. Blau, Oak Ridge National Laboratory

Introduction

THE SURFACES OF SOLIDS play many different and important roles in technology. Their functions range from imparting a pleasing appearance to protecting the underlying material from wear and corrosion, and from bearing contact loads to serving as the substrates for coatings. The properties of free surfaces differ from those of bulk materials. A variety of specialized testing methods, therefore, have been developed specifically for characterizing the mechanical behavior of surfaces and the treatments and coatings applied to them.

In some engineering applications, like the bonding or fastening of parts, surfaces are placed in intimate contact with the intention that they will not move relative to one another. In other cases, as in bearings, gears, brakes, and rotating face seals, adjacent surfaces are intended to move relative to one another in a smooth and stable fashion, while at the same time supporting a normal load. Sometimes, as in the attachment of protective coatings to a surface, strong adhesion is desirable, but in other instances, as in the seizure and galling of sliding bearings, strong adhesion is not desirable. Likewise, low friction might be desirable for a face seal but undesirable for a brake pad. A high rate of abrasive wear for a paper mill slitter-knife blade is to be avoided, yet the high abrasive wear rate associated with grinding prepares the surfaces of castings for mating with other parts. Consequently, adhesion, friction, and wear are neither inherently good nor bad. Rather, they are important to both the cosmetic and engineering functions of parts and must, therefore, be measured and controlled.

Under some conditions, adhesion, friction, and wear are directly related, but under other conditions they are not. For example, when clean metals rub against one another, adhesion can occur, raising the friction and promoting the deformation and fracture of the softer material. The more extensive these processes are, the more the wear. By contrast, there are cases in which the sliding friction of an interface can be relatively high (disc brake pads against rotors), but the wear of the materials involved is relatively low. While appearing contrary to intuition, the high-friction/low-wear situation becomes understandable when friction is viewed as the energy available to do work on a material, and wear is but one of the possible ways in which a system can dissipate that energy—conversion into heat being another. Thus, two sliding couples can possess nearly the same friction coefficients but greatly different wear rates.

In this Section, tests designed specifically to evaluate the adhesion, friction, and wear behavior of various material systems are described. Included within the wear category are other forms of surface damage, like galling and scuffing. Unlike other mechanical properties, such as the elastic constants or shear strength, properties of adhesion, friction, and wear depend strongly upon the surface conditions of the solid and not exclusively upon its bulk structure. The selection of appropriate test methods to meet engineering requirements for adhesion, friction, and wear, therefore, is somewhat complicated. Each functional requirement must be analyzed on a case-by-case basis, and no one test is universally the best for measuring either adhesion, friction, or wear.

Introduction to Adhesion, Friction, and Wear Testing

Peter J. Blau, Oak Ridge National Laboratory

Adhesion Testing

The article “Adhesion Testing” in this Section describes many different techniques and test methods that have been devised for measuring the adhesion between solids. There is little standardization in this field, although some investigators tend to favor one method over another. Most adhesion test methods are designed to assess the ability of two materials to remain connected to one another despite the application of external or internal body forces in various directions with respect to the interface. For example, different types of adhesion tests have been designed to measure resistance to peeling, shearing, and delamination. In a few instances, adhesion tests are used in the study of frictional phenomena that occur at a fine scale between protuberances on mating surfaces. The article on adhesion testing contains a more complete discussion of these test methods and a bibliography.

Introduction to Adhesion, Friction, and Wear Testing

Peter J. Blau, Oak Ridge National Laboratory

Friction Testing

Friction and wear are not basic properties of materials but rather represent the response of a material pair in a certain environment to imposed forces, which tend to produce relative motion between the paired materials. Friction and wear behavior is, therefore, subject to the considerations of testing geometry, the characteristics of the relative motion, the contact pressure between the surfaces, the temperature, the stiffness and vibrational properties of the supporting structures, the presence or absence of third bodies, the duration of contact, and the chemistry of the environment in and around the interface. Tables of friction coefficients should not be trusted to provide applicable numerical values unless the conditions used to develop the data closely mimic those of the application for which the data are intended. Since frictional interactions occur under a wide variety of contact conditions and size scales, selecting test methods for screening materials or lubricants for frictional behavior should be done with care.

The article “Testing Methods for Solid Friction” describes a variety of methods that have proven useful in measuring friction coefficients, both under static and kinetic conditions. Since frictional response is sometimes sensitive to the preparation and cleaning of surfaces, these factors should be addressed when developing friction testing procedures. Other testing variables, some of them rather subtle (like the fixture stiffness or thermal conductivity), can affect friction test results in some cases. Frictional transitions, like running-in, are common in engineering systems (Ref 1), so they should be considered when deciding on the type of data collection method.

Standard test methods, like those produced by ASTM, can be useful not only as guides to friction testing procedures but also as a source of information on which test variables should be controlled. Published standards, like friction test methods in general, do not address all possible needs for friction measurement, and thus, the engineer might need to devise his or her own tests to fit the situation.

Reference cited in this section

1. P.J. Blau, *Friction Science and Technology*, Marcel Dekker, Inc., 1996

Introduction to Adhesion, Friction, and Wear Testing

Peter J. Blau, Oak Ridge National Laboratory

Scratch Testing

Scratch tests are used for two main purposes:(a) to measure the adhesion of a coating or film to a surface, or (b) to measure the resistance of a surface to damage from a harder opposing body. Scratch testing methods for the former purpose are described in the article “Adhesion Testing.” Scratch tests used for the latter purpose are described in the article “Scratch Testing” in this Volume. The use of scratch tests has a relatively long history, having been introduced by the German mineralogist Friedrich Mohs in 1822 for identifying different mineral species. The ability of a mineral to scratch or be scratched by another mineral is an important clue to its identification, and use of the Mohs test persists to this day.

During recent years, scratch tests have been instrumented using force and acoustic emission sensors to provide additional information for materials and coatings characterization. Diamond is the material of choice for most scratch testing indenters, but diamond is not the only material used in scratch tests. Hardened steel files, for example, are used for scratch testing under certain circumstances. New testing parameters, such as the critical load for coating failure and the scratching coefficient (i.e., the normal force divided by the tangential force that resists scratching), have been introduced to measure other surface properties. Scratch tests can be useful for obtaining numerical rankings of the resistance of a material to single-point abrasion and for assessing the mechanisms of material removal under abrasive conditions.

Introduction to Adhesion, Friction, and Wear Testing

Peter J. Blau, Oak Ridge National Laboratory

Testing for Wear and Surface Damage of Various Kinds

Because wear and surface damage take on many different forms, several articles on wear and surface damage testing have been included in this Volume. Wear is a form of mechanically induced surface damage that results in the progressive removal of material from a surface. Galling, chipping, or scratching can occur with one contact event, and not being progressive, these phenomena are not strictly forms of wear. However, they still fall under the category of surface damage. Because a great many types of surface damage occur in machinery, different types of tests have been developed. The chapters in this Section describe quite a few of them, but it is possible that a specialized method must be developed to effect a simulation of specific conditions or to isolate a certain form of wear for detailed study.

Selection of the right type of test becomes critically important in order to achieve engineering relevance. In fact, materials and surface treatments can rank in opposite order when tested for resistance to different forms of wear (Ref 2). More than one type of wear can attack the same part, like both sliding and impact wear in printing presses, and both erosive and abrasive wear on plastic extrusion machine screws. Sometimes wear can operate in the presence of corrosive or chemically active environments, and synergistic chemomechanical effects are possible. The selection of an appropriate wear testing method begins with an assessment of the type of wear involved as well as the mechanical conditions and the environment that produced it.

Having a structured classification of wear types can make test selection easier. Different classification schemes for wear have been developed because those who developed them have come from different backgrounds with different experiences with wear. No one scheme is universally accepted, but most systems have similar features. For example, mechanical wear can be classified by the type of relative motion: (a) tangential motion (sliding), (b) impact, and (c) rolling (Ref 3). An abbreviated summary of the common wear and surface damage types, categorized in this way, is given in Table 1. Formal definitions for the important types of wear are provided in the *ASM Handbook*, Vol 18, *Friction, Lubrication and Wear Technology* (Ref 4). That Volume also contains reviews of each major form of wear and comprehensive discussions of wear mechanisms, the wear of different types of materials, and application-specific methods for wear control.

Table 1 Common types of wear and mechanical surface damage

Category	Characteristics
Sliding wear	Tangential motion and traction between surfaces
2 body abrasive wear	Wear by fixed hard particles moving along a surface
3 body abrasive wear	Wear by hard particles passing between opposing bodies
Adhesive wear	Wear arising from the localized adhesion of one surface to another, which results in plastic deformation and fracture with the transfer of detached material to the opposing surface
Fretting wear	Wear arising from short-amplitude oscillations or tangential contact vibrations
Fatigue wear	Wear involving the nucleation and propagation of surface and/or subsurface cracks under cyclic tangential forces arising from sliding contact
Polishing wear	Fine-scale wear by the action of hard particles, chemomechanical processes, or both
Impact wear	Normal forces acting cyclically on surfaces
Single-body impact wear	Wear from the repeated impact of a second body
Multibody impact wear	Wear from the repeated impact of particles, bubbles, droplets, or energy discharges. Examples include particle impingement erosion, cavitation erosion (wear by imploding bubbles), slurry erosion, and spark erosion.
Rolling contact wear	Wear from the accumulation of surface damage during the cyclic stressing of one body rolling over or along another
Surface damage other than wear (examples)	Loss or displacement of material from a surface owing to mechanical contact in some form
Chipping	Removal of material from a surface, generally involving brittle crack propagation and the production of shell-like features. Chipping commonly occurs at sharp corners or edges of brittle contact surfaces.
Scuffing	Plastic deformation of surface material by rubbing, which generally produces a smooth appearance and is often localized in certain areas of the surface. Scuffing is sometimes referred to as <i>incipient galling</i> .
Scratching	Production of one or more shallow grooves in a surface by a hard counter body moving tangentially along the surface
Galling	A severe form of surface material displacement involving plastic deformation and the loss of fit between counter surfaces
Gouging	A severe form of localized plastic deformation in which relatively deep, localized troughs are produced
Scoring	Production of one or more deep scratches in a body generally involving plowing by a hard particle or protuberance on an opposing body
False Brinelling	Production of clusters of craters similar in appearance to hardness indentations with a spherical indenter
Frosting	The production of a dull appearance, typically on a bearing surface, due to a random pattern of fine scratches or gouges

The descriptions given in the “Characteristics” column of Table 1 suggest that the use of wear terminology is not without ambiguities. It is therefore important, when discussing or reporting on wear problems, to describe the phenomena sufficiently well so that terminology ambiguities are avoided. Wear problems can be further complicated by environmental interactions, such as oxidation or other surface chemical reactions, which occur along with wear. In fact, some wear classification schemes list oxidational or chemical wear as major forms of wear. Tests for most of the important forms of wear listed in Table 1 are described in this section. Sources for information regarding impact wear, polishing wear, and other types not covered here are listed in the bibliography.

Abrasive wear is one of the most economically important types of wear. The cost of damaged equipment, down time, and materials loss attributable to abrasive wear in the mining and agriculture industries alone is staggering. Several types of two-body and three-body abrasive wear tests are described. As with other types of

wear, more than one kind of test can be needed to establish the suitability of a given material, coating, or surface treatment for complex abrasive environments.

Erosive wear, as indicated in Table 1, can involve removal of material by impinging solids, liquids, liquid-entrained or gas-entrained solids, bubbles (cavitation erosion), or sparks. Like abrasive wear, erosive wear is a costly form of wear in industry. It attacks piping, pumping equipment, turbomachinery, and conveyor systems. Loose particles from erosive wear can also travel to other parts of a machine, creating secondary damage and loss of function. The variables associated with different types of erosive wear tests commonly include impingement angle, impingement velocity, screening by rebounding particles, and the shapes and sizes of the erodent particles.

Sliding contact, like galling or scuffing, can produce surface damage with only one contact event, or it can be a progressive form of wear like fretting or other repetitive contact types of wear. The article “Testing for Sliding Contact Damage” in this Section describes several forms of sliding contact damage and the methods commonly used to evaluate the resistance of materials to these damages.

Just as machines and their parts exist in a spectrum of sizes, friction and wear phenomena can also occur in various size scales. Obviously, the fine-scale interfacial contact processes involved in nanoscale coatings on hard disks require a different testing approach than the macroscale wear that occurs on the digger teeth of mining equipment and on the bows of icebreakers. Therefore, not only are there different types of wear, like abrasive wear, erosive wear, and so on, but there are also different size-scales of wear phenomena.

References cited in this section

2. H. Czichos, *Tribology: A Systems Approach*, Elsevier, Amsterdam, Netherlands, 1978, p 322–325
3. P.J. Blau, Wear Testing, *Metals Handbook Desk Edition*, ASM International, 1998, p 1342–1347
4. P.J. Blau, Glossary, *Friction, Lubrication, and Wear Technology*, Vol 18, ASM Handbook, ASM International, 1992, p 1–21

Introduction to Adhesion, Friction, and Wear Testing

Peter J. Blau, Oak Ridge National Laboratory

Testing for Wear and Surface Damage of Various Kinds

Because wear and surface damage take on many different forms, several articles on wear and surface damage testing have been included in this Volume. Wear is a form of mechanically induced surface damage that results in the progressive removal of material from a surface. Galling, chipping, or scratching can occur with one contact event, and not being progressive, these phenomena are not strictly forms of wear. However, they still fall under the category of surface damage. Because a great many types of surface damage occur in machinery, different types of tests have been developed. The chapters in this Section describe quite a few of them, but it is possible that a specialized method must be developed to effect a simulation of specific conditions or to isolate a certain form of wear for detailed study.

Selection of the right type of test becomes critically important in order to achieve engineering relevance. In fact, materials and surface treatments can rank in opposite order when tested for resistance to different forms of wear (Ref 2). More than one type of wear can attack the same part, like both sliding and impact wear in printing presses, and both erosive and abrasive wear on plastic extrusion machine screws. Sometimes wear can operate in the presence of corrosive or chemically active environments, and synergistic chemomechanical effects are possible. The selection of an appropriate wear testing method begins with an assessment of the type of wear involved as well as the mechanical conditions and the environment that produced it.

Having a structured classification of wear types can make test selection easier. Different classification schemes for wear have been developed because those who developed them have come from different backgrounds with different experiences with wear. No one scheme is universally accepted, but most systems have similar features. For example, mechanical wear can be classified by the type of relative motion: (a) tangential motion (sliding), (b) impact, and (c) rolling (Ref 3). An abbreviated summary of the common wear and surface damage types, categorized in this way, is given in Table 1. Formal definitions for the important types of wear are provided in the *ASM Handbook*, Vol 18, *Friction, Lubrication and Wear Technology* (Ref 4). That Volume also contains reviews of each major form of wear and comprehensive discussions of wear mechanisms, the wear of different types of materials, and application-specific methods for wear control.

Table 1 Common types of wear and mechanical surface damage

Category	Characteristics
Sliding wear	Tangential motion and traction between surfaces
2 body abrasive wear	Wear by fixed hard particles moving along a surface
3 body abrasive wear	Wear by hard particles passing between opposing bodies
Adhesive wear	Wear arising from the localized adhesion of one surface to another, which results in plastic deformation and fracture with the transfer of detached material to the opposing surface
Fretting wear	Wear arising from short-amplitude oscillations or tangential contact vibrations
Fatigue wear	Wear involving the nucleation and propagation of surface and/or subsurface cracks under cyclic tangential forces arising from sliding contact
Polishing wear	Fine-scale wear by the action of hard particles, chemomechanical processes, or both
Impact wear	Normal forces acting cyclically on surfaces
Single-body impact wear	Wear from the repeated impact of a second body
Multibody impact wear	Wear from the repeated impact of particles, bubbles, droplets, or energy discharges. Examples include particle impingement erosion, cavitation erosion (wear by imploding bubbles), slurry erosion, and spark erosion.
Rolling contact wear	Wear from the accumulation of surface damage during the cyclic stressing of one body rolling over or along another
Surface damage other than wear (examples)	Loss or displacement of material from a surface owing to mechanical contact in some form
Chipping	Removal of material from a surface, generally involving brittle crack propagation and the production of shell-like features. Chipping commonly occurs at sharp corners or edges of brittle contact surfaces.
Scuffing	Plastic deformation of surface material by rubbing, which generally produces a smooth appearance and is often localized in certain areas of the surface. Scuffing is sometimes referred to as <i>incipient galling</i>.
Scratching	Production of one or more shallow grooves in a surface by a hard counter body moving tangentially along the surface
Galling	A severe form of surface material displacement involving plastic deformation and the loss of fit between counter surfaces
Gouging	A severe form of localized plastic deformation in which relatively deep, localized troughs are produced
Scoring	Production of one or more deep scratches in a body generally involving plowing by a hard particle or protuberance on an opposing body
False Brinelling	Production of clusters of craters similar in appearance to hardness indentations with a spherical indenter
Frosting	The production of a dull appearance, typically on a bearing surface, due to a

random pattern of fine scratches or gouges

The descriptions given in the “Characteristics” column of Table 1 suggest that the use of wear terminology is not without ambiguities. It is therefore important, when discussing or reporting on wear problems, to describe the phenomena sufficiently well so that terminology ambiguities are avoided. Wear problems can be further complicated by environmental interactions, such as oxidation or other surface chemical reactions, which occur along with wear. In fact, some wear classification schemes list oxidational or chemical wear as major forms of wear. Tests for most of the important forms of wear listed in Table 1 are described in this section. Sources for information regarding impact wear, polishing wear, and other types not covered here are listed in the bibliography.

Abrasive wear is one of the most economically important types of wear. The cost of damaged equipment, down time, and materials loss attributable to abrasive wear in the mining and agriculture industries alone is staggering. Several types of two-body and three-body abrasive wear tests are described. As with other types of wear, more than one kind of test can be needed to establish the suitability of a given material, coating, or surface treatment for complex abrasive environments.

Erosive wear, as indicated in Table 1, can involve removal of material by impinging solids, liquids, liquid-entrained or gas-entrained solids, bubbles (cavitation erosion), or sparks. Like abrasive wear, erosive wear is a costly form of wear in industry. It attacks piping, pumping equipment, turbomachinery, and conveyor systems. Loose particles from erosive wear can also travel to other parts of a machine, creating secondary damage and loss of function. The variables associated with different types of erosive wear tests commonly include impingement angle, impingement velocity, screening by rebounding particles, and the shapes and sizes of the erodent particles.

Sliding contact, like galling or scuffing, can produce surface damage with only one contact event, or it can be a progressive form of wear like fretting or other repetitive contact types of wear. The article “Testing for Sliding Contact Damage” in this Section describes several forms of sliding contact damage and the methods commonly used to evaluate the resistance of materials to these damages.

Just as machines and their parts exist in a spectrum of sizes, friction and wear phenomena can also occur in various size scales. Obviously, the fine-scale interfacial contact processes involved in nanoscale coatings on hard disks require a different testing approach than the macroscale wear that occurs on the digger teeth of mining equipment and on the bows of icebreakers. Therefore, not only are there different types of wear, like abrasive wear, erosive wear, and so on, but there are also different size-scales of wear phenomena.

References cited in this section

2. H. Czychos, *Tribology: A Systems Approach*, Elsevier, Amsterdam, Netherlands, 1978, p 322–325
3. P.J. Blau, Wear Testing, *Metals Handbook Desk Edition*, ASM International, 1998, p 1342–1347
4. P.J. Blau, Glossary, *Friction, Lubrication, and Wear Technology*, Vol 18, ASM Handbook, ASM International, 1992, p 1–21

Introduction to Adhesion, Friction, and Wear Testing

Peter J. Blau, Oak Ridge National Laboratory

Adhesion, Friction, and Wear Testing Devices

Literally hundreds of devices for measuring adhesion, friction, and wear have been developed. Some of these are commercially manufactured but most of them probably have been custom-designed for specific purposes. This situation makes it difficult to compare the results from one study with those of another study unless the appropriate correlation has been established. There is no simple answer to the problems arising from the

proliferation of different testing machines for adhesion, friction, and wear. The use of established voluntary standards can help, but only if the standard applies directly to the problem of current concern. In the absence of widespread, commonly used test methods, it is necessary to analyze the applied conditions associated with each set of results carefully to determine the extent to which they can be compared to other work.

As with mechanical testing in general, commercial adhesion, friction, and wear testing machines are becoming increasingly computer automated. While automation has obvious advantages, it also necessitates conscientious calibration to ensure that the sensors and control mechanisms provide accurate readings to the computer.

In adhesion, friction, and wear testing, as in other forms of mechanical testing, the four most important requirements are (a) understanding the characteristics of the test method being applied, (b) expecting differing degrees of repeatability from different material types, (c) selecting the right testing tool for the job, and (d) coupling measurements with physical observations of contact surfaces to ascertain the causes for the measured behavior.

Introduction to Adhesion, Friction, and Wear Testing

Peter J. Blau, Oak Ridge National Laboratory

References

1. P.J. Blau, *Friction Science and Technology*, Marcel Dekker, Inc., 1996
2. H. Czichos, *Tribology: A Systems Approach*, Elsevier, Amsterdam, Netherlands, 1978, p 322–325
3. P.J. Blau, Wear Testing, *Metals Handbook Desk Edition*, ASM International, 1998, p 1342–1347
4. P.J. Blau, Glossary, *Friction, Lubrication, and Wear Technology*, Vol 18, ASM Handbook, ASM International, 1992, p 1–21
5. D.F. Moore, *Principles and Applications of Tribology*, Pergamon Press, Oxford, 1975, p 62–85

Introduction to Adhesion, Friction, and Wear Testing

Peter J. Blau, Oak Ridge National Laboratory

Selected References

- B. Bhushan and B.K. Gupta, *Handbook of Tribology*, McGraw-Hill, 1991
- *Friction and Wear Testing Source Book*, ASM International, 1997
- *Friction, Lubrication, and Wear Technology*, Vol 18, ASM Handbook, ASM International, 1992
- *Metals Handbook Desk Edition*, 2nd ed., ASM International, 1998
- R.G. Bayer, *Mechanical Wear Prediction and Prevention*, Marcel Dekker, Inc., 1995
- Special Technical Publications, ASTM
- W.A. Glaeser, *Characterization of Tribological Materials*, Butterworth-Heinemann Ltd., Boston, 1993
- *Wear Control Handbook*, M.B. Peterson and W.O. Winer, Ed., American Society of Mechanical Engineers, 1980

Adhesion Testing

Introduction

ADHESION refers to the interfacial bond strength between two materials in close proximity with one another. Adhesive bond strength can be described in several ways, depending on the nature of the interface. In physical chemistry, for example, adhesion is a fundamental term that refers to the attractive force between a solid surface and a second phase in either liquid or solid form. In this context, adhesion is a manifestation of the innate interatomic and intermolecular bonds that occur between the surfaces of two materials.

Other meanings of adhesion also arise in different disciplines related to mechanical engineering and the evaluation of coatings and films. In railway engineering, for example, adhesion often means friction (Ref 1) or the sliding resistance between two materials. In this context, the term adhesion refers to mechanical adhesion, which is defined as the adhesion produced by the interlocking of protuberances on the surfaces in an interface (Ref 1).

Adhesion also has important practical meaning in the evaluation of coatings, adhesives, and composite materials. Thin films ($<1\ \mu\text{m}$, or 0.04 mil), thick films ($>1\ \mu\text{m}$), and bulk coatings ($>25\ \mu\text{m}$, or 98 mils) all depend on adhesion, which can be evaluated and measured in a variety of ways, depending on the product configuration and application requirements. Therefore, it is not surprising that many methods are used to measure adhesion for films, coatings, and adhesive-bonded joints. Indeed, there are so many variations on adhesion measurements in coatings, surface films, and adhesives (Ref 2, 3, 4, 5, 6) that it would be impossible to describe them fully here.

Therefore, the purpose of this article is to describe briefly common adhesion measurement techniques for the three basic types of adhesion outlined by Mittal (Ref 2 and 6):

1. Fundamental (or basic) adhesion
2. Thermodynamic adhesion
3. Practical adhesion

Common measurement methods for each type of adhesion are briefly discussed, with the main focus on practical adhesion testing of coatings and thin films. However, to illustrate the use of adhesion testing in materials research, this article also includes a section on the use of adhesion tests in the evaluation of stress-corrosion cracking (SCC) within bimaterial interfaces.

References cited in this section

1. P.J. Blau, Glossary of Terms, *Friction, Lubrication, and Wear Technology*, Vol 18, *ASM Handbook*, ASM International, 1992
2. K.L. Mittal, Ed., *Adhesion Measurements of Films and Coatings*, VSP, 1995
3. K.L. Mittal, Ed., *Adhesive Joints*, Plenum Press, 1984
4. G.L. Schneberger, Ed., *Adhesives in Manufacturing*, Marcel Dekker, 1983
5. G.P. Anderson, S.J. Bennett, and K.L. DeVries, *Analysis and Testing of Adhesive Bonds*, Academic Press, 1977
6. K.L. Mittal, Ed., *Adhesion Measurement of Thin Films, Thick Films and Bulk Coatings*, STP 640, ASTM, 1978

Fundamental Adhesion

Fundamental adhesion refers to the basic intermolecular forces that occur whenever two materials are in close proximity. These intermolecular forces that act between the surfaces of bodies are called surface forces (Ref 7, 8), and adhesion is one manifestation of the existence of surface forces.

Surface Forces

Fundamental adhesion arises from innate surface forces, which have their origins in well-understood interatomic and intermolecular forces (Ref 7). Such forces are always present, and they can be described by the summation of individual bond strengths over a unit area or by the energy required to break chemical bonds at the weakest plane or loci of points within an interface (Ref 2).

It is sometimes convenient to classify surface forces as either short-range or long-range surface forces. Short-range surface forces are those that act between atoms and molecules that are essentially in contact, say within 0.1 or 0.2 nm of each other. Examples of this are covalent and hydrogen bonding, as well as Born repulsions. Long-range surface forces act between surfaces that are farther apart, which in this context means on the order of a few nanometers. Examples of long-range surface forces include van der Waals and electrostatic forces. However, some short-range surface forces also produce effects over a longer range. An example of this is steric repulsion. In this case, surfactant molecules adsorbed on a solid surface (via short-range bonding) can prevent a second surface from approaching the first. Boundary lubricants operate in this way to keep solid surfaces separated.

In general, short-range forces are stronger than long-range forces and make the most important contributions to adhesion. Unfortunately, long-range forces are easier to both measure and model. Therefore, knowledge of surface forces, from both a theoretical and experimental standpoint, is much sounder for long-range effects. This is why an understanding of fundamental adhesion based on short-range surface forces has proven to be difficult (Ref 9).

Measurement of Surface Forces

“Long-range” surface forces act over surface separations from 1 to 100 nm and cause forces levels in the range of about 10^{-7} to 10^{-4} N. Measuring these forces is not a trivial matter. The magnitude of the forces increases with surface area (or, as shown below, with the radius of curved surfaces). Thus, in order to have measurable forces, it is desirable to have extended areas of surface. At the same time, to make sensible measurements of surface separation on a nanometer scale, it is necessary for the surfaces to be extremely smooth. A method of detecting small forces is required, as are methods of controlling and measuring very small surface separations.

Although surface force measurements have been made for several decades, the inherent difficulties of surface preparation and cleanliness limited the number of materials studied and the amount of data to a small level, until about 1970. The most popular technique has been the crossed-cylinder apparatus devised by Tabor (Ref 10) and further developed by Israelachvili (Ref 11). This technique uses a surface force apparatus (SFA), which is commercially available. A review of the field up until 1982 is also provided in Ref 12.

The SFA consists of a closed stainless steel chamber designed to enclose a variety of liquid or vapor media and is usually operated at ambient temperature and pressure. Force is measured between two cylindrical surfaces, with the axes of the cylinders at right angles to each other (Fig. 1). The reason for choosing this geometry is for purposes of practicality. If two planar surfaces were to be used (as one might have supposed), then there would be extreme difficulties in forming surfaces of sufficient flatness, mounting them exactly parallel, maintaining parallelism while moving the surfaces together or apart, and avoiding edge effects, all while working on a nanometer scale. As shown in the next section, “The Derjaguin Approximation,” it turns out that there is no difficulty interpreting the forces measured in this odd geometry because there is a simple relationship between the force measured between crossed cylinders and the energy of interaction between flat surfaces.

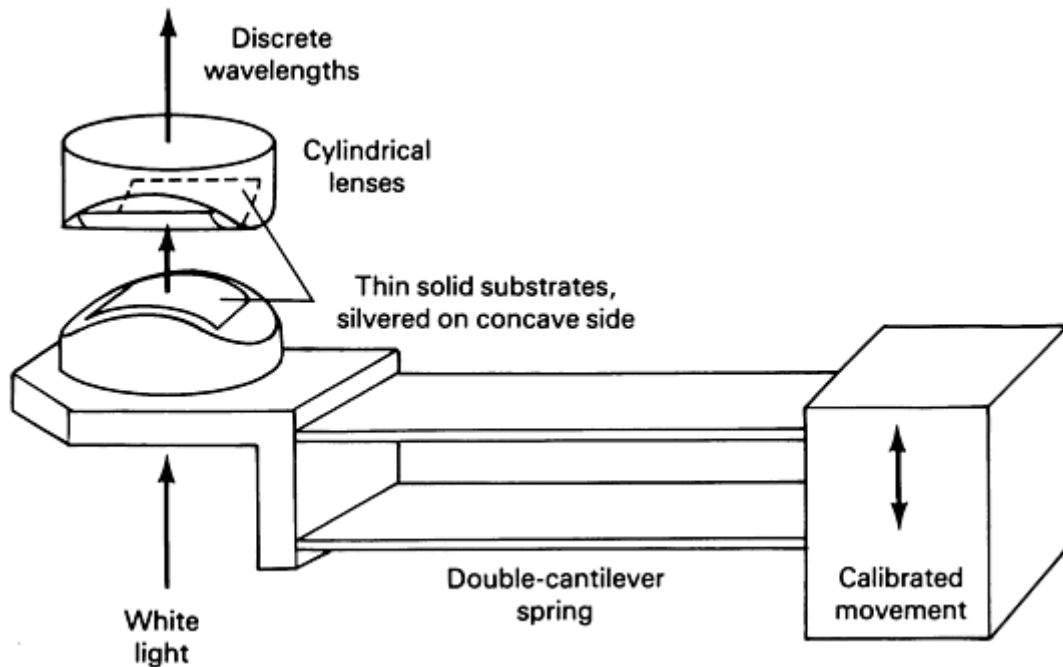


Fig. 1 Surface force apparatus, in which two thin solid substrates are mounted as cross cylinders, with one of them supported by a cantilever spring whose deflection measures the force. An optical interferometric technique is used to measure the distance between the surfaces.

In order to measure surface separation, the SFA employs an optical interference technique (Ref 11, 13, 14). Under optimal conditions, this gives a resolution of 0.1 nm or better. Of course, one drawback is that it places a limitation on the solid materials that can be investigated; namely, that at least one of the pair whose surfaces approach contact must be transparent and rather thin (ideally, a few nm). Most of the measurements made with this apparatus have been made with thin foils of mica bent around and glued to cylindrical glass lenses.

To implement the optical method, a 95% reflecting silver layer is coated on the outer (that is, remote) surface of each solid substrate. Collimated white light is shone through the two substrates and whatever medium separates them (Fig. 1). Multiple-beam interference between the two silver layers selects only certain wavelengths of light, which are passed by the interferometer. All other wavelengths interfere destructively and are not transmitted. The transmitted light is collected and directed to a grating spectrometer, which spreads it according to wavelength, so that discrete wavelengths appear at the exit port of the spectrometer as spatially separated fringes of equal chromatic order.

The wavelengths depend on the thicknesses and refractive indices of the materials that are included in the interferometer: usually, the two transparent substrates and whatever fluid medium is between them. Measurement and analysis of the wavelengths allow computation of these thicknesses (Ref 13, 14). Because the two solids are of fixed thickness, those values can be subtracted from the total to give the thickness of the intervening medium, that is, the separation, D , between the inner (adjacent) surfaces of the solids at their closest point of approach.

The surface force that one solid substrate exerts on the others is measured by a simple spring-deflection method. One solid is mounted on a cantilever spring, the remote end of which is moved up or down using a three-stage drive mechanism. The first stage is a micrometer that allows coarse positioning of the surfaces from a separation of a few mm to a few μm . The second stage is a micrometer that acts through a differential spring mechanism, which reduces the motion a thousand-fold, allowing positioning to approximately 1 nm. Finally, voltage applied to a piezoelectric tube expander gives positioning to a fraction of 1 nm.

After calibrating the drive mechanisms, it is straightforward to monitor any differences between a movement of the remote end of the spring and the distance moved by the end that bears one of the solids. This difference corresponds to a deflection of the spring. Multiplying it by the spring stiffness (typically 100 N/m, or 7 lbf/ft) gives the increment in force resulting from the movement. Because both the calibration and the movement of the solid are measured with a resolution of ~ 0.1 nm, it is possible to measure very small force changes (10^{-7} to 10^{-8} N) using this technique.

The Derjaguin Approximation. The force, F_c , between two gently curved surfaces is proportional to the interaction energy per unit area, E_f , between two flat ones at the same separation. This relationship, known as the Derjaguin approximation, allows straightforward interpretations to be made of surface force measurements between crossed cylinders (or between one sphere and another or between a sphere and a flat plate). It is also helpful in certain adhesion measurements, as described below.

The Derjaguin approximation is derived (see Ref 7, for example) by considering the force between each element of one curved surface and each element of the other, and then integrating over the two surfaces to obtain the total force. As long as the radius of curvature is much larger than the range of the surface force, this is approximately equivalent to integrating the force per unit area, F_f , between flat surfaces, from the minimum separation of the curved surfaces, D , to an effectively infinite upper limit, with some geometrical factors to account for the shape of the surfaces. The integral simply gives the interaction energy between flats, $E_f(D)$, which is the work done against the surface forces in moving the flat surfaces from infinity to D . For two spheres of radius R_1 and R_2 , the geometrical factor is a constant, giving:

$$F_c(D) = 2\pi R E_f(D)$$

where $1/R = 1/R_1 + 1/R_2$. It can be shown that the geometry of crossed cylinders of equal radii, R_c , is equivalent to a sphere of radius R_c approaching a flat plate, or to two spheres of radius $2R_c$ approaching each other.

Substrate Materials. The original and still most common solid material used in surface force measurements is mica, chosen because it satisfies the requirements (thin and transparent) of the optical interference technique used in the SFA and because it is easy to prepare large areas of molecularly smooth surface by cleavage. Experiments have been conducted on mica surfaces immersed in many different liquid and vapor environments (Ref 8).

Recently, there has been some success in extending these measurements to a wider range of surfaces. One approach is to coat mica surfaces by various techniques, including Langmuir-Blodgett deposition, surfactant or polymer adsorption from solution, plasma modification, and evaporative coating of thin metal, carbon, and metal-oxide films. An alternative approach is to find a means of preparing other transparent materials as micron-thick foils with very smooth surfaces. This has been done for sapphire, silica, pyrex glass, and certain polymers. It is reasonable to expect that the range of materials studied will continue to increase in the near future.

Currently, the best way to prepare metal surfaces for SFA appears to be thin-film evaporation onto mica or another smooth substrate. Because the optical technique requires some light to pass through the two films, their thicknesses cannot be more than a few tens of nanometers. It is possible to use the metal films themselves as one or both optical interferometer mirrors, but the fringes of equal chromatic order would disappear from the visible spectrum if the two metal surfaces were brought closer together than about $1\ \mu\text{m}$ ($40\ \mu\text{in.}$). In that case, an alternative method of measuring separation, such as capacitance, would be required.

Environments. Tests with the surface force apparatus can be conducted in many different liquids or vapors, as long as they are compatible with the materials of the SFA system (namely, stainless steel, silica, Kel-F, and Teflon). There is a provision to heat the chamber to around $100\ \text{°C}$ ($212\ \text{°F}$). Use of an appropriate heating jacket could extend the temperature range from, perhaps, -50 to $150\ \text{°C}$ (-60 to $300\ \text{°F}$). At about $150\ \text{°C}$ ($300\ \text{°F}$), the silver layers used for interferometer mirrors degrade. This limit might be raised by using other optical coatings. The next limitation of the current design would be the maximum operating temperature of the Teflon seals, which is $250\ \text{°C}$ ($480\ \text{°F}$). In principle, the same or comparable techniques could be extended to operate at several hundred degrees, but in practice this would require a major redesign of the apparatus.

At present, the SFA is intended only to operate at or near ambient pressure. With some modifications to the seals, it could be made to hold moderate vacuum, say 10^{-4} Pa (10^{-6} torr). A total redesign would be required to build a device for making comparable measurements in ultrahigh vacuum (UHV) conditions.

Preparation of Surfaces and Fluids. Any solid to be investigated by the SFA method should be smooth, compared to the range of forces under examination. Because the adhesion between surfaces is often dominated by very short-range forces, atomically smooth surfaces would be required to make fundamental and reproducible measurements of these. However, rough surfaces still adhere, and so measurements can be made without insisting on atomic smoothness. The drawback, in that case, is that it would be more difficult to obtain a straightforward interpretation of the results.

Because SFA measurements involve extremely small surface separations, there are stringent requirements for cleanliness. One speck of dust in the wrong place can spoil the entire test. The relative importance of surface cleanliness is again related to the range of force under investigation. For very short-range forces, even a

monolayer of adsorbed vapor will dramatically influence results. Considerable care must also be taken in preparing any liquid or vapor environment. Vapors must be free of dust, and liquids must be free of both particulate and molecular (for example, polymer or surfactant) contamination that can easily adsorb to solid surfaces and affect the results.

Other Measurements with SFA. The SFA method can be used to measure other properties of thin liquid or vapor films and solids at or near contact. These properties include the thickness of an adsorbed layer, the refractive index of very thin liquid films or adsorbed layers (Ref 13), the viscosity of ultrathin liquid films (Ref 15, 16), and the friction between two molecularly smooth solids (Ref 17).

References cited in this section

2. K.L. Mittal, Ed., *Adhesion Measurements of Films and Coatings*, VSP, 1995
7. J.N. Israelachvili, *Intermolecular and Surface Forces*, Academic Press, London, 1985
8. R.G. Horn, Surfaces Forces and Their Action in Ceramic Materials, *J. Am. Ceram. Soc.*, Vol 73, 1990, p 1117–1135
9. R.G. Horn, Measurement of Surface Forces and Adhesion, *Friction, Lubrication, and Wear Technology*, Vol 18, *ASM Handbook*, ASM International, 1992, p 399
10. D. Tabor and R.H.R. Winterton, The Direct Measurement of Normal and Retarded van der Waals Forces, *Proc. R. Soc. (London) A*, Vol 312, 1969, p 435–450
11. J.N. Israelachvili and G.E. Adams, Measurement of Forces between Two Mica Surfaces in Aqueous Electrolyte Solutions in the Range 0 to 100 nm, *J. Chem. Soc. Faraday Trans. I*, Vol 74, 1978, p 975–1001
12. K.B. Lodge, Techniques for the Measurement of Forces between Solids, *Adv. Colloid Interface Sci.*, Vol 19, 1983, p 27–73
13. J.N. Israelachvili, Thin Film Studies Using Multiple-Beam Interferometry, *J. Colloid Interface Sci.*, Vol 44, 1973, p 259–272
14. R.G. Horn and D.T. Smith, Analytic Solution for the Three-Layer Multiple Beam Interferometer, *Appl. Opt.*, Vol 30, 1991, p 59–65
15. D.Y.C. Chan and R.G. Horn, The Drainage of Thin Liquid Films between Solid Surfaces, *J. Chem. Phys.*, Vol 83, 1985, p 5311–5324
16. J. Peachey, J. Van Alsten, and S. Granick, Design of an Apparatus to Measure the Shear Response of Ultrathin Liquid Films, *Rev. Sci. Instrum.*, Vol 62, 1991, p 463–473
17. A.M. Homola, J.N. Israelachvili, M.L. Gee, and P.M. McGuiggan, Measurement of and Relation between the Adhesion and Friction of Two Surfaces Separated by Molecularly Thin Liquid Films, *J. Tribol.*, Vol 111, 1989, p 675–682

Adhesion Testing

Thermodynamic Adhesion

Thermodynamic adhesion refers to the change in free energy when an interface is formed or separated. This concept of adhesion is defined in terms of surface energy, interfacial energy, and the work of adhesion.

Surface energy (γ_s) is the work required to create a unit area of new surface from bulk material. It is commonly defined as half the reversible work (W_c) required to first divide a monolithic solid into two new surfaces and then to pull the two surfaces far apart in a vacuum (where far apart means beyond the range of the applicable surface forces). The term W_c is also called the work of cohesion.

In general, the creation of a new surface from a separation of materials involves the breaking of interatomic bonds, whose number (and possibly strength) depend on crystallographic orientation. Therefore, surface energy varies from one crystal face to another (Ref 18). The act of creating two surfaces requires work to be done against the attractive surface forces, and thus the integration of surface force, as a function of separation from 0 to ∞ , gives a quantity:

$$W_{SF} = - \int_0^{\infty} F_f(D) dD \quad (\text{Eq 1})$$

where $F_f(D)$ is the surface force between flat solids at a separation, D , using the convention that $F < 0$ for an attractive force. The subscript SF indicates that this is the contribution to W_c from the surface forces.

Sometimes W_{SF} is equated to twice the surface energy, but this is not generally correct because other energetic processes are likely to occur during the creation of new surfaces. In particular, the new surfaces are likely to reconstruct. Atoms near the new surface rearrange their positions to a configuration that is more favorable near a surface than was their original configuration in the bulk of the solid. Furthermore, there is the delicate issue of assigning the energy associated with breaking strong, short-ranged atomic bonds when the original solid is “magically” cleaved. This is certainly a contribution (probably the major one) to W_c , but it is unclear whether or not it should be included in the definition of W_{SF} .

Interfacial Energy. When a solid is not in vacuum but is in contact with a liquid or vapor, it is considered in terms of interfacial energy, γ_{SL} or γ_{SV} , respectively, rather than surface energy. If the above process is carried out in either a liquid or vapor environment, the work of cohesion equals twice the interfacial (solid-liquid or solid-vapor) energy. The same remarks about reversibility and reconstruction still apply. Furthermore, in this situation there is also the likelihood that molecules of the liquid or vapor will adsorb to the new solid surface (which could be thought of as “reconstruction” of the fluid at the interface). Adsorption reduces the interfacial energy.

Note that the reconstruction of both solid and fluid depends on which materials are involved. For example, a given solid material may reconstruct differently in water than in a hydrocarbon liquid. The details of the interfacial structure are also likely to depend on the distance between one interface and the other. Careful consideration also must be given to the question of reversibility. If the adsorption is irreversible, then bringing the two solids back together after they have been separated will not remove the adsorbate, and the surfaces will never return to their original intimate contact and will not reform the original atomic bonding that existed in the monolithic solid.

The interfacial energy, γ_{LV} , between a liquid and its own vapor is also called the surface energy, or, more commonly, the surface tension of that liquid. The term “tension” comes from a real force that resists any attempt to increase the surface area of a given volume of liquid. Surface tension of a liquid can be measured directly. Determining either the surface or interfacial energy of a solid is much more problematic. Solid-liquid and solid-vapor surface energies are related to the liquid surface tension and the contact angle, θ , made by the liquid on the solid through Young's equation:

$$\gamma_{SV} = \gamma_{SL} + \gamma_{LV} \cos \theta \quad (\text{Eq 2})$$

Work of adhesion (W_A) refers to the energetic cost of creating new interfaces of each solid material in contact with the environment, γ_{1E} and γ_{2E} , where the subscript E could be liquid or vapor, as appropriate, less the energetic gain from removing the original solid-solid interface. The energy associated with the solid-solid interface is also termed an interfacial energy, γ_{12} , which is defined by the Dupré equation:

$$W_A = \gamma_{1E} + \gamma_{2E} - \gamma_{12} \quad (\text{Eq 3})$$

Adhesion is sometimes used to mean work of adhesion. In a similar way, one could define the work of adhesion between two pieces of the same solid material. This would differ from the work of cohesion if the two pieces were brought together in an environment so that adsorbate remained at the interface or if they were formed with their crystal orientations misaligned, giving a grain boundary at the interface. In that case, the quantity γ_{12} would be nonzero and would correspond to a grain-boundary energy, with or without extrinsic molecules

present. Because grain-boundary energy depends on grain-boundary angle, the adhesion between two crystals of the same material depends on their relative orientation.

Note that there is another effect that can make the above definition of work of adhesion problematic. When two solids are pulled apart, it is quite possible, and often observed in practice, that separation does not occur precisely between the two materials. Many solids diffuse into one another when in contact, particularly at high temperature. This makes it almost impossible to separate them in the ideal way that the simple thought experiment would imply. Even without diffusion, it is frequently found that joints break parallel to, but not precisely at, the interface. Many experimentalists have detected at least one of the materials on both sides of the division following separation (Ref 18).

When the environment includes a condensable vapor, an additional contribution to the adhesion between two solids occurs from an effect known as capillary condensation. Liquid condenses (as long as the contact angle is less than 90°) to form a bridge wherever the gap between the solids is small. Curvature of the liquid-vapor meniscus results in a negative Laplace pressure in the liquid, which acts as a cohesive force that holds the solids together. The magnitude of this force depends on the relative vapor pressure of the liquid and on the geometry of the solids (Ref 7 and 19). In some situations, this is the predominant factor in adhesion.

References cited in this section

7. J.N. Israelachvili, *Intermolecular and Surface Forces*, Academic Press, London, 1985
18. D.H. Buckley, *Surface Effects in Adhesion, Friction, Wear and Lubrication*, Elsevier, Amsterdam, 1981
19. F.M. Orr, L.E. Scriven, and A.P. Rivas, Pendular Rings between Solids: Meniscus Properties and Capillary Force, *J. Fluid Mech.*, Vol 67, 1975, p 723–742

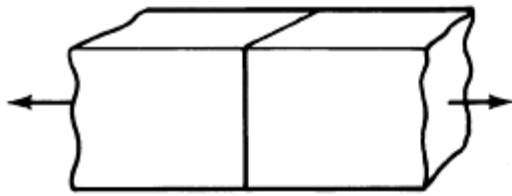
Adhesion Testing

Practical Adhesion

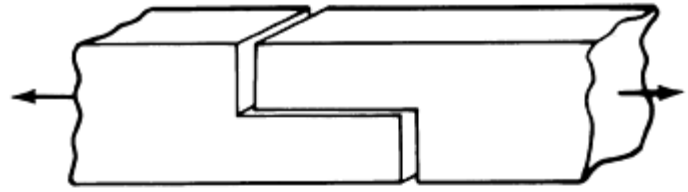
There are many types of adhesion tests for specific geometries and modes of separation for coatings, films, and adhesive joints (Ref 2, 3, 4, 5, 6). A number of them are either empirical or semiempirical. Others give only a comparative test of adhesion, such as whether the adhesion between a thin film and a substrate is greater or less than the adhesion between the film and some reference material.

In general, practical adhesion tests involve the application of a known stress to a joint or interface to determine when it fails. However, the force required to separate two bodies with mating surfaces depends very much on the manner in which they are separated. For example, two microscope slides held together by a thin film of moisture are extremely difficult to separate in simple tension or even by wedging them apart, whereas they separate easily in shear. The reason for this lies partly in the fact that the work of adhesion can be done by applying a large force over a small distance (uniform tension) or a small force over a large distance (as in peeling or sliding). In a similar way, the fracture threshold also depends on the mode of separation, such as tension versus shear. Therefore, an adhesion test carried out in one mode might reveal little about failure in another.

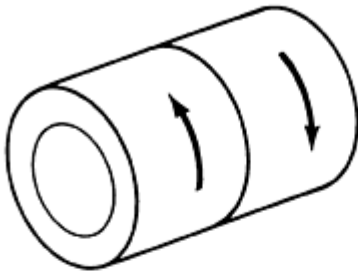
Adhesive Joints. Various arrangements that can be employed in adhesion tests are illustrated in Fig. 2. For large pieces (as opposed to films or coatings), the most obvious arrangement is the butt joint (Fig. 2a). Although it may look simple, the ease of fracture or failure can depend strongly on the presence of flaws in the joint and on how and whether a crack/separation is initiated at the edges of the sample. A lap joint (Fig. 2b) is appropriate to test shear strength, for example, in laminates. Care must be taken to avoid excessive bending of the beams during the test, because that introduces some tensile component. The ring shear, or “napkin ring,” test (Fig. 2c) applies a more uniform shear stress to the joint, whereas the peg topple test (Fig. 2d) is closer to ideal tension, but not straightforward to analyze.



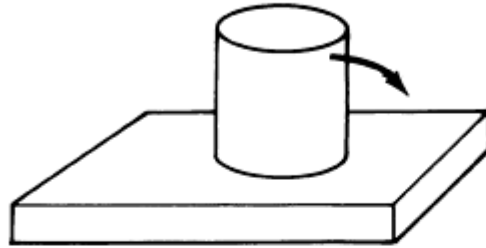
(a) Butt joint



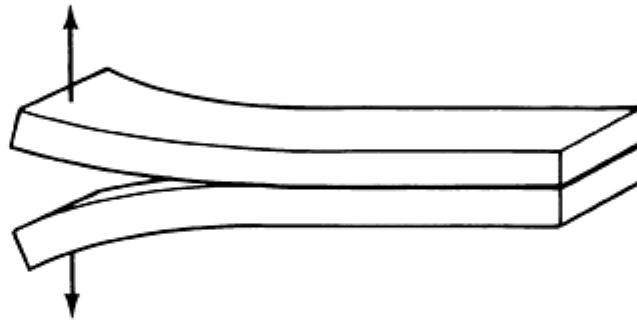
(b) Lap joint



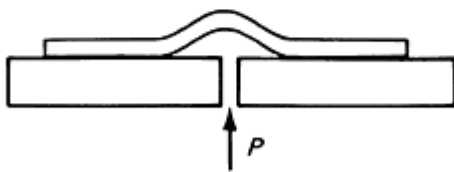
(c) Napkin ring



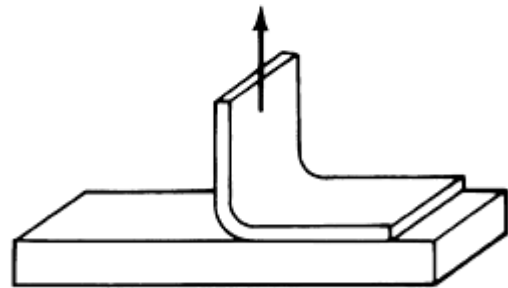
(d) Peg topple



(e) Double-cantilever beam



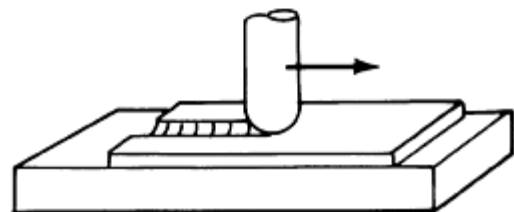
(f) Blister



(g) Peel



(h) Delamination



(i) Scratch

Fig. 2 Various arrangements for adhesion tests

The double-cantilever-beam geometry (Fig. 2e) provides an excellent fracture-mechanics type of test if suitable samples can be prepared. A clever variation on this is to profile the beams in such a way that the fracture

threshold is independent of the length of the crack (Ref 20), making the analysis very simple. These types of practical adhesion tests are most commonly applied to adhesive-joint testing, which is described in more detail in the article “Testing of Adhesive Joints” in this Volume.

Films and Coatings. When thin films, thick films, or coatings are involved, there is another set of test geometries that can be used. The peel test is very common, with the force applied at various angles, not just the 90° angle shown in Fig. 2(g). Blister and delamination tests (Fig. 2f and h) can be very well controlled and properly analyzed in terms of fracture mechanics (Ref 2 and 21). The scratch test (Fig. 2i) is much more difficult to analyze, but it at least has the merit of being the only one of these configurations that tests adhesion under dynamic sliding conditions. More detailed coverage of the various methods is contained in Ref 2 and 6. Mechanical testing and indentation testing of thin films are also covered in the article “Evaluation of Mechanical Properties of Thin Films” in the *ASM Handbook*, Volume 5, *Surface Engineering* (p 642–646).

References cited in this section

2. K.L. Mittal, Ed., *Adhesion Measurements of Films and Coatings*, VSP, 1995
3. K.L. Mittal, Ed., *Adhesive Joints*, Plenum Press, 1984
4. G.L. Schneberger, Ed., *Adhesives in Manufacturing*, Marcel Dekker, 1983
5. G.P. Anderson, S.J. Bennett, and K.L. DeVries, *Analysis and Testing of Adhesive Bonds*, Academic Press, 1977
6. K.L. Mittal, Ed., *Adhesion Measurement of Thin Films, Thick Films and Bulk Coatings*, STP 640, ASTM, 1978
20. W.D. Bascom, P.F. Becher, J.L. Bitner, and J.S. Murday, Use of Fracture Mechanics Concepts in Testing of Film Adhesion, *Adhesion Measurement of Thin Films, Thick Films and Bulk Coatings*, STP 640, K.L. Mittal, Ed., ASTM, 1978, p 63–81
21. D.B. Marshall and A.G. Evans, Measurement of Adherence of Residually Stressed Thin Films by Indentation. Mechanics of Interface Delamination, *J. Appl. Phys.*, Vol 56, 1984, p 2632–2638

Adhesion Testing

Adhesion and Interfacial Degradation

Natalia Tymiak and W. Gerberich, University of Minnesota

Gaining an insight into mechanisms of environmentally induced interfacial degradation requires an understanding of the fundamental aspects of adhesion between two dissimilar materials. For any application involving multilayers, fiber/matrix, or film/substrate systems, strength of bonding between two materials is one of the critical reliability issues. Environmental exposure is also a key factor in the interfacial degradation of various bond interfaces of metal/polymer (Ref 22, 23), ceramic/polymer (Ref 24), metal/ceramic (Ref 25, 26), and so forth. For interfaces involving metals, the possibility of hydrogen-induced interfacial degradation exists under exposure to gaseous hydrogen (Ref 27) or during cathodic hydrogen discharge (Ref 28). The latter may

result from an appropriate combination of local galvanic electrocoupling and moisture environment that is quite common for microelectronics applications.

References cited in this section

22. A. Carre and J. Shultz, Polymer-Aluminum Adhesion. III. Effect of a Liquid Environment, *J. Adhesion*, Vol 18, 1984, p 171–184
23. J.D. Venables, Review: Adhesion and Durability of Metal-Polymer Bonds, *J. Mater. Sci.*, Vol 19, 1984, p 2431–2453
24. H. Wu, J.T. Dickinson, and S.C. Langford, Dynamic Measurements of Humidity Attack on Polymer/Glass Interfaces under Stress, *J. Adhes. Sci.*, Vol 11, 1997, p 695–717
25. S.X. Mao and A.G. Evans, The Influence of Blunting on Crack Growth at Oxide/Metal Interfaces, *Acta Mater.*, Vol 45, 1997, p 4263–4270
26. T.S. Oh, J. Rodel, R.M. Cannon, and R.O. Ritchie, Ceramic/Metal Interfacial Crack Growth Toughening by Controlled Microcracks and Interfacial Geometries, *Acta Metall.*, Vol 36, 1988, p 2083–2093
27. N.R. Moody, S.K. Venkataraman, B. Bastaez, J.E. Angelo, and W.W. Gerberich, Hydrogen Effects on the Fracture of Thin Tantalum Nitride Films, *Mater. Res. Soc. Symp. Proc.*, Vol 356, 1995, p 827–832
28. N.I. Tymiak, M. Li, A. Volinsky, Y. Katz, and W.W. Gerberich, The Role of Plasticity in Bi-material Fracture with Ductile Interlayers, *Metall. Trans. A*, Vol 31, 2000, p 863–871

Adhesion Testing

Fundamental Aspects of Bimaterial Interfacial Adhesion

The practical work of adhesion, W_{prac} , refers to the total energy necessary for separation along an interface between two materials as affected by several energy absorption mechanisms. In terms of the critical strain energy release rate, G_{crit} , that is, elastic energy released per unit of fracture area:

$$W_{\text{prac}} = G_{\text{crit}} = \Gamma_0 + \Gamma_p + \text{other forms of dissipation} \quad (\text{Eq 4})$$

Here, Γ_0 is the work consumed by the fracture process per unit area of new surfaces. Interfacial fracture energy, Γ_0 , accounts for both the thermodynamic work of adhesion, W_a , and microstructural effects in the fracture process zone such as crack bridging (Ref 29), interdiffusion, mechanical interlocking (Ref 30), and/or existing defects along an interface. The thermodynamic work of adhesion is determined mainly by attractive interatomic or intermolecular forces. The most common interfacial attractive forces result from van der Waals and Lewis acid-base interactions (Ref 31). A contribution of electrostatic forces should also be considered (Ref 32).

The magnitude of W_a is determined by the Dupré equation (Eq 3) (Ref 33) and is defined as:

$$W_a = \gamma_1 + \gamma_2 - \gamma_{12}$$

where γ_1 , γ_2 , and γ_{12} are surface energies of materials along an interface and of the interface respectively. The term Γ_p in Eq 4 accounts for plastic energy dissipation rate at the interfacial crack tip. For interfaces involving polymers, viscoelastic-plastic deformation may result in additional dissipational losses, Γ_v . The stronger the interface (higher Γ_0), the more energy is dissipated through plastic and/or viscoelastic deformation (as well as through any other dissipation process). Other factors affecting Γ_p and Γ_v are viscoelastic-plastic properties of two materials forming an interface and geometry of a system. The latter implies crack configuration and

volumes of materials involved. For example, experimental results for ductile films on brittle substrates such as copper on SiO₂ suggest plastic energy dissipation scaling with the copper film thickness (Ref 34). As a result, the practical work of adhesion can increase by orders of magnitude when film thickness increases from the nanometer to the micron scale. Among other mechanical properties determining Γ_p , yield stress appears to be of a critical concern due to its high sensitivity to microstructure, chemistry, and gradient constraints. Frictional losses may be significant for rough interfaces with the effect increasing with the decreasing film thickness (Ref 35). For strong interfaces, additional dissipation mechanisms may be present. These include void nucleation (Ref 36), second-phase debonding, microcracking, and shear band formation (Ref 37, 38).

Measurements of the practical work of adhesion can also be strongly dependent on the mode mixity or a relative fraction of mode I and mode II. Mode mixity is determined by sample/applied load geometry and can be defined as (Ref 39):

$$\Psi = \arctan\left(\frac{K_{II}}{K_I}\right) + \text{elastic mismatch term} \quad (\text{Eq 5})$$

Generally, G_{crit} increases as the crack tip becomes increasingly heavy under mode II conditions (Ref 40). Possible mechanisms responsible for this trend include frictional losses (Ref 35) and/or plastic energy dissipation rates (Ref 41, 42), which increase with increasing mode II contribution.

It is clear that even in the absence of an environment there is no single value of adhesion for a bimaterial couple. The reasoning is that the practical work of adhesion depends on the volumes of materials involved as well as the loading modes and the microstructural characteristics determined by a particular processing route.

References cited in this section

29. Y.Y. Wang, F.P. Chiang, and R.S. Barsoum, A Photoelastic Study of Extending Cracks in Adhesion Joints, *J. Adhes.*, 1995
30. A.G. Evans and J.W. Hutchinson, Effects of Non-Planarity on the Mixed Mode Fracture Resistance of Bi-material Interfaces, *Acta Met. Mater.*, Vol 37, 1989, p 909–916
31. F.M. Fowkes, D.W. Dwight, and D.A. Cole, Acid-Base Properties of Glass Surfaces, *J. Non-Cryst. Solids*, Vol 120, 1990, p 47–60
32. J.T. Dickinson, L.C. Jensen, S. Lee, L. Scuderio, and S.C. Langford, Fracto-Emission and Electrical Transients due to Interfacial Failure, *J. Adhes. Sci. Technol.*, Vol 8, 1994, p 1285–1309
33. A. Dupre, *Theorie Mechanique de la Chaleur*, Paris, 1989
34. A. Bagchi and A.G. Evans, Measurements of the Debond Energy for Thin Metallization Lines on Dielectrics, *Thin Solid Films*, Vol 286, 1996, p 203–212
35. R.G. Stringfellow and L.B. Freund, The Effect of Interfacial Friction on the Buckle-Driven Spontaneous Delamination of a Compressed Thin Film, *Int J. Solid Structures*, Vol 30, 1993, p 1379–1395
36. A. Needleman, An Analysis of Tensile Decohesion along an Interface, *J. Mech. Phys. Solids*, Vol 38, 1990, p 289–324
37. W.D. Bascom, R.L. Cottingham, R.C. Jones, and P. Peyster, Fracture of Epoxy and Elastomer Epoxy Polymers in Bulk and as Adhesives, *Organic Coat. Plast. Chem.*, Vol 34, 1974, p 300
38. J.N.B. Sutton, McGary, *Polym. Eng. Sci.*, Vol 13, 1973, p 29
39. J.W. Hutchinson and Z. Suo, *Adv. Appl. Mech.*, Vol 29, 1992, p 63

40. K.M. Liechti and Y.S. Chai, Biaxial Loading Experiments for Determining Interfacial Fracture Toughness. *J. Appl. Mech.*, Vol 58, 1991, p 680–687
41. V. Tvergaard V and J.W. Hutchinson, The Influence of Plasticity on Mixed Mode Interface Toughness, *J. Mech. Phys. Solids*, Vol 41, 1993, p 1119–1135
42. P.A. Mataga and P. Ponte Castaneda, Stable Crack Growth along a Brittle/Ductile Interface-II Small Scale Yielding Solutions and Interfacial Toughness, *Int. J. Solids Struct.*, Vol 36 (No. 1), 1998, p 1–35

Adhesion Testing

Environment-Interface Interactions

An environmentally induced reduction in interfacial fracture energy may result from the following:

- Change in the thermodynamic work of adhesion
- Microstructural degradation such as microcracking
- Yield stress and/or viscoelastic property changes affecting dissipation losses
- Chemical or electrochemical reactions along an interface or in one or both materials, for example, hydride formation

Depending on the bimaterial couple and the environment, any of the above may be prevalent.

Similarly, as in the case of bulk solids, environments may be considered as chemically reactive if their reaction with either materials at the interface leads to dissolution or compound formation. Nonreactive environments include media that influence mechanical behavior of one or both joining materials. The other part of nonreactive media regarded as “inert” comprises environments that only may induce changes in surface energies of joining materials (γ_1 and γ_2) and that of an interface (γ_{12}). Note that specific interfacial crack-tip conditions may change environment/material interactions. Thus, any experimental results for a bulk material/environment may not be directly applicable to the same material along an interfacial crack. For example, varying ionic species concentrations unique to the crack tip region may adversely affect either side of an interface. This could involve oxygen reduction along a metal/polymer interface leading to polymer degradation. Another example is hydrogen evolution leading to metal embrittlement. It is also necessary to emphasize that diffusion along an interface may be much higher than in any of the two joining materials. Thus, after the same time of environmental exposure, the effect may be much stronger for a fracture along an interface compared to fracture in bulk materials.

Adhesion Testing

Polymer/Inorganic Interfaces

Factors Determining Polymer/Inorganic Material Adhesion. The thermodynamic work of adhesion for polymers is determined mainly by intermolecular bonds and Lewis acid-base (donor-acceptor) interactions (Ref 31). With a significant difference between acidities of joining materials, donor-acceptor bonds would be prevalent compared to intermolecular bonds (Ref 43). There is experimental evidence of adhesion strength decreasing with decreasing difference in acidities of joining surfaces (Ref 31). Environmental exposure resulting in change of surface acidity may affect adhesion strength. A so-called weak boundary layer may exist in some cases determining strength of an interface (Ref 44). It should be cautioned that bonding may be distinctively different

for metal-on-polymer compared to polymer-on-metal for a given couple. This would imply different response to environment/deformation exposure.

Environmental Effects on Different Contributions of Interfacial Toughness. The considerations for fracture in bulk polymers are relevant for interfaces involving polymers as well.

Special attention should be given to:

- Specific interactions between a polymer and an environment within a specific highly stressed near-crack-tip region
- Liquid transport toward a crack tip
- Temperature effects
- Rate dependence (loading and/or crack growth)

Environment/inorganic material interactions should be accounted for with specific attention to the environmentally induced surface modification. These may range from change in surface acidity to formation of a reaction product with the chemical and/or mechanical properties distinctively different from those of the original material.

For a particular system, environmental effects on the dominant contribution of adhesion strength would probably be most apparent. Depending on the structure of an interface and viscoelastic-plastic properties of joining materials, the thermodynamic work of adhesion may be small compared to dissipation and microstructural contributions. For several polymer-on-metal systems, adhesion strength is governed by mechanical/microstructural factors. On the other hand, viscoelastic-plastic dissipation may be dominant for strong interfaces involving polymers that exhibit viscoelastic flow. In some cases, it is possible to identify and evaluate environmental effects on a specific mechanism of adhesion, as discussed in the next sections.

Thermodynamic Work of Adhesion. With the peel test, Carre and Shultz (Ref 22) were able to evaluate environmentally induced relative change in the thermodynamic work of adhesion for rubber films on aluminum tested in various alcohols. These results agree very well with the theoretical calculations.

Microstructural/Mechanical Effects. The strongest effects may be expected here from exposure to “reactive” environments causing structural and/or chemical changes in one or both components of an interface. For interfaces where a dominant fraction of adhesion strength comes from a mechanical interlocking between a polymer and underlying metal oxide, environmentally induced changes in the chemistry and morphology of an oxide may be critical. Examples include aluminum oxide conversion to a hydroxide that is less strong and adheres poorly to the underlying metal (Ref 23). Similarly, adhesion to Ti/TiO₂ substrate may deteriorate with titanium oxide undergoing a polymorphic transformation to anatase (Ref 23). Such a transformation is highly temperature and moisture dependent. In other systems, such as epoxy-coated phosphated steel, exposure to humid environments results in formation of a porous, moisture-retaining metal oxide layer (Ref 45). This facilitates adhesion strength losses. It should be noted that reactions between a solid and an environment may be strongly affected by the presence of a joining material. For example, galvanic coupling between an exposed metal and an adjacent polymer-coated surface results in oxygen reduction along an intact interface (Ref 46). This leads to the transformation of a near-interface layer of polymer into a gel-like structure with subsequent gradual interface deterioration. In many cases involving degradation of a near-interface region in one of the joining materials, a cohesive rather than adhesive fracture occurs.

Dissipation Losses. Environmental exposure may result in both *direct* and *indirect* effects on plastic/viscoplastic dissipation. First, environmentally induced changes in viscoelastic plastic behavior would influence dissipation *directly*. Second, degradation of the thermodynamic work of adhesion and/or microstructural component of adhesion strength may result in lower dissipation contributions. Moisture-affected viscoplastic deformation may be regarded as a major source of humidity-induced interfacial strength degradation for a glass/pressure sensitive adhesive (PSA) interface (Ref 47). There was no apparent difference between exposed and nonexposed samples prior to the “yield point” corresponding to fibril formation. In contrast, the capacity for viscoplastic deformation associated with interfacial fracture appeared greatly deteriorated in the presence of a humid environment. This resulted from local moisture absorption in the vicinity of the crack tip rather than humidity-induced changes in the bulk viscoelastic behavior of the polymer. Sometimes, moisture effects are complicated by the possible change of mechanisms at different humidity levels. In general, moisture has been shown to decrease interfacial toughness for polyimide films on glass substrates. For low humidity levels, adhesion strength decreased with the increasing moisture content.

However, for moisture content levels above 60%, adhesion strength increased with the further humidity increase as shown in Fig. 3 (Ref 48). Here, formation of a boundary layer along an interface has been suggested as the possible mechanism responsible for adhesion strength increase at relative humidities above 60%.

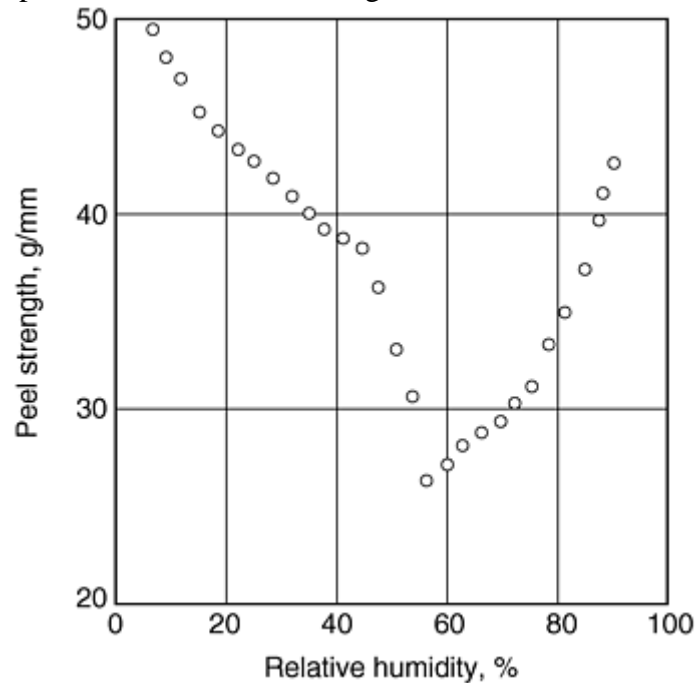


Fig. 3 Peel strength of 14.3 μm polyimide film with a peeling rate of 0.5 mm/min as a function of relative humidity. Source: Ref 49

References cited in this section

22. A. Carre and J. Shultz, Polymer-Aluminum Adhesion. III. Effect of a Liquid Environment, *J. Adhesion*, Vol 18, 1984, p 171–184
23. J.D. Venables, Review: Adhesion and Durability of Metal-Polymer Bonds, *J. Mater. Sci.*, Vol 19, 1984, p 2431–2453
31. F.M. Fowkes, D.W. Dwight, and D.A. Cole, Acid-Base Properties of Glass Surfaces, *J. Non-Cryst. Solids*, Vol 120, 1990, p 47–60
43. K.W. Allen, A Review of Contemporary Views of Theories of Adhesion, *J. Adhes.*, Vol 21, 1987, p 261–277
44. J.W. Severin, R. Hokke, H. Van der Wel, and G. de With, The Influence of Thermal Treatments on the Adhesion of Electrolessly Deposited Ni(P) Layers on Alumina Ceramic, *J. Electrochem. Soc.*, Vol 141, 1994, p 816–824
45. Y.M. Aravot and A. Albu-Yaron, The Effect of Environmental Moisture on the Adhesion Toughness of Epoxy-Coated Phosphated Steels, *J. Mater. Sci. Lett.*, Vol 12, 1993, p 1437–1438
46. A. Leng, H. Streckel, and M. Stratman, The Delamination of Polymeric Coatings from Steel, Parts 1–4, *Corros. Sci.*, Vol 41, 1999, p 547–620
47. H. Wu, J.T. Dickinson, and S.C. Langford, Dynamic Measurements of Humidity Attack on Polymer/Glass Interfaces under Stress, *J. Adhes. Sci. Technol.*, Vol 11, 1997, p 695–717

48. D.-C. Hu and H.-Ch. Chen, Humidity Effect on Polyimide Film Adhesion, *J. Mater. Sci.*, Vol 27, 1992, p 5262–5268
49. K. Suganuma, K. Niihara, T. Fujita, and T. Okamoto, *Metal-Ceramic Joints*, Vol 8, Proc. MRS Int. Meeting (Pittsburgh, PA), Doyamma et al., Ed., Materials Research Society, 1989, p 113

Adhesion Testing

Interfaces between Inorganic Materials

As of the late 1990s, there appears to be only limited experimental data available on environmental degradation of inorganic interfaces. As for polymer/inorganic interfaces, environment could affect the thermodynamic work of adhesion as well as deteriorate an interfacial bond via reaction with one or both joining materials. *Direct* environmental effects on the dissipation losses would not be considered here, except possibly for interfaces where one material is susceptible to environmentally induced changes (e.g., via hydrogen charging) in plastic behavior. In contrast, *indirect* changes in dissipation losses are possible via environmental effects on the thermodynamic work of adhesion and/or microstructure.

Metal Films on Ceramic Substrates. As of the late 1990s, environmental effects for metal films on ceramic substrates have only been evaluated for very few metal/ceramic systems. All of these studies examined humidity or hydrogen effects on interfaces between metallic films and ceramic substrates. From these studies, the condition of a ceramic surface appeared to be very important in determining susceptibility to environmental cracking as shown by the Al/Si₃N₄ (Ref 49) system tested in water. Presence of a damaged near-surface region in Si₃N₄ seemed to increase propensity for SCC. With such a layer, a crack propagated through this layer rather than along an interface. Removal of the damaged material yielded interfacial strength approaching that for bulk Si₃N₄.

In contrast, with the deliberately patterned SiO₂ surface, Cu/SiO₂ interfaces exhibit much higher toughness in both dry and humid environments (Ref 26) as shown in Fig. 4. The effect was attributed to crack bridging. Indicating similarity of mechanisms, the form of velocity-energy release rate (*V-G*) dependencies was essentially the same for smooth and patterned interfaces. Likewise for bulk materials, the kinetic curves for interfacial crack growth exhibit three characteristic regions. The strong environmental effect on both threshold (~20% reduction) and crack growth rates (more than 3 orders of magnitude increase) is evident from comparison of *V-G* curves in wet and dry nitrogen. Enhanced crack growth rates in humid environments were attributed to absorbed-water-induced weakening of interfacial bonds, which limits the extent of plastic stretching of the bridging segments of copper film. Namely, indirect changes in plastic energy dissipation were present there. It should be noted that observed interfacial crack velocities exhibited higher sensitivity to stress intensity and were more than 3 orders of magnitude greater than crack velocities for bulk soda lime glass in water vapor (Ref 50).

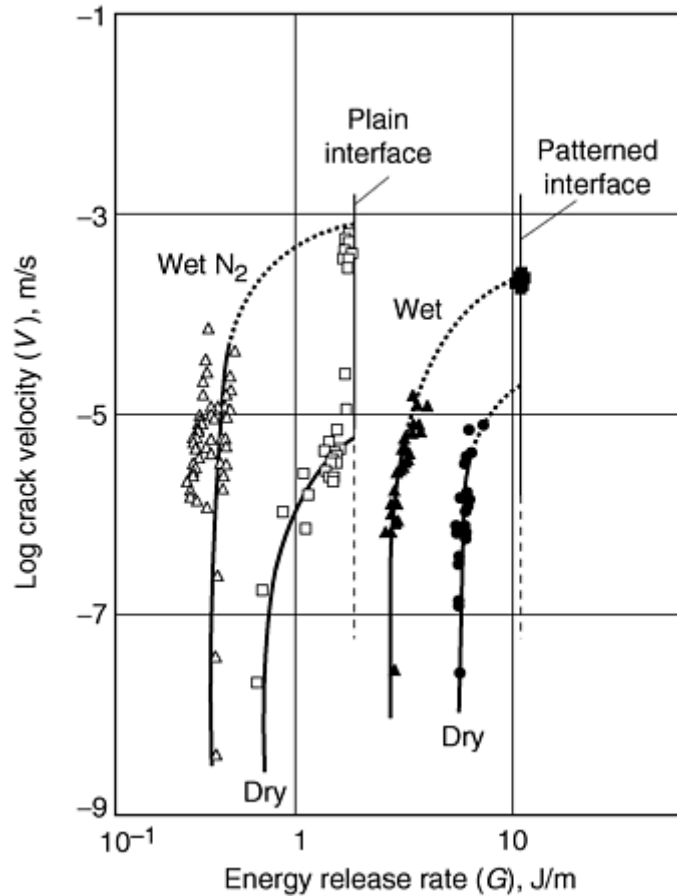


Fig. 4 Crack growth rates along plain and patterned glass/copper interfaces in wet and dry gaseous nitrogen environments

Experimental results for gold films on Al_2O_3 substrates tested in laboratory air and dry nitrogen indicate a moisture-induced reduction in adhesion strength (Ref 25). Examination of fracture surfaces indicated separation along an interface with no crack kinking into joining materials. With no apparent changes in any joining material, observed adhesion strength reduction would be attributed to the environmental effects on the interfacial fracture energy. Similarly, as in the previous example, a decrease of the interfacial bond strength resulted in less plastic deformation of the metal.

Hydrogen effects have been examined for thin 200 to 1000 nm copper film on oxidized silicon with 10 nm titanium interlayers between copper and SiO_2 (Ref 51). For both charged and noncharged films, the practical work of adhesion (W_{prac}) increased with the increasing film thickness, as shown in Fig. 5. Based on previous studies (Ref 52), this trend was attributed to plastic energy dissipation scaling with the film thickness. Hydrogen charging induced degradation of the practical work of adhesion. The possibility of a direct decrease in Γ_p has been eliminated as there was no change in the copper film yield stress following hydrogen charging. Based on the W_{prac} values and a theoretical model (Ref 53), a hydrogen-induced decrease of Γ_0 from 4 to 2 J/m^2 , independent of film thickness, had been determined. An additional investigation would be required to determine whether this change is attributed to the decreased thermodynamic work of adhesion, microstructural effects, or both. Examination of chemical composition and topography of fracture surfaces would clearly be necessary here. Also, to eliminate the possibility of a contribution from humidity, charging with gaseous hydrogen could be utilized.

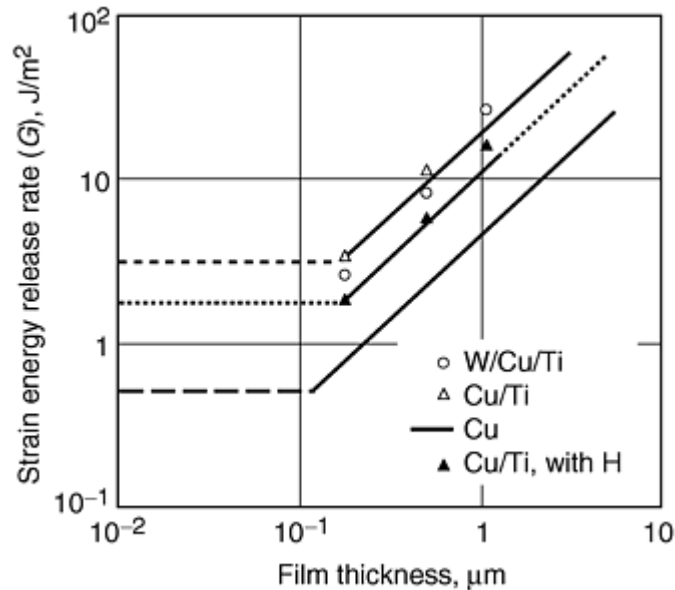


Fig. 5 Hydrogen effects on strain energy release rates for Cu/Ti/SiO₂ interfaces

Ceramic Films on Metallic Substrates. Studies of environmental stability of ceramic coatings on metallic substrates have shown interfacial strength degradation during long-term aging without applied stress. For example, a substantial adhesion loss was observed for flame sprayed Al₂O₃ coatings on 316L stainless steel aged in aerated Ringers solution (Ref 54). Ferber and Brown (Ref 55) evaluated alumina coatings on 316L stainless steel and titanium alloy Ti-6Al-4V in distilled water under applied four-point bending. With the lower “inert” strength, alumina/stainless-steel interface exhibited higher susceptibility to environmental stress cracking. For both systems, the extent of slow crack growth was much greater than that reported for porous alumina (Ref 56). With increasing temperature, adhesion strength degradation increased for both types of coatings. Reaction between water and strained crack-tip bonds was suggested as a governing mechanism for environmentally assisted interfacial crack growth. At ambient temperature, fracture was always 100% adhesive for the alumina/stainless-steel interface. In contrast, for the alumina/titanium-alloy interface, fraction of adhesive fracture decreased with increasing fatigue life. This indicated that slow crack growth in a coating became the dominant mechanism at lower stress levels where longer environmental exposure was involved. For alumina/stainless steel, an observed environmental effect may be attributed to interfacial strength degradation. The situation is more complex for the alumina/titanium-alloy interface. Here, cohesive energy reduction for alumina becomes more significant with increasing time and, eventually, becomes less than the adhesive energy. For the weaker alumina/stainless-steel interface, the cohesive energy still exceeds the adhesive energy of an interface.

Ceramic-Ceramic Interfaces. Similarly, as for metal/ceramic interfaces, only very few systems have been evaluated. Only humidity or hydrogen effects have been investigated in these studies. Several studies (Ref 57, 58) address subcritical crack growth along SiO₂/TiN interfaces exposed to aqueous environments. Here environmental effects were evaluated both ex situ and in situ. For the ex situ experiments, crack growth velocities have been found to be highly sensitive to humidity exposure time (Ref 57). With the above, it was suggested that subcritical crack growth involved the diffusion of environmental species along the interface ahead of a crack. In fact, ion mass spectroscopy (SIMS) measurements (Ref 59) revealed that moisture diffusion along an interface was about 10⁴ times faster than diffusion in the bulk SiO₂. In situ experiments (Ref 58) were conducted under controlled humidity (40% RH) and temperature. It was suggested that mechanisms responsible for SCC in bulk glasses may also be involved in the environmentally assisted interfacial fracture (Ref 58).

Moody et al. (Ref 60) evaluated deuterium effects on adhesion between 600 nm thick tantalum nitride films and sapphire. As revealed by a microscratch test, deuterium exposure resulted in an interfacial toughness decrease from 24.5 to 9.1 MPa√m. At the same time, indentation testing indicated no changes in the mechanical properties of TaN films. Thus, direct deuterium effects on plastic energy dissipation could be eliminated. Therefore, decreasing interfacial toughness was attributed to an interfacial fracture energy decrease. Available experimental evidence supported hydrogen-induced decohesion. However, deuterium could also affect adhesion

strength by affecting the interfacial microstructure. Thus, the necessity of a more precise microstructural evaluation was suggested.

References cited in this section

25. S.X. Mao and A.G. Evans, The Influence of Blunting on Crack Growth at Oxide/Metal Interfaces, *Acta Mater.*, Vol 45, 1997, p 4263–4270
26. T.S. Oh, J. Rodel, R.M. Cannon, and R.O. Ritchie, Ceramic/Metal Interfacial Crack Growth Toughening by Controlled Microcracks and Interfacial Geometries, *Acta Metall.*, Vol 36, 1988, p 2083–2093
49. K. Suganuma, K. Niihara, T. Fujita, and T. Okamoto, *Metal-Ceramic Joints*, Vol 8, Proc. MRS Int. Meeting (Pittsburgh, PA), Doyamma et al., Ed., Materials Research Society, 1989, p 113
50. J.M. Howe, Bonding, Structure, and Properties of Metal/Ceramic Interface: Part 2, Interface Fracture Behavior and Property Measurement, *Int. Mater. Rev.*, Vol 38, 1993, p 257–271
51. N.I. Tymiak, M. Li, A.A. Volinsky, Y. Katz, and W.W. Gerberich, Environmental Effects on Cu/SiO₂ and Cu/Ti/SiO₂ Thin Film Adhesion, *Reliability in Microelectronics* MRS Proc., 1999
52. W.W. Gerberich, D.E. Kramer, N.I. Tymiak, A.A. Volinsky, D.F. Bahr, and M.D. Kriese, Nanoindentation-Induced Defect-Interface Interactions: Phenomena Methods and Limitations *Acta Mater.*, Vol 47, 1999, p 4115–4123
53. Y. Katz, N.I. Tymiak, and W.W. Gerberich, Nano-mechanical Probes as New Approaches to Hydrogen/Deformation Interaction Studies, An Invited Paper for Recent Advances in the Engineering Aspects of Hydrogen Embrittlement, *Eng. Fract. Mech.*, 2000
54. C.M. Baldwin and J.D. Mackenzie, Flame Sprayed Alumina on Stainless Steel for Possible Prosthetic Application, *J. Biomed. Mater. Res.*, Vol 10, 1976, p 445–453
55. M.K. Ferber and S.D. Brown, Delayed Failure of Plasma-Sprayed Al₂O₃ Applied to Metallic Substrates, *J. Am. Ceram. Soc.*, Vol 64, 1981, p 737–741
56. D. Avigdor and S.D. Brown, Delayed Failure of a Porous Alumina, *J. Am. Ceram. Soc.*, Vol 61, 1978, p 97–99
57. G. Xu, M.Y. He, and D.R. Clarke, The Effect of Moisture on the Fracture Energy of TiN/SiO₂ Interfaces in Multi-layer Thin Films, *Acta Mater.*, Vol 47, 1999, p 4131–4141
58. M. Lane and R.H. Dauskardt, Subcritical Debonding of Multilayer Interconnect Structures: Temperature and Humidity Effects, *Reliability in Microelectronics*, MRS Proc., Spring meeting, 1999
59. G. Xu, T. Mates, and D.R. Clarke, Moisture Diffusivity Measurement along SiO₂/TiN Interface Using Secondary Ion Mass Spectroscopy (SIMS), *Reliability in Microelectronics*, MRS Proc., 1999
60. N.R. Moody, S.K. Venkataraman, B. Bastaez, J.E. Angelo, and W.W. Gerberich, Hydrogen Effects on the Fracture of Thin Tantalum Nitride Films, *Mater. Res. Soc. Symp. Proc.*, Vol 356, 1995, p 827–832

Testing Methods

Testing techniques for in situ environmental testing of thin-film adhesion are briefly reviewed. The focus is on quantitative methods where a characteristic of interfacial toughness is extracted from experimental results utilizing an appropriate model. In most cases, modeling is based on elasticity solutions. It is necessary to emphasize that these are applicable only under small-scale-yielding crack-tip conditions with the remaining material being elastic. However, extensive plastic deformation or even general yielding may develop in a ductile counterpart of an interface. Lai and Dillard (Ref 61) determined general yielding conditions for the most common test configurations and suggest appropriate types of test and sample dimensions for interfaces with different elastic mismatch and residual stresses. Even under conditions where general yielding is not expected, the local crack-tip region may experience extensive plastic deformation and associated dissipation losses. Several studies evaluate plastic energy dissipation associated with interfacial fracture (Ref 62, 63, 64). Results of these studies may be applied to practical specimen configurations that approximate situations treated in the above analyses. As for specific testing methods, either finite element analysis (FEM) analysis (Ref 65) or analytical approximation may be available (Ref 66) in some cases.

Methods suitable for in situ environmental testing of thin-film adhesion are briefly described below and are summarized in Tables 1 and 2 (Ref 65, 66, 67, 68, 69, 70, 71, 72, 73, 74, 75, 76, 77, 78, 79, 80, 81, 82, 83, 84, 85, 86, 87, 88, 89, 90, 91, 92, 93, 94, 95). For ease of evaluation and to obtain useful quantitative data, the following criteria are suggested for these tests:

- Simple sample preparation with no or minimum effect on the properties of interfaces and/or joining materials
- A simple testing procedure with a possibility for in situ environmental exposure and/or testing shortly after an environmental exposure
- Precision and reliability in measurements of loading and crack growth characteristics
- Availability of an adequate model for a *quantitative* analysis. Ideally, not only a characteristic value of interfacial toughness should be determined, but also corresponding mode mixity and possible contributions of various dissipation processes
- Close approximation of service conditions (geometry and environment)

Examination of fracture surfaces may also provide useful information.

Table 1 Summary of adhesion testing methods

Test	Driving force for delamination	Sample preparation	Analysis	Mode mixity	Applicability	Requirements	Advantages	Disadvantages
Sandwich (Ref 65, 67, 68, 69)	External load	Diffusion bonding	Relatively simple, analytical solutions available	Between 0 and 90°, depending on a particular sample geometry	All types of interfaces	Film thickness small with any in-plane dimension	In situ testing; film residual stresses not required.	Sample preparation may change interfacial properties.
Peel test (Ref 70, 71, 72, 73)	External load	Simple partial delamination needs to be introduced.	A variety of dissipational processes to account for	...	Thick films; relatively weak adhesion	Mode mixity range out of practical interest range; not directly applicable to very brittle and/or very thin films
Blister (Ref 74, 75, 76, 77, 78)	Pressurization-environmental effects may be evaluated by pressurization with the media of interest.	Complex removing a “window” of a substrate (direct) or a fil (invert)	...	-60° to -30°	Challenging sample preparation; a direct method is not suitable for brittle films.

Table 2 Summary of indentation (contact mechanics) methods for adhesion testing

Test	Driving force for delamination	Sample preparation	Analysis	Mode mixity	Applicability	Requirements	Advantages	Disadvantages
Axisymmetric indentation (Ref 81, 82, 83)	Film residual stress plus stress due to indentation-induced plastic deformation in a film	None	Analytical	...	Plastically deforming films on harder substrates	More accurate for indentation depth smaller than film thickness	Simple sample preparation, procedure, and analysis	In general, not applicable for very ductile films and/or strong adhesion. Residual stress measurements are required.

Microwedge indentation (Ref 84, 85)	Indentation-induced plastic deformation in a film; or indentation-induced plastic deformation in a substrate	May involve microlithography	Analytical	-37° to -53°	Fine lines of ductile material on a brittle substrate and brittle films on ductile substrates	...	Directly applicable for microelectronic structures	...
Superlayer and axisymmetric indentation (Ref 86, 87, 88)	Same as above plus an additional driving force from a superlayer	None	Numerical	...	Ductile films on brittle substrates	...	Simple procedure; may be applied for very ductile film and/or strong interfaces	Challenges in analysis. Residual stress measurements are required.
Axisymmetric indentation (Ref 89, 90)	Indentation-induced plastic deformation of a substrate	None	Analytical approximation utilizing fem results	Pure mode II assumed	Brittle films on ductile substrates	Indentation depth much smaller than film thickness	Simple procedure	Not applicable for very strongly adherent films where very large penetration depth with the associated pileup are required. Here, film might experience out of plane bending
Microwedge scratch (Ref 84)	...	Microlithography or may be applied directly to fin lines	Analytical	...	Same as above	Same as above	Simple procedure	...
Scratch (Ref 91, 92, 93, 94)	...	None	Crude analytical approximations	Close to mode II	...	Thin films	Simple procedure may be applied to films on very ductile substrates	Very challenging analysis

Sandwich Specimen Testing. A thin film is sandwiched between two halves of a different material to make a fracture specimen tested either in tension or flexural bending. With the crack growing along an interface of interest, fracture toughness can be determined (Ref 65, 67, 68, 69).

Peel Test. A film is detached from a substrate under a fixed angle (Ref 70, 71). Elastic-plastic dissipation losses for a fixed-arm peel test have been analyzed by Kinloch et al. (Ref 72). The symmetrical double-peel arrangement for peel testing at variable angle and constant rate has been described in Ref 73.

Blister Test. A window in a substrate (direct method) (Ref 74, 75, 76, 77) or in a film (invert method) (Ref 78) is removed, and a remaining counterpart is pressurized by a liquid or a gas. An environmental effect may be evaluated by pressurization with the media of interest. With the electrolytic hydrogen charging of a thin metallic film, spontaneous blisters may form. Interfacial toughness may be estimated in this case, providing hydrogen fugacity is known.

Shear test under uniform plane stress loading along an interface (Ref 79, 80).

Contact Mechanics Testing. In this test, an indenter is driven into film/substrate system in order to induce film debonding. The driving force for delamination in contact mechanics methods is indenter-induced deformation. Little or no sample preparation is required (Table 2) and so there are no interfacial property changes from sample preparation. Based on the load and delamination dimensions, adhesion strength may be evaluated (Ref 81, 82, 83, 84, 85, 86, 87, 88, 89, 90, 91, 92, 93, 94, 95).

References cited in this section

61. Y.-H. Lai and D.A. Dillard, Using Fracture Efficiency to Compare Adhesion Tests, *Int. J. Solids Struct.*, Vol 34, 1997, p 509–525
62. V. Tvergaard and J.W. Hutchinson, Toughness of an Interface along a Thin Ductile Layer Joining Elastic Solids, *Philos. Mag. A*, 1994, p 641–656
63. Y. Wei and J.W. Hutchinson, Models of Interface Separation Accompanied by Plastic Dissipation at Multiple Scales, *Int. J. Fract.*, Vol 95, 1999, p 1–17
64. K.J. Hsia, Z. Suo, and W. Yang, Cleavage due to Dislocation Confinement in Layered Materials, *J. Mech. Phys. Sol.*, Vol 42, 1994, p 877–896
65. R.H. Dauskardt, M. Lane, Q. Ma, and N. Krishna, Adhesion and Debonding of Multi-Layer Thin Film Structures, *Eng. Fract. Mech.*, Vol 61, 1998, p 141–162
66. W.W. Gerberich, A.A. Volinsky, N.I. Tymiak, and N.R. Moody, A Brittle to Ductile Transition in Adhered Thin Films, *Fall MRS 1999* (Boston), Vol 594, 2000
67. P.G. Charalambides, J. Lund, A.G. Evans, and R.M. McMeeking, A Test Specimen for Determining the Fracture Resistance of Bimaterial Interfaces, *J. Appl. Mech.*, Vol 101, 1989, p 77–82
68. A.G. Evans and B.J. Dalgleish, The Fracture Resistance of Metal-Ceramic Interfaces, *Acta Metall. Mater.*, Vol 40, Suppl. Issue, 1992, p S295–306
69. G. Elssner, T. Suga, and M. Turwitt, Determination of the Fracture Energy and the Fracture Resistance of Interfaces, *J. Phys. Coll. (Orsay)*, Vol 46, 1985, p 657–663
70. R.M. Cannon, V. Jayaram, B.J. Dalgleish, and R.M. Fisher, *MRS Symp. Proc.*, Vol 72, 1986, p 121
71. T.S. Oh, R.M. Cannon, and R.O. Ritchie, *J. Am. Ceram. Soc.*, Vol 70, 1987, p C532
72. A.J. Kinloch, C.C. Lau, and J.G. Williams, The Peeling of Flexible Laminates, *Int. J. Fract.*, Vol 66, 1994, p 45–70

73. A.P. Jackson, The Peeling of Surgical Pressure-Sensitive Adhesives at Different Angles, *J. Mater. Sci. Lett.*, Vol 7, 1988, p 1368–1370
74. E.H. Andrews and A. Stevenson, Fracture Energy of Epoxy Resin under Plane Strain Conditions, *J. Mater. Sci.*, Vol 13, 1978, p 1680–1688
75. H.M. Jensen, The Blister Test for Interface Toughness Measurement, *Eng. Fract. Mech.*, Vol 40, 1991, p 475–486
76. R.J. Hohlfelder, H. Luo, J.J. Vlassak, C.E.D. Chidsey, and W.D. Nix, Measuring Interfacial Fracture Toughness with the Blister Test, Thin Films: Stresses and Mechanical Properties VI. Symposium, Materials Research Society, 1997, p 115–120
77. M. Dupeux, A. Bosseboeuf, and D. Buttard, Investigation of the Mechanical Properties and Adhesion of P.V.D. Tungsten Films on Si and Si Compounds by Bulge and Blister Tests, MRS Spring Meeting (San Francisco), 13–17 April 1998
78. K.R. Jiang and L.S. Penn, Use of the Blister Test to Study the Adhesion of Brittle Materials, *J. Adhes.*, Vol 32, 1990, Part I, p 203–216; Part II, p 217–226
79. L. Arcan, Y.M. Aravot, M.E. Arcan, and A. Albu-Yaron, *Ultramicroscopy*, Vol 23, 1987, p 234
80. Y.M. Aravot and A. Albu-Yaron, *Ultramicroscopy*, Vol 26, 1991, p 6423
81. D.B. Marshal and A.G. Evans, Measurement of Adherence of Residually Stressed Thin Film by Indentation. I. Mechanics of Interface Delamination, *J. Appl. Phys.*, Vol 56, 1984, p 2632–2638
82. M.J. Matthewson, Axi-Symmetric Contact on Thin Compliant Coatings, *J. Mech. Phys. Solids*, Vol 29, 1981, p 89–113
83. L.G. Rosenfeld, J.E. Ritter, T.J. Lerner, and M.R. Lin, Use of the Microindentation Technique for Determining Interfacial Fracture Energy, *J. Appl. Phys.*, Vol 67, 1990, p 3291–3296
84. M. De Boer and W.W. Gerberich, Microwedge Indentation of the Thin Film Fine Line, I. Mechanics, *Acta Mater.*, Vol 44, 1996, p 3169–3175
85. J.J. Vlassak, M.D. Drory, and W.D. Nix, A Simple Technique for Measuring the Adhesion of Brittle Films to Ductile Substrates with Applications to Diamond-Coated Titanium, *J. Mater. Res.*, Vol 12, 1997, p 1900–1910
86. M.D. Kriese, W.W. Gerberich, and N.R. Moody, Quantitative Adhesion Measures of Multilayer Films. Part I. Indentation Mechanics, *J. Mater. Res.*, Vol 14, 1999, p 3007–3018
87. N.I. Tymiak, A.A. Volinsky, M.D. Kriese, S.A. Downs, and W.W. Gerberich, The Role of Plasticity in Bi-Material Fracture with Ductile Underlayers, *Metall. Trans. A*, Vol 31, 2000, p 863–871
88. A.A. Volinsky, N.I. Tymiak, M.D. Kriese, W.W. Gerberich, and J.W. Hutchinson, Qualitative Modelling and Measurement of Copper Thin Film Adhesion, *Fall 1998 MRS (Boston)*, Vol 539, 1998, p 277–290
89. M.D. Drory and J.W. Hutchinson, Measurement of Brittle-Film Adhesion on a Ductile Substrate by Indentation, *Proc. R. Soc. (London) A*, 1996, p 2319–2341

90. D.F. Bahr and W.W. Gerberich, Effect of In and Out of Plane Stresses during Indentation of Diamond Films on Metal Substrates, Thin Films, *Stresses and Mechanical Properties VI, Symposium. Mater. Res. Soc.*, 1997, p 85–90
91. P.R. Chalker, S.J. Bull, and D.S. Rickerby, A Review of the Methods for the Evaluation of Coating-Substrate Adhesion, *Mat. Sci. & Engng., A*, Vol A140, 1991, p 583–592
92. S.V. Hainsworth, S.J. Bull, and T.F. Page, Scratch Deformation Response of Thin CN_x Coatings at Ultra-Low Loads, *Fundamentals of Nanindentation and Nanotribology, Symposium. Mater. Res. Soc.*, 1998, p 433–438
93. T.W. Wu, Microscratch and Load Relaxation Tests for Ultra-Thin Films, *J. Mater. Res.*, Vol 6, 1991, p 407–426
94. S. Venkataraman, D.L. Kohlstedt, and W.W. Gerberich, Continuous Microscratch Measurements of the Practical and True Works of Adhesion for Metal/Ceramic Systems, *J. Mater. Res.*, Vol 11, 1996, p 3133–3145
95. J.E. Ritter, T.J. Lardner, L.G. Rosenfeld, and M.R. Linn, Measurement of Adhesion of Thin Polymer Coatings by Indentation, *J. Appl. Phys.*, Vol 66, 1989, p 3627–3634

Adhesion Testing

Surface and Adhesive Energies

Surface energies of fracture surfaces for environmentally exposed and nonexposed interfaces can be evaluated with the contact angle method (Ref 96, 97). Measured values may be compared to these for corresponding bulk material (Ref 98). Contact mechanics approaches provide an alternative measure of adhesive strength between flat and spherical surfaces (Ref 99, 100). Swadener et al. (Ref 98) measured adherence of an epoxy sphere to both pure glass surface and that obtained after fracture along an interface with epoxy. Similarly, environmental effects on interfacial fracture surfaces may be evaluated. Finally, an alternative way to measure adhesion strength using fracture surface examination was proposed by Sharma and coworkers (Ref 101). The method is based on digital image processing. A special sample preparation involving microlithography is required here.

References cited in this section

96. J.M. Howe, Bonding, Structure, and Properties of Metal/Ceramic Interfaces: Part 1 Chemical Bonding, *Int. Mater. Rev.*, Vol 38, 1993, p 233–256
97. A. Carre and J. Shultz, Polymer-Aluminum Adhesion. I. The Surface Energy of Aluminum in Relation to its Surface Treatment, *J. Adhes.*, Vol 15, 1983, p 151–162
98. J. Swadener, K.M. Liechti, and A.L. de Lozanne, The Intrinsic Toughness and Adhesion Mechanisms of a Glass/Epoxy Interface, *J. Mech. Phys. Solids*, Vol 47, 1999, p 223–258
99. K.L. Johnson, K. Kendall, and A.D. Roberts, Surface Energy and the Contact of Elastic Solids, *Proc. R. Soc. (London) A*, Vol 324, 1971, p 301–313
100. D. Maugis and M. Barquins, Fracture Mechanics and the Adherence of Viscoelastic Bodies, *J. Phys. D., Appl. Phys.*, Vol 11, 1978, p 1989–2023

101. R. Sharma, J.-K. Lin, and J. Drye, A New Method to Evaluate Thin Film Adhesion, *J. Adhes.*, Vol 40, 1993, p 257–265

Adhesion Testing

References

1. P.J. Blau, Glossary of Terms, *Friction, Lubrication, and Wear Technology*, Vol 18, *ASM Handbook*, ASM International, 1992
2. K.L. Mittal, Ed., *Adhesion Measurements of Films and Coatings*, VSP, 1995
3. K.L. Mittal, Ed., *Adhesive Joints*, Plenum Press, 1984
4. G.L. Schneberger, Ed., *Adhesives in Manufacturing*, Marcel Dekker, 1983
5. G.P. Anderson, S.J. Bennett, and K.L. DeVries, *Analysis and Testing of Adhesive Bonds*, Academic Press, 1977
6. K.L. Mittal, Ed., *Adhesion Measurement of Thin Films, Thick Films and Bulk Coatings*, STP 640, ASTM, 1978
7. J.N. Israelachvili, *Intermolecular and Surface Forces*, Academic Press, London, 1985
8. R.G. Horn, Surfaces Forces and Their Action in Ceramic Materials, *J. Am. Ceram. Soc.*, Vol 73, 1990, p 1117–1135
9. R.G. Horn, Measurement of Surface Forces and Adhesion, *Friction, Lubrication, and Wear Technology*, Vol 18, *ASM Handbook*, ASM International, 1992, p 399
10. D. Tabor and R.H.R. Winterton, The Direct Measurement of Normal and Retarded van der Waals Forces, *Proc. R. Soc. (London) A*, Vol 312, 1969, p 435–450
11. J.N. Israelachvili and G.E. Adams, Measurement of Forces between Two Mica Surfaces in Aqueous Electrolyte Solutions in the Range 0 to 100 nm, *J. Chem. Soc. Faraday Trans. I*, Vol 74, 1978, p 975–1001
12. K.B. Lodge, Techniques for the Measurement of Forces between Solids, *Adv. Colloid Interface Sci.*, Vol 19, 1983, p 27–73
13. J.N. Israelachvili, Thin Film Studies Using Multiple-Beam Interferometry, *J. Colloid Interface Sci.*, Vol 44, 1973, p 259–272
14. R.G. Horn and D.T. Smith, Analytic Solution for the Three-Layer Multiple Beam Interferometer, *Appl. Opt.*, Vol 30, 1991, p 59–65
15. D.Y.C. Chan and R.G. Horn, The Drainage of Thin Liquid Films between Solid Surfaces, *J. Chem. Phys.*, Vol 83, 1985, p 5311–5324

16. J. Peachey, J. Van Alsten, and S. Granick, Design of an Apparatus to Measure the Shear Response of Ultrathin Liquid Films, *Rev. Sci. Instrum.*, Vol 62, 1991, p 463–473
17. A.M. Homola, J.N. Israelachvili, M.L. Gee, and P.M. McGuiggan, Measurement of and Relation between the Adhesion and Friction of Two Surfaces Separated by Molecularly Thin Liquid Films, *J. Tribol.*, Vol 111, 1989, p 675–682
18. D.H. Buckley, *Surface Effects in Adhesion, Friction, Wear and Lubrication*, Elsevier, Amsterdam, 1981
19. F.M. Orr, L.E. Scriven, and A.P. Rivas, Pendular Rings between Solids: Meniscus Properties and Capillary Force, *J. Fluid Mech.*, Vol 67, 1975, p 723–742
20. W.D. Bascom, P.F. Becher, J.L. Bitner, and J.S. Murday, Use of Fracture Mechanics Concepts in Testing of Film Adhesion, *Adhesion Measurement of Thin Films, Thick Films and Bulk Coatings*, STP 640, K.L. Mittal, Ed., ASTM, 1978, p 63–81
21. D.B. Marshall and A.G. Evans, Measurement of Adherence of Residually Stressed Thin Films by Indentation. Mechanics of Interface Delamination, *J. Appl. Phys.*, Vol 56, 1984, p 2632–2638
22. A. Carre and J. Shultz, Polymer-Aluminum Adhesion. III. Effect of a Liquid Environment, *J. Adhesion*, Vol 18, 1984, p 171–184
23. J.D. Venables, Review: Adhesion and Durability of Metal-Polymer Bonds, *J. Mater. Sci.*, Vol 19, 1984, p 2431–2453
24. H. Wu, J.T. Dickinson, and S.C. Langford, Dynamic Measurements of Humidity Attack on Polymer/Glass Interfaces under Stress, *J. Adhes. Sci.*, Vol 11, 1997, p 695–717
25. S.X. Mao and A.G. Evans, The Influence of Blunting on Crack Growth at Oxide/Metal Interfaces, *Acta Mater.*, Vol 45, 1997, p 4263–4270
26. T.S. Oh, J. Rodel, R.M. Cannon, and R.O. Ritchie, Ceramic/Metal Interfacial Crack Growth Toughening by Controlled Microcracks and Interfacial Geometries, *Acta Metall.*, Vol 36, 1988, p 2083–2093
27. N.R. Moody, S.K. Venkataraman, B. Bastaez, J.E. Angelo, and W.W. Gerberich, Hydrogen Effects on the Fracture of Thin Tantalum Nitride Films, *Mater. Res. Soc. Symp. Proc.*, Vol 356, 1995, p 827–832
28. N.I. Tymiak, M. Li, A. Volinsky, Y. Katz, and W.W. Gerberich, The Role of Plasticity in Bi-material Fracture with Ductile Interlayers, *Metall. Trans. A*, Vol 31, 2000, p 863–871
29. Y.Y. Wang, F.P. Chiang, and R.S. Barsoum, A Photoelastic Study of Extending Cracks in Adhesion Joints, *J. Adhes.*, 1995
30. A.G. Evans and J.W. Hutchinson, Effects of Non-Planarity on the Mixed Mode Fracture Resistance of Bi-material Interfaces, *Acta Met. Mater.*, Vol 37, 1989, p 909–916
31. F.M. Fowkes, D.W. Dwight, and D.A. Cole, Acid-Base Properties of Glass Surfaces, *J. Non-Cryst. Solids*, Vol 120, 1990, p 47–60
32. J.T. Dickinson, L.C. Jensen, S. Lee, L. Scuderio, and S.C. Langford, Fracto-Emission and Electrical Transients due to Interfacial Failure, *J. Adhes. Sci. Technol.*, Vol 8, 1994, p 1285–1309
33. A. Dupre, *Theorie Mechanique de la Chaleur*, Paris, 1989

34. A. Bagchi and A.G. Evans, Measurements of the Debond Energy for Thin Metallization Lines on Dielectrics, *Thin Solid Films*, Vol 286, 1996, p 203–212
35. R.G. Stringfellow and L.B. Freund, The Effect of Interfacial Friction on the Buckle-Driven Spontaneous Delamination of a Compressed Thin Film, *Int J. Solid Structures*, Vol 30, 1993, p 1379–1395
36. A. Needleman, An Analysis of Tensile Decohesion along an Interface, *J. Mech. Phys. Solids*, Vol 38, 1990, p 289–324
37. W.D. Bascom, R.L. Cottington, R.C. Jones, and P. Peyster, Fracture of Epoxy and Elastomer Epoxy Polymers in Bulk and as Adhesives, *Organic Coat. Plast. Chem.*, Vol 34, 1974, p 300
38. J.N.B. Sutton, McGary, *Polym. Eng. Sci.*, Vol 13, 1973, p 29
39. J.W. Hutchinson and Z. Suo, *Adv. Appl. Mech.*, Vol 29, 1992, p 63
40. K.M. Liechti and Y.S. Chai, Biaxial Loading Experiments for Determining Interfacial Fracture Toughness. *J. Appl. Mech.*, Vol 58, 1991, p 680–687
41. V. Tvergaard V and J.W. Hutchinson, The Influence of Plasticity on Mixed Mode Interface Toughness, *J. Mech. Phys. Solids*, Vol 41, 1993, p 1119–1135
42. P.A. Mataga and P. Ponte Castaneda, Stable Crack Growth along a Brittle/Ductile Interface-II Small Scale Yielding Solutions and Interfacial Toughness, *Int. J. Solids Struct.*, Vol 36 (No. 1), 1998, p 1–35
43. K.W. Allen, A Review of Contemporary Views of Theories of Adhesion, *J. Adhes.*, Vol 21, 1987, p 261–277
44. J.W. Severin, R. Hokke, H. Van der Wel, and G. de With, The Influence of Thermal Treatments on the Adhesion of Electrolessly Deposited Ni(P) Layers on Alumina Ceramic, *J. Electrochem. Soc.*, Vol 141, 1994, p 816–824
45. Y.M. Aravot and A. Albu-Yaron, The Effect of Environmental Moisture on the Adhesion Toughness of Epoxy-Coated Phosphated Steels, *J. Mater. Sci. Lett.*, Vol 12, 1993, p 1437–1438
46. A. Leng, H. Streckel, and M. Stratman, The Delamination of Polymeric Coatings from Steel, Parts 1–4, *Corros. Sci.*, Vol 41, 1999, p 547–620
47. H. Wu, J.T. Dickinson, and S.C. Langford, Dynamic Measurements of Humidity Attack on Polymer/Glass Interfaces under Stress, *J. Adhes. Sci. Technol.*, Vol 11, 1997, p 695–717
48. D.-C. Hu and H.-Ch. Chen, Humidity Effect on Polyimide Film Adhesion, *J. Mater. Sci.*, Vol 27, 1992, p 5262–5268
49. K. Suganuma, K. Niihara, T. Fujita, and T. Okamoto, *Metal-Ceramic Joints*, Vol 8, Proc. MRS Int. Meeting (Pittsburgh, PA), Doyamma et al., Ed., Materials Research Society, 1989, p 113
50. J.M. Howe, Bonding, Structure, and Properties of Metal/Ceramic Interface: Part 2, Interface Fracture Behavior and Property Measurement, *Int. Mater. Rev.*, Vol 38, 1993, p 257–271
51. N.I. Tymiak, M. Li, A.A. Volinsky, Y. Katz, and W.W. Gerberich, Environmental Effects on Cu/SiO₂ and Cu/Ti/SiO₂ Thin Film Adhesion, *Reliability in Microelectronics MRS Proc.*, 1999

52. W.W. Gerberich, D.E. Kramer, N.I. Tymiak, A.A. Volinsky, D.F. Bahr, and M.D. Kriese, Nanoindentation-Induced Defect-Interface Interactions: Phenomena Methods and Limitations *Acta Mater.*, Vol 47, 1999, p 4115–4123
53. Y. Katz, N.I. Tymiak, and W.W. Gerberich, Nano-mechanical Probes as New Approaches to Hydrogen/Deformation Interaction Studies, An Invited Paper for Recent Advances in the Engineering Aspects of Hydrogen Embrittlement, *Eng. Fract. Mech.*, 2000
54. C.M. Baldwin and J.D. Mackenzie, Flame Sprayed Alumina on Stainless Steel for Possible Prosthetic Application, *J. Biomed. Mater. Res.*, Vol 10, 1976, p 445–453
55. M.K. Ferber and S.D. Brown, Delayed Failure of Plasma-Sprayed Al₂O₃ Applied to Metallic Substrates, *J. Am. Ceram. Soc.*, Vol 64, 1981, p 737–741
56. D. Avigdor and S.D. Brown, Delayed Failure of a Porous Alumina, *J. Am. Ceram. Soc.*, Vol 61, 1978, p 97–99
57. G. Xu, M.Y. He, and D.R. Clarke, The Effect of Moisture on the Fracture Energy of TiN/SiO₂ Interfaces in Multi-layer Thin Films, *Acta Mater.*, Vol 47, 1999, p 4131–4141
58. M. Lane and R.H. Dauskardt, Subcritical Debonding of Multilayer Interconnect Structures: Temperature and Humidity Effects, *Reliability in Microelectronics*, MRS Proc., Spring meeting, 1999
59. G. Xu, T. Mates, and D.R. Clarke, Moisture Diffusivity Measurement along SiO₂/TiN Interface Using Secondary Ion Mass Spectroscopy (SIMS), *Reliability in Microelectronics*, MRS Proc., 1999
60. N.R. Moody, S.K. Venkataraman, B. Bastaez, J.E. Angelo, and W.W. Gerberich, Hydrogen Effects on the Fracture of Thin Tantalum Nitride Films, *Mater. Res. Soc. Symp. Proc.*, Vol 356, 1995, p 827–832
61. Y.-H. Lai and D.A. Dillard, Using Fracture Efficiency to Compare Adhesion Tests, *Int. J. Solids Struct.*, Vol 34, 1997, p 509–525
62. V. Tvergaard and J.W. Hutchinson, Toughness of an Interface along a Thin Ductile Layer Joining Elastic Solids, *Philos. Mag. A*, 1994, p 641–656
63. Y. Wei and J.W. Hutchinson, Models of Interface Separation Accompanied by Plastic Dissipation at Multiple Scales, *Int. J. Fract.*, Vol 95, 1999, p 1–17
64. K.J. Hsia, Z. Suo, and W. Yang, Cleavage due to Dislocation Confinement in Layered Materials, *J. Mech. Phys. Sol.*, Vol 42, 1994, p 877–896
65. R.H. Dauskardt, M. Lane, Q. Ma, and N. Krishna, Adhesion and Debonding of Multi-Layer Thin Film Structures, *Eng. Fract. Mech.*, Vol 61, 1998, p 141–162
66. W.W. Gerberich, A.A. Volinsky, N.I. Tymiak, and N.R. Moody, A Brittle to Ductile Transition in Adhered Thin Films, *Fall MRS 1999* (Boston), Vol 594, 2000
67. P.G. Charalambides, J. Lund, A.G. Evans, and R.M. McMeeking, A Test Specimen for Determining the Fracture Resistance of Bimaterial Interfaces, *J. Appl. Mech.*, Vol 101, 1989, p 77–82
68. A.G. Evans and B.J. Dalgleish, The Fracture Resistance of Metal-Ceramic Interfaces, *Acta Metall. Mater.*, Vol 40, Suppl. Issue, 1992, p S295–306

69. G. Elssner, T. Suga, and M. Turwitt, Determination of the Fracture Energy and the Fracture Resistance of Interfaces, *J. Phys. Coll. (Orsay)*, Vol 46, 1985, p 657–663
70. R.M. Cannon, V. Jayaram, B.J. Dalgleish, and R.M. Fisher, *MRS Symp. Proc.*, Vol 72, 1986, p 121
71. T.S. Oh, R.M. Cannon, and R.O. Ritchie, *J. Am. Ceram. Soc.*, Vol 70, 1987, p C532
72. A.J. Kinloch, C.C. Lau, and J.G. Williams, The Peeling of Flexible Laminates, *Int. J. Fract.*, Vol 66, 1994, p 45–70
73. A.P. Jackson, The Peeling of Surgical Pressure-Sensitive Adhesives at Different Angles, *J. Mater. Sci. Lett.*, Vol 7, 1988, p 1368–1370
74. E.H. Andrews and A. Stevenson, Fracture Energy of Epoxy Resin under Plane Strain Conditions, *J. Mater. Sci.*, Vol 13, 1978, p 1680–1688
75. H.M. Jensen, The Blister Test for Interface Toughness Measurement, *Eng. Fract. Mech.*, Vol 40, 1991, p 475–486
76. R.J. Hohlfelder, H. Luo, J.J. Vlassak, C.E.D. Chidsey, and W.D. Nix, Measuring Interfacial Fracture Toughness with the Blister Test, Thin Films: Stresses and Mechanical Properties VI. Symposium, Materials Research Society, 1997, p 115–120
77. M. Dupeux, A. Bosseboeuf, and D. Buttard, Investigation of the Mechanical Properties and Adhesion of P.V.D. Tungsten Films on Si and Si Compounds by Bulge and Blister Tests, MRS Spring Meeting (San Francisco), 13–17 April 1998
78. K.R. Jiang and L.S. Penn, Use of the Blister Test to Study the Adhesion of Brittle Materials, *J. Adhes.*, Vol 32, 1990, Part I, p 203–216; Part II, p 217–226
79. L. Arcan, Y.M. Aravot, M.E. Arcan, and A. Albu-Yaron, *Ultramicroscopy*, Vol 23, 1987, p 234
80. Y.M. Aravot and A. Albu-Yaron, *Ultramicroscopy*, Vol 26, 1991, p 6423
81. D.B. Marshal and A.G. Evans, Measurement of Adherence of Residually Stressed Thin Film by Indentation. I. Mechanics of Interface Delamination, *J. Appl. Phys.*, Vol 56, 1984, p 2632–2638
82. M.J. Matthewson, Axi-Symmetric Contact on Thin Compliant Coatings, *J. Mech. Phys. Solids*, Vol 29, 1981, p 89–113
83. L.G. Rosenfeld, J.E. Ritter, T.J. Lerner, and M.R. Lin, Use of the Microindentation Technique for Determining Interfacial Fracture Energy, *J. Appl. Phys.*, Vol 67, 1990, p 3291–3296
84. M. De Boer and W.W. Gerberich, Microwedge Indentation of the Thin Film Fine Line, I. Mechanics, *Acta Mater.*, Vol 44, 1996, p 3169–3175
85. J.J. Vlassak, M.D. Drory, and W.D. Nix, A Simple Technique for Measuring the Adhesion of Brittle Films to Ductile Substrates with Applications to Diamond-Coated Titanium, *J. Mater. Res.*, Vol 12, 1997, p 1900–1910
86. M.D. Kriese, W.W. Gerberich, and N.R. Moody, Quantitative Adhesion Measures of Multilayer Films. Part I. Indentation Mechanics, *J. Mater. Res.*, Vol 14, 1999, p 3007–3018

87. N.I. Tymiak, A.A. Volinsky, M.D. Kriese, S.A. Downs, and W.W. Gerberich, The Role of Plasticity in Bi-Material Fracture with Ductile Underlayers, *Metall. Trans. A*, Vol 31, 2000, p 863–871
88. A.A. Volinsky, N.I. Tymiak, M.D. Kriese, W.W. Gerberich, and J.W. Hutchinson, Qualitative Modelling and Measurement of Copper Thin Film Adhesion, *Fall 1998 MRS (Boston)*, Vol 539, 1998, p 277–290
89. M.D. Drory and J.W. Hutchinson, Measurement of Brittle-Film Adhesion on a Ductile Substrate by Indentation, *Proc. R. Soc. (London) A*, 1996, p 2319–2341
90. D.F. Bahr and W.W. Gerberich, Effect of In and Out of Plane Stresses during Indentation of Diamond Films on Metal Substrates, Thin Films, *Stresses and Mechanical Properties VI, Symposium. Mater. Res. Soc.*, 1997, p 85–90
91. P.R. Chalker, S.J. Bull, and D.S. Rickerby, A Review of the Methods for the Evaluation of Coating-Substrate Adhesion, *Mat. Sci. & Engng.*, A, Vol A140, 1991, p 583–592
92. S.V. Hainsworth, S.J. Bull, and T.F. Page, Scratch Deformation Response of Thin CN_x Coatings at Ultra-Low Loads, *Fundamentals of Nanindentation and Nanotribology, Symposium. Mater. Res. Soc.*, 1998, p 433–438
93. T.W. Wu, Microscratch and Load Relaxation Tests for Ultra-Thin Films, *J. Mater. Res.*, Vol 6, 1991, p 407–426
94. S. Venkataraman, D.L. Kohlstedt, and W.W. Gerberich, Continuous Microscratch Measurements of the Practical and True Works of Adhesion for Metal/Ceramic Systems, *J. Mater. Res.*, Vol 11, 1996, p 3133–3145
95. J.E. Ritter, T.J. Lardner, L.G. Rosenfeld, and M.R. Linn, Measurement of Adhesion of Thin Polymer Coatings by Indentation, *J. Appl. Phys.*, Vol 66, 1989, p 3627–3634
96. J.M. Howe, Bonding, Structure, and Properties of Metal/Ceramic Interfaces: Part 1 Chemical Bonding, *Int. Mater. Rev.*, Vol 38, 1993, p 233–256
97. A. Carre and J. Shultz, Polymer-Aluminum Adhesion. I. The Surface Energy of Aluminum in Relation to its Surface Treatment, *J. Adhes.*, Vol 15, 1983, p 151–162
98. J. Swadener, K.M. Liechti, and A.L. de Lozanne, The Intrinsic Toughness and Adhesion Mechanisms of a Glass/Epoxy Interface, *J. Mech. Phys. Solids*, Vol 47, 1999, p 223–258
99. K.L. Johnson, K. Kendall, and A.D. Roberts, Surface Energy and the Contact of Elastic Solids, *Proc. R. Soc. (London) A*, Vol 324, 1971, p 301–313
100. D. Maugis and M. Barquins, Fracture Mechanics and the Adherence of Viscoelastic Bodies, *J. Phys. D., Appl. Phys.*, Vol 11, 1978, p 1989–2023
101. R. Sharma, J.-K. Lin, and J. Drye, A New Method to Evaluate Thin Film Adhesion, *J. Adhes.*, Vol 40, 1993, p 257–265

Testing Methods for Solid Friction

K.G. Budinski, Eastman Kodak Company; P.J. Blau, Oak Ridge National Laboratory

Introduction

IN MACHINERY WITH MOVING PARTS, friction control can make the difference between acceptable operation and catastrophic failure. Friction in moving parts also reduces the energy-efficiency of machines, making them more costly to operate than if friction were reduced. Therefore, the measurement of friction force and the calculation of the coefficient of friction is warranted for many kinds of machines. In machine design, friction characteristics must be known for friction drives, for sizing motors, for determining work forces, for braking, for rotary seals, and for designing any part of the machine in which changes in forces between sliding members could affect operation. There is a close parallel between the history of friction science and the development of transportation systems, because friction problem solving has enabled the development of all kinds of engines, motor bearings, brakes, transmissions, seals, tires, and other vehicle components (Ref 1). To emphasize the importance of friction in machine design, it has been estimated that one-third to one-half the energy production of the world is wasted through friction (Ref 2).

Friction is not a measure of wear or the tendency to wear; therefore, it does not determine service life. Frictional heating sometimes causes a part to fail, but this usually occurs when circumstances cause abnormal friction effects. Articles describing a variety of measurement methods for different types of wear can be found in other articles in this Section of the Handbook and in *Friction, Lubrication, and Wear Technology*, Vol 18, *ASM Handbook*.

This article describes techniques for measuring friction. Emphasis is on solid/solid sliding friction, but in several instances, lubricated testing methods are described. Many different methods have been developed to measure friction because frictional behavior is dependent not only on the properties of the materials involved, but also on the manner in which they come together and interact (Ref 4). The objective of this article, therefore, is to provide enough information so that a person who has never conducted a friction test can do so. Depending on the method of measurement and the way in which the data are to be used, friction data can be obtained in various forms. The last section of this article therefore, describes how to report friction data and how these data can be entered into a database.

References cited in this section

1. D. Dowson, *History of Tribology*, Longman, 1979
2. A.Z. Szeri, *Tribology: Friction, Lubrication, and Wear*, Hemisphere Publishing Corp., 1980, p 2
4. P.J. Blau, *Friction Science and Technology*, Marcel Dekker, Inc., 1996

Testing Methods for Solid Friction

K.G. Budinski, Eastman Kodak Company; P.J. Blau, Oak Ridge National Laboratory

Definition of the Friction Coefficient

The static friction force, F_s , is that force which is just sufficient to resist the onset of relative motion between two bodies in contact under an applied normal force, N . The kinetic friction force, F_k , is that force which must

be overcome to allow the continuance of motion between two bodies. F_s and F_k act along or tangent to contact surface or interface in a direction so as to directly oppose relative motion. Thus, the static friction coefficient, μ_s , and the kinetic friction coefficient, μ_k , can be defined as a dimensionless ratio of forces as follows:

$$\mu_s = \frac{F_s}{N} \quad (\text{Eq 1})$$

and

$$\mu_k = \frac{F_k}{N} \quad (\text{Eq 2})$$

Elsewhere in this article, if there is no subscript for μ and it is not otherwise stated, it should be assumed that μ_k is implied.

In Eq 1 and 2, both N and F are expressed in units of force. For example, a 1 kg mass resting on a plane exerts a downward force of 9.81 newtons. Strictly speaking, the applied “load” is only equivalent to the normal force if it is applied downward. Thus, it is appropriate to say a load of 9.8 newtons was applied only if the weight acts downward, as in deadweight loading. If, as in a horizontally loaded component, the N acts in a direction other than parallel to the gravitational force, the expression “normal force,” not “load,” must be used. In practice, it is always better to use the general term “normal force” to avoid having to make this distinction.

Testing Methods for Solid Friction

K.G. Budinski, Eastman Kodak Company; P.J. Blau, Oak Ridge National Laboratory

Methods for Measuring Friction

Surface Preparation. Before one conducts any kind of friction test, surfaces of the test pieces should be properly prepared, and their method of preparation should be documented. Since frictional behavior reflects the condition of the contact surfaces and the interface conditions between them, it can be affected by the initial cleanliness of surfaces as well as the method used to produce those surfaces (i.e., machining conditions, polishing methods, etc.). The degree to which the cleanliness and other initial preparation factors will affect the results depends to some extent on the applied test conditions. For example, lightly loaded contacts tend to be more sensitive to surface cleanliness than heavily loaded surfaces in which the onset of sliding quickly wipes films away and can even alter the surface roughness and the subsurface microstructure.

In preparing surfaces for application-oriented testing, including lubricated testing, the conditions of the tribosystem should be simulated as closely as possible. For example, if brake rotor surfaces become rusty during long idle periods in a parking lot, then rusty surfaces should be used for brake rotor friction testing to simulate this condition. Absorbed films from the atmosphere can be another source of contamination. In tests of ultrahigh-molecular weight polyethylene used for conveyor tracks, for example, it was found that if the material sat unused for 48 h or more, as over a weekend, the starting friction was unacceptably high due to the formation of a film on the material. Thus, the laboratory test conditions should mimic such practical operating considerations.

The effects of specimen surface preparation and handling are not further discussed here, but the reader can consult Ref 2 and 3 for additional details. The next sections describe friction testing geometries and the major considerations implicit in their use.

Inclined-Plane Method. Most commonly used friction coefficient measuring methods require the measurement of both the friction force and the normal force, but not all friction coefficient measuring methods do. For example, the inclined-plane static friction coefficient measurement method depicted in Fig. 1 and dating back over 400 years to Leonardo da Vinci's notebooks, requires only a block of material resting on a flat surface, which can be tilted gradually. The weight of the block need not be known, only the angle of tilt. In this case, μ_s is obtained from the following expression:

$$\mu_s = \tan \theta \quad (\text{Eq 3})$$

The specimen is placed on the plane in a horizontal position, and the plane is gradually raised. At some angle, θ , movement of the specimen begins, and the static friction coefficient can be determined. This simple and straightforward test lends itself to standardization. The ease of repetition allows many measurements to be made to obtain an average and standard deviation for μ_s . If the static friction coefficient is relatively low (less than 0.09, $\theta = \sim 5^\circ$), additional precautions in leveling and measuring the tilt angle are required. In fact, alternative means for friction measurement should be considered if such low values are to be accurately measured.

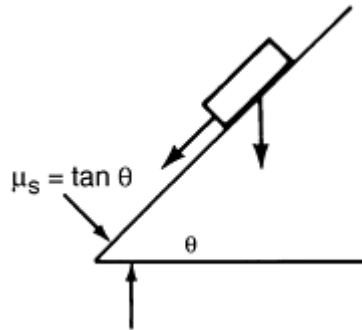


Fig. 1 Inclined plane measurement of the static coefficient of friction (μ_s)

Inclined-plane tests form the basis for ASTM D 3248 (for measuring cardboard friction) and D 3334 (for measuring the friction of woven fabrics), but they can be used for a wide variety of other solid materials. This method does not require the weight of slider block to be known, but research on metals has shown that the results are not independent of the normal force, especially at light loads (Ref 5). The problem with this technique is that it does not simulate many real-life tribosystems. Machine designers do not design systems that involve only inclined planes, and friction is not dependent on just the materials making up the couple. Therefore, more complex machines that simulate the frictional contact of the specific applications can be required. The same argument holds true for simple pulley and weight methods described in the next section.

Friction Test Methods Using Weights and Pulleys. The friction coefficient can be calculated for simple geometries using arrangements of weights and pulleys. Some typical arrangements for measuring static friction coefficients are shown in Fig. 2. Mass is added until the block or cylinder of known weight just begins to move. Equation 1 can then be used.

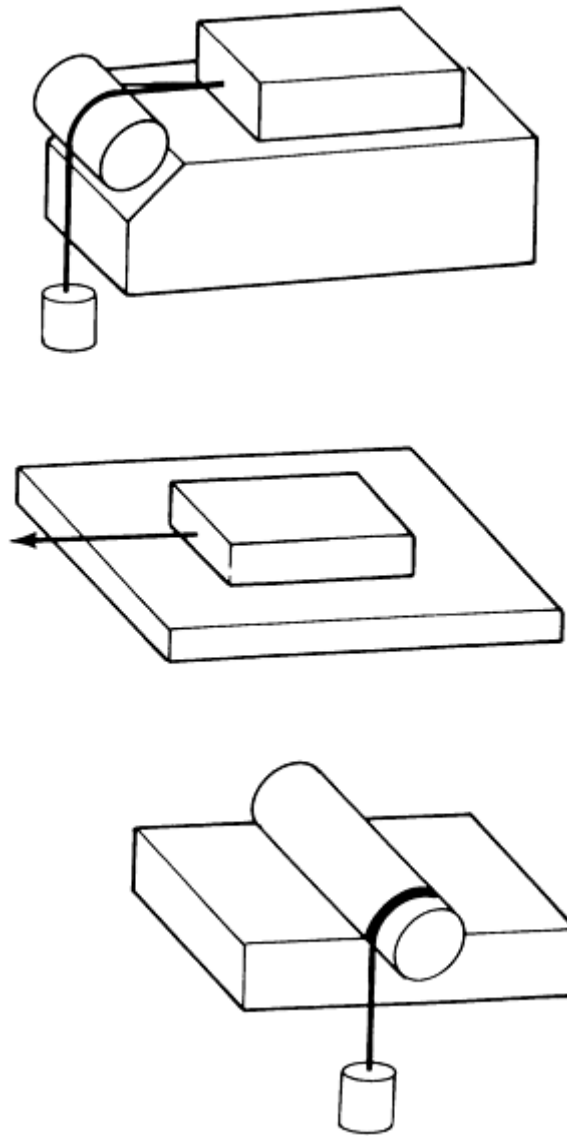


Fig. 2 Schematics of friction-measuring devices based on early work of Leonardo da Vinci

Like the inclined plane method, the problem with block and pulley methods is that the precision and repeatability of the measurement tends to be not very high. One has to account for such things as the stretching of the connecting wires or cords, the friction in the pulleys, pulling any knots tight before motion begins, and more. It is thus, desirable when possible to use force sensors. With force sensors and smooth motor drives, sled-type, block-on-plane methods can be used to measure not only the static but the kinetic friction coefficient as well.

Pulling a block on a flat surface with a load sensor yields the friction force, F in the basic friction equation, $F = \mu N$, where N is the normal force. This is probably the most common method of measuring friction force. Although there are countless variations of this test, most devices use a force sensor that is essentially a calibrated spring. This spring has a spring constant that determines the sensitivity of the system; there is probably some damping associated with the system. A free-body diagram of a sled friction tester is shown in Fig. 3.

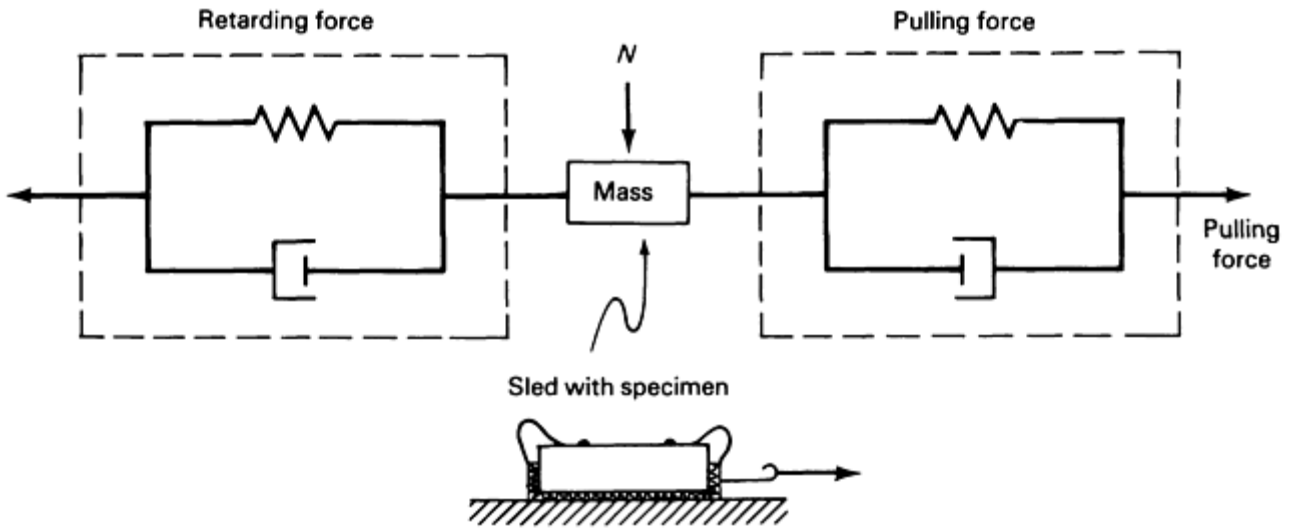


Fig. 3 Free-body diagram of a sled friction tester. N , normal force

Certain system parameters can affect the results of a friction study. All that is measured is the friction force, F , by means of an electrical signal or a mechanical device. Both types of sensors have elastic and damping characteristics that can affect the measurement. The major concern is static friction. If the pulling system shown in Fig. 3 were replaced by a steel rod, which would have much smaller time-dependent strain behavior, the system model could be simplified as shown in Fig. 4. The measured force would still involve the elastic properties of the steel rod (spring a), but any time-dependent component of the friction force would come from the system under study, that is, the elasticity, a , and viscous behavior, b , of the surface contacts.

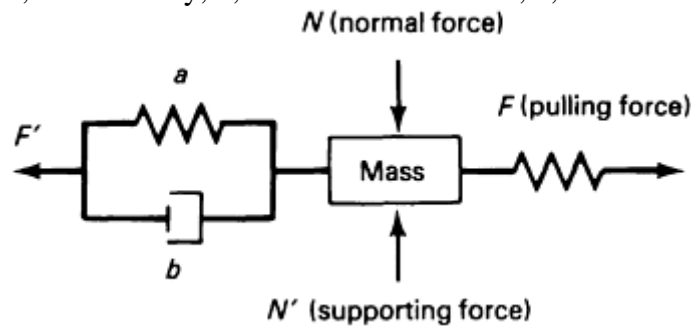


Fig. 4 Free-body diagram of a sled friction tester with a nonelastic driver.

Friction Tests of Shafts and Capstans. The friction of shafts turning in journal bearings and of flexible materials sliding over curved surfaces represents two important classes of practical frictional problems. In each case, the plane of interaction is not flat, and the resistance to rotation is of interest. The directions of the friction force represent a family of vectors of tangency to the curved surface acting along the contact zone.

Figure 5 shows a diagram of a journal bearing. The Petrov equation, developed in the late 19th century, can be used to calculate the friction coefficients as follows:

$$\mu_k = \left(\frac{4\pi^2 l}{c} \right) \left(\frac{\eta \omega}{N} \right) \quad (\text{Eq 4})$$

where r is shaft radius, l is bushing length, c is lubricant film thickness, η is lubricant viscosity, ω is shaft velocity, and N is normal force.

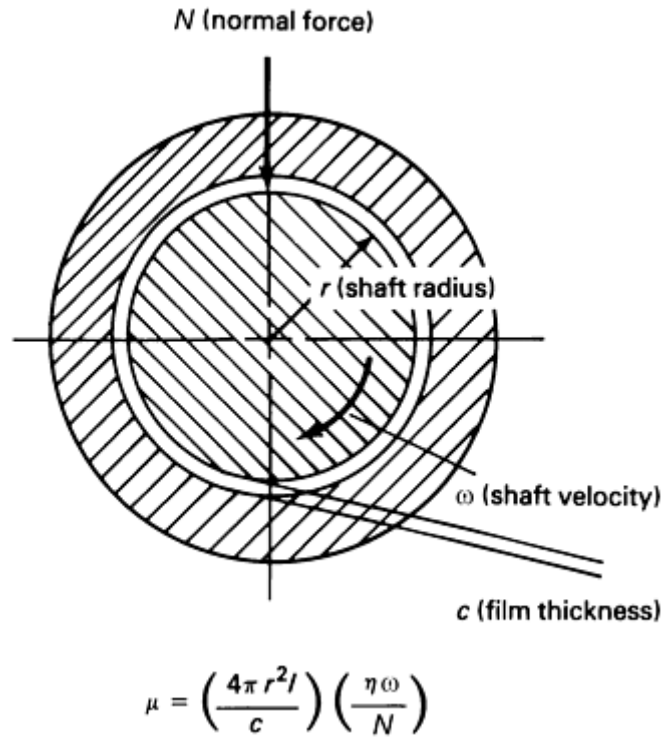


Fig. 5 Petrov equation for the coefficient of friction of a lubricated tribosystem. See text for details.

The friction of a journal bearing or rotating bushing can be measured using an arrangement such as that shown in Fig. 6. The use of a calibrated spring of some kind (as in Fig. 4) is probably the most common method of measuring friction force. The spring has a spring constant that determines the sensitivity of the system, but as shown in Fig. 3 and 4, there is probably some damping associated with this kind of system as well.

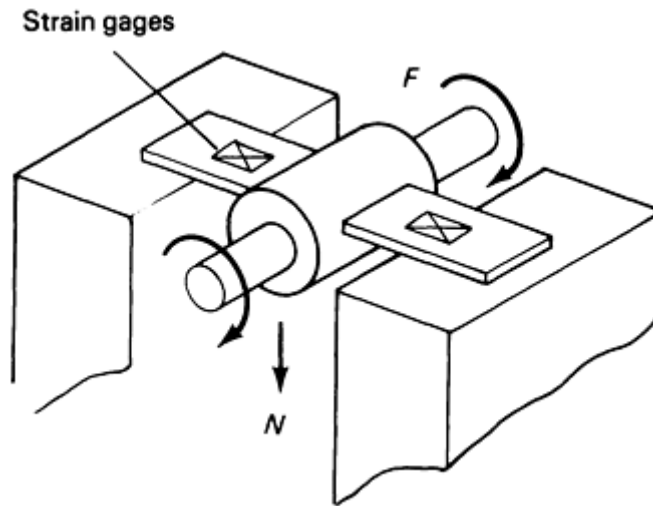


Fig. 6 Use of load cells for measurement of friction force

In another case of non-flat sliding contact, a flexible web is wrapped around a capstan. Figure 7 shows this geometry. The tension T_1 , which can be measured by a force sensor, is given by the following:

$$T_1 = We^{\mu b} \tag{Eq 5}$$

where W is the weight (or another tension force), μ is the friction coefficient (either static or kinetic depending on the use for the test), b is the wrap angle around the capstan or shaft (in radians), and e is the base of natural logarithms (2.7183). Solving for μ as a function of the measured tension, applied tension or weight, and the wrap angle in radians is possible, as follows:

$$\mu = b \ln \frac{T_1}{W} \tag{Eq 6}$$

The capstan test has become a standard ASTM test method ASTM G 143. When using multiple wraps, as in ASTM D 3412, the value of b is adjusted accordingly to equal the number of wraps, or wraps plus fractions of complete wraps, times 2 radians.

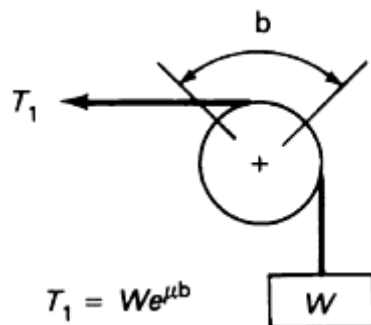


Fig. 7 Schematics of friction-measuring concept for non-flat sliding contact

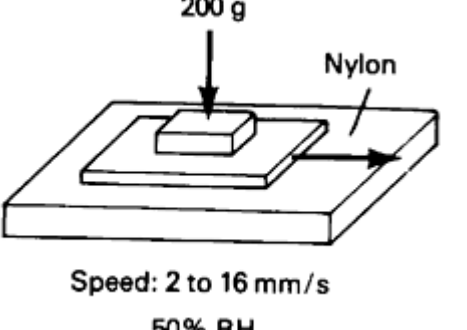
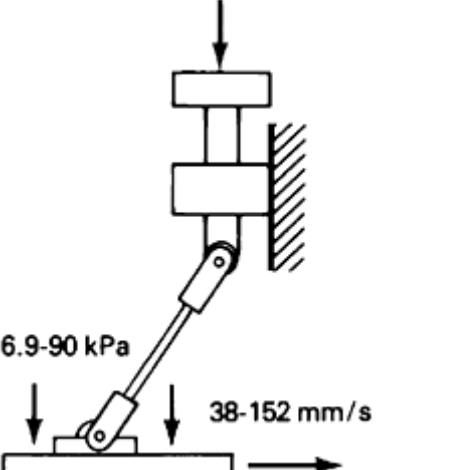
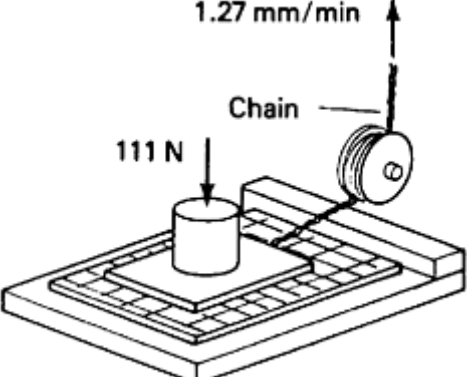
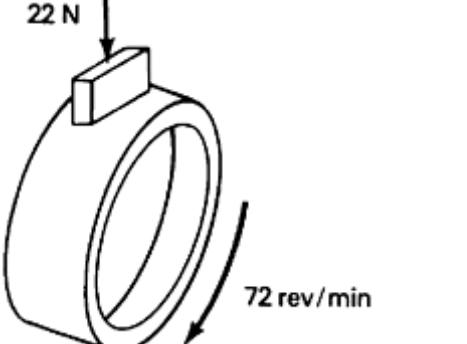
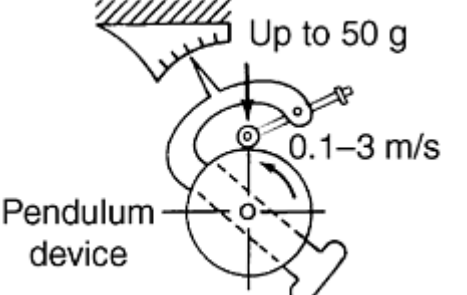
Other Types of Friction Tests, Including Standards. As mentioned, earlier, there are many types of friction tests because there are many reasons for obtaining friction data. In some cases, one might wish to simulate a certain tribosystem. In other cases, one might wish to screen new materials, lubricants, or coatings in a more generic sense and without a specific application in mind. Sometimes, the fine-scale frictional interaction of surfaces is studied purely for scientific purposes.

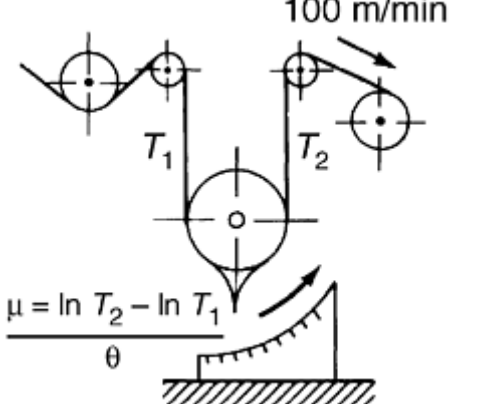
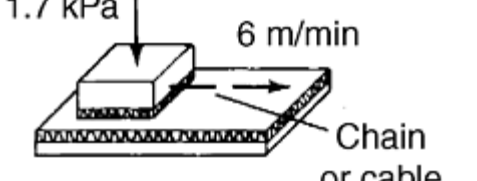
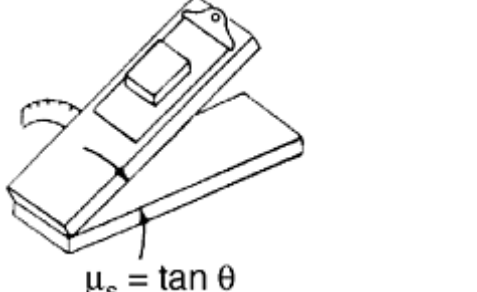
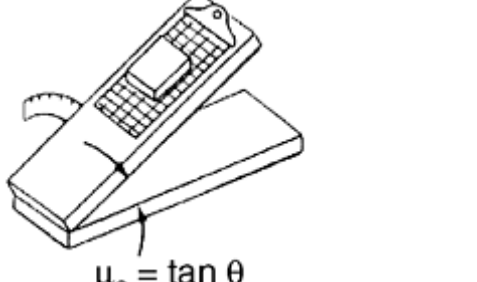
Sometimes, only a limited quantity of a new or experimental material or lubricant is available, and it is necessary to use small, easy-to-fabricate test specimens. A variety of commercial friction testing machines is available for friction testing using simple test geometries, like block-on-ring and pin-on-disk.

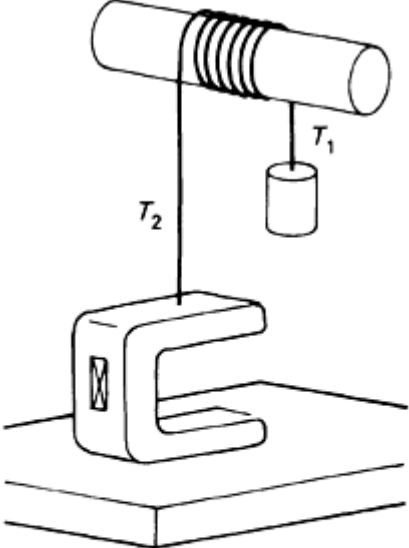
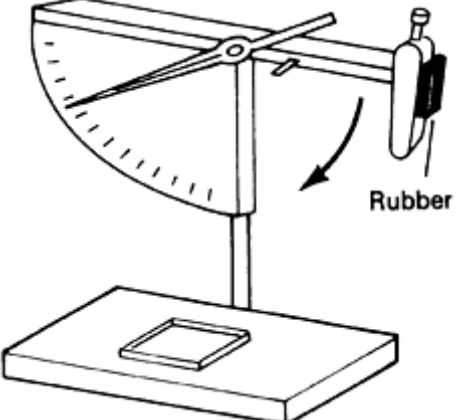
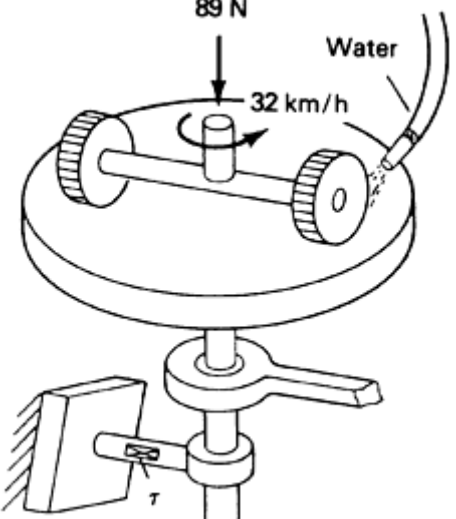
Table 1 shows ASTM friction test methods. Standards documents generally describe the characteristics of a method, as well as its applicability, precision, and accuracy.

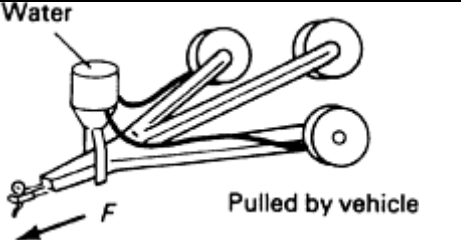
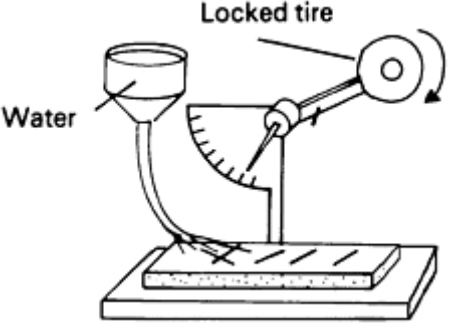
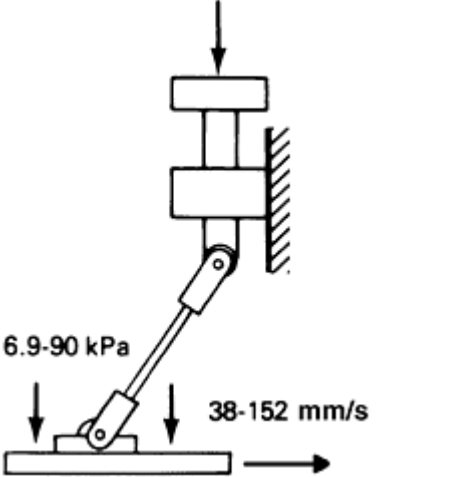
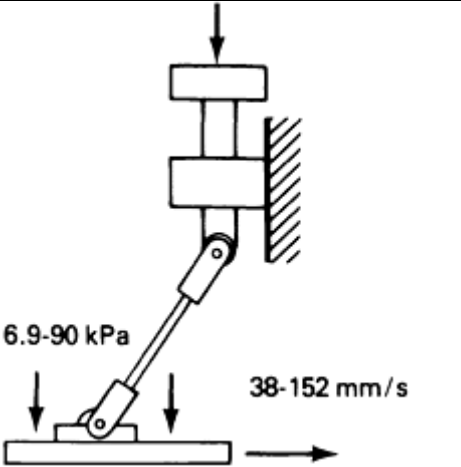
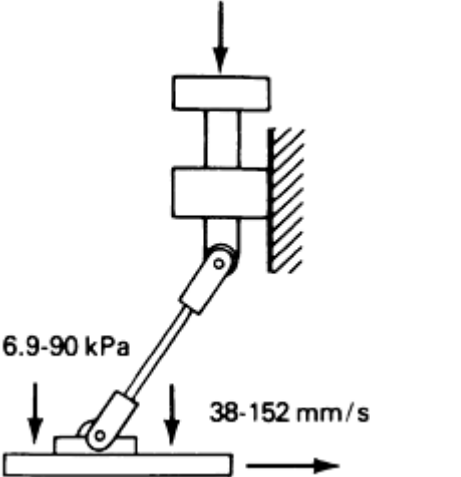
Table 1 Selected solid friction tests per ASTM standards

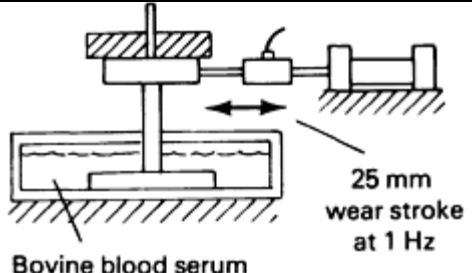
Standard (committee), title	Material couple (measured parameters)	Test configuration
B 460 (B-9 on metal powders), Dynamic Coefficient on Friction and Wear of Sintered Metal Friction Materials under Dry conditions	Friction materials versus metal (μ_k versus temperature)	
B 461 (B-9 on metal powders), Frictional Characteristics of Sintered Metal Friction Materials Run in Lubricants	Friction materials versus metal (μ_k versus number of engagements) (μ_k versus velocity)	
B 526 (B-9 metal powders), Coefficient of Friction and Wear of Sintered Metal	Friction materials versus gray case iron (μ_s and μ_k)	
C 808 (C-5 on carbon/graphite), Reporting Friction and Wear Test Results of	Carbon versus other materials (μ_s and μ_k)	Any apparatus

<p>Manufactured Carbon and Graphite Bearing and Seal Materials</p>		
<p>D 1894 (D-20 on plastics), Static and Kinetic Coefficients of Friction of Plastic Films and Sheeting</p>	<p>Plastic film versus stiff or other solids (μ_s and μ_k)</p>	 <p>200 g Nylon Speed: 2 to 16 mm/s 50% RH</p>
<p>D 2047 (D-21 on polishes), Static Coefficient of Friction of Polish Coated Floor Surfaces as Measured by the James Machine</p>	<p>Flooring Materials versus shoe heels and soles (μ_s and μ_k)</p>	 <p>6.9-90 kPa 38-152 mm/s</p>
<p>D 2394 (D-7 on wood), Simulated Service Testing of Wood and Wood-Base Finish Flooring</p>	<p>Wood and wood-base flooring versus sole leather (μ_s and μ_k)</p>	 <p>111 N Chain 1.27 mm/min</p>
<p>D 2714 (D-2 on lubricants), Calibration and Operation of Alpha Model LFW-1 Friction and Wear Testing Machine</p>	<p>Steel ring versus steel block (lubricated with standard oil) (μ_k)</p>	 <p>22 N 72 rev/min</p>
<p>D 3028 (D-20 on plastics), Kinetic Coefficient of Friction of Plastic Solids and Sheeting</p>	<p>Plastic sheets or solids versus other solids (μ_s and μ_k)</p>	 <p>Up to 50 g 0.1-3 m/s Pendulum device</p>

<p>D 3108 (D-13 on textiles), Coefficient of Friction Yarn to Solid Material</p>	<p>Textile yarns versus solids (μ_k)</p>	 <p>100 m/min</p> <p>T_1 T_2</p> <p>$\mu = \frac{\ln T_2 - \ln T_1}{\theta}$</p>
<p>D 3247 (D-6 on paper), Coefficient of Static Friction of Corrugated and Solid Fiberboard</p>	<p>Self-mated cardboard (μ_s)</p>	 <p>1.7 kPa</p> <p>6 m/min</p> <p>Chain or cable</p>
<p>D 3248 (D-6 on paper), Coefficient of Static Friction of Corrugated and Solid Fiberboard (inclined plane method)</p>	<p>Self-mated cardboard (μ_s)</p>	 <p>$\mu_s = \tan \theta$</p>
<p>D 3334 (D-13 on textiles), Testing of Fabrics Woven from Polyolefin Monofilaments</p>	<p>Self-mated woven fabric (μ_s)</p>	 <p>$\mu_s = \tan \theta$</p>

<p>D 3412 (D-13 on textiles), Coefficient of Friction, Yarn to Yarn</p>	<p>Continuous filament and spun yarns self-mated (μ_s and μ_k)</p>	 $\mu = [\ln (T_2 / T_1)] / \theta$ <p>where: μ = coefficient of friction θ = wrap angle, rad T_1 = input tension, gf (or mN) T_2 = output tension, gf (or mN)</p>
<p>D 4103 (D-21 on polishes), Preparation of Substrate Surfaces for Coefficient of Friction</p>	<p>Vinyl and wool tiles (preparation only)</p>	<p>Any apparatus</p>
<p>E 303 (E-17 on traveled surfaces) Measuring Surface Frictional Properties using the British Pendulum Tester</p>	<p>Rubber versus pavement (BPN, British pendulum number)</p>	
<p>E 510 (E-17 on traveled surfaces), Determining Pavement Surface Frictional and Polishing Characteristics using a Small Torque Device</p>	<p>Rubber versus pavement (TN, torque number)</p>	

<p>E 670 (E-17 on traveled surfaces), Side Force Friction on Paved Surfaces using the Mu-Meter</p>	<p>Tires versus pavement (μ) ($F_{dry} - F_{wet}$)</p>	
<p>E 707 (E-17 on traveled surfaces), Skid Resistance of paved surfaces using the North Carolina State University Variable Speed Friction Tester</p>	<p>Rubber tire versus pavement (variable speed number)</p>	
<p>F 489 (F-13 on footwear), Rating of Static Coefficient of Shoe Sole and Heel Materials as Measured by the James Machine</p>	<p>Leather and rubber sole and heel material versus walking surfaces (μ_s)</p>	
<p>F 609, Test Method for Static Slip Resistance of Footwear, Sole, Heel, or Related Materials by Horizontal Pull Slipmeter (HPS)</p>	<p>Footwear materials versus walking surface (μ_s)</p>	
<p>F 695-81 (F-13 on footwear), Evaluation of Test Data Obtained by Using the Horizontal Slipmeter or the James Machine for Measurement of Static Slip Resistance of Footwear, Sole, Heel, or Related Materials</p>	<p>Footwear materials versus walking surfaces (reliable ranking of footwear for slip resistance) (μ_k)</p>	

F 732 (F-4 on medical and surgical materials), Reciprocating Pin-on-Flat Evaluation of Friction and Wear Properties of Polymeric Materials for Use in Total Joint Prostheses	Materials for human joints (μ_k)	
-------------------------------------------------------------------------------------------------------------------------------------------------------------------------------------	--------------------------------------------------------	-------------------------------------------------------------------------------------

(a) Note: Used with permission of the G-2 Committee on Wear and Erosion

Microscale Friction Tests. In recent years, the ability to perform friction-type tests at scales approaching the atomic level has been developed in research laboratories. This field has been called “microtribology” or “nanotribology.” Microscale tests address a special class of friction and adhesion problems. The results can fail to directly agree with test results on similar materials conducted at more macroscales of contact, such as those described in Table 1. Fine-scale friction test results can relate to such applications as thin films on computer hard disks, read-write heads, and microelectromechanical systems (MEMS). They can provide information on the behavior of monolayers of lubricating films, but they tend not to be able to address issues such as particulate contamination and embedment effects, microstructural inhomogeneity, thick film behavior, and surfaces with the scales of roughness typical of many present-day engineering components. Therefore, it is important to conduct such fine-scale tests with a full understanding of the implications and limitations of the results.

In conducting microscale friction tests, the typical apparatus contains an elastic beam of some kind on which a needlelike probe is affixed. A full range of materials is not generally available in the form of these tiny slider tips, so the ability to examine many different material combinations is limited. There are various sensing modes, some of which reflect a laser beam off the back side of the elastic beam and measure its deflection to infer the bending force produced by frictional drag. In other cases, capacitive sensors or piezoelectric sensors are used. Providing details on these specialized, largely basic-research oriented test methods is beyond the scope of this article. The reader is referred instead to Ref 6 and the article by R.G. Horn in Ref 3 for more details.

Friction Testing under Well-Lubricated Conditions. If sliding members are fully separated by a film of lubricant (oil, water, gas, and so forth), the friction coefficient of the system is essentially the friction coefficient of the fluid. When boundary lubrication exists, the surfaces are partially in contact, and the coefficient of friction of the system is a function of the combined properties of the fluid and surfaces. When dry-film lubricants are used, the friction coefficient of the system can be related to the properties of the dry-film lubricant slipping on itself or to those of an uncoated solid on the lubricant film. Lubrication with graphite, molybdenum disulfide, or fluorocarbons is an example of this.

With fluid separation, the friction coefficients can be several orders of magnitude lower than they are for systems that involve solid contact. The Stribeck-Hersey curve shown in Fig. 8 allows calculation of the coefficient of friction from lubricant properties ($\eta N/P$), where η is the viscosity, N is the velocity, and P is the pressure (load). Empirical measurement of friction in film-separated systems is complicated by the need to maintain the fluid separation. With oils and greases, it usually involves testing at high velocities. If circumstances allow, the use of a friction coefficient calculated from the fluid parameters is much easier.

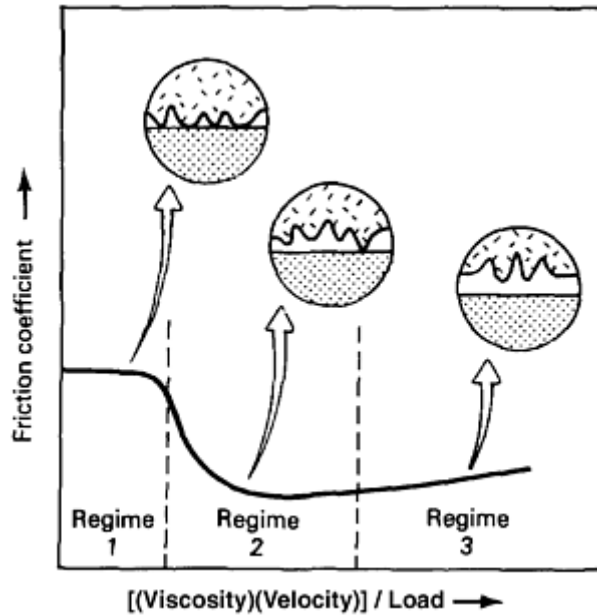


Fig. 8 Plot of friction coefficient, μ , versus $[(\text{viscosity})(\text{velocity})]/\text{load}$, $(\eta_0 U)/P$, to show range of the three regimes of lubrication. Regime 1, boundary lubrication; regime 2, thin-film lubrication; regime 3, thick-film lubrication

A number of test methods, like the lubricated block-on-ring test (ASTM D 2714) and the four-ball test, are used for determining the effects of lubricant additives on frictional behavior. A pin-in-Vee block test is used for assessing load carrying capacity and seizure. Additional information on lubricant friction testing is available in, for example, the ASTM standards developed by committee D-2 and in Ref 7.

References cited in this section

2. A.Z. Szeri, *Tribology: Friction, Lubrication, and Wear*, Hemisphere Publishing Corp., 1980, p 2
3. *Friction, Lubrication, and Wear Technology*, Vol 18, *ASM Handbook*, ASM International, 1992
5. E. Rabinowicz, Friction Coefficients of Noble Metals over a Range of Loads, *Wear*, Vol 159, p 89
6. B. Bhushan, *Handbook of Micro/ Nanotribology*, 2nd ed., CRC Press, Inc., 1998
7. R. Booser, Ed., *CRC Handbook of Lubrication*, Vol 1–3, CRC Press, Inc.

Testing Methods for Solid Friction

K.G. Budinski, Eastman Kodak Company; P.J. Blau, Oak Ridge National Laboratory

Performing a Valid Test

The procedural considerations that should be addressed to ensure that valid data are derived from a friction test are discussed in this section. Investigators often run a friction test that is convenient to use but that has no resemblance to the system under study. Friction is a system property, and systems must be modeled carefully (same materials, same surface treatments, and so forth). Other factors that can affect the validity of a friction test include sample preparation, method of friction measurement, and interpretation of data.

System Modeling. Essentially three types of geometries prevail in systems where friction is a concern. These include:

- Hertzian contact
- Flat-on-flat
- Conforming surfaces (belt on a drum, plain bearings, and so forth)

These systems are illustrated in Fig. 9. It could be argued that when wear occurs, all surfaces become conforming. This is true for all systems except those where the triboelements remain Hertzian in contact. For example, railroad wheels wear significantly in service, but they still contact the track in a Hertzian manner by line or point contact. With regard to wear of the sliding surfaces, this can be the most important aspect of modeling a tribosystem. If the system under study will wear, and it is the desired goal of the study to determine the friction characteristics under conditions of steady-wear, friction should be measured in a wear test. If the system of concern will not change with time, a friction test that does not involve wear can be conducted. Figure 10 shows how wear can affect friction forces. Figure 10(a) illustrates the friction force variation with time for a system that does not experience any wear or changes in behavior when wear occurs. If, for example, paper is conveyed over a fixed roller with a smooth finish, it is highly likely that the friction force will remain the same as the roller wears by polishing abrasion, and the friction force will be constant with time, as will the nature of the tribosystem. The roller constantly wears, but the surface is always polished. The wear debris is carried away with the product, and nothing in the system changes. This statement must be qualified by noting that the environment (humidity, temperature, and so forth) can cause friction to change with time. Environmental effects are discussed later in this article.

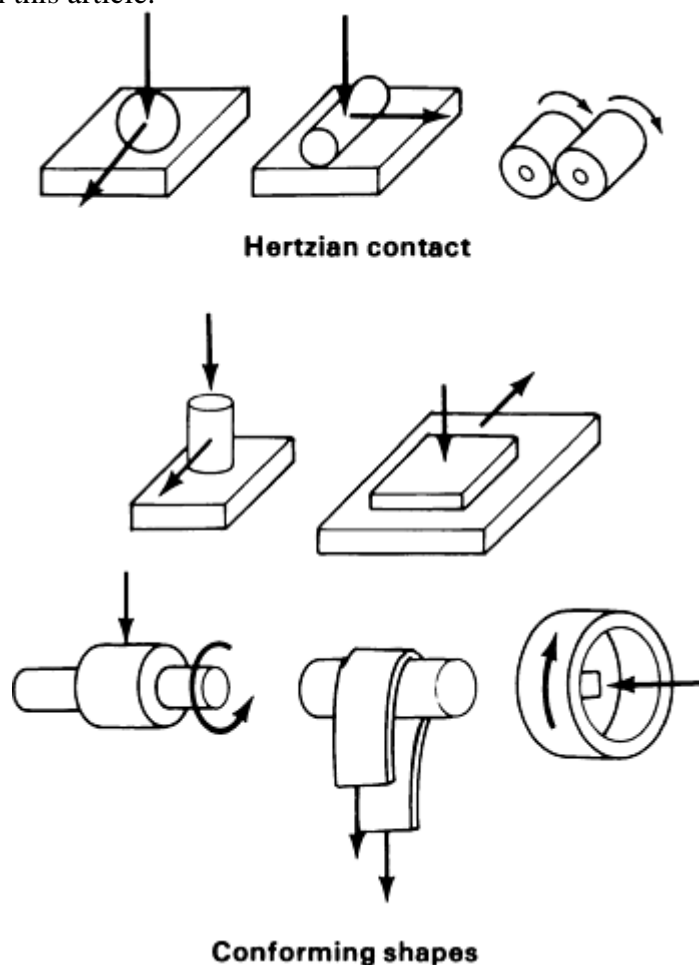


Fig. 9 Friction test specimen configuration options

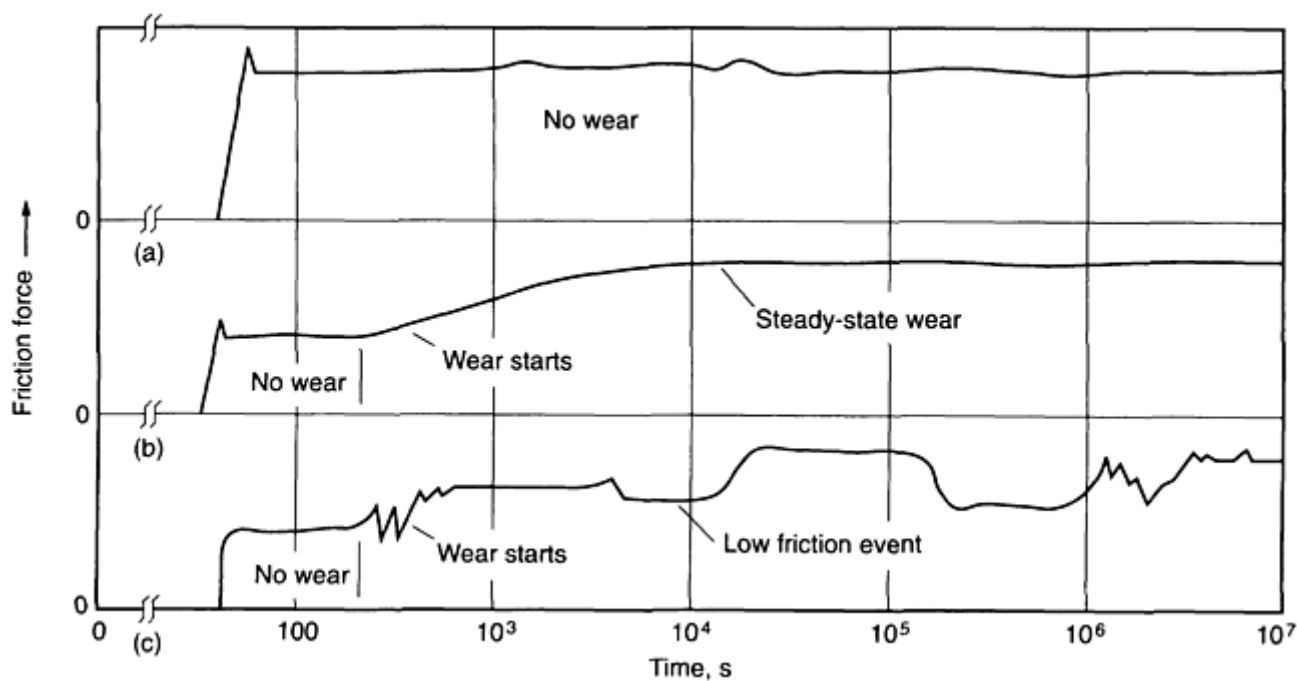


Fig. 10 Effect of system wear on friction force. (a) System that does not experience any wear or changes in behavior when wear occurs. (b) System where friction force increases with time until reaching a steady-state conditions. (c) System where friction force varies with each event in the wear process

Figure 10(b) illustrates a tribosystem where the friction force increases with time and then reaches steady state. This type of behavior might occur in a system experiencing severe wear. Friction is low when both members have their original surfaces. When the original surfaces start to wear, friction increases, and from that point on, the worn surfaces remain the same. It is comparable to a machining operation in that material is constantly being removed, but the cutting forces remain constant.

Figure 10(c) illustrates a system where the friction force varies with events in the wear process. This type of behavior often occurs in a tribosystem where wear debris remains in the system. Depending on how it separates the surfaces, wear debris can have lubricating or nonlubricating effect on the system. The friction will be constant when the triboelements have their original surfaces; when they wear, there will be a friction event followed by another when both surfaces become coated and are separated by wear debris. Because wear is a statistical process, some other event can take place to remove the separating wear debris, and still another cycle or friction event will occur. This phenomenon is seen in many machines. The machine can run quietly for a year, but then a squeal occurs that lasts for two weeks and then stops. The noise can come back in two months, or it might never return. It is quite possible that significant fluctuations in friction force with time are the result of environmental events. For example, it is well documented that the friction characteristics of photographic films are significantly affected by relative humidity. Photographic emulsions are gelatin based. Many gelatins have mechanical properties that are directly proportional to their water content. Mechanical properties vary with humidity, and these property changes in turn affect friction characteristics. Temperature has a similar influence on many materials, particularly plastics.

The illustrations shown in Fig. 10 are presented in order to emphasize that it is important to closely model the system under consideration. The test should simulate the mode of contact and the environment, and the length of time that the system is tested should be typical for the intended service. If new materials are being screened for friction characteristics, short-term and long-term tests should be conducted to explore friction events that change with time. If a service problem is being studied, the test should simulate the important aspects of the service, the environment, the type of contact, and the materials. It is not necessary to exactly duplicate the sliding speed and load unless they are likely to change some properties of the test materials (temperature, chemical environment, and so forth).

Material Documentation. Problems concerning repeatability of a friction test with time can be related to subtle or major changes in the nature of one of the tribocomponents. For this reason, it is important to provide adequate documentation of the materials in a tribosystem where friction measurement is the goal. As shown in Table 2, the necessary documentation varies with the type of material (metal, plastic, ceramic, or composite).

Table 2 Material parameters that should be documented to ensure repeatability when testing tribosystems

Metals

- **Chemical composition**
- **Manufacturer name and address**
- **Manufacturing process [wrought (cold finished or hot finished), cast, extruded, etc.]**
- **Generic designation**
- **Trade name (if applicable)**
- **ASTM or similar designation**
- **Condition of heat treatment**
- **Surface finish**
- **Surface treatments**
- **Grain direction**
- **Microstructure**

Plastics

- **Polymer species (If a blend, state ratio of blended polymers)**
- **Fillers, lubricants, and so forth (percentage)**
- **Manufacturing process (injection molded, extruded, cast)**
- **Generic name**
- **Applicable specifications (MIL, ASTM, and so on)**
- **Trade name and manufacturer number**
- **Manufacturer name and address**
- **Process used to generate wear surfaces, orientation of wear surfaces to original shape (wear surfaces flatwise on as-molded flatwise plate, wear surfaces end grain in extruded shape, and so on)**
- **Lubricants on the surface or in the material**
- **Surface texture of wear surface or in the material**
- **Surface texture of wear surfaces (R_a , lay, waviness)**
- **Heat treatments applied**

Composites

- **Detailed description of composite components (filament winding details, number of plies, components in laminate)**
- **Generic name and applicable specifications on composite components**
- **Trade names of components**
- **Manufacturer name and address**
- **Method of manufacture**
- **How wear surfaces were generated**
- **Orientation of wear surfaces to reinforcement**
- **Heat treatments**
- **Surface texture (R_a , lay, waviness)**
- **Surface treatments, lubricants, mold releases, and so forth**

Ceramics

- **Basic type and composition**
- **Percent theoretical density**
- **Manufacturer name and address**
- **Trade name**

- Manufacturing process (HIP, vacuum sintering, chemical vapor deposition, and so on)
- Method used to generate wear surfaces (grinding, polishing, and so on)
- Texture of wear surfaces (R_a , lay, waviness)
- Heat treatment
- Surface treatments
- Grain size
- Microstructure
- Morphology (degree of crystallinity, phases present, crystal structure)
- Lubricants/impregnants

R_a , surface roughness in terms of arithmetic average

More items undoubtedly could be added to Table 2, but the point to be made is that all of the variables that have been mentioned thus far could affect sliding friction. If the surfaces are lubricated, the tester must add related details of the type of lubricant and its distribution on the sliding surfaces. It is imperative that documentation on all members in the tribosystem be included. It is quite easy to cite examples where each of the factors listed in Table 2 has affected friction results in laboratory tests; more importantly, these factors influence friction properties in service. Heat treatment, structure, and so forth can affect mechanical properties. Surface films affect sliding forces; surface texture affects early friction. A cast polyester has different mechanical properties than a tentered and drafted polyester web, and a hot isostatically pressed silicon carbide has different mechanical properties than pressed and sintered material. The tester should be meticulous about material documentation.

Surface Condition. Few tribologists will argue with the statement that friction can be affected by surface condition. If the loads are light enough, only the outer one or two mono-layers on the surface might take part in sliding interactions. In lubricated systems, surface roughness plays a role in determining whether the surfaces are separated. Full-film separation will not occur unless the film thickness is greater than the composite surface roughness. Even with hydrodynamic lubrication, there are some investigators who claim that the system friction is affected by the surface roughness and lay (Fig. 11). In the normal range of roughness on rolling-element bearings and plain metal bearings (0.1 to 1 $\mu m R_a$), it is likely that the surface features do not significantly affect lubricated sliding. In nonlubricated sliding, the effect of roughness can be negligible to significant, depending on the system (Ref 8). With normal machined surfaces with a roughness less than about 1.5 μm , the effect will be slight. Roughness becomes a meaningful factor when the roughness interactions result in mechanical locking effects. This usually happens only with very rough surfaces. Sometimes, very smooth surfaces cause adhesion—for example, gage blocks or plastic webs on smooth surfaces. Conversely, in some applications such as high-speed sliding of yarns and filaments over stationary guide pins, the friction coefficient is low when the pin surfaces are rough (0.5 to 2 $\mu m R_a$) and becomes very high when the pins become polished from wear.

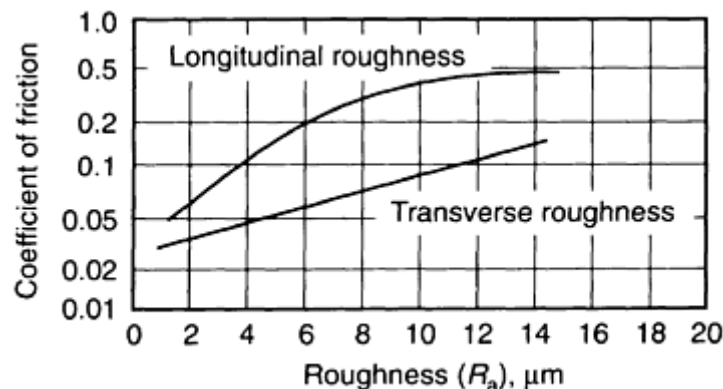


Fig. 11 Effect of surface roughness on the friction coefficient of a lubricated sliding system. Adapted from Ref 8

A valid wear test considers the effect of surface texture. For many systems, the effect is not significant. If, however, surface texture is considered a variable for a given wear study, a few quick tests using the high and

low of the expected range of surface texture will determine whether this is a parameter to be pursued in a friction study.

Surface films are important in most tribosystems, especially unlubricated systems. The recommended practice in friction testing is to leave the films in place if they are likely to occur in the tribosystem of interest. If they are not part of the system of interest, they should be removed by cleaning. Valid wear results require that a cleaning procedure be used that will remove contaminants and not leave another contaminating film. The cleanest surface is the as-machined or as-ground surface (without coolants and the like). These types of surfaces prevent cleaning-solution contamination problems. If metal surfaces must be cleaned of contaminating films, then a refluxed solvent system should be used. Plastics are difficult to clean with solvents because of the risk of chemical alteration of the surface. Commercial glass-cleaning solutions have been employed to clean plastic test surfaces with favorable results. Ceramics can also be cleaned by these solutions. Sometimes even water-based cleaners can chemically alter a ceramic surface. The safest technique for removing contaminants on ceramics is dry lapping or similar abrasive finishing.

Absorbed films from the atmosphere can be another source of contamination. To cite an example, many plastics were tested in a comprehensive laboratory program as a track material for conveyance of plastic parts. Test results indicated that an ultrahigh-molecular-weight poly-ethylene had the lowest friction. Hundreds of feet of this track were installed in the manufacturing plant, but within a month the track was pulled out and replaced because of an environmental factor that had not been considered during laboratory testing. Although there were no problems with the track during the week when there was a three-shift operation, after the weekend, parts would stick to the track with great frequency. Only after several hours of downtime and frequent “nudging” of the parts would the system begin working properly. Further study indicated that when the track material was allowed to sit idle for a period of 48 h, some type of film formed that deleteriously altered the friction characteristics.

This example points out the importance of carefully duplicating the system environment, even to the extent of allowing surfaces to sit idle in production environments. Many manufacturing plants have an atmosphere that can leave a condensate on a surface. If this is likely to occur in a tribosystem under study, then it should be made part of the friction testing.

Reference cited in this section

8. Y.-R. Jeng, Experimental Study of the Effects of Surface Roughness on Friction, *Tribol. Trans.*, Vol 33 (No. 3), 1980, p 402–410

Testing Methods for Solid Friction

K.G. Budinski, Eastman Kodak Company; P.J. Blau, Oak Ridge National Laboratory

Test Parameters

Friction test parameters, such as speed and load, should be as close as possible to actual conditions. Sometimes, however, it is difficult to simulate these parameters in a laboratory environment. The speeds and loads can be out of the range of the lab equipment, or testing at actual conditions might take too long. A valid friction test does not require that speeds and loads be exactly duplicated. Friction coefficients are relatively insensitive to speed and loads up to the point where these parameters affect the properties of the test surfaces. Speed will affect friction results on most metals when it is sufficiently high to soften the surface and alter mechanical properties. With plastics, this temperature can be only a few hundred degrees Fahrenheit. With metals, the critical temperature is close to the stress-relief temperature for a given alloy.

Sliding speed for a friction test can range from 10 mm/s (0.4 in./s) for an inclined plane test to 100 m/s (325 ft/s) for high-speed yarn friction tests. For optimum results, test equipment should yield a wide range of sliding speeds. If the actual operating speed is unusually high or low, unique friction conditions can be produced that

can be simulated only by test speeds in the range of concern. For example, a laboratory study was conducted on plastic and competitive plain bearings for a compact-disk drive scanner that had to slide (bushings versus hardened steel shafts) in a linear motion at a speed of $1.6 \mu\text{m/s}$ (0.00006 in./s). The slow speed caused many materials to display stick-slip behavior. When higher speeds were used, this did not occur. Under such conditions, the speed of the tribosystem should be duplicated as closely as possible.

The same type of reasoning should be applied to test loads. If a system under study uses loads of only a few grams, this should be duplicated. If the system under study is subject to extreme forces, such as those that occur in threaded fasteners, there is little recourse other than to use these very high forces. When studying bolt friction, most investigators use actual bolts and nuts and a washer equipped with a strain gage for measurement of bolt tension. This is because of the difficulty in obtaining a bench-top friction tester that can apply a 45 kN ($10,000 \text{ lbf}$) normal force.

As a rule of thumb, if it is not possible to simulate the service load, then the highest load that does not exceed the compressive strength of either member in the test couple should be used. This is particularly applicable to Hertzian loading situations. If the compressive strength of the material is exceeded, the friction test only yields the forces to plastically deform the surfaces. Test speeds and loads that produce significant wear should be avoided unless that is part of the tribosystem under study.

As previously mentioned, friction force might not be constant throughout a test, and questions can arise as to the value that should be reported. The most meaningful data are the minimum, the maximum, the mean, and the standard deviations. These allow the use of statistical analysis to determine whether friction coefficients for various systems are really different. Erratic systems such as that described in Fig. 10(c) will be treated with statistics. In friction tests where the goal is to find a couple with the smoothest motion, a suitable test parameter for ranking materials is the standard deviation of the friction force. This shows the variability of the friction forces for the various systems. In fact, for all friction tests it is recommended that statistical tests be used. The simplest test of differences is illustrated in Fig. 12. If the mean of test data is plotted with error bars coinciding with plus or minus two standard deviations, a visual test of differences can be made. If the error bars overlap, the test results are not statistically different. In Fig. 12, couples B, C, and D have the same frictional characteristics; only couple A differs.

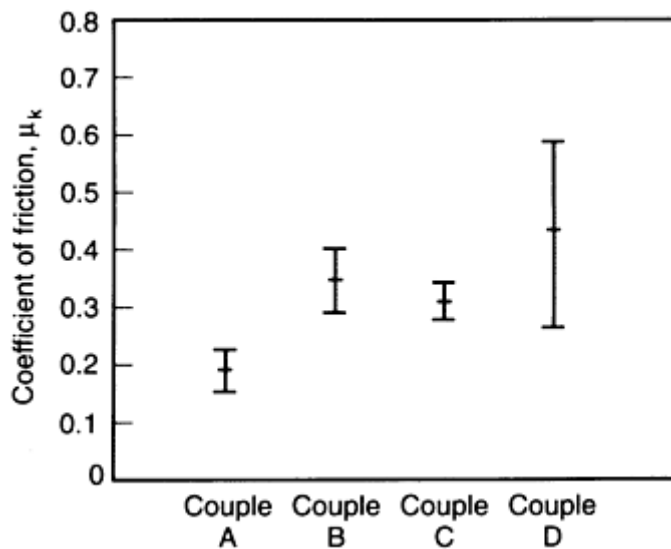


Fig. 12 Graphical use of statistics to show differences in friction coefficients between various material couples

Sample size must also be considered in statistic tests. There are a number of ways to calculate sample size, but most statisticians prefer a large number (for example, 40) of replicate tests. Because most friction tests are very repeatable within a laboratory, this number may be a bit high. Most studies using a bench-top friction tester can have statistical accuracy with as few as 10 replicates per system.

Friction Measurements

A number of precautions must be observed during friction measurements, and most have to do with the measuring equipment. Some of the more commonly used force-measuring systems are illustrated in Fig. 13. Probably the most important consideration with regard to instruments for measuring friction forces is selection of a force-measuring system that is suitably sized for the task. If the tribosystem being tested will produce friction forces of about 4.5 N (1 lbf), it is recommended that a force-measuring system with a capacity of only about 45 N (10 lbf) be used. In other words, a sensor with a capacity not more than 10 times the force to be measured should generally be selected for a given application.

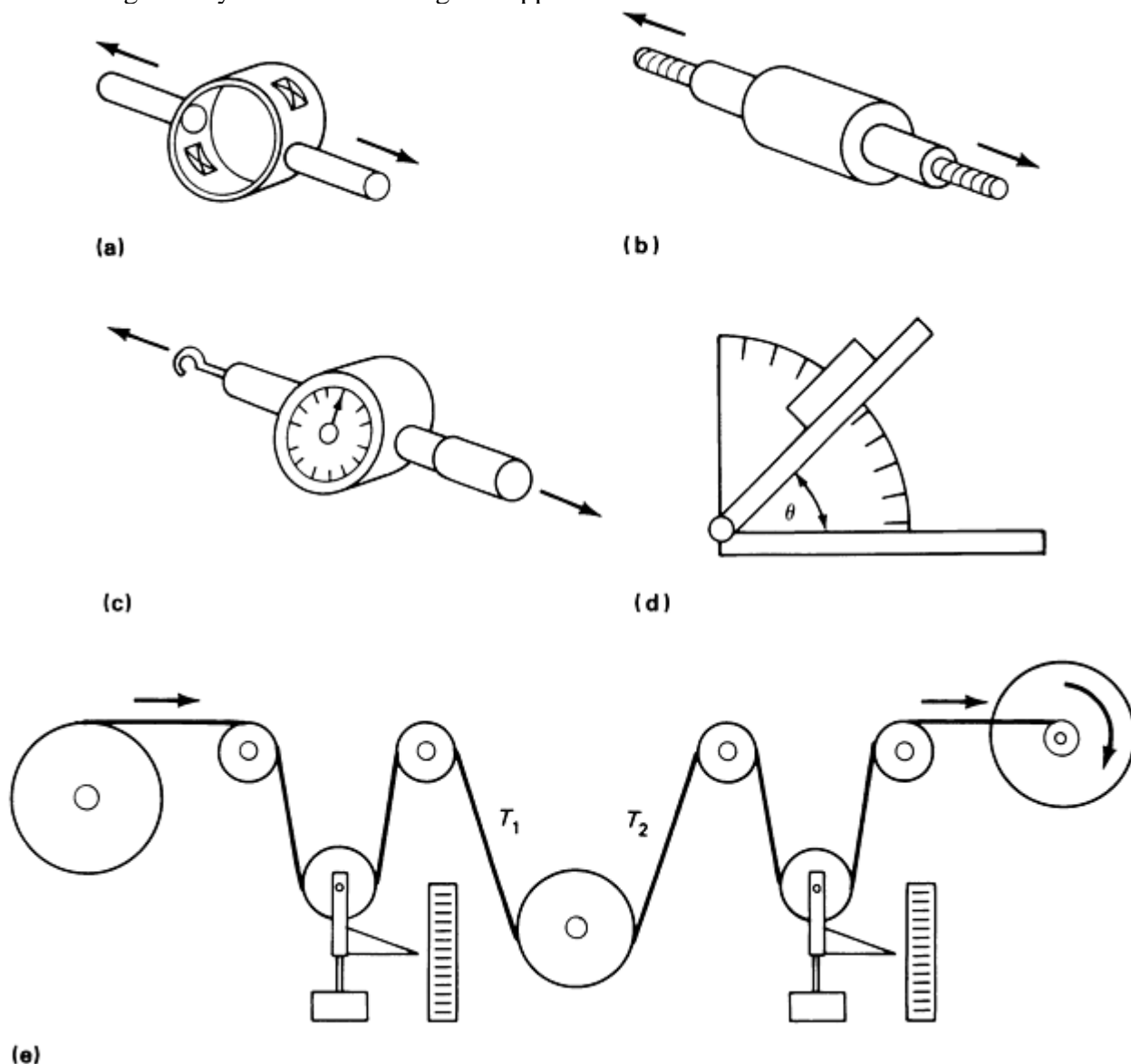


Fig. 13 Friction force sensors. (a) Strain ring with strain gages. (b) Strain gage load cell. (c) Mechanical force gage. (d) Inclined plane. (e) Web tension tester (tension is measured by the position of the weighted sheaves)

The strain ring illustrated in Fig. 13(a) is assembled in the laboratory and features four strain gages adhesively bonded to the ring to form a Wheatstone bridge strain rosette. This type of system can be very accurate, because

the ring can be made as heavy or as light as desired. The disadvantages are that such gages are more fragile than purchased gages, and humidity and temperature can affect the adhesion of the gages. This system also requires assembly by a person with some expertise in strain gages.

The commercially available strain-gage load cells shown in Fig. 13(b) are quite durable. Most have some type of internal diaphragm that is instrumented with strain gages. However, these devices can be destroyed by a momentary load greater than its capacity, necessitating expensive replacement. Many companies offer these gages with mechanical stops to prevent overload damage.

Mechanical force gages (Fig. 13c) work much like strain gages, except that force measurements are made by a spring and sliding system arrangement. The greatest disadvantage of such devices is that they have no recording capability. They are also prone to inaccurate readings by operators.

Friction coefficients measured on inclined planes (Fig. 13d) require only the measurement of the angle at which motion of the test block occurs. The most common technique for measuring this angle is the simple incorporation of a protractor scale in the device. A more accurate system uses an electronic level on the inclined plane. These devices have digital readout capability and are much more accurate than visual assessment of the angle of an inclined plane. One precaution in using this type of device is that the speed at which the plane is raised will affect the breakaway angle. The more reliable inclined plane rigs have a motorized raising device on the table.

The device illustrated in Fig. 13(e) is commonly used to measure the friction coefficient of a moving web over a stationary surface or over a roll where relative slip is occurring. The tension in the web on either side of the test roll will yield the coefficient of kinetic friction when the capstan formula is used. The tension-measuring roll, called a "dancer roll," moves up and down with changes in web tension. The disadvantage of these systems is that they are not very easy to gage electronically, and, thus, continuous recording can be difficult. Most dancer rolls are being replaced by cantilever rolls with strain gages incorporated in their mounting brackets.

Whichever force-measuring technique is used, it is most important that the device be sized correctly and that friction forces be recorded over a sufficient period of time to ensure that steady-state conditions exist.

Computerized data acquisition systems may be used for high-speed digital recording if the details of frictional behavior are needed. The digital data can be used to rapidly calculate average friction force, standard deviation, and other statistical parameters. Sometimes, however, high-speed friction recordings can produce hash in the signal, and a filtering algorithm must be used to reveal the general trends. The response of common chart recorders is usually slow enough to eliminate the hash problem, and, therefore, such chart recorders are still useful for recording trends in the overall friction behavior.

The final precaution that warrants consideration is the system stiffness. If a system is prone to stick-slip behavior or high static friction, a highly compliant force-measuring system should be used. From a practical standpoint, an elastic force-measuring system usually consists of nylon fishing line to pull member A along member B. If a stiff-movement system such as a screw drive is used to produce specimen motion, phenomena such as stick-slip behavior might not be produced. The decision as to whether a high-stiffness (steel) or low-stiffness (plastic) system should be used must be based on the intended application. If the tribosystem of interest is highly elastic, the plastic-movement system should be used. If the system is rigid, the screw-drive system (or a similar system) should be used.

Testing Methods for Solid Friction

K.G. Budinski, Eastman Kodak Company; P.J. Blau, Oak Ridge National Laboratory

Overall System Considerations

A proposed method for analyzing wear problems is to look at the tribosystem and tabulate all of the system inputs, outputs, and disturbances (Fig. 14). Friction is considered to be a system loss, but certain components of friction should be noted and recorded. From the aspect of system usability, sometimes these system losses are more important than the friction force. For example, in a study on the wear of various cemented carbide couples, it was learned that some carbide couples produced squealing. The friction coefficient was slightly

higher than comparable metal-to-metal couples (about 0.5 compared with 0.4) while the wear was very low, but this couple was deemed unacceptable for use because of the noise.

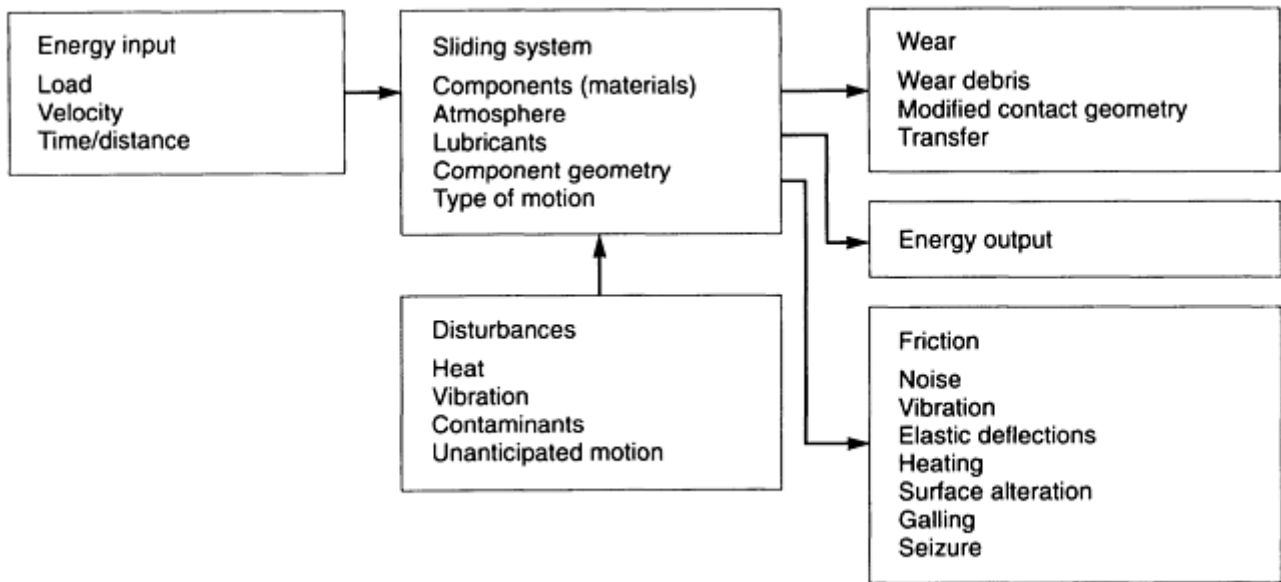


Fig. 14 Systems approach for analyzing friction and wear problems

In Fig. 14, important losses include vibration, elastic deflections, heating, surface alteration, galling, and even seizure. Vibration as an output of a sliding system often indicates that stick-slip behavior is prevalent. Noise is often the result of stick-slip behavior, but a system that exhibits such behavior does not necessarily emanate noise. Although vibration is not always apparent on friction force traces, it can show up on deflection or displacement transducers. This type of behavior from a sliding system is usually undesirable. Accurate measurement of vibration can require the use of accelerometers on one of the members of the sliding system. Likewise, elastic deflection, which can occur at a sliding interface, does not always show up on the friction force recording. This deflection can mean that the couple under study has unacceptable frictional characteristics. For example, when several elastomers that were undergoing friction tests were slid on a paper counterface, they bent over in the direction of motion; the contact geometry was changed from the point contact of a hemispherical rider to a line contact of a bent hemispherical-ended rod. The friction force was apparently high enough to cause this deflection.

Although heating is an obvious result of friction between sliding members, it is often not measured. The temperature rise is often significant, and it is easy to measure. The mechanical properties of plastics are susceptible to degradation by heating to relatively low temperatures. The temperature rise at a sliding interface is the result of the properties of the materials in contact in addition to the sliding conditions. It will be different for different couples that can have the same friction coefficient. Therefore, for sliding systems that can be affected by frictional heating of the interfaces, a valid friction test should record the temperature rise.

Surface alteration is another important aspect of many wear and friction tests. Whenever wear occurs in a sliding test, the friction coefficient is not that of the test couple alone, but it is the system that comprises the couple as well as wear debris in the interface. When wear testing couples that are not supposed to wear during friction testing, it is important to examine both surfaces for alterations. Damage often can be caused by polishing or scratching. When friction alters the prevailing surface texture, a wear test has been performed, not a friction test. The friction force measured and coefficient of friction must be reported for a worn surface.

Galling and seizing are the worst possible results of a friction test. Galling is characterized by the formation of microscopic cumulative material transfer during sliding, and seizure (stopping of motion) can be the net result. If a couple seizes, there will be no friction coefficient to report, but merely the fact that the couple seized. If galling occurs, the friction force will often decrease (Fig. 15), but the surfaces will be damaged. This can produce data that misleads a user, who may think that the couple works fairly well because the friction coefficient was low, when actually galling occurred and the material couple is not compatible.

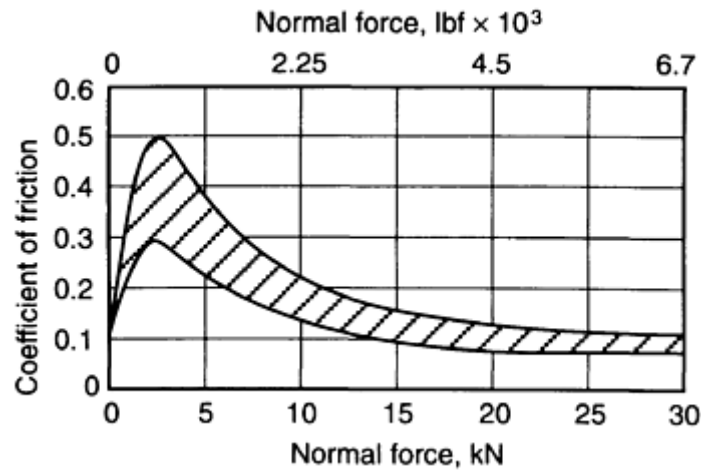


Fig. 15 Typical friction coefficients derived from galling tests (various metal/metal couples)

Testing Methods for Solid Friction

K.G. Budinski, Eastman Kodak Company; P.J. Blau, Oak Ridge National Laboratory

Friction Databases

The first friction database was compiled by J.T. Desagulies around 1725 (as reported by Dowson in Ref 1). Desagulies tabulated the friction coefficients for the couples of interest at the time. Some current handbooks list friction coefficients for 50 or so materials, with limited documentation regarding test conditions. These tabulations are of little use if the application requires knowing a friction coefficient within an accuracy of ± 0.2 . Differences in the tribosystem used to make the measurements can, for example, produce a result of 0.1 for a couple on device No. 1 and a result of 0.3 for the same couple tested on device No. 2. It can be stated with a high degree of confidence that measuring techniques will have a significant effect on the friction coefficient of a particular couple in the unlubricated condition. Differences can exist in lubricated systems, but the coefficients will be much lower. An accuracy of $\pm 20\%$ results in a much smaller number. For example, well-lubricated steel couples can have a kinetic coefficient of friction of 0.05 ($\pm 20\%$ makes the number 0.04 to 0.06). In other words, existing friction databases have limited utility unless the test conditions used to develop the data are stated and the application conditions are similar.

In order to determine how friction databases should be formulated and used, ASTM Committee G-2 on wear and erosion developed a standard format for friction databases in 1987. Although this work is ongoing, progress has been made as to the type of data that should go into databases. The minimum results to be reported are the following:

- Test couple (member 1 and member 2)
- Static coefficient of friction
- Kinetic coefficient of friction

The minimum test condition information includes the following:

- Apparent pressure
- Normal force
- Velocity
- Temperatures (bulk) of samples
- Test atmosphere
- Lubricant

- Sliding distance (when μ was measured)

Other types of data would also be desirable, but even the ASTM-recommended list is difficult to deal with in database or spreadsheet types of software. The strategy is to have these data in a database so that selective data can be tabulated (see Table 3). The motivation for establishing friction databases is the elimination of repetitive tests. Even within a single laboratory, it is not uncommon to see the same couples brought in for study several times over a period of several years. Without a database, the tests are rerun each time. The long-range goal is to have published data that can be used by design engineers in the same way that designers use corrosion data generated by countless sources over many years.

Table 3 Friction and wear data of selected plastics tested against polycarbonate containing 12% polytetrafluoroethylene

Plastic ^(a)	Kinetic coefficient of friction, μ_k	Specific wear rate of selected plastic ^(b) , $K \times 10^{-6}$
PC	0.19	7.00
PC + PET	0.19	7.26
PCTG + 30% GF	0.36	9.00
PET + 30% GF	0.27	9.00
PET + 30% GF + mica	0.29	8.00
PC + 10% aramid	0.09	4.00
PA + 10% aramid	0.08	0.80
PA + 15% aramid + 10% TFE	0.70	0.50
LCP wear grade	0.10	2.00
LCP + mineral	0.07	0.60
PC + 40% aramid	0.18	9.00
PC/IPN + 2% aramid	0.15	2.00
PC + 20% aramid	0.20	7.00

(a) PC, polycarbonate; PET, polyethylene terephthalene; GF, glass fiber, PA, polyamide; LCP, liquid crystal polymer; IPN, interpenetrating networks; TPE, tetrafluoroethylene.

(b) Parameters; friction force, F , 9.86 N (2.20lbf); velocity, V , 0.208 m/s (0.682 ft/s); sliding distance, D , 732.0 m (2402 ft)

Reference cited in this section

1. D. Dowson, *History of Tribology*, Longman, 1979

Testing Methods for Solid Friction

K.G. Budinski, Eastman Kodak Company; P.J. Blau, Oak Ridge National Laboratory

References

1. D. Dowson, *History of Tribology*, Longman, 1979
2. A.Z. Szeri, *Tribology: Friction, Lubrication, and Wear*, Hemisphere Publishing Corp., 1980, p 2
3. *Friction, Lubrication, and Wear Technology*, Vol 18, *ASM Handbook*, ASM International, 1992

4. P.J. Blau, *Friction Science and Technology*, Marcel Dekker, Inc., 1996
5. E. Rabinowicz, Friction Coefficients of Noble Metals over a Range of Loads, *Wear*, Vol 159, p 89
6. B. Bhushan, *Handbook of Micro/Nanotribology*, 2nd ed., CRC Press, Inc., 1998
7. R. Booser, Ed., *CRC Handbook of Lubrication*, Vol 1–3, CRC Press, Inc.
8. Y.-R. Jeng, Experimental Study of the Effects of Surface Roughness on Friction, *Tribol. Trans.*, Vol 33 (No. 3), 1980, p 402–410

Scratch Testing

Vispi Homi Bulsara, Cummins Engine Company; Srinivasan Chandrasekar and Thomas N. Farris, Purdue University

Introduction

TO UNDERSTAND the basis and applications of scratch testing, it is useful first to consider it relative to indentation hardness testing (described in detail in the Section “Hardness Testing” in this Volume). It is well established that indentation hardness testing measures the resistance of a material to permanent, plastic deformation (Ref 1). Indentation hardness has a direct correlation with the yield strength of a solid, and for most materials the hardness is directly proportional to the yield strength. Thus, indentation hardness may be said to “measure” the plastic properties of a material. In a typical hardness test, a sharp (e.g., pyramid) or blunt (sphere) indenter is pressed into the material being tested, and the hardness is estimated as the load divided by the contact area of the indentation. The indentation hardness test is widely used both in academic laboratories and in industry as a tool for characterizing mechanical properties of a material and also as a quality control measure (Ref 2, 3).

In contrast to indentation hardness, scratch hardness is a parameter that is determined by sliding a hard indenter tip across the surface of the material (Ref 4). The scratch hardness is again obtained as the load over a load-bearing area, which is representative of the indenter track. Scratch hardness has some correlation with indentation hardness in that it also measures the response of a material to plastic deformation. Furthermore, since scratch formation is a form of controlled abrasive wear, it would seem reasonable to use the test as a means of ranking materials for their resistance to abrasion in service. This must, however, be done with some caution since the geometry of the indenter tip may be substantially different from that of the asperities present on a surface. In practice, scratch testing is typically used to determine the scratch hardness of materials, characterize the mechanisms of deformation and material removal, compare the abrasive wear resistance of materials, and measure the adhesion strength of coatings. An examination of its application in these areas indicates that it is used more as a quality control technique, and furthermore the measure obtained is more qualitative than quantitative.

This article reviews the origins and development of scratch tests, the experimental configurations used in these tests, and the application of the tests to characterize the mechanical response of materials.

References cited in this section

1. D. Tabor, *The Hardness of Metals*, Oxford University Press, 1951
2. M.M. Chaudhri and Y. Enomoto, *Philos. Mag. A.*, Special Issues on Indentation Hardness, 1996

3. S. Jayaraman, G.T. Hahn, W.C. Oliver, C.A. Rubin, and P.C. Bastias, Determination of Monotonic Stress-Strain Curve of Hard Materials from Ultra-Low-Load Indentation Tests, *Int. J. Solids Struct.*, Vol 35 (No. 5–6), 1998, p 365–381
4. S. Jacobsson, M. Olsson, P. Hedenqvist, and O. Vingsbo, Scratch Testing, *Friction, Lubrication, and Wear Technology*, Vol 18, *ASM Handbook*, ASM International, 1992, p 430–437

Scratch Testing

Vispi Homi Bulsara, Cummins Engine Company; Srinivasan Chandrasekar and Thomas N. Farris, Purdue University

Origins of Scratch Testing and the Mohs Scale

Perhaps the earliest attempt to develop a scale of scratch hardness for different materials was made by Reaumur in 1722 (Ref 5), who measured the hardness of a substance as the point at which it started scratching a bar whose hardness decreased from one end to the other. A similar method was used by Werner (Ref 5), who developed the first real scale of hardness, which was further extended by Hauy (Ref 5). In Hauy's scale, there were four groups of hardness listed in order of their mutual scratchability.

The Austrian mineralogist Mohs is credited with developing the first semiquantitative measure for scratch hardness in 1822. This measure is expressed on a scale called the Mohs scale. The Mohs scale consists of 10 minerals, arranged in an order such that each mineral will scratch the one on the scale below it, but will not scratch any mineral that is above it on the scale. In measuring scratch hardness using the Mohs scale, the sharp corner of a material is rubbed against the flat surface of another, and the flat surface is checked for scratches. A material higher up on the Mohs scale would scratch all materials with a lower Mohs number. The Mohs hardness number for the material being tested is given by the number corresponding to the hardest of the 10 reference materials that does not scratch this material.

Since the scratching process and the indentation process are both determined by the plastic properties of the material, one may expect to find some correlation between Mohs hardness and the indentation hardness for minerals. Such a correlation does in fact exist, as shown in Fig. 1, which is based on Williams (Ref 6). Some of the indentation hardness measurements in this figure were made with the standard Vickers indenter, others with the Knoop indenter. Both of the indenters produce a pyramidal indentation and give roughly the same hardness values for materials.

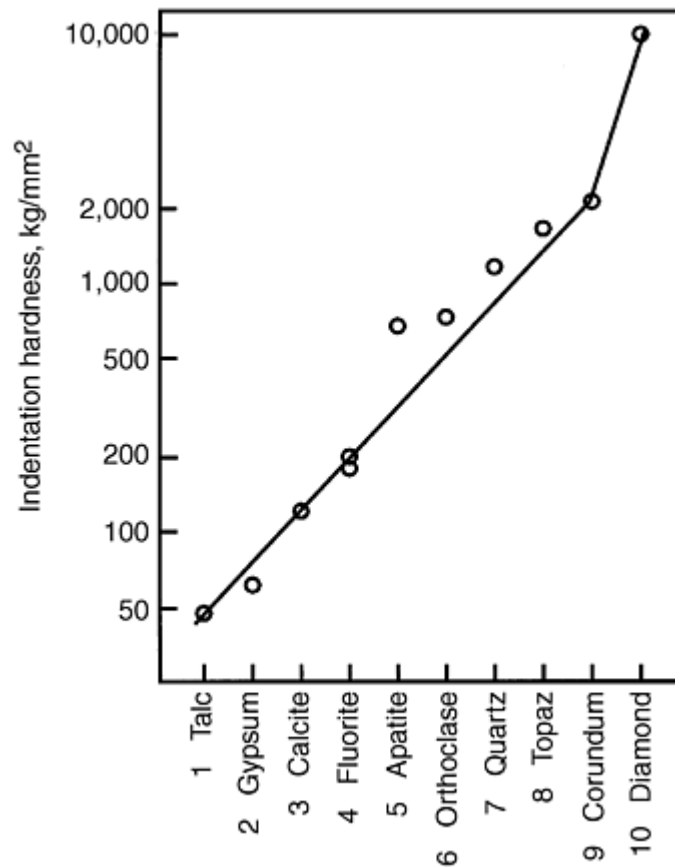


Fig. 1 Variation of indentation hardness with Mohs number. The slope of the line indicates that a unit change in Mohs number corresponds to a factor of ~1.6 in the indentation hardness. The logarithm of hardness is plotted in the figure. Source: Ref 6

The gradient of the logarithmic plot of Fig. 1 indicates that each skip in the Mohs scale is equivalent to an increase in indentation hardness by a factor of ~1.6, with the exception of that between corundum (a form of aluminum oxide with a Mohs number of 9) and diamond (which has a Mohs number of 10). The uniformity of this scale in terms of the indentation hardness of the 10 minerals reflects the high quality of the experimental work of Mohs, who was himself also well aware of the much larger increase on the scale between the Mohs values of 9 and 10.

The relation between Mohs scale and indentation hardness embodied in Fig. 1 may be interpreted in terms of the following simple experiment performed by Tabor (Ref 7). By suitable heat treatment, a strip of metal is rendered soft at one end and hard at the other, with a fairly uniform increase in indentation hardness along its length. Another metal specimen of uniform intermediate hardness is prepared with a sharp point at one end, and the point is dragged over the strip from the soft to the hard end. It is found that under well-lubricated conditions, the friction is high over the soft portion, and a fine chip is produced during sliding. This behavior changes rather abruptly at a critical value of hardness, where the friction quickly drops to a low value (Fig. 2) and there is little material removal or surface damage. In terms of Fig. 2 it is seen that a point of Vickers hardness 930 kg/mm^2 just ceases to scratch the surface when the hardness of the mating surface exceeds about 830 kg/mm^2 . Based on such experiments, it has been generally accepted that for one material to scratch another the indenter material must be at least 20% harder than the damaged surface. Additional experiments carried out since this early work have shown that this difference depends on the shape of the indenter, varying between a few percent harder for a spherical indenter to about 60% harder for a much more angular indenter.

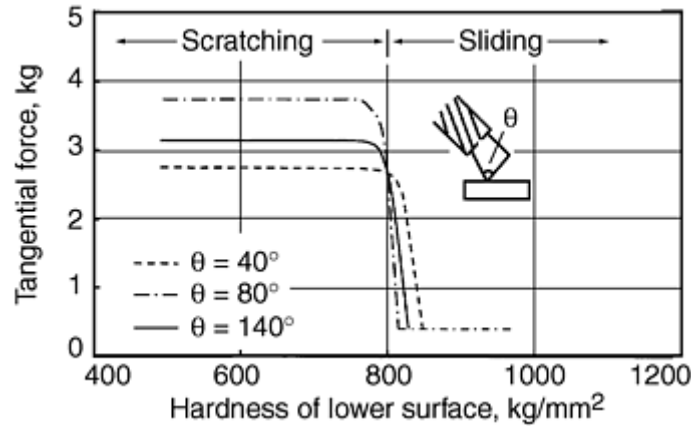


Fig. 2 Frictional force plotted as a function of surface hardness for a metal point of hardness $H_p = 930 \text{ kg/mm}^2$ traversing a steel surface (load 4.2 kg). Lubricated surfaces. Scratching ceases, and the friction falls to a low value if the hardness of the surface exceeds 830 kg/mm^2 . Source: Ref 7

The apparently linear variation of the logarithm of indentation hardness with Mohs number seen in Fig. 1 can be easily explained in light of the above results pertaining to scratching. If one assumes that scratching just begins when $H \geq kH_s$, where H is indentation hardness and H_s is scratch hardness, then we can construct a hardness scale in which every unit is k times as hard as the preceding one. The Mohs number (M) is then related to indentation hardness (H) by a relation of the form:

$$H = C(k)^M \quad (\text{Eq 1})$$

where C is a proportionality constant. Taking the logarithm of both sides of Eq 1 gives:

$$\log H = M \log k + \text{Constant} \quad (\text{Eq 2})$$

Thus a plot of $\log H$ against M should give a straight line. From experimental results reported earlier, k has a value slightly greater than one for a spherical indenter and ~ 1.6 for a much more angular indenter.

Equation 2 and Fig. 1 can be used to obtain an approximate estimate of indentation hardness of a material when its Mohs number is specified. Even though Mohs number is not very much used to specify hardness of a material, it has been the experience of the authors that, not infrequently, they have seen it arise in various contexts.

References cited in this section

5. S.R. Williams, *Hardness and Hardness Measurements*, American Society for Metals, 1942
6. J.A. Williams, Analytical Models of Scratch Hardness, *Tribol. Int.*, Vol 29 (No. 8), 1996, p 675–694
7. F.P. Bowden and D. Tabor, *The Friction and Lubrication of Solids*, Oxford University Press, Vol I, 1951; Vol II, 1964

Scratch Testing

Vispi Homi Bulsara, Cummins Engine Company; Srinivasan Chandrasekar and Thomas N. Farris, Purdue University

Experimental Devices

Scratch tests can be classified into two categories—low speed and high speed—based on the velocity of the scratching element with respect to the material surface.

Low-Speed Devices. The scratch element (i.e., indenter) is usually mounted on a linear slide and moved along the material surface at speeds of no more than a few millimeters per second to generate a single-pass scratch. The element may be reciprocated against the sample to generate a multipass scratch. Another method used to generate a multipass scratch is to mount the sample on a rotating turntable and slide it against a stationary scratch element. These three configurations are shown in Fig. 3(a) to (c).

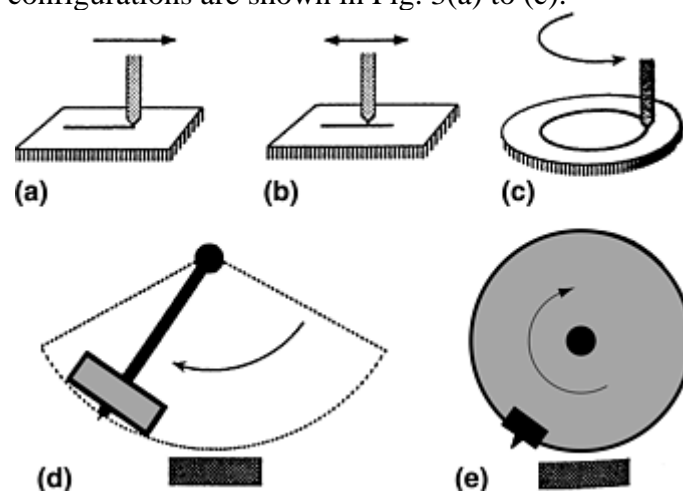


Fig. 3 Different scratch devices. (a) and (b) Linear. (c) Rotary. (d) Pendulum. (e) Grinding type. Source: Ref 4

High-Speed Devices. A high-speed, linear slide can be used to provide relative motion of the sample surface with respect to the scratch element. In this configuration, which is simple and easily instrumented, it is difficult to achieve speeds greater than about 3 m/s. Single-pass as well as multipass scratches can be generated with this device. Other high-speed scratching devices utilize a scratch element that is mounted on the end of a pendulum (Fig. 3d) or on the periphery of a rotating metal disk (Fig. 3e) to generate high speeds, while the sample is mounted on a slide, which may or may not be moving. Speeds much higher than 3 m/s can be easily achieved with the rotating-disk device; in fact by mounting the disk on the spindle of high-speed grinding machines it is feasible to achieve speeds as high as 90 m/s.

In-Situ Scratch Devices. There is a third category of scratching devices that are somewhat less often used. These may be termed as in situ scratching devices because scratch formation can be directly observed in these devices, in situ, using an optical or a scanning electron microscope (SEM). The indenter is stationary, and the sample is slid at a very low velocity by mounting it on a linear slide. In the device, which is mounted inside the chamber of an SEM, the electron beam is focused at the contact between the scratch element tip and the sample surface, thereby enabling scratch formation to be observed at high magnification, but at speeds of the order of a few microns per second. The ambient atmosphere within the chamber may also be varied between a vacuum ($\sim 10^{-7}$ torr) to low pressures of various gases. The authors have developed a simple, in situ device that utilizes an optical microscope to study scratch formation in optically transparent solids (Fig. 4). A high-magnification optical microscope with a large working distance objective is mounted behind the sample, enabling observation of the scratch interface through the sample. The sample is traversed against the scratch element using a high-pressure linear slide at speed between 25 nm/s and 200 mm/s. A high-speed camera may be attached to the microscope for high-speed observation. This has made possible a study of scratch mechanisms ranging from ductile scratching to brittle fracture during scratching of transparent brittle materials like glass, spinel, sapphire, and several oxide polycrystals, and observation of ductile chip formation during scratching of brittle materials. Indentation and scratch damage on coatings deposited over transparent substrates can also be studied using this device.

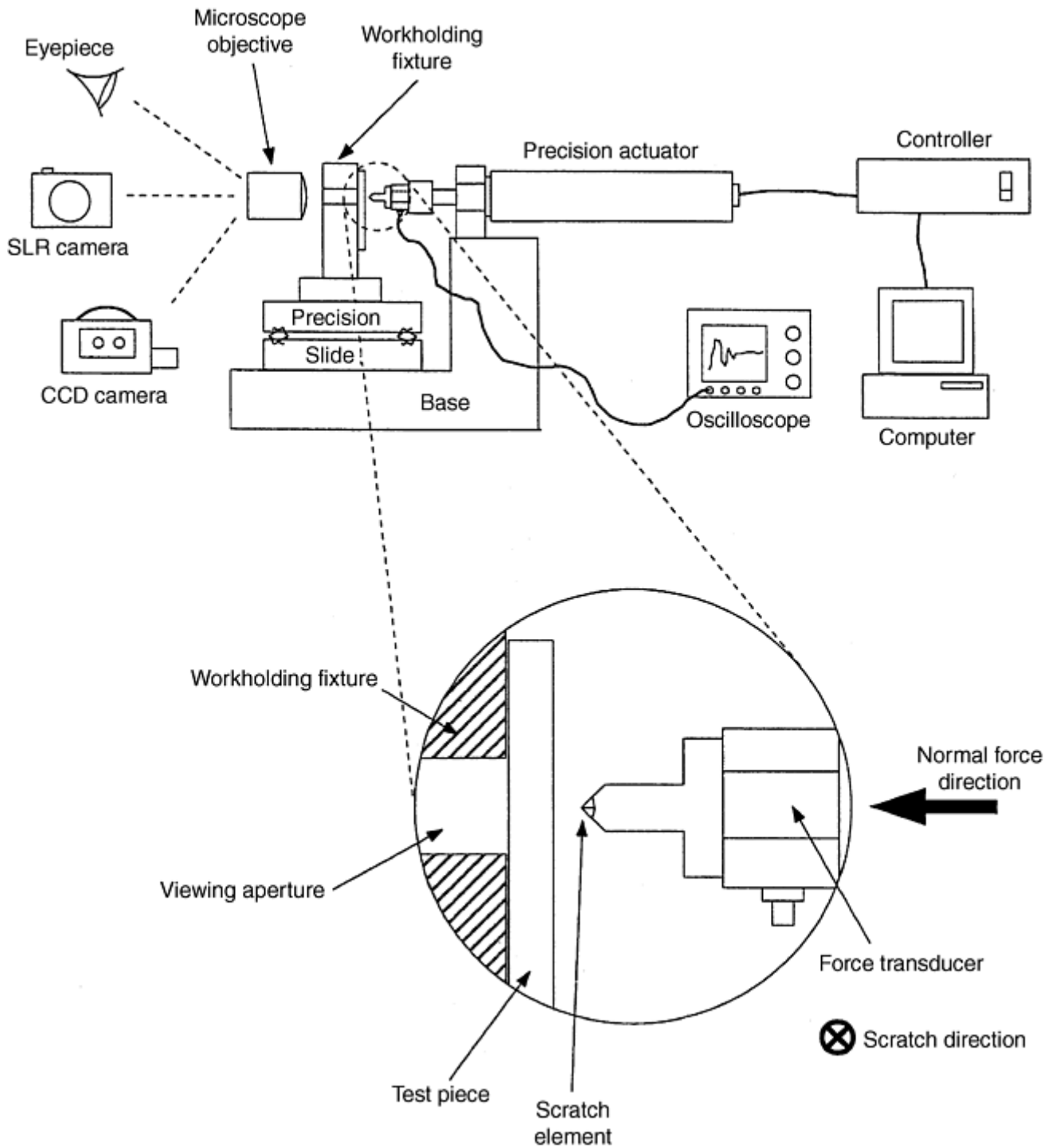


Fig. 4 Purdue scratch apparatus for in situ viewing of scratch formation

Reference cited in this section

4. S. Jacobsson, M. Olsson, P. Hedenqvist, and O. Vingsbo, *Scratch Testing, Friction, Lubrication, and Wear Technology*, Vol 18, *ASM Handbook*, ASM International, 1992, p 430–437

Test Parameters

When a scratch test is used to determine the scratch hardness of a material, the test has to be performed in a controlled or standard configuration. The important parameters of the test are highlighted and briefly described.

Indenter Material. For most tests, a diamond indenter is used to minimize the wear on the indenter and to reduce the influence of wear on the mechanism of scratching. Other hard materials, such as sapphire and tungsten carbide, may also be used as indenters provided they are much harder than the material being scratched. It should be noted that for wear tests—since wear properties of a pair of materials, that is, a material system, are usually studied—the scratch element is made of one material, not necessarily a hard material such as diamond, while the sample may be made of another material.

Indenter Shape. The shape of the indenter is usually spherical (or ball), conical with a sharp tip, a four-faced pyramid (Vickers, Knoop), or a triangular (Berkovich) pyramid. The radius of the indenter tip for a sharp indenter should not be larger than a prescribed amount, and it should be at least an order of magnitude less than the depth of the scratch. Typical indenter radius for a Vickers indenter is $<2\ \mu\text{m}$. It is important that the indenter tip shape is carefully characterized before testing. Conical or pyramid indenters are commonly used in scratch tests, since they can produce a plastic scratch even in brittle materials.

Orientation of the Indenter Relative to the Scratch Direction. In the case of a nonaxisymmetric indenter, such as a pyramid indenter, the diagonal of the indenter is aligned parallel to the scratch direction to reduce cracking in brittle materials and formation of a chip in ductile materials.

Indenter Angle of Attack. This is the angle made by the leading face of the indenter with the sample surface. Usually, the axis of the indenter is aligned perpendicular to the sample surface with the sharp tip (apex) digging in to the sample. However, in some scratch tests this is not necessarily the case. For example, in the Birnbaum scratch hardness test, the leading edge of the cubic indenter (formed by the corner of a cube) is at 35° to the sample surface, hence orienting the main diagonal at 80° to the sample surface.

Sample Preparation. The sample surface is usually polished to a micron or submicron arithmetic average roughness (R_a) to minimize the influence of roughness on the test results. The R_a of the surface should be an order of magnitude less than the depth of the scratch. By a suitable series of polishing steps, it is feasible to achieve R_a values as small as 10 nm fairly easily.

Scratch Velocity. The relative velocity between the indenter and the work surface is held constant during the test. In older scratch devices, the velocity was controlled by weights, attached to the slide (on which the work material or indenter is installed), which was passed over a pulley; by varying the weights it was possible to obtain different scratch velocities. In devices used at the time of publication, the slide is driven by a motor with precise velocity and position control.

Scratch Length or Duration. In order to avoid end effects associated with sample edges and obtain steady-state data, the length of the scratch should be at least 20 times greater than the depth or width of the scratch (whichever is larger).

Scratch Load or Depth. Either scratch load or the depth of indenter penetration can be set at a fixed amount throughout the test. It should be noted that for testing the strength of coatings, the depth of the scratch or the normal load on the indenter is increased at a fixed rate as the indenter is traversed across the sample. The scratch depth is controlled by aligning the scratch direction parallel to the surface of the test material. The scratch load is held constant by the use of deadweights to apply the load. Alternatively, load cells can be used to monitor the scratch load and a feedback mechanism used to move the indenter into or away from the sample surface to maintain constant load.

Number of Passes. This is the number of times the indenter passes over the same scratch track. In most scratch tests, only a single scratch track is made in the sample. Wear tests involve several passes of the scratch element over the same scratch track.

Determination of Scratch Width or Depth. If the scratch width and depth are determined visually using an optical microscope, the magnification, lighting, and grid/scale used should be standardized to enable

reproducibility of results. If the scratch cross-section profile is determined by contact (stylus)-based methods, parameters such as filter type, cutoff length, stylus travel velocity, and stylus tip radius have to be standardized. In the recent past, techniques such as scanning probe microscopy (atomic force microscopy and scanning tunneling microscopy), confocal microscopy, and light-interference-based profilometry have improved the accuracy and resolution of measurement of scratch width and depth. The techniques also provide information about the three-dimensional geometry of the scratch including material pileup, elastic recovery, and so forth (Fig. 5).

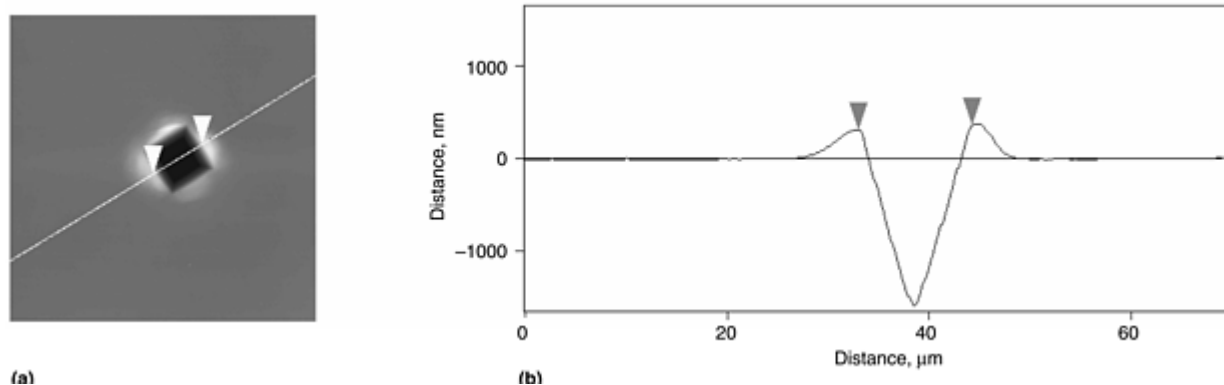


Fig. 5 Cross section of a Vickers indentation in iron along a line joining the midpoints of opposite edges of the indentation (load ≈ 40 g). (a) Plan view of the indent. (b) Atomic force microscopy line profile along the section line marked in (a). Section details: surface distance, $29.7 \mu\text{m}$; horizontal distance, $28.8 \mu\text{m}$; vertical distance, 46.8 nm ; angle, 0.093°

Scratch Testing

Vispi Homi Bulsara, Cummins Engine Company; Srinivasan Chandrasekar and Thomas N. Farris, Purdue University

Application and Interpretation of Results

Before discussing the application of the scratch test to determine different parameters pertaining to the deformation and fracture of solids, it is instructive to briefly review the measurement of indentation hardness (which is discussed in more detail in the Section “Hardness Testing” in this Volume).

Overview of Indentation Hardness. The indentation hardness test has found widespread application in analyzing the mechanical properties of materials. The most common method of estimating indentation hardness of a solid is by slowly loading an indenter, sharp or blunt, into the surface and estimating the contact pressure applied by the indenter in producing a well-developed plastic zone. In practice, the contact dimensions of the indentation, that is, the contact circle diameter for a spherical indenter and the diagonal lengths for pyramidal indenters, are measured after the indenter is unloaded from the surface. The hardness is obtained most commonly as the load (P) divided by the surface area of the indentation. A better hardness value, referred to as true hardness, is obtained by dividing the load by the projected area of the indentation. This value can be directly identified with the mean pressure, p_m , applied by the indenter, if it is assumed, as is commonly done, that the projected area of the indentation is negligibly changed by the elastic recovery taking place during unloading of the indenter.

Applying these definitions to the case of quasistatic loading of a solid by a Vickers indenter, which produces a pyramid indentation, the Vickers indentation hardness (H_V) is obtained as:

$$H_V = \frac{P}{\text{Surface area of indentation}}$$

$$\approx \frac{P}{d^2} \times 1.854 \tag{Eq 3}$$

Here d is the diagonal length of the indentation and P is the maximum load applied by the indenter. A true value for the Vickers hardness, namely the true Vickers hardness (H_{TV}), is estimated as:

$$H_{TV} = \frac{P}{\text{Projected area of indentation}} = \frac{2P}{d^2} \quad (\text{Eq 4})$$

Note that $H_V = 0.927 H_{TV}$. For most materials, it is commonly assumed that $H_{TV} \approx 3\sigma_y$ where σ_y is the yield strength of the material.

It is most often the case that during indentation part of the displaced material is piled up in the form of a ridge surrounding the indentation. This is well illustrated by the atomic force microscopy image and associated line trace of a Vickers indentation shown in Fig. 5. When obtaining the contact area for Eq 3 and 4, it is assumed that the pileup of the material produced during indentation does not support any load. In practice, the piled-up material does, in fact, support a load.

Scratch Hardness Estimation. Now consider what happens to a Vickers indenter if it is moved along the sample surface, after a load, P , has been applied. This corresponds to a scratch test. For the purpose of discussion it shall be assumed, without loss of generality, that the pyramid indenter is being moved along the direction of one of the indentation diagonals. As the indenter is quasi-statically loaded and then slid against the surface, the indenter first sinks further into the surface due to loss of load-carrying capacity of the two rear faces. As sliding proceeds, the indenter will “climb up,” pushing a ridge of deforming material ahead of it. A steady state is soon reached in which the normal force, P , the tangential force, F , and the extent of plastic deformation as characterized by the width of the scratch track become constant. A schematic of a scratch track and an optical micrograph of the plan views of a track made by a Vickers indenter are shown in Fig. 6 and 7, respectively. Figure 8 is a schematic of the relevant load-bearing areas associated with the normal and tangential force, respectively, which enter into the calculation of scratch hardness.

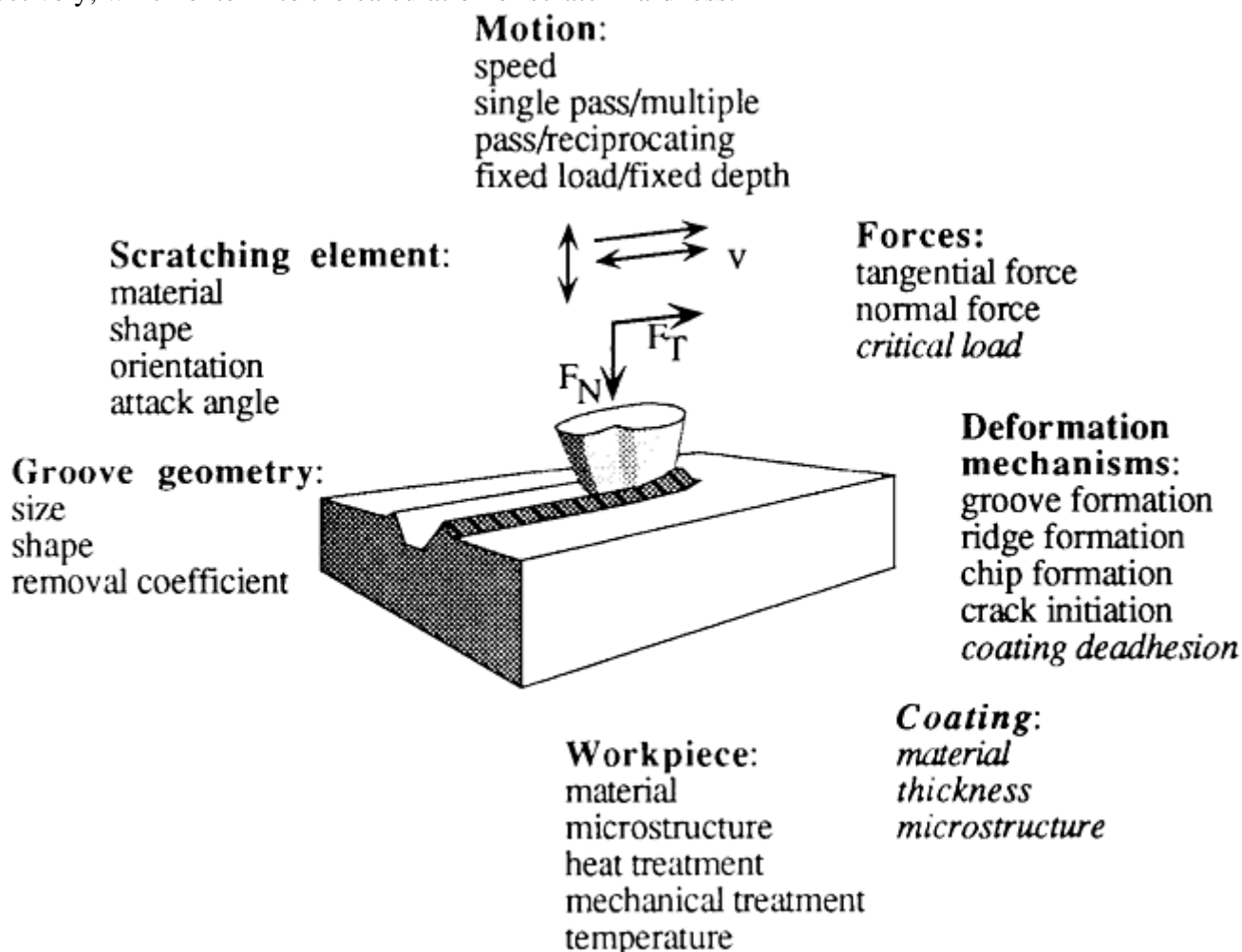


Fig. 6 Parameters encountered in scratch testing. F_T , tangential friction force; F_N , normal load; v , scratching speed

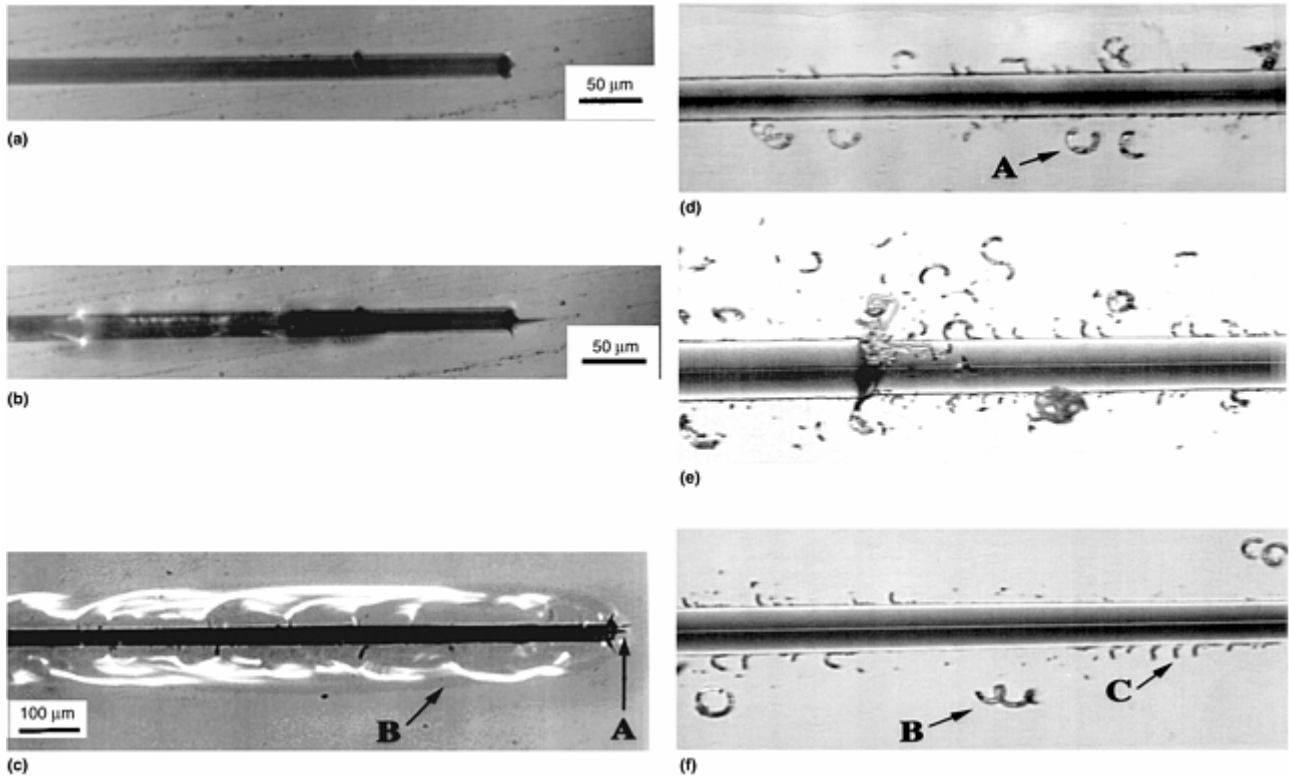


Fig. 7 The load dependence of fracture and deformation about scratches made by a Vickers indenter in soda-lime glass. These photographs were taken in tests conducted in the Purdue scratch apparatus. (a) Scratch appears plastic until end of traverse. Load, 120 g. (b) Lateral and median cracks pop up around the scratch track, shown in (a), when the indenter is unloaded. (c) Lateral and median cracks after unloading. Load, 90 g. A, extent of median crack; B, extent of lateral crack. (d), (e), and (f), different parts of the same scratch track showing ductile chip formation at low loads. A, curly chip; B, spiral chip; C, chips attached to groove surface

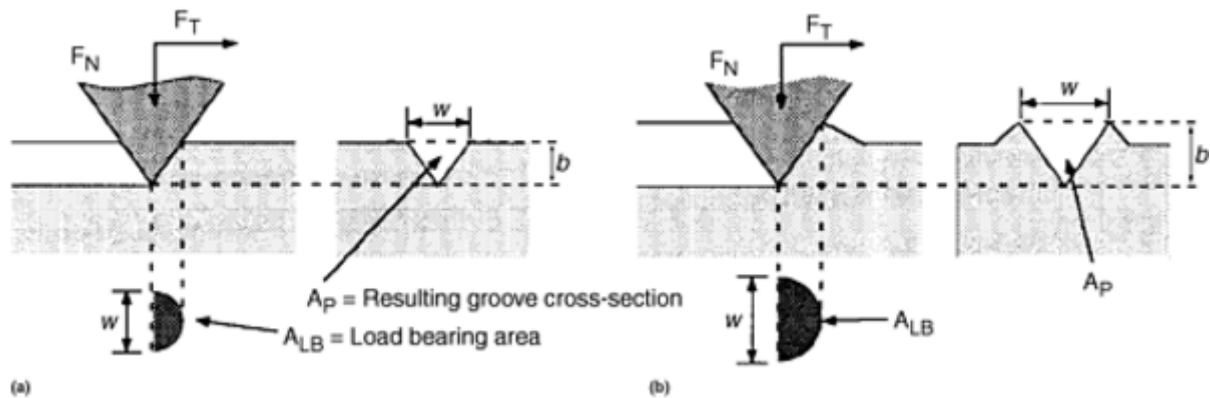


Fig. 8 Effect on load-bearing area, A_{LB} , of scratching with a conical tool. (a) Pure cutting (no ridge formation). (b) A more realistic situation of ridge formation (that is, mixed microplowing and microcutting). w , groove width; b , groove height

The scratch hardness may also be defined with reference to Fig. 8. By analogy with quasi-static indentation, the scratch hardness H_S is defined as (Ref 6):

$$H_S = \frac{P}{A_{LB}} \quad (\text{Eq 5})$$

The projected load-bearing area, A_{LB} , is estimated from measurements of the scratch track width, w . In practice, if w is measured with an optical microscope, some part of the piled-up region along the lateral edges of the track will be included in the measurement. For a Vickers indenter, A_{LB} is obtained as:

$$A_{LB} = \frac{w^2}{4} \quad (\text{Eq 6})$$

Similar relations can be obtained easily for other indenter geometries. Note that A_{LB} for a Vickers indenter calculated using Eq 6 is independent of whether the indenter is moved edge first or face first.

It is reasonable to expect that the scratch hardness, H_S , is equal to the associated indentation hardness (Vickers, Knoop, Brinell), H , since both parameters are associated with the plastic response of a material. However, experimental results indicate otherwise. Table 1 is a comparison of indentation hardness (H) and scratch hardness, H_S , for a selection of materials. It is seen that the ratio H_S/H is not only different from a value of one, but also varies widely, depending on material type and properties. In order to understand these variations, it is necessary to analyze a detailed model of the plastic scratching process (Ref 6), but this is beyond the scope of this article. Suffice to say that H_S may be used in an analogous way to indentation hardness, but with considerable caution. From a measurement point of view, the measurement of scratch width, including the pileup region, is much easier and can be more accurately carried out than indentation diagonal measurement. For example, profilometry of the scratch track provides an accurate measurements of w .

Table 1 Comparison of indentation hardness H and scratch hardness H_S for a range of materials

Material	H		H_S		H_S/H
	MPa	ksi	MPa	ksi	
0.9% carbon steel	2,800	405	3,300	480	1.16
	3,340	485	4,200	610	1.26
	4,330	630	5,650	820	1.31
	7,530	1,090	8,800	1,275	1.17
	9,420	1,365	10,700	1,550	1.14
Aluminum	216	31	196	28	0.91
Annealed					
Worked	422	61	245	35	0.58
Copper	530	76	903	130	1.70
Annealed					
Worked	1,079	155	853	125	0.79
0.2% carbon steel	1,265	185	1,295	190	1.02
Annealed					
Worked	2,354	340	2,247	325	0.95

Source: Ref 6

Plowing Hardness. When performing a scratch test, the tangential force (F) on the indenter is also measured. This leads to the definition of another hardness parameter that is based on the groove cross-sectional area, A_P , and the tangential force (see Fig. 8). This hardness parameter is usually referred to as plowing hardness (H_P) and is defined as (Ref 6):

$$H_P = \frac{F}{A_P} \quad (\text{Eq 7})$$

For a Vickers indenter, or more generally for scratching with a wedge indenter of wedge apex angle 2α ,

$$A_P = b^2 \tan \alpha \quad (\text{Eq 8})$$

where b is the depth of the scratch groove measured either from the original surface or from the peak of the piled-up region. The corresponding area A_P for this wedge indenter is $b^2 \tan^2 \alpha$. It must be noted that b cannot be estimated from track width, w , and the indenter angle 2α , because of elastic recovery of the scratch. Consequently, b has to be obtained from a measurement. The quantity H_P can be interpreted in more than one way. For example, it can be thought of as the energy expended in displacing a unit volume of material. It is also related to the minimum load required for a chip to be formed during scratching. However, the demarcation between the deformation regimes in which chip formation is the preferred mode rather than indentation is primarily dependent on the attack angle of the indenter, and to a lesser extent on indenter tip radius.

Specific Energy of Abrasive Machining. The scratch test, with a pyramid indenter or an abrasive particle, can be used to estimate the specific energy (u) in abrasive machining, that is, the energy required to remove unit volume of material by chip formation. The specific energy can be obtained as:

$$u = \frac{\text{Power}}{\text{Volume of material removed}} \quad (\text{Eq 9})$$

$$= \frac{Fv}{Vbw} = \frac{F}{bw}$$

where F is the tangential or cutting force on the particle, b is the depth of material removed, and w is the width of the scratch track.

The specific energy is an important parameter used to evaluate the efficiency of machining processes. It can also be a useful parameter in studying the cutting action of abrasive grits of different type, shape, and composition. The challenge in using this approach is that high-frequency dynamometers capable of measuring the force on a single indenter or particle that is imposed over a duration of a few tens of microseconds are not currently available. There are other approaches to estimating the energy consumed during cutting, but these are not sufficiently accurate, nor do they have high resolution.

Efficiency of Material Removal. The scratch test can be used to evaluate the efficiency of material removal by calculating a parameter that compares the amount of material removed by chip formation with the volume displaced by indentation. This parameter, sometimes called the removal coefficient, η , is defined as:

$$\eta = \frac{\text{Volume of material removed}}{\text{Volume of material displaced}} \quad (\text{Eq 10})$$

The challenge in estimating this parameter is quantifying the amount of material that is piled up (see earlier discussion).

Stress analysis of scratch testing is used to determine whether information more detailed than scratch hardness is available within the test. Analysis of the stress field induced by scratch testing is difficult due to the complicated geometry imposed by the contact problem and the inelastic behavior of the material in the presence of concentrated stresses. Stress analysis of scratch testing can be classified broadly into indentation of ductile or brittle materials by spherical or pyramidal indenters. The elastic stresses associated with a sliding spherical indenter are well characterized, for example, in Ref 8. However, detailed elastic stress fields for pyramid indenters are not available due to the singular nature of the stresses. These singularities require special care when using finite elements to resolve elastic-plastic stress fields for normal indentation (Ref 9). An accurate finite element solution for scratching using pyramid indenters is not available.

For spherical indenters, the finite-element method is capable of resolving the stresses associated with scratch testing of ductile materials (Ref 10). However, an assumed constitutive behavior that is capable of accurately predicting the ratcheting strain for repeated sliding of a range of materials eludes researchers (Ref 11). These elastic-plastic calculations yield much information that is difficult to present in a compact form that can be used to interpret experimental results over a range of loads. However, an approximate solution for ductile materials subjected to normal indentation based on the “expanding cavity” are available (Ref 8). This solution relies on an observation that strain fields are spherically symmetric. It provides a convenient classification of spherical indentations into elastic, elastic-plastic, and fully plastic regimes. This model has not been applied to scratching.

References cited in this section

6. J.A. Williams, Analytical Models of Scratch Hardness, *Tribol. Int.*, Vol 29 (No. 8), 1996, p 675–694
8. K.L. Johnson, *Contact Mechanics*, Cambridge, 1985
9. Y. Murakami and K. Matsuda, Analysis of Vickers Hardness by the Finite Element Method, *J. Appl. Mech.*, Vol 61 (No. 4), 1994, p 822–828

10. S.M. Kulkarni, G.T. Hahn, C.A. Rubin, and V. Bhargava, Elasto-plastic Finite Element Analysis of Three-Dimensional Pure Rolling Contact above the Shakedown Limit, *J. Appl. Mech.*, Vol 58 (No. 2), 1991, p 347–353
11. C. Sakae and L.M. Keer, Application of Direct Method for a Nonlinear-Kinematic-Hardening Material under Rolling/Sliding Line Contact: Constant Ratchetting Rate, *J. Mech. Phys. Solids*, Vol 45 (No. 9), 1997, p 1577–1594

Scratch Testing

Vispi Homi Bulsara, Cummins Engine Company; Srinivasan Chandrasekar and Thomas N. Farris, Purdue University

Sliding Indentation Fracture of Brittle Materials

The Blister Field. Recent interest in fracture induced by sliding indentation of brittle materials warrants special attention. When a sharp indenter is quasi-statically applied onto a surface of a brittle solid, the classical theory relating the hardness to the yield stress of metals (Ref 1) no longer applies since yielding no longer occurs at a constant maximum shear stress or at a constant volume (Ref 12). A large body of experimental observations have shown that in brittle materials the volume of material displaced by the penetration of the indenter is accommodated by compaction or shear deformation, or both, and this may occur either uniformly or irregularly. In silicate glasses, which have a relatively open structure, the displaced material is most readily accommodated by compaction within a zone underneath the indenter. However, in soda-lime glasses and in most ceramics shear deformation dominates, with some compaction also taking place underneath the indenter. The experimental model used by Yoffe (Ref 13) to describe the deformation underneath a sharp conical indenter in soda-lime glass is based on the work of Peter (Ref 14), among others, who showed that the mean contact pressure under a sharp indenter remains constant and relatively independent of the indenter geometry. This model assumes that as a conical indenter is applied to the solid surface, yielding initially occurs in a hemispherical bowl under the indenter and continues until the yielded zone attains its stable preferred state for that pressure. As the indenter is loaded further, no additional flow occurs within this bowl, but fresh yielding takes place in an adjoining thin hemispherical shell. This process continues, and “it is as if a set of nested hemispherical bowls separated by plastic filler were forced down in turn, one within the other” (Ref 13). The yielding process occurs through a combination of shear deformation and compaction within the yielded zone. Part of the material displaced by the indenter is accommodated by compaction within the yielded zone, while the remaining material is pushed into the surroundings. At the end of the indentation process, the elastic half-space is left with an overlarge hemispheroid fixed in a hemispherical cavity on its surface. This misfit leads to a residual stress in the region outside of the cavity. Consequently, as the material reacts to this residual stress, cracking may occur within the solid.

The “blister” field proposed by Yoffe (Ref 13) was for describing the development of cracks below a conical indenter acting on a brittle solid. The stress distribution in the surrounding elastic zone was obtained as the superposition of two stress fields—the Boussinesq field for the point force, which idealized the indentation pressure distribution, and a doublet force system, which idealized the localized inelastic deformation. The doublet force system for the blister field consisted of superposition of a point center of expansion in an infinite elastic solid with an additional doublet to satisfy the free surface normal stress boundary condition. Such a doublet force system leads to a volume increase of the inelastic deformation zone that must be taken up by compaction or elastic deformation of the remainder of the solid. The volume increase is a measure of the “strength” of the blister field. The strength of the blister field varies with the applied force; this variation is characterized by a material property that has thus far defied a precise estimation. Qualitatively, Yoffe's model has predicted the origin and growth of radial, median, and lateral crack systems quite well. In particular it is consistent with the observation that for a certain range of loads, the lateral crack forms and grows during

unloading. Its only disadvantage is from a quantitative point of view, as a procedure for determining the strength of the blister field for various indenter geometries is not yet available.

Models to describe the sliding indentation fracture process in ceramics have not yet evolved to a stage where the inelasticity under the indenter is accounted for completely (Ref 15, 16, 17). This is in large part due to the difficulty introduced by a lack of information concerning the constitutive behavior of ceramics in large hydrostatic compressive stress fields such as that existing underneath a microindentation. It seems that a reasonable first step for modeling the sliding indentation stress fields would be to extend Yoffe's work on static indentation to the sliding situation (Ref 18). This extension includes the load-history effects of inelastic deformation left behind by the sliding indenter and the elastic effects due to the frictional force.

Sliding Indentation Fracture Observations. The sliding indentation stress field (Ref 18) provides interpretation of observations of the microcracking about scratches in brittle solids (Ref 15, 16, 19, 20). Figure 9(a) shows a schematic view of the crack patterns that have emerged from the studies, most of which have been carried out at light loads in soda-lime glass, silicon, polycrystalline alumina, and nickel-zinc ferrite. The typically observed crack patterns are median, lateral, and chevron (radial) cracks. The load regimes at which the various cracks occur in soda-lime glass are summarized in Table 2, which is obtained based on observations of the fractured specimen.

Table 2 Classification of fracture patterns in soda-lime glass under a sliding Vickers indenter

Normal load (N)	Fracture pattern
~0–0.05	No crack
~0.05–0.8	Median cracking
~0.8–3	Median and lateral cracking with lateral crack growth to the surface at higher loads
~3–6	Median cracking and crushed scratch track

Source: Ref 19

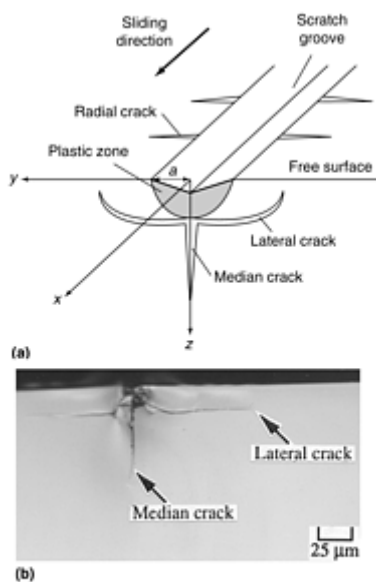


Fig. 9 (a) Cracks induced by sliding microindentation of brittle solids. (b) Photograph of cross section

In situ observations indicate that these cracks initiate at or close to the boundary between the inelastic deformation zone and the surrounding elastic solid. The subsequent growth of these cracks occurs in the elastic region. Bulsara (Ref 20) observes that for most loads at which median and lateral cracks occur, the cracks propagate such that the crack front moves with the load. However, near loads of about 1 N applied with a Vickers indenter in soda-lime glass, the lateral crack does not appear until the indenter is lifted from the surface. Once the load is removed, the lateral crack forms beneath the end of the scratch and propagates rapidly along the entire length of the scratch and until the beginning of the scratch track, where it stops. Fracture and

deformation patterns about scratches in soda-lime glass, which is often used as a model brittle material, as shown in Fig. 7, which also shows ductile chips formed by scratching in glass.

The assumption that these cracks are initiated and propagated by tensile stresses that occur in the elastic material immediately adjoining the inelastic zone allows for predictions of crack formation and growth through a consideration of the stress fields. It has been shown that the present analytical model provides reasonably good descriptions of the crack patterns observed around sliding indentations in brittle materials. In particular, the analysis accounts for the occurrence of lateral cracking under sliding indenters above an experimentally observed threshold load (Ref 18).

The sliding blister field does not reveal any information about details of deformation in the inelastic zone near the indenter. Recently, investigators have been examining this issue using nanoscratch testing. However, the sliding blister field is a simple analytical tool that can be used to explain many interesting aspects of failure mechanisms in glass that occur near sliding microindentations.

Sliding Indentation Modeling of Polishing. A common method for making surfaces smooth is by rubbing them against a block with an abrasive slurry interspersed between them. This process is called polishing or, sometimes, lapping. The block is typically made of a metal, for example, cast iron or tin, or it consists of a soft, flexible material such as cloth, nylon, or leather attached to the surface of a metal block. The polishing slurry is composed of hard, abrasive particles (e.g., diamond, silicon carbide, alumina) suspended in a fluid medium such as deionized water, glycol, or viscous oil. A force is applied to the work surface by the polishing block; this force typically corresponds to a polishing pressure of 7 to 14 kPa (1–2 psi), where polishing pressure is the polishing force divided by the work surface area. The relative sliding velocity between the block and the work surface is usually less than 0.5 m/s and randomly oriented through the course of the process so as to produce a smooth surface devoid of directional scratches. This velocity is one to two orders of magnitude less than the relative velocity between an abrasive wheel and workpiece in grinding. An early, important application of polishing was lens making, and indeed it was for this purpose that the process was studied by Newton, Herschel, and Rayleigh (Ref 21). Since then, polishing has become a critical process in many applications ranging from the manufacture of precision mechanical components to electronic substrates and optical windows.

While the applied polishing force is low and in itself insufficient even to cause considerable elastic deformation of the work surface, this force is transmitted to the surface, not uniformly, but at the microscopic contacts between the abrasive particles and the work surface (Ref 22, 23). At these contacts the pressure imposed by a particle on the surface should be quite high, often comparable to the hardness of the work material. Consequently, the mechanism of material removal in polishing, which varies from brittle fracture to plastic microcutting, is not so much dictated by the applied polishing force as by the manner in which this force is transmitted locally by the particles to the work surface. This is consistent with microscopic observations of polished surfaces and polishing debris, which indicate that the abrasive particles act like single-point cutting tools or indenters (Ref 22, 24). The force applied by an abrasive particle also plays a major role in determining polishing temperatures (Ref 25) and the extent of plastically deformed layers and residual stresses on polished surfaces (Ref 22, 26, 27). Because of the critical importance of these forces to the mechanics of polishing, it is of interest to deduce the magnitude and distribution of these forces and their dependence on polishing parameters.

A model has been developed to determine the number and size of abrasive particles involved in material removal in polishing and the forces acting on these particles (Ref 28). This model assumes that each particle acts as a sliding microindentation. The effect of particle size on these parameters has been simulated for a range of particle sizes. It is shown that when polishing with abrasive powders having relatively broad size distributions, only a very small percentage of the particles are involved in material removal. Further, these particles comprise the larger particles occurring in the tail end of the particle size distribution. The average force on a particle is found to be in the range of 5 to 200 mN under typical polishing conditions, which is of the order of loads used in microindentation hardness testing. These predictions of the model are consistent with observations pertaining to polished surfaces and the polishing process.

References cited in this section

1. D. Tabor, *The Hardness of Metals*, Oxford University Press, 1951

12. P.W. Bridgman and I. Simon, Effects of Very High Pressure on Glass, *J. Appl. Phys.*, Vol 24 (No. 4), 1953, p 405–413
13. E.H. Yoffe, Elastic Stress Fields Caused by Indenting Brittle Materials, *Philos. Mag. A*, Vol 46 (No. 4), 1982, p 617–628
14. K.W. Peter, Densification and Flow Phenomena of Glass in Indentation Experiments, *J. Non-Cryst. Solids*, Vol 5, 1970, p 103–115
15. M.V. Swain, Microfracture about Scratches in Brittle Solids, *Proc. R. Soc. A*, Vol 366, 1979, p 575–597
16. A. Misra and I. Finnie, On the Scribing and Subsequent Fracturing of Silicon Semiconductor Wafers, *J. Mater. Sci.*, Vol 14, 1979, p 2567–2574
17. S.Y. Chen, T.N. Farris, and S. Chandrasekar, Sliding Microindentation Fracture of Brittle Materials, *STLE Tribol. Trans.*, Vol 34 (No. 2), 1991, p 161–168
18. Y. Ahn, T.N. Farris, and S. Chandrasekar, Sliding Microindentation Fracture of Brittle Materials: Role of Elastic Stress Fields, *Mech. Mater.*, Vol 29, 1998, p 1087–1093
19. Y. Ahn, “Deformation about Sliding Indentation in Ceramics and Its Application to Lapping,” Ph.D. thesis, Purdue University, 1992
20. V.H. Bulsara, “Scratch Formation in Brittle Solids and its Application to Polishing,” Ph.D. thesis, Purdue University, 1997
21. Lord Rayleigh, Polish, *Nature*, Vol 64, 1901, p 385
22. L.E. Samuels, *Metallographic Polishing by Mechanical Methods*, 3rd ed., American Society for Metals, 1982
23. E.C. Rabinowicz, Polishing, *Sci. Am.*, Vol 218 (No. 6), 1968, p 91–99
24. R.L. Aghan and L.E. Samuels, Mechanisms of Abrasive Polishing, *Wear*, Vol 16, 1970, p 293–301
25. V.H. Bulsara, Y. Ahn, S. Chandrasekar, and T.N. Farris, Polishing and Lapping Temperatures, *J. Tribol.*, Vol 119 (No. 1), 1997, p 163–170
26. S. Chandrasekar and M.M. Chaudhri, Indentation Cracking in Soda-Lime Glass and Ni-Zn Ferrite under Knoop and Conical Indenters and Residual Stress Measurements, *Philos. Mag. A*, Vol 67 (No. 5), 1993, p 1187–1218
27. B.J. Hockey, Plastic Deformation of Alumina by Indentation and Abrasion, *J. Am. Ceram. Soc.*, Vol 54 (No. 5), 1971, p 223–231
28. V.H. Bulsara S. Chandrasekar, and T.N. Farris, Mechanics of Polishing, *J. Appl. Mech. (Trans. ASME)*, Vol 65 (No. 2), 1998, p 410–416

Scratch Testing

Vispi Homi Bulsara, Cummins Engine Company; Srinivasan Chandrasekar and Thomas N. Farris, Purdue University

Summary

Scratch testing is useful and simple as a means of comparing the hardness of materials. The ubiquitous presence of the Mohs scale is testament to the usefulness of scratch testing. The scratch test also provides the basis for developing models of more complicated processes such as wear or polishing. However, it is not currently used to obtain more fundamental information, such as stress-strain curves, due to the lack of a robust model of the process.

Scratch Testing

Vispi Homi Bulsara, Cummins Engine Company; Srinivasan Chandrasekar and Thomas N. Farris, Purdue University

Acknowledgments

The authors acknowledge support from the Materials Processing and Tribology Center at Purdue.

Scratch Testing

Vispi Homi Bulsara, Cummins Engine Company; Srinivasan Chandrasekar and Thomas N. Farris, Purdue University

References

1. D. Tabor, *The Hardness of Metals*, Oxford University Press, 1951
2. M.M. Chaudhri and Y. Enomoto, *Philos. Mag. A.*, Special Issues on Indentation Hardness, 1996
3. S. Jayaraman, G.T. Hahn, W.C. Oliver, C.A. Rubin, and P.C. Bastias, Determination of Monotonic Stress-Strain Curve of Hard Materials from Ultra-Low-Load Indentation Tests, *Int. J. Solids Struct.*, Vol 35 (No. 5–6), 1998, p 365–381
4. S. Jacobsson, M. Olsson, P. Hedenqvist, and O. Vingsbo, Scratch Testing, *Friction, Lubrication, and Wear Technology*, Vol 18, *ASM Handbook*, ASM International, 1992, p 430–437
5. S.R. Williams, *Hardness and Hardness Measurements*, American Society for Metals, 1942
6. J.A. Williams, Analytical Models of Scratch Hardness, *Tribol. Int.*, Vol 29 (No. 8), 1996, p 675–694
7. F.P. Bowden and D. Tabor, *The Friction and Lubrication of Solids*, Oxford University Press, Vol I, 1951; Vol II, 1964
8. K.L. Johnson, *Contact Mechanics*, Cambridge, 1985

9. Y. Murakami and K. Matsuda, Analysis of Vickers Hardness by the Finite Element Method, *J. Appl. Mech.*, Vol 61 (No. 4), 1994, p 822–828
10. S.M. Kulkarni, G.T. Hahn, C.A. Rubin, and V. Bhargava, Elasto-plastic Finite Element Analysis of Three-Dimensional Pure Rolling Contact above the Shakedown Limit, *J. Appl. Mech.*, Vol 58 (No. 2), 1991, p 347–353
11. C. Sakae and L.M. Keer, Application of Direct Method for a Nonlinear-Kinematic-Hardening Material under Rolling/Sliding Line Contact: Constant Ratchetting Rate, *J. Mech. Phys. Solids*, Vol 45 (No. 9), 1997, p 1577–1594
12. P.W. Bridgman and I. Simon, Effects of Very High Pressure on Glass, *J. Appl. Phys.*, Vol 24 (No. 4), 1953, p 405–413
13. E.H. Yoffe, Elastic Stress Fields Caused by Indenting Brittle Materials, *Philos. Mag. A*, Vol 46 (No. 4), 1982, p 617–628
14. K.W. Peter, Densification and Flow Phenomena of Glass in Indentation Experiments, *J. Non-Cryst. Solids*, Vol 5, 1970, p 103–115
15. M.V. Swain, Microfracture about Scratches in Brittle Solids, *Proc. R. Soc. A*, Vol 366, 1979, p 575–597
16. A. Misra and I. Finnie, On the Scribing and Subsequent Fracturing of Silicon Semiconductor Wafers, *J. Mater. Sci.*, Vol 14, 1979, p 2567–2574
17. S.Y. Chen, T.N. Farris, and S. Chandrasekar, Sliding Microindentation Fracture of Brittle Materials, *STLE Tribol. Trans.*, Vol 34 (No. 2), 1991, p 161–168
18. Y. Ahn, T.N. Farris, and S. Chandrasekar, Sliding Microindentation Fracture of Brittle Materials: Role of Elastic Stress Fields, *Mech. Mater.*, Vol 29, 1998, p 1087–1093
19. Y. Ahn, “Deformation about Sliding Indentation in Ceramics and Its Application to Lapping,” Ph.D. thesis, Purdue University, 1992
20. V.H. Bulsara, “Scratch Formation in Brittle Solids and its Application to Polishing,” Ph.D. thesis, Purdue University, 1997
21. Lord Rayleigh, Polish, *Nature*, Vol 64, 1901, p 385
22. L.E. Samuels, *Metallographic Polishing by Mechanical Methods*, 3rd ed., American Society for Metals, 1982
23. E.C. Rabinowicz, Polishing, *Sci. Am.*, Vol 218 (No. 6), 1968, p 91–99
24. R.L. Aghan and L.E. Samuels, Mechanisms of Abrasive Polishing, *Wear*, Vol 16, 1970, p 293–301
25. V.H. Bulsara, Y. Ahn, S. Chandrasekar, and T.N. Farris, Polishing and Lapping Temperatures, *J. Tribol.*, Vol 119 (No. 1), 1997, p 163–170
26. S. Chandrasekar and M.M. Chaudhri, Indentation Cracking in Soda-Lime Glass and Ni-Zn Ferrite under Knoop and Conical Indenters and Residual Stress Measurements, *Philos. Mag. A*, Vol 67 (No. 5), 1993, p 1187–1218

27. B.J. Hockey, Plastic Deformation of Alumina by Indentation and Abrasion, *J. Am. Ceram. Soc.*, Vol 54 (No. 5), 1971, p 223–231
28. V.H. Bulsara S. Chandrasekar, and T.N. Farris, Mechanics of Polishing, *J. Appl. Mech. (Trans. ASME)*, Vol 65 (No. 2), 1998, p 410–416

Scratch Testing

Vispi Homi Bulsara, Cummins Engine Company; Srinivasan Chandrasekar and Thomas N. Farris, Purdue University

Selected References

- A. Broese van Groenou, N. Maan, and J.B.D. Veldkamp, Single-Point Scratches as a Basis for Understanding Grinding and Lapping, *The Science of Ceramic Machining and Surface Finishing II*, B.J. Hockey and R.W. Rice, Ed., pages 43–60. NBS SP 562, National Bureau of Standards, 1979, p 43–60
- V. Bulsara, S. Chandrasekar, and T.N. Farris, Direct Observation of Contact Damage Produced by Vickers Indentation in Diamond-Like Films, *Proc. IMECE Symp Dissimilar Material Systems: Manufacturing Processes, Design, and Mechanics*, (Dallas, TX, Nov 1997), Volume MD-80, p 287–292
- M.M. Chaudhri and E.H. Yoffe, The Area of Contact between a Small Sphere and a Flat Surface, *Philos. Mag.*, Vol 44 (No. 3), 1981, p 667–675
- W. Cheng, E. Ling, and I. Finnie, Median Cracking of Brittle Solids due to Scribing with Sharp Indenters, *J. Am. Ceram. Soc.*, Vol 73 (No. 3), 1990, p 580–586
- W. Cheng and I. Finnie, A Mechanism for Sub-surface Median Crack Initiation in Glass During Indenting and Scribing, *J. Mater. Sci.*, Vol 25, 1990, p 575–579
- K. Miyoshi and D.H. Buckley, Ceramic Wear in Indentation and Sliding Contact, *ASLE Trans.*, Vol 28 (No. 3), 1985, p 296–302
- T.O. Mulhearn, The Deformation of Metals by Vickers-Type Pyramidal Indenters, *J. Mech. Phys. Solids*, Vol 7, 1959, p 85–96
- J.D.B. Veldkamp, N. Hattu, and V.A.C. Snijders, Crack Formation During Scratching of Brittle Materials, *Fracture Mechanics of Ceramics*, R.C. Bradt, A.G. Evans, D.P.H. Hasselman, and F.F. Lange, Ed., Vol 3, Plenum, 1978, p 273–301
- Sh. Wada, Micro-fracture of Ceramics and Tribology, *Jpn. J. Tribol.* Vol 35 (No. 8), 1990, p 859–866

Abrasive Wear Testing

Jeffrey A. Hawk, U.S. Department of Energy, Albany Research Center

Introduction

ABRASIVE WEAR is a major problem for the excavation, earth moving, mining, and minerals processing industries and occurs in a wide variety of equipment, such as bulldozer blades, excavator teeth, rock drill bits, crushers, slushers, ball mills and rod mills, chutes, slurry pumps, and cyclones. Figure 1 shows the extent of abrasion that can occur on a bulldozer blade. However, abrasive wear is not limited to these activities. Abrasion is a problem in most wear environments at one point or another, even though it may not be the primary wear mechanism initially. In any tribosystem where dust and wear debris are not controlled and excluded, abrasive

wear will be a problem. The wear of parts, the cost of repair and replacement of these parts, and the associated downtime related to these activities results in significant costs to many industries. As a result, some sort of preliminary indication of the wear resistance of these parts is desirable. For the most part, however, wear tests of specific machinery or parts are costly to perform, are very labor intensive, and require a long time to complete. In addition, the environmental variables change over the course of the test, making correlations between tests run at different times and in different places difficult. In order to reduce testing costs and speed up component development laboratory wear tests have been developed (Ref 1, 2, 3, 4). Many of these tests are company specific and consist of data collected over many years. These data are then used in conjunction with experience to design and select alloys for use as wear components within that company. However, these data are not usually available to other competitors or to the general public. Consequently, laboratory abrasive wear tests that are not specific to any particular tribological environment have also been developed over the years.



Fig. 1 Extent of abrasion on a bulldozer blade. Notice the width and depth of the wear scars.

In general, abrasive wear processes have typically been divided into two broad regimes: high-stress abrasion or low-stress abrasion. High-stress, or grinding abrasion, occurs when abrasive particles are compressed between two solid surfaces, as for example, between grinding rods or balls. The high-stress abrasion that occurs, for example, in grinding mills takes place over a very small contact region, where the ore particles are caught between the grinding balls or between the grinding balls and the mill liner. The high contact pressure produces indentations and scratching of the wearing surfaces and fractures and pulverizes the abrasive particles. Hard minerals such as quartz will indent and scratch martensitic steels having yield strengths of 2100 MPa (300 ksi). High-stress abrasion is often referred to as three-body abrasion, although two-body, high-stress conditions can also exist. High-stress abrasion implies that the abrasive particle is fractured and broken apart during the wear process. Exactly how these small abrasive particles affect the actual removal of the material is not well understood. It has been speculated that high-stress grinding abrasion facilitates material removal by a combination of cutting, plastic deformation, and surface fracture on a microscopic scale, as well as by tearing and fatigue or spalling on a macroscopic scale.

Low-stress, or scratching, abrasion occurs when lightly loaded abrasive particles impinge upon and move across the wearing surface, cutting and ploughing on a microscopic scale. In aqueous or other liquid environments, corrosion may also contribute to the overall wear rate, in which case erosion-corrosion is the operative wear mechanism. In both cases, low-stress abrasion is the primary mode of wear. The wear rates in

terms of metal thickness removed per day are quite low in low-stress abrasion, so a significant portion of the total wear is probably due to the abrasion of a continually reforming oxide film. This may be especially true in the handling of particulates in a wet environment, such as agricultural operations and the movement of slurries.

References cited in this section

1. P.A. Swanson, Comparison of Laboratory and Field Abrasion Tests, *Wear of Materials*, K.C. Ludema, Ed., ASME, 1985, p 519–525.
2. M.A. Moore, Laboratory Simulation Testing for Service Abrasive Wear Environments, *Wear of Materials: Volume II*, K.C. Ludema, Ed., ASME, 1987, p 673–687
3. P.A. Swanson, Comparison of Laboratory Abrasion Tests and Field Tests, *Tribology: Wear Test Selection for Design and Application*, STP 1199, A.W. Ruff and R.G. Bayer, Ed., ASTM, 1993, p 80–99
4. J.H. Tylczak, J.A. Hawk, and R.D. Wilson, A Comparison of Laboratory Abrasion and Field Wear Results, *Wear*, Vol 225–229, 1999, p 1059–1069

Abrasive Wear Testing

Jeffrey A. Hawk, U.S. Department of Energy, Albany Research Center

Parameters Influencing Wear

A variety of parameters influence all wear mechanisms and thus influence the abrasive wear behavior of materials. To a certain extent, abrasive wear tests have been designed to emphasize one or more of these parameters, especially the dominant one in an application. These parameters can be categorized as follows (Ref 5, 6):

- *Material parameters*: Material parameters of importance include composition, microstructure (e.g., grain size), mechanical properties (e.g., yield strength, elastic modulus, ductility), fracture toughness, thermal conductivity, degree of work hardening, hardness, and so on.
- *Design parameters*: Design parameters also influence the wear mechanisms, and some of the more important ones are shape, loading, force/impact level, type of motion (e.g., sliding/rolling), roughness, vibration, and cycle time.
- *Environmental parameters*: Of particular importance is the environment of the wear event and parameters such as temperature, humidity, atmosphere, wet/dry conditions, pH, contamination, and so on.
- *Lubrication parameters*: In certain nonabrasive applications, the type of lubricant, lubricant stability, type of fluid lubrication, and so on are all important.

In abrasive wear, the characteristics of the abrasive particle are also important. Some factors of influence are particle shape, particle size, hardness, yield strength, fracture properties, and concentration (Ref 7). These characteristics will influence the severity of the abrasion.

References cited in this section

5. H. Czichos, *A Systems Approach to the Science and Technology of Friction, Lubrication and Wear*, Elsevier Science Publishers BV, Amsterdam, Netherlands, 1978

6. R.G. Bayer, Wear Testing, *Mechanical Testing*, Vol 8, Metals Handbook, 9th ed., ASM International, 1985, p 601–608
7. P.J. Mutton, *Abrasion Resistant Materials: Volume 1*, AMIRA, Melbourne, Australia, 1988, p 5–17

Abrasive Wear Testing

Jeffrey A. Hawk, U.S. Department of Energy, Albany Research Center

Elements of a Wear Test

The general elements of all laboratory wear tests are simulation, acceleration, specimen preparation, test control, wear measurement, and data reporting (Ref 5, 6). Simulation is the most important element of the wear test because it ensures that the behavior experienced in the laboratory test is the same as in the application. The ideal wear test will exactly duplicate the wear situation, but in most cases only an actual field test of the component will accomplish that. It is important, at the very least, that the laboratory wear test generate the same wear mechanisms as the application and that the primary wear mechanism in the application is the primary one in the laboratory test. Other factors of attention include test geometry, load range, surface conformity, break-in, and so on.

Acceleration of the wear test is important because it reduces the overall time and cost of the testing effort. Accelerating the wear test, however, can influence or change the material response. For example, if the load or the speed of the test is increased, one wear mechanism may be emphasized more than another or the wear regime may pass from mild to severe. Even so, all laboratory wear tests are accelerated to one degree or another, either through continuous operation, measurement of smaller quantities of wear, or by applying higher loads, speeds, or temperatures.

Attention to specimen preparation and test control are important in laboratory wear testing because they determine the degree of scatter in the data (i.e., they either improve or degrade precision and reproducibility). In any test method, it is important to reduce as much as possible the number of factors that can influence the result of that test. Ideally, the wear test should reflect differences in the material and not differences in the operation of the test. Specimen preparation is critical because each test should start with a specimen that is identical to the last in terms of geometry, surface finish, break-in, and so on. Therefore, it is important that each specimen is prepared for the test in exactly the same manner (i.e., cleaning, drying, storage, weighing, etc.). In addition, accurate control of wear test apparatus operating parameters such as load, speed, instrument construction, ambient environment, location and alignment, and supply of abrasive is critical to controlling the reproducibility of the test data. Of particular importance in a wear test is the use of a reference material. The use of a reference material allows the operation of the wear test apparatus to be checked periodically for conformance to the operating parameters, to test the skill of the operator, and to determine such factors as the influence of environment (Ref 6).

Determining the most efficient way to measure the extent of wear loss from a test depends primarily on the type of wear test and the amount of wear generated from the test. Common wear measuring techniques include the measurement of mass loss, volume loss or displacement, scar width or depth or some other geometrical measure, or other indirect measures, such as the time required to wear through a coating or the load required to cause severe wear or a change in surface reflectance (Ref 6). The way in which the degree of wear is measured is based on convenience, the nature of the wear specimen, and the available measuring techniques. In abrasive wear, large amounts of material are typically removed, and as a result, mass loss measurements are typically favored. In the case of microabrasion, where mass loss is minimal, geometrical methods are more effective. Material wear behavior in terms of the wear rate can be described by either producing a wear curve or by measuring wear at a single point in the test (Ref 6). Because wear is nonlinear, a wear curve generally provides more information and allows evaluation of more complex behavior than a single-point measurement (Ref 6).

However, once a wear curve has been established for a material or class of materials, the wear test can be designed so that a single-point measurement can be used.

Wear is a system response, and when reporting data, a complete description of the system is needed to put the data in context. Information that should be supplied includes the following where applicable (Ref 5, 6):

- Apparatus
- Geometry of contact
- Type of motion
- Load
- Speed
- Environmental conditions
- Conditions of wearing mediums
- Description of materials
- Description of lubricants and lubrication used
- Description of wear-in period, if appropriate
- Unusual observations (e.g., evidence of material transfer)
- Surface and materials preparations
- Sample surface roughness

The report should describe the material tested, the general nature of the test, conditions of the counterface, testing environment, and any other significant features.

Wear test data scatter can be significantly reduced by careful testing methods. The number of tests that should be conducted to provide accurate results depends on the type of wear test being conducted, but it is suggested that several tests, rather than one, should form the basis for conclusions. In general, a minimum of three tests is preferred, and the need for replication depends on the testing purpose, degree of control, and scatter (Ref 6).

References cited in this section

5. H. Czichos, *A Systems Approach to the Science and Technology of Friction, Lubrication and Wear*, Elsevier Science Publishers BV, Amsterdam, Netherlands, 1978
6. R.G. Bayer, *Wear Testing, Mechanical Testing*, Vol 8, Metals Handbook, 9th ed., ASM International, 1985, p 601–608

Abrasive Wear Testing

Jeffrey A. Hawk, U.S. Department of Energy, Albany Research Center

Standardized Abrasive Wear Tests

Wear testing in general, and abrasion testing in particular, has few standardized tests with well-defined experimental procedures. In many cases, the standardized tests do not adequately represent the actual wear environment of interest, and as a result, many ad hoc wear tests have been developed over the years within specific industries and companies. The American Society for Testing and Materials (ASTM) has tried to standardize the most popular of these wear tests so that the tests can be performed in a like manner from one laboratory to the next with a reasonable degree of precision and bias.

The following abrasion and erosion test procedures are listed in the *Annual Book of ASTM Standards*, Volume 03.02 (Ref 8):

Standard No.	Description
G 56	Abrasiveness of Ink-Impregnated Fabric Printer Ribbons
G 76	Conducting Erosion Tests by Solid Particle Impingement Using Gas Jets
G 65	Measuring Abrasion Using the Dry Sand/Rubber Wheel Apparatus
G 132	Pin Abrasion Testing
G 75	Slurry Abrasivity (Miller Number) and Slurry Abrasion Response of Materials (SAR No.)
G 105	Conducting Wet Sand/Rubber Wheel Abrasion Tests
G 81	Jaw Crusher Gouging Abrasion Test

The first six items in the table are all ASTM test methods, while the seventh is an ASTM practice. In the following sections, some of the test procedures and practices are described in more detail, while others are left for the reader to explore. Additional nonstandard ASTM abrasive wear tests are also described. For anyone wishing to do abrasive wear testing, it is useful to read the various ASTM standards and practices in order to gain an understanding of how to structure a wear test (abrasive or otherwise), calculate mass/volume losses and wear rates, and report the measures of precision and bias in the data.

Reference cited in this section

8. “Wear and Erosion: Metal Corrosion,” *Annual Book of ASTM Standards*, ASTM

Description of Tests and Equipment

In the following section, abrasive wear testing is broken up into the following general topics: scratch testing, dry abrasion against fixed particles, dry abrasion against loose particles, wet abrasion against fixed or loose particles, gouging-abrasion, small particle erosion, impact abrasion, slurry abrasion, and microabrasion. For these abrasion categories, the general test procedures are outlined, some in more detail than others, selected results are given, and the advantages and limitations of the tests are discussed.

Scratch Wear Testing

Scratch wear testing is a method of mechanically testing a specimen by moving a stylus or indenter over its surface (Ref 9). This wear test is important because it provides information on the micromechanics of material removal for the stylus-material tribosystem. Typically, a single abrasive particle, in the form of a well-defined and oriented stylus, is moved across the surface of a material in some controlled manner (load and velocity) generating a groove. By controlling the shape of the stylus and its orientation with the wear surface, information as to the volume of material removed and the wear mechanism controlling material removal can be obtained (i.e., cutting or plowing) (Ref 9, 10). The following simple expression has been used as a starting point for quantifying the volume of material removed from a surface during two-body abrasion by a single conical abrasive particle (Ref 11):

$$W_v = \left(\frac{2 \tan \alpha}{\pi} \right) \cdot \frac{s \cdot F_N}{H} \quad (\text{Eq 1})$$

where W_v is the volume of material lost to abrasive wear, s is the sliding distance, F_N is the normal load on the conical abrasive particle, H is the yield pressure or the hardness of the wearing surface, and α is the angle of attack of the abrasive particle. Equation 1 is more typically written as:

$$W_v = k_{ab} \frac{s \cdot F_N}{H} \quad (\text{Eq 2})$$

where k_{ab} is known as the wear coefficient for abrasion and replaces the first factor (i.e., a geometrical one) in Eq 1. Many preconditions exist for using Eq 2, the most important of which is that microcutting occurs during the abrasive process. As a consequence, Eq 2 provides an upper limit for the amount of material removed from a surface during abrasion. Values of k_{ab} fall between 10^{-2} and 10^{-4} for ductile materials, with the lower values of k_{ab} associated with three-body wear and the greater values with that of two-body wear (Ref 11).

Although diamond indenters are usually used in scratch testing because of their prevalence in hardness testing, any material can be used as the scratch stylus. Although details of scratch testing are not covered here (see the article "Scratch Testing" in this Volume), it is important to realize that scratch testing can aid in understanding the large-scale abrasive wear behavior of materials by fixed particles through understanding what occurs as one particle moves across the surface (Ref 12). Figure 2 shows the damage mechanisms that occur in a white cast iron as a result of a single scratch using a diamond stylus.

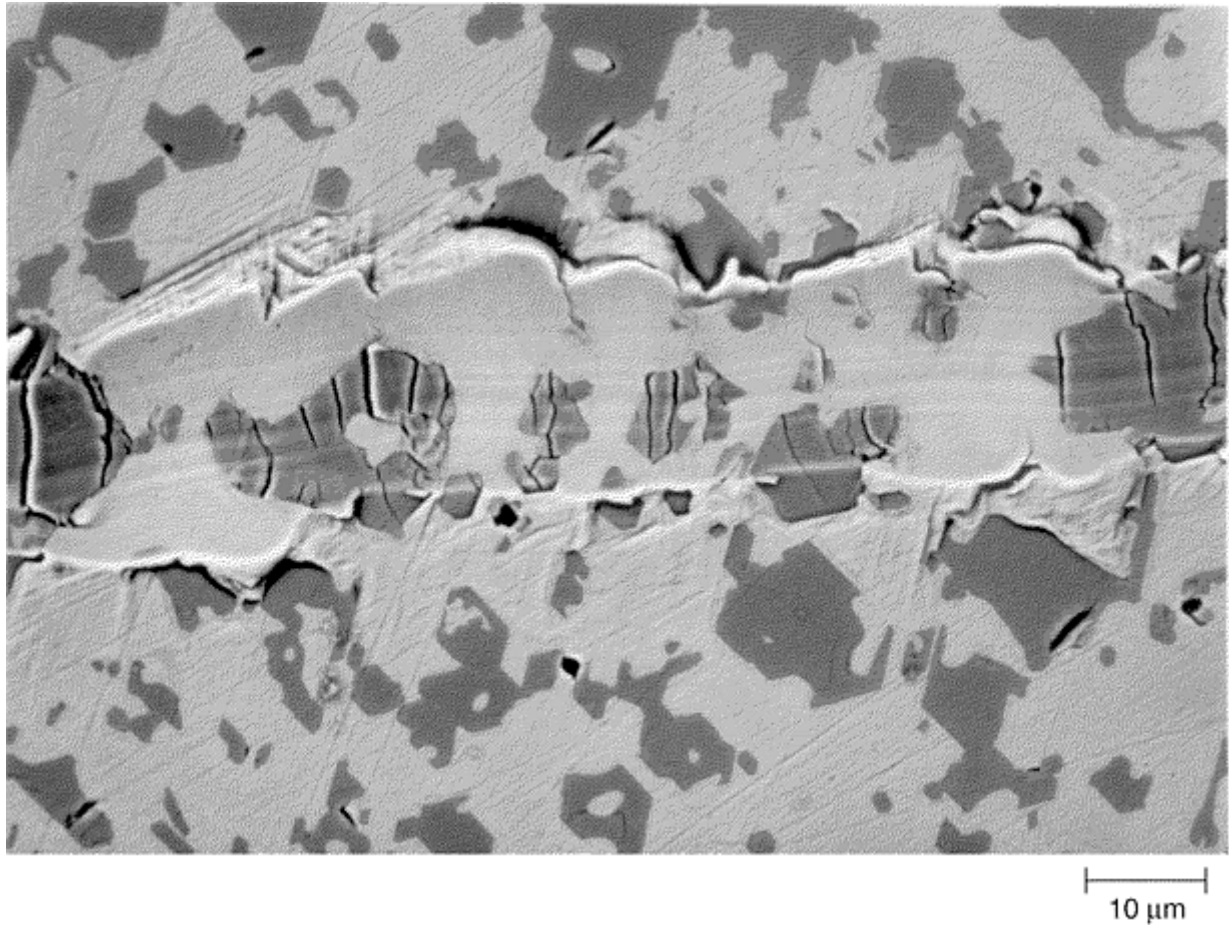


Fig. 2 Single scratch, using a 20 μm conical diamond stylus under a 100 g load, on a high-Cr white cast iron. Notice the matrix transformation to martensite and the cracking of the carbides. Source: Ref 12

Dry Abrasion against Fixed Particles

Dry abrasion against fixed particles is typically performed using a pin abrasion wear tester. Pin abrasion wear testing simulates high-stress, quasi-two-body abrasive wear. The wear test is high stress because the abrasive grains are frequently fractured during the test. It is quasi-two-body because at the onset of the test, the abrasive particles are fixed to the cloth backing with an adhesive. As the test progresses, fractured bits of the abrasive and wear debris become trapped in the interfacial region between the end of the pin and the abrasive cloth, thus adding a third body to the system.

Many different pin abrasion wear testers have been developed over the years (Table 1). All these devices have one thing in common; that is, they expose a specimen to an environment where the abrasive grains are initially fixed to a substrate. Table 1 also provides some of the pertinent operating conditions for various pin abrasion wear testers. ASTM G 132 provides a useful guide to the general features of pin abrasion wear testing (Ref 27). In the discussion that follows, details specific to the operation of the pin-on-drum are provided (Fig. 3) (Ref 23, 28), although these same conditions also hold for many of the other pin abrasion wear testers.

Table 1 Comparison of various pin abrasion wear tests

Author(s) (reference)	Machine type	Geometry of wear track	Pin diam, mm	Normal load, N	Unit load, N/cm^2	Speed, m/s	Abrasive area, m^2	Total available path length, m	Pin rotation, rpm
Robin (13)	Pin-on- disk	Circular	15	12.4	9.8	1.14	N/A	N/A	No
Khruschov	Pin-on-	Spiral	2	2.9	94	0.5	0.05	45	No

(14)	disk								
Richardson (15)	Pin-on-disk	Spiral	2.5	4.9	100	0.17	0.05	20	No
Nathan and Jones (16)	Pin-on-belt	Linear	5	4.9–98	25–500	0–2.5	0.36	70	Optional
Khruschov (17)	Pin-on-drum	Helical	2	Impact	0.06	25	No
Larsen-Basse (18)	Pin-on-table	Linear	9.5	0.98–17.6	1.4–25	N/A	N/A	N/A	No
Muscara and Sinnott (19)	Pin-on-table	Rectilinear	6.35	66.7	210	0.042	0.10	15	20
Mutton (20)	Pin-on-drum	Helical	6.35	66.7	210	0.042	0.49	75	20
Allen et al. (21)	Pin-on-belt	Linear	10	4.9–98	5–98	0–0.45	0.72	15	No
Berns and Fischer (22)	Pin-on-table	Rectilinear	6	37.2	132	0.005	0.30	50	48
Blickensderfer and Laird (23)	Pin-on-drum	Helical	6.35	17.4–103.4	54.9–326.5	0.045	0.97	150	17
Sin et al. (24)	Pin-on-disk	Spiral	6.35	4.9–39.2	15.5–123.8	0.02–0.06	0.03	4	No
Axén and Jacobsson (25)	Pin-on-drum	Helical	5 × 5	0.9–39.1	3.6–156.4	0.08	N/A	7	No
Moore and King (26)	Pin-on-disk	Spiral	5	2.5–29.5	12.5–150.0	0.5	N/A	8	No

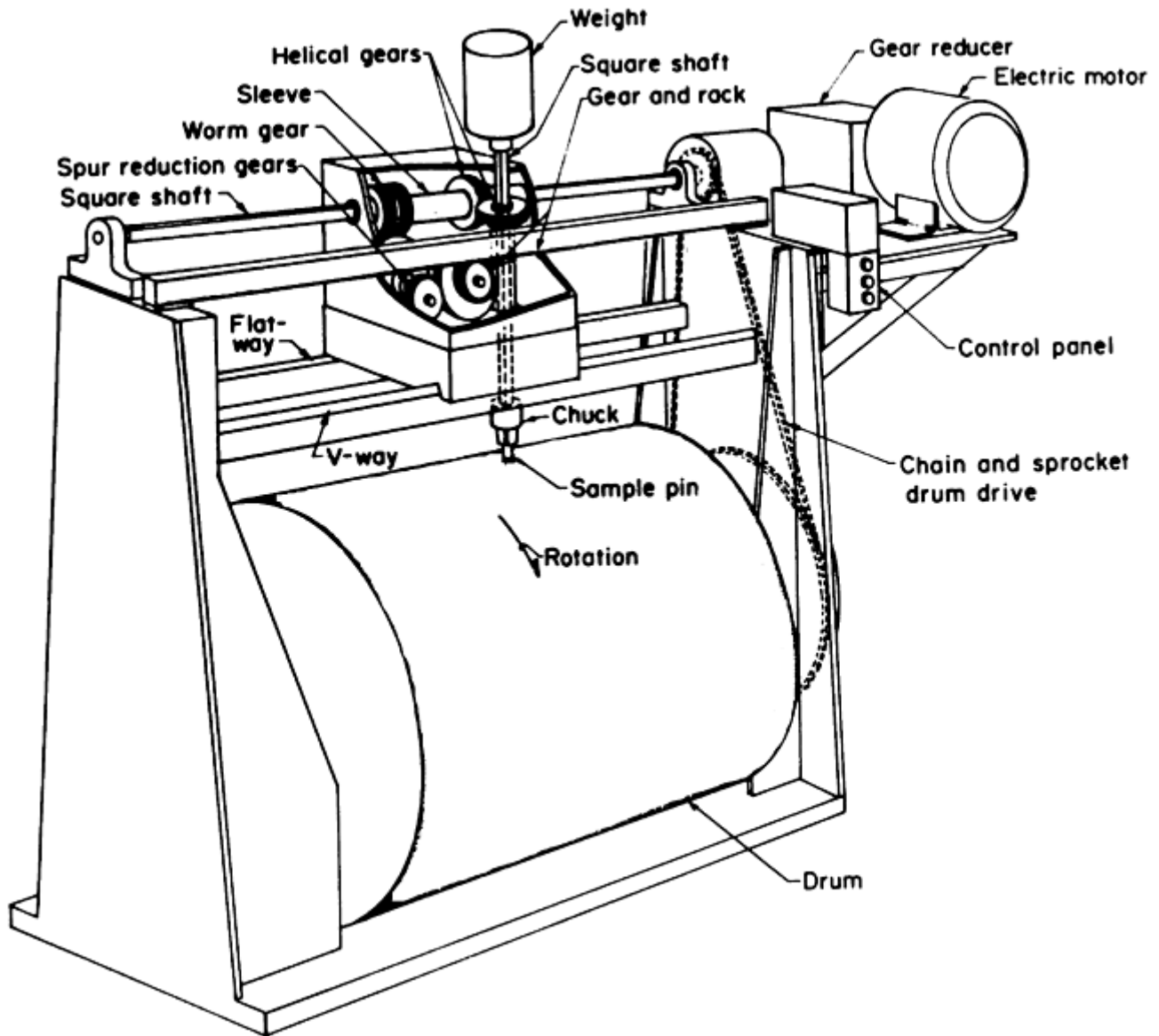


Fig. 3 Schematic diagram of the pin-on-drum wear apparatus. Source: Ref 23, 28

Selection of the Abrasive Media. Selecting the appropriate abrasive to use in the wear test is important. The most common abrasive in the earth's environment is silica (SiO_2), with a hardness of about 1000 HV. To more closely simulate the actual abrasion that occurs in a particular application, however, the same type of abrasive encountered should be used in the pin abrasion test. Commercially available abrasive cloths are produced with garnet (1300 HV), alumina (2000 HV), and silicon carbide (2500 HV) as the abrasives. Sometimes flint abrasives (common sandpaper) are used, although silicon carbide is probably the easiest abrasive particle to find in the variety of paper sizes needed to fit on the pin abrasion testers.

Another consideration in abrasive selection is the amount of abrasive wear desired during the course of the wear test, and this is a function of the abrasive used in the test, the sliding distance, and the hardness of the material being investigated. For "soft" metals and alloys such as aluminum and mild steel, garnet, alumina, and silicon carbide abrasive particles of the same size remove approximately the same mass of material during a test of the same duration. Any minor variations in material removed when using these abrasives is due to slight variations in the characteristics of the abrasive particles, such as their shape (angularity), their fracture characteristics (sharp or blunt fragments upon fracture), and their packing on the backing cloth during manufacture (different abrasive types pack differently on the cloth as a result of their shape). For "hard" materials such as tool steels and high-chromium white cast iron, some change in the relative wear ranking may occur when different abrasives are used (Ref 29). For hard-particle reinforced composites and ceramics, a harder abrasive such as alumina or silicon carbide should be used in order to give reasonable mass losses for reasonable sliding distance.

Pin Abrasion Test Procedures. During a pin abrasion test, a pin (of whatever diameter used for that particular machine) is first broken in by running it across the abrasive to be used in the actual wear test. This act accomplishes two purposes: it creates a uniform surface for testing and conforms the specimen surface to the counterface. The pin specimen is cleaned and then weighed (typically to an accuracy of 0.1 mg). The actual wear test is then performed, with the sliding distance being determined to give a reasonable amount of mass loss, usually on the order of 20 to 40 mg. (This way, measurement errors are kept low, that is, 1 part in 200–400.) Sometimes the sliding distance is determined by the physical constraints of the pin abrasion test apparatus (especially for the phonograph-style or table machines). Once an abrasion test is completed, the specimens are cleaned in some manner to remove any loosely adherent wear debris, rinsed in some manner to remove surface contamination, and then air dried or stored in a vacuum desiccator before weighing.

At some point in the analytical investigation of the wear properties of the material, the density of the material should be determined using standard techniques. The density can then be used to convert specimen mass loss to a volume loss. This allows the wear rates for different materials classes to be directly compared when determined under identical conditions.

In pin abrasion wear testing, a reference pin is also typically used so that variations in the abrasives can be accounted for and so that the relative abrasion rate of different classes of materials (e.g., steels, cast irons, ceramics, metal matrix composites, etc.) can be compared (Table 2). Typically, the reference material is an alloy that is easily obtainable so that it can be used by anyone with a pin abrasion tester in order to compare results with those of other researchers. Usually, the heat treated condition of the reference pin is given by a hardness value (e.g., ASTM A 514/A 514M, type B hardened to HB 269).

Table 2 Typical pin-on-drum wear data for ferrous alloys

Alloy and designation	Hardness, HB	Abrasive wear ^(a)	
		WF	mm ³ /m
Stainless steel, type 304	207	0.73	0.86
Low-alloy steel, ASTM A 514	256	0.98	1.11
Low-alloy steel, AISI 4340	540	0.73	0.95
Tool steel, type D2	698	0.42	0.49
High-chromium white cast iron	661	0.27	0.31
Carbon steel, AISI 1060	785	0.50	0.56

Note: Load, 66.7 N (15 lbf); pin diameter, 6.35 mm (0.25 in.).

(a) WF, relative wear factor

If a reference material is used in the pin abrasion test, a ratio of the volume loss of the specimen of interest and the reference pin can be calculated from the following relationship:

$$WF = \frac{V_x}{V_r} \quad (\text{Eq 3})$$

where WF is the relative wear factor for a given set of abrasive test conditions (i.e., load, sliding distance, and abrasive), and these conditions should always be stated. The term V_x is the volume of material lost to abrasion for the test specimen under the given test conditions, while V_r is the volume lost to abrasion for the reference specimen. In ASTM G 132, the normalized wear is calculated in the following manner (Ref 27):

$$\text{wear rate} = \frac{CW_x}{\rho S_x}, \text{ mm}^3/\text{Nm} \quad (\text{Eq 4})$$

where W_x is the mass loss of the specimen (in any units), S_x is the mass loss of the reference specimen (in the same units as W_x), ρ is the density of the test specimen (known or measured to three significant figures) in g/cm^3 or mg/mm^3 , and C is the reference constant equal to the mean mass loss (also in grams or milligrams) of the reference pin per unit track length (in meters) per unit load (in newtons) for the abrasive type and test parameters used. The ratio $C:S_x$ functions as a normalizing factor. (The value of C should be determined for each abrasive particle type and size used in a pin abrasion test. Using many rolls of abrasive over a number of years can cause large errors in the determination of C .)

As an alternative method for determining wear rate from the mass loss data, one of the many equations listed in the literature can be used (Ref 30). Typically, these equations represent the wear as either the specific wear rate

(mm³/Nm), a dimensionless wear coefficient, or as the volume wear (mm³/m). Wear rate can also be represented as the total volume of material lost (mm³) for a specific set of test conditions (i.e., abrasive size, abrasive type, applied load, and sliding distance). Table 3 lists some of the ways in which wear rate can be represented.

Table 3 General definitions of wear rate

Definition	Equation	Relationships between wear rates
Time-dependent wear rate	$\dot{W}_t = \frac{\Delta h}{t}$	$\dot{W}_t = \dot{W}_s p v$ $\dot{W}_t = \dot{W}_v$
Distance-dependent wear rate	$\dot{W}_L = \frac{\Delta h}{L}$	$\dot{W}_t = \dot{W}_L p^2 v$
Dimensionless wear rate	$\dot{W} = \frac{\Delta V}{LA}$	$\dot{W} = \dot{W}_L p^2$
Specific wear rate	$\dot{W}_s = \frac{\Delta V}{L F_n} = \frac{\Delta m}{L \rho F_n}$	$\dot{W}_s = \dot{W}_L p$

Note: Δh , height loss of specimen; t , time of operation; L , sliding distance; ΔV , volume loss; A , apparent contact area; F_n , normal load on specimen; Δm , specimen mass loss; ρ , density of specimen; p , pressure; v , velocity.

Source: Ref 30

Variation in test results for the pin-on-drum abrasion test at a single facility is consistently less than 5% for homogeneous metals, alloys, and ceramics, and in some cases, less than 1%. For composite materials and composite-type materials such as high-chromium white cast irons, the variance is typically between 5 and 10%, depending on the reinforcement and the strength of the interfacial bond between matrix and reinforcement (Ref 31, 32, 33).

In addition to ranking materials, the pin-on-drum abrasive wear test is very effective in discerning volume wear and wear mechanisms for a wide range of metals, alloys, composites, ceramics, and polymers. The surface area remains constant during the test, and consequently, different materials can be compared directly for volume loss and material-removal mechanisms.

Dry Abrasion against Loose Particles

Many cases of abrasive wear occur where the abrasive particles are not fixed but are free to slide and rotate. The dry sand, rubber wheel (DSRW) abrasion test apparatus simulates one such environment (i.e., low-stress, three-body abrasive wear) (Ref 34, 35). This type of wear occurs in the mining industry in linkages, pivot pins, and wire ropes, which suffer slow wear from the sliding and rolling action of abrasive fragments of rock and ore trapped between metal surfaces. It also occurs in agricultural tillage tools. Since this type of wear is slow, field trials alone are much too long to be effective in evaluating new materials. The DSRW abrasion test presents researchers with a quick and easy way to perform numerous tests, rank materials, and correlate the result with selected field tests. Even before the test became an ASTM standard (G65) in 1980, it had been used by a number of laboratories for many year. Since becoming an ASTM standard, it has become one of the most popular abrasive wear tests in the United States for ranking materials. As such, many companies have developed a qualitative understanding of how their materials perform in a particular wear environment relative to other materials.

DSRW Equipment and Specimen. The basic ASTM machine (Fig. 4) consists of a chlorobutyl rubber-rimmed steel wheel, 228 mm (9 in.) diam \times 12.7 mm (0.5 in.) wide; a sand hopper connected by a tube to a nozzle that allows 300 to 400 g/min sand flow; a revolution counter that stops the drive motor after a set number of revolutions; and a weighted lever arm that holds the specimen and produces a horizontal force against the wheel where the sand is flowing. The sand is 50/70 mesh Ottawa sand (although other rounded quartz sands may be used). The mesh size corresponds to a particle size range of 212 to 300 μ m. The hardness of the chlorobutyl rubber on the wheel must be durometer A - 60 \pm 2.

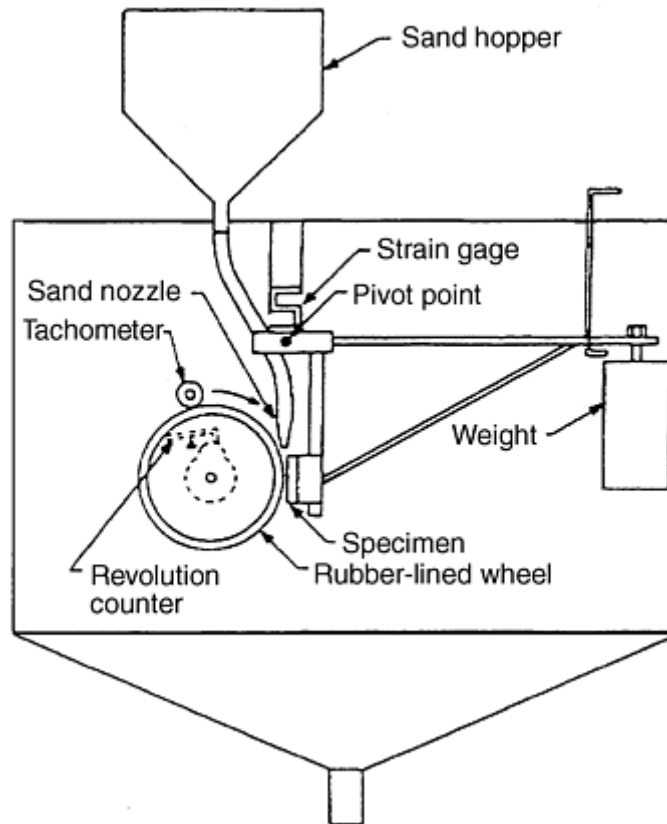


Fig. 4 Schematic diagram of the dry sand, rubber wheel wear apparatus. Source: Ref 35

A typical test specimen is a rectangle, 25 mm (1 in.) wide \times 75 mm (3 in.) long, that is 3 to 13 mm (0.1 to 0.5 in.) thick. The wear surface is ground flat with a surface finish of at least 0.8 μm . The density of the test material must be known in order to calculate the volume of material lost during the course of the test.

DSRW Test Procedure. The equipment has two test parameters: the sliding distance (i.e., the number of wheel revolutions) and the specimen load. ASTM recognizes five procedures using variations of these two test parameters (Table 4).

Table 4 Standard conditions for the dry sand, rubber wheel abrasion test

ASTM procedure	Force on specimen		Wheel revolutions	Distance abraded	
	N	lbf		m	ft
A	130	29	6,000	4,309	14,137
B	130	29	2,000	1,436	4,711
C	130	29	100	71.8	235.6
D	45	10	6,000	4,309	14,137
E	130	29	1,000	718	2,356

A test consists of the following eight steps:

1. Cleaning and weighing the specimen
2. Mounting the specimen in the lever arm fixture and loading the lever arm fixture
3. Starting the sand flow through the nozzle
4. Starting the rubber-wheel drive motor
5. Releasing the lever arm so that the specimen contacts the wheel, starting the revolution counter
6. Stopping the motor (automatic) and sand flow
7. Removing the test specimen
8. Cleaning and reweighing the test specimen to determine the mass loss during the course of the test.

From the mass loss and the density of the material, the volume loss is calculated. The test is repeated one or more times. The coefficient of variation between two or more tests for a material must not exceed 7% in order to meet ASTM specifications for a valid test. Wear-scar nonuniformity is another reason for invalidating test results. A nonuniform wear scar is an indication that the sample lever arm was misaligned or that the chlorobutyl rubber wheel has deteriorated and must be redressed.

Two points need to be kept in mind when performing DSRW tests. First, moisture in the sand may affect the flow rate of the sand through the nozzle (agglomeration of sand particles) and thus affect test results. In order to prevent this from occurring, it is good practice to dry the sand prior to use in some sort of oven at approximately 100 °C (210 °F), typically for more than 1 h. However, before using the sand in a test, it must be allowed to cool to room temperature. Reproducibility will also be improved if the sand is sieved prior to its use in the DSRW to remove foreign debris that may have inadvertently been included when the sand was bagged. Using a 40 mesh (425 µm) sieve will allow the sand to pass through while trapping agglomerations and other debris. A second factor that may adversely affect the results is softening of the chlorobutyl rubber wheel. After any test, the friction between the rubber wheel, sand, and specimen causes the rubber to heat up and soften. Consequently, the rubber must be allowed to cool to room temperature before another test is run. Typically, 1 h between tests is sufficient.

For most ferrous materials, testing is performed using a 130 N (29 lbf) load for 2000 revolutions of the rubber wheel (ASTM procedure B in Table 4), leading to volume losses ranging from 20 to 120 mm³. The reproducibility of the test is highest for volume losses in the range of 20 to 100 mm³.

Typically, in tests in which less than 20 mm³ is lost, any small material inhomogeneities are greatly magnified; therefore, a more severe test should be run by using either a greater sliding distance or higher load. Above 100 mm³ of material loss, the wear groove becomes so deep that it may contact the edge of the rubber wheel and cause erratic results. Therefore, a less severe procedure may be necessary. Using another procedure has a disadvantage in that test results cannot be directly compared among different procedures.

The DSRW test should be used only for the ranking of various materials, not for determining the absolute values of wear. For example, a material that wears half as much as another in this test probably will not last twice as long in the field because the test tends to exaggerate differences. Field factors such as the hardness and particle size of the abrading material will affect the absolute values of wear more than they affect the ranking. Typical wear data are presented in Table 5. In general, there is reasonable correlation between hardness and wear, with the amount of material removed decreasing as the hardness of the material increases.

Table 5 Typical dry sand, rubber wheel abrasive wear data

Alloy	Hardness, HV	Volume loss, mm ³	
		Procedure A	Procedure B
Stainless steel, type 304	207	408.0	170.8
Low-alloy steel, ASTM A 514	256	...	134.1
Low-alloy steel, AISI 4340	540	...	74.0
Tool steel, type D2	689	45.3	14.6
High-chromium white cast iron	661	31.5	12.7
Carbon steel, AISI 1060	785	...	32.1

One criticism of the DSRW test is that the area of contact changes as the test proceeds. That is, as the volume of material removed by abrasion increases, the surface area of contact between the rubber wheel and the DSRW sample increases. Thus, the effective contact area increases continually during the course of the test. This circumstance makes direct comparison of material loss between specimens impracticable, especially for those situations where material volume loss is greater than 20 mm³.

An advantage of DSRW testing over pin abrasion testing is that different types of abrasive particles can be used. Of course, doing this moves the test away from the ASTM standard 50/70 mesh Ottawa sand, but more realistic information can be obtained concerning the wear that occurs to a material as a result of a particular abrasive. The process of creating sand for use in the DSRW is straightforward. The ore of interest must be crushed, sized, washed, and dried. The sand should then be tested to determine whether the flow rate falls within the ASTM specifications (i.e., 300–400 g/min). If not, another nozzle should be fabricated that provides this flow rate. The wear test is then run as per the procedures specified in Table 4.

DSRW Test Variants. In order to obtain more information about the three-body abrasive wear process and to exert more control over test parameters, modifications to the standard DSRW test have been made (Ref 36, 37). Aside from a change in the position of the wear specimen (where it is placed in a horizontal configuration instead of the vertical one specified in G 65), major differences in operation include better control of particle feed rate (and the use of less abrasive during the course of the test), the ability to change wheel material (metal, polyurethane rimmed in addition to the usual rubber rimmed), the measurement of tangential traction forces (leading to calculation of the coefficient of friction), shorter duration tests, and the ability to use different abrasives. These configurations permit the load per particle and the packing density of the abrasive within the contact region to be determined. Research has shown that the steady state wear rate is reached at approximately 200 wheel revolutions, so tests of shorter duration can be run, with multiple tests run on the same specimen.

Wet Abrasion against Fixed or Loose Particles

Two significantly different test approaches have been developed to perform wet abrasive wear tests. One approach, similar to the DSRW, is defined in ASTM G 105, "Standard Test Method for Conducting Wet Sand/Rubber Wheel Abrasion Tests" (Ref 38). The other wet abrasion tests use the principles associated with the grinding, polishing, and lapping of materials (Ref 39). The former test can be roughly classified as a macroabrasion wear test, while the latter one is more of a microabrasion wear test.

Wet Sand/Rubber Wheel Abrasion Test. The wet sand, rubber wheel (WSRW) test is almost identical to the DSRW test. In this test (i.e., ASTM G 105) (Ref 38), a test specimen is abraded in a slurry containing abrasive grit of controlled size and composition. As in the DSRW test, the abrasive is introduced between the test specimen and a rotating neoprene rubber-rimmed wheel of specified hardness. Unlike the DSRW test, however, where the abrasive is directed between the specimen and the rubber-rimmed wheel using a gravity feed system, the wheel and specimen in the WSRW test sit in the slurry with stirring paddles agitating the mixture of sand and water. This constant agitation facilitates the movement of abrasive particles to the specimen rubber-rimmed wheel interface where they are caught and used to abrade the specimen in the direction of wheel rotation.

Figure 5 is a schematic diagram of the WSRW apparatus. The test apparatus consists of the following major parts: rubber-rimmed wheel with stirring paddles, slurry chamber, and specimen holder and loading assembly. The rubber-rimmed wheel and paddle assembly is nominally 178 mm (7 in.) in diameter (including the rubber rim) by 13 mm (0.5 in.) in width. Neoprene GW is used as the elastomer for the rubber rim with other constituents added to give the desired durometer A hardness (Ref 38). The slurry chamber must be large enough to hold the 0.940 kg of deionized water-1.5 kg rounded grain quartz sand (AFS 50/70) slurry. The slurry is typically only used once and then discarded because multiple use of the sand-water slurry may affect test comparisons.

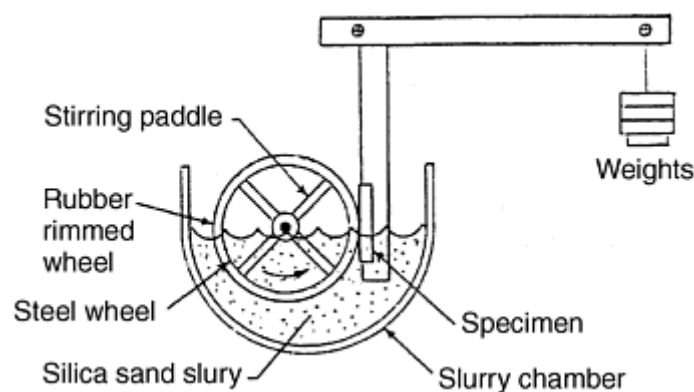


Fig. 5 Schematic diagram of wet sand, rubber wheel wear apparatus. Source: Ref 38

For the DSRW test, only one rubber-rimmed wheel of specified hardness (Shore A durometer 60 ± 2) is used. In the case of the WSRW test, three rubber-rimmed wheels of different hardnesses (Shore A durometer 50, 60, and 70, all of ± 2 variance) are used to determine the wear rate. The WSRW test procedure is very straightforward. First, the test specimen (nominal dimensions: 57 mm, or 2.2 in., long \times 25 mm, or 1 in., wide \times 6.5 - 16 mm, or 0.26 - 0.63 in., thick) is placed in the specimen holder and immersed in the sand-water slurry. It is then loaded with a mass equivalent of 222 N (50 lbf) force and run in for 1000 revolutions of the wheel (total sliding distance of 558.6 m, or 1833 ft). The run-in eliminates the machined surface layer and exposes fresh

material that has not been affected by the surface preparation procedure. The test specimen is then removed, thoroughly cleaned, dried, and weighed (to the nearest 0.0001 g). The slurry chamber is drained and rinsed to remove any remnants of sand-water slurry from the run-in step.

The actual test begins at this point and is conducted in the run-in wear scar using either the same durometer 50 wheel used in the run-in or with another durometer 50 rubber-rimmed wheel. (Before each test is run, the durometer A hardness must be measured for the rubber-rimmed wheel at several points around the periphery.) The actual test follows the same procedure used to perform the run-in; that is, a 222 N (50 lbf) force is used to press the test specimen into the wheel in the presence of fresh sand-water slurry for an additional 1000 revolutions of the wheel. After the test, the sample is removed, cleaned, and weighed. The slurry is discarded and the chamber is rinsed out. Additional 1000 revolution tests are then performed using the durometer 60 and 70 wheels (in increasing order of hardness). From each of these tests, the normalized mass loss is calculated. The normalized mass loss for each durometer A hardness is then graphed on semilog coordinates as a function of the wheel hardness. The mass loss is plotted on the log scale while the wheel hardness is plotted on the linear scale. The reportable mass loss is obtained by fitting a least square line to the three data points and solving the equation for a hardness value of exactly durometer 60. The durometer 60 normalized mass loss can be converted to a volume loss by dividing by the density of the test material.

As with any wear test apparatus, the WSRW unit should be periodically checked to make sure it continues to operate within normal conditions. As with all ASTM tests, a reference specimen is used to establish and periodically verify machine variance. For a specific reference material, a minimum of five tests should be run to establish the machine operating parameters and precision. Subsequently, additional tests can be run with the reference specimens and these results compared against the baseline operating parameters. If the variation is greater than 7%, the machine should be considered out of control and steps taken to bring it back into compliance.

One advantage of the WSRW test is that variations in the hardness of the rubber-rimmed wheel, which plague the DSRW test, are lessened. For example, it has been observed that a difference in the durometer A hardness of 3 points produces a variation of 30% in the total mass loss (Ref 40). By using wheels of three different hardnesses, and normalizing the mass loss to the durometer 60 value on the least square line, more consistent values of wear rate are obtained. The linear nature of the lines on the semilog plot supports this approach. In addition to rubber-wheel hardness variations, the following variables also affect the reproducibility of the wear data: "loss of diameter" of the rubber wheel (accounted for by normalized mass loss calculations) (Ref 38), rubber wheel surface finish (a freshly dressed wheel holds abrasive grains better than a glazed wheel (Ref 40), rpm of the rubber wheel, specimen surface finish, pressure, slurry density, and slurry temperature. All of these variables, except slurry temperature, are addressed specifically in ASTM G 105.

For very wear-resistant materials, the number of wheel revolutions may need to be increased in order to obtain mass loss with the required statistical accuracy. If this is done, the procedure used is the same as just outlined.

Other abrasive-type slurry mixtures can be used in this test as needed to simulate applications. However, doing this makes the test nonstandard, and all operating parameters should be carefully controlled and noted so comparisons can be appropriately made. This wear test is not as widely used as the DSRW test because of the time and effort required to produce a valid result.

Metallographic Polishing Microabrasion Wear Tests. In order to determine the wear rate of a material, a metallographic polishing wheel can be used as the abrasive application device, where the sample can be abraded against alumina or silicon carbide paper, or against a diamond polishing disk, using water as a fluid lubricant for two-body abrasive wear conditions, and against a metal lapping wheel using a slurry of some composition for three-body abrasive wear conditions. The wear sample may be rigidly fixed relative to the wheel and abrasive (i.e., moving in the same wear track with the wear rate decreasing as a function of sliding distance, a result of the interstices between the abrasive particles becoming clogged with wear debris). Or, the sample may undergo a complicated movement relative to the wheel and abrasive (as in the case of an automatic polisher where the head rotates the samples so that they encounter fresh abrasive and so that the wear debris can be flushed from between the abrasive particles). A third type of wear tester that makes use of a modified pin-on-disk sliding wear tester and resin bonded grinding disks has been developed. The wet abrasion tests in this section are nonstandard, but they offer different ways to perform abrasion testing on materials.

In using metallographic grinding, polishing, or lapping equipment as the wear test apparatus, care must be taken to identify and monitor all operating conditions used, such as wheel velocity, sample holder velocity (if necessary), applied load, test duration, abrasive delivery system (i.e., abrasive size, particle loading, liquid

suspension, delivery rate), sample dimensions and configuration, and wear loss determination method. One technique, the Struers Micro Wear Test (Ref 39, 41), has standardized these operating features using the Struers Abrapol-2. In this test, three identical samples are abraded during one wear-test cycle.

Sample preparation is critical to the success of this test because a modified metallographic sample holder is used to hold the wear specimens. Typically, the wear samples are cut into cubes (e.g., $10 \times 10 \times 10 \text{ mm}^3$) and embedded into epoxy resin under controlled conditions using a special mounting device (Fig. 6a). In this way, a small thickness (~1 mm) of material protrudes from the mount so that abrasion occurs only to the specimen material and not the mounting resin. The samples are then lapped to a mirror finish using $3 \mu\text{m}$ diamonds (i.e., to make sure all samples start with a uniform and planar surface). They are then thoroughly cleaned, dried, and weighed before being mounted into the specimen holder. The specimens are separated from each other by 120° in the holder.

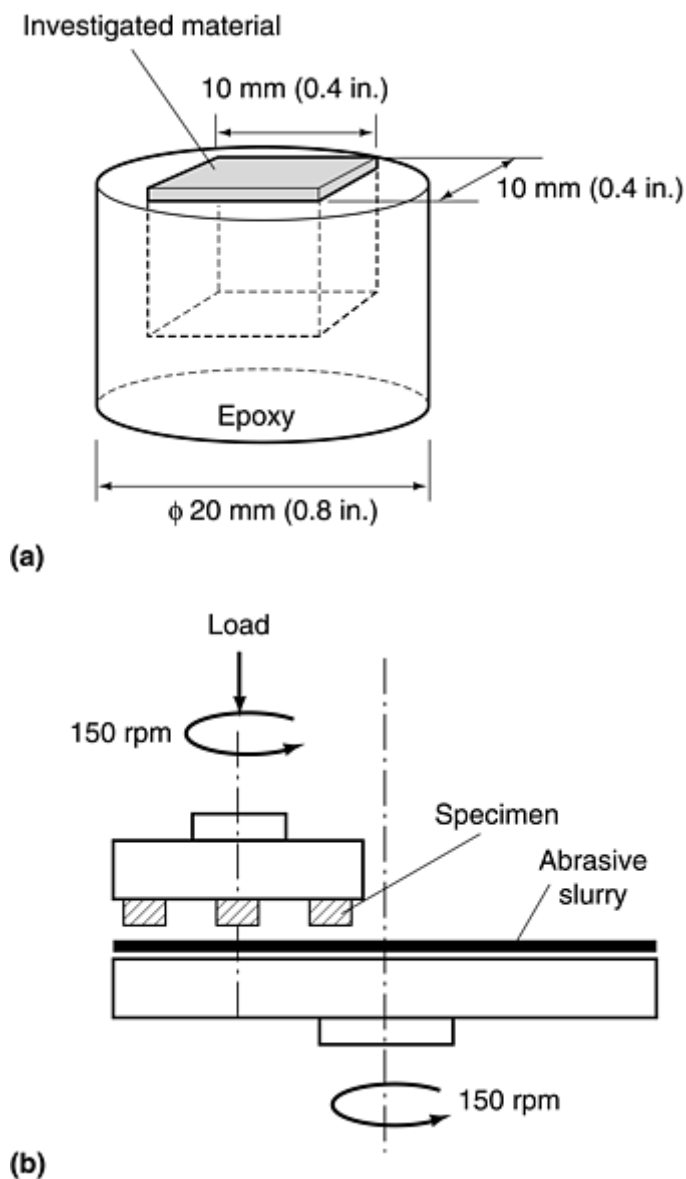


Fig. 6 Schematic diagram of (a) sample and (b) wear apparatus used for performing microabrasion wear tests. Source: Ref 41

The sample holder with specimens is then inserted in the polishing unit. As with most automatic metallographic polishing units, the sample holder is rotated at high speed (in this case, 150 rpm) relative to the rotating 300 mm (12 in.) diameter disk (Fig. 6b). In this way, the samples do not follow the same wear path on the disk but sweep the whole working area, thus encountering fresh abrasive as determined by the slurry handling system throughout the test. A cast iron disk (210 HV) is used with the slurry, and off-center concentric grooves are machined into its surface to hold slurry and wear debris. The load on the wear samples can be varied, from between 20 and 1200 N (4.5 and 270 lbf), depending on the sample cross-sectional area. Disk and specimen holder velocity is also variable, yielding specimen velocities of between 1.0 and 7.5 m/s . Test duration is

variable, but a typical test can last up to 2 minutes. However, the test time ultimately depends on the hardness of the material being tested and the type and size of abrasive particle being used. After the operating conditions have been determined, a test cycle is run on the three samples. After each test cycle, the samples are moved, ultrasonically cleaned in alcohol, and dried. Mass loss is determined for each sample, and the average value is used to calculate a wear rate from one of the equations in Table 3. If needed, a second, third, or additional wear cycle is run to achieve the precision and accuracy required.

In the case of the pin-on-abrasive disk (Ref 42), different fluids, either corrosive or noncorrosive in nature, can be used so that the effect of corrosion can be investigated while a sample is being abraded. Using ASTM G 119 (Ref 43), the effect of corrosion on wear and wear on corrosion can be determined for a given material. Figure 7 is a schematic representation of the corrosive-abrasive wear apparatus. Although the geometrical configuration is different from the pin-on-drum in that the pin is abraded against a flat disk of abrasive (in this case, a resin bonded grinding disk), the same general principles hold as with the pin-on-drum with one exception. In the pin-on-drum test, the sample is traversed in a helical fashion so that only fresh abrasive is encountered by the pin. In this test, the pin remains in the same position relative to the disk, but the disk deteriorates with time in such a manner as to constantly expose fresh abrasive grains for abrasion. The use of a circulating liquid facilitates the flushing of wear debris from the wear track on the disk. Thus, a wear curve can be generated that shows the typical linear increase in mass/volume loss with sliding distance (Fig. 8).

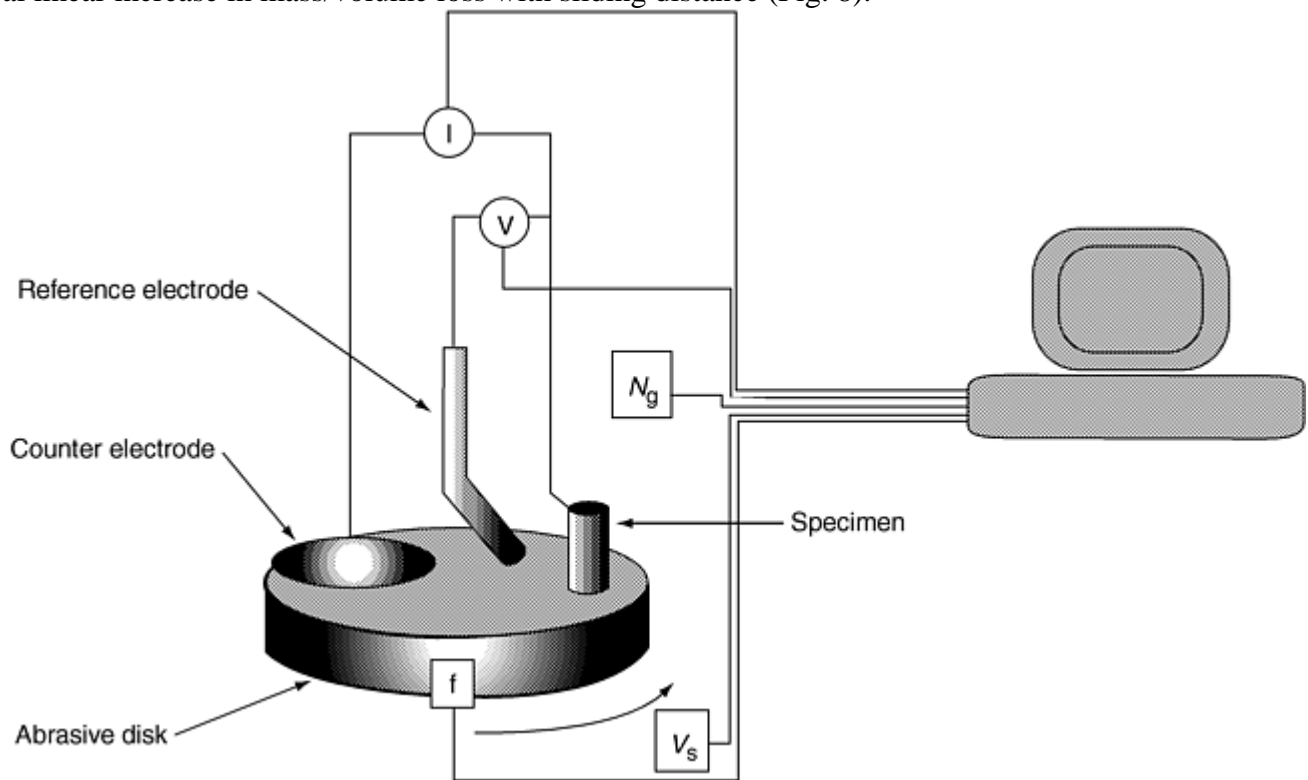


Fig. 7 Schematic diagram of pin-on-abrasive disk wear apparatus. I , current; V , potential; N_g , normal acceleration (up and down motion of pin specimen as a result of interaction with abrasive disk); f , frictional force of pin-abrasive disk couple; V_s , sliding speed of disk. Source: Ref 42

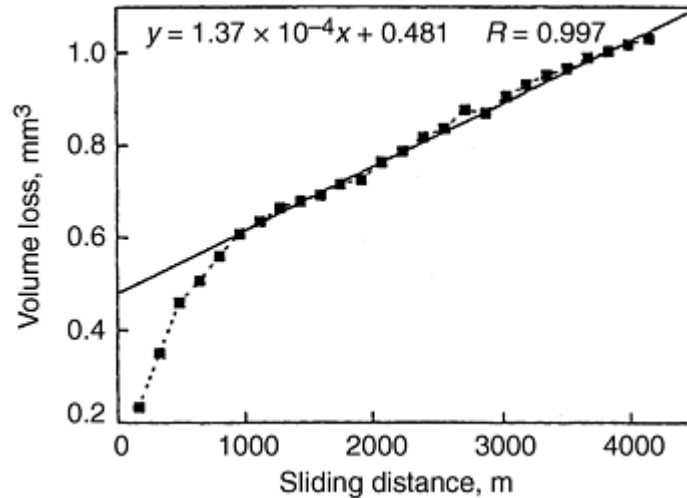


Fig. 8 Wear curve for ASTM A 514, type B low-alloy steel showing nonlinear and linear portions of volume loss versus sliding distance data. Normal force, 1.4 N (0.3 lbf); sliding speed, 0.1 m/s. Source: Ref 42

The general procedure for performing a wear test is exactly the same as with the other abrasion tests described so far. The sample is broken in, thoroughly cleaned, dried, and weighed before use. The pin is placed in a holder, then pressed against the surface of the grinding disk (either alumina or silicon carbide of different grit sizes), and the deionized circulating water is started. The sliding speed, distance to be traveled, and load are then selected. The test is run and the mass loss is measured. The wear rate is calculated in the normal way using one of the equations in Table 3. Research has shown that for any pin specimen-grinding disk couple, a curve of sliding distance versus cumulative mass/volume loss can be constructed. Typically, there is a nonlinear portion to the curve at short sliding distances where the pin is conforming to the disk surface. In essence, this test requires that both the pin and disk be conditioned before recording wear data. Once the nonlinear region has been identified for a material-disk couple under a specific set of operating conditions, then single-point wear tests can be subsequently run to determine the wear rate. The use of a deionized water lubricant usually does not introduce problems in determining the wear rate since the test is short enough (typically 2–3 hours), and the abrasive wear rate is large enough to obscure the effects of corrosion. However, if another lubricant, either more acidic or basic, is used, then the test becomes one of abrasion-corrosion. In this case, the component of corrosion is more significant.

Gouging-Abrasion Wear Testing

Gouging-abrasive wear is identified by the removal of a significant amount of material (a gouge) from the wear object during an encounter with an abrasive object in which the abrasive object also suffers damage. It is a type of high-stress wear that may be produced by either two-body or three-body conditions. The jaw crusher test gives high-stress, three-body abrasive wear. Jaw crusher wear tests were pioneered in the United States by Borik (Ref 44, 45) and used abroad by Sare and Hall (Ref 46). The jaws that crush the rock are taken as the test specimen. A number of investigators believe that the jaw crusher test gives the closest correlation to wear that occurs on earth-penetrating equipment, such as excavator teeth, power shovel buckets, scoops, and grader blades, as well as real jaw crusher wear.

Jaw Crusher Equipment and Specimen. One test plate and one reference plate are attached to the stationary jaw, and the other test and reference plates are attached to the movable jaw such that a test plate and a reference plate oppose each other. A rock hopper and rock chute are attached above the jaw crusher. The arrangement of the jaw crusher test equipment is shown in Fig. 9.

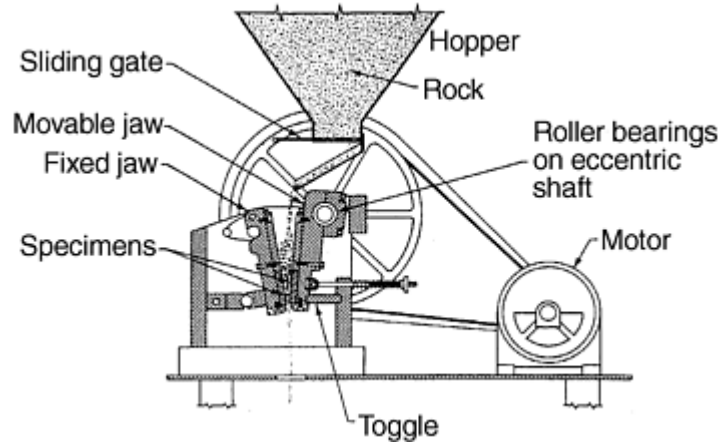


Fig. 9 Schematic diagram of jaw crusher wear apparatus. Source: Ref 47, 49

The test as used provides an average of the mass or volume loss of a pair of test plates, one from the stationary and the other from the movable jaw of the test machine. As specified by ASTM G 81 (Ref 47), jaw crusher data are presented as the ratio of the mass loss of the test specimen to that of a reference material. However, there is some disagreement (Ref 48) regarding the most efficient way to perform multiple tests and interpret the data. Complete details of the ASTM procedure can be found in Ref 47. The procedure described subsequently is an alternative test procedure that determines the absolute wear rate for a pair of jaw crusher specimens (Ref 49).

Jaw Crusher Procedure. In the nonstandard ASTM jaw crusher test, a set of four wear plates are cleaned and weighed and then clamped into the jaws of the jaw crusher (one set of specimens, A and B, in the stationary jaw, and another set of specimens, B and A, in the movable jaw). One specimen plate in the stationary jaw (A, for example) opposes that of another specimen (B) in the movable jaw. The minimum jaw opening is set (as per ASTM standard G 81), and rock is processed through the jaw crusher. The specimens are removed and cleaned thoroughly to remove any microscopic wear and/or crushed ore debris. The samples are rinsed in ethanol and then warm air dried. The mass loss is determined for each of the four jaw crusher plates. The samples are then reversed in the jaw assembly (i.e., the plates in the A position of the stationary jaw are now placed in the A position of the movable jaw), and the plates in the movable jaw are now placed in the stationary jaw, again in positions that oppose each other. The assembly is then placed back into the jaw crusher, the gap is reset, and a second run is made. The samples are once again removed, thoroughly cleaned, dried, and weighed. At this point, an average of the mass loss during the test is calculated for each of the two plates of the same material. This value is converted to a volume loss by dividing the mass loss by the density of the material. Table 6 shows data from both the ASTM method and the method just described.

Table 6 Typical jaw crusher wear data for ferrous alloys

Alloy and designation	Hardness ^(a) , HV	Volume loss ^(b) , mm ³ /kg
Stainless steel, type 304	207	27.7 ± 4.9
Austenitic steel, 13% Mn	230	13.2 ± 2.1
Low-alloy steel, ASTM A 514	256	23.9 ± 3.3
Low-alloy steel, AISI 4340	540	13.8 ± 1.4
Tool steel, type D2	698	15.9 ± 2.5
High-chromium white cast iron	661	15.6 ± 2.2

Tests conducted using high-silica quartzite ore.

(a) Hardness measurements were calculated from the average of ten readings from each wear face of the two jaw crusher specimens, for a total of 20 measurements.

(b) Volume loss is in cubic millimeters of material lost per kilogram of ore crushed.

In the ASTM procedure, a reference material is run with every test. Therefore, only one specimen material can be run at a time, and the ratio calculated refers to the wear of the specimen compared with the wear of the standard. By running the test with a standard material in all positions, the operation of the jaw crusher can be checked to see whether it still operates within performance limits. By using a nonstandard approach, data from

two sets of test specimens can be obtained during one test. Using reference materials mixed in with the other specimens will also provide information on whether the jaw crusher is performing within specified limits. An advantage in using the nonstandard method is that it allows the specimen materials to be matched according to their hardness so that the wear rates from both sets of materials will be similar in magnitude. Doing this eliminates the possibility of a softer material wearing at an accelerated rate, skewing the ratio with respect to the reference material. Another advantage of the jaw crusher is that the abrasive used for the test can be exactly matched to the field application. Table 7 gives some representative data for different ore types.

Table 7 Jaw crusher wear data for ferrous alloys using different ores

Alloy and designation	Volume loss, mm ³ /kg		
	Quartzite	Limestone	Granite
Stainless steel, type 304	27.7 ± 4.9	6.3 ± 0.1	6.3 ± 1.0
Low-alloy steel, ASTM A 514	23.9 ± 3.3	6.1 ± 1.0	6.9 ± 0.5
Low-alloy steel, REM 500	11.3 ± 1.5	1.2 ± 0.0(2)	0.8 ± 0.0(3)
Low-alloy steel, AISI 4340	13.8 ± 1.4	1.5 ± 0.2	0.9 ± 0.1

Erosion Testing

Solid particle erosion is the loss of material from repeated impacts by small, solid particles. Erosion by solid particles using gas jets is a standard ASTM test method, G 76 (Ref 50), which provides specific guidelines on erosion testing. This test is briefly discussed here because it is another example of an impact-abrasion process. When referring to solid particle erosion, it is implied that the erosive particle size is relatively small (tens to hundreds of micrometers), and particle velocities are relatively high (i.e., >1 m/s but usually in the range of ten to several hundred m/s).

Material removal via erosion is a complicated process, dependent upon the incident angle of impact. For example, at incident angles approaching 90°, material is lost in a sequential process of platelet formation and detachment. In this process, material is extruded from the impact crater in the form of a lip or platelet through plastic deformation. These lips or platelets are subsequently deformed by further impacts, leading eventually to detachment as a wear flake. At impact angles of less than 20°, the abrasive particles form shallow craters and grooves as they impact and move across the surface. Material removal is via a process of plastic deformation, extrusion, microplowing, and microcutting, where any extruded material from an impact or plowed groove is subsequently detached as a result of further particle impact (Ref 51, 52).

As in scratch testing, erosion testing using either single or multiple particles of controlled size and mass (e.g., 1 mm, or .04 in., diameter WC-Co spheres) provides information on the micromechanics of damage and mass loss mechanisms in homogeneous and complex materials. The degree of damage from single impacts can be determined using surface profilometry measurements and scanning electron microscopy. In multiple impact solid particle erosion using controlled particles, mass loss is determined by weighing. For the interested reader, the following references describe the procedure used in single- and multiple-impact particle erosion and the methods used to measure damage (Ref 53, 54). These tests require consistent specimen preparation of the samples in order to obtain representative mass loss measurements and to assess damage.

Contrasted with the controlled erosion tests just described are those tests that are related directly to applications such as erosion in coal combustion power plants and gas turbines in coal-fired combined cycle power generation (Ref 55, 56, 57). In these cases, the effects of environment, especially temperature and atmosphere, complicate the analysis process.

Impact Abrasion Wear Testing

Bond (Ref 58) developed a laboratory scale test to accurately simulate the wear conditions that exist in the impact crushing of ores (both soft and hard) by impact hammers and blow bars. The rationale for the development of the test apparatus was to be able to predict the wear, and hence the energy consumption, that occurred in the crushing and grinding of ore (Ref 59, 60). However, this test is applicable to any wear process in which impact occurs during the abrasion process. Impact-abrasion testing can be performed in an impeller-

in-drum apparatus, which is also a nonstandard wear test. Unlike solid particle erosion, where the size of the erosive particle is in the range of 10 to 100 μm , particle sizes using the impeller-in-drum are on the order of 25 to 30 mm (1.0 to 1.2 in.). Consequently, the size of the impact craters can be several hundred micrometers in diameter.

Impeller-in-Drum Apparatus and Test Specimens. The impeller-in-drum wear test apparatus uses an impeller-in-a- (rotating) drum arrangement (Fig. 10). The central impeller holds the three paddles, which impact the abrasive media at a high linear velocity. The impeller and abrasive particles reside inside a nominally closed and slowly rotating larger drum (a 3.0 mm, or 0.12 in., gap exists between the covering plate and the drum so that the smaller wear debris can escape the drum during operation). When operating, the drum and the impeller rotate in the same direction. The large drum, which is rubber lined (to both reduce noise and to provide some friction between the drum and the abrasive particles), rotates slowly at 45 rpm, lifting the abrasive particles until they overcome the frictional forces of the rubber lining and fall into the path of the rapidly rotating paddles. The impeller-in-drum wear test apparatus uses three metal paddles as wear test specimens instead of the one used in the Bond apparatus. These paddles are $75 \times 25 \times 12.5$ mm ($3 \times 1 \times 0.5$ in.). Approximately 38 mm (1.5 in.) of the length of the paddle extends from the impeller hub assembly and is available for particle impact. This translates into approximately 950 mm^2 of impact surface area. During operation, the paddles rotate at 620 ± 5 rpm (a velocity equal to about 6 m/s at the tip of the paddle), causing them to impact against particles of a hard abrasive mineral, for example, quartzite or granite or limestone. The abrasive particle-wear specimen collisions cause wear to occur on the broad faces of the paddles from a combination of impact-type events as well as from abrasion. The impeller-in-drum wear test provides quantitative information on the impact-abrasion wear rate of the three test specimens through measurements of the mass loss before and after the wear test schedule. Wear test variance is typically less than 10% for a duplicate set of specimens, although this test does have the potential for greater wear variance than either the dry sand, rubber wheel or the pin-on-drum. (Note: Certain safety precautions must also be exercised when using the impeller-in-drum wear test apparatus. Because the test can cause a large amount of very fine particulate matter, when working with high silica quartzite, ventilation through the use of a cyclone exhaust system, as well as through the use of a respirator or small particle dust mask, is required. The silica-rich dust will irritate the mucus membranes in the throat and nasal passages in the short term and can cause silicosis, a form of lung cancer, if exposed for longer times.)

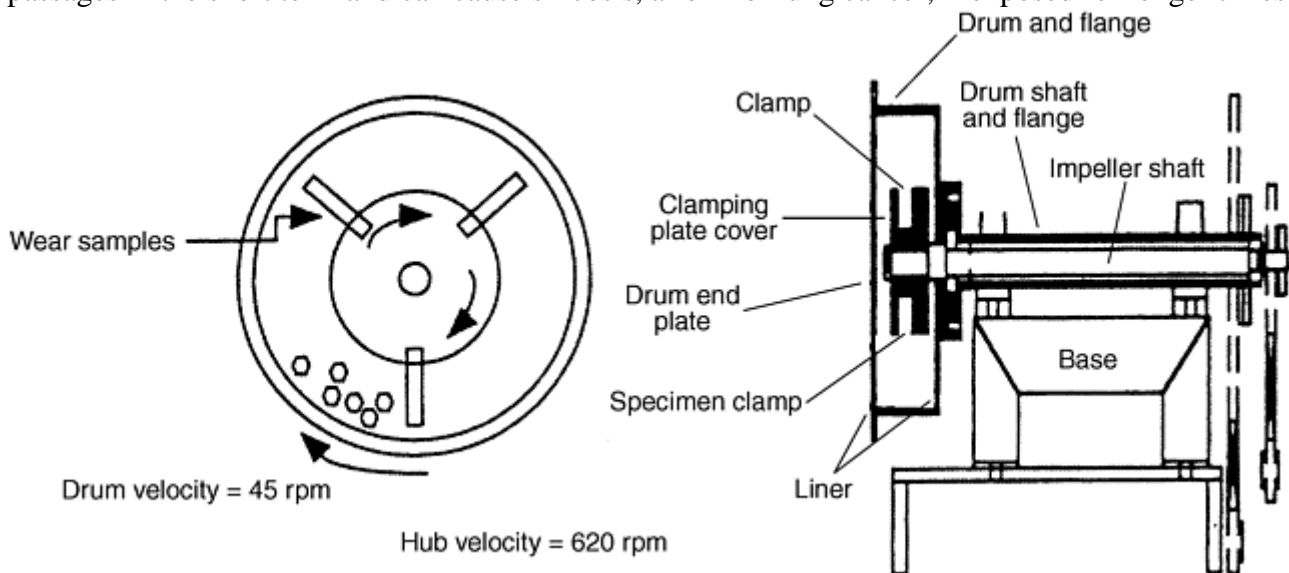


Fig. 10 Schematic diagram of impeller-in-drum impact-abrasion wear apparatus. Source: Ref 61

Impeller-in-drum test procedures include a one hour procedure and a multihour procedure.

One Hour Test Procedure. The general test procedure for the impeller-in-drum starts with the sizing of abrasive particles in the range of -25 to +19 mm (-1 to +0.75 in.). After this step, 0.6 kg of abrasive is measured, and the number of particles that make up the charge is counted. Typically, for a 0.6 kg charge of high-silica quartzite, the number of particles range from 38 to 44. The 0.6 kg charge is then loaded into the impeller and the cover is bolted into place. An empty bag is positioned under the discharge chute to catch any abrasive debris that escapes from the drum during operation and is not vented by the cyclone exhaust system. Typically, 30 to 50 g

of fines will escape from the drum during a 15 min milling run. The cyclone exhaust system collects and traps the very finest dust. In this way, only the larger abrasive fragments are comminuted in the drum.

The drum and impeller are then set into motion. This marks the beginning of the first of two 1 h tests. The speed of the impeller is adjusted to 620 rpm for the first 15 min interval. After the first 15 min test interval has elapsed, the impeller and drum are stopped, the cover is removed, and the abrasive is collected. A fresh 0.6 kg charge of abrasive is placed in the drum, and the procedure is repeated for a second 15 min interval. This is done twice more, for a total running time of 1 h. During this time, the total amount of abrasive passed through the impeller-in-drum system is 2.4 kg. After the first four 15 min tests, the paddle samples are removed, thoroughly cleaned, and then hot-air dried. They are weighed to the nearest tenth of a milligram to determine the mass loss. The specimen face is then reversed, and a duplicate series of four 15 min tests are run. The results of these two series of tests are averaged and the standard deviation is calculated.

Multihour Test Procedure. In the multihour impeller-in-drum test, only one side of the sample is tested. In this case, four or five 1 h test segments are run on one side of the specimen paddle in the same manner as the single hour test. After each 1 h time period, the sample is removed, thoroughly cleaned, and weighed. It is then placed back into the impeller-in-drum and another hour of testing is performed. In each case, fresh abrasive is placed in the drum at 15 min intervals. For a 4 h test, 9.6 kg of abrasive is processed, while for the 5 h test, 12 kg of abrasive is comminuted.

The results of the multihour test are presented in graphical form (i.e., a wear curve) in terms of the cumulative mass or volume loss for the specimen as a function of time. In this way, the steady state wear impact-abrasion wear rate can be determined, if one exists, from the linear portion of the mass/volume loss versus time curve. Figure 11 shows examples of wear curves generated from impeller-in-drum wear tests.

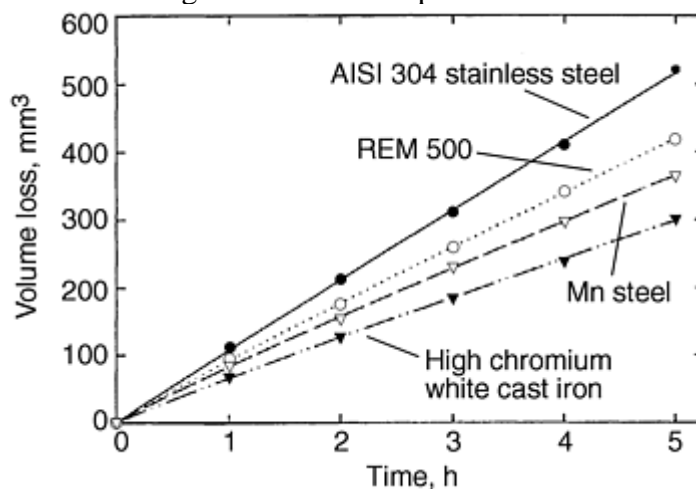


Fig. 11 Wear curves of volume loss versus time for different materials worn against high silica quartzite. Source: Ref 61

Previous research has shown that the 1 h impact-abrasion wear test represents an upper limit as far as the wear rate is concerned (Ref 61). During the 1 h test, break-in is occurring during which the wear specimen conforms to the wear environment. In this case, the sharp edges are being rounded and the surface is work hardening. Development of the wear curves indicate that this process occurs during the first 1 to 2 h of the test, after which the material reaches a steady state in terms of mass loss. Table 8 shows the results for both the 1 h impact-abrasion test and the multiple hour test. Notice that the steady state wear rates are consistently lower than those of the average of the 1 h tests.

Table 8 Typical impeller-tumbler wear data for ferrous alloys

Alloy and designation	Hardness, HV	Wear rate, mm ³ /h		Difference ^(a) , %
		1 h test	5 h test	
304 stainless steel	207	112.2	102.3	-8.8
12% Mn steel	230	84.2	69.7	-17.2
ASTM A 514	256	101.3	96.7	-4.5

AISI 4340	540	96.2	76.6	-20.4
REM 500	505	93.7	81.0	-13.6
D2 tool steel	698	70.2	57.0	-18.8
High-chromium white cast iron	661	69.1	58.0	-16.1

(a) Comparison is made to the wear rate of that material after the first hour of testing.

Comparable to the jaw crusher test, the impeller-in-drum has the advantage of simulating more than one wear mechanism (i.e., both abrasion and impact). The test also can use many different ores as abrasive particles, thus matching the environment of the application more closely.

Slurry Abrasion Wear Testing

A slurry is a mixture of solid particles and a liquid (usually water) of a consistency that allows it to be pumped. This mixture is by nature abrasive and causes extensive damage to pump housings and impellers, tee junctions, elbows, and hydrocyclones. ASTM test method G 75 specifies a test for performing slurry abrasion tests (Ref 62). Other tests using slurries that allow different conditions from those in G 75 to be evaluated also have been developed. These tests include low-angle slurry pot (Ref 63, 64, 65), pipeline (Ref 66, 67), and jet impingement (Ref 68) type tests. All of these tests involve lowstress, two-body abrasive wear. One such device, illustrated in Fig. 12, consists of a slurry pot with an impeller that rotates the slurry past an array of specimens located around the inside of the pot (Ref 65, 69, 70, 71). In this apparatus, the impingement angle is low or nearly tangential.

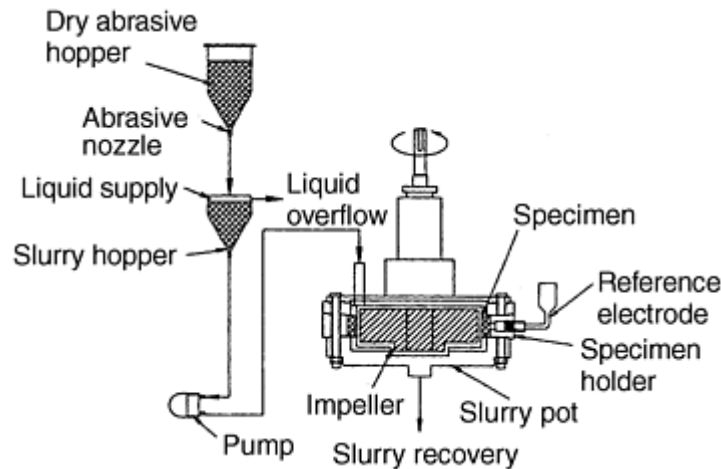


Fig. 12 Schematic diagram for slurry wear apparatus. Source: Ref 65, 69, 70, 71

ASTM G 75, or the Miller number, is used to determine the abrasivity of slurries, based on the rate of metal loss from a standard 27% Cr white cast iron test block that reciprocates through any slurry, on a rubber lap, with an imposed load of 22.2 N (5.0 lbf) placed on the 27% Cr white cast iron test block. The higher the Miller number is, the more aggressive the slurry will be on the part. Although not specifically addressed in ASTM G 75, the effect of corrosion on the slurry abrasion process must be accounted for in the operation of any slurry-handling system (Ref 72). Information on equipment, the specifics of the test procedure, and factors affecting slurry abrasivity can be found in Ref 62.

A limitation on the Miller number is that it is based on a high-chromium white cast iron. Consequently, the slurry-abrasion response (SAR) was developed so that different materials could be tested against a standard slurry to see how they performed. In essence, the SAR is the determination of the Miller number in reverse, and it is based on the same Miller number procedure. This test tends to emphatically highlight the effects of corrosion on a material for a particular slurry.

A slurry wear test apparatus of a general nature comprises a slurry pot and the equipment to feed the slurry to the pot at a controlled rate. The feeding of slurry can be accomplished in one of two ways: flow-through mode where the slurry passes through the system once and is discarded, and recirculating mode where the slurry is passed through the system many times. In the recirculating mode of this slurry-pot apparatus, abrasive degradation and wear debris contamination influence the wear rate over time. Figure 13 shows what can happen when the slurry is recirculated, compared with when it passes through the system only one time. In general,

when the slurry passes through once, a linear volume loss-versus-time curve is generated. The wear rate will vary with slurry loading (i.e., the solids concentration in the slurry), size of abrasive particle, angularity of the abrasive particle, slurry flow rate, temperature, liquid composition and pH, and the material being tested. As in other wear tests, the inclusion of reference standards is important to maintaining proper operation of the equipment and normalizing the wear data between different material classes.

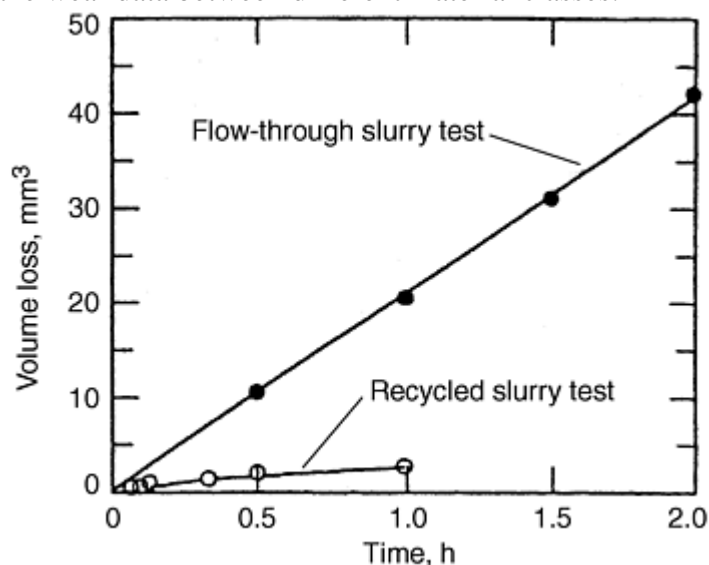


Fig. 13 Wear curves from slurry wear tests showing different wear rates when slurry is recirculated versus a once-through test. Source: Ref 65

Microabrasion Wear Testing

The tests described to this point are typically used to determine the abrasive wear response of materials on a macroscopic scale. Many advanced composites for abrasive wear applications consist of layered structures where the outermost material is meant to be wear resistant, or are materials that have a hard or soft outer coating. In these cases, a test is needed that can investigate the properties of the layer or coating without complicating the result with the effect of the underlying material. In some cases, information on the wear behavior of materials is needed where the abrasive interaction results from the contact of submicron to nanometer scale particles with a surface (e.g., as in the effects of flow of a nanometer size slurry used for polishing silicon wafers in the semiconductor industry).

Two different techniques for measuring microabrasion have been developed (Ref 73, 74, 75, 76, 77, 78, 79). Both techniques use a cratering approach where the rotation of some tool in the presence of a fine abrasive slurry results in the production of a circular depression. At some point during the test, the coating is worn through, and a “bull's-eye” depression is seen where the substrate shows through. Using geometrical relationships, the thickness of the coating can be determined. If the rotational speed of the tool, applied load, and number of rotations (i.e., sliding distance) of the tool are accurately monitored, the wear rate can be determined for the coating and underlying material. This is done by interrupting the test at different points in the process and making visual measurements of the wear scar using optical or scanning electron microscopy (SEM). Another way to measure the diameter and depth of the wear scar is to use a surface profilometer. Although these testing techniques are relatively new, their importance grows as a result of efforts to create new materials with wear-resistant hard surfaces for possible use as components in micron-scale machines.

By imposing a spherical geometry on the wear scar, the overall wear behavior can be described by a classical model for abrasive wear:

$$SN = \frac{V}{\kappa} \quad (\text{Eq 5})$$

where S is the total relative sliding distance between counterbody and specimen, N is the normal load on the contact area, and V is the wear volume. κ is the wear coefficient and represents the wear properties of the material.

The imposed geometrical condition means that the wear volume can be calculated from a single measurement of the wear scar diameter. The sliding distance is equal to the total number of revolutions of the spherical tool multiplied by the circumference of the tool. Thus, in terms of measured quantities, Eq 5 becomes:

$$SN \approx \left(\frac{\pi b^4}{64R} \right) \frac{1}{\kappa} \quad (\text{Eq 6})$$

where b is the diameter of the circular wear scar, and R is the radius of the rotating spherical tool. Note, however, that this equation is only valid for wear scar depths much less than R .

In one microabrasion test method (Ref 76, 77, 78, 79), a rotating steel sphere is pressed against the test specimen in the presence of a slurry of small abrasive particles (Fig. 14). The steel sphere can be any diameter but in these references is approximately 25 mm (1 in.). The abrasive slurry is typically an aqueous suspension of small abrasive particles (e.g., 4 μm silicon carbide abrasive particles with an initial concentration of 0.75 g/cm^3 , although silica, alumina, diamond, or any other abrasive can be used in any desired concentration). The sliding speed of the steel sphere can be varied from 30 to 150 rpm (i.e., 0.04 to 0.20 m/s for a 25 mm, or 1 in., steel sphere) to control the rate of wear, but a typical value is 0.05 m/s. The normal load can also be varied (0.05–5 N, or 0.01–1.1 lbf), but a value of 0.18 N (0.04 lbf) is typical. The normal load is monitored by a load cell. The wear coefficient can be calculated by measuring the progressive increase in the diameter of the wear scar with respect to total sliding distance. The gradient of the linear relationship between wear volume and the product of sliding distance and normal load yields the wear resistance of the material. Figure 15 shows one such calculation.

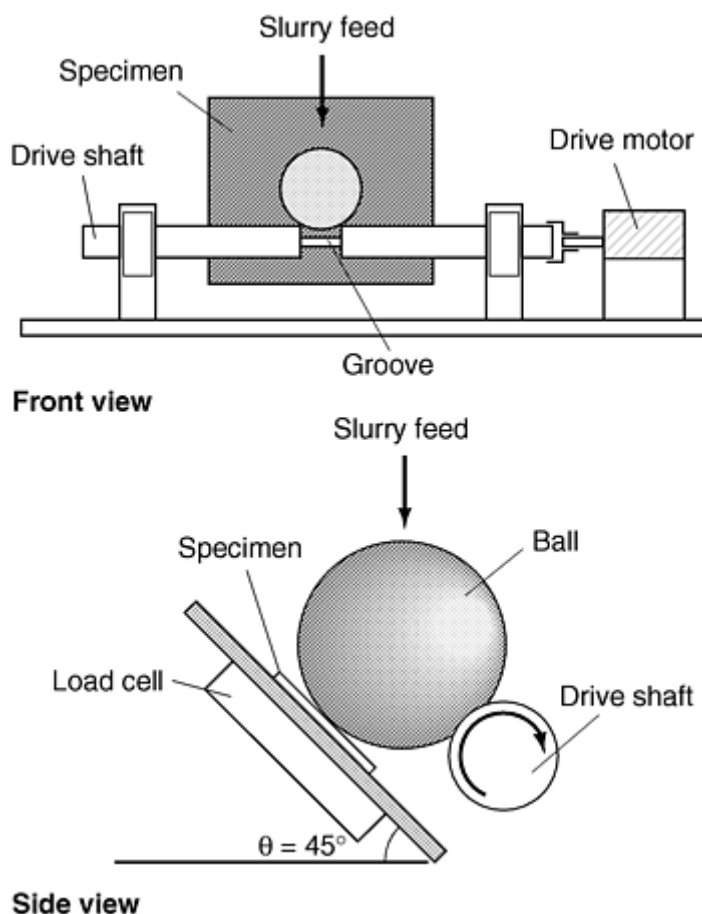


Fig. 14 Schematic diagram of microabrasion ball cratering wear apparatus. Source: Ref 76

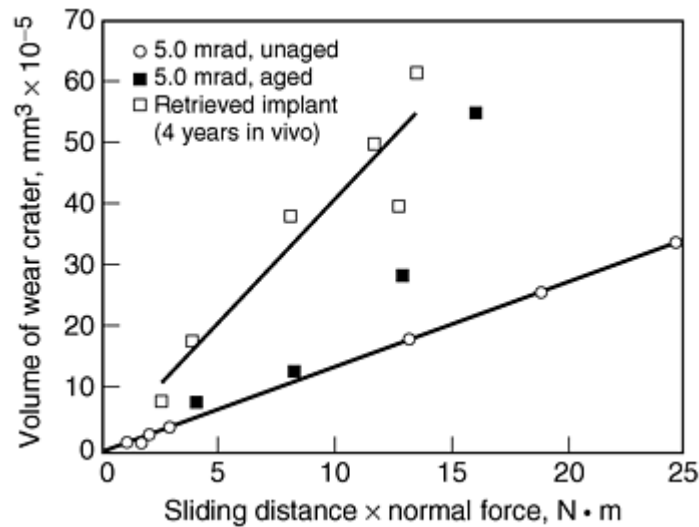


Fig. 15 Wear curves from microabrasion wear tests, mrad, milliradians. Source: Ref 76

References cited in this section

9. S. Jacobsson, M. Olsson, P. Hedenqvist, and O. Vingsbo, Scratch Testing, *Friction, Lubrication, and Wear Technology*, Vol 18, *ASM Handbook*, ASM International, 1992, p 430–437
10. K.-H. Zum Gahr, *Microstructure and Wear of Materials*, Elsevier Science Publishers BV, Amsterdam, Netherlands, 1987, p 132–350
11. E. Rabinowicz, *Friction and Wear of Materials*, 2nd ed., John Wiley & Sons, Inc., 1995, p 191–238
12. Ö.N. Doğan and J.A. Hawk, Effect of Carbide Orientation on Abrasion of High Cr White Cast Iron, *Wear*, Vol 189, 1995, p 136–142
23. R. Blickensderfer and G. Laird III, A Pin-on-Drum Abrasive Wear Test And Comparison to other Pin Tests, *J. Test. Eval.*, Vol 16, 1988, p 516–526
27. “Standard Test Method for Pin Abrasion Testing,” G 132, *Wear and Erosion: Metal Corrosion*, Vol 03.02, ASTM
28. R. Blickensderfer, J.H. Tylczak, and B.W. Madsen, “Laboratory Wear Testing Capabilities of the Bureau of Mines,” Bureau of Mines IC 9001, 1985, 36 pages
29. Ö.N. Doğan, J.A. Hawk, J.H. Tylczak, R.S. Wilson, and R.D. Govier, Wear of TiC Reinforced Metal Matrix Composites, *Wear*, Vol 225–229, 1999, p 758–769
30. A.M. Häger and M. Davies, Short-Fibre Reinforced High-Temperature Resistant Polymers for a Wide Field of Tribological Applications, *Advances in Composite Tribology*, Elsevier Science Publishers BV, Amsterdam, Netherlands, 1973, p 115–116
31. J.A. Hawk and D.E. Alman, Abrasive Wear Behavior of NiAl and NiAl-TiB₂ Composites, *Wear*, Vol 225–229, 1999, p 544–556
32. Ö.N. Doğan, J.A. Hawk, and G. Laird II, Solidification Structure and Abrasion Resistance of High Cr White Irons, *Metall. Mater. Trans. A*, Vol 28, 1997, p 1315–1328
33. C.P. Doğan and J.A. Hawk, Role of Composition and Microstructure in the Abrasive Wear of High-Alumina Ceramics, *Wear*, Vol 225–229, 1999, p 1050–1058

34. H.S. Avery, An Analysis of the Rubber Wheel Abrasion Test, *Wear of Materials*, A.W. Ruff and K.C. Ludema, Ed., ASME, 1981, p 367–378
35. “Standard Practice for Conducting Dry Sand/Rubber Wheel Abrasion Tests,” G 65, *Wear and Erosion: Metal Corrosion*, Vol 03.02, ASTM
36. A.N.J. Stevenson and I.M. Hutchings, Development of the Dry Sand/Rubber Wheel Abrasion Test, *Wear*, Vol 195, 1996, p 232–240
37. G.J. Gore and J.D. Gates, Effect of Hardness on Three Different Forms of Wear, *Wear*, Vol 203–204, 1997, p 544–563
38. “Standard Practice for Conducting Wet Sand/Rubber Wheel Abrasion Tests,” G 105, *Wear and Erosion: Metal Corrosion*, Vol 03.02, ASTM
39. E. Fundal, *Application of the LABORMAT Lapping and Micro Wear Testing*, Fundal Consulting, Borup, Denmark
40. F. Borik, “Rubber Wheel Abrasion Test,” SAE Paper 700687, Society of Automotive Engineers, 1970
41. T. Yamamoto, M. Olsson, and S. Hogmark, Three-body Abrasive Wear of Ceramic Materials, *Wear*, Vol 174, 1994, p 21–31
42. F.J. Friedersdorf and G.R. Holcomb, Pin-on-Disk Corrosion-Wear Test, *J. Test. Eval.*, Vol 26, 1998, p 352–357
43. “Standard Guide for Determining Synergism between Wear and Corrosion,” G 119, *Wear and Erosion: Metal Corrosion*, Vol 03.02, ASTM
44. F. Borik and D.L. Sponseller, Gouging Abrasion Test for Materials Used in Ore and Rock Crushing, Part I: Description of the Test, *J. Mater.*, Vol 6, 1971, p 576–589
45. F. Borik and W.G. Scholz, Gouging Abrasion Test for Material Used in Ore and Rock Crushing, Part II: Effect of Metallurgical Variables on Gouging Wear, *J. Mater.*, Vol 6, 1971, p 590–605
46. I.R. Sare and W.B. Hall, The Determination of Gouging Abrasion by Jaw Crusher Tests, *Conference on Lubrication, Friction, and Wear in Engineering*, 1–5 Dec 1980, (Melbourne, Australia), Inst. Eng., Barton, A.C.T., Australia, 1982, p 94–98
47. “Standard Practice for Jaw Crusher Gouging Abrasion Test,” G 81, *Wear and Erosion: Metal Corrosion*, Vol 03.02, ASTM
48. I.R. Sare and A.G. Constantine, Design and Analysis of Jaw Crusher Gouging Abrasion Tests, *J. Test. Eval.*, Vol 19, 1991, p 115–122 (see also Discussion: F.W. Wood, *J. Test. Eval.*, Vol 19, 1991, p 408–409. Author's closure: I.R. Sare and A.G. Constantine, *J. Test. Eval.*, Vol 19, 1991, p 410–412)
49. J.A. Hawk, R.D. Wilson, J.H. Tylczak, and Ö.N. Doğan, Laboratory Wear Tests: Investigation of Test Methods and Alloy Correlation, *Wear*, Vol 225–229, 1999, p 1031–1042
50. “Standard Test Method for Conducting Erosion Tests by Solid Particle Impingement Using Gas Jets,” G 76, *Wear and Erosion: Metal Corrosion*, Vol 03.02, ASTM
51. I.M. Hutchings, R.E. Winter, and J.E. Field, Solid Particle Erosion of Metals: The Removal of Surface Material by Spherical Projectiles, *Proc. R. Soc. (London) A*, Vol 348, 1976, p 379–392

52. A.V. Levy, *Solid Particle Erosion and Erosion-Corrosion of Materials*, ASM International, 1995, p 11–33
53. R.M. Anderson, T.A. Adler, and J.A. Hawk, Scale of Microstructure Effects on Impact Resistance of Al_2O_3 , *Wear*, Vol 162–164, 1993, p 1073–1080
54. T.A. Adler and Ö.N. Doğan, Erosive Wear and Impact Damage of High Chromium White Cast Irons, *Wear*, Vol 225–229, 1999, p 174–180
55. J. Stringer, Practical Experience with Wastage at Elevated Temperatures in Coal Combustion Systems, *Wear*, Vol 186–187, 1995, p 11–27
56. J.Y. Tu, C.A.J. Fletcher, M. Behnia, J.A. Reizes, D. Owens, and P. Jones, Prediction of Flow and Erosion in Power Utility Boilers and Comparison with Measurement, *J. Eng. Gas Turbines Power*, Vol 119, 1997, p 709–716
57. N.J. Simms, J.E. Oakey, D.J. Stephenson, P.J. Smith, and J.R. Nicholls, Erosion-Corrosion Modelling of Gas Turbine Materials for Coal-Fired Combined Cycle Power Generation, *Wear*, Vol 186–187, 1995, p 247–255
58. F.C. Bond, Lab Equipment and Tests Help Predict Metal Consumption in Crushing and Grinding, *Eng. Min. J.*, Vol 165, 1964, p 169–175
59. F.C. Bond, The Third Theory of Comminution, *Min. Eng.*, Vol 4, 1952, p 484–494
60. F.C. Bond, New Ideas Clarify Grinding Principles, *Chem. Eng.*, Vol 69, 1962, p 103–108
61. R.D. Wilson and J.A. Hawk, Impeller Wear Impact-Abrasive Wear Test, *Wear*, Vol 225–229, 1999, p 1248–1257
62. “Standard Test Method for Determination of Slurry Abrasivity (Miller Number) and Slurry Abrasion Response of Materials (SAR Number),” G 75, *Wear and Erosion: Metal Corrosion*, Vol 03. 02, ASTM
63. L.D.A. Jackson, Controlling Abrasion in Slow Slurry Pipeline Systems, *Can. Min. J.*, Vol 95, 1974, p 42
64. W. Tsai, J.A.C. Humphrey, I. Cornet, and A.V. Levy, “Experimental Measurement of Accelerated Erosion in a Slurry Pot Tester,” *Wear*, Vol 68, 1981, p 289–303
65. B.W. Madsen, Measurements of Wear and Corrosion Rates Using a Novel Slurry Wear Test, *Mater. Perform.*, Vol 26, 1987, p 21–28
66. J. Postlethwaite, B.J. Brady, M.W. Hawrylak, and E.B. Tinker, Effects of Corrosion on the Wear Patterns in Horizontal Slurry Pipelines, *Corrosion*, Vol 34, 1978, p 245–250
67. A. Elkholy, Prediction of Abrasive Wear for Slurry Pump Materials, *Wear*, Vol 84, 1983, p 39–49
68. H. Hocke and H.N. Wilkinson, Testing Abrasion Resistance of Slurry Pipeline Materials, *Tribol. Int.*, Vol 5, 1978, p 289–294
69. B.W. Madsen, A Study of Parameters Using a New Constant-Wear-Rate Slurry Test, *Wear of Materials*, K.C. Ludema, Ed., ASME, 1985, p 345–354

70. B.W. Madsen and R. Blickensderfer, A New Flow-Through Slurry Erosion Wear Test, *Slurry Erosion: Uses, Applications, and Test Methods*, STP 946, J.E. Miller and F.E. Schmidt, Jr., Ed., ASTM 1987, p 169–184
71. B.W. Madsen, Corrosive Wear, *Friction, Lubrication, and Wear Technology*, Vol 18, *ASM Handbook*, ASM International, 1992, p 271–279
72. J.E. Miller, Slurry Erosion, *Friction, Lubrication, and Wear Technology*, Vol 18, *ASM Handbook*, ASM International, 1992, p 233–235
73. A. Kassman, S. Jacobsson, L. Erickson, P. Hedenqvist, and M. Olsson, A New Test Method for the Intrinsic Abrasion Resistance of Thin Coatings, *Surf. Coat. Technol.*, Vol 50, 1991, p 75–84
74. G. Nothnagel, Wear Resistance Determination of Coatings from Cross-Section Measurements of Ball-Ground Craters, *Surf. Coat. Technol.*, Vol 57, 1993, p 151–154
75. P. Hedenqvist, M. Bromark, M. Olsson, S. Hogmark, and E. Bergmann, Mechanical and Tribological Characterization of Low Temperature Deposited PVD TiN Coatings, *Surf. Coat. Technol.*, Vol 63, 1994, p 115–122
76. K.L. Rutherford and I.M. Hutchins, A Micro-Abrasive Wear Test, with Particular Application to Coated Systems, *Surf. Coat. Technol.*, Vol 79, 1996, p 231–239
77. K.L. Rutherford and I.M. Hutchings, Micro-Scale Abrasive Wear Testing of PVD Coatings on Curved Surfaces, *Tribology Letters*, Vol 2, 1996, p 1–11
78. K.L. Rutherford, R.I. Trezona, A.C. Ramamurthy, and I.M. Hutchings, The Abrasive and Erosive Wear of Polymeric Paint Films, *Wear*, Vol 203–204, 1997, p 325–334
79. M. Choudhury and I.M. Hutchings, The Effect of Irradiation and Ageing on the Abrasive Wear Resistance of Ultra High Molecular Weight Polyethylene, *Wear*, Vol 203–204, 1997, p 335–340

Abrasive Wear Testing

Jeffrey A. Hawk, U.S. Department of Energy, Albany Research Center

Summary and Conclusions

This discussion on abrasive wear testing attempts to show that both standard (ASTM) and nonstandard laboratory abrasive wear tests are available. All these wear tests have similarities in terms of application simulation, acceleration, specimen preparation, test control, wear measurement, and data reporting (Ref 5, 6). The most important fact to keep in mind is that in any laboratory wear test, application simulation of the wear mechanisms is of utmost importance. It is critical to run a test where the operative wear mechanisms in the laboratory are the ones observed in the field. It is also important to make sure that all equipment variables are noted and controlled so that any differences in the wear behavior of a suite of materials are due to the physical and mechanical differences in the materials and not to variations in the sample preparation, test procedures, or operation of the test equipment.

In running abrasive wear tests for the first time, or in the investigation of new classes of materials, it is important to perform multiple tests and generate wear curves of volume loss versus sliding distance. Doing this has several advantages. First, any nonlinearities will show up, thus providing a guide of how the test should be

run. Second, the steady state wear behavior will yield more accurate wear rates. In many cases, this procedure will subsequently verify the use of single test wear measurements for obtaining wear rates (as in the pin-on-drum).

References cited in this section

5. H. Czichos, *A Systems Approach to the Science and Technology of Friction, Lubrication and Wear*, Elsevier Science Publishers BV, Amsterdam, Netherlands, 1978
6. R.G. Bayer, Wear Testing, *Mechanical Testing*, Vol 8, Metals Handbook, 9th ed., ASM International, 1985, p 601–608

Abrasive Wear Testing

Jeffrey A. Hawk, U.S. Department of Energy, Albany Research Center

References

1. P.A. Swanson, Comparison of Laboratory and Field Abrasion Tests, *Wear of Materials*, K.C. Ludema, Ed., ASME, 1985, p 519–525.
2. M.A. Moore, Laboratory Simulation Testing for Service Abrasive Wear Environments, *Wear of Materials: Volume II*, K.C. Ludema, Ed., ASME, 1987, p 673–687
3. P.A. Swanson, Comparison of Laboratory Abrasion Tests and Field Tests, *Tribology: Wear Test Selection for Design and Application*, STP 1199, A.W. Ruff and R.G. Bayer, Ed., ASTM, 1993, p 80–99
4. J.H. Tylczak, J.A. Hawk, and R.D. Wilson, A Comparison of Laboratory Abrasion and Field Wear Results, *Wear*, Vol 225–229, 1999, p 1059–1069
5. H. Czichos, *A Systems Approach to the Science and Technology of Friction, Lubrication and Wear*, Elsevier Science Publishers BV, Amsterdam, Netherlands, 1978
6. R.G. Bayer, Wear Testing, *Mechanical Testing*, Vol 8, Metals Handbook, 9th ed., ASM International, 1985, p 601–608
7. P.J. Mutton, *Abrasion Resistant Materials: Volume 1*, AMIRA, Melbourne, Australia, 1988, p 5–17
8. “Wear and Erosion: Metal Corrosion,” *Annual Book of ASTM Standards*, ASTM
9. S. Jacobsson, M. Olsson, P. Hedenqvist, and O. Vingsbo, Scratch Testing, *Friction, Lubrication, and Wear Technology*, Vol 18, *ASM Handbook*, ASM International, 1992, p 430–437
10. K.-H. Zum Gahr, *Microstructure and Wear of Materials*, Elsevier Science Publishers BV, Amsterdam, Netherlands, 1987, p 132–350
11. E. Rabinowicz, *Friction and Wear of Materials*, 2nd ed., John Wiley & Sons, Inc., 1995, p 191–238

12. Ö.N. Doğan and J.A. Hawk, Effect of Carbide Orientation on Abrasion of High Cr White Cast Iron, *Wear*, Vol 189, 1995, p 136–142
13. F. Robin, The Wear of Steels by Abrasives, *Rev. Metall. (Paris)*, Vol 8, 1911, p 47–84 (in French)
14. M.M. Khrushchov, Resistance of Metals to Wear by Abrasion as Related to Hardness, *Proc. Conf. Lub. Wear*, Inst. Mech. Eng., London, UK, 1957, 1957, p 655–659
15. R.C.D. Richardson, The Wear of Metals by Hard Abrasives, *Wear*, Vol 10, 1967, p 291–309
16. G.K. Nathan and W.J.D. Jones, The Empirical Relationship between Abrasive Wear and the Applied Conditions, *Wear*, Vol 9, 1966, p 300–309
17. M.M. Kruschov, Principles of Abrasive Wear, *Wear*, Vol 28, 1974, p 69–88
18. J. Larsen-Basse, Influence of Grit Size on the Groove Formation during Sliding Abrasion, *Wear*, Vol 11, 1968, p 213–222
19. J. Muscara and M.J. Sinnott, Construction and Evaluation of a Versatile Abrasive Wear Testing Apparatus, *Metall. Eng. Q.*, Vol 12, 1972, p 21–32
20. P.J. Mutton, “High Stress Abrasion Testing of Wear Resistant Steels and Cast Irons,” Laboratory Report MRL/PM3/78/001, Broken Hill Proprietary Co., Melbourne Res. Lab., Clayton, Victoria, Australia, Aug 1978, 49 pages
21. C. Allen, B.E. Protheroe, and A. Ball, the Selection of Abrasion-Corrosion-Resistant Materials for Gold-Mining Equipment, *S. Afr. Inst. Min. Metall.*, Vol 81, 1981, p 289–297
22. H. Berns and A. Fischer, Wear Resistance of Fe-Cr-C Hard Surfacing with Additions of B, Ti, and Mn, *Wear of Mater.*, K.C. Ludema, Ed., ASME, 1983, p 298–302
23. R. Blickensderfer and G. Laird III, A Pin-on-Drum Abrasive Wear Test And Comparison to other Pin Tests, *J. Test. Eval.*, Vol 16, 1988, p 516–526
24. H. Sin, N. Saka, and N.P. Suh, Abrasive Wear Mechanisms and the Grit Size Effect, *Wear*, Vol 55, 1979, p 163–190
25. N. Axén and S. Jacobsson, A Model for the Abrasive Wear Resistance of Multiphase Materials, *Wear*, Vol 174, 1994, p 187–199
26. M.A. Moore and F.S. King, Abrasive Wear of Brittle Materials, *Wear*, Vol 60, 1980, p 123–140
27. “Standard Test Method for Pin Abrasion Testing,” G 132, *Wear and Erosion: Metal Corrosion*, Vol 03.02, ASTM
28. R. Blickensderfer, J.H. Tylczak, and B.W. Madsen, “Laboratory Wear Testing Capabilities of the Bureau of Mines,” Bureau of Mines IC 9001, 1985, 36 pages
29. Ö.N. Doğan, J.A. Hawk, J.H. Tylczak, R.S. Wilson, and R.D. Govier, Wear of TiC Reinforced Metal Matrix Composites, *Wear*, Vol 225–229, 1999, p 758–769
30. A.M. Häger and M. Davies, Short-Fibre Reinforced High-Temperature Resistant Polymers for a Wide Field of Tribological Applications, *Advances in Composite Tribology*, Elsevier Science Publishers BV, Amsterdam, Netherlands, 1973, p 115–116

31. J.A. Hawk and D.E. Alman, Abrasive Wear Behavior of NiAl and NiAl-TiB₂ Composites, *Wear*, Vol 225–229, 1999, p 544–556
32. Ö.N. Doğan, J.A. Hawk, and G. Laird II, Solidification Structure and Abrasion Resistance of High Cr White Irons, *Metall. Mater. Trans. A*, Vol 28, 1997, p 1315–1328
33. C.P. Doğan and J.A. Hawk, Role of Composition and Microstructure in the Abrasive Wear of High-Alumina Ceramics, *Wear*, Vol 225–229, 1999, p 1050–1058
34. H.S. Avery, An Analysis of the Rubber Wheel Abrasion Test, *Wear of Materials*, A.W. Ruff and K.C. Ludema, Ed., ASME, 1981, p 367–378
35. “Standard Practice for Conducting Dry Sand/Rubber Wheel Abrasion Tests,” G 65, *Wear and Erosion: Metal Corrosion*, Vol 03.02, ASTM
36. A.N.J. Stevenson and I.M. Hutchings, Development of the Dry Sand/Rubber Wheel Abrasion Test, *Wear*, Vol 195, 1996, p 232–240
37. G.J. Gore and J.D. Gates, Effect of Hardness on Three Different Forms of Wear, *Wear*, Vol 203–204, 1997, p 544–563
38. “Standard Practice for Conducting Wet Sand/Rubber Wheel Abrasion Tests,” G 105, *Wear and Erosion: Metal Corrosion*, Vol 03.02, ASTM
39. E. Fundal, *Application of the LABORMAT Lapping and Micro Wear Testing*, Fundal Consulting, Borup, Denmark
40. F. Borik, “Rubber Wheel Abrasion Test,” SAE Paper 700687, Society of Automotive Engineers, 1970
41. T. Yamamoto, M. Olsson, and S. Hogmark, Three-body Abrasive Wear of Ceramic Materials, *Wear*, Vol 174, 1994, p 21–31
42. F.J. Friedersdorf and G.R. Holcomb, Pin-on-Disk Corrosion-Wear Test, *J. Test. Eval.*, Vol 26, 1998, p 352–357
43. “Standard Guide for Determining Synergism between Wear and Corrosion,” G 119, *Wear and Erosion: Metal Corrosion*, Vol 03.02, ASTM
44. F. Borik and D.L. Sponseller, Gouging Abrasion Test for Materials Used in Ore and Rock Crushing, Part I: Description of the Test, *J. Mater.*, Vol 6, 1971, p 576–589
45. F. Borik and W.G. Scholz, Gouging Abrasion Test for Material Used in Ore and Rock Crushing, Part II: Effect of Metallurgical Variables on Gouging Wear, *J. Mater.*, Vol 6, 1971, p 590–605
46. I.R. Sare and W.B. Hall, The Determination of Gouging Abrasion by Jaw Crusher Tests, *Conference on Lubrication, Friction, and Wear in Engineering*, 1–5 Dec 1980, (Melbourne, Australia), Inst. Eng., Barton, A.C.T., Australia, 1982, p 94–98
47. “Standard Practice for Jaw Crusher Gouging Abrasion Test,” G 81, *Wear and Erosion: Metal Corrosion*, Vol 03.02, ASTM
48. I.R. Sare and A.G. Constantine, Design and Analysis of Jaw Crusher Gouging Abrasion Tests, *J. Test. Eval.*, Vol 19, 1991, p 115–122 (see also Discussion: F.W. Wood, *J. Test. Eval.*, Vol 19, 1991, p 408–409. Author's closure: I.R. Sare and A.G. Constantine, *J. Test. Eval.*, Vol 19, 1991, p 410–412)

49. J.A. Hawk, R.D. Wilson, J.H. Tylczak, and Ö.N. Doğan, Laboratory Wear Tests: Investigation of Test Methods and Alloy Correlation, *Wear*, Vol 225–229, 1999, p 1031–1042
50. “Standard Test Method for Conducting Erosion Tests by Solid Particle Impingement Using Gas Jets,” G 76, *Wear and Erosion: Metal Corrosion*, Vol 03.02, ASTM
51. I.M. Hutchings, R.E. Winter, and J.E. Field, Solid Particle Erosion of Metals: The Removal of Surface Material by Spherical Projectiles, *Proc. R. Soc. (London) A*, Vol 348, 1976, p 379–392
52. A.V. Levy, *Solid Particle Erosion and Erosion-Corrosion of Materials*, ASM International, 1995, p 11–33
53. R.M. Anderson, T.A. Adler, and J.A. Hawk, Scale of Microstructure Effects on Impact Resistance of Al₂O₃, *Wear*, Vol 162–164, 1993, p 1073–1080
54. T.A. Adler and Ö.N. Doğan, Erosive Wear and Impact Damage of High Chromium White Cast Irons, *Wear*, Vol 225–229, 1999, p 174–180
55. J. Stringer, Practical Experience with Wastage at Elevated Temperatures in Coal Combustion Systems, *Wear*, Vol 186–187, 1995, p 11–27
56. J.Y. Tu, C.A.J. Fletcher, M. Behnia, J.A. Reizes, D. Owens, and P. Jones, Prediction of Flow and Erosion in Power Utility Boilers and Comparison with Measurement, *J. Eng. Gas Turbines Power*, Vol 119, 1997, p 709–716
57. N.J. Simms, J.E. Oakey, D.J. Stephenson, P.J. Smith, and J.R. Nicholls, Erosion-Corrosion Modelling of Gas Turbine Materials for Coal-Fired Combined Cycle Power Generation, *Wear*, Vol 186–187, 1995, p 247–255
58. F.C. Bond, Lab Equipment and Tests Help Predict Metal Consumption in Crushing and Grinding, *Eng. Min. J.*, Vol 165, 1964, p 169–175
59. F.C. Bond, The Third Theory of Comminution, *Min. Eng.*, Vol 4, 1952, p 484–494
60. F.C. Bond, New Ideas Clarify Grinding Principles, *Chem. Eng.*, Vol 69, 1962, p 103–108
61. R.D. Wilson and J.A. Hawk, Impeller Wear Impact-Abrasive Wear Test, *Wear*, Vol 225–229, 1999, p 1248–1257
62. “Standard Test Method for Determination of Slurry Abrasivity (Miller Number) and Slurry Abrasion Response of Materials (SAR Number),” G 75, *Wear and Erosion: Metal Corrosion*, Vol 03.02, ASTM
63. L.D.A. Jackson, Controlling Abrasion in Slow Slurry Pipeline Systems, *Can. Min. J.*, Vol 95, 1974, p 42
64. W. Tsai, J.A.C. Humphrey, I. Cornet, and A.V. Levy, “Experimental Measurement of Accelerated Erosion in a Slurry Pot Tester,” *Wear*, Vol 68, 1981, p 289–303
65. B.W. Madsen, Measurements of Wear and Corrosion Rates Using a Novel Slurry Wear Test, *Mater. Perform.*, Vol 26, 1987, p 21–28
66. J. Postlethwaite, B.J. Brady, M.W. Hawrylak, and E.B. Tinker, Effects of Corrosion on the Wear Patterns in Horizontal Slurry Pipelines, *Corrosion*, Vol 34, 1978, p 245–250

67. A. Elkholy, Prediction of Abrasive Wear for Slurry Pump Materials, *Wear*, Vol 84, 1983, p 39–49
68. H. Hocke and H.N. Wilkinson, Testing Abrasion Resistance of Slurry Pipeline Materials, *Tribol. Int.*, Vol 5, 1978, p 289–294
69. B.W. Madsen, A Study of Parameters Using a New Constant-Wear-Rate Slurry Test, *Wear of Materials*, K.C. Ludema, Ed., ASME, 1985, p 345–354
70. B.W. Madsen and R. Blickensderfer, A New Flow-Through Slurry Erosion Wear Test, *Slurry Erosion: Uses, Applications, and Test Methods*, STP 946, J.E. Miller and F.E. Schmidt, Jr., Ed., ASTM 1987, p 169–184
71. B.W. Madsen, Corrosive Wear, *Friction, Lubrication, and Wear Technology*, Vol 18, *ASM Handbook*, ASM International, 1992, p 271–279
72. J.E. Miller, Slurry Erosion, *Friction, Lubrication, and Wear Technology*, Vol 18, *ASM Handbook*, ASM International, 1992, p 233–235
73. A. Kassman, S. Jacobsson, L. Erickson, P. Hedenqvist, and M. Olsson, A New Test Method for the Intrinsic Abrasion Resistance of Thin Coatings, *Surf. Coat. Technol.*, Vol 50, 1991, p 75–84
74. G. Nothnagel, Wear Resistance Determination of Coatings from Cross-Section Measurements of Ball-Ground Craters, *Surf. Coat. Technol.*, Vol 57, 1993, p 151–154
75. P. Hedenqvist, M. Bromark, M. Olsson, S. Hogmark, and E. Bergmann, Mechanical and Tribological Characterization of Low Temperature Deposited PVD TiN Coatings, *Surf. Coat. Technol.*, Vol 63, 1994, p 115–122
76. K.L. Rutherford and I.M. Hutchings, A Micro-Abrasive Wear Test, with Particular Application to Coated Systems, *Surf. Coat. Technol.*, Vol 79, 1996, p 231–239
77. K.L. Rutherford and I.M. Hutchings, Micro-Scale Abrasive Wear Testing of PVD Coatings on Curved Surfaces, *Tribology Letters*, Vol 2, 1996, p 1–11
78. K.L. Rutherford, R.I. Trezona, A.C. Ramamurthy, and I.M. Hutchings, The Abrasive and Erosive Wear of Polymeric Paint Films, *Wear*, Vol 203–204, 1997, p 325–334
79. M. Choudhury and I.M. Hutchings, The Effect of Irradiation and Ageing on the Abrasive Wear Resistance of Ultra High Molecular Weight Polyethylene, *Wear*, Vol 203–204, 1997, p 335–340

Solid Particle Erosive Wear Testing

Ian M. Hutchings, University of Cambridge (England)

Introduction

EROSION is defined as “progressive loss of original material from a solid surface due to mechanical interaction between that surface and a fluid, a multicomponent fluid, or impinging liquid or solid particles” (Ref 1). Because of the broad scope of this term, it is usually qualified to indicate the relevant mechanism or context, for example, as cavitation erosion, liquid impingement erosion, slurry erosion, or solid particle erosion. This article addresses the topic of erosion by the impact of solid particles, which can be a serious cause of wear in

powder handling and transport systems, gas wells, chemical plant, and gas turbine engines. The particles responsible for erosion are typically between 5 and 500 μm in size, and impact velocities can range from less than 10 m/s up to supersonic speeds. Erosive particles are usually, but not inevitably, suspended in a flowing gas stream, although the particle velocity may differ significantly from that of the gas.

The amount of material removed from a surface by erosion generally increases with the time of exposure to the particle stream, as shown schematically in Fig. 1. Several methods can be used to express the dependence of erosion on exposure time. Because in erosion testing it is often most convenient, as well as most accurate, to determine material removal by periodically weighing the specimen, erosion is often quoted in terms of mass removed from the surface by unit mass of erodent particles striking it (e.g., in milligrams eroded per kilogram). This measure of erosion has the advantage that it is dimensionless, but for practical purposes, it is sometimes preferable to express it as volume removed per unit mass of erodent (e.g., mm^3 eroded per kilogram of erodent). In many applications the surface is exposed to a constant flux of erodent particles, and it is straightforward to convert a value of erosion expressed, for example, as mass removed per unit mass of particles striking the surface to depth removed in unit time. However the erosion is expressed, it is important to note that under some circumstances, the rate of material removal will not be constant and that a significant incubation period may occur after a fresh surface is exposed to the particle stream before the rate of erosion reaches a steady state (Fig. 1).

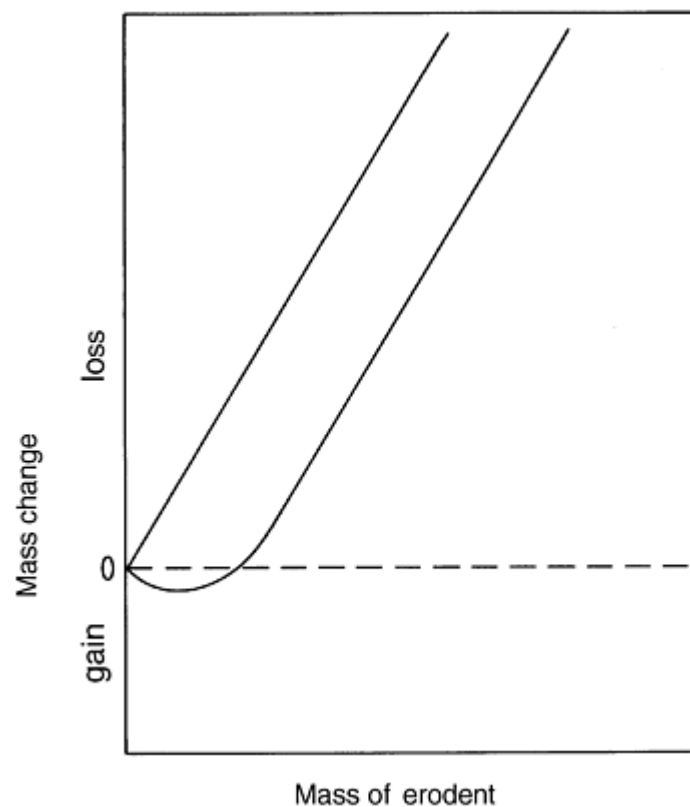


Fig. 1 Typical dependence of mass lost from a specimen on the total mass of erodent particles that have struck it. In many cases, the mass loss increases linearly with mass of erodent from the start of the test, but under some conditions there may be a significant incubation period when the specimen gains mass.

Reference cited in this section

1. "Standard Terminology Relating to Wear and Erosion," G 40, *Annual Book of ASTM Standards*, ASTM, 1998

Important Variables in Erosion

Erosion, defined as mass removed from the surface per unit mass of impacting particles, depends strongly on the following:

- Particle impact velocity
- Particle impact angle
- Particle size, shape, and material
- Ambient temperature

as well as on the properties of the material being eroded. In a reproducible erosion test, all these factors should be well controlled and, if possible, measured.

The most important variable in erosion is the particle velocity because, under most conditions, it has a very strong influence on erosion rate. For many materials, once steady state conditions have been reached, the erosion, E (expressed as the mass removed by unit mass of erodent particles), can be expressed as a simple power function of particle impact velocity, V (Ref 2):

$$E = kV^n \quad (\text{Eq 1})$$

where the constant of proportionality, k , includes the effects of all the other variables. The value of n , the velocity exponent, is typically between 2 and 3, although much higher exponents are seen under some circumstances. A value of approximately 2.4 is commonly seen for the erosion of ductile metals. The value of n does not vary much with impact angle, although there is some suggestion that higher values of n are associated with steeper impact angles.

Erosion also depends markedly on impact angle, often in one of two distinctive ways. Ductile metals eroded by angular particles show maximum erosion (expressed as mass loss per unit mass of particles) at shallow angles of incidence. The impact angle in erosion is almost invariably defined as the angle between the direction of particle motion and the plane of the surface, so that normal incidence corresponds to an impact angle of 90° . Peak erosion for ductile metals occurs typically at an angle of 20 to 30° and is associated with impact under the most favorable conditions for the removal of material by ductile ploughing and cutting mechanisms. The erosion of a ductile metal at 90° incidence may be about $\frac{1}{2}$ to $\frac{1}{3}$ of the peak value. An example of this angular dependence is illustrated in Fig. 2.

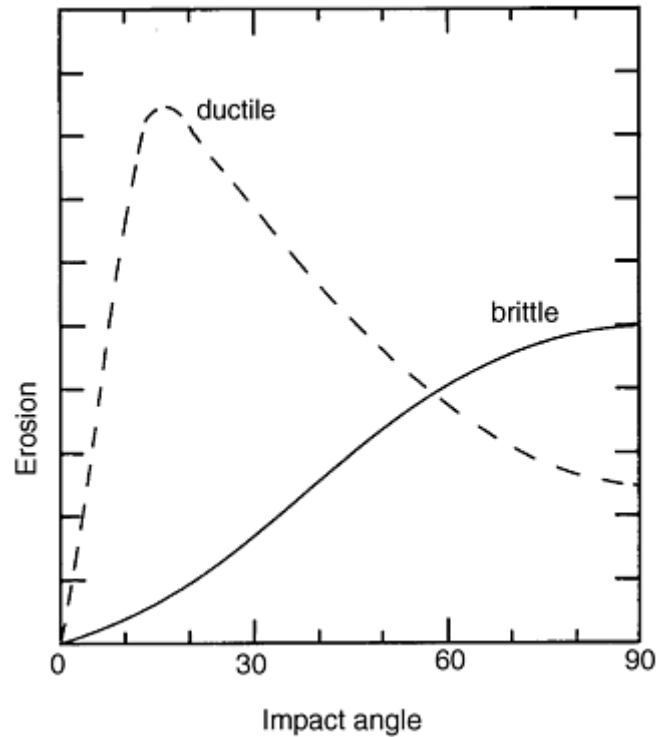


Fig. 2 Typical dependence of erosion (defined as mass lost per unit mass of impinging particles) on impact angle (defined as the angle between the impact direction and the surface)

Materials that erode by the formation and intersection of brittle fractures, such as inorganic glasses impacted by hard angular particles that are large enough to cause local cracking, show peak erosion for normal incidence and a steady reduction in erosion as the impact angle falls. Figure 2 also shows this behavior. The two types of behavior are often referred to as *ductile* and *brittle*, respectively. However, it is not safe to deduce the mechanisms of material removal on the basis of the angular dependence of erosion, since in some systems ductile processes can lead to peak erosion at 90°, and transitions in fracture behavior can result in atypical angular dependence of erosion even in a “classically brittle” material. Intermediate behavior, with peak erosion at 45 to 60°, is not unknown.

The particles used in an erosion test must be well characterized. The size of the particles can influence the erosion rate in two important and distinct ways. Particles of different sizes, striking the surface at the same angle and velocity, will generally remove different amounts of material per unit mass of particles, although for particles larger than about 100 μm striking a ductile metal this variation may be small. This dependence of erosion on particle size represents a genuine size effect. In some erosion test methods, as discussed later, the impact velocity will itself vary with particle size, and since erosion is generally a strong function of velocity, this effect contributes to a further dependence of the measured erosion rate on particle size. For these reasons, it is clear that, wherever possible, the size range of the particles used in an erosion test should be known and should be as narrow as possible. Particles are often classified by sieving, and standard sources that discuss the principles and optimal procedures for this method are available (Ref 3, 4). Specification of the sieve sizes may be sufficient to define the range of particle size used in a test; however, laser granulometry is a readily available technique that can be used to provide a more accurate description of the particle size distribution.

The erodent particle material is an important factor, as illustrated in Fig. 3, that shows results for the erosion of a glass-bonded alumina (a common erosion-resistant ceramic), tested with silicon carbide, alumina, and silica particles, all of the same size (125–150 μm). The erosion caused by the silicon carbide particles was more than ten times that caused by the same mass of silica particles. A major factor responsible for this effect is the relative hardness of the erodent particles and the surface being eroded. In this example, both the silicon carbide and the alumina particles, which were commercial abrasives, were significantly harder than the alumina specimen. The silica, in contrast, had about the same hardness as the specimen:

Specimen or erodent	Vickers microhardness	
	GPa	10 ⁶ psi
Alumina specimen	12.7	1.84
Silicon carbide particles	33.4	4.84
Alumina particles	26.5	3.84
Silica particles	13.1	1.90

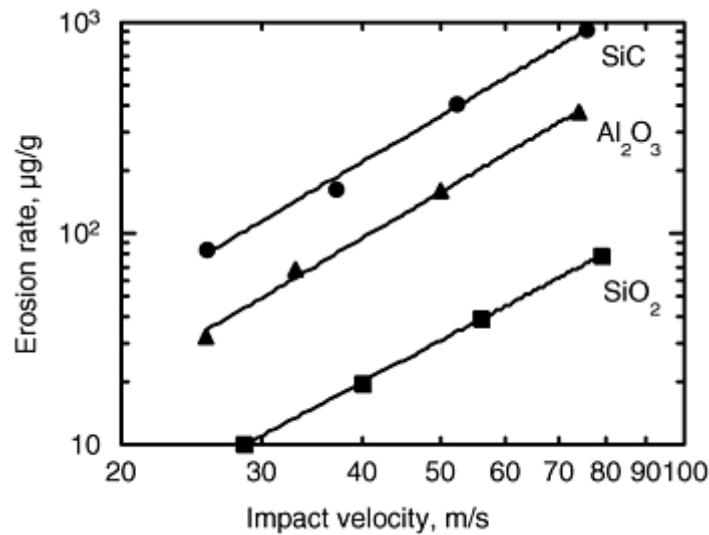


Fig. 3 Influence of particle material on erosion rate, for erosion of a sintered glass-bonded alumina ceramic by silica, alumina, and silicon carbide particles, 125–150 µm in diameter, at normal incidence. Adapted from Ref 5

Shape also plays a role in determining the relative erosivity of different particles (Ref 6) and is difficult to separate from other particle properties, since particle shape is often determined by the fracture processes by which the particles themselves are formed. As in the case of particle size, there is an intrinsic effect of shape on the erosion rate, which can lead to angular particles producing up to ten or more times the erosion caused by spherical particles of the same material. Measurement of particle shape is not straightforward because, although there are many possible methods of assessing shape, it is unclear which method is most appropriate in the context of erosive wear testing. Qualitative descriptors such as “rounded,” “subangular,” “angular,” and so on, are often used and may be adequate in conjunction with a more detailed specification of the material and source of the erodent particles.

For these reasons, it is important that if the purpose of erosion testing is to compare material behavior or obtain quantitative measurements of erosion rate in the context of a particular engineering application, appropriate erodent particles are used in the test. Not only should the particle size and shape be representative of the application in question, but the particle material should also provide a realistic simulation of the properties of the actual particles. Although the ready availability of reproducible commercial abrasive particles such as silicon carbide or alumina with well-defined size may suggest their use in erosion testing, it is important to appreciate that they are much harder than most naturally occurring erosive particles, which are often silica or silicate minerals. Not only may the absolute values of erosion rate measured with very hard particles be misleading, but the mechanisms of damage and even the ranking of erosion rates of materials may be different. Because damage is suffered by the erodent particles when they strike a surface, the properties of the particles after they have been used in an erosion test will differ, often significantly, from those of fresh particles. Even if gross fracture of the particles is avoided, subtle changes in shape can occur. If at all possible, erodent particles should, therefore, not be reused for erosion testing.

References cited in this section

2. I.M. Hutchings, *Tribology: Friction and Wear of Engineering Materials*, CRC Press, Inc., 1992, p 171–197

3. *Manual on Testing Sieving Methods, ASTM Manual 32*, ASTM, 1998
4. "Test Sieving," BS 1796-1, British Standards Institution, London (also ISO 2591-1)
5. P.H. Shipway and I.M. Hutchings, The Role of Particle Properties in the Erosion of Brittle Materials, *Wear*, Vol 193, 1996, p 105–113
6. S. Bahadur and R. Badruddin, Erodent Particle Characterization and the Effect of Particle Size and Shape on Erosion, *Wear of Materials 1989*, K.C. Ludema, Ed., ASME, 1989, p 143–153

Solid Particle Erosive Wear Testing

Ian M. Hutchings, University of Cambridge (England)

Erosion Test Methods

Laboratory-scale erosion testing is performed for several reasons: to provide data on absolute or relative wear rates under specific conditions, to examine the validity of theoretical models, or to study the mechanisms of wear. The first of these objectives can include data on the relative behavior of different materials and provides information of direct value to the design engineer, while the others are of more value in improving understanding of erosive wear.

Methods used for laboratory erosion testing can be divided into those in which the particles are accelerated in a gas stream and those where circular motion is used to achieve the impact velocity. Four methods are shown schematically in Fig. 4 and are discussed in detail subsequently. Of these, the gas-blast test rig (Fig. 4a) and the centrifugal accelerator (Fig. 4b) are the most widely used methods.

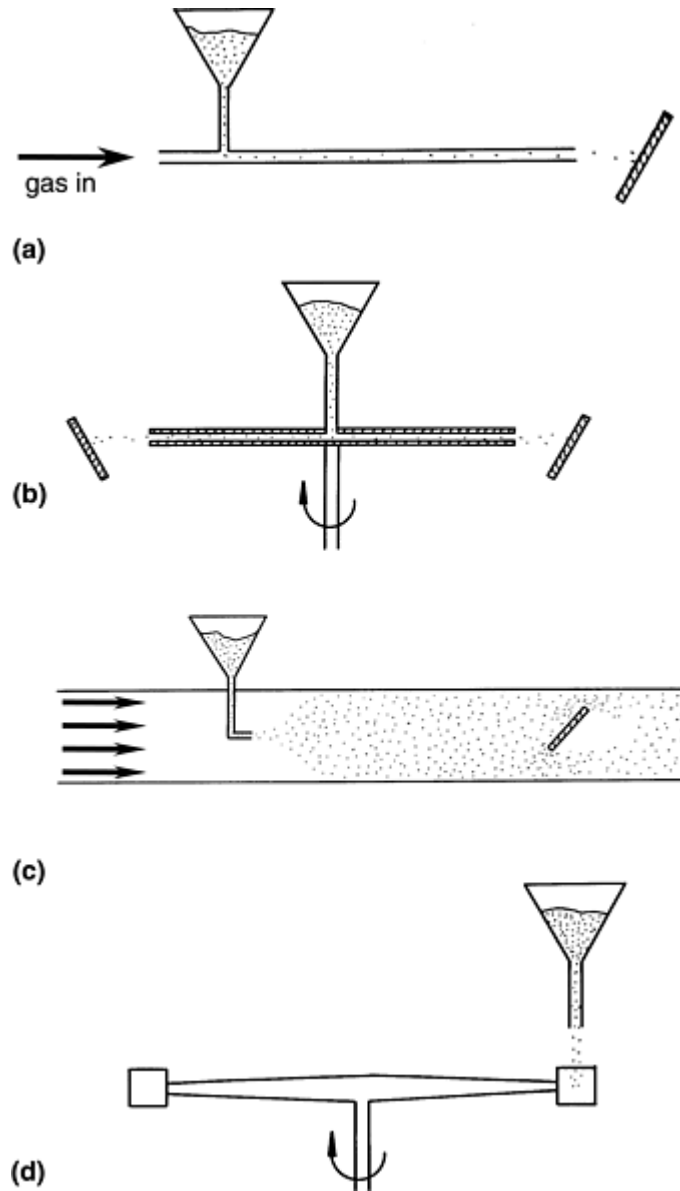


Fig. 4 Schematic diagrams showing four classes of erosion test methods. (a) Gas-blast rig. (b) Centrifugal accelerator. (c) Wind tunnel. (d) Whirling arm tester

Gas-Blast Method. In the gas-blast or jet impingement test, particles are entrained into a gas stream and accelerated along a nozzle. The particles leave the end of the nozzle and then strike the test specimen, which is fixed at a known angle to the axis of the nozzle some distance from its end. The acceleration nozzle used in this test method is generally a plain cylindrical tube for ease of construction and replacement. There are national standards relating to this type of test method, but nonstandard designs are also commonly used.

In ASTM standard G 76 (Ref 7), the use of a nozzle 50 mm (2 in.) long with a bore of 1.50 mm (0.06 in.) is recommended. A former German standard (DIN 50332) suggested the use of a nozzle 120 mm (4.7 in.) long with an internal diameter of either 8 or 18 mm (0.3 or 0.7 in.), depending on the test conditions. Sheldon and coworkers (Ref 8) used a nozzle 305 mm (12 in.) long with an internal diameter of 4.95 mm (0.19 in.), and similar dimensions have been used in many other experimental programs. The aspect ratio (length:diameter) of this nozzle is 61.6, approximately twice that of the ASTM standard nozzle. Other investigators have used considerably longer nozzles. For example, Marshall and others (Ref 9) used a nozzle 3 m (9.8 ft) long with a bore of 9.5 mm (0.37 in.) (aspect ratio = 316), while Andrews and others (Ref 10) used nozzles 4 m (13.1 ft) long with 25 mm (1 in.) internal diameter (aspect ratio = 160), and 1 m (3.3 ft) long with an internal diameter of 10 mm (0.4 in.) (aspect ratio = 100). The ASTM standard suggests that a length:diameter ratio of at least 25 is desirable to achieve an acceptable particle velocity distribution in the stream.

The velocity with which the particles leave the nozzle and strike the specimen will depend on the velocity of the gas stream, on the drag forces acting on the particles, and on the distance over which the particles accelerate

along the nozzle. In long nozzles of large diameter, the particles may reach essentially the same speed as the gas stream, but in short or narrow nozzles, the particle velocity may be significantly lower than that of the gas. Accurate knowledge of the particle exit velocity is therefore essential unless the purpose of the test is simply to compare material behavior under constant, but unspecified, erosion conditions.

A long nozzle might be considered to be beneficial on the grounds that it might lead to a higher particle exit velocity for a given gas pressure. It might also be assumed that the divergence of the erodent particle stream on leaving the nozzle would be less, leading to less uncertainty in the angle with which the particles strike the target. A long nozzle might also have the advantage of reducing the spread in the velocities of particles where there is a distribution of particle sizes in the erodent supply. However, the assumption that longer nozzles give higher particle exit velocities is not necessarily correct. It is true that with a longer nozzle the particles reach a higher proportion of the gas exit velocity than in shorter nozzles, but on the other hand, for the same overall pressure drop, the gas velocity will be lower than with a shorter nozzle due to friction between the gas and the nozzle wall. A second important influence on particle exit velocity arises from the collision of the particles against the nozzle wall, which causes a retarding effect. The internal surface topography (i.e., roughness) of the nozzle wall therefore affects the particle exit velocity.

Particles can be fed into the gas stream in various ways. One simple method is to use a pressurized particle feeder in which particles are metered by the rotation of an electrically driven disk carrying a groove from which the powder is supplied through a pressurized tube to a mixing chamber at the high-pressure end of the nozzle. Powder feeders of this type are commercially available, for example, to supply plasma-spray guns. An alternative method of erodent feeding uses a rotating grooved disk at atmospheric pressure from which the powder is sucked through a feed tube into a constricted portion of the airstream in which a low pressure region is created. Screw feeders can also be used. However the erodent particles are metered, good control over the feed rate is desirable.

Figure 5 shows the layout of a typical laboratory-scale gas-blast erosion rig. Suction created in the ejector causes the erodent particles to be drawn into a feed tube from a groove in a slowly rotating turntable, which is fed by gravity from a hopper. The particles are then mixed into the main gas stream. By controlling the speed of rotation of the turntable, a constant particle feed rate can be accurately maintained. The acceleration nozzle is a stainless steel tube, typically 5 mm (0.2 in.) in internal diameter and 300 mm (11.8 in.) long. Since the nozzle wears progressively in use, the diameter should be regularly monitored to ensure constant test conditions. The test sample is clamped at an accurately known angle to the axis at a standoff distance of about 5 nozzle diameters from the end of the nozzle. Arrangements are made to collect the erodent particles and debris from the airstream before it is vented from the apparatus. Since the particle velocity is controlled by maintaining a fixed pressure drop between the ends of the nozzle, it is relatively straightforward to achieve reproducible and well-characterized conditions in such a rig.

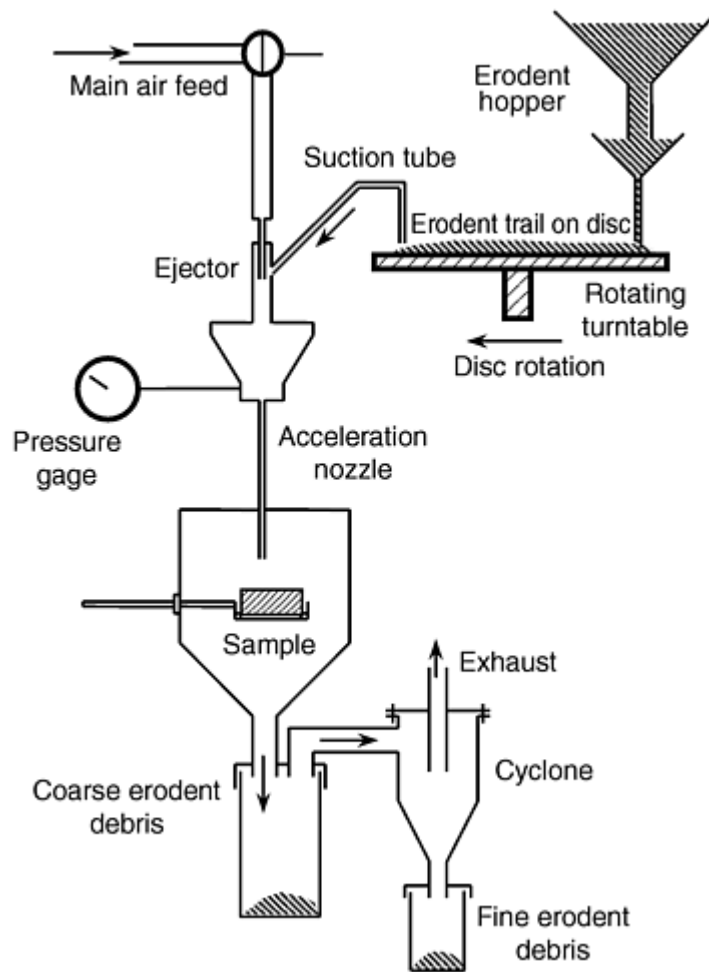


Fig. 5 Typical small-scale laboratory gas-blast erosion rig. Eroder particles are accelerated in a gas stream along a cylindrical nozzle and strike a specimen fixed at the end of the nozzle. Source: Ref 11

A typical test procedure would involve mounting the specimen at the appropriate distance and angle from the end of the nozzle, filling the particle feeder with a weighed quantity of sieved erodent particles, setting the pressure at the nozzle entry to the level needed to achieve the desired particle velocity, starting the particle feeder at an appropriate rate, checking and adjusting the nozzle pressure if necessary, and running the test until all the particles have passed through the apparatus. The specimen is handled carefully, cleaned (to remove loose particles), and weighed before and after the test. The specimen is then replaced in the apparatus in the same position and orientation, and the test run is repeated to produce further erosion of the same region of the surface until sufficient data have been gathered (see the section “Data Analysis and Interpretation” in this article).

The use of preweighed quantities of erodent in each test, and running the test until the particles have all passed through the rig, is preferable to running the test for a set time at a preset feed rate because a constant feed rate cannot always be assured.

Computational models are available to predict particle velocities in gas-blast erosion testing, but in order to make accurate predictions they must take account not only of the size, density, and drag coefficient (which will depend on the shape) of the particles, but also of the nozzle wall friction and the effects of particle-wall and even particle-particle interactions. The plume of particles leaving the end of a cylindrical nozzle contains some particles that diverge quite markedly from the nozzle axis, showing that impacts between particles and the nozzle wall can be significant (Ref 11). Theoretical models for particle velocity are therefore no substitute for accurate measurements under realistic operating conditions performed by one of the methods discussed in the section “Measurement of Particle Velocity” in this article.

For some purposes, however, a simple empirical model has been found to be useful. The following equation provides a good fit to the dependence of particle velocity on air pressure for a cylindrical nozzle 4.9 mm (0.19

in.) in diameter and 308 mm (12.1 in.) long, with one end at atmospheric pressure, along which particles are accelerated in an airstream (Ref 12):

$$V^2 = \frac{kP}{d^{0.57}\rho^{1.08}} \quad (\text{Eq 2})$$

where V is the exit velocity of the particles (in m/s), P is the gage pressure at the high-pressure end of the nozzle (in kPa; 100 kPa = 1 bar), d is the diameter of the particles (in micrometers), and ρ is the density of the particles (in Mg/m³). For these conditions and with the data expressed in the units given, $k = 7900$. As shown in Fig. 6, this equation provides a good fit to measured particle velocities up to about 80 m/s. A linear variation of (particle velocity)² with gas pressure has also been demonstrated for cylindrical nozzles with other aspect ratios, and the functional dependence of velocity on particle size and density has been shown to be similar to that of Eq 2. It is likely that an empirical relationship similar to Eq 2 can be used, after suitable calibration, for many designs of gas-blast erosion rig.

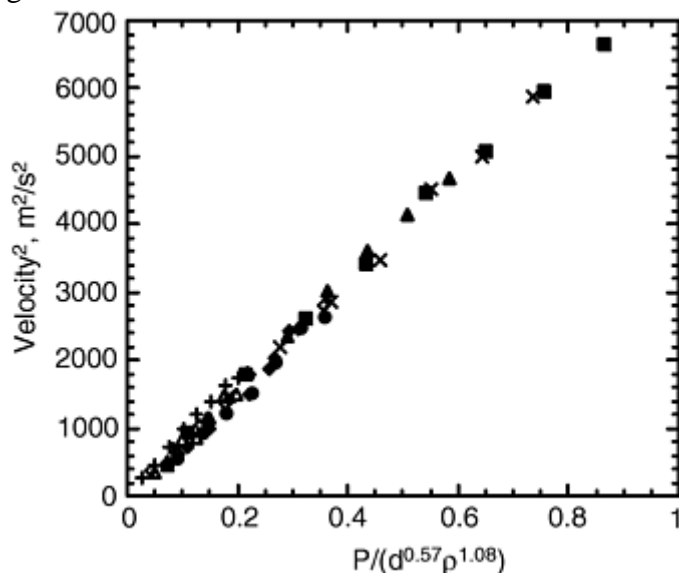


Fig. 6 Empirical correlation between particle velocity and nozzle pressure drop, P ; mean particle diameter, d ; and particle material density, ρ , for erodent particles of a wide range of sizes and materials in an air-blast erosion rig with a nozzle 308 mm (12 in.) long and 4.90 mm (0.19 in.) internal diameter. The data are well fitted by Eq 2. Adapted from Ref 12

The stream of particles leaving the nozzle diverges significantly because of particle-wall collisions and particle-particle interactions. This divergence can be described by a simple function (Ref 11). The proportion of particles traveling at angles between θ and $\theta + d\theta$ to the nozzle axis, $p(\theta)d\theta$, is given by:

$$p(\theta) = \beta^2 \frac{\sin \theta}{\cos^3 \theta} \exp(-\beta \tan \theta) \quad (\text{Eq 3})$$

where β is a dimensionless quantity that describes the spreading of the plume and has been termed the *focus coefficient*. The value of β depends on the shape of the erodent particles and on the internal roughness of the nozzle wall, as well as on the impact velocity; typical values lie in the range of approximately 10 to 25, with a low value of β corresponding to a highly divergent stream. Because of this divergence, the area of the specimen exposed to the erodent stream must be significantly greater than the cross-sectional area of the end of the nozzle in order to ensure that most of the particles strike the specimen. For a typical nozzle diameter of 5 mm (0.2 in.) and a specimen mounted at a distance of 20 mm (0.8 in.) from the end of the nozzle, a specimen width of at least 25 mm (1 in.) is necessary to avoid significant error from this source.

Centrifugal Accelerator. In the centrifugal accelerator, illustrated by the apparatus shown in Fig. 7, the erodent particles are fed to the center of a rotating disk, usually with a screw or vibratory feeder, and then travel outwardly along radial slots or tubes in the disk. They leave the disk at the periphery with a tangential component of velocity equal to that of the disk itself and a radial velocity component that depends on their motion within the radial channels. Specimens are mounted at points surrounding the periphery of the disk and are exposed to a series of streams of erodent particles as the radial tubes sweep past. The use of a centrifugal

accelerator for erosion testing was specified in a national standard of the former Soviet Union (GOST 23.201.78), and examples of such apparatus have been described in Ref 13, 14, and 15.

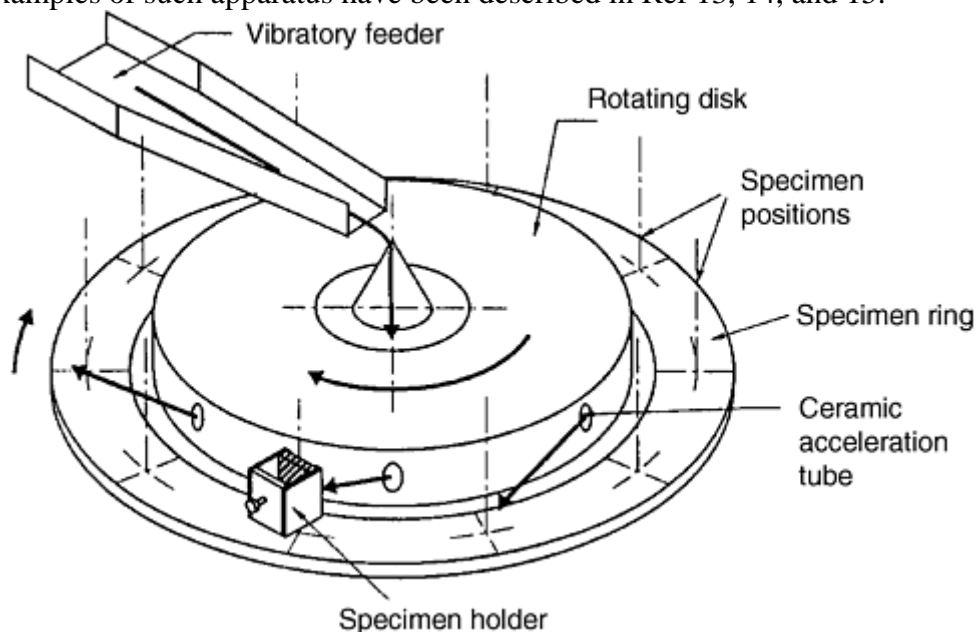


Fig. 7 Typical centrifugal accelerator test rig. Erodent particles are fed into the center of a rotating disk and emerge through radial tubes to strike the specimens, which are arranged in a ring around the periphery of the disk. Source: Ref 13

The method has the advantage over the gas-blast method in that a large number of specimens can be subjected to the same erosion conditions simultaneously, and it is therefore well suited to performing screening tests on many different materials. The specimens are often mounted on a ring that rotates slowly around the rotating disk, to eliminate any possible bias associated with specific specimen locations. Maximum numbers of specimens per test have ranged up to 30 in different designs of rig, with rotating disk diameters between 200 and 600 mm (8 and 24 in.). The apparatus shown in Fig. 7 (Ref 13) has a disk 240 mm (9.4 in.) in diameter, containing six radial tubes, each with an internal bore diameter of 2.6 mm (0.10 in.). The particles are supplied to the center of the disk by a vibratory feeder at a constant rate, and care is taken in the design to ensure that the particle flow is split evenly between the six tubes. Typically, ten samples are placed symmetrically around the carrier ring; each specimen holder can be angled independently to achieve impact angles in the range of 5 to 90°. The specimens are all mounted in the vertical plane.

Constant particle impact velocity is achieved through control of the disk speed, which is readily measured. However, the velocity of the particles results from both radial and tangential motion; typical particle trajectories are illustrated in Fig. 8. Accurate determination of the impact velocity, and of the impact angle at the specimen surface, thus requires a knowledge of the ratio of the velocity components or the angle of motion relative to the radial direction. Probably the simplest method of determining these is to measure the direction of motion of the particles experimentally, by allowing them to pass through a slotted shield and noting the position of impact on a specimen surface fixed beyond the shield. The particle trajectory, defined by the line joining the centers of the erosion scar and the slot, allows the relative velocity components, as well as the true angle of impact on the specimens, to be calculated. For one particular design of centrifugal accelerator (Ref 15), the radial velocity component was found to be about 0.8 times the tangential component and independent of velocity and particle size. The particle trajectories were therefore at an angle of about 39° to the tangential direction.

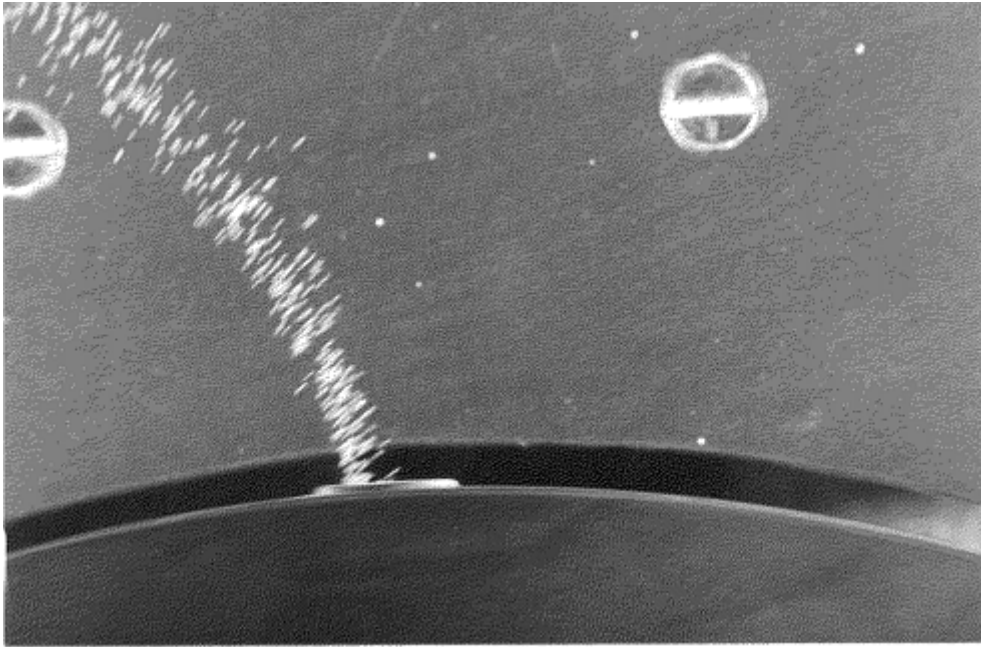


Fig. 8 Single flash exposure showing streak images of particle trajectories for olivine sand particles, 150–250 μm in diameter, leaving an acceleration tube at the rim of the rotating disk in a centrifugal accelerator of the design shown in Fig. 7. The disk was rotating clockwise and the mean particle velocity was 7 m/s. Courtesy of T. Deng and M.S.A. Bradley, University of Greenwich, UK

Erosion at different impact angles can be achieved by varying the angles at which the specimens are mounted in the apparatus. Because of the pattern of motion of the particles in this test, the impingement angle and the particle flux vary in a complex but geometrically predictable way across the surface of a finite-sized specimen. These effects have been analyzed in detail (Ref 15). At least one edge of the specimen will also, in general, be exposed to the erodent stream, and it is common practice to mask both the leading and trailing edges of samples in order to prevent erosion occurring at unwanted angles of impingement. The total amount of erodent striking each specimen surface will be only a small fraction of the total fed into the rig and must be calculated from the specimen and rig dimensions. The erosion of each specimen can then be calculated, in terms of mass removed per unit mass of impinging erodent particles, from measurements of mass loss.

As in the gas-blast method discussed in the previous section, it is desirable to run the test to consume a preweighed total mass of erodent, rather than rely on maintaining and measuring a steady particle feed rate and running the test for a fixed time.

Wind-Tunnel Tests. Because of the large size and expense of the test rig, the wind-tunnel method shown schematically in Fig. 4(c) is used predominantly where information on the performance of shaped components such as turbine blades is required, rather than for studies of material response alone. For tests of the former type, the wind tunnel method, in which the test specimen is immersed in a rapidly flowing stream of air or other gas containing erodent particles, is invaluable. Figure 9 shows a typical wind tunnel test facility (Ref 17). The specimen is located in a rectangular section (dimensions 25.4×76.2 mm, or 1×3 in.) of the wind tunnel, following a long (approximately 4 m, or 13 ft) acceleration duct. With this length of acceleration tunnel, relatively large particles ($200 \mu\text{m}$) are accelerated to up to 85% and smaller particles ($20 \mu\text{m}$) to up to 98% of the air speed. In order to avoid disturbing the airflow too much, the specimen area in the test section is typically restricted to $<10\%$ of the total cross-sectional area of the flow. After impact with the specimen, the erodent particles, which have been supplied from a preweighed batch in the particle feeder, are separated from the main airstream by a cyclone separator and filter.

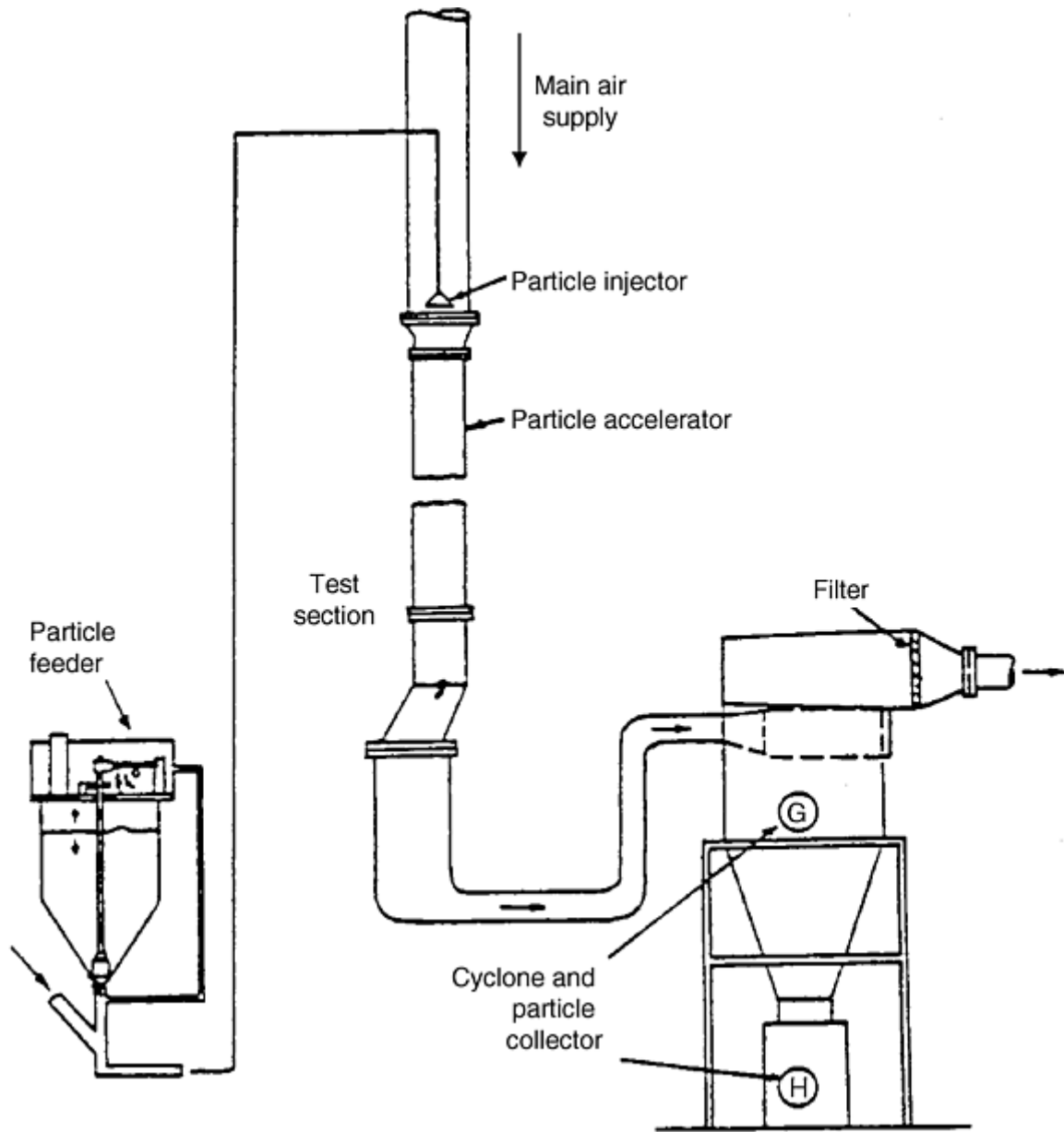


Fig. 9 Schematic diagram of wind tunnel test rig. Source: Ref 16

Whirling Arm Testers. Figure 10 shows an example of a whirling arm test rig in which impact occurs between a moving specimen and a slowly falling stream of erodent particles. In this approach, which is particularly useful in studying erosion at very high impact velocities, the specimens are carried at the ends of a rotating arm (Ref 14, 18). At high speeds, accurate balancing of both the arm and the specimens becomes important and introduces extra complexity to the process of specimen preparation. Specimen materials must have sufficient strength and ductility to withstand the high centrifugal stresses to which they are subjected during testing, and satisfactory methods must be used to attach the specimens to the rotor. In some designs, aerodynamic effects are eliminated by operating the rig in a vacuum or reduced air pressure, and this is essential if very high speeds are required. There are then engineering problems associated with the sealing of the vacuum against the rapidly rotating drive shaft, unless the method shown in Fig. 10 is adopted, where the motor casing itself provides the vacuum seal.

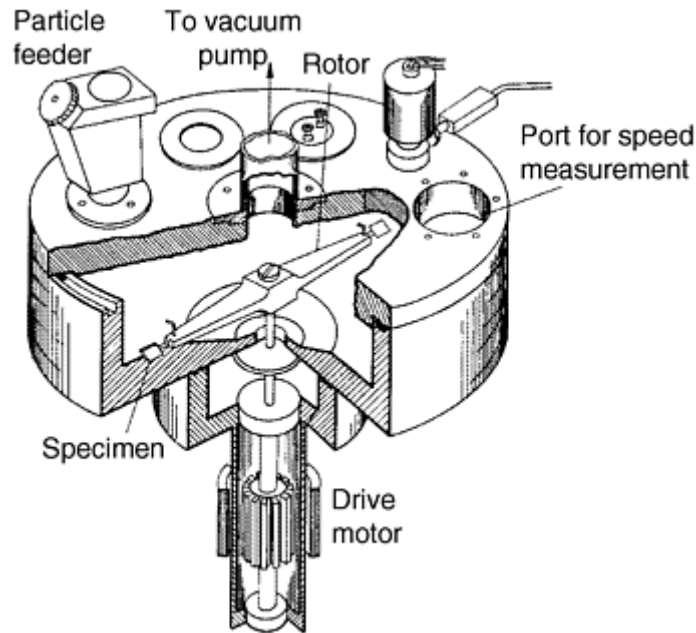


Fig. 10 Schematic diagram of whirling arm erosion rig, in which particles are dropped into the path of two specimens attached to the ends of a rapidly rotating arm. Adapted from Ref 18

Both electric motors and air turbines have been used to rotate the specimen arm, and specimen speeds up to at least 550 m/s have been achieved. The impact velocity can be accurately calculated from the rotor radius and the rotational speed, while the impact angle can be controlled by fixing the specimens to the rotor arm at an appropriate angle. This often involves the use of different rotors for different impact angles. The fate of erodent particles after striking the specimen must be considered since they will rebound and may cause secondary impacts, from intact particles or fragments, during subsequent rotation of the arm. Some method of capturing the particles after impact is required. The design described in Ref 18 used sheet metal traps coated with silicone oil to catch small dust fragments as well as whole particles.

The whirling arm method involves greater effort in specimen preparation and in conducting the test than other methods; the time taken to load and unload the specimens, and to pump the chamber down if it is an evacuated rig, may be significant. The specimens must be of accurate dimensions, form a dynamically balanced pair on the whirling arm, and be sufficiently strong and tough to withstand the high centrifugal stresses imposed during testing. These requirements have tended to restrict the method to metallic samples. Despite these considerations, the whirling arm method can achieve the highest particle velocities, and in order to obtain erosion data under such conditions, it has great value.

References cited in this section

7. "Standard Test Method for Conducting Erosion Tests by Solid Particle Impingement Using Gas Jets," G 76, *Annual Book of ASTM Standards*, ASTM
8. G.L. Sheldon, J. Maji, and C.T. Crowe, Erosion of a Tube by Gas-Particle Flow, *J. Eng. Mater. Technol. (Trans. ASME)*, Vol 99, 1977, p 138–142
9. D.B. Marshall et al., Particle Size Distribution Effects on the Solid Particle Erosion of Brittle Materials, *Wear*, Vol 71, 1981, p 363–373
10. D.R. Andrews, S.M. Walley, and J.E. Field, Solid Particle Erosion Studies in the Cavendish Laboratory, Paper 36, *Proc. 6th Int. Conf. on Erosion by Liquid and Solid Impact*, Cavendish Laboratory, Cambridge, UK, 1983
11. P.H. Shipway and I.M. Hutchings, Influence of Nozzle Roughness on Conditions in a Gas-Blast Erosion Rig, *Wear*, Vol 162–164, 1993, p 148–158

12. A.N.J. Stevenson and I.M. Hutchings, Scaling Laws for Particle Velocity in the Gas-Blast Erosion Test, *Wear*, Vol 181–183, 1995, p 56–62
13. A.J. Burnett, S.R. De Silva, and A.R. Reed, Comparisons between Sand Blast and Centripetal Effect Accelerator Type Erosion Testers, *Wear*, Vol 186–187, 1995, p 168–178
14. I.R. Kleis and K.K. Uuemyis, Mechanical Rigs for Studying Abrasive Erosion, *Russ. Eng. J.*, Vol 51, 1971, p 13–15
15. S. Söderberg, S. Hogmark, U. Engman, and H. Swahn, Erosion Classification of Materials Using a Centrifugal Erosion Tester, *Tribol. Int.*, Dec 1981, p 333–343
16. W. Tabakoff, Experimental Study on the Effects of Specimen Sizes on Erosion, *Wear*, Vol 86, 1983, p 65–72
17. W. Tabakoff, M.F. Malak, and A. Hamed, *AIAA J.*, Vol 25, 1987, p 721–726
18. J.E. Goodwin, W. Sage, and G.P. Tilly, Study of Erosion by Solid Particles, *Proc. Inst. Mech. Eng.*, Vol 184, 1969, p 279–291

Solid Particle Erosive Wear Testing

Ian M. Hutchings, University of Cambridge (England)

Measurement of Particle Velocity

Since impact velocity is a very important variable in erosion, accurate measurement of impact velocity is essential in any quantitative erosion test.

Various methods of velocity measurement have been employed. Potentially, the most accurate is laser Doppler velocimetry (LDV), which can provide statistical information on particle speed and direction of motion at any selected point close to, or distant from, the specimen surface. Laser Doppler velocimetry has been applied to gas-blast, centrifugal accelerator, and wind tunnel tests (Ref 17, 19), but the apparatus can be bulky and expensive, and for many purposes simpler methods are adequate.

An early method, still valuable and widely used, is the rotating double-disk method (Ref 20) illustrated in Fig. 11. Two disks are rotated on a common shaft, and the stream of erodent particles is arranged to strike the upper disk, which has a thin radial slot cut in it. The lower disk is coated with a thin paint or dye film to show where particles strike it. Two erosion scars are formed: one with the disks stationary, with the particles passing through the slit in the upper disk, and the other with the disks rotating at a known speed. The angular displacement, θ , between the two scars is measured and can be used to calculate the time taken for the particles to travel the distance, L , between the disks, and hence their velocity, V . The velocity is given by:

$$V = \frac{L\omega}{\theta} \quad (\text{Eq 4})$$

where ω is the angular velocity of the rotating disks. In practical examples of this device, a high rotational speed is needed to achieve reasonable displacement of the scars and thus accuracy of measurement of the angle, θ . Values between 3000 and 10,000 revolutions per minute (rpm) are common, with a distance, L , of about 20 to 40 mm (0.8 to 1.6 in.). The method is well suited to use in an air-blast erosion test, since velocity calibration can be carried out under exactly the same conditions of particle feed rate and air pressure as used in the erosion test. Typically, the random error in measuring velocity in this way is $\pm 10\%$. There can also be a systematic error due to the aerodynamic influence of the rotating disks on particle stream, which may be 10% or even greater for very small particles of low density. A comparison of velocities measured by both the double-disk

method and LDV suggests that for a typical velocity in a gas-blast rig (45 m/s) and for rather small particles (50 μm silicon carbide or alumina), the double-disk method systematically underestimates the velocity by some 10%, although the error would be expected to be less for larger particles (Ref 19).

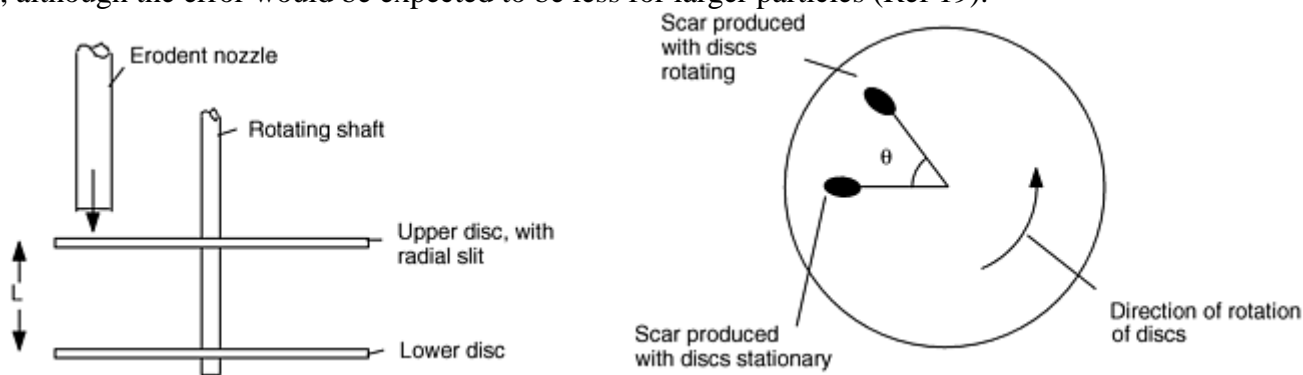


Fig. 11 Rotating disk method for measuring particle velocity. Adapted from Ref 20

Another relatively simple method, which is well suited to use with the gas-blast method, involves measuring the time of flight of the particles between two transverse light beams a short distance apart (Ref 11, 21). In one version of this method, illustrated in Fig. 12, the sensor contains a short glass tube that can be attached to the end of the nozzle; the small increase in length has been shown to have a negligible effect on the particle exit velocity (Ref 11). The timer uses infrared emitters and detectors, and the beams are collimated by two pairs of holes 1 mm (0.04 in.) in diameter, aligned perpendicularly to the axis of the nozzle. The electronic timing system contains a clock that is triggered by a decrease in light intensity of approximately 0.5%. The velocity is determined from the time taken for the particle to pass between the two beams. Inevitably, there will be some particles that will interrupt one beam but not the other, while in some cases, the particle that stops the clock may not be the one that started it. It can be shown by computer simulation of the system that even for a stream of particles all traveling with the same velocity, these effects will lead to a distribution of recorded flight times. However, in all cases, the peak in the distribution corresponds to the true flight time, from which the particle velocity can be calculated. The use of a low concentration of particles in the gas stream helps to provide a well-defined peak in the time distribution. Figure 13 shows typical data from this method, for spherical glass Ballotini particles, about 130 μm in diameter, accelerated along a straight nozzle at two different driving pressures. In this plot the times of flight have been converted into equivalent velocities over the timing distance.

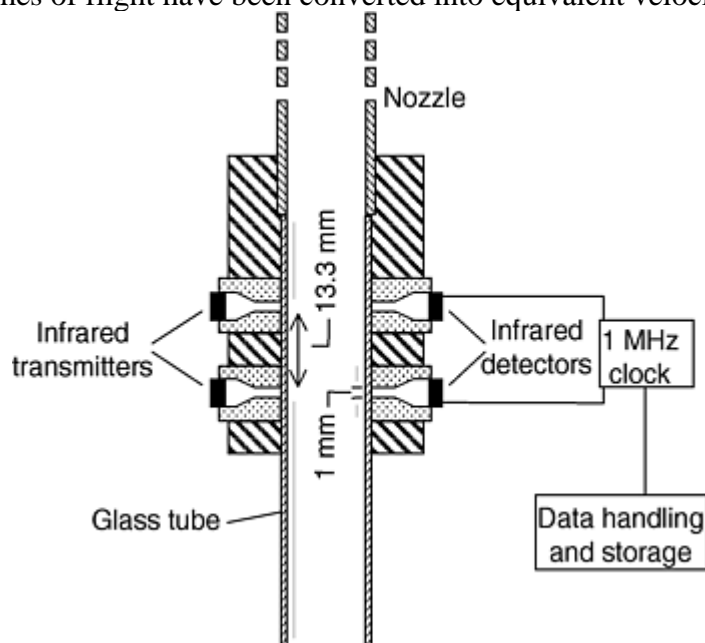


Fig. 12 Optoelectronic method of determining particle velocity, by time-of-flight measurement. Source: Ref 11

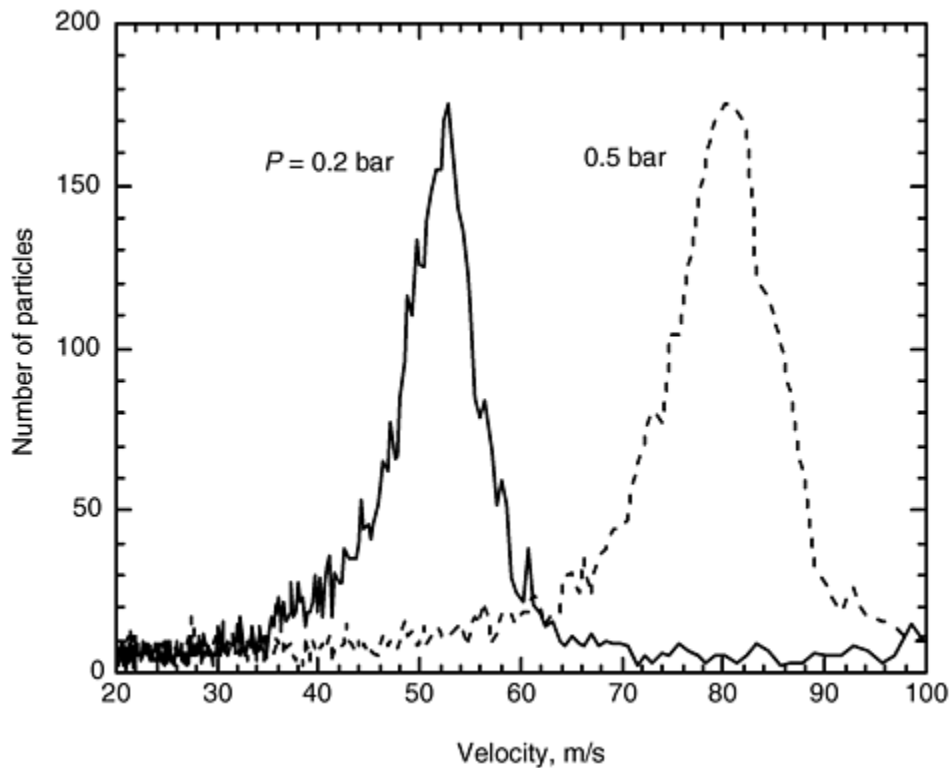


Fig. 13 Typical data from the time-of-flight method shown in Fig. 12, for 125–150 μm glass Ballotini accelerated in a gas blast rig at nozzle pressure (P) of 0.2 and 0.5 bar. Source: Ref 11

High-speed multiple-flash photography has also been successfully used to measure particle velocities and can provide a more economical alternative to LDV. Specialist equipment is needed to produce flashes of sufficiently short duration to freeze the motion of rapidly moving particles, with accurately known interflash timing. To image the small particles used in erosion testing, a relatively small field of view is needed, with sharp focus and a small depth of field. Conventional stroboscopic light sources tend to be too slow to be useful and of insufficient brightness when used at the high speeds that are needed; a means of triggering separate short-duration flash sources at precise time intervals provides a better method. Although two flashes alone are sufficient in principle to determine a velocity, confusion can occur in identifying which images correspond to each particle if there are several images in the frame, and a sequence of several flashes can provide more reliable data. Figure 14 illustrates this method and shows images of olivine sand particles leaving a horizontal gas-blast nozzle at a mean speed of 30 m/s, produced with a four-flash sequence. The image was captured with a video camera and computer frame-grabber card synchronized with the flashes. This method provides very quick image acquisition, and since the image is already in digital form, particle velocity vectors can easily and quickly be determined by suitable image analysis software.

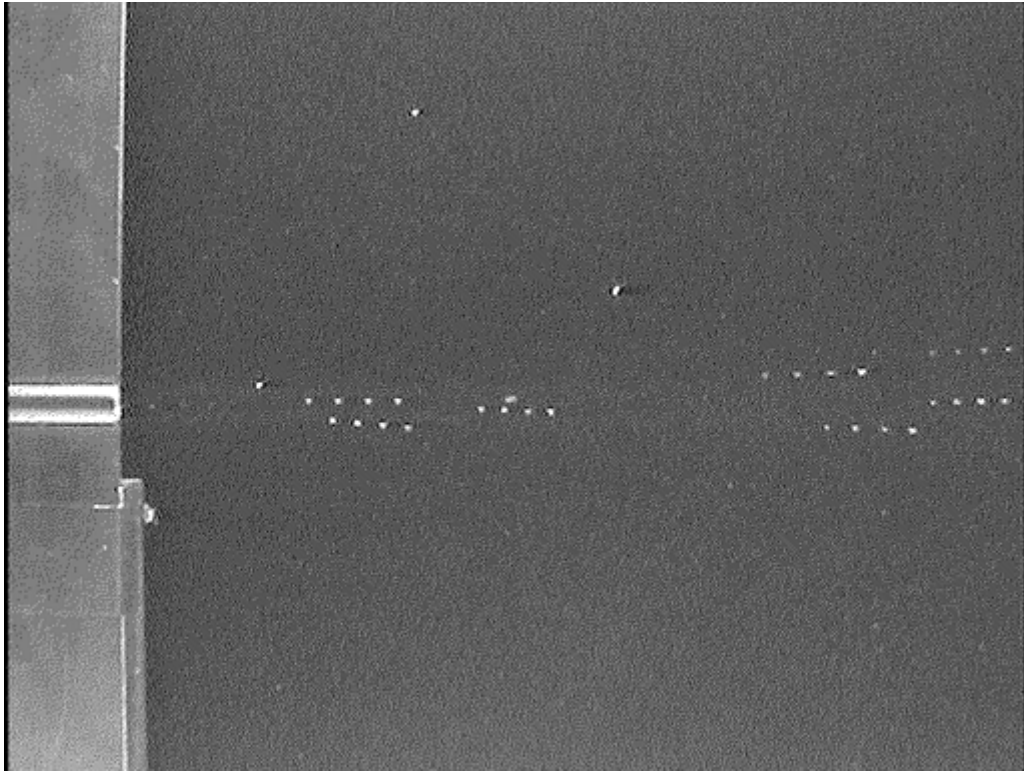


Fig. 14 Multiple flash image showing olivine sand particles leaving a horizontal gas-blast nozzle (at the left of the frame) and traveling to the right at a mean velocity of 30 ms. The particles were imaged with four short duration flashes at 0.2 ms intervals, and the frame was acquired with a video camera and computer image-grabber card. Courtesy of D.N. Allsopp and I.M. Hutchings, University of Cambridge, UK

References cited in this section

11. P.H. Shipway and I.M. Hutchings, Influence of Nozzle Roughness on Conditions in a Gas-Blast Erosion Rig, *Wear*, Vol 162–164, 1993, p 148–158
17. W. Tabakoff, M.F. Malak, and A. Hamed, *AIAA J.*, Vol 25, 1987, p 721–726
19. V. Ponnaganti, D.E. Stock, and G.L. Sheldon, Measurement of Particle Velocities in Erosion Processes, *Polyphase Flow and Transport Technology*, R.A. Bajura, Ed., ASME, 1980, p 217–222
20. A.W. Ruff and L.K. Ives, Measurement of Solid Particle Velocity in Erosive Wear, *Wear*, Vol 35, 1975, p 195–199
21. T.H. Kosel and K. Anand, An Optoelectronic Erodent Particle Velocimeter, *Corrosion and Particle Erosion at High Temperatures*, V. Srinivasan and K. Vedula, Ed., The Minerals, Metals and Materials Society, 1989, p 349–368

Solid Particle Erosive Wear Testing

Ian M. Hutchings, University of Cambridge (England)

Data Analysis and Interpretation

Most erosion tests are performed to determine the rate of material removal, and the primary measurement of material loss is by weighing. Since the mass loss to be measured will usually be small, often less than 1 mg, it is very important that the balance used to weigh the specimen has adequate sensitivity and long-term stability. The latter point is important, since an erosion experiment may last for several hours or even days, and the measurement involves determining small changes in the mass of a specimen that has a much larger mass itself. The balance must be carefully zeroed before each weighing. Temperature control in the balance room may be necessary, and a “control” specimen similar in mass to the erosion specimen but not exposed to erosion may be useful to reduce random errors in weighing. A well-defined protocol must be adopted to clean the specimen (for example, with a clean, dry blast of compressed air) before each weighing. With such precautions, and by using a well-characterized erosion test operated under stable conditions, it is possible to achieve highly reproducible measurements of erosion rate. Figure 15(a)(a) shows data from a low carbon steel specimen eroded by three 100 g quantities of olivine sand in a gas-blast erosion test at 20 m/s and 30° impact angle. The plot is linear (with a regression coefficient of 0.9997), leading to high confidence in the measured erosion value, and in this case, a single test in which the specimen was exposed to 300 g of erodent would have yielded essentially the same erosion rate.

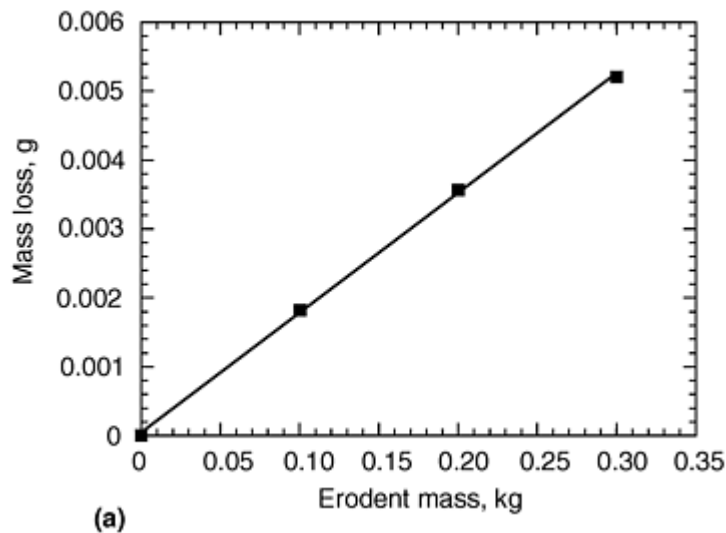


Fig. 15(a)

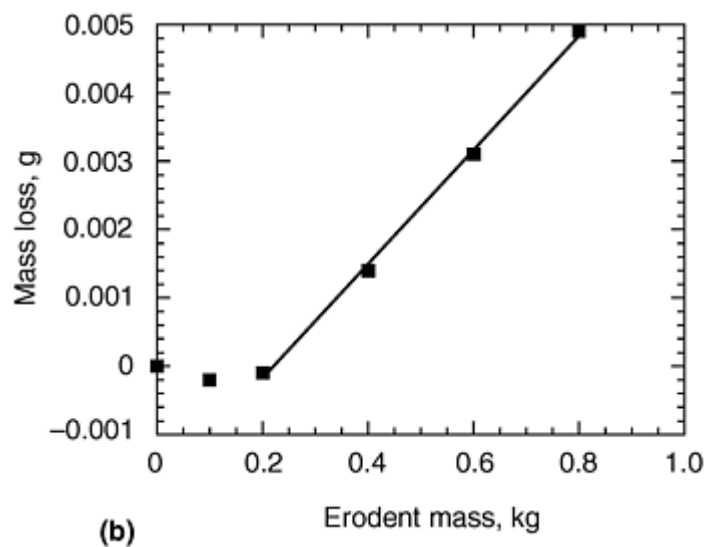


Fig. 15(b)

Typical erosion data from tests in a gas-blast rig with 300–425 μm olivine sand particles. (a) Mild steel specimen, 20 m/s, 30° impact angle. (b) Glass-bonded alumina ceramic specimen, 30 m/s, 90° impact angle. Courtesy of D.N. Allsopp and I.M. Hutchings, University of Cambridge, UK

In some circumstances, as just noted, materials may exhibit an incubation period of lower mass loss, or even mass gain, before steady state erosion occurs. Data showing this effect are illustrated in Fig. 15(b)(b) for a sintered alumina ceramic sample eroded at 30 m/s and 90 ° impact angle. Linear behavior was exhibited only after some 200 g of erodent had struck the specimen, but if a single measurement of mass loss had been made after exposure to, for example, 400 or even 800 g of erodent, the resulting value of mean erosion rate would not have accurately reflected the true steady state behavior of the sample. It is therefore essential that enough data are gathered from the sample to enable its steady state erosion behavior to be accurately assessed. This may involve preliminary testing to establish the exposure needed to achieve steady state conditions.

Although reproducibility within a single laboratory can be good, erosion test results obtained in different laboratories often show greater variability (Ref 22). The most important source of this is in the method and accuracy of measurement of particle velocity. Different methods of erosion testing may also introduce subtle, but important, differences in the particle motion. For example, there is evidence (Ref 23) that particle rotation plays an important role in explaining differences in erosion rate seen with gas-blast and rotating disk erosion testers (Ref 13).

References cited in this section

13. A.J. Burnett, S.R. De Silva, and A.R. Reed, Comparisons between Sand Blast and Centripetal Effect Accelerator Type Erosion Testers, *Wear*, Vol 186–187, 1995, p 168–178
22. A.W. Ruff, Analysis of Interlaboratory Test Results of Solid Particle Impingement Erosion, *Wear*, Vol 108, 1986, p 323–335
23. M.S.A. Bradley, University of Greenwich, UK, 1999, private communication

Solid Particle Erosive Wear Testing

Ian M. Hutchings, University of Cambridge (England)

Data Analysis and Interpretation

Most erosion tests are performed to determine the rate of material removal, and the primary measurement of material loss is by weighing. Since the mass loss to be measured will usually be small, often less than 1 mg, it is very important that the balance used to weigh the specimen has adequate sensitivity and long-term stability. The latter point is important, since an erosion experiment may last for several hours or even days, and the measurement involves determining small changes in the mass of a specimen that has a much larger mass itself. The balance must be carefully zeroed before each weighing. Temperature control in the balance room may be necessary, and a “control” specimen similar in mass to the erosion specimen but not exposed to erosion may be useful to reduce random errors in weighing. A well-defined protocol must be adopted to clean the specimen (for example, with a clean, dry blast of compressed air) before each weighing. With such precautions, and by using a well-characterized erosion test operated under stable conditions, it is possible to achieve highly reproducible measurements of erosion rate. Figure 15(a)(a) shows data from a low carbon steel specimen eroded by three 100 g quantities of olivine sand in a gas-blast erosion test at 20 m/s and 30° impact angle. The plot is linear (with a regression coefficient of 0.9997), leading to high confidence in the measured erosion value, and in this case, a single test in which the specimen was exposed to 300 g of erodent would have yielded essentially the same erosion rate.

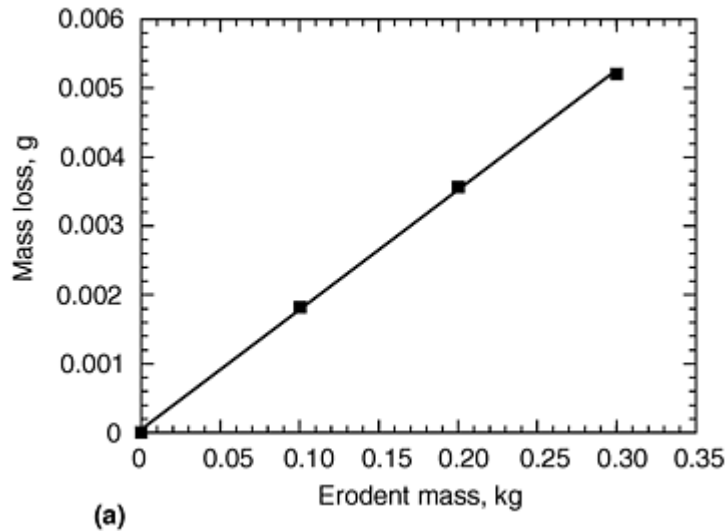


Fig. 15(a)

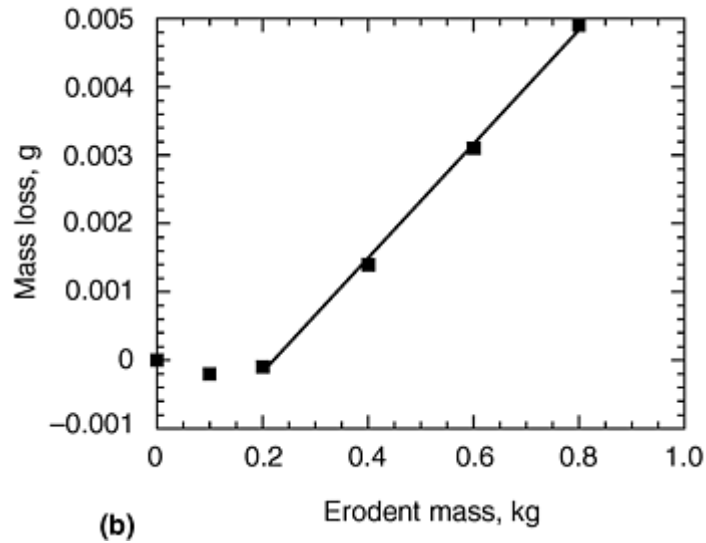


Fig. 15(b)

Typical erosion data from tests in a gas-blast rig with 300–425 μm olivine sand particles. (a) Mild steel specimen, 20 m/s, 30° impact angle. (b) Glass-bonded alumina ceramic specimen, 30 m/s, 90° impact angle. Courtesy of D.N. Allsopp and I.M. Hutchings, University of Cambridge, UK

In some circumstances, as just noted, materials may exhibit an incubation period of lower mass loss, or even mass gain, before steady state erosion occurs. Data showing this effect are illustrated in Fig. 15(b)(b) for a sintered alumina ceramic sample eroded at 30 m/s and 90° impact angle. Linear behavior was exhibited only after some 200 g of erodent had struck the specimen, but if a single measurement of mass loss had been made after exposure to, for example, 400 or even 800 g of erodent, the resulting value of mean erosion rate would not have accurately reflected the true steady state behavior of the sample. It is therefore essential that enough data are gathered from the sample to enable its steady state erosion behavior to be accurately assessed. This may involve preliminary testing to establish the exposure needed to achieve steady state conditions.

Although reproducibility within a single laboratory can be good, erosion test results obtained in different laboratories often show greater variability (Ref 22). The most important source of this is in the method and accuracy of measurement of particle velocity. Different methods of erosion testing may also introduce subtle, but important, differences in the particle motion. For example, there is evidence (Ref 23) that particle rotation plays an important role in explaining differences in erosion rate seen with gas-blast and rotating disk erosion testers (Ref 13).

References cited in this section

13. A.J. Burnett, S.R. De Silva, and A.R. Reed, Comparisons between Sand Blast and Centripetal Effect Accelerator Type Erosion Testers, *Wear*, Vol 186–187, 1995, p 168–178
22. A.W. Ruff, Analysis of Interlaboratory Test Results of Solid Particle Impingement Erosion, *Wear*, Vol 108, 1986, p 323–335
23. M.S.A. Bradley, University of Greenwich, UK, 1999, private communication

Solid Particle Erosive Wear Testing

Ian M. Hutchings, University of Cambridge (England)

References

1. “Standard Terminology Relating to Wear and Erosion,” G 40, *Annual Book of ASTM Standards*, ASTM, 1998
2. I.M. Hutchings, *Tribology: Friction and Wear of Engineering Materials*, CRC Press, Inc., 1992, p 171–197
3. *Manual on Testing Sieving Methods*, *ASTM Manual 32*, ASTM, 1998
4. “Test Sieving,” BS 1796-1, British Standards Institution, London (also ISO 2591-1)
5. P.H. Shipway and I.M. Hutchings, The Role of Particle Properties in the Erosion of Brittle Materials, *Wear*, Vol 193, 1996, p 105–113
6. S. Bahadur and R. Badruddin, Erodent Particle Characterization and the Effect of Particle Size and Shape on Erosion, *Wear of Materials 1989*, K.C. Ludema, Ed., ASME, 1989, p 143–153
7. “Standard Test Method for Conducting Erosion Tests by Solid Particle Impingement Using Gas Jets,” G 76, *Annual Book of ASTM Standards*, ASTM
8. G.L. Sheldon, J. Maji, and C.T. Crowe, Erosion of a Tube by Gas-Particle Flow, *J. Eng. Mater. Technol. (Trans. ASME)*, Vol 99, 1977, p 138–142
9. D.B. Marshall et al., Particle Size Distribution Effects on the Solid Particle Erosion of Brittle Materials, *Wear*, Vol 71, 1981, p 363–373
10. D.R. Andrews, S.M. Walley, and J.E. Field, Solid Particle Erosion Studies in the Cavendish Laboratory, Paper 36, *Proc. 6th Int. Conf. on Erosion by Liquid and Solid Impact*, Cavendish Laboratory, Cambridge, UK, 1983
11. P.H. Shipway and I.M. Hutchings, Influence of Nozzle Roughness on Conditions in a Gas-Blast Erosion Rig, *Wear*, Vol 162–164, 1993, p 148–158
12. A.N.J. Stevenson and I.M. Hutchings, Scaling Laws for Particle Velocity in the Gas-Blast Erosion Test, *Wear*, Vol 181–183, 1995, p 56–62

13. A.J. Burnett, S.R. De Silva, and A.R. Reed, Comparisons between Sand Blast and Centripetal Effect Accelerator Type Erosion Testers, *Wear*, Vol 186–187, 1995, p 168–178
14. I.R. Kleis and K.K. Uuemyis, Mechanical Rigs for Studying Abrasive Erosion, *Russ. Eng. J.*, Vol 51, 1971, p 13–15
15. S. Söderberg, S. Hogmark, U. Engman, and H. Swahn, Erosion Classification of Materials Using a Centrifugal Erosion Tester, *Tribol. Int.*, Dec 1981, p 333–343
16. W. Tabakoff, Experimental Study on the Effects of Specimen Sizes on Erosion, *Wear*, Vol 86, 1983, p 65–72
17. W. Tabakoff, M.F. Malak, and A. Hamed, *AIAA J.*, Vol 25, 1987, p 721–726
18. J.E. Goodwin, W. Sage, and G.P. Tilly, Study of Erosion by Solid Particles, *Proc. Inst. Mech. Eng.*, Vol 184, 1969, p 279–291
19. V. Ponnaganti, D.E. Stock, and G.L. Sheldon, Measurement of Particle Velocities in Erosion Processes, *Polyphase Flow and Transport Technology*, R.A. Bajura, Ed., ASME, 1980, p 217–222
20. A.W. Ruff and L.K. Ives, Measurement of Solid Particle Velocity in Erosive Wear, *Wear*, Vol 35, 1975, p 195–199
21. T.H. Kosel and K. Anand, An Optoelectronic Eroding Particle Velocimeter, *Corrosion and Particle Erosion at High Temperatures*, V. Srinivasan and K. Vedula, Ed., The Minerals, Metals and Materials Society, 1989, p 349–368
22. A.W. Ruff, Analysis of Interlaboratory Test Results of Solid Particle Impingement Erosion, *Wear*, Vol 108, 1986, p 323–335
23. M.S.A. Bradley, University of Greenwich, UK, 1999, private communication

Solid Particle Erosive Wear Testing

Ian M. Hutchings, University of Cambridge (England)

Selected References

- W.F. Adler, Ed., Erosion: Prevention and Useful Applications, *ASTM Special Technical Publication 664*, ASTM, 1977
- I. Finnie, Erosion of Surfaces by Solid Particles, *Wear*, Vol 3, 1960, p 87–103
- I.M. Hutchings, *Tribology: Friction and Wear of Engineering Materials*, CRC Press, Inc. and Edward Arnold, London, 1992
- I.M. Hutchings and J.A. Little, Eds., *Proc. 8th Int. Conf. on Erosion by Liquid and Solid Impact*, Cambridge, UK, published in *Wear*, Vol 186–187, 1995
- A.V. Levy, *Solid Particle Erosion and Erosion-Corrosion of Materials*, ASM International, 1995
- J.A. Little, Ed., *Proc. Int. Conf. on Erosive and Abrasive Wear, Incorporating 9th Int. Conf. on Erosion by Liquid and Solid Impact*, Cambridge, UK, published in *Wear*, Vol 235, 1999
- C.M. Preece, Ed., Erosion, *Treatise on Materials Science and Technology*, Vol 16, Academic Press, New York, 1979

- J.E. Ritter, Ed., *Erosion of Ceramic Materials*, Trans Tech Publications, Switzerland; also published as *Key Engineering Materials*, Vol 71, 1992

Sliding Contact Damage Testing

Introduction

SURFACE DAMAGE from sliding contact is related to the adhesion of the mating surfaces in contact. Adhesion is a major contributor to sliding resistance (friction) and can cause loss of material at the surface (i.e., wear) or surface damage without a loss of material at the surface (e.g., galling or scuffing). Adhesion is clearly demonstrated in sliding systems when a shaft seizes in a bearing.

The types of surface damage caused by sliding contact include adhesive wear, galling, and fretting. These three damage mechanisms are all influenced by adhesion of the mating surfaces, but these categories also reflect the nature of the surface damage and the type of sliding contact. For example, galling is considered a severe form of adhesive wear that occurs when two surfaces slide against each other at relatively low speeds and high loads. Fretting is also a special case of adhesive wear that occurs from oscillatory motion of relatively small amplitude.

The third damage type, adhesive wear, is a little more ambiguous. Often adhesive wear is defined by excluding other forms of wear. For example, if no abrasive substances are found, if the amplitude of sliding is greater than that in fretting, and if the rate of material loss is not governed by the principles of oxidation, adhesive wear is said to occur. In most cases, however, adhesive wear involves a transfer of material from one surface to another. Adhesive wear also occurs typically from the sliding contact of two surfaces, where interfaces in contact are made to slide and the locally adhered regions must separate, leaving transferred material. Breakout of this transferred material will form additional debris. This separation of material results in a wide range of wear rates, depending on the type of contact and the adhesion between the mating surfaces.

This article describes the methods for evaluation of surface damage caused by sliding contact. The first section, "Adhesive Wear," describes wear testing from long-distance sliding of nominally clean and dry (unlubricated) surfaces. This is followed by sections on test methods for galling and fretting wear, which are more unique forms of adhesive wear and surface damage. Additional information on sliding contact damage can be found in *Friction, Lubrication, and Wear Technology*, Volume 18 of *ASM Handbook*.

Sliding Contact Damage Testing

Adhesive Wear

W.A. Glaeser, Battelle

Adhesive wear typically occurs from sliding contact and is often manifested by a transfer of material between the contacting surfaces. As an example, Fig. 1 shows bronze transfer to a steel surface under sliding contact. Transfer can be minute and only visible in the microscope. Deformation wear, or plastic deformation of a thin surface layer during sliding contact, can also fall under the definition of adhesive wear. Adhesive wear can occur along with abrasive or chemical wear conditions. A transfer layer can build up on the harder surface of a sliding pair in the form of a mechanically mixed material (Ref 1). The transfer layer can also contain compacted wear debris. This layer will tend to break out and form wear debris.

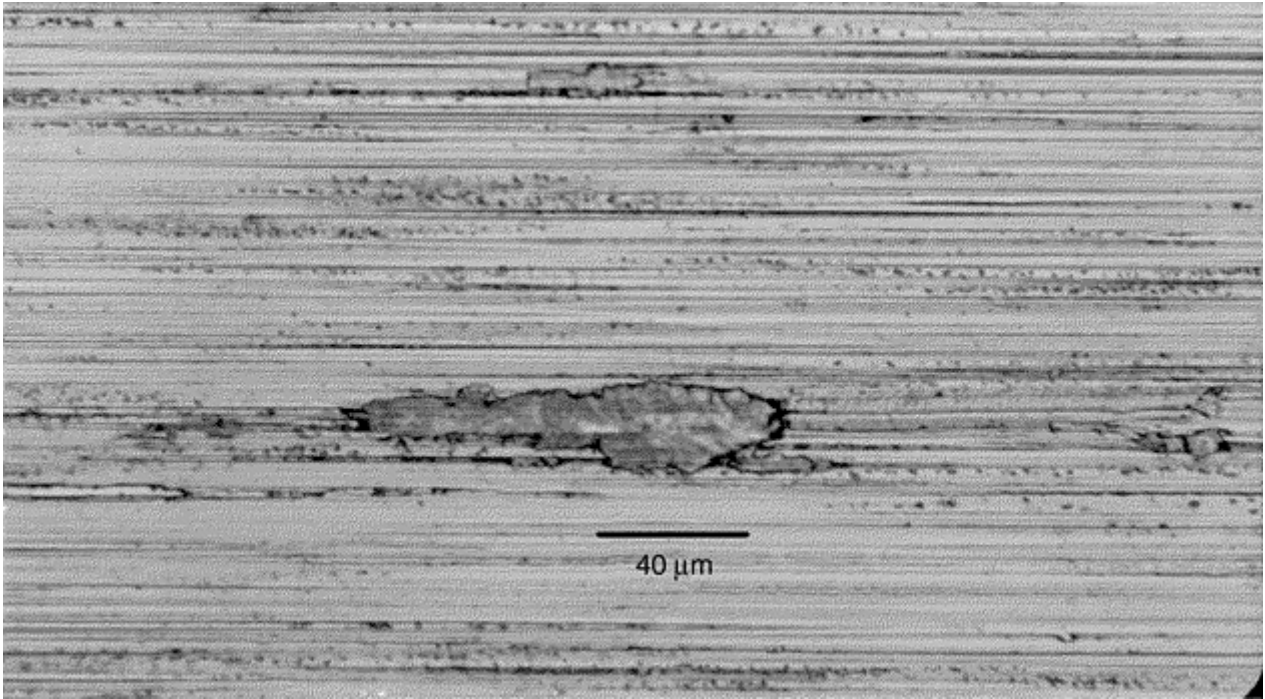


Fig. 1 Bronze transfer to a steel surface after adhesive wear during sliding contact

Adhesive wear is a function of material combination, lubrication, and environment. For instance, austenitic stainless steels (AISI 304, 316, etc.) sliding against themselves are very likely to transfer and gall with severe surface damage. Other materials that are prone to adhesive wear include titanium, nickel, and zirconium. These materials make very poor unlubricated sliding pairs and can wear severely in adhesive mode even when lubricated. Other metals are apt to show adhesive wear when dry sliding contact occurs. Rubber tends to bond to smooth, dry surfaces (glass and polymers) by weak van der Waals forces and slide in a stick-slip mode that involves adhesion.

A gaseous environment is an important factor in promoting adhesive wear. The lack of oxygen and water vapor in a wear environment can aggravate adhesive wear. High vacuum conditions as found in outer space will make adhesive wear likely. Wear tests run in simulated space conditions (10^{-10}) torr reveal tendencies for various material combinations to develop adhesive wear in that environment (Ref 2).

Adhesive wear testing can be carried out with a variety of sliding contact systems. These include four-ball, block-on-ring, pin-on-disk, crossed cylinders, flat-on-flat, and disk machines. Examples are shown in Fig. 2.

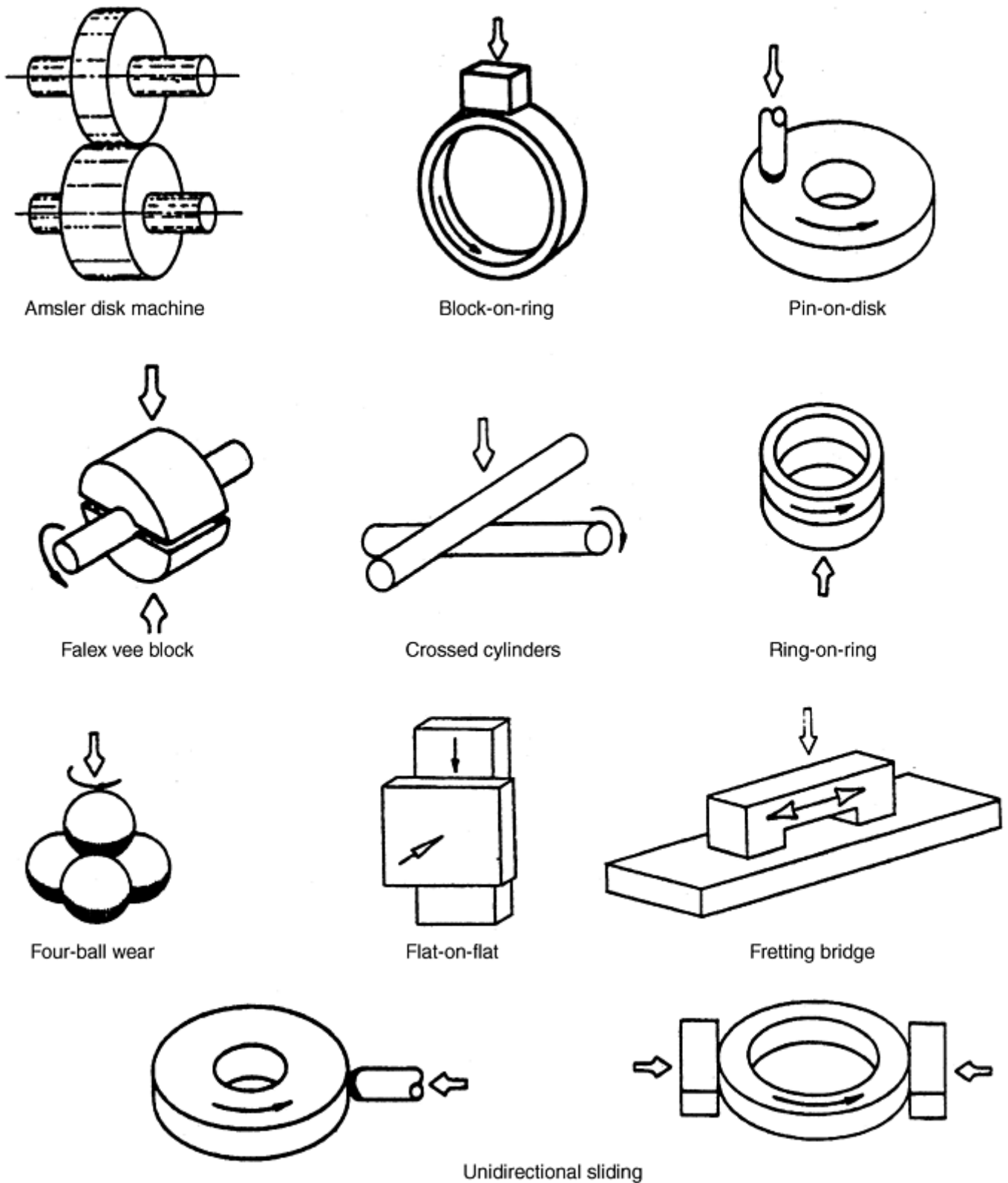


Fig. 2 Diagrams of contact types for various test machines

Adhesive wear testing (sliding contact wear, no lubrication, slow motion, heavy load) may be chosen deliberately to investigate the resistance of a material to excessive wear and material transfer for a given application. Adhesive wear can also occur unexpectedly in a sliding contact test and should be recognized from the wear morphology. Typical wear scars associated with adhesive wear are shown in Fig. 3 and 4. Figure 4(a) shows a scanning electron microscope (SEM) micrograph of an embedded steel particle in an aluminum bearing surface; the particle is identified by the energy-dispersive x-ray spectrometry (EDX) pattern for iron shown in Fig. 4(b). The test can be designed to determine load capacity or effects of temperature on the onset of

adhesive wear. These data would then be used in the design of a bearing or gear system that could operate safely in the conditions simulated in the test.



Fig. 3 SEM micrograph of adhesive wear of cast iron

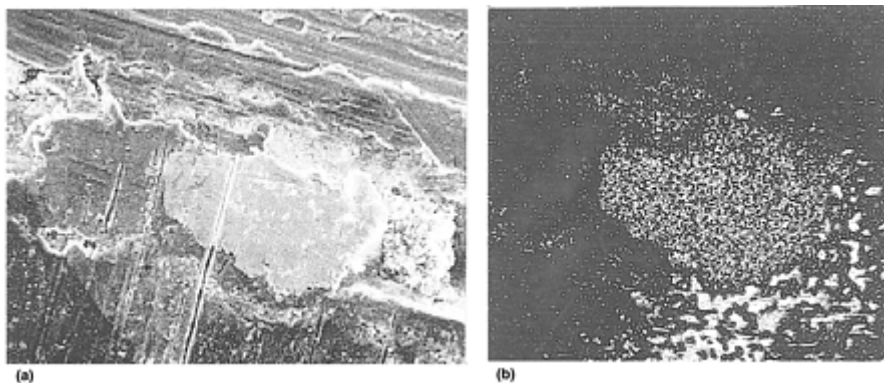


Fig. 4 Scar from adhesive wear. (a) SEM micrograph of wear scar on an aluminum bearing with embedded steel particle from the shaft. 200× (b) EDX pattern for iron in the particle. 200×

References cited in this section

1. P. Heilman, J. Don, T.C. Sun, W.A. Glaeser, and D.A. Rigney, Sliding Wear and Transfer, *Proc. Int. Conf. Wear of Materials*, American Society of Mechanical Engineers, 1989, p 1–8
2. W.R. Jones, S. Pepper, et al., The Preliminary Evaluation of Liquid Lubricants for Space Applications by Vacuum Tribometry, *28th Aerospace Mechanisms Symposium*, National Aeronautics and Space Administration, May 1994

Adhesive Wear Terms

Adhesive wear from sliding contact occurs from the transference of material from one surface to another due to a process of solid-phase welding (Ref 3). Particles that are removed from one surface are either permanently or temporarily attached to the other surface. There are also a number of other terms used to describe adhesive wear conditions, defined as follows.

Asperity refers to an isolated high spot in a given surface-roughness profile or a protuberance in the small-scale topographical irregularities of a solid surface.

Cold welding is the bonding of surface contact points after localized softening or melting caused by the frictional heating of contacting asperities during sliding.

Galling is a severe form of scuffing and is often associated with gross damage to the surfaces or failure. The usage of the term galling has different intents, and therefore its meaning must be ascertained from the specific context of the usage. Galling can be considered to be a severe form of adhesive wear, where cold welding of asperities causes heavy transfer of surface material.

Scuffing is the formation of severe scratches in the sliding direction. Also referred to as *scoring*, scuffing is considered a milder form of galling. It occurs when cold-welded junctions leave hardened protrusions, which tend to plow and scratch the softer mating surface much like abrasion.

Seizure is the stopping of relative motion as a result of interfacial friction or by gross surface welding. Seizure is an adhesive wear condition, where cold welding and material transfer result in loss of clearance between mating surfaces.

Wear coefficient is a nondimensional number that is typically defined as the proportionality k factor in the Archard wear formula (Ref 4):

$$W = kLD/H$$

where W is wear volume, L is normal load or force, D is distance of sliding, H is hardness, and k is wear coefficient.

This equation *assumes a linear process*; that is, wear is proportional to the applied load and distance, and inversely proportional to hardness. This equation is used extensively in developing data from wear tests. As an example, assume a pin-on-disk wear test is run using a copper pin. The operating conditions are as follows (a detailed description of the calculation and use of the wear coefficient can be found in Ref 5):

Normal load, N (kgf)	19.6 (2)
Disk speed, rpm	80
Track diameter, mm (in.)	32 (1.3)
Test duration, h	2
Pin weight loss, mg (grains)	23.1 (0.35)
Hardness of pin, HV	80
Density of copper, g/cm³ (lb/in.³)	8.9 (0.3)

The wear coefficient is calculated as follows:

$$W = 23.1 / 8.9 = 260 \text{ mm}^3$$

$$D = \pi \times 32 \times 80 \times 120 = 9.65 \times 10^5 \text{ mm}$$

$$k = 2.60 \times 80 / 9.65 \times 10^5 \times 2 = 1.08 \times 10^{-4}$$

Wear Life Determination. Assume a 10 mm diam copper pin electrode rides against a rotating steel surface running at 100 rpm and the allowable shortening of the pin due to wear is 10 mm. The pin load is 1 kg. The track diameter is 70 mm. What is the approximate life of the pin?

$$k = 1.08 \times 10^{-4}$$

$$\text{Pin wear volume} = \pi \times 100 \times 10 = kLD/H$$

$$D = (3.14 \times 10^3 \times 80) / 1.08 \times 10^{-4}$$

$$= 2.32 \times 10^9 \text{ mm}$$

$$D = \pi \times 70 \times 100 \times \text{time}$$

$$\text{Time} = 2.32 \times 10^9 / 2.2 \times 10^4$$

$$= 1.05 \times 10^5 \text{ min, or 1750 h}$$

Specific wear is similar to wear coefficient, except that the hardness factor is not included. This is often used when determining the wear properties of materials of similar hardness.

References cited in this section

3. Glossary of Terms, *Friction, Lubrication, and Wear Technology*, Vol 18, *ASM Handbook*, P. Blau, Ed., ASM International, 1992
4. E. Rabinowicz, Wear Coefficient—Metals, *Wear Control Handbook*, American Society of Mechanical Engineers, 1980, p 475–506
5. E. Rabinowicz, Wear Coefficient—Metals, *Wear Control Handbook*, American Society of Mechanical Engineers, 1980, p 475–484

Sliding Contact Damage Testing

Selecting Standard Adhesive Wear Tests

Generally, adhesive wear testing involves sliding contact between unlubricated parts. For instance, such testing might help identify a material combination for a slow-moving brake or clutch system. Testing also could assist in operating a sleeve bearing in a high vacuum or oxygen and water-vapor-free environment. The purpose might be to estimate the wear life of such an operating system. The wear coefficient can be obtained from an appropriate wear test apparatus, and the maximum wear loss can be specified.

Simulation of Operating Conditions. In selecting a standard wear test, it is important that the test come close to simulating the prospective operating conditions of the mechanism of concern. The test should simulate the following conditions:

Contact
Point contact (ball-on-flat, ball-on-ball, crossed cylinders)
Line contact (roller-on-flat; roller-on-roller, axes parallel)
Flat-on-flat
Conforming (sleeve or journal bearing)
Velocity and load (high speed, low load; low speed, high load; low speed, low load)
Temperature
Vibration
Gaseous environment

Contact conditions can be selected from a number of wear test configurations as are shown in Fig. 2. These are taken from standard wear tests, and many can be found in ASTM specifications. The Amsler and Falex vee block represent line contact systems. Point contact is represented in pin-on-disk, crossed cylinders and four-ball tests, while flat-on-flat is shown in ring-on-ring, fretting bridge, and flat-on-flat configurations.

The following ASTM standards apply to the configurations shown in Fig. 2:

Test	ASTM No.	Title
Block-on-ring	G 77	Standard Test Method for Ranking Resistance of Materials to Sliding Wear, Using Block-on-Ring Test
Crossed cylinders	G 83	Standard Test Method for Wear Testing with a Crossed Cylinder Apparatus
Pin-on-disk	G 99	Standard Test Method for Wear Testing with a Pin-on-Disk Apparatus
Falex vee block	D 2670	Standard Test Method for Measuring Wear Properties of Fluid Lubricants (Falex Pin and Fee Block Method)
Four-ball	D 4172	Standard Test Method for Wear Preventive Characteristics of Lubrication Fluid (Four-Ball Method)

These standards are also available in Ref 6.

Temperature and Friction. Wear tests should have continuous measurement of both specimen temperature and friction. Temperature can be measured by a thermocouple inserted in the stationary specimen near the contact surface. A number of standard tests found in ASTM specifications have friction measuring devices included in the description of the apparatus.

Velocity and Load. Archard's equation, as a general model of wear, assumes that wear is proportional to the applied load and sliding distance. Distance and velocity are related, and so wear is also proportional to velocity by Archard's equation. Because it is desirable and economical to run wear tests as quickly as possible, both the load and the velocity can be increased to speed up a test. However, increasing these parameters will also increase the frictional heat generation and can lead to overheating. Overheating will change the wear mode (increasing galling and surface damage) and will result in misleading wear data. This is particularly important in wear testing of polymers. Polymers have low thermal conductivity and low melting and softening points compared to metals. Therefore, before embarking on a series of wear tests for statistical analysis, a set of preliminary tests should be run to establish the most efficient method, while keeping the wear mode as expected in the application.

Reference cited in this section

6. *Friction and Wear Testing: Source Book of Selected References from ASTM Standards and ASM Handbooks*, ASM International, 1997

Sliding Contact Damage Testing

Statistical Analysis of Wear Data

Data scatter is inherent in any testing, and using a statistical approach to the analysis of wear data is desirable. The method in ASTM G 83 (Ref 7) recommends sample sizes over 10. However, because 10 samples may not be possible owing to availability of samples and cost, ASTM G 83 does provide a method for analysis with sample sizes less than 10. The method uses the range of test results, where the range, R , is the difference between the highest and lowest test values for an initial set (2 to 10 samples) of measurements. For these small sample sizes, the standard deviation (s) can be calculated from the R value instead of from the root mean square value. For sample sizes from 2 to 10, the standard deviation is calculated from the range of the first few test results as follows:

$$s = R/d_2$$

where the values for d_2 are listed in Table 1 for different sample sizes.

Table 1 Factors for estimating standard deviation for sample sizes 10 and less

Sample size	d_2
2	1.128
3	1.693
4	2.059
5	2.326
6	2.534
7	2.704
8	2.847
9	2.970
10	3.078

Standard deviation $s = R/d_2$ for small sample size, where the range R is the difference between the highest and lowest test values for an initial set (2 to 10 samples) of measurements.

Source: Ref 7

Sample size (n) estimate can be derived from the relation:

$$n = 1.96 v/e^2$$

where v is the percent coefficient of variation = $(s/x) \times 100(\%)$, e is the sampling error, and x is the average for n tests. For example, if $s = 0.9$ mg and $x = 8$ mg, then the coefficient of variation is 11%. If an allowable sampling error (e) is selected as 10%, the sample size for 95% confidence limits should be $(1.9 \cdot 11/10)^2 = 5$.

The results of round-robin tests from several laboratories using block-on-ring test apparatus are reported in the appendix of ASTM G 77 (and also Ref 8). This reference shows the expected scatter in such wear tests.

References cited in this section

7. "Standard Test Method for Wear Testing with a Crossed-Cylinder Apparatus," ASTM G 83, *Annual Book of ASTM Standards*
8. *Friction and Wear Testing: Source Book of Selected References from ASTM Standards and ASM Handbooks*, ASM International, 1997, p 110–114

Sliding Contact Damage Testing

Measuring Wear

A wear test should be run long enough to produce measurable wear. What constitutes measurable wear depends on the measuring method. The easiest way to determine measurable wear is to measure weight loss. This is also the coarsest method. Weight loss must be sufficient to be uninfluenced by condensed moisture, contaminants such as dust and oil, and minute transfer. Dimensional change is a more sensitive method. If a well-defined contact geometry is used such as ball-on-flat, ball-on-ball, or ring-on-flat, a scar length can be translated to volume loss. Equations for calculating wear volume from scar dimensions are shown in Fig. 5.

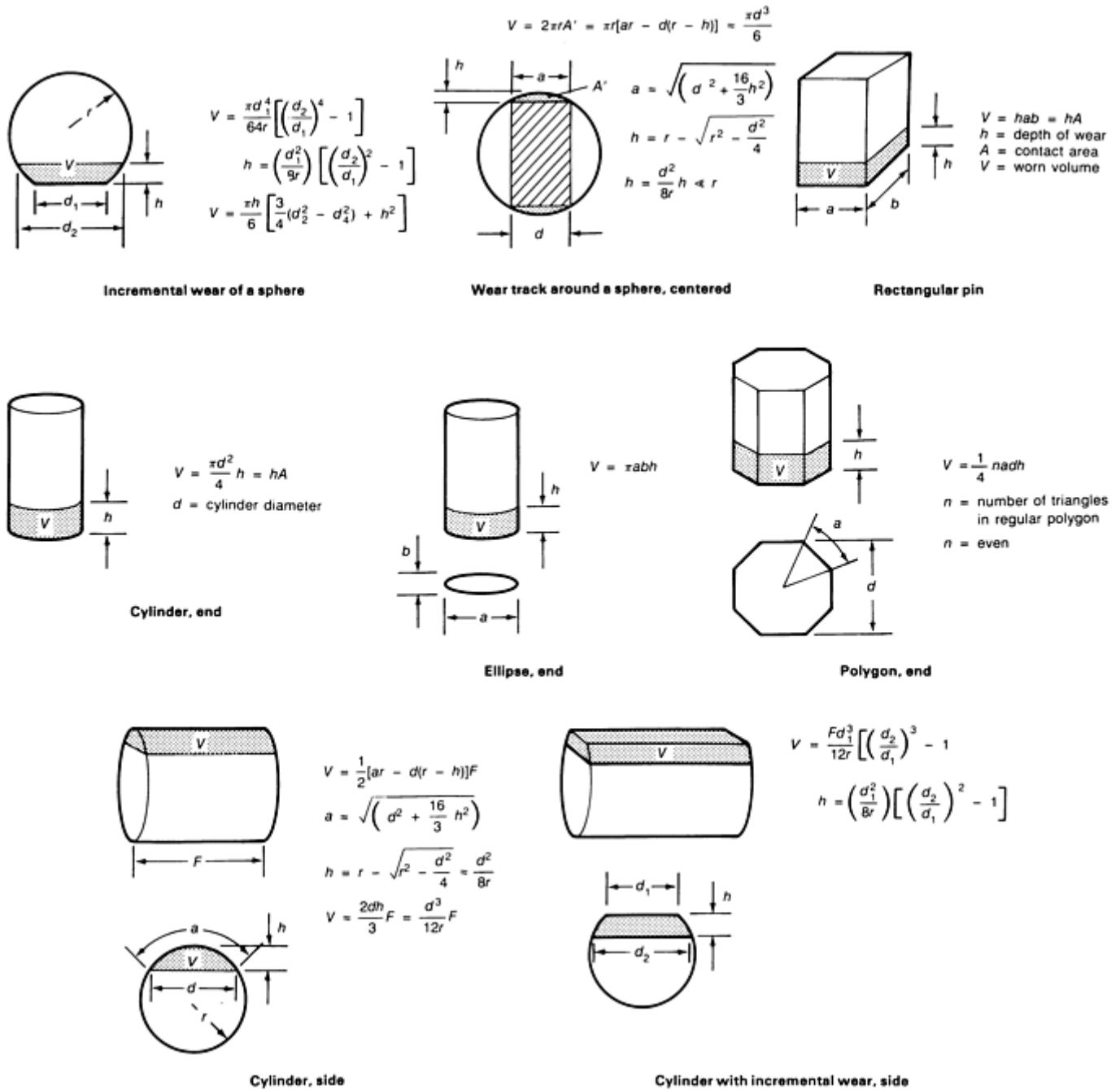


Fig. 5 Wear volume calculations for various shapes in contact with a flat surface. Source: Ref 9

Adhesive wear testing often involves some transfer from one surface to another. It is good practice to use two methods to measure wear: scar measurement and weight loss. The volumes determined from both methods can be compared, and effects of transfer, deformation, or pitting can be detected.

Reference cited in this section

9. A.W. Ruff, *Wear Measurement, Friction, Lubrication, and Wear Technology*, Vol 18, *ASM Handbook*, P. Blau, Ed., ASM International, 1992, p 362–369

Galling

John H. Magee, Carpenter Specialty Alloys

Galling is a severe form of adhesive wear or surface damage that occurs when the surface of two components slide against each other at relatively low speeds and high loads. Lubricants or coatings, designed to reduce friction and prevent galling, are sometimes either ineffective or cannot be used due to product contamination concerns. Thus, gross surface damage occurs and is characterized by localized material transfer or removal. This gross surface damage is known as galling and can occur after just a few cycles of relative movement between the mating surfaces. Severe galling can cause seizure of these parts.

When galling takes place, mated surfaces typically show distinct junctions where severe plastic deformation has occurred (Fig. 6). These contact surfaces contain areas where asperities, or surface protrusions, from one surface have bonded together with those on the other surface. Under low stresses, these junctions are minute and break apart with movement resulting in adhesive wear debris. However, higher stresses produce much larger junctions and galling (Ref 11).

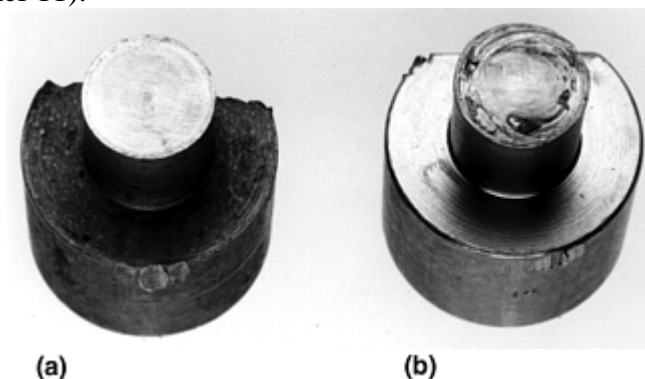


Fig. 6 Galling test button specimens, after testing. (a) No galling exhibited. (b) Severe galling. Source: Ref 10

Components that encounter galling conditions include threaded fasteners from a typical bolt/nut connection to large threaded tubular used in oil exploration. Valve parts have mating surfaces that are designed to encounter infrequent sliding movement. Galling damage on these surfaces affects valve performance, for example, leaking. The interface of a roller and side plate on a continuous chain-link conveyor belt can gall when lubrication is not used. This is an important design consideration for the conveyance of food and drug products because lubricants are prohibited due to contamination concerns (Ref 12).

The term galling has also been used to describe surface damage caused during metalworking. Metalworking processes include rolling, extrusion, wire drawing, deep drawing of sheet, and press-forming operations. Insufficient lubrication sometimes causes metal transfer and galling. In Japan, the term galling is used mainly to describe damage in sheet metalforming processes. Tests to characterize this gross surface damage usually involve production equipment or laboratory simulation of various plastic metalworking processes. Additional information can be found in Ref 13 and in *Friction, Lubrication, and Wear Technology*, Volume 18 of *ASM Handbook*.

This section describes in detail the ASTM G 98 button-on-block galling test. The purpose of this test is to rank material couples resistant to galling. Several variations of this test are also discussed that either increase the severity of the test or attempt to quantify the surface damage using profilometry. Data obtained from button-on-block testing are very useful in screening materials for prototype testing.

This section also describes prototype testing of threaded fasteners. Three threaded connection tests are discussed as examples of prototype tests designed to closely simulate field service for a specific application. This type of testing tends to be expensive, but vital before use in-service. Also, these tests can be used to solve a specific galling problem.

References cited in this section

10. J.H. Magee, Stainless Steels That Resist Wear and Galling, *Stainl. Steel World*, May 1997
11. J.H. Magee, Two Galling Resistant Stainless Steels Used for Bridge Hinge Pins, *14th Annual Bridge Conference*, June 1997 (Pittsburgh, PA), 1997, p 161–165
12. J.H. Magee, Wear of Stainless Steels, *Friction, Lubrication, and Wear Technology*, Vol 18, *ASM Handbook*, P. Blau, Ed., ASM International, 1992, p 710–724
13. H.D. Merchant and K.J. Bhansali, “Metal Transfer and Galling in Metallic Systems,” Symposium Proceeding, Oct 1986 (Orlando, FL), ASTM, 1987

Sliding Contact Damage Testing

Button-on-Block Galling Test

In the 1950s, a simple button-on-block test was developed to evaluate the galling resistance of material couples (Ref 14). A specific version of this test is defined in ASTM G 98 (Ref 6, 15). This test is generally performed on bare metals; however, nonmetallics, coatings, solid lubricants, and surface-modified alloys can be tested as well.

The button-on-block test uses available laboratory equipment capable of maintaining a constant, compressive load between two flat surfaces. Both a Brinell hardness tester and a tension-test machine have been used to perform this test. Also, Falex Corporation, a designer and manufacturer of wear test equipment, has an apparatus specifically designed for button-on-block testing.

For bare metal evaluations, both galling specimens (button and block) are ground with abrasive paper or machine ground with an abrasive wheel. Both test surfaces should have a surface finish between 0.25 and 1.1 μm (10 and 45 $\mu\text{in.}$) for the arithmetic average surface roughness (R_a). Specimen flatness should be maintained at 0.33 mm/m (0.004 in./ft) to ensure 100% contact between the specimens during testing. The only critical dimension for either specimen is the button diameter that constitutes the contact area. The standard diameter is 13 mm (0.5 in.); however, other button diameters can be used. If a different diameter is used, then it should be reported since it can affect the test result. The block specimen must have sufficient area to accommodate at least one test; however, most users have found that a block length between 75 and 150 mm (3 and 6 in.) is ideal for this multiple sample test procedure. A reasonable block width is 19 mm (0.75 in.), and a minimum width of 17 mm (0.625 in.) is necessary for testing a 13 mm (0.5 in.) button. Thickness is not critical.

Immediately prior to testing, both galling specimens are cleaned to remove machinery oils and metallic particles. The following cleaning technique is suggested for metals in ASTM G 98. First, ultrasonically clean the button and block in trichloroethane. Then, use a methanol rinse to remove any traces of trichloroethane residue. Materials with open grains (powder metals or hardfaced alloys) must be dried to remove all traces of the cleaning solvent that may be entrapped in the material. Note that because the use of trichloroethane is being discouraged, any nonchlorinated, non-film-forming cleaning agent and solvent can be used as a substitute.

Once cleaned, the specimens are mounted in the loading device, and a light compressive load, for example, 110 N (25 lb), is applied to make sure the button is properly seated on the block. The button-on-block test setup is shown in Fig. 7. A selected compressive load is then placed on the button specimen. This results in a specific compressive stress for a 13 mm (0.5 in.) button sample. The selected load is dependent on educated judgment of the galling resistance of the mated couples, that is, light loads for poor galling resistance and heavy loads for excellent galling-resistant couples. Stress cannot exceed the compressive yield strength of the button material.

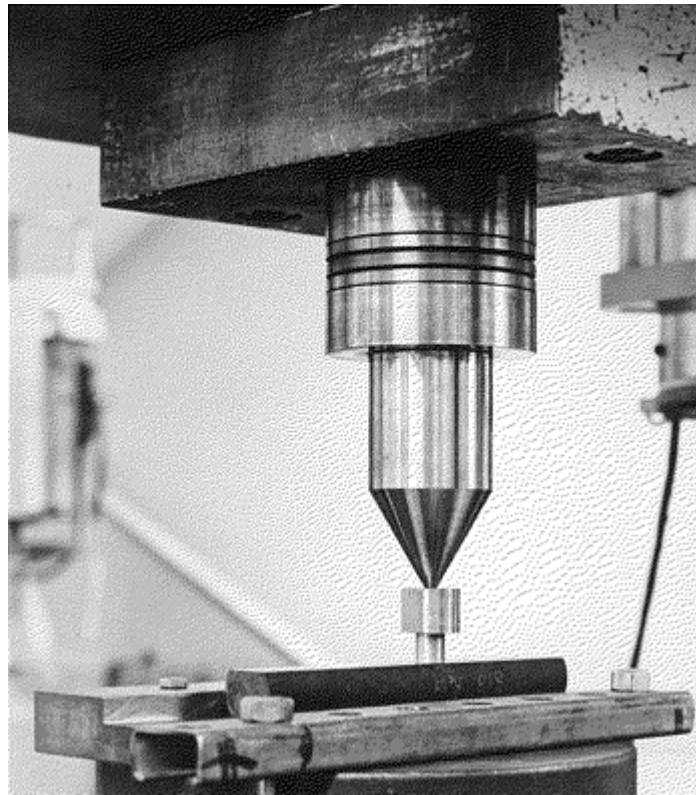


Fig. 7 Button-on-block galling test arrangement using a tension test machine. Source: Ref 16

Once loaded, the button is rotated slowly one revolution (360°) using either an open-end wrench, an adjustable wrench, or some other special tool for rotating by hand. A mechanized system may also be used to rotate one specimen relative to the other. The latter may allow torque measurement during testing. Actual sliding time should be between 3 and 20 s. Rotation direction, clockwise or counterclockwise, is not specified in ASTM G 98; however, it should be noted. The compressive load is then removed, and the mated surfaces are visually examined for galling. If specimens appear smooth and undamaged, to the unaided eye, the procedure is repeated at a higher load with an untested button specimen at a new location on the block sample. A burnished surface does not constitute a galled surface, nor does a scored surface. At least one of the contacting surfaces must exhibit torn metal. Galling has a distinct, macroscopic appearance with protrusions of metal above the original surface (Fig. 6).

If galling has occurred, testing is done at a lower load with a new button and block location to establish an interval between the highest nongalled stress and galled stress. This interval is used to define the threshold galling stress (TGS) and should be no greater than 34.5 MPa (5 ksi) for threshold stresses greater than 138 MPa (20 ksi) and no greater than 21 MPa (3 ksi) for threshold stresses of 138 MPa (20 ksi) or less. If galling is questionable or borderline, the test is repeated at a higher load to confirm the previous test result.

A typical series of galling tests is shown in Fig. 8. The reported TGS for the example is 34.5 MPa (4.5 ksi). Since the galling stress is based on the button diameter contact, the button impression on the block should be measured to determine if full contact occurred. At light loads, that may not be the case.



Fig. 8 Sequence of galling tests on block specimens. Source: Ref 17

Experience has shown that galling is most prevalent in sliding systems that are slow moving and operate intermittently. The movement of threaded components or the opening and closing of valve components are classic examples that this test method attempts to simulate. This test method has proved valuable in screening

materials for further prototypical testing that more closely simulates actual service conditions. The button and block material do not have to be the same material and hardness. When dissimilar, the selection of the button material should be the same as the sliding component being screened for the specific application. Table 2 lists threshold galling stress data for a variety of material couples using the button-on-block test. Additional data can be found in Ref 12. This test is most popular for galling-prone materials, such as stainless steels.

Table 2 Galling resistance of selected material couples (metal A vs. metal B)

Contact metal A		Contact metal B		Threshold galling stress ^(a)	
Alloy	Hardness, HB	Alloy	Hardness, HB	MPa	ksi
Silicon bronze	200	Silicon bronze	200	28	4
	200	Type 304	140	304	44
A286 (S66286)	270	A286	270	21	3
AISI 4337	484	AISI 4337	415	14	2
AISI 1034	415	AISI 1034	415	14	2
Waukesha 88	141	Type 303	180	345+	50+
	141	Type 201	202	345+	50+
	141	Type 316	200	345+	50+
	141	S17400	405	345+	50+
	141	20Cr-80Ni	180	345+	50+
Type 201	202	Type 201	202	104	15
	202	Type 304	140	14	2
	202	S17400	382	14	2
	202	Nitronic 32	231	248	36
Type 301	169	Type 416	342	21	3
	169	Type 440C	560	21	3
Type 410	322	Type 420	472	21	3
Type 416	342	Type 416	372	90	13
	372	Type 410	322	28	4
	342	Type 430	190	21	3
	342	20Cr-80Ni	180	48	7
Type 440C	560	Type 440C	604	76	11
S17400	311	Type 304	140	14	2
	380	Nitronic 32	401	90	13
	435	Type 304	140	14	2
	400	S17700	400	21	3
	435	S17700	435	14	2
Nitronic 32 (S24100)	235	S17400	380	76	11
	401	Nitronic 32	401	235	34
	235	Nitronic 32	401	235	34
	235	Type 304	140	48	7
	401	Type 304	140	90	13
Nitronic 50 (S20910)	205	AISI 1034	205	14	2
	205	Nitronic 50	205	14	2
	321	Nitronic 50	321	14	2
	205	Nitronic 32	401	90	13
	321	Nitronic 32	235	55	8
	205	Type 304	140	28	4
Nitronic 60 (S21800)	205	Type 301	169	345+	50+
	205	Type 420	472	345+	50+

	213	S17400	313	345+	50+
	205	S17400	332	345+	50+
	205	Nitronic 50	205	345+	50+
	205	S13800	297	345+	50+
	205	S13800	437	345+	50+
	205	AISI 4337	448	345+	50+
	205	Stellite 6B	415	345+	50+
	205	A286	270	338+	49+
	205	20Cr-80Ni	180	248	36
	205	Ti-6Al-4V	332	345+	50+

(a) Values shown are unlubricated threshold galling stress for the button-on-block galling test. Values given as 50+ indicate the samples did not gall.

Source: Ref 14

Multiple-Rotation Button-on-Block Testing. A modification of the standard single-rotation test is a multiple-rotation procedure. This change is designed to simulate the action of valve components. Also, repetitive sliding across the same surface results in galling at lower stress values. Thus, alloys or coatings with good-to-excellent galling resistance can be evaluated. This procedure is especially useful for screening materials for service conditions known to be severe. One example of this multiple procedure is the triple-rotation test where the button is turned counterclockwise (360°), clockwise (360°), and counterclockwise (360°). This modified button-on-block test has been used to evaluate stainless steels with improved galling resistance and for testing solid lubricants, such as molybdenum-disulfide. Table 3 compares various stainless steels using the single- and triple-rotation tests. Most stainless alloys tested have significantly lower TGS values using the triple-rotation tests. Those who use cobalt-base alloys, hardfaced materials, and metallic coatings, should consider a multiple-rotation type of test procedure.

Table 3 Threshold galling stress results for selected self-mated stainless steels

Contact alloy	UNS No.	Hardness	Threshold galling stress			
			Single rotation ^(a)		Triple rotation	
			MPa	ksi	MPa	ksi
Gall-Tough	S20161	95 HRB	104+	15+	104+	15+
		28 HRC	104+	15+	104+	15+
Nitronic 60	S21800	92 HRB	104+	15+	48	7
Nitronic 50	S24100	23 HRC	97	14	14	2
18-18 Plus	S28200	96 HRB	166	24	7	1
Type 303	S30300	85 HRB	138	20	<7	<1
Type 304	S30400	86 HRB	55	8	<7	<1
Type 420	S42000	49 HRC	55	8	14	2
Trimrita	S42010	50 HRC	104+	15+	21	3
Type 430	S43000	98 HRB	10	1.5	<7	<1
Custom 630	S44004	55 HRC	124	18	14	2
Custom 455	S45500	48 HRC	97	13	<7	<1
A 286	S66286	30 HRC	14	2	<7	<1

(a) Button-on-block test, unlubricated ground finish. +, did not gall. <, galled at this stress.

(b) ASTM G 98.

Source: Ref 12

References cited in this section

6. *Friction and Wear Testing: Source Book of Selected References from ASTM Standards and ASM Handbooks*, ASM International, 1997

12. J.H. Magee, Wear of Stainless Steels, *Friction, Lubrication, and Wear Technology*, Vol 18, *ASM Handbook*, P. Blau, Ed., ASM International, 1992, p 710–724
14. Committee of Stainless Steel Producers, “Review of the Wear and Galling Characteristics of Stainless Steels,” American Iron and Steel Institute, April 1978, p 8
15. “Standard Test Method for Galling Resistance of Materials,” ASTM G 98, *Annual Book of ASTM Standards*
16. J.H. Magee, Austenitic Stainless Steels with Improved Galling Resistance, *High Manganese Austenitic Stainless Steels*, ASM International, 1987, p 62
17. J.H. Magee, “Development of Stainless Steel Galling Test,” Carpenter Technology Corporation, 1987

Sliding Contact Damage Testing

Profilometry Evaluation of Galling Damage

Instead of a visual determination to assess galling damage, surface profilometry has been used. Several test procedures can be found in the literature (Ref 18, 19, 20). One example is a galling procedure that involves the twisting of a cylindrical 16 mm ($\frac{5}{8}$ in.) diameter pin against a block. Tests are performed at three selected loads. Cylindrical pins are slowly tested back and forth 10 times, through an arc of 120° at each load, using a new pin and block location per load. Scar profiles are measured using a profilometer. The difference in peak-to-valley amplitudes between the final roughness and the initial roughness (measured in microns) is plotted versus load. Resistance to galling is quantified by the degree of damage (measured in microns) as shown in Fig. 9. This 10-turn test is designed to evaluate excellent galling-resistant materials such as Stellite alloy No. 6, against other materials. Damage measured by this test typically does not reach the level of surface damage observed in the button-on-block test, that is, macroscopic protrusions of metal above the surface. Note that when stainless steels, such as type 304, 316, and 410, are evaluated self-mated using this procedure, severe damage occurs at relatively low loads with only one or two twists possible before total seizure.

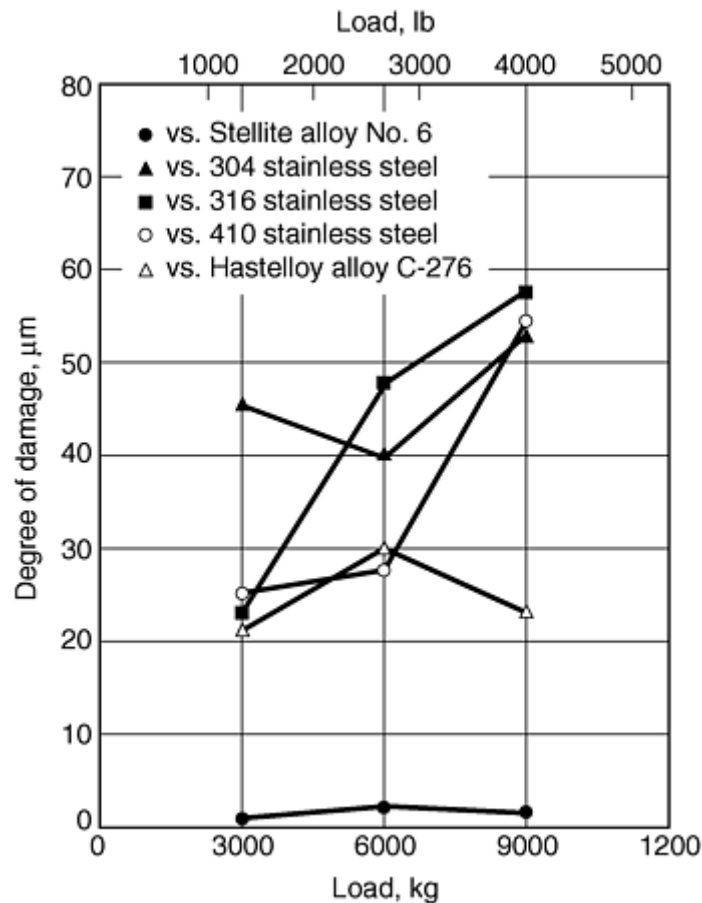


Fig. 9 Resistance to galling of Stellite alloy No. 6 (surface ground counterface) versus selected materials. Source: Ref 20

References cited in this section

18. P. Crook, The Development of a Series of Wear Resistant Materials Akin to Those of the Cobalt-Chromium Alloys, *Wear of Materials Conf. (1981)*, S.K. Rhee, A.W. Ruff, and K. Ludema, Ed., American Society of Mechanical Engineers, 1981, p 202–209
19. W. Schumacher, The Galling Resistance of Silver, Tin and Chrome Plated Stainless Steels, *Wear of Materials Conf. 1981*, S.K. Rhee, A.W. Ruff, and K. Ludema, Ed., American Society of Mechanical Engineers, 1981, p 186–196
20. R.W. Kirchner, P. Crook, and A. Asphahani, “Wear/Corrosion-Resistant High Performance Alloys for the Food Industries,” Paper 102, presented at Corrosion 1984, April 1984 (New Orleans), National Association of Corrosion Engineers, 1984

Sliding Contact Damage Testing

Pin-on-Flat Galling Test

A second example of a procedure that uses surface profilometry to measure galling damage is the pin-on-flat test (Ref 21). In this test, a spherically tipped pin slides in a straight line against a flat surface (Fig. 10). Unlike the procedures previously discussed, there is no twisting action, nor is the button surface flat. A single pass with a distance of 40 mm (1.5 in.) is employed at a speed of 2 mm/s (0.8 in./s) and a load of 130 N (30 lb). Surface

finish of the specimens is produced by a 6 μm polish, and the pin diameter is 13 mm (0.5 in.). A pin tip radius of 25 mm (1 in.) is used. As with all galling evaluations discussed, specimens are thoroughly cleaned in an ultrasonic bath and then alcohol rinsed prior to testing.

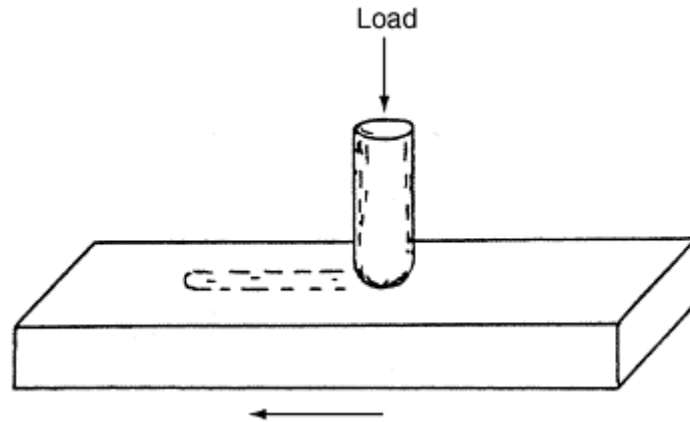


Fig. 10 Pin-on-flat galling test configuration. Source: Ref 21

The topography of the damage is measured on the flat specimen by means of a stylus profilometer. A series of parallel traces at a spacing of approximately 0.3 mm (0.012 in.) is taken over the entire length of the track. The tracing direction is perpendicular to the sliding direction. Profile data are acquired in digital form, yielding a matrix of values that specify the elevation of points on the surface. A significant parameter, R_t , determined by these profilometry measurements, is the average maximum peak-to-valley distances (microns) for traces taken across the surface damage area. This parameter reflects the importance of the large protrusions and deep gouges that are characteristic of galling. Galling tendency of material is a function of the R_t value. Figure 11 plots damage severity (R_t) versus Knoop hardness for a wide variety of materials. The results show there is no overall correlation of damage severity with hardness. Aluminum-bronze, a known galling-resistant material, had no surface damage, while galling-prone alloys (such as type 410 stainless steel) had significant damage.

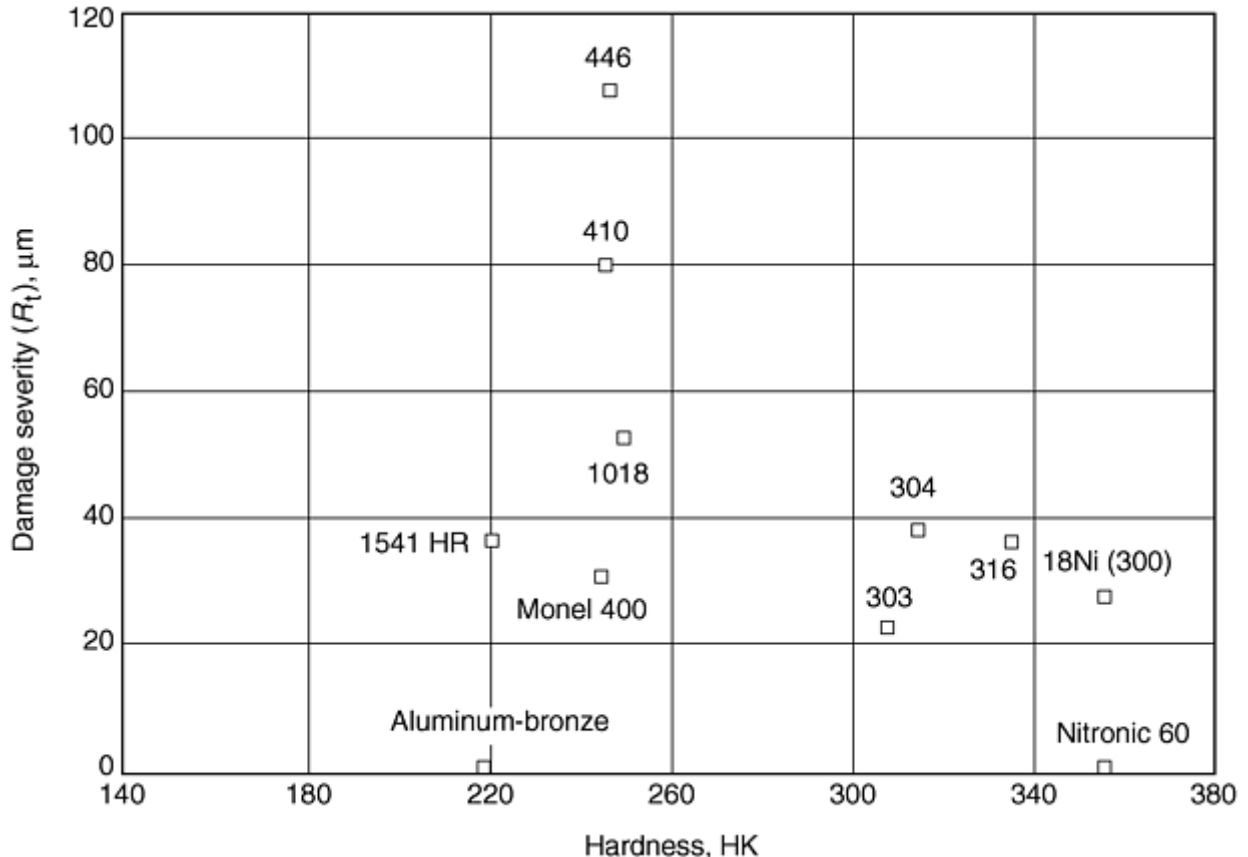


Fig. 11 Damage severity (R_t) as measured by profilometry plotted against hardness for several commercial alloys. Source: Ref 21

Reference cited in this section

21. L.K. Ives, M.B. Peterson, and E.P. Whinton, "Galling: Mechanism and Measurement," National Bureau of Standards Report, 1987, p 33–40

Sliding Contact Damage Testing

Threaded Connection Galling Tests

The galling tests described previously have been designed to rank material couples as a screening evaluation for prototype testing. Prototype tests tend to be more expensive and are designed for a specific application. Several threaded connections tests exemplify prototype testing (Ref 22, 23, 24). They are designed to determine if galling or seizure is a problem when inserting and removing threaded connections.

The first example involves evaluating a bolted joint design consisting of a socket head captive screw, a stainless flat washer, a helical lock washer, a stainless steel threaded insert, and a 19 mm ($\frac{3}{4}$ in.) thick drawer manifold to be bolted to the casting of a computer cabinet. In this test, each screw was inserted manually to minimize the chance of cross-threading, then torqued to a specified level, loosened, and removed completely. This sequence was repeated until galling or severe thread damage occurred. Variables evaluated were screw and insert material, molybdenum-disulfide lubricant, cadmium or nickel-plated screws, and thread type. The life-cycle design requirement was 900 cycles. Results of two of these tests can be found in Table 4.

Table 4 Sample results of two threaded connection galling tests

Test	Screw material	Insert material	Number of cycles to galling of threads
1	17-4 PH stainless steel, $\frac{3}{8}$ -24 in., UNF-3A, 41 HRC, nonlubricated	Type 303 stainless steel hole, $\frac{3}{8}$ -24 in., UNF-3B, 89 HRB	225
2	17-4 PH stainless steel, H1050, $\frac{3}{8}$-24 in., UNF-3A, 31 HRC, nonlubricated	Nitronic 60 hole, $\frac{3}{8}$-24 in., UNF-3B, 96 HRB	1000

Source: Ref 22

Other examples of prototype tests involve threaded tubular products for deep and gas wells. These connections are prone to galling due to the high torque applied in the makeup operation, that is, near the yield strength of some alloys. Prototype tests were developed to evaluate this condition especially to determine the effectiveness of lubricants or surface treatments. A bolt-nut test apparatus was designed to closely simulate a threaded tubular makeup (Fig. 12) (Ref 23). Lubricants were applied to bolts and nuts according to manufacturer directions, and the makeup torque was applied. The calculated surface stress on the threaded parts and bolt-to-washer mating parts corresponded to metal-to-metal seal parts in actual threads. The makeup speed was slow: 3 rpm. Torque and clamping force were measured. After each makeup and break operation, the threaded parts and bolt-to-washer mating parts were inspected for galling. The lubricant performance was evaluated principally by noting the number of makeup and break cycles until galling was first observed. Also, the variation of torque coefficient was monitored during the test. Typical results are shown in Table 5. Longer test times of 30 days in the fastened state prior to breakout have been evaluated by this method as have higher-temperature test conditions to simulate deep-well service.

Table 5 Bolt-nut test results on the lubrication performance of various lubricants under different test condition

Lubricant	Test and condition	Makeup and break cycles until galling observed	Torque coefficient ^(a) at first makeup	Variation of torque coefficient, %
MoS ₂ -Sb ₂ O ₃ -epoxyester film	None	20	73 × 10 ⁻³	+7, -6
		^(b)	102	-16
	API grease	^(b)	121	+9
		^(b)	124	+11
	API grease + sand	9	139	+3, -2
		^(b)	125	+18
	API grease + water	24	146	-14
		^(b)	125	+5, -6
	API grease + brine	22	149	+7, -7
		^(b)	127	+9, -13
Commercial organic resin bonded lubricant containing MoS ₂ (MIL-L-23398, 46147, 8937B)	None	9	189	+21
		8	314	-14
	API grease	6	165	-16
		^(b)	164	-22
	API grease + sand	14	202	-31
		7.5	175	-14
	API grease + water	22	146	-23
		19	167	-30
	API grease + brine	18	159	-16
		10	159	-21
Commercial paste containing polyalkyleneglycol, lithium soap and MoS ₂	None	8	161	+9
	API grease	9	153	-7
		15	152	-11
	API grease + sand	11	160	-10
		7.5	154	-3
	API grease + water	8	124	+10
		7	145	-9
	API grease + brine	8	158	-15
		7.5	140	+11, -1
	Electroplated copper film ^(c)	None	1	310 × 10 ⁻³
API grease		^(b)	171	+1, -14
API grease + sand		10	191	-17
API grease + water		23	157	+10
API grease + brine		^(b)	158	-17
Heat treated films				
MoS ₂ -Sb ₂ O ₃ -epoxyester film, heat treated at 250 °C (480 °F) × 30 min in air	None	^(b)	82	-16
	API grease	^(b)	147	+21, -3
	API grease + sand	^(b)	135	+10
	API grease + water	^(b)	136	+13

	API grease + brine	^(b)	140	+7, -3
Commercial organic resin-bonded lubricant containing MoS ₂ (MIL-L-23398, 46147, 8937B), heat treated at 250 °C (480 °F) × 30 min in air	None	22	57	+2, -11
	API grease	^(b)	125	+5, -12
	API grease + sand	20	127	+32
	API grease + water	^(b)	124	+29
	API grease + brine	^(b)	120	+26

(a) Torque coefficient (C) relates torque (T) to bolt tension (F) and bolt diameter (D) as follows: $T = CDF$.

(b) No galling after 25 makeup and break cycles.

(c) Copper striking followed by electroplating in CuSO₄ bath (15 μm, or 40 μin. thick). API, American Petroleum Institute.

Source: Ref 23

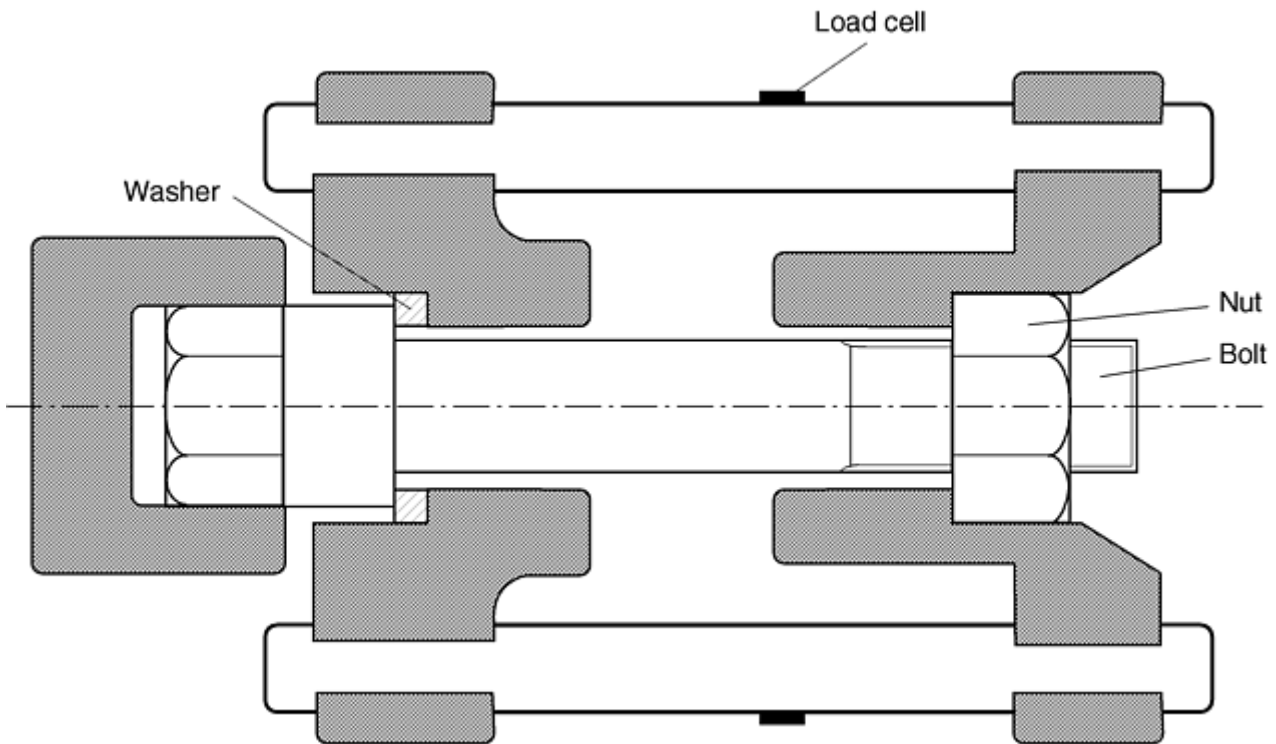


Fig. 12 Bolt-nut galling test apparatus. Source: Ref 23

Another oil-country threaded tubular test involves thick-walled, high-alloy products such as nonmagnetic drill collars. These 9 m (30 ft) long collars are prone to galling when their threaded box and pin connections are released after being joined with high makeup torques. These connections require an antigalling lubricant or surface treatment, such as ion implantation (Ref 25). To evaluate their effectiveness, make/break galling tests are performed. Full-size connections are machined with threads and lubricant/surface treatments are applied. A large torque machine then “makes” the connection at a specified torque, appropriate for the threaded tubular size, then breaks the connection. The breakout torque is recorded. This procedure is repeated several times (typically 5 to 10 times). Alignment of the box/pin connection is important to prevent galling. After testing, the threads and seal surfaces of the box and pin tubulars are examined for galling. Test results simply report whether or not galling occurred.

References cited in this section

22. D.D. Vo and C.E. Wissing, Jr., Failures of Bolted Connections Due to Wear and Galling in Bolt Threads, *Proc. Use of New Technology to Improve Mechanical Readiness, Reliability and Maintainability*, Cambridge, 1985

23. E. Yamamoto, K. Wada, T. Fukyuka, K. Shimogori, K. Fukiwara, and K. Tsuji, "Lubricating Films to Prevent Galling of Stainless Steel Parts," 38th ASLE Meeting, April 1983 (Houston), American Society of Lubrication Engineers
24. D.G. Frick, "Drill Collar Connection Trial," Report DGF2-85, Carpenter Technology Corporation, July 1985
25. G.W. White, Eliminating Galling of High-Alloy Tubular Threads by High-Energy Ion Deposition Process, *J. Pet. Technol.*, Aug 1984, p 1345–1351

Sliding Contact Damage Testing

Prevention of Galling

Preventing galling damage is a critical part in applications where parts are sliding against each other under high loads and low speeds. It becomes a bigger issue when corrosion-resistant alloys, such as stainless steels, are required under nonlubrication conditions. Despite the best efforts of designers and users, occasions also arise when close clearances result in the contact and rubbing of components in rotating machinery. Of key importance in this case is the prevention of galling, because this can cause seizure and severe damage.

Galling can be resisted in several ways. For applications in which galling is of concern, the following guidelines should be considered:

- Lubricate where possible.
- Keep load, temperature, and speed as low as possible.
- Parts should be dimensionally tight with sufficient clearance.
- Use a surface finish between 0.25 and 1.75 μm (10 and 70 $\mu\text{in.}$) whenever possible (many stainless parts are electropolished, which can lead to galling and wear).
- Increase contact area, so that there is less stress on parts and less depth of wear.
- Carefully select alloys in unlubricated systems, or where insufficient lubrication may be present. Dissimilar-mated couples with high threshold galling stress values can be chosen or high work-hardening rate austenitic stainless alloys can be selected for improved adhesive and cavitation wear resistance and galling resistance.
- Use surface treatments, such as nitriding, carburizing, and hardface coating, or solid lubricant coatings (i.e., molybdenum disulfide or graphite).

Galling resistance can sometimes be aided by heat treating the opposing parts so that they have a hardness difference of at least 50 HB, which encourages wear of the softer material rather than adhesion and resultant part-to-part material transfer (Ref 26). Another method of discouraging galling is to machine grooves in one or both of the close-clearance components, so that as wear takes place the debris can collect somewhere other than at the close running clearance. This also promotes rapid heat transfer at rubbing interfaces, keeping parts cool and hard. Local surface temperatures can become very high even with grooving, because of the flash-temperature effect, but such temperatures decay in short distances and do not result in galling if surface heat removal is effective (Ref 27). Grooving the surfaces results in a design compromise, however. Although grooving reduces clearance leakage, it also reduces the beneficial shaft support provided by the Lomakin effect (Ref 28).

Finally, the test methods described in this article also provide a basis in the evaluation and prevention of galling. The general comparison of galling potential for different materials can be done by the measurement of the contact stress required for cold welding and subsequent material pullout for a material mated against itself. This is called threshold galling stress. A complete listing of threshold galling data for stainless steels can be found in Ref 12.

References cited in this section

12. J.H. Magee, Wear of Stainless Steels, *Friction, Lubrication, and Wear Technology*, Vol 18, *ASM Handbook*, P. Blau, Ed., ASM International, 1992, p 710–724
26. W. Marscher, A Phenomenological Model of Abradable Wear in High Performance Turbomachinery, *Wear*, Vol 59, 1980, p 191–211
27. W. Marscher, “A Critical Evaluation of the Flash Temperature Concept,” Preprint 81-Am-1D-3, American Society of Lubrication Engineers, 1981
28. W. Marscher, Wear of Pumps, *Friction, Lubrication, and Wear Technology*, Vol 18, *ASM Handbook*, P. Blau, Ed., ASM International, 1992, p 594, 595

Sliding Contact Damage Testing

Fretting Wear

R.B. Waterhouse, University of Nottingham (United Kingdom)

Fretting refers to a special form of surface wear that occurs from small-amplitude tangential oscillations between two surfaces in contact. The amplitude (or magnitude) of the relative motion in fretting wear is what distinguishes it from other forms of wear during unidirectional and reciprocating sliding contact. In practical cases, fretting wear occurs from extremely small repetitive motion, usually less than 25 μ m peak-to-peak amplitude.

One immediate consequence of the fretting process in normal atmospheric conditions is the production of oxide debris; hence the terms “fretting wear” and “fretting corrosion” are used for this phenomenon. Surface damage from fretting begins with local adhesion between mating surfaces and progresses when adhered particles are removed from a surface. When adhered particles are removed from the surface, they may react with air or other corrosive environments. Affected surfaces show pits or grooves with surrounding corrosion products.

The movement is usually the result of external vibration, but movement also occurs from cyclic contact stresses (fatigue) between mated parts. This fact gives rise to another and usually more damaging aspect of fretting, namely the early initiation of fatigue cracks. This is termed *fretting fatigue* or *contact fatigue*. Fatigue cracks may also be initiated where the contacting surfaces are under a very heavy normal load or where there is a static tensile stress in one of the surfaces. There are cases where the movement is not simply tangential, but is complicated by the normal force also oscillating to the extent that the surfaces lose contact in each cycle. This leads to a hammering effect, which is termed *impact fatigue*. In this case, the phase relationship between the two motions can be an important factor. Fretting fatigue and the associated methods of testing are described in more detail in the article “Fretting Fatigue” in this Volume.

This section describes the testing and the special problems in the evaluation of fretting wear. For example, one important feature of fretting is that the debris or wear product remains between the surfaces and can play a role in the development of the process. This is particularly true where the surfaces are flat or conforming as in, for example, a hub on an axle. In many experimental investigations, the common type of geometry has been the sphere or cylinder on a flat.

Another problem in investigating fretting wear in the laboratory has been devising systems to produce controlled movement of extremely small amplitude and the ability to measure and monitor that amplitude in the very area of the contact. It follows, of course, that the amount of wear debris produced is also very small, which creates problems where quantitative measurements are required. This section describes how these problems have been overcome by investigators in the past.

Fretting Mechanism

In general, fretting occurs between two tight-fitting surfaces that are subjected to a cyclic, relative motion of extremely small amplitude. Although certain aspects of the mechanism of fretting are still not thoroughly understood, the fretting process is generally divided into the following three parts: initial conditions of surface adhesion, oscillation accompanied by the generation of debris, and fatigue and/or wear in the region of contact. Fretting wear occurs from repeated shear stresses that are generated by friction during small amplitude oscillatory motion or slip between two surfaces pressed together in intimate contact. In fretting, the term *slip* is used to denote small amplitude surface displacements, in contrast to *sliding*, which denotes macroscopic displacements. In many cases, slip only occurs over part of the contacting surfaces and is therefore referred to as partial slip. Fretting damage has been detected at amplitudes of less than 1 μm (Ref 29). As the amplitude is increased, the process resembles unidirectional or reciprocating sliding wear. The upper limit has been suggested as 75 μm (Ref 30), and Fig. 13 shows the volume of wear damage as a function of slip amplitude.

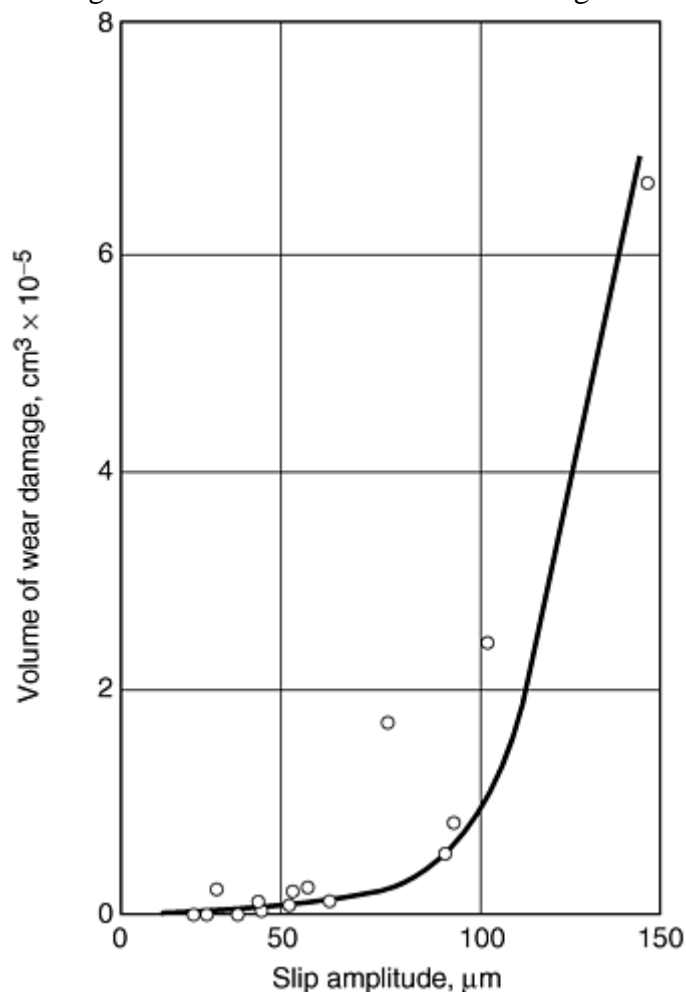


Fig. 13 Effect of slip amplitude on fretting damage of mild steel. Source: Ref 30

The severity of fretting damage is influenced by several factors including:

- *Contact Load*. As long as fretting amplitude is not reduced, fretting wear will increase linearly with increasing load.

- *Amplitude*. There appears to be no measurable amplitude below which fretting does not occur. However, if the contact conditions are such that deflection is only elastic, it is not likely that fretting damage will occur. Fretting wear loss increases with amplitude. The effect of amplitude can be linear, or there can be a threshold amplitude above which a rapid increase in wear occurs (Ref 30). The transition is not well established and probably depends on the geometry of the contact.
- *Frequency*. When fretting is measured in volume of material removed per unit sliding distance, there does not appear to be a frequency effect.
- *Number of Cycles*. An incubation period occurs during which fretting wear is negligible. After the incubation period, a steady-state wear rate is observed, and a more general surface roughening occurs as fretting continues.
- *Relative Humidity*. For materials that rust in air, fretting wear is higher in dry air than in saturated air.
- *Temperature*. The effect of elevated temperature on fretting depends on the oxidation characteristics of the material.

The effects of these factors are discussed in more detail in Ref 30 and 31. The article “Fretting Fatigue Testing” in this Volume also provides additional details on the effects of these test variables. The main focus of this section is on fretting test rigs and wear measurements.

References cited in this section

29. S.R. Brown, *Materials Evaluation under Fretting Conditions*, STP 780, ASTM, 1981, p 30
30. R.B. Waterhouse, *Fretting Corrosion*, Pergamon, 1972, p 69, 133
31. R.B. Waterhouse, *Fretting Wear, Friction, Lubrication, and Wear Technology*, Vol 18, *ASM Handbook*, P. Blau, Ed., ASM International, 1992, p 242–256

Sliding Contact Damage Testing

Fretting Rigs

Experimental rigs for investigating fretting wear are either driven mechanically or by an electromagnetic vibrator. Figure 14 shows a mechanical rig driven by an electric motor with eccentric loading device. Other methods of producing small amplitude have been the use of rotating out-of-balance weights, but control here is much more difficult.

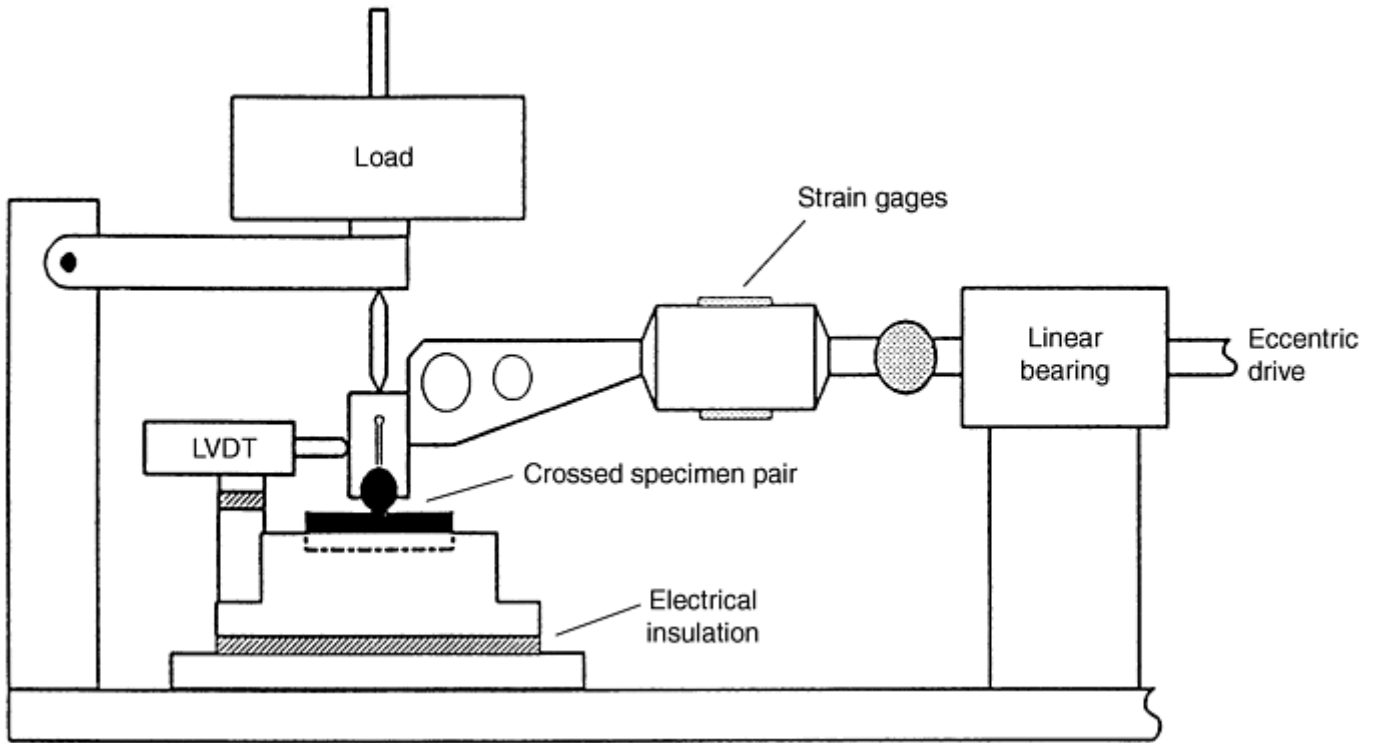


Fig. 14 Mechanical fretting wear rig. LVDT, linear variable differential transformer

A key factor in test rigs is the type of contact, because the ease with which debris can escape from the contact region influences the fretting process itself. For example, the escape of debris in the crossed-cylinder arrangement (Fig. 15) is greatly influenced by the direction of motion (Ref 32). The arrangement shown in Fig. 15(b) allows the debris to escape by being pushed out by the axial movement of the upper cylinder, leading to more frequent metal-to-metal contact and a higher wear rate than the arrangement shown in Fig. 15(a).

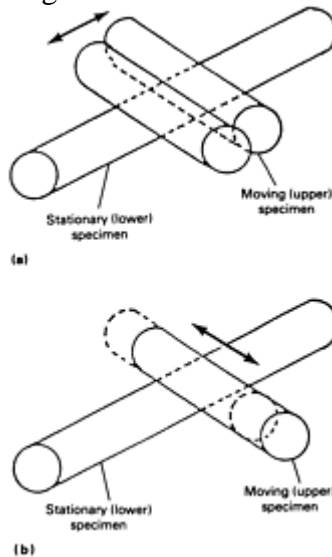


Fig. 15 Two test directions for determining fretting in a crossed-cylinder arrangement. (a) Parallel to axis of lower specimen. (b) At right angles to axis of lower specimen. Source: Ref 31

The original machine designed by Tomlinson (Fig. 16) comprised a long horizontal lever connected to an annular specimen in contact with a horizontal flat specimen with the load applied by a vertical rod through the center of the specimen passing through a hole in the flat specimen. By applying an oscillating circumferential motion to the end of the lever of, for example, 5 mm (0.2 in.), this would be reduced at the specimen to 5 μm (200 $\mu\text{in.}$) for a lever 1 m (3.28 ft) in length. More recent machines (e.g., Fig. 14) use an adjustable eccentric producing a horizontal movement that is transmitted via a sleeve bearing to the upper specimen, which can be a ball bearing, a spherical-ended slider, or a flat in contact with a fixed-flat specimen. The normal load can be

applied by a dead-weight system. It is advisable to have as few junctions as possible between the eccentric and the specimen since movement will be lost in them. The motor driving the eccentric should have sufficient power to force the movement, particularly as considerable changes in the coefficient of friction can occur during fretting. Amplitude is measured with a proximity or capacitance gage. Rotational movement can be measured with an optical lever.

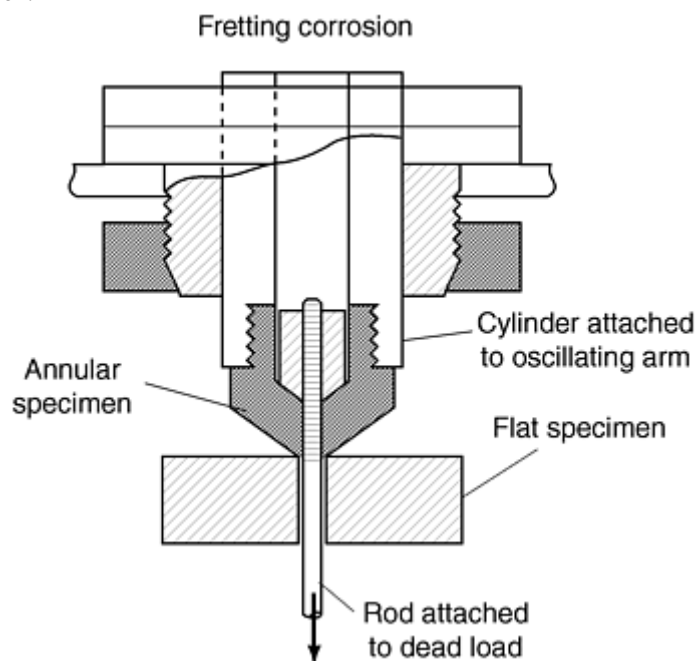


Fig. 16 Fretting test of Tomlinson involving contact between annular ring and flat. Source: Ref 30

In experimental investigations, the ease and cost of preparing specimens are significant factors, and the crossed-cylinder arrangement (Fig. 15) is one of the most convenient. However, as previously noted, the ease with which debris escapes can influence results. In this regard, Tomlinson's original design of an apparatus with torsional vibration of annulus on flat has much to commend it because no part of the contacting surfaces becomes exposed, and, for debris to escape, it must move at right angles to the direction of motion. A further slight advantage is that the amplitude of slip has a small variation from the inner to the outer edge and can therefore be used to investigate the effect of amplitude in one test. With flat contact surfaces, however, the initiation and development of areas of wear damage are sporadic no matter how carefully the surfaces are prepared and the alignment controlled. Contact pressure is usually expressed as the nominal value calculated from the apparent area of contact and the applied load.

Friction Monitoring. It is usually necessary to monitor the friction during a test. This can be accomplished by strain gaging the connecting rod to the specimen to measure the tangential force. Such an arrangement can be made more sensitive by using a tubular member. This arrangement can also provide cooling if the fretting couple is to be enclosed in a furnace.

Frequency is controlled by driving the device with a variable-speed dc motor. Using electromagnetic vibrators requires them to be of sufficient power for the purpose and has the same problems in transmitting the movement to the fretting specimens. For low frequencies of less than 5 Hz, mechanical machines have the advantage, but for higher frequencies even up to kHz, electromagnetic rigs (Fig. 14) are recommended. For very high frequencies and small fretting amplitude piezoelectric rigs have been used (Ref 33). Other methods of producing the small-amplitude movement have been to use rotating out-of-balance weights, but control here is much more difficult.

The environment is an important feature of fretting testing. Humidity can have a marked effect, particularly with reactive materials such as aluminum and titanium, and it should be controlled by enclosing the fretting couple in a suitable container. This can also be used to provide other environments such as argon or carbon dioxide. More specialized environments such as high temperature, low temperature, seawater or body fluids, and even vacuum require more complicated equipment, but have all been successfully accomplished and are documented in the literature. The author's most difficult task was to study fretting of stainless steels in an

atmosphere of carbon dioxide at 4050 kPa (40 atm) pressure and 600 °C (1110 °F). Descriptions of this rig and others can be found in Ref 29 and 30.

References cited in this section

29. S.R. Brown, *Materials Evaluation under Fretting Conditions*, STP 780, ASTM, 1981, p 30
30. R.B. Waterhouse, *Fretting Corrosion*, Pergamon, 1972, p 69, 133
31. R.B. Waterhouse, Fretting Wear, *Friction, Lubrication, and Wear Technology*, Vol 18, *ASM Handbook*, P. Blau, Ed., ASM International, 1992, p 242–256
32. M. Kuno and R.B. Waterhouse, The Effect of Oscillatory Direction on Fretting Wear under Crossed Cylinder Contact Conditions, Eurotrib 89, *Proc. 5th International Congress on Tribology*, 12–15 June 1989 (Helsinki), Vol 3, p 30–35
33. P. Rehbein and J. Wallaschek, *Wear*, Vol 216 (No. 2), 1998, p 97–105

Sliding Contact Damage Testing

Measurement of Fretting Wear

The amount of material removed in fretting wear is extremely small, particularly in the partial slip regime, so determining it by loss in weight of the specimen is impractical. The minute amount of debris, usually an oxide, is difficult to remove for the purpose of weighing. The debris is often compacted. On steel, it is the α ferric oxide, which is red in color but, when compacted, is blackish gray. It is the mineral hematite, which is black in massive form but red when powdered.

It is much more satisfactory to attempt to measure the volume of material removed. One of the earliest methods was to measure the area of damage (A) and then to find the depth by carefully machining the surface until the last trace of damage had just disappeared and to estimate the depth (d) from the weight of material machined off. The product Ad was thus a measure of the volume of material lost as wear. Nowadays computerized profilometers are available that can survey the scar and produce a view of it as in Fig. 17. The computer can also provide information on the volume below the datum of the original surface as well as material above the datum, since often there is local plastic deformation arising from the fretting action. It is usual to express the wear as the difference between these two figures.

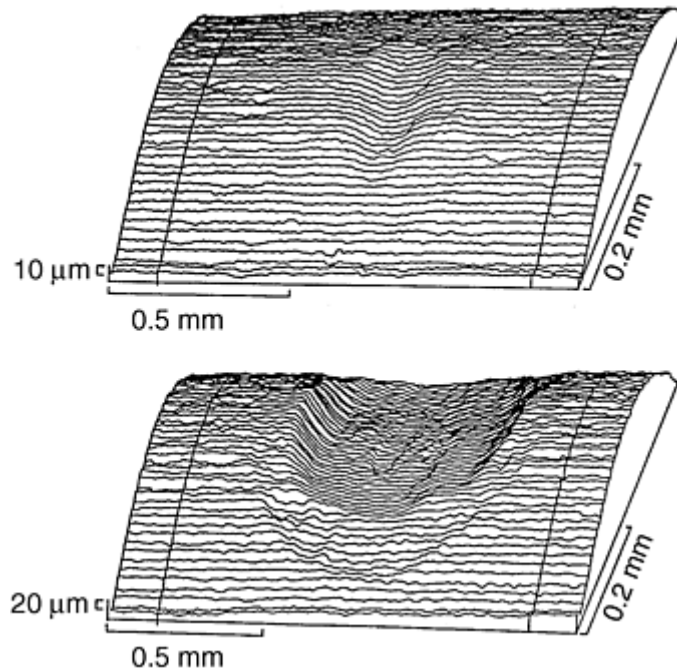


Fig. 17 Profilometer projections of wear scars on two crossed-cylinder contacting specimens

Obviously if the wear is to be accurately determined, all the debris must be completely removed. This can usually be achieved by ultrasonic cleaning. There have been chemical methods that involve the use of complex selenium compounds that remove the debris but do not attack the underlying material. Removal of the debris assists subsequent examination in the scanning microscope. Fretting wear is usually expressed, as are other types of wear, as a specific wear rate, that is, the volume of material lost per unit distance of sliding per unit of applied load.

A more sophisticated method of assessing fretting wear is to use thin-layer activation (TLA). It involves irradiation of one of the surfaces with protons from the cyclotron, which results in the formation of radionuclides, which in the case of steel is mainly cobalt-56. Measurement of the γ radiation from the debris or transferred material is claimed to give accurate results with a minute amount of debris (Ref 34).

Reference cited in this section

34. S.R. Brown, *Materials Evaluation under Fretting Conditions*, STP 780, 1981, p 7

Sliding Contact Damage Testing

Specimen Preparation

There are two factors that can influence the results in fretting wear tests. These are the surface roughness of the specimens and the existence of residual stresses in the specimen surface. Generally speaking, the more highly polished the surface the greater the wear. This is attributed to the fact that the oxide debris is an abrasive material and participates in the wear process. On a rough surface, contact is via well-defined asperities and the debris can drop into the adjacent grooves. Residual stress has an effect because one of the basic mechanisms is surface fatigue as exemplified in Suh's delamination theory (Ref 35). A residual tensile stress increases the amount of wear, whereas a compressive stress reduces it (Ref 36). This is an argument for the application of shot peening to prevent fretting wear since it roughens the surface and generates a compressive residual stress in the surface. In most experimental investigations, it is usual to give the specimens a light polish with 000

emery paper followed by degreasing in acetone or ultrasonic cleaning. The SEM is a very suitable piece of equipment for examining the surface damage. Figure 18 shows a typical example.

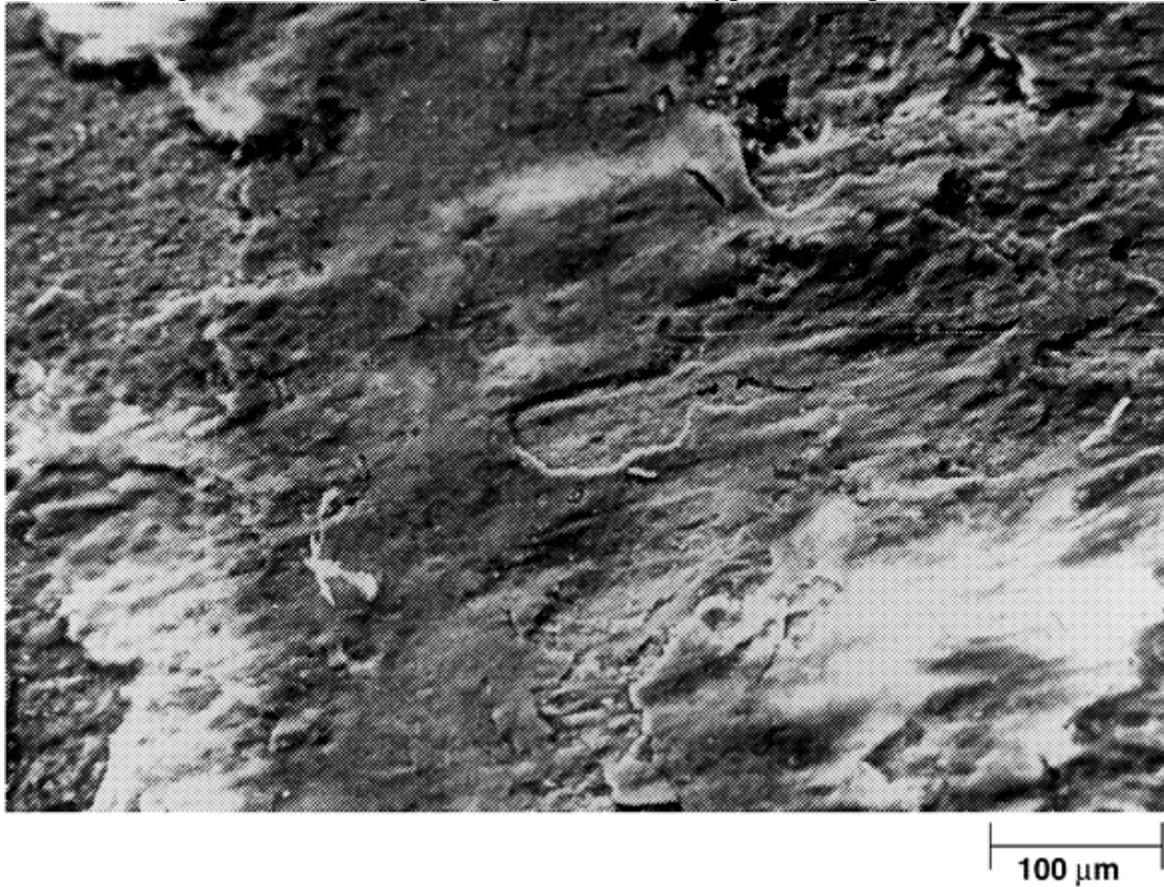


Fig. 18 SEM micrograph of fretting damage on a mild steel specimen showing compacted debris and delamination

References cited in this section

35. P. de Baets and K. Strickmans, *Tribology Int.*, Vol 29 (No. 4), 1996, p 307–312
36. J. Labedz, *Metal Treatments against Wear, Corrosion, Fretting and Fatigue*, A. Niku-Lari and R.B. Waterhouse, Ed., Pergamon, 1988, p 87–98

Sliding Contact Damage Testing

Reducing Fretting Wear

The first approach to a fretting problem is to consider the basic design of the contacting components. This is particularly so if the fretting is the result of one of the members of the contact being subjected to a cyclic stress, that is, fatigued. In this case, it is important if possible to reduce stress concentrations in the region of the contact. In the case of a hub on a shaft, this is achieved by increasing the shaft diameter at the wheel seat with a generous fillet radius. A similar effect can be achieved by providing a stress-relieving groove. Such design changes are those customarily recommended in designing against fatigue. If the problem cannot be tackled in this way, then recourse has to be made to surface treatments. Increasing the hardness of the surface by work hardening, for example, by shot peening or surface rolling, or by diffusion treatments such as carburizing or nitriding in the case of steel can be effective. Beyond that there is now a wide variety of treatments

encompassed in the term “surface engineering.” Hard coatings such as titanium nitride (TiN) can be recommended if the substrate material is sufficiently strong to support them (Ref 37). However, if breakdown occurs the result can be disastrous because one then has a very abrasive material in the contact. Ion implantation has the advantage of surface alloying not possible by other means and also the development of residual compressive stress. More information on the control of fretting wear is given in Ref 31 and the article “Fretting Fatigue Testing” in this Volume.

References cited in this section

31. R.B. Waterhouse, Fretting Wear, *Friction, Lubrication, and Wear Technology*, Vol 18, *ASM Handbook*, P. Blau, Ed., ASM International, 1992, p 242–256
37. M. Shima, J. Okado, I.R. McColl, R.B. Waterhouse, T. Hasegawa, and M. Kasaya, *Wear*, 225–229; Part I, 1999, p 38–45

Sliding Contact Damage Testing

References

1. P. Heilman, J. Don, T.C. Sun, W.A. Glaeser, and D.A. Rigney, Sliding Wear and Transfer, *Proc. Int. Conf. Wear of Materials*, American Society of Mechanical Engineers, 1989, p 1–8
2. W.R. Jones, S. Pepper, et al., The Preliminary Evaluation of Liquid Lubricants for Space Applications by Vacuum Tribometry, *28th Aerospace Mechanisms Symposium*, National Aeronautics and Space Administration, May 1994
3. Glossary of Terms, *Friction, Lubrication, and Wear Technology*, Vol 18, *ASM Handbook*, P. Blau, Ed., ASM International, 1992
4. E. Rabinowicz, Wear Coefficient—Metals, *Wear Control Handbook*, American Society of Mechanical Engineers, 1980, p 475–506
5. E. Rabinowicz, Wear Coefficient—Metals, *Wear Control Handbook*, American Society of Mechanical Engineers, 1980, p 475–484
6. *Friction and Wear Testing: Source Book of Selected References from ASTM Standards and ASM Handbooks*, ASM International, 1997
7. “Standard Test Method for Wear Testing with a Crossed-Cylinder Apparatus,” ASTM G 83, *Annual Book of ASTM Standards*
8. *Friction and Wear Testing: Source Book of Selected References from ASTM Standards and ASM Handbooks*, ASM International, 1997, p 110–114
9. A.W. Ruff, Wear Measurement, *Friction, Lubrication, and Wear Technology*, Vol 18, *ASM Handbook*, P. Blau, Ed., ASM International, 1992, p 362–369
10. J.H. Magee, Stainless Steels That Resist Wear and Galling, *Stainl. Steel World*, May 1997

11. J.H. Magee, Two Galling Resistant Stainless Steels Used for Bridge Hinge Pins, *14th Annual Bridge Conference*, June 1997 (Pittsburgh, PA), 1997, p 161–165
12. J.H. Magee, Wear of Stainless Steels, *Friction, Lubrication, and Wear Technology*, Vol 18, *ASM Handbook*, P. Blau, Ed., ASM International, 1992, p 710–724
13. H.D. Merchant and K.J. Bhansali, “Metal Transfer and Galling in Metallic Systems,” Symposium Proceeding, Oct 1986 (Orlando, FL), ASTM, 1987
14. Committee of Stainless Steel Producers, “Review of the Wear and Galling Characteristics of Stainless Steels,” American Iron and Steel Institute, April 1978, p 8
15. “Standard Test Method for Galling Resistance of Materials,” ASTM G 98, *Annual Book of ASTM Standards*
16. J.H. Magee, Austenitic Stainless Steels with Improved Galling Resistance, *High Manganese Austenitic Stainless Steels*, ASM International, 1987, p 62
17. J.H. Magee, “Development of Stainless Steel Galling Test,” Carpenter Technology Corporation, 1987
18. P. Crook, The Development of a Series of Wear Resistant Materials Akin to Those of the Cobalt-Chromium Alloys, *Wear of Materials Conf. (1981)*, S.K. Rhee, A.W. Ruff, and K. Ludema, Ed., American Society of Mechanical Engineers, 1981, p 202–209
19. W. Schumacher, The Galling Resistance of Silver, Tin and Chrome Plated Stainless Steels, *Wear of Materials Conf. 1981*, S.K. Rhee, A.W. Ruff, and K. Ludema, Ed., American Society of Mechanical Engineers, 1981, p 186–196
20. R.W. Kirchner, P. Crook, and A. Asphahani, “Wear/Corrosion-Resistant High Performance Alloys for the Food Industries,” Paper 102, presented at Corrosion 1984, April 1984 (New Orleans), National Association of Corrosion Engineers, 1984
21. L.K. Ives, M.B. Peterson, and E.P. Whinton, “Galling: Mechanism and Measurement,” National Bureau of Standards Report, 1987, p 33–40
22. D.D. Vo and C.E. Wissing, Jr., Failures of Bolted Connections Due to Wear and Galling in Bolt Threads, *Proc. Use of New Technology to Improve Mechanical Readiness, Reliability and Maintainability*, Cambridge, 1985
23. E. Yamamoto, K. Wada, T. Fukyuka, K. Shimogori, K. Fukiwara, and K. Tsuji, “Lubricating Films to Prevent Galling of Stainless Steel Parts,” 38th ASLE Meeting, April 1983 (Houston), American Society of Lubrication Engineers
24. D.G. Frick, “Drill Collar Connection Trial,” Report DGF2-85, Carpenter Technology Corporation, July 1985
25. G.W. White, Eliminating Galling of High-Alloy Tubular Threads by High-Energy Ion Deposition Process, *J. Pet. Technol.*, Aug 1984, p 1345–1351
26. W. Marscher, A Phenomenological Model of Abradable Wear in High Performance Turbomachinery, *Wear*, Vol 59, 1980, p 191–211
27. W. Marscher, “A Critical Evaluation of the Flash Temperature Concept,” Preprint 81-Am-1D-3, American Society of Lubrication Engineers, 1981

28. W. Marscher, Wear of Pumps, *Friction, Lubrication, and Wear Technology*, Vol 18, *ASM Handbook*, P. Blau, Ed., ASM International, 1992, p 594, 595
29. S.R. Brown, *Materials Evaluation under Fretting Conditions*, STP 780, ASTM, 1981, p 30
30. R.B. Waterhouse, *Fretting Corrosion*, Pergamon, 1972, p 69, 133
31. R.B. Waterhouse, Fretting Wear, *Friction, Lubrication, and Wear Technology*, Vol 18, *ASM Handbook*, P. Blau, Ed., ASM International, 1992, p 242–256
32. M. Kuno and R.B. Waterhouse, The Effect of Oscillatory Direction on Fretting Wear under Crossed Cylinder Contact Conditions, Eurotrib 89, *Proc. 5th International Congress on Tribology*, 12–15 June 1989 (Helsinki), Vol 3, p 30–35
33. P. Rehbein and J. Wallaschek, *Wear*, Vol 216 (No. 2), 1998, p 97–105
34. S.R. Brown, *Materials Evaluation under Fretting Conditions*, STP 780, 1981, p 7
35. P. de Baets and K. Strikckmans, *Tribology Int.*, Vol 29 (No. 4), 1996, p 307–312
36. J. Labedz, *Metal Treatments against Wear, Corrosion, Fretting and Fatigue*, A. Niku-Lari and R.B. Waterhouse, Ed., Pergamon, 1988, p 87–98
37. M. Shima, J. Okado, I.R. McColl, R.B. Waterhouse, T. Hasegawa, and M. Kasaya, *Wear*, 225–229; Part I, 1999, p 38–45

Introduction to Creep and Stress-Relaxation Testing

James C. Earthman, University of California at Irvine

Introduction

THE FIELD of materials behavior at elevated temperatures has seen a formidable wealth of advancements over the last century. These accomplishments were made possible by the work of many scientists and engineers throughout the world who developed critical technologies necessary to make high-temperature materials stronger and more reliable (Ref 1, 2, 3). Applications for these materials include jet engines, power generation facilities, automobile engines, and electronic devices (Ref 4, 5). The potential efficiency of these systems typically increases with increasing operating temperature. This natural trend provides a strong demand for materials that can withstand higher temperatures. For aerospace applications, there is also a strong need for reducing weight, and it is often the high-temperature materials that have the highest densities in the aerospace structure. Reduced weight has been achieved by reducing component geometry, leading to greater stresses in high-temperature materials. Naturally, the importance of reliable creep and stress-rupture testing increases with increasing service stress. Introducing new high-temperature materials that have lower densities is another means by which weight reduction goals have been met for aerospace structures.

References cited in this section

1. *Creep and Fracture of Engineering Materials and Structures: Proc. of the Seventh International Conf. in honor of Prof. Oleg D. Sherby*, (University of California, Irvine), 10–15 Aug 1997, J.C. Earthman and F.A. Mohamed, Ed., Minerals, Metals and Materials Society/AIME, 1997
2. *Creep Behavior of Advanced Materials for the 21st Century*, proc. from 1999 TMS annual meeting (San Diego, CA), 28 Feb to 4 March 1999, R.S. Mishra, A.K. Mukherjee, and K.L. Murty, Ed., Minerals, Metals and Materials Society/AIME, 1999
3. *Advanced Materials for the 21st Century: The 1999 Julia R. Weertman Symposium*, proc. from 1999 TMS fall meeting (Cincinnati, OH), 31 Oct to 4 Nov 1999, Y-W. Chung, D.C. Dunand, P.K. Liaw, and G.B. Olson, Ed., Minerals, Metals and Materials Society/AIME, 1999
4. H.T. Lin, P.F. Becher, M.K. Ferber, and V. Parthasarathy, “Verification of Creep Performance of a Ceramic Gas Turbine Blade,” paper presented at the Science of Engineering Ceramics II, an International Symposium, (Osaka, Japan), 1998
5. *Frontiers in Electronics: High Temperature and Large Area Applications*, proc. of Symposium A on High Temperature Electronics, Materials, Devices, and Applications, and proc. of Symposium B on Thin Film Materials for Large Area Electronics of the 1996 E-MRS Spring Conference (Strasbourg, France), 4–7 June 1996, J. Camassel et al., Ed., Elsevier, Amsterdam, 1997

Introduction to Creep and Stress-Relaxation Testing

James C. Earthman, University of California at Irvine

Trends and New Technologies in Materials Testing

Considerable resources and effort have been spent over the last few decades on developing new methods of materials synthesis in order to satisfy the demand for better high-temperature materials. For example, mechanical alloying, sol gel processing, and various spray processing technologies have developed rapidly (Ref 6). These and other processing methods have successfully provided new materials systems that exhibit significantly higher creep strengths compared to those for conventional alloys. These new materials are typically tested extensively at elevated service temperatures before they can be approved for use (Ref 3). The demand for reliable data has led to the advancement of high-temperature testing methodologies that incorporate computer-based data acquisition and control.

Creep deformation and rupture experiments are used to determine the strength and lifetime of materials under quasi-static conditions at elevated temperatures. This testing typically involves imposing constant stress or displacement conditions as well as a constant elevated temperature. In addition to simulating service environments, these quasi-static conditions typically induce a physical behavior that is quite tractable from a theoretical perspective. Accordingly, there have been a considerable number of advancements in the theory of creep and creep rupture that can provide a physically based understanding of the microstructural mechanisms that govern the observed behavior. For the practicing engineer, an understanding of the physics of creep behavior can be quite useful for determining how a material might be altered microstructurally to perform better at elevated temperatures. This knowledge can also be used to improve methods of predicting high-temperature behavior from extrapolations of available laboratory data. With a good fundamental understanding, an engineer might also exercise more wisdom in selecting the best material for a given application. In light of these benefits, the following article in this Section, “Creep Deformation of Metals, Polymers, Ceramics, and Composites,” reviews the current theoretical underpinnings of creep deformation of engineering materials. This article provides the theoretical background for understanding many of the physical processes relevant to the testing methods, experimental results, and analytical approaches described in the subsequent articles.

Our best understanding of creep behavior has been developed for constant stress conditions. For relatively small strains (less than about 1%), constant load conditions suffice as a good approximation of constant stress in a creep experiment. For larger strains, constant stress conditions must be strictly imposed in order to obtain valid data. Accordingly, various approaches for imposing constant stress conditions in a creep test are presented in the article “Creep and Creep-Rupture Testing” in this Section. This article has been updated in the present volume to include two computer-aided approaches that are emerging as the preferred methods for creep laboratories.

Creep rupture often presents a severe risk in high-temperature applications when not addressed using appropriate testing and data interpretation methods. The article “Assessment and Use of Creep-Rupture Properties” covers methods for accurately assessing creep rupture properties. These methods include established interpolation and extrapolation procedures and properties-estimation schemes when data is sparse. The methods presented in this Section are primarily useful for testing under constant stress conditions.

Stress relaxation testing involves imposing a constant displacement under load at elevated temperatures. As mentioned above, this approach represents another quasi-static loading condition that can provide useful information about creep properties. The term *stress relaxation* refers to the time-dependent decrease in stress as creep deformation reduces elastic strain in the specimen under a fixed displacement. One of the primary advantages of this approach is that it can often provide an assessment of creep properties in a fraction of the time it takes using constant stress methods. It is also the most appropriate testing scheme when the target application, such as high-temperature bolting, undergoes a constant displacement condition. The article “Stress Relaxation Testing” gives an overview of methods that may be used to rapidly generate creep data over several orders of magnitude in strain rate.

Creep properties have for the most part been studied under uniaxial stress conditions in which the loading is applied parallel to the longitudinal axis of a cylindrical or plate specimen. Although uniaxial stress experiments have led to a good understanding of the physical processes involved, they often do not provide sufficient information to predict the behavior of high-temperature components. Load bearing parts at elevated temperatures are often subjected to multiaxial loading conditions that drive the deformation and rupture mechanisms in a manner that is different from uniaxial loads. Multiaxial conditions are particularly relevant for pressurized pipe and vessel components subjected to high temperatures. Hence, it is generally necessary to impose multiaxial stress conditions in creep and creep-rupture testing so that the effects of multiaxial stress states can be appropriately addressed. Accordingly, an article is also presented in this Section that describes the current state-of-the-art for testing tubular samples at elevated temperatures under multiaxial conditions.

Superplastic behavior refers to the ability of some fine-grained materials to achieve strains at elevated temperatures exceeding 300% and, in some cases, in excess of 2000%. From an industrial perspective, superplastic materials are of great interest because of the ability to produce complex shapes in a single inexpensive forming operation, eliminating labor-intensive machining costs. Naturally, exceptional testing methods are generally required for superplastic materials due to the large strains that are realized. A comprehensive overview entitled “Superplastic Deformation at Elevated Temperatures” is provided in this Section. Considerations for determining the optimum strain rate and impurity level are also discussed in this article.

References cited in this section

3. *Advanced Materials for the 21st Century: The 1999 Julia R. Weertman Symposium*, proc. from 1999 TMS fall meeting (Cincinnati, OH), 31 Oct to 4 Nov 1999, Y-W. Chung, D.C. Dunand, P.K. Liaw, and G.B. Olson, Ed., Minerals, Metals and Materials Society/AIME, 1999
6. *Non-Equilibrium Processing of Materials*, C. Suryanarayana, Ed, *Pergamon Materials Series*, Vol 2, Pergamon, 1998

Introduction to Creep and Stress-Relaxation Testing

James C. Earthman, University of California at Irvine

References

1. *Creep and Fracture of Engineering Materials and Structures: Proc. of the Seventh International Conf. in honor of Prof. Oleg D. Sherby*, (University of California, Irvine), 10–15 Aug 1997, J.C. Earthman and F.A. Mohamed, Ed., Minerals, Metals and Materials Society/AIME, 1997
2. *Creep Behavior of Advanced Materials for the 21st Century*, proc. from 1999 TMS annual meeting (San Diego, CA), 28 Feb to 4 March 1999, R.S. Mishra, A.K. Mukherjee, and K.L. Murty, Ed., Minerals, Metals and Materials Society/AIME, 1999
3. *Advanced Materials for the 21st Century: The 1999 Julia R. Weertman Symposium*, proc. from 1999 TMS fall meeting (Cincinnati, OH), 31 Oct to 4 Nov 1999, Y-W. Chung, D.C. Dunand, P.K. Liaw, and G.B. Olson, Ed., Minerals, Metals and Materials Society/AIME, 1999
4. H.T. Lin, P.F. Becher, M.K. Ferber, and V. Parthasarathy, “Verification of Creep Performance of a Ceramic Gas Turbine Blade,” paper presented at the Science of Engineering Ceramics II, an International Symposium, (Osaka, Japan), 1998
5. *Frontiers in Electronics: High Temperature and Large Area Applications*, proc. of Symposium A on High Temperature Electronics, Materials, Devices, and Applications, and proc. of Symposium B on Thin Film Materials for Large Area Electronics of the 1996 E-MRS Spring Conference (Strasbourg, France), 4–7 June 1996, J. Camassel et al., Ed., Elsevier, Amsterdam, 1997
6. *Non-Equilibrium Processing of Materials*, C. Suryanarayana, Ed, *Pergamon Materials Series*, Vol 2, Pergamon, 1998

Creep Deformation of Metals, Polymers, Ceramics, and Composites

Jeffery C. Gibeling, University of California, Davis

Introduction

CREEP DEFORMATION is any permanent inelastic strain that occurs when a material is subjected to a sustained stress. The rate at which this deformation occurs depends not only on the magnitude of the applied stress, but also on time and temperature. Thus, it is appropriate to consider creep to be a kinetic process and to write an appropriate rate law. In addition, the rate at which a material creeps depends on the size, spacing, and distribution of relevant microstructural features. As a consequence, it is also necessary to write equations that describe how the internal structure changes with respect to time or strain (Ref 1, 2).

Creep is considered to be a high-temperature phenomenon, although it is important to recognize that temperature is a relative quantity for any material. In crystalline solids such as metals and ceramics, creep is of concern when the service temperature is greater than or equal to approximately $0.5 T_m$, where T_m is the absolute melting temperature, commonly expressed on the Kelvin scale (Ref 3, 4). In the creep literature, it is common to refer to the ratio of T/T_m as the *homologous temperature*. Because homologous rather than absolute temperature is the relevant quantity, nickel-base superalloys undergo creep in gas turbine engine blades and vanes at 900 to 1400 K (1160–2060 °F), whereas the solder used to attach integrated circuits to their packages can deform at a service temperature of 400 K (260 °F). In both cases, the service temperature is high with respect to the melting point of the material. However, some crystalline materials exhibit measurable creep strains at temperatures as low as $0.25 T_m$. In noncrystalline materials such as polymers and glasses, the relevant reference is the glass transition temperature, T_g , above which creep occurs at measurable rates.

These observations suggest that a material with a sufficiently high melting temperature be chosen to achieve the creep resistance needed in a particular application. To do so, however, is rarely practical because of a variety of other design requirements including cost, density, and environmental stability. For this reason, the goal of materials engineers is to identify compositions and microstructures that will lead to improved creep strength at a given service temperature. To do so requires an understanding of the mechanisms by which creep deformation occurs.

References cited in this section

1. W.D. Nix and J.C. Gibeling, Mechanisms of Time-Dependent Flow and Fracture of Metals, *Flow and Fracture at Elevated Temperatures*, R. Raj, Ed., American Society for Metals, 1985, p 1–63
2. B. Ilshner and W.D. Nix, Mechanisms Controlling Creep of Single Phase Metals and Alloys, *Strength of Metals and Alloys*, Vol 3, P. Haasen et al., Ed., Pergamon Press, New York, 1980, p 1503–1530
3. O.D. Sherby and P.M. Burke, Mechanical Behavior of Crystalline Solids at Elevated Temperature, *Prog. Mater. Sci.*, Vol 13 (No. 7), 1967, p 325–390
4. A.K. Mukherjee, J.E. Bird, and D.E. Dorn, Experimental Correlations for High Temperature Creep, *ASM Trans. Quart.*, Vol 62, 1969, p 155–179

Creep Testing

Creep deformation is normally studied by applying either a constant load (equivalent to a constant engineering stress) or a constant true stress to a material at a sufficiently high homologous temperature that a measurable amount of creep strain occurs in a reasonable time. Constant load testing is normally employed for engineering purposes, because this situation most accurately represents service loading conditions. In contrast, constant true stress testing is used to study deformation mechanisms. At small strains, the two methods give essentially the same results. However, since the focus of this article is on creep mechanisms, primary consideration is given to the outcome of constant true stress experiments. The basic record of such a test is a plot of creep strain, ϵ , versus time, t , as illustrated schematically in Fig. 1(a) for loading in tension. It is often useful to numerically differentiate these data to determine the creep rate, $d\epsilon/dt$, or $\dot{\epsilon}$, as shown in Fig. 1(b). Normally, a small permanent loading strain, ϵ_0 , is observed when the creep stress is first applied. This strain occurs so rapidly that it is generally treated as instantaneous. With increasing strain, the creep rate gradually decreases. This hardening transient is called *primary creep*. Eventually, however, the creep rate reaches a constant value, known as the *steady state creep rate*, $\dot{\epsilon}_{ss}$, or minimum creep rate in the secondary region. This value is commonly used to characterize the creep resistance of materials and to identify the mechanism that control the creep process. In addition, the steady state region often represents the largest fraction of time during the creep test because the strain rate is the lowest. As strain continues to occur, however, microstructural damage also begins to accumulate, and the creep rate increases. This final stage, known as *tertiary creep*, immediately precedes failure or creep rupture of the test specimen. The tertiary creep strains may be quite large in some materials, especially at high stresses.

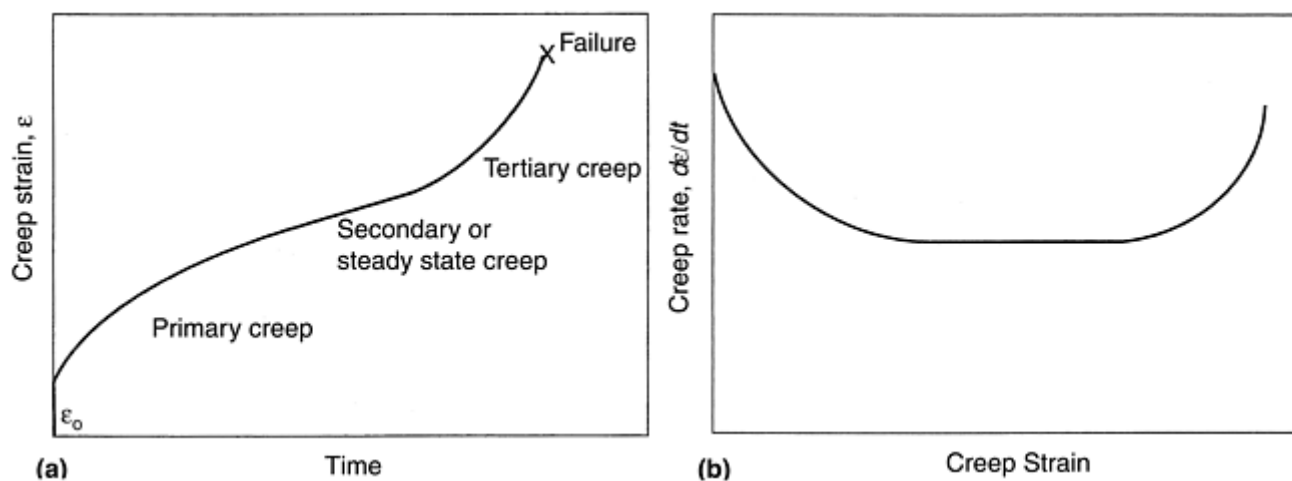


Fig. 1 Schematic illustration of the dependence for pure materials of (a) creep strain on time and (b) creep rate on creep strain

A variety of empirical relations have been proposed to describe the shape of the creep curve shown in Fig. 1(a). At low temperatures ($T < 0.3T_m$), the primary creep transient is often logarithmic with time, and steady state may not be reached. The resulting creep response can be represented by a logarithmic dependence of strain on time. At higher temperatures, the transition from primary to secondary creep can be described by an equation of the form:

$$\epsilon = \epsilon_0 + \beta t^m + \dot{\epsilon}_{ss}t \quad (\text{Eq 1})$$

where m is typically equal to $\frac{1}{3}$ and β is a constant. A more recent approach is based on an empirical fitting procedure to describe all three regions given by:

$$\varepsilon = \theta_1(1 - e^{-\theta_2 t}) + \theta_3(e^{\theta_4 t} - 1) \quad (\text{Eq 2})$$

where the θ parameters include both the stress and temperature dependence of the creep process (Ref 5). It should be noted that this approach is based on the inherent assumption that the minimum creep rate represents a transition from primary to tertiary creep without the presence of any true steady state creep rate. This approach is especially relevant for many high-strength metals, intermetallic compounds, and ceramics for which the steady state region does not persist over large strains or long times.

As noted earlier, this discussion of creep mechanisms is based on data obtained primarily from constant true stress testing. However, the form of the creep curve is very similar under constant load testing. Since creep deformation occurs under conditions of constant volume (until internal voids begin to form during tertiary creep), the cross-sectional area must decrease as the sample length increases for deformation in tension. If the load is held constant, then the true stress must increase with increasing strain. As a consequence, a steady state is not expected under constant load conditions, and the tertiary region includes the effects of both microstructural and geometric softening. It is important to note, however, that this distinction between the two loading modes is only apparent at large strains.

While the characteristic creep response shown in Fig. 1 represents the behavior of a large number of materials, there are other important cases in which the creep response is quite different. For example, some solid solution strengthened alloys exhibit an inverted primary transient when the interaction between the solute atoms and the gliding dislocations is rate controlling. This observation is illustrated schematically in Fig. 2(a). Other materials may exhibit a behavior that combines a normal transient with an inverted transient, resulting in a sigmoidal primary region. This behavior is shown in Fig. 2(b).

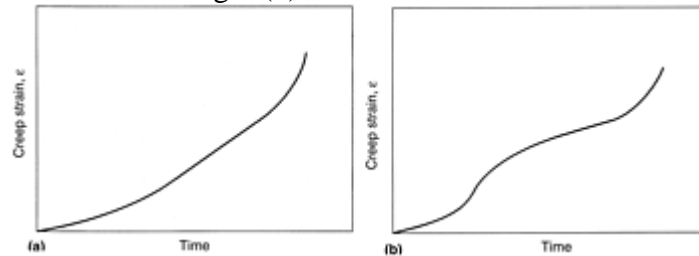


Fig. 2 Schematic illustrations of the variation of creep strain with time. (a) Behavior exhibited by some solid solution strengthened materials characterized by an inverted primary transient. (b) Behavior of some other materials that combines a normal transient with an inverted transient

Reference cited in this section

5. R.W. Evans and B. Wilshire, *A New Theoretical and Practical Approach to Creep and Creep Fracture*, *Proc. Seventh International Conf. Strength of Metals and Alloys*, H.J. McQueen, J.-P. Bailon, J.I. Dickson, J.J. Jonas, and M.G. Akben, Ed., Pergamon Press, Oxford, 1986, p 1807–1830

Creep Deformation of Metals, Polymers, Ceramics, and Composites

Jeffery C. Gibeling, University of California, Davis

Phenomenological Descriptions of Creep

Current knowledge of the mechanisms that control creep deformation is based on a combination of empirical correlations of results and micromechanical models (Ref 1, 2, 3, 4). Although a number of significant theoretical descriptions of creep have been presented, current understanding is based primarily on a correlation of the results from hundreds of independent investigations. In simplest form, creep of a variety of materials exhibiting a variety of mechanisms can be described by a phenomenological rate equation of the form:

$$\dot{\epsilon} = A \left(\frac{\sigma}{G} \right)^n \exp \left(\frac{-Q_c}{kT} \right) \quad (\text{Eq 3})$$

where A is approximately constant for a given material, n is the stress exponent, G is the elastic shear modulus, and Q_c is the activation energy for creep. This equation describes the dependence of the creep rate on the two key external variables, temperature and stress. Specific values of n and Q_c are associated with specific creep mechanisms. Thus, by characterizing the stress and temperature dependence of the creep rate, it is often possible to identify the rate-controlling mechanism for a particular material. Commonly, it is observed that the activation energy for creep is the same as that for diffusion; hence, the term $\exp -Q_c/kT$ is replaced by the relevant diffusivity, D (Ref 3, 4).

In the following sections, the creep behavior of crystalline and amorphous materials are considered separately. The emphasis in all cases is on correlating the macroscopic behavior with the underlying microscopic mechanisms. This requires that a variety of internal variables that describe the microstructural features that control the rate of deformation be considered.

References cited in this section

1. W.D. Nix and J.C. Gibeling, Mechanisms of Time-Dependent Flow and Fracture of Metals, *Flow and Fracture at Elevated Temperatures*, R. Raj, Ed., American Society for Metals, 1985, p 1–63
2. B. Ilshner and W.D. Nix, Mechanisms Controlling Creep of Single Phase Metals and Alloys, *Strength of Metals and Alloys*, Vol 3, P. Haasen et al., Ed., Pergamon Press, New York, 1980, p 1503–1530
3. O.D. Sherby and P.M. Burke, Mechanical Behavior of Crystalline Solids at Elevated Temperature, *Prog. Mater. Sci.*, Vol 13 (No. 7), 1967, p 325–390
4. A.K. Mukherjee, J.E. Bird, and D.E. Dorn, Experimental Correlations for High Temperature Creep, *ASM Trans. Quart.*, Vol 62, 1969, p 155–179

Creep Deformation of Metals, Polymers, Ceramics, and Composites

Jeffery C. Gibeling, University of California, Davis

Creep Behavior of Crystalline Solids

The mechanisms of creep in crystalline solids primarily include dislocation motion and atomic diffusion. Each process dominates in certain regimes of stress and temperature for a given material. Accordingly, the stress and temperature dependencies of the creep rate can be used to identify the relevant creep mechanisms.

Diffusional Creep. Mechanistically, diffusional creep leads to deformation of grains when the transport of atomic vacancies (opposite to the direction of atom transport) is biased by an applied stress. As a consequence, it is necessary to include a grain-size dependence in the phenomenological creep equation, resulting in an expression of the form:

$$\dot{\epsilon} = A \frac{DGb}{kT} \left(\frac{\mathbf{b}}{d} \right)^2 \left(\frac{\sigma}{G} \right) \quad (\text{Eq 4})$$

where d is the grain size and \mathbf{b} is the Burgers vector. This grain size dependence is introduced because the grain boundaries serve as sources and sinks for the diffusing vacancies. Equation 4 reflects a linear dependence of creep rate on stress; hence, $n = 1$. When diffusion through the grain interiors provides the most rapid path, then the diffusivity, D , is equal to the lattice or bulk self-diffusion coefficient. This process is known as Nabarro-

Herring creep. Alternatively, diffusion may be more rapid through the grain boundaries, in which case D in Eq 4 is replaced by $\delta D_{gb}/d$, where δ is the grain boundary width and D_{gb} is the grain boundary diffusivity. As a consequence, the creep rate varies as d^{-3} when diffusion occurs via grain boundaries; this mechanism is known as Coble creep. Thus, the grain size exponent can be used to distinguish between mechanisms that exhibit the same stress exponent.

Diffusional creep is favored at high temperatures, low stresses, and fine grain sizes. As a consequence, this mechanism is especially important in ceramic materials, where dislocation motion may be restricted by the strong lattice friction associated with ionic and covalent bonding. Small, stable grains result from common processing methods. Conversely, resistance to diffusional creep can be improved by increasing the grain size or developing an elongated grain structure through directional solidification.

Dislocation Creep. When many crystalline metals and ceramics are tested at intermediate temperatures and stresses, the predominant deformation mechanism involves the motion of dislocations. Upon initial application of a stress to a well-annealed material, dislocations move rapidly, as there are few obstacles to their motion. However, they also multiply rapidly, and the subsequent strain hardening causes the creep rate to decrease dramatically during the primary transient as represented in Fig. 1. This strain hardening arises as the number of dislocations increases and they begin to serve as barriers to glide motion of other dislocations. During the primary creep transient, the dislocation structure gradually becomes organized into low-angle boundaries that define subgrains within the grains. This substructure becomes more stable as deformation approaches steady state. Through careful study of deformed materials, it is possible to demonstrate that the size of several key microstructural features scales with the applied stress in the steady state regime. Specifically, the subgrain size, the spacing of dislocations in the subgrain interiors, and the dislocation spacing within subgrain walls all vary as σ^{-1} . These microstructural features remain in dynamic equilibrium during steady state deformation as dislocations are continuously generated and annihilated (Ref 2, 6).

One of the most influential and compelling observations regarding creep of single-phase materials is that the temperature dependence is the same as that for lattice self-diffusion. This evidence supports the concept that power law creep is diffusion controlled. Diffusion is needed to enable dislocations to climb past obstacles to their continued glide. Thus, creep occurs by the sequential processes of dislocation glide and climb. As the climb step is slower than glide, it is rate controlling. A compilation of creep activation energy data (Q_c) for a wide variety of metals and ceramics shows that it is inevitably equal to the activation energy for self diffusion Q_L (Fig. 3). It should be noted that both species must diffuse to enable dislocation creep to occur in ceramics, but the creep rate is controlled by the rate of diffusion of the slower moving ions. While there are a few notable exceptions to the rule that $Q_c = Q_L$, the preponderance of evidence supports the concept that the rate of power law creep is controlled by lattice self-diffusion at homologous temperatures greater than 0.5. At lower temperatures, the activation energy falls to lower values, as shown in Fig. 4. The lower plateau (in the range $0.25 < T_H < 0.5$) generally corresponds to the activation energy for vacancy diffusion along dislocation cores. In this temperature range, the creep rate also depends on the density of dislocations to serve as diffusion paths. Since dislocation density varies inversely with stress, this leads to an effective diffusivity, D_{eff} , given by:

$$D_{eff} = D_L + \beta \left(\frac{\sigma}{G} \right)^2 D_c \quad (\text{Eq 5})$$

where D_c is the self-diffusion coefficient in the dislocation core and β is a constant about equal to 10. As a consequence of this additional stress dependence, the expected stress exponent is $n = 7$ in this temperature range.

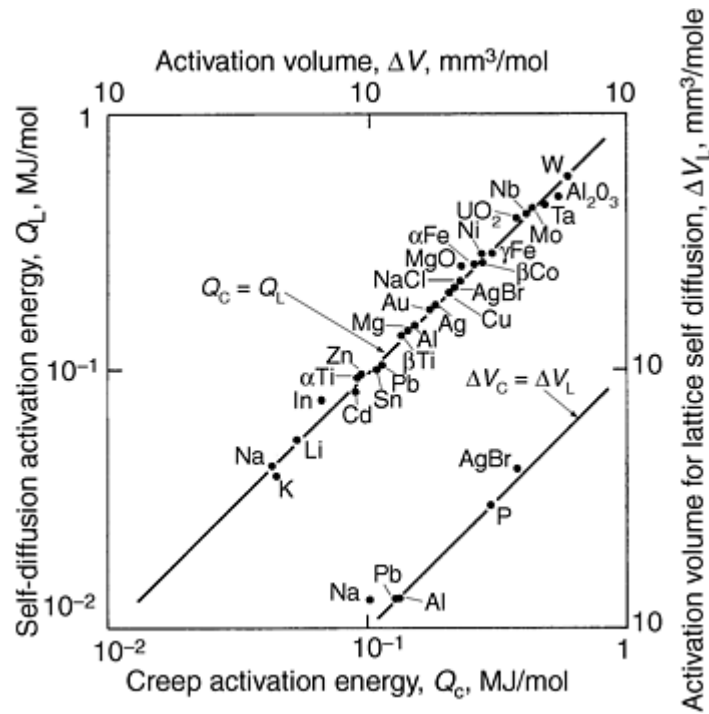


Fig. 3 Comparison of activation energies and activation volumes for steady state creep and lattice self-diffusion for various materials above $0.5T_m$ (Ref 1)

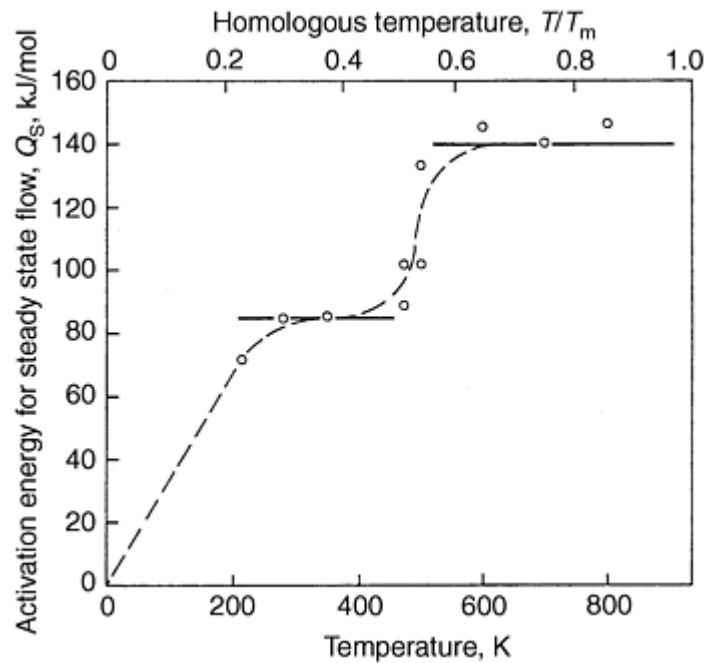


Fig. 4 Activation energy for steady state creep of pure aluminum as a function of temperature. Source: Ref 1

The observation that high-temperature creep is controlled by lattice self-diffusion can be confirmed by measuring the hydrostatic pressure dependence of creep. The relevant measured quantity is the activation volume, ΔV . As shown in Fig. 3 for a limited set of available data, the activation volume for creep, ΔV_C , is equal to the activation volume for lattice self diffusion, ΔV_L .

Creep of single phase materials exhibits a power law stress dependence as given by Eq 3, where n is normally in the range of 4.5 to 5. Accordingly, this regime is often called power law creep. Although the observation of $n = 5$ in the power law region is well documented for a variety of materials, it is important to recognize that theoretical treatments can only rationalize a value of 3 or 4. This is often termed the *natural creep law*. Representative data for pure aluminum are plotted in Fig. 5. These data illustrate that power law creep is

observed over many orders of magnitude of strain rate. However, above a normalized stress of about $\sigma/E = 10^{-3}$ (or a normalized shear stress, $\tau/G = 10^{-3}$), the creep rate begins to increase more strongly with applied stress. From the perspective of power law creep, this region is described as power law breakdown and can be described mathematically by an exponential or hyperbolic sine function as indicated in the figure. Alternatively, this change in behavior may be considered a natural transition between high-temperature (power law) deformation and low-temperature flow (Ref 1, 2).

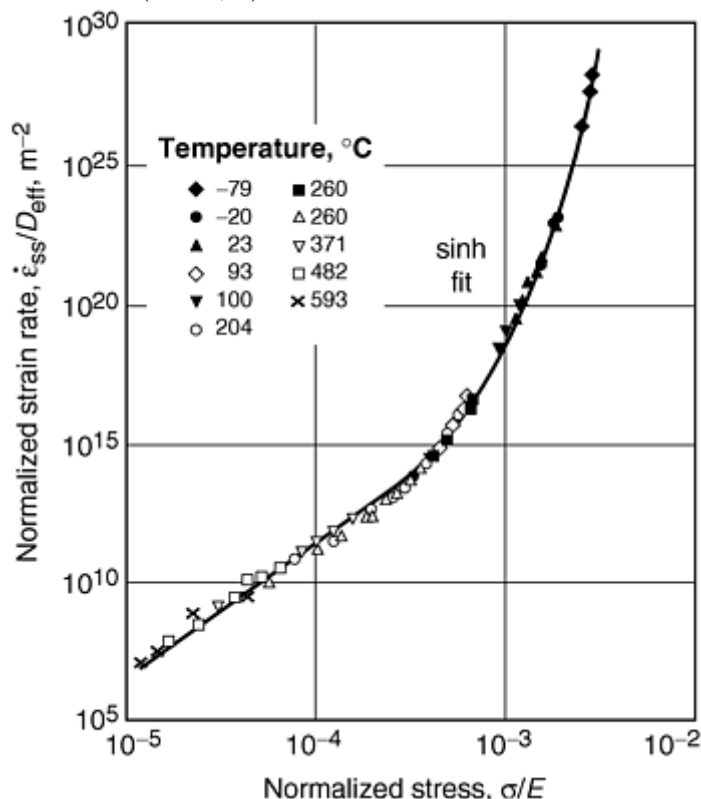


Fig. 5 Steady state creep properties of pure aluminum presented as normalized strain rate as a function of normalized stress. Source: Ref 1

Dislocation creep involves the interaction of the stress fields of moving dislocations with those of stationary dislocations. Since the stresses surrounding a dislocation depend on the elastic modulus of the solid, the creep rate is also expected to depend on elastic modulus. The most important contribution of modulus to understanding the mechanisms of creep is that it introduces an additional temperature dependence to the creep expression. For that reason, it is not important whether the elastic or shear modulus is considered, as long as the correct variation with temperature is taken into account. In particular, analysis of creep data to determine the activation energy must be based on a comparison of creep rates measured at constant values of stress normalized by modulus, not at constant values of stress.

When these factors are taken into account, the resulting empirical creep equation can be written as:

$$\dot{\epsilon} = A \frac{D G b}{k T} \left(\frac{\sigma}{G} \right)^n \quad (\text{Eq 6})$$

where A is essentially a fitting parameter that includes additional effects of microstructure such as stacking fault energy (Ref 3, 4). The parameter A must be determined from the data in order to calculate absolute values of the creep rate. As noted earlier, most pure materials and solid solution alloys that exhibit pure metal behavior are characterized by n values in the range of 4 to 8. Accordingly, measurement of values in this range can be taken as evidence that the creep mechanism involves climb-controlled dislocation motion.

In ceramics, the high lattice friction, or Peierls stresses, low dislocation densities, and lack of sufficient slip systems suggest that dislocation creep should be difficult. Nevertheless, at similar homologous temperatures and normalized stresses, the creep behavior of many ceramics is similar to that of metals (Ref 3, 7, 8). In particular, many ceramic materials also exhibit dislocation climb-controlled creep with $n \approx 5$, although in other cases a stress exponent closer to 3 is observed. Because subgrain structures are observed in these materials, dislocation climb from Bardeen-Herring sources has been identified as the principal mechanism of deformation

in the latter case. In general, the observation of $n = 3$ in essentially pure ceramics provides evidence that the material is not fully ductile, because it lacks the five independent slip systems required for general dislocation glide deformation. This situation may be attributed to both crystallographic orientation effects and the relatively high friction stresses associated with glide on some atomic planes in ceramics.

Creep in Alloys. As noted earlier, the creep curve for many solid solution strengthened alloys has a different form (Fig. 2a) than that observed for pure materials (Fig. 1) (Ref 3, 9). In these materials, solute atom clusters strongly interact with the stress fields of dislocations, and viscous glide of dislocations is the rate-controlling process. The principal interaction mechanisms that impede dislocation glide include segregation of solute atoms to dislocations, the destruction of short-range atomic order by gliding dislocations, and chemical interaction of solute atoms with dissociated (partial) dislocations. In addition to the characteristic shape of the creep curve, the behavior of these alloys differs from that of pure metals in that the stress exponent typically has a value of 3, and dislocations do not form extensive subgrain structures during deformation. Finally, the activation energy for creep generally equals that for self-diffusion of the solute atoms in the matrix. Together, these characteristics identify a material that exhibits class A (for alloy) behavior, which can be contrasted with the class M (for pure metal) response evidenced by alloys in which the dislocation/solute interactions are weaker and n is typically equal to 5. Similar viscous glide behavior has been observed in ceramic solid solutions. Here it is necessary to distinguish between glide-controlled creep and climb creep, described earlier. Both are characterized by $n = 3$, but subgrain structures do not form when creep is glide controlled.

An empirical analysis of the creep behavior of a number of solid solution alloys indicates that it is possible to predict whether an alloy will exhibit class M (climb-controlled) or class A (glide-controlled) behavior based on knowledge of fundamental physical quantities (Ref 9). In particular, deformation by viscous dislocation glide is expected when:

$$\left(\frac{kT}{ec^{1/2}Gb^3} \right)^2 < B \left(\frac{\gamma}{Gb} \right)^3 \left(\frac{\sigma}{G} \right)^2 \quad (\text{Eq 7})$$

where e is the solute-solvent atom size difference, c is the solute concentration, γ is the stacking fault energy of the alloy, and B is a constant, which is estimated from creep data for the Al-3%Mg alloy. This relationship correctly predicts the creep response of nearly all of the alloys to which it has been applied. As an example, data for a number of solid solution alloys are plotted in Fig. 6 along with the line representing the predictions of Eq 7. These data illustrate that the creep behavior of some alloys is controlled by the rate of dislocation glide while other alloys exhibit climb controlled deformation. In contrast, the data for some alloys, such as Al-3%Mg, reveal a transition from climb-controlled creep ($n = 5$) at low normalized stresses and normalized creep rates to glide-controlled deformation ($n = 3$) at high stresses.

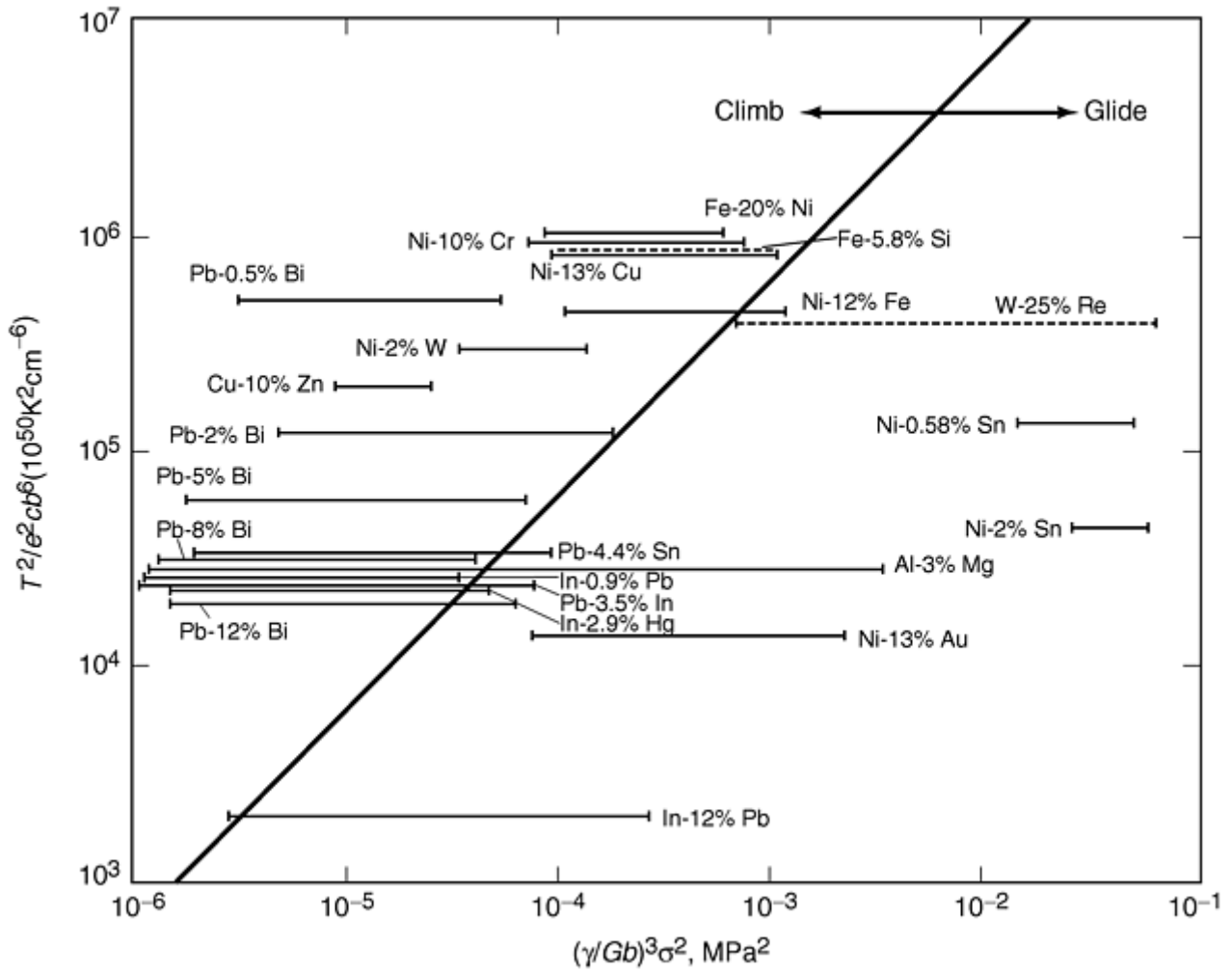


Fig. 6 Criterion for viscous glide controlled creep and dislocation climb controlled creep in solid solution strengthened alloys. Source: Ref 9

Creep of Dispersion Strengthened Materials. One method to improve the creep resistance of materials for elevated temperature applications is to add a uniform distribution of fine particles that block the motion of dislocations. Creep tests of dispersion strengthened materials commonly reveal high stress exponents (on the order of 20–100) and activation energies that are up to twice those for lattice diffusion (Ref 10). An example of results for thoria-dispersed nickel-chromium alloys is illustrated in Fig. 7 (Ref 11). Phenomenologically, creep of dispersion strengthened metals can be rationalized by introducing a threshold stress denoted by σ_0 into Eq 3 to account for the effect of the particles on the moving dislocations. The modified creep equation then takes the form:

$$\dot{\epsilon} = A \left(\frac{\sigma - \sigma_0}{G} \right)^n \exp\left(\frac{-Q_c}{RT} \right) \quad (\text{Eq 8})$$

When a threshold stress is calculated from the creep data and included in the creep equation, the observed stress exponents are approximately equal to 5, and the calculated activation energies agree with those for lattice self-diffusion.

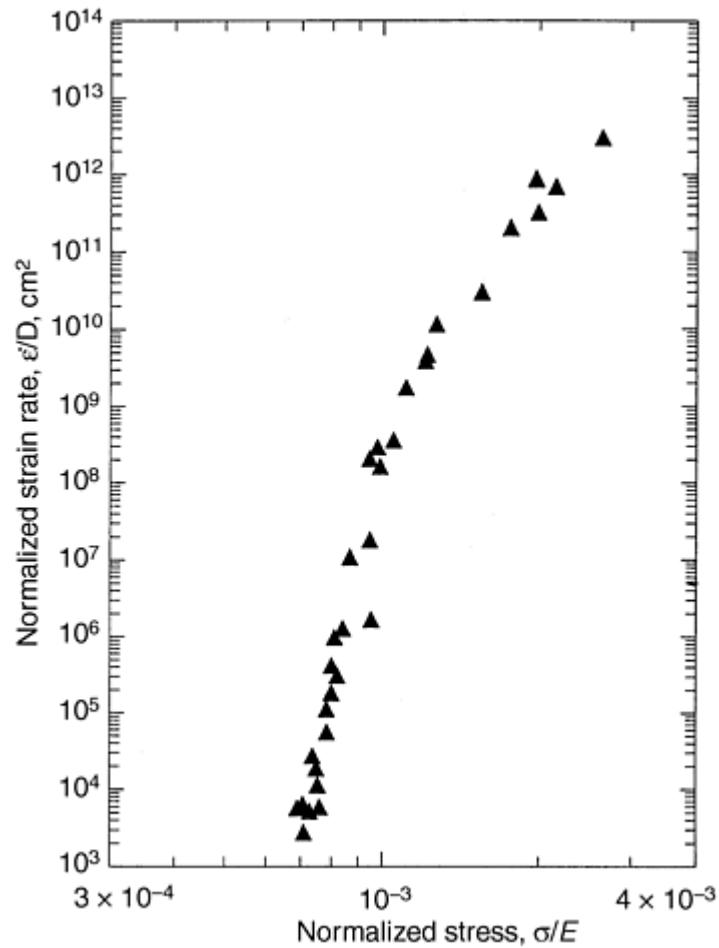


Fig. 7 Steady state creep results for a Ni-Cr alloy dispersion strengthened with ThO₂. Source: Ref 11

At high stresses, gliding dislocations can pass the dispersoid particles by the process of Orowan bowing. However, at the high temperatures and lower stresses that characterize creep deformation, it is more likely that dislocations climb out of their glide planes to overcome the particles. Theoretical treatments of climb are based on a mechanism in which only the segment of dislocation in the particle/matrix interface climbs (local climb) or one in which a significant length of dislocation line near the particle leaves the glide plane (general climb). While the climb process may introduce a threshold stress, its magnitude, as calculated from various models, is generally too low to explain the experimental observations. Further, the relatively strong temperature dependence of the threshold stress cannot be adequately explained by these theories. Thus, the threshold stress approach provides a powerful method to correlate creep data for dispersion strengthened materials, but cannot be fully justified on a theoretical basis.

A number of investigators have presented evidence from transmission electron microscopy (TEM) of creep tested dispersion strengthened metals showing dislocations that appear to be bound to particles (Ref 10). The distinctive feature of these micrographs is that the dislocations are stopped on the departure side of the particles after having climbed over them. These observations demonstrate that the line energy of the dislocations is reduced in the particle/matrix interface. Assuming that climb over the particles is relatively rapid, creep can then be modeled by considering the thermally activated release of dislocations from the departure side of the particles to be rate controlling. The resulting equation differs substantially from the usual form and contains several parameters that are difficult to evaluate from the creep data. A satisfactory fit has been obtained for creep data for a limited number of dispersion strengthened materials (Ref 10). Nevertheless, the TEM observations present compelling evidence that dislocations interact strongly with particles on a very local scale. Deformation Mechanism Maps. The mechanisms of dislocation glide, dislocation climb, and diffusional flow exhibit different stress and temperature dependencies. Thus, the relative contribution of each process will depend on the value of the applied stress, the temperature and microstructural features such as grain size. Ashby has developed a graphical method to represent the conditions under which the various creep mechanisms predominate (Ref 12).

An example of this graphical approach, known as a deformation mechanism map, is presented in Fig. 8 for creep of pure alumina (Al_2O_3) with a grain size of $100\ \mu\text{m}$. The axes of this map represent shear stress normalized by the shear modulus and homologous temperature. Each field of the map represents the range of stress and temperature over which a particular mechanism is expected to be the principal creep process. These maps are created using experimental data to determine the necessary material properties and constants in equations that describe each mechanism (such as Eq 4 and 6). Field boundaries are drawn where two mechanisms contribute equally to the overall creep rate. In addition, lines of constant total strain rate are superimposed as shown in Fig. 8.

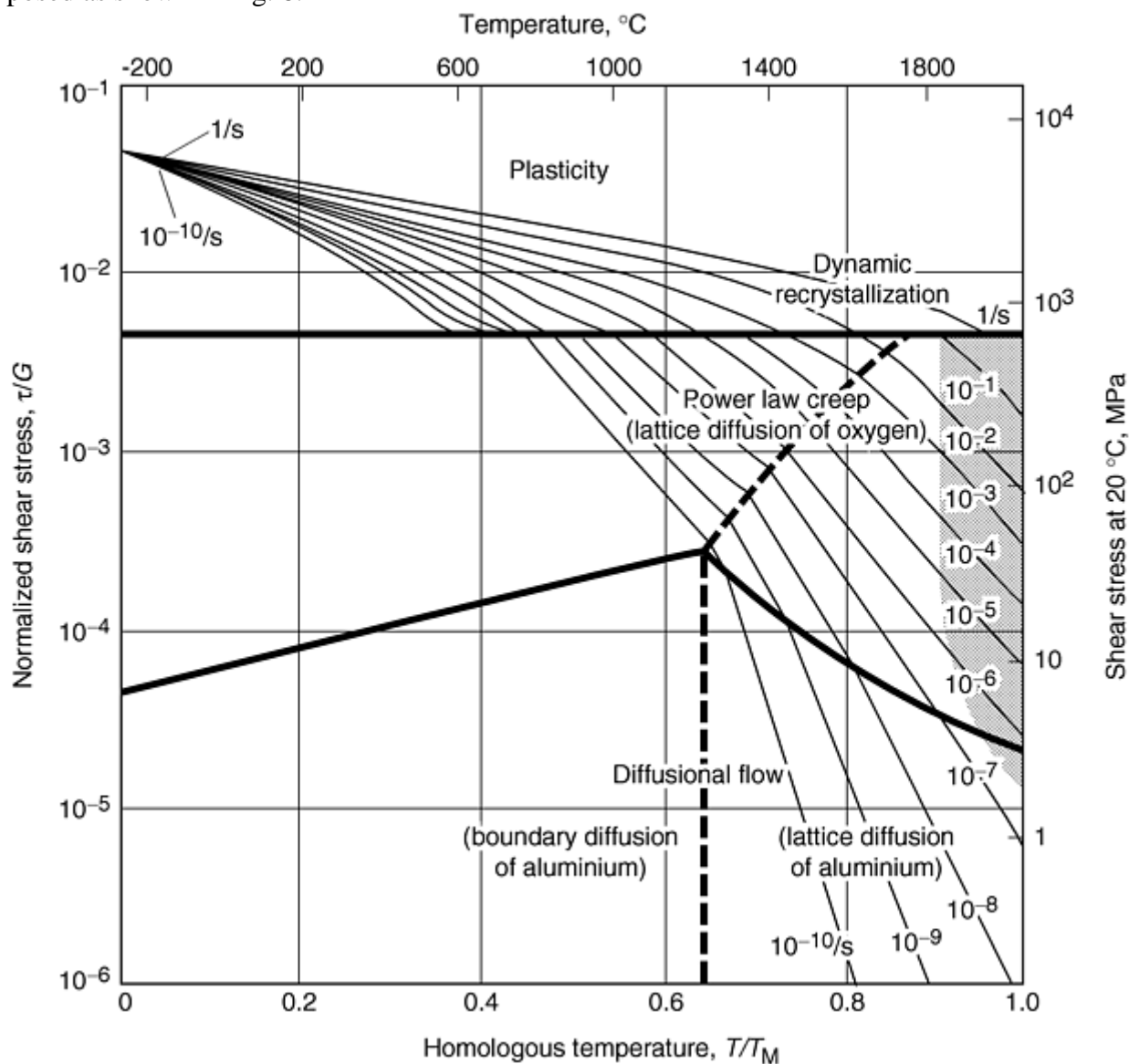


Fig. 8 Deformation mechanism map for creep of pure alumina (Al_2O_3) with a grain size (d) of $100\ \mu\text{m}$. Source: Ref 12

Maps of this type have been constructed for a variety of metals and ceramics (Ref 12). Specific knowledge of the stress and temperature dependence of the various mechanisms provides a guide to material selection and component design and suggests equations that should be used in a particular design analysis. Perhaps most importantly, these maps can be used to identify an approach to designing materials for improved creep resistance.

Creep of Composites. Structural composite materials are generally created by adding a reinforcing phase to improve some aspect of the mechanical behavior of a matrix material. The primary goal in developing metal matrix composites (MMCs) is to improve the specific stiffness and/or strength. In contrast, the motivation for adding a reinforcing phase to a ceramic matrix composite (CMC) is usually to enhance fracture toughness. Nevertheless, both MMCs and CMCs have generated considerable attention as candidate materials for high-temperature applications where creep resistance is also of concern.

In most MMCs the reinforcement is a discontinuous ceramic phase (in the form of short fibers, whiskers, or particulates). Further, these reinforcements are assumed to remain elastic, even at elevated temperatures. As a consequence, the applied stress is shared by the matrix and reinforcement, resulting in a decreased stress in the matrix compared to an unreinforced material. This load sharing effectively increases the creep resistance of the composite. It is also important to recognize that the reinforcements are generally too large to interact with individual dislocations as do precipitates and dispersoids.

The results of numerous investigations of metal matrix composites suggest that their creep behavior is largely determined by the creep characteristics of the matrix in terms of the stress exponent and activation energy (Ref 13). When the effects of load sharing and redistribution are taken into account, the magnitude of the creep rate can also be predicted with reasonable accuracy. In many cases, MMCs appear to exhibit characteristics similar to dispersion-strengthened metals, including high stress exponents and activation energies as well as apparent threshold behavior. These characteristics generally reflect the fact that the material is prepared by powder processing methods that may also incorporate fine dispersoids in the matrix. These dispersoids control the matrix creep response, which dominates the response of the composite.

The creep response of multiphase ceramics depends on the relative volume fractions of the matrix and reinforcement phase (Ref 14). As with MMCs, it is usually assumed that the reinforcing phase is rigid and that deformation occurs in the matrix, although this idealization may not always hold true for CMCs. At low volume fractions of reinforcement, the particles behave independently of one another. In this case, creep is controlled by power law deformation in a crystalline matrix or (linear) viscous flow (if the matrix is amorphous). The results of creep studies of low volume fraction materials reveal little improvement in creep strength. As the volume fraction of reinforcement is increased, the creep resistance increases dramatically. For example, when the volume fraction of whiskers in a CMC exceeds 15%, the creep rate falls by 1 to 2 orders of magnitude from the rate observed in the unreinforced matrix. This improvement appears to be essentially independent of volume fraction of reinforcement in the range 15 to 50%. Finally, at high volume fractions, the creep behavior can be described as highly constrained flow of the matrix material coupled with cavitation. Often, this situation arises in liquid phase sintered materials with an amorphous grain boundary phase. Additional complications in describing creep arise if the reinforcements form a continuous network.

References cited in this section

1. W.D. Nix and J.C. Gibeling, Mechanisms of Time-Dependent Flow and Fracture of Metals, *Flow and Fracture at Elevated Temperatures*, R. Raj, Ed., American Society for Metals, 1985, p 1–63
2. B. Ilshner and W.D. Nix, Mechanisms Controlling Creep of Single Phase Metals and Alloys, *Strength of Metals and Alloys*, Vol 3, P. Haasen et al., Ed., Pergamon Press, New York, 1980, p 1503–1530
3. O.D. Sherby and P.M. Burke, Mechanical Behavior of Crystalline Solids at Elevated Temperature, *Prog. Mater. Sci.*, Vol 13 (No. 7), 1967, p 325–390
4. A.K. Mukherjee, J.E. Bird, and D.E. Dorn, Experimental Correlations for High Temperature Creep, *ASM Trans. Quart.*, Vol 62, 1969, p 155–179
6. W. Blum, High-Temperature Deformation and Creep of Crystalline Solids, *Plastic Deformation and Fracture of Materials*, H. Mughrabi., Ed., VCH, 1993, p 359–405
7. W.R. Cannon and T.G. Langdon, Review: Creep of Ceramics, Part 1, *J. Mater. Sci.*, Vol. 18, 1983, p 1–50
8. W.R. Cannon and T.G. Langdon, Review: Creep of Ceramics, Part 2, *J. Mater. Sci.*, Vol 23, 1988, p 1–20
9. F.A. Mohamed and T.G. Langdon, The Transition from Dislocation Climb to Viscous Glide in Creep of Solid Solution Alloys, *Acta Metall.*, Vol 22 (No. 6), 1974, p 779–788

10. E. Arzt, Creep of Dispersion Strengthened Materials: A Critical Assessment, *Res Mech.*, Vol. 31, 1991, p 399–453
11. R.W. Lund and W.D. Nix, High Temperature Creep of Ni-20Cr-2ThO₂ Single Crystals, *Acta Metall.*, Vol 24, 1976, p 469–481
12. H.J. Frost and M.F. Ashby, *Deformation Mechanism Maps: The Plasticity and Creep of Metals and Ceramics*, Pergamon Press, Oxford, 1982
13. J.C. Gibeling, Interpretation of Threshold Stresses and Obstacle Strengths in Creep of Particle-Strengthened Materials, *Creep Behavior of Advanced Materials for the 21st Century*, R.S. Mishra, A.K. Mukherjee, and K.L. Murty, Ed., The Minerals, Metals and Materials Society, 1999, p 239–253
14. D.S. Wilkinson, Creep Mechanisms in Multiphase Ceramic Materials, *J. Am. Ceram. Soc.*, Vol 81, 1998, p 275–299

Creep Deformation of Metals, Polymers, Ceramics, and Composites

Jeffery C. Gibeling, University of California, Davis

Creep Response of Amorphous Solids

In contrast to the crystalline solids described in the previous section, glasses and many polymers have an amorphous atomic or molecular structure. Although these materials are not usually intended for structural applications in which resistance to creep deformation is a design consideration, their creep behavior is important in both processing and service. Many amorphous materials undergo viscoelastic deformation, which includes elastic, anelastic, and viscous plastic strain. Both anelastic and viscous deformation are commonly referred to as creep, although only the latter is permanent. To remain consistent with previous descriptions of creep, only the permanent, viscous deformation of amorphous solids is considered here.

A useful representation of the creep response of amorphous solids above the glass transition temperature is given by a simple expression for the rate of linear viscous flow:

$$\dot{\gamma} = \frac{\tau}{\eta} \quad (\text{Eq 9})$$

where τ is the shear stress, $\dot{\gamma}$ is the shear strain rate, and η is the structure- and temperature-dependent viscosity that is a function of the activation enthalpy (ΔH) as follows:

$$\eta = \eta_0 \exp \frac{\Delta H}{RT} \quad (\text{Eq 10})$$

Thus, creep in amorphous solids is a thermally activated process. In terms of tensile quantities, Eq 9 can be rewritten as:

$$\dot{\epsilon} = \frac{\sigma}{3\eta} \quad (\text{Eq 11})$$

While the preceding expressions adequately represent the behavior of both glasses and polymers, these two classes of materials differ significantly in their mechanisms of creep. These microstructural differences are reflected in the viscosities of the materials. In polymers, particularly those characterized as thermoplastics, the rate controlling creep mechanism involves cooperative motion of molecular chain segments with respect to one another. The rate and extent of creep strain decreases with increasing density of cross links between the molecular chains. Increasing molecular weight (resulting in longer molecular chains) also reduces the creep rate, but to a less significant extent. In glasses, the mobility of groups of atoms within the network of glass

forming oxides (such as SiO₂) determines the resistance to creep deformation. Network modifiers that break up the continuity of the network reduce the viscosity, thereby promoting higher creep rates (and easier formability).

Many engineering polymers also exhibit a phenomenon known as stress relaxation. In essence, stress relaxation is creep under conditions of constant total length, such that elastic strain is gradually converted to permanent plastic strain. This causes both the stress and the strain rate to decrease with time. However, the underlying mechanisms are essentially the same as for creep deformation.

Finally, we note that polymer matrix composites (PMCs) also exhibit creep deformation (Ref 15). In general, measurements of activation energy and activation volume reveal that the addition of stiff fibers does not alter the mechanism of deformation in the polymer matrix. However, an adequate description of the creep behavior of PMCs requires consideration of the volume replacement effect that gives rise to a stress redistribution and the role of constraint of deformation as the fibers essentially stiffen the matrix. Thus, the role of the reinforcements is similar in the case of crystalline matrix and amorphous matrix composites.

Reference cited in this section

15. J. Raghavan and M. Meshii, Creep of Polymer Composites, *Compos. Sci. Technol.*, Vol 57, 1997, p 1673–1688

Creep Deformation of Metals, Polymers, Ceramics, and Composites

Jeffery C. Gibeling, University of California, Davis

References

1. W.D. Nix and J.C. Gibeling, Mechanisms of Time-Dependent Flow and Fracture of Metals, *Flow and Fracture at Elevated Temperatures*, R. Raj, Ed., American Society for Metals, 1985, p 1–63
2. B. Ilshner and W.D. Nix, Mechanisms Controlling Creep of Single Phase Metals and Alloys, *Strength of Metals and Alloys*, Vol 3, P. Haasen et al., Ed., Pergamon Press, New York, 1980, p 1503–1530
3. O.D. Sherby and P.M. Burke, Mechanical Behavior of Crystalline Solids at Elevated Temperature, *Prog. Mater. Sci.*, Vol 13 (No. 7), 1967, p 325–390
4. A.K. Mukherjee, J.E. Bird, and D.E. Dorn, Experimental Correlations for High Temperature Creep, *ASM Trans. Quart.*, Vol 62, 1969, p 155–179
5. R.W. Evans and B. Wilshire, A New Theoretical and Practical Approach to Creep and Creep Fracture, *Proc. Seventh International Conf. Strength of Metals and Alloys*, H.J. McQueen, J.-P. Bailon, J.I. Dickson, J.J. Jonas, and M.G. Akben, Ed., Pergamon Press, Oxford, 1986, p 1807–1830
6. W. Blum, High-Temperature Deformation and Creep of Crystalline Solids, *Plastic Deformation and Fracture of Materials*, H. Mughrabi., Ed., VCH, 1993, p 359–405
7. W.R. Cannon and T.G. Langdon, Review: Creep of Ceramics, Part 1, *J. Mater. Sci.*, Vol. 18, 1983, p 1–50
8. W.R. Cannon and T.G. Langdon, Review: Creep of Ceramics, Part 2, *J. Mater. Sci.*, Vol 23, 1988, p 1–20

9. F.A. Mohamed and T.G. Langdon, The Transition from Dislocation Climb to Viscous Glide in Creep of Solid Solution Alloys, *Acta Metall.*, Vol 22 (No. 6), 1974, p 779–788
10. E. Arzt, Creep of Dispersion Strengthened Materials: A Critical Assessment, *Res Mech.*, Vol. 31, 1991, p 399–453
11. R.W. Lund and W.D. Nix, High Temperature Creep of Ni-20Cr-2ThO₂ Single Crystals, *Acta Metall.*, Vol 24, 1976, p 469–481
12. H.J. Frost and M.F. Ashby, *Deformation Mechanism Maps: The Plasticity and Creep of Metals and Ceramics*, Pergamon Press, Oxford, 1982
13. J.C. Gibeling, Interpretation of Threshold Stresses and Obstacle Strengths in Creep of Particle-Strengthened Materials, *Creep Behavior of Advanced Materials for the 21st Century*, R.S. Mishra, A.K. Mukherjee, and K.L. Murty, Ed., The Minerals, Metals and Materials Society, 1999, p 239–253
14. D.S. Wilkinson, Creep Mechanisms in Multiphase Ceramic Materials, *J. Am. Ceram. Soc.*, Vol 81, 1998, p 275–299
15. J. Raghavan and M. Meshii, Creep of Polymer Composites, *Compos. Sci. Technol.*, Vol 57, 1997, p 1673–1688

Creep and Creep-Rupture Testing*

Introduction

CREEP PROPERTIES are important in the design of components that are subjected to stresses at elevated temperatures for prolonged periods. In order to use materials for high-temperature components, it is essential to measure and evaluate the creep behavior of the material as a function of time. This may include creep tests and/or creep-rupture tests. Creep tests measure the amount of creep strain as a function of time, while creep-rupture tests measure the time to fracture for a given temperature and stress levels. Both tests have engineering application depending on design criteria. In some cases, the amount of creep strain is a design factor, while stress rupture is the design criterion in other cases. For example, Tables 1 and 2 list maximum-use temperatures in specific applications with different design criteria.

Table 1 Temperature limits of superheater tube materials covered in ASME Boiler Codes

Material	Maximum-use temperature			
	Oxidation/graphitization criteria, metal surface ^(a)		Strength criteria, metal midsection	
	°C	°F	°C	°F
SA-106 carbon steel	400–500	750–930	425	795
Ferritic alloy steels 0.5Cr-0.5Mo	550	1020	510	950
1.2Cr-0.5Mo	565	1050	560	1040
2.25Cr-1Mo	580	1075	595	1105
9Cr-1Mo	650	1200	650	1200
Austenitic stainless steel	760	1400	815	1500

Type 304H				
-----------	--	--	--	--

(a) In the fired section, tube surface temperatures are typically 20–30 °C (35–55 °F) higher than the tube midwall temperature. In a typical U.S. utility boiler, the maximum metal surface temperature is approximately 625 °C (1155 °F).

Table 2 Suggested maximum temperatures in petrochemical operations for continuous service based on creep or rupture data

Material	Maximum temperature based on creep rate		Maximum temperature based on rupture	
	°C	°F	°C	°F
Carbon steel	450	850	540	1000
C-0.5 Mo steel	510	950	595	1100
$\frac{1}{2}$ Cr-1Mo steel	540	1000	650	1200
Type 304 stainless steel	595	1100	815	1500
Alloy C-276 nickel-base alloy	650	1200	1040	1900

The purpose of this article is to review the basic equipment and methods for creep and creep-rupture testing. The article begins with a brief review of steady state creep behavior with subsequent sections on testing equipment, constant-load testing, and constant-stress testing. However, another engineering aspect of creep behavior is stress relaxation. Stress relaxation is the reduction of applied or residual stresses as a function of time when a stressed material is held at constant strain (i.e., held at a constant length without further deformation). Stress relaxation occurs over time, because the elastic strain within a stressed material is transformed into permanent (i.e., plastic) strain by creep deformation. This transformation, in effect, causes a reduction in elastic strain, which in turn, results in a reduction of the applied stress over time. For example, a common practical example of stress relaxation is when the tightness of high-temperature bolting undergoes progressive stress relaxation at a rate that depends on the creep strength of the material.

Stress relaxation testing principally has been used to measure and predict the relaxation of stress as a function of time and temperature. However, stress relaxation testing can also be considered as a type of creep test. Traditional creep-test methods involve the measurement of creep strain as a function of time with a fixed load (or stress) at constant temperature. Stress relaxation is a test of the same behavior but under the opposite set of test conditions, where the reduction of stress is measured with the total strain held constant at a given temperature. Stress relaxation testing is thus a complementary creep-test method that, in a short time, can generate creep-rate data as a function of stress covering five or more orders of magnitude in creep rate (see the section “Accelerated Testing” in the article “Stress Relaxation Testing” in this Volume).

Footnote

* The section “Creep Properties” was adapted from Ref 1 with additional content by R.W. Hayes, Metals Technology, Inc. The remaining sections of this article were adapted from “Creep, Stress-Rupture, and Stress-Relaxation Testing” in Volume 8 of the 9th Edition *Metals Handbook*. The section “Constant-Stress Testing” was updated by N.L. Carroll, Applied Test Systems Inc.

Reference cited in this section

1. R. Viswanathan, *Damage Mechanisms and Life Assessment of High-Temperature Components*, ASM International, 1989, p 59–69

Creep Properties

Creep properties are generally determined by means of a test in which a constant uniaxial load or stress is applied to the specimen and the resulting creep strain is recorded as a function of time. Typical shapes of creep curves are shown in Fig. 1. After the instantaneous strain, ϵ_0 , a decelerating strain-rate stage (primary creep) leads to a steady minimum creep rate (or secondary creep strain rate, $\dot{\epsilon}$), which is finally followed by an accelerating stage (tertiary creep) that ends in fracture at a rupture time, t_r . The strain at rupture, ϵ_r , represents the rupture ductility.

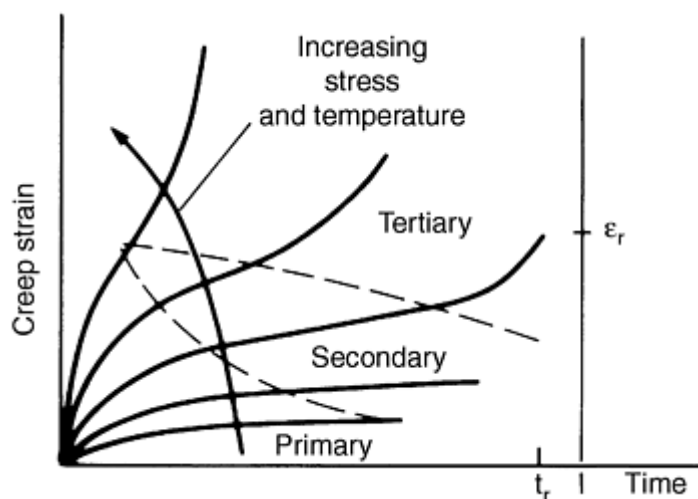


Fig. 1 Schematic illustration of creep-curve shapes. Source: Ref 1

The shape of the creep curve is determined by several competing reactions, including:

1. Strain hardening
2. Softening processes such as recovery, recrystallization, strain softening, and precipitate overaging
3. Damaging processes, such as cavitation and cracking, and specimen necking.

Of these factors, strain hardening tends to decrease the creep rate, whereas the other factors tend to increase the creep rate. The balance among these factors determines the shape of the creep curve. During primary creep, the decreasing slope of the creep curve is attributed to strain hardening. Secondary-stage creep is explained in terms of a balance between strain hardening and the softening and damaging processes, resulting in a nearly constant creep rate. The tertiary stage marks the onset of internal- or external-damage processes (item 3 in the preceding numbered list), which result in a decrease in the resistance to load or a significant increase in the net section stress. Coupled with the softening processes (item 2), the balance achieved in stage 2 is now offset, and a rapidly increasing tertiary stage of creep is reached.

Footnote

* The section “Creep Properties” was adapted from Ref 1 with additional content by R.W. Hayes, Metals Technology, Inc. The remaining sections of this article were adapted from “Creep, Stress-Rupture, and Stress-Relaxation Testing” in Volume 8 of the 9th Edition *Metals Handbook*. The section “Constant-Stress Testing” was updated by N.L. Carroll, Applied Test Systems Inc.

Reference cited in this section

1. R. Viswanathan, *Damage Mechanisms and Life Assessment of High-Temperature Components*, ASM International, 1989, p 59–69

Creep and Creep-Rupture Testing*

Stress and Temperature Dependence

Of all the parameters pertaining to the creep curve, the most important for engineering applications are the secondary creep, or minimum strain rate ($\dot{\epsilon}_{\min}$), and the time to rupture (t_r). Specifically, their dependence on temperature and applied stress are of utmost interest to the designer. This dependence varies with the applicable creep mechanism. A variety of mechanisms and equations have been proposed in the literature and have been reviewed elsewhere (Ref 2, 3, 4). Fortunately, all these mechanisms can be fitted into two basic categories: diffusional creep and dislocation creep.

In diffusional creep, diffusion of single atoms or ions either by bulk transport (Nabarro-Herring creep) or by grain-boundary transport (Coble creep) leads to a Newtonian viscous type of flow. The flow of atoms is envisaged to occur from regions of local compressive stress toward regions of local tensile stress, balanced by a counterflow of vacancies in the opposite direction. No motion of dislocations is envisaged. In this form of creep, the steady state creep rates are postulated to vary linearly with stress (i.e., $\dot{\epsilon} \propto \sigma$). At low stresses, diffusional creep is seen only at very high temperatures above $0.6 T_m$, where T_m is the melting point of the material. This high-temperature regime is not generally of engineering significance for design of components.

For structural applications and high-temperature components, the pertinent temperature regime is about 0.4 to $0.6 T_m$ (Ref 5). Most engineering applications for high-temperature components fall within this intermediate temperature regime of 0.4 to $0.6 T_m$.

Creep deformation in the “intermediate” temperature regime can be associated with a combination of mechanisms from the low-temperature regime ($T < 0.4 T_m$) and high-temperature regime ($T > 0.6 T_m$). At temperatures below $0.4 T_m$, deformation is primarily controlled by dislocation glide. Recovery processes within the low-temperature regime involve the cross slip of dislocations and are therefore considered as dynamic recovery processes. Within the low-temperature regime, diffusional processes are considered negligible and do not contribute to the deformation process. As temperatures are increased above $0.4 T_m$, dislocations move on their glide planes just as at low temperatures, although more systems may become operative due to the increased temperature. The most important difference, however, is that now dislocations acquire a new degree of freedom, the ability to climb from one slip system to another by diffusional processes, a static recovery process. This contribution of diffusion to creep deformation has been discussed extensively with much of our current understanding coming from the work of Sherby (Ref 5). Sherby and Miller (Ref 6) have also compiled a large body of data that clearly suggest a one-to-one relationship between the activation energy for lattice self-diffusion and the activation energy for creep deformation.

Power Law Model of Steady State Creep Rates. In the intermediate temperature regime ($0.4 T_m < T < 0.6 T_m$), the creep rate varies nonlinearly with stress, as either a power function or an exponential function of stress, in contrast to the linear stress dependence of diffusional creep. At stresses and temperatures of interest to the engineer, the following behavior proposed by Norton (Ref 7) and Bailey (Ref 8) is generally obeyed:

$$\dot{\epsilon} = A\sigma^n \quad (\text{Eq 1})$$

where A and n are stress-independent constants. In addition, because one contribution to creep is a thermally activated diffusion process, its temperature sensitivity would be expected to obey an Arrhenius-type expression, with a characteristic activation energy Q for the rate-controlling mechanism. Equation 1 can, therefore, be rewritten as (Ref 9):

$$\dot{\epsilon} = A\sigma^n \exp\left(\frac{-Q}{RT}\right) \quad (\text{Eq 2})$$

where A and n are constants (for a given condition), and R is the universal gas constant.

Equation 2 is a power-law relation that provides a basis for modeling creep rates as a function of temperature and stress. However, A , n , and Q are parameters that depend on the particular material condition, stress level, and temperature. The parameter A , for example, includes microstructural factors that influence the modes of creep deformation. Therefore, the parameter A must be determined from data in order to calculate absolute values of creep rates (see “Deformation-Mechanism Maps” in this article for a discussion on how the power-law regime may vary for a material).

Creep deformation results also indicate that the values for n and Q in Eq 2 are both variable with respect to stress and temperature. An example of the change in the value of n is shown in Fig. 2 for a normalized-and-tempered $\frac{1}{4}\text{Cr}-\frac{1}{2}\text{Mo}$ steel (Ref 10). A distinct break in the curve is evident, with $n = 4$ at low stresses and $n = 10$ at higher stresses. The breaks in the curves occurred at stresses at which the fracture mode changed from intergranular (I) to transgranular (T) at high stresses.

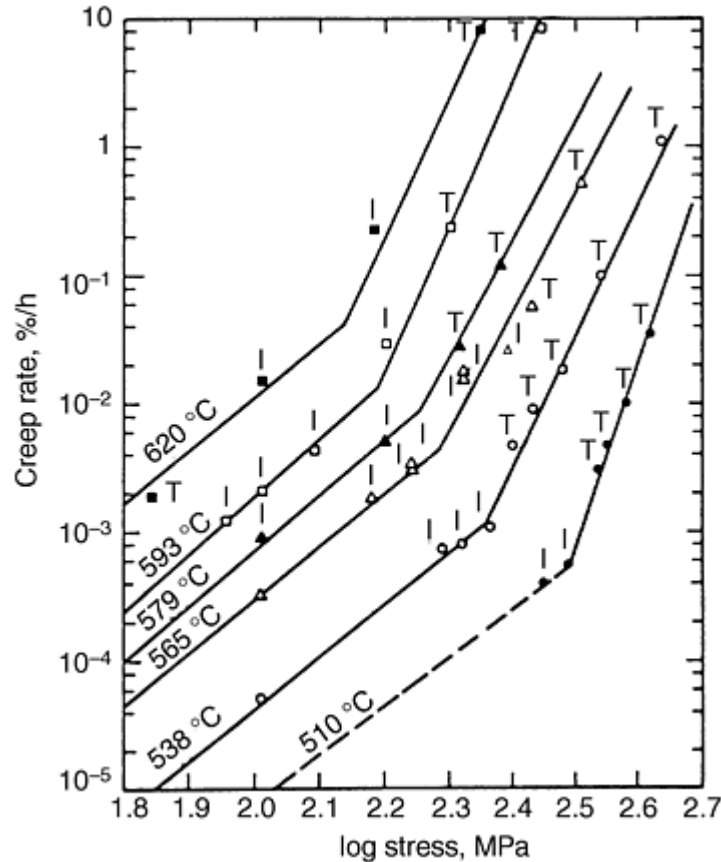


Fig. 2 Variation of minimum creep rate with stress for a normalized-and-tempered $\frac{1}{4}\text{Cr}-\frac{1}{2}\text{Mo}$ steel. T and I denote transgranular and intergranular failure, respectively. Source: Ref 10

Values of n ranging from $n = 1$ at low stresses to $n = 14$ at high stresses have been reported (Ref 10 11 12 13 14 15 16), and Table 3 is a sample of studies selected to illustrate this point. Although many investigators report a distinct break in the curve, others view the value of n as continuously changing with stress and temperature.

Table 3 Examples of reported values of stress exponent and activation energy for creep of steels

System	Temperature (T)		Coefficients in the low-stress region		Coefficients in the high-stress region		Interpretation of coefficients	Reference
	°C	°F	n	Q , kJ/mole	n	Q , kJ/mole		
$\frac{1}{4}\text{Cr}-\frac{1}{2}\text{Mo}$ steel	510–620	950–1150	4	400	10	625	Grain boundary sliding at low stresses and matrix deformation at high stresses	10

$\frac{1}{24}$ Cr-1Mo steel	565	1050	2.5	...	12	...	Deformation governed by matrix deformation	11
1Cr- $\frac{1}{2}$ Mo steel, heat-affected zone	550–605	1020–1120	3	300	6	300	Diffusive mechanism at low stresses and dislocation mechanism at high stresses	12
1Cr- $\frac{1}{2}$ Mo steel, base metal	550–605	1020–1120	5.6	...	5.6	13
Cr-Mo-V-steel	550–600	1020–1110	4.9	326	14.3	503	Dislocation climb over particles at low stresses and bowing between particles at high stresses	14 (p 230)
20Cr-25Ni-Nb steel	750	1380	3–4.7	465–532	8–12	440–494	Metallographic measurement showed that $\dot{\epsilon}_{gb} = A\sigma^m$, where $m = 3.4$. Transition from low- σ to high- σ behavior was attributed to change from grain-boundary sliding to matrix deformation.	14 (p 106)
20Cr-25Ni-Nb steel	750	1380	2–5	250–390; average, 320	$n \sim$ corresponds to boundary sliding; $n > 3$ corresponds to matrix deformation. From scratch displacements it was found that $\dot{\epsilon}_{gbs} = A^{3.7}$ and $Q_{gbs} = 385$ kJ/mole.	14 (p 122)
20Cr-25Ni-Nb steel	700–750	1290–1380	n varied from 6 to 8.4 with increasing T. Q varied with σ. At $\sigma = 79$ MPa, $Q = 678$ kJ/mole.		Values of n and Q are only “apparent” unless a back stress due to NbC precipitate is considered.	14 (p 86)

To account for these changes, it has been suggested (Ref 11, 13, 14, 17, 18) that the effective stress changes with test conditions due to changes in an “internal back stress σ_0 ” and that the stress term in Eq 2 should be modified to $(\sigma - \sigma_0)^n$. The internal back stress represents a resisting force and is postulated to arise from a variety of microstructural factors such as dislocation configurations, precipitate dispersion, and solid-solution effects.

While discussions continue regarding the natures of n and Q and the reasons for their variations, industrial practice has continued to ignore these controversies and to use a simple power law (Eq 2) with discretely chosen values of n and Q . Because variations in n and Q are generally interrelated and self-compensating, no major discrepancies in the end results have been noted in the low-stress region, as indicated in Table 3. At higher stress levels, the power-law model of creep strain rates begins to break down, as discussed later in the section “Power-Law Breakdown.”

Deformation-Mechanism Maps. With a knowledge of the stress and temperature dependence of the creep rate for each mechanism, it is possible to construct plots showing the regimes for the various mechanisms in the stress/temperature space. These plots, which are usually called deformation-mechanism maps or Ashby maps, are constructed by plotting the shear stress (σ_s) normalized by the shear modulus (G), against the homologous temperature. Ashby maps for a turbine-blade alloy (MAR-M 200) are shown in Fig. 3 (Ref 1). As discussed previously, the diffusional creep mechanism operates at low stresses and high temperatures, whereas at intermediate stresses, dislocation creep or power-law creep is operative. By comparing Fig. 3(a) and (b), it can

be seen that increasing the grain size from 100 μm (3.9 mils) to 1 cm (0.39 in.) expands the power-law creep regime and appreciably decreases the creep rate of the turbine-blade material. These maps are thus very useful in providing insight into the operative creep mechanisms.

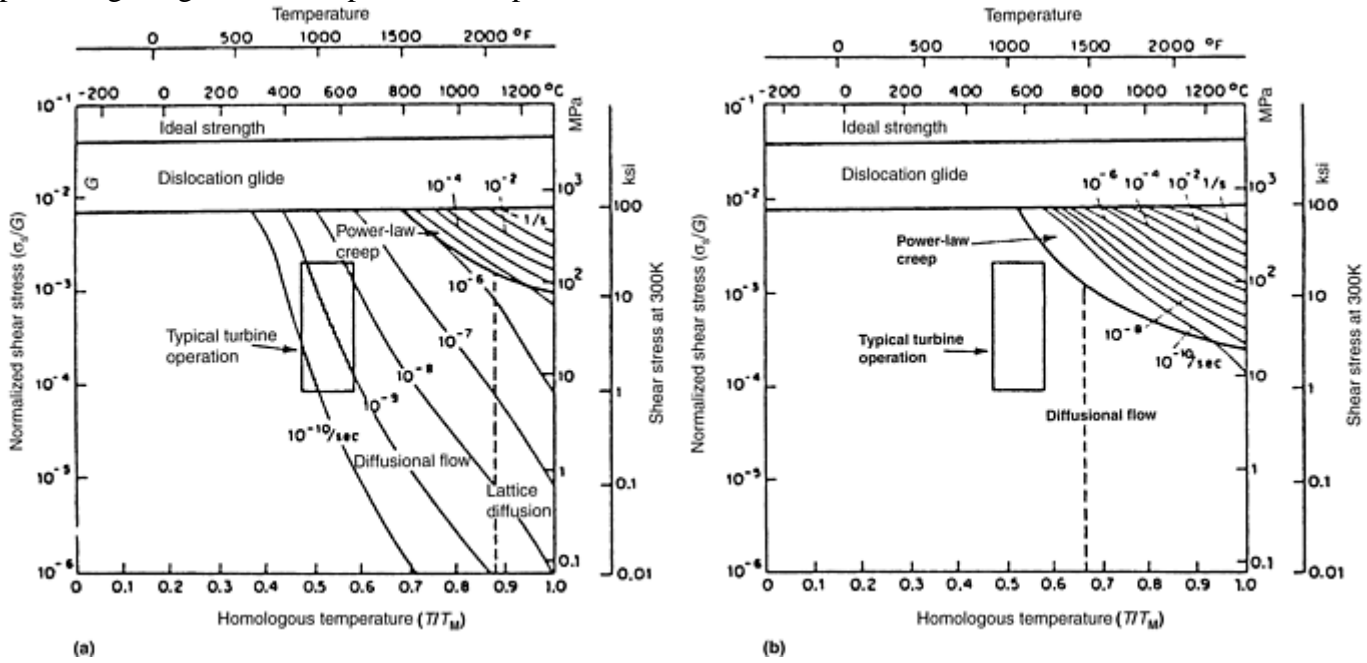


Fig. 3 Ashby deformation maps for MAR-M 200. A turbine blade will deform rapidly by boundary diffusion at a grain size of (a) 100 μm but not a grain size of (b) 1 cm

The two maps in Fig. 3 for the same material with different grain sizes also illustrate the wide variation in creep rates at a given combination of stress and temperature. This wide variation is reflected by the determination of parameter A (in Eq 2), which must be determined experimentally for calculation of creep rates.

Power-Law Breakdown. Steady state creep rate at high temperatures can be described well by a power law (Eq 2), where the stress exponent (n) ranges from 4 to 5 for face-centered cubic (fcc) metals (Fig. 4) and about 3 for body-centered cubic (bcc) metals (Fig. 5), and where the activation energy (Q) for creep is equal to that for lattice self-diffusion. The data presented in Fig. 4 and 5 (Ref 19) indicate that this holds for a wide variety of pure metals for normalized stress values below about $\sigma_s/G = 10^{-3}$.

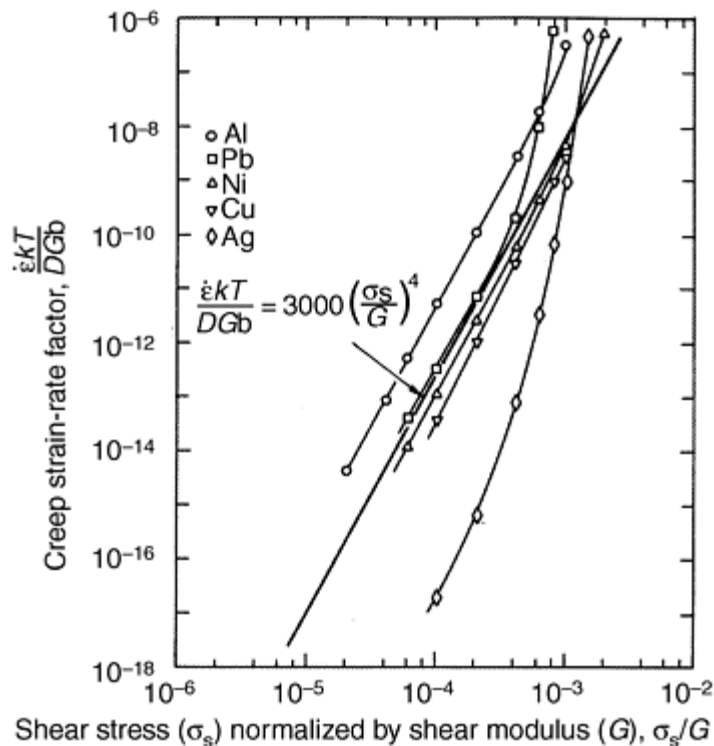


Fig. 4 Creep data for several fcc metals plotted as a function of normalized shear stress (σ_s/G) compared with a power-law stress exponent of $n = 4$. Because the activation for creep (Q in Eq 2) is the same as that for diffusion, the term $\exp(-Q/RT)$ in Eq 2 is replaced here by the diffusion coefficient, D . b = Burgers vector. Source: Ref 5 with data largely from Ref 19

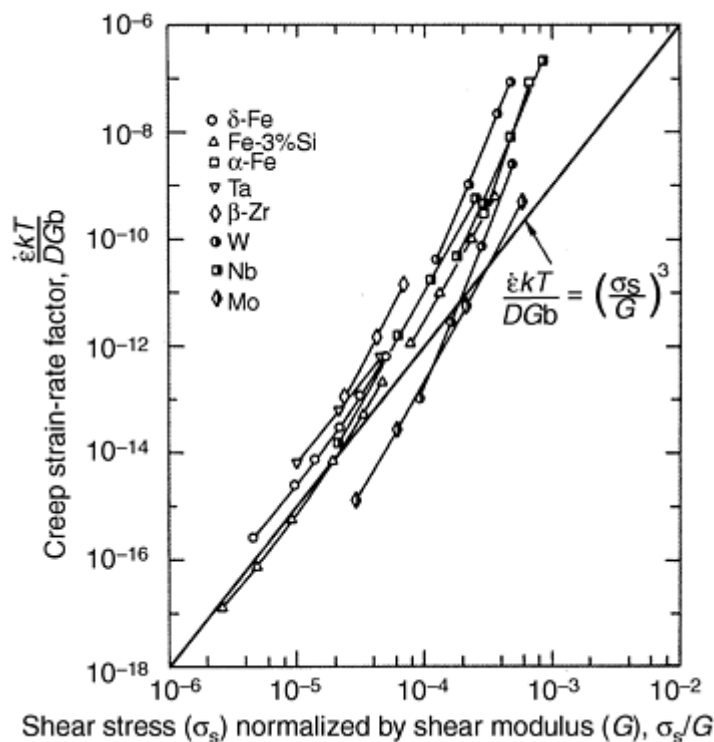


Fig. 5 Creep data for several bcc metals plotted as a function of normalized shear stress (σ_s/G) compared with a power-law stress exponent of $n = 3$. Source: Ref 5 with data largely from Ref 19

At normalized stresses above $(\sigma_s/G) = 10^{-3}$, creep rates begin to increase more strongly with stress, and the power-law model breaks down. This failure of the power law at higher stress levels is known in the literature as the *power-law breakdown*. In this high-stress region, an exponential or sink function appears to be more applicable. For example, an exponential relationship, although not generally used, has been proposed (Ref 9) to explain the behavior at very high stresses, as follows:

$$\dot{\epsilon} = A \exp(C_7\sigma) \quad (\text{Eq 3})$$

where A and C_7 are stress-independent constants. A sink function has also been used in the high-stress region (see Fig. 5 in the article “Creep Deformation of Metals, Polymers, Ceramics, and Composites” in this Volume). In addition to the increased effect of stress on steady state creep rates, the activation energies for creep within the high-stress regime also tend to decrease to values well below those for lattice self-diffusion. Robinson and Sherby (Ref 20) were among the first to suggest increasing stress exponents and decreasing activation energies at the stress levels associated with power-law breakdown. This has led to the concept of effective diffusivity. The effective diffusion coefficient is higher than the lattice diffusion coefficient, and strong evidence in favor of the effective diffusion concept can be found in the work of Luthy et al. (Ref 21). It was found that the steady state strain rates within the high stress-low temperature regime could be correlated with those obtained within the high-temperature regime by using an effective diffusivity to normalize the steady state strain rate. However, the concept of an effective diffusivity does not fully account for power-law breakdown. Spingarn et al. (Ref 22) have pointed out that the stress exponent and the activation energy should change together within the power-law breakdown regime. In analyzing the creep behavior of several metals within the intermediate regime, Spingarn et al. (Ref 22) found that for some metals, the activation energy decreased at lower temperatures, but the stress exponent remains constant. In other cases, the stress exponent is found to increase with decreasing temperature, but the activation energy remains constant. In the case of nickel, the activation energy decreases while the stress exponent increases as expected; however, the transition temperatures and stress levels are not in agreement with the predictions of the effective diffusivity. Perhaps the most limiting factor regarding the

effective diffusivity concept is that it does not provide a natural explanation of the increased effect of stress in the breakdown regime.

Composite Model and Constant-Structure Creep. At sufficiently high temperatures where creep is controlled by lattice self-diffusion steady state creep can be described quite well using a power-law approach. However, at higher stress levels (or lower temperatures), the power-law description begins to break down. As just described, an effective diffusion coefficient into the power-law equation provides an explanation for the increasing stress exponents and decreasing activation energies obtained within the high-stress/low-temperature region, but in many cases, it is not consistent with experiment.

A composite model of plastic flow, which involves diffusion-controlled recovery at high temperatures and cross-slip-controlled recovery at low temperatures, has been developed to unify the high- and low-temperature regimes (Ref 1, 23). In the framework of the composite model, power-law breakdown is considered as a natural transition from diffusion-controlled recovery at high temperatures (low stresses) to cross-slip-controlled recovery at lower temperatures (higher stresses).

The composite model is also the foundation upon which the concept of constant structure creep is derived. Constant structure creep, as it fits within the framework of the composite model, describes the kinetics of dislocation glide, multiplication, and annihilation within the cell interiors. Gibeling and coworkers (Ref 24, 25, 26, 27, 28) have argued that the power-law approach does not provide an adequate description of creep under constant structure condition.

Instead, it was suggested that the creep rate under constant structure conditions ($\dot{\epsilon}_{cs}$) can best be described by an exponential kinetic law of the form derived by Kocks et al. (Ref 25) for obstacle-controlled dislocation glide.

Stress and Temperature Dependence of Time to Rupture. The behavior of t_r with respect to σ and T is similar to that of $\dot{\epsilon}$, with the differences being that the signs are reversed for the stress exponent and the activation energy. The parameter A in Eq 2 also has slightly altered values. This behavior occurs when $\dot{\epsilon}$ and t_r are inversely related through Monkman-Grant-type relationships (i.e., $\dot{\epsilon}t_r \simeq \text{constant}$).

Footnote

* The section “Creep Properties” was adapted from Ref 1 with additional content by R.W. Hayes, Metals Technology, Inc. The remaining sections of this article were adapted from “Creep, Stress-Rupture, and Stress-Relaxation Testing” in Volume 8 of the 9th Edition *Metals Handbook*. The section “Constant-Stress Testing” was updated by N.L. Carroll, Applied Test Systems Inc.

References cited in this section

1. R. Viswanathan, *Damage Mechanisms and Life Assessment of High-Temperature Components*, ASM International, 1989, p 59–69
2. F. Garofalo, *Fundamentals of Creep and Creep Rupture in Metals*, M. Fine, J. Weertman, and J.R. Weertman, Ed., MacMillan Series in Materials Science, The MacMillan Co., New York, 1965
3. S.K. Mitra and D. McLean, Work Hardening and Recovery in Creep, *Proc. R. Soc.*, Vol 295, 1966, p 288–299
4. G. Bernasconi and G. Piatti, Ed., *Creep of Engineering Materials and Structures*, Applied Science Publishers, London, 1979
5. O.D. Sherby, *Acta Metallurgica*, Vol 10, 1962, p 135–147
6. O.D. Sherby and A.K. Miller, *ASME Journal of Materials and Technology*, Vol 101, 1979, p 387
7. F.H. Norton, *The Creep of Steel at High Temperatures*, McGraw-Hill, 1929
8. R.W. Bailey, *Creep of Steel under Simple and Compound Stress*, *Engineering*, Vol 121, 1930, p 265

9. O.D. Sherby and P.M. Burke, Mechanical Behavior of Crystalline Solids at Elevated Temperatures, *Prog. Mater. Sci.*, Vol 13, 1967, p 325
10. R. Viswanathan, The Effect of Stress and Temperature on the Creep and Rupture Behavior of a 1.25 pct. Chromium -0.5 pct. Molybdenum Steel, *Metall. Trans. A*, Vol 8A, 1977, p 877–883
11. B.J. Cane, “The Process Controlling Creep and Creep Fracture of $2\frac{1}{4}$ Cr-1Mo Steel,” CEGB Report RD/LR 1979, Central Electricity Generating Board Research Laboratories, Leatherhead, England, 1979
12. M.S. Shammas, “Estimating the Remaining Life of Boiler Pressure Parts,” EPRI Final Report on RP 2253-1, Vol 4, Electric Power Research Institute, Palo Alto CA, 1987
13. M.C. Askins et al., EPRI Final Report on RP 2253-1, Vol 5, Electric Power Research Institute, Palo Alto, CA, 1987
14. I.R. McLaughlin, in *Creep Strength in Steel and High Temperature Alloys*, The Metals Society, London, 1974, p 8, 71, 86, 106, 122, 217, 230
15. K.E. Amin and J.E. Dorn, *Acta Metall.*, Vol 17, 1969, p 1429
16. V. Foldyna, A. Jakobova, T. Prnka, and J. Sabotka, *Creep Strength in Steels and High Temperature Alloys*, The Metals Society, London, 1974, p 130
17. K.R. Williams and B. Wilshire, *Metall. Sci. J.*, Vol 7, 1973, p 176
18. C.N. Ancecuist, R. Gasca-Neri, and W.D. Nix, A Phenomenological Theory of Steady State Creep Based on Average Internal and Effective Stress, *Acta Metall.*, Vol 18, June 1970, p 663–671
19. A.K. Mukherjee, J.E. Bird, and J.E. Dorn, *ASM Trans. Quart.*, Vol 62, 1969, p 155
20. S.L. Robinson and O.D. Sherby, *Acta Metall.*, Vol 17, 1969, p 109
21. H. Luthy, A.K. Miller, and O.D. Sherby, *Acta Metall.*, Vol 28, 1980, p 169
22. J.R. Spingarn, D.M. Barnett, and W.D. Nix, *Acta Metall.*, Vol 27, 1979, p 1549
23. W.D. Nix, J.C. Gibeling, and D.A. Hughes, *Metall. Trans. A.*, Vol 16, 1985, p 2215
24. M. Biberger and J.C. Gibeling, *Acta Metall. Mater.*, Vol 43, 1995, p 3247
25. U.F. Kocks, A.S. Argon, and M.F. Ashby, *Thermodynamics and Kinetics of Slip*, Pergamon Press, Oxford, 1975, p 141
26. G.S. Nakayama and J.C. Gibeling, *Acta Metall.*, Vol 38, 1990, p 2023
27. G.S. Nakayama and J.C. Gibeling, *Scr. Metall. Mater.*, Vol 24, 1990, p 2031
28. G.S. Nakayama and J.C. Gibeling, *Modeling the Deformation of Crystalline Solids*, T.C. Lowe et al., Ed., TMS, Warrendale, PA, 1991, p 589

Extrapolation Techniques

Because many high-temperature components are designed to operate over long periods of time (sometimes in excess of 100,000 h), extrapolation of laboratory creep and rupture data to actual service conditions is unavoidable. Even if long-time data are available for selected heats of material, heat-to-heat variations in properties make it necessary to estimate the long-time behavior for other heats. Greater difficulty is encountered in estimating the remaining creep lives of in-service components, where decisions have to be made based on very short-time laboratory tests (usually less than 1000 h). The need for extrapolation techniques that permit estimation of the long-term creep and rupture strengths of materials based on short-duration tests is thus a very real and important one in design, quality control, and plant evaluation.

Basically, parametric techniques incorporate time stress and temperature test data into a single expression. When test data recorded over adequate times and at temperatures above the service temperature are incorporated into a single “master curve,” the stress for the service-temperature conditions can be read directly from the master curve.

Extensive reviews of parametric techniques have been given elsewhere (Ref 29 and 30). Their historical evolution up to the present time has been reviewed by Manson and Ensign (Ref 31). More detailed information on extrapolation is also provided in the article “Assessment and Use of Creep-Rupture Properties” in this Volume.

Footnote

* The section “Creep Properties” was adapted from Ref 1 with additional content by R.W. Hayes, Metals Technology, Inc. The remaining sections of this article were adapted from “Creep, Stress-Rupture, and Stress-Relaxation Testing” in Volume 8 of the 9th Edition *Metals Handbook*. The section “Constant-Stress Testing” was updated by N.L. Carroll, Applied Test Systems Inc.

References cited in this section

29. J.B. Conway, *Stress Rupture Parameters: Origin, Calculations and Use*, Gordon and Breach, 1969
30. S.S. Manson, *Time-Temperature Parameters—A Re-Evaluation of Some New Approaches*, ASM Publication D-8-100, American Society for Metals, 1968, p 1–115
31. S.S. Manson and C.R. Ensign, A Quarter Century of Progress in the Development of Correlation and Extrapolation Methods for Creep Rupture Data, *ASME J. Eng. Mater. Technol.*, Vol 101, 1979, p 317–325

Methods and Equipment

Determination of creep characteristics of metals at high temperatures requires the use of a loading device or test stand, an electric furnace with suitable temperature control, and an extensometer. Equipment discussed in this section is for uniaxially loaded specimens in tension. More information on creep and stress-rupture testing equipment and methods can be found in the following standard:

Designation	Title
ASTM E 139	Standard Test Methods for Conducting Creep, Creep-Rupture, and Stress-Rupture Tests of Metallic Materials
BS 3500	Methods for Creep and Rupture Testing of Metals
DIN 51226	Creep Testing Machines for Tensile Stress Testing of Metallic Materials
ISO 204	Uninterrupted Uniaxial Creep Testing in Tension of Metallic Materials
ISO 7500 (Part 2)	Verification of Applied Load—Tension Creep Testing Machines

Footnote

* The section “Creep Properties” was adapted from Ref 1 with additional content by R.W. Hayes, Metals Technology, Inc. The remaining sections of this article were adapted from “Creep, Stress-Rupture, and Stress-Relaxation Testing” in Volume 8 of the 9th Edition *Metals Handbook*. The section “Constant-Stress Testing” was updated by N.L. Carroll, Applied Test Systems Inc.

Creep and Creep-Rupture Testing*

General Methods and Test Factors

Creep behavior is generally determined by uniaxial loading of test specimens heated to temperature in some environment. Creep-rupture experiments measure the deformation as a function of time to failure. If strain-time behavior is measured, but the test is stopped before failure, this is termed an *interrupted creep experiment*. Finally, if an inadequate strain-measuring system or no attempt to determine length is employed, and the test is run to fracture, a stress-rupture experiment results.

In terms of data that characterize creep, the stress-rupture test provides the least amount, because only the time-to-rupture and strain-at-rupture data are available for correlation with temperature and stress. These data and other information, however, can be obtained from creep-rupture experiments. Such additional measurements can include elastic strain on loading, amount of primary creep strain, time to onset of secondary, creep, steady state creep rate, amount of secondary creep, time to onset of tertiary creep, time to 0.5% strain, time to 1.0% strain, and so on. All of these data can be fitted to equations involving temperature and stress. An interrupted creep test provides much the same data as a creep-rupture experiment within the imposed strain-time limitations.

Direction of Loading. Most creep-rupture tests of metallic materials are conducted in uniaxial tension. Although this method is suitable for ductile metals, compressive testing is more appropriate for brittle, flaw-sensitive materials. In compression, cracks perpendicular to the applied stress do not propagate as they would in tension; thus, a better measure of the inherent plastic properties of a brittle material can be obtained.

In general, loading direction has little influence on many creep properties—for example, steady state creep rate in ductile materials (Ref 32). However, even in these materials, the onset of third-stage creep and fracture is usually delayed in compression compared with tension. This delay is due to the minimized effect of microstructural flaws and the inability to form a “neck-like” mechanical instability. For brittle materials, the difference in behavior between tension and compression can be extreme, primarily due to the response to flaws. Consequently, care must be exercised when using compressive creep properties of a brittle material to estimate tensile behavior.

Test specimens for uniaxial tensile creep-rupture tests are the same as those used in short-term tensile tests. Solid round bars with threaded or tapered grip ends or thin sheet specimens with pin and clevis grip ends are typical. However, many other types and sizes of specimens have been used successfully where the choice of geometry was dictated by the available materials. For example, small threaded round bars with a 12 mm (0.47 in.) overall length and a 1.52 mm (0.06 in.) diameter by 5 mm (0.2 in.) long reduced section have been used to

measure transverse stress-rupture properties of a 13 mm (0.51 in.) diameter directionally solidified eutectic alloy bar (Ref 33).

In the case of uniaxial compression testing, specimen design can be simple small-diameter right cylinders or parallelepipeds with length-to-diameter ratios ranging from approximately 2 to 4. Larger ratios tend to enhance elastic buckling, and smaller ratios magnify the effects of friction between the test specimen and the load-transmitting member. These specimen geometries are well suited for creep testing when only a small amount of material is available or when the material is difficult to machine.

Environment. The optimum conditions for a creep-rupture test are those in which the specimen is influenced only by the applied stress and temperature. This rarely occurs, particularly at elevated temperatures, and these conditions do not exist for real structures and equipment operating under creep conditions. For example, turbine blades are continuously exposed to hot, reactive gases that cause corrosion and oxidation.

Reactions between the test environment and material vary greatly, ranging from no visible effect to large-scale attack. For example, creep-rupture testing of aluminum, iron-chromium-aluminum, nickel-chromium, and nickel-base superalloys at elevated temperatures in air can generally be accomplished without problems because these materials form thin, stable, protective oxide films. This is not the case for refractory metals (molybdenum, niobium, tantalum, and tungsten) and their alloys, due to their strong reaction with oxygen, which leads to the formation of porous, nonprotective, and in some cases, volatile oxides. Environmental effects such as oxidation and corrosion reduce the load-bearing cross-sectional area and can also facilitate the formation and growth of cracks.

Reactions are also possible in inert atmospheres (such as vacuum) and in reducing gas environments. Elevated-temperature testing in vacuum can result in the loss of volatile alloying elements and subsequent loss of strength. Exposure to reducing gases can result in the absorption of interstitial atoms (carbon, hydrogen, and nitrogen), which may increase strength, but also induce brittleness.

A “perfect” environment does not exist for all creep testing. The appropriate choice depends on the material, its intended use, and the available environmental protection methods. If creep mechanisms are being determined, then the atmosphere should be as inert, or nonreactive, as possible. However, if the material is to be used in an unprotected state in a reactive atmosphere, then creep testing should reflect these conditions.

Creep data from inert atmosphere tests cannot be used for design purposes when the material will be exposed to conditions of severe oxidation. However, if environmental protection methods, such as oxidation- or corrosion-resistant coatings, are available, then testing in inert gas is acceptable, and the resulting data can be used for design.

If reactions occur between the test environment and the specimen, the resultant creep-rupture data will not reflect the true creep properties of the material. Rather, the measured data are indicative of a complex interaction between creep and environmental attack, where the effects of environmental attack become more important in long-term exposure.

Footnote

* The section “Creep Properties” was adapted from Ref 1 with additional content by R.W. Hayes, Metals Technology, Inc. The remaining sections of this article were adapted from “Creep, Stress-Rupture, and Stress-Relaxation Testing” in Volume 8 of the 9th Edition *Metals Handbook*. The section “Constant-Stress Testing” was updated by N.L. Carroll, Applied Test Systems Inc.

References cited in this section

32. G.P. Tilly and G.F. Harrison, Interpretation of Tensile and Compressive Creep Behavior of Two Nickel Alloys, *J. Strain Anal.*, Vol 8, 1973, p 124–131
33. H.H. Gray, “Transverse Tensile and Stress Rupture Properties of $\gamma/\gamma' - \delta$ Directionally Solidified Eutectic,” NASA TMX-73451, 1979

On the specimen side of the machine, a balance beam leveling motor is recommended to compensate for elongation of the test specimen. If this is not available, the balance beam may become unlevel, thus changing the calibration of the weight system. However, properly designed creep testing machines will maintain load accuracy well within ASTM requirements, even when out of level by as much as $\pm 10^\circ$.

The procedure for calibration of weights is given in ASTM E 4, "Standard Practice for Force Verification of Testing Machines." The weights should be verified within a limit of 1% at least every 5 years. Additionally, the weight of the overall load train system should be verified within a limit of 1% at least once a year, except for test stands for long-term tests that last more than 1 year.

The test specimen is connected to the balance beam through the load train, a system of pull rods and couplings manufactured from high-temperature alloys that are capable of maintaining strength and corrosion resistance at the test temperatures encountered. The load train should be machined and assembled such that minimum bending moments are imposed on the test specimen. ASTM recommends a maximum of 10% bending strain, compared with the axial strain due to misalignment of the load train. To overcome this problem, alignment couplings (such as ball and socket or knife-edge systems) are used in the load train to facilitate self-alignment.

Vibration and shock loads can have a significant effect on the end results in creep and stress-rupture testing. Care must be taken in selecting the test site to ensure that vibration or shock is minimal. Additionally, the test stand should be isolated from the floor with a vibration-damping material such as cork or rubber. The leveling motor can introduce vibration that may affect long-term creep tests, or shorter tests if the vibration is significant.

A timer that automatically records the time to rupture is also included on most test stands. During creep tests, the time must be recorded with the creep values.

Footnote

* The section "Creep Properties" was adapted from Ref 1 with additional content by R.W. Hayes, Metals Technology, Inc. The remaining sections of this article were adapted from "Creep, Stress-Rupture, and Stress-Relaxation Testing" in Volume 8 of the 9th Edition *Metals Handbook*. The section "Constant-Stress Testing" was updated by N.L. Carroll, Applied Test Systems Inc.

Creep and Creep-Rupture Testing*

Furnaces

Furnaces used in creep and stress-rupture testing generally are tubular, with an electrical-resistance winding that heats the test specimen through radiation in an air atmosphere. These furnaces can have single or multiple heating zones. The tube is located in a vertical position, with the pull rods connected to the specimen. Care must be taken to seal the opening of the furnace without interfering with the alignment of the load train or the action of the linkage for creep tests.

Temperature Control and Measurement. Materials properties frequently are affected by temperature. The requirement for temperature control of creep and stress-rupture tests is $\pm 1.7^\circ\text{C}$ ($\pm 3^\circ\text{F}$) when testing at 982°C (1800°F) and below, and $\pm 2.8^\circ\text{C}$ ($\pm 5^\circ\text{F}$) above that value. Maintaining control requires practice.

Temperature measurement systems require a transducer to convert a temperature differential to an electrical signal. The transducer typically is a thermocouple that is attached directly to the specimen. Specimens with gage length 25.4 mm (1.0 in.) or greater require two thermocouples; specimens with gage lengths 50.8 mm (2.0 in.) or greater require a third thermocouple.

The thermocouple should maintain in firm and close contact with the test specimen during the entire test. Inherent errors are associated with thermocouples, including calibration error, drift due to metallurgical changes to the thermocouple junction during the test, lead wire error, attachment gap error, radiation error, and conduction error.

Footnote

* The section “Creep Properties” was adapted from Ref 1 with additional content by R.W. Hayes, Metals Technology, Inc. The remaining sections of this article were adapted from “Creep, Stress-Rupture, and Stress-Relaxation Testing” in Volume 8 of the 9th Edition *Metals Handbook*. The section “Constant-Stress Testing” was updated by N.L. Carroll, Applied Test Systems Inc.

Creep and Creep-Rupture Testing*

Extensometers

When creep data are required, the specimen strain must be measured as a function of time. With most metals this is difficult because use of strain-measuring transducers generally is not practical at the test temperatures encountered. A mechanical linkage must then be attached to the specimen to transmit the strain to the strain-measuring equipment outside the high-temperature environment.

The most commonly used strain transducer is the linear variable differential transformer, which consists of a movable metal core that changes the electrical characteristics with the small motion associated with strain measurements (Fig. 7). Linkages that attach to the specimen typically are made of alloys that can withstand the test temperatures encountered. The linkage can be attached either to the gage length or on the shoulders outside the gage length.

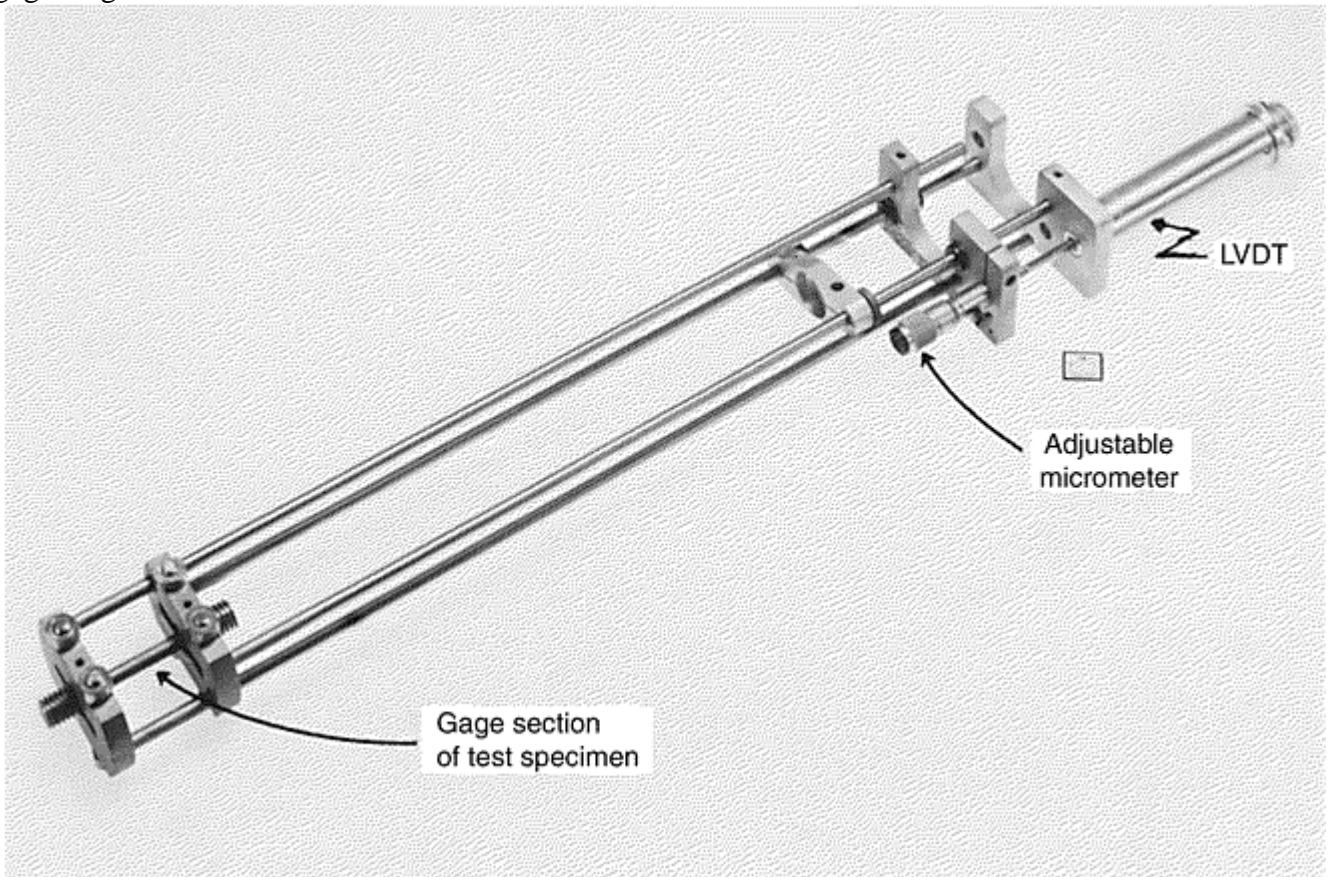


Fig. 7 Typical rod-and-tube-type extensometer for elevated-temperature creep testing. Extensometer is clamped to grooves machined in the shoulders of the test specimen.

Care must be taken to ensure that the measured deformation occurs only in the gage section. Thus, measurements based on the relative motion of parts of the gripping system above and below the test specimen are generally inaccurate because the site of deformation is unknown. Extensometry systems are currently available that attach directly to the specimen (shoulders, special ridges machined on the reduced section, or the gage section itself) and transmit the relative motion of the top and bottom of the gage section via tubes and rods

to a sensing device such as a linear variable differential transformer (LVDT). Figure 7 illustrates such a system. These systems are quite accurate and stable over long periods of time.

Typical problems encountered with the use of extensometers include:

- Error due to strain in the fillet of the test specimen when the extensometer linkage is attached to the shoulder (see Ref 34 for strain corrections)
- Fracture where the extensometer linkage attaches to the specimen gage length
- Error in strain measurement when the extensometer linkage is attached such that it measures the strain only on one side of the specimen
- Error due to slippage of extensometer linkage on the gage section of ductile specimens
- Damage to linkages and extensometers when the specimen fails
- Bending strain introduced to smaller test specimens, particularly strip specimens, due to the weight of the linkage and extensometer

Other methods of direct strain measurement exist and, under certain circumstances, are suitable. At low temperatures, strain gages can be directly bonded to the gage section and can be used to follow deformation over the range of extension for which the strain gage is valid. For specimens that will undergo reasonable deformations ($\epsilon > 1.0\%$), the distance between two gage marks can be optically tracked with a cathetometer as a function of time. While the location of strain is known, use of this technique is operator dependent and is generally limited to tests of less than 8 h or greater than 100 h in duration in order to permit sufficient readings to properly define the creep curve.

Footnote

* The section “Creep Properties” was adapted from Ref 1 with additional content by R.W. Hayes, Metals Technology, Inc. The remaining sections of this article were adapted from “Creep, Stress-Rupture, and Stress-Relaxation Testing” in Volume 8 of the 9th Edition *Metals Handbook*. The section “Constant-Stress Testing” was updated by N.L. Carroll, Applied Test Systems Inc.

Reference cited in this section

34. J.M. Thomas and J.F. Carlson, Errors in Deformation Measurements for Elevated Temperature Tension Tests, *ASTM Bulletin*, May 1955, p 47–55

Creep and Creep-Rupture Testing*

Other Testing Considerations

Constant Load Versus Constant Stress Testing. Most uniaxial creep and stress-rupture tests are conducted under constant-load conditions. Although the method is simple, the stress in the gage section varies with strain (time). This can be seen by considering a bar of length L_0 and cross-sectional area A_0 subjected to a tensile load P . At time $t = 0$, the initial engineering stress on the bar is:

$$s_0 = \frac{P}{A_0} \quad (\text{Eq 4})$$

With the assumption of uniform deformation during creep, the bar lengthens to L and the cross-sectional area decreases to A , because volume must be conserved:

$$LA = L_0A_0 \quad (\text{Eq 5})$$

Therefore:

$$A = A_0 \left(\frac{L_0}{L} \right) \quad (\text{Eq 6})$$

and the true stress on the bar is:

$$\sigma = \left(\frac{P}{A} \right) = s_0 \left(\frac{L}{L_0} \right) \quad (\text{Eq 7})$$

Methods have been devised to account for the change in cross-sectional area during creep. These are based on a rearranged form of Eq 7, where:

$$\sigma = \frac{P}{A} = \frac{PL}{L_0 A_0} \quad (\text{Eq 8})$$

By maintaining PL at a fixed value, a constant stress test can be conducted. In general, the strain-time behavior under constant stress conditions follows the general forms of primary, secondary, and tertiary stages (Fig. 1). However, the period of time spent in primary and secondary creep under constant stress can be much longer than under an identical engineering stress (constant load). Hence, rupture life is longer under constant stress conditions.

Failure under constant stress conditions eventually occurs due to some microstructural and/or mechanical instability in the same manner as a constant load experiment. Once a local variation in cross-sectional area is formed, the actual stress is higher than the imposed constant stress, and further deformation concentrates at this location.

In reality, the basic assumptions of conservation of volume and/or uniform deformation have been violated; therefore, Eq 8 is no longer valid. When nonuniform deformation starts in either a constant load or constant stress test, the local strain and strain rate vary along the gage section in an unknown manner.

Engineering Strain Versus True Strain. In creep experiments, there is little difference between strains calculated by the engineering strain or true strain definitions when the length change is approximately 10% or less. For greater length changes, the calculated values of strain deviate greatly. Although this is of no consequence for tension, the limit of a maximum engineering strain of -1.00 in compression places an artificial barrier on the description of compressive creep. Hence, true strain is a much better indicator of compressive ductility and creep characteristics. In particular, creep behavior measured in tension and compression can be compared only when both are expressed as true strain due to the limiting engineering strain in compression.

Microstructure. During creep, significant microstructural changes occur on all levels. On the atomic scale, dislocations are created and forced to move through the material. This leads to work hardening as the dislocation density increases and the dislocations encounter barriers to their motion. At low temperatures, an ever-diminishing creep rate results; however, if the temperature is sufficiently high, dislocations rearrange and annihilate through recovery events.

The combined action of hardening and recovery processes during primary creep can lead to the formation of a stable distribution of subgrains or loose three-dimensional dislocation networks in some materials, or an approximately uniform dislocation distribution without subgrains in other materials. These stable dislocation configurations are maintained and are characteristic of second-stage creep.

Creep deformation also produces change in the light optical macro- and microstructures. Such changes include slip bands, grain-boundary sliding, cavity formation and growth, and cracking (grain-boundary, interphase boundary, and transgranular). The extent of these microstructural changes is generally increased near fracture sites compared with other regions.

The microstructure of an elevated-temperature creep or stress-rupture test specimen rarely resembles the initial microstructure. Most materials are not thermodynamically stable; hence, prolonged exposure under creep conditions can result in the precipitation of new phases, dissolution or growth of desired phases, grain growth, and so on. Although many of the structural changes can be duplicated through simple heat treatment, some changes will only occur under the combined influence of stress and temperature.

Microstructural changes due to the combined influence of temperature and stress are the most difficult to control. These changes enhance creep and therefore contribute to the observed strain. Even if the changes are essentially complete after primary creep, and the resultant microstructure is more creep resistant than the original structure, the creep strain from such changes may be so great that the material cannot be used. To circumvent these changes, simulation of creep exposure prior to actual use may be necessary.

Complete microstructural examination of tested and untested materials should be an essential part of any creep experiment. As a minimum, the as-received microstructure should be compared with those at and away from the fracture site for the shortest-lived and longest-lived test specimens at each temperature. Comparison of these specimens aids identification of the relevant deformation mechanism, indicates whether environment is affecting creep, and reveals any significant microstructural changes. Such information is vital for interpreting and understanding creep behavior.

Interrupted Tests. Power failure or some other problem may make it necessary to interrupt a test, during which time the specimen cools and must then be reheated. For many materials, this appears to have little effect on either creep properties or time to rupture if cooling and heating times are not too long. However, such treatment may affect the test material. Any interruption of a test should be reported.

Footnote

* The section “Creep Properties” was adapted from Ref 1 with additional content by R.W. Hayes, Metals Technology, Inc. The remaining sections of this article were adapted from “Creep, Stress-Rupture, and Stress-Relaxation Testing” in Volume 8 of the 9th Edition *Metals Handbook*. The section “Constant-Stress Testing” was updated by N.L. Carroll, Applied Test Systems Inc.

Creep and Creep-Rupture Testing*

Constant-Load Testing

Most uniaxial creep and stress-rupture tests are conducted under constant-load conditions. The load is usually maintained constant throughout the test, and as the specimen elongates and decreases in cross-sectional area, the axial stress increases. The initial stress that was applied to the specimen is usually the reported value of stress. Methods of compensating for the change in dimensions of the specimen so as to carry out the creep test under constant-stress conditions have been developed (see the section “Constant-Stress Testing” in this article).

Footnote

* The section “Creep Properties” was adapted from Ref 1 with additional content by R.W. Hayes, Metals Technology, Inc. The remaining sections of this article were adapted from “Creep, Stress-Rupture, and Stress-Relaxation Testing” in Volume 8 of the 9th Edition *Metals Handbook*. The section “Constant-Stress Testing” was updated by N.L. Carroll, Applied Test Systems Inc.

Creep and Creep-Rupture Testing*

Specimen Preparation

Test specimens for creep and stress-rupture tests in tension are similar to those used for short-time tensile tests. Notched specimens are discussed later in this article.

Specimens with round cross sections have threaded ends, except those used at very high temperatures or those of materials that are difficult to machine or display high sensitivity to notches. Specimens with shouldered ends (no threads), or “buttonhead” fittings, are used for tests conducted at very high temperatures, particularly those in vacuum. At high temperatures, threaded specimens tend to seize in the adapters after testing due to oxidation or diffusion. The method of gripping buttonhead specimens provides self-alignment, which is advantageous with brittle materials.

For sheet or plate specimens, the load is often applied via pins placed in through holes in the shoulder ends of the specimens. If the specimen is sufficiently large, it may have elongated shoulder ends extending outside the furnace. Extension tabs sometimes are welded or brazed to the specimen shoulder and extend outside the furnace. Specially designed grips that fit the fillets at the end of the gage length are also used to apply load.

The gage length of a specimen should be uniform. The diameter or width at the ends of the reduced section should not be less than the diameter or width at the center. It is sometimes desirable to have the diameter or width of the reduced section slightly smaller at its center. The difference should range from maximums of 0.5% for a 2.54 mm (0.100 in.) diameter or width specimen to 0.2% for a 12.8 mm (0.505 in.) diameter or width specimen. Specimens should be smooth and free from scratches or other stress raisers and should be machined to minimize cold working or surface distortion. In computing the stress or the load required to provide a certain stress, the smallest original cross-sectional area should be used.

Misalignment can cause high local stresses and premature failure. If threaded specimens are used, the threaded adapters that the specimens fit into should be inspected frequently to ensure proper alignment. These devices may creep during a test and, after several tests, may undergo appreciable misalignment.

Buttonhead specimens and adapters tend to be self-aligning and pose fewer alignment problems. With sheet specimens, it is important that any brazing or welding of extension tabs be done in an alignment fixture. For sheet specimens using a pin in each tab to apply the load, the pin holes must be centered on a line running through the center of the reduced section rather than centered on the tabs. Brittle materials are more sensitive to misalignment than ductile materials.

Footnote

* The section "Creep Properties" was adapted from Ref 1 with additional content by R.W. Hayes, Metals Technology, Inc. The remaining sections of this article were adapted from "Creep, Stress-Rupture, and Stress-Relaxation Testing" in Volume 8 of the 9th Edition *Metals Handbook*. The section "Constant-Stress Testing" was updated by N.L. Carroll, Applied Test Systems Inc.

Creep and Creep-Rupture Testing*

Specimen Loading

Care is required to avoid straining the specimen when mounting it in the adapters and load train, particularly if the specimen is small or brittle. With the specimen in place, the load train (specimen adapters or grips, pull rods, etc.) should be examined carefully for any misalignment that may cause bending of the specimen under load.

The upper load train should be suspended from the lever arm and the compensating weight adjusted so that the lever arm balances. Strain-measuring clamps and an extensometer or platinum strips are attached to the specimen, and the load train is inserted into the furnace with the specimen centered. The specimen must be stabilized at temperature before loading. Also, the extensometer should be adjusted and zeroed.

Loading the weight pan should be done smoothly and without excessive shock. If the specimen is to be step-loaded, the weight is placed on the weight pan in measured increments, and the strain corresponding to each step of loading is recorded. The loading curve thus obtained is used in determining the elastic modulus and plastic strain from load application. If step-loading is not used, a method of smoothly applying the load must be used. This can be done by placing a support such as a scissors jack under the load pan during loading. When all weights are in place, the supporting jack is lowered smoothly from under the weight pan.

Footnote

* The section "Creep Properties" was adapted from Ref 1 with additional content by R.W. Hayes, Metals Technology, Inc. The remaining sections of this article were adapted from "Creep, Stress-Rupture, and Stress-

Relaxation Testing” in Volume 8 of the 9th Edition *Metals Handbook*. The section “Constant-Stress Testing” was updated by N.L. Carroll, Applied Test Systems Inc.

Creep and Creep-Rupture Testing*

Temperature Control

The specimen should not be overheated while brought to temperature. A common practice is first to bring the specimen to about 10 °C (18 °F) below the desired temperature in about 1 to 4 h. Then, over a longer period, the specimen is brought to the desired temperature.

A period of time above the desired temperature is not “cancelled out” by an equal period at a temperature the same amount below the desired temperature. If the temperature rises above the desired temperature by more than a small amount, the test should be rejected. Specified limits are ± 1.7 °C (± 3 °F) up to 982 °C (1800 °F) and ± 2.8 °C (± 5 °F) above 982 °C (1800 °F). At temperatures significantly above 1093 °C (2000 °F), the limits are broadened. Variations of temperature along the specimen from the nominal test temperature should vary no more than these limits at these temperatures. These limits refer to indicated variations in temperature according to the temperature recorder.

The indicated temperature must be as close to the true temperature as possible to prevent thermocouple error or instrument error. Thermocouples, particularly base-metal thermocouples, drift in calibration with use or when contaminated. Other sources of error are incorrect lead wires, lead wires that are connected incorrectly, and direct radiation on the thermocouple bead.

Representative thermocouples should be calibrated from each lot of wires used for base-metal thermocouples. At high temperatures, base-metal thermocouples should not be reused without first removing the wire exposed to high temperature and rewelding. Noble-metal thermocouples generally are more stable. However, they are also subject to error due to contamination and must be annealed periodically by connecting a variable transformer and passing sufficient current through the wires to make them incandescent.

When attaching the thermocouple to the specimen, the junction must be kept in intimate contact with the specimen. The bead at the junction should be as small as possible, and there must be no twisting of the thermocouple that could cause shorting. Any other metal contact across the two wires will cause shorting and erroneous readings. Shielding of the thermocouple junction from radiant heating is also recommended.

Most creep and stress-rupture machines are equipped with a switch that automatically shuts off a timer when the specimen breaks. In creep tests, the load usually is low enough that rupture does not occur. The microswitch that shuts off the timer often also shuts off or lowers the temperature of the furnace. In some furnaces, the life of the heating element is reduced significantly if the furnace is shut off after each test; instead, the temperature is merely lowered.

Footnote

* The section “Creep Properties” was adapted from Ref 1 with additional content by R.W. Hayes, Metals Technology, Inc. The remaining sections of this article were adapted from “Creep, Stress-Rupture, and Stress-Relaxation Testing” in Volume 8 of the 9th Edition *Metals Handbook*. The section “Constant-Stress Testing” was updated by N.L. Carroll, Applied Test Systems Inc.

Creep and Creep-Rupture Testing*

Notched-Specimen Testing

Notched specimens are used principally as a qualitative alloy selection tool for comparing the suitability of materials for components that may contain deliberate or accidental stress concentrations. The rupture life of notched specimens is an indication of the ability of a material to deform locally without cracking under multiaxial stresses. Because this behavior is typical of superalloys, the majority of notched-specimen testing is performed on superalloys.

The most common practice is to use a circumferential 60° V-notch in round specimens, with a cross-sectional area at the base of the notch one-half that of the unnotched section. However, size and shape of test specimens should be based on requirements necessary for obtaining representative samples of the material being investigated.

In a notch test, the material being tested most severely is the small volume at the root of the notch. Therefore, surface effects and residual stresses can be very influential. The notch radius must be carefully machined or ground, because it can have a pronounced effect on test results. The root radius is generally 0.13 mm (0.005 in.) or less and should be measured using an optical comparator or other equally accurate means. Size effects, stress-concentration factors introduced by notches, notch preparation, grain size, and hardness are all known to affect notch-rupture life.

Notch-rupture properties can be obtained by using individual notched and unnotched specimens, or by using a specimen with a combined notched and unnotched test section. The ratio of rupture strength of notched specimens to that of unnotched specimens varies with notch shape and acuity, specimen size, rupture life (and therefore stress level), testing temperature, and heat treatment and processing history.

To avoid introducing large experimental errors, notched and unnotched specimens must be machined from adjacent sections of the same piece of material, and the gage sections must be machined to very accurate dimensions. For the combination specimen, the diameter of the unnotched section and the diameter at the root of the notch should be the same within ± 0.025 mm (± 0.001 in.).

Notch sensitivity in creep rupture is influenced by various factors, including material and test conditions. The presence of a notch may increase life, decrease life, or have no effect. When the presence of a notch increases life over the entire range of rupture time, the alloy is said to be notch strengthened; that is, the notched specimen can withstand higher nominal stresses than the unnotched specimen. Conversely, when the notch-rupture strength is consistently below the unnotched-rupture strength, the alloy is said to be notch sensitive, or notch weakened. Many investigators have defined a notch-sensitive condition as one for which the notch strength ratio is below unity. However, this ratio is unreliable and can vary according to class of alloy and rupture time.

Certain alloys and test conditions show notch strengthening at high nominal stresses and notch weakening at lower nominal stresses. Changes in heat treatment of some alloys may also alter notch sensitivity significantly. For example, single low-temperature aging of some alloys may produce very low rupture ductilities because the structure is not sufficiently stabilized. Consequently, exposure of such materials for prolonged rupture times will further reduce rupture ductility because of continued precipitation of particles that enhance notch sensitivity. On the other hand, multiple aging usually stabilizes the structure and thus reduces notch sensitivity. Generally, notch sensitivity increases as temperature is reduced.

Notch configuration can have a profound effect on test results, particularly in notch-sensitive alloys. Most studies on notch configuration present results in terms of the elastic stress-concentration factor. The design criterion for the weakening effect of notches at normal and low temperatures is that of complete elasticity. The design stress is the yield stress divided by the elastic stress-concentration factor K_t . The value of the peak axial (design) stress depends on the configuration of the notch.

There is no simple relationship for the effect of notches at elevated temperatures. For ductile metals, the ratio of rupture strength of notched specimens to that of unnotched specimens usually increases to some maximum as the stress-concentration factor is increased. For very insensitive alloys, there may be little further change. Metals that are more notch sensitive may undergo a reduction in ratio as the notch sharpness (stress-concentration factor) is increased beyond the maximum and may show notch weakening for even sharper notches. Very notch-sensitive alloys may undergo little or no notch strengthening, even for very blunt notches (low stress-concentration factor) and may undergo progressive weakening as notch sharpness increases.

Footnote

* The section “Creep Properties” was adapted from Ref 1 with additional content by R.W. Hayes, Metals

Technology, Inc. The remaining sections of this article were adapted from “Creep, Stress-Rupture, and Stress-Relaxation Testing” in Volume 8 of the 9th Edition *Metals Handbook*. The section “Constant-Stress Testing” was updated by N.L. Carroll, Applied Test Systems Inc.

Creep and Creep-Rupture Testing*

Constant-Stress Testing

Norman L. Carroll, Applied Test Systems

Creep and stress-rupture data usually are obtained under constant-load test conditions. However, it is sometimes desirable or necessary to obtain test data under constant-stress conditions. In this case, the applied load is adjusted as the length of the specimen changes to maintain constant stress on the specimen.

Constant-stress testing is necessary to accurately determine differences between the temperature dependence and the stress dependence of a material. Early quantitative work on creep of materials demonstrated that the tensile creep of several pure metals and a selection of alloys under constant stress could best be represented by (Ref 35):

$$L = L_0(1 + \beta t^{1/3})e^{Kt}$$

where L is length of specimen after time, t , L_0 is the length immediately after loading, and β and K are material parameters. Typical creep curves and the effect of temperature and stress on the constants β and K in the Andrade creep equation (Ref 36) are shown in Fig. 8. The sensitivity to stress should be noted. In principle, a constant-stress test can be much more meaningful than a constant-load test. However, constant-stress tests are much more difficult to conduct because load reduction must be commensurate with the degree of straining. Furthermore, in reducing the load to keep the stress constant at a neck, the stress at other points along the gage length of the specimen is reduced. Under these conditions, the strain measured over the gage length of the specimen is no longer a representative strain. The constant-stress test, therefore, may be more meaningful when specimen elongation occurs uniformly rather than locally by necking (Ref 1) because the strain at the neck is also not simply related to the applied stress. Nonetheless, constant-stress creep tests are useful engineering tests that continue to be improved with computer-controlled test machines, as described later in this section.

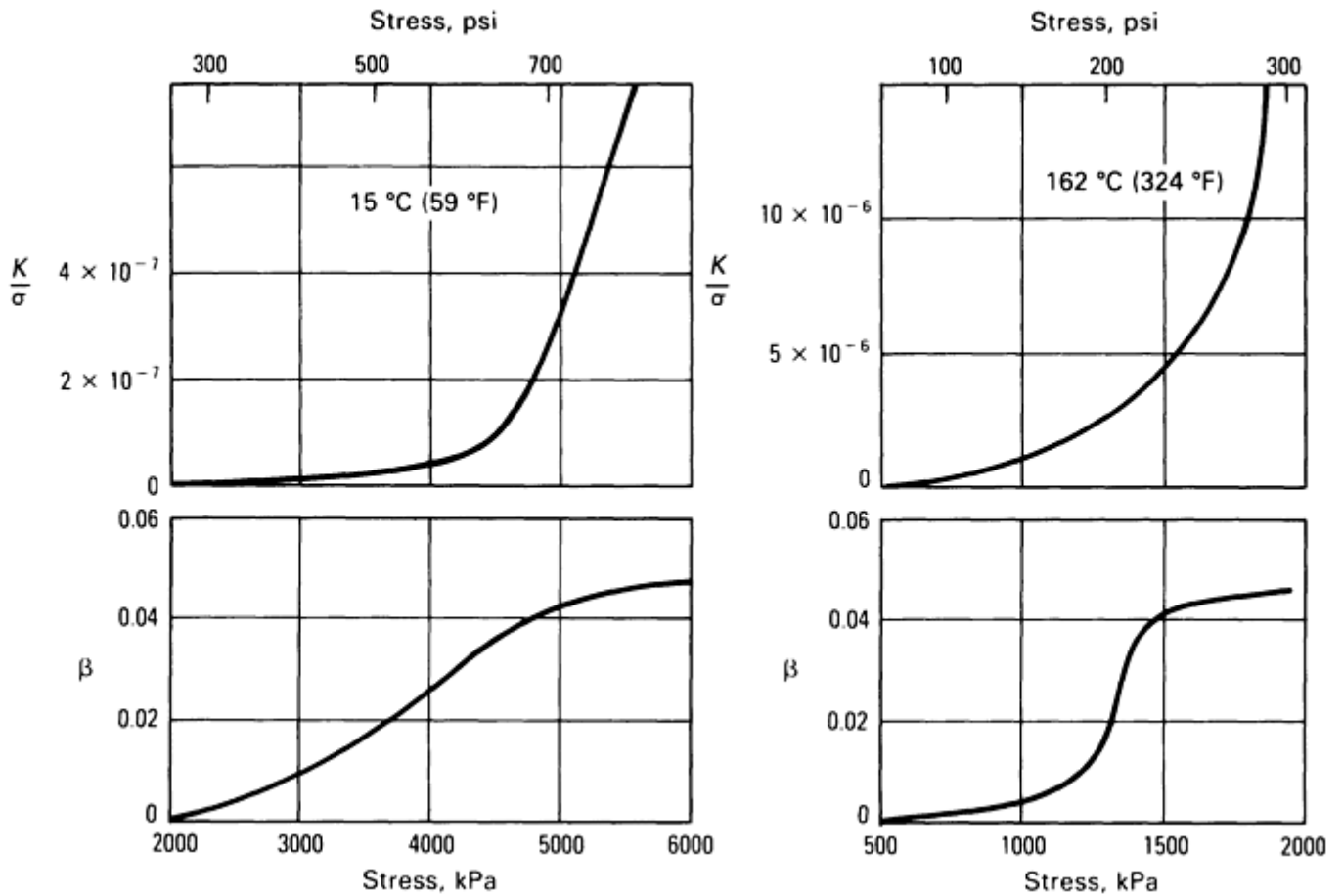


Fig. 8 Creep expression constants β and K/σ plotted as a function of stress at two temperatures

Footnote

* The section “Creep Properties” was adapted from Ref 1 with additional content by R.W. Hayes, Metals Technology, Inc. The remaining sections of this article were adapted from “Creep, Stress-Rupture, and Stress-Relaxation Testing” in Volume 8 of the 9th Edition *Metals Handbook*. The section “Constant-Stress Testing” was updated by N.L. Carroll, Applied Test Systems Inc.

References cited in this section

1. R. Viswanathan, *Damage Mechanisms and Life Assessment of High-Temperature Components*, ASM International, 1989, p 59–69
35. A. Fox, Lecture Notes, ASM Continuing Education Seminar, *Creep and Stress Relaxation Testing*, March 1980
36. E.N. Da C. Andrade, On the Viscous Flow in Metals and Allied Phenomena, *Proc. R. Soc. (London)* Vol 84, Series A, 1910–11, p 1

Creep and Creep-Rupture Testing*

Test Methods

Hyperbolic-Weight Constant-Stress Apparatus. An early application of constant-stress methods in creep testing was the use of a hyperbolic weight by Andrade (Ref 36) in which load was reduced with extension of the specimen as the weight was lowered into a liquid (Fig. 9). The required shape of the weight is given by an equation of a hyperbola:

$$y = \sqrt{\frac{ML_0}{\rho\pi} \cdot \frac{1}{L+x}} \quad (\text{Eq 9})$$

where M is the mass of the load, L_0 is the initial length of the wire, and ρ is the density of the liquid, usually water. The coordinates of the hyperbola, x and y , are shown in Fig. 9. After selecting a particular M and L_0 , the exact size of the weight is given. A weight, once constructed, is exact for one particular initial load, but with reasonable approximation, the same weight can be used over a limited range of loads.

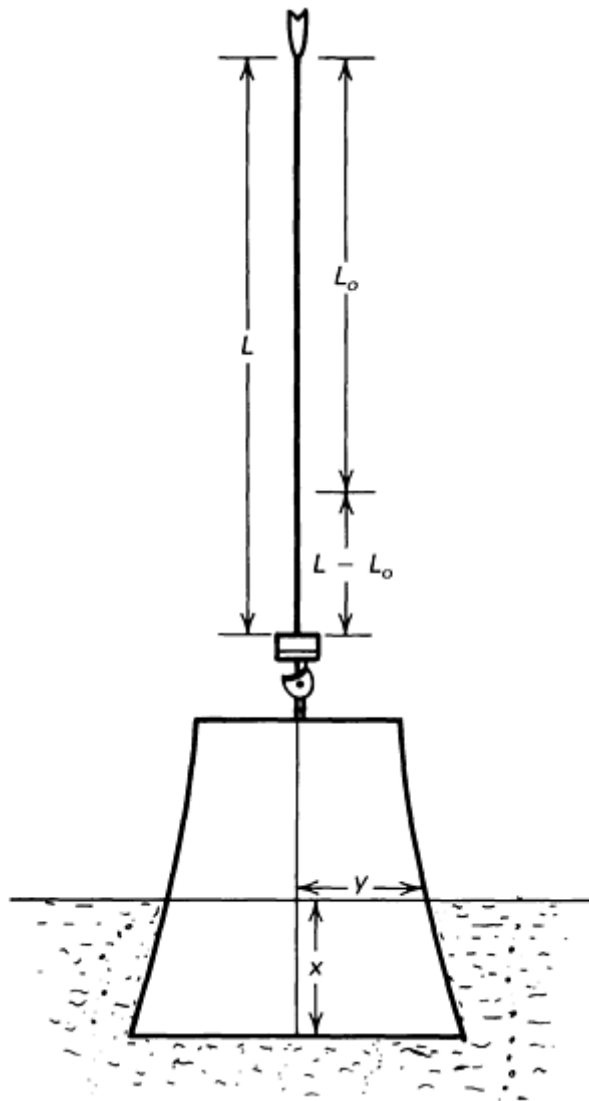


Fig. 9 Hyperbolic-weight constant-stress apparatus. Source: Ref 36

Andrade's tests on lead wire showed a significant difference between results on constant-load and constant-stress tests for the same initial length and the same initial load (Fig. 10). Under constant stress, the rate per unit length, once past the initial effect, is constant up to breaking.

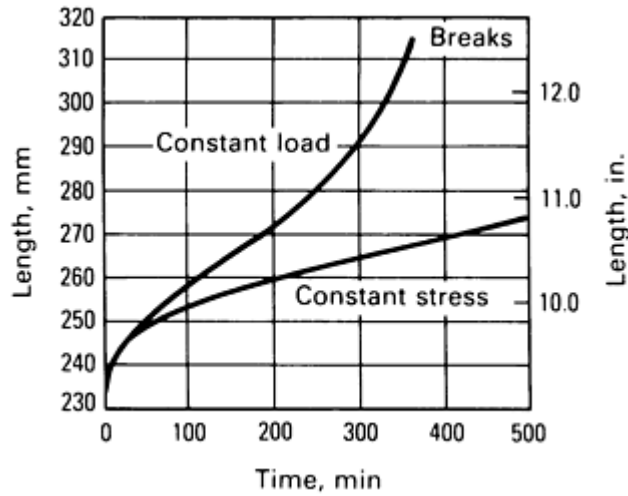


Fig. 10 Results of tests on lead wire under constant-load and constant-stress conditions. Source: Ref 36

Balanced Beam with Cams. A more convenient and useful method uses a balanced beam with shaped cams (Ref 37). A beam (PH in Fig. 11) is supported by a knife edge B and carries two plates, F and C, one at each end. Plate C has a groove along its outer edge HK; the profile HK is an arc of a circle with center B. D is a thin steel wire resting in the groove that is fixed to the adjusting screw, E. The lower end of D is attached to the upper end of the wire to be stretched. F is the second plate, in the groove of which lies a thin steel wire supporting a weight W. The profile of the bottom of the groove PQR is made such that the moment of the weight W about the axis through B is inversely proportional to the length of the wire undergoing stretch, which (assuming that any change in density of the metal that may occur during stretch is negligible) will make the stretching force proportional to the cross section of the wire.

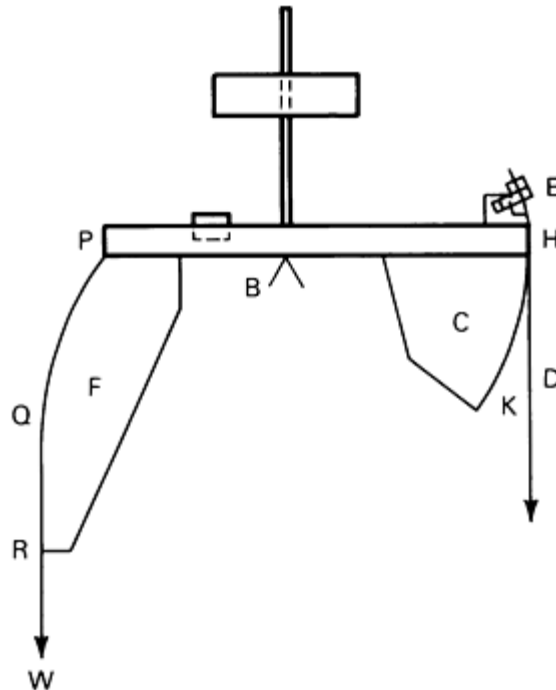


Fig. 11 Balanced beam with cams. See text for explanation of symbols. Source: Ref 37

A compact cam-lever apparatus for application of either constant stress or constant load in tension for large uniform deformations has been developed (Ref 38). Systems of this type have been used for constant-stress testing at loads up to 45 kN (10,000 lbf).

The profile of the constant-stress cam lever is similar to that of the balanced beam with cams (Ref 37), except that exact parametric equations for the cam profile have been determined. The load to the specimen is applied through a circular disk of radius R (Fig. 12). The initial mechanical advantage is r_0/R , but the ratio is reduced as the specimen elongates.

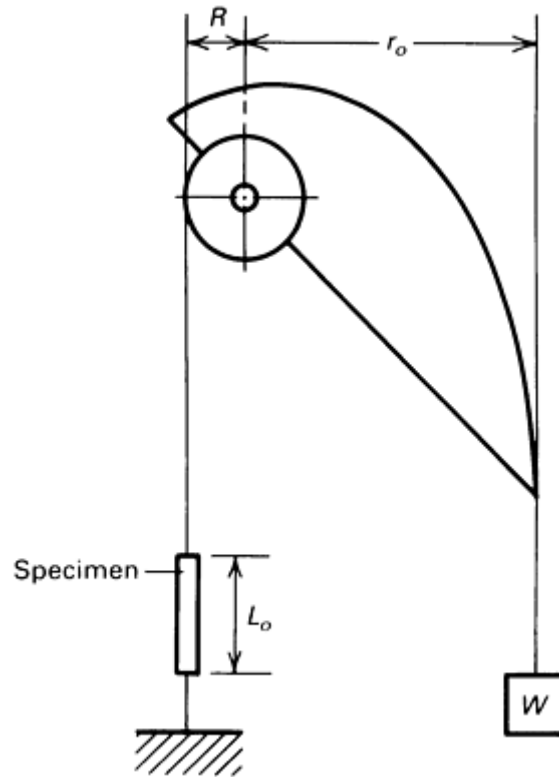


Fig. 12 Constant-stress cam-lever apparatus. Source: Ref 38

To maintain constant stress, the load P on the specimen must be reduced as the specimen elongates to compensate for the reduction in area A . Thus, the instantaneous stress P/A must remain constant. By assuming constant specimen volume and uniform strain, LA (where L is the specimen length) must remain constant. Therefore, it follows that PL also remains constant. In Fig. 12, under equilibrium conditions, $P = Wr/R$, where W is the applied weight and r is the instantaneous moment arm of the applied weight. Thus, to maintain a constant stress, the following condition must be satisfied:

$$rL = \text{constant} - r_0L_0 \quad (\text{Eq 10})$$

where L_0 is the initial specimen length and r_0 is the initial value of r .

As the length of the specimen increases, the arc of contact on the small wheel increases by an equivalent amount. Thus, the instantaneous specimen length may be written as:

$$L = L_0 + (\theta - \theta_0)R \quad (\text{Eq 11})$$

where θ_0 is the angle for the initial positioning of the constant-stress cam. Eliminating L from Eq 10 and 11 leads to:

$$r = \frac{r_0L_0}{L_0 + R(\theta - \theta_0)} \quad (\text{Eq 12})$$

This is the equation of the profile of a constant-stress cam. To design an actual cam profile, it is desirable to transform Eq 12 into a fixed Cartesian coordinate system (x, y) . These design considerations are discussed in Ref 37 and 38.

To provide balance and proper control of loading on the specimen, a balancing cam is added to the loading cam. As shown in Fig. 13, a circular disk or constant-load wheel also may be added to the cam for the purpose of performing constant-load testing. The load can be transmitted by a number of methods; steel bands or roller chain are used most frequently. The shaft of the cam assembly usually is supported by pillow block bearings. Another method of support is the use of hardened and ground knife edges and V-blocks (Fig. 14), although this method results in reduced cam rotation and specimen elongation.

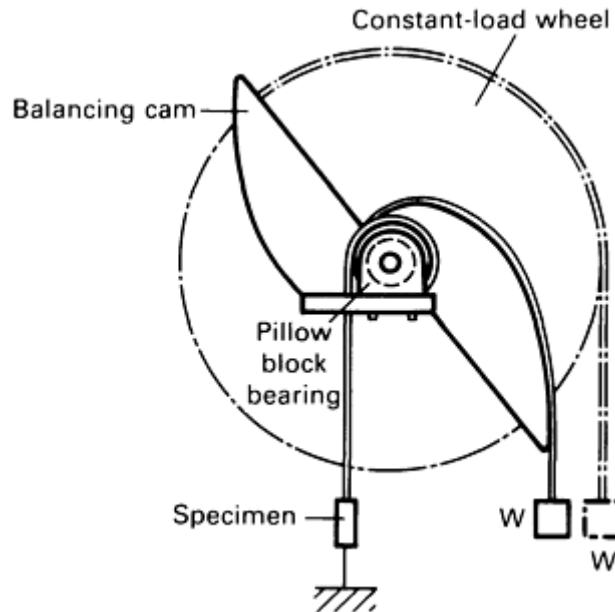


Fig. 13 Constant-stress testing system with balancing cam and constant-load wheel

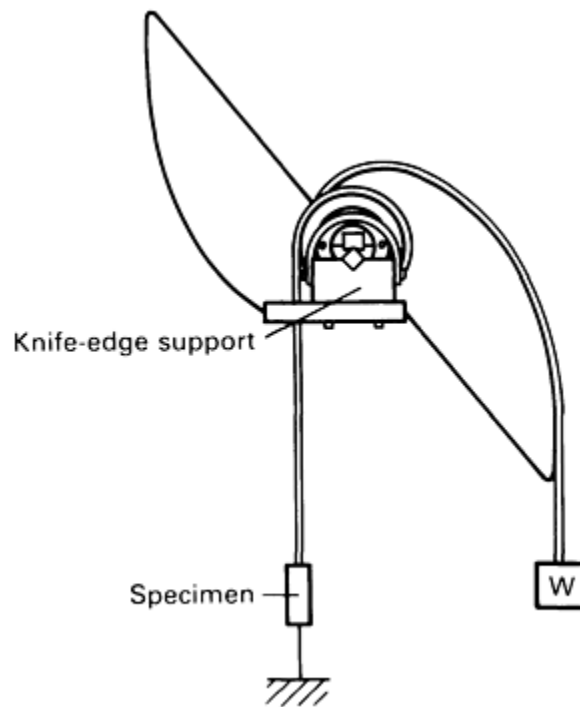


Fig. 14 Constant-stress testing system using V-block and knife-edge support

Typical systems of this type include a counterbalance cam, a pillow block bearing support, and a three-zone furnace for elevated temperature testing. A motorized automatic weight elevator with a platform usually provides gradual load application, reduces labor in handling weights, and minimizes shock upon specimen failure. The cams for these systems are programmed and machined on a computer numeric control (CNC) milling machine to provide optimum accuracy and minimum cost.

A constant-stress apparatus for use with low forces has been developed to eliminate frictional effects of hinges or bearings (Ref 39). Reference 40 describes a method of cam assembly support by means of steel tapes. Modifications of this method were designed to achieve the accurate maintenance of constant stress when forces as low as 0.1 N (0.022 lbf) are involved (Fig. 15).

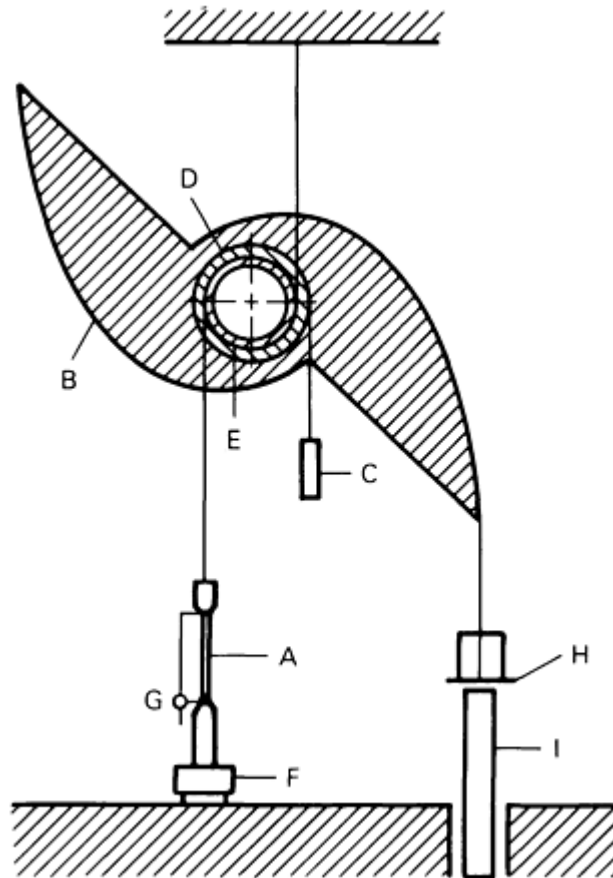


Fig. 15 Constant-stress testing system for use with low forces. A, specimen; B, double cam; C, counterweight; D, pulley for counterweight; E, hollow cylinder from which specimen is suspended; F, force cell; G, tape displacement gage; H, loaded mass pan; I, hydraulic ram

To balance the mass of the cam about the point of suspension and thereby ensure that the only force on the specimen is the applied force due to the mass M , the counterweight C is necessary. With the modified suspension, the cam profile equation becomes:

$$r = \frac{(r_0 - R)L_0}{L_0 + 2R(\theta - \theta_0)} + R \quad (\text{Eq 13})$$

For actually determining the cam profile, Eq 13 usually is transformed into two profile equations that express the Cartesian coordinates x and y in terms of a single parameter.

In the absence of frictional forces, the lower limit on the applied force P is determined by the sensitivity with which the suspension system can be balanced. For the present apparatus, the lower limit was 0.1 N (0.022 lbf), which corresponds to 5.0 kPa (0.72 psi) if the specimen diameter is 5 mm (0.2 in.). Thus, the apparatus is suitable for use at small stresses, such as may be encountered in studies of plastic flow at temperatures close to the melting point. The system demonstrated accuracy within $\pm 0.50\%$.

High-Temperature Constant-Stress Compression Creep Apparatus. A constant-stress apparatus has been developed for high-temperature compression testing of ceramic materials in controlled atmospheres (Ref 41). The creep frame is based on the fundamental concepts developed in Ref 42 for the application of constant compressive stress loading using the Andrade fulcrum principle via a lever arm mechanism from a weight pan loaded system. The following equation ensures maintenance of constant stress:

$$L_3 = \frac{L_1 L_2}{L} \quad (\text{Eq 14})$$

where L_1 , L_2 , and L_3 are the distances between the various knife edges (Fig. 16 and 17) and L is the sample length.

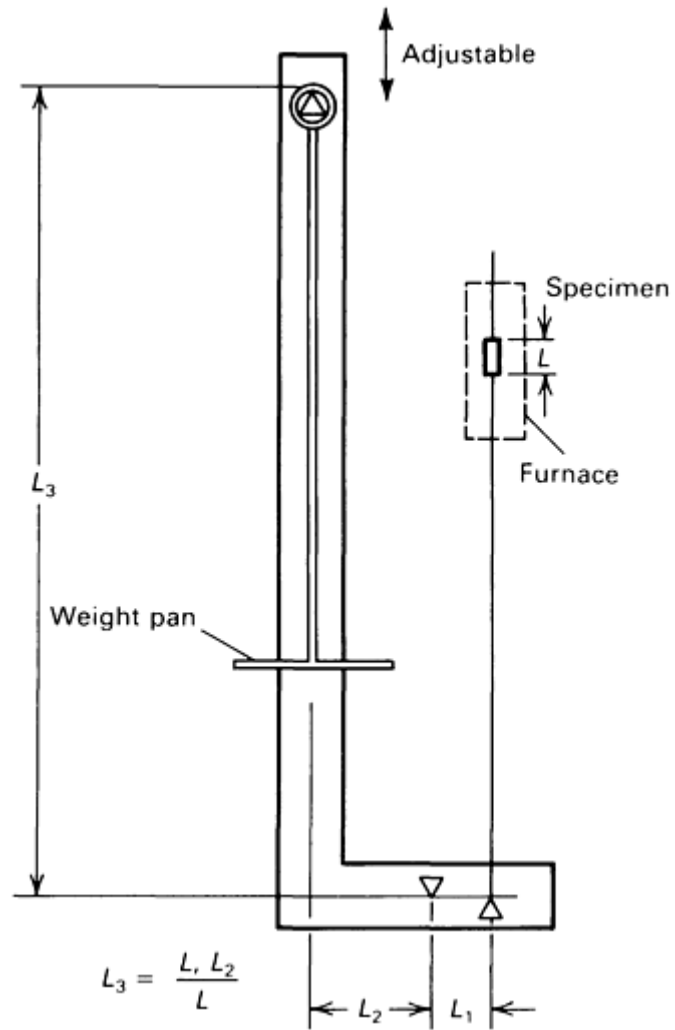


Fig. 16 Knife-edge configuration for constant-stress compression testing. Source: Ref 41

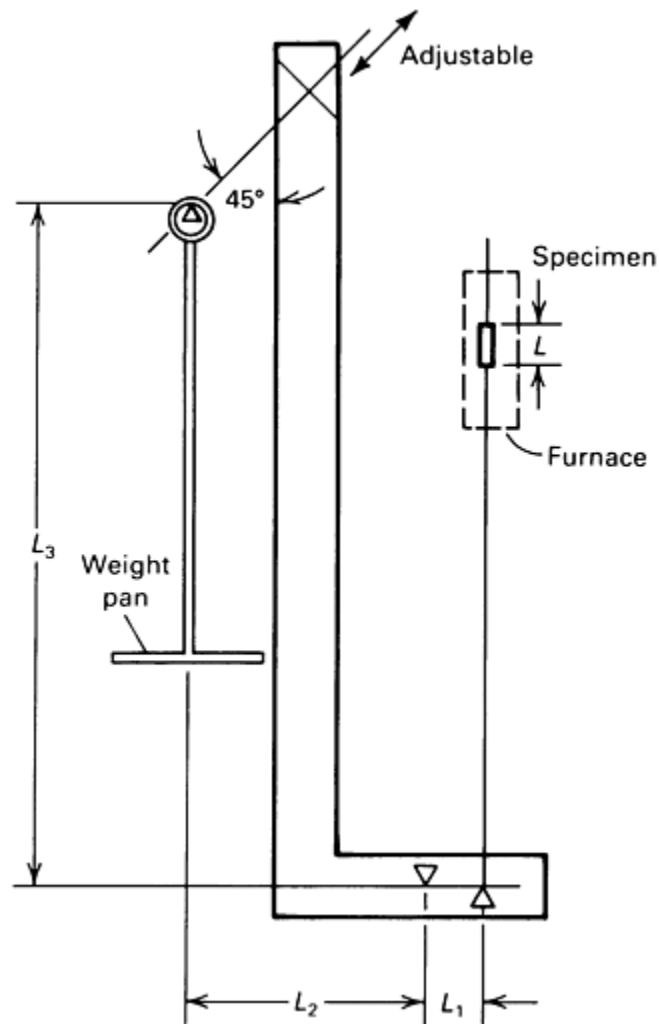


Fig. 17 Alternate knife-edge construction providing a greater range of sample lengths. Source: Ref 41

Two knife edges provide the fulcrum for the lever arm, another supports the weight pan, and a fourth applies the force to the lower sample push rod. When the load pan support columns are vertical, the frame acts as a simple fulcrum to apply a force on the lower push rod that is greater than the force on the weight pan by a factor of L_2/L_1 . When the sample deforms, the frame tilts backward and the columns are no longer vertical.

This movement, which is proportional to the preset L_3 and the amount of deformation, increases the force applied to the push rod and also to the sample. The increase in force compensates for the increase in area of the sample as it is compressed, thus maintaining a constant stress. Shorter samples require a greater L_3 because the area of the sample becomes greater for the same amount of deformation than for a sample of greater height. Sample area is not important in making L_3 calculations because changes in area for a given amount of creep are of the same proportion for samples having either a large or a small area if both are of the same height. The system described also allows L_3 to be adjusted.

By increasing or decreasing the range of L_3 , the range of sample lengths can be changed. This is done by using longer or shorter weight pan support columns or by using an adjusting system that simultaneously changes L_3 and L_2 by moving the weight pan knife edge, as shown in Fig. 17. Two bars with weights are used to balance the frame.

The unit maintains constant stress to within 1%, as long as the total strain does not exceed 10% and the test is initiated with the weight pan columns in a vertical position. However, if an approximation of the total strain during the run can be predicted and if the unit is set such that it passes through the vertical position when approximately one-half of the total strain has occurred, the stress can be held to within 0.5% up to a total strain of 10%.

Footnote

* The section “Creep Properties” was adapted from Ref 1 with additional content by R.W. Hayes, Metals Technology, Inc. The remaining sections of this article were adapted from “Creep, Stress-Rupture, and Stress-Relaxation Testing” in Volume 8 of the 9th Edition *Metals Handbook*. The section “Constant-Stress Testing” was updated by N.L. Carroll, Applied Test Systems Inc.

References cited in this section

36. E.N. Da C. Andrade, On the Viscous Flow in Metals and Allied Phenomena, *Proc. R. Soc. (London)* Vol 84, Series A, 1910–11, p 1
37. E.N. Da C. Andrade and G. Chalmers, The Resistivity of Polycrystalline Wires in Relation to Plastic Deformation and the Mechanism of Plastic Flow, *Proc. R. Soc. (London)* Vol 138, Series A, 1932, p 348
38. F. Garofalo, O. Richmond, and W.F. Domis, Design of Apparatus for Constant-Stress or Constant-Load, *J. Basic Eng.*, Vol 84, 1962, p 287–293
39. M.F. Holmes and P.J. Wray, A Constant Stress Apparatus Suitable for Use with Small Forces, *J. Phys. E, Sci. Instrum.*, Vol 3, 1970
40. L.M.T. Hopkin, A Simple Constant Stress Apparatus for Creep Testing, *Proc. Phys. Soc. B*, Vol 63, 1950, p 346–349
41. C.H. Carter, Jr., C.A. Stone, and R.F. Davis, High-Temperature Multi-atmosphere Constant Stress Compression Creep Apparatus, *Rev. Sci. Instrum.*, Vol 51 (No. 10), Oct 1980, p 1352–1357
42. R.L. Fullman, R.P. Carreker, and J.C. Fisher, Simple Devices for Approximating Constant Stress During Tensile Creep Tests, *J. Met.*, Vol 5, 1953, p 657

Creep and Creep-Rupture Testing*

Computer-Controlled Constant-Stress Testing

As previously noted, precision-machined cam-lever systems are designed to mechanically adjust the load with respect to the change in length of a specimen with a fixed initial gage length and overall length. Although the disadvantage of this type of testing system is the physical constraint on the initial geometry of the specimens to be tested, the lever arm lends a significant mechanical advantage to the testing machine. Moreover, by using the increased compliance, reduced force, and increased travel on the weight pan end of the lever system (e.g., with a ratio of 10:1 or 20:1), a significant increase in control parameters and sensitivity results in higher precision testing.

The use of a computer control system for constant-stress testing can overcome the constraints on specimen geometry imposed by the cam-lever and similar systems. The computer control system can be programmed to accommodate a wide variety of specimens as well as provide control over test parameters such as rate of load application and removal, step-loading, cyclic loading, test time, furnace or oven temperature, and so on. The computer control system can also be used for data acquisition and analysis and for emergency test situations.

Dynamically Adjusted Constant-Stress Creep Test Machine. A novel computer-controlled creep testing system, developed at the University of California, Davis, is called the dynamically adjusted constant-stress creep machine (DACSCM) (Ref 43). This system integrates the positive and beneficial aspects of the lever-arm test system with a computer-control system that modulates load control apparatus to perform constant-stress creep

experiments. The testing system, at the time of writing, accumulated well over 1200 experimental hours of usage by various investigators. The longest test lasted for more than 274 h at a single constant stress rate. The specific algorithm that relates load and tensile elongation to cross-sectional area is based on the assumption of volume constancy within the deforming gage length. The following expression can be written:

$$P_i = \sigma_0 \left(\frac{A_0 l_0}{l_0 + x_i} \right) \quad (\text{Eq 15})$$

where for the i_{th} data point, σ_0 is the desired stress, A_0 is the initial cross-sectional area, l_0 is the initial gage length, and x_i is the total accumulated specimen displacement. The expression will be assumed to be valid throughout the entire deformation process until the onset of necking (i.e., localized straining) within the specimen takes place. Also, since a significant amount of the experimental creep work is carried out at strain levels that are much less than those typically required to initiate necking, this assumption can be considered reasonable and acceptable.

Typical Computer-Controlled Constant-Stress Testing System. A typical constant-stress testing system with a lever arm and computer control and data acquisition is shown in Fig. 18. With proper programming and selection of lever arm ratios, a system of this type provides precision control and also data acquisition and analysis. The versatility of these systems makes it feasible to perform various test functions, such as creep/stress rupture testing, stress relaxation testing, constant-stress testing, and cyclic load or cyclic strain testing. This type of system can be easily converted from one test mode to any of the other modes. In addition, compression testing can be performed in any of the test modes by using an appropriate compression test fixture. Testing systems such as the one shown in Fig. 18, are available with dual ratio lever arms (e.g., 20:1 and 3:1), which extend the range and provide optimum control and sensitivity.

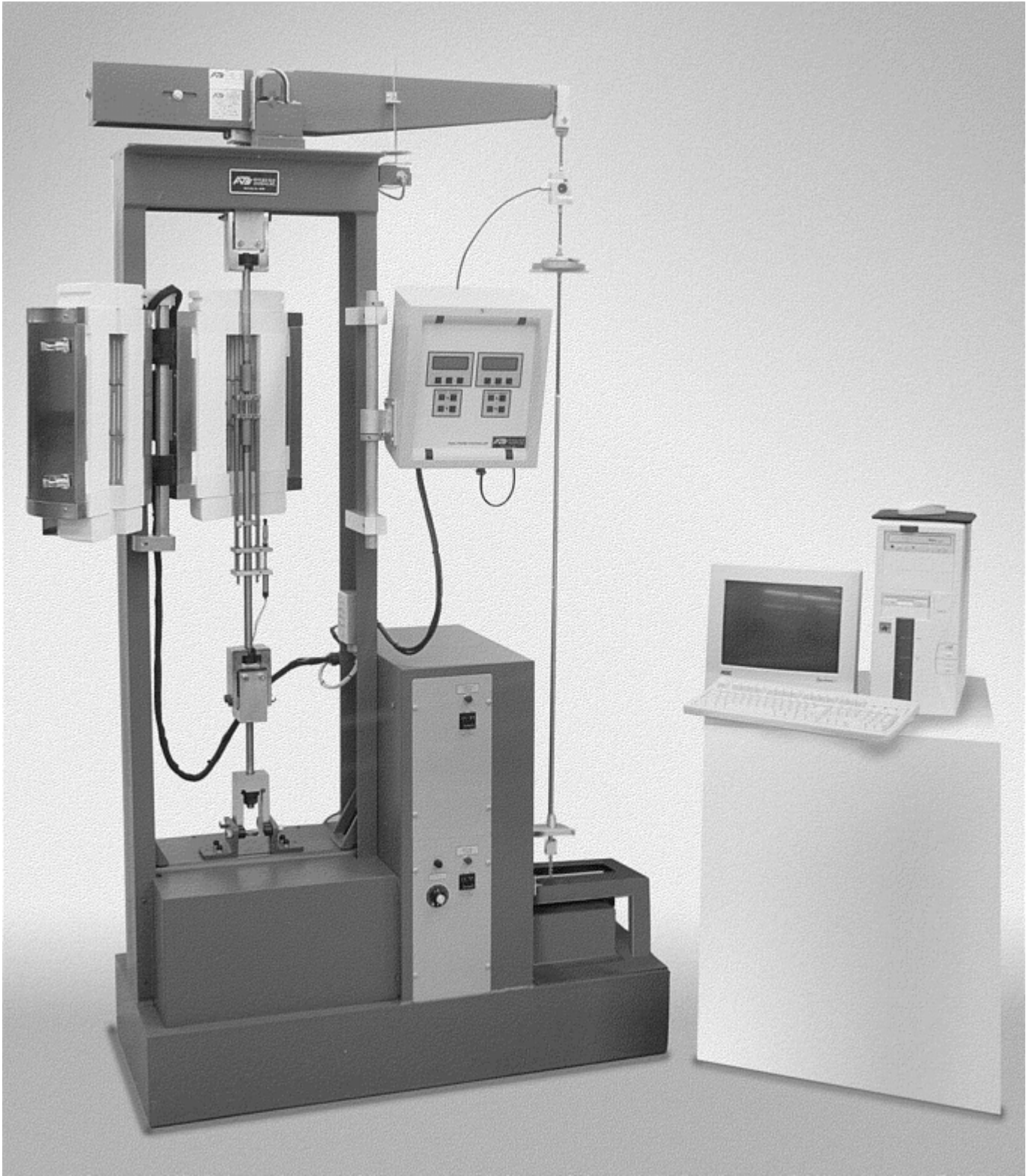


Fig. 18 Typical computer-controlled constant-stress test system with 90-kN (20,000 lbf) load capacity and furnace system.

In order to achieve precise test results, measurement is required on the specimen gage length and sometimes on the specimen diameter(s) as well. A typical extensometer is an averaging extensometer with dual high-precision capacitance transducers. Extensometers are also available to gage specimen diameter(s) change during testing, using similar transducers.

Footnote

* The section “Creep Properties” was adapted from Ref 1 with additional content by R.W. Hayes, Metals Technology, Inc. The remaining sections of this article were adapted from “Creep, Stress-Rupture, and Stress-Relaxation Testing” in Volume 8 of the 9th Edition *Metals Handbook*. The section “Constant-Stress Testing” was updated by N.L. Carroll, Applied Test Systems Inc.

Reference cited in this section

43. R.B. Grishaber, R.H. Lu, D.M. Farkas, and A.K. Mukherjee, A Novel Computer Controlled Constant Stress Lever Arm Creep Testing Machine, *Rev. Sci. Instrum.*, Vol 68 (No. 7), July 1997, p 2812–2817

Creep and Creep-Rupture Testing*

Stress Relaxation

Traditional creep testing to develop descriptions of strain rate, stress, and temperature behavior can be time intensive and expensive, involving many creep test stands, specimens, and thousands of hours of testing. Stress relaxation offers the potential to eliminate this difficulty by producing strain rate/stress data over a wide range of rates from a single specimen (see the article “Stress Relaxation Testing” in this Volume). This information is developed when the elastic strain of a specimen extended (or compressed) to a certain constant length is converted to plastic strain. As the specimen slowly deforms, the load required to maintain the constant length is reduced, hence the term *stress relaxation* test. In addition, this type of experiment simulates the real engineering problem of the long-term loosening of tightened bolts and other fasteners.

In its simplest form, a stress relaxation test involves loading (straining) a specimen to some predetermined load (strain), fixing the position of the specimen (halting the crosshead motion in a universal test machine, for example), and measuring the load as a function of time. With knowledge of the elastic modulus of the specimen and the stiffness of the testing machine, the load-time data can be converted to stress/strain-rate data. This information can then be used to determine the stress components and activation energies of creep for deformation.

In stress relaxation testing, a material is loaded with an initial stress level (σ_0 , in the idealized graphic representation in Fig. 19). Depending on the application, the initial stress may be below, at, or above the yield stress on loading. Whether or not there is permanent plastic strain on loading, there is an elastic strain that, in linear elastic materials, is proportional to the stress through the appropriate temperature-dependent modulus. Most reported data concern stress relaxation in materials initially stressed below their yield strength. Conversely, if initial yielding occurs, an initial permanent or plastic strain develops (Fig. 20). The elastic strain remaining, EC, is directly proportional to the remaining stress, DC in Fig. 20, so that in effect, after the initial yielding, stress relaxation is a time-dependent conversion of elastic to plastic irrecoverable strain. As time progresses, line ED in Fig. 20 shifts to the right and the relaxation of stress ($\Delta\sigma$) is defined as equivalent to the stress required to produce an equal amount of elastic deformation, where (assuming that the modulus of elasticity is constant and that the change in cross-sectional area is negligible during the test):

$$\Delta\sigma = \sigma_0 - \sigma_t = E\varepsilon_p$$

where σ_t is the stress at time t , E is the elastic modulus, and ε_p is the plastic strain at time t . The quantity ε_p is equal to the residual strain after load removal.

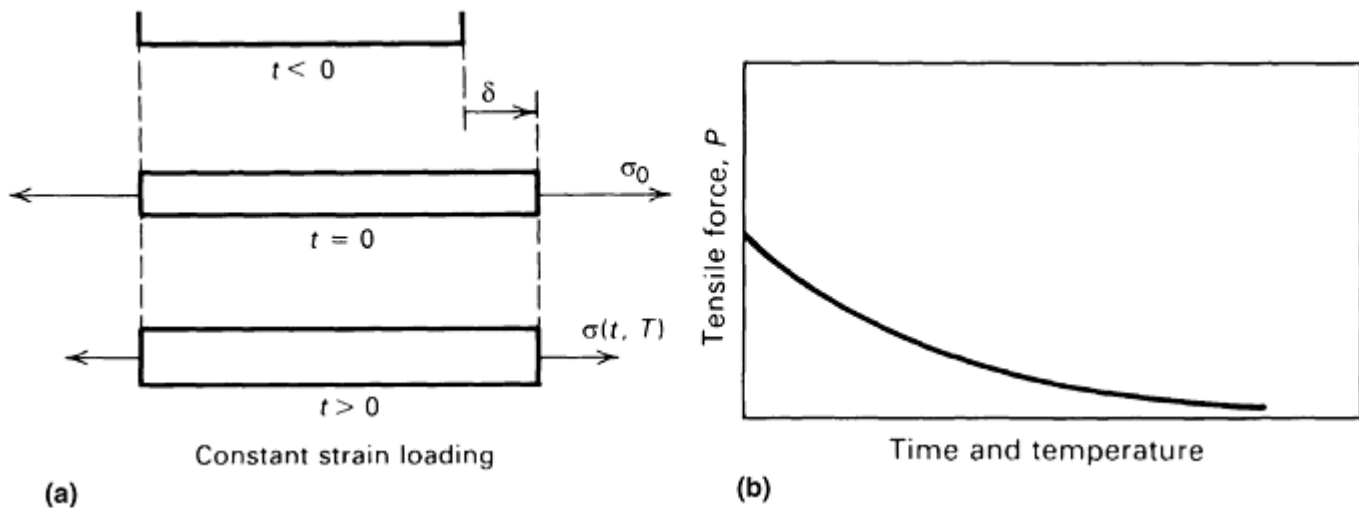


Fig. 19 Idealized concept of stress relaxation. (a) Constant strain loading in tension. (b) Stress-relaxation curves in tension

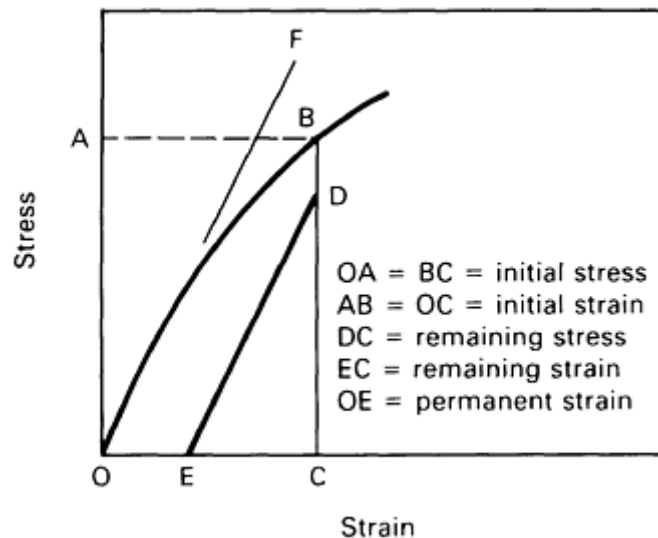


Fig. 20 Stress-strain diagram for determining relaxation in stress

One major drawback of many stress relaxation tests is the number of demands placed on the experimental equipment. The load-measuring system must be capable of making accurate measurements of very small changes as a function of time. The effect of the loading rate on the relaxation rate should be evident. In addition, room temperature, as well as specimen temperature, must be precisely controlled throughout the experiment. This is critical, because even small fluctuations in temperature will produce thermal expansion effects that can mask changes due to relaxation. Also, the calculated stress exponents and activation energies may not be the same as those determined from creep testing. The processes that produce plastic flow could be different for these two situations. Only comparison of the results from both types of testing can detect equivalent behavior.

Footnote

* The section "Creep Properties" was adapted from Ref 1 with additional content by R.W. Hayes, Metals Technology, Inc. The remaining sections of this article were adapted from "Creep, Stress-Rupture, and Stress-Relaxation Testing" in Volume 8 of the 9th Edition *Metals Handbook*. The section "Constant-Stress Testing" was updated by N.L. Carroll, Applied Test Systems Inc.

References

1. R. Viswanathan, *Damage Mechanisms and Life Assessment of High-Temperature Components*, ASM International, 1989, p 59–69
2. F. Garofalo, *Fundamentals of Creep and Creep Rupture in Metals*, M. Fine, J. Weertman, and J.R. Weertman, Ed., MacMillan Series in Materials Science, The MacMillan Co., New York, 1965
3. S.K. Mitra and D. McLean, Work Hardening and Recovery in Creep, *Proc. R. Soc.*, Vol 295, 1966, p 288–299
4. G. Bernasconi and G. Piatti, Ed., *Creep of Engineering Materials and Structures*, Applied Science Publishers, London, 1979
5. O.D. Sherby, *Acta Metallurgica*, Vol 10, 1962, p 135–147
6. O.D. Sherby and A.K. Miller, *ASME Journal of Materials and Technology*, Vol 101, 1979, p 387
7. F.H. Norton, *The Creep of Steel at High Temperatures*, McGraw-Hill, 1929
8. R.W. Bailey, *Creep of Steel under Simple and Compound Stress*, *Engineering*, Vol 121, 1930, p 265
9. O.D. Sherby and P.M. Burke, Mechanical Behavior of Crystalline Solids at Elevated Temperatures, *Prog. Mater. Sci.*, Vol 13, 1967, p 325
10. R. Viswanathan, The Effect of Stress and Temperature on the Creep and Rupture Behavior of a 1.25 pct. Chromium -0.5 pct. Molybdenum Steel, *Metall. Trans. A*, Vol 8A, 1977, p 877–883
11. B.J. Cane, “The Process Controlling Creep and Creep Fracture of $2\frac{1}{4}$ Cr-1Mo Steel,” CEGB Report RD/LR 1979, Central Electricity Generating Board Research Laboratories, Leatherhead, England, 1979
12. M.S. Shamma, “Estimating the Remaining Life of Boiler Pressure Parts,” EPRI Final Report on RP 2253-1, Vol 4, Electric Power Research Institute, Palo Alto CA, 1987
13. M.C. Askins et al., EPRI Final Report on RP 2253-1, Vol 5, Electric Power Research Institute, Palo Alto, CA, 1987
14. I.R. McLaughlin, in *Creep Strength in Steel and High Temperature Alloys*, *The Metals Society*, London, 1974, p 8, 71, 86, 106, 122, 217, 230
15. K.E. Amin and J.E. Dorn, *Acta Metall.*, Vol 17, 1969, p 1429
16. V. Foldyna, A. Jakobova, T. Prnka, and J. Sabotka, *Creep Strength in Steels and High Temperature Alloys*, *The Metals Society*, London, 1974, p 130
17. K.R. Williams and B. Wilshire, *Metall. Sci. J.*, Vol 7, 1973, p 176
18. C.N. Ancecuist, R. Gasca-Neri, and W.D. Nix, A Phenomenological Theory of Steady State Creep Based on Average Internal and Effective Stress, *Acta Metall.*, Vol 18, June 1970, p 663–671

19. A.K. Mukherjee, J.E. Bird, and J.E. Dorn, *ASM Trans. Quart.*, Vol 62, 1969, p 155
20. S.L. Robinson and O.D. Sherby, *Acta Metall.*, Vol 17, 1969, p 109
21. H. Luthy, A.K. Miller, and O.D. Sherby, *Acta Metall.*, Vol 28, 1980, p 169
22. J.R. Spingarn, D.M. Barnett, and W.D. Nix, *Acta Metall.*, Vol 27, 1979, p 1549
23. W.D. Nix, J.C. Gibeling, and D.A. Hughes, *Metall. Trans. A.*, Vol 16, 1985, p 2215
24. M. Biberger and J.C. Gibeling, *Acta Metall. Mater.*, Vol 43, 1995, p 3247
25. U.F. Kocks, A.S. Argon, and M.F. Ashby, *Thermodynamics and Kinetics of Slip*, Pergamon Press, Oxford, 1975, p 141
26. G.S. Nakayama and J.C. Gibeling, *Acta Metall.*, Vol 38, 1990, p 2023
27. G.S. Nakayama and J.C. Gibeling, *Scr. Metall. Mater.*, Vol 24, 1990, p 2031
28. G.S. Nakayama and J.C. Gibeling, *Modeling the Deformation of Crystalline Solids*, T.C. Lowe et al., Ed., TMS, Warrendale, PA, 1991, p 589
29. J.B. Conway, *Stress Rupture Parameters: Origin, Calculations and Use*, Gordon and Breach, 1969
30. S.S. Manson, *Time-Temperature Parameters—A Re-Evaluation of Some New Approaches*, ASM Publication D-8-100, American Society for Metals, 1968, p 1–115
31. S.S. Manson and C.R. Ensign, A Quarter Century of Progress in the Development of Correlation and Extrapolation Methods for Creep Rupture Data, *ASME J. Eng. Mater. Technol.*, Vol 101, 1979, p 317–325
32. G.P. Tilly and G.F. Harrison, Interpretation of Tensile and Compressive Creep Behavior of Two Nickel Alloys, *J. Strain Anal.*, Vol 8, 1973, p 124–131
33. H.H. Gray, “Transverse Tensile and Stress Rupture Properties of γ/γ' - δ Directionally Solidified Eutectic,” NASA TMX-73451, 1979
34. J.M. Thomas and J.F. Carlson, Errors in Deformation Measurements for Elevated Temperature Tension Tests, *ASTM Bulletin*, May 1955, p 47–55
35. A. Fox, Lecture Notes, ASM Continuing Education Seminar, *Creep and Stress Relaxation Testing*, March 1980
36. E.N. Da C. Andrade, On the Viscous Flow in Metals and Allied Phenomena, *Proc. R. Soc. (London)* Vol 84, Series A, 1910–11, p 1
37. E.N. Da C. Andrade and G. Chalmers, The Resistivity of Polycrystalline Wires in Relation to Plastic Deformation and the Mechanism of Plastic Flow, *Proc. R. Soc. (London)* Vol 138, Series A, 1932, p 348
38. F. Garofalo, O. Richmond, and W.F. Domis, Design of Apparatus for Constant-Stress or Constant-Load, *J. Basic Eng.*, Vol 84, 1962, p 287–293

39. M.F. Holmes and P.J. Wray, A Constant Stress Apparatus Suitable for Use with Small Forces, *J. Phys. E, Sci. Instrum.*, Vol 3, 1970
40. L.M.T. Hopkin, A Simple Constant Stress Apparatus for Creep Testing, *Proc. Phys. Soc. B*, Vol 63, 1950, p 346–349
41. C.H. Carter, Jr., C.A. Stone, and R.F. Davis, High-Temperature Multi-atmosphere Constant Stress Compression Creep Apparatus, *Rev. Sci. Instrum.*, Vol 51 (No. 10), Oct 1980, p 1352–1357
42. R.L. Fullman, R.P. Carreker, and J.C. Fisher, Simple Devices for Approximating Constant Stress During Tensile Creep Tests, *J. Met.*, Vol 5, 1953, p 657
43. R.B. Grishaber, R.H. Lu, D.M. Farkas, and A.K. Mukherjee, A Novel Computer Controlled Constant Stress Lever Arm Creep Testing Machine, *Rev. Sci. Instrum.*, Vol 68 (No. 7), July 1997, p 2812–2817

Footnote

* The section “Creep Properties” was adapted from Ref 1 with additional content by R.W. Hayes, Metals Technology, Inc. The remaining sections of this article were adapted from “Creep, Stress-Rupture, and Stress-Relaxation Testing” in Volume 8 of the 9th Edition *Metals Handbook*. The section “Constant-Stress Testing” was updated by N.L. Carroll, Applied Test Systems Inc.

Assessment and Use of Creep-Rupture Properties

Howard R. Voorhees, Materials Technology Corporation Martin Prager, Materials Properties Council

Introduction

USE OF CREEP-RUPTURE PROPERTIES to determine allowable stresses for service parts has evolved with experience, although guidelines for use differ among specifications.

Pioneering efforts by ASME (Ref 1 and earlier versions) to improve safety in use of metals for long-time operation at temperatures in the creep range set allowable stresses by considering the following criteria among others:

- 100% of the stress to produce a creep rate of 0.01%/1000 h, based on a conservative average of reported tests as evaluated by an ASME committee. In assessing data, greater weight is given to those tests run for longer times.
- 63% of the average stress or 80% of the minimum stress reported to produce rupture at the end of 100,000 h, as determined from available extrapolated data

These criteria continue to find wide acceptance.

For most commercial steels and alloys, available raw data come from tests with durations ranging from a few hundred to several thousand hours. Tests seldom run longer than 10,000 h, and durations of 100,000 h are rare. Measured secondary creep rates as low as 0.01%/1000 h are also unusual. Allowable stresses recommended in existing specifications usually are derived from extrapolations. Considerable scatter in test results may be observed even for a given heat of an alloy, so interpolated creep and rupture strengths are not precisely established.

Although measurement and application of creep-rupture properties is often imprecise, general trends are evident. Methods for assessing creep-rupture properties (including nonclassical creep behavior), common

interpolation and extrapolation procedures, and properties estimation based on insufficient data are discussed in this article.

Reference cited in this section

1. Basis for Estimating Stress Values, Paragraph A-150, Rules for Construction of Power Boilers, *ASME Boiler and Pressure Vessel Code*, Section I, American Society of Mechanical Engineers, New York, 1983

Assessment and Use of Creep-Rupture Properties

Howard R. Voorhees, Materials Technology Corporation Martin Prager, Materials Properties Council

Scatter of Creep-Rupture Test Data

Reliable creep-rupture property measurements require that the test specimens be representative of the material to be used in service, preferably in the product form and condition of intended service. Testing results may vary significantly with sampling procedures. For example, heavy sections may exhibit variations in strength level with depth after normalizing or quenching and tempering treatments. A common practice is to take samples midway between the center and the surface of the specimen.

Similar variations in strength can occur for fully annealed plate or bar that has been cold straightened. Reannealing may be required before valid testing results can be obtained. For some materials (e.g., stainless steel castings several inches thick, or alloys subjected to elevated temperature after critical prior plastic deformation), the grains may become so coarse that a specimen cross section contains only one or several grains. Local creep rates may then vary considerably along the specimen gage length according to the orientation of the individual large grains with respect to the loading direction.

Sampling direction seldom affects creep and rupture properties for materials with uniform single-phase structures of small equiaxed grains. For such materials, specimen size also exhibits minimal influence, except for the greater relative importance of surface oxidation and similar effects in small specimens. Due to solidification and processing conditions, preferred orientation of secondary phases or grains can alter test results. In critical situations, the loading direction in the test specimen should parallel the major stress direction expected under service loading. For rolled materials, ASTM E 139 (Ref 2) recommends that specimens be taken in the direction of rolling, unless otherwise specified.

The presence of large discrete particles of lower ductility and strength (e.g., graphite flakes in gray cast iron, or large glassy inclusions in steel) may significantly lower the sound cross section of a small specimen, but have a lesser influence in a larger specimen. Specimen size may have the opposite effect if only a few scattered low-strength particles are present; consequently, a specimen small enough could be free of these large-scale areas of weakness. More subtle variations in local creep and rupture strengths arise at grain boundaries, precipitates, voids, composition gradients, and other regions of microscale nonuniformity.

Specimen Size. For many steels, the influence of specimen size is minimal compared to other variables. During testing of a low-alloy steel (ASTM A 193, grade B16) and a high-alloy steel (ASTM A 453, grade 660) using five different specimen diameters ranging from 5 to 84 mm (0.2–3.3 in.), rupture strength appeared to be independent of size for unnotched specimens (Ref 3). Variation in rupture time with size was erratic for notched specimens, but the largest size had about three quarters of the strength of the smallest geometrically similar specimen.

Scatter from Heterogeneities. Heterogeneities in a low-alloy steel of commercial quality have been found to cause much of the typical 30% scatter encountered in determining creep rates under strict testing conditions (Ref 4). Scatter for rupture times is approximately half that magnitude with materials that are specially prepared to be uniform.

Temperature and Other Testing Variables. Even with the use of precise temperature controllers and high-quality pyrometric practice, care is required to hold the average indicated specimen temperature within usual specifications of ± 2 °C (± 3.6 °F) (Ref 2) with time. Variation from one location to another along the specimen gage length typically approaches this magnitude, even in furnaces with independent adjustment of power input within zones.

These variations in indicated temperature do not include errors in initial thermocouple and pyrometer calibrations, leadwire mismatch, or drift in thermocouple output with time. Actual temperature can differ from the reported value by at least 5 °C (9 °F) during some portion of a representative creep or rupture test.

For steel at 450 °C (842 °F), a temperature disparity of 5 °C (9 °F) corresponds approximately to 20% variation in rupture time (Ref 4). A 10% change in creep rate results from a load change of 1.5%, or a temperature change of 2.5 °C (4.5 °F) (Ref 3). An error of more than 1% in the applied load is unlikely under typical conditions.

Equipment for creep-rupture testing commonly includes features to promote uniform axial loading. However, bending loads may still occur. The increase in secondary creep rates and reduction in rupture life with eccentricity of loading is analyzed in Ref 5, which reports that extreme cases of bending introduced by threaded ends on cylindrical specimens reduce rupture life by as much as 60%. The largest effects occur for short or notched specimens and for materials with low ductility to rupture.

Eccentric loading exerts maximum influence on creep measurements in the early stages of a test. With initially bowed specimens, which are common when specimens are as-cast or are strip-type machined from thin material, early creep indications may be erroneous if the extensometer fails to accurately average the strains at opposite sides of the specimen.

Typical Data Scatter. Rolled bars from a single heat of 2.25Cr-1Mo steel were tested by 21 laboratories in eight countries (Ref 6). The largest deviations in average results for one laboratory from the arithmetic mean of values from all laboratories for the stress to cause rupture in 1000, 3000, and 10,000 h were:

Temperature		Deviation
°C	°F	
550	1022	+14.3 and -16.6%
600	1112	+21.2 and -12.1%

Another group of 18 laboratories in seven countries cooperated in tests of Nimonic 105 alloy bars at 900 °C (1652 °F) (Ref 7). Mean rupture times adjusted to a common stress for individual laboratories (four tests each) ranged from a high of 1491.4 h to a low of 1090.2 h (15.5% deviation). Time to 0.5% total deformation varied from 75.4 to 182.3 h for 16 of these laboratories; deviation from the mean value thus increased to 41.5%.

Temperature control was found to be the most serious source of variation in rupture measurement. In particular, calibration drift of Chromel-Alumel thermocouples at this high test temperature was responsible for the long mean rupture times found by five of the laboratories. Not more than about 15% scatter generally can be attributed to testing variables, if a laboratory has followed standard procedures.

Multiple Heats and Product Forms. Scatter bands become much broader when data originate from tests on numerous heats, particularly when data include a broad range of product forms and sizes. Elevated-temperature properties for steel and superalloys are available (see, for example, Ref 8, 9, 10, 11, 12, 13, 14, 15, 16, 17, and 18). Typically, data for each grade of steel include plots of the stress for rupture in 1000, 10,000, or 100,000 h versus the test temperature. Where appropriate, distinctive shapes of data points identify different product forms or heat treatments.

When data at a given temperature are extensive, the reported range of derived stresses to produce rupture in a given time typically consists of a two-fold ratio of the highest to the lowest stress level. The corresponding spread of rupture times for a given test stress is on the order of 100-fold.

If a new set of test results does not fall within the broad scatter bands, careful review and confirmation is required before the new data are accepted as valid. Bias of new data tends toward the upper half of the scatter bands compiled for older data because the increase of residual alloying elements from scrap recycling, higher nitrogen content, and improved alignment and temperature control in modern testers tend to raise indicated creep and rupture properties.

At a test temperature of 593 °C (1100 °F) and at a stress of 207 MPa (30 ksi), rupture life ranged from 84 to 2580 h and secondary creep rate ranged from 0.16 to 0.00077%/h for 20 heats of type 304 stainless steel in the reannealed condition (Ref 19). Corresponding large variations were observed at all test temperatures and for

tests on seven heats of type 316 stainless steel. Reannealing of as-received material lowered time to rupture in some cases, but the degree of variation persisted in properties among heats.

Good linear correlation was obtained when the logarithm of rupture strength was plotted against ultimate tensile strength at the same temperature for various types of austenitic stainless steels in the annealed and cold-worked conditions at temperatures ranging from 538 to 816 °C (1000–1500 °F) and for test times approaching 10,000 h. Tensile strength, in turn, was reported to be essentially proportional to $(C + N)d^{-1/2}$, where C and N represent the weight percentage of carbon and nitrogen content, respectively, and d is average grain diameter.

Although long-time performance generally cannot be accurately predicted from short-time data, the location of a particular set of rupture data within a published scatter band should agree with the relative tensile strength of the material being tested in the range of tensile strengths spanned by all heats and product forms. Tests to measure low rates of secondary creep frequently are terminated after the creep rate appears to have become reasonably constant. If the test duration had been prolonged substantially, a continued slow decline in creep rate may have been observed.

A “false” minimum rate may occur in some tests before the classical secondary creep period has been reached. Observations of many comparative creep and rupture strengths for steels has established the following general relationships:

$$\frac{0.0001\% / \text{h creep strength}}{10,000 \text{ h rupture strength}} = 0.7 \text{ to } 0.8$$

$$\frac{0.00001\% / \text{h creep strength}}{100,000 \text{ h rupture strength}} = 0.5 \text{ to } 0.6$$

If a new set of test results differs from these patterns, verification is suggested before the new results are accepted.

References cited in this section

2. “Standard Recommended Practice for Conducting Creep, Creep-Rupture, and Stress-Rupture Tests of Metallic Materials,” E 139, *Annual Book of ASTM Standards*, Vol 03.01, ASTM, 1984, p 283–297.
3. A.K. Schmieder, Size Effect During Rupture Tests of Unnotched and Notched Specimens of Cr-Mo-V and Cr-Ni Steels, in *Ductility and Toughness Considerations in Elevated Temperature Service*, American Society of Mechanical Engineers, New York, 1978, p 31–48
4. B. Aronsson and A. Hede, Some Observations on the Reproducibility of Creep Rate Determinations, in *High-Temperature Properties of Steel*, Iron and Steel Institute, London, 1967, p 41–45
5. D.R. Hayhurst, The Effects of Test Variables on Scatter in High-Temperature Tensile Creep-Rupture Data, *Int. J. Mech. Sci.*, Vol 16, 1974, p 829–841
6. W. Ruttman, M. Krause, and K.J. Kremer, International Community Tests on Long-Term Behavior of $2\frac{1}{4}\%$ Cr-1%Mo Steel, in *High-Temperature Properties of Steel*, Iron and Steel Institute, London, 1967, p 23–29
7. D. Coutsouradis and D.K. Faurschou, “Cooperative Creep Testing Program,” AGARD Report 581, North Atlantic Treaty Organization, Advisory Group for Aerospace Research & Development, Neuilly-sur-Seine, France, 1971
8. “Report on the Elevated-Temperature Properties of Stainless Steels,” DS 5-S1, ASTM, 1965
9. “An Evaluation of the Yield, Tensile, Creep, and Rupture Strengths of Wrought 304, 316, 321, and 347 Stainless Steels at Elevated Temperatures,” DS 5-S2, ASTM, 1969

10. "Supplemental Report on the Elevated-Temperature Properties of Chromium-Molybdenum Steels," DS 6-S1, ASTM, 1966
11. "Supplemental Report on the Elevated-Temperature Properties of Chromium-Molybdenum Steels," DS 6-S2, ASTM, 1971
12. "Report on the Elevated-Temperature Properties of Selected Super-Alloys," DS 7-S1, ASTM, 1968
13. "An Evaluation of the Elevated-Temperature Tensile and Creep-Rupture Properties of Wrought Carbon Steel," DS 11-S1, ASTM, 1969
14. "Evaluation of the Elevated-Temperature Tensile and Creep-Rupture Properties of C-Mo, Mn-Mo and Mn-Mo-Ni Steels," DS 47, ASTM, 1971
15. "Evaluation of the Elevated-Temperature Tensile and Creep-Rupture Properties of Steel," DS 50, ASTM, 1973
16. "Evaluation of the Elevated-Temperature Tensile and Creep-Rupture Properties of 3 to 9 Percent Cr-Mo Steels," DS 58, ASTM, 1975
17. "Evaluations of the Elevated-Temperature Tensile and Creep-Rupture Properties of 12 to 27 Percent Chromium Steels," DS 59, ASTM, 1980
18. "Compilation of Stress-Relaxation Data for Engineering Alloys," DS 60, ASTM, 1982
19. V.K. Sikka, H.E. McCoy, Jr., M.K. Booker, and C.R. Brinkman, "Heat-to-Heat Variation in Creep Properties of Types 304 and 316 Stainless Steels," ASME Paper 75-PVP-26, American Society of Mechanical Engineers, New York, 1975

Assessment and Use of Creep-Rupture Properties

Howard R. Voorhees, Materials Technology Corporation Martin Prager, Materials Properties Council

Nonclassical Creep Behavior

The curve of creep deformation versus time traditionally displays three consecutive stages (Fig. 1). The longest period of substantially constant creep rate is preceded by a primary stage during which the rate declines from an initial high value and is followed by a tertiary stage of rising creep rate as rupture is approached (Fig. 2).

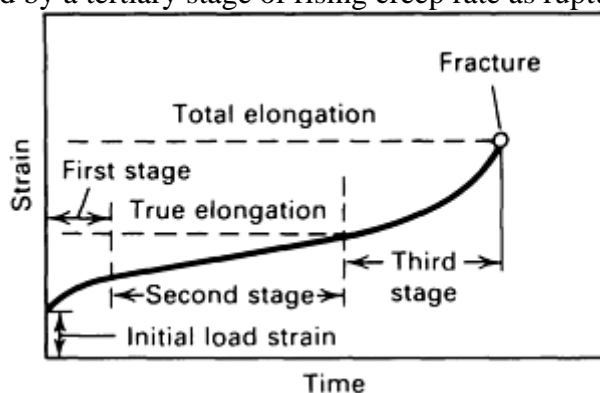


Fig. 1 Schematic tension-creep curve showing the three stages of creep

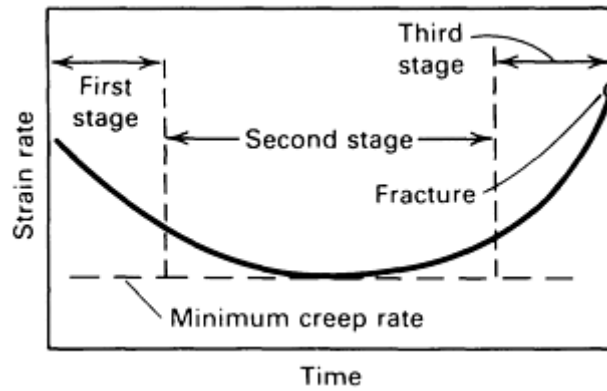


Fig. 2 Relationship of strain rate, or creep rate, and time during a constant-load creep test. The minimum creep rate is attained during second-stage creep.

Although this classical pattern can be made to fit many materials and test conditions, the relative duration of the three periods differs widely with materials and conditions. For example, in many superalloys and other materials in which a strengthening precipitate continues to age at creep temperatures, brief primary creep often shows transition to a long upward sweep of creep rate, with hardly more than a point of inflection for the secondary period.

Aging of normalized and tempered 0.5Cr-0.5Mo-0.25V steel during creep under 80 MPa (11.6 ksi) stress at 565 °C (1050 °F) has been reported to cause the creep curve to effectively exhibit only a continuously increasing creep rate to fracture (Ref 20). For twice the amount of stress, the creep curve in this case followed the classical trends. In other alloys, such as titanium alloys, with limited elongation before fracture, the tertiary stage may be brief and may show little increase in creep rate before rupture occurs.

A more obvious departure from classical behavior develops during the early portion of many tests when precise creep measurements are taken. When 34 ferritic steels were studied for as long as 100,000 h at temperatures ranging from 450 to 600 °C (842–1112 °F), step-form irregularities were observed, with an extended period of secondary creep preceded by a lower steady creep rate of shorter duration during primary creep (Ref 21).

Negative Creep. Because a variety of metallurgical processes can be involved and because the rates and direction of these processes can vary with time and temperature, departures from classical creep curves can take many forms and can be overlooked unless accurate creep readings are taken at sufficiently close intervals, particularly during early stages of the test. For 2.25Cr-1Mo, Cr-Ni-Mo, and Cr-Mo-V steels, some tests have demonstrated an abrupt drop to negative creep rate (contraction) after a brief beginning period of positive primary creep. Once this contraction ceased, the remaining portion of the test displayed the classical succession of declining, steady, and then rising creep rates. Figure 3 gives an example for normalized and tempered 2.25Cr-1Mo steel, tested at 275.8 MPa (40 ksi) at 482 °C (900 °F) (Ref 22).

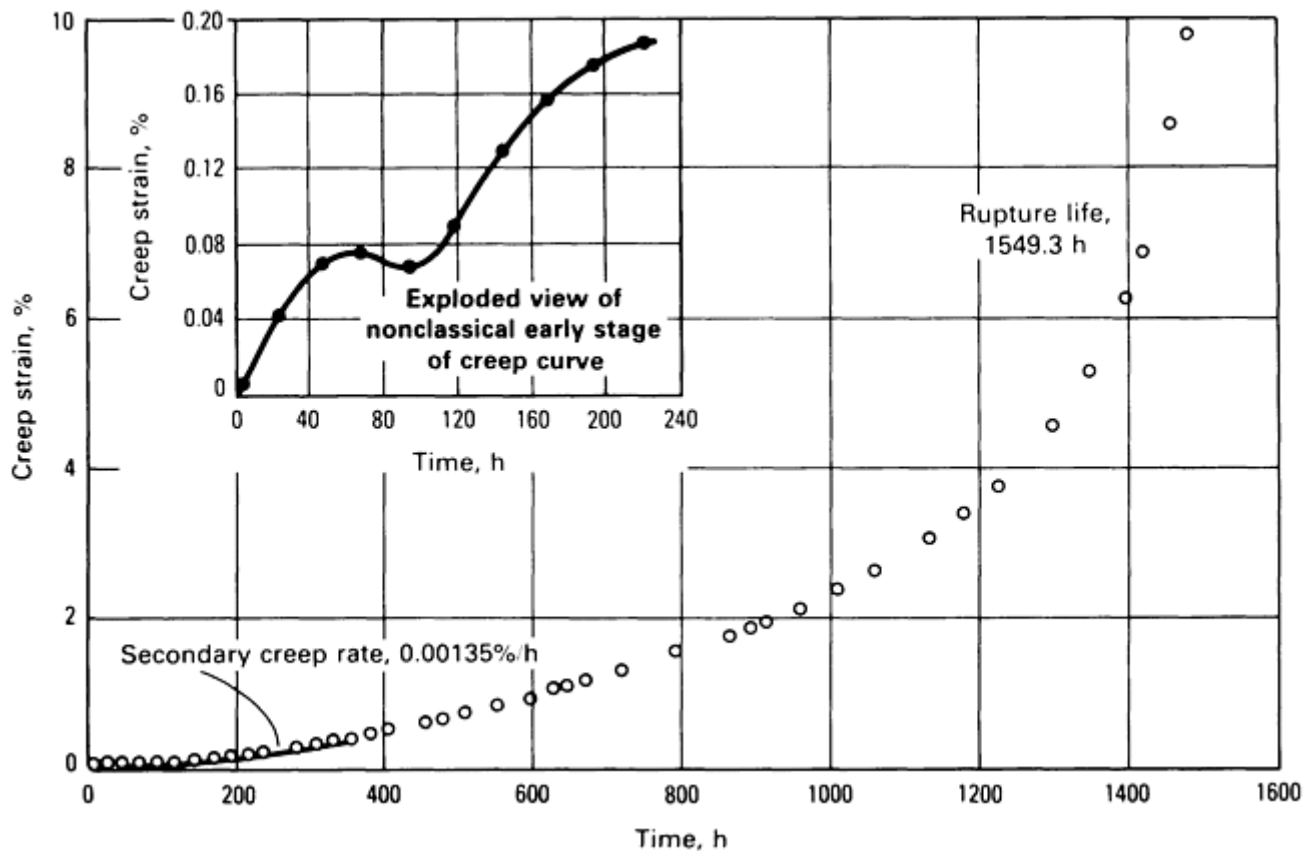


Fig. 3 Creep curve of 2.25Cr-1Mo steel with nonclassical early stage. Normalized and tempered to 607 MPa (88 ksi) tensile strength at room temperature. Tested at 482 °C (900 °F) at 275.8 MPa (40 ksi)

Definite negative creep was noted in at least one test each at 482, 704, 816, and 871 °C (900, 1300, 1500, and 1600 °F) for cast CF8 austenitic stainless steel in tests of boiler and pressure-vessel materials (Ref 22). Rupture times for these tests ranged from 1000 h to longer than 30,000 h. For some combinations of material lots and test temperatures, nearly all creep curves of these tests showed an early “false” minimum rate during part of the primary stage. Structural changes responsible for the measured contraction were undetermined.

Short-term negative creep also was observed in tests on quenched and tempered 2.25Cr-1Mo steel at 482 °C (900 °F) and at 482 and 538 °C (900 and 1000 °F) for the same steel in the normalized and tempered condition. Two steady-state creep stages for annealed 2.25Cr-1Mo steel have been reported (Ref 23), which were due to the interaction of molybdenum and carbon atoms with dislocations and the subsequent decrease in the number of these atoms as Mo_2C precipitated. A volume decrease associated with the precipitation process also could account for the observed creep curve trends.

Interstitial diffusion of carbon and hydrogen into dislocations has been observed, and alloy strain-aging effects have been found to cause creep rate transitions noted for carbon steels and normalized 0.5% Mo steel (Ref 24). Negative creep in Nimonic 80A appears related to an ordering reaction in the Ni-Cr matrix and possible formation of Ni_3Cr (Ref 25).

Oxide and Nitride Strengthening. An entirely different source of variation from classical patterns occurs in creep tests at high temperature due to reaction with the air that forms the environment. Tests longer than 50 h with 80Ni-20Cr alloys at 816 and 982 °C (1500 and 1800 °F) showed a deceleration of creep after the normal tertiary stage was reached, resulting in a second period of steady-state creep and later another period of last-stage creep (Ref 26). Figure 4 illustrates a creep curve showing the effect of oxide strengthening.

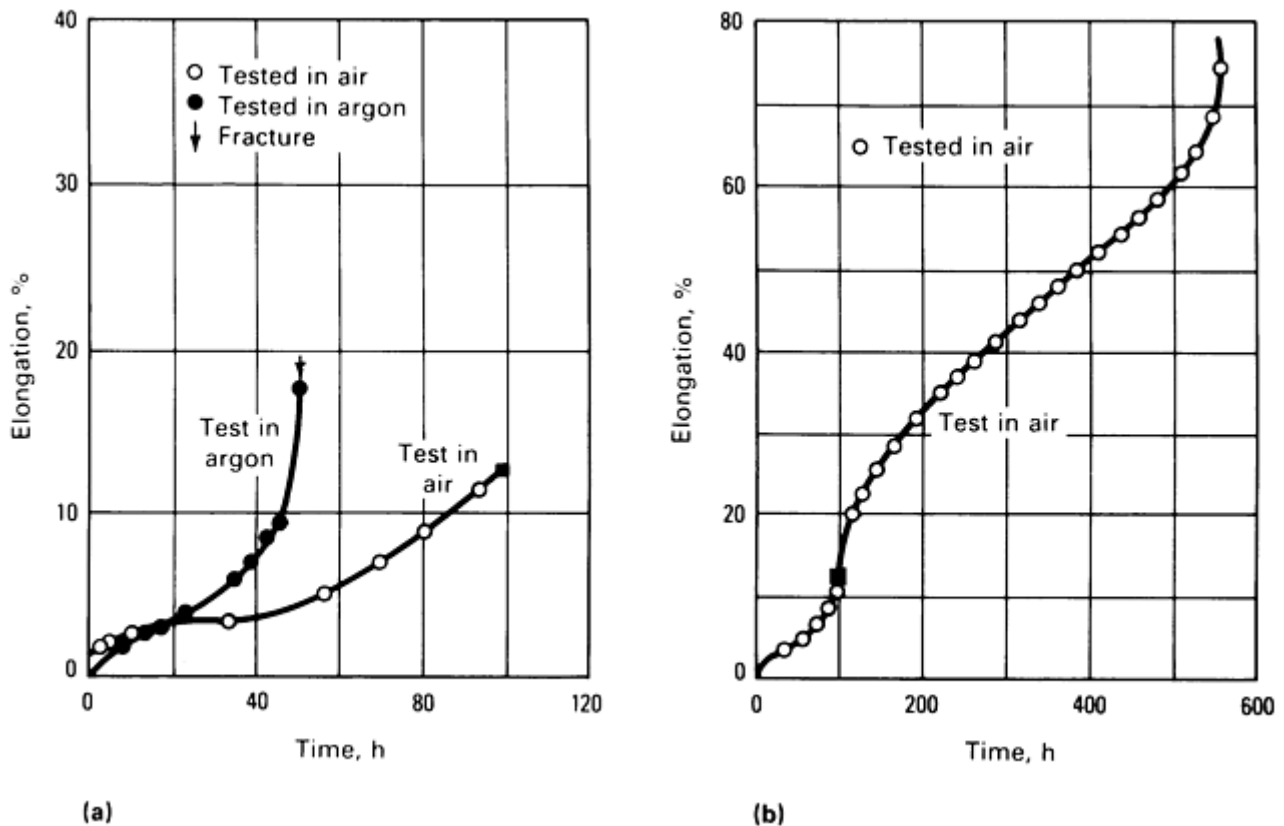


Fig. 4 Creep curves of alloy 2V tested at 980 °C (1800 °F) and 17.2 MPa (2500 psi). (a) Tests in argon and air for same duration. (b) Entire curve of specimen tested in air is shown. Filled square on both graphs represents same point.

This behavior, which prolonged rupture life and caused a slope decrease in curves of log stress versus log rupture life, was due to oxide and nitride formation on surfaces of the intercrystalline cracks that form extensively during tertiary creep. Observed interconnection of the bulk of these cracks added substantially to strengthening against creep deformation in the late stages of the tests.

This effect also was observed in 99.8% Ni tested at 815 °C (1500 °F) under 20.7 MPa (3000 psi) stress (Ref 27). Fracture after a prolonged time occurred in a lower stressed section of the fillet. Fewer intergranular cracks in this region resulted in less oxidation strengthening than in the gage section.

References cited in this section

20. K.R. Williams and B. Wilshire, Effects of Microstructural Instability on the Creep and Fracture Behavior of Ferritic Steels, *Mat. Sci. Eng.*, Vol 28, 1977, p 289–296
21. M. Wild, Analysis of Creep Behavior of Heat-Resistant Ferritic Steels at Temperatures from 450 to 600 °C, *Archiv. Eisenhüttenwes.*, Vol 34, Dec 1963, p 935–950 (in German)
22. Private business communication, Materials Technology Corporation data sheets submitted to the Metal Properties Council for tests under MPC Contract No. 174-1
23. R.L. Klueh, Interaction Solid Solution Hardening in 2.25 Cr-1Mo Steel, *Mat. Sci. Eng.*, Vol 35, 1978, p 239–253
24. J. Glen, The Shape of Creep Curves, *Trans. ASME J. Basic Eng.*, Vol 85 (No. 4), Series D, Dec 1963, p 595–600
25. J.P. Milan et al., Negative Creep in Ni-Cr-Ti Alloys, Fourth Interamerican Conference on Materials Technology, Caracas, June–July 1975, p 102–106

26. R. Widmer and N.J. Grant, The Role of Atmosphere in the Creep-Rupture Behavior of 80Ni-20Cr Alloys, *Trans. ASME J. Basic Eng.*, Vol 82 (No. 4), Series D, Dec 1960, p 882–886
27. P. Shahinian and M.R. Achter, Creep-Rupture of Nickel of Two Purities in Controlled Environments, Joint International Conference on Creep, Institute of Mechanical Engineers, London, 1963, p 7-49 to 7-57

Assessment and Use of Creep-Rupture Properties

Howard R. Voorhees, Materials Technology Corporation Martin Prager, Materials Properties Council

Extrapolation and Interpolation Procedures

The determination of creep-rupture behavior under the conditions of intended service requires extrapolation and/or interpolation of raw data. No single method for determination of properties exists; rather, various techniques have evolved for data handling of most materials and applications of engineering interest. These techniques include graphical methods, time-temperature parameters, and methods used for estimations when data are sparse or hard to obtain. Recent developments for predicting remaining life of components in creep service are described in this section.

Graphical Methods

Test results frequently are displayed as plots of log stress versus log rupture time and log stress versus log secondary creep rate, with a separate curve (isotherm) for each test temperature. For limited ranges of test variables, test points frequently fall in a straight line for each temperature. Nonlinearity of isotherms with broader ranges of test parameters has been treated variously, but common practice is to represent the data by two or more intersecting straight line segments. Figure 5 illustrates such treatment for an aluminum alloy.

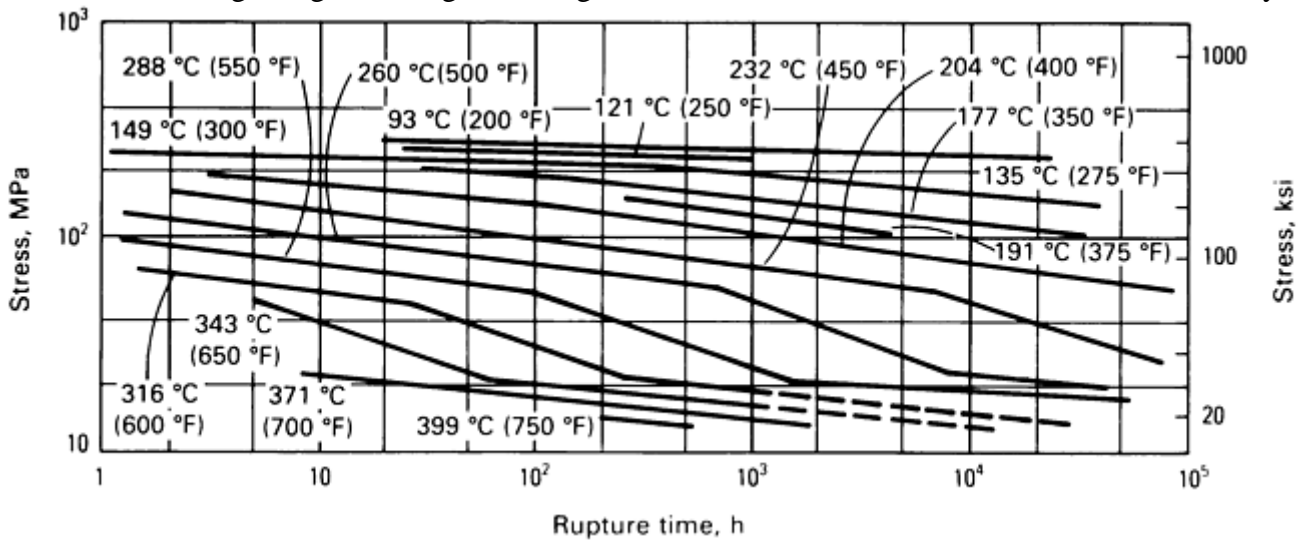


Fig. 5 Logarithmic plot of stress versus rupture life for aluminum alloy 6061-T651

Isotherms for lower temperatures characteristically display a flatter slope than those for higher temperatures. At a given temperature, when the test stresses drop below a given level that varies with alloy composition and metallurgical condition, the slope of the isotherm usually steepens. This steeper slope often approximates the slope for early times at the next higher test temperature.

Early investigators of engineering creep behavior introduced a “conservative” practice of using the slope from the next higher temperature when an isotherm had to be extended to longer times. Use of this method is limited to the specific temperatures of the test runs. Even under these conditions, extrapolations should be only in the direction of longer times for the lower range of test temperatures.

Because the change in slope of log stress versus log time isotherms historically appeared to be associated with a gradual change in fracture mode from transgranular at lower temperatures and higher stress to intergranular at relatively high temperatures and low stress, the belief developed that once the slope of the longer time portion became established, further slope change would not occur. Experimental data available at that time provided no indication that these linear plots could not be extrapolated to long times with confidence. Subsequent long-time data demonstrate that such extrapolations may lead to erroneous results.

Upward Inflection of Log-Log Rupture Plots at Long Times

Review of 52 heats from 31 wrought and cast steels, each with test times longer than 50,000 h, indicated that some portion of the log stress versus log rupture time curves for all ferritic steels showed a decrease in slope when tests were of sufficiently long durations (Ref 28). The degree of this upward inflection depends on composition, heat treatment, and, particularly, test temperature.

A sharp inflection at one temperature (e.g., 500 °C, or 930 °F) was usually accompanied by a less distinct inflection covering a broader time range at a higher test temperature (e.g., 550 °C, or 1022 °F). Generally, these inflections shifted to shorter times and lower stresses with increasing test temperature. Existence of inflections appeared to be related to precipitation phenomena.

For the heat-treatable aluminum alloy 6061-T651, test stresses between about 20 and 50 MPa (2900 and 7250 psi) for temperatures ranging from 260 to 343 °C (500–650 °F) exhibited nearly the same slope on a plot of log stress versus log rupture time, which was steeper than for either higher or lower stress levels (Ref 29). The long-time rupture results obtained had been predicted (Ref 30) by separate graphical extrapolation of each of three regimes of rather constant slope (see Fig. 5).

In this instance, the curves that were actually extended were lines for fixed stress levels (isostress lines) on plots of log rupture time versus temperature, or the reciprocal of absolute temperature. However, extrapolation could have been carried out on the usual log stress versus log rupture time plot by treating the data as a family of curves, with different portions of each curve falling into different slope regimes. Direct graphical extension of isostress lines appeared to provide better extrapolation of rupture data than other common methods (Ref 31).

Curves of log stress versus log rupture life for two chromium-molybdenum steels (ASTM A 387, grades 22 and 11) typically show an increase followed by a decrease in steepness for tests at 538 to 566 °C (1000–1050 °F). Consequently, correct prediction of 100,000 h strengths requires that these changes in slope be incorporated into the analysis (Ref 32). This requirement applies to all evaluation methods. Unless the input data include results that encompass structural changes of the type expected under intended service conditions, accurate extrapolation cannot be expected.

Some metallurgists prefer a semilogarithmic plot of stress versus log rupture time. The sigmoidal shape of isotherms is thus more evident, but extrapolation difficulties remain. The double inflections (or sigmoidal shape) for rupture curves can be greatly accentuated when notched specimens are tested. In the intermediate stress regime, rupture life can actually decrease as the level of test stress is lowered.

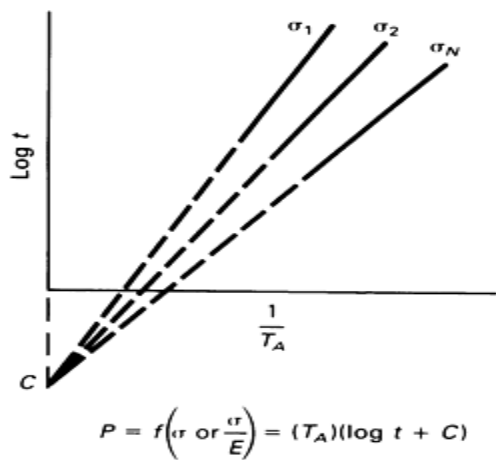
Time-Temperature Parameters

Temperatures that are higher than those encountered in service have traditionally been used to shorten the time required to obtain creep-rupture results. One such approach incorporates time and temperature into an expression or parameter, such that a single master curve of stress or log stress can represent all data obtained for a given lot of material over a wide range of test conditions.

When the parameter calculated for a desired service time and temperature falls within the range of the master curve, the corresponding stress can be read directly from that curve. More than 30 parameters have been proposed; although not always developed that way, several can be derived from the following:

$$P = \frac{\frac{\log t}{\sigma^Q} - \log t_A}{(T - T_A)^R} \quad (\text{Eq 1})$$

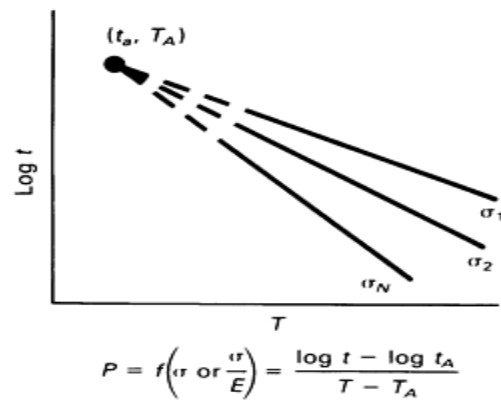
where t is rupture time in hours; σ is stress in psi; T is test temperature in °F; and T_A , $\log t_A$, Q , and R are constants determined from the experimental test data. Geometric requirements for lines of constant stress for several parametric models are shown in Fig. 6 (Ref 23), a plot of logarithm of time versus either temperature or its reciprocal. Of these, the Larson-Miller and Manson-Haferd parameters represent early developments in time-temperature parameters that retain considerable application.



$$P = f\left(\sigma \text{ or } \frac{\sigma}{E}\right) = (T_A)(\log t + C)$$

Larson-Miller

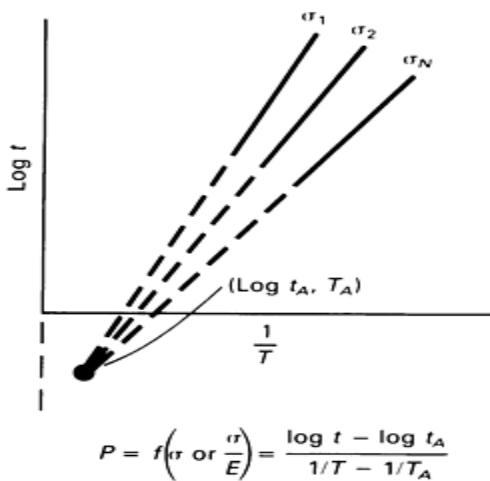
(a)



$$P = f\left(\sigma \text{ or } \frac{\sigma}{E}\right) = \frac{\log t - \log t_A}{T - T_A}$$

Manson-Haferd

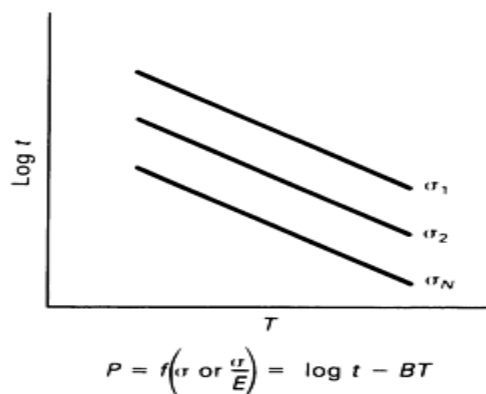
(b)



$$P = f\left(\sigma \text{ or } \frac{\sigma}{E}\right) = \frac{\log t - \log t_A}{1/T - 1/T_A}$$

Goldhoff-Sherby

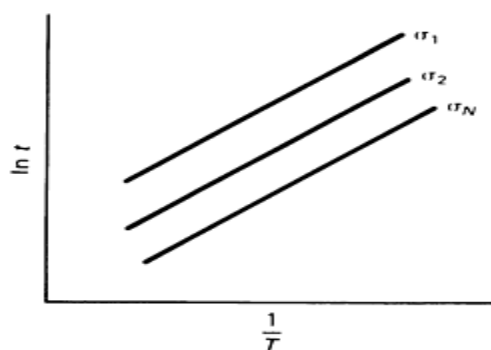
(c)



$$P = f\left(\sigma \text{ or } \frac{\sigma}{E}\right) = \log t - BT$$

Manson-Succop

(d)



$$P = f\left(\sigma \text{ or } \frac{\sigma}{E}\right) = AT\theta^{-B/T}$$

Orr-Sherby-Dorn

(e)

Fig. 6 Schematic representation of several parametric models. In the equations given for each parameter, σ is applied stress, t is time, T is temperature in $^{\circ}\text{C}$ or $^{\circ}\text{F}$, T_A is absolute temperature in K or $^{\circ}\text{R}$, Q is the activation energy, R is the gas constant, and B and C are numerical constants characteristic of the material and its metallurgical condition.

The Larson-Miller Parameter. In 1953, Larson and Miller introduced the concept of time-temperature parameters to correlate and extrapolate creep-rupture data (Ref 34) for absolute temperature, T_A , and time to

rupture, t_r . Their parameter $P = f(\sigma) = T_A (\log t_r + C)$ is depicted on a graph of $\log t$ or $\log (t_r)$ versus $1/T_A$ by straight constant stress lines converging to a point at $1/T_A = 0$ (Fig. 6a). At that point, $\log t = C$ defines the optimum value of C for the data involved.

In Fig. 7(a), an actual set of stress-rupture data is shown for the nickel-base alloy Inconel 718 as log stress versus log time to rupture. The data are then replotted as constant-time curves on coordinates of stress versus temperature in Fig. 7(b). To that graph dashed horizontal lines have been added for stress levels of 550, 620, 760, and 830 MPa (80, 90, 110, and 120 ksi). Values for T at the intercepts of these dashed lines and the constant-time curves have been read off and plotted in Fig. 7(c) on coordinates of $\log t$ versus $10^4/T_A$. By extending the data in Fig. 7(c), a plausible set of converging isostress lines meeting on the ordinate at a value of $\log t = -25$ can be obtained. The Larson-Miller equation for this set of data is:

$$P = T_A (\log t_r + 25) \tag{Eq 2}$$

where absolute temperature, T_A , is in units of the Kelvin or Rankine temperature scales.

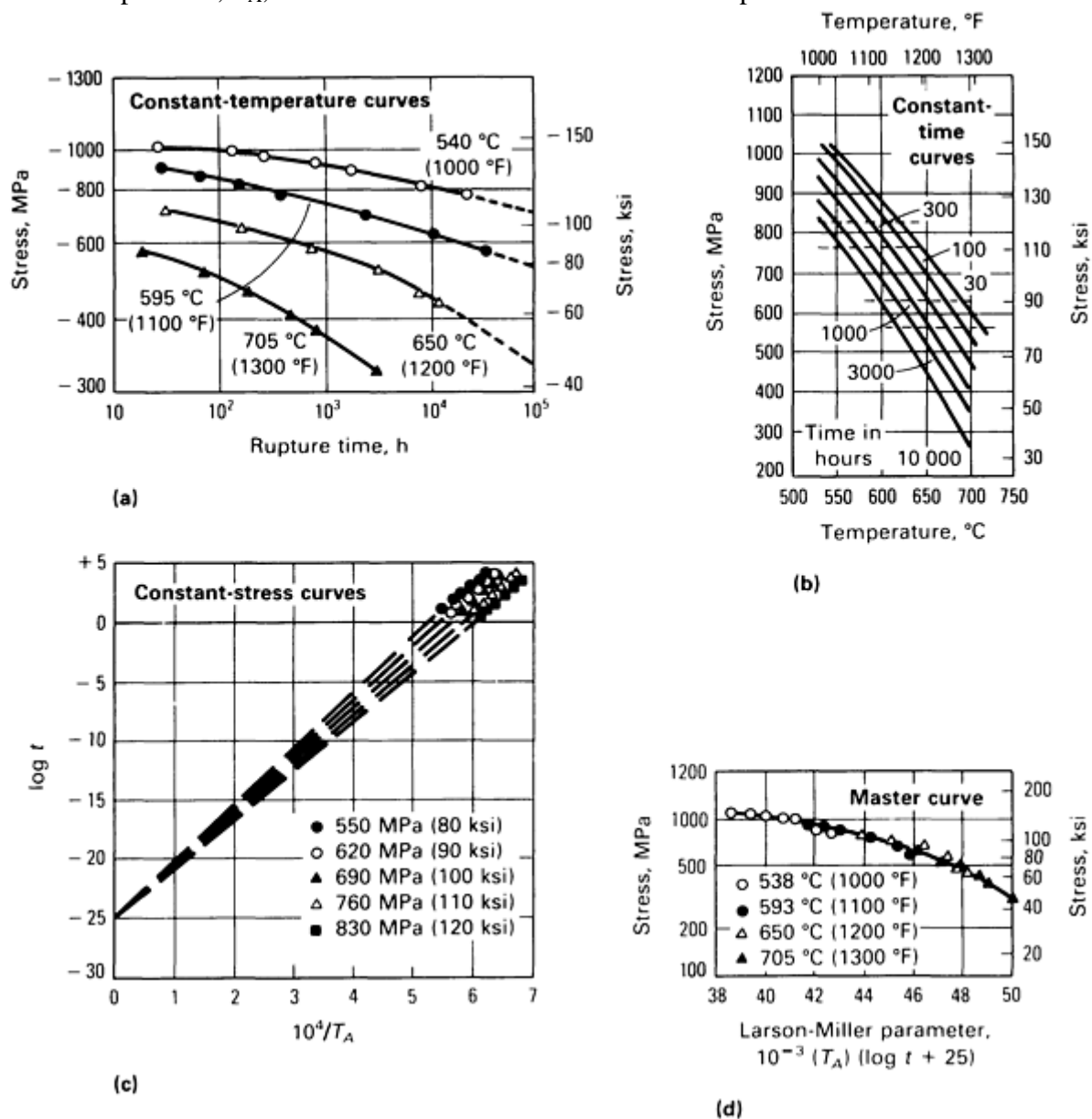


Fig. 7 Method of creating master Larson-Miller curve for Inconel 718 from experimental stress-rupture curves

For each data point in the original set of stress, time, and temperature data, the proper value can be substituted in Eq 2 and plotted as shown in Fig. 7(d). This is the compact parameter form of graphical representation known as the “master curve.” A common practice when input data are limited is to assume that $C = 20$, which has been found to be reasonably true for many materials.

Other Parameters. The Manson-Haferd parameter predicts a constant stress plot from log time, t , versus temperature, T (in °F, °C, or K), from the parametric relation:

$$P = f(\sigma) = \frac{(\log t - \log t_1)}{T - T_1}$$

This equation yields a family of straight lines converging to a point $t(T_A, t_A)$, which defines the optimum constants for that particular data set (Fig. 6b). On these same coordinates, the Manson-Succop parameter requires that isostress lines be straight and parallel (Fig. 6d). These conflicting patterns and still different patterns for the additional parameters cannot occur simultaneously over the entire range of data from a given set.

A frequent finding is that different parameters provide best fit to different portions of the same data. For example, using data obtained from tests on a 1Cr-1Mo-0.25V steel, the Larson-Miller parameter gave the best extrapolation at 482 °C (900 °F), and the Manson-Haferd parameter was preferable at 538 °F (1000 °F). However, the Orr-Sherby-Dorn parameter gave the best fit at 593 °C (1100 °F) (Ref 35, 36).

Although numerous studies have considered the relative merits of these and other proposed parameters, no one parameter has emerged as universally superior to all others. Five representative parameters were compared in terms of correlating and extrapolating extensive sets of data on the creep and rupture properties of seven steels and superalloys (Cr-Mo, Cr-Mo-V, 12%Cr, A 286, Astroloy, René 41, and Inconel 718) (Ref 37). The difference in fit among parameter methods was found to be relatively small and inconsistent from one alloy to another. The largest source of variation in the fitted values for time to rupture, time to 1% creep, and minimum creep rate was the difference between alloys, regardless of the parameter used.

Results were marginal to poor when extrapolation was beyond the range of the fitted master curve. When prediction of long-time data was confined to the master curve derived using only short-time data, no one parametric method gave consistently superior results.

For critical evaluation of the comparative ability to predict known long-time rupture lives (11,000–64,000 h) for the ferritic steels, data up to 10,000 h were applied to establish fit to the parametric model. For the superalloys, only data up to 1000 h were used to predict known rupture times between 1200 and 33,000 h. Table 1 lists ranges for the ratio (predicted life/actual life) extracted from Ref 37 for 46 extrapolations, including one in which slight extension was required beyond the fit of each master curve.

Table 1 Comparative extrapolation abilities of methods used to determine creep-rupture behavior

Parameter or method	Ratio: predicted life/actual life		
	Minimum	Average	Maximum
Larson-Miller	0.34	1.57	5.64
Manson-Haferd	0.44	1.51	6.30
Goldhoff-Sherby	0.36	1.64	8.85
Manson-Succop	0.39	1.53	4.96
Orr-Sherby-Dorn	0.11	1.09	4.01
Monkman-Grant	0.33	0.93	1.82

Studies on 0.5Cr-0.5Mo-0.25V steel pipe (Ref 38) found the Manson-Haferd parameter significantly superior to predict known rupture times (8712–20,664 h) from data points of less than 6000 h duration than either the Larson-Miller or Orr-Sherby-Dorn parameters. The latter two parameters generally provide optimistic prediction of behavior. According to Ref 38, very short-time data should be eliminated from the analysis if predictions beyond 10,000 h are desired, because their inclusion distorts the correlation at long times. As with graphical methods, the accuracy of parametric extrapolations is related to the interval of test variables on which the prediction is based.

Minimum Commitment Method. Experimental data may deviate from the requirement imposed by the form of each parameter for linearity of isostress curves or for parallelism or convergence of families of such curves. The minimum commitment method starts with a time-temperature-stress relationship sufficiently general to include all commonly used parameters. The pattern of the data is not forced in advance; instead, the actual experimental data naturally lead to the most appropriate functional relationship for the particular material.

Manson applied a “station-function” approach to $f(\log t) + p(T) = g(\sigma)$; all parametric formulations can reduce to this equation. Each of the functions f , p , and g were represented by their discrete numerical magnitudes at

specific values of the corresponding independent variable. Figure 8 illustrates treatment of Astroloy data given in Ref 37.

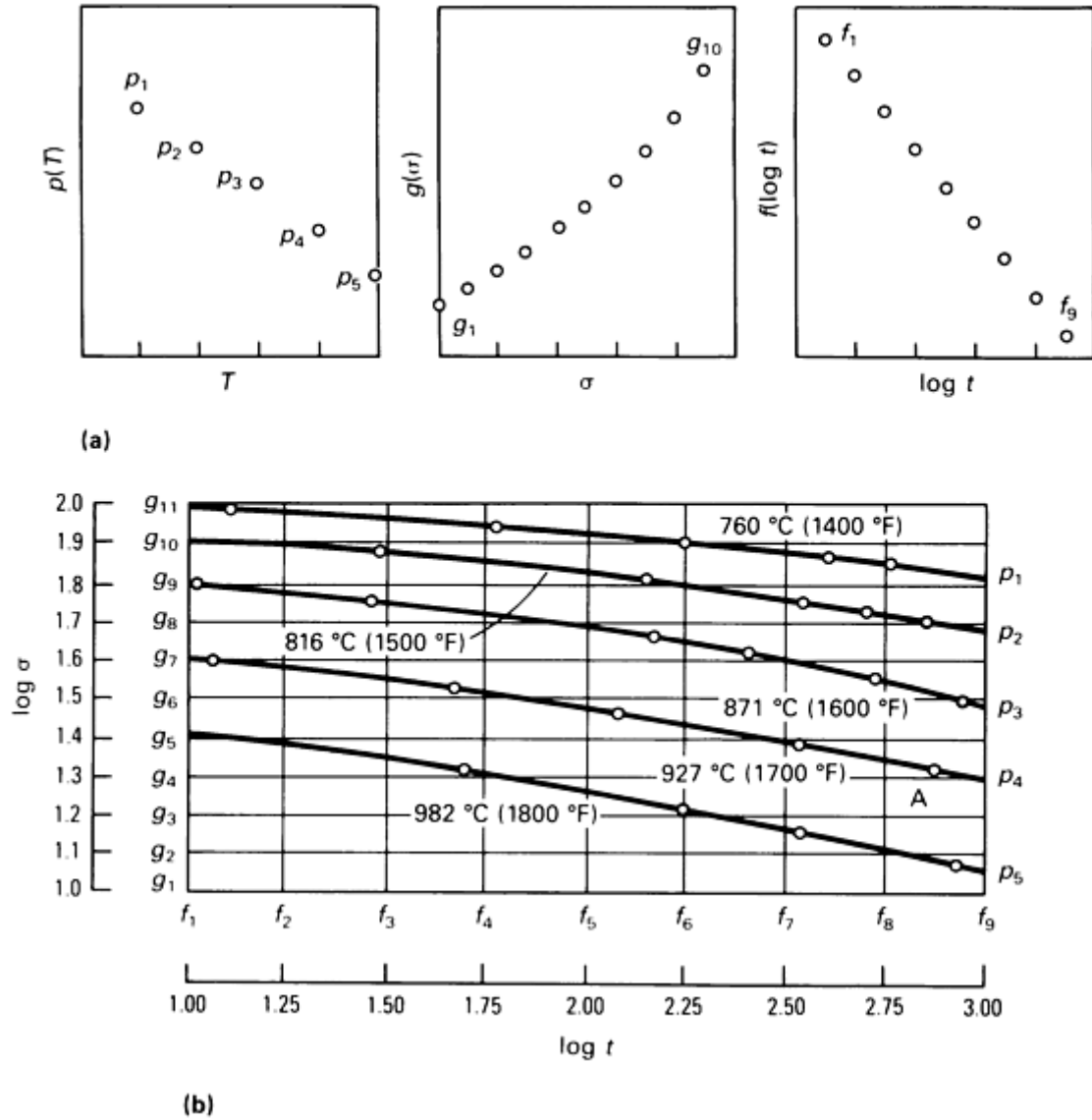


Fig. 8 Application of station function approach to Astroloy data. (a) Station-function representation of $p(T)$, $g(\sigma)$, and $f(\log t)$ at specific values of T , σ , and $\log t$. (b) Net point selections for solution. Source: Ref 39

Temperature stations were arbitrarily chosen at $T = 760, 816, 871, 927,$ and 982 °C (1400, 1500, 1600, 1700, and 1800 °F); the values of the p functions at these respective temperatures are designated $p_1, p_2, p_3, p_4,$ and p_5 . For times such that $\log t = 1.0, 1.25, 1.5, \dots, 3.0$, the respective corresponding f values are $f_1, f_2, f_3, \dots, f_9$. The g values are designated $g_1, g_2, g_3, \dots, g_{11}$ for levels of $\log \sigma = 1.0, 1.1, 1.2, \dots, 2.0$, with σ given in ksi. Consider the experimental point A ($T = 927$ °C, or 1700 °F); $\log t = 2.873$, $\log \sigma = 1.322$). At this point, p is directly p_4 , but values of f and g must be interpolated. Higher order interpolation can be easily accomplished, but simple linear interpolation was chosen for this illustration. For A between $\log t$ of $f_8 = 2.75$ and $f_9 = 3.00$:

$$\begin{aligned}
 f(2.873) &= \frac{3.0 - 2.873}{3.0 - 2.75} f_8 + \frac{2.873 - 2.75}{3.0 - 2.75} f_9 \\
 &= 0.508 f_8 + 0.492 f_9
 \end{aligned}
 \tag{Eq 3}$$

In a similar manner, the relation for stress at this point becomes:

$$g(1.322) = \frac{1.4 - 1.322}{1.4 - 1.3} g_4 + \frac{1.322 - 1.3}{1.4 - 1.3} g_5$$

$$= 0.78 g_4 + 0.22 g_5$$
(Eq 4)

Introducing these results into the original general equation yields:

$$0.508 f_8 + 0.492 f_9 + p_4 = 0.78 g_4 + 0.22 g_5$$
(Eq 5)

A similar equation can be written for each experimental point. By choosing a sufficient number of stations, the number of equations available will exceed the number of unknowns, so that a least-squares solution can be used to determine the unknowns. Once the equations have been solved, the function $f(\log t)$ may be extrapolated using graphical, polynomial, or recurrence relations.

Although a better fit to the data should result by the minimum commitment method than by forcing fit to an arbitrary parameter, extrapolations can still be imprecise. As with other methods, the degree of accuracy of predictions relies on having accurate and representative raw data from tests that reflect any structural changes expected to occur in the regime of the extrapolated conditions.

A specialized form of the general equation developed in 1971 (Ref 40) contains a characteristic material constant A :

$$\log t + AP(T) \log t + P(T) = G(\log \sigma)$$
(Eq 6)

The parameter A is a measure of structural stability, because the more unstable the material, the higher the negative value of A required to fit the data. On a plot of log stress versus log time, all isothermals converge at the extrapolated point $\log t = -(1/A)$ (Ref 41). For the parallel isotherms of the Orr-Sherby-Dorn parameter, $A = 0$; Miller-Larson requires $A = +0.5$. With data fitting the Manson-Haferd parameter, negative A values result; the Astroloy data discussed above converge at about $t = 6.36$, resulting in $A = -0.157$.

Establishing an accurate individualized value of A for a specific material is difficult from a short-life database. One acceptable approach is to use universalized values of $A = 0$ for aluminum alloys and pure metals, and $A = -0.05$ for most steels and superalloys (Ref 41). Highly unstable materials like Astroloy, as well as carbon steels, require higher negative values of A ; for these materials, $A = -0.15$ was found to be adequate in most instances. The minimum commitment method was initially developed for use with single-heat data. Application to multiple-heat analyses is discussed in Ref 42, including information on suitable computer programs.

References cited in this section

23. R.L. Klueh, Interaction Solid Solution Hardening in 2.25 Cr-1Mo Steel, *Mat. Sci. Eng.*, Vol 35, 1978, p 239–253
28. J.H. Bennowitz, On the Shape of the Log Stress-Log Time Curve of Long Time Creep-Rupture Tests, Joint International Conference on Creep, Institute of Mechanical Engineers, London, 1963, p 5-81 to 5-92
29. W.C. Leslie, J.W. Jones, and H.R. Voorhees, Long-Time Creep-Rupture Tests of Aluminum Alloys, *J. Test. Eval.*, Vol 8 (No. 1), 1980, p 32–41
30. D.J. Wilson and H.R. Voorhees, Creep Rupture Testing of Aluminum Alloys to 100,000 Hours, *J. Mat.*, Vol 7 (No. 4), 1972, p 501–509
31. S.P. Agrawal, L.E. Byrnes, J.A. Yaker, and W.C. Leslie, Creep Rupture Testing of Aluminum Alloys: Metallographic Studies of Fractured Test Specimens, *J. Test. Eval.*, Vol 5 (No. 3), May 1977, p 161–173
32. D.J. Wilson, Extrapolation of Rupture Data for Type 304 (18Cr-10Ni), Grade 22 ($2\frac{1}{4}$ Cr-1Mo), and Grade 11 ($1\frac{1}{4}$ Cr- $\frac{1}{2}$ Mo- $\frac{3}{4}$ Si) Steels,” *Trans. ASME J. Eng. Mat. Technol.*, Jan 1974, p 22–33

34. F.R. Larson and J. Miller, A Time-Temperature Relationship for Rupture and Creep Stresses, *Trans. ASME*, Vol 74, 1952, p 765
35. R.M. Goldhoff, Comparison of Parameter Methods for Extrapolating High-Temperature Data, *Trans. ASME J. Basic Eng.*, Vol 81 (No. 4), Series D, Dec 1959, p 629–644
36. R.L. Orr, O.D. Sherby, and J.E. Dorn, Correlations of Rupture Data for Metals at Elevated Temperatures, *Trans. ASM*, Vol 46, 1954, p 113–118
37. R.M. Goldhoff and G.J. Hahn, Correlation and Extrapolation of Creep-Rupture Data of Several Steels and Superalloys Using Time-Temperature Parameters, in *Time-Temperature Parameters for Creep-Rupture Analysis*, American Society for Metals, 1968, p 199–245
38. W.M. Cummings and R.H. King, Extrapolation of Creep Strain and Rupture Properties of $\frac{1}{2}\text{Cr}-\frac{1}{2}\text{Mo}-\frac{1}{4}\text{V}$ Pipe Steel, *Proc. Inst. Mech. Eng.*, Vol 185, 1970–71, p 285–299
39. S.S. Manson, Time-Temperature Parameters—A Re-evaluation and Some New Approaches, in *Time-Temperature Parameters for Creep-Rupture Analysis*, American Society for Metals, 1968, p 1–113
40. S. Manson and C.R. Ensign, “A Specialized Model for Analysis of Creep Rupture Data by the Minimum Commitment Station-Function Approach,” NASA TM X-52999, 1971, p 1–14
41. S.S. Manson and C.R. Ensign, Interpolation and Extrapolation of Creep Rupture Data by the Minimum Commitment Method. Part I: Focal-Point Convergence, in *Characterization of Materials for Service at Elevated Temperature*, American Society of Mechanical Engineers, New York, 1978, p 299–398
42. S.S. Manson and A. Muralidharen, Analysis of Creep Rupture Data for Five Multiheat Alloys by the Minimum Commitment Method Using Double Heat Centering Technique, in *Progress in Analysis of Fatigue and Stress Rupture*, American Society of Mechanical Engineers, New York, 1984, p 1–46

Assessment and Use of Creep-Rupture Properties

Howard R. Voorhees, Materials Technology Corporation Martin Prager, Materials Properties Council

Estimation of Required Properties Based on Insufficient Data

Complete independent evaluation of creep-rupture properties for a new lot of material, whether by graphical, parametric, or minimum commitment methods, requires numerous test points covering an extensive range of test variables. Frequently, the amount of data available is too limited for full treatment by usual procedures. Experimental difficulties often limit obtaining accurate test results at conditions of interest, such as evaluation of creep-rupture properties near the low end of the temperature range in which time-dependent effects are significant.

Tests of short or moderate duration at these temperatures frequently require use of such high stress levels that the immediate high plastic strains at load application alter the nature of the material from that which exists during service under lower stresses. Testing at or near a stress of intended application often requires more time and/or expense than is feasible before the material is to be put into use. Approximate methods permit such difficulties to be treated in a generally satisfactory manner. Established correlations also permit estimation of some unmeasured properties from other types of available results.

The Monkman-Grant Relationship. Analysis of data for a variety of aluminum-, iron-, nickel-, titanium-, cobalt-, and copper-base alloys led Monkman and Grant to the following empirical relationship (Ref 43):

$$\log t_r + m \log (\text{mcr}) = C$$

(Eq 7)

where t_r is time to rupture; mcr is minimum creep rate; and m and C are constants that differ significantly among alloy groups, but exhibit nearly fixed values for a given heat of material, or for different lots within the same alloy group.

Equation 7 enables assessment of the reliability of each individual test by examining its fit within the scatter band for all tests. Once a minimum creep rate has been determined in a low-stress test, rupture life can be estimated without running the test to failure. Although Monkman and Grant stated that this relationship was not intended for extrapolation, it can be used for that purpose, particularly when only low-stress tests are acceptable to prevent large initial plastic strains.

Table 1 includes the results obtained when the Monkman-Grant relationship is applied to data obtained on these same seven materials (Ref 37). Overall prediction of rupture life for these 46 extrapolations using this technique was more accurate than that provided by any of the five time-temperature parameters.

For additional materials (Ref 44) where good fit is obtained to a single linear plot on the coordinates of log time versus log secondary creep rate, extrapolation of a known secondary creep rate to the corresponding rupture life appears to be as good or better than by other extrapolation methods. One advantage of Eq 7 is that it can be applied successfully to as few as four to six data points, in contrast to the approximately 30 tests needed to establish the entire Manson-Haferd master curve (Ref 45). For the minimum commitment method, even more data points are usually required.

One advantage of this correlation, particularly with materials that exhibit structural instability under testing, is that the specimens used to determine the input data for secondary creep rates experience the same history of structural change that exists during the corresponding period of a test carried to rupture. Best predictions result by concentrating on tests encompassing a limited range of stresses and temperatures.

Reduced scatter was noted (Ref 46) for eight nonferrous alloys and two superalloys when the term $\log t_r$ in Eq 7 was replaced by $\log (t_r/\epsilon_c)$, where ϵ_c is the total creep deformation at fracture. This trend was confirmed by Ref 47 in tests on a 2.25Cr-1Mo steel.

Although deformation-modified rupture time may improve correlation in some instances, other cases exist where use of the original relationship is sufficient or better. Data for 17 test points for 4% cold-worked type 304 stainless steel (Ref 48) exhibited a spread in creep elongation from 1.5 to 24%. Goodness of fit was identical (coefficient of determination $r_2 = 0.86$) for linear regression of the data treated by the original versus the modified log-log relationships.

Extrapolation is fast and direct when using the Monkman-Grant coordinates, but with the modified relationship, creep elongation at the given temperature and corresponding to the rupture time sought must first be estimated. This usually requires subjective extrapolation of only a few elongation values displaying wide scatter and with no evident single trend. Introduction of a creep elongation factor may have value when only correlation or interpolation of test results is desired, but it is not recommended for extrapolation.

One occasional problem in estimation of rupture life from creep data is uncertainty whether secondary creep has truly been established. Changes in creep rate with continuing test time are often sufficiently gradual and so close to the sensitivity of measurement that what appears to be a steady-rate condition may in fact still be a late portion of primary creep. Reference 49 illustrates successive apparent minimum creep rates of 2.05, 1.7, and 1.40%/10,000 h for respective test durations of 1000, 2000, and 5000 h.

A distinctive slope change in a plot of log creep rate versus time or log time often provides better assurance that the secondary creep period has been entered than study of the deformation-time curve itself. Although an equation expressing true strain in terms of elapsed time, secondary creep rate, and three constants deviates markedly from actual behavior during the early portion of primary creep, a statistical analysis such as that detailed in Ref 50 may predict acceptable values of secondary creep rate from transient data.

For type 316 stainless steel tested at 704 to 830 °C (1300–1525 °F), the initial transient rate at $t = 0$ was found to be almost equal to 3.3 times the secondary creep rate in the same test (Ref 51). A significantly different magnitude (near 1000) for this ratio of initial and secondary creep rates was found in Ref 52 for a high-temperature alloy. A simple proportionality of this type and the more general analysis cited above are tempting alternatives to permit shortened test durations, but both suffer from the need for creep measurements that are more precise than those commonly obtained. Currently, neither method is capable of replacing long-time testing.

The Gill-Goldhoff Method. Many designs for elevated-temperature service require that deformation not exceed some maximum value; in these cases, creep strain rather than rupture life becomes the focus. Although

published compilations and computer banks of data include rupture properties for most materials of engineering interest, corresponding information on the time-dependency of strain is frequently sparse or nonexistent. Many early studies did not include strain measurement during rupture tests. When creep data were obtained, accuracy was sometimes questionable due to inadequate control of temperature or low precision of strain measurements. Frequently, the only listed creep data are minimum creep rates. Most of these results were obtained from tests that were terminated after a few thousand hours, or even less, and true secondary creep rate may not have become established.

Studies by the Metal Properties Council (now the Materials Properties Council, or MPC) and similar groups attempt to report both the total strain on loading and the times to various levels of creep strain. Until such results are more universally available, creep strain to be expected in given design situations must still be estimated.

Gill and Goldhoff (Ref 49, 53) found a log-log correlation between stress to cause rupture and stress for a given creep strain for the same time and temperature. Figure 9 shows their composite plot for aluminum-base alloys and stainless steels, including several superalloys.

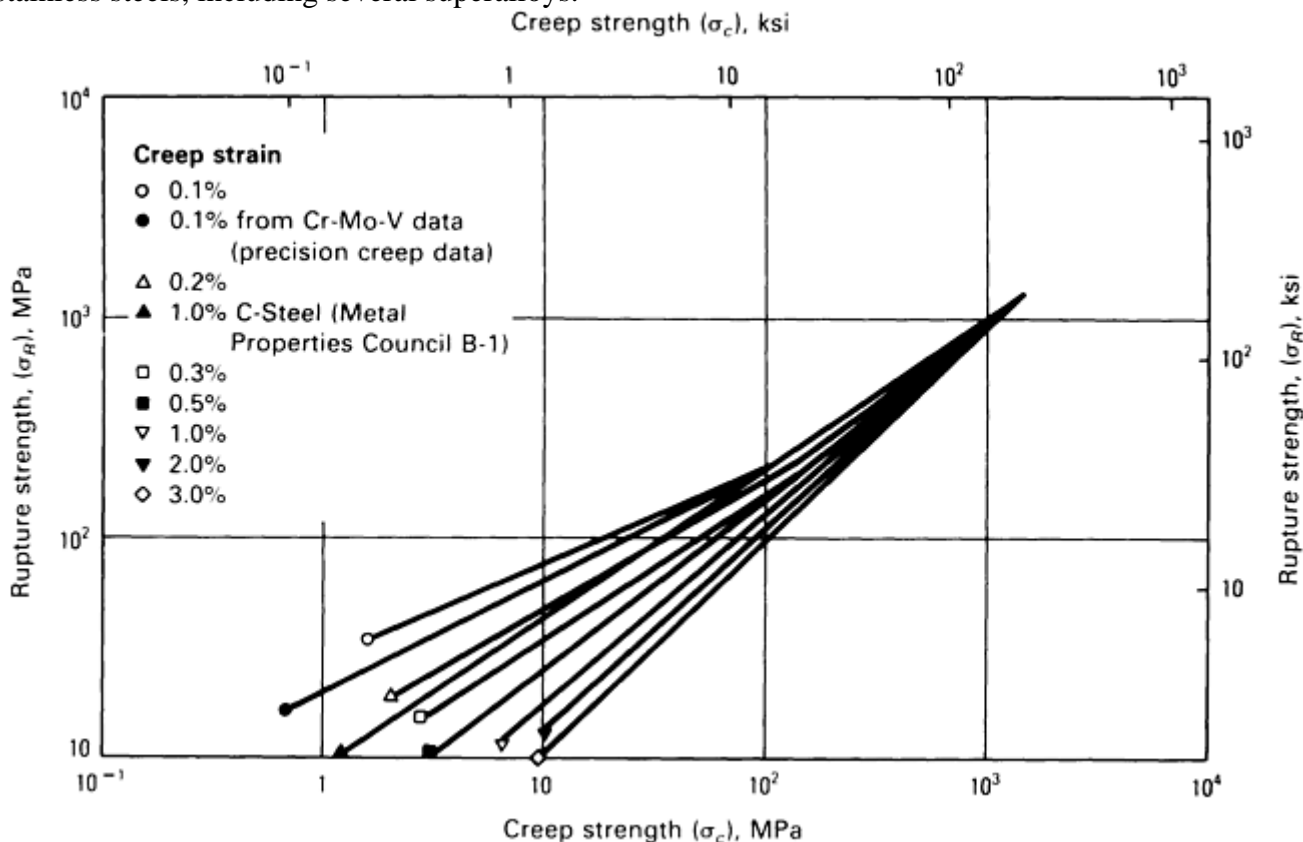


Fig. 9 Composite graph for the Gill-Goldhoff correlation. Source: Ref 53

To obtain this correlation, tests in which 0.1% creep occurred in less than 100 h were rejected to prevent intolerable data scatter. Despite this, the “universal” curves of Fig. 9 can be associated with fairly wide data scatter, particularly at low creep strains. Some deviations from the correlation were related to microstructural instabilities, which produce differing proportions of primary, secondary, and tertiary creep among alloys and for varying test conditions.

Despite occasional anomalies, the Gill-Goldhoff correlation meets some preliminary design needs, particularly if the technique is tailored to grades of alloys similar to those of immediate concern. In principle, this technique can also be used to predict rupture properties from early creep measurements from tests that are not continued to rupture. This use is limited by the short rupture times that are derived from tests terminated at creep strains of 1% or less. If these tests were continued to higher levels of creep, improved predictions of rupture should be obtained by determining the secondary creep rate and then applying the Monkman-Grant relationship.

Treatment of Isolated Test Points. Particularly at the start of a testing program, the need may arise to extract information from a single available test. The form of most parameters limits their use to situations in which multiple test results are available. The Larson-Miller parameter is an exception if the generalized constant $C = 20$ is used.

For the stress of the test, longer rupture times within a factor of ten from the test duration frequently can be estimated satisfactorily for temperatures below that of the test. If a master curve or graph of isothermals is available for another lot of like or similar alloy, a parallel curve passed through the coordinates of the test point for the new lot can serve as an approximate representation of expected behavior for limited ranges of variables from the test conditions.

References cited in this section

37. R.M. Goldhoff and G.J. Hahn, Correlation and Extrapolation of Creep-Rupture Data of Several Steels and Superalloys Using Time-Temperature Parameters, in *Time-Temperature Parameters for Creep-Rupture Analysis*, American Society for Metals, 1968, p 199–245
43. F.C. Monkman and N.J. Grant, An Empirical Relationship Between Rupture Life and Minimum Creep Rate in Creep-Rupture Tests, *Proc. ASTM*, Vol 56, 1956, p 593–605
44. H.R. Voorhees, “Determination of Rupture Strength at Temperatures Near the Lower End of the Time-Dependent Range,” findings reported to the Metal Properties Council, Inc., New York, 1984
45. S. Manson and W.F. Brown, Jr., Discussion to a Paper by F. Garofalo et al., *Trans. ASME*, Vol 78 (No. 7), Oct 1956, p 143
46. F. Dobeš and K. MiliXXke, The Relation Between Minimum Creep Rate and Time to Fracture, *Met. Sci.*, Vol 10, Nov 1976, p 382–384
47. D. Lonsdale and P.E.J. Flewitt, Relationship Between Minimum Creep Rate and Time to Fracture for 2- $\frac{1}{2}$ %Cr-1%Mo Steel, *Met. Sci.*, May 1978, p 264–265
48. M. Gold, W.E. Leyda, and R.H. Zeisloft, The Effect of Varying Degree of Cold Work on the Stress-Rupture Properties of Type 304 Stainless Steel, *Trans. ASME J. Eng. Mat. Technol.*, Vol 97 (No. 4), Series H, Oct 1975, p 305–312
49. R.F. Gill and R.M. Goldhoff, Analysis of Long-Time Creep Data for Determining Long-Term Strength, *Met. Eng. Quart.*, Vol 10 (No. 3), Aug 1970, p 30–39
50. P.L. Threadgill and B.L. Mordike, The Prediction of Creep Life From Transient Creep Data, *Z. Metallkd.*, Vol 68 (No. 4), 1977, p 266–269
51. F. Garofalo, C. Richmond, W.F. Domis, and F. von Gemmingen, Strain-Time, Rate-Stress and Rate-Temperature Relations During Large Deformations in Creep, Joint International Conference on Creep, Institution of Mechanical Engineers, London, 1963, p 1-31 to 1-39
52. P.L. Threadgill and B. Wilshire, Mechanisms of Transient and Steady-State Creep in a γ' -Hardened Austenitic Steel, in *Creep Strength in Steel and High-Temperature Alloys*, The Metals Society, London, 1974, p 8–14
53. R.M. Goldhoff and R.F. Gill, A Method for Predicting Creep Data for Commercial Alloys on a Correlation Between Creep Strength and Rupture Strength, *Trans. ASME J. Basic Eng.*, Vol 94 (No. 1), Series D, March 1972, p 1–6

Evaluating Remaining Creep-Rupture Life

Expected residual rupture life following a discrete change in service conditions may at times be estimated without further tests. The more usual practice is to test creep-exposed samples at increased stress and/or temperature than they had seen in service, to reduce testing duration. Results are then extrapolated back to nominal service conditions. In addition to parametric methods and isostress methods, at least three others procedures have found recent promotion:

- The MPC Omega Method
- Analysis on restricted-range Monkman-Grant coordinates
- Accelerated creep-test methodology of David Woodford

These methods are described in the section “Other Evaluation Methods” in this article.

Discrete Changes in Temperature or Stress. When a creep-rupture test is interrupted by cooling and reheating at a moderate rate at constant load, and if the time under changing temperature is brief compared to the original test duration, the effect of the interruption on either the creep curve or rupture life usually cannot be readily detected, unless thermal gradients cause gross plastic deformation or spalling of surface layers.

Similar results can be expected when temperature and stress rise and fall in unison, as during start-up and shutdown of a steam boiler. For the alternate situation in which unloading occurs while the creep temperature is maintained, significant recovery of primary creep can ensue; reapplying the load results in a period of primary creep.

Under step-wise alteration of load, temperature, or both during a test or service, performance often roughly follows the “life-fraction rule” or “linear cumulative damage rule” (Ref 54), in which the percentage of total life consumed for each period of fixed temperature and stress is represented as:

$$\% \text{ total life} = \frac{\text{actual time at the given conditions}}{\text{rupture life at those conditions without alteration}} \times 100$$

Accuracy of this rule ranges from excellent to rather poor, with best results for multiple small excursions (Ref 55). Although solid-state reactions, which can reverse at different exposure temperatures, may introduce complications under some conditions, investigators have found the life-fraction rule more appropriate for steels under temperature changes than under stress changes (Ref 56).

Life-fraction summations at failure as low as 0.36 and as high as 2.43 have been reported (Ref 57). The spread was only from 0.75 to 1.50 for the same tests using damage fractions defined by $K(t/t_r) + (1 - K)(\epsilon/\epsilon_r)$, where t and ϵ are the time and strain under a period of fixed conditions, for which the rupture time and fracture strain are t_r and ϵ_r . K is a material constant ranging from zero to 1; the zero limit applies to materials that develop cracks early in life, and K approaches 1 for materials that exhibit no cracking until rupture is imminent. Typical values of K (Ref 57) are as follows:

Material and test temperature	K
Copper at 250 °C (482 °F)	0.3
A 286 alloy at 649 °C (1200 °F), solution treated at 1204 °C (2200 °F)	0.47
A 286 alloy at 649 °C (1200 °F), solution treated at 982 °C (1800 °F)	0.43
Inconel X-750 at 732 °C (1350 °F)	0.625

When data are insufficient for determination of K , acceptable results frequently can be obtained with an empirical rule (Ref 58), by which the life-fractions added are defined by $\sqrt{(t/t_r)(\epsilon/\epsilon_r)}$. With any of these cumulative damage rules, comparison usually is against rupture life from constant-load tests—that is, with actual stress rising as creep reduces the cross section. When the same specimen undergoes load changes for

different periods, respective stress levels have been based on the initial cross section. This corresponds to using the same original load if an interrupted test must be restarted. The actual stress at the time of test restart is $(\sigma_n(A_o/A_c))$, where σ_n is the present nominal stress, A_o is the initial specimen cross section, and A_c is the specimen cross section after creep deformation up to the time of the test interruption.

When the specimen for a test in a later portion of creep has been machined from a part that has already undergone considerable reduction in cross section by prior creep, a corresponding area-modified stress must be employed for consistent interpretation of the results (Ref 59). The load applied to produce the desired nominal stress σ_n , related to the virgin material is calculated to make the actual stress $\sigma_a = \sigma_n(A_o/A_c)$, where the latter term relates cross-sectional areas of the original part before and after creep. Use of such an area-modified stress has been reported to improve prediction of remaining life from post-service rupture tests (Ref 59, 60).

An approximation of remaining rupture life for components that have undergone prolonged service can be calculated by introducing best estimates for operating temperatures and stresses into the above damage rules. More exact evaluation, however, can be obtained by testing representative samples removed from service.

Measurement of Creep-Rupture Properties After Service. Dependable application of techniques to estimate remaining life requires that the loading direction for the final test corresponds to the largest principal stress of service and that the specimen is representative of surface deterioration or other damage present in the part. Possible temperature and loading gradients in service must be kept in mind when selecting a sampling site and when applying test results to predictions of further serviceability. Despite these possible additional variables, assessments of post-service rupture properties require only about the same number and duration of tests as conventional evaluation of any new lot of familiar material.

Large specimens are recommended to limit relative loss in cross section from oxidation, unless surfaces are protected from the usual air environment of tests.

For samples from tubes or similar shapes subjected to internal-pressure service and consequent major service stress in the circumferential direction, uniaxial creep tests are preferred to have the test load act in that direction. Specimens from tube and pipe can have wedges of similar material welded to the outside-diameter face near the ends of a ring segment from the sample. Electron-beam welded attachments of imaginative design make possible the testing of many samples available only in small sizes or inconvenient shapes.

Isostress Tests. A typical study involves testing three or four specimens all at a single stress similar to, or slightly above, the stress of service, and each at a different temperature higher than that of service. Results are extrapolated to service temperature on coordinates of log rupture time versus either absolute temperature or its reciprocal.

The principal drawback of this procedure is that at least some tests must usually be conducted at a higher temperature than is needed in other evaluation methods.

Allowance for Data Scatter. In an effort to minimize uncertainties from extrapolation procedures, undue emphasis may be placed on a test with the longest affordable duration. Normal data scatter still limits evaluation of expected performance from isolated points. Indeed, a more reliable prediction may be obtained when the same total test time is devoted to performing a greater number of tests with intermediate duration rather than only a few with extended life. An exception is when instabilities occur only with very long testing.

Some researchers study scatter by running multiple tests at one or more fixed combinations of stress and temperature. Again, a series of tests, each at different conditions, permits equally good statistical treatment to evaluate the scatter, while providing a broader indication of the material characteristics. Although emphasis has been placed on time to rupture, the extra expense of obtaining complete creep deformation data in all tests is often justified by the insight afforded into the effects of structural changes.

References cited in this section

54. E.L. Robinson, Effect of Temperature Variation on the Creep Strength of Steels, *Trans. ASME*, Vol 60, 1938, p 253–259
55. P.N. Randall, Cumulative Damage in Creep-Rupture Tests of a Carbon Steel, *Trans. ASME J. Basic Eng.*, Vol 84 (No. 2), Series D, June 1962, p 239–242
56. D.A. Woodford, Creep Damage and Remaining Life Concept, *Trans. ASME J. Eng. Mat. Technol.*, Vol 101 (No. 4), Dec 1979, p 311–316

57. M.M. Abo El Ata and I. Finnie, A Study of Creep Damage Rules, *Trans. ASME J. Basic Eng.*, Vol 94 (No. 3), Series D, Sept 1972, p 533–543
58. J.W. Freeman and H.R. Voorhees, “Notch Sensitivity of Aircraft Structural and Engine Alloys, Part II: Further Studies with A-286 Alloys,” Wright Air Development Center, Technical Report 57–58, ASTIA Document 207,850, Jan 1959
59. R.V. Hart, Concept of Area-Modified Stress for Life-Fraction Summation During Creep, *Met. Technol.*, Sept 1977, p 447–448
60. R.V. Hart, Assessment of Remaining Creep Life Using Accelerated Stress-Rupture Tests, *Met. Technol.*, Jan 1976, p 1–7

Assessment and Use of Creep-Rupture Properties

Howard R. Voorhees, Materials Technology Corporation Martin Prager, Materials Properties Council

Evaluating Remaining Creep-Rupture Life

Expected residual rupture life following a discrete change in service conditions may at times be estimated without further tests. The more usual practice is to test creep-exposed samples at increased stress and/or temperature than they had seen in service, to reduce testing duration. Results are then extrapolated back to nominal service conditions. In addition to parametric methods and isostress methods, at least three others procedures have found recent promotion:

- The MPC Omega Method
- Analysis on restricted-range Monkman-Grant coordinates
- Accelerated creep-test methodology of David Woodford

These methods are described in the section “Other Evaluation Methods” in this article.

Discrete Changes in Temperature or Stress. When a creep-rupture test is interrupted by cooling and reheating at a moderate rate at constant load, and if the time under changing temperature is brief compared to the original test duration, the effect of the interruption on either the creep curve or rupture life usually cannot be readily detected, unless thermal gradients cause gross plastic deformation or spalling of surface layers.

Similar results can be expected when temperature and stress rise and fall in unison, as during start-up and shutdown of a steam boiler. For the alternate situation in which unloading occurs while the creep temperature is maintained, significant recovery of primary creep can ensue; reapplying the load results in a period of primary creep.

Under step-wise alteration of load, temperature, or both during a test or service, performance often roughly follows the “life-fraction rule” or “linear cumulative damage rule” (Ref 54), in which the percentage of total life consumed for each period of fixed temperature and stress is represented as:

$$\% \text{ total life} = \frac{\text{actual time at the given conditions}}{\text{rupture life at those conditions without alteration}} \times 100$$

Accuracy of this rule ranges from excellent to rather poor, with best results for multiple small excursions (Ref 55). Although solid-state reactions, which can reverse at different exposure temperatures, may introduce complications under some conditions, investigators have found the life-fraction rule more appropriate for steels under temperature changes than under stress changes (Ref 56).

Life-fraction summations at failure as low as 0.36 and as high as 2.43 have been reported (Ref 57). The spread was only from 0.75 to 1.50 for the same tests using damage fractions defined by $K(t/t_r) + (1 - K)(\epsilon/\epsilon_r)$, where t and ϵ are the time and strain under a period of fixed conditions, for which the rupture time and fracture strain are t_r and ϵ_r . K is a material constant ranging from zero to 1; the zero limit applies to materials that develop cracks early in life, and K approaches 1 for materials that exhibit no cracking until rupture is imminent. Typical values of K (Ref 57) are as follows:

Material and test temperature	K
Copper at 250 °C (482 °F)	0.3
A 286 alloy at 649 °C (1200 °F), solution treated at 1204 °C (2200 °F)	0.47
A 286 alloy at 649 °C (1200 °F), solution treated at 982 °C (1800 °F)	0.43
Inconel X-750 at 732 °C (1350 °F)	0.625

When data are insufficient for determination of K , acceptable results frequently can be obtained with an empirical rule (Ref 58), by which the life-fractions added are defined by $\sqrt{(t/t_r)(\epsilon/\epsilon_r)}$. With any of these cumulative damage rules, comparison usually is against rupture life from constant-load tests—that is, with actual stress rising as creep reduces the cross section. When the same specimen undergoes load changes for different periods, respective stress levels have been based on the initial cross section. This corresponds to using the same original load if an interrupted test must be restarted. The actual stress at the time of test restart is $(\sigma_n(A_o/A_c))$, where σ_n is the present nominal stress, A_o is the initial specimen cross section, and A_c is the specimen cross section after creep deformation up to the time of the test interruption.

When the specimen for a test in a later portion of creep has been machined from a part that has already undergone considerable reduction in cross section by prior creep, a corresponding area-modified stress must be employed for consistent interpretation of the results (Ref 59). The load applied to produce the desired nominal stress σ_n , related to the virgin material is calculated to make the actual stress $\sigma_a = \sigma_n(A_o/A_c)$, where the latter term relates cross-sectional areas of the original part before and after creep. Use of such an area-modified stress has been reported to improve prediction of remaining life from post-service rupture tests (Ref 59, 60).

An approximation of remaining rupture life for components that have undergone prolonged service can be calculated by introducing best estimates for operating temperatures and stresses into the above damage rules. More exact evaluation, however, can be obtained by testing representative samples removed from service.

Measurement of Creep-Rupture Properties After Service. Dependable application of techniques to estimate remaining life requires that the loading direction for the final test corresponds to the largest principal stress of service and that the specimen is representative of surface deterioration or other damage present in the part. Possible temperature and loading gradients in service must be kept in mind when selecting a sampling site and when applying test results to predictions of further serviceability. Despite these possible additional variables, assessments of post-service rupture properties require only about the same number and duration of tests as conventional evaluation of any new lot of familiar material.

Large specimens are recommended to limit relative loss in cross section from oxidation, unless surfaces are protected from the usual air environment of tests.

For samples from tubes or similar shapes subjected to internal-pressure service and consequent major service stress in the circumferential direction, uniaxial creep tests are preferred to have the test load act in that direction. Specimens from tube and pipe can have wedges of similar material welded to the outside-diameter face near the ends of a ring segment from the sample. Electron-beam welded attachments of imaginative design make possible the testing of many samples available only in small sizes or inconvenient shapes.

Isostress Tests. A typical study involves testing three or four specimens all at a single stress similar to, or slightly above, the stress of service, and each at a different temperature higher than that of service. Results are extrapolated to service temperature on coordinates of log rupture time versus either absolute temperature or its reciprocal.

The principal drawback of this procedure is that at least some tests must usually be conducted at a higher temperature than is needed in other evaluation methods.

Allowance for Data Scatter. In an effort to minimize uncertainties from extrapolation procedures, undue emphasis may be placed on a test with the longest affordable duration. Normal data scatter still limits evaluation of expected performance from isolated points. Indeed, a more reliable prediction may be obtained when the same total test time is devoted to performing a greater number of tests with intermediate duration rather than only a few with extended life. An exception is when instabilities occur only with very long testing.

Some researchers study scatter by running multiple tests at one or more fixed combinations of stress and temperature. Again, a series of tests, each at different conditions, permits equally good statistical treatment to evaluate the scatter, while providing a broader indication of the material characteristics. Although emphasis has been placed on time to rupture, the extra expense of obtaining complete creep deformation data in all tests is often justified by the insight afforded into the effects of structural changes.

References cited in this section

54. E.L. Robinson, Effect of Temperature Variation on the Creep Strength of Steels, *Trans. ASME*, Vol 60, 1938, p 253–259
55. P.N. Randall, Cumulative Damage in Creep-Rupture Tests of a Carbon Steel, *Trans. ASME J. Basic Eng.*, Vol 84 (No. 2), Series D, June 1962, p 239–242
56. D.A. Woodford, Creep Damage and Remaining Life Concept, *Trans. ASME J. Eng. Mat. Technol.*, Vol 101 (No. 4), Dec 1979, p 311–316
57. M.M. Abo El Ata and I. Finnie, A Study of Creep Damage Rules, *Trans. ASME J. Basic Eng.*, Vol 94 (No. 3), Series D, Sept 1972, p 533–543
58. J.W. Freeman and H.R. Voorhees, “Notch Sensitivity of Aircraft Structural and Engine Alloys, Part II: Further Studies with A-286 Alloys,” Wright Air Development Center, Technical Report 57–58, ASTIA Document 207,850, Jan 1959
59. R.V. Hart, Concept of Area-Modified Stress for Life-Fraction Summation During Creep, *Met. Technol.*, Sept 1977, p 447–448
60. R.V. Hart, Assessment of Remaining Creep Life Using Accelerated Stress-Rupture Tests, *Met. Technol.*, Jan 1976, p 1–7

Assessment and Use of Creep-Rupture Properties

Howard R. Voorhees, Materials Technology Corporation Martin Prager, Materials Properties Council

References

1. Basis for Estimating Stress Values, Paragraph A-150, Rules for Construction of Power Boilers, *ASME Boiler and Pressure Vessel Code*, Section I, American Society of Mechanical Engineers, New York, 1983
2. “Standard Recommended Practice for Conducting Creep, Creep-Rupture, and Stress-Rupture Tests of Metallic Materials,” E 139, *Annual Book of ASTM Standards*, Vol 03.01, ASTM, 1984, p 283–297.
3. A.K. Schmieder, Size Effect During Rupture Tests of Unnotched and Notched Specimens of Cr-Mo-V and Cr-Ni Steels, in *Ductility and Toughness Considerations in Elevated Temperature Service*, American Society of Mechanical Engineers, New York, 1978, p 31–48
4. B. Aronsson and A. Hede, Some Observations on the Reproducibility of Creep Rate Determinations, in *High-Temperature Properties of Steel*, Iron and Steel Institute, London, 1967, p 41–45

5. D.R. Hayhurst, The Effects of Test Variables on Scatter in High-Temperature Tensile Creep-Rupture Data, *Int. J. Mech. Sci.*, Vol 16, 1974, p 829–841
6. W. Ruttman, M. Krause, and K.J. Kremer, International Community Tests on Long-Term Behavior of $2\frac{1}{4}\%$ Cr-1%Mo Steel, in *High-Temperature Properties of Steel*, Iron and Steel Institute, London, 1967, p 23–29
7. D. Coutsouradis and D.K. Faurschou, “Cooperative Creep Testing Program,” AGARD Report 581, North Atlantic Treaty Organization, Advisory Group for Aerospace Research & Development, Neuilly-sur-Seine, France, 1971
8. “Report on the Elevated-Temperature Properties of Stainless Steels,” DS 5-S1, ASTM, 1965
9. “An Evaluation of the Yield, Tensile, Creep, and Rupture Strengths of Wrought 304, 316, 321, and 347 Stainless Steels at Elevated Temperatures,” DS 5-S2, ASTM, 1969
10. “Supplemental Report on the Elevated-Temperature Properties of Chromium-Molybdenum Steels,” DS 6-S1, ASTM, 1966
11. “Supplemental Report on the Elevated-Temperature Properties of Chromium-Molybdenum Steels,” DS 6-S2, ASTM, 1971
12. “Report on the Elevated-Temperature Properties of Selected Super-Alloys,” DS 7-S1, ASTM, 1968
13. “An Evaluation of the Elevated-Temperature Tensile and Creep-Rupture Properties of Wrought Carbon Steel,” DS 11-S1, ASTM, 1969
14. “Evaluation of the Elevated-Temperature Tensile and Creep-Rupture Properties of C-Mo, Mn-Mo and Mn-Mo-Ni Steels,” DS 47, ASTM, 1971
15. “Evaluation of the Elevated-Temperature Tensile and Creep-Rupture Properties of Steel,” DS 50, ASTM, 1973
16. “Evaluation of the Elevated-Temperature Tensile and Creep-Rupture Properties of 3 to 9 Percent Cr-Mo Steels,” DS 58, ASTM, 1975
17. “Evaluations of the Elevated-Temperature Tensile and Creep-Rupture Properties of 12 to 27 Percent Chromium Steels,” DS 59, ASTM, 1980
18. “Compilation of Stress-Relaxation Data for Engineering Alloys,” DS 60, ASTM, 1982
19. V.K. Sikka, H.E. McCoy, Jr., M.K. Booker, and C.R. Brinkman, “Heat-to-Heat Variation in Creep Properties of Types 304 and 316 Stainless Steels,” ASME Paper 75-PVP-26, American Society of Mechanical Engineers, New York, 1975
20. K.R. Williams and B. Wilshire, Effects of Microstructural Instability on the Creep and Fracture Behavior of Ferritic Steels, *Mat. Sci. Eng.*, Vol 28, 1977, p 289–296
21. M. Wild, Analysis of Creep Behavior of Heat-Resistant Ferritic Steels at Temperatures from 450 to 600 °C, *Archiv. Eisenhüttenwes.*, Vol 34, Dec 1963, p 935–950 (in German)
22. Private business communication, Materials Technology Corporation data sheets submitted to the Metal Properties Council for tests under MPC Contract No. 174-1

23. R.L. Klueh, Interaction Solid Solution Hardening in 2.25 Cr-1Mo Steel, *Mat. Sci. Eng.*, Vol 35, 1978, p 239–253
24. J. Glen, The Shape of Creep Curves, *Trans. ASME J. Basic Eng.*, Vol 85 (No. 4), Series D, Dec 1963, p 595–600
25. J.P. Milan et al., Negative Creep in Ni-Cr-Ti Alloys, Fourth Interamerican Conference on Materials Technology, Caracas, June–July 1975, p 102–106
26. R. Widmer and N.J. Grant, The Role of Atmosphere in the Creep-Rupture Behavior of 80Ni-20Cr Alloys, *Trans. ASME J. Basic Eng.*, Vol 82 (No. 4), Series D, Dec 1960, p 882–886
27. P. Shahinian and M.R. Achter, Creep-Rupture of Nickel of Two Purities in Controlled Environments, Joint International Conference on Creep, Institute of Mechanical Engineers, London, 1963, p 7-49 to 7-57
28. J.H. Bennewitz, On the Shape of the Log Stress-Log Time Curve of Long Time Creep-Rupture Tests, Joint International Conference on Creep, Institute of Mechanical Engineers, London, 1963, p 5-81 to 5-92
29. W.C. Leslie, J.W. Jones, and H.R. Voorhees, Long-Time Creep-Rupture Tests of Aluminum Alloys, *J. Test. Eval.*, Vol 8 (No. 1), 1980, p 32–41
30. D.J. Wilson and H.R. Voorhees, Creep Rupture Testing of Aluminum Alloys to 100,000 Hours, *J. Mat.*, Vol 7 (No. 4), 1972, p 501–509
31. S.P. Agrawal, L.E. Byrnes, J.A. Yaker, and W.C. Leslie, Creep Rupture Testing of Aluminum Alloys: Metallographic Studies of Fractured Test Specimens, *J. Test. Eval.*, Vol 5 (No. 3), May 1977, p 161–173
32. D.J. Wilson, Extrapolation of Rupture Data for Type 304 (18Cr-10Ni), Grade 22 ($2\frac{1}{4}$ Cr-1Mo), and Grade 11 ($1\frac{1}{4}$ Cr- $\frac{1}{2}$ Mo- $\frac{3}{4}$ Si) Steels,” *Trans. ASME J. Eng. Mat. Technol.*, Jan 1974, p 22–33
33. R.M. Goldhoff, Appendix
 - 3: Time-Temperature Parameters, *Properties and Selection: Stainless Steels, Tool Materials, and Special-Purpose Metals*, Vol 3, *Metals Handbook*, 9th ed., American Society for Metals, 1980, p 237–241
34. F.R. Larson and J. Miller, A Time-Temperature Relationship for Rupture and Creep Stresses, *Trans. ASME*, Vol 74, 1952, p 765
35. R.M. Goldhoff, Comparison of Parameter Methods for Extrapolating High-Temperature Data, *Trans. ASME J. Basic Eng.*, Vol 81 (No. 4), Series D, Dec 1959, p 629–644
36. R.L. Orr, O.D. Sherby, and J.E. Dorn, Correlations of Rupture Data for Metals at Elevated Temperatures, *Trans. ASM*, Vol 46, 1954, p 113–118
37. R.M. Goldhoff and G.J. Hahn, Correlation and Extrapolation of Creep-Rupture Data of Several Steels and Superalloys Using Time-Temperature Parameters, in *Time-Temperature Parameters for Creep-Rupture Analysis*, American Society for Metals, 1968, p 199–245

38. W.M. Cummings and R.H. King, Extrapolation of Creep Strain and Rupture Properties of $\frac{1}{2}\text{Cr}-\frac{1}{2}\text{Mo}-\frac{1}{4}\text{V}$ Pipe Steel, *Proc. Inst. Mech. Eng.*, Vol 185, 1970–71, p 285–299
39. S.S. Manson, Time-Temperature Parameters—A Re-evaluation and Some New Approaches, in *Time-Temperature Parameters for Creep-Rupture Analysis*, American Society for Metals, 1968, p 1–113
40. S. Manson and C.R. Ensign, “A Specialized Model for Analysis of Creep Rupture Data by the Minimum Commitment Station-Function Approach,” NASA TM X-52999, 1971, p 1–14
41. S.S. Manson and C.R. Ensign, Interpolation and Extrapolation of Creep Rupture Data by the Minimum Commitment Method. Part I: Focal-Point Convergence, in *Characterization of Materials for Service at Elevated Temperature*, American Society of Mechanical Engineers, New York, 1978, p 299–398
42. S.S. Manson and A. Muralidharen, Analysis of Creep Rupture Data for Five Multiheat Alloys by the Minimum Commitment Method Using Double Heat Centering Technique, in *Progress in Analysis of Fatigue and Stress Rupture*, American Society of Mechanical Engineers, New York, 1984, p 1–46
43. F.C. Monkman and N.J. Grant, An Empirical Relationship Between Rupture Life and Minimum Creep Rate in Creep-Rupture Tests, *Proc. ASTM*, Vol 56, 1956, p 593–605
44. H.R. Voorhees, “Determination of Rupture Strength at Temperatures Near the Lower End of the Time-Dependent Range,” findings reported to the Metal Properties Council, Inc., New York, 1984
45. S. Manson and W.F. Brown, Jr., Discussion to a Paper by F. Garofalo et al., *Trans. ASME*, Vol 78 (No. 7), Oct 1956, p 143
46. F. Dobeš and K. MiliXXke, The Relation Between Minimum Creep Rate and Time to Fracture, *Met. Sci.*, Vol 10, Nov 1976, p 382–384
47. D. Lonsdale and P.E.J. Flewitt, Relationship Between Minimum Creep Rate and Time to Fracture for $2-\frac{1}{2}\%$ Cr-1%Mo Steel, *Met. Sci.*, May 1978, p 264–265
48. M. Gold, W.E. Leyda, and R.H. Zeisloft, The Effect of Varying Degree of Cold Work on the Stress-Rupture Properties of Type 304 Stainless Steel, *Trans. ASME J. Eng. Mat. Technol.*, Vol 97 (No. 4), Series H, Oct 1975, p 305–312
49. R.F. Gill and R.M. Goldhoff, Analysis of Long-Time Creep Data for Determining Long-Term Strength, *Met. Eng. Quart.*, Vol 10 (No. 3), Aug 1970, p 30–39
50. P.L. Threadgill and B.L. Mordike, The Prediction of Creep Life From Transient Creep Data, *Z. Metallkd.*, Vol 68 (No. 4), 1977, p 266–269
51. F. Garofalo, C. Richmond, W.F. Domis, and F. von Gemmingen, Strain-Time, Rate-Stress and Rate-Temperature Relations During Large Deformations in Creep, Joint International Conference on Creep, Institution of Mechanical Engineers, London, 1963, p 1-31 to 1-39
52. P.L. Threadgill and B. Wilshire, Mechanisms of Transient and Steady-State Creep in a γ' -Hardened Austenitic Steel, in *Creep Strength in Steel and High-Temperature Alloys*, The Metals Society, London, 1974, p 8–14
53. R.M. Goldhoff and R.F. Gill, A Method for Predicting Creep Data for Commercial Alloys on a Correlation Between Creep Strength and Rupture Strength, *Trans. ASME J. Basic Eng.*, Vol 94 (No. 1), Series D, March 1972, p 1–6

54. E.L. Robinson, Effect of Temperature Variation on the Creep Strength of Steels, *Trans. ASME*, Vol 60, 1938, p 253–259
55. P.N. Randall, Cumulative Damage in Creep-Rupture Tests of a Carbon Steel, *Trans. ASME J. Basic Eng.*, Vol 84 (No. 2), Series D, June 1962, p 239–242
56. D.A. Woodford, Creep Damage and Remaining Life Concept, *Trans. ASME J. Eng. Mat. Technol.*, Vol 101 (No. 4), Dec 1979, p 311–316
57. M.M. Abo El Ata and I. Finnie, A Study of Creep Damage Rules, *Trans. ASME J. Basic Eng.*, Vol 94 (No. 3), Series D, Sept 1972, p 533–543
58. J.W. Freeman and H.R. Voorhees, “Notch Sensitivity of Aircraft Structural and Engine Alloys, Part II: Further Studies with A-286 Alloys,” Wright Air Development Center, Technical Report 57–58, ASTIA Document 207,850, Jan 1959
59. R.V. Hart, Concept of Area-Modified Stress for Life-Fraction Summation During Creep, *Met. Technol.*, Sept 1977, p 447–448
60. R.V. Hart, Assessment of Remaining Creep Life Using Accelerated Stress-Rupture Tests, *Met. Technol.*, Jan 1976, p 1–7
61. D.A. Woodford, “Accelerated Testing for High Temperature Materials Performance and Remaining Life Assessment,” EPRI 114045, 1999
62. W.L. Williams, “Parameter and Long-Life Creep Rupture Tests of Type 304 Steel,” ASTM Technical Report D8-9.6. (Presented at the 1968 Materials Engineering Exposition and Congress, Detroit, 14–17 Oct 1968)
63. V. Biss, D.L. Sponseller, and M. Semchyshen, Metallographic Examination of Type 304 Stainless Steel Creep Rupture Specimens, *ASTM J. Mater.*, Vol 7 (No. 1), March 1972, p 88–94
64. Independent tests by Materials Technology Corporation, Ann Arbor, MI
65. M. Prager, Development of the MPC Omega Method for Life Assessment in the Creep Range, *Pressure Vessel Technol. (Trans. ASME)*, Vol 117, May 1995, p 95–103

Assessment and Use of Creep-Rupture Properties

Howard R. Voorhees, Materials Technology Corporation Martin Prager, Materials Properties Council

Selected References

- F.R. Larson and J. Miller, Time-Temperature Relationship for Rupture and Creep Stress, *Trans. ASME*, Vol 74, 1952
- S.S. Manson and A. M Haferd, “A Linear Time-Temperature Relation for Extrapolation of Creep and Stress-Rupture Data,” NACA TN 1890, March 1953

Stress Relaxation Testing

D.A. Woodford, MPa, Inc.

Introduction

THE MAJORITY OF CREEP TESTING, as described in this Volume, uses a fixed load (or stress) at a constant temperature and measures the increase in strain as a function of time. However, materials may also creep under constraint with little or no dimensional change. This constraint then approximates a constant total strain, so a more appropriate test in such situations is one in which the material is deformed to a fixed strain, which is then held constant. Depending on the application, the corresponding initial stress may be below, at, or above the yield stress on loading. Whether or not there is permanent plastic strain on loading, there is an elastic strain that, in linear elastic materials, is proportional to the stress through the appropriate temperature sensitive modulus. If the temperature and stress are sufficiently high creep will occur, but since the total strain is held constant, this can only be achieved if the elastic strain decreases with a corresponding decrease in the stress. Creep at a fixed total strain, therefore, results in a time dependent stress relaxation.

A common practical example where stress relaxation is a major design issue is in high temperature bolting. After being initially torqued to ensure joint tightness the stress progressively relaxes at a rate that depends on the creep strength of the material. For major components such as steam turbine shell flanges, it is essential to avoid leakage by periodic bolt retightening. Alloys have to be used, which will ensure steam tight joints at least up to normal turbine overhaul periods that may now extend to 50,000 h (Ref 1).

In addition to many such mechanical fastener problems, stress relaxation is important in the wire of prestressed concrete (Ref 2), all types of springs (Ref 3), electrical contacts (Ref 4), soldered joints (Ref 5), and the relief of stress gradients induced by differential swelling in in-pile nuclear reactor tubes (Ref 6).

Stress relaxation is not limited to externally applied stresses. Residual stresses caused by metal working (Ref 7) or welding (Ref 8) may have to be reduced by stress relieving treatments prior to placing parts in service. Finally, parts such as gas turbine blades with internal cooling may develop severe stress and temperature gradients in service that will lead to stress redistribution under constraint, and temperature changes in cyclic operation may lead to residual stresses that relax at temperature. For repeated cycles the accumulated creep strain may eventually lead to cracking as a result of thermal fatigue (Ref 9).

From this discussion it is clear that stress relaxation and stress redistribution are major manifestations of creep deformation in practical applications. This is especially true for high-temperature cyclic operation. In many cases, however, suitable relaxation data does not exist, and analysis has to be made using existing constant load isothermal creep data. Thus there is much interest in predicting relaxation from creep data and vice versa. The problem is that most structural materials experience strong deformation path dependence. Thus, a material creeping under constant load and accumulating strain experiences a different deformation path from one subjected to a fixed total strain and decreasing stress. To convert one to the other requires a damage law such as time hardening or strain hardening or a mechanical equation of state, which incorporates one or more internal state variables (Ref 10). These approaches have varying degrees of success and will not be further considered.

This article concentrates on metallic materials as covered by ASTM E 328 (Ref 11), although stress relaxation is very important in plastics. For plastics a separate ASTM testing standard (Ref 12) is available that recognizes the viscoelastic behavior. This means that the creep strain may be mostly or fully recoverable upon removal of the load. Recent work on engineering ceramics suggests that these materials also show viscoelastic behavior (Ref 13). Composites of all types are expected to show internal stress redistribution between the components as well as complex macroscopic stress relaxation depending on the component phases.

References cited in this section

1. J. Bolton, Design Considerations for High Temperature Bolting, *Performance of Bolting Materials in High Temperature Plant Applications*, Institute of Materials, 1995

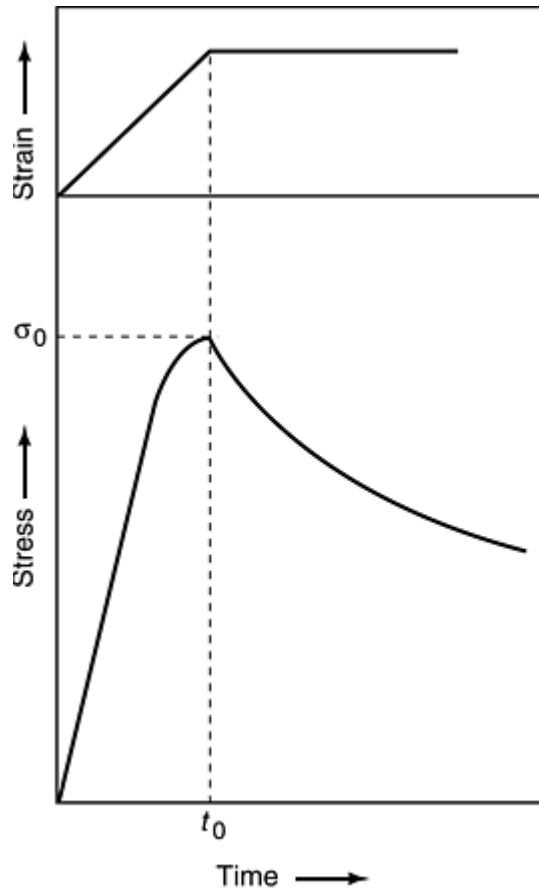
2. R.J. Glodowski and G.E. Hoff, Stress Relaxation of Steel Tendons Used in Prestressed Concrete under Conditions of Changing Applied Stress, STP 676, *Stress Relaxation Testing*, A. Fox, Ed., ASTM, 1978, p 42–58
3. S.U.V. Idermark and E.R. Johansson, Room Temperature Stress Relaxation of High Strength Strip and Wire Spring Steels-Procedure and Data, STP 676, *Stress Relaxation Testing*, A. Fox, Ed., ASTM, 1978, p 61–77
4. J. Miyake, T. Kimura, and T. Endo, Stress Relaxation of Cu-Ti Alloy C199, *Creep and Stress Relaxation in Miniature Structures and Components*, H.D. Merchant, Ed., TMS, 1996, p 57–74
5. H. Mavoori, J. Chin, S. Aaynman, B. Moran, L. Keer, and M. Fine, *Creep, Stress Relaxation and Plastic Deformation in Sn-Ag and Sn-Zn Eutectic Solders*, H.D. Merchant, Ed., TMS, 1996, p 173–190
6. J.M. Beeston and T.K. Burr, In-Reactor Stress Relaxation of Type 348 Stainless Steel In-Pile Tube, STP 676, *Stress Relaxation Testing*, A. Fox, Ed., ASTM, 1978, p 155–170
7. F.T. Geyling and P.L. Key, Stress Relaxation of Residual Metalworking Stresses, STP 676, *Stress Relaxation Testing*, A. Fox, Ed., ASTM, 1978, p 143–154
8. R.M. Chenko, Weld Residual Stress Measurements on Austenite Stainless Steel Pipes, *Weldments: Physical Metallurgy and Failure Phenomena*, Fifth Bolton Landing Conference, 1978, p 195–206
9. D.A. Woodford and D.F. Mowbray, Effect of Material Characteristics and Test Variables on Thermal Fatigue of Cast Superalloys, *Mater. Sci. Eng.*, Vol 16, 1974, p 5–43
10. G.A. Webster and R.A. Ainsworth, *High Temperature Component Life Assessment*, Chapman and Hall, 1994
11. Standard Methods for Stress Relaxation Tests for Materials and Structures, E 328-86, *Annual Book of ASTM Standards*, ASTM, 1991
12. Practice for Testing Stress Relaxation of Plastics, D 2991, *Annual Book of ASTM Standards*, ASTM
13. D.A. Woodford, Stress Relaxation, Creep Recovery, and Newtonian Viscous Flow in Silicon Nitride, *J. Am. Ceram. Soc.*, Vol 81 (No. 9), 1998, p 2327–2332

Stress Relaxation Testing

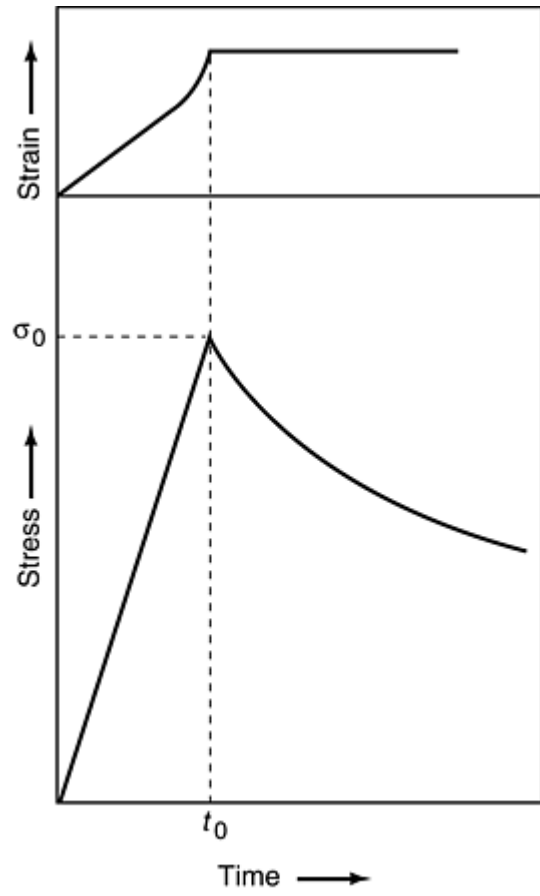
D.A. Woodford, MPa, Inc.

Testing Considerations

Figures 1 and 2 illustrate load characteristics and data representation for stress relaxation testing for the most convenient and common uniaxial tensile test (Ref 2). The constraint is obtained by the application of the external load at either a constant strain rate or constant load rate. Figure 3 shows the response in each case for an initial stress, σ_0 , exceeding the proportional limit. If the stress and temperature are sufficiently high, the extent of nonelastic strain on loading will depend on the loading rate, which will in turn affect the initial relaxation rate. The loading rate should therefore be reasonably high. The stress relaxation test starts at $t = t_0$ when the desired level of constraint is obtained. The relaxation can be plotted in the form of remaining stress (Fig. 2a) or relaxed stress (Fig. 2b), which is the initial stress minus the remaining stress.

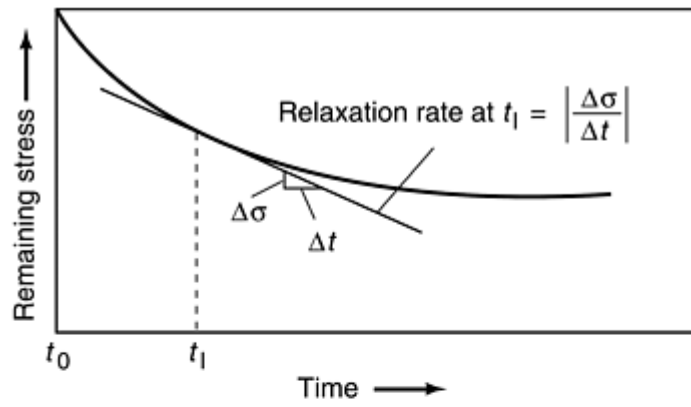


(a)

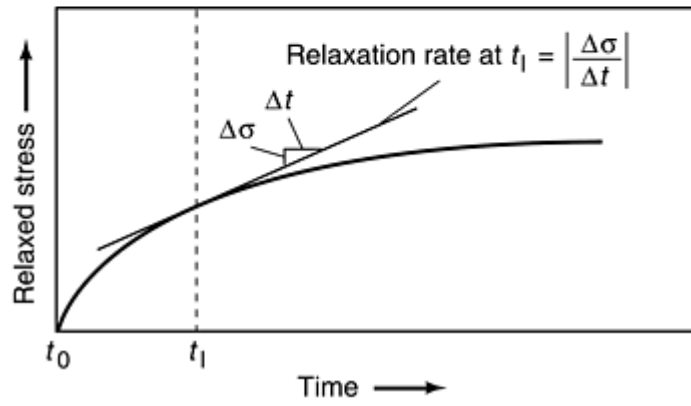


(b)

Fig. 1 Characteristic behavior during loading period in a stress relaxation test. (a) Constant strain rate. (b) Constant load rate. Source: Ref 11



(a)



(b)

Fig. 2 Typical stress relaxation curves plotted for (a) remaining stress and (b) relaxed stress (the initial stress minus the remaining stress). Source: Ref 11

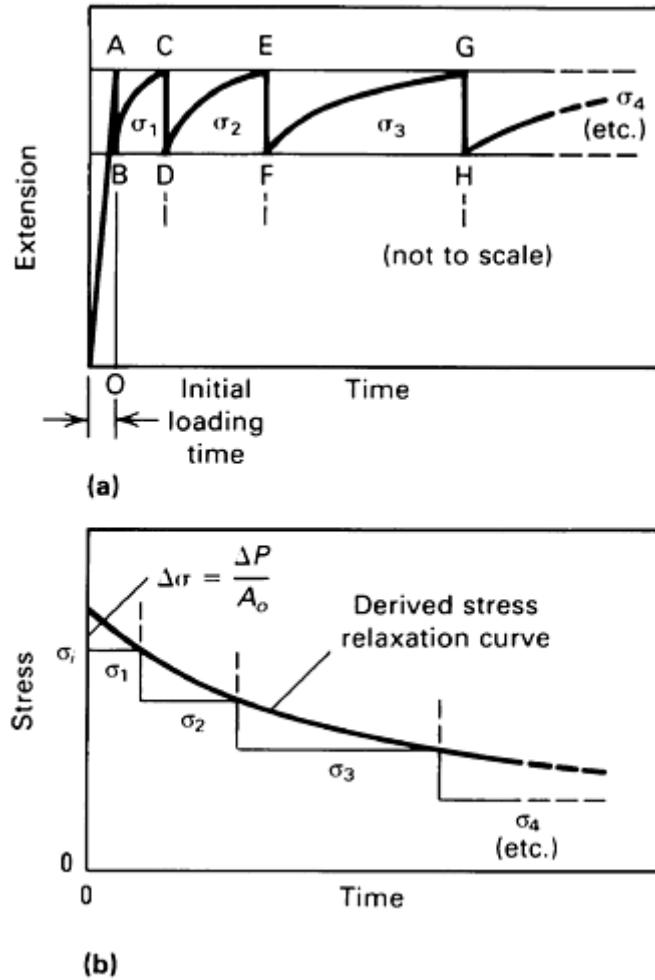


Fig. 3 Derivation of stress-relaxation curve for step-down creep test. (a) Constant extension approximated by a step-down creep test. (b) Stress-time relation

The components of strain can be considered to be elastic strain, ϵ_e , time-independent plastic strain (e.g., on loading), ϵ_p , and time-dependent creep strain, ϵ_c . The creep strain can further be designated as nonrecoverable and recoverable (or anelastic strain). For example, unloading after creep in plastics can lead to contraction at zero stress to the extent that the creep strain is fully recovered. In metals this recoverable strain is usually only a small fraction of the total creep strain (less than 10%). In ceramics the situation is intermediate with typically about 40 to 50% of the creep strain recovering (Ref 13). The total strain after loading is given as:

$$\epsilon_t = \epsilon_e + \epsilon_p + \epsilon_c = \text{constant} \quad (\text{Eq 1})$$

There is no need in Eq 2 to separate the creep strain into its two components of recoverable and nonrecoverable time-dependent strain. However, for ceramics and certainly for plastics, this does become a design consideration if deformation path dependence is important. Differentiating and remembering that the plastic strain on loading, by definition, is not time dependent, and that the total strain is constant:

$$0 = \dot{\epsilon}_e + 0 + \dot{\epsilon}_c \quad (\text{Eq 2})$$

Rearranging Eq 2:

$$\dot{\epsilon}_c = \frac{-\dot{\sigma}}{E} \quad (\text{Eq 3})$$

where E is the elastic modulus.

Equation 3 shows how the creep rate is equal in magnitude to the elastic strain rate and can be calculated at any time during relaxation from the stress rate divided by the elastic modulus. Thus the test is a self-programmed variable stress creep test and should be independent of the test machine characteristics.

Until recently the stress relaxation test has been used principally to measure and predict the relaxation of stress as a function of time and temperature. However, it is now recognized as a unique creep test, which in a short

time, can generate creep rate data as a function of stress covering five or more orders of magnitude in creep rate. This new application of the test is discussed in a subsequent section.

References cited in this section

2. R.J. Glodowski and G.E. Hoff, Stress Relaxation of Steel Tendons Used in Prestressed Concrete under Conditions of Changing Applied Stress, STP 676, *Stress Relaxation Testing*, A. Fox, Ed., ASTM, 1978, p 42–58
11. Standard Methods for Stress Relaxation Tests for Materials and Structures, E 328-86, *Annual Book of ASTM Standards*, ASTM, 1991
13. D.A. Woodford, Stress Relaxation, Creep Recovery, and Newtonian Viscous Flow in Silicon Nitride, *J. Am. Ceram. Soc.*, Vol 81 (No. 9), 1998, p 2327–2332

Stress Relaxation Testing

D.A. Woodford, MPA, Inc.

Stress Relaxation in Tension

There are now two types of stress relaxation tests performed in tension. They are distinguished by the test objectives and to a lesser extent by the type of equipment used and the stress levels covered. The long-term tests are designed to give specific data on the amount of stress relaxation that results in a particular time at a specific temperature. It assumes that predictions from traditional creep tests would be insufficiently accurate. The bolting problem is the most commonly cited example. In contrast, the accelerated tests are designed to give comprehensive information on the creep strength of the material, which can then be used in many ways. It provides an alternative to the traditional creep test as a basis for materials selection, design, and life prediction. Both types of test are described in the following.

Long-Term Tests

Because the objective in these tests is to measure quantitatively the amount of relaxation in very long times from a given stress, which is often below the yield stress, great precision and stability is required of the test equipment. Moreover, because the test will often be run for years to relate to actual service times, it is normal to use inexpensive load frames. Lever arm type creep machines with a means periodically to adjust the weight to maintain constant specimen constraint have been commonly used (Ref 14). The practicalities of testing have been discussed in detail recently (Ref 15) and emphasize the need for accurate control of strain and temperature and measurement of stress. For example, ASTM E 328-86 (Ref 11) requires strain control within $\pm 0.0025\%$ and temperature control that does not exceed $\pm 3^\circ\text{C}$ or $\pm 0.5\%$, whichever is greater. This must be true for the test duration, which can be several years. Moreover, the relaxation can be quite sensitive to the setup and loading procedure, including the loading rate, which can have a very significant effect on subsequent relaxation (Ref 15).

The use of a motor driven lever arm system for load adjustments offers a number of advantages: the force (torque) required on the motor drive is reduced by the lever arm ratio, which leads to less inertia, increased sensitivity, smoother action, and finer control. However, such systems generally are not designed for continuous control. Typically, the strain is held between limits, and one common procedure is shown schematically in Fig. 3 is taken from ASTM E 328-86. In this step-down test, when the upper limit of strain is reached, a small reduction in stress is made that leads to an instantaneous elastic contraction. The specimen then creeps under the reduced stress until the limit is reached when the stress is again reduced by the same

amount, and so on. An alternative approach is to allow a small amount of strain to occur beyond the set strain before reducing the load. Depending on the magnitude of the stress decrements the two results will differ slightly because the average strains will differ and the deformation paths will differ. There are also options as far as the choice of the appropriate stress to use in plotting the data from each cycle (i.e., the maximum, minimum, or average). Clearly the smaller imposed stress reduction is preferred in both cases.

Figure 4 shows a typical stress-relaxation system equipped for step-down tension testing. This has a three-zone furnace, a temperature-compensated extensometer system, an electronic control module, and a data recorder. It is constructed with a precision balanced lever arm supported on knife edges. The output from the load cell is used directly to construct a stress versus time relaxation curve.

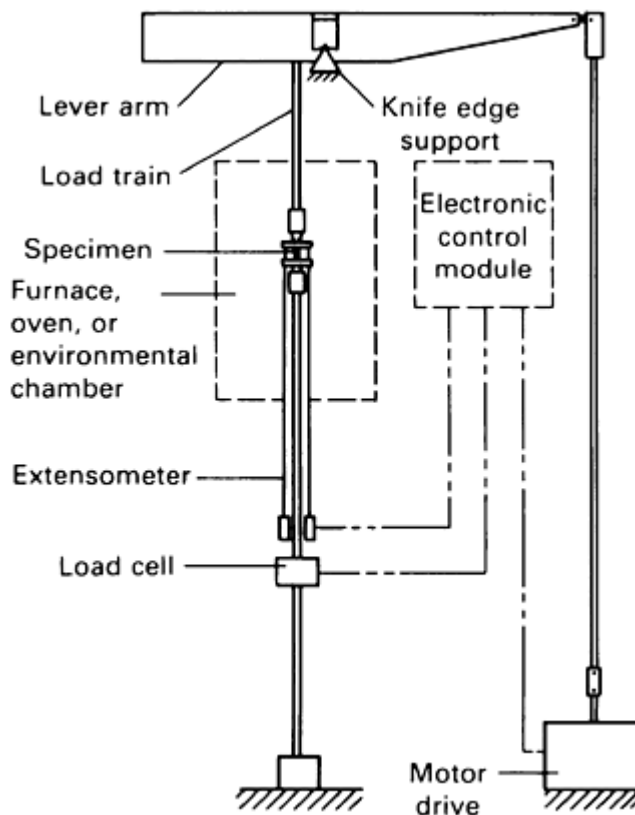


Fig. 4 Schematic of stress-relaxation test system equipped for step-down tension testing

A useful measure of the precision expected for relaxation of a 1%Cr-Mo-V bolting steel at 500 °C is shown in Fig. 5. Results from nine British and six German laboratories are summarized on rolled, oil quenched, and tempered bars deformed to 0.2% strain (Ref 16). Both manual and mechanical load reduction techniques were used to maintain the strain nearly constant. The following mean values were found: initial stress, 319 MPa, residual stress at 2000 h, 107 MPa, and ratio of residual stress at 2000 h to initial stress, 0.34. Each of these mean values had a scatter of about $\pm 15\%$.

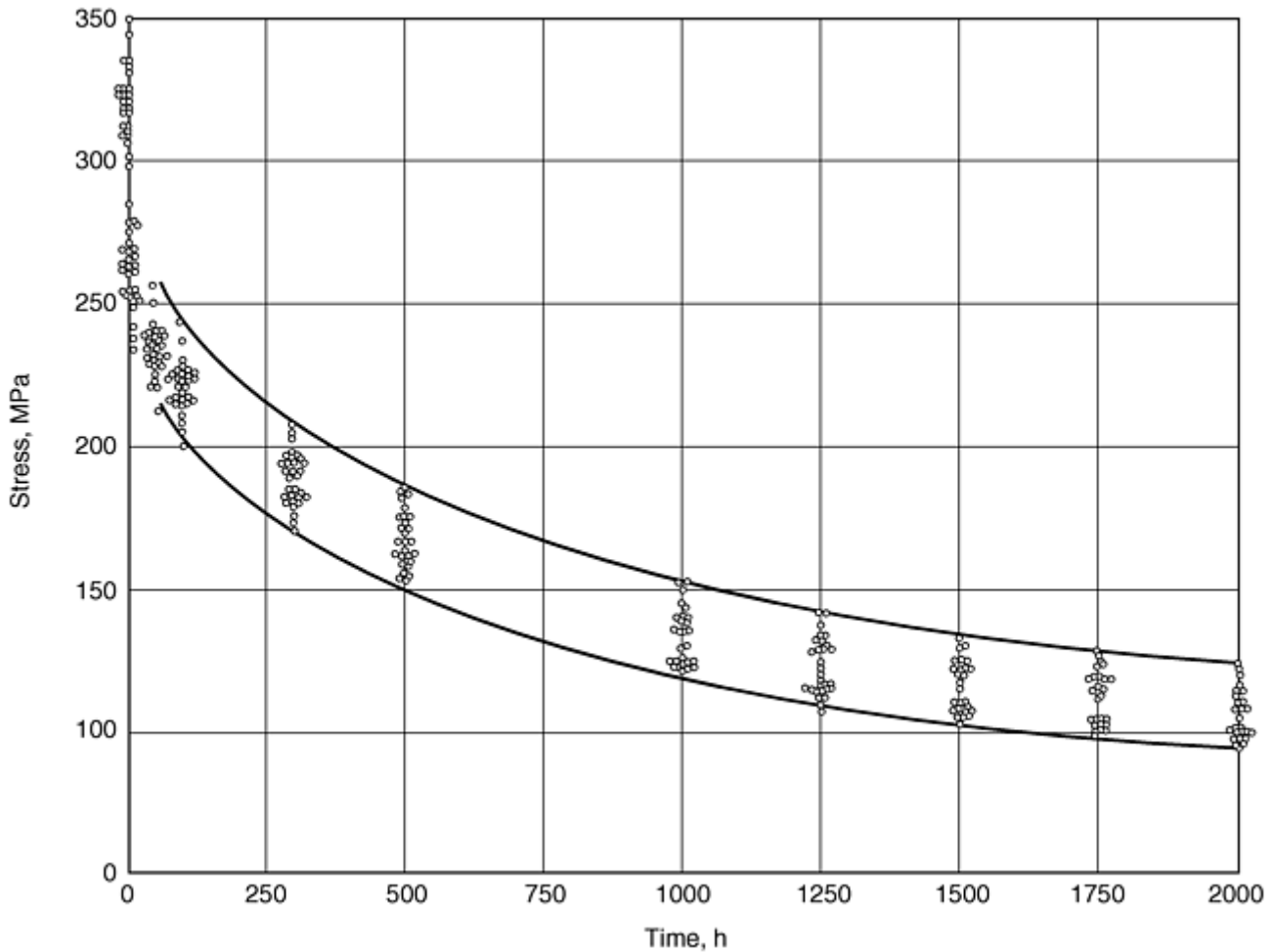


Fig. 5 Repeatability among fifteen laboratories for relaxation of Cr-Mo-V bolting steel from 0.2% strain at 500 °C

Accelerated Testing

As previously noted, the stress relaxation test is a self-programmed variable stress creep test that can reach extremely low creep rates in quite short times. Hart (Ref 17) was the first to recognize and exploit the comprehensive creep rate data that could be generated from the load relaxation test. Hart's objective was to express a plastic equation of state in terms of the stress versus creep rate relationship, and much of his work was confined to pure aluminum at room temperature. Hart used a screw-driven tensile machine and calculated the nonelastic extension rate of the specimen from the load record without the use of an extensometer. When the crosshead was stopped this nonelastic extension rate (\dot{L}) is given as:

$$\dot{L} = -C\dot{P} \quad (\text{Eq 4})$$

where \dot{P} is the rate of change of load and C is the elastic compliance of the entire load train including the load cell and specimen. To achieve the necessary accuracy with this method, a digital data acquisition and analysis technique was developed. It was necessary not only to control the specimen temperature accurately but also the ambient temperature for the machine to maintain constant system compliance. Considerable progress was made in developing a plastic equation of state for aluminum and identifying scaling laws for this and other pure metals and some alloys.

One of the early attempts to use this technique as a basis for creep strength evaluation in engineering materials was reported on Cr-Mo-V steel at temperatures up to 538 °C (Ref 18). Because the system compliance was not constant during the test at this temperature, an extensometer was used. Although this was a fixed crosshead test, the creep strain was able to be calculated directly. At any time during the test, it was the sum of the increase in overall strain, which was measured directly, plus the decrease in elastic strain on the specimen, which was calculated from the load record and specimen modulus.

In tests lasting two days, creep rates covering up to six decades in creep rate were obtained using the previously described method (Ref 18). However, in subsequent tests on all classes of materials, it was decided to use a fixed strain on the specimen rather than depending on the compliance of the machine. With suitable computer control for continuous strain adjustment, the tests could be conducted on any type of universal test machine (Ref 19). Because the specimen total strain was held constant, this was equivalent to using an infinitely stiff system so that, in principle, test results should be independent of the test equipment. This approach has been used on a wide range of steels (Ref 18, 20), superalloys (Ref 21), ceramics (Ref 13), and polymers (Ref 22). An example of this methodology is illustrated in Fig. 6 7 8 for Cr-Mo-V steel (Ref 20). Figure 6 gives the stress versus natural logarithm (ln) time curves at 500, 550, and 600 °C. The strain was held constant at 0.4%, which is just beyond the elastic limit ($\approx 0.3\%$) to minimize transient effects. These curves were fitted with polynomial expressions, which could then be differentiated to give stress versus creep rate curves directly using the elastic modulus as described previously (see Fig. 7). As with several other studies, it was found that the data could be superimposed by horizontal translation with good precision. This means that the curves can be parameterized using an exponential temperature function. This function was optimized and used to construct the creep rate/temperature parameter plot of Fig. 8. Also included in the figure are three minimum creep rate data points at the same three temperatures on the same heat. These were from tests lasting several thousand hours. The agreement is quite good despite the different deformation paths, especially at the highest temperature (or longest time) of 600 °C. The parameter plot can also be used as a basis for creep design. As an example, possible design points at different temperatures are identified on the figure at creep rates of $3 \times 10^{-11} \text{ s}^{-1}$. This is a rate corresponding to 1% in 100,000 h. The total test time for all the stress relaxation data shown in Fig. 6 was three days.

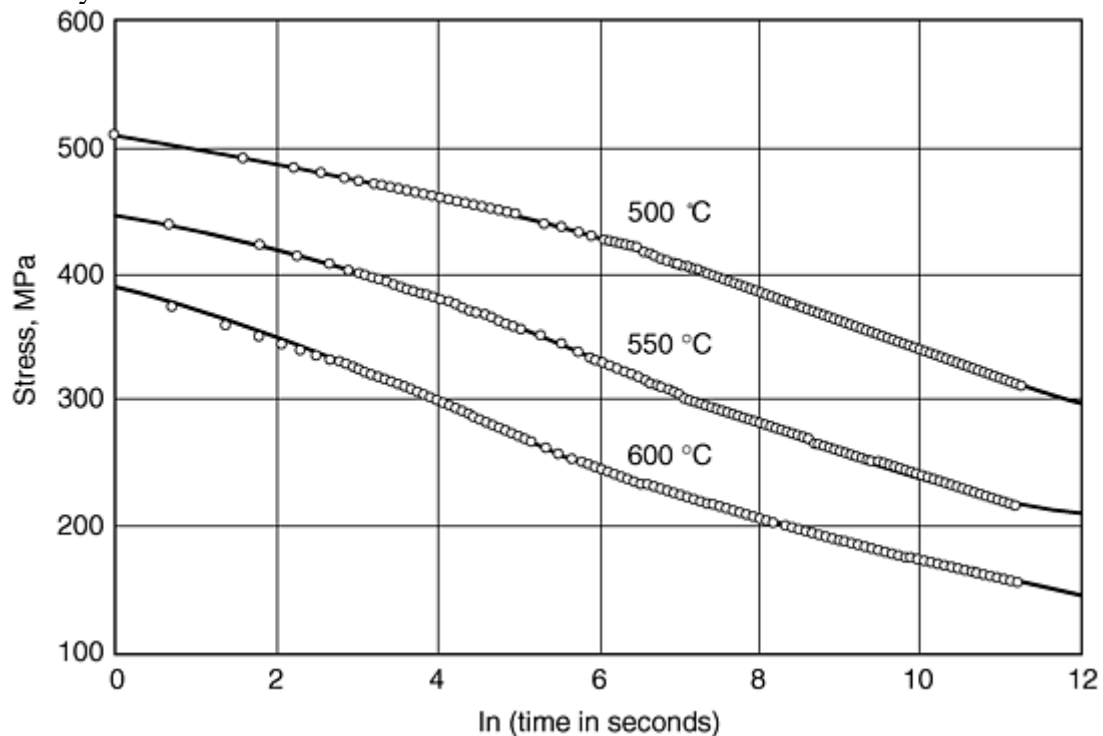


Fig. 6 Stress versus natural logarithm for Cr-Mo-V rotor steel at three temperatures from 0.4% strain

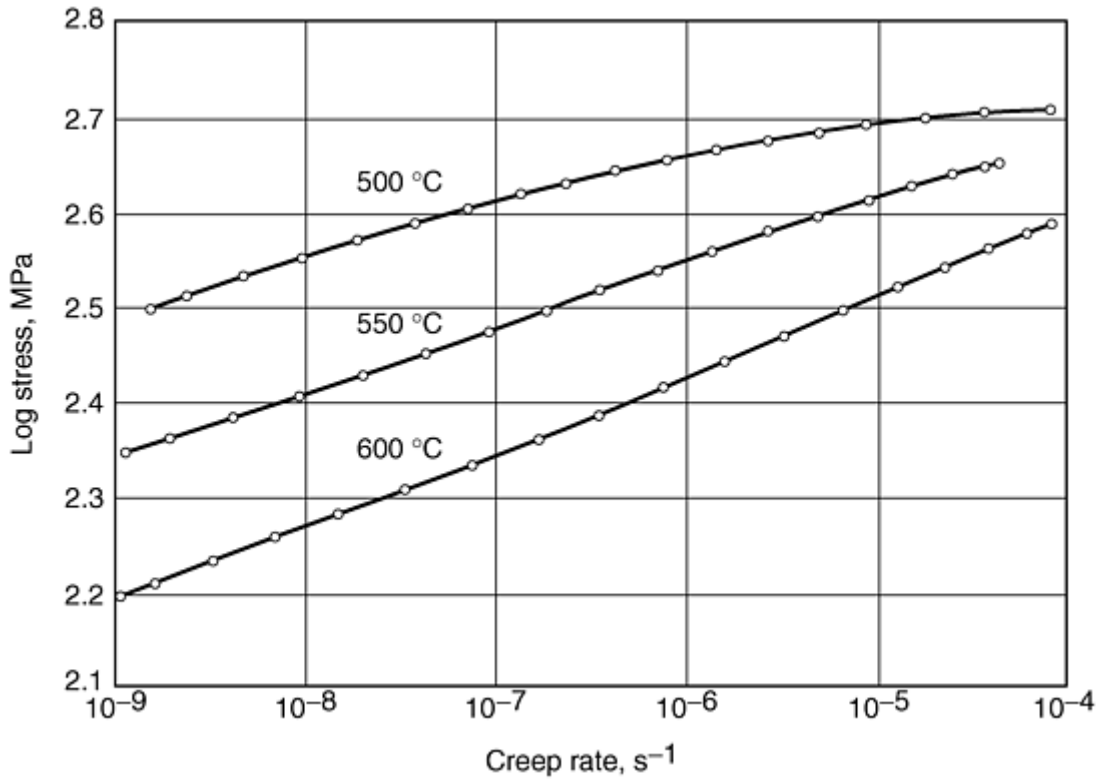


Fig. 7 Calculated stress versus creep rate behavior for Cr-Mo-V steel at three temperatures

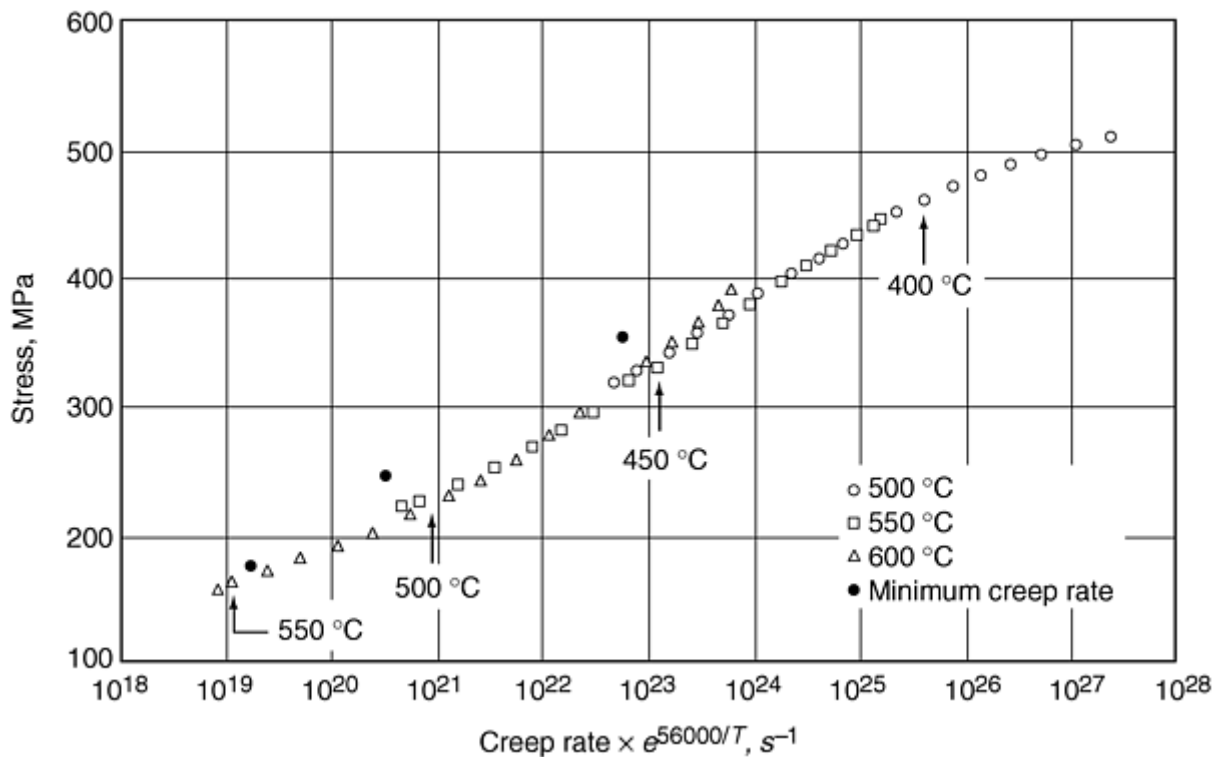


Fig. 8 Parametric plot for Cr-Mo-V steel of stress versus temperature compensated creep rate (with absolute temperature, T , in K) compared with long time minimum creep rate (MCR) data. Possible design points are indicated at various temperatures.

References cited in this section

11. Standard Methods for Stress Relaxation Tests for Materials and Structures, E 328-86, *Annual Book of ASTM Standards*, ASTM, 1991

13. D.A. Woodford, Stress Relaxation, Creep Recovery, and Newtonian Viscous Flow in Silicon Nitride, *J. Am. Ceram. Soc.*, Vol 81 (No. 9), 1998, p 2327–2332
14. M.S. Loveday and B. King, Uniaxial Testing Apparatus and Testpieces, *High Temperature Mechanical Properties of Materials*, M.S. Loveday, M.F. Day, and B.F. Dyson, Ed., NPL, 1982, p 128–157
15. A. Strang, Review of Current International Stress Relaxation Testing Standards, *Performance of Bolting Materials in High Temperature Plant Applications*, Institute of Materials, 1995, p 97–114
16. J. Hacon and A Krause, Relaxation Properties of a 1CrMoV Bolting Steel under Uniaxial Tensile Load, Paper 51, *Proceedings Conference Properties of Creep Resistant Steels*, VDEL, Dusseldorf, 1972
17. E. Hart, Load Relaxation Testing and Material Constitutive Relations, *Stress Relaxation Testing*, STP 676, A. Fox, Ed., ASTM, 1978, p 5–20
18. D.A. Woodford, Measurement of the Mechanical State of a Low Alloy Steel at Elevated Temperature, *Metall. Trans. A*, Vol 6, 1975, p 1693–1697
19. D.A. Woodford, Test Methods for Accelerated Development, Design, and Life Assessment of High Temperature Materials, *Mater. Des.*, Vol 14 (No. 4), 1993, p 231–242
20. D.A. Woodford and K. Iijima, Creep Strength Evaluation, Design, and Life Management of Cr-Mo-V Rotor Steel Using Stress Relaxation Testing, *Advances in Turbine Materials, Design, and Manufacturing*, Fourth International Charles Parsons Turbine Conference, A. Strang, W.M. Banks, R.D. Conroy, and M.J. Goulette, Ed., Institute of Materials, 1997, p 613–624
21. D.A. Woodford, Accelerated High Temperature Performance Evaluation of Superalloys for Process Optimization and Remaining Life Assessment, *ASME IGTI Turbo Expo Conference* (Indianapolis, IN), ASME, 1999
22. G.G. Gryzywinski and D.A. Woodford, Creep Analysis of Thermoplastics Using Stress Relaxation Data, *J. Polym. Eng. Sci.*, Vol 35 (No. 24), 1995, p 1931–1937

Stress Relaxation Testing

D.A. Woodford, MPa, Inc.

Other Stress States

For the operation of many devices and the relief of residual stresses, the stress state can be complex so that relaxation tests other than simple tension are more appropriate. The ASTM E 328 testing standard (Ref 11) covers some of these.

Compression Testing

Figure 9 shows a simple apparatus for conducting long-term compression stress relaxation tests. In this equipment, the specimen is subjected to an increasing compressive load using a hydraulic ram until the specified strain is attained. The nut on the load strut is adjusted to maintain a constant compressive strain on the test specimen. The force required to maintain a constant compressive strain drops as a function of time and temperature, and it is recorded by a pressure transducer, shown schematically as a pressure gage.

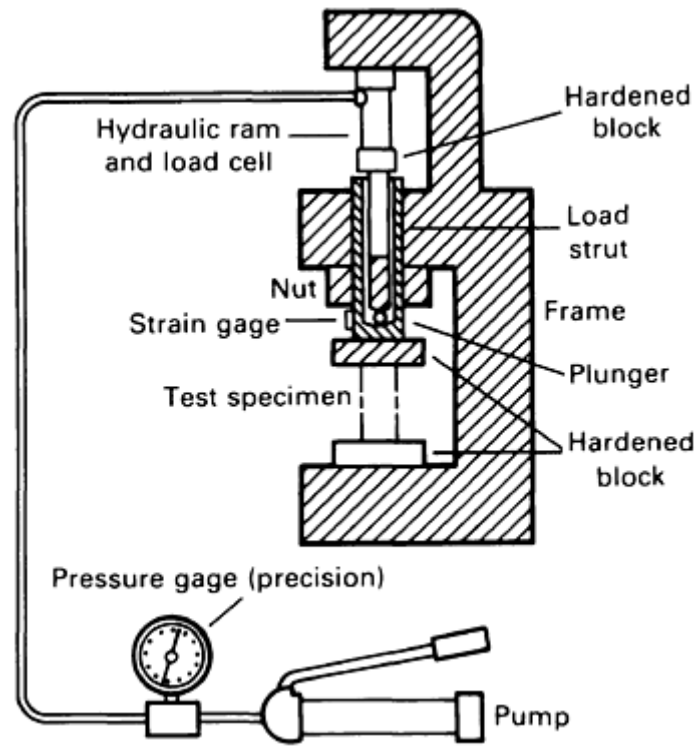


Fig. 9 Apparatus for conducting stress-relaxation compression test

As with tensile testing, the remaining stress can be measured continuously, periodically using step unloading, or by elastic springback at the end of the test period. In the latter method, the elastic strain calculated from the difference between the set total strain and the remaining plastic strain is proportional through the elastic modulus to the relaxed stress. If it is demonstrable that periodic reloading has no effect on the stress relaxation curve, the same specimen can be reloaded to the same compressed gage length to establish the stress relaxation curve as a function of time. This method is not accurate if significant anelastic recovery occurs.

In compression testing, the possibility of buckling and barreling must be minimized, and special consideration, thus, must be given to specimen alignment, precision of the bearing surfaces, and geometry of the test specimen. It is also possible to use a compression cage in a universal test machine and control directly on an extensometer positioned on the test specimen. This method would be more suitable for the accelerated testing method.

Bend Testing

Stress relaxation in bending is very common in flat springs, electronic connectors, and relay springs, and a number of extensive studies have been reported (Ref 4, 23, 24). In these methods, the outer fiber strain during bending is held constant.

The change in bending moment during relaxation is determined either by monitoring the applied force continuously using an apparatus such as that shown in Fig. 10 or by intermittently lifting the specimen just off its reaction point and measuring the force (or moment) required to accomplish this (see Fig. 11). Alternatively, the loss in moment can be determined either by using a mandrel (Fig. 12) or a tapered constant curvature specimen (Fig. 13) and measuring elastic springback upon unloading. A compressive study (Ref 25) at three different laboratories found that agreement was $\pm 5\%$ stress remaining (Fig. 14) for the following three methods:

- Continuously reading force indicator
- Force required to lift the specimen free of one or more constraints during the test period
- Elastic springback upon unloading at the end of the test period

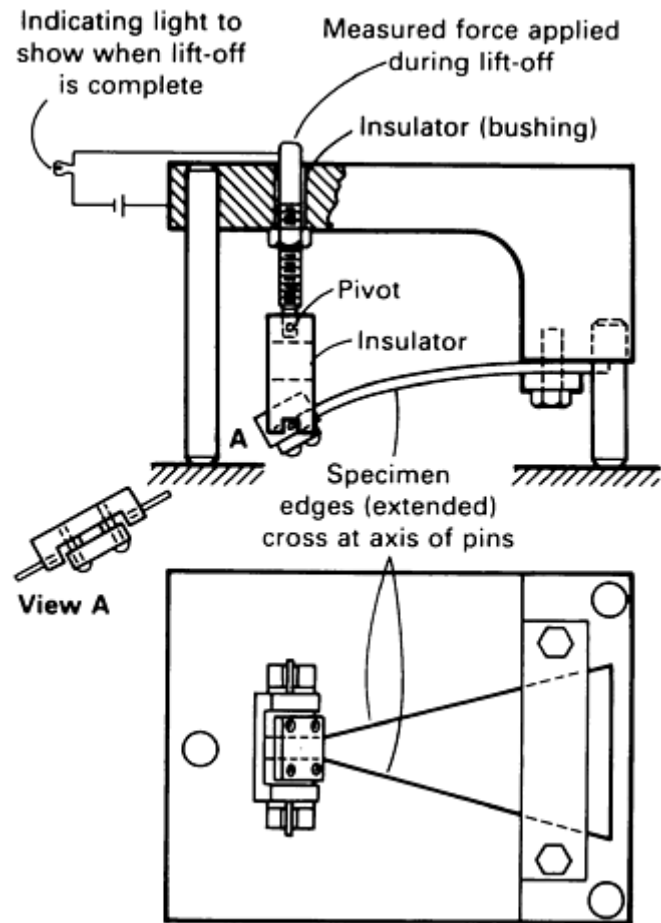


Fig. 11 Stress-relaxation bend test specimen in static fixture for lift-off measurements

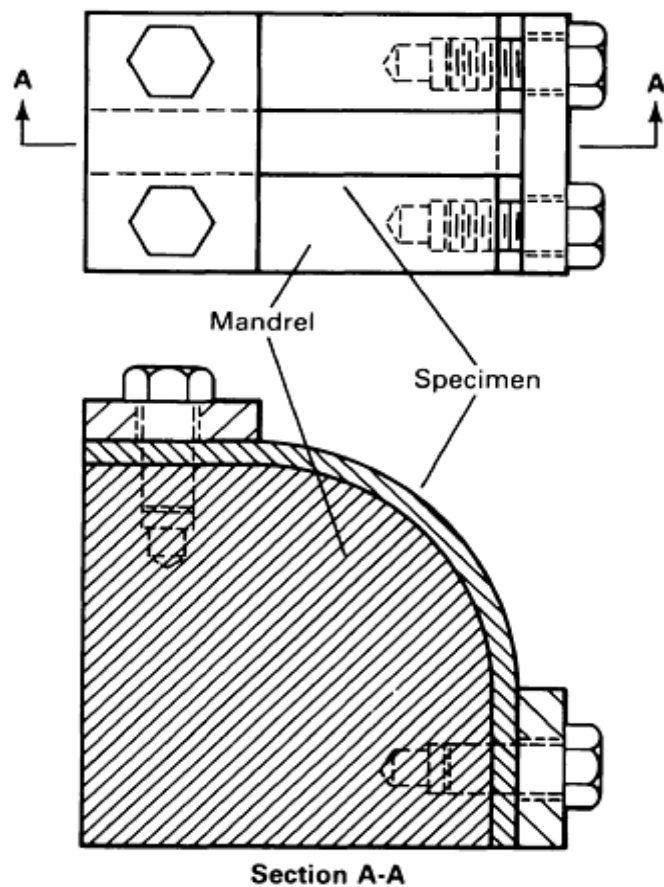


Fig. 12 Mandrel type stress relaxation bending test

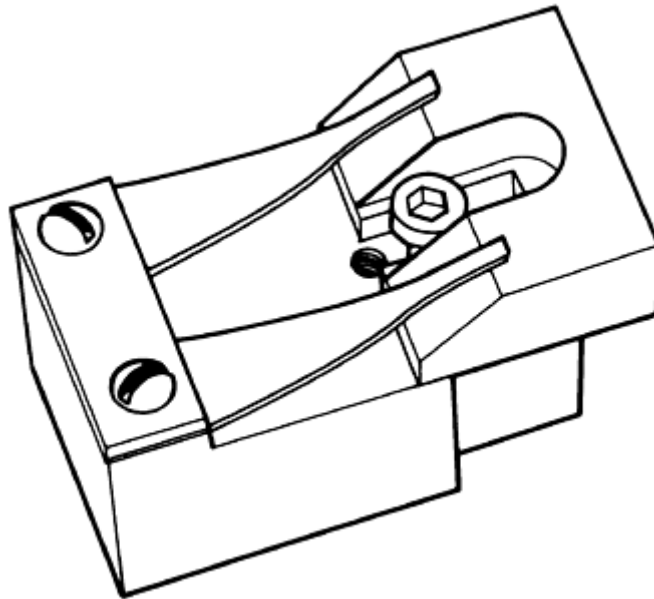


Fig. 13 Tapered, constant curvature cantilever beam strip specimen bending test

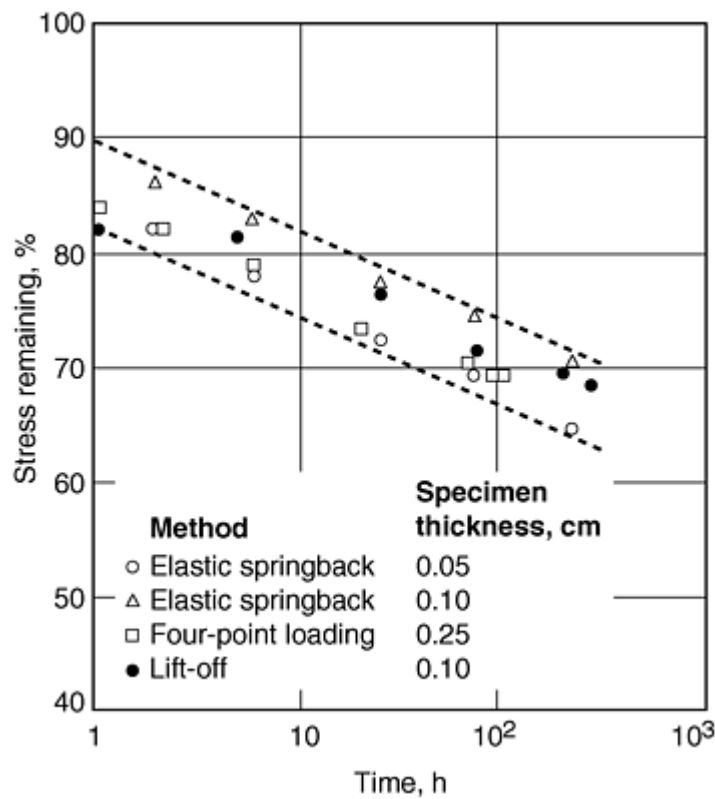


Fig. 14 Percent stress remaining versus time for 70-30 brass (C26000) for test using three methods at three laboratories. Initial stress equals 80% of 0.2% yield strength.

Torsion Testing

In torsion testing, a cylindrical or tubular specimen is subjected to a constant torsional strain. The change in restraining torque associated with the stress relaxation can be determined by continuous monitoring with a torque transducer or by periodically applying a slight torque to transfer the remaining torque from the end grips to the transducer. Alternatively, the twist springback on unloading can be used to determine how much remanent twist angle remains, and consequently, how much torque would be required to twist the specimen back to its original angle of twist prior to relaxation.

Because of the increased complexity of testing and analysis of torsion stress relaxation, there is interest in predicting torsion stress relaxation based on tensile data. Using combined tension and torsion relaxation tests, it has been shown that in thin-walled copper tubes tested at 250 °C, the results of pure tensile stress relaxation tests can be used to predict complex stress relaxation behavior on the basis of octahedral shear stress equivalence (Ref 26).

Test on Springs

Designers need to be able to estimate how much force remains in a spring after a given service exposure. The experimental methods are similar to those for the other stress states and include:

- Monitoring the decrease in spring force at a constant temperature after deflection to a given displacement
- Determining the remaining spring load by transferring the load periodically from the deflecting member to a load measuring device
- Using the elastic springback on unloading to calculate the spring force remaining immediately prior to unloading using the spring constant

Figures 15 and 16 (Ref 27) illustrate the latter two methods.

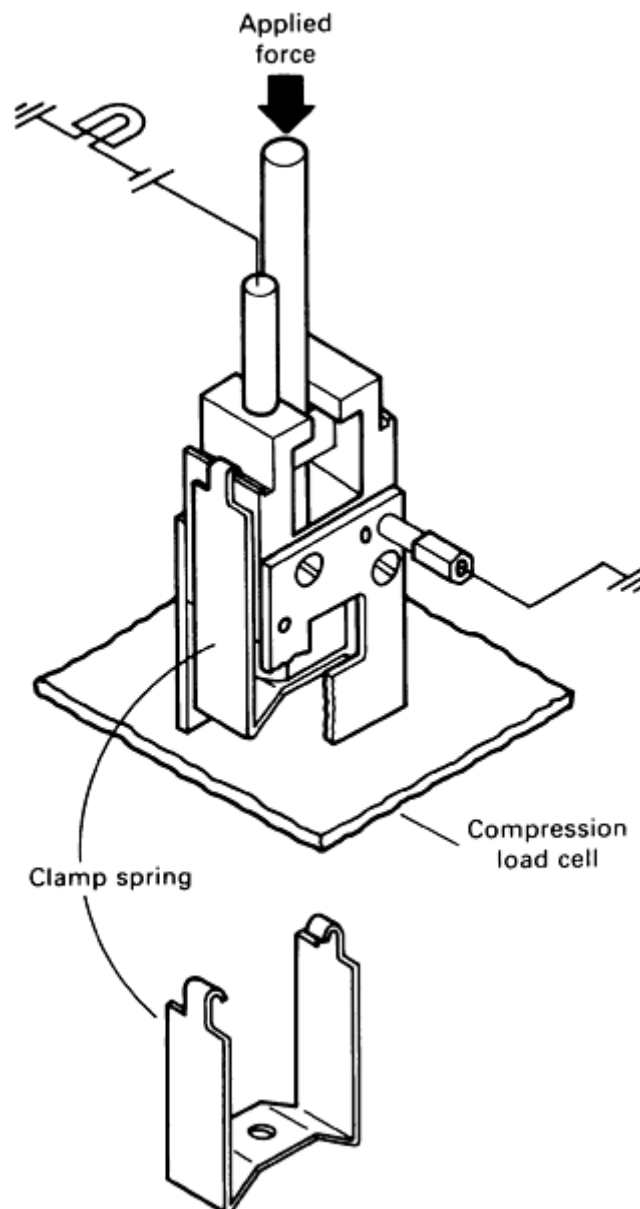


Fig. 15 Setup for stress relaxation testing of a clamp spring

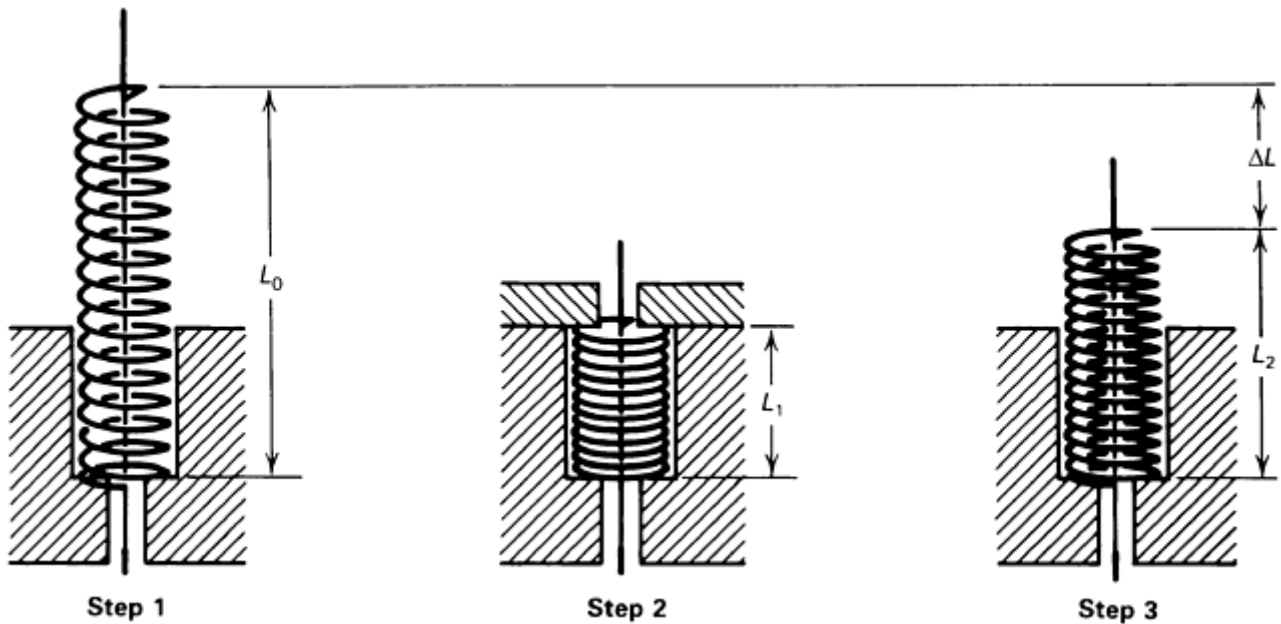


Fig. 16 Application of load during a stress-relaxation test of a helical compression spring at room temperature. Original free length, L_0 , compressed length, L_1 ; free length upon release from load at temperature, L_2 ; permanent set, ΔL

Figure 15 shows the apparatus used to determine the force remaining as a function of time and temperature in a complex relay pileup clamp spring. To measure the force of the spring on the pileup, the spring is clamped into a rigid steel fixture that is on a compression load cell. Force is applied using a universal testing machine by means of a plunger, which is depressed and then twisted to lock in place. Electrical contact is made between the plunger and a spring-loaded contact. The force required to break the electrical contact is measured as a function of time to give the relaxation curve.

In Fig. 16, a helical compression spring is deflected and held at the test temperature. The force remaining after time, t , is determined by measuring the permanent set, ΔL , on unloading by the relationship:

$$\frac{\Delta P}{P_0} = \frac{\Delta L}{L_0}$$

where P_0 is the initial load, ΔP is the change in load, L_0 is the initial length, and L is the permanent set.

References cited in this section

4. J. Miyake, T. Kimura, and T. Endo, Stress Relaxation of Cu-Ti Alloy C199, *Creep and Stress Relaxation in Miniature Structures and Components*, H.D. Merchant, Ed., TMS, 1996, p 57–74
11. Standard Methods for Stress Relaxation Tests for Materials and Structures, E 328-86, *Annual Book of ASTM Standards*, ASTM, 1991
23. A. Fox, Ed., Stress Relaxation in Bending of AISI 301 Type Corrosion Resistant Steel Strip, STP 676, *Stress Relaxation Testing*, ASTM, 1978, p 78–88
24. E.W. Filer and C.R. Scorey, Stress Relaxation in Beryllium Copper Strip, STP 676, *Stress Relaxation Testing*, A. Fox, Ed., ASTM, 1978, p 89–111
25. P. Parikh, Report on Bending Stress Relaxation Round Robin, STP 676, *Stress Relaxation Testing*, A. Fox, Ed., ASTM, 1978, p 112–125

26. J. Henderson and J.D. Sneddon, Complex Stress Creep Relaxation on Commercially Pure Copper at 250 °C, *Advances in Creep Design*, A.I. Smith and A.M. Nicolson, Ed., John Wiley & Sons, Inc., 1971, p 163–180
27. A. Fox, Effect of Temperature on Stress Relaxation of Several Metallic Materials, *Residual Stress and Stress Relaxation*, Proceedings 28th Sagamore Army Materials Research Conference, E. Kula and V. Weiss, Ed., Plenum Press, 1982, p 181–203

Stress Relaxation Testing

D.A. Woodford, MPa, Inc.

Acknowledgments

In preparing this chapter, extensive use was made of the article by A. Fox, under the same title, which appeared in the previous edition of Volume 8 of this Handbook. ASTM E 328-86 (1991) was also extremely useful.

Stress Relaxation Testing

D.A. Woodford, MPa, Inc.

References

1. J. Bolton, Design Considerations for High Temperature Bolting, *Performance of Bolting Materials in High Temperature Plant Applications*, Institute of Materials, 1995
2. R.J. Glodowski and G.E. Hoff, Stress Relaxation of Steel Tendons Used in Prestressed Concrete under Conditions of Changing Applied Stress, STP 676, *Stress Relaxation Testing*, A. Fox, Ed., ASTM, 1978, p 42–58
3. S.U.V. Idermark and E.R. Johansson, Room Temperature Stress Relaxation of High Strength Strip and Wire Spring Steels-Procedure and Data, STP 676, *Stress Relaxation Testing*, A. Fox, Ed., ASTM, 1978, p 61–77
4. J. Miyake, T. Kimura, and T. Endo, Stress Relaxation of Cu-Ti Alloy C199, *Creep and Stress Relaxation in Miniature Structures and Components*, H.D. Merchant, Ed., TMS, 1996, p 57–74
5. H. Mavoori, J. Chin, S. Aaynman, B. Moran, L. Keer, and M. Fine, *Creep, Stress Relaxation and Plastic Deformation in Sn-Ag and Sn-Zn Eutectic Solders*, H.D. Merchant, Ed., TMS, 1996, p 173–190
6. J.M. Beeston and T.K. Burr, In-Reactor Stress Relaxation of Type 348 Stainless Steel In-Pile Tube, STP 676, *Stress Relaxation Testing*, A. Fox, Ed., ASTM, 1978, p 155–170
7. F.T. Geyling and P.L. Key, Stress Relaxation of Residual Metalworking Stresses, STP 676, *Stress Relaxation Testing*, A. Fox, Ed., ASTM, 1978, p 143–154

8. R.M. Chenko, Weld Residual Stress Measurements on Austenite Stainless Steel Pipes, *Weldments: Physical Metallurgy and Failure Phenomena*, Fifth Bolton Landing Conference, 1978, p 195–206
9. D.A. Woodford and D.F. Mowbray, Effect of Material Characteristics and Test Variables on Thermal Fatigue of Cast Superalloys, *Mater. Sci. Eng.*, Vol 16, 1974, p 5–43
10. G.A. Webster and R.A. Ainsworth, *High Temperature Component Life Assessment*, Chapman and Hall, 1994
11. Standard Methods for Stress Relaxation Tests for Materials and Structures, E 328-86, *Annual Book of ASTM Standards*, ASTM, 1991
12. Practice for Testing Stress Relaxation of Plastics, D 2991, *Annual Book of ASTM Standards*, ASTM
13. D.A. Woodford, Stress Relaxation, Creep Recovery, and Newtonian Viscous Flow in Silicon Nitride, *J. Am. Ceram. Soc.*, Vol 81 (No. 9), 1998, p 2327–2332
14. M.S. Loveday and B. King, Uniaxial Testing Apparatus and Testpieces, *High Temperature Mechanical Properties of Materials*, M.S. Loveday, M.F. Day, and B.F. Dyson, Ed., NPL, 1982, p 128–157
15. A. Strang, Review of Current International Stress Relaxation Testing Standards, *Performance of Bolting Materials in High Temperature Plant Applications*, Institute of Materials, 1995, p 97–114
16. J. Hacon and A Krause, Relaxation Properties of a 1CrMoV Bolting Steel under Uniaxial Tensile Load, Paper 51, *Proceedings Conference Properties of Creep Resistant Steels*, VDEL, Dusseldorf, 1972
17. E. Hart, Load Relaxation Testing and Material Constitutive Relations, *Stress Relaxation Testing*, STP 676, A. Fox, Ed., ASTM, 1978, p 5–20
18. D.A. Woodford, Measurement of the Mechanical State of a Low Alloy Steel at Elevated Temperature, *Metall. Trans. A*, Vol 6, 1975, p 1693–1697
19. D.A. Woodford, Test Methods for Accelerated Development, Design, and Life Assessment of High Temperature Materials, *Mater. Des.*, Vol 14 (No. 4), 1993, p 231–242
20. D.A. Woodford and K. Iijima, Creep Strength Evaluation, Design, and Life Management of Cr-Mo-V Rotor Steel Using Stress Relaxation Testing, *Advances in Turbine Materials, Design, and Manufacturing*, Fourth International Charles Parsons Turbine Conference, A. Strang, W.M. Banks, R.D. Conroy, and M.J. Goulette, Ed., Institute of Materials, 1997, p 613–624
21. D.A. Woodford, Accelerated High Temperature Performance Evaluation of Superalloys for Process Optimization and Remaining Life Assessment, *ASME IGTI Turbo Expo Conference* (Indianapolis, IN), ASME, 1999
22. G.G. Gryzywinski and D.A. Woodford, Creep Analysis of Thermoplastics Using Stress Relaxation Data, *J. Polym. Eng. Sci.*, Vol 35 (No. 24), 1995, p 1931–1937
23. A. Fox, Ed., Stress Relaxation in Bending of AISI 301 Type Corrosion Resistant Steel Strip, STP 676, *Stress Relaxation Testing*, ASTM, 1978, p 78–88
24. E.W. Filer and C.R. Scorey, Stress Relaxation in Beryllium Copper Strip, STP 676, *Stress Relaxation Testing*, A. Fox, Ed., ASTM, 1978, p 89–111

25. P. Parikh, Report on Bending Stress Relaxation Round Robin, STP 676, *Stress Relaxation Testing*, A. Fox, Ed., ASTM, 1978, p 112–125
26. J. Henderson and J.D. Sneddon, Complex Stress Creep Relaxation on Commercially Pure Copper at 250 °C, *Advances in Creep Design*, A.I. Smith and A.M. Nicolson, Ed., John Wiley & Sons, Inc., 1971, p 163–180
27. A. Fox, Effect of Temperature on Stress Relaxation of Several Metallic Materials, *Residual Stress and Stress Relaxation*, Proceedings 28th Sagamore Army Materials Research Conference, E. Kula and V. Weiss, Ed., Plenum Press, 1982, p 181–203

Influence of Multiaxial Stresses on Creep and Creep Rupture of Tubular Components

R.C. Hurst and J.H. Rantala, European Commission, Joint Research Centre, Institute for Advanced Materials (The Netherlands)

Introduction

DESIGN OF PRESSURIZED COMPONENTS is normally based on uniaxial data because all the material data is generated using uniaxial tests. However, typical industrial piping components operate under a multiaxial state of stress as a result of the internal pressure, temperature gradients, and system stresses. Very general effective stress concepts have been used in component design codes to calculate the creep life of the material under triaxial state of stress. These concepts are based on the principle that the life of a component with a multiaxial effective stress corresponds to the rupture time at the same uniaxial stress according to the uniaxial design data.

Influence of Multiaxial Stresses on Creep and Creep Rupture of Tubular Components

R.C. Hurst and J.H. Rantala, European Commission, Joint Research Centre, Institute for Advanced Materials (The Netherlands)

Multiaxiality and Principal Stresses

Any complex stress combination with stresses in three directions and six different shear stresses can be reduced to just three stresses, the principal stresses $\sigma_1 > \sigma_2 > \sigma_3$. The highest of these is called the maximum principal stress (MPS). In the principal stress coordinate system there are no shear stresses.

The stress state is biaxial if $\sigma_3 = 0$, as is often assumed for thin-walled tubes. The stress system is reduced to uniaxial when $\sigma_1 = \sigma$ and $\sigma_2 = \sigma_3 = 0$. In thick-walled pipes and components the stress state is triaxial.

In the stress distribution figures in this article, a tube under internal pressure that has a ratio of inner radius to outer radius of 0.6 has been used as an example.

Effective Stress Equations

The basic idea of effective stresses is to calculate a stress for complex stress situations with a value that gives the correct failure time when applied to uniaxial data, which is often the basis for engineering design—and often the only data available in absence of representative multiaxial test data.

The effective stresses can be calculated for different cases, each of which will be described in detail in this article:

- Elastic stresses (see the section “Elastic Stress Distribution in a Tube”)
- Steady-state creep stresses (see the section “Steady-State Creep Stress Distribution in a Tube”)
- Stresses in a fully plastic case (see the section “Plastic Stresses in a Tube”)
- Thermal stresses (see the section “Thermal Stresses in a Tube”)

The thermal stresses are often superimposed with one of the former stress systems.

Von Mises Criterion. The most commonly used effective stress concept is the one presented in 1913 by von Mises, based on a concept of maximum energy of distortion:

$$\sigma_{VM} = \frac{1}{\sqrt{2}} [(\sigma_1 - \sigma_2)^2 + (\sigma_2 - \sigma_3)^2 + (\sigma_3 - \sigma_1)^2]^{1/2} \quad (\text{Eq 1})$$

The von Mises effective stress is most widely used in engineering design, both in the low and high temperature ranges. It has been found to govern the deformation of materials under complex loading situations. It is also the controlling parameter for creep rupture at high stresses where the rupture is associated with large deformations and a ductile failure mechanism. However, in long-term service, the rupture is controlled either by MPS or a mixed MPS-von Mises criterion. Also in brittle materials, the rupture tends to be more MPS controlled.

Much work has been focused on whether or not creep rupture would occur under a complete tensile triaxiality when $\sigma_1 = \sigma_2 = \sigma_3 = \sigma$. Under these circumstances, von Mises would go to zero, which means that there is no deformation or rupture in the short term, but it is believed that creep rupture would occur under MPS control after a long exposure time with a constrained grain-boundary cavity nucleation and growth mechanism. Experimentally this is extremely difficult to verify because of the difficulty of triaxial loading using a cruciform specimen, for example.

For practical reasons, the von Mises equation is often used in engineering design in a different form where, instead of principal stresses, the engineering stresses are used, including torsion stress:

$$\sigma_{VM} = \frac{1}{\sqrt{2}} [(\sigma_h - \sigma_a)^2 + (\sigma_a - \sigma_r)^2 + (\sigma_r - \sigma_h)^2 + 3\tau^2]^{1/2} \quad (\text{Eq 2})$$

where σ_h is hoop stress (circumferential), σ_a is axial stress, σ_r is radial stress, and τ is torsion stress.

Often an effective stress concept has been used in the background when design rules have been determined, but it is not always apparent to the user from the design code itself. Similarly, plenty of detailed analyses have often been hidden behind the design safety factors.

Tresca Criterion. The yield criterion generally known as the Tresca criterion is based on the concept of maximum shear stress energy and is expressed simply as:

$$\sigma_{TR} = \sigma_1 - \sigma_3 \quad (\text{Eq 3})$$

Huddleston Criterion. This multiaxial effective stress concept is a modified version of the von Mises stress, and it is claimed to better take the multiaxiality into account (Ref 1, 2). Here the equation is shown in the simplified form.

$$\sigma_{\text{HUD}} = \sigma_{\text{VM}} \exp \left[0.24 \left(\frac{J_1}{S_S} - 1 \right) \right] \quad (\text{Eq 4})$$

$$J_1 = \sigma_1 + \sigma_2 + \sigma_3 \quad (\text{Eq 5})$$

$$S_S = \sqrt{\sigma_1^2 + \sigma_2^2 + \sigma_3^2} \quad (\text{Eq 6})$$

While under the steady-state creep conditions, the von Mises predicts highest stresses on the inner surface; the Huddleston distribution, on the other hand, is quite contrary and would probably provide a more reliable basis for damage and life predictions than von Mises, at least if only stress is considered in life prediction and not ductility. (See Fig. 1 in the section “Steady-State Creep Stress Distribution in a Tube” in this article.) This criterion was originally developed for stainless steels but has proved to be useful for ferritic high-temperature engineering materials as well. The Huddleston criterion was incorporated into ASME Code Case N-47-29.

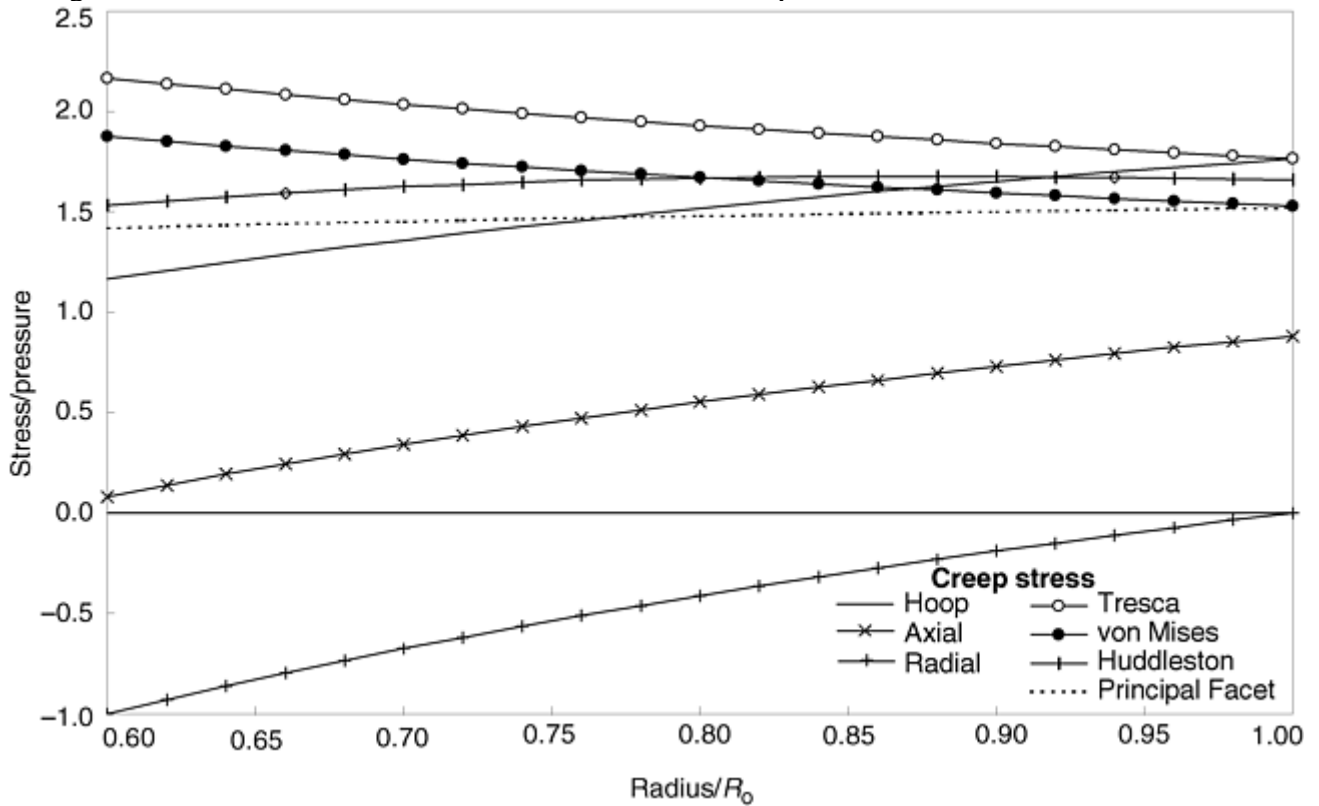


Fig. 1 Distribution of normalized steady-state creep stresses in a pressurized tube with a ratio of inner radius, R_i , to outer radius, R_o , of 0.6. The principal facet stress values have been normalized by dividing by a factor of 2.24

Mixed Criteria. Often mixed criteria have been proposed because, in practical cases, none of the classical parameters describe the material behavior sufficiently in various stress cases. One of the most common criterion is the one developed at the former Central Electricity Generating Board in the United Kingdom, presented by Cane and Hayhurst (Ref 3, 4):

$$\sigma_{\text{eff}} = \alpha \sigma_1 + (1-\alpha) \bar{\sigma} \quad (\text{Eq 7})$$

where α is the coefficient of thermal expansion. A similar empirical effective stress concept for high-temperature materials has been proposed by the Russian research institute CKTI:

$$\sigma_{\text{CKTI}} = (\sigma_{\text{MPS}}^n + 0.47 \sigma_{\text{VM}}^n)^{1/n} \quad (\text{Eq 8})$$

where n is the Norton creep exponent.

The concept of principal facet stress σ_F has been developed (Ref 5) based on the observations that creep damage will first appear on grain boundaries transverse to the axis of MPS, and that on inclined boundaries there will be shear deformation, which is mainly controlled by von Mises effective stress:

$$\sigma_F = 2.24\sigma_1 - 0.62(\sigma_2 + \sigma_3) \quad (\text{Eq 9})$$

The principal facet stress has been found to bring uniaxial and multiaxial data together especially for ferritic and austenitic steels. However, this stress does not apply directly to engineering calculations because the stress values calculated by Eq 9 are high. Therefore, in Fig. 1, σ_F has been normalized by a factor of 2.24. The principal facet stress is then seen to coincide with the von Mises stress on the outer surface of the pressurized tube. Normalization by a factor of 2 would make σ_F coincide with the von Mises stress in the skeletal point and with the distribution of the Huddleston stress.

The Effect of Stress System on the Damage Processes. At least in the short term, the creep damage process of cavity nucleation seems to be von Mises controlled because cavity nucleation requires accumulation of shear strain. On the contrary, for brittle materials the number of cavities formed is a function of MPS and intergranular fracture is promoted by the increasing ratio of σ_1/σ_{VM} (Ref 3). Similarly, the effect of MPS becomes more pronounced under long service times, under which the uniaxial ductility is known to reduce remarkably and fracture becomes more brittle.

According to Cane (Ref 3), the growth of grain-boundary cavities is controlled by MPS at low effective stress levels and by von Mises at high stress levels. If component-integrity and life-assessment methods do not give proper consideration to the change of the damage mechanism, they are likely to be conservative at high stresses and short times when $\sigma_1/\sigma_{VM} < 1$ and not conservative at low stress levels in the long term when $\sigma_1/\sigma_{VM} > 1$.

References cited in this section

1. R.L. Huddleston, An Improved Multiaxial Creep-Rupture Strength Criterion, *J. Pressure Vessel Technol. (Trans. ASME)*, Vol 107, Nov 1985, p 421–429
2. R.L. Huddleston, Assessment of an Improved Multiaxial Strength Theory Based on Creep-Rupture Data for Type 316 Stainless Steel, *J. Pressure Vessel Technol. (Trans. ASME)*, Vol 115, May 1993, p 177–184
3. B.J. Cane, Creep Damage Accumulation and Fracture under Multiaxial Stresses, *Proc. Advances in Fracture Research (Fracture 81)*, 1981 (Cannes, France), Vol 3, Pergamon Press, 1982
4. B.J. Cane, Representative Stresses for Creep Deformation and Failure of Pressurised Tubes and Pipes, *Int. J. Pressure Vessel Piping*, Vol 10, 1982, p 119–128
5. H.K. Kim, F.A. Mohamed, and J.C. Earthman, “High Temperature Rupture of Microstructurally Unstable 304 Stainless Steel Under Uniaxial and Triaxial Stress States,” *Metall. Trans. A*, Vol 22, 1991, 2629–2635

Influence of Multiaxial Stresses on Creep and Creep Rupture of Tubular Components

R.C. Hurst and J.H. Rantala, European Commission, Joint Research Centre, Institute for Advanced Materials (The Netherlands)

Effective Strain

In a multiaxial stress system as well, strains occur in three different directions, which are assumed to coincide with the principal stress axes. It is assumed that failure will occur when the effective strain reaches the uniaxial rupture strain value. The effective strain equation is almost identical with the respective stress equation (Eq 2):

$$\bar{\varepsilon} = \frac{\sqrt{2}}{3} [(\varepsilon_1 - \varepsilon_2)^2 + (\varepsilon_2 - \varepsilon_3)^2 + (\varepsilon_3 - \varepsilon_1)^2]^{0.5} \quad (\text{Eq 10})$$

Similarly, the effective strain rate can be expressed as:

$$\dot{\bar{\varepsilon}} = \frac{\sqrt{2}}{3} [(\dot{\varepsilon}_1 - \dot{\varepsilon}_2)^2 + (\dot{\varepsilon}_2 - \dot{\varepsilon}_3)^2 + (\dot{\varepsilon}_3 - \dot{\varepsilon}_1)^2]^{0.5} \quad (\text{Eq 11})$$

The relationship between stress and strain rate can then be expressed:

$$\frac{\dot{\varepsilon}_1 - \dot{\varepsilon}_2}{\sigma_1 - \sigma_2} = \frac{\dot{\varepsilon}_2 - \dot{\varepsilon}_3}{\sigma_2 - \sigma_3} = \frac{\dot{\varepsilon}_3 - \dot{\varepsilon}_1}{\sigma_3 - \sigma_1} = \frac{3}{2} \frac{\dot{\varepsilon}}{\sigma} \quad (\text{Eq 12})$$

Further, a simple criterion comes from the fact that most engineering materials are considered to be incompressible. This rule applies for both strains and strain rates:

$$\dot{\varepsilon}_1 + \dot{\varepsilon}_2 + \dot{\varepsilon}_3 = 0 \quad (\text{Eq 13})$$

Influence of Multiaxial Stresses on Creep and Creep Rupture of Tubular Components

R.C. Hurst and J.H. Rantala, European Commission, Joint Research Centre, Institute for Advanced Materials (The Netherlands)

Elastic Stress Distribution in a Tube

The equations for the elastic stress distribution for hoop, axial, and radial stress (Ref 6) were first published by Lamé in 1852 and can be expressed as:

$$\sigma_h = \frac{p}{Y^2 - 1} \left[1 + \left(\frac{R_o}{r} \right)^2 \right] \quad (\text{Eq 14})$$

$$\sigma_a = \frac{p}{Y^2 - 1} \quad (\text{Eq 15})$$

$$\sigma_r = \frac{p}{Y^2 - 1} \left[1 - \left(\frac{R_o}{r} \right)^2 \right] \quad (\text{Eq 16})$$

where p is pressure, Y is the outer radius divided by the inner radius (R_o/R_i), and r is the radius. The elastic stress distribution is shown in Fig. 2 for an example tube ($R_i = 0.6R_o$) without any stress relaxation due to plasticity or creep.

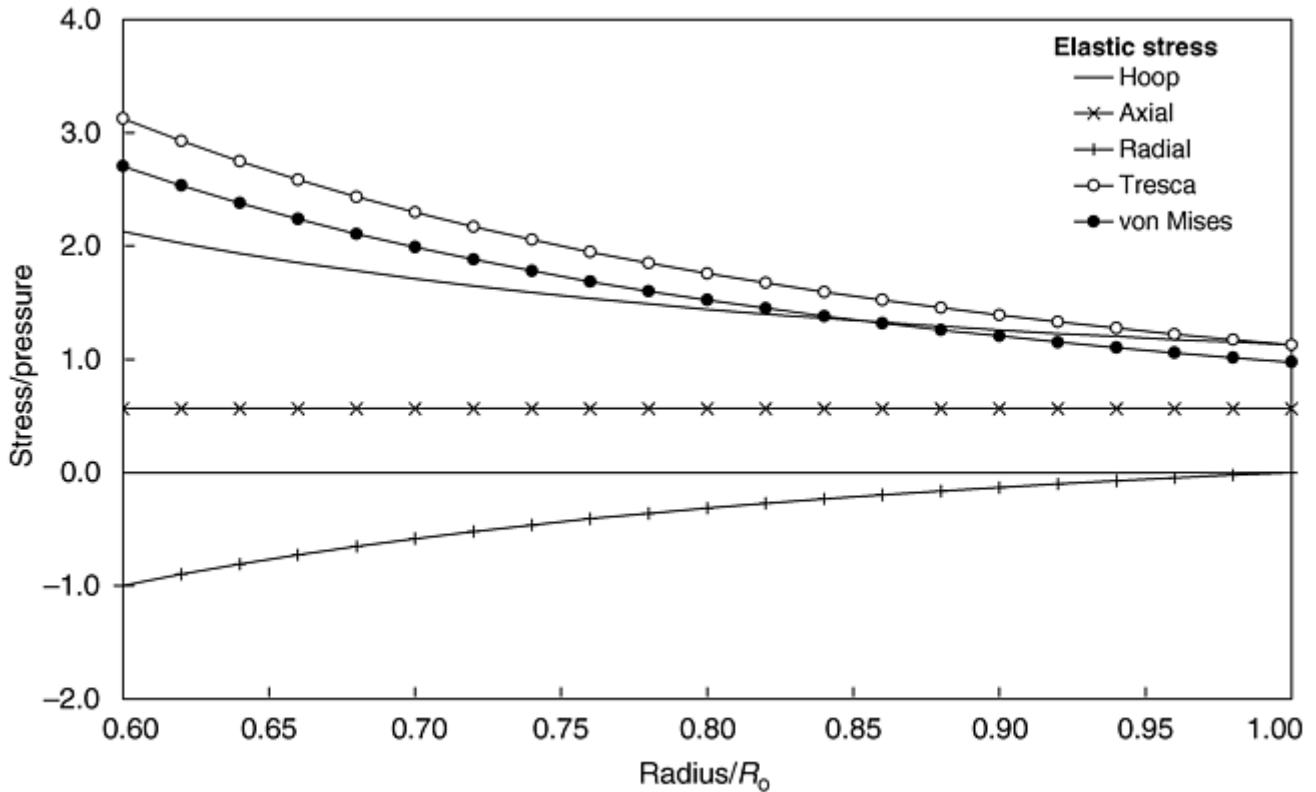


Fig. 2 Distribution of normalized elastic stresses in a pressurized tube with a ratio of inner radius, R_i , to outer radius, R_o , of 0.6

The thicker the tube, the steeper the stress gradient becomes. The radial (compressive) stress on the inside is, by definition, equal to the inner pressure and gradually decreases to zero towards the outer surface. This radial stress has to be taken into account when calculating the effective stress. On the other hand, in a thin-walled tube, the radial stress is often considered negligible, and, therefore, the stress state is simplified to biaxial.

Reference cited in this section

6. R. Seshardi, Design and Life Prediction of Fired Heater Tubes in the Creep Range, *J. Pressure Vessel Technol. (Trans. ASME)*, Vol 110, Aug 1988, p 322–328

Influence of Multiaxial Stresses on Creep and Creep Rupture of Tubular Components

R.C. Hurst and J.H. Rantala, European Commission, Joint Research Centre, Institute for Advanced Materials (The Netherlands)

Steady-State Creep Stress Distribution in a Tube

The analytical solutions for a tube under steady-state creep (Ref 6, 7, 8) were published first in 1935 by Bailey, and therefore, the following equations for hoop, axial, and radial stresses are often referred to as the Bailey equations:

$$\sigma_h = \frac{p}{(Y)^{2/n} - 1} \left[1 + \frac{2-n}{n} \left(\frac{R_o}{r} \right)^{2/n} \right] \quad (\text{Eq 17})$$

$$\sigma_a = \frac{p}{(Y)^{2/n} - 1} \left[1 + \frac{1-n}{n} \left(\frac{R_o}{r} \right)^{2/n} \right] \quad (\text{Eq 18})$$

$$\sigma_r = \frac{p}{(Y)^{2/n} - 1} \left[1 - \left(\frac{R_o}{r} \right)^{2/n} \right] \quad (\text{Eq 19})$$

The stress distribution is shown in Fig. 1.

These stresses are related by a correlation, which can be used to check numerical calculations:

$$\sigma_a = 0.5(\sigma_h + \sigma_r) \quad (\text{Eq 20})$$

With creep, the initial elastic stresses are redistributed and the stresses are “reversed.” Under pressurization, the maximum elastic stresses appear on the inner surface of the tube, but, due to creep, these stresses relax and, under steady-state conditions, the maximum stresses move to the outer surface. The maximum initial elastic hoop stress of $2.13p$ on the inner surface is reduced to only $1.16p$ under steady-state creep. Meanwhile, on the outside, the initial elastic hoop stress of $1.13p$ increases to 1.76 under creep conditions. It should also be noted that the elastic stress distribution is a special case of creep stress distribution when $n = 1$.

References cited in this section

6. R. Seshardi, Design and Life Prediction of Fired Heater Tubes in the Creep Range, *J. Pressure Vessel Technol. (Trans. ASME)*, Vol 110, Aug 1988, p 322–328
7. R.W. Bailey, Creep Relationships and Their Application to Pipes, Tubes and Cylindrical Parts under Internal Pressure, *Proc. Inst. Mech. Eng. A*, Vol 164, 1951, p 425
8. I. Finnie and W.R. Heller, *Creep of Engineering Materials*, McGraw-Hill, 1959

Influence of Multiaxial Stresses on Creep and Creep Rupture of Tubular Components

R.C. Hurst and J.H. Rantala, European Commission, Joint Research Centre, Institute for Advanced Materials (The Netherlands)

Plastic Stresses in a Tube

These equations assume a completely plastic case:

$$\sigma_h = p \left[\frac{1 + \ln\left(\frac{r}{R_o}\right)}{\ln\left(\frac{R_o}{R_i}\right)} \right] \quad (\text{Eq 21})$$

$$\sigma_a = p \left[\frac{1 + 2 \ln\left(\frac{r}{R_o}\right)}{2 \ln\left(\frac{R_o}{R_i}\right)} \right] \quad (\text{Eq 22})$$

$$\sigma_r = p \left[\frac{\ln\left(\frac{r}{R_o}\right)}{\ln\left(\frac{R_o}{R_i}\right)} \right] \quad (\text{Eq 23})$$

A reference stress equal to the von Mises effective stress value can be calculated for the fully plastic case using Eq 24:

$$\sigma_M = \frac{p\sqrt{3}}{2 \ln\left(\frac{R_o}{R_i}\right)} \quad (\text{Eq 24})$$

The plastic stress distribution for the example tube is shown in Fig. 3. It should be noted that the plastic stress distribution in a cylindrical body is very similar to the creep stress distribution. This similarity has been used in the limit load analysis where plastic finite-element (FE) stress analysis is used to determine representative failure loads for various components. Second, both von Mises and Tresca distributions are constant through the wall thickness. Third, it should be noted that the Tresca value is equal to the maximum hoop stress value on the outer surface.

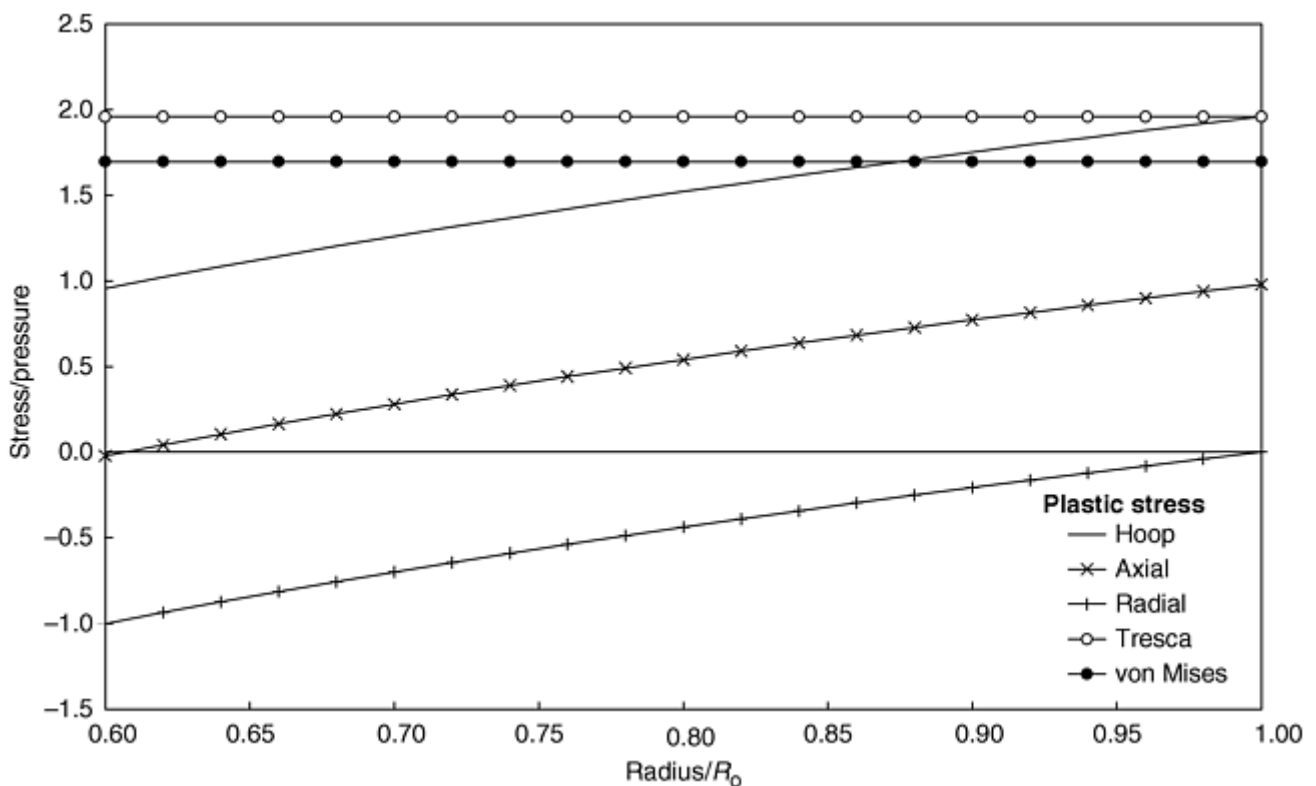


Fig. 3 Distribution of normalized plastic stresses in a pressurized tube with a ratio of inner radius, R_i , to outer radius, R_o , of 0.6

Influence of Multiaxial Stresses on Creep and Creep Rupture of Tubular Components

R.C. Hurst and J.H. Rantala, European Commission, Joint Research Centre, Institute for Advanced Materials (The Netherlands)

Thermal Stresses in a Tube

Often thermal stresses appear in plant components, which can have a significant influence on the stresses. In heat exchangers, tubes operate continuously under a thermal gradient, and, in many plants, thick-walled

components experience severe thermal gradients, especially during transition periods like start-up and shut-down of the plant. Often these thick-walled components set a limit to the start-up speed just because of the maximum allowable thermal stress in the wall.

During operation, thermal stresses are often superimposed on primary stresses originating from the pressure. The thermal stresses are called secondary because, in long-term operation, they may relax as a result of creep. In that case, after long-term operation (after complete stress redistribution), the stresses follow the steady state distribution; at shut-down, the initial elastic stresses and thermal stresses have to be subtracted. Then the remaining stress at zero pressure with zero temperature gradient becomes:

$$\text{Remaining stress} = \text{steady state stress} - \text{elastic stress}$$

from pressure - thermal stress

The thermal hoop, axial, and radial stresses can be calculated using the following equations. Here the temperature gradient has been defined as a result of external heating. For the cases of internal heating (applicable to the start-up of a cold component), the thermal gradient, ΔT , becomes negative and the stress distribution is reversed.

$$\sigma_h = \frac{E\alpha(\Delta T)}{2(1-\nu)\ln Y} \times \left[\ln(R_o/r) + \frac{(R_o/r)^2}{Y^2 - 1} \ln Y - 1 \right] \quad (\text{Eq 25})$$

$$\sigma_a = \frac{E\alpha(\Delta T)}{2(1-\nu)\ln Y} \times \left[2 \ln(R_o/r) + \frac{2 \ln Y}{Y^2 - 1} \ln Y - 1 \right] \quad (\text{Eq 26})$$

$$\sigma_r = \frac{E\alpha(\Delta T)}{2(1-\nu)\ln Y} \times \left[\ln(R_o/r) + \frac{1 - (R_o/r)^2}{Y^2 - 1} \ln Y \right] \quad (\text{Eq 27})$$

where E is the modulus of elasticity and ν is Poisson's ratio. An example of the distribution of multiaxial thermal stresses is shown in Fig. 4 for the example tube.

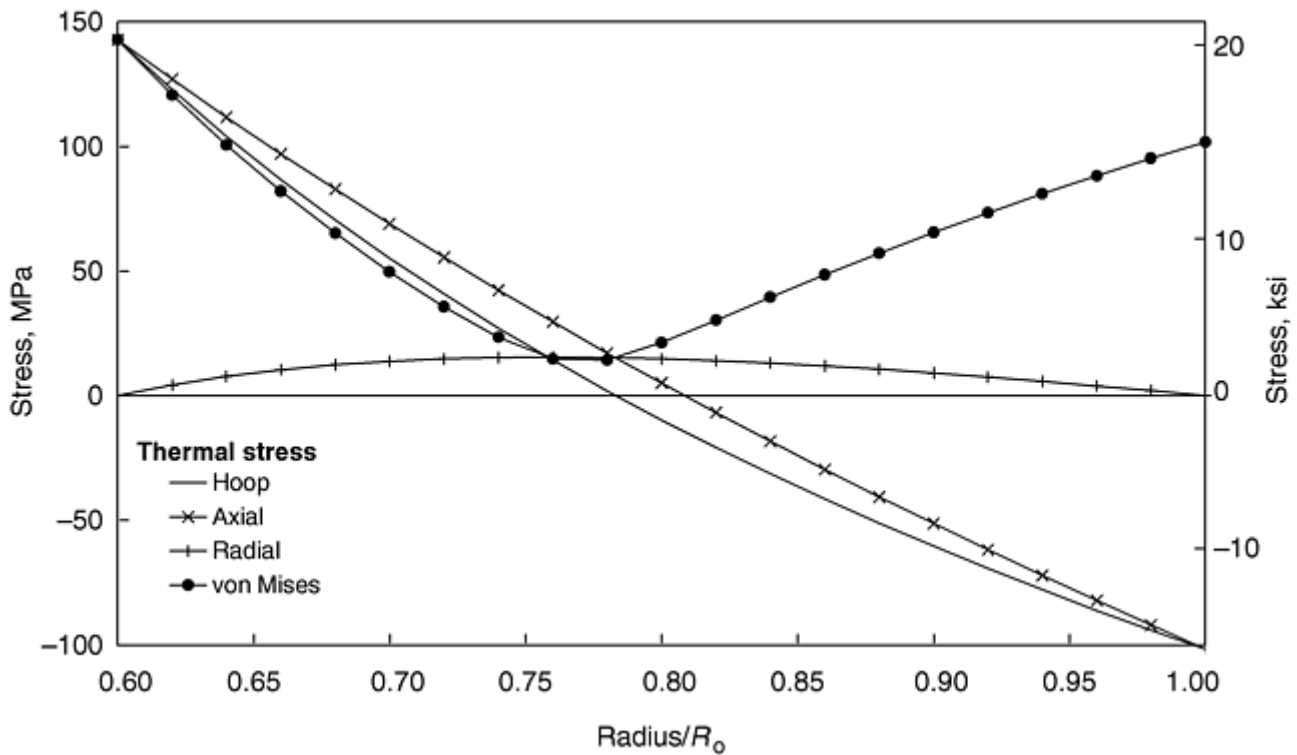


Fig. 4 Distribution of normalized thermal stresses in a pressurized tube with a ratio of inner radius, R_i , to outer radius, R_o , of 0.6 and with a temperature gradient of 50 °C (90 °F) under external heating

Influence of Multiaxial Stresses on Creep and Creep Rupture of Tubular Components

R.C. Hurst and J.H. Rantala, European Commission, Joint Research Centre, Institute for Advanced Materials (The Netherlands)

Comparison of Life Predictions By Different Effective Stress Criterion

Figure 5 contains data generated for P91 steel at 600 °C (1100 °F) using tubular specimens (outside diam 38×2 mm, thinner than the example tube in other figures) under internal pressure and axial end load with different ratios of hoop and axial stress. It should be noted that all the tests were started with the same initial von Mises stress. In the same figure, the continuum damage mechanics (CDM) model predictions are shown for three different multiaxial stress rupture criterion: von Mises, Tresca, and Huddleston.

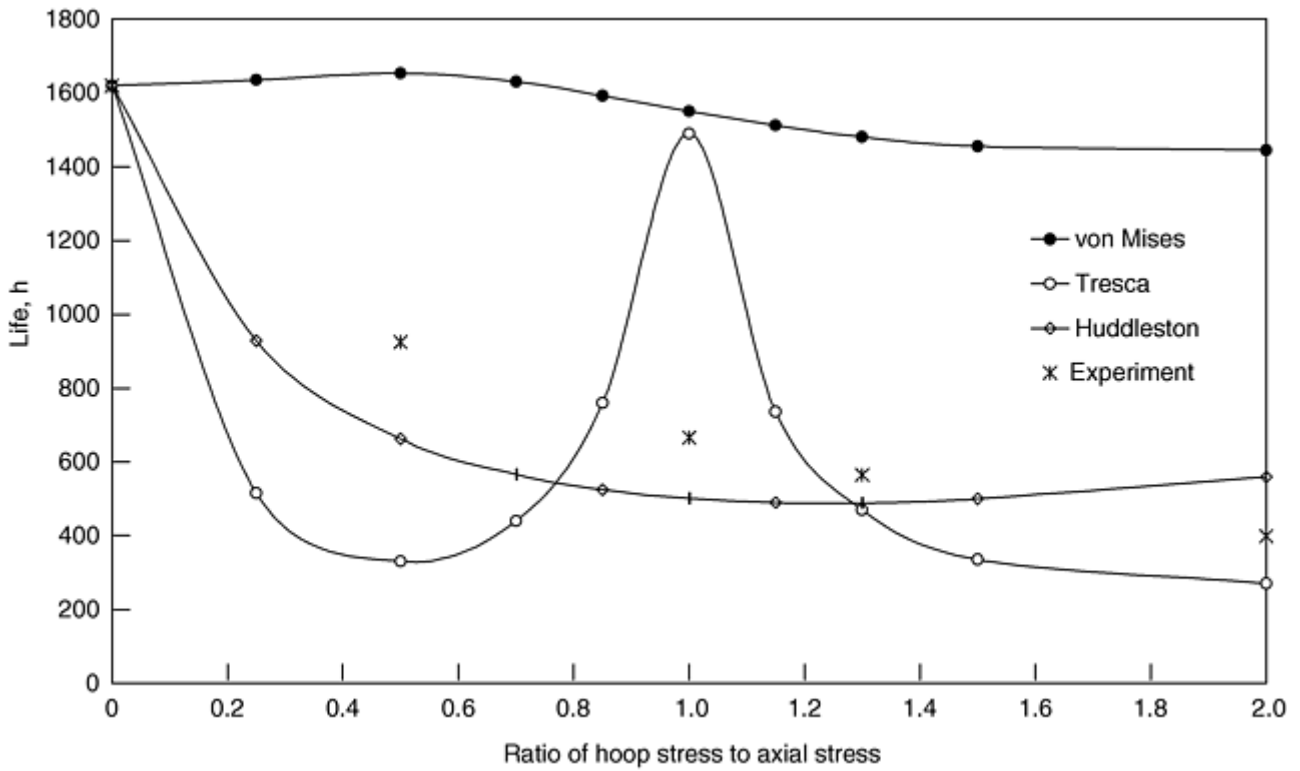


Fig. 5 Multiaxial creep test results for a pressurized P91 tube with end load at 600 °C (1100 °F) under various ratios of hoop stress to axial stress and with constant initial von Mises stress

One would assume then that the von Mises prediction would be a flat curve, but the CDM model predicts always a slightly curved shape. Similarly, one would assume that at stress ratios of 2 and 0.5, the life would be the same, but it does not seem to be the case. The reason for this is that at a stress ratio of 2, the hoop stress is dominant and the hoop strain leads to an increase of the inner diameter, which will reduce the life in a pressurized test. On the other hand, at a stress ratio of 0.5 (hoop stress is half of the axial), the axial stress is dominant and the diameter actually remains constant (the necking as a result of the axial stress is balanced by the internal pressure). This leads to a slightly increased life.

When the initial von Mises stress is the same in all tests, the shape of the Tresca (or MPS) curve is explained by the hoop and axial stress components. Figure 6 clarifies this. The MPS in this figure consists of axial stress between stress ratios 0 to 1 and hoop stress when stress ratio is greater than unity. The MPS life curve in Fig. 5 is a “mirror image” of the MPS curve in Fig. 6.

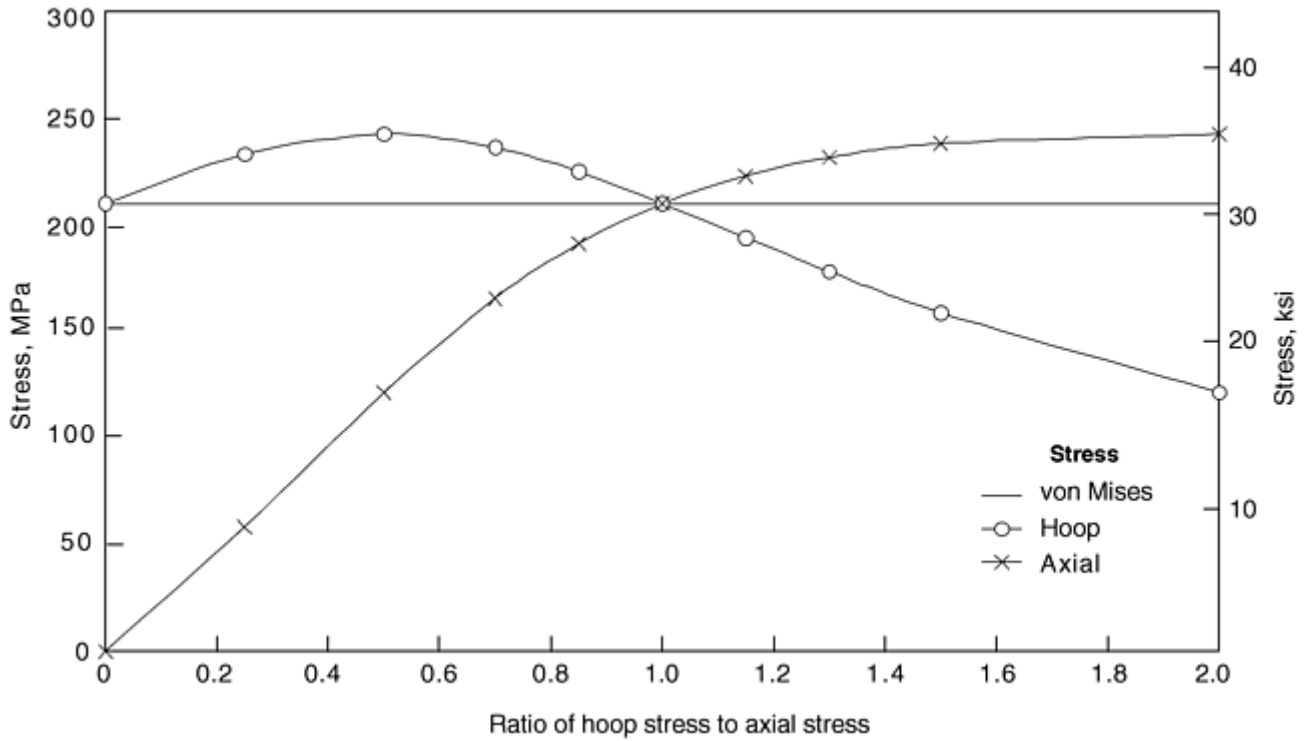


Fig. 6 Hoop and axial strain components in an internally pressurized tube when the von Mises effective stress is kept constant

The plots like Fig. 5 can be used to tell whether the stress rupture criterion is von Mises or MPS. For many materials, the experimental points lie somewhere in the middle. It has been observed that the Huddleston stress, described by, Eq 4 correlates fairly well with this data. It should be noted, however, that plots like Fig. 5 are time dependent. This figure describes the short-term behavior where the failure is associated with large deformation. In long-term service, the damage mechanism is constrained grain-boundary cavitation, which is associated with very little deformation. Therefore, under the long-term service conditions, the creep behavior tends to become more MPS dominated.

Influence of Multiaxial Stresses on Creep and Creep Rupture of Tubular Components

R.C. Hurst and J.H. Rantala, European Commission, Joint Research Centre, Institute for Advanced Materials (The Netherlands)

Commonly Used Stress Equations for Design

Often, the design of pressurized components is based on simple and desirably conservative design rules, and, in many cases, a simple mean diameter hoop (MDH) stress equation is used only because experience has proved it to be conservative in most cases:

$$\text{MDH} = \frac{p(d_o - t)}{2t} \quad (\text{Eq 28})$$

where d_o is the outside diameter, and t is the tube thickness. According to Cane (Ref 4), the mean diameter hoop stress well describes the life at high pressures and underestimates it at low stresses; that is, MDH is conservative in design for long-term operation.

The axial stress component in a pressurized tube with axial loading can be calculated using the following equation:

$$\sigma_a = 0.5\text{MDH} + \frac{4F}{\pi (d_o^2 - d_i^2)} \quad (\text{Eq 29})$$

where F is the axial load and d_i is the inside diameter. These simple stress equations are insensitive to system (bending) stresses, which may appear, for example, in a piping as a result of thermal expansion between fixed points. This can result in severe secondary bending stresses, which should be taken into account in piping design. Omission of bending stresses can lead to premature failure in, for example, welds close to fixed points (type IV cracking).

For tubes, a skeletal stress has been found to correlate fairly well with the stress rupture data:

$$\sigma_{\text{skel}} = p \frac{\left(\frac{2-n}{n}\right) \left(\frac{R_o}{r}\right)^{2/n} + 1}{\left(\frac{R_o}{R_i}\right)^{2/n} - 1} \quad (\text{Eq 30})$$

The basis for this definition is the observation that in approximately the middle of the wall thickness there is a point where the stresses are not dependant on the Norton creep exponent, n , as demonstrated in Fig. 7. Calculation of the von Mises stress in the mid-wall using the steady-state creep stresses leads to Eq 30. The skeletal stress value for the tube used in the example of Fig. 7 becomes $1.71p$.

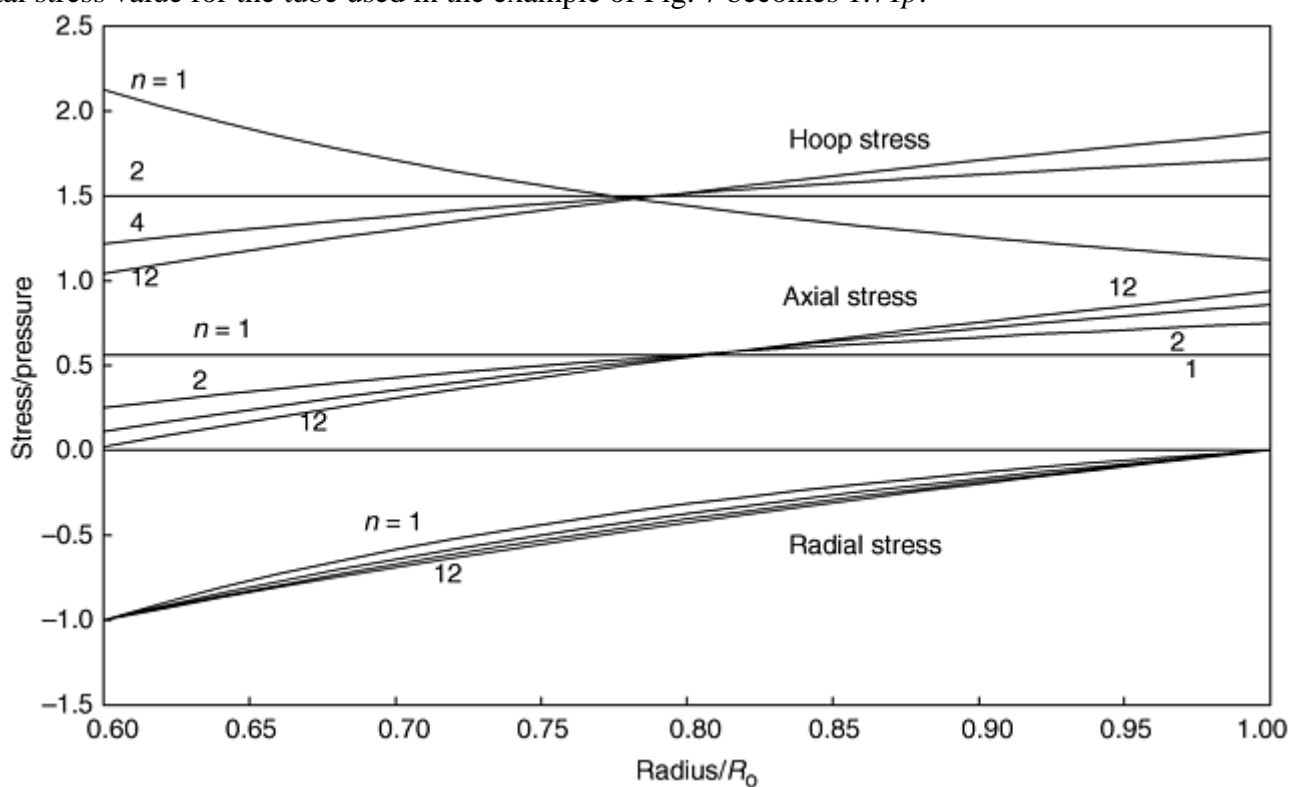


Fig. 7 Stress distributions in a creeping tube at different creep exponents showing the appearance of a skeletal stress in a point where the hoop stress value is practically independent of the Norton creep exponent (n). R_o , outside radius of tube

Reference cited in this section

4. B.J. Cane, Representative Stresses for Creep Deformation and Failure of Pressurised Tubes and Pipes, *Int. J. Pressure Vessel Piping*, Vol 10, 1982, p 119–128

Multiaxial Creep Ductility

It is well known that triaxiality has a strong effect on the ductility of materials. Under high degrees of tensile triaxiality, ductility will decrease remarkably. Therefore, a constraint parameter, h , is introduced (Ref 9):

$$h = \frac{\sigma_1 + \sigma_2 + \sigma_3}{3\sigma_{VM}} \tag{Eq 31}$$

Then the ratio of multiaxial and uniaxial ductility can be expressed by an exponential equation:

$$\frac{\epsilon_{fmx}}{\epsilon_f} = 1.65 \exp\left(\frac{-3h}{2}\right) \tag{Eq 32}$$

where ϵ_f is failure strain and ϵ_{fmx} is the failure strain under multiaxial conditions. An alternative solution is to define a triaxiality factor (TF), which is three times the h parameter:

$$TF = \frac{\sigma_1 + \sigma_2 + \sigma_3}{\sigma_{VM}} = 3h \tag{Eq 33}$$

Then multiaxial ductility (Ref 10) can then be calculated from a simple formula:

$$\frac{\epsilon_{fmx}}{\epsilon_f} = \frac{1}{TF} \tag{Eq 34}$$

These ductility equations give very different predictions of the multiaxial behavior at both extremes. The reciprocal Eq 34 gives very high values when TF approaches zero (equal tensile principal stresses) and does not work if TF is negative. The exponential Eq 32 gives lower multiaxial ductility values at small and negative values of h and is more conservative at high degrees of multiaxiality. Both curves go through the uniaxial point, which is $TF = 1$ and $h = 1/3$ (Fig. 8).

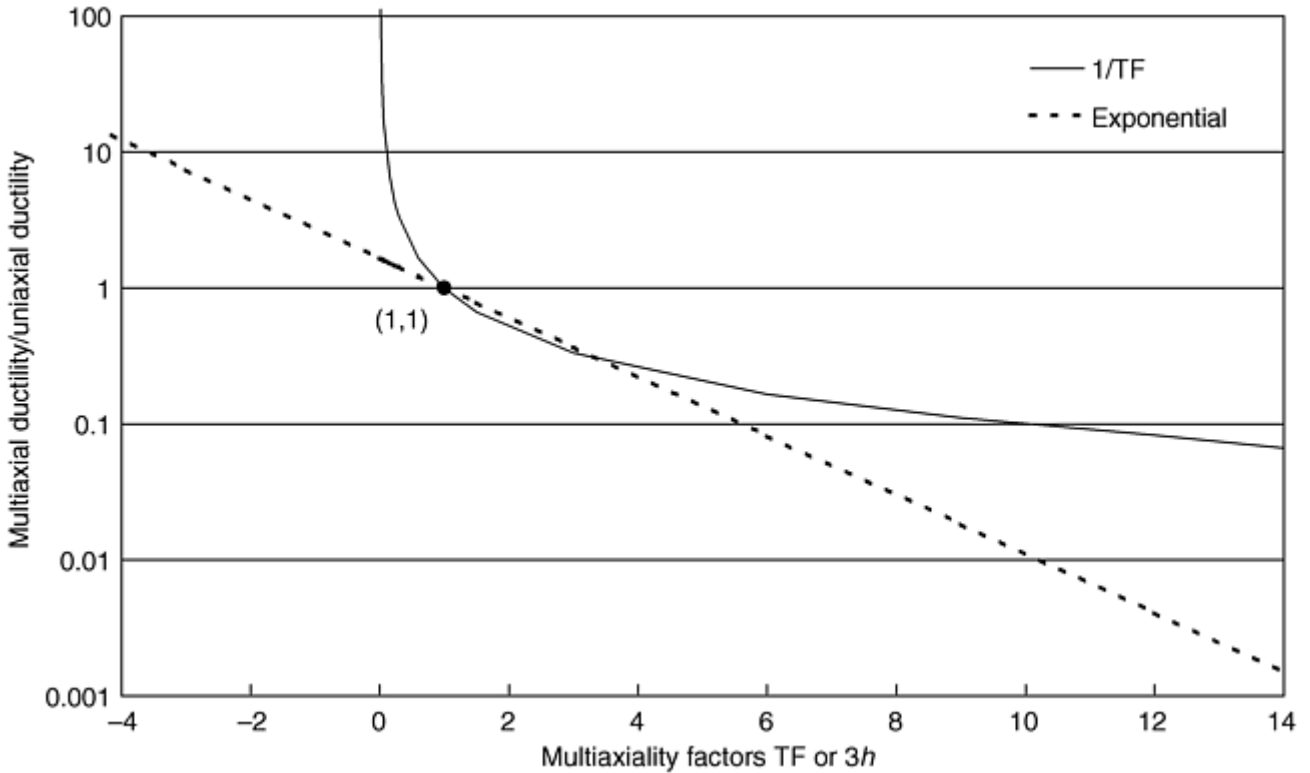


Fig. 8 Multiaxial ductility as a function of the triaxiality factor using Eq 32 and 34

High degrees of multiaxiality can be found especially at notch roots or in front of a crack tip. Also, in the soft zone of the heat-affected zone of a weld there is a strong element of tensile triaxiality, which will have an effect on the life.

The multiaxial ductility for our model tube ($R_i = 0.6R_o$) gives the values shown in Table 1 when calculated using the Eq 32 and 34. This result is extremely important because it explains the discrepancy between the two observations:

- Creep stress analysis for a cylindrical body gives always the maximum effective stress values on the *inner* surface of the tube.
- The service experience shows that the creep damage always appears on the *outer* surface of the tube—at least for materials other than the most brittle ones.

Table 1 Ratio of multiaxial and uniaxial ductility calculated at various locations in the wall of a tube

Location on tube wall	Ratio of multiaxial ductility to uniaxial ductility	
	$1/TF^{(a)}$	$1.65 \exp(-3h/2)^{(b)}$
Inner surface	7.60	1.54
Mid wall	1.01	1.00
Outer surface	0.58	0.69

Tube has a ratio of inner radius to outer radius of 0.6.

(a) See Eq 34.

(b) See Eq 32.

In a creeping tube, the strains are proportional to $1/\text{radius}$. Therefore, both the effective stress and the strain on the inner surface of the tube are the highest, but the multiaxial ductility is clearly higher than the uniaxial ductility, as shown in Table 1. This is why the damage does not initiate on the inside of the tube (except in materials where the uniaxial creep ductility is very low—then the relaxation of the high initial elastic stresses can cause failure on the inside). On the other hand, according to Eq 32 and 34, the ductility on the outer surface is much less than the uniaxial ductility, which leads to the initiation of the damage on the outer surface first.

Fortunately, the nature of creep rupture itself seems to simplify the problem of multiaxiality in plant components. In long-term service, creep rupture occurs with a constrained grain-boundary cavity nucleation and growth mechanism, it seems to be more MPS controlled, and damage appears predominantly on the outer surface (which is fortunate from an inspection point of view).

This finding could simplify the necessary engineering calculations of multiaxial stress systems to some extent. However, the present-day design codes for plant equipment do not necessarily reflect this idea, although design lives can be well above 100,000 h where MPS would become the controlling parameter. Further, it should be remembered that for components in the creep regime, the MPS should not be calculated according to the initial elastic distribution but according to the steady-state creep stress distribution.

References cited in this section

9. P. Segle, P. Andersson, and L.Å. Samuelson, A parametric study of creep crack growth in heterogeneous CT specimens by use of finite element simulations, *Mater. High Temp.*, Vol 15, 1998, p 101
10. B.W. Roberts, Influence of Multiaxial Stressing on Creep and Creep Rupture, *Mechanical Testing*, Vol 8, *ASM Handbook*, ASM International, 1985, p 343–345

Influence of Multiaxial Stresses on Creep and Creep Rupture of Tubular Components

R.C. Hurst and J.H. Rantala, European Commission, Joint Research Centre, Institute for Advanced Materials (The Netherlands)

Multiaxial Testing Methods

The vast majority of material creep tests have been performed using uniaxial tests and this will probably continue to be in the future. For modeling and validation purposes, multiaxial tests are indispensable due to their more representative stress state. The following multiaxial test methods have been used (Ref 11):

- Tubular specimen under tension and torsion
- Pressurized tube under internal pressure and end loading
- Notched uniaxial specimen (“Bridgman notch”)
- Fracture mechanic specimen (for example, compact tension or single-edge notched bend)
- Biaxial plate
- Triaxial cruciform specimen under triaxial tension (Ref 12)

A tubular specimen under combined tension and torsion provides a small and inexpensive specimen tested in machines that are commercially available. However, the stress state in the tension-plus-torsion test is such that the second principal stress, σ_2 , is negative, which is not representative of pressurized industrial components.

A tube under internal pressure and axial end load provides also a relatively small specimen, and test services are available from many laboratories. The loading is relatively well representative of the piping components, with axial loading giving the possibility to vary the stress ratio of σ_1/σ_2 . For thin-walled tubes with negligible radial stress, the stress state is close to biaxial, but the stress state becomes triaxial when thick-walled tubes or pipes are used with considerable (negative) radial stress. Pressurized tubes can be also tested with axial or circumferential notches or cracks. For safety reasons, pressure tests should be carried out only in dedicated concrete test cells.

A notched uniaxial specimen is certainly the cheapest multiaxial specimen and can be tested in a conventional creep testing machine. Axial and diametral extensometry will provide information about the deformation during the test. Recent work on notched bars provides detailed information about the stress distribution in the test specimen with various notch geometries (Ref 13).

In a fracture-mechanics specimen, there is a high degree of tensile triaxiality at the notch tip when the local deformation has been constrained by the surrounding material. This multiaxiality will probably enhance the creep damage process.

The biaxial plate and the three-dimensional cruciform specimen provide an ideal tool for the researcher with a possibility to vary the individual stress components, but they are extremely expensive to test in highly specialized test rigs and only very few laboratories in the world can offer these services.

References cited in this section

11. J. Henderson and B.F. Dyson, *Measurement of High Temperature Mechanical Properties of Materials*, M.S. Loveday, M.F. Day, and B.F. Dyson, Ed., National Physical Laboratory, London, 1982, p 171–184.
12. D.J. Gooch and I.M. How, *Techniques for Multiaxial Creep Testing*, Elsevier, 1986, p 241
13. G.A. Webster, S.R. Holdsworth, M.A. Loveday, I.J. Perrin, and H. Purper, *A Code of Practice for Conducting Notched Bar Creep Rupture Tests and the Interpretation of the Data*, High Temperature Mechanical Testing Committee, ESIS TC11, 1999 (draft)

References

1. R.L. Huddleston, An Improved Multiaxial Creep-Rupture Strength Criterion, *J. Pressure Vessel Technol. (Trans. ASME)*, Vol 107, Nov 1985, p 421–429
2. R.L. Huddleston, Assessment of an Improved Multiaxial Strength Theory Based on Creep-Rupture Data for Type 316 Stainless Steel, *J. Pressure Vessel Technol. (Trans. ASME)*, Vol 115, May 1993, p 177–184
3. B.J. Cane, Creep Damage Accumulation and Fracture under Multiaxial Stresses, *Proc. Advances in Fracture Research (Fracture 81)*, 1981 (Cannes, France), Vol 3, Pergamon Press, 1982
4. B.J. Cane, Representative Stresses for Creep Deformation and Failure of Pressurised Tubes and Pipes, *Int. J. Pressure Vessel Piping*, Vol 10, 1982, p 119–128
5. H.K. Kim, F.A. Mohamed, and J.C. Earthman, “High Temperature Rupture of Microstructurally Unstable 304 Stainless Steel Under Uniaxial and Triaxial Stress States,” *Metall. Trans. A*, Vol 22, 1991, 2629–2635
6. R. Seshardi, Design and Life Prediction of Fired Heater Tubes in the Creep Range, *J. Pressure Vessel Technol. (Trans. ASME)*, Vol 110, Aug 1988, p 322–328
7. R.W. Bailey, Creep Relationships and Their Application to Pipes, Tubes and Cylindrical Parts under Internal Pressure, *Proc. Inst. Mech. Eng. A*, Vol 164, 1951, p 425
8. I. Finnie and W.R. Heller, *Creep of Engineering Materials*, McGraw-Hill, 1959
9. P. Segle, P. Andersson, and L.Å. Samuelson, A parametric study of creep crack growth in heterogeneous CT specimens by use of finite element simulations, *Mater. High Temp.*, Vol 15, 1998, p 101
10. B.W. Roberts, Influence of Multiaxial Stressing on Creep and Creep Rupture, *Mechanical Testing*, Vol 8, *ASM Handbook*, ASM International, 1985, p 343–345
11. J. Henderson and B.F. Dyson, *Measurement of High Temperature Mechanical Properties of Materials*, M.S. Loveday, M.F. Day, and B.F. Dyson, Ed., National Physical Laboratory, London, 1982, p 171–184.
12. D.J. Gooch and I.M. How, *Techniques for Multiaxial Creep Testing*, Elsevier, 1986, p 241
13. G.A. Webster, S.R. Holdsworth, M.A. Loveday, I.J. Perrin, and H. Purper, *A Code of Practice for Conducting Notched Bar Creep Rupture Tests and the Interpretation of the Data*, High Temperature Mechanical Testing Committee, ESIS TC11, 1999 (draft)

Mechanical Behavior

Superplasticity is regarded as a creep phenomenon because it has been observed at temperatures at or above 50% of the melting point. Accordingly, in studying the mechanical behavior of superplastic alloys, it is essential to establish the following four relationships that define the basic deformation characteristics associated with a creep process: (a) the relationship between stress and strain rate, (b) the relationship between strain rate or stress and temperature, (c) the relationship between strain rate or stress and grain size, and (d) the relationship between strain contributed by boundary sliding and total strain.

The Relationship between Stress and Strain Rate

In general, the relationship between stress and strain rate is determined from two types of presentation. In the first type of presentation, the data are plotted as stress against strain rate on a logarithmic scale. The slope of this plot yields the value of the strain-rate sensitivity, m . In the second type of presentation, the data are plotted logarithmically as strain rate against stress. The slope of such a plot represents the stress exponent, n . Under steady-state conditions, n is equal to $1/m$.

In early work on the mechanical behavior of superplastic alloys, the plots of stress versus strain rate and the strain-rate sensitivity, m , were determined using several procedures in which specimens were tested in tension using a machine operated at a constant crosshead speed (a screw-driven type or a servohydraulic system) (Ref 7, 8, 9, 10, 11, 12). A summary of these procedures is given in Table 1. While the application of these procedures has provided useful information on the variation of m with strain rate during superplastic deformation, there are several problems that need attention when some of the procedures are used. Primary among these problems is the fact that true steady-state conditions cannot be achieved with a tensile machine operated at constant crosshead speed. As a result, the plot of stress against strain rate, using logarithmic scales, can produce erroneous results when used to determine the steady-state characteristics of superplastic flow, such as the activation energy for deformation or grain-size sensitivity. In addition, the stress-relaxation method can lead to inaccurate data if the procedure is not corrected for the effect of the stiffness of the testing machine. Furthermore, it is difficult to obtain very low strain-rate data on machines with constant crosshead speed or a constant strain rate. Due to this difficulty, it is not possible to unambiguously establish the characteristics of superplastic flow in this range of strain rates.

Table 1 Early procedures for calculating strain-rate sensitivity, m

Method	m	Representation	Procedure	Reference
A	$m = \frac{\log(P_b/P_a)}{\log(V_2/V_1)}$		The curve for V_1 is extrapolated to point a' such that the total strain at a' is equal to the strain at that of point b' (max load) on the curve for V_2	Ref 7

B	$m = \frac{\log(\sigma_b/\sigma_a)}{\log(V_2/V_1)}$		<p>The true stress and true strain rate at points <i>a</i> and <i>b</i> which represent the maximum loads on curves V_1 and V_2</p>	Ref 8
C	$m = \frac{\log(P_c/P_d)}{\log(V_2/V_1)}$		<p>The curve for V_2 is extrapolated to point <i>c</i> which is above point <i>d</i> at which the velocity change is made</p>	Ref 9
D	$m = \frac{\log(P_e/P_d)}{\log(V_2/V_1)}$		<p>The load values immediately before (point <i>d</i>) and after (point <i>e</i>) the velocity change are used</p>	Ref 10
E	$m = \frac{\partial \ln \sigma}{\partial \ln(d\varepsilon/dt)}$		<p>The values of true stress and true strain rate are calculated at various points along the load-time curve and $\log \sigma$ is then plotted against $d\varepsilon/dt$</p>	Ref 11
F	$m = \frac{\partial \ln \sigma}{\partial \ln(d\sigma/dt)}$		<p>The cross-head is stopped at <i>S</i> and the values of the true stresses are then estimated at different points along the relaxation curve. <i>m</i> is determined from the slope of the plot of $\log \sigma$ vs $\log d\sigma/dt$</p>	Ref 12

Recently, the stress dependence of strain rate, or, equivalently, the strain-rate dependence of stress in superplastic materials has been established under double-shear conditions (Ref 13, 14, 15). As indicated by experimental evidence, double shear specimens, shown in Fig. 2(a), have the following advantages over tensile specimens (Ref 16, 17, 18). First, a constant stress condition is maintained under constant load, and, as a result, it is not necessary to use a creep machine with a compact cam lever to maintain constant stress as is required in the case of a tensile specimen. Figure 2(b) schematically represents a simple creep machine that can be used in testing double shear specimens. Second, the problem of plastic instability can be avoided. Finally, shear deformation remains completely uniform over the gauge length of the specimen up to 120% strain. In conducting double-shear experiments, two different, but complimentary, procedures are used.

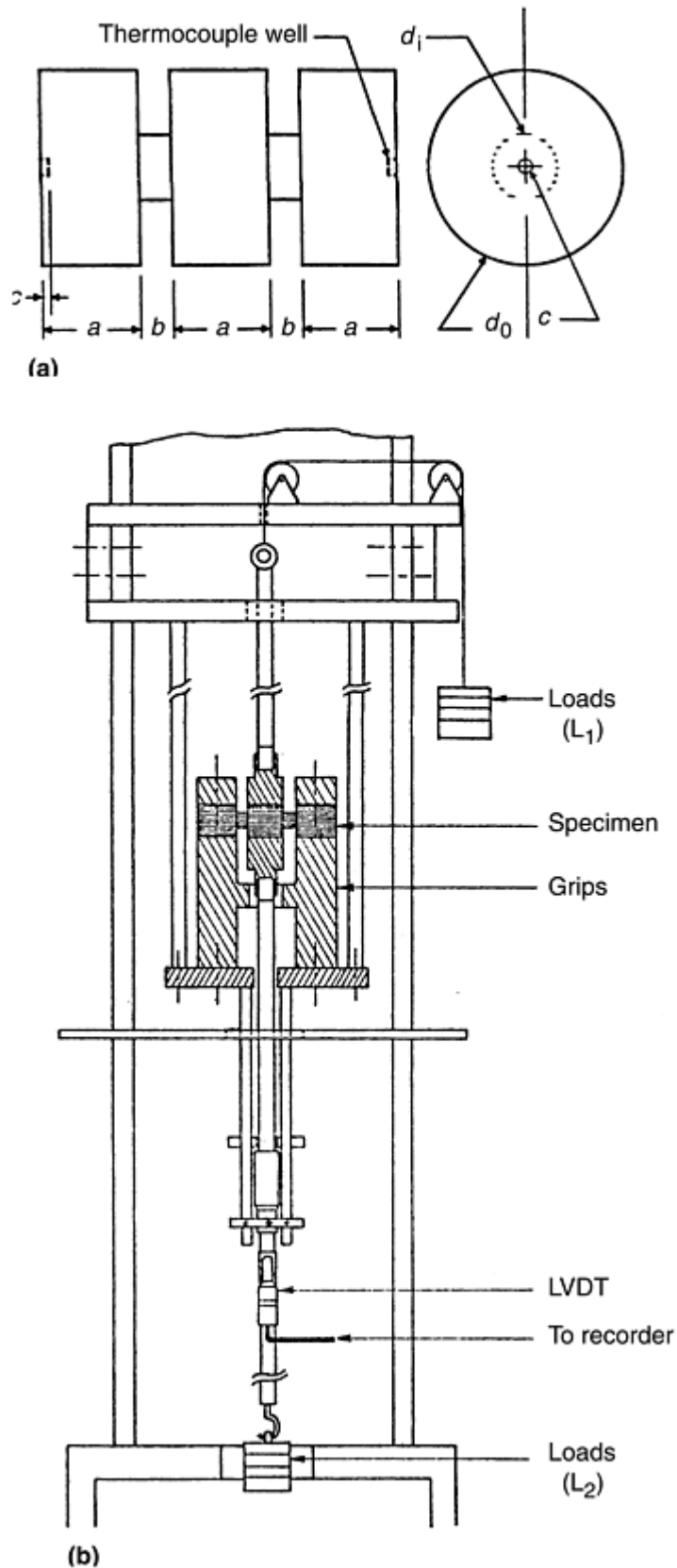


Fig. 2 Double shear testing. (a) Specimen configuration. $a = \frac{3}{8}$ in., $b = \frac{1}{8}$ in., $c = \frac{1}{16}$ in., $d_1 = \frac{3}{8}$ in., $d_0 = \frac{3}{4}$ in. (b) Creep machine for testing double shear specimens

In the first procedure, specimens are deformed under creep conditions of constant load (equivalent to true constant stress due to the use of double-shear specimen geometry). In this case, the steady-state strain rate is recorded for the imposed stress and the data are plotted logarithmically as strain rate against stress. Steady

strain rates are obtained by performing uninterrupted tests and/or stress-change tests. In uninterrupted tests, several identical specimens are tested at different stresses (constant temperature and constant grain size), and steady-state strain rates are calculated from creep curves that represent plots of strain against time. Typical examples of creep curves reported for commercial grade Zn-22Al at intermediate and low stresses are given in Fig. 3(a) and (b) respectively (Ref 14). Examination of these creep curves shows that the alloy exhibits a normal primary stage followed by a well-defined steady-state stage, and that the duration of the primary stage increases with decreasing applied stress. In stress-change tests, the steady-state strain rates are measured at several different stresses on a single specimen. In this procedure, a single specimen is crept at a constant stress to within steady-state creep, and then the initial stress is changed in successive steps to a final value. For each stress change, whether an increase or a decrease, sufficient strain is allowed to ascertain whether the new steady-state stage has been reached. Figures 4(a) and (b), in which the creep rate is plotted as a function of creep strain, provide typical examples of the application of this procedure to high purity Zn-22Al (Ref 14). The data presented in these figures reveal the following features: (a) After a stress increase, the creep rate decreases and reaches the new steady-state value (Fig. 4a), and by contrast, after a stress reduction, the creep rate increases and reaches the new steady-state value (Fig. 4a); (b) After a stress decrease or a stress increase, the amount of transient strain preceding steady-state creep is small, approximately 0.01 to 0.02.

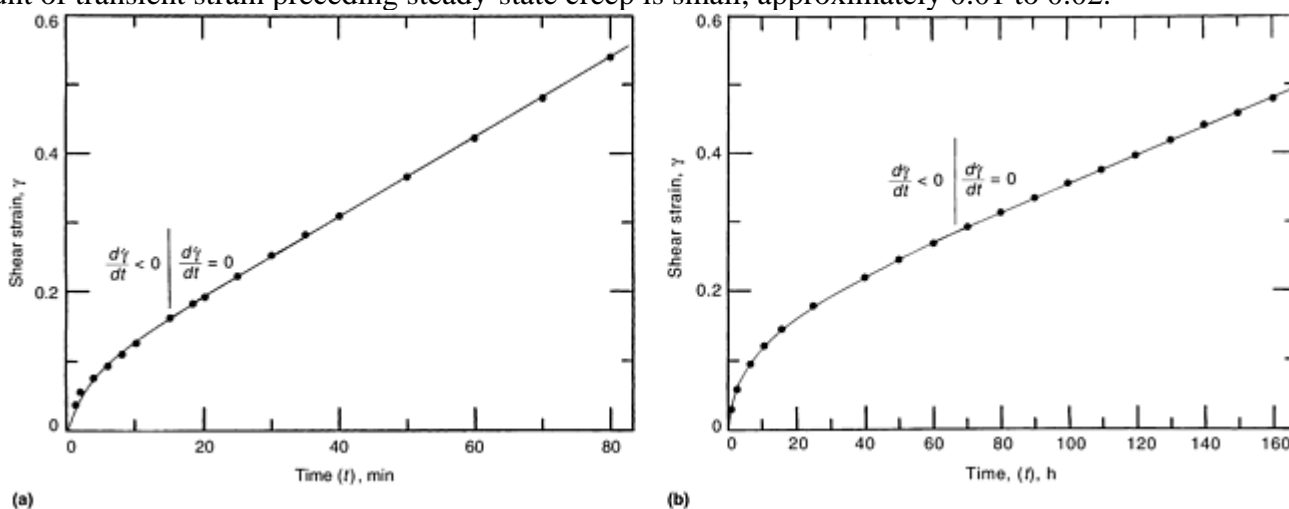


Fig. 3 Shear strain versus time (creep curve) for commercial purity Zn-22Al having a grain size of 3.5 μm . Temperature, 463 K. (a) $\tau = 4.14$ MPa. (b) $\tau = 0.825$ MPa. Source: Ref 14

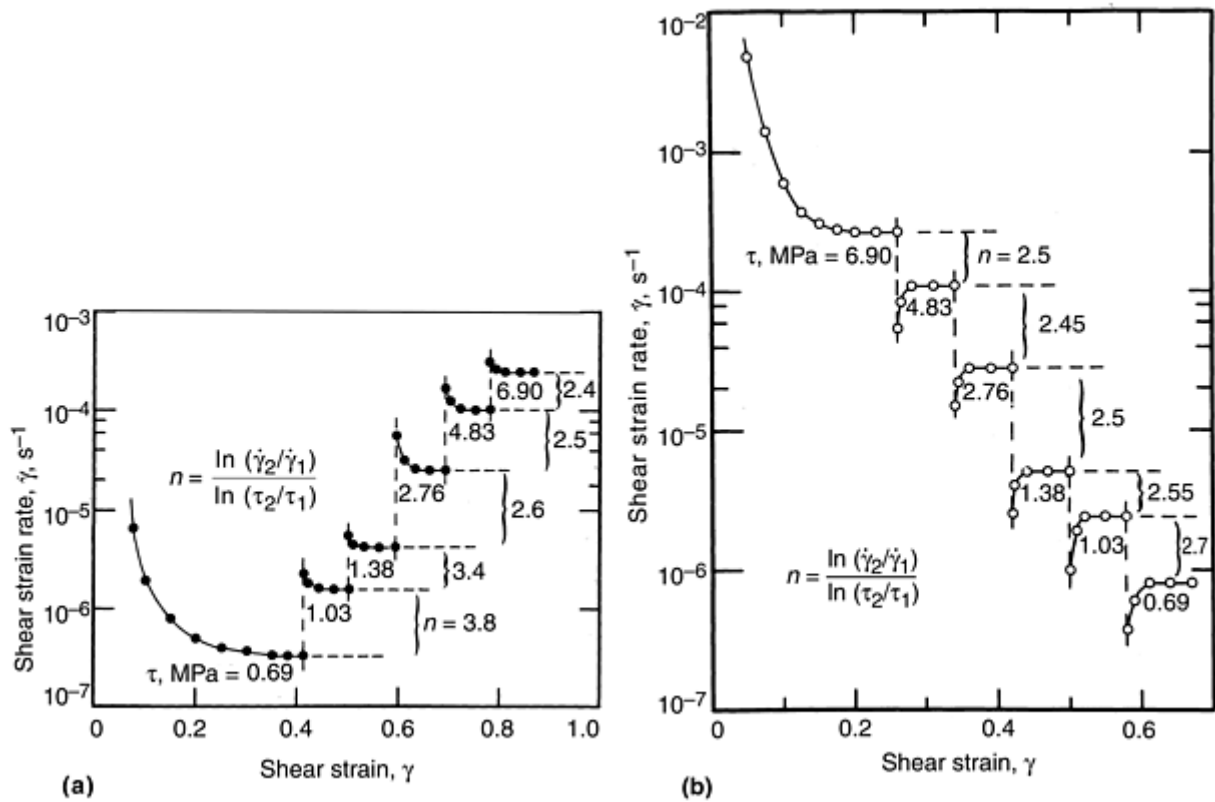


Fig. 4 The results of stress-change experiments for high-purity Zn-22Al having a grain size of 3.5 μm . Temperature, 463 K. (a) Stress is increased from $\tau = 0.69$ MPa in steps to $\tau = 6.0$ MPa. (b) Stress is decreased from $\tau = 6.9$ MPa in steps to $\tau = 0.69$ MPa. Source: Ref 14

In the second procedure, specimens are deformed using a testing machine that imposes a constant rate of crosshead displacement (equivalent to a true constant strain rate due to the double-shear configuration of the specimen). In this case, the steady-state flow stress is recorded for an imposed strain rate and the data are plotted as stress against strain rate on logarithmic scales. The steady-state stresses are obtained from tests conducted on several specimens at true strain rates (uninterrupted tests) or from cycling tests conducted on the same specimen (strain rate-change tests). Figure 5 illustrates both types of tests using double-shear specimens. In Fig. 5, the results on Zn-22Al are plotted as shear stress against shear strain up to strains of 125% (Ref 19). The solid lines show the individual stress-strain curves for the various specimens tested at different constant strain rates; the strain rates are indicated for each curve. The broken line shows the composite stress-strain curve obtained by cycling a single specimen through a number of constant strain rates.

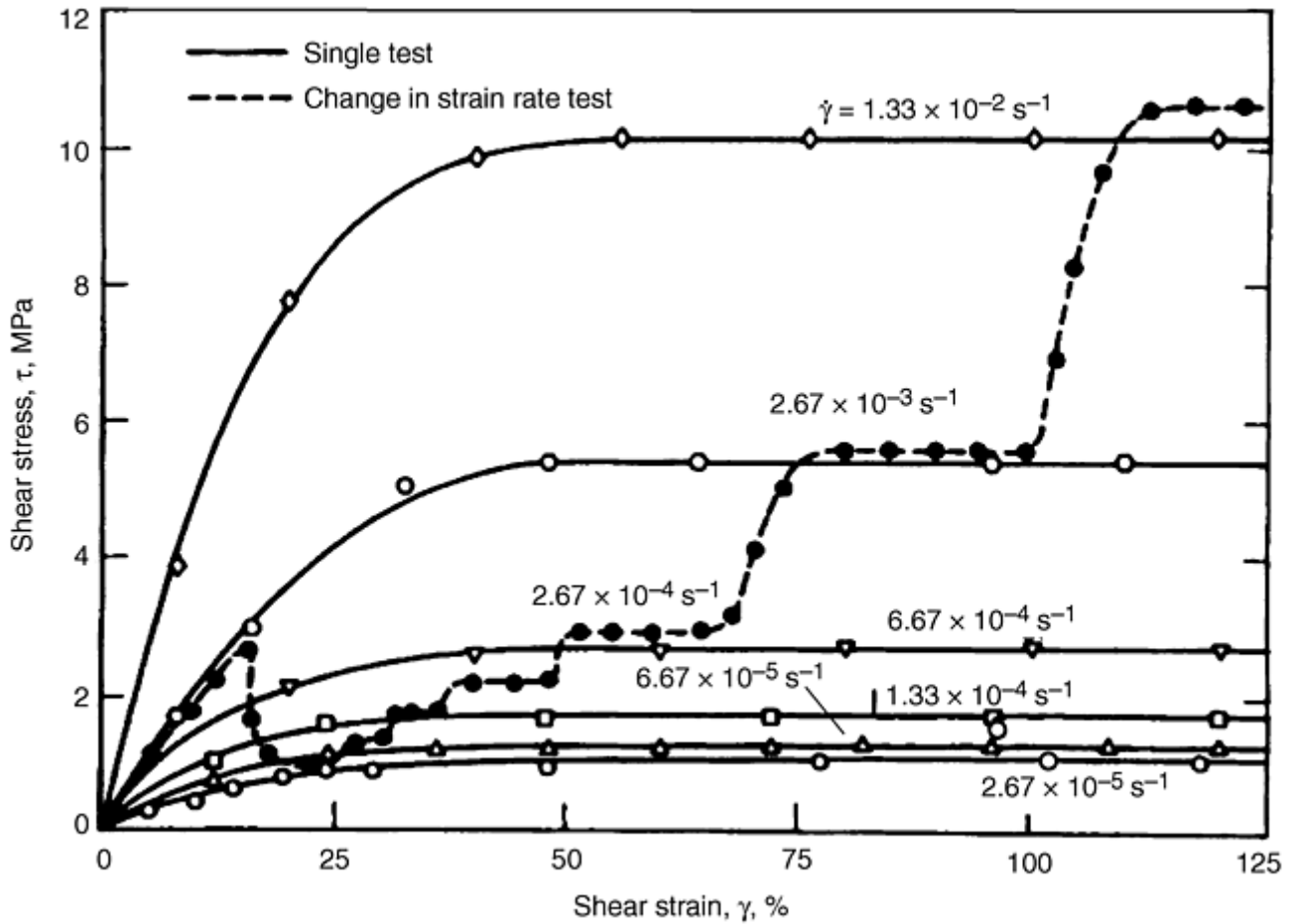


Fig. 5 Shear stress plotted against shear strain for specimens of Zn-22Al at a temperature of 484 K, obtained either by testing each specimen at a single constant strain rate (solid line) or by cycling a single specimen through a number of constant strain rates (broken line). Source: Ref 19

Typical experimental results on the stress dependence of strain rate in commercial purity Zn-22Al (Ref 14) are shown in Fig. 6, in which shear strain rate, $\dot{\gamma}$, is plotted as a function of shear stress, τ , on a logarithmic scale. By identifying the individual datum points from the creep machine and universal testing machine (UTM) (a screw-driven machine operated at a constant cross-head speed), it is clear that there is excellent agreement between the two experimental procedures over intermediate stresses (and intermediate strain rates). In obtaining the data for Fig. 6, the creep machine (constant-stress and stress-change experiments) was primarily used to establish the deformation at low and intermediate stresses whereas the UTM (constant-strain-rate and strain-rate-cycling experiments) was used to establish behavior at intermediate and high stresses.

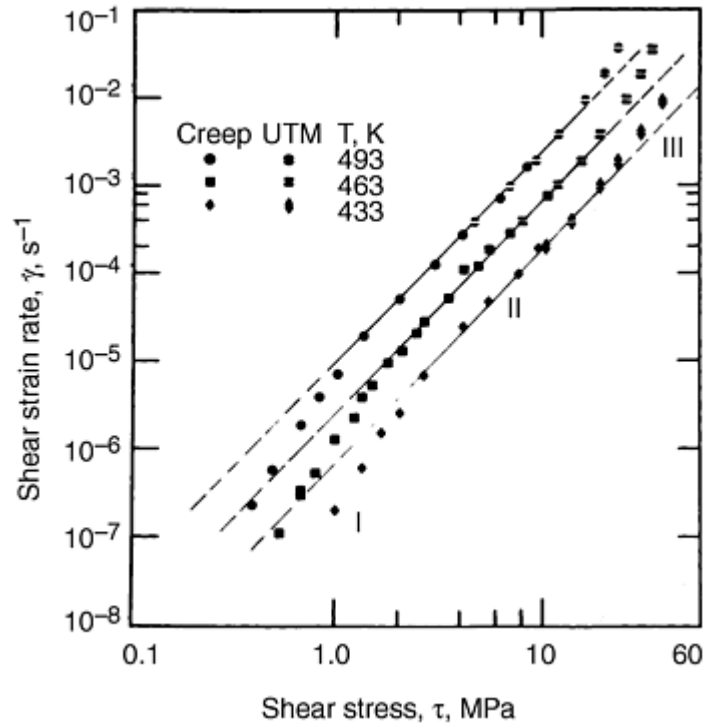


Fig. 6 Shear strain rate versus shear stress (logarithmic scale) for commercial purity Zn-22Al having a grain size of 3.5 μm at various temperatures from 433 to 493 K. Source: Ref 14

The Relationship between Strain Rate and Temperature

When the plastic deformation of a material is dictated by a thermally activated process, the strain rate for the i th deformation mechanism may be expressed in terms of rate reaction theory as:

$$\dot{\gamma}_i = A_i(\tau, T, d) \exp\left(-\frac{\Delta H_i}{RT}\right) \quad (\text{Eq 1})$$

where A_i is the frequency factor, τ is the applied stress, T is the absolute temperature, d is the grain size, ΔH_i is the activation enthalpy, and R is the gas constant. The activation enthalpy (ΔH_i) is an important component in the deformation equation, and its determination plays a key role in the process of identifying the rate-controlling mechanism. According to Eq 2, ΔH_i is uniquely defined by the expression:

$$\Delta H_i = R \left(\frac{\partial \ln \dot{\gamma}}{\partial (-1/T)} \right)_{\tau, d} \quad (\text{Eq 2})$$

Equation 2 suggests a simple and direct method of estimating ΔH_i , which is referred to as an activation enthalpy at constant stress and which, under creep conditions, is equivalent to the apparent activation energy, Q_a .

Superplasticity is a thermally activated process, and Eq 2 provides the basis of various methods adopted to determine the activation energy associated with the flow process. The following section outlines three methods for measuring the activation energy for super-plastic deformation.

Rapid Change in Temperature at Constant Stress. If the temperature is changed very rapidly during a test and the stress level remains constant, the apparent activation energy may be obtained from Eq 2 through the expression:

$$Q_a \approx \frac{R \ln(\dot{\gamma}_2 / \dot{\gamma}_1)}{(T_2 - T_1) / T_2 T_1} \quad (\text{Eq 3})$$

where $\dot{\gamma}_1$ and $\dot{\gamma}_2$ are the instantaneous creep rates immediately preceding and following a small increase in temperature from T_1 to T_2 (Ref 20, 21). Figure 7 provides an example of the application of this temperature change procedure to commercial purity Zn-22Al (Ref 14).

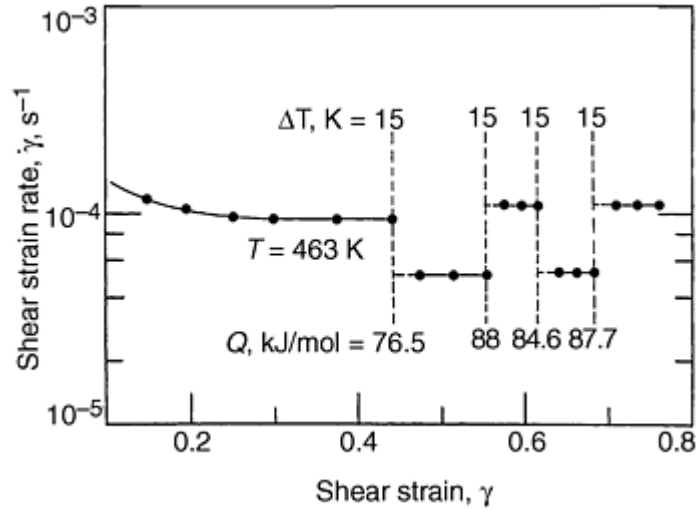


Fig. 7 Shear strain rate versus strain for commercial purity Zn-22Al having a grain size of 3.5 μm , showing the determination of the activation energy (Q) from the temperature change procedure. $\tau = 4.14$ MPa; $Q_{\text{ave}} = 84.2$ kJ/mole. Source: Ref 14

Variation of Strain Rate at Constant Stress. Under conditions of constant stress and grain size, Q_a is given by Eq 2. A plot of logarithmic $\dot{\gamma}$ versus $1/T$ at a constant stress has a slope of $-Q_a/2.3R$. The data of such a plot are obtained from a logarithmic plot of strain rate against stress at a constant grain size and with a range of temperatures (Fig. 6).

Variation of Stress at Constant Strain Rate. As mentioned earlier, tests on superplastic behavior are also conducted at constant strain rate. According to an analysis of the activation energy for superplastic flow, under conditions of constant strain rate, Q_a is given by:

$$Q_a = nR \left(\frac{\partial \ln \tau}{\partial (1/T)} \right)_{d, \dot{\gamma}} \quad (\text{Eq 4})$$

Therefore, a plot of logarithmic τ versus $1/T$ has a slope of $Q_a/2.3nR$ (Ref 21).

It is worth noting that due to the small values of the stress exponent for superplastic flow, the difference between the apparent activation energy and the true activation energy is not significant and falls in the range of the experimental error involved in measurement of Q_a , that is, the correction for the temperature dependence of the shear modulus may not be necessary (Ref 22).

The Relationship between Strain Rate or Stress and Grain Size

The relationship between strain rate and grain size can be established by conducting a series of tests at a constant temperature and with a range of grain sizes. The data obtained from these tests are then plotted as strain rate against stress on a logarithmic scale, as shown in Fig. 8. Finally, the grain-size exponent, s , is obtained from the logarithmic plot of strain rate against stress by logarithmically plotting strain rate against grain size at constant stress (Ref 14, 23).

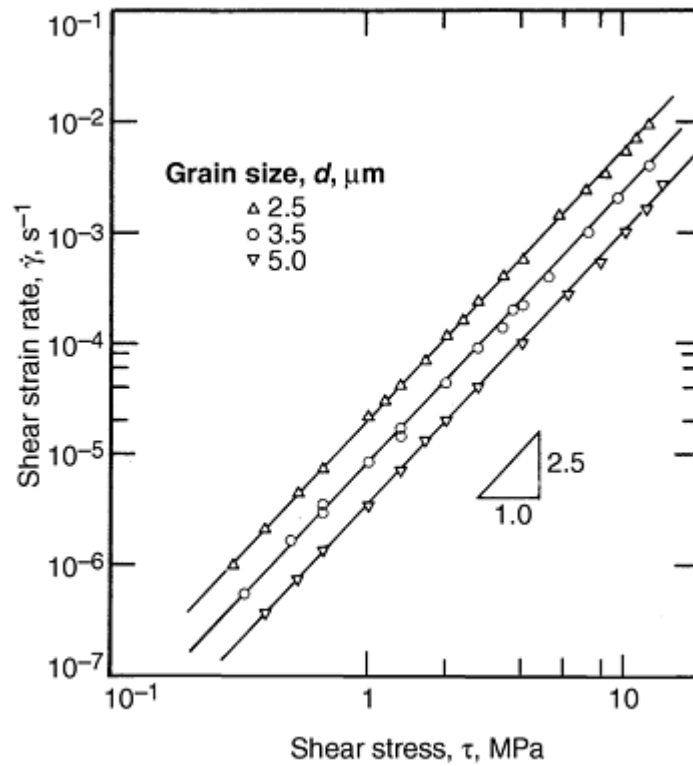


Fig. 8 Shear strain rate versus shear stress (logarithmic scale) for high purity Zn-22Al for various grain sizes at 493 K. Source: Ref 14

The Relationship between Strain Contributed by Boundary Sliding and Total Strain

Grain-boundary sliding (GBS) is a process that occurs during the high-temperature creep of polycrystalline materials and in which one grain slides over another grain under the action of a shear stress. Sliding is shown schematically in Fig. 9. As a result of the sliding of the two grains offsets are produced at their common boundary; \mathbf{pr} is the sliding vector, u is the component of sliding resolved along the stress axis, v is the component measured perpendicular to both the stress axis and the specimen surface, and w is the component measured perpendicular to the stress axis but in the plane of the surface. Also, as shown in Fig. 9, the orientation of the grain boundary is defined by two angles θ and α : θ is the angle between the stress axis and the trace of the boundary in the plane of the surface, and α is the internal angle made by the boundary trace on a longitudinal section cut perpendicular to the surface.

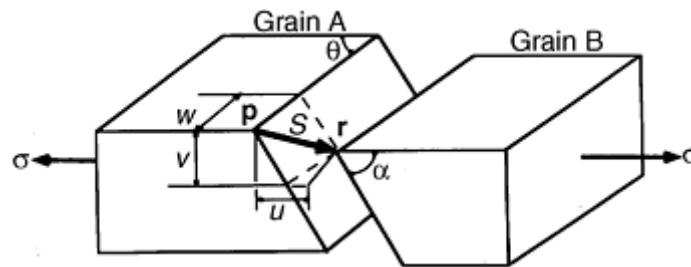


Fig. 9 Schematic representation of grain-boundary sliding

In superplasticity experiments, the longitudinal offset, u , and/or the transverse offsets, w , are considered in calculating the strain contribution from boundary sliding to total strain. As described elsewhere (Ref 24, 25), the strain due to boundary sliding, ϵ_{gbs} , is obtained from \bar{u} and \bar{w} through the following expressions:

$$\epsilon_{\text{gbs}} = \Psi \bar{u} / \bar{L} \quad (\text{Eq 5a})$$

$$\epsilon_{\text{gbs}} = \phi \bar{w} / \bar{L} \quad (\text{Eq 5b})$$

where Ψ is a geometric constant equal to 0.8 (Ref 24) for the longitudinal offset, \bar{u} is the average offset, \bar{L} is the average linear intercept grain size, ϕ is a geometric constant equal to 1.5 for the transverse offset, and \bar{w} is the average transverse offset (Ref 24, 25). The method of calculating ε_{gbs} from u is applicable only when the grains are equiaxed, a condition that is satisfied during superplastic deformation. The contribution of boundary sliding to the total strain, ξ , is calculated from the equation:

$$\xi = \varepsilon_{\text{gbs}} / \varepsilon_t \quad (\text{Eq 6})$$

In taking measurements of GBS, several steps are carried out. First, prior to testing, one of the flat surfaces of each specimen is polished to a mirror-like scratch-free surface, and very fine lines (marker lines) are placed on the polished gage surface, either parallel or perpendicular to the specimen axis. One method of creating such lines is by drawing a lens tissue containing 1 μm diamond paste across the surface only once in either the longitudinal or the transverse direction. Longitudinal marker lines are used to measure the sliding offset perpendicular to the stress axis, w . Transverse marker lines are used to measure the sliding offset parallel to the stress axis, u . Figure 10 illustrates the two types of marker lines, longitudinal and transverse, and the two classes of offset, w and u . It is also possible to take measurements of sliding using a printed-grid technique. However, as reported elsewhere, the technique can be unsatisfactory due to the resolution difficulties in the scanning electron microscope (SEM) (Ref 24). Second, tensile specimens are deformed at a constant temperature on a testing machine operated at a constant crosshead speed. Tensile tests are conducted to a predetermined strain in the range of 20 to 100% at various initial strain rates. Third, after testing and cleaning in an ultrasonic cleaner, the specimens are examined in the SEM and a number of representative photomicrographs are taken within the gage length. These micrographs are enlarged, and individual sliding offsets are measured. In general, about 200 to 500 readings are taken on each one of the specimens.

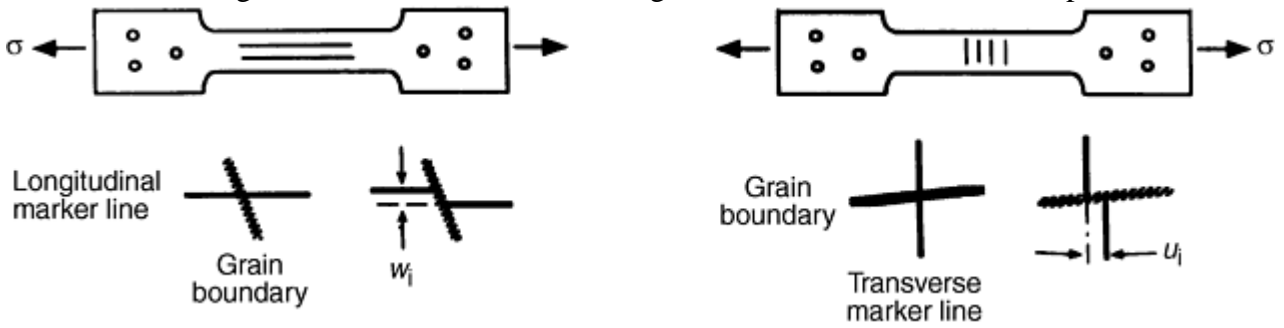


Fig. 10 Schematic configuration of maker lines, longitudinal and transverse, and their offsets, w (perpendicular to stress axis) and u (parallel to the stress axis), respectively

Superplastic alloys such as Zn-22Al and Pb-62Sn have two phases, and in this case, there are two intercrystalline boundaries (e.g., Al-Al and Zn-Zn) and an interphase boundary (e.g., Al-Zn). To ensure that sampling of measurement for GBS does not favor a certain type of boundary, the number of each type of boundary counted experimentally should be selected according to an approach proposed by Gifkins (Ref 26). Such an approach, which was adopted in examining sliding behavior in high-purity Pb-62Sn (Ref 26, 27) and Zn-22Al (Ref 28), is extended here to describe the general case of a superplastic material consisting of two phases.

The approach by Gifkins (Ref 26) is based on the following assumptions: (a) the ratio of the volume fraction of the two phases of a micrograin superplastic alloy is equivalent to the ratio in the linear transverse intercept, and (b) grains make a single transverse array. If the ratio of the volume fraction of α and β phases in the alloy is f , then this ratio, on the basis of the above assumptions, may be expressed as:

$$X\bar{L}_\alpha / Y\bar{L}_\beta = f \quad (\text{Eq 7a})$$

where X and Y are the number of α and β grains respectively, and \bar{L}_α and \bar{L}_β are the linear sizes of α and β phases, respectively. This expression may be rewritten using the following consideration. If x (α - α) boundaries and y (α - β) boundaries are counted, there would be x (α) grains forming (α - α) boundaries and $y/2$ (α) grains forming α - β boundaries, that is, $X = x + y/2$. Then, the number of β grains, Y , and the number of (β - β) boundaries, z , are given, respectively, by:

$$Y = \frac{1}{f} \left(\frac{\bar{L}_\alpha}{\bar{L}_\beta} \right) \left(x + \frac{y}{2} \right) \quad (\text{Eq 7b})$$

and

$$z = Y - y/2 \quad (\text{Eq 7c})$$

The following example, based on the recent results reported for the superplastic Zn-22Al alloy (Ref 28), illustrates the application of Eq 7b(b) and (c) to boundary-sliding measurements. For this alloy, α is the aluminum-rich phase, β is the zinc-rich phase, and $f = 0.75$. Accordingly, Eq 7a(a) gives 100 zinc grains for every 88 aluminum grains when $\bar{L}_{\text{Zn}} = 303 \mu\text{m}$ and $\bar{L}_{\text{Al}} = 2.8 \mu\text{m}$. In performing sliding measurements, the number of Al-Al and Zn-Al boundaries sampled were close to 60 and 150, respectively. Using $x = 60$, $y/2 = 75$, $\bar{L}_{\text{Al}} = 2.8 \mu\text{m}$, and $\bar{L}_{\text{Zn}} = 3.3 \mu\text{m}$, Eq 7b(b) and (c) result in 78 Zn-Zn boundaries, a number used in the analysis reported in Ref 28.

Figures 11(a) and (b) show typical photographs of commercial purity Zn-22Al tested to an elongation of about 20% at $4 \times 10^{-5} \text{ s}^{-1}$ in the superplastic region (Ref 28). The photographs show several features associated with the occurrence of sliding in the alloy: (a) grain displacements are often large and sharp, as illustrated, for example, by Fig. 11(a); (b) striated bands (Fig. 11a) are usually observed at Zn-Al boundaries and Zn-Zn boundaries; and (c) grain rotation is observed to occur in both phases, the aluminum-rich phase (dark) and the zinc-rich phase (bright) (Fig. 11b).

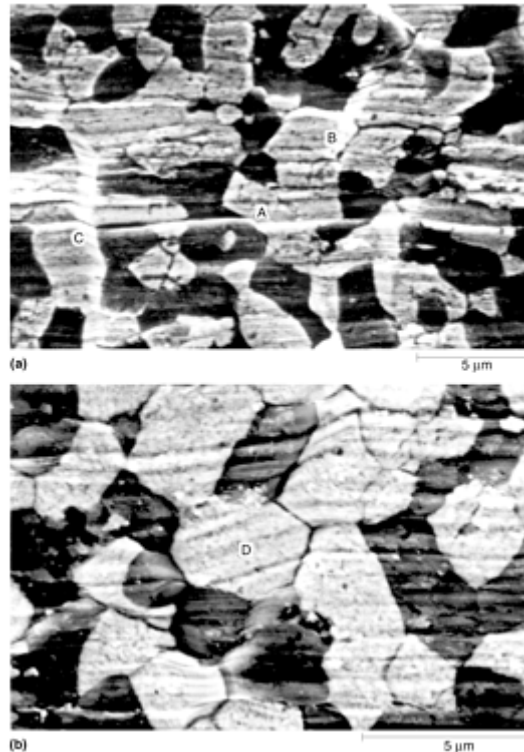
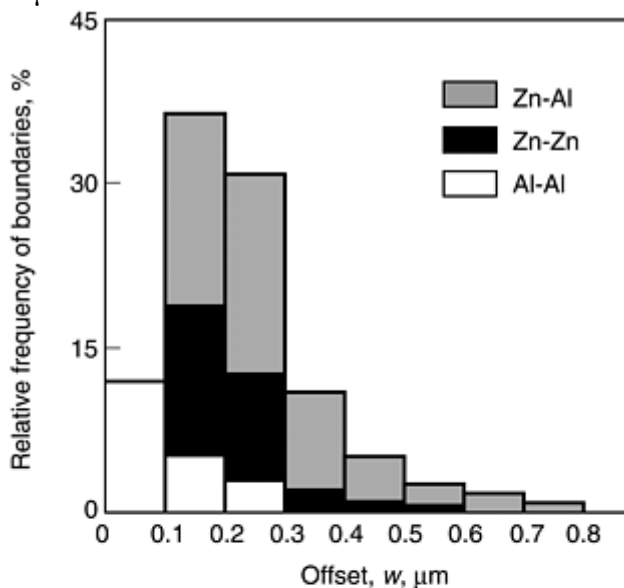


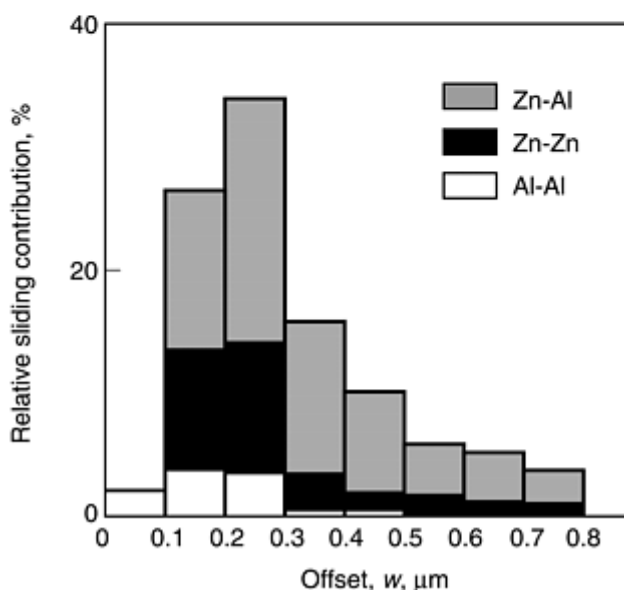
Fig. 11 Typical area of the gage length for a Zn-22Al sample tested at $4 \times 10^{-5} \text{ s}^{-1}$ to an elongation of 20%. (a) A large offset at a Zn-Al boundary is shown at A and a striated band at a Zn-Zn boundary is marked at B and at C. (b) Grain rotation in a zinc-rich phase is shown at D. Source: Ref 28

To characterize the offset measurements, two types of histograms are normally constructed (Ref 24, 27, 28, 29). The first type is based on the relative frequency of various boundaries, whereas the second type is based on the relative sliding contribution of these boundaries. These two types of histograms are illustrated using some of the recent results reported for Zn-22Al (Ref 27). In Fig. 12(a), the histogram of the relative frequency of boundaries is shown. In this case, the relative frequency of the number of each boundary (Al-Al, Zn-Al, and Zn-Zn) is plotted against the offset w in increments of $0.1 \mu\text{m}$ at $\dot{\epsilon}_0 = 4 \times 10^{-5} \text{ s}^{-1}$, which corresponds to the super-plastic region. As noted in the figure, the largest displacements occur at Zn-Al interphase boundaries, the smallest displacements occur at Al-Al intercrystalline boundaries, and Zn-Zn intercrystalline boundaries exhibit slightly lower values than those at Zn-Al boundaries. In addition, the histogram shows the following features:

(a) all displacements are in the range of 0 to 0.8 μm ; (b) the maximum frequency occurs at the boundaries with the offset interval of 0.1 to 0.2 μm ; and (c) the largest sliding offsets at Al-Al intercrystalline boundaries are found in the interval of 0.4 to 0.5 μm .



(a)



(b)

Fig. 12 Histograms for commercial purity Zn-22Al with a grain size of 5.4 μm for offset increments of 0.1 μm at $\dot{\epsilon}_0 = 4 \times 10^{-5} \text{ s}^{-1}$ and 493 K. (a) Histogram showing the relative frequency of the number of boundaries. (b) Histogram showing the relative sliding contribution to the total sliding for each type of boundary

In Fig. 12(b), the histogram of relative sliding is presented. As shown in the figure, the percentage contributions to the total sliding for each type of boundary in Zn-22Al are plotted for the offset w in increments of 0.1 μm $\dot{\epsilon}_0 = 4 \times 10^{-5} \text{ s}^{-1}$. This histogram is more practical than that based on the frequency of the number of each type of boundary (Fig. 12a) because a small number of boundaries with a large amount of offsets can significantly contribute to the total sliding. According to the histogram, maximum contribution occurs at boundaries with displacement offsets in the interval of 0.2 to 0.3 μm .

References cited in this section

7. W.A. Backofen, I.R. Turner, and D.H. Avery, Superplasticity in an Al-Zn Alloy, *Trans. ASM*, Vol 57, 1964, p 980
8. W.B. Morrison, Superplasticity of Low-Alloy Steels, *Trans. ASM*, Vol 61, 1968, p 423
9. J. Hedworth and M.J. Stowell, The Measurement of Strain-Rate Sensitivity in Superplastic Alloys, *J. Mater. Sci.*, Vol 6, 1971, p 1061
10. G.B. Gibbs, Creep and Stress Relaxation Studies with Polycrystalline Magnesium, *Philos. Mag.*, Vol 13, 1966, p 317
11. A. Arieli and A. Rosen, Measurement of Strain-Rate Sensitivity Coefficient in Superplastic Ti-6Al-4V Alloy, *Scr. Metall.*, Vol 10, 1976, p 471
12. E.W. Hart, A Phenomenological Theory for Plastic Deformation of Polycrystalline Metals, *Acta Metall.*, Vol 18, 1970, p 599
13. P.K. Chaudhury and F.A. Mohamed, Effect of Impurity Content on Superplastic Flow in the Zn-22% Al Alloy, *Acta Metall.*, Vol 36, 1988, p 1099
14. P.K. Chaudhury, V. Sivaramakrishnan, and F.A. Mohamed, Superplastic Deformation Behavior in Commercial and High Purity Zn-22 pct Al, *Metall. Trans. A*, Vol 19, 1988, p 2741
15. S. Yan, J.C. Earthman, and F.A. Mohamed, Effect of Cd on Superplastic Flow in the Pb-62 wt% Sn Eutectic, *Philos. Mag. A*, Vol 69, 1994, p 1017
16. B.Y. Chirouze, D.M. Schwartz, and J.E. Dorn, The Mechanism of Basal Creep in Mg-12 at.% Li from 500 to 885 K, *Trans. ASM*, Vol 51, 1967, p 51
17. K.L. Murty, F.A. Mohamed, and J.E. Dorn, Viscous Glide, Dislocation Climb and Newtonian Viscous Deformation Mechanisms of High Temperature Creep in Al-3Mg, *Acta Metall.*, Vol 20, 1972, p 1009
18. M.S. Soliman, T.J. Ginter, and F.A. Mohamed, *Philos. Mag. A*, Vol 48, 1993, p 63
19. F.A. Mohamed and T.G. Langdon, A Comparison of Constant Strain Rate and Creep Testing Procedures in Superplasticity, *J. Mater. Sci.*, Vol 17, 1982, p 1925
20. H.I. Huang, O.D. Sherby, and J.E. Dorn, Activation Energy for High Temperature Creep of High Purity Aluminum, *Trans. MS/AIME*, Vol 23, 1956, p 117
21. F.A. Mohamed and T.G. Langdon, The Determination of the Activation Energy for Superplastic Flow, *Phys. Status Solidi (a)*, Vol 33, 1976, p 375
22. J.E. Bird, A.K. Mukerjee, and J.E. Dorn, Correlations between High-Temperature Creep Behavior and Structure, *Proc. of a Symp. on Quantitative Relation Between Properties and Microstructure*, D.G. Brandon and A. Rosen, Ed., Israel University Press, 1969, p 22
23. F.A. Mohamed and T.G. Langdon, Creep at Low Stress Levels in the Superplastic Zn-22% Al Eutectoid, *Acta Metall.*, Vol 23, 1975, p 117
24. P. Shariat, R.B. Vastava, and T.G. Langdon, An Evaluation of the Roles of Intercrystalline and Interphase Boundary Sliding in Two-Phase Supersonic Alloys, *Acta Metall.*, Vol 30, 1982, p 285

25. T.G. Langdon, The Effect of Surface Configuration on Grain Boundary Sliding, *Metall. Trans.*, Vol 3, 1972, p 797
26. R.C. Gifkins, Factors Influencing Deformation of Superplastic Alloys, *Mater. Forum*, Vol 15, 1991, p 82
27. K.T. Park, S. Yan, and F.A. Mohamed, Boundary Sliding Behavior in High-Purity Pb-62% Sn, *Philos. Mag. A*, Vol 72, 1995, p 891
28. K. Duong and F.A. Mohamed, Effect of Impurity Content on Boundary Sliding Behavior in the Superplastic Zn-22% Al Alloy, *Acta Mater.*, Vol 46, 1998, p 4571
29. R.B. Vastava and T.G. Langdon, An Investigation of Intercrystalline and Interphase Boundary Sliding in the Superplastic Pb-62% Sn Eutectic, *Acta Metall.*, Vol 27, 1979, p 251

Superplastic Deformation at Elevated Temperatures

Farghalli A. Mohamed, University of California, Irvine

Deformation Regions and Their Characteristics

Over the past three decades, the mechanical behavior of micrograin superplastic alloys has been extensively studied. As a result of these investigations, two findings are well documented. First, micrograin superplasticity is a diffusion-controlled process that can be represented by the following dimensionless equation (Ref 22):

$$\frac{\dot{\gamma}kT}{DG\mathbf{b}} = A \left(\frac{\mathbf{b}}{d} \right)^s \left(\frac{\tau}{G} \right)^n \quad (\text{Eq 8a})$$

with

$$D = D_0 \exp\left(-\frac{Q}{RT}\right) \quad (\text{Eq 8b})$$

where $\dot{\gamma}$ is the shear creep, k is Boltzmann's constant, T is the absolute temperature, D is the diffusion coefficient that characterizes the creep process, G is the shear modulus, \mathbf{b} is the Burgers vector, A is a dimensionless constant, d is the grain size, s is the grain-size sensitivity, τ is the applied shear stress, n is the stress exponent, Q is the activation energy for the diffusion process that controls the creep behavior, and D_0 is the frequency factor for diffusion.

Second, the relationship between stress (τ) and strain rate ($\dot{\gamma}$) is often sigmoidal (Ref 23, 30, 31, 32). Under creep-testing conditions, this sigmoidal relationship is manifested by the presence of three regions (Fig. 6): region I (low-stress region), region II (intermediate-stress region), and region III (high-stress region). The characterization of the sigmoidal trend in terms of these regions is mainly based on the value of the stress exponent, n ($n = (\partial \ln \dot{\gamma} / \partial \ln \tau)_{T,d}$) or strain rate sensitivity, m [$m = (\partial \ln \tau / \partial \ln \dot{\gamma})_{T,d}$] at constant temperature and grain size. Of these three regions, regions I and II have been the subject of many studies that have aimed at not only establishing the deformation characteristics of both regions but also providing interpretations of these characteristics in terms of deformation mechanisms. The characteristics of these three regions are briefly described below.

Region III. In this region (the high-stress region), the stress exponent is higher than 3, the apparent activation energy is higher than that for grain boundary diffusion, and the creep rates are sensitive to changes in grain size. **Region II** (the intermediate-stress region) covers several orders of magnitude of strain rate and is characterized by a stress exponent, n , of 1.5 to 2.5, an apparent activation energy, Q_a , that is close to that for boundary

diffusion, Q_{gb} , and a grain size sensitivity, s , of about 2. Contribution of GBS to the total strain is high and maximum ductility occurs. Because of these characteristics, region II is often referred to as the superplastic region. Experimental data show that superplastic behavior in this region is not sensitive to the presence of impurities. This finding is demonstrated in Fig. 13, where the experimental data of (a) Pb-62Sn and (b) Zn-22Al are plotted in terms of 8aEq 8b, as normalized creep rate versus normalized shear stress, τ/G , on a logarithmic scale. Normalized creep rate is given by $(\dot{\gamma}kT / D_{gb}Gb)(d/b)^s$, where $D_{gb} = D_0 \exp(-Q_{gb}/RT)$. In plotting the data on Pb-62Sn, the values of D_0 , Q_{gb} , b , and s were taken as $1 \text{ cm}^2/\text{s}$, 61 kJ/mol , $3.2 \times 10^{-8} \text{ cm}$, and 2.3 , respectively (Ref 17). In plotting the data on Zn-22Al, the values of D_0 , Q_{gb} , b , and s were taken as $1 \text{ cm}^2/\text{s}$, 78 kJ/mol , $2.7 \times 10^{-8} \text{ cm}$, and 2.4 , respectively (Ref 33). In addition to demonstrating that the creep rates of two grades of Pb-62Sn, having different impurity content, are identical in this region, Fig. 13(a) indicates that the same creep data cluster about a single straight line that extends over four orders of magnitude of strain rate. This result, which is similar to that shown for Zn-22Al in Fig. 13(b), confirms not only that region II behavior is insensitive to impurity atoms, but also that region II (the superplastic region) does not represent a transition region between region I (low-stress region) and region III (high-stress region), that is, region II is a consequence of the operation of a distinct deformation process.

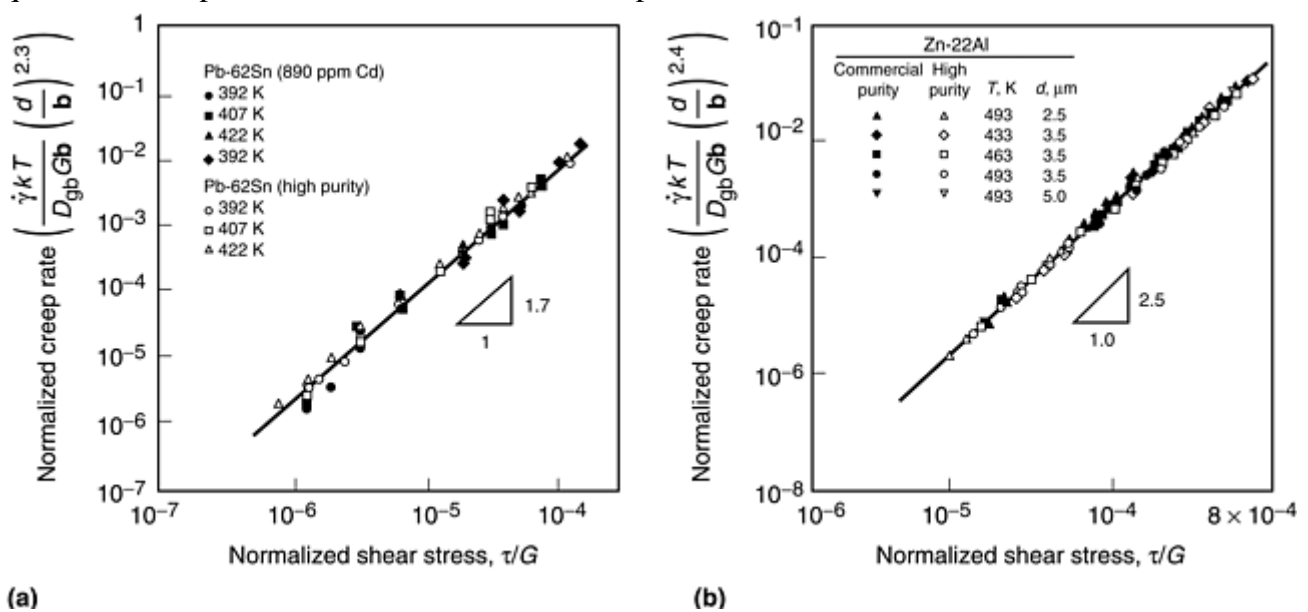
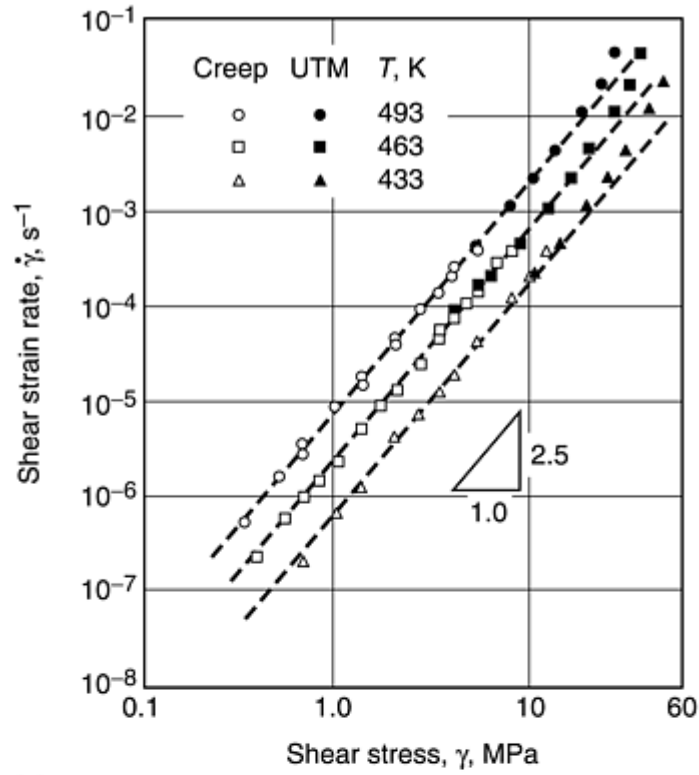
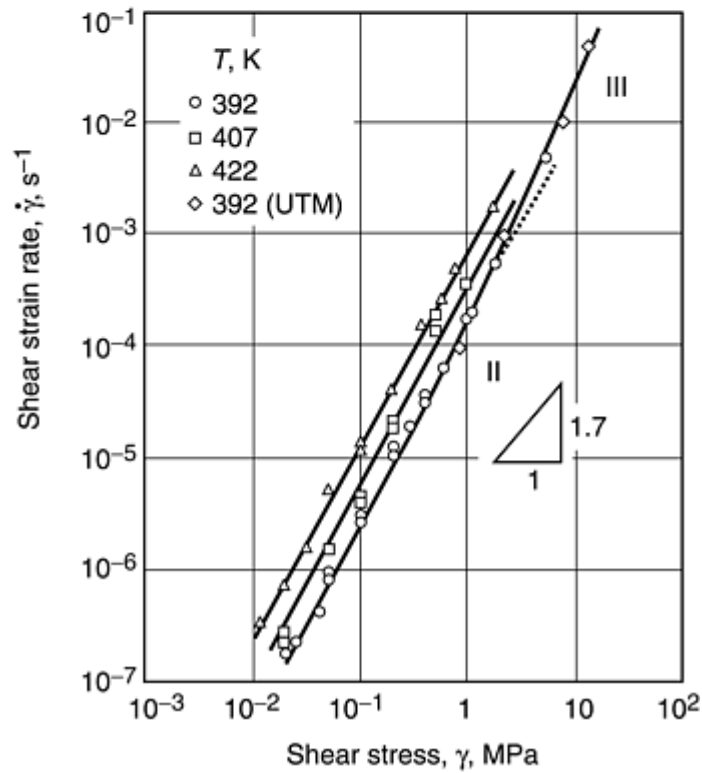


Fig. 13 Normalized creep rate versus normalized shear stress (logarithmic scale). (a) For Pb-62Sn doped with cadmium at intermediate stresses (region II) and for high-purity Pb-62Sn at both intermediate and low stresses. Source: Ref 15. (b) For commercial-purity Zn-22Al at intermediate stresses (region II) and for high-purity Zn-22Al at both intermediate and low stresses. Source: Ref 14

Region I (the low-stress region) is characterized by a stress exponent of 3 to 5 (Ref 23, 30, 31, 32), an apparent activation energy higher than that for grain-boundary diffusion, and a decrease in both ductility and contribution of GBS to total strain. However, the creep behavior in this region exhibits essentially the same grain-size sensitivity noted in region II. Recent experimental evidence (Ref 13, 14, 15, 33) has revealed that steady-state creep in region I, unlike that in region II, is influenced by impurities. This evidence has been demonstrated by two main experimental observations: (a) Zn-22Al (Ref 13, 14) and Pb-62Sn (Ref 15) do not exhibit region I when the impurity level in the alloy is reduced to about 6 ppm; and (b) the stress exponent, n , and the apparent activation energy for creep, Q_a , in region I, unlike those in region II, are sensitive to impurity content (Ref 13, 33). Observation (a) is demonstrated by Fig. 14(a) and (b), which show the absence of region I in high-purity Zn-22Al (Ref 13, 14) and high-purity Pb-62Sn (Ref 15), respectively. As indicated by Fig. 6, region I is present in commercial purity Zn-22Al that contains 100 ppm of impurities (Ref 14). Observation (b) is demonstrated by Fig. 15, in which the values of the apparent activation energy in regions I and II are plotted as a function of applied stress for three grades of Zn-22Al containing different impurity levels; grades 1, 2, and 3 contain 180, 100, and 6 ppm of impurities. As shown by the figure, Q_a in grade 3 (high-purity grade) is equal to 85 kJ/mol ($\sim Q_{gb}$), even at stresses typical of those used in investigating region I in grades 1 and 2; under the condition of constant stress, Q_a in region I for grade 2 (100 ppm of impurities) is smaller than that for grade 1 (180 ppm of impurities).



(a)



(b)

Fig. 14 Shear strain rate versus shear stress (logarithmic scale). (a) For high-purity Zn-22Al having a grain size of 3.5 μm at various temperatures from 433 to 493 K. Source: Ref 14. (b) For high-purity Pb-62Sn having a grain size of 8 μm at various temperatures from 392 to 422 K. Source: Ref 15

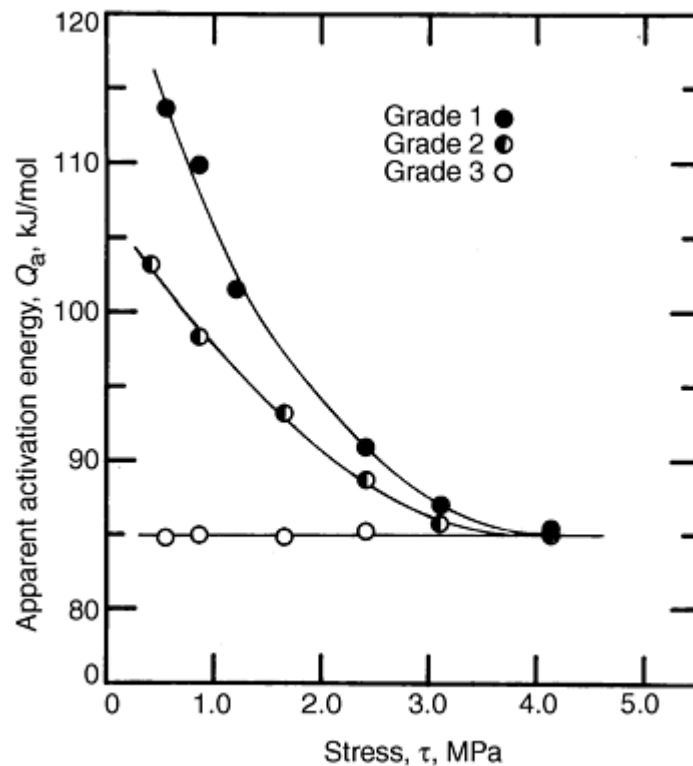


Fig. 15 The dependence of the average apparent activation energy on stress for grades 1, 2, and 3 of Zn-22Al containing 180, 100, and 6 ppm of impurities, respectively (grain size = 2.5 μm). Source: Ref 13

References cited in this section

13. P.K. Chaudhury and F.A. Mohamed, Effect of Impurity Content on Superplastic Flow in the Zn-22% Al Alloy, *Acta Metall.*, Vol 36, 1988, p 1099
14. P.K. Chaudhury, V. Sivaramakrishnan, and F.A. Mohamed, Superplastic Deformation Behavior in Commercial and High Purity Zn-22 pct Al, *Metall. Trans. A*, Vol 19, 1988, p 2741
15. S. Yan, J.C. Earthman, and F.A. Mohamed, Effect of Cd on Superplastic Flow in the Pb-62 wt% Sn Eutectic, *Philos. Mag. A*, Vol 69, 1994, p 1017
17. K.L. Murty, F.A. Mohamed, and J.E. Dorn, Viscous Glide, Dislocation Climb and Newtonian Viscous Deformation Mechanisms of High Temperature Creep in Al-3Mg, *Acta Metall.*, Vol 20, 1972, p 1009
22. J.E. Bird, A.K. Mukerjee, and J.E. Dorn, Correlations between High-Temperature Creep Behavior and Structure, *Proc. of a Symp. on Quantitative Relation Between Properties and Microstructure*, D.G. Brandon and A. Rosen, Ed., Israel University Press, 1969, p 22
23. F.A. Mohamed and T.G. Langdon, Creep at Low Stress Levels in the Superplastic Zn-22% Al Eutectoid, *Acta Metall.*, Vol 23, 1975, p 117
30. F.A. Mohamed, S. Shen-Ann, and T.G. Langdon, The Activation Energies Associated with Superplastic Flow, *Acta Metall.*, Vol 23, 1975, p 1443
31. F.A. Mohamed and T.G. Langdon, Creep Behavior in the Superplastic Pb-62% Sn Eutectic, *Philos. Mag. A*, Vol 32, 1975, p 697
32. S.H. Vale, D.J. Eastgate, and P.M. Hazzledine, The Low Strain Rate Behavior of Superplastic Zn-Al Eutectoid Alloy, *Scr. Metall.*, Vol 13, 1979, p 1157

Superplastic Deformation at Elevated Temperatures

Farghalli A. Mohamed, University of California, Irvine

Deformation Mechanisms

Region III Deformation Mechanisms. The deformation mechanism responsible for this region is not well established. Early observations suggest that region III in superplastic alloys represents normal power-law creep, which controls the behavior of large-grained metals at elevated temperatures (Ref 22). These observations (Ref 3) include (a) measurements of high stress exponents in several superplastic alloys, (b) the presence of extensive dislocation activity in the interiors of grains, (c) the occurrence of changes in grain shape, (d) increases in the texture after deformation, and (e) the close correspondence between the transition stresses from region II (the superplastic region) to region III and those predicted from the equation that describes the dependence of the average subgrain size, λ , formed during the creep of metals on the applied stress (Ref 22, 34). This correspondence implies that region III occurs at higher stresses where a stable subgrain structure begins to develop (Ref 35). However, the above suggestion that the creep behavior of superplastic alloys in region III is controlled by the same type of dislocation process that is dominant in metals at high temperatures is not entirely satisfactory for two primary reasons. First, experimental results in a superplastic copper alloy have revealed an inverse dependence of creep rate on grain size in region III (Ref 36); this behavior contrasts with that of pure metals at high stresses where creep rates are essentially insensitive to changes in grain size. Second, experimental evidence indicates that at high stresses no well-developed subgrains are formed in the interiors of grains; only dislocation tangles are present (Ref 3). On the basis of these findings, it seems most likely that region III is the result of the operation of some form of an intragranular dislocation process, which is influenced by the presence of grain boundaries. It is worth mentioning that there are difficulties in establishing the mechanical characteristics of region III due to the fast creep rates associated with this region.

Region II Deformation Mechanisms. As a result of considerable efforts over the past three decades, a number of deformation mechanisms were proposed or speculated to explain the origin of superplastic flow, especially in region II. Of these mechanisms, the most commonly considered ones are based on grain-boundary sliding (GBS) (Ref 37, 38, 39, 40, 41, and 42-43). Depending on the nature of the accommodation process that is necessary to relieve stress concentration, the GBS models may be divided into two types: diffusional accommodation and dislocation accommodation.

GBS accommodated by diffusion flow is the basis of the model by Ashby and Verrall (Ref 37). This model, which involves a grain-switching event, predicts the presence of a sigmoidal relationship between stress and strain rate, the retention of an equiaxed grain structure, and the absence of a significant dislocation activity. While these predictions are in harmony with experimental evidence, there are several problems associated with the model. Of these problems, which are stated elsewhere in detail (Ref 14, 23, 30, and 31), the following two are worth mentioning. First, the nature of the sigmoidal relationship between stress and strain rate, as predicted by the model, is not consistent with experimental findings. According to the model, the stress exponent for creep in region II is not constant, but varies continuously with stress (Ref 37). This trend contrasts the results reported for superplastic alloys, in which region II exhibits a constant stress exponent over several orders of magnitude of strain rate. Second, the model predicts that the apparent activation energies in region I and II are the same. This prediction is in conflict with the finding that region I is associated with a higher apparent activation energy.

Models based on GBS accommodated by dislocation motion were developed by several investigators (Ref 38, 39, 40, 41, 42, and 43). While these models, in general, involve GBS and some form of dislocation motion, their details and assumptions are different (Table 2). However, despite their different details and assumptions, all of the models mentioned can be described by a rate-controlling equation:

$$\dot{\gamma} = C \frac{DGb}{kT} \left(\frac{b}{d} \right)^2 \left(\frac{\tau}{G} \right)^2 \quad (\text{Eq 9})$$

where C is a constant that can be estimated from the details of each mode; values of C for the models mentioned are given in Table 2. For all models, with the exception of that proposed by Gittus, $D = D_{gb}$; in the case of Gittus's model, $D = D_{IPB}$, where D_{IPB} is the interphase boundary diffusion (Ref 41). As indicated by 8aEq 8b, the models of GBS accommodated by dislocation motion predict the correct stress, temperature, and grain-size dependencies. In addition, the fact that for each model C does not depend on the impurity level of the superplastic alloy is in line with the experimental finding that region II behavior is insensitive to this parameter. Despite this excellent agreement, various objections were raised against the assumptions and details of some of the models mentioned. These objections are discussed in detail elsewhere (Ref 2, 45). In addition to these objections, the agreement between the values of the experimental creep rates in region II and those rates predicted from the models is not satisfactory (Ref 33); for example, in case of Pb-62Sn (Ref 15, 33), the experimental creep rates of Pb-62Sn at low stresses are two orders of magnitude faster than those estimated from the model by Ball and Hutchinson (Ref 38), which predicts the fastest rate among the GBS models listed in Table 2.

Table 2 Grain-boundary-sliding models accommodated by dislocation motion (Eq 9)

Model	Values for C (Eq 9)	Comments	Reference
Sliding of groups of grains	300	Sliding of group of grains. Dislocations are created at triple points and annihilated by the process of climb into grain boundaries.	38
Individual grain sliding	12	Grain slide individually. Dislocations are produced by ledges and protrusions. $D = D_{gb}$	39
Dislocation glide and climb	384	Dislocation movement by glide and climb in the mantle along the adjacent grains $D = D_{gb}$	40
Dislocation pile up	320	Pile-up of boundary dislocations at interphase boundaries $D = D_{IPB}$. τ_0 is ignored for region II.	41
Bardeen-Herring source	480	The creation of dislocations on a solute-free mantle by Bardeen-Herring multiplication $D = D_{gb}$	42
Grain rolling	30	Grain rolling. Grain-boundary sliding by the glide of grain-boundary dislocations on sliding grain facets. Accommodation by the climb of grain-boundary-sliding dislocations on facets with normal stresses $D = D_{gb}$ $\Omega = \text{atomic size} = 0.7b^3$ $\delta = \text{boundary thickness} \sim 2b$	43

Note: The table does not include a model (Ref 44) that predicts a grain-size exponent of 3 and is based on boundary sliding controlled by intragranular dislocation motion.

Region I Deformation Mechanisms. In earlier analyses of superplastic flow, region I behavior in superplastic materials was explained in terms of three possibilities: (a) the presence of threshold stress processes that are not sensitive to temperature, such as the interaction between boundary dislocations and ledges (Ref 41), and fluctuations in the grain boundary area (Ref 37); (b) the operation of a new deformation process related to pure boundary sliding (Ref 40), and for which $Q = 0.2 Q_L$, where Q_L is an activation energy for lattice diffusion; and (c) the occurrence of concurrent grain growth (Ref 46, 47). Possibilities (a) and (b) have been ruled out because they cannot account for the higher activation energy measured in region I (Ref 30, 31). Possibility (c) is not

supported by experimental evidence that has shown the presence of a well-defined region I under experimental conditions involving negligible grain growth (Ref 13, 14, 15, 23, 30, 31).

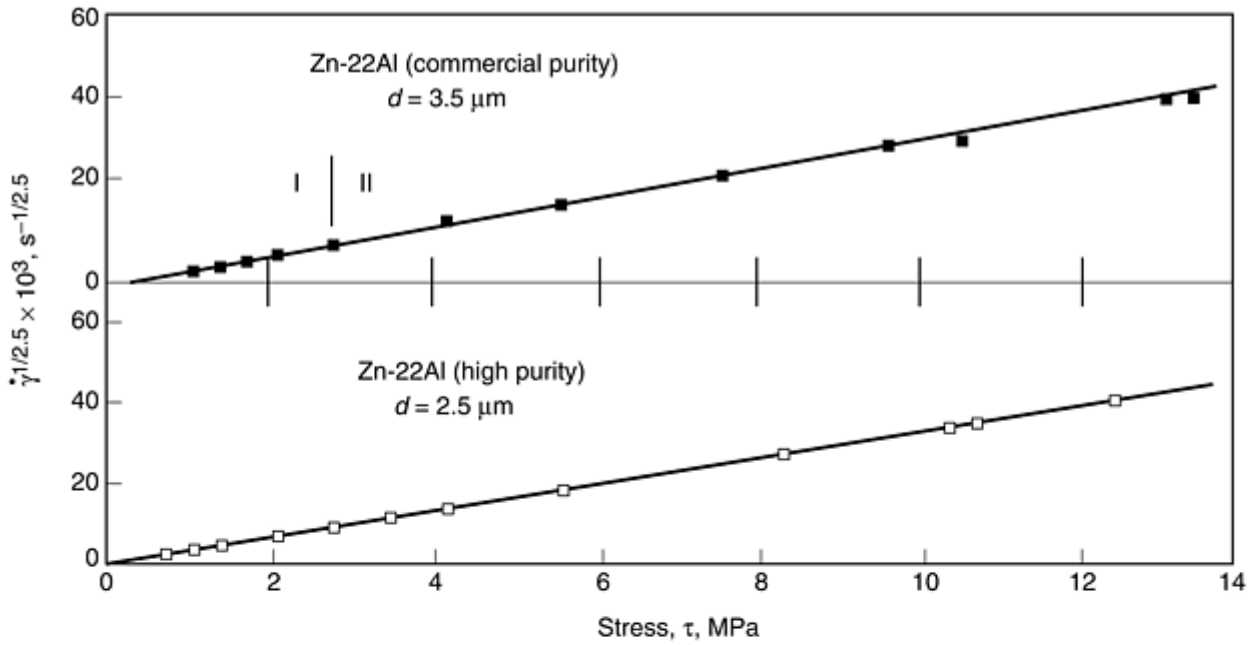
Recent experimental work shows that the characteristics of creep in region I are influenced by impurity level (Ref 13, 14, 15, 33). On the basis of this evidence, it is most likely that region I behavior is related to one of the following processes: (a) viscous glide (Ref 13, 48), (b) grain-boundary migration controlled by impurities (Ref 49), and (c) an impurity-dominated threshold stress (Ref 50). Consideration of the details of processes (a) and (b) suggests that they do not provide a satisfactory explanation for all the creep characteristics associated with region I for two reasons.

First, viscous glide creep, whether it is dominant in the interiors of grains or along the mantle in case of "mantle-and core" models, leads to an activation energy (equal to that for impurity diffusion) that is higher than Q_{gb} , in agreement with available experimental evidence; however, it fails to account for grain size and stress dependencies in region I. In addition, the observation of extensive primary creep in the creep curves at low stresses is not compatible with the characteristics of viscous glide creep as reported in solid-solution alloys of class I (Ref 51).

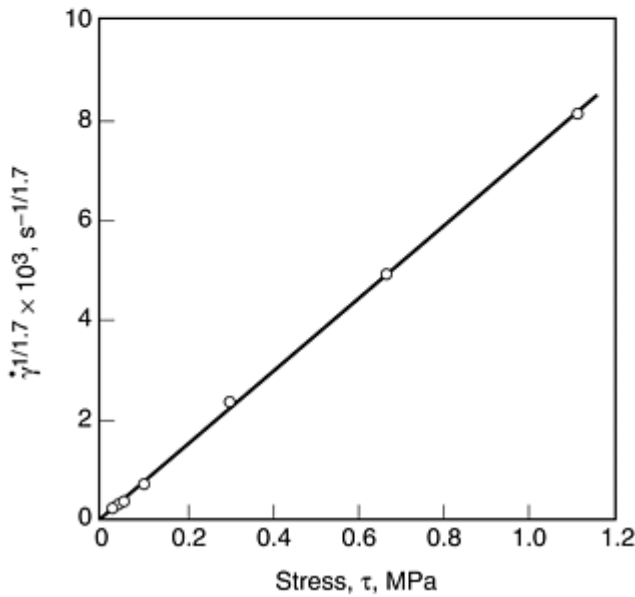
Second, grain boundary migration controlled by impurity drag, which was proposed by Gifkins (Ref 49) and represents a modification of his original grain-emergence model (Ref 52), is associated with two characteristics that are consistent with region I behavior: an activation energy higher than Q_{gb} and a high stress exponent. However, the occurrence of grain emergence, a feature on which the model is based, is debatable (Ref 53), and the exact value of the stress exponent is not predicted. In addition, the model has not been developed quantitatively, and, as a result, no comparison regarding the experimental values of creep rates in Zn-22Al can be made.

It has been suggested on the basis of an analysis of superplastic flow at low stresses (Ref 50), that region I behavior may be a consequence of the operation of a threshold-stress process whose origin is related to the segregation of impurity atoms at boundaries and their interaction with boundary dislocations; in this case, the threshold stress (τ_0) is equivalent to the stress that must be exceeded before boundary dislocations can break away from the impurity atmosphere and produce deformation. Recent creep data reported for several grades of Zn-22Al containing different levels of impurities, in particular iron, have revealed the presence of a threshold stress with characteristics consistent with various phenomena associated with boundary segregation, as summarized in the following paragraphs (Ref 54, 55, 56, 57, and 58).

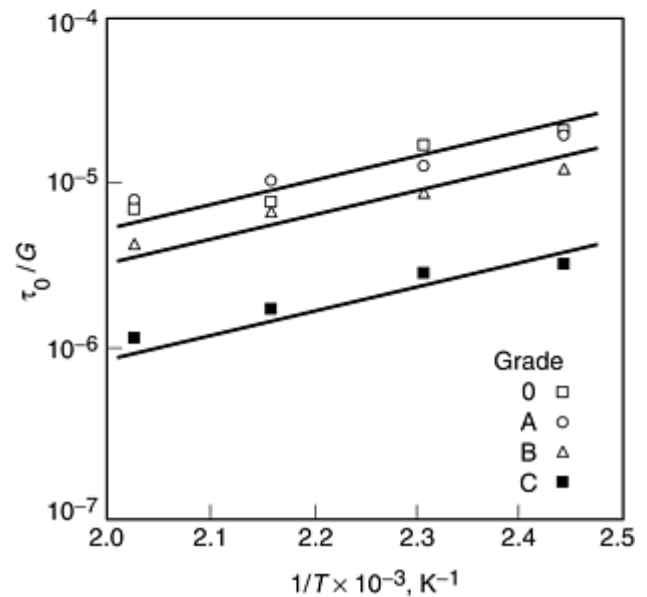
No threshold stress is observed for super-plastic flow in high-purity Zn-22Al as shown by Fig. 16(a) (Ref 13, 14). A similar trend for high-purity Pb-62Sn is shown in Fig. 16(b). As reported elsewhere (Ref 13, 14, 15, 33, and 50) and illustrated by Fig. 16(a) and (b), τ_0 is determined from experimental creep data obtained for a superplastic alloy by plotting $\dot{\gamma}^{1/n}$ ($n = 2.5$) against τ at a single temperature on a double linear scale and extrapolating the resultant line to zero strain rate.



(a)



(b)



(c)

Fig. 16 Threshold stress behavior. (a) Determination of the threshold stress (τ_0) for superplastic flow in Zn-22Al at 433K. Source: Ref 14. (b) Determination of the threshold stress for superplastic flow in high-purity Pb-62Sn at 392 K. Source: Ref 15. (c) A plot of the logarithm of τ_0/G as a function of $1/T$ for grades 0, A, B, and C of Zn-22Al having a grain size of $2.5 \mu m$ and containing 1460 ppm, 423 ppm, 125 ppm, and 40 ppm of iron, respectively

According to the experimental data reported for superplastic alloys (Ref 13, 14, 15, 33) the temperature dependence of the threshold stress is described by the following (Ref 13, 14, 15, 33, and 54):

$$\frac{\tau_0}{G} = B_0 \exp(-Q_0 / RT) \quad (\text{Eq 10})$$

where B_0 is a constant and Q_0 is an activation energy term. The plot of Fig. 16(c), in which experimental data on the threshold-stress behavior of several grades of Zn-22Al doped with iron are plotted as τ_0/G versus $1/T$ on a logarithmic scale, provides a graphical presentation for this relation. Equation 10 resembles in form the following equation (Ref 55) that gives, to a first approximation, the concentration of impurity atoms segregated to boundaries, c , as a function of temperature:

$$c = c_0 \exp(-W / RT) \quad (\text{Eq 11})$$

where c_0 is the average concentration of impurity, and W is the interaction energy between a boundary and a solute atom.

As indicated by Fig. 13(a) and (b), the experimental data for two superplastic alloys, Pb-62Sn and Zn-22Al, in region II (the superplastic region) can be best described by the following:

$$\frac{\dot{\gamma}kT}{D_{gb}Gb} = A \left(\frac{b}{d} \right)^s \left(\frac{\tau}{G} \right)^n \quad (\text{Eq 12})$$

The concept of an impurity-dominated threshold stress signifies that the same deformation process controls both region II (the superplastic region) and region I (the low-stress region) and that the apparent difference in stress and temperature dependencies between the two regions are the result of the increasing importance of τ_0 with decreasing creep stress in grades containing sufficient impurity levels. On this basis, it is expected that the experimental data obtained for superplastic alloys in regions I and II at various temperatures can be described by a single deformation process that incorporates τ_0 and may be given by:

$$\frac{\dot{\gamma}kT}{D_{gb}Gb} = B \left(\frac{b}{d} \right)^s \left(\frac{\tau - \tau_0}{G} \right)^n \quad (\text{Eq 13})$$

The data for both Pb-62Sn and Zn-22Al are plotted as normalized creep rate, $(\dot{\gamma}kT / D_{gb}Gb) (d/b)^s$ versus $(\tau - \tau_0)/G$ on a logarithmic scale in Fig. 17(a) and (b), respectively (for high-purity Pb-62Sn and Zn-22Al, $(\tau - \tau_0)$ is equivalent to τ for all stresses, and $s = 2.3$ and 2.4 for Pb-62Sn and Zn-22Al, respectively). Examination of the figures demonstrates that the data of each alloy can be represented by a straight line that extends over several orders of magnitude of normalized creep rate.

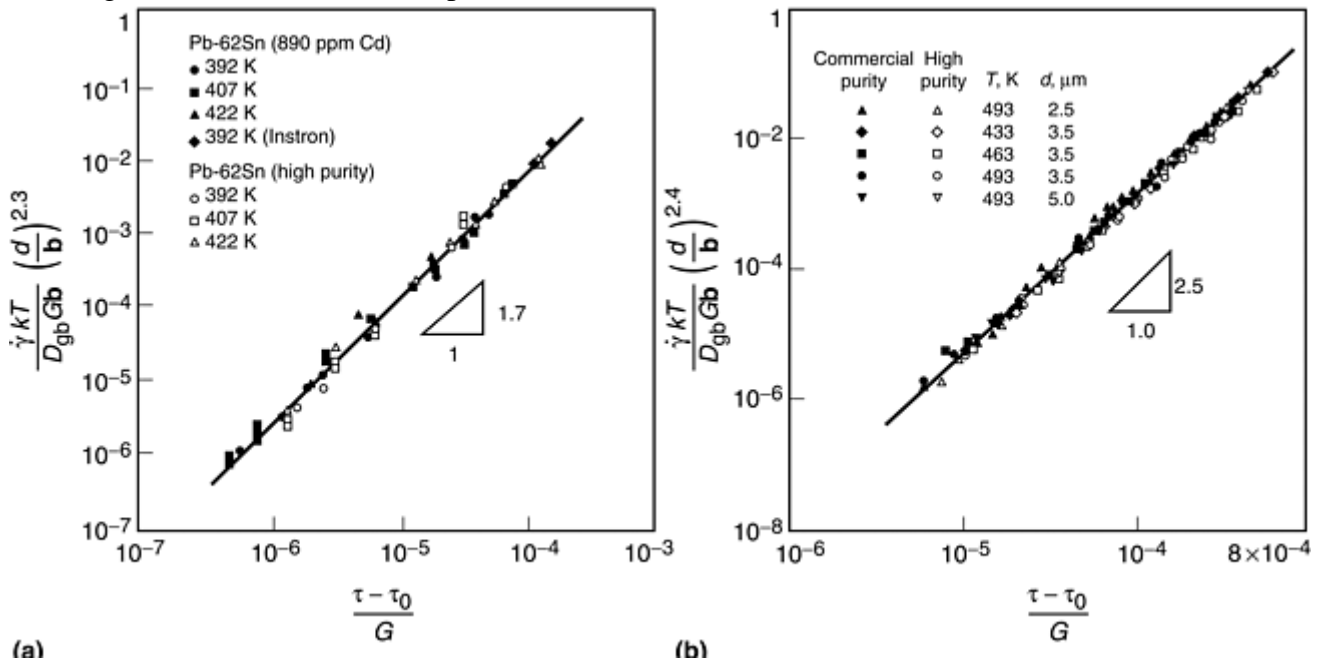


Fig. 17 Normalized creep rate versus normalized effective stress, $(\tau - \tau_0)/G$. (a) For both Pb-62Sn doped with cadmium and high-purity Pb-62Sn under intermediate and low stresses. Source: Ref 15. (b) For both commercial-purity Zn-22Al and high-purity Zn-22Al under intermediate and low stresses. Source: Ref 14

References cited in this section

2. A.K. Mukherjee, Deformation Mechanisms in Superplasticity, *Annu. Rev. Mater. Sci.*, Vol 9, 1979, p 191
3. R.C. Gifkins, Mechanisms of Super-plasticity, *Proc. of a Symp. on Superplastic Forming of Structural Alloys*, N.E. Paton and C.H. Hamilton, Ed. (San Diego), Metallurgical Society of AIME, 1980, p 2

13. P.K. Chaudhury and F.A. Mohamed, Effect of Impurity Content on Superplastic Flow in the Zn-22% Al Alloy, *Acta Metall.*, Vol 36, 1988, p 1099
14. P.K. Chaudhury, V. Sivaramakrishnan, and F.A. Mohamed, Superplastic Deformation Behavior in Commercial and High Purity Zn-22 pct Al, *Metall. Trans. A*, Vol 19, 1988, p 2741
15. S. Yan, J.C. Earthman, and F.A. Mohamed, Effect of Cd on Superplastic Flow in the Pb-62 wt% Sn Eutectic, *Philos. Mag. A*, Vol 69, 1994, p 1017
22. J.E. Bird, A.K. Mukerjee, and J.E. Dorn, Correlations between High-Temperature Creep Behavior and Structure, *Proc. of a Symp. on Quantitative Relation Between Properties and Microstructure*, D.G. Brandon and A. Rosen, Ed., Israel University Press, 1969, p 22
23. F.A. Mohamed and T.G. Langdon, Creep at Low Stress Levels in the Superplastic Zn-22% Al Eutectoid, *Acta Metall.*, Vol 23, 1975, p 117
30. F.A. Mohamed, S. Shen-Ann, and T.G. Langdon, The Activation Energies Associated with Superplastic Flow, *Acta Metall.*, Vol 23, 1975, p 1443
31. F.A. Mohamed and T.G. Langdon, Creep Behavior in the Superplastic Pb-62% Sn Eutectic, *Philos. Mag. A*, Vol 32, 1975, p 697
33. P.K. Chaudhury, K.T. Park, and F.A. Mohamed, Effect of Fe on the Superplastic Deformation of Zn-22 pct Al, *Metall. Mater. Trans. A*, Vol 25, 1994, p 2391
34. F.A. Mohamed and T.J. Ginter, The Stress Dependence of Subgrain Size in Al, *J. Mater. Sci.*, Vol 17, 1982, p 2007
35. F.A. Mohamed and T.G. Langdon, Deformation Mechanism Maps for Superplastic Materials, *Scr. Metall.*, Vol 10, 1976, p 759
36. S.A. Shei and T.G. Langdon, The Mechanical Properties of a Superplastic Quasi-Single Phase Copper Alloy, *Acta Metall.*, Vol 26, 1978, p 638
37. M.F. Ashby and R.A. Verrall, Diffusion-Accommodated Flow and Superplasticity, *Acta Metall* Vol 21, 1973, p 149
38. A. Ball and M.M Hutchinson, Super-plasticity in the Aluminum-Zinc Eutectoid, *Met. Sci.*, Vol 3, 1969, p 1
39. A.K. Mukherjee, The Rate Controlling Mechanism in Superplasticity, *Mater. Sci. Eng.*, Vol 8, 1971, p 83
40. R.C. Gifkins, Grain-Boundary Sliding and Its Accommodation during Creep and Superplasticity, *Metall. Trans. A*, Vol 7, 1976, p 1225
41. J.H. Gittus, Theory of Superplastic Flow in Two-Phase Materials: Role of Interphase-Boundary Dislocations, Ledges, and Diffusion, *J. Eng. Mater. Technol. (Trans. ASME)*, Vol 99, 1977, p 244
42. A. Arieli and A.K. Mukherjee, A Model for the Rate-Controlling Mechanism in Superplasticity, *Mater. Sci. Eng.*, Vol 45, 1980, p 61
43. V. Paidar and S. Takeuchi, Superplastic Deformation Carried by Grain Boundaries, *Acta Metall. Mater.*, Vol 40, 1992, p 1773

44. H.W. Hayden, S. Floreen, and P.D. Goodell, The Deformation Mechanisms of Superplasticity, *Metall. Trans.*, Vol 3, 1972, p 833
45. R.C. Gifkins and T.G Langdon, Comments on Theories of Structural Superplasticity, *Mater. Sci. Eng.*, Vol 36, 1978, p 27
46. G. Rai and N.J. Grant, On the Measurements of Superplasticity in an Al-Cu Alloy, *Metall. Trans. A*, Vol 6, 1975, p 385
47. A. Arieli and A.K. Mukherjee, On Concurrent Grain Growth and Deformation Mechanism in Region I for Superplastic Zn-22% Eutectoid Alloy, *Scr. Metall.*, Vol 13, 1979, p 331
48. J. Weertman, Steady-State Creep of Crystals, *J. Appl. Phys.*, Vol 28, 1957, p 1185
49. R.C. Gifkins, "Mechanisms for Low-Stress Region I of Superplasticity," in *Proceedings of a Symposium on Strength of Metals and Alloys*, R.C. Gifkins, Ed., Pergamon, Oxford, 1982, p 701
50. F.A. Mohamed, Interpretation of Superplastic Flow in Terms of Threshold Stress, *J. Mater. Sci.*, Vol 18, 1983, p 582
51. F.A. Mohamed and T.G. Langdon, The Transition from Viscous Glide to Dislocation Climb, *Acta Metall.*, Vol 22, 1974, p 779
52. R.C. Gifkins, Grain Rearrangements during Superplastic Deformation, *J. Mater. Sci.*, Vol 13, 1978, p 1926
53. I.I. Novikov, V.K. Portnoy, and V.S. Levchenko, Investigation of Structural Changes during Superplastic Deformation of Zn-22% Al Alloy by Replica Locating Technique, *Acta Metall.*, Vol 29, 1981, p 1077
54. S.T. Yang and F.A. Mohamed, On the Characteristics of the Threshold Stress for Superplastic Flow in Zn-22 pct Al, *Metall. Mater. Trans. A*, Vol 26, 1995, p 493
55. H. Gleiter and B. Chalmers, High Angle Grain Boundaries, *Prog. Mater. Sci.*, Vol 16, 1973
56. X.G. Jiang, S.T. Yang, J.C. Earthman, and F.A. Mohamed, Effect of Fe on Ductility and Cavitation in the Superplastic Zn-22 pct Al Eutectoid, *Metall. Mater. Trans. A*, Vol 27, 1996, p 863
57. M.P. Seah, Grain Boundary Segregation and the T-t Dependence of Temper Brittleness, *Acta Metall.*, Vol 25, 1977, p 34
58. P. Gas, M. Guttman, and J. Bernardini, The Interactive Co-Segregation of Sb and Ni at the Grain Boundaries of Ultra-High Purity Fe-Base Alloys, *Acta Metall.*, Vol 30, 1982, p 1309

Superplastic Deformation at Elevated Temperatures

Farghalli A. Mohamed, University of California, Irvine

Effect of Impurities on Superplastic Flow

The preceding discussion indicates that the creep characteristics, including the stress exponent and the activation energy for deformation, are influenced by the presence of impurities. In the following section, the effects of impurities on boundary sliding, cavitation, and ductility are presented.

Grain-Boundary Sliding. The occurrence of micrograin superplasticity in metallic systems requires a stable and equiaxed grain size of less than 10 μm . This requirement, along with the strong sensitivity of steady-state creep rates measured during superplastic flow to changes in grain size, d , has demonstrated the significant influence of boundaries on the superplastic behavior. Over the past three decades, considerable efforts have been made to characterize the nature and significance of their role. For example, as mentioned previously, the concept of boundary sliding accommodated by some form of dislocation activity was adopted in developing several deformation models that treated steady-state superplastic deformation in region II (Ref 38, 39, 40, 41, 42, and 43). In addition, many investigations have been performed in tension on several different superplastic alloys to evaluate the significance of grain-boundary sliding in the three regions of behavior previously mentioned.

In these investigations, measurements were taken of sliding offsets along prescribed marker lines on the surface of tensile specimens, and the contribution of boundary sliding to the total strain was estimated using appropriate equations. Despite minor differences in the procedures and equations used in boundary-sliding estimates, the results reported in the investigations are generally consistent and show that, at low elongations (typically of the order of 20–30%), the percentage contribution of boundary sliding to total strain generally ranges from 50 to 70% in region II, but it decreases sharply to approximately 20 to 30% in regions I and III (Ref 24, 29).

In a very recent study (Ref 28), the effect of impurity level on the contribution of boundary sliding to the total strain was examined in the superplastic Zn-22Al alloy. The results of that study follow.

Figure 18 shows a plot of the contribution from boundary sliding to the total strain, ξ , against initial strain rate, $\dot{\epsilon}_0$, for three grades of Zn-22Al (Ref 28). Grades 1 and 2 contain 180 and 100 ppm of impurities, respectively, whereas grade 3 is a high-purity grade containing 6 ppm of impurities. In this plot, the vertical lines *A* and *B* represent the transitions from region I to region II and from region II to region III, respectively. (As mentioned previously, these three regions characterize the sigmoidal relation between stress and strain rate.) An examination of such a plot reveals that the values of the contribution of boundary sliding to the total strain in Zn-22Al at low strain rates (region I) are affected by the presence of impurities, unlike those at intermediate and high strain rates (region II and region III, respectively). This finding is reflected in the following observations: (a) for all three grades, ξ exhibits the same value of 20% at high-strain rates, (b) for grade 3 (high-purity Zn-22Al), ξ at low strain rates is not only significant (61%) but also comparable to that at intermediate strain rates (~60%), (c) at the same strain rate in region I, the values of ξ in grades 1 and 2 are less than that in grade 3, and (d) at the same strain rate in region I, ξ in region I (180 ppm of impurities) is less than that in grade 2 (100 ppm of impurities).

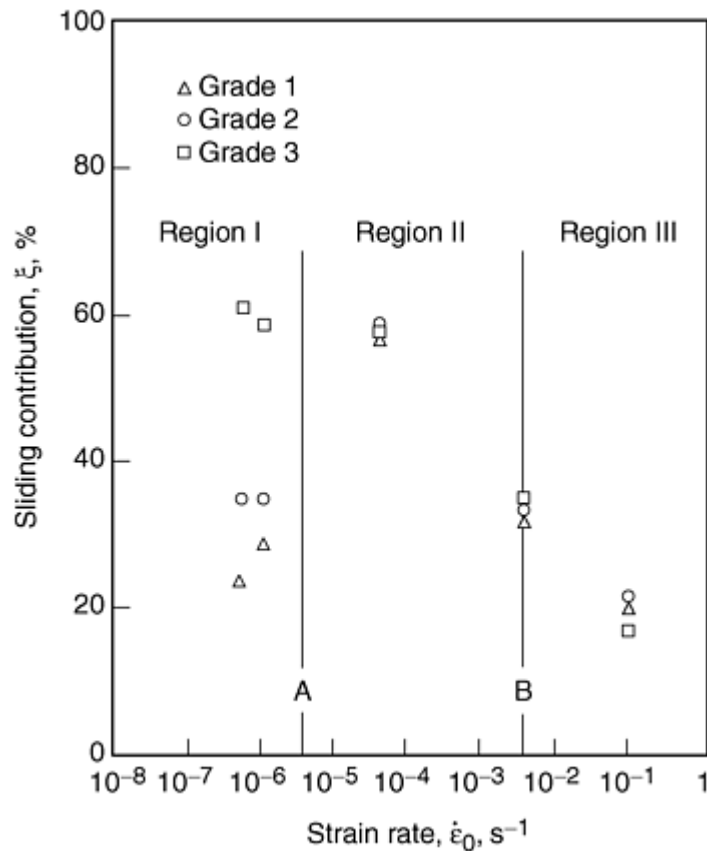


Fig. 18 The contribution of boundary sliding to the total strain, ξ , as a function of strain rates for grades 1, 2, and 3 of Zn-22Al containing 180, 100, and 6 ppm of impurities, respectively. Grain size 5.4 μm ; temperature, 493 K. Source: Ref 59

As mentioned earlier, the sensitivity of region I to impurity level is most likely a reflection of the presence of a threshold stress for creep in Zn-22Al (Ref 13, 14, 33, 50), which is related to strong impurity segregation at boundaries and which strongly depends on temperature, according to Eq 9. The interpretation of the creep behavior of superplastic alloys, in terms of a threshold stress arising from impurity atom segregation, signifies that region I and II are controlled by the same deformation mechanism. However, it is not immediately clear why, as shown by the results on grades 1 and 2, ξ in region I is lower than that in region II if the rate-controlling mechanism is the same in the two regions. It is quite possible that the correlation between impurity level and the sliding contribution at low strain rates is a reflection of the influence of impurities on accommodation processes for boundary sliding such as boundary migration (Ref 49, 52) and lattice dislocation motion (Ref 59). This possibility is discussed in detail in Ref 28.

According to the preceding discussion, the effect of impurity level on the boundary-sliding contribution corresponds well with the effect of impurity level on steady-state creep characteristics reported for the present alloy (Ref 13, 14, and 33). This correspondence, the main aspects of which are summarized in Table 3, indicates that under the present experimental conditions, boundary sliding is an important feature of the deformation process that controls steady-state superplastic flow. Further studies are needed to investigate the effect of impurities on the contribution of boundary sliding to the total strain in Zn-22Al and other superplastic alloys at large strains (>30%). The data of such studies can be used to clarify whether the characteristics of boundary sliding reflect those of steady-state superplastic flow at all strains (small and large) (Ref 24, 60, 61, 62, and 63).

Table 3 Correspondence between effect of impurity level on the sliding contribution and that on steady-state superplastic flow

Strain rate region	Effect of impurity level on the sliding contribution	Effect of impurity level on steady-state superplastic flow
High-strain-rate region (region III)	Impurity level has no effect on the contribution of boundary sliding to the total strain, $\xi \cdot \xi \sim 24\%$.	Impurity level has no effect on the advent of region III.
Intermediate-strain-rate region (region II or the superplastic region)	Impurity level has no noticeable effect on the contribution of boundary sliding. Sliding contribution to the total strain is equal to $\sim 60\%$.	Impurity level has no effect on the values of the stress exponent and the activation energy for superplastic flow. $n = 2.5$ and $Q_c = Q_{gb}$
Low-strain-rate region (region I in grades 1 and 2)	For a high purity alloy, ξ is equal to that in the intermediate strain rates. The sliding contribution decreases with increasing impurity level.	For a high-purity alloy, the intermediate-stress region (region II) extends to the lowest strain rate with no evidence for region I. Both n and Q_c increase with increasing impurity level.

Cavitation. It is well-established that during superplastic deformation most materials develop internal cavities, which grow and coalesce, leading to cavitation damage. Such damage in turn gives rise to premature failure of the material, thereby imposing a serious limitation on the mechanical properties of components prepared by superplastic forming. A solution of this problem necessitates (a) a detailed understanding of the cavitation process in superplastic alloys over wide ranges of experimental conditions, and (b) an identification of various factors that may control the nucleation and growth of cavities. In recent years, the effect of impurities on cavitation during superplastic flow has received considerable attention.

As mentioned previously, segregation of impurities at boundaries has been suggested as a probable cause for occurrence of region I, which micrograin superplastic alloys often exhibit at low stresses. In support of the previously mentioned concept regarding impurity segregation, experimental results have revealed the following observations: (a) cavities are not observed in high-purity Zn-22Al (Ref 56, 64, 65, and 66), and (b) the extent of cavitation in Zn-22Al depends on the impurity content of the alloy (Ref 56, 60). Figure 19 illustrates these two observations. The observed correlation between the level of impurities and the extent of cavitation in Zn-22Al is most probably related to effects associated with the presence of excessive impurities at boundaries due to their segregation. As mentioned elsewhere (Ref 56, 59, 60, 61, and 67), impurity segregation may lead to accelerated cavitation rates through the following processes: (a) reduction of the surface energy, (b) formation of precipitates that serve as cavity nucleation sites, (c) reduction of grain-boundary diffusivity, (d) reduction of boundary cohesive strength, and (e) retardation of grain growth that involves boundary migration.

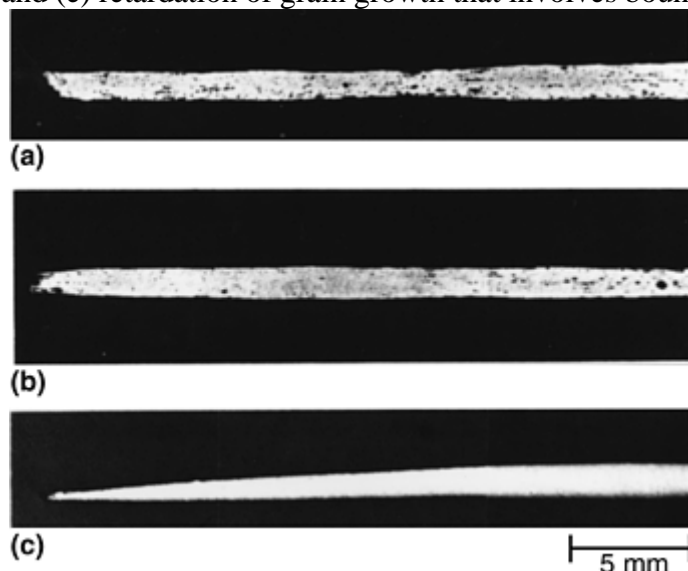


Fig. 19 Cavitation in Zn-22Al grades at 1.33×10^{-4} . (a) Grade 1 (180 ppm of impurities). (b) Grade 2 (100 ppm of impurities). (c) Grade 3 (6 ppm of impurities). Source: Ref 60

Ductility. The results of several analyses have demonstrated that ductility, defined as the percentage of elongation to fracture, is a sensitive function of the stress exponent n , which equals $1/m$ (Ref 68, 69, 70, 71). In general, ductility increases as the value of the stress exponent decreases (or as the value of the strain rate sensitivity increases), because, as suggested by several investigators, the lower the stress exponent, the larger the necking resistance (Ref 68, 69, 70, and 71). Mathematically, the dependence of ductility on the stress exponent can, for example, be expressed by the following equation, the development of which is based on consideration of plastic instabilities in a tensile specimen (Ref 68):

$$e\% = [\exp(c/n) - 1]\% \quad (\text{Eq 14})$$

where $c = \ln(400/n)$ and e represents elongation.

For a superplastic alloy, such as Zn-22Al, the stress exponent (n) exhibits a minimum at intermediate stresses or intermediate strain rates where the superplastic region dominates (Ref 13, 14, 23, and 30). Accordingly, it is expected that the ductility of the alloy, when plotted as the elongation to fracture versus stress or strain rate, would exhibit a maximum at intermediate stresses or intermediate strain rates. This behavior is presented in Fig. 20, where the average elongation for Zn-22Al is plotted as a function of initial strain rate (Ref 72).

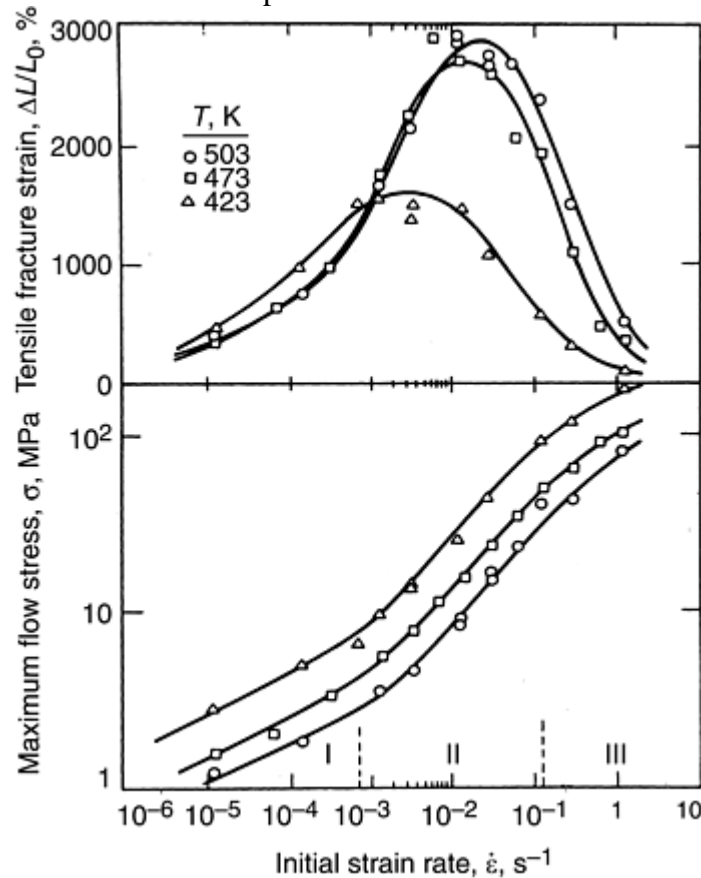


Fig. 20 Tensile fracture strain as a function of initial strain rate for a testing temperature of 473 K and a grain size of $2.5 \mu\text{m}$ (upper); the corresponding plots of maximum flow stress versus initial strain rate (lower). Source: Ref 72

The effect of iron on the ductility of the superplastic Zn-22Al alloy was recently investigated (Ref 56). Some of the results of the investigation are shown in Fig. 21, where the average elongation to failure (e_f) estimated from several specimens that were pulled to failure at $1.33 \times 10^{-4} \text{ s}^{-1}$ in region II (the superplastic region), where $n = 2.5$, is plotted as a function of iron content. As shown by the figure, there are two regions of behavior: (a) e_f decreases slowly for iron concentrations less than 125 ppm, and (b) e_f decreases rapidly at higher iron levels. It has been suggested in Ref 56 that introducing high iron levels in Zn-22Al, while not changing the stress exponent for creep in region II, leads to a loss in the ductility of the alloy in this region for the following reason. Well documented experimental evidence has implied that during superplastic flow, segregation of impurities at

boundaries occurs. According to information previously mentioned, segregation of impurities at interfaces can lead to several different phenomena that involve a reduction in the value of the following materials parameters: surface energy, grain-boundary diffusivity, and boundary cohesive strength (Ref 56, 59, 60, 61, and 67). The occurrence of one or more of these phenomena would adversely influence ductility, either by resulting in nucleating cavities (the growth and interlinkage of which during deformation may cause premature failure) or by weakening boundaries.

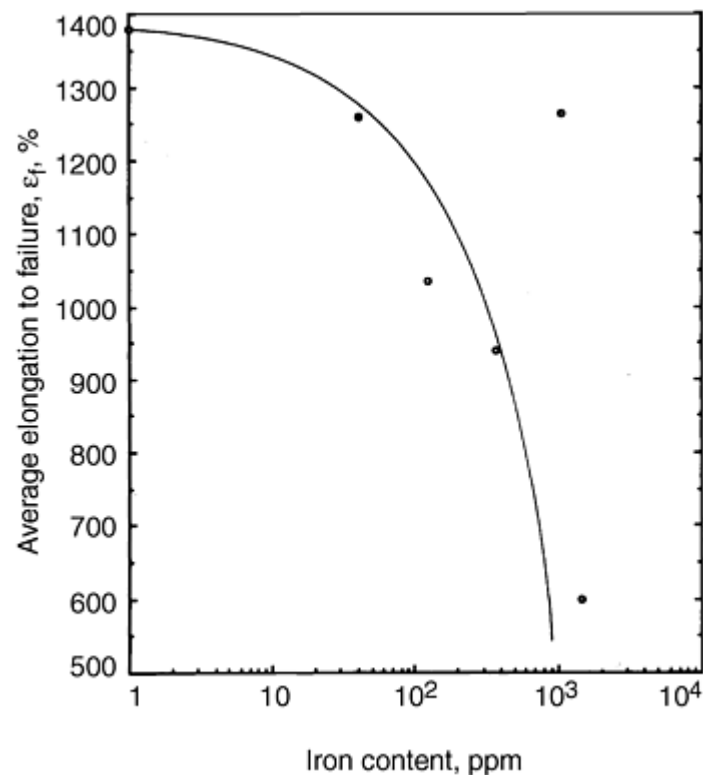


Fig. 21 The average elongation to failure as a function of iron content for an initial grain size of 2.5 μm, testing temperature of 473 K, and an initial strain rate of $1.33 \times 10^{-4} \text{ s}^{-1}$. Source: Ref 56

References cited in this section

13. P.K. Chaudhury and F.A. Mohamed, Effect of Impurity Content on Superplastic Flow in the Zn-22% Al Alloy, *Acta Metall.*, Vol 36, 1988, p 1099
14. P.K. Chaudhury, V. Sivaramakrishnan, and F.A. Mohamed, Superplastic Deformation Behavior in Commercial and High Purity Zn-22 pct Al, *Metall. Trans. A*, Vol 19, 1988, p 2741
23. F.A. Mohamed and T.G. Langdon, Creep at Low Stress Levels in the Superplastic Zn-22% Al Eutectoid, *Acta Metall.*, Vol 23, 1975, p 117
24. P. Shariat, R.B. Vastava, and T.G. Langdon, An Evaluation of the Roles of Intercrystalline and Interphase Boundary Sliding in Two-Phase Supersonic Alloys, *Acta Metall.*, Vol 30, 1982, p 285
28. K. Duong and F.A. Mohamed, Effect of Impurity Content on Boundary Sliding Behavior in the Superplastic Zn-22% Al Alloy, *Acta Mater.*, Vol 46, 1998, p 4571
29. R.B. Vastava and T.G. Langdon, An Investigation of Intercrystalline and Interphase Boundary Sliding in the Superplastic Pb-62% Sn Eutectic, *Acta Metall.*, Vol 27, 1979, p 251
30. F.A. Mohamed, S. Shen-Ann, and T.G. Langdon, The Activation Energies Associated with Superplastic Flow, *Acta Metall.*, Vol 23, 1975, p 1443

33. P.K. Chaudhury, K.T. Park, and F.A. Mohamed, Effect of Fe on the Superplastic Deformation of Zn-22 pct Al, *Metall. Mater. Trans. A*, Vol 25, 1994, p 2391
38. A. Ball and M.M Hutchinson, Super-plasticity in the Aluminum-Zinc Eutectoid, *Met. Sci.*, Vol 3, 1969, p 1
39. A.K. Mukherjee, The Rate Controlling Mechanism in Superplasticity, *Mater. Sci. Eng.*, Vol 8, 1971, p 83
40. R.C. Gifkins, Grain-Boundary Sliding and Its Accommodation during Creep and Superplasticity, *Metall. Trans. A*, Vol 7, 1976, p 1225
41. J.H. Gittus, Theory of Superplastic Flow in Two-Phase Materials: Role of Interphase-Boundary Dislocations, Ledges, and Diffusion, *J. Eng. Mater. Technol. (Trans. ASME)*, Vol 99, 1977, p 244
42. A. Arieli and A.K. Mukherjee, A Model for the Rate-Controlling Mechanism in Superplasticity, *Mater. Sci. Eng.*, Vol 45, 1980, p 61
43. V. Paidar and S. Takeuchi, Superplastic Deformation Carried by Grain Boundaries, *Acta Metall. Mater.*, Vol 40, 1992, p 1773
49. R.C. Gifkins, "Mechanisms for Low-Stress Region I of Superplasticity," in *Proceedings of a Symposium on Strength of Metals and Alloys*, R.C. Gifkins, Ed., Pergamon, Oxford, 1982, p 701
50. F.A. Mohamed, Interpretation of Superplastic Flow in Terms of Threshold Stress, *J. Mater. Sci.*, Vol 18, 1983, p 582
52. R.C. Gifkins, Grain Rearrangements during Superplastic Deformation, *J. Mater. Sci.*, Vol 13, 1978, p 1926
56. X.G. Jiang, S.T. Yang, J.C. Earthman, and F.A. Mohamed, Effect of Fe on Ductility and Cavitation in the Superplastic Zn-22 pct Al Eutectoid, *Metall. Mater. Trans. A*, Vol 27, 1996, p 863
59. R.Z. Valiev and T.G. Langdon, An Investigation of the Role of Intragranular Dislocation Strain in the Superplastic Pb-62% Sn Eutectic Alloy, *Acta Metall. Mater.*, Vol 41, 1991, p 949
60. Z.R. Lin, A.H. Chokshi, and T.G. Langdon, An Investigation of Grain Boundary Sliding in Superplasticity at High Elongations, *J. Mater. Sci.*, Vol 23, 1988, p 2712
61. R.C. Gifkins, Ductility and Strain-Rate Control Mechanisms in Superplasticity, *Scr. Metall. Mater.*, Vol 25, 1991, p 1397
62. M.J. Mayo and W.D. Nix, A Micro-Indentation Study of Superplasticity in Pb, Sn, and Sn-38 wt.% Pb, *Acta Metall.*, Vol 36, 1988, p 2183
63. M.J. Mayo and W.D. Nix, Direct Observation of Superplastic Flow Mechanisms in Torsion, *Acta Metall.*, Vol 37, 1989, p 1121
64. K.T. Park and F.A. Mohamed, Effect of Impurity Content on Cavitation in the Superplastic Zn-22 pct Al Alloy, *Metall. Trans. A*, Vol 21, 1990, p 2605
65. K.T. Park, S.T. Yang, J.C. Earthman, and F.A. Mohamed, The Effect of Impurities on Ductility and Cavitation in the Superplastic Zn-22% Al Alloy, *Mater. Sci. Eng. A*, Vol 188, 1994, p 59

66. A. Yousefiani, J.C. Earthman, and F.A. Mohamed, Formation of Cavity Stringers during Superplastic Deformation, *Acta. Mater.*, Vol 46, 1998, p 3557
67. H. Riedel in *Fracture at High Temperatures*, B. Ilschner and N. Grant, Ed., MRE Springer-Verlag, 1986, p 116
68. F.A. Mohamed, Modification of the Burke-Nix Ductility Expression, *Scripta Metall.*, Vol 13, 1979, p 87
69. F.A. Nichols, Plastic Instabilities and Uniaxial Tensile Ductilities, *Acta Metall.*, Vol 27, 1980, p 663
70. L.H. Lin, J.P. Hirth, and E.W. Hart, Plastic Instability in Uniaxial Tension Tests, *Acta Metall.*, Vol 29, 1981, p 819
71. F.A. Mohamed and T.G. Langdon, Flow Localization and Neck Formation in a Superplastic Metal, *Acta Metall.*, Vol 29, 1981, p 911
72. F.A. Mohamed, M.I. Ahmed, and T.G. Langdon, Factors Influencing Ductility in the Superplastic Zn-22 Pct Al Eutectoid, *Metall. Trans. A*, Vol 8, 1977, p 933

Superplastic Deformation at Elevated Temperatures

Farghalli A. Mohamed, University of California, Irvine

Grain Growth during Testing

During superplastic flow, concurrent grain growth (deformation-enhanced grain growth or strain-induced grain growth) takes place. In some cases, the amount of concurrent grain growth is more significant than that arising from stress-free annealing or in the shoulder of a tensile specimen (static grain growth) (Ref 73). The occurrence of significant concurrent grain growth during superplastic flow can lead to the following effects: (a) the observation of a false region I (Ref 46, 47), (b) a loss of ductility in region II (Ref 56, 74), (c) erroneous values for creep rates measured in region II when the applied stress acting on a single specimen was changed during stress-increase experiments from a very low value (Ref 74), (d) the predominance of strain hardening in the stress-strain curves at high temperatures (Ref 75), and (e) an increase in the level of cavitation (Ref 76). (Excessive concurrent grain growth results in less accommodation of boundary sliding by boundary migration or boundary diffusion.)

Three comments are in order regarding concurrent grain growth. First, concurrent grain growth is very significant, and its associated effects, such as strain hardening, become noticeable when experiments are performed without an annealing treatment before testing (Ref 46, 75). Second, the results of a recent investigation on the superplastic flow of Zn-22Al doped with iron have shown that the effect of concurrent grain growth on cavitation is not as significant as that of the level of iron (Ref 56). Third, region I behavior is genuine and is not related to the occurrence of concurrent grain growth; a well-defined region I, with high values of the apparent stress exponent and the apparent activation energy, was observed in creep experiments involving negligible grain growth.

References cited in this section

46. G. Rai and N.J. Grant, On the Measurements of Superplasticity in an Al-Cu Alloy, *Metall. Trans. A*, Vol 6, 1975, p 385

47. A. Arieli and A.K. Mukherjee, On Concurrent Grain Growth and Deformation Mechanism in Region I for Superplastic Zn-22% Eutectoid Alloy, *Scr. Metall.*, Vol 13, 1979, p 331
56. X.G. Jiang, S.T. Yang, J.C. Earthman, and F.A. Mohamed, Effect of Fe on Ductility and Cavitation in the Superplastic Zn-22 pct Al Eutectoid, *Metall. Mater. Trans. A*, Vol 27, 1996, p 863
73. C.H. Cacers and D.S. Wilkinson, Superplastic Behavior of a Zn-22 pct Al-0.5 Pct Cu Alloy, *Metall. Trans. A*, Vol 17, 1985, p 1873
74. A. Yousefiani and F.A. Mohamed, Superplastic Flow and Cavitation in Zn-22% pct Al Doped with Cu, *Metall. Mater. Trans. A*, Vol 29, 1998, p 1653
75. B.P. Kashyap and T. Tangi, On the Contribution of Concurrent Grain Growth to Strain Sensitive Flow of a Superplastic Al-Cu Eutectic Alloy, *Metall. Trans. A*, Vol 18, 1987, p 417
76. D.W. Livesey and N. Ridley, Effect of Grain Size on Cavitation in Superplastic Zn-22% Al Eutectoid, *J. Mater. Sci.*, Vol 17, 1982, p 2257

Superplastic Deformation at Elevated Temperatures

Farghalli A. Mohamed, University of California, Irvine

Acknowledgments

This work was supported by the National Science Foundation under grant No. DMR-810422. Thanks are also due to Professor James Earthman for useful discussion, and to my graduate students, Ahmadali Yousefiani, Kim Duong, and Zhigang Lin, for their assistance.

Superplastic Deformation at Elevated Temperatures

Farghalli A. Mohamed, University of California, Irvine

References

1. M.M.I. Ahmed, F.A. Mohamed, and T.G. Langdon, Neck Formation and Cavitation in the Superplastic Zn-22 pct Al Eutectoid, *J. Mater. Sci.*, Vol 14, 1979, p 2913
2. A.K. Mukherjee, Deformation Mechanisms in Superplasticity, *Annu. Rev. Mater. Sci.*, Vol 9, 1979, p 191
3. R.C. Gifkins, Mechanisms of Super-plasticity, *Proc. of a Symp. on Superplastic Forming of Structural Alloys*, N.E. Paton and C.H. Hamilton, Ed. (San Diego), Metallurgical Society of AIME, 1980, p 2
4. O.D. Sherby and J. Wadsworth, Superplasticity—Recent Advanced and Future Directions, *Prog. Mater. Sci.*, Vol 33, 1989, p 169

5. A.H. Chokshi, A.K. Mukherjee, and T.G. Langdon, Superplasticity in Advanced Materials, *Mater. Sci. Rep.*, Vol 10, 1993, p 237
6. R. Sawle, Commercial Application of Superplastic Sheet Forming, *Proc. of a Symp. on Superplasticity Forming of Structural Alloys*, N.E. Paton and C.H. Hamilton, Ed. (Warrendale, PA), TMS-AIME, 1982, p 307
7. W.A. Backofen, I.R. Turner, and D.H. Avery, Superplasticity in an Al-Zn Alloy, *Trans. ASM*, Vol 57, 1964, p 980
8. W.B. Morrison, Superplasticity of Low-Alloy Steels, *Trans. ASM*, Vol 61, 1968, p 423
9. J. Hedworth and M.J. Stowell, The Measurement of Strain-Rate Sensitivity in Superplastic Alloys, *J. Mater. Sci.*, Vol 6, 1971, p 1061
10. G.B. Gibbs, Creep and Stress Relaxation Studies with Polycrystalline Magnesium, *Philos. Mag.*, Vol 13, 1966, p 317
11. A. Arieli and A. Rosen, Measurement of Strain-Rate Sensitivity Coefficient in Superplastic Ti-6Al-4V Alloy, *Scr. Metall.*, Vol 10, 1976, p 471
12. E.W. Hart, A Phenomenological Theory for Plastic Deformation of Polycrystalline Metals, *Acta Metall.*, Vol 18, 1970, p 599
13. P.K. Chaudhury and F.A. Mohamed, Effect of Impurity Content on Superplastic Flow in the Zn-22% Al Alloy, *Acta Metall.*, Vol 36, 1988, p 1099
14. P.K. Chaudhury, V. Sivaramakrishnan, and F.A. Mohamed, Superplastic Deformation Behavior in Commercial and High Purity Zn-22 pct Al, *Metall. Trans. A*, Vol 19, 1988, p 2741
15. S. Yan, J.C. Earthman, and F.A. Mohamed, Effect of Cd on Superplastic Flow in the Pb-62 wt% Sn Eutectic, *Philos. Mag. A*, Vol 69, 1994, p 1017
16. B.Y. Chirouze, D.M. Schwartz, and J.E. Dorn, The Mechanism of Basal Creep in Mg-12 at.% Li from 500 to 885 K, *Trans. ASM*, Vol 51, 1967, p 51
17. K.L. Murty, F.A. Mohamed, and J.E. Dorn, Viscous Glide, Dislocation Climb and Newtonian Viscous Deformation Mechanisms of High Temperature Creep in Al-3Mg, *Acta Metall.*, Vol 20, 1972, p 1009
18. M.S. Soliman, T.J. Ginter, and F.A. Mohamed, *Philos. Mag. A*, Vol 48, 1993, p 63
19. F.A. Mohamed and T.G. Langdon, A Comparison of Constant Strain Rate and Creep Testing Procedures in Superplasticity, *J. Mater. Sci.*, Vol 17, 1982, p 1925
20. H.I. Huang, O.D. Sherby, and J.E. Dorn, Activation Energy for High Temperature Creep of High Purity Aluminum, *Trans. MS/AIME*, Vol 23, 1956, p 117
21. F.A. Mohamed and T.G. Langdon, The Determination of the Activation Energy for Superplastic Flow, *Phys. Status Solidi (a)*, Vol 33, 1976, p 375
22. J.E. Bird, A.K. Mukerjee, and J.E. Dorn, Correlations between High-Temperature Creep Behavior and Structure, *Proc. of a Symp. on Quantitative Relation Between Properties and Microstructure*, D.G. Brandon and A. Rosen, Ed., Israel University Press, 1969, p 22

23. F.A. Mohamed and T.G. Langdon, Creep at Low Stress Levels in the Superplastic Zn-22% Al Eutectoid, *Acta Metall.*, Vol 23, 1975, p 117
24. P. Shariat, R.B. Vastava, and T.G. Langdon, An Evaluation of the Roles of Intercrystalline and Interphase Boundary Sliding in Two-Phase Supersonic Alloys, *Acta Metall.*, Vol 30, 1982, p 285
25. T.G. Langdon, The Effect of Surface Configuration on Grain Boundary Sliding, *Metall. Trans.*, Vol 3, 1972, p 797
26. R.C. Gifkins, Factors Influencing Deformation of Superplastic Alloys, *Mater. Forum*, Vol 15, 1991, p 82
27. K.T. Park, S. Yan, and F.A. Mohamed, Boundary Sliding Behavior in High-Purity Pb-62% Sn, *Philos. Mag. A*, Vol 72, 1995, p 891
28. K. Duong and F.A. Mohamed, Effect of Impurity Content on Boundary Sliding Behavior in the Superplastic Zn-22% Al Alloy, *Acta Mater.*, Vol 46, 1998, p 4571
29. R.B. Vastava and T.G. Langdon, An Investigation of Intercrystalline and Interphase Boundary Sliding in the Superplastic Pb-62% Sn Eutectic, *Acta Metall.*, Vol 27, 1979, p 251
30. F.A. Mohamed, S. Shen-Ann, and T.G. Langdon, The Activation Energies Associated with Superplastic Flow, *Acta Metall.*, Vol 23, 1975, p 1443
31. F.A. Mohamed and T.G. Langdon, Creep Behavior in the Superplastic Pb-62% Sn Eutectic, *Philos. Mag. A*, Vol 32, 1975, p 697
32. S.H. Vale, D.J. Eastgate, and P.M. Hazzledine, The Low Strain Rate Behavior of Superplastic Zn-Al Eutectoid Alloy, *Scr. Metall.*, Vol 13, 1979, p 1157
33. P.K. Chaudhury, K.T. Park, and F.A. Mohamed, Effect of Fe on the Superplastic Deformation of Zn-22 pct Al, *Metall. Mater. Trans. A*, Vol 25, 1994, p 2391
34. F.A. Mohamed and T.J. Ginter, The Stress Dependence of Subgrain Size in Al, *J. Mater. Sci.*, Vol 17, 1982, p 2007
35. F.A. Mohamed and T.G. Langdon, Deformation Mechanism Maps for Superplastic Materials, *Scr. Metall.*, Vol 10, 1976, p 759
36. S.A. Shei and T.G. Langdon, The Mechanical Properties of a Superplastic Quasi-Single Phase Copper Alloy, *Acta Metall.*, Vol 26, 1978, p 638
37. M.F. Ashby and R.A. Verrall, Diffusion-Accommodated Flow and Superplasticity, *Acta Metall* Vol 21, 1973, p 149
38. A. Ball and M.M Hutchinson, Super-plasticity in the Aluminum-Zinc Eutectoid, *Met. Sci.*, Vol 3, 1969, p 1
39. A.K. Mukherjee, The Rate Controlling Mechanism in Superplasticity, *Mater. Sci. Eng.*, Vol 8, 1971, p 83
40. R.C. Gifkins, Grain-Boundary Sliding and Its Accommodation during Creep and Superplasticity, *Metall. Trans. A*, Vol 7, 1976, p 1225

41. J.H. Gittus, Theory of Superplastic Flow in Two-Phase Materials: Role of Interphase-Boundary Dislocations, Ledges, and Diffusion, *J. Eng. Mater. Technol. (Trans. ASME)*, Vol 99, 1977, p 244
42. A. Arieli and A.K. Mukherjee, A Model for the Rate-Controlling Mechanism in Superplasticity, *Mater. Sci. Eng.*, Vol 45, 1980, p 61
43. V. Paidar and S. Takeuchi, Superplastic Deformation Carried by Grain Boundaries, *Acta Metall. Mater.*, Vol 40, 1992, p 1773
44. H.W. Hayden, S. Floreen, and P.D. Goodell, The Deformation Mechanisms of Superplasticity, *Metall. Trans.*, Vol 3, 1972, p 833
45. R.C. Gifkins and T.G Langdon, Comments on Theories of Structural Superplasticity, *Mater. Sci. Eng.*, Vol 36, 1978, p 27
46. G. Rai and N.J. Grant, On the Measurements of Superplasticity in an Al-Cu Alloy, *Metall. Trans. A*, Vol 6, 1975, p 385
47. A. Arieli and A.K. Mukherjee, On Concurrent Grain Growth and Deformation Mechanism in Region I for Superplastic Zn-22% Eutectoid Alloy, *Scr. Metall.*, Vol 13, 1979, p 331
48. J. Weertman, Steady-State Creep of Crystals, *J. Appl. Phys.*, Vol 28, 1957, p 1185
49. R.C. Gifkins, "Mechanisms for Low-Stress Region I of Superplasticity," in *Proceedings of a Symposium on Strength of Metals and Alloys*, R.C. Gifkins, Ed., Pergamon, Oxford, 1982, p 701
50. F.A. Mohamed, Interpretation of Superplastic Flow in Terms of Threshold Stress, *J. Mater. Sci.*, Vol 18, 1983, p 582
51. F.A. Mohamed and T.G. Langdon, The Transition from Viscous Glide to Dislocation Climb, *Acta Metall.*, Vol 22, 1974, p 779
52. R.C. Gifkins, Grain Rearrangements during Superplastic Deformation, *J. Mater. Sci.*, Vol 13, 1978, p 1926
53. I.I. Novikov, V.K. Portnoy, and V.S. Levchenko, Investigation of Structural Changes during Superplastic Deformation of Zn-22% Al Alloy by Replica Locating Technique, *Acta Metall.*, Vol 29, 1981, p 1077
54. S.T. Yang and F.A. Mohamed, On the Characteristics of the Threshold Stress for Superplastic Flow in Zn-22 pct Al, *Metall. Mater. Trans. A*, Vol 26, 1995, p 493
55. H. Gleiter and B. Chalmers, High Angle Grain Boundaries, *Prog. Mater. Sci.*, Vol 16, 1973
56. X.G. Jiang, S.T. Yang, J.C. Earthman, and F.A. Mohamed, Effect of Fe on Ductility and Cavitation in the Superplastic Zn-22 pct Al Eutectoid, *Metall. Mater. Trans. A*, Vol 27, 1996, p 863
57. M.P. Seah, Grain Boundary Segregation and the T-t Dependence of Temper Brittleness, *Acta Metall.*, Vol 25, 1977, p 34
58. P. Gas, M. Guttman, and J. Bernardini, The Interactive Co-Segregation of Sb and Ni at the Grain Boundaries of Ultra-High Purity Fe-Base Alloys, *Acta Metall.*, Vol 30, 1982, p 1309

59. R.Z. Valiev and T.G. Langdon, An Investigation of the Role of Intragranular Dislocation Strain in the Superplastic Pb-62% Sn Eutectic Alloy, *Acta Metall. Mater.*, Vol 41, 1991, p 949
60. Z.R. Lin, A.H. Chokshi, and T.G. Langdon, An Investigation of Grain Boundary Sliding in Superplasticity at High Elongations, *J. Mater. Sci.*, Vol 23, 1988, p 2712
61. R.C. Gifkins, Ductility and Strain-Rate Control Mechanisms in Superplasticity, *Scr. Metall. Mater.*, Vol 25, 1991, p 1397
62. M.J. Mayo and W.D. Nix, A Micro-Indentation Study of Superplasticity in Pb, Sn, and Sn-38 wt.% Pb, *Acta Metall.*, Vol 36, 1988, p 2183
63. M.J. Mayo and W.D. Nix, Direct Observation of Superplastic Flow Mechanisms in Torsion, *Acta Metall.*, Vol 37, 1989, p 1121
64. K.T. Park and F.A. Mohamed, Effect of Impurity Content on Cavitation in the Superplastic Zn-22 pct Al Alloy, *Metall. Trans. A*, Vol 21, 1990, p 2605
65. K.T. Park, S.T. Yang, J.C. Earthman, and F.A. Mohamed, The Effect of Impurities on Ductility and Cavitation in the Superplastic Zn-22% Al Alloy, *Mater. Sci. Eng. A*, Vol 188, 1994, p 59
66. A. Yousefiani, J.C. Earthman, and F.A. Mohamed, Formation of Cavity Stringers during Superplastic Deformation, *Acta Mater.*, Vol 46, 1998, p 3557
67. H. Riedel in *Fracture at High Temperatures*, B. Ilschner and N. Grant, Ed., MRE Springer-Verlag, 1986, p 116
68. F.A. Mohamed, Modification of the Burke-Nix Ductility Expression, *Scripta Metall.*, Vol 13, 1979, p 87
69. F.A. Nichols, Plastic Instabilities and Uniaxial Tensile Ductilities, *Acta Metall.*, Vol 27, 1980, p 663
70. L.H. Lin, J.P. Hirth, and E.W. Hart, Plastic Instability in Uniaxial Tension Tests, *Acta Metall.*, Vol 29, 1981, p 819
71. F.A. Mohamed and T.G. Langdon, Flow Localization and Neck Formation in a Superplastic Metal, *Acta Metall.*, Vol 29, 1981, p 911
72. F.A. Mohamed, M.I. Ahmed, and T.G. Langdon, Factors Influencing Ductility in the Superplastic Zn-22 Pct Al Eutectoid, *Metall. Trans. A*, Vol 8, 1977, p 933
73. C.H. Cacers and D.S. Wilkinson, Superplastic Behavior of a Zn-22 pct Al-0.5 Pct Cu Alloy, *Metall. Trans. A*, Vol 17, 1985, p 1873
74. A. Yousefiani and F.A. Mohamed, Superplastic Flow and Cavitation in Zn-22% pct Al Doped with Cu, *Metall. Mater. Trans. A*, Vol 29, 1998, p 1653
75. B.P. Kashyap and T. Tangi, On the Contribution of Concurrent Grain Growth to Strain Sensitive Flow of a Superplastic Al-Cu Eutectic Alloy, *Metall. Trans. A*, Vol 18, 1987, p 417
76. D.W. Livesey and N. Ridley, Effect of Grain Size on Cavitation in Superplastic Zn-22% Al Eutectoid, *J. Mater. Sci.*, Vol 17, 1982, p 2257

Introduction to High Strain Rate Testing

Sia Nemat-Nasser, University of California, San Diego

Introduction

HIGH STRAIN RATE TESTING is important for many engineering structural applications and metalworking operations. In structural applications, various components must be designed to function over a broad range of strain rates and temperatures. In metalworking operations, materials undergo large amounts of strains at various temperatures and strain rates. The constituent materials must, therefore, be characterized at the strain rates and temperatures of the intended application. Conventional servohydraulic machines are generally used for testing at quasi-static strain rates of 1 s^{-1} or less (Fig. 1). With special design, it is possible to attain greater strain rates, up to about 100 s^{-1} , with conventional load frames. For higher strain rates, other test methods are required. Table 1 summarizes various methods in terms of the ranges of the strain rates that they can achieve.

Table 1 Experimental methods for high strain rate testing

Applicable strain rate, s^{-1}	Testing technique
Compression tests	
<0.1	Conventional load frames
0.1–100	Special servohydraulic frames
0.1–500	Cam plastometer and drop test
200– 10^4	Hopkinson (Kolsky) bar in compression
10^3 – 10^5	Taylor impact test
Tension tests	
<0.1	Conventional load frames
0.1–100	Special servohydraulic frames
100– 10^3	Hopkinson (Kolsky) bar in tension
10^4	Expanding ring
$>10^5$	Flyer plate
Shear and multiaxial tests	
<0.1	Conventional shear tests
0.1–100	Special servohydraulic frames
10– 10^3	Torsional impact
100– 10^4	Hopkinson (Kolsky) bar in torsion
10^3 – 10^4	Double-notch shear and punch
10^4 – 10^7	Pressure-shear plate impact

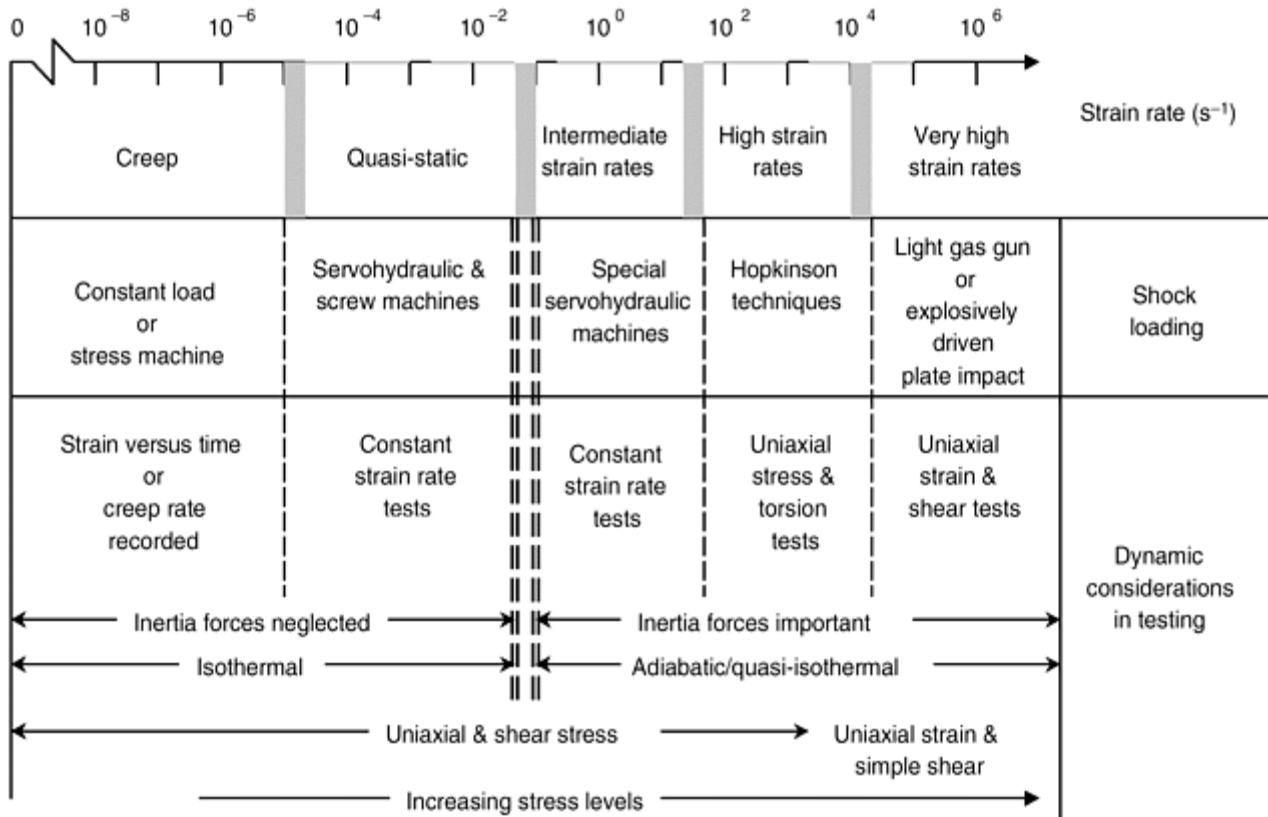


Fig. 1 Strain rate regimes and associated instruments and experimental conditions

The articles in this Section describe various methods for high strain rate testing. Several methods have been developed, starting with the pioneering work of John Hopkinson (Ref 1) and his son, Bertram Hopkinson (Ref 2, 3). Based on these contributions and also on an important paper by Davies (Ref 4), Kolsky (Ref 5) invented the split-Hopkinson pressure bar, which allows the deformation of a sample of a ductile material at a high strain rate, *while maintaining a uniform uniaxial state of stress within the sample*. The basic concept of the Kolsky apparatus involves a test sample sandwiched between an input and output bar, as described in detail in the article “Classic Split-Hopkinson Pressure Bar Testing” in this section. This technique provides a capability to measure the stress-strain response of ductile materials at a high strain rate, usually between approximately 50 s^{-1} and 10^4 s^{-1} , depending on the sample size, over the entire stress-strain curve. Strains exceeding 100% can be achieved with the Hopkinson bar method. The maximum strain rate that can be attained in a Hopkinson bar varies inversely with the length of the test specimen. The maximum strain rate is also limited by the elastic limit of the Hopkinson bars that are used to transmit the stress pulse to the test sample. These basic factors of the Hopkinson bar method and some specialized compression and tension tests are discussed in the article “High Strain Rate Tension and Compression Tests” in this section. An overview of shear test methods (other than the torsional Kolsky bar method) is also provided in the article “High Strain Rate Shear Testing.”

The most important characteristic of Kolsky's split-Hopkinson compression apparatus is that it allows high strain rate deformation while the sample is, in fact, in *dynamic equilibrium*, that is, the stress gradient is essentially zero along the sample. It is thus possible to develop the uniaxial stress-strain response of many materials at a variety of strain rates. Because the response of most materials depends on both the strain rate and the temperature, the technique allows developing constitutive relations that express the uniaxial stress to the corresponding strain rate and temperature. From such results, one is able to produce experimentally based, three-dimensional constitutive models for numerous materials.

The series of articles on split-Hopkinson compression testing begins with the article “Classic Split-Hopkinson Pressure Bar Testing,” which is followed by the article “Recovery Hopkinson Bar Techniques.” One limitation of the classic split-Hopkinson bar technique had been the repeated loading of the sample by the stress pulses that travel back and forth along the bars. During the 1990s, techniques were developed to trap the reflected pulses at the free ends of the Hopkinson bars, making it possible to subject a sample to a single stress pulse and then recover the sample without it being subjected to any additional loading (Ref 6). Using this recovery

technique, it is possible to develop isothermal stress-strain curves for many materials at a desired temperature and strain rate (Ref 7). This technique is described in the article “Recovery Hopkinson Bar Techniques.”

References cited in this section

1. J. Hopkinson, *Original Papers by J. Hopkinson*, Vol 2, B. Hopkinson, Ed., Cambridge: At the University Press, 1901, p 316–324
2. B. Hopkinson, The Effects of Momentary Stresses in Metals, *Proc. R. Soc. (London) A*, Vol 74, 1905, p 498
3. B. Hopkinson, A Method of Measuring the Pressure Produced in the Detonation of High Explosives or by the Impact of Bullets, *Philos. Trans. R. Soc. (London) A*, Vol 213, 1914, p 437–456
4. R.M. Davies, A Critical Study of the Hopkinson Pressure Bar, *Philos. Trans. R. Soc. (London) A*, Vol 240, 1948, p 375–457
5. H. Kolsky, An Investigation of the Mechanical Properties of Materials at Very High Rates of Loading, *Proc. Phys. Soc.*, Vol 62, 1949, p 676–700
6. S. Nemat-Nasser, J.B. Isaacs, and J.E. Starrett, Hopkinson Techniques for Dynamic Recovery Experiments, *Proc. R. Soc. (London) A*, Vol 435, 1991, p 371–391
7. S. Nemat-Nasser and J.B. Isaacs, Direct Measurement of Isothermal Flow Stress of Metals at Elevated Temperatures and High Strain Rates with Application to Ta and Ta-W Alloys, *Acta Metall.*, Vol 45, 1997, p 907–919

Introduction to High Strain Rate Testing

Sia Nemat-Nasser, University of California, San Diego

Techniques Required for Split-Hopkinson Testing of Very Soft or Hard Materials

In order to render the split-Hopkinson technique useful and reliable for the testing of very soft and very hard materials, special techniques must be used. These techniques are described in the articles “Split-Hopkinson Pressure Bar Testing of Soft Materials” and “Split-Hopkinson Pressure Bar Testing of Ceramics,” respectively. The Hopkinson technique can also be used to study the strain rate dependence of the compressive failure stress of very hard materials. At room temperature, the strain in such a sample can be measured directly by attaching strain gages to the sample (see the articles “Recovery Hopkinson Bar Techniques” and “Split-Hopkinson Pressure Bar Testing of Ceramics”). For high-temperature tests new techniques are required, such as elevated-temperature testing discussed in the article “Recovery Hopkinson Bar Techniques.”

The split-Hopkinson technique has also been extended to include testing ductile materials in tension, in torsion (Ref 8, 9, 10, 11), and even in combined torsion and uniaxial stress (Ref 12). Torsional testing is described in detail in the article “Torsional Kolsky Bar Testing.” The Hopkinson technique can also be used for high strain rate indentation tests, as discussed in the article “Dynamic Indentation Testing.” another interesting development based on the split-hopkinson bar is the deformation of a sample at high strain rates while it is under a triaxial state of stress for both static and dynamic lateral confinement. (This is discussed in the article “Triaxial Hopkinson Techniques.”)

For yet higher strain rates beyond the range of Hopkinson techniques (Fig. 1) other special techniques are necessary. For very high strain rates, plate-impact experiments are used. The uniaxial Hopkinson experiments

provide a uniaxial stress in the sample (ideally speaking). The normal plate-impact experiment is designed to provide a uniaxial strain state in the central portion of the sample. In the oblique plate impact experiment, the uniaxial strain is accompanied by simple shearing. Strain rates of 10^5 and 10^6 s⁻¹, and even greater, have been achieved. This technique is discussed in the article “Low Velocity Impact Testing.” the strains that can be produced by the plate impact experiments are, however, limited. To obtain large strains at high strain rates, one may employ hat-shaped experiments and cylinder-collapse tests as described in the article “High Strain Rate Shear Testing.”

References cited in this section

8. J. Harding, E.O. Wood, and J.D. Campbell, Tensile Testing of Materials at Impact Rates of Strain, *J. Mech. Eng. Sci.*, Vol 2, 1960, p 88–96
9. U.S. Lindholm, Some Experiments with the Split Hopkinson Pressure Bar, *J. Mech. Phys. Solids*, Vol 12, 1964, p 317–335
10. U.S. Lindholm and L.M. Yeakley, High Strain-Rate Testing: Tension and Compression, *Exp. Mech.*, Vol 8, 1968, p 1–9
11. K.A. Hartley, J. Duffy, and R.H. Hawley, Measurement of the Temperature Profile During Shear Band Formation in Steels Deforming at High Strain Rates, *J. Mech. Phys. Solids*, Vol 35, 1987, p 283–301
12. J.L. Lewis and W. Goldsmith, A Biaxial Split Hopkinson Bar for Simultaneous Torsion and Compression, *Rev. Sci. Instrum.*, Vol 44, 1979, p 812–814

Introduction to High Strain Rate Testing

Sia Nemat-Nasser, University of California, San Diego

References

1. J. Hopkinson, *Original Papers by J. Hopkinson*, Vol 2, B. Hopkinson, Ed., Cambridge: At the University Press, 1901, p 316–324
2. B. Hopkinson, The Effects of Momentary Stresses in Metals, *Proc. R. Soc. (London) A*, Vol 74, 1905, p 498
3. B. Hopkinson, A Method of Measuring the Pressure Produced in the Detonation of High Explosives or by the Impact of Bullets, *Philos. Trans. R. Soc. (London) A*, Vol 213, 1914, p 437–456
4. R.M. Davies, A Critical Study of the Hopkinson Pressure Bar, *Philos. Trans. R. Soc. (London) A*, Vol 240, 1948, p 375–457
5. H. Kolsky, An Investigation of the Mechanical Properties of Materials at Very High Rates of Loading, *Proc. Phys. Soc.*, Vol 62, 1949, p 676–700
6. S. Nemat-Nasser, J.B. Isaacs, and J.E. Starrett, Hopkinson Techniques for Dynamic Recovery Experiments, *Proc. R. Soc. (London) A*, Vol 435, 1991, p 371–391

7. S. Nemat-Nasser and J.B. Isaacs, Direct Measurement of Isothermal Flow Stress of Metals at Elevated Temperatures and High Strain Rates with Application to Ta and Ta-W Alloys, *Acta Metall.*, Vol 45, 1997, p 907–919
8. J. Harding, E.O. Wood, and J.D. Campbell, Tensile Testing of Materials at Impact Rates of Strain, *J. Mech. Eng. Sci.*, Vol 2, 1960, p 88–96
9. U.S. Lindholm, Some Experiments with the Split Hopkinson Pressure Bar, *J. Mech. Phys. Solids*, Vol 12, 1964, p 317–335
10. U.S. Lindholm and L.M. Yeakley, High Strain-Rate Testing: Tension and Compression, *Exp. Mech.*, Vol 8, 1968, p 1–9
11. K.A. Hartley, J. Duffy, and R.H. Hawley, Measurement of the Temperature Profile During Shear Band Formation in Steels Deforming at High Strain Rates, *J. Mech. Phys. Solids*, Vol 35, 1987, p 283–301
12. J.L. Lewis and W. Goldsmith, A Biaxial Split Hopkinson Bar for Simultaneous Torsion and Compression, *Rev. Sci. Instrum.*, Vol 44, 1979, p 812–814

High Strain Rate Tension and Compression Tests

Introduction

MECHANICAL BEHAVIOR at high strain rates differs considerably from that observed at quasi-static or intermediate strain rates, and many engineering applications require characterization of mechanical behavior under dynamic conditions. For example, strain rates ranging from 100 s^{-1} to more than 10^4 s^{-1} occur in many processes or events of practical importance, such as foreign object damage, explosive forming, earthquakes, blast loading, structural impacts, terminal ballistics, and metalworking.

This introductory article briefly reviews the dynamic factors and experimental methods for high strain rate tension testing and compression testing methods listed in Table 1. Considerable data on the high strain rate behavior of many materials (including steels, aluminum and copper alloys, titanium, beryllium, magnesium, and zinc) are available in the literature (see the Selected References at the end of this article). Results indicate that for many metals a linear relation exists between flow stress and the logarithm of plastic strain rate in the range from quasi-static rates to about 10^3 s^{-1} . Above this range, however, the flow stress generally rises far more rapidly with strain rate. Thus, the linear relationship is no longer valid, and extrapolation from the lower strain rate regime becomes unreliable. Fewer data are available at the higher strain rates, particularly at very high strain rates above 10^3 or 10^4 s^{-1} , at which testing becomes more difficult. At strain rates in excess of 10^4 s^{-1} , the lower yield stress is often found to be directly proportional to strain rate, rather than to the logarithm of strain rate. This implies a new region of mechanical response controlled in part by a viscous damping mechanism in contrast to thermally activated processes at strain rates below 10^4 s^{-1} .

Table 1 Experimental methods for high strain rate testing

Mode	Applicable strain rate, s ⁻¹	Testing technique
Compression	<0.1	Conventional load frames
	0.1–100	Special servohydraulic frames
	0.1–500	Cam plastometer and drop test
	200–10 ⁴	Hopkinson pressure bar in compression
	10 ⁴ –10 ⁵	Taylor impact test
Tension	<0.1	Conventional load frames
	0.1–100	Special servohydraulic frames
	100–10 ⁴	Hopkinson pressure bar in tension
	10 ⁴	Expanding ring
	>10 ⁵	Flyer plate

High Strain Rate Tension and Compression Tests

Test Effects at High Strain Rates

Strain rate, $\dot{\epsilon}$, is the rate of change of strain, ϵ , with time, t :

$$\dot{\epsilon} = \frac{d\epsilon}{dt} \quad (\text{Eq 1})$$

where ϵ can be either the engineering or the true strain. Although compressive strain and strain rate are negative quantities, the negative sign is often omitted when it is understood that the test is a compression test. For a constant strain rate experiment, the strain rate is simply the total strain divided by the duration of the test:

$$\dot{\epsilon} = \frac{\epsilon}{t} \quad (\text{Eq 2})$$

When ϵ in Eq 1 is the engineering strain, then:

$$\frac{d\epsilon}{dt} = \frac{1}{L_0} \frac{dL}{dt} = \frac{V}{L_0} \quad (\text{Eq 3})$$

where L is the length of the specimen of original length, L_0 , and V is the velocity at which the specimen is being deformed. A constant crosshead speed in a mechanical testing machine yields a constant engineering strain rate defined by Eq 3.

A typical (quasi-static) mechanical test is performed at a strain rate of around 10^{-3} s^{-1} , which yields a strain of 0.5 in 500 seconds. The equipment and techniques generally can be extended to strain rates as high as 0.1 s^{-1} without difficulty. Tests at higher strain rates may necessitate other experimental techniques and additional dynamic considerations, such as inertia effects, wave propagation effects, and shock wave effects (Fig. 1). Thermal effects and the difficulties of strain measurement are additional factors in high strain rate testing.

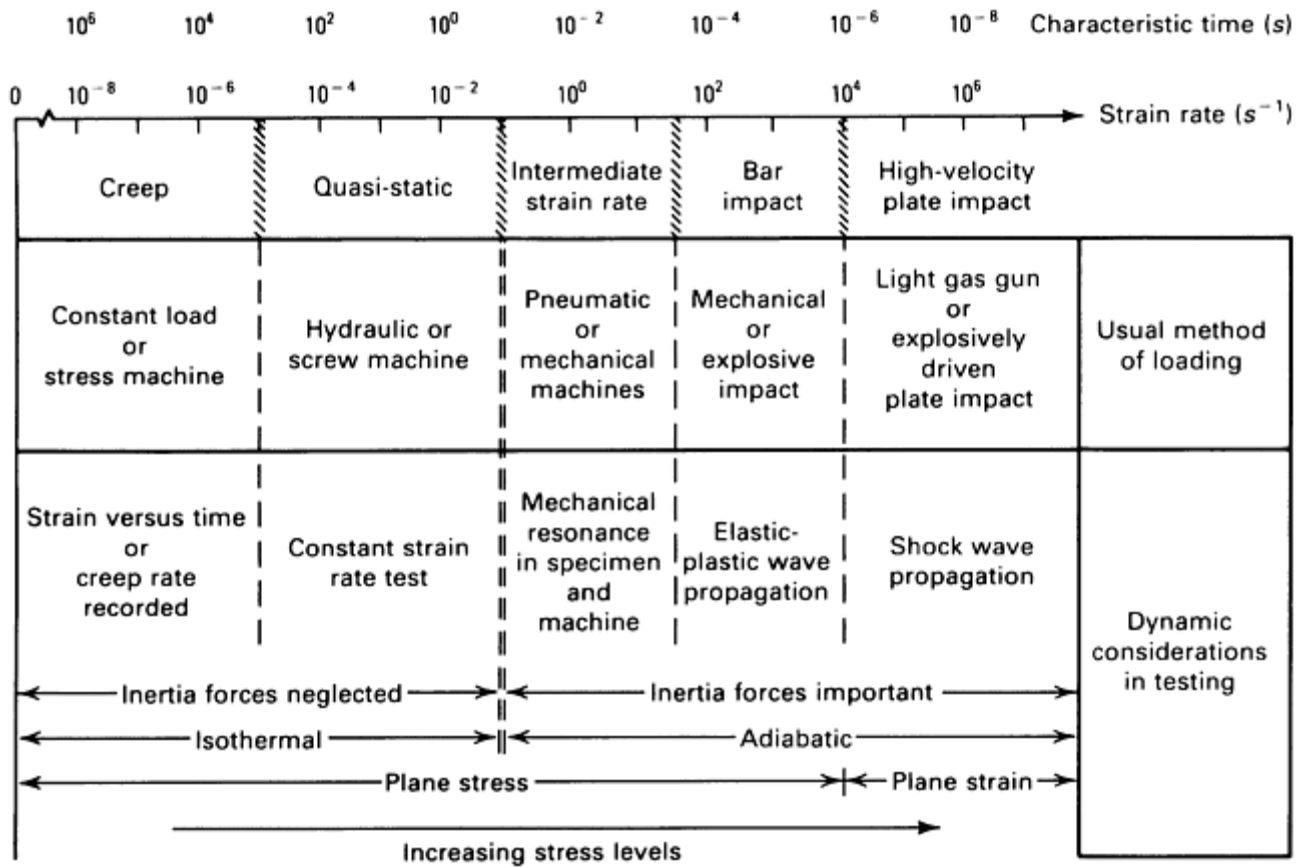


Fig. 1 Dynamic aspects of materials testing. Source: Ref 1

Dynamic Factors

A fundamental difference between a high strain rate test and a quasi-static test is that inertia and wave propagation effects become more pronounced at higher strain rates (Fig. 1). These dynamic effects on test results become more pronounced at higher strain rates, as shown in Table 2, for low, medium, high, and very high strain rate regimes. When the strain rate is increased through the medium strain rate regime, the measurement of load is the first to be affected by stress wave propagation. As the strain rate is increased even further, uniform deformation within the specimen becomes more critical. At very high strain rates (beginning at about 10^4 or 10^5 s^{-1}), shock wave propagation becomes critical. Shock wave propagation is discussed in more detail in the article “Shock Wave Testing of Ductile Materials” in this Volume.

Table 2 Experimental techniques for various strain rate regimes in compression testing

Strain rate regime	Experimental techniques	Wave propagation
Low rate: $\dot{\epsilon} < 0.1 s^{-1}$	Standard mechanical testing procedures	Not significant
Medium rate: $0.1 s^{-1} \leq \dot{\epsilon} \leq 200 s^{-1}$	Servo-hydraulic frames, cam plastometer, drop test	Influences load measurement
High rate: $200 s^{-1} \leq \dot{\epsilon} \leq 10^5 s^{-1}$	Hopkinson pressure bar	Affects uniform stress approximation
	Rod impact (Taylor) test	Analysis required for interpretation of results
Very high rate: $\dot{\epsilon} > 10^5 s^{-1}$	Flyer plate impact	Critical

Source: Ref 2

Conventional Load Frames at Medium Strain Rates. Strain rate effects in uniaxial tension or compression are determined by tests with conventional load frames up to approximately 100 or 200 s^{-1} . Conventional test machines are available with increased ram velocities, as are high-speed pneumatic and hydraulic machines. The speed capability of a machine may be influenced by several factors. Speed may be a function of the load that

the ram is attempting to apply, and the no-load speed may be much higher than the full-load speed. The distance traveled may also affect the speed capability. A long-stroke machine may attain a given speed only after a significant amount of travel. Depending on the specimen length, considerable specimen strain could occur before final maximum velocity is obtained in a tension test. Finally, the ability to control speed is a function of the response capability of a servo-controlled machine working in a closed-loop mode. Open-loop machines provide speeds that can be influenced by specimen strength and cannot easily reproduce predetermined velocities or strain rates on materials with different yield strengths or strain hardening behaviors. Load cell ringing at intermediate or medium strain rates may be negligible. However, even if wave propagation effects in the test piece can be neglected, the characteristic response time of load cells must still be checked. At intermediate strain rates, “ringing” of a load cell can mask the desired measurement. Load cell ringing is frequently encountered in high-rate tensile testing. Generally, the load-cell response time (which is the reciprocal of its natural frequency in hertz) must be small compared to the total duration of the test. For example, if a load cell has a natural frequency of 1 kHz, its period of vibration is 10^{-3} s. This load cell could then be used only for experiments that lasted over ten times that amount, or over 10 μ s.

Another condition that must be satisfied is the distance of the load cell from the end of the specimen. If a sufficient distance exists between the specimen and load cell, the finite elastic wave transit time may result in load data that are not time-coincident with strain data. To prevent phase lags from obscuring the experimental data, the wave transit time from the specimen to load cell should be negligibly small compared to the test duration. Otherwise, the load data must be corrected for the delay, and such corrections seldom are precise.

Wave Propagation Effects. At high strain rates, uniform deformation within the test piece becomes a factor. Inertia initially opposes uniform deformation, and a stress wave is transmitted and reflected within the test piece at the speed of sound. If the deformation is purely elastic, then the longitudinal sound velocity, c_{EL} , is simply $c_{EL} = \sqrt{E/\rho}$, where E is the elastic modulus and ρ is density. If the material has deformed into the plastic region, the plastic-wave velocity is more appropriate and generally can be an order of magnitude smaller than the elastic wave velocity. One-dimensional strain-rate-independent theory predicts that the plastic wave propagates at a velocity, c_{PL} , determined by:

$$c_{PL} = \sqrt{\frac{d\sigma/d\varepsilon}{\rho}} \quad (\text{Eq 4})$$

where $d\sigma/d\varepsilon$ is the slope of the true stress/true strain curve. For many materials, the initial work-hardening rate $d\sigma/d\varepsilon$ is approximately 1% of E ; thus for these materials, the plastic wave velocity is approximately 10% of the elastic-wave velocity.

However, experimental evidence in a variety of metals suggests that the above estimate is too conservative. The stress waves generated by impacts at stress levels far in excess of the yield stress appear to travel, at least initially, closer to the elastic wave velocity rather than at the plastic wave velocity (Eq 4). This implies that the wave propagation behavior can be more complicated than described by Eq 4. The velocity of the plastic wave is

sometimes estimated as $\sqrt{B/\rho}$ where B is the bulk modulus.

The velocity of waves and the size of the test piece determine the upper limit of strain rate for accurate measurement of stress-strain curves. If many wave transits occur during a test, the use of average stresses and strains can be justified. However, if only a few wave reflections occur before the specimen fails, then individual wave propagation must be considered. In this case, average values alone cannot be considered, and the use of this test to determine dynamic stress-strain response is precluded. As a first approximation, Davies and Hunter (Ref 3): have estimated that three reverberations are required for stress equilibration in compression testing.

To illustrate the importance of stress wave propagation, consider compression testing of a 10 mm (0.4 in.) specimen, in which the elastic wave velocity is 5.0×10^3 m/s (16.4×10^3 ft/s) and the initial plastic wave velocity may be approximated as 5.0×10^2 m/s (16.4×10^2 ft/s). Assuming that three reverberations of the slower moving plastic wave are required for uniform stress within the deforming specimen, the time for these reverberations is computed to equal 60 μ s. At a strain rate of 10^3 s $^{-1}$, the specimen will have compressed to a strain of 6% during this interval. Thus, data at strains less than this may be invalid, because it cannot be assumed that the specimen was deforming uniformly. Even if the elastic wave velocity is used in the above example, the critical strain at which uniform stress within the specimen is achieved is computed to be equal to 0.6%. At a strain rate of 10^4 s $^{-1}$, this critical strain becomes 6%.

The above example illustrates that wave propagation becomes an important consideration affecting test validity in the high strain rate regime of Table 2. It also illustrates a major advantage of compression testing over tension testing at high strain rates; a compression test specimen can be fabricated to relatively small dimensions to minimize wave propagation times. Another way to determine whether or not wave propagation effects limit the validity of a test is the sample ring-up time, which is the time required for a sample to achieve a uniform state of stress. Generally, measurements are not valid for times such that $L \sim ct$, where c is the speed of stress wave propagation. This corresponds to a situation in which strain $\epsilon \gg \dot{\epsilon}L/c$. Consequently, small strain measurements are difficult to obtain at very high strain rates. Sample length can also be reduced, although there are limits in reducing specimen dimensions.

Another concern is that local failure may occur at the end to which the load is applied. The magnitude of the stress transient (σ_m) associated with the sudden application of velocity v_0 is $\sigma_m = \rho cv_0$ (where ρ is density of the material). Tension tests must be designed so that $\sigma_m < \sigma_{yy}$, the tensile yield stress. For example, consider a bar 25 mm (1 in.) in length that is accelerated at one end to 2.5 m/s (8.2 ft/s). For many engineering materials, including steels, aluminum alloys, and titanium alloys, the elastic wave velocity is about 5000 m/s (16,400 ft/s). The maximum stress generated at the accelerated end of the bar is ρcv , where v is the deformation speed ($v = \dot{\epsilon}L$). For a steel bar, the first stress pulse is 100 MPa (14.5 ksi) and the average strain rate is 100 s^{-1} . If a steel with a strength of 1 GPa (145 ksi) is being tension tested, the maximum allowable driving velocity is 25 m/s (82 ft/s). At that velocity, instantaneous failure would occur at the driven end.

Departure from Isothermal Test Conditions

It is well known that most of the work of deformation is expended as heat; only 5 to 10% of this work is actually stored in the defect structure of the deformed specimen. As the strain rate increases, there is insufficient time for the transport of this heat from the specimen to the grips, platens, or atmosphere. Thus, the specimen temperature can increase during deformation.

The work of deformation, W , is simply:

$$W = \int^{L_f} L P dL \quad (\text{Eq 5})$$

where P is the applied load, and L is the length of the specimen of final length, L_f , and original length, L_o . Equation 5 can be rewritten as:

$$W = A_o L_o \int^e s(e) de \quad (\text{Eq 6})$$

where A_o and L_o are the original specimen area and length, respectively, s is the engineering stress, and e is the engineering strain.

If it is assumed that this work is transformed to heat adiabatically (i.e., without heat flow), then the specimen temperature increase, ΔT , is defined by:

$$\Delta T = \frac{1}{\rho C_p} \int^{e_f} s(e) de \quad (\text{Eq 7})$$

where ρ is the density, and C_p is the heat capacity of the test piece material at constant pressure. As an example, consider the deformation of a stainless steel specimen to a strain of 0.5, and, for simplicity, also assume that the flow stress of the material is constant and equal to 750 MPa (109 ksi). With a density of 8 g/cm^3 (0.29 lb/in.^3) and a heat capacity of $500 \text{ J/kg} \cdot \text{K}$ ($0.120 \text{ cal/g} \cdot \text{°C}$), the temperature increase at a strain of 0.5 is estimated to be 94 K calculated from Eq 7. This is a significant increase and demonstrates that this is not an isothermal test.

The above estimate assumed adiabatic conditions, which are only the case in the high strain rate regime. However, at least under these conditions, the temperature increase can be estimated fairly accurately, and deformation within the specimen remains uniform. The medium strain rate regime is further complicated by heat flow, which in quiescent environments is dominated by conduction through the ends of the specimen. In this regime, there is the possibility of generating a substantial axial temperature gradient from the end to the midpoint of the specimen. This gradient can result in nonuniform deformation throughout the specimen, which complicates interpretation of the experimental results. In fact, if the temperature dependence of the flow stress is high enough, deformation may become highly localized at the center of the specimen; this situation is less likely in a compression specimen than it is in a tensile specimen, which has a much higher aspect ratio.

Measurement of Stress and Strain

Measurement of stress and strain and data acquisition becomes more difficult as the strain rate increases. For example, the frequency response of the load cell must be considered, as previously noted. The frequency response of other measurement devices, such as extensometers or strain gages, must also be considered, along with any signal conditioning and the sampling rates during digital data acquisition. Computer data acquisition systems with sampling at rates as fast as 100 kHz should be sufficient for tests at strain rates as high as 10^2 s^{-1} . For analog-to-digital processing, the sampling rate is inversely related to the desired accuracy or byte size of the digitized "word." For example, with a byte size of 10 bits, sampling rates with typical processors can be as fast as 20 MHz.

In some cases, the standard measurement techniques for stress or strain at low strain rates become unsuitable for testing at higher strain rates. For example, the use of fragile devices, such as extensometers, may not be appropriate for tests that involve large, rapid deformations. Specific procedures for each of the experimental techniques are discussed in more detail in the following sections, but a few general comments concerning strain measurement during tension tests with conventional load frames are summarized here. Additional information on compression testing at medium strain rates is also in the article "Uniaxial Compression Testing" in this Volume.

Measurement of strain is a major problem in high strain rate testing. In quasi-static tension testing, for example, the diameter of the minimum cross section in a cylindrical specimen is easily measured. In contrast, such measurements are virtually impossible or highly impractical in high-rate testing. Furthermore, although strains are easily measured over a uniform gage length section in quasi-static tension testing, the same measurements are considerably more difficult to obtain at high strain rates. Mechanical extensometers also are of little use at high strain rates due to the effects of inertia.

In high strain rate tests, strain measurements typically utilize strain gages, optical extensometers, and displacement measurements between loading fixtures to determine or infer the dynamic tensile in a test piece. At very high rates of strain, strains may be measured in some experimental configurations only through wave propagation analysis. This procedure generally requires that assumptions be made about the constitutive behavior, that wave propagation analysis be carried out, and that predictions and experimental observations be compared. Unique solutions cannot be guaranteed because some other constitutive model may conceivably provide similar results in a particular wave propagation problem.

Electrical resistance strain gages are the most direct, reliable method for strain measurement in high-speed testing. The frequency response capability of strain gages is considerably greater than the mechanical response of the combination of load train, specimen, and load cell. Another method of measuring strain involves the use of optical extensometers, in which displacement measurements across the loading fixtures are divided by an actual or effective gage length. When using crosshead displacement in tension test, caution must be exercised to ensure that these represent only specimen elongation and not machine, ram, or load train elongations. The same precautions that apply in quasi-static tests also apply in dynamic tests. If these precautions are observed, valid stress-strain data from tension testing in conventional load frames can be obtained up to maximum strain rates in the range of 10 to 100 s^{-1} . For higher strain rates, or for cases in which the above criteria are not met, more specialized testing techniques may have to be used, as discussed in this article and in the remaining articles in this Section.

References cited in this section

1. U.S. Lindholm, High Strain Rate Tests, *Measurement of Mechanical Properties*, Vol 5, Part I, *Techniques of Metals Research*, R.F. Bunshah, Ed., Interscience, 1971, p 199–271
2. High Strain Rate Compression Testing, *Mechanical Testing*, Vol 8, *ASM Handbook*, ASM International, 1985 p 190–207
3. E.D.H. Davies and S.C. Hunter, The Dynamic Compression Testing of Solids by the Method of the Split Hopkinson Pressure Bar, *J. Mech. Phys. Solids*, Vol 11, 1963, p 155

Compression Tests at High Strain Rates

As listed in Tables 1 and 2, several methods are available for compression testing at strain rates up to about 10^4 to 10^5 s⁻¹. These high strain rate compression tests are briefly reviewed in this section with a focus on the general principles, advantages, and limitations of each test method.

Cam Plastometer

The cam plastometer is designed specifically for compression testing at strain rates from 0.5 to more than 200 s⁻¹. The axial load to compress the specimen is transferred from massive rotating flywheels through a cam; this provides the distinct advantage of being able to obtain a constant true strain rate experiment. The cam plastometer is used to obtain the resistance to compressive deformation of materials, principally metals, at constant strain rates over a useful and significant range of strain rates and a practical range of testing temperatures. Most plastometers have a capacity to compress cylindrical specimens homogeneously to a 50% reduction in height, assuming the material is tested at temperatures at which it is ductile enough to permit this reduction.

The development of the cam plastometer in the 1950s was significant because it allowed an extension of mechanical testing capability by three orders of magnitude in strain rate over that obtained in standard mechanical test machines. Furthermore, the cam plastometer mechanism lends itself to the generation of a constant true strain rate experiment, which is ideally suited for metal deformation studies. Most cam plastometer facilities have elevated-temperature testing capabilities. Some of these are equipped for testing in vacuum or in selected atmospheres. These require a vacuum chamber around the specimen-platen assembly and the use of O-ring or bellows grips. The elevated-temperature capability for some facilities is up to 1300 K through the use of in situ induction heating in a reducing atmosphere and the use of aluminum oxide platens. These platens appear to dampen some load cell ringing that occurs when using much denser tungsten carbide platens.

The cam plastometer was originally used to study the rolling characteristics of uranium plate and sheet by the classic Orowan method (Ref 4). This machine underwent several revisions in both mechanical design and instrumentation for compression testing of pure lead (Ref 5), commercial-purity aluminum (Ref 6), and steels (Ref 7). The first constant true strain rate cam plastometer was designed and built by Orowan at the British Iron and Steel Research Association (BISRA) in 1950. It was used to obtain true stress-strain curves for 12 steels at true strain rates of 0.05 to 100 s⁻¹ and temperatures from 1173 to 1473 K (Ref 7). Others have built cam plastometers to perform specific studies. Machines have been built to study the compressive deformation of aluminum and aluminum alloys (Ref 8, 9), depleted uranium (Ref 4, 10), zinc and zinc alloys (Ref 11, 12), and other ferrous and nonferrous metals (Ref 13). A modern version of the cam plastometer has also been designed and built at the Canadian Department of Mines, Energy, and Resources (Ref 14).

True strain rate compression tests are achieved in all cam plastometers by designing the load-applying mechanism in the form of a logarithmic cam (as true strain is, by definition, logarithmic strain). The true strain rate is constant only if the rotational speed of the cam is constant. This is achieved by storing large amounts of energy in flywheels and in the many rotating parts of transmissions, as well as in the cam. To maintain a constant strain rate, this stored energy must greatly exceed the energy required to compress the specimen. A typical cam plastometer setup is shown in Fig. 2, in which a 37 kW direct-current motor (behind the belt guard) and the 40 kV generator are depicted. The motor drives three flywheels distributed between and at both ends of the drive train, which consists of two large off-highway-type transmissions. Cam plastometers can be massive pieces of equipment. Size introduces problems in dynamically balancing the cam and in providing sufficient strength and minimum deflection of the loading frame and drive train. Some cam plastometers in Japan have been equipped with four-post loading frames to circumvent these problems.



Fig. 2 Typical cam plastometer facility. Direct-current motor and generator are on the left; three flywheels and two transmissions are on the right; two-post loading frame is at rear. Courtesy of Los Alamos National Laboratory

Effects of Friction and Lubricants. As in all compression tests, deformation is homogeneous throughout the test only if frictional constraint is minimized at the interfaces between the platens and the specimen ends. That is, the specimen should start out as a cylinder and maintain this cylindrical geometry throughout the test. This requires the use of a suitable lubricant at the interfaces.

Minimizing the effects of friction in a compression test involves selection of a suitable length-to-diameter (L/D) ratio for the specimen and the selection of proper lubrication for the specimen/platen interfaces. An L/D ratio of 1.56 is generally considered optimum. Ratios much larger than this lead to buckling, whereas ratios much smaller than this yield higher stress-strain curves, indicating excessive specimen-platen frictional constraint. An L/D ratio of 1.56 is within the range specified in ASTM E 9, "Compression Testing of Metallic Materials at Room Temperature."

Many lubricants (e.g., viscous oils, powdered graphite, or powdered, liquid-based, and grease-based molybdenum disulfide) have been used for room-temperature testing. A satisfactory lubricant for room-temperature and lower-temperature (to 77 K) testing is "Motor-Mica," which is a mixture of finely ground powdered mica and a highly viscous commercial automotive oil.

At slightly elevated temperatures, powdered tungsten disulfide has been used successfully. At higher temperatures, various glass frits exhibiting viscosities in the range 4000 to 6000 Pa · s (400–600 poise) at temperature can be used. For a series of tests on a titanium alloy, the commercial glaze Deltaglaze 347m was used above 1283 K, and Deltaglaze 349m has been used between 900 and 1010 °C (1650 and 1850 °F).

Coefficient of friction measurements by the method proposed in Ref 15 may be helpful in the preliminary selection of lubricants. Concentric grooves in the ends of the specimen are necessary for most plastometer testing. Depth, spacing, and included angle of the grooves must be determined empirically.

Drop Tower Compression Test

The drop tower compression test, as the name implies, uses a falling weight to provide a compressive load to the specimen. The test technique has the capability to generate high loads at medium strain rates, which cannot be readily obtained by servohydraulic load frames or cam plastometers. Load capacities of 900 kN (100 tons) have been demonstrated for this technique, with test durations from 0.1 to 20 μ s resulting in loading rates as high as 1 GN/s (115×10^3 tons/s).

The drop tower compression test has been used to measure compressive fracture strengths, to determine the compressive stress-strain behavior of material at medium strain rates, and to evaluate the dimensional stability of components subjected to impact compressive loads. Two general approaches can be used for drop tower compression testing. Fracture or compressive stress-strain tests require that the strain rate does not vary significantly during the test. This is accomplished in the drop tower test by ensuring that the available energy of the crosshead (weight times height) is no less than three times (preferably an order of magnitude) greater than the energy absorbed by the specimen and the test system.

The second test approach is used to evaluate the effect of subcritical, or low blow, loadings on the test specimen or components. In this case, the available energy of the crosshead is selected to generate a specific load. During the test, the crosshead comes to a stop and then rebounds. To avoid secondary loadings, a device for removing the specimen or catching the crosshead on the rebound must be used.

Limitations. The drop tower compression test is neither a constant-displacement rate nor a constant-loading rate test. The rate and form of the compressive loading depend on the specimen and test system compliances, as well as the impact velocity and available energy of the falling weight. Test conditions must be determined by trial and error or from empirically derived parameters. The test velocities and, therefore, the loading and strain rates are limited by both the response time of the instrumentation and the inertia loading of the system. In many cases, it is the latter that limits the test velocity. In general, it is better to drop a larger weight from a lower height than the converse when energy requirements are a consideration. The lower velocity will reduce the inertia loading and still generate comparable maximum loads.

Specimen displacement and energy calculations, which are commonly made for instrumented impact (i.e., Charpy) tests, are based on measuring the momentum impulse acting on the falling weight and calculating the resultant temporal impact velocity. These calculated values can be highly inaccurate for the drop tower compression test because deformations in the systems can be greater than the specimen deflections.

Equipment. A typical drop tower compression system is shown in Fig. 3. The test system consists of a drop tower with a massive foundation, a dynamic compression fixture, and stop blocks. The 900 kN (100 ton) capacity system utilizes a commercially available drop tower with an adjustable crosshead weight of 225 to 1000 kg (500–2200 lb) and a maximum drop height of 1.5 m (5 ft). A 12,000 kg (26,500 lb) steel-reinforced concrete foundation is used to provide maximum rigidity to the drop tower.

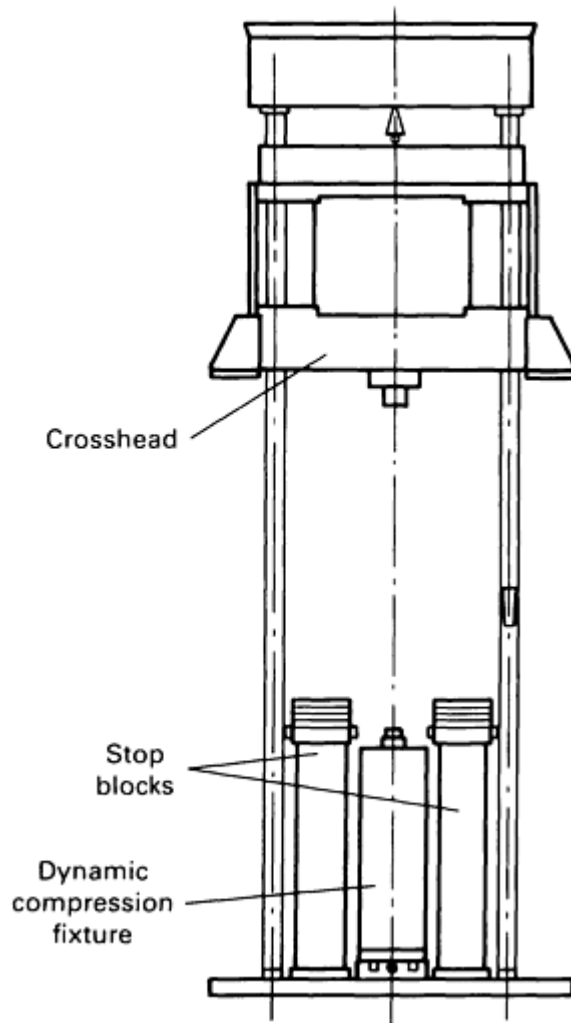


Fig. 3 Drop tower with compression fixture and stop blocks in place

The dynamic compression fixture (Fig. 4) transfers the impact load from the crosshead to the specimen through a shaft. Proper alignment of the shaft with the specimen axis is maintained throughout the test by linear ball bearings. Small nonparallelisms in the specimen ends are accommodated by a spherical seat beneath the lower platen. The impact load is sensed by a load cell located directly below the spherical seat. Stop blocks arrest the falling crosshead to avoid continued loading of the dynamic compression fixture after the shaft has reached its maximum travel. The development of the dynamic compression fixture is described in Ref 16.

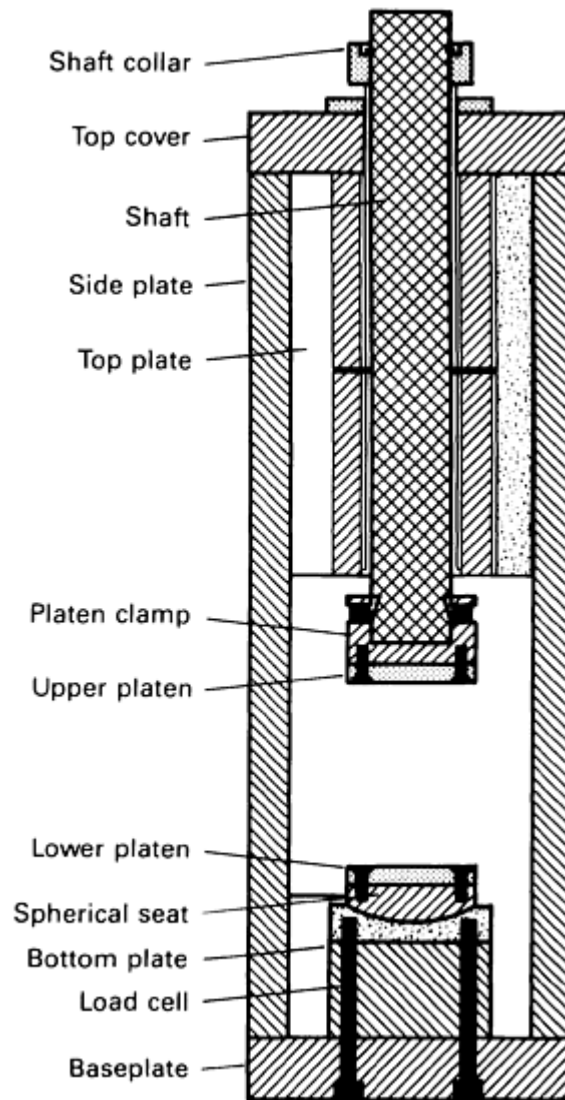


Fig. 4 Dynamic compression test fixture

A principal consideration in the design of the dynamic compression system is that the entire load train compliance must be kept quite low to achieve high loads. Gaps, mismatches, and foreign material at any of the interfaces in the load train adversely alter the rate and form of the impact loading. A second consideration is to minimize the mass of the fixture between the specimen and the centerline of the load cell. Acceleration of this mass to the test velocity causes inertia loads (Ref 17) that can obscure the actual mechanical loading of the specimen. The control of inertia effects is described in Ref 18.

Instrumentation. Equipment designed specifically for instrumented impact testing is used to acquire the load-versus-time data for the drop tower compression test. Minimum instrumentation requirements are a transducer to sense the specimen loading, the associated signal conditioning equipment, and recording instruments to provide a permanent record of the load-sensing transducer. The integrated system must be capable of sampling rates as fast as 35 kHz. The specific requirements for the load instrumentation, as well as the effect of limiting the frequency response, are described in Ref 17 and 19.

Specimen Requirements. Specific specimen requirements have not been developed for the drop tower compression test. However, several specimen configurations based on right-circular cylinders and lengths greater than two times their diameter have been used. As with all compression tests, the end constraint of the specimen due to friction is a primary concern. Hardened steel and modulus-matched inserts have been used between the platens and the specimen to minimize the constraint.

The Hopkinson Bar

Development of test techniques based on the Hopkinson bar has led to significant advances in high strain rate testing capabilities. These techniques yield the highest possible strain rates in a uniaxial compression test under uniform deformation conditions. In addition, the determination of stress within the deforming specimen is made without use of a load cell, and the measurement of strain is made without directly monitoring the specimen length.

The Hopkinson bar derives its name from its developer, who in 1914 used a long elastic bar to study the pressures produced by the impact of a bullet or by the detonation of an explosive (Ref 20). In designing this experiment, Hopkinson recognized that as long as the pressure bar remains elastic, the displacements in the pressure bar are directly related to the stresses and that the length of the wave in the bar is related to the duration of the impact through the velocity of sound in the bar, a quantity that is well known. A significant feature of this work is that the pressures were estimated by measuring the momentum (with a ballistic pendulum) acquired by a small section of the bar placed in contact with the bar at the far end. Further developments in the experimental techniques occurred a few decades after these original experiments, when Davies (Ref 21) and Kolsky (Ref 22) designed condensers to measure displacements in the pressure bars. Kolsky also introduced the split-Hopkinson pressure bar technique, in which the specimen is sandwiched between two pressure bars. He demonstrated how stress and strain within the deforming specimen are related to displacements in the pressure bars. Because of these contributions, the split-Hopkinson pressure bar is often referred as the Kolsky bar.

There are two basic configurations for Hopkinson pressure bar testing: the split-Hopkinson pressure bar (Fig. 5a) and the single pressure bar configuration (Fig. 5b). The basic principles of the two techniques are similar, and several investigators have used the single pressure bar configuration. The most widely used method is the split-Hopkinson pressure bar method, which consists of two elastic pressure bars that sandwich the specimen between them. Upon impact of a striker bar on an incident bar, an elastic compressive wave is generated within the incident bar, and the time-dependent strain in the pressure bar is measured at strain gage A at the midpoint of the incident bar (Fig. 5a). At the incident bar/specimen interface, the wave is partially reflected and partially transmitted into the specimen. A portion of the incident wave is reflected back along the incident bar as a tensile wave. This reflected strain is measured by strain gage A. Strain measurements are also taken on the output bar with strain gage B. These strain measurements on the pressure bars are used to determine the stress-strain behavior of the specimen if two basic conditions are met. First, the wave propagation within the pressure bars must be one-dimensional. Secondly, the specimen must deform uniformly. Under these two conditions, stress-strain behavior of the specimen can be determined as described below. More details are also in the article "Classic Split-Hopkinson Pressure Bar Testing" in this Volume.

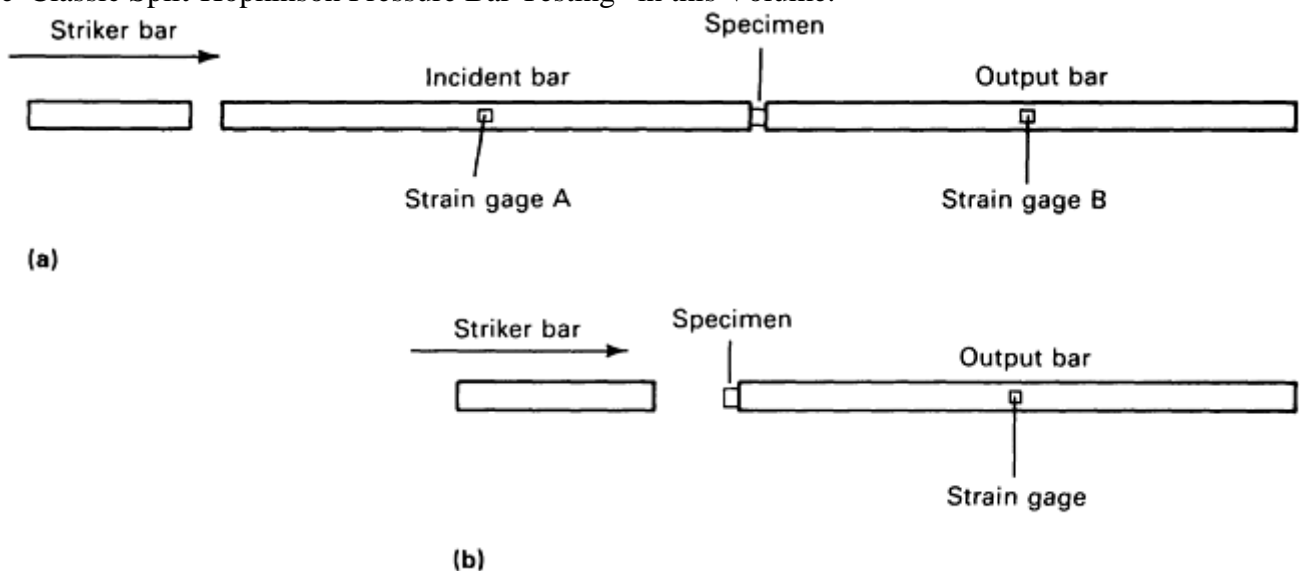


Fig. 5 Typical configurations of the Hopkinson bar. (a) Split-Hopkinson pressure bar with specimen sandwiched between two long elastic pressure bars, each of which is instrumented at its midpoint with a strain gage. (b) Single pressure bar with striker bar impacting the specimen directly. With this configuration, the motion of the striker bar or displacement within the specimen must be monitored independently.

Relating Hopkinson Bar Strain Gage Measurements to Specimen Stress-Strain Behavior. The strain rate in the deforming specimen is:

$$\frac{d\varepsilon}{dt} = \frac{V_1 - V_2}{L} \quad (\text{Eq 8})$$

where V_1 and V_2 are the velocities at the incident bar/specimen and specimen/output bar interfaces, respectively. The velocity V_1 is the product of the longitudinal sound velocity, C_o , in the pressure bar and the total strain at the incident bar/specimen interface, which is $\varepsilon_I - \varepsilon_R$. Similarly, the velocity V_2 is equal to $C_o \varepsilon_T$. In this development the incident and transmitted strains (ε_I , ε_T) and ε are all compressive strains, but are considered positive, whereas the reflected strain (ε_R) represents a tensile strain and is negative. Replacing V_1 and V_2 in Eq 8 with these expressions yields:

$$\frac{d\varepsilon(t)}{dt} = \frac{C_o}{L} [\varepsilon_I(t) - \varepsilon_R(t) - \varepsilon_T(t)] \quad (\text{Eq 9})$$

The average stress on the specimen is:

$$\sigma(t) = \frac{P_1(t) + P_2(t)}{2A} \quad (\text{Eq 10})$$

where P_1 and P_2 are the forces at the incident bar/specimen and specimen/output bar interfaces, respectively, and A is the instantaneous cross-sectional area of the specimen. At the incident bar/specimen interface, the force is:

$$P_1(t) = E[\varepsilon_I(t) + \varepsilon_R(t)]A_o \quad (\text{Eq 11})$$

where E is Young's modulus and A_o is the cross-sectional area of the bar. Likewise, the force at the specimen/output bar interface is:

$$P_2(t) = E\varepsilon_T(t)A_o \quad (\text{Eq 12})$$

Combining Eq 11 and 12 with Eq 10 yields:

$$\sigma(t) = \frac{E}{2} \frac{A_o}{A} [\varepsilon_I(t) + \varepsilon_R(t) + \varepsilon_T(t)] \quad (\text{Eq 13})$$

When the specimen is deforming uniformly, the stress at the incident bar/specimen interface equals that at the specimen/output bar interface and from Eq 11 and 12.

$$\varepsilon_I(t) + \varepsilon_R(t) = \varepsilon_T(t) \quad (\text{Eq 14})$$

from which Eq 9 and 13 may be simplified:

$$\frac{d\varepsilon(t)}{dt} = \frac{-2C_o}{L} \varepsilon_R(t) \quad (\text{Eq 15})$$

$$\sigma(t) = E \frac{A_o}{A} \varepsilon_T(t) \quad (\text{Eq 16})$$

Thus, the stress-strain behavior of the specimen is determined simply by measurements made on the elastic pressure bars in a split-Hopkinson pressure bar test. The analysis applies as well to the single bar configuration shown in Fig. 5(b). However, because the striker bar impacts directly with the specimen in this test, the strain $\varepsilon_R(t)$, which now represents the wave generated in the striker bar, cannot be measured with a strain gage, and another measurement technique is required, such as with high-speed photography.

As previously noted, the above equations relating strain gage measurement to stress-strain behavior in the deforming specimen require that two important conditions be met. The first is that wave propagation within the pressure bars must be one-dimensional if surface displacement measurements are used to represent the axial displacement over the entire cross-sectional area of the pressure bar. The second condition is that the specimen must deform uniformly; this is opposed by both radial and longitudinal inertia and by frictional constraint at the specimen/pressure bar interfaces. These two conditions are discussed in more detail in the article "Classic Split-Hopkinson Pressure Bar Testing" in this Volume.

Rod Impact (Taylor) Testing

The rod impact test is based on the Taylor test for measuring the dynamic yield strength (Ref 23). The technique has been improved so that the entire stress-strain flow curve can be determined at high strain rates (around 10^4 or 10^5 s⁻¹) and large plastic strains (50–150%) for materials at ambient or elevated temperatures. The availability of this technique has been useful in determining constitutive behavior at high strain rates and the evaluation of dynamic compressive fracture.

The classic Taylor test (Ref 23, 24) involves a cylindrical specimen rod that impacts a “rigid” plate (Fig. 6a). The plastic deformation at the impact end shortens the rod, and the fractional change in rod length can, by one-dimensional rigid-plastic analysis, be related to the dynamic yield strength. This relationship was shown to be independent of both the rod aspect ratio and the impact velocity for a wide variety of materials, including copper, lead, paraffin wax, and various steels.

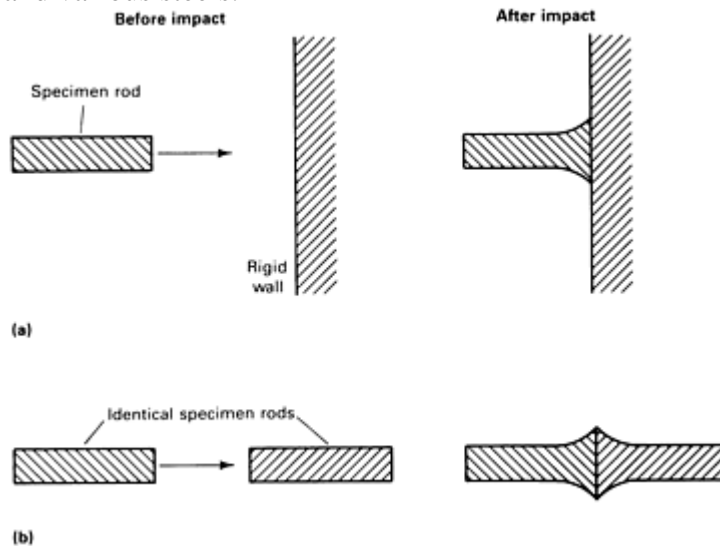


Fig. 6 Two-rod impact configurations. (a) Classic Taylor test. (b) Symmetric rod impact test

Although this method is appealing in its simplicity, the Taylor test received only moderate interest. Twenty-five years after the original Taylor tests, the use of two-dimensional wave propagation codes enabled a better understanding of and renewed interest in this technique. In 1972, Wilkins and Guinan (Ref 25), using a two-dimensional finite difference code and an elastic-plastic model with work hardening, were able to correctly simulate the final shapes and final lengths of Taylor test specimens of several metallic alloys at ambient temperatures. Their results showed good correlation between the dynamic yield strength and the fractional change in rod length for a wide range of impact velocities and rod aspect ratios, thus confirming many of the Taylor/Whiffin conclusions (Ref 23, 24).

Further improvements have led to two types of tests: symmetric rod impact tests and asymmetric rod impact tests. The advantage of the asymmetric rod impact test is that elevated temperature tests can be performed without heating a moving projectile, as required with the symmetric rod impact test. These types of tests are used in evaluation of constitutive models (Ref 26) and dynamic deformation and fracture behavior (Ref 27, 28). Determination of the dynamic flow curve of a material from a rod impact test is made by computationally simulating the experiment with a two-dimensional wave propagation computer code. The flow parameters are varied until the computed profiles agree with those determined experimentally at various times during the deformation history.

Symmetric Rod Impact Test. In the early 1980s, Erlich et al. (Ref 29) implemented two major modifications to the classic Taylor technique as a method for obtaining the entire stress-strain flow curve for materials undergoing high strain rate compressive and shear loading to large plastic strains. The first was to use ultrahigh-speed photography to monitor the deformation history of the specimen rod. This allows intermediate as well as final deformation states to be compared with two-dimensional computer simulations, thus improving the reliability of the flow curve determination.

The second modification was to replace the rigid plate with another rod of the same geometry and material as the impacting rod (Fig. 6b). This arrangement, referred to as the “symmetric rod impact” technique, allows the impacting ends of the two specimen rods to deform together symmetrically, thus eliminating boundary condition uncertainties in the analysis that arise from the unknown friction conditions at the rod/plate interface and from the deformation of the rigid plate adjacent to that interface. By using the symmetric rod impact

technique, dynamic flow curves at ambient temperature were obtained for 6061-T6 aluminum (Ref 29), a titanium alloy, and 4340 steel over a wide range of initial hardnesses (Ref 30).

A typical experimental arrangement for the symmetric rod impact test at ambient temperature is shown in Fig. 7. The specimen rods are identical right circular cylinders, the ends of which are machined flat and parallel to within about 0.01 mm (0.0004 in.). The impacting rod is mounted on the front end of a projectile, which is accelerated by expanding helium in a gas gun. Projectile velocity is recorded by a series of contact pins located near the end of the gun barrel. The stationary rod is held in place by six ceramic fingers attached to a target-mounting fixture, which in turn is affixed to an alignment plate at the muzzle of the gun. The position of the latter rod can be adjusted by rotating the threaded bars into which the ceramic fingers are inserted. Alignment of the two rods is critical to ensure that the impacting ends are parallel and coaxial.

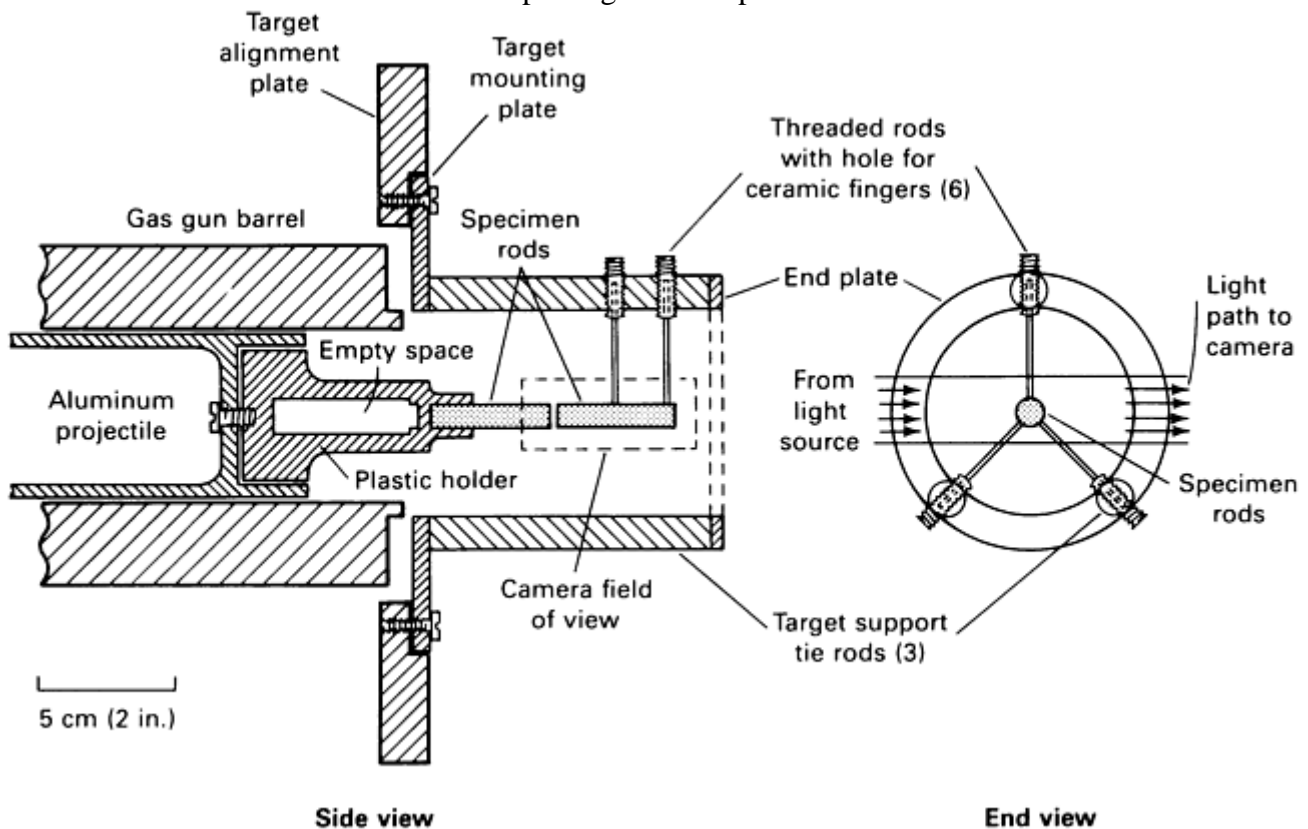


Fig. 7 Symmetric rod impact tests at ambient temperature

The specimen rods are backlit by a quick-pulse, high-intensity light source (xenon flash tube or exploding bridge wires) triggered just before impact. The silhouettes of the deforming rods are recorded by a high-speed framing camera at framing rates between one half and one million frames per second. After deformation is complete (about 30–40 μ s after impact), the specimen rods fly into a recovery pipe filled with rags or other energy-absorbing materials that minimize additional deformation. The pipe is sufficiently narrow to prevent the projectile from entering the specimen and impacting it again. The recovered rods are then sectioned along the axis and examined metallographically to ascertain the extent of internal damage.

The impact velocity must be low enough to suppress the formation of tensile voids (which can occur at early times by the focusing of the radial release waves on the rod axis) or shear bands (which can occur at later times as a result of large plastic deformation near the impact end). Although a small amount of incipient damage can be tolerated, any significant amount of damage can affect the shape of the deforming rod profiles.

Asymmetric Rod Impact Test. As mentioned previously, one advantage of the asymmetric rod impact test is that elevated temperature tests can be performed without heating a moving projectile, as required with the symmetric rod impact test. In this variation, a rigid plate is launched into a stationary specimen rod that is preheated to the desired temperature. An elevated-temperature test with the asymmetric rod impact technique only requires that the target specimen be preheated to the desired test temperature. The specimen is preheated with three infrared line heaters. Radiation from each linear filament is focused onto the specimen by an elliptical reflector. In 1982, Gust (Ref 31) used a reverse ballistics variation of the classic Taylor test to measure fractional changes in the length of various metallic rods at initial temperatures up to about 1000 $^{\circ}$ C (1830 $^{\circ}$ F). If

frictional effects in the impact area are not a significant factor for a given specimen material and target, the asymmetric rod impact technique may be used to determine dynamic flow curves at ambient or elevated temperatures.

References cited in this section

4. E. Orowan, The Calculation of Roll Pressure in Hot and Cold Flat Rolling, *Proc. Inst. Mech. Eng.*, Vol 150, 1943, p 143
5. N. Loizou and R.B. Sims, The Yield Stress of Pure Lead in Compression, *J. Mech. Phys. Solids*, Vol 1, 1953, p 234
6. J.F. Alder and V.A. Phillips, The Effect of Strain Rate and Temperature on the Resistance of Aluminum, Copper, and Steel to Compression, *J. Inst. Met.*, Vol 83, 1954–1955, p 80
7. P.M. Cook, True Stress-Strain Curves for Steel in Compression at High Temperatures and Strain Rates for Application to the Calculation of Load and Torque in Hot Rolling, Conf. on The Properties of Materials at High Rates of Strain, Institution of Mechanical Engineers, 1957, p 86
8. R.R. Arnold and R.J. Parker, Resistance to Deformation of Aluminum and Some Aluminum Alloys, *J. Inst. Met.*, Vol 88, 1959–1960, p 255
9. J.A. Bailey and A.R.E. Singer, A Plane-Strain Cam Plastometer for Use in Metal-Working Studies, *J. Inst. Met.*, Vol 92, 1963–1964, p 288
10. J.E. Hockett, Compression Testing at Constant True Strain Rates, *Proc. ASTM*, Vol 59, 1959, p 1309
11. J.M. Jacquerie, The Plasticity of Zinc, *C.R.M. Metall. Rep.*, No. 9, 1966, p 51 (in French)
12. A. Hannick and J.M. Jacquerie, The Compression Test with the Cam Plastometer and its Application to the Determination of Rolling Pressures, *C.R.M. Metall. Rep.*, No. 3, 1965, p 49 (in French)
13. H. Suzuki, S. Hashizume, Y. Yabuki, Y. Ichihara, S. Nakajima, and K. Kenmochi, Studies on the Flow Stress of Metals and Alloys, *Rep. Inst. Ind. Sci., Univ. Tokyo*, Vol 18 (No. 3, Serial No. 117), 1968
14. M.J. Stewart, Hot Deformation of C-Mn Steels From 1000 to 2200 F (600 to 1200 C) With Constant True Strain Rates From 0.5 to 140 s⁻¹, *The Hot Deformation of Austenite*, J.B. Ballance, Ed., The Metallurgical Society of AIME, 1977, p 47
15. G.T. van Rooyen and W.A. Backofen, A Study of Interface Friction in Plastic Compression, *Int. J. Mech. Sci.*, Vol 1, 1960, p 1
16. W.F. Adler, T.W. James, and P.E. Kukuchek, “Development of a Dynamic Compression Fixture for Brittle Materials,” Technical Report CR-81-918, Effects Technology, Inc., Santa Barbara, April 1981
17. D.R. Ireland, “Procedures and Problems Associated with Reliable Control of the Instrumented Impact Test,” in “Instrumented Impact Testing,” STP 563, ASTM, 1974, p 3–29
18. H.J. Saxton, D.R. Ireland, and W.L. Server, “Analysis and Control of Inertial Effects During Instrumented Impact Testing,” in “Instrumented Impact Testing,” STP 563, ASTM, 1974, p 50–73
19. D.R. Ireland, “Critical Review of Instrumented Impact Testing,” Paper 5 presented at the Dynamic Fracture Toughness Conference, London, July 1976

20. B. Hopkinson, A Method of Measuring the Pressure Produced in the Detonation of Explosives or by the Impact of Bullets, *Philos. Trans. A*, Vol 213, 1914, p 437
21. R.M. Davies, A Critical Study of the Hopkinson Pressure Bar, *Philos. Trans. R. Soc. (London) A*, Vol 240, 1948, p 375
22. H. Kolsky, An Investigation of the Mechanical Properties of Materials at Very High Rates of Loading, *Proc. R. Soc. (London) B*, Vol 62, 1949, p 676
23. G.I. Taylor, The Use of Flat-Ended Projectiles for Determining Dynamic Yield Strength, Part I: Theoretical Considerations, *Proc. R. Soc. (London) A*, Vol 194, 1948, p 289–299
24. A.C. Whiffin, The Use of Flat-Ended Projectiles for Determining Dynamic Yield Strength, Part II: Tests on Various Metallic Materials, *Proc. R. Soc. (London) A*, Vol 194, 1948, p 200–232
25. M.L. Wilkins and M.W. Guinan, Impact of Cylinders on a Rigid Boundary, *J. Appl. Phys.*, Vol 44, 1973, p 1200–1206
26. J. Buchar, S. Rolc, V. Hruby, On the Explosive Welding of a Ring to the Axisymmetric Body, *J. Mater. Process. Technol.*, Vol 85 (No. 1–3), Jan 1999, 171–174
27. R.W. Armstrong, F.J. Zerilli, Deformation Twinning: From Atomic Modeling to Shock Wave Loading, *Advances in Twinning*, Minerals, Metals and Materials Society/AIME, 1999, p 67–81
28. H. Couque, On the Use of the Symmetric Taylor Test to Evaluate Dynamic Ductile Compression Fracture Properties of Metals, *Structures under Shock and Impact V*, Computational Mechanics Publications, 1998, p 579–589
29. D.C. Erlich, D.A. Shockey, and L. Seaman, Symmetric Rod Impact Technique for Dynamic Yield Determination, Second Topical Conference on Shock Waves in Condensed Matter, Menlo Park, CA, *AIP Conf. Proc.*, No. 78, 1981, p 402–406
30. D.C. Erlich, D.A. Shockey, and L. Seaman, Symmetric Rod Impact Test for Dynamic Yield Determination, *Shock Waves in Condensed Matter*, American Institute of Physics, 1983, p 402–406
31. W.H. Gust, High Impact Deformation of Metal Cylinders at Elevated Temperatures, *J. Appl. Phys.*, Vol 53 (No. 5), 1982, p 3566–3575

High Strain Rate Tension and Compression Tests

High Strain Rate Tension Testing

As previously noted, valid stress-strain data can be obtained in conventional load frames for strain rates in a range up to about 10 to 100 s⁻¹ if suitable precautions are observed with regard to wave propagation effects and instrument response times. For tension testing at higher strain rates, or for cases when wave propagation effects are important, then more specialized testing techniques may have to be used, as described subsequently.

Expanding Ring Test

The expanding ring test is a highly sophisticated technique for subjecting metals to tensile strain rates over 10^4 s^{-1} (Ref 32, 33, 34). Although the testing principle is simple, its performance requires specialized equipment available in only a few laboratories. The ring test can determine the high-rate stress-strain relationships, but a simplified, more widely used version can be employed to determine ultimate strain only (Ref 35, 36).

This test involves the sudden radial acceleration of a ring due to detonation of an explosive charge or electromagnetic loading. The ring rapidly becomes a free-flying body, expanding radially and decelerating due to its own internal circumferential stresses. A thin ring must be used for the analysis to be valid; the wall thickness should be less than one-tenth the ring diameter, which is typically 25 mm (1 in.). If R is the radius of the ring and σ is the hoop stress:

$$\sigma = -\rho R \frac{d^2 R}{dt^2} \quad (\text{Eq 17})$$

To obtain stress-strain data, radial displacement as a function of time must be calculated. Strain is proportional to change in radius (just as engineering strain in tension is $\Delta L/L_0$); thus:

$$\epsilon = \ln \frac{R}{R_0} \quad (\text{Eq 18})$$

where R_0 is the initial radius. Stress may be computed from Eq 17 by double differentiation of radial displacement data as a function of time. Ring displacement can be obtained through the use of high-speed photography, streak cameras, displacement interferometers, or other methods for measuring radius as a function of time.

It is difficult to determine stress accurately by double differentiation of displacement data. Several laboratories have used a laser velocity interferometer to measure ring velocity directly (Ref 37, 38). Thus, only a single differentiation is necessary to calculate stress, and precision is improved considerably.

Advantages of the Ring Test. The ring test has two principal advantages. The expanding ring test subjects the material to a state of dynamic uniaxial stress without the wave propagation complications that accompany other high strain rate tests. Also, the maximum strain rate available in the ring test is higher than in any other common tension tests involving large plastic strains.

Limitations of the Ring Test. Strain rate in the expanding ring test is not usually constant. The strain rate is computed from $(dR/dt)/R$, and both of these terms vary continually. Strain rate is usually greatest at the start of ring deceleration, when strain is smallest. Values in excess of 10^4 s^{-1} are readily obtained. If the ring does not rupture, the strain rate falls to zero at the end of the test.

Ring specimens also experience a compressive preload in the radial direction that often exceeds the yield stress during the acceleration phase. Because load history is known to affect the subsequent stress-strain behavior of many materials, data obtained from expanding ring tests do not always agree with results from other tests at slightly lower strain rates.

The difficulties, expenses, and limitations of the expanding ring test preclude its use as a standard test technique for generating high strain rate stress-strain data in tension. Only a few laboratories are capable of performing this test. However, if subjecting a material to high strain rates in tension without determining stress-strain data is of primary interest, the expanding ring test is much easier to conduct. A number of investigators have used this test to determine strain to failure under dynamic loading (Ref 35, 36). Here, the accurate determination of radial displacement versus time is not as critical because stresses are not calculated. Less precise displacement data provide reasonably accurate determinations of strain rate. The ambiguity arising from possible strain rate history effects still exists when the expanding ring test is used in this simpler manner.

The expanding cylinder test, a variation of the ring test, provides a dynamic stress state equivalent to that produced in a quasi-static tensile test on a wide sheet versus a thin strip of material. A difficulty encountered in this type of test is the need for an impulse to be generated simultaneously in time along the axis of the cylinder. Because explosive detonation along a wire, for example, propagates at a finite wave speed, uniform deformation along the length of the axis cannot be ensured. Dimensions, detonation wave speeds, and synchronization of multiple detonation all must be considered carefully to ensure that the cylinder is deformed as uniformly as possible and that axial stress waves are not generated (Ref 39).

Flyer Plate and Short Duration Pulse Loading

Traditionally, flat plate impact tests have been used to obtain high strain rate yield data, shock wave response data, and equation of state data for materials undergoing uniaxial strain. Uniaxial strain refers to a three-dimensional state of stress in which deformation or strain occurs in only one direction—the direction of loading. The uniaxial strain condition persists for only a short period of time until stress waves originating at lateral boundaries reach the specimen interior. In a typical experiment, this time period is on the order of several to tens of microseconds. Uniaxial strain is defined mathematically as:

$$u_x \neq 0, u_y = u_z = 0 \quad (\text{Eq 19})$$

where x is the direction of loading, u_x is the displacement in that direction, and y and z are orthogonal directions in a plane normal to x . The strains are obtained from the displacement derivatives, thus:

$$\varepsilon_x \neq 0, \varepsilon_y = \varepsilon_z = 0 \quad (\text{Eq 20})$$

The flat plate impact test is performed by launching a flat flyer plate against a second stationary target plate. Compressed gas guns, propellant guns, magnetic accelerators, and explosives have all been used to launch the flyer plate (Ref 40). Extreme precision must be achieved to eliminate relative tilt at the instant of impact. A typical experimental setup using a gas gun is shown in Fig. 8. The flyer plate is carried in the gas gun in a plastic sabot. Velocity of the flyer is determined from the transit time between the shorting pin in the gun barrel and time-of-arrival pins in the target. The target is supported by a spall ring that suppresses late-time radial tensile waves.

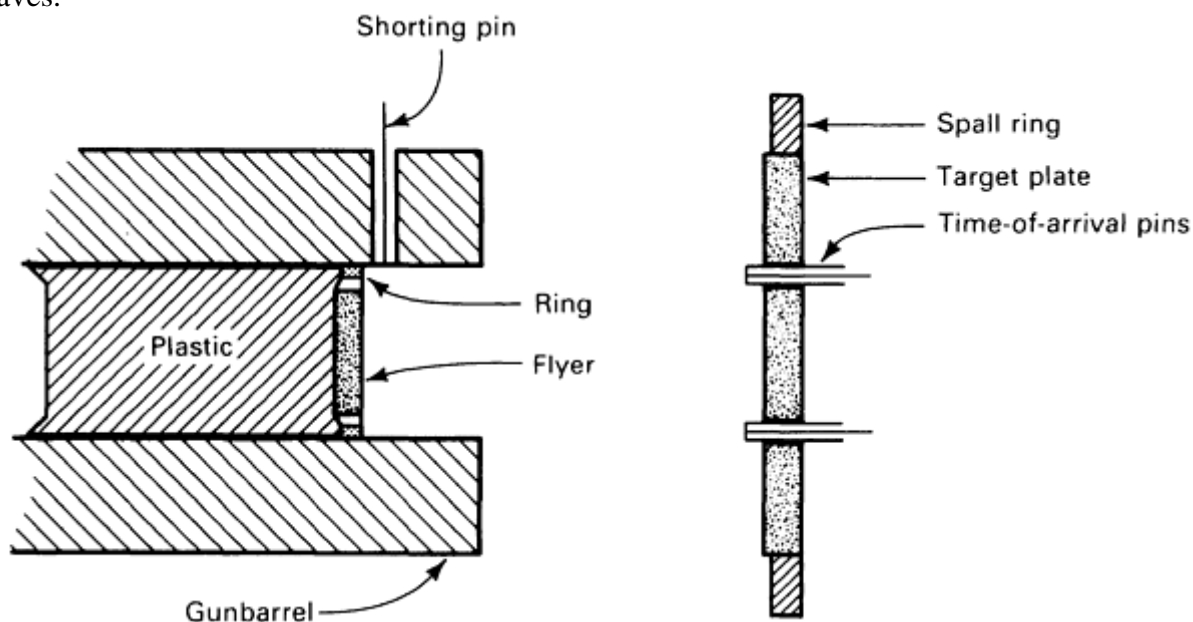


Fig. 8 Schematic of gas-gun-launched flyer plate impact test setup

The stress waves along the axis normal to the impact plane are shown in Fig. 9. A flyer plate of thickness d , moving left to right, strikes an initially stationary target of thickness T ; the impact occurs at the origin, O , of the (x, t) coordinates. Elastic-plastic behavior is assumed in Fig. 9. Elastic waves propagate at approximately c_{EL} , the longitudinal elastic sound speed. Plastic waves propagate at approximately $\sqrt{B/\rho}$ where B is the bulk modulus. The arrivals of the elastic and plastic waves at the target rear surface are denoted as E and P .

$$\sigma = \rho U v$$

(Eq 22)

where U is shock propagation speed and v is particle velocity. Peak particle velocity is half the impact velocity, v_0 , for a symmetric impact. For steel-on-steel impacts, Eq 22 becomes approximately $\sigma = 200 v_0$. For $\sigma > \sigma_{\text{HEL}} = 15$ kbar, a v_0 greater than 75 m/s (245 ft/s) is required. This presents no problem when a gas gun is used. Experiments with $v_0 < 100$ m/s (330 ft/s) are often difficult because of impact tilt, which becomes more critical at low velocities. Also, impact velocity must not be so high that the velocity of the P wave (Fig. 9) exceeds c_{EL} . That limit for steels usually is greater than 1 km/s (0.6 mile/s). The limit for other materials can be found by consulting the tables in Ref 43.

Given an appropriate impact velocity, to determine σ_{HEL} one of the following measurements must be made. The peak particle velocity behind the E wave can be measured. This can be accomplished at the free surface with capacitor gages, sloping mirrors, or a velocity interferometer. The velocity behind the wave is half the free surface velocity. The stress is related to the free surface velocity by Eq 22 with $v = c_{\text{EL}}$.

Direct measurement of σ_{HEL} can be obtained by embedded piezoresistive gages. Manganin and carbon gages frequently are used for this purpose. This technique requires sectioning the target or using a backing plate and correcting for partial transmission of the wave transmitted through the interface. Magnetic particle velocity gages can be used for nonconducting targets, such as plastics and rocks, but they are not suitable for metals.

Spall stress can be determined by two methods. The simplest, in terms of analysis, interpretation, and experimental technique, is to vary systematically the flyer plate thickness, d , and impact velocity, v_0 , to determine the critical values at which rupture occurs. As the flyer plate thickness is increased, the duration of the compressive and tensile load increases; the load duration is approximately $2d/c_{\text{EL}}$.

Eventually, for flyer plate thicknesses exceeding about 5 mm (0.2 in.), the spall stress reaches a load duration limit. In many metals, the limiting spall strength is several times the value of σ_{HEL} . Figure 10 illustrates typical spall stress data for low-carbon steel. The data illustrate that for pulse durations longer than a few microseconds, the greatest tensile stress that the material can sustain without rupture is 25 kbar.

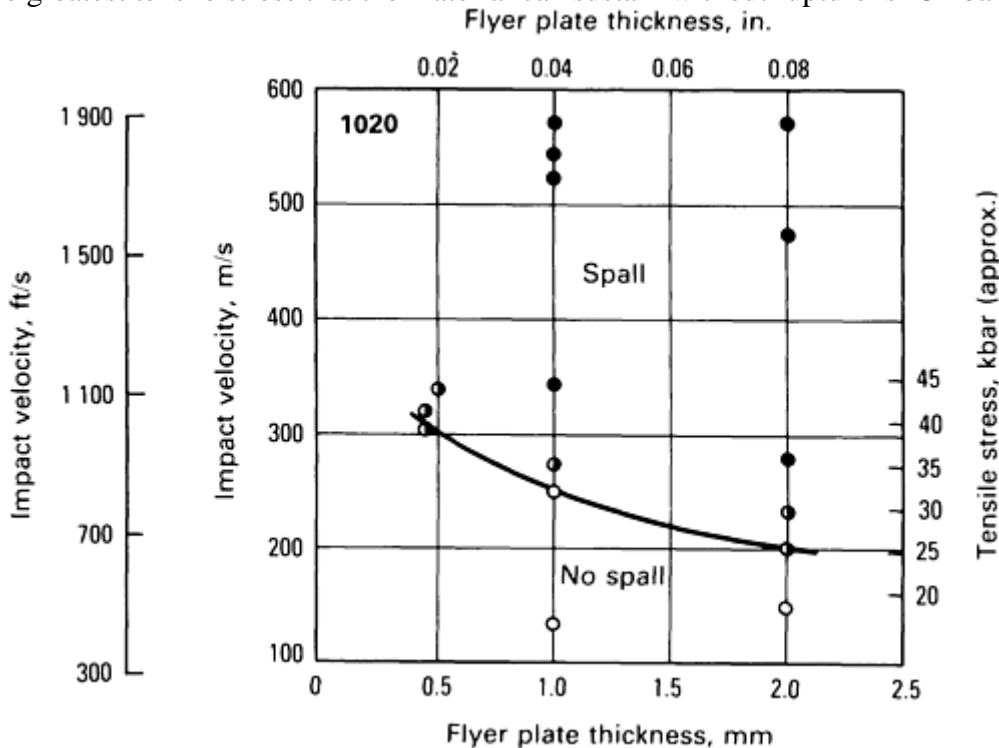


Fig. 10 Spall data for low-carbon 1020 steel

Interpretation of experiments using thinner flyer plates is more complex because a computer code must be used to calculate the stress history on the spall plane. Finite difference codes (Ref 41) or method of characteristics codes (Ref 44) can be used. Finite difference codes are more accurate and more widely applicable than method of characteristics codes, but the user must be specially trained in this subject.

Another approach to spall characterization is to initiate impact above the spall threshold and to deduce the material behavior from the free surface velocity, Δv_s , data. Figure 11 illustrates a typical free surface velocity

history with spalling. E, P, R, and S refer to the same arrivals as explained in text for Fig. 9. The spall stress is given approximately by $\rho_{CEL} \Delta v_s/2$. However, a more exact determination requires code analysis.

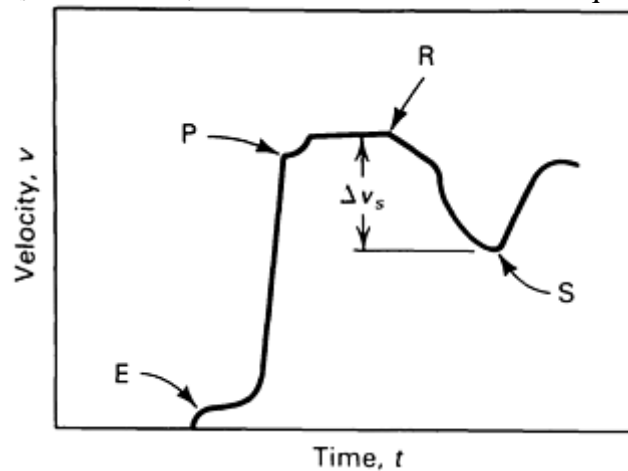
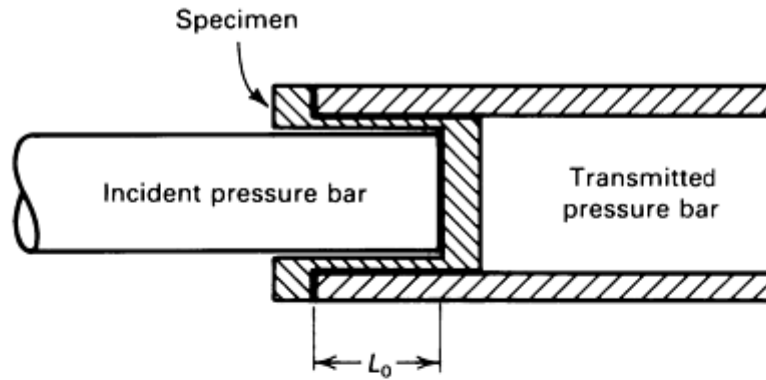


Fig. 11 Free surface velocity data when spall occurs

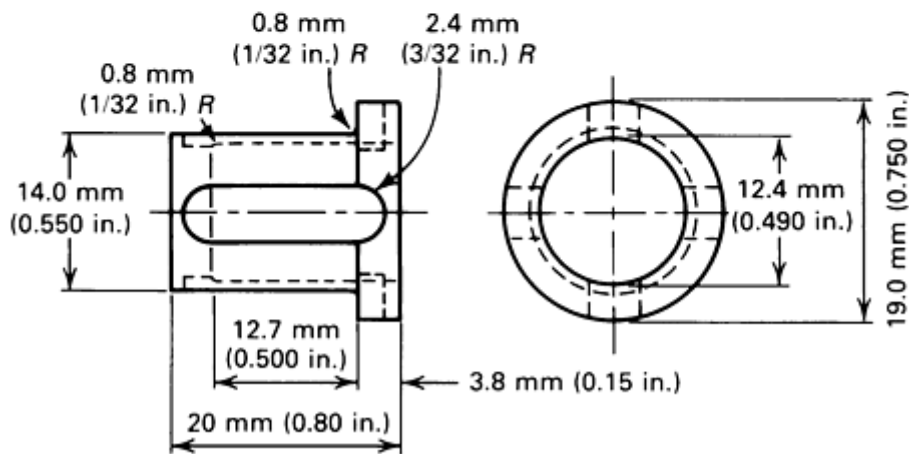
Split-Hopkinson Bar in Tension

The principles of the split-Hopkinson bar in tension are similar to those in compression, as discussed in the article “Classic Split-Hopkinson Pressure Bar Testing” in this Volume. The primary differences are the methods of generating a tensile loading pulse, specimen geometry, and the method of attaching the specimen to the two bars (incident and transmitter).

Basically, three types of tension split-Hopkinson bars have been developed. The first (Ref 45) involves the use of compressive pulses in the input and transmitter bars, as in the compressive test. The input bar is solid, while the transmitter or output bar is a hollow tube of the same cross-sectional area as the input bar. The specimen is a complex “top-hat” type of geometry, as shown in Fig. 12. The specimen actually is comprised of four parallel tensile bars of equal cross-sectional area. Although specimen machining is somewhat complex, the test is conducted in the same manner as compressive testing.



Specimen configuration



Dimensions of test specimen

Fig. 12 Details of the split-Hopkinson tension specimen. Source: Ref 45

The second type of tension split-Hopkinson bar test involves the use of a smaller standard type of threaded tension specimen and generation of a tensile pulse directly on the end of the loading or input bar (Ref 46, 47). This can be accomplished in several ways, as shown in Fig. 13. In Fig. 13(a), a mass is impacted directly on an anvil attached to the end of the input bar. In Fig. 13(b), an anvil is loaded by a compressive wave transmitted through another loading bar that is a hollow tube. The compressive pulse in the loading tube is generated by the same techniques as the compression split-Hopkinson bar. In Fig. 13(c), a pulse is generated by the detonation of an explosive against the anvil. In Fig. 13(a) and (c), it is difficult to generate a pulse of constant amplitude, while in Fig. 13(b) a long time duration is accomplished in the same manner as in compressive testing.

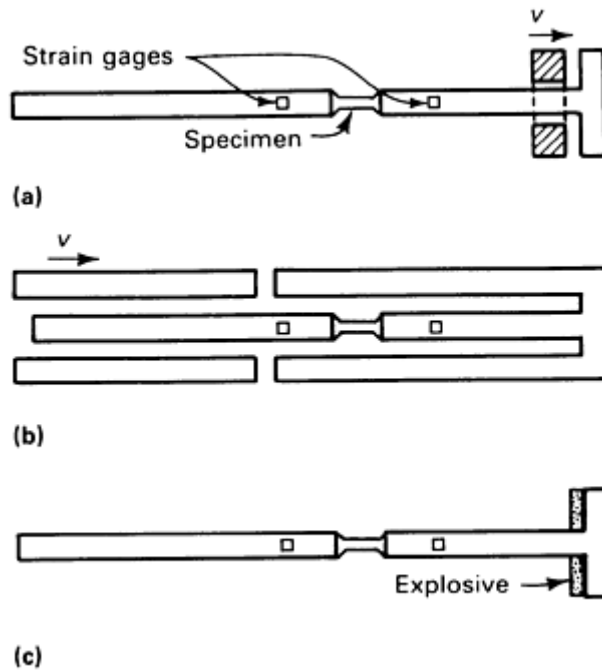


Fig. 13 Schematic of three types of split-Hopkinson tension-loading techniques

The third type of tension test also uses a threaded specimen but uses the reflection of a compression pulse at a free end and a collar to protect the specimen from initial precompression (Ref 48). Figure 14(a) illustrates an experimental setup. Figure 14(b) is a Lagrangian $x-t$ diagram, which illustrates the details of wave propagation in the bars and the experimental procedures. When the striker bar is accelerated against bar No. 1, the impact generates a compression pulse, the amplitude of which depends on the striker velocity and the length of which is twice the elastic wave transit time in the striker bar. The pulse travels down the bar until it reaches the specimen. The threaded tensile specimen is attached to the two pressure bars, as shown in detail "A" of Fig. 14(a).

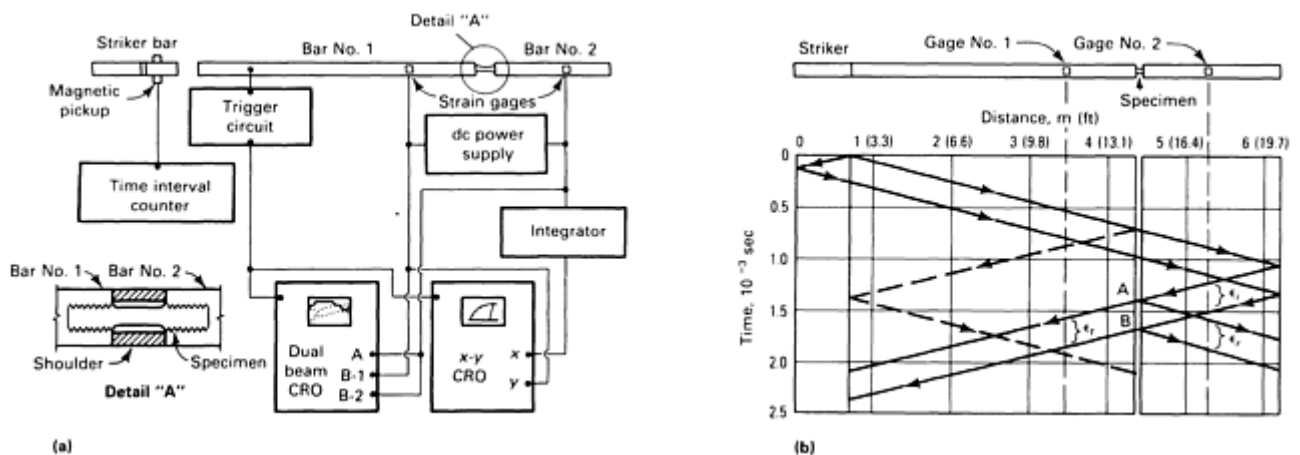


Fig. 14 Split-Hopkinson bar test using threaded tension specimen. (a) Schematic of tensile loading apparatus. Source: Ref 48. (b) Lagrangian diagram for tensile loading apparatus. CRO, cathode ray oscilloscope

After the specimen has been screwed into the bars, a split shoulder or collar is placed over the specimen, and it is screwed in until the pressure bars fit tightly against the shoulder. The shoulder is made of the same material as the pressure bars, has the same outer diameter, and has an inner diameter that just clears the specimen. The ratio of the cross-sectional area of the shoulder to that of the pressure bars is typically 3:4, while the ratio of the area of the shoulder to the net cross-sectional area of the specimen is typically 12:1.

The compression pulse travels through the composite cross section of the shoulder and specimen in an essentially undispersed manner. Tightening of the specimen by twisting the pressure bars, the relatively loose

fit of the threaded joint of the specimen into the bars, and the large area ratio of the shoulder to the specimen ensure that no compression beyond the elastic limit is transmitted to the specimen.

Ideally, the entire compression pulse passes through the supporting shoulder as if the specimen were not present, although in practice it is difficult to prevent prestraining of the specimen. The compression pulse continues to propagate until it reaches the free end of bar No. 2. There it reflects and propagates back as a tensile pulse, ϵ_i , and passes gage No. 2. Upon reaching the specimen at point A as shown in Fig. 14(b), the tensile pulse is partially transmitted through the specimen, ϵ_t , and partially reflected back into bar No. 2, ϵ_r . Note that the shoulder, which carried the entire compressive pulse around the specimen, is unable to support any tensile loads because it is not fastened to the bars.

Tight fitting of the shoulder against the bars is critical in transmitting the compression pulse down the bars without significant wave dispersion. Similarly, the tight fit of the threaded tensile specimen against the bars is essential to achieve smooth and rapid loading of the specimen as the tensile pulse arrives. Failure to remove all "play" from the threaded joint results in uneven loading of the specimen and spurious wave reflections.

Analysis of the tensile split-Hopkinson bar test is almost identical to that of the compression test. The major difference is the actual or effective gage length of the specimen. Contrary to the compression test, in which a right circular cylinder is used, the tensile test uses a cylindrical specimen with an attached shoulder and additional gripping, such as threads. Because the split-Hopkinson bar test can only provide data on the relative displacement between the ends of the incident and transmitter bars, an effective gage length generally must be used. This is equivalent to determining strain in a tensile test through crosshead displacement measurement. The use of strain gages on test samples to determine an effective gage length is strongly recommended. This calibration is accomplished easily at low strain rates, preferably in a conventional test machine in which the crosshead displacement is monitored separately.

As with any uniaxial tensile test, once localized necking occurs, it is no longer possible to simply convert load-displacement data to stress-strain data. The range of application of the Hopkinson bar test can be extended by high-speed photography of necking specimens. An analysis that allows estimation of effective stress and strain from the profile of the necking specimen is described in Ref 49. Photographs can be made with a suitable high-speed camera system through windows provided in the collar. The major technical difficulty is the precise synchronization of the exposures with the Hopkinson bar record (Ref 50).

References cited in this section

32. T. Nicholas and S.J. Bless, High Strain Rate Tension Testing, *Mechanical Testing*, Vol 8, *ASM Handbook*, ASM International, 1985, p 208–214
33. F.I. Niordson, A Unit for Testing Materials at High Strain Rates, *Exp. Mech.*, Vol 5, 1965, p 29–32
34. C.R. Hoggatt and R.F. Recht, Stress-Strain Data Obtained at High Strain Rates Using an Expanding Ring, *Exp. Mech.*, Vol 9, 1969, p 441–448
35. D.E. Grady and D.A. Benson, Fragmentation of Metal Rings by Electromagnetic Loading, *Exp. Mech.*, Vol 28, 1983, p 393–400
36. A.M. Rajendran and I.M. Fyfe, Inertia Effects on the Ductile Failure of Thin Rings, *J. Appl. Mech. (Trans. ASME)*, Vol 104, 1982, p 31–36
37. L.M. Barker and R.E. Hollenback, Laser Interferometer for Measuring High Velocities of Any Reflecting Surface, *J. Appl. Phys.*, Vol 43, 1972, p 4669–4674
38. R.H. Warnes, T.A. Duffey, R.R. Karpp, and A.E. Carden, An Improved Technique for Determining Dynamic Material Properties Using the Expanding Ring, *Shock Waves and High-Strain-Rate Phenomena in Metals*, M.A. Meyers and L.E. Murr, Ed., Plenum Press, 1981
39. D. Bauer and S.J. Bless, Strain Rate Effects on Ultimate Strain of Copper, *Shock Waves in Condensed Matter*, North Holland, Amsterdam, 1983

40. G.R. Fowles, Experimental Technique and Instrumentation, *Dynamic Response of Materials to Intense Impulse Loading*, P.C. Chou and A.K. Hopkins, Ed., Air Force Materials Laboratory, Wright-Patterson Air Force Base, 1973
41. J.A. Zukas, T. Nicholas, H.F. Swift, L.B. Greszczuk, and D.R. Curran, *Impact Dynamics*, John Wiley & Sons, New York, 1982, p 452
42. R.G. McQueen, S.P. Marsh, J.W. Taylor, J.N. Fritz, and W.J. Carter, The Equation of State of Solids from Shock Wave Studies, *High Velocity Impact Phenomena*, R. Kinslow, Ed., Academic Press, 1970
43. S.P. Marsh, *LASL Shock Hugoniot Data*, University of California Press, 1980
44. L.M. Barker and E.G. Young, "SWAP-9: An Improved Stress Wave Analyzing Program," Sandia National Laboratories Report SLA-74-0009, Albuquerque, NM, 1974
45. U.S. Lindholm and L.M. Yeakley, High Strain Rate Testing: Tension and Compression, *Exp. Mech.*, Vol 8, 1968, p 1–9
46. J. Harding, E.D. Wood, and J.D. Campbell, Tensile Testing of Material at Impact Rates of Strain, *J. Mech. Eng. Sci.*, Vol 2, 1960, p 88–96
47. C. Albertini and M. Montagnani, Testing Techniques Based on the Split Hopkinson Bar, *Mechanical Properties at High Rates of Strain*, J. Harding, Ed., Institute of Physics, London, 1974
48. T. Nicholas, Tensile Testing of Materials at High Rates of Strain, *Exp. Mech.*, Vol 21, 1980, p 177–185
49. P.W. Bridgeman, Chapter 1, *Studies in Large Plastic Flow and Fracture*, 1st ed., McGraw-Hill, 1952
50. L.A. Cross, S.J. Bless, A.M. Ranjendran, E.A. Strader, and D.S. Dawicke, New Technique to Investigate Necking in a Tensile Hopkinson Bar, *Exp. Mech.*, Vol 24 (No. 3), 1984, p 184–186

High Strain Rate Tension and Compression Tests

Rotating Wheel

Another method for tension testing at high strain rates consists of a rotating wheel with claws or noses that quickly stroke a yoke containing test pieces. An early test machine was developed by Mann in 1936 (Ref 51), and in 1944 Fehr et al. (Ref 52) reached strain rates of nearly 10^3 s^{-1} with some bearable ringing. In the 1960s, Schopper produced and sold about 100 "rotating wheel machines," which also had a 200 kg (440 lb) wheel with a releasable claw and a specimen within a yoke fixed in front of the wheel (Fig. 15). By careful adjustments, velocities of about 40 m/s (130 ft/s) were reached without any bending moments. However, the overall frequency response of the fixture (despite the 50 kHz quartz transducer for force-time recording) was only 2.5 kHz, which is too low for high-rate testing.

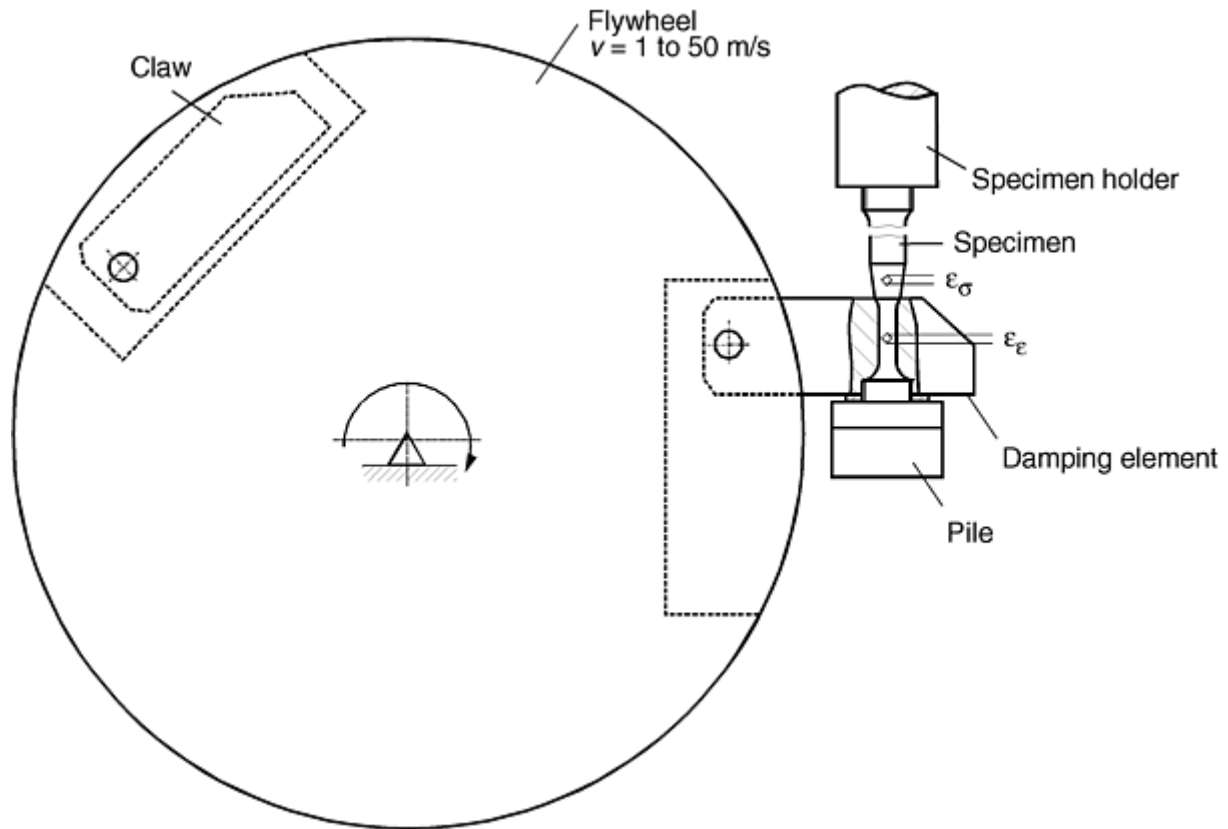


Fig. 15 Principle of high-rate tensile testing with flywheel setup

The essential improvement has been to introduce load-measuring gages as close to the gage length as possible. This is realized by measuring elastic strains and converting to stresses by the elastic modulus. To assure low barriers for reflections of stress wave propagation, the strain gages for load measurement are positioned at cones of 8° on the smallest possible diameter. With this technique, stress-strain records are possible up to velocities of 30 m/s, which corresponds to strain rates of $\dot{\epsilon} = 2500 \text{ s}^{-1}$ with a gage length of 10.5 mm (0.41 in.) and a diameter of 3.5 mm (0.14 in.) ($L/D = 3$). Even with high strain hardening and highly deformable materials, there is practically no influence of the tested materials on the history of velocity or strain rate like in a Hopkinson bar setup because the energy content of the rotating wheel exceeds the fracture energy of the specimen more than 10 times (for striking velocities $v > 10 \text{ m/s}$, or 33 ft/s).

A similar setup, but based on a moving mass of a few kilograms guided along straight bars, has also been developed by Stelly and Dorneval at CEA, France with good results (Ref 53). Higher strain rates of $\dot{\epsilon} = 10^4 \text{ s}^{-1}$, for example, can be reached with short gage length. To provide easy strain recording for the complete loading up to fracture, electro-optical cameras or noncontact laser interferometers can be used. The advantage of this instrumentation is that the strain is measured, not calculated under certain assumptions.

In order to avoid more reflections of the stress wave from the upper end of the specimen, the length beside the gage length is extended to $2s > v_c \cdot t$ (where s is the rod length between gage length and fixture, v_c is the sound velocity, and t is the time to fracture at the used striking velocity). In the case of short lengths, a wave transmitter bar is connected to the specimen. This procedure requires the evaluation of impedance transfer between the sample and bar. Figure 16 shows stress-time diagrams of screwed, brazed, and welded joints tested under high strain rate conditions at about $\dot{\epsilon} = 1000 \text{ s}^{-1}$. These results reveal that screwing and brazing are insufficient methods to obtain stress-time diagrams of good quality. Therefore, in this test setup welded joints are most suitable to perform tensile tests at high and very high strain rates.

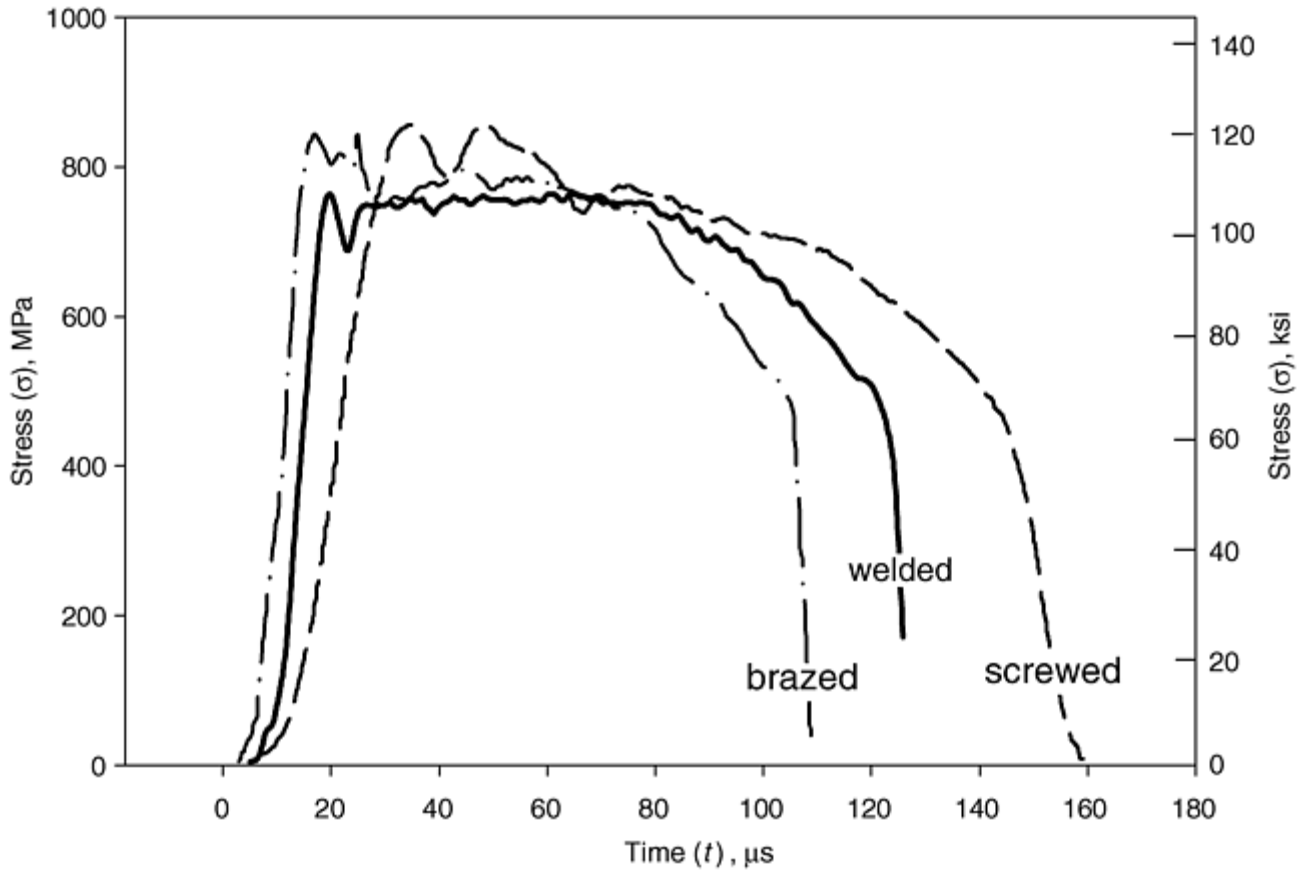


Fig. 16 Influence of joining method on stress-time curves for high strain rate tension test specimens

This procedure was successfully applied for high-rate, high-temperature tests (Fig. 17). Notice the occurrence of the upper and lower yielding and the following nearly undisturbed stress-time records. The wave transmitter bar was used for a stress measurement because the strain gages at the gage length were unsuitable at test temperature. Temperatures up to 600 °C (1100 °F) are reached with heated air; higher temperatures should be possible using small infrared ovens (Ref 54, 55) or induction heating.

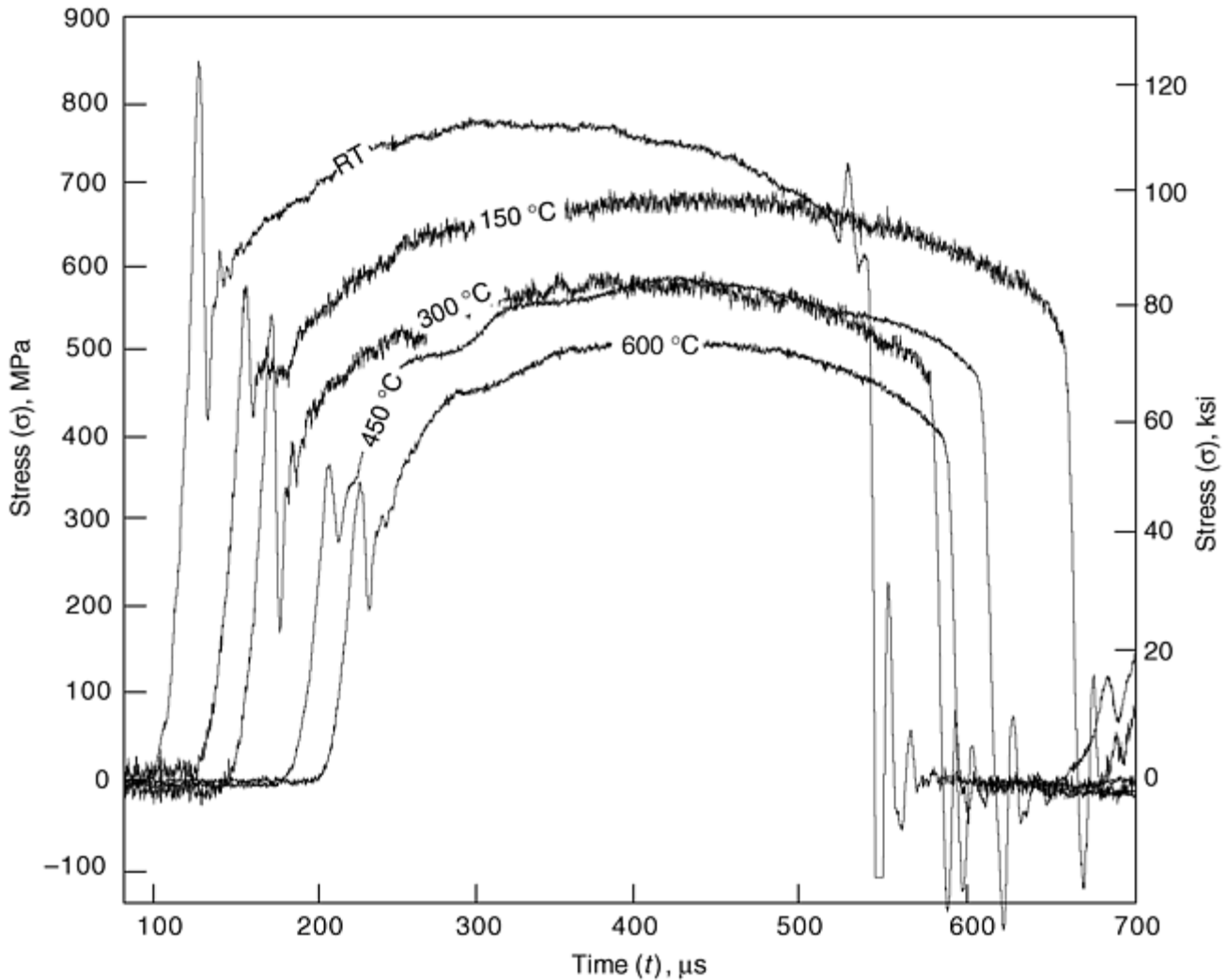


Fig. 17 Stress-time diagrams from high rate tension testing of carbon steel (0.45% C) between room temperature and 600 °C (1100 °F)

References cited in this section

51. H. C. Mann, High Velocity Tension Impact Tests, *Proc. ASTM*, Vol 36 (part 2), 1936, p 85–109
52. R.O. Fehr, E. Parker, and D.J. DeMichael, Measurement of Dynamic Stress and Strain in Tensile Test Specimens, *J. Appl. Mech. (Trans. ASME)*, Vol 6A, 1944, p 65–71
53. R. Dormeival and M. Stelly, Influence of Grain Size and Strain Rate of the Mechanical Behavior of High-Purity Polycrystalline Copper, Second Conf. on Mechanical Properties at High Rates of Strain, 1979 (Oxford), Institute of Physics, London, Serial No. 47, p 154–165
54. C.E. Frantz, P.S. Follansbee, and W.E. Wright, New Experimental Techniques with the Split Hopkinson Pressure Bar, *High Energy Rate Forming*, Berman and Schroeder, Ed., American Society of Mechanical Engineers, 1984, p 229
55. A.M. Lennon and K.T. Ramesh, A Technique for Measurement the Dynamic Behaviour of Materials at High Temperatures, *Int. J. Plast.*, Vol 14 (No. 12), 1998, p 1279–1292

Acknowledgments

The discussion of rotating wheel tension testing was prepared for this Volume by L.W. Meyer, S. Abdel-Malek, and T. Halle, Technical University Chemnitz and Nordmetall GbR, Germany. Other portions of this article were adapted from the following articles in Volume 8 of the 9th Edition *Metals Handbook*:

- “Drop Tower Compression Testing” by G.B. Dudder (p 196–198)
- “Rod Impact (Taylor) Test” by D.C. Erlich (p 203–207)
- “High Strain Rate Compression Testing: Introduction” by P.S. Follensbee (p 190–192)
- “The Hopkinson Bar” by P.S. Follensbee (p 198–203)
- “Compression Testing by Conventional Load Frames at Medium Strain Rates” by P.S. Follansbee and P.E. Armstrong (p 192–193)
- “The Cam Plastometer” by J.E. Hockett (p 193–196)
- “High Strain Rate Tension Testing” by T. Nicholas and S.J. Bless (p 208–214)
- “Introduction to High Strain Rate Testing” by M.R. Staker (p 187–189)

High Strain Rate Tension and Compression Tests

References

1. U.S. Lindholm, High Strain Rate Tests, *Measurement of Mechanical Properties*, Vol 5, Part I, *Techniques of Metals Research*, R.F. Bunshah, Ed., Interscience, 1971, p 199–271
2. High Strain Rate Compression Testing, *Mechanical Testing*, Vol 8, *ASM Handbook*, ASM International, 1985 p 190–207
3. E.D.H. Davies and S.C. Hunter, The Dynamic Compression Testing of Solids by the Method of the Split Hopkinson Pressure Bar, *J. Mech. Phys. Solids*, Vol 11, 1963, p 155
4. E. Orowan, The Calculation of Roll Pressure in Hot and Cold Flat Rolling, *Proc. Inst. Mech. Eng.*, Vol 150, 1943, p 143
5. N. Loizou and R.B. Sims, The Yield Stress of Pure Lead in Compression, *J. Mech. Phys. Solids*, Vol 1, 1953, p 234
6. J.F. Alder and V.A. Phillips, The Effect of Strain Rate and Temperature on the Resistance of Aluminum, Copper, and Steel to Compression, *J. Inst. Met.*, Vol 83, 1954–1955, p 80
7. P.M. Cook, True Stress-Strain Curves for Steel in Compression at High Temperatures and Strain Rates for Application to the Calculation of Load and Torque in Hot Rolling, Conf. on The Properties of Materials at High Rates of Strain, Institution of Mechanical Engineers, 1957, p 86
8. R.R. Arnold and R.J. Parker, Resistance to Deformation of Aluminum and Some Aluminum Alloys, *J. Inst. Met.*, Vol 88, 1959–1960, p 255

9. J.A. Bailey and A.R.E. Singer, A Plane-Strain Cam Plastometer for Use in Metal-Working Studies, *J. Inst. Met.*, Vol 92, 1963–1964, p 288
10. J.E. Hockett, Compression Testing at Constant True Strain Rates, *Proc. ASTM*, Vol 59, 1959, p 1309
11. J.M. Jacquerie, The Plasticity of Zinc, *C.R.M. Metall. Rep.*, No. 9, 1966, p 51 (in French)
12. A. Hannick and J.M. Jacquerie, The Compression Test with the Cam Plastometer and its Application to the Determination of Rolling Pressures, *C.R.M. Metall. Rep.*, No. 3, 1965, p 49 (in French)
13. H. Suzuki, S. Hashizume, Y. Yabuki, Y. Ichihara, S. Nakajima, and K. Kenmochi, Studies on the Flow Stress of Metals and Alloys, *Rep. Inst. Ind. Sci., Univ. Tokyo*, Vol 18 (No. 3, Serial No. 117), 1968
14. M.J. Stewart, Hot Deformation of C-Mn Steels From 1000 to 2200 F (600 to 1200 C) With Constant True Strain Rates From 0.5 to 140 s⁻¹, *The Hot Deformation of Austenite*, J.B. Ballance, Ed., The Metallurgical Society of AIME, 1977, p 47
15. G.T. van Rooyen and W.A. Backofen, A Study of Interface Friction in Plastic Compression, *Int. J. Mech. Sci.*, Vol 1, 1960, p 1
16. W.F. Adler, T.W. James, and P.E. Kukuchek, “Development of a Dynamic Compression Fixture for Brittle Materials,” Technical Report CR-81-918, Effects Technology, Inc., Santa Barbara, April 1981
17. D.R. Ireland, “Procedures and Problems Associated with Reliable Control of the Instrumented Impact Test,” in “Instrumented Impact Testing,” STP 563, ASTM, 1974, p 3–29
18. H.J. Saxton, D.R. Ireland, and W.L. Server, “Analysis and Control of Inertial Effects During Instrumented Impact Testing,” in “Instrumented Impact Testing,” STP 563, ASTM, 1974, p 50–73
19. D.R. Ireland, “Critical Review of Instrumented Impact Testing,” Paper 5 presented at the Dynamic Fracture Toughness Conference, London, July 1976
20. B. Hopkinson, A Method of Measuring the Pressure Produced in the Detonation of Explosives or by the Impact of Bullets, *Philos. Trans. A*, Vol 213, 1914, p 437
21. R.M. Davies, A Critical Study of the Hopkinson Pressure Bar, *Philos. Trans. R. Soc. (London) A*, Vol 240, 1948, p 375
22. H. Kolsky, An Investigation of the Mechanical Properties of Materials at Very High Rates of Loading, *Proc. R. Soc. (London) B*, Vol 62, 1949, p 676
23. G.I. Taylor, The Use of Flat-Ended Projectiles for Determining Dynamic Yield Strength, Part I: Theoretical Considerations, *Proc. R. Soc. (London) A*, Vol 194, 1948, p 289–299
24. A.C. Whiffin, The Use of Flat-Ended Projectiles for Determining Dynamic Yield Strength, Part II: Tests on Various Metallic Materials, *Proc. R. Soc. (London) A*, Vol 194, 1948, p 200–232
25. M.L. Wilkins and M.W. Guinan, Impact of Cylinders on a Rigid Boundary, *J. Appl. Phys.*, Vol 44, 1973, p 1200–1206
26. J. Buchar, S. Rolc, V. Hruby, On the Explosive Welding of a Ring to the Axisymmetric Body, *J. Mater. Process. Technol.*, Vol 85 (No. 1–3), Jan 1999, 171–174

27. R.W. Armstrong, F.J. Zerilli, Deformation Twinning: From Atomic Modeling to Shock Wave Loading, *Advances in Twinning*, Minerals, Metals and Materials Society/AIME, 1999, p 67–81
28. H. Couque, On the Use of the Symmetric Taylor Test to Evaluate Dynamic Ductile Compression Fracture Properties of Metals, *Structures under Shock and Impact V*, Computational Mechanics Publications, 1998, p 579–589
29. D.C. Erlich, D.A. Shockey, and L. Seaman, Symmetric Rod Impact Technique for Dynamic Yield Determination, Second Topical Conference on Shock Waves in Condensed Matter, Menlo Park, CA, *AIP Conf. Proc.*, No. 78, 1981, p 402–406
30. D.C. Erlich, D.A. Shockey, and L. Seaman, Symmetric Rod Impact Test for Dynamic Yield Determination, *Shock Waves in Condensed Matter*, American Institute of Physics, 1983, p 402–406
31. W.H. Gust, High Impact Deformation of Metal Cylinders at Elevated Temperatures, *J. Appl. Phys.*, Vol 53 (No. 5), 1982, p 3566–3575
32. T. Nicholas and S.J. Bless, High Strain Rate Tension Testing, *Mechanical Testing*, Vol 8, *ASM Handbook*, ASM International, 1985, p 208–214
33. F.I. Niordson, A Unit for Testing Materials at High Strain Rates, *Exp. Mech.*, Vol 5, 1965, p 29–32
34. C.R. Hoggatt and R.F. Recht, Stress-Strain Data Obtained at High Strain Rates Using an Expanding Ring, *Exp. Mech.*, Vol 9, 1969, p 441–448
35. D.E. Grady and D.A. Benson, Fragmentation of Metal Rings by Electromagnetic Loading, *Exp. Mech.*, Vol 28, 1983, p 393–400
36. A.M. Rajendran and I.M. Fyfe, Inertia Effects on the Ductile Failure of Thin Rings, *J. Appl. Mech. (Trans. ASME)*, Vol 104, 1982, p 31–36
37. L.M. Barker and R.E. Hollenback, Laser Interferometer for Measuring High Velocities of Any Reflecting Surface, *J. Appl. Phys.*, Vol 43, 1972, p 4669–4674
38. R.H. Warnes, T.A. Duffey, R.R. Karpp, and A.E. Carden, An Improved Technique for Determining Dynamic Material Properties Using the Expanding Ring, *Shock Waves and High-Strain-Rate Phenomena in Metals*, M.A. Meyers and L.E. Murr, Ed., Plenum Press, 1981
39. D. Bauer and S.J. Bless, Strain Rate Effects on Ultimate Strain of Copper, *Shock Waves in Condensed Matter*, North Holland, Amsterdam, 1983
40. G.R. Fowles, Experimental Technique and Instrumentation, *Dynamic Response of Materials to Intense Impulse Loading*, P.C. Chou and A.K. Hopkins, Ed., Air Force Materials Laboratory, Wright-Patterson Air Force Base, 1973
41. J.A. Zukas, T. Nicholas, H.F. Swift, L.B. Greszczuk, and D.R. Curran, *Impact Dynamics*, John Wiley & Sons, New York, 1982, p 452
42. R.G. McQueen, S.P. Marsh, J.W. Taylor, J.N. Fritz, and W.J. Carter, The Equation of State of Solids from Shock Wave Studies, *High Velocity Impact Phenomena*, R. Kinslow, Ed., Academic Press, 1970
43. S.P. Marsh, *LASL Shock Hugoniot Data*, University of California Press, 1980

44. L.M. Barker and E.G. Young, "SWAP-9: An Improved Stress Wave Analyzing Program," Sandia National Laboratories Report SLA-74-0009, Albuquerque, NM, 1974
45. U.S. Lindholm and L.M. Yeakley, High Strain Rate Testing: Tension and Compression, *Exp. Mech.*, Vol 8, 1968, p 1–9
46. J. Harding, E.D. Wood, and J.D. Campbell, Tensile Testing of Material at Impact Rates of Strain, *J. Mech. Eng. Sci.*, Vol 2, 1960, p 88–96
47. C. Albertini and M. Montagnani, Testing Techniques Based on the Split Hopkinson Bar, *Mechanical Properties at High Rates of Strain*, J. Harding, Ed., Institute of Physics, London, 1974
48. T. Nicholas, Tensile Testing of Materials at High Rates of Strain, *Exp. Mech.*, Vol 21, 1980, p 177–185
49. P.W. Bridgeman, Chapter 1, *Studies in Large Plastic Flow and Fracture*, 1st ed., McGraw-Hill, 1952
50. L.A. Cross, S.J. Bless, A.M. Ranjendran, E.A. Strader, and D.S. Dawicke, New Technique to Investigate Necking in a Tensile Hopkinson Bar, *Exp. Mech.*, Vol 24 (No. 3), 1984, p 184–186
51. H. C. Mann, High Velocity Tension Impact Tests, *Proc. ASTM*, Vol 36 (part 2), 1936, p 85–109
52. R.O. Fehr, E. Parker, and D.J. DeMichael, Measurement of Dynamic Stress and Strain in Tensile Test Specimens, *J. Appl. Mech. (Trans. ASME)*, Vol 6A, 1944, p 65–71
53. R. Dormeival and M. Stelly, Influence of Grain Size and Strain Rate of the Mechanical Behavior of High-Purity Polycrystalline Copper, Second Conf. on Mechanical Properties at High Rates of Strain, 1979 (Oxford), Institute of Physics, London, Serial No. 47, p 154–165
54. C.E. Frantz, P.S. Follansbee, and W.E. Wright, New Experimental Techniques with the Split Hopkinson Pressure Bar, *High Energy Rate Forming*, Berman and Schroeder, Ed., American Society of Mechanical Engineers, 1984, p 229
55. A.M. Lennon and K.T. Ramesh, A Technique for Measurement the Dynamic Behaviour of Materials at High Temperatures, *Int. J. Plast.*, Vol 14 (No. 12), 1998, p 1279–1292

High Strain Rate Tension and Compression Tests

Selected References

1990 to 1999

- T.J. Ahrens, G.Q. Chen, W. Yang, and J.K. Knowles, Effect of Irreversible Phase Change on Shock-Wave Propagation, *J. Mech. Phys. Solids*, Vol 47 (No. 4), 1999, p 763–783
- T. Aizawa, K. Ito, and M. Tsuchida, Intense High-Strain-Rate Loading Devices for Advanced Materials Synthesis and Processing, *J. School Eng.*, Univ. Tokyo, Vol 45, 1998, p 41–86
- A. Al-Tounsi, M.S.J. Hashmi, Effect of Sintering Temperature on High Strain Rate Properties of Iron Powder Compacts, *3rd International Conference on Mechanical and Physical Behaviour of Materials under Dynamic Loading (DYMAT 91)*, 14–18 Oct 1991 (Strasbourg, France) or *J. Phys. (France) IV*, Vol 1 (Colloq. 3, Suppl. JP III, 8), 1991, p 203–208

- C. Albertini, M. Montagnani, E.V. Pizzinato, and A. Rodis, Comparison of Mechanical Properties in Tension and Shear at High Strain Rate for AISI 316 and Armco Iron, *Mechanical Behaviour of Materials VI*, Vol I, 29 July–2 Aug 1991 (Kyoto, Japan), Pergamon Press plc, Oxford, UK, 1992, p 351–356
- C. Albertini, M. Montagnani, E.V. Pizzinato, A. Rodis, S. Berleghi, G. Berrini, G. Pazienza, and A. Paluffi, Mechanical Properties in Shear at Very High Strain Rate of AISI 316 Stainless Steel and of a Pure Iron Comparison with Tensile Properties, *Shock-Wave and High-Strain-Rate Phenomena in Materials*, Marcel Dekker, Inc., 1992, p 681–691
- R.W. Armstrong, X.J. Zhang, C. Feng, J.D. Williams, and F.J. Zerilli, High Strain Rate Deformation Behavior of Tantalum, *Tantalum*, 5–8 Feb 1996 (Anaheim, CA), Minerals, Metals and Materials Society/AIME, Warrendale, PA, 1996, p 157–162
- R.W. Armstrong and F.J. Zerilli, Deformation Twinning: From Atomic Modeling to Shock Wave Loading, Advances in Twinning, 28 Feb–4 Mar 1999 (San Diego), *Advances in Twinning*, Minerals, Metals and Materials Society/AIME, 1999, p 67–81
- R. Asfahani, E. Chen, and A. Crowson, *High Strain Rate Behavior of Refractory Metals and Alloys*, Minerals, Metals and Materials Society, Warrendale, PA, 1992, p 316
- P.B. Berbon, M. Furukawa, Z. Horita, M. Nemoto, N.K. Tsenev, R.Z. Valiev, and T.G. Langdon, Processing of Aluminum Alloys for High Strain Rate Superplasticity, Second Symp. on Hot Deformation of Aluminum Alloys II, 11–15 Oct 1998 (Rosemont, IL), *Hot Deformation of Aluminum Alloys II*, Minerals, Metals and Materials Society/AIME, 1998, p 111–124
- T.R. Bieler and A.K. Mukherjee, Region I Deformation Mechanisms in High Strain Rate Superplastic IN9021, *Superplasticity and Superplastic Forming 1995*, 13–15 Feb 1995 (Las Vegas, NV), Minerals, Metals and Materials Society/AIME, Warrendale, PA, 1995, p 153–160
- J.J. Blandin, B. Baudalet, and R. Dendievel, Mechanical Approach of High Strain Rate Superplastic Behavior of Composite Materials, *Towards Innovation in Superplasticity I*, 23–24 July 1996 (Kyoto, Japan), 1997 or *Mater. Sci. Forum*, Vol 233–234, 1997, p 3–20
- M. Carsi, A. Fernandez-Vicente, O.A. Ruano, and O.D. Sherby, Processing, Microstructure, Strength, and Ductility Relationships in Ultrahigh Carbon Steel Assessed by High Strain Rate Torsion Testing, *Mater. Sci. Technol.*, Vol 15 (No. 9), 1999, p 1087–1095
- E.P. Carton, M. Stuivinga, H. Keizers, H.J. Verbeek, and P.J. Van Der Put, Shock Wave Fabricated Ceramic-Metal Nozzles, *Appl. Compos. Mater.*, Vol 6 (No. 3), 1999, p 139–165
- D.R. Chichili, K.T. Ramesh, and K.J. Hemker, High Strain Rate Deformation Mechanisms in Alpha Titanium, *The Johannes Weertman Symposium*, 4–8 Feb 1996 (Anaheim, CA), Minerals, Metals and Materials Society/AIME, Warrendale, PA, 1996, p 437–448
- Y. Estrin and A. Molinari, Constitutive Modelling of High Strain-Rate Deformation: Application to Adiabatic Shear Banding, *Advances in Fracture Research*, ICF9, Vol 6, High Strain Rate Fracture and Impact Mechanics, 1–5 April 1997 (Sydney, Australia), Elsevier Science Ltd., Oxford, UK, 1997, p 2755–2769
- J.C. Fu, C. Labbe, J.L. Lataillade, F. Collombet, E. Sellier, and Y. Le Petitcorps, Mechanical Properties of Composite Materials (SiC/224 and SiC/8090) in Torsion and Tension at High Strain Rate and Temperature, *EURODYMAT 94*, 26–30 Sept 1994 (Oxford, UK), Les Editions de Physique Les Ulis, Les Ulis cedex A, France, 1994 or *J. Phys. (France) IV*, Vol 4, (C8), p 219–224 Sept 1994
- Y. Gordeev, V. Redkin, and A. Staver, Influence Of Shock-Wave Ultrafine Particles on Some Properties of Hard Metals Composites, *1996 European Conference on Advances in Hard Materials Production*, 27–29 May 1996 (Stockholm, Sweden), European Powder Metallurgy Association, Shrewsbury, UK, 1996, p 135–140
- D. Grady, Scattering as a Mechanism for Structured Shock Waves in Metals, Dynamic Deformation and Failure Mechanics of Materials, 22–24 May 1997 (Pasadena), *J. Mech. Phys. Solids*, Vol 46 (No. 10), 1998, p 2017–2032
- G.T. Gray III, Influence of High-Strain Rate and Temperature on the Mechanical Behavior of Ni-, Fe-, and Ti-Based Aluminides, *Deformation and Fracture of Ordered Intermetallic Materials III*, 6–10 Oct 1996 (Cincinnati, OH), Minerals, Metals and Materials Society/AIME, Warrendale, PA, 1996, p 57–73

- B.Q. Han, S.R. Agnew, and D.C. Dunand, High-Strain-Rate Deformation of Pure Aluminum Reinforced with 25% Alumina Submicron Particles near the Solidus Temperature, *Scr. Mater.*, Vol 40 (No. 7), 1999, p 801–808
- M.S.J. Hashmi and M.M. Haque, High Strain Rate Properties of an Aluminum Alloy and High Purity Copper at Room Temperature (Retroactive Coverage), *International Symposium on Intense Dynamic Loading and Its Effects*, 3–7 June 1986 (Beijing, China), Science Press, Beijing, China, 1986, p 637–648
- K. Higashi, T. Mukai, K. Kaizu, S. Tanimura, and S. Tsuchida, Influence of Temperature on Stability of High Strain Rate Deformation in Some Commercial Aluminum Alloys, *Mechanical Behaviour of Materials—VI*, Vol I, 29 July–2 Aug 1991 (Kyoto, Japan), Pergamon Press plc, Oxford, UK, 1992, p 307–312.
- K. Higashi, T. Mukai, S. Tanimura, T.G. Nieh, and J. Wadsworth, Temperature Dependence of Mechanical Properties at High Strain Rate in Three Mechanically Alloyed Aluminum Alloys, *Proceedings of the Thirty-Seventh Japan Congress on Materials Research*, Sept 1993 (Kyoto, Japan), Society of Materials Science, Kyoto, Japan, 1994, p 27–32
- M.F. Horstemeyer and D.A. Mosher, High Strain Rate Effects on Cast A356 Aluminum Alloy, *Materials Solutions* 98, 12–15 Oct 1998 (Rosemont, IL), *Advances in Aluminum Casting Technology*, ASM International, 1998, p 149–150
- J.W. House, L.L. Wilson, and M.E. Nixon, High Strain-Rate Material Behavior Using Taylor Anvil Experiments, *Mechanical Behaviour of Materials—VI*, Vol I, 29 July–2 Aug 1991 (Kyoto, Japan), Pergamon Press plc, Oxford, UK, 1992, p 343–349
- N. Igata, K. Kawata, M. Itabashi, H. Yumoto, K. Sawada, and H. Kitahara, Plastic Deformation of Iron and Steel at High Strain Rate, *Advanced Materials for Future Industries: Needs and Seeds*, 11–14 Dec 1991 (Chiba, Japan), International Convention Management, Inc., Tokyo, Japan, 1991, p 1121–1129
- International Workshop on Industrial Applications of Explosion, Shock-Wave and High Pressure Phenomena (ESHP Workshop), 27–28 Oct 1997 (Kumamoto, Japan), *J. Mater. Process. Technol.*, Vol 85 (No. 1–3), 1999
- Z. Jin and T.R. Bieler, An Investigation of High Strain Rate Superplastic Deformation Mechanisms by Means of Texture Analysis, *Advances in Superplasticity and Superplastic Forming*, 2–5 Nov 1992 (Chicago, IL), Minerals, Metals and Materials Society, Warrendale, PA, 1993, p 121–132
- Z. Jin, G.T. Gray III, and M. Yamaguchi, Deformation of Polysynthetically Twinned (PST) TiAl Crystals at High-Strain Rate and High Temperature, *High-Temperature Ordered Intermetallic Alloys VII*, 2–5 Dec 1996 (Boston, MA), Materials Research Society, Pittsburgh, PA, 1997, p 189–194
- G.I. Kanel, Some New Data on Deformation and Fracture of Solids under Shock-Wave Loading, *Dynamic Deformation and Failure Mechanics of Materials*, 22–24 May 1997 (Pasadena, CA), *J. Mech. Phys. Solids*, Vol 46 (No. 10), 1998, p 1869–1886
- L.J. Kecskes and I.W. Hall, High-Strain-Rate Response of Hot-Explosively Consolidated W-Ti Alloys, *J. Mater. Res.*, Vol 14 (No. 7), 1999, p 2838–2848
- W.-J. Kim and J.-K. Kim, High Strain-Rate Superplasticity in a Fine-Grained PM 7475 Al Alloy, *Metals and Mater.*, Vol 4 (No. 6), 1998, p 1133–1141
- D.W. Kum, W.J. Kim, and G. Frommeyer, High Strain Rate Superplasticity of an Ultra-Fine Grained Al-Ti-Fe Alloy, *Scr. Mater.*, Vol 40 (No. 2), 1988, p 223–228
- J. Lankford, A. Bose, and H. Couque, High Strain Rate Behavior of Tungsten Heavy Alloys, *High Strain Rate Behavior of Refractory Metals and Alloys*, Oct 1991 (Cincinnati, OH), Minerals, Metals and Materials Society, Warrendale, PA, 1992, p 267–287
- J. Lankford, H. Couque, A. Bose, and C.E. Anderson, Microstructure Dependence of High-Strain-Rate Deformation and Damage Development in Tungsten Heavy Alloys, *Shock-Wave and High-Strain-Rate Phenomena in Materials*, Marcel Dekker, Inc., 1992, p 137–145
- D.H. Lassila, M. Leblanc, and G.T. Gray III, High-Strain-Rate Deformation Behavior of Shocked Copper, *Shock-Wave and High-Strain-Rate Phenomena in Materials*, Marcel Dekker, Inc., 1992, p 587–595
- B.F. Levin, K.S. Vecchio, J.N. DuPont, and A.R. Marder, Solid Particle Erosion Resistance and High Strain Rate Deformation Behavior of Inconel-625 Alloy, *Superalloys 718, 625, 706 and Various*

Derivatives, 15–18 June 1997 (Pittsburgh, PA), Minerals, Metals and Materials Society/AIME, Warrendale, PA, 1997, p 479–488

- Y. Liu, Y. Li, K.T. Ramesh, and J. Van Humbeeck, High Strain Rate Deformation of Martensitic NiTi Shape Memory Alloy, *Scr. Mater.*, Vol 41 (No. 1), 1999, p 89–95
- M. Mabuchi, T. Imai, and K. Higashi, High Strain Rate Superplastic Behavior in Si₃N₄/Aluminum Composites, *Aspects of High Temperature Deformation and Fracture in Crystalline Materials*, 28–31 July 1993 (Nagoya, Japan), The Japan Institute of Metals, Sendai, Japan, 1993, p 471–478
- M. Mabuchi and K. Higashi, Processing, Properties and Applications of High Strain Rate Superplastic Materials, Second Symp. on Hot Deformation of Aluminum Alloys II, 11–15 Oct 1998 (Rosemont, IL), *Hot Deformation of Aluminum Alloys II*, Minerals, Metals and Materials Society/AIME, 1998, p 87–99
- D. Macdougall, A Radiant Heating Method for Performing High-Temperature High-Strain-Rate Tests, *Meas. Sci. Technol.*, Vol 9 (No. 10), 1998, p 1657–1662
- L.S. Magness, Jr., High Strain Rate Deformation Behaviors of Kinetic Energy Penetrator Materials during Ballistic Impact, *Shear Instabilities and Viscoplasticity Theories*, 14–16 Sept 1992 (San Diego, CA) or *Mech. Mater.*, Vol 17 (No. 2–3), 1994, p 147–154
- T. Maki, Microstructural Evolution during High Strain Rate Superplastic Deformation in Microduplex Stainless Steel, *Towards Innovation in Superplasticity I*, 23–24 July 1996 (Kyoto, Japan) or *Mater. Sci. Forum*, Vol 233–234, 1997, p 139–146
- S.A. Maloy and G.T. Gray III, High Strain Rate Deformation of Cast Ti-48Al-2Nb-2Cr in the Duplex Morphology, *Gamma Titanium Aluminides*, 13–16 Feb 1995 (Las Vegas, NV), Minerals, Metals and Materials Society/AIME, Warrendale, PA, 1995, p 307–314
- K. Matsuki, M. Tokizawa, and Y. Murakami, Microstructure Change during High Strain Rate Superplastic Deformation in a PM 7475 Al-0.7Zr Alloy, *Superplasticity in Metals, Ceramics, and Intermetallics*, 16–19 April 1990 (San Francisco, CA), Materials Research Society, Pittsburgh, PA, 1990, p 265–270
- K. Matsuki, H. Kawakami, M. Tokizawa, Y. Murakami, and S. Murakami, High Strain Rate Superplasticity and Mechanical Properties after Superplastic Deformation of MA 2024Al-SiC Particulate Composites, *Aluminum Alloys: Their Physical and Mechanical Properties, ICAA5, Part 2*, 1–5 July 1996 (Grenoble, France) or *Mater. Sci. Forum*, Vol 217–222 (No. 2), 1996, p 1163–1174
- H. Matsumoto, Analysis of State Compressed by a Plane Shock Wave, *Nippon Zairyo Kyodo Gakkaishi (J. Jpn. Soc. Strength Fract. Mater.)*, Vol 32 (No. 3), 1998, p 81–90
- H. Matsumoto, Estimation of Shock-Compressed Region by Analysis of Propagation of Shock Wave and Rarefaction Wave, *Nippon Zairyo Kyodo Gakkaishi (J. Jpn. Soc. Strength Fract. Mater.)*, Vol 33 (No. 1), 1999, p 17–24
- L.G. Melin, P. Stahle, and K.G. Sundin, High Strain Rate Tensile Testing Using Microscopic High Speed Photography, 11th Int. Conf. on Experimental Mechanics, 24–28 Aug 1998 (Oxford, UK), *Experimental Mechanics: Advances in Design, Testing and Analysis I*, 1998, p 175–179
- L.A. Merzhievsky and A.V. Tyagel'sky, Dislocation Kinetics of Shock Wave Metal Deformation, *3rd International Conference on Mechanical and Physical Behaviour of Materials under Dynamic Loading (DYMAT 91)*, 14–18 Oct 1991 (Strasbourg, France), *J. Phys. (France) IV*, Vol 1, (Colloq. No. 3, Suppl. JP III, No. 8), 1991, p 525–531
- Y. Meunier, R. Roux, and G. Pont, Experimental and Theoretical Approaches to the High Strain Rate Effect on the Properties of Armour Steels, *Structures under Shock and Impact*, July 1989 (Cambridge, MA), Computation Mechanics Publications, Southampton, UK, 1989, p 193–202
- M.A. Meyers, *Dynamic Behavior of Materials*, John Wiley & Sons, 1994
- M.A. Meyers, Dynamic Failure: Mechanical and Microstructural Aspects, *EURODYMAT 94*, Les Editions de Physique Les Ulis, 112 or *J. Phys. (France) IV*, Vol 4, (C8), Sept 1994, p 597–621
- M.A. Meyers, U. Andrade, K.S. Vecchio, A.H. Chokshi, J. Beatty, and L.W. Meyer, High Strain, High-Strain-Rate Deformation of Copper, *Shock-Wave and High-Strain-Rate Phenomena in Materials*, Marcel Dekker, Inc., 1992, p 529–542
- M.A. Meyers, U.R. Andrade, and A.H. Chokshi, The Effect of Grain Size on the High-Strain, High-Strain-Rate Behavior of Copper, *Metall. Mater. Trans. A*, Vol 26A (No. 11), 1995, p 2881–2893
- M.A. Meyers, Y.-J. Chen, F.D.S. Marquis, and D.S. Kim, High Strain, High-Strain-Rate Behavior of Tantalum, *Metall. Mater. Trans. A*, Vol 26A (No. 10), 1995, p 2493–2501

- M.A. Meyers, Y.-J. Chen, and V.F. Nesterenko, Spontaneous and Forced Shear Localization in High-Strain-Rate Deformation of Tantalum, *Mater. Sci. Eng. A*, Vol 268 (No. 1–2), 1999, p 70–82
- M.A. Meyers, L.E. Murr, and K.P. Staudhammer, *Shock-Wave and High-Strain-Rate Phenomena in Materials*, Marcel Dekker, Inc., 1992
- R.S. Mishra, R.Z. Valiev, S.X. McFadden, R.K. Islamgaliev, and A.K. Mukherjee, Severe Plastic Deformation Processing and High Strain Rate Superplasticity in an Aluminum Matrix Composite, *Scr. Mater.*, Vol 40 (No. 10), 1999, p 1151–1155
- K. Miura, S. Takagi, O. Furukimi, T. Obara, and S. Tanimura, High Strain Rate Deformation Behaviour of High Strength Steel Sheet for Automobile, *29th International Symposium on Automotive Technology and Automation*, Vol I, 3–6 June 1996 (Florence, Italy), Automotive Automation Limited, Croydon, UK, 1996, p 77–84
- A.J. Mukherjee and R.S. Mishra, The Rate Controlling Deformation Mechanism in High Strain Rate Superplasticity, *11th International Conference on the Strength of Materials*, 25–29 Aug 1997 (Prague, Czech Republic) or *Mater. Sci. Eng. A*, Vol A234–236, 30 Aug 1997, p 1023–1025
- R.J. Mundekis and J.F. Muller, Effects of Rolling Schedule and Annealing on the High Strain Rate Behavior of Tantalum, *High Strain Rate Behavior of Refractory Metals and Alloys*, Oct 1991 (Cincinnati, OH), Minerals, Metals and Materials Society, Warrendale, PA, 1992, p 77–96
- L.E. Murr, S. Pappu, C. Kennedy, C.-S. Niou, and M.A. Meyers, Tantalum Microstructures for High-Strain-Rate Deformation: Shock Loading, Shaped Charges, and Explosively Formed Penetrators, *Tantalum*, 5–8 Feb 1996 (Anaheim, CA), Minerals, Metals and Materials Society/AIME, Warrendale, PA, 1996, p 145–155
- T. Ninomiya, H. Hira, N. Kanetake, and T. Choh, High Strain Rate Superplastic Bulge Forming of SiC Particle Reinforced 2124 Aluminum Alloy Composite, *J. Jpn. Inst. Light Met.*, Vol 48 (No. 8), 1998 p 380–384
- L.N. Oklei and I.V. Chkartishvili, The Deformation Process and the Conditions of the Shock Wave Origination (Retroactive Coverage), *International Symposium on Intense Dynamic Loading and Its Effects*, 3–7 June 1986 (Beijing, China), Science Press, Beijing, China, 1986, p 294–299
- P.O. Pashkov, D.P. Cheprasov, and S. Peitsch, Effect of Shock Waves on the Structure and Properties of Quenched Steels, *Fiz. Met. Metalloved.*, Vol 87 (No. 2), 1999, p 54–58
- A. Peikrishvili, L. Japaridze, G. Gotsiridze, and N. Chikhradze, Shock-Wave Deformation of W-Ni-Fe Heavy Alloys at Elevated Temperatures, *Shock-Wave and High-Strain-Rate Phenomena in Materials*, Marcel Dekker, Inc., New York, 1992, p 223–229
- B.M. Powers, J.R. Vinson, I.W. Hall, and V. Nardone, High Strain Rate Mechanical Properties of Silicon Carbide Reinforced Aluminum Matrix Composites, *Tenth International Conference on Composite Materials, Part II: Metal Matrix Composites*, 14–18 Aug 1995 (Whistler, British Columbia), Woodhead Publishing Limited, c/o Turpin Distribution Services Ltd., Herts, UK, 1995, p 317–322
- J. Rodriguez, C. Navarro, and J. Llorca, Tensile Properties of Metal-Matrix Composites at High Strain Rate and Elevated Temperatures, *ICCM/9, Metal Matrix Composites*, Vol I, 12–16 July 1993 (Madrid, Spain,) University of Zaragoza, Zaragoza, Spain, 1993, p 533–540
- Z. Rosenberg, New Experimental Techniques for the Determination of High Strain Rate Properties of Materials, *Strength of Metals and Alloys*, Vol I, 14–19 July 1991 (Haifa, Israel), Freund Publishing House, Ltd., London, UK, 1991, p 101–109
- S.K. Schiferi and P.J. Maudlin, Texture-Induced Anisotropy and High-Strain Rate Deformation in Metals, *Shock-Wave and High-Strain-Rate Phenomena in Materials*, Marcel Dekker, Inc., 1992, p 213–221
- J. Svejcar, P. Ptacek, J. Krejci, and J. Buchar, Dislocation Substructure Induced by High Strain Rate Deformation in Fcc Poly and Single Crystals, *EUROMAT 97: 5th European Conference on Advanced Materials and Processes and Applications*, Vol 1, *Metals and Composites*, 21–23 April 1997 (Maastricht, Netherlands), Netherlands Society for Materials Science, Zwijndrecht, Netherlands, 1997, p 141–144
- W. Tong, G. Ravichandran, T. Christman, and T. Vreeland Jr., Processing and Properties of SiC-Particulate Reinforced Titanium Matrix Composites by Shock Wave Consolidation, *EURODYMAT 94*, 26–30 Sept 1994 (Oxford, UK), Les Editions de Physique Les Ulis, France, 1994 or *J. Phys. (France) IV*, Vol 4 (C8), Sept 1994, p 331–336

- J.-C. Tsai, J.-B. Duh, and S.-C. Cheuh, Flow Stress Behavior of Cast Co-Cr-Mo Alloy Evaluated by High Strain Rate of Compression Tests, *EMRS 1992 Fall Meeting, Symposium B: Materials under Extreme Conditions*, 3–6 Nov 1992 (Strasbourg, France), *Mater. Sci. Eng. A*, Vol A168 (No. 1), 30 Aug 1993, p 1–3
- K.S. Vecchio, High-Strain, High-Strain-Rate Deformation of Tantalum and Tantalum-Tungsten Alloys, *EURODYMAT 94*, 26–30 Sept 1994 (Oxford, UK), Les Editions de Physique Les Ulis, France, 1994, *J. Phys. (France) IV*, Vol 4 (C8), Sept 1994, p 301–306
- D.V. Voronin, Modeling of Initiation of Shock Waves in Tubes by Gas Detonation, *Fiz. Goren. Vzryva*, Vol 35 (No. 2), 1999, p 75–80
- H. Watanabe, T. Mukai, M. Mabuchi, and K. Higashi, High-Strain-Rate Superplasticity at Low Temperature in a ZK61 Magnesium Alloy Produced by Powder Metallurgy, *Scr. Mater.*, Vol 41 (No. 2), 1999, p 209–213
- C.L. Wittman, C.M. Lopatin, J.P. Swensen, and T.J. Holmquist, High Strain Rate Properties and Modeling of a Tungsten Alloy in Compression and Tension, *High Strain Rate Behavior of Refractory Metals and Alloys*, Oct 1991 (Cincinnati, OH), Minerals, Metals and Materials Society, Warrendale, PA, 1992, p 167–178
- C. Wolff, O. Pawelski, and W. Rasp, Analysis of the Asymmetric Upsetting Test with Extremely High Strain Rate as Tool for Friction Measurement, *Metal Forming 98*, 1–3 Sep 1998 (Birmingham, UK), *J. Mater. Process. Technol.*, Vol 80-81, 1998, p 287–291
- X. Xu, D. Zhang, Z. Shi, C. Zhao, and R. Wu, High Strain Rate Superplasticity of Aluminum Matrix Composite Made by Squeeze Casting, *Chin. J. Nonferrous Met.*, Vol 9 (No. 2), 1999, p 231–235
- L.-W. Yang and P.-W. Kao, High Temperature Tensile Behavior of MA Al-Ti Alloys at High Strain-Rate, *THERMEC '97: International Conference on Thermomechanical Processing of Steels and Other Materials*, Vol II, 7–11 July 1997 (Wollongong, Australia), Minerals, Metals and Materials Society/AIME, Warrendale, PA, 1997, p 1457–1463
- L. Zernow and L. Lowry, High-Strain-Rate Deformation of Copper in Shaped Charge Jets, *Shock-Wave and High-Strain-Rate Phenomena in Materials*, Marcel Dekker, Inc., 1992, p 503–519

1985 to 1990

- A.M. Abdelhay, A Study of High Strain Rate Generation of Adiabatic Shear Bands in a Titanium Alloy, Ph.D. diss., University of Alabama, *Diss. Abstr. Int.*, Vol 49 (No. 11), 1989, p 167
- C. Albertini, M. Montagnani, and E.V. Pizzinato, Specimen Size and Shape Effects at High Strain-Rate on the Mode of Yielding and Flow of AISI 316, *Impact Loading and Dynamic Behavior of Materials*, Vol 1, DGM Informationsgesellschaft mbH, 1988, p 461–468
- T.N.M. Al-Haddid, High Strain Rate Properties of Structural Aluminum, *Diss. Abstr. Int.*, Vol 49 (No. 2), 1988, p 385
- B. Avitzur and J. Kowalski, Analytical Model of the High Strain-Rate Expansion of a Hollow Cylinder, *J. Mech. Work. Technol.*, Vol 16 (No. 3), 1988, p 299–313
- D.L. Baragar, The High Temperature and High Strain-Rate Behaviour of a Plain Carbon and an HSLA Steel, *J. Mech. Work. Technol.*, Vol 14 (No. 3), 1987, p 295–307
- D.C. Drucker, High Strain-Rate Response Regimes for Dislocated Alloy Microstructures, *Macro- and Micro-Mechanics of High Velocity Deformation and Fracture*, Springer-Verlag, 1987, 137–148
- P.S. Follansbee, “High-Strain-Rate Deformation of FCC Metals and Alloys,” paper presented at the Int. Conf. on Metallurgical Applications of Shock-Wave and High-Strain-Rate Phenomena (EXPLOMET 85), 28 July–1 Aug 1985 (Portland, OR)
- P.S. Follansbee and G.T. Gray III, An Analysis of the Low Temperature, Low and High Strain-Rate Deformation of Ti-6Al-4V, *Metall. Trans. A*, Vol 20 (No. 5), 1989, p 863–874
- L.B. Freund, J.W. Hutchinson, and P.S. Lam, Analysis of High-Strain-Rate Elastic-Plastic Crack Growth, *Eng. Fract. Mech.*, Vol 23 (No. 1), 1986, p 119–129
- T.G. George, “High-Strain-Rate, High-Temperature Biaxial Testing of DOP-26 Iridium,” Report DE88010471/XABMA, Los Alamos National Laboratory, May 1988, p 47
- V.R. Golubev, A.I. Korshunov, and S.A. Novikov, Strength and Failure of Tantalum Alloy TaV10 With Shock-Wave Loading, *Strength Mater. (USSR)*, 1988, p 605–610 (translation)

- V.K. Golubev, A.I. Korshunov, S.A. Novikov, Sobolev, S. Yu, and N.A. Yukina, Strength and Failure of Aluminum Alloy AMg6 with Shock-Wave Loading, *J. Appl. Mech. Tech. Phys. (Russia)*, Vol 29 (No. 2), 1988, p 274–280 (translation)
- W.H. Gourdin, Electromagnetic Ring Expansion: Experiment, Analysis, and Application to High-Strain-Rate Testing, *Impact Loading and Dynamic Behavior of Materials*, Vol 2, Informationsgesellschaft mbH, 1988, p 533–540.
- J Harding, The Effect of High Strain Rate on Material Properties, *Materials at High Strain Rates*, Elsevier Applied Science Publishers, 1987, p 133–186
- J. Harding, M. Taya, B. Derby, and S. Pickard, An Investigation of the High Strain Rate Deformation of SiCw/2124 Aluminum Composite, Sixth Int. Conf. on Composite Materials and Second European Conference on Composite Materials, 20–24 July 1987 (London), *ICCM & ECCM*, Vol 2, Elsevier Applied Science Publishers Ltd., 1987, p 2.224–2.233
- A.A. Johnson and J.A. Von Fraunhofer, Fractographic Observations on a Splined Shaft Which Failed by High Strain-Rate Torsional Overload, *Surf. Coat. Technol.*, Vol 29 (No. 2), 1986, p 153–156
- P. Kasiraj, Shock-Wave Consolidation of Metallic Powders, *Diss. Abstr. Int.*, Vol 46 (No. 1), 1985, p 174
- I. Lauber-Altmann and F. Muller, Failure of the Shock-Wave Model in the Low-Pressure Region, *J. Phys. D, Appl. Phys.*, Vol 19 (No. 11), 1986, p 2157–2169
- P.A. Lush and N. Sanada, Pitting in Aluminum Alloys Produced by Air Bubble-Shock Wave Interaction, *Erosion by Liquid and Solid Impact, Seventh Int. Conf.*, 7–10 Sep 1987 (Cambridge, UK), Cavendish Laboratory, 1987, p 24.1–24.5
- M.A. Meyers, N.N. Thadhani, and L.-H. Yu, Explosive Shock Wave Consolidation of Metal and Ceramic Powders, *Shock Waves for Industrial Applications*, Noyes Publications, 1988, p 265–334
- M.A. Meyers, C.L. Wittman, H.-R. Pak, and S. Kuriyama, Observation and Modeling of High-Strain-Rate Shear Localization, *Impact Loading and Dynamic Behavior of Materials*, Vol 2, DGM Informationsgesellschaft mbH, 1988, p 719–728
- A.H. Mutz, N.N. Thadhani, and T. Vreeland, Jr., Tensile Properties of Shock-Wave Consolidated and Hot-Isostatically Pressed Compacts of Rapidly Solidified Pyromet 718 Powder, *Impact Loading and Dynamic Behavior of Materials*, Vol 2, DGM Informationsgesellschaft mbH, 1988, p 661–668
- C. Nagasaki, A. Aizawa, and J. Kihara, Influence of Manganese and Sulfur on Hot Ductility of Carbon Steels at High Strain Rate, *Trans. Iron Steel Inst. Jpn.*, Vol 27 (No. 6), 1987, p 506–512
- K. Ogawa, Mechanical Behavior of Metals Under Tension-Compression Loading at High Strain Rate, *Int. J. Plast.*, Vol 1 (No. 4), 1985, p 347–358
- F. Ornath and I. Minkoff, Fracture Behaviour of Cast Steels Under High Strain Rate Conditions, *Solidification Processing 1987*, 21–24 Sep 1987 (Sheffield, UK), The Institute of Metals, 1988, p 428–431
- R.C. Ortiz, “High Strain Rate, High Temperature Deformation of Stainless Steel,” Ph.D. diss., University of Sheffield, *Diss. Abstr. Int.*, Vol 49 (No. 10), 1989, p 446
- Y.-H. Pao, A Theoretical and Experimental Study of Dynamic Plasticity Over a Wide Range of Strain Rates and Temperatures, Ph.D. diss., Ohio State University, *Diss. Abstr. Int.*, Vol 49 (No. 8), 1989, p 193
- A.M. Rajendran and S.J. Bless, Determination of Tensile Flow Stress Beyond Necking at Very High Strain Rate, *Exp. Mech.*, Vol 26 (No. 4), 1986, p 319–323
- A.M. Rajendran, S.J. Bless, and D.S. Dawicke, Evaluation of Bodner-Partom Model Parameters at High Strain Rate, *J. Eng. Mater. Technol. (Trans. ASME)*, Vol 108 (No. 1), 1986, p 75–80
- O.V. Roman and V.G. Gorobtsov, Shock Wave Powder Compaction: State of the Art and Trends in the USSR, *Shock Waves for Industrial Applications*, Noyes Publications, 1988, p 335–379
- F.H. Samuel, R. Barbosa, F. Boratto, S. Yue, and J.J. Jonas, Laboratory Simulation of Flow Stresses During Strip Rolling Using High Strain Rate Torsion Testing, Int. Conf. on Physical Metallurgy of Thermomechanical Processing of Steels and Other Metals, 6–10 June 1988 (Tokyo), *THERMEC-88*, Vol 2, The Iron and Steel Institute of Japan, 1988, p 721–728
- D.A. Shockey, D.C. Erlich, J.F. Kalthoff, and H. Homma, Short Pulse Fracture Mechanics, *Eng. Fract. Mech.*, Vol 23, 1986, p 311–319

- D.A. Shockey, Material Aspects of the Adiabatic Shear Phenomenon, *Metallurgical Applications of Shock Wave Phenomena*, Marcel Dekker, 1986, p 633–656
- K.P. Staudhammer, Shock Wave Effects and Metallurgical Parameters, *Impact Loading and Dynamic Behavior of Materials*, Vol 1, DGM Informationsgesellschaft mbH, 1988, p 93–110
- D.J. Steinberg, Constitutive Model Used in Computer Simulation of Time-Resolved, Shock-Wave Data, Hypervelocity Impact, 21–24 Oct 1986 (San Antonio, TX), *Int. J. Impact Eng.*, Vol 5 (No. 1–4), 1987, p 603–611
- D.J. Steinberg, “Constitutive Models Used in Computer Simulation of Time-Resolved, Shock-Wave Data,” Lawrence Livermore National Laboratory, Report DE87008471/GAR, 1987, p 9
- D.J. Steinberg, Constitutive Models Used in Computer Simulation of Time-Resolved, Shock-Wave Data, *Impact Loading and Dynamic Behavior of Materials*, Vol 2, DGM Informationsgesellschaft mbH, 1988, p 645–651
- J.W. Swegle and D.E. Grady, Shock Viscosity and the Prediction of Shock Wave Rise Times, *J. Appl. Phys.*, Vol 58 (No. 2), 1985, p 692–701
- S.M. Taya, I.W. Hall, and H. Yoon, Void Growth in Single Crystal Cu-SiO₂ During High Strain-Rate Deformation, *Acta Metall.*, Vol 33 (No. 12), 1985, p 2143–2153
- L. Vasquez and H.J. McQueen, Restoration of Copper During Stress Relaxation Between Stages of High Strain Rate, Hot Torsion, Strength of Metals and Alloys, 12–16 Aug 1985 (Montreal), *ICSMA 7*, Vol 2, Pergamon Press Ltd., 1985, p 905–910
- H.S. Yadav and N.K. Gupta, Study of Collapse of a Free Surface Conical Cavity Due to a Plane or Spherical Shock Wave, *Int. J. Impact Eng.*, Vol 3 (No. 4), 1985, p 217–232
- S. Yoshimura, K.L. Chen, and S.N. Atluri, A Study of Two Alternate Tangent Modulus Formulations and Attendant Implicit Algorithms for Creep as Well as High-Strain-Rate Plasticity, *Int. J. Plast.*, Vol 3 (No. 4), 1987, p 391–413
- S. Yoshimura, G. Yagawa, and S.N. Atluri, Generation and Propagation Analyses of High-Strain-Rate Dynamic Crack Propagation in a Visco-Plastic Solid, *Nucl. Eng. Des.*, Vol 3 (No. 2), 1989, p 273–289
- J. Zhou and K. Guan, Research on Flow Stress in Alloy Structural Steels at High Temperature and High Strain Rate, *Acta Metall. Sin. (China)*, Vol 22 (No. 1), 1986, p B31–B39

Until 1985

- K. Bitans and P.W. Whitton, High-Strain-Rate Investigations with Particular Reference to Stress-Strain Characteristics, *Int. Met. Rev.*, Vol 17, review 161, 1972, p 66–78
- J.D. Campbell, Dynamic Plasticity of Metals, *International Centre for Mechanical Sciences, Course and Lectures*, No. 46, Springer-Verlag, 1970
- R.J. Clifton, Dynamic Plasticity, *J. Appl. Mech. (Trans. ASME)*, Vol 50, 1983, p 941–952
- L. Davison and R.A. Graham, Shock Compression of Solids, *Phys. Rep.*, Vol 55 (No. 4), 1979, p 255–370
- S.J. Green and S.G. Babcock, “Response of Materials to Suddenly Applied Stress Loads,” Part I: “High Strain-Rate Properties of Eleven Reentry-Vehicle Materials at Elevated Temperatures,” Report TR66-83, General Motors Defense Research Laboratories, Aerospace Operations Dept., Santa Barbara, CA, 1966
- A.J. Holzer and P.K. Wright, Dynamic Plasticity: A Comparison Between Results from Mechanical Testing and Machining, *Mater. Sci. Eng.*, Vol 51, 1981, p 81–92
- K. Kawata and J. Shioiri, Ed., *High Velocity Deformation of Solids*, Springer-Verlag, Berlin, 1978
- H. Kolsky, *Stress Waves in Solids*, Oxford University Press, London, 1953
- L.H.N. Lee, Dynamic Plasticity, *Nucl. Eng. Des.*, Vol 27, 1974, p 386–397
- U.S. Lindholm, Ed., *Mechanical Behavior of Materials Under Dynamic Loads*, Springer-Verlag, 1968
- U.S. Lindholm and R.L. Bessey, “A Survey of Rate Dependent Strength Properties of Metals,” Technical Report 69–199, Air Force Materials Laboratory, Wright-Patterson Air Force Base, Dayton, OH, 1969
- M.A. Meyers and L.E. Murr, Ed., *Shock Waves and High-Strain-Rate Phenomena in Metals*, Plenum Press, 1981

- T. Nicholas, Material Behavior at High Strain Rates, *Impact Dynamics*, J. Zukas, T. Nicholas, H.F. Swift, L.B. Greszczuk, and D.R. Curran, Ed., John Wiley & Sons, 1981, p 277–331
- H.C. Rogers, Adiabatic Plastic Deformation, *Ann. Rev. Mater. Sci.*, Vol 9, 1979, p 283–311
- R.W. Rohde, B.M. Butcher, J.R. Holland, and C.H. Karnes, Ed., *Metallurgical Effects at High Strain Rates*, Plenum Press, 1973
- D.A. Shockey, *Fracture of Structural Materials under Dynamic Loading*, SRI International, 1981
- R. Sutterlin, Sur la Plasticite Dynamique: Son Application a l'Etude du Forgeage (Dynamic Plasticity: Its Application to Studies of Forging), Memorial de l'Artilerie Francaise, *Sci. Tech. Armement*, Vol 46 (No. 4), 1972, p 909–989; Vol 47 (No. 3), 1973, p 567–646

High Strain Rate Shear Testing

Introduction

SHEAR DEFORMATION is encountered in several types of processing operations, such as punching, grinding, machining, forming, and events or processes that result in penetration. Using adequate models (like von Mises, Tresca, Nadai-Tresca, and Nadai-von Mises), one can convert mechanical properties from tension and compression testing to shear stress and shear strain; however, this conversion seldom extends into a high strain range. The limit is frequently about 20% strain, which is far less than the strains reached in the aforementioned applications. At higher plastic strains, the deviation between results can become quite significant, with axial tests invariably providing higher values on flow stress than shear tests provide (after conversion by either the von Mises or Tresca flow rule). Therefore, to accurately predict mechanical behavior at high strain (especially for nonisotropic materials), testing for shear behavior should be performed directly in shear at the appropriate level of strain, temperature, and strain rate for a given operation. In addition to immediate practical applications, high strain rate shear data are invaluable for the development of macroscopic constitutive models and for studies into possible deformation mechanisms for metals. Macroscopic results can be combined with microscopic observations to make fundamental contributions to the development of constitutive equations based on the micromechanisms that are dominant during deformation at a particular rate and temperature.

Shear and torsion testing also have some advantages over uniaxial testing in tension or compression testing. In particular, with the absence of a Poisson ratio effect, complications caused by radial expansion or contraction are eliminated during shear and torsion testing. The problems of necking, which occurs in tension tests, and barreling, which occurs in compression tests, thus, do not occur in shear and torsion testing. Furthermore, due to the Poisson ratio effect, radial expansion or contraction of stress waves during the initial phase of axial high-speed tests is opposed by a radial inertia that becomes greater with a shorter pulse and larger amplitude. This results in a short-pulse radial stress component in the specimen superposed on the axial stress component. Hence, in axial loading, the state of stress in the specimen is only at constant strain rates. In torsional testing, however, the inertial and frictional effects from radial expansion or contraction do not occur. The torsional inertia stresses still remain. Nevertheless, this is one consideration that originally led to the development of the torsional Kolsky bar, and it has since been shown that the strain rate sensitivities determined by torsion tests on a variety of materials compare more or less well with those determined by axial tests.

Another advantage of torsion testing at high strain rates is the absence of geometric dispersion. When an axial stress pulse (tension or compression) travels down a cylindrical bar, the pulse undergoes geometric dispersion; that is, the different frequency components in an axial pulse have different velocities. In contrast, there is no geometric dispersion when a torsional pulse travels along an elastic bar in its primary mode; that is, all frequency components of the torsional pulse have the same velocity. Hence, a torsional pulse initiated either by explosive detonation or by the release of a stored torque does not change its shape as it propagates toward the specimen.

On the other hand, with torsion testing, some disadvantages must be considered:

- All tube specimens imply a stress and strain gradient from the inner to the outer wall diameter that can be diminished by using a relative thin-wall thickness and a large diameter. The limit of “slenderness” is given by elastic buckling before yielding or plastic buckling while yielding.
- Upper and lower yield stresses, connected with Lüders bands, are flattened out because of the inability to local compliance.
- Flat products are often unsuited for torsion testing because of nonrotational texture distribution.

This article briefly reviews the dynamic factors and experimental methods for high strain rate shear testing by the methods listed in Table 1. As for axial loading, a variety of testing machines are available for shear loading. Selection usually depends on the rate of deformation required. A servo-hydraulic machine provides the most convenient testing method for rates up to about 10^2 s^{-1} , provided that precautions are observed for wave propagation effects within the loading column. Wave propagation effects place an upper theoretical limit on the attainable strain rates. Hence, other methods of testing become necessary. Torsional impact loading has been widely used to obtain strain rates up to about 10^2 s^{-1} . Between strain rates of 10^2 and 10^4 s^{-1} , the torsional Kolsky (or split-Hopkinson) bar has proven to be a very convenient method of testing. Other methods of high strain rate shear testing include double shear and punching, which provide somewhat higher rates than the torsional Kolsky bar. For rates above 10^4 up to approximately 10^7 s^{-1} , plate impact tests are used to subject thin specimens to combined pressure and shear.

Table 1 Shear tests for high strain rate conditions

Testing technique	Application strain rate, s^{-1}
Conventional shear	<0.1
Special servo-hydraulic frames	0.1 to 100
Torsional impact	10 to 10^3
Hopkinson (Kolsky) bar in torsion	10^2 to 10^4
Double-notch shear and punch	10^3 to 10^4
Pressure-shear plate impact	10^4 to 10^7

All of the techniques described in this article are capable of producing a complete stress-strain curve for a given material. Based on a combination of results obtained from tests using the methods already described, a complete analysis of material behavior in shear over a wide range of dynamic rates (10 to 10^7 s^{-1}) can be obtained. For penetration, punching, machining, etc., a strain rate range of 10^3 to 10^5 s^{-1} is of particular interest, but knowledge of material response over the entire range is very useful. For strain rates up to approximately 10^4 s^{-1} , the lower yield stress is often found to be proportional to the logarithm of strain rate. At strain rates in excess of 10^4 s^{-1} , the lower yield stress is often found to be directly proportional to strain rate, rather than to the logarithm of strain rate. This implies a new region of mechanical response controlled by a viscous damping mechanism, in contrast to thermally activated processes at strain rates below 10^4 s^{-1} .

High Strain Rate Shear Testing

High Strain Rate Torsion Testing

High strain rate torsion testing involves the use of high-speed hydraulic machines, torsional impact devices, or the Kolsky (split-Hopkinson) bar.

High-Speed Hydraulic Torsional Machines

Hydraulic torsion test machines can be used as an alternative to mechanically driven torsional devices to provide transient loading. High-speed hydraulic torsion machines are analogous to axial test machines, but a torsional actuator is used instead of a standard linear hydraulic actuator. A typical high-speed torsional system without the possibility of compensating axial loads is illustrated schematically in Fig. 1 (Ref 1). As in the torsional impact device discussed in the next section of this article, a stiff loading system and reaction frame are required, as well as low inertia in the moving parts. As illustrated in Fig. 1, these requirements are accomplished by enclosing the system, which features an integral actuator shaft, specimen, and load transducer, within a rigid housing. The vaned torsional actuator allows a rotation of about 3 rad.

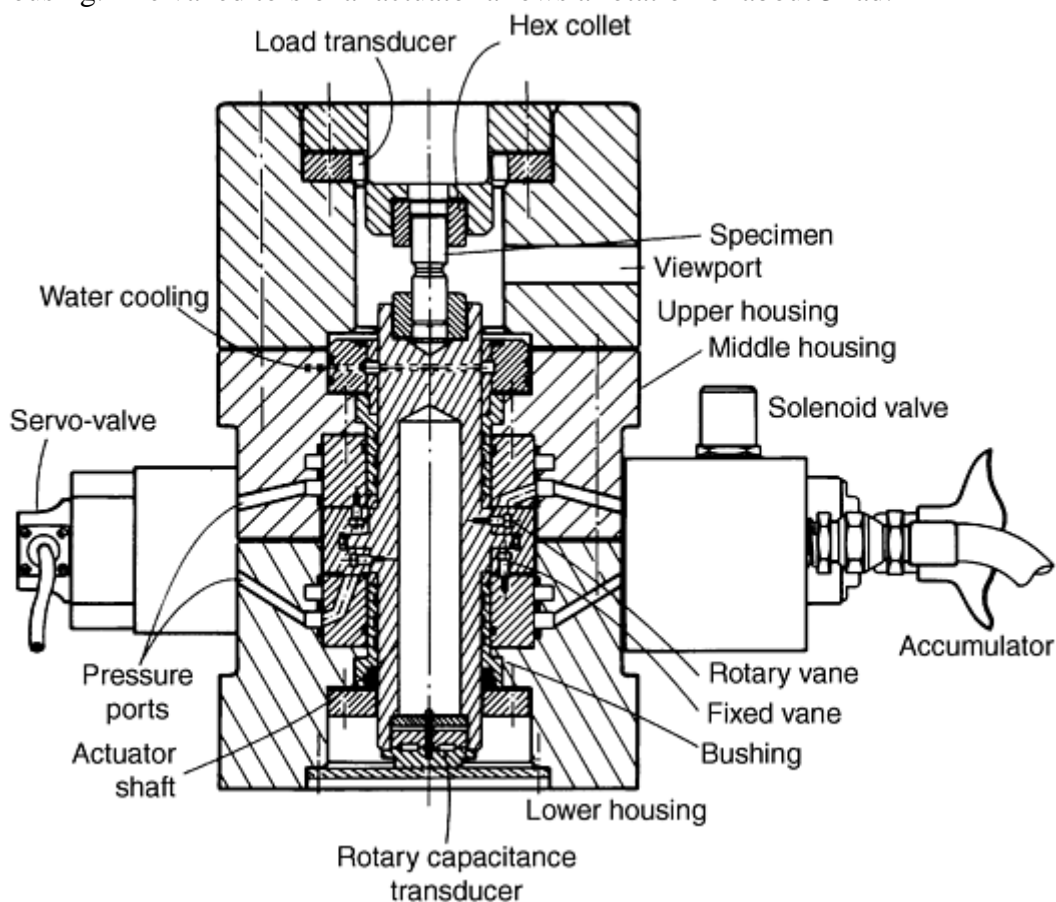


Fig. 1 Dynamic hydraulic torsion test facility. Source: Ref 1

Hydraulic loading of the actuator is maintained by a servovalve and servo-control loop for operating at low rotational velocities, which provide shear strain rates to about 10 s^{-1} . For higher velocities, a solenoid-triggered quick-release valve conveys pressure from an accumulator directly to the actuator. In this open-loop mode, strain rates of up to 300 s^{-1} have been reported.

In contrast to mechanical impact devices, the rotary actuator shaft, specimen, and load transducer are initially attached (as in a standard test machine), and no transient mechanical engagement or impact is involved. This facilitates maintenance of coaxiality and alignment. However, the specimen still undergoes a rapid acceleration at the higher speeds, and inertial or resonance effects are still experienced by the load transducer.

Figure 2 illustrates a typical record of shear stress, τ , and shaft rotation, θ , as a function of time. The rotation is obtained from a rotary capacitance transducer that is attached to the bottom of the actuator shaft. The load transducer is a strain-gage element placed between the specimen and upper housing. Dynamic effects or “ringing” in the load signal are evident. Finite element analysis of the shaft, specimen, and load transducer

system can be used to ensure that the mean signal from the load transducer is an accurate representation of the shear stress in the specimen. The computed and measured stresses are compared in Fig. 2. Such dynamic analysis is often required for proper interpretation or verification of dynamic test procedures. The specimen geometry is similar to that used with torsional impact devices (thin-walled with a gage length of 3.2 mm, 6.4 mm inner radius $\theta_{\max} \approx 2.5$ radians).

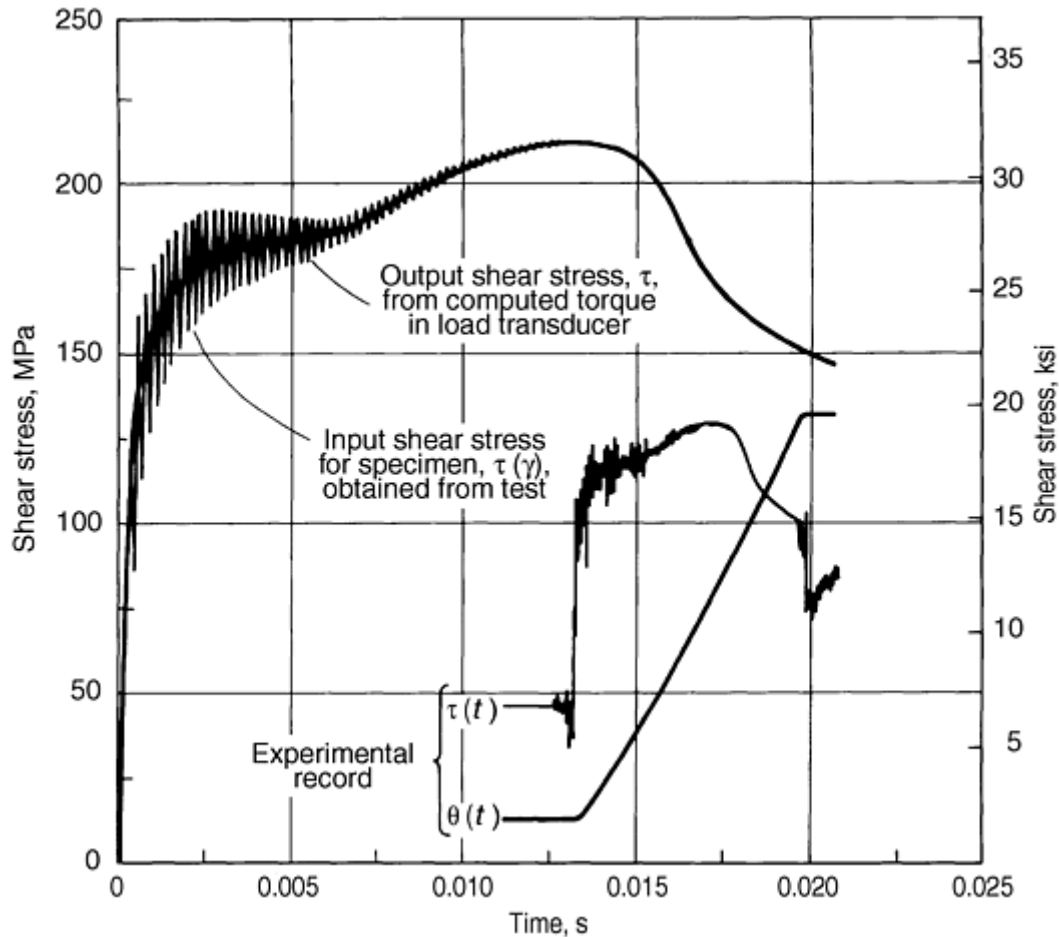


Fig. 2 Comparison of computed response with experimental results for dynamic torsion test. Source: Ref 1

Such short specimens of $L/D = \frac{1}{4}$ are preferable for reading high strain at high-strain rates. In order to reach a stress and strain field as homogeneous as possible, longer gage lengths than the gage radius must be taken. An L/D ratio of 1 seems to be a minimum (Ref 2). An L/D ratio of 2 is better.

References cited in this section

1. U.S. Lindholm, A. Nagy, G.R. Johnson, and J.M. Hoegfeldt, Large Strain, High Strain Rate Testing of Copper, *J. Eng. Mater. Technol. (Trans. ASME)*, Vol 102, 1980, p 376–381
2. K. Stiebler, Beitrag zum Fließverhalten der Stähle Ck35 und X2CoNiMnMoNNb211653 unter zweiachsiger dynamischer Belastung, Ph.D. thesis, RWTH Aachen, Germany, 1989

High Strain Rate Shear Testing

Torsional Impact Testing

Torsional impact loading methods have been used with a number of testing devices that were developed to test metals at strain rates up to about 10^3 s^{-1} (Ref 3, 4, 5, 6, 7). Early tests of this type used solid, round specimens. More recently, short, thin-walled tubular specimens in which nearly homogeneous stress and strain states can be achieved have been used.

The devices generally consist of a stationary supported specimen, initially uncoupled from the drive mechanism. The energy to deform the specimen is stored in a rotating flywheel and/or a drive shaft. The rotating system is brought to the desired angular velocity, and a release and engagement mechanism quickly couples the torsional load to the specimen.

Torsional impact systems require the following conditions:

- Alignment and concentricity of the specimen with the drive and engagement system
- Low inertia and high stiffness of the load train to minimize inertial effects and resonances during impact
- Adequate frequency response in the load-measuring and strain-measuring devices
- Sufficient energy in the drive system to maintain nearly constant strain rate in the test specimen during deformation

A typical torsional impact system is illustrated in Fig. 3. In this device, a commercial lathe bed and drive mechanism are utilized; however, the arrangement is typical of all torsional impact systems. The specimen is rotated in the chuck of the lathe, which has speeds from 500 to 2000 rpm. Other devices attach either the drive unit or the specimen to a flywheel, which is driven by a variable-speed motor. In either case, the drive unit is brought up to constant rotational speed before engagement of the specimen.

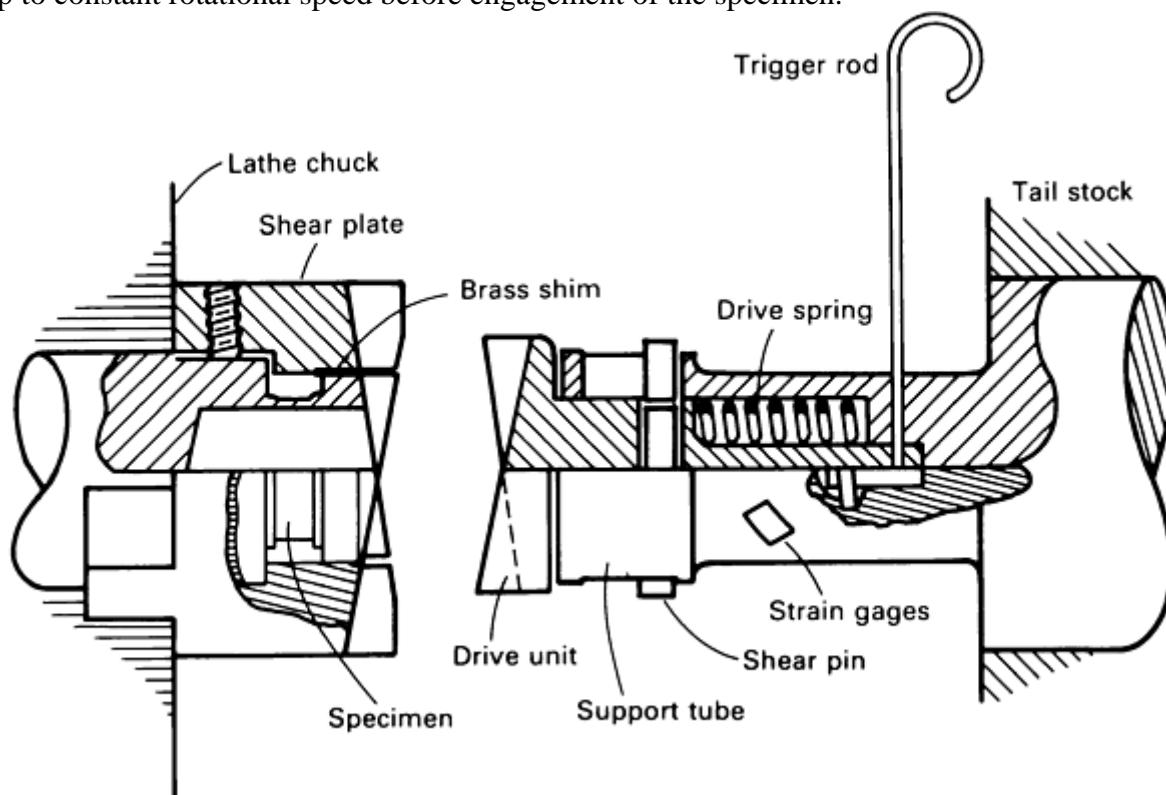


Fig. 3 Cross section of torsional impact machine. Source: Ref 4

When the rotational speed is established, a release mechanism (the trigger rod in Fig. 3) allows a compressed drive spring to engage the drive unit with the specimen by means of mated, tapered engagement beads. In the mechanical design of this type of device, alignment, coaxiality, and details of the engagement mechanism are important. An alternative to the arrangement in Fig. 3 consists of a stationary specimen and load cell and a rotating drive unit. Such an arrangement is described in Ref 4.

Torsional load is measured with a strain-gage elastic tubular element in the load train. The stiffness of this gage section should be as high as possible so that torsional resonances of the system induced by the impact on engagement do not produce excessive “ringing” in the load signal. These resonant frequencies are also governed by the total length of the load train between the rigid supports.

The mean shear strain rate, $\dot{\gamma}_m$, in the specimen is related to the angular velocity of the two ends of the specimen by:

$$\dot{\gamma}_m = \dot{\gamma}_a \frac{R_a + R_i}{2R_a}$$

where

$$\dot{\gamma}_a = \frac{Ra\dot{\theta}}{L} \quad (\text{Eq 1})$$

and where R_a and R_i are the outer and inner radii, respectively, and L is the length of the specimen gage section. Typical gage section dimensions are on the order of 3.2 mm (0.125 in.) in length, 6.4 mm (0.250 in.) in radius, and 0.76 mm (0.030 in.) in wall thickness. Thus, the shear strain rate is approximately twice the rotational speed of the drive mechanism.

Depending on the total angle of twist (θ) allowed, very large strains can be achieved, often in the range of $\gamma = 1$ to 5. Because such large strains generally are involved, the rotational velocity (either initial or transient) is used to determine strain rate (Eq 1) or strain. If the energy stored in the drive mechanism is large compared with the strain energy to deform the specimen, a nearly constant strain rate can be assumed to be proportional to the initial θ . Generally, direct strain measurements on the specimen are seldom made. Only Stiebler (Ref 2 and 3) has used strain gages; Meyer and Hahn have used strain gages as high-speed electro-optical devices. A photographic technique employing a drum camera to record the transient strain distribution in the specimen during deformation is described in Ref 4.

A significant aspect of dynamic torsion testing is the occurrence of plastic instabilities due to thermal feedback when the test conditions approach adiabatic deformation (Ref 2, 7, 8). For fully adiabatic conditions, the temperature rise, ΔT_a , in the specimen is given by:

$$\Delta T_a = \frac{k}{\rho C} \int_0^\gamma \tau d\gamma \quad (\text{Eq 2})$$

where τ and γ are the shear stress and strain, respectively; k is a proportionality constant (ratio of plastic work converted to thermal energy); ρ is density; and C is specific heat. Instability occurs when the thermal softening due to the adiabatic temperature rise overcomes the intrinsic strain-hardening capacity of the test material.

Observation of adiabatic shear instabilities in torsion test specimens are reported in Ref 2, 4, and 8. Depending on material properties and specimen geometry, such instabilities occur in the strain rate range from 10 to 10^3 s^{-1} . When instability occurs, sharp temperature and strain gradients may arise in the specimen. Transient measurement of these profiles is difficult, but post-test examination of the test specimen may reveal the existence of localized straining in the form of either deformation bands or, in some cases (e.g., steels), transformation bands (Ref 7, 8).

References cited in this section

2. K. Stiebler, Beitrag zum Fließverhalten der Stähle Ck35 und X2CoNiMnMoNNb211653 unter zweiachsiger dynamischer Belastung, Ph.D. thesis, RWTH Aachen, Germany, 1989
3. K. Stiebler, H.-D. Kunze, and E. El-Magd, Description of the Flow Behaviour of a High Strength Austenitic Steel under Biaxial Loading by a Constitutive Equation, *Nuclear Engineering and Design*, Vol 127, 1991
4. R.S. Culver, Torsional-Impact Apparatus, *Exp. Mech.*, Vol 12, 1972, p 398–405
5. C.E. Work and T.J. Dolan, The Influence of Strain Rate and Temperature on the Strength and Ductility of Mild Steel in Torsion, *Proc. ASTM*, Vol 53, 1953, p 611–626
6. N.G. Calvert, Impact Torsion Experiments, *Inst. Mech. Eng.*, Vol 169 (No. 44), 1955, p 897

7. R.S. Culver, Thermal Instability Strain in Dynamic Plastic Deformation, *Metallurgical Effects at High Strain Rates*, R.W. Rohde, B.M. Butcher, J.R. Holland, and C.H. Karnes, Ed., Plenum Press, 1973, p 519–530
8. U.S. Lindholm and G.R. Johnson, Strain-Rate Effects in Metals at Large Shear Strains, *Material Behavior under High Stress and Ultrahigh Loading Rates*, J. Mescall and V. Weiss, Ed., Plenum Press, 1983, p 61–79

High Strain Rate Shear Testing

Torsional Kolsky (Split-Hopkinson) Bar

The torsional Kolsky bar is a reliable apparatus for testing materials in the 10^2 to 10^4 s⁻¹ strain rate regime (Ref 9). In general, the torsional Kolsky bar is well suited for conducting quasi-static and incremental strain rate tests, as well as dynamic strain rate tests. Thus, strain rate and strain rate history studies can be conducted using the same apparatus, thereby eliminating differences in test apparatus as a source of error in determining these effects. In the torsional Kolsky bar, a dynamic strain rate can be superposed on the quasi-static strain rate so that unloading does not occur, and the stress and strain rate increments can be measured directly for greater accuracy (Ref 10).

As previously noted, testing materials in torsion has some advantages over axial loading due to the absence of Poisson's ratio effects and geometric dispersion. When a torsional pulse travels along an elastic bar in its primary mode, all its frequency components have the same velocity. Hence, a torsional pulse initiated either by explosive detonation or by the release of a stored torque does not change its shape as it propagates toward the specimen. In Kolsky bar experiments, the absence of geometric dispersion in torsion means that a pulse initiated with a short rise time will maintain this rise time until it reaches the specimen, independent of the length of the Kolsky bar. Also, the torsional strain gage stations can be located as near or as far from the specimen as desired and still reveal the correct-shaped pulse incident on or reflected from the specimen. In an axial Kolsky bar, however, a gage placed too close to the specimen is subject to errors due to three-dimensional end effects, while a gage placed too far from the specimen produces unsatisfactory results because of geometric dispersion.

There is, however, a disadvantage in a non-dispersive pulse. If a torsional pulse is noisy when initiated (i.e., if some high-frequency components are superposed on the main pulse), this characteristic will be maintained, regardless of the length of the Kolsky bar. As a result, the strain rate imposed on the specimen will not be constant. In an axial Kolsky bar, such high-frequency components gradually disappear. Hence, an axial pulse tends to become flat—that is, tends to smooth out—as it travels along an elastic bar. A noisy torsional pulse such as that associated with explosive initiation of the pulse (Ref 11) will retain this characteristic; it will never become flat and, hence, will not provide deformation at a constant strain rate. As a result, for explosive initiation of a torsional pulse, a mechanical filter or pulse smoother is required to eliminate the high-frequency components. This type of device usually is not required when the torsional pulse is initiated by the stored-torque technique, because the amplitude is constant.

Torsional split-Hopkinson bar testing is described in more detail in the article “Torsional Kolsky Bar Testing” in this Volume. As in the case of pressure bar testing, values of torsional stress and strain in the specimen can be inferred from the measured records of the torsional strain in the incident and transmitter bars. These relations, which were first derived by Kolsky for the axial bar, can be transposed to shear values. In accordance with the analysis of Kolsky, the reflected pulse in a torsion bar provides a measure of the shear strain rate in the specimen $\dot{\gamma}(t)$ and, through a single integration, provides the shear strain in the specimen, $\gamma_s(t)$. The shear strain in the specimen is given by the difference in rotation between its two ends divided by its length:

$$\gamma_s = \frac{D_s\phi_1 - D_s\phi_2}{2L_s} \quad (\text{Eq 3})$$

where ϕ_1 and ϕ_2 are the angles of twist in the incident and transmitter bars, respectively; D_s is the mean diameter of the thin-walled specimen; and L_s is its length. The value of ϕ_2 can be determined from the shear strain measured at the surface of the transmitter bar through:

$$\gamma_T = \frac{D}{2} \frac{\partial \phi_2}{\partial x} = \frac{D}{2c} \frac{\partial \phi_2}{\partial t}$$

where D is the diameter of the Kolsky bar, and $c = \sqrt{G/\rho}$ is the torsional velocity in the Kolsky bar. As a result:

$$\phi_2 = \frac{2c}{D} \int_0^t \gamma_T(t) dt \quad (\text{Eq 4})$$

Similarly, ϕ_1 can be determined from the difference in strains due to the incident and reflected pulses:

$$\phi_1 = \frac{2c}{D} \int_0^t [\gamma_I(t) - \gamma_R(t)] dt \quad (\text{Eq 5})$$

where the negative sign is necessary because the reflected pulse travels in the $-x$ direction. If Eq 3 is differentiated and Eq 4 and 5 are utilized:

$$\dot{\gamma}_s(t) = \frac{c}{L_s} \frac{D_s}{D} [\dot{\gamma}_T(t) - \{\dot{\gamma}_I(t) - \dot{\gamma}_R(t)\}] \quad (\text{Eq 6})$$

where the strains are all functions of time. For a homogenous state of strain in the specimen, the transmitted pulse is the difference between the incident and reflected pulses, so that $\gamma_T = \gamma_I - (-\gamma_R)$ and hence:

$$\dot{\gamma}_s(t) = \frac{2cD_s}{L_s D} \dot{\gamma}_R(t) \quad (\text{Eq 7})$$

Because $\dot{\gamma}_R$ is determined from the output of the strain gages on the incident bar during passage of the reflected pulse and because all other quantities in Eq 7 are known, it provides a measure of the strain rate in the specimen as a function of time. The signal is integrated electronically to yield $\gamma_s(t)$, which is the strain in the specimen. Kolsky also showed that the transmitted pulse provides a direct measure of the average shear stress in the specimen, $\tau_s(t)$. For a thin-walled tube in torsion, the stress is given by:

$$\tau_s = \frac{2T_s}{(\pi D_s^2) t_s} \quad (\text{Eq 8})$$

where t_s is the wall thickness, and T_s is the average torque. The average torque in the specimen is also given by the average of the torques at each of its ends:

$$T_s = \frac{1}{2}(T_1 + T_2) \quad (\text{Eq 9})$$

where T_1 is the torque at the interface with the incident bar, and T_2 is the torque at the interface with the transmitter bar. The former is given in terms of the strain at the surface of the bar—that is, by the strain in the incident and reflected pulses—by $T_1 = G(\gamma_I + \gamma_R)\pi D^3/16$. For the homogeneous state of stress in the specimen, $\gamma_I + \gamma_R \approx \gamma_T$ so that:

$$\tau_s(t) = \frac{GD^3}{8} \frac{\dot{\gamma}_T(t)}{D_s^2 t_s} \quad (\text{Eq 10})$$

Thus, Eq 7 and 10 provide stress and strain in the specimen as functions of time. Eliminating time yields the stress-strain curve for the material at the strain rate provided through Eq 7.

References cited in this section

9. K.A. Hartley, J. Duffy, and R.H. Hawley, The Torsional Kolsky (Split-Hopkinson) Bar, *Mechanical Testing*, Vol 8, *Metals Handbook*, 9th ed., American Society for Metals, 1985, p 218–230
10. R.A. Frantz and J. Duffy, The Dynamic Stress-Strain Behavior in Torsion of 1100-O Aluminum Subjected to a Sharp Increase in Strain Rate, *J. Appl. Mech.*, Vol 39, 1972, p 939–945

11. J. Duffy, J.D. Campbell, and R.H. Hawley, On the Use of a Torsional Split Hopkinson Bar to Study Rate Effects in 1100-O Aluminum, *J. Appl. Mech.*, Vol 38, 1971, p 83–91

High Strain Rate Shear Testing

Double-Notch Shear Testing and Punch Loading

Kolsky or split-Hopkinson bar testing in compression, tension, or torsion is governed by an upper limit (on the strain rate that can be achieved) of approximately 3000 s^{-1} . However, situations arise where strain rates of several orders of magnitude greater than this limit are expected, such as in high-speed metal forming operations or around rapidly propagating cracks. Attempts have thus been made to modify the Kolsky bar technique for use at strain rates in this range.

The most common method involves a drastic reduction in the effective gage length of the specimen, either by the use of a miniaturized version of the Kolsky bar, which is generally associated with an increase in the velocity of impact (Ref 12, 13, and 14), or by the use of specialized specimen designs. Two examples of specialized specimen designs are the double-notch shear test and the high-speed punching test. In both, the specimen material is subjected to a high rate of shear.

References cited in this section

12. U.S. Lindholm, Deformation Maps in the Region of High Dislocation Velocity, *High Velocity Deformation of Solids*, K. Kawata and J. Shioiri, Ed., International Union of Theoretical and Applied Mechanics Symposium, Springer-Verlag, Berlin, 1978
13. G.L. Wulf, Dynamic Stress-Strain Measurements at Large Strains, *Mechanical Properties at High Rates of Strain*, J. Harding, Ed., Institute of Physics Conf. Series (No. 21), 1974, p 48–52
14. D.A. Gorham, Measurement of Stress-Strain Properties of Strong Metals at Very High Rates of Strain, *Mechanical Properties at High Rates of Strain*, J. Harding, Ed., Institute of Physics Conf. Series (No. 47), 1979, p 16

High Strain Rate Shear Testing

Double-Notch Shear Testing

In double-notch shear testing, the output bar is replaced by a tube into which the input bar can slide (Fig. 4). The lower end of the input bar and the upper end of the output tube are slotted to accommodate the thin plate specimen (see Fig. 5) into which two pairs of notches have been cut. With an effective gage length in this specimen of 0.84 mm (0.033 in.), a maximum shear strain rate of $40,000 \text{ s}^{-1}$, an order of magnitude greater than that reached in the standard Kolsky bar apparatus, has been achieved (Ref 15, 16).

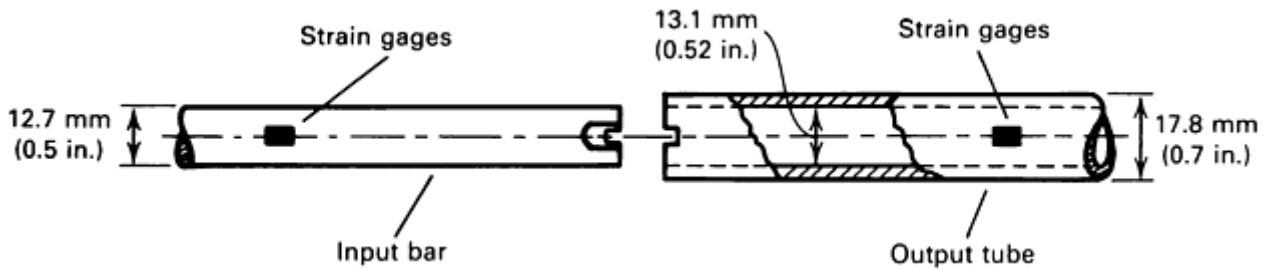


Fig. 4 Kolsky bar apparatus for double-notch shear testing at very high strain rates

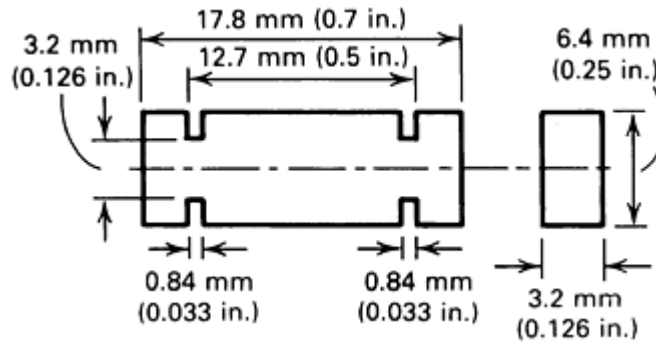


Fig. 5 Double-notch shear specimen

The principal disadvantage of this technique is that at shear strains greater than about 20%, the specimen ceases to deform in pure shear. Reliable results can only be obtained at relatively low values of shear strain (Ref 17). Because about 20 μ s are required for a constant strain rate to become established, results obtained at low strains can only be associated with an average value of strain rate.

References cited in this section

15. W.G. Ferguson, J.E. Hauser, and J.E. Dorn, The Dynamic Punching of Metals, Dislocation Damping in Zinc Single Crystals, *Brit. J. Appl. Phys.*, Vol 18, 1967, p 411–417
16. J.D. Campbell and W.G. Ferguson, The Temperature and Strain Rate Dependence of Shear Strength of Mild Steel, *Philos. Mag.*, Vol 21, 1970, p 63–82
17. J. Harding and J. Huddart, The Use of the Double-Notch Shear Test in Determining the Mechanical Properties of Uranium at Very High Rates of Strain, *Proc. 2nd International Conf. Mechanical Properties at High Rates of Strain*, J. Harding, Ed., The Institute of Physics, London, 1979, p 49–61

High Strain Rate Shear Testing

Punch Loading

This version of the Kolsky bar is similar to the modification described above. In punch loading, however, the specimen is a flat plate in which a circular hole is punched. A typical setup is shown in Fig. 6. Although the clearance between the punch bar and the die tube is about 0.025 mm (0.001 in.) in Fig. 6, the effective gage length—that is, the width of the shear zone in an actual test specimen—was found to be considerably greater. The width of the shear zone is not very clearly defined, so in this case the quoted shear strains and strain rates are only approximate. Estimates of the effective gage width for the test may be made by optical microscopy with microhardness traverses across the shear zone or by comparing a derived shear stress/shear strain curve

based on an assumed gage width with the results of a conventional torsion test at a similar strain rates. Using this technique, shear strain rates in excess of 10^4 s^{-1} have been obtained (Ref 18).

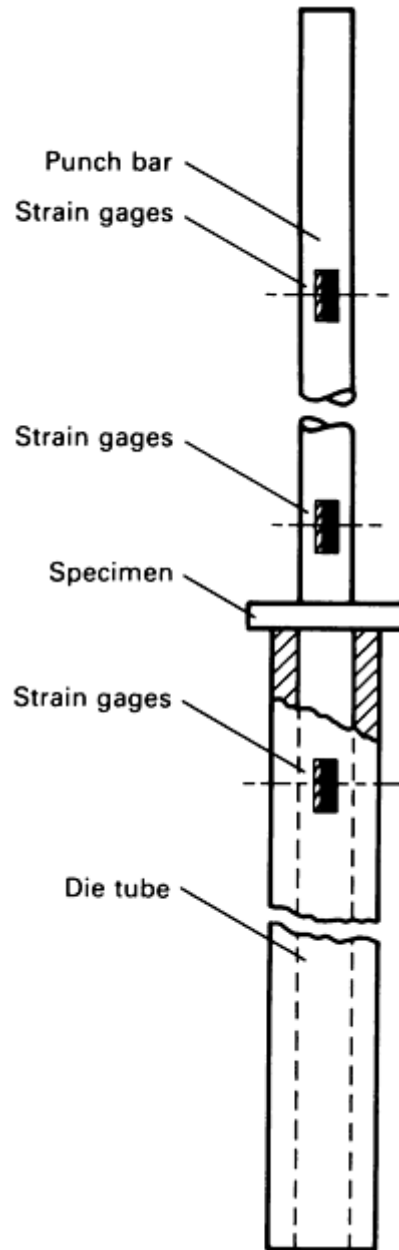


Fig. 6 Punch-loading Kolsky bar apparatus

Reference cited in this section

18. A.R. Dowling, J. Harding, and J.D. Campbell, The Dynamic Punching of Metals, *J. Inst. Metals*, Vol 98, 1970, p 215–224

High Strain Rate Shear Testing

Shear Testing with Hat-Shaped Specimen

L.W. Meyer and L. Krüger, Materials and Impact Engineering at Technical University Chemnitz and Nordmetall GbR, Germany

A special type of shear test configuration involves the use of a hat-shaped specimen to evaluate shear deformation and failure of metallic materials from high shear deformation at high strain rates (Ref 19, 20, 21, 22, 23, 24, 25, 26 27, 28, 29, 30). In this method, the material is forced to shear when a hat-shaped specimen is compressed in a Hopkinson bar or drop-weight machine. Depending on the material properties, broad or narrow shear areas develop, which may lead to a localization or concentrated adiabatic shear failure. The main advantage is that the shear tests can be stopped at any point of deformation, and the subsequent microstructures developed can be investigated in detail (Ref 21, 22, 23, 24, 25, 26, 27, and 28). Shear stress and work of deformation can also be estimated, because the force and displacement during shearing are measured (Ref 30, 31).

References cited in this section

19. K.-H. Hartmann, H.D. Kunze, and L.W. Meyer, Metallurgical Effects on Impact Loaded Materials, *Shock Wave and High-Strain-Rate Phenomena in Metals*, M.A. Meyers and L.E. Murr, Ed., Plenum Press, 1981, p 325–337
20. L.W. Meyer and S. Manwaring, Critical Adiabatic Shear Strength of Low Alloyed Steel under Compressive Loading, *Metallurgical Applications of Shock Wave and High-Strain-Rate Phenomena*, L.E. Murr, K.P. Staudhammer, and M.A. Meyers, Ed., Marcell Dekker, 1986, p 657–674
21. J.A. Hines and K.S. Vecchio, Dynamic Recrystallization in Adiabatic Shear Bands in Shock-Loaded Copper, *Metallurgical and Materials Application of Shock Wave and High-Strain-Rate Phenomena*, L.E. Murr, K.P. Staudhammer, and M.A. Meyers, Ed., Elsevier Science B.V., 1995, p 421–428
22. F.D.S. Marquis, M.A. Meyers, Y.J. Chen, and D.S. Kim, High-Strain, High-Strain-Rate Of Tantalum, *Metall. Mater. Trans. A, Physical Metallurgy and Materials Science*, Vol 26 (No. 10), 1995, p 2493–2501
23. S. Nemat-Nasser, Y.-F. Li, and J.B. Isaacs, Experimental/Computational Evaluation of Flow Stress at High Strain Rates with Application to Adiabatic Shear Banding, *Mech. Mater.*, Vol 17 (No. 2–3), 1994, p 111–134
24. R.W. Chen and K.S. Vecchio, Microstructural Characterization of Shear Band Formation in Al-Li Alloys, *J. Physique IV (France)*, tome 4, Coll. C8, 1994, p 459–463
25. U. Andrade, “High-Strain, High-Strain-Rate Deformation of Copper,” Ph.D. thesis, University of California, San Diego, 1993
26. M.A. Meyers, L.W. Meyer, J. Beatty, U. Andrade, K.S. Vecchio, and A.H. Chokshi, High Strain, High-Strain Rate Deformation of Copper, *Shock Wave and High-Strain-Rate Phenomena in Materials*, M.A. Meyers, L.E. Murr, and K.P. Staudhammer, Ed., Marcel Dekker, 1992, p 529–542
27. M.A. Meyers, G. Subhash, B.K. Kad, and L. Prasad, Evolution of Microstructure and Shear-Band Formation in α -hcp Titanium, *Mech. Mater.*, Vol 17 (No. 2–3), 1994, p 175–193
28. M.A. Meyers, Y.-J. Chen, F.D.S. Marquis, and D.S. Kim, High-Strain, High-Strain-Rate Behavior of Tantalum, *Metall. Mater. Trans. A*, Vol 26, Oct 1995, p 2493–2501
29. L.W. Meyer and A. Schrödter, Mechanical Reduction of Oscillations on a Split Hopkinson Bar—A Simple, but Efficient Method for High Strain Rate Material Testing, *ACAM*, Canberra, ISBN 0-7334-0558-4, 1999

30. J.H. Beatty, L.W. Meyer, M.A. Meyers, and S. Nemat-Nasser, Formation of Controlled Adiabatic Shear Bands in AISI 4340 High Strength Steel, *Shock Wave and High-Strain-Rate Phenomena in Materials*, M.A. Meyers, L.E. Murr, and K.P. Staudhammer, Ed., Marcel Dekker, 1992, p 645–656
31. S. Nemat-Nasser, J.B. Isaacs, and J. Starrett, Hopkinson Techniques for Dynamic Recovery Experiments, *Proc. R. Soc. (London) A*, Vol 435, 1991, p 371–391

High Strain Rate Shear Testing

Test Setup and Operation

The test setup (Fig. 7a) (Ref 19, 30) is a specimen placed between the input and output bars. To reduce ringing effects during the shear test, a small lead or copper disc of 3 to 5 mm (0.12 to 0.20 in.) in diameter and 0.25 to 0.5 mm (0.01 to 0.02 in.) thickness is placed in between the striker bar and the input bar (Fig. 7b). This creates a trapezoidal or ramp-shaped input wave, which reduces the Pochhammer-Chree ringing (Ref 29, 30). The force applied to the sample is measured by strain gages on the output bar, and specimen displacement is measured with a precise high-speed electrooptical camera system. The force-time ($F-t$) and displacement-time ($s-t$) signals are recorded, and stress measurements are calculated from the transmitted and reflected elastic waves in the bars.

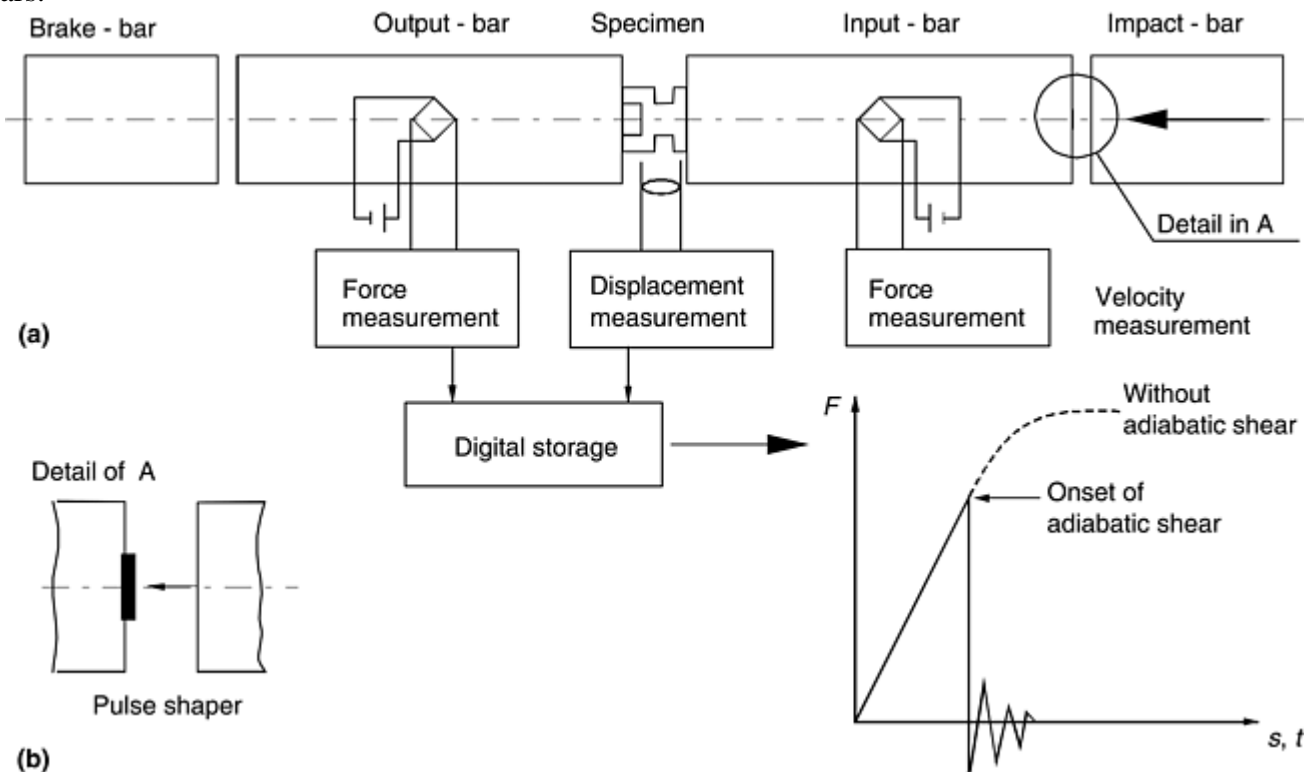


Fig. 7 Test setup for shear testing with hat-shaped specimen. (a) Specimen placed between input and output bar. (b) Detail of pulse shaper

Test Specimen. The specimen is machined from one piece in a cylindrical form and consists essentially of a tube on one side and a bar on the other side (Fig. 8). The region between the tube and bar section is the shear area (Fig. 8). To investigate the development of the shear-band formation and to stop the shear displacement at any desired stage, it is beneficial to use spacer rings of different thicknesses while testing (Fig. 9). This use of spacer rings allows the manufacturing of one fixed (or standard) specimen geometry for different test levels of shear displacement. Regarding the thickness of the spacer rings and the cut in width of the hat-shaped specimen

(E in Fig. 8), the possible shear displacement (Δs) is predetermined before the test. The advantage of this geometry and testing procedure is the symmetry in the left and right regions of the shear zone. Without the same properties of the material and the same geometry, the shear stresses inside and around the shear zone would have an asymmetrical distribution (Ref 32).

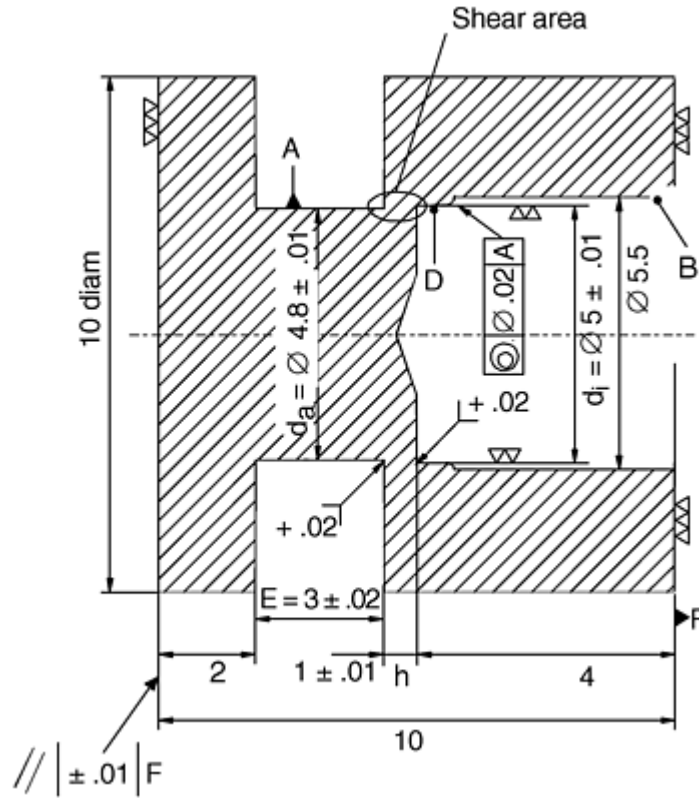


Fig. 8 Hat-shaped specimen to produce shear deformation under axial compression loading. All dimensions are in millimeters.

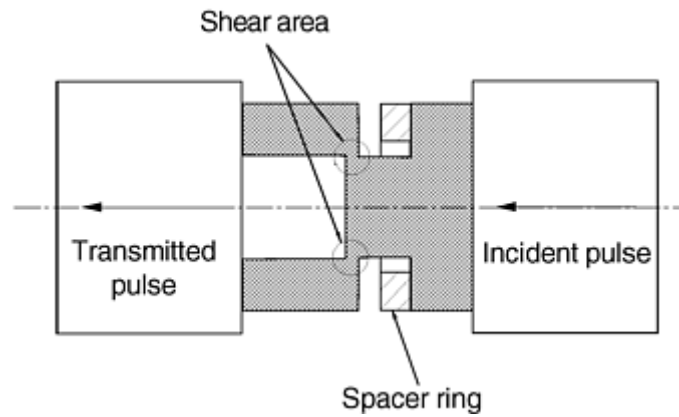


Fig. 9 Detail of loading with spacer ring for controlled shear displacement

The stress state in the plastic deformation region is fairly close to simple shear, and plastic strain is approximately equal to the ratio between the shear displacement and the thickness of the plastically deformed band. The stress pulse, produced by impacting the incident bar, generates controlled plastic shear deformation in the shear area (Fig. 9), while the rest of the specimen undergoes elastic deformation. The mean shear stress, τ , is estimated by the force, F , divided by the area of resisting shearing:

$$\tau = \frac{F}{\pi h \left(\frac{d_i + d_e}{2} \right)}$$

where d_i and d_e are the internal and external diameter, respectively, and h is the height of the area of the shear zone in the axial direction (Ref 27).

The shear strain γ can be determined from the ratio of the controlled displacement, δ , and the width of the shear band, x :

$$\gamma = \frac{\delta}{x}$$

and as shown by Andrade (Ref 25), the shear strain γ can be related to the uniaxial strain (Ref 33):

$$\varepsilon = \ln \left(\frac{\gamma^2}{2} + \gamma + 1 \right)^{1/2}$$

Using this test setup, it is possible to study microstructural changes just before and just after the initiation of the instability, even in the range of $\Delta s/h$ displacement ratios on the order of a hundred or more (Ref 19, 26, 27, 31). The onset of localized deformation is evident from the drop in the shear stress displacement diagram. This is shown schematically in the output graph in Fig. 10. Depending on the properties of materials, the drop may be very sharp (Fig. 10) or may be less sudden (Fig. 11). The influence of strain rate on strength and deformability under hat-shaped configurations is shown in Fig. 10. The statically loaded material exhibits a deformability of about 0.5 mm or 50% shear strain. Under dynamic loading in the same geometry, the deformability is reduced to low amounts (about 10% of the static values). In general, this can be interpreted as a velocity-induced “embrittlement,” expressed by the drastic reduction of energy absorption. Locally, very high shear strains are observed, and the shear strain rates are evaluated by means of micrographs of the measured thickness of the shear zones and the velocity of shear displacements. For the CrMoV steel, a strain rate $\dot{\varepsilon} = 10^5 - 10^6 \text{ s}^{-1}$ within shear band widths of approximately 5 to 10 μm is calculated.

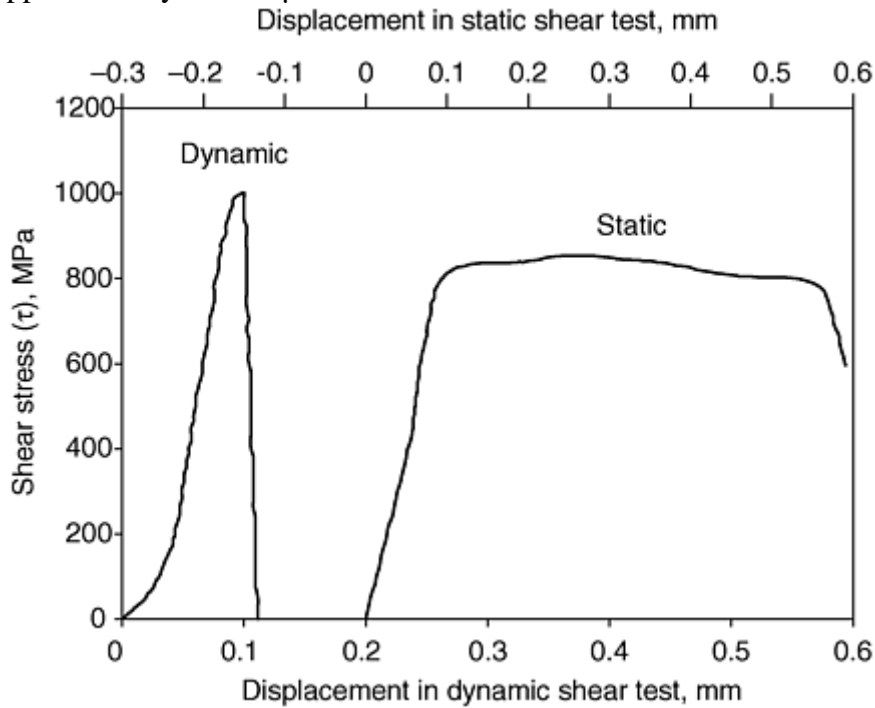


Fig. 10 Shear stress-displacement diagram for a CrMoV steel under dynamic and quasi-static loading. Source: Ref 19

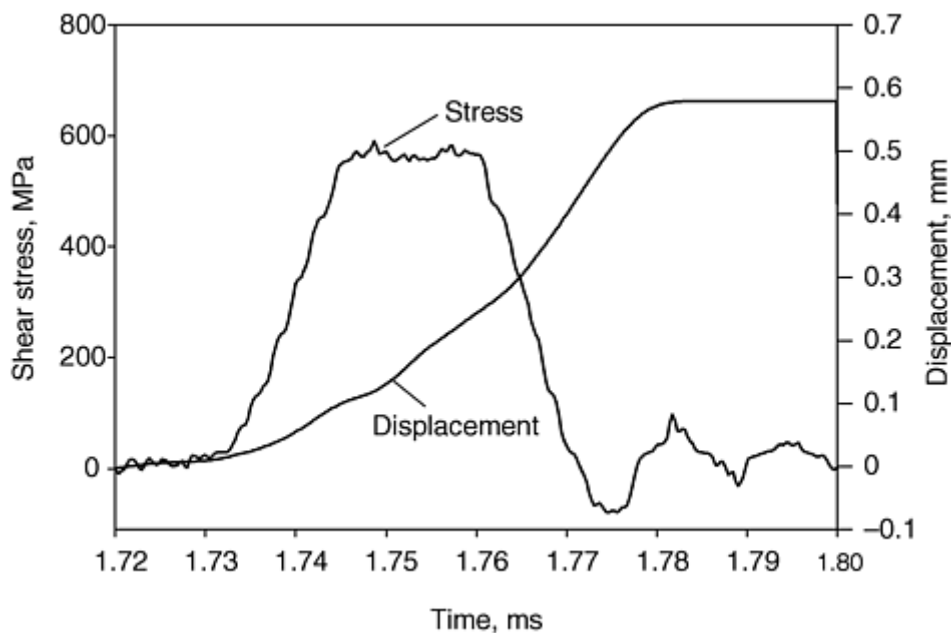


Fig. 11 Shear stress and displacement versus time for rolled homogeneous armor steel

References cited in this section

19. K.-H. Hartmann, H.D. Kunze, and L.W. Meyer, Metallurgical Effects on Impact Loaded Materials, *Shock Wave and High-Strain-Rate Phenomena in Metals*, M.A. Meyers and L.E. Murr, Ed., Plenum Press, 1981, p 325–337
25. U. Andrade, “High-Strain, High-Strain-Rate Deformation of Copper,” Ph.D. thesis, University of California, San Diego, 1993
26. M.A. Meyers, L.W. Meyer, J. Beatty, U. Andrade, K.S. Vecchio, and A.H. Chokshi, High Strain, High-Strain Rate Deformation of Copper, *Shock Wave and High-Strain-Rate Phenomena in Materials*, M.A. Meyers, L.E. Murr, and K.P. Staudhammer, Ed., Marcel Dekker, 1992, p 529–542
27. M.A. Meyers, G. Subhash, B.K. Kad, and L. Prasad, Evolution of Microstructure and Shear-Band Formation in α -hcp Titanium, *Mech. Mater.*, Vol 17 (No. 2–3), 1994, p 175–193
29. L.W. Meyer and A. Schrödter, Mechanical Reduction of Oscillations on a Split Hopkinson Bar—A Simple, but Efficient Method for High Strain Rate Material Testing, *ACAM*, Canberra, ISBN 0-7334-0558-4, 1999
30. J.H. Beatty, L.W. Meyer, M.A. Meyers, and S. Nemat-Nasser, Formation of Controlled Adiabatic Shear Bands in AISI 4340 High Strength Steel, *Shock Wave and High-Strain-Rate Phenomena in Materials*, M.A. Meyers, L.E. Murr, and K.P. Staudhammer, Ed., Marcel Dekker, 1992, p 645–656
31. S. Nemat-Nasser, J.B. Isaacs, and J. Starrett, Hopkinson Techniques for Dynamic Recovery Experiments, *Proc. R. Soc. (London) A*, Vol 435, 1991, p 371–391
32. T. Pintat, Ph.D. thesis, University Bremen, Germany, 1993
33. M.A. Meyers, U.R. Andrade, and A.H. Chokshi, The Effect of Grain Size on the High-Strain, High-Strain-Rate Behavior of Copper, *Metall. Mater. Trans. A*, Vol 26, Nov 1995, p 2881–2893

Analysis of Shear Zones

The hat-shaped specimen is a suitable configuration to investigate the evolved microstructure and to compare materials under shear loading. For example, Pintat et al. (Ref 34, 35) analyzed the influence of predeformation and grain size on the work of deformation during shearing of two plain carbon steels (Ck 10, Ck 45) with 0.1 and 0.45 wt% C content. The energy consumption of the shear process was estimated by the integral of the force/displacement curve. With increasing predeformation or strain rate, the shear failure occurred at minor displacements, limiting the absorbed work of deformation. Furthermore, the work of deformation decreases with increasing shear rate.

Many investigators have also used this specimen to investigate the hardness, size, and shape of shear zones in different materials (e.g., Fig. 12) and the change in microstructure during shearing (Ref 21, 23, 31, 34, 36, and 37). For example, Beatty et al. (Ref 31) showed that 4340 steels with the same hardness but different distributions of carbon absorb varying amounts of energy. They analyzed adiabatic shear bands in 4340 steel, finding a structure of a large number of micrograins with grain sizes between 10 and 50 nm (Ref 31).

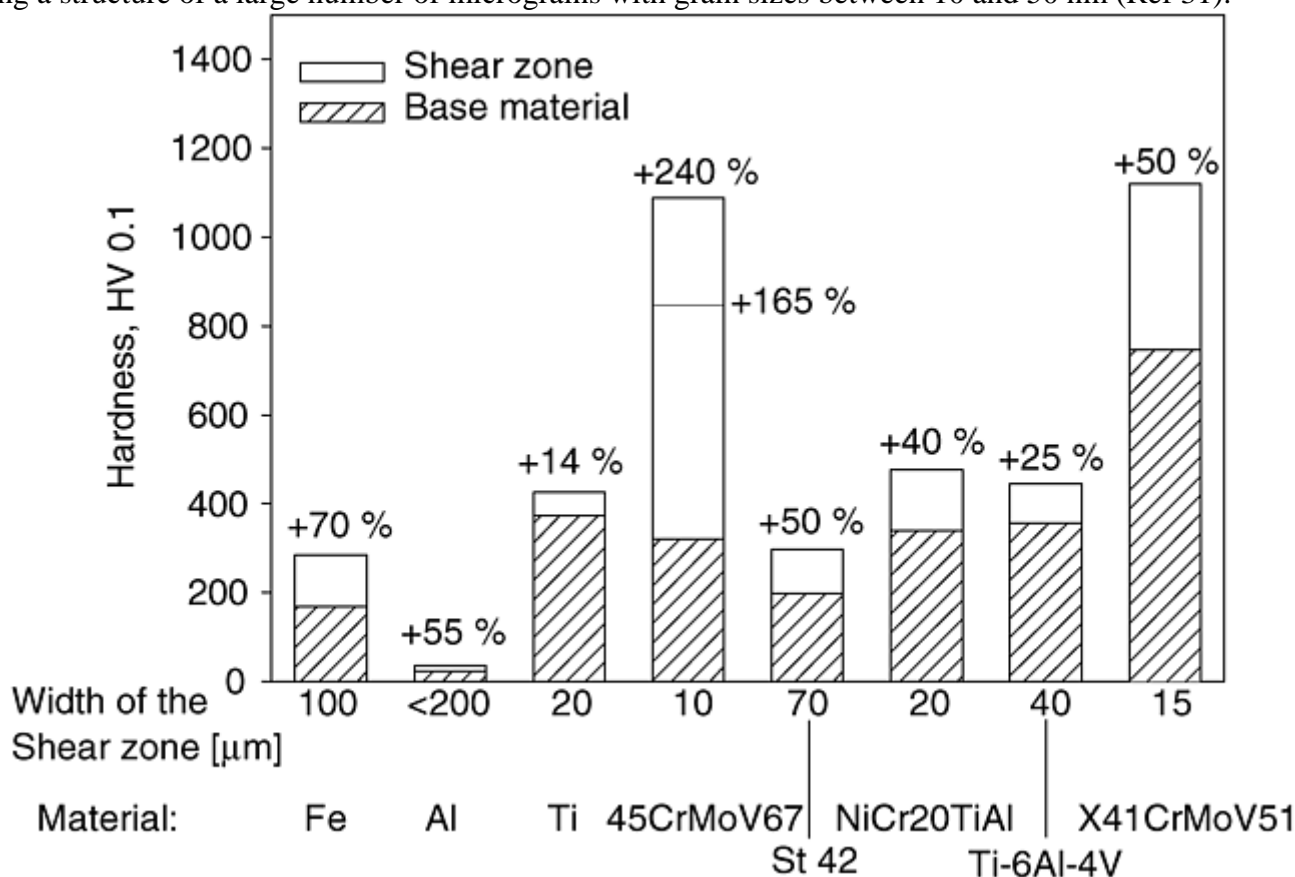


Fig. 12 Hardness of base material and hardness and width of shear bands for different materials. Source: Ref 34

References cited in this section

21. J.A. Hines and K.S. Vecchio, Dynamic Recrystallization in Adiabatic Shear Bands in Shock-Loaded Copper, *Metallurgical and Materials Application of Shock Wave and High-Strain-Rate Phenomena*, L.E. Murr, K.P. Staudhammer, and M.A. Meyers, Ed., Elsevier Science B.V., 1995, p 421–428

23. S. Nemat-Nasser, Y.-F. Li, and J.B. Isaacs, Experimental/Computational Evaluation of Flow Stress at High Strain Rates with Application to Adiabatic Shear Banding, *Mech. Mater.*, Vol 17 (No. 2–3), 1994, p 111–134
31. S. Nemat-Nasser, J.B. Isaacs, and J. Starrett, Hopkinson Techniques for Dynamic Recovery Experiments, *Proc. R. Soc. (London) A*, Vol 435, 1991, p 371–391
34. T. Pintat, L.W. Meyer, and H. Schrader, Properties of Inhomogeneous Shear Zones in Different Materials, *J. Phys., Coll. C5*, 1985
35. T. Pintat, B. Scholz, H.D. Kunze, and O. Vöhringer, The Influence of Carbon Content and Grain Size on Energy Consumption during Adiabatic Shearing, *J. Phys., Coll. C3*, 1988, p 237–244
36. M.A. Meyers, L.W. Meyer, K.S. Vecchio, and U. Andrade, High Strain, High-Strain Rate Deformation of Copper, *J. Phys. (France) IV, Coll. C3*, 1991, p 11–17
37. K. Minnaar and M. Zhou, An Analysis of the Dynamic Shear Failure Resistance of Structural Metals, *J. Mech. Phys. Solids*, Vol 46 (No. 10), 1998, p 2155–2170

High Strain Rate Shear Testing

Drop-Weight Compression Shear Testing

L.W. Meyer and L. Krüger, Materials and Impact Engineering at Technical University Chemnitz and Nordmetall GbR, Germany

The distribution of stress and strains in materials is often inhomogeneous when materials are subjected to high strain rates and strains in various situations such as high-speed cutting, forging processes, ballistic impact, and crash behavior of structures. These very complex loading conditions at high strain rates may lead to localized regions of increased shear deformation (Fig. 13); when heat cannot be dissipated at high strain rates, adiabatic shear bands may develop, depending on the strain rate and the thermal properties of a material. For example, titanium alloys are very susceptible to adiabatic shear failure even under uniaxial dynamic compression loading. In contrast, sintered or sintered and swaged tungsten alloys are less sensitive to adiabatic shear failure (Ref 38), although shear localizations are observed in the tip of tungsten penetrators. Thus, conditions exist where even tungsten alloys may fail by adiabatic shear.

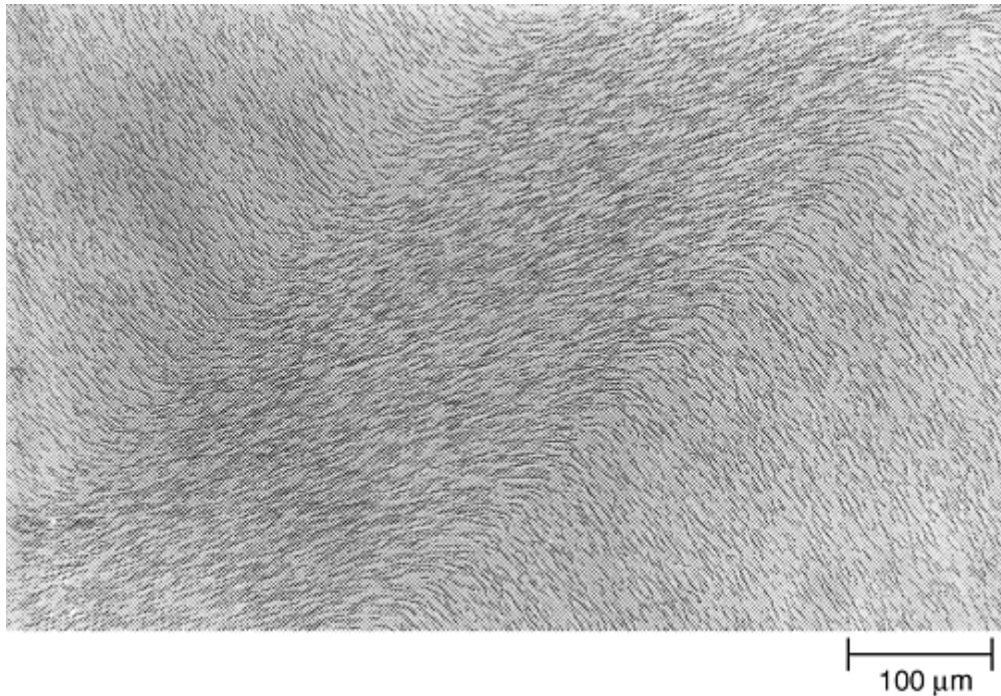


Fig. 13 Localized shear deformation band in tungsten alloy W90

The susceptibility to adiabatic shear failure under pure shear loads can be examined by dynamic torsion tests on tube specimens (Ref 39, 40, 41, 42) and shear tests using hat-shaped specimens (Ref 19, 21, 22, 23, 24, 25, 26, 27, 28, 31, 32, 33, 34, 35, 36, 43, 44, and 45). The torsion test allows the determination of stresses, shear strains, and strain rate conditions in a thin cross section at the initiation of adiabatic shear failure. The hat-shaped specimen method, as previously described in this article, has the advantage of applying very high strains and very high strain rates and, by geometry, can produce narrow shear bands, even in materials not susceptible to shear band formation. The disadvantage of the hat-shaped specimen method is that the stress concentration at both sides of the shear plane prevents a local stress determination.

It is also known that adiabatic shear failure occurs in uniaxial compression tests (Ref 46, 47, 48). This is observed mostly in high-strength materials like thermomechanically treated steels, titanium alloys, or ultrahigh-strength steels. Additionally, in most impact applications, pure shear or compression stress states are few. This leads to a necessity for biaxial dynamic loading systems that allow reproducible experiments under defined stress conditions of solid specimens instead of thin tubes (Ref 49, 50, and 51). This approach has been developed based on drop-weight testing with high strain rates as a way to evaluate the materials sensitivity or susceptibility for adiabatic shear failures. The advantage of the drop-weight testing (in contrast to typical Hopkinson setups) is that large amounts of stored energy can be applied, so that the strain-rate history is not influenced by the strain hardening of the test material under compressive and compression/shear loading. The drop-weight method also allows high strain testing of $\frac{3}{4}$ in. (20 mm) cross sections, even of high-strength materials. This may be of interest if there are geometry-dependent gradients in the hardness or stress-strain behavior.

References cited in this section

19. K.-H. Hartmann, H.D. Kunze, and L.W. Meyer, Metallurgical Effects on Impact Loaded Materials, *Shock Wave and High-Strain-Rate Phenomena in Metals*, M.A. Meyers and L.E. Murr, Ed., Plenum Press, 1981, p 325–337
21. J.A. Hines and K.S. Vecchio, Dynamic Recrystallization in Adiabatic Shear Bands in Shock-Loaded Copper, *Metallurgical and Materials Application of Shock Wave and High-Strain-Rate Phenomena*, L.E. Murr, K.P. Staudhammer, and M.A. Meyers, Ed., Elsevier Science B.V., 1995, p 421–428

22. F.D.S. Marquis, M.A. Meyers, Y.J. Chen, and D.S. Kim, High-Strain, High-Strain-Rate Of Tantalum, *Metall. Mater. Trans. A*, Physical Metallurgy and Materials Science, Vol 26 (No. 10), 1995, p 2493–2501
23. S. Nemat-Nasser, Y.-F. Li, and J.B. Isaacs, Experimental/Computational Evaluation of Flow Stress at High Strain Rates with Application to Adiabatic Shear Banding, *Mech. Mater.*, Vol 17 (No. 2–3), 1994, p 111–134
24. R.W. Chen and K.S. Vecchio, Microstructural Characterization of Shear Band Formation in Al-Li Alloys, *J. Physique IV (France)*, tome 4, Coll. C8, 1994, p 459–463
25. U. Andrade, “High-Strain, High-Strain-Rate Deformation of Copper,” Ph.D. thesis, University of California, San Diego, 1993
26. M.A. Meyers, L.W. Meyer, J. Beatty, U. Andrade, K.S. Vecchio, and A.H. Chokshi, High Strain, High-Strain Rate Deformation of Copper, *Shock Wave and High-Strain-Rate Phenomena in Materials*, M.A. Meyers, L.E. Murr, and K.P. Staudhammer, Ed., Marcel Dekker, 1992, p 529–542
27. M.A. Meyers, G. Subhash, B.K. Kad, and L. Prasad, Evolution of Microstructure and Shear-Band Formation in α -hcp Titanium, *Mech. Mater.*, Vol 17 (No. 2–3), 1994, p 175–193
28. M.A. Meyers, Y.-J. Chen, F.D.S. Marquis, and D.S. Kim, High-Strain, High-Strain-Rate Behavior of Tantalum, *Metall. Mater. Trans. A*, Vol 26, Oct 1995, p 2493–2501
31. S. Nemat-Nasser, J.B. Isaacs, and J. Starrett, Hopkinson Techniques for Dynamic Recovery Experiments, *Proc. R. Soc. (London) A*, Vol 435, 1991, p 371–391
32. T. Pintat, Ph.D. thesis, University Bremen, Germany, 1993
33. M.A. Meyers, U.R. Andrade, and A.H. Chokshi, The Effect of Grain Size on the High-Strain, High-Strain-Rate Behavior of Copper, *Metall. Mater. Trans. A*, Vol 26, Nov 1995, p 2881–2893
34. T. Pintat, L.W. Meyer, and H. Schrader, Properties of Inhomogeneous Shear Zones in Different Materials, *J. Phys.*, Coll. C5, 1985
35. T. Pintat, B. Scholz, H.D. Kunze, and O. Vöhringer, The Influence of Carbon Content and Grain Size on Energy Consumption during Adiabatic Shearing, *J. Phys.*, Coll. C3, 1988, p 237–244
36. M.A. Meyers, L.W. Meyer, K.S. Vecchio, and U. Andrade, High Strain, High-Strain Rate Deformation of Copper, *J. Phys. (France) IV*, Coll. C3, 1991, p 11–17
38. L.W. Myer, F.-J. Behler, K. Frank, and L.S. Magness, Interdependencies between the Dynamic Mechanical Properties and the Ballistic Behaviour of Materials, *Proc. of the 12th International Symposium on Ballistics*, Vol 1, p 419–428
39. L.S. Costin, E.E. Crisman, R.H. Hawley, and J. Duffy, On the Localization of Plastic Flow in Mild Steel Tubes under Dynamic Torsional Loading, *Mechanical Properties at High Rate of Strain*, Institute of Physics Conf. Series (No. 47), J. Harding, Ed., 1979, p 90–100
40. J.H. Giovanola, Observation of Adiabatic Shear Banding in Simple Torsion, *Impact Loading and Dynamic Behaviour of Materials*, C.Y. Chiem, H.-D. Kunze, and L.W. Meyer, Ed., DGM Informationsgesellschaft, Oberursel, 1988, p 705–710

41. J. Duffy, Experimental Studies of Shear Band Formation Through Temperature Measurements and High Speed Photography, *Proc. 3rd International Conf. on Mechanical and Physical Behaviour of Materials under Dynamic Loading*, DYMAT Association, Paris, 1991, p 645–652
42. K.T. Ramesh, On the Localization of Shearing Deformations in Tungsten Heavy Alloys, *Mech. Mater.*, Vol 17 (No. 2–3), Elsevier, 1994, p 165–173
43. K.-H. Hartmann, H.D. Kunze, and L.W. Meyer, Metallurgical Effects on Impact Loaded Materials, *Shock Wave and High-Strain-Rate Phenomena in Metals*, M.A. Meyers and L.E. Murr, Ed., Plenum Press, 1981, p 325–337
44. L.W. Meyer and S. Manwaring, Critical Adiabatic Shear Strength of Low Alloyed Steel under Compressive Loading, *Metallurgical Applications of Shock Wave and High-Strain-Rate Phenomena*, L.E. Murr, K.P. Staudhammer, and M.A. Meyers, Ed., Marcell Dekker, 1986, p 657–674
45. S. Nemat-Nasser, Y.-F. Li, and J.B. Isaacs, Experimental/Computational Evaluation of Flow Stress at High Strain Rates with Application to Adiabatic Shear Banding, *Mech. Mater.*, Vol 17 (No. 2–3), 1994, p 111–134
46. L.W. Myer, Dynamic Behavior of Thermomechanically Treated Ultra High Strength Steel under Tensile and Compressive Loading, I. Berman and J.W. Schroeder, Ed., *High Energy Rate Fabrication*, ASME, 1984, p 245–252
47. C.H. Nguyen, Evaluation of the Elastic Response to Impact for High-Strength Steels, *Metallurgical and Materials Applications of Shock-Wave and High-Strain-Rate Phenomena*, L.E. Murr, K.P. Staudhammer, and M.A. Meyers, Ed., Elsevier, 1995, p 699–706
48. M. Stelly and R. Dorneval, Adiabatic Shearing, *Metallurgical Applications of Shock-Wave and High-Strain-Rate Phenomena*, L.E. Murr, K. Staudhammer, and M.A. Meyers, Ed., Marcel Dekker, 1986, p 607–632
49. L.W. Meyer, E. Staskewitsch, and A. Burblied, Adiabatic Shear Failure under Biaxial Dynamic Compression/Shear Loading, *Mech. Mater.*, Vol 17 (No. 2–3), 1994, p 203–214
50. L.W. Meyer, L. Krueger, W. Gooch, and M. Burkins, Analysis of Shear Band Effects in Titanium Relative to High Strain-Rate Laboratory/Ballistic Impact Tests, *J. Phys. (France) IV*, Vol 7, 1997, p 415–422
51. L.W. Meyer, L. Krüger, and S. Abdel-Malek, Adiabatic Shearing Banding: Strength and Deformation Behaviour as well as Damage Process, *Materialprüfung*, Vol 41, Hanserverlag, 1999, p 31–34 (in German)

High Strain Rate Shear Testing

Test Setup and Operation

A drop-weight tower consists essentially of a heavy weight that drops on a specimen placed on an anvil (Fig. 14). The frame (A) and all other parts of the test setup are of high stiffness, and the weight is guided in a special ball-bearing system in order to ensure a precise alignment of the hammer. Below the weight, a small tup is fixed to give a precise loading condition. To measure the load time history, calibrated strain gages are glued on

the top. The displacement can be measured with both a high-speed electro-optical camera and a light gate system from which the strain rate can be calculated. All measured data are amplified and stored in a fast oscilloscope. Special stopping devices and high-speed brakes allow evaluation of test results including recovery tests at any stage in the deformation history. The strain-rate limit is about 200 s^{-1} , compared to strain rates of about $2 \times 10^3 \text{ s}^{-1}$ for Hopkinson-bar methods (Ref 51).

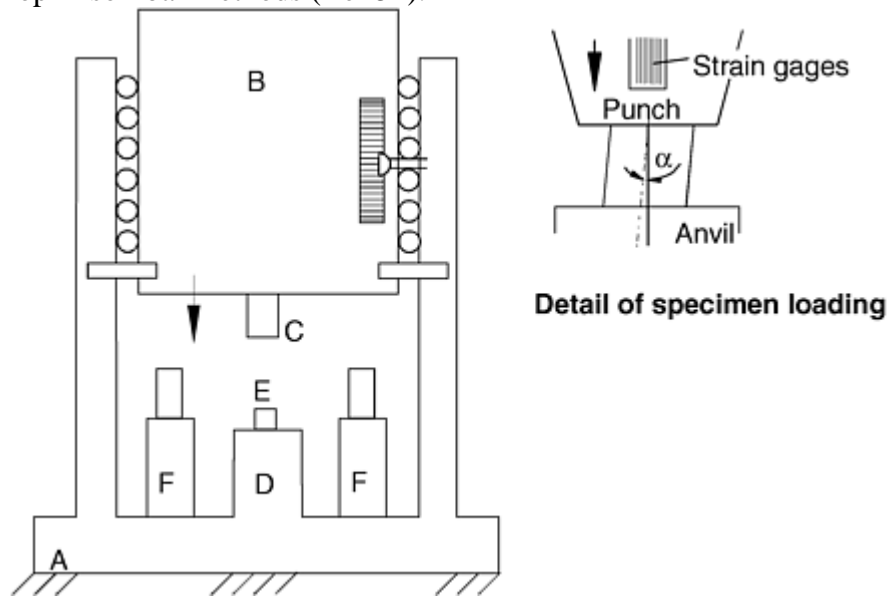


Fig. 14 Tower and specimen for drop-weight compression-shear testing, A, frame; B, falling weight; C, tup with force measurement; D, anvil; E, specimen; F, stopping device; α , angle of inclination

Reference cited in this section

51. L.W. Meyer, L. Krüger, and S. Abdel-Malek, Adiabatic Shearing Banding: Strength and Deformation Behaviour as well as Damage Process, *Materialprüfung*, Vol 41, Hanserverlag, 1999, p 31–34 (in German)

High Strain Rate Shear Testing

Application and Analysis of Results

Drop-weight testing is a method for high strain rate compression testing that can produce combined compression-shear loading by using cylindrical specimens with a relatively small inclination angle along the loading axis of up to 10° (Fig. 14). This type of specimen configuration leads to nearly the same compressive stress distribution but applies additional shear stress. For example, an inclination of 3° to the loading axis gives an additional shear loading of 5.2% of the axial compression load (Fig. 15). Compared to the hat-shaped specimen with its shear forcing geometry, the inclined cylindrical specimen geometry just “offers” a dynamic biaxial stress state, and the material responds with its own specific behavior of sensitivity to adiabatic shear failure. Therefore, with this testing procedure, the tendency of failure under adiabatic shearing can be successfully evaluated under high-rate biaxial compression-shear loading. With the aid of stopping devices (Fig. 14), the history of the shear band development also can be explored thoroughly.

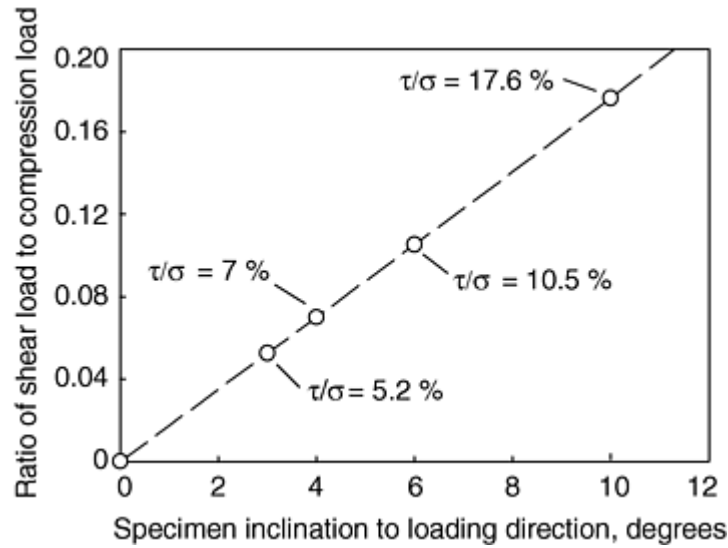


Fig. 15 Ratio of shear load to compressive load as a function of specimen inclination to the loading axis

The general effect of shear-band formation on uniaxial compression behavior is shown in Fig. 16 and 17. At low strains, the compressive stress-strain behavior is nearly the same for uniaxial and biaxial conditions. At high strains, however, biaxial loading leads to a turning point (point A in Fig. 17) and a stress maximum (B in Fig. 17). This behavior is explained by the development of shear bands (Ref 49). Depending on the material behavior, the subsequent adiabatic shear failure follows immediately or after few percent of strain (point C in Fig. 17). For example, Fig. 16 plots the dynamic compressive stress-strain behavior of a sintered and swaged tungsten alloy. Under (pure) compressive loading, the material can be compressed to high amounts of deformation without any shear bands or cracks. With the increase of an additional stress component in shear, the compressive strength and deformation behavior is changed beyond $\tau/\sigma = 7\%$. At a loading state of $\tau/\sigma = 10.5\%$, the adiabatic shear failure leads to a sharp reduction in axial deformation of about 30%. A further increase of additional shear stress causes a failure at 20% axial deformation.

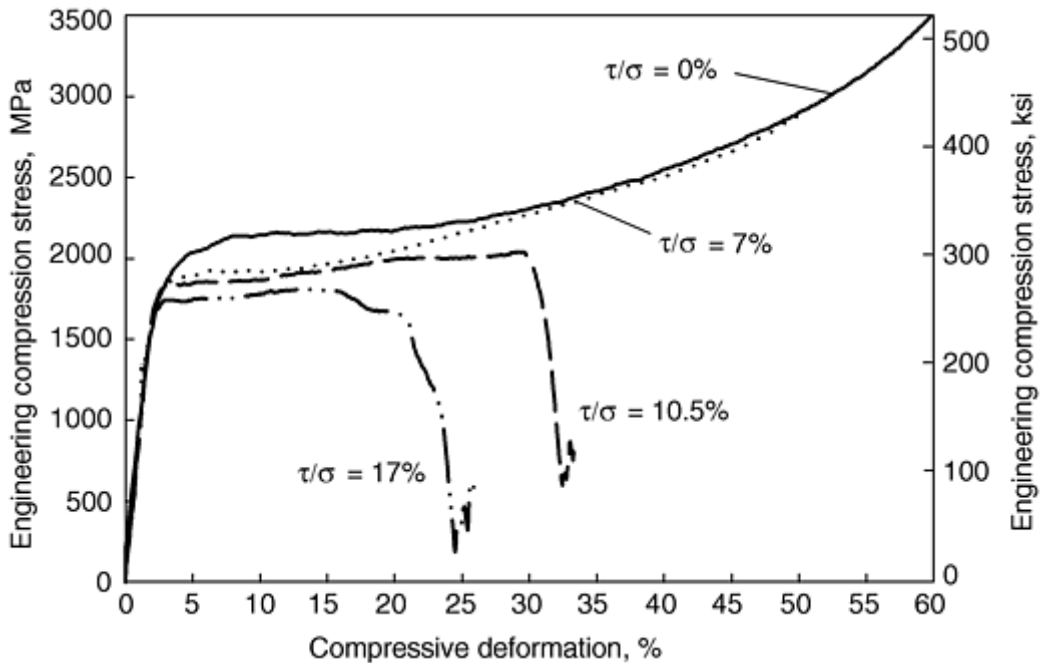


Fig. 16 Engineering compression stress-strain behavior of a swaged tungsten (W-Ni-Co-Fe) alloy cylindrical specimen with inclination to the loading axis varying between 0 and 10°

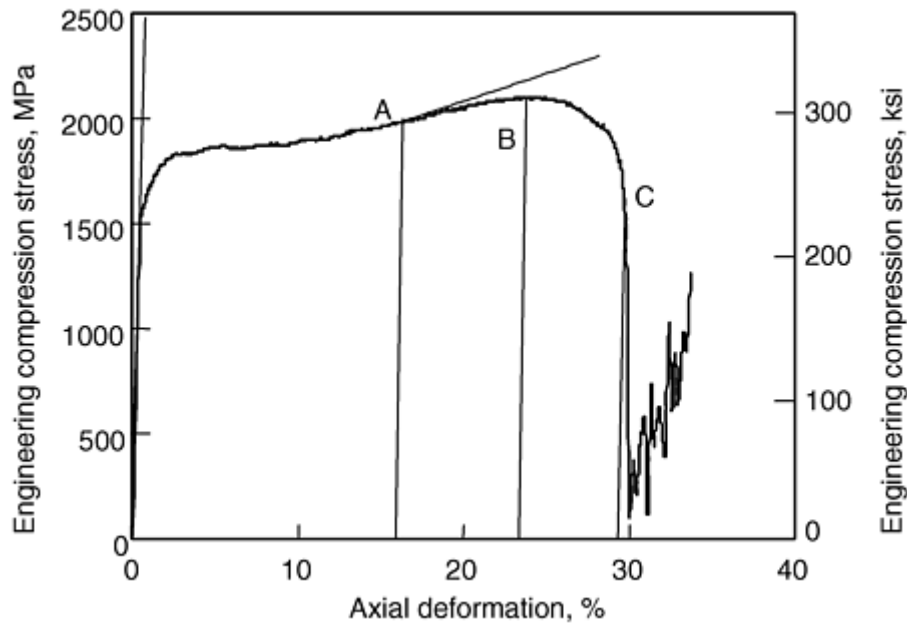


Fig. 17 Typical behavior of engineering compression stress and axial deformation under a biaxial compression-shear load

In order to evaluate the influence of the biaxial compression-shear loading, data were developed for tungsten alloys and a high-strength, α - β titanium alloy, Ti-62222Si (Ti-6Al-2Sn-2Zr-2Mo-0.25Si). The titanium alloy was tested at room temperature under a wide range of strain rates. Under quasi-static loading, the material failed at about 32% compressive deformation with a nearly homogeneous distributed deformation around the 45° shear plane (Fig. 18). With increasing strain rates to 10^2 s^{-1} and 10^3 s^{-1} , the deformability is limited by adiabatic shear failure. The compressive deformation is reduced to about half of that under quasi-static loading. With increasing inclination of the specimen at $\dot{\epsilon} = 200 \text{ s}^{-1}$, the increase in the ratio of shear to compression stress leads additionally to both a strong reduction of the deformability and compressive strength (Fig. 19).

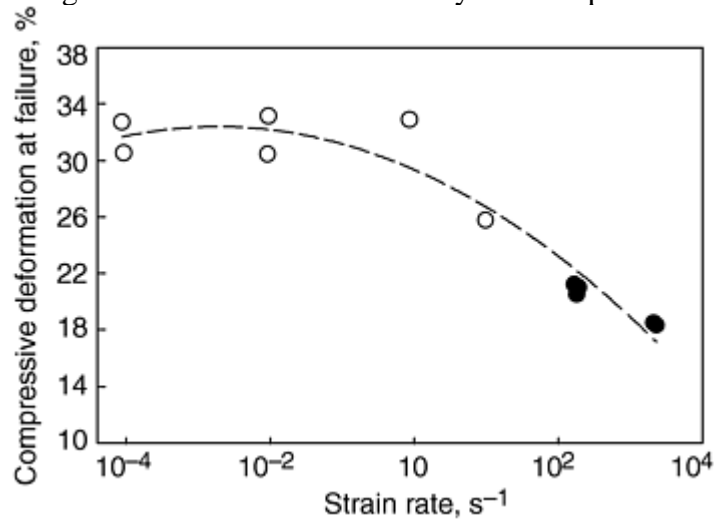


Fig. 18 Deformability behavior under pure compressive loading as function of strain rate for titanium alloy Ti-62222Si. Open circles, failure under stable plastic flow; solid circles, failure with adiabatic shear bands

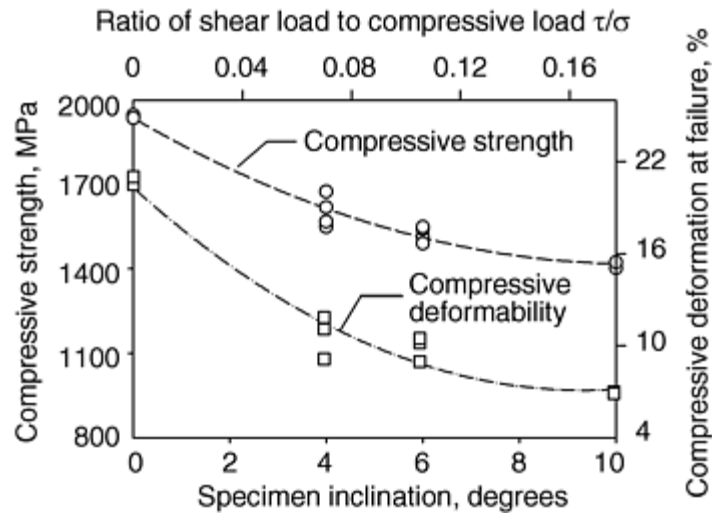


Fig. 19 Effect of shear-compression stress ratio on the compressive strength and deformability of titanium alloy Ti-62222Si with initial strain rate of about $2 \times 10^2 \text{ s}^{-1}$

Figure 20 shows a comparison of the deformability of different materials as a function of induced stress state under dynamic loading of about 200 s^{-1} for titanium alloy Ti-6Al-4V and four tungsten-heavy alloys in different heat treatment and swaging conditions. The state of deformation just prior to failure is indicated by the symbols in the figure. The open symbols represent a nearly uniform broad strain distribution in the specimen without any additional cracks or strain concentrations. The diamonds with a cross inside represent the first occurrence of a crack in the specimen, such as small tensile or shear cracks or shear failure over a broad shear zone. Solid symbols indicate sharp and concentrated, nonuniform strain distribution where failure occurs by adiabatic shear. The size was 6 mm in diameter and 6 mm in height.

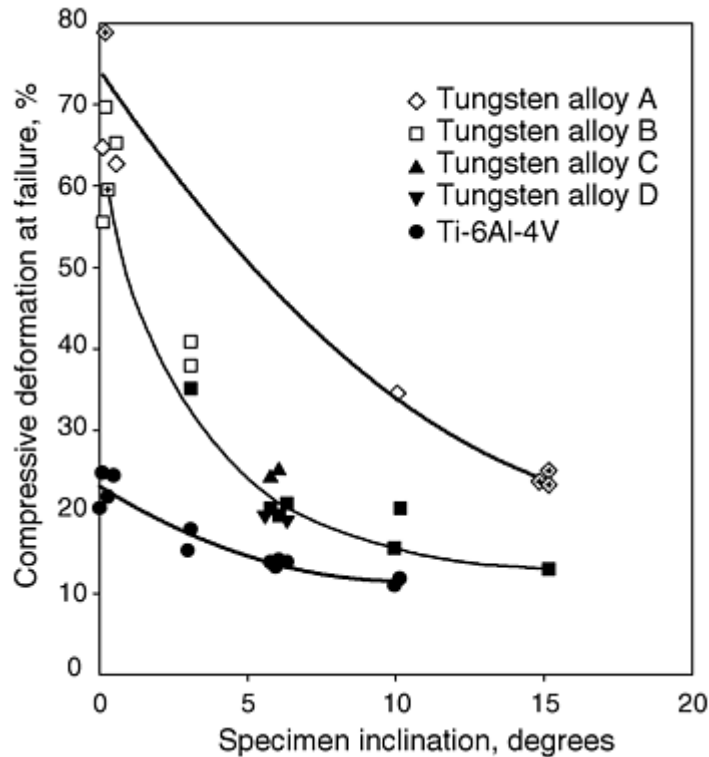


Fig. 20 Compressive deformation versus the biaxial shear-compression load ratio for titanium alloy Ti-6Al-4V and several tungsten alloys (see text). Open symbols: uniform deformation, no cracks, no failures; symbols with a cross inside: first tensile or shear cracks, (normal) shear failure (not concentrated); solid symbols: adiabatic shear failure

Tungsten alloy A (diamond symbol) is used in a sintered condition and reaches the highest deformation. Under uniaxial compression, this material can be compressed beyond 70% deformation without shear failure. First

shear cracks appear at 45° to the loading axis. Under a combined compression/shear loading with 15 ° inclination to the loading axis, only 23% axial strain is required for a broad (but not concentrated) shear failure. At 10° inclination and 34% axial strain, the test was stopped. Investigation of the deformed microstructure in the sample revealed that no cracks had appeared. The width of the shear band was about 0.5 mm in thickness. Response of tungsten alloy B (in the sintered and swaged condition and plotted with square symbols) shows a different failure behavior. Under pure uniaxial dynamic compression, the evolution of small cracks was detected on the surface. With the influence of combined shear stress, the compressive deformation to failure is reduced. At a loading of $\tau/\sigma = 5.2\%$ (3° inclination to the loading axis), one adiabatic shear failure at 34% axial deformation was measured in a group of three tests. At $\tau/\sigma = 10.5\%$ or 6 ° inclination, all three specimens failed by adiabatic shear at around 20% deformation. With further increase in additional amount of shear stress, the compressive deformation to failure decreases continuously without any change in failure mode. This diagram demonstrates that the method employed can distinguish between different materials as well as between materials within the same group.

Stopping devices also make it possible to arrest the dynamic test at any point of deformation. This possibility allows the recovery and subsequent analysis of the evolution of shear-band formation and shear-failure development by means of optical or transmission electron microscopy. For example, metallographic examination of Ti-6Al-4V (Ref 49) revealed that the beginning of the adiabatic shear formation leads to a decrease of the slope of the stress-strain curve. With the use of stopping devices, an intermediate stage of the developing shear band is shown (Fig. 13).

Reference cited in this section

49. L.W. Meyer, E. Staskewitsch, and A. Burblies, Adiabatic Shear Failure under Biaxial Dynamic Compression/Shear Loading, *Mech. Mater.*, Vol 17 (No. 2–3), 1994, p 203–214

High Strain Rate Shear Testing

Thick-Walled Cylinder Testing

Vitali F. Nesterenko, Department of Mechanical and Aerospace Engineering, University of California, San Diego

The thick-walled cylinder (TWC) method is used for high strain rate testing of solid materials (Ref 52, 53, 54, 55, 56) and porous mixtures (Ref 57, 58). Figure 21 shows the basic experimental configuration used to produce the radial collapse of the metallic specimens. The system uses the controlled detonation of an explosive to generate the pressures required for the collapse of metallic samples. The specimens are placed within a copper jacket (copper-driver tube); the system extremities are composed of steel plugs. Annealed polycrystalline oxygen-free high-conductivity copper with grain size 100 μm or less was chosen as a driver because of the high resistance of this material to shear localization. Stopper tubes of copper can be used inside the hollow specimen to decrease strain. Driver and stopper tubes can also be constructed from tantalum, which can dissipate more energy during collapse.

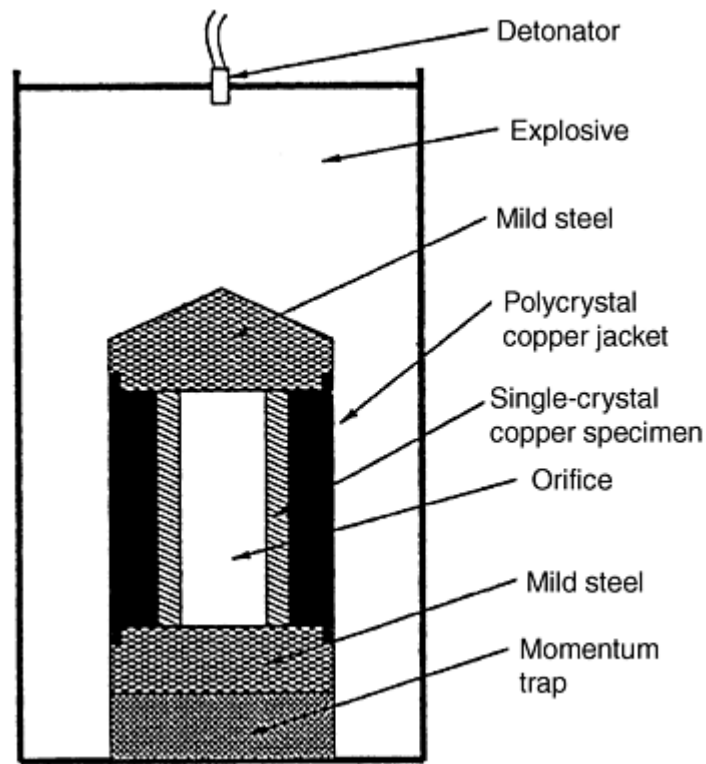


Fig. 21 The basic experimental setup for explosion-driven collapse of a metallic sample

The TWC method is a valuable technique because it allows testing under conditions more complex than uniaxial conditions. Practically all applications under high strain rates involve either two-dimensional or three-dimensional deformation. With the exception of the before-mentioned shear-compression test, the Taylor impact test, the tensile/torsion tests of Stiebler (Ref 2, 3), other shear and torsional tests, and cavity expansion experiments by Klopp and Shockey et al. (Ref 59), most high strain rate testing is uniaxial.

Multiaxial testing is useful in the evaluation of localized regions of high deformation such as shear bands (Ref 60, 61, 62). The observations of shear bands under controlled strain conditions is very important for comparison of material behavior. The role of pressure is very important for localization in solid materials, and the strain-controlled TWC method is well suited for this application. An important feature of this method is that a relatively large amount of material is in the state of pure shear before the start of instability. This provides conditions for spontaneous shear localization, which is different, for example, than “forced” localization in the hat-shaped specimens method (Ref 63) discussed previously in this article.

Plastic flow of single crystals at high strains, and high strain rates is another example where the symmetry breakdown due to crystal structure can result in complex three-dimensional flow, which has been analyzed through numerical modeling and experiments (Ref 64). High strain rate flow of damaged ceramics also requires three-dimensional tests, because it involves localization of deformation on early stages of flow (Ref 65, 66) and, as a result, a broken symmetry of any initially symmetric one-dimensional or even two-dimensional configuration. The development of computational models for the flow of fragmented ceramics under armor penetration conditions, like the FRAGBED model by Curran, Seaman, Cooper and Shockey (Ref 67, 68) needs adequate support by three-dimensional experiments. Especially important are experiments that may allow separation of the volume distributed and the deformation localized inside shear bands (Ref 69, 70). The experimental validation of this type of modeling needs tests that subject prefractured ceramics to high strain, high strain rate compressive flow with controlled conditions and with the ability to recover the heavily damaged ceramics with very small postevent deformation. The last condition is very important because it allows the test to reveal the brittle fracture details of contacting ceramic particles and microstructural features of localized flow—such as shear-induced dynamic sintering of SiC within shear bands for fine particle size/granular material (Ref 71).

References cited in this section

2. K. Stiebler, Beitrag zum Fließverhalten der Stähle Ck35 und X2CoNiMnMoNNb211653 unter zweiachsiger dynamischer Belastung, Ph.D. thesis, RWTH Aachen, Germany, 1989
3. K. Stiebler, H.-D. Kunze, and E. El-Magd, Description of the Flow Behaviour of a High Strength Austenitic Steel under Biaxial Loading by a Constitutive Equation, *Nuclear Engineering and Design*, Vol 127, 1991
52. V.F. Nesterenko, A.N. Lazaridi, and S.A. Pershin, Localization of Deformation in Copper by Explosive Compression of Hollow Cylinders, *Fiz. Goren. Vzryva*, Vol 25 (No. 4), 1989, p 154–155 (in Russian)
53. M.P. Bondar and V.F. Nesterenko, Strain Correlation at Different Structural Levels for Dynamically Loaded Hollow Copper Cylinders, *J. Phys. (France) IV Coll. C3*, Vol 1, supplement to *J. Phys. (France) III*, p 163–170
54. V.F. Nesterenko, M.P. Bondar, and I.V. Ershov, Instability of Plastic Flow at Dynamic Pore Collapse, *High-Pressure Science and Technology 1993 (Joint International Association for Research and Advancement of High Pressure Science and Technology and American Physical Society Topical Group on Shock Compression of Condensed Matter Conf.)*, (Colorado Springs), 28 June to 2 July 1993, AIP Conf. Proceedings, Part 2 (No. 309), p 1173–1176
55. V.F. Nesterenko and M.P. Bondar, Localization of Deformation in Collapse of a Thick Walled Cylinder, *Fiz. Goren. Vzryva*, Vol 30 (No. 4), 1994, p 99–111 (in Russian)
56. V.F. Nesterenko and M.P. Bondar, Investigation of Deformation Localization by the “Thick-Walled Cylinder” Method, *DYMAT J.*, Vol 1 (No. 3), 1994, p 245–251
57. V.F. Nesterenko, M.A. Myers, C.H. Chen, and J.C. LaSalvia, Controlled High-Rate Localized Shear in Porous Reactive Media, *Appl. Phys. Lett.*, Vol 65 (No. 24), 1994, p 3069–3071
58. V.F. Nesterenko, M.A. Myers, C.H. Chen, and J. LaSalvia, The Structure of Controlled Shear Bands in Dynamically Deformed Reactive Mixtures, *Metall. Mater. Trans. A*, Vol 26, 1995, p 2511–2519
59. R.W. Klopp, D.A. Shockey, L. Seaman, D.R. Curran, J.T. McGinn, and T. Resseguier, A Spherical Cavity Expansion Experiment for Characterizing Penetration Resistance of Armor Ceramics, *Mech. Test. Ceram. Ceram. Comp.*, AMD, Vol 197, ASME, 1996, p 41–55
60. D.E. Grady and M.E. Kipp, The Growth of Unstable Thermoplastic Shear with Application to Steady-Wave Shock Compression in Solids, *J. Mech. Phys. Solids*, Vol 35, 1987, p 95–119
61. T.W. Wright and H. Ockendon, Research Note: a Scaling Law for the Effect of Inertia on the Formation of Adiabatic Shear Bands, *Int. J. Plast.*, Vol 12 (No. 7), 1996, p 927–934
62. A. Molinari, Collective Behavior and Spacing of Adiabatic Shear Bands, *J. Mech. Phys. Solids*, Vol 45 (No. 9), 1997, p 1551–1575
63. Y.-J. Chen, M.A. Myers, and V.F. Nesterenko, Spontaneous and Forced Shear Localization in High-Strain-Rate Deformation of Tantalum, *Mater. Sci. Eng., A*, Vol 268, 1999, p 70–82
64. S. Nemat-Nasser, T. Okinaka, and V.F. Nesterenko, Experimental Observation and Computational Simulation of Dynamic Void Collapse in Single Crystal Copper, *Mater. Sci. Eng. A*, Vol 249 (No. 1–2), 1998, p 22–29
65. W. Chen and G. Ravichandran, Static and Dynamic Compressive Behavior of Aluminum Nitride under Moderate Confinement, *J. Am. Ceram. Soc.*, Vol 79, 1996, p 579–584

66. W. Chen and G. Ravichandran, Dynamic Compressive Failure of a Glass Ceramic under Lateral Confinement, *J. Mech. Phys. Solids*, Vol 45 (No. 8), 1997, p 1303–1328
67. D.R. Curran, L. Seaman, T. Cooper and D.A. Shockey, Micromechanical Model for Comminution and Granular Flow of Brittle Material under High Strain Rate Application to Penetration of Ceramic Targets, *Int. J. Impact Eng.*, Vol 13, 1993, p 53–83
68. R.W. Klopp, D.A. Shockey, D.R. Curran, and T. Copper, “A Granular Flow Model for Developing Smart Armor Ceramics,” *Final Technical Report on Contract DAAH04-94-K-0001*, Jan 1998, p 85
69. V.F. Nesterenko, M.A. Myers, and H.C. Chen, Shear Localization in High-Strain-Rate Deformation of Granular Alumina, *Acta Mater.*, Vol 44 (No. 5), 1996, p 2017–2026
70. C.J. Shih, V.F. Nesterenko, and M.A. Myers, High-Strain-Rate Deformation and Comminution of Silicon Carbide, *J. Appl. Phys.*, Vol 83 (No. 9), 1998, p 4660–4671
71. C.J. Shih, M.A. Meyers, and V.F. Nesterenko, High-Strain-Rate Deformation of Granular Silicon Carbide, *Acta Mater.*, Vol 46 (No. 11), 1998, p 4037–4065

High Strain Rate Shear Testing

Test Setup

As previously noted, the basic setup is configured for radial collapse of metallic specimens. The system uses the controlled detonation of an explosive, which is placed coaxially along with the specimen. Detonation is initiated at the top, propagating along the cylinder axis. The explosive parameters in the TWC method (detonation velocity, density, and thickness) are carefully selected to provide a “smooth” pore collapse. The geometry of the experiment should be such that implosion should be practically stopped due to the dissipation processes inside the sample and driver tube. Wave reflection effects are minimized, and spalling of the internal cylinder surface is nonexistent. A low-detonation explosive (detonation speed, $D \approx 4000$ m/s, or 13,100 ft/s) with low initial density (0.9 to 1 g/cm³) is typically used. A description of the method can be found in Ref 69, 70, 71, and 52, 53, 54, 55, 56, 57, 58. The velocity of the inner wall of the tube is measured by an electromagnetic gage placed in the center of a cavity collapsing in external magnetic field (Ref 54, 55).

The collapse also can be driven by impulse magnetic field with detailed measurements of collapse geometry. The great advantage of this type of driver is the minimization of axial movement and very well-controlled boundary conditions represented by magnetic field (pressure) history on the outside surface of the driver tube. The results obtained with this method for thin aluminum alloy shells (Ref 72) as well as for thick-walled titanium and 304 stainless steel cylinders (Ref 73) are very encouraging. For example the dynamic of collapse of the titanium and stainless steel cylinders was apparently different, despite the domination of total mass of the assembly by the copper driver. That may be associated with damage induced by earlier shear localization in titanium.

A simple model to calculate the kinematics of implosion driven by explosion can be used with the assumption of instantaneous detonation. This assumption is applied because the velocity of the collapse is more than an order of magnitude less than the detonation speed. In this model, the initial conditions in the detonation products correspond to the uniform pressure, P_D ; density, ρ_D ; and sound speed, c_D , as follows:

$$P_D = \frac{\rho_o D^2}{k+1} \quad \rho_D = \frac{\rho_o (k+1)}{k} \quad c_D = \frac{k}{k+1} D$$

where ρ_0 is the initial density of explosive, D is the detonation speed, and k is the coefficient in the polytropic law for detonation products. The dependence of sound speed, c , on current density, ρ , in expanding detonation products has the following form:

$$c = c_D \left(\frac{\rho_D}{\rho} \right)^{1-k}$$

Material of the cylinder is considered to be incompressible and elastic-plastic with strain, strain rate, and temperature-dependent strength. This approach results in excellent agreement of calculations with measured time of collapse $8 \mu\text{s}$ for standard conditions of testing where the outside diameter of explosive was 60 mm (2.4 in.), the inside diameter was 30 mm (1.2 in.), $D = 4000 \text{ m/s}$ (13,100 ft/s), $\rho_0 = 1000 \text{ kg/m}^3$, and $k = 2.5$.

References cited in this section

52. V.F. Nesterenko, A.N. Lazaridi, and S.A. Pershin, Localization of Deformation in Copper by Explosive Compression of Hollow Cylinders, *Fiz. Goren. Vzryva*, Vol 25 (No. 4), 1989, p 154–155 (in Russian)
53. M.P. Bondar and V.F. Nesterenko, Strain Correlation at Different Structural Levels for Dynamically Loaded Hollow Copper Cylinders, *J. Phys. (France) IV Coll. C3*, Vol 1, supplement to *J. Phys. (France) III*, p 163–170
54. V.F. Nesterenko, M.P. Bondar, and I.V. Ershov, Instability of Plastic Flow at Dynamic Pore Collapse, *High-Pressure Science and Technology 1993 (Joint International Association for Research and Advancement of High Pressure Science and Technology and American Physical Society Topical Group on Shock Compression of Condensed Matter Conf.)*, (Colorado Springs), 28 June to 2 July 1993, AIP Conf. Proceedings, Part 2 (No. 309), p 1173–1176
55. V.F. Nesterenko and M.P. Bondar, Localization of Deformation in Collapse of a Thick Walled Cylinder, *Fiz. Goren. Vzryva*, Vol 30 (No. 4), 1994, p 99–111 (in Russian)
56. V.F. Nesterenko and M.P. Bondar, Investigation of Deformation Localization by the “Thick-Walled Cylinder” Method, *DYMAT J.*, Vol 1 (No. 3), 1994, p 245–251
57. V.F. Nesterenko, M.A. Myers, C.H. Chen, and J.C. LaSalvia, Controlled High-Rate Localized Shear in Porous Reactive Media, *Appl. Phys. Lett.*, Vol 65 (No. 24), 1994, p 3069–3071
58. V.F. Nesterenko, M.A. Myers, C.H. Chen, and J. LaSalvia, The Structure of Controlled Shear Bands in Dynamically Deformed Reactive Mixtures, *Metall. Mater. Trans. A*, Vol 26, 1995, p 2511–2519
69. V.F. Nesterenko, M.A. Myers, and H.C. Chen, Shear Localization in High-Strain-Rate Deformation of Granular Alumina, *Acta Mater.*, Vol 44 (No. 5), 1996, p 2017–2026
70. C.J. Shih, V.F. Nesterenko, and M.A. Myers, High-Strain-Rate Deformation and Comminution of Silicon Carbide, *J. Appl. Phys.*, Vol 83 (No. 9), 1998, p 4660–4671
71. C.J. Shih, M.A. Meyers, and V.F. Nesterenko, High-Strain-Rate Deformation of Granular Silicon Carbide, *Acta Mater.*, Vol 46 (No. 11), 1998, p 4037–4065
72. J. Stokes, D. Oro, R.D. Fulton, D. Morgan, A. Obst, H. Oona, W. Anderson, E. Chandler, and P. Egan, Material Failure and Pattern Growth in Shock-Driven Aluminium Cylinders at the Pegasus Facility, *Bull. Amer. Phys. Soc.*, Vol 44 (No. 2), 1999, p 33
73. J.L. Stokes, V.F. Nesterenko, J.S. Shlachter, and R.D. Fulton, Comparative Behavior of Ti and 304 Stainless Steel in Magnetically-Driven Implosion at the Pegasus-II Facility, personal communication

Test Factors

The implosion of relatively thin shell results in flow instability of geometrical nature (Ref 74, 75, 76, 77). In conditions of thick-walled cylinder experiments, the number of waves due to the growth of small perturbations on the inner wall caused by this geometric instability (any departures from circular form and uniform velocity grow during collapse) can be evaluated and is less than 1. The geometry of the TWC method is selected in such a way that material instability breaks the symmetry of the cylindrical collapse, resulting in shear localization.

The state of strain generated within the collapsing cylinder is one of pure shear before shear localization starts. This is shown in Fig. 22, in which the distortion of an elemental cube at radius r_o is followed as it moves toward the axis of the cylinder. There is no rotation of the elemental cube. The strain in the axial direction of the cylinder is zero, and the planes of maximum shear lie at 45° to a radius, as indicated at r_o in Fig. 22. In pressure insensitive materials, the planes are also inclined at 45° to the cylinder axis. The strains for material points being collapsed to different final radii r_f , are depicted on Fig. 23 for the initial inner and outer radii of a sample 7 and 10.5 mm (0.28 and 0.41 in.) respectively. Each line designates the strain of a material point as it converges inward. The extremity of the line designates the radius and strain of the inside surface of a sample with radius after collapse R_f equal to 3.1 and 4.3 mm (0.12 and 0.17 in.). As the tube collapses inward, the inner surfaces experience increasing strains as the final radius of the cavity (R_f) approaches zero.

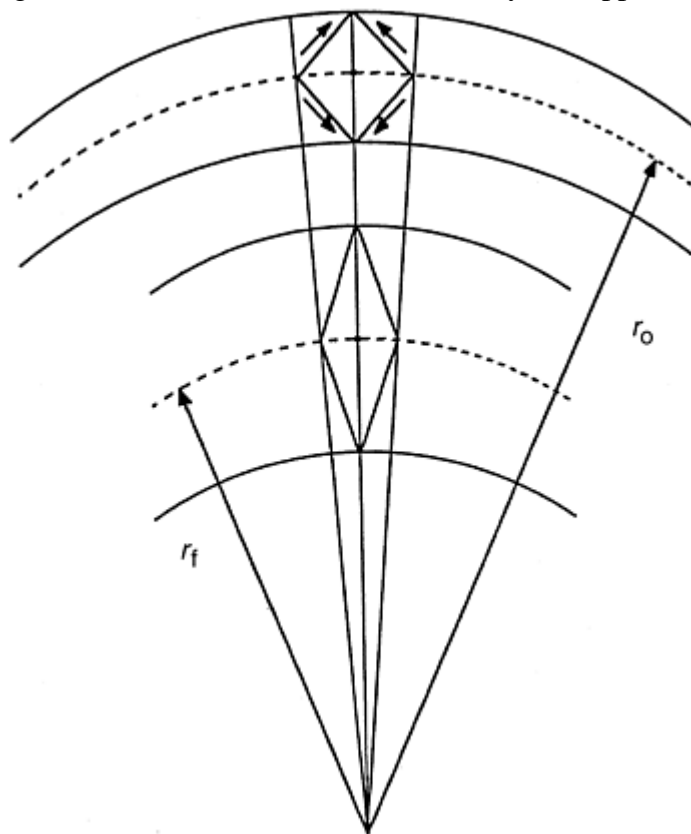


Fig. 22 Geometry of pure shear in incompressible thick-walled cylinder under uniform plastic deformation. r_o and r_f are initial and final radii of element. Source: Ref 78

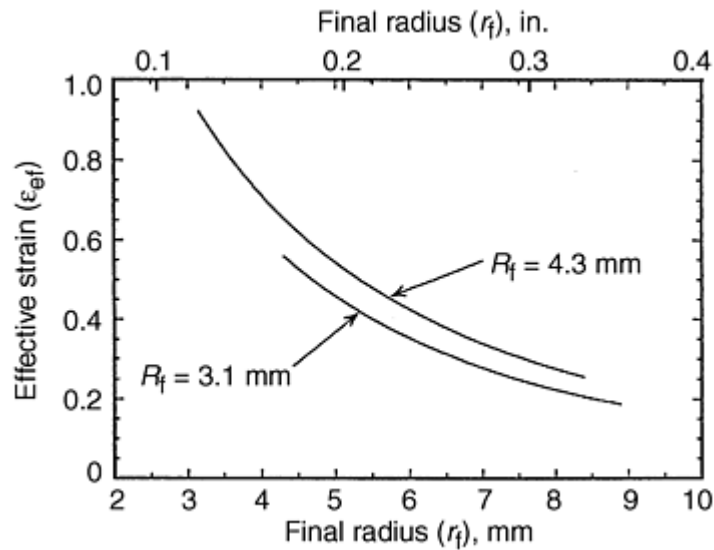


Fig. 23 Effective strain in titanium sample as a function of final radius of element r_f in partially collapsed geometry for two configurations with final inner sample radii R_f equal to 3.1 and 4.3 mm (0.12 and 0.17 in.)

Strain Rates. The main step in establishing strain rates is connected with determination of velocity field in the sample. The radial velocity of the cylindrical cavity $v(t)$ can be measured by an electromagnetic technique (Ref 54, 55). The insertion of samples from different materials inside a copper driver tube does not significantly change the time of collapse in comparison with the uniform copper cylinder having the same geometrical dimensions. This is because the replacement of the central part of copper by sample material does not essentially change the overall mass, which is dominated by the mass of outside copper (and initial velocity) of the assembly. That is why the velocity data obtained for a monolithic copper cylinder can be used as a first approximation to calculate the strain rate. Figure 24 shows the shear strain rates during the collapse process for two points corresponding to two values of final radii, which are the ends of shear bands in titanium. The strain rate is seen to fluctuate around corresponding mean values, and the variation ($\pm 15\%$) is not significant. That is why, to a first approximation, the strain rates for these material points can be considered as constant and equal to $3.5 \times 10^4 \text{ s}^{-1}$ and $6 \times 10^4 \text{ s}^{-1}$.

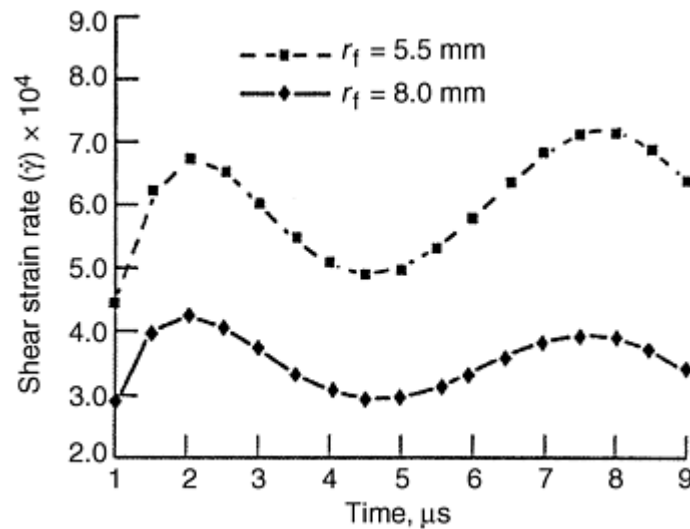


Fig. 24 Shear strain rate versus time in titanium sample as a function of final radii of element r_f . Source: Ref 78

Stresses in the TWC method are found experimentally or are based on the measured kinematics of implosion and corresponding constitutive equations. The situation is the same as in the impact rod (Taylor) test. The advantage of the TWC method is that it involves a very simple state of strain (pure shear during uniform flow and plane strain after instability starts). Also in the TWC method, stress gages can be used more effectively for

the same reason. Although the main dynamic input to stresses is from inertial effects due to the gradient of particle velocity in the cylinder, the effect of dynamic stresses on shear localization in solid materials can be neglected to a first approximation. In general, the distribution of stresses during implosion depends on material strength and cannot be controlled in this method. Therefore, numerical modeling should be used to extract the stress field during the collapse process. Two-dimensional models reflecting plane-strain conditions can be successfully applied, predicting the stress field and the relatively complex shape of the cavity (Ref 68, 79).

References cited in this section

54. V.F. Nesterenko, M.P. Bondar, and I.V. Ershov, Instability of Plastic Flow at Dynamic Pore Collapse, *High-Pressure Science and Technology 1993 (Joint International Association for Research and Advancement of High Pressure Science and Technology and American Physical Society Topical Group on Shock Compression of Condensed Matter Conf.)*, (Colorado Springs), 28 June to 2 July 1993, AIP Conf. Proceedings, Part 2 (No. 309), p 1173–1176
55. V.F. Nesterenko and M.P. Bondar, Localization of Deformation in Collapse of a Thick Walled Cylinder, *Fiz. Goren. Vzryva*, Vol 30 (No. 4), 1994, p 99–111 (in Russian)
68. R.W. Klopp, D.A. Shockey, D.R. Curran, and T. Copper, “A Granular Flow Model for Developing Smart Armor Ceramics,” *Final Technical Report on Contract DAAH04-94-K-0001*, Jan 1998, p 85
74. S.V. Serikov, Stability of a Viscoplastic Ring, *Zh. Prikl. Mekh. Tekh. Fiz.*, Vol 25 (No. 1), 1984, p 157–168 or *Appl. Mech. Tech. Phys.*, July 1984, Vol 25, p 142–153
75. H.E. Lindberg, Buckling of a Very Thin Cylindrical Shell due to an Impulsive Pressure, *Trans. ASME E, J. Appl. Mech.*, Vol 31, 1964, p 267–273
76. A.L. Florence and G. R. Abrahamson, Critical Velocity for Collapse of Viscoplastic Cylindrical Shells without Buckling, *J. Appl. Mech. (Trans. ASME)*, March 1977, p 89–94
77. A.G. Ivanov, V.A. Ogorodnikov, and E.S. Tyun'kin, The Behavior of Shells under Impulsive Loading: Small Perturbations, *Zh. Prikl. Mekh. Tekh. Fiz.*, Vol 33 (No. 6), 1992, p. 112–115 or *J. Appl. Mech. Tech. Phys. (USSR)*, May 1993, p 871–874
78. V.F. Nesterenko, M.A. Meyers, and T.W. Wright, Self-Organization in the Initiation of Adiabatic Shear Bands, *Acta Mater.*, Vol 46 (No. 1), 1998, p 327–340
79. S. Nemat-Nasser, T. Okinaka, V.F. Nesterenko, and M. Liu, Dynamic Void Collapse in Crystals: Computational Modeling and Experiments, *Philos. Mag.*, Vol 78 (No. 5), 1998, p 1151–1174

High Strain Rate Shear Testing

Advantages and Limitations

The TWC method allows investigation of the material instability during the high-strain flow. The use of a TWC (with a ratio of cylinder-wall thickness to hole diameter of approximately 1) is very important for reproducible tests involving instability phenomena. A thick wall stabilizes the symmetry of implosion and creates macroscopically uniform boundary conditions, even when instability breaks symmetry at the internal parts of the setup.

Internal patterning induced by deformation in this method can also be clarified, depending on the precise control of overall strain due to the developed, simple “soft” self-recovery setup. This allows comparative analysis of the stages of shear localization in solids, chemical reactions, and deformation localization in ceramics in high strain rate deformation. Also, it allows investigation of material instabilities from implosion phenomena.

The TWC method could benefit from several improvements in the technique, such as these:

- In situ measurements of stresses during the collapse process, at least during the stage of uniform flow before instability
- Development of driver systems (such as magnetically driven systems) with greater precision during implosion to reduce the axial component of strain
- Development of continuous measurements of the kinematics of inner and outer surfaces of the assembly
- Methods to investigate the influence of boundary conditions on shear instability
- Methods to investigate nucleation sites using high-quality interfaces between the sample and the stopper tube

High Strain Rate Shear Testing

Pressure-Shear Plate Impact Testing

Pressure-shear plate impact testing is a procedure that is used to obtain stress-strain curves at the highest strain rates attainable under well-characterized loading conditions (Ref 80). Shear strain rates on the order of 10^5 s^{-1} are obtained for specimens thinned to thicknesses of about 0.2 mm (0.008 in.). Even higher strain rates, up to 10^7 s^{-1} , can be obtained for very thin specimens (with thicknesses of 2.5 μm) prepared by vapor deposition. In addition to providing high strain rates, this type of testing provides simple shearing deformation and controllable levels of nearly hydrostatic pressure.

Pressure-shear plate impact testing is limited to fine-grained materials, because the grain size must be small compared to specimen thickness to ensure that a representative average polycrystalline response is measured. The specimen material should also be soft relative to the plate materials used to impose the deformation so that these plates will remain elastic under the impact loading conditions.

Pressure-shear experiments require a plate impact facility and instrumentation for measuring the shear waves that are generated by pressure-shear impact. Such experiments are lengthy because of the time required for specimen preparation. Although these limitations restrict the materials that can be studied and the facilities that can perform the testing, the scientific and technical importance of understanding the plastic response of metals at strain rates up to 10^5 s^{-1} and above necessitates further development of the technique. The method has been used successfully to obtain dynamic stress-strain curves of several face-centered cubic and body-centered cubic metals at strain rates of 10^5 s^{-1} and higher.

The method is based on concepts drawn from plate impact experiments and Kolsky bar experiments. From the former is taken the concept that plane waves should be used in experiments designed to measure dynamic material properties to simplify the interpretation of experimental results by making a one-dimensional wave theory applicable. Plate impact experiments also provide the methodology and instrumentation required for conducting such experiments. From Kolsky bar experiments is taken the concept of sandwiching a thin, soft specimen between two hard, elastic materials in order to sustain high strain rates in the specimen and to allow its response to be determined from measurements of wave profiles in the elastic materials. These measured profiles are related to the stresses and nominal strain rates in the specimen by one-dimensional elastic wave theory.

The pressure-shear loading configuration was introduced originally as a means of generating shear waves in symmetric plate impact experiments involving the impact of two plates of the same material. Shear waves are used, because shear wave profiles provide a more sensitive indication of the dynamic plastic response of materials than do longitudinal waves generated in conventional normal impact of plates. Shear waves have been

generated by the impact of parallel plates inclined relative to their direction of approach (Ref 81, 82) and by the normal impact of an anisotropic elastic plate of y -cut quartz (Ref 83, 84). Shear wave profiles have been monitored by means of a transverse displacement interferometer (Ref 83), two normal-velocity interferometers (Ref 85) with beams at nonnormal incidence (Ref 84), and, for nonmetallic targets, an embedded electromagnetic gage (Ref 82).

Pressure-shear waves have been used to study the plastic response of 6061-T6 aluminum (Ref 84, 86, 87, 88) and alpha-titanium (Ref 46). These studies are important because of the greater sensitivity of the shear wave profiles to the plastic flow characteristics of materials and because of the information they provide on the effects of nonproportional loading on the dynamic plastic response of materials. However, as with other wave propagation experiments, limitations include the fact that the constitutive relation between stress, strain, and strain rate is not obtained directly but must be inferred by comparison of the recorded wave profiles with those predicted for various assumed constitutive models.

Another limitation of plastic wave propagation experiments is that, although high shear strain rates are generated near the impact face, the recorded wave profiles are determined primarily by plastic response of the material at remote positions where the wave profiles have spread and strain rates have decreased. Both of these drawbacks to pressure-shear wave propagation experiments are overcome in the high strain rate pressure-shear plate experiment.

The following is a brief description of the basic concepts of plate impact tests. More detailed discussions are in the article "Low Velocity Impact Testing" in this Volume.

References cited in this section

46. L.W. Myer, Dynamic Behavior of Thermomechanically Treated Ultra High Strength Steel under Tensile and Compressive Loading, I. Berman and J.W. Schroeder, Ed., *High Energy Rate Fabrication*, ASME, 1984, p 245–252
80. R.J. Clifton and R.W. Klopp, Pressure-Shear Plate Impact Testing, *Mechanical Testing*, Vol 8, *Metals Handbook*, 9th ed., American Society for Metals, 1985, p 231–237
81. A.S. Abou-Sayed, R.J. Clifton, and L. Hermann, The Oblique Plate Impact Experiment, *Exp. Mech.*, Vol 16, 1976, p 127–132
82. Y.M. Gupta, Shear Measurements in Shock Loaded Solids, *Appl. Phys. Lett.*, Vol 29, 1976, p 694–697
83. K.S. Kim, R.J. Clifton, and P. Kumar, A Combined Normal and Transverse Displacement Interferometer with an Application to Impact of Y-Cut Quartz, *J. Appl. Phys.*, Vol 48, 1977, p 4132–4139
84. L.C. Chhabildas, H.J. Sutherland, and J.R. Asay, Velocity Interferometer Technique to Determine Shear-Wave Particle Velocity in Shock-Loaded Solids, *J. Appl. Phys.*, Vol 50, 1979, p 5196–5201
85. L.M. Barker and R.E. Hollenbach, Laser Interferometer for Measuring High Velocities of Any Reflecting Surface, *J. Appl. Phys.*, Vol 43, 1972, p 4669–4675
86. K.S. Kim and R. J. Clifton, Pressure-Shear Impact of 6061-T6 Aluminum and Alpha-Titanium, *J. Appl. Mech.*, Vol 47, 1980, p 11–16
87. L.C. Chhabildas and J.W. Swegle, Dynamic Pressure-Shear Loading of Materials Using Anisotropic Crystals, *J. Appl. Phys.*, Vol 51, 1980, p 4799–4807
88. A. Gilat and R.J. Clifton, Pressure-Shear Waves in 6061-T6 Aluminum and Alpha-Titanium, *J. Mech. Phys. Solids*, Vol 33, 1985, p 263–284

Basic Concepts

High strain rate pressure-shear impact testing is performed by impacting a thin, soft specimen plate with a hard, elastic flyer plate inclined at an angle, θ , as shown in Fig. 25. The thin specimen plate is backed by a thick elastic anvil plate, which creates a state of high pressure and high shear strain rate in the thin specimen. Because the flyer and anvil plate remain elastic during the experiment, the stresses in the elastic plates can be inferred by measuring the projectile velocity and the particle velocity at the rear surface of the anvil plate.

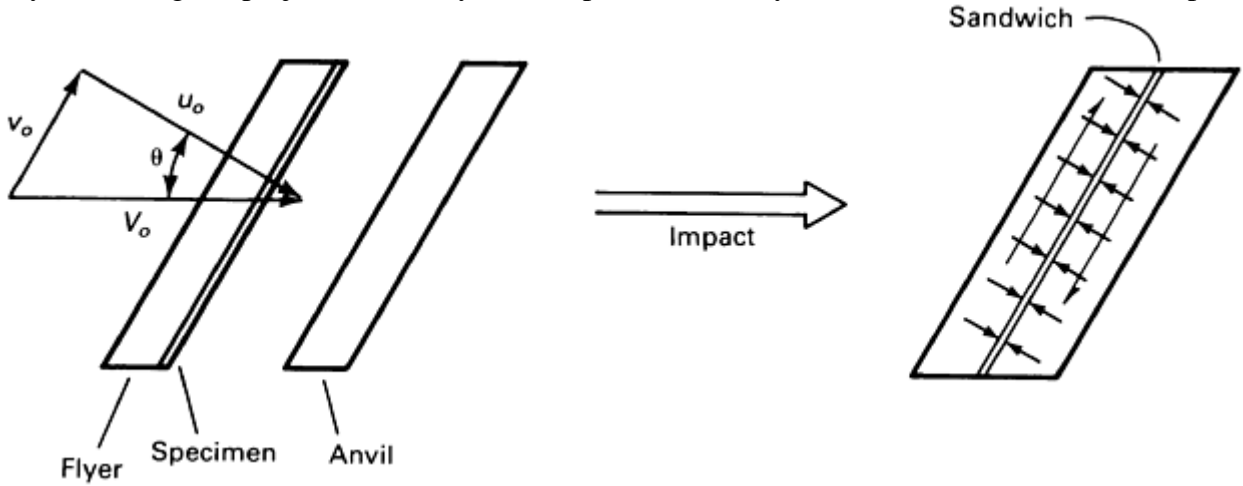


Fig. 25 Schematic representation of high strain rate pressure-shear impact configuration. u_0 is the initial velocity of the flyer plate in the normal direction, and v_0 is the initial velocity of the flyer plate in the transverse direction. V_0 is the projectile velocity and θ is the flyer plate angle.

During early stages of the test, before release waves reach the center of the plate from the periphery, one-dimensional wave theory applies. All states at the impact face of an elastic flyer plate must satisfy the following characteristic relations (Ref 89):

$$-\sigma + \rho c_1 u = \rho c_1 u_0 \quad (\text{Eq 11})$$

$$\tau + \rho c_2 v = \rho c_2 v_0 \quad (\text{Eq 12})$$

All states at the impact face of an elastic anvil plate must satisfy:

$$-\sigma - \rho c_1 u = 0 \quad (\text{Eq 13})$$

$$\tau - \rho c_2 v = 0 \quad (\text{Eq 14})$$

where σ is the normal stress in the x -direction, τ is the shear traction in the transverse direction, ρc_1 is the longitudinal acoustic impedance, ρc_2 is the shear impedance, u is the particle velocity in the normal direction, and v is the particle velocity in the transverse direction. The initial normal and transverse components of the velocity of the flyer plate are u_0 and v_0 , respectively.

The loci of stress and particle velocity states for the flyer and anvil plates are shown in Fig. 26 for the normal components and in Fig. 27 for the transverse components. At impact, shear waves and longitudinal waves are sent forward into the anvil and backward into the specimen, as shown in the $x-t$ diagram in Fig. 28. The flyer and anvil plates are selected to have impedances that are greater than or equal to that of the specimen so that unloading does not occur as the waves reflect back and forth.

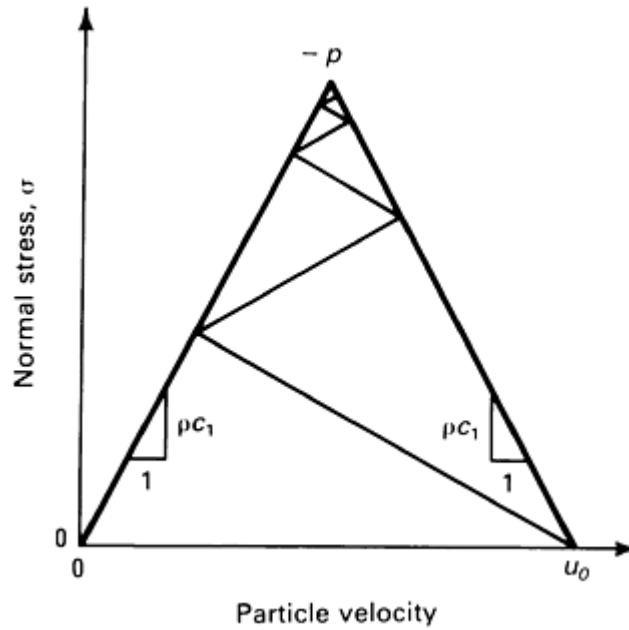


Fig. 26 Loci of normal stress-particle velocity states for flyer, anvil, and specimen, ρc_1 is the longitudinal acoustic impedance; u_0 is the particle velocity state for the flyer and anvil plates in the normal direction.

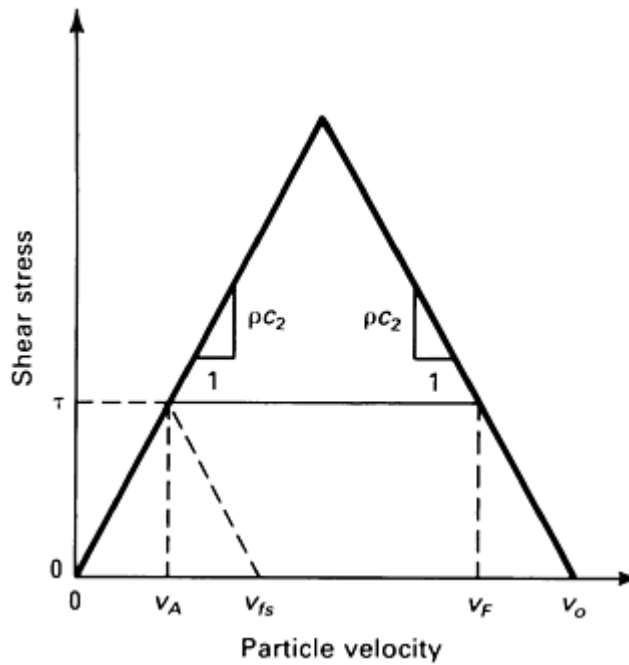


Fig. 27 Loci of shear stress/transverse particle velocity states for flyer, anvil, and specimen. v_A is the anvil particle velocity and v_{fs} is the transverse particle velocity at the free surface of the anvil. v_F is the particle velocity; v_0 is the particle velocity state for the flyer and anvil plates in the transverse direction.

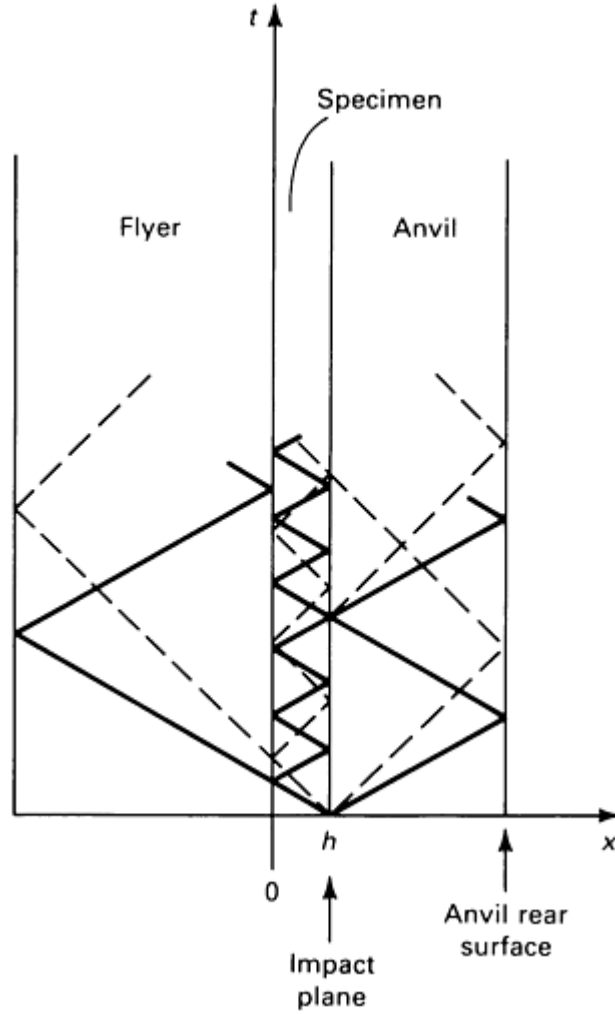


Fig. 28 $x-t$ diagram illustrating the shear waves and longitudinal waves at impact

Because the waves in the specimen are plastic, they are quickly attenuated, and the stress state in the specimen becomes nominally homogeneous. This has been verified computationally for aluminum specimens sandwiched between steel plates (Ref 89). It was also verified that after a few reflections, the hydrostatic pressure in the specimen becomes nearly equal to the value of the homogeneous normal stress (Ref 89). The homogeneous normal stress attained is the value at the point of intersection of the two lines given by Eq 3 and 5.

$$-p \approx \sigma = \frac{1}{2} \rho c_1 u_0 \quad (\text{Eq 15})$$

This point, which is the apex in Fig. 26, is attained because the elastic resistance of the specimen to volume change will not allow a finite normal velocity difference to be maintained across the thickness of the specimen, while flow in the radial direction is prohibited.

It is possible, however, to maintain a finite transverse velocity difference across the thin specimen for the duration of the experiment. If the specimen behaves viscoplastically and if the stress state is homogeneous, then the shear stress will equilibrate at a value τ in Fig. 27, and the flyer and anvil particle velocities will be v_F and v_A , respectively. The nominal shear strain rate is:

$$\dot{\gamma} = \frac{v_F - v_A}{h} \quad (\text{Eq 16})$$

where h is the specimen thickness. Note that:

$$v_F - v_A = v_0 - v_{fs} \quad (\text{Eq 17})$$

where v_{fs} is the transverse particle velocity at the free surface of the anvil. The shear strain rate can be integrated over time to give the shear strain. From Eq 14, the shear stress is:

$$\tau = \rho c_2 v_A = \frac{1}{2} \rho c_2 v_{fs} \quad (\text{Eq 18})$$

Thus, it is only necessary to measure the incident projectile velocity, the skew angle, and the particle velocity at the rear surface of the anvil to construct a shear stress versus shear strain curve at high strain rates and high hydrostatic pressures.

Reference cited in this section

89. C.H. Li, A Pressure-Shear Experiment for Studying the Dynamic Plastic Response of Metals and Shear Strain Rates of 10^5 s^{-1} , Ph.D. thesis, Brown University, Providence, RI, 1982

High Strain Rate Shear Testing

Acknowledgments

Portions of this article were adapted from the following articles published in *Mechanical Testing*, Volume 8, *ASM Handbook*, 1985:

- R.J. Clifton and R.W. Klopp, Pressure-Shear Plate Impact Testing, p 230–238
- Harding, Double-Notch Shear Testing and Punch Loading, p 228–230
- K.A. Hartley and J. Duffy, High Strain Rate Shear Testing: Introduction, p 215
- K.A. Hartley, J. Duffy, and R.H. Hawley, The Torsional Kolsky (Split-Hopkinson) Bar, p 218–228
- U.S. Lindholm, High-Speed Hydraulic Torsional Machines, p 215–216
- U.S. Lindholm, Torsional Impact Testing, p 216–218

High Strain Rate Shear Testing

References

1. U.S. Lindholm, A. Nagy, G.R. Johnson, and J.M. Hoegfeldt, Large Strain, High Strain Rate Testing of Copper, *J. Eng. Mater. Technol. (Trans. ASME)*, Vol 102, 1980, p 376–381
2. K. Stiebler, Beitrag zum Fließverhalten der Stähle Ck35 und X2CoNiMnMoNb211653 unter zweiachsiger dynamischer Belastung, Ph.D. thesis, RWTH Aachen, Germany, 1989
3. K. Stiebler, H.-D. Kunze, and E. El-Magd, Description of the Flow Behaviour of a High Strength Austenitic Steel under Biaxial Loading by a Constitutive Equation, *Nuclear Engineering and Design*, Vol 127, 1991
4. R.S. Culver, Torsional-Impact Apparatus, *Exp. Mech.*, Vol 12, 1972, p 398–405
5. C.E. Work and T.J. Dolan, The Influence of Strain Rate and Temperature on the Strength and Ductility of Mild Steel in Torsion, *Proc. ASTM*, Vol 53, 1953, p 611–626
6. N.G. Calvert, Impact Torsion Experiments, *Inst. Mech. Eng.*, Vol 169 (No. 44), 1955, p 897

7. R.S. Culver, Thermal Instability Strain in Dynamic Plastic Deformation, *Metallurgical Effects at High Strain Rates*, R.W. Rohde, B.M. Butcher, J.R. Holland, and C.H. Karnes, Ed., Plenum Press, 1973, p 519–530
8. U.S. Lindholm and G.R. Johnson, Strain-Rate Effects in Metals at Large Shear Strains, *Material Behavior under High Stress and Ultrahigh Loading Rates*, J. Mescall and V. Weiss, Ed., Plenum Press, 1983, p 61–79
9. K.A. Hartley, J. Duffy, and R.H. Hawley, The Torsional Kolsky (Split-Hopkinson) Bar, *Mechanical Testing*, Vol 8, *Metals Handbook*, 9th ed., American Society for Metals, 1985, p 218–230
10. R.A. Frantz and J. Duffy, The Dynamic Stress-Strain Behavior in Torsion of 1100-O Aluminum Subjected to a Sharp Increase in Strain Rate, *J. Appl. Mech.*, Vol 39, 1972, p 939–945
11. J. Duffy, J.D. Campbell, and R.H. Hawley, On the Use of a Torsional Split Hopkinson Bar to Study Rate Effects in 1100-O Aluminum, *J. Appl. Mech.*, Vol 38, 1971, p 83–91
12. U.S. Lindholm, Deformation Maps in the Region of High Dislocation Velocity, *High Velocity Deformation of Solids*, K. Kawata and J. Shioiri, Ed., International Union of Theoretical and Applied Mechanics Symposium, Springer-Verlag, Berlin, 1978
13. G.L. Wulf, Dynamic Stress-Strain Measurements at Large Strains, *Mechanical Properties at High Rates of Strain*, J. Harding, Ed., Institute of Physics Conf. Series (No. 21), 1974, p 48–52
14. D.A. Gorham, Measurement of Stress-Strain Properties of Strong Metals at Very High Rates of Strain, *Mechanical Properties at High Rates of Strain*, J. Harding, Ed., Institute of Physics Conf. Series (No. 47), 1979, p 16
15. W.G. Ferguson, J.E. Hauser, and J.E. Dorn, The Dynamic Punching of Metals, Dislocation Damping in Zinc Single Crystals, *Brit. J. Appl. Phys.*, Vol 18, 1967, p 411–417
16. J.D. Campbell and W.G. Ferguson, The Temperature and Strain Rate Dependence of Shear Strength of Mild Steel, *Philos. Mag.*, Vol 21, 1970, p 63–82
17. J. Harding and J. Huddart, The Use of the Double-Notch Shear Test in Determining the Mechanical Properties of Uranium at Very High Rates of Strain, *Proc. 2nd International Conf. Mechanical Properties at High Rates of Strain*, J. Harding, Ed., The Institute of Physics, London, 1979, p 49–61
18. A.R. Dowling, J. Harding, and J.D. Campbell, The Dynamic Punching of Metals, *J. Inst. Metals*, Vol 98, 1970, p 215–224
19. K.-H. Hartmann, H.D. Kunze, and L.W. Meyer, Metallurgical Effects on Impact Loaded Materials, *Shock Wave and High-Strain-Rate Phenomena in Metals*, M.A. Meyers and L.E. Murr, Ed., Plenum Press, 1981, p 325–337
20. L.W. Meyer and S. Manwaring, Critical Adiabatic Shear Strength of Low Alloyed Steel under Compressive Loading, *Metallurgical Applications of Shock Wave and High-Strain-Rate Phenomena*, L.E. Murr, K.P. Staudhammer, and M.A. Meyers, Ed., Marcell Dekker, 1986, p 657–674
21. J.A. Hines and K.S. Vecchio, Dynamic Recrystallization in Adiabatic Shear Bands in Shock-Loaded Copper, *Metallurgical and Materials Application of Shock Wave and High-Strain-Rate Phenomena*, L.E. Murr, K.P. Staudhammer, and M.A. Meyers, Ed., Elsevier Science B.V., 1995, p 421–428

22. F.D.S. Marquis, M.A. Meyers, Y.J. Chen, and D.S. Kim, High-Strain, High-Strain-Rate Of Tantalum, *Metall. Mater. Trans. A*, Physical Metallurgy and Materials Science, Vol 26 (No. 10), 1995, p 2493–2501
23. S. Nemat-Nasser, Y.-F. Li, and J.B. Isaacs, Experimental/Computational Evaluation of Flow Stress at High Strain Rates with Application to Adiabatic Shear Banding, *Mech. Mater.*, Vol 17 (No. 2–3), 1994, p 111–134
24. R.W. Chen and K.S. Vecchio, Microstructural Characterization of Shear Band Formation in Al-Li Alloys, *J. Physique IV (France)*, tome 4, Coll. C8, 1994, p 459–463
25. U. Andrade, “High-Strain, High-Strain-Rate Deformation of Copper,” Ph.D. thesis, University of California, San Diego, 1993
26. M.A. Meyers, L.W. Meyer, J. Beatty, U. Andrade, K.S. Vecchio, and A.H. Chokshi, High Strain, High-Strain Rate Deformation of Copper, *Shock Wave and High-Strain-Rate Phenomena in Materials*, M.A. Meyers, L.E. Murr, and K.P. Staudhammer, Ed., Marcel Dekker, 1992, p 529–542
27. M.A. Meyers, G. Subhash, B.K. Kad, and L. Prasad, Evolution of Microstructure and Shear-Band Formation in α -hcp Titanium, *Mech. Mater.*, Vol 17 (No. 2–3), 1994, p 175–193
28. M.A. Meyers, Y.-J. Chen, F.D.S. Marquis, and D.S. Kim, High-Strain, High-Strain-Rate Behavior of Tantalum, *Metall. Mater. Trans. A*, Vol 26, Oct 1995, p 2493–2501
29. L.W. Meyer and A. Schrödter, Mechanical Reduction of Oscillations on a Split Hopkinson Bar—A Simple, but Efficient Method for High Strain Rate Material Testing, *ACAM*, Canberra, ISBN 0-7334-0558-4, 1999
30. J.H. Beatty, L.W. Meyer, M.A. Meyers, and S. Nemat-Nasser, Formation of Controlled Adiabatic Shear Bands in AISI 4340 High Strength Steel, *Shock Wave and High-Strain-Rate Phenomena in Materials*, M.A. Meyers, L.E. Murr, and K.P. Staudhammer, Ed., Marcel Dekker, 1992, p 645–656
31. S. Nemat-Nasser, J.B. Isaacs, and J. Starrett, Hopkinson Techniques for Dynamic Recovery Experiments, *Proc. R. Soc. (London) A*, Vol 435, 1991, p 371–391
32. T. Pintat, Ph.D. thesis, University Bremen, Germany, 1993
33. M.A. Meyers, U.R. Andrade, and A.H. Chokshi, The Effect of Grain Size on the High-Strain, High-Strain-Rate Behavior of Copper, *Metall. Mater. Trans. A*, Vol 26, Nov 1995, p 2881–2893
34. T. Pintat, L.W. Meyer, and H. Schrader, Properties of Inhomogeneous Shear Zones in Different Materials, *J. Phys.*, Coll. C5, 1985
35. T. Pintat, B. Scholz, H.D. Kunze, and O. Vöhringer, The Influence of Carbon Content and Grain Size on Energy Consumption during Adiabatic Shearing, *J. Phys.*, Coll. C3, 1988, p 237–244
36. M.A. Meyers, L.W. Meyer, K.S. Vecchio, and U. Andrade, High Strain, High-Strain Rate Deformation of Copper, *J. Phys. (France) IV*, Coll. C3, 1991, p 11–17
37. K. Minnaar and M. Zhou, An Analysis of the Dynamic Shear Failure Resistance of Structural Metals, *J. Mech. Phys. Solids*, Vol 46 (No. 10), 1998, p 2155–2170

38. L.W. Myer, F.-J. Behler, K. Frank, and L.S. Magness, Interdependencies between the Dynamic Mechanical Properties and the Ballistic Behaviour of Materials, *Proc. of the 12th International Symposium on Ballistics*, Vol 1, p 419–428
39. L.S. Costin, E.E. Crisman, R.H. Hawley, and J. Duffy, On the Localization of Plastic Flow in Mild Steel Tubes under Dynamic Torsional Loading, *Mechanical Properties at High Rate of Strain, Institute of Physics Conf. Series* (No. 47), J. Harding, Ed., 1979, p 90–100
40. J.H. Giovanola, Observation of Adiabatic Shear Banding in Simple Torsion, *Impact Loading and Dynamic Behaviour of Materials*, C.Y. Chiem, H.-D. Kunze, and L.W. Meyer, Ed., DGM Informationsgesellschaft, Oberursel, 1988, p 705–710
41. J. Duffy, Experimental Studies of Shear Band Formation Through Temperature Measurements and High Speed Photography, *Proc. 3rd International Conf. on Mechanical and Physical Behaviour of Materials under Dynamic Loading*, DYMAT Association, Paris, 1991, p 645–652
42. K.T. Ramesh, On the Localization of Shearing Deformations in Tungsten Heavy Alloys, *Mech. Mater.*, Vol 17 (No. 2–3), Elsevier, 1994, p 165–173
43. K.-H. Hartmann, H.D. Kunze, and L.W. Meyer, Metallurgical Effects on Impact Loaded Materials, *Shock Wave and High-Strain-Rate Phenomena in Metals*, M.A. Meyers and L.E. Murr, Ed., Plenum Press, 1981, p 325–337
44. L.W. Meyer and S. Manwaring, Critical Adiabatic Shear Strength of Low Alloyed Steel under Compressive Loading, *Metallurgical Applications of Shock Wave and High-Strain-Rate Phenomena*, L.E. Murr, K.P. Staudhammer, and M.A. Meyers, Ed., Marcell Dekker, 1986, p 657–674
45. S. Nemat-Nasser, Y.-F. Li, and J.B. Isaacs, Experimental/Computational Evaluation of Flow Stress at High Strain Rates with Application to Adiabatic Shear Banding, *Mech. Mater.*, Vol 17 (No. 2–3), 1994, p 111–134
46. L.W. Myer, Dynamic Behavior of Thermomechanically Treated Ultra High Strength Steel under Tensile and Compressive Loading, I. Berman and J.W. Schroeder, Ed., *High Energy Rate Fabrication*, ASME, 1984, p 245–252
47. C.H. Nguyen, Evaluation of the Elastic Response to Impact for High-Strength Steels, *Metallurgical and Materials Applications of Shock-Wave and High-Strain-Rate Phenomena*, L.E. Murr, K.P. Staudhammer, and M.A. Meyers, Ed., Elsevier, 1995, p 699–706
48. M. Stelly and R. Dormeival, Adiabatic Shearing, *Metallurgical Applications of Shock-Wave and High-Strain-Rate Phenomena*, L.E. Murr, K. Staudhammer, and M.A. Meyers, Ed., Marcel Dekker, 1986, p 607–632
49. L.W. Meyer, E. Staskewitsch, and A. Burblies, Adiabatic Shear Failure under Biaxial Dynamic Compression/Shear Loading, *Mech. Mater.*, Vol 17 (No. 2–3), 1994, p 203–214
50. L.W. Meyer, L. Krueger, W. Gooch, and M. Burkins, Analysis of Shear Band Effects in Titanium Relative to High Strain-Rate Laboratory/Ballistic Impact Tests, *J. Phys. (France) IV*, Vol 7, 1997, p 415–422
51. L.W. Meyer, L. Krüger, and S. Abdel-Malek, Adiabatic Shearing Banding: Strength and Deformation Behaviour as well as Damage Process, *Materialprüfung*, Vol 41, Hanserverlag, 1999, p 31–34 (in German)

52. V.F. Nesterenko, A.N. Lazaridi, and S.A. Pershin, Localization of Deformation in Copper by Explosive Compression of Hollow Cylinders, *Fiz. Goren. Vzryva*, Vol 25 (No. 4), 1989, p 154–155 (in Russian)
53. M.P. Bondar and V.F. Nesterenko, Strain Correlation at Different Structural Levels for Dynamically Loaded Hollow Copper Cylinders, *J. Phys. (France) IV Coll. C3*, Vol 1, supplement to *J. Phys. (France) III*, p 163–170
54. V.F. Nesterenko, M.P. Bondar, and I.V. Ershov, Instability of Plastic Flow at Dynamic Pore Collapse, *High-Pressure Science and Technology 1993 (Joint International Association for Research and Advancement of High Pressure Science and Technology and American Physical Society Topical Group on Shock Compression of Condensed Matter Conf.)*, (Colorado Springs), 28 June to 2 July 1993, AIP Conf. Proceedings, Part 2 (No. 309), p 1173–1176
55. V.F. Nesterenko and M.P. Bondar, Localization of Deformation in Collapse of a Thick Walled Cylinder, *Fiz. Goren. Vzryva*, Vol 30 (No. 4), 1994, p 99–111 (in Russian)
56. V.F. Nesterenko and M.P. Bondar, Investigation of Deformation Localization by the “Thick-Walled Cylinder” Method, *DYMAT J.*, Vol 1 (No. 3), 1994, p 245–251
57. V.F. Nesterenko, M.A. Myers, C.H. Chen, and J.C. LaSalvia, Controlled High-Rate Localized Shear in Porous Reactive Media, *Appl. Phys. Lett.*, Vol 65 (No. 24), 1994, p 3069–3071
58. V.F. Nesterenko, M.A. Myers, C.H. Chen, and J. LaSalvia, The Structure of Controlled Shear Bands in Dynamically Deformed Reactive Mixtures, *Metall. Mater. Trans. A*, Vol 26, 1995, p 2511–2519
59. R.W. Klopp, D.A. Shockey, L. Seaman, D.R. Curran, J.T. McGinn, and T. Resseguier, A Spherical Cavity Expansion Experiment for Characterizing Penetration Resistance of Armor Ceramics, *Mech. Test. Ceram. Ceram. Comp.*, AMD, Vol 197, ASME, 1996, p 41–55
60. D.E. Grady and M.E. Kipp, The Growth of Unstable Thermoplastic Shear with Application to Steady-Wave Shock Compression in Solids, *J. Mech. Phys. Solids*, Vol 35, 1987, p 95–119
61. T.W. Wright and H. Ockendon, Research Note: a Scaling Law for the Effect of Inertia on the Formation of Adiabatic Shear Bands, *Int. J. Plast.*, Vol 12 (No. 7), 1996, p 927–934
62. A. Molinari, Collective Behavior and Spacing of Adiabatic Shear Bands, *J. Mech. Phys. Solids*, Vol 45 (No. 9), 1997, p 1551–1575
63. Y.-J. Chen, M.A. Myers, and V.F. Nesterenko, Spontaneous and Forced Shear Localization in High-Strain-Rate Deformation of Tantalum, *Mater. Sci. Eng., A*, Vol 268, 1999, p 70–82
64. S. Nemat-Nasser, T. Okinaka, and V.F. Nesterenko, Experimental Observation and Computational Simulation of Dynamic Void Collapse in Single Crystal Copper, *Mater. Sci. Eng. A*, Vol 249 (No. 1–2), 1998, p 22–29
65. W. Chen and G. Ravichandran, Static and Dynamic Compressive Behavior of Aluminum Nitride under Moderate Confinement, *J. Am. Ceram. Soc.*, Vol 79, 1996, p 579–584
66. W. Chen and G. Ravichandran, Dynamic Compressive Failure of a Glass Ceramic under Lateral Confinement, *J. Mech. Phys. Solids*, Vol 45 (No. 8), 1997, p 1303–1328
67. D.R. Curran, L. Seaman, T. Cooper and D.A. Shockey, Micromechanical Model for Comminution and Granular Flow of Brittle Material under High Strain Rate Application to Penetration of Ceramic Targets, *Int. J. Impact Eng.*, Vol 13, 1993, p 53–83

68. R.W. Klopp, D.A. Shockey, D.R. Curran, and T. Copper, "A Granular Flow Model for Developing Smart Armor Ceramics," *Final Technical Report on Contract DAAH04-94-K-0001*, Jan 1998, p 85
69. V.F. Nesterenko, M.A. Myers, and H.C. Chen, Shear Localization in High-Strain-Rate Deformation of Granular Alumina, *Acta Mater.*, Vol 44 (No. 5), 1996, p 2017–2026
70. C.J. Shih, V.F. Nesterenko, and M.A. Myers, High-Strain-Rate Deformation and Comminution of Silicon Carbide, *J. Appl. Phys.*, Vol 83 (No. 9), 1998, p 4660–4671
71. C.J. Shih, M.A. Meyers, and V.F. Nesterenko, High-Strain-Rate Deformation of Granular Silicon Carbide, *Acta Mater.*, Vol 46 (No. 11), 1998, p 4037–4065
72. J. Stokes, D. Oro, R.D. Fulton, D. Morgan, A. Obst, H. Oona, W. Anderson, E. Chandler, and P. Egan, Material Failure and Pattern Growth in Shock-Driven Aluminium Cylinders at the Pegasus Facility, *Bull. Amer. Phys. Soc.*, Vol 44 (No. 2), 1999, p 33
73. J.L. Stokes, V.F. Nesterenko, J.S. Shlachter, and R.D. Fulton, Comparative Behavior of Ti and 304 Stainless Steel in Magnetically-Driven Implosion at the Pegasus-II Facility, personal communication
74. S.V. Serikov, Stability of a Viscoplastic Ring, *Zh. Prikl. Mekh. Tekh. Fiz.*, Vol 25 (No. 1), 1984, p 157–168 or *Appl. Mech. Tech. Phys.*, July 1984, Vol 25, p 142–153
75. H.E. Lindberg, Buckling of a Very Thin Cylindrical Shell due to an Impulsive Pressure, *Trans. ASME E, J. Appl. Mech.*, Vol 31, 1964, p 267–273
76. A.L. Florence and G. R. Abrahamson, Critical Velocity for Collapse of Viscoplastic Cylindrical Shells without Buckling, *J. Appl. Mech. (Trans. ASME)*, March 1977, p 89–94
77. A.G. Ivanov, V.A. Ogorodnikov, and E.S. Tyun'kin, The Behavior of Shells under Impulsive Loading: Small Perturbations, *Zh. Prikl. Mekh. Tekh. Fiz.*, Vol 33 (No. 6), 1992, p. 112–115 or *J. Appl. Mech. Tech. Phys. (USSR)*, May 1993, p 871–874
78. V.F. Nesterenko, M.A. Meyers, and T.W. Wright, Self-Organization in the Initiation of Adiabatic Shear Bands, *Acta Mater.*, Vol 46 (No. 1), 1998, p 327–340
79. S. Nemat-Nasser, T. Okinaka, V.F. Nesterenko, and M. Liu, Dynamic Void Collapse in Crystals: Computational Modeling and Experiments, *Philos. Mag.*, Vol 78 (No. 5), 1998, p 1151–1174
80. R.J. Clifton and R.W. Klopp, Pressure-Shear Plate Impact Testing, *Mechanical Testing*, Vol 8, *Metals Handbook*, 9th ed., American Society for Metals, 1985, p 231–237
81. A.S. Abou-Sayed, R.J. Clifton, and L. Hermann, The Oblique Plate Impact Experiment, *Exp. Mech.*, Vol 16, 1976, p 127–132
82. Y.M. Gupta, Shear Measurements in Shock Loaded Solids, *Appl. Phys. Lett.*, Vol 29, 1976, p 694–697
83. K.S. Kim, R.J. Clifton, and P. Kumar, A Combined Normal and Transverse Displacement Interferometer with an Application to Impact of Y-Cut Quartz, *J. Appl. Phys.*, Vol 48, 1977, p 4132–4139
84. L.C. Chhabildas, H.J. Sutherland, and J.R. Asay, Velocity Interferometer Technique to Determine Shear-Wave Particle Velocity in Shock-Loaded Solids, *J. Appl. Phys.*, Vol 50, 1979, p 5196–5201

85. L.M. Barker and R.E. Hollenbach, Laser Interferometer for Measuring High Velocities of Any Reflecting Surface, *J. Appl. Phys.*, Vol 43, 1972, p 4669–4675
86. K.S. Kim and R. J. Clifton, Pressure-Shear Impact of 6061-T6 Aluminum and Alpha-Titanium, *J. Appl. Mech.*, Vol 47, 1980, p 11–16
87. L.C. Chhabildas and J.W. Swegle, Dynamic Pressure-Shear Loading of Materials Using Anisotropic Crystals, *J. Appl. Phys.*, Vol 51, 1980, p 4799–4807
88. A. Gilat and R.J. Clifton, Pressure-Shear Waves in 6061-T6 Aluminum and Alpha-Titanium, *J. Mech. Phys. Solids*, Vol 33, 1985, p 263–284
89. C.H. Li, A Pressure-Shear Experiment for Studying the Dynamic Plastic Response of Metals and Shear Strain Rates of 10^5 s^{-1} , Ph.D. thesis, Brown University, Providence, RI, 1982

Classic Split-Hopkinson Pressure Bar Testing

George T. (Rusty) Gray III, Los Alamos National Laboratory

Introduction

EXPERIMENTAL TECHNIQUES in characterizing the behavior of materials at high rates of strain are concerned with measuring the change in mechanical properties, such as yield strength, work hardening, and ductility, which can vary with strain rate. Strain rate, $\dot{\epsilon}$, is defined as the rate of change of strain (defined as the ratio of change in the length of a mechanical test sample) with respect to time, t . Minimal scientific or engineering attention was historically paid to the effects of high strain rates on material behavior until increased manufacturing production techniques (Ref 1, 2, 3, 4, 5), such as high-speed wire drawing and cold rolling, as well as studies supporting military technologies concerned with ballistics (Ref 6, 7), armor, and detonation physics, required further knowledge. Interest in the high-rate mechanical behavior of materials has continued to expand during the last 40 years, driven by demands for increased understanding of material response subjected to high-rate loading and impact events. High-rate-loading experiments provide the critically needed data required for the development of predictive constitutive model descriptions of materials.

Constitutive models strive to capture the fundamental relationships between how independent variables, such as stress, strain rate, strain, stress state, and temperature, independently affect the constitutive behavior of materials (Ref 8, 9, 10). Robust material models capturing the controlling physics of high-rate materials response are required for large-scale finite-element simulations of many complex engineering systems and processes, including the following:

- Automotive crashworthiness
- Aerospace impacts, including foreign-object damage, such as during bird ingestion in jet engines, blade containment in engines, and meteorite impact on satellites
- Dynamic structural loadings, such as those occurring during an earthquake
- High-rate manufacturing processes, including high-rate forging, machining, shot peening, shock welding, and laser surface processing
- Cavitation and particulate erosion in turbines and marine propulsion
- Defense applications, including projectile/armor and explosive or propellant/material interactions

Measurement of the mechanical properties of materials is normally conducted via loading test samples in compression, tension, or torsion. Conventional mechanical testing frames can be used to achieve nominally

constant loading rates for limited plastic strains and thereby a constant engineering strain rate. Typical screw-driven or servohydraulic testing machines are routinely used to measure the stress-strain response of materials up to strain rates as high as 1 s^{-1} . Specially designed testing machines, typically equipped with high-capacity servohydraulic valves and high-speed control and data acquisition instrumentation, can be used during compression and tensile testing to achieve strain rates as high as 200 s^{-1} . Above this strain rate regime, $\dot{\epsilon} > 200 \text{ s}^{-1}$, alternate techniques employing projectile driven impacts have been developed to directly or indirectly induce stress-wave propagation in a sample material.

Chief among these techniques is the split-Hopkinson pressure bar, which is capable of achieving the highest uniform uniaxial stress loading of a specimen in compression at nominally constant strain rates of the order of 10^3 s^{-1} . Hopkinson bar techniques have also been developed to probe the high-rate response of materials in tensile- and torsion-loading stress states. In each instance, stress is directly measured using elastic elements in series with the specimen of interest. Stress waves are generated via an impact event, and the elastic elements used are long bars such that the duration of the loading pulse is less than the wave transit time in the bar. In each of the Hopkinson bar techniques, the dynamic stress-strain response of materials at strain rates up to $2 \times 10^4 \text{ s}^{-1}$ in compression, and somewhat lower in tension or torsion, and true strains of 0.3 can be readily achieved in a single test.

References cited in this section

1. U.S. Lindholm, High Strain Rate Testing, Part 1: Measurement of Mechanical Properties, *Techniques of Metals Research*, Vol 5, R.F. Bunshah, Ed., Wiley Interscience, New York, 1971, p 199–271
2. U.S. Lindholm, Review of Dynamic Testing Techniques and Material Behaviour, *Inst. Phys. Conf. Ser.*, Vol 21, 1974, p 3–21
3. P.S. Follansbee, The Hopkinson Bar, *Mechanical Testing*, Vol 8, *ASM Handbook*, American Society for Metals, 1985, p 198–203
4. J.E. Field, S.M. Walley, N.K. Bourne, and J.M. Huntley, Experimental Methods at High Rates of Strain, *J. Phys. (France) IV Colloq.*, C8 (DYMAT 94), Vol 4, 1994, p 3–22
5. J.E. Field, S.M. Walley, N.K. Bourne, and J.M. Huntley, Review of Experimental Techniques for High Rate Deformation Studies, *Proc. Acoustics and Vibration Asia '98* (Singapore), 1998, p 9–38
6. W.E. Carrington and M.L.V. Gayler, The Use of Flat Ended Projectiles for Determining Yield Stress, Part III: Changes in Microstructure Caused by Deformation at High Striking Velocities, *Proc. R. Soc. (London) A*, Vol 194, 1948, p 323–331
7. B. Hopkinson, A Method of Measuring the Pressure Produced in the Detonation of High Explosives or by the Impact of Bullets, *Philos. Trans. R. Soc. (London) A*, Vol 213, 1914, p 437–456
8. P.S. Follansbee and U.F. Kocks, A Constitutive Description of Copper Based on the Use of the Mechanical Threshold Stress as an Internal State Variable, *Acta Metall.*, Vol 36, 1988, p 81–93
9. S.R. Chen and G.T. Gray III, Constitutive Behaviour of Tantalum and Tantalum-Tungsten Alloys, *Metall. Trans. A*, Vol 27, 1996, p 2994–3006
10. J.R. Klepaczko, Constitutive Modeling in Dynamic Plasticity Based on Physical State Variables—A Review, *J. Phys. (France) Colloq.*, C3 (DYMAT 88), Vol 49, 1988, p 553–560

Historical Background of the Hopkinson Bar Technique

The split-Hopkinson pressure bar technique is named for Bertram Hopkinson (Ref 7) who, in 1914, used the induced-wave propagation in a long elastic metallic bar to measure the pressures produced during dynamic events. Through the use of momentum traps of differing lengths, Hopkinson studied the shape and evolution of stress pulses as they propagated down long metallic rods as a function of time. Based on this pioneering work, the experimental apparatus using elastic stress-wave propagation in long rods to study dynamic processes in materials was named the Hopkinson pressure bar. Later work by Davies (Ref 11, 12) and Kolsky (Ref 13) used two Hopkinson pressure bars in series, with the sample sandwiched in between, to measure the dynamic stress-strain response of materials. This technique thereafter has been referred to as either the split-Hopkinson pressure bar (Ref 3, 14), Davies bar (Ref 15), or Kolsky bar (Ref 3, 13, 16, 17, 18). The generalized split-Hopkinson pressure bar technique in its current form owes a debt of gratitude to each of these innovative scientists, as well as to the engineers and scientists responsible for the development of high-precision strain gages, signal conditioners, and high-speed digital oscilloscopes, without which the sensitivity, accuracy, and reproducibility of this technique would not be possible.

Following the original split-Hopkinson pressure bar apparatus developed to measure the compressive mechanical behavior of a material, alternate Hopkinson bar schemes were designed for loading samples in uniaxial tension (Ref 14, 19, 20), torsion (Ref 21), simultaneous torsion compression (Ref 22), and simultaneous compression torsion (Ref 23). High-strain-rate testing in a Hopkinson bar under an imposed lateral confinement has also been demonstrated using shrink-fit metallic containment sleeves on a sample (Ref 24). Split-Hopkinson bars have also been used to load notched samples to measure either the shear strength (Ref 25, 26, 27, 28, 29) or the fracture toughness (Ref 30) of an impact-loaded material. The basic theory of how to reduce the pressure bar data based upon one-dimensional stress wave analysis, as presented in the theory of the split-Hopkinson pressure bar section, is common to all three loading stress states. Of the different Hopkinson bar techniques (i.e., compression, tension, and torsion) the compression bar remains the most readily analyzed and least complex method to achieve a uniform high-rate stress state. In addition, the compression bar uses simple right-regular solid samples. Details of the dynamic loading of materials in tension using either the tensile split-Hopkinson pressure bar or expanding ring test are compared and contrasted with the compression Hopkinson bar technique discussed in the section "Stress-State Equilibrium during Split-Hopkinson Pressure Bar Testing" in this article.

An alternate method of probing the mechanical behavior of materials at high strain rates, of the order of 10^3 s^{-1} , is the Taylor rod impact test. This technique, named after G.I. Taylor (Ref 31), who developed the test, entails firing a solid cylinder of the material of interest against a rigid target. The deformation induced in the rod due to the impact in the Taylor test shortens the rod as radial flow occurs at the impact surface. The fractional change in the rod length can then, by assuming one-dimensional rigid-plastic analysis, be related to the dynamic yield strength. By measuring the overall length of the impacted cylinder and the length of the undeformed (rear) section of the projectile, the dynamic yield stress of the material can be calculated (Ref 31). The Taylor test technique offers an apparently simplistic method to ascertain information concerning the dynamic strength properties of a material. However, this test represents an integrated test rather than a unique experiment with a uniform stress state or strain rate, as does the split-Hopkinson pressure bar. Accordingly, the Taylor test has been used most prevalently as a validation experiment in concert with two-dimensional finite-element calculations.

This article describes the techniques involved in measuring the high-strain-rate stress-strain response of materials using a split-Hopkinson pressure bar, hereafter abbreviated as SHPB (Ref 18). The focus of this article is on the generalized techniques applicable to all SHPBs, whether compressive, tensile, or torsion. Emphasis is given to the methods of collecting and analyzing compressive high-rate mechanical property data and a discussion of the critical experimental variables that must be controlled to yield valid and reproducible

high-strain-rate stress-strain data. Comparisons and contrasts to the differences invoked when using a tensile Hopkinson bar in terms of loading technique, sample design, and stress-state stability also are discussed.

References cited in this section

3. P.S. Follansbee, The Hopkinson Bar, *Mechanical Testing*, Vol 8, *ASM Handbook*, American Society for Metals, 1985, p 198–203
7. B. Hopkinson, A Method of Measuring the Pressure Produced in the Detonation of High Explosives or by the Impact of Bullets, *Philos. Trans. R. Soc. (London) A*, Vol 213, 1914, p 437–456
11. R.M. Davies, A Simple Modification of the Hopkinson Pressure Bar, *Proc. 7th Int. Cong. on Applied Mechanics*, Vol 1, 1948, p 404
12. R.M. Davies, A Critical Study of the Hopkinson Pressure Bar, *Philos. Trans. R. Soc. (London) A*, Vol 240, 1948, p 375–457
13. H. Kolsky, An Investigation of the Mechanical Properties of Materials at Very High Rates of Loading, *Proc. Phys. Soc. (London)*, Vol 62B, 1949, p 676–700
14. U.S. Lindholm and L.M. Yeakley, High Strain Rate Testing: Tension and Compression, *Exp. Mech.*, Vol 8, 1968, p 1–9
15. H. Kolsky, Stress Waves in Solids, *J. Sound Vib.*, Vol 1, 1964, p 88–110
16. V.P. Muzychenko, S.I. Kashchenko, and V.A. Guskov, Use of the Split Hopkinson Pressure Bar Method for Examining the Dynamic Properties of Materials: Review, *Ind. Lab. (USSR)*, Vol 52, 1986, p 72–83
17. H. Zhao and G. Gary, On the Use of SHPB Techniques to Determine the Dynamic Behavior of Materials in the Range of Small Strains, *Int. J. Solids Struct.*, Vol 33, 1996, p 3363–3375
18. G.T. Gray III, High-Strain-Rate Testing of Materials: The Split-Hopkinson Pressure Bar, *Methods in Materials Research*, E. Kaufmann, Ed., John Wiley Press, 1999, in press
19. J. Harding, E.O. Wood, and J.D. Campbell, Tensile Testing of Materials at Impact Rates of Strain, *J. Mech. Eng. Sci.*, Vol 2, 1960, p 88–96
20. G.H. Staab and A. Gilat, A Direct-Tension Split Hopkinson Bar for High Strain-Rate Testing, *Exp. Mech.*, Vol 31, 1991, p 232–235
21. J. Duffy, J.D. Campbell, and R.H. Hawley, On the Use of a Torsional Split Hopkinson Bar to Study Rate Effects in 1100-O Aluminum, *J. Appl. Mech. (Trans. ASME)*, Vol 38, 1971, p 83–91
22. J.L. Lewis and W. Goldsmith, A Biaxial Split Hopkinson Bar for Simultaneous Torsion and Compression, *Rev. Sci. Instrum.*, Vol 44, 1973, p 811–813
23. D.R. Chichili and K.T. Ramesh, Recovery Experiments for Adiabatic Shear Localization: A Novel Experimental Technique, *Trans. ASME*, Vol 66, 1999, p 10–20
24. W. Chen and G. Ravichandran, Static and Dynamic Compressive Behavior of Aluminum Nitride under Moderate Confinement, *J. Amer. Ceram. Soc.*, Vol 79, 1996, p 579–584

25. J.D. Campbell and W.G. Ferguson, The Temperature and Strain Rate Dependence of the Shear Strength of Mild Steel, *Philos. Mag.*, Vol 21, 1970, p 63–82
26. J. Harding and J. Huddart, The Use of the Double-Notch Shear Test in Determining the Mechanical Properties of Uranium at Very High Rates of Strain, *Inst. Phys. Conf. Ser.*, Vol 47, 1980, p 49–61
27. D. Ruiz, J. Harding, and C. Ruiz, The Double Notch Shear Test—Analysis and Development for Material Testing at Very High Strain Rates, *Structures under Shock and Impact*, P.S. Bulson, Ed., Elsevier, Amsterdam, p 145–154
28. J.R. Klepaczko, An Experimental Technique for Shear Testing at High and Very High Strain Rates: The Case of a Mild Steel, *Int. J. Impact Eng.*, Vol 15, 1994, p 25–40
29. J.R. Klepaczko, H.V. Nguyen, and W.K. Nowacki, Quasi-Static and Dynamic Shearing of Sheet Metals, *Eur. J. Mech. A-Solids*, Vol 18, 1999, p 271–289
30. J. Klepaczko, Application of the Split Hopkinson Pressure Bar to Fracture Dynamics, *Inst. Phys. Conf. Ser.*, Vol 47, 1980, p 201–214
31. G.I. Taylor, The Use of Flat Ended Projectiles for Determining Yield Stress, Part I: Theoretical Considerations, *Proc. R. Soc. (London) A*, Vol 194, 1948, p 289–299

Principles of the Split-Hopkinson Pressure Bar

While there is no universal standard design for SHPB test apparatus, all facilities share common design elements. A compression Hopkinson bar test apparatus consists of the following:

- Two long, symmetrical bars
- Bearing and alignment fixtures to allow the bars and striking projectile to move freely while retaining precise axial alignment
- Compressed gas launcher/gun tube or alternate propulsion device for accelerating a projectile, termed the striker bar, to produce a controlled compressive pulse in the incident bar
- Strain gages mounted on both bars to measure the stress-wave propagation in the bars
- Associated instrumentation and data acquisition system to control, record, and analyze the stress-wave data in the bars (Ref 18)

In a compression split-Hopkinson pressure bar, a sample is sandwiched between an elastic incident and a transmitted bar (Fig. 1). The terms *incident/input* and *transmitted/output* are used interchangeably throughout this article to describe the two pressure bars used in the SHPB. The elastic displacements measured in these bars are in turn used to determine the stress-strain conditions at each end of the sample.

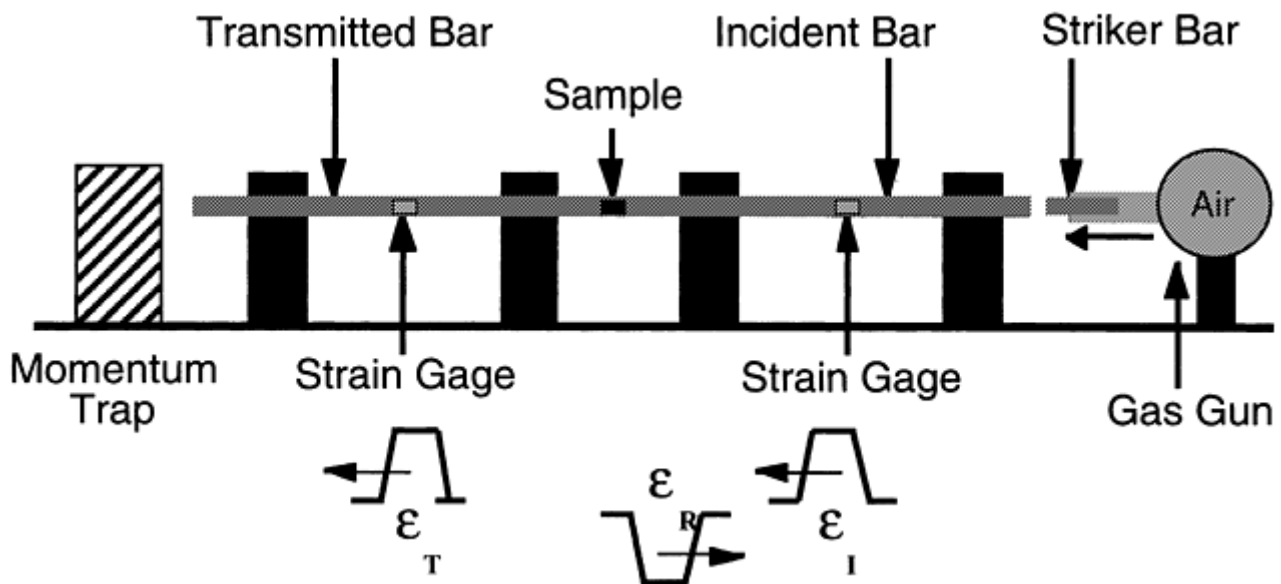


Fig. 1 Schematic of a compression split-Hopkinson pressure bar

The bars used in a split-Hopkinson bar setup are traditionally constructed from a high-strength structural metal, AISI-SAE 4340 steel, maraging steel, or a nickel alloy such as Inconel. Such construction is used because the yield strength of the selected pressure bar material determines the maximum stress attainable within the deforming specimen given that the pressure bars must remain elastic. Inconel bars have been previously used for elevated-temperature Hopkinson bar testing because this alloy's elastic properties are essentially invariant up to 800 °C (Ref 3). Because a lower-modulus material increases the signal-to-noise level, the selection of a bar material with lower strength and lower elastic modulus material for the bars is sometimes desirable to facilitate high-resolution dynamic testing of low-strength materials such as polymers or foams. Researchers have selected bar materials possessing a range of elastic stiffnesses from maraging steel (210 GPa) to titanium (110 GPa) to aluminum (90 GPa) to magnesium (45 GPa) (Ref 5, 32), and finally, to polymer bars (<20 GPa) (Ref 17, 33, 34, 35). Alternately, the signal-to-noise of a Hopkinson bar used to test polymeric materials can be

increased using a hollow tubular transmitted pressure bar (Ref 36). While this technique can yield increased transmitted wave measurement sensitivity, the absolute resolution of the sample stress-strain data for polymeric materials must still address the elastic wave dispersion in the tubular-transmitted bar (Ref 37, 38).

The length, l , and diameter, d , of the pressure bars are chosen to meet a number of criteria for test validity as well as the maximum strain rate and strain level desired in the sample. The length of the pressure bars must first ensure one-dimensional wave propagation for a given pulse length; for experimental measurements on most engineering materials, this propagation requires approximately 10 bar diameters. To readily allow separation of the incident and reflected waves for data reduction, each bar should exceed a length-to-diameter (L/D) ratio of ~ 20 . In addition, the maximum strain rate desired will influence the selection of the bar diameter because the highest strain-rate tests require the smallest diameter pressure bars (this aspect of bar design is discussed in a later section). The third consideration affecting the selection of the bar length is the amount of total strain desired to be imparted into the specimen; the absolute magnitude of this strain is related to the length of the incident wave. The pressure bar must be at least twice as long as the incident wave if the incident and reflected waves are to be recorded without interference. In addition, because the bars must remain elastic during the test, the displacement and velocity of the bar interface between the sample and the bar can be accurately determined. Depending on the sample size, for strains $>30\%$ it may be necessary for the split-Hopkinson bars to have an L/D ratio of 100 or more (Ref 3). There are similar requirements for bar L/D ratios to allow wave separation for compression, tensile, and torsion Hopkinson bars.

For proper Hopkinson bar operation, the bars must be physically straight, free to move without binding, and carefully mounted to ensure optimal axial alignment. Precision bar alignment is required for both uniform and one-dimensional wave propagation within the pressure bars as well as for uniaxial compression within the specimen during loading. Bar alignment cannot be forced by overconstraining or forceful clamping of curved pressure bars in an attempt to straighten them because this clamping violates the boundary conditions for one-dimensional wave propagation in an infinite cylindrical solid. Lack of free movement of the bars will lead to additional noise on the wave forms measured on the pressure bars. Bar motion must not be impeded by the mounting bushings but rather must remain free to readily move along the bar axis. Accordingly, it is essential to apply precise dimensional specifications during construction and assembly. Pressure bars are often centerless ground along their length to achieve the uniform diameter and straightness required. In typical bar installations, as schematically shown in Fig. 1, the pressure bars are mounted to a common rigid base to provide a rigid and straight mounting platform. Construction of the Hopkinson pressure bar facility, compression, tension, or torsion, on an optical rail beam rigidly attached to an I-beam, can be used to facilitate reproducible alignment. Figure 2 shows one of the compression Hopkinson bar facilities at Los Alamos National Laboratory, where an optical rail is used to maintain accurate pressure bar alignment. Individual mounting brackets or stanchions with slip bearings through which the bars pass are typically spaced every 200 to 300 mm (8 to 12 in.), depending on the bar diameter and stiffness. Mounting brackets are generally designed so that they can be individually translated to adjust bar alignment within each stanchion.

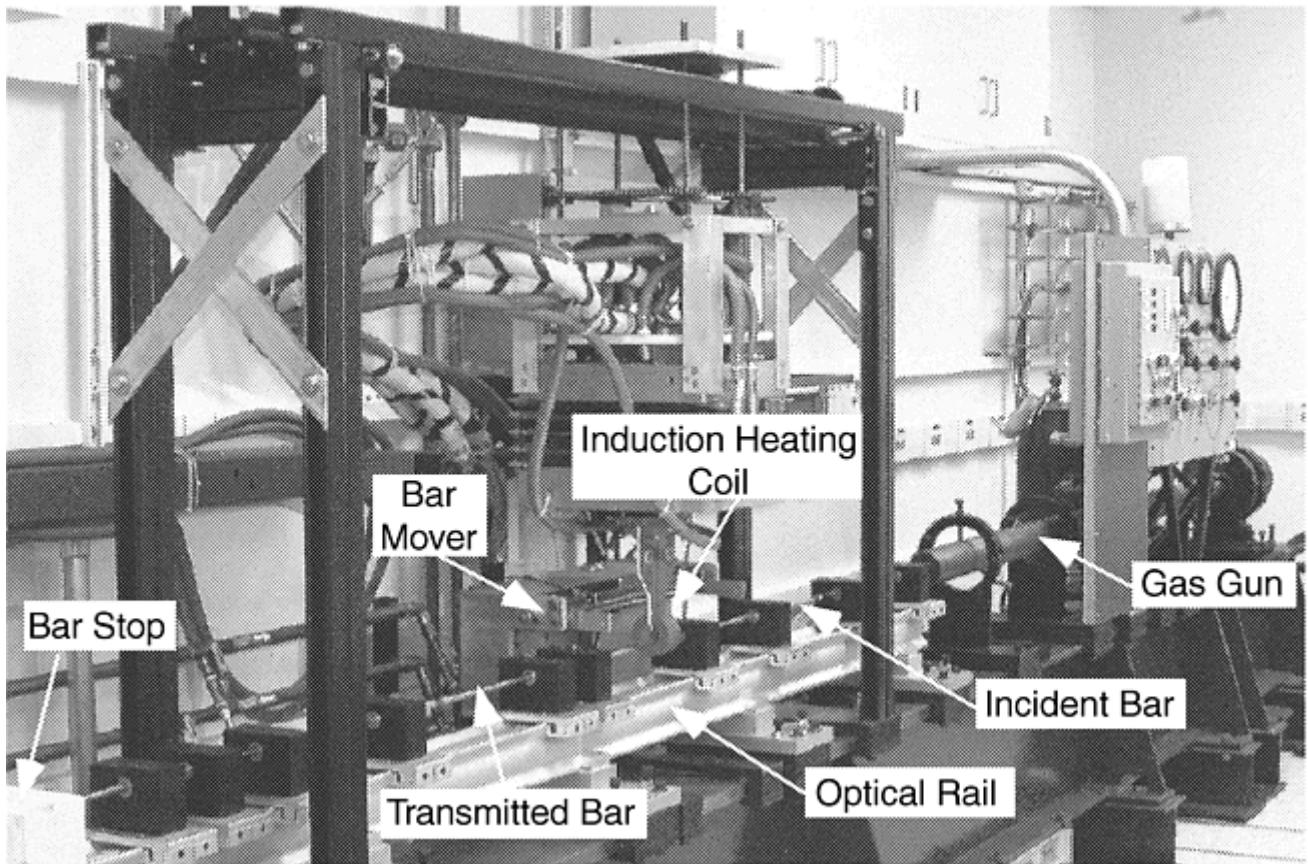


Fig. 2 A compression split-Hopkinson pressure bar facility at Los Alamos National Laboratory

The most common method of generating an incident wave in the input bar is to propel a striker bar to impact the end of the incident bar. The striker bar is normally fabricated from the same material and is of the same diameter as the pressure bars. The length and velocity of the striker bar are chosen to produce the desired total strain and strain rate within the test specimen. While elastic waves can also be generated in an incident bar through the adjacent detonation of explosives at the free end of the incident bar, as Hopkinson did (Ref 7), it is more difficult to ensure a one-dimensional excitation within the incident bar by direct explosive loading.

The impact of a striker bar on the free end of the incident bar develops a longitudinal compressive incident wave in this bar, designated ϵ_i , as denoted in Fig. 3. Once this wave reaches the bar-specimen interface, a part of the pulse, designated ϵ_r , is reflected while the remainder of the stress pulse passes through the specimen and, upon entering the output bar, is termed the transmitted wave, ϵ_t . The time of passage and magnitude of these three elastic pulses through the incident and transmitted bars are recorded by strain gages normally cemented at the midpoint positions along the length of the two pressure bars. Figure 3 shows an illustration of the strain-gage data measured as a function of time for the three wave signals during the testing of a 304L stainless steel sample using maraging steel pressure bars. The incident and transmitted wave signals represent compressive loading pulses, while the reflected wave is a tensile wave.

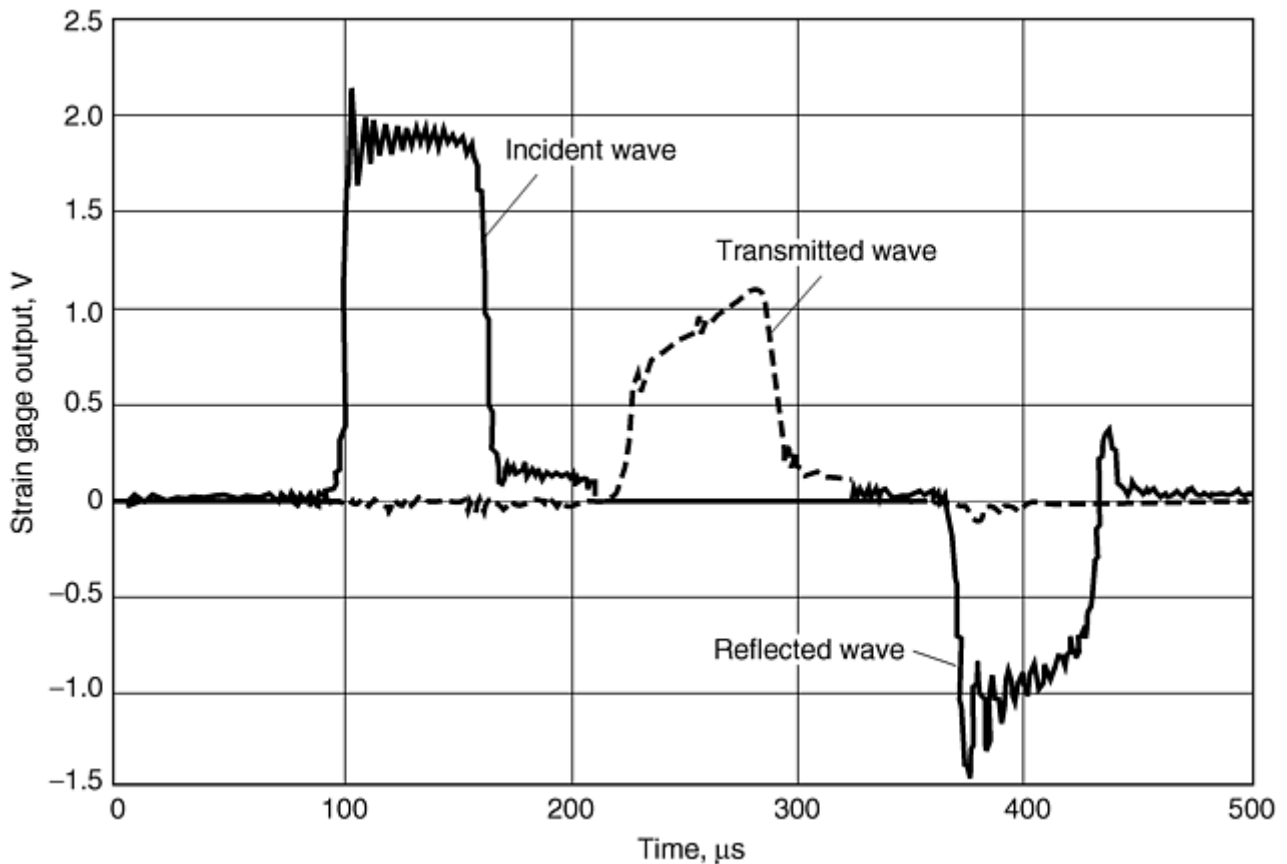


Fig. 3 Strain-gage data, after signal conditioning and amplification, from a compression split-Hopkinson pressure bar test of a 304 stainless steel sample showing the three stress waves measured as a function of time. Note that the wave positions in time are arbitrarily superimposed due to the time delays used during data acquisitions.

Using the wave signals from the gages on the incident and transmitted bars as a function of time, the forces and velocities at the two interfaces between the pressure bars and the specimen can be determined. When the specimen is deforming uniformly, the strain rate within the specimen is directly proportional to the amplitude of the reflected wave. Similarly, the stress within the sample is directly proportional to the amplitude of the transmitted wave. (termed the 1-wave stress as discussed later). The reflected wave is also integrated to obtain strain and is plotted against stress to give the dynamic stress-strain curve for the specimen.

References cited in this section

3. P.S. Follansbee, The Hopkinson Bar, *Mechanical Testing*, Vol 8, *ASM Handbook*, American Society for Metals, 1985, p 198–203
5. J.E. Field, S.M. Walley, N.K. Bourne, and J.M. Huntley, Review of Experimental Techniques for High Rate Deformation Studies, *Proc. Acoustics and Vibration Asia '98* (Singapore), 1998, p 9–38
7. B. Hopkinson, A Method of Measuring the Pressure Produced in the Detonation of High Explosives or by the Impact of Bullets, *Philos. Trans. R. Soc. (London) A*, Vol 213, 1914, p 437–456
17. H. Zhao and G. Gary, On the Use of SHPB Techniques to Determine the Dynamic Behavior of Materials in the Range of Small Strains, *Int. J. Solids Struct.*, Vol 33, 1996, p 3363–3375
18. G.T. Gray III, High-Strain-Rate Testing of Materials: The Split-Hopkinson Pressure Bar, *Methods in Materials Research*, E. Kaufmann, Ed., John Wiley Press, 1999, in press

32. G.T. Gray III, D.J. Idar, W.R. Blumenthal, C.M. Cady, and P.D. Peterson, High- and Low-Strain Rate Compression Properties of Several Energetic Material Composites as a Function of Strain Rate and Temperature, *11th Detonation Symposium*, 1998 (Snow Mass, CO), J. Short, Ed., in press
33. G. Gary, J.R. Klepaczko, and H. Zhao, Generalization of Split Hopkinson Bar Technique to Use Viscoelastic Materials, *Int. J. Impact Eng.*, Vol 16, 1995, p 529–530
34. G. Gary, L. Rota, and H. Zhao, Testing Viscous Soft Materials at Medium and High Strain Rates, *Constitutive Relation in High/Very High Strain Rates*, K. Kawata and J. Shioiri, Ed., Springer-Verlag, Tokyo, 1996, p 25–32
35. G.T. Gray III, W.R. Blumenthal, C.P. Trujillo, and R.W. Carpenter II, Influence of Temperature and Strain Rate on the Mechanical Behavior of Adiprene-L100, *J. Phys. (France)*, C3 (DYMAT 97), Vol 7, 1997, p 523–528
36. W. Chen, B. Zhang, and M.J. Forrestal, A Split Hopkinson Bar Technique for Low-Impedance Materials, *Exp. Mech.*, Vol 39, 1999, p 1–5
37. I. Mirsky and G. Herrmann, Axially Symmetric Motions of Thick Cylindrical Shells, *J. Appl. Mech. (Trans. ASME)*, Vol 25, 1958, p 97–102
38. G. Herrmann and I. Mirsky, Three-Dimensional and Shell-Theory Analysis of Axially Symmetric Motions of Cylinders, *J. Appl. Mech. (Trans. ASME)*, Vol 23, 1956, p 563–568

Classic Split-Hopkinson Pressure Bar Testing

George T. (Rusty) Gray III, Los Alamos National Laboratory

Theory of the Split-Hopkinson Pressure Bar

The determination of the stress-strain behavior of a material being tested in a Hopkinson bar, whether it is loaded in compression as in the present illustration or in a tensile or torsion bar configuration, is based on the same principles of one-dimensional elastic-wave propagation within the pressure loading bars as previously reviewed (Ref 1, 3, 16, 18, 39).

As identified originally by Hopkinson (Ref 7) and later refined by Kolsky (Ref 13), the use of a long elastic bar to study high-strain-rate mechanical behavior of materials is feasible using remote elastic bar measures of sample response because the wave propagation behavior in such a geometry is well understood and mathematically predictable. Accordingly, the displacements or stresses generated at any point can be deduced by measuring the elastic wave at any point, x , as it propagates along the bar (Ref 3, 18, 40).

The subscripts 1 and 2 are used in this description to denote the incident and transmitted bar ends of the specimen, respectively. The strains in the bars are then designated as ϵ_i , ϵ_r , and ϵ_t (incident, reflected, and transmitted strains, respectively) and the displacements of the ends of the specimen as u_1 and u_2 at the incident bar-specimen and specimen-transmitted bar interfaces as given schematically in the enlarged view of the test specimen in Fig. 4.

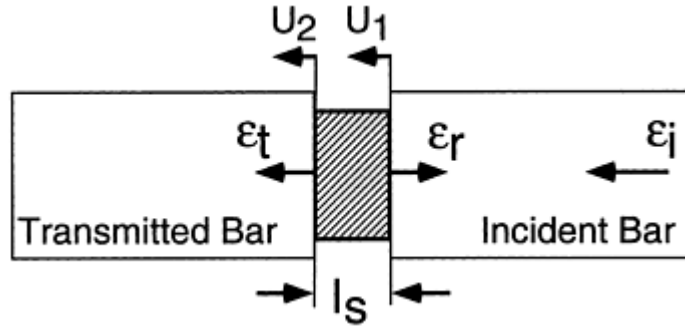


Fig. 4 Expanded view of incident (input) bar/specimen/transmitted (output) bar region

From elementary wave theory, it is known that the solution to the wave equation:

$$\frac{\partial^2 u}{\partial x^2} = \frac{1}{c_b^2} \frac{\partial^2 u}{\partial t^2} \quad (\text{Eq 1})$$

can be written as:

$$u = f(x - c_b t) + g(x + c_b t) = u_i + u_r \quad (\text{Eq 2})$$

for the incident (input) bar, where f and g are functions describing the incident and reflected wave shapes, and c_b is the longitudinal wave speed in the pressure bars.

By definition, the 1-D strain is given by:

$$\epsilon = \frac{\partial u}{\partial x} \quad (\text{Eq 3})$$

Therefore, differentiating Eq 2 with respect to x , the strain in the incident rod is given by:

$$\epsilon = f' + g' = \epsilon_i + \epsilon_r \quad (\text{Eq 4})$$

Differentiating Eq 2 with respect to time and using Eq 4 gives:

$$\dot{u} = c_b (-f' + g') = c_b (-\epsilon_i + \epsilon_r) \quad (\text{Eq 5})$$

for the incident bar.

The time derivative of the displacement in the transmitted bar, $u = h(x - c_b t)$, yields:

$$\dot{u} = -c_b \epsilon_t \quad (\text{Eq 6})$$

in the transmitted bar. Equations 5 and 6 are true everywhere, including at the ends of the pressure bars. The strain rate in the test specimen is:

$$\dot{\epsilon} = \frac{(\dot{u}_1 - \dot{u}_2)}{l_s} \quad (\text{Eq 7})$$

where l_s is the instantaneous length of the specimen, and \dot{u}_1 and \dot{u}_2 are the velocities at the incident bar-specimen and specimen-transmitted bar interfaces, respectively.

Substituting Eq 5 and 6 into Eq 7 gives:

$$\dot{\epsilon} = \frac{c_b}{l_s} (-\epsilon_i + \epsilon_r + \epsilon_t) \quad (\text{Eq 8})$$

By definition, the forces in the two bars are:

$$F_1 = AE(\epsilon_i + \epsilon_r) \quad (\text{Eq 9})$$

and

$$F_2 = AE\epsilon_t \quad (\text{Eq 10})$$

where A is the cross-sectional area of the pressure bar, and E is the Young's elastic modulus of the bars (normally equal, given that identical material is used for both the incident and transmitted pressure bars).

After an initial "ringing-up" period, where the exact duration or period depends on the sample sound speed and sample geometry (in particular, its length), it is assumed that the specimen is in force equilibrium, and the

specimen is deforming uniformly. If these assumptions are valid, a simplification can be made equating the forces on each side of the specimen (i.e., $F_1 = F_2$). Comparing Eq 9 and 10, therefore, means that

$$\varepsilon_t = \varepsilon_i + \varepsilon_r \quad (\text{Eq 11})$$

Substituting this criterion into Eq 8 yields:

$$\dot{\varepsilon} = \frac{2 c_b \varepsilon_r}{l_s} \quad (\text{Eq 12})$$

The engineering stress, or conventional stress, in conventional mechanical testing of materials is calculated from the force divided by the sample original area, A_0 . Because of the constancy of volume in incompressible solids, $A_0 l_0 = A_s l_s$, (where l_0 is the original length of the specimen, A_0 is the original cross-sectional area, and A_s is the instantaneous cross-sectional area of the sample) (Ref 41). Expressions for the strain can therefore be written in terms of either the length or the area of the test sample. Accordingly, the true stress is calculated from the strain-gage-signal measure of the transmitted force divided by the instantaneous cross-sectional area, A_s , of the specimen over which it acts:

$$\sigma(t) = \frac{AE\varepsilon_t}{A_s} \quad (\text{Eq 13})$$

The importance of this requirement to all types of Hopkinson bar testing using the one-dimensional wave assumptions detailed is that true stress in a sample in the Hopkinson bar cannot be extracted for materials whose volumes are not conserved. The instantaneous sample area used in Eq 13 is deduced from the reflected strain signal in the incident bar assuming that the constancy of volume assumption is valid in the sample (i.e., there is a fixed relationship between sample cross-sectional area and its length). Without this assumption, there is no basis for using the transmitted signal to measure force and the reflected wave to extract strain in the sample. Materials for which this problem exists include metallic and polymeric foams, honeycomb structures, and porous compacts for which mechanical loading produces compaction, densification, or porosity during testing. Valid Hopkinson bar testing of materials for which the constant volume criterion is not valid, therefore, requires additional sample diagnostics during the duration of the test to calculate true stress. Simultaneous use of high-resolution high-speed photography can be used to monitor sample length and diameter during testing. The photographic data, once digitized, can then be used to measure the actual strain rate and true strain as a function of time in the sample. Such data, when combined with the transmitted wave-data measuring force, can provide the needed data to calculate true stress.

Given that the volume constancy requirement is satisfied in the sample, Eq 12 and 13 can be used to determine the dynamic stress-strain curve of the sample. This analysis is termed a 1-wave analysis because it uses only the reflected wave to calculate strain in the sample, and only the transmitted wave is used to calculate the stress in the sample. The 1-wave analysis assumes that stress equilibrium is ensured in the sample (i.e., as a function of time, the stress and strain in the sample are uniform along its length). Conversely, the stress in the sample at the incident bar-sample interface can be calculated using a momentum balance of the incident and reflected wave pulses, termed a 2-wave stress analysis because it is a summation of the two waves at this interface. However, it is known that such a condition cannot be correct at the early stages of any test because of the transient effect that occurs when loading starts at the incident bar-specimen interface while the other sample face remains at rest. Given finite stress-wave propagation through the sample, time is required for stress-state equilibrium to be achieved. Reduced sound speed and high radial inertia in the sample will increase this problem (Ref 32).

Previous researchers have additionally adopted a 3-wave stress analysis, which averages the forces on both ends of the specimen to track the ringup of the specimen to a state of stable stress (Ref 18, 40). The term *3-wave* indicates the use of all three waves to calculate an average stress in the sample, the transmitted wave to calculate the stress at the specimen-transmitted interface (back stress), and the combined incident and reflected pulses to calculate the stress at the incident bar-specimen interface (front stress). In the 3-wave case, the specimen stress is then simply the average of the two forces divided by the combined interface areas:

$$\sigma(t) = \frac{F_1(t) + F_2(t)}{2 A_s} \quad (\text{Eq 14})$$

Substituting Eq 9 and 10 into Eq 14 then gives:

$$\sigma(t) = \frac{AE}{2A_s}(\epsilon_i + \epsilon_r + \epsilon_t) \quad (\text{Eq 15})$$

From these equations, the average stress-strain curve of the specimen can be computed from the measured reflected and transmitted strain pulses as long as the volume of the specimen remains constant and the sample is free of barreling (i.e., friction effects are minimized).

References cited in this section

1. U.S. Lindholm, High Strain Rate Testing, Part 1: Measurement of Mechanical Properties, *Techniques of Metals Research*, Vol 5, R.F. Bunshah, Ed., Wiley Interscience, New York, 1971, p 199–271
3. P.S. Follansbee, The Hopkinson Bar, *Mechanical Testing*, Vol 8, *ASM Handbook*, American Society for Metals, 1985, p 198–203
7. B. Hopkinson, A Method of Measuring the Pressure Produced in the Detonation of High Explosives or by the Impact of Bullets, *Philos. Trans. R. Soc. (London) A*, Vol 213, 1914, p 437–456
13. H. Kolsky, An Investigation of the Mechanical Properties of Materials at Very High Rates of Loading, *Proc. Phys. Soc. (London)*, Vol 62B, 1949, p 676–700
16. V.P. Muzychenko, S.I. Kashchenko, and V.A. Guskov, Use of the Split Hopkinson Pressure Bar Method for Examining the Dynamic Properties of Materials: Review, *Ind. Lab. (USSR)*, Vol 52, 1986, p 72–83
18. G.T. Gray III, High-Strain-Rate Testing of Materials: The Split-Hopkinson Pressure Bar, *Methods in Materials Research*, E. Kaufmann, Ed., John Wiley Press, 1999, in press
32. G.T. Gray III, D.J. Idar, W.R. Blumenthal, C.M. Cady, and P.D. Peterson, High- and Low-Strain Rate Compression Properties of Several Energetic Material Composites as a Function of Strain Rate and Temperature, *11th Detonation Symposium*, 1998 (Snow Mass, CO), J. Short, Ed., in press
39. M.M. Al-Mousawi, S.R. Reid, and W.F. Deans, The Use of the Split Hopkinson Pressure Bar Techniques in High Strain Rate Materials Testing, *Proc. Inst. Mech. Eng., Part C: J. Mech. Eng. Sci.*, Vol 211, 1997, p 273–292
40. P.S. Follansbee and C. Frantz, Wave Propagation in the SHPB, *J. Eng. Mater. Technol. (Trans. ASME)*, Vol 105, 1983, p 61–66
41. G.E. Dieter, *Mechanical Metallurgy*, McGraw-Hill, Inc., 1976

Classic Split-Hopkinson Pressure Bar Testing

George T. (Rusty) Gray III, Los Alamos National Laboratory

Practical Aspects of the Split-Hopkinson Pressure Bar

Calibration. To analyze the strain-gage data from a split-Hopkinson pressure bar test, the system must be calibrated prior to testing (Ref 3, 18). Calibration of the entire Hopkinson bar setup is obtained in situ by comparing the constant amplitude of a wave pulse with the impact velocity of the striker bar for each bar

separately, termed “bars apart.” Operationally, this calibration is accomplished by inputting a known velocity pulse into the input bar, and then, in turn, the transmitted bar, with no sample present. Thereafter, impact of the striker with the input bar in direct contact with the transmitted bar, with no specimen, gives the coefficient of transmission, termed “bars together.” Accurate measurement of the velocity, V , of the striker bar impact into a pressure bar is linearly related by:

$$\varepsilon_j = \frac{V}{2c_b} \quad (\text{Eq 16})$$

where ε_j is the strain in the incident or transmitted bar, depending on which is being calibrated, and c_b is the longitudinal wave speed in the bar if the impacting striker bar and the pressure bar are the same material and have the same cross-sectional area. Careful measurement of the striker velocity, using a laser interruption scheme or shorting pins, for example, in comparison with the elastic strain signal in a pressure bar, can then be used to calculate a calibration factor for the pressure bar being calibrated. Accurate measurement of the longitudinal-wave velocity in the pressure bars being used is critical. The use of textbook values is not advised. Variations in alloy chemistry, microstructure, and heat treatment from the manufacturer can all lead to measurable variations in the longitudinal wave speed in the pressure bars and should not be assumed to be a constant but rather measured for each set of bars used. Calibration values also include validation due to strain-gage response, including cement or epoxy interfaces, wiring, amplifiers, and so on. Calibrations should be verified periodically, especially when changes are made to either mechanical or electronic components.

Optimal data resolution also requires careful design of the sample size for a given material as well as the selection of an appropriate striker bar length and velocity to achieve test goals. The determination of the optimal sample length first requires consideration of the sample rise time, t , required for a uniform uniaxial stress state to be achieved within the sample. It has been estimated (Ref 42) that this rise time is the time required for three (actually π) reverberations of the stress pulse within the specimen (Ref 3). For a plastically deforming solid that obeys the Taylor-von Karman theory, time follows the relationship:

$$t^2 \geq \frac{\pi^2 \rho_s l_s^2}{\partial\sigma/\partial\varepsilon} \quad (\text{Eq 17})$$

Here, ρ_s is the density of the specimen, l_s is the specimen length, and $\partial\sigma/\partial\varepsilon$ is the stage 2 work-hardening rate of the true stress/true strain curve for the material to be tested. For rise times less than that given by Eq 17, the sample should not be assumed to be deforming uniformly, and stress-strain data will accordingly be in error. Materials possessing either high work-hardening rates, slow sound speeds, and/or high densities will require shorter sample lengths to facilitate rapid ringup and, therefore, rapid attainment of a uniaxial stress state in the sample.

One approach for achieving a uniform stress state during split-Hopkinson pressure bar testing is to decrease the sample length such that the rise time, t , from Eq 17 is as small as possible. Other considerations of scale, which are described in the sample design section, limit the range of L/D ratios appropriate for a given material; the specimen length may not be decreased without a concomitant decrease in the specimen and bar diameters. The use of small diameter bars (<6 mm) to achieve higher strain rates is a common practice in split-Hopkinson pressure bar testing (Ref 3).

Pulse Shaping. Because the value of t from Eq 17 has a practical minimum, an alternate method to facilitate stress-state equilibrium at low strains is to increase the rise time of the incident wave. Use of impedance-matched materials for the striker and incident bar (i.e., a symmetric impact) yields a short rise-time pulse, which approximates a square wave. The rise time of such a square-wave pulse is likely to be less than t in Eq 16 in most instances. Contrarily, if the rise time of the incident wave pulse is increased to a value more comparable with the time to ring up the specimen, then the data will be valid at an earlier strain. Furthermore, because the highly dispersive short wavelength components arise from the leading and trailing edges in the incident wave, a longer rise-time pulse will contain fewer of these components than will a sharply rising pulse (Ref 3, 43). The consequence of this solution is a lower applied strain rate.

Experimentally, the rise time of the incident wave can be increased by placing a soft, deformable metal shim between the striker and the incident bar during impact. The choice of material and thickness for this shim, or tip material (Ref 43), depends on the desired strain rate and the strength of the specimen. Typically, the tip material is selected to have the same strength as the specimen and is 0.1 to 2 mm (0.004 to 0.08 in.) in thickness. An additional benefit of this layer is that it can result in a more uniform strain rate throughout the experiment. However, for thick shims the strain rate will not be constant and will ramp up during the test. The exact

selection of the optimal tip material and thickness for a given test sample is not readily calculated and remains a matter of experience via trial and error. The use of tip materials to shape the incident pulse is particularly effective in attaining constant strain rates and stress-state equilibrium in modest- and high-strength materials exhibiting steep strain-hardening rates.

A recent proposed alternative to the use of tip material to increase the incident pulse rise time is to use a three-bar Hopkinson configuration (Ref 44, 45). In the three-bar configuration, an additional pressure bar and a dummy sample are positioned between the striker bar and the traditional incident bar. The pulse transmitted by the dummy specimen becomes the new incident pulse applied to the incident bar. With this method, the transmitted pulse sent into the incident pressure bar is ramp shaped, with only a minor amount of oscillations (Ref 45). The disadvantages of this method are the need for an additional pressure bar and an additional sample for each test. Alternately, a lower-strength preloading bar can be substituted, which damps many of the high-frequency oscillations and removes the need for a second sample (Ref 45).

Hopkinson Bar Test Setup. Once the Hopkinson bar system has been calibrated and the optimal specimen length, l_s , has been selected, preparations for testing can proceed (Ref 3). At a constant strain rate, the maximum strain that can be achieved in the specimen is directly proportional to the length of the striker bar utilized, L :

$$\epsilon = 2\dot{\epsilon} \frac{L}{c_b} \quad (\text{Eq 18})$$

The nominal strain rate in the specimen may be conservatively approximated by considering momentum conservation between the striker bar and incident bar. It can similarly be shown that (Ref 3):

$$\dot{\epsilon} = \frac{V}{l_s} \quad (\text{Eq 19})$$

where V is the striker bar velocity, and l_s is the length of the specimen. This equation overestimates the strain rate but can provide a useful value for test design. At higher striker-bar velocities, this relationship has been found to be a good first approximation for soft metals, such as annealed copper or aluminum. Equations 18 and 19 can be used to approximate the striker-bar length and striker-bar velocity required to achieve a desired strain and strain rate for a given sample size. These formulas provide a good starting point for selecting test parameters to achieve a valid SHPB test. However, samples possessing high initial yield strengths, yield drops such as those often seen in low-carbon steels or other refractory metals, and/or very high strain-hardening responses, will require increased striker-bar lengths and impact velocities to achieve the desired strain value.

Stress-State Equilibrium during Split-Hopkinson Pressure Bar Testing. The classic split-Hopkinson pressure bar equations relating strain-gage measurement to stress-strain behavior in the deforming specimen require that the specimen deform uniformly. This behavior is opposed by both radial and longitudinal inertia and by frictional constraint at the specimen-pressure bar interfaces. To understand the procedure to validate attainment of a uniform stress state in the sample in an SHPB test, it is instructive to review the different analyses discussed, which are used to calculate sample stress from the pressure bar strains and what they indicate. In the 1-wave analysis, the sample stress is directly proportional to the bar strain measured in the output bar as calculated using Eq 13. This waveform characteristically exhibits low oscillation amplitude because the deforming sample effectively damps much of the high-frequency oscillations inherent in the incident pulse as it propagates through the sample. More importantly, the 1-wave stress analysis reflects the conditions at the sample-transmitted bar interface and is often referred to as the sample back stress.

Alternatively, in a 2-wave analysis, the sum of the synchronized incident and reflected bar waveforms (which are opposite in sign) is proportional to the sample front stress and represents the conditions at the incident bar-sample interface. Unfortunately, both the incident and reflected waveforms contain substantial inherent oscillations which, compared to the transmitted waveform, cause uncertainty in the interpretation of stress, especially near the yield point. In addition, these harmonic oscillations are subject to dispersion due to the wavespeed dependence of different frequencies that causes asynchronization of the raw overlapped waveforms and, therefore, inaccuracy in the calculation of the front stress (Ref 18, 32).

A dispersion-correction analysis has been developed (Ref 3, 40, 43) to account for these changes in phase angle of the primary mode harmonic oscillation of all three strain signals. This analysis results in more accurate and smoother stress-strain curves, especially near the yield point. Finally, a third stress-calculation variation that

considers the complete set of three measured bar waveforms, the 3-wave analysis, is simply the average of the front and the back stress. The 3-wave average is calculated as described by Eq 15.

Sample equilibrium can be checked by comparing the 1-wave and 2-wave (or 3-wave) stress-strain response (Ref 18, 40, 46, 47, 48). Recent studies have demonstrated that both inertia and wave propagation effects can significantly affect the stress differences across the length of a specimen deformed in a compression SHPB (Ref 18, 32, 47, 49).

The validity of an SHPB test may be verified by examining the incident and transmitted pressure-bar data for stress-state equilibrium as well as a constant strain rate. When the stress state is uniform throughout the sample, the 2-wave stress oscillates equally above and below the 1-wave stress. Figure 5 shows the 1-wave, 2-wave, and strain-rate data as a function of strain for an SHPB test conducted on a 304L stainless steel sample. In this illustration, the front and back stress data reductions exhibit very similar response beyond ~ 0.02 strain, verifying that the sample attained a uniform stress state. Verification of attaining an essentially constant strain rate throughout an SHPB test will serve as validation of a careful balance of striker-bar length, striker-bar velocity, and the use of tip material. In addition to a check of the stress equilibrium in the specimen, a constant strain rate demonstrates a high-precision, valid material characterization measurement.

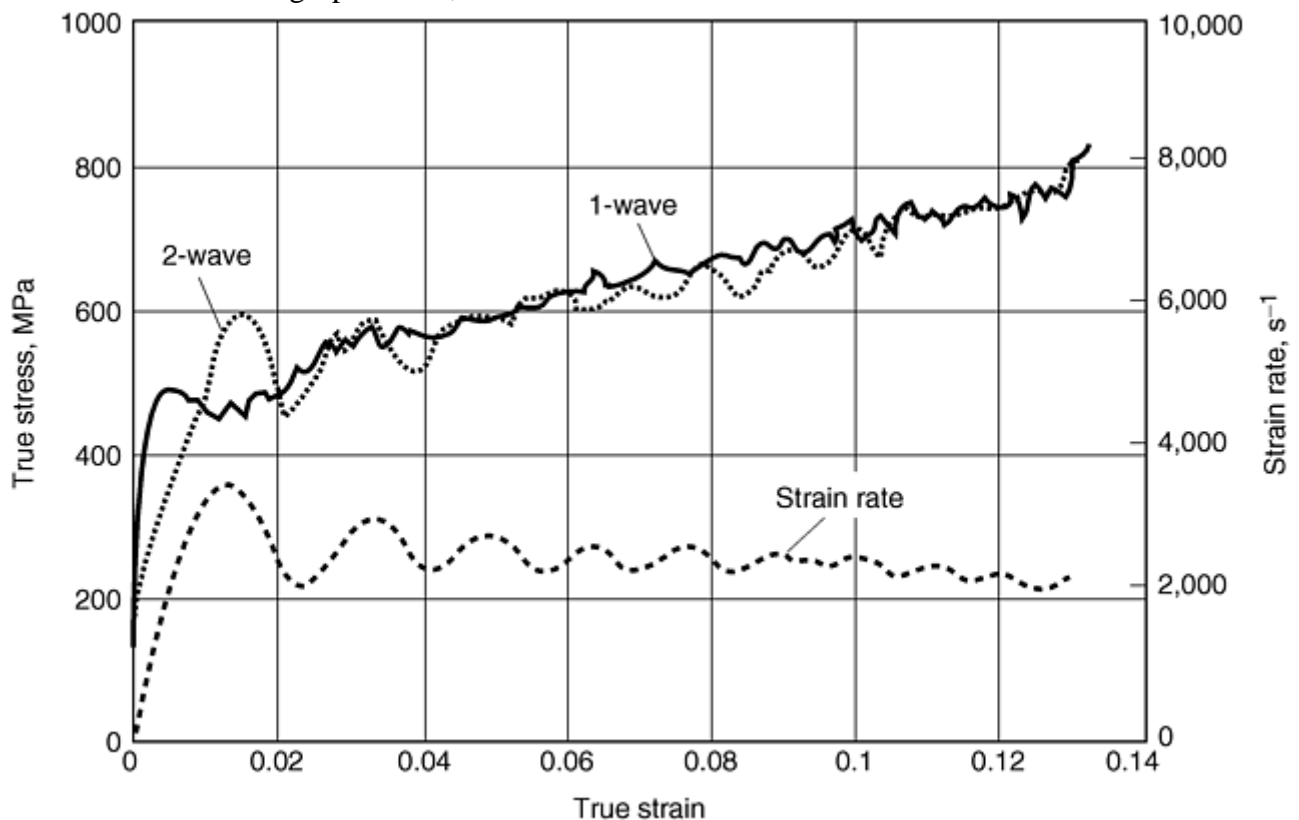


Fig. 5 Stress-strain response of a 304 stainless steel specimen showing the 1- and 2-wave stress curves and the strain rate

Contrarily, when the stress state is *not* uniform throughout the SHPB sample, the 2-wave stress diverges and exceeds the 1-wave stress values. Previous Hopkinson bar studies of ceramic materials using this 1-wave versus 2-wave comparison have shown quite dramatically that a sample is not in stress equilibrium when divergence is observed (Ref 50). In ceramic and cermet materials, this divergence correlates very well with the onset of nonuniform plastic flow and/or premature fracture events. Split-Hopkinson bar analysis for attenuating materials, such as in the case of testing soils, has shown that the time required to achieve stress uniformity can be considerable (Ref 51). Valid analysis of the dynamic stress-strain behavior of the soil samples during the course of testing required the use of a Lagrangian analysis coupled with a standard analysis.

Results have revealed that the slow longitudinal sound speeds typical for some polymeric materials make stress equilibrium during SHPB testing difficult to achieve (Ref 32, 34, 52, 53). The pronounced difference in the initial 1-wave and 2-wave signals for a 6.35 mm (0.25 in.) long, 1 to 1 aspect ratio, high-purity lead sample is shown in Fig. 6. This behavior can be viewed as an indication of a sluggish sample ringup to stress-state equilibrium, compared with the incident wave rise time and a marginally valid Hopkinson bar test at strains

>6%, even though a reasonably stable strain rate is indicated throughout the entire test. The data in Fig. 6 and recent studies on polymeric materials, therefore, assert the need to examine the technique of using thinner sample aspect ratios when studying the high strain rate constitutive response of low sound speed, dispersive materials (Ref 47, 49) and low-strength, high-density solids. Based on the data in Fig. 6, all subsequent testing for this sample material used 3.2 mm (0.12 in.) long samples with a length-to-diameter aspect ratio of 0.5 and lower striker-bar velocities to reduce the strain rate, thereby helping sample ringup. The combination of these measures proved successful in attaining stress equilibrium at lower strain levels in metallic lead samples.

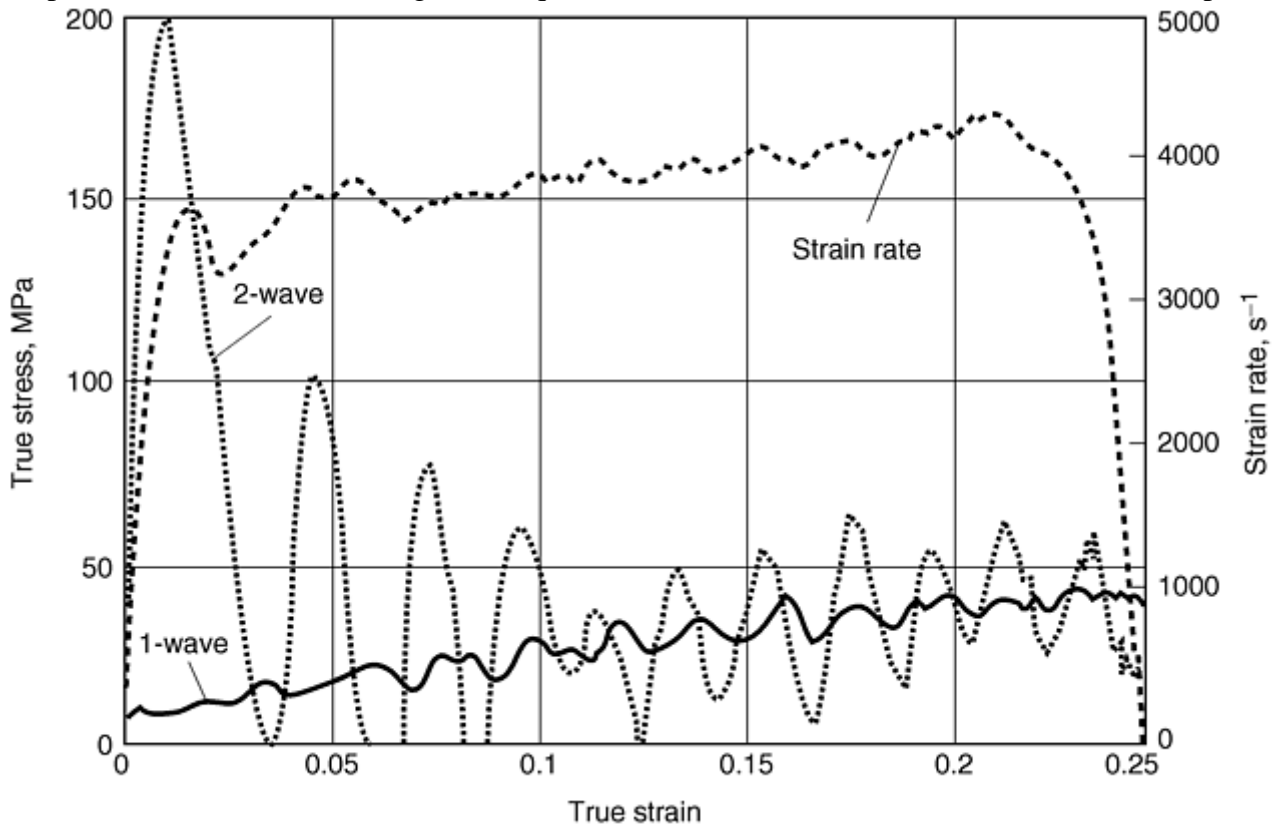


Fig. 6 Room-temperature stress-strain response of a high-purity lead (6.35 mm long by 6.35 mm diam) sample showing the 1- and 2-wave stress curves in addition to strain rate

The finite time to achieve stress-state equilibrium demonstrates that the high-rate elastic modulus of a sample cannot be measured by any Hopkinson bar. Because the stress equilibrium does not occur until well over 1% plastic strain, it is impossible to accurately measure the compressive Young's modulus of materials at high strain rates using the SHPB. The compressive Young's modulus of a material is best measured using ultrasonic techniques.

Increased resolution of the ringup during SHPB testing of materials possessing high sound speeds and/or low fracture toughness values can be achieved by measuring the strain in the sample via strain gages bonded directly on the sample (Ref 54). Testing of ceramics, cermets, thermoset epoxies, and geological materials requires accurate measurement of the local strains. The difficulties with this technique are that reproducible gage application on small samples is challenging and labor intensive, and the specimens often deform to strains greater than the gages can survive (nominally, 5% strain) so they can only be used once.

Split-Hopkinson Bar Testing as a Function of Temperature. The development of robust constitutive material model descriptions of a material's mechanical behavior often requires quantitative knowledge of the coincident influence of temperature and strain rate variations. Accurate measurement of the high strain-rate mechanical response of a material using an SHPB at temperatures other than ambient, however, presents several technical and scientific challenges. Because the stress and strain as a function of time within the deforming specimen are determined by strain-gage measurements made using the elastic pressure bars, the longitudinal sound speed and elastic modulus of the pressure bars, both of which vary with temperature, are important parameters. The pronounced effect of temperature on the elastic properties of viscoelastic materials, which have been proposed as alternate bar materials to achieve increased stress resolution, has been a chief barrier to their adoption to measuring the high-rate response of polymers over a range of temperatures (Ref 32, 35). In this case, both a rate

and temperature-dependent constitutive model for elastomer pressure bars themselves would be required to reduce SHPB data for a sample of interest because an assumption of linear elasticity cannot be invoked for polymeric pressure bars over a range of strain rates and temperatures.

Various techniques have been developed to heat samples in an SHPB depending on whether it is a compression or tensile Hopkinson bar. The combined length of both pressure bars (which can easily exceed 2 m, or 6.5 ft) while simultaneously maintaining alignment within the supporting stanchions makes it operationally impossible to heat or cool the entire bar assembly, either tensile or compressive, with any uniformity of temperature. Even if heating or cooling were feasible, it would require a bar material capable of withstanding the high/low temperatures desired as well as the development of new temperature-calibrated strain gages and robust adhesives/epoxies to rigidly attach them to the bars. Operationally, therefore, the most common techniques for elevated-temperature testing include the following (Ref 3, 5):

- Heating only the sample and perhaps a short section of the pressure bars and then correcting for the temperature gradient effects on the properties of the pressure bars if they are significant (Ref 55)
- Correcting the temperature-dependent sound velocity and elastic modulus of the bars based on an assessment of the temperature gradient, either estimated or measured with a thermocouple. The strain-gage signals are then corrected for the temperature-dependent sound velocity and elastic modulus of the bars (Ref 14).
- Tapering the bars to maintain the mechanical impedance constant along the length of the bars (Ref 56). A disadvantage of this method is that a bar of a particular profile can only compensate for one particular temperature gradient and is, therefore, of minimal use.
- Using mechanical devices that bring the ambient temperature pressure bars into contact with the heated sample a fraction of a second before the stress pulse arrives at the end of the incident bar (Ref 57)

In the first method, heat input into the pressure bars can be minimized in the case of tensile Hopkinson bar testing by rapid heating of the sample gage section using either high-speed radiant (Ref 58) or induction heating (Ref 59, 60). This technique of sample heating will not avoid the altering of the elastic properties of the pressure bars in the case of compressive Hopkinson bar testing unless heating of the bars can be avoided. The second method has been used at temperatures up to 613 °C (Ref 14). Alternately, the selection of a bar material, such as Inconel, which exhibits only a small variability in its elastic properties up to ~600 °C, can alternately be used without the need for corrections up to modest temperatures. Heating/cooling to modest temperatures (-55 to +55 °C) of interest for polymer testing over which the elastic properties of Ti-6Al-4V or Mg bars are unaffected can also be achieved using heated/cooled helium (He) gas as a heat transfer medium (Ref 32, 49).

The last heating technique provides a solution that eliminates the need for corrections to the strain-gage data because heat is applied only to the specimen and not to any part of the bars. This method, however, is only practical in the case of a compression SHPB because in a tensile or a torsion bar the sample is mechanically coupled to the pressure bars. In the case of a compression SHPB, this heating method is accomplished by starting with the bars separated from the sample. The sample is heated independently in a specially designed resistance furnace (a vacuum furnace minimizes radiant heating), by direct radiant heating, or by an induction-heating coil. Just prior to firing the striker bar, the pressure bars are mechanically positioned into contact with the heated sample using bar movers (Ref 43). If the contact time between the sample and the bars is minimized to less than 200 milliseconds, the specimen temperature and the temperature at the ends of the bars remain approximately constant. This approach, while requiring careful attention to the timing between the movement of the pressure bars and the firing of the striker bar, has been used successfully at temperatures up to 1200 °C (Ref 61).

References cited in this section

3. P.S. Follansbee, The Hopkinson Bar, *Mechanical Testing*, Vol 8, *ASM Handbook*, American Society for Metals, 1985, p 198–203
5. J.E. Field, S.M. Walley, N.K. Bourne, and J.M. Huntley, Review of Experimental Techniques for High Rate Deformation Studies, *Proc. Acoustics and Vibration Asia '98* (Singapore), 1998, p 9–38

14. U.S. Lindholm and L.M. Yeakley, High Strain Rate Testing: Tension and Compression, *Exp. Mech.*, Vol 8, 1968, p 1–9
18. G.T. Gray III, High-Strain-Rate Testing of Materials: The Split-Hopkinson Pressure Bar, *Methods in Materials Research*, E. Kaufmann, Ed., John Wiley Press, 1999, in press
32. G.T. Gray III, D.J. Idar, W.R. Blumenthal, C.M. Cady, and P.D. Peterson, High- and Low-Strain Rate Compression Properties of Several Energetic Material Composites as a Function of Strain Rate and Temperature, *11th Detonation Symposium*, 1998 (Snow Mass, CO), J. Short, Ed., in press
34. G. Gary, L. Rota, and H. Zhao, Testing Viscous Soft Materials at Medium and High Strain Rates, *Constitutive Relation in High/Very High Strain Rates*, K. Kawata and J. Shioiri, Ed., Springer-Verlag, Tokyo, 1996, p 25–32
35. G.T. Gray III, W.R. Blumenthal, C.P. Trujillo, and R.W. Carpenter II, Influence of Temperature and Strain Rate on the Mechanical Behavior of Adiprene-L100, *J. Phys. (France)*, C3 (DYMAT 97), Vol 7, 1997, p 523–528
40. P.S. Follansbee and C. Frantz, Wave Propagation in the SHPB, *J. Eng. Mater. Technol. (Trans. ASME)*, Vol 105, 1983, p 61–66
42. E.D.H. Davies and S.C. Hunter, The Dynamic Compression Testing of Solids by the Method of the Split Hopkinson Pressure Bar (SHPB), *J. Mech. Phys. Solids*, Vol 11, 1963, p 155–179
43. C.E. Frantz, P.S. Follansbee, and W.T. Wright, Experimental Techniques with the SHPB, *High Energy Rate Fabrication—1984*, I. Berman and J.W. Schroeder, Ed., American Society of Mechanical Engineers, 1984, p 229–236
44. S. Ellwood, L.J. Griffiths, and D.J. Parry, Materials Testing at High Constant Strain Rates, *J. Phys. E, Sci. Instrum.*, Vol 15, 1982, p 280–282
45. D.J. Parry, A.G. Walker, and P.R. Dixon, Hopkinson Bar Pulse Smoothing, *Meas. Sci. Technol.*, Vol 6, 1995, p 443–446
46. P.S. Follansbee, High Strain Rate Deformation of FCC Metals and Alloys, *Metallurgical Applications of Shock Wave and High Strain Rate Phenomena*, L.E. Murr, K.P. Staudhammer, and M.A. Meyers, Ed., Marcel Dekker, 1986, p 451–480
47. X.J. Wu and D.A. Gorham, Stress Equilibrium in the Split Hopkinson Pressure Bar Test, *J. Phys. (France) IV Colloq.*, C3 (EURODYMAT 97), Vol 7, 1997, p 91–96
48. G.T. Gray III, W.R. Blumenthal, C.P. Trujillo, and R.W. Carpenter, Influence of Temperature and Strain Rate on the Mechanical Behavior of Adiprene L-100, *J. Phys. IV Colloq.*, C3 (DYMAT 97), 1997, p 523–528
49. G.T. Gray III, W.R. Blumenthal, C.P. Trujillo, and R.W. Carpenter II, Influence of Temperature and Strain Rate on the Mechanical Behavior of Adiprene L-100, *J. Phys. (France) IV Colloq.*, C3 (EURODYMAT 97), Vol 7, 1997, p 523–528
50. W.R. Blumenthal and G.T. Gray III, Structure-Property Characterization of Shock-Loaded B₄C-Al, *Inst. Phys. Conf. Ser.*, Vol 102, 1989, p 363–370
51. C.W. Felice, E.S. Gaffney, and J.A. Brown, Extended Split-Hopkinson Bar Analysis for Attenuating Materials, *J. Eng. Mech.*, Vol 117, 1991, p 1119–1135

52. S.M. Walley and J.E. Field, Strain Rate Sensitivity of Polymers in Compression from Low to High Strain Rates, *DYMAT J.*, Vol 1, 1994, p 211–228
53. S.M. Walley, J.E. Field, and N.A. Safford, A Comparison of the High Strain Rate Behaviour in Compression of Polymers at 300K and 100K, *J. Phys. (France) IV Colloq.*, C3 (DYMAT 91), Vol 1, 1991, p 185–190
54. W.R. Blumenthal and G.T. Gray III, *Structure-Property Characterization of Shock-Loaded B₄C-Al*, Oxford, 1989, p 363–370
55. C. Bacon, Numerical Prediction of the Propagation of Elastic Waves in Longitudinally Impacted Rods: Applications to Hopkinson Testing, *Int. J. Impact Eng.*, Vol 13, 1993, p 527–539
56. A.M. Eleiche, Impedance Matching in Non-Homogeneous Elastic Bars, *J. Phys. D, Appl. Phys.*, Vol 8, 1975, p 505–511
57. C.E. Frantz, P.S. Follansbee, and W.J. Wright, *New Experimental Techniques with the Kolsky Bar*, I. Berman and J.W. Schroeder, Ed., American Society of Mechanical Engineers, 1984, p 229–236
58. D. Macdougall, A Radiant Heating Method for Performing High-Temperature High-Strain-Rate Tests, *Meas. Sci. Technol.*, Vol 9, 1998, p 1657–1662
59. Z. Rosenberg, D. Dawicke, E. Strader, and S.J. Bless, A New Technique for Heating Specimens in Split-Hopkinson-Bar Experiments Using Induction Coil Heaters, *Exp. Mech.*, Vol 26, 1986, p 275–278
60. Z. Rosenberg, D. Dawicke, and S.J. Bless, A New Technique for Heating Specimens in Split Hopkinson Bar Experiments Using Induction Coil Heaters, *Metallurgical Applications of Shock Wave and High Strain Rate Phenomena*, L.E. Murr, K.P. Staudhammer, and M.A. Meyers, Ed., Marcel Dekker, 1986, p 543–552
61. H.W. Sizek and G.T. Gray III, Deformation of Polycrystalline Ni₃Al at High Strain Rates and Elevated Temperatures, *Acta Metall. Mater.*, Vol 41, 1993, p 1855–1860

Classic Split-Hopkinson Pressure Bar Testing

George T. (Rusty) Gray III, Los Alamos National Laboratory

Split-Hopkinson Pressure Bar in Tension

Tensile-Loading Techniques. The principles and the data analysis for the tensile split-Hopkinson pressure bar are similar to those discussed for the compression SHPB (Ref 62, 63, 64). The primary differences are the methods of generating a tensile-loading pulse, specimen geometry, and the method of attaching the specimen to the two bars (incident and transmitted). Three separate general types of tension split-Hopkinson pressure bar design have been developed (Ref 63). All three loading techniques use measures of the tensile pulses in the input and transmitter bars, as in the compressive SHPB, to study the dynamic tensile response of a material.

Method 1. In the first method, developed by Lindholm and Yeakley (Ref 14), the incident bar is solid, while the transmitted bar is a hollow tube of the same cross-sectional area as the input bar. A complex “top-hat” type of sample geometry, as shown in Fig. 7, is machined from the material of interest. The specimen essentially comprises four parallel tensile bars of equal cross-sectional area. Although specimen machining is somewhat complex in this method, the actual SHPB test is conducted in the identical manner because compressive testing

and the data analysis is identical to that outlined previously. The advantage of this tensile loading method is that, given a suitable hollow transmitted bar matched to the incident bar, tensile Hopkinson bar tests can be conducted using a standard compressive SHPB loading setup as shown in Fig. 1 and 2.

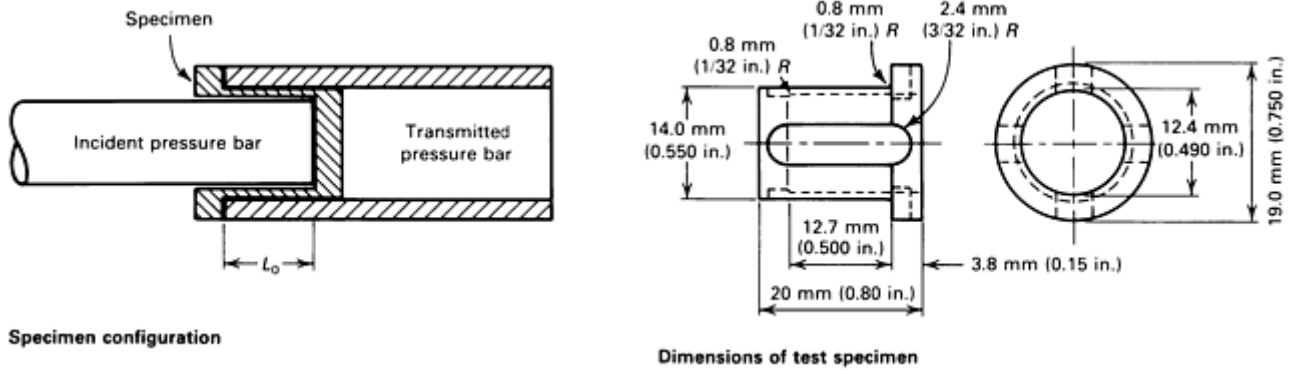


Fig. 7 “Top-hat” tensile split-Hopkinson bar sample design. Source: Ref 14

Method 2. The second type of tensile split-Hopkinson bar test, and the most commonly implemented mode of loading (Ref 5), involves direct tensile loading of the incident bar to subject a sample in a uniaxial tensile stress state. This loading mode can be accomplished using a standard type of axisymmetric circular tension specimen threaded directly into the ends of the incident and transmitted pressure bars, a dumbbell-shaped sample loaded through flanges attached to the incident and transmitted bars, or a flat tensile sample loaded using a small compression grip assembly designed into the ends of the incident and transmitted bars. A tensile pulse in each instance is generated in the incident bar either by loading the end of the incident bar through direct impact of a mass with a flange on the end of the incident bar (Ref 19) or by releasing a tensile pulse stored in the incident bar using a clamping fixture (Ref 20). Figure 8 shows a schematic of a tensile split-Hopkinson bar setup using the hollow-striker-bar loading method. In this loading method, a long tensile pulse, similarly stable as in a compressive bar, can be imparted using a hollow striker tube accelerated along the incident bar from a compressed gas breech or from a falling weight in a vertically configured tensile bar. In the second variation, tensile wave loading in the incident bar is generated through the release of a tensile load that is initially stored in a section of the incident bar.

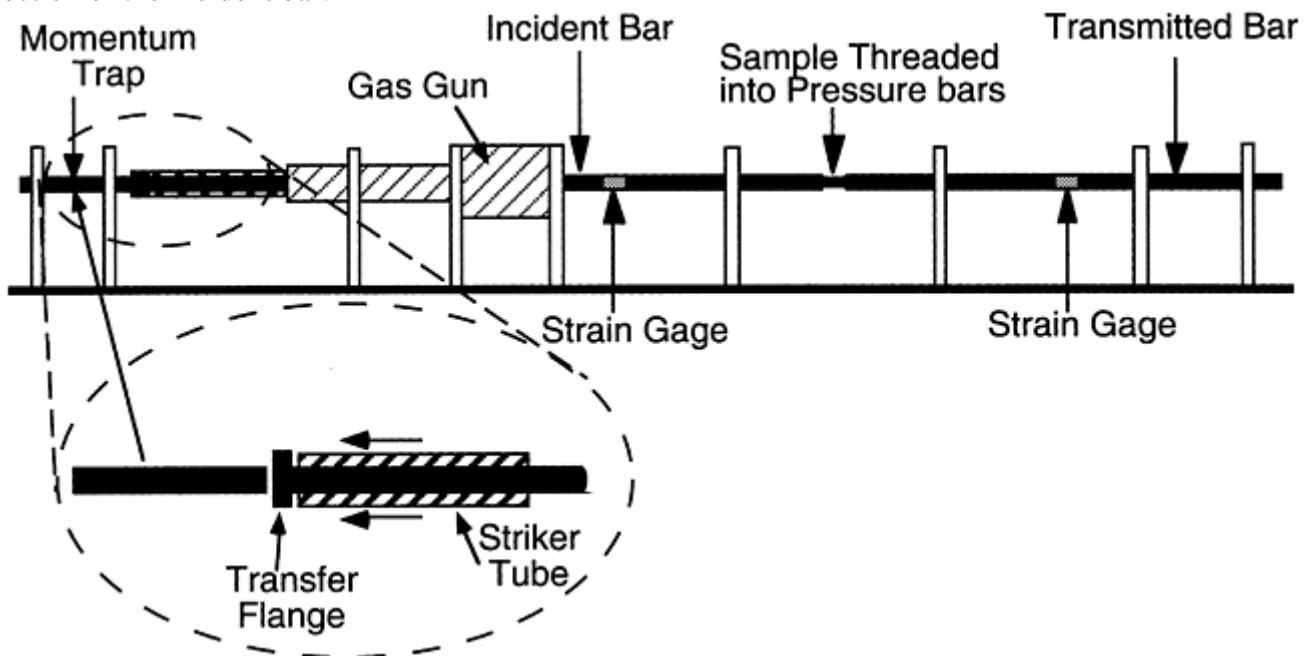


Fig. 8 Schematic of a tensile split-Hopkinson pressure bar test setup

Method 3. The third type of Hopkinson bar loading in tension also uses a circular specimen threaded into the ends of the two pressure bars but uses the reflection of the compression pulse at the free end of the transmitted bar to load the sample in tension and a circular collar to protect the specimen from the initial compressive pulse

(Ref 62). After the specimen has been screwed into the incident and transmitted bars, a split shoulder or collar is placed over the specimen, and it is screwed in until the pressure bars fit tightly against the shoulder. The shoulder is made of the same material as the pressure bars, has the same outer diameter, and has an inner diameter that just clears the specimen. The ratio of the cross-sectional area of the shoulder to that of the pressure bars is typically 3 to 4, while the ratio of the area of the shoulder to the net cross-sectional area of the specimen is typically 12 to 1 (Ref 62, 63). When the striker bar impacts the incident bar, a compressive pulse travels down the incident bar until it reaches the specimen. The amplitude of the pulse, which is a function of the striker velocity and length, is twice the elastic wave transit time in the striker bar.

In this loading method, the compression pulse travels through the composite cross section of the loading collar and specimen in an essentially undisturbed manner. The relatively loose fit of the threaded joint of the specimen into the bars and the large area ratio of the collar to the specimen ensure that no compression beyond the elastic limit is transmitted through the specimen (Ref 63). Ideally, the entire compression pulse passes through the supporting circular collar as if the specimen were not present, although in practice it is operationally difficult to prevent prestraining of the specimen to some degree. The compression pulse continues to propagate until it reaches the free end of the transmitted bar where it reflects and propagates back as a tensile pulse. Upon reaching the specimen, the tensile pulse is partially transmitted through the specimen and partially reflected back into the bar, which is now acting as the incident bar. Because the shoulder, which carried the entire compressive pulse around the specimen, is not rigidly connected to the pressure bars, it will not support any tensile load. Tight fitting of the collar against the two pressure bars is critical in transmitting the compression pulse down the bars without significant wave dispersion or prestraining of the sample. Similarly, the fit of the threaded tensile specimen against the bars is essential to achieve smooth and rapid loading of the specimen as the tensile pulse arrives. Failure to remove all play from the threaded joint results in uneven loading of the specimen and spurious wave reflections because of the open gaps in the loading thread area.

Data analysis for a tensile split-Hopkinson bar test is essentially identical to that of the compression Hopkinson bar analysis detailed previously. The additional complications encountered in the tensile and torsional Hopkinson techniques are related to the following:

- Modification of the pressure bar ends to accommodate gripping of complex samples, which alter wave propagation in the sample and bars
- Potential need for additional diagnostics to calculate true stress
- Increased need to accurately incorporate inertial effects into data reduction to extract quantitative material constitutive behavior
- More complicated stress pulse generation systems required for tensile and torsion bars

Alteration of the bar ends to accommodate threaded or clamped samples leads to complex boundary conditions at the bar specimen interface and, therefore, introduces uncertainties in the wave mechanics description of the test (Ref 14).

When complex sample geometries are used, signals measured in the pressure bars record the structural response of the entire sample, not just the gage section, where plastic deformation is assumed to be occurring. When plastic strain occurs in the sections adjacent to the sample's uniform gage area, accurate determination of the stress-strain response of the material is more complicated. In these cases, additional diagnostics, such as high-speed photography, are mandatory to quantify the loaded section of the deforming sample. In the tensile bar case, an additional requirement is that exact quantification of the deforming sample cross-sectional area as a function of strain is necessary to achieve true-stress data. Contrary to a compressive SHPB test, in which a right-circular cylindrical sample is most often utilized, the tensile SHPB test uses a cylindrical specimen with an attached shoulder and additional gripping, including threads. Because the split-Hopkinson bar data analysis only provides data on the relative displacement between the ends of the incident and transmitter bars, an effective gage length generally must be used. This is equivalent to determining strain in a tensile test through cross-head displacement measurement. The use of strain gages on test samples to determine an effective gage length is strongly recommended. This calibration is accomplished easily at low strain rates, preferably in a conventional test machine in which the cross-head displacement is monitored separately.

As with any uniaxial tensile test, once localized necking occurs, it is no longer possible to simply convert load-displacement data to stress-strain data. This lack of valid stress-state analysis is related to both the lack of uniform plastic deformation in the sample and the attendant volumetric sample expansion, which damage-

evolution processes represent. The range of application of the Hopkinson bar test can be extended by high-speed photography of necking specimens, although an accurate measure of the deforming volume of the sample as necking proceeds is difficult at best, given a lack of knowledge of the damage processes evolving within the sample. An analysis that allows estimation of effective stress and strain from the profile of the necking specimen can be obtained. Using the apparatus described in method 3, photographs can be made with a suitable high-speed camera system through windows provided in the collar (Ref 65, 66).

The final complexity inherent to the tension Hopkinson loading configurations has to do with the increased sample dimensions required. Valid dynamic characterization of many material product forms, such as thin sheet materials and small-section bar stock, may be significantly complicated or completely impractical using either tensile or torsion Hopkinson bars because of an inability to fabricate test samples. Techniques have been developed, however, to address these concerns in the case of testing sheet materials in the Hopkinson bar (Ref 66).

References cited in this section

5. J.E. Field, S.M. Walley, N.K. Bourne, and J.M. Huntley, Review of Experimental Techniques for High Rate Deformation Studies, *Proc. Acoustics and Vibration Asia '98* (Singapore), 1998, p 9–38
14. U.S. Lindholm and L.M. Yeakley, High Strain Rate Testing: Tension and Compression, *Exp. Mech.*, Vol 8, 1968, p 1–9
19. J. Harding, E.O. Wood, and J.D. Campbell, Tensile Testing of Materials at Impact Rates of Strain, *J. Mech. Eng. Sci.*, Vol 2, 1960, p 88–96
20. G.H. Staab and A. Gilat, A Direct-Tension Split Hopkinson Bar for High Strain-Rate Testing, *Exp. Mech.*, Vol 31, 1991, p 232–235
62. T. Nicholas, Tensile Testing of Materials at High Rates of Strain, *Exp. Mech.*, Vol 21, 1981, p 177–185
63. T. Nicholas and S.J. Bless, High Strain-Rate Tension Testing, *Mechanical Testing*, Vol 8, *ASM Handbook*, American Society for Metals, 1985, p 208–214
64. S. Ellwood, L.J. Griffiths, and D.J. Parry, A Tensile Technique for Materials Testing at High Strain Rates, *J. Phys. E, Sci. Instrum.*, Vol 15, 1982, p 1169–1172
65. L.A. Cross, S.J. Bless, A.M. Rajendran, E.A. Strader, and D.S. Dawicke, New Technique to Investigate Necking in a Tensile Hopkinson Bar, *Exp. Mech.*, Vol 24, 1984, p 184–186
66. M.M. LeBlanc and D.H. Lassila, Dynamic Tensile Testing of Sheet Materials Using the Split-Hopkinson Bar Technique, *Exp. Tech.*, Vol 17, 1993, p 37–42

Classic Split-Hopkinson Pressure Bar Testing

George T. (Rusty) Gray III, Los Alamos National Laboratory

Data Reduction Measurement and Analysis Automation

Acquisition of split-Hopkinson bar data requires a high degree of automation because of the high-speed nature of the stress loading inherent to the Hopkinson bar and the need for signal measurement and storage equipment capable of these acquisition speeds (Ref 18, 67, 68, 69). The measurement instrumentation required for a split-

Hopkinson pressure bar test includes two strain-gage signal conditioners and a means of recording these signals. The strain-gage signal conditioners must have a frequency response of at least 1 MHz to achieve adequate data resolution. Units with sampling frequencies as high as 1 GHz are now available. In addition, modern signal conditioners possess variable gain amplification, up to 1000 times, while retaining high signal-to-noise levels. Gain settings in excess of 500 are critical to the high-resolution measurement of the very low flow stresses typical of many polymer and polymeric composites. Until recently, oscilloscopes were used almost exclusively to capture and record the strain-gage signal pulses. When using one oscilloscope to capture the strain-gage data, the transmitted wave and integrated reflected wave can be fed to an oscilloscope with x - y capability to directly yield the dynamic stress-strain curve for the specimen. The reflected wave may be fed through an operational amplifier to yield a signal directly proportional to the strain in the specimen but without dispersion correction.

The three wave signals are now often captured using high-speed analog-to-digital (A/D) recorders or high-speed A/D data-acquisition computer modules, which are directly interfaced with a personal computer. Using either platform, it is now possible to digitize the raw data directly and perform the integration numerically. With the improved availability of the digitized data, more robust Hopkinson bar data reduction software is now regularly used by research labs conducting split-Hopkinson bar testing. This software can be used to calibrate the bars and store the calibration information, adjust the timing between the transmitted and reflected waves to account for the transit time through the specimen, and calculate the elastic wave dispersion in the measured data.

References cited in this section

18. G.T. Gray III, High-Strain-Rate Testing of Materials: The Split-Hopkinson Pressure Bar, *Methods in Materials Research*, E. Kaufmann, Ed., John Wiley Press, 1999, in press
67. J. Yuan, N. Takeda, and A.M. Waas, A Note on Data Processing in the Split Hopkinson Pressure Bar Tests, *Exp. Tech.*, Vol 1, 1998, p 21–24
68. J.M. Lifshitz and H. Leber, Data Processing in the Split Hopkinson Pressure Bar Tests, *Int. J. Impact Eng.*, Vol 15, 1994, p 723–733
69. T. Yokoyama and K. Kishida, A Microcomputer-Based System for the High-Speed Compression Test by the Split Hopkinson Pressure Bar Technique, *J. Test. Eval.*, Vol 14, 1986, p 236–242

Classic Split-Hopkinson Pressure Bar Testing

George T. (Rusty) Gray III, Los Alamos National Laboratory

Wave Dispersion in the Split-Hopkinson Pressure Bar

Applying the equations given in the theory of the Hopkinson bar section, the stress-strain behavior of the specimen can be computed from the measured incident, reflected, and transmitted strain pulses made on the elastic bars (Ref 3, 18, 67). Knowing the timing required for the elastic wave signals to traverse from the specimen to the gages on the input and output bars based on the calibration procedure, the reflected and transmitted pulses can be synchronized to coincide at the specimen interface. By integrating Eq 13, and remembering that $\varepsilon = \ln(l_0/l_s)$ in compression, $\varepsilon(t)$ and $l_s(t)$ can be calculated in the specimen. Assuming constancy of volume of the specimen during the course of deforming the specimen, $A_s(t)$ and, therefore, $\sigma(t)$ can now be calculated from Eq 13. The average true stress-true strain curve is then produced by removing time as a variable between the stress and strain data.

The 1- and 2-wave analyses used to calculate average stress discussed in the theory section implicitly assume that the strain-time pulses measured at the strain gages are identical with those at the ends of the bars in contact with the specimen. This assumption, however, is not correct because the specimen is normally smaller in diameter than the bar such that the bar ends are not uniformly loaded across their diameter and, therefore, will indent elastically. In addition, as the bars are compressed longitudinally, albeit elastically, they expand radially in response to the applied force (i.e., the Poisson effect). While the exact mathematical descriptions of these effects on the propagation of an elastic pulse through a large elastic rod are very complex, the result is that different frequencies of pulses induced in the bars disperse with distance traveled in the bar. The result of this dispersion is such that the pulse induced in the input bar through the impact of the striker bar does not immediately rise into a steady square-wave impulse of fixed amplitude but rather “rings” up. These end effects quickly dampen after the wave has propagated about ten bar diameters (Ref 40, 67).

The wave propagation behavior thereafter becomes fully described by the equation of motion in an infinite cylindrical solid. The solution of the equation of motion for these boundary conditions was derived independently during the late 19th century by the mathematicians Pochhammer (Ref 70) and Chree (Ref 71). These relations were later specifically applied to address dispersion in the SHPB (Ref 12, 15, 40, 72, 73, 74). The pressure bars have been determined to vibrate predominantly in a fundamental mode (i.e., while there are an infinite number of potential solutions to the equation of motion according to the vibrational mode, only one frequency appears to dominate in long elastic bars).

This vibration of the bar leads to wave dispersion that can mask resolution of the fine details in the stress-strain data of interest, particularly at higher strain rates where the period of the oscillations can be a large fraction of the total strain measured. While this elastic dispersion cannot be eliminated, techniques have been adopted based on the Pochhammer-Chree equation of motion to correct for any additional dispersion that occurs during the wave propagation from the specimen/bar interfaces to the gage locations (Ref 40, 72, 74, 75, 76, 77).

At any position, z , along the pressure bar, the wave, $f(t)$, may be represented by an infinite cosine Fourier series:

$$f(t) = \frac{A_0}{2} + \sum_{n=1}^{\infty} D_n \cos(n\omega_0 t - \delta_n) \quad (\text{Eq 20})$$

where ω_0 is the frequency of the longest wavelength component ($n = 1$), and δ_n is the phase angle of component $n\omega_0$. The wave dispersion in the pressure bars occurs because higher-frequency components travel more slowly than lower-frequency components and thus lag behind the leading edge of the wave. The dispersion results in a change of relative position and amplitude of the oscillations, together with a gradual increase in the rise time of the pulse as it travels along the bar. Because the strains measured in the pressure bars are measured by strain gages located some distance from the specimen, the pulse shapes at the strain-gage positions will be modified because of the dispersion effects and therefore do not accurately represent the pulse shapes at the specimen location.

The dispersion of the waves alters the phase angle, δ , such that at a position, $z + \Delta z$, the new phase angle can be calculated:

$$\delta(z + \Delta z) = \delta(z) + \frac{n\omega_0 \Delta z}{C_0} \left(\frac{C_0}{C_n} - 1 \right) \quad (\text{Eq 21})$$

where C_0 is the longitudinal wave speed in the bar, and C_n is the velocity of component $n\omega_0$. The value of C_n depends on the wavelength and on the mode of vibration; in the SHPB case, this is dominated by the fundamental mode (Ref 12). The phase angle at any position along the bar can be calculated using Eq 21, and the wave reconstructed at that new position using Eq 20. Accordingly, the raw stress-versus-strain data calculated using either the 1- or 2-wave analysis can be dispersion corrected by mathematically moving the wave to a common point on the bar (e.g., the bar-sample interface). This correction removes a large amount of the inherent wave dispersion, thereby yielding smoother final stress-strain curves (Ref 40, 43, 55, 72, 73, 78, 79).

Direct-Impact Compression Hopkinson Pressure Bar. Several researchers have suggested that one way to avoid the dispersion problem in the incident bar is to dispense with the incident bar altogether and impact the sample directly with the striker bar (Ref 72, 80 81 82 83 84 85 86 87 88). The initial intent of the direct-impact bar was to be used as a means of increasing the maximum strain rate achievable. While maximum higher strain rates can, in principle, be achieved using this technique, direct Hopkinson bars pose several difficulties. The first difficulty is that, because there is no incident bar, there is no means to calculate the strain rate and thereby the strain. Direct strain measurement on the sample and/or high-speed photography must be used to track diametral

sample expansion and therefore the strain. Careful study has shown that this is problematic, but this limitation can be overcome (Ref 83, 89). The second problem is that it is more difficult to achieve a constant strain rate in the sample because the direct impact of the striker bar on the sample lacks the equilibrium pulse achieved during the ringup in the incident bar in the split-Hopkinson configuration.

References cited in this section

3. P.S. Follansbee, The Hopkinson Bar, *Mechanical Testing*, Vol 8, *ASM Handbook*, American Society for Metals, 1985, p 198–203
12. R.M. Davies, A Critical Study of the Hopkinson Pressure Bar, *Philos. Trans. R. Soc. (London) A*, Vol 240, 1948, p 375–457
15. H. Kolsky, Stress Waves in Solids, *J. Sound Vib.*, Vol 1, 1964, p 88–110
18. G.T. Gray III, High-Strain-Rate Testing of Materials: The Split-Hopkinson Pressure Bar, *Methods in Materials Research*, E. Kaufmann, Ed., John Wiley Press, 1999, in press
40. P.S. Follansbee and C. Frantz, Wave Propagation in the SHPB, *J. Eng. Mater. Technol. (Trans. ASME)*, Vol 105, 1983, p 61–66
43. C.E. Frantz, P.S. Follansbee, and W.T. Wright, Experimental Techniques with the SHPB, *High Energy Rate Fabrication—1984*, I. Berman and J.W. Schroeder, Ed., American Society of Mechanical Engineers, 1984, p 229–236
55. C. Bacon, Numerical Prediction of the Propagation of Elastic Waves in Longitudinally Impacted Rods: Applications to Hopkinson Testing, *Int. J. Impact Eng.*, Vol 13, 1993, p 527–539
67. J. Yuan, N. Takeda, and A.M. Waas, A Note on Data Processing in the Split Hopkinson Pressure Bar Tests, *Exp. Tech.*, Vol 1, 1998, p 21–24
70. L. Pochhammer, About the Initiation of the Velocities of Small Oscillations in Unbounded Isotropic Circular Cylinders, *J. Reine Angew. Math.*, Vol 81, 1876, p 324–336 (in German)
71. C. Chree, The Equations of an Isotropic Elastic Solid in Polar and Cylindrical Coordinates: Their Solution and Application, *Trans. Camb. Philos. Soc.*, Vol 14, 1889, p 250–369
72. D.A. Gorham, Measurement of Stress-Strain Properties of Strong Metals at Very High Strain Rates, *Inst. Phys. Conf. Series*, Vol 47, 1980, p 16–24
73. J.C. Gong, L.E. Malvern, and D.A. Jenkins, Dispersion Investigation in the Split Hopkinson Pressure Bar, *J. Eng. Mater. Technol. (Trans. ASME)*, Vol 112, 1990, p 309–314
74. C. Bacon, An Experimental Method for Considering Dispersion and Attenuation in a Viscoelastic Hopkinson Bar, *Exp. Mech.*, Vol 38, 1998, p 242–249
75. C.K.B. Lee, R.C. Crawford, K.A. Mann, P. Coleman, and C. Petersen, Evidence of Higher Pochhammer-Chree Modes in an Unsplit Hopkinson Bar, *Meas. Sci. Technol.*, Vol 6, 1995, 853–859
76. C.K.B. Lee and R.C. Crawford, A New Method for Analyzing Dispersed Bar Gauge Data, *Meas. Sci. Technol.*, Vol 4, 1993, p 931–937
77. D.A. Gorham, A Numerical Method for the Correction of Dispersion in Pressure Bar Signals, *J. Phys. E*, Vol 16, 1983, p 477–479

78. G. Gary, J.R. Klepaczko, and H. Zhao, Corrections for Wave Dispersion and Analysis of Small Strains with Split Hopkinson Bar, *J. Phys. (France) IV Colloq.*, C3 (DYMAT 91), Vol 1, 1991, p 403–410 (in French)
79. D.A. Gorham and X.J. Wu, An Empirical Method for Correcting Dispersion in Pressure Bar Measurements of Impact Stress, *Meas. Sci. Technol.*, Vol 7, 1996, p 1227–1232
80. C.K.H. Dharan and F.E. Hauser, Determination of Stress-Strain Characteristics at Very High Strain Rates, *Exp. Mech.*, Vol 10, 1970, p 370–376
81. A.L. Wingrove, A Device for Measuring Strain-Time Relationships in Compression at Quasi-Static and Dynamic Strain Rates, *J. Phys E, Sci. Instrum.*, Vol 4, 1971, p 873–875
82. G.L. Wulf and G.T. Richardson, The Measurement of Dynamic Stress-Strain Relationships at Very High Strain Rates, *J. Phys. E*, Vol 7, 1974, p 167–169
83. D.A. Gorham, P.H. Pope, and J.E. Field, An Improved Method for Compressive Stress-Strain Measurements at Very High Strain Rates, *Proc. R. Soc. (London) A*, Vol 438, 1992, p 153–170
84. C.W. Fong, Crack Initiation in Perforated Propellants under High Strain Rate Impact Conditions, *Propell. Explos. Pyrotech.*, Vol 10, 1985, p 91–96
85. S.M. Walley, J.E. Field, and S.J.P. Palmer, Impact Sensitivity of Propellants, *Proc. R. Soc. (London) A*, Vol 438, 1992, p 571–583
86. S.Y. Ho, High Strain Rate Impact Studies of Predamaged Rocket Propellants, Part I: Characterization of Damage Using a Cumulative Damage Criterion, *Combustion & Flame*, Vol 104, 1996, p 524–534
87. S.M. Walley, J.E. Field, P.H. Pope, and N.A. Safford, A Study of the Rapid Deformation Behaviour of a Range of Polymers, *Philos. Trans. R. Soc. (London) A*, Vol 328, 1989, p 1–33
88. O.S. Lee, S.S. You, J.H. Chong, and H.S. Kang, Dynamic Deformation under a Modified Split Hopkinson Pressure Bar Experiment, *KSME Int. Journal*, Vol 12, 1998, p 1143–1149
89. P.H. Pope and J.E. Field, Determination of Strain in a Dynamic Compression Test, *J. Phys. E, Sci. Instrum.*, Vol 17, 1984, p 817–820

Classic Split-Hopkinson Pressure Bar Testing

George T. (Rusty) Gray III, Los Alamos National Laboratory

Sample Design and Preparation

The errors due to radial and longitudinal inertia as well as friction effects can be reduced by choosing a sample size that minimizes the areal mismatch between the sample and the bar diameter and maintains a sample L/D ratio of 0.5 to 1.0.

For a given bar diameter, the sample diameter is typically chosen to be ~80% of the bar diameter for a compression bar test. Such a ratio allows ~30% true strain to be imparted into the sample before the sample exceeds the bar diameter. Samples for compressive split-Hopkinson bar testing similar to conventional low-rate compression testing need to be machined such that the two loading faces are flat, parallel to a 0.001 in. (0.01

mm) tolerance or better, as well as having the sides of the sample orthogonal to the loading faces. For brittle materials, this tolerance must be an order of magnitude greater. Orthogonality, as well as precision machining of parallel flat loading faces, is crucial to attaining uniform elastic loading in a compressive Hopkinson bar test and thereafter achieving a uniform stress-state in the sample.

While most investigators using the split-Hopkinson bar routinely use right-regular cylindrical samples, cubes and other square-sided shapes can be used. Ease of machining on a lathe to achieve accurate and reproducible sample specifications also favors cylindrical samples. The selection of the optimal sample diameter and L/D ratio is dependent on the maximum strain rate desired as well as the sample size requirement necessary to have specimens sufficiently large to ensure measurement of bulk properties of the material of interest. Coarse-scaled microstructures or composite materials require larger sample sizes than fine-scaled ones. An approximate rule of thumb is that the specimen diameter needs to be at least ten times the representative microstructural unit size for polycrystalline metals and alloys. Coarse-scaled materials, particularly, engineering composites such as concrete (Ref 90) or polymeric layups, require careful sample-size selection as well as specifically designed split-Hopkinson bars to achieve valid high-strain-rate stress-strain data.

Sample designs for Hopkinson bar testing of materials exhibiting a low resistance to axial cracking, such as ceramics, and/or composite matrix/reinforcement debonding, require the use of specialized sample designs. The use of “dog-bone” samples, originally designed by Tracy (Ref 91), allow the achievement of stable uniaxial stress in ceramics during Hopkinson bar testing. By suppressing axial cracking and/or brittle fracture processes in ceramic or cermet samples, because of the larger diameter ends of the samples, valid Hopkinson bar tests can be achieved (Ref 92). Accurate measurement of the high-strain-rate mechanical behavior of fiber-reinforced composite samples also requires a specialized sample design. Uniaxial testing of composites can be achieved using tapered compression samples with end sections constrained with chamfered rings to suppress axial splitting (Ref 93).

References cited in this section

90. C. Albertini, E. Cadoni, and K. Labibes, Dynamic Mechanical Behaviour of Large Concrete Specimens by Means of a Hopkinson Bar Bundle, *Proc. 2nd Int. Symp. on Impact Eng.*, C.Y. Chiem, L.L. Wang, and S. Tanimura, Ed., Chinese Journal of Mechanics Press, Beijing, 1996, p 214–219
91. C.A. Tracy, A Compression Test for High Strength Ceramics, *J. Test. Eval.*, Vol 15, 1987, p 14–19
92. W.R. Blumenthal and G.T. Gray III, *Characterization of Shock-Loaded Aluminum-Infiltrated Boron Carbide Cermets*, S.C. Schmidt, J.N. Johnson, and L.W. Davison, Ed., North-Holland Press, 1990, p 393–396
93. H. Couque, C. Albertini, and J. Lankford, Failure Mechanisms in a Unidirectional Fire-Reinforced Thermoplastic Composite under Uniaxial, In-Plane Biaxial and Hydrostatically Confined Compression, *J. Mater. Sci. Lett.*, Vol 12, 1993, p 1953–1957

Classic Split-Hopkinson Pressure Bar Testing

George T. (Rusty) Gray III, Los Alamos National Laboratory

High-Rate Uniaxial Stress-Loading Effects on Materials

High-rate testing is conducted on a large number of materials of scientific and engineering interest to support the development of materials constitutive models (Ref 46, 94, 95, 96, 97, 98). Figure 9 shows the stress-strain response of electrical-grade iron measured in compression at various strain rates and temperatures. The range of temperatures and strain rates is conducted to facilitate a robust constitutive modeling fit for this metal. The

lower strain-rate tests were performed on a standard screw-driven Instron testing machine using the same specimen geometry as the dynamic tests. All the stress-strain curves, as a function of temperature and strain rate, are true values. Although the SHPB data at strains below ~ 1 to 2% are not in stress-state equilibrium, the curves are plotted in their entirety from load inception. Increasing strain rate at ambient temperature, 298 K, is seen to increase the flow stress of iron (Fe) equivalent to a decrease in temperature at a constant strain rate.

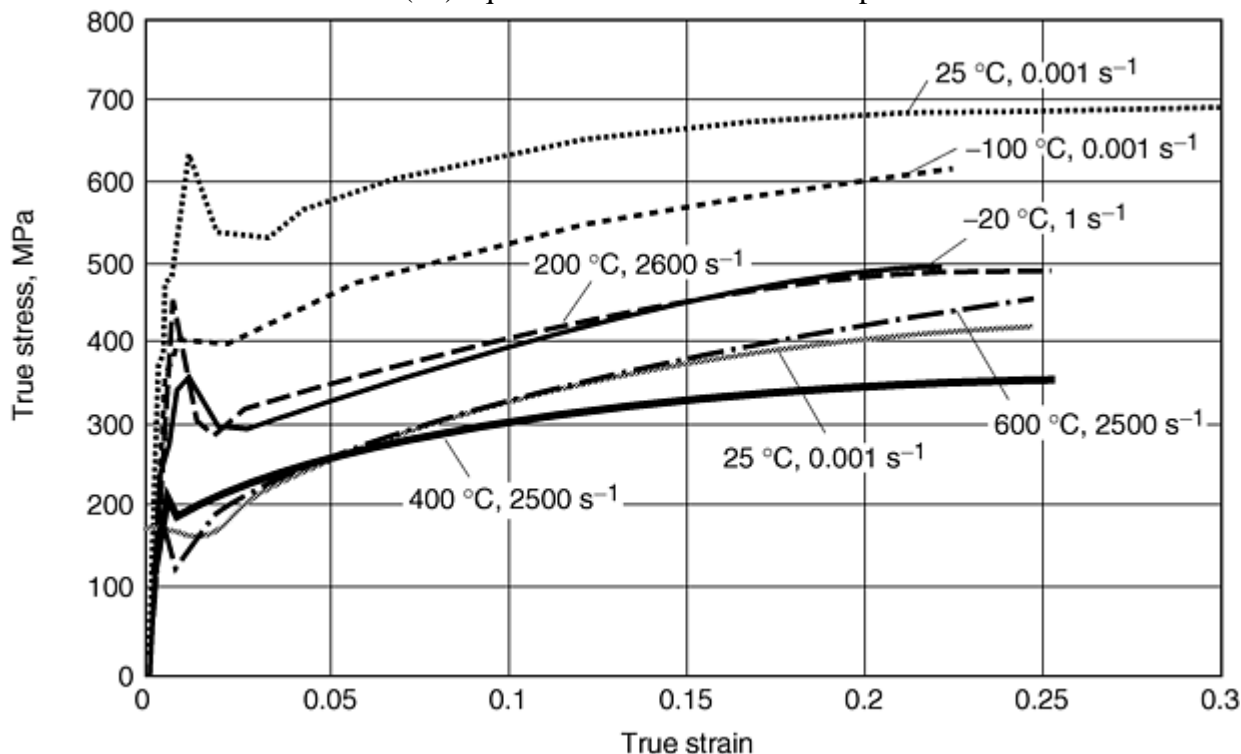


Fig. 9 Stress-strain response of electrical iron as a function of strain rate and temperature

The response of the iron in Fig. 9 is similar to that of other body-centered-cubic (bcc) metals and alloys, such as tantalum (Ta), tungsten (W), molybdenum (Mo), and niobium (Nb) (Ref 94) and hexagonal-close-packed (hcp) metals and alloys, such as zirconium (Zr), beryllium (Be), zinc (Zn), and titanium (Ti) (Ref 99, 100). In this class of metals, strain-hardening responses after yielding are nearly invariant as a function of strain rate (i.e., the stress-strain curves are all nearly parallel in slope although offset in their initial yields). This response is typical of bcc, hcp, and lower-symmetry metals where the Peierls stress dominates low-temperature and high-strain-rate mechanical behavior (Ref 94).

Other materials, including high-purity, face-centered cubic metals in an annealed condition, such as copper (Cu), nickel (Ni), aluminum (Al), and silver (Ag), conversely exhibit nearly strain-rate independent yielding behavior while their post-yield strain hardening is strongly rate dependent. The stress-strain behavior of high-purity silver given in Fig. 10 is typical of this class of materials. In-depth knowledge of the simultaneous influence of temperature and strain rate is used as the basis for advanced materials model development to describe high-strain-rate material response.

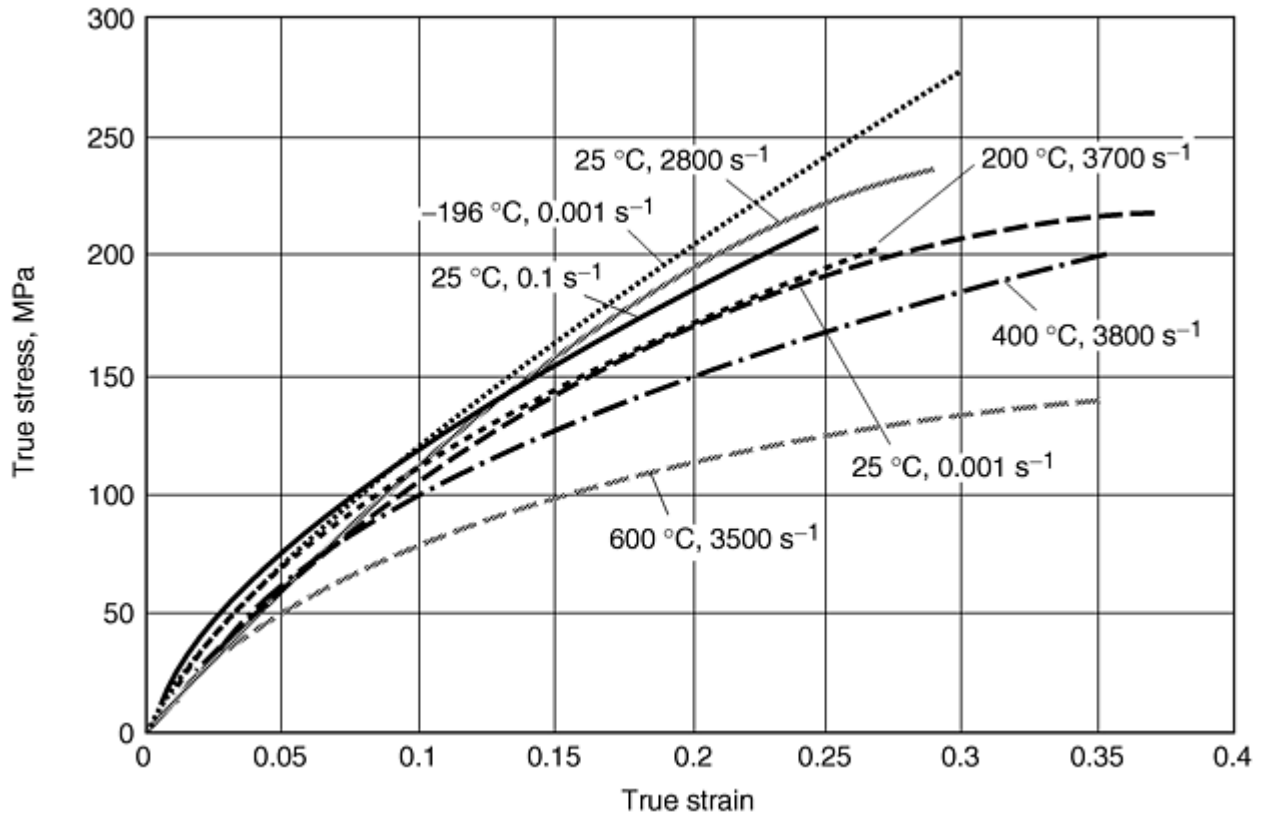


Fig. 10 Stress-strain response of high-purity silver as a function of strain rate and temperature

In addition to the direct influence of strain rate on stress-strain behavior by modifying defect generation and storage processes, high-rate deformation also alters the measured mechanical response due to the adiabatic heating accompanying high-rate plastic deformation. While adiabatic heating can be neglected during quasistatic deformation, the effect of adiabatic heating on the measured high-rate stress-strain behavior of materials must be considered. To extract an isothermal curve of the material response at a high rate, a relationship between temperature and stress must be assumed, and the data corrected accordingly. The temperature increase, ΔT , for mechanical tests at strain rates above 500 s^{-1} can be calculated assuming a certain percentage, Ψ of the work of plastic deformation is converted into heat (Ref 101, 102):

$$\Delta T = \frac{\Psi}{\rho C_p} \int \sigma(\epsilon) \delta \epsilon \quad (\text{Eq 22})$$

where σ and ϵ are the true stress and strain, respectively; ρ is the density; and C_p is the heat capacity that can be written in the form (Ref 103):

$$C_p = A_0 + A_1 \cdot T + \frac{A_2}{T^2} \quad (\text{Eq 23})$$

Adiabatic heating may be significant in samples deformed at high strain rates, particularly at higher strains. Careful consideration of adiabatic effects on overall constitutive response is crucial to accurate material model development.

References cited in this section

46. P.S. Follansbee, High Strain Rate Deformation of FCC Metals and Alloys, *Metallurgical Applications of Shock Wave and High Strain Rate Phenomena*, L.E. Murr, K.P. Staudhammer, and M.A. Meyers, Ed., Marcel Dekker, 1986, p 451–480
94. S.R. Chen and G.T. Gray III, Constitutive Behavior of Tantalum and Tantalum-Tungsten Alloys, *Metall. Mater. Trans. A*, Vol 27, 1996, p 2994–3006

95. E. El-Magd, H. Scholles, and H.P. Weissaupt, The Stress-Strain Behaviour of Pure Metals and Composite Materials in the Region of the Lüders Deformation under Dynamic Load Conditions, *DYMAT J.*, Vol 2, 1995, p 151–166
96. J. Harding, High-Rate Straining and Mechanical Properties of Materials, *Explosive Welding, Forming and Compaction*, T.Z. Blazynski, Ed., Applied Science Publishers, London, 1983, p 123–158
97. T. Nicholas and A.M. Rajendran, Material Characterization at High Strain Rates, *High Velocity Impact Dynamics*, J.A. Zukas, Ed., John Wiley & Sons Inc., 1990, p 127–296
98. J. Macdougall and J. Harding, Materials Testing for Constitutive Equations, *J. Phys. (France) IV Colloq.*, C3 (EURODYMAT 97), Vol 7, 1997, p 103–108
99. U.F. Kocks, Constitutive Equations for Slip, *Constitutive Equations in Plasticity*, A.S. Argon, Ed., MIT Press, 1975, p 81–116
100. G.T. Gray III, Influence of Strain Rate on the Structure Property Behavior of Ti-48Al-1V, *Microstructure/Property Relationships in Titanium Aluminides and Alloys*, Y.W. Kim and R.R. Boyer, Ed., The Minerals, Metals and Materials Society, 1991, p 263–274
101. H. Quinney and G.I. Taylor, The Emission of the Latent Energy due to Previous Cold Working when a Metal is Heated, *Proc. R. Soc. (London) A*, Vol 163, 1937, p 157–181
102. G.I. Taylor and W.S. Farren, The Heat Developed during Plastic Extension of Metals, *Proc. R. Soc. (London) A*, Vol 107, 1925, p 422–451
103. D.R. Stull and G.C. Stinke, *Thermodynamic Properties of the Elements*, American Chemical Society, 1956

Classic Split-Hopkinson Pressure Bar Testing

George T. (Rusty) Gray III, Los Alamos National Laboratory

Limitations and Problem Areas

In addition to the care needed to ensure the achievement of stress equilibrium during SHPB testing, several other problems can be encountered during experimental investigations studying the mechanical behavior of materials at high rates of loading. These problems are associated with inertia effects in the test machine, sample constraint due to friction at the points of contact, and issues related to assuring accurate strain gage measurements on the pressure bars.

Inertia. Even when the specimen has been evaluated to be deforming uniformly, longitudinal and radial inertia caused by the rapid particle accelerations imposed during high strain-rate testing can influence the measured stress-strain behavior (Ref 3, 104). The errors due to both longitudinal and radial inertia have been analyzed, and corrections have been derived for these errors (Ref 42). This analysis states that:

$$\sigma(t) = \sigma_m(t) + \rho_s \left(\frac{l_s^2}{6} - \nu_s \frac{d^2}{8} \right) \frac{\delta^2 \epsilon(t)}{\delta t^2} \quad (\text{Eq 24})$$

where σ_m is the measured stress, ρ_s is the density of the specimen, ν is the Poisson's ratio, l_s is the specimen length, and d is the specimen diameter. This expression predicts that errors are minimized if the strain rate is held constant or if the term inside the brackets is set to zero by choosing specimen dimensions such that

$$\frac{l_s}{d} = \sqrt{\frac{3v_s}{4}} \quad (\text{Eq 25})$$

For a Poisson's ratio of 0.33, Eq 25 suggests that the optimum sample l_s/d ratio to minimize errors caused by inertia is 0.5. Further work by Bertholf and Karnes (Ref 105) using a full two-dimensional finite-difference, elastoplastic finite-element analysis confirmed these results. This l_s/d ratio is less than that determined to be the most favorable for the minimization of errors due to friction in ASTM E 9, which specifies that $1.5 < l_s/d < 2.0$ (Ref 3). However, because the total strain in a split-Hopkinson pressure bar test is typically limited to approximately 25% to reduce the area mismatch between the specimen and the pressure bar, samples with an l_s/d of 0.5 are not expected to introduce any serious errors.

Radial inertia considerations limit the strain rate for which the SHPB technique is valid to about 10^5 s^{-1} for a high sound-speed material. The reason for this limitation is that as the strain rate is increased, the specimen size must be decreased accordingly. The specimen required eventually becomes so small that it no longer represents bulk material response. Only very fine-grained materials, such as nanocrystalline-structured materials, with high sound speeds can be tested with valid results at the very highest strain rates using this technique.

Friction is an important consideration in determining the validity of all compression testing (Ref 106). Further, the assumption of uniaxial stress conditions in the specimen can be affected by the presence of frictional forces that can cause radial traction at the interfaces between the pressure bars and the specimen. Lubrication is therefore required at the specimen/pressure bar interfaces. The optimum l_s/d ratio to minimize friction for a split-Hopkinson pressure bar compression test specimen is approximately one-half that determined to be most favorable for minimizing errors caused by friction for low-rate tests.

Early workers studying the SHPB were concerned about longitudinal inertial effects (i.e., how long it takes the forces on the ends of the specimen to become equal, that is, the ringing up time). Accordingly, they tested thin wafers of material with a thickness-to-diameter ratio of 0.1. Such extreme sample aspect ratios are known to maximize the effect of friction as the measured yield pressure, p , is related to the material flow stress, σ_f , according to the relation (Ref 107):

$$p = \left(\frac{1 + mD}{3\sqrt{3}l_s} \right) \sigma_f \quad (\text{Eq 26})$$

where m is the ratio of the friction stress to the shear strength of the material, D is the specimen diameter, and l_s is the specimen thickness (or length). Bell (Ref 108) identified that the absence of proper lubrication at the pressure bar/sample interfaces can cause large discrepancies between the measured strain on the radial surface of the specimen and the average strain obtained from the relative displacement of its two faces in the compression split-Hopkinson bar test.

Care must be exercised, therefore, in lubricating samples prior to testing as well as to limiting the strain in a single test to strains less than ~20 to 25%. Repeated reloading of a sample, with intermediate remachining to ensure flat and parallel sample loading surfaces, can be utilized to achieve higher total strains. Repetitive reloading offers the added benefit of minimizing adiabatic heating effects on the measured stress-strain behavior. The size of the sample can also have a significant effect on the friction condition during an SHPB test. Gorham (Ref 104) showed that larger samples of copper deformed at the same strain rate involve longer radial displacement at higher velocities than in the case of smaller samples. Breakdown in the lubricant is more likely under large displacements, and loss of lubricant by jetting is enhanced at increased strain rates. Care must therefore be exercised to avoid velocity-dependent frictional constraints altering the stress-strain response if larger test samples are used.

The use of an oil-based molybdenum disulfide lubricant has been shown to be effective for room-temperature SHPB testing (Ref 3). For elevated-temperature tests, a thin layer of fine boron nitride powder can be used to lubricate the specimen/pressure bar interfaces. So far, no lubricant has been found that completely eliminates friction for metallic specimens in this geometry, although the frictional stresses can be reduced to about 4% of the metal's shear strength. Friction can, in principle, be measured using annular specimens, the idea being that the higher the friction, the smaller the ratio of the internal to external diameter for a given strain (Ref 107, 109). However, the presence of a layer of lubricant at these interfaces can influence the timing between the waves recorded on the incident and output pressure bars. Consequently, it is important to maintain as thin as possible the layer of lubricant on the bar ends. Routine examination of the surface finish and flatness of the pressure-bar-

loading faces, in addition to checking for any possible cracking or erosion of the bar ends, are also critical elements influencing valid SHPB data acquisition.

Strain-Gage Measurements. Because the stress-strain behavior of the material of interest is deduced from the elastic strain signals in the pressure bars, the details of the conditions controlling the accuracy and reproducibility of the strain gages are crucial. A number of considerations related to strain-gage installation and usage can affect the elastic strain measurements obtained. Two gages generally are mounted at diametrically opposite positions on each bar and connected so as to average out most bending strains in the bars and increase the magnitude of the strain signal measured by a factor of two. The use of four gages arranged equidistantly around the bar diameter, comprising a complete Wheatstone strain gage bridge, will totally eliminate any bending effects on the strain data. The four-gage arrangement additionally corrects for any magnetostriction effects (induced voltage in the strain gages due to stress wave propagation in a ferromagnetic bar material). Use of nonmagnetic pressure bar materials, such as Ti-6Al-4V or Mg, eliminates any potential magnetostriction errors in the strain-gage outputs. In addition to the elimination of bending forces through the use of multiple gage locations, shielding of the wire leads from the strain gages to the signal conditioners is important for minimizing external noise given the small magnitude of the absolute strain signals and the level of amplification required to boost the signals to the levels required by the data acquisition system.

Finally, bonded strain gages have a finite-time-response capability that is linked to the stiffness of the epoxy used to bond the gages to the bars as well as the thickness of the interface. Using an epoxy that is too compliant can dampen the signals transferred from the bar surface to the strain gages. Conversely, an epoxy that is too stiff and brittle will require frequent replacement. Careful selection, application, and maintenance of the gages bonded to the SHPB is required to ensure accurate bar operation. Periodic calibration is used to monitor the gage/epoxy bond degradation.

References cited in this section

3. P.S. Follansbee, The Hopkinson Bar, *Mechanical Testing*, Vol 8, *ASM Handbook*, American Society for Metals, 1985, p 198–203
42. E.D.H. Davies and S.C. Hunter, The Dynamic Compression Testing of Solids by the Method of the Split Hopkinson Pressure Bar (SHPB), *J. Mech. Phys. Solids*, Vol 11, 1963, p 155–179
104. D.A. Gorham, The Effect of Specimen Dimensions on High Strain Rate Compression Measurements of Copper, *J. Phys. D, Appl. Phys.*, Vol 24, 1991, p 1489–1492
105. I.D. Bertholf and C.H. Karnes, 2D Analysis of the Split Hopkinson Pressure Bar System, *J. Mech. Phys. Solids*, Vol 23, 1975, p 1–19
106. J. Klepaczko and Z. Malinowski, Dynamic Frictional Effects as Measured from the Split Hopkinson Pressure Bar, *High Velocity Deformation of Solids*, K. Kawata and J. Shioiri, Ed., Springer-Verlag (Berlin), 1978, p 403–416
107. D.A. Gorham, P.H. Pope, and O. Cox, Sources of Error in Very High Strain Rate Compression Tests, *Inst. Phys. Conf. Series*, Vol 70, 1984, p 151–158
108. J.F. Bell, An Experimental Diffraction Grating Study of the Quasi-Static Hypothesis of the SHPB Experiment, *J. Mech. Phys. Solids*, Vol 14, 1966, p 309–327
109. S.M. Walley, P.D. Church, M. Furth, and J.E. Field, A High-Speed Photographic Study of the Rapid Deformation of Metal Annuli: A Comparison of Theory with Experiment, *J. Phys. (France) IV Colloq.*, C3 (EURODYMAT 97), Vol 7, 1997, p 317–322

New Developments in Split-Hopkinson Bar Testing

The Hopkinson pressure bar, as a research and engineering tool for the quantitative measurement of the high-rate stress-strain behavior of materials, is a technique that is far from static. In recent years, a number of new improvements have been designed and their value proven to improve both the accuracy and timeliness of measurements. One-, two-, and three-dimensional finite-element models of the split-Hopkinson pressure bar have proven their ability to simulate test parameters and allow pretest setup validation checks as an aid to planning. Finite-element models additionally offer a means in the future to validate the data and dispersion analysis used in the Hopkinson bar to probe for the effects of inertia and friction, for example, and provide an opportunity to extend the use of the Hopkinson bar to the characterization of materials for which the SHPB technique was previously unable to achieve a valid uniaxial stress state. Previous research using this approach on the SHPB testing and analysis of soil samples has shown the utility of such a finite element method (FEM)/standard SHPB analysis (Ref 51). A current example of this promising line of research is applied to split-Hopkinson bar testing of viscoplastic materials (more information can be found in the article “Split-Hopkinson Pressure Bar Testing of Soft Materials” in this Volume).

Novel methods of characterizing sample diametrical strains are also being developed for the Hopkinson bar using optical diagnostic techniques (Ref 110, 111). This technique offers an alternate mechanism to measure the diametrical strain in a Hopkinson pressure bar sample as a function of time using a linear laser line-measuring diagnostic device. This technique offers a valuable additional way to accurately measure sample dimensional changes without the use of strain gages attached to the sample. This technique, however, must also be cautiously approached as a stand-alone technique where anisotropic plasticity in the sample could falsely portray the sample diametral strain unless multiple viewing points are surveyed. Additional optical techniques are emerging that may provide a quantitative means of measuring axial and radial strains in SHPB samples during testing. These techniques include monitoring strains on a cylindrical sample using Bragg grating sensors (Ref 112) and the measurement of tangential displacements on samples and/or the pressure bars themselves using speckle interferometry (Ref 113).

Finally, careful attention to controlling wave reflections in the SHPB has also opened new opportunities to study defect/damage evolution in brittle materials during high-rate loading histories (Ref 114). Careful momentum trapping of the transmitted and reflected wave pulses in the pressure bars can be utilized to facilitate single pulse loading of the sample. Researchers are also exploring exciting new methods for in situ dispersion measurements (Ref 47) on pressure bars, which offer opportunities for increased signal resolution in the future.

References cited in this section

47. X.J. Wu and D.A. Gorham, Stress Equilibrium in the Split Hopkinson Pressure Bar Test, *J. Phys. (France) IV Colloq.*, C3 (EURODYMAT 97), Vol 7, 1997, p 91–96
51. C.W. Felice, E.S. Gaffney, and J.A. Brown, Extended Split-Hopkinson Bar Analysis for Attenuating Materials, *J. Eng. Mech.*, Vol 117, 1991, p 1119–1135
110. V. Vallé, M. Cottron, and A. Lagarde, Dynamic Optical Method for Local Strain Measurements: Principle and Characteristics, *J. Phys. (France) IV Colloq.*, C8 (DYMAT 94), Vol 4, 1994, p 59–64
111. K.T. Ramesh and S. Narasimhan, Finite Deformations and the Dynamic Measurement of Radial Strain on Compression Kolsky Bar Experiments, *Int. J. Solids Struct.*, Vol 33, 1996, p 3723–3738
112. S.W. James, R.P. Tatam, S.R. Fuller, and C. Crompton, Monitoring Transient Strains on a Gun Barrel Using Fibre Bragg-Grating Sensors, *Meas. Sci. Technol.*, Vol 10, 1999, p 63–67

113. F. Gascon, A. Bayon, and A. Varade, Measurement of Longitudinal Vibrations in a Slender Rod by Optical Heterodyne Interferometry, *Eur. J. Mech.-A/Solids*, Vol 17, 1998, p 167–177
114. S. Nemat-Nasser, J.B. Isaacs, and J.E. Starrett, Hopkinson Techniques for Dynamic Recovery Experiments, *Proc. R. Soc. (London) A*, Vol 435, 1991, p 371–391

Classic Split-Hopkinson Pressure Bar Testing

George T. (Rusty) Gray III, Los Alamos National Laboratory

Acknowledgments

The author would like to thank Thomas A. Mason and George C. Kaschner for their assistance in this work. Helpful discussions with Stephen Walley, John E. Field, Neil K. Bourne, Paul F. Follansbee, Robert K. Garrett, D. Goto, and Kenneth S. Vecchio are gratefully acknowledged. This work was supported in part by the U.S. Department of Energy.

Classic Split-Hopkinson Pressure Bar Testing

George T. (Rusty) Gray III, Los Alamos National Laboratory

References

1. U.S. Lindholm, High Strain Rate Testing, Part 1: Measurement of Mechanical Properties, *Techniques of Metals Research*, Vol 5, R.F. Bunshah, Ed., Wiley Interscience, New York, 1971, p 199–271
2. U.S. Lindholm, Review of Dynamic Testing Techniques and Material Behaviour, *Inst. Phys. Conf. Ser.*, Vol 21, 1974, p 3–21
3. P.S. Follansbee, The Hopkinson Bar, *Mechanical Testing*, Vol 8, *ASM Handbook*, American Society for Metals, 1985, p 198–203
4. J.E. Field, S.M. Walley, N.K. Bourne, and J.M. Huntley, Experimental Methods at High Rates of Strain, *J. Phys. (France) IV Colloq.*, C8 (DYMAT 94), Vol 4, 1994, p 3–22
5. J.E. Field, S.M. Walley, N.K. Bourne, and J.M. Huntley, Review of Experimental Techniques for High Rate Deformation Studies, *Proc. Acoustics and Vibration Asia '98* (Singapore), 1998, p 9–38
6. W.E. Carrington and M.L.V. Gayler, The Use of Flat Ended Projectiles for Determining Yield Stress, Part III: Changes in Microstructure Caused by Deformation at High Striking Velocities, *Proc. R. Soc. (London) A*, Vol 194, 1948, p 323–331
7. B. Hopkinson, A Method of Measuring the Pressure Produced in the Detonation of High Explosives or by the Impact of Bullets, *Philos. Trans. R. Soc. (London) A*, Vol 213, 1914, p 437–456
8. P.S. Follansbee and U.F. Kocks, A Constitutive Description of Copper Based on the Use of the Mechanical Threshold Stress as an Internal State Variable, *Acta Metall.*, Vol 36, 1988, p 81–93

9. S.R. Chen and G.T. Gray III, Constitutive Behaviour of Tantalum and Tantalum-Tungsten Alloys, *Metall. Trans. A*, Vol 27, 1996, p 2994–3006
10. J.R. Klepaczko, Constitutive Modeling in Dynamic Plasticity Based on Physical State Variables—A Review, *J. Phys. (France) Colloq.*, C3 (DYMAT 88), Vol 49, 1988, p 553–560
11. R.M. Davies, A Simple Modification of the Hopkinson Pressure Bar, *Proc. 7th Int. Cong. on Applied Mechanics*, Vol 1, 1948, p 404
12. R.M. Davies, A Critical Study of the Hopkinson Pressure Bar, *Philos. Trans. R. Soc. (London) A*, Vol 240, 1948, p 375–457
13. H. Kolsky, An Investigation of the Mechanical Properties of Materials at Very High Rates of Loading, *Proc. Phys. Soc. (London)*, Vol 62B, 1949, p 676–700
14. U.S. Lindholm and L.M. Yeakley, High Strain Rate Testing: Tension and Compression, *Exp. Mech.*, Vol 8, 1968, p 1–9
15. H. Kolsky, Stress Waves in Solids, *J. Sound Vib.*, Vol 1, 1964, p 88–110
16. V.P. Muzychenko, S.I. Kashchenko, and V.A. Guskov, Use of the Split Hopkinson Pressure Bar Method for Examining the Dynamic Properties of Materials: Review, *Ind. Lab. (USSR)*, Vol 52, 1986, p 72–83
17. H. Zhao and G. Gary, On the Use of SHPB Techniques to Determine the Dynamic Behavior of Materials in the Range of Small Strains, *Int. J. Solids Struct.*, Vol 33, 1996, p 3363–3375
18. G.T. Gray III, High-Strain-Rate Testing of Materials: The Split-Hopkinson Pressure Bar, *Methods in Materials Research*, E. Kaufmann, Ed., John Wiley Press, 1999, in press
19. J. Harding, E.O. Wood, and J.D. Campbell, Tensile Testing of Materials at Impact Rates of Strain, *J. Mech. Eng. Sci.*, Vol 2, 1960, p 88–96
20. G.H. Staab and A. Gilat, A Direct-Tension Split Hopkinson Bar for High Strain-Rate Testing, *Exp. Mech.*, Vol 31, 1991, p 232–235
21. J. Duffy, J.D. Campbell, and R.H. Hawley, On the Use of a Torsional Split Hopkinson Bar to Study Rate Effects in 1100-O Aluminum, *J. Appl. Mech. (Trans. ASME)*, Vol 38, 1971, p 83–91
22. J.L. Lewis and W. Goldsmith, A Biaxial Split Hopkinson Bar for Simultaneous Torsion and Compression, *Rev. Sci. Instrum.*, Vol 44, 1973, p 811–813
23. D.R. Chichili and K.T. Ramesh, Recovery Experiments for Adiabatic Shear Localization: A Novel Experimental Technique, *Trans. ASME*, Vol 66, 1999, p 10–20
24. W. Chen and G. Ravichandran, Static and Dynamic Compressive Behavior of Aluminum Nitride under Moderate Confinement, *J. Amer. Ceram. Soc.*, Vol 79, 1996, p 579–584
25. J.D. Campbell and W.G. Ferguson, The Temperature and Strain Rate Dependence of the Shear Strength of Mild Steel, *Philos. Mag.*, Vol 21, 1970, p 63–82
26. J. Harding and J. Huddart, The Use of the Double-Notch Shear Test in Determining the Mechanical Properties of Uranium at Very High Rates of Strain, *Inst. Phys. Conf. Ser.*, Vol 47, 1980, p 49–61

27. D. Ruiz, J. Harding, and C. Ruiz, The Double Notch Shear Test—Analysis and Development for Material Testing at Very High Strain Rates, *Structures under Shock and Impact*, P.S. Bulson, Ed., Elsevier, Amsterdam, p 145–154
28. J.R. Klepaczko, An Experimental Technique for Shear Testing at High and Very High Strain Rates: The Case of a Mild Steel, *Int. J. Impact Eng.*, Vol 15, 1994, p 25–40
29. J.R. Klepaczko, H.V. Nguyen, and W.K. Nowacki, Quasi-Static and Dynamic Shearing of Sheet Metals, *Eur. J. Mech. A-Solids*, Vol 18, 1999, p 271–289
30. J. Klepaczko, Application of the Split Hopkinson Pressure Bar to Fracture Dynamics, *Inst. Phys. Conf. Ser.*, Vol 47, 1980, p 201–214
31. G.I. Taylor, The Use of Flat Ended Projectiles for Determining Yield Stress, Part I: Theoretical Considerations, *Proc. R. Soc. (London) A*, Vol 194, 1948, p 289–299
32. G.T. Gray III, D.J. Idar, W.R. Blumenthal, C.M. Cady, and P.D. Peterson, High- and Low-Strain Rate Compression Properties of Several Energetic Material Composites as a Function of Strain Rate and Temperature, *11th Detonation Symposium*, 1998 (Snow Mass, CO), J. Short, Ed., in press
33. G. Gary, J.R. Klepaczko, and H. Zhao, Generalization of Split Hopkinson Bar Technique to Use Viscoelastic Materials, *Int. J. Impact Eng.*, Vol 16, 1995, p 529–530
34. G. Gary, L. Rota, and H. Zhao, Testing Viscous Soft Materials at Medium and High Strain Rates, *Constitutive Relation in High/Very High Strain Rates*, K. Kawata and J. Shioiri, Ed., Springer-Verlag, Tokyo, 1996, p 25–32
35. G.T. Gray III, W.R. Blumenthal, C.P. Trujillo, and R.W. Carpenter II, Influence of Temperature and Strain Rate on the Mechanical Behavior of Adiprene-L100, *J. Phys. (France)*, C3 (DYMAT 97), Vol 7, 1997, p 523–528
36. W. Chen, B. Zhang, and M.J. Forrestal, A Split Hopkinson Bar Technique for Low-Impedance Materials, *Exp. Mech.*, Vol 39, 1999, p 1–5
37. I. Mirsky and G. Herrmann, Axially Symmetric Motions of Thick Cylindrical Shells, *J. Appl. Mech. (Trans. ASME)*, Vol 25, 1958, p 97–102
38. G. Herrmann and I. Mirsky, Three-Dimensional and Shell-Theory Analysis of Axially Symmetric Motions of Cylinders, *J. Appl. Mech. (Trans. ASME)*, Vol 23, 1956, p 563–568
39. M.M. Al-Mousawi, S.R. Reid, and W.F. Deans, The Use of the Split Hopkinson Pressure Bar Techniques in High Strain Rate Materials Testing, *Proc. Inst. Mech. Eng., Part C: J. Mech. Eng. Sci.*, Vol 211, 1997, p 273–292
40. P.S. Follansbee and C. Frantz, Wave Propagation in the SHPB, *J. Eng. Mater. Technol. (Trans. ASME)*, Vol 105, 1983, p 61–66
41. G.E. Dieter, *Mechanical Metallurgy*, McGraw-Hill, Inc., 1976
42. E.D.H. Davies and S.C. Hunter, The Dynamic Compression Testing of Solids by the Method of the Split Hopkinson Pressure Bar (SHPB), *J. Mech. Phys. Solids*, Vol 11, 1963, p 155–179

43. C.E. Frantz, P.S. Follansbee, and W.T. Wright, Experimental Techniques with the SHPB, *High Energy Rate Fabrication—1984*, I. Berman and J.W. Schroeder, Ed., American Society of Mechanical Engineers, 1984, p 229–236
44. S. Ellwood, L.J. Griffiths, and D.J. Parry, Materials Testing at High Constant Strain Rates, *J. Phys. E, Sci. Instrum.*, Vol 15, 1982, p 280–282
45. D.J. Parry, A.G. Walker, and P.R. Dixon, Hopkinson Bar Pulse Smoothing, *Meas. Sci. Technol.*, Vol 6, 1995, p 443–446
46. P.S. Follansbee, High Strain Rate Deformation of FCC Metals and Alloys, *Metallurgical Applications of Shock Wave and High Strain Rate Phenomena*, L.E. Murr, K.P. Staudhammer, and M.A. Meyers, Ed., Marcel Dekker, 1986, p 451–480
47. X.J. Wu and D.A. Gorham, Stress Equilibrium in the Split Hopkinson Pressure Bar Test, *J. Phys. (France) IV Colloq.*, C3 (EURODYMAT 97), Vol 7, 1997, p 91–96
48. G.T. Gray III, W.R. Blumenthal, C.P. Trujillo, and R.W. Carpenter, Influence of Temperature and Strain Rate on the Mechanical Behavior of Adiprene L-100, *J. Phys. IV Colloq.*, C3 (DYMAT 97), 1997, p 523–528
49. G.T. Gray III, W.R. Blumenthal, C.P. Trujillo, and R.W. Carpenter II, Influence of Temperature and Strain Rate on the Mechanical Behavior of Adiprene L-100, *J. Phys. (France) IV Colloq.*, C3 (EURODYMAT 97), Vol 7, 1997, p 523–528
50. W.R. Blumenthal and G.T. Gray III, Structure-Property Characterization of Shock-Loaded B₄C-Al, *Inst. Phys. Conf. Ser.*, Vol 102, 1989, p 363–370
51. C.W. Felice, E.S. Gaffney, and J.A. Brown, Extended Split-Hopkinson Bar Analysis for Attenuating Materials, *J. Eng. Mech.*, Vol 117, 1991, p 1119–1135
52. S.M. Walley and J.E. Field, Strain Rate Sensitivity of Polymers in Compression from Low to High Strain Rates, *DYMAT J.*, Vol 1, 1994, p 211–228
53. S.M. Walley, J.E. Field, and N.A. Safford, A Comparison of the High Strain Rate Behaviour in Compression of Polymers at 300K and 100K, *J. Phys. (France) IV Colloq.*, C3 (DYMAT 91), Vol 1, 1991, p 185–190
54. W.R. Blumenthal and G.T. Gray III, *Structure-Property Characterization of Shock-Loaded B₄C-Al*, Oxford, 1989, p 363–370
55. C. Bacon, Numerical Prediction of the Propagation of Elastic Waves in Longitudinally Impacted Rods: Applications to Hopkinson Testing, *Int. J. Impact Eng.*, Vol 13, 1993, p 527–539
56. A.M. Eleiche, Impedance Matching in Non-Homogeneous Elastic Bars, *J. Phys. D, Appl. Phys.*, Vol 8, 1975, p 505–511
57. C.E. Frantz, P.S. Follansbee, and W.J. Wright, *New Experimental Techniques with the Kolsky Bar*, I. Berman and J.W. Schroeder, Ed., American Society of Mechanical Engineers, 1984, p 229–236
58. D. Macdougall, A Radiant Heating Method for Performing High-Temperature High-Strain-Rate Tests, *Meas. Sci. Technol.*, Vol 9, 1998, p 1657–1662

59. Z. Rosenberg, D. Dawicke, E. Strader, and S.J. Bless, A New Technique for Heating Specimens in Split-Hopkinson-Bar Experiments Using Induction Coil Heaters, *Exp. Mech.*, Vol 26, 1986, p 275–278
60. Z. Rosenberg, D. Dawicke, and S.J. Bless, A New Technique for Heating Specimens in Split Hopkinson Bar Experiments Using Induction Coil Heaters, *Metallurgical Applications of Shock Wave and High Strain Rate Phenomena*, L.E. Murr, K.P. Staudhammer, and M.A. Meyers, Ed., Marcel Dekker, 1986, p 543–552
61. H.W. Sizek and G.T. Gray III, Deformation of Polycrystalline Ni₃Al at High Strain Rates and Elevated Temperatures, *Acta Metall. Mater.*, Vol 41, 1993, p 1855–1860
62. T. Nicholas, Tensile Testing of Materials at High Rates of Strain, *Exp. Mech.*, Vol 21, 1981, p 177–185
63. T. Nicholas and S.J. Bless, High Strain-Rate Tension Testing, *Mechanical Testing*, Vol 8, *ASM Handbook*, American Society for Metals, 1985, p 208–214
64. S. Ellwood, L.J. Griffiths, and D.J. Parry, A Tensile Technique for Materials Testing at High Strain Rates, *J. Phys. E, Sci. Instrum.*, Vol 15, 1982, p 1169–1172
65. L.A. Cross, S.J. Bless, A.M. Rajendran, E.A. Strader, and D.S. Dawicke, New Technique to Investigate Necking in a Tensile Hopkinson Bar, *Exp. Mech.*, Vol 24, 1984, p 184–186
66. M.M. LeBlanc and D.H. Lassila, Dynamic Tensile Testing of Sheet Materials Using the Split-Hopkinson Bar Technique, *Exp. Tech.*, Vol 17, 1993, p 37–42
67. J. Yuan, N. Takeda, and A.M. Waas, A Note on Data Processing in the Split Hopkinson Pressure Bar Tests, *Exp. Tech.*, Vol 1, 1998, p 21–24
68. J.M. Lifshitz and H. Leber, Data Processing in the Split Hopkinson Pressure Bar Tests, *Int. J. Impact Eng.*, Vol 15, 1994, p 723–733
69. T. Yokoyama and K. Kishida, A Microcomputer-Based System for the High-Speed Compression Test by the Split Hopkinson Pressure Bar Technique, *J. Test. Eval.*, Vol 14, 1986, p 236–242
70. L. Pochhammer, About the Initiation of the Velocities of Small Oscillations in Unbounded Isotropic Circular Cylinders, *J. Reine Angew. Math.*, Vol 81, 1876, p 324–336 (in German)
71. C. Chree, The Equations of an Isotropic Elastic Solid in Polar and Cylindrical Coordinates: Their Solution and Application, *Trans. Camb. Philos. Soc.*, Vol 14, 1889, p 250–369
72. D.A. Gorham, Measurement of Stress-Strain Properties of Strong Metals at Very High Strain Rates, *Inst. Phys. Conf. Series*, Vol 47, 1980, p 16–24
73. J.C. Gong, L.E. Malvern, and D.A. Jenkins, Dispersion Investigation in the Split Hopkinson Pressure Bar, *J. Eng. Mater. Technol. (Trans. ASME)*, Vol 112, 1990, p 309–314
74. C. Bacon, An Experimental Method for Considering Dispersion and Attenuation in a Viscoelastic Hopkinson Bar, *Exp. Mech.*, Vol 38, 1998, p 242–249
75. C.K.B. Lee, R.C. Crawford, K.A. Mann, P. Coleman, and C. Petersen, Evidence of Higher Pochhammer-Chree Modes in an Unsplit Hopkinson Bar, *Meas. Sci. Technol.*, Vol 6, 1995, 853–859
76. C.K.B. Lee and R.C. Crawford, A New Method for Analyzing Dispersed Bar Gauge Data, *Meas. Sci. Technol.*, Vol 4, 1993, p 931–937

77. D.A. Gorham, A Numerical Method for the Correction of Dispersion in Pressure Bar Signals, *J. Phys. E*, Vol 16, 1983, p 477–479
78. G. Gary, J.R. Klepaczko, and H. Zhao, Corrections for Wave Dispersion and Analysis of Small Strains with Split Hopkinson Bar, *J. Phys. (France) IV Colloq.*, C3 (DYMAT 91), Vol 1, 1991, p 403–410 (in French)
79. D.A. Gorham and X.J. Wu, An Empirical Method for Correcting Dispersion in Pressure Bar Measurements of Impact Stress, *Meas. Sci. Technol.*, Vol 7, 1996, p 1227–1232
80. C.K.H. Dharan and F.E. Hauser, Determination of Stress-Strain Characteristics at Very High Strain Rates, *Exp. Mech.*, Vol 10, 1970, p 370–376
81. A.L. Wingrove, A Device for Measuring Strain-Time Relationships in Compression at Quasi-Static and Dynamic Strain Rates, *J. Phys E, Sci. Instrum.*, Vol 4, 1971, p 873–875
82. G.L. Wulf and G.T. Richardson, The Measurement of Dynamic Stress-Strain Relationships at Very High Strain Rates, *J. Phys. E*, Vol 7, 1974, p 167–169
83. D.A. Gorham, P.H. Pope, and J.E. Field, An Improved Method for Compressive Stress-Strain Measurements at Very High Strain Rates, *Proc. R. Soc. (London) A*, Vol 438, 1992, p 153–170
84. C.W. Fong, Crack Initiation in Perforated Propellants under High Strain Rate Impact Conditions, *Propell. Explos. Pyrotech.*, Vol 10, 1985, p 91–96
85. S.M. Walley, J.E. Field, and S.J.P. Palmer, Impact Sensitivity of Propellants, *Proc. R. Soc. (London) A*, Vol 438, 1992, p 571–583
86. S.Y. Ho, High Strain Rate Impact Studies of Predamaged Rocket Propellants, Part I: Characterization of Damage Using a Cumulative Damage Criterion, *Combustion & Flame*, Vol 104, 1996, p 524–534
87. S.M. Walley, J.E. Field, P.H. Pope, and N.A. Safford, A Study of the Rapid Deformation Behaviour of a Range of Polymers, *Philos. Trans. R. Soc. (London) A*, Vol 328, 1989, p 1–33
88. O.S. Lee, S.S. You, J.H. Chong, and H.S. Kang, Dynamic Deformation under a Modified Split Hopkinson Pressure Bar Experiment, *KSME Int. Journal*, Vol 12, 1998, p 1143–1149
89. P.H. Pope and J.E. Field, Determination of Strain in a Dynamic Compression Test, *J. Phys. E, Sci. Instrum.*, Vol 17, 1984, p 817–820
90. C. Albertini, E. Cadoni, and K. Labibes, Dynamic Mechanical Behaviour of Large Concrete Specimens by Means of a Hopkinson Bar Bundle, *Proc. 2nd Int. Symp. on Impact Eng.*, C.Y. Chiem, L.L. Wang, and S. Tanimura, Ed., Chinese Journal of Mechanics Press, Beijing, 1996, p 214–219
91. C.A. Tracy, A Compression Test for High Strength Ceramics, *J. Test. Eval.*, Vol 15, 1987, p 14–19
92. W.R. Blumenthal and G.T. Gray III, *Characterization of Shock-Loaded Aluminum-Infiltrated Boron Carbide Cermets*, S.C. Schmidt, J.N. Johnson, and L.W. Davison, Ed., North-Holland Press, 1990, p 393–396
93. H. Couque, C. Albertini, and J. Lankford, Failure Mechanisms in a Unidirectional Fire-Reinforced Thermoplastic Composite under Uniaxial, In-Plane Biaxial and Hydrostatically Confined Compression, *J. Mater. Sci. Lett.*, Vol 12, 1993, p 1953–1957

94. S.R. Chen and G.T. Gray III, Constitutive Behavior of Tantalum and Tantalum-Tungsten Alloys, *Metall. Mater. Trans. A*, Vol 27, 1996, p 2994–3006
95. E. El-Magd, H. Scholles, and H.P. Weisshaupt, The Stress-Strain Behaviour of Pure Metals and Composite Materials in the Region of the Lüders Deformation under Dynamic Load Conditions, *DYMAT J.*, Vol 2, 1995, p 151–166
96. J. Harding, High-Rate Straining and Mechanical Properties of Materials, *Explosive Welding, Forming and Compaction*, T.Z. Blazynski, Ed., Applied Science Publishers, London, 1983, p 123–158
97. T. Nicholas and A.M. Rajendran, Material Characterization at High Strain Rates, *High Velocity Impact Dynamics*, J.A. Zukas, Ed., John Wiley & Sons Inc., 1990, p 127–296
98. J. Macdougall and J. Harding, Materials Testing for Constitutive Equations, *J. Phys. (France) IV Colloq.*, C3 (EURODYMAT 97), Vol 7, 1997, p 103–108
99. U.F. Kocks, Constitutive Equations for Slip, *Constitutive Equations in Plasticity*, A.S. Argon, Ed., MIT Press, 1975, p 81–116
100. G.T. Gray III, Influence of Strain Rate on the Structure Property Behavior of Ti-48Al-1V, *Microstructure/Property Relationships in Titanium Aluminides and Alloys*, Y.W. Kim and R.R. Boyer, Ed., The Minerals, Metals and Materials Society, 1991, p 263–274
101. H. Quinney and G.I. Taylor, The Emission of the Latent Energy due to Previous Cold Working when a Metal is Heated, *Proc. R. Soc. (London) A*, Vol 163, 1937, p 157–181
102. G.I. Taylor and W.S. Farren, The Heat Developed during Plastic Extension of Metals, *Proc. R. Soc. (London) A*, Vol 107, 1925, p 422–451
103. D.R. Stull and G.C. Stinke, *Thermodynamic Properties of the Elements*, American Chemical Society, 1956
104. D.A. Gorham, The Effect of Specimen Dimensions on High Strain Rate Compression Measurements of Copper, *J. Phys. D, Appl. Phys.*, Vol 24, 1991, p 1489–1492
105. I.D. Bertholf and C.H. Karnes, 2D Analysis of the Split Hopkinson Pressure Bar System, *J. Mech. Phys. Solids*, Vol 23, 1975, p 1–19
106. J. Klepaczko and Z. Malinowski, Dynamic Frictional Effects as Measured from the Split Hopkinson Pressure Bar, *High Velocity Deformation of Solids*, K. Kawata and J. Shioiri, Ed., Springer-Verlag (Berlin), 1978, p 403–416
107. D.A. Gorham, P.H. Pope, and O. Cox, Sources of Error in Very High Strain Rate Compression Tests, *Inst. Phys. Conf. Series*, Vol 70, 1984, p 151–158
108. J.F. Bell, An Experimental Diffraction Grating Study of the Quasi-Static Hypothesis of the SHPB Experiment, *J. Mech. Phys. Solids*, Vol 14, 1966, p 309–327
109. S.M. Walley, P.D. Church, M. Furth, and J.E. Field, A High-Speed Photographic Study of the Rapid Deformation of Metal Annuli: A Comparison of Theory with Experiment, *J. Phys. (France) IV Colloq.*, C3 (EURODYMAT 97), Vol 7, 1997, p 317–322
110. V. Vallé, M. Cottron, and A. Lagarde, Dynamic Optical Method for Local Strain Measurements: Principle and Characteristics, *J. Phys. (France) IV Colloq.*, C8 (DYMAT 94), Vol 4, 1994, p 59–64

111. K.T. Ramesh and S. Narasimhan, Finite Deformations and the Dynamic Measurement of Radial Strain on Compression Kolsky Bar Experiments, *Int. J. Solids Struct.*, Vol 33, 1996, p 3723–3738
112. S.W. James, R.P. Tatam, S.R. Fuller, and C. Crompton, Monitoring Transient Strains on a Gun Barrel Using Fibre Bragg-Grating Sensors, *Meas. Sci. Technol.*, Vol 10, 1999, p 63–67
113. F. Gascon, A. Bayon, and A. Varade, Measurement of Longitudinal Vibrations in a Slender Rod by Optical Heterodyne Interferometry, *Eur. J. Mech.-A/Solids*, Vol 17, 1998, p 167–177
114. S. Nemat-Nasser, J.B. Isaacs, and J.E. Starrett, Hopkinson Techniques for Dynamic Recovery Experiments, *Proc. R. Soc. (London) A*, Vol 435, 1991, p 371–391

Recovery Hopkinson Bar Techniques

Sia Nemat-Nasser, University of California, San Diego

Introduction

THE CLASSICAL split-Hopkinson bar technique is described in separate articles in this Section for tension, compression, and torsion tests. For all three cases, the stress pulse travels along the incident bar and is partly transmitted to the transmission bar by the specimen sandwiched between the two bars. The remaining part of the stress pulse is reflected back in the incident bar as tension in the compression bars, as compression in the tension bars, and as reverse torsion in the torsion bars. Both the transmitted and reflected pulses travel along the corresponding bar and are then reflected back and eventually reload the sample. If the sample does not fail in the course of the first loading, it will then be subjected to repeated loading by these elastic waves traveling back and forth along the bars.

There are many applications where it is necessary to subject a sample to a single loading and then recover it, without the sample having been subjected to any additional loads. Such a capability allows, for example, to relate the microstructural changes to the loading history or, as is shown later, to produce isothermal stress-strain relations for certain metals, at high strain rates (Ref 1, 2, 3).

For compression tests, special fixtures, such as “stopper rings,” can be used to limit the total axial strain of the sample and to transmit the remaining compression pulse through the stopper ring once the sample length equals that of the ring (Ref 4, 5, 6). A similar technique, however, does not apply to the tension or torsion tests. Moreover, even in compression, such a technique works only if large axial permanent straining of the sample is involved, and even then, the sample with the stopper ring is repeatedly loaded elastically. For hard, brittle materials, such as ceramics and their composites, the total axial strain to failure is very small, and, therefore, a “stopper-ring approach” is difficult, if not impossible, to implement. For this class of materials, once the initial compressive pulse has produced microcracks in the brittle sample, the subsequent reflected compression pulses may shatter the specimen, making recovery essentially impossible by that technique. For tension tests, and in the absence of wave trapping, both the transmitted and reflected pulses load the sample repeatedly.

The stopper-ring approach fails also when recovery tests are to be performed at high temperatures. For high strain-rate tests at elevated temperatures, it is necessary to heat the sample to the required temperature, while keeping the incident and transmission bars at suitably low temperatures. If the bars are in contact with the specimen within the furnace, their temperature will increase, having a variable distribution along the bars. This affects the elastic properties of the bar and, hence, the stress pulses. Moreover, the bars being good heat conductors (usually of maraging steel), the considerable heat loss that occurs makes controlling the experiment difficult.

To remedy these major problems, techniques have been developed where, for compression and tension tests (Ref 7), both the reflected and transmitted pulses are trapped at the far end of the bars, once the sample is

subjected to the initial loading. Moreover, this can be done at elevated temperatures, where the sample is heated within an attached furnace, with the Hopkinson bars held outside the furnace. These bars are then brought into contact with the specimen microseconds before the stress pulse reaches the end of the incident bar. The method ensures that the sample is subjected to a single stress pulse with a time variation that is also fully controlled.

In addition to the compression and tension recovery Hopkinson bar techniques, a technique has been worked out that allows recovery of the sample after it has been subjected to a compression followed by a tension pulse (Ref 7). This technique permits the study of the Bauschinger effect and the strain-rate history effects on the mechanical properties and microstructural evolution of materials under various dynamic loading conditions (Ref 8, 9).

The dynamic tests of hard materials (e.g., ceramics) at elevated temperatures present a new challenge. At suitably low temperatures, the sample strain can be measured directly by placing a strain gage on the sample (Ref 10, 11, 12, 13). This, however, may not be possible at elevated temperatures. Even at low temperatures, indentation of the bars by the sample must be prevented in order to obtain reliable results and preclude damaging of the bars. This latter problem is solved by using properly confined tungsten carbide (WC) inserts, placed between the sample and the bars (Ref 12). The impedance of the inserts is carefully matched with that of the bars. For strain measurements at high temperatures, a new technique is *differential strain measurement* (DSM), which can be used to obtain accurate and reliable values of the strain in the dynamic test of very hard ceramics at elevated temperatures. This method is briefly discussed in the section “High-Temperature, High Strain Rate Testing of Hard, Brittle Materials” in this article.

References cited in this section

1. S. Nemat-Nasser and J.B. Isaacs, Direct Measurement of Isothermal Flow Stress of Metals at Elevated Temperatures and High Strain Rates with Application to Ta and Ta-W Alloys, *Acta Metall.*, Vol 45, 1997, p 907–919
2. S. Nemat-Nasser and Y. Li, Flow Stress of FCC Polycrystals with Application to OFHC Cu, *Acta Mater.*, Vol 46, 1998, p 565–577
3. S. Nemat-Nasser, W. Guo, and M. Liu, Experimentally-Based Micromechanical Modeling of Dynamic Response of Molybdenum, *Scr. Mater.*, Vol 40, 1999, p 859–872
4. K.H. Hartman, H.D. Kunze, and L.W. Meyer, Metallurgical Effects in Impact Loaded Materials, *Shock Waves and High-Strain-Rate Phenomena in Metals*, M.A. Meyers and L.E. Murr, Ed., Plenum, London, 1986, p 325
5. S. Nemat-Nasser, J.B. Isaacs, G. Ravichandran, and J.E. Starrett, High Strain Rate Testing in the U.S., *Proc. TTCP TTP-1 Workshop on Techniques of Small Scale High Strain Rate Studies*, 26 April 1988, Materials Science Laboratory, Melbourne, Australia, 1988
6. S. Nemat-Nasser and S.N. Chang, Compression-Induced High Strain Rate Void Collapse, Tensile Cracking, and Recrystallization in Ductile Single and Polycrystals, *Mech. Mater.*, Vol 10, 1990, p 1–17
7. S. Nemat-Nasser, J.B. Isaacs, and J.E. Starrett, Hopkinson Techniques for Dynamic Recovery Experiments, *Proc. R. Soc. (London) A*, Vol 435, 1991, p 371–391
8. A. Thakur, S. Nemat-Nasser, and K.S. Vecchio, Bauschinger Effect in Haynes 230 Alloy: Influences of Strain Rate and Temperature, *Metall. Mater. Trans.*, Vol 27A, 1996, p 1739–1748
9. A. Thakur, S. Nemat-Nasser, and K.S. Vecchio, Dynamic Bauschinger Effect, *Acta Mater.*, Vol 44, 1996, p 2797–2807
10. W.P. Rogers, J.B. Isaacs, and S. Nemat-Nasser, Effect of Microstructural Damage on Ultrasonic Velocity and Elastic Moduli of Partially Stabilized Zirconia, *Review of Progress in Quantitative*

11. W.P. Rogers and S. Nemat-Nasser, Transformation Plasticity at High Strain Rate in Magnesia-Partially-Stabilized Zirconia, *J. Am. Ceram. Soc.*, Vol 73, 1990, p 136–139
12. V. Sharma, S. Nemat-Nasser, and K.S. Vecchio, Dynamic-Compression Fatigue of Hot-Pressed Silicon-Nitride, *Exp. Mech.*, Dec 1994, p 315–323
13. G. Subhash and S. Nemat-Nasser, Dynamic Stress-Induced Transformation and Texture Formation in Uniaxial Compression of Zirconia Ceramics, *J. Am. Ceram. Soc.*, Vol 76, 1993, p 153–165

Recovery Hopkinson Bar Techniques

Sia Nemat-Nasser, University of California, San Diego

Momentum Trapping for Hopkinson Bars

In a tension recovery Hopkinson bar, both the reflected compression and the transmitted tension pulses must be trapped once the loading of the sample is completed. In a compression bar, on the other hand, only the tension pulse, which reflects off the sample, must be trapped since the transmitted compression cannot reload the sample.

Figure 1(a) shows the momentum trapping scheme for a tension pulse. The free end of the bar terminates with a transfer flange F in contact with a momentum-trap tube MT, which has the same impedance as the bar (e.g., the tube has the same cross-sectional area and is made of the same material as the bar). The tensile pulse T in Fig. 1(a) reflects off the free end F of the transfer flange as compression. This compressive pulse is then fully transferred into the momentum-trap tube MT in contact with the flange because of the matched impedances. The compression then reflects off the free end of the tube as tension and is trapped in the tube, which begins to move away from the transfer flange once the reflected tension reaches the tube's end in contact with the flange. This process is similar to transferring compression pulses across contacting bars with fully matched impedances. As shown in Fig. 1(b), the compression pulse C will be completely transmitted from bar A to bar B across the contact surface S_c when the bars have the same impedance. This transmitted compressive pulse then reflects from the free end of the bar B as tension and is fully trapped in B.

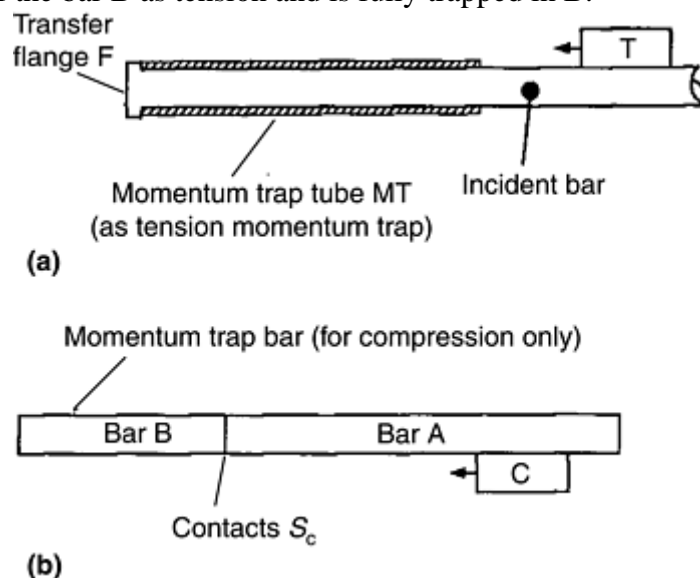


Fig. 1 Momentum trapping in recovery Hopkinson bar testing. (a) Momentum-trap tube MT in contact with transfer flange F traps the tension pulse T upon reflection off the flange F. (b) Bar B in contact with bar A traps compression pulse C. Source: Ref 7

Tension Hopkinson Bar with Momentum Traps. In a tension Hopkinson bar, the momentum trapping scheme shown in Fig. 1(a) and (b) can be used to trap the compression pulse (Fig. 1b), which reflects off the sample, back into the incident bar, and the tension pulse (Fig. 1a), which is transmitted through the sample into the transmission bar, respectively.

Figures 2, 3, 4 show a complete system that includes at the loading end a tubular striker, an incident bar with a transfer flange at its free end, a gas gun through which the incident bar passes, and a momentum-trap bar. The far end of the transmission bar terminates in a momentum-trap tube (not shown), which is the mirror image of the one shown in Fig. 1(a).

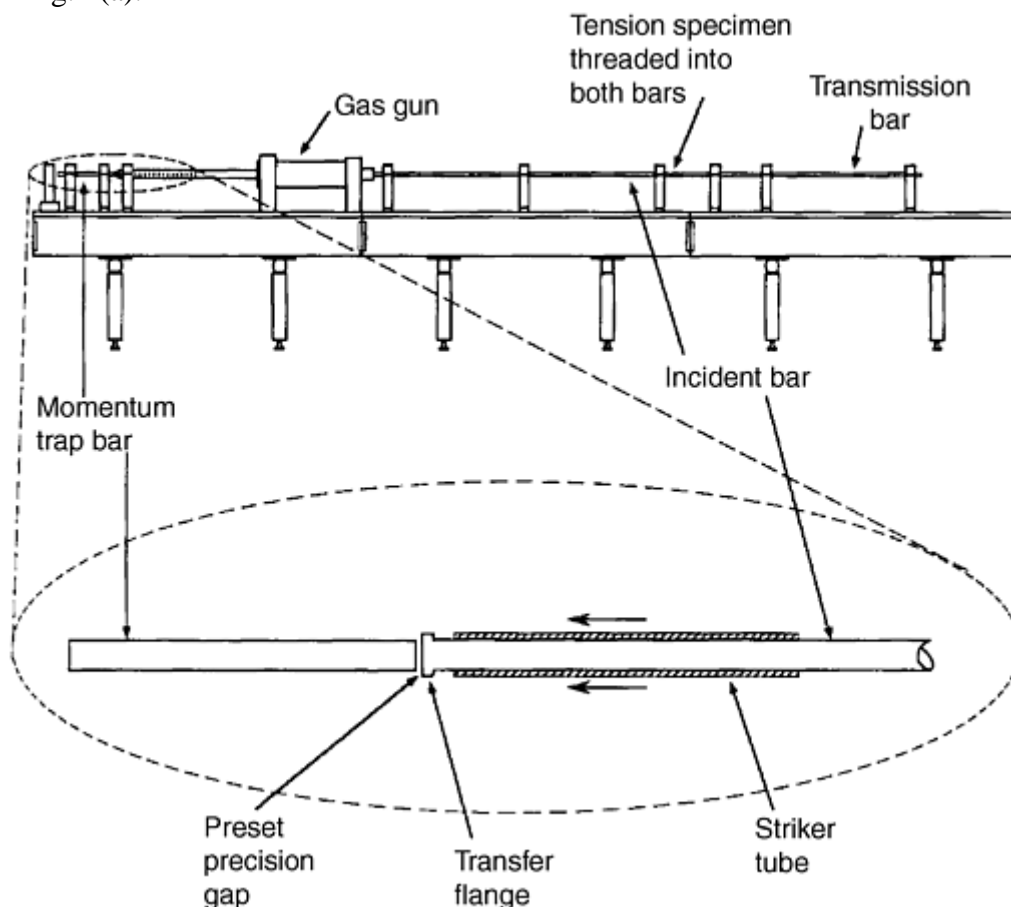


Fig. 2 Recovery tension Hopkinson bar setup. Source: Ref 7

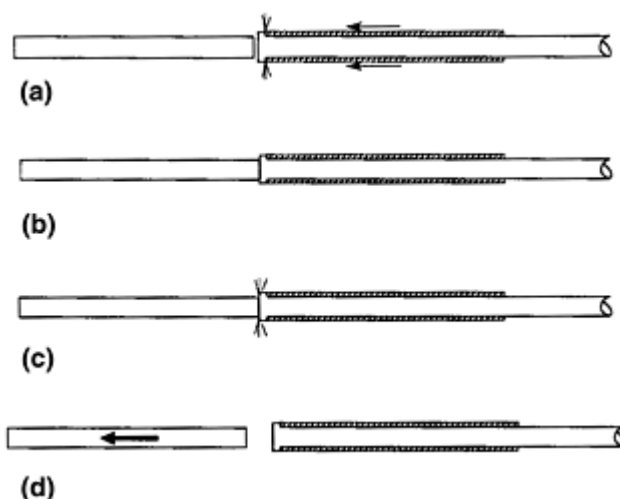


Fig. 3 Operation of the recovery tension Hopkinson bar. (a) Striker tube impacts transfer flange. (b) The resulting tensile pulse closes the preset precision gap. (c) The compression pulse, which reflects off the sample into the incident bar, reaches the transfer flange and is transmitted into the momentum-trap bar. (d) The momentum in the trapped pulse causes the bar to fly off. Source: Ref 7

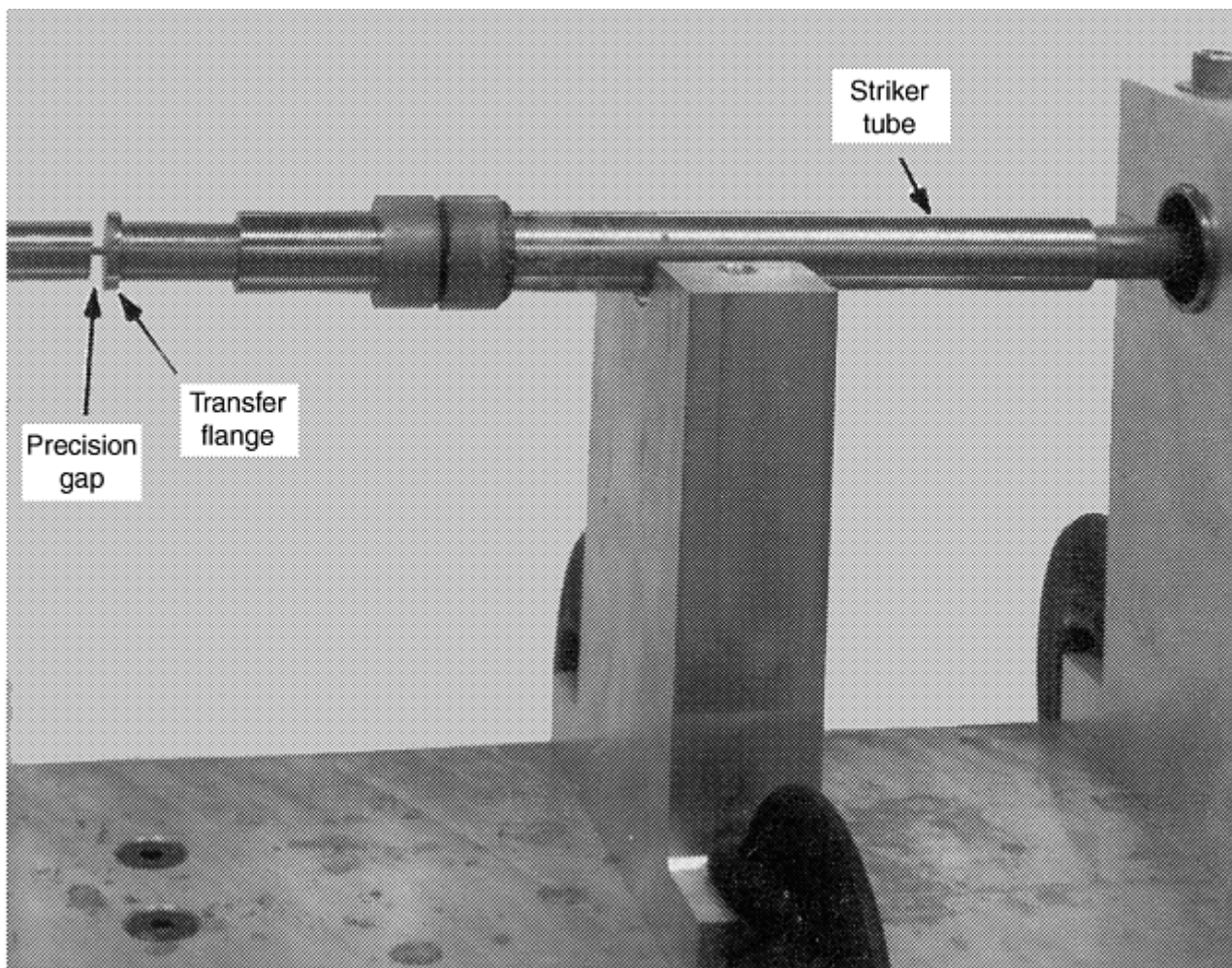


Fig. 4 Photograph of tension Hopkinson bar momentum-trap construction. Source: Ref 7

A preset precision gap separates the momentum-trap bar and the transfer flange of the incident bar. The precision gap is set such that the end of the momentum-trap bar and the face of the transfer flange are brought into contact, once the entire tensile pulse, produced by the tubular striker, is transferred into the incident bar through the transfer flange. This tensile pulse then travels toward the sample, where it is partly transmitted into the transmission bar and is partly reflected as compression back into the incident bar. This reflected compression (often nearly the same as the incident pulse) is then transmitted into the momentum-trap bar and reflects off the other (free) end of this bar as a tensile pulse. This pulse is then trapped in the momentum-trap bar since the contact interface with the transfer flange cannot support tension. The momentum of the trapped pulse causes the bar to fly off. The incident bar then is everywhere at rest. The pulse, which is transmitted through the sample into the transmission bar, is also trapped at the free end of this bar by a momentum-trap tube. This free end of the transmission bar includes a transfer flange and a momentum-trap tube in contact with the flange, similar to those in Fig. 1(a).

At the striker end of the incident bar, the precision gap between the transfer flange and the momentum-trap bar must be calculated and set with some care to obtain satisfactory results, as illustrated in Fig. 5(a). If the gap is too large, the reflected compression pulse in the incident bar will not be transmitted to the momentum-trap bar. On the other hand, if the gap is too small, it will be closed during the loading of the incident bar by the striker. This affects the stress pulse, moves the momentum-trap bar into an improper position, and, hence, produces undesirable results. An example is shown in Fig. 5(b), where the gap was much too large.

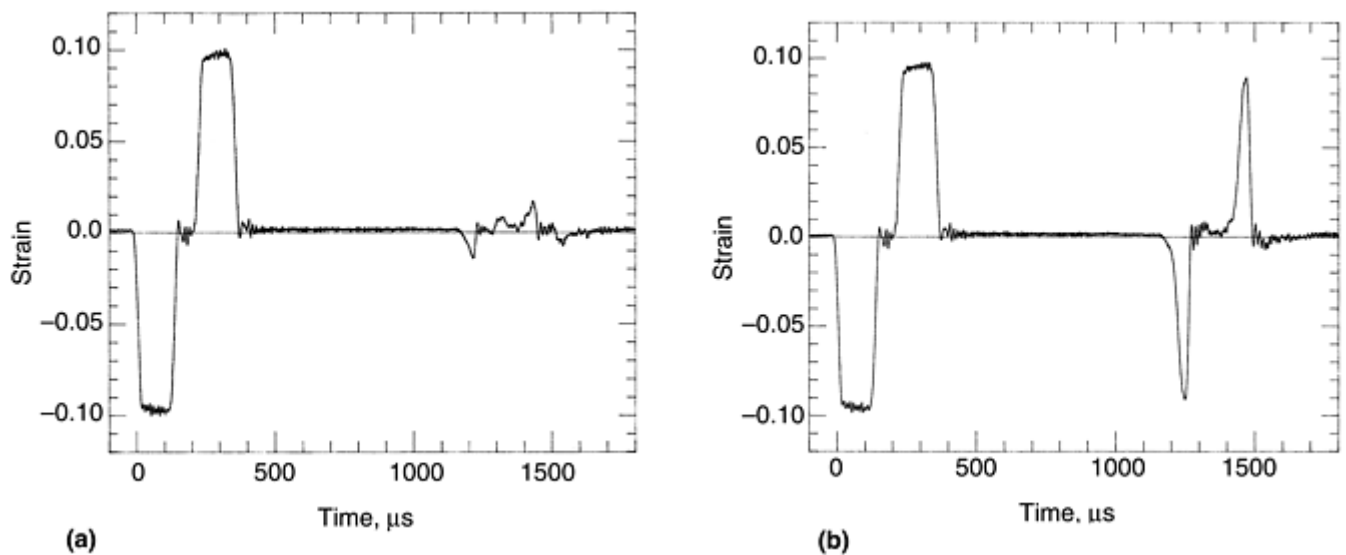


Fig. 5 (a) A typical tensile stress pulse, its reflected compression pulse, and its residue after trapping. (b) A poorly trapped reflected compression; the gap between the momentum-trap and incident bars was too big. Source: Ref 7

The momentum-trap bar is correctly positioned when the gap is set such that when the initial collision between the striker and the incident bar is complete, the incident bar is fully in contact with the momentum-trap bar. While the necessary separation can be calculated, in practice this provides a starting point that then is optimized by trial and error. If the breech pressure of the gas gun and the striker velocity are kept constant while adjusting the gap, within a few trials the correct gap for a given striker bar and breech pressure will be obtained. With data of this kind, a calibration curve of breech pressure versus gap can be established for further use. Calibration curves of this kind are not universal and must be rechecked periodically for the same system and reestablished each time a change in the system is made.

Reference cited in this section

7. S. Nemat-Nasser, J.B. Isaacs, and J.E. Starrett, Hopkinson Techniques for Dynamic Recovery Experiments, *Proc. R. Soc. (London) A*, Vol 435, 1991, p 371–391

Recovery Hopkinson Bar Techniques

Sia Nemat-Nasser, University of California, San Diego

Stress-Reversal and Strain Rate Jump Hopkinson Techniques

Using a flange and a momentum-trap tube, it is possible to produce a compression pulse followed by a tension pulse and to create a sudden jump (an increase or a decrease) in the strain rate. These techniques are discussed in this section.

Stress-Reversal Technique. Figure 6 shows the overall design of this stress-reversal Hopkinson bar. The loading end of the incident bar begins with a transfer flange, as shown in Fig. 6 and 7 (see also Fig. 8). In this setup, the incident tube, the striker bar, and the incident bar have the same impedance. The incident tube rests against the transfer flange at one end and against a reaction mass at the other, as shown in Fig. 6 and 7. The reaction mass is a large steel cylinder through which the incident bar passes.

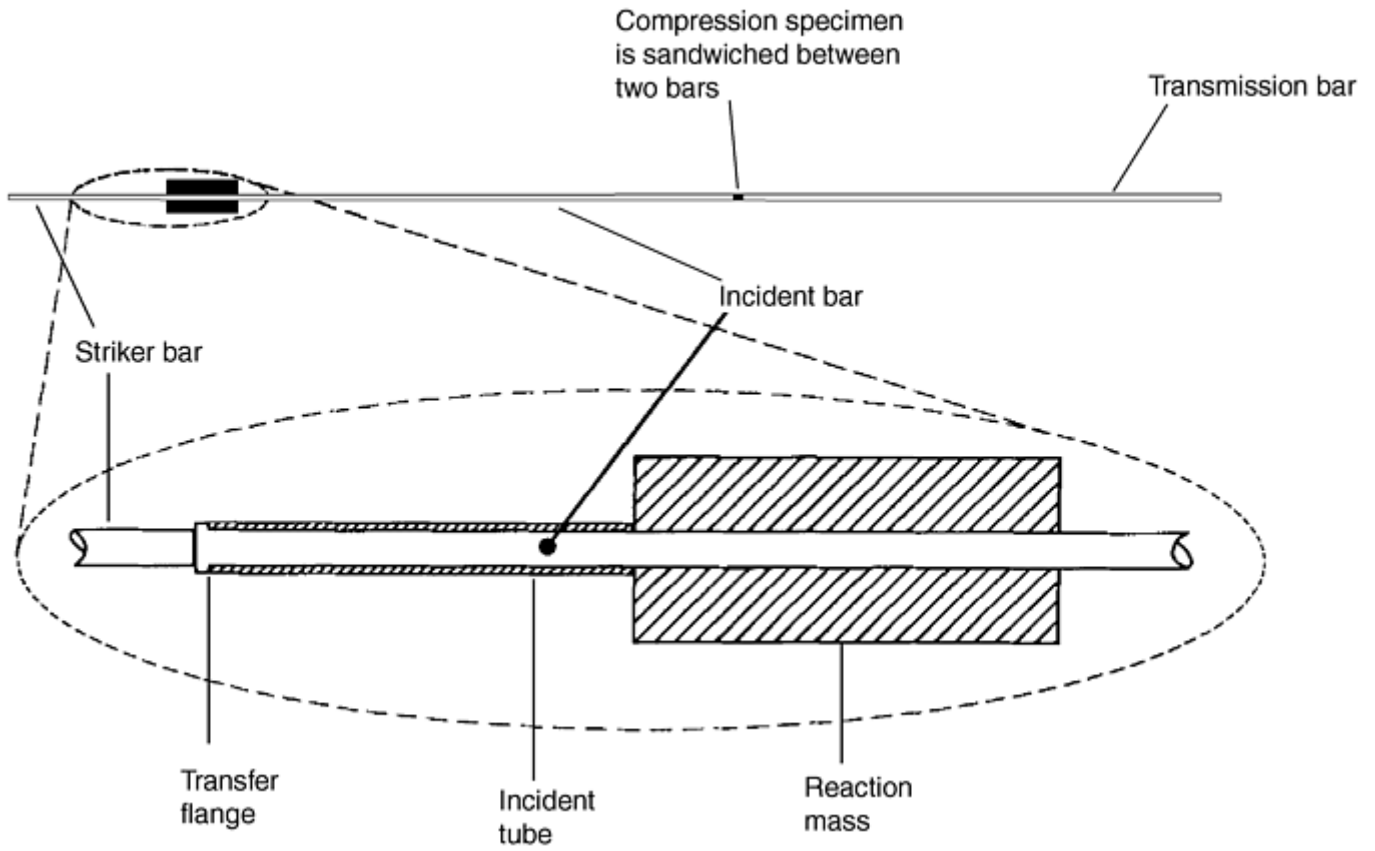


Fig. 6 A stress-reversal Hopkinson bar setup. Source: Ref 7

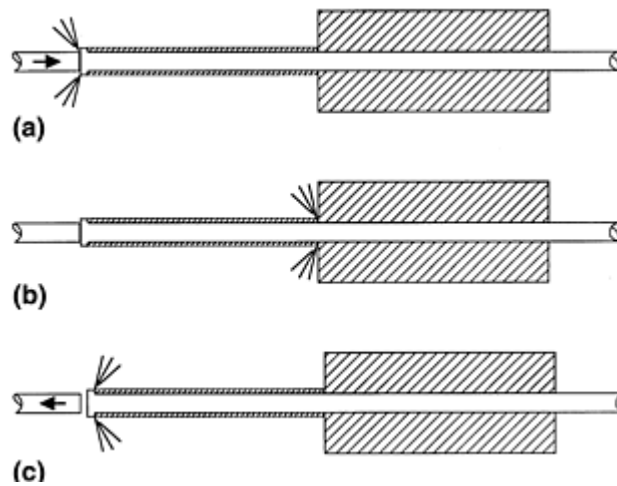


Fig. 7 Operation of stress-reversal Hopkinson bar. (a) Striker bar impacts transfer flange. (b) Compressive pulse in the incident tube reflects from the reaction mass. (c) Striker bar bounces away. Source: Ref 7

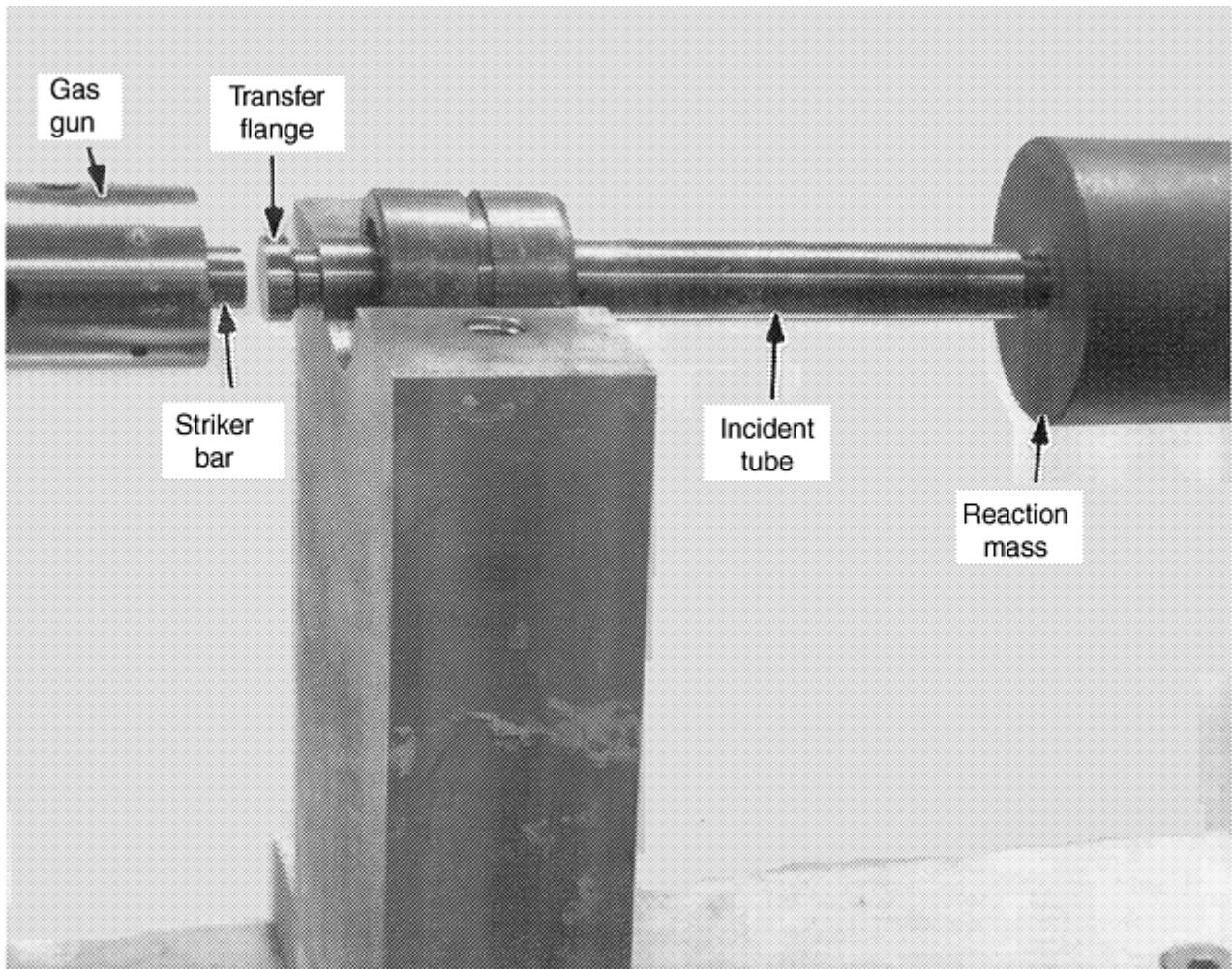


Fig. 8 Photograph of a stress-reversal loading fixture. Source: Ref 7

When the striker bar impacts the transfer flange at velocity V_0 , it imparts a common axial strain to the incident tube and incident bar. The compression pulse in the incident bar travels along this bar toward the specimen. The compression pulse in the incident tube reflects from the reaction mass as compression and reaches the transfer flange at the same instant that the tension release pulse—which is reflected from the free end of the striker—reaches the end of the striker bar in contact with the transfer flange. Since the combined cross section of the incident bar and tube is twice that of the striker bar, having the same material properties, the striker bar begins to bounce back, away from the transfer flange, as the transfer flange is loaded by the compression pulse traveling along the incident tube. This compression pulse then imparts a tensile pulse to the incident bar, which follows the then-existing compression pulse in the incident bar, both pulses traveling toward the sample. Figure 9 illustrates a typical result.

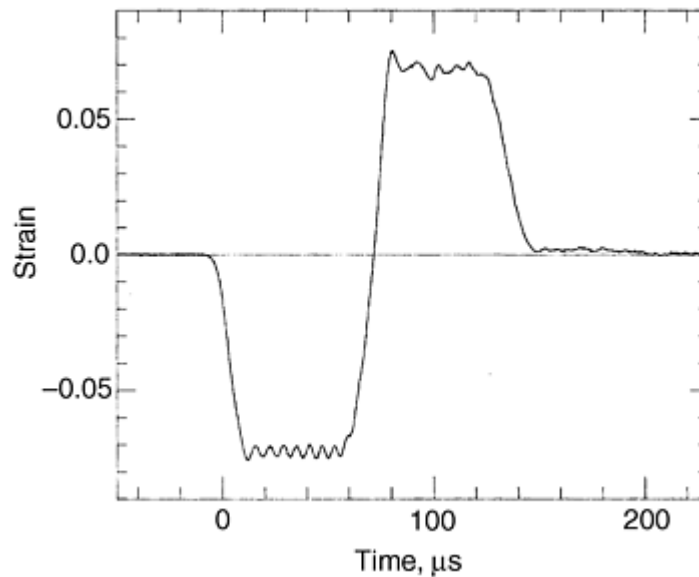


Fig. 9 A typical stress pulse generated by the stress-reversal Hopkinson bar technique. Source: Ref 7

It is important to bear in mind the significance of the perfect impedance matching of the striker bar, incident bar, and incident tube, as well as the configuration of the transfer flange in the design of the loading fixture for proper functioning of the stress-reversal Hopkinson technique.

From the equality of particle velocities at contacting surfaces and the conservation of linear momentum, it follows that the particle velocity in the incident bar and incident tube at impact is $V_0/3$. The particle velocity of the compressed portion of the striker bar, relative to its unstressed part, then is $2V_0/3$. When the reflected release-wave front in the striker reaches the contact with the transfer flange, the striker bar begins to move at velocity $V_0/3$ away from the transfer flange. At the same instant, the compression wave in the incident tube imparts to the transfer flange exactly the same particle velocity (i.e., $V_0/3$) in exactly the same direction. Thus, the contact surfaces remain in contact for a short period, $t_0 = 2l_0/C_0$, until the striker separates at a third of its initial impact velocity, as the flange comes to rest; here, l_0 is the common length of the striker bar and the incident tube, and C_0 is their common longitudinal elastic-wave speed.

Strain Rate Jump. The stress-reversal technique can be used to change the strain rate during the course of Hopkinson bar compression or tension experiments (Ref 14). Consider a recovery compression system first. The loading (striker) end of the incident bar includes a transfer flange, an incident tube, and a reaction mass, as sketched in Fig. 10(a). Suppose the transfer tube is in contact with the transfer flange. Then, as the striker bar impacts the incident bar over the transfer flange, elastic compressive stresses are induced in both the incident bar and the incident tube, as well as in the striker bar, in accordance with their impedances. To change (decrease) the stress (and, hence, the strain) in the incident bar in the course of the experiment, a predetermined gap is introduced between the transfer flange and the incident tube (Fig. 10b). As the striker bar now impacts the incident bar, a compressive stress pulse is imparted into this bar, resulting in the shortening of the bar. Once the incident bar is sufficiently shortened to come in contact with the incident tube over the transfer flange, a stress pulse is also imparted into the incident tube, reducing the compressive stress (and, hence, the compressive strain) in the incident bar. Since the sample strain rate is a linear function of the incident strain in the incident bar, the procedure allows implementation of a change in the sample strain rate during the course of the experiment. By proper choice of the gap and the involved impedances, a desired change in the sample strain rate can be achieved.

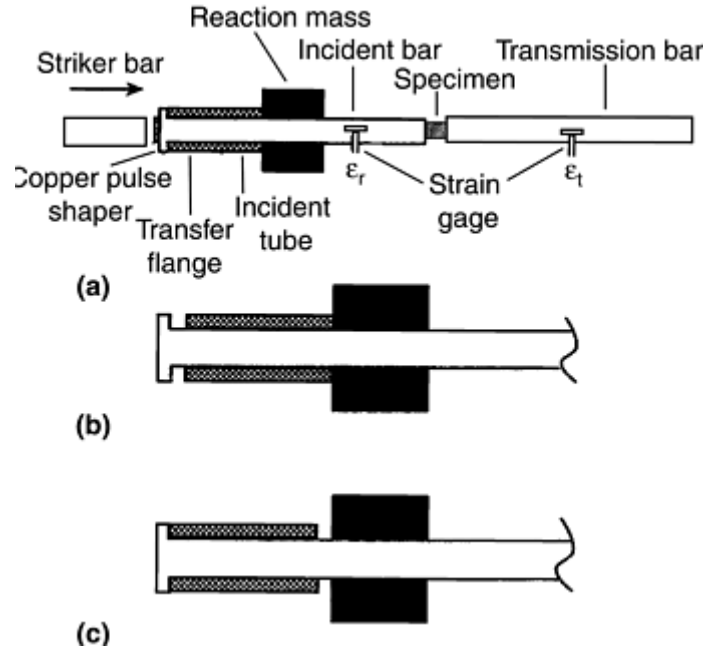


Fig. 10 Recovery Hopkinson bar compression testing. (a) Test configuration. (b) A gap between the incident tube and the transfer flange leads to a decrease in the strain rate, once the gap is closed. (c) A gap between the incident tube and the reaction mass leads to an increase in the strain rate. Source: Ref 8

It is also possible to increase the sample strain rate using the same construction. For this purpose, the incident tube first rests against the transfer flange, as the striker bar impacts the flange (Fig. 10c). If the length of the incident tube is suitably smaller than that of the striker, and if the other end of this tube (which is not in contact with the transfer flange) is free, the compressive pulse in the tube will be reflected off its free end as a tensile release pulse, reaching the transfer flange before the tensile release wave in the striker reaches there. The incident tube then separates from the transfer flange while the striker bar continues to impart a stress pulse into the incident bar. Upon separation of the tube from the flange, the stress (and, hence, the strain) in the incident bar is increased accordingly. Thus, the incident strain at the sample-incident bar interface is increased, resulting in a corresponding increase in the sample strain rate.

For numerical estimates, ρ , C , E , A , u , ϵ , and σ denote the mass density, longitudinal wave speed, Young's modulus, area, particle velocity, axial strain, and axial stress, respectively, and subscripts st, i, and tb represent the striker bar, incident bar, and the incident tube, respectively. Set $k = \rho CA$, and note that $C^2 = E/\rho$. Since the bar and the tube remain elastic throughout the experiment, in general:

$$\sigma = \rho Cu = \sqrt{\rho E} u = E\epsilon \quad (\text{Eq 1})$$

$$\epsilon = \frac{u}{C} = \frac{\sigma}{E}$$

While a gap separates the incident tube and the transfer flange (Fig. 4b):

$$k_i u_i = k_{st} u_{st} \quad (\text{Eq 2})$$

$$V_0 - u_{st} = u_i$$

where V_0 is the (constant) initial velocity of the striker bar. From Eq 1 and 2, it follows that:

$$\epsilon_i = \frac{k_{st}}{k_{st} + k_i} \frac{V_0}{C_i} \quad (\text{Eq 3})$$

This strain in the incident bar is the incident strain at the sample end of the incident bar. If the strain in the transmission bar is denoted by ϵ_t , then the strain rate in the sample, $\dot{\epsilon}_s$, is given by:

$$\begin{aligned}\dot{\epsilon}_s &= 2 \frac{C_i}{l_s} (\epsilon_i - \epsilon_t) \\ &= 2 \frac{C_i}{l_s} \left(\frac{k_{st}}{k_{st} + k_i} \frac{V_0}{C_i} - \epsilon_t \right)\end{aligned}\quad (\text{Eq 4})$$

where l_s is the sample length. Note that, in general, the incident and transmission bars have common area, wave speed, and so on.

When the gap between the transfer flange and the incident tube is closed (Fig. 10c), the incident strain is reduced to:

$$\epsilon_i = \frac{k_{st}}{k_{st} + k_i + k_{tb}} \frac{V_0}{C_i} \quad (\text{Eq 5})$$

resulting in the sample strain rate of:

$$\dot{\epsilon}_s = 2 \frac{C_i}{l_s} \left(\frac{k_{st}}{k_{st} + k_i + k_{tb}} \frac{V_0}{C_i} - \epsilon_t \right) \quad (\text{Eq 6})$$

If the sample material is rate independent, ϵ_t will be the same in Eq 4 and 6, and the change in the sample strain rate becomes:

$$\begin{aligned}\Delta \dot{\epsilon}_s &= 2 \frac{V_0}{l_s} \left(\frac{k_{st}}{k_{st} + k_i + k_{tb}} - \frac{k_{st}}{k_{st} + k_i} \right) \\ &= -2 \frac{V_0}{l_s} \left[\frac{k_{st} k_{tb}}{(k_{st} + k_i)(k_{st} + k_i + k_{tb})} \right]\end{aligned}\quad (\text{Eq 7})$$

When $k_{st} = k_i = k_{tb}$:

$$\Delta \dot{\epsilon}_s = -\frac{1}{3} \frac{V_0}{l_s} \quad (\text{Eq 8})$$

For example, with a striker velocity of 30 m/s (98 ft/s) and sample length of 5 mm (0.2 in.), $\Delta \dot{\epsilon}_s = 2 \times 10^3 \text{ s}^{-1}$. Note that these results apply to both reduction and increase in the sample strain rate.

For rate-dependent materials, the flow stress changes with the strain rate. Hence, the transmitted strain ϵ_t in the transmission bar is changed:

$$\epsilon_t = \frac{\sigma_s A_s}{E_t A_t}$$

where subscripts s and t refer to the sample and transmission bar, respectively. Hence, if the change in the sample flow stress is $\Delta \sigma_s$:

$$\begin{aligned}\Delta \dot{\epsilon}_s &= -2 \frac{V_0}{l_s} \left[\frac{k_{st} k_{tb}}{(k_{st} + k_i)(k_{st} + k_i + k_{tb})} \right] \\ &\quad - 2 \frac{C_i A_s}{l_s E_t A_t} \Delta \sigma_s\end{aligned}\quad (\text{Eq 9})$$

where $\Delta \dot{\epsilon}_s$ is negative when the strain rate (and, hence, the flow stress) is decreased.

Figure 11 illustrates the results of this method. Point A on the lower curve in this figure marks the strain in the sample, at which the strain rate is changed from about 1600 s^{-1} to about 850 s^{-1} ; the strain rate difference is about 750 s^{-1} . The impact velocity of the striker bar is 8 m/s (26 ft/s); the Young's modulus of the incident bar is 200 GPa (29×10^6 psi). The diameter of the transmission bar is 1.27 cm (0.5 in.). The length of the sample is 0.35 cm (0.14 in.). The stress difference in Fig. 11 due to the change of the strain rate is 350 MPa (50 ksi). From Eq 9 and these data, a strain rate difference of 757 s^{-1} is obtained (Ref 8). This calculated result is very close to the observed one.

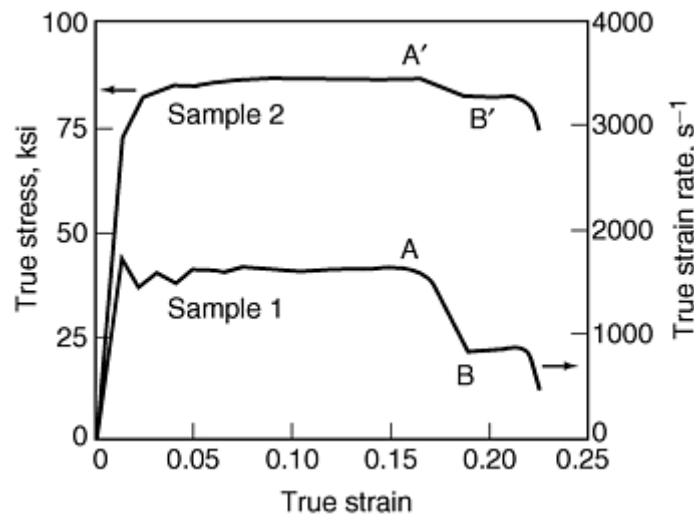


Fig. 11 Illustration of strain rate jump. At point A the strain rate is changed from about 1600 s^{-1} to about 850 s^{-1} , leading to a stress difference of about 350 MPa (50 ksi). Source: Ref 8

Strain Rate Jump in Tension. The tension bar with a momentum trap can be used to change the strain rate during the course of tension Hopkinson tests. First, consider a case in which it is required to decrease the strain rate during a test. To accomplish this, a gap is provided between the momentum-trap bar and the transfer flange of the incident bar in Fig. 1(a) such that this gap is closed while the striker tube is transferring the load to the transfer flange. By suitable choices of the impedances of the incident bar, momentum-trap bar, and the striker tube, it is then possible to suddenly decrease the strain rate by a desired amount. The basic equations follow from those given in the previous section.

To increase the strain rate in a tension Hopkinson test, a suitably short momentum-trap bar in contact with the flange is used (Fig. 1a), *before* the striker tube impacts the transfer flange. Then, the striker bar imparts a tensile pulse into the incident bar and, simultaneously, a compression pulse into the momentum-trap bar. This compression pulse reflects off the other end of the momentum-trap bar as a tensile release wave, separating the bar from the flange, once it reaches the contact between the bar and the flange. For a suitably long striker tube, this can occur while the striker is continuing to load the transfer flange. Again, the necessary equations are similar to those given in the previous section. Note that the impedances must be properly selected in order to achieve a desired increase or decrease in the strain rate.

Recovery after Combined Compression-Tension Loading. In many high strain rate applications, materials may be subjected to dynamic compressive loads, followed by tension. An example is the examination of the dynamic Bauschinger effect and its relation to the microstructure of the material. Experimental investigations of this kind require techniques to recover the sample after it has been subjected to a cycle of compression followed by tension, or tension followed by compression.

The stress-reversal technique can be used to subject a specimen to a combined compression-tension pulse without interruption and then recover it for post-test characterization (Ref 7). The loading fixture is the same as shown in Fig. 6 7 8. The sample configuration and the manner by which it is attached to the incident and transmission bars are designed such that, after the specimen is subjected to the desired compression-tension pulse, it is detached from the incident bar without additional loading of its central gage portion. This process is accomplished as follows.

As shown in Fig. 12 (see also photograph in Fig. 13), in addition to the reaction mass R_0 , there are two other reaction masses, denoted by R_1 and R_2 . The sample construction (Fig. 14) includes two threaded ends and a reaction flange F_S , which, at the start of the experiment, rests against the reaction mass R_1 , with the sample end fully threaded into the incident bar.

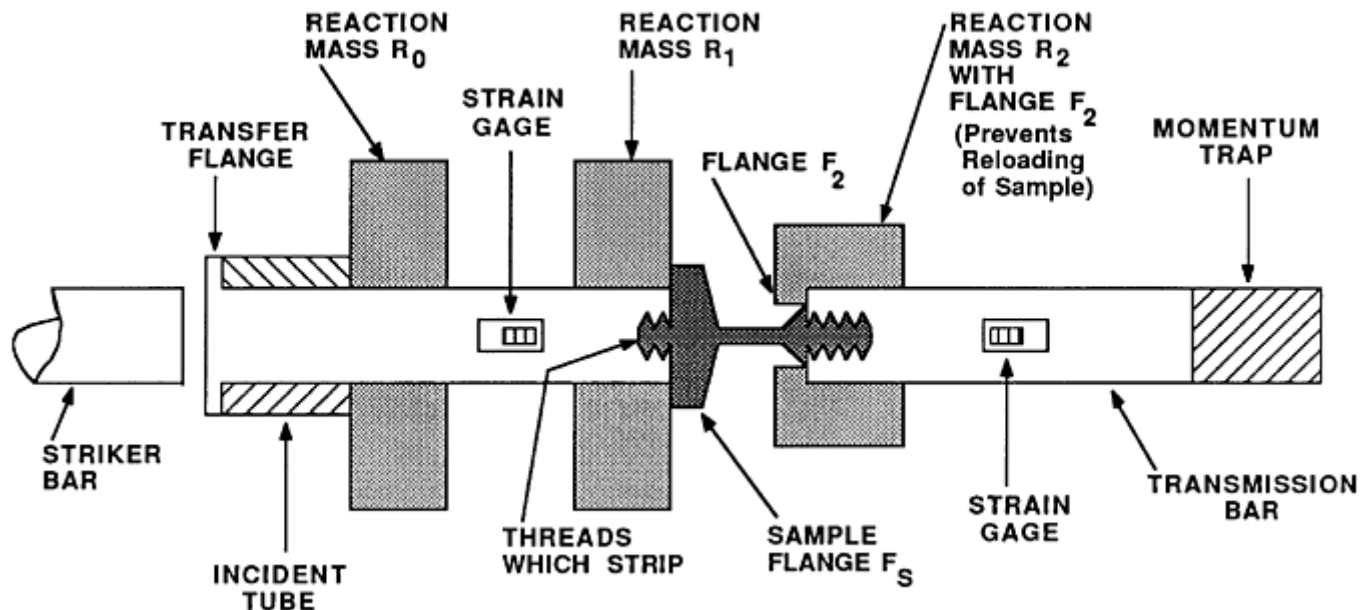


Fig. 12 Combined compression-tension dynamic recovery experiment. Source: Ref 7

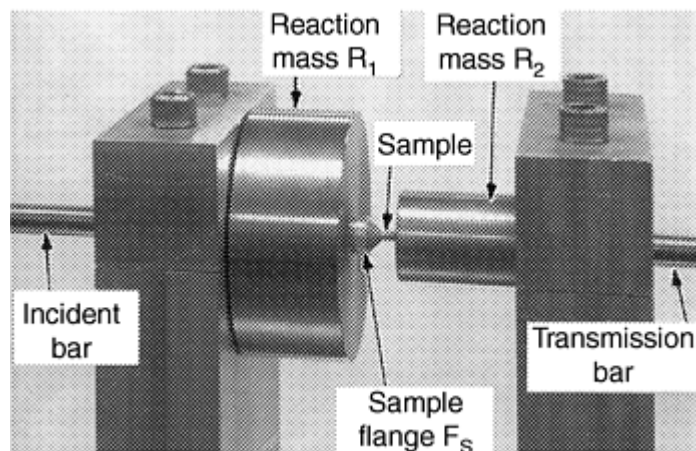


Fig. 13 Photograph of combined compression-tension setup showing the manner by which the sample is connected to the incident and transmission bars. Source: Ref 7

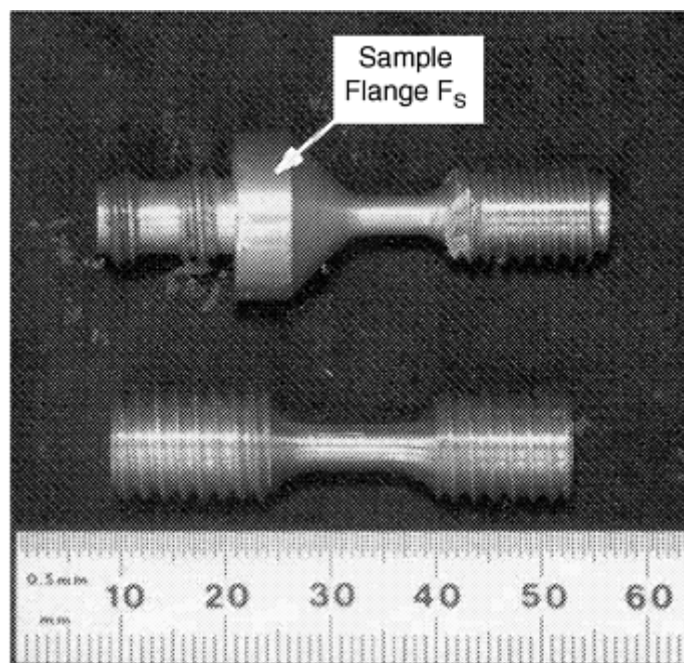


Fig. 14 Two samples of the same material (Al-Cu), one flanged for recovery test and the other unflanged for data acquisition. Source: Ref 7

The sample is threaded into the transmission bar through the reaction mass R_2 . The transmission bar rests against a thin flange F_2 , constructed in R_2 by reducing its opening diameter around the sample, as shown in Fig. 12. The other (output) end of the transmission bar is in contact with a bar of the same impedance, which can trap compression pulses transmitted through the sample into the transmission bar. When the striker hits the transfer flange of the incident bar, a compression pulse followed by a tension pulse is imparted into the incident bar, as discussed in the section “Stress-Reversal Technique” in this article. The compression-tension pulse travels toward the sample and subjects the sample to compression first (which shortens the sample), followed by tension (which almost restores the initial length of the sample). A part of the compression pulse is transmitted through the sample into the transmission bar and is trapped at the far end of this bar by the momentum-trap bar (hatched in Fig. 12). The remaining part of the compression pulse is reflected off the specimen into the incident bar as tension. This tension then reflects back from the striker end of the incident bar and returns to the sample as tension because of the presence of the transfer flange, incident tube, and the reaction mass R_0 .

When the tensile segment of the initial compression-tension pulse reaches the specimen, it is partly transmitted through the sample into the transmission bar and is partly reflected off the sample as compression, back into the incident bar. As the sample shortens during the compressive loading, prior to the arrival of the tension pulse, its flange, F_S , separates from the reaction mass R_1 . The subsequent tensile loading (almost) restores the sample's initial length, bringing the sample's flange (almost) in contact with the reaction mass R_1 . The tensile pulse, which reflects as compression from the far end of the transmission bar, returns to the sample, loading it (just slightly) until the transmission bar comes in contact with the flange F_2 of the reaction mass R_2 . At this instant, the sample flange F_S is in complete contact with the reaction mass R_1 . Shortly after, the tensile pulses, which are reflected from the loading end of the incident bar, reach the sample, pulling the incident bar away from the sample, while the sample flange F_S is engaged against the reaction mass R_1 . (As discussed previously, both compression and tension pulses are reflected as tension from the loading end back into the incident bar.) The threads that connect the sample to the incident bar are designed to strip off during this final tensile-loading process. Note that the threads are pulled against the flange F_S resting on R_1 . This prevents loading the sample over its gage length during this recovery stage. The sample is then recovered, having been subjected to a cycle of compression-tension loading over its gage length.

The flange F_S in combination with the threaded ends of the sample makes the impedance matching difficult and, hence, complicates the interpretation of the resulting data. This problem can be overcome to a great extent by performing two tests, one to recover the sample (which has a flange) for post-test analysis and the other (using a sample that does not have a flange) to collect the required data. Figure 12 shows the two samples. The corresponding data are given in Fig. 15. Even though the data obtained with the flanged sample are noisy, they agree quite well with those obtained with the unflanged sample. The unflanged sample, on the other hand, is subjected to additional tensile pulses, which may cause necking, or even tensile failure of the sample.

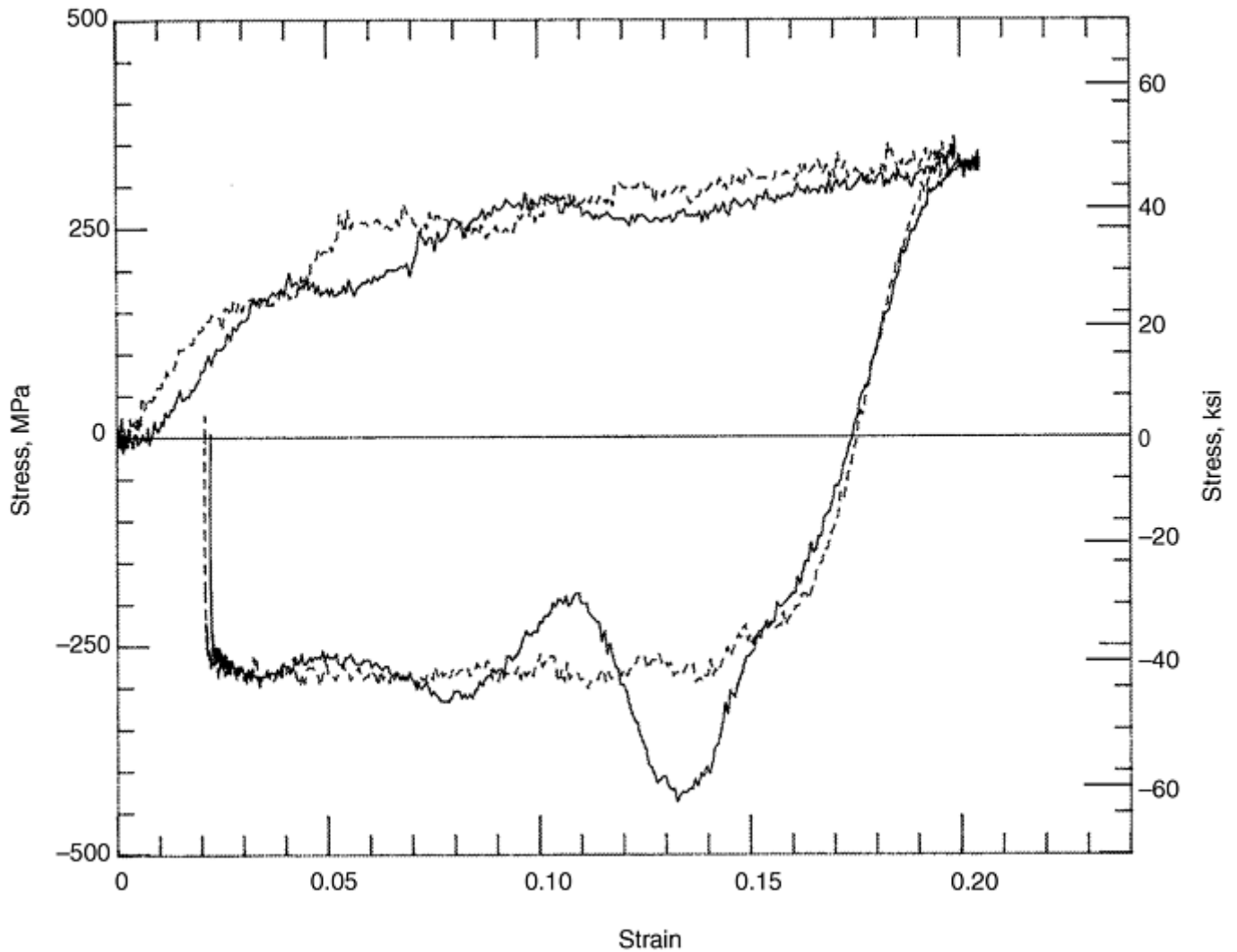
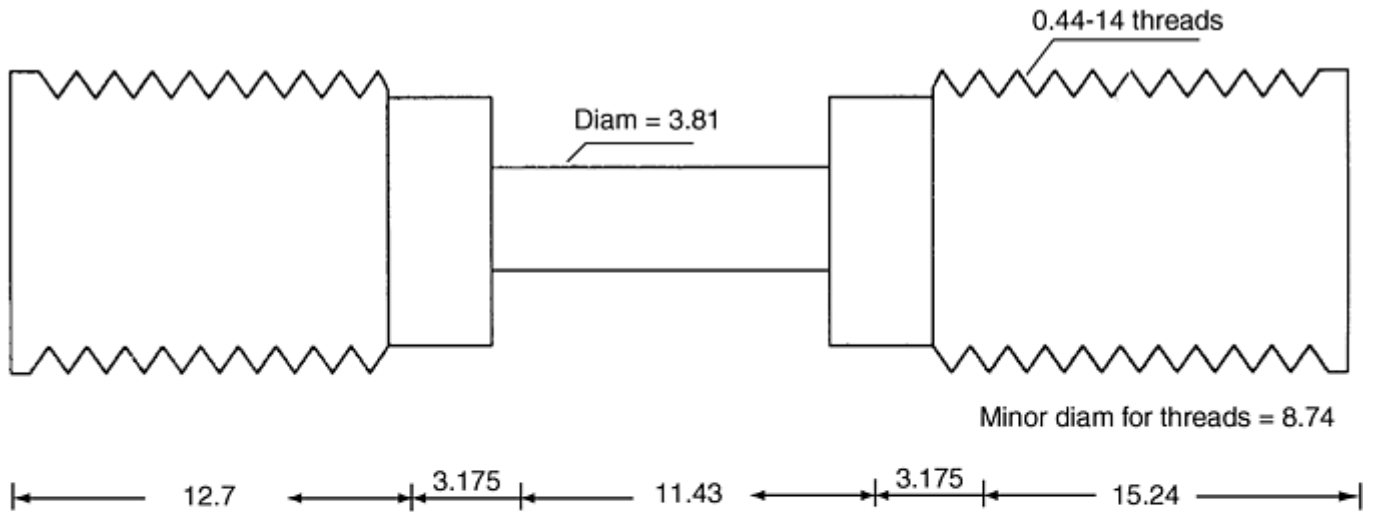
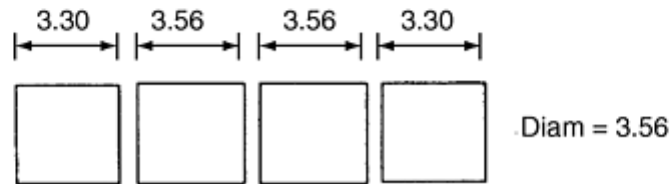


Fig. 15 Data at 3200 s^{-1} strain rate, using flanged (solid curve) and unflanged (dashed curve) specimens (compression is positive). Source: Ref 7

Recovery after Tension and Compression Loading. The recovery tension and compression Hopkinson techniques can be used to subject a sample to a tensile pulse, recover the sample, produce from it compression samples (Fig. 16), and then subject these samples to compression and recover them. This allows the studying of the response and microstructural changes when the material is subjected to a tension, recovered, and then subjected to a compression (Ref 8, 9). In this approach, the tensile loading is not followed immediately by a compression pulse. Hence, if there are any microstructural changes during the recovery and preparation of the compression samples from the original tension sample, these changes may affect the subsequent compression test results. Indeed, the effects of such changes on the response of the material can be studied by this method.



Tension test specimen



Compression test specimen (after tension experiment)

Fig. 16 Sample geometry for high strain rate Bauschinger experiments. Dimensions in millimeters. Source: Ref 14

References cited in this section

7. S. Nemat-Nasser, J.B. Isaacs, and J.E. Starrett, Hopkinson Techniques for Dynamic Recovery Experiments, *Proc. R. Soc. (London) A*, Vol 435, 1991, p 371–391
8. A. Thakur, S. Nemat-Nasser, and K.S. Vecchio, Bauschinger Effect in Haynes 230 Alloy: Influences of Strain Rate and Temperature, *Metall. Mater. Trans.*, Vol 27A, 1996, p 1739–1748
9. A. Thakur, S. Nemat-Nasser, and K.S. Vecchio, Dynamic Bauschinger Effect, *Acta Mater.*, Vol 44, 1996, p 2797–2807
14. S. Nemat-Nasser, Y Li, and J.B. Isaacs, Experimental/Computational Evaluation of Flow Stress at High Strain Rates with Application to Adiabatic Shearbanding, *Mech. Mater.*, Vol 17, 1994, p 111–134

Recovery Hopkinson Bar Techniques

Sia Nemat-Nasser, University of California, San Diego

Recovery Dynamic Testing of Hard Materials

Most ceramics are extremely hard and undergo very little strain prior to failing. Their response is essentially linear, up to failure. Thus, special techniques are necessary in order to perform high strain rate recovery experiments on these materials.

In the classical compression split-Hopkinson bar, the yield stress of the sample must be considerably smaller than the yield stress of the bars. The ends of the incident and transmission bars, in contact with the specimen, therefore remain essentially flat as the sample deforms. Furthermore, the impedance of the sample generally is considerably smaller than that of the bars throughout the entire loading history. Therefore, the tensile pulse that reflects off the sample into the incident bar is a good measure of the velocity of the sample end of the incident bar relative to that of the transmission bar.

When very hard materials, such as ceramics and ceramic composites, are being tested in the compression split-Hopkinson bar, the reflected pulse, in general, no longer accurately measures the strain rate in the sample. Indeed, if the diameter of the sample is not considerably smaller than the diameter of the bar, the impedance of the sample may be close to, or, in certain cases, even greater than that of the incident bar, resulting in a very small reflected tensile pulse, or even a reflected compressive pulse. On the other hand, as is often required, when the diameter of the sample is considerably smaller than that of the bars, the hard sample indents the ends of the bars (Fig. 17). Furthermore, since the total strain to failure for hard ceramics and their composites is usually quite small (1 or 2%), the indentation, in general, introduces significant errors in the results if the reflected pulse is used to calculate the strain in the sample. The reflected wave in the incident bar no longer is an accurate measure of the strain rate in the sample of hard, brittle materials, although the transmitted pulse is still a good indication of the stress in the sample.

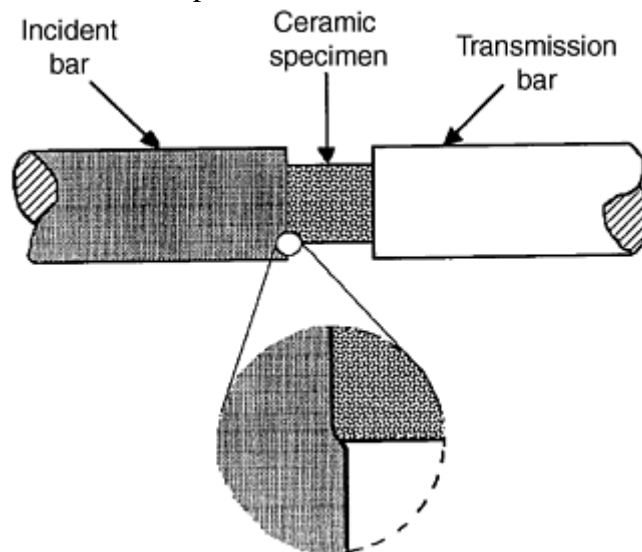


Fig. 17 Indentation of the bar by a hard (ceramic) specimen. Source: Ref 7

As can be seen from Eq 4, for the sample strain rate to be constant it is necessary that $\dot{\epsilon}_r = -(\dot{\epsilon}_i - \dot{\epsilon}_t)$ be constant. In the classical Hopkinson technique, this is accomplished by seeking to impart a constant stress pulse into the incident bar. A constant stress pulse, however, does not produce a constant strain rate in an elastic sample. Instead, such a pulse deforms the sample in three distinct regimes, namely, an initial regime of positive strain rate when the stress in the sample increases to a constant level, followed by a regime of zero strain rate, which is then followed by a regime of negative strain rate. Thus, for hard ceramics, it is necessary to render the strain differential, $\epsilon_i - \epsilon_t$, as nearly constant as possible. This can be achieved by using a ramp pulse.

These basic problems have been solved (Ref 10, 11, 12, 13) using the following techniques:

- The strain is measured directly by attaching strain gages to the sample. For samples with square cross sections, two strain gages are used, one to measure the axial strain and the other to measure the lateral strain (Ref 10, 11).
- A thin metal cushion is placed at the striker end of the incident bar to produce a ramp stress pulse in the incident bar. Figure 18 shows typical stress and strain pulses that can be obtained in this manner. In Ref 7, a detailed analysis of the finite deformation of the copper cushion is given, together with experimental verification of the results. It is shown that the pulse shape depends on the cushion

geometry and the length and velocity of the striker and that it can be reliably predicted using finite plasticity theory.

- The yielding of the bars by the hard ceramic samples can be prevented using an impedance-matched small platen of polished tungsten carbide. When necessary, a composite of the tungsten carbide, which is press fitted within a ring of, for example, Kovar, may be used. Figure 19(a) shows the construction used by Sharma et al. (Ref 12), and Fig. 19(b) shows a composite tungsten-carbide platen. It is important to attain a good impedance match between the inserts and the bars in such constructions.

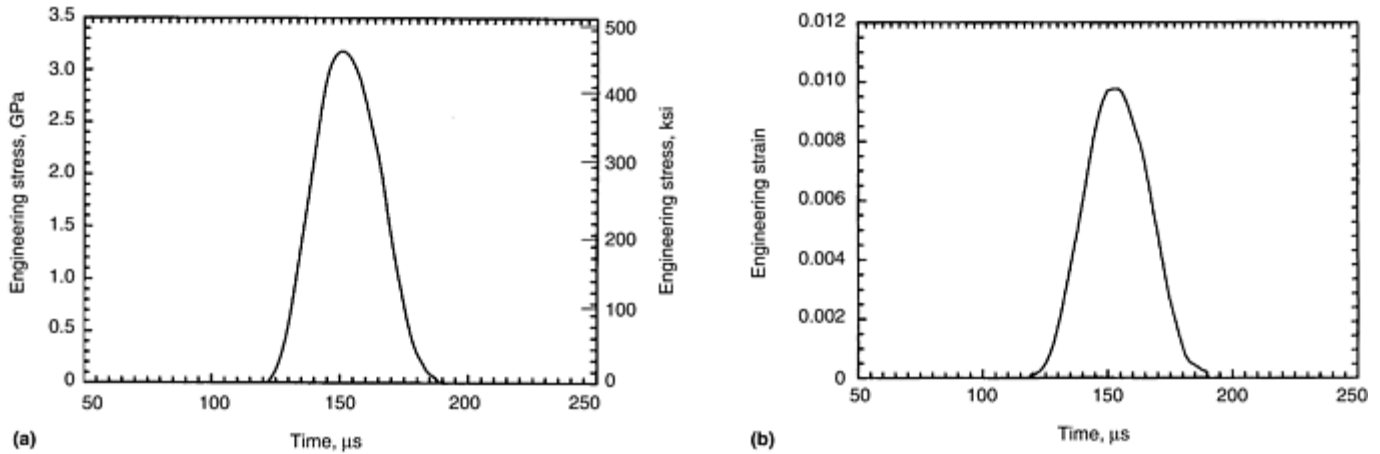


Fig. 18 Typical (a) stress and (b) strain pulses obtained by pulse shaping to produce constant strain rate in an elastic sample. Source: Ref 12

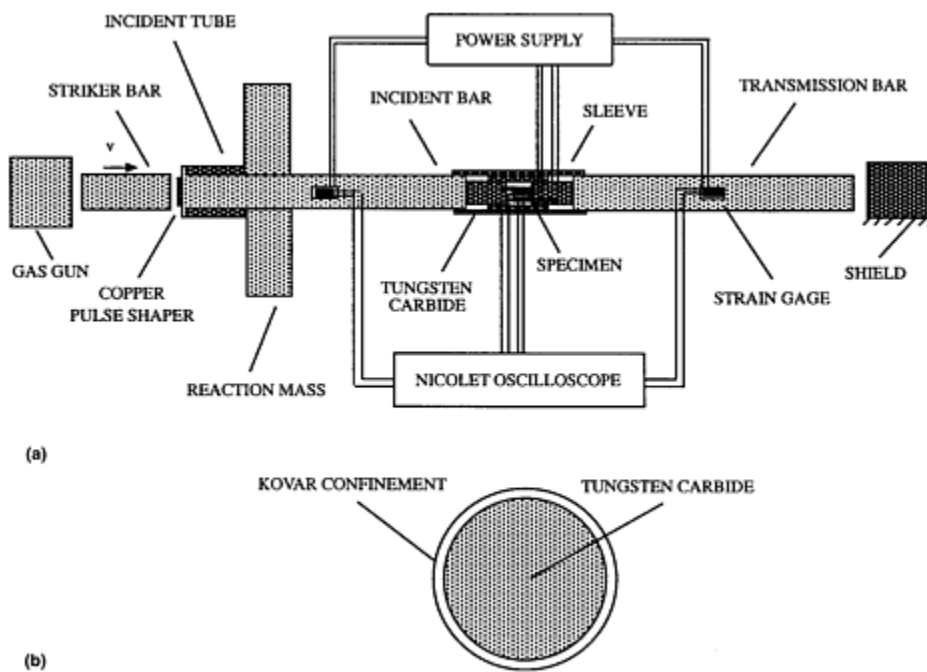


Fig. 19 Modified split-Hopkinson compression bar to test hard ceramics at high strain rates. (a) Test configuration. (b) Tungsten-carbide platen with Kovar confinement. Source: Ref 12

References cited in this section

7. S. Nemat-Nasser, J.B. Isaacs, and J.E. Starrett, Hopkinson Techniques for Dynamic Recovery Experiments, *Proc. R. Soc. (London) A*, Vol 435, 1991, p 371–391
10. W.P. Rogers, J.B. Isaacs, and S. Nemat-Nasser, Effect of Microstructural Damage on Ultrasonic Velocity and Elastic Moduli of Partially Stabilized Zirconia, *Review of Progress in Quantitative*

11. W.P. Rogers and S. Nemat-Nasser, Transformation Plasticity at High Strain Rate in Magnesia-Partially-Stabilized Zirconia, *J. Am. Ceram. Soc.*, Vol 73, 1990, p 136–139
12. V. Sharma, S. Nemat-Nasser, and K.S. Vecchio, Dynamic-Compression Fatigue of Hot-Pressed Silicon-Nitride, *Exp. Mech.*, Dec 1994, p 315–323
13. G. Subhash and S. Nemat-Nasser, Dynamic Stress-Induced Transformation and Texture Formation in Uniaxial Compression of Zirconia Ceramics, *J. Am. Ceram. Soc.*, Vol 76, 1993, p 153–165

Recovery Hopkinson Bar Techniques

Sia Nemat-Nasser, University of California, San Diego

Applications of Recovery Hopkinson Techniques

The recovery of the sample that has been subjected to a single stress pulse allows a number of interesting applications, a few of which are reviewed in this section.

Isothermal Flow Stress of Ductile Materials at High Strain Rates. Incremental straining can be used to measure the strain softening produced by the temperature rise associated with the high strain rate plastic deformation of ductile samples. The effect of any recovery on the flow stress that may occur during unloading and cooling to room temperature, and reloading of the sample, is assessed by overlapping the incremental straining of similar samples of the material. Figure 20 provides results for a tantalum-tungsten alloy (Ta-10%W). Curves 1 and 2 are obtained quasi-statically (Instron machine) at 10^{-3} and 1 s^{-1} strain rates. Curve 3 is the adiabatic stress-strain relation at a 5700 s^{-1} strain rate, starting with $25 \text{ }^\circ\text{C}$ ($77 \text{ }^\circ\text{F}$) initial temperature; different samples are used. To obtain the (quasi-) isothermal flow stress at a 5700 s^{-1} strain rate, a fourth sample is deformed incrementally in the recovery Hopkinson system, obtaining curves 4, 5, and 6. Then, curve 7 is constructed using these results.

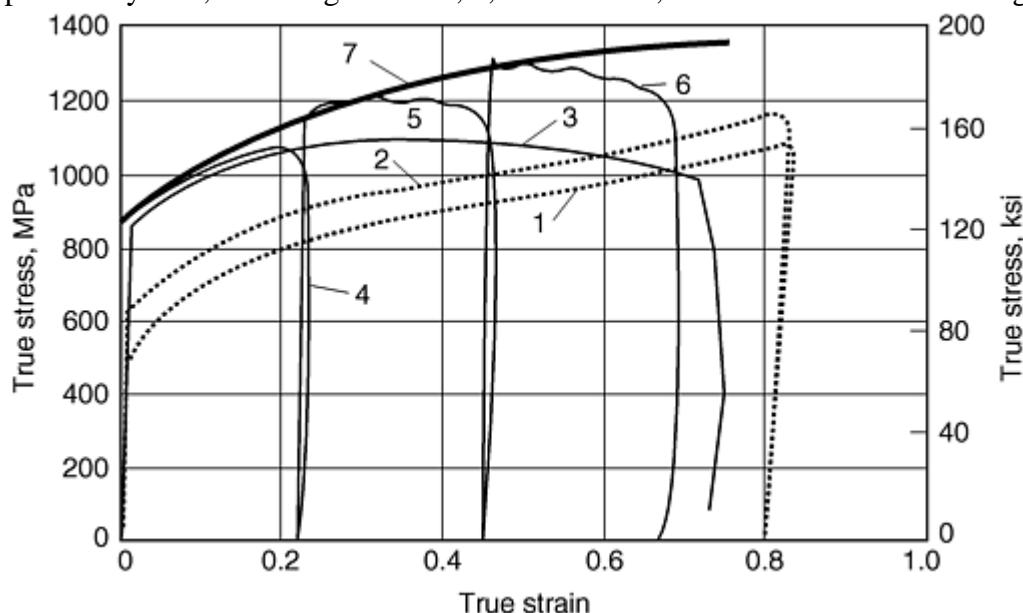


Fig. 20 The true stress-true strain relations for Ta-10%W at $25 \text{ }^\circ\text{C}$ ($77 \text{ }^\circ\text{F}$). Curves 1, 2, and 7 are isothermal relations at strain rates of 10^{-3} , 1, and 5700 s^{-1} . Curve 5 is adiabatic at 5700 s^{-1} strain rate. Source: Ref 1

Before accepting curve 7 as the quasi-isothermal stress-strain relation of this material, it is necessary to establish whether a uniform stress state is attained in the sample prior to yielding in each straining increment. The sample in this experiment was 3.8 mm (0.15 in.) long. The duration of the elastic wave to travel the length of the sample is about 1.2 μs . Hence, the stress in the sample is essentially uniform after 5 μs . The time required to bring the sample to its yield point is greater than 10 μs . Hence, a uniform stress is attained in each incremental loading prior to yielding.

The results in Fig. 20 also show that the differences among curves 1, 2, and 7 are only due to the change in the strain rate because the effect of temperature is now removed. It is interesting to note that these three curves are essentially parallel, their common slope being a measure of the material's work hardening. Moreover, the thermal softening can be read off directly from the difference between curves 3 and 7.

It is also possible to check whether there have been any substantial changes in the microstructure of the material, when the sample is unloaded and cooled to room temperature, in each incremental loading. In addition, it is possible to evaluate the part of the plastic work, which is used to increase the sample temperature during its high strain rate deformation. This is illustrated by the results given in Fig. 21 for the same Ta-10% W alloy, tested at the same 5700 s^{-1} strain rate. The dashed curve in this figure is the adiabatic result. Curve 1 is obtained by an incremental deformation of a new sample of the same material, at the same strain rate, in the recovery Hopkinson system. It follows the dashed curve closely, indicating the repeatability of the experiment. The area under this solid curve can be used to calculate the total plastic work per unit mass. The change in the temperature of the sample can then be computed from:

$$\Delta T = \int_0^\epsilon \frac{\eta \sigma}{\rho C_v} d\epsilon \quad (\text{Eq 10})$$

where ϵ and σ are the axial strain and stress in the sample, respectively; ρ is the mass density of the sample; and C_v is the (temperature-dependent) heat capacity at constant volume. In Eq 10, η is the fraction of the energy used to increase the sample temperature. To obtain curve 2 in Fig. 21, it was necessary to assume that all the plastic work was used to increase the sample temperature, setting $\eta = 1$. The results show that, to within experimental errors, this is a good assumption for the present case (see Ref 15 for comments and comparison with infrared measurements using several different materials).

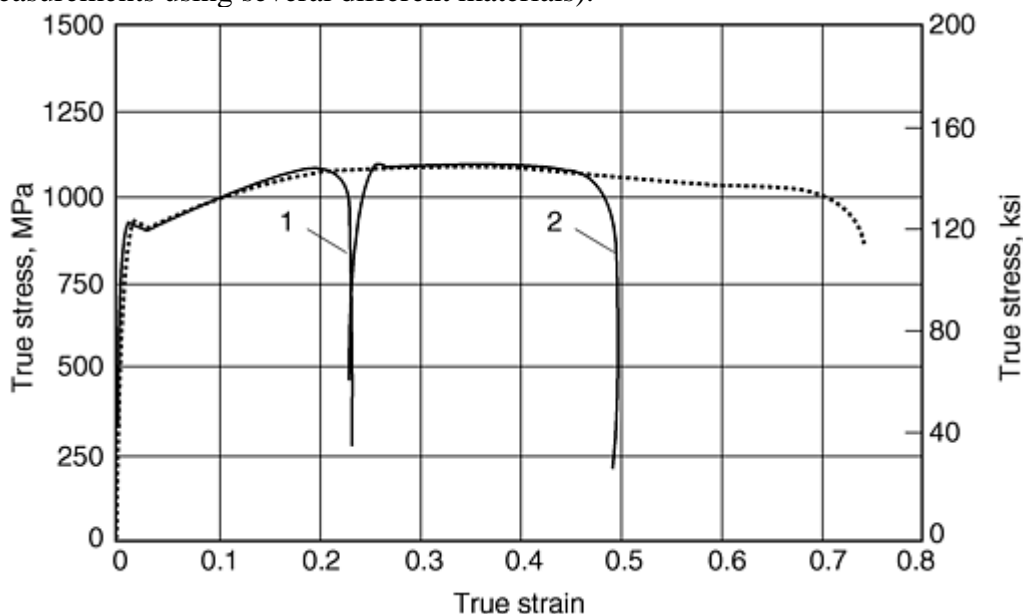


Fig. 21 The true stress-true strain relations for Ta-10%W at 5700 s^{-1} strain rate; all three curves are adiabatic, with an initial temperature of 25 °C (77 °F) for the dashed curve and for curve 1 and an initial temperature of 135 °C (275 °F) for curve 3. Source: Ref 1

References cited in this section

1. S. Nemat-Nasser and J.B. Isaacs, Direct Measurement of Isothermal Flow Stress of Metals at Elevated Temperatures and High Strain Rates with Application to Ta and Ta-W Alloys, *Acta Metall.*, Vol 45, 1997, p 907–919

Recovery Hopkinson Bar Techniques

Sia Nemat-Nasser, University of California, San Diego

High-Temperature Dynamic Recovery Tests

For high strain rate tests at elevated temperatures, it is necessary to heat the sample to the required temperature while keeping the incident and transmission bars at suitably low temperatures. If the bars are in contact with the specimen within the furnace, their temperature will increase, having a variable distribution along the bars. This affects the elastic properties of the bars and, hence, the stress pulses. Moreover, the bars being good heat conductors (usually of maraging steel), the considerable heat loss that occurs makes controlling the experiment difficult.

Different techniques are required in order to alleviate these difficulties when testing metals that are ductile and ceramics that are hard and brittle, as discussed subsequently.

High-Temperature, High Strain Rate Testing of Ductile Materials. In this case, the bars are kept outside the range of the heating unit in the furnace, while keeping the specimen at the center of the furnace. The bars are then brought into contact with the specimen microseconds before the stress pulse reaches the end of the incident bar. This is accomplished by two bar movers that are activated by the same gas gun that propels the striker bar toward the incident bar. Figure 22(a) illustrates the experimental setup just before the gun is fired, and Fig. 22(b) shows the configuration after the bar movers have brought the incident and transmission bars in contact with the sample. The motion of the bar movers is controlled by the area of its piston and the gas pressure in the breech of the gas gun. In a properly designed system of this kind (Ref 1), the bars are brought into contact with the specimen microseconds before the sample is loaded by the elastic pulse traveling in the incident bar. Once the sample is loaded, the bars move out, and the sample is recovered without having been subjected to any stresses other than the initial one.

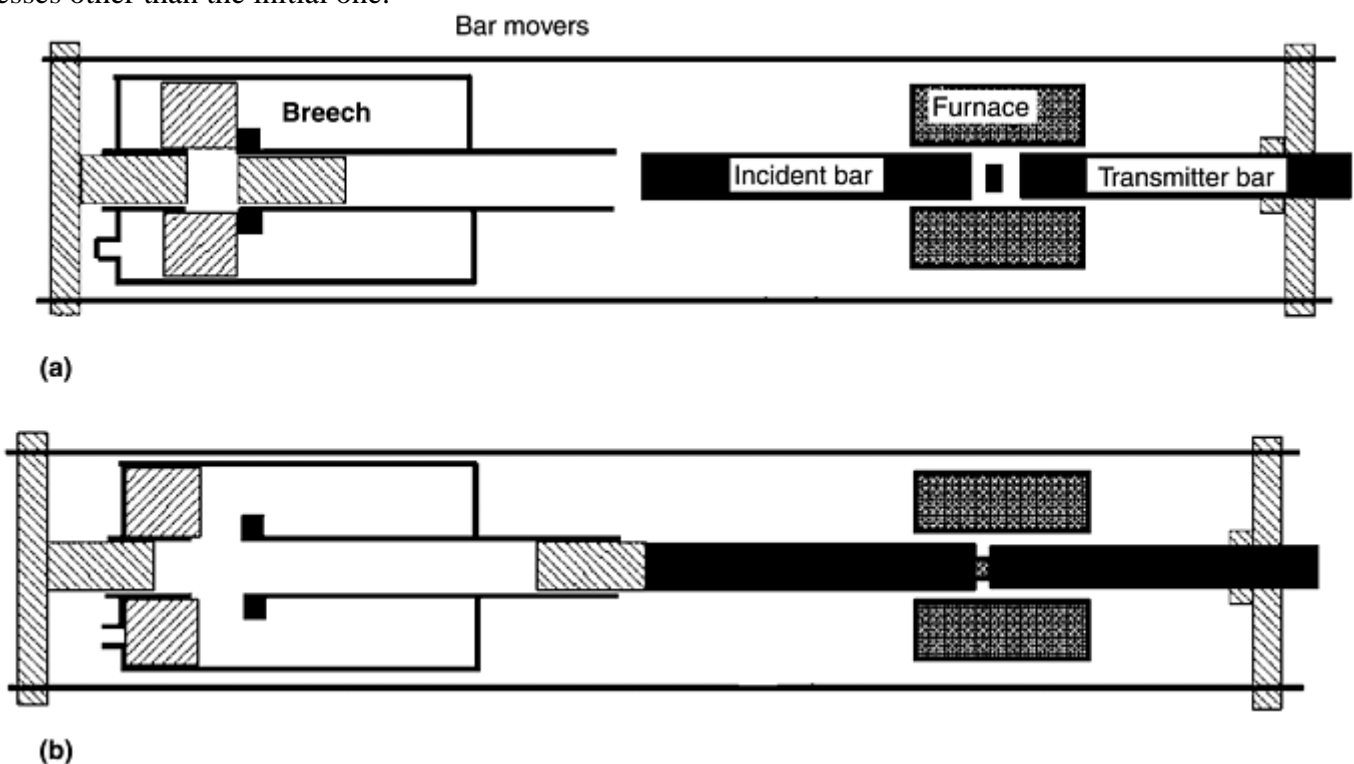


Fig. 22 Operation of the high-temperature recovery Hopkinson bar (a) before and (b) during the test. Source: Ref 1

Figure 23(a) shows the furnace and the ends of the incident and transmission bars. Figure 23(b) shows the relative position of the sample held by thermocouples, and the ends of the incident and transmission bars; this is the configuration maintained in the furnace just before firing the gas gun. The sample is attached by suitable wires to a sleeve, which is a thin tube. The bar movers then move the transmission bar, bring it into contact with the sample, and then the sample, the sleeve, and the transmission bar are brought into contact with the incident bar. Figure 23(c) shows the furnace and the sample attached to the sleeve outside of the furnace. Figure 23(d) shows the bar movers attached to the breech of the gas gun of the Hopkinson construction.

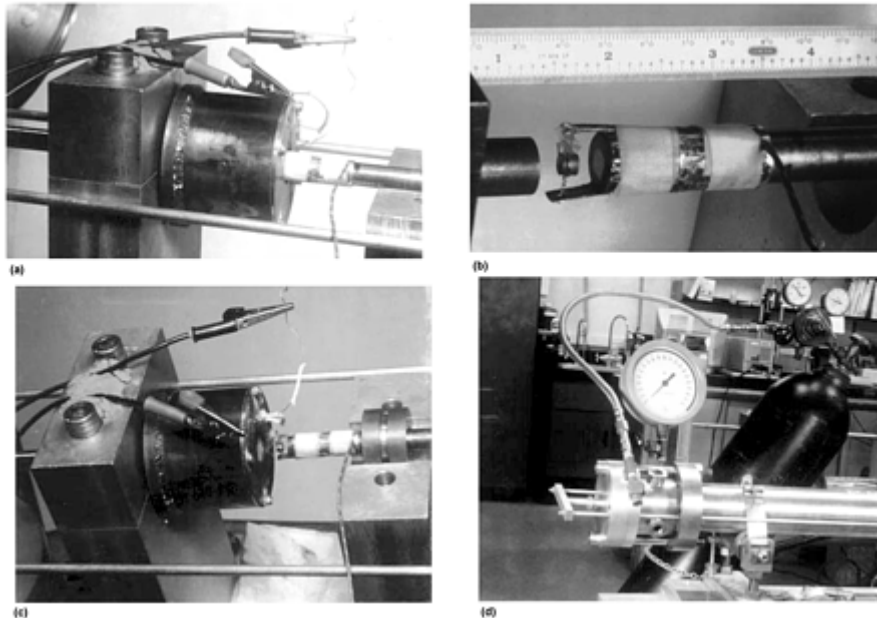


Fig. 23 Dynamic recovery testing at high temperatures. (a) Furnace over the end of the incident and transmission bars. (b) Position of the sample when held by thermocouples. (c) Furnace and the sample attached to the sleeve. (d) Bar movers attached to the breech of the gas gun of the Hopkinson construction. Source: Ref 1

Isothermal Flow Stress of Ductile Materials at High Temperatures and High Strain Rates. To produce an isothermal flow stress at a high strain rate and high temperature, the sample is heated to the required temperature in the furnace attached to the recovery Hopkinson bar and then loaded incrementally. After the application of each load increment, the sample is unloaded without being subjected to any additional stress pulses. The sample is then allowed to return to room temperature, its dimensions are measured, and it is reheated in the furnace to its initial temperature before the application of the next strain increment.

Since the unloading, the cooling of the sample, the reheating to its initial temperature, and the reloading may affect the microstructure and, hence, the thermomechanical properties of the material, it is necessary to check this in each case. To this end, a sample that has been loaded, unloaded, and cooled to its initial temperature may then be reheated to the temperature it had reached just prior to its unloading. If there are no substantial changes in the microstructure that affect the flow-stress properties, then the flow stress, upon reloading, should follow the previous stress-strain curve. The procedure is similar to that described for Fig. 21. The only difference is the initial temperature.

As an application, consider measurement of the high strain-rate isothermal flow stress of the Ta-10%W alloy at 325 °C (615 °F); see Fig. 24. The room-temperature results are the same as in Fig. 20. Figure 24 includes the high strain rate, room-temperature results reported in Fig. 20; for example, curve 3 in Fig. 24 is the same as curve 7 of Fig. 20.

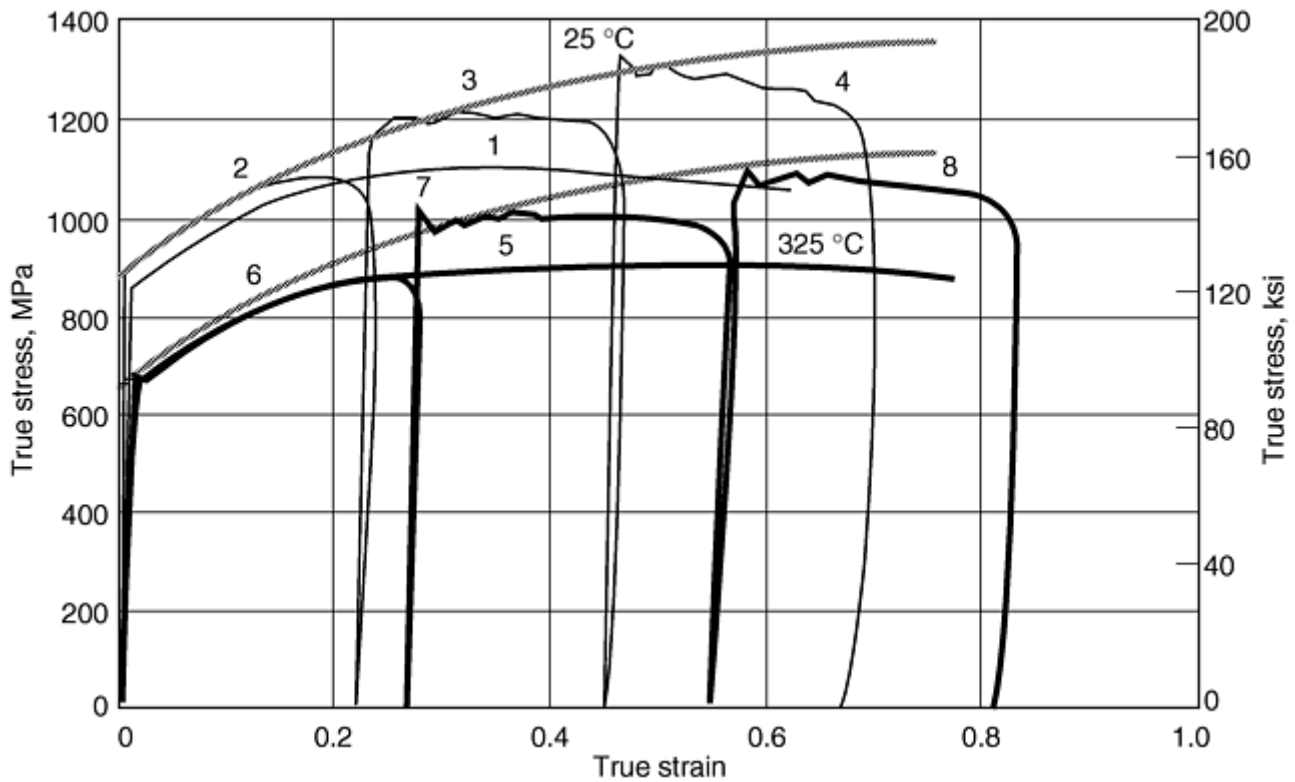


Fig. 24 True stress-true strain relations for Ta-10%W at 5700 s^{-1} strain rate. Curves 1, 2, 3, and 4 are for $25 \text{ }^{\circ}\text{C}$ ($77 \text{ }^{\circ}\text{F}$), and curves 5, 6, 7, and 8 are for $325 \text{ }^{\circ}\text{C}$ ($615 \text{ }^{\circ}\text{F}$) initial temperatures. The isothermal curves for $25 \text{ }^{\circ}\text{C}$ ($77 \text{ }^{\circ}\text{F}$) and $325 \text{ }^{\circ}\text{C}$ ($615 \text{ }^{\circ}\text{F}$) are essentially parallel.

With an approach similar to that for the room-temperature tests of Fig. 20, but now using an attached furnace, the results given in Fig. 24 for a $325 \text{ }^{\circ}\text{C}$ ($615 \text{ }^{\circ}\text{F}$) initial temperature have been obtained. As is seen, the quasi-isothermal curves for 25 and $325 \text{ }^{\circ}\text{C}$ (77 and $615 \text{ }^{\circ}\text{F}$) initial temperatures are almost parallel, showing essentially the same work hardening for the Ta-10%W alloy. Comparing these results with those of Fig. 24, it is seen that the isothermal work hardening seems to be independent of the temperature for this material, within the considered temperature and strain rate ranges. Hence, the work hardening due to plastic straining is not coupled with either temperature or strain rate. This is an important property since the flow stress then can be divided into an athermal part and a thermally activated part where the athermal part may be assumed to depend solely on the microstructure. The thermal part is due to the short-range barriers to the motion of dislocations (Ref 16). Note that here again it is necessary to establish whether a uniform stress state is attained in the sample, prior to yielding in each incremental straining, and whether the structure of the material is affected by the cycle of unloading, cooling, reheating, and reloading, as discussed in the section “Isothermal Flow Stress of Ductile Materials at High Strain Rates.”

High-temperature, high strain rate testing of hard, brittle materials poses the following challenges:

- It is necessary to prevent the indentation of the bars by the sample.
- It is necessary to heat the sample while keeping the bars outside the heating zone within the furnace.
- It is necessary to measure the strain of the sample at high temperatures within the furnace.

In compression, these qualifications can be met as follows. First, in addition to the techniques outlined in the section “Recovery Dynamic Testing of Hard Materials,” long inserts (e.g., 1 in.) are used for elevated-temperature tests. The use of longer inserts ensures that while the sample is heated to the required temperature, the bars remain at a suitably low temperature. Second, since strain gages have a limited temperature range of operation and cannot be used at elevated temperatures, differential strain measurement (DSM) has been developed to obtain accurate and reliable measurements of strains for dynamic tests of hard ceramics at elevated temperatures.

The DSM technique is based on the observation that an error is introduced due to the presence of the inserts and their interfaces with the sample and the bars. Hence, the displacement recorded by the strain gage on the

incident bar may be considerably greater than the actual sample displacement. For two tests, if the experimental conditions and the area of contact between the sample and the inserts and that between the inserts and the bars are kept the same, the error produced by the presence of the inserts will also be essentially the same in both tests.

To apply the DSM technique, two high strain rate tests are conducted on the Hopkinson bar, with two samples of different lengths. All other experimental conditions such as the striker bar length, the striker velocity, the pulse-shaper dimensions, and the sample temperature are maintained the same in both tests. After the two tests are conducted for the same stress, the difference in the strain can be attributed to the difference in the sample lengths. The displacement of the shorter sample is subtracted from that of the longer sample at several stress levels, and the differential displacement is obtained as a function of the stress. The displacement data thus obtained correspond to the displacement data for a sample with a length equaling the difference in the lengths of the two test samples. Thus, the stress-displacement data obtained now are the actual data that would correspond to a sample with a length equal to the difference in the lengths of the test samples.

Using a well-designed ramped loading, it is possible to measure the elastic modulus of ceramics at high temperatures and high strain rates by this procedure with considerable accuracy. Figure 25 shows the strain as a function of time for two samples of silicon nitride tested at 730 °C (1350 °F). The samples are of different lengths and are both tested in the elastic regime. It may be noted that the strain rate is nearly the same for the two tests.

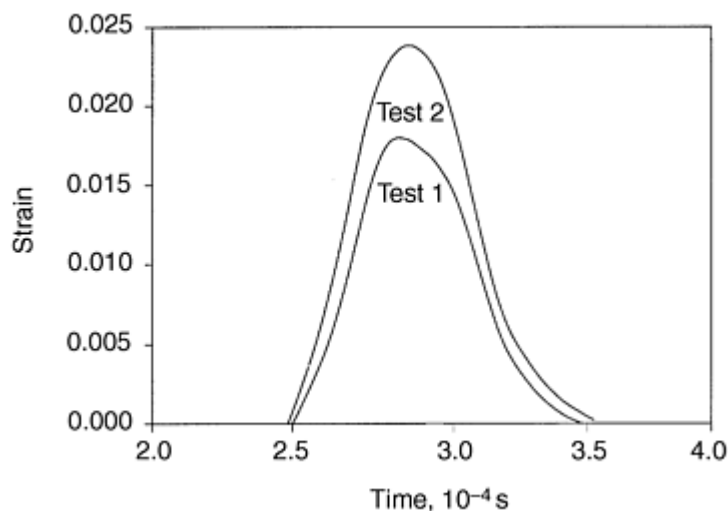


Fig. 25 Strain-time data for two samples of different lengths tested at 730 °C (1350 °F)

References cited in this section

1. S. Nemat-Nasser and J.B. Isaacs, Direct Measurement of Isothermal Flow Stress of Metals at Elevated Temperatures and High Strain Rates with Application to Ta and Ta-W Alloys, *Acta Metall.*, Vol 45, 1997, p 907–919
16. U.F. Kocks, A.S. Argon, and M.F. Ashby, Thermodynamics and Kinetics of Slip, *Prog. Mater. Sci.*, Pergamon Press, New York, Vol 19, p 68–170

Recovery Hopkinson Bar Techniques

Sia Nemat-Nasser, University of California, San Diego

Acknowledgments

This work has been supported by an ARO/MURI DAAH04-96-1-0376 grant to the University of California, San Diego.

Recovery Hopkinson Bar Techniques

Sia Nemat-Nasser, University of California, San Diego

References

1. S. Nemat-Nasser and J.B. Isaacs, Direct Measurement of Isothermal Flow Stress of Metals at Elevated Temperatures and High Strain Rates with Application to Ta and Ta-W Alloys, *Acta Metall.*, Vol 45, 1997, p 907–919
2. S. Nemat-Nasser and Y. Li, Flow Stress of FCC Polycrystals with Application to OFHC Cu, *Acta Mater.*, Vol 46, 1998, p 565–577
3. S. Nemat-Nasser, W. Guo, and M. Liu, Experimentally-Based Micromechanical Modeling of Dynamic Response of Molybdenum, *Scr. Mater.*, Vol 40, 1999, p 859–872
4. K.H. Hartman, H.D. Kunze, and L.W. Meyer, Metallurgical Effects in Impact Loaded Materials, *Shock Waves and High-Strain-Rate Phenomena in Metals*, M.A. Meyers and L.E. Murr, Ed., Plenum, London, 1986, p 325
5. S. Nemat-Nasser, J.B. Isaacs, G. Ravichandran, and J.E. Starrett, High Strain Rate Testing in the U.S., *Proc. TTCP TTP-1 Workshop on Techniques of Small Scale High Strain Rate Studies*, 26 April 1988, Materials Science Laboratory, Melbourne, Australia, 1988
6. S. Nemat-Nasser and S.N. Chang, Compression-Induced High Strain Rate Void Collapse, Tensile Cracking, and Recrystallization in Ductile Single and Polycrystals, *Mech. Mater.*, Vol 10, 1990, p 1–17
7. S. Nemat-Nasser, J.B. Isaacs, and J.E. Starrett, Hopkinson Techniques for Dynamic Recovery Experiments, *Proc. R. Soc. (London) A*, Vol 435, 1991, p 371–391
8. A. Thakur, S. Nemat-Nasser, and K.S. Vecchio, Bauschinger Effect in Haynes 230 Alloy: Influences of Strain Rate and Temperature, *Metall. Mater. Trans.*, Vol 27A, 1996, p 1739–1748
9. A. Thakur, S. Nemat-Nasser, and K.S. Vecchio, Dynamic Bauschinger Effect, *Acta Mater.*, Vol 44, 1996, p 2797–2807
10. W.P. Rogers, J.B. Isaacs, and S. Nemat-Nasser, Effect of Microstructural Damage on Ultrasonic Velocity and Elastic Moduli of Partially Stabilized Zirconia, *Review of Progress in Quantitative Nondestructive Evaluation*, D.B. Thomson and D.E. Chimenti, Ed., Plenum, New York, 1989, p 1827–1832
11. W.P. Rogers and S. Nemat-Nasser, Transformation Plasticity at High Strain Rate in Magnesia-Partially-Stabilized Zirconia, *J. Am. Ceram. Soc.*, Vol 73, 1990, p 136–139
12. V. Sharma, S. Nemat-Nasser, and K.S. Vecchio, Dynamic-Compression Fatigue of Hot-Pressed Silicon-Nitride, *Exp. Mech.*, Dec 1994, p 315–323

13. G. Subhash and S. Nemat-Nasser, Dynamic Stress-Induced Transformation and Texture Formation in Uniaxial Compression of Zirconia Ceramics, *J. Am. Ceram. Soc.*, Vol 76, 1993, p 153–165
14. S. Nemat-Nasser, Y Li, and J.B. Isaacs, Experimental/Computational Evaluation of Flow Stress at High Strain Rates with Application to Adiabatic Shearbanding, *Mech. Mater.*, Vol 17, 1994, p 111–134
15. R. Kapoor and S. Nemat-Nasser, Determination of Temperature Rise during High Strain Rate Deformation, *Mech. Mater.*, Vol 27, 1998, p 1–12
16. U.F. Kocks, A.S. Argon, and M.F. Ashby, Thermodynamics and Kinetics of Slip, *Prog. Mater. Sci.*, Pergamon Press, New York, Vol 19, p 68–170

Split-Hopkinson Pressure Bar Testing of Soft Materials

George T. (Rusty) Gray III and William R. Blumenthal, Los Alamos National Laboratory

Introduction

THE HIGH-STRAIN-RATE, STRESS-STRAIN RESPONSE of polymers and polymeric-composite materials has received increased scientific and industrial attention in recent years. This interest is driven by the need for predictive constitutive model descriptions to support large-scale finite-element simulations of polymers subjected to high-strain-rate (impact) loading. Applications for which high-strain-rate loading represents an important service environment for polymers include:

- Automotive crashworthiness, where polymers, polymer foams, and polymeric composites have seen significantly increased structural usage
- Aerospace damage tolerance, including foreign-object damage such as during bird ingestion in jet engines equipped with polymeric composite blades and vanes
- Sporting goods applications where dynamic behavior and impact resistance of polymer composites is critical, such as tennis rackets, golf shafts, mountain bike frames, and so on
- Polymeric binder constituents used in polymer-bonded explosives (PBXs) and rocket propellants

The establishment of more physically based constitutive models to describe complex loading paths and to understand the effect of manufacturing processes on polymers and polymeric composites subjected to dynamic loading environments requires a detailed knowledge of the separate and synergistic effects of temperature and strain rate on their mechanical response. Split-Hopkinson pressure bar (SHPB), or Kolsky-bar, testing remains the main experimental method to characterize the high-strain-rate mechanical behavior of these materials. The specialized aspects required to accurately quantify the behavior of these “soft” materials using the SHPB is the subject of this article.

Split-Hopkinson Pressure Bar Testing of Soft Materials

George T. (Rusty) Gray III and William R. Blumenthal, Los Alamos National Laboratory

Background

A significant number of previous studies have probed the high-rate constitutive response of a wide variety of polymers and polymer composites, starting with Kolsky in 1949 through the present (Ref 1, 2, 3, 4, 5, 6, 7, 8, 9, 10, 11). Several in-depth reviews by Walley and others summarize the broad spectrum of polymers (Ref 12, 13, 14). Beginning with the high-rate pressure-bar studies of Kolsky (Ref 1) on polythene (polymerized ethylene) and rubber, it has been shown that:

- The effective elastic moduli of polymeric materials are strongly influenced by strain rate.
- The flow stress of a ductile polymer reaches a maximum strength at some moderate strain level under constant, high-strain-rate loading.
- Some polymers exhibit no permanent plastic flow after substantial high rate straining, the strain recovery effect being time dependent.
- Stress-wave propagation through some polymers, such as polythene, is so dispersive that over a certain sample length no transmitted Hopkinson bar signal is measured.

Experimental results for a large number of polymers over a wide range of strain rates have exhibited a linear relationship between the compressive yield stress of the polymer and log (strain rate) (Ref 13, 14).

The low inherent flow strength and low elastic impedance of polymers and polymeric composites pose additional challenges to the accurate measurement of their high-strain-rate uniaxial stress mechanical response using an SHPB (Ref 3). Resolution of the low flow strengths in polymers has prompted the adoption of alternate pressure-bar materials in deference to the high-strength steels classically used. Because lower modulus bar materials increase the signal-to-noise level of measurement strain gages, their selection is desirable to facilitate high-resolution dynamic testing of low-strength materials such as polymers, as long as the yield strength of the sample material remains well below that of the bar materials. Researchers have documented the use of bar materials possessing a range of elastic stiffnesses from maraging steel to titanium to aluminum to magnesium (Ref 15, 16) and, finally, to polymer bars (Ref 3, 17, 18, 19). Table 1 summarizes the elastic modulus and impedance values for a range of typical pressure-bar materials.

Table 1 Comparison of the impedance properties of bar materials for split-Hopkinson pressure bar testing

Bar material	Elastic modulus (E)		Wave impedance (ρ/C_0), $\text{km} \cdot \text{g/s} \cdot \text{cm}^3$	Impedance relative to steel, $(\rho/C_0)_x/(\rho/C_0)_{\text{steel}}$, %
	GPa	10^6 ksi		
Steel	212	31	40.8	100
Ti-6Al-4V	115	17	22.8	56
Aluminum	90	13	13.5	33
Magnesium	45	7	8.6	21
Polymethyl methacrylate (PMMA)	4	1	2.2	5

The ideal materials properties desired for pressure bars used in an SHPB are multifaceted and reflect a range of effects to control physical parameters that either improve measurement fidelity and robustness or are the chief sources of potential errors that can complicate data analysis and resolution and, thereby, test accuracy. The selection of an appropriate pressure-bar material represents a balance of the tradeoffs pursuant to a given material. The traditional use of metallic pressure bars reflects the fact that many metals and alloys exhibit a number of positive attributes in regard to their use as “load cells” in parallel with the sample and as wave guides for high-fidelity wave propagation. Ideal pressure bars should exhibit all of the following properties, and any deviations in practice constitute a compromise:

Good wave guide properties:

- Very low attenuation. Signal loss in perfectly elastic materials is essentially zeroed.
- Little or no time-dependent response, including frequency dependence, anelasticity, and dispersion

- Little radial wave attenuation. A low Poisson ratio is desirable.
- Large thermal range, both above and below ambient, over which the elastic properties are constant
- Low interference potential—low susceptibility to picking up stray signals during testing (high impedance mismatch with air, little coupling between bar and bar stanchions due to large impedance mismatch)
- Large input range before bars exhibit distortion—high strength/high elastic limit

Good load cell properties:

- High sensitivity for high-gage signal-to-noise, low-modulus bars
- Large input range—high-strength and high-elastic-limit bars
- High-wave-speed bar material resulting in good dynamic range (high bandwidth)
- Little signal interference from strain gages and glue joints—high modulus ratio between the pressure bar material and the glue and strain gages
- Minimal coupling of pressure bars with stanchions, strain-gage cables, and connections
- Low Poisson ratio of pressure bars to maximize one-dimensional strain conditions in pressure bars since longitudinal strain is measured (i.e., minimize two-dimensional strain effects on gage measurements)

The adoption of increasingly lower impedance pressure bar materials for Hopkinson bar testing over the past ten years is a direct result of the desire to increase the signal-to-noise gain to adequately resolve the low elastic strains produced in the pressure bars during testing of low-strength materials. Even with a high-gain, strain-gage signal conditioner using a 500× gain, it can be difficult or impossible to resolve the transmitted pressure pulse of a soft polymer using traditional steel pressure bars. In essence, if the wave impedance (ρC_0) of the sample material under investigation is much lower than that of the pressure bars, the magnitude of the transmitted pulse can become very weak. In addition, as described in the article “Classic Split-Hopkinson Pressure Bar Testing,” several different wave analyses should be used to calculate the sample stress from the incident, reflected, and transmitted bar time-resolved measured strains to validate stress-state equilibrium. Issues of stress-state equilibrium are addressed subsequently as pertains to polymer testing.

The additional complications inherent to testing viscoelastic materials and the care that must be exercised to accurately measure their mechanical behavior in an SHPB were introduced in the seminal work of Kolsky (Ref 1) on plastics and rubber. Kolsky (Ref 1, 20) discussed the difficulty in resolving the low-magnitude transmitted pulses for rubber or polythene and, thereafter, the importance of using thin sample thicknesses to reduce the time a sample takes to “ring up” to a state of uniform uniaxial stress. His studies demonstrated that thin samples were critical when studying the high-rate constitutive response of plastics and rubber or the “assumption that the pressure on both sides of the specimen are sensibly the same is no longer valid” (Ref 1). In this article, some of the specialized SHPB developments within the last ten years to facilitate testing soft materials are detailed. These techniques include the data-reduction techniques and assumptions required to use polymer pressure bars, the importance of sample-size considerations to polymer testing, and temperature-control methodologies germane to measuring the high-strain-rate uniaxial stress response of polymers and other soft materials.

References cited in this section

1. H. Kolsky, An Investigation of the Mechanical Properties of Materials at Very High Rates of Loading, *Proc. Phys. Soc. (London) B*, Vol 62, 1949, p 676–700
2. S.H. Ahmad, Flow Stress of High Density Polyethylene and Nylon 66 at High Rates of Strain, *Polym. Int.*, Vol 28, 1992, p 291–294
3. G.T. Gray III, W.R. Blumenthal, C.P. Trujillo, and R.W. Carpenter II, Influence of Temperature and Strain Rate on the Mechanical Behavior of Adiprene L-100, *J. Phys. (France) IV Colloq.*, C3 (EURODYMAT 97), Vol 7, 1997, p 523–528

4. N.N. Diah, A. Ivankovic, P.S. Leever, and J.G. Williams, The High Strain Rate Behaviour of Polymers, *J. Phys. (France) IV Colloq.*, C8 (DYMAT 94), Vol 4, 1994, p 119–124
5. A. Trojanowski, C. Ruiz, and J. Harding, Thermomechanical Properties of Polymers at High Rates of Strain, *J. Phys. (France) IV Colloq.*, C3 (EURODYMAT 97), Vol 7, 1997, p 447–452
6. A.M. Bragov and A.K. Lomunov, Mechanical Properties of Some Polymers and Composites at Strain Rate of 1000/s, *J. Phys. (France) IV Colloq.*, C8 (DYMAT 94), Vol 4, 1994, p 337–342
7. S.M. Walley, D. Xing, and J.E. Field, Mechanical Properties of Three Transparent Polymers in Compression at a Very High Rate of Strain, *Impact and Dynamic Fracture of Polymers and Composites*, J.G. Williams and A. Pavan, Ed., Mechanical Engineering Publications Ltd., 1995, p 289–303
8. S.M. Walley, J.E. Field, G.M. Swallowe, and S.N. Mentha, The Response of Various Polymers to Uniaxial Compressive Loading at Very High Rates of Strain, *J. Phys. (France) Colloq.*, C5 (DYMAT 85), Vol 46, 1985, p 607–616
9. S.M. Walley, J.E. Field, P.H. Pope, and N.A. Safford, The Rapid Deformation Behaviour of Various Polymers, *J. Phys. (France) III*, Vol 1, 1991, p 1889–1925
10. S.M. Walley, J.E. Field, and N.A. Safford, A Comparison of the High Strain Rate Behaviour in Compression of Polymers at 300K and 100K, *Proc. 8th Int. Conf. on Deformation, Yield, and Fracture of Polymers*, edited by p. paper 16, Plastics and Rubber Institute, London, 1991
11. S. Hamdan and G.M. Swallowe, The Strain-Rate and Temperature Dependence of the Mechanical Properties of Polyetherketone and Polyetheretherketone, *J. Mater. Sci.*, Vol 31, 1996, p 1415–1423
12. S.M. Walley, J.E. Field, P.H. Pope, and N.A. Safford, A Study of the Rapid Deformation Behaviour of a Range of Polymers, *Philos. Trans. R. Soc. (London) A*, Vol 328, 1989, p 1–33
13. S.M. Walley and J.E. Field, Strain Rate Sensitivity of Polymers in Compression from Low to High Strain Rates, *DYMAT J.*, Vol 1, 1994, p 211–228
14. S.N. Kukureka and I.M. Hutchings, Yielding of Engineering Polymers at Strain Rates of up to 500 s⁻¹, *Int. J. Mech. Sci.*, Vol 26, 1984, p 617–623
15. G.T. Gray III, D.J. Idar, W.R. Blumenthal, C.M. Cady, and P.D. Peterson, High- and Low-Strain Rate Compression Properties of Several Energetic Material Composites as a Function of Strain Rate and Temperature, *11th Detonation Symposium*, (Snow Mass, CO), J. Short, Ed., Amperstand Publishing, 2000
16. J.E. Field, S.M. Walley, N.K. Bourne, and J.M. Huntley, Review of Experimental Techniques for High Rate Deformation Studies, *Proc. Acoustics and Vibration Asia '98*, 1998 (Singapore), p 9–38
17. G. Gary, J.R. Klepaczko, and H. Zhao, Generalization of Split Hopkinson Bar Technique to Use Viscoelastic Materials, *Int. J. Impact Eng.*, Vol 16, 1995, p 529–530
18. G. Gary, L. Rota, and H. Zhao, Testing Viscous Soft Materials at Medium and High Strain Rates, *Constitutive Relation in High/Very High Strain Rates*, K. Kawata and J. Shioiri, Ed., Springer-Verlag, Tokyo, 1996, p 25–32
19. H. Zhao and G. Gary, On the Use of SHPB Techniques to Determine the Dynamic Behavior of Materials in the Range of Small Strains, *Int. J. Solids Struct.*, Vol 33, 1996, p 3363–3375

Split-Hopkinson Pressure Bar Testing of Soft Materials

George T. (Rusty) Gray III and William R. Blumenthal, Los Alamos National Laboratory

Split-Hopkinson Bar Testing of Polymers

The quantification of the uniaxial stress-strain compressive response of low mechanical impedance soft materials in the SHPB has been the subject of significant innovation since 1992. Higher-resolution measurement of the stress-strain responses of increasingly lower-flow-strength materials has led to the adoption of lower-impedance pressure bars, specifically titanium-alloy, aluminum-alloy, magnesium or magnesium-alloy, and, finally, polymer pressure bars. The technical advantages and disadvantages of each are discussed in this section.

Polymer Pressure Bars

Based on the low impedance of many structural plastics, such as polymethyl methacrylate (PMMA) and polycarbonate (PC), a number of researchers have explored the benefits of using polymers for the pressure bars in an SHPB to test low-impedance polymers and foams (Ref 17, 18, 21, 22, 23, 24, 25, 26, 27, 28, 29, 30, 31, 32, and 33). These researchers have pursued the use of polymer bars to access the significant signal-to-noise gains that polymeric bars promise, as summarized in Table 1. While the lower inherent impedance of polymers offers positive attributes to SHPB testing of soft materials, their use requires additional analysis for data reduction, temperature complications, and additional restrictions compared with traditional metallic pressure bars.

Polymeric materials, unlike metals and alloys loaded in their elastic regime, are not ideally linear elastic, nor do they exhibit undistorted wave propagation. Polymeric materials, on the contrary, exhibit significant stress-wave attenuation, wave dispersion due to time and frequency dependency, a strong temperature dependency between ± 50 °C (± 90 °F), and are susceptible to gradual degradation in their “elastic” properties during prolonged usage due to the effects of oxidation and ultraviolet radiation. Notwithstanding these shortcomings, numerous researchers have explored the opportunities that the lower impedance and low modulus of polymers offers to the field of SHPB testing.

Researchers exploring the high-strain-rate, stress-strain response of lower-impedance soft materials have worked to quantify how the nonlinear response of polymeric bars alters the classic SHPB data reduction. In metallic bars, the linear elastic response of the bars defines that the measured strain pulse describes not only the local strain wave but also the associated stress wave and the particle velocity at different positions along the pressure bar. On the contrary, a viscoelastic material, such as PMMA, exhibits both wave attenuation and wave dispersion. As a wave travels down a polymer pressure bar, the wave amplitude decreases due to attenuation, and the shape of the waveform becomes distorted. Accordingly, strains measured at a given position on a viscoelastic bar do *not* represent the strain pulse at another position along the pressure bar without complex manipulation and corrections. Therefore, the “classic” SHPB analysis based on the undistorted character of wave propagation must be modified when viscoelastic bars are used instead of linear-elastic metallic bars. The measured strain pulse on a viscoelastic bar represents the strain wave *only* at the measured point, but neither the stress nor the particle velocity can be directly deduced from a measured strain signal in a viscoelastic bar by simply using a proportional coefficient as in the case of metals where the elastic modulus is used. This fact has been demonstrated by a number of researchers (Ref 17, 21, 23, 24, and 25). Quantification of the stresses, strains, and strain rates in a sample to be tested in an SHPB equipped with polymeric pressure bars, therefore, requires a viscoelastic wave analysis of the pressure-bar responses. Use of a simple linear elastic data reduction

for polymeric bars is inappropriate and will lead to errors as large as 52% as quantified by Wang and others (Ref 23).

Use of polymeric bars in an SHPB, therefore, requires the derivation of an accurate predictive material constitutive model description of the dispersion and dissipation in the viscoelastic bars to deduce the stress-strain behavior of the sample being tested. Zhao and Gary (Ref 24) proposed using a stress-strain constitutive model derived by using the wave recorded at one point on the incident bar as input data. The model parameters are thereafter determined through comparison with the predicted wave and the wave recorded at another point on the incident bar. A similar model reduction can be conducted for the transmitted pressure bar. Once the model parameters have been identified, this data can also be used for the wave dispersion correction (Ref 34).

Quantification and comparison of the forces in the transmitted bar are conducted using a bars-together configuration, where no sample is present. Here, the stress in the incident and transmitted bars are ideally equal. Using this technique, Zhao and Gary (Ref 24) characterized the frequency and phase velocity of their viscoelastic bars. The complex modulus of the polymer pressure bars is then calculated from the phase velocity and attenuation. Both of these quantities are bar-diameter dependent, and the frequency characteristics become less and less accurate as the wave frequency and the bar diameter increase. The work of Zhao and Gary (Ref 24) showed that in the case of PMMA pressure bars, selection of bar with diameters less than 10 mm (0.4 in.) minimized errors.

Sawas, Brar, and Brockman (Ref 33) similarly proposed measurement of the strain or particle velocity at two different locations along a polymer pressure bar. The strain measurements for the two positions were then reduced analytically to derive the model parameters for a viscoelastic description of the pressure bars. Figure 1 presents an example of the similitude of stress-strain mechanical property for 1100 aluminum alloy using a conventional SHPB and what can be obtained using cast acrylic pressure bars. In the experimental setup described by Sawas, Brar, and Brockman (Ref 33), high-strength titanium anvils were placed between the aluminum alloy sample and the two polymeric pressure bars to prevent damage to the bars during testing and to minimize elastic deformation at the specimen bar interface.

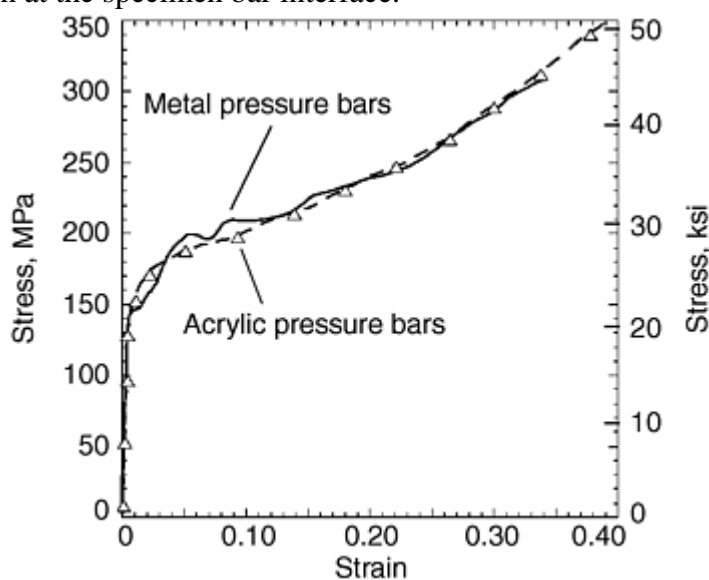


Fig. 1 Comparison of the stress-strain data measured for 1100 aluminum alloy using a conventional metallic pressure bar and an acrylic pressure bar for split-Hopkinson pressure bar testing. Source: Ref 33

Zhao, Gary, and Klepaczko (Ref 29) have additionally analyzed the use and modeling of polymeric pressure bars in the SHPB. In this model, a Fourier stationary wave approach is presented. This modeling approach was proposed because the numerical efficiency and precision are independent of the distance between the bar/specimen interface and the gage location. Additionally, this approach addresses the need to deal with the three-dimensional effects, such as bar-diameter effects, without introducing additional computational penalties. Their analysis of the solution of the propagation of the harmonic waves in an elastic bar reduces to the Pochhammer-Chree frequency equation, which gives the relation between the wave number and the frequency of the wave. Further analysis by Bacon (Ref 35, 36) supports the accuracy of harmonic wave modeling and its applicability to any solid cylindrical cross-sectional linear viscoelastic-infinite pressure bar.

The constitutive behavior of the polymeric bars, independent of whether a transient wave analysis (Ref 23) or a Fourier stationary harmonic wave analysis (Ref 29) is employed, is modeled using a Maxwell element-based approach to describe linear viscoelastic behavior. Zhao, Gary, and Klepaczko (Ref 29) proposed using a 4 Voigt element and 1 spring in a series Maxwell element rather than a more classic 3-element Maxwell model (a mechanical analog composed of a spring in parallel with a dashpot in series with a spring). Due to the almost constant damping and phase velocity, they selected the more complex form rather than a 3-element Maxwell model to model the high frequencies. Upon implementation of this model, Zhao, Gary, and Klepaczko (Ref 29) demonstrated that analyses of an SHPB test cannot be performed by simply shifting the effects of elastic geometry dispersion and the effects of the one-dimensional viscoelastic wave propagation. This is because of the strong effect of bar geometry on wave attenuation in the polymeric pressure bars.

Researchers interested in implementing one of these constitutive modeling approaches should examine in detail the appropriate papers. The main problem with using polymeric pressure bars to quantify the constitutive response of soft materials is the dependency on a complex geometry-dependent viscoelastic model analysis of the pressure bar signals to deduce sample behavior. This is in contrast to the relatively simple “classic” linear elastic data reduction where metallic pressure bars are used. These papers have demonstrated that a detailed solution to the dissipation and dispersion behavior of polymeric pressure bars can be accurately obtained for constant ambient temperature testing. Accordingly, sufficiently accurate dynamic stress-strain behavior of soft materials can be measured using polymeric pressure bars.

However, modeling to date of the polymer pressure-bar constitutive response has only been successfully demonstrated for ambient-temperature testing. In the case of metallic bars, the elastic properties are essentially constant well above and below ambient temperature. This allows testing without modification of the analysis and without the extremely difficult task of controlling the entire bar system and sample temperature to within a few degrees. In the case of polymer bars, testing at temperatures below and above ambient temperature also requires a strain-rate- and temperature-dependent constitutive model and a thermal profile of each test if the temperature of the entire bar cannot be maintained at the same level for accurate modeling of the pressure-bar response and thereafter the data reduction of the sample mechanical behavior.

Lower-Impedance Metallic Pressure Bars

The use of increasingly lower impedance titanium (Ti) (Ref 3, 16), aluminum (Al) (Ref 13, 37, 38), and magnesium (Mg) (Ref 15, 16, 39) metallic pressure bars to achieve higher-resolution transmitted bar signals requires no additional data reduction assumptions or caveats. Analysis of the stresses and strains in test samples using any metallic pressure bar material maintained in their elastic regimes can be readily conducted per the linear-elastic bar analysis detailed in the article “Classic Split-Hopkinson Pressure Bar Testing.” Unlike the case of using polymeric pressure bars, the data reduction to determine the stress-strain response of a sample tested using metallic pressure bars benefits from not only the validity of a simple linear-elastic bar response but also the relatively undistorted character of wave propagation in metallic bars (wave dispersion must still be corrected for maximum fidelity, as discussed in the article “Classic Split-Hopkinson Pressure Bar Testing”).

The absolute resolution of metallic pressure bars can be additionally increased through the concurrent use of high-gain, wide bandwidth, strain-gage signal amplifiers. Low-noise signal conditioners capable of gains up to 1000× and 3 MHz bandwidths are now commercially available (Ref 15). The use of pressure bars of 6061-T6 aluminum alloy or AZ31B magnesium alloy have proved capable of accurately resolving the mechanical response of a number of polymeric materials. Figure 2 illustrates the measurement of the dynamic stress-strain behavior of a soft Estane (B.F. Goodrich, Richfield, OH)-based binder material using magnesium pressure bars (Ref 15). The resolution of the 1- and 2-wave stress-strain responses for this binder material at stress levels below 1 MPa (145 psi) demonstrates that a classic metallic SHPB using magnesium bars can accurately resolve low-amplitude transmitted strain pulses. The delay in equilibrium, which is evident in Fig. 2 by the difference between the 1- and 2-wave signals, is consistent with the pronounced dispersive damping of stress-wave propagation through low-strength viscoelastic specimens. The ramifications of this pronounced lag in stress-state stability is discussed in the next section of this article.

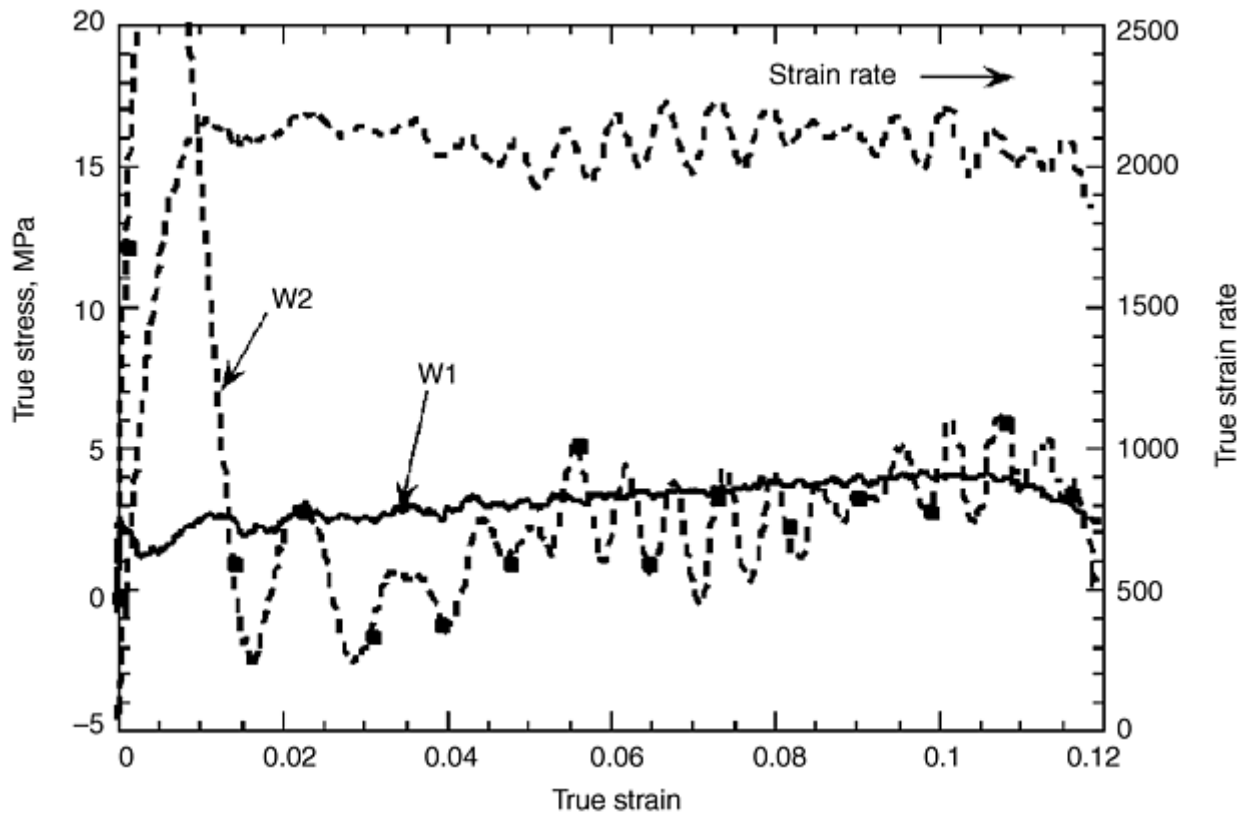


Fig. 2 Stress-strain response of a viscoelastic estane-based polymeric energetic binder tested at 0 °C (30 °F) measured with magnesium pressure bars and using an incident bar strain-gage gain of 200× and transmitted bar strain-gage gain of 500×. W1, one-wave signal; W2, two-wave signal. Source: Ref 15

An additional recent approach to increase the sensitivity of an SHPB to resolve the stress-strain behavior of polymers is the use of a hollow aluminum transmitted pressure bar. Chen and others (Ref 38) have demonstrated that using a hollow high-strength aluminum alloy transmitted pressure bar can significantly increase the signal to noise measured during the SHPB testing of RTV630 silicon rubber. A pulse shaper was used with the hollow aluminum alloy transmitted bar to simultaneously increase the rise time of the incident pulse as well as to filter out the high-frequency components of the incident waveform, thereby reducing the effect of the end cap of the hollow transmitted bar (Ref 38). While an end cap can be used to suppress damage to the ends of the bar and not interfere with the transmitted stress signal, the presence of an additional interface at the end cap/incident bar intersection will significantly complicate the reflected strain signal, which is needed to calculate the sample strain and strain rate. The influence of an end cap on a hollow pressure bar on stress-state equilibrium in a polymer sample should be evaluated by comparing the 1- and 2-wave analyses of the state of stress in the sample, as described subsequently.

While lower-impedance metallic bars can significantly increase the signal to noise to resolve the stress-strain response of low-strength solids, there remain classes of soft polymeric materials that cannot be analyzed using conventional split-Hopkinson bar data analysis. For all types of Hopkinson bar testing, the assumption of one-dimensional wave propagation in the bar and sample requires that true stress in a sample in the Hopkinson bar cannot be extracted for materials whose volumes are not conserved. The instantaneous sample area used in Eq 6 in the article “Classic Split-Hopkinson Pressure Bar Testing” is deduced from the reflected strain signal in the incident bar, assuming that the constancy of volume assumption is valid in the sample (i.e., there is a fixed relationship between sample cross-sectional area and its length). In addition, samples not possessing constant volumes by their very nature of compacting or exhibiting nonhomogeneous deformation processes prior to achieving a “bulk” response during testing will exhibit significant time delays before the sample attains a uniform state of uniaxial stress-state equilibrium (if at all) during testing. These materials include metallic and polymeric foams, honeycomb structures, and porous compacts, including types of wood, for which mechanical loading produces densification or porosity during testing.

Valid Hopkinson bar testing of materials for which the constant volume criterion is not valid, therefore, requires additional sample diagnostics during the duration of the test to calculate true stress; simultaneous use of high-

resolution, high-speed photography can be used to monitor sample strain during testing. The photographic data, once digitized, can then be used to measure the actual instantaneous sample area as a function of time in the sample for use in determining the true sample strain and strain rate. Finally, this data, when combined with the transmitted wave data, can provide the means to calculate true stress in the sample.

References cited in this section

3. G.T. Gray III, W.R. Blumenthal, C.P. Trujillo, and R.W. Carpenter II, Influence of Temperature and Strain Rate on the Mechanical Behavior of Adiprene L-100, *J. Phys. (France) IV Colloq.*, C3 (EURODYMAT 97), Vol 7, 1997, p 523–528
13. S.M. Walley and J.E. Field, Strain Rate Sensitivity of Polymers in Compression from Low to High Strain Rates, *DYMAT J.*, Vol 1, 1994, p 211–228
15. G.T. Gray III, D.J. Idar, W.R. Blumenthal, C.M. Cady, and P.D. Peterson, High- and Low-Strain Rate Compression Properties of Several Energetic Material Composites as a Function of Strain Rate and Temperature, *11th Detonation Symposium*, (Snow Mass, CO), J. Short, Ed., Amperstand Publishing, 2000
16. J.E. Field, S.M. Walley, N.K. Bourne, and J.M. Huntley, Review of Experimental Techniques for High Rate Deformation Studies, *Proc. Acoustics and Vibration Asia '98*, 1998 (Singapore), p 9–38
17. G. Gary, J.R. Klepaczko, and H. Zhao, Generalization of Split Hopkinson Bar Technique to Use Viscoelastic Materials, *Int. J. Impact Eng.*, Vol 16, 1995, p 529–530
18. G. Gary, L. Rota, and H. Zhao, Testing Viscous Soft Materials at Medium and High Strain Rates, *Constitutive Relation in High/Very High Strain Rates*, K. Kawata and J. Shioiri, Ed., Springer-Verlag, Tokyo, 1996, p 25–32
21. L.L. Wang, K. Labibes, Z. Azari, and G. Pluvinage, On the Use of a Viscoelastic Bar in the Split Hopkinson Bar Technique, *Proc. Int. Symp. on Impact Eng.*, I. Maekawa, Ed., ISIE, Sendai, Japan, 1992, p 532–537
22. G. Gary, J.R. Klepaczko, and H. Zhao, Corrections for Wave Dispersion and Analysis of Small Strains with Split Hopkinson Bar, *Proc. Int. Symp. on Impact Eng.*, I. Maekawa, Ed., ISIE, Sendai, Japan, 1992, p 73–78
23. L. Wang, K. Labibes, Z. Azari, and G. Pluvinage, Generalization of Split Hopkinson Bar Technique to Use Viscoelastic Bars, *Int. J. Impact Eng.*, Vol 15, 1994, p 669–686
24. H. Zhao and G. Gary, A Three Dimensional Analytical Solution of the Longitudinal Wave Propagation in an Infinite Linear Viscoelastic Cylindrical Bar: Application to Experimental Techniques, *J. Mech. Phys. Solids*, Vol 43, 1995, p 1335–1348
25. L. Wang, K. Labibes, Z. Azari, and G. Pluvinage, Authors Reply to “Generalization of Split Hopkinson Bar Technique to Use Viscoelastic Bars,” *Int. J. Impact Eng.*, Vol 16, 1995, p 530–531
26. G. Gary and H. Zhao, Inverse Methods for the Dynamic Study of Nonlinear Materials with a Split Hopkinson Bar, *IUTAM Symposium on Nonlinear Waves in Solids*, J.L. Wegner and F.R. Norwood, Ed., American Society of Mechanical Engineers, 1995, p 185–189
27. O. Sawas, N.S. Brar, and A.C. Ramamurthy, High Strain Rate Characterization of Plastics Using Polymeric Split Hopkinson Bar, *Shock Compression of Condensed Matter—1995*, S.C. Schmidt and W.C. Tao, Ed., American Institute of Physics, Woodbury, NY, 1996, p 581–584

28. S. Rao, V.P.W. Shim, and S.E. Quah, Dynamic Mechanical Properties of Polyurethane Elastomers Using a Nonmetallic Hopkinson Bar, *J. Appl. Polym. Sci.*, Vol 66, 1997, p 619–631
29. H. Zhao, G. Gary, and J.R. Klepaczko, On the Use of a Viscoelastic Split Hopkinson Pressure Bar, *Int. J. Impact Eng.*, Vol 19, 1997, p 319–330
30. H. Zhao, Testing of Polymeric Foams at High and Medium Strain Rates, *Polym. Test.*, Vol 16, 1997, p 507–516
31. H. Zhao, A Study of Specimen Thickness Effects in the Impact Tests on Polymers by Numeric Simulations, *Polymer*, Vol 39, 1998, p 1103–1106
32. O. Sawas, N.S. Brar, and R.A. Brockman, High Strain Rate Characterization of Low-Density Low-Strength Materials, *Shock Compression of Condensed Matter—1997*, S.C. Schmidt, D.P. Dandekar, and J.W. Forbes, Ed., American Institute of Physics, Woodbury, NY, 1998, p 855–858
33. O. Sawas, N.S. Brar, and R.A. Brockman, Dynamic Characterization of Compliant Materials Using an All-Polymeric Split Hopkinson Bar, *Exp. Mech.*, Vol 38, 1998, p 204–210
34. P.S. Follansbee and C. Frantz, Wave Propagation in then SHPB, *J. Eng. Mater. Technol. (Trans. ASME)*, Vol 105, 1983, p 61–66
35. C. Bacon, An Experimental Method for Considering Dispersion and Attenuation in a Viscoelastic Hopkinson Bar, *Exp. Mech.*, Vol 38, 1998, p 242–249
36. C. Bacon, Separation of Waves Propagating in an Elastic or Viscoelastic Hopkinson Pressure Bar with Three-Dimensional Effects, *Int. J. Impact Eng.*, Vol 22, 1999, p 55–69
37. S.F. Wang and A.A. Ogale, Effects of Physical Aging on Dynamic Mechanical and Transient Properties of Polyetheretherketone, *Polym. Eng. Sci.*, Vol 29, 1989, p 1273–1278
38. W. Chen, B. Zhang, and M.J. Forrestal, A Split-Hopkinson Bar Technique for Low Impedance Materials, *Exp. Mech.*, Vol 39, 1999, p 1–5
39. G.T. Gray III, C.M. Cady, and W.R. Blumenthal, Influence of Temperature and Strain Rate on the Constitutive Behavior of Teflon and Nylon, *Plasticity 99: Constitutive and Damage Modeling of Inelastic Deformation and Phase Transformation*, A.S. Khan, Ed., Neat Press, Fulton, MD, 1998, p 955–958

Split-Hopkinson Pressure Bar Testing of Soft Materials

George T. (Rusty) Gray III and William R. Blumenthal, Los Alamos National Laboratory

Stress-State Equilibrium of Soft Materials

The stress-state equilibrium in a sample during testing in an SHPB can be checked by comparing the 1- and 2-wave (or 3-wave) stress-strain response of the sample as described in the article “Classic Split-Hopkinson Pressure Bar Testing” and illustrated in Fig. 2 (Ref 34, 40, 41, 42, and 43). Recent studies have documented that both inertia and wave propagation effects during testing of a compression SHPB sample can significantly affect the stress differences across the length of a specimen during loading (Ref 3, 15, 41, and 43). Experimental results have revealed that the slow longitudinal sound speeds typical of some polymeric materials make longitudinal stress equilibrium during SHPB testing difficult to achieve (Ref 13, 15, 18, and 44).

Assuming frictional effects on the stress state are insignificant, the validity of an SHPB test on polymeric materials can be evaluated by examining the incident and transmitted pressure-bar data for stress-state equilibrium in addition to assessing whether a constant strain-rate condition has been achieved during a test. When the stress state is uniform throughout an SHPB sample, the 2-wave stress oscillates equally above and below the 1-wave stress. In the 1-wave analysis, the sample stress is directly proportional to the bar strain measured from the transmitted bar. This waveform characteristically exhibits low oscillation amplitude because the deforming sample effectively damps much of the ringing inherent in the incident pulse as it propagates through the sample. This damping can be quite significant in low-sound-speed materials such as polymers.

The 1-wave stress analysis represents the conditions at the sample transmitted bar interface and is referred to as the sample “back stress.” In a 2-wave analysis, the sum of the synchronized incident and reflected bar waveforms is proportional to the sample “front stress” and represents the conditions at the incident bar sample interface. However, both the incident and reflected waveforms contain substantial inherent oscillations that give rise to large uncertainty in the stress level, especially near the yield point, compared with the stress calculated from the transmitted waveform. These harmonic oscillations are also subject to dispersion due to the wave-speed dependence of different frequencies propagating through the pressure bars. This causes asynchronization of the overlapped waveforms and, therefore, inaccuracy in the calculation of the front stress. Mathematical methods have been developed to correct the primary mode of wave dispersion, and this dispersion correction results in higher-accuracy calculations of the stress at low strains (Ref 34). Finally, a third stress-calculation variation that considers the complete set of three measured bar waveforms, the 3-wave analysis, is simply the average of the front and the back stress.

Figure 2 shows the 1-wave, 2-wave, and strain-rate data as a function of strain for an SHPB test conducted on an Estane-based polymer binder sample. In this illustration, the front and back stress data reductions exhibit substantially different responses up to moderate strain values, verifying that the sample did not attain a uniform stress state until after a strain of 0.06. Attempts to achieve higher strain rates ($>5000 \text{ s}^{-1}$) at $25 \text{ }^{\circ}\text{C}$ ($77 \text{ }^{\circ}\text{F}$) proved difficult to unsuccessful. For example, at a strain rate of 7000 s^{-1} , the 1- and 2-wave signals diverged for the entire test (invalidating the stress analysis as discussed previously). The data in Fig. 2 illustrate the difficulty in testing polymeric materials possessing low impedance independent of whether a conventional metallic SHPB or polymeric-pressure-bar SHPB setup is used. Achievement of stress-state equilibrium in the sample is dependent on both the viscoelastic nature of the sample material and on sample geometry, which is discussed subsequently.

Achievement of a constant strain rate in a polymer sample throughout an SHPB test serves as validation of the careful balance of striker-bar length, striker-bar velocity, and tip material and thickness. In addition, a constant strain rate is a further qualitative check of the attainment of stress equilibrium in the specimen.

References cited in this section

3. G.T. Gray III, W.R. Blumenthal, C.P. Trujillo, and R.W. Carpenter II, Influence of Temperature and Strain Rate on the Mechanical Behavior of Adiprene L-100, *J. Phys. (France) IV Colloq.*, C3 (EURODYMAT 97), Vol 7, 1997, p 523–528
13. S.M. Walley and J.E. Field, Strain Rate Sensitivity of Polymers in Compression from Low to High Strain Rates, *DYMAT J.*, Vol 1, 1994, p 211–228
15. G.T. Gray III, D.J. Idar, W.R. Blumenthal, C.M. Cady, and P.D. Peterson, High- and Low-Strain Rate Compression Properties of Several Energetic Material Composites as a Function of Strain Rate and Temperature, *11th Detonation Symposium*, (Snow Mass, CO), J. Short, Ed., Amperstand Publishing, 2000
18. G. Gary, L. Rota, and H. Zhao, Testing Viscous Soft Materials at Medium and High Strain Rates, *Constitutive Relation in High/Very High Strain Rates*, K. Kawata and J. Shioiri, Ed., Springer-Verlag, Tokyo, 1996, p 25–32
34. P.S. Follansbee and C. Frantz, Wave Propagation in then SHPB, *J. Eng. Mater. Technol. (Trans. ASME)*, Vol 105, 1983, p 61–66

40. P.S. Follansbee, High Strain Rate Deformation of FCC Metals and Alloys, *Metallurgical Applications of Shock Wave and High Strain Rate Phenomena*, L.E. Murr, K.P. Staudhammer, and M.A. Meyers, Ed., Marcel Dekker, 1986, p 451–480
41. X.J. Wu and D.A. Gorham, Stress Equilibrium in the Split Hopkinson Pressure Bar Test, *J. Phys. (France) IV Colloq.*, C3 (EURODYMAT 97), Vol 7, 1997, p 91–96
42. G.T. Gray III, W.R. Blumenthal, C.P. Trujillo, and R.W. Carpenter, Influence of Temperature and Strain Rate on the Mechanical Behavior of Adiprene L-100, *J. Phys. (France) IV Colloq.*, C3 (EURODYMAT 97), 1997, p 523–528
43. G.T. Gray III, High-Strain-Rate Testing of Materials: The Split-Hopkinson Pressure Bar, *Methods in Materials Research*, John Wiley Press, 2000
44. S.M. Walley, J.E. Field, and N.A. Safford, A Comparison of the High Strain Rate Behaviour in Compression of Polymers at 300K and 100K, *J. Phys. (France) IV Colloq.*, C3 (DYMAT 91), Vol 1, 1991, p 185–190

Split-Hopkinson Pressure Bar Testing of Soft Materials

George T. (Rusty) Gray III and William R. Blumenthal, Los Alamos National Laboratory

Sample-Size Effects

The sample thickness used in an SHPB test is constrained by the need to assure a uniform stress state for accurate and reproducible constitutive data (Ref 3, 4, 38, and 45). Given the documented influence of temperature on the elastic and plastic properties of ductile polymers, it is also important to evaluate sample geometry effects over a range of temperatures (Ref 3).

The pronounced difference in the initial 1-, 2-, and 3-wave signals for several polymers has demonstrated the importance of carefully assessing sample size to achieve a uniform uniaxial stress state in the sample (Ref 3, 15). Differences in the 1- and 2-wave stress levels for sample length/diameter (l/d) aspect ratio = 1 samples (6.35 mm, or 0.25 in., thick) of a polyurethane elastomer (Adiprene [Uniroyal Chemical Company Inc., Middlebury, CT] L100) (Ref 3), polyamide (nylon), or Teflon (E.I. DuPont de Nemours & Co., Inc., Wilmington, DE) (Ref 39) indicate a sluggish ringup to stress-state equilibrium and, therefore, a marginally valid Hopkinson bar test at strains <5%, even though a constant strain rate is indicated throughout the entire test. Similar to the early findings of Kolsky (Ref 1) and more recent studies of Diah and others (Ref 4, 45) and Chen and others (Ref 38), the high-rate stress-strain response of polymeric samples exhibits pronounced sample-size dependence. The 1-wave stress analysis for Adiprene L100 samples tested at ambient temperature were found to depend on sample thickness as shown in Fig. 3. While the maximum flow stress attained for each sample thickness was nominally the same for a strain of 10%, the details of the ringing up of the sample and the falloff in flow stress after the maximum stress level was reached is seen to be significantly different. The 1 to 1 aspect ratio sample exhibits the most dispersive oscillatory ringup, as well as the most rapid falloff in flow stress for the three sample thicknesses. The 3.2 mm (0.125 in.) thick sample ($l/d = 0.5$) exhibited a clear yield strength and the lowest ringing amplitude. Chen and others (Ref 38) similarly observed substantial wave attenuation in 6.34 mm (0.25 in.) thick RTV630 rubber samples compared with 1.54 mm (0.06 in.) thick samples, which exhibited significantly faster ringup during testing.

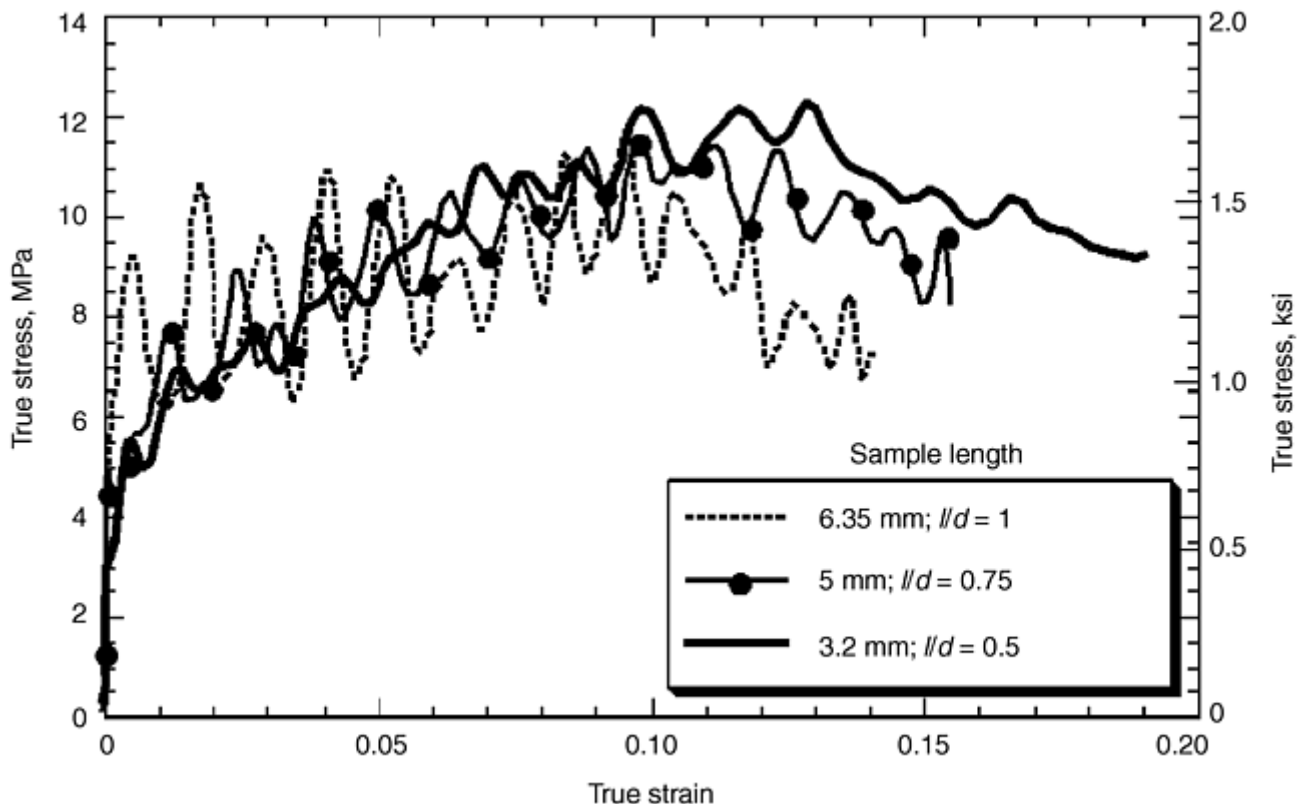


Fig. 3 Stress-strain response of 6.35 mm (0.25 in.) diam Adiprene L100 samples as a function of sample length at high strain rate (2500 s^{-1})

The ambient temperature data in Fig. 3 for Adiprene L100 illustrates the need to use lower sample aspect ratios when studying the entire high-strain-rate constitutive response of low-sound-speed dispersive materials such as polymers. The measurements on Adiprene L100 (Ref 3) and RTV630 rubber (Ref 38) suggest that, depending on the polymer and temperature range of testing, sample aspect ratios (l/d) of 0.5 or 0.25 can be effective in minimizing wave attenuation while also keeping frictional effects under control. Another interesting observation from Fig. 3 is the difference in the stress falloff as a function of sample thickness at strains over 10%. Taking into account that the lubrication conditions were the same for all samples, these results suggest that the dynamic stress relaxation of Adiprene L100 is also a function of sample size. The sample aspect ratio needed to achieve satisfactory uniaxial stress-state equilibrium also was found to be strongly dependent on the test temperature. While an $l/d = 0.5$ sample facilitated achieving equilibrium at $25 \text{ }^\circ\text{C}$ ($77 \text{ }^\circ\text{F}$) on Adiprene L100, samples with higher aspect ratios, such as $l/d = 1$, proved suitable at temperatures below approximately 240 K ($-28 \text{ }^\circ\text{F}$). These observations clearly demonstrate that achievement of stress equilibrium within polymeric samples is influenced by their initial elastic properties. Further experiments also are needed to quantify the stress-relaxation kinetics of viscoelastic materials as well as damage evolution processes in polymeric composites (Ref 43). A novel approach to studying these processes is to compare finite-element modeling (FEM) predictions for the bar outputs with actual bar outputs using proposed material models. This work is described in detail later.

References cited in this section

1. H. Kolsky, An Investigation of the Mechanical Properties of Materials at Very High Rates of Loading, *Proc. Phys. Soc. (London) B*, Vol 62, 1949, p 676–700
3. G.T. Gray III, W.R. Blumenthal, C.P. Trujillo, and R.W. Carpenter II, Influence of Temperature and Strain Rate on the Mechanical Behavior of Adiprene L-100, *J. Phys. (France) IV Colloq.*, C3 (EURODYMAT 97), Vol 7, 1997, p 523–528

4. N.N. Diah, A. Ivankovic, P.S. Leever, and J.G. Williams, The High Strain Rate Behaviour of Polymers, *J. Phys. (France) IV Colloq.*, C8 (DYMAT 94), Vol 4, 1994, p 119–124
15. G.T. Gray III, D.J. Idar, W.R. Blumenthal, C.M. Cady, and P.D. Peterson, High- and Low-Strain Rate Compression Properties of Several Energetic Material Composites as a Function of Strain Rate and Temperature, *11th Detonation Symposium*, (Snow Mass, CO), J. Short, Ed., Amperstand Publishing, 2000
38. W. Chen, B. Zhang, and M.J. Forrestal, A Split-Hopkinson Bar Technique for Low Impedance Materials, *Exp. Mech.*, Vol 39, 1999, p 1–5
39. G.T. Gray III, C.M. Cady, and W.R. Blumenthal, Influence of Temperature and Strain Rate on the Constitutive Behavior of Teflon and Nylon, *Plasticity 99: Constitutive and Damage Modeling of Inelastic Deformation and Phase Transformation*, A.S. Khan, Ed., Neat Press, Fulton, MD, 1998, p 955–958
43. G.T. Gray III, High-Strain-Rate Testing of Materials: The Split-Hopkinson Pressure Bar, *Methods in Materials Research*, John Wiley Press, 2000
45. N.N. Diah, P.S. Leever, and J.G. Williams, Thickness Effects in Split Hopkinson Pressure Bar Tests, *Polymer*, Vol 34, 1993, p 4230–4234

Split-Hopkinson Pressure Bar Testing of Soft Materials

George T. (Rusty) Gray III and William R. Blumenthal, Los Alamos National Laboratory

Split-Hopkinson Bar Testing as a Function of Temperature

While numerous studies have investigated the influence of strain rate on the constitutive response of a range of polymers, the influence of temperature at high strain rate on polymer mechanical behavior has been less extensively researched (Ref 14, 44). This lack of data is in contradiction to the fact that robust constitutive modeling descriptions of polymers used in structural applications must accurately describe polymer response as a function of service temperature. Polymer and polymer-composite responses for temperatures from -40 to +40 °C (-40 to 105 °F) are relevant for arctic to desert service environments. Testing at temperatures below 25 °C (77 °F) for a range of polymers has shown that both the measured “loading elastic” modulus and the measured peak flow stresses increase with decreasing temperature (Ref 14, 44). Based on these results, it is apparent that the construction of robust material models for polymeric constitutive behavior requires systematic knowledge of the independent effects of temperature and strain rate.

Constant temperature conditions between 200 and 350 K (-100 and 170 °F) on a split-Hopkinson bar have been achieved with the use of a specially designed gas manifold system developed at the Los Alamos National Laboratory. Here, samples can be cooled and heated using helium gas within a type 304 stainless steel containment chamber held at a partial vacuum, as shown in Fig. 4. Helium gas, due to its inertness and high thermal conductivity, was selected as the heat-transfer medium to heat/cool a range of materials including polymers, energetics, and propellant materials. The helium gas is cooled below ambient temperature by passing the helium through a copper coil positioned within a liquid nitrogen dewar, while elevated temperatures are achieved by heating the helium in a parallel coil within a glycerin-filled beaker warmed to approximately 450 K (350 °F) by a heating plate.

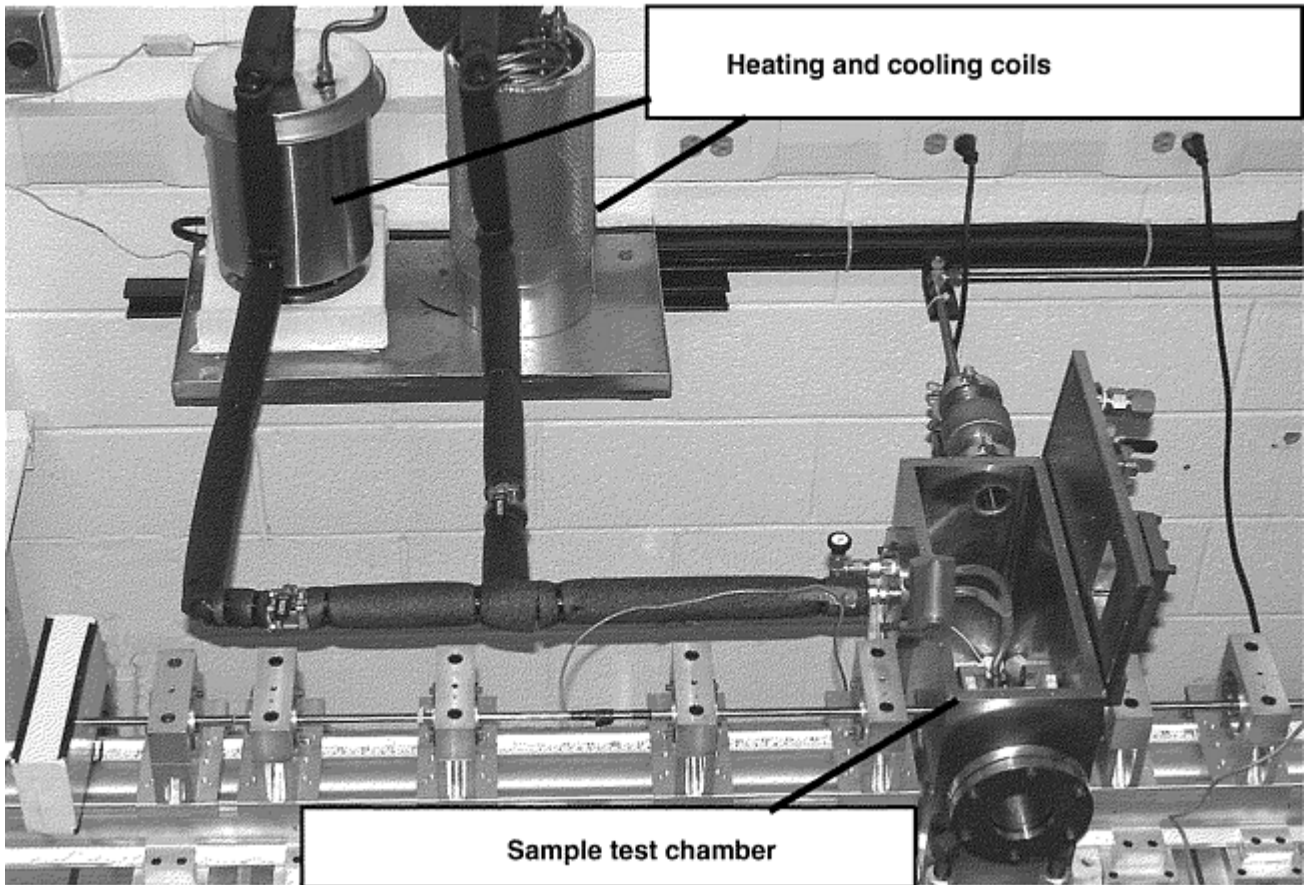


Fig. 4 Photograph of specialized split-Hopkinson pressure bar setup using either Ti-6Al-4V or magnesium pressure bars and a helium-gas manifold heating/cooling system to allow controlled temperature testing at high strain rates of polymers

Sample temperature in this heating/cooling scheme is monitored using a thermocouple positioned to lightly contact the outside of the sample. Regulating the helium gas flow rate to the manifold surrounding the sample allows fine temperature control. The heat transfer time required to heat or cool a 1 to 1 aspect ratio sample of Adiprene L-100 was determined using a thermocouple inserted into the middle of a dummy sample. A time duration of 5 min was determined to be necessary to equilibrate a polymer sample at temperature after attaining a stable helium gas temperature within the manifold surrounding the sample. A similar procedure is being used at Los Alamos National Laboratory for evaluating the temperature dependency of the high-strain-rate response of a range of engineering polymers and energetic materials (Ref 39, 43). An example of the type of data that can be measured for a polymer is shown in Fig. 5 for Teflon.

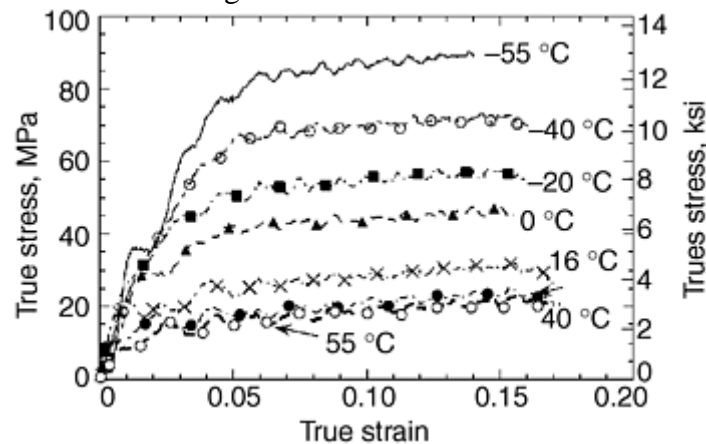


Fig. 5 Stress-strain response of Teflon at 2500 s^{-1} as a function of temperature

To yield the highest fidelity stress measurements while still testing below the yield strength of the pressure bars themselves using either Ti-6Al-4V or magnesium pressure bars and $l/d = 0.5$ aspect ratio samples, the high-strain-rate response of Teflon as a function of test temperature from -55 to $+55$ °C (-65 to 130 °F) was measured (Ref 39). The anelastic flow stress response (post-yield behavior) of Teflon is shown in Fig. 5 to exhibit nominally parallel stress-strain curves as a function of temperature. This nominally constant “hardening” behavior suggests that the deformation mechanisms controlling post-yield anelastic flow in Teflon is not substantially temperature dependent, while its yield strength varies with temperature for a fixed loading rate. Invariant strain hardening as a function of temperature is similar to the response of body-centered-cubic (bcc) metals where a Peierls stress dominates yielding behavior. This suggests that a thermally activated approach to modeling polymer constitutive behavior appears fruitful and demonstrates the importance of studying temperature effects on polymer constitutive behavior.

References cited in this section

14. S.N. Kukureka and I.M. Hutchings, Yielding of Engineering Polymers at Strain Rates of up to 500 s^{-1} , *Int. J. Mech. Sci.*, Vol 26, 1984, p 617–623
39. G.T. Gray III, C.M. Cady, and W.R. Blumenthal, Influence of Temperature and Strain Rate on the Constitutive Behavior of Teflon and Nylon, *Plasticity 99: Constitutive and Damage Modeling of Inelastic Deformation and Phase Transformation*, A.S. Khan, Ed., Neat Press, Fulton, MD, 1998, p 955–958
43. G.T. Gray III, High-Strain-Rate Testing of Materials: The Split-Hopkinson Pressure Bar, *Methods in Materials Research*, John Wiley Press, 2000
44. S.M. Walley, J.E. Field, and N.A. Safford, A Comparison of the High Strain Rate Behaviour in Compression of Polymers at 300K and 100K, *J. Phys. (France) IV Colloq.*, C3 (DYMAT 91), Vol 1, 1991, p 185–190

Split-Hopkinson Pressure Bar Testing of Soft Materials

George T. (Rusty) Gray III and William R. Blumenthal, Los Alamos National Laboratory

Test Sample Preparation

Due to the soft, viscoelastic nature of some polymers and polymeric composites at ambient temperatures, a special procedure has been adopted at Los Alamos National Laboratory and other facilities to machine SHPB specimens with parallel loading surfaces within a tolerance of 0.03 mm (0.001 in.). First, the rough-cut specimens are slowly cooled (<20 °C/min, or 36 °F/min) on a metal platen surrounded by liquid nitrogen. Then, during machining, the polymeric specimens are sprayed with cold nitrogen gas from the vaporization of liquid nitrogen to keep the sample in a hardened state well below the glass transition temperature. The increased stiffness of the cooled samples significantly increases the ease of single-point turning of samples. Similarly, the specimens must be slowly warmed back to ambient conditions to minimize thermal shock, residual stresses, and specimen distortion.

Finite-Element Modeling (FEM) of the Split-Hopkinson Bar

In recent years, a number of new innovations have been demonstrated for the SHPB, and their value has been demonstrated in improving both the accuracy and timeliness of high-rate testing measurements. One-, two-, and three-dimensional FEMs of the SHPB have proved their ability to simulate test parameters and allow pretest setup validation checks as an aid to planning. Finite-element models, therefore, offer a means to validate the data and dispersion analysis used in the Hopkinson bar to probe for the effects of inertia and friction and to provide an opportunity to extend the use of the Hopkinson bar. An example is the characterization of polymeric materials for which a uniaxial stress state cannot be achieved. Previous research using this approach on soil samples has shown the utility of a combined FEM/SHPB analysis (Ref 46).

Systematic FEM modeling of the SHPB with concurrent experimental SHPB measurements is a means to extend the use of the SHPB technique beyond that of a conventional measurement apparatus (Ref 47). It can afford the characterization of materials for which the SHPB technique was previously invalid using classic one-dimensional data analysis, serving as a validation tool for complex sample geometries, and facilitating data analysis and constitutive model development for sample materials exhibiting nonuniform and/or nonconservative behaviors such as compaction, shear band formation, and fracture.

In the first instance, a coupled experimental and FEM approach can facilitate the high rate characterization of materials for which the attainment of a stable uniaxial stress state during testing is problematic or impossible, such as polymer foams. In the second case, FEM can provide a valuable tool to verify and validate sample geometry design where equilibrium considerations are paramount, such as tensile SHPB specimens. Unlike the compressive Hopkinson bar where right-regular sample shapes are most often used, tensile Hopkinson bar testing uses complex sample geometries. During tensile Hopkinson bar testing, the signals measured in the pressure bars record the structural response of the entire tensile sample, not just the gage section, where plastic deformation is assumed to be occurring. Because the split-Hopkinson bar data analysis only provides data on the relative displacement between the ends of the incident and transmitter bars, an effective gage length generally must be used. Finite-element modeling coupled with high-speed photographic characterization of the sample gage section as a function of time also may provide a technique to extract quantitative stress-strain constitutive data from a tensile SHPB test, even in the presence of unavoidable strain gradients in the sample. The time-resolved local measurement of strain in the sample gage length is also important to validate modeling of the constitutive response of the sample material.

In the final instance, FEM can be used to examine the validity of constitutive and damage evolution models for sample materials for which conventional Hopkinson-bar analysis is limited. Examples include the high-rate deformation response of materials such as metallic and polymeric foams and honeycomb structures where nonuniform compaction occurs, materials that undergo nonuniform plasticity such as shear banding and kinking, and materials that undergo damage or fracture processes that invalidate the tacit SHPB data analysis assumption of homogeneous deformation in the calculation of sample stress. Local strain quantification using high-speed photographic techniques coupled with FEM modeling of “crush-up” densification could use SHPB test data to validate the accuracy of the densification modeling scheme for a metallic foam. In this approach, the stress-time histories for the incident and transmitted pressure bars are used as a validation check against FEM simulations of the metallic foam response for a range of applied strain rates, sample geometries, and temperatures.

The SHPB configuration can be modeled using a Lagrangian mesh as shown in Fig. 6 (Ref 47). In this example, solid cylindrical lengths of steel, titanium, aluminum, or magnesium alloy can represent the striker, incident, and transmitted bars. An axis of symmetry can be presumed about the longitudinal (length) axis of the pressure bars, and as such, modeling of the pressure bars is performed assuming two-dimensional axisymmetry and linear elasticity. The specimen, however, must be modeled using a three-dimensional Lagrangian mesh such that nonuniform deformation processes within the sample, such as compaction in the case of foams, shear banding, kinking, and so on, are to be physically described. Elemental and nodal quantities in the finite-element

model are then recorded at various positions along the longitudinal (length) axis of the SHPB model. Figure 6 presents an FEM simulation snapshot plotting sample strain rate for an SHPB test of a Teflon sample using Ti-6Al-4V pressure bars. The graphical data in Fig. 6 illustrate the nonuniformity in strain rate in a polymeric sample during the initial stages of ringup prior to the achievement of a uniform uniaxial stress state in the sample or a nominally constant strain rate of loading (Ref 47).

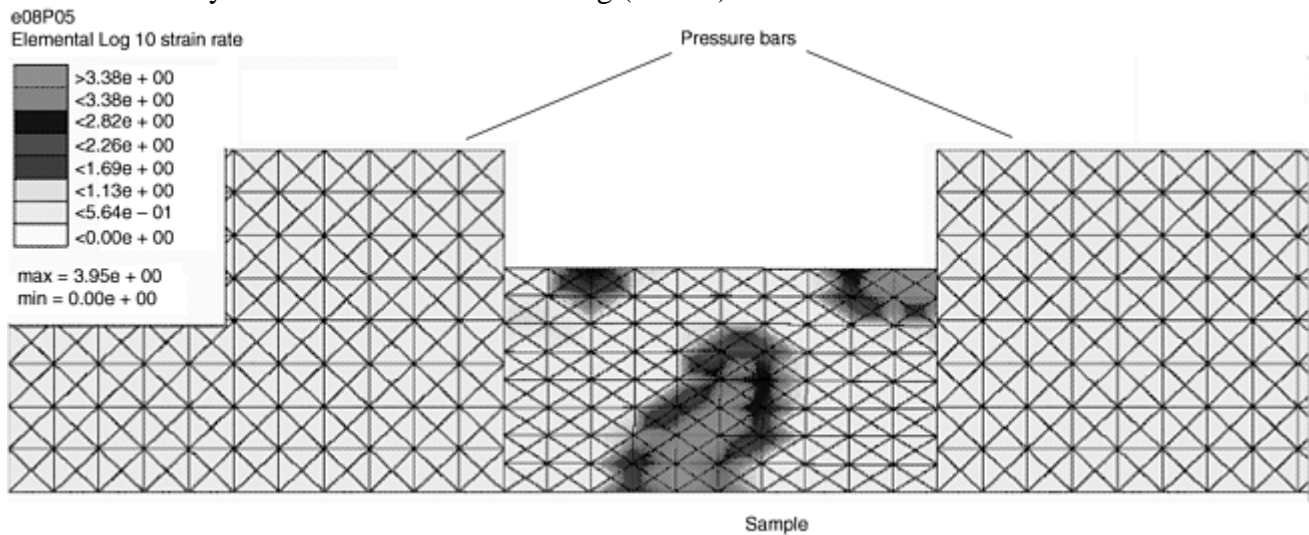


Fig. 6 Finite-element simulation of a Teflon. $l/d = 1$ sample in a split-Hopkinson pressure bar test. The early stages of the ringup of the Teflon sample toward achieving a uniform uniaxial stress state is reflected by the nonuniform strain rate as a function of position within the sample. Source: Ref 47

References cited in this section

46. C.W. Felice, E.S. Gaffney, and J.A. Brown, Extended Split-Hopkinson Bar Analysis for Attenuating Materials, *J. Eng. Mech.*, Vol 117, 1991, p 1119–1135
47. D.M. Goto, R.K. Garrett Jr., and G.T. Gray III, Finite Element Modeling of the Split-Hopkinson Pressure Bar: Stress State Stability, *Exp. Mech.*, in preparation

Split-Hopkinson Pressure Bar Testing of Soft Materials

George T. (Rusty) Gray III and William R. Blumenthal, Los Alamos National Laboratory

Summary

The Hopkinson pressure bar, as a research and engineering tool for the quantitative measurement of the high-rate stress-strain behavior of soft materials, has undergone significant evolution in the past 5 years. Higher-resolution measurements of the constitutive responses of viscoelastic solids under ambient conditions have been developed using both polymeric and magnesium pressure bars compared with measurements with high-strength steel bars. Due to their time- and temperature-dependent dispersive and dissipative nature, viscoelastic solids pose unique challenges during Hopkinson bar testing. The most daunting of these challenges is the attainment of stress-state equilibrium. Careful selection of sample geometry and the use of 1- and 2-wave stress-wave analyses are crucial to verifying the attainment of a uniaxial stress state during Hopkinson bar testing. Finite-element modeling of SHPB measurements coupled with experimental SHPB measurements offers great promise as a means to extend the use of the SHPB technique beyond that of solely a measurement method. Finite-element modeling of the SHPB can support the quantification of the constitutive behavior of materials, which were previously invalid using only classic one-dimensional SHPB stress-wave analysis. These

simulations can serve as a validation and verification tool for complex sample geometries and facilitate data analysis and constitutive model development for materials exhibiting nonuniform and/or nonconservative behaviors such as compaction (foams), shear band formation, and fracture.

Split-Hopkinson Pressure Bar Testing of Soft Materials

George T. (Rusty) Gray III and William R. Blumenthal, Los Alamos National Laboratory

Acknowledgments

This work was supported under the auspices of the United States Department of Energy. The authors wish to acknowledge the assistance of M.F. Lopez for conducting the quasi-static mechanical testing and B. Jacquez, C.P. Trujillo, and T. Bell for conducting the dynamic mechanical testing. The authors wish to acknowledge T.A. Mason for critically reviewing this manuscript.

Split-Hopkinson Pressure Bar Testing of Soft Materials

George T. (Rusty) Gray III and William R. Blumenthal, Los Alamos National Laboratory

References

1. H. Kolsky, An Investigation of the Mechanical Properties of Materials at Very High Rates of Loading, *Proc. Phys. Soc. (London) B*, Vol 62, 1949, p 676–700
2. S.H. Ahmad, Flow Stress of High Density Polyethylene and Nylon 66 at High Rates of Strain, *Polym. Int.*, Vol 28, 1992, p 291–294
3. G.T. Gray III, W.R. Blumenthal, C.P. Trujillo, and R.W. Carpenter II, Influence of Temperature and Strain Rate on the Mechanical Behavior of Adiprene L-100, *J. Phys. (France) IV Colloq.*, C3 (EURODYMAT 97), Vol 7, 1997, p 523–528
4. N.N. Dioh, A. Ivankovic, P.S. Leever, and J.G. Williams, The High Strain Rate Behaviour of Polymers, *J. Phys. (France) IV Colloq.*, C8 (DYMAT 94), Vol 4, 1994, p 119–124
5. A. Trojanowski, C. Ruiz, and J. Harding, Thermomechanical Properties of Polymers at High Rates of Strain, *J. Phys. (France) IV Colloq.*, C3 (EURODYMAT 97), Vol 7, 1997, p 447–452
6. A.M. Bragov and A.K. Lomunov, Mechanical Properties of Some Polymers and Composites at Strain Rate of 1000/s, *J. Phys. (France) IV Colloq.*, C8 (DYMAT 94), Vol 4, 1994, p 337–342
7. S.M. Walley, D. Xing, and J.E. Field, Mechanical Properties of Three Transparent Polymers in Compression at a Very High Rate of Strain, *Impact and Dynamic Fracture of Polymers and Composites*, J.G. Williams and A. Pavan, Ed., Mechanical Engineering Publications Ltd., 1995, p 289–303
8. S.M. Walley, J.E. Field, G.M. Swallowe, and S.N. Mentha, The Response of Various Polymers to Uniaxial Compressive Loading at Very High Rates of Strain, *J. Phys. (France) Colloq.*, C5 (DYMAT 85), Vol 46, 1985, p 607–616

9. S.M. Walley, J.E. Field, P.H. Pope, and N.A. Safford, The Rapid Deformation Behaviour of Various Polymers, *J. Phys. (France) III*, Vol 1, 1991, p 1889–1925
10. S.M. Walley, J.E. Field, and N.A. Safford, A Comparison of the High Strain Rate Behaviour in Compression of Polymers at 300K and 100K, *Proc. 8th Int. Conf. on Deformation, Yield, and Fracture of Polymers*, edited by p. paper 16, Plastics and Rubber Institute, London, 1991
11. S. Hamdan and G.M. Swallowe, The Strain-Rate and Temperature Dependence of the Mechanical Properties of Polyetherketone and Polyetheretherketone, *J. Mater. Sci.*, Vol 31, 1996, p 1415–1423
12. S.M. Walley, J.E. Field, P.H. Pope, and N.A. Safford, A Study of the Rapid Deformation Behaviour of a Range of Polymers, *Philos. Trans. R. Soc. (London) A*, Vol 328, 1989, p 1–33
13. S.M. Walley and J.E. Field, Strain Rate Sensitivity of Polymers in Compression from Low to High Strain Rates, *DYMAT J.*, Vol 1, 1994, p 211–228
14. S.N. Kukureka and I.M. Hutchings, Yielding of Engineering Polymers at Strain Rates of up to 500 s^{-1} , *Int. J. Mech. Sci.*, Vol 26, 1984, p 617–623
15. G.T. Gray III, D.J. Idar, W.R. Blumenthal, C.M. Cady, and P.D. Peterson, High- and Low-Strain Rate Compression Properties of Several Energetic Material Composites as a Function of Strain Rate and Temperature, *11th Detonation Symposium*, (Snow Mass, CO), J. Short, Ed., Amperstand Publishing, 2000
16. J.E. Field, S.M. Walley, N.K. Bourne, and J.M. Huntley, Review of Experimental Techniques for High Rate Deformation Studies, *Proc. Acoustics and Vibration Asia '98*, 1998 (Singapore), p 9–38
17. G. Gary, J.R. Klepaczko, and H. Zhao, Generalization of Split Hopkinson Bar Technique to Use Viscoelastic Materials, *Int. J. Impact Eng.*, Vol 16, 1995, p 529–530
18. G. Gary, L. Rota, and H. Zhao, Testing Viscous Soft Materials at Medium and High Strain Rates, *Constitutive Relation in High/Very High Strain Rates*, K. Kawata and J. Shioiri, Ed., Springer-Verlag, Tokyo, 1996, p 25–32
19. H. Zhao and G. Gary, On the Use of SHPB Techniques to Determine the Dynamic Behavior of Materials in the Range of Small Strains, *Int. J. Solids Struct.*, Vol 33, 1996, p 3363–3375
20. H. Kolsky, The Propagation of Stress Pulses in Viscoelastic Solids, *Philos. Mag.*, 8th series, Vol 1, 1956, p 693–710
21. L.L. Wang, K. Labibes, Z. Azari, and G. Pluvinage, On the Use of a Viscoelastic Bar in the Split Hopkinson Bar Technique, *Proc. Int. Symp. on Impact Eng.*, I. Maekawa, Ed., ISIE, Sendai, Japan, 1992, p 532–537
22. G. Gary, J.R. Klepaczko, and H. Zhao, Corrections for Wave Dispersion and Analysis of Small Strains with Split Hopkinson Bar, *Proc. Int. Symp. on Impact Eng.*, I. Maekawa, Ed., ISIE, Sendai, Japan, 1992, p 73–78
23. L. Wang, K. Labibes, Z. Azari, and G. Pluvinage, Generalization of Split Hopkinson Bar Technique to Use Viscoelastic Bars, *Int. J. Impact Eng.*, Vol 15, 1994, p 669–686
24. H. Zhao and G. Gary, A Three Dimensional Analytical Solution of the Longitudinal Wave Propagation in an Infinite Linear Viscoelastic Cylindrical Bar: Application to Experimental Techniques, *J. Mech. Phys. Solids*, Vol 43, 1995, p 1335–1348

25. L. Wang, K. Labibes, Z. Azari, and G. Pluinage, Authors Reply to “Generalization of Split Hopkinson Bar Technique to Use Viscoelastic Bars,” *Int. J. Impact Eng.*, Vol 16, 1995, p 530–531
26. G. Gary and H. Zhao, Inverse Methods for the Dynamic Study of Nonlinear Materials with a Split Hopkinson Bar, *IUTAM Symposium on Nonlinear Waves in Solids*, J.L. Wegner and F.R. Norwood, Ed., American Society of Mechanical Engineers, 1995, p 185–189
27. O. Sawas, N.S. Brar, and A.C. Ramamurthy, High Strain Rate Characterization of Plastics Using Polymeric Split Hopkinson Bar, *Shock Compression of Condensed Matter—1995*, S.C. Schmidt and W.C. Tao, Ed., American Institute of Physics, Woodbury, NY, 1996, p 581–584
28. S. Rao, V.P.W. Shim, and S.E. Quah, Dynamic Mechanical Properties of Polyurethane Elastomers Using a Nonmetallic Hopkinson Bar, *J. Appl. Polym. Sci.*, Vol 66, 1997, p 619–631
29. H. Zhao, G. Gary, and J.R. Klepaczko, On the Use of a Viscoelastic Split Hopkinson Pressure Bar, *Int. J. Impact Eng.*, Vol 19, 1997, p 319–330
30. H. Zhao, Testing of Polymeric Foams at High and Medium Strain Rates, *Polym. Test.*, Vol 16, 1997, p 507–516
31. H. Zhao, A Study of Specimen Thickness Effects in the Impact Tests on Polymers by Numeric Simulations, *Polymer*, Vol 39, 1998, p 1103–1106
32. O. Sawas, N.S. Brar, and R.A. Brockman, High Strain Rate Characterization of Low-Density Low-Strength Materials, *Shock Compression of Condensed Matter—1997*, S.C. Schmidt, D.P. Dandekar, and J.W. Forbes, Ed., American Institute of Physics, Woodbury, NY, 1998, p 855–858
33. O. Sawas, N.S. Brar, and R.A. Brockman, Dynamic Characterization of Compliant Materials Using an All-Polymeric Split Hopkinson Bar, *Exp. Mech.*, Vol 38, 1998, p 204–210
34. P.S. Follansbee and C. Frantz, Wave Propagation in then SHPB, *J. Eng. Mater. Technol. (Trans. ASME)*, Vol 105, 1983, p 61–66
35. C. Bacon, An Experimental Method for Considering Dispersion and Attenuation in a Viscoelastic Hopkinson Bar, *Exp. Mech.*, Vol 38, 1998, p 242–249
36. C. Bacon, Separation of Waves Propagating in an Elastic or Viscoelastic Hopkinson Pressure Bar with Three-Dimensional Effects, *Int. J. Impact Eng.*, Vol 22, 1999, p 55–69
37. S.F. Wang and A.A. Ogale, Effects of Physical Aging on Dynamic Mechanical and Transient Properties of Polyetheretherketone, *Polym. Eng. Sci.*, Vol 29, 1989, p 1273–1278
38. W. Chen, B. Zhang, and M.J. Forrestal, A Split-Hopkinson Bar Technique for Low Impedance Materials, *Exp. Mech.*, Vol 39, 1999, p 1–5
39. G.T. Gray III, C.M. Cady, and W.R. Blumenthal, Influence of Temperature and Strain Rate on the Constitutive Behavior of Teflon and Nylon, *Plasticity 99: Constitutive and Damage Modeling of Inelastic Deformation and Phase Transformation*, A.S. Khan, Ed., Neat Press, Fulton, MD, 1998, p 955–958
40. P.S. Follansbee, High Strain Rate Deformation of FCC Metals and Alloys, *Metallurgical Applications of Shock Wave and High Strain Rate Phenomena*, L.E. Murr, K.P. Staudhammer, and M.A. Meyers, Ed., Marcel Dekker, 1986, p 451–480

41. X.J. Wu and D.A. Gorham, Stress Equilibrium in the Split Hopkinson Pressure Bar Test, *J. Phys. (France) IV Colloq.*, C3 (EURODYMAT 97), Vol 7, 1997, p 91–96
42. G.T. Gray III, W.R. Blumenthal, C.P. Trujillo, and R.W. Carpenter, Influence of Temperature and Strain Rate on the Mechanical Behavior of Adiprene L-100, *J. Phys. (France) IV Colloq.*, C3 (EURODYMAT 97), 1997, p 523–528
43. G.T. Gray III, High-Strain-Rate Testing of Materials: The Split-Hopkinson Pressure Bar, *Methods in Materials Research*, John Wiley Press, 2000
44. S.M. Walley, J.E. Field, and N.A. Safford, A Comparison of the High Strain Rate Behaviour in Compression of Polymers at 300K and 100K, *J. Phys. (France) IV Colloq.*, C3 (DYMAT 91), Vol 1, 1991, p 185–190
45. N.N. Diah, P.S. Leever, and J.G. Williams, Thickness Effects in Split Hopkinson Pressure Bar Tests, *Polymer*, Vol 34, 1993, p 4230–4234
46. C.W. Felice, E.S. Gaffney, and J.A. Brown, Extended Split-Hopkinson Bar Analysis for Attenuating Materials, *J. Eng. Mech.*, Vol 117, 1991, p 1119–1135
47. D.M. Goto, R.K. Garrett Jr., and G.T. Gray III, Finite Element Modeling of the Split-Hopkinson Pressure Bar: Stress State Stability, *Exp. Mech.*, in preparation

Split-Hopkinson Pressure Bar Testing of Ceramics

G. Subhash, Michigan Technological University G. Ravichandran, California Institute of Technology

Introduction

SPLIT-HOPKINSON PRESSURE BAR (SHPB) TESTING, described elsewhere in this Section, was originally developed by Kolsky (Ref 1) and has been traditionally used for determining the plastic properties of metals (which are softer than the pressure bar material) at high strain rates in the range of 10^2 to 10^4 s⁻¹. Ceramics, on the other hand, are hard and brittle and typically exhibit higher compressive strength than metals. Because most of the ceramics reveal only elastic strains to failure, accurate measurement of these strains using the traditional SHPB technique is often not a trivial task.

In this article, the inherent limitations of the traditional SHPB technique for testing ceramics and the modifications necessary in design and test procedures are discussed. Before describing the test method for ceramics, a brief discussion of the operational principle of the traditional SHPB technique and the relevant assumptions in the derivation of the stress-strain relationship are presented. This is followed by discussion of the inherent limitations on the validity of these assumptions while testing ceramics and the necessary modifications in SHPB design and test procedure for high-strength brittle ceramics. Other topics covered in this article include maximum strain rate that can be obtained in ceramics using an SHPB, the necessity of incident pulse shaping, specimen design considerations, interpretation of experimental results obtained from SHPB testing of ceramics, and the effectiveness of the proposed modifications.

Reference cited in this section

1. H. Kolsky, An Investigation of the Mechanical Properties of Materials at Very High Rates of Loading, *Proc. R. Soc. (London) B*, Vol 62, 1949, p 676–700

Review of Traditional Split-Hopkinson Pressure Bar Operational Principles

A traditional SHPB configuration (Fig. 1) consists of a striker bar, an incident bar (AB), and a transmission bar (CD). A specimen of suitable dimensions is sandwiched between the incident and transmission bars. The striker bar is launched from a gas gun at a predetermined velocity towards the incident bar. Upon impact at A , a compressive pulse is generated in the incident bar and travels towards the specimen. The duration of the pulse is equal to the round trip travel time of the longitudinal wave in the striker bar. Upon reaching the specimen, a portion of the incident pulse is transmitted into the transmission bar as a compression pulse, and the remaining portion is reflected back into the incident bar traveling toward the impact end, A . Strain gages are mounted at midpoints along the length of the incident and transmission bars to capture the stress pulses as they pass by. In general, the specimen is chosen to have a lower impedance (product of density, wave velocity, and area of cross section) than the bar material, and, hence, the reflected pulse is rendered tensile in nature. Based on one-dimensional analysis, it can be shown that the equations for stress, strain, and strain rate in the specimen are given by (Ref 1, 2):

$$\sigma_s(t) = \frac{A_o E_o}{A_s} \varepsilon_T(t) \quad (\text{Eq 1})$$

$$\dot{\varepsilon}_s = -\frac{2c_o}{l_s} \varepsilon_R(t) \quad (\text{Eq 2})$$

$$\varepsilon_s(t) = \int_0^t \dot{\varepsilon}_s(t) dt \quad (\text{Eq 3})$$

where A is cross-sectional area, E is Young's modulus, l is length, σ is stress, ε is strain, $\dot{\varepsilon}$ is strain rate, and t is time. The subscripts o , s , T , and R correspond to the bar, specimen, transmitted pulse, and reflected pulse, respectively; and c_o is the longitudinal bar wave velocity, which is given by $\sqrt{E_o/\rho_o}$, where ρ_o is density. In deriving Eq 1 2 3, the following assumptions are made:

1. The specimen is under a uniform and uniaxial state of stress during deformation.
2. The incident and transmission bars remain elastic at all times during the experiment, and the end surfaces of the bars in contact with the specimen remain flat and parallel during the deformation of the specimen.
3. The incident, transmitted, and reflected pulses undergo minimal dispersion as they travel along the length of the bar.
4. The stress distribution across the cross section of the incident and transmission bars is fairly uniform (meaning that the measured strains on the surface of the bar using strain gages are representative of the stress in the elastic bars).
5. The accumulated strain in the specimen (determined from the reflected strain gage signal in Eq 3) is solely due to a single incident compression pulse reaching the specimen; in other words, the specimen is subjected to only a single incident stress pulse to cause the observed deformation.

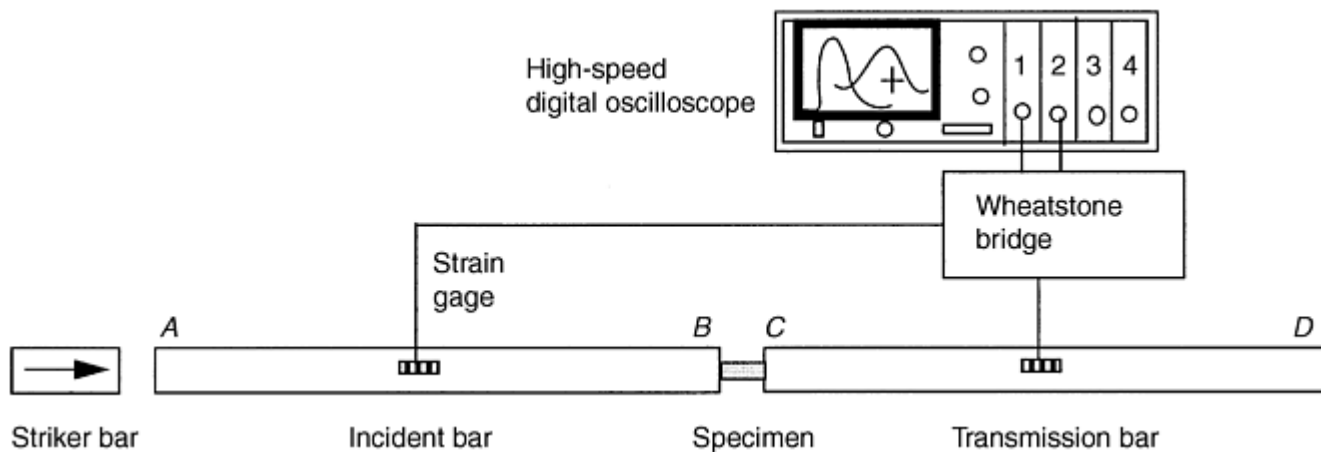


Fig. 1 Schematic of the traditional split-Hopkinson pressure bar test configuration. AB, incident bar; CD, transmission bar; A, impact location

These assumptions (except the fifth one) are easily satisfied while testing metals where plastic deformation is desired. Ceramics, on the other hand, are hard, have high strength, and exhibit no more than 1 to 2% strains before fracture. Therefore, several of the above assumptions are violated while testing ceramics using the traditional SHPB procedure, and, thus, caution must be exercised while interpreting the experimental data. Proper modifications must also be made in the testing procedure to ensure the accuracy and reliability of the stress and strain measurements. Each of the five assumptions (and related issues in SHPB testing of ceramics) is discussed in the following section.

References cited in this section

1. H. Kolsky, An Investigation of the Mechanical Properties of Materials at Very High Rates of Loading, *Proc. R. Soc. (London) B*, Vol 62, 1949, p 676–700
2. H. Kolsky, *Stress Waves in Solids*, Dover, 1963, p 41–94

Split-Hopkinson Pressure Bar Testing of Ceramics

G. Subhash, Michigan Technological University G. Ravichandran, California Institute of Technology

Limitations of Testing Ceramics by Traditional Split-Hopkinson Pressure Bar Techniques

The first assumption (that the specimen is under a uniform and uniaxial state of stress) ensures that the stress within the specimen is in equilibrium before the required data (e.g., failure strength) about the ceramic behavior is extracted from the strain-gage signals. Stress equilibrium in the entire specimen is ensured by choosing the duration of the incident loading pulse to be sufficiently longer than the travel time of the longitudinal wave within the specimen. This allows for sufficient wave reflections to occur within the specimen, after which a state of uniaxial and uniform stress is expected to prevail. While testing metals where plastic properties are of interest, the specimen undergoes elastic deformation during the initial few reflections of the incident wave within the specimen, during which a nonuniform state of stress prevails. Therefore, the elastic deformation obtained for metals using a SHPB test is often neglected, and only plastic strains are plotted.

In the case of ceramics (where only elastic strains form a significant portion of the overall response), specimen failure can occur before sufficient reflections occur or before stress equilibrium within the specimen has been established. Thus, the failure strength data obtained under these conditions does not represent the true uniaxial compressive strength of a ceramic. Ravichandran and Subhash (Ref 3) demonstrated that if the impedance

mismatch between a ceramic specimen and the steel bars is taken into account, it is possible to derive the magnitude of the stress difference between the two end surfaces of the specimen at any given instant while the specimen is being loaded by an incident pulse in SHPB testing. Figure 2 illustrates the result of their analysis. On the y -axis is the normalized parameter $R(t)$ defined as the ratio of stress difference, $\Delta\sigma(t)$, between the two end surfaces of the specimen, B and C , at a given instant to the mean stress, $\sigma_m(t)$, in the specimen at that instant, that is:

$$R(t) = \left| \frac{\Delta\sigma(t)}{\sigma_m(t)} \right| \quad (\text{Eq 4})$$

On the x -axis is the normalized time, where t_s is the time required for one single transit of the longitudinal wave within the specimen, that is, $t_s = l_s/c_s$. The results are plotted as a function of impedance mismatch parameter, r , between the specimen and the steel bars, which is defined as:

$$r = \frac{\rho_o c_o A_o}{\rho_s c_s A_s} \quad (\text{Eq 5})$$

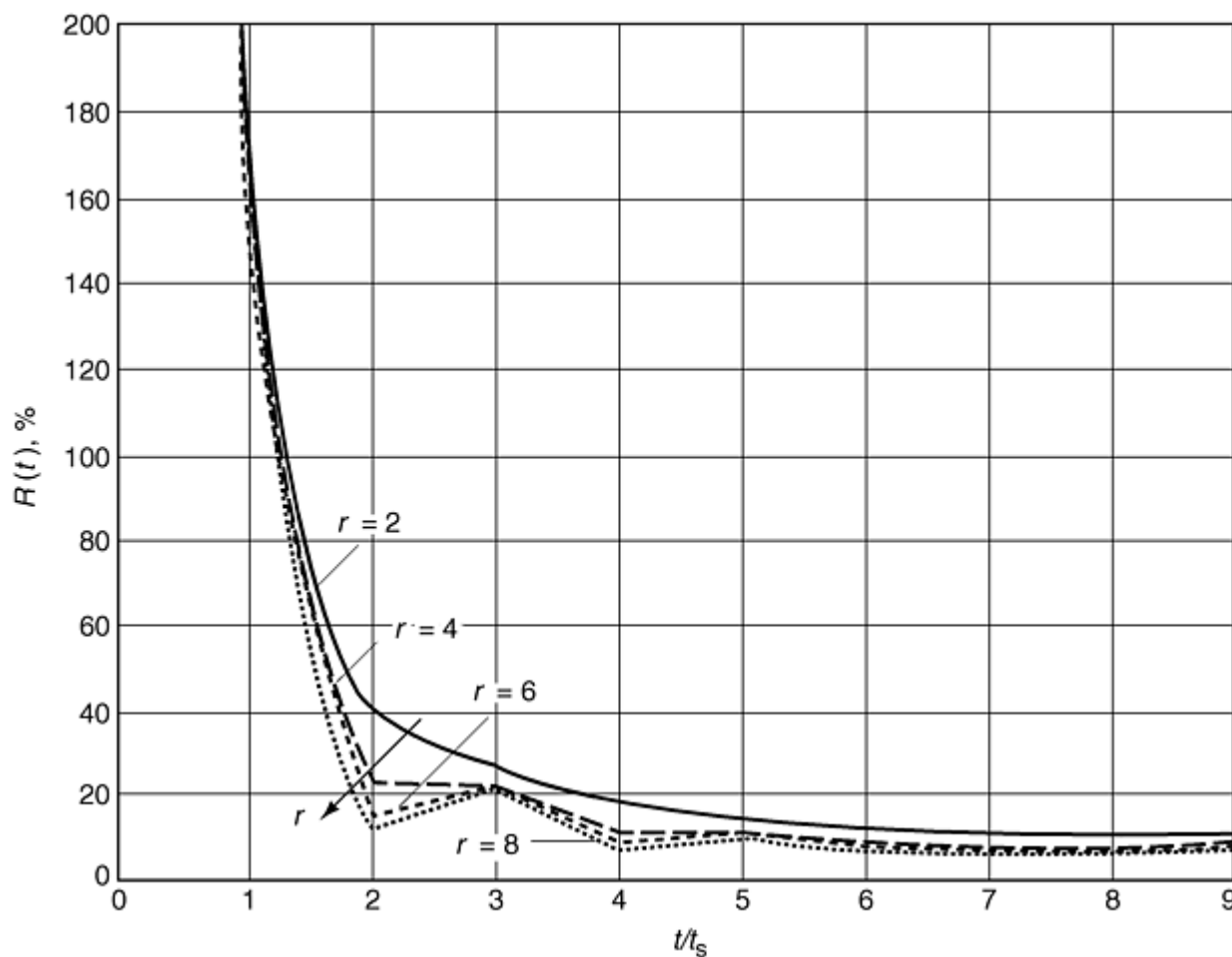


Fig. 2 A plot of normalized stress difference between the two ends of a ceramic specimen versus number of wave reflections within the specimen. See discussion in text. Source: Ref 3

The plot shown in Figure 2 indicates that several reflections are needed before complete stress equilibrium is achieved within a ceramic specimen. For practical purposes, a stress difference of 5% between the two end surfaces of the specimen with respect to the mean stress is assumed reasonable. It takes at least four transit times to reach this value, and, therefore, for the fracture strength data to be valid, the failure of the ceramic specimen should occur at least after this time has elapsed during loading of the incident pulse. These results were also confirmed by Chen et al. (Ref 4) using finite element simulations. A typical incident stress pulse containing equal loading and unloading portions should, therefore, have a total duration, T , of at least eight transit times (assuming failure occurs only during the loading phase) of the longitudinal wave within a ceramic specimen, that is:

$$T = 8t_s = \frac{8l_s}{c_s} \quad (\text{Eq 6})$$

The maximum length, l_s , of a ceramic specimen for a given incident pulse duration is now limited to:

$$l_s = \frac{Tc_s}{8} \quad (\text{Eq 7})$$

The equation clearly reflects the fact that the time required for stress equilibration increases with specimen length.

The second assumption (that the incident and transmission bars remain elastic at all times during the experiment, and the end surfaces of the bars in contact with the specimen remain flat and parallel during deformation of the specimen) is usually met by making the incident and transmission bars out of a high-strength material, for example, maraging steel. Notice that the equation for the stress (Eq 1) in the specimen contains the area of the bar in the numerator and the area of the specimen in the denominator. Therefore, by making the specimen diameter smaller (or the bar diameter bigger) one can impose a sufficiently high stress level to cause fracture in a high-strength ceramic specimen while keeping the stress level in the incident and transmission bars within the elastic limit of the bar material. Because ceramics are harder than steel, however, they can indent into the steel bars, as illustrated in Fig. 3(a), thus violating the later part of the second assumption (i.e., the end surfaces of the bars in contact with the specimen remain flat and parallel during the deformation). The indentation into the steel bars can also cause stress concentration along the circumference of the specimen end faces and lead to a nonuniform (or nonhomogeneous deformation) and nonuniaxial stress state within the specimen, thus also violating the first assumption. The stress concentration can lead to premature failure (e.g., chipping) of the ceramic by initiating microcracking at these locations. This problem can be reduced by sandwiching the ceramic specimen between two identical high-strength tungsten-carbide (WC) inserts and placing this whole assembly in the SHPB testing setup, as shown schematically in Fig. 3(b). The main requirement in this approach is that the tungsten-carbide inserts should not alter the incident, reflected, and transmitted stress-wave characteristics as the wave crosses the specimen-bar interfaces to avoid misinterpretation of strains measured by the strain gages on the bars. This requirement can be achieved by matching the impedance of the tungsten-carbide inserts to that of the bar material, that is:

$$(\rho c A)_{WC} = \rho_o c_o A_o \quad (\text{Eq 8})$$

This requirement can also be achieved by accordingly choosing the diameter of the inserts. The length of the inserts is typically chosen to be one fourth of the length of the specimen.

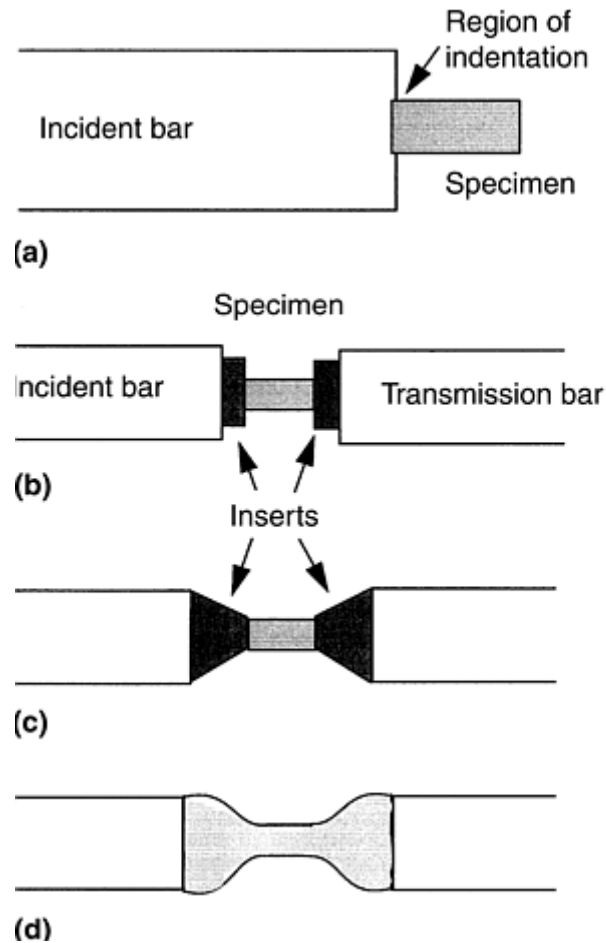


Fig. 3 Problem caused by the hardness of ceramic specimens and techniques developed to solve the problem. (a) Schematic illustration of indentation of hard ceramic into the bars. (b) Specimen-insert assembly with impedance matched tungsten carbide inserts. (c) Specimen-insert assembly with matching diameter conical inserts. (d) Dog-bone shaped specimen with end diameters sized to match the incident and transmission bars

Alternate insert geometry to reduce the indentation into the bars was proposed by Anderson et al. (Ref 5). In this design, conical ceramic inserts with matching diameters at both ends, as shown in Fig. 3(c), were used. Finite element analysis on various specimen-insert configurations (Ref 4) has confirmed that the magnitude of indentation into the steel bars, as well as the stress concentrations in the specimen, can be eliminated by using conical inserts. However, the analysis also revealed that conical inserts can alter the reflected and transmitted wave characteristics considerably due to the impedance mismatch with the steel bars. Other disadvantages of ceramic conical inserts compared to the constant-diameter impedance-matched tungsten-carbide inserts are higher manufacturing cost and need to customize the inner diameter of the cone whenever the specimen dimensions change. A dog-bone shaped ceramic specimen with an end diameter matched to that of the bar, shown in Fig. 3(d), has also been used in the literature to reduce the stress concentration and avoid indentation into the bars (Ref 6, 7). Again, this specimen geometry is prohibitively expensive to manufacture from a ceramic material.

While using inserts to avoid indentation into the bars, it is assumed that the strength of inserts is considerably greater than the ceramic being tested. However, smaller-diameter high-strength ceramic specimens can cause stress concentration on the inserts and cause fracture of the inserts before the ceramic specimen. Once the failure of insert occurs, the ceramic fractures invariably (due to stress concentration caused by the insert fragments on the ceramic), thus rendering the data on ceramic fracture strength invalid. To eliminate this possibility, it is recommended that the inserts be laterally confined using steel rings that can provide adjustable confining pressures, as shown in Fig. 4. To avoid impedance mismatch at the contact surface between the bar and the insert, the thickness of the steel ring is made slightly smaller than that of the inserts.

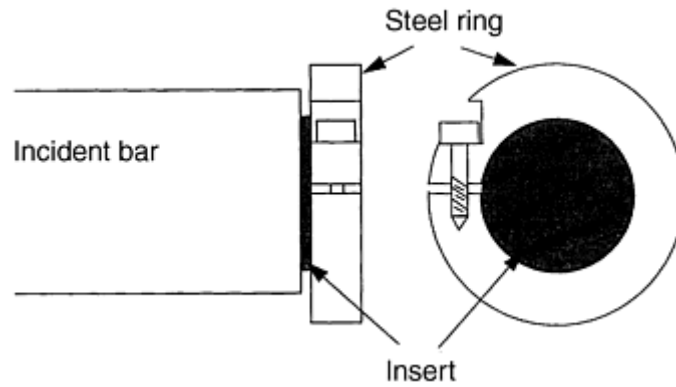


Fig. 4 Schematic of the adjustable lateral confinement ring to avoid premature fracture of inserts

The third assumption (that the incident, transmitted, and reflected pulses undergo minimal dispersion as they travel along the length of the bar) points to the fact that stress-strain response of a ceramic is not measured on the specimen during its deformation, but at distances farther away from the specimen (and at a time different from that of specimen deformation) using strain gages on the incident and transmission bar surfaces (Fig. 1). Under these circumstances, it is imperative that the reflected (which is a measure of strain) and transmitted (which is a measure of stress) strain-gage signals reflect the true response of the specimen. If dispersion is present in the propagating pulse, the amplitude and duration of the pulse changes by the time it reaches the strain gages and results in erroneous measurement of stress and strain within a ceramic. The extent of dispersion depends on the dominant frequency components present in (or the shape of) a propagating stress pulse (Ref 3). When the diameter of the bar is comparable to the wavelength of the dominant frequency component (or when the period of the pulse is comparable to the transit time of the bar wave across the diameter of the bar), dispersion effects become extremely severe, and the use of surface measurements at distances farther away from the specimen lead to erroneous measurement of the stress-strain response. It is suggested that the pulse duration should at least be 10 times larger than the transit time of the longitudinal wave across the diameter of the bar to minimize the dispersion in a propagating stress pulse (Ref 2, 8). Because the minimum pulse duration of the incident stress pulse and the maximum obtainable strain within a ceramic are limited, the maximum strain rate that can be imposed on to a ceramic specimen using SHPB testing is also limited. This concept is discussed in detail in the section “Limiting (Maximum) Strain Rate” in this article.

One way to avoid the problems associated with the dispersion is to eliminate the use of strain-gage signals from the bars. Instead, one can mount strain gages directly on the ceramic specimen and record the axial and transverse strains in situ during the deformation of the specimen. This procedure is also expected to give a more accurate measure of strain in a ceramic. Because the majority of ceramics undergo only linear elastic response until failure, the stress to fracture, σ_f , can be determined from the measured strain to fracture, ϵ_f , using Hooke's law ($\sigma_f = E\epsilon_f$). However, caution should be exercised while adopting this linear elastic approach on ceramics that exhibit significant inelastic strain before fracture. For example, zirconia ceramics, such as MgO-PSZ and Y-TZP, exhibit considerable inelastic strains due to stress-induced transformation and associated microcracking (Ref 9, 10), as discussed in the section “Pulse Shaping” in this article. In such cases, use of linear elastic response until fracture can overestimate the failure strength.

The fourth assumption (that the stress distribution across the cross section of the steel bars at a given instant is uniform) implies that the strain-gage measurements on the surface of the bars are representative of the stress at any interior point at that cross section of the bar. To further illustrate this concept, consider the stress distributions in the bar shown in Fig. 5. Obviously, for the stress distribution shown in Fig. 5(a), the measured strains on the surface of the bars will represent those at any interior point on the bar cross section. For the stress distributions shown in Fig. 5(b) the strain-gage measurements are not representative of the strains inside the bars, and, hence, the surface measurements will be meaningless. The nonuniform stress distribution can occur if either a planar impact is not ensured between the striker and the incident bars or when the duration of the incident stress pulse is comparable to that of the time required for transit of the longitudinal wave across the diameter of the bar, which can amplify the dispersion effects (Ref 3).

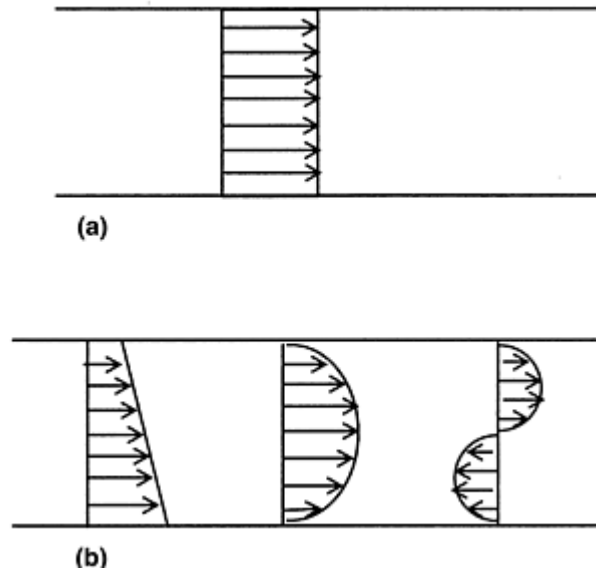


Fig. 5 Examples of (a) uniform stress and (b) nonuniform stress distribution in split-Hopkinson pressure bar testing

The fifth assumption (that the accumulated strain in the specimen is due solely to a single incident compression pulse reaching the specimen) emphasizes the fact that in traditional SHPB testing, a ceramic specimen is subjected to repeated loading (due to wave reflections within the incident bar) unless it is fractured during the first compression pulse loading. In the traditional design, shown in Fig. 1, the reflected pulse off the specimen is tensile in nature, and when it reaches the striker end of the incident bar, A, it reflects back as a compression pulse and travels once again toward the specimen, thus reloading the specimen. This process repeats several times causing multiple loadings on the specimen. Notice that the stress-strain response obtained from the initial transmitted (Eq 1) and reflected (Eq 3) strain-gage signals does not account for the accumulated damage in the specimen due to multiple loadings. Therefore, the microstructural changes (or the accumulated strain) in a specimen cannot be correlated to the macroscopic stress-strain response. For example, in the case of ceramics, suppose that the amplitude of the incident stress pulse is such that it is slightly below the stress level required for complete fracture but well above the stress level for initiating microcracking in a ceramic specimen (e.g., zirconia ceramics). The repeated loading due to reflected pulses can completely fracture the already weakened (or microcracked) specimen, but the stress-strain response may indicate otherwise because this is derived from the first transmitted and reflected pulses only.

The reloading of the specimen due to reflected pulses can be eliminated by using the modified SHPB technique shown in Fig. 6. In this design, the tensile pulse reflected off the specimen into the incident bar is captured by the “momentum-trap” assembly designed at the striker end of the incident bar. The technique is described in the article “Recovery Hopkinson Bar Techniques” in this Volume. Upon impact of the striker, the momentum-trap design also introduces a tensile pulse following the traditional compression pulse into the incident bar. Moreover, once a specimen is subjected to the initial compression pulse, all other pulses travelling towards the specimen end are rendered tensile and, therefore, cannot reload the specimen as the incident bar retracts away from the specimen. The trapping of the tensile pulse reflected off the specimen has overriding importance in recovery experiments on some ceramics (e.g., zirconia ceramics), where considerable microcracking and inelastic deformation can occur before complete fracture of the specimen (Ref 9, 10).

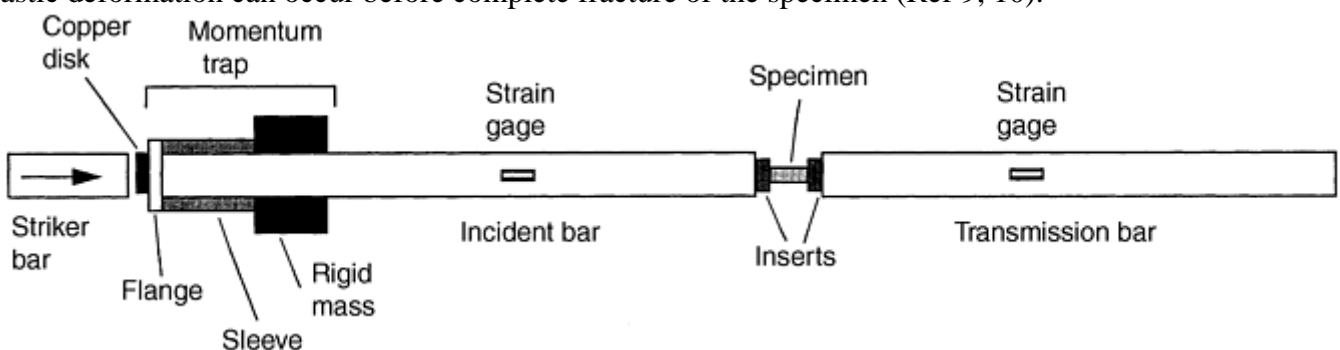


Fig. 6 Schematic of a split-Hopkinson pressure bar test configuration modified with momentum trap.
Source: Ref 11

References cited in this section

2. H. Kolsky, *Stress Waves in Solids*, Dover, 1963, p 41–94
3. G. Ravichandran and G. Subhash, Critical Appraisal of Limiting Strain Rates for Compression Testing of Ceramics in a Split-Hopkinson Pressure Bar, *J. Am. Ceram. Soc.*, Vol 77, 1994, p 263–267
4. W. Chen, G. Subhash, and G. Ravichandran, Evaluation of Ceramic Specimen Geometries Used in Split-Hopkinson Pressure Bar, *Dymat*, Vol 1, 1994, p 191–210
5. C. Anderson, Jr., P. O'Donoghue, J. Lankford, and J. Walker, Numerical Simulations of SHPB Experiments for the Dynamic Compressive Strength and Failure of Ceramics, *Int. J. Frac.*, Vol 55, 1992, p 193–208
6. A. Cosculluela, J. Cagnoux, and F. Collombet, Two Types of Experiments for Studying Uniaxial Dynamic Compression of Alumina, *Shock Compression of Condensed Matter*, S.C. Schmidt, R.D. Dick, J.W. Forbes, and D.G. Tasker, Ed., Elsevier Science Publishers, 1991, p 951–954
7. W.R. Blumenthal, High Strain Rate Compression and Fracture of B4C-Aluminum Cermets, *Shock-Wave and High-Strain-Rate Phenomena in Materials*, M.A. Meyers, L.E. Murr, and K.P. Staudhammer, Ed., Marcel Dekker, 1992, p 1093–1100
8. P.S. Follansbee and C. Frantz, Wave Propagation in the Split-Hopkinson Pressure Bar, *J. Eng. Mater. Technol. (Trans. ASME)*, Vol 105, 1983, p 61–66
9. G. Subhash and S. Nemat-Nasser, Dynamic Stress-Induced Transformation and Texture Formation in Uniaxial Compression of Zirconia Ceramics, *J. Am. Ceram. Soc.*, Vol 76, 1993, p 153–165
10. G. Subhash and S. Nemat-Nasser, Uniaxial Stress Behavior of Y-TZP, *J. Mater. Sci.*, Vol 25, 1993, p 5949–5952
11. S. Nemat-Nasser, J.B. Isaacs, and J.E. Starrett, Hopkinson Techniques for Dynamic Recovery Experiments, *Proc. R. Soc. (London) A*, Vol 435, 1991, p 371–391

Split-Hopkinson Pressure Bar Testing of Ceramics

G. Subhash, Michigan Technological University G. Ravichandran, California Institute of Technology

Limiting (Maximum) Strain Rate

The concept of limiting strain rate for ceramics using a SHPB test originates from the fact that ceramics are hard and exhibit extremely small strains (<1%) before fracture. Consequently, several of the assumptions previously discussed are violated. For failure strength data obtained from SHPB experiments to be valid, the stress in a specimen must be made to reach equilibrium, which means that enough wave reflections must occur within the specimen before fracture is initiated. This condition imposes limits on either the pulse duration (Eq 6) or the specimen length (Eq 7). The following simple calculations further illustrate this concept (Ref 3). The time required for an incident wave to travel from one end of the specimen to the other is given by:

$$t_s = \frac{l_s}{c_s} \quad (\text{Eq 9})$$

Let τ be the time required for stress equilibration within the specimen and t_f be the time to fracture during loading by the incident pulse. For failure strength data to be valid, t_f should be greater than or equal to τ . Assume that the time required for stress to reach equilibrium is an integer multiple of transit time, t_s , that is:

$$\tau = \alpha t_s \quad (\text{Eq 10})$$

where α represents the number of wave reflections within the specimen. The nominal strain rate at the time of failure in a ceramic that exhibits only elastic strains is given by:

$$\dot{\epsilon} = \frac{\epsilon_f}{t_f} \quad (\text{Eq 11})$$

where ϵ_f is the failure strain. Because t_f has to be at least equal to τ for failure strength data to be valid, substituting Eq 9 and 10 in Eq 11 gives the maximum (or limiting) strain rate that can be achieved in a ceramic, that is:

$$\dot{\epsilon}_l = \frac{\epsilon_f c_s}{\alpha l_s} \quad (\text{Eq 12})$$

As illustrated in Fig. 2, at least four transit times in a ceramic specimen are required for stress equilibrium to be achieved ($\alpha = 4$). Typical ceramic specimen lengths used in SHPB testing are around 9.5 mm (0.375 in.), and assuming a wave speed of 10,000 m/s (32,800 ft/s) and a failure strain of around 1% in a ceramic, the maximum strain rate that can be achieved in a ceramic specimen using SHPB testing is around 2600/s. Because the failure strain and wave velocity are fixed for a given ceramic, acquiring failure strength data beyond this strain rate requires further reduction in specimen length (and a corresponding reduction in diameter to keep the length-to-diameter ratio of 2 to 1). For various structural ceramics, this limiting strain rate is found to be in the range of 2500 to 3000/s (Ref 3).

The concept of limiting (or maximum) strain rate in a ceramic using SHPB testing can also be approached from the dispersion effects of propagating stress pulses in a slender bar, discussed earlier under the third assumption. Let us assume that the incident pulse propagating in the bar has a fundamental frequency, ω_o , and a period, T , where:

$$\omega_o = \frac{2\pi}{T} \quad (\text{Eq 13})$$

Because a typical input pulse in SHPB testing is composed of multiple frequencies, all of which are assumed to be integer multiples of the fundamental frequency, a characteristic wave velocity is associated with each of the frequencies, ω , and the corresponding phase velocity, c_p , is given by:

$$c_p = \frac{\omega}{2\pi} \Lambda \quad (\text{Eq 14})$$

where Λ is the wave length associated with a particular frequency component. The phase velocity can be obtained from the approximate dispersion relation (Ref 2, 8) given by:

$$\frac{c_p}{c_o} = 1 - \nu^2 \pi^2 \left(\frac{a}{\Lambda} \right)^2 \quad (\text{Eq 15})$$

where ν is the Poisson's ratio and a is the radius of the bar. For propagating longitudinal stress pulses in a cylindrical bar, it has been shown that when $a/\Lambda > 0.1$, dispersion effects become dominant, and the stress and displacement fields become highly nonuniform across the cross section of the bar (e.g., Fig. 5b). Therefore, the data obtained from the surface measurements at distances farther away from the specimen lead to erroneous results (violation of assumptions 3 and 4). To minimize dispersion, the dominant frequency component in the frequency spectrum of the incident pulse should be such that $a/\Lambda < 0.1$ (Ref 2, 8). This condition can be rewritten using Eq 13 and 14 as:

$$\left(\frac{c_o}{c_p} \right) \left(\frac{\omega}{\omega_o} \right) < 0.1 \quad (\text{Eq 16})$$

where the fundamental frequency can be determined in terms of bar geometry and material properties as:

$$\omega_o = 2\pi \frac{c_o}{a} \quad (\text{Eq 17})$$

Using relevant numbers for a 9.5 mm (0.375 in.) diameter SHPB made of maraging steel ($a = 4.75$ mm, or 0.19 in., $\nu = 0.3$, and $c_o = 4970$ m/s), ω_o can be calculated from Eq 17 as 6.574×10^6 rad/s. For $a/\Lambda = 0.1$, c_p can be calculated from Eq 15 to obtain a limiting value of the fundamental frequency, ω , from Eq 16 as 6.516×10^5 rad/s. Finally, the corresponding period, T , of the pulse is calculated from Eq 13 to be $9.64 \mu\text{s}$. A given pulse typically consists of equal durations of loading and unloading phases. Assuming the failure of the specimen coincides with the peak input load (i.e., at $4.82 \mu\text{s}$) for a failure strain of 1% in a ceramic specimen, the maximum strain rate that can be achieved based on dispersion relation is calculated using Eq 11 to be 2074/s. This value should be deemed as a lower bound for the limiting strain rate because in $4.8 \mu\text{s}$ approximately 5 wave reflections can occur for a ceramic specimen of length 9.5 mm (0.375 in.).

From the preceding discussions, it is clear that the maximum strain rate that can be achieved in a ceramic specimen using SHPB testing can be derived from two approaches: one based on time required for stress to reach equilibrium in the specimen and the other based on dispersion effects in the propagating pulse. Both approaches yield the maximum strain rate limit between 2000 and 2600/s. However, this value can be further extended by reducing the specimen length, decreasing the bar diameter, or increasing the failure strain of the ceramic material (through microstructural control). However, decreasing the bar diameter will warrant further reductions in the specimen dimensions so as to obtain the required stress level to cause fracture in a ceramic specimen.

References cited in this section

2. H. Kolsky, *Stress Waves in Solids*, Dover, 1963, p 41–94
3. G. Ravichandran and G. Subhash, Critical Appraisal of Limiting Strain Rates for Compression Testing of Ceramics in a Split-Hopkinson Pressure Bar, *J. Am. Ceram. Soc.*, Vol 77, 1994, p 263–267
8. P.S. Follansbee and C. Frantz, Wave Propagation in the Split-Hopkinson Pressure Bar, *J. Eng. Mater. Technol. (Trans. ASME)*, Vol 105, 1983, p 61–66

Split-Hopkinson Pressure Bar Testing of Ceramics

G. Subhash, Michigan Technological University G. Ravichandran, California Institute of Technology

Pulse Shaping

Traditionally, a rectangular shaped incident pulse is generated in the incident bar through a planar impact between the striker and the incident bars. For metallic specimens, this wave form is ideally suited because metals undergo large plastic strains and the rectangular shaped loading pulse imposes a nominally uniform strain rate throughout the plastic deformation (Fig. 7a). In the case of a ceramic specimen, use of rectangular incident pulse is not recommended because ceramics undergo only elastic strain before fracture, and the total energy contained in the rectangular pulse can be too large to cause excessive fragmentation of ceramics without any possibility for recovery of the intact but microcracked specimen for post-test quantification and analysis. Moreover, the rectangular pulse with its steep rise in stress level can impose a nonuniform strain rate during the elastic deformation of the ceramic due to the differences between the slopes of the imposed loading rate and the stress-strain response, as shown in Fig. 7(b). Therefore, modification in the incident pulse shape that matches the slope of the elastic response of the ceramic is recommended. Figure 7(c) illustrates the advantage of using a ramp pulse while testing ceramics. When incident stress amplitude of the ramp pulse is greater than the stress required for microcracking in a ceramic, the total energy contained in the ramp pulse beyond the fracture

strength is much smaller than the traditional rectangular pulse of similar duration. At the onset of inelasticity (such as microcracking or transformation plasticity in the case of zirconia ceramics), the remaining duration of the pulse with excess energy is considerably shorter, and, hence, the cracks have less available time and energy to propagate, coalesce, and cause catastrophic failure of the ceramic, which can occur if the traditional rectangular incident pulse of constant duration is imposed. By matching the slopes of the incident ramp pulse and the stress-strain response, one can also attain a constant strain rate throughout the elastic deformation of the ceramic.

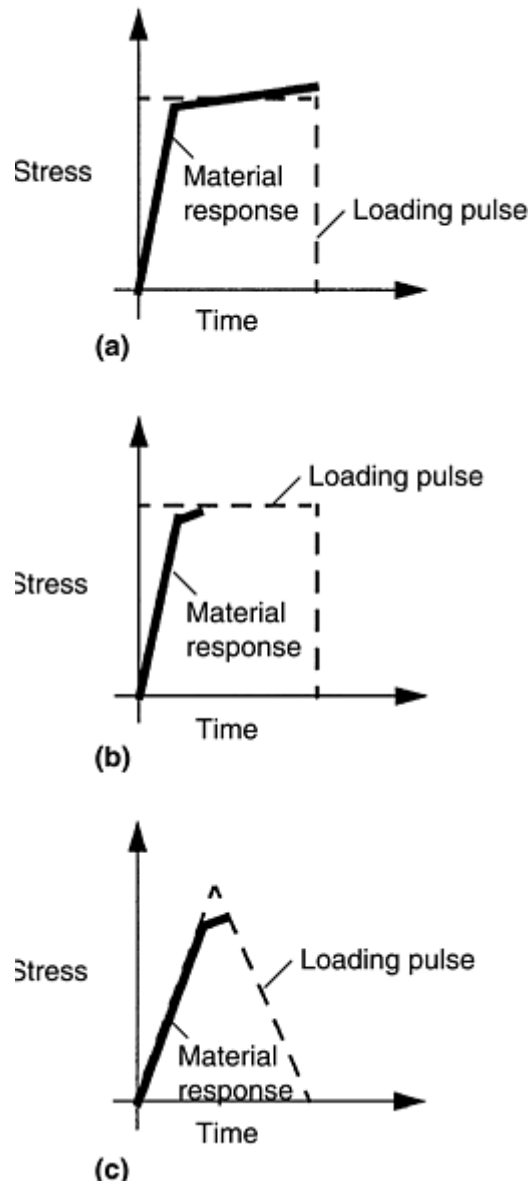


Fig. 7 Schematic illustration of the influence of incident pulse shaping on the stress-strain response of a ceramic specimen. (a) Rectangular-shaped pulse on a ductile specimen. (b) Rectangular pulse on a ceramic specimen. (c) Ramp-shaped pulse on a ceramic specimen

A ramp pulse can be produced by placing a thin ductile (e.g., copper, aluminum) metallic disk of 0.5 to 1 mm (0.02–0.04 in.) thick and 2 to 3 mm (0.08–0.12 in.) diameter on the impact end of the incident bar, as shown in Fig. 6. Upon impact by a striker, the plastic deformation of the disk generates a ramp pulse in the incident bar. The rise and fall times in the ramp pulse can be controlled by changing the material of the pulse shaper as well as the velocity and length of the striker bar. Figure 8(a) illustrates the traditional rectangular pulse; Fig. 8(b) shows the typical ramp stress pulse obtained using a copper disk. Note that, although both the pulses are obtained with the same striker bar, the ramp pulse duration is almost twice that of the rectangular pulse. In-depth discussions on pulse shaping can be found in Ref 11.

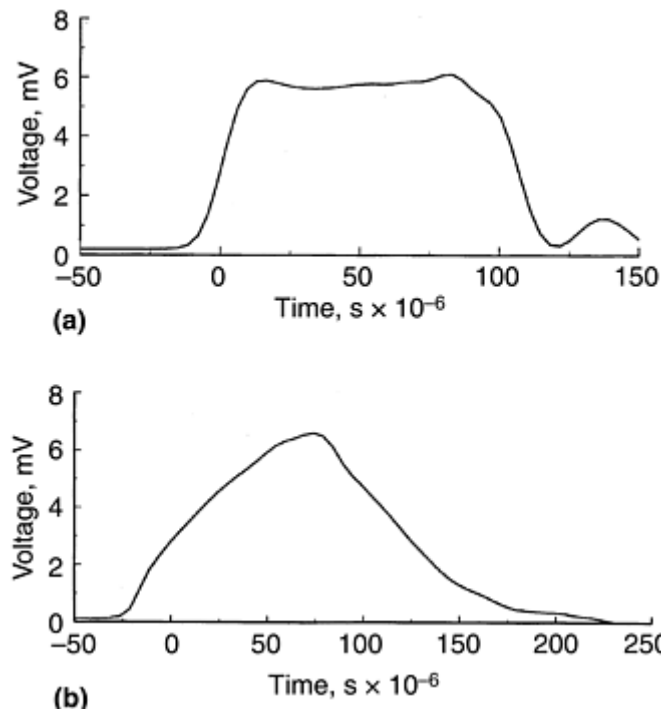


Fig. 8 Comparison of (a) rectangular-shaped pulse with (b) ramp-shaped pulse obtained from the same length striker bar

Although pulse shaping allows controlled damage in a ceramic specimen at a constant strain rate, use of traditional SHPB does not preclude the possibility for repeated reloading of the specimen due to wave reflections in the incident bar. Even if the amplitude of the incident stress pulse is carefully adjusted such that it is just enough to cause microcracking in the ceramic (but not complete fracture), the reloading of the specimen by reflected pulses in a traditional SHPB test will suffice to cause complete fracture of the already weakened (due to microcracking during the first loading) specimen, further emphasizing the need for momentum trapping discussed previously. With the above modifications, precise stress-strain curves can be obtained in microcracking ceramics, such as zirconia ceramics, even after significant inelastic strain (due to the stress-induced transformation) and extensive microcracking have accumulated in the specimen. A typical stress-strain curve revealing transformation and microcracking phases for magnesia partially stabilized zirconia (MgO-PSZ), obtained using a ramp loading pulse in a modified SHPB is shown in Fig. 9. In these experiments, strain gages were mounted on the specimen to obtain the axial and transverse strains during the deformation.

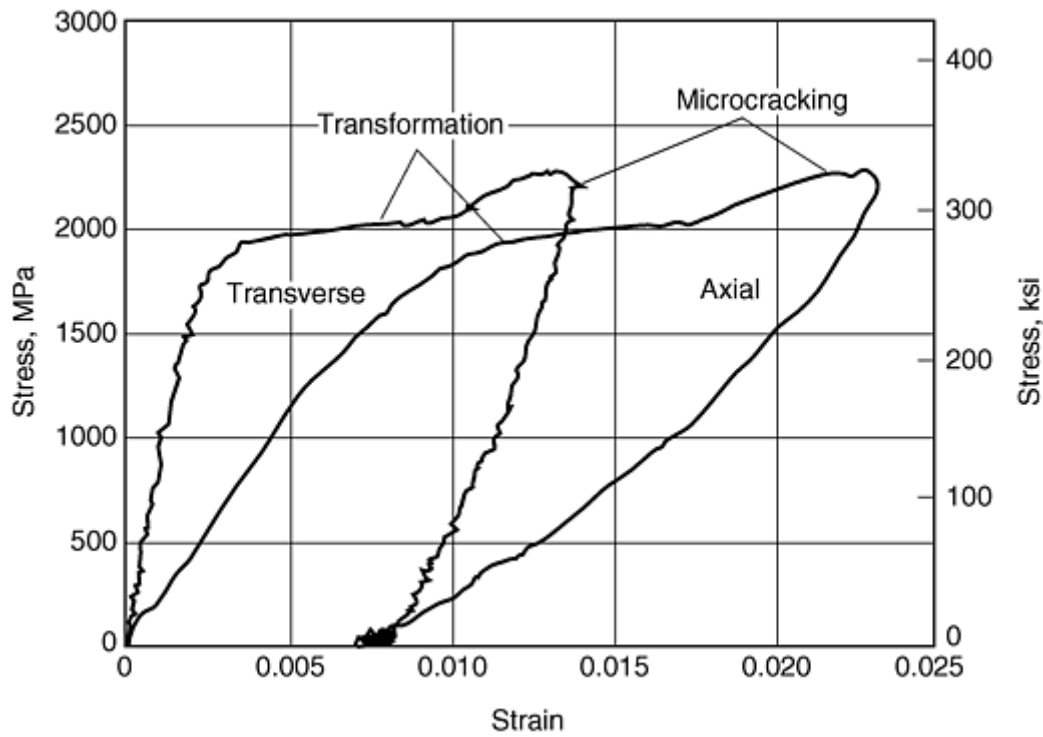


Fig. 9 Stress-strain response obtained using a ramp-shaped pulse in a modified split-Hopkinson pressure bar test for zirconia ceramic exhibiting inelastic strains associated with stress-induced transformation and microcracking. Source: Ref 9, 10

References cited in this section

9. G. Subhash and S. Nemat-Nasser, Dynamic Stress-Induced Transformation and Texture Formation in Uniaxial Compression of Zirconia Ceramics, *J. Am. Ceram. Soc.*, Vol 76, 1993, p 153–165
10. G. Subhash and S. Nemat-Nasser, Uniaxial Stress Behavior of Y-TZP, *J. Mater. Sci.*, Vol 25, 1993, p 5949–5952
11. S. Nemat-Nasser, J.B. Isaacs, and J.E. Starrett, Hopkinson Techniques for Dynamic Recovery Experiments, *Proc. R. Soc. (London) A*, Vol 435, 1991, p 371–391

Specimen Design

The stress-strain response and failure strength data on ceramics obtained from SHPB is strongly influenced by the tolerances in the ceramic specimen dimensions, such as parallelism between the end faces, normality of the end faces with the axis of the specimen, and surface finish. Similar to uniaxial static compression testing of metals and ceramics, a length-to-diameter ratio of 2 to 1 is recommended for high-strain-rate testing. Because ceramics have a high elastic modulus (nearly 1.5 to 2 times that of steel) and small failure strains (<1%), small variations in the parallelism between the end surfaces can cause high stress concentrations at these locations leading to chipping or initiation of fracture during deformation. Therefore, it is extremely important to grind the end surfaces to a high degree of flatness (at least 0.01 mm, or 0.0004 in.) and parallelism (within 0.001 mm, or 0.00004 in.) to avoid premature failure of the specimen. Because ceramics are also flaw sensitive, it is recommended that all surfaces be polished to reduce the influence of machining induced surface flaws.

Interpretation of Test Results

High-strain-rate response of brittle materials, in particular ceramics, differs from quasi-static response in two ways. First, there is an increase in fracture strength at high strain rates. Figure 10 illustrates data on aluminum-nitride uniaxial compressive fracture strength as a function of strain rate. Similar trends were also observed in several other structural ceramics, such as alumina, silicon carbide, and rocks (Ref 13, 14, 15). Note that, beyond a critical strain rate, the fracture strength increases with strain rate dramatically. Second, there is an increased propensity for multiple microcrack initiation from several locations in the specimen. Both these effects are intimately connected to the inherent microstructure. A brief discussion on the mechanisms of brittle fracture and damage evolution follows. The discussion is expected to assist a nonspecialist in this field in proper interpretation of the experimental results obtained using an SHPB test.

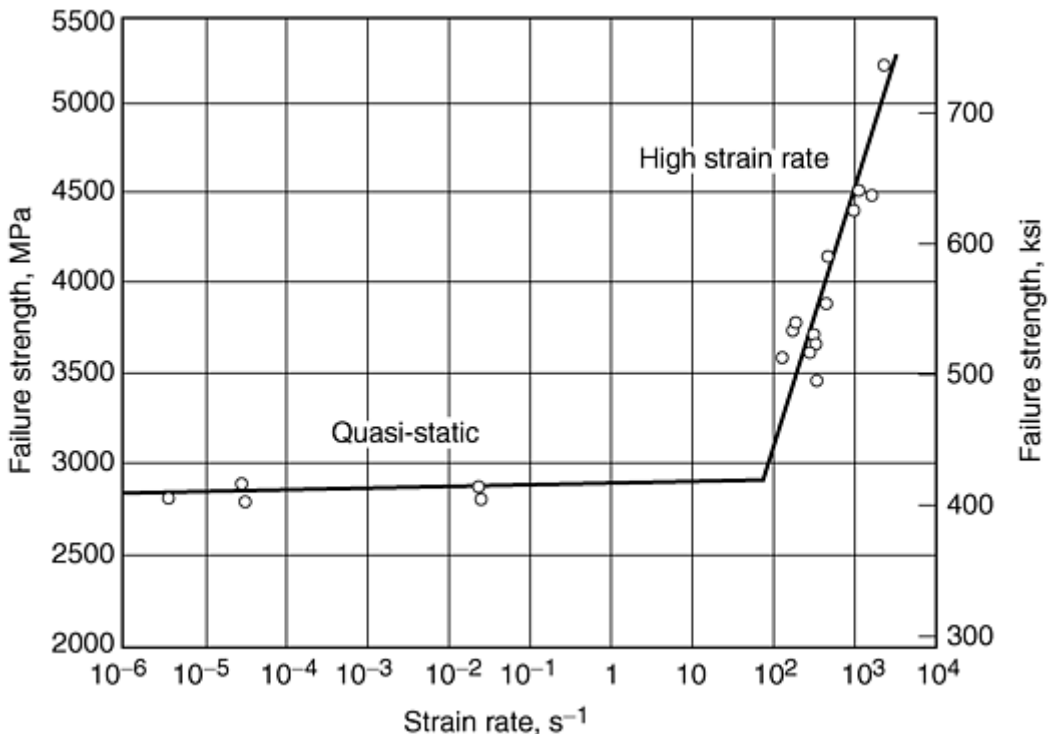


Fig. 10 Plot of variation of fracture strength as a function of strain rate for aluminum nitride (AlN) ceramic. Source: Ref 12

Mechanisms of Brittle Failure Under High-Strain-Rate Loading. It has been well established that processing-induced microstructural inhomogeneities, such as inclusions, grain boundary impurities, second phases, triple junctions, and pores are mainly responsible for the nucleation of microcracks that lead to fracture in ceramics (Ref 14, 16, 17). However, the difference in the characteristics of crack growth from these inhomogeneities is mainly responsible for the rate-sensitive nature of fracture strength in brittle materials. At low strain rates, typically below 100/s, both sintered and hot-pressed ceramics, in general, do not exhibit rate-sensitive failure strength. This behavior has been attributed to unstable crack growth from inhomogeneities and their instantaneous coalescence, which inhibits any subcritical crack growth.

At high strain rates, beyond a critical strain rate, both sintered and hot-pressed ceramics exhibit a high rate-sensitive fracture stress due to inertia-dominated crack growth (Ref 14, 15, 17); that is, as the loading rate increases, the time available for a crack to initiate and grow reduces. The inertia associated with the crack-growth acceleration will inhibit early fracture initiation while the applied stress continues to rise rapidly, thus elevating the compressive failure strength under dynamic loads. The critical strain rate at which transition from the rate-insensitive (unstable) to rate-sensitive (inertia dominated) crack growth in microcracking solids has been found to depend on material properties. Grady and Lipkin (Ref 18) proposed the following relationship for the transitional strain rate:

$$\dot{\epsilon} = \frac{K_{Ic}}{\rho c r_o^{3/2}} \quad (\text{Eq 18})$$

where K_{Ic} is the fracture toughness, ρ is material density, c is wave velocity, and r_o is the average initial microcrack size, which is typically assumed to be the same as the grain size in ceramics. Ravichandran and Subhash (Ref 17) proposed this equation:

$$\dot{\epsilon} = \frac{\sigma_f \tilde{c}}{E l_s} \quad (\text{Eq 19})$$

where σ_f is the quasi-static compressive strength and \tilde{c} is the characteristic crack velocity which is taken as the speed at which inertia effects become significant, that is, when the crack velocity reaches approximately 0.2 of shear wave velocity. Equation 19 is a modified version of the equation proposed by Lankford (Ref 14) where the length is replaced by radius of the specimen and by shear wave speed. Both Eq 18 and 19 predict the transitional strain rate to be between 1200 and 1500/s.

In the inertia-dominated (high-strain-rate) regime, the relationship between the compressive fracture strength, σ_f , and strain rate at fracture for a variety of brittle ceramics has been found to follow a relationship (Ref 18):

$$\sigma_f \propto \dot{\epsilon}^{1/3} \quad (\text{Eq 20})$$

A micromechanical damage model for brittle materials developed by Ravichandran and Subhash (Ref 17) shows a similar relationship, $\sigma_f \propto \dot{\epsilon}^n$, where n ranges from $1/4$ to $1/3$. The value of n depends on the relationship describing the dynamic fracture toughness as a function of crack speed. Although the relationship discussed previously has been found to reasonably represent the failure behavior of coarse-grained ceramics, recent experimental results on fine-grained, high-purity ceramics revealed a complete absence of such a transitional strain rate (Ref 19, 20). In these ceramics, the uniaxial compressive fracture strength increased linearly with strain rate in the range between 10^{-3} and 10^5 /s. This behavior has been attributed to fine grain size, significant reduction in the process induced flaws, and elimination of inhomogeneities during processing, all of which resulted in enhanced dislocation activity and microshear banding similar to those observed in ductile metals.

Damage Evolution. One of the major characteristics of crack growth during uniaxial compressive loading of brittle materials is that crack growth occurs in a direction parallel to the loading axis. On a plane perpendicular to the loading axis, the cracks can be randomly oriented, thereby making the specimen transversely isotropic. The problem of tensile crack growth from preexisting microcracks has been analyzed in detail (Ref 21, 22). Under uniaxial compressive loading, tensile cracks nucleate from the preexisting flaws in the direction of maximum tensile stress. The major difference in crack growth under static and dynamic loading is that in static loading, a single crack typically dominates the fracture behavior. This is because once the stress required for crack initiation is reached, the weakest crack starts to grow first, and the stored elastic energy continues to provide the necessary driving force for unstable crack growth to continue and cause eventual failure of the specimen. Here the rate of loading is extremely slow compared to the crack growth rate, and, hence, once crack growth is initiated it cannot be controlled. In the case of dynamic loading, the inertia associated with the crack tip opening delays the crack growth while the applied stress rises much more rapidly beyond that required for

several cracks to grow; therefore, multiple cracks grow simultaneously. The difference in the crack growth phenomena between static and dynamic loading rates is illustrated schematically in Fig. 11. If the loading process continues during dynamic testing, the energy required for crack growth continues to be supplied to the crack tips, leading to complete fragmentation of the specimen. Through proper pulse shaping, the amount of input energy can be controlled (Fig. 7, 8), and microcrack growth can be limited, allowing for recovery of the intact but microcracked specimen.

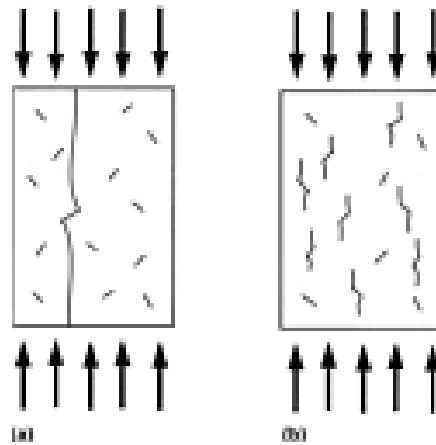


Fig. 11 Schematic of crack growth from preexisting flaws under (a) static and (b) dynamic uniaxial compressive loads

In order to confirm multiple crack growth during dynamic loading, Subhash and Nemat-Nasser (Ref 9) conducted dynamic uniaxial compression experiments on a MgO-PSZ ceramic specimen in a modified SHPB with a ramp-shaped input pulse. They subjected the specimen to uniaxial compressive loads successively in two perpendicular directions. The first loading caused axial crack growth parallel to the first loading direction. The second loading (in a direction perpendicular to the first one) also induced axial crack growth parallel to this loading direction. The micrograph provided in Fig. 12 reveals the network of cracks developed parallel to the two loading directions. Notice that the microcracks developed during the first loading do not seem to influence the crack growth during the second loading, suggesting that in uniaxial compression, cracks always grow parallel to the loading axis even in the presence of some material anisotropy caused during the first loading. Complete recovery of the specimen after multiple microcrack growth was possible due to the controlled energy input through pulse shaping and ensuring a single loading through modified SHPB testing. With continued loading, one could expect the specimen to break into columnar fragments due to crack growth from several locations. Investigations by Kipp and Grady (Ref 23) and Lankford and Blanchard (Ref 16) have confirmed that fragment size is inversely proportional to the applied strain rate. Smaller fragment size and its narrow distribution in high-strain-rate experiments imply nucleation and rapid coalescence of numerous microcracks under dynamic loading, a conclusion that was also supported by the modeling studies on strain-rate effects on brittle fracture in compression by Nemat-Nasser and Deng (Ref 24).

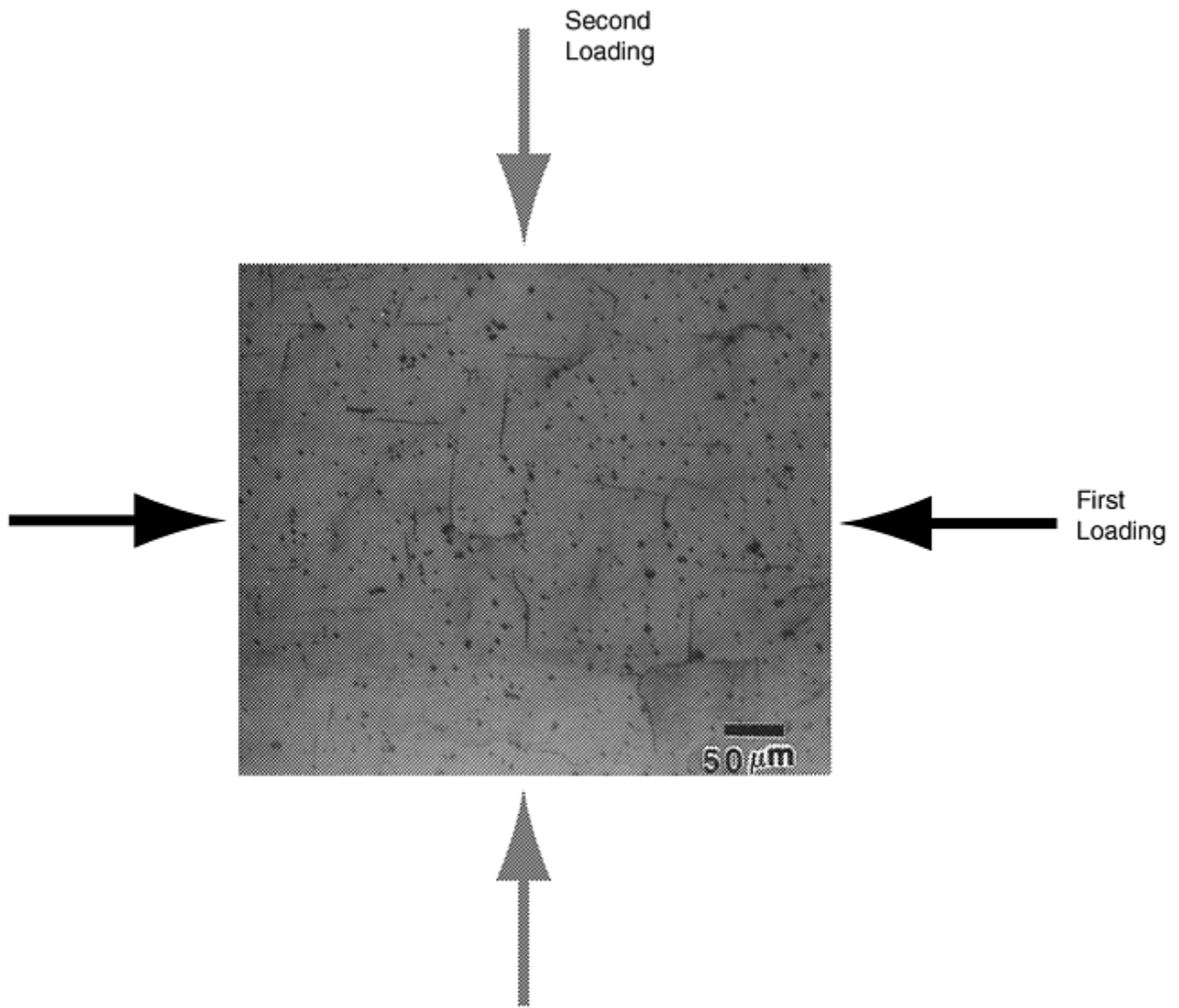


Fig. 12 Micrograph of axial cracking during dynamic uniaxial loading of magnesia partially stabilized zirconia. Arrows indicate directions from two loadings perpendicular to one another

References cited in this section

9. G. Subhash and S. Nemat-Nasser, Dynamic Stress-Induced Transformation and Texture Formation in Uniaxial Compression of Zirconia Ceramics, *J. Am. Ceram. Soc.*, Vol 76, 1993, p 153–165
12. G. Subhash and G. Ravichandran, Mechanical Behavior of Hot-Pressed Aluminum Nitride Under Uniaxial Compression, *J. Mater. Sci.*, Vol 33, 1997, p 1933–1939
13. J. Lankford, Compressive Strength and Microplasticity in Polycrystalline Alumina, *J. Mater. Sci.*, Vol 12, 1977, p 791–796
14. J. Lankford, Mechanisms Responsible for Strain-Rate Dependent Compressive Strength in Ceramic Materials, *J. Am. Ceram. Soc.*, Vol 64, 1981, p 25–33
15. J. Lankford, Dynamic Compressive Fracture in Fiber-reinforced Ceramic Matrix Composites, *Mater. Sci. Eng. A*, Vol 107, 1989, p 261–268
16. J. Lankford and C.R. Blanchard, Fragmentation of Brittle Materials at High rates of Loading, *J. Mater. Sci.*, Vol 26, 1991, p 3067–3072

17. G. Ravichandran and G. Subhash, A Micro Mechanical Model for High Strain Rate Behavior of Ceramics, *Int. J. Solids Struct.*, Vol 32 (No. 17/18), 1995, p 2627–2650
18. D.E. Grady and J. Lipkin, Criteria for Impulsive Rock Fracture, *Geophy. Res. Lett.*, Vol 7, 1980, p 255–258
19. J. Staehler, W.W. Predebon, B.J. Pletka, and G. Subhash, Micromechanisms of Deformation in High Purity Hot Pressed Alumina, *Mater. Sci. Eng.*, 1999 (in review)
20. J. Lankford, W.W. Predebon, J.M. Staehler, G. Subhash, B.J. Pletka, and C.E. Anderson, The Role of Plasticity as Limiting Factor in the Compressive Failure of High Strength Ceramics, *Mech. Mater.*, Vol 29, 1998, p 205–218
21. S. Nemat-Nasser and M. Horii, Compression-Induced Nonplanar Crack Extension with Application to Splitting, Exfoliation, and Rockburst, *J. Geophys. Res.*, Vol 87, 1982, p 6805–6821
22. M.F. Ashby and S.D. Hallam, The Failure of Brittle Solids Containing Small Cracks under Compressive Stress States, *Acta Metall.*, Vol 34, 1986, p 497–510
23. M.E. Kipp and D.E. Grady, Dynamic Fracture Growth and Interaction in One Dimension, *J. Mech. Phys. Solids*, Vol 33, 1985, p 399–415
24. S. Nemat-Nasser and H. Deng, Strain-Rate Effects on Brittle Failure in Compression, *Acta Metall. Mater.*, Vol 42, 1994, p 1013–1024

Split-Hopkinson Pressure Bar Testing of Ceramics

G. Subhash, Michigan Technological University G. Ravichandran, California Institute of Technology

Conclusions

The inherent limitations of the traditional SHPB technique for testing of brittle materials necessitate modifications in the SHPB design and testing procedure. In order to obtain accurate and reliable data on the behavior of ceramics at high strain rates, modifications such as strain gaging the specimen, sandwiching the specimen between high-strength impedance matching inserts, momentum trapping, and incident pulse shaping should be employed. Because ceramics exhibit only elastic strains to failure, one should also be aware of the maximum strain rate that can be achieved using the SHPB technique. This limiting strain rate depends on specimen size, its elastic properties, incident pulse duration, and the bar diameter. For more accurate measurement of fracture strains and identification of true failure modes, it is emphasized that close tolerances should be maintained for flatness and parallelism of the loading surfaces, and the specimens should be carefully ground and polished to reduce machining-induced damage on the surfaces.

Split-Hopkinson Pressure Bar Testing of Ceramics

G. Subhash, Michigan Technological University G. Ravichandran, California Institute of Technology

References

1. H. Kolsky, An Investigation of the Mechanical Properties of Materials at Very High Rates of Loading, *Proc. R. Soc. (London) B*, Vol 62, 1949, p 676–700
2. H. Kolsky, *Stress Waves in Solids*, Dover, 1963, p 41–94
3. G. Ravichandran and G. Subhash, Critical Appraisal of Limiting Strain Rates for Compression Testing of Ceramics in a Split-Hopkinson Pressure Bar, *J. Am. Ceram. Soc.*, Vol 77, 1994, p 263–267
4. W. Chen, G. Subhash, and G. Ravichandran, Evaluation of Ceramic Specimen Geometries Used in Split-Hopkinson Pressure Bar, *Dymat*, Vol 1, 1994, p 191–210
5. C. Anderson, Jr., P. O'Donoghue, J. Lankford, and J. Walker, Numerical Simulations of SHPB Experiments for the Dynamic Compressive Strength and Failure of Ceramics, *Int. J. Frac.*, Vol 55, 1992, p 193–208
6. A. Cosculluela, J. Cagnoux, and F. Collombet, Two Types of Experiments for Studying Uniaxial Dynamic Compression of Alumina, *Shock Compression of Condensed Matter*, S.C. Schmidt, R.D. Dick, J.W. Forbes, and D.G. Tasker, Ed., Elsevier Science Publishers, 1991, p 951–954
7. W.R. Blumenthal, High Strain Rate Compression and Fracture of B4C-Aluminum Cermets, *Shock-Wave and High-Strain-Rate Phenomena in Materials*, M.A. Meyers, L.E. Murr, and K.P. Staudhmmmer, Ed., Marcel Dekker, 1992, p 1093–1100
8. P.S. Follansbee and C. Frantz, Wave Propagation in the Split-Hopkinson Pressure Bar, *J. Eng. Mater. Technol. (Trans. ASME)*, Vol 105, 1983, p 61–66
9. G. Subhash and S. Nemat-Nasser, Dynamic Stress-Induced Transformation and Texture Formation in Uniaxial Compression of Zirconia Ceramics, *J. Am. Ceram. Soc.*, Vol 76, 1993, p 153–165
10. G. Subhash and S. Nemat-Nasser, Uniaxial Stress Behavior of Y-TZP, *J. Mater. Sci.*, Vol 25, 1993, p 5949–5952
11. S. Nemat-Nasser, J.B. Isaacs, and J.E. Starrett, Hopkinson Techniques for Dynamic Recovery Experiments, *Proc. R. Soc. (London) A*, Vol 435, 1991, p 371–391
12. G. Subhash and G. Ravichandran, Mechanical Behavior of Hot-Pressed Aluminum Nitride Under Uniaxial Compression, *J. Mater. Sci.*, Vol 33, 1997, p 1933–1939
13. J. Lankford, Compressive Strength and Microplasticity in Polycrystalline Alumina, *J. Mater. Sci.*, Vol 12, 1977, p 791–796
14. J. Lankford, Mechanisms Responsible for Strain-Rate Dependent Compressive Strength in Ceramic Materials, *J. Am. Ceram. Soc.*, Vol 64, 1981, p 25–33
15. J. Lankford, Dynamic Compressive Fracture in Fiber-reinforced Ceramic Matrix Composites, *Mater. Sci. Eng. A*, Vol 107, 1989, p 261–268
16. J. Lankford and C.R. Blanchard, Fragmentation of Brittle Materials at High rates of Loading, *J. Mater. Sci.*, Vol 26, 1991, p 3067–3072
17. G. Ravichandran and G. Subhash, A Micro Mechanical Model for High Strain Rate Behavior of Ceramics, *Int. J. Solids Struct.*, Vol 32 (No. 17/18), 1995, p 2627–2650

18. D.E. Grady and J. Lipkin, Criteria for Impulsive Rock Fracture, *Geophy. Res. Lett.*, Vol 7, 1980, p 255–258
19. J. Staehler, W.W. Predebon, B.J. Pletka, and G. Subhash, Micromechanisms of Deformation in High Purity Hot Pressed Alumina, *Mater. Sci. Eng.*, 1999 (in review)
20. J. Lankford, W.W. Predebon, J.M. Staehler, G. Subhash, B.J. Pletka, and C.E. Anderson, The Role of Plasticity as Limiting Factor in the Compressive Failure of High Strength Ceramics, *Mech. Mater.*, Vol 29, 1998, p 205–218
21. S. Nemat-Nasser and M. Horii, Compression-Induced Nonplanar Crack Extension with Application to Splitting, Exfoliation, and Rockburst, *J. Geophys. Res.*, Vol 87, 1982, p 6805–6821
22. M.F. Ashby and S.D. Hallam, The Failure of Brittle Solids Containing Small Cracks under Compressive Stress States, *Acta Metall.*, Vol 34, 1986, p 497–510
23. M.E. Kipp and D.E. Grady, Dynamic Fracture Growth and Interaction in One Dimension, *J. Mech. Phys. Solids*, Vol 33, 1985, p 399–415
24. S. Nemat-Nasser and H. Deng, Strain-Rate Effects on Brittle Failure in Compression, *Acta Metall. Mater.*, Vol 42, 1994, p 1013–1024

Torsional Kolsky Bar Testing

Amos Gilat, The Ohio State University

Introduction

THE TORSIONAL KOLSKY BAR TEST is a reliable technique for testing materials in the 10^2 to 10^4 s^{-1} strain-rate regime (Fig. 1). In this technique, shown schematically in Fig. 2, a short material specimen is placed between two bars. The specimen is loaded by a torsional wave that is generated in one of the bars. Once loaded, the wave is partially reflected back and partially transmitted to the other bar. The history of load and deformation in the specimen is determined by monitoring the waves in the bars, which remain elastic throughout the test. The technique is a variation of a technique proposed by Kolsky (Ref 2), in which the specimen is loaded in compression. It is described in the article “Classic Split-Hopkinson Pressure Bar Testing” in this Volume.

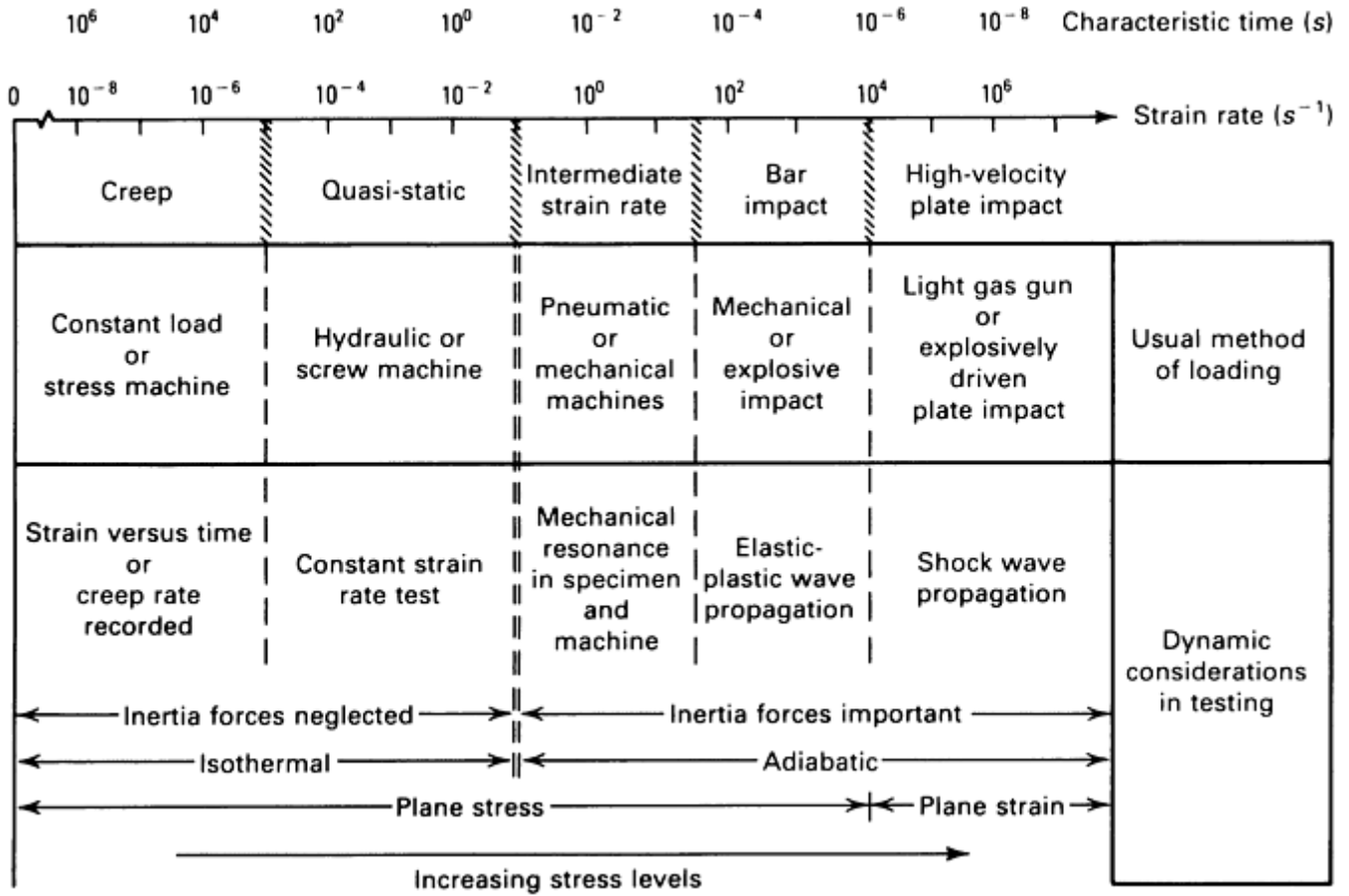


Fig. 1 Dynamic aspects of material testing. Source Ref 1

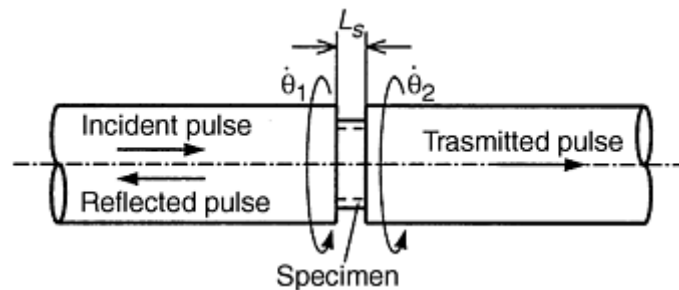


Fig. 2 Schematic of the torsional Kolsky bar apparatus. Angular velocities of the ends of the specimen are denoted by $\dot{\theta}_1$ and $\dot{\theta}_2$.

References cited in this section

1. U.S. Lindholm, High Strain Rate Tests, in *Measurement of Mechanical Properties*, Vol 5, Part I, Techniques of Metals Research, R.F. Bunshah, Ed., Interscience, 1971, p 199–271
2. H. Kolsky, An Investigation of the Mechanical Properties of Materials at Very High Rates of Loading, *Proc. Phys. Soc. London*, Vol 62-B, 1949, p 676–700

Historical Perspective

In 1949 Kolsky devised an experiment in which short specimens are placed between two long elastic cylindrical bars that act as wave guides for a loading pulse. The experiment was referred to as the split-Hopkinson bar, although the purpose of the test, the instrumentation, and the specimen were quite different from those in Hopkinson's original experiment (Ref 3).

In Kolsky's test, loading is accomplished by a compressive wave propagating along one of the bars and through the specimen. This wave is partially transmitted into the second bar and partially reflected by the specimen. The bars in this configuration are used for applying the load to the specimen and as transducers for measuring the displacements and loads at the specimen ends, which are in contact with the bars. Kolsky showed that the portion of the incident loading wave that is transmitted through the specimen provides a measure of the axial stress in the specimen, while the magnitude of the wave that is reflected back is proportional to its strain rate. It is assumed that the specimen is under a state of uniaxial stress and that the stress and strain are uniform along the specimen because the wave transit time through the specimen is very short compared to the duration of the loading wave.

The first torsional Kolsky bar was introduced in 1966 by Baker and Yew, who produced a torsional wave by a sudden release of a clamped pretwisted end section of an elastic bar (Ref 4). They showed that the stress-strain curves in shear for the specimen could be obtained by an analysis of the waves measured in the elastic bars on both sides of the specimen. Originally, a torsional version of the Kolsky bar was developed to eliminate radial inertia effect in the specimen and in the bars and the radial traction component that can be imposed (if friction is not eliminated) at the interfaces between the specimen and the bars in the compression test. Today these reasons no longer seem as important because the results from torsional tests have been found to be consistent with those of compression. However, torsional loading has other advantages, as described later in this article.

In the early 1970s, several configurations of torsional Kolsky bar were introduced by several investigators (Ref 5, 6, and 7). The various machines differ mainly in the method used for generating the torsional loading wave. Duffy et al. originally used explosive loading to initiate the loading pulse (Ref 5). Others used a sudden release of a stored torque. Explosive loading produces a short pulse with a short rise time. A stored-torque loading system provides a longer pulse, which produces larger strains in the specimen. The pulse, however, has a longer rise time that depends on the details of the clamp design.

The torsional Kolsky bar has also been modified for studying strain-rate history effects by conducting incremental and decremental strain-rate tests. In incremental strain-rate tests, the specimen is first twisted quasi-statically, and then a dynamic strain rate is imposed with no intermediate unloading (Ref 8, 9). In decremental strain rate tests an initial high strain rate deformation is suddenly reduced and continues at a lower strain rate (Ref 10, 11). Both strain rates are within the range of the torsional Kolsky bar.

The technique has also been adapted for testing materials at temperatures below and above the ambient (Ref 12, 13). For temperatures below the ambient and above the ambient up to about 150 °C, or 302 °F the technique is used without any modifications. In tests at higher temperatures (up to 1000 °C, or 1832 °F), the effect of heating the specimen on the adjacent elastic bars must be addressed.

The torsional Kolsky bar also provides means for studying localization of plastic deformation through the formation of adiabatic shear bands (Ref 14, 15, and 16). The evolution of the localization is recorded by high-speed photography and associated temperature increase is measured by detecting infrared radiation. Recently, a recovery experiment, in which the specimen was loaded up to a predetermined strain and then unloaded and recovered for microscopic examination, has also been introduced (Ref 17).

References cited in this section

3. B. Hopkinson, The Effects of Momentary Stresses in Metals, *Proc. Phys. Soc. London*, Vol 74-A, 1905, p 498–506

4. W.W. Baker and C.H. Yew, Strain Rate Effects in the Propagation of Torsional Plastic Waves, *J. Appl. Mech.*, Vol 33, 1966, p 917–923
5. J. Duffy, J.D. Campbell, and R.H. Hawley, On the Use of a Torsional Split Hopkinson Bar to Study Rate Effects in 1100-O Aluminum, *J. Appl. Mech.*, Vol 38, 1971, p 83–91
6. T. Nicholas and J.E. Lawson, On the Determination of the Mechanical Properties of Materials at High Shear-Strain Rates, *J. Mech. Phys. Solids*, Vol 20, 1972, p 57–64
7. J.L. Lewis and J.D. Campbell, The Development and Use of a Torsional Hopkinson Bar Apparatus, *Exp. Mech.*, Vol 12 (No. 11), 1972, p 520–524
8. R.A. Frantz and J. Duffy, The Dynamic Stress-Strain Behavior in Torsion of 1100-O Aluminum Subjected to a Sharp Increase in Strain Rate, *J. Appl. Mech.*, Vol 39, 1972, p 939–945
9. J.D. Campbell, A.M. Eleiche, and M.C.C. Tsao, Strength of Metals and Alloys at High Strains and Strain Rates, in *Fundamental Aspects of Structural Alloy Design*, R.J. Jaffee and B.A. Wilcox, Ed., Plenum Press, 1977, p 545–563
10. J. Lipkin, J.D. Campbell, and J.D. Swearingen, The Effects of Strain-Rate Variations on the Flow Stress of OFHC Copper, *J. Mech. Phys. Solids*, Vol 26, 1978, p 251–268
11. A. Gilat and Y.H. Pao, High Rate Decremental-Strain Rate Test, *Exp. Mech.*, Vol 28 (No. 3), 1988, p 322–325
12. A.M. Eleiche and J. Duffy, Effects of Temperature on the Static and Dynamic Stress-Strain Characteristics in Torsion of 1100-O Aluminum, *Int. J. Mech. Sci.*, Vol 17, 1975, p 85–95
13. A. Gilat and X. Wu, Elevated Temperature Testing with the Torsional Split Hopkinson Bar, *Exp. Mech.*, Vol 34 (No. 2), 1994, p 166–170
14. L.S. Costin, E.E. Crisman, R.H. Hawley, and J. Duffy, On the Localization of Plastic Flow in Mild Steel Tubes Under Dynamic Torsional Loading, in *Proc. 2nd Int. Conf. Mechanical Properties of Materials at High Rates of Strain*, J. Harding, Ed., The Institute of Physics, 1979, p 287–282
15. A. Marchand and J. Duffy, An Experimental Study of the Formation Process of Adiabatic Shear Bands in a Structural Steel, *J. Mech. Phys. Solids*, Vol 36, 1988, p 251–283
16. J.H. Giovanola, Adiabatic Shear Banding Under Pure Shear Loading, Part I: Direct Observation of Strain Localization and Energy Dissipation Measurements, *Mech. Mater.*, Vol 7, 1988, p 59–71
17. Q. Xue, L.T. Shen, and Y.L. Bai, A Modified Split Hopkinson Torsional Bar in Studying Shear Localization, *Meas. Sci. Technol.*, Vol 6, 1995, p 1557–1565

Torsional Kolsky Bar Testing

Amos Gilat, The Ohio State University

Comparison with Compression Kolsky Bar

The torsional Kolsky bar was originally introduced in order to verify strain-rate effects that were observed in tests with the compression Kolsky bar. Concerns have been raised with regard to the effects of inertia and friction on the experimental results when a compression load is used. Although the compressive and torsional Kolsky bar techniques are based on the same principles, there are significant differences between the two. In addition to the difference in the states of stress, the techniques use specimens that have different geometry, and the boundary conditions at the specimen ends are different. The two techniques are now compared in detail.

Inertia Effects in the Specimen. Due to the Poisson's ratio effect, loading in the compressional test is accompanied by radial expansion of the specimen. This radial expansion is opposed by a radial inertia that becomes greater with a shorter pulse and larger amplitude. This effect results in a radial stress component in the specimen superposed on the axial stress component. Hence, in axial loading, the state of stress in the specimen is not fully uniaxial. Furthermore, the radial component of stress is difficult to evaluate because it depends on dynamic material properties that have not yet been determined. In torsional testing, due to the absence of Poisson's ratio effect, radial expansion or contraction does not occur and inertial effects do not exist.

Friction Effects. In the compression Kolsky bar, radial deformation accompanies the axial motion. Radial traction is imposed at the interfaces between the specimen and the bars because the Poisson's ratio of the specimen is not necessarily the same as of the bars, and because the specimen undergoes plastic deformation. The radial traction causes unknown stresses and barreling in the specimen. Although friction can be minimized by proper lubrication, it cannot be completely eliminated. In torsional testing, friction does not exist.

Wave Dispersion in the Bars. In the compression Kolsky bar, the elastic waves that travel in the bars undergo geometric dispersion because different frequency components in the compressive pulse have different velocities. In particular, the higher frequency components travel at a lower velocity than the main pulse. In contrast, there is no geometric dispersion when a torsional pulse travels along an elastic bar in its primary mode; that is, all frequency components of the torsional pulse have the same velocity. Hence, a torsional pulse does not change its shape as it propagates toward the specimen.

The absence of geometric dispersion in torsion means that a pulse initiated with a short rise time will maintain this rise time until it reaches the specimen, independent of the length of the Kolsky bar. Also, the torsional strain gage stations can be located as near or as far from the specimen as desired and still reveal the correct shape pulse incident on, or reflected from, the specimen. In an axial Kolsky bar, however, a gage placed too close to the specimen is subject to errors due to three-dimensional end effects, while a gage placed too far from the specimen may produce unsatisfactory results due to geometric dispersion.

If a torsional pulse is noisy when initiated (i.e., if some high-frequency components are superposed on the main pulse), this characteristic will be maintained, regardless of the length of the Kolsky bar. As a result, the strain rate imposed on the specimen will not be constant. In axial Kolsky bar, such high-frequency components gradually disappear. Hence, an axial pulse tends to become flat—that is, tends to smooth out—as it travels along an elastic bar. A noisy torsional pulse will retain this characteristic; it will never become flat and, hence, will not provide deformation at a constant strain rate.

Specimens. Polycrystalline specimens tested in a torsional Kolsky bar experiment are shaped as short, thin-wall tubes. These specimens require substantially more material and are more expensive to machine than the specimens used in a compression Kolsky bar, which are shaped as short cylinders. In addition, gripping tubular specimen is more difficult, and special care must be taken that the specimens are attached firmly to the bars and that there are no wave reflections due to the gripping method.

Torsional Kolsky Bar Testing

Amos Gilat, The Ohio State University

Description

The torsional Kolsky (split-Hopkinson) bar apparatus is made up of two collinear bars that face each other and are supported by bearings that allow them to rotate freely. The specimen, which is usually a short, thin-wall tube, is attached between the two bars. To conduct a test, a torsional wave is generated in one of the bars

(incident bar). The wave propagates toward the specimen, and, when it arrives, the specimen is loaded and the wave is partially reflected back to the incident bar and partially transmitted to the other bar (transmitter bar). The apparatus and the specimen are designed such that the amplitude of the incident wave is much larger than the torque required for deforming the specimen or causing the specimen to fail. Consequently, most of the wave is reflected back to the incident bar and only a small portion is transmitted to the transmitter bar. As a result, the end of the incident bar where the specimen is attached rotates with an angular velocity that is much larger than the angular velocity of the other end of the specimen that is connected to the transmitter bar. The difference in the angular velocity between the specimen ends causes the specimen, which is very short, to deform at a high rate. In addition, because the specimen is short, and hence, the time it takes for the wave to propagate through is very short, the deformation is uniform. The history of load and deformation of the specimen is determined by monitoring the waves in the bars, which remain elastic throughout the test.

The Bars

The bars typically have a diameter of about 25 mm (1 in.) and are made of aluminum. Steel and titanium have also been used. The bars must be aligned properly and supported along the length by a series of bearings that allow free rotation. Aluminum bars are easy to use and are suitable for most applications. For an elastic torsional wave that propagates in a bar, the relationship between the torque, T , and the angular velocity, $\dot{\theta}$, is given by:

$$\dot{\theta} = \frac{T}{\rho J c} \quad (\text{Eq 1})$$

where ρ is the density, J is the polar moment of inertia, and c is the torsional wave speed. The maximum torque that can propagate in an elastic bar is limited by the yield stress of the material, τ_Y , which is related to the torque by:

$$T = \frac{\tau_Y J}{r} \quad (\text{Eq 2})$$

where r is the radius of the bar. Substituting T from Eq 2, and $c = \sqrt{G/\rho}$, where G is the shear modulus, in Eq 1 gives:

$$\dot{\theta} = \frac{\tau_Y}{r \sqrt{\rho G}} \quad (\text{Eq 3})$$

Equation 3 shows that, theoretically, a higher angular velocity can be achieved with bars made of a material that has high yield stress and low density and shear modulus. Titanium is a material that has a high value of $\tau_Y/\sqrt{\rho G}$. Practically, however, it is difficult to produce a torsion pulse in the incident bar with an amplitude high enough for the shearing stress to approach the yield stress of alloyed titanium. With this limitation, an aluminum bar has an advantage because, for the same torque, it will have a higher angular velocity than titanium.

Generating the Incident Wave

To conduct a test, a torsional wave has to be generated in the incident bar. The wave is characterized by its rise time, shape, amplitude, and duration. The most common method for generating the wave is a sudden release of a stored torque. The torsional wave can also be initiated by explosives. Descriptions of both methods follow.

Stored-Torque Torsional Kolsky Bar. A stored-torque Kolsky bar is shown schematically in Fig. 3. The loading wave in the incident bar is produced by the release of a torque that is initially stored at the section of the bar between the clamp and the loading end. The stored torque is generated by first tightening the clamp and then turning the end of the bar. It is important that the section of the bar with the stored torque will be loaded with pure torque without bending moment or axial force. This can be done by rotating a wheel, attached at the end of incident bar, with a hydraulic system of a cable and pulleys that applies a pure couple to the wheel. The design of the clamp is crucial for good results. The clamp must be able to hold the desired torque without slipping and release the torque rapidly enough to produce a sharp-fronted stress pulse traveling toward the specimen.

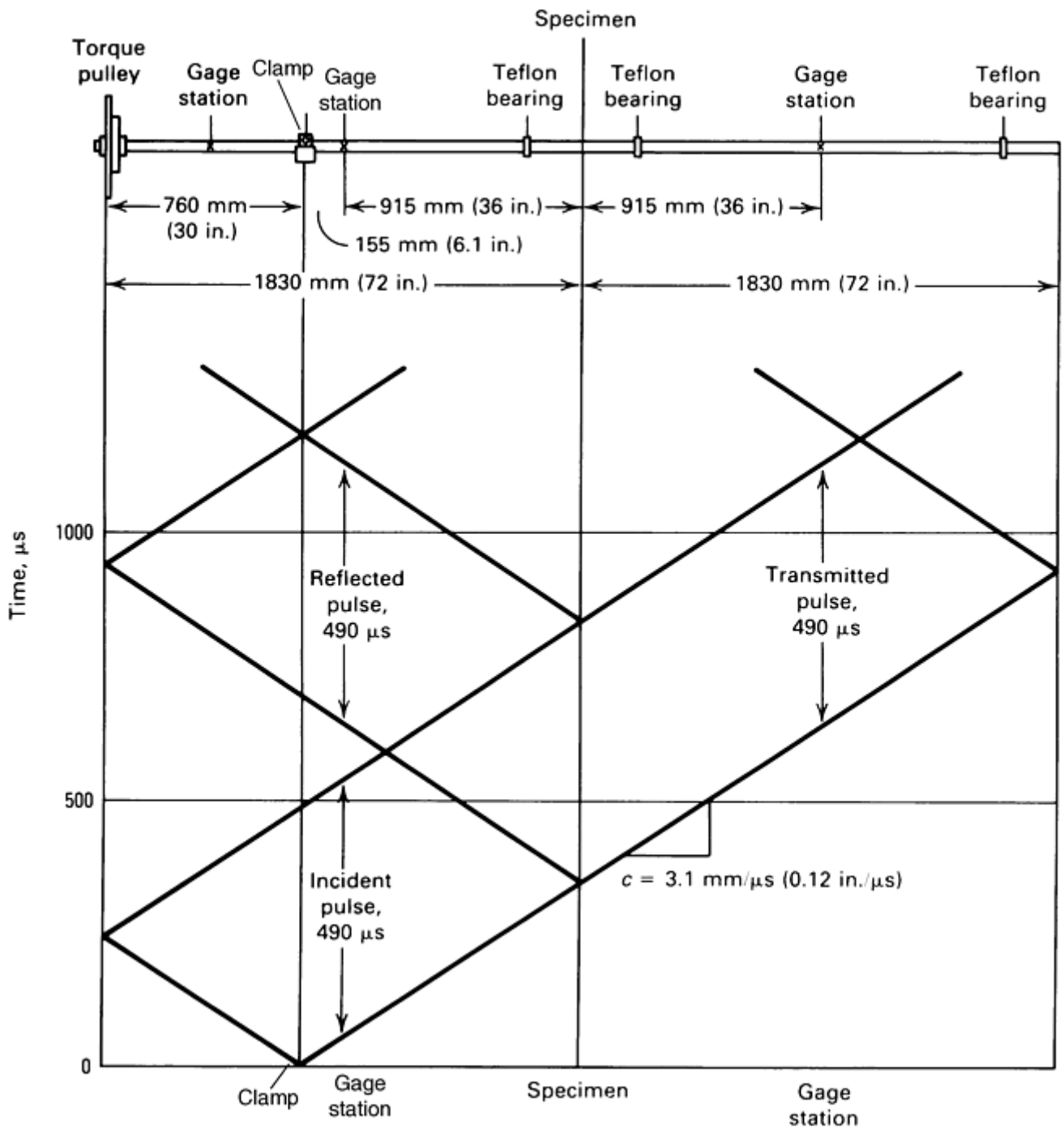


Fig. 3 Schematic of a stored-torque torsional Kolsky bar and its wave characteristic diagram. Torsional wave speed is denoted by c .

Clamping Techniques. The design of the quick-release clamp has a direct influence on the quality of the incident loading wave. Ideally, the incident pulse should rise instantly to a constant amplitude and then drop off immediately to zero at the end of the pulse, thus forming a square loading pulse. In practice, a finite time (rise time) is required to achieve maximum torque in the loading pulse.

A clamp designed by Duffy (Ref 18) is shown in Fig. 4. It consists of two arms that are held together at the top by a notched pin and are hinged at the bottom to a fixed peg on one side and to a sliding peg on the other. The clamp is tightened by a hydraulic ram that pushes the lower ends of the clamp arms together. After the desired torque is loaded between the loading end and the clamp, the hydraulic pressure is increased until the notched pin at the top fractures, releasing the stored torque.

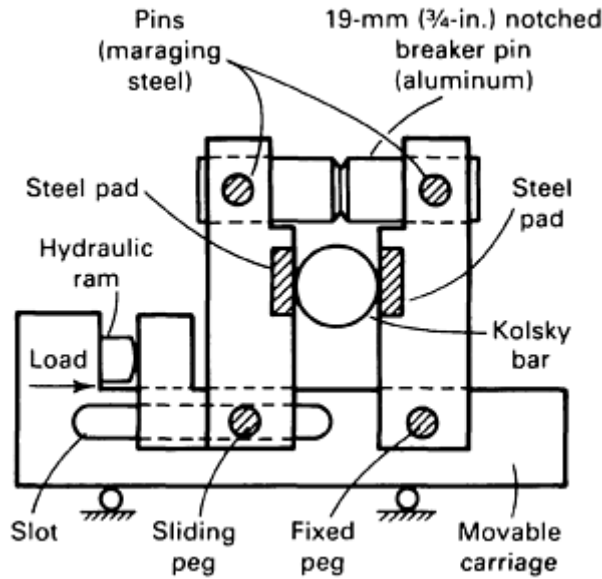


Fig. 4 Clamp designed by Duffy for the torsional Kolsky bar. Source: Ref 18

A variation of this design introduced by Gilat is illustrated in Fig. 5. In this design, both arms can slide at the bottom. The clamp is tightened by a hydraulic C-clamp that pushes the lower ends of the clamp arms against each other. The hydraulic C-clamp is attached to the frame by means of a cable, a pulley, and a soft spring. In this way the C-clamp is “floating,” adjusting itself to the location of the bar. In this design, the clamp arms are shaped to match the circumference of the loading bar. Between tests, the bare surfaces of the bar and the arms that are in contact are cleaned with acetone to ensure good gripping.

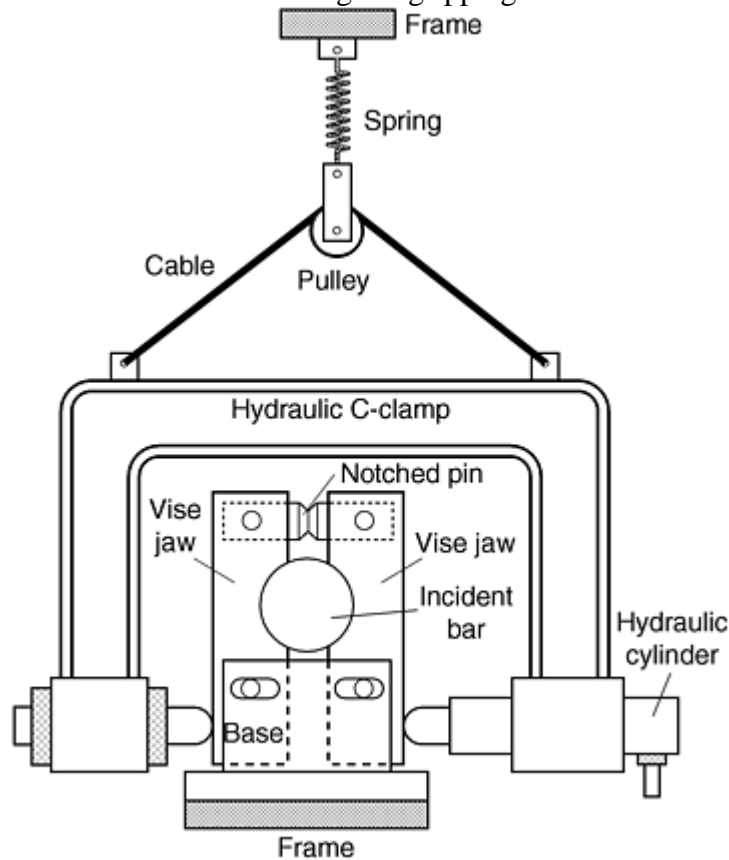


Fig. 5 Clamp designed by Gilat for the torsional Kolsky bar

The amount of torque required to achieve the desired strain rate is a determining factor in selecting the notched-pin material and the depth of the notch. Pulse rise time is also affected by the choice of material for the notched pin. The pin material must exhibit minimal ductility, but must not be brittle enough to fracture before the clamp

is tight enough to hold the desired stored torque. Functional pin materials include 6061-T6 and 7075-T6 aluminum alloys. The desired clamping force and fracture point are achieved by varying the depth of the notch. Steel pins can also be used, but even brittle steels produce a longer rise time than aluminum alloys. It might be expected that the mass of the clamp would affect the rise time of the pulse, but this appears not to be the case. The rise time of the pulse can be decreased much more significantly by proper selection of pin material.

Misalignment of the various components of the Kolsky bar can result in a small unloading pulse immediately preceding the incident loading pulse, particularly if misalignment is caused by the action of the clamp. The entire clamp mechanism must be allowed to slide relative to the bar. This is achieved with the movable carriage and the floating hydraulic C-clamp in the designs shown in Fig. 4 and 5, respectively. Care should be taken to prevent bending of the incident bar when the clamp is tightened.

Explosively Loaded Torsional Kolsky Bar. An explosively loaded torsional Kolsky bar is shown schematically in Fig. 6. The torsional pulse is generated by the simultaneous detonation of two small charges at the loading end (Fig. 7). To obtain a pure torque with no bending, each charge must provide an equal impulse, and they must be detonated at the same instant. The first requirement is met by using equal weights of explosive and the second by using a single detonator connected to the explosive charge by means of "leaders" that are also made of the explosive. These leaders are of equal length, and tests have shown that the explosive charges are detonated less than 0.1 μs apart. Although the pulse that is initiated is almost entirely torsional, some low-amplitude axial and bending stress pulses are also initiated. The amplitude of these undesirable pulses can be decreased by inserting a mechanical filter in the bar. The filter, resembling a rather stiff bellows, is shown at the top of Fig. 8. It is made of an aluminum alloy, such as 6061-T6, with relatively high yield stress.

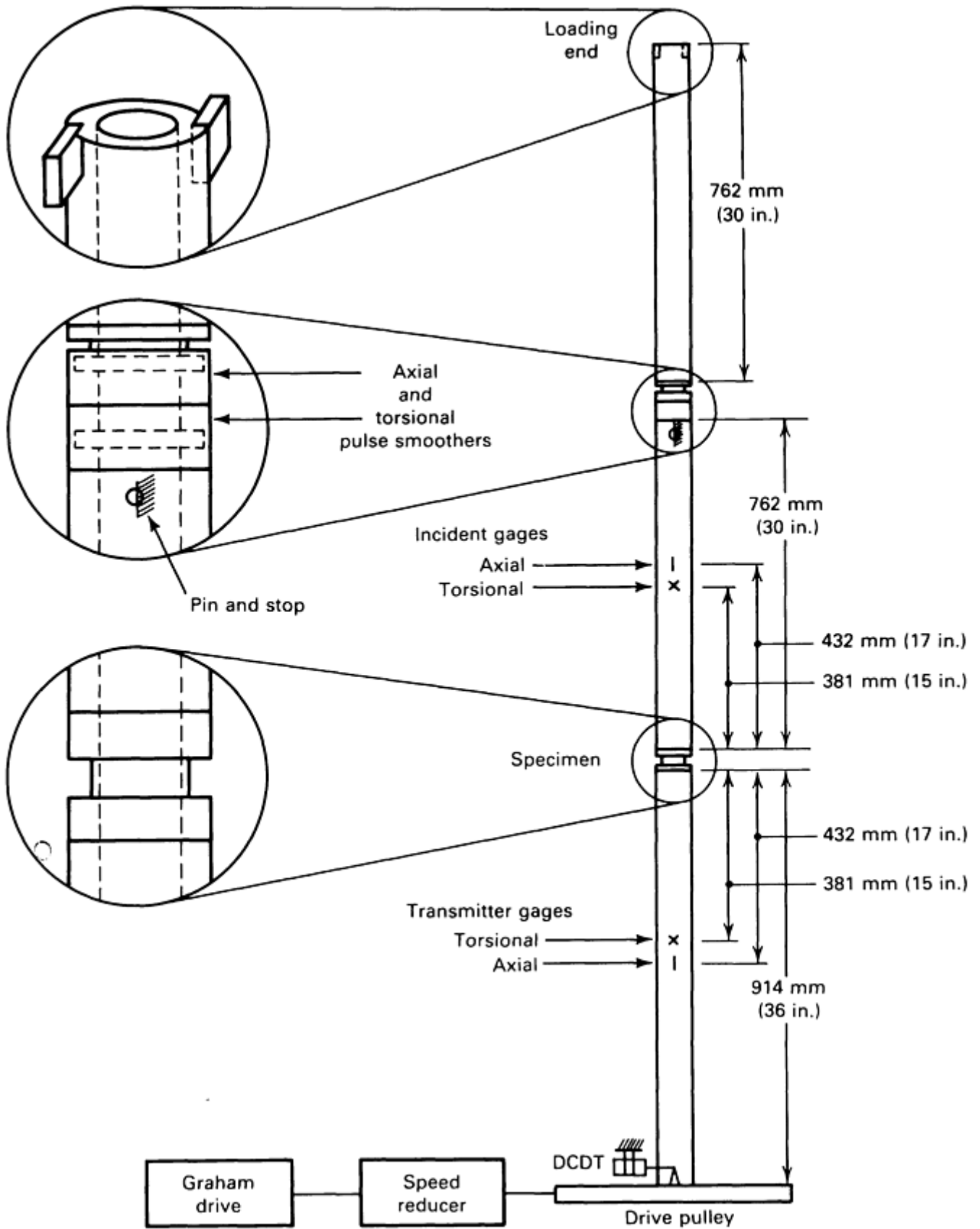


Fig. 6 Schematic of explosively loaded torsional Kolsky bar

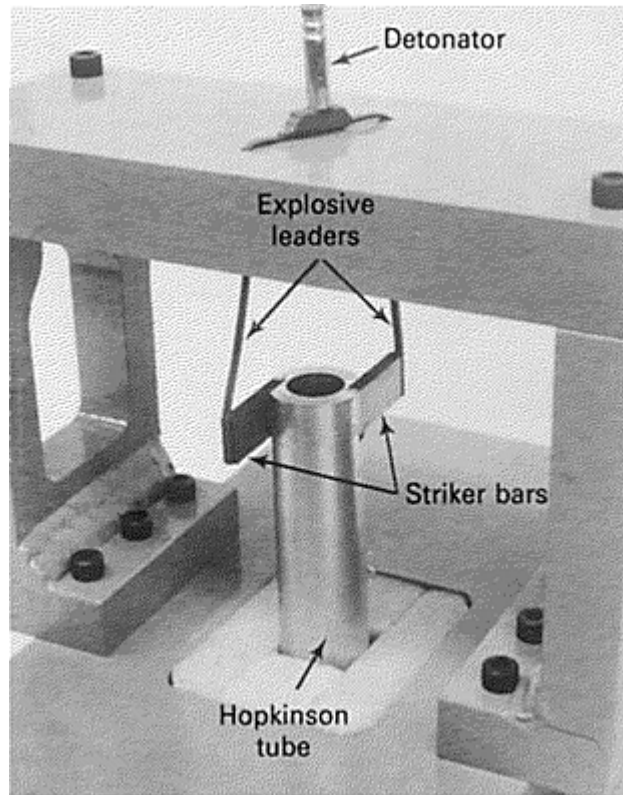


Fig. 7 Loading end of explosively loaded torsional Kolsky bar

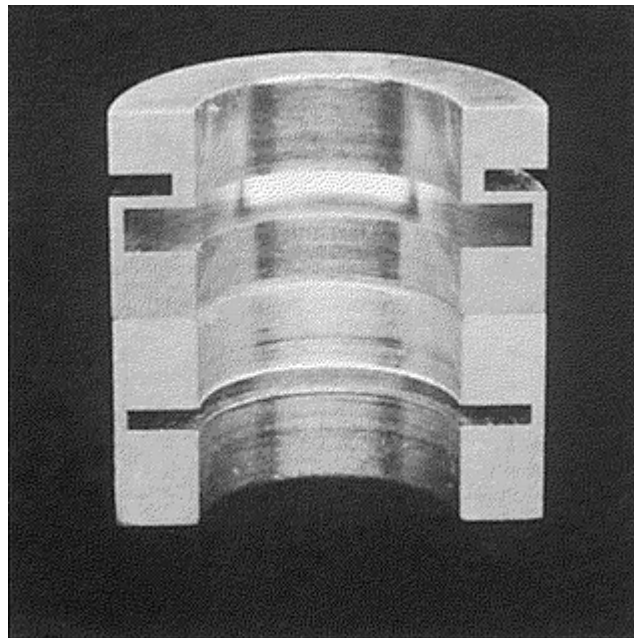


Fig. 8 Cross section of pulse filter showing the axial pulse attenuator (top) and the torsional pulse smoother (bottom)

The advantage of explosive loading is the short rise time in the loading pulse compared to a stored-torque system. A typical rise time is only 7 to 10 μs , compared with 20 to 40 μs with the stored-torque system, depending on pulse amplitude. The pulse produced by the explosion at the loading end, however, is neither “square” nor “smooth.” The amplitude of the pulse varies considerably with time. Because no geometric dispersion occurs for a torsional pulse in its first mode, the pulse profile remains unchanged as the pulse propagates toward the specimen. The variation in amplitude is undesirable because it results in loading the specimen at a variable strain rate. The pulse profile can be smoothed by a second mechanical filter (pulse smoother). The pulse smoother is a short length of tubing with a narrow neck made of 1100-O aluminum so that it deforms plastically during the passage of the pulse. It reduces the magnitude of the higher-frequency

components, smoothing the pulse. As shown in Fig. 8, the two filters are placed next to each other in the incident bar.

The explosive charges produce a relatively short pulse so that the total strain is generally small. With a stored-torque bar, the distance between the loading end and the clamp can be increased to produce as long a pulse as the available laboratory space will allow.

Test Specimens

Polycrystalline specimens used in the torsional Kolsky bar experiments usually are short, thin-wall tubes with integral flanges machined from bar stock (Fig. 9). The specimen is held in position by either cementing its flanges to the Kolsky bars with epoxy cement, shown in Fig. 9(a), or by mechanical means, shown in Fig. 9(b).

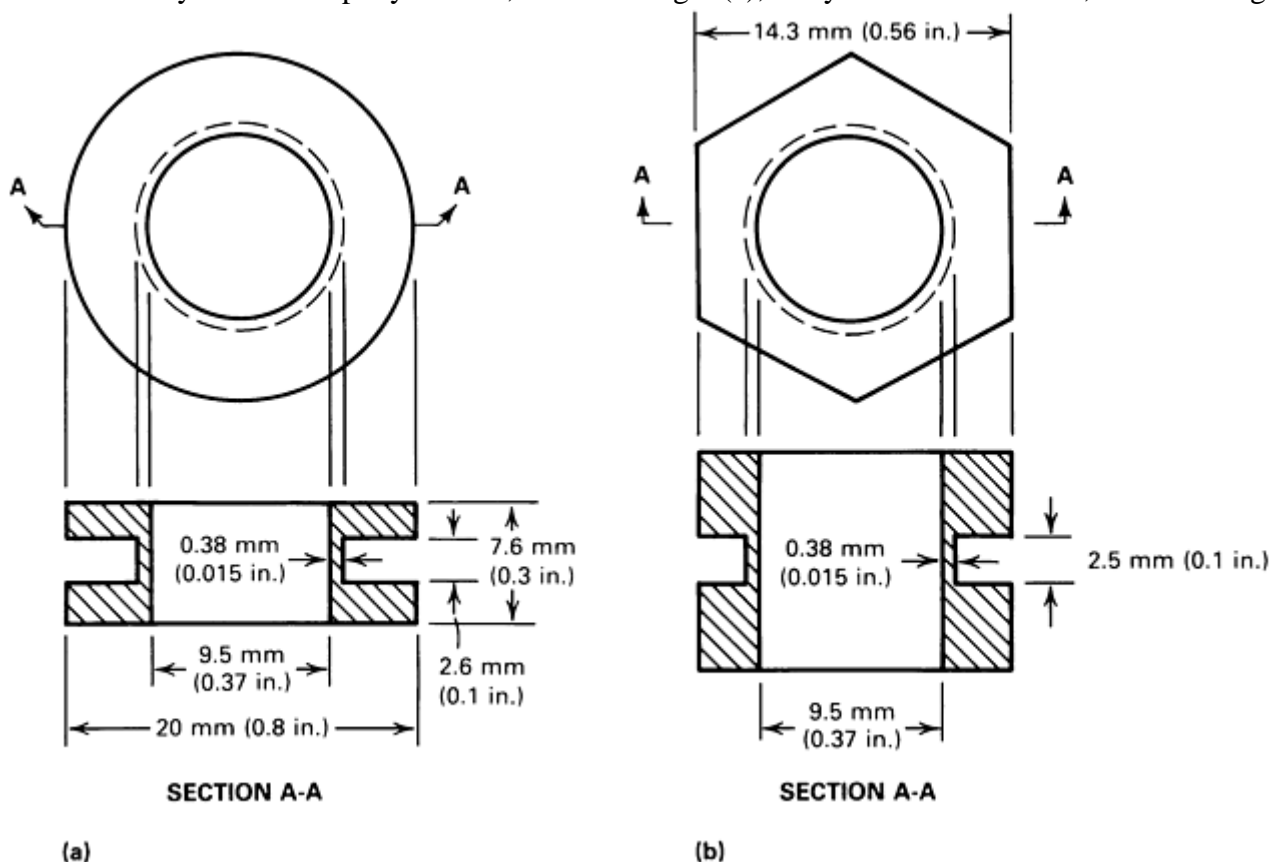


Fig. 9 Details of the polycrystalline specimen used in the torsional Kolsky bar experiment. (a) Tubular specimen with cylindrical flanges for cementing. (b) Tubular specimen with hexagonal flanges

Cemented connections where the faces of the flanges are glued directly to the bar ends are rigid and provide sufficient strength for specimens that have relatively low flow stress (e.g., 1100-O aluminum, OFHC copper, or zinc). Specimens made of materials with higher flow stress can still be cemented by using an adapter that increases the surface area of the glue. Cemented connections are less convenient to use because it takes a long time for the epoxy to cure and the bar ends have to be cleaned after each test. In addition, cemented connections cannot be used in tests at elevated temperatures.

Mechanical connections must be as rigid as possible to prevent loss of motion between the specimen and the bars as the stress pulses pass. Threaded connections do not meet this requirement. However, success has been achieved using hexagonal flanges on the specimen with matching sockets in the ends of the Kolsky bars. To prevent lost motion between the socket and the flanges, small set screws are used to hold the specimen flanges against the driving faces of the hexagonal sockets. For specimen materials with high flow stress, such as alloy steel, the set screws may not grip the specimen tightly enough to prevent relative rotation. To enhance rigidity, the hexagonal socket can be filled with warm glycol phthalate, the specimen inserted, and the set screws tightened.

The dimensions of the flanges and the design of any adapter or mechanical connection device must be such that the torsional mechanical impedance matches that of the bar so that the stress pulses do not undergo reflection when propagating through. This condition requires that the product ρcJ is constant along the bar. The use of short specimens in the torsional Kolsky bar implies that a nearly homogenous state of strain is obtained after a few reflections of the loading pulse from the ends of the specimen. To examine the development of the elastic-plastic boundary within the wall thickness of the tubular specimen, a finite-element analysis of the strain distribution is performed (Ref 19). In this analysis, a bilinear elastic-plastic stress-strain relation is used with an elastic modulus and a plastic-hardening rate approximately equal to those of commercially pure aluminum. Figure 10 illustrates the growth of the plastic zone (the dark areas) at various stages of deformation.

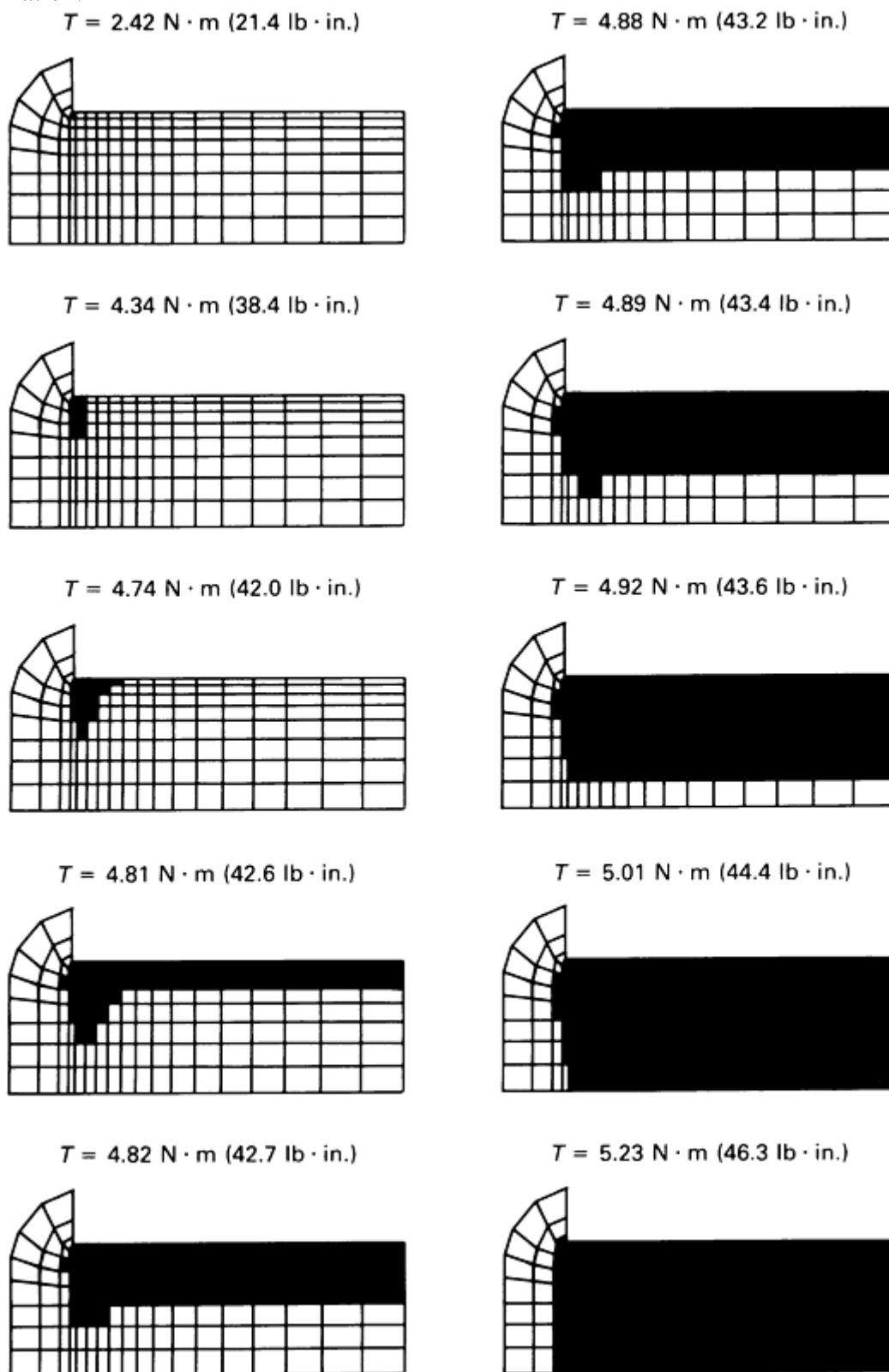


Fig. 10 Results of a finite-element analysis showing the growth of the plastic zone within the tubular specimen used in the torsional Kolsky bar. Each diagram shows a cross section through half the length of the tube wall, plus the adjacent flange. The plastic zone is represented by the dark area and the applied torque is T . Source: Ref 19

The plastic zone begins at the reentrant corner between the thin-wall tube and the flange, and from there spreads gradually throughout the thickness of the wall. Each diagram in Fig. 10 represents one quarter of the cross section of the tube and the adjacent part of the flange; thus, the central axis of the specimen lies below in each diagram. The values of the applied torque are given.

The plastic zone proceeds radially toward the inside wall surface and then across the gage length along the outside surface of the specimen. The plastic zone is contained until almost the entire specimen begins to flow. These results are based on a static analysis, but because the wavelength of the pulse is much longer than the specimen, these data can be applied to the dynamic deformation and appear to agree well with experimental results.

With continued loading into the plastic range, the strain distribution in the thin-wall tube may not remain homogeneous. For example, depending on the material, shear bands may form that completely encircle the thin-wall tube. Whenever the strain is not homogeneous, interpretation of the strain gage records is significantly altered because the strain rate and, hence, the strain that are calculated from the strain-gage records are average values based on the assumption that the deformation is homogeneous. If shear bands develop, they are not encountered until some plastic deformation has accumulated. For instance, Costin et al. observed shear bands in 1018 cold-rolled steel at plastic strain of 8 to 10% (Ref 14). The presence of shear bands in a thin-wall tubular specimen is easy to detect by scribing fine axial lines on the inside-wall surface of the specimen before loading. If the strain remains homogeneous throughout the deformation process, after testing, each of these lines appears tilted at the shear angle within the gage length of the specimen, but remains straight and axial in the flange area (Fig. 11b). Any departure from a straight line within the gage length is evidence of nonhomogeneous strain. When nonuniform strain is present, as in the case of a shear band, the lines depart drastically from straight lines (Fig. 11a).

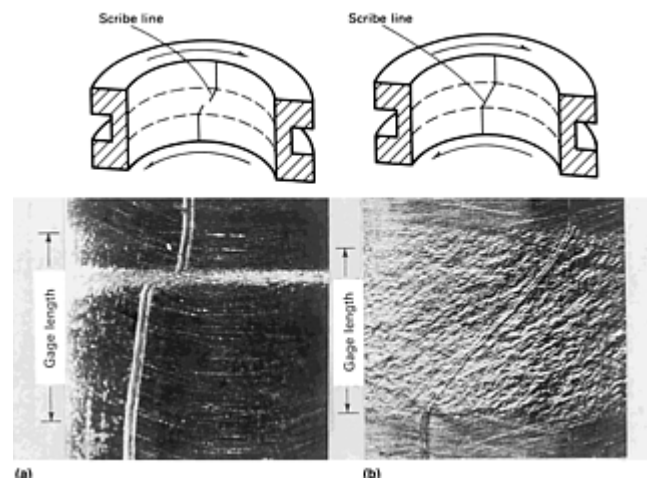


Fig. 11 Section of specimen showing scribe line after testing. (a) Specimen with nonhomogenous strain distribution due to the formation of a shear band. (b) Specimen with homogenous strain distribution

Single-crystal specimens can be tested in the torsional Kolsky bar using a small rectangular parallelepiped. A matched set of four single-crystal specimens with the same crystallographic orientation are tested together. The specimens are arranged circumferentially at 90° intervals (Fig. 12).

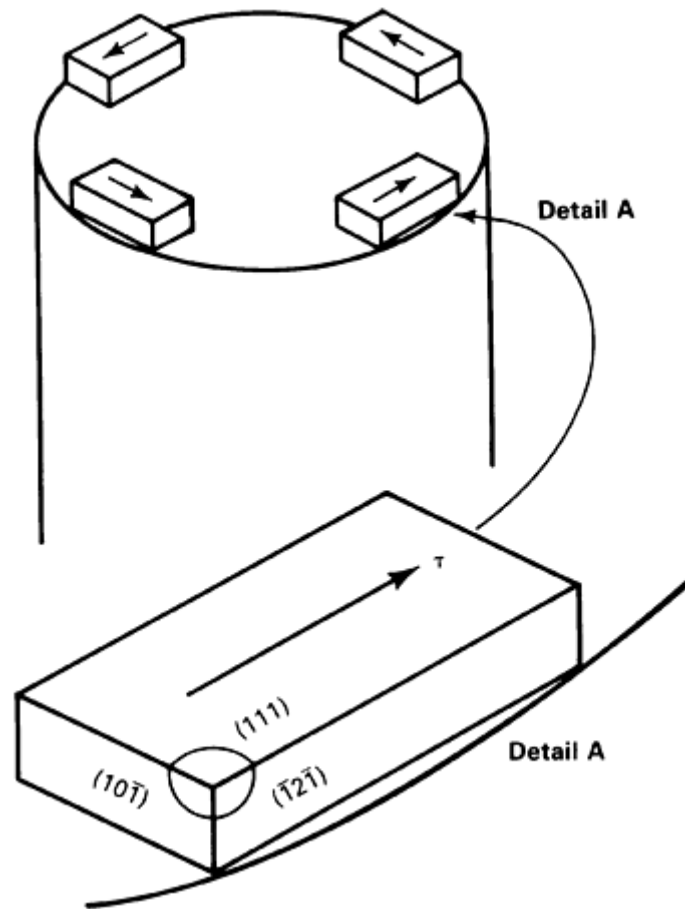


Fig. 12 Aluminum single-crystal specimens showing the arrangement relative to the Kolsky bar

The specimens are secured with an epoxy cement. These cements are sufficiently strong to test pure metals, which generally have a low flow stress. With strong metals, the epoxy might break before any significant amount of strain accumulates. Each test yields the average stress-strain properties of the four specimens (Ref 20).

Measuring the Waves in the Bars

The torsional waves in the Kolsky bars are detected by electrical-resistance strain gages. At each measuring station, four strain gages, equally spaced around the circumference, are placed on the bar. Two gages on opposite sides are at $+45^\circ$ to the axis of the bar, and the other two gages, also on opposite sides but rotated 90° relative to the first two, are at -45° to the axis of the bar. The four gages are connected in a four-arm Wheatstone bridge.

Location of Measuring Stations. A wave-characteristic diagram for a stored-torque Kolsky bar that shows the positions of the wave fronts with time is shown in Fig. 3. Upon release of the clamp, the torsional pulse, with a torque of amplitude equal to half that of the stored torque, propagates down the bar toward the specimen. Simultaneously, an unloading pulse of equal magnitude propagates from the clamp toward the loading pulley. The torsional mechanical impedance of the pulley is sufficiently large so that the reflected unloading wave reduces the torque in the incident bar to zero as it propagates back along the bar. The duration of the loading pulse is the time required for the pulse to travel twice the distance along the bar between the clamp and the loading end.

The waves are measured on the incident and transmitter bars. On the transmitter bar, the wave is measured in one location. On the incident bar, the wave can be measured at either one or two locations.

When the pulse on the incident bar is measured at one location, as shown in Fig. 3, the location must be at a sufficient distance from the specimen so that a clear record of both the incident and the reflected pulses is obtained without overlap or interference. For example, if the distance between the clamp and the loading end is 760 mm (30 in.), the pulse length would be $490 \mu\text{s}$ for an aluminum bar with a shear wave speed of 3100 m/s

(10,200 ft/s). To ensure that the reflected pulse does not overlap with the incident pulse at the gage station and thus cause interference, the gage station must be placed at least 760 mm (30 in.) from the specimen. Furthermore, to ensure that the stress in the bar returns to zero after the pulse has passed, the station should be located at an even greater distance from the specimen. For example, for the bar shown in Fig. 3, the gage station is located 915 mm (36 in.) from the specimen. A gage station for monitoring the transmitted pulse is located at the same distance from the specimen (915 mm, or 36 in.). Figure 13 shows an oscilloscope record from a test with the stored-torque Kolsky bar in which the pulse on the incident bar was recorded at one location.

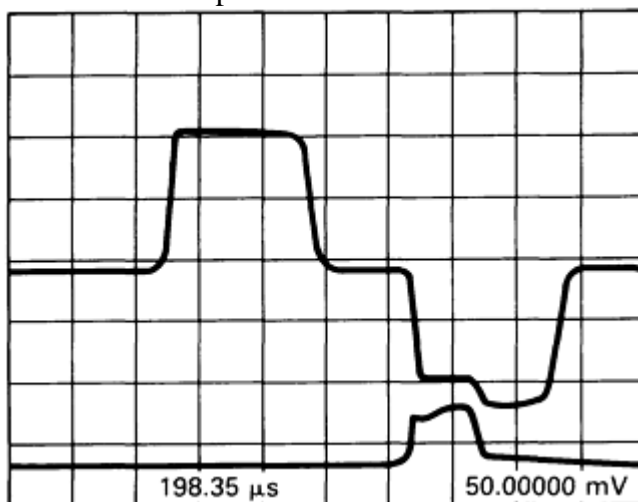


Fig. 13 Oscilloscope record from a test with a stored-torque Kolsky bar in which the pulse in the incident bar is recorded at one gage station. Each horizontal division equals 200 μs. Transmitted output magnified 2×. Fracture of the specimen causes transmitted pulse magnitude to drop to zero.

When the pulse in the incident bar is measured at two locations, one station is located near the clamp and the other near the specimen (Fig. 14). The angular velocity and torque at the interface between the incident bar and the specimen can be determined from the recorded pulses in the two stations. The duration of the experiment that can be analyzed depends on the location of the gage stations. A longer duration is obtained if stations *A* and *B* are placed close to the clamp and the specimen, respectively. To have a uniform wave in the gage station *A*, it should not be located too close to the clamp (a distance of 3–4 bar diameters appears to be appropriate). The length of the clamped section of the incident bar should be designed such that the reflected wave from the loading wheel reaches gage station *A* just after the reflected wave from the specimen arrives there. When processing the data it is also convenient (though not necessary) to place gage stations *B* and *C* at the same distance from the specimen. Figure 15 shows oscilloscope records from a test with the stored-torque Kolsky bar in which the pulse on the incident bar was recorded at two locations (Ref 21).

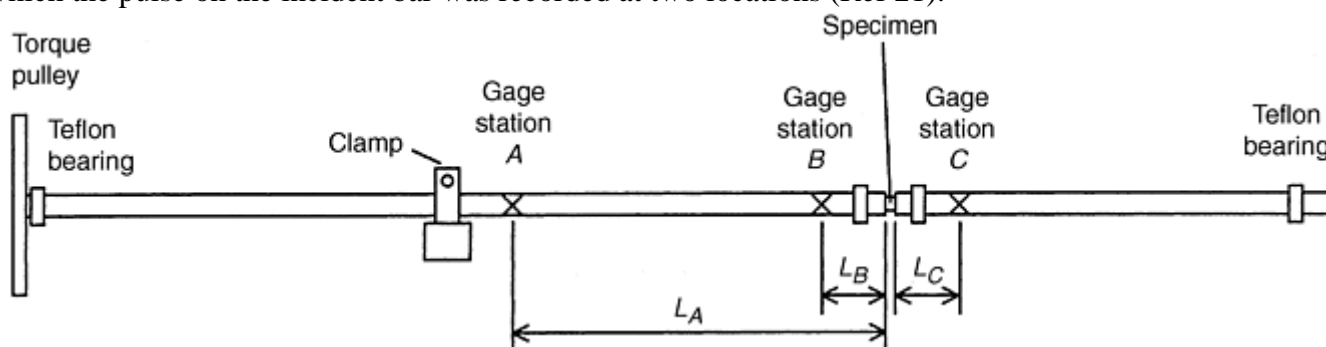


Fig. 14 Schematic of a torsional Kolsky bar with two gage stations on the incident bar

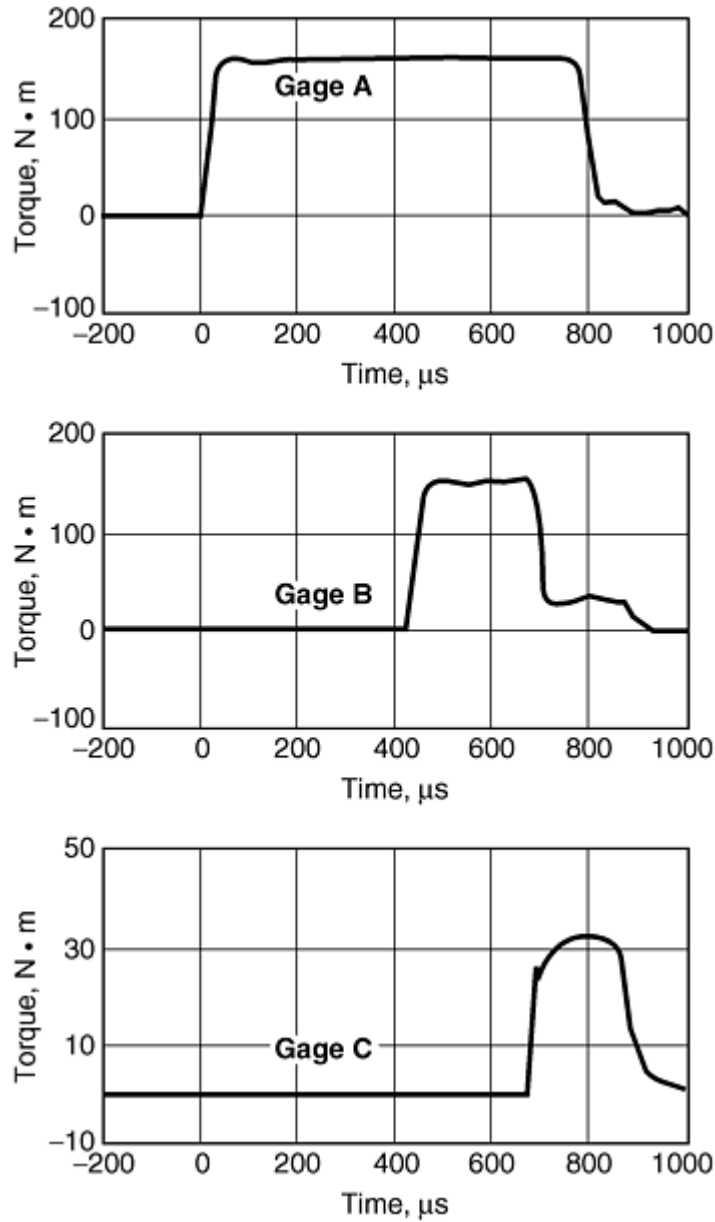


Fig. 15 Oscilloscope record from a test with a stored-torque Kolsky bar in which the pulse in the incident bar is recorded at two gage stations. Source: Ref 21

Calculating Stress, Strain, and Strain Rate. The average shear strain rate in the specimen as a function of time, $\dot{\gamma}_s(t)$, is determined from the difference in the angular velocity between its two ends by:

$$\dot{\gamma}_s(t) = \frac{r_s}{L_s} [\dot{\theta}_1(t) - \dot{\theta}_2(t)] \quad (\text{Eq 4})$$

where $\dot{\theta}_1(t)$ and $\dot{\theta}_2(t)$ are the angular velocities of the specimen ends where it attaches to the incident and transmitter bars, respectively; r_s is the mean radius of the thin-wall specimen; and L_s is the length of the specimen.

When one gage station is used to measure the waves on the incident bar $[\dot{\theta}_1(t) - \dot{\theta}_2(t)]$ is determined from the reflected pulse by:

$$[\dot{\theta}_1(t) - \dot{\theta}_2(t)] = \frac{2[-T_R(t)]}{\rho J c} \quad (\text{Eq 5})$$

where $T_R(t)$ is the amplitude of the torque of the reflected pulse. Equation 5 is derived by assuming that the specimen is under a uniform state of stress such that the torque at both ends is equal. The torque, T , at a gage station is related to the measured shear strain on the surface of the bar, γ , by:

$$T = \frac{GJ}{r_b} \gamma \quad (\text{Eq 6})$$

where r_b is the radius of the bar. Using Eq 6 to replace T_R with γ_R in Eq 5 and substituting in Eq 4 gives the strain rate in the specimen as a function of strain of the reflected pulse:

$$\dot{\gamma}_s(t) = \frac{r_s}{L_s} \frac{2c}{r_b} [-\gamma_R(t)] \quad (\text{Eq 7})$$

When two strain gage stations are used to measure the waves on the incident bar, $[\dot{\theta}_1(t) - \dot{\theta}_2(t)]$ is determined by:

$$\begin{aligned} [\dot{\theta}_1(t) - \dot{\theta}_2(t)] = & \frac{1}{\rho J c} [T_A(t - t_A) + T_A(t - t_A + 2t_B) \\ & - T_B(t + t_B) - T_C(t + t_C)] \end{aligned} \quad (\text{Eq 8})$$

where T_A , T_B , and T_C are the torques in the bars at gage stations A , B , and C , respectively; and $t_A = L_A/c$, $t_B = L_B/c$, and $t_C = L_C/c$ are the times required for the elastic waves in the bars to propagate the distance from the specimen to gage stations A , B , and C , respectively. The strain rate in the specimen at time t is obtained by using Eq 6 and substituting Eq 8 in Eq 4:

$$\begin{aligned} \dot{\gamma}_s(t) = & \frac{c}{r_b} \frac{r_s}{L_s} [\gamma_A(t - t_A) + \gamma_A(t - t_A + 2t_B) \\ & - \gamma_B(t + t_B) - \gamma_C(t + t_C)] \end{aligned} \quad (\text{Eq 9})$$

where γ_A , γ_B , and γ_C are the strains measured at gage stations A , B , and C , respectively. The shear strain in the specimen γ_s is obtained by integrating the strain rate (given by Eq 7 or 9, depending on the configuration of gage stations on the incident bar):

$$\gamma_s(t) = \int_0^t \dot{\gamma}_s(t) dt \quad (\text{Eq 10})$$

Figure 16 shows the strain rate and strain versus time calculated from the pulse records shown in Fig. 15.

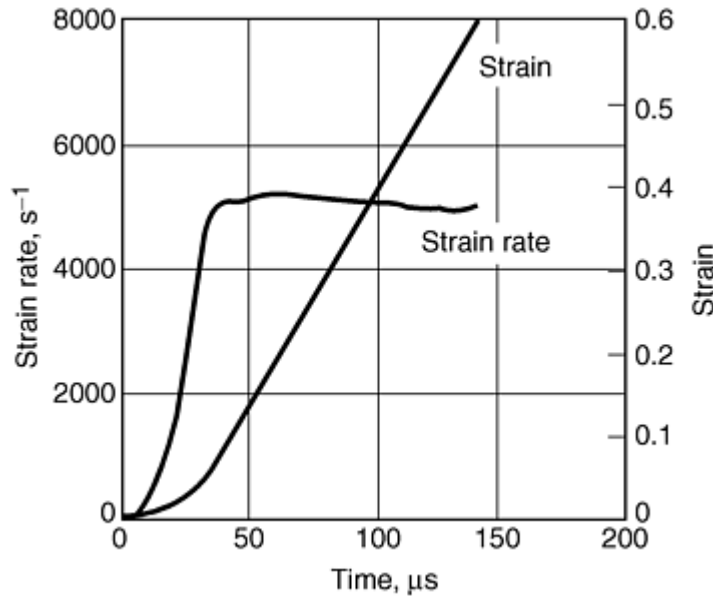


Fig. 16 Strain rate in the A533B steel specimen as calculated from the pulses in Fig. 15

The shear stress in the specimen, τ_s , is determined from the torque in the specimen, T_s . For a thin-wall tube the stress is given by:

$$\tau_s = \frac{T_s}{2 \pi r_s^2 t_s} \quad (\text{Eq 11})$$

where t_s is the wall thickness. Because the stress in the specimen is assumed to be uniform, the torque at each end of the specimen is the same, and the torque of the pulse transmitted to the output bar is the torque in the specimen. In terms of the strain measured by the strain gage station on the output bar, the shear stress in the specimen at time t is given by:

$$\tau_s(t) = \frac{Gr_b^3}{4r_s^2 t_s} \gamma_C(t + t_C) \quad (\text{Eq 12})$$

Figure 17 shows the stress-strain curve that is obtained from the records in Fig. 15 and 16.

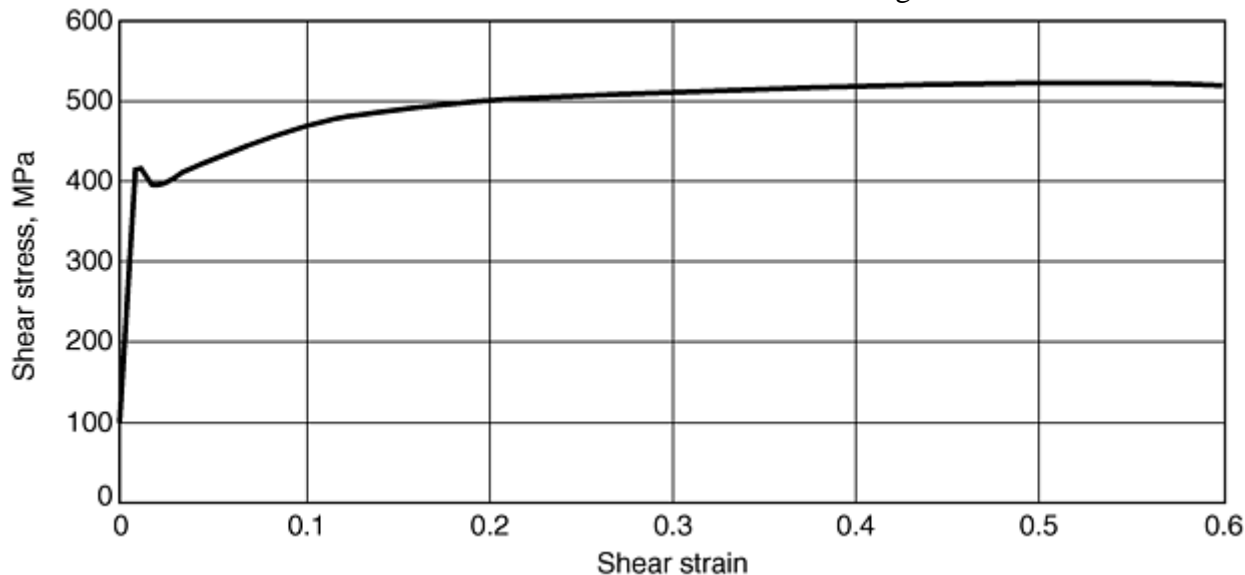


Fig. 17 Stress-strain curve for A533B steel obtained from the records in Fig. 15 and 16. Test temperature, 25 °C (77 °F); strain rate, 5000 s⁻¹

Data Recording. The signals from the Wheatstone bridges are typically recorded by a digital oscilloscope with a frequency response of at least 1 MHz. The signals can then be processed with the oscilloscope to determine the strain rate, strain, and strain in the specimen. Alternatively, the digitized signals can be transferred for processing and plotting to a computer. With the availability of fast data-acquisition boards for personal computers, recording and processing can be also done by a computer directly.

References cited in this section

14. L.S. Costin, E.E. Crisman, R.H. Hawley, and J. Duffy, On the Localization of Plastic Flow in Mild Steel Tubes Under Dynamic Torsional Loading, in *Proc. 2nd Int. Conf. Mechanical Properties of Materials at High Rates of Strain*, J. Harding, Ed., The Institute of Physics, 1979, p 287–282
18. K.A. Hartley, J. Duffy, and R.H. Hawley, The Torsional Kolsky (Split-Hopkinson) Bar, *Mechanical Testing*, Vol 8, *ASM Handbook*, ASM International, 1985, p 218–228
19. E.K.C. Leung, An Elastic-Plastic Stress Analysis of the Specimen Used in the Torsional Kolsky Bar, *J. Appl. Mech.*, Vol 47, 1980, p 278–282
20. C.Y. Chiem and J. Duffy, Strain Rate History Effects and Observations of Dislocation Substructure in Aluminum Single Crystals Following Dynamic Deformation, *Mater. Sci. Eng.*, Vol 57, 1963, p 233–247
21. Y.H. Pao and A. Gilat, High Strain Rate Deformation and Failure of A533B Steel at Various Temperatures, *Acta Metall. Mater.*, Vol 40, 1992, p 1271–1280

Application Areas

Limitations on Strain Rate. The practical upper limit on the strain rate that can be achieved in tests with the torsional Kolsky bar is about 10^4 s^{-1} . This can be observed by combining Eq 4 and 5 to write the strain rate as a function of the reflected torque, and substituting $T_I - T_T$ for $-T_R$, which gives:

$$\dot{\gamma}_s = \frac{r_s}{L_s} \frac{2}{\rho J c} (T_I - T_T) \quad (\text{Eq 13})$$

where T_I is the incident torque and T_T is the transmitted torque. For a solid circular cylinder, the incident torque is related to the shear stress in the incident bar (τ_b) by:

$$T_I = \frac{J}{r_b} \tau_b \quad (\text{Eq 14})$$

Using Eq 11 and 14, the strain rate in the specimen can be obtained as:

$$\dot{\gamma}_s = \frac{2}{L_s \rho c} \left[\tau_I \left(\frac{r_s}{r_b} \right) - 4 \left(\frac{r_s}{r_b} \right)^3 \left(\frac{r_s}{r_b} \right) \tau_s \right] \quad (\text{Eq 15})$$

Where τ_I is the incident shear stress. From Eq 15, it is evident that the maximum strain rate is attained when the quantity on the right side is maximized. One means is to make the specimen shorter, that is, to decrease L_s . However, with very short specimens, the end effects can become important; that is, the strain in the specimen may never be uniform.

Because the second term in Eq 15 generally is small, another method of increasing the strain rate is to increase the ratio r_s/r_b by decreasing the radius of the bar, or by increasing the mean radius of the specimen. The limiting ratio of r_s/r_b that can be used is 1 because r_s cannot be greater than r_b without a significant change in the impedance.

Yet another method of increasing the strain rate is to select a bar material with a high yield stress in order to maximize τ_I in Eq 15. This would appear to have an advantage because a much greater torque can be stored in the bar. However, two other factors affect the selection of the bar material. First, the mass density, ρ , of the bar material has to be considered. For example, the mass density of steel is about three times that of aluminum. Thus, unless the steel has a yield stress that is more than three times that of aluminum, there will be no increase in strain rate when using a steel bar. With this regard, a material with a high ratio of yield stress to density, such as a titanium alloy, will theoretically maximize the strain rate. Secondly, the ability to clamp a high torque has to be considered. As discussed earlier, it is difficult, if not impossible, to clamp a torque such that the shear stress in the bar approaches the yield stress. High clamping pressures may also produce an axial pulse upon the release of the clamp.

It is evident from Eq 15 that an increase in the diameter of the Kolsky bar will not increase strain rate significantly. Increased diameter alters only the second term in Eq 15, which is considerably smaller than the first term. From Eq 14, it is evident that, although optimum bar dimensions and material exist to achieve a maximum strain rate, there is a physical limit of strain rate of about 10^4 s^{-1} that is attainable.

The practical lower limit on strain rate in the Kolsky bar is about 10^2 s^{-1} because a lower strain rate cannot be held constant throughout the test. A constant value of strain rate requires that the magnitude of the reflected pulse be held constant, and this in turn requires that the input pulse be considerably larger than that of the transmitted pulse. Depending on the rate of work hardening of the specimen material, this imposes a lower limit on the strain rate that can be attained with the Kolsky bar.

In practice, it is easiest to design a torsional Kolsky bar to reach a strain rate of about 10^3 s^{-1} . This value is easily doubled by shortening the specimen, or can be reduced by imposing less torque. Tests outside the range of 500 to 2000 s^{-1} require special consideration.

Low- and High-Temperature Testing. Theoretically, the torsional Kolsky bar technique can be used for testing at any temperature without further modifications (other than heating or cooling) if either the whole apparatus is at the same temperature, or only the specimen is at the testing temperature and the rest of the system is at constant (room) temperature. Practically, it is very difficult, if not impossible, to conduct tests in either manner. Changing the temperature of the specimen introduces a temperature gradient in the incident and transmitter bars. Such gradients produce a variation in the shear modulus of the bars and, hence, variations in the impedance. An impedance that is not constant along the bars causes reflections of the elastic waves that make interpretation of the recorded wave data very difficult.

In tests below room temperature, or at mildly elevated temperatures of up to about 200 °C (392 °F), a possible change in the elastic constants along the bars, due to temperature gradient caused by the heating or cooling of the specimen, is small and can be neglected.

For testing at higher temperatures, various methods have been introduced. They can be divided into two categories. One approach is to allow and monitor temperature gradients in the bars and correct for their effects. Using this approach, Chiddister and Malvern corrected for this effect, in tests with a compression Kolsky bar, through a calculation of the repeated partial reflections as the pulse propagated along the bar in the heat-affected zone (Ref 22). Although this approach is acceptable, the calculations can be cumbersome. This method can be adapted to the torsional configuration. A different solution was proposed by Eleiche and Duffy, who tapered the Kolsky bars to counteract the effect of the thermal gradients (Ref 12). In this approach, the taper in the Kolsky bar, which provides a variable impedance, is determined by calculation to counteract the change in the impedance due to the temperature gradient, resulting in a constant impedance. An example of a tapered bar used for tests conducted at 250 °C (482 °F) is shown in Fig. 18. The disadvantage of this method is that it requires a temperature survey before testing so that the Kolsky bar can be machined to the right taper. Furthermore, a bar tapered for testing at one temperature cannot be used for testing at a different temperature. The advantage of this method is that the data recorded at the strain gage stations requires no further interpretation beyond the usual treatment for room-temperature tests. Results for 1020 steel, obtained at a variety of temperatures at a dynamic strain rate of 10^3 s^{-1} , are shown in Fig. 19.

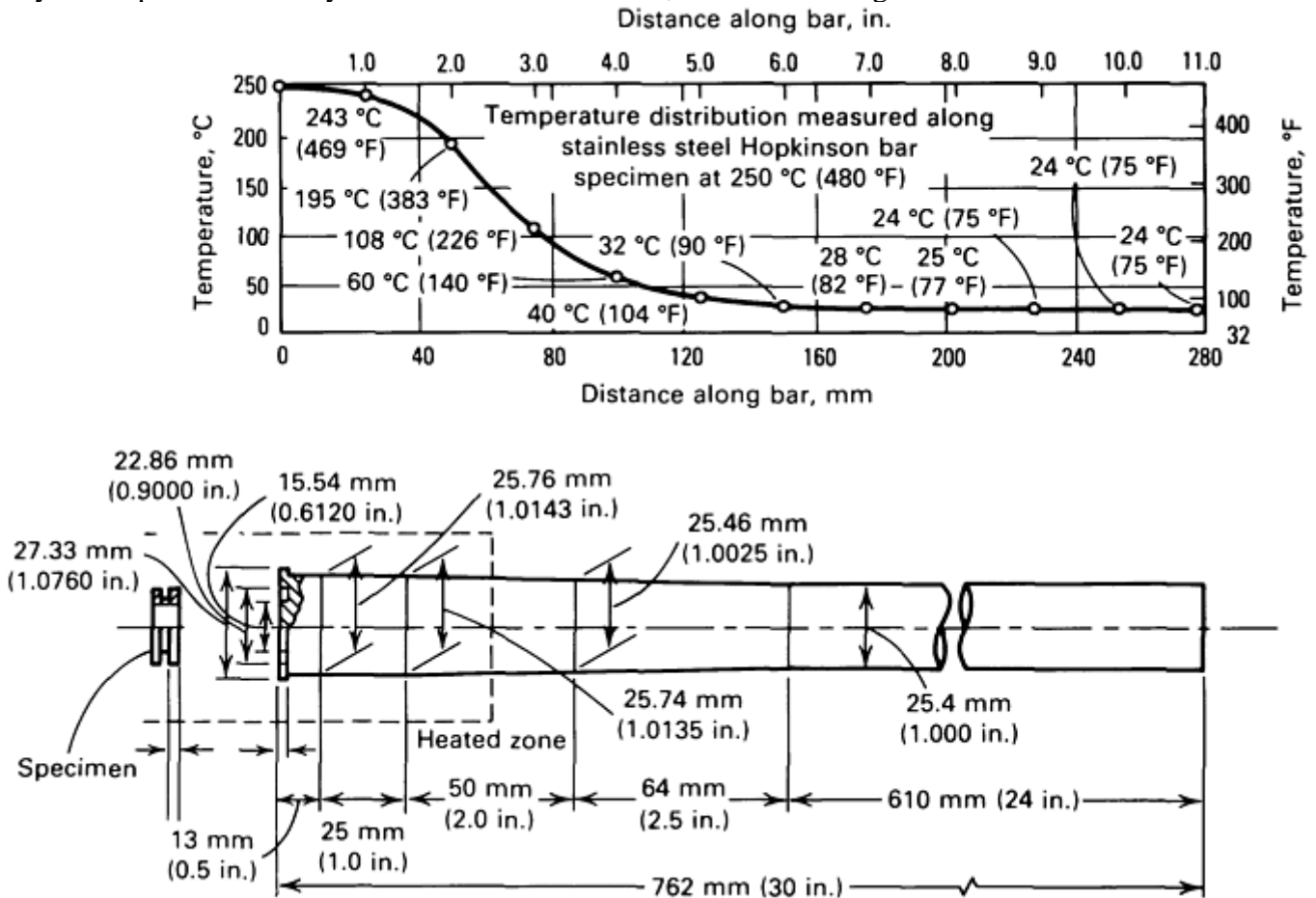


Fig. 18 Tapered steel torsional Kolsky bar for test at 250 °C (482 °F). Source: Ref 12

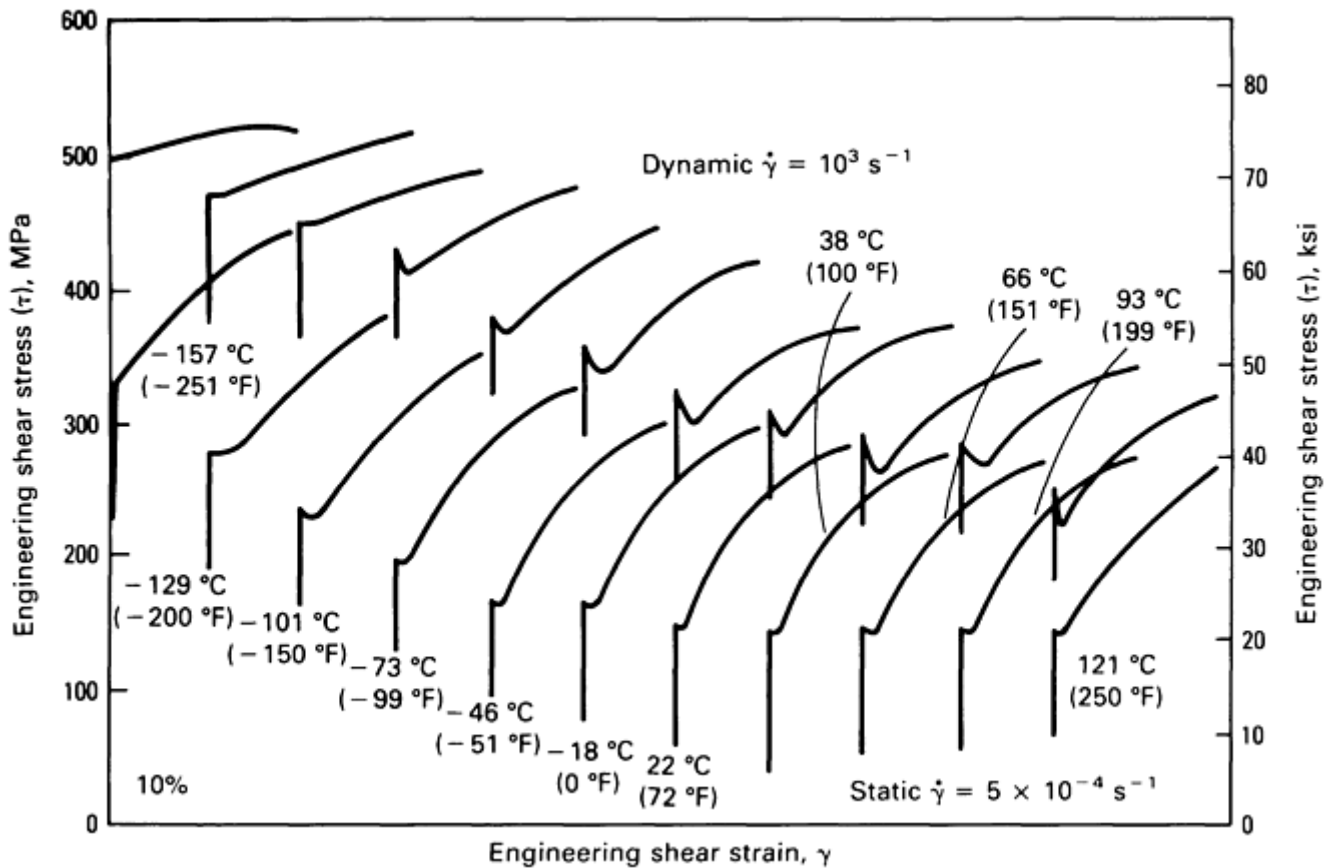


Fig. 19 Static and dynamic shear stress-strain curves at various temperatures for 1020 hot-rolled steel

Another approach is to heat the specimen and minimize the temperature increase and the length of the affected regions of the bars. This approach was used by Gilat and Wu for tests at temperatures up to 1060 °C (1940 °F) (Ref 13). They used a rapid-heating device and a connection between the specimen and the bars that allows transmission of the torsional wave with constant impedance and minimizes heat conduction to the bars. The heat-affected zone was only 20 mm (0.79 in.) long and did not have a noticeable effect on the propagating pulses. This allows recording and processing of the data in the same manner as in room-temperature tests. In a similar method, inserts, made of a material with elastic constants that are not affected significantly by temperature of the magnitude used in the test, are placed between the specimen and the bars (Ref 23). The specimen and the adjacent ends of the inserts are heated to the testing temperature while the temperature gradient is confined to the inserts.

Quasi-Static and Incremental Strain-Rate Testing. Specimens can also be tested in torsion quasi-statically using a stored-torque Kolsky bar, as shown schematically in Fig. 20. In this case, the incident bar is clamped against rotation as in the dynamic test, but quasi-static loading is applied by a pulley system at the far end of the transmitter bar by means of a variable-drive low-speed electric motor.

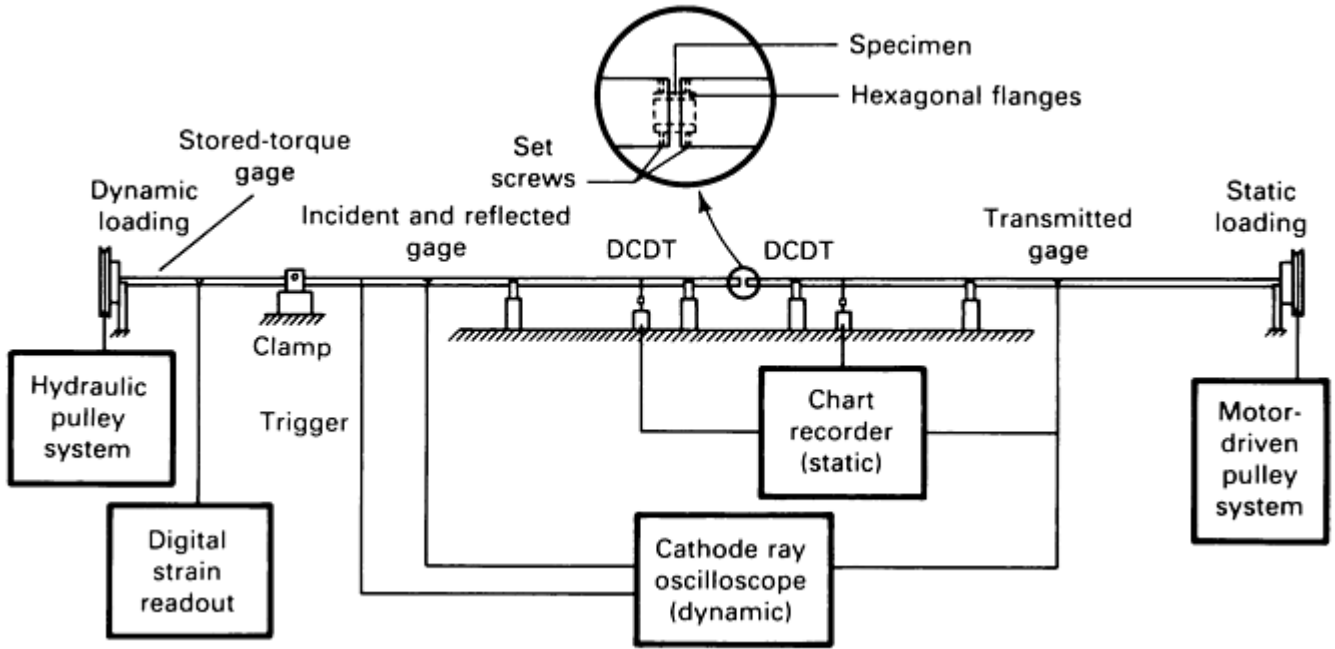


Fig. 20 Schematic of a stored-torque torsional Kolsky bar modified for quasi-static and incremental strain rate tests. DCDT, direct current differential transformer

The stress during the quasi-static loading is measured, as in the dynamic test, by a four-arm bridge on the transmitter bar. To determine the strain in the specimen, two linear direct-current differential transformers are placed equidistant from the specimen. Extremely fine wires attached to the cores of the differential transformers are wound around the bars. As the bars rotate, the cores are pulled vertically out of the transformer coils. The difference between the output signals from the direct-current differential transformers is directly proportional to the amount of twist undergone by the specimen plus the elastic twist of the portion of the Kolsky bar between the differential transformers. To obtain the shear strain in the specimen, the elastic rotation of the bar between the two differential transformers is subtracted from the total rotation. The elastic rotation is measured by cementing the bars together without a specimen and loading them quasi-statically. Results for 1020 steel obtained at a variety of temperatures at a quasi-static strain rate of $5 \times 10^{-4} \text{ s}^{-1}$ are included in Fig. 19.

In incremental strain-rate testing, the incident bar is clamped and a torque for the dynamic test is stored. Then, a quasi-static loading is applied by a pulley system at the far end of the transmitter bar. When the strain in the specimen reaches the predetermined value, the clamp is released and the specimen is dynamically loaded (Ref 8, 9).

Constant strain-rate tests and incremental strain-rate tests can be used for determining the apparent and true strain-rate sensitivity. The apparent strain-rate sensitivity, μ_a , is defined by:

$$\mu_a = \frac{\partial \tau_a}{\partial \ln \dot{\gamma}} \approx \frac{\Delta \tau}{\ln \left(\frac{\dot{\gamma}_r}{\dot{\gamma}_i} \right)} \quad (\text{Eq 16})$$

where $\Delta \tau$, as shown in Fig. 21, is the difference in flow stress between two constant strain-rate curves at $\dot{\gamma}_i$ and $\dot{\gamma}_r$. Experiments are performed at various constant strain rates, and the stress (at a given value of strain) is plotted as a function of strain rate on a logarithmic scale. The slope of this line provides the value of the derivative in Eq 16.

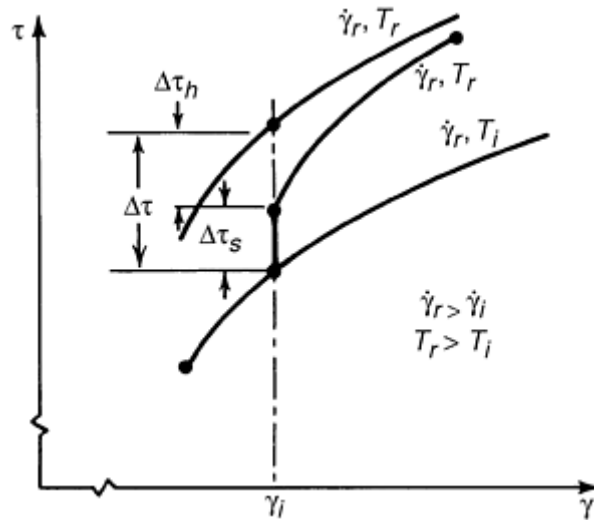


Fig. 21 Schematic representation of the effect of rapid changes in strain rate on flow stress for face-centered-cubic metals

The true strain-rate sensitivity, $\bar{\mu}_T$, is defined by:

$$\bar{\mu}_T = \frac{\partial \tau_a}{\partial \ln \dot{\gamma}} \approx \frac{\Delta \tau_s}{\ln \left(\frac{\dot{\gamma}_r}{\dot{\gamma}_i} \right)} \quad (\text{Eq 17})$$

where $\Delta \tau_s$ is the difference in flow stress due to an increment in strain rate from $\dot{\gamma}_i$ to $\dot{\gamma}_r$. The true strain-rate sensitivity is determined from the incremental strain-rate test. Figure 21 illustrates a typical stress-strain curve obtained in such a test. As shown, the flow stress after the strain-rate increment is different from the flow stress at the same value of strain in a specimen strained entirely at the dynamic strain rate. This leads to a difference between the apparent and true strain-rate sensitivities. For face-centered-cubic (fcc) and hexagonal-close-packed (hcp) metals, the all-dynamic flow stress is greater than the flow stress immediately after the increment in strain rate. This difference is commonly referred to as the strain-rate history effect because in both cases the strain is the same, but the history of strain rate is different (Ref 8, 9, and 24).

Frequently, with further deformation, the difference between the two values of flow stress diminishes, and eventually the two dynamic curves merge. In this case, the material is said to have a “fading memory” (Ref 25). Body-centered cubic metals, under certain conditions and particularly at very low temperatures, may exhibit a negative strain-rate history effect; that is, the flow stress after an increment in strain rate is greater than the flow stress for the material strained entirely at the dynamic rate (Ref 26). At room temperature, bcc metals generally show only a small history effect, although the influence of strain rate on flow stress usually is considerably greater than that for fcc metals.

In incremental strain rate tests, the Kolsky bar provides an important advantage: the transmitted signal furnishes a measure not of the total stress in the specimen, but of the excess stress, $\Delta \tau_s$, imposed by the stress pulse above the existing stress as a result of loading at the quasi-static strain rate (Fig. 22). Thus, rather than evaluation of a small difference between two large numbers, measurement of the stress increment, $\Delta \tau_s$, can be made directly from oscilloscope records. Results of incremental strain-rate tests on aluminum are shown in Fig. 23.

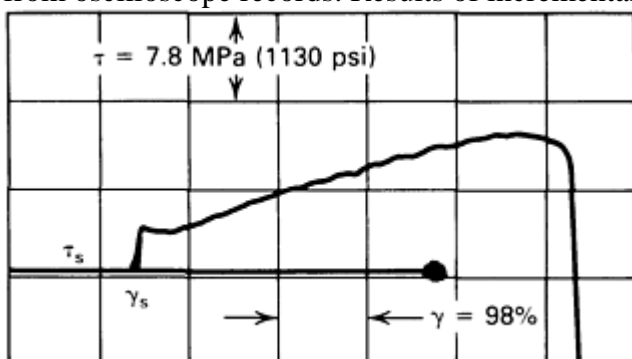


Fig. 22 Oscilloscope record of dynamic portion of incremental strain-rate test. Vertical deflection represents excess stress over τ_s , the maximum static stress. Horizontal deflection represents excess strain over γ_s .

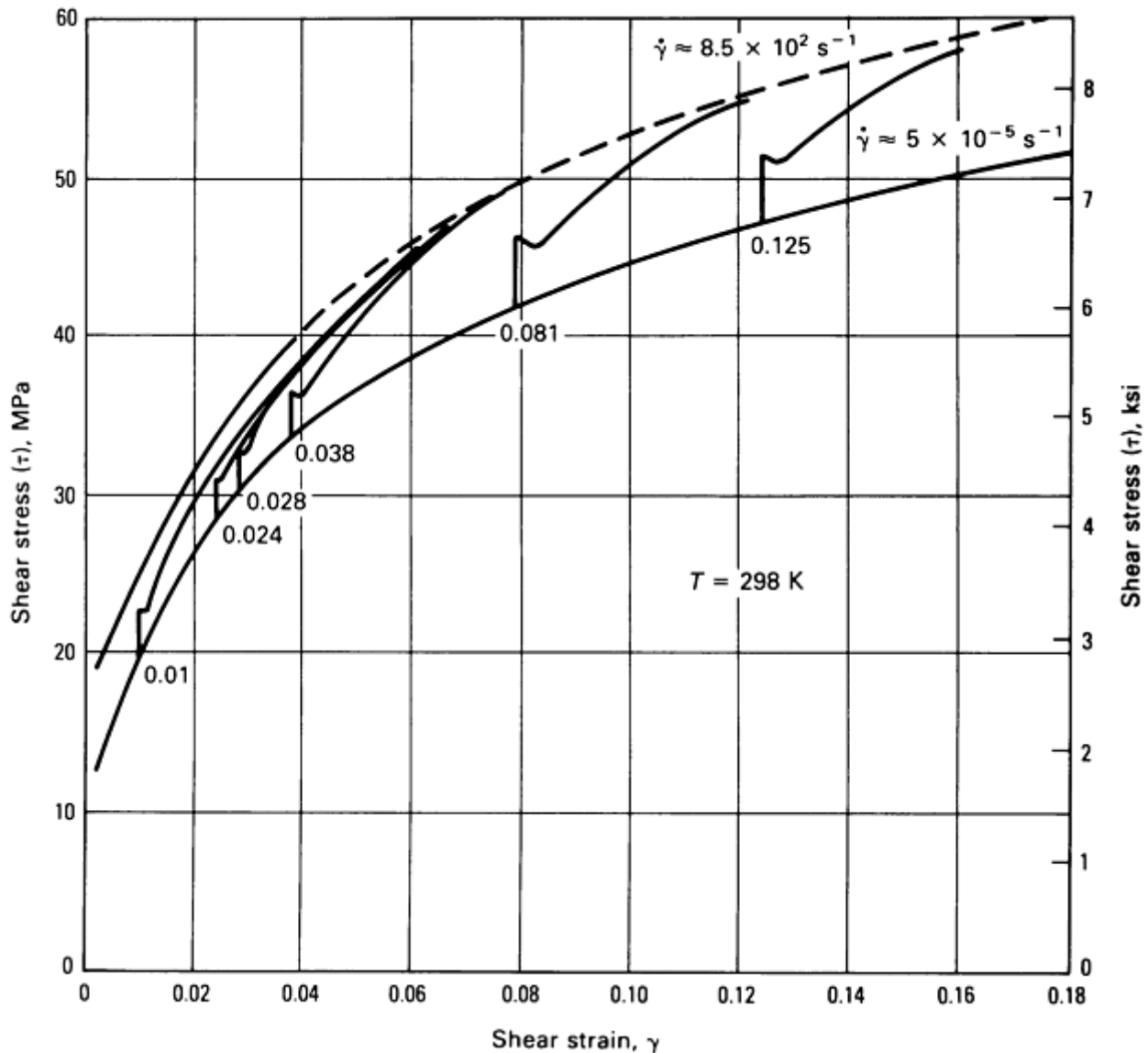


Fig. 23 Behavior of 1100-O aluminum under static, dynamic, and incremental strain-rate loading in shear. Strain rate changes from 5×10^{-5} to 850 s^{-1} in incremental rate test. Source: Ref 8

Localization and Shear-Banding Experiments. The torsional Kolsky bar has been used for studying localization of plastic deformation and the formation of adiabatic shear bands (Ref 14, 15, and 16). As already mentioned, the existence of localized deformation is evident when a scribed line along the gage length of the specimen appears to be discontinuous after the test (Fig. 11). A detailed study of the evolution of the localization is done by taking high-speed photographs of deforming grid lines on the specimen (Ref 15, 16). Strain profiles, obtained by analyzing the deformed grid at different times along the specimen gage length, are shown in Fig. 24. Attempts have also been made to measure the increase in temperature at the shear band during the deformation process (Ref 15). This was done by measuring the infrared radiation emitted from the surface of the specimen.

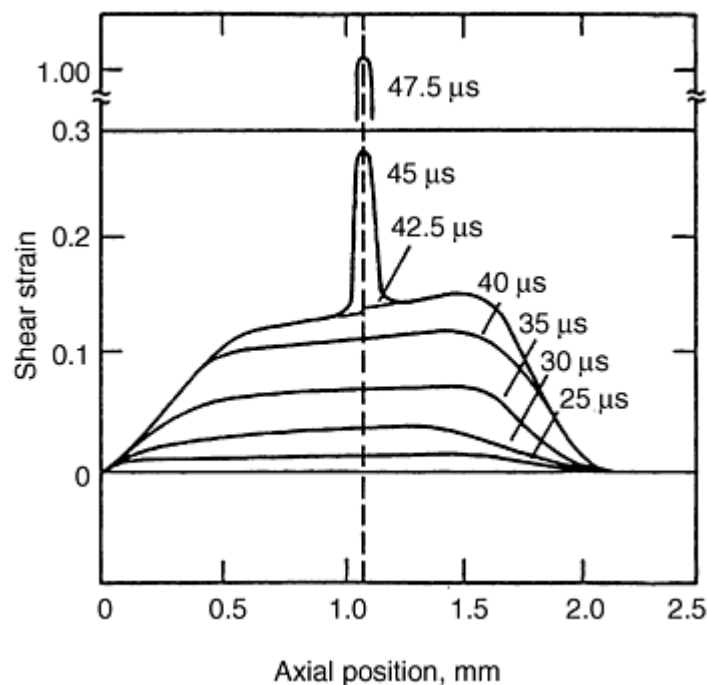


Fig. 24 Shear strain profiles across the specimen width during the formation of adiabatic shear band. Source: Ref 16

Recently, a recovery experiment, in which the specimen is loaded up to a predetermined strain and then unloaded and recovered for microscopic examination, has also been introduced (Ref 17). In a standard test, the actual material testing takes place during loading by the first wave that arrives to the specimen. The transmitted and reflected waves, however, are reflected back toward the specimen from the far ends of the bars and continue to reverberate in the system. If the specimen does not break during the first loading, it is subjected to further loading as the waves reflect back and forth. Consequently, when the specimen is removed after the test, its microstructure cannot be related to the deformation that took place during the initial loading.

In a recovery experiment, the specimen is loaded only once, which means that after the test the specimen can be removed and examined. In Ref 17, reloading of the specimen by the reflected transmitted pulse is eliminated by trapping the wave. Reloading by a reflection of the incident wave is avoided by designing the test so that the amplitude of the reflected wave is reduced to a level below the elastic limit. Recovery experiments are simpler to conduct with the compression version of the Kolsky bar.

References cited in this section

8. R.A. Frantz and J. Duffy, The Dynamic Stress-Strain Behavior in Torsion of 1100-O Aluminum Subjected to a Sharp Increase in Strain Rate, *J. Appl. Mech.*, Vol 39, 1972, p 939-945
9. J.D. Campbell, A.M. Eleiche, and M.C.C. Tsao, Strength of Metals and Alloys at High Strains and Strain Rates, in *Fundamental Aspects of Structural Alloy Design*, R.J. Jaffee and B.A. Wilcox, Ed., Plenum Press, 1977, p 545-563
12. A.M. Eleiche and J. Duffy, Effects of Temperature on the Static and Dynamic Stress-Strain Characteristics in Torsion of 1100-O Aluminum, *Int. J. Mech. Sci.*, Vol 17, 1975, p 85-95
13. A. Gilat and X. Wu, Elevated Temperature Testing with the Torsional Split Hopkinson Bar, *Exp. Mech.*, Vol 34 (No. 2), 1994, p 166-170
14. L.S. Costin, E.E. Crisman, R.H. Hawley, and J. Duffy, On the Localization of Plastic Flow in Mild Steel Tubes Under Dynamic Torsional Loading, in *Proc. 2nd Int. Conf. Mechanical Properties of Materials at High Rates of Strain*, J. Harding, Ed., The Institute of Physics, 1979, p 287-282

15. A. Marchand and J. Duffy, An Experimental Study of the Formation Process of Adiabatic Shear Bands in a Structural Steel, *J. Mech. Phys. Solids*, Vol 36, 1988, p 251–283
16. J.H. Giovanola, Adiabatic Shear Banding Under Pure Shear Loading, Part I: Direct Observation of Strain Localization and Energy Dissipation Measurements, *Mech. Mater.*, Vol 7, 1988, p 59–71
17. Q. Xue, L.T. Shen, and Y.L. Bai, A Modified Split Hopkinson Torsional Bar in Studying Shear Localization, *Meas. Sci. Technol.*, Vol 6, 1995, p 1557–1565
22. J.L. Chiddister and L.E. Malvern, Compression Impact Testing Of Aluminum at Elevated Temperatures, *Exp. Mech.*, Vol 3, 1963, p 81–90
23. C.G. Schmidt, R.D. Caligiuri, J.H. Giovanola, and D.C. Erlich, Effect of Grain Size on High Strain Rate Deformation of Copper, *Metall. Trans. A*, Vol 22, 1991, p 2349–2357
24. J. Duffy, Strain Rate History Effects and Dislocation Substructure at High Strain Rates, in *Materials Behavior Under High Stress and Ultrahigh Loading Rates*, J. Mescall and V. Weiss, Ed., Plenum Press, 1983, p 21–37
25. J. Klepaczko, Strain-Rate History Effects for Polycrystalline Aluminum and the Theory of Intersections, *J. Mech. Phys. Solids*, Vol 16, 1968, p 255–266
26. K.A. Hartley and J. Duffy, Strain Rate and Temperature History Effects During Deformation of FCC and BCC Metals, in *Mechanical Properties of Materials at High Rates of Strain*, J. Harding, Ed., The Institute of Physics, 1984, p 21–30

Torsional Kolsky Bar Testing

Amos Gilat, The Ohio State University

Acknowledgments

The present article is a revision of the article The Torsional Kolsky (Split-Hopkinson) Bar by K.A. Hartley, J. Duffy, and R.H. Hawley, which appeared in *Mechanical Testing*, Vol 8, *ASM Handbook*, ASM International, 1985, p 218–228. Some sections and paragraphs from the original article are included here without alteration.

Torsional Kolsky Bar Testing

Amos Gilat, The Ohio State University

References

1. U.S. Lindholm, High Strain Rate Tests, in *Measurement of Mechanical Properties*, Vol 5, Part I, Techniques of Metals Research, R.F. Bunshah, Ed., Interscience, 1971, p 199–271

2. H. Kolsky, An Investigation of the Mechanical Properties of Materials at Very High Rates of Loading, *Proc. Phys. Soc. London*, Vol 62-B, 1949, p 676–700
3. B. Hopkinson, The Effects of Momentary Stresses in Metals, *Proc. Phys. Soc. London*, Vol 74-A, 1905, p 498–506
4. W.W. Baker and C.H. Yew, Strain Rate Effects in the Propagation of Torsional Plastic Waves, *J. Appl. Mech.*, Vol 33, 1966, p 917–923
5. J. Duffy, J.D. Campbell, and R.H. Hawley, On the Use of a Torsional Split Hopkinson Bar to Study Rate Effects in 1100-O Aluminum, *J. Appl. Mech.*, Vol 38, 1971, p 83–91
6. T. Nicholas and J.E. Lawson, On the Determination of the Mechanical Properties of Materials at High Shear-Strain Rates, *J. Mech. Phys. Solids*, Vol 20, 1972, p 57–64
7. J.L. Lewis and J.D. Campbell, The Development and Use of a Torsional Hopkinson Bar Apparatus, *Exp. Mech.*, Vol 12 (No. 11), 1972, p 520–524
8. R.A. Frantz and J. Duffy, The Dynamic Stress-Strain Behavior in Torsion of 1100-O Aluminum Subjected to a Sharp Increase in Strain Rate, *J. Appl. Mech.*, Vol 39, 1972, p 939–945
9. J.D. Campbell, A.M. Eleiche, and M.C.C. Tsao, Strength of Metals and Alloys at High Strains and Strain Rates, in *Fundamental Aspects of Structural Alloy Design*, R.J. Jaffee and B.A. Wilcox, Ed., Plenum Press, 1977, p 545–563
10. J. Lipkin, J.D. Campbell, and J.D. Swearingen, The Effects of Strain-Rate Variations on the Flow Stress of OFHC Copper, *J. Mech. Phys. Solids*, Vol 26, 1978, p 251–268
11. A. Gilat and Y.H. Pao, High Rate Decremental-Strain Rate Test, *Exp. Mech.*, Vol 28 (No. 3), 1988, p 322–325
12. A.M. Eleiche and J. Duffy, Effects of Temperature on the Static and Dynamic Stress-Strain Characteristics in Torsion of 1100-O Aluminum, *Int. J. Mech. Sci.*, Vol 17, 1975, p 85–95
13. A. Gilat and X. Wu, Elevated Temperature Testing with the Torsional Split Hopkinson Bar, *Exp. Mech.*, Vol 34 (No. 2), 1994, p 166–170
14. L.S. Costin, E.E. Crisman, R.H. Hawley, and J. Duffy, On the Localization of Plastic Flow in Mild Steel Tubes Under Dynamic Torsional Loading, in *Proc. 2nd Int. Conf. Mechanical Properties of Materials at High Rates of Strain*, J. Harding, Ed., The Institute of Physics, 1979, p 287–282
15. A. Marchand and J. Duffy, An Experimental Study of the Formation Process of Adiabatic Shear Bands in a Structural Steel, *J. Mech. Phys. Solids*, Vol 36, 1988, p 251–283
16. J.H. Giovanola, Adiabatic Shear Banding Under Pure Shear Loading, Part I: Direct Observation of Strain Localization and Energy Dissipation Measurements, *Mech. Mater.*, Vol 7, 1988, p 59–71
17. Q. Xue, L.T. Shen, and Y.L. Bai, A Modified Split Hopkinson Torsional Bar in Studying Shear Localization, *Meas. Sci. Technol.*, Vol 6, 1995, p 1557–1565
18. K.A. Hartley, J. Duffy, and R.H. Hawley, The Torsional Kolsky (Split-Hopkinson) Bar, *Mechanical Testing*, Vol 8, *ASM Handbook*, ASM International, 1985, p 218–228

19. E.K.C. Leung, An Elastic-Plastic Stress Analysis of the Specimen Used in the Torsional Kolsky Bar, *J. Appl. Mech.*, Vol 47, 1980, p 278–282
20. C.Y. Chiem and J. Duffy, Strain Rate History Effects and Observations of Dislocation Substructure in Aluminum Single Crystals Following Dynamic Deformation, *Mater. Sci. Eng.*, Vol 57, 1963, p 233–247
21. Y.H. Pao and A. Gilat, High Strain Rate Deformation and Failure of A533B Steel at Various Temperatures, *Acta Metall. Mater.*, Vol 40, 1992, p 1271–1280
22. J.L. Chiddister and L.E. Malvern, Compression Impact Testing Of Aluminum at Elevated Temperatures, *Exp. Mech.*, Vol 3, 1963, p 81–90
23. C.G. Schmidt, R.D. Caligiuri, J.H. Giovanola, and D.C. Erlich, Effect of Grain Size on High Strain Rate Deformation of Copper, *Metall. Trans. A*, Vol 22, 1991, p 2349–2357
24. J. Duffy, Strain Rate History Effects and Dislocation Substructure at High Strain Rates, in *Materials Behavior Under High Stress and Ultrahigh Loading Rates*, J. Mescall and V. Weiss, Ed., Plenum Press, 1983, p 21–37
25. J. Klepaczko, Strain-Rate History Effects for Polycrystalline Aluminum and the Theory of Intersections, *J. Mech. Phys. Solids*, Vol 16, 1968, p 255–266
26. K.A. Hartley and J. Duffy, Strain Rate and Temperature History Effects During Deformation of FCC and BCC Metals, in *Mechanical Properties of Materials at High Rates of Strain*, J. Harding, Ed., The Institute of Physics, 1984, p 21–30

Triaxial Hopkinson Techniques

Sia Nemat-Nasser, Jon Isaacs, and Jacob Rome, University of California, San Diego

Introduction

COMPRESSIVE PROPERTIES AND FAILURE MODES of many materials, particularly brittle materials, are dramatically affected by stress triaxiality. This has been demonstrated through various laboratory experiments, since the early work of Bridgman (Ref 1), who demonstrated several failure modes peculiar to high pressures, leading to paradoxical results. The common feature of these paradoxes is that failure always occurs by the formation of *tension* cracks in specimens subjected to *pure compression*. While all these paradoxes have been fully understood (Ref 2), they do emphasize the importance of controlled triaxial experiments in materials characterization. Indeed, in axial compression, brittle materials such as rocks or ceramics fail by axial splitting, faulting, or plastic deformation (barreling), depending on the relative magnitude of the confining pressure that may accompany the axial compression (Ref 3, 4, 5, and 6). Model studies show that similar results emerge at high strain rate.

Triaxial Hopkinson techniques can be used to simultaneously subject a sample to axial and lateral compressions. The lateral compression may be applied through a pneumatic pressure vessel (Ref 7, 8, and 9) or dynamically using a special Hopkinson technique. These two techniques are reviewed in this article.

References cited in this section

1. P.W. Bridgman, *The Physics of High Pressure*, Bell, London, 1931

2. C.H. Scholtz, G. Boitnott, and S. Nemat-Nasser, The Bridgman Ring Paradox Revisited, *Pure and Applied Geophysics (PAGEOPH)*, Vol 124, 1986, p 587–599
3. S. Nemat-Nasser and H. Horii, Compression-Induced Nonplanar Crack Extension with Application to Splitting, Exfoliation, and Rockburst, *J. Geophys. Res.*, Vol 87 (No. B8), 1982, p 6805–6821
4. S. Nemat-Nasser, J.B. Isaacs, and J.E. Starrett, Hopkinson Techniques for Dynamic Recovery Experiments, *Proc. R. Soc. (London) A*, Vol 435, 1991, p 371–391
5. H. Horii and S. Nemat-Nasser, Compression-Induced Microcrack Growth in Brittle Solids: Axial Splitting and Shear Failure, *J. Geophys. Res.*, Vol 90 (No. B4), 1985, p 3105–3125
6. H. Horii and S. Nemat-Nasser, Brittle Failure in Compression: Splitting, Faulting and Brittle-Ductile Transition, *Philos. Trans. R. Soc. (London) A*, Vol 319 (No. 1549), 1986, p 337–374
7. R.J. Christensen, S.R. Swanson, and W.S. Brown, Split Hopkinson Bar Test on Rock under Confining Pressure, *Exp. Mech.*, Vol 12, 1972, p 508–541
8. L.E. Malvern, D.A. Jenkins, T. Tang, and S. McClure, Dynamic Testing of Laterally Confined Concrete, *Micromechanics of Failure of Quasi Brittle Materials*, Elsevier Applied Science, 1991, p 343–352
9. G. Gary and B. Bailly, Behaviour of Quasi-Brittle Material at High Strain Rate, Experiment and Modelling, *Eur. J. Mech., A/Solids*, Vol 17 (No. 3), 1998, p 403–420

Triaxial Hopkinson Techniques

Sia Nemat-Nasser, Jon Isaacs, and Jacob Rome, University of California, San Diego

Pneumatic Pressure Vessel

Figures 1 and 2 are a photograph and a schematic, respectively, of a 75 mm (3 in.) Hopkinson system, particularly designed to test large samples of concrete, rock, polymeric composites, and other materials with relatively coarse microstructures. Except for a 6 ft brake bar to absorb the momentum and dissipate the energy, the system is similar to the classical Hopkinson bar discussed in the article “Classic Split-Hopkinson Pressure Bar Testing” in this section. The brake bar acts as a simple friction brake. Two clamps are secured around the brake bar, and the tightness is adjusted to ensure that the brake bar absorbs the energy efficiently.

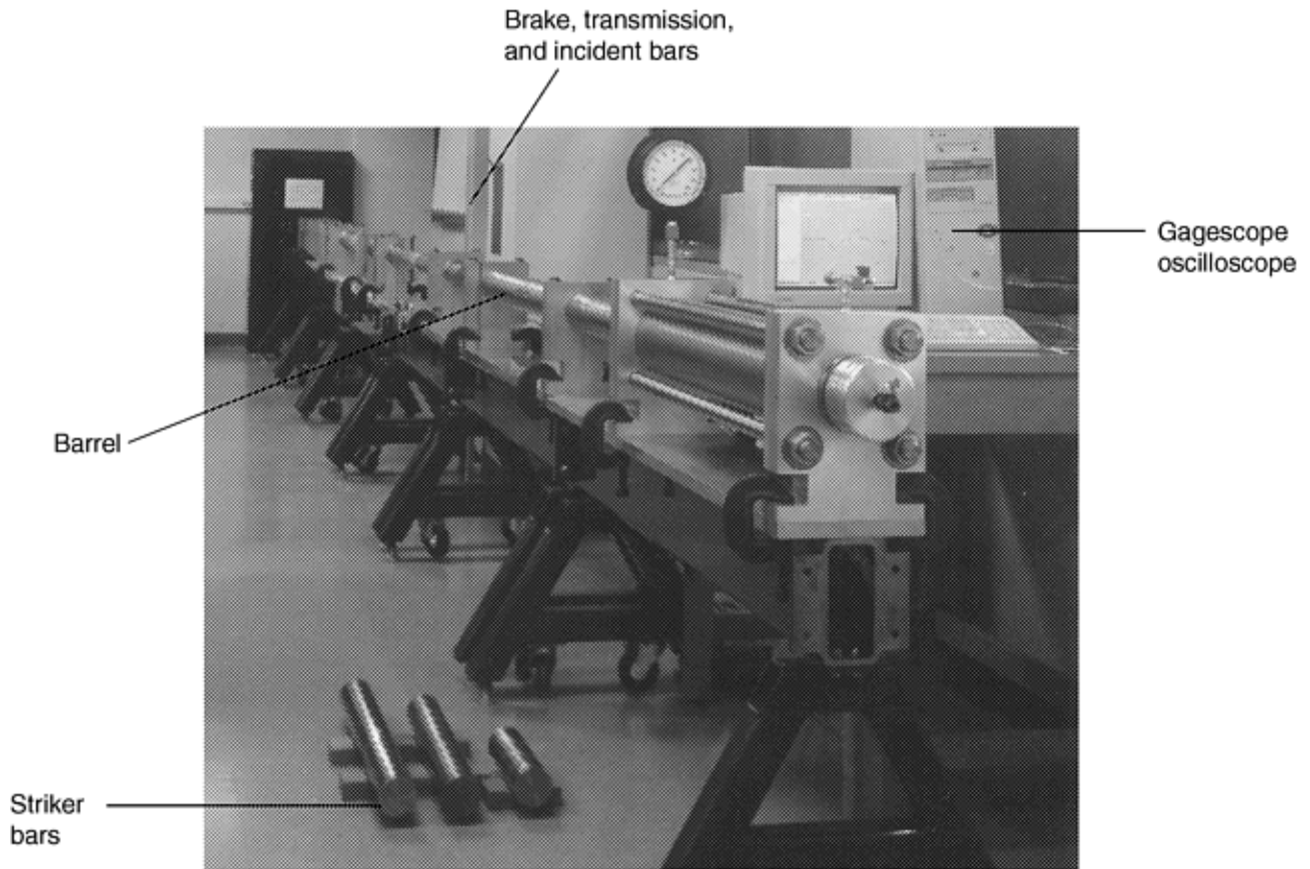


Fig. 1 Photograph of a 75 mm (3 in.) diam Hopkinson bar test system

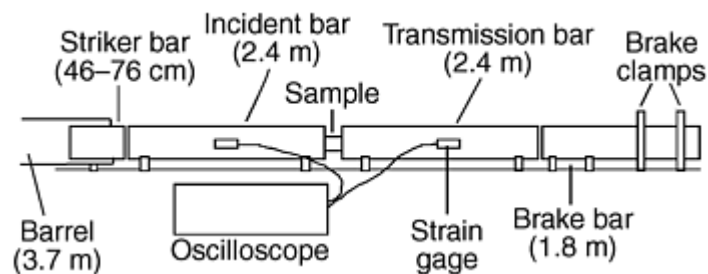


Fig. 2 Schematic of a 75 mm (3 in.) diam Hopkinson bar test system

A large diameter pressure vessel provides the pneumatic confinement (Fig. 3, 4). A steel cylinder of 150 mm (6 in.) outside diameter (OD) and 13 mm ($\frac{1}{2}$ in.) wall thickness surrounds the sample. The aluminum end plates are each 25 mm (1 in.) thick and are held together by four 9.5 mm ($\frac{3}{8}$ in.) bolts. A rubber sleeve, secured by hose clamps, is placed over the sample to prevent direct contact between the sample and the high-pressure gas. O-rings are used to seal the pressurized chamber. A band clamp and the brake bar restrain the incident and transmission bars, respectively, to prevent them from moving apart. This pressure vessel provides a constant radial confinement of up to 7 MPa (1000 psi).

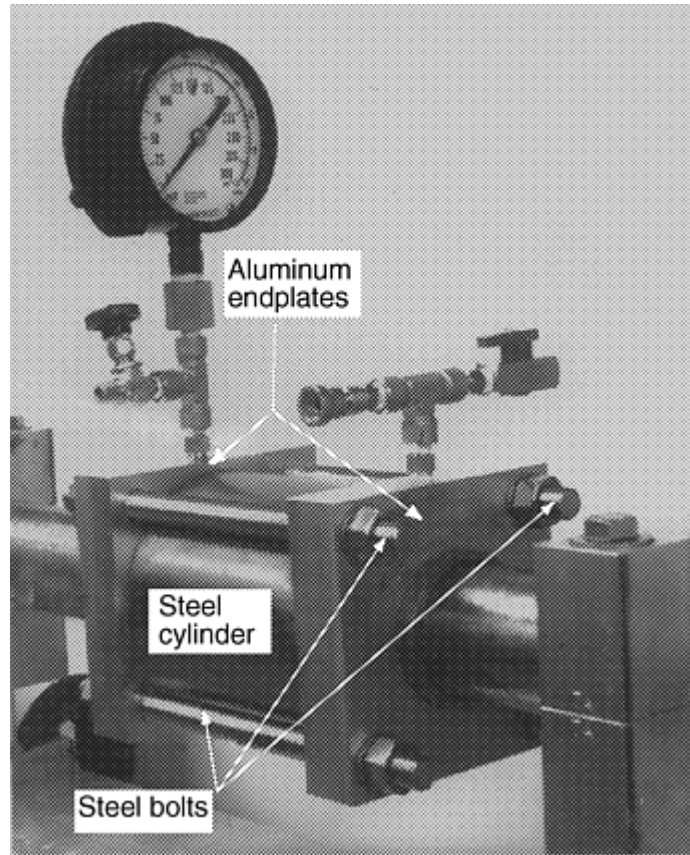


Fig. 3 Photograph of a pneumatic pressure vessel for a 75 mm (3 in.) Hopkinson bar test system

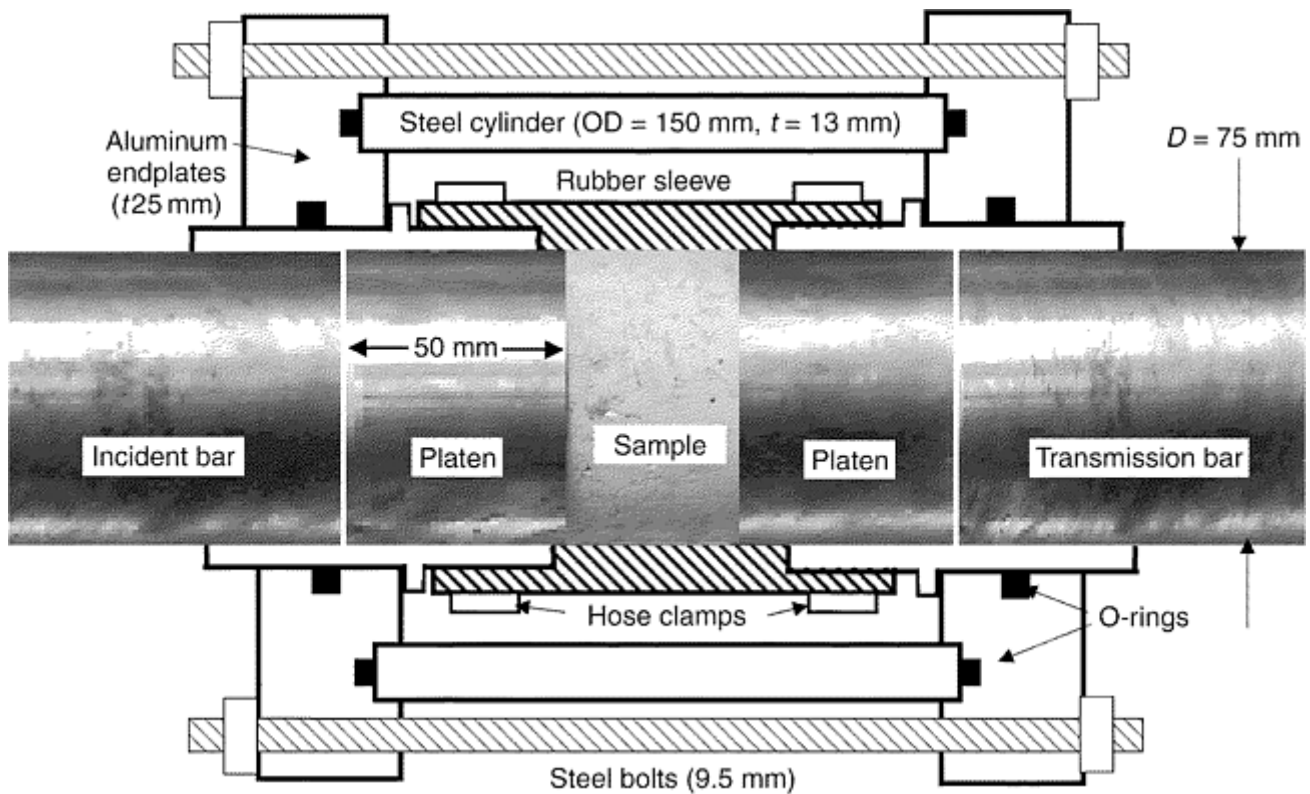


Fig. 4 Schematic of a pneumatic pressure vessel for a 75 mm (3 in.) Hopkinson bar test system. t , thickness; D , diameter; OD, outside diameter

Dynamic Confinement

The classical Hopkinson Bar can be modified to allow dynamic triaxial compressive loading of a sample. This technique simultaneously loads the sample in the axial and radial directions. Figures 5 and 6 are a photograph and schematic, respectively, of this system. The striker (A) impacts the first incident bar (B), generating the incident pulse. The wave is transmitted to the second incident bar (C) and the incident tube (F). (Note: With this design, the reflected pulse cannot be measured directly, so it is calculated as the difference between the transmitted pulse and the incident pulse.) The sample (D) is inside a Teflon (E.I. DuPont de Nemours & Co., Inc., Wilmington, DE) tube (G), which in turn is inside an aluminum sleeve (H).

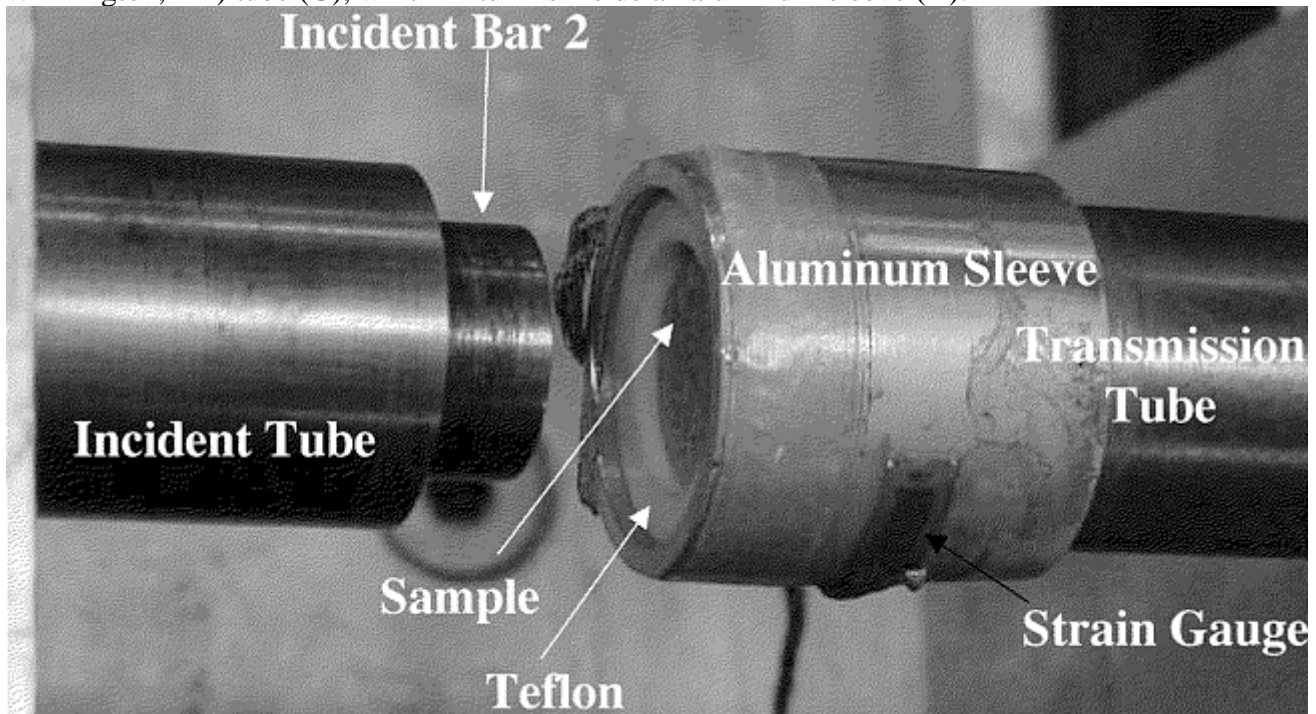


Fig. 5 Close-up photograph of dynamic triaxial load cell on a 19 mm ($\frac{3}{4}$ in.) Hopkinson bar

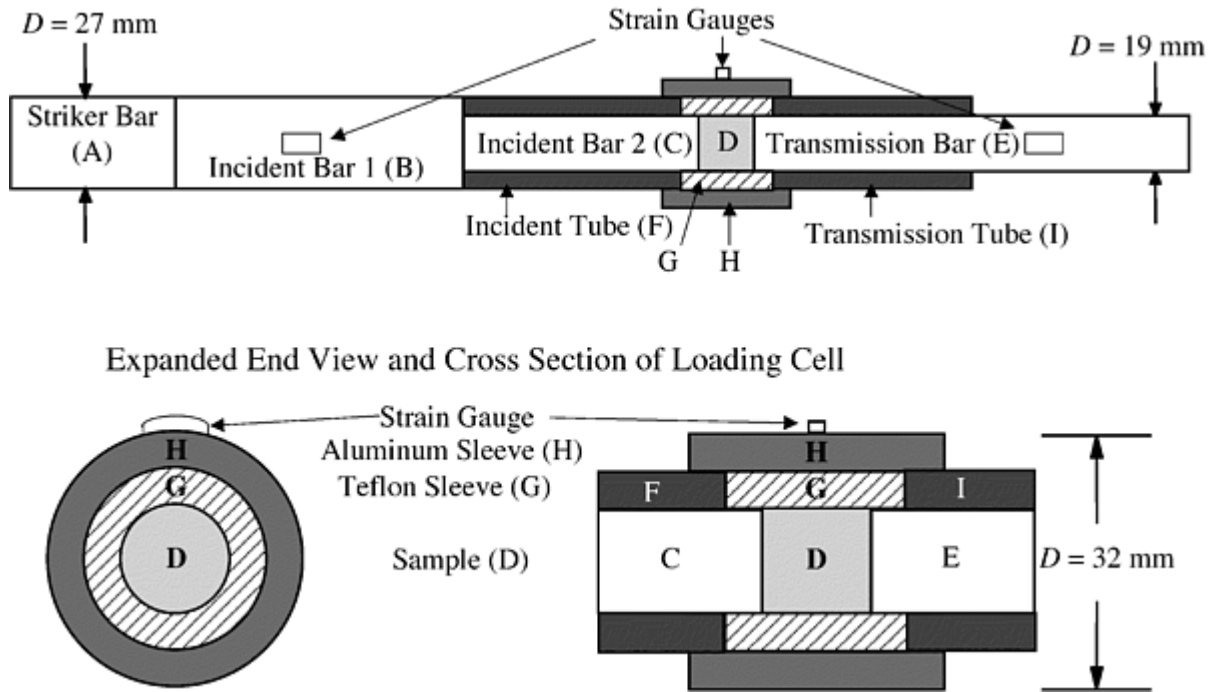
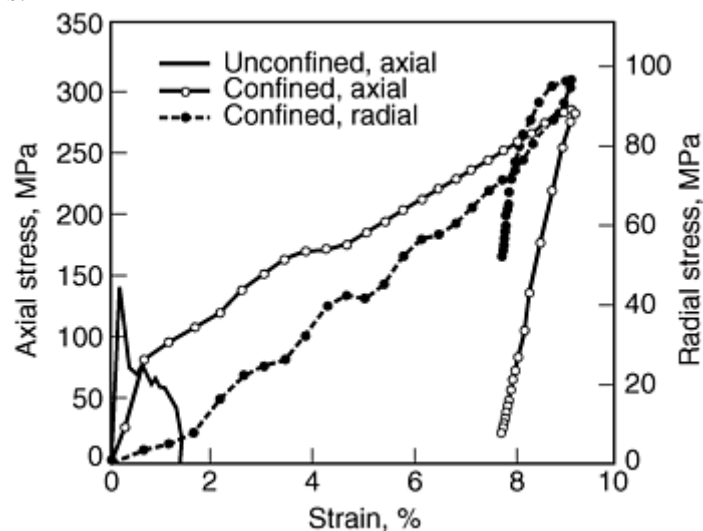


Fig. 6 Schematic of a 19 mm ($\frac{3}{4}$ in.) Hopkinson bar featuring the dynamic triaxial load cell

The confinement is provided by the Teflon, which is dynamically compressed between the incident tube (F) and the transmission tube (I). Restrained laterally by the aluminum sleeve, a large hydrostatic stress is produced in the Teflon. This pressure creates a large radial stress on the sample. The hoop strain in the aluminum sleeve is measured, and the radial confining stress is calculated. The radial stress can be controlled independently from the axial stress and strain to a limited extent by, for example, altering the thickness of the aluminum sleeve to control when the sleeve yields.

The simultaneous loading in the radial and axial directions is ensured by the design of the bar. The stress waves in the incident bar and the incident tube are generated at the same time. The bar and the tube are made of the same material and they have nearly the same length. Thus, the stress wave in the incident bar reaches the sample (loading it axially) at the same time as the stress wave in the incident tube reaches the Teflon (loading the sample radially).

This method has been used to test several samples. In Fig. 7, the response of a mortar sample tested in uniaxial compression is compared with another mortar sample tested in triaxial compression. These results demonstrate both the effect radial confinement can have on a brittle material and the simultaneous loading of the sample in the axial and radial directions.



Triaxial Hopkinson Techniques

Sia Nemat-Nasser, Jon Isaacs, and Jacob Rome, University of California, San Diego

References

1. P.W. Bridgman, *The Physics of High Pressure*, Bell, London, 1931
2. C.H. Scholtz, G. Boitnott, and S. Nemat-Nasser, The Bridgman Ring Paradox Revisited, *Pure and Applied Geophysics (PAGEOPH)*, Vol 124, 1986, p 587–599
3. S. Nemat-Nasser and H. Horii, Compression-Induced Nonplanar Crack Extension with Application to Splitting, Exfoliation, and Rockburst, *J. Geophys. Res.*, Vol 87 (No. B8), 1982, p 6805–6821
4. S. Nemat-Nasser, J.B. Isaacs, and J.E. Starrett, Hopkinson Techniques for Dynamic Recovery Experiments, *Proc. R. Soc. (London) A*, Vol 435, 1991, p 371–391
5. H. Horii and S. Nemat-Nasser, Compression-Induced Microcrack Growth in Brittle Solids: Axial Splitting and Shear Failure, *J. Geophys. Res.*, Vol 90 (No. B4), 1985, p 3105–3125
6. H. Horii and S. Nemat-Nasser, Brittle Failure in Compression: Splitting, Faulting and Brittle-Ductile Transition, *Philos. Trans. R. Soc. (London) A*, Vol 319 (No. 1549), 1986, p 337–374
7. R.J. Christensen, S.R. Swanson, and W.S. Brown, Split Hopkinson Bar Test on Rock under Confining Pressure, *Exp. Mech.*, Vol 12, 1972, p 508–541
8. L.E. Malvern, D.A. Jenkins, T. Tang, and S. McClure, Dynamic Testing of Laterally Confined Concrete, *Micromechanics of Failure of Quasi Brittle Materials*, Elsevier Applied Science, 1991, p 343–352
9. G. Gary and B. Bailly, Behaviour of Quasi-Brittle Material at High Strain Rate, Experiment and Modelling, *Eur. J. Mech., A/Solids*, Vol 17 (No. 3), 1998, p 403–420

Dynamic Indentation Testing

G. Subhash, Michigan Technological University

Introduction

STATIC INDENTATION TESTING is one of the oldest and most widely used methods for characterizing materials properties. Its immense popularity stems from the simplicity of the testing procedure and its ability to

characterize material response in a wide range of engineering applications. The technique has been used extensively for determining hardness, which has been related to mechanical properties of materials (e.g., yield stress, tensile strength, work-hardening rate, wear resistance, and fracture toughness of brittle materials), for evaluating the effectiveness of heat treatment processes and surface modification techniques, and for measuring the adhesive strength of thick films and surface coatings. A comprehensive review on static hardness testing and its applications is available in Ref 1, 2, 3 and in the section "Hardness Testing" in this Volume.

Indentation hardness is defined as the intensity of the indentation load (i.e., indentation load over the projected area of the indentation imprint). Depending upon its intended application, indentation hardness has been interpreted broadly. For a machinist, hardness is a measure of resistance to cutting, for a metallurgist, it is resistance to penetration, and for a tribologist, it is resistance to wear. All these definitions relate to a material's resistance to permanent deformation (i.e., a measure of yield stress in metals and fracture strength in brittle ceramics). Therefore, static hardness basically refers to plastic properties that are indirectly derived (or related) through this method without laborious specimen preparation. However, it is well established in high-strain-rate literature (e.g., Ref 4) that plastic properties of materials are strongly a function of strain rate for a vast majority of materials.

The use of static hardness as a measure of yield stress, for example, in a high-speed machining process or under high-velocity impact applications, may not be appropriate. This is because in a static indentation hardness test, a predetermined indentation load is applied over 5 to 15 s, causing an imprint of the indenter on a given material. The rate of deformation (or strain rate) during this test is typically of the order of $10^{-5}/s$. A machinist may use this hardness data for selecting suitable process parameters, such as speed, feed, tooling, and so on, to effectively perform a desired machining operation on a workpiece. Note that the selection of process parameters is based on a static measure, whereas in a high-speed machining operation, material removal occurs in less than several hundred microseconds, resulting in a strain rate in excess of $10^3/s$. This strain rate is at least 5 to 6 orders of magnitude greater than that achieved in a static indentation test. At such high strain rates, it is well established that the inelastic properties of materials are considerably different from their quasi-static counterparts. For example, metals exhibit an increase in yield strength (Ref 4, 5), and ceramics exhibit an increase in fracture strength (e.g., Ref 6, 7, 8, 9) and fracture toughness (Ref 10, 11).

Similar situations also may arise while characterizing impact and dynamic wear behavior of materials where the deformation rates are several orders of magnitude greater than that achieved in a typical static indentation or uniaxial tension test. In addition, high-strain-rate deformation also results in a significant rise in temperature due to the adiabatic nature of deformation and strongly influences the plastic response, which also is not captured in a static indentation test where isothermal conditions prevail during the deformation. Under such circumstances, use of dynamic hardness where the indentation load is applied in microsecond duration may lead to a more accurate assessment of material behavior and process parameter selection.

Recently, there has been an increased interest in dynamic indentation technique because of its ability to predict dynamic plastic properties of materials at high strain rates ($>10^3/s$). Such studies have considerable relevance in the analysis of structures subjected to impact, high-velocity sliding wear, crash, and so on. For example, in the field of wear of materials, Meng and Ludema (Ref 12) pointed out that 28 generic erosion models have been used to predict the wear properties of materials. Several inelastic properties such as hardness, yield strength, and fracture toughness appear in a majority of these equations. However, the exponent of the velocity term in these models has been observed to range between 2 and 5. Based on the momentum considerations, these authors argue that the velocity exponent should be around 2. One of the reasons for the observed variability is rationalized in terms of inappropriate use of static properties. Since wear is a dynamic process, they suggest the use of dynamic materials properties, such as dynamic hardness, dynamic strength, and dynamic fracture toughness, which they speculate could make a difference by a factor of 10 in estimating the wear rates. Although several established techniques, such as split Hopkinson pressure bar and plate-impact experiments, exist to evaluate the properties of materials at high strain rates, none of these techniques offer the ease and simplicity that parallel a typical hardness test. Therefore, several approaches have been adopted to evaluate indentation hardness in time scales much shorter than a few seconds. This article describes a method (based on split Hopkinson pressure bar testing) for determining the dynamic indentation response of metals and ceramics. This method of dynamic indentation testing can determine rate-dependent characteristics of metals and ceramics at moderate strain rates. For example, dynamic indentation testing reveals a significant effect of loading rates on the hardness and the induced plastic zone size in metals and the hardness and induced crack sizes of brittle materials.

References cited in this section

1. D. Tabor, A Simple Theory of Static and Dynamic Hardness, *Proc. R. Soc. (London)*, Vol 192A, 1948, p 247–274
2. D. Tabor, *The Hardness of Metals*, Oxford University Press, London, 1951, p 1–173
3. H.T. Angus, The Significance of Hardness, *Wear*, Vol 54, 1979, p 33–78
4. M.A. Meyers, *Dynamic Behavior of Materials*, John Wiley & Sons, Inc., 1994, p 323–563
5. G. Subhash, The Constitutive Behavior of Refractory Metals as a Function of Strain Rate, *JOM*, Vol 47 (No. 5), 1995, p 55–58
6. J. Lankford, Mechanisms Responsible for Strain-Rate Dependent Compressive Strength in Ceramic Materials, *J. Am. Ceram. Soc.*, Vol 64, 1981, p 25–33
7. J. Lankford and C.R. Blanchard, Fragmentation of Brittle Materials at High Rates of Loading, *J. Mater. Sci.*, Vol 26, 1991, p 3067–3072
8. H.D. Espinosa, G. Raiser, R.J. Clifton, and M. Ortiz, Experimental Observations and Numerical Modeling of Inelasticity in Dynamically Loaded Ceramics, *J. Hard Mater.*, 1992, Vol 3 (No. 3–4), p 285–295
9. G. Subhash and G. Ravichandran, Mechanical Behavior of Hot-Pressed Aluminum Nitride under Uniaxial Compression, *J. Mater. Sci.*, Vol 33, 1997, p 1933–1939
10. S. Suresh, T. Nakamura, Y. Yeshurun, K.H. Yang, and J. Duffy, Tensile Fracture Toughness of Ceramic Materials: Effects of Dynamic Loading and Elevated Temperatures, *J. Am. Ceram. Soc.*, Vol 73 (No. 8), 1990, p 2457–2480
11. K.H. Yang and A.S. Kobayashi, A Hybrid Procedure for Dynamic Characterization of Ceramics at Elevated Temperatures, *Proc. Conf. Hostile Environments and High Temperature Measurements*, Society of Experimental Mechanics, 1989, p 41–44
12. H.C. Meng and K.C. Ludema, Wear Models and Predictive Equations: Their Form and Content, *Wear*, Vol 181, 1995, p 443–457

Dynamic Indentation Testing

G. Subhash, Michigan Technological University

Dynamic Hardness Testing: A Review

Rebound Method. To determine dynamic hardness, several methods based on rigid body dynamics have been used previously (Ref 1, 13, 14, 15). The majority of these techniques use gravity to accelerate an indenter from a predetermined height onto a specimen and measure the rebound height to determine the hardness of a specimen. A similar principle is adopted in projectiles shot from a gas gun where both the incident and rebound velocities are measured. Based on the kinetic energy of the impacting projectile and the energy required to form the resulting crater, an expression for dynamic hardness is derived. However, unlike a static hardness test,

where the load is directly measured, these methods warrant measurement of incident velocity, V_i , of the indenter for determining the dynamic hardness, H_d , as per the following equation (Ref 15, 16):

$$H_d = \frac{MV_i^2}{2U} \quad (\text{Eq 1})$$

where M is the mass of the indenter and U is the unrelaxed volume of the indentation imprint on the specimen. This relationship assumes that the ratio of decrease in indentation volume due to the elastic recovery to unrelaxed volume is the same as the ratio of rebound velocity to incident velocity of a spherical ball. Another assumption is that the resistance to indentation is constant throughout the deformation, but this assumption has been questioned by several authors (Ref 16, 17). Moreover, it is difficult to control the loading duration in this approach because it depends on the frictional properties and coefficient of restitution (which itself varies with indenter velocity) between the specimen and the indenter. The loading duration and the strain rate during the deformation are estimated (not directly measured) based on the energy absorbed to create the crater and the rebound height of the indenter. Therefore, these rebound methods do not parallel the simplicity of the static indentation test method where the indentation load and the contact time are directly measured to determine the static indentation hardness.

Commercial devices, such as Equotip hardness testers, based on rebound techniques also have emerged in the market (Ref 18). In this method, the hardness of a material is not determined, but a numerical measure called an "Equotip hardness number," which is proportional to the ratio of rebound velocity to impact velocity, is used to represent the hardness. However, this number has not been correlated to the established hardness measures such as Rockwell, Brinell, or Vickers hardness numbers.

Pendulum Method. Nobre and others (Ref 16) used a pendulum machine to investigate the surface resistance of a ductile steel to impact by hard ceramic balls. The pendulum is equipped with a piezoelectric transducer that enables the history of impact as well as the velocity of pendulum before and after the impact to be obtained. Obviously, the impact force or indentation load can be controlled by the amplitude of displacement from the mean position where the specimen is situated. Similar to the rebound method, the duration of contact with the specimen cannot be controlled in this technique because it depends on the resistance offered by the specimen material, which is a function of the geometry and materials properties. Therefore, assumptions similar to those in the rebound technique also should be made in this method to determine the dynamic hardness, and all these factors render this technique different from the method for static hardness determination.

The basic disadvantage of these methods is that neither the indentation load nor the duration of the indentation are precisely controlled a priori. This makes the determination of dynamic hardness nontrivial compared with the static hardness testing where the hardness is determined by a simple relationship based on the measured load and the size of the indentation imprint. Therefore, a technique that parallels the method for static indentation hardness determination, where the indentation load and the size of indentation are directly measured, can be of significant practical value for comparison of the static and dynamic hardness measurements and for determination of strain-rate-sensitive properties of materials.

References cited in this section

1. D. Tabor, A Simple Theory of Static and Dynamic Hardness, *Proc. R. Soc. (London)*, Vol 192A, 1948, p 247–274
13. D.B. Marshall, A.G. Evans, and Z. Nisenholz, Measurement of Dynamic Hardness by Controlled Sharp-Projectile Impact, *J. Am. Ceram. Soc.*, Vol 66 (No. 8), 1983, p 580–585
14. G. Sundararajan and P.G. Shewmon, The Use of Dynamic Impact Experiments in the Determination of the Strain Rate Sensitivity of Metals and Alloys, *Acta Metall.*, Vol 31, 1983, p 101–109
15. Y. Tirupataiah and G. Sundararajan, A Dynamic Indentation Technique for the Characterization of the High Strain Rate Plastic Flow Behavior of Ductile Metals and Alloys, *J. Mech. Phys. Solids*, Vol 39, 1991, p 243–271

16. J.P. Nobre, A.M. Dias, and R. Gras, Resistance of Ductile Steel Surface to Spherical Normal Impact Indentation: Use of Pendulum Machine, *Wear*, Vol 211, 1997, p 226–236
17. C.H. Mok and J. Duffy, The Dynamic Stress-Strain Relation of Metals as Determined from Impact Tests with Hard Ball, *Int. J. Mech. Sci.*, Vol 7, 1965, p 355–371
18. “Standard Test Method for Equotip Hardness Testing of Steel Products,” A 956–96, *Annual Book of ASTM Standards*, ASTM, Vol 01.05, 1997

Dynamic Indentation Testing

G. Subhash, Michigan Technological University

Dynamic Indentation Hardness Testing

One of the basic requirements for conducting indentation testing is the ability to deliver a single indentation load. Methods based on the split Hopkinson pressure bar (SHPB) were adopted by Mok and Duffy (Ref 17), where repeated loading due to wave reflections that occur in an incident bar were avoided by using a rigid stopper. Again, the load was not directly measured but calculated based on several assumptions. Although this method offers an ad hoc, or temporary, solution to create a single dynamic indentation, none of the methods offer the elegance and simplicity of the recovery bar momentum-trapping device developed for SHPB (see Ref 19 and the article “Recovery Hopkinson Bar Testing” in this Volume). With proper instrumentation, this technique can be effectively used (Ref 20, 21, 22) to determine the dynamic indentation hardness of metals and ceramics. The method does not use any of the theoretical formulations developed in previously described methods to determine either the load or the duration of impact. The hardness is determined by directly measuring the load and the size of indentation, exactly similar to the procedure used for static-hardness determination. The velocity of the indenter during the penetration of the indenter into the specimen is also measured directly to obtain a more accurate picture of the resistance of the specimen and the velocity of the indenter during the impact. This information is later used to calculate the strain rate of deformation and to verify the hardness measurements with the yield stress values obtained from uniaxial stress-strain response at similar strain rates.

Test Setup. The test setup comprises four major parts: a gas gun to propel a short striker rod; a long, slender rod with a strain gage mounted at the center; a high-frequency load cell; and a cantilever beam with a strain gage. The long, slender rod (length-to-diameter ratio >20) is designed with an integral “flange-sleeve-rigid mass” assembly, called the momentum trap (MT), at one end and an indenter mounted in a housing at the other end. The long, slender rod is the same as the incident bar in the modified SHPB (Ref 19) described in the article “Recovery Hopkinson Bar Techniques” in this Volume. The assembly is made of heat treated high-strength maraging steel. The inner diameter of the sleeve and the rigid mass is designed to slide smoothly over the incident bar. The outer diameter of the sleeve is designed to match the impedance of the incident rod, where impedance is defined as the product of the area of cross section, density, and wave velocity. Since both the sleeve and the incident rod are made of the same material, the outer diameter of the sleeve is calculated based on the cross-sectional area of the rod. The outer diameter and the length of the rigid mass are arbitrary but typically range between 8 and 10 times the diameter of the incident bar. The flange diameter is the same as the outer diameter of the sleeve. All the contact surfaces between the flange, sleeve, and rigid mass are carefully polished to a high degree of flatness for effective transfer of wave energy during the operation. More details of the momentum-trap design can be found in Ref 19 and the article “Recovery Hopkinson Bar Techniques” in this Volume.

A high-frequency (200 kHz) load cell is mounted on a separate rigid base at the indenter end of the incident bar. The load-cell signal is passed through a charge amplifier into a digital oscilloscope. A specimen material of suitable dimensions, preferably the same diameter and length of the load cell (6 mm), is sandwiched between

the indenter and the load cell. A thin metallic strip mounted with a $350\ \Omega$ strain gage in the center is held fixed at one end with its free end resting against the indenter base in the housing. This metallic strip acts as a cantilever beam with its free end moving in unison with the indenter during the hardness testing. The configuration of the dynamic indentation testing device is shown in Fig. 1. A short striker bar is launched from a gas gun to make a planar impact on the sleeve end of the incident bar. The diameter of the striker bar is the same as that of the incident bar, and the length is typically kept the same as the sleeve length. The impacting surfaces are made flat and perpendicular to the bar axis so that a planar impact is ensured during the operation.

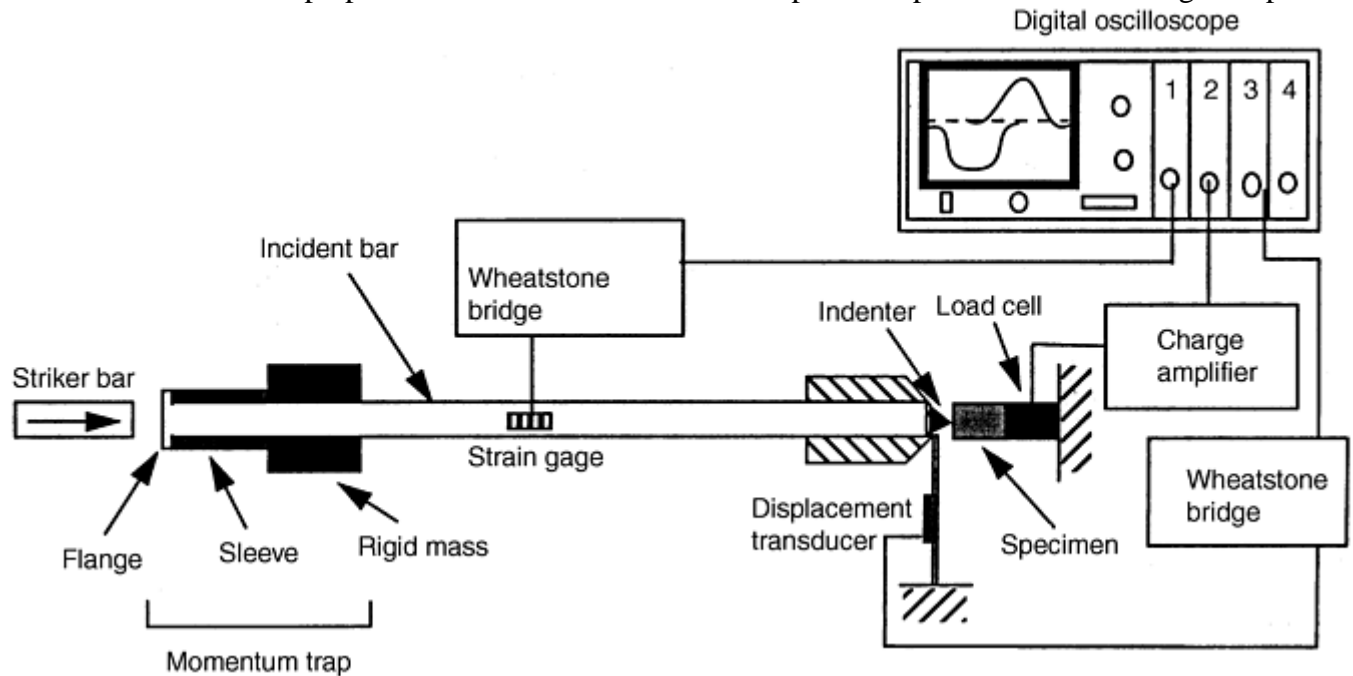
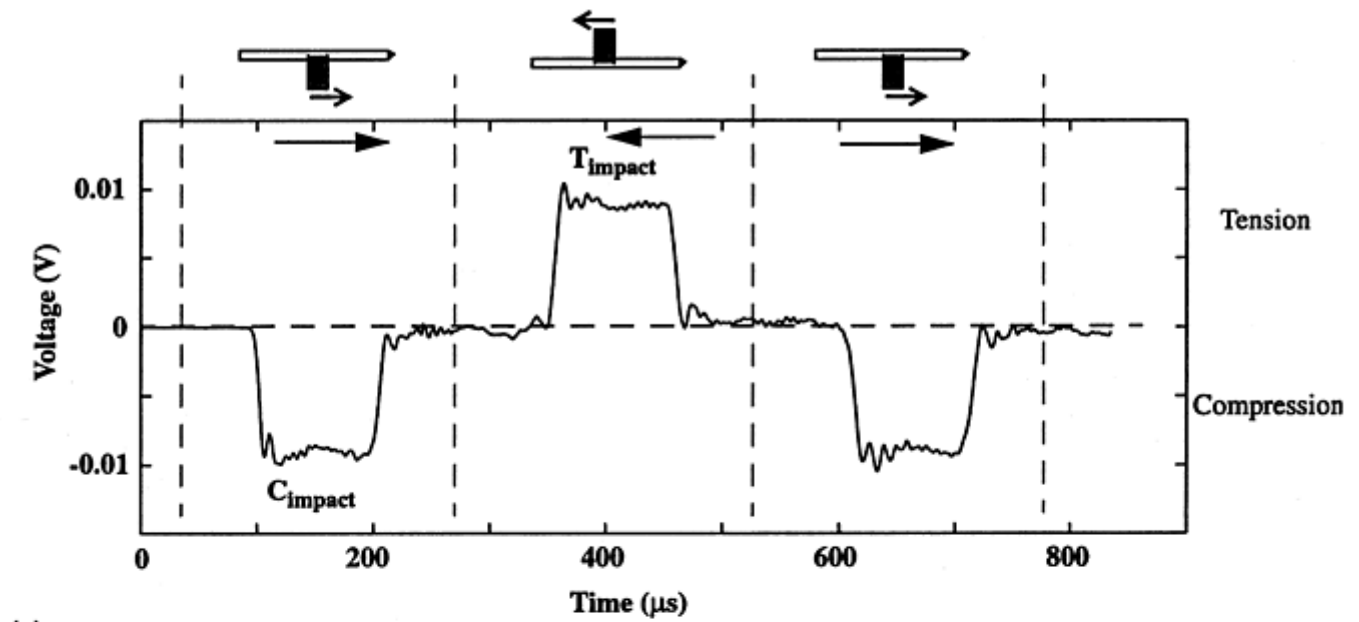


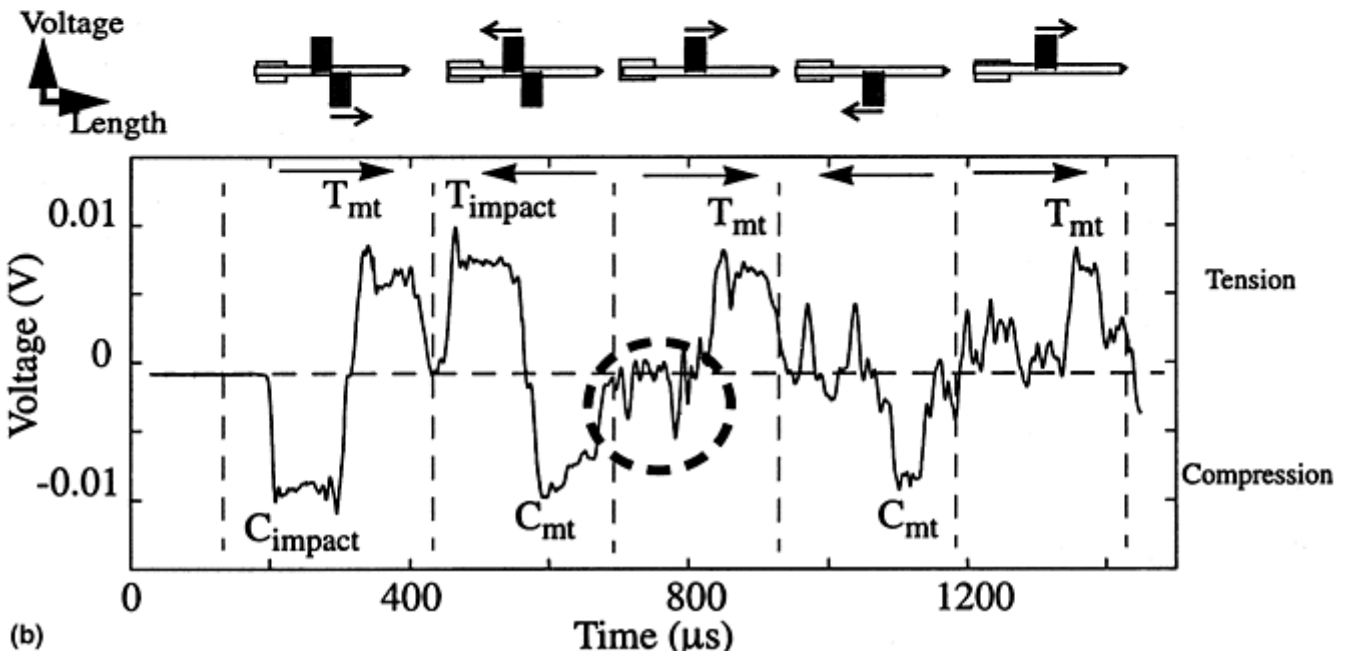
Fig. 1 Experimental setup for dynamic indentation hardness measurements

An alternate design (Ref 21) places the load cell between the indenter and the incident bar. This configuration is suitable when indentation hardness measurements are to be performed on large specimens. Although the hardness measurements were statistically the same in both configurations, the signal generated by the load cell in the later configuration was extremely noisy due to the stress-wave interactions at the interface between the load cell and the incident bar.

Operation. Before describing the operation of the dynamic hardness tester or the incident bar with a momentum trap, it is imperative to understand the elastic stress-wave-propagation phenomena in a slender rod *without* the momentum trap. Assume an incident bar with a strain gage mounted at the center of the rod *without* the momentum trap. A short striker bar is propelled from a gas gun to cause an impact at one end of the incident bar. Figure 2(a) illustrates the strain-gage signal obtained from an incident bar without the momentum trap. Upon impact of the striker bar onto an incident bar, a single compression pulse (C_{impact}) is generated in the incident bar whose amplitude is proportional to the velocity of the impacting striker bar, and the duration is equal to the round-trip travel time of the longitudinal wave in the striker bar. If an indenter is attached to the other end of the incident bar (illustrated on the top of the strain-gage signals), the compression wave will reach the indenter end and cause the indenter to penetrate the specimen. Since the indenter tip has a negligible area, it acts as a free end, and the compression pulse will reflect as a tensile pulse (T_{impact}) traveling back toward the impact end. Upon reaching this end, this tensile pulse reflects back again as a compression pulse and travels toward the indenter to cause another indentation. This process will repeat several times, causing multiple indentations, thus making the incident bar without the momentum trap unsuitable for indentation investigations and hardness determination where a single indentation imprint is desired.



(a)



(b)

Fig. 2 Strain-gage signals revealing the stress pulses in the incident bar (a) in the absence of the momentum trap and (b) with the momentum trap. The illustrations on top of the strain signals indicate the physical position of these pulses in the bar.

To avoid multiple indentations, a momentum-trap assembly is designed at the impact end of the incident bar, as shown in Fig. 1. Upon impact of the striker onto the flange end of the incident bar, compressive stress pulses are generated in both the incident bar and the sleeve. The pulse in the sleeve travels toward the rigid mass and reflects back as a compressive pulse at the rigid mass. Since the particle velocity in a compression wave is in the direction of wave travel, upon reaching the flange end, the materials particles within the wave push against the flange, thus loading a tensile pulse into the incident bar. Therefore, the strain gage mounted at the center of the incident bar will record a compressive pulse (C_{impact}) followed by a tensile pulse (T_{mt})—as indicated in the strain-gage signal shown in Fig. 2(b)—both traveling toward the indenter. The compression pulse causes the desired indentation upon reaching the indenter and reflects back as a tension pulse (T_{impact}) similar to the situation in the incident bar without the momentum trap described previously. The original tensile pulse (T_{mt}),

upon reaching the indenter, retracts the indenter away from the specimen and reflects back as a compression pulse (C_{mt}) into the incident bar.

Both these reflected pulses (T_{impact} and C_{mt}) now travel toward the flange end (shown in the illustrations with arrows on top of the strain-gage signals). Upon reaching the sleeve end, the T_{impact} is captured by the momentum-trap assembly and separates the contact between the flange and the sleeve. Therefore, the strain gage on the incident bar will not sense this pulse in its subsequent readings. A circle indicating the position of the trapped pulse is illustrated in Fig. 2(b). The C_{mt} will reflect back as a tensile pulse, T_{mt} (due to the free-boundary condition at the flange end), and travel toward the indenter. This pulse will travel back and forth in the incident bar as a tensile pulse while traveling toward the indenter and as a compressive pulse while traveling toward the flange, until it is eventually dissipated. In both situations, the incident bar moves farther away from the specimen, thus avoiding repeated indentations. *Thus, by designing the momentum trap suitably, it can be ensured that only a single compression pulse reaches the indenter end, thus allowing dynamic indentation tests to be performed at high strain rates.*

In this method, the incident pulse impact duration and amplitude are independent of the indenter-specimen interactions, and hence, the impact duration is maintained irrespective of the specimen properties. The reflected pulse (i.e., T_{impact}) contains information on the specimen and, therefore, can provide some estimate of the indentation load. However, any effort to obtain the load estimate from the reflected signal will warrant a prior knowledge of the specimen properties and some assumptions on the energy absorbed in the specimen, thus making this method different from that of static indentation testing, where the load is directly measured. To accomplish this objective, a high-frequency load cell is mounted rigidly on a separate base. The specimen is sandwiched between the indenter and the load cell and is held by a small compression force.

Similar to static testing, the indenter is placed in contact with the specimen before the striker is impacted onto the incident bar. By choosing a long incident bar, normal impact is ensured in the experiment without causing any rotation of the indenter. After the dynamic indentation, the load experienced by the specimen during the indentation is captured by the load cell and recorded on a digital oscilloscope. Figure 3 is a typical load-cell signature during indentation of a metallic specimen. The peak indentation load is measured from this pulse. The size of the indentation imprint on the specimen is measured after the experiment to calculate the dynamic hardness according to ASTM E 92-82 (Ref 23):

$$\text{Vickers hardness} = 1.8544 P/d^2 \quad (\text{Eq 2})$$

where d is the average indentation diagonal, and P is the peak load measured by the load cell. For comparison purposes, static hardness measurements were made using a hardness tester at suitable loads of 15 s duration. In both static and dynamic cases, a diamond Vickers indenter with a 136° apex angle is used.

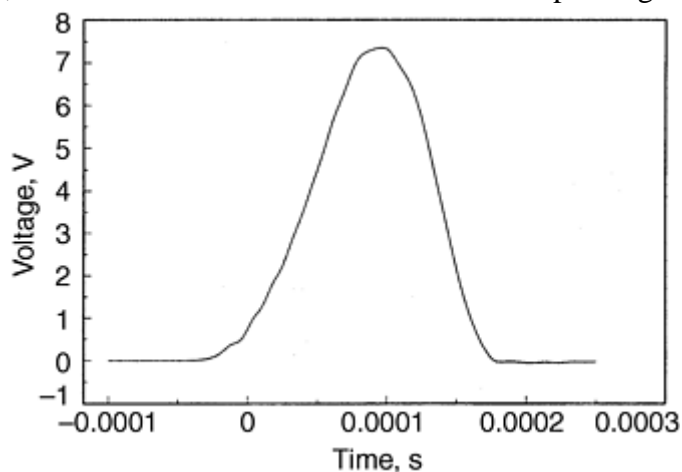


Fig. 3 Typical load-cell signal during indentation on a metal

Measurement of Time of Contact. The displacement of the indenter is fully controlled by the duration and amplitude of the initial compression pulse (C_{impact}), and hence, the time of contact between the indenter and the specimen is the same as the duration of the initial compression pulse. Note that in a rebound method the time of contact is controlled by specimen and indenter properties (e.g., coefficient of restitution, frictional characteristics, and so on). In the current method, the velocity of the indenter is measured using a steel strip as a cantilever beam with its free end resting against the indenter base as shown in Fig. 1. A strain gage mounted on

the steel strip monitors the displacements of the free end as the indenter penetrates into the specimen. The voltage generated by the strain gage is converted to the deflection at the free end using simple beam theory. Figure 4 illustrates a typical profile of the movement of the tip of the cantilever beam during the indentation on a steel specimen.

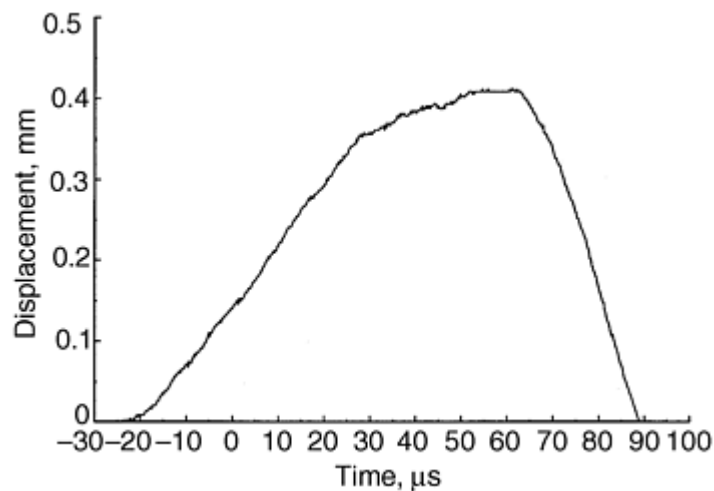


Fig. 4 Profile of strain-gage signal mounted on the cantilever beam, indicating the depth of indentation as a function of time

References cited in this section

17. C.H. Mok and J. Duffy, The Dynamic Stress-Strain Relation of Metals as Determined from Impact Tests with Hard Ball, *Int. J. Mech. Sci.*, Vol 7, 1965, p 355–371
19. S. Nemat-Nasser, J.B. Isaacs, and J.E. Starrett, Hopkinson Techniques for Dynamic Recovery Experiments, *Proc. R. Soc. (London) A*, Vol 435, 1991, p 371–391
20. B.J. Koepell and G. Subhash, Characteristics of Residual Plastic Zone under Static and Dynamic Indentations, *Wear*, Vol 224, 1999, p 56–67
21. G. Subhash, B.J. Koepell, and A. Chandra, Dynamic Indentation Hardness and Rate Sensitivity in Metals, *J. Eng. Mater. Technol. (Trans. ASME)*, Vol 121, 1999, p 257–263
22. R.J. Anton and G. Subhash, Dynamic Vickers Indentation of Brittle Materials, *Wear*, in press
23. “Standard Test Method for Vickers Hardness of Metallic Materials,” E 92–82, *Annual Book of ASTM Standards*, Vol 03.01, ASTM, 1996

Dynamic Indentation Testing

G. Subhash, Michigan Technological University

Test Results

A range of commercially available metals and ceramics have been tested by this method. Dynamic indentation hardness measurements on metals, when compared with the yield stress obtained at similar strain rates, verify the validity of the Tabor's relationship $H = 3 \times Y$, where H is the hardness and Y is the yield strength at 8% strain. To further validate the dynamic indentation results, the plastic zone size beneath the indentation in

metals also has been measured as a function of the rate of indentation. Indentation hardness measurements on brittle materials also have been done. The extent of cracks generated from the corners of the indentation can be correlated to the strain-rate effects in these ceramics.

Dynamic indentation hardness of metals has been tested on several commercial aluminum, copper, steel, and titanium alloys with specimens of 4 to 6 mm diameter and 8 to 10 mm length. The diameter of the specimens was limited by the size of the load cell used in the experimental setup. The loading surfaces of each specimen were metallographically prepared and polished down to 6 μm surface finish. Figure 5 presents the load versus the square of the average indentation diagonal for both static and dynamic indentations on the test materials. A regression line is plotted through each set of data. The slope of this line multiplied by 1.8544 (Eq 2) gives the hardness. Note that the slope of the dynamic Vickers hardness (DHV) data is consistently greater than the static Vickers hardness (HV) data. The straight-line nature of the data indicates that the hardness is relatively constant in the range of loads used in these experiments. The hardness measurements obtained from these plots, as well as the percent increase in dynamic hardness over the static hardness, that is, $([\text{DHV}-\text{HV}]/\text{HV}) \times 100$, are summarized in Fig. 6. For aluminum and copper alloys, which have a face-centered cubic (fcc) structure, the percentage increase in hardness at higher rates varies between 2 and 10%. For steels (most of the commercial steels have complex crystal structure), this increase is between 10 and 20%, and for titanium and its alloys (hexagonal closed-pack structures), it is well above 20%.

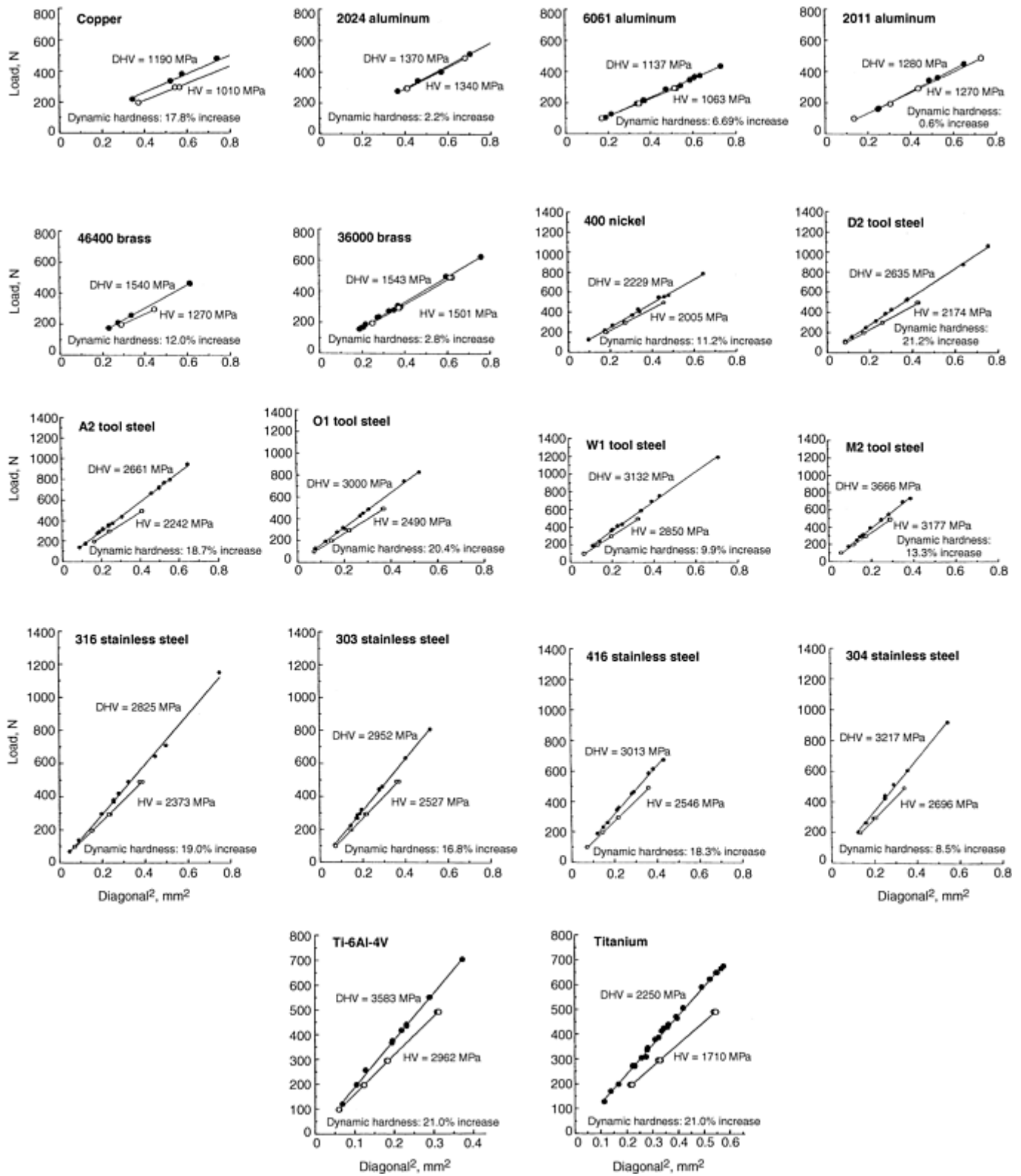


Fig. 5 Plots of load versus square of the mean indentation diagonal for selected metals and alloys

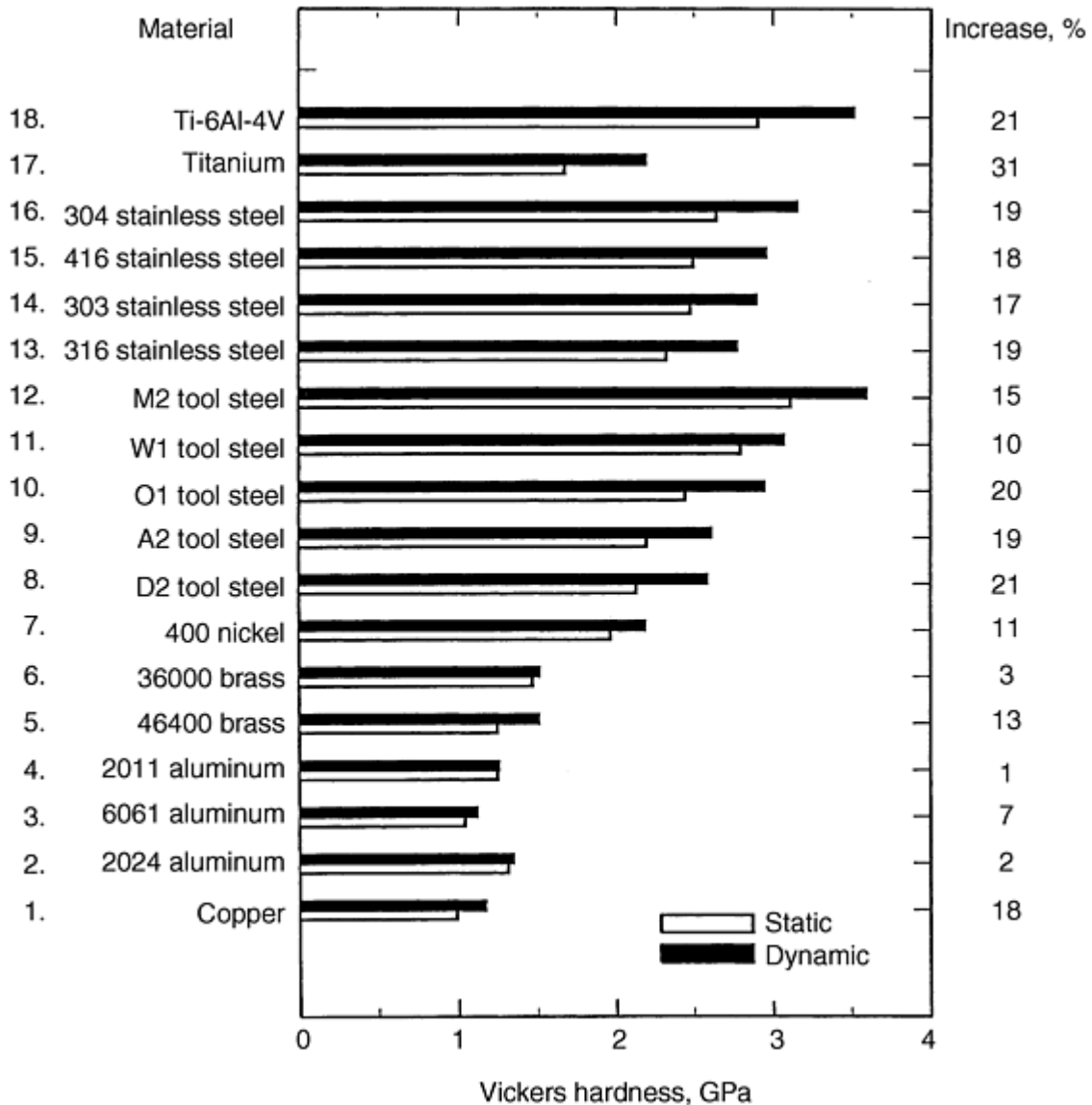


Fig. 6 Summary of static and dynamic Vickers hardness data for the metals and alloys included in Fig. 5. The numbers on the right indicate the percentage increase in dynamic hardness over the static hardness.

Velocity of the Indenter and Deformation Strain Rate. The velocity of the indenter during the penetration is calculated from the recorded strain (Fig. 4) from a gage (mounted on the cantilever beam) signal. The strain signal is converted to the displacement at the free end of the cantilever beam using basic beam-theory equations. The slope of this curve gives an estimate of the velocity of indenter during penetration. Note that the profile of this curve is considerably different from the incident compression (C_{impact}) pulse shown in Fig. 2(b), but the duration of both curves is close to 100 μs . The plot indicates that the indenter penetrates with a higher velocity close to 7.25 m/s during the early stages and then slows down to 1.5 m/s before unloading. The initial high velocity is due to the low resistance encountered by the indenter sharp-tip as it penetrates the specimen. With continued penetration, the area resisting the indenter increases due to the pyramidal shape of the indenter, and the velocity decreases. It is cautioned here that the velocity of the indenter in the current method is measured while the indenter is in contact with the specimen and should not be confused with the free velocity of the indenter in air used in the rebound method.

Hardness has been related to yield stress of metallic materials through Tabor's relationship ($H = 3 \times Y$), where H is the indentation hardness and Y is the yield stress at 8% strain (Ref 1, 2). However, this equation has been verified only for static indentations. To verify the current results on dynamic hardness and to establish the validity of Tabor's relationship in the dynamic regime, it is necessary to estimate the strain rate of deformation during the dynamic indentation process. However, in an indentation experiment, the accumulated plastic strain varies considerably within the plastic zone. The residual strain is maximum in a region closer to the tip of the indentation and decreases rapidly at distances farther away. The nonhomogeneity of plastic strain results in a

nonuniform strain rate within the plastic zone. Therefore, an average measure of strain rate will be defined from global velocity measurements as follows:

$$\text{Average strain rate} = \frac{\text{velocity of the indenter}}{\text{size of the indentation}} \quad (\text{Eq 3})$$

Any measure of the size of indentation, such as the diagonal or the depth of indentation, could be used because the order of strain rate does not vary significantly with either of the measurements. Based on the loading range employed in this investigation, the size of the diagonal of the indentation was measured to be approximately 0.6 to 0.7 mm. The velocity of the indenter was chosen as the lesser of the two velocities (1.5 m/s) in Fig. 4. This is because the deformation volume is greater during the later stages of the penetration process. Accordingly, the average strain rate was determined to be around 2200/s. This value of strain rate is in reasonable agreement with the dynamic spherical indentation experiments by Mok and Duffy (Ref 17), who used a split Hopkinson pressure bar and determined the strain rate to be around 1500/s. Finite element simulations of the dynamic indentation process also confirmed that a large portion of the plastic volume experiences a strain rate in the range of 1000 to 2000/s (Ref 24).

Validation of Tabor's Relationship in Dynamic Indentation Experiments. To verify the validity of Tabor's equation in the dynamic regime, uniaxial compressive stress-strain response was obtained at a quasi-static strain rate of around 0.001/s and a dynamic strain rate of around 2000/s for all the materials. The quasi-static experiments were performed on a servohydraulic machine, and the high-strain-rate experiments were performed using a compression split Hopkinson pressure bar. Specimen sizes of 4 to 6 mm diameter and 8 to 12 mm length were used in these experiments. The stress-strain curves at these two strain rates are given in Fig. 7 for the same materials included in Fig. 5 and 6. For rate-sensitive materials, significant increase in yield strength can be observed. From the given stress-strain curves, yield stress at 8% strain was obtained and plotted against the corresponding hardness in Fig. 8. For static data, the regression line yields a slope of 3, thus validating the Tabor relationship. Similar analysis of the dynamic data yields a slope slightly less than 3. This slight variation may be expected because the strain rate in the indentation test determined according to Eq 3 is an average measure. Moreover, the stress-strain data generated from the Hopkinson pressure bar experiment was not exactly at one constant strain rate but varied between 1800 and 2200/s for different materials. Nevertheless, the data validate the Tabor's relationship under dynamic conditions also (i.e., $DHV=3Y_d$, where Y_d is the yield stress at 8% strain).

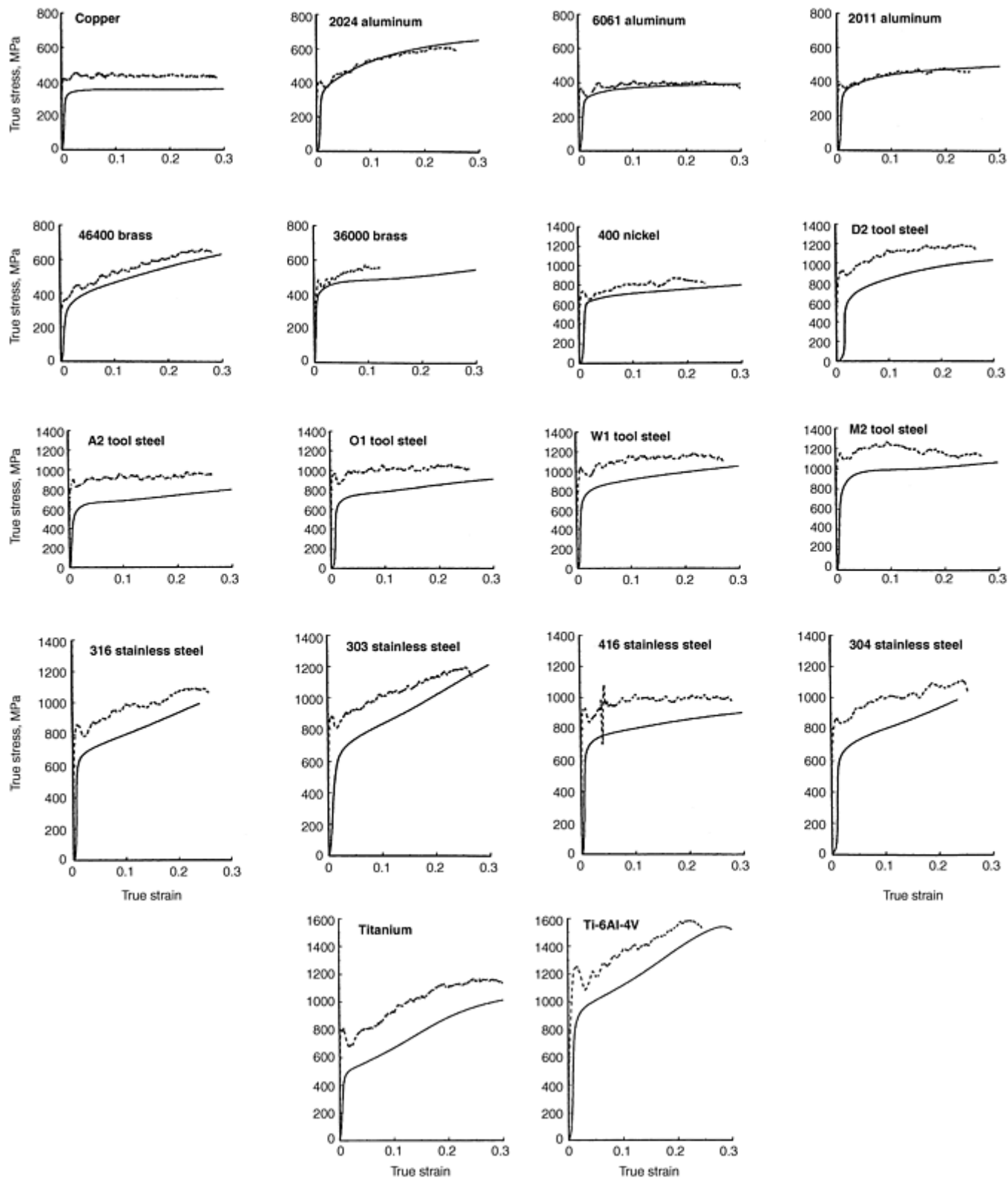


Fig. 7 Stress-strain response for metals at quasi-static and high strain rates

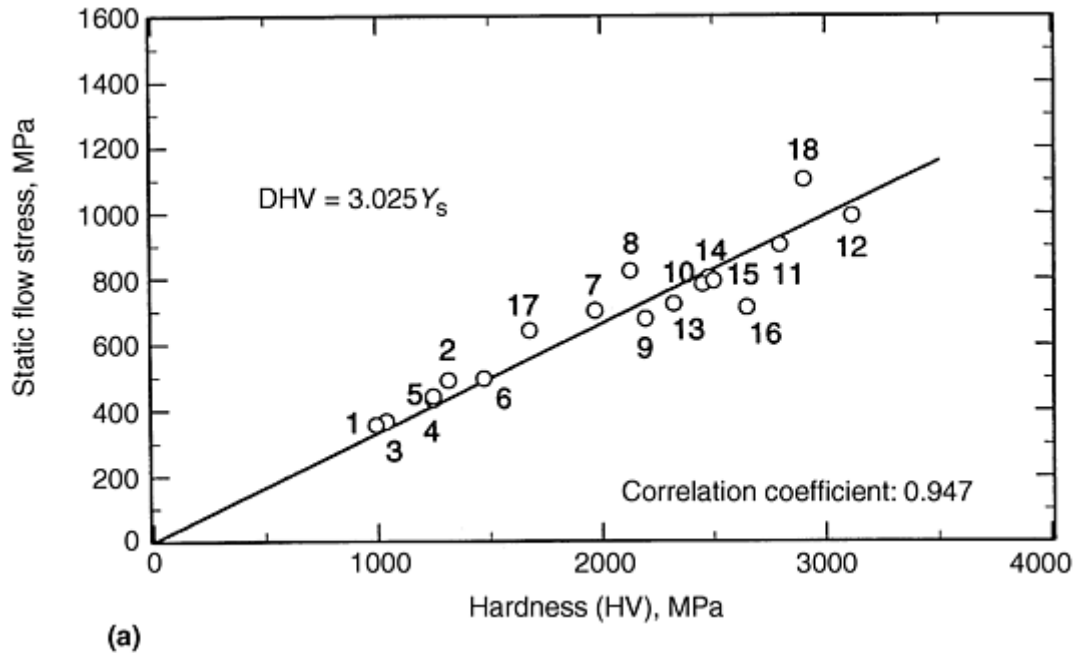


Fig. 8 Hardness versus yield stress at 8% strain for metals under (a) static loading and (b) dynamic loading. The numbers next to the data points refer to metals and alloys listed in Fig. 6.

Characteristics of the Indentation Plastic Zone. To estimate the differences in plastic zone size with respect to the loading rate, microhardness measurements have been performed within the indentation zones of two materials that exhibited a strain-rate-sensitive and a strain-rate-insensitive stress-strain response. Static and dynamic indentations were performed at similar load levels (approximately 490 N) on 2024 aluminum (rate insensitive) and 316 stainless steel (rate sensitive) (Fig. 7). The specimens were then sectioned just outside of the indentation zone using a low-speed diamond saw and then carefully ground and polished such that the final polished surface passed through the midsection of the indentation as shown in Fig. 9 (Ref 20). In the region surrounding the indentation, static microhardness measurements (which are basically hardness measurements at much lower load levels) were performed as per ASTM E 384-89 (Ref 25), and the data were contoured to give an indication of the accumulated plastic strains as a function of depth beneath the indentation. For the present work, loads of 100 g for aluminum and 200 g for stainless steel were used with microindentation spacing of 0.12 mm and 0.16 mm, respectively.

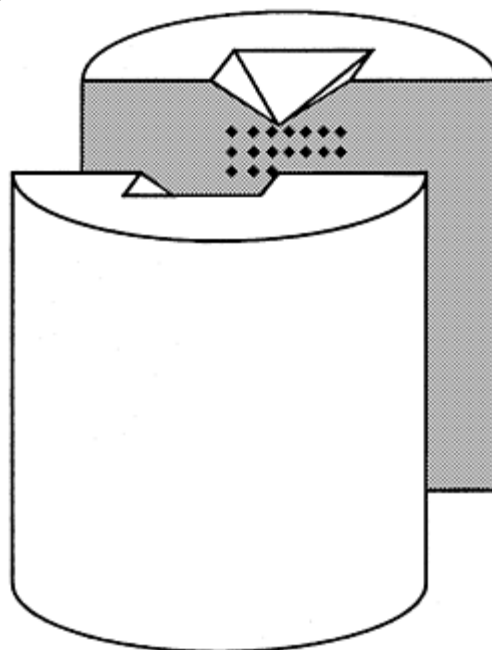


Fig. 9 Schematic of the plane illustrating the grid of microhardness measurements surrounding the macroindentation

Contours of microhardness for static and dynamic indentations on aluminum and steel are shown in Fig. 10. The exact magnitude of the accumulated plastic strains closest to the surface or the tip of indentation could not be obtained with this procedure due to the constraint imposed by the ASTM standard (Ref 25) (i.e., hardness measurements should be performed at a distance at least 2.5 times the diagonal of indentation from a free surface). The position of the free surface of the specimen is denoted by a solid line in the figure. For comparison purposes, all the contours are plotted on the same scale, with shaded regions representing the area where the microindentations were performed.

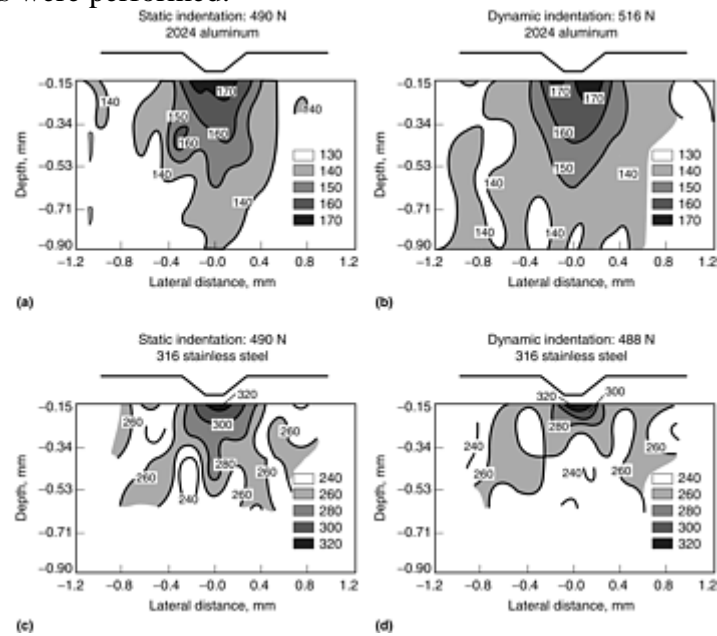


Fig. 10 Contours of microhardness measurements revealing the plastic zone size beneath static and dynamic indentations. (a) 2024 aluminum, static indentation. (b) 2024 aluminum, dynamic indentation. (c) 316 stainless steel, static indentation. (d) 316 stainless steel, dynamic indentation

Two major observations can be made from these plots. The first observation is that the size of the plastic zone for 2024 aluminum is almost the same under static and dynamic loads. The contours of microhardness are also approximately similar in terms of their depth, width, and magnitude of microhardness. This is expected since this material exhibits no rate sensitivity in both its hardness (Fig. 6) and constitutive response (Fig. 7). The minor scatter seen in the microhardness contours may be a result of the natural scatter in microhardness measurements and minor compositional and microstructural variations between the two specimens. In contrast, the contours of microhardness for 316 stainless steel reveal that the plastic zone size is considerably smaller under dynamic indentation compared with the static indentation for similar loads. This is consistent with the rate-sensitive nature of steel—that is, a higher yield stress at higher strain rates (Fig. 7).

The second observation is that the static yield stress at 8% strain for 316 stainless steel is around 750 MPa and that of aluminum is close to 500 MPa. Correspondingly, the plastic volume size in steel under static indentation is significantly smaller compared with that of aluminum. A similar result also is seen for dynamic loads where the effect is further enhanced due to an increase in yield strength in steel and relatively no change in aluminum.

To avoid single crystal effects associated with individual grains, this analysis should be used only when the grain size is considerably smaller than the size of microindentation. For large-grained materials one can take advantage of the micromechanisms of deformation (other than dislocation plasticity) to identify the extent of residual plastic zone. For example, in the case of titanium, which undergoes mechanical twinning during plastic deformation, the extent of twinned region beneath the indentation can be used to estimate the plastic zone size (Ref 20). However, caution should be used in interpreting the results based on such microstructural features because twinning is a preferred mode of plastic deformation at high strain rates in body-centered cubic (bcc) and hexagonal close-packed (hcp) materials (Ref 26). Moreover, the orientation of individual grains with respect to the local stress axis may also play a major role in inducing twins in a specific grain irrespective of its distance from the indentation within the plastic zone. It also is important to be aware of the fact that plastic strain also is accommodated by the dislocation activity and should be considered before any definite conclusions can be drawn.

References cited in this section

1. D. Tabor, A Simple Theory of Static and Dynamic Hardness, *Proc. R. Soc. (London)*, Vol 192A, 1948, p 247–274
2. D. Tabor, *The Hardness of Metals*, Oxford University Press, London, 1951, p 1–173
17. C.H. Mok and J. Duffy, The Dynamic Stress-Strain Relation of Metals as Determined from Impact Tests with Hard Ball, *Int. J. Mech. Sci.*, Vol 7, 1965, p 355–371
20. B.J. Koepf and G. Subhash, Characteristics of Residual Plastic Zone under Static and Dynamic Indentations, *Wear*, Vol 224, 1999, p 56–67
24. B.J. Koepf, “Dynamic Indentation Hardness of Materials,” Ph.D. dissertation, Michigan Technological University, Houghton, MI, 1997
25. “Standard Test Method for Microhardness of Materials,” E 384–89, *Annual Book of ASTM Standards*, Vol 03.01, ASTM, 1996
26. G.T. Gray III, Deformation Substructures Induced by High Strain Rate Deformation, *Modeling the Deformation of Crystalline Solids*, T.C. Lowe, A.D. Rollett, P.S. Follansbee, and G.S. Daehn, Ed., The Minerals, Metals, Materials Society, Warrendale, 1991, p 145–157

Dynamic Indentation Testing

G. Subhash, Michigan Technological University

Dynamic Indentation of Brittle Materials

Static indentation investigations were used extensively to analyze the fracture characteristics of brittle materials (Ref 27, 28, 29, and 30). The approach also has been extended to model material-removal mechanisms during grinding and sliding wear of ceramics (Ref 31, 32). In order to develop a representative model of material removal during machining of brittle materials, the interaction of an abrasive grit with the workpiece has been viewed as an indentation event where the indenter is attempting to penetrate the workpiece surface in the normal direction, while being dragged in the lateral direction. Such a premise forms the basis for the “indentation fracture” models for machining of brittle materials. During static Vickers indentation studies, it was noted that penny-shaped median cracks develop during loading of the indenter, and lateral cracks parallel to the surface develop during unloading of the indenter. In a surface-grinding operation, the lateral cracks assist in chip formation and material removal, whereas median cracks leave residual damage in a workpiece. The role of these cracks is reversed in a dicing operation (i.e., median cracks assist material separation and lateral cracks induce surface damage). These model studies were typically performed using static indentations where the rate effects are not sufficiently captured as described previously. Therefore, a technique for performing dynamic Vickers indentations is of significant practical value for better characterizing the indentation fracture behavior of brittle materials at similar strain rates.

Static and dynamic Vickers indentation hardness have been compared for six commercially available brittle materials: Pyrex (Corning, Inc., Corning, NY) (borosilicate) glass, sintered alumina (Al_2O_3), hot pressed pure aluminum nitride (AlN), 3% yttria-doped AlN (Y_2O_3 -AlN), maximum-strength-grade magnesia, partially stabilized zirconia (MgO-PSZ), and yttria tetragonal zirconia polycrystal (Y_2O_3 -TZP or Y-TZP) (as described further in Ref 22). A plot of indentation load (P) versus the square of the mean indentation diagonal (d^2) is plotted for all the brittle materials in Fig. 11. A regression line was fit through the static and dynamic data

separately. Note that, similar to metals, the dynamic indentation hardness measurements on brittle materials were consistently greater than the static hardness measurements, and there seems to be no apparent dependence of hardness on the indentation load in the range of loads used in this investigation. In the case of AlN, notice that both the pure and doped AlN had essentially the same static hardness of 11.45 GPa. However, the pure AlN revealed a 19% increase in the dynamic hardness over the static hardness compared with 8% in the doped AlN. This may suggest that the addition of the yttria dopant in AlN decreased the rate sensitivity by half. The commercially sintered alumina exhibited a 12% increase in the dynamic hardness over its static hardness. The static Vickers hardness for this commercial-grade alumina is around 9.54 GPa, which is considerably lower than that for a dense and pure alumina, which typically has hardness in the range of 19 to 26 GPa (Ref 33). The lower hardness of the commercial alumina is attributed to extensive porosity and impurities present in the material. Similarly, data for zirconia ceramics revealed that there is an increase of 9.0% for MgO-PSZ and a 12% increase for Y-TZP in their dynamic hardness.

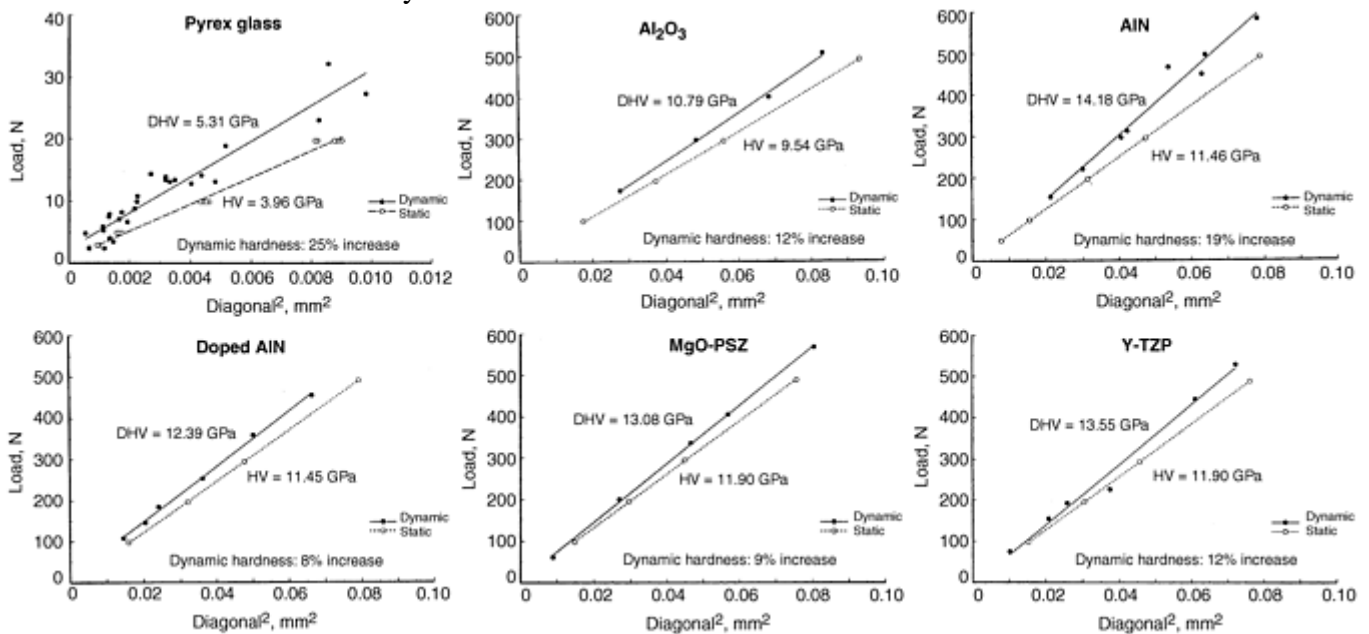


Fig. 11 Plots of load versus square of the mean indentation diagonal for brittle materials

The current results on brittle materials (i.e., increase in hardness under dynamic loading compared with that of static loading) is consistent with the previous results on glass by Fairbanks and others (Ref 34). The hardness results also are supported by the observed rate-dependent uniaxial strength of structural ceramics where an increase in fracture strength with increase in loading rate has been observed in Pyrex glass (Ref 35), alumina (Ref 36), zirconia ceramics (Ref 37, 38), and aluminum nitride ceramics (Ref 9). However, for ceramics, the Tabor relationship between hardness and fracture strength cannot be established because of absence of significant plastic strain and the resulting early onset of unstable fracture. Lankford and others (Ref 36) rationalized the reasons for the nonexistence of Tabor's relationship in ceramics and concluded that, even if plasticity initiates in ceramics at high confining stresses, the accompanying stress concentration will initiate microcracking simultaneously and cause catastrophic fracture well before a stress magnitude of $H/3$ is reached. Induced Crack Morphology. Typical crack systems induced in brittle materials due to an indentation by a rigid indenter have been summarized by Cook and Pharr (Ref 27). Of specific interest are radial and median cracks because these crack systems leave a surface trace on the specimen and can be easily measured for quantification of damage and fracture toughness calculations. Figure 12 illustrates the effect of loading rate on static and dynamic indentations in zirconia ceramics. It is clear from the micrographs that the median crack lengths are considerably larger during static indentations compared with the dynamic indentations at similar load levels.

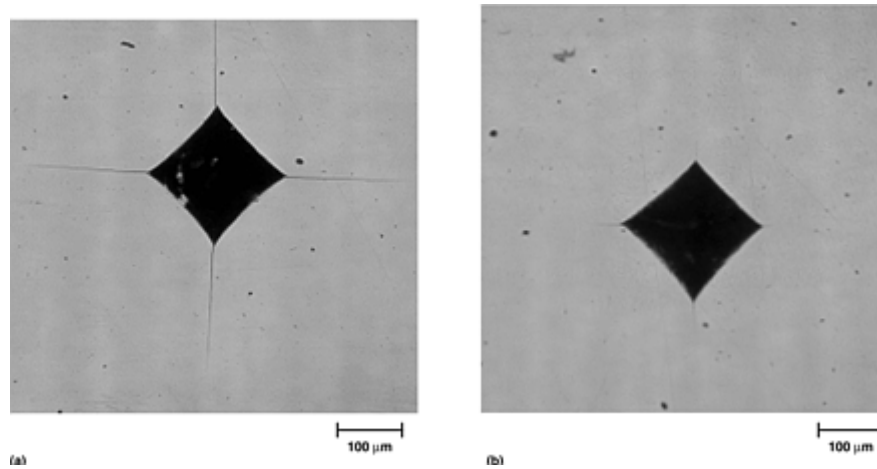


Fig. 12 Micrographs revealing the extent of induced median cracks in MgO-PSZ under (a) static and (b) dynamic indentations

A plot of half median crack length, c , versus the half indentation diagonal, a , is presented in Fig. 13 for Pyrex glass and MgO-PSZ. The inset in this figure gives a pictorial representation of c and a . Similar plots for AlN and Al₂O₃ revealed no significant differences in the induced crack sizes between the static and dynamic indentations (Ref 22). This is because only a limited number of specimens for each ceramic were tested, and the data did not exhibit any specific trends in the extent of damage with loading rate. From Fig. 13, it can be noticed that in the case of Pyrex glass, the median crack size induced under dynamic loading is consistently greater than in the static loading. This is contrary to the observed behavior in zirconia ceramics where the median crack sizes are significantly smaller under dynamic loads compared with the static loads. This difference has been attributed to transformation toughening in these ceramics (Ref 39). Under dynamic loading, the zirconia ceramics exhibit higher yield strength and large inelastic strains close to 2% (Ref 37, 38). Such large inelastic strains can effectively absorb the imposed dynamic loads and result in the reduced cracking and enhanced fracture toughness.

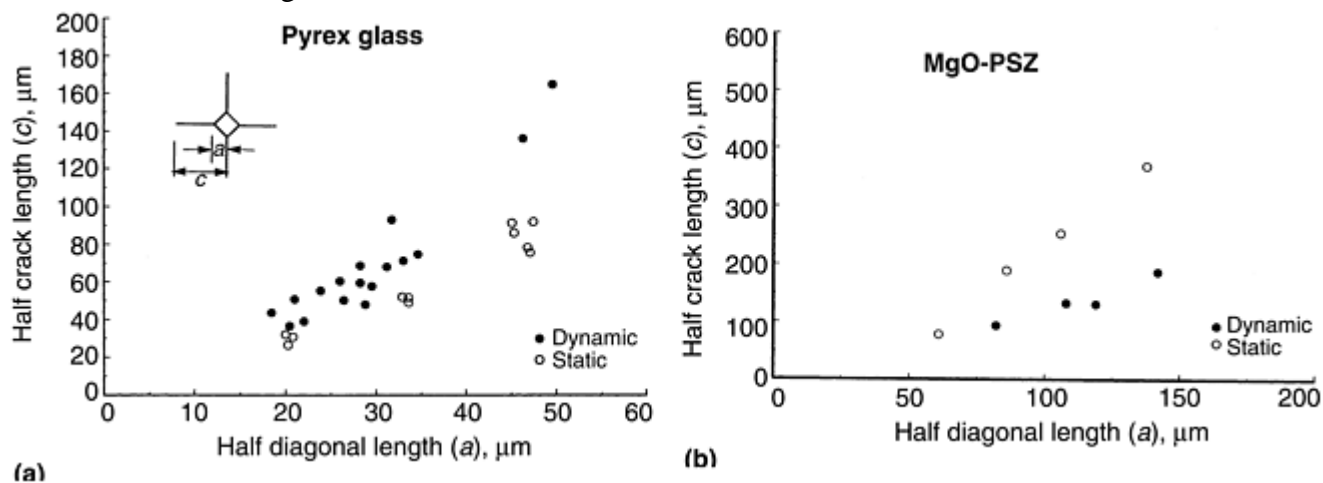


Fig. 13 Plots of half median crack length versus half indentation diagonal for (a) Pyrex glass and (b) MgO-PSZ under static and dynamic indentations

It is interesting to see that the trends in hardness are similar for Pyrex glass and structural ceramics, but the extent of induced damage in Pyrex glass is contrary to that observed in zirconia ceramics. The fracture behavior of glasses has been viewed as a representative behavior in brittle ceramics (Ref 27, 29, 30, and 32). Although the fracture patterns may be similar in glasses and ceramics under static loading, the current study reveals that the rate effects are significantly different in glasses compared with those in structural ceramics. Similar studies in glasslike materials (such as ZnS) also confirm these observations (i.e., an increase in hardness as well as induced damage—or decrease in fracture toughness—under impact loading compared with static loading) (Ref 13). This implies that the use of static models based on the observations on static fracture behavior of glasses may not be appropriate when modeling the material-removal rates of structural ceramics under high-velocity

grinding and sliding conditions. These results also support the observations of Meng and Ludema (Ref 12) on erosion model predictions discussed previously. One of the reasons for such contrasting behavior in glasses and structural ceramics under static and dynamic loads is that glasses are amorphous in structure whereas ceramics are polycrystalline materials with microstructural features such as grain boundaries, second phases, impurities, voids, and triple junction, which can promote crack deflection and contribute to radically different crack growth characteristics and fracture toughness. These inhomogeneities that form during processing have also been found to be responsible for early fracture as well as the rate-sensitive nature of failure in brittle materials (Ref 6, 40). Several empirical models for fracture-toughness estimation based on the indentation hardness and the induced crack sizes have been proposed in the literature. Recently, Ponton and Rawlings (Ref 41, 42) have summarized these equations and provided standardized indentation toughness equations for several classes of ceramics.

References cited in this section

6. J. Lankford, Mechanisms Responsible for Strain-Rate Dependent Compressive Strength in Ceramic Materials, *J. Am. Ceram. Soc.*, Vol 64, 1981, p 25–33
9. G. Subhash and G. Ravichandran, Mechanical Behavior of Hot-Pressed Aluminum Nitride under Uniaxial Compression, *J. Mater. Sci.*, Vol 33, 1997, p 1933–1939
12. H.C. Meng and K.C. Ludema, Wear Models and Predictive Equations: Their Form and Content, *Wear*, Vol 181, 1995, p 443–457
13. D.B. Marshall, A.G. Evans, and Z. Nisenholz, Measurement of Dynamic Hardness by Controlled Sharp-Projectile Impact, *J. Am. Ceram. Soc.*, Vol 66 (No. 8), 1983, p 580–585
22. R.J. Anton and G. Subhash, Dynamic Vickers Indentation of Brittle Materials, *Wear*, in press
27. R.F. Cook and G.M. Pharr, Direct Observation and Analysis of Indentation Cracking in Glasses and Ceramics, *J. Am. Ceram. Soc.*, Vol 73 (No. 4), 1990, p 787–817
28. B.R. Lawn and A.G. Evans, Elastic-Plastic Indentation Damage in Ceramics: the Median/ Radial Crack System, *J. Am. Ceram. Soc.*, Vol 63 (No. 9/10), 1980, p 574–581
29. S.S. Chiang, D.B. Marshall, and A.G. Evans, The Response of Solids to Elastic/Plastic Indentation: (a) Stresses and Residual Stresses and (b) Fracture Initiation, *J. Appl. Phys.*, Vol 53, 1982, p 298–317
30. D.B. Marshall, B.R. Lawn, and A.G. Evans, Elastic-Plastic Indentation Damage in Ceramics: the Lateral Crack System, *J. Am. Ceram. Soc.*, Vol 65 (No. 11), 1982, p 561–566
31. A.G. Evans and D.B. Marshall, Wear Mechanisms in Ceramics, *Fundamentals of Friction and Wear of Materials*, D.A. Rigney, Ed., American Society for Metals, 1981, p 439–450
32. B.R. Lawn, *Fracture of Brittle Solids*, Cambridge University Press, 1993, p 249–304
33. M.W. Barsoum, *Fundamentals of Ceramics*, McGraw-Hill, 1997, p 401
34. C.J. Fairbanks, R.S. Polvani, S.M. Wiederhorn, B.J. Hockey, and B.R. Lawn, Rate Effects in Hardness, *J. Mater. Sci. Lett.*, Vol 1, 1982, p 391–393
35. J.E. Loukus, G. Subhash, and A. Chandra, “Observations on High Strain Rate Single Grit Scratching of Brittle Materials,” presented at NSF Grantees Conference (Vancouver, British Columbia), 4–7 Jan 2000

36. J. Lankford, W.W. Predebon, J.M. Staehler, G. Subhash, B.J. Pletka, and C.E. Anderson, The Role of Plasticity as Limiting Factor in the Compressive Failure of High Strength Ceramics, *Mech. Mater.*, Vol 29, 1998, p 205–218
37. G. Subhash and S. Nemat-Nasser, Dynamic Stress-Induced Transformation and Texture Formation in Uniaxial Compression of Zirconia Ceramics, *J. Am. Ceram. Soc.*, Vol 76 (No. 1), 1993, p 153–165
38. G. Subhash and S. Nemat-Nasser, Uniaxial Stress Behavior of Y-TZP, *J. Mater. Sci.*, Vol 25, 1993, p 5949–5952
39. D.J. Green, R.H.J. Hannink, and M.V. Swain, *Transformation Toughening of Ceramics*, CRC Press Inc., 1989, p 5–93
40. G. Ravichandran and G. Subhash, A Micro Mechanical Model for High Strain Rate Behavior of Ceramics, *Int. J. Solids Struct.*, Vol 32 (No. 17/18), 1995, p 2627–2650
41. C.B. Ponton and R.D. Rawlings, Vickers Indentation Fracture Test, Part 1: Review of Literature and Formulation of Standardised Indentation Toughness Equations, *Mater. Sci. and Technol.*, Vol 5, 1989, p 865–960
42. C.B. Ponton and R.D. Rawlings, Vickers Indentation Fracture Test, Part 2: Application and Critical Evaluation of Standardised Indentation Toughness Equations, *Mater. Sci. and Technol.*, Vol 5, 1989, p 961–976

Dynamic Indentation Testing

G. Subhash, Michigan Technological University

Acknowledgments

This work was supported by the National Science Foundation under Grant DMI 9610545 and NASA/Michigan Space Grant Consortium.

Dynamic Indentation Testing

G. Subhash, Michigan Technological University

References

1. D. Tabor, A Simple Theory of Static and Dynamic Hardness, *Proc. R. Soc. (London)*, Vol 192A, 1948, p 247–274
2. D. Tabor, *The Hardness of Metals*, Oxford University Press, London, 1951, p 1–173
3. H.T. Angus, The Significance of Hardness, *Wear*, Vol 54, 1979, p 33–78

4. M.A. Meyers, *Dynamic Behavior of Materials*, John Wiley & Sons, Inc., 1994, p 323–563
5. G. Subhash, The Constitutive Behavior of Refractory Metals as a Function of Strain Rate, *JOM*, Vol 47 (No. 5), 1995, p 55–58
6. J. Lankford, Mechanisms Responsible for Strain-Rate Dependent Compressive Strength in Ceramic Materials, *J. Am. Ceram. Soc.*, Vol 64, 1981, p 25–33
7. J. Lankford and C.R. Blanchard, Fragmentation of Brittle Materials at High Rates of Loading, *J. Mater. Sci.*, Vol 26, 1991, p 3067–3072
8. H.D. Espinosa, G. Raiser, R.J. Clifton, and M. Ortiz, Experimental Observations and Numerical Modeling of Inelasticity in Dynamically Loaded Ceramics, *J. Hard Mater.*, 1992, Vol 3 (No. 3–4), p 285–295
9. G. Subhash and G. Ravichandran, Mechanical Behavior of Hot-Pressed Aluminum Nitride under Uniaxial Compression, *J. Mater. Sci.*, Vol 33, 1997, p 1933–1939
10. S. Suresh, T. Nakamura, Y. Yeshurun, K.H. Yang, and J. Duffy, Tensile Fracture Toughness of Ceramic Materials: Effects of Dynamic Loading and Elevated Temperatures, *J. Am. Ceram. Soc.*, Vol 73 (No. 8), 1990, p 2457–2480
11. K.H. Yang and A.S. Kobayashi, A Hybrid Procedure for Dynamic Characterization of Ceramics at Elevated Temperatures, *Proc. Conf. Hostile Environments and High Temperature Measurements*, Society of Experimental Mechanics, 1989, p 41–44
12. H.C. Meng and K.C. Ludema, Wear Models and Predictive Equations: Their Form and Content, *Wear*, Vol 181, 1995, p 443–457
13. D.B. Marshall, A.G. Evans, and Z. Nisenholz, Measurement of Dynamic Hardness by Controlled Sharp-Projectile Impact, *J. Am. Ceram. Soc.*, Vol 66 (No. 8), 1983, p 580–585
14. G. Sundararajan and P.G. Shewmon, The Use of Dynamic Impact Experiments in the Determination of the Strain Rate Sensitivity of Metals and Alloys, *Acta Metall.*, Vol 31, 1983, p 101–109
15. Y. Tirupataiah and G. Sundararajan, A Dynamic Indentation Technique for the Characterization of the High Strain Rate Plastic Flow Behavior of Ductile Metals and Alloys, *J. Mech. Phys. Solids*, Vol 39, 1991, p 243–271
16. J.P. Nobre, A.M. Dias, and R. Gras, Resistance of Ductile Steel Surface to Spherical Normal Impact Indentation: Use of Pendulum Machine, *Wear*, Vol 211, 1997, p 226–236
17. C.H. Mok and J. Duffy, The Dynamic Stress-Strain Relation of Metals as Determined from Impact Tests with Hard Ball, *Int. J. Mech. Sci.*, Vol 7, 1965, p 355–371
18. “Standard Test Method for Equotip Hardness Testing of Steel Products,” A 956–96, *Annual Book of ASTM Standards*, ASTM, Vol 01.05, 1997
19. S. Nemat-Nasser, J.B. Isaacs, and J.E. Starrett, Hopkinson Techniques for Dynamic Recovery Experiments, *Proc. R. Soc. (London) A*, Vol 435, 1991, p 371–391
20. B.J. Koepf and G. Subhash, Characteristics of Residual Plastic Zone under Static and Dynamic Indentations, *Wear*, Vol 224, 1999, p 56–67

21. G. Subhash, B.J. Koeppel, and A. Chandra, Dynamic Indentation Hardness and Rate Sensitivity in Metals, *J. Eng. Mater. Technol. (Trans. ASME)*, Vol 121, 1999, p 257–263
22. R.J. Anton and G. Subhash, Dynamic Vickers Indentation of Brittle Materials, *Wear*, in press
23. “Standard Test Method for Vickers Hardness of Metallic Materials,” E 92–82, *Annual Book of ASTM Standards*, Vol 03.01, ASTM, 1996
24. B.J. Koeppel, “Dynamic Indentation Hardness of Materials,” Ph.D. dissertation, Michigan Technological University, Houghton, MI, 1997
25. “Standard Test Method for Microhardness of Materials,” E 384–89, *Annual Book of ASTM Standards*, Vol 03.01, ASTM, 1996
26. G.T. Gray III, Deformation Substructures Induced by High Strain Rate Deformation, *Modeling the Deformation of Crystalline Solids*, T.C. Lowe, A.D. Rollett, P.S. Follansbee, and G.S. Daehn, Ed., The Minerals, Metals, Materials Society, Warrendale, 1991, p 145–157
27. R.F. Cook and G.M. Pharr, Direct Observation and Analysis of Indentation Cracking in Glasses and Ceramics, *J. Am. Ceram. Soc.*, Vol 73 (No. 4), 1990, p 787–817
28. B.R. Lawn and A.G. Evans, Elastic-Plastic Indentation Damage in Ceramics: the Median/ Radial Crack System, *J. Am. Ceram. Soc.*, Vol 63 (No. 9/10), 1980, p 574–581
29. S.S. Chiang, D.B. Marshall, and A.G. Evans, The Response of Solids to Elastic/Plastic Indentation: (a) Stresses and Residual Stresses and (b) Fracture Initiation, *J. Appl. Phys.*, Vol 53, 1982, p 298–317
30. D.B. Marshall, B.R. Lawn, and A.G. Evans, Elastic-Plastic Indentation Damage in Ceramics: the Lateral Crack System, *J. Am. Ceram. Soc.*, Vol 65 (No. 11), 1982, p 561–566
31. A.G. Evans and D.B. Marshall, Wear Mechanisms in Ceramics, *Fundamentals of Friction and Wear of Materials*, D.A. Rigney, Ed., American Society for Metals, 1981, p 439–450
32. B.R. Lawn, *Fracture of Brittle Solids*, Cambridge University Press, 1993, p 249–304
33. M.W. Barsoum, *Fundamentals of Ceramics*, McGraw-Hill, 1997, p 401
34. C.J. Fairbanks, R.S. Polvani, S.M. Wiederhorn, B.J. Hockey, and B.R. Lawn, Rate Effects in Hardness, *J. Mater. Sci. Lett.*, Vol 1, 1982, p 391–393
35. J.E. Loukus, G. Subhash, and A. Chandra, “Observations on High Strain Rate Single Grit Scratching of Brittle Materials,” presented at NSF Grantees Conference (Vancouver, British Columbia), 4–7 Jan 2000
36. J. Lankford, W.W. Predebon, J.M. Staehler, G. Subhash, B.J. Pletka, and C.E. Anderson, The Role of Plasticity as Limiting Factor in the Compressive Failure of High Strength Ceramics, *Mech. Mater.*, Vol 29, 1998, p 205–218
37. G. Subhash and S. Nemat-Nasser, Dynamic Stress-Induced Transformation and Texture Formation in Uniaxial Compression of Zirconia Ceramics, *J. Am. Ceram. Soc.*, Vol 76 (No. 1), 1993, p 153–165
38. G. Subhash and S. Nemat-Nasser, Uniaxial Stress Behavior of Y-TZP, *J. Mater. Sci.*, Vol 25, 1993, p 5949–5952

39. D.J. Green, R.H.J. Hannink, and M.V. Swain, *Transformation Toughening of Ceramics*, CRC Press Inc., 1989, p 5–93
40. G. Ravichandran and G. Subhash, A Micro Mechanical Model for High Strain Rate Behavior of Ceramics, *Int. J. Solids Struct.*, Vol 32 (No. 17/18), 1995, p 2627–2650
41. C.B. Ponton and R.D. Rawlings, Vickers Indentation Fracture Test, Part 1: Review of Literature and Formulation of Standardised Indentation Toughness Equations, *Mater. Sci. and Technol.*, Vol 5, 1989, p 865–960
42. C.B. Ponton and R.D. Rawlings, Vickers Indentation Fracture Test, Part 2: Application and Critical Evaluation of Standardised Indentation Toughness Equations, *Mater. Sci. and Technol.*, Vol 5, 1989, p 961–976

Shock Wave Testing of Ductile Materials

George T. (Rusty) Gray III, Los Alamos National Laboratory

Introduction

THE STUDY of the physical properties of ductile solids subjected to shock wave loading is undertaken to understand how the thermodynamic conditions and strain rate affect material response. Much of the development of the field of shock wave physics and metal plasticity has taken place since World War II and stems from the engineering importance and scientific interest in this technical area related to conventional and nuclear weapons. In contrast to quasi-static loading, the stress applied during shock loading is the result of the inertial response of the sample to a rapidly applied external load. As with quasi-static loading, the behavior of a material during shock loading is uniquely controlled by its stress-volume response or equation of state (EOS) (Ref 1, 2). The Rankine-Hugoniot or “Hugoniot” of a material is the locus of end states obtained through a shock process defining the pressure-volume relationship of a solid (Ref 3). Contrary to quasi-static loading, in the case of shock loading, conservation of mass and momentum applied to the shock transition give extra constraints allowing exact information on the stress, density, and material energy behind the shock. Numerous review papers chronicle the EOS of materials during shock loading (Ref 3, 4, 5, 6, 7, 8, 9, 10, 11, and 12). The focus of this review is an introduction to the experimental techniques used to study the effects of shock wave loading on ductile materials (primarily metals, although the techniques apply equally to polymeric solid), and the scientific and engineering applications motivating these studies.

References cited in this section

1. W.J.M. Rankine, On the Thermodynamic Theory of Waves of Finite Longitudinal Disturbance, *Philos. Trans. R. Soc. (London)*, Vol 160, 1870, p 277–288
2. J.N. Johnson and R. Chéret, Shock Waves in Solids: An Evolutionary Perspective, *Shock Waves*, Vol 9, 1999, p 193–200
3. M.H. Rice, R.G. McQueen, and J.M. Walsh, Compression of Solids by Strong Shock Waves, *Solid State Phys.*, Vol 6, 1958, p 1–63
4. J.M. Walsh and R.H. Christian, Equation of State of Metals from Shock Wave Measurements, *Phys. Rev.*, Vol 97, 1955, p 1544–1556

5. J.M. Walsh, M.H. Rice, R.G. McQueen, and F.L. Yarger, Shock-Wave Compressions of Twenty-Seven Metals: Equations of State of Metals, *Phys. Rev.*, Vol 108, 1957, p 196–216
6. R.G. McQueen and S.P. Marsh, Equation of State for Nineteen Metallic Elements from Shock-Wave Measurements to Two Megabars, *J. Appl. Phys.*, Vol 31, 1960, p 1253–1269
7. R.G. McQueen, Laboratory Techniques for Very High Pressures and the Behavior of Metals under Dynamic Loading, *Metallurgy at High Pressures and High Temperatures*, K.A. Gschneidner, Jr., M.T. Hepworth, and N.A.D. Parlee, Ed., Gordon and Breach, 1964, p 44–132
8. R.G. McQueen, S.P. Marsh, J.W. Taylor, J.N. Fritz, and W.J. Carter, The Equation of State of Solids from Shock Wave Studies, *High Velocity Impact Phenomena*, R. Kinslow, Ed., Academic Press, 1970, p 293–417, 515–568
9. C.P. Morris, *Los Alamos Shock Wave Profile Data*, University of California Press, 1981
10. L.V. Altshuler, K.K. Krupnikov, and M.I. Brazhnik, Dynamic Compressibility of Metals under Pressures from 400,000 to 4,000,000 Atmospheres, *Sov. Phys. JETP*, Vol 7, 1958, p 614–619
11. C.E. Anderson, J.S. Wilbeck, J.C. Hokanson, J.R. Asay, D.E. Grady, R.A. Graham, and M.E. Kipp, Sandia Shock Compression Database, *Shock Waves in Condensed Matter—1985*, Y.M. Gupta, Ed., Plenum, 1986, p 185–190
12. L.V. Altshuler, R.F. Trunin, V.D. Urlin, V.E. Fortov, and A.I. Funtikov, Development of Dynamic High-Pressure Techniques in Russia, *Phys. Usp.*, Vol 42, 1999, p 261–280

Shock Wave Testing of Ductile Materials

George T. (Rusty) Gray III, Los Alamos National Laboratory

Development of Shock Wave Studies

The earliest study of the relation between the propagation of elastic pulses and the formation of brittle fracture was documented in the work of John Hopkinson in 1872 (Ref 13). Hopkinson studied the strength of steel wires subjected to impulsive tensile loading. He explained the observed phenomena in terms of one-dimensional elastic wave propagation. Studies concerned with the response of ductile metals subjected to shock wave loading date to the seminal work of Bertram Hopkinson, John Hopkinson's son, in 1921. Hopkinson described how shock wave loading influenced mechanical behavior and fracture response of iron and steel samples subjected to an impulse load generated from exploding “gun cotton” placed in contact with a metal sample (Ref 14).

Hopkinson was the first to document how shock-induced fracture in a ductile metal could be initiated due to the interaction of the reflected wave from the rear surface of a sample assembly with the tail of the release wave from the impactor. Bertram Hopkinson documented in his paper “The Pressure of a Blow” (Ref 14) that when gun cotton was exploded on a 12.7 mm (0.5 in.) thick steel plate it punched out a hole of its own diameter through the plate. When the same explosive charge was detonated on a 19 mm (0.75 in.) thick plate, a scab of steel was formed. Experimenting with a still thicker plate revealed the formation of an internal crack parallel to the surface of the plate. This formation of internal damage and cracking, but not complete separation of the target plate to form a scab, is now called *incipient spall* (Ref 15). Rinehart (Ref 16) in 1952 referred to this process as *scabbing* following the terminology previously used by Hopkinson. This impulse-driven fracture

process, previously termed *Hopkinson fracture* (Ref 17, 18), or scabbing (Ref 16), is today more generically called *spallation* (Ref 15). Spallation is known to be strongly influenced not only by bulk mechanical properties but also by microstructure in materials as summarized in several reviews (Ref 15, 19, 20, 21, 22, and 23).

Work on the EOS, strength effects, and development of shock recovery techniques on ductile metals has its origins with the research of Walsh, McQueen, Marsh, and Rice (Ref 3, 5, and 6). The beginning of studies of metallurgical substructure and postmortem strengthening effects of shock wave loading on metals began with the pioneering article of Cyril Stanley Smith (Ref 24) in 1958. In this article Smith describes how the uniaxial strain, high-strain-rate loading, characteristic of shock wave loading, affects the generation and storage of defect structures in metals and alloys. His article further describes the genesis of the method of shock recovery first developed at Los Alamos National Laboratory during the Manhattan Project era. Through the use of shock recovery experiments, samples can be subjected to high-pressure shock through impact and subsequently recovered for the purpose of allowing postmortem metallurgical evaluation of the effects of the shock straining on the microstructure of a material. This technique, which introduced the use of impedance-matched radial momentum trapping rings, as well as a backing plate to prevent radial release and spallation, respectively, within the sample, when coupled with water deceleration of the sample, lead to recovery of intact shocked samples.

Studying the physical properties of materials during the very rapid loading rate and short time interval during the actual passage of a shock wave through a material is difficult. Shock recovery experiments provide insights into the processes occurring during shock wave loading through the analysis of carefully recovered samples. Characterization and quantification of “soft” recovered samples provides a mechanism to quantify the defect generation and storage mechanisms operative in materials subjected to impulse loading histories (Ref 25).

Smith (Ref 24) in his study using optical metallography first described how substructural studies of shock-recovered samples can provide valuable insight into the hydrodynamic effects of shock loading on materials. Since 1958, a number of in-depth reviews have summarized the systematic changes in structure and the commensurate property changes produced by the passage of shock waves through metals and alloys (Ref 26, 27, 28, 29, 30, 31, 32, 33, 34, and 35). In each of these reviews, the microstructure/mechanical property changes observed in shock-recovered samples have been correlated with the shock compression characteristics imposed (e.g., peak pressure, duration, rarefaction rate, and temperature) and the specific shock-induced defects produced. In addition, for a variety of metals and alloys, the defects produced during shock prestraining have been compared and contrasted with those typically observed following quasi-static deformation.

Applications of Shock Wave Tests. Interest in studying the effects of shock wave loading on materials has two components. The first gives knowledge of its pressure-volume (EOS) behavior during the actual time interval of the shock process. These studies include “real-time” shock physics diagnostic experimental methods, which quantify the response of a material during the passage of the shock wave through it as registered in the shock wave profile and other measurements, such as temperature, resistivity, and x-ray diffraction (Ref 36). The second experimental aspect of shock wave research includes analysis of samples subjected to an impact excursion to examine the postmortem signature of the shock prestraining and/or Hopkinson fracture process as described above. Postmortem studies are a type of Sherlock Holmes exercise in which scientific quantification of the structure/property manifestations in a material, due to exposure to a shock wave, is utilized to provide insight into the physical processes during shock wave loading. Experimental programs that couple both real-time and postmortem aspects offer the most promising opportunities to the understanding of shock processes in ductile materials and to the support of the development of physically based theoretical models describing shock loading (Ref 37, 38, and 39).

Types of Shock Waves. In typical shock-loading experiments, there are up to three distinct waves (Ref 40, 41, and 42):

- Elastic wave
- Plastic wave (termed the plastic I wave)
- Phase transformation wave (termed the plastic II wave)

The magnitude of the imposed shock on a material determines whether a “purely” elastic wave or an elastic plus a plastic wave traverses a sample. In the case of materials that undergo a pressure-induced change of phase, such as iron, tin, bismuth, titanium, zirconium, and hafnium, a third wave that we call the second plastic wave traverses the sample (Ref 40, 42, 43, and 44). Figure 1 is the wave profile for a sample configured to

study the spallation of tin. This profile illustrates the fundamental aspects of elastic-plastic behavior in a ductile metal, which are observed during shock loading of a ductile material. Relative scales are given in Fig. 1 to illustrate the high velocities and short times typical for shock wave profiles. The range of possible experimental techniques to quantify the structure/property effects of planar shock waves on ductile materials (specifically metals and alloys) due to the manifestations of wave propagation through a material are presented in this article.

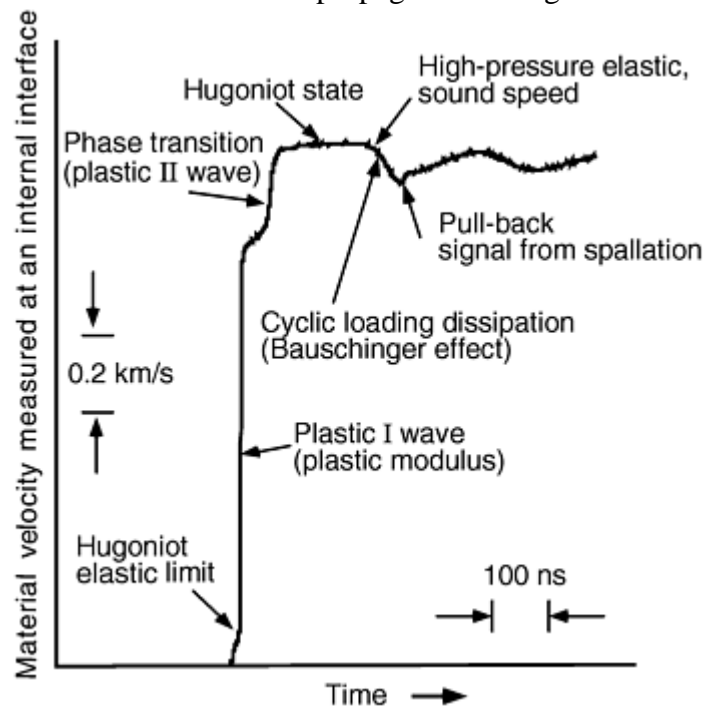


Fig. 1 Shock wave profile for tin illustrating various shock processes. Source: Ref 45

References cited in this section

3. M.H. Rice, R.G. McQueen, and J.M. Walsh, Compression of Solids by Strong Shock Waves, *Solid State Phys.*, Vol 6, 1958, p 1–63
5. J.M. Walsh, M.H. Rice, R.G. McQueen, and F.L. Yarger, Shock-Wave Compressions of Twenty-Seven Metals: Equations of State of Metals, *Phys. Rev.*, Vol 108, 1957, p 196–216
6. R.G. McQueen and S.P. Marsh, Equation of State for Nineteen Metallic Elements from Shock-Wave Measurements to Two Megabars, *J. Appl. Phys.*, Vol 31, 1960, p 1253–1269
13. B. Hopkinson, A Method of Measuring the Pressure Produced in the Detonation of High Explosives or by the Impact of Bullets, *Philos. Trans. R. Soc. (London) A*, Vol 213, 1914, p 437–456
14. B. Hopkinson, The Pressure of a Blow, *The Scientific Papers of Bertram Hopkinson*, Cambridge University Press, 1921, p 423–437
15. M.A. Meyers and C.T. Aimone, Dynamic Fracture (Spalling) of Metals, *Prog. Mater. Sci.*, Vol 28, 1983, p 1–96
16. J.S. Rinehart, Scabbing of Metals under Explosive Attack: Multiple Scabbing, *J. Appl. Phys.*, Vol 23, 1952, p 1229–1233
17. I.C. Skidmore, An Introduction to Shock Waves in Solids, *Appl. Mater. Res.*, Vol 4, 1965, p 131–147
18. H. Kolsky, The Waves Generated by Brittle Fracture in Glass, *Trans. Soc. Rheology*, Vol 20, 1976, p 441–454

19. D.R. Curran, L. Seaman, and D.A. Shockey, Dynamic Failure of Solids, *Phys. Rep.*, Vol 147, 1987, p 253–388
20. D.R. Curran, L. Seaman, and D.A. Shockey, Linking Dynamic Fracture to Microstructural Processes, *Shock Waves and High Strain-Rate Phenomena in Metals*, M.A. Meyers and L.E. Murr, Ed., Plenum, 1981, p 129–167
21. D.R. Curran, L. Seaman, and D.A. Shockey, Dynamic Failure in Solids, *Phys. Today*, Vol 30 (No. 1), 1977, p 46–55
22. A.K. Zurek and M.A. Meyers, Microstructural Aspects of Dynamic Failure, *High Pressure Shock Compression of Solids II: Dynamic Fracture and Fragmentation*, L. Davison, D.E. Grady, and M. Shahinpoor, Ed., Springer-Verlag, 1996, p 25–70
23. P. Chevrier and J.R. Klepaczko, Spall Fracture: Mechanical and Microstructural Aspects, *Eng. Fract. Mech.*, Vol 63, 1999, p 273–294
24. C.S. Smith, Metallographic Studies of Metals after Explosive Shock, *Trans. Metall. Soc. AIME*, Vol 214, 1958, p 574–589
25. G.T. Gray III, Influence of Shock-Wave Deformation on the Structure/Property Behavior of Materials, *High-Pressure Shock Compression of Solids*, J.R. Asay and M. Shahinpoor, Ed., Springer-Verlag, 1993, p 187–216
26. D.G. Doran and R.K. Linde, Shock Effects in Solids, *Solid State Phys.*, Vol 19, 1966, p 230–290
27. S. Mahajan, Metallurgical Effects of Planar Shock Waves in Metals and Alloys, *Phys. Status Solidi (a)*, Vol 2, 1970, p 187–201
28. W.C. Leslie, Microstructural Effects of High Strain Rate Deformation, *Metallurgical Effects at High Strain Rates*, R.W. Rhode, B.M. Butcher, J.R. Holland, and C.H. Karners, Ed., Plenum Press, 1973, p 571
29. L.E. Murr, Residual Microstructure—Mechanical Property Relationships in Shock-Loaded Metals and Alloys, *Shock Waves and High Strain Rate Phenomena in Metals*, M.A. Meyers and L.E. Murr, Ed., Plenum, 1981, p 607–673
30. L.E. Murr, Metallurgical Effects of Shock and High-Strain-Rate Loading, *Materials at High Strain Rates*, T.Z. Blazynski, Ed., Elsevier Applied Science, 1987, p 1–46
31. D. Raybould and T.Z. Blazynski, Non-Metallic Materials under Shock Loading, *Materials at High Strain Rates*, T.Z. Blazynski, Ed., Elsevier Applied Science, 1987, p 71–132
32. K.P. Staudhammer, Shock Wave Effects and Metallurgical Parameters, *Impact Loading and Dynamic Behaviour of Materials*, C.Y. Chiem, H.-D. Kunze, and L.W. Meyer, Ed., DGM Informationsgesellschaft mbH, 1988, p 93–112
33. G.T. Gray III, Shock Recovery Experiments: An Assessment, *Shock Compression of Condensed Matter—1989*, S.C. Schmidt, J.N. Johnson, and L.W. Davidson, Ed., Elsevier, 1990, p 407–414
34. G.T. Gray III, Shock Experiments in Metals and Ceramics, *Shock-Wave and High-Strain-Rate Phenomena in Materials*, M.A. Meyers, L.E. Murr, and K.P. Staudhammer, Ed., Marcel-Dekker, 1992, p 899–912

35. G.T. Gray III, Shock Loading Response of Advanced Materials, *High Pressure Science and Technology 1993*, S.C. Schmidt, J.W. Shaner, G.A. Samara, and M. Ross, Ed., American Institute of Physics, 1994, p 1161–1164
36. R.A. Graham, Impact Techniques for the Study of Physical Properties of Solids under Shock Wave Loading, *J. Basic Eng. (Trans. ASME)*, Vol 89, 1967, p 911–918
37. G.T. Gray III, R.S. Hixson, and C.E. Morris, Bauschinger Effect During Shock Loading, *Shock Compression of Condensed Matter—1991*, S.C. Schmidt, R.D. Dick, J.W. Forbes, and D.G. Tasker, Ed., Elsevier, 1992, p 427–430
38. J.N. Johnson, R.S. Hixson, D.L. Tonks, and G.T. Gray III, Shock Compression and Quasielastic Release in Tantalum, *High Pressure Science and Technology 1993*, S.C. Schmidt, J.W. Shaner, G.A. Samara, and M. Ross, Ed., American Institute of Physics, 1994, p 1095–1098
39. J.N. Johnson, G.T. Gray III, and N.K. Bourne, Effect of Pulse Duration and Strain Rate on Incipient Spall Fracture in Copper, *J. Appl. Phys.*, Vol 86, 1999, p 4892–4901
40. E.G. Zukas, Shock-Wave Strengthening, *Met. Eng. Q.*, Vol 6, 1966, p 1–20
41. C.M. Fowler, F.S. Minshall, and E.G. Zukas, A Metallurgical Method for Simplifying the Determination of Hugoniot Curves for Iron Alloys in the Two-Wave Region, *Response of Metals to High Velocity Deformation*, P.G. Shewmon and V.F. Zackay, Ed., Interscience, 1961, p 275–308
42. G.T. Gray III, Shock-Induced Defects in Bulk Materials, *Materials Research Society Symp. Proc.*, Vol 499, 1998, p 87–98
43. E. Hornbogen, Shock-Induced Dislocations, *Acta Metall.*, Vol 10, 1962, p 978–980
44. S. Mahajan, Metallurgical Effects of Planar Shock Waves in Metals and Alloys, *Phys. Status Solidi (a)*, Vol 2, 1970, p 187–201
45. L.M. Barker and R.E. Hollenbach, Interferometer Technique for Measuring the Dynamic Mechanical Properties of Materials, *Rev. Sci. Instrum.*, Vol 36, 1965, p 1617–1620

Shock Wave Testing of Ductile Materials

George T. (Rusty) Gray III, Los Alamos National Laboratory

Techniques for Shock-Loading Materials

Samples are most frequently shock loaded under laboratory or controlled firing-point conditions using either high-exposure (HE) explosives, gun-launched impactors (also referred to as flyer or driver plates), exploding foils, or direct radiation impingement, including lasers and electron beams (Ref 3, 7, 8, 12, 25, 34, 36, 46, 47, 48, 49, and 50). Given sufficient lateral extent of the load and sufficiently thin sample thickness, a sample is shocked in a one-dimensional plane strain manner; the sample experiences uniaxial strain loading and uniaxial unloading. Each of these techniques offers advantages and disadvantages as summarized below.

Explosive-Driven Shock-Loading Methods. A controlled shock history can be imparted to a sample of interest using several different explosive-driven system designs. A review of HE-driven shock assemblies used for shock experimentation is detailed in several reviews including Dieter (Ref 46), Zukas (Ref 40), Duvall (Ref

51), Graham (Ref 36), Fowles (Ref 47), and McQueen (Ref 49). Explosive-driven shock-loading systems offer the advantage of shock loading very large sample assemblies and components. Impact velocities up to approximately $6 \text{ mm}/\mu\text{s}$ ($\frac{15}{64} \text{ in.}/\mu\text{s}$) and a large range in shock pressures up to approximately 5 Mbar in ductile metals can be readily obtained. HE-driven experiments can be relatively low cost. The disadvantages of using HE-driven shock-loading methods are that they provide less control over flyer-plate velocity than other methods and they cause tilt and bow of the driver plate.

Figure 2 shows several common HE-driven shock assembly designs. A driver plate is positioned either parallel or inclined and displaced at the necessary standoff distance from the target. An explosive is detonated by a line wave or plane wave generator that then either directly drives a driver plate or serves to uniformly ignite a main HE charge that accelerates a driver plate into a sample assembly.

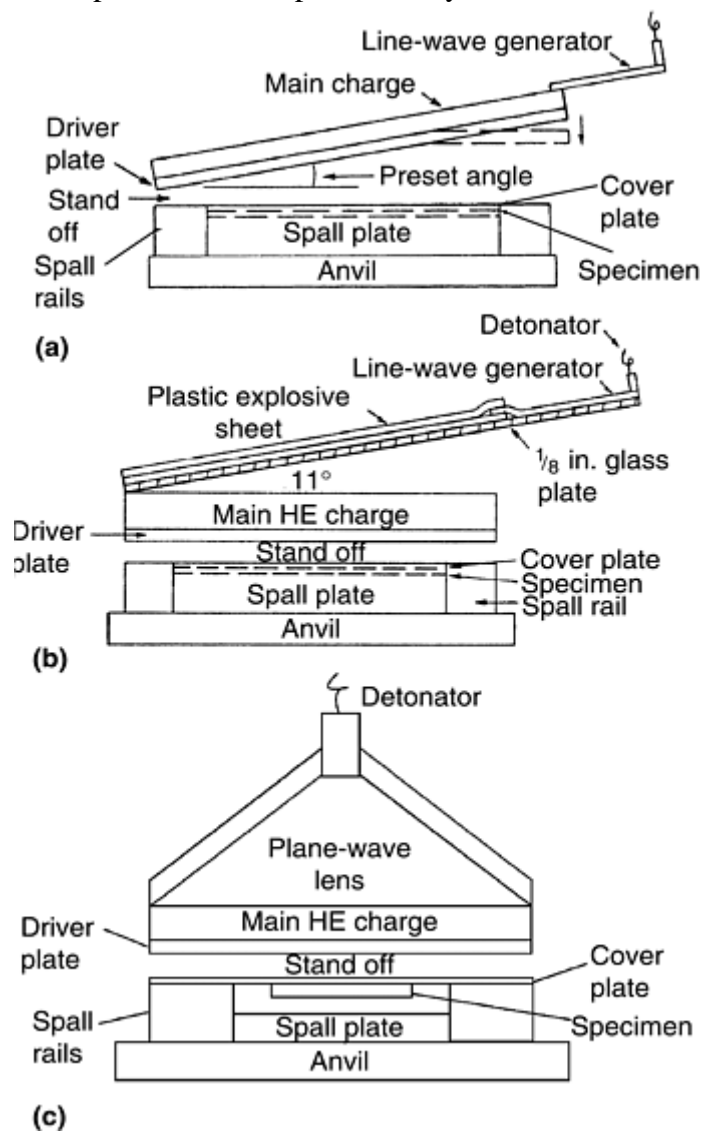


Fig. 2 Explosive-driven shock-loading assemblies. (a) Inclined-plate system. (b) Parallel-plate glass system. (c) Plane wave generator lens

The inclined-plate assembly, sometimes termed a “mouse-trap plane wave initiator” (Ref 47), as seen in Fig. 2(a), has been used for low-velocity ($<15 \text{ GPa}$, or $2.2 \times 10^6 \text{ psi}$), peak shock pressure shock experiments. A line wave generator is comprised of a perforated triangle of HE sheet that is initiated at one end of the generator with a blasting cap and a small starter charge. Passage of the detonation front between the series of carefully spaced holes in the line generator results in an essentially linear wave front arrival at the base of the generator. The “mouse-trap” loading technique is used only when a rough approximation to planar impact is required due to limitations imposed by edge effects and the requirement for high precision during assembly manufacture (Ref 47).

Parallel Plate Glass Assembly. At higher pressures a parallel-plate-driven or plane wave lens-driven assembly design is used (Ref 40, 46). Parallel plate-driven shock assemblies offer the opportunity to shock load large assemblies to high peak pressures while still retaining plane wave loading. In a parallel-plate design (Fig. 2b), point detonation of a line wave generator is used to produce line detonation of a starter charge of HE sheet, such as plastic explosive with a pentaerythritol tetranitrate (PETN) base, placed on top of a thin sheet of steel or of glass. In the first case, a thin steel sheet positioned at a preset angle above the main charge is made to impact uniformly across the main charge to provide plane wave loading of the driver plate (Ref 52). In the second instance, shown in Fig. 2(b), two overlapping sheets of plastic explosive fracture a glass sheet upon which they are resting. The preset angle of the glass sheet above the main charge provides a planar shower of high-speed glass fragments resulting in simultaneous detonation over the entire main charge surface.

Plane-Wave Generator Lens Assembly. As shown in Fig. 2(c), a driver plate in a parallel-plate configuration can be driven using a plane wave generator lens placed directly above the main explosive charge (Ref 6, 7). In a plane wave lens, a pyramidal construct of HE is fabricated using an outer layer of higher-detonation explosive surrounding a lower-detonation inner explosive. Careful design of the lens geometry and explosives used will produce planar shock arrival at the base of the lens. Plane wave lenses offer the highest degree of planar shock wave drive. The disadvantage of using a plane wave generator lens is the substantially increased cost associated with the fabrication, casting, and machining of HE lenses.

Diagnostic Techniques. For real-time shock-physics experiments the assembly designs shown in Fig. 2 can be modified to allow placement of diagnostics immediately behind or adjacent to the shock assembly. The range of diagnostic techniques applied to quantifying the physical property changes occurring during the passage of a shock wave through a sample is diverse, including:

- Shorting pins to measure the impactor velocity and tilt
- Free surface velocity using capacitors (Ref 53), interferometric techniques (Ref 45, 54), or magnetic technique (Ref 53) to record the particle-velocity time history at the rear of the specimen
- High-speed or streak photography to record shock wave breakout at the rear of the specimen (Ref 55, 56)
- Electrical conductivity or piezoelectric or piezoresistance response
- X-ray diffraction to quantify sample structural changes (currently a developmental technique)

Wave profile measurements, manganin pressure gages, or interferometry (specifically velocity interferometer system for any reflector, or VISAR), can be used to quantify the broad range of phenomena illustrated in Fig. 1 for shock-loaded tin. For experimental configurations where the intent is to recover the shock-prestrained sample, the HE-driven sample assembly is placed above a deceleration medium, such as a water tank or soft wet sand (Ref 52). Deceleration and simultaneous cooling of the sample by firing the sample into water has been shown to be effective in minimizing the microstructural and substructural changes that slow cooling can allow (Ref 46, 52). The water effectively minimizes these changes by removing the residual heat induced in the sample due to the dissipative shock compression process.

Gas/Powder Launcher-Driven Shock Loading. Based on the reproducibility of projectile launch velocity and impact planarity, convenience of use in a laboratory setting, and ability to perform controlled oblique impact (such as for combined pressure-shear studies, described in Ref 57), guns or launchers have become the method of choice for many ductile material EOS, shock recovery, and spallation studies. For impacts at peak shock stresses below approximately 700 GPa (100×10^6 psi) the precise control afforded by launchers is unequaled. Gas- and propellant-driven launchers additionally offer unequaled control of impactor-target alignment and impact planarity through the use of long-axis projectiles to minimize tilt (Ref 58, 59). Angular misorientations between the projectile and target assembly of a few tenths of a milliradian are routinely achieved. Higher velocities (up to 2 km/s, or 1.2 miles/s) can be achieved using propellant-driven launchers. Projectile velocities up to 8 km/s (5.0 miles/s) are routinely achieved using a two-stage light-gas gun (Ref 60). Launchers and/or guns of various designs usually possess smooth-bore launch tubes with barrel lengths from 3 to 30 m (10–100 ft). Acceleration of the projectile is accomplished using a compressed light gas (air, nitrogen, helium), hydrogen, a propellant, or a combination of these. While hydrogen can result in substantially increased launcher performance, the environmental and safety hazards commensurate with the use of hydrogen have reduced its use except in the case of two-stage launchers. The disadvantages of fixed launchers are their high initial cost, limited sample sizes (typically <100 mm, or 4 in., in diameter), and their significant facility sizes, making them

less portable than explosive-driven systems. Figure 3 illustrates many of the key design features of a launcher, including its breech, launch tube, experimental chamber, and catch tank. As in the case of HE-driven shock experiments, a broad range of diagnostics can be positioned directly adjacent to the sample during loading to facilitate real-time measurements. Deceleration of samples for post mortem evaluation following shock prestraining or Hopkinson fracture (spallation) testing can be achieved using a water-filled catch assembly or soft rags positioned immediately behind the shock assembly in the catch tank (Ref 61, 62). Details of the parameters used to design either real-time or recovery fixtures for postmortem studies using either HE- or launcher-driven shock loading are discussed below.

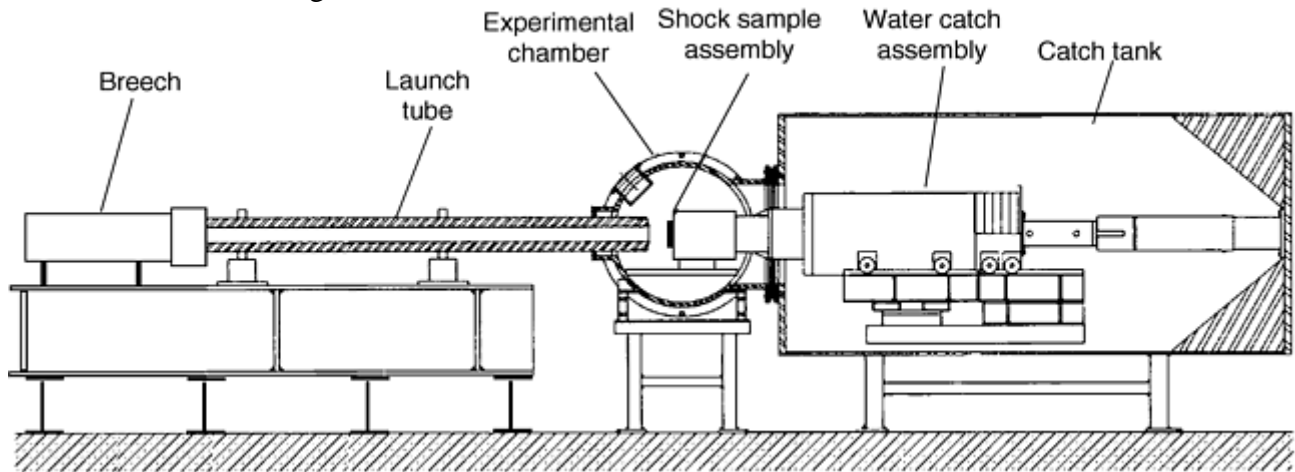


Fig. 3 Schematic of 80 mm (3.1 in.) launcher at Los Alamos designed to facilitate soft recovery shock wave testing

Shock-Loading Methods Using Exploding Foil and Laser-Driven Impactors. Shock loading of samples can also be accomplished using impactors accelerated with an exploding foil (Ref 47) or a laser-driven flyer plate (Ref 63).

In the exploding-foil technique, shock loading is accomplished by discharging a high-energy capacitor bank through a metallic foil, causing it to explode (Ref 64, 65). A flyer plate positioned adjacent to the exploding foil is thereby accelerated. The impact velocity of the flyer plate is controlled by the energy of the discharge, the mass per unit area of the foil, and the standoff distance between the flyer plate and the specimen. The electrical energy transferred into the flyer can be augmented by placing a sheet of explosive between the foil and flyer plate. An intermediate layer of explosive positioned in this manner is used to generate higher-amplitude, longer-duration pulses. The principal advantage of this technique is its ability to generate very-short-duration pulses facilitating attenuation shock studies and the ability to do many experiments in a short time. Disadvantages of the exploding-foil technique include the fact that flyer-plate planarity is lower than achievable with gas and propellant launchers, and tilt is generally not measured. Additionally, small flyer-plate dimensions impose restrictions on the pulse durations and sample thicknesses that can be loaded in one dimension, and the electrical fields commensurate with the capacitance-bank loading technique yield a high electrical field.

Laser-driven impactors are also used to shock load materials. In this technique a high-power laser is directed through a quartz substrate to a metal-substrate interface (Ref 66). The metal layer, made from aluminum or copper, is physically vapor deposited to a thickness of 0.5 to 50 μm thick on the quartz substrate. The laser energy is deposited into the ablative layer, thus accelerating the metal layer (Ref 66). The high-temperature and high-pressure ablative layer serves to accelerate the remaining tamped solid metal as a miniature flyer plate. The flyer plate launched is the same diameter as the laser beam, which is typically 0.4 to 1 mm (0.016–0.04 in.) in diameter. Miniature flyer plates using this technique can be accelerated to velocities ranging from 0.5 to more than 6 mm/ μs (0.02–0.24 in.). The advantage of this loading technique is its compact size scale, ability to produce very-short-duration shock pulses, and potential as a means to interrogate interfaces in bicrystals (Ref 67). The disadvantages of this technique include the fact that the very thin flyer plate limits the shock pulse duration to short times (e.g., <100 ns), and the short pulse duration and the rapid attenuation of the short pulse lengths produced by the thin flyer plates will not support steady shocks in thicker samples (>0.5 mm, or 0.02 in., thick), thereby limiting the usefulness of this technique to studying bulk phenomena, such as spallation, in polycrystals.

Radiation-Driven Shock-Loading Methods. Shock loading of materials can also be achieved through direct application of a penetrating radiation impulse to a ductile material (Ref 47). This can be achieved using electron beam impulse loading (Ref 68), direct laser impingement (Ref 69), or exposure to an underground near-nuclear weapon (Ref 12).

Pulsed electron beam machines can produce electron energies of more than 5 MeV, fluences of several hundred calories per square centimeter, and pulse durations of a few tens of nanoseconds (Ref 68). Electron beams can be used to produce beams of essentially uniform power over areas of a few square centimeters. The stress pulse in the sample is generated by the extremely rapid heating of the sample at depths in the material, which cannot be relaxed by a rarefaction wave during the deposition time of the pulse.

Direct laser impingement on the surface of a sample can similarly be used to induce a shock wave in a material (Ref 69, 70, 71, 72, and 73). In this type of shock-loading experiment a high-power laser is focused on a thin sample. Testing is conducted in a vacuum to avoid air ionization. The irradiated metallic surface is vaporized producing a plasma, which induces a compressive shock wave in the target. The duration of the pressure pulse in the target is of the same order of magnitude as that of the laser pulse, typically 0.5 to approximately 30 ns. The amplitude of the stress pulses induced by laser heating can induce strong shocks up to 200 GPa (29×10^6 psi) depending on the irradiation intensity. Uniaxial strain can be achieved in a central portion of thin samples as long as the diameter of the irradiated spot is larger than the sample thickness. The advantages and disadvantages of this technique are analogous to the miniature flyer discussed above. The principal disadvantage to direct laser irradiation for shock wave studies is the attainment of a steady shock wave through a polycrystalline material. The short pulse duration and the attenuation of these pulses restricts testing to samples typically less than 1 mm (0.04 in.) thick.

Exposure to Nuclear Explosion. The final direct radiation-driven shock wave technique results from the placement of samples in the near zone of an underground nuclear explosion. Such experiments proved capable of supporting studies of the compressibility of metals such as iron, lead, copper, and uranium in the pressure range up to 20 TPa (29×10^{12} psi) (Ref 12, 74, 75, and 76). Experimental tests of this type have yielded extremely high-pressure compressibility and EOS information on a range of ductile metals, as summarized in the references, but has not produced absolute EOS information.

References cited in this section

3. M.H. Rice, R.G. McQueen, and J.M. Walsh, Compression of Solids by Strong Shock Waves, *Solid State Phys.*, Vol 6, 1958, p 1–63
6. R.G. McQueen and S.P. Marsh, Equation of State for Nineteen Metallic Elements from Shock-Wave Measurements to Two Megabars, *J. Appl. Phys.*, Vol 31, 1960, p 1253–1269
7. R.G. McQueen, Laboratory Techniques for Very High Pressures and the Behavior of Metals under Dynamic Loading, *Metallurgy at High Pressures and High Temperatures*, K.A. Gschneidner, Jr., M.T. Hepworth, and N.A.D. Parlee, Ed., Gordon and Breach, 1964, p 44–132
8. R.G. McQueen, S.P. Marsh, J.W. Taylor, J.N. Fritz, and W.J. Carter, The Equation of State of Solids from Shock Wave Studies, *High Velocity Impact Phenomena*, R. Kinslow, Ed., Academic Press, 1970, p 293–417, 515–568
12. L.V. Altshuler, R.F. Trunin, V.D. Ustinov, V.E. Fortov, and A.I. Funtikov, Development of Dynamic High-Pressure Techniques in Russia, *Phys. Usp.*, Vol 42, 1999, p 261–280
25. G.T. Gray III, Influence of Shock-Wave Deformation on the Structure/Property Behavior of Materials, *High-Pressure Shock Compression of Solids*, J.R. Asay and M. Shahinpoor, Ed., Springer-Verlag, 1993, p 187–216
34. G.T. Gray III, Shock Experiments in Metals and Ceramics, *Shock-Wave and High-Strain-Rate Phenomena in Materials*, M.A. Meyers, L.E. Murr, and K.P. Staudhammer, Ed., Marcel-Dekker, 1992, p 899–912

36. R.A. Graham, Impact Techniques for the Study of Physical Properties of Solids under Shock Wave Loading, *J. Basic Eng. (Trans. ASME)*, Vol 89, 1967, p 911–918
40. E.G. Zukas, Shock-Wave Strengthening, *Met. Eng. Q.*, Vol 6, 1966, p 1–20
45. L.M. Barker and R.E. Hollenbach, Interferometer Technique for Measuring the Dynamic Mechanical Properties of Materials, *Rev. Sci. Instrum.*, Vol 36, 1965, p 1617–1620
46. G.E. Dieter, Metallurgical Effects of High-Intensity Shock Waves in Metals, *Response of Metals to High Velocity Deformation*, P.G. Shewmon and V.F. Zackay, Ed., Interscience, 1961, p 409–446
47. G.R. Fowles, Experimental Technique and Instrumentation, *Dynamic Response of Materials to Intense Impulsive Loading*, P.C. Chou and A.K. Hopkins, Ed., Air Force Materials Laboratory, Wright Patterson Air Force Base, 1972, p 405–480
48. P.S. DeCarli and M.A. Meyers, Design of Uniaxial Shock Recovery Experiments, *Shock Waves and High Strain Rate Phenomena in Metals*, M.A. Meyers and L.E. Murr, Ed., Plenum, 1981, p 341–373
49. R.G. McQueen and S.P. Marsh, High Explosive Systems for Equation-of-State Studies, *Shock Waves in Condensed Matter—1987*, S.C. Schmidt and N.C. Holmes, Ed., Elsevier, 1988, p 107–110
50. M.A. Meyers, *Dynamic Behavior of Materials*, Wiley Interscience, 1994
51. G.E. Duvall, Shock Waves in the Study of Solids, *Appl. Mech. Rev.*, Vol 15, 1962, p 849–854
52. E.G. Zukas, Shock-Wave Strengthening, *Met. Eng. Q.*, Vol 6 (No. 2), 1966, p 1–20
53. J.N. Fritz and J.A. Morgan, An Electromagnetic Technique for Measuring Material Velocity, *Rev. Sci. Instrum.*, Vol 44, 1973, p 215–221
54. L.M. Barker and R.E. Hollenbach, Laser Interferometer for Measuring High Velocities of Any Reflecting Surface, *J. Appl. Phys.*, Vol 43, 1972, p 4669–4675
55. R.G. McQueen, J.W. Hopson, and J.N. Fritz, Optical Technique for Determining Rarefaction Wave Velocities at Very High Pressures, *Rev. Sci. Instrum.*, Vol 53, 1982, p 245–250
56. J.N. Fritz, C.E. Morris, R.S. Hixson, and R.G. McQueen, Liquid Sound Speeds at Pressure from the Optical Analyzer Technique, *High Pressure Science and Technology 1993*, S.C. Schmidt, J.W. Shaner, G.A. Samara, and M. Ross, Ed., American Institute of Physics, 1994, p 149–152
57. R.J. Clifton, Pressure Shear Impact and the Dynamic Plastic Response of Metals, *Shock Waves in Condensed Matter—1983*, J.R. Asay, R.A. Graham, and G.K. Straub, Ed., North-Holland, 1984, p 105–111
58. R.A. Graham and J.R. Asay, Measurement of Wave Profiles in Shock Loaded Solids, *High Temp.—High Press.*, Vol 10, 1978, p 355–390
59. G.R. Fowles, G.E. Duvall, J. Asay, P. Bellamy, F. Feistman, D. Grady, T. Michaels, and R. Mitchell, Gas Gun for Impact Studies, *Rev. Sci. Instrum.*, Vol 41, 1970, p 984–996
60. J.W. Taylor, Experimental Methods in Shock Wave Physics, *Metallurgical Effects at High Strain Rates*, R.W. Rohde, B.M. Butcher, J.R. Holland, and C.H. Karnes, Ed., Plenum Press, 1973, p 107–128

61. G.T. Gray III, Deformation Twinning in Aluminum-4.8 wt.% Mg, *Acta Metall.*, Vol 36, 1988, p 1745–1754
62. G.T. Gray III, P.S. Follansbee, and C.E. Frantz, Effect of Residual Strain on the Substructure Development and Mechanical Response of Shock-Loaded Copper, *Mater. Sci. Eng. A*, Vol 111, 1989, p 9–16
63. D.L. Paisley, Laser-Driven Miniature Flyer Plates for Shock Initiation of Secondary Explosives, *Shock Compression of Condensed Matter—1989*, S.C. Schmidt, J.N. Johnson, and L.W. Davidson, Ed., Elsevier, 1990, p 733–736
64. D.E. Mikkola and R.N. Wright, Dislocation Generation and Its Relation to the Dynamic Plastic Response of Shock Loaded Metals, *Shock Waves in Condensed Matter—1983*, J.R. Asay, R.A. Graham, and G.K. Straub, North-Holland, 1984, p 415–418
65. S. Larouche, E.T. Marsh, and D.E. Mikkola, Strengthening Effects of Deformation Twins and Dislocations Introduced by Short Duration Shock Pulses in Cu-8.7Ge, *Metall. Trans. A*, Vol 12, 1981 p 1777–1785
66. D.L. Paisley, Laser-Driven Miniature Plates for One-Dimensional Impacts at 0.5– ϵ 6 km/s, *Shock-Wave and High-Strain-Rate Phenomena in Materials*, M.A. Meyers, L.E. Murr, and K.P. Staudhammer, Ed., Marcel Dekker, 1992, p 1131–1141
67. D.L. Paisley, R.H. Warnes, and R.A. Kopp, Laser-Driven Flat Plate Impacts to 100 GPa with Sub-Nanosecond Pulse Duration and Resolution for Material Property Studies, *Shock Compression of Condensed Matter—1991* S.C. Schmidt, R.D. Dick, J.W. Forbes, and D.G. Tasker, Ed., Elsevier, 1992, p 825–828
68. J.H. Shea, A. Mazzella, and L. Avrami, Equation of State Investigation of Granular Explosives Using a Pulsed Electron Beam, *Proc. Fifth Symp. (Int.) on Detonation*, Office of Naval Research, Arlington, Virginia, 1970, p 351–359
69. F. Cottet and J.P. Romain, Formation and Decay of Laser-Generated Shock Waves, *Phys. Rev. A*, Vol 25, 1982, p 576–579
70. F. Cottet, J.P. Romain, R. Fabbro, and B. Faral, Measurements of Laser Shock Pressure and Estimate of Energy Lost at 1.05 μ m Wavelength, *J. Appl. Phys.*, Vol 55, 1984, p 4125–4127
71. F. Cottet and M. Boustie, Spallation Studies in Aluminum Targets Using Shock Waves Induced by Laser Irradiation at Various Pulse Durations, *J. Appl. Phys.*, Vol 66, 1989, p 4067–4073
72. T. de Rességuier and M. Hallouin, Stress Relaxation and Precursor Decay in Laser Shock-Loaded Iron, *J. Appl. Phys.*, Vol 84, 1998, p 1932–1938
73. T. de Rességuier and M. Deleignies, Spallation of Polycarbonate under Laser Driven Shocks, *Shock Waves*, Vol 7, 1997, p 319–324
74. C.E. Ragan, Equation-of-State Experiments using Nuclear Explosions, *Proc. Int. Symp. on Behaviour of Condensed Matter at High Dynamic Pressures*, Commissariat à l'Energie Atomique, Saclay, Paris, 1978, p 477
75. C.E. Ragan III, Shock Compression Measurements at 1 to 7 TPa, *Phys. Rev. A*, Vol 25, 1982, p 3360–3375

Shock Wave Testing of Ductile Materials

George T. (Rusty) Gray III, Los Alamos National Laboratory

Design of Shock Recovery and Spallation Fixtures

The structure/property relationships in materials subjected to shock wave deformation are very difficult to conduct and complex to interpret due to the dynamic nature of the shock process and the very short time of the test. Due to these imposed constraints, the majority of real-time shock process measurements are limited to studying the interactions of the transmitted wave arrival at the free surface or at target-window interfaces. To augment these in situ wave profile measurements, shock recovery techniques were developed in the late 1950s to experimentally assess the residual effects of shock wave compression, release, and shock-induced fracture events on materials. The object of soft recovery experiments is to examine the terminal structure-property relationships of a material that has been subjected to a known uniaxial shock history then returned to ambient conditions without experiencing radial release tensile wave loading or collateral recovery strains. Tensile wave interactions may be mostly mitigated by surrounding the sample with tightly fitting material of the same (or nearly the same) shock impedance, both laterally and axially around the sample. This technique, termed *momentum trapping*, has continued to evolve to prevent large radial release waves from entering the sample and to prevent Hopkinson fracture (spallation) for a variety of sample configurations and shock-loading methods. When ideally trapped, the residual strain, ϵ_{res} , in the recovered sample (defined here as the final sample thickness divided by the initial sample thickness) should be on the order of only a few percent. Since the inception of shock recovery studies, the use of momentum trapping techniques has been successfully applied to a large number of metallic systems and a more limited number of brittle solids.

Several review papers chronicle the development and design of shock recovery techniques (Ref 25, 26, 34, 40, 48, 77, and 78). To correctly assess the influence of shock wave deformation on ductile material structure and properties, it is crucial to systematically control the experimental loading parameters and design the shock fixtures to recover the test sample with minimum residual strain. With higher peak pressures (from 10 GPa, or 1.5×10^6 psi, upward) however, recovery of shock-loaded samples becomes increasingly difficult. For low-pressure shocks, for example, a few times the Hugoniot elastic limit of the material, shock recovery is straightforward independent of whether the shock is generated via HE, launcher impact, or radiation impingement. At pressures in excess of 50 to 60 GPa (7.3×10^6 to 8.7×10^6 psi) recovery of bulk metallic samples that have not been seriously compromised by significant shock heating and/or radial release strains is nearly impossible. At shock pressures greater than 100 GPa (14.5×10^6 psi) recovery of samples is essentially impossible. The techniques described below have been used for both HE- and launcher-driven shock recovery experiments.

References cited in this section

25. G.T. Gray III, Influence of Shock-Wave Deformation on the Structure/Property Behavior of Materials, *High-Pressure Shock Compression of Solids*, J.R. Asay and M. Shahinpoor, Ed., Springer-Verlag, 1993, p 187–216
26. D.G. Doran and R.K. Linde, Shock Effects in Solids, *Solid State Phys.*, Vol 19, 1966, p 230–290

34. G.T. Gray III, Shock Experiments in Metals and Ceramics, *Shock-Wave and High-Strain-Rate Phenomena in Materials*, M.A. Meyers, L.E. Murr, and K.P. Staudhammer, Ed., Marcel-Dekker, 1992, p 899–912
40. E.G. Zukas, Shock-Wave Strengthening, *Met. Eng. Q.*, Vol 6, 1966, p 1–20
48. P.S. DeCarli and M.A. Meyers, Design of Uniaxial Shock Recovery Experiments, *Shock Waves and High Strain Rate Phenomena in Metals*, M.A. Meyers and L.E. Murr, Ed., Plenum, 1981, p 341–373
77. R.N. Orava and R.H. Wittman, Techniques for the Control and Application of Explosive Shock Waves, *Proc. of Fifth Int. Conf. on High Energy Fabrication*, University of Denver, 1975, p 1.1.1
78. M.A. Mogilevskii, Shock-Wave Loading of Specimens with Minimum Permanent Set, *Combust. Explos. Shock Waves*, Vol 21, 1985, p 639–640

Shock Wave Testing of Ductile Materials

George T. (Rusty) Gray III, Los Alamos National Laboratory

Design Parameters for Flyer-Plate Experiments

The variation of the shock parameters (peak pressure and pulse duration) for recovery experiments can be calculated using several simple formulations. Equations have been developed by Orava and Wittman (Ref 77) for the design of recovery assemblies to achieve a given peak pressure and pulse duration and to protect the sample from significant radial release and possible subsequent spallation. Design of the target-flyer variables to achieve a given set of shock parameters in a shock recovery experiment is typically started by fixing the desired peak shock pressure or true transient strain. This is linked to the fact that changes in peak shock pressure are known to produce the most significant variation in post shock material structure-property relations (Ref 24, 25, 26, 28, 29, 30, 40, 42, 44, and 46). When the flyer plate and target assembly are the same material, called symmetric impact, the material velocity behind the shock is exactly one half of the projectile velocity (Ref 77, 79):

$$V_p = \frac{U_P^D}{2} + \frac{U_P^T}{2} = U_p \quad (\text{Eq 1})$$

where V_p is the projectile velocity and U_p is the particle velocity partitioned between the driver plate, $\frac{U_P^D}{2}$, and the target, $\frac{U_P^T}{2}$. Symmetric impact is generally preferred because it is most easily analyzed. In the case of dissimilar materials, the particle velocity is divided according to the Hugoniot equations of each by the impedance matching method (Ref 6). In this situation, complex release behavior is typical. Hugoniot data for a wide range of materials can be found tabulated in Ref 79. The total equivalent or effective transient strain induced in the sample due to this impact (encompassed as a sum of both the elastic and plastic compression and elastic and plastic release portions of the shock process), ϵ_t , is determined from the measured Hugoniot data, which is the dynamic compressibility of the material as a function of pressure where V_0 and V are the initial and final volumes of the material during the peak of the shock. Assuming that the residual strain remaining in the sample after the shock release is zero (Ref 80), the transient or equivalent total strain imparted to the sample due to the shock-loading impulse and release is given by:

$$\epsilon_t = \frac{4}{3} \ln \left(\frac{V}{V_0} \right) \quad (\text{Eq 2})$$

In Fig. 4, a time-distance diagram of a symmetric impact by a driver plate with the target backed by a spall plate is presented that ignores strength in the sample. The symmetry of impact is reflected in the similar slope

of the shock velocity, labeled U_s , into the driver and target starting at time zero. The length of time the sample remains at pressure is determined by combining the shock wave and release wave transit times through the flyer. When the rarefaction wave reaches the flyer-target interface the pressure in the sample is released. The release process is stretched in time in the form of a “rarefaction fan” due to the variation in longitudinal and bulk wave speeds as a function of pressure. The pulse duration time, t_p , at the front of the sample is approximated by (Ref 77):

$$t_p = d^D \left(\frac{1}{U_s^D} + \frac{\rho_0^D}{\rho_s^D C^D} \right) \quad (\text{Eq 3})$$

where d^D is the driver plate thickness, U_s^D is the shock velocity in the driver in shock, ρ_0^D and ρ_s^D are density of driver at ambient pressure and under shock, respectively, and C^D is the bulk sound speed in the compressed (shocked-state) driver.

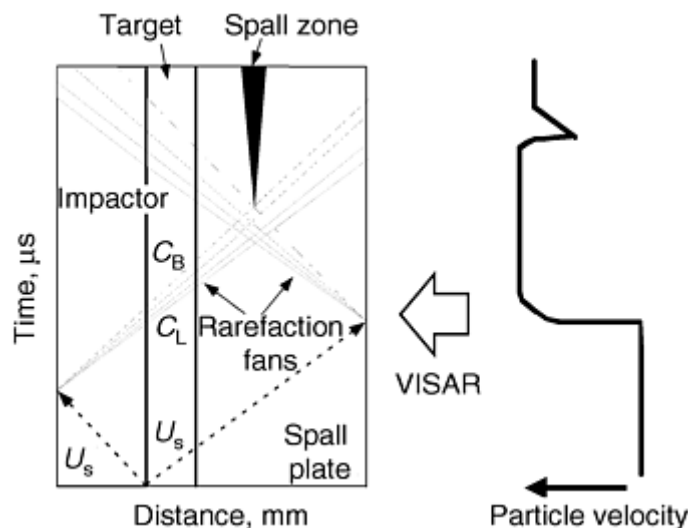


Fig. 4 Time-distance diagram of a symmetric shock wave impact

To assure the recovery specimen experiences uniaxial strain, that is, one-dimensional strain, in nature during both loading and unloading it is necessary to protect the sample from radial release prior to uniaxial release. Figure 4 schematically represents the time distance for a symmetric impact and the commensurate particle-velocity time history, which would be visible to an interferometer, such as a VISAR, looking at the rear surface of the sample assembly. If the driver plate and target assembly have the same dimension, then immediately after the target assembly is impacted by the driver, radial release waves will be directed toward the interior of the target assembly from the driver edges. In order to mitigate these lateral release waves, the sample within the target assembly is surrounded by momentum traps comprised of rings or rails of material similar to the sample. The width of the momentum trapping necessary must be sufficient to contain the total shock event in the flyer and target of time, t_s (Ref 77).

Given simple centered flow conditions where the driver, target, and momentum trapping materials are the same, the minimum trapping width w is given by (Ref 77):

$$w \geq \frac{C}{C_0} \left[\left(\frac{U_s + C_0}{U_s} \right) d^D + d^T \right] \quad (\text{Eq 4})$$

After the shock has traversed the sample, if it is not obstructed, it will reflect off the back surface of the specimen as a release wave. This further complicates the loading history of the sample, indeed, if the rear surface release wave is allowed to interact with the forward-moving release wave propagating in from the driver that releases the sample to ambient pressure. In this case the two tensile release fans will meet and cause spall fracture when the amplitude is above the dynamic tensile strength of the material. To prevent this from occurring in the sample intended for postshock characterization, a spall plate is placed behind the sample to isolate the release wave interactions in the spall plate, thereby protecting the sample spallation (Fig. 4). The release time, t_R , must be greater than or equal to the shock time. To protect the sample from spall interactions, the spall plate thickness must equal or exceed the dimension (Ref 77):

$$h \geq \frac{C}{C_0} \left[\left(\frac{U_s + C_0}{U_s + C} \right) d^D + \left(\frac{U_s - C_0}{U_s + C} \right) d^T \right] \quad (\text{Eq 5})$$

As an example, a 10 GPa (1.5×10^6 psi), 1 μ s pulse shock in a 5 mm (0.2 in.) thick high-purity copper sample (symmetric impact, $C_0 = 3.94$ mm/ μ s, $C = 4.425$ mm/ μ s, $U_s = 4.326$ mm/ μ s, and $V/V_0 = 0.94$) requires an impactor traveling at 0.518 mm/ μ s ($U_p = 0.259$ mm/ μ s) using a 2.25 mm (0.09 in.) thick copper impactor or driver plate. The minimum momentum trapping and spall plate requirements are then calculated to be 10.45 mm (0.41 in.) and 10.56 mm (0.42 in.), respectively. While Eq 4 and 5 pertaining to the momentum trapping and spallation requirements can be corrected for nonsymmetrical impact, this is not usually done. Internal impedance mismatching within the assembly will cause additional wave reflections that compromise the simple compression loading history of the sample. In instances where symmetric assembly design is impossible, as is typically the case for most brittle solids, other techniques are necessary.

Figure 5 illustrates an example of a soft shock recovery fixture positioned on a shock support or impact assembly for conducting shock recovery experiments on a gas- and/or propellant-driven launcher. Following release of the shock through the sample, the two opposing release waves are designed to interact within the spall plate, thereby isolating the sample from the high tensile stresses resulting from the overlap of the two release fans. The central opening in the impact is thereafter utilized to facilitate the escape of the sample assembly into the recovery catch tank area for deceleration. This central passageway additionally serves as a mechanism to separate the sample assembly from the continued forward momentum on the projectile. Inadequate assembly design to ensure a one-dimensional shock loading and release sequence has been shown to alter the sample shock history and subsequent structure-property response due to the additional plastic work imposed on the sample due to late-time radial release effects (Ref 80, 81). Careful attention to momentum trapping of samples during shock recovery experimentation is therefore required if the structure-property effects quantified in postmortem recovered samples are to be correlated to processes occurring during shock loading.

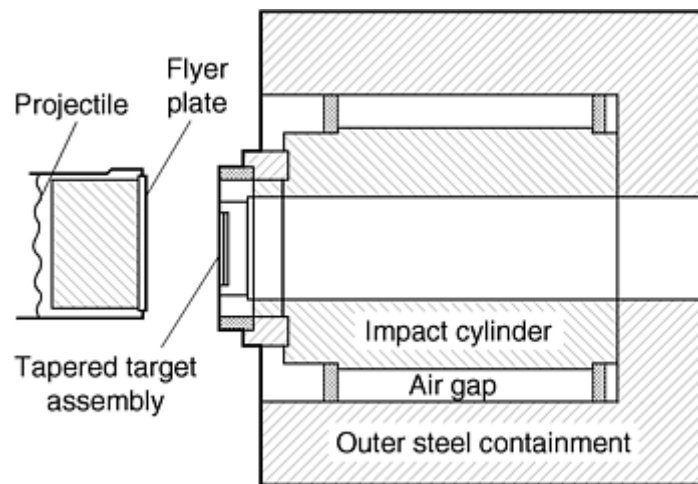


Fig. 5 Schematic of a soft shock recovery fixture used on a gas/powder launcher assembly

References cited in this section

6. R.G. McQueen and S.P. Marsh, Equation of State for Nineteen Metallic Elements from Shock-Wave Measurements to Two Megabars, *J. Appl. Phys.*, Vol 31, 1960, p 1253–1269
24. C.S. Smith, Metallographic Studies of Metals after Explosive Shock, *Trans. Metall. Soc. AIME*, Vol 214, 1958, p 574–589
25. G.T. Gray III, Influence of Shock-Wave Deformation on the Structure/Property Behavior of Materials, *High-Pressure Shock Compression of Solids*, J.R. Asay and M. Shahinpoor, Ed., Springer-Verlag, 1993, p 187–216
26. D.G. Doran and R.K. Linde, Shock Effects in Solids, *Solid State Phys.*, Vol 19, 1966, p 230–290

28. W.C. Leslie, Microstructural Effects of High Strain Rate Deformation, *Metallurgical Effects at High Strain Rates*, R.W. Rhode, B.M. Butcher, J.R. Holland, and C.H. Karners, Ed., Plenum Press, 1973, p 571
29. L.E. Murr, Residual Microstructure—Mechanical Property Relationships in Shock-Loaded Metals and Alloys, *Shock Waves and High Strain Rate Phenomena in Metals*, M.A. Meyers and L.E. Murr, Ed., Plenum, 1981, p 607–673
30. L.E. Murr, Metallurgical Effects of Shock and High-Strain-Rate Loading, *Materials at High Strain Rates*, T.Z. Blazynski, Ed., Elsevier Applied Science, 1987, p 1–46
40. E.G. Zukas, Shock-Wave Strengthening, *Met. Eng. Q.*, Vol 6, 1966, p 1–20
42. G.T. Gray III, Shock-Induced Defects in Bulk Materials, *Materials Research Society Symp. Proc.*, Vol 499, 1998, p 87–98
44. S. Mahajan, Metallurgical Effects of Planar Shock Waves in Metals and Alloys, *Phys. Status Solidi (a)*, Vol 2, 1970, p 187–201
46. G.E. Dieter, Metallurgical Effects of High-Intensity Shock Waves in Metals, *Response of Metals to High Velocity Deformation*, P.G. Shewmon and V.F. Zackay, Ed., Interscience, 1961, p 409–446
77. R.N. Orava and R.H. Wittman, Techniques for the Control and Application of Explosive Shock Waves, *Proc. of Fifth Int. Conf. on High Energy Fabrication*, University of Denver, 1975, p 1.1.1
79. S.P. Marsh, *LASL Shock Hugoniot Data*, University of California Press, 1980
80. G.T. Gray III, P.S. Follansbee, and C.E. Frantz, Effect of Residual Strain on the Substructure Development and Mechanical Response of Shock-Loaded Copper, *Mater. Sci. Eng. A*, Vol 111, 1989, p 9–16
81. A.L. Stevens and O.E. Jones, Radial Stress Release Phenomena in Plate Impact Experiments: Compression-Release, *J. Appl. Mech. (Trans. ASME)*, Vol 39, 1972, p 359–366

Shock Wave Testing of Ductile Materials

George T. (Rusty) Gray III, Los Alamos National Laboratory

Shock Recovery and Spallation Studies of Ductile Materials

As described previously, shock wave research includes analysis of samples subjected to an impact excursion to examine the postmortem signature of the shock prestraining on the substructure and mechanical behavior of a material in addition to damage evolution of a ductile material when subjected to a spallation uniaxial strain loading history. A few examples of the types of experimental data and post mortem characterization results typically quantified for both shock recovery and spallation research are introduced below.

Defect Generation during Shock Loading as Quantified Using Shock Recovery Experiments. In an ideal isotropic homogeneous material, the passage of an elastic shock through a bulk material should leave behind no lattice defects or imperfections. In practice, the severe loading path conditions imposed during a shock induce a high density of defects in most materials (i.e., dislocations, point defects, and/or deformation twins). In addition, during the shock process some materials may undergo a pressure-induced phase transition that affects

the material response. If the high-pressure phase persists upon release of pressure to ambient conditions (although metastable) the postmortem substructure and mechanical response will also reflect the high-pressure excursion. Interpretation of the results of shock wave effects on materials must therefore address all of the details of the shock-induced deformation substructure in light of the operative metallurgical strengthening mechanisms in the material under investigation and the experimental conditions under which the material was deformed and recovered.

Microstructural examinations of shock-recovered samples have characterized the differing types of lattice defects (dislocations, point defects, stacking faults, deformation twins, and, in some instances, high-pressure phase products) generated during shock loading. The specific type of defect or defects activated and their density and morphology within the shock-recovered material have, in turn, been correlated to the details of the starting material chemistry, microstructure, and initial mechanical behavior or hardness, and the postmortem mechanical behavior of the shock-prestrained material. Several in-depth reviews have summarized the microstructural and mechanical response of shock-recovered metals and alloys (Ref 24, 25, 26, 28, 29, 30, 40, 42, 44, and 46). In general, the deformation substructures resulting from modest shock loading (up to 40 GPa, or 6×10^6 psi) in metals are observed to be very uniformly distributed on a grain-to-grain scale.

The specific type of substructure developed in the shock in a given metal (e.g., dislocation cells, twins, or faults) has been shown to critically depend on a number of factors. These include the crystal structure of the metal or alloy, the relevant strengthening and deformation mechanisms in the material (such as alloying, grain size, second phases, and interstitial content), temperature, stacking fault energy, and the shock-loading parameters and experimental conditions. The overall substructure, while macroscopically uniform, can vary within single grains. The substructure can consist of homogeneously distributed dislocation tangles or cells, coarse planar slip, stacking faults, or twins (i.e., be locally heterogeneous). The type of substructure formed depends on the deformation mechanisms operative in the specific material under the specific shock conditions. These shock-induced microstructural changes in metallic systems in turn correlate with variations in the postmortem mechanical properties. For example, the formation of deformation twins is facilitated in many materials due to the very high strain rate during shock loading (Ref 61).

Shock loading in most metals and alloys has been shown to manifest greater hardening than quasi-static deformation for the same total strain, particularly if the metal undergoes a polymorphic phase transition, such as is observed in pure iron (Ref 42). Figure 6 compares the stress-strain response of annealed copper and annealed tantalum samples that have been quasi-statically loaded with the quasi-static reloading responses of the samples that have been shock prestrained. The shock-loaded stress-strain curves are plotted offset at the approximate total transient shock strains, calculated as $\frac{1}{3} \ln(V/V_0)$ for the shock (where V and V_0 are the compressed volumes during the shock and the initial volumes, respectively). The offset curve for copper shows that the reload behavior of the shock-prestrained sample (compared at an equivalent strain level) exhibits a reload flow stress considerably higher than the unshocked copper. Other face-centered cubic metals and alloys (e.g., copper, nickel, and aluminum) have been seen to exhibit similar behavior (Ref 24, 25, 26, 28, 29, 30, 40, 42, 44, and 46). On the contrary, the reload stress-strain response of tantalum shock prestrained to 7 and 20 GPa (1 and 3×10^6 psi) is observed to display essentially no enhanced shock hardening in comparison to quasi-static loading to an equivalent plastic strain.

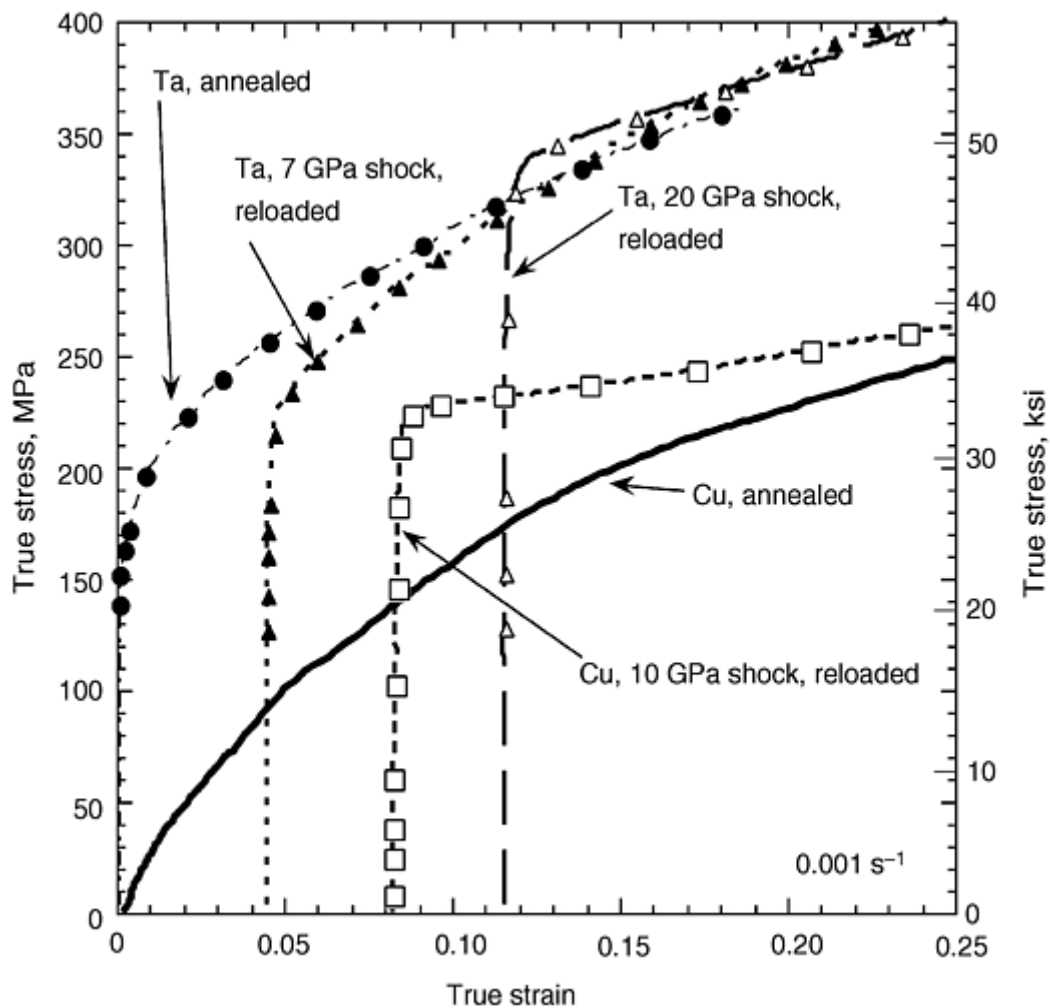


Fig. 6 Stress-strain response of tantalum and copper illustrating the varied effect of shock prestraining on postshock mechanical behavior

Spallation “Hopkinson Fracture” Studies of Ductile Materials. Spallation is the failure in a material due to the action of tensile stresses developed in the interior of a sample or component through the overlap of two release waves. Since the early work of Hopkinson (Ref 14), numerous researchers have studied this phenomena (Ref 15, 16, 20, 22, and 82). Early work by Rinehart (Ref 16), through systematic studies on a range of engineering metals and alloys, demonstrated that a critical shock stress is needed to produce scabbing in a material. The characteristic nature of this material quantity, as well as its importance to understanding interactions between shock and the structure, continues to make spallation research of primary scientific and engineering interest. A systematic representation of the idealized process of release wave overlap driving a material into a dynamic tension, uniaxial strain, loading state is shown in Fig. 4. The elastic wave in this figure is assumed to be negligible compared to the plastic I wave; no additional waves, such as a phase transition plastic II wave, are present.

Measurements of the spall strength are based on analysis of the one-dimensional motion of compressible, contiguous, condensed matter following the reflection of the shock pulse from the surface of the sample or component. Figure 4 shows the shock trajectory that a sample undergoes during the path in a spallation experiment. The shock that is imparted into the target through the jump in particle velocity upon impact with the driver plate (or impactor) is thereafter unloaded through the release wave originating (in one dimension) from the rear surface of the driver plate that diminishes the free surface velocity. If the impactor is sufficiently thin, the rarefaction will overtake the shock because the release wave is traveling into the precompressed solid and, therefore, its wave speed is higher than the shock velocity. In this case, the rarefaction will attenuate the shock. This unloading wave is actually a fan of characteristics, which erodes the shock down toward ambient pressure. This reduces the particle velocity from the peak Hugoniot State achieved by the imposed shock. For thicker impactors, as in Fig. 4, the release fan arrives at the rear surface of the target well after the arrival of the main shock. At the free rear surface of the target, the shock wave is reflected as an unloading wave that travels

back toward the interior of the target. Overlap of the release fans causes the material in the overlap region to be loaded in tension. The maximum tensile stress is reached in the central area of the overlap of the two release fans, termed the spall plane.

If the maximum tensile stress achieved exceeds the local fracture strength, damage is initiated in the target. Fracture of the material at the spall plane causes the tensile stress to decrease rapidly to zero. As a result, a compression wave forms in the matter adjacent to the spall plane region. These waves propagate in each direction away from the spall plane. At the rear surface of the target, as in Fig. 4 where the particle velocity is monitored, this compression wave is manifested as a jump in velocity. When the target spalls, a stress wave is trapped between the spall plane and the rear of the target. Later reverberations of this stress wave lead to a damped oscillation in the particle velocity record. This “ringing,” or period of oscillations, can be used to determine the thickness of the spalled layer or scab produced.

Monitoring of the rear surface velocity of the sample or of the sample-window interface using a manganin pressure gage or VISAR quantifies the sample particle velocity history. A representation of the correlation between the spallation process within a sample and its manifestation on the sample rear surface or sample-window surface is shown on the right side of Fig. 4. Measurements of the wave profile of a sample driven to spall provides information on the time-dependent wave propagation and intersection processes leading to damage evolution in a material if the tensile stresses are sufficiently high. Shock studies designed to study spallation in a material therefore use the wave profile and, specifically, the details of the magnitude of the “pull-back” signal to quantify the energy necessary to nucleate and propagate damage. Figure 7 presents a VISAR wave profile of high-purity zirconium subjected to spall loading (Ref 83). The arrow A identifies the Hugoniot elastic limit for this material and the pull-back signal documents that this shock amplitude is sufficient to cause damage evolution in this material; in this case, however, no scab was formed but rather only incipient spall.

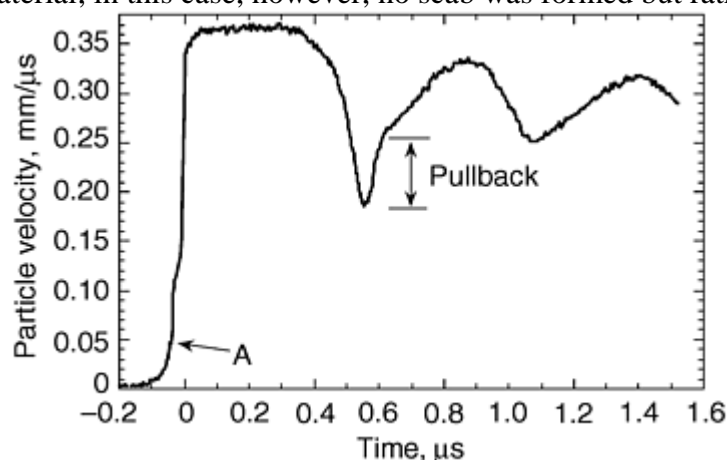


Fig. 7 Rear surface velocity shock wave profile (developed using VISAR interferometry) showing spallation in zirconium. Source: Ref 83

Profiles such as Fig. 7 provide quantitative data to compare with one-dimensional wave propagation finite-difference and finite-volume code calculations that model dynamic fracture. Additional insight into the physics and materials science controlling the process of spallation can be provided through examining the postshocked and damaged samples, just as Hopkinson did in his first steel studies. Figure 8 shows a metallographic cross section through an incipiently spalled high-purity tantalum sample following impact loading. In this example, nearly spherical ductile voids are observed to have nucleated and grown, as a function of position from the central fracture plane, and begun to coalesce under the imposed tensile stress history. Given sufficient tensile stress amplitude and appropriate geometry, damage can lead to scab formation and, therefore, complete separation of the sample into multiple pieces. Identification of the final fracture modes manifesting complete separation can be obtained by soft recovering the scab formed and then examining its fracture surface. Figure 9 presents an example of a fracture surface of a spalled Ta-10W sample illustrating cleavage fracture behavior.

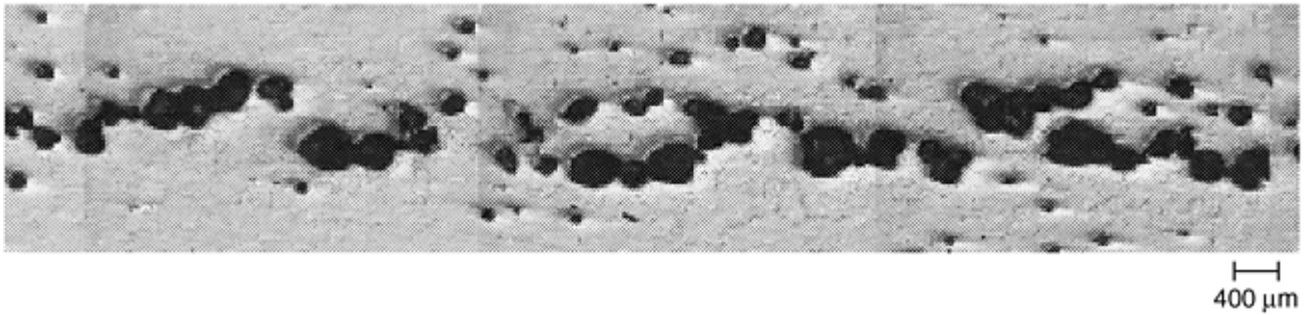


Fig. 8 Metallographic cross section of soft-recovered tantalum sample following spallation

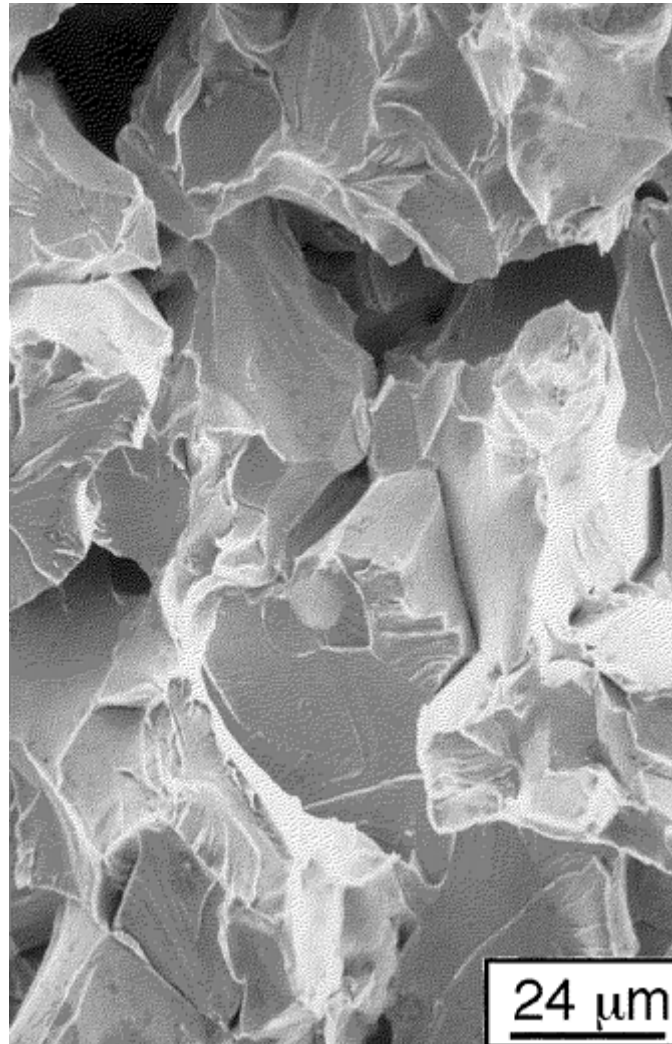


Fig. 9 Scanning-electron microscopy (SEM) image of transgranular cleavage fracture in Ta-10W spallation sample. Source: Ref 84

Quantification of the damage nucleation and evolution processes leading to dynamic failure provide the critical physical insight into the micromechanisms governing this complex dynamic fracture process (Ref 22). Documentation of the time- and stress-dependent loading parameters, specific damage mechanisms controlling nucleation and growth, and the microstructural factors influencing these processes is needed to develop physically based models describing the spallation of ductile materials.

References cited in this section

14. B. Hopkinson, The Pressure of a Blow, *The Scientific Papers of Bertram Hopkinson*, Cambridge University Press, 1921, p 423–437

15. M.A. Meyers and C.T. Aimone, Dynamic Fracture (Spalling) of Metals, *Prog. Mater. Sci.*, Vol 28, 1983, p 1–96
16. J.S. Rinehart, Scabbing of Metals under Explosive Attack: Multiple Scabbing, *J. Appl. Phys.*, Vol 23, 1952, p 1229–1233
20. D.R. Curran, L. Seaman, and D.A. Shockey, Linking Dynamic Fracture to Microstructural Processes, *Shock Waves and High Strain-Rate Phenomena in Metals*, M.A. Meyers and L.E. Murr, Ed., Plenum, 1981, p 129–167
22. A.K. Zurek and M.A. Meyers, Microstructural Aspects of Dynamic Failure, *High Pressure Shock Compression of Solids II: Dynamic Fracture and Fragmentation*, L. Davison, D.E. Grady, and M. Shahinpoor, Ed., Springer-Verlag, 1996, p 25–70
24. C.S. Smith, Metallographic Studies of Metals after Explosive Shock, *Trans. Metall. Soc. AIME*, Vol 214, 1958, p 574–589
25. G.T. Gray III, Influence of Shock-Wave Deformation on the Structure/Property Behavior of Materials, *High-Pressure Shock Compression of Solids*, J.R. Asay and M. Shahinpoor, Ed., Springer-Verlag, 1993, p 187–216
26. D.G. Doran and R.K. Linde, Shock Effects in Solids, *Solid State Phys.*, Vol 19, 1966, p 230–290
28. W.C. Leslie, Microstructural Effects of High Strain Rate Deformation, *Metallurgical Effects at High Strain Rates*, R.W. Rhode, B.M. Butcher, J.R. Holland, and C.H. Karners, Ed., Plenum Press, 1973, p 571
29. L.E. Murr, Residual Microstructure—Mechanical Property Relationships in Shock-Loaded Metals and Alloys, *Shock Waves and High Strain Rate Phenomena in Metals*, M.A. Meyers and L.E. Murr, Ed., Plenum, 1981, p 607–673
30. L.E. Murr, Metallurgical Effects of Shock and High-Strain-Rate Loading, *Materials at High Strain Rates*, T.Z. Blazynski, Ed., Elsevier Applied Science, 1987, p 1–46
40. E.G. Zukas, Shock-Wave Strengthening, *Met. Eng. Q.*, Vol 6, 1966, p 1–20
42. G.T. Gray III, Shock-Induced Defects in Bulk Materials, *Materials Research Society Symp. Proc.*, Vol 499, 1998, p 87–98
44. S. Mahajan, Metallurgical Effects of Planar Shock Waves in Metals and Alloys, *Phys. Status Solidi (a)*, Vol 2, 1970, p 187–201
46. G.E. Dieter, Metallurgical Effects of High-Intensity Shock Waves in Metals, *Response of Metals to High Velocity Deformation*, P.G. Shewmon and V.F. Zackay, Ed., Interscience, 1961, p 409–446
61. G.T. Gray III, Deformation Twinning in Aluminum-4.8 wt.% Mg, *Acta Metall.*, Vol 36, 1988, p 1745–1754
82. L. Davison and R.A. Graham, Shock Compression of Solids, *Phys. Rep.*, Vol 55, 1979, p 255–379
83. G.T. Gray III, N.K. Bourne, M.A. Zoicher, P.J. Maudlin, and J.C.F. Millett, Influence of Crystallographic Anisotropy on the Hopkinson Fracture “Spallation” of Zirconium, *Shock Compression of Condensed Matter—1999*, AIP Conference Proceedings, M.D. Furnish, L.C. Chhabildas, and R.S. Hixson, Ed., American Institute of Physics Press, Woodbury, NY, 2000, p 509–512

84. G.T. Gray III and A.D. Rollett, The High-Strain-Rate and Spallation Response on Tantalum, TA-10W and T-111, *High Strain Rate Behaviour of Refractory Metals and Alloys*, R. Asfahani, E. Chen, and A. Crowson, The Minerals, Metals and Materials Society, 1992, p 303–315

Shock Wave Testing of Ductile Materials

George T. (Rusty) Gray III, Los Alamos National Laboratory

Summary

Systematic shock-loading studies of materials, in which microstructural “real-time” shock physics processes, mechanical property, and dynamic fracture effects are characterized quantitatively, provide important diagnostic tools to understand the constitutive behavior of materials. A variety of loading techniques can be used to shock load materials including HE-driven gas/powder launchers, exploding foils, laser-driven flyer plates, and direct radiation impingement (including lasers and electron beams). Shock recovery experiments provide a post mortem snapshot of the structure-property response of a material to the extreme conditions of strain rate, triaxial stress, and temperature imposed by the shock for comparison with in situ wave profile and shock-reload data. Postmortem characterization of shock-loaded materials will continue to contribute valuable data to the understanding of real-time wave profile and shock wave data.

Shock Wave Testing of Ductile Materials

George T. (Rusty) Gray III, Los Alamos National Laboratory

Acknowledgments

This work was supported under the auspices of the United States Department of Energy. The author acknowledges the assistance of B. Jacquez and C.P. Trujillo in conducting the shock recovery and spallation testing. The author wishes to acknowledge R.S. Hixson and Dennis Hayes for critically reviewing this manuscript.

Shock Wave Testing of Ductile Materials

George T. (Rusty) Gray III, Los Alamos National Laboratory

References

1. W.J.M. Rankine, On the Thermodynamic Theory of Waves of Finite Longitudinal Disturbance, *Philos. Trans. R. Soc. (London)*, Vol 160, 1870, p 277–288
2. J.N. Johnson and R. Chéret, Shock Waves in Solids: An Evolutionary Perspective, *Shock Waves*, Vol 9, 1999, p 193–200

3. M.H. Rice, R.G. McQueen, and J.M. Walsh, Compression of Solids by Strong Shock Waves, *Solid State Phys.*, Vol 6, 1958, p 1–63
4. J.M. Walsh and R.H. Christian, Equation of State of Metals from Shock Wave Measurements, *Phys. Rev.*, Vol 97, 1955, p 1544–1556
5. J.M. Walsh, M.H. Rice, R.G. McQueen, and F.L. Yarger, Shock-Wave Compressions of Twenty-Seven Metals: Equations of State of Metals, *Phys. Rev.*, Vol 108, 1957, p 196–216
6. R.G. McQueen and S.P. Marsh, Equation of State for Nineteen Metallic Elements from Shock-Wave Measurements to Two Megabars, *J. Appl. Phys.*, Vol 31, 1960, p 1253–1269
7. R.G. McQueen, Laboratory Techniques for Very High Pressures and the Behavior of Metals under Dynamic Loading, *Metallurgy at High Pressures and High Temperatures*, K.A. Gschneidner, Jr., M.T. Hepworth, and N.A.D. Parlee, Ed., Gordon and Breach, 1964, p 44–132
8. R.G. McQueen, S.P. Marsh, J.W. Taylor, J.N. Fritz, and W.J. Carter, The Equation of State of Solids from Shock Wave Studies, *High Velocity Impact Phenomena*, R. Kinslow, Ed., Academic Press, 1970, p 293–417, 515–568
9. C.P. Morris, *Los Alamos Shock Wave Profile Data*, University of California Press, 1981
10. L.V. Altshuler, K.K. Krupnikov, and M.I. Brazhnik, Dynamic Compressibility of Metals under Pressures from 400,000 to 4,000,000 Atmospheres, *Sov. Phys. JETP*, Vol 7, 1958, p 614–619
11. C.E. Anderson, J.S. Wilbeck, J.C. Hokanson, J.R. Asay, D.E. Grady, R.A. Graham, and M.E. Kipp, Sandia Shock Compression Database, *Shock Waves in Condensed Matter—1985*, Y.M. Gupta, Ed., Plenum, 1986, p 185–190
12. L.V. Altshuler, R.F. Trunin, V.D. Urlin, V.E. Fortov, and A.I. Funtikov, Development of Dynamic High-Pressure Techniques in Russia, *Phys. Usp.*, Vol 42, 1999, p 261–280
13. B. Hopkinson, A Method of Measuring the Pressure Produced in the Detonation of High Explosives or by the Impact of Bullets, *Philos. Trans. R. Soc. (London) A*, Vol 213, 1914, p 437–456
14. B. Hopkinson, The Pressure of a Blow, *The Scientific Papers of Bertram Hopkinson*, Cambridge University Press, 1921, p 423–437
15. M.A. Meyers and C.T. Aimone, Dynamic Fracture (Spalling) of Metals, *Prog. Mater. Sci.*, Vol 28, 1983, p 1–96
16. J.S. Rinehart, Scabbing of Metals under Explosive Attack: Multiple Scabbing, *J. Appl. Phys.*, Vol 23, 1952, p 1229–1233
17. I.C. Skidmore, An Introduction to Shock Waves in Solids, *Appl. Mater. Res.*, Vol 4, 1965, p 131–147
18. H. Kolsky, The Waves Generated by Brittle Fracture in Glass, *Trans. Soc. Rheology*, Vol 20, 1976, p 441–454
19. D.R. Curran, L. Seaman, and D.A. Shockey, Dynamic Failure of Solids, *Phys. Rep.*, Vol 147, 1987, p 253–388

20. D.R. Curran, L. Seaman, and D.A. Shockey, Linking Dynamic Fracture to Microstructural Processes, *Shock Waves and High Strain-Rate Phenomena in Metals*, M.A. Meyers and L.E. Murr, Ed., Plenum, 1981, p 129–167
21. D.R. Curran, L. Seaman, and D.A. Shockey, Dynamic Failure in Solids, *Phys. Today*, Vol 30 (No. 1), 1977, p 46–55
22. A.K. Zurek and M.A. Meyers, Microstructural Aspects of Dynamic Failure, *High Pressure Shock Compression of Solids II: Dynamic Fracture and Fragmentation*, L. Davison, D.E. Grady, and M. Shahinpoor, Ed., Springer-Verlag, 1996, p 25–70
23. P. Chevrier and J.R. Klepaczko, Spall Fracture: Mechanical and Microstructural Aspects, *Eng. Fract. Mech.*, Vol 63, 1999, p 273–294
24. C.S. Smith, Metallographic Studies of Metals after Explosive Shock, *Trans. Metall. Soc. AIME*, Vol 214, 1958, p 574–589
25. G.T. Gray III, Influence of Shock-Wave Deformation on the Structure/Property Behavior of Materials, *High-Pressure Shock Compression of Solids*, J.R. Asay and M. Shahinpoor, Ed., Springer-Verlag, 1993, p 187–216
26. D.G. Doran and R.K. Linde, Shock Effects in Solids, *Solid State Phys.*, Vol 19, 1966, p 230–290
27. S. Mahajan, Metallurgical Effects of Planar Shock Waves in Metals and Alloys, *Phys. Status Solidi (a)*, Vol 2, 1970, p 187–201
28. W.C. Leslie, Microstructural Effects of High Strain Rate Deformation, *Metallurgical Effects at High Strain Rates*, R.W. Rhode, B.M. Butcher, J.R. Holland, and C.H. Karners, Ed., Plenum Press, 1973, p 571
29. L.E. Murr, Residual Microstructure—Mechanical Property Relationships in Shock-Loaded Metals and Alloys, *Shock Waves and High Strain Rate Phenomena in Metals*, M.A. Meyers and L.E. Murr, Ed., Plenum, 1981, p 607–673
30. L.E. Murr, Metallurgical Effects of Shock and High-Strain-Rate Loading, *Materials at High Strain Rates*, T.Z. Blazynski, Ed., Elsevier Applied Science, 1987, p 1–46
31. D. Raybould and T.Z. Blazynski, Non-Metallic Materials under Shock Loading, *Materials at High Strain Rates*, T.Z. Blazynski, Ed., Elsevier Applied Science, 1987, p 71–132
32. K.P. Staudhammer, Shock Wave Effects and Metallurgical Parameters, *Impact Loading and Dynamic Behaviour of Materials*, C.Y. Chiem, H.-D. Kunze, and L.W. Meyer, Ed., DGM Informationsgesellschaft mbH, 1988, p 93–112
33. G.T. Gray III, Shock Recovery Experiments: An Assessment, *Shock Compression of Condensed Matter—1989*, S.C. Schmidt, J.N. Johnson, and L.W. Davidson, Ed., Elsevier, 1990, p 407–414
34. G.T. Gray III, Shock Experiments in Metals and Ceramics, *Shock-Wave and High-Strain-Rate Phenomena in Materials*, M.A. Meyers, L.E. Murr, and K.P. Staudhammer, Ed., Marcel-Dekker, 1992, p 899–912
35. G.T. Gray III, Shock Loading Response of Advanced Materials, *High Pressure Science and Technology 1993*, S.C. Schmidt, J.W. Shaner, G.A. Samara, and M. Ross, Ed., American Institute of Physics, 1994, p 1161–1164

36. R.A. Graham, Impact Techniques for the Study of Physical Properties of Solids under Shock Wave Loading, *J. Basic Eng. (Trans. ASME)*, Vol 89, 1967, p 911–918
37. G.T. Gray III, R.S. Hixson, and C.E. Morris, Bauschinger Effect During Shock Loading, *Shock Compression of Condensed Matter—1991*, S.C. Schmidt, R.D. Dick, J.W. Forbes, and D.G. Tasker, Ed., Elsevier, 1992, p 427–430
38. J.N. Johnson, R.S. Hixson, D.L. Tonks, and G.T. Gray III, Shock Compression and Quasielastic Release in Tantalum, *High Pressure Science and Technology 1993*, S.C. Schmidt, J.W. Shaner, G.A. Samara, and M. Ross, Ed., American Institute of Physics, 1994, p 1095–1098
39. J.N. Johnson, G.T. Gray III, and N.K. Bourne, Effect of Pulse Duration and Strain Rate on Incipient Spall Fracture in Copper, *J. Appl. Phys.*, Vol 86, 1999, p 4892–4901
40. E.G. Zukas, Shock-Wave Strengthening, *Met. Eng. Q.*, Vol 6, 1966, p 1–20
41. C.M. Fowler, F.S. Minshall, and E.G. Zukas, A Metallurgical Method for Simplifying the Determination of Hugoniot Curves for Iron Alloys in the Two-Wave Region, *Response of Metals to High Velocity Deformation*, P.G. Shewmon and V.F. Zackay, Ed., Interscience, 1961, p 275–308
42. G.T. Gray III, Shock-Induced Defects in Bulk Materials, *Materials Research Society Symp. Proc.*, Vol 499, 1998, p 87–98
43. E. Hornbogen, Shock-Induced Dislocations, *Acta Metall.*, Vol 10, 1962, p 978–980
44. S. Mahajan, Metallurgical Effects of Planar Shock Waves in Metals and Alloys, *Phys. Status Solidi (a)*, Vol 2, 1970, p 187–201
45. L.M. Barker and R.E. Hollenbach, Interferometer Technique for Measuring the Dynamic Mechanical Properties of Materials, *Rev. Sci. Instrum.*, Vol 36, 1965, p 1617–1620
46. G.E. Dieter, Metallurgical Effects of High-Intensity Shock Waves in Metals, *Response of Metals to High Velocity Deformation*, P.G. Shewmon and V.F. Zackay, Ed., Interscience, 1961, p 409–446
47. G.R. Fowles, Experimental Technique and Instrumentation, *Dynamic Response of Materials to Intense Impulsive Loading*, P.C. Chou and A.K. Hopkins, Ed., Air Force Materials Laboratory, Wright Patterson Air Force Base, 1972, p 405–480
48. P.S. DeCarli and M.A. Meyers, Design of Uniaxial Shock Recovery Experiments, *Shock Waves and High Strain Rate Phenomena in Metals*, M.A. Meyers and L.E. Murr, Ed., Plenum, 1981, p 341–373
49. R.G. McQueen and S.P. Marsh, High Explosive Systems for Equation-of-State Studies, *Shock Waves in Condensed Matter—1987*, S.C. Schmidt and N.C. Holmes, Ed., Elsevier, 1988, p 107–110
50. M.A. Meyers, *Dynamic Behavior of Materials*, Wiley Interscience, 1994
51. G.E. Duvall, Shock Waves in the Study of Solids, *Appl. Mech. Rev.*, Vol 15, 1962, p 849–854
52. E.G. Zukas, Shock-Wave Strengthening, *Met. Eng. Q.*, Vol 6 (No. 2), 1966, p 1–20
53. J.N. Fritz and J.A. Morgan, An Electromagnetic Technique for Measuring Material Velocity, *Rev. Sci. Instrum.*, Vol 44, 1973, p 215–221

54. L.M. Barker and R.E. Hollenbach, Laser Interferometer for Measuring High Velocities of Any Reflecting Surface, *J. Appl. Phys.*, Vol 43, 1972, p 4669–4675
55. R.G. McQueen, J.W. Hopson, and J.N. Fritz, Optical Technique for Determining Rarefaction Wave Velocities at Very High Pressures, *Rev. Sci. Instrum.*, Vol 53, 1982, p 245–250
56. J.N. Fritz, C.E. Morris, R.S. Hixson, and R.G. McQueen, Liquid Sound Speeds at Pressure from the Optical Analyzer Technique, *High Pressure Science and Technology 1993*, S.C. Schmidt, J.W. Shaner, G.A. Samara, and M. Ross, Ed., American Institute of Physics, 1994, p 149–152
57. R.J. Clifton, Pressure Shear Impact and the Dynamic Plastic Response of Metals, *Shock Waves in Condensed Matter—1983*, J.R. Asay, R.A. Graham, and G.K. Straub, Ed., North-Holland, 1984, p 105–111
58. R.A. Graham and J.R. Asay, Measurement of Wave Profiles in Shock Loaded Solids, *High Temp.—High Press.*, Vol 10, 1978, p 355–390
59. G.R. Fowles, G.E. Duvall, J. Asay, P. Bellamy, F. Feistman, D. Grady, T. Michaels, and R. Mitchell, Gas Gun for Impact Studies, *Rev. Sci. Instrum.*, Vol 41, 1970, p 984–996
60. J.W. Taylor, Experimental Methods in Shock Wave Physics, *Metallurgical Effects at High Strain Rates*, R.W. Rohde, B.M. Butcher, J.R. Holland, and C.H. Karnes, Ed., Plenum Press, 1973, p 107–128
61. G.T. Gray III, Deformation Twinning in Aluminum-4.8 wt.% Mg, *Acta Metall.*, Vol 36, 1988, p 1745–1754
62. G.T. Gray III, P.S. Follansbee, and C.E. Frantz, Effect of Residual Strain on the Substructure Development and Mechanical Response of Shock-Loaded Copper, *Mater. Sci. Eng. A*, Vol 111, 1989, p 9–16
63. D.L. Paisley, Laser-Driven Miniature Flyer Plates for Shock Initiation of Secondary Explosives, *Shock Compression of Condensed Matter—1989*, S.C. Schmidt, J.N. Johnson, and L.W. Davidson, Ed., Elsevier, 1990, p 733–736
64. D.E. Mikkola and R.N. Wright, Dislocation Generation and Its Relation to the Dynamic Plastic Response of Shock Loaded Metals, *Shock Waves in Condensed Matter—1983*, J.R. Asay, R.A. Graham, and G.K. Straub, North-Holland, 1984, p 415–418
65. S. Larouche, E.T. Marsh, and D.E. Mikkola, Strengthening Effects of Deformation Twins and Dislocations Introduced by Short Duration Shock Pulses in Cu-8.7Ge, *Metall. Trans. A*, Vol 12, 1981 p 1777–1785
66. D.L. Paisley, Laser-Driven Miniature Plates for One-Dimensional Impacts at 0.5– ϵ 6 km/s, *Shock-Wave and High-Strain-Rate Phenomena in Materials*, M.A. Meyers, L.E. Murr, and K.P. Staudhammer, Ed., Marcel Dekker, 1992, p 1131–1141
67. D.L. Paisley, R.H. Warnes, and R.A. Kopp, Laser-Driven Flat Plate Impacts to 100 GPa with Sub-Nanosecond Pulse Duration and Resolution for Material Property Studies, *Shock Compression of Condensed Matter—1991* S.C. Schmidt, R.D. Dick, J.W. Forbes, and D.G. Tasker, Ed., Elsevier, 1992, p 825–828
68. J.H. Shea, A. Mazzella, and L. Avrami, Equation of State Investigation of Granular Explosives Using a Pulsed Electron Beam, *Proc. Fifth Symp. (Int.) on Detonation*, Office of Naval Research, Arlington, Virginia, 1970, p 351–359

69. F. Cottet and J.P. Romain, Formation and Decay of Laser-Generated Shock Waves, *Phys. Rev. A*, Vol 25, 1982, p 576–579
70. F. Cottet, J.P. Romain, R. Fabbro, and B. Faral, Measurements of Laser Shock Pressure and Estimate of Energy Lost at 1.05 μ m Wavelength, *J. Appl. Phys.*, Vol 55, 1984, p 4125–4127
71. F. Cottet and M. Boustie, Spallation Studies in Aluminum Targets Using Shock Waves Induced by Laser Irradiation at Various Pulse Durations, *J. Appl. Phys.*, Vol 66, 1989, p 4067–4073
72. T. de Ressaiguiet and M. Hallouin, Stress Relaxation and Precursor Decay in Laser Shock-Loaded Iron, *J. Appl. Phys.*, Vol 84, 1998, p 1932–1938
73. T. de Ressaiguiet and M. Deleignies, Spallation of Polycarbonate under Laser Driven Shocks, *Shock Waves*, Vol 7, 1997, p 319–324
74. C.E. Ragan, Equation-of-State Experiments using Nuclear Explosions, *Proc. Int. Symp. on Behaviour of Condensed Matter at High Dynamic Pressures*, Commissariat à l'Energie Atomique, Saclay, Paris, 1978, p 477
75. C.E. Ragan III, Shock Compression Measurements at 1 to 7 TPa, *Phys. Rev. A*, Vol 25, 1982, p 3360–3375
76. R.F. Trunin, Shock Compressibility of Condensed Materials in Strong Shock Waves Generated by Underground Nuclear Explosions, *Physics Usp.*, Vol 37, 1994, p 1123–1145
77. R.N. Orava and R.H. Wittman, Techniques for the Control and Application of Explosive Shock Waves, *Proc. of Fifth Int. Conf. on High Energy Fabrication*, University of Denver, 1975, p 1.1.1
78. M.A. Mogilevskii, Shock-Wave Loading of Specimens with Minimum Permanent Set, *Combust. Explos. Shock Waves*, Vol 21, 1985, p 639–640
79. S.P. Marsh, *LASL Shock Hugoniot Data*, University of California Press, 1980
80. G.T. Gray III, P.S. Follansbee, and C.E. Frantz, Effect of Residual Strain on the Substructure Development and Mechanical Response of Shock-Loaded Copper, *Mater. Sci. Eng. A*, Vol 111, 1989, p 9–16
81. A.L. Stevens and O.E. Jones, Radial Stress Release Phenomena in Plate Impact Experiments: Compression-Release, *J. Appl. Mech. (Trans. ASME)*, Vol 39, 1972, p 359–366
82. L. Davison and R.A. Graham, Shock Compression of Solids, *Phys. Rep.*, Vol 55, 1979, p 255–379
83. G.T. Gray III, N.K. Bourne, M.A. Zoicher, P.J. Maudlin, and J.C.F. Millett, Influence of Crystallographic Anisotropy on the Hopkinson Fracture “Spallation” of Zirconium, *Shock Compression of Condensed Matter—1999*, AIP Conference Proceedings, M.D. Furnish, L.C. Chhabildas, and R.S. Hixson, Ed., American Institute of Physics Press, Woodbury, NY, 2000, p 509–512
84. G.T. Gray III and A.D. Rollett, The High-Strain-Rate and Spallation Response on Tantalum, TA-10W and T-111, *High Strain Rate Behaviour of Refractory Metals and Alloys*, R. Asfahani, E. Chen, and A. Crowson, The Minerals, Metals and Materials Society, 1992, p 303–315

Low-Velocity Impact Testing

Horacio Dante Espinosa, Northwestern University, Sia Nemat-Nasser, University of California, San Diego

Introduction

IMPACT TESTS are used to study dynamic deformation and failure modes of materials. Low-velocity impact techniques can be classified as plate-on-plate, rod-on-plate, plate-on-rod, or rod-on-rod experiments. Two types of plate-on-plate impact tests have been developed: wave propagation experiments and thin-layer high-strain-rate experiments. The plate-on-plate experiments are further classified as nonrecovery or recovery experiments. The focus of this article is on plate-on-plate experimental techniques. At the end of this article, rod-on-plate and plate-on-rod experiments are briefly examined.

Observation of plane waves in materials provides a powerful method for understanding and quantifying their dynamic response (Ref 1, 2, 3, 4, 5, 6, 7, 8, and 9) and failure modes (Ref 10, 11, 12, 13, 14, 15, 16, 17, 18, 19, 20, 21, 22, 23, 24, 25, 26, 27, 28, and 29). Plate impact experiments are used to generate such plane waves (Ref 30, 31, and 32). These experiments provide controlled extreme stress-state loading conditions, involving one-dimensional stress-pulse propagation. The recovery configurations in plate-on-plate impact experiments are performed with the objective of examining the microstructural changes in the specimen after it is subjected to loading under a uniaxial strain condition. The experiments are designed to achieve a controlled plane-wave loading of the specimens. In practice, this is limited by the finite size of the plates employed, which generate radial release waves. This has the potential for significant contribution to the damage processes by introducing causes other than the uniaxial straining of the material. Hence, this aspect of the plate impact experiment has been a subject of considerable research in the past (Ref 11, 13, 33, 34, 35, 36, 37, 38, and 39).

The plate impact experiments are performed in two main modes: *normal impact* and *pressure-shear*, or *oblique impact*. Both modes have been specialized to several new configurations to achieve different aspects of control over the imposed loading. In these experiments, the time histories of the stress waves are recorded and used to infer the response of the specimen with the goal of constitutive modeling. To enable the formulation of correct constitutive behavior for the considered material, knowledge of the micromechanisms of deformation that occur during the passage of the stress waves is necessary. Such knowledge is also necessary for damage-evolution studies. Hence, it is important that the specimen is recovered after it is subjected to a well-characterized loading pulse so that it can be analyzed for any changes in its microstructure. This is achieved in the normal plate impact mode by using an impedance-matched momentum trap behind the specimen (Ref 1, 7, and 11). Ideally, the momentum-trap plate captures the momentum of the loading pulse and flies away, leaving the specimen at rest.

Initially, the recovery technique was developed for the normal plate experiments (Ref 1, 38, and 39), and it has been implemented in the pressure-shear mode to study shear stress-sensitive, high-rate deformation mechanisms. The difficulty in conducting pressure-shear recovery experiments stems from the fact that both the shear and longitudinal momenta must be trapped and that there is a large difference in the longitudinal and shear wave velocities for any given material. To overcome this problem, one idea that had been proposed was to use a composite flyer made of two plates of the same material that are separated by a thin layer of a low shear resistance film, such as a lubricant (Ref 40, 41). This design would enable the shear pulse to be unloaded at the interface, while the pressure pulse would be transmitted to the next plate. The pressure pulse would return to the specimen momentum-trap interface as an unloading wave after the unloading of the shear wave has taken place. The thickness of the momentum-trap plate is chosen such that the normal unloading wave from its rear surface arrives at this interface much later, and hence, the momentum trap would separate just as in the normal recovery experiment, but after trapping both the shear and normal momenta.

The plate impact experiments can be performed at different temperatures by providing temperature-control facilities in the test chamber. This may consist of a high-frequency (0.5 MHz) induction heating system, for high-temperature tests, or a cooling ring with liquid nitrogen circulating through an inner channel, for low-temperature experiments (Ref 42, 43, and 44).

Confined and unconfined rod experiments have been performed (Ref 45, 46) with the aim of extending the uniaxial strain deformation states imposed in the plate impact experiments. The bar impact and pressure-shear experiments provide a measurement of yield stress at rates of 10^3 to $10^5/s^{-1}$. They also allow the experimental verification and validation of constitutive models and numerical solution schemes under two-dimensional states of deformation. In-material stress measurements, with embedded manganin gages, are used to obtain axial and lateral stress histories. Stress decay, pulse duration, release structure, and wave dispersion are well defined in these plate and rod experiments.

References cited in this section

1. P. Kumar and R.J. Clifton, Dislocation Motion and Generation in LiF Single Crystals Subjected to Plate-Impact, *J. Appl. Phys.*, Vol 50 (No. 7), 1979, p 4747–4762
2. K.S. Kim and R.J. Clifton, Pressure-Shear Impact of 6061-T6 Aluminum and Alpha-Titanium, *J. Appl. Mech.*, Vol 47, 1980, p 11–16
3. A. Gilat and R.J. Clifton, Pressure-Shear Waves in 6061-T6 Aluminum and Alpha-Titanium, *J. Mech. Phys. Solids*, Vol 33 (No. 3), 1985, p 263–284
4. C.H. Li, “A Pressure-Shear Experiment for Studying the Dynamic Plastic Response of Metals and Shear Strain Rates of $10^5 s^{-1}$,” Ph.D. thesis, Brown University, Providence, RI, 1982
5. R.J. Clifton and R.W. Klopp, Pressure-Shear Plate Impact Testing, *Mechanical Testing*, Vol 8, *ASM Handbook*, 9th ed., ASM International, 1985, p 230–239
6. K.T. Ramesh and R.J. Clifton, A Pressure-Shear Plate Impact Experiment for Studying the Rheology of Lubricants at High Pressures and High Strain Rates, *J. Tribology*, 1987, Vol 109, p 215
7. H.D. Espinosa and R.J. Clifton, Plate Impact Experiments for Investigating Inelastic Deformation and Damage of Advanced Materials, *Symposium on Experiments in Micromechanics of Fracture-Resistant Materials* (ASME Winter Annual Meeting), 1–6 Dec 1991 (Atlanta, GA), K.S. Kim, Ed., 1991, p 37–56
8. J.C. Escobar and R.J. Clifton, On Pressure-Shear Plate Impact for Studying the Kinetics of Stress-Induced Phase Transformations, *Mater. Sci. Eng. A: Structural Materials: Properties, Microstructure & Processing*, No. 1–2, 1 Oct 1993, p 125–142
9. Y. Sano, S.-N. Chang, M.A. Meyers, and S. Nemat-Nasser, Identification of Stress Induced Nucleation Sites for Martensite in Fe-31.8wt%Ni-0.02wt%C Alloy, *Acta Metall. Mater.*, Vol 40 (No. 2), 1992, p 413–417
10. G. Ravichandran and R.J. Clifton, Dynamic Fracture under Plane Wave Loading. *Int. J. Fract.*, Vol 40 (No. 3), 1989, p 157–201
11. G. Raiser, R.J. Clifton, and M. Ortiz, A Soft-Recovery Plate Impact Experiment for Studying Microcracking in Ceramics, *Mech. Mater.*, Vol 10, 1990, p 43–58
12. H.D. Espinosa, G. Raiser, R.J. Clifton, and M. Ortiz, Inelastic Mechanisms in Dynamically Loaded Ceramics, *Mechanics Computing in 1990s and Beyond*, *ASCE Proceedings*, 20–22 May 1991 (Columbus, OH), H. Adeli and R. Sierakowski, Ed., American Society of Civil Engineers, 1991, p 293–297
13. H.D. Espinosa, G. Raiser, R.J. Clifton, and M. Ortiz, Performance of the Star-Shaped Flyer in the Study of Brittle Materials: Three Dimensional Computer Simulations and Experimental Observations, *J. Appl. Phys.*, Vol 72 (No. 8), 1992, p 3451–3457

14. H.D. Espinosa, G. Raiser, R.J. Clifton, and M. Ortiz, Experimental Observations and Numerical Modeling of Inelasticity in Dynamically Loaded Ceramics, *J. Hard Mater.*, Vol 3 (No. 3–4), 1992, p 285–313
15. V. Prakash, L.B. Freund, and R.J. Clifton, Stress Wave Radiation from a Crack Tip during Dynamic Initiation, *J. Appl. Mech. (Trans. ASME)*, Vol 59 (No. 2), June 1992, p 356–365
16. A.R. Machcha and S. Nemat-Nasser, Pressure-Shear Recovery Experiments, *Mech. Mater.*, Vol 18, 1994, p 49–53
17. H.D. Espinosa, M. Mello, and Y. Xu, A Desensitized Displacement Interferometer Applied to Impact Recovery Experiments, *J. Appl. Phys. Lett.*, Vol 69 (No. 21), 1996, p 3161–3163
18. H.D. Espinosa, A. Patanella, and Y. Xu, Dynamic Compression-Shear Loading of Brittle Materials with Specimen Recovery, *Proceedings of the 11th Int. Conf. on Experimental Mechanics*, 24–28 Aug 1998 (Oxford, UK), I.M. Allison, Ed., 1998, p 223–229
19. H.D. Espinosa, A. Patanella, and Y. Xu, Dynamic Compression-Shear Response of Brittle Materials with Specimen Recovery, to appear in *Exp. Mech.*, 2000
20. M. Zhou, A. Needleman, and R.J. Clifton, Finite Element Simulations of Shear Localization in Plate Impact, *J. Mech. Phys. Solids*, Vol 42 (No. 3), 1994, p 423–458
21. H.D. Espinosa, On the Dynamic Shear Resistance of Ceramic Composites and its Dependence on Applied Multiaxial Deformation, *Int. J. Solids Struct.*, Vol 32 (No. 21), 1995, p 3105–3128
22. P.D. Zavattieri, P.V. Raghuram, and H.D. Espinosa, A Computational Model of Ceramic Microstructures Subjected to Multi-Axial Dynamic Loading, to appear in *J. Mech. Phys. Solids*, 2000
23. A.R. Machcha and S. Nemat-Nasser, Effects of Geometry in Pressure-Shear and Normal Plate Impact Experiments: Three-Dimensional Finite Element Simulations and Experimental Observations, *J. Appl. Phys.*, Vol 80 (No. 6), 1996, p 3267–3274
24. H.D. Espinosa, Y. Xu, and N.S. Brar, Micromechanics of Failure Waves in Glass: Experiments, *J. Am. Ceram. Soc.*, Vol 80 (No. 8), 1997, p 2061–2073
25. H.D. Espinosa, Y. Xu, and N.S. Brar, Micromechanics of Failure Waves in Glass: Modeling, *J. Am. Ceram. Soc.*, Vol 80 (No. 8), 1997, p 2074–2085
26. H.D. Espinosa, Y. Xu, and H.-C. Lu, Inelastic Behavior of Fiber Composites Subjected to Out-of-Plane High Strain Rate Shearing, *Acta Mater.*, Vol 45 (No. 11), 1997, p 4855–4865
27. H.V. Arrieta and H.D. Espinosa, High and Low Temperature Dynamic Testing of Advanced Materials, *Shock Compression of Condensed Matter*, APS Conference (Snowbird, UT), American Physics Society, 1999
28. H.D. Espinosa, P.D. Zavattieri, and G.L. Emore, Adaptive FEM Computation of Geometric and Material Nonlinearities with Application to Brittle Failure, *Mech. Mater.*, H.D. Espinosa and R.J. Clifton, Ed., Vol 29, 1998, p 275–305
29. H.D. Espinosa, P.D. Zavattieri, and S. Dwivedi, A Finite Deformation Continuum/Discrete Model for the Description of Fragmentation and Damage in Brittle Materials, *J. Mech. Phys. Solids*, Vol 46 (No. 10), 1998, p 1909–1942

30. A.S. Abou-Sayes, R.J. Clifton, and L. Hermann, The Oblique Plate Impact Experiment, *Exp. Mech.*, Vol 16, 1976, p 127–132
31. L.C. Chhabildas and J.W. Swegle, Dynamic Pressure-Shear Loading of Materials Using Anisotropic Crystals, *J. Appl. Phys.*, Vol 51, 1980, p 4799–4807
32. T. Nicholas and S.J. Bless, High Strain Rate Tension Testing, *Mechanical Testing*, Vol 8, *ASM Handbook*, 9th ed., ASM International, 1985, p 208–214
33. W.F. Hartman, Determination of Unloading Behavior of Uniaxially Strained 6061-T Aluminum from Residual Strain Measurements, *J. Appl. Phys.*, Vol 35, 1964, p 2090
34. R. Dandliker and J.-F. Willemin, Measuring Microvibrations by Heterodyne Speckle Interferometry, *Opt. Lett.*, Vol 6, 1981, p 165
35. J.E. Vorthman and G.E. Duvall, Dislocations in Shocked and Recovered LiF, *J. Appl. Phys.*, Vol 53, 1982, p 3607–3615
36. S.-N. Chang, D.-T. Chung, G. Ravichandran, and S. Nemat-Nasser, Plate Impact Experiments on Mg-PSZ and Improved Target Configuration, *Proceedings of 1989 APS Topical Conference on Shock Compression of Condensed Matter*, 14–17 Aug 1989, S.C. Schmidt, J.N. Johnson, and L.W. Davidson, Ed., American Physics Society, 1990, p 389–392
37. S.-N. Chang, D.-T. Chung, Y.F. Li, and S. Nemat-Nasser, Target Configurations for Plate-Impact Recovery Experiments, *J. Appl. Mech.*, Vol 92-APM-18, 1992, p 1–7
38. P. Kumar and R.J. Clifton, A Star-Shaped Flyer for Plate Impact Recovery Experiments, *J. Appl. Phys.*, Vol 48, 1977b, p 4850
39. R.J. Clifton, G. Raiser, M. Ortiz, and H.D. Espinosa, A Soft Recovery Experiment for Ceramics, *Proceedings of 1989 APS Conference on Shock Compression of Condensed Matter*, American Physics Society, 1990, p 437–440
40. S. Nemat-Nasser, J.B. Isaacs, G. Ravichandran, and J.E. Starrett, High Strain Rate Testing in the U.S., *Proceedings of the TTCP TTP-1 Workshop on New Techniques of Small Scale High Strain Rate Studies*, 26 April 1988 (Melbourne, Australia)
41. H.D. Espinosa, Micromechanics of the Dynamic Response of Ceramics and Ceramic Composites, Ph.D. thesis, Brown University, Providence, RI, 1992
42. K.J. Frutschy and R.J. Clifton, High-Temperature Pressure-Shear Plate Impact Experiments on OFHC Copper, *J. Mech. Phys. Solids*, Vol 46 (No. 10), 1998, p 1723–1743
43. K.J. Frutschy and R.J. Clifton, High-Temperature Pressure-Shear Plate Impact Experiments Using Pure Tungsten Carbide Impactors, *Exp. Mech.*, Vol 38 (No. 2), 1998, p 116–125
44. H.V. Arrieta and H.D. Espinosa, The Role of Thermal Activation on Dynamic Stress Induced Inelasticity and Damage in Ti-6Al-4V, submitted to *Mech. Mater.*, 2000
45. N.S. Brar and S.J. Bless, Failure Waves in Glass under Dynamic Compression, *High Pressure Res.*, Vol 10, 1992, p 773–784
46. D. Grady and J.L. Wise, “Dynamic Properties of Ceramic Materials,” Sandia Report SAND93-0610, Sandia National Laboratories, 1993

Low-Velocity Impact Testing

Horacio Dante Espinosa, Northwestern University, Sia Nemat-Nasser, University of California, San Diego

Plate Impact Facility

Gas Gun. The low-velocity impact experiments are generally performed in single-stage gas guns that are capable of firing projectiles of complex shapes as well as various materials and weights at limited velocities. Plate impact experiments discussed in this section were carried out on single-stage light-gas guns capable of projectile velocities from a few tens of meters per second to 1200 m/s (3940 ft/s).

A light gas gun facility generally has four interconnected parts: a pressure chamber or breech, a gun barrel, a target chamber, and a catcher tank (Fig. 1). Different types of breeches have been used. The most common is a wraparound breech, which employs no moving parts under pressure except the projectile itself as a fast-opening valve. The projectile back piston, which closes the breech, is designed to withstand the gas pressure. The breech holds gas at pressures between 1.4 and 20.7 MPa (200 and 3000 psi) to accelerate the projectile through the gun barrel and into the target chamber. The gun barrel diameter and length may be different, depending on the design. Examples include:

- 76.2 mm (3 in.) diameter and 6.09 m (20 ft) long gun with velocities in the range of 50 to 1000 m/s (165 to 3280 ft/s)
- 60 mm (2.4 in.) diameter and 1.2 m (3.9 ft) long gun with moderate velocities up to 200 m/s (660 ft/s)
- 56 mm (2.2 in.) diameter and 10 m (33 ft) long high-velocity gun with velocities up to 1200 m/s (3940 ft/s)
- 152 mm (6 in.) diameter and 5 m (16.4 ft) long gun with moderate velocities up to 400 m/s (1300 ft/s)
- 25 mm (1 in.) diameter and 5 m (16.4 ft) long gun with velocities up to 1200 m/s (3940 ft/s)

The inner surface of the barrel is honed to an almost mirror polish to reduce friction. To prevent projectile rotation, either a keyway is machined along the barrel, or the barrel is lightly broached. The target chamber is equipped with a special mounting system to hold the target assembly at normal or oblique angles. This system may allow remote rotation of the target, in any direction, to preserve the alignment upon target heating/cooling or simply prior to firing. The chamber and gun barrel are evacuated using a vacuum pump to a pressure of approximately 50 mtorr. Among other things, this prevents the formation of an air cushion between the target and flyer at impact. To avoid overpressure in the target chamber, after gas expansion, an exhaust system to ambient air may have to be implemented if the volume of the target chamber and the catcher tank is not adequate. The target and specimen leave the vacuum chamber through a rear port. A catcher tank filled with cotton rugs is used to decelerate and recover the projectile and target.

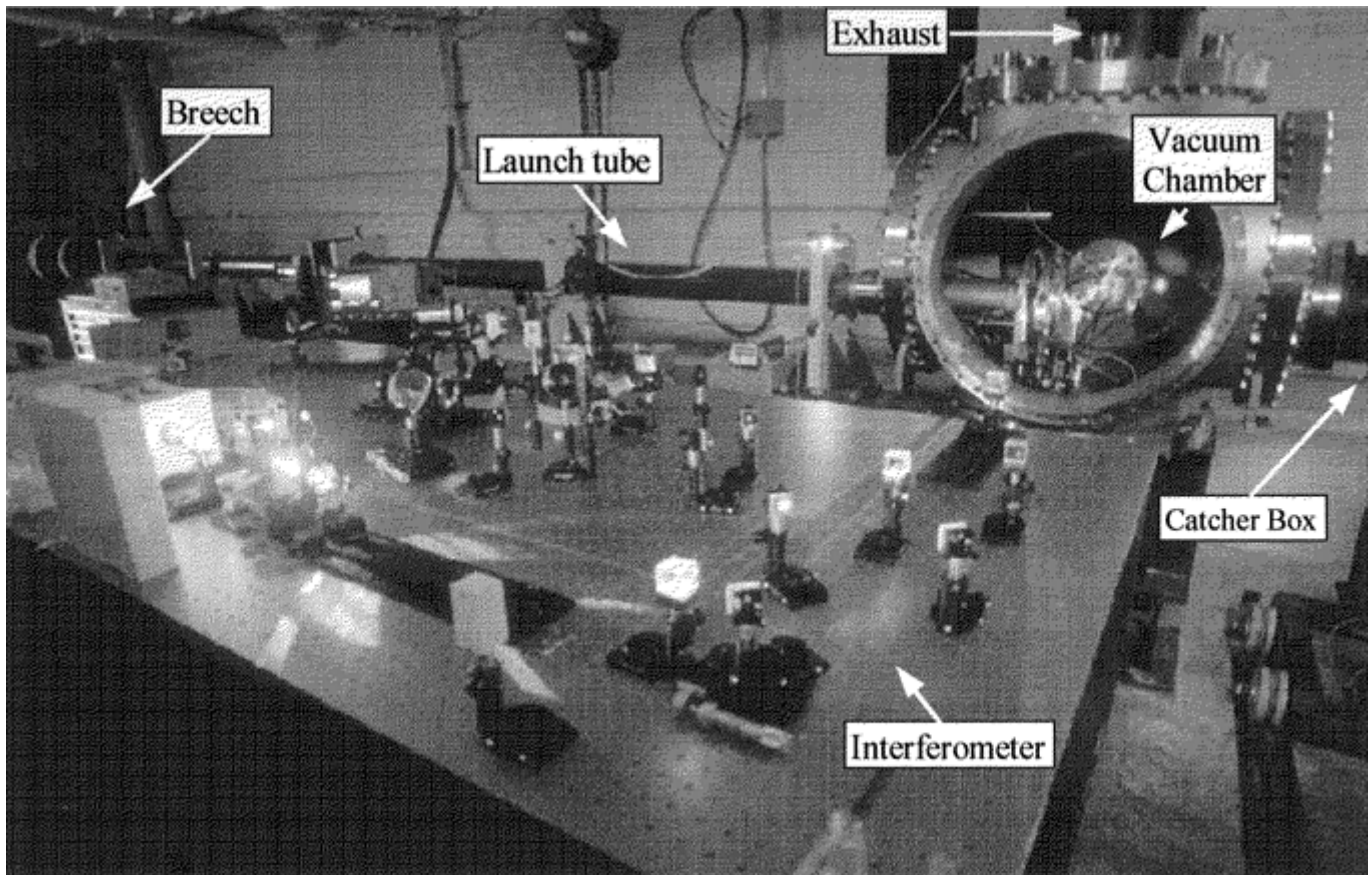


Fig. 1 Gas gun facility for low-velocity impact testing

Projectile. The projectile used for these experiments consists of a fiberglass tube, usually about 25 cm (10 in.) in length, with an aluminum back piston on the rear end and a polyvinyl chloride (PVC) holder on the front. The flyer plate or rod is glued to the PVC holder, which has a machined cavity. The fiberglass tube is centerless ground so that it slides smoothly in the gun barrel. A set of two holes in the fiberglass tube ensures that the pressure inside the projectile remains essentially the same as that on the outside. This prevents unwanted deformation of the projectile when the system is under vacuum. The aluminum back piston is screwed or glued to the fiberglass tube for high and low velocities, respectively. It holds a sealing set of two O-rings to withstand the breech pressure. A plastic key fitting the barrel keyway is placed in a slot machined on the wall of the fiberglass tube. The PVC holder carries the flyer backed by foam material to achieve wave release. All the pieces are glued together with five min epoxy.

Velocity Measurements. The velocity of the projectile just prior to impact is measured by means of a method that is similar to the one described in Ref 47. Ten pins of constantan wire, less than 0.1 mm (0.004 in.) in diameter, are positioned in pairs at the exit of the gun barrel. The pins are connected to an electronic box in which output, recorded in an oscilloscope, consists of steps every time a pair of pins closes the circuit. The PVC holder is coated with a silver paint to achieve conductivity between pins. The distance between the positive pins is measured with a traveling microscope with a resolution of 1 μm or better. When this distance is divided by the time between steps, as recorded in the oscilloscope, an average velocity is obtained. The accuracy of the system is better than 1%.

The motion of the target or anvil velocity is measured by interferometric techniques (Ref 48, 49, 50, and 51). In the case of low-velocity experiments, the variable sensitivity displacement interferometer (VSDI) is employed (Ref 52). Alternatively, for high- and low-temperature planar impact tests, an air-delay-leg normal velocity interferometer for any reflecting surface (ADL-VISAR) is used. In both cases, disposable mirrors are positioned at a certain distance from the rear surface of the specimen to allow illumination and interrogation of the target back surface. A side window on the target chamber provides access to the laser beam of the interferometer. Two digital oscilloscopes record the interferometer traces and velocity/tilt signals. Maximum sample rate, up to 4 million samples per second, 1 GHz bandwidth and 8 MB of memory may be used. The oscilloscopes are employed at full bandwidth and with a sample rate of 1 million samples per second or higher.

Tilt Measurement. The tilt during impact is measured by means of four contact pins placed on the surface of the target (Ref 1). When the target or the anvil plate can be drilled, four self-insulated metallic pins lapped flush with the front surface of the target/anvil plate are positioned in the periphery. When these pins are grounded by the flyer, a staircase signal is recorded on the oscilloscope at a ratio of 1 to 2 to 4 to 8. The tilt can be estimated by fitting a plane through the tilt pins by a least-square analysis. When the previous technique cannot be used, a special shape-conductive coating can be applied, using a mask, to the target impact surface and the same principle applied (Ref 7, 11). In some cases, such as in high-temperature testing, neither of the previous approaches is feasible, and tilt cannot be measured without major modifications.

High-and Low-Temperature Facilities. A high-temperature facility consists of an induction heating system and a heat exchanger for cooling the device and the coil around the specimen. A schematic of the high-temperature target assembly is shown in Fig. 2. This type of system is capable of delivering 25 kW of constant power at high frequency (0.5 MHz). Temperatures up to 1200 °C (2200 °F) in metallic and ceramic materials have been achieved in calibration tests. A photograph of the target chamber and high-temperature setup is shown in Fig. 3. The temperature is externally monitored by a K-type thermocouple glued close to the back face of the sample. An electronic control is employed to regulate the temperature. The system adjusts the heating ramp to minimize thermal shock and deformation in the specimen.

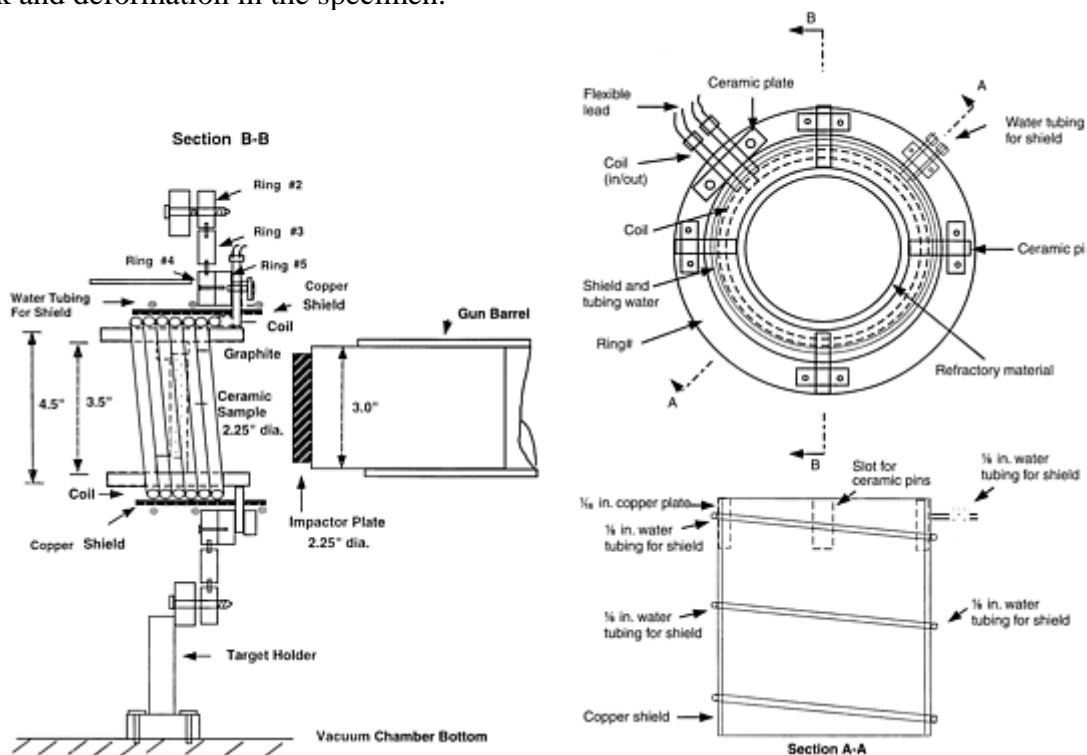


Fig. 2 Target assembly for high-temperature, low-velocity impact tests. Dimensions in inches. Source: Ref 44

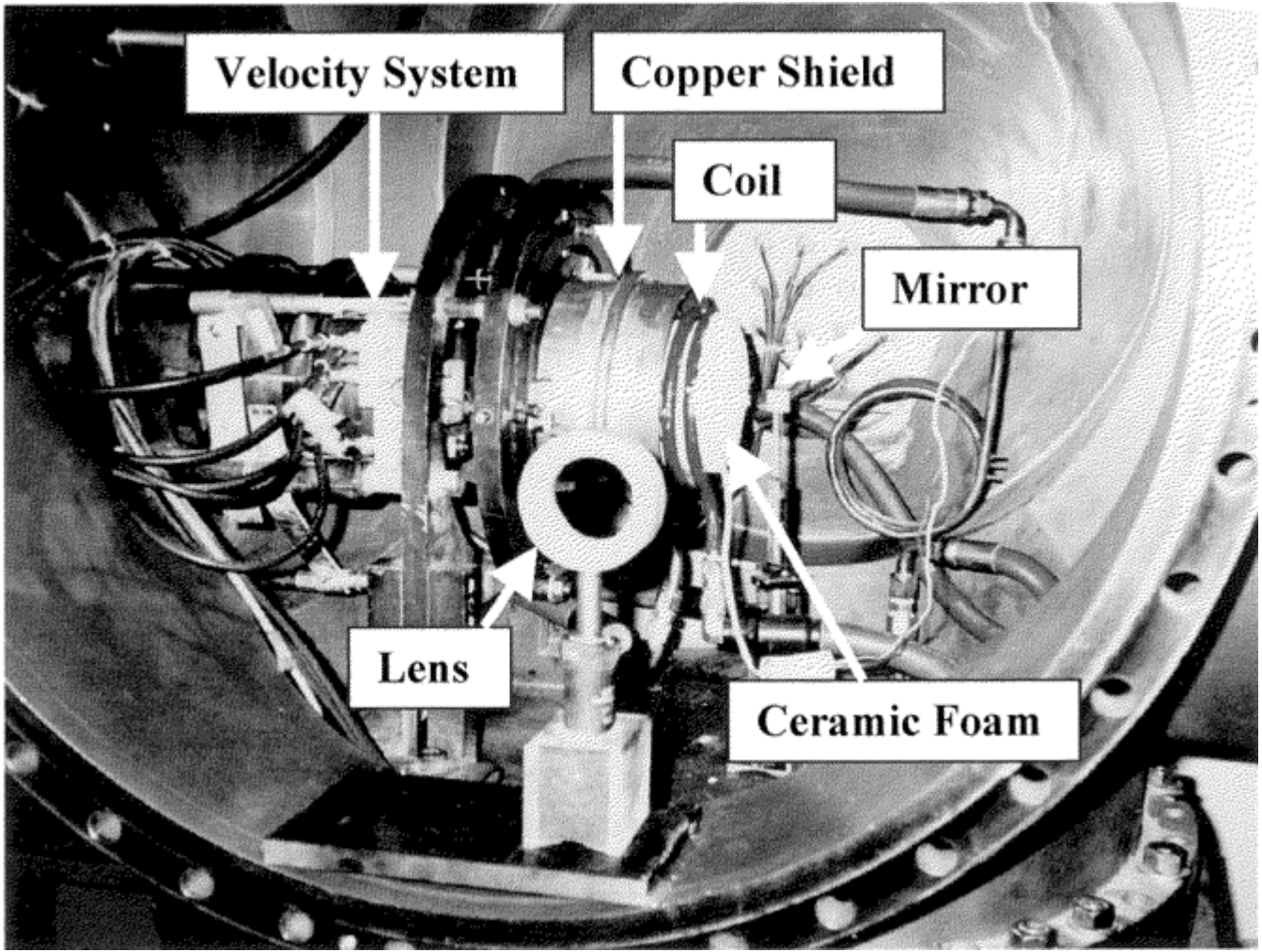


Fig. 3 Gas gun vacuum chamber with high-temperature setup. Source: Ref 44

The induction copper coil is mounted in the mentioned target holder and connected to the heating system by means of a specially designed feedthrough. The coil is made from copper tubing. The copper section conducts the high-frequency electrical energy, whereas the inner core carries refrigeration water. The intense electromagnetic field inside the coil induces parasite currents in the magnetic target. A graphite susceptor holder is employed to position the target and heat nonconductive materials. Ceramic foam is placed between the sample and the copper coil to confine heat to the sample. A copper tube is connected to a water line to keep its temperature low and shield electromagnetic radiation. This shield is attached to the alignment rings, which support the whole target assembly.

For low-temperature testing, a cooling ring with liquid nitrogen circulating through an inner channel is used to reduce the temperature of the samples down to $-150\text{ }^{\circ}\text{C}$ ($-238\text{ }^{\circ}\text{F}$). The ring consists of two pieces of aluminum machined to fit together with special seals for low temperature to make the holder leak proof. Appropriated stainless steel hoses are used to drive liquid nitrogen from an external reservoir tank. The sample is kept in place inside the cooling ring by means of a disposable aluminum ring and polymethyl methacrylate (PMMA) pins. The liquid nitrogen is provided by a 175 kPa (25 psi) external tank. Once the heat exchange has taken place, the nitrogen in gaseous state is bled from the vacuum chamber. The temperature is monitored by means of a type J thermocouple glued to the rear surface of the specimen (Ref 27).

References cited in this section

1. P. Kumar and R.J. Clifton, Dislocation Motion and Generation in LiF Single Crystals Subjected to Plate-Impact, *J. Appl. Phys.*, Vol 50 (No. 7), 1979, p 4747–4762

7. H.D. Espinosa and R.J. Clifton, Plate Impact Experiments for Investigating Inelastic Deformation and Damage of Advanced Materials, *Symposium on Experiments in Micromechanics of Fracture-Resistant Materials* (ASME Winter Annual Meeting), 1–6 Dec 1991 (Atlanta, GA), K.S. Kim, Ed., 1991, p 37–56
11. G. Raiser, R.J. Clifton, and M. Ortiz, A Soft-Recovery Plate Impact Experiment for Studying Microcracking in Ceramics, *Mech. Mater.*, Vol 10, 1990, p 43–58
27. H.V. Arrieta and H.D. Espinosa, High and Low Temperature Dynamic Testing of Advanced Materials, *Shock Compression of Condensed Matter*, APS Conference (Snowbird, UT), American Physics Society, 1999
44. H.V. Arrieta and H.D. Espinosa, The Role of Thermal Activation on Dynamic Stress Induced Inelasticity and Damage in Ti-6Al-4V, submitted to *Mech. Mater.*, 2000
47. G.R. Fowles, Gas Gun for Impact Studies, *Rev. Sci. Instrum.*, Vol 41, 1970, p 984
48. L.M. Barker and R.E. Hollenbach, Interferometer Technique for Measuring the Dynamic Mechanical Properties of Materials, *Rev. Sci. Instrum.*, Vol 36 (No. 11), 1965, p 1617–1620
49. L.M. Barker and R.E. Hollenbach, Laser Interferometry for Measuring High Velocities of Any Reflecting Surface, *J. Appl. Phys.*, Vol 43 (No. 11), 1972, p 4669–4675
50. K.S. Kim, R.J. Clifton, and P. Kumar, A Combined Normal and Transverse Displacement Interferometer with an Application to Impact of Y-Cut Quartz, *J. Appl. Phys.*, Vol 48, 1977, p 4132–4139
51. L.C. Chhabildas, H.J. Sutherland, and J.R. Asay, Velocity Interferometer Technique to Determine Shear-Wave Particle Velocity in Shock-Loaded Solids, *J. Appl. Phys.*, Vol 50, 1979, p 5196–5201
52. H.D. Espinosa, M. Mello, and Y.Xu, A Variable Sensitivity Displacement Interferometer with Application to Wave Propagation Experiments, *J. Appl. Mech.*, Vol 64, 1997, p 123–131

Low-Velocity Impact Testing

Horacio Dante Espinosa, Northwestern University, Sia Nemat-Nasser, University of California, San Diego

Specimen Preparation and Alignment

To generate plane waves at impact and upon reflection off interfaces, the faces of the flyer and specimen plates must be flat. The flyer plate and specimen are lapped flat (using, e.g., 15 μm alumina abrasive first, and then 6 μm diamond abrasive). The accepted flatness of these surfaces is around 1.5 to 2 wavelengths of green light ($\lambda = 550 \text{ nm}$). This is measured by counting the number of interference fringes (Newton's rings) formed between the polished surface and an optical flat. The procedure is continued until only two fringes are visible over the whole surface. The rear surface of the target plate is polished using 1 μm and $\frac{1}{4}\mu\text{m}$ diamond abrasive to obtain a reflective surface for interferometric purposes. For a pressure-shear recovery experiment, the surfaces corresponding to the solid or liquid lubricant interface are highly polished. All other surfaces are roughened by lapping with 15 μm diamond paste. This is to ensure sufficient surface roughness to transfer the shear loading by dry friction. The specimen is cleaned ultrasonically in ethyl alcohol. The polished surface is wiped clean with acetone and ethyl alcohol, in that order, and stored. The final surface is often scanned using a profilometer.

When certain materials are tested at high temperatures, oxide thin films may form, which can reduce reflectivity significantly. For instance, Ti-6Al-4V surfaces oxidize very fast. Thin layers of oxide form at temperatures between 315 and 650 °C (600 and 1200 °F). The film is barely perceptible, but with increasing temperature and time, it becomes thicker and darker, acquiring a straw-yellow color at about 370 °C (700 °F) and dark blue at 480 °C (900 °F). Temperatures high enough to produce oxidation may be reached even under a vacuum of less than 50 mtorr. This oxide layer reduces the reflectivity of the titanium surface, making it difficult to obtain a good interferometric signal. To overcome this difficulty in Ti-6Al-4V, a platinum coating (0.1 μm thick) has been applied to the back surface of the specimen. A pre-etching of the surface guarantees a good adhesion of the coating. Platinum is stable at high temperature; however, due to mismatch in coefficients of thermal expansion, debonding may occur if the surface temperature of the specimen is increased too fast. Therefore, the induction heating power must be controlled at all times with a feedback loop and coating materials selected to match the target thermal properties.

The plate dimensions are selected such that at the center of the specimen, a unidimensional strain state is kept for a few microseconds before release waves from the periphery arrive to the observation point(s). These dimensions are a function of the type of experiment and configuration and are therefore discussed separately.

The plates are optically aligned at room temperature using the technique described in Ref 1. For this technique, the projectile is advanced to a position near the target, and a specially coated precision prism is placed between the two surfaces to be impacted. An autocollimator is used to first align the prism to the flyer and then the specimen to the prism. In this way, the surfaces of the flyer and the specimen are aligned with an accuracy of 0.02 milliradians. After alignment, the projectile is pulled back to the other end of the launch tube. To preserve target alignment, especially in the case of high- and low-temperature experiments, the position of a collimated laser beam, reflected from the rear surface of the target plate, is monitored on a stationary screen roughly 12 m (40 ft) away. A target plate tilt of 1 milliradian results in a beam translation of 1.2 cm (0.47 in.) on this screen. This remote beam system allows monitoring of the tilt along the vacuum process and during the heating or cooling of the sample. Remote mechanical controls attached to the target holder screws are employed to drive the target back to its original position, thereby ensuring that the target and the flyer plates maintain their original room-temperature alignment. The quality of the interferometric signals is usually an indication of the parallelism at impact.

Reference cited in this section

1. P. Kumar and R.J. Clifton, Dislocation Motion and Generation in LiF Single Crystals Subjected to Plate-Impact, *J. Appl. Phys.*, Vol 50 (No. 7), 1979, p 4747–4762

Low-Velocity Impact Testing

Horacio Dante Espinosa, Northwestern University, Sia Nemat-Nasser, University of California, San Diego

Surface Velocity Measurements with Laser Interferometric Techniques

Barker and Hollenbach (Ref 48) developed a normal velocity interferometer (NVI), where normally reflected laser light from a target plate was collected and split into two separate beams, which are subsequently interfered after traveling through different path lengths. The sensitivity of the interferometer is a function of the delay time between the interfering beams. The resulting fringe signal is related directly to changes in the normal particle velocity. Barker and Hollenbach (Ref 49) then introduced a significantly improved NVI system termed a velocity interferometer for any reflecting surface (VISAR), developed based on the wide-angle Michelson interferometer (WAM) concept, resulting in an interferometer capable of velocity measurements from either a spectrally or diffusely reflecting specimen surface. Another improvement incorporated into the VISAR was the simultaneous monitoring of two fringe signals 90° out of phase. In most VISAR systems, three signals are recorded—the two quadrature optical signals obtained from horizontally and vertically polarized components of

light that differ in phase because of the retardation plate and the intensity-monitoring signal used in data reduction. However, higher signal-to-noise ratios can be obtained by subtracting the two s-polarized beams and the two p-polarized beams, both pairs 180° out of phase (Ref 53). This feature, known as *push-pull*, significantly reduces the noise introduced by incoherent light entering the interferometer.

Another laser interferometer to emerge in the 1970s was the laser Doppler velocimeter (LDV) developed by Sullivan and Ezekiel (Ref 54). The LDV can be used to monitor in-plane motion but does not lend itself to the simultaneous monitoring of normal motion. The need to measure both normal and in-plane displacements prompted the development of the transverse displacement interferometer (TDI) by Kim et al. (Ref 50). The TDI takes advantage of diffracted laser beams generated by a grating deposited or etched onto the specimen rear surface. In this technique, the 0th order reflected beam is used to monitor longitudinal motion in a conventional way, for example, by means of an NVI or normal displacement interferometer (NDI), while any pair of n th order symmetrically diffracted beams is interfered to obtain a direct measure of the transverse particle displacement history. The sensitivity of the TDI is given by $\frac{1}{2\sigma} n$ (mm/fringe) where σ is the grating frequency and n represents the order of the interfering diffracted beams.

Chhabildas et al. (Ref 55) presented an alternative interferometric technique particularly suited for monitoring in-plane particle velocities in shock wave experiments. The technique employs two VISARs that monitor specific diffracted laser beams from a target surface.

Both techniques, the two-VISAR and the NDI-TDI, have advantages and disadvantages. The combined NDI-TDI system has a much better resolution at low velocities but requires the deposition of grids on the free surface of the target plate. On the other hand, the two-VISAR technique provides velocity profiles directly without the need to differentiate displacement profiles. Although the two-VISAR technique is simpler to use when optical window plates are needed, it was shown that a combined NVI-TDI with window interferometer is feasible (Ref 56).

The relatively small range of velocities that can be measured by the NDI motivated the development of the NVI. The sensitivity of the NDI is given by $\lambda/2$ (mm/fringe) where λ represents the laser light wavelength. The extreme sensitivity of this interferometer severely limits its application in wave propagation experiments due to the inordinately high signal frequencies that may be generated. An NVI or a VISAR, on the other hand, has a variable sensitivity given by $\lambda/[2\tau + (1 + \delta)]$ (mm/ μ s/fringe), where τ represents a time delay between the interfering light beams introduced by an air-delay leg or etalon in the interferometer. The factor $(1 + \delta)$ is a correction term to account for the refractive index of the etalon. An appealing feature of this interferometer is that the fringe record is a direct measure of particle velocity, thereby alleviating the need for differentiation of the reduced signal. Moreover, signal frequencies generated by an NVI are proportional to particle acceleration and are, therefore, lower than equivalent signal frequencies generated by an NDI. However, during an initial time period τ , an NVI is functioning as an NDI since the delayed light arriving at the detector from the delay leg or etalon is reflected from a stationary target (Ref 57). Ironically, it is the interpretation of the NVI in the interval where it operates as an NDI that limits the usefulness of the NVI in the low-velocity range (0.1–0.25 mm/ μ s). In this velocity range, values of τ in the neighborhood of 5 ns or more are required to obtain records with at least three or four fringes. This in turn leads to a greater averaging of the velocity measurements. Furthermore, elastic precursors causing velocity jumps of more than 0.1 mm/ μ s in a time less than τ cannot be detected because the early time NDI signal frequency may exceed the frequency response of the light-detection system. This feature is described as *lost fringes* in Ref 58.

Clearly, the NDI and VISAR principles described here indicate that there is a velocity range between 0.1 and 0.25 mm/ μ s over which particle velocities may not be measured with the desired accuracy. Barker and Hollenbach (Ref 49) investigated the accuracy of the VISAR experimentally. They found that measurements with 2% accuracy could be obtained when a delay time of approximately 1 ns corresponding to a velocity per fringe constant equal to 0.2 mm/ μ s is used. Certainly, velocities below 0.2 mm/ μ s can be measured, but the uncertainty of the measurement increases because only a fraction of a fringe is recorded. In this case, signals in quadrature have to be recorded immediately before the experiment and assume the amplitude remains the same during the experiment (Ref 59). It should be pointed out that the VISAR data reduction is very sensitive to the position and shape of the Lissajous (Ref 59). Despite these minor subtleties, the VISAR is currently the more versatile and easy-to-set-up interferometer. Many laboratories around the world have adopted the VISAR as a routine tool for particle velocity measurement in normal impact experiments. Typically, delay times between 1 and 1.5 ns are employed. In this working range, the VISAR possesses a very high accuracy and sensitivity.

A common feature of all interferometers discussed in this section is that successful signal acquisition requires good fringe contrast during the time of the experiment. Contrast losses arise from two main causes, interferometer imperfections and target motion (displacement and tilt). These losses can be, in general, time varying. For instance, a beam splitter that does not split light equally will produce a constant loss of contrast, while unevenly curved surfaces will produce a variable contrast change as a function of the light path in the interferometer. Target rotations that change the light path can be very detrimental to most interferometers. In this respect, interferometers that use scatter light from the target and fiber optics to transfer the laser light will minimize the loss in fringe contrast because the light path in the interferometer is fixed. Furthermore, even target rotations of a few milliradians will not result in signal loss in such systems. By contrast, standard interferometer setups, without fiber optics, require tilts smaller than 1 milliradian to avoid a change in the light path that can offset the beam from the optical components of the interferometer. This feature is particularly relevant in two- and three-dimensional wave propagation problems (e.g., penetration experiments, in which significant surface rotations are expected at diagnostic points). In the early 1990s, Barker developed a VISAR with these features (Ref 58). In 1998, the same company introduced a multipoint fiber optics VISAR to the market.

Espinosa et al. (Ref 52) introduced a variable sensitivity displacement interferometer (VSDI) to provide an alternative to the NDI, as well as to VISAR interferometers as applied to plate impact experiments, particularly when normal and in-plane velocity measurements need to be recorded simultaneously in the range of 50 to 250 m/s (165 to 820 ft/s). The sensitivity of such an interferometer is variable, and thus, it can operate over a wide range of particle velocities without exceeding the frequency response of the light-detection system. The VSDI interferometer is discussed in more detail subsequently.

Variable Sensitivity Displacement Interferometer (VSDI) Theory. To examine the results of this method, consider the effect of interfering a normally reflected beam with a beam diffracted at an angle θ with respect to the specimen normal as shown in Fig. 4. The normally reflected beam is split at beam splitter BS1. Each half of the normal beam is then made to interfere with one of the diffracted beams via beam splitters BS2 and BS3. The resulting signals generated by each interfering beam pair are monitored by photodetectors. The combined field for either pair of interfering plane waves leads to a classical interference expression, from which the following result is deduced (Ref 52).

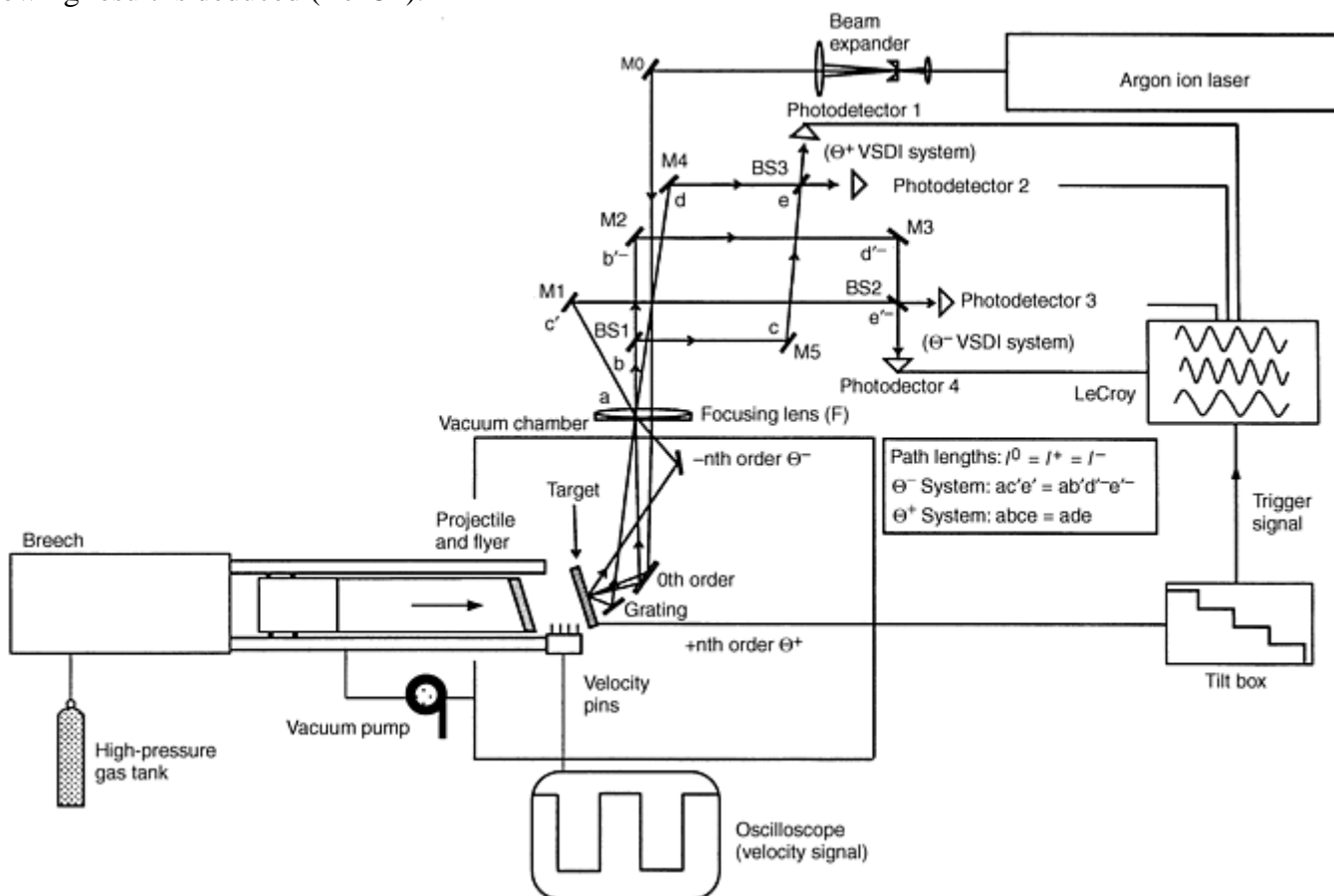


Fig. 4 Optical layout of a variable sensitivity displacement interferometer (VSDI) system. The Θ^\pm system is obtained by combining a normally reflected beam and a diffracted beam at an angle Θ^\pm . In this figure, mirrors M0-M5 and beam splitters BS1-BS3 are used to obtain the VSDI systems. The lens with focal length F is used to focus the beam at the grating plane in the anvil back surface. Source: Ref 52

For *purely normal motion* (desensitized normal displacement interferometer, DNDI):

$$\frac{\text{normal displacement}}{\text{fringe}} = \frac{\lambda}{1 - \cos \theta} = \frac{\lambda}{1 - \sqrt{1 - (n\lambda\sigma)^2}}$$

where $\sigma = 1/d$ represents the frequency of a diffraction grating with pitch d . The fringe constant varies from infinity at $\theta = 0^\circ$ to λ (mm/fringe) at $\theta = 90^\circ$. Therefore, a VSDI is obtained that is particularly well suited for normal plate impact experiments with particle velocities in excess of 100 m/s (330 ft/s). Clearly, the selection of the appropriate angle θ should be based on deductive knowledge of the frequency range that will be spanned. For *purely in-plane motion* (desensitized transverse displacement interferometer, DTDI):

$$\frac{\text{transverse displacement}}{\text{fringe}} = \frac{\lambda}{\sin \theta} = \frac{1}{\sigma n}$$

The DTDI sensitivity ranges from a complete loss of sensitivity at $\theta = 0^\circ$ to a theoretical sensitivity limit of λ (mm/fringe) at $\theta = 90^\circ$. The interferometer is “desensitized” in the sense that, for the same diffraction orders, it exhibits one-half the sensitivity of the transverse displacement interferometer (TDI) (Ref 50).

For *combined normal and in-plane motions* (VSDI system):

$$\frac{\text{normal displacement}}{\text{fringe}} = \frac{\lambda}{2(1 - \cos \theta)}$$

$$\frac{\text{transverse displacement}}{\text{fringe}} = \frac{\lambda}{2 \sin \theta}$$

This last sensitivity is the same as the one exhibited by the TDI (Ref 50). It should also be noted that the normal displacement sensitivity is twice the sensitivity obtained by a single VSDI system in the case of pure normal motion principally because the signal obtained by the addition of two VSDI systems exhibits a double recording of the normal displacement.

References cited in this section

48. L.M. Barker and R.E. Hollenbach, Interferometer Technique for Measuring the Dynamic Mechanical Properties of Materials, *Rev. Sci. Instrum.*, Vol 36 (No. 11), 1965, p 1617–1620
49. L.M. Barker and R.E. Hollenbach, Laser Interferometry for Measuring High Velocities of Any Reflecting Surface, *J. Appl. Phys.*, Vol 43 (No. 11), 1972, p 4669–4675
50. K.S. Kim, R.J. Clifton, and P. Kumar, A Combined Normal and Transverse Displacement Interferometer with an Application to Impact of Y-Cut Quartz, *J. Appl. Phys.*, Vol 48, 1977, p 4132–4139
52. H.D. Espinosa, M. Mello, and Y.Xu, A Variable Sensitivity Displacement Interferometer with Application to Wave Propagation Experiments, *J. Appl. Mech.*, Vol 64, 1997, p 123–131
53. W.F. Hemsing, Velocity Sensing Interferometer (VISAR) Modification, *Rev. Sci. Instrum.*, Vol 50 (No. 1), 1979, p 73–78
54. J.P. Sullivan and S. Ezekiel, A Two-Component Laser Doppler Velocimeter for Periodic Flow Fields, *J. Phys.*, Vol E7, 1974, p 272–274

55. L.C. Chhabildas, H.J. Sutherland, and J.R. Asay, A Velocity Interferometer Technique to Determine Shear-Wave Particle Velocity in Shock-Loaded Solids, *J. Appl. Phys.*, Vol 50 (No. 8), 1979, p 5196–5201
56. H.D. Espinosa, Dynamic Compression Shear Loading with In-Material Interferometric Measurements, *Rev. Sci. Instrum.*, Vol 67 (No. 11), 1996, p 3931–3939
57. R.J. Clifton, Analysis of the Laser Velocity Interferometer, *J. Appl. Phys.*, Vol 41 (No. 13), 1970, p 5335–5337
58. Valyn VISAR, *User's Handbook*, Valyn International, Albuquerque, NM, 1995
59. Valyn VISAR Data Reduction Program, *User's Handbook*, Valyn International, Albuquerque, NM, 1995

Low-Velocity Impact Testing

Horacio Dante Espinosa, Northwestern University, Sia Nemat-Nasser, University of California, San Diego

Plate Impact Soft-Recovery Experiments

Normal and pressure-shear plate impact soft-recovery experiments (Ref 16, 17, and 18) offer attractive possibilities for identifying the principal mechanisms of inelasticity under dynamic tension and compression, with and without an accompanying shearing. The samples are recovered, allowing their study by means of microscopic characterization. This feature, together with the real-time stress histories, may be used to assess the validity of constitutive models (Ref 8, 14, 20, 21, 22, 29, and 60). This kind of experiment on brittle materials provides information on the onset of elastic precursor decay, spall strength, and material softening due to microcracking.

A plate impact experiment involves the impact of a moving flat plate, called a *flyer*, with another stationary plate, called the *target*, which may be the specimen. In the normal plate impact experiment, the specimen is subjected to a compression pulse, and the material at the center of the specimen is under a strictly uniaxial strain condition. In the pressure-shear experiment, the specimen undergoes a combined compression and shearing. Thus, the material undergoes a transverse shearing while it is in a compressed condition. The wave propagation is one dimensional, since both the pressure and shear pulses travel along the same axis.

The recovery configuration in the normal impact mode employs a backing plate for the target to capture the longitudinal momentum. In the pressure-shear recovery mode (Ref 16, 17, 18, 19, and 52) two flyer plates that are separated by a thin lubricant layer (which is a thin film of minimal shearing resistance and very high bulk modulus) are used along with the backing plate to capture the longitudinal and shear momenta. A liquid lubricant was used by Machcha and Nemat-Nasser (Ref 16), while a solid lubricant (photoresist AZ 1350J-from Hoechst Celanese) was used by Espinosa and coworkers (Ref 17, 18, 19, and 52). In practice, the amount of the trapped shear momentum depends on the shear properties of the lubricant thin film. All plates have to be reasonably impedance matched to obtain good results. Good discussions of the requirements for normal recovery can be found in Ref 7, 11, and 38. Figure 5 shows the configuration of the plates and the time-distance, t - X , diagram for the normal impact recovery experiment (Ref 1, 7, 11). Figures 6 and 7 show the experimental layouts and t - X diagrams for the high-strain-rate (Ref 17, 18, and 19) and wave propagation (Ref 16, 18, and 19) pressure-shear recovery experiments, respectively.

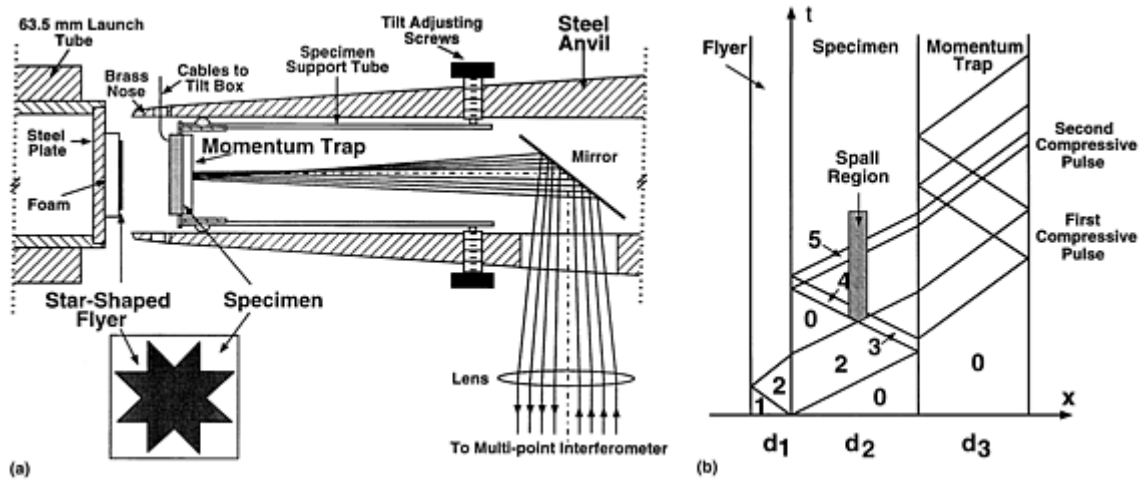


Fig. 5 Soft-recovery, normal impact testing. (a) Test configuration. (b) Lagrangian time-distance (t - X) diagram for soft recovery experiment. Source: Ref 7

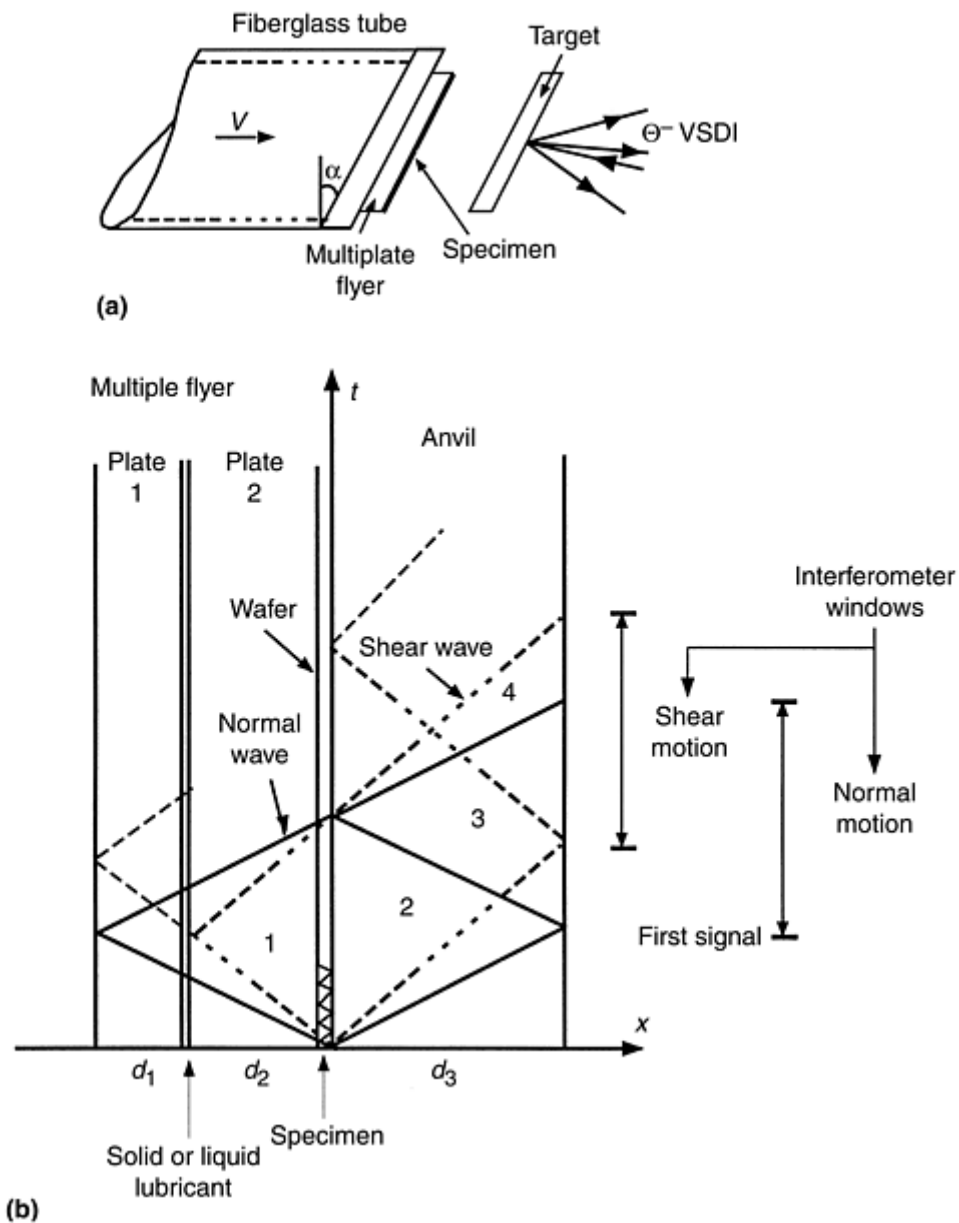


Fig. 6 Pressure-shear high-strain-rate testing. (a) Test configuration. (b) Lagrangian t - X diagram for pressure-shear high-strain-rate recovery experiment. Source: Ref 18, 19

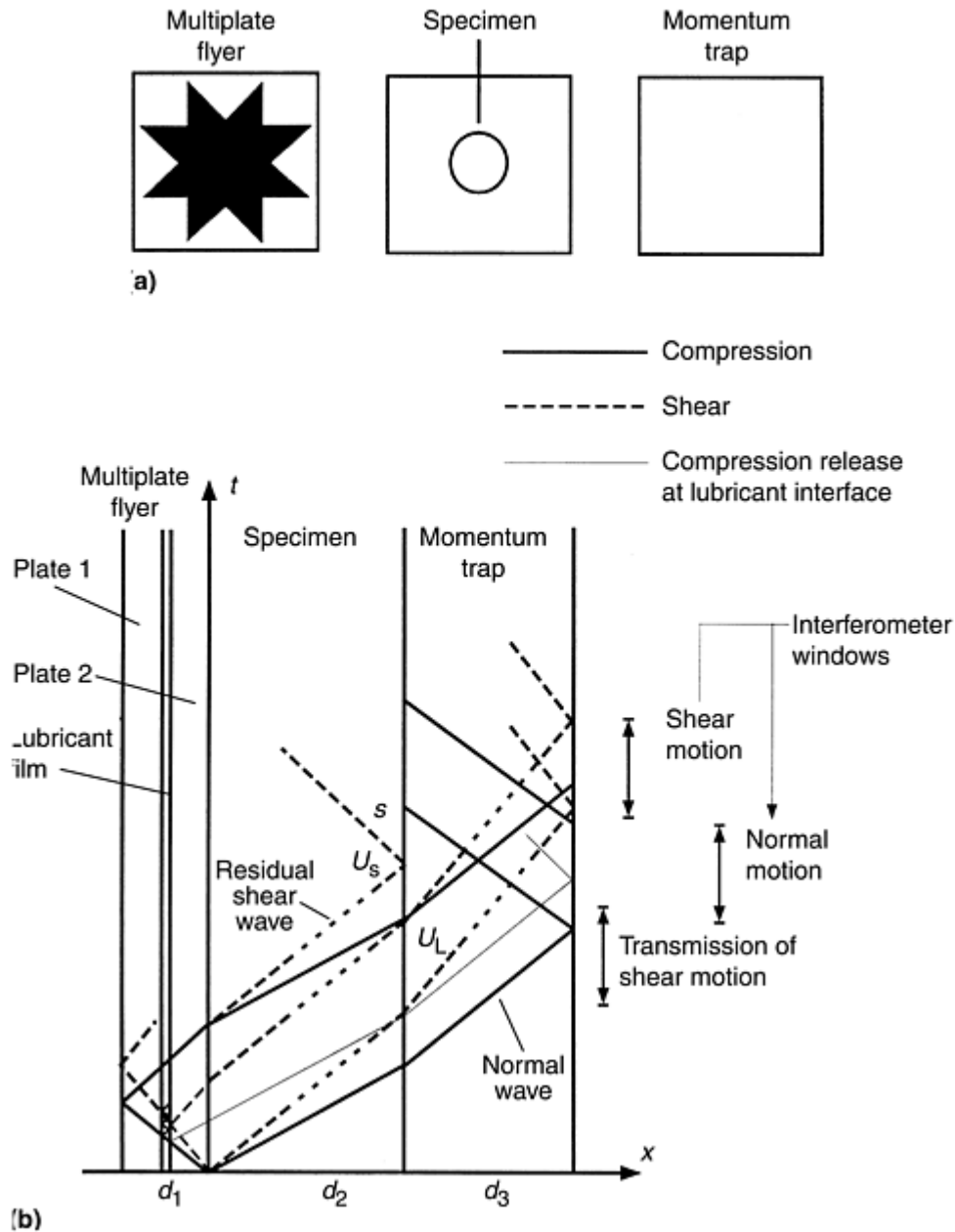


Fig. 7 Pressure-shear wave propagation testing. (a) Test configuration. (b) Lagrangian t - X diagram for pressure-shear wave propagation recovery experiment. Source: Ref 18, 19

To reduce the boundary release wave effects, guard rings and confining fixtures have been used around the circumference of the sample (Ref 33, 36, and 37). This requires close tolerances in machining, making the specimen preparation and assembly difficult. A better approach was proposed by Kumar and Clifton (Ref 38), who made use of a star geometry for the flyer to redirect the release waves and decrease their damaging effect at the center. This approach was implemented in experimental studies by a number of researchers (Ref 11, 13, 14, 35, 37, 61, and 62). Three-dimensional simulations on different configurations have also been conducted by many authors (Ref 13, 36, 63, and 64) for the normal impact configuration, leading to several recommendations to improve this configuration. Experimental evidence shows that it is difficult to recover brittle specimens intact, even at moderate stresses of about 2.0 GPa (290 ksi). Results from numerical simulations suggest that thin flyer plates must be used, which lead to short loading duration. This is difficult to implement in the pressure-shear recovery experiments since very thin plates produce negligible shear pulse duration. Investigation of the release effects in the pressure-shear and normal plate impact recovery experiments on brittle materials shows that the geometry of the plates may be used to mitigate release effects (Ref 16, 17, 18, and 19). Independently of the geometry of the pressure-shear configuration, some fraction of the energy always

remains in the sample as shear momentum and may affect the radial release waves before they are trapped. The question of the residual shear pulse, which arises because of the shear strength of the lubricant layer, must always be addressed.

Normal Plate Impact

Experimental facilities, projectile characteristics, measurement techniques, and specimen preparation and alignment are discussed in the preceding sections of this article. To illustrate the basic procedure and the corresponding results, consider first the normal configuration shown in Fig. 5(a), with the t - X diagram of Fig. 5b, in the context of the investigation of inelasticity in a ceramic composite (Ref 7). The fiberglass tube projectile carries steel and star-shaped Ti-6Al-4V flyer plates that are separated by a low-impedance foam to prevent reloading of the specimen by reflected waves. The Ti-6Al-4V flyer has sufficiently high yield strength and acoustic impedance lower than the tested ceramic composite sample. The target assembly consists of an inner cylinder for supporting the specimen and an outer anvil for stopping the projectile. The anvil has a disposable brass nose, which absorbs part of the impact energy. The 22 by 22 mm² (0.87 by 0.87 in.²) specimen is a thin plate of AlN/AlN/Al composite, backed up by the same size plate, which, ideally, has matching impedance. This plate flies off the back of the specimen after the main compressive pulse reflects from the rear surface and returns to the interface.

Experimental Procedure. A 63 mm (2.5 in.) gas gun was used (Ref 7). The specimen characteristics and relevant test data are reported in Tables 1 and 2. For the purpose of aligning and triggering the oscilloscopes, a multilayer thin film mask was sputtered onto the impact face of the specimen. Since the AlN/AlN/Al composite is conductive, a 1 μm thick insulating layer of Al₂O₃ was first sputtered. Then, by using a mask, a 0.1 μm thick layer of aluminum was sputtered in the form of four diagonal strip pins at the corners and two ground strips crossing at the center. Tilt and impactor velocity were measured using the techniques discussed in the section “Plate Impact Facility” in this article. The normal motion at four points on the rear surface of the momentum-trap plate was monitored by means of a normal displacement interferometer (NDI) to identify nonplanar motions that can be correlated with the microcracking process and the unloading waves from the star-shaped flyer.

Table 1 Properties of materials used in normal impact recovery experiments

Material	Density, g/cm ³	Longitudinal wave speed, mm/μs	Transverse wave speed, mm/μs	Acoustic impedance, GPa · μs/mm	Shear impedance, GPa · μs/mm
Hampden steel	7.86	5.983	3.264	47.03	25.66
Ti-6Al-4V	4.43	6.255	3.151	27.71	13.96
AlN/AlN/Al	3.165	9.50	5.5	30.07	17.41

Source: Ref 7

Table 2 Summary of results from normal impact recovery experiments

Shot No.	Projectile velocity, mm/μs	Normal stress		Shear stress	
		GPa	ksi	MPa	ksi
91-01	0.0804	1.417	206	475	69
91-02	0.1070	1.889	273	633	92

Source: Ref 7

Wave Propagation Analysis. At impact, plane compression waves are produced in both the thin star-shaped flyer and the specimen. The reflection from the foam-flyer interface unloads the compressive wave, resulting in a compressive pulse of duration equal to the round-trip travel time through the thickness of the star flyer. When the compressive pulse reaches the rear surface of the specimen, the gap between the specimen and the momentum-trap plate produces a reflected wave, which unloads the compressive pulse. Tensile stresses are generated after crossing the compressed region. By the time this pulse reaches the flyer-specimen interface,

separation between the flyer and specimen has taken place, and the pulse reflection causes compressive stresses. The initial compressive pulse, minus the pulse reflected at the gap, propagates into the momentum trap and reflects back. When this tensile pulse reaches the interface between the specimen and the momentum trap, the momentum trap separates because this interface cannot withstand tension. At this time, the specimen is left unstressed and without momentum. Because of the impedance mismatch between the specimen and the momentum trap, an additional compressive wave is reflected at the interface and makes a round trip through the specimen. This relatively small compressive reloading occurs later than the principal loading of interest and is expected to have minor influence on the observed damage.

This one-dimensional analysis is valid in the central region of the specimen (Ref 38), where the effects of diffracted waves from the corners and the edges of the flyer are minimized. The only cylindrical wave, which passes through the central octagonal region, is a shear wave diffracted from the boundary upon the arrival of a cylindrical unloading wave at 45° . To fully assess the role of the cylindrical waves diffracted from the edges of the star and the spherically diffracted waves from the corners of the flyer and the specimen, three-dimensional elastic computations have been performed (Ref 13). The principal unloading waves that travel in the central octagonal region are diffracted spherical waves emanating from the corners of the flyer. These waves produce tensile stresses within the sample. The maximum amplitudes of such stresses occur for transverse tensile stresses at the rear surface of the specimen. These amplitudes are of the order of 15% of the longitudinal compressive stress in the incident plane wave. It should be pointed out that this amplitude represents an upper bound for such stresses. First, in real experiments there is a lack of simultaneity for the time of contact of the eight corners due to the tilt between the flyer and the specimen. Second, the divergence of the unloading waves from the corners will induce microcracking near these corners and thereby reduce the level of tensile stresses that propagate into the central octagonal region to a value below a fracture stress threshold. These features have been observed systematically in Al_2O_3 and $\text{AlN}/\text{AlN}/\text{Al}$ composite tested samples.

Experimental Results. A summary of the experiments is given in Tables 1 and 2. The velocity-time histories of two typical results are given in Fig. 8(a) and (b). The reported stresses are at the interface between the specimen and the momentum trap. The maximum shear stress is given. The stress-time histories at the front surface of the momentum trap can be read from the secondary vertical axis. Dashed lines in the plot are the elastic solution results, which are used as a reference to discuss several observed inelastic effects. The main compressive pulse, with duration between 240 and 195 ns, is followed by a second compressive pulse corresponding to the tensile pulse generated by an intentional gap of 30 and 85 ns in Fig. 8(a) and (b), respectively. The third pulse results from the reflection of the main pulse at the interface between the specimen and the momentum trap. Its close resemblance to the main pulse is an indication of the dominance of plane waves in the central region of the sample. In the experiment at lower impact velocity (Fig. 8a), the compressive pulse has the full amplitude of the elastic prediction. This implies that, initially, the material did not undergo inelastic processes at this level of stresses. The small reduction in amplitude at the end of the pulse can be interpreted from the analysis of release waves from the star-shaped flyer corners (Ref 13). The tail at the end of the first compressive pulse appears to be the result of the inelastic strain rate produced by the nucleation and propagation of microcracks (Fig. 8a). If so, the duration of the tail can be associated with the time required for the stress, at the wave front, to relax to the threshold value required for initiating crack propagation. Strong evidence of microcracking is found in the attenuation and spreading of the second compressive pulse. In Fig. 8(b), some indication of inelasticity in compression appears toward the end of the pulse. This feature is consistent with the increase in dislocation density, within the AlN filler particles, the AlN reaction product, and the Al phase, observed in transmission electron microscopy (TEM) samples made from the recovered specimens (details can be found in Ref 7).

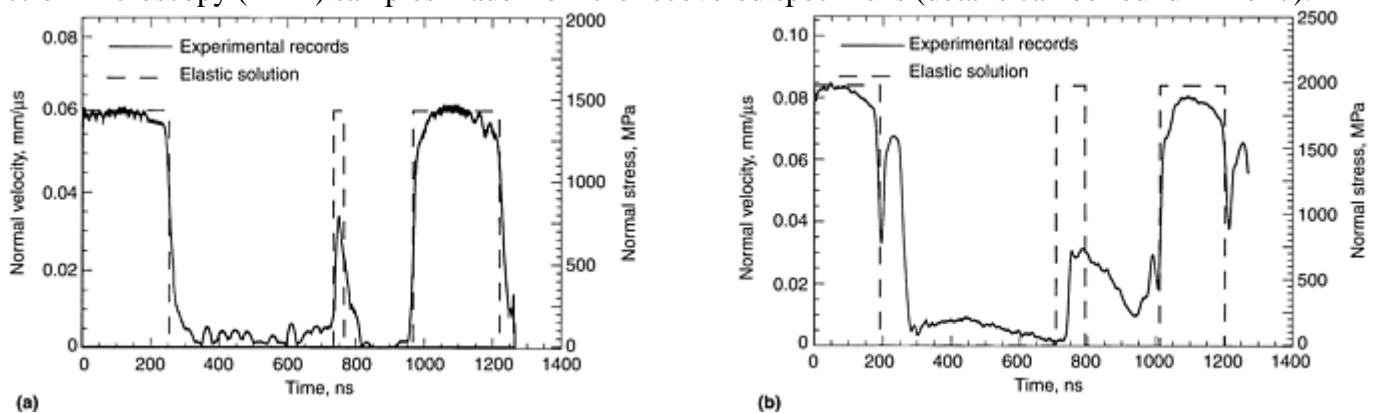


Fig. 8 Velocity-time profiles for normal impact recovery experiments. (a) Profile for shot No. 91-01 in Table 2. Second compressive pulse is attenuated due to material dynamic failure in tension. (b) Profile for shot No. 91-02 in Table 2. A strong spall signal and attenuation of the first compressive pulse are observed. Source: Ref 7

Pressure-Shear Plate Impact

Inclining the flyer, specimen, and target plates with respect to the axis of the projectile produces compression-shear loading. By varying the inclination angle, a variety of loading states may be achieved. For small angles of inclination, small shear stresses are produced, which can be used to probe the damage induced by the accompanying pressure. This pressure-shear plate impact experiment was modified by Ramesh and Clifton (Ref 6) to study the elastohydrodynamic lubricant response at very high strain rates. The idea of recovery pressure-shear plate impact experiment was presented by Nemat-Nasser et al. (Ref 40), Espinosa (Ref 41), and Yadav et al. (Ref 65) and was first successfully implemented to study the response and failure modes of alumina ceramics by Machcha and Nemat-Nasser (Ref 16) and later by Espinosa et al. (Ref 17, 18, 19, and 52) in their studies of dynamic friction and failure of brittle materials.

Wave Propagation Analysis. The Lagrangian time-distance (t - X) diagrams for pressure-shear high-strain-rate and wave propagation configurations, designed for specimen recovery, are shown in Fig. 6(b) and 7(b). In the case of pressure-shear high-strain-rate experiments, the specimen is a thin wafer, 100 to 500 μm thick, sandwiched between two anvil plates. At impact, plane compression waves and shear waves are produced in both the impactor and the target. Since the shear wave velocity is approximately half the longitudinal wave velocity, a thin film with very low shear resistance needs to be added to the flyer plate such that the arrival of the unloading shear wave, to the impact surface, precedes the arrival of the unloading longitudinal wave generated at the back surface of the second flyer plate. The longitudinal and shear wave fronts arriving to the anvil-free surface are shown in Fig. 6(b). These wave fronts determine the longitudinal and shear windows measured interferometrically. These velocity histories contain information on the sample stress history as discussed in the next paragraph. A similar wave analysis applies to the wave propagation pressure-shear configuration (Fig. 7b).

According to one-dimensional elastic wave theory (Ref 5), the normal stress is given by $\sigma = \rho c_1 u_0/2$, in which ρc_1 is the flyer and anvil longitudinal impedance, and u_0 is the normal component of the impact velocity V (i.e., $u_0 = V \cos \theta$). The strain rate is given by the velocity difference between the two faces of the sample divided by its thickness (i.e., $\dot{\lambda} = (v_f - v_a)/h = (v_0 - v_{fs})/h$), where v_f and v_a are the flyer and anvil transverse velocities, respectively, at their interfaces with the specimen, and $v_0 = V \sin \theta$ and v_{fs} are, respectively, the transverse components of the impact velocity and the velocity of the free surface of the anvil plate. The integration of the strain rate over time gives the shear strain $\gamma(t)$. One-dimensional elastic wave theory can be used again to express the shear stress in terms of the measured free surface transverse velocity (i.e., $\tau = \rho c_2 v_{fs}/2$), where ρc_2 is the anvil shear impedance. These equations can be used to construct $\tau - \gamma$ curves at strain rates as high as $1 \times 10^5 \text{ s}^{-1}$ and pressures in the range of 2 to 5 GPa (290 to 725 ksi). It must be emphasized that this analysis is based on the assumption that inelasticity takes place only in the specimen. An investigation of this requirement at high strain rate and temperatures can be found in Ref 42.

Numerical simulations have been performed by Machcha and Nemat-Nasser (Ref 23) for the pressure-shear recovery experiments. The results confirm the advantages of the star-shaped geometry. Machcha and Nemat-Nasser positioned the star-shaped flyer as a second flyer plate, which does not fully mitigate lateral release waves, in the central portion of the sample. Espinosa and coworkers (Ref 18, 19) positioned the star-shaped flyer plate as the first plate of the multiplate flyer assembly. The selection of materials for the manufacturing of flyer plates depends on the application for which experiments are conducted. In the characterization of hard materials, demanding requirements are placed on the manufacturing of flyer and momentum-trap plates. These plates must be hard enough in compression and shear to remain elastic at the high stress levels required for the inelastic deformation of the specimen. The momentum trap must be strong enough in tension to prevent failure at 45° when the shear wave propagates through the unloaded region adjacent to the rear surface of the momentum trap. These requirements are met by using Speed Star (Carpenter Technology Corp.—Specialty Alloys, Reading, PA) steel plates with a 0.2% offset yield stress greater than 2200 MPa (320 ksi) in shear and a tensile strength in excess of 1500 MPa (220 ksi). Another important feature in the selection of the flyer material is that its longitudinal and shear impedances must be smaller or equal to those of the specimen. In this way, a

single compression-shear pulse is introduced in the sample. Moreover, the longitudinal and shear impedances of the momentum-trap plate must match the impedances of the sample to avoid wave reflections at the specimen momentum-trap interface. Density, wave speeds, and impedances for the materials used in this investigation are reported in Table 3.

Table 3 Properties of materials used in pressure-shear impact recovery experiments

Material	Density kg/m ³	Wave speed, mm/μs		Impedance, GPa · mm/μs	
		<i>c</i> ₁	<i>c</i> ₂	ρc ₁	ρc ₂
Speed-Star Steel	8138	5.852	3.128	47.62	25.46
TiB ₂	4452	10.93	7.3	48.66	32.5
Al ₂ O ₃ /SiC	3890	10.56	6.24	41.08	24.27

Source: Ref 19

Experimental Procedure. The 76 mm (3.0 in.) gas gun described in the section “Plate Impact Facility” was used. The multiplate flyer and target plates were made of Speed Star steel. The specimens were made with two types of ceramics. In the high-strain-rate pressure-shear experiment, an Al₂O₃/SiC nanocomposite wafer was used. TiB₂ plates were employed in the wave propagation pressure-shear experiments. In the latter case, two specimen configurations were investigated. The first one consisted of a square specimen with the same dimensions as the star-shaped flyer. The second configuration consisted of a hollow square steel plate in which a TiB₂ ceramic rod 12.7 mm (0.5 in.) in diameter was shrunk fitted.

The target rear surface was polished, and then a thin layer of positive photoresist was deposited using a spinning machine. A holographic phase grating was constructed by interference of two laser beams. The angle between the beams was selected such that a sinusoidal profile with 1000 lines/mm was obtained. This grating was used to measure the normal and transverse displacements by means of a variable sensitivity displacement interferometer (VSDI) (Ref 52). The signals generated by each interfering beam pair were monitored by silicon photodetectors.

Experimental Results. A summary of these experiments is presented in Table 4. The normal velocity-time profile obtained from the high-strain-rate pressure-shear recovery configuration is shown in Fig. 9(a). The normal particle velocity shows a velocity reduction after an initial jump indicating the presence of a small gap between the Al₂O₃/SiC nanocomposite and the multiplate flyer. Upon reverberation of waves within the specimen, the normal velocity rises to a value of about 140 m/s (460 ft/s) at approximately 0.4 μs and remains almost constant until release waves from the boundary reach the observation point. The peak normal stress in this shot, computed according to $\sigma = \rho c_1 u_{fs}/2$, reaches 3.45 GPa (500 ksi). The transverse particle velocity history for this experiment is shown in Fig. 9(b). The velocity rises progressively and then drops for a few nanoseconds. Since in this experiment, shear motion is transferred by friction, a reduction in normal traction at the specimen-steel plate interface results in a drop of the transmitted shear motion. When the gap closes, the transverse velocity increases until it reaches a maximum value of 22 m/s (72 ft/s) at about 500 ns. It then decays continuously while the normal velocity remains constant (Fig. 9a). The maximum shear stress, given by $\tau = \rho c_2 v_{fs}/2$, is 280 MPa (41 ksi). This value is well below the expected shear stress of 575 MPa (83 ksi), assuming elastic material response. The progressive reduction in anvil-free surface transverse velocity implies a variable strain rate and absence of a homogeneous stress state in the sample. In this experiment, round plates were used and the sample was precracked through a sequence of microindentations in a diameter of 38 mm (1.5 in.) Lateral trapping of release waves was attempted by forming a circular crack with the unloaded sample in the central region. Despite these efforts, the degree of damage was severe enough that the ceramic sample was reduced to fine powder upon unloading. This feature of material pulverization upon unloading was investigated by Zavattieri et al. (Ref 22) by simulating compression-shear loading on representative volume elements at the grain level. These investigators show that a ceramic microstructure containing a dilute set of microcracks may pulverize in unloading due to the stored elastic energy within the grains.

Table 4 Summary of parameters for pressure-shear recovery experiments

Shot No.	Specimen	Specimen thickness	Impactor thickness	Target thickness	Projectile velocity	Tilt, mrad	Configuration
----------	----------	--------------------	--------------------	------------------	---------------------	------------	---------------

		mm	in.	mm	in.	mm	in.	m/s	ft/s		
7-1025	Al ₂ O ₃ /SiC	0.54	0.021	2.42–3.65	0.095–0.144	7.99	0.31	148	486	1.3	High strain-rate recovery
7-1115	TiB ₂	4.15	0.163	1.04–2.55	0.041–0.100	4.53	0.18	130	427	20.3	Wave propagation recovery
8-0131	TiB ₂	8.9	0.35	0.92–3.0	0.036–0.12	4.05	0.16	133	436	1.32	Wave propagation recovery

Source: Ref 19

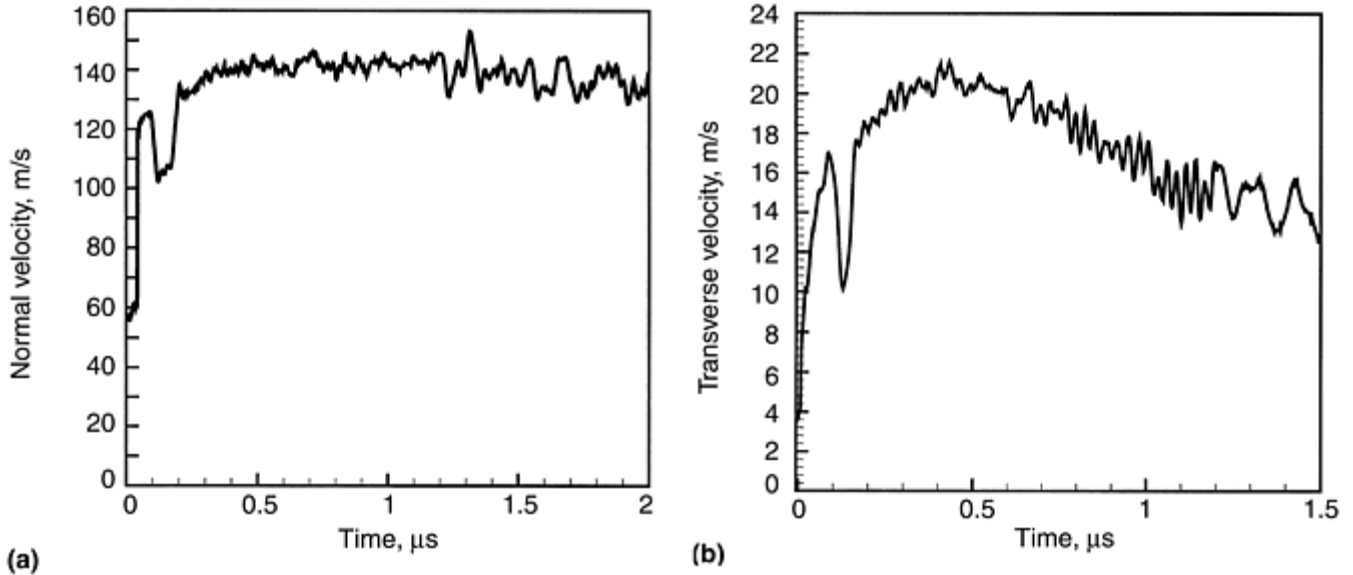


Fig. 9 Velocity histories from a pressure-shear high-strain-rate experiment (shot No. 7-1025 in Table 4). (a) Normal velocity history. The time scale starts with the arrival of the longitudinal wave to the anvil-free surface. (b) Transverse velocity history. The time scale starts with the arrival of the shear wave to the anvil-free surface. Source: Ref 18, 19

In the case of the wave propagation pressure-shear recovery configuration, round and square-shaped TiB₂ plate specimens were used. The longitudinal and shear waves recorded in the case of the square-shaped TiB₂ specimen are shown in Fig. 10(a) and 10(b), respectively. The velocity profile in the first microsecond is shown in solid lines, while the remaining part of the signal is shown in dashed lines. Figure 10(a) shows the normal velocity rises to a value predicted by one-dimensional elastic wave theory. After approximately 200 ns, the longitudinal particle velocity progressively decays and then rises again at approximately 500 ns. This longitudinal velocity history is very close to the one-dimensional elastic wave propagation prediction if the effect of spherical waves emanating from the star-shaped flyer corners is taken into account (Ref 13). Another source of stress decay is the presence of a thin polymer layer in the multiplate flyer. As previously discussed, longitudinal stress decay occurs until a homogeneous deformation state is reached in the polymer film. The transverse particle velocity shown in Fig. 10(b) also presents clear features. Upon wave arrival to the back surface of the momentum-trap plate, an in-plane velocity of about 10 m/s (33 ft/s) is measured interferometrically. After shear wave arrival, according to the *t-X* diagram discussed previously, the transverse velocity rises to a maximum of 38 m/s (125 ft/s). This value is below the shear wave velocity predicted by one-dimensional wave propagation theory. Hence, the material clearly exhibits an inelastic behavior in shear. At approximately 800 ns, the transverse velocity decays progressively.

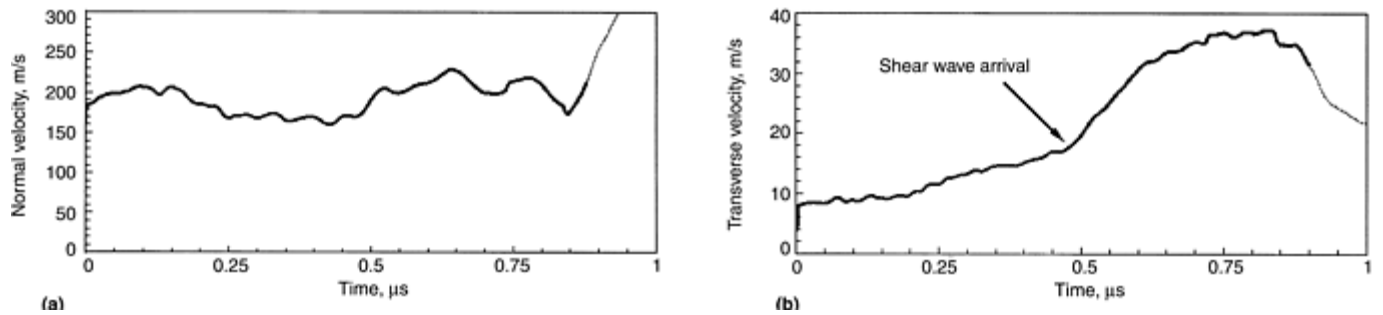


Fig. 10 Velocity histories from a pressure-shear wave propagation experiment (shot No. 8-0131 in Table 4). (a) Normal velocity history. The time scale starts with the arrival of the longitudinal wave to the momentum-trap-free surface. (b) Transverse velocity history. The time scale starts with the arrival of the shear wave to the momentum-trap-free surface. Source: Ref 19

Understanding these complex velocity histories requires complete three-dimensional simulations of the compression-shear experiment including damage and tilt effects. In this experiment, the steel plates are fully recovered. In contrast to the shrink-fitted specimen, the ceramic specimen is fragmented with varying fragment sizes (Fig. 11). The larger fragment is several millimeters in size, but its location in the square plate could not be identified unambiguously. In this case, the star-shaped flyer also is fragmented in the central region. In addition, long cracks are observed running parallel to the edges. Severe indentation is observed in the second flyer plate, although its hardness was measured to be 55 HRC. In this configuration, the momentum-trap plate remains intact with no cracks observable to the naked eye. Additional details can be found in Ref 18 and 19.

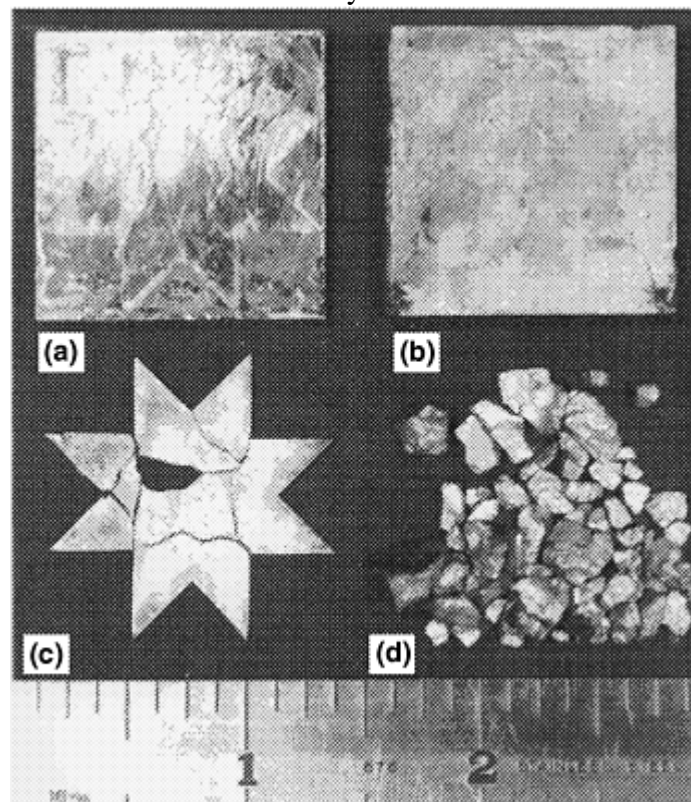


Fig. 11 Optical micrograph of recovered plates from a pressure-shear wave propagation experiment (shot No. 8-0131 in Table 4). (a) Second flyer plate. (b) Back momentum-trap plate. (c) Star-shaped flyer plate. (d) Fragmented specimen. Source: Ref 19

References cited in this section

1. P. Kumar and R.J. Clifton, Dislocation Motion and Generation in LiF Single Crystals Subjected to Plate-Impact, *J. Appl. Phys.*, Vol 50 (No. 7), 1979, p 4747–4762

5. R.J. Clifton and R.W. Klopp, Pressure-Shear Plate Impact Testing, *Mechanical Testing*, Vol 8, *ASM Handbook*, 9th ed., ASM International, 1985, p 230–239
6. K.T. Ramesh and R.J. Clifton, A Pressure-Shear Plate Impact Experiment for Studying the Rheology of Lubricants at High Pressures and High Strain Rates, *J. Tribology*, 1987, Vol 109, p 215
7. H.D. Espinosa and R.J. Clifton, Plate Impact Experiments for Investigating Inelastic Deformation and Damage of Advanced Materials, *Symposium on Experiments in Micromechanics of Fracture-Resistant Materials* (ASME Winter Annual Meeting), 1–6 Dec 1991 (Atlanta, GA), K.S. Kim, Ed., 1991, p 37–56
8. J.C. Escobar and R.J. Clifton, On Pressure-Shear Plate Impact for Studying the Kinetics of Stress-Induced Phase Transformations, *Mater. Sci. Eng. A: Structural Materials: Properties, Microstructure & Processing*, No. 1–2, 1 Oct 1993, p 125–142
11. G. Raiser, R.J. Clifton, and M. Ortiz, A Soft-Recovery Plate Impact Experiment for Studying Microcracking in Ceramics, *Mech. Mater.*, Vol 10, 1990, p 43–58
13. H.D. Espinosa, G. Raiser, R.J. Clifton, and M. Ortiz, Performance of the Star-Shaped Flyer in the Study of Brittle Materials: Three Dimensional Computer Simulations and Experimental Observations, *J. Appl. Phys.*, Vol 72 (No. 8), 1992, p 3451–3457
14. H.D. Espinosa, G. Raiser, R.J. Clifton, and M. Ortiz, Experimental Observations and Numerical Modeling of Inelasticity in Dynamically Loaded Ceramics, *J. Hard Mater.*, Vol 3 (No. 3–4), 1992, p 285–313
16. A.R. Machcha and S. Nemat-Nasser, Pressure-Shear Recovery Experiments, *Mech. Mater.*, Vol 18, 1994, p 49–53
17. H.D. Espinosa, M. Mello, and Y. Xu, A Desensitized Displacement Interferometer Applied to Impact Recovery Experiments, *J. Appl. Phys. Lett.*, Vol 69 (No. 21), 1996, p 3161–3163
18. H.D. Espinosa, A. Patanella, and Y. Xu, Dynamic Compression-Shear Loading of Brittle Materials with Specimen Recovery, *Proceedings of the 11th Int. Conf. on Experimental Mechanics*, 24–28 Aug 1998 (Oxford, UK), I.M. Allison, Ed., 1998, p 223–229
19. H.D. Espinosa, A. Patanella, and Y. Xu, Dynamic Compression-Shear Response of Brittle Materials with Specimen Recovery, to appear in *Exp. Mech.*, 2000
20. M. Zhou, A. Needleman, and R.J. Clifton, Finite Element Simulations of Shear Localization in Plate Impact, *J. Mech. Phys. Solids*, Vol 42 (No. 3), 1994, p 423–458
21. H.D. Espinosa, On the Dynamic Shear Resistance of Ceramic Composites and its Dependence on Applied Multiaxial Deformation, *Int. J. Solids Struct.*, Vol 32 (No. 21), 1995, p 3105–3128
22. P.D. Zavattieri, P.V. Raghuram, and H.D. Espinosa, A Computational Model of Ceramic Microstructures Subjected to Multi-Axial Dynamic Loading, to appear in *J. Mech. Phys. Solids*, 2000
23. A.R. Machcha and S. Nemat-Nasser, Effects of Geometry in Pressure-Shear and Normal Plate Impact Experiments: Three-Dimensional Finite Element Simulations and Experimental Observations, *J. Appl. Phys.*, Vol 80 (No. 6), 1996, p 3267–3274
29. H.D. Espinosa, P.D. Zavattieri, and S. Dwivedi, A Finite Deformation Continuum/Discrete Model for the Description of Fragmentation and Damage in Brittle Materials, *J. Mech. Phys. Solids*, Vol 46 (No. 10), 1998, p 1909–1942

33. W.F. Hartman, Determination of Unloading Behavior of Uniaxially Strained 6061-T Aluminum from Residual Strain Measurements, *J. Appl. Phys.*, Vol 35, 1964, p 2090
35. J.E. Vorthman and G.E. Duvall, Dislocations in Shocked and Recovered LiF, *J. Appl. Phys.*, Vol 53, 1982, p 3607–3615
36. S.-N. Chang, D.-T. Chung, G. Ravichandran, and S. Nemat-Nasser, Plate Impact Experiments on Mg-PSZ and Improved Target Configuration, *Proceedings of 1989 APS Topical Conference on Shock Compression of Condensed Matter*, 14–17 Aug 1989, S.C. Schmidt, J.N. Johnson, and L.W. Davidson, Ed., American Physics Society, 1990, p 389–392
37. S.-N. Chang, D.-T. Chung, Y.F. Li, and S. Nemat-Nasser, Target Configurations for Plate-Impact Recovery Experiments, *J. Appl. Mech.*, Vol 92-APM-18, 1992, p 1–7
38. P. Kumar and R.J. Clifton, A Star-Shaped Flyer for Plate Impact Recovery Experiments, *J. Appl. Phys.*, Vol 48, 1977b, p 4850
40. S. Nemat-Nasser, J.B. Isaacs, G. Ravichandran, and J.E. Starrett, High Strain Rate Testing in the U.S., *Proceedings of the TTCP TTP-1 Workshop on New Techniques of Small Scale High Strain Rate Studies*, 26 April 1988 (Melbourne, Australia)
41. H.D. Espinosa, Micromechanics of the Dynamic Response of Ceramics and Ceramic Composites, Ph.D. thesis, Brown University, Providence, RI, 1992
42. K.J. Frutschy and R.J. Clifton, High-Temperature Pressure-Shear Plate Impact Experiments on OFHC Copper, *J. Mech. Phys. Solids*, Vol 46 (No. 10), 1998, p 1723–1743
52. H.D. Espinosa, M. Mello, and Y.Xu, A Variable Sensitivity Displacement Interferometer with Application to Wave Propagation Experiments, *J. Appl. Mech.*, Vol 64, 1997, p 123–131
60. M.A. Zikry and S. Nemat-Nasser, High Strain-Rate Localization and Failure of Crystalline Materials, *Mech. Mater.*, Vol 10 (No. 3), 1990, p 215–237
61. F. Longy and J. Cagnoux, Plasticity and Microcracking in Shock-Loaded Alumina, *J. Am. Ceram. Soc.*, Vol 72 (No. 6), 1989, p 971
62. D. Yaziv, “Shock Fracture and Recompaction of Ceramics,” Ph.D. thesis, University of Dayton, 1985
63. A.L. Stevens and O.E. Jones, Radial Stress Release Phenomena in Plate Impact Experiments: Compression-Release, *J. Appl. Mech.*, Vol 39, 1972, p 359–366
64. R.L. Rabie, J.E. Vorthman, and J.K. Dienes, Three-Dimensional Computer Modeling of a Shock Recovery Experiment, *Shock Waves in Condensed Matter*, Vol 5, J.R. Asay, R.A. Graham, and G.K. Straub, Ed., 1983
65. S. Yadav, J.A. Davis, and K.T. Ramesh, Damage and Recovery Experiments Using Pressure-Shear Plate Impact, *Experimental Techniques in the Dynamics of Deformable Solids*, Vol 165, ASME, Applied Mechanics Division (AMD), 1993, p 71–78

Low-Velocity Impact Testing

Pressure-Shear Friction Experiments

This technique was originally introduced by Prakash and Clifton (Ref 66). Its main objective was to investigate time-resolved friction at slipping speeds (5 to 30 m/s, or 16 to 98 ft/s) and pressures (1 to 3 GPa, or 145 to 435 ksi) typical of high-speed machining processes. As discussed in Ref 66, the technique can be easily interpreted within the one-dimensional wave propagation theory. By using characteristic equations it can be shown that the shear and normal stresses at the sliding interface are given by:

$$\tau(t) = 0.5(\rho c_2)_t v_{fs}(t)$$

$$\sigma(t) = 0.5(\rho c_1)_t u_{fs}(t)$$

in which $(\rho)_t$ is the target material density, $(c_1)_t$ and $(c_2)_t$ are the longitudinal and shear wave velocities of the target material, and v_{fs} and u_{fs} are the shear and longitudinal free-surface velocities interferometrically measured. Furthermore, the slipping velocity is given by:

$$V_{\text{slip}} = V \sin \theta - \left[\frac{(\rho c_2)_t + (\rho c_2)_f}{2(\rho c_2)_f} \right] v_{fs}$$

The friction coefficient is obtained by the ratio $\tau(t)/\sigma(t)$. More details about the derivation of these formulas can be found in Ref 67.

The pressure-shear friction experimental technique discussed in this section is an extension of the technique introduced by Prakash and Clifton (Ref 66) in the sense that the experiment is designed for specimen recovery. Here, the specimen is the interface formed after impact by the flyer and target plates rather than the thin specimen shown in Fig. 6. Certainly, a coating may be deposited on the flyer and/or the target plates to examine its frictional properties under pressure and sliding velocities typical of manufacturing processes or ballistic penetration events. The preparation of the plates, assembly of the target, and alignment follow the procedures outlined in the section ‘‘Specimen Preparation and Alignment’’ in this article.

In an experiment reported in Ref 52, 4340 steel tribopair was used. Typical VSDI signals obtained in these experiments are shown in Fig. 12(a) and (b). In Fig. 12(a), the normal free-surface velocity history is plotted together with the Θ VSDI amplitude corrected signal. Upon arrival of the longitudinal wave to the target-free surface, the normal velocity exhibits an increase in velocity to a level of approximately 80 m/s (260 ft/s) followed by a reduction and increase in velocity due to wave reverberations in the thin polymer layer used in the multiplate flyer. A few bumps are observed in the first 900 ns of the normal velocity history. These variations in normal velocity are likely the result of the low signal-to-noise ratio in the early part of the record (Fig. 12a). They are also due in part to errors in data reduction arising from the insensitivity of the displacement interferometer at the peaks and valleys of the trace (Ref 7). Experience suggests that signals with higher frequencies are less sensitive to errors caused by signal noise. The noise level can be observed in the part of the record preceding the longitudinal wave arrival. In later experiments, the angle θ used in the Θ VSDI has been increased with good results. An approximately constant velocity of 115 m/s (377 ft/s) is monitored in the next 1.8 μ s, which is in agreement with the elastic prediction. It should be noted that this normal velocity would lead to a frequency of 450 MHz in an NDI, while in the VSDI system, a much smaller frequency is recorded.

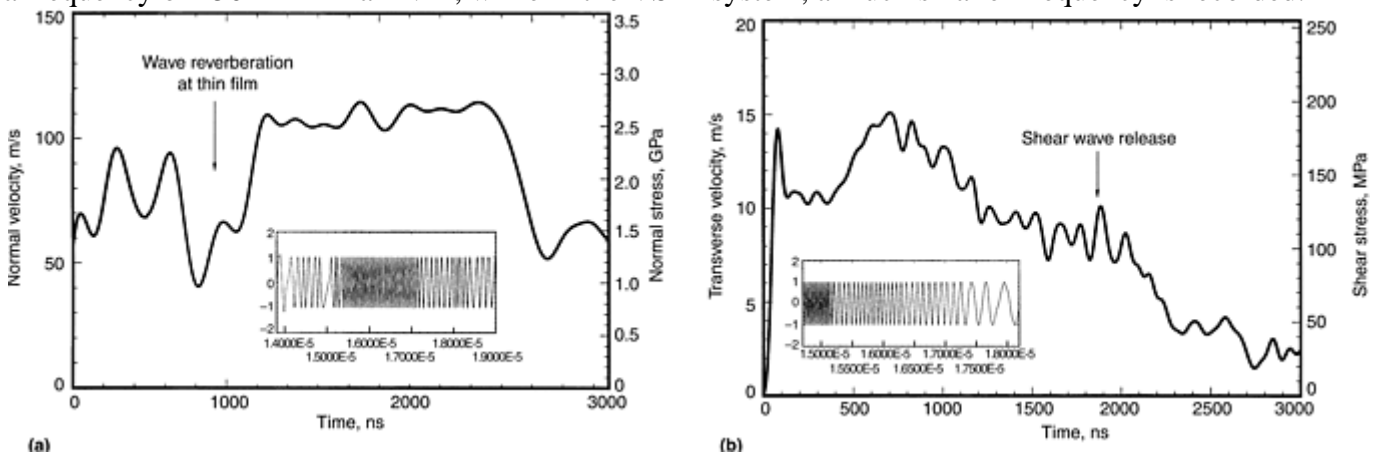


Fig. 12 Particle velocity-time profiles for a dynamic friction recovery experiment. (a) Normal profile; impact velocity, 125 m/s (410 ft/s). The inset shows the Θ VSDI trace after amplitude correction. (b) Transverse profile; impact shear velocity, 38.62 m/s (126.7 ft/s). The inset shows the TDI trace after amplitude correction. Source: Ref 52

In Fig. 12(b) the transverse velocity history and the TDI amplitude corrected signal are shown. A transverse velocity well below the impact shear velocity is measured, indicating interface sliding. Small fluctuations in the transverse velocity are due in part to errors in data reduction arising from the insensitivity of the TDI at the peaks and valleys of the trace (Ref 7). An in-plane wave release is observed at approximately 2 μ s. This wave release is in agreement with the wave release predicted by one-dimensional elastic wave theory. It should be noted that the reduction in in-plane motion is progressive. A residual transverse velocity of 5 m/s (16 ft/s) is recorded, likely due to the shear resistance of the thin polymer film used in the multiplate flyer. Modeling of the experiment, including the frictional behavior of the steel interface and the nonlinear behavior of the polymer thin film, is required to fully interpret the transverse velocity history. Further evidence on the shear wave duration can be observed in Fig. 13 in which an optical micrograph shows sliding marks, approximately 50 μ m in length. From the transverse velocity history, an average sliding velocity of 26 m/s (85 ft/s) is computed. This velocity during 2 μ s leads to a sliding length of 52 μ m, which correlates very well with the sliding marks observed on the micrographs.

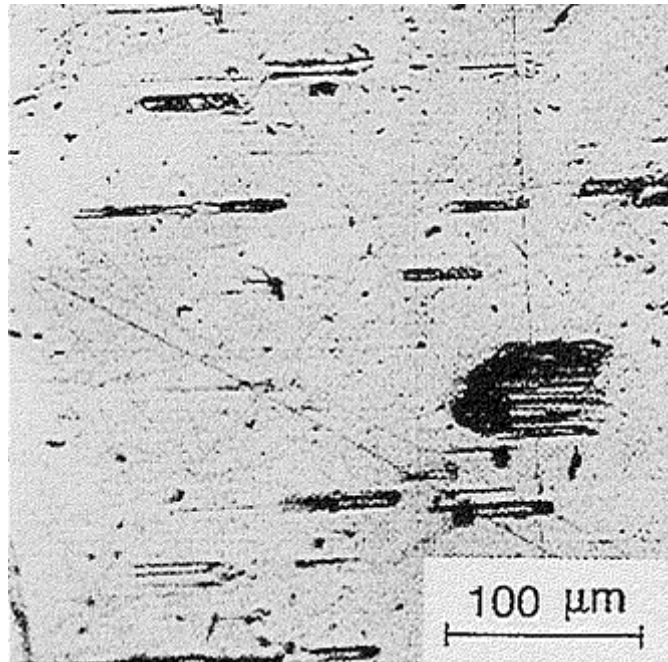


Fig. 13 Optical micrograph of impact surface from recovered flyer plate. Sliding marks approximately 50 μ m in length are observed. Source: Ref 52

Prakash and Clifton (Ref 66) and Prakash (Ref 67) reported dynamic friction coefficients for various tribopairs, namely, WC/4340 steel and WC/Ti-6Al-4V. This work was later extended by Rajagopalan et al. (Ref 68) concerning the estimate of temperature histories in the two plates. Pressure-shear friction experiments on preheated target plates were conducted by Frutsky and Clifton (Ref 69). In their work, the friction phenomenon is investigated at high temperatures. Additional insight into the dynamic friction experimental technique can be found in these references.

References cited in this section

7. H.D. Espinosa and R.J. Clifton, Plate Impact Experiments for Investigating Inelastic Deformation and Damage of Advanced Materials, *Symposium on Experiments in Micromechanics of Fracture-Resistant Materials* (ASME Winter Annual Meeting), 1–6 Dec 1991 (Atlanta, GA), K.S. Kim, Ed., 1991, p 37–56

52. H.D. Espinosa, M. Mello, and Y.Xu, A Variable Sensitivity Displacement Interferometer with Application to Wave Propagation Experiments, *J. Appl. Mech.*, Vol 64, 1997, p 123–131
66. V. Prakash and R.J. Clifton, Time Resolved Dynamic Friction Measurements in Pressure Shear, *Experimental Techniques in the Dynamics of Deformable Solids*, Vol 165, ASME, Applied Mechanics Division (AMD), 1993, p 33–48
67. V. Prakash, Pressure-Shear Plate Impact Experiment for Investigating Transient Friction, *Exp. Mech.*, Vol 35 (No. 4), 1995, p 329–336
68. S. Rajagopalan, M.A. Irfan, and V. Prakash, Novel Experimental Techniques for Investigating Time Resolved High Speed Friction, *Wear*, Vol 225 (No. 2), 1999, p 1222–1237
69. K.J. Frutschy and R.J. Clifton, Plate-Impact Technique for Measuring Dynamic Friction at High Temperatures, *J. Tribology (Trans. ASME)*, Vol 119 (No. 3), July 1997, p 590–593

Low-Velocity Impact Testing

Horacio Dante Espinosa, Northwestern University, Sia Nemat-Nasser, University of California, San Diego

High-Temperature Plate Impact Testing

Understanding materials response at high temperatures and high strain rates is essential to the development of constitutive models describing dynamic failure of advanced materials. Such models are of crucial importance to many applications, for example, crack arrest in engineering structures, failure of turbine engine blades, foreign object impact on satellites, automotive crashworthiness, and military applications such as projectile deformation and armor penetration. Current understanding of basic properties such as plastic flow and dynamic fracture strength in the high-temperature and high-strain-rate regime is very limited. This is due to the scarcity of experimental studies with the needed spatial and temporal resolution to identify damage and failure mechanisms.

It has been shown that high strain rates increase the yield stress in metals (Ref 70, 71, 72, and 73), whereas it is generally accepted that a rise in temperature tends to reduce the resistance to flow by lowering activation barriers associated with the atomic mechanisms of deformation (Ref 74, 75, 76, and 77). When a metallic material is subjected to dynamic and high-temperature loading, a competition process between work hardening (resulting from the production, motion, and interaction of dislocations and other defects) and thermal softening occurs. Extensive research on the stress-strain temperature-dependent behavior in many body-centered cubic and face-centered cubic metals has been carried out (Ref 78, 79, 80, and 81). These results show that temperature has a much greater effect on material strength than strain rate if the deformation is performed under both high-strain-rate and high-temperature conditions.

Even though inelastic mechanisms at high strain rates are not completely understood, researchers agree on the definition of the Hugoniot elastic limit (HEL) as the axial stress, under one-dimensional strain, leading to the onset of material inelasticity. Hence, the evolution of the HEL or its equivalent, the dynamic yield stress, with temperature can be identified by means of normal impact high-temperature experiments. Frutschy and Clifton (Ref 42) carried out pioneer work on the temperature and rate dependence of the dynamic yield stress in oxygen-free high-conductivity copper. Instead of the normal impact experiment described, they performed pressure-shear high-temperature experiments.

Simultaneous nucleation, growth, and coalescence of microvoids or microcracks govern the spall process in advanced materials. Thermal energy plays an important role in the deformation mechanisms leading to strain inhomogeneities that drive the failure process. Limited experimental work exists to define the role of thermal

activation on spall behavior of materials. Recently, studies from Kanel et al. (Ref 82) and Golubev and Sobolev (Ref 83) on aluminum and magnesium have been published. It has been found that spall strength drops with temperature, but no further investigations have been carried out to establish the role of the microstructure in the spallation process.

This section describes the experimental technique developed for shock impact testing at high temperature and reports the variation of HEL and spallation with temperature in Ti-6Al-4V. Microstructural analyses that provide insight into the deformation mechanisms of high-temperature-shocked materials are reported in Ref 44 and 84.

Wave Propagation Analysis for HEL and Spallation Identification. The Dynamic Inelasticity Laboratory described in the section “Plate Impact Facility” in this article possesses the instrumentation to perform planar impact experiments at different temperatures. The setup is similar to the one developed by Frutsky and Clifton (Ref 42, 43) for pressure-shear impact experiments.

The selected experimental configuration is a symmetric planar impact or spall configuration (Fig. 14a). The elastic wave fronts and their interaction can be understood by examining the Lagrangian (t - X) diagram shown in Fig. 14(b). At impact, plane compression waves are produced in both the flyer and the specimen (state 1). Reflection from the foam-flyer interface unloads almost completely the compressive wave, resulting in a compressive pulse duration equal to the round-trip travel time through the flyer thickness. When the compressive pulse reaches the rear surface of the specimen, a reflected wave is generated. This wave unloads the compressive pulse (state 2). Tensile stresses are generated when the two unloading waves, one from the flyer and the other from the specimen back surface, meet in the central part of the specimen (state 3). By the time this pulse reaches the flyer-specimen interface, separation takes place and the pulse reflection causes further compressive stresses (state 4).

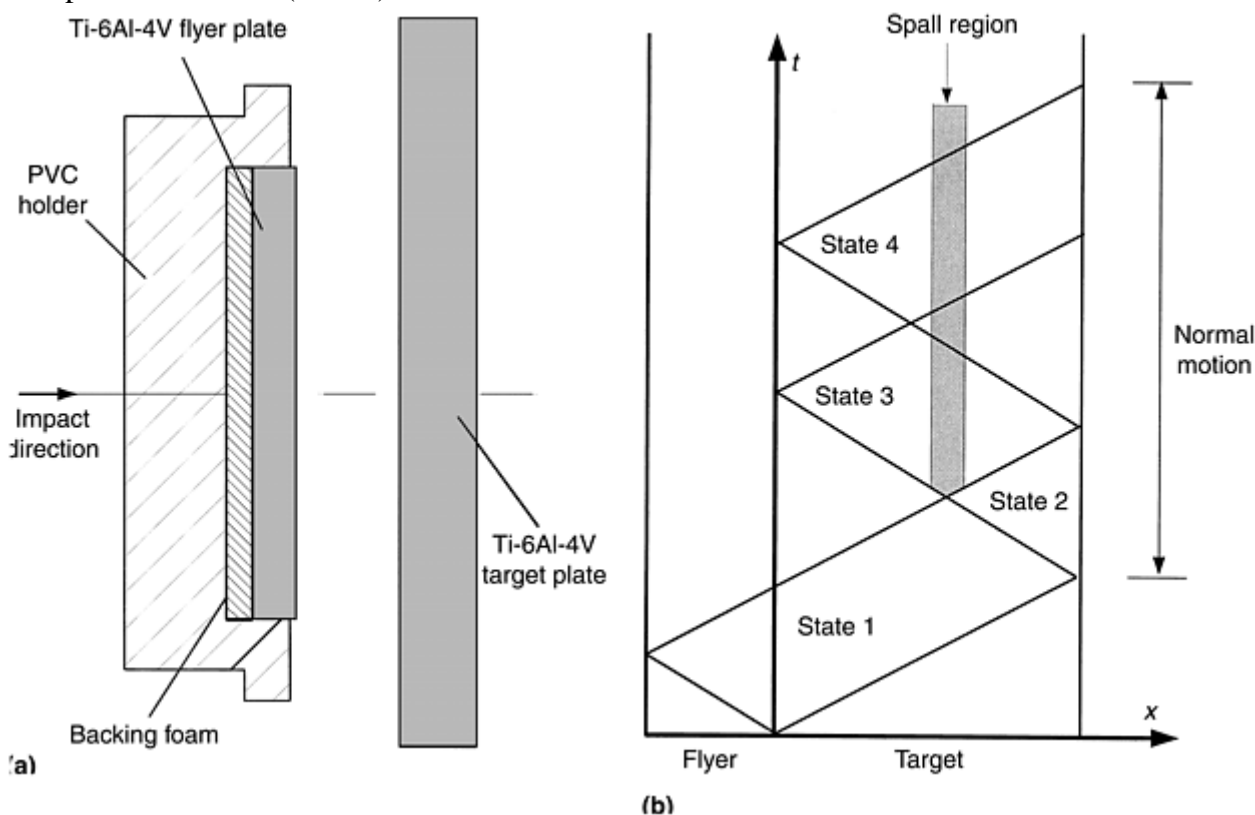


Fig. 14 High-temperature spall experiments. (a) Impact configuration. (b) Lagrangian t - X diagram of spall configuration. Source: Ref 44

For the experiments reported in this subsection, the thickness of the targets was close to 8 mm (0.3 in.) for all specimens with a corresponding half thickness for the flyers. Hence, the spall plane was located near the middle of the target plate. The impact velocity range was selected such that the lowest velocity was enough to induce dynamic yield in Ti-6Al-4V (about 900 MPa, or 130 ksi, according to Ref 85), whereas the highest velocity would induce spallation.

Experimental Procedure. The experimental procedure follows the technique discussed in the section “Specimen Preparation and Alignment.” Something unique to the high-temperature target setup is the assembly of the target plate to the target holder. The Ti-6Al-4V sample is placed hand tight inside a graphite susceptor and glued using high-temperature epoxy. The two pieces together are slipped into a ceramic-foam sleeve that fits inside the coil shown in Fig. 2 and 3. The sleeve is firmly attached by high-temperature epoxy and four ceramic pins to the surrounding copper coil.

The induction heating process generates a temperature gradient in the sample. In fact, the induced currents tend to stay on the surface of the specimen, generating more heat at the surface than in the bulk of the material (Ref 86). Titanium alloys have low thermal conductivity; therefore, the heating gradient can be important. A reduction in the coil diameter generates a denser electromagnetic field that can penetrate the shield generated by the induced currents, achieving a more homogeneous heating (Ref 86). A more practical approach is to employ a material with high electrical conductivity and heat thermal capacity to hold the target and minimize transient time. The graphite susceptor shown in Fig. 2 is introduced in the developed setup with this aim. Temperature is measured by a thermocouple attached to the rear face of the specimen, as close as possible to the center point.

The high velocities required in this study generated a strong shock wave within the target chamber upon the exit of the projectile from the launch tube. To protect the high-temperature assembly, an extension was added to the gun barrel. Following aerodynamic considerations, the extension was designed to keep the high-temperature target assembly outside of the gas-flow cone emanating from the end of the gun barrel. An exploded view of the described experimental assembly is presented in Fig. 15. The assembly and alignment of the plates and the measurement of projectile velocity follow the techniques described in the section “Specimen Preparation and Alignment.”

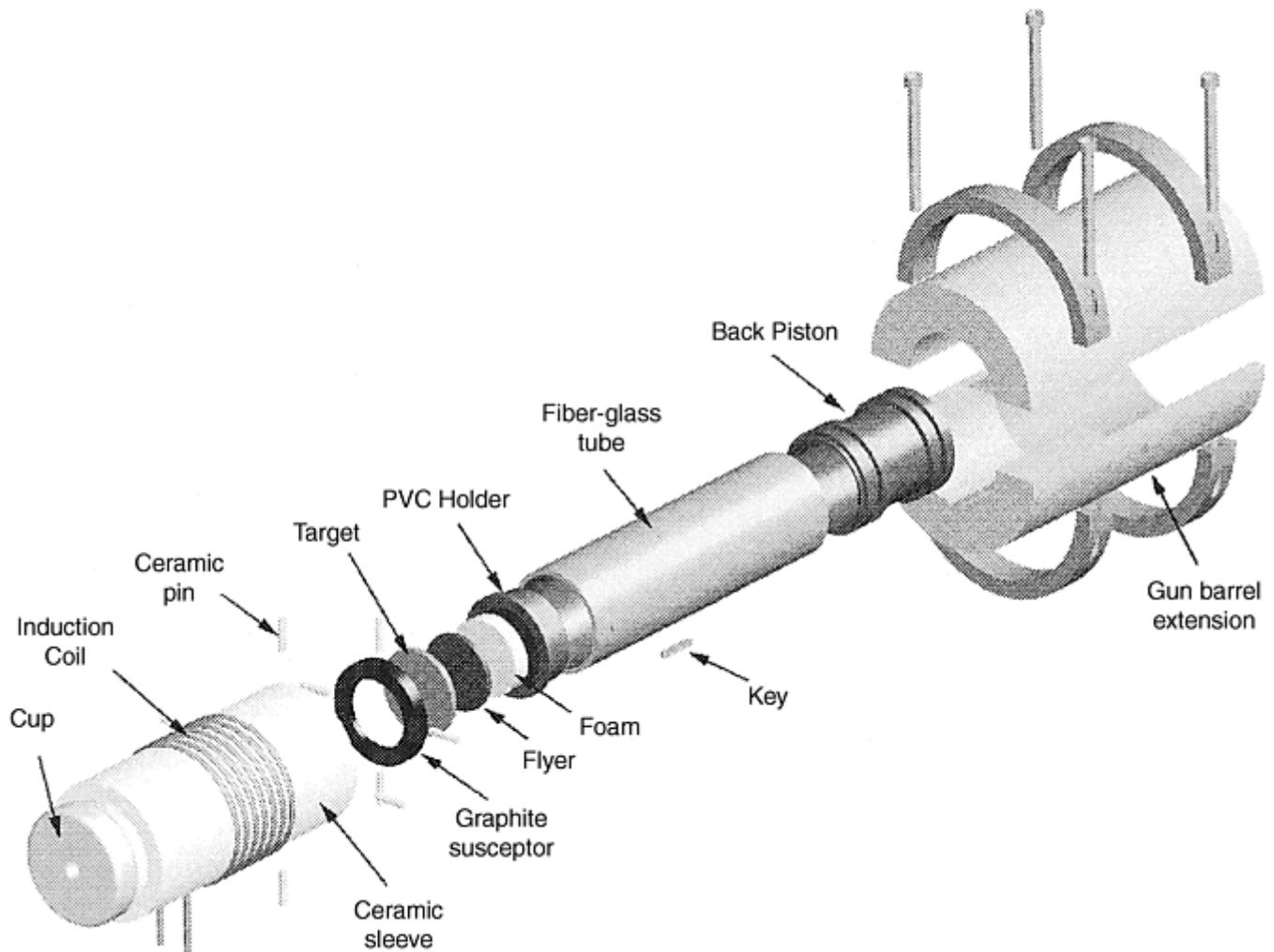


Fig. 15 Exploded view of gas gun extension. Source: Ref 44

A disposable mirror is suspended at a certain distance from the rear face of the specimen to allow the laser beam to monitor the motion of the rear surface of the specimen. The target chamber has a side window to

provide access for the laser beam that is used in the air-delay-leg normal velocity interferometer for any reflecting surface (ADL-VISAR) (Ref 44) depicted in Fig. 16. To avoid overheating of the mirror employed to collect light for the interferometer, a ceramic foam is used to close the ceramic sleeve that contains the target (Fig. 2). A small hole is drilled on the center of the cup, and the laser light is sent in and collected back through it.

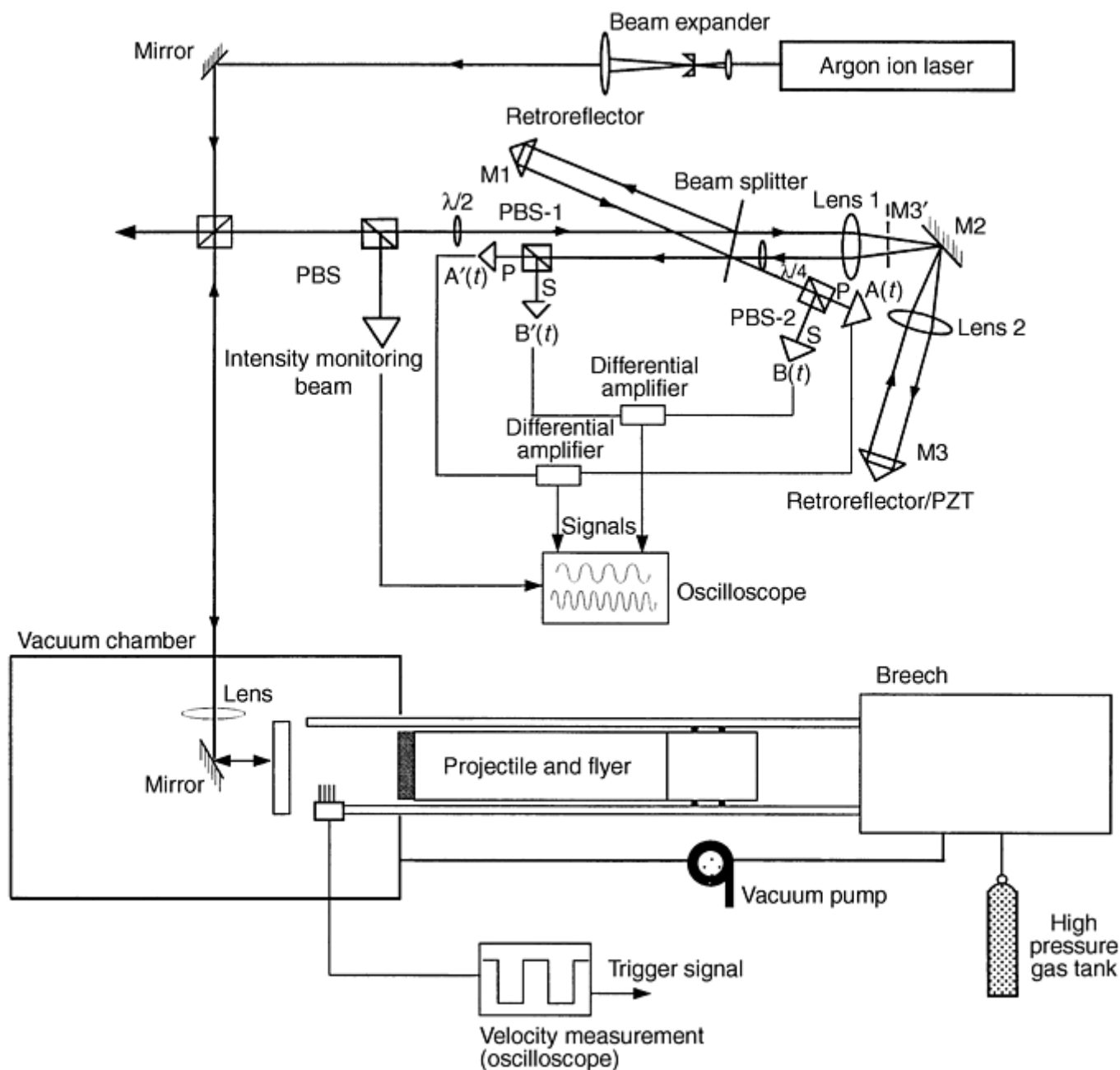


Fig. 16 Schematic of ADL-VISAR interferometer. Source: Ref 87

Tested Material. Details on the hot-rolled commercial grade plates Ti-6Al-4V, its chemical composition, and metallographic examination of the as-received plates can be found in Ref 44. It is interesting to point out the high interstitial oxygen content (0.18%) and grain elongation in the rolling direction. The target and flyer plates were all machined from the as-received plates in such a way that the impact axis was perpendicular to the rolling direction. The hardness was measured to be 35.6 HRC. At room temperature, the longitudinal wave speed, ultrasonically measured, is $c_L = 6232$ m/s (20,446 ft/s), and the material density is 4430 kg/m³; therefore, the acoustic impedance is 27.608 GPa/mm/ μ s.

Experimental Results. A summary of performed high-temperature impact experiments is presented in Tables 5 and 6. A first experiment, 98-0924, was performed to have a reference of the material behavior at room temperature. Its time-velocity history is shown in Fig. 17. As can be observed in this figure, the elastic precursor in this experiment was lost due to the low velocity per fringe (18.75 m/s, or 62 ft/s) employed in the

interferometer. Twelve fringes were added to the fringe count to match the boundary conditions (Ref 49). The velocity jump corresponding to the HEL is 200.5 m/s (657.8 ft/s) in good agreement with the 201 m/s (659 ft/s) reported in Ref 88.

Table 5 Summary of parameters for high-temperature impact experiments

Shot No.	Impactor thickness		Target thickness		Impact velocity		Normal stress	
	mm	in.	mm	in.	m/s	ft/s	GPa	ksi
T98-0924	3.60	0.142	7.6	0.30	251	823	3.46	506
T98-1210	3.51	0.138	7.79	0.307	272	892	3.56	516
T99-0602	3.32	0.131	6.69	0.263	417	1368	5.44	789
T99-1008	3.61	0.142	6.795	0.268	594	1949	7.45	1080

Source: Ref 44, 84

Table 6 Summary of results for high-temperature impact experiments

Short No.	Preheat temperature		Strain rate, $s^{-1} \times 10^5$	Transient strain	Hugoniot elastic limit		Dynamic yield stress		Spall strength	
	°C	°F			GPa	ksi	MPa	ksi	GPa	ksi
T98-0924	22	72	1.47	0.0135	2.77	402	1402	203.3	5.10 ^(a)	740^(a)
T98-1210	298	568	1.61	0.0153	2.11	306	917	133.0
T99-0602	315	599	2.27	0.0239	2.105	305	914	132.6	4.47	648
T99-1008	513	955	3.26	0.0356	1.98	287	858	124.4	4.30	624

(a) Reported in the literature

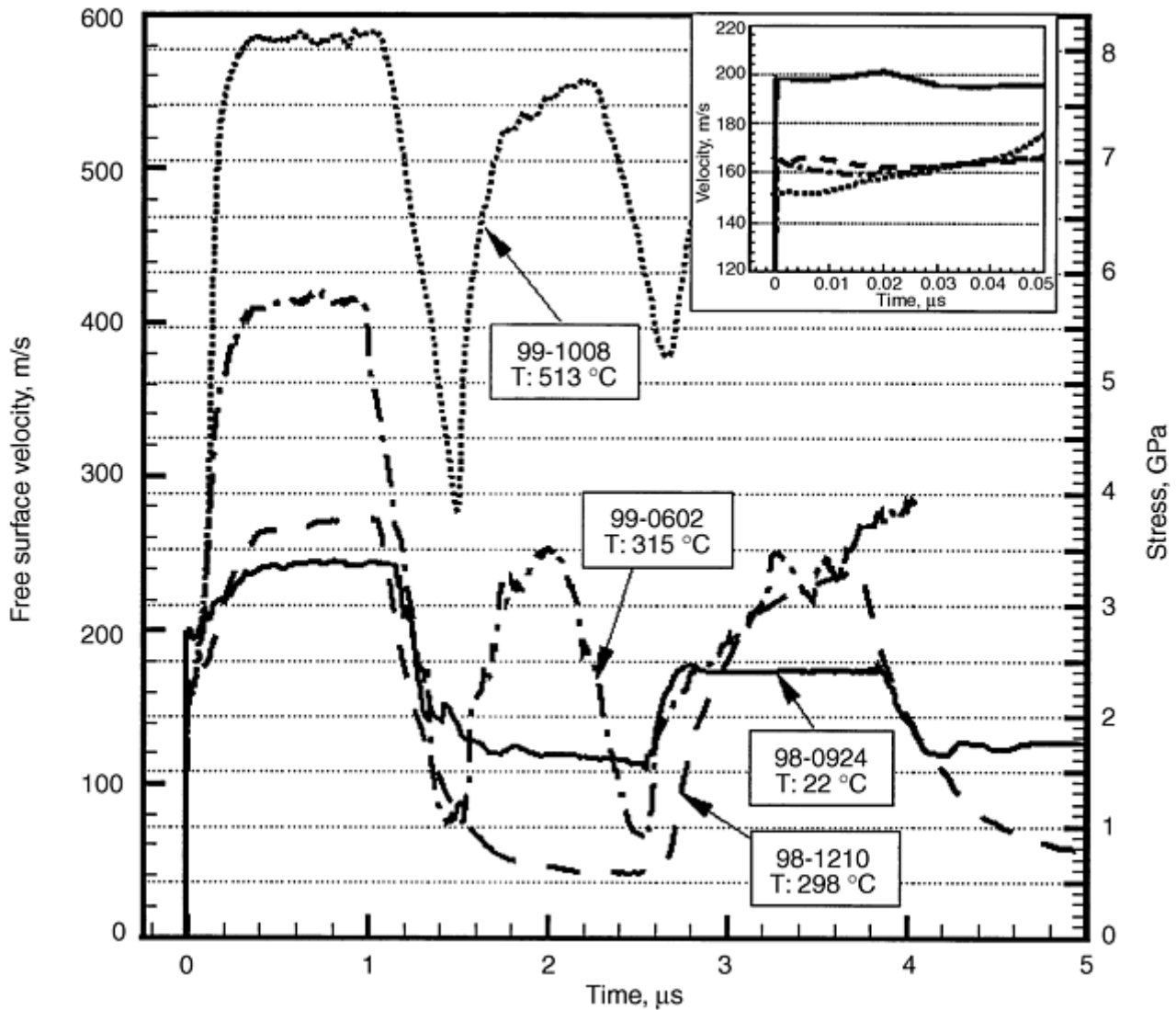


Fig. 17 Velocity histories of normal high-temperature impact experiments. Source: Ref 44, 84

The transition between elastic-plastic behavior is clearly captured; there is a sharp elastic unloading followed by a dispersive unloading tail. The dispersion in the unloading tail is due to the severe plastic deformation the material underwent in the loading phase. The reloading pulse that is generated by the reflection at the flyer-specimen interface is greatly reduced with respect to the expected elastic behavior. Even though some hardening is expected due to the passage of the first loading pulse, the hardening must appear as a change in the slope of the second loading pulse instead of the observed attenuation. The attenuation indicates that part of the energy is dissipated in the form of shock-induced damage at the applied stress level. Note that no spall signal is observed in the free-surface velocity record. Hence, the stress-pulse attenuation is indicative of damage initiation without the formation of a spall region within the sample. This was confirmed by scanning electron microscopy (SEM) studies performed on the recovered samples. Microvoids at the α - β interface were observed through the thickness of the target plate. Details can be found in Ref 44.

An interesting feature of experiment 98-0924 is the oscillation of the velocity profile close to the end of the first unloading. Mescheryakov et al. (Ref 89) reported that oscillations in their VISAR signal appeared to indicate a shock-induced phase transformation in Ti-6Al-4V. Their post-test SEM studies performed over samples recovered right after the experiment in a water chamber presented evidence of an ω residual phase in the microstructure. The setup for this experiment did not allow for cooling the samples right after impact, but the similarity with Mescheryakov et al. (Ref 89) in the interferometric records indicates the presence of a shock-induced phase transformation in Ti-6Al-4V. The stress level for the transformation is 2.17 GPa (315 ksi), close to ω -start pressure reported by Vohra et al. (Ref 90) but lower than the phase transition reported by Mescheryako, 2.95 GPa (428 ksi). The direct transformation is not observed because it is overcome by the elastic wave.

A second experiment, 98-1210, performed at 298 °C (568 °F) shows the effect of temperature on damage kinetics at similar stress and strain rate levels. The elastic precursor is also lost in this experiment; several fringes were added to match boundary conditions. A higher plastic deformation expected at high temperature makes the slope of the plastic wave more pronounced, as can be observed in Fig. 17. The smoothness of the velocity profile shows a progressive deformation of the free surface, which is a clear indication of high plastic deformation within the target plate. The velocity jump corresponding to the HEL is lower, 166 m/s (545 ft/s), showing a decrease in the dynamic yield stress with temperature. The so-called precursor decay is also more pronounced due to the increased rate of plastic deformation. In this experiment, the temperature rise was estimated to be 17 °C (31 °F), giving a final temperature of 315 °C (600 °F) well below the β -transus temperature range for Ti-6Al-4V (570–650 °C, or 1060 to 1200 °F). No evidence of shock-induced phase transition appears in this experiment (see first unloading in Fig. 17).

Experiment 99-0602 was carried out at 315 °C (600 °F). This temperature is close to the temperature in experiment 98-1210, but the impact velocity is higher. For this experiment the interferometer was modified to a higher velocity per fringe, 95.1 m/s (312 ft/s). Even though a shorter delay leg was used, part of the elastic precursor overcame the recording system, and one fringe needed to be added to match the boundary conditions. According to the velocity profile shown in Fig. 17, the velocity jump corresponding to the HEL coincides with the one in experiment 98-1210 (same temperature). The plastic wave slope is higher, indicating a stronger hardening due to the higher inelastic strain rate. The unloading is dispersive and shows again the reverse-phase transformation. Between the first and second loading pulse, a clear spall signal appears. Spallation occurs at a lower stress than the one reported by other investigators (e.g., Ref 91). Some researchers attribute this to an incomplete fracture at the spall plane. There are several approaches to calculate spall strength. For consistency with results reported in the literature, for other metallic materials, the approach stated by Kanel et al. (Ref 82) is employed. Such an approach establishes the spall strength for a symmetric impact, according to $0.5 \rho C_0 \Delta V$, where ΔV is the velocity drop from the peak velocity to the spall signal. According to this equation, experiment 99-0602 presents spall strength of 4.47 GPa (648 ksi). This value represents a reduction of ~10% from the value of 5.1 GPa (740 ksi) at room temperature, reported in Ref 88 and 91. The reduction in spall strength with temperature was previously reported by Kanel et al. (Ref 82) in magnesium and aluminum. Oscillations in the free-surface velocity profile during unloading again indicate the phase transition $\omega \rightarrow \alpha$. This phase transition happens at a compressive stress level of approximately 2.25 GPa (434 ksi), slightly higher than the phase transition at room temperature. The temperature rise was estimated to be 40 °C (72 °F), giving a final temperature of 351 °C (664 °F). As in the previous case, the final temperature is well below the β -transus; hence, allotropic transformations were not likely to occur.

To further explore the spall behavior, experiment 99-1008 was carried out at a temperature close to the limit of applicability of Ti-6Al-4V, that is, ~500 °C (930 °F). The impact velocity was set to about 590 m/s (1935 ft/s) to ensure a clear spallation process. The velocity per fringe in the interferometer was 97.2 m/s (318.9 ft/s), resulting in a partial loss of the elastic precursor as in experiment 98-1210. The free-surface velocity profile for this last experiment is shown in Fig. 17. A consistent reduction of the HEL with temperature can be observed. The plastic wave slope is steeper than in the other discussed experiments, indicating an even stronger hardening. A Hugoniot state is clearly achieved followed by a dispersive unloading pulse as in previous experiments. The overall wave profile is smooth, indicating a progressive deformation when the wave travels through the target. Between the expected first and second loading pulses, a fast-rising pull-back signal and clear spallation signal appear, which indicates the formation of a well-defined spall fracture plane. The higher rate of velocity increase during spallation is evidence that the fracture process is more violent than the one in experiment 99-0602. In fact, the recovered target was split into two pieces (Ref 44). Using the approach developed by Kanel et al. (Ref 82), the spall strength was estimated at 4.30 GPa (624 ksi). This indicates a reduction of 5% in the spall strength with an increment of ~200 °C (360 °F). The decrease in spall strength is in agreement with the results reported in Ref 82 for magnesium and aluminum. The inverse shock phase transformation $\alpha - \omega$ was not present in this experiment. The spall signal rings at a higher stress than the level corresponding to the inverse shock transformation previously observed. Therefore, it is not possible to conclude whether the increase of the peak shock stress can trigger the inverse shock transformation despite the increase in temperature. The temperature rise for this experiment was estimated to be 81 °C (146 °F), resulting in a final temperature of 593 °C (1100 °F). The final value is close to the β -transus temperature. Thermomechanical properties change with allotropic transformations in Ti-6Al-4V (Ref 92).

A comprehensive microscopy study on the failure and damage modes of Ti-6Al-4V as a function of temperature can be found in Ref 44 and 84.

References cited in this section

42. K.J. Frutschy and R.J. Clifton, High-Temperature Pressure-Shear Plate Impact Experiments on OFHC Copper, *J. Mech. Phys. Solids*, Vol 46 (No. 10), 1998, p 1723–1743
43. K.J. Frutschy and R.J. Clifton, High-Temperature Pressure-Shear Plate Impact Experiments Using Pure Tungsten Carbide Impactors, *Exp. Mech.*, Vol 38 (No. 2), 1998, p 116–125
44. H.V. Arrieta and H.D. Espinosa, The Role of Thermal Activation on Dynamic Stress Induced Inelasticity and Damage in Ti-6Al-4V, submitted to *Mech. Mater.*, 2000
49. L.M. Barker and R.E. Hollenbach, Laser Interferometry for Measuring High Velocities of Any Reflecting Surface, *J. Appl. Phys.*, Vol 43 (No. 11), 1972, p 4669–4675
70. S. Yadav and K.T. Ramesh, The Mechanical Properties of Tungsten-Based Composites at Very High Strain Rates, *Mater. Sci. Eng. A*, Vol A203, 1995, p 140
71. D.R. Chichili, K.T. Ramesh, and K.J. Hemker, High-Strain-Rate Response of Alpha-Titanium: Experiments, Deformation Mechanisms and Modeling, *Acta Mater.*, Vol 46 (No. 3), 1998, p 1025–1043
72. R. Kapoor and S. Nemat-Nasser, High-Rate Deformation of Single Crystal Tantalum: Temperature Dependence and Latent Hardening, *Scr. Mater.*, Vol 40 (No. 2), 18 Dec 1998, p 159–164
73. K.-S. Kim, R.M. McMeeking, and K.L. Johnson, Adhesion, Slip, Cohesive Zones and Energy Fluxes for Elastic Spheres, *J. Mech. Phys. Solids*, Vol 46, 1998, p 243–266
74. W. Johnson, Processes Involving High Strain Rates, *Int. Phys. Conference Series*, Vol 47, 1979, p 337
75. J.D. Campbell, High Strain Rate Testing of Aluminum, *Mater. Sci. Eng.*, Vol 12, 1973, p 3
76. Hirschvogel, Metal Working Properties, *Mech. Working Technol.*, Vol 2, 1978, p 61
77. S. Yadav and K.T. Ramesh, Mechanical Behavior of Polycrystalline Hafnium: Strain-Rate and Temperature Dependence, *Mater. Sci. Eng. A: Structural Materials: Properties, Microstructure & Processing*, No. 1–2, 15 May 1998, p 265–281
78. L.X. Zhou and T.N. Baker, Deformation Parameters in b.b.c., *Met. Mater. Sci. Eng.*, Vol A177, 1994, p 1
79. S. Nemat-Nasser and J.B. Isaacs, Direct Measurement of Isothermal Flow Stress of Metals at Elevated Temperatures and High Strain Rates with Application to Ta and Ta-W Alloys, *Acta Mater.*, Vol 45 (No. 3), 1997, p 907–919
80. A.M. Lennon and K.T. Ramesh, Technique for Measuring the Dynamic Behavior of Materials at High Temperatures, *Inter. J. Plast.*, Vol 14 (No. 12), 1998, p 1279–1292
81. T. Sakai, M. Ohashi, and K. Chiba, Recovery and Recrystallization of Polycrystalline Nickel after Hot Working, *Acta Metall.*, Vol 36, 1988, p 1781
82. G.I. Kanel, S.V. Razorenov, A. Bogatch, A.V. Utkin, and V.E. Fortov, Spall Fracture Properties of Aluminum and Magnesium at High Temperatures, *J. Appl. Phys.*, Vol 79, 1996, p 8310

83. V.K. Golubev and Y.S. Sobolev, Effect of Temperature on Spall Failure of Some Metal Alloys, *11th APS Topical Group Meeting on Shock Compression of Condensed Matter* (Snowbird, UT), American Physics Society, 1999
84. H.V. Arrieta, "Dynamic Testing of Advanced Materials at High and Low Temperatures," MSc thesis, Purdue University, West Lafayette, IN, 1999
85. R.A. Wood, *Titanium Alloy Handbook*, Metals and Ceramic Center, Battelle, Publication MCIC-HB-02, 1972
86. G.Q. Chen and T.J. Ahrens, Radio Frequency Heating Coils for Shock Wave Experiments, *Mater. Res. Symp. Proc.*, Vol 499, 1998, p 131
87. H.D. Espinosa, Recent Developments in Velocity and Stress Measurements Applied to the Dynamic Characterization of Brittle Materials, *Mech. Mater.*, H.D. Espinosa and R.J. Clifton, Ed., Vol 29, 1998, p 219–232
88. N.S. Brar and A. Hopkins, Shock Hugoniot and Shear Strength of Ti-6Al-4V, *11th APS Topical Group Meeting on Shock Compression of Condensed Matter*, (Snowbird, UT), American Physics Society, 1999
89. Y. Mescheryakov, A.K. Divakov, and N.I. Zhigacheva, Shock-Induced Phase Transition and Mechanisms of Spallation in Shock Loaded Titanium Alloys, *11th APS Topical Group Meeting on Shock Condensed Matter*, Snowbird, UT, 1999
90. Y.K. Vohra, S.K. Sikka, S.N. Vaidya, and R. Chidambaram, Impurity Effects and Reaction Kinetics of the Pressure-Induced Alpha to Omega Transformation in Ti, *J. Phys. Chem. Solids*, Vol 38, 1977, p 1293
91. Y. Me-Bar, M. Boas, and Z. Rosenberg, Spall Studies on Ti-6Al-4V, *Mater. Sci. Eng.*, Vol 85, 1987, p 77
92. J.E. Shrader and M.D. Bjorkman, High Temperature Phase Transformation in the Titanium Alloy Ti-6Al-4V, *American Physics Society Conference Proc.*, No. 78, American Physics Society, 1981, p 310–314

Low-Velocity Impact Testing

Horacio Dante Espinosa, Northwestern University, Sia Nemat-Nasser, University of California, San Diego

Impact Techniques with In-Material Stress and Velocity Measurements

Several research efforts have been made for in-material measurements of longitudinal and shear waves in dynamically loaded solids. Successful experiments where velocity histories have been obtained at interior surfaces by inserting metallic gages in a magnetic field and measuring the current generated by their motion have been reported (Ref 93, 94, and 95); these gages are called electromagnetic particle velocity (EMV) gages. This technique can be applied only to nonmetallic materials.

Another technique developed for in-material measurements employs manganin gages placed between the specimen and a back plate to measure the time history of the longitudinal stress, or by placing a manganin gage at an interface made in the direction of wave propagation to measure lateral stresses (Ref 96, 97). In this

configuration, the dynamic shear resistance of the material can be obtained by simultaneously measuring the axial and lateral stresses.

An alternative technique for the in-material measurement of the dynamic shear resistance of materials is the use of oblique impact with the specimen backed by a window plate (Ref 56). In this technique, longitudinal and shear wave motions are recorded by a combined normal displacement interferometer (NDI) or a normal velocity interferometer (NVI) (Ref 48) and a transverse displacement interferometer (TDI) (Ref 50). Alternatively, the VSDI interferometer previously discussed can be used. The velocity measurements are accomplished by manufacturing a high-pitch diffraction grating at the specimen-window interface (Ref 56).

In-Material Stress Measurements with Embedded Piezoresistant Gages. Many materials exhibit a change in electrical resistivity as a function of both pressure and temperature. Manganin, an alloy with 24 wt% Cu, 12 wt% Mn, and 4 wt% Ni, was first used as a pressure transducer in a hydrostatic apparatus by Bridgman in 1911 (Ref 98). Manganin is a good pressure transducer because it is much more sensitive to pressure than it is to temperature changes. Impact experiments performed by Bernstein and Keough (Ref 99) and DeCarli et al. (Ref 100) showed a linear relationship between axial stress σ_1 , in the direction of wave propagation, and resistance change; namely, $\sigma_1 = \Delta R / kR_0$ in which R_0 is the initial resistance and k is the piezoresistance coefficient. For manganin, DeCarli et al. (Ref 100) found $k = 2.5 \times 10^{-2} \text{ GPa}^{-1}$. The value of this coefficient is a function of the gage alloy composition; therefore, a calibration is required. Manganin gages are well suited for stress measurements above 4 GPa (580 ksi) and up to 100 GPa (15×10^6 psi). At lower stresses, carbon and ytterbium have a higher-pressure sensitivity (Ref 101), resulting in larger resistance changes and, hence, more accurate measurements. Carbon gages can be accurately used up to pressures of 2 GPa (290 ksi), while ytterbium can be used up to pressures of 4 GPa (580 ksi).

In plate impact experiments, the gage element is usually embedded between plates to measure either longitudinal or transverse axial stresses. A schematic of the experimental configuration is shown in Fig. 18. If the gage is placed between conductive materials, it needs to be electrically insulated by packaging the gage using polyester film, mica, or polytetrafluoroethylene. Another reason for using a gage package is to provide additional protection in the case of brittle materials undergoing fracture.

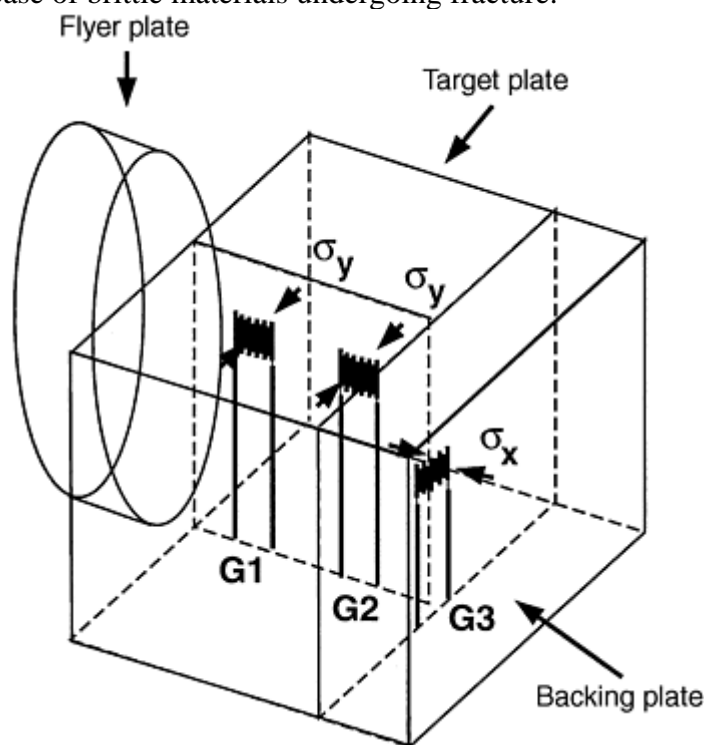


Fig. 18 Manganin gage experiment configuration. Gages G1 and G2 record transverse stress at two locations. Gage G3 records the longitudinal stress at the specimen back plate interface. Source: Ref 87

Through the use of metallic leads, the gage is connected to a power supply that energizes the gage prior to the test. The power supply comprises a capacitor that is charged to a selected voltage and discharged upon command into a bridge network by the action of a timer and a power transistor. The current pulse that is delivered to the bridge is quasi-rectangular with duration between 100 and 800 μs . The bridge network is

basically a Wheatstone bridge that is externally completed by the gage. The gage, which is nominally $50\ \Omega$, is connected to the bridge with a $50\ \Omega$ coaxial cable. The reason for using a pulse excitation of the bridge, rather than a continuous excitation, is that such an approach permits high outputs without the need for signal amplification and avoids excessive Joule heating effects that can result in gage failure. The bridge output is connected to an oscilloscope for the recording of voltage changes resulting from changes in resistance. The relation between voltage and resistance change is obtained by means of a calibration with a variable resistor.

A concern with this technique is the perturbation of the one dimensionality of the wave propagation due to the presence of a thin layer, perpendicular to the wave front, filled with a material having a different impedance and mechanical response. Calculations by Wong and Gupta (Ref 102) show that the inelastic response of the material being studied affects the gage calibration. In 1994, Rosenberg and Brar (Ref 103) reported that in the elastic range of the gage material, its resistance change is a function of the specimen elastic moduli. In a general sense, this is a disadvantage in the lateral stress-gage concept. Nonetheless, their analysis shows that in the plastic range of the lateral gage response, a single calibration curve for all specimen materials exists. These findings provide a methodology for the appropriate interpretation of lateral gage signals and increase the reliability of the lateral stress-measuring technique.

Example: Identification of Failure Waves in Glass. In-material axial and transverse stress measurements have been successfully used in the interpretation of so-called failure waves in glass (Ref 24, 25, and 45). By using the configuration shown in Fig. 18 with the longitudinal gage backed by a PMMA plate, the dynamic tensile strength of the material was determined (Ref 45). In these experiments, manganin gages were used. Soda-lime and aluminosilicate glass plates were tested. The density and longitudinal wave velocity for the soda-lime glass were $2.5\ \text{g/cm}^3$ and $5.84\ \text{mm}/\mu\text{s}$, respectively. The aluminosilicate glass properties were density = $2.64\ \text{g/cm}^3$, Young's modulus = $86\ \text{GPa}$ ($12 \times 10^6\ \text{psi}$), and Poisson's ratio = 0.24.

By appropriate selection of the flyer-plate thickness, the plane at which tension occurs for the first time within the sample was located close to the impact surface or close to the specimen-PMMA interface. In experiment 7-0889, a 5.7 mm (0.22 in.) thick soda-lime glass target was impacted with a 3.9 mm (0.15 in.) aluminum flyer at a velocity of 906 m/s (2972 ft/s). The manganin gage profile is shown in Fig. 19. The spall plane in this experiment happened to be behind the failure wave. The profile shows the arrival of the compressive wave with a duration of approximately $1.5\ \mu\text{s}$, followed by a release to a stress of about 3 GPa (435 ksi) and a subsequent increase to a constant stress level of 3.4 GPa (493 ksi). The stress increase after release is the result of reflection of the tensile wave from material that is being damaged under dynamic tension and represents the dynamic tensile strength of the material (spall strength). From this trace, it was concluded that soda-lime glass shocked to a stress of 7.5 GPa (1088 ksi) has a spall strength of about 0.4 GPa (58 ksi) behind the so-called failure wave. The experiment was repeated with a 2.4 mm (0.09 in.) thick aluminum flyer (7-1533); the result was complete release from the back of the aluminum impactor (Fig. 19). A pull-back signal was observed after approximately $0.45\ \mu\text{s}$ with a rise in stress of about 2.6 GPa (377 ksi). It should be noted that the spall plane in this experiment was in front of the failure wave. These two experiments clearly show that the spall strength of glass depends on the location of the spall plane with respect to the propagating failure wave. For soda-lime glass, a dynamic tensile strength of 2.6 and 0.4 GPa (377 and 58 ksi) was measured with manganin gages in front of and behind the failure wave, respectively. Dandekar and Beaulieu (Ref 104) obtained similar results using a VISAR.

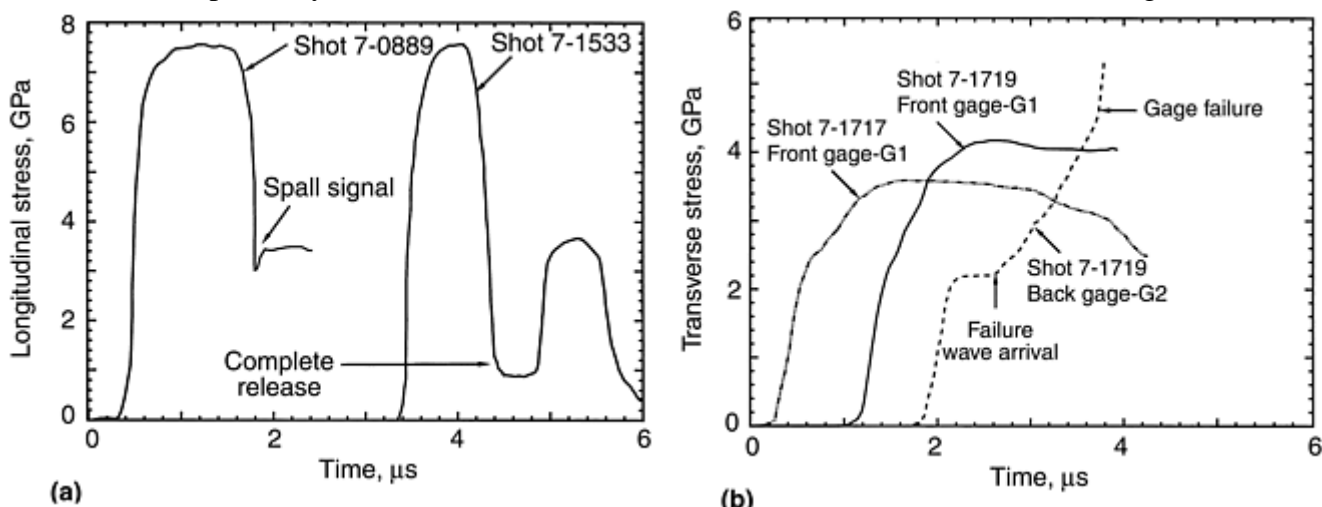


Fig. 19 In-material gage profiles from spall experiments. (a) Longitudinal profiles. Gage profile on the left shows a strong reduction in spall strength (measurement behind the so-called failure wave front). (b) Transverse profiles showing transverse stress histories at two locations within the glass specimen. Source: Ref 87

Additional features of the failure-wave phenomenon were obtained from transverse gage experiments performed on soda-lime and aluminosilicate glasses (Ref 24). In these experiments, one or two narrow 2 mm (0.08 in.) wide manganin gages (type C-8801113-B) were embedded in the glass target plates in the direction transverse to the shock direction as shown in Fig. 18. A thick back plate of the same glass was used in the target assembly. Aluminum or glass impactor plates were used to induce failure waves. The transverse stress, σ_2 , was obtained from the transverse gage record. Figure 19 shows measured transverse gage profile at two locations (shot 7-1719) in the aluminosilicate glass. The two-wave structure that results from the failure wave following the longitudinal elastic wave can clearly be seen. The first gage, at the impact surface, shows an increase in lateral stress to the value predicted by one-dimensional wave theory, 2.2 GPa (319 ksi) in Fig. 19, immediately followed by a continuous increase to a stress level of 4.2 GPa (609 ksi). The second gage, at 3 mm (0.12 in.) from the impact surface, initially measures a constant lateral stress of 2.2 GPa (319 ksi) followed by an increase in stress level on arrival and passage of the failure wave. It should be noted that the initial slope was measured by lateral gage G2. This can only be the case if the failure wave does not have an incubation time so the increase in lateral stress with the sweeping of the failure wave through the gage increases the initial slope in gage G1. By contrast, gage G2 sees the arrival of the failure wave about 700 ns after the arrival of the elastic wave (see step at 2.2 GPa). Furthermore, these traces also confirm that the failure wave initiates at the impact surface and propagates to the interior of the sample. This interpretation is in agreement with the impossibility of monitoring impact surface velocity with a VISAR system (Ref 104) when failure waves are present. The impact parameters used in these experiments are summarized in Table 7. Measured profiles of manganin gages were converted to stress-time profiles following the calibrations of longitudinal and transverse manganin gages under shock loading given in Ref 105 and 103, respectively.

Table 7 Summary of parameters and results for manganin gage experiments

Shot No.	Material	Thickness of aluminum impactor		Target thickness		Impact velocity		Normal stress	
		mm	in.	mm	in.	m/s	ft/s	GPa	ksi
7-0889	Soda-lime glass	3.9	0.15	5.7	0.22	906	2972	7.5	1088
7-1533	Soda-lime glass	2.4	0.09	5.7	0.22	917	3009	7.6	1102
7-1717	Aluminosilicate glass	12.7	0.50	19.4	0.76	770	2526	6.1	885
7-1719	Aluminosilicate glass	14.5	0.57	19.4	0.76	878	2881	6.97	1011

References cited in this section

24. H.D. Espinosa, Y. Xu, and N.S. Brar, Micromechanics of Failure Waves in Glass: Experiments, *J. Am. Ceram. Soc.*, Vol 80 (No. 8), 1997, p 2061–2073
25. H.D. Espinosa, Y. Xu, and N.S. Brar, Micromechanics of Failure Waves in Glass: Modeling, *J. Am. Ceram. Soc.*, Vol 80 (No. 8), 1997, p 2074–2085
45. N.S. Brar and S.J. Bless, Failure Waves in Glass under Dynamic Compression, *High Pressure Res.*, Vol 10, 1992, p 773–784
48. L.M. Barker and R.E. Hollenbach, Interferometer Technique for Measuring the Dynamic Mechanical Properties of Materials, *Rev. Sci. Instrum.*, Vol 36 (No. 11), 1965, p 1617–1620
50. K.S. Kim, R.J. Clifton, and P. Kumar, A Combined Normal and Transverse Displacement Interferometer with an Application to Impact of Y-Cut Quartz, *J. Appl. Phys.*, Vol 48, 1977, p 4132–4139

56. H.D. Espinosa, Dynamic Compression Shear Loading with In-Material Interferometric Measurements, *Rev. Sci. Instrum.*, Vol 67 (No. 11), 1996, p 3931–3939
87. H.D. Espinosa, Recent Developments in Velocity and Stress Measurements Applied to the Dynamic Characterization of Brittle Materials, *Mech. Mater.*, H.D. Espinosa and R.J. Clifton, Ed., Vol 29, 1998, p 219–232
93. Y.M. Gupta, Shear Measurements in Shock Loaded Solids, *Appl. Phys. Lett.*, Vol 29, 1976, p 694–697
94. Z. Young and O. Dubugnon, A Reflected Shear-Wave Technique for Determining Dynamic Rock Strength, *Int. J. Rock Mech. Min. Sci.*, 1977, p 247–259
95. Y.M. Gupta, D.D. Keough, D.F. Walter, K.C. Dao, D. Henley, and A. Urweider, Experimental Facility to Produce and Measure Compression and Shear Waves in Impacted Solids, *Rev. Sci. Instrum.*, Vol 51(a), 1980, p 183–194
96. R. Williams and D.D. Keough, Piezoresistive Response of Thin Films of Calcium and Lithium to Dynamic Loading, *Bull. Am. Phys. Soc. Series II*, Vol 12, 1968, p 1127
97. Z. Rosenberg and S.J. Bless, Determination of Dynamic Yield Strengths with Embedded Manganin Gages in Plate-Impact and Long-Rod Experiments, *Exp. Mech.*, 1986, p 279–282
98. P.W. Bridgman, *Proc. Am. Acad. Arts Sci.*, Vol 47, 1911, p 321
99. D. Bernstein and D.D. Keough, Piezoresistivity of Manganin, *J. Appl. Phys.*, Vol 35, 1964, p 1471
100. P.S. DeCarli, D.C. Erlich, L.B. Hall, R.G. Bly, A.L. Whitson, D.D. Keough, and D. Curran, “Stress-Gage System for the Megabar (100 MPa) Range,” Report DNA 4066F, Defense Nuclear Energy, SRI Intl., Palo Alto, CA, 1976
101. L.E. Chhabildas and R.A. Graham, *Techniques and Theory of Stress Measurements for Shock-Wave Applications*, Symposia Series, ASME, Applied Mechanics Division (AMD), AMD-83, 1987, p 1–18
102. M.K.W. Wong and Y.M. Gupta, Dynamic Inclusion Analyses of Lateral Piezoresistance Gauges under Shock Wave Loading, *Shock Compression of Condensed Matter*, S.C. Schmidt, R.D. Dick, J.W. Forbes, and D.J. Tasker, Ed., Elsevier, Essex, U.K., 1991
103. Z. Rosenberg and N.S. Brar, Hysteresis of Lateral Piezoresistive Gauges, *High Pressure Science and Technology*, Joint AIRAPT-APS Conference (Colorado Springs, CO), S.C. Schmidt, Ed., 1994, p 1707–1710
104. D.P. Dandekar and P.A. Beaulieu, Failure Wave under Shock Wave Compression in Soda Lime Glass, *Metallurgical and Material Applications of Shock-Wave and High-Strain-Rate Phenomena*, L.E. Murr et al., Ed., Elsevier, 1995
105. Z. Rosenberg and Y. Partom, Longitudinal Dynamic Stress Measurements with In-Material Piezoresistive Gauges, *J. Appl. Phys.*, Vol 58, 1985, p 1814

Low-Velocity Impact Testing

Low-Velocity Penetration Experiments

In many ballistic impact tests, often only the incident and residual velocities are recorded. To understand how targets defeat projectiles, the complete velocity history of the projectile must be recorded. Moreover, multiple instrumentation systems are highly desirable because they provide enough measurements for the identification of failure through modeling and analysis. In this section, a new experimental configuration that can record tail-velocity histories of penetrators and target back surface out-of-plane motion in penetration experiments is presented. The technique provides multiple real-time diagnostics that can be used in model development. Laser interferometry is used to measure the surface motion of both projectile tail and target plate with nanosecond resolution. The investigation of penetration in woven glass fiber reinforced polyester (GRP) composite plates also is discussed.

Experimental Setup. Penetration experiments were conducted with a 75 mm (3 in.) light gas gun with keyway. The experiments were designed to avoid complete destruction of the target plate so that microscopy studies could be performed in the samples. Impactor tail velocity and back surface target plate velocity histories were successfully measured by using the setups shown in Fig. 20(a) and (b), direct and reverse penetration experiments, respectively.

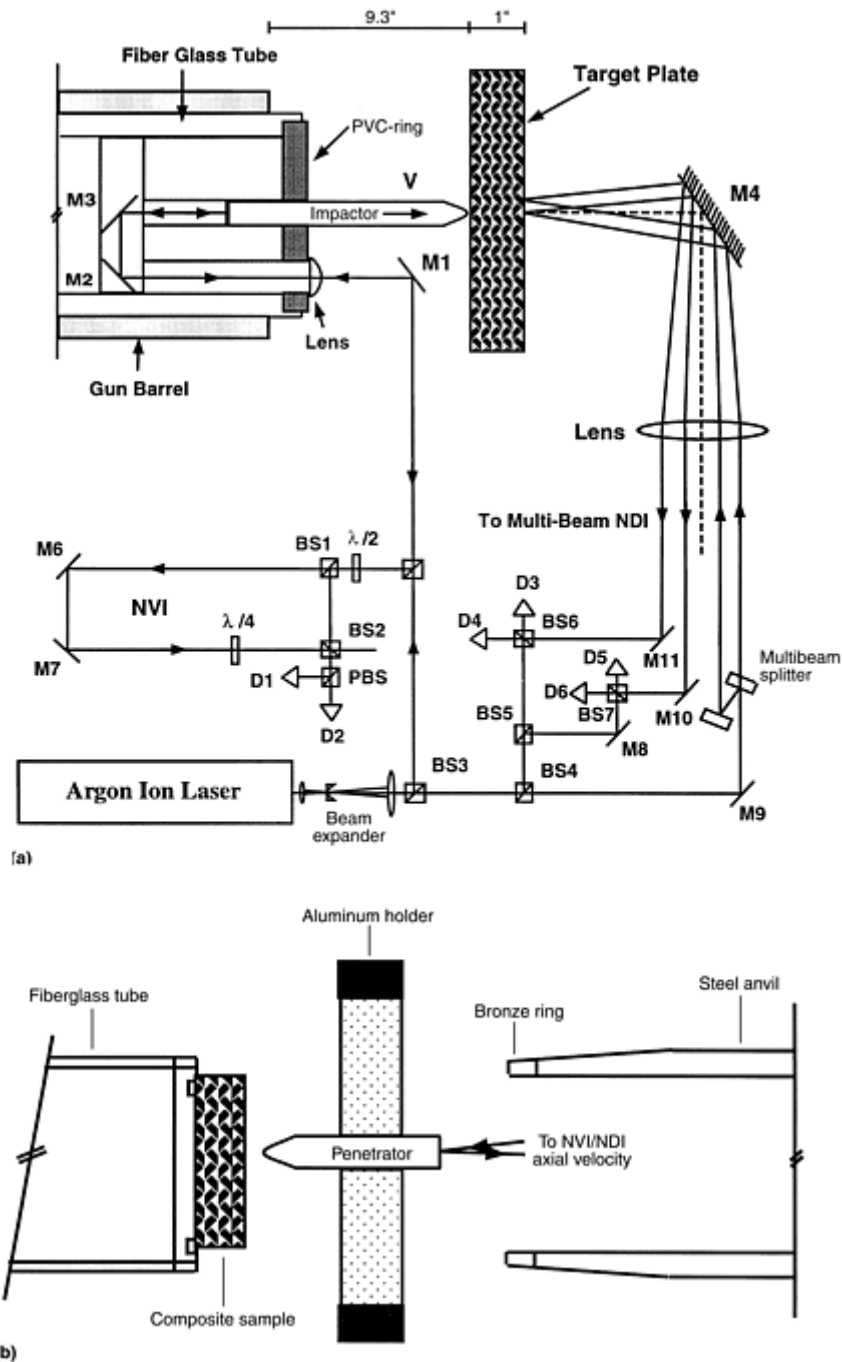


Fig. 20 Low-velocity penetration experiments. (a) Setup for direct penetration experiment (rod-on-plate). (b) Setup for reverse penetration experiment (plate-on-rod). Source: Ref 107

In the case of direct penetration experiments (Fig. 20a), the projectile holder was designed such that a normal velocity interferometer could be obtained on a laser beam reflected from the back surface of the projectile. In addition to this measurement, a multipoint interferometer was used to continuously record the motion of the target back surface. It should be noted that the NVI system used in this configuration has variable sensitivity so its resolution can be adjusted to capture initiation and evolution of failure. The NVI records contain information on interply delamination, fiber breakage and kinking, and matrix inelasticity as these events start and progress in time.

A cylindrical target plate 100 mm (4 in.) in diameter and 25 mm (1 in.) thick was positioned in a target holder with alignment capabilities. The target was oriented so that impact at normal incidence was obtained. A steel penetrator with a 30° conical tip was mounted in a fiberglass tube by means of a PVC holder. This holder contained two mirrors and a plano-convex lens along the laser beam path. The focal distance of the plano-convex lens was selected to focus the beam at the penetrator back surface. Penetrator tail velocities were measured by means of the normal velocity interferometer (NVI), with signals in quadrature (Fig. 20a). The

interferometer beams were aligned while the penetrator was at the end of the gun barrel (i.e., on conditions similar to the conditions occurring at the time of impact). The alignment consisted of adjusting mirrors M1, M2, and M3 such that the laser beam, reflected from the penetrator tail, coincided with the incident laser beam. Through motion of the fiberglass tube along the gun barrel, it was observed that the present arrangement preserves beam alignment independently of the position of the penetrator in the proximity of the target. Therefore, a considerable recording time could be expected before the offset of the interferometer. A few precautions were taken to avoid errors in the measurement. First, the PVC holder was designed such that the penetrator could move freely along a cylindrical cavity (i.e., no interaction between the steel penetrator and PVC holder was allowed and, therefore, true deceleration was recorded). The penetrator was held in place during firing by means of epoxy deposited at the penetrator periphery on the front face of the PVC holder. Second, in order to avoid projectile rotation that could offset the interferometer alignment, a polytetrafluoroethylene key was placed in the middle of the fiberglass tube. Target back surface velocities were measured with a multipoint normal displacement interferometer (NDI). Since woven composites are difficult to polish, the reflectivity of the back surface was enhanced by gluing a 0.025 mm (0.001 in.) mylar sheet, and then a thin layer of aluminum was vapor deposited.

In the case of reverse-penetration experiments (Fig. 20b), composite flyer plates were cut with a diameter of 57 mm (2.25 in.) and a thickness of 25 mm (1 in.). The composite plates were lapped flat using 15 μ m silicon carbide powder slurry. These plates were mounted on a fiberglass tube by means of a backing aluminum plate. The penetrator, a steel rod with a 30° conical tip, was mounted on a target holder and aligned for impact at normal incidence. In these experiments, the penetrator back-surface velocity was simultaneously measured by means of NDI and NVI systems. A steel anvil was used to stop the fiberglass tube and allow the recovery of the sample.

Experimental Results: Velocity Measurements. A summary of experiments is given in Table 8. The NVI signals in quadrature were analyzed following the procedure described in Ref 106. The NDI signals were converted to particle velocities according to the procedure described in Ref 52. The impactor velocity during the penetration event, in experiments 5-1122 and 6-1117, is given in Fig. 21. A velocity reduction of approximately 32 m/s (105 ft/s) in shot 5-1122 and about 20 m/s (66 ft/s) in shot 6-1117 are observed after 100 μ s of the recorded impact. A progressive decrease in velocity is observed in the first 30 μ s followed by an almost constant velocity and a sudden velocity increase of 7 m/s (23 ft/s) at approximately 60 μ s. Further reduction in velocity is measured in the next 40 μ s. In the case of shot 6-1117, the tail velocity shows a profile with features similar to the one recorded in shot 5-1122. These velocity histories present a structure that should be indicative of the contact forces that develop between penetrator and target, as well as the effect of damage in the penetration resistance of GRP target plates. It should be noted that a projectile traveling at 200 m/s (656 ft/s) moves a distance of 20 mm (0.8 in.) in 100 μ s.

Table 8 Summary of parameters for rod-on-plate and plate-on-rod impact experiments

Experiment No.	Impact velocity		Specimen diameter		Type of experiment
	m/s	ft/s	mm	in.	
5-1122	200 ^(a)	656 ^(a)	102	4	Direct penetration
6-0308	200 ^(a)	656 ^(a)	57	2.25	Reverse penetration
6-0314	500 ^(a)	1640 ^(a)	57	2.25	Reverse penetration
6-0531	181.6	596	102	4	Direct penetration
6-1117	180.6	593	102	4	Direct penetration

Note: For all experiments, specimen thickness was 24 mm (1 in.); impactor dimensions were 14 mm (0.56 in.) diam; 30° conical, 64 mm (2.5 in.) length.

(a) Velocity estimated from gas gun calibration curve based on breech pressure.

Source: Ref 107

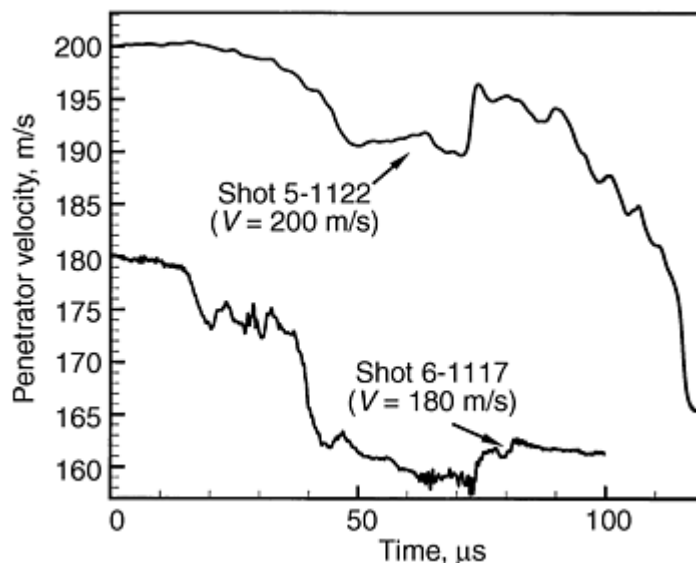


Fig. 21 Penetrator tail velocity histories recorded with normal velocity interferometer (NVI) using the direct penetration configuration. V , velocity. Source: Ref 107

Back-surface velocity histories at the specimen center measured by means of a normal displacement interferometer (NDI) are shown in Fig. 22 for shot 5-1122, 6-0531, and 6-1117. A velocity increase to a value of 22 m/s (72 ft/s), followed by a decrease and increase to a maximum velocity of about 50 m/s (164 ft/s), after 20 μ s, is measured in shot 5-1122. The trace from shot 6-0531 and 6-1117 shows features similar to the features present in the velocity history recorded in experiment 5-1122. However, significant differences in amplitude are observed. A maximum particle velocity of 18 m/s (59 ft/s) is observed at about 37.5 μ s. These velocity histories present variations such as small humps with some apparent periodicity. Numerical simulation of the experiments, incorporating the observed failure modes, is required to interpret the various features observed in the velocity traces.

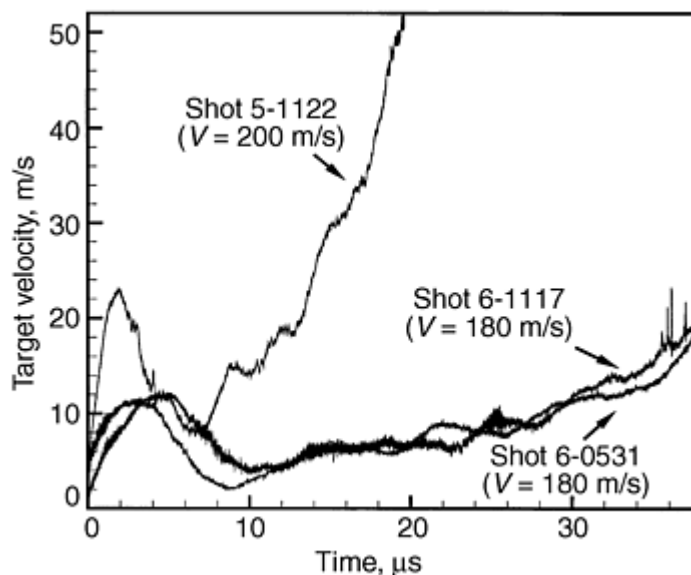


Fig. 22 Back surface normal velocity histories at the center of glass fiber-reinforced epoxy composite target. V , velocity. Source: Ref 107

To confirm the velocities measured in the direct penetration experiment, two reverse penetration experiments were conducted at impact velocities of 200 and 500 m/s (656 and 1640 ft/s), experiments 6-0308 and 6-0314, respectively. Another objective of these experiments was to examine rate effects in the penetration resistance of woven-fiber composites. The interferometrically measured penetrator tail velocities are plotted in Fig. 23. The steel penetrator velocity shows a progressive increase and a decrease to almost zero velocity upon arrival of an unloading wave generated at the penetrator-free surface. The arrival time of approximately 14 μ s coincides with

the round-trip time of the wave through the penetrator nose back to the penetrator tail. This feature is observed in both experiments. A continuous increase in velocity is recorded with velocities of 20 m/s and 32 m/s (66 and 105 ft/s) after 42 μ s, respectively. A maximum velocity of 50 m/s (164 ft/s) is recorded in experiment 6-0314 after 65 μ s. A comparison of the velocity histories in these two experiments clearly reveals that composite failure presents moderate rate sensitivity. Moreover, velocities recorded in experiment 6-0308 appear to confirm the velocity reduction interferometrically recorded in experiment 5-1122 (direct-penetration experiment).

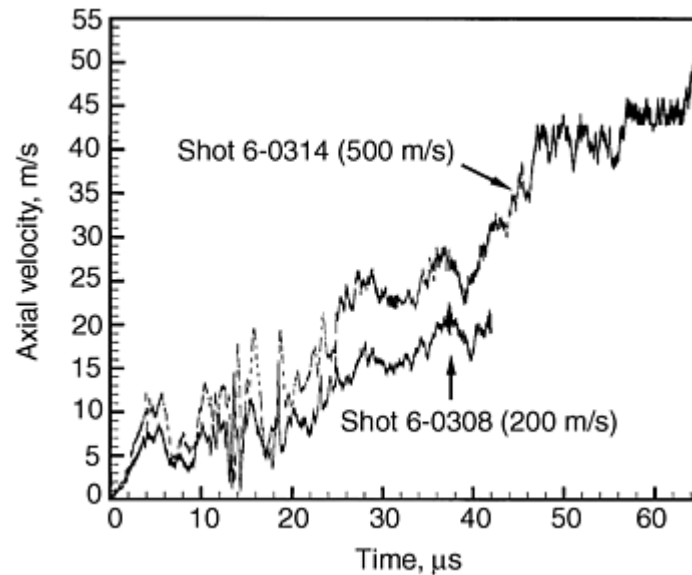


Fig. 23 Penetrator tail velocity histories recorded with normal displacement interferometer (NDI) in reverse penetration configuration. Source: Ref 107

Microscopy studies were performed in recovered samples to assess the amount of delamination and fiber fracture and kinking. The details of this study can be found in Ref 107.

References cited in this section

52. H.D. Espinosa, M. Mello, and Y. Xu, A Variable Sensitivity Displacement Interferometer with Application to Wave Propagation Experiments, *J. Appl. Mech.*, Vol 64, 1997, p 123–131
106. L. Barker, “VISAR88—A New Data Reduction Program for VISARs,” Sandia Report, Sandia National Laboratory, 1988
107. H.D. Espinosa, H.-C. Lu, and Y. Xu, A Novel Technique for Penetrator Velocity Measurement and Damage Identification in Ballistic Penetration Experiments, *J. Compos. Mater.*, Vol 32 (No. 8), 1998

Low-Velocity Impact Testing

Horacio Dante Espinosa, Northwestern University, Sia Nemat-Nasser, University of California, San Diego

References

1. P. Kumar and R.J. Clifton, Dislocation Motion and Generation in LiF Single Crystals Subjected to Plate-Impact, *J. Appl. Phys.*, Vol 50 (No. 7), 1979, p 4747–4762

2. K.S. Kim and R.J. Clifton, Pressure-Shear Impact of 6061-T6 Aluminum and Alpha-Titanium, *J. Appl. Mech.*, Vol 47, 1980, p 11–16
3. A. Gilat and R.J. Clifton, Pressure-Shear Waves in 6061-T6 Aluminum and Alpha-Titanium, *J. Mech. Phys. Solids*, Vol 33 (No. 3), 1985, p 263–284
4. C.H. Li, “A Pressure-Shear Experiment for Studying the Dynamic Plastic Response of Metals and Shear Strain Rates of 10^5 s^{-1} ,” Ph.D. thesis, Brown University, Providence, RI, 1982
5. R.J. Clifton and R.W. Klopp, Pressure-Shear Plate Impact Testing, *Mechanical Testing*, Vol 8, *ASM Handbook*, 9th ed., ASM International, 1985, p 230–239
6. K.T. Ramesh and R.J. Clifton, A Pressure-Shear Plate Impact Experiment for Studying the Rheology of Lubricants at High Pressures and High Strain Rates, *J. Tribology*, 1987, Vol 109, p 215
7. H.D. Espinosa and R.J. Clifton, Plate Impact Experiments for Investigating Inelastic Deformation and Damage of Advanced Materials, *Symposium on Experiments in Micromechanics of Fracture-Resistant Materials* (ASME Winter Annual Meeting), 1–6 Dec 1991 (Atlanta, GA), K.S. Kim, Ed., 1991, p 37–56
8. J.C. Escobar and R.J. Clifton, On Pressure-Shear Plate Impact for Studying the Kinetics of Stress-Induced Phase Transformations, *Mater. Sci. Eng. A: Structural Materials: Properties, Microstructure & Processing*, No. 1–2, 1 Oct 1993, p 125–142
9. Y. Sano, S.-N. Chang, M.A. Meyers, and S. Nemat-Nasser, Identification of Stress Induced Nucleation Sites for Martensite in Fe-31.8wt%Ni-0.02wt%C Alloy, *Acta Metall. Mater.*, Vol 40 (No. 2), 1992, p 413–417
10. G. Ravichandran and R.J. Clifton, Dynamic Fracture under Plane Wave Loading. *Int. J. Fract.*, Vol 40 (No. 3), 1989, p 157–201
11. G. Raiser, R.J. Clifton, and M. Ortiz, A Soft-Recovery Plate Impact Experiment for Studying Microcracking in Ceramics, *Mech. Mater.*, Vol 10, 1990, p 43–58
12. H.D. Espinosa, G. Raiser, R.J. Clifton, and M. Ortiz, Inelastic Mechanisms in Dynamically Loaded Ceramics, *Mechanics Computing in 1990s and Beyond*, *ASCE Proceedings*, 20–22 May 1991 (Columbus, OH), H. Adeli and R. Sierakowski, Ed., American Society of Civil Engineers, 1991, p 293–297
13. H.D. Espinosa, G. Raiser, R.J. Clifton, and M. Ortiz, Performance of the Star-Shaped Flyer in the Study of Brittle Materials: Three Dimensional Computer Simulations and Experimental Observations, *J. Appl. Phys.*, Vol 72 (No. 8), 1992, p 3451–3457
14. H.D. Espinosa, G. Raiser, R.J. Clifton, and M. Ortiz, Experimental Observations and Numerical Modeling of Inelasticity in Dynamically Loaded Ceramics, *J. Hard Mater.*, Vol 3 (No. 3–4), 1992, p 285–313
15. V. Prakash, L.B. Freund, and R.J. Clifton, Stress Wave Radiation from a Crack Tip during Dynamic Initiation, *J. Appl. Mech. (Trans. ASME)*, Vol 59 (No. 2), June 1992, p 356–365
16. A.R. Machcha and S. Nemat-Nasser, Pressure-Shear Recovery Experiments, *Mech. Mater.*, Vol 18, 1994, p 49–53
17. H.D. Espinosa, M. Mello, and Y. Xu, A Desensitized Displacement Interferometer Applied to Impact Recovery Experiments, *J. Appl. Phys. Lett.*, Vol 69 (No. 21), 1996, p 3161–3163

18. H.D. Espinosa, A. Patanella, and Y. Xu, Dynamic Compression-Shear Loading of Brittle Materials with Specimen Recovery, *Proceedings of the 11th Int. Conf. on Experimental Mechanics*, 24–28 Aug 1998 (Oxford, UK), I.M. Allison, Ed., 1998, p 223–229
19. H.D. Espinosa, A. Patanella, and Y. Xu, Dynamic Compression-Shear Response of Brittle Materials with Specimen Recovery, to appear in *Exp. Mech.*, 2000
20. M. Zhou, A. Needleman, and R.J. Clifton, Finite Element Simulations of Shear Localization in Plate Impact, *J. Mech. Phys. Solids*, Vol 42 (No. 3), 1994, p 423–458
21. H.D. Espinosa, On the Dynamic Shear Resistance of Ceramic Composites and its Dependence on Applied Multiaxial Deformation, *Int. J. Solids Struct.*, Vol 32 (No. 21), 1995, p 3105–3128
22. P.D. Zavattieri, P.V. Raghuram, and H.D. Espinosa, A Computational Model of Ceramic Microstructures Subjected to Multi-Axial Dynamic Loading, to appear in *J. Mech. Phys. Solids*, 2000
23. A.R. Machcha and S. Nemat-Nasser, Effects of Geometry in Pressure-Shear and Normal Plate Impact Experiments: Three-Dimensional Finite Element Simulations and Experimental Observations, *J. Appl. Phys.*, Vol 80 (No. 6), 1996, p 3267–3274
24. H.D. Espinosa, Y. Xu, and N.S. Brar, Micromechanics of Failure Waves in Glass: Experiments, *J. Am. Ceram. Soc.*, Vol 80 (No. 8), 1997, p 2061–2073
25. H.D. Espinosa, Y. Xu, and N.S. Brar, Micromechanics of Failure Waves in Glass: Modeling, *J. Am. Ceram. Soc.*, Vol 80 (No. 8), 1997, p 2074–2085
26. H.D. Espinosa, Y. Xu, and H.-C. Lu, Inelastic Behavior of Fiber Composites Subjected to Out-of-Plane High Strain Rate Shearing, *Acta Mater.*, Vol 45 (No. 11), 1997, p 4855–4865
27. H.V. Arrieta and H.D. Espinosa, High and Low Temperature Dynamic Testing of Advanced Materials, *Shock Compression of Condensed Matter*, APS Conference (Snowbird, UT), American Physics Society, 1999
28. H.D. Espinosa, P.D. Zavattieri, and G.L. Emore, Adaptive FEM Computation of Geometric and Material Nonlinearities with Application to Brittle Failure, *Mech. Mater.*, H.D. Espinosa and R.J. Clifton, Ed., Vol 29, 1998, p 275–305
29. H.D. Espinosa, P.D. Zavattieri, and S. Dwivedi, A Finite Deformation Continuum/Discrete Model for the Description of Fragmentation and Damage in Brittle Materials, *J. Mech. Phys. Solids*, Vol 46 (No. 10), 1998, p 1909–1942
30. A.S. Abou-Sayes, R.J. Clifton, and L. Hermann, The Oblique Plate Impact Experiment, *Exp. Mech.*, Vol 16, 1976, p 127–132
31. L.C. Chhabildas and J.W. Swegle, Dynamic Pressure-Shear Loading of Materials Using Anisotropic Crystals, *J. Appl. Phys.*, Vol 51, 1980, p 4799–4807
32. T. Nicholas and S.J. Bless, High Strain Rate Tension Testing, *Mechanical Testing*, Vol 8, *ASM Handbook*, 9th ed., ASM International, 1985, p 208–214
33. W.F. Hartman, Determination of Unloading Behavior of Uniaxially Strained 6061-T Aluminum from Residual Strain Measurements, *J. Appl. Phys.*, Vol 35, 1964, p 2090

34. R. Dandliker and J.-F. Willemin, Measuring Microvibrations by Heterodyne Speckle Interferometry, *Opt. Lett.*, Vol 6, 1981, p 165
35. J.E. Vorthman and G.E. Duvall, Dislocations in Shocked and Recovered LiF, *J. Appl. Phys.*, Vol 53, 1982, p 3607–3615
36. S.-N. Chang, D.-T. Chung, G. Ravichandran, and S. Nemat-Nasser, Plate Impact Experiments on Mg-PSZ and Improved Target Configuration, *Proceedings of 1989 APS Topical Conference on Shock Compression of Condensed Matter*, 14–17 Aug 1989, S.C. Schmidt, J.N. Johnson, and L.W. Davidson, Ed., American Physics Society, 1990, p 389–392
37. S.-N. Chang, D.-T. Chung, Y.F. Li, and S. Nemat-Nasser, Target Configurations for Plate-Impact Recovery Experiments, *J. Appl. Mech.*, Vol 92-APM-18, 1992, p 1–7
38. P. Kumar and R.J. Clifton, A Star-Shaped Flyer for Plate Impact Recovery Experiments, *J. Appl. Phys.*, Vol 48, 1977b, p 4850
39. R.J. Clifton, G. Raiser, M. Ortiz, and H.D. Espinosa, A Soft Recovery Experiment for Ceramics, *Proceedings of 1989 APS Conference on Shock Compression of Condensed Matter*, American Physics Society, 1990, p 437–440
40. S. Nemat-Nasser, J.B. Isaacs, G. Ravichandran, and J.E. Starrett, High Strain Rate Testing in the U.S., *Proceedings of the TTCP TTP-1 Workshop on New Techniques of Small Scale High Strain Rate Studies*, 26 April 1988 (Melbourne, Australia)
41. H.D. Espinosa, Micromechanics of the Dynamic Response of Ceramics and Ceramic Composites, Ph.D. thesis, Brown University, Providence, RI, 1992
42. K.J. Frutschy and R.J. Clifton, High-Temperature Pressure-Shear Plate Impact Experiments on OFHC Copper, *J. Mech. Phys. Solids*, Vol 46 (No. 10), 1998, p 1723–1743
43. K.J. Frutschy and R.J. Clifton, High-Temperature Pressure-Shear Plate Impact Experiments Using Pure Tungsten Carbide Impactors, *Exp. Mech.*, Vol 38 (No. 2), 1998, p 116–125
44. H.V. Arrieta and H.D. Espinosa, The Role of Thermal Activation on Dynamic Stress Induced Inelasticity and Damage in Ti-6Al-4V, submitted to *Mech. Mater.*, 2000
45. N.S. Brar and S.J. Bless, Failure Waves in Glass under Dynamic Compression, *High Pressure Res.*, Vol 10, 1992, p 773–784
46. D. Grady and J.L. Wise, “Dynamic Properties of Ceramic Materials,” Sandia Report SAND93-0610, Sandia National Laboratories, 1993
47. G.R. Fowles, Gas Gun for Impact Studies, *Rev. Sci. Instrum.*, Vol 41, 1970, p 984
48. L.M. Barker and R.E. Hollenbach, Interferometer Technique for Measuring the Dynamic Mechanical Properties of Materials, *Rev. Sci. Instrum.*, Vol 36 (No. 11), 1965, p 1617–1620
49. L.M. Barker and R.E. Hollenbach, Laser Interferometry for Measuring High Velocities of Any Reflecting Surface, *J. Appl. Phys.*, Vol 43 (No. 11), 1972, p 4669–4675
50. K.S. Kim, R.J. Clifton, and P. Kumar, A Combined Normal and Transverse Displacement Interferometer with an Application to Impact of Y-Cut Quartz, *J. Appl. Phys.*, Vol 48, 1977, p 4132–4139

51. L.C. Chhabildas, H.J. Sutherland, and J.R. Asay, Velocity Interferometer Technique to Determine Shear-Wave Particle Velocity in Shock-Loaded Solids, *J. Appl. Phys.*, Vol 50, 1979, p 5196–5201
52. H.D. Espinosa, M. Mello, and Y.Xu, A Variable Sensitivity Displacement Interferometer with Application to Wave Propagation Experiments, *J. Appl. Mech.*, Vol 64, 1997, p 123–131
53. W.F. Hemsing, Velocity Sensing Interferometer (VISAR) Modification, *Rev. Sci. Instrum.*, Vol 50 (No. 1), 1979, p 73–78
54. J.P. Sullivan and S. Ezekiel, A Two-Component Laser Doppler Velocimeter for Periodic Flow Fields, *J. Phys.*, Vol E7, 1974, p 272–274
55. L.C. Chhabildas, H.J. Sutherland, and J.R. Asay, A Velocity Interferometer Technique to Determine Shear-Wave Particle Velocity in Shock-Loaded Solids, *J. Appl. Phys.*, Vol 50 (No. 8), 1979, p 5196–5201
56. H.D. Espinosa, Dynamic Compression Shear Loading with In-Material Interferometric Measurements, *Rev. Sci. Instrum.*, Vol 67 (No. 11), 1996, p 3931–3939
57. R.J. Clifton, Analysis of the Laser Velocity Interferometer, *J. Appl. Phys.*, Vol 41 (No. 13), 1970, p 5335–5337
58. Valyn VISAR, *User's Handbook*, Valyn International, Albuquerque, NM, 1995
59. Valyn VISAR Data Reduction Program, *User's Handbook*, Valyn International, Albuquerque, NM, 1995
60. M.A. Zikry and S. Nemat-Nasser, High Strain-Rate Localization and Failure of Crystalline Materials, *Mech. Mater.*, Vol 10 (No. 3), 1990, p 215–237
61. F. Longy and J. Cagnoux, Plasticity and Microcracking in Shock-Loaded Alumina, *J. Am. Ceram. Soc.*, Vol 72 (No. 6), 1989, p 971
62. D. Yaziv, “Shock Fracture and Recompaction of Ceramics,” Ph.D. thesis, University of Dayton, 1985
63. A.L. Stevens and O.E. Jones, Radial Stress Release Phenomena in Plate Impact Experiments: Compression-Release, *J. Appl. Mech.*, Vol 39, 1972, p 359–366
64. R.L. Rabie, J.E. Vorthman, and J.K. Dienes, Three-Dimensional Computer Modeling of a Shock Recovery Experiment, *Shock Waves in Condensed Matter*, Vol 5, J.R. Asay, R.A. Graham, and G.K. Straub, Ed., 1983
65. S. Yadav, J.A. Davis, and K.T. Ramesh, Damage and Recovery Experiments Using Pressure-Shear Plate Impact, *Experimental Techniques in the Dynamics of Deformable Solids*, Vol 165, ASME, Applied Mechanics Division (AMD), 1993, p 71–78
66. V. Prakash and R.J. Clifton, Time Resolved Dynamic Friction Measurements in Pressure Shear, *Experimental Techniques in the Dynamics of Deformable Solids*, Vol 165, ASME, Applied Mechanics Division (AMD), 1993, p 33–48
67. V. Prakash, Pressure-Shear Plate Impact Experiment for Investigating Transient Friction, *Exp. Mech.*, Vol 35 (No. 4), 1995, p 329–336

68. S. Rajagopalan, M.A. Irfan, and V. Prakash, Novel Experimental Techniques for Investigating Time Resolved High Speed Friction, *Wear*, Vol 225 (No. 2), 1999, p 1222–1237
69. K.J. Frutschy and R.J. Clifton, Plate-Impact Technique for Measuring Dynamic Friction at High Temperatures, *J. Tribology (Trans. ASME)*, Vol 119 (No. 3), July 1997, p 590–593
70. S. Yadav and K.T. Ramesh, The Mechanical Properties of Tungsten-Based Composites at Very High Strain Rates, *Mater. Sci. Eng. A*, Vol A203, 1995, p 140
71. D.R. Chichili, K.T. Ramesh, and K.J. Hemker, High-Strain-Rate Response of Alpha-Titanium: Experiments, Deformation Mechanisms and Modeling, *Acta Mater.*, Vol 46 (No. 3), 1998, p 1025–1043
72. R. Kapoor and S. Nemat-Nasser, High-Rate Deformation of Single Crystal Tantalum: Temperature Dependence and Latent Hardening, *Scr. Mater.*, Vol 40 (No. 2), 18 Dec 1998, p 159–164
73. K.-S. Kim, R.M. McMeeking, and K.L. Johnson, Adhesion, Slip, Cohesive Zones and Energy Fluxes for Elastic Spheres, *J. Mech. Phys. Solids*, Vol 46, 1998, p 243–266
74. W. Johnson, Processes Involving High Strain Rates, *Int. Phys. Conference Series*, Vol 47, 1979, p 337
75. J.D. Campbell, High Strain Rate Testing of Aluminum, *Mater. Sci. Eng.*, Vol 12, 1973, p 3
76. Hirschvogel, Metal Working Properties, *Mech. Working Technol.*, Vol 2, 1978, p 61
77. S. Yadav and K.T. Ramesh, Mechanical Behavior of Polycrystalline Hafnium: Strain-Rate and Temperature Dependence, *Mater. Sci. Eng. A: Structural Materials: Properties, Microstructure & Processing*, No. 1–2, 15 May 1998, p 265–281
78. L.X. Zhou and T.N. Baker, Deformation Parameters in b.b.c., *Met. Mater. Sci. Eng.*, Vol A177, 1994, p 1
79. S. Nemat-Nasser and J.B. Isaacs, Direct Measurement of Isothermal Flow Stress of Metals at Elevated Temperatures and High Strain Rates with Application to Ta and Ta-W Alloys, *Acta Mater.*, Vol 45 (No. 3), 1997, p 907–919
80. A.M. Lennon and K.T. Ramesh, Technique for Measuring the Dynamic Behavior of Materials at High Temperatures, *Inter. J. Plast.*, Vol 14 (No. 12), 1998, p 1279–1292
81. T. Sakai, M. Ohashi, and K. Chiba, Recovery and Recrystallization of Polycrystalline Nickel after Hot Working, *Acta Metall.*, Vol 36, 1988, p 1781
82. G.I. Kanel, S.V. Razorenov, A. Bogatch, A.V. Utkin, and V.E. Fortov, Spall Fracture Properties of Aluminum and Magnesium at High Temperatures, *J. Appl. Phys.*, Vol 79, 1996, p 8310
83. V.K. Golubev and Y.S. Sobolev, Effect of Temperature on Spall Failure of Some Metal Alloys, *11th APS Topical Group Meeting on Shock Compression of Condensed Matter* (Snowbird, UT), American Physics Society, 1999
84. H.V. Arrieta, “Dynamic Testing of Advanced Materials at High and Low Temperatures,” MSc thesis, Purdue University, West Lafayette, IN, 1999
85. R.A. Wood, *Titanium Alloy Handbook*, Metals and Ceramic Center, Battelle, Publication MCIC-HB-02, 1972

86. G.Q. Chen and T.J. Ahrens, Radio Frequency Heating Coils for Shock Wave Experiments, *Mater. Res. Symp. Proc.*, Vol 499, 1998, p 131
87. H.D. Espinosa, Recent Developments in Velocity and Stress Measurements Applied to the Dynamic Characterization of Brittle Materials, *Mech. Mater.*, H.D. Espinosa and R.J. Clifton, Ed., Vol 29, 1998, p 219–232
88. N.S. Brar and A. Hopkins, Shock Hugoniot and Shear Strength of Ti-6Al-4V, *11th APS Topical Group Meeting on Shock Compression of Condensed Matter*, (Snowbird, UT), American Physics Society, 1999
89. Y. Mescheryakov, A.K. Divakov, and N.I. Zhigacheva, Shock-Induced Phase Transition and Mechanisms of Spallation in Shock Loaded Titanium Alloys, *11th APS Topical Group Meeting on Shock Condensed Matter*, Snowbird, UT, 1999
90. Y.K. Vohra, S.K. Sikka, S.N. Vaidya, and R. Chidambaram, Impurity Effects and Reaction Kinetics of the Pressure-Induced Alpha to Omega Transformation in Ti, *J. Phys. Chem. Solids*, Vol 38, 1977, p 1293
91. Y. Me-Bar, M. Boas, and Z. Rosenberg, Spall Studies on Ti-6Al-4V, *Mater. Sci. Eng.*, Vol 85, 1987, p 77
92. J.E. Shrader and M.D. Bjorkman, High Temperature Phase Transformation in the Titanium Alloy Ti-6Al-4V, *American Physics Society Conference Proc.*, No. 78, American Physics Society, 1981, p 310–314
93. Y.M. Gupta, Shear Measurements in Shock Loaded Solids, *Appl. Phys. Lett.*, Vol 29, 1976, p 694–697
94. Z. Young and O. Dubugnon, A Reflected Shear-Wave Technique for Determining Dynamic Rock Strength, *Int. J. Rock Mech. Min. Sci.*, 1977, p 247–259
95. Y.M. Gupta, D.D. Keough, D.F. Walter, K.C. Dao, D. Henley, and A. Urweider, Experimental Facility to Produce and Measure Compression and Shear Waves in Impacted Solids, *Rev. Sci. Instrum.*, Vol 51(a), 1980, p 183–194
96. R. Williams and D.D. Keough, Piezoresistive Response of Thin Films of Calcium and Lithium to Dynamic Loading, *Bull. Am. Phys. Soc. Series II*, Vol 12, 1968, p 1127
97. Z. Rosenberg and S.J. Bless, Determination of Dynamic Yield Strengths with Embedded Manganin Gages in Plate-Impact and Long-Rod Experiments, *Exp. Mech.*, 1986, p 279–282
98. P.W. Bridgman, *Proc. Am. Acad. Arts Sci.*, Vol 47, 1911, p 321
99. D. Bernstein and D.D. Keough, Piezoresistivity of Manganin, *J. Appl. Phys.*, Vol 35, 1964, p 1471
100. P.S. DeCarli, D.C. Erlich, L.B. Hall, R.G. Bly, A.L. Whitson, D.D. Keough, and D. Curran, “Stress-Gage System for the Megabar (100 MPa) Range,” Report DNA 4066F, Defense Nuclear Energy, SRI Intl., Palo Alto, CA, 1976
101. L.E. Chhabildas and R.A. Graham, *Techniques and Theory of Stress Measurements for Shock-Wave Applications*, Symposia Series, ASME, Applied Mechanics Division (AMD), AMD-83, 1987, p 1–18

102. M.K.W. Wong and Y.M. Gupta, Dynamic Inclusion Analyses of Lateral Piezoresistance Gauges under Shock Wave Loading, *Shock Compression of Condensed Matter*, S.C. Schmidt, R.D. Dick, J.W. Forbes, and D.J. Tasker, Ed., Elsevier, Essex, U.K., 1991
103. Z. Rosenberg and N.S. Brar, Hysteresis of Lateral Piezoresistive Gauges, *High Pressure Science and Technology*, Joint AIRAPT-APS Conference (Colorado Springs, CO), S.C. Schmidt, Ed., 1994, p 1707–1710
104. D.P. Dandekar and P.A. Beaulieu, Failure Wave under Shock Wave Compression in Soda Lime Glass, *Metallurgical and Material Applications of Shock-Wave and High-Strain-Rate Phenomena*, L.E. Murr et al., Ed., Elsevier, 1995
105. Z. Rosenberg and Y. Partom, Longitudinal Dynamic Stress Measurements with In-Material Piezoresistive Gauges, *J. Appl. Phys.*, Vol 58, 1985, p 1814
106. L. Barker, “VISAR88—A New Data Reduction Program for VISARs,” Sandia Report, Sandia National Laboratory, 1988
107. H.D. Espinosa, H.-C. Lu, and Y. Xu, A Novel Technique for Penetrator Velocity Measurement and Damage Identification in Ballistic Penetration Experiments, *J. Compos. Mater.*, Vol 32 (No. 8), 1998

Fracture Toughness and Fracture Mechanics

Introduction

FRACTURE may be defined as the mechanical separation of a solid owing to the application of stress. Fractures of engineering materials are broadly categorized as ductile or brittle, and fracture toughness is related to the amount of energy required to create fracture surfaces. In ideally brittle materials such as glass, the energy required for fracture is simply the intrinsic surface energy of the material, as demonstrated by Griffith (Ref 1). For structural alloys at room temperature, considerably more energy is required for fracture because plastic deformation accompanies the fracture process.

Fracture-mechanics technology has significantly improved the ability to design safe and reliable structures. The application of fracture-mechanics concepts has identified and quantified the primary parameters that affect structural integrity. These parameters include the magnitude and range of the applied stresses; the size, shape orientation, and rate of propagation of the existing crack; and the fracture toughness of the material.

Two categories of fracture mechanics are linear-elastic fracture mechanics (LEFM) and elastic-plastic fracture mechanics (EPFM). Linear-elastic fracture mechanics is used if the crack tip in a body is sharp and there is only a small amount of plastic deformation at or near the crack tip. Some materials that are designed using LEFM concepts are high-strength steels, titanium, and aluminum alloys. Elastic-plastic fracture mechanics is used when the crack tip is not sharp and there is some crack-tip plasticity (blunting). Elastic-plastic fracture mechanics is used to design materials such as lower-strength, higher-toughness steels. Elastic-plastic fracture mechanics is also used in the evaluation of ceramic matrix composites (see the article “Fracture Toughness of Ceramics and Ceramic Matrix Composites” in this Volume).

The LEFM approach to fracture analysis assumes a part or specimen contains a crack or other flaw, the crack is a flat surface in a linear-elastic stress field, and the energy released during rapid crack propagation is a basic material property and is not influenced by part size.

Linear-elastic fracture-mechanics technology is based on an analytical procedure that relates the stress-field magnitude and distribution in the vicinity of a crack tip to the nominal stress applied to the structure: to the size, shape, and orientation of the crack or cracklike imperfection; and to the material properties.

A crack in a loaded part or specimen generates its own stress field ahead of a sharp crack, which can be characterized by a single parameter called stress intensity (K). Relations between the stress-intensity factors and various body configurations; crack sizes, shapes, and orientations; and loading conditions are available in the published literature (e.g., Ref 2).

K represents a single parameter that includes both the effect of the stress applied to a sample and the effect of a crack of given size in the sample. It can have a simple relation to applied stress and crack length, or the relation can involve complex geometry factors for complex loading, various configurations of real structural components, and variations in crack shapes.

Rapid crack propagation is controlled solely by a material constant, called the critical stress-intensity factor (K_c) where crack propagation becomes rapid. The greater the value of K_c , the higher the stress required to produce rapid propagation and the greater the resistance of the material to brittle fracture. The critical stress-intensity factor is determined using relatively simple laboratory specimens.

Figure 1 defines three modes of loading: mode I, opening, or tensile, mode; mode II, sliding, or shear, mode; and mode III, tearing mode. Fracture-mechanics concepts are essentially the same for each mode. However, the great majority of all actual cracking and fracture cases are mode I problems. A crack in the very early stage of development will turn into a direction in which it experiences only mode I loading, unless it is prevented from doing so by geometrical confinement. For this reason, fracture mechanics is generally confined to mode I.

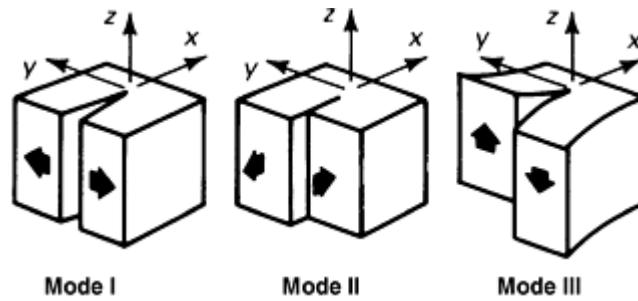


Fig. 1 Modes of loading. Mode I (opening mode): tension stress in the y direction, or perpendicular to crack surfaces. **Mode II (edge-sliding mode):** shear stress in the x direction, or perpendicular to crack tip. **Mode III (tearing mode):** shear stress in z direction, or parallel to crack tip

The nomenclature for K_c is modified to include the loading mode. For example, K_{Ic} is the critical stress-intensity factor or fracture toughness under mode I loading. The vast majority of testing to determine fracture toughness is performed in mode I; therefore, most of the published fracture-toughness values are K_{Ic} .

The stress-intensity factor, K_I , for a crack tip in any body that is subjected to tensile stresses, σ , perpendicular to the plane of the crack (mode I deformation) is given by the relationship:

$$K_I = \sigma \sqrt{\pi a} f(g) \quad (\text{Eq 1})$$

where a is crack length and $f(g)$ is a function that accounts for crack geometry and structural configuration. This general relationship makes it possible to translate laboratory results into practical design information without the need for extensive service experience or correlations.

References cited in this section

1. A.A. Griffith, The Phenomena of Rupture and Flow in Solids, *Philos. Trans. Soc. (London) A*, Vol 221, 1920, p 163–198
2. S.T. Rolfe and J.M. Barsom, *Fracture and Fatigue Control in Structures—Applications of Fracture Mechanics*, Prentice-Hall, 1977

Fracture Toughness and Fracture Mechanics

Fracture Toughness

Toughness is defined as the ability of a material to absorb energy. It is usually characterized by the area under a stress-strain curve for a smooth (unnotched) tension specimen loaded slowly to fracture. Notch toughness represents the ability of a material to absorb energy usually determined under impact loading in the presence of a notch. Notch toughness is measured by using a variety of specimens such as the Charpy V-notch impact specimen, the dynamic-tear specimen, and plane-strain fracture-toughness specimens under static loading (K_{Ic}) and under impact loading (K_{Id}).

Ductile-to-Brittle Fracture Transition. Traditionally, the notch-toughness characteristics of low- and intermediate-strength steels have been described in terms of the transition from ductile to brittle behavior as test temperature increases. Most structural steels can fail in either a ductile or a brittle manner depending on several conditions such as temperature, loading rate, and constraint.

The most widely used specimen for characterizing the ductile-to-brittle transition behavior of steels has been the Charpy V-notch impact specimen, which is described in ASTM E 23 (Ref 3). These specimens may be tested at different temperatures and the impact notch toughness at each test temperature may be determined from the energy absorbed during fracture, the percent shear (fibrous) fracture on the fracture surface, or the

change in the width of the specimen (lateral expansion). An example of the ductile-to-brittle transition with temperature for each of these parameters is presented in Fig. 2. The actual values for each parameter and the locations of the curves along the temperature axis are usually different for different steels and even for a given steel composition.

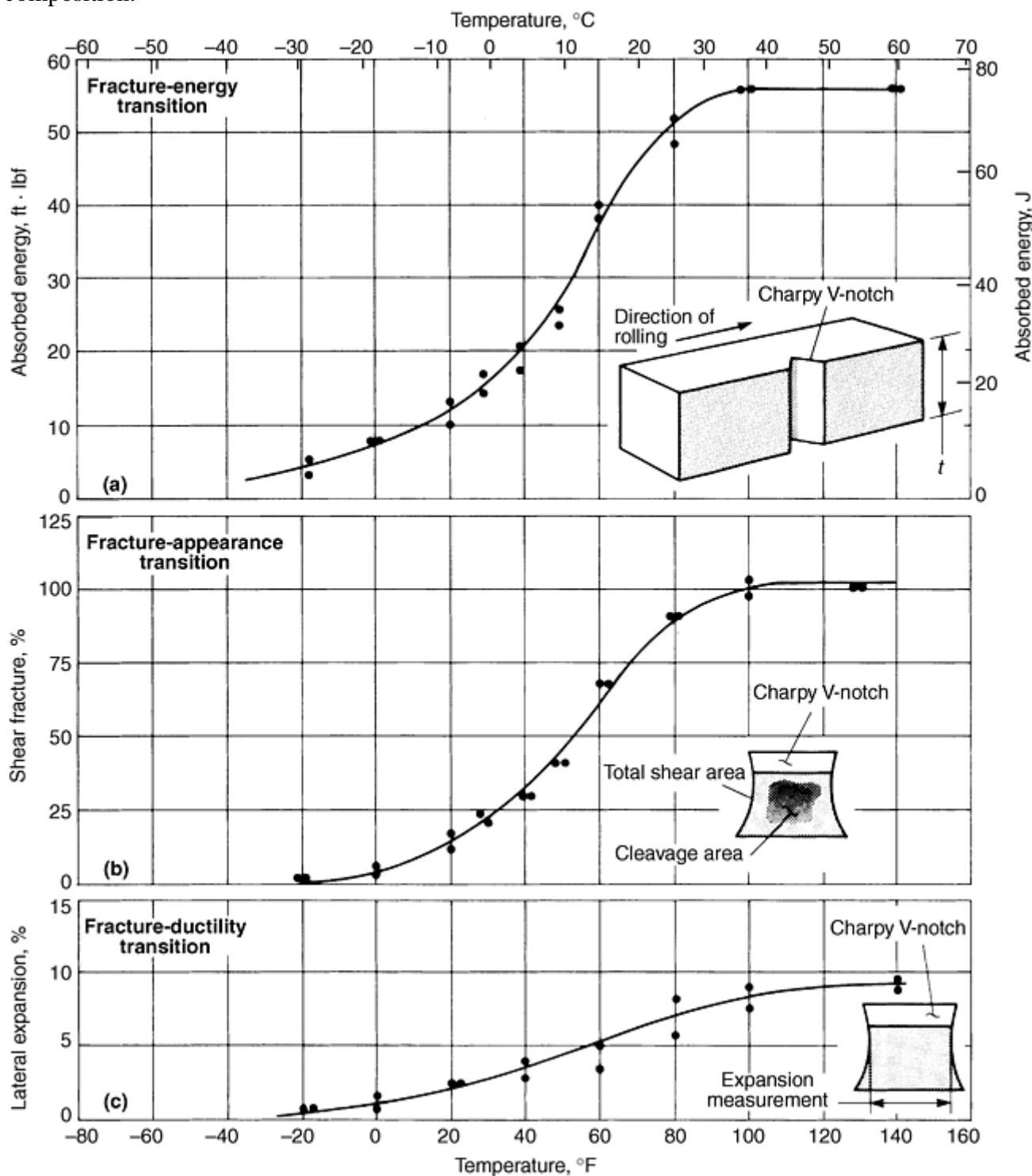


Fig. 2 Characteristics of the transition-temperature range for Charpy V-notch testing of low-carbon steel plate, as determined by (a) fracture energy, (b) fracture appearance, and (c) fracture ductility. The drawings at lower right in the graphs indicate: (a) orientation of the specimen notch with plate thickness, t , and direction of rolling; (b) location of the total shear area on the fracture surface; and (c) location of the expansion measurement in this series of tests—all illustrated for a Charpy V-notch specimen. Percentage of shear fracture and lateral expansion were based on the original dimensions of the specimen. Material is semikilled low-carbon steel plate (0.18% C, 0.54% Mn, 0.07% Si)

The rate of change from ductile to brittle behavior depends on many parameters, including strength and composition of the material. Because the transition occurs over a range of temperatures, it has been customary to define a single temperature within the transition range that reflects the behavior of the steel under consideration. Several equally useful definitions are in use, including the 20 J (15 ft · lbf) temperature, the 380 μm (15 mil) temperature, and the 50% shear temperature.

Fracture Mechanics. Fracture-toughness behavior, or the ability of a material to withstand fracture in the presence of cracks, can be established best by using fracture-mechanics concepts. The stress-intensity value for a given applied stress increases with increasing crack length, and for a given crack length increases with increasing applied stress. One of the underlying principles of fracture mechanics is that unstable fracture occurs when the stress-intensity factor at the crack tip reaches a critical value, K_c . For mode I loading (opening, or tensile mode) and for small crack-tip plastic deformation (plane-strain conditions), the critical stress-intensity factor for fracture instability, K_{Ic} , represents the inherent ability of a material to resist progressive tensile crack extension. However, this fracture-toughness property varies with constraint, and like other material properties such as yield strength, varies with temperature and loading rate as follows:

K_c	Critical stress-intensity factor for static loading and plane-stress conditions of variable constraint. Thus, this value depends on specimen thickness and geometry, as well as on crack size.
K_{Ic}	Critical stress-intensity factor for static loading and plane-strain conditions of maximum constraint. Thus, this value is a minimum value for thick plates.
K_{Id}	Critical stress-intensity factor for dynamic (impact) loading and plane-strain conditions of maximum constraint
$K_c, K_{Ic},$ or K_{Id}	$C\sigma\sqrt{a}$

where C is a constant that is a function of specimen and crack geometry, σ is nominal stress in MPa or ksi, and a is flaw size in millimeters or inches.

Each of these values (K_c , K_{Ic} , and K_{Id}) is also a function of temperature, particularly for those structural materials exhibiting a transition from brittle to ductile behavior.

By knowing the critical value of K_I at failure (K_c , K_{Ic} , or K_{Id}) for a given material of a particular thickness and at a specific temperature and loading rate, the designer can determine flaw sizes that can be tolerated in structural members for a given design stress level. Conversely, the designer can determine the design stress level that can be safely used for an existing crack that may be present in a structure. In general, the relationship among fracture toughness (K_c), stress (σ), and crack size (a) is shown schematically in Fig. 3 (Ref 4) for a through-thickness crack in a plate. The figure shows that there are many combinations of stress and crack size (e.g., σ_f and a_f) that may cause fracture, and many combinations (e.g., σ_0 and a_0) that will not cause fracture, of the particular material under slow loading and at test temperature.

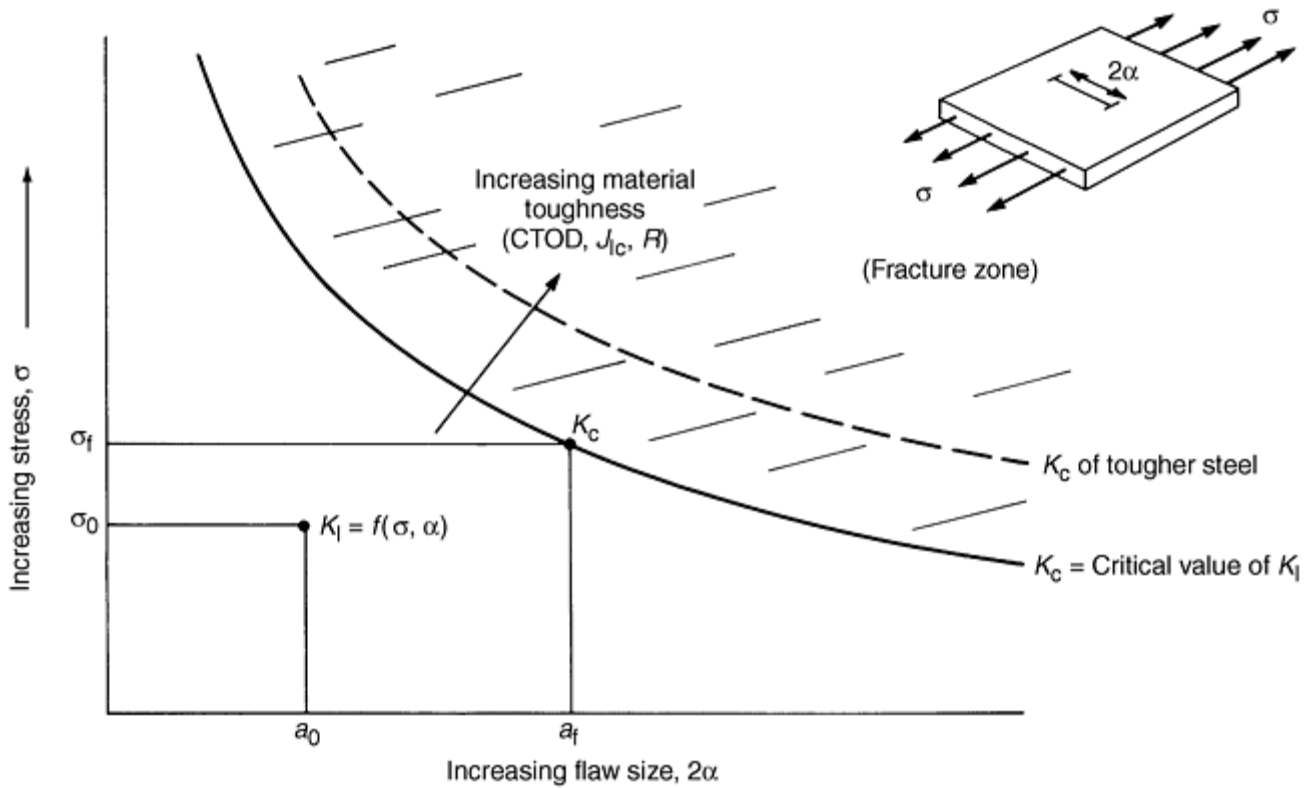


Fig. 3 Relationship among stress, flaw size, and material toughness. CTOD, crack tip opening displacement

Fracture toughness properties are obtained by testing standard specimens at a given test temperature and loading rate. These are discussed in more detail in the article “Fracture Toughness Testing” in this Volume.

Effects of Constraint, Temperature, and Loading Rate. Fracture toughness, K_c , varies with the degree of localized constraint to plastic flow along the tip of the fatigue crack. Thus, cracks in very thick members are subjected to higher constraints than are cracks in thinner members. The maximum constraint, as defined in ASTM E 399 (Ref 5), occurs under plane-strain conditions and results in the lowest value of fracture toughness, K_{Ic} . Under identical test conditions, the K_c values for thinner plates are usually higher than those observed under plane-strain conditions (i.e., $K_c > K_{Ic}$).

Fracture toughness, K_{Ic} , of constructional steels under a constant rate of loading increases with increasing temperature (Ref 2, 4). The rate of increase of K_{Ic} with temperature does not remain constant, but increases markedly above a given test temperature. An example of this behavior is shown in Fig. 4 (Ref 2, 6) for A36 steel plate tested at three different loading rates. This transition in plane-strain fracture toughness is related to a change in the microscopic mode of crack initiation at the crack tip from cleavage to increasing amounts of ductile tearing.

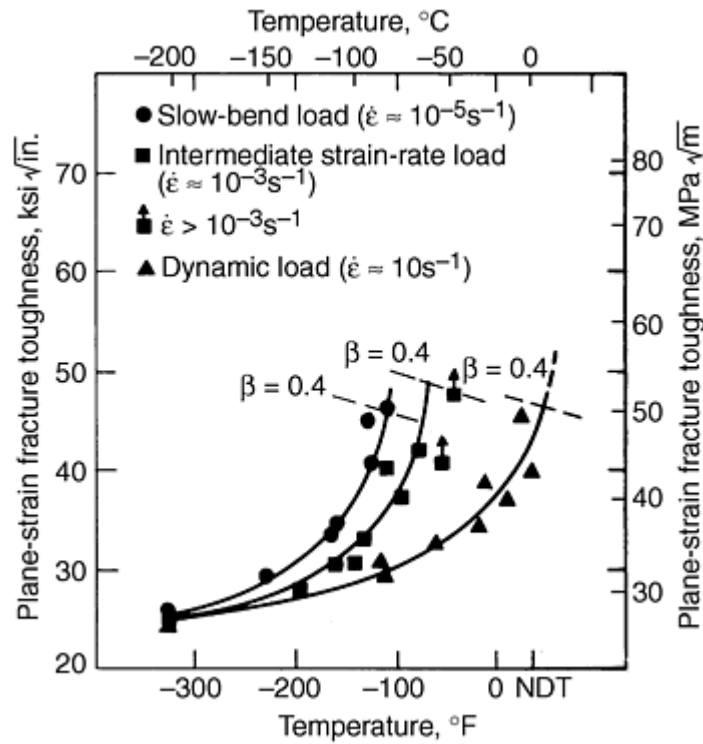


Fig. 4 Effect of temperature and strain rate on plane-strain fracture-toughness behavior of ASTM type A36 steel

An analysis of plane-strain fracture-toughness data that were obtained for constructional steels and that were valid according to ASTM standard procedures shows that the fracture-toughness transition curve is translated (shifted) to higher temperature values as the loading rate is increased. Thus, at a given temperature, fracture toughness values measured at high loading rates are generally lower than those measured at lower loading rates. Also, the fracture-toughness values for constructional steels decrease with decreasing test temperature to a minimum K_{Ic} value that is equal to about $27.5 \text{ MPa} \sqrt{m}$ ($25 \text{ ksi} \sqrt{11\text{in.}}$). This minimum fracture-toughness value is independent of the loading rate used to obtain the fracture-toughness transition curve.

Data for steels having yield strengths between 36 and 250 ksi, such as those presented in Fig. 5 (Ref 2, 6), show that the shift between static and impact plane-strain fracture-toughness curves is given (Ref 2) by:

$$T_{\text{shift}} = 215 - 1.5 \sigma_{ys} \quad (\text{Eq 2a})$$

$$\text{for } 28 \text{ ksi} < \sigma_{ys} \leq 130 \text{ ksi}$$

and

$$T_{\text{shift}} = 0 \text{ for } \sigma_{ys} > 130 \text{ ksi} \quad (\text{Eq 2b})$$

where T is temperature in °F and σ_{ys} is room-temperature yield strength. The temperature shift between static and any intermediate or impact plane-strain fracture-toughness curves is given (Ref 7) by:

$$T_{\text{shift}} = (150 - \sigma_{ys}) \dot{\epsilon}^{0.17} \quad (\text{Eq 3})$$

where T is temperature in °F, σ_{ys} is room-temperature yield strength in ksi, and $\dot{\epsilon}$ is strain rate in s^{-1} . The strain rate is calculated for a point on the elastic-plastic boundary (Ref 8) according to:

$$\dot{\epsilon} = \frac{2 \sigma_{ys}}{tE} \quad (\text{Eq 4})$$

where t is the loading time for the test and E is the elastic modulus for the material.

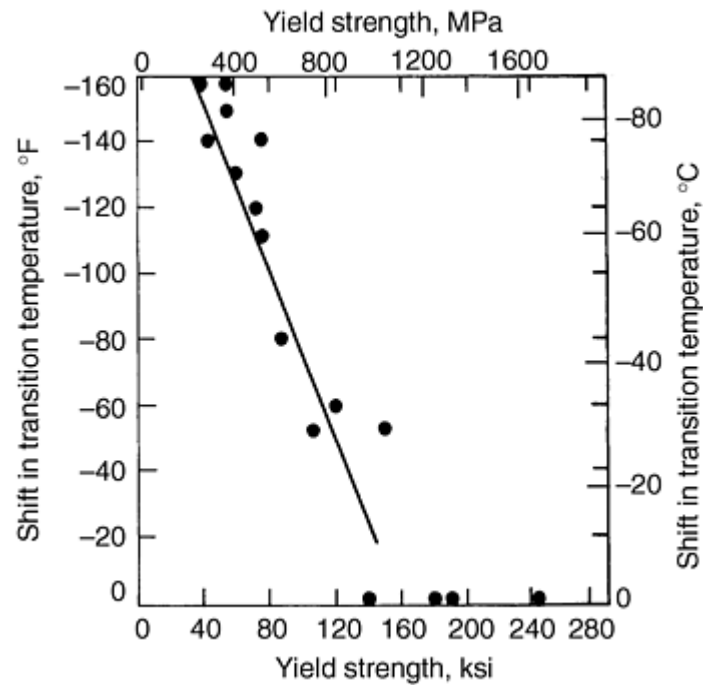


Fig. 5 Effect of yield strength on shift in transition temperature between impact and static plane-strain fracture-toughness curves

A proper use of fracture-mechanics methodology for fracture control of structures necessitates the determination of fracture toughness for the material at the temperature and loading rate representative of the intended application.

The morphology of fracture surfaces for steel can be understood by considering the fracture-toughness transition behavior under static and impact loading (Fig. 6). The static fracture-toughness transition curve depicts the mode of crack initiation at the crack tip. The dynamic fracture-toughness transition curve depicts the mode of crack propagation.

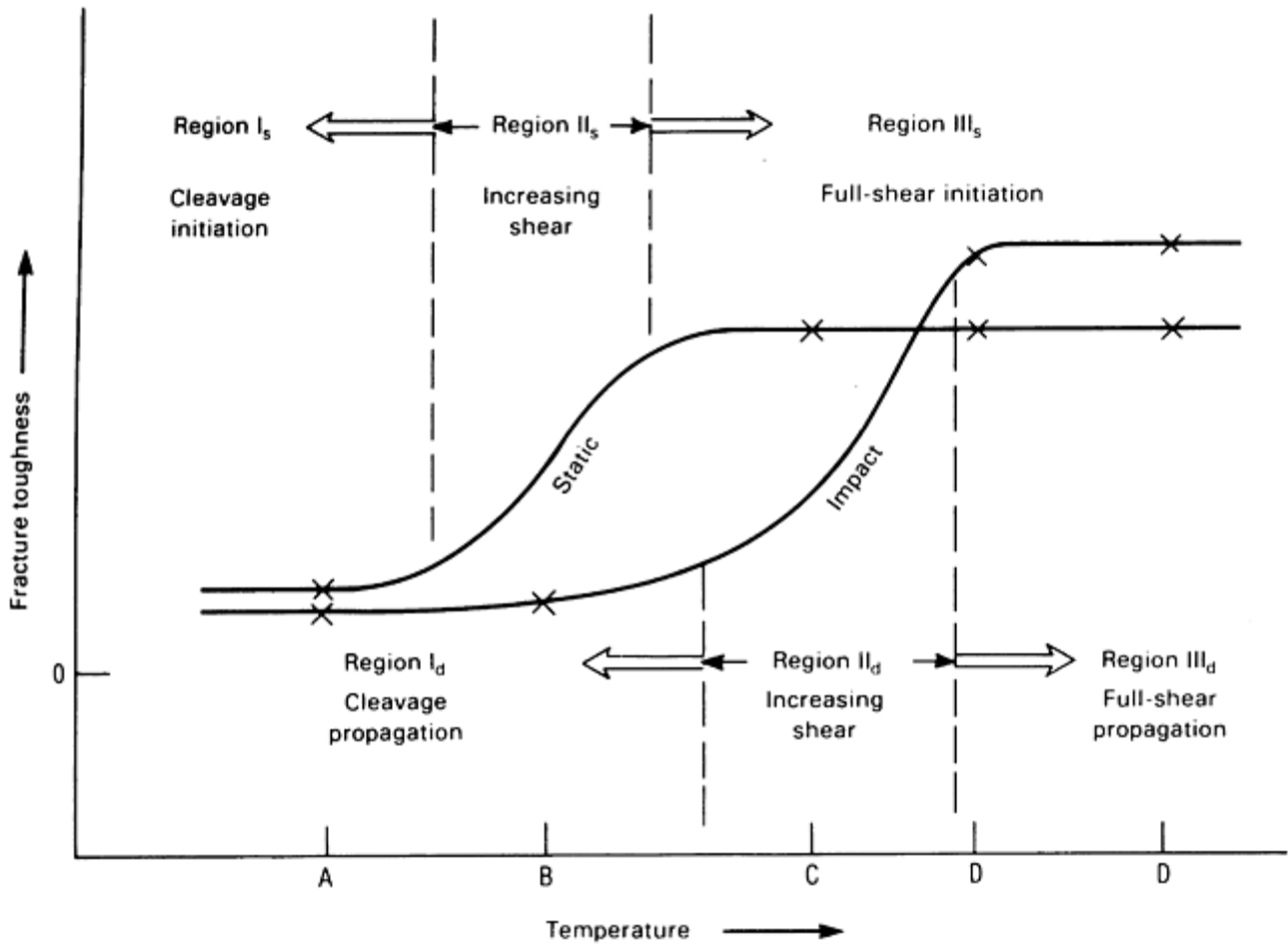


Fig. 6 Fracture-toughness transition behavior of steel under static and impact loading

The fracture-toughness curve for either static or dynamic loading can be divided into three regions as shown in Fig. 6. In region I_s for the static curve, the crack initiates in a cleavage mode from the tip of the fatigue crack. In region II_s, the fracture toughness to initiate unstable crack propagation increases with increasing temperature. This increase in crack-initiation toughness corresponds to an increase in the size of the plastic zone and in the zone of ductile tearing (shear) at the tip of the crack prior to unstable crack extension. In this region, the ductile-tearing zone is usually very small and is difficult to delineate by visual examination. In region III_s, the static fracture toughness is quite large and somewhat difficult to define, but the fracture initiates by ductile tearing (shear).

Once a crack has initiated under a static load, the morphology (cleavage or shear) of the fracture surface for the propagating crack is determined by the dynamic behavior and degree of plane strain at the temperature. Regions I_d, II_d, and III_d in Fig. 6 correspond to cleavage, increasing ductile tearing (shear), and full-shear crack propagation, respectively. Thus, at temperature A, the crack initiates and propagates in cleavage. At temperatures B and C, the crack exhibits ductile initiation, but propagates in cleavage. The only difference between the behaviors at temperatures B and C is that the ductile-tearing zone for crack initiation is larger at temperature C than at temperature B. At temperatures D, cracks initiate and propagate in full shear. Consequently, full-shear fracture initiation and propagation occur only at temperatures for which the static and dynamic (impact) fracture behaviors are on the upper shelf.

Correlations of K_{I_d} , K_{I_c} , and Charpy V-Notch Impact Energy Absorption. The Charpy V-notch impact specimen is the most widely used specimen for material development, specifications, and quality control. Moreover, because the Charpy V-notch impact energy absorption curve for constructional steels undergoes a transition in the same temperature zone as the impact plane-strain fracture toughness (K_{I_d}), a correlation among these test results has been developed for the transition region and is given (Ref 2, 6) by:

$$\frac{(K_{I_d})^2}{E} = 5(\text{CVN}) \quad (\text{Eq 5})$$

where K_{I_d} is in $\text{ksi} \sqrt{\text{in}}$, E is in ksi , and CVN is in $\text{ft} \cdot \text{lb}$. The validity of this correlation is apparent from the data presented in Fig. 7 for various grades of steel ranging in yield strength from about 36 to about 140 ksi and in Fig. 8 for eight heats of SA 533B, class 1, steel. Consequently, a given value of CVN impact energy absorption corresponds to a given K_{I_d} value (Eq 5), which in turn corresponds to a given toughness behavior at lower rates of loading. The behavior for loading rates less than impact are established by shifting the K_{I_d} value to lower temperatures by using Eq 2a, 2b, or 3. Conversely, for a desired behavior at the minimum operating temperature and maximum in-service loading rate, the corresponding behavior under impact loading can be established by using Eq 2a, 2b, or 3, and the equivalent CVN impact value can be established by using Eq 5.

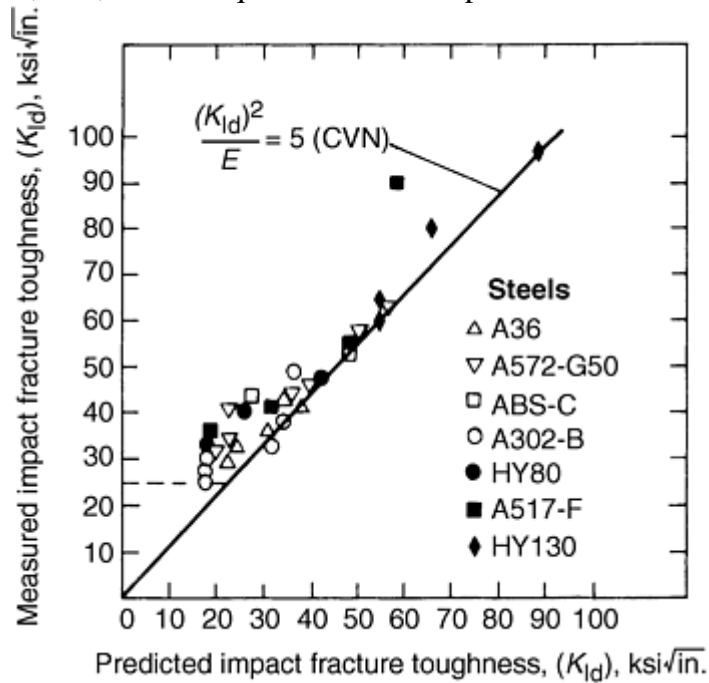


Fig. 7 Correlation of plane-strain impact fracture toughness and impact Charpy V-notch energy absorption for various grades of steel

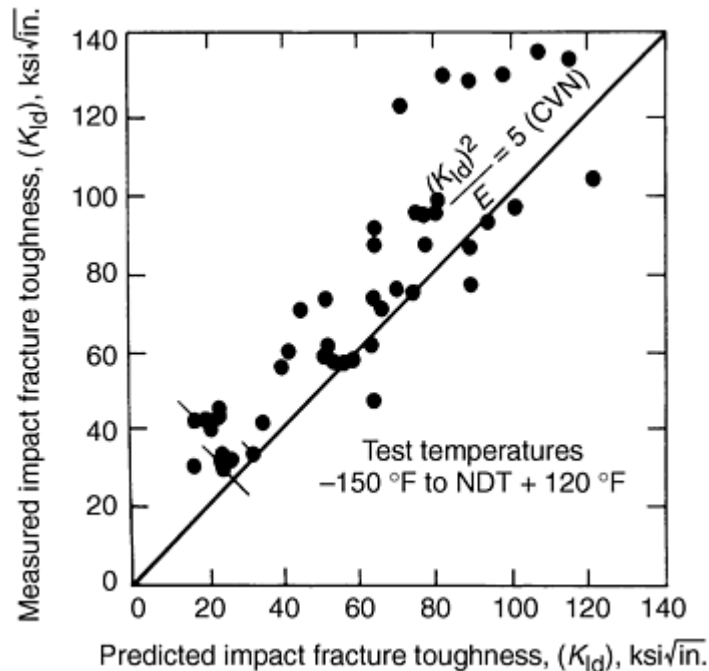


Fig. 8 Correlation of plane-strain impact fracture toughness and impact Charpy V-notch energy absorption for SA 533B, class 1, steel

Barsom and Rolfe (Ref 2) suggested a relationship between K_{Ic} and upper-shelf Charpy V-notch impact energy absorption. This upper-shelf correlation, shown in Fig. 9, was developed empirically for steels having room-temperature yield strength, σ_{ys} , higher than about 110 ksi and is given by:

$$\left(\frac{K_{Ic}}{\sigma_{ys}}\right)^2 = \frac{5}{\sigma_{ys}} \left(CVN - \frac{\sigma_{ys}}{20} \right) \quad (\text{Eq 6})$$

where K_{Ic} is in ksi $\sqrt{\text{in}}$, σ_{ys} is in ksi, and CVN is energy absorption in ft · lbf for a Charpy V-notch impact specimen tested in the upper-shelf (100% shear fracture) region.

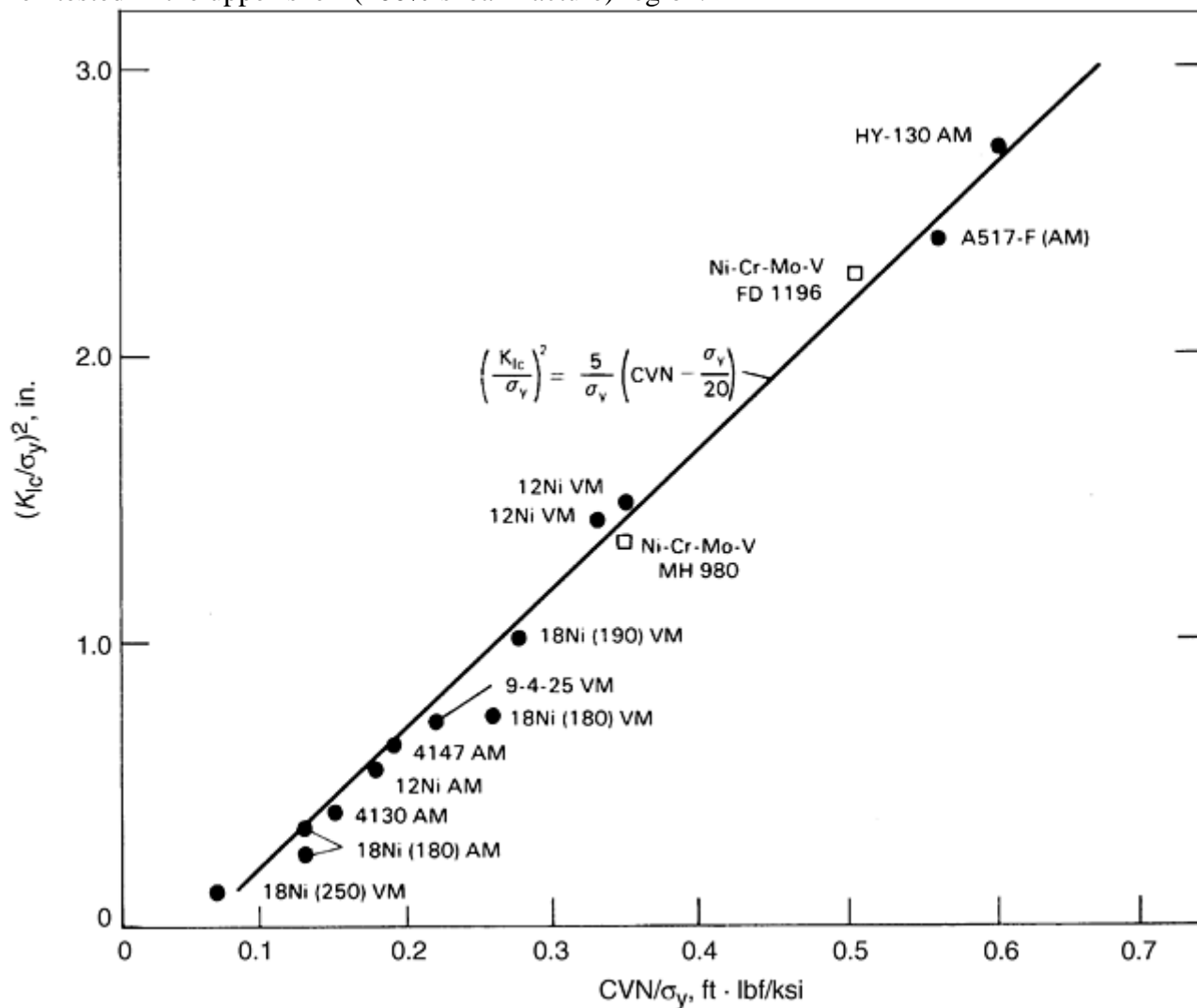


Fig. 9 Relation between plane-strain fracture toughness (K_{Ic}) and Charpy V-notch (CVN) impact energy. Tests conducted at 27 °C (80 °F). VM, vacuum melted; AM, air melted

At the upper shelf, the effects of loading rate and notch acuity are not as critical as in the transition region. The effect of loading rate is to elevate the yield strength by about 25 ksi. Thus, Eq 6 may be used to calculate K_{Ic} values by replacing σ_{ys} with the dynamic yield strength, σ_{yd} , where $\sigma_{yd} \approx \sigma_{ys} + 25$ ksi. This use of Eq 6 to calculate K_{Ic} is consistent with the observation that, in the upper-shelf region, the dynamic fracture toughness of steels is higher than the static fracture toughness.

References cited in this section

2. S.T. Rolfe and J.M. Barsom, *Fracture and Fatigue Control in Structures—Applications of Fracture Mechanics*, Prentice-Hall, 1977

3. "Standard Test Methods for Notched Bar Impact Testing of Metallic Materials," E 23-98, *Annual Book of ASTM Standards*, Vol 03.01, ASTM, 1999, p 138–162
4. J.M. Barsom and S.T. Rolfe, K_{Ic} Transition Temperature Behavior of A517-F Steel, *Eng. Fract. Mech.*, Vol 2 (No. 4), June 1971
5. "Standard Test Method for Plane-Strain Fracture Toughness of Metallic Materials," E 399-90, *Annual Book of ASTM Standards*, Vol 03.01, ASTM, 1999, p 422–452
6. J.M. Barsom, Development of the AASHTO Fracture-Toughness Requirements for Bridge Steels, *Eng. Fract. Mech.*, Vol 7 (No. 3), Sept 1975
7. J.M. Barsom, Effect of Temperature and Rate of Loading on the Fracture Behavior of Various Steels, *Dynamic Fracture Toughness*, The Welding Institute, 1976
8. A.K. Shoemaker and S.T. Rolfe, The Static and Dynamic Low-Temperature Crack-Toughness Performance of Seven Structural Steels, *Eng. Fract. Mech.*, Vol 2 (No. 4), June 1971

Fracture Toughness and Fracture Mechanics

Fracture Mechanics

Fracture mechanics is the study of the influence of loading, crack size, and structural geometry on the fracture resistance of materials containing natural flaws and cracks. When applied to design, the objective of the fracture-mechanics analysis is to limit operating stresses so that a preexisting flaw of assumed initial size will not grow to critical size during the desired service life of the structure. Service life is calculated on the basis of probable initial flaw sizes limited by inspection, a stress analysis of the structure, and experimental data relating crack growth and fracture to fracture-mechanics parameters.

Linear Elastic Fracture Mechanics

The fundamental ideas underlying the foundation of fracture mechanics stem from the work of Griffith (Ref 1), who demonstrated that the strain energy released upon crack extension is the driving force for fracture in a cracked material under linear-elastic conditions. The elastic strain energy, U , is the work done by a load, P , causing a displacement, Δ :

$$U = P\Delta/2 = CP^2/2 \quad (\text{Eq 7})$$

where $C = \Delta/P$, the elastic compliance.

The loss of elastic potential energy with crack extension of unit area, A , is defined as the strain-energy release rate, G . For a crack extending at constant deflection or at constant load:

$$G = dU/dA = (P^2/2)dC/dA \quad (\text{Eq 8})$$

This relationship characterizes the fracture resistance of structural materials by defining a critical strain-energy release rate, G_c , at the critical load, P_c , when fracture occurs in a specimen with a known compliance function, dC/dA .

Stress-Intensity Factor. Fracture mechanics is based on a stress analysis of the stress distribution near the tip of a crack located in a linear-elastic body. The magnitude of the crack-tip stress field, σ_{ij} , is proportional to a single parameter, K , the stress-intensity factor:

$$\sigma_{ij} = K(2\pi r)^{-1/2} f_{ij}(\theta) = K \cdot f(\text{position}) \quad (\text{Eq 9})$$

where r and θ are cylindrical position coordinates, $r = 0$ at the crack tip, and $\theta = 0$ in the crack plane. K is a function of the applied stress, σ , a is the crack length, and $Y(a)$ is a factor dependent on structural geometry:

$$K = Y(a)\sigma(\pi a)^{1/2} \quad (\text{Eq 10})$$

The strain-energy release rate and stress-intensity approaches are related:

$$K^2 = E'G \quad (\text{Eq 11})$$

where for plane stress, $E' = E$, the elastic modulus; for plane strain, $E' = E/(1 - \nu^2)$, where ν is Poisson's ratio. Thus, it is equivalent to attribute the driving force for fracture to the crack-tip stress field, which is proportional to K or to the elastic strain-energy release rate, G . The stress intensity, K , is used more commonly than G , because K can be computed for different structural geometries using stress-analysis techniques.

Fracture occurs when the crack-tip stress field reaches a critical magnitude, that is, when K reaches K_c , the fracture toughness of the material. K_c is a mechanical property that is a function of temperature, loading rate, and microstructure, much the same as yield strength is; K_c is also a function of the extent of plastic strain at the crack tip relative to the other specimen or structure dimensions. If the plastic zone is small compared with the specimen dimensions and the crack size, then K_c approaches a constant minimum value defined as the plane-strain fracture toughness, K_{Ic} .

Crack Tip Plasticity. Applicability of the linear-elastic analysis has been extended to conditions approaching net section yielding by correcting for the zone of plasticity that exists at the crack tip (Ref 9). The assumption is that the plastic material at the crack tip strains without carrying the incremental load; therefore, the crack behaves as if it were a slightly longer crack in a linear-elastic material. The adjustment is made by adding the radius of the plastic zone, r_y , to the crack length, a , such that the expression for the stress-intensity factor becomes:

$$K = Y(a + r_y) \sigma [\pi(a + r_y)]^{1/2} \quad (\text{Eq 12})$$

where

$$r_y = 1/2\pi (K/\sigma_y)^2 \quad (\text{Eq 13})$$

where σ_y is the yield strength at the crack tip. The r_y correction modifies the crack-tip stress field to account for the elastic stress redistribution that is due to the localized plasticity.

Size Effect. A two-dimensional stress state is assumed in a bulk material when one of the dimensions of the body is small relative to the others. A two-dimensional stress state called plane strain develops when plastic deformation at the crack tip is severely limited. This is promoted by thick sections, high strength and limited ductility. In contrast, a two-dimensional stress state called plane stress develops when much more plastic deformation occurs around the crack tip. This is promoted by low-strength ductile materials and very thin sections of high-strength materials. The difference between plane strain and plane stress is based on the presence or absence, respectively, of transverse constraint in material deformation in the vicinity of the crack tip.

As specimen thickness, B , increases, σ_y increases from σ_{ys} (the engineering yield stress of the material at 0.2% strain) to $(3\sigma_{ys})^{1/2}$ because of a geometric constraint to plastic deformation associated with a transition from plane-stress to plane-strain conditions. The maximum value of σ_y is reached when the plastic zone size is limited to about 5% of the thickness. Thus, in a given material, the plastic zone size as computed by Eq 13 may vary with thickness by a factor of 3, leading to a strong dependence of K_c on thickness, as shown in Fig. 10. The inflection point of the curve in Fig. 10 occurs at approximately $(K_{Ic}/\sigma_{ys})^2$. Therefore, for maximum toughness:

$$B < (K_{Ic}/\sigma_{ys})^2 \text{ or } K_{Ic} > \sigma_{ys}(B)^{1/2} \quad (\text{Eq 14})$$

Equation 14 is useful in material selection.

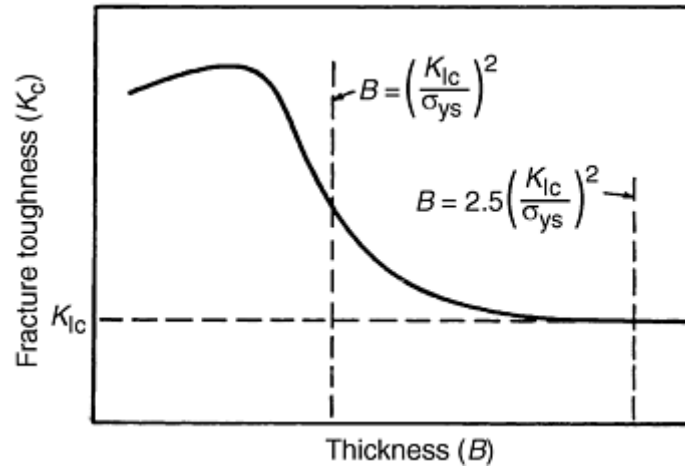


Fig. 10 Fracture toughness transition in structural alloys

Of great importance is the fact that the curve in Fig. 10 approaches an asymptote at a thickness of $B \geq 2.5 \left(\frac{K_{Ic}}{\sigma_{ys}}\right)^2$. At this point the fracture toughness value, K_{Ic} , is a material constant, independent of further increase of thickness.

Elastic-Plastic Fracture Mechanics

High-toughness structural materials undergo extensive plastic deformation prior to fracture. Therefore, the concepts of linear-elastic fracture mechanics need to account for elastic-plastic behavior. The general concepts of EPFM, as they relate to metallic materials and ceramic composites, are described in more detail in the article “Feature Toughness of Ceramics and Ceramic Matrix Composites” in this Volume.

Three basic methods of EPFM include the crack-tip opening displacement (CTOD), the J -integral, and the R -curve methods. These tests are intended to provide specialized measurements of fracture properties as follows:

- CTOD: full range of fracture toughness; for slow loading rates
- J -integral: elastic-plastic fracture toughness; for slow loading rates
- R -curve: resistance to fracture extension; for elastic-plastic fracture and slow loading rates

Crack-Tip Opening Displacement. The concept of the CTOD and crack-mouth opening displacement (CMOD) is shown schematically in Fig. 11, which shows a sample specimen before and after (hidden lines) deformation (Ref 10). Note that the CMOD is evaluated at the load line (centerline of the loading) and the CTOD is evaluated at the crack tip. Some test methods used for evaluating the CTOD are British Standard 7448, Part 1 and ASTM E 1290 (Ref 11, 12).

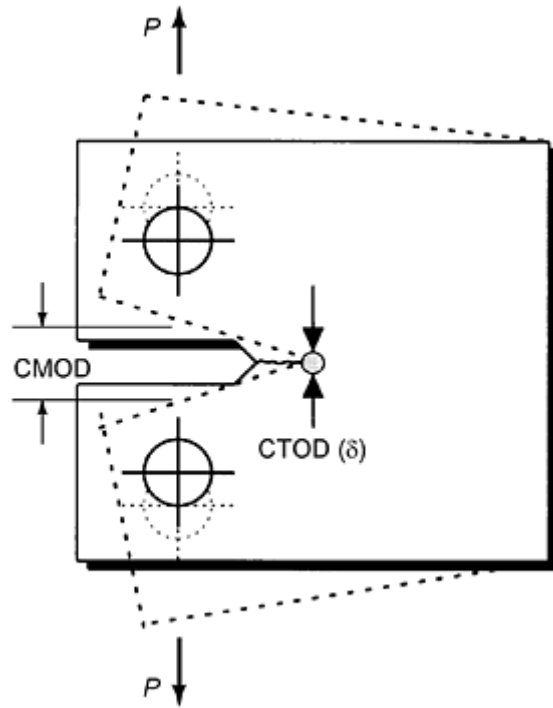


Fig. 11 Sample specimen showing the definition of crack-mouth opening displacement (CMOD) and crack-tip opening displacement (CTOD). CTOD is the diameter of the circular arc at the blunted crack tip and should not be confused with the plastic zone. Source: Ref 10

The CTOD concept is a crack tip strain criterion for fracture. For a crack in an elastic body, the crack-opening displacement, v , at a distance r from the crack tip is given by the displacement equation:

$$v = 2K/\pi E' (2\pi r)^{1/2} \quad (\text{Eq 15})$$

Under conditions of small-scale yielding, the displacement at the crack tip, δ , can be calculated by assuming the effective crack tip ($a_{\text{eff}} = a + r_y$) is at a distance, r_y , from the actual crack tip:

$$\delta = 2v = 4K/\pi E' (2\pi r_y)^{1/2} = 4K^2/\pi E' \sigma_y \quad (\text{Eq 16})$$

Theoretically, fracture occurs when $\delta = \delta_c$, the critical CTOD. In practice, a characteristic value for δ exists only for the crack initiation event; significantly more scatter exists for δ measured at maximum load or final fracture. The CTOD approach is limited by the analytical and experimental uncertainties of the crack-tip region. Analytically, δ is defined as the CTOD at the interface of the elastic-plastic boundary and the crack surface. Experimentally, δ is calculated from displacement measurements taken remotely from the crack tip because direct physical measurements are not precise. Further uncertainty is introduced by the term σ_y in Eq 16, which may vary by 75%, depending on the degree of elastic constraint—a crack-tip characteristic that cannot be measured directly.

The CTOD approach offers a significant improvement over linear-elastic methods in the plastic range. An empirical correlation, known as a design curve, relates CTOD, crack size, and applied strain for a wide range of structural and material combinations.

For many years, only the CTOD test measured toughness for a brittle, unstable fracture event using a nonlinear-fracture parameter. In addition, the method allows the measurement of toughness after a “pop-in,” which is described as a discontinuity in the load-versus-displacement record usually caused by a sudden, unstable advance of the crack that is subsequently arrested.

The J -integral (Ref 13) characterizes the elastic-plastic field in the vicinity of the crack tip. J is defined as the line integral:

$$J = \int_{\Gamma} [w dy - \bar{T}(\partial \bar{u} / \partial x) ds] \quad (\text{Eq 17})$$

where Γ is any contour surrounding the crack tip, w is the strain-energy density, \bar{T} is the force vector normal to Γ , \bar{u} is the displacement vector, and s is the arc length along Γ . The J -integral is path independent for linear and nonlinear elastic materials and nearly so for most structural materials (elastic-plastic) under monotonic loading conditions (Ref 14). Thus, J can be computed using numerical methods by analyzing loads and displacements

along a contour away from the crack tip, that is, in a region where the analysis methods are quite accurate. This eliminates the uncertainties of the crack-tip region—a problem that seriously limits the usefulness of the CTOD method.

An equivalent interpretation is that J is equal to the change of the pseudopotential energy (the area under the load-displacement curve), U , upon an increment of crack extension of unit area, A ;

$$J = dU/dA \quad (\text{Eq 18})$$

For the linear-elastic case, the potential energy equals the strain energy ($U = V$), and therefore, Eq 18 is the same as Eq 8 and $J = G$. Thus, J appears to be a logical extension of LEFM into the elastic-plastic range.

Because of the irreversibility of plastic deformation, the energy interpretation of the J -integral does not apply to the process of crack extension, and J is not equal to the energy available for crack extension in elastic-plastic materials as G is for elastic materials. J is simply an analytically convenient, measurable parameter that is a characteristic of the elastic-plastic field at the crack tip.

Crack initiation under elastic-plastic conditions occurs at a characteristic value of J , called J_{Ic} ; J_{Ic} is related to the linear-elastic plane-strain toughness, K_{Ic} , in the same way G is related to K in Eq 11. Thus, J -integral methods can be used to determine K_{Ic} in specimens significantly smaller than the size requirements for linear-elastic response.

The J -integral concept is not only applicable to crack initiation, but also is applicable to crack propagation. For most materials that fail in the elastic-plastic range, significant fracture resistance exists after crack initiation. Therefore, in some cases the J -integral may be unduly conservative as a fracture criterion.

J -integral analysis must properly account for the stress-strain characteristics of the material. Thus, for a given structural configuration, J -integral solutions are required for each distinct material instead of the single solution needed for K analyses.

The R -curve concept, introduced by Krafft, Sullivan, and Boyle (Ref 15), is a characterization of the increase in fracture resistance accompanying the slow crack extension that precedes unstable fracture. ASTM E 561 covers the standard practice for R -curve determination. The R -curve is constructed by plotting crack extension, Δa , as a function of the driving force for fracture expressed in terms of G , K , J , or δ . The level of driving force required to extend the crack is defined as the resistance, R , of the material. An R -curve is shown in Fig. 12, where R is expressed in terms of K and is denoted by K_R . The R -curve may be used as a fracture criterion when crack-driving-force curves expressed in terms of K versus a at constant load in Fig. 12 are shown on the same plot. Fracture is predicted when the following conditions are met:

$$K = K_R \text{ and } \partial K/\partial a = \partial K_R/\partial a \quad (\text{Eq 19})$$

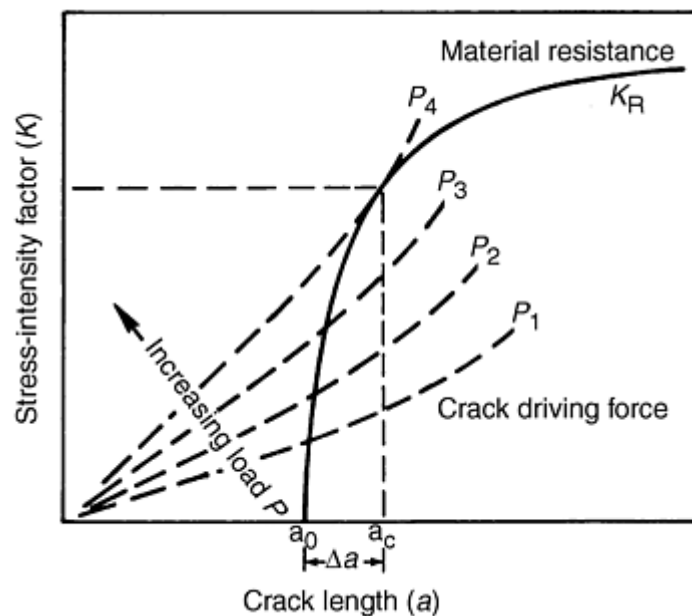


Fig. 12 Crack growth resistance curve and crack driving force curves in R -curve format. Source: Ref 16

K_R and K are computed for the test specimen and structure, respectively, using the appropriate value of $Y(a + r_y)$ in Eq 12.

In applying the R -curve concept as a fracture criterion, it is assumed that the R -curve is a property of the material for a given thickness and temperature, and the influence of planar geometry on the predicted instability point is considered in the calculation of K for the driving-force curves.

The conditions for tearing instability are shown in Fig. 13. The dashed line segment, tangent to the R -curve, shows the magnitude and slope of K versus a , calculated for a structural application at a loading condition where the application values of K and dK/da match the values of K_R and dK_R/da . As with R -curve K -values, an r_Y -type plastic zone adjustment is used for calculation of application K values. The values of K_R and of dK_R/da must be calculated for the applications crack using r_Y -corrected estimates of K_R .

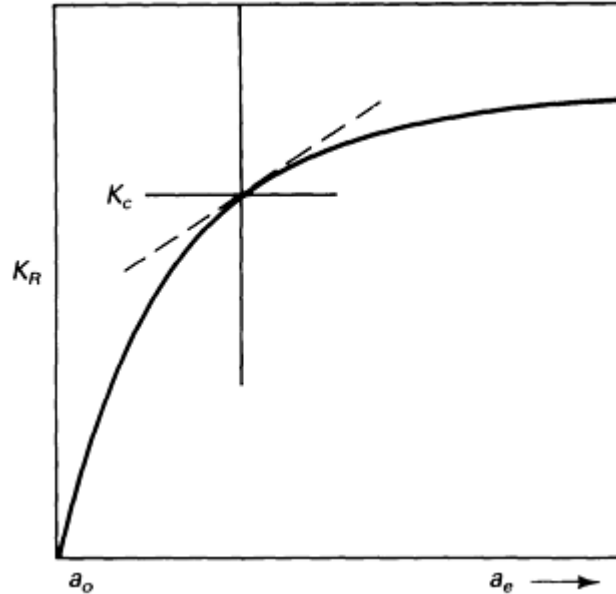


Fig. 13 Schematic R -curve. Dashed line shows a segment of the driving K -value, for which dK/da and K match the slope of the K -value of the R curve.

There is a close relationship between basic concepts used in R -curve testing and in J - R testing. However, with R -curve testing, the main emphasis is on the crack front conditions of plane stress; with J - R testing, emphasis is on crack front conditions of plane strain.

The R -curve approach is used as a measure of fracture toughness for plate thicknesses where valid K_{Ic} data cannot be obtained because of the size requirements for linear elasticity. For example, nickel steels have been evaluated at temperatures down to 76 K using the R -curve approach (Ref 17). The results can be misleading if one compares materials on the basis of fracture toughness; that is, an initiation criterion, such as K_{Ic} , indicates a substantially lower toughness than an instability criterion, such as the R -curve.

Fracture Toughness Testing

Fracture toughness is a single-parameter characterization of the fracture resistance of a material containing a crack. The single parameter depends on the fracture criterion chosen and varies as a function of temperature, loading rate, and microstructure. In this section, K_{Ic} is used as the linear-elastic fracture criterion and J_{Ic} is used as the fracture criterion for the elastic-plastic and fully plastic cases. Load-displacement records representing the three fracture cases are shown in Fig. 14.

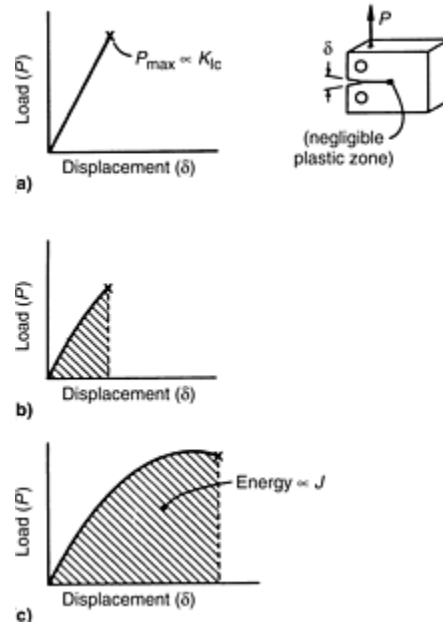


Fig. 14 Load-displacement behavior observed in fracture toughness tests. (a) Linear-elastic. (b) Elastic-plastic (failure before limit load). (c) Fully plastic (exhibits a limit load). (a) shows brittle behavior (K_{Ic} is measured). (b) and (c) show ductile behavior (J_{Ic} is measured).

Although the J_{Ic} value can be used to obtain an estimate of K_{Ic} , denoted $K_{Ic}(J)$, it should be understood that K_{Ic} and $K_{Ic}(J)$ may represent significantly different fracture behavior. K_{Ic} is the critical K level for the linear-elastic case, at which significant measurable extension of the crack occurs, often triggering unstable fracture. For valid measurements of K_{Ic} , the critical K level must be reached prior to significant plastic deformation; that is, the plastic zone size is negligible, less than 2% of the crack length and the thickness. In contrast, $K_{Ic}(J)$ for elastic-plastic or fully plastic fracture indicates an estimate K_{Ic} calculated from J_{Ic} , the J -integral value at which the first measurable extension of the crack occurs. Since plastic deformation prior to the onset of cracking does not invalidate the J_{Ic} measurement, smaller specimens can be used. Either: (a) significant amount of stable crack extension under rising load is displayed before final fracture occurs or (b) the elastic-plastic behavior culminates in plastic instability (Ref 18). The differences in K_{Ic} and $K_{Ic}(J)$ may be clarified by consideration of their test methods.

Linear-Elastic Fracture Toughness. Standard test method ASTM E 399 (Ref 5) is used to measure plane-strain fracture toughness, K_{Ic} . The standard is designed to ensure that linear-elastic conditions prevail throughout the test. This is achieved by requiring a sufficiently large specimen for the particular toughness and yield strength of the material being tested. Planar dimensions are sized to ensure elastic response of the specimen, and the thickness is sized to ensure sufficient through-thickness constraint. The dimensional criteria in ASTM E 399 are:

$$B, a \geq 2.5(K_{Ic}/\sigma_{ys})^2 \quad (\text{Eq 20})$$

where B and a are defined in Fig. 15 for the compact specimen.

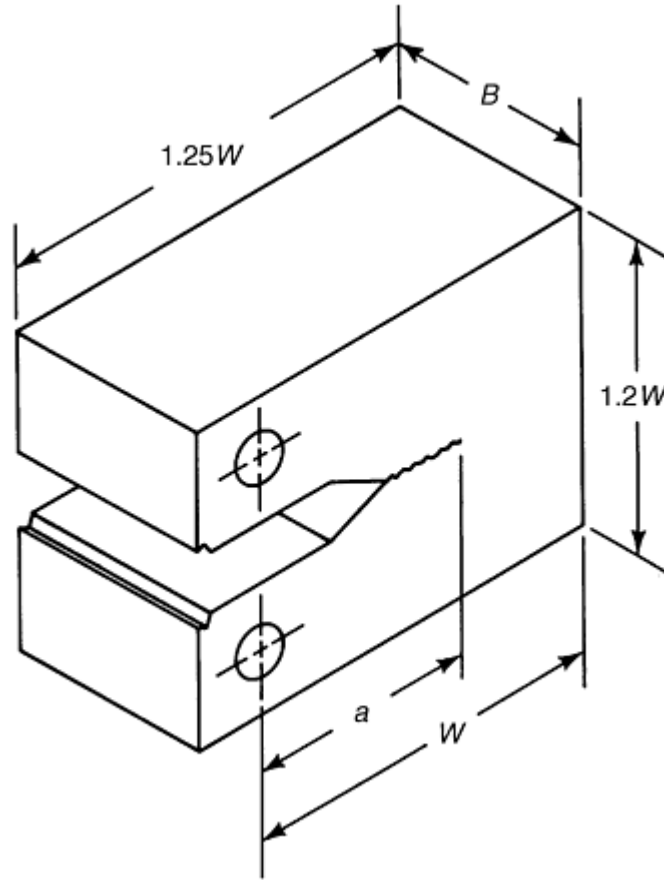


Fig. 15 ASTM E 399 compact specimen for fracture toughness testing

The specimens are precracked by fatigue cycling to an initial relative crack length of $a/W \simeq 0.5$. Precracking loads are limited to low values to keep the plastic zone size at the crack tip small; the fatigue loads must be such that the maximum K level during fatigue is less than $0.6 K_{Ic}$. (Changes in yield strength must be taken into account if precracking is performed at room temperature and testing at cryogenic temperatures.) Subsequently, the specimens are monotonically loaded to failure. During loading, load, P , and displacement, Δ , are measured and a P - Δ curve is recorded. The critical load, P_Q , as defined in ASTM E 399, is either the maximum load or the load at a 5% secant offset from the linear part of the P - Δ test record. If the maximum load in the test exceeds $1.10 P_Q$, the test is invalid. A trial value of fracture toughness, K_Q , is calculated from the critical load, the measured crack length, the specimen dimensions, and the specimen calibration function $Y(a/W)$, as follows:

$$K_Q = P_Q Y(a/W) / B W^{1/2} \quad (\text{Eq 21})$$

If all the conditions of ASTM E 399 are met, such as precracking procedures, load-displacement record, and specimen dimensions, then $K_Q = K_{Ic}$.

The K_{Ic} test method was standardized by ASTM in 1970. Uncertainties in K_{Ic} measurements obtained by this method lie between 4 and 10% (Ref 19). Three tests per material per temperature are considered sufficient to demonstrate reproducibility.

J-integral fracture toughness. J_{Ic} measurement is based largely on the method proposed in 1974 (Ref 20, 21), as shown schematically in Fig. 16. Typically, a series of deeply notched compact specimens are precracked to $a/W \simeq 0.6$, and each specimen is loaded to a J -level in the region where crack extension is anticipated. The load-displacement curve is recorded on an X - Y recorder, with displacement being measured at the load line. Then the specimen is unloaded and heated to tint the region of crack extension. The specimen is fractured, and the crack extension, Δa , is measured from the exposed fracture surface. J is calculated from the load-displacement record and specimen dimensions using:

$$J = (A/Bb)f(a_0/W) \quad (\text{Eq 22})$$

where A is the area under the load-displacement curve, $b = (W - a)$ is the uncracked ligament, and $f(a_0/W)$ is a function of crack length.

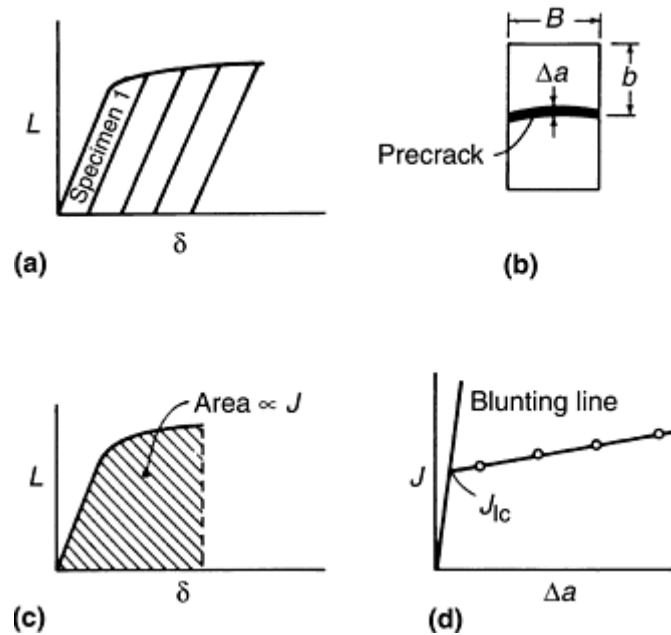


Fig. 16 J -resistance curve test method for J_{Ic} determination. (a) Test records. (b) Heat-tinted fracture surface. (c) J calculation. (d) Resistance curve

The results of a test series are plotted as J versus Δa . On the same graph, the line defined by Eq 23 is drawn:

$$J = 2\bar{\sigma}\Delta a \quad (\text{Eq 23})$$

where $\bar{\sigma}$ is the flow stress (the average of the yield and ultimate strengths). The intersection of the J - Δa plot and the $J/2\bar{\sigma}$ line is defined as J_{Ic} , the value of J at the onset of crack extension. Apparent crack extension at Δa values of less than $J/2\bar{\sigma}$ is attributed to deformation at the crack tip instead of material separation. The linear-elastic plane-strain fracture toughness can be estimated from J_{Ic} as follows:

$$K_{Ic}(J) = [J_{Ic}E/(1 - \nu^2)]^{1/2} \quad (\text{Eq 24})$$

where E is Young's modulus and ν is Poisson's ratio.

The J -integral method has been combined into ASTM E 1820 (Ref 22), and the individual standard E 813 was withdrawn from the *Annual Book of ASTM Standards* in 1998.

Other Test Methods. Fracture toughness data can be obtained using test methods other than the currently favored K_{Ic} and J_{Ic} methods. Care must be taken in comparing these data with K_{Ic} and J_{Ic} values and in applying the data to materials selection or design. Difficulties arise owing to differences in measurement criteria and fracture criteria.

In both K_{Ic} and J_{Ic} testing, the measurement point (i.e., P_Q for K_{Ic} and the $J/2\bar{\sigma}$ intersection for J_{Ic}) is near the onset of crack extension. Fracture toughness data are frequently reported where the maximum load values are used to calculate fracture toughness, and the results are reported in terms of K or J values—often with a change of subscript (e.g., K_{max} , K_{IE} , K_C , J_C).

Significant differences in toughness also may be attributed to differences in the fracture criteria. Data obtained by the CTOD or R -curve methods evaluate the fracture toughness of ductile materials after significant crack extension and plasticity have occurred. Consequently, the toughness values for the same material are higher than those obtained by the K_{Ic} or J_{Ic} methods. Advantages and disadvantages of various fracture toughness tests are shown in Table 1.

Table 1 Fracture toughness tests

Method	Advantages	Disadvantages
K_{Ic} , ASTM E 399	This method is the most reliable to get fracture toughness values at lower temperatures. The success of all other methods is based on their ability to give data comparable to this method.	The high cost of testing the large specimens required for higher temperature tends to reduce the number of data points. Linear extrapolation from valid K_{Ic} at lower temperature to higher temperature

		produces conservatism. No valid K_{Ic} values at higher temperature.
<i>J</i> -integral, ASTM E 813	Provides fracture toughness values that agree with K_{Ic} method. Yields realistic fracture toughness data at higher temperature. Has the advantage (over CTOD) of a sound theoretical basis, which permits evaluation of stable crack growth. Determination of dJ/da is a measure of the resistance to continued crack propagation. Testing many small <i>J</i> specimens provides an indication of material toughness variation.	Not able to evaluate irregular crack propagation due to residual stress or at HAZ near welds. Not accurate enough at low temperatures. Measurements are inaccurate due to irregular crack fronts. Not valid for thin materials where K_J is 2.5 K_{Ic} . When heat tinting is used, the additional number of specimens adds to testing costs.
CTOD, BS 7448, ASK-AAN 220	Provides fracture toughness values that agree with ASTM K_{Ic} method. Yields realistic fracture toughness data at higher temperatures. CTOD results have shown good consistency and comparability with toughness values using other methods. Simultaneous measurement of CTOD and <i>J</i> -integral is possible for a minor extra cost.	Variations in the measurement of δ results in variations of K_{Ic} of up to a factor of 2. This method restricted to temperatures above -60 °C.
Simple equal energy	Provides fracture toughness values that agree with ASTM K_{Ic} method. Yields realistic fracture toughness data at higher temperatures. Toughness data are identical or closely similar to <i>J</i> -integral data.	Limitations similar to those of the <i>J</i> -integral method. This method is more empirical in nature, so <i>J</i> -integral testing is preferred.
Instrumented Charpy testing	Requires small specimens. Practically suited for determination of toughness variations in small regions of complex parts, in HAZ of welds, and in other locally embrittled zones. Error in K_{Ic} is small (in comparison to ASTM K_{Ic} method) for predominantly brittle failure.	Can provide very pessimistic values, particularly at higher temperatures. K_{Ic} is slightly underestimated at low temperatures, but considerable scatter of measurements exists above the brittle-transition temperature within a factor of 3 due to small size of specimens. Difficulty in separating the crack-initiation and crack propagation components of fracture.
Empirical methods per Begley and Logsdon	Requires small specimens. Offers a rapid and inexpensive technique to estimate K_{Ic} for wrought ferritic steels. This method indicates that Charpy K_{Ic} values are scattered and lie entirely below ASTM K_{Ic} data. Conservative by a factor of up to 3. K_{Ic} by this method provides narrow scatter band with the results below ASTM K_{Ic} by a factor of 2.	Can provide very pessimistic values, particularly at higher temperatures. Cannot give information relevant to small regions such as HAZ at welds, castings, or materials other than the ferritic steels.

CTOD, crack-tip opening displacement; HAZ, heat-affected zones.

Source: Ref 10

Specimens. There are many fracture-specimen types and sizes, each offering specific advantages and disadvantages. Some of these are listed in Table 2. The choice of a particular specimen geometry depends on technical purposes and test requirements. The three-point bend and compact specimens (standard specimens of the ASTM E 399 and E 813 methods) are often preferred for general laboratory materials evaluation, because *K* and *J* calibrations for these specimens are accurately known and relatively low loads are required during testing. Data obtained with nonstandard specimens must be evaluated carefully to ensure that the same fracture criteria are used, such as the onset of cracking.

Table 2 Advantages and disadvantages of selected fracture toughness test specimens

Specimen type	Advantages	Disadvantages
Compact specimen	High K_{Ic} measurement capability for size Standard specimen (ASTM E 399) Low loads required	Expense of machining
Three-point bend	Standard specimen (ASTM E 399) Low loads required Suitable for wide range of orientations	A long span transverse to loading direction, which may be a disadvantage for some cryostats
Center-cracked tension	Pure tensile loading	High loads and large material requirements
Double-edge notched	Pure tensile loading	High loads and large material requirements
Single-edge notched	Easy notch preparation	High loads and material requirements
Double cantilever beam	Tapered specimens, can be designed such that the value of K is independent of crack length	Long span transverse to loading direction Side grooving may be necessary to guide cracking direction Machining expenses
Surface-flawed specimen (part-through crack)	Simulates a flaw type commonly found in service	Size requirements are difficult to establish K solution not precisely known High loads are required
C-shaped specimen	Special geometry suitable for bar stock	Limited applicability
Wedge-opening-load specimen	Larger width than compact specimen May be bolt loaded at one end	Expense of machining

For K_{Ic} measurements, ASTM E 399 describes procedures using test specimens such as those shown in Fig. 17. The crack-tip plastic region is small compared with crack length and to the specimen dimension in the constraint direction. A compact-type (CT) specimen, shown in Fig. 17(d), often is used to experimentally determine fracture toughness and other fracture properties. From a record of load versus crack opening and from previously determined relations of crack configuration to stress intensity, plane-strain fracture toughness can be accurately measured if all the criteria for a valid test are met.

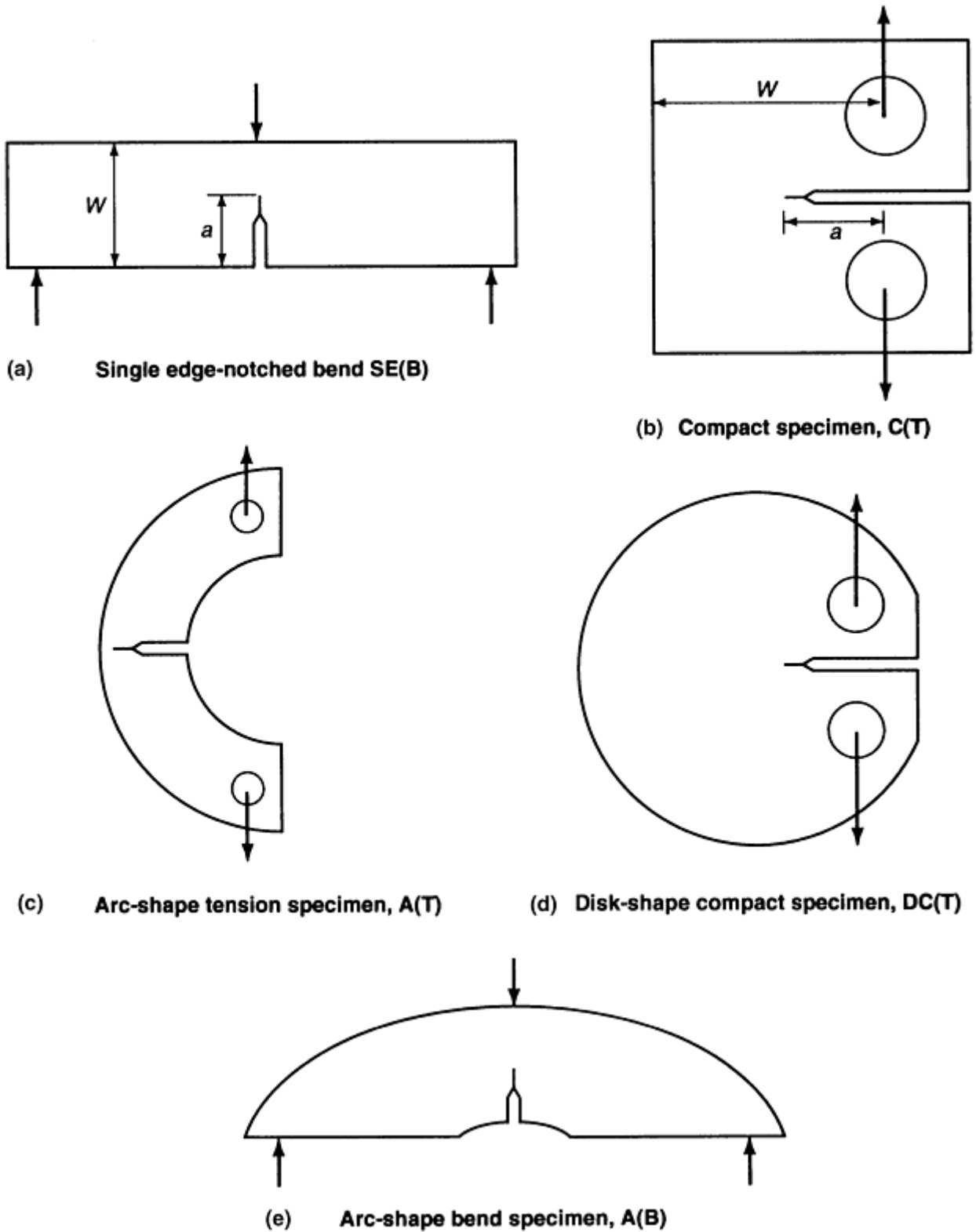


Fig. 17 Specimen types used in plane-strain fracture-toughness (K_{Ic} testing (ASTM E 399)

Compliance-based fracture testing uses a CMOD gage. Direct-current signals are amplified and conditioned to control and monitor the test. Generally, the load is monitored using a load cell mounted within the test frame in the load train.

Specimen Orientation. Most structural alloys are anisotropic—their fracture toughness varies with direction. Fracture anisotropy is caused by microstructural inhomogeneities, such as irregular grain structure, chemical segregation, crystallographic texturing, or inclusion morphology. Specimen orientation is important since it determines the direction of crack propagation through the microstructure.

In some alloys, nearly equiaxial microstructures are achieved. Then, fracture properties may be nearly isotropic. The fracture resistance of most alloys, however, is quite dependent on orientation, more so than some tensile properties. Rolled plates having elongated grains may exhibit J_{Ic} variations of up to 2 to 1. Knowledge of anisotropy can be used to advantage by orienting components judiciously in relation to the maximum service stress.

Loading Rate. Plastic deformation is a time-dependent process that can be suppressed at high loading rates. High loading rates produce higher yield strengths and reduce the toughness of some alloys, particularly the body-centered cubic (bcc) alloys. Dynamic tests are typically performed at high rates between 10^4 and 10^6 $\text{MPa}\sqrt{\text{m}} \cdot \text{s}^{-1}$, whereas static K_{Ic} tests are conducted at stress-intensity-factor rates of about $1 \text{ MPa}\sqrt{\text{m}} \cdot \text{s}^{-1}$. As a rule, alloys that show rate-sensitive tensile behavior also show rate-sensitive fracture behavior. If the tensile yield strength of an alloy is raised significantly while its ductility is lowered at high strain rates, reduced fracture toughness values may be expected for dynamic loading. This is typically the case for low-strength ferritic steels.

Thermal and Metallurgical Effects on Toughness

As shown in Fig. 18, fracture toughness may increase or decrease as temperature is lowered, depending on metallurgical factors.

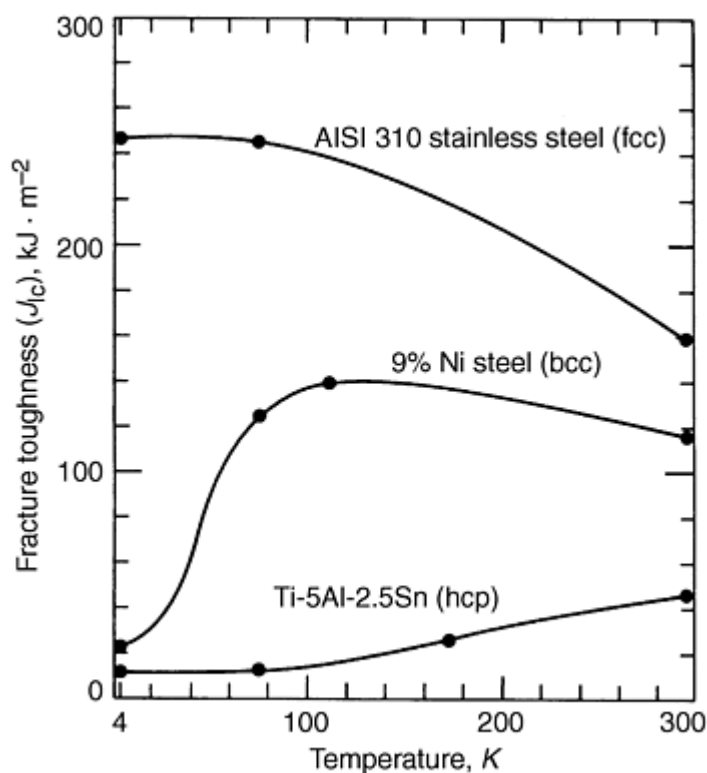


Fig. 18 Temperature dependence of fracture toughness for alloys, illustrating characteristic behavior for three different crystal structures

To be suitable for cryogenic applications, structural alloys should fracture in a ductile manner at all service temperatures. Ductile fracture is caused by the formation and growth of the voids that eventually comprise the fracture surface. Thus, the toughness of ductile metals is related to the factors that influence the nucleation and growth of voids. Voids nucleate most readily at second-phase particles, such as inclusions and precipitates (1 to 10 μm in size), as a result of interfacial separation, fracture of the particle, or matrix separation caused by strain concentration near the particle. Voids grow and coalesce by ductile tearing of the matrix. Ductile tearing resistance is a function of the strength and ductility of the matrix. As matrix strength increases, less energy is dissipated by plastic deformation during tearing, and toughness is reduced. Increased matrix strength also tends to activate additional void nucleation sites. Consequently, yield strength is inversely proportional to fracture toughness, as shown in Fig. 19.

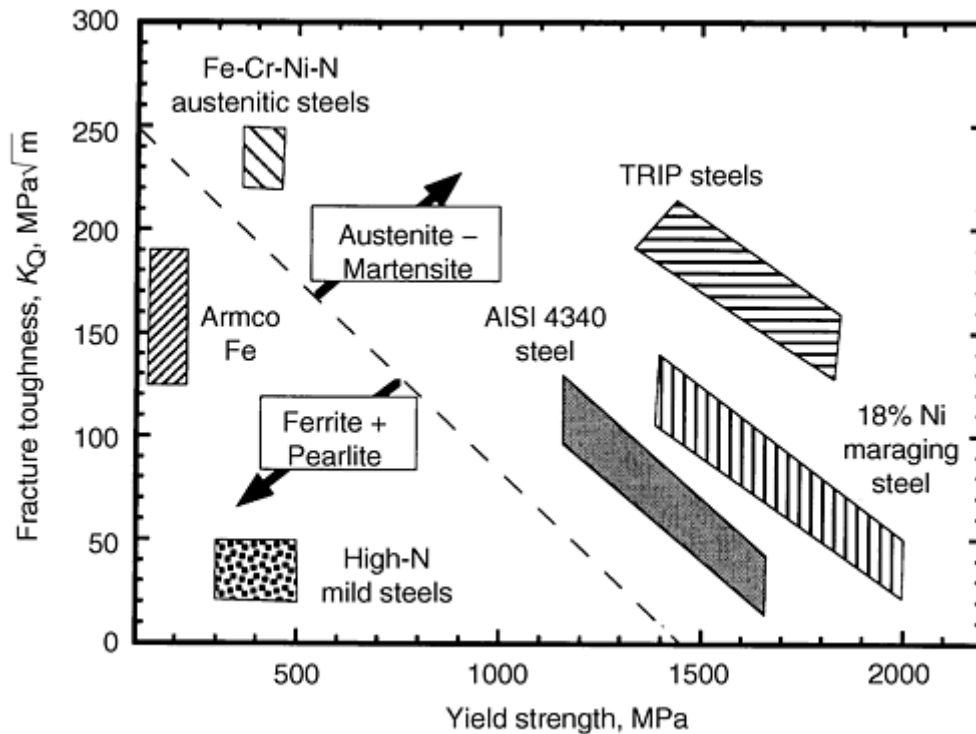


Fig. 19 Fracture toughness versus yield strength for some structural steels, TRIP, transformation-induced plasticity

Brittle fracture requires less energy for surface formation than ductile fracture. Lower energy fracture modes include cleavage and intercrystalline (grain-boundary) fracture. Cleavage is a fracture mode in which material separation proceeds along preferred crystallographic planes without sizable plastic deformation prior to fracture. Metals subject to cleavage usually have a large increase in yield strength as temperature is decreased. Cleavage occurs when the cleavage fracture stress is reached before the energy required for void formation is exceeded. Intercrystalline fracture occurs when the cohesive strength of the grain boundary is exceeded before cleavage or ductile fracture occurs. As matrix strength increases with decreasing temperature, intergranular failure may occur more readily in a susceptible alloy.

The influence of selected metallurgical factors on toughness at low temperatures is discussed in the following sections.

Crystal Structure. Figure 18 indicates that crystal structure is a reliable guide for qualitative prediction of temperature dependence: face-centered cubic (fcc) alloys typically exhibit high toughness throughout the ambient-to-cryogenic range; body-centered cubic (bcc) alloys exhibit precipitous decreases in fracture toughness at critical transition temperatures; and hexagonal close-packed (hcp) alloys are noted for comparatively low toughness at all temperatures. Metallurgical factors (composition, purity, and processing) can strongly modify the fracture behavior, and in every crystal structure class there are exceptional alloys.

Face-Centered Cubic Alloys. Annealed fcc alloys have low strength and high fracture toughness. Included in this group are copper alloys, aluminum alloys, austenitic stainless steels, and nickel-base superalloys. Ductile tearing is typical, even in thick sections. Fracture toughness values for these alloys usually increase between 295 and 4 K, often showing a broad maximum at temperatures near 77 K.

Body-Centered Cubic Alloys. Because of their ductile-to-brittle transitions, alloys having bcc structure are of limited use at cryogenic temperatures. The transitions are associated with a change in fracture mode from void coalescence to cleavage as temperature is reduced. The transition temperature range is a function of the metallurgical and mechanical variables that alter matrix strength. Factors tending to raise the transition temperature for a given alloy and heat treatment combination include increasing grain sizes, thicker sections, and higher loading rates. Nickel alloying decreases the transition temperatures of ferritic steels.

Hexagonal Close-Packed Alloys. The fracture toughness of hcp metals and alloys is usually quite low, and many exhibit transitional behavior such as that observed in bcc alloys. Beryllium, for example, exhibits room temperature, K_{Ic} values of about 7 to 23 $\text{MPa}\sqrt{m}$, and a 30% decrease occurs as temperature is reduced to 77

K. Low-temperature ductile-to-brittle transitions have been observed in zinc, beryllium, and magnesium, but not in cadmium. Under certain conditions, titanium alloys have exhibited abrupt toughness reductions. The chemical composition of an alloy determines its crystal structure, phase balance, and potential strengthening and deformation mechanisms. Thus, composition has the primary influence on material behavior, including fracture toughness. Chemical composition includes impurities dissolved in the matrix or present as precipitates and inclusions.

Alloy additions increase the stability of the fcc phase in austenitic stainless steels. For example, toughness of nitrogen-strengthened Fe-Cr-Ni-Mn stainless steels at 76 and 4 K may increase with increasing austenite stability. However, the influence of austenite stability on low-temperature toughness is not clear in the Fe-Cr-Ni stainless steels such as AISI 304, 310, and 316.

Phase balance can have a marked effect on toughness at cryogenic temperatures. For example, 308L and 316L stainless steel weld metals are formulated to provide 5 to 10% ferrite, a bcc phase, and the balance austenite. The ferrite is needed to prevent hot cracking, but at cryogenic temperatures the ferrite is brittle and lowers the toughness of the weld metal. Other examples of phase balance are the 5, 6, and 9% Ni steels, where the nickel content results in a 5 to 10% retained austenite after the alloys have been properly heat treated. Retained austenite contributes to improved toughness of these alloys at temperatures from 300 to 76 K.

Potential strengthened mechanisms are a function of alloy content. Solid-solution strengthening of austenitic stainless steels by interstitial nitrogen provides a large increase in yield strength at cryogenic temperatures and a corresponding decrease in fracture toughness. By comparison, solid-solution strengthening by substitutional elements, such as magnesium in aluminum, has a relatively small effect on the temperature dependence of strength and toughness. For precipitation-hardened alloys having an fcc matrix, changes in strength and toughness at low temperatures are also small.

In addition to intentional alloying elements, commercial alloys inevitably contain impurity elements that cannot be economically removed during processing. In most cases, impurities either dissolve interstitially, thereby reducing matrix toughness, or precipitate in the solidifying metal because they are less soluble upon cooling. Precipitates formed in this way increase the ease of void formation and reduce toughness. Occasionally impurities segregate to grain boundaries, causing severe toughness losses that are due to intergranular embrittlement. A classic example is temper brittleness in steels where small concentrations of impurities segregate to the grain boundaries and form a continuous intergranular fracture path.

Processing includes producing, refining, and casting of the alloy; working the ingot into a suitable product form; and heat treating the final product. Within the limits imposed by chemical composition, processing controls the alloy microstructure and, consequently, the properties. Production, refining, and casting operations determine the cleanliness and homogeneity of the alloy. Working the ingot into a suitable product form influences anisotropy, grain size, homogeneity, and cold working. Heat treatment provides the final microstructural control. All of these processes influence toughness at all temperatures. Table 3 summarizes the effects of microstructure on toughness.

Table 3 Effects of microstructural variables on fracture toughness of steels

Microstructural parameter	Effect on toughness
Grain size	Increase in grain size increases K_{Ic} in austenite and ferritic steels
Unalloyed retained austenite	Marginal increase in K_{Ic} by crack burning
Alloyed retained austenite	Significant increase in K_{Ic} by transformation-induced toughening
Interlath and intralath carbides	Decrease K_{Ic} by increasing the tendency to cleave
Impurities (P, S, As, Sn)	Decrease K_{Ic} by temper embrittlement
Sulfide inclusions and coarse carbides	Decrease K_{Ic} by promoting crack or void nucleation
High carbon content (>0.25%)	Decrease K_{Ic} by easily nucleating cleavage
Twinned martensite	Decrease K_{Ic} due to brittleness
Martensite content in quenched steels	Increase K_{Ic}
Ferrite and pearlite in quenched steels	Decrease K_{Ic} of martensitic steels

Processing to minimize grain size is desirable because matrix strength is increased with a minimum change in toughness. Grain refinement is particularly beneficial to alloys that undergo a ductile-to-brittle transition, such as the ferritic steels, because it lowers the transition temperature.

Processing treatments that cause grain-boundary precipitation of intermetallic compounds, usually carbides, can reduce toughness at cryogenic temperatures. Embrittlement due to grain-boundary precipitates only occurs when the matrix strength exceeds the grain-boundary strength; that is, it may occur at cryogenic temperatures but not necessarily at room temperature.

Fatigue Crack Growth

Fatigue progresses in three stages: crack initiation, crack growth, and fracture on the final cycle. Therefore, the fatigue lifetime of a component is determined by the number of cycles required to initiate and propagate a crack to critical proportions. In complex structures, cracks already exist as a result of manufacturing or fabrication or are assumed to exist because inspection methods are not sensitive enough to verify their absence. In low-cycle fatigue applications, crack initiation occurs quickly and may account for little of the total fatigue life.

In reviews of extensive crack propagation data, Paris (Ref 23) observed that a log-log plot of the crack growth rate, da/dN , versus the stress-intensity range, ΔK , is a straight line, obeying an equation of the form:

$$da/dN = c(\Delta K)^n \quad (\text{Eq 25})$$

where c and n are empirical constants and $\Delta K = K_{\max} - K_{\min}$ (K_{\max} and K_{\min} are the maximum and minimum stress-intensity factors of the fatigue cycle). This relation, known as the Paris equation, implies that the cyclic crack-tip stress field described by ΔK is the driving force for fatigue crack extension. Cyclic profile, frequency, mean load, and stress state are of secondary importance. The principal limitation of Eq 25 is the failure to account for environmentally enhanced fatigue crack growth, but Eq 25 still provides a useful basis for the empirical analysis of crack growth data. Accordingly, most data are presented as log-log plots of da/dN versus ΔK . When fatigue crack growth rates are measured over a more complete range (10^{-8} to 1 mm/cycle), the curve has three distinct regions, as shown in Fig. 20. At low growth rates, the curve approaches a threshold value of ΔK , denoted ΔK_{th} , below which fatigue crack growth does not occur. At intermediate growth rates, the curve is linear on a log-log-scale and conforms to Eq 25. Finally, accelerated crack growth occurs when K_{\max} approaches K_c .

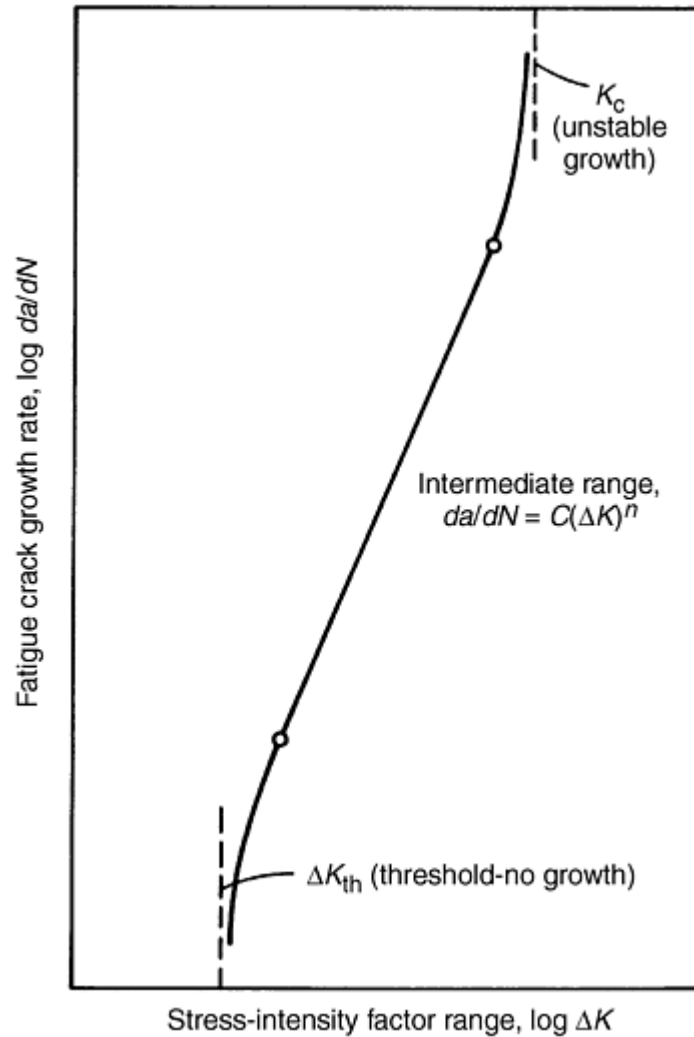


Fig. 20 Fatigue crack growth rate data trends, illustrating the sigmoidal curve of da/dN versus ΔK

Test Methods. Fatigue crack growth rate measurements are generally conducted in fatigue test machines capable of applying a constant load amplitude cycle at frequencies on the order of 10 Hz. The standard method for constant amplitude fatigue crack growth rate measurements above 10^8 m/cycle is designated ASTM E 647 (Ref 24). Specimens are precracked by fatigue cycling at a load amplitude equal to or less than the test-load amplitude. During the test, crack length is measured as a function of number of cycles and the data are plotted and reduced in terms of da/dN versus ΔK , as shown in Fig. 20. The growth rate, da/dN , is the slope of the a versus N curve at a given value of a , and the stress intensity range is the ΔK level at that value of a calculated for the specific specimen configuration. For the case of the compact specimens:

$$\Delta K = (P_{\max} - P_{\min})Y(a/W)/B(W)^{1/2} \quad (\text{Eq 26})$$

where P_{\max} and P_{\min} are the maximum and minimum values of the constant-amplitude load cycle.

The basic data in fatigue crack propagation tests are the cycle number and crack length. The cycle number is readily monitored by electronic or mechanical counters. Several methods of crack length determination have been successfully used in room-temperature studies: direct visual measurement, ultrasonic sensing, electrical potential measurements, and the compliance method.

The compliance method is an indirect technique, applicable at all temperatures. It is based on the correlation between specimen compliance (displacement per unit load) and crack length: compliance increases as crack length increases.

The basic procedures for calibrating the compliance method are illustrated schematically in Fig. 21. Crack-front striations (beach marks) on specimen fracture surfaces are created by changes in the minimum fatigue load. The crack lengths are then measured, averaged, and plotted against their compliance values. The resultant curve is then fit using a polynomial expression that is used to infer crack lengths from compliance data recorded during fatigue crack growth tests.

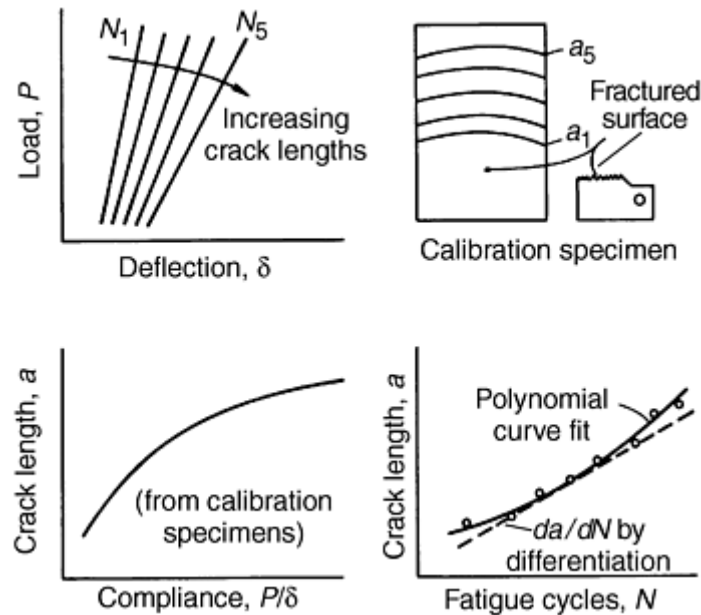


Fig. 21 Compliance method for fatigue crack growth rate measurements

The compliance method offers advantages for testing thick specimens, because the crack-front curvature is accounted for in the average crack length derived from the compliance value. In contrast, the visual method measures the crack length at the specimen surface. Otherwise, the accuracies of the visual and compliance methods are comparable.

Today, laboratory testing for fracture toughness relies more on servohydraulic equipment, which consists of mechanical test apparatus with sophisticated computer data acquisition and controls. In compliance-based fracture testing, the displacement usually is measured across the crack mouth opening using cantilever beam clip gages, optical (laser and white light) extensometry, or back face strain gages. Each of these techniques has its own advantages and may be used to continuously monitor crack length. An additional benefit of compliance techniques is that the same signal can be used for determining crack closure.

Mechanical Test Variables. The data trends illustrated in Fig. 20 should hold as long as ΔK is a valid descriptive parameter for the crack-tip stress field. In cases of extreme plasticity, ΔJ is a better parameter for correlating fatigue crack growth.

Mean stress is proportional to the stress-intensity ratio, $R = K_{\min}/K_{\max}$, and can significantly influence fatigue crack growth rates. In general, for constant ΔK values, da/dN often increases as R increases.

The stress-intensity ratio is usually held constant at a value between 0 and 0.1 for laboratory tests. However, in service applications, R may be higher or variable, and this must be considered in fatigue crack growth predictions.

Cyclic frequency and waveform are important variables for tests at elevated temperatures and in corrosive environments because creep and corrosion are time-dependent processes. However, at cryogenic temperatures, cyclic frequency and waveform have little influence on fatigue crack growth rates.

Test Environment. The room temperature fatigue properties of some alloys are more sensitive to the chemical environment than static tensile properties or fracture toughness. Most cryogenic environments are inert or their chemical reactivity is abated, so that few problems with structural alloys are encountered. Some room-temperature environments, normally considered benign, may actually cause accelerated cracking. For example, unconditioned room-temperature air contains enough moisture to accelerate the fatigue crack growth rates of a wide variety of steel and aluminum alloys. This moisture effect must be recognized when comparing data for inert cryogenic environments with data for unconditioned laboratory air at room temperature. Unless data for dehumidified air are available, it may be difficult to differentiate between temperature effects and chemical reaction.

Specimen Orientation. Crack growth rates in the intermediate range are relatively insensitive to specimen orientation. At high ΔK values, however, orientation effects become obvious and are usually associated with inhomogeneities due to grain structure, second-phase particles, or inclusion distribution and morphology. Some wrought alloys having elongated grain structures also exhibit nearly isotropic fatigue crack growth resistance.

Fatigue Life Calculations. Equation 25 is frequently used to estimate the life of a cracked structure subject to fatigue. For a crack assumed to exist at a selected location in a structure, the relationship between K_c , respectively. Life is calculated by integrating Eq 25 between the limits set by the initial flaw size and the final size, based on fracture toughness data:

$$N = \int_{a_i}^{a_c} da / [c(\Delta K)^n]$$

$$= 1/[c(\Delta \sigma)^n] \int_{a_i}^{a_c} da / [f(a)]^n \quad (\text{Eq 27})$$

For complex load histories, $\Delta\sigma$ takes on many values as a function of time, and Eq 27 must be integrated sequentially using numerical methods. Several computerized techniques have been developed to evaluate Eq 27, including some to account for load interaction effects. A load interaction effect is the beneficial effect of peak loads on subsequent low-load growth rates. For example, da/dN is frequently reduced below expected values during the low-stress amplitude cycles that follow high-stress amplitude cycles.

Fatigue Life Calculations for Brittle Materials. For safety-critical applications involving most metallic materials, integration of crack growth data is frequently done according to Eq 27. This approach is more difficult with brittle materials like ceramics and intermetallics, which have fatigue crack growth rates that are more sensitive to the applied stress intensities than are rates for metallic materials (e.g., Fig. 22). This higher sensitivity results in a higher exponent, n , in the Paris equation and makes life projection from integration more difficult for brittle materials. Accordingly, a more appropriate approach for brittle materials may be to design on the basis of threshold levels below which fatigue failure cannot occur.

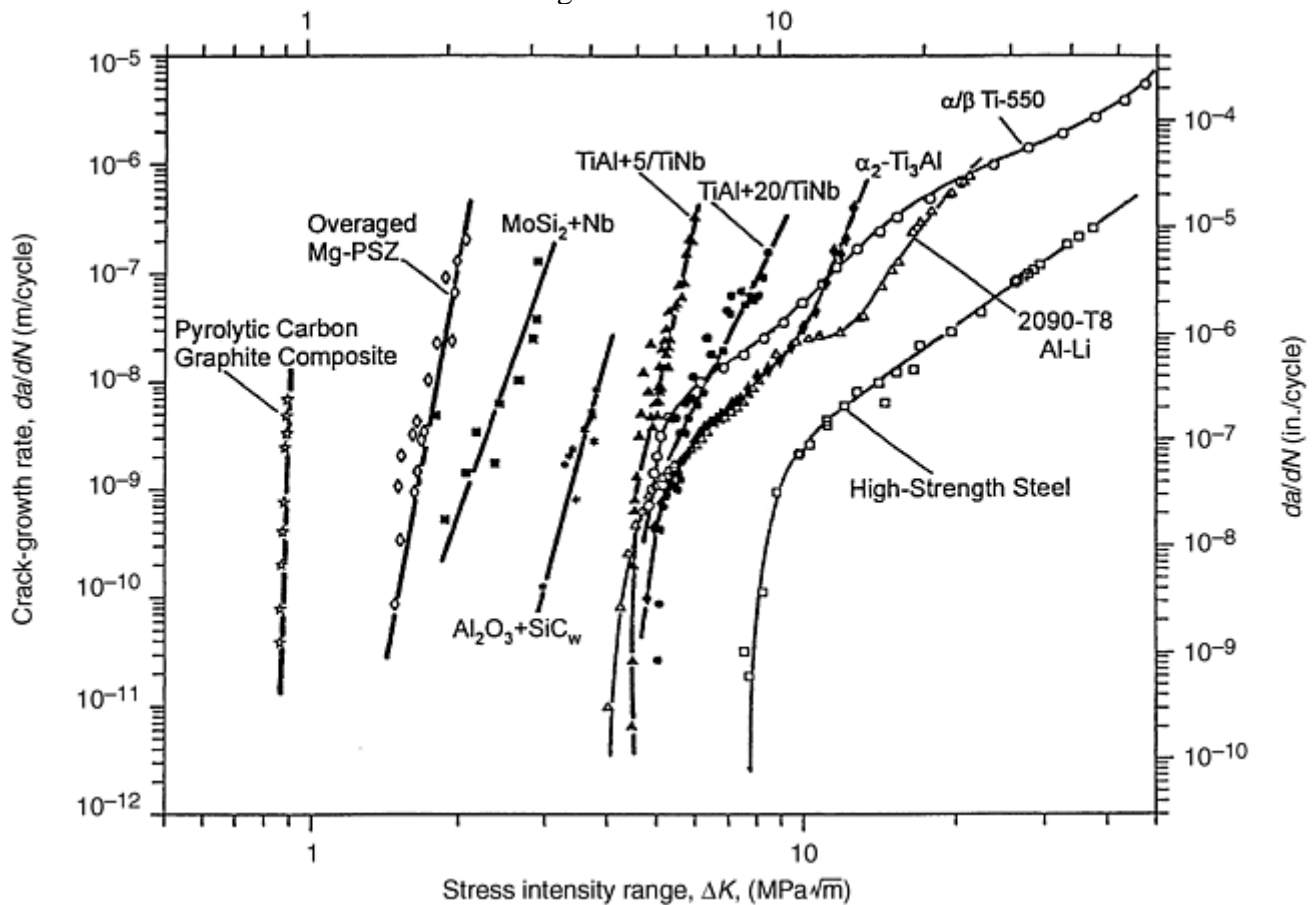


Fig. 22 Schematic variation of fatigue-crack propagation rate (da/dN) with applied stress intensity range (ΔK), for metals, intermetallics, and ceramics. Source: Ref 25

References cited in this section

1. A.A. Griffith, The Phenomena of Rupture and Flow in Solids, *Philos. Trans. Soc. (London) A*, Vol 221, 1920, p 163–198

5. "Standard Test Method for Plane-Strain Fracture Toughness of Metallic Materials," E 399-90, *Annual Book of ASTM Standards*, Vol 03.01, ASTM, 1999, p 422–452
9. G.R. Irwin, Plastic Zone near a Crack and Fracture Toughness, *Proc. Seventh Sagamore Ordnance Materials Research Conference*, Syracuse University Press, 1960, p IV63–IV78
10. R.D. Venter and D.W. Hoepfner, "Crack and Fracture Behavior in Tough Ductile Materials," report submitted to the Atomic Energy Control Board of Canada, Oct 1985
11. "Fracture Mechanics Tests, Part 1: Method for Determination of K_{Ic} , Critical CTOD and Critical J Values of Metallic Materials," BS 7448: Part 1, The British Standards Institution, 1991
12. "Standard Test Method for Crack Tip Opening Displacement (CTOD) Fracture Toughness Measurement," E 1290-93, *Annual Book of ASTM Standards*, Vol 03.01, ASTM, 1999, p 831–840
13. J.R. Rice, A Path Independent Integral and Approximate Analysis of Strain Concentration by Notches and Cracks, *J. Appl. Mech.*, Vol 35, 1968, p 379–386
14. D.J. Hayes, "Some Applications of Elastic Plastic Analysis to Fracture Mechanics," Ph.D. thesis, University of London, 1970
15. J.M. Krafft, A.M. Sullivan, and R.W. Boyle, Effect of Dimensions on Fast Fracture Instability of Notched Sheets, *Proc., Crack Propagation Symposium*, Vol I, College of Aeronautics, Cranfield, England, 1961, p 8–28
16. D.E. McCabe and R.H. Heyer, R-Curve Determination Using a Crack-Line-Wedge-Loaded (CLWL) Specimen, *Fracture Toughness Evaluation by R-Curve Methods*, STP 527, 1973, p 17–35
17. D.A. Sarno, J.P. Bruner, and G.E. Kampschafer, Fracture Toughness of 5% Nickel Steel Weldments, *Weld J.*, Vol 53, 1974, p 486
18. P.C. Paris, H. Tada, A. Zahoor, and H. Ernst, The Theory of Instability of the Tearing Mode of Elastic-Plastic Crack Growth, *Elastic-Plastic Fracture*, STP 668, J.D. Landes, J.A. Begley, and G.A. Clarke, Ed., ASTM, 1977, p 5–36
19. S.D. Antolovich and G.R. Chanai, Errors Associated with Fracture Toughness Testing, Paper II-242, *Third Int. Conf. Fracture*, Verein Deutscher Eisenhüttenleute, Dusseldorf, 1975, p 1–5
20. J.D. Landes and J.A. Begley, Test Results from J-Integral Studies—An Attempt to Develop a J-Integral Test Procedure, *Fracture Analysis*, STP 560, ASTM, 1974, p 170–186
21. "Standard Test Method for J_{Ic} , A Measure of Fracture Toughness," E 813, *Annual Book of ASTM Standards*, Vol 03.01, ASTM, (before 1998)
22. "Standard Test Method for Measurement of Fracture Toughness," E 1820-99, *Annual Book of ASTM Standards*, Vol 03.01, ASTM, 1999, p 972–1005
23. P.C. Paris, The Fracture Mechanics Approach to Fatigue, *Fatigue—An Interdisciplinary Approach*, Syracuse University Press, 1964, p 107–133
24. "Standard Test Method for Measurement of Fatigue Crack Growth Rates," E 647-95a, *Annual Book of ASTM Standards*, Vol 03.01, ASTM, 1999, p 577–613

25. R.O. Ritchie and R.H. Dauskardt, Cyclic Fatigue of Ceramics: A Fracture Mechanics Approach to Subcritical Crack Growth and Life Prediction, *J. Ceram. Soc. J.*, Vol 99, 1991, p 1047–1062

Fracture Toughness and Fracture Mechanics

Acknowledgments

The material in this article is largely taken from:

- J.M. Barsom, Fracture Mechanics—Fatigue and Fracture, *Metals Handbook Desk Edition*, American Society for Metals, 1985, p 32–2 to 32–5
- J.M. Barsom, Fracture Toughness, *Metals Handbook Desk Edition*, American Society for Metals, 1985, p 32–5 to 32–8
- M.P. Blinn and R.A. Williams, Design for Fracture Toughness, *Materials Selection and Design*, Vol 20, *ASM Handbook*, ASM International, 1997, P 533–544
- R.L. Tobler and H.I. McHenry, Fracture Mechanics, *Materials at Low Temperatures*, American Society for Metals, 1983, p 269–293

Fracture Toughness and Fracture Mechanics

References

1. A.A. Griffith, The Phenomena of Rupture and Flow in Solids, *Philos. Trans. Soc. (London) A*, Vol 221, 1920, p 163–198
2. S.T. Rolfe and J.M. Barsom, *Fracture and Fatigue Control in Structures—Applications of Fracture Mechanics*, Prentice-Hall, 1977
3. “Standard Test Methods for Notched Bar Impact Testing of Metallic Materials,” E 23-98, *Annual Book of ASTM Standards*, Vol 03.01, ASTM, 1999, p 138–162
4. J.M. Barsom and S.T. Rolfe, K_{Ic} Transition Temperature Behavior of A517-F Steel, *Eng. Fract. Mech.*, Vol 2 (No. 4), June 1971
5. “Standard Test Method for Plane-Strain Fracture Toughness of Metallic Materials,” E 399-90, *Annual Book of ASTM Standards*, Vol 03.01, ASTM, 1999, p 422–452
6. J.M. Barsom, Development of the AASHTO Fracture-Toughness Requirements for Bridge Steels, *Eng. Fract. Mech.*, Vol 7 (No. 3), Sept 1975
7. J.M. Barsom, Effect of Temperature and Rate of Loading on the Fracture Behavior of Various Steels, *Dynamic Fracture Toughness*, The Welding Institute, 1976
8. A.K. Shoemaker and S.T. Rolfe, The Static and Dynamic Low-Temperature Crack-Toughness Performance of Seven Structural Steels, *Eng. Fract. Mech.*, Vol 2 (No. 4), June 1971

9. G.R. Irwin, Plastic Zone near a Crack and Fracture Toughness, *Proc. Seventh Sagamore Ordnance Materials Research Conference*, Syracuse University Press, 1960, p IV63–IV78
10. R.D. Venter and D.W. Hoepfner, “Crack and Fracture Behavior in Tough Ductile Materials,” report submitted to the Atomic Energy Control Board of Canada, Oct 1985
11. “Fracture Mechanics Tests, Part 1: Method for Determination of K_{Ic} , Critical CTOD and Critical J Values of Metallic Materials,” BS 7448: Part 1, The British Standards Institution, 1991
12. “Standard Test Method for Crack Tip Opening Displacement (CTOD) Fracture Toughness Measurement,” E 1290-93, *Annual Book of ASTM Standards*, Vol 03.01, ASTM, 1999, p 831–840
13. J.R. Rice, A Path Independent Integral and Approximate Analysis of Strain Concentration by Notches and Cracks, *J. Appl. Mech.*, Vol 35, 1968, p 379–386
14. D.J. Hayes, “Some Applications of Elastic Plastic Analysis to Fracture Mechanics,” Ph.D. thesis, University of London, 1970
15. J.M. Krafft, A.M. Sullivan, and R.W. Boyle, Effect of Dimensions on Fast Fracture Instability of Notched Sheets, *Proc., Crack Propagation Symposium*, Vol I, College of Aeronautics, Cranfield, England, 1961, p 8–28
16. D.E. McCabe and R.H. Heyer, R -Curve Determination Using a Crack-Line-Wedge-Loaded (CLWL) Specimen, *Fracture Toughness Evaluation by R-Curve Methods*, STP 527, 1973, p 17–35
17. D.A. Sarno, J.P. Bruner, and G.E. Kampschaefer, Fracture Toughness of 5% Nickel Steel Weldments, *Weld J.*, Vol 53, 1974, p 486
18. P.C. Paris, H. Tada, A. Zahoor, and H. Ernst, The Theory of Instability of the Tearing Mode of Elastic-Plastic Crack Growth, *Elastic-Plastic Fracture*, STP 668, J.D. Landes, J.A. Begley, and G.A. Clarke, Ed., ASTM, 1977, p 5–36
19. S.D. Antolovich and G.R. Chanai, Errors Associated with Fracture Toughness Testing, Paper II-242, *Third Int. Conf. Fracture*, Verein Deutscher Eisenhüttenleute, Dusseldorf, 1975, p 1–5
20. J.D. Landes and J.A. Begley, Test Results from J -Integral Studies—An Attempt to Develop a J -Integral Test Procedure, *Fracture Analysis*, STP 560, ASTM, 1974, p 170–186
21. “Standard Test Method for J_{Ic} , A Measure of Fracture Toughness,” E 813, *Annual Book of ASTM Standards*, Vol 03.01, ASTM, (before 1998)
22. “Standard Test Method for Measurement of Fracture Toughness,” E 1820-99, *Annual Book of ASTM Standards*, Vol 03.01, ASTM, 1999, p 972–1005
23. P.C. Paris, The Fracture Mechanics Approach to Fatigue, *Fatigue—An Interdisciplinary Approach*, Syracuse University Press, 1964, p 107–133
24. “Standard Test Method for Measurement of Fatigue Crack Growth Rates,” E 647-95a, *Annual Book of ASTM Standards*, Vol 03.01, ASTM, 1999, p 577–613
25. R.O. Ritchie and R.H. Dauskardt, Cyclic Fatigue of Ceramics: A Fracture Mechanics Approach to Subcritical Crack Growth and Lite Production, *J. Ceram. Soc. J.*, Vol 99, 1991, p 1047–1062

Fracture Toughness Testing

John D. Landes, University of Tennessee, Knoxville

Introduction

FRACTURE TOUGHNESS is defined as a “generic term for measures of resistance to extension of a crack” (Ref 1). The term fracture toughness is usually associated with the fracture mechanics methods that deal with the effect of defects on the load-bearing capacity of structural components. Fracture toughness is an empirical material property that is determined by one or more of a number of standard fracture toughness test methods. In the United States, the standard test methods for fracture toughness testing are developed by ASTM (formerly the American Society for Testing and Materials). These standards are developed by volunteer committees and are subjected to consensus balloting. This means that all objecting points of view to any part of the standard must be accounted for. Other industrial countries have equivalent standards writing organizations that develop fracture toughness test standards. In addition, international bodies such as the International Organization for Standardization (ISO) develop fracture toughness test standards that have an influence on products intended for the international market. In this review of fracture toughness testing, the ASTM approach is emphasized to provide a consistent point of view.

The standard fracture toughness test methods were written primarily for the testing of metallic materials. Toughness testing of nonmetals is also important. For many nonmetals, standards are developed based on procedures, analyses, and methods used for metallic fracture toughness tests with some possible modification to account for special needs of the nonmetal material behavior. Fracture toughness test methods written specifically for a particular nonmetal are relatively new. Therefore, this review emphasizes those standards written for metals without intent to make them apply exclusively to metals. A short discussion of fracture toughness testing for ceramics and polymers is included at the end of this article.

General Fracture Toughness Behavior. As a general background before discussing the details of fracture toughness testing and analysis, fracture toughness behavior and the parameters used to describe it are discussed. Fracture toughness is defined as resistance to the propagation of a crack. This propagation is often thought to be unstable, resulting in a complete separation of the component into two or more pieces. Actually, the fracture event can be stable or unstable. With unstable crack extension, often associated with a brittle fracture event, the fracture occurs at a well-defined point, and the fracture characterization can be given by a single value of the fracture parameter. With stable crack extension, often associated with a ductile fracture process, the fracture is an ongoing process that cannot be readily described by a point (Ref 2). This fracture process is characterized by a crack growth resistance curve, or *R*-curve. This is a plot of a fracture parameter versus the ductile crack extension, Δa . An example *K*-based *R*-curve is shown in Fig. 1. Sometimes a single point is chosen on the *R*-curve to describe the entire process; this is mostly done for convenience and does not give a complete quantitative description of the fracture behavior.

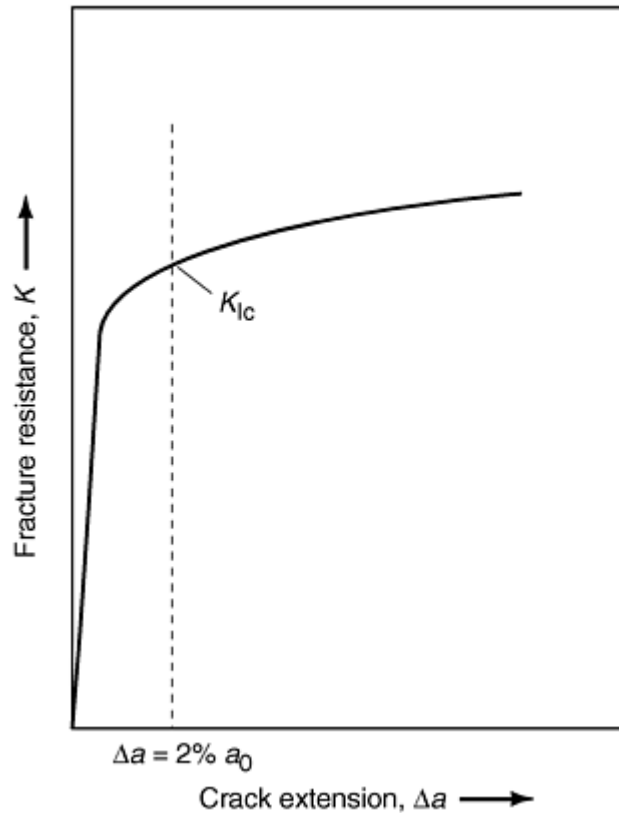


Fig. 1 Schematic of K -based crack resistance, R , curve with definition of K_{Ic}

Whether the fracture is ductile or brittle does not directly influence the deformation process that a component or specimen might undergo during the measurement of toughness (Ref 2). The deformation process is generally described as being linear-elastic or nonlinear. This determines which parameter is used in the fracture toughness test characterization. All loading begins as linear-elastic. For this, the primary fracture parameter is the well-known crack-tip stress-intensity factor, K (Ref 3). If the toughness is relatively high, the loading may progress from linear-elastic to nonlinear during the toughness measurement, and a nonlinear parameter is needed. The nonlinear parameters that are most often used in toughness testing are the J -integral (Ref 4), labeled J , and the crack tip opening displacement (CTOD), labeled δ (Ref 5). Because all loading starts as linear-elastic, the nonlinear parameters are all written as a sum of a linear component and a nonlinear component. This is illustrated with the individual descriptions of the various methods in this article.

Test Methods Covered. The test methods covered include linear-elastic and nonlinear loading, slow and rapid loading, crack initiation, and crack arrest. The development of the test methods followed a chronological pattern; that is, a standard was written for a particular technology soon after that technology was developed. Standards written in this manner tend to become exclusive to a particular procedure or parameter. Because most fracture toughness tests use the same specimens and procedures, this exclusive nature of each new standard did not allow much flexibility in the determination of a fracture toughness value. The newer approach is to write standards to encompass all parameters and measures of toughness into a single test procedure. This approach is labeled the common fracture toughness test method approach and has resulted in a new standard developed by ASTM as well as similar standards from organizations in other countries. The test standards for fracture toughness testing are not completed; revision and expansion of existing standards are in progress at this time. It is a requirement of ASTM that standards be reevaluated every five years and be updated if necessary. Therefore, work on revising and updating standards is continually in progress.

The fracture toughness test is generally conducted on a test specimen containing a preexisting defect; usually the defect is a sharp crack introduced by fatigue loading and called the precrack. The test is conducted on a machine that loads the specimen at a prescribed rate. Measurements of load and a displacement value are taken during the test. The data resulting from these measurements are subjected to an analysis procedure to evaluate the desired toughness parameters. These toughness results are then subjected to qualification procedures (or validity criteria) to see if they meet the conditions for which the toughness parameters can be accepted. Values meeting these qualification conditions are labeled as acceptable standard measures of fracture toughness. The

standard fracture toughness test, thus, has these ingredients: test specimens, types, and preparation; loading machine, test fixture, and instrumentation requirements; measurement taking; data analysis; and qualification of results. The following sections discuss the various standard fracture toughness test methods following this format. The fracture toughness test methods written as ASTM standards follow a prescribed format. It is not always easy to determine the step-by-step procedure required to conduct the test from the standard. The sections below, which describe the various methods, follow a format of a step-by-step procedure rather than the format of the actual standards. The application of the fracture toughness result to the evaluation of structural components containing defects is not explicitly covered in the ASTM standard test methods, nor is it covered in this article. The description of the fracture toughness test methods follows a somewhat chronological outline, beginning with the methods that use the linear-elastic parameter K . After this, the methods that use the nonlinear parameters J and δ are discussed. Next, some of the work in progress to update the standards and the newest standards is discussed. Finally, a brief overview of fracture toughness testing for ceramic and polymer materials is given (see the articles “Fracture Resistance Testing of Plastics” and “Fracture Toughness of Ceramics and Ceramic Matrix Composites” in this Volume for additional information about testing of these materials).

References cited in this section

1. “Standard Terminology Relating to Fracture Testing,” E 616, *Annual Book of ASTM Standards*, Vol 3.01, ASTM
2. J.D. Landes and R. Herrera, Micro-mechanisms of Elastic/Plastic Fracture Toughness, J_{Ic} , *Proc. 1987 ASM Materials Science Seminar*, ASM International, 1989, p 111–130
3. G.R. Irwin, Analysis of Stresses and Strains near the End of a Crack Traversing a Plate, *J. Appl. Mech.*, Vol 6, 1957, p 361–364
4. J.R. Rice, A Path Independent Integral and the Approximate Analysis of Strain Concentrations by Notches and Cracks, *J. Appl. Mech.*, Vol 35, 1968, p 379–386
5. A.A. Wells, Unstable Crack Propagation in Metals: Cleavage and Fast Fracture, *Proc. Cranfield Crack Propagation Symposium*, Vol 1, Paper 84, 1961

Fracture Toughness Testing

John D. Landes, University of Tennessee, Knoxville

Linear-Elastic Fracture Toughness Testing

Fracture mechanics and fracture toughness testing began with a strictly linear-elastic methodology using the crack-tip stress-intensity factor, K . Later, nonlinear parameters were developed. However, the first test methods developed used the linear-elastic parameters and were based on K . These methods are described first in this article.

The linear-elastic methods of fracture toughness testing are used to measure a single-point fracture toughness value. For fracture by a brittle mechanism, this is no problem. Fracture occurs at a distinct point, and the fracture toughness measurement is taken as a value of the fracture parameter at that point. For fracture by a ductile mechanism, the fracture is a process, and the fracture toughness measurement is an R -curve. To get a single value for this fracture toughness, a point on the R -curve must be chosen. This usually involves a construction procedure. The ASTM E 399 K_{Ic} standard fracture toughness test method, which is described next,

gives an example of a construction procedure that is used to get a single-point measurement of fracture toughness on the R -curve.

Plane-Strain Fracture Toughness (K_{Ic}) Test (ASTM E 399)

The first fracture toughness test that was written as a standard was the K_{Ic} test method, ASTM E 399. This test measures fracture toughness that develops under predominantly linear-elastic loading with the crack-tip region subjected to near-plane-strain constraint conditions through the thickness. The test was developed for essentially ductile fracture conditions, but can also be used for brittle fracture. As a ductile fracture test, a single point to define the fracture toughness is desired. To accomplish this, a point where the ductile crack extension equals 2% of the original crack length is identified. This criterion is illustrated schematically with a K - R curve in Fig. 1. This criterion gives a somewhat size-dependent measurement, and so validity criteria are chosen to minimize the size effects as well as to restrict the loading to essentially the linear-elastic regime. The various elements of the K_{Ic} test are discussed in a little more detail than are some of the other tests for fracture toughness measurement. In this way, the K_{Ic} test can serve as a model for the other discussions. The details of this test can be found in Ref 6.

Test Specimen Selection. The first element of the test is the selection of a test specimen. Five different specimen geometries are allowed (Fig. 2). These are the single edge-notched bend specimen, SE(B), compact specimen, C(T), arc-shaped tension specimen, A(T), disk-shaped compact specimen, DC(T), and the arc-shaped bend specimen, A(B). Many of these specimen geometries are used in the other standards as well. The acronyms are standard ASTM nomenclature given in Ref 1. The bend and compact specimens (Fig. 2a and b, respectively) are traditional fracture toughness specimens used in nearly every fracture toughness test method. The other three are special geometries that represent structural component forms. Therefore, most fracture toughness tests are conducted with either the edge-notched bend or compact specimens. The choice between the bend and compact specimen is based on the following:

- The amount of material available (the bend takes more)
- Machining capabilities (the compact has more detail and costs more to machine)
- The loading equipment available for testing (discussed next)

All of the specimens for the K_{Ic} test must be precracked in fatigue before testing. This means that a sharp crack is developed at the end of a notch by repeated loading and unloading of the specimen, that is, fatigue loading. Refer to ASTM E 399 (Ref 6) for details on precracking.

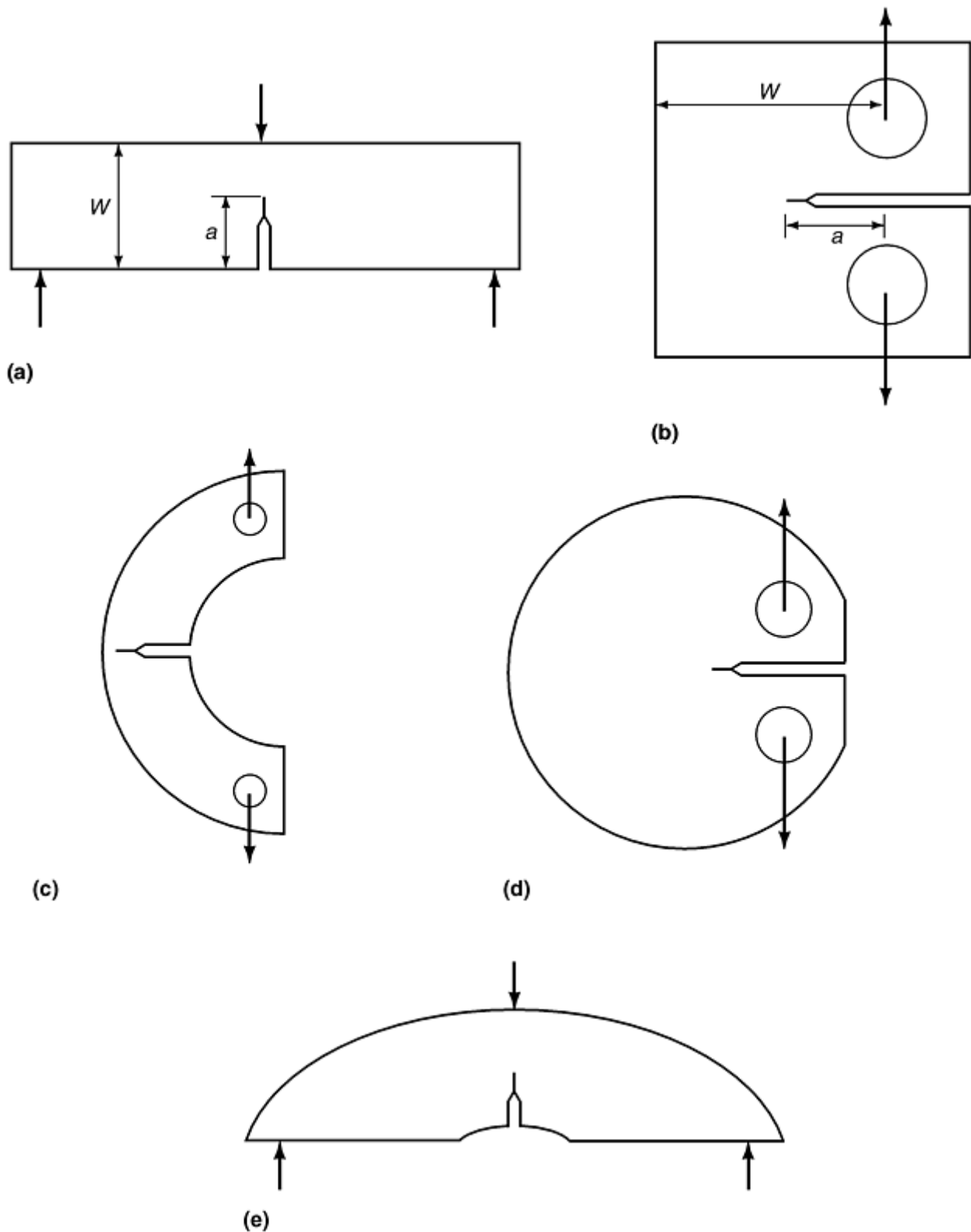


Fig. 2 Specimen types used in the K_{Ic} test (ASTM E 399). (a) Single edge-notched bend, SE(B). (b) Compact specimen, C(T). (c) Arc-shaped tension specimen, A(T). (d) Disk-shaped compact specimen, DC(T). (e) Arc-shaped bend specimen, A(B)

The choice of the specimen also requires a choice of the size. Because the validity criteria depend on the size of the specimen, it is important to select a sufficient specimen size before conducting the test. However, the validity criteria cannot be evaluated until the test is completed; therefore, choosing the correct size is a guess that may turn out to be wrong. There are guidelines (Ref 6) for choosing a correct size, but no guarantee that the chosen size will pass the validity requirement. The test specimens must also be chosen so that the proper material is sampled. This means that the location in the material source and the orientation of the sample must

be correct and accounted for. The ASTM standards have a letter system to specify orientation (Ref 1). As the specimens are being prepared, requirements for tolerances on such things as locations of surfaces, size and location of the notch and pin holes, and surface finishes must be followed.

Loading Machines and Instrumentation. The next step in the test procedure is the choice of a loading machine and the preparation of loading fixtures and instrumentation for recording the test data. Most tests are conducted on either closed-loop servo-hydraulic machines or constant-rate crosshead drive machines. The first machines allow load, displacement, or other transducer control but are more expensive. They are preferred for precracking, which is usually done at a constant load range so load control is desired. The second type of loading machine is less expensive and may give more stability but allows only crosshead control. Because this is required in most of the fracture toughness tests, this type of machine is quite satisfactory for the actual fracture toughness testing but is not so good for precracking.

Loading fixtures must be designed for the test. Two types can be used (3); choice of loading fixture depends on the test specimen chosen. The bend specimens SE(B) and A(B) use a bend fixture. The tension specimens C(T), DC(T), and A(T) require a pin-and-clevis loading. Note in Fig. 3(a) that the bend loading is three point; this is the case for all bend- loaded specimens. Also note in Fig. 3(b) that the clevis has a loading flat at the bottom of the pin hole. This allows free rotation of the specimen arms during the test and is essential for getting good results.

For the K_{Ic} test, a continuous measurement of load and displacement is required during testing. The load is measured by a load cell, which should be on all loading machines. The measurement of displacement is usually done with a strain-gaged clip gage that is positioned over the mouth of the crack in the specimen. An example of a clip gage is shown in Fig. 4. Figure 3(a) shows the bend specimen with a clip gage in place. The standards give guidelines for the accuracies and working requirements of the load and displacement gages used in the tests.

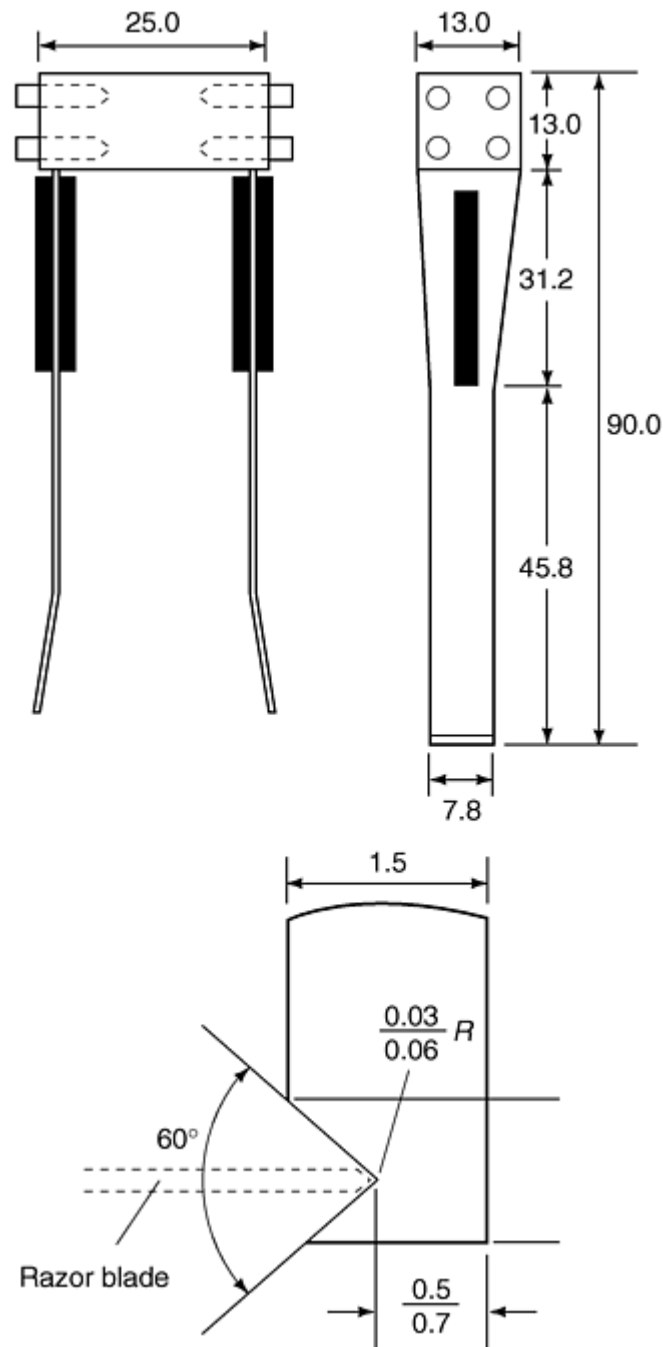


Fig. 4 An example clip gage for displacement measurement (all dimensions in mm)

The loading of the specimen is done at a prescribed rate. It must be done fast enough so that any environmental or temperature interactions are not a problem. On the other hand, it must be done slowly enough so that it is not considered a dynamically loaded test. For the K_{Ic} test, the load must be applied at a rate so that the increase in K is given by the range 0.55 to $2.75 \text{ MPA} \sqrt{m/s}$. The loading is done in displacement control, which usually means test machine crosshead control. During the loading, the load and displacement are measured continuously. This can be done autographically or digitally.

Test Data and Analysis. The load-and-displacement record provides the basic data of the test. The data are then analyzed to determine a provisional K_{Ic} value, labeled K_Q . This provisional value is determined from a

provisional load, P_Q , and the crack length. The P_Q value is determined with a secant line of reduced slope on the load-and-displacement record (Fig. 5). The construction for P_Q involves drawing the original loading slope of the load-versus-displacement record. A slope of 5% less than the original (secant slope) is then drawn. For a monotonically increasing load, the P_Q is taken where the 5% secant slope intersects the load-versus-displacement curve; this is illustrated as type I in Fig. 5. For other records in which an instability or other maximum load is reached before the 5% secant, the maximum load reached up to and including the possible intersection of the 5% secant is the P_Q . Type II illustrated in Fig. 5 is an example of one of the other types of load-versus-displacement records. The 5% secant corresponds to about 2% ductile crack extension; this may be physical crack extension or effective crack extension related to plastic zone development. Unstable failure before reaching the 5% offset also marks a measurement point for P_Q at the maximum load reached at the point of instability.

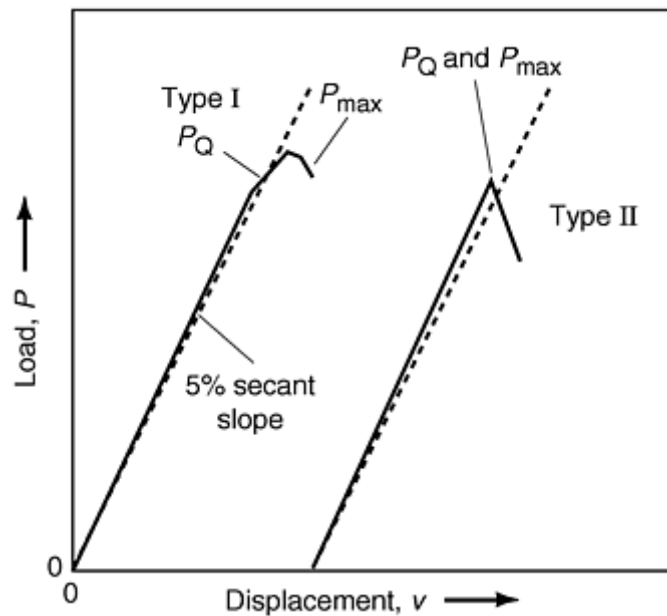


Fig. 5 Typical load-versus-displacement record for the two types of K_{Ic} testing

The P_Q value is used to determine the corresponding K_Q value. This is calculated from the equation:

$$K = P f(a/W) / \sqrt{W} \quad (\text{Eq 1})$$

where P is load, B and W are specimen thickness and width, and $f(a/W)$ is a calibration function that depends on the ratio of crack length to specimen width, a/W , and is given in the standard. For the calculation of K , a crack length value, a , is required. This comes from a physical measurement on the fracture surface of a broken specimen half. The specimen must be fractured into halves if it is not already that way from the test. The crack length is measured to the tip of the precrack using an averaging formula given in the test standard. This value of crack length normalized with width, W , is used in the calibration function $f(a/W)$ to determine the K_Q value.

The K_Q is a provisional K value that may be the K_{Ic} if it passes the validity requirements. The first of the two major validity requirements is quantified as:

$$\frac{P_{\max}}{P_Q} \leq 1.10 \quad (\text{Eq 2})$$

which limits the R -curve behavior to an essentially flat trend and ensures some physical crack extension. The second requirement is:

$$a, B \geq 2.5 \left(\frac{K_Q}{\sigma_{ys}} \right) \quad (\text{Eq 3})$$

which guarantees linear-elastic loading and plane-strain thickness. P_{\max} is the maximum value of load reached during the test. An example of P_{\max} is shown in Fig. 5; σ_{ys} is the 0.2% offset yield strength. Other validity requirements relating to specimen preparation, precracking, and crack front straightness must also be met.

Values of K_Q that pass all validity requirements are labeled as valid K_{Ic} and are reported as such. The ASTM E 399 standard lists all of the information required for the test report.

Rapid-Load $K_{Ic}(t)$ Test

A value of fracture toughness labeled $K_{Ic}(t)$ can be determined for a rapid-load test. Details of this method are given in a special annex to ASTM E 399 (Ref 6). For the static loading rate K_{Ic} value, the maximum loading rate is $2.75 \text{ MPA } \sqrt{\text{m}}/\text{s}$. Anything faster than that is labeled as a rapid-load fracture toughness. The specimens, apparatus, and procedure are much the same as for the regular K_{Ic} test. Special instructions are given to ensure that the instrumentation can handle the rapidly changing signals. The interpretation of results must be based on a dynamic value of the yield stress, σ_{YD} . An equation for σ_{YD} is given in the Annex to ASTM E 399. Results are reported as $K_{Ic}(t)$, where the loading time of the test, t , is written in parentheses after the measured toughness value.

K-R Curve Test (ASTM E 561)

Ductile fracture toughness behavior is measured by a crack growth resistance curve, or R -curve, which is defined as “a plot of crack-extension resistance as a function of slow-stable crack extension” (Ref 1). Although many ductile fracture processes can be measured as a single-point, such as with K_{Ic} , the R -curve is a more complete description of the fracture toughness. When the R -curve increases significantly with increased loading, a single-point measurement is even less descriptive of the actual fracture toughness. Steeply rising R -curves occur in many metallic materials but especially in thin plate or sheet materials. The steeply rising R -curve makes the single-point definition of fracture toughness more size-dependent and geometry-dependent and does not lend itself to correct structural evaluation.

The K - R curve is a good method for fracture toughness characterization in cases where the R curve is steeply rising but the fracture behavior occurs under predominantly linear-elastic loading conditions. The K - R curve procedure is given by ASTM E 561 (Ref 7). The objective of the method is to develop a plot of K , the resistance parameter, versus effective crack extension, Δa_e . The method allows three different test specimens, the compact, C(T), the center-cracked tension panel, M(T), and the crack-line-wedge-loaded specimen, C(W). The compact specimen is shown in Fig. 2(b). The center-cracked tension panel and the crack-line-wedge-loaded specimens are shown in Fig. 6(a) and (b), respectively. The first two specimens use a conventional loading machine with fixtures that are specified in the test method. The C(W) specimen is wedge loaded to provide a stiff, displacement-controlled loading system (Fig. 6b). This can prevent rapid, unstable failure of the specimen under conditions where the R -curve toughness is low so that the R curve can be measured to larger values of Δa_e . All specimens must be precracked in fatigue.

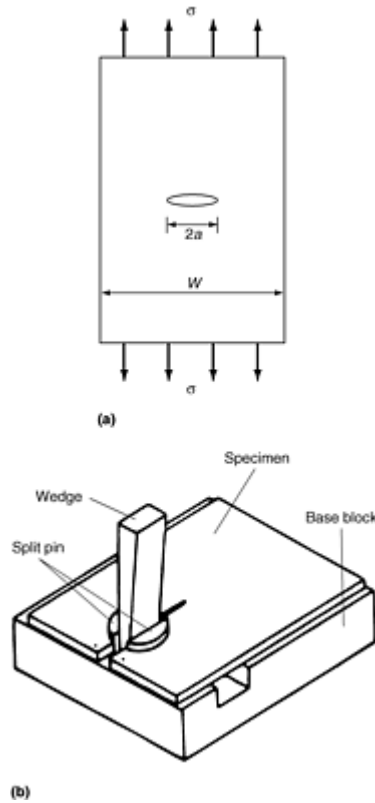


Fig. 6 Specimens for the K - R curve test (ASTM E 561). (a) Center-cracked tension specimen, M(T). (b) Crack-line-wedge-loaded compact specimen, C(W), in loading fixture

The instrumentation required on the specimens is similar to that for the K_{Ic} test, except for the case of the C(W) specimen. The basic test result is a plot of load versus a displacement measured across the specimen mouth. From this, an effective crack length is determined from secant slopes on the load-versus-displacement record (Fig. 7). An effective crack extension is the difference between the original and effective crack lengths. Effective crack length is determined from the slope of the secant offset using the appropriate compliance function, which relates this slope to crack length. The K is determined as a function of the applied load, P , and corresponding effective crack length. This is given by:

$$K = P f(a_c / W) / \sqrt{W} \quad (\text{Eq 4})$$

The resulting plot of K versus effective crack length is the desired K - R curve fracture toughness. The result is subjected to a validity requirement that limits the amount of plasticity. For the C(T) and C(W) specimens

$$b = (W - a) \geq (4/\pi)/(K_{\max}\sigma_{ys})^2 \quad (\text{Eq 5})$$

where b is the uncracked ligament length, σ_{ys} is the 0.2% offset yield strength, and K_{\max} is the maximum level of K reached in the test. For the M(T) specimen, the net section stress based on the physical crack size must be less than the yield strength.

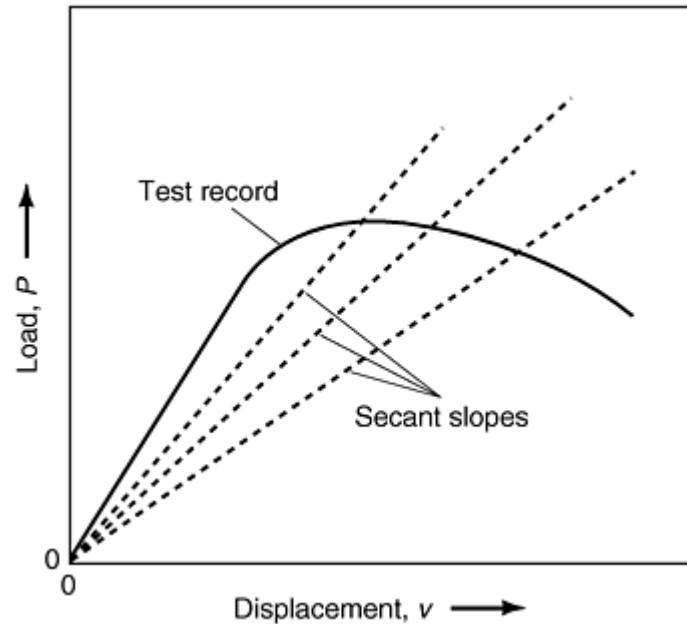


Fig. 7 Secant measurement of effective crack length

For the C(W) specimen, a load is not measured. The data collected are a series of displacement values taken at two different points along the crack line, one near the crack mouth and one nearer the crack tip. From the two different displacement values, an effective crack length can be determined from the ratio of the two displacement values and from calibration values given in ASTM E 561. From the crack length and displacement a K value can be determined and the K - R curve constructed. The toughness result is then a curve of K versus Δa_e , somewhat similar to the one in Fig. 1. The K - R curve fracture toughness is a function of the material thickness; all results are given for a specified thickness. There is no validity requirement relating to a thickness level as with the K_{Ic} standard.

Crack Arrest, (K_{Ia}) Test (ASTM E 1221)

This procedure allows a toughness value to be determined based on the arrest of a rapidly growing crack. The specimen and procedure are somewhat different from those for the previously discussed toughness test methods, which determine initiation toughness values only. The specimen for crack arrest testing is called the compact crack-arrest specimen (Fig. 8). It is similar to the crack-line-wedge-loaded specimen, C(W), of the K - R curve method and requires wedge loading in order to provide a very stiff loading system to arrest the crack. The specimen also requires side grooves—machined notches on the specimen planar face (Fig. 8)—to aid in getting a straight-running crack during the test. The notch preparation is different from that used in the other standards in that the specimen has a notch with no precrack. A brittle weld bead is placed at the notch tip to start the running crack. The running crack advances rapidly into the test material and must be arrested by the test material to produce a K_{Ia} result. The only instrumentation on the specimen is a displacement gage. A load cell is placed on the loading wedge, but it does measure the load on the specimen. The displacements at the beginning of the unstable crack extension and at the crack arrest position are measured and converted to K values. To eliminate effects of nonlinear deformation, which cannot be directly measured with only a displacement gage, a series of loads and unloads are conducted on the specimen until the unstable cracking occurs.

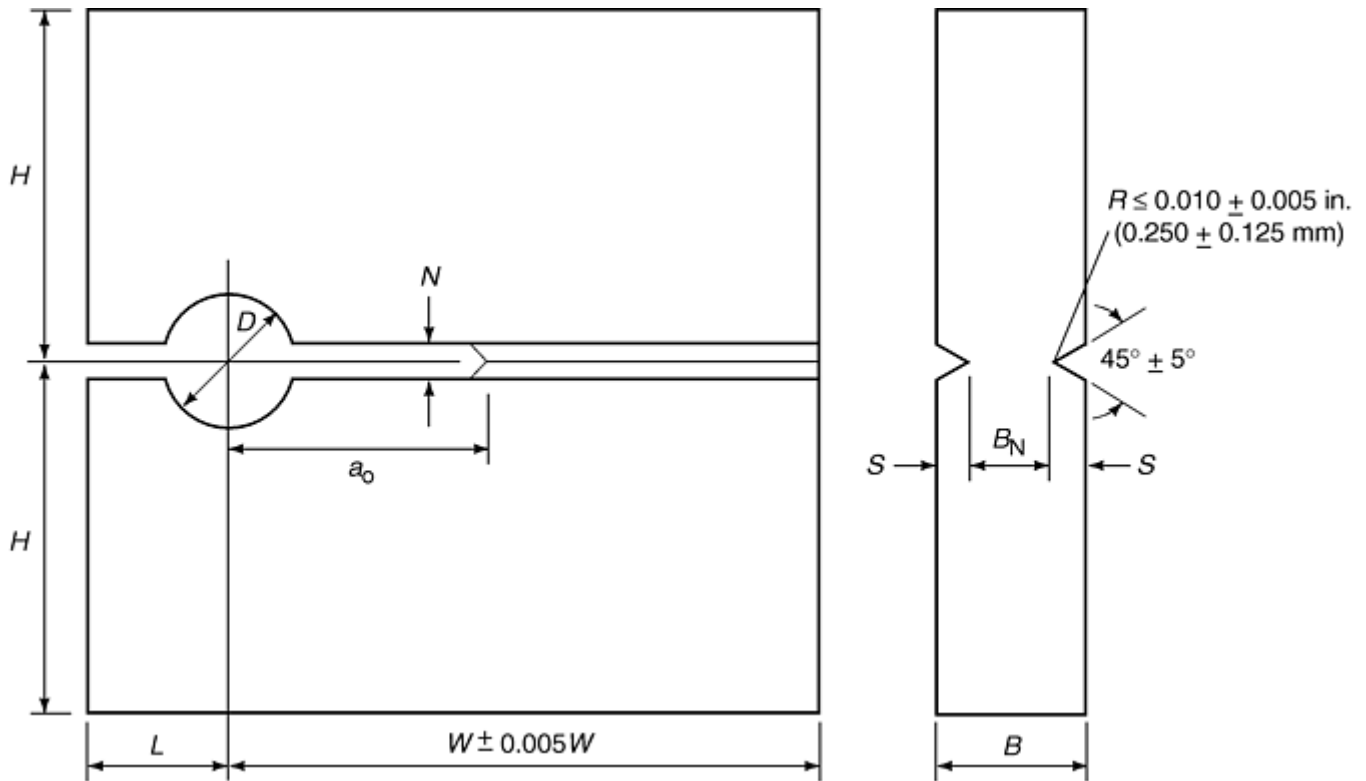


Fig. 8 Crack-line-wedge-loaded compact crack-arrest specimen

The value of K_{Ia} is determined from a displacement value and the crack length at the arrest point. Validity is determined from the size criterion:

$$W - a \geq 1.25 (K/\sigma_{YD})^2 \quad (\text{Eq 6})$$

where σ_{YD} is a dynamic yield strength. To complete a successful K_{Ia} test, careful attention must be paid to the instructions in ASTM E 1221 (Ref 8).

References cited in this section

1. "Standard Terminology Relating to Fracture Testing," E 616, *Annual Book of ASTM Standards*, Vol 3.01, ASTM
6. "Standard Method for Plane-Strain Fracture Toughness of Metallic Materials," E 399, *Annual Book of ASTM Standards*, Vol 3.01, ASTM
7. "Standard Practice for R-Curve Determination," E 561, *Annual Book of ASTM Standards*, Vol 3.01, ASTM
8. "Standard Method for Determining Plane-Strain Crack Arrest Toughness, K_{Ia} , of Ferritic Steels," E 1221, *Annual Book of ASTM Standards*, Vol 3.01, ASTM

Fracture Toughness Testing

John D. Landes, University of Tennessee, Knoxville

Nonlinear Fracture Toughness Testing

Linear-elastic parameters are used to measure fracture toughness for relatively low toughness materials, which fracture under or near the linear-loading portion of the test. For many materials used in structures, it is desirable to have high toughness, a value at least high enough so that the structure would not reach fracture toughness before significant yielding occurs. For these materials, it is necessary to use the nonlinear fracture parameters to measure fracture toughness properties. The two leading nonlinear fracture parameters are J and δ .

For many of the nonlinear fracture toughness measurements, the fracture mode is a ductile one. In this case the fracture toughness is measured by an R -curve, that is, a plot of the fracture-characterizing parameter as a function of the ductile crack advance. The evaluation of the R -curve toughness requires three measurements during the test: load, displacement, and crack length. The load and displacement are standard measurements. The crack length requires a special monitoring system. In the standards, the crack length has been measured visually on the fracture surface and by an elastic unloading compliance method that uses the elastic properties of the specimen geometry to evaluate crack length. Methods that have also been used are an electrical potential drop method and a key curve, or normalization, method. The electrical potential method uses the electrical resistance of the material to evaluate crack length. The method of normalization uses the plastic deformation properties of the material to evaluate crack length.

The visual method was the first and longest used of the methods. It has a disadvantage in that it requires a number of specimens to evaluate one R -curve. Each specimen generates only one point on the R -curve. It is often called the multiple-specimen method. The other methods require only one specimen to generate an R -curve and are often called single-specimen methods. The elastic unloading compliance method is the most often used of the single-specimen methods and is used in many of the standards to measure fracture toughness during nonlinear loading. It cannot be used under rapid loading conditions or for materials that do not have a linear-elastic loading character. This would include polymer materials. The electrical potential drop method requires a material that has a measurable electrical resistance. It is mostly used for metallic materials. In the past it has been in some standard test methods, but presently it is withdrawn from all existing standards because it has not always given accurate crack length measurement during a fracture toughness test. The method of normalization has not been standardized. It is advantageous in that it can be used for any material that generates nonlinear loading that is similar to plastic deformation in metals. It can be used to measure crack length both for polymers and for rapid loading test conditions.

J_{Ic} Testing (ASTM E 813)

The first standard test developed using the J parameter is the J_{Ic} test, originally standardized as ASTM E 813 (Ref 9). (Changes to this standard will be discussed later.) In this test an R -curve is developed using J versus Δa pairs. A point near the beginning of the R -curve is defined as J_{Ic} , “a value of J near the onset of stable crack extension” (Ref 9). The specimens for the J_{Ic} test are the bend, SE(B), and compact, C(T). These are similar to the ones used for K_{Ic} testing (Fig. 2a and b); however, the compact specimen for J testing allows for a load line displacement measurement in the line of the applied loads. Therefore, a cutout is machined in the front of the specimen to accommodate the placement of a clip gage on the load line (Fig. 9). Also, side grooving is recommended on this specimen to assist in maintaining a straight crack front during the stable crack growth. The loading fixtures required are the bend fixture for the bend specimen (Fig. 3a) and the pin and clevis for the compact specimen (Fig. 3b). As with the K_{Ic} test, the clevis has a loading flat at the bottom of the pinhole, which is essential for free rotation of the specimen. The instrumentation required is the load cell and a displacement measuring clip gage. The clip gage for the J_{Ic} test requires more resolution than that for the K_{Ic} test if a single-specimen test method is used. For the bend specimen, a loadline clip gage is needed to measure J . Additionally, a second clip gage can be used over the crack mouth if a single-specimen method is used.

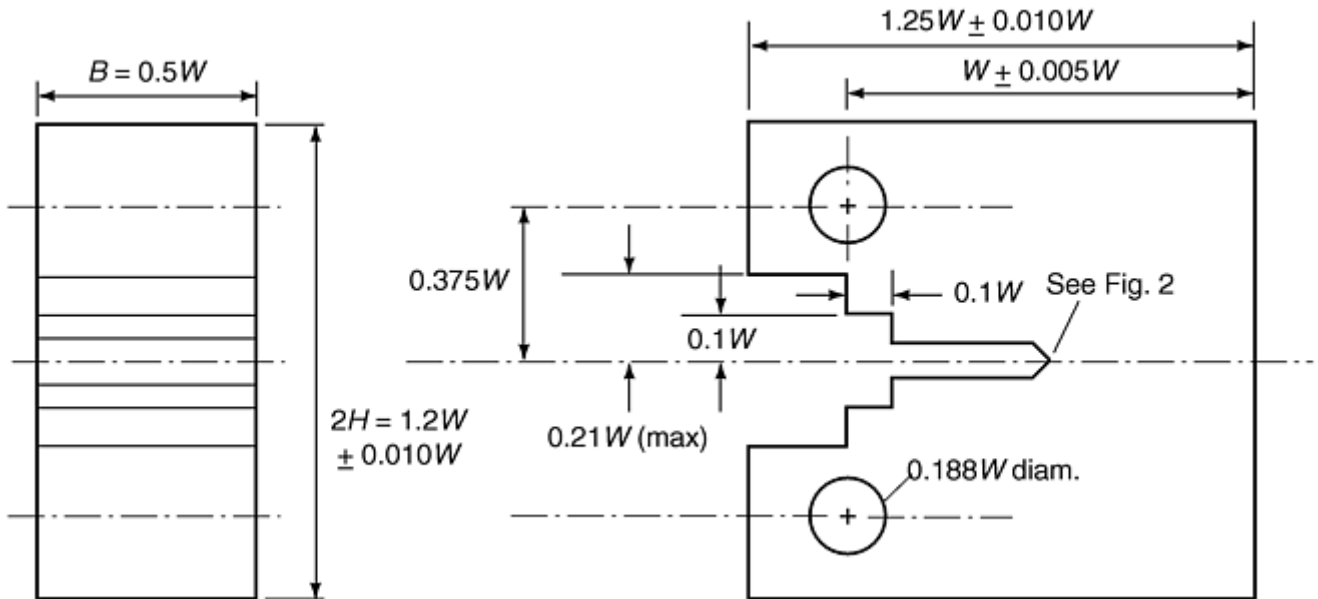


Fig. 9 J_{Ic} compact specimen with load line cutout

J_{Ic} Test Procedures. The basic output of the test is a plot of J versus physical crack extension (Δa). (Unlike the $K-R$ curve method, which uses effective crack extension, the J_{Ic} test uses physical crack extension.) To obtain the required J versus Δa data, measurements of load, displacement, and physical crack length are required during the test. Two techniques are used to develop these data. The first is the multiple-specimen test method, in which each specimen develops a single value of J and Δa , but no special crack monitoring equipment is needed during the test. Crack extension is measured on the fracture surface at the conclusion of the test. However, for this technique a number of specimens (usually five or more) are required to develop the plot of J versus Δa from which the J_{Ic} is evaluated. The other test method is the elastic unloading compliance method, a single-specimen test from which all of the J and Δa values needed for the result are developed from one test specimen.

The test procedure depends on the method of crack length monitoring. For the multiple-specimen test, five or more identical specimens are loaded to prescribed displacement values that are expected to give some physical crack extension without complete separation of the specimen. This results in a number of individual load-versus-displacement records as shown in Fig. 10. When the prescribed displacement is reached, the specimen is unloaded, and the crack tip is marked by a procedure called heat tinting. Heat tinting consists of marking the physical crack extension by heating the specimen until oxidation occurs on the crack. The specimen is then broken open, and the crack extension is measured on the fracture surface.

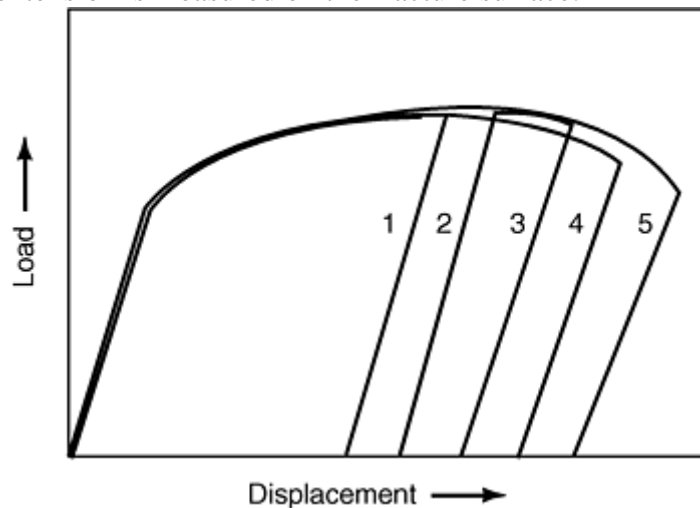


Fig. 10 Load versus displacement for multiple-specimen tests

The single-specimen method using elastic compliance is initially loaded in the same way; however, during the test, partial unloadings are taken to develop elastic slopes from which crack length can be evaluated using compliance relationships (Fig. 11). The compliance relationships are given in ASTM E 813 (Ref 9).

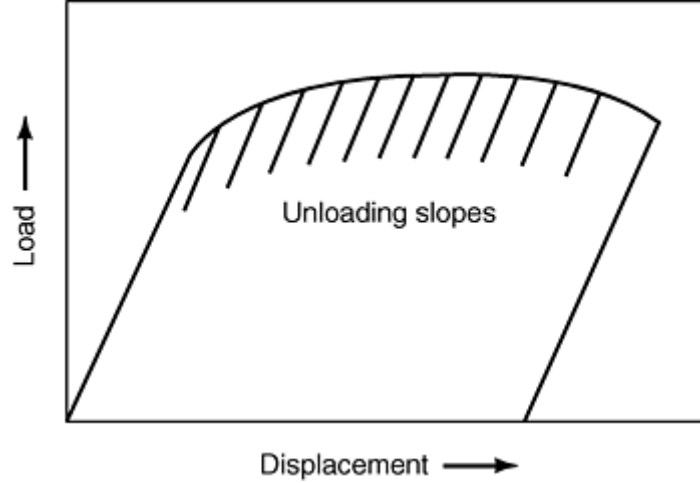


Fig. 11 Load versus displacement with unloading slopes

Data Evaluation. From these test results, J is evaluated from the load-versus-loadline displacement record. The J is calculated from a linear combination of an elastic term and a plastic term given as:

$$J = J_{el} + J_{pl} \frac{K^2(1-\nu^2)}{E} + \frac{\eta_{pl}}{Bb} \int_0^{v_{pl}} P dv_{pl} \quad (\text{Eq 7})$$

where K is the stress-intensity factor, E is elastic modulus, ν is Poisson's ratio, P is load, v_{pl} is plastic displacement, B is specimen thickness, b is specimen uncracked ligament ($W - a$, where W is specimen width) and η_{pl} is a coefficient that has values of $\eta_{pl} = 2$ for the SE(B) specimen of Fig. 2(a) and $\eta_{pl} = 2 + 0.522b/W$ for the compact specimen of Fig. 9.

The crack length is used to determine $\Delta a = a - a_0$, where a_0 is the original crack length at the beginning of the test. For the multiple-specimen method, all Δa values are determined from measurements taken from the fracture surface of the test specimen. For some metals, heat tinting does not oxidize the crack surfaces, and another method of marking the crack extension, for example posttest fatiguing, can be used. The specimen is broken in two after the heat-tint procedure, usually at a low temperature to induce brittle fracture for easy reading of the ductile crack extension and to otherwise minimize plastic deformation during this procedure. Typically, this is done by cooling the specimen to the temperature of liquid nitrogen before breaking it in two. Crack lengths a_0 and a_f , original and final, are measured on the fracture surface. A nine-point measurement and averaging method is used because the crack front is usually neither straight or regular. This procedure is described in ASTM E 813 (Ref 9). For the single-specimen methods for which crack length monitoring systems are used, the crack length is evaluated at prescribed points during the test. In the elastic unloading compliance method, a crack length can be determined at each unload. Typically, about 20 of 50 unloading data pairs, P , v , and a are evaluated for each test. For single-specimen tests, a physical measurement of the final crack length is made at the end of the test using the same procedure that is followed for the multiple-specimen test, so that this measured crack length can be compared with the final crack length evaluated by the crack monitoring system.

The J versus Δa results form a part of the J - R curve and are the basic data of the J_{Ic} method. The objective is to get J versus Δa values in a certain restricted range. These data are then subjected to a prescribed evaluation scheme to choose a point on the J - R curve that is near the initiation of stable cracking. The method for developing the J_{Ic} is somewhat complicated, and the details are given in ASTM E 813 (Ref 9). Basically, the J versus Δa pairs are evaluated to see which fall in a prescribed range. The pairs falling in the correct range are fitted with a power-law equation:

$$J = C_1(\Delta a)^{C_2} \quad (\text{Eq 8})$$

where C_1 and C_2 are constants. A construction line is drawn, and the intersection of this with the fitted line, Eq 8, is the evaluation point for a candidate J_{Ic} value. This candidate value is labeled J_Q . A schematic of the process of J_{Ic} evaluation is shown in Fig. 12.

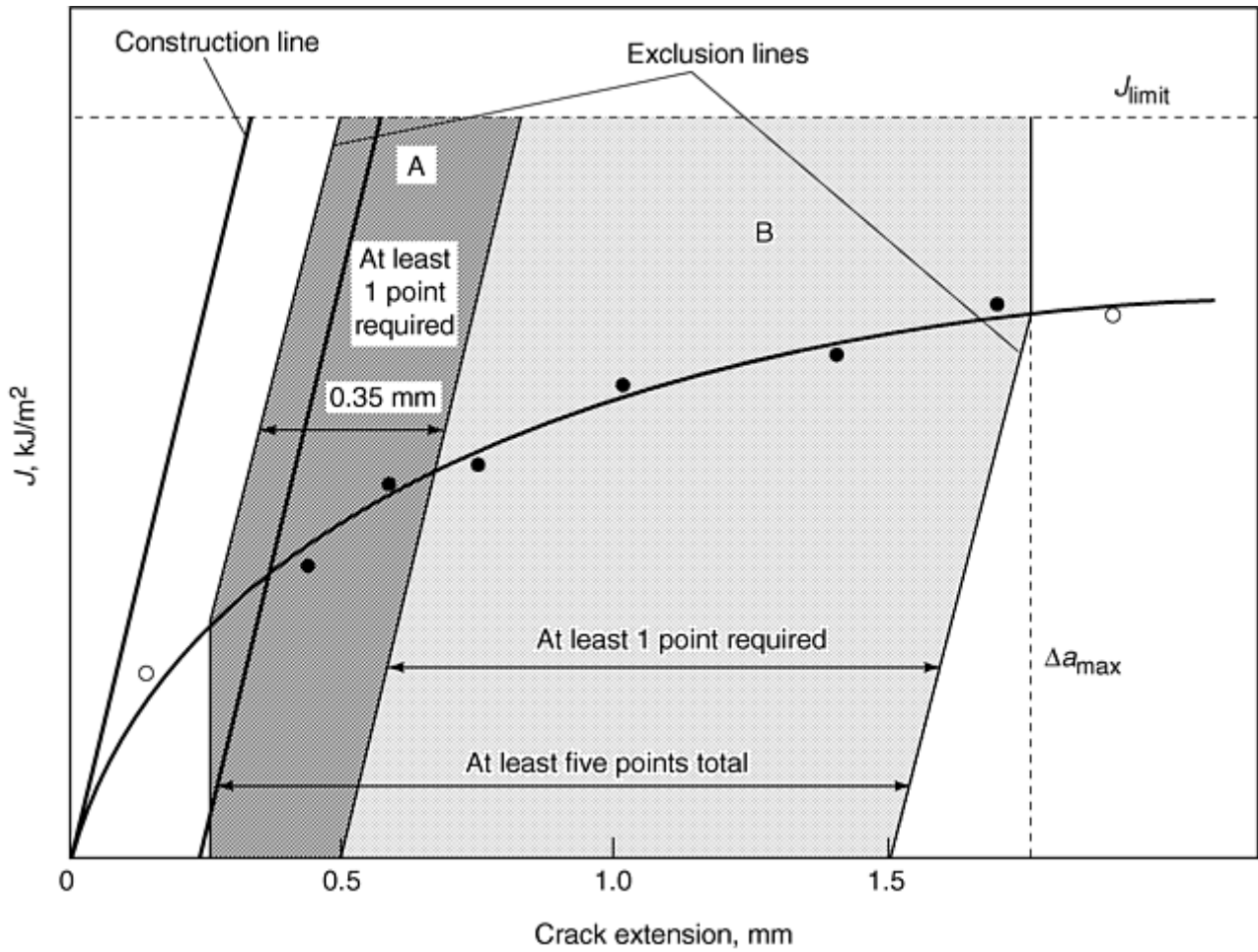


Fig. 12 J_{Ic} evaluation scheme

The candidate J_Q value is subjected to qualification criteria to see if it constitutes an acceptable value. The basic one is to guarantee a sufficient specimen size:

$$b, B \geq 25(J_Q / \sigma_Y) \quad (\text{Eq 9})$$

where σ_Y is an effective yield strength and

$$\sigma_Y = (\sigma_{ys} + \sigma_{uts})/2 \quad (\text{Eq 10})$$

where σ_{ys} and σ_{uts} are the yield strength and ultimate tensile strength, respectively.

If the qualification requirements are met, the J_Q is J_{Ic} and the results are reported following the prescribed format in ASTM E 813 (Ref 9).

J-R Curve Evaluation (ASTM E 1152)

A more complete evaluation of fracture toughness for ductile fracture based on J is the J - R curve. The test procedure was originally standardized as ASTM E 1152 (Ref 10). This standard uses the same specimens, instrumentation, and test procedures as the J_{Ic} test. The J - R curve test cannot be conducted with the multiple-specimen test procedure; it must use a single-specimen procedure. The purpose of the J - R curve is to develop points of J versus Δa ; these comprise the fracture toughness evaluation. A single value of J is not specifically measured as it is for the J_{Ic} procedure. The single-specimen method used is again primarily the elastic unloading compliance method. Equation 7 is the basic J formula for the case of a nongrowing crack. It is based on a K equivalence for the elastic component of J and an area term for the plastic component of J . Alternate J formulas are given in ASTM E 1152 (Ref 10) for the growing crack. Qualification criteria are also given in the standard (Ref 10). The J_{Ic} and J - R curve methods are very similar; hence the two have recently been combined into one standard, ASTM E 1820 (Ref 11). The individual standard ASTM E 813 and E 1152 were withdrawn from the *Annual Book of ASTM Standards* beginning in 1998.

Crack Tip Opening Displacement (CTOD) Test (ASTM E 1290)

The crack tip opening displacement method of fracture toughness measurement was the first one that used a nonlinear fracture parameter to evaluate toughness (Ref 5). The first CTOD standard was written by the British Standards Institution (Ref 12). Subsequently, ASTM E 1290 was written as the U.S. version of this test method (Ref 13). The basic idea of the test method is to evaluate a fracture toughness point for brittle fracture or to evaluate a safe point for the case of ductile fracture. The primary measurements of toughness are at unstable fracture before significant ductile crack extension, labeled δ_c , unstable fracture after significant crack extension, δ_u , or the point of maximum load in the test, δ_m . The method originally had a point near the beginning of stable crack extension, δ_i , that was measured as a point on an R -curve in a similar manner to J_{Ic} . This point was subsequently removed from the test method.

The CTOD standard uses the same bend and compact specimens that are used in the J_{Ic} test; thus the same loading fixtures are used. The method requires measurement of load and displacement during the test. As for J , the formulas for δ calculation use a combination of an elastic and a plastic component:

$$\delta = \frac{K^2(1-\nu^2)}{2\sigma_{ys}E} + \frac{r_p(W-a_0)v_p}{r_p(W-a_0) + a_0 + z} \quad (\text{Eq 11})$$

In this equation, the elastic component of δ is based on a K equivalence, and the plastic component is based on a rigid plastic rotation of the specimen about a neutral stress point at $r_p(W-a_0)$ from the crack tip. In Eq 11, ν is Poisson's ratio, σ_{ys} is the yield strength, r_p is a rotation factor, v_p is a plastic component of displacement, $W-a_0$ is the uncracked ligament length, and z is the distance from the clip gage measurement position to the front face for an SE(B) specimen or to the load line for a C(T) specimen (Fig. 13). The rotation factor, r_p , is 0.44 for the bend specimen and a variable ranging from 0.46 to 0.47 for the compact specimen.

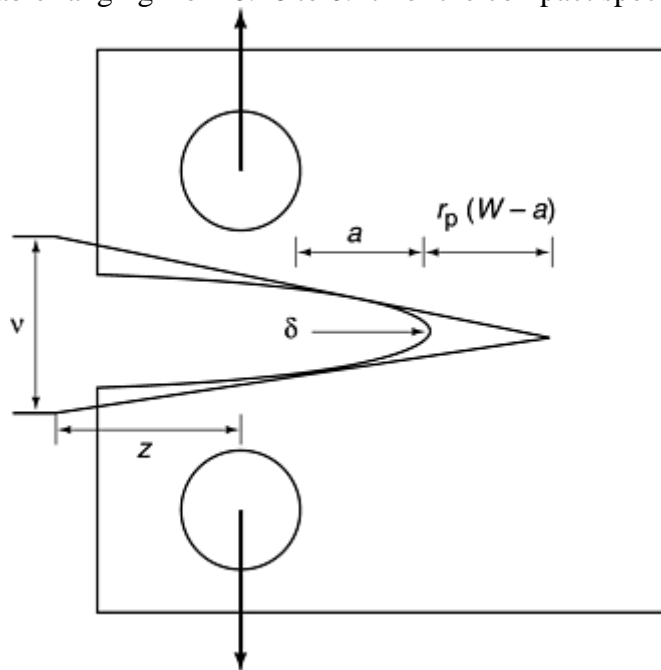


Fig. 13 Definitions of length parameters used in plastic CTOD

For many years the CTOD test was the only one that measured toughness for a brittle, unstable fracture event using a nonlinear fracture parameter. Now fracture toughness can be measured for unstable fracture using J in ASTM E 1820. The ASTM E 1290 method also allows the measurement of toughness after a pop-in, which is described as a discontinuity in the load-versus-displacement record usually caused by a sudden, unstable advance of the crack that is subsequently arrested.

References cited in this section

5. A.A. Wells, Unstable Crack Propagation in Metals: Cleavage and Fast Fracture, *Proc. Cranfield Crack Propagation Symposium*, Vol 1, Paper 84, 1961
9. "Standard Method for J_{Ic} , a Measure of Fracture Toughness," E 813, *Annual Book of ASTM Standards*, Vol 3.01, ASTM
10. "Standard Method for Determining J-R Curves," E 1152, *Annual Book of ASTM Standards*, Vol 3.01, ASTM
11. "Standard Test Method for Measurement of Fracture Toughness," E 1820, *Annual Book of ASTM Standards*, Vol 3.01 ASTM
12. "Methods for Crack Opening Displacement (COD) Testing," BS5762: 1979, The British Standards Institution, 1979
13. "Standard Method for Crack-Tip Opening Displacement (CTOD) Fracture Toughness Measurement," E 1290, *Annual Book of ASTM Standards*, Vol 3.01, ASTM

Fracture Toughness Testing

John D. Landes, University of Tennessee, Knoxville

New Standards for Metallic Materials

The development of standard fracture toughness test methods is not completed. In the past five years, two new standards have been developed, successfully balloted, and placed in the *Annual Book of ASTM Standards*. They are the common test method, a new fracture toughness standard that combines most of the standard test methods discussed above into a single standard, and the transition fracture toughness standard. A standard for testing of weldments is still being developed.

Common Fracture Toughness Test Method

Because the J_{Ic} and J - R curve test standards are similar in many respects, they have been combined into a single test standard, ASTM E 1820 (Ref 11). This standard method also allows a measurement of fracture toughness using the linear elastic parameter, K , and the nonlinear parameters, J and δ . The idea of a common method is that most of the fracture toughness tests use the same specimens, instrumentation, and test procedures. However, the analysis part of the standard gives each an exclusive quality that was derived from the historical development of the fracture mechanics methodology. The way individual methods were written in the past allows for the likelihood that a test can produce an invalid or unqualified result with no way to use the analysis procedure of another test method to try to obtain an acceptable result. The common method combines all measurements of fracture toughness into a single standard instead of many specialized standards. Therefore, after the test has been completed, the behavior of the material can dictate the nature of the analysis used, and a satisfactory fracture toughness result can be achieved for most tests. The analysis can use a linear elastic or an elastic-plastic parameter; it can use a single point fracture measurement or an R -curve toughness measurement. The way that each test is evaluated depends on the nature of the deformation and fracture behavior during the test. Therefore, the actual test result has a major influence on how the data are analyzed.

An additional feature of the new common method is an initialization procedure to assure that the initial portion of the J - R curve is aligned properly with the initial measured crack length. The ASTM E 813 method of J_{Ic} measurement did not specifically align the initial portion of the curve and could give artificially raised or lowered values of J_{Ic} reflecting the misalignment in the initial J - R curve. The ASTM E 1820 method includes

all of the fracture toughness methods discussed in the previous section except for the K - R curve method and the crack arrest test method.

Transition Fracture Toughness Testing

The measurement of transition fracture toughness for ferritic steels has long been a problem. The fracture behavior is usually brittle sometimes after an initial period of ductile crack extension. The toughness values show extensive scatter and size dependency that cause difficulty in the characterization of toughness for the evaluation of structures. The scatter and size dependency has been attributed to statistical influences and constraint differences (Ref 14). Characterization of the toughness relies mainly on the statistical handling of the data.

Test method ASTM E 1921 has been developed recently to handle the problems of transition fracture toughness testing (Ref 15). The specimens, fixtures, instrumentation, test procedures, and calculation of toughness parameters follow existing standards, for example, ASTM E 1820. The evaluation of the statistical aspects are handled with a weakest-link Weibull statistical distribution (Ref 15). Six or more fracture toughness test results are required at a given temperature. If the specimen size is not the unit size prescribed in the standard, a statistical size adjustment is made to the fracture toughness values. From the toughness results and using a statistical evaluation, a median value of toughness is identified. All median values of the distribution are aligned on a master curve (Fig. 14). The assumption is made that in the standard, the master curve of median toughness values is reproducible for the range of steel alloys with yield strengths between 275 and 825 MPa. The master curve is positioned with a reference temperature, T_0 , which is the temperature where a median toughness has a value of $100 \text{ MPa}\sqrt{m}$. All of the equations relating to the application of the Weibull statistics and the determination of T_0 for the placement of the master curve are given in the ASTM E 1921 (Ref 15). From the master curve and Weibull statistics, the toughness distribution at other temperatures can be determined. Also, from the statistical distribution, a percentage lower bound confidence level of toughness can be identified. For example, a 95% lower bound confidence level can be determined from the statistical distribution as a function of temperature.

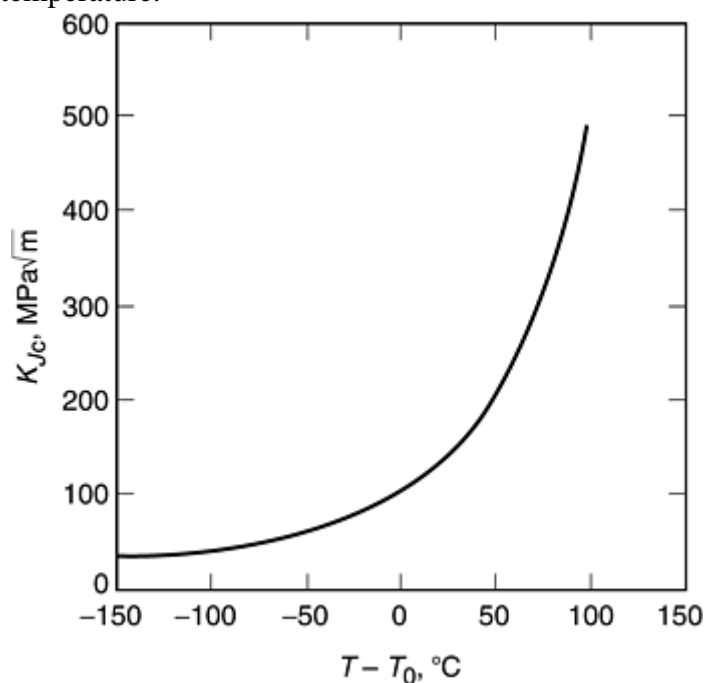


Fig. 14 Master curve of transition fracture toughness, K_{Jc} , critical stress intensity based on the J integral

Fracture Testing of Weldments

Preparation of a test method for the fracture toughness testing of weldments is ongoing. Weldments do not require a different set of parameters, specimens, or equipment for toughness testing; however, special problems exist for the testing of weldments. Solutions to these problems are not covered in the other standards.

Weldments have a composite of materials containing base metal, heat-affected zone, and weld metal regions. Such things as the placement of the notch for the sampling of the correct material, the precracking procedure to get the crack to grow into the correct area, and the handling of such thing as distortion and residual stresses present problems. These will be covered in the weldment standard. The parts that are common with the other standards are not covered in this method, but the tester is referred to the other standards to complete the testing and analysis after the special problems inherent to the testing of weldments have been addressed. In its first version, this standard will be annexed to the existing ASTM E 1290 method on CTOD testing, and the test result will be analyzed primarily with the δ parameter.

References cited in this section

11. "Standard Test Method for Measurement of Fracture Toughness," E 1820, *Annual Book of ASTM Standards*, Vol 3.01 ASTM
14. J.D. Landes and D.H. Shaffer, Statistical Characterization of Fracture in the Transition Region, *Fracture Mechanics: Twelfth Conference*, STP 700, ASTM, 1980, p 368–382
15. "Standard Test Method for Determination of Reference Temperature, T_0 , for Ferritic Steels in the Transition Range," E 1921, *Annual Book of ASTM Standards*, Vol 3.01, ASTM

Fracture Toughness Testing

John D. Landes, University of Tennessee, Knoxville

Fracture Toughness Test for Nonmetals

The standardization of fracture toughness test methods for nonmetals is relatively new compared to standardization for metallic materials. However, in the past ten years, several new standards have been written for ceramic and polymer materials. These are usually patterned after similar standards for metallic materials. The requirements to use the fracture mechanics approach for fracture toughness determination are that the materials are homogeneous, isotropic, and have a macroscopic defect. Because no material meets this requirement at all levels, it is required that it fits this criterion at some scale. Usually, this could be a scale of the same approximate size as the defect length.

To develop the correct test procedure, the deformation behavior of the material must be considered to determine the fracture parameter to be used to characterize the fracture toughness results. To determine whether the fracture is characterized by a single point or by an R -curve, the fracture behavior of the material must be considered. Brief discussion of fracture toughness testing of ceramics and polymer materials follows. A more complete description is given in other articles in this Section specifically written for these materials. Some fracture toughness standards have been developed for other nonmetallic materials including glass, rock, and polymer matrix composites. These standards are not discussed in this article.

Fracture Toughness Testing for Ceramics

Discussion of the fracture toughness testing of ceramics considers two different groups, monolithic ceramics and ceramic matrix composites.

Monolithic ceramics are brittle and fracture in a linear-elastic manner. The toughness, therefore, can be characterized by the K parameter. A fracture toughness test procedure could be similar to the K_{Ic} test procedure given in ASTM E 399 or ASTM E1820 following the methods used for metallic materials. A major problem for the fracture toughness testing of ceramics is the introduction of the defect. Because the toughness is so low, failure can occur during a fatigue precracking procedure. One fracture toughness method that has been used for

brittle materials including ceramics is the chevron-notch fracture toughness test, ASTM E 1304 (Ref 16). This is one of the test methods that do not require a fatigue precrack. The ASTM E 1304 method was developed for metallic materials but can often be used for brittle ceramic materials. Because the fracture behavior of ceramics is brittle, the toughness can be measured as a single point value. A new and provisional standard, PS 70 (Ref 17), has been developed for the fracture toughness testing of advanced ceramics at ambient temperatures. In this standard, a defect may be introduced as a precrack, or a hardness indentation or a chevron notch can be used to start the defect, as in ASTM E 1304. The precrack is popped in using a compression loading fixture; fatigue loading is not used for precracking advanced ceramics.

Ceramic-matrix composites have a more ductile looking toughness character. These materials exhibit more of an *R*-curve behavior. In some cases the deformation has a nonlinear characteristic. Although the nonlinear behavior may not be the same as plasticity in metallic materials, the nonlinear fracture parameters may still apply. Fracture toughness testing for these materials is largely in the experimental stages, and testing information is available in a variety of articles on the subject. The article “Fracture Toughness of Ceramics and Ceramic Matrix Composites” includes a good set of references relative to the fracture testing of ceramic matrix materials.

Fracture Toughness Testing for Polymers

The fracture toughness behavior for polymers usually falls into two classes, below the glass transition temperature T_g , and above T_g . Below T_g , the deformation is nearly linear elastic, and fracture is unstable. Therefore, a single-point toughness value, characterized by K , can be used. Above T_g , the deformation is nonlinear, and the fracture behavior is stable cracking. A *J*-based *R*-curve approach can be used. Two problems that must be addressed in developing test standards for polymers that make them different from metals are the viscoelastic nature of the polymer deformation behavior and the problem of introducing a defect by fatigue loading. The viscoelastic deformation character makes the fracture toughness result dependent on the loading rate, and that must always be specified in the test report. Comparison of toughness results for polymers should always be made with awareness of the effect of loading rate. Also, due to the viscoelastic nature of polymers, introduction of the defect is not easily accomplished with fatigue loading, and the crack is usually introduced with a razor blade cut.

Fracture toughness testing of polymer materials has been standardized in the past few years. The ASTM D 5045 method, standardized in 1996 (Ref 18), is used for determining fracture toughness of plastic materials that fail under essentially plane-strain and linear-elastic conditions. It has a basis in the ASTM E 399 method and follows a lot of the same methods. For more ductile polymers, the ASTM D 6068 method, also standardized in 1996 (Ref 19), develops the *J*-*R* curve fracture toughness for plastic materials. It follows the ASTM E 813 method in that it is a multiple specimen technique used where each test generates a single point on the *J*-*R* curve. It does not have a J_{Ic} analysis as ASTM E 813 does, but it uses the entire *R*-curve as the fracture toughness characterization. Both of these standard test methods for plastics require a reporting of the loading rate during the test and an introduction of the defect with a razor blade cut. A single specimen method for developing the *J*-*R* curve has not been standardized for polymers; however, the normalization method for developing the *J*-*R* curve has been shown to work well as a single-specimen method for several of the more ductile polymers (Ref 20).

More detailed information is provided in the article “Fracture Resistance Testing of Plastics” in this Volume.

References cited in this section

16. “Standard Test Method for Plane Strain (Chevron Notch) Fracture Toughness of Metallic Materials,” E 1304, *Annual Book of ASTM Standards*, Vol 3.01, ASTM
17. “Provisional Test Methods for Determination of Fracture Toughness of Advanced Ceramics at Ambient Temperatures,” PS 70, *Annual Book of ASTM Standards*, Vol 15.01, ASTM
18. “Standard Test Methods for Plane-Strain Fracture Toughness and Strain Energy Release Rate of Plastic Materials,” D 5045, *Annual Book of ASTM Standards*, Vol 8.03, ASTM

19. "Standard Test Method Determining J - R Curves of Plastic Materials," D 6068, *Annual Book of ASTM Standards*, Vol 8.03, ASTM
20. Z. Zhou, J.D. Landes, and D.D. Huang, J - R Curve Calculation with the Normalization Method for Toughened Polymers, *Polym. Eng. Sci.*, Vol 34 (No. 2), Jan 1994, p 128–134

Fracture Toughness Testing

John D. Landes, University of Tennessee, Knoxville

References

1. "Standard Terminology Relating to Fracture Testing," E 616, *Annual Book of ASTM Standards*, Vol 3.01, ASTM
2. J.D. Landes and R. Herrera, Micro-mechanisms of Elastic/Plastic Fracture Toughness, J_{Ic} , *Proc. 1987 ASM Materials Science Seminar*, ASM International, 1989, p 111–130
3. G.R. Irwin, Analysis of Stresses and Strains near the End of a Crack Traversing a Plate, *J. Appl. Mech.*, Vol 6, 1957, p 361–364
4. J.R. Rice, A Path Independent Integral and the Approximate Analysis of Strain Concentrations by Notches and Cracks, *J. Appl. Mech.*, Vol 35, 1968, p 379–386
5. A.A. Wells, Unstable Crack Propagation in Metals: Cleavage and Fast Fracture, *Proc. Cranfield Crack Propagation Symposium*, Vol 1, Paper 84, 1961
6. "Standard Method for Plane-Strain Fracture Toughness of Metallic Materials," E 399, *Annual Book of ASTM Standards*, Vol 3.01, ASTM
7. "Standard Practice for R-Curve Determination," E 561, *Annual Book of ASTM Standards*, Vol 3.01, ASTM
8. "Standard Method for Determining Plane-Strain Crack Arrest Toughness, K_{Ia} , of Ferritic Steels," E 1221, *Annual Book of ASTM Standards*, Vol 3.01, ASTM
9. "Standard Method for J_{Ic} , a Measure of Fracture Toughness," E 813, *Annual Book of ASTM Standards*, Vol 3.01, ASTM
10. "Standard Method for Determining J - R Curves," E 1152, *Annual Book of ASTM Standards*, Vol 3.01, ASTM
11. "Standard Test Method for Measurement of Fracture Toughness," E 1820, *Annual Book of ASTM Standards*, Vol 3.01, ASTM
12. "Methods for Crack Opening Displacement (COD) Testing," BS5762: 1979, The British Standards Institution, 1979
13. "Standard Method for Crack-Tip Opening Displacement (CTOD) Fracture Toughness Measurement," E 1290, *Annual Book of ASTM Standards*, Vol 3.01, ASTM

14. J.D. Landes and D.H. Shaffer, Statistical Characterization of Fracture in the Transition Region, *Fracture Mechanics: Twelfth Conference*, STP 700, ASTM, 1980, p 368–382
15. “Standard Test Method for Determination of Reference Temperature, T_0 , for Ferritic Steels in the Transition Range,” E 1921, *Annual Book of ASTM Standards*, Vol 3.01, ASTM
16. “Standard Test Method for Plane Strain (Chevron Notch) Fracture Toughness of Metallic Materials,” E 1304, *Annual Book of ASTM Standards*, Vol 3.01, ASTM
17. “Provisional Test Methods for Determination of Fracture Toughness of Advanced Ceramics at Ambient Temperatures,” PS 70, *Annual Book of ASTM Standards*, Vol 15.01, ASTM
18. “Standard Test Methods for Plane-Strain Fracture Toughness and Strain Energy Release Rate of Plastic Materials,” D 5045, *Annual Book of ASTM Standards*, Vol 8.03, ASTM
19. “Standard Test Method Determining J - R Curves of Plastic Materials,” D 6068, *Annual Book of ASTM Standards*, Vol 8.03, ASTM
20. Z. Zhou, J.D. Landes, and D.D. Huang, J - R Curve Calculation with the Normalization Method for Toughened Polymers, *Polym. Eng. Sci.*, Vol 34 (No. 2), Jan 1994, p 128–134

Fracture Toughness Testing

John D. Landes, University of Tennessee, Knoxville

Selected References

- T.L. Anderson, *Fracture Mechanics, Fundamentals and Applications*, 2nd ed., CRC Press, 1995
- J.M. Barsom and S.T. Rolfe, *Fracture and Fatigue Control in Structures*, 2nd ed., Prentice-Hall, 1987
- J.A. Begley and J.D. Landes, The J Integral as a Fracture Criterion, *Fracture Toughness, Proc. 1971 National Symposium on Fracture Mechanics*, Part II, STP 514, ASTM, 1972, p 1–20
- D. Broek, *Elementary Fracture Mechanics*, 4th rev. ed., Martinus Nijhoff, 1986
- W.F. Brown, Jr. and J.E. Srawley, Plane-Strain Crack Toughness Testing of High Strength Metallic Materials, STP 410, ASTM, 1966
- G.A. Clarke, W.R. Andrews, P.C. Paris, and D.W. Schmidt, Single Specimen Tests for J_{Ic} Determination, *Mechanics of Crack Growth*, STP 590, ASTM, 1976, p 24–42
- G.A. Clarke, W.R. Andrews, J.A. Begley, J.K. Donald, G.T. Embley, J.D. Landes, D.E. McCabe, and J.H. Underwood, A Procedure for the Determination of Ductile Fracture Toughness Values Using J Integral Techniques, *J. Test. Eval.*, Vol 7 (No. 1), Jan 1979, p 49–56
- M.G. Dawes, Elastic-Plastic Fracture Toughness Based on CTOD and J -Contour Integral Concepts, *Elastic-Plastic Fracture*, STP 668, J.D. Landes, J.A. Begley, and G.A. Clarke, Ed., ASTM, 1979, p 307–333
- *Fracture Toughness Testing and Its Applications*, STP 381, ASTM, 1965
- A. Joyce and J.P. Gudas, Computer Interactive J_{Ic} Testing of Navy Alloys, *Elastic-Plastic Fracture*, STP 668, J.D. Landes, J.A. Begley, and G.A. Clarke, Ed., ASTM, 1979, p 451–468
- J.D. Landes and J.A. Begley, The Effect of Specimen Geometry on J_{Ic} , *Fracture Toughness, Proc. 1971 National Symposium on Fracture Mechanics*, Part II, STP 514, ASTM, 1972, p 24–39
- J.D. Landes and J.A. Begley, Test Results from J_{Ic} Studies—An Attempt to Establish a J_{Ic} Testing Procedure, *Fracture Analysis*, STP 560, ASTM, 1974, p 170–186

- J.D. Landes and J.A. Begley, Recent Developments in J_{Ic} Testing, *Developments in Fracture Mechanics Test Methods Standardization*, STP 632, ASTM, 1977, p 57–81
- P.C. Paris and G.C. Sih, Stress Analysis of Cracks, *Fracture Toughness Testing and Its Applications*, STP 381, ASTM, 1965, p 30–81
- K.H. Schwalbe and D. Hellmann, Application of the Electrical Potential Method of Crack Length Measurement Using Johnson's Formula, *J. Test. Eval.*, Vol 9 (No. 3), 1981, p 218–221
- H. Tada, P.C. Paris, and G.R. Irwin, “The Stress Analysis of Cracks Handbook,” Paris Productions, St. Louis, MO, 1985.
- K. Wallin, Statistical Modeling of Fracture in the Ductile to Brittle Transition Region, *Defect Assessment in Components—Fundamentals and Applications*, J.G. Blauel and K.H. Schwalbe, Ed.,ESIS/EGF, Mechanical Engineering Publications, 1991, p 1–31
- K. Wallin, Fracture Toughness Transition Curve Shape for Ferritic Structural Steels, *Proc. Joint FEFG/ICF International Conference on Fracture of Engineering Materials* (Singapore), 6–8 Aug 1991, p 83–88
- J.G. Williams, *Fracture Mechanics of Polymers*, John Wiley & Sons, New York, 1984

Creep Crack Growth Testing

B.E. Gore, Northwestern University, W. Ren, Air Force Materials Laboratory, P.K. Liaw, The University of Tennessee

Introduction

HIGH-TEMPERATURE APPLICATIONS in the chemical processing, aerospace, nuclear and fossil power-generation industries, and waste incineration industries are realizing a need for materials that can withstand increasingly more strenuous working environments for longer periods of time. While many of the methods used to predict the service life of a structural component involve tests based on the behavior of a material under pure creep conditions, many applications require an understanding of how creep-fatigue conditions affect the life of a component.

Using the fossil energy industry as an example, their systems are rarely operated under steady-state conditions. Due to factors such as shutdowns for safety inspections and changing demands, there is often a thermal-mechanical fatigue process introduced during service (Ref 1). These processes can affect the service life of a material by inducing a redistribution of crack-tip stresses and by affecting the creep zone growth behavior (Ref 2) or by changing the creep crack propagation mechanisms (Ref 3). Therefore, the interaction of creep and fatigue damage is an important concern in structural life assessments. There is also an increasing demand to develop methods of increasing the service life of existing systems, as well as to develop more accurate techniques of predicting the initial life span of a material (Ref 4). These demands are a result of not only economic concerns but safety considerations as well (Ref 5).

Test methods for the evaluation of creep-fatigue interactions include fatigue-life testing with hold times and creep crack growth testing with hold times. Fatigue-life testing involves stress-controlled ($S-N$) or strain-controlled ($\epsilon-N$) cyclic loading, where hold times and waveform patterns are used to evaluate the time-dependent effects of creep conditions on fatigue life. These fatigue-life test methods are used to evaluate materials for safe-life designs by either infinite life ($S-N$) or finite life ($\epsilon-N$) criteria. Test methods for this approach are discussed in more detail in the article “Fatigue, Creep-Fatigue, and Thermomechanical Fatigue-Life Testing” in this Volume.

Creep crack growth testing is based on the concepts of fracture mechanics where subcritical crack growths are evaluated from a preexisting flaw or crack. Although careful measures are taken to ensure that materials, especially those designed for high-temperature applications, do not contain potentially damaging internal errors, it is true that small defects, such as those due to machining or inclusions in the material, may elude inspections

(Ref 5, 6). Unintended defects typically serve as the point of origin of a crack, which can ultimately lead to the failure of the material. For these reasons, it is important to understand not only the mechanisms by which a crack propagates in a particular material, but also to be able to predict the rate of crack growth and to use experimental data in order to develop a model for the behavior of a material prior to its application in real-world situations. This article focuses on a description of the experimental method that should be followed in conducting tests of creep-fatigue crack growth (CFCG) with various hold times and also provides an overview of some suitable life-prediction models.

References cited in this section

1. W. Ren, "Time-Dependent Fracture Mechanics Characterization of Haynes HR160 Superalloy," Ph.D. dissertation, School of Material Science and Engineering, University of Tennessee, 1995
2. H. Riedel and J.R. Rice, Tensile Cracks in Creep Solids, *Fracture Mechanics: Twelfth Conf.*, STP 700, ASTM, 1980, p 112–130
3. M. Okazaki, I. Hattori, F. Shiraiwa, and T. Koizumi, Effect of Strain Wave Shape on Low-Cycle Fatigue Crack Propagation of SUS 304 Stainless Steel at Elevated Temperatures, *Metal. Trans. A*, Vol 14, 1983, p 1649–1659
4. A. Saxena and P.K. Liaw, "Remaining Life Estimations of Boiler Pressure Parts—Crack Growth Studies," Final Report CS 4688 per EPRI Contract RP 2253-7, Electric Power Research Institute, 1986
5. R.H. Norris, P.S. Grover, B.C. Hamilton, and A. Saxena, Elevated Temperature Crack Growth, *Fatigue and Fracture*, Vol 19, *ASM Handbook*, ASM International, 1996
6. A. Saxena, "Life Assessment Methods and Codes," EPRI TR-103592, Electric Power Research Institute, 1996

Creep Crack Growth Testing

B.E. Gore, Northwestern University, W. Ren, Air Force Materials Laboratory, P.K. Liaw, The University of Tennessee

Creep and Creep Fatigue

Static Loading (Creep Conditions). Testing involving a static load could also be characterized as a crack growth test conducted with an infinite hold time. In such a case, there is little or no fatigue effect to be accounted for; however, depending on the environment, there can be significant and sometimes fatal damage due to creep (permanent deformation resulting from a steady load). A final failure would either occur due to widespread or localized creep damage (Ref 5, 7). Creep damage is liable to be widespread if the material is in a uniform stress and temperature environment. In this case, failure is likely to occur due to creep rupture. Failure of this kind is most commonly observed in a component, such as a steam pipe or an inlet casing, where the material is thin (Ref 8). Correspondingly, in a structural component, such as a turbine blade, one is apt to observe failure due to creep crack propagation as opposed to creep rupture. In this case, the creep is localized as a result of nonuniform stresses and temperatures (Ref 5).

Cyclic Loading (Creep-Fatigue Conditions). In a test run under cyclic loading conditions, the constant load is periodically interrupted by unloading and reloading. In this case, the effects of creep-fatigue interactions during transitory load periods play a major role in the initiation and growth of cracks along with the effects of creep during the intervals of steady-state loads. This type of scenario might occur in a fossil energy system, for example, when there are pressure and temperature fluctuations due to changes in output energy demands (Ref

1). Creep-fatigue damage might also be of foremost concern in turbine casings where it is often the primary cause of crack initiation and propagation (Ref 8). It remains that creep contributes to crack growth in regions where temperatures exceed 427 °C (800 °F), while thermal stresses are considered responsible for fatigue and creep-fatigue crack growth in the lower temperature regions (Ref 5, 6).

References cited in this section

1. W. Ren, "Time-Dependent Fracture Mechanics Characterization of Haynes HR160 Superalloy," Ph.D. dissertation, School of Material Science and Engineering, University of Tennessee, 1995
5. R.H. Norris, P.S. Grover, B.C. Hamilton, and A. Saxena, Elevated Temperature Crack Growth, *Fatigue and Fracture*, Vol 19, *ASM Handbook*, ASM International, 1996
6. A. Saxena, "Life Assessment Methods and Codes," EPRI TR-103592, Electric Power Research Institute, 1996
7. A. Saxena, "Recent Advances in Elevated Temperature Crack Growth and Models for Life Prediction," *Advances in Fracture Research: Proc. Seventh Int. Conf. on Fracture*, March 1989 (Houston, TX), K. Salama, K. Ravi-Chander, D.M.R. Taplin, and P. Rama Rao, Ed., Pergamon Press, 1989, p 1675–1688
8. W.A. Logsdon, P.K. Liaw, A. Saxena, and V.E. Hulina, Residual Life Prediction and Retirement for Cause Criteria for Ships Service Turbine Generator (SSTG) Upper Casings, Part I: Mechanical Fracture Mechanics Material Properties Development, *Eng. Fract. Mech.*, Vol 25, 1986, p 259–288

Creep Crack Growth Testing

B.E. Gore, Northwestern University, W. Ren, Air Force Materials Laboratory, P.K. Liaw, The University of Tennessee

Material Characterization

Creep-Ductile Materials. Materials that are classified as being creep-ductile have the ability to sustain significant amounts of crack growth before failure. Examples of these materials would include Cr-Mo steels, stainless steels, and Cr-Mo-V steels (Ref 5). Crack growth in this type of material is normally accompanied by substantial creep deformation at the crack tip. As a result, in order to be able to make accurate predictions for the lives of high-temperature components made from such materials, a complete understanding of the crack growth mechanics and damage mechanisms is necessary. An example of the characteristic flow of this methodology is shown in Fig. 1.

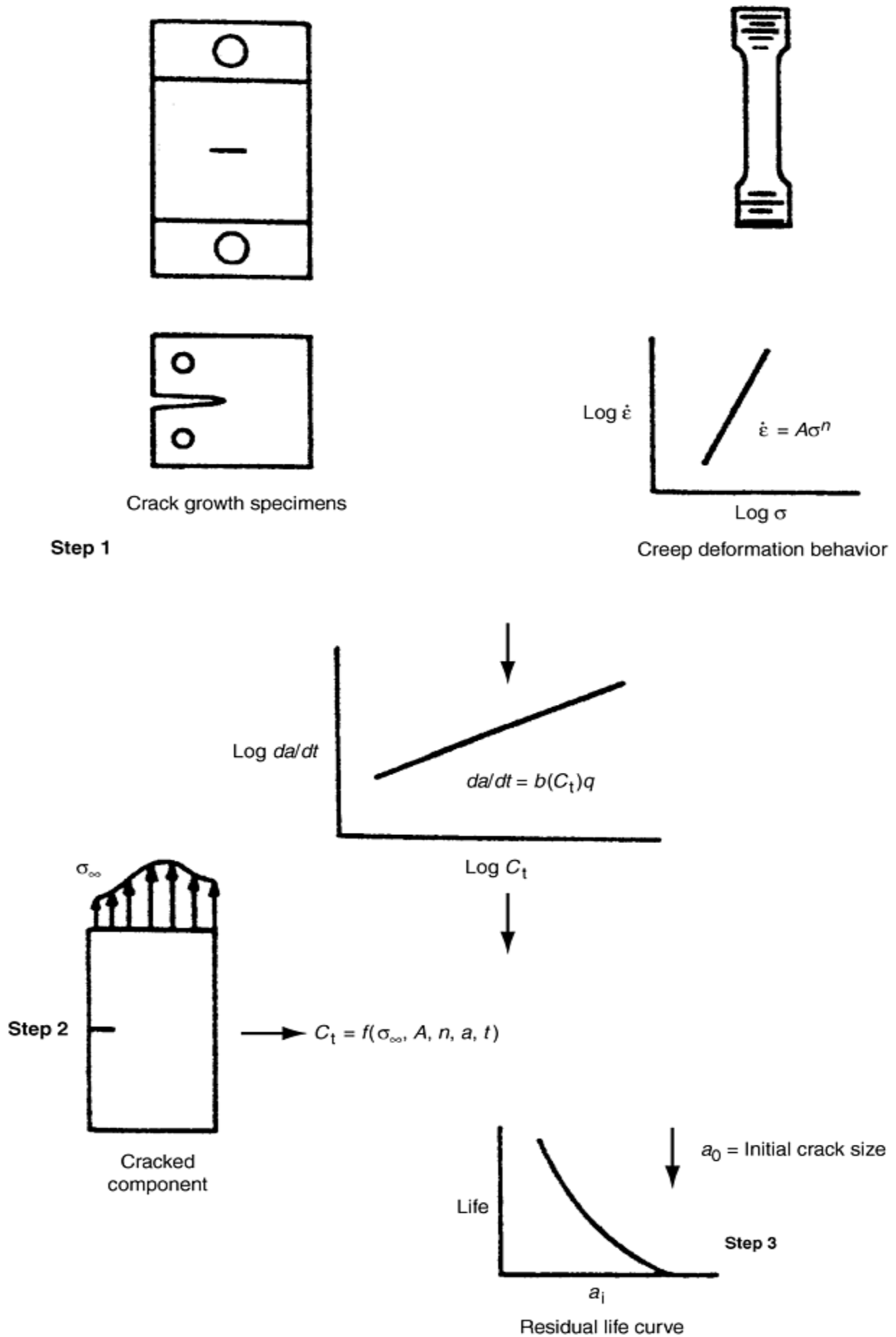


Fig. 1 The methodology for predicting crack propagation life using time-dependent fracture mechanics concepts. Source: Ref 9

Typically, crack growth in this type of material is due to grain boundary cavitation. The cavitation is commonly seen to initiate at second-phase particles or at defects along the grain boundaries (Ref 10). As the cavities nucleate and grow larger, a coalescence of the cavities is observed that will eventually lead to crack propagation and, ultimately, failure (Ref 11). This mechanism is considered to be characteristic of creep crack growth. Other mechanisms for fatigue crack growth with hold times include an alternating slip mechanism (a crack-tip blunt mechanism) and the influence of corrosive environment (Ref 5).

Creep-Brittle Materials. A second type of material is the creep-brittle material. These materials are typified by the fact that creep crack growth is normally accompanied by small-scale creep deformation and by crack growth rates that are comparable to the rates at which creep deformation spreads in the cracked body (Ref 5). This can substantially influence the crack-tip parameters that characterize their crack propagation rates. Examples of this type of material include nickel-base superalloys, titanium alloys, high-temperature aluminum alloys, intermetallics, and ceramic materials.

References cited in this section

5. R.H. Norris, P.S. Grover, B.C. Hamilton, and A. Saxena, Elevated Temperature Crack Growth, *Fatigue and Fracture*, Vol 19, *ASM Handbook*, ASM International, 1996
9. P.K. Liaw, A. Saxena, and J. Schaefer, Predicting the Life of High-Temperature Structural Components in Power Plants, *JOM*, Feb 1992
10. J.T. Staley, Jr., "Mechanisms of Creep Crack Growth in a Cu-1 wt. % Sb Alloy," MS thesis, Georgia Institute of Technology, 1988
11. J.L. Bassani and V. Vitek, *Proc. Ninth National Congress of Applied Mechanics—Symposium on Non-Linear Fracture Mechanics*, L.B. Freund and C.F. Shih, Ed., American Society of Mechanical Engineers, 1982, p 127–133

Creep Crack Growth Testing

B.E. Gore, Northwestern University, W. Ren, Air Force Materials Laboratory, P.K. Liaw, The University of Tennessee

Time-Dependent Fracture Mechanics

Parameters for Static Loading

In time-dependent fracture mechanics, parameters have been defined for static loading and cyclic loading. There are six crack-tip parameters considered to be applicable for cases of static loading. Each parameter is specific to a particular set of testing conditions. These conditions are outlined below along with the definitions and calculations that correspond to each parameter. All of the following information on parameters is found in Ref 1.

In order to be able to characterize the creep crack behavior of a cracked body, the creep deformation and the relationship among the creep strain, stress, and strain rate must first be considered. For cracks in creeping solids under conditions of static loading, the following equation is most frequently used to describe this relationship (Ref 12):

$$\dot{\epsilon} = \frac{\dot{s}}{E} + A_1 e^{-P_2 n_1 (1+P)} + A_2 s^n \quad (\text{Eq 1})$$

where $\dot{\epsilon}$ is the engineering creep strain rate, \dot{s} is the applied engineering stress rate, e is the engineering strain, s is the engineering (nominal) stress, E is Young's modulus, A_1 is the primary creep coefficient, p and n_1 are the primary creep exponents, A_2 is the secondary creep coefficient, and n is the secondary creep exponent. Under extensive creep conditions, the first term in Eq 1 can be neglected. This term is due to the elastic strain rate, which is only of importance during small-scale creep. The second term is due to primary creep, and thus, under extensive primary creep conditions, Eq 1 can be reduced to:

$$\dot{\epsilon} = A_1 e^{-p} s^{n_1(1+p)} \quad (\text{Eq 2})$$

Similarly, the third term is due to secondary creep, and so under extensive secondary creep conditions, Eq 1 reduces to:

$$\dot{\epsilon} = A_2 s^n \quad (\text{Eq 3})$$

All of the coefficients and exponents in the above equations may be obtained from creep deformation test results.

C^* Parameter. The conditions for the application of C^* can be described as extensive secondary creep conditions (Ref 1). In cases where the pure secondary creep condition is emphasized, one might see the use of the notation C_s^* instead of C^* . The level of load and, accordingly, the characterization of the loading have a negligible effect on the material behavior because, under extensive creep conditions, the creep strain rate dominates the elastic or plastic strain rate throughout the cracked specimen (Ref 1). The C^* parameter is analogous to the path-independent J -integral discussed previously. The basic definition of the integral, as given by Landes and Begley (Ref 13), Nikbin et al. (Ref 14), and Taira et al. (Ref 15) is as follows:

$$C^* = \int_{\Gamma} \left(W_s^* dy - T_i \frac{\partial \dot{u}_i}{\partial x} ds \right) \quad (\text{Eq 4})$$

where Γ is a counter-clockwise contour of the integral that encloses the crack tip (Fig. 2), T_i is the outward stress vector acting on the contour around the crack, \dot{u}_i is the displacement rate vector, and ds is an increment of the contour path. W_s^* is the strain energy rate density defined by the equation:

$$W_s^* = \int \dot{\epsilon}^{mn} \sigma_{ij} d\dot{\epsilon}_{ij}$$

Overall, C^* is a calculation of the energy input rate in the crack-tip area, similar to the J -integral. It could also be referred to as the stress-power dissipation rate in the cracked body (Ref 13).

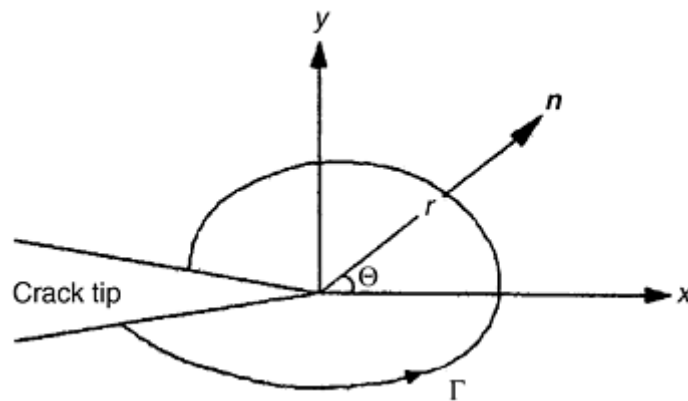


Fig. 2 Schematic of the contour integral in terms of crack-tip coordinate system used to define C^* . n is the unit normal vector. Source: Ref 5

An approximation for estimating C^* can be found in the Electric Power Research Institute (EPRI) Handbook solution (Ref 1). In this case, C^* is indirectly calculated from the material power-law creep constants, A_2 and n , from Eq 3. When under plane strain conditions, the equation for a compact-type (CT) specimen is given by:

$$C^* = \frac{A_2}{(W-a)^n} h_1 \left(\frac{a}{W}, n \right) \left(\frac{P}{1.445 \zeta_B} \right)^{n+1} \quad (\text{Eq 5})$$

with

$$\xi = \left[\left(\frac{2a}{W-a} \right)^2 + 2 \left(\frac{2a}{W-a} \right) + 2 \right]^{1/2} - \left(\frac{2a}{W-a} \right) - 1 \quad (\text{Eq 6})$$

where W is the compact tension specimen width, a is the crack length, P is the applied load, B is the thickness of the cracked body, and h_1 is a function of a/W and the strain-hardening exponent (the numerical values of h_1 can be found in Ref 16).

In addition, C^* can also be described as the energy input rate difference between two identically loaded bodies with incrementally differing crack lengths, da :

$$C^* = - \frac{1}{B} \frac{dU^*}{da} \quad (\text{Eq 7})$$

where U^* is the power input in the cracked body. From this last equation, an expression has been derived for experimentally determining C^* :

$$C^* = \frac{P\dot{V}_c}{B_N W} \eta \left(n, \frac{a}{W} \right) \quad (\text{Eq 8})$$

where \dot{V}_c is the load-line deflection due to creep, B_N is the net specimen thickness (in side-grooved specimens, B_N is equal to the distance between the roots of the grooves), and η is a function of crack length, the exponent on stress in Norton's creep equation, and specimen geometry (Ref 1).

Because as the cracked body is under extensive secondary creep conditions and the stress and strain rates are related by Eq 3, the crack-tip stress and strain rate fields can be described in terms of C^* as follows (Ref 17, 18):

$$\sigma_{ij} = \left[\frac{C^*}{I_n A_2 r} \right]^{1/(n+1)} \tilde{\sigma}_{ij}(\theta; n) \quad (\text{Eq 9})$$

$$\epsilon_{ij} = \left[\frac{C^*}{I_n A_2 r} \right]^{n/(n+1)} \dot{\epsilon}_{ij}(\theta; n) \quad (\text{Eq 10})$$

where I_n is a dimensionless factor (Ref 19), $\tilde{\sigma}_{ij}(\theta; n)$ is the dimensionless stress angular distribution (Ref 19), $\dot{\epsilon}_{ij}$ is the strain rate tensor, and $\dot{\epsilon}_{ij}(\theta; n)$ is the dimensionless strain rate angular distribution.

$C^*(t)$ Parameter. For the $C^*(t)$ parameter, the conditions are extensive primary and/or secondary creep conditions (Ref 1). Again, the level of the load has little effect on the material behavior. The $C^*(t)$ parameter is essentially the extension of C^* from extensive secondary creep conditions into extensive primary creep conditions. This parameter can be defined as:

$$C^*(t) = \int_{\Gamma} \left[W^*(t) dy - T_i \frac{\partial u_i}{\partial x} ds \right] \quad (\text{Eq 11})$$

where $W^*(t)$ is the instantaneous stress-power or energy rate per unit volume.

One can see in Eq 11 that when the specimen is under pure secondary creep conditions, $W^*(t)$ is replaced by W_s^* , and thus, $C^*(t)$ is equal to C^* (as shown in Eq 4).

Conditions of extensive creep are not always associated with pure secondary or pure primary creep. Often, a mixture of primary and secondary creep is found. Under such conditions, the $C^*(t)$ integral is no longer path independent. However, an approximation of $C^*(t)$ can still be calculated path-independently with an error of 2% (Ref 20).

Under extensive primary-secondary creep conditions, the value of $C^*(t)$ can also be approximated by the sum of $C^*(t)$ under extensive primary creep conditions and $C^*(t)$ or C^* under extensive secondary creep conditions. This approximation is given by:

$$C^*(t) \approx \frac{C_h^*}{(1+p)t^{p/(1+p)}} + C_s^* \quad (\text{Eq 12})$$

where C_h^* is the stress-dependent part of the path-independent integral $C^*(t)$ under extensive primary creep conditions. In Eq 12, the first term on the right-hand side is the value of $C^*(t)$ under extensive pure primary creep conditions, while the second term is the $C^*(t)$ or C^* value under extensive pure secondary creep conditions. Another expression of Eq 12 would be:

$$C^*(t) \approx [1 + (t_2/t)^{p/(1+p)}] C_s^* \quad (\text{Eq 13})$$

where t_2 is the time of the transition from extensive primary creep to extensive secondary creep. Here t_2 can be determined by:

$$t_2 = \left[\frac{C_h^*}{(1+p)C_s^*} \right]^{(1+p)/p} \quad (\text{Eq 14})$$

Knowing that C^* can be estimated experimentally from Eq 8, $C^*(t)$ can similarly be measured in test specimens under extensive secondary creep conditions using this equation:

$$C^*(t) = \frac{P\dot{V}_c}{B_N W} \eta \left(n_1, n, \frac{a}{W} \right) \quad (\text{Eq 15})$$

Equation 15 differs from Eq 8 in that the function, η , is a function of the primary creep exponent, n_1 , in addition to the secondary creep exponent, n , and the ratio of crack size to specimen width, a/W . The expression for η is given by (Ref 21):

$$\eta = \left[\frac{n}{n+1} \frac{t}{t_2} + \frac{n_1}{n_1+1} \left(1 - \frac{t}{t_2} \right) \right] \times \left(\frac{2}{1-a/W} + 0.522 \right) \quad (\text{Eq 16})$$

For CT specimens, it has been shown that there is little dependence of η on n and n_1 . For this reason, it is recommended that for these specimens, η can be approximated using the following equation (Ref 22):

$$\eta = \frac{n}{n+1} \left(\frac{2}{1-a/W} + 0.522 \right) \quad (\text{Eq 17})$$

This equation has been adopted by ASTM E 1457, "Standard Test Method for Measurement of Creep Crack Growth Rates in Metals" (Ref 23).

C_h^* Parameter. The conditions for C_h^* can be expressed as extensive primary creep conditions (Ref 1). This parameter was defined as a path-independent integral by Riedel (Ref 24). As such, C_h^* is the stress-dependent part of $C^*(t)$ under extensive primary creep conditions shown as:

$$C^*(t) = \frac{C_h^*}{(1+p)t^{p/(1+p)}} \quad (\text{Eq 18})$$

C_h^* can be determined by the equation:

$$C_h^* = \frac{[A_1(1+p)]^{1/(1+p)}}{(W-a)^{n_1}} h_1 \left(\frac{a}{W}, n_1 \right) \times \left(\frac{P}{1.445\zeta B} \right)^{n_1} \quad (\text{Eq 19})$$

$C(t)$ Parameter. The conditions for the $C(t)$ parameter are frequently found at the crack tip. These conditions can be described as small-scale, elastic, primary and/or secondary creep conditions (Ref 1). Ohji et al. (Ref 25), Bassani and McClintock (Ref 26), and Ehlers and Riedel (Ref 27) studied the crack-tip stress fields under these conditions, and the $C(t)$ integral was defined as follows:

$$C(t) = \int_{\Gamma_s} \left(W_s^* dy - T_i \frac{\partial \dot{u}_i}{\partial x} ds \right) \quad (\text{Eq 20})$$

where Γ_s is a counter-clockwise contour of the integral that encloses the crack within the crack-tip creep zone. This differs from the counter-clockwise contour of the C^* integral because, in that case, the contour of the integral was not limited to the crack-tip creep zone. The reason for this limitation is that it is only in the creep zone that the creep strain rate may dominate the elastic strain rate. The loading is confined to elastic loading for this parameter due to the fact that the creep strain rate may not be able to dominate the plastic strain rate under small-scale creep zone conditions. This is because the plastic zone size may be larger than the creep zone size. Just from the definition of the $C(t)$ parameter, it is evident that when the creep zone scale transitions from small to extensive conditions, the definition of the parameter becomes indistinguishable from that of the $C^*(t)$ parameter.

When experiencing small-scale, elastic, secondary creep conditions in the case of plane strain, the value of $C(t)$ can be approximated by this equation (Ref 25, 26, and 27):

$$C(t) \approx \frac{K^2(1-\nu^2)}{(n+1)Et} \quad (\text{Eq 21})$$

where K is the stress intensity factor, and ν is Poisson's ratio.

Another approximation for $C(t)$ under the same conditions is given as (Ref 27):

$$C(t) = [1 + t_T / t] C_s^* \quad (\text{Eq 22})$$

where t_T is the transition time from small-scale to extensive creep given by the equation:

$$t_T = \frac{K^2(1-\nu^2)}{E(n+1)C_s^*} \quad (\text{Eq 23})$$

The approximations from Eq 22 have been confirmed in several numerical studies and have been determined to be reasonably accurate (Ref 20, 28).

When under small-scale, elastic conditions with primary and/or secondary creep conditions, the $C(t)$ parameter can be approximated as follows (Ref 20, 29):

$$C(t) = [1 + t_{TP}/t + (t_2/t)^{p/(1+p)}] C_s^* \quad (\text{Eq 24})$$

where t_{TP} is the transition time from the small-scale primary creep to extensive primary creep conditions as determined by:

$$t_{TP} = \left[\frac{K^2(1-\nu^2)}{EC_s^*} \right]^{1+p} \frac{1}{1+n_1} \quad (\text{Eq 25})$$

For creep deformation ranging from small-scale to extensive creep, Ehlers and Riedel (Ref 27) proposed that $C(t)$ can be determined from the sum of the small-scale and extensive creep solutions as follows:

$$C(t) = \frac{K^2(1-\nu^2)}{(n+1)Et} + C^* \quad (\text{Eq 26})$$

Their analytical work, along with that of Ohji et al. (Ref 25), shows that similar to C^* for the extensive, secondary creep conditions, $C(t)$ may be used to describe the crack-tip stress and strain fields under the small-scale, elastic creep conditions:

$$\sigma_{ij} = \left[\frac{C(t)}{I_n A_2 r} \right]^{1/(n+1)} \tilde{\sigma}_{ij}(\theta; n) \quad (\text{Eq 27})$$

$$\epsilon_{ij} = \left[\frac{C(t)}{I_n A_2 r} \right]^{n/n+1} \dot{\epsilon}_{ij}(\theta; n) \quad (\text{Eq 28})$$

Even though $C(t)$ can be applied to both small-scale and extensive creep conditions, this parameter has a severe drawback. The values of $C(t)$ can only be calculated with the given equations and cannot be experimentally measured, as was the case with C^* and $C^*(t)$. In addition, the accuracy of its calculated values depends heavily on the accuracy of the constitutive equations employed for the calculation (Ref 1).

$C_{st}(t)$ Parameter. The conditions for the $C_{st}(t)$ parameter can be described as small-scale, elastic, primary and/or secondary creep conditions during the time shortly after t_1 is reached and long before t_2 is reached (Ref 1). In

this case, t_1 is the transition time from small-scale primary creep in the elastic field to extensive primary creep conditions. McDowell et al. (Ref 30) have shown that in a compact tension (CT) specimen during this time, $C(t)$ becomes essentially path independent because a stationary stress field is achieved across the remaining ligament. Under such conditions, $C(t)$ is defined as $C_{st}(t)$, and can be determined from the following equation:

$$C_{st}(t) = [1 + (t_2/t)^{p/(1+p)}] C_s^* \quad (\text{Eq 29})$$

C_t Parameter. For C_t , the conditions can best be described as small-scale or transition, elastic, and primary and/or secondary creep conditions (Ref 1). The C_t parameter was originally proposed by Saxena (Ref 31) in order to avert the disadvantage of $C(t)$, which cannot be experimentally measured. This parameter can be thought of as an extension of the C^* integral into the small-scale and transition creep regions, and, under extensive creep conditions, the C_t parameter approaches the value of $C^*(t)$ in much the same way as the $C(t)$ parameter does (Ref 1). Under small-scale conditions, however, the C_t parameter behaves differently from $C(t)$. Whereas $C(t)$ is the amplitude of the crack-tip stress field, C_t , as defined by Saxena, is uniquely related to the rate of expansion of the creep zone size under small-scale creep conditions (Ref 28):

$$(C_t)_{SSC} = \frac{2}{3} (1 - \nu^2) \frac{K^2}{EW} (F'/F) \beta \dot{\gamma}_c \quad (\text{Eq 30})$$

where $(C_t)_{SSC}$ is the value of C_t when the small-scale creep condition is emphasized, F is the K -calibration factor [$F = (K/P)BW/2$], F' is the a/W derivative of F [$F' = dF/da(a/W)$], and $\dot{\gamma}_c$ is the rate of expansion of the creep zone size.

For the rate of expansion of the creep zone size, $\dot{\gamma}_c$, expressions have been derived for elastic, primary creep and elastic, secondary creep conditions (Ref 21, 28). An analytical estimation of $(C_t)_{SSC}$ may be found by substituting the corresponding $\dot{\gamma}_c$ expressions into Eq 30 (Ref 1).

When the specimen is under small-scale, elastic primary creep conditions, the rate of expansion of the creep zone is given by the following equation:

$$\begin{aligned} \dot{\gamma}_c &= \frac{K^2}{2\pi} \left[\frac{I_{n_1} E}{2\pi(1-\nu^2)} \right]^{2/(n_1-1)} \\ &\times [(1+n_1)(1+p)A_1]^{2/(1+p)(n_1-1)} \\ &\times \left[\frac{\tilde{\gamma}_c(\theta)}{1+p} \right] \times \left[\frac{2}{n_1+1} \right]^{[2/(1+p)(n_1-1)-1]} \end{aligned} \quad (\text{Eq 31})$$

where I_{n_1} is a nondimensional factor dependent upon n_1 , and $\tilde{\gamma}_c(\theta)$ is the dimensionless function defining the creep zone shape (Ref 1).

Under small-scale, elastic secondary creep conditions, the rate of expansion of the creep zone size is given by:

$$\dot{\gamma}_c = \frac{2\alpha}{n-1} K^2 t^{-(n-3)/(n-1)} (EA)^{2/(n-1)} \tilde{\gamma}_c(\theta) \quad (\text{Eq 32})$$

where α is a dimensionless constant dependent on n .

C_t may also be estimated over a range, from small-scale to extensive creep conditions, using the following:

$$C_t = (C_t)_{SSC} + C^*(t) \quad (\text{Eq 33})$$

where $(C_t)_{SSC}$ and $C^*(t)$ are both calculated rather than experimentally measured values. Again, it is important to note that C_t changes from $(C_t)_{SSC}$ to $C^*(t)$ as conditions progress from small-scale to extensive creep (Ref 1).

An equation has been included in the ASTM handbook (Ref 23) that allows the experimental measure of C_t under small-scale creep conditions. This equation is included as follows:

$$(C_t)_{SSC} = \frac{P\dot{V}_c}{\sqrt{B_N B W}} \left(\frac{F'}{F} \right) \quad (\text{Eq 34})$$

Parameters for Cyclic Loading

For cyclic loading, there are two parameters considered to be applicable for tests involving cyclic loading. Again, the testing conditions, definitions, and necessary calculations for each parameter are outlined below.

ΔJ_c Parameter. The ΔJ_c parameter is simply a time integral of C^* or J^* over the hold time, t_h , involved in trapezoidal waveform loading (Ref 1). The parameter was first introduced by Jaske and Begley (Ref 32) and Taira et al. (Ref 33) in order to correlate with the time-dependent creep crack growth during a trapezoidal waveform loading at elevated temperatures. Its definition is:

$$\Delta J_c = \int_0^{t_h} C^* (dt) \quad (\text{Eq 35})$$

where t_h is the hold time at the maximum load of a trapezoidal load form.

When a material is subjected to trapezoidal waveform loading, its response can be divided into two parts: the loading portion and the hold time portion. Creep deformation may occur at the crack tip during both portions. When integrated over the hold time, the ΔJ_c parameter gives the total energy input in the crack-tip area due to creep deformation that occurs during the hold time (Ref 1). During the loading portion, the amount of creep deformation generally depends on the rate of loading. If the loading is conducted quickly, the creep deformation is small compared to the elastic and plastic deformation. Thus, it is usually a negligible effect, and, therefore, no time-dependent fracture-mechanics parameter has been defined for such instances. However, in the case of slow loading, creep deformation can dominate the elastic and plastic deformation. In this instance, Ohtani et al. (Ref 34) and other researchers (Ref 35, 36, and 37) have proposed a method to use for estimation of ΔJ_c . This method functions on the assumption that creep deformation occurs under extensive creep conditions.

Because trapezoidal waveform loading involves both elastic and plastic deformations, the total energy output for the entire cycle should be described by the sum of the cycle-dependent and time-dependent parts (Ref 1). Therefore, the ΔJ_c parameter can be integrated into the total J -integral (ΔJ_T) defined as:

$$\Delta J_T = \Delta J_f + \Delta J_c \quad (\text{Eq 36})$$

where ΔJ_f is the cycle-dependent integral associated with time-independent plasticity (Ref 1).

$(C_t)_{\text{avg}}$ Parameter. The $(C_t)_{\text{avg}}$ parameter is, as the notation denotes, the average value of the C_t parameter during the hold time periods of a trapezoidal waveform (Ref 1). The parameter was first defined by Saxena as the following (Ref 38, 39, and 40):

$$(C_t)_{\text{avg}} = \frac{1}{t_h} \int_0^{t_h} C_t dt \quad (\text{Eq 37})$$

The definition of the $(C_t)_{\text{avg}}$ parameter given in Eq 37 is applicable only for creep deformation encountered during the hold time, t_h . In general, along with the creep deformation during this time, there is elastic deformation as a result of stress relaxation. With longer hold times, the creep zone expands from small-scale to extensive creep, so eventually the elastic deformation will become insignificant. As can be seen through Eq 37, as C_t approaches C^* , $(C_t)_{\text{avg}} \cdot t_h$ becomes equal to ΔJ_c (Ref 1). It is important to note, however, that under small-scale creep conditions, the $(C_t)_{\text{avg}} \cdot t_h$ and ΔJ_c parameters will not be equal. This is especially true when the values are calculated as opposed to being experimentally obtained (Ref 1).

According to which method is used to estimate the deflection rate of the cracked body, there are two ways to determine the value of $(C_t)_{\text{avg}}$. For a CT specimen test, where the load and load-line deflection as functions of time can be determined experimentally, the value of $(C_t)_{\text{avg}}$ is experimentally measured. However, for the case of a cracked component, where the deflection rate can only be predicted analytically, $(C_t)_{\text{avg}}$ is found by calculation.

When measured experimentally, $(C_t)_{\text{avg}}$ can be obtained from the following:

$$(C_t)_{\text{avg}} = \frac{\Delta P \Delta V_c}{B W_{t_h}} \frac{F'}{F} - C^* \left(\frac{F'}{F} \frac{1}{\eta} - 1 \right) \quad (\text{Eq 38})$$

where ΔP is the applied load range and ΔV_c is the load-line deflection due to creep during the hold period. The value of $(C_t)_{\text{avg}}$, when determined analytically, is found through the employment of equations that depend on material conditions. If a material has low resistance to cyclic plasticity, where the cyclic plastic zone is larger than the creep zone during the first hold time, $(C_t)_{\text{avg}}$ may be determined from the following equation (Ref 39) as elastic-cyclic plastic-secondary creep conditions:

$$(C_1)_{\text{avg}} = \frac{2\alpha\beta\tilde{\gamma}_c(\theta)}{E} (1 - \nu^2) \frac{\Delta K^4}{W} \frac{F'}{F} (EA_2)^{2/n-1} \times \left[\frac{(t_h + t_{\text{pl}})^{2/n-1} - (t_{\text{pl}})^{2/n-1}}{t_h} \right] + C^* \quad (\text{Eq 39})$$

where ΔK is the range of the stress intensity factor, t_{pl} is the factor added to account for retardation in the creep zone expansion rate due to cyclic plasticity, and α and β are constants. In order to estimate t_{pl} , the following may be used:

$$t_{\text{pl}} = \frac{1}{EA_2} \left[\xi \left(\frac{m' - 1}{m' + 1} \right) \left(\frac{1}{2\sigma_{\text{YS}}^c} \right)^2 \times \frac{1}{\alpha\tilde{\gamma}_c(90^\circ)} \right]^{(n-1)/2} \quad (\text{Eq 40})$$

where m' is the cyclic strain-hardening exponent, σ_{YS}^c is the cyclic yield strength determined as the stress amplitude ($\Delta\sigma/2$) corresponding to a plastic strain amplitude ($\Delta\varepsilon_p/2$) of 0.2%, and ξ is a constant.

On the other hand, for materials having high resistance to cyclic deformations, where creep rates are high and the creep zone size quickly exceeds the cyclic plastic zone size, the value of $(C_1)_{\text{avg}}$ may be calculated from a different equation (Ref 41):

$$(C_1)_{\text{avg}} = \frac{4\alpha n\beta\tilde{\gamma}_c(\theta)}{EW} (1 - \nu^2) \times \Delta K^4 \frac{F'}{F} \times (EA_2)^{2/(n-1)} (N_{t_h})^{-(n-1)/(n-3)} + C^* \quad (\text{Eq 41})$$

where N is the number of fatigue cycles. For more detail concerning these last few equations, consult Ref 39 and 41.

References cited in this section

1. W. Ren, "Time-Dependent Fracture Mechanics Characterization of Haynes HR160 Superalloy," Ph.D. dissertation, School of Material Science and Engineering, University of Tennessee, 1995
5. R.H. Norris, P.S. Grover, B.C. Hamilton, and A. Saxena, Elevated Temperature Crack Growth, *Fatigue and Fracture*, Vol 19, *ASM Handbook*, ASM International, 1996
12. A. Saxena, Fracture Mechanics Approaches for Characterizing Creep-Fatigue Crack Growth, *Int. J. JSME A*, Vol 36 (No. 1), 1993, p 15, 16
13. J.D. Landes and J.A. Begley, A Fracture Mechanics Approach to Creep Crack Growth, *Mechanics of Crack Growth*, STP 590, ASTM, 1976, p 128–148
14. K.M. Nikbin, G.A. Webster, and C.E. Turner, Relevance of Nonlinear Fracture Mechanics to Creep Cracking, *Cracks and Fracture*, STP 601, ASTM, 1976, p 47–62
15. S. Taira, R. Ohtani, and T. Kitamura, Application of J-integral to High-Temperature Crack Propagation, *J. Eng. Mater. Technol. (Trans. ASME)*, Vol 101, 1979, p 154
16. V. Kumar, M.D. German, and C.F. Shih, "An Engineering Approach to Elastic-Plastic Analysis," Technical Report EPRI NP-1931, Electric Power Research Institute, 1981

17. J. Hutchinson, Singular Behavior at the End of a Tensile Crack in a Hardening Material, *J. Mech. Phys. Solids*, Vol 16, 1968, p 13
18. J. Rice and G.F. Rosengren, Plane Strain Deformation near a Crack Tip in a Power-Law Hardening Material, *J. Mech. Phys. Solids*, Vol 16, 1968, p 1–12
19. N.L. Goldman and J.W. Hutchinson, Fully Plastic Crack Problems: The Center-Cracked Strip Under Plane Strain, *Int. J. Solids Struct.*, Vol 11, 1975, p 575–591
20. C.P. Leung, D.L. McDowell, and A. Saxena, Consideration of Primary Creep at Stationary Crack Tips: Implications for the C_t Parameter, *Int. J. Fract.*, Vol 36, 1988
21. A. Saxena, Creep Crack Growth in Creep-Ductile Materials, *Eng. Fract. Mech.*, Vol 40 (No. $\frac{1}{5}$), 1991, p 721
22. P.K. Liaw, A. Saxena, and J. Schaefer, Estimating Remaining Life of Elevated Temperature Steam Pipes, Part I: Material Properties, *Eng. Fract. Mech.*, Vol 32, 1989, p 675
23. “Standard Test Method for Measurement of Creep Crack Growth Rates in Metals,” ASTM E 1457, American Society for Testing and Materials, 1998
24. H. Riedel, Creep Deformation at Crack Tips in Elastic-Viscoelastic Solids, *J. Mech. Phys. Solids*, Vol 29, 1981, p 35
25. K. Ohji, K. Ogura, and S. Kubo, Stress-Strain Field and Modified J-Integral in the Vicinity of a Crack Tip Under Transient Creep Conditions, *Int. J. JSME*, Vol 790 (No. 13), p 18, 1979
26. J.D. Bassani and F.A. McClintock, Creep Relaxation of Stress Around a Crack Tip, *Int. J. Solids Struct.*, Vol 7, 1981, p 479
27. R. Ehlers and H. Riedel, A Finite Element Analysis of Creep Deformation in a Specimen Containing a Macroscopic Crack, *Advances in Fracture Research: Proc. of the Fifth Int. Conf. of Fracture, ICF-5*, Vol 2, Pergamon Press, 1981, p 691–698
28. J.L. Bassani, K.E. Hawk, and A. Saxena, Evaluation of the C_t Parameter for Characterizing Creep Crack Growth Rate in the Transient Regime, *Time-Dependent Fracture*, Vol 1, *Nonlinear Fracture Mechanics*, STP 995, ASTM, 1986, p 7–26
29. H. Riedel and V. Hetampel, Creep Crack Growth in Ductile, Creep Resistant Steels, *Int. J. Fract.*, Vol 34, 1987, p 179
30. D.L. McDowell and C.P. Leung, Implication of Primary Creep and Damage for Creep Crack Extension Criteria, *Structural Design for Elevated Temperature Environments—Creep, Ratchet, Fatigue and Fracture, Pressure Vessel and Piping Division*, Vol 163, July 23–27 1989 (Honolulu), American Society of Mechanical Engineers
31. A. Saxena, Creep Crack Growth Under Nonsteady-State Conditions, ASTM STP 905, *Seventeenth ASTM National Symposium on Fracture Mechanics*, American Society for Testing and Materials, 1986, p 185–201
32. B.E. Jaske and J.A. Begley, An Approach to Assessing Creep/Fatigue Crack Growth, *Ductility and Toughness Considerations in Elevated Temperature Service*, MPC-8, ASTM, 1978, p 391

33. S. Taira, R. Ohtani, and T. Komatsu, Application of J-Integral to High Temperature Crack Propagation, Part II: Fatigue Crack Propagation, *J. Eng. Mater. Technol. (Trans. ASME)*, Vol 101, 1979, p 162
34. R. Ohtani, T. Kitamura, A. Nitta, and K. Kuwabara, High-Temperature Low Cycle Fatigue Crack Propagation and Life Laws of Smooth Specimens Derived from the Crack Propagation Laws, STP 942, H. Solomon, G. Halford, L. Kaisand, and B. Leis, Ed., ASTM, 1988, p 1163
35. K. Kuwabara, A. Nitta, T. Kitamura, and T. Ogala, Effect of Small-Scale Creep on Crack Initiation and Propagation under Cyclic Loading, STP 924, R. Wei and R. Gangloff, Ed., ASTM, 1988, p 41
36. R. Ohtani, T. Kitamura, and K. Yamada, A Nonlinear Fracture Mechanics Approach to Crack Propagation in the Creep-Fatigue Interaction Range, *Fracture Mechanics of Tough and Ductile Materials and Its Application to Energy Related Structures*, H. Liu, I. Kunio, and V. Weiss, Ed., Materials Nijhoff Publishers, 1981, p 263
37. K. Ohji, *Fracture Mechanics Approach to Creep-Fatigue Crack Growth in Role of Fracture Mechanics in Modern Technology*, Fukuoka, Japan, 1986
38. K.B. Yoon, A. Saxena, and P.K. Liaw, *Int. J. Fract.*, Vol 59, 1993, p 95
39. K. B. Yoon, A. Saxena, and D. L. McDowell, Influence of Crack-Tip Cyclic Plasticity on Creep-Fatigue Crack Growth, *Fracture Mechanics: Twenty Second Symposium*, STP 1131, ASTM, 1992, p 367
40. A. Saxena and B. Gieseke, Transients in Elevated Temperature Crack Growth, *International Seminar on High Temperature Fracture Mechanics and Mechanics*, EGF-6, Elsevier Publications, 1990, p iii-19
41. N. Adefris, A. Saxena, and D.L. McDowell, Creep-Fatigue Crack Growth Behavior in 1Cr-1Mo-0.25V Steels I: Estimation of Crack Tip Parameters, *J. Fatigue Mater. Struct.*, 1993

Creep Crack Growth Testing

B.E. Gore, Northwestern University, W. Ren, Air Force Materials Laboratory, P.K. Liaw, The University of Tennessee

Creep-Fatigue Crack Growth Testing

The following description of the experimental test method for creep crack growth tests using a compact specimen geometry, under cyclic or static loading, is in agreement with the ASTM E 1457 "Standard Test Method for Measurement of Creep Crack Growth Rates in Metals" (Ref 23). The aforementioned technique entails applying a constant load to a heated, precracked specimen until significant crack extension or failure occurs. During the test, the crack length, load, and load-line deflections must be monitored and recorded, and upon test completion, the final crack length must be measured. Analysis of the test data involves an examination of the crack growth rate with respect to time, da/dt , in terms of the magnitude of an appropriate elevated-temperature crack growth parameter (Ref 5, 23). The various crack growth parameters are presented earlier in this article.

Specimen Configuration and Dimensions. The recommended specimen for creep crack growth testing is the CT specimen. Figure 3 illustrates the specimen geometry, including details of the design specifications. Although other configurations have also been used, such as the center-cracked tensile (CCT) panel and the single-edge notch (SEN) specimen, the CT specimen is considered to be more suitable for creep and creep-fatigue crack growth testing (Ref 5) and remains most convenient. In terms of suitability, the transition time for extensive creep conditions to develop is longer in CT than in CCT specimens for the same K and a/W for samples of

identical width (Ref 42). Due to the extended transition time, during creep-fatigue testing, the necessary condition that $t_c/t_1 \ll 1$, with t_c representing cyclic time, and t_1 being the aforementioned transition time, is more easily met. In terms of convenience, an advantage of the CT specimen is that a clip gage can be easily attached for the measurement of load-line deflection, which is one of the components required in the calculation of crack-tip parameters. In addition, one of the most important advantages is that the magnitude of the applied load needed to obtain a particular value of K is significantly lower for CT than for CCT specimens. Hence, machines with smaller load capacities and small fixtures can be used for testing (Ref 5).

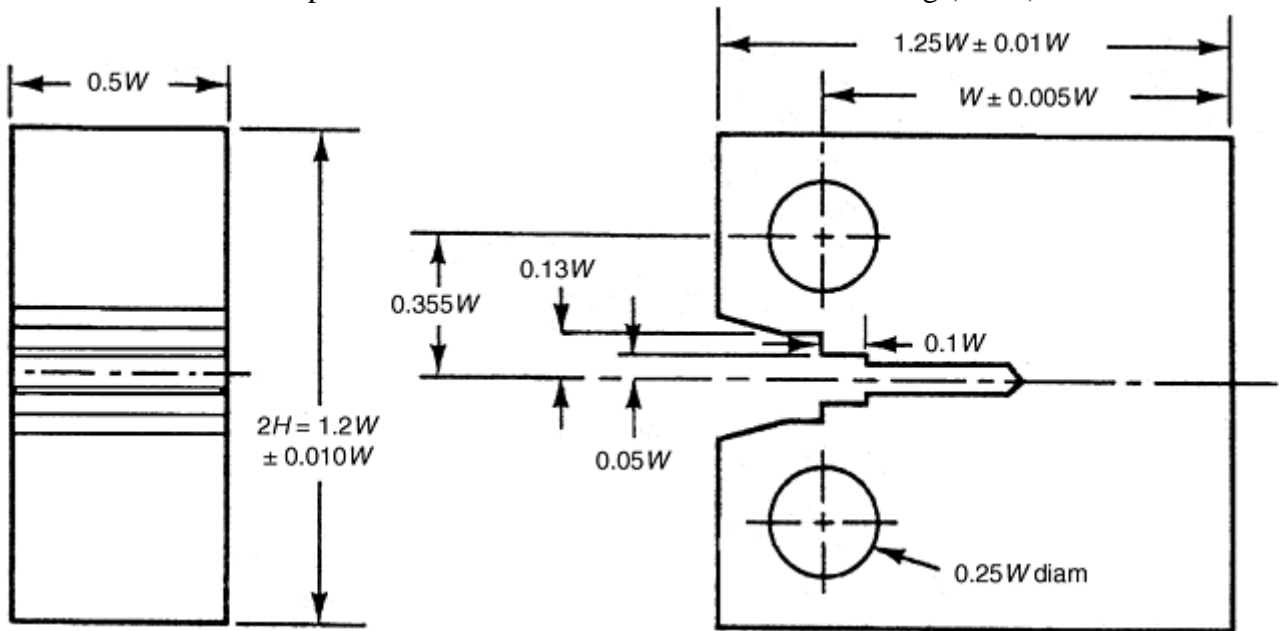


Fig. 3 Drawing of standard CT specimen. Source: Ref 22

Testing Machines. Three different types of machines can be used to run crack growth tests: dead-weight, servomechanical, and servohydraulic machines. Regardless of the choice of machine, it is necessary to be able to maintain a constant load over an extended period of time (variations are not to exceed $\pm 1.0\%$ of the nominal load value at any time). Note that to fulfill this requirement, if lever-type, dead-weight creep machines are used, care must be taken to ensure that the lever arm remains in a horizontal position. More detailed specifications of the testing machine may be found in ASTM E 4, "Practices for Load Verification of Testing Machines" (Ref 43). Additionally, it is recommended that precautions be taken to ensure that the load is applied as nearly axial as possible.

Control Parameter. For those tests run under creep-fatigue conditions where a trapezoidal waveform is employed, a choice between testing conducted under a load-controlled or displacement-controlled conditions must be made. Figure 4(a) shows a schematic representation of the displacement versus time and crack size versus time for a load-controlled case. Displacement-controlled testing schematics of the load versus time and crack size versus time are shown in Fig. 4(b) for comparison (Ref 5).

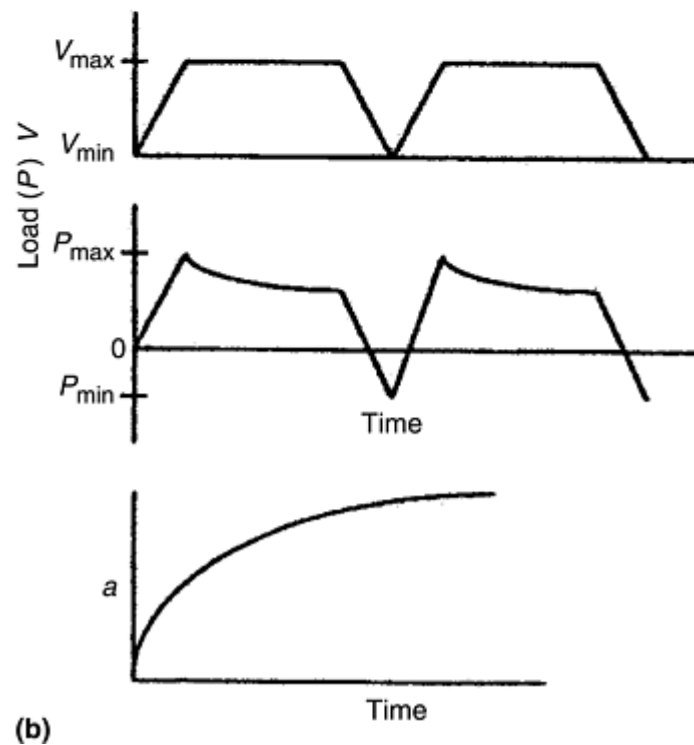
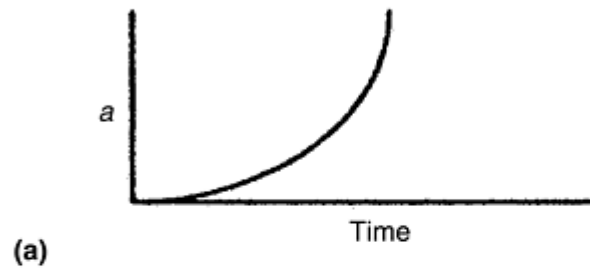
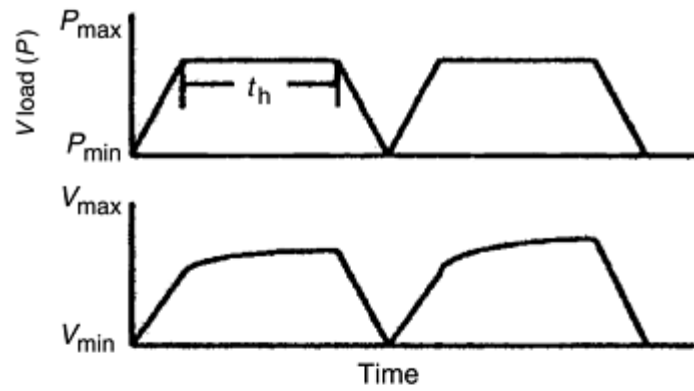


Fig. 4 Schematic comparison of (a) load-controlled and (b) displacement-controlled testing under trapezoidal loading. Source: Ref 5

Due to matters of convenience, tests are most frequently conducted under load-controlled conditions. However, there are a few advantages of displacement-controlled testing that should be considered. For instance, due to a continuous rise in the net section stress ahead of the crack in load-controlled tests during crack growth, K continually increases as the size of the remaining ligament decreases. Consequently, this means that the scale of creep in the specimen increases as the test progresses, which causes ratcheting in the specimen as the inelastic deflection accumulates with the completion of each cycle (Ref 5). Comparatively, as can be seen in Fig. 4(b), the applied load decreases with crack extension in displacement-controlled tests, so ratcheting is avoided (Ref

44). Also, data can be collected for greater crack extensions in displacement-controlled tests than in load-controlled tests. Overall, load-controlled tests are more suitable for low crack growth rates, and displacement-controlled tests are suited for higher crack growth rates (greater than 4×10^{-6} mm/cycle) and tests with extensive hold times (Ref 5).

Grips and Fixtures. For the CT specimen, a pin and clevis assembly should be used at both the top and bottom of the specimen. This assembly will allow in-plane rotation as the specimen is loaded. Materials for the grips and pull rods should be creep resistant and able to withstand the temperature environment to which they will be exposed during the test. Examples of current elevated-temperature materials being used include AISI grade 304 and 316 stainless steels, grade A 286 steel, Inconel 718, and Inconel X750. The loading pins should be machined from temperature-resistant steels, such as A 286, and should be heat treated to ensure that they acquire a high resistance to creep deformation and rupture.

Heating Devices. Samples are generally heated by means of either an electric resistance furnace or a laboratory convection oven. Before the application of load and for the duration of the test, the difference between the temperature indicated by the device and the nominal test temperature is not to exceed ± 2 °C (± 3 °F) for temperatures at or below 1000 °C (1800 °F). It is to remain within ± 3 °C (± 5 °F) for temperatures above 1000 °C (1800 °F). In the initial heating of the specimen, it is important to avoid temperature overshoots that could potentially affect test results. In order to measure the specimen temperature, a thermocouple must be attached to the specimen. The thermocouple should be placed in the uncracked ligament region of the sample 2 to 5 mm (0.08–0.2 in.) above or below the crack plane. If the width of the specimen exceeds 50 mm (2 in.), it is advisable to attach multiple thermocouples at evenly spaced intervals in the uncracked ligament region around the crack plane, as stated previously. Thermocouples must be kept in intimate contact with the specimen. In order to avoid short circuiting, ceramic insulators should cover the individual wires of the temperature circuit.

Fatigue Precracking. In order to eliminate the effects of the machined notch and to provide a sharp crack tip for crack initiation, it is necessary to precrack creep and/or creep-fatigue test specimens. An extensively detailed method for the process can be found in ASTM E 399, “Test Method for Plane-Strain Fracture Toughness of Metallic Materials” (Ref 45). Specimen precracking must be conducted in the same condition as it is going to be tested. The temperature is to be at or above room temperature and must not exceed the designed test temperature. For the process of precracking, equipment must be used that is capable of applying a symmetric load with respect to the machined notch and must be able to control the maximum stress intensity factor, K_{max} , to within $\pm 5\%$. The fatigue load used during the process must remain below the following maximum value (Ref 23):

$$P_f = \frac{0.4B_N(W - a_0)^2 \sigma_{ys}}{(2W + a_0)} \quad (\text{Eq 42})$$

where B_N is the corrected specimen thickness, W is the specimen width, a_0 is the initial crack length measured from the load line, and σ_{ys} is the yield strength. While the fatigue precrack is in the final 0.64 mm (0.025 in.) of extension, the maximum load shall not exceed P_f or a load such that the ratio of the stress intensity factor range to Young's modulus ($\Delta K/E$) is equal to or less than 0.0025 mm^{1/2} (0.0005 in.^{1/2}), whichever is less (Ref 23). In this manner, it is ensured that the final precrack loading will not exceed that of the initial creep or creep-fatigue crack growth test.

The crack length for the fatigue precrack can be measured using the same methods described in the next section, “Test Procedure,” for monitoring crack length during crack growth testing. Measurements of the fatigue precrack must be accurate to within 0.1 mm (0.004 in.). Measurements must be taken on both surfaces, and their values must not differ by more than 1.25 mm (0.05 in.). If surface cracks are allowed to exceed this limit, further extension will be required until the aforementioned criteria are met (Ref 5). The total initial crack length (the starter notch plus fatigue precrack) must be at least 0.45 times the width, but no longer than 0.55 times the width.

References cited in this section

5. R.H. Norris, P.S. Grover, B.C. Hamilton, and A. Saxena, Elevated Temperature Crack Growth, *Fatigue and Fracture*, Vol 19, *ASM Handbook*, ASM International, 1996

22. P.K. Liaw, A. Saxena, and J. Schaefer, Estimating Remaining Life of Elevated Temperature Steam Pipes, Part I: Material Properties, *Eng. Fract. Mech.*, Vol 32, 1989, p 675
23. "Standard Test Method for Measurement of Creep Crack Growth Rates in Metals," ASTM E 1457, American Society for Testing and Materials, 1998
42. A. Saxena, Limits of Linear Elastic Fracture Mechanics in the Characterization of High-Temperature Fatigue Crack Growth, *Basic Questions in Fatigue*, Vol 2, STP 924, R. Wei and R. Gangloff, Ed., ASTM, 1989, p 27–40
43. "Practices of Load Verification of Testing Machines," E 4 94, *Annual Book of Standards*, Vol 3.01, ASTM, 1994
44. A. Saxena, R.S. Williams, and T.T. Shih, *Fracture Mechanics—13*, STP 743, ASTM, 1981, p 86
45. "Test Method for Plane-Strain Fracture Toughness of Metallic Materials," E 399, *Annual Book of ASTM Standards*, Vol 3.01, ASTM, 1994, p 680–714

Creep Crack Growth Testing

B.E. Gore, Northwestern University, W. Ren, Air Force Materials Laboratory, P.K. Liaw, The University of Tennessee

Test Procedure

Number of Tests. Data collected during creep crack growth rate testing will inherently exhibit scatter. Values of da/dt at a given value of $C^*(t)$ can vary by as much as a factor of two (Ref 23, 46). This inherent scatter can be further augmented by variables, such as microstructural differences, load precision, environmental control, and data processing techniques (Ref 23). It is thus advised that replicate tests be conducted; when this is impractical, multiple specimens must be tested in order to obtain regions of overlapping da/dt versus $C^*(t)$ data. Assurance of the inferences drawn from the data is augmented by increasing the number of tests conducted.

Test Setup. Prior to testing, it is necessary to take measures to prepare for the measurements of the crack length, load-line displacement, temperature, and number of completed cycles. As discussed in subsequent sections, the electric potential drop method, in which fluctuations in potential in a constructed voltage loop are monitored, is often used to calculate the crack length during testing. In order to prepare for this method, the specimen must be fitted with current input and voltage leads to the current source and potentiometer, respectively. The fitting can be conducted either prior to or just after specimen installation according to preference. In order to avoid contact with other components in the test setup that could potentially skew results, the leads can be covered with protective ceramic insulators. In order to begin installation of the specimen, both clevis pins must be inserted, after which a small load of approximately 10% of the intended test load should be applied in order to bolster the axial stability of the load train. At this point, the extensometer must be placed along the load line of the specimen in order to monitor load-line displacements. Care must be taken to make sure that the device is in secure contact with the knife edges. Subsequently, the thermocouples must be attached to the specimen by being placed in contact with the crack plane in the uncracked ligament region. Lastly, the furnace must be brought into position, and heating of the specimen should begin. The initialization of the current for the electric potential system must be in concordance with the point of turning on the furnace. This is because resistance heating of the specimen will occur as a result of the applied current.

In order to avoid overshoots in temperature exceeding the limits set forth previously, it is recommended that the heating of the specimen be slow and steady. It may even be desirable to stabilize the temperature at an increment of 5 to 30 °C (10–50 °F) below the final testing temperature and then make adjustments as necessary. Once the appropriate test temperature is achieved and stabilized, it should be held for a given amount of time

necessary to ensure that the temperature will be able to be maintained within the aforementioned limits. This time is to be, at minimum, 1 hour per 25 mm (1 in.) of specimen thickness. After these requirements have been met, a set of measurements must be recorded while in the initial no-load state for reference. It follows that the next step is the application of the load. The load must be applied carefully in order that shock loads or inertial loads can be avoided, and the length of time for the application of the load should remain as short as possible. The load or K -level chosen depends on the required crack growth rates during the test. For effective testing, the crack growth rates must be selected to mimic those encountered during the service life of a material. Without delay, upon the completion of loading the sample, another set of measurements of electric potentials and displacements must be taken to be used as the initial loading condition (time = 0).

Data Acquisition during Testing. The electric potential voltage, load, load-line displacement, test temperature, and number of cycles must be monitored and recorded continuously throughout the test if autographic strip chart recorders or voltmeters are used. If digital data acquisition systems are employed, a full set of readings must be taken no less frequently than once every fifteen minutes. The resolution of these data acquisition systems must be at least one order of magnitude better than the measuring instrument (Ref 5).

Crack Length Measurement. When monitoring creep crack propagation, the chosen technique should be able to resolve crack extensions of at least 0.1 mm (0.004 in.). Surface crack length measurements by optical means, such as a travelling microscope, are not considered reliable as a primary method due to the fact that crack extension across the thickness of the specimen is not always uniform. However, optical observation may be used as an auxiliary measurement method. For the aforementioned reason, the selected crack length measurement technique must be capable of measuring the average crack length across the specimen thickness. The most commonly used method for the determination of crack length in creep-fatigue crack growth testing is the electric potential drop method. This method involves applying a fixed electric current and monitoring any changes in the output voltage across the output locations. Because any increase in crack length (corresponding to a decrease in the uncracked ligament) would result in an increase in the electric resistance, the final result is an increase in the output voltage (Ref 5). The electric potential drop method is considered to be the most compatible with elevated-temperature creep crack growth testing.

The input current and voltage lead locations for a typical CT specimen are shown in Fig. 5. The leads may be attached either by welding them to the material or by connecting them to the material with screws. The choice of the method essentially depends on the material and test conditions. For a soft material tested at relatively low temperatures, threaded connections are fine, but for harder materials, it is recommended that the leads be welded, especially for tests conducted at elevated temperatures (Ref 5). The leads must be long enough to allow current input devices and output voltage measuring instruments to be far enough away from the furnace so as to avoid excessive heating. In addition, leads should be about the same length to minimize lead resistance, which contributes to the thermal voltage, V_{th} , as described below. Concerning material choice for the leads, 2 mm (0.08 in.) diameter stainless steel wires have been shown to work very well due to excellent oxidation resistance at elevated temperatures. Nonetheless, any material that is resistant to oxidation and is capable of carrying a current that is stable at the test temperature should be suitable. In the past, nickel and copper wires have been effectively used as a lead material for tests conducted at lower temperatures (Ref 5).

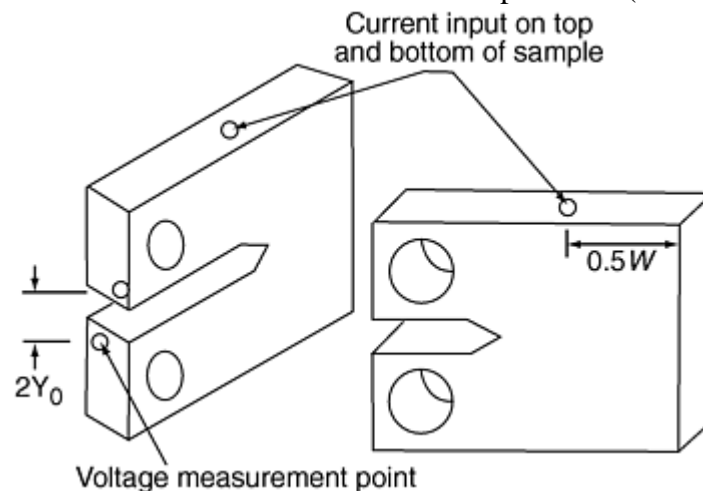


Fig. 5 Input current and voltage lead locations for which Eq 43 applies. Source: Ref 22

In order to calculate the crack size for the setup shown in Fig. 5 from the measured output voltage and initial voltage values, V and V_0 , the following closed-form equation should be used (Ref 47, 48):

$$a_i = \frac{2W}{\pi} \cos^{-1} \left(\frac{\cosh(\pi Y_0 / 2W)}{\cosh \left[\frac{V}{V_0} \cosh^{-1} \left(\frac{\cosh(\pi Y_0 / 2W)}{\cos(\pi a_0 / 2W)} \right) \right]} \right) \quad (\text{Eq 43})$$

where a_i is the instantaneous crack length, W is the specimen width, Y_0 is the half distance between the output voltage leads, V is the instantaneous output voltage, and a_0 is the reference crack size with respect to the reference voltage, V_0 . Usually a_0 is the initial crack size after precracking, and V_0 is the initial voltage. Often the voltages, V and V_0 , used for determining the crack size in the equation differ from their respective indicated readings when using a direct current technique. This is due to V_{th} , which can be caused by many factors, including differences in the junction properties of the connectors, differences in the resistance of the output leads, varying output lead lengths, and temperature fluctuations in output leads themselves (Ref 5). Measured values of V_{th} should be recorded before the load application and periodically throughout testing. To make these measurements, the current source must be turned off; then the output voltage should be recorded. Before calculations are made, the V_{th} value must be subtracted from the respective V and V_0 so that the actual crack extension length can be established.

When testing materials that have high electrical conductivity, fluctuations in V_{th} are often seen. This type of fluctuation can be of the same magnitude as the fluctuation in voltage that accompanies crack growth and could, therefore, veil this information. Because of this potential variation, it is recommended that the direct current electric potential drop method not be the only nonvisual method for crack length measurements chosen. Other more sophisticated techniques, such as the reversing current potential method, are recommended for use. The reversing direct current electrical potential drop (RDCEPD) method is simply a variation of the electrical potential drop method described by Johnson (Ref 47). This method is more sensitive to crack growth near the specimen surface. In the RDCEPD method, a direct current is used, but the polarity is reversed at a fairly low frequency (Ref 49). This step compensates for zero drift errors. Refer to Caitlin, et al. (Ref 50) for a more detailed description of this crack length monitoring method.

It is imperative to keep in mind, while performing creep crack propagation tests, the importance of maintaining a nearly straight crack front. The initial and final crack lengths must fluctuate no more than 5% across the specimen thickness. Often the maintenance of a straight crack front depends on the material and the sample thickness. It has been noted before that thicker specimens sometimes experience crack tunneling, or nonstraight crack extension. Crack tunneling (thumbnail-shaped crack fronts) is common in specimen configurations that are not side grooved (parallel-sided) (Ref 5, 7). Side-grooving the specimens can minimize the occurrence of crack tunneling. Side grooves of 20% reduction have been found to work well in several materials, although reductions of up to 25% are considered to be acceptable. The included angle of the grooves is usually less than 90° with a root radius less than or equal to 0.4 ± 0.2 mm (0.016 ± 0.008 in.). It is important to perform the precracking of the specimen before the side grooving, as it is difficult to detect the precrack when located in the grooves.

Load-Line Displacement Measurements. Load-line displacements can be described as those that occur at the loading pins due to the crack associated with the accumulation of creep strains. In order to be able to ultimately determine the crack-tip parameters, it is necessary to continually record the displacement measurements. These displacement measurements must be taken as close to the load line as possible. The measuring device must be attached on the knife edges of a CT specimen. Alternatively, for CCT specimens, the displacement should be measured on the load line at points ±35 mm (±1.40 in.) from the crack centerline (Ref 5). In order to directly measure the displacement, an elevated-temperature clip gage may be attached to the specimen (strain gages for up to approximately 150 °C, or 300 °F, or capacitance gages for higher temperatures), and then the entire assembly should be placed in the furnace. Instead, if the devices mentioned previously are not available, the displacements can be transferred outside the furnace using a rod and tube assembly. In this case, the transducer—a direct current displacement transducer (DCDT), linear variable displacement transducer (LVDT), or capacitance gage—is placed outside the furnace. It is important that the rod and tube be made of materials

that are thermally stable and be fabricated of the same material to avoid any adverse effects caused by differences in thermal expansion coefficients (Ref 23). The deflection measurement devices should have a resolution of at least 0.01 mm (0.0004 in.) (Ref 5).

Post-Test Measurements. When the test has been completed, whether due to specimen failure or to the acquisition of sufficient crack growth data, the load should be removed, and the furnace be turned off. Once the specimen has cooled down adequately, it should be removed from the machine. The initial crack length (due to precracking) and the final crack length (resulting from creep crack growth) should be measured at nine points equidistant from each other along the face of the crack. The collected data can be processed using a computer program that uses either the secant method or the seven-point polynomial method to calculate the deflection rates, dV/dt , crack growth rates, da/dt , and the crack-tip parameters. For a more detailed description of these methods refer to ASTM E 1457 (Ref 23).

References cited in this section

5. R.H. Norris, P.S. Grover, B.C. Hamilton, and A. Saxena, Elevated Temperature Crack Growth, *Fatigue and Fracture*, Vol 19, *ASM Handbook*, ASM International, 1996
7. A. Saxena, "Recent Advances in Elevated Temperature Crack Growth and Models for Life Prediction," *Advances in Fracture Research: Proc. Seventh Int. Conf. on Fracture*, March 1989 (Houston, TX), K. Salama, K. Ravi-Chander, D.M.R. Taplin, and P. Rama Rao, Ed., Pergamon Press, 1989, p 1675–1688
22. P.K. Liaw, A. Saxena, and J. Schaefer, Estimating Remaining Life of Elevated Temperature Steam Pipes, Part I: Material Properties, *Eng. Fract. Mech.*, Vol 32, 1989, p 675
23. "Standard Test Method for Measurement of Creep Crack Growth Rates in Metals," ASTM E 1457, American Society for Testing and Materials, 1998
46. A. Saxena and J. Han, "Evaluation of Crack Tip Parameters for Characterizing Crack Growth Behavior in Creeping Materials," ASTM Task Group E24-04-08/E24.08.07, American Society for Testing and Materials, 1986
47. H.H. Johnson, *Mater. Res. Stand.*, Vol 5 (No. 9), 1965, p 442–445
48. K.H. Schwalbe and D.J. Hellman, *Test Evaluation*, Vol 9 (No. 3), 1981, p 218–221
49. P.F. Browning, "Time Dependent Crack Tip Phenomena in Gas Turbine Disk Alloys," doctoral thesis, Rensselaer Polytechnic Institute, Troy, NY, 1998
50. W.R. Caitlin, D.C. Lord, T.A. Prater, and L.F. Coffin, The Reversing D-C Electrical Potential Method, *Automated Test Methods for Fracture and Fatigue Crack Growth*, STP 877, W.H. Cullen, R.W. Landgraf, L.R. Kaisand, and J.H. Underwood, Ed., ASTM, 1985, p 67–85

Creep Crack Growth Testing

B.E. Gore, Northwestern University, W. Ren, Air Force Materials Laboratory, P.K. Liaw, The University of Tennessee

Life-Prediction Methodology

In recent years, the subject of remaining-life prediction has drawn considerable attention. The interest in the issue of remaining-life prediction stems from the necessity to avoid costly forced outages, from the need to

extend the component life beyond the original design life for economic reasons, and from safety considerations (Ref 7, 50, 51, 52, 53, 54, 55, 56, 57, 58, 59, 60, 61, and 62). A closer look at the method of predicting the life of materials can be found in Ref 61. Here, high-temperature structural components in power plants are analyzed. Steam pipes, for example, are generally subject to elevated-temperature operating conditions. Because of the high-temperature exposure and the simultaneous internal-pressure loading, the pipes are prone to creep damage. Thus, material properties including creep data of in-service or ex-service steels are critical input parameters for accurate life assessment of steam-pipe systems.

Figure 1, again, shows a schematic of the general remaining-life-prediction methodology for high-temperature components (Ref 52). The life-prediction methodology can be separated into three steps. In step 1, two kinds of pertinent material testing are performed (i.e., creep crack growth and creep deformation and rupture experiments). By combining the results of these two tests and tensile tests, the rates of creep crack propagation, da/dt , can be characterized by the creep crack growth rate correlating parameter (C_t) (Ref 9, 31, 51, 52, and 63). In step 2, the value of C_t for a structural component containing a defect is calculated and used to estimate the creep crack growth rate. In step 3, the creep crack propagation rate equation— da/dt versus C_t —and the calculated value of C_t for the structural component are combined to develop residual life curves, such as a plot of initial crack size versus remaining life. The final life of the structural component can be determined based on certain failure criteria (e.g., fracture toughness).

References cited in this section

7. A. Saxena, "Recent Advances in Elevated Temperature Crack Growth and Models for Life Prediction," *Advances in Fracture Research: Proc. Seventh Int. Conf. on Fracture*, March 1989 (Houston, TX), K. Salama, K. Ravi-Chander, D.M.R. Taplin, and P. Rama Rao, Ed., Pergamon Press, 1989, p 1675–1688
9. P.K. Liaw, A. Saxena, and J. Schaefer, Predicting the Life of High-Temperature Structural Components in Power Plants, *JOM*, Feb 1992
31. A. Saxena, Creep Crack Growth Under Nonsteady-State Conditions, ASTM STP 905, *Seventeenth ASTM National Symposium on Fracture Mechanics*, American Society for Testing and Materials, 1986, p 185–201
50. W.R. Caitlin, D.C. Lord, T.A. Prater, and L.F. Coffin, The Reversing D-C Electrical Potential Method, *Automated Test Methods for Fracture and Fatigue Crack Growth*, STP 877, W.H. Cullen, R.W. Landgraf, L.R. Kaisand, and J.H. Underwood, Ed., ASTM, 1985, p 67–85
51. P.K. Liaw, A. Saxena, and J. Schaefer, *Eng. Fract. Mech.*, Vol 32, 1989, p 675, 709
52. P.K. Liaw and A. Saxena, "Remaining-Life Estimation of Boiler Pressure Parts—Crack Growth Studies," Electric Power Research Institute, EPRI CS-4688, Project 2253-7, final report, July 1986
53. P.K. Liaw, M.G. Burke, A. Saxena, and J.D. Landes, *Met. Trans. A*, Vol 22, 1991, p 455
54. P.K. Liaw, G.V. Rao, and M.G. Burke, *Mater. Sci. Eng. A*, Vol 131, 1991, p 187
55. P.K. Liaw, M.G. Burke, A. Saxena, and J.D. Landes, Fracture Toughness Behavior in Ex-Service Cr-Mo Steels, *22nd ASTM National Symposium on Fracture Mechanics*, STP 1131, ASTM, 1992, p 762–789
56. P.K. Liaw and A. Saxena, "Crack Propagation Behavior under Creep Conditions," *Int. J. Fract.*, Vol 54, 1992, p 329–343
57. W.A. Logsdon, P.K. Liaw, A. Saxena, and V.E. Hulina, *Eng. Fract. Mech.*, Vol 25, 1986, p 259
58. A. Saxena, P.K. Liaw, W.A. Logsdon, and V.E. Hulina, *Eng. Fract. Mech.*, Vol 25, 1986, p 289

59. V.P. Swaminathan, N.S. Cheruvu, A. Saxena, and P.K. Liaw, "An Initiation and Propagation Approach for the Life Assessment of an HP-IP Rotor," paper presented at the *EPRI Conference on Life Extension and Assessment of Fossil Plants*, 2–4 June 1986 (Washington, D.C.)
60. N.S. Cheruvu, *Met. Trans. A*, Vol 20, 1989, p 87
61. R. Viswanathan, *Damage Mechanisms and Life Assessment of High-Temperature Components*, ASM International, 1989
62. C.E. Jaske, *Chem. Eng. Prog.*, April 1987, p 37
63. P.K. Liaw, A. Saxena, and J. Schaefer, Creep Crack Growth Behavior of Steam Pipe Steels: Effects of Inclusion Content and Primary Creep, *Eng. Fract. Mech.*, Vol 57, 1997, p 105–130

Creep Crack Growth Testing

B.E. Gore, Northwestern University, W. Ren, Air Force Materials Laboratory, P.K. Liaw, The University of Tennessee

Acknowledgments

B.E. Gore is thankful for the support of the University of Tennessee, Knoxville, especially her fellow group members, Dr. Yuehui He, Bing Yang, Liang Jiang, J.T. Broome, Glen Porter, and Leslie Miller. P.K. Liaw is grateful for the financial support provided by the National Science Foundation (DMI-9724476 and EEC-9527527 with Dr. D. Durham and Ms. M. Poats as contract monitors, respectively).

Creep Crack Growth Testing

B.E. Gore, Northwestern University, W. Ren, Air Force Materials Laboratory, P.K. Liaw, The University of Tennessee

References

1. W. Ren, "Time-Dependent Fracture Mechanics Characterization of Haynes HR160 Superalloy," Ph.D. dissertation, School of Material Science and Engineering, University of Tennessee, 1995
2. H. Riedel and J.R. Rice, Tensile Cracks in Creep Solids, *Fracture Mechanics: Twelfth Conf.*, STP 700, ASTM, 1980, p 112–130
3. M. Okazaki, I. Hattori, F. Shiraiwa, and T. Koizumi, Effect of Strain Wave Shape on Low-Cycle Fatigue Crack Propagation of SUS 304 Stainless Steel at Elevated Temperatures, *Metal. Trans. A*, Vol 14, 1983, p 1649–1659
4. A. Saxena and P.K. Liaw, "Remaining Life Estimations of Boiler Pressure Parts—Crack Growth Studies," Final Report CS 4688 per EPRI Contract RP 2253-7, Electric Power Research Institute, 1986
5. R.H. Norris, P.S. Grover, B.C. Hamilton, and A. Saxena, Elevated Temperature Crack Growth, *Fatigue and Fracture*, Vol 19, *ASM Handbook*, ASM International, 1996

6. A. Saxena, "Life Assessment Methods and Codes," EPRI TR-103592, Electric Power Research Institute, 1996
7. A. Saxena, "Recent Advances in Elevated Temperature Crack Growth and Models for Life Prediction," *Advances in Fracture Research: Proc. Seventh Int. Conf. on Fracture*, March 1989 (Houston, TX), K. Salama, K. Ravi-Chander, D.M.R. Taplin, and P. Rama Rao, Ed., Pergamon Press, 1989, p 1675–1688
8. W.A. Logsdon, P.K. Liaw, A. Saxena, and V.E. Hulina, Residual Life Prediction and Retirement for Cause Criteria for Ships Service Turbine Generator (SSTG) Upper Casings, Part I: Mechanical Fracture Mechanics Material Properties Development, *Eng. Fract. Mech.*, Vol 25, 1986, p 259–288
9. P.K. Liaw, A. Saxena, and J. Schaefer, Predicting the Life of High-Temperature Structural Components in Power Plants, *JOM*, Feb 1992
10. J.T. Staley, Jr., "Mechanisms of Creep Crack Growth in a Cu-1 wt. % Sb Alloy," MS thesis, Georgia Institute of Technology, 1988
11. J.L. Bassani and V. Vitek, *Proc. Ninth National Congress of Applied Mechanics—Symposium on Non-Linear Fracture Mechanics*, L.B. Freund and C.F. Shih, Ed., American Society of Mechanical Engineers, 1982, p 127–133
12. A. Saxena, Fracture Mechanics Approaches for Characterizing Creep-Fatigue Crack Growth, *Int. J. JSME A*, Vol 36 (No. 1), 1993, p 15, 16
13. J.D. Landes and J.A. Begley, A Fracture Mechanics Approach to Creep Crack Growth, *Mechanics of Crack Growth*, STP 590, ASTM, 1976, p 128–148
14. K.M. Nikbin, G.A. Webster, and C.E. Turner, Relevance of Nonlinear Fracture Mechanics to Creep Cracking, *Cracks and Fracture*, STP 601, ASTM, 1976, p 47–62
15. S. Taira, R. Ohtani, and T. Kitamura, Application of J-integral to High-Temperature Crack Propagation, *J. Eng. Mater. Technol. (Trans. ASME)*, Vol 101, 1979, p 154
16. V. Kumar, M.D. German, and C.F. Shih, "An Engineering Approach to Elastic-Plastic Analysis," Technical Report EPRI NP-1931, Electric Power Research Institute, 1981
17. J. Hutchinson, Singular Behavior at the End of a Tensile Crack in a Hardening Material, *J. Mech. Phys. Solids*, Vol 16, 1968, p 13
18. J. Rice and G.F. Rosengren, Plane Strain Deformation near a Crack Tip in a Power-Law Hardening Material, *J. Mech. Phys. Solids*, Vol 16, 1968, p 1–12
19. N.L. Goldman and J.W. Hutchinson, Fully Plastic Crack Problems: The Center-Cracked Strip Under Plane Strain, *Int. J. Solids Struct.*, Vol 11, 1975, p 575–591
20. C.P. Leung, D.L. McDowell, and A. Saxena, Consideration of Primary Creep at Stationary Crack Tips: Implications for the C_1 Parameter, *Int. J. Fract.*, Vol 36, 1988
21. A. Saxena, Creep Crack Growth in Creep-Ductile Materials, *Eng. Fract. Mech.*, Vol 40 (No. $\frac{4}{5}$), 1991, p 721
22. P.K. Liaw, A. Saxena, and J. Schaefer, Estimating Remaining Life of Elevated Temperature Steam Pipes, Part I: Material Properties, *Eng. Fract. Mech.*, Vol 32, 1989, p 675

23. "Standard Test Method for Measurement of Creep Crack Growth Rates in Metals," ASTM E 1457, American Society for Testing and Materials, 1998
24. H. Riedel, Creep Deformation at Crack Tips in Elastic-Viscoelastic Solids, *J. Mech. Phys. Solids*, Vol 29, 1981, p 35
25. K. Ohji, K. Ogura, and S. Kubo, Stress-Strain Field and Modified J-Integral in the Vicinity of a Crack Tip Under Transient Creep Conditions, *Int. J. JSME*, Vol 790 (No. 13), p 18, 1979
26. J.D. Bassani and F.A. McClintock, Creep Relaxation of Stress Around a Crack Tip, *Int. J. Solids Struct.*, Vol 7, 1981, p 479
27. R. Ehlers and H. Riedel, A Finite Element Analysis of Creep Deformation in a Specimen Containing a Macroscopic Crack, *Advances in Fracture Research: Proc. of the Fifth Int. Conf. of Fracture, ICF-5*, Vol 2, Pergamon Press, 1981, p 691–698
28. J.L. Bassani, K.E. Hawk, and A. Saxena, Evaluation of the C_t Parameter for Characterizing Creep Crack Growth Rate in the Transient Regime, *Time-Dependent Fracture*, Vol 1, *Nonlinear Fracture Mechanics*, STP 995, ASTM, 1986, p 7–26
29. H. Riedel and V. Hetampel, Creep Crack Growth in Ductile, Creep Resistant Steels, *Int. J. Fract.*, Vol 34, 1987, p 179
30. D.L. McDowell and C.P. Leung, Implication of Primary Creep and Damage for Creep Crack Extension Criteria, *Structural Design for Elevated Temperature Environments—Creep, Ratchet, Fatigue and Fracture, Pressure Vessel and Piping Division*, Vol 163, July 23–27 1989 (Honolulu), American Society of Mechanical Engineers
31. A. Saxena, Creep Crack Growth Under Nonsteady-State Conditions, ASTM STP 905, *Seventeenth ASTM National Symposium on Fracture Mechanics*, American Society for Testing and Materials, 1986, p 185–201
32. B.E. Jaske and J.A. Begley, An Approach to Assessing Creep/Fatigue Crack Growth, *Ductility and Toughness Considerations in Elevated Temperature Service*, MPC-8, ASTM, 1978, p 391
33. S. Taira, R. Ohtani, and T. Komatsu, Application of J-Integral to High Temperature Crack Propagation, Part II: Fatigue Crack Propagation, *J. Eng. Mater. Technol. (Trans. ASME)*, Vol 101, 1979, p 162
34. R. Ohtani, T. Kitamura, A. Nitta, and K. Kuwabara, High-Temperature Low Cycle Fatigue Crack Propagation and Life Laws of Smooth Specimens Derived from the Crack Propagation Laws, STP 942, H. Solomon, G. Halford, L. Kaisand, and B. Leis, Ed., ASTM, 1988, p 1163
35. K. Kuwabara, A. Nitta, T. Kitamura, and T. Ogala, Effect of Small-Scale Creep on Crack Initiation and Propagation under Cyclic Loading, STP 924, R. Wei and R. Gangloff, Ed., ASTM, 1988, p 41
36. R. Ohtani, T. Kitamura, and K. Yamada, A Nonlinear Fracture Mechanics Approach to Crack Propagation in the Creep-Fatigue Interaction Range, *Fracture Mechanics of Tough and Ductile Materials and Its Application to Energy Related Structures*, H. Liu, I. Kuno, and V. Weiss, Ed., Materials Nijhoff Publishers, 1981, p 263
37. K. Ohji, *Fracture Mechanics Approach to Creep-Fatigue Crack Growth in Role of Fracture Mechanics in Modern Technology*, Fukuoka, Japan, 1986
38. K.B. Yoon, A. Saxena, and P.K. Liaw, *Int. J. Fract.*, Vol 59, 1993, p 95

39. K. B. Yoon, A. Saxena, and D. L. McDowell, Influence of Crack-Tip Cyclic Plasticity on Creep-Fatigue Crack Growth, *Fracture Mechanics: Twenty Second Symposium*, STP 1131, ASTM, 1992, p 367
40. A. Saxena and B. Gieseke, Transients in Elevated Temperature Crack Growth, *International Seminar on High Temperature Fracture Mechanics and Mechanics*, EGF-6, Elsevier Publications, 1990, p iii-19
41. N. Adefris, A. Saxena, and D.L. McDowell, Creep-Fatigue Crack Growth Behavior in 1Cr-1Mo-0.25V Steels I: Estimation of Crack Tip Parameters, *J. Fatigue Mater. Struct.*, 1993
42. A. Saxena, Limits of Linear Elastic Fracture Mechanics in the Characterization of High-Temperature Fatigue Crack Growth, *Basic Questions in Fatigue*, Vol 2, STP 924, R. Wei and R. Gangloff, Ed., ASTM, 1989, p 27-40
43. "Practices of Load Verification of Testing Machines," E 4 94, *Annual Book of Standards*, Vol 3.01, ASTM, 1994
44. A. Saxena, R.S. Williams, and T.T. Shih, *Fracture Mechanics—13*, STP 743, ASTM, 1981, p 86
45. "Test Method for Plane-Strain Fracture Toughness of Metallic Materials," E 399, *Annual Book of ASTM Standards*, Vol 3.01, ASTM, 1994, p 680-714
46. A. Saxena and J. Han, "Evaluation of Crack Tip Parameters for Characterizing Crack Growth Behavior in Creeping Materials," ASTM Task Group E24-04-08/E24.08.07, American Society for Testing and Materials, 1986
47. H.H. Johnson, *Mater. Res. Stand.*, Vol 5 (No. 9), 1965, p 442-445
48. K.H. Schwalbe and D.J. Hellman, *Test Evaluation*, Vol 9 (No. 3), 1981, p 218-221
49. P.F. Browning, "Time Dependent Crack Tip Phenomena in Gas Turbine Disk Alloys," doctoral thesis, Rensselaer Polytechnic Institute, Troy, NY, 1998
50. W.R. Caitlin, D.C. Lord, T.A. Prater, and L.F. Coffin, The Reversing D-C Electrical Potential Method, *Automated Test Methods for Fracture and Fatigue Crack Growth*, STP 877, W.H. Cullen, R.W. Landgraf, L.R. Kaisand, and J.H. Underwood, Ed., ASTM, 1985, p 67-85
51. P.K. Liaw, A. Saxena, and J. Schaefer, *Eng. Fract. Mech.*, Vol 32, 1989, p 675, 709
52. P.K. Liaw and A. Saxena, "Remaining-Life Estimation of Boiler Pressure Parts—Crack Growth Studies," Electric Power Research Institute, EPRI CS-4688, Project 2253-7, final report, July 1986
53. P.K. Liaw, M.G. Burke, A. Saxena, and J.D. Landes, *Met. Trans. A*, Vol 22, 1991, p 455
54. P.K. Liaw, G.V. Rao, and M.G. Burke, *Mater. Sci. Eng. A*, Vol 131, 1991, p 187
55. P.K. Liaw, M.G. Burke, A. Saxena, and J.D. Landes, Fracture Toughness Behavior in Ex-Service Cr-Mo Steels, *22nd ASTM National Symposium on Fracture Mechanics*, STP 1131, ASTM, 1992, p 762-789
56. P.K. Liaw and A. Saxena, "Crack Propagation Behavior under Creep Conditions," *Int. J. Fract.*, Vol 54, 1992, p 329-343
57. W.A. Logsdon, P.K. Liaw, A. Saxena, and V.E. Hulina, *Eng. Fract. Mech.*, Vol 25, 1986, p 259

58. A. Saxena, P.K. Liaw, W.A. Logsdon, and V.E. Hulina, *Eng. Fract. Mech.*, Vol 25, 1986, p 289
59. V.P. Swaminathan, N.S. Cheruvu, A. Saxena, and P.K. Liaw, "An Initiation and Propagation Approach for the Life Assessment of an HP-IP Rotor," paper presented at the *EPRI Conference on Life Extension and Assessment of Fossil Plants*, 2–4 June 1986 (Washington, D.C.)
60. N.S. Cheruvu, *Met. Trans. A*, Vol 20, 1989, p 87
61. R. Viswanathan, *Damage Mechanisms and Life Assessment of High-Temperature Components*, ASM International, 1989
62. C.E. Jaske, *Chem. Eng. Prog.*, April 1987, p 37
63. P.K. Liaw, A. Saxena, and J. Schaefer, Creep Crack Growth Behavior of Steam Pipe Steels: Effects of Inclusion Content and Primary Creep, *Eng. Fract. Mech.*, Vol 57, 1997, p 105–130

Impact Toughness Testing

Introduction

DYNAMIC FRACTURE occurs under a rapidly applied load, such as that produced by impact or by explosive detonation. In contrast to quasi-static loading, dynamic conditions involve loading rates that are greater than those encountered in conventional tensile tests or fracture mechanics tests. Dynamic fracture includes the case of a stationary crack subjected to a rapidly applied load, as well as the case of a rapidly propagating crack under a quasi-stationary load. In both cases the material at the crack tip is strained rapidly and, if rate sensitive, may offer less resistance to fracture than at quasi-static strain rates. For example, values for dynamic fracture toughness are lower than those for static toughness (K_{Ic}) in the comparison shown in Fig. 1.

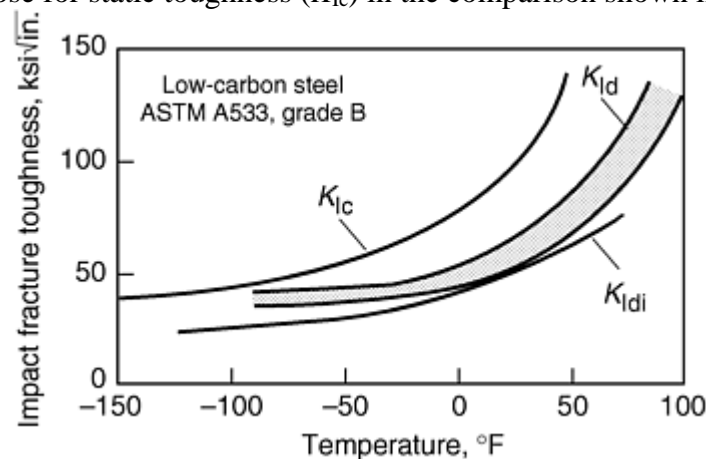


Fig. 1 Comparison of static (K_{Ic}), dynamic (K_{Id}), and dynamic-instrumented (K_{Idi}) impact fracture toughness of precracked specimens of ASTM A 533 grade B steel, as a function of test temperature. The stress-intensity rate was about $1.098 \times 10^4 \text{ MPa}\sqrt{\text{m}} \cdot \text{s}^{-1}$ ($10^4 \text{ ksi}\sqrt{\text{in.}} \cdot \text{s}^{-1}$) for the dynamic tests and about $1.098 \times 10^6 \text{ MPa}\sqrt{\text{m}} \cdot \text{s}^{-1}$ ($10^6 \text{ ksi}\sqrt{\text{in.}} \cdot \text{s}^{-1}$) for the dynamic-instrumented tests. Source: Ref 1

Because many structural components are subjected to high loading rates in service, or must survive high loading rates during accident conditions, high strain rate fracture testing is of interest and components must be designed against crack initiation under high loading rates or designed to arrest a rapidly running crack.

Furthermore, because dynamic fracture toughness is generally lower than static toughness, more conservative analysis may require consideration of dynamic toughness.

Measurement and analysis of fracture behavior under high loading rates is more complex than under quasi-static conditions. There are also many different test methods used in the evaluation of dynamic fracture resistance. Test methods based on fracture mechanics, as discussed extensively in other articles of this Section, produce quantitative values of fracture toughness parameters that are useful in design. However, many qualitative methods have also been used in the evaluation of impact energy to break a notched bar, percent of cleavage area on fracture surfaces, or the temperature for nil ductility or crack arrest. These qualitative tests include methods such as the Charpy impact test, the Izod impact test, and the drop-weight test. Other less common tests are the explosive bulge test, the Robertson test, the Esso test, and the Navy tear test (described in the 8th Edition *Metals Handbook*, Volume 10, p 38–40).

This article focuses exclusively on notch-toughness tests with emphasis on the Charpy impact test. The Charpy impact test has been used extensively to test a wide variety of materials. Because of the simplicity of the Charpy test and the existence of a large database, attempts also have been made to modify the specimen, loading arrangement, and instrumentation to extract quantitative fracture mechanics information from the Charpy test. Other miscellaneous notch-toughness test methods are also discussed in this article.

Reference cited in this section

1. Use of Precracked Charpy Specimens, *Fracture Control and Prevention*, American Society for Metals, 1974, p 255–282

Impact Toughness Testing

History of Impact Testing

Before fracture mechanics became a scientific discipline, notched-bar impact tests were performed on laboratory specimens to simulate structural failures, eliminating the need to destructively test large engineering components. The simulation of structural component failure by notched-bar impact tests is based on severe conditions of high loading rate, stress concentration, and triaxial stress state. These tests have been extensively used in the evaluation of ductile-to-brittle transition temperature of low- and medium-strength ferritic steels used in structural applications such as ships, pressure vessels, tanks, pipelines, and bridges.

The initial development of impact testing began around 1904 when Considère discovered and noted in a published document that increasing strain rate raises the temperature at which brittle fracture occurs. In 1905 another Frenchman, George Charpy, developed a pendulum-type impact testing machine based on an idea by S.B. Russell. This machine continues to be the most widely used machine for impact testing. In 1908 an Englishman by the name of Izod developed a similar machine that gained considerable popularity for a period of time but then waned in popularity because of inherent difficulties in testing at temperatures other than room temperature.

Impact testing was not widely used, and its significance not fully understood, until World War II when many all-welded ships were first built (approximately 3000 of them). Of these 3000 ships, approximately 1200 suffered hull fractures, 250 of which were considered hazardous. In fact, 19 or 20 of them broke completely in two. These failures did not necessarily occur under unusual conditions; several occurred while the ships were at anchor in calm waters. In addition to ship failures, other large, rigid structures, such as pipelines and storage tanks, failed in a similar manner. All failures had similar characteristics. They were sudden, had a brittle appearance, and occurred at stresses well below the yield strength of the material. It was noted that they originated at notches or other areas of stress concentration, such as sharp corners and weld defects. These failures were often of considerable magnitude: in one case a pipeline rupture ran for 20 miles.

The Naval Research Laboratory, along with others, launched a study of the cause of these fractures. It was noted that often, but not always, failures occurred at low temperatures. More detailed historical research

revealed that similar failures had been recorded since the 1800s but had been largely ignored. The results of this study renewed interest, and further investigation revealed that materials undergo a transition from ductile behavior to brittle behavior as the temperature is lowered. In the presence of a stress concentrator such as a notch, it takes little loading to initiate a fracture below this transition temperature, and even less to cause such a fracture to propagate. These transitions were not predictable by such tests as hardness testing, tensile testing, or, for the most part, chemical analysis, which were common tests of the times. It was then discovered that a ductile-to-brittle transition temperature could be determined by impact testing using test specimens of uniform configuration and standardized notches. Such specimens were tested at a series of decreasing temperatures, and the energy absorbed in producing the fracture was noted. The Charpy pendulum impact testing machine was used. At first, test results were difficult to reproduce. The problem was partly resolved by producing more uniformly accurate test equipment. The notch most often used was of a keyhole type created by drilling a small hole and then cutting through the test bar to the hole by sawing or abrasive cutting. It was soon found that by using specimens with sharper notches, better-defined transition temperatures that were more reproducible could be determined. A well-defined notch with a V configuration became the standard. Steels in particular could then be tested and the ductile-to-brittle transition temperature obtained.

Two problems remained. First, testing machines had to be standardized very carefully or the results were not reproducible from one machine to another. The other problem was that the transition temperature found by testing small bars was not necessarily the same as that for full-size parts.

Fortunately, the problem with standardization was resolved by the Army. They learned that impact testing was a necessity for producing successful armor plate and gun tubes. Research at the Watertown Arsenal resulted in the development of standard test specimens of various impact levels. The Army made these available to their various vendors so that the vendors could standardize their own testing machines. This program was so successful that such specimens were made available to the public, at a nominal charge, starting in the 1960s. Next, the manufacturers of testing equipment were pressured into making equipment available that would meet these exacting standards.

The problem of differing transition temperatures for full-size parts and test specimens was discovered when a series of full-size parts was tested using a giant pendulum-type impact machine and these results were compared with those determined using small standard test bars made from the same material. A partial solution to this problem was the development of the drop-weight test (DWT) and the drop-weight tear test (DWTT). These tests produced transition temperatures similar to those found when testing full-size parts. Unfortunately, such tests are adaptable only for plate specimens of limited sizes and have not become widely used.

The Charpy V-notch test continues to be the most used and accepted impact test in use in the industry. However, the restricted applicability of the Charpy V-notch impact test has been recognized for many years (Ref 2). Charpy test results are not directly applicable for designs, and the observed ductile-to-brittle transition depends on specimen size. Nonetheless, the Charpy V-notch test is useful in determining the temperature range of ductile-to-brittle transition.

Reference cited in this section

2. C.E. Turner, *Impact Testing of Metals*, STP 466, ASTM, 1970, p 93

Impact Toughness Testing

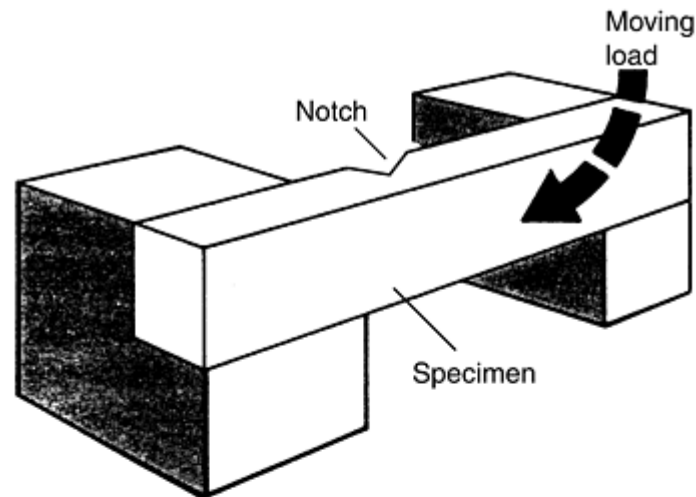
Types of Notch-Toughness Tests

In general, notch toughness is measured in terms of the absorbed impact energy needed to cause fracturing of the specimen. The change in potential energy of the impacting head (from before impact to after fracture) is determined with a calibrated dial that measures the total energy absorbed in breaking the specimen. Other quantitative parameters, such as fracture appearance (percent fibrous fracture) and degree of ductility/deformation (lateral expansion or notch root contraction), are also often measured in addition to the

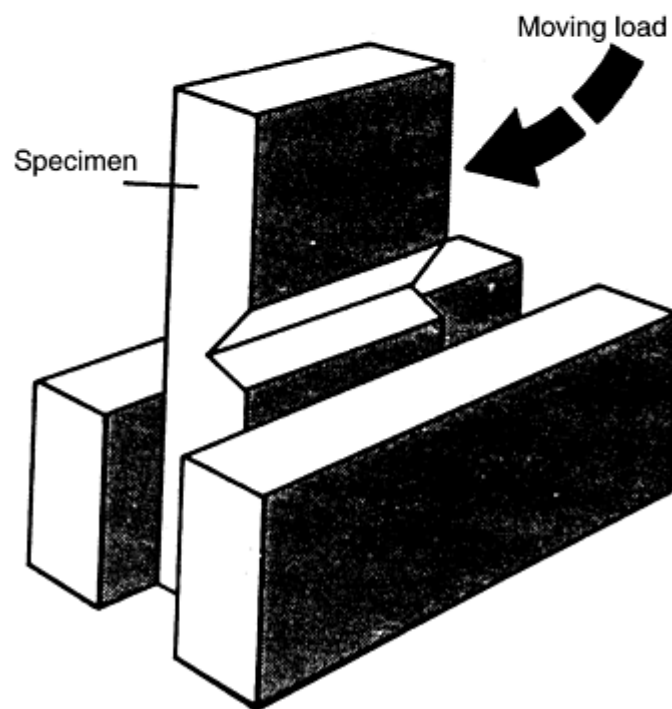
fracture energy. Impact tests may also be instrumented to obtain load data as a function of time during the fracture event. In its simplest form, instrumented impact testing involves the placement of a strain gage on the tip (the striker).

Many types of impact tests have been used to evaluate the notch toughness of metals, plastics, and ceramics. In general, the categories of impact tests can be classified in terms of loading method (pendulum stroke or drop-weight loading) and the type of notched specimen (e.g., Charpy V-notch, Charpy U-notch, or Izod). The following descriptions briefly describe the key types of impact tests that are used commonly in the evaluation of steels or structural alloys.

The Charpy and Izod impact tests are both pendulum-type, single-blow impact tests. The principal difference, aside from specimen and notch dimensions, is in the configuration of the test setup (Fig. 2). The Charpy test involves three-point loading, where the test piece is supported at both ends as a simple beam. In contrast, the Izod specimen is set up as a cantilever beam with the falling pendulum striking the specimen above the notch (Fig. 2b).



(a)



(b)

Fig. 2 Specimen types and test configurations for pendulum impact toughness tests. (a) Charpy method. (b) Izod method

The Charpy V-notch test continues to be the most utilized and accepted impact test in use in the industry. It is written into many specifications. While this test may not reveal exact ductile-to-brittle transition temperatures for large full-size parts, it is easily adaptable as an acceptability standard on whether or not parts are apt to behave in a brittle manner in the temperature range in which they are likely to be used.

The drop-weight test is conducted by subjecting a series (generally four to eight) of specimens to a single impact load at a sequence of selected temperatures to determine the maximum temperature at which a specimen breaks. The impact load is provided by a guided, free-falling weight with an energy of 340 to 1630 J (250 to 1200 ft · lbf) depending on the yield strength of the steel to be tested. The specimens are prevented by a stop from deflecting more than a few tenths of an inch.

This is a “go, no-go” test in that the specimen will either break or fail to break. It is surprisingly reproducible. For example, Pellini made 82 tests of specimens from one plate of semikilled low-carbon steel. At -1 °C (30 °F) and 4 °C (40 °F), all specimens remained unbroken. At -7 °C (20 °F), only one of 14 specimens broke; however, at -12 °C (10 °F), 13 of the 14 specimens broke. At temperatures below -12 °C (10 °F), all specimens broke.

The drop-weight tear test (DWTT) uses a test specimen that resembles a large Charpy test specimen. The test specimen is 76 mm (3 in.) wide by 305 mm (12 in.) long, supported on a 254 mm (10 in.) span. The thickness of the specimen is the full thickness of the material being examined. The specimens are broken by either a falling weight or a pendulum machine. The notch in the specimen is pressed to a depth of 5 mm (0.20 in.) with a sharp tool-steel chisel having an angle of 45°. The resulting notch root radius is approximately 0.025 mm (0.001 in.). One result of the test is the determination of the fracture appearance transition curve. The “average” percent shear area of the broken specimens is determined for the fracture area neglecting a region “one thickness” in length from the root of the notch and “one thickness” from the opposite side of the specimen. These regions are ignored because it is believed that the pressing of the notch introduces a region of plastically deformed material which is not representative of the base material. Similarly the opposite side of the specimen is plastically deformed by the hammer tup during impact. The fracture appearance plotted versus temperature defines an abrupt transition in fracture appearance. This transition has been shown to correlate with the transition in fracture propagation behavior in cylindrical pressure vessels and piping.

Impact Toughness Testing

Charpy Impact Testing

As previously noted, the specimen in the Charpy test is supported on both ends and is broken by a single blow from a pendulum that strikes the middle of the specimen on the unnotched side. The specimen breaks at the notch, the two halves fly away, and the pendulum passes between the two parts of the anvil. The height of fall minus the height of rise gives the amount of energy absorption involved in deforming and breaking the specimen. To this is added frictional and other losses amounting to 1.5 or 3J (1 or 2 ft · lbf). The instrument is calibrated to record directly the energy absorbed by the test specimen.

Methods for Charpy testing of steels are specified in several standards including:

Designation	Title
ASTM E 23	Standard Test Methods for Notched Bar Impact Testing of Metallic Materials
BS 131-2	The Charpy V-Notch Impact Test on Metals
BS 131-3	The Charpy U-Notch Impact Test on Metals
BS 131-6	Method for Precision Determinations of Charpy V-Notch Impact Energies for Metals
ISO 148	Steel—Charpy Impact Test (V-Notch)
ISO 83	Steel—Charpy Impact Test (U-Notch)
DIN-EN 10045	Charpy Impact Test of Metallic Materials

These standards provide requirements of test specimens, anvil supports and striker dimensions and tolerances, the pendulum action of the test machine, the actual testing procedure and machine verification, and the determination of fracture appearance and lateral expansion.

The general configuration of the Charpy test, as shown in Fig. 3 for a V-notch specimen, is common to the requirements of most standards for the Charpy test. Differences between ASTM E 23 and other standards include differences in machining tolerances, dimensions of the striker tip (Fig. 4), and the ASTM E 23 requirements for testing of reference specimens. The most pronounced difference between standards is the different geometry for the tip of the striker, or tup. The tup in the ASTM specification (Fig. 4a) is slightly flatter than in many other specifications (Fig. 4b). From a comparison of results from Charpy tests with the two different tup geometries, differences appeared more pronounced for several steels at impact energies above 100 J (74 ft · lbf) (Ref 3). From this evaluation, a recommendation was also made to use the sharper and smoother tup (Fig. 4b) if the national standards are unified further.

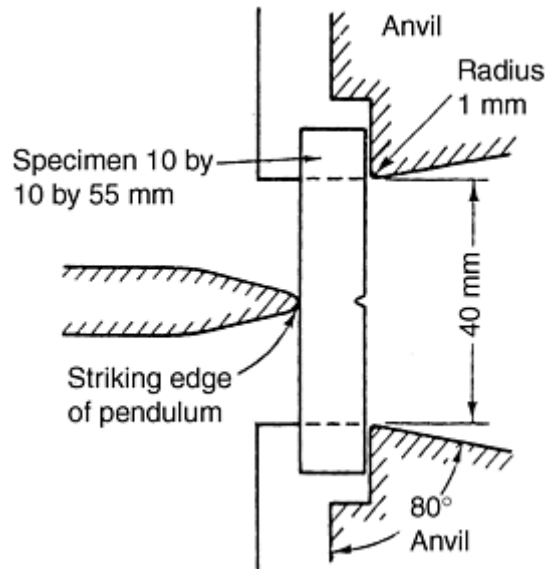


Fig. 3 General configuration of anvils and specimen in Charpy test

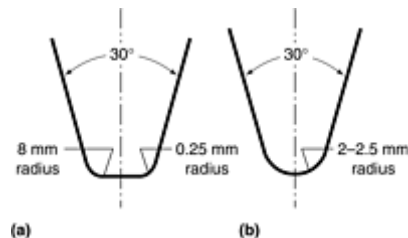
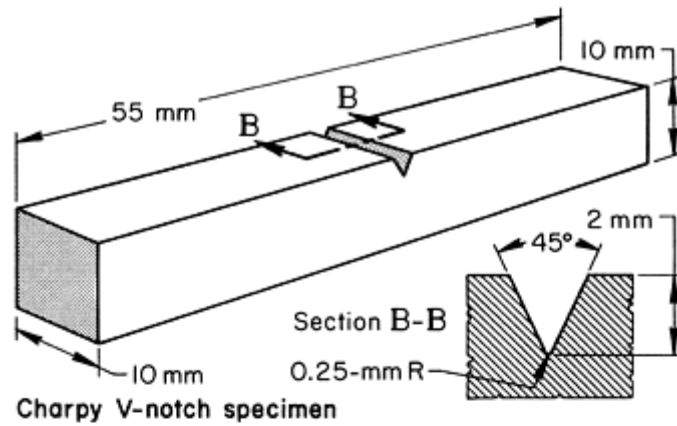
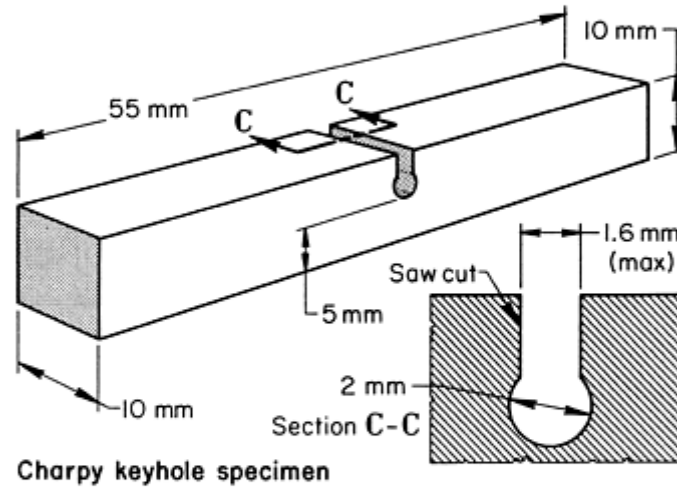


Fig. 4 Comparison of striker profiles for Charpy testing. (a) ASTM E 23. (b) Other national and international codes: AS1544, Part 2; BS 131, Part 2; DIN 51222; DS10 230; GOST 9454; ISO R148; JIS B7722; NF A03-161; NS 1998; UNI 4713-79. Source: Ref 3

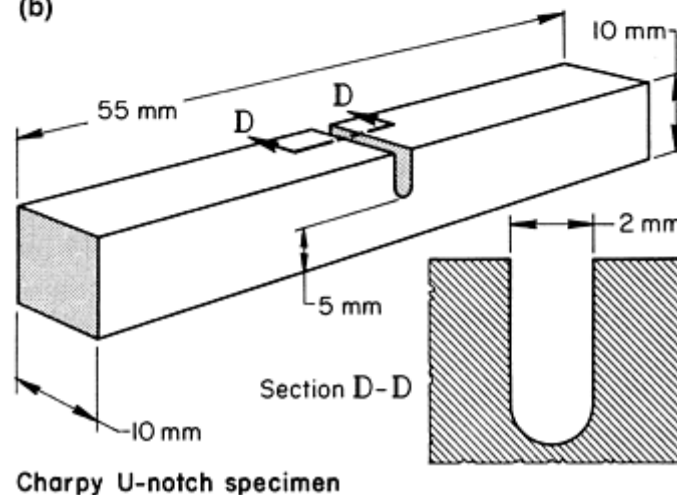
There are also three basic types of standard Charpy specimens (Fig. 5): the Charpy V-notch, the Charpy U-Notch, and the Charpy keyhole specimen. These dimensions are based on specifications in ASTM E 23, ISO 148, and ISO 83. The primary specimen and test procedure involves the Charpy V-notch test. Other Charpy-type specimens are not used as extensively because their degree of constraint and triaxiality is considerably less than the V-notch specimen.



(a)



(b)



(c)

Fig. 5 Dimensional details of Charpy test specimens most commonly used for evaluation of notch toughness. (a) V-notch specimen (ASTM E 23 and ISO 148). (b) Keyhole specimen (ASTM E 23). (c) U-notch specimen (ASTM E 23 and ISO 83)

The Charpy V-notch impact test has limitations due to its blunt notch, small size, and total energy measurement (i.e., no separation of initiation and propagation components of energy). However, this test is used widely because it is inexpensive and simple to perform. Thus, the Charpy V-notch test commonly is used as a screening test in procurement and quality assurance for assessing different heats of the same type of steel. Also, correlation with actual fracture toughness data is often devised for a class of steels so that fracture mechanics analyses can be applied directly. Historically, extensive correlation with service performance has indicated its usefulness.

The keyhole and U-notches were early recognized (1945) as giving inadequate transition temperatures because of notch bluntness. Even the V-notch does not necessarily produce a transition temperature that duplicates that of a full-size part. Under current testing procedures, the Charpy V-notch test is reproducible and produces close approximations of transition temperatures found in full-size parts. It is widely used in specifications to ensure that materials are not likely to initiate or propagate fractures at specific temperature levels when subjected to impact loads.

Equipment

Charpy testing requires good calibration methods. Machine belting should be examined regularly for looseness, and broken specimens should be examined for unusual side markings. Anvils should also be examined for wear. Testing Machines. Charpy impact testing machines are available in a variety of types. Some are single-purpose machines for testing Charpy specimens only. Others are adaptable to testing Izod and tension impact specimens also. They are offered in a range of loading capacities. The most common of these capacities are 325 and 160 J (240 and 120 ft · lbf). Some machines have variable load capabilities, but most are of a single-fixed-load type. When purchasing or using a machine, be sure that the available loading is such that specimens to be tested will break with a single blow, within 80° of the machine capacity (as shown by the scale on the machine).

While loading capacity depends on the anticipated strength of specimens to be tested, the maximum value of such specimens is the principal consideration. Very tough specimens may stop the hammer abruptly without breaking. A number of such load applications have been known to cause breakage of the pendulum arm. On the other hand, lower-capacity machines may be more accurate and more likely to meet standardization requirements. For most ordinary steel testing applications, the machine with a capacity of 160 J (120 ft · lbf) makes a good compromise choice. Testing of a large number of very tough specimens may require a machine with a capacity of 325 to 400 J (240–300 ft · lbf).

Charpy impact machines are of a pendulum type. They must be very rigid in construction to withstand the repeated hammering effect of breaking specimens without affecting the operation of the pendulum mechanism. The machine must be rigidly mounted. Special concrete foundations are sometimes used, but at least the machine must be bolted down to an existing concrete foundation, which should be a minimum of 150 mm (6 in.) thick. The pendulum should swing freely with a minimum of friction. Any restriction in movement of the pendulum will increase the energy required to fracture the specimen. This produces a test value that is higher than normal. There will always be small effects of this type, and they are usually compensated for, along with windage friction effects, by scale-reading adjustments built into the equipment.

While the pendulum must be loose enough to swing freely with little friction, it must not be loose enough to produce inaccuracies, such as nonuniform striking of the specimen. The components must be sturdy enough to resist deformation at impact. This is particularly true of the anvil and pendulum. It is important that the instrument be level. Some machines have a built-in bubble-type level. Others have machined surfaces where a level can be used. In operation, the pendulum is raised to the proper height and held by a cocking mechanism that can be instantly released.

ASTM E 23 specifies that tests should be made at velocities between 3 and 6 m/s (10 and 20 ft/s) and that this is defined as “the maximum tangential velocity of the striking member at the center of strike.” When hanging freely, the striking tip of the pendulum should be within 2.5 mm (0.10 in.) of touching the area of the specimen where first contact will be made. The anvil that retains the test specimen must be made such that the specimen can be squarely seated. The notch must be centered so that the pendulum tip hits directly behind it.

Most impact testing machines have scales that read directly in foot-pounds (scales also may read in degrees). As noted, the scale can be adjusted to compensate for windage, pendulum friction, and other variations. The scale should read zero when the pendulum is released without a specimen being present. Pendulum and anvil design, configuration, and dimensions are important. It is also important that the broken specimens be able to fly freely without being trapped in the anvil by the pendulum. Proper anvil design, such as that shown in Fig. 6, can minimize jamming.

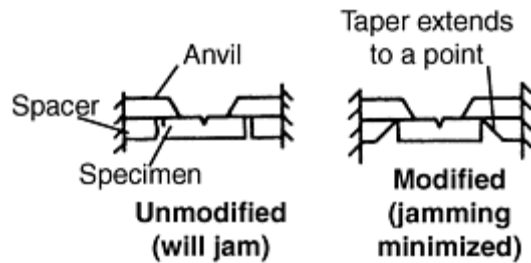


Fig. 6 Typical anvil arrangement with modification that reduces the possibility of jamming

Specimens. As previously noted, there are three commonly used standard Charpy impact test specimens, which are similar except for the notch (Fig. 5). The V-notch bar is the most frequently used specimen, although some specific industries still use the other types of test bars. The steel casting industry, for instance, uses the keyhole-notch specimen more frequently. There are also many varieties of subsized specimens that should be used only when insufficient material is available for a full-size specimen, or when the shape of the material will not allow removal of a standard specimen.

It is important that specimens be machined carefully and that all dimensional tolerances be followed. Care must be exercised to ensure that specimens are square. It is easy to grind opposite sides parallel, but this does not ensure squareness. The machining of the notch is the most critical factor. The designated shape and size of the notch must be strictly followed, and the notch must have a smooth (not polished) finish. Special notch-broaching machines are available for V-notching. A milling machine with a fly cutter can also be used.

In preparing keyhole-notch specimens, the hole should be drilled at a low speed to avoid heat generation and work hardening. Use of a jig with a drill bushing ensures accuracy. After the hole has been drilled, slotting can be done by almost any method that meets specifications, but care should be exerted to prevent the slotting tool from striking the back of the hole. In all cases it is desirable to examine the notch at some magnification. A stereoscopic microscope or optical comparator is suitable for this examination. In fact, a V-notch template for use with the optical comparator can be used to ensure proper dimensions.

Specimens must generally be provided with identification markings. This is best done on the ends of the specimen. In preparing specimens where structural orientation is a factor (e.g., rolling direction of wrought materials), such orientation should be taken into consideration and noted, because orientation can cause wide variations in test results. If not otherwise noted, the specimen should be oriented in the rolling direction of the plate (forming direction of any formed part) and the notch should be perpendicular to that surface (orientation A in Fig. 7). This produces maximum impact values. All notching must be done after any heat treatment that might be performed.

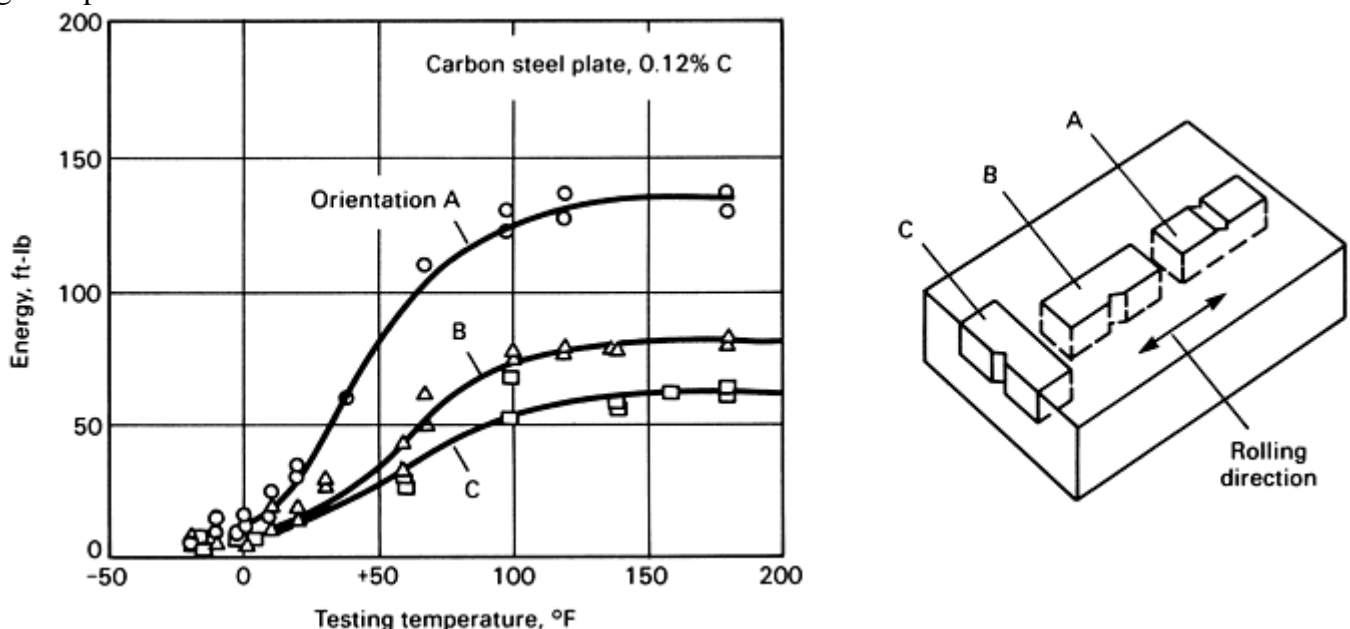


Fig. 7 Effect of specimen orientation on impact test results

While correlation exists between full-size specimens and subsize specimens, such correlation is not direct. Many specifications (ASTM and ASME, for example) specify differing acceptable values for various specimen sizes (Table 1).

Table 1 Conversion table for subsize Charpy impact-test specimens

Size of specimens ^(a) , mm	Minimum average impact strength for three specimens		Minimum impact strength for one specimen or for set of three specimens	
	J	ft · lbf	J	ft · lbf
10 × 10 (full size)	20.3	15.0	13.6	10.0
10 × 7.5	16.9	12.5	11.5	8.5
10 × 5	13.6	10.0	9.5	7.0
10 × 2.5	6.8	5.0	4.7	3.5

(a) Insofar as possible, full-size Charpy keyhole specimens should be used. However, where absolutely necessary, it is permissible to use specimens with width (in direction of the length of the notch; see ASME Section VIII, U-84, Unfired Pressure Vessels) reduced in accordance with the above tabulation.

Calibration. ASTM E 23 goes into considerable detail to ensure proper calibration of testing machines. Other relevant standards for qualification or calibration of the test machines are:

ASTM E 1236	Standard Practice for Qualifying Charpy Impact Machines as Reference Machines
BS 131-7	Verification of the Test Machine Used for Precision Determination of Charpy V-Notch Impact
BS-EN 10045-2	Charpy Impact Test on Metallic Materials Part 2: Method for the Verification of Impact Testing Machines
ISO 148-2	Metallic Materials—Charpy Pendulum Impact Test Part 2: Verification of Test Machines

These publications should be consulted for a basic understanding of machine calibration. Calibration and test variables are also reviewed in Ref 4 and 5. These publications help identify causes of improper results.

Standard test bars for calibration can be purchased from: Director, Army Materials and Mechanics Research Center, Attention AMXMR-MQ, Watertown, MA 02172 (formerly known as the Watertown Arsenal). Standard specimens are tested as per instructions, and the results, along with a filled-out questionnaire and the broken specimens, are returned. A report is then sent stating if the machine meets calibration standards and, if not, what should be done to ensure qualification.

Test Method

Once the equipment has been properly set up and calibrated and the specimens have been correctly prepared, testing can be done. Prior to each testing session, the pendulum should be allowed at least one free fall with no test specimen present, to confirm that zero energy is indicated. Specimen identification and measurements are then recorded along with test temperature. The pendulum is cocked, and the specimen is carefully positioned in the anvil using special tongs (Fig. 8) that ensure centering of the notch. The quick-release mechanism is actuated, and the pendulum falls and strikes the specimen, generally causing it to break. The amount of energy absorbed is recorded (normally in foot-pounds), and this data is noted adjacent to the specimen identification on the data sheet. The broken specimens are retained for additional evaluation of the fracture appearance and for measurement of lateral expansion where required. The broken halves are often placed side by side, taped together, and labeled for identification.

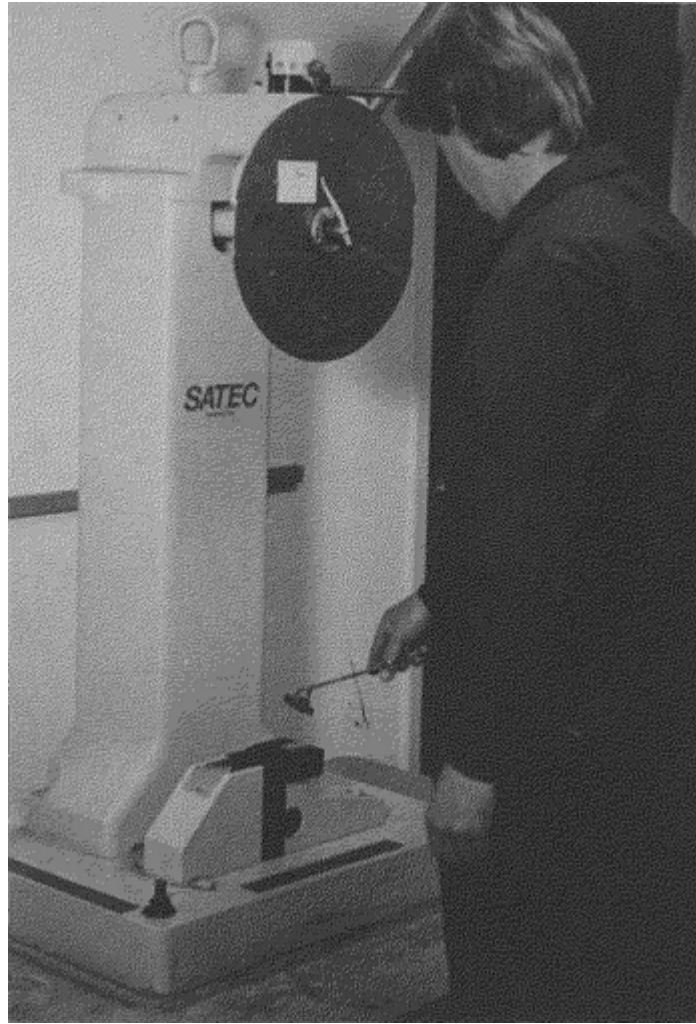


Fig. 8 Use of tongs to place a specimen in a Charpy impact testing machine for testing

The release mechanism must be consistent and smooth. Test specimens must leave the impact machine freely, without jamming or rebounding into the pendulum; requirements on clearances and containment shrouds are specific to individual machine types. The test specimen must be accurately positioned on the anvil support within 5 s of removal from the heating (or cooling) medium; requirements for heating time depend on the heating medium. Identification marks on test specimens must not interfere with the test; also, any heat treatment of specimens should be performed prior to final machining.

A daily check procedure of the apparatus must be conducted to ensure proper performance. Verification of the testing system is required using Army Materials and Mechanics Research Center (AMMRC) standardized specimens; verification should be completed at least once a year or after any parts are replaced or any repairs or adjustments are made to the machine. An operational testing sequence is recommended, as well as specifics on dial energy reading, lateral expansion measurement (technique and measuring fixture), and fracture appearance estimation.

Test Temperature. Specimen temperature can drastically affect the results of impact testing. If not otherwise stated, testing should be done at temperatures from 21 to 32 °C (70–90 °F). Much Charpy impact testing is done at temperatures lower than those commonly designated as room temperature. Of these low-temperature tests, the majority are made between room temperature and -46 °C (-50 °F), because it is within this range that most ductile-to-brittle transition temperatures occur. A certain amount of testing is also done down to -196 °C (-320 °F) for those materials that may be used in cryogenic service. Some additional testing (mainly research) is done at the liquid helium and liquid hydrogen temperatures (-269 and -251 °C, or -452 and -420 °F). Such testing requires special techniques and will not be discussed here. For testing at temperatures down to or slightly below -59 °C (-75 °F), ethyl alcohol and dry ice are most commonly used. This combination solidifies at around -68 °C (-90 °F). A suitable insulated container should be used to cool the test specimens (a container insulated with a layer of styrofoam works fine). A screen-type grid raised at least 25 mm (1 in.) above the bottom of the container allows cooling liquid to circulate beneath the specimens. A calibrated temperature-measuring device,

such as a low-temperature glass or metal thermometer or a thermocouple device, should be placed so as to read the temperature near the center of a group of specimens being cooled. The solution should be agitated sufficiently to ensure uniformity of bath temperature. The cooling liquid should cover the specimen by at least 25 mm (1 in.). The specimen-handling tongs should be placed in the same cooling bath as the specimens. When the specimens have been placed in the alcohol bath along with the tongs, chips of solid CO₂ (dry ice) can be added and the solution agitated. Experience will dictate the amount of dry ice required to reach a certain temperature. Once the temperature is reached, it seems to hold steady with only an occasional addition of a small chip of dry ice. The specimens in a liquid bath should be held within +0 and -1.5 °C (+0 and -3 °F) of test temperature for at least 5 min prior to testing. The specimens should then be removed one at a time with the cooled tongs and tested within 5 s of removal from the bath. Watch the temperature between tests because the tongs can raise the bath temperature if left out of the bath too long. The commercial cooling baths that are available range from insulated stainless steel containers to containers with self-contained refrigeration units. Also available are thermocouple devices that can be placed in the cooling bath and will give a digital temperature readout. Dry ice cannot be stored for any length of time, but there is a device that produces “instant” dry ice from a CO₂ compressed gas bottle. Testing between -59 and -196 °C (-75 and -320 °F) requires a liquid medium that will not solidify at these temperatures. Various liquids are available. One that has been successfully used is isohexane (adequate ventilation should be provided and care exercised to avoid inhalation of the volatile organic fumes). Liquid nitrogen replaces the dry ice as a coolant material, and the procedure is then similar to that for dry ice and alcohol. It is wise to keep handy a large, easy-to-handle piece of metal to serve as a temperature moderator in case the temperature becomes lower than desired. It can be plunged into the bath and, acting as a heat sink, can cause the temperature to rise quickly.

High-Temperature Testing. Occasionally, high-temperature impact testing is performed. This can be done using an agitated, high-flashpoint oil (heat treating quenching oils may work) or other liquid medium that is stable at the desired test temperature. The bath and specimens are then held at temperature in a furnace or oven for at least 10 min prior to testing.

Test Results

Results of impact testing are determined in three ways. In the first method, already discussed, they can be read directly from the testing machine (in joules or foot-pounds). This is the most commonly specified test result. It is desirable to test three specimens at each test temperature; the average value of the three is the test result used. If a minimum test value is specified for material acceptance, not more than one test result of the three should fall below that value. If the value of one of the three specimens is about 6 J (5 ft · lbf) lower than the average, or lower than the average value by greater than $\frac{2}{3}$ of the specified acceptance value, the material should be either rejected or retested. In retesting, three additional specimens must be tested, and all must equal or exceed the specified acceptance value. Since it is often required or important to determine the ductile-to-brittle transition temperature, impact test results are plotted against test temperature. Somewhere in that transition zone between the high-energy and low-energy values is an energy value that can be defined as the transition temperature. When the transition is very pronounced, this value is easily determined. However, because the more common case is a less sharply defined transition, an energy value may be specified below which the material is considered to be brittle (below the ductile-to-brittle transition temperature). Such a value may vary with material type and requirements, but the value of 20 J (15 ft · lbf) is often used as a specified value.

Fracture Appearance Method. Other methods of specifying ductile-to-brittle transition temperature are sometimes presented along with the energy values obtained. The first of these auxiliary tests is the *fracture-appearance method*. The fractured impact bars are examined and the fractures compared with a series of standard fractures or overlays of such fractures. By this method the percentage of shear fracture is determined. The amount of shear fracture can also be determined in another way. This is done by carefully measuring the dimensions of the brittle cleavage exhibited on the specimen fracture surface (Fig. 9), and then referring to Table 2. These methods are described in detail in ASTM A 370. The percentage of shear can be plotted against test temperature and the transition temperature can be ascertained using the shear percentage value specified.

Table 2 Tables of percent shear for measurements made in both inches and millimeters for impact-test specimens

Because these tables are set up for finite measurements or dimensions *A* and *B* (see Fig. 9), 100% shear is to be reported when either *A* or *B* is zero.

Dimension B, in.	Dimension A, in.																
	0.05	0.10	0.12	0.14	0.16	0.18	0.20	0.22	0.24	0.26	0.28	0.30	0.32	0.34	0.36	0.38	0.40
0.05	98	96	95	94	94	93	92	91	90	90	89	88	87	86	85	85	84
0.10	96	92	90	89	87	85	84	82	81	79	77	76	74	73	71	69	68
0.12	95	90	88	86	85	83	81	79	77	75	73	71	69	67	65	63	61
0.14	94	89	86	84	82	80	77	75	73	71	68	66	64	62	59	57	55
0.16	94	87	85	82	79	77	74	72	69	67	64	61	59	56	53	51	48
0.18	93	85	83	80	77	74	72	68	65	62	59	56	54	51	48	45	42
0.20	92	84	81	77	74	72	68	65	61	58	55	52	48	45	42	39	36
0.22	91	82	79	75	72	68	65	61	57	54	50	47	43	40	36	33	29
0.24	90	81	77	73	69	65	61	57	54	50	46	42	38	34	30	27	23
0.26	90	79	75	71	67	62	58	54	50	46	41	37	33	29	25	20	16
0.28	89	77	73	68	64	59	55	50	46	41	37	32	28	23	18	14	10
0.30	88	76	71	66	61	56	52	47	42	37	32	27	23	18	13	9	3
0.31	88	75	70	65	60	55	50	45	40	35	30	25	20	18	10	5	0

Dimension B, mm	Dimension A, mm																		
	1.0	1.5	2.0	2.5	3.0	3.5	4.0	4.5	5.0	5.5	6.0	6.5	7.0	7.5	8.0	8.5	9.0	9.5	10
1.0	99	98	98	97	96	96	95	94	94	93	92	92	91	91	90	89	89	88	88
1.5	98	97	96	95	94	93	92	92	91	90	89	88	87	86	85	84	83	82	81
2.0	98	96	95	94	92	91	90	89	88	86	85	84	82	81	80	79	77	76	75
2.5	97	95	94	92	91	89	88	86	84	83	81	80	78	77	75	73	72	70	69
3.0	96	94	92	91	89	87	85	83	81	79	77	76	74	72	70	68	66	64	62
3.5	96	93	91	89	87	85	82	80	78	76	74	72	69	67	65	63	61	58	56
4.0	95	92	90	88	85	82	80	77	75	72	70	67	65	62	60	57	55	52	50
4.5	94	92	89	86	83	80	77	75	72	69	66	63	61	58	55	52	49	46	44
5.0	94	91	88	85	81	78	75	72	69	66	62	59	56	53	50	47	44	41	37
5.5	93	90	86	83	79	76	72	69	66	62	59	55	52	48	45	42	38	35	31
6.0	92	89	85	81	77	74	70	66	62	59	55	51	47	44	40	36	33	29	25
6.5	92	88	84	80	76	72	67	63	59	55	51	47	43	39	35	31	27	23	19
7.0	91	87	82	78	74	69	65	61	56	52	47	43	39	34	30	26	21	17	12
7.5	91	86	81	77	72	67	62	58	53	48	44	39	34	30	25	20	16	11	6
8.0	90	85	80	75	70	65	60	55	50	45	40	35	30	25	20	15	10	5	0

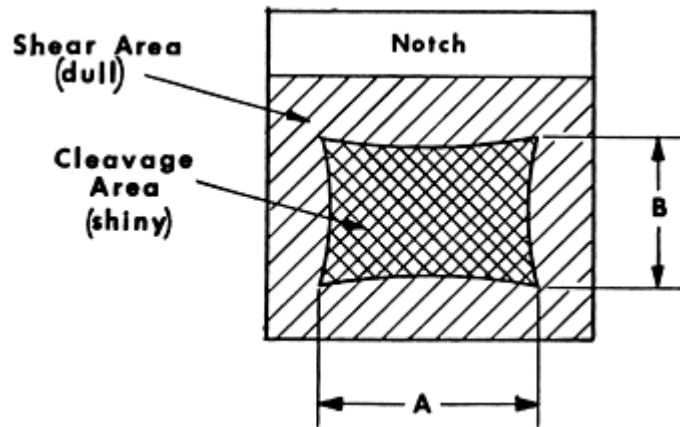


Fig. 9 Sketch of a fractured impact test bar. The method used in calculating percent shear involves measuring average dimensions A and B to the nearest 0.5 mm (0.02 in.) and then consulting a chart (Table 2) to determine the percent shear fracture. (Courtesy of ASTM)

Unlike Charpy energy, fracture appearance is indicative of how a specimen failed. It is therefore useful when attempting to correlate results of Charpy testing with other toughness test methods that use different specimen geometries and loading rates. However, the fracture-appearance method can also be subjective. In one round-robin test survey of 20 specimens (Ref 6), results showed that agreement was best when operators are experienced, samples are close to the fracture-appearance transition, and when simple, two-dimensional figures are used for assessment.

Lateral-Expansion Method. The other auxiliary method of determining transition temperature is the *lateral-expansion method*. This procedure is based on the fact that protruding shear lips are produced (perpendicular to the notch) on both sides of each broken specimen. The greater the ductility, the larger the protrusions. This lateral expansion can be expressed as a measure of acceptable ductility at a given test temperature. The broken halves from each end of each specimen are measured. The higher values from each side are added together, and this total is the lateral-expansion value. A minimum value of lateral expansion must be specified as a transition value. These test results are then plotted against test temperature and a curve interpolated. The impact energy (in joules or foot-pounds) is also reported. These methods are described in detail in ASTM A 370 and E 23.

Applications

Test criteria for Charpy V-notch impact testing usually involve:

- A minimum impact energy value
- Shear appearance of fractured test bars expressed in percent
- Lateral expansion

For steels, the minimum acceptable values most commonly specified for these three evaluation methods are, respectively: 20 J (15 ft · lbf), 50% shear, and 1.3 mm (50 mil). As a general rule of thumb, Charpy V-notch impact strengths of 14 J (10 ft · lbf) and lower are likely to initiate fractures. An impact strength of 27 J (20 ft · lbf) is likely to propagate brittle fracture once initiated, and values well above 27 J (20 ft · lbf) are necessary to arrest fracturing once it has been initiated.

Charpy impact testing does not produce numbers that can be used for design purposes, but is widely used in specifications such as ASTM A 593, “Specification for Charpy V-Notch Testing Requirements for Steel Plates for Pressure Vessel.” Other applications are briefly described below.

Nuclear Pressure Vessel Design Code. For nuclear pressure vessels, the American Society of Mechanical Engineers (ASME) Boiler and Pressure Vessel Code (Ref 7) and the Code of Federal Regulations (Ref 8) currently use fracture mechanics principles that dictate toughness requirements for pressure vessel steels and weldments. The specified toughness requirements are obtained using Charpy V-notch test specimens coupled with the nil-ductility transition temperature (NDTT) per ASTM E 208. The actual approach involves a reference temperature, designated RT_{NDT} , and the reference fracture toughness curve, K_{IR} . The reference fracture toughness curve defined in Appendix G, Section III, of the ASME Code uses an experimentally

determined relationship between toughness and temperature that is adjusted along the temperature axis according to an index reference temperature.

The reference toughness curve, K_{IR} , is assumed to describe the minimum (lower bound) fracture toughness for all ferritic materials approved for nuclear pressure boundary applications having a minimum specified yield strength of 345 MPa (50 ksi) or less. The value of RT_{NDT} is obtained by measuring the drop-weight nil-ductility transition temperature and performing standard Charpy V-notch tests. The nil-ductility transition temperature is determined initially, and then a set of three Charpy V-notch specimens is tested at a temperature that is 33 °C (60 °F) higher than the nil-ductility transition temperature to measure the temperature, T_{CV} , which ensures an increase in toughness with temperature. Charpy energies of 68 J (50 ft · lbf) and lateral expansion of 0.89 mm (35 mil) are used to ensure this condition.

The nil-ductility transition temperature becomes the RT_{NDT} temperature if the Charpy results equal or exceed the above limits. If the Charpy values at T_{CV} or the nil-ductility transition temperature plus 33 °C (60 °F) are lower than required, additional Charpy tests should be performed at higher test temperatures, usually in increments of 5.6 °C (10 °F), until the requirements are satisfied and T_{CV} is measured. The RT_{NDT} temperature then becomes the temperature (T_{CV}) at which the criteria are met minus 33 °C (60 °F). Thus, the reference temperature is always either greater than or equal to the nil-ductility transition temperature.

Steel Bridge Toughness Criteria. The American Association of State Highway and Transportation Officials (AASHTO) has adopted Charpy impact toughness requirements for primary tension members in bridge steels based on section thickness, yield strength, and expected service temperature. They are based on the fracture toughness corresponding to the maximum loading rate expected in service (Ref 9).

Correlations with Fracture Toughness. Empirical attempts have been made to correlate the Charpy impact energy with K_{Ic} to allow a quantitative assessment of critical flaw size and permissible stress levels. Most of these correlations are dimensionally incompatible, ignore differences between the two measures of toughness (in particular, loading rate and notch acuity), and are valid only for limited types of materials and ranges of data. Additionally, these correlations can be widely scattered. However, some correlations can provide a useful guide to estimating fracture toughness; in fact, the preceding design criteria for nuclear pressure vessel and bridge steels are partially based on such correlative procedures.

Some of the more common correlations are listed in Table 3 (Ref 9, 10, 11, 12, 13, 14, 15, and 16) with appropriate units. Note that some of the correlations attempt to eliminate the effects of loading rate; the dynamic fracture toughness, K_{Id} , is correlated with Charpy energy. Other attempts have been made to improve and explain some of the correlations (see, for example, Ref 17). A study has also been conducted using a portion of the Charpy energy to separate initiation and propagation components in the Charpy test (Ref 18). The results from this study for an upper-shelf J_{Ic} correlation for pressure vessel steels were not significantly better than the Rolfe-Novak correlation listed in Table 3. A statistically based correlation for lower-bound toughness has also been developed for pressure vessel steels (Ref 19, 20). Thus, simple and empirical correlations can be used as general guidelines for estimating K_{Ic} or K_{Id} within the limits of the specific correlation.

Table 3 Typical Charpy/ K_{Ic} correlation for steels

Correlation	Transition temperature regime
Barsom (Ref 9)	
$K_{Id}^2/E = 5$ (CVN)	$K_{Ic} K_{Id} = \text{psi} \sqrt{\text{in.}}$ $E = \text{psi}$ $\text{CVN} = \text{ft} \cdot \text{lbf}$
Barsom-Rolfe (Ref 10) $K_{Ic}^2/E = 2(\text{CVN})^{3/2}$	
Sailors-Corten (Ref 11)	
$K_{Ic}^2/E = 8$ (CVN)	$K_{Id} = \text{ksi} \sqrt{\text{in.}}$ $\text{CVN} = \text{ft} \cdot \text{lbf}$
$K_{Id}^2 = 15.873(\text{CVN})^{3/8}$	
Begley-Logsdon—three points (Ref 12)	
$(K_{Ic})_1 = 0.45 \sigma_y$ at 0% shear fracture temperature	$K_{Ic} = \text{ksi} \sqrt{\text{in.}}$ $\sigma_y = \text{ksi}$
$(K_{Ic})_2$ From Rolfe-Novak Correlation at 100% shear fracture temperature	
$(K_{Ic})_3 = \frac{1}{2}[(K_{Ic})_1 + (K_{Ic})_2]$ at 50% shear fracture temperature	

Marandet-Sanz—three steps (Ref 13)	
$T_{100} = 9 + 1.37 T_{28J}$	$T_{100} = \text{°C, for which } K_{Ic} = 100 \text{ MPa}\sqrt{m}$ $T_{28} = \text{°C, for which CVN} = 28J$ $K_{Ic} = \text{MPa}\sqrt{m}$ $\text{CVN} = J$
$K_{Ic} = 19 \text{ (CVN)}^{1/2}$ Shift K_{Ic} curve through T_{100} point	
Wullaert-Server (Ref 14)	
$K_{Ic,d} = 2.1 (\sigma_y \text{ CVN})^{1/2}$	$K_{Ic,d} = \text{ksi}\sqrt{\text{in.}}$ $\text{CVN} = \text{ft} \cdot \text{lbf}$ $\sigma_y = \text{ksi corresponding to approximate loading rate}$
Upper-shelf region	
Rolfe-Novak— $\sigma_y > 100 \text{ ksi}$ (Ref 15)	
$(K_{Ic}/\sigma_y)^2 = 5 \text{ (CVN}/\sigma_y - 0.05)$	$K_{Ic} = \text{ksi}\sqrt{\text{in.}}$ $\text{CVN} = \text{ft} \cdot \text{lbf}$ $\sigma_y = \text{ksi}$
Ault-Wald-Bertolo—ultrahigh-strength steels (Ref 16)	
$(K_{Ic}/\sigma_y)^2 = 1.37 \text{ (CVN}/\sigma_y) - 0.045$	$K_{Ic} = \text{ksi}\sqrt{\text{in.}}$ $\text{CVN} = \text{ft} \cdot \text{lbf}$ $\sigma_y = \text{ksi}$

1.0 ksi = 6.8948 MPa; $1.0 \text{ ksi}\sqrt{\text{in.}} = 1.099 \text{ MPa}\sqrt{m}$; $1.0 \text{ ft} \cdot \text{lbf} = 1.356 \text{ J}$; CVN is the designation for Charpy impact energy; σ_y is the yield stress; and E is the Young's modulus.

As previously described, a lower-bound K_{IR} toughness curve is shifted relative to a reference temperature, RT_{NDT} , and used to define the ductile-to-brittle transition. The RT_{NDT} is a critical value and is defined very conservatively in terms of Charpy and dynamic tear specimen results. Continued application of these requirements is now a principal limitation to continued operation of several commercial nuclear power plants (Ref 21). Recent work by ASTM Committee E-8 has proposed a method to obtain a new reference temperature and a method to define, using a probabilistic approach, a median ductile-to-brittle transition curve from a set of six properly tested small samples that would, in many cases, be precracked Charpy specimens. Statistical confidence bounds would then be available for this median transition “master curve,” which would be specific to the particular nuclear plant of interest and could be used to assure that the pressure vessel had adequate toughness for continued operation.

A generalized prediction method to predict K_{Ic} transition curves has also been developed with data from various steels including 2.25Cr-1Mo, 1.25Cr-0.50Mo, 1Cr and 0.50Mo chemical pressure vessel steels, and ASTM A 508 C1.1, A 508 C1.2, A 508 C1.3 and A 533 Gr.B C1.1 nuclear pressure vessel steels (Ref 22). This method consists of a master curve of K_{Ic} and a temperature shift, ΔT , between fracture toughness and Charpy V-notch impact transition curves versus yield strength relationship for T_0 , where T_0 is the temperature showing 50% of the upper-shelf K_{Ic} value. The K_{Ic} transition curves predicted using both methods showed a good agreement with the lower bound of measured K_{Ic} values obtained from elastic-plastic, J_c , tests.

References cited in this section

- O.L. Towers, Effects of Striker Geometry on Charpy Results, *Met. Constr.*, Nov 1983, p 682–685
- J.M. Holt, Ed., *Charpy Impact Test: Factors and Variables*, STP 1072, ASTM, 1990
- T.A. Siewert and A.K. Schmieder, Ed., *Pendulum Impact Machines: Procedures and Specimens for Verification*, STP 1248, ASTM, 1995
- B.F. Dixon, Reliability of Fracture Appearance Measurement in the Charpy Test, *Weld. J.*, Vol 73 (No. 8), Aug 1994, p 39–46

7. “Rules for Construction of Nuclear Power Plant Components,” ASME Boiler and Pressure Vessel Code, Section III, Division 1³₄, Appendices, Nonmandatory Appendix G, American Society for Mechanical Engineers, 1983
8. Energy (Title 10), Domestic Licensing of Production and Utilization Facilities (Part 50), *Code of Federal Regulations*, U.S. Government Printing Office, 1981
9. J.M. Barsom, The Development of AASHTO Fracture Toughness Requirements for Bridge Steels, *Eng. Fract. Mech.*, Vol 7 (No. 3), Sept 1975, p 605–618
10. J.M. Barsom and S.T. Rolfe, Correlations Between K_{Ic} and Charpy V-Notch Test Results in the Transition Temperature Range, *Impact Testing of Materials*, STP 466, ASTM, 1979, p 281–302
11. R.H. Sailors and H.T. Corten, Relationship Between Material Fracture Toughness Using Fracture Mechanics and Transition Temperature Tests, *Fracture Toughness, Proceedings of the 1971 National Symposium on Fracture Mechanics—Part II*, STP 514, ASTM, 1972, p 164–191
12. J.A. Begley and W.A. Logsdon, “Correlation of Fracture Toughness and Charpy Properties for Rotor Steels,” WRL Scientific Paper 71-1E7-MSLRF-P1, Westinghouse Research Laboratory, Pittsburgh, PA, July 1971
13. B. Marandet and G. Sanz, Evaluation of the Toughness of Thick Medium-Strength Steels by Using Linear Elastic Fracture Mechanics and Correlations Between K_{Ic} and Charpy V-Notch, *Flaw Growth and Fracture*, STP 631, ASTM, 1977, p 72–95
14. R.A. Wullaert, Fracture Toughness Predictions from Charpy V-Notch Data, *What Does the Charpy Test Really Tell Us?: Proceedings of the American Institute of Mining, Metallurgical and Petroleum Engineers*, American Society for Metals, 1978
15. S.T. Rolfe and S.R. Novak, Slow-Bend K_{Ic} Testing of Medium-Strength High-Toughness Steels, *Review of Developments in Plane-Strain Fracture Toughness Testing*, STP 463, ASTM, 1970, p 124–159
16. “Rapid Inexpensive Tests for Determining Fracture Toughness,” National Materials Advisory Board, National Academy of Sciences, Washington, D.C., 1976
17. *What Does the Charpy Test Really Tell Us?: Proceedings of the American Institute of Mining, Metallurgical and Petroleum Engineers*, American Society for Metals, 1978
18. D.M. Norris, J.E. Reaugh, and W.L. Server, A Fracture-Toughness Correlation Based on Charpy Initiation Energy, *Fracture Mechanics: Thirteenth Conference*, STP 743, ASTM, 1981, p 207–217
19. W.L. Server et al., “Analysis of Radiation Embrittlement Reference Toughness Curves,” EPRI NP-1661, Electric Power Research Institute, Palo Alto, CA, Jan 1981
20. Metal Properties Council MPC-24, Reference Fracture Toughness Procedures Applied to Pressure Vessel Materials, *Proceedings of the Winter Annual Meeting of the American Society for Mechanical Engineers*, American Society of Mechanical Engineers, New York, 1984
21. J.A. Joyce, Predicting the Ductile-to-Brittle Transition in Nuclear Pressure Vessel Steels from Charpy Surveillance Specimens, *Recent Advances in Fracture*, Minerals, Metals and Materials Society/AIME, 1997, p 65–75

22. T. Iwadate, Y. Tanaka, and H. Takemata, Prediction of Fracture Toughness K_{Ic} Transition Curves of Pressure Vessel Steels from Charpy V-Notch Impact Test Results, *J. Pressure Vessel Technol. (Trans. ASME)*, Vol 116 (No. 4), p 353–358

Instrumented Charpy Impact Test

The use of additional instrumentation (typically an instrumented tup) allows a standard Charpy impact machine to monitor the analog load-time response of Charpy V-notch specimen deformation and fracturing. The primary advantage of instrumenting the Charpy test is the additional information obtained while maintaining low cost, small specimens, and simple operation. The most commonly used approach is application of strain gages to the striker to sense the load-time behavior of the test specimen. In some cases, gages are placed on the specimen as well, such as for the example shown in Fig. 10 (Ref 23).

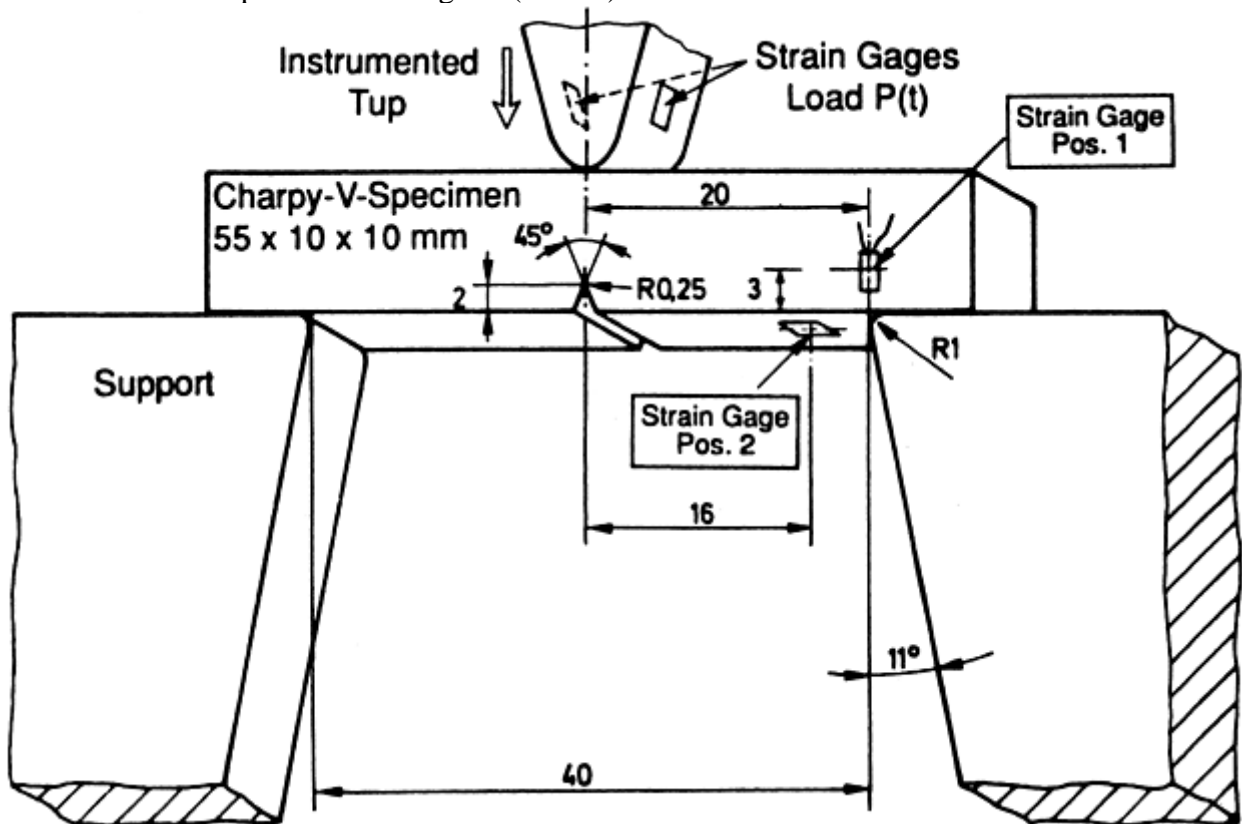


Fig. 10 Charpy specimen with additional instrumentation at the supports

General Description

Instrumentation of the tup provides valuable data in terms of the load-time, $P-t$, history during impact. Extensive efforts have been made to help determine the dynamic fracture toughness, K_{Id} , over a range of behavior in linear-elastic, elastic-plastic, and fully plastic regimes. An overview of these efforts is given in Ref 24.

Figure 11 schematically illustrates the change in Charpy behavior as a function of temperature for a medium-strength steel. As shown, instrumentation clearly allows the various stages in the fracture process to be identified. The energy value, W_M , is associated with the area under the load-time ($P-t$) curve up to maximum load, P_M . This impulse value is converted to energy by using Newton's second law, which accounts for the pendulum velocity decrease during the deformation-fracture process. This velocity decrease is proportional to the instantaneous load on the specimen at any particular time, t_i ; the actual energy absorbed, ΔE_i , simplifies to (Ref 25):

$$\Delta E = E_a \left[1 - \left(\frac{E_a}{4E_o} \right) \right] \tag{Eq 1}$$

where E_0 is the total available kinetic energy of the pendulum ($\frac{1}{2}m \cdot V_0^2$) and:

$$E_a = V_0 \int_0^{t_i} P \cdot dt \quad (\text{Eq 2})$$

where V_0 is the initial impact velocity, and m is the effective mass of the pendulum. The ability to separate the total absorbed energy into components greatly augments the information gained by instrumentation. Load-time diagrams can be constructed to illustrate the various fracture process stages indicative of the fracture mode transition from brittle to ductile behavior (Ref 26).

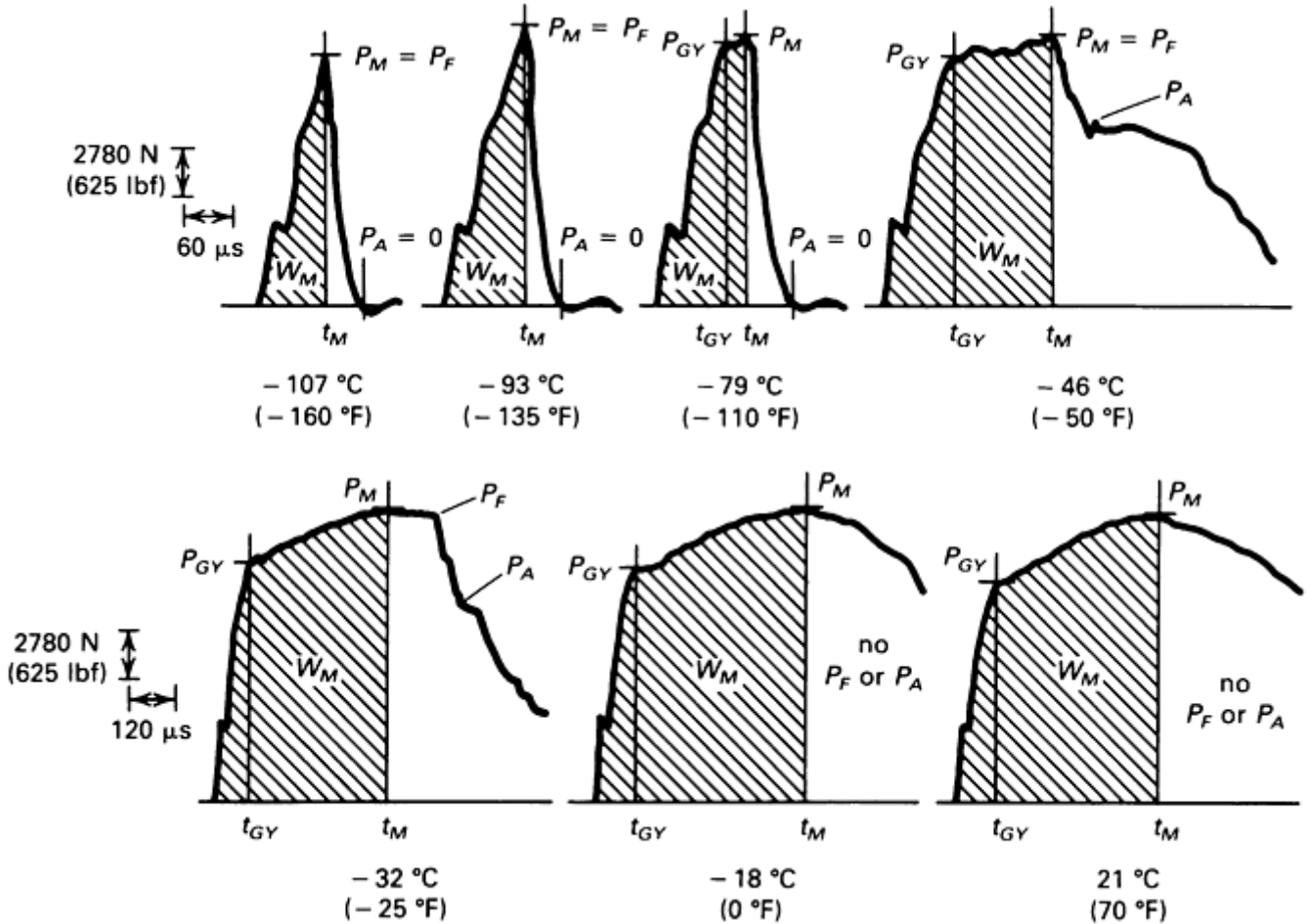


Fig. 11 Load-time response for a medium-strength steel. P_M , maximum load; P_{GY} , general yield load; P_F , fast fracture load (generally cleavage); P_A , arrest load after fast fracture propagation; t_M , time to maximum load; t_{GY} , time to general yield; W_M , energy absorbed up to maximum load

One of the primary reasons for the development of the instrumented Charpy test was to apply existing notch bend theories (slow bend) to the dynamic three-point bend Charpy impact test. Obtaining load information during the standard Charpy V-notch impact test establishes a relationship between metallurgical fracture parameters and the transition temperature approach for assessing fracture behavior (Ref 27). Initial studies concentrated on the full range of mechanical behavior from fully elastic in the lower Charpy shelf region to elastic-plastic in the transition region to fully plastic in the upper shelf region (see Fig. 11).

Most studies have been performed on structural steels, with primary emphasis on the effect of composition, strain rate, and radiation on the notch bend properties. Interest in instrumented impact testing has expanded to include testing of different types of specimens (e.g., precracked, large bend), variations in test techniques (e.g., low blow, full-size components), and testing of many different materials (e.g., plastics, composites, aerospace materials, ceramics). The many variations in test methods is a motivation for standardized test methods, although standardization for instrumented Charpy testing has been slow (see the section "Standards and Requirements" in this article).

Instrumentation

Instrumentation for a typical Charpy impact testing system includes an instrumented striker, a dynamic transducer amplifier, a signal-recording and display system, and a velocity-measuring device. The instrumented striker is the dynamic load cell, which is securely attached to the falling weight assembly. The striker has cemented strain gages to sense the compression loading of the tup while it is in contact with the test specimen. The dynamic transducer amplifier provides direct-current power to the strain gages and typically amplifies the strain gage output after passing through a selectable upper-frequency cutoff.

The impact signal is recorded and stored either on a storage oscilloscope or through the use of a transient signal recorder. Digital data from a transient recorder can be reconverted back to analog form and plotted on an x - y recorder, or the digital data can be transferred to a computer for direct analysis.

Triggering is best accomplished through an internal trigger that has the ability to capture the signal preceding the trigger; external triggering from the velocity-sensing device is often used instead of an appropriate internal trigger. The velocity-measuring system should be a noncontacting, optical system that clocks a flag on the impacting mass immediately before impact so that initial velocity measurements can be made. Velocities must be determined for all impact drop heights used.

The impact machine and the instrumentation package must be calibrated to ensure reliable data. Calibration of the Charpy pendulum impact machine is performed in accordance with ASTM E 23, as discussed previously in this article in terms of periodic proof testing of AMMRC calibration specimens to ensure reliable dial energy values.

Instrumentation calibration consists of a time base and load-cell calibration with a system frequency response measurement. The time base calibration consists of passing a known time mark pulse through the system and calibrating accordingly. The load-cell calibration is typically accomplished by testing notched specimens of 6061-T651 aluminum that are only slightly loading-rate sensitive over the range used (Ref 28). The load cell is calibrated when the measured dynamic limit load is only slightly higher than the predetermined quasi-static limit load (measured using the same loading arrangement and anvil dimensions) and when the dial energy (or velocity-determined energy measurement) matches the integrated total energy. The relationship used for obtaining total absorbed energy, ΔE_o , from the area under the load-time record follows the approach in Eq 1 and 2.

The calculated ΔE_o value will match the dial energy reading when the system is calibrated (in addition to the limit load check). Because the aluminum limit load is fairly low (around 7.1 kN, or 1600 lbf), a check on load-cell linearity at higher loads is also needed. To accomplish this, the integrated energy/dial energy requirement for a quenched and tempered 4340 specimen (52 HRC) that has a higher fracture load (near 27 kN, or 6000 lbf) is checked.

Low-energy AMMRC calibration specimens can be used for this procedure. If the energies match for the 4340 test at the same amplifier gain as for the aluminum calibration, the load-cell calibration is usually linear throughout the usable load range. Static linearity checks can also be made if the static loading system exactly duplicates the dynamic loading conditions. Daily test checks using the aluminum calibration specimens are suggested to verify load-cell calibration.

The system frequency response is determined experimentally by superimposing a constant-amplitude sine wave signal on the output of the strain gage bridge circuit (Ref 29). The peak-to-peak amplitude of the signal should be equivalent to approximately half the full-scale capacity of the load transducer at a frequency low enough to ensure no signal attenuation. The frequency of the sine wave is then increased until the amplitude is attenuated 10% (0.915 dB), and the response time, t_R , is calculated as:

$$t_R = \frac{0.35}{f_{0.915}} \quad (\text{Eq 3})$$

where $f_{0.915}$ is the frequency at 0.915 dB (10%) attenuation.

Standards and Requirements

Instrumented impact tests that generate P - t plots from instrumented tups require careful attention to test procedures and analytical methods in order to determine dynamic fracture toughness values with the accuracy and reliability required for engineering purposes. Extensive efforts have been made to standardize instrumented impact tests, but many inherent difficulties in analysis and interpretation have impeded the formal development of standard methods. Nonetheless, instrumented impact testing is an accepted method in the evaluation of

irradiation embrittlement of nuclear pressure vessel steels (Ref 30). Several instrumented impact tests have also been developed for plastics (Ref 31) with the ISO standard 179-2 on instrumented Charpy testing of plastics (Ref 32). The following discussions focus on requirements for steels, while more information on impact testing of plastics and ceramics are addressed in the article “Mechanical Testing of Polymers and Ceramics” in this Volume. For nonmetallic materials, such as plastics and ceramics, the application of available models involving energy considerations may be necessary for arriving at the true toughness values (Ref 24).

Standard Methods. Extensive efforts in the development of instrumented Charpy tests began in the 1960s and 1970s with the advent of fracture mechanics and precracked Charpy V-notch specimens, when a series of seminars and conferences in the 1970s (Ref 33, 34, 35, and 36) examined the role of instrumented impact testing in the evaluation of dynamic fracture toughness (Ref 24). The International Institute of Welding first attempted to standardize the instrumented Charpy test, but concluded that the test was not sufficiently documented, and the effort was discontinued (Ref 37). A few years later, two significant events prompted serious consideration of standardization. The development of the K_{IR} curve by the Pressure Vessel Research Committee and its inclusion in the ASME Code, Section III, created the need for dynamic initiation toughness, K_{Id} , data. Simultaneously, two other related groups began formulating procedures and conducting interlaboratory round robins. The Pressure Vessel Research Committee/Metals Property Council Task Group on Fracture Toughness Properties for Nuclear Components developed procedures for measuring K_{Id} values from precracked Charpy specimens (Ref 38).

The Electric Power Research Institute (EPRI) funded work to develop procedures known as the “EPRI Procedures” (Ref 28, 39). This procedure is summarized in the following section, “General Test Requirements.” Since that time, important theoretical and technical developments have occurred, as outlined in Ref 24. Efforts have also been made in the development of standards. In 1992, the European Structural Integrity Society (ESIS) formed a working party (formed within ESIS Technical Subcommittee 5) devoted to instrumented impact testing on subsize Charpy-V specimens of metallic materials. In 1994, ESIS issued a draft of a standard method for the instrumented Charpy V-notch test on metallic materials (Ref 40). This method allows one to estimate an approximate value of the proportion of ductile fracture surface by one of the following formulas:

$$\% \text{ shear} = [1 - (P_{IU} - P_A) / P_M] \times 100\%$$

$$\% \text{ shear} = [1 - (P_{IU} - P_A) / (P_M - P_{GY})] \times 100\%$$

$$\% \text{ shear} = \{1 - (P_{IU} - P_A) / [P_M + 0.5(P_M - P_{GY})]\} \times 100\%$$

$$\% \text{ shear} = \left(1 - \sqrt{[(P_{GY} / P_M) + 2]} / 3 \right)$$

$$\times \left[\left(\sqrt{P_{IU} - P_M} \right) - \left(\sqrt{P_A / P_M} \right) \right] \times 100\%$$

where P_{GY} , P_M , P_{IU} , and P_A are characteristic points on the load-time diagram shown in Fig. 12.

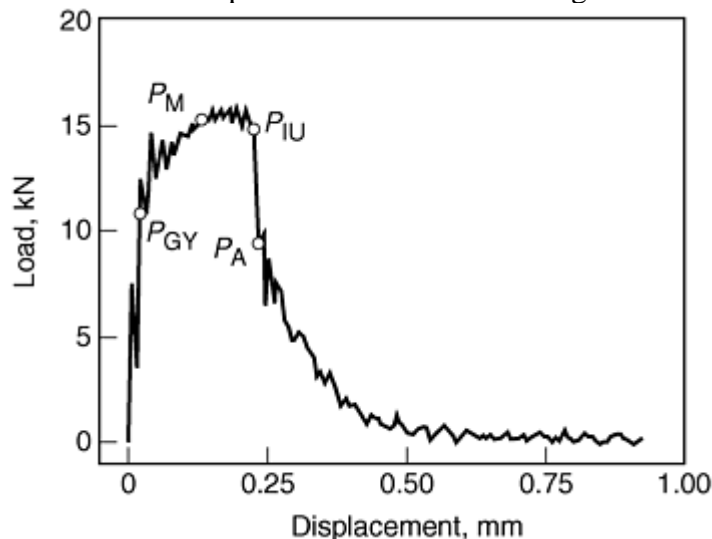


Fig. 12 Load vs. time record showing the definitions of the various load points used in various models to estimate the percent shear fracture; P_{GY} , characteristic value for onset of plastic deformation; P_M , maximum load; P_{IU} , load at the initiation of unstable crack propagation; P_A , load at the end of unstable crack propagation.

The working group also performed round-robin testing to help develop the state of knowledge on the dynamic behavior of miniaturized impact specimens (Ref 41). In 1992, a formal committee also was formed for development of a possible JIS standard for evaluation of dynamic fracture toughness by the instrumented Charpy impact testing method. Problems to be resolved before the standardization of the instrumented Charpy impact test method are pointed out in Ref 42.

General Test Requirements. Only subtle differences exist between the “EPRI Procedures” (Ref 28) and the Pressure Vessel Research Committee procedures for measuring K_{Id} values from precracked Charpy specimens (Ref 38, 43). The following test requirements are taken from the EPRI procedures.

The load signal obtained from an instrumented striker during an impact test oscillates about the actual load required to deform the specimen. Therefore, the signal analysis procedure employed should minimize the deviation of the apparent load from the actual specimen deformation load. A simplistic view of the impact event allows three major areas for test specification to be identified: initial loading, limited frequency response, and electronic curve fitting.

The impact loading of a specimen will create inertial oscillations in the contact load between striker and specimen, and a time interval between 2τ and 3τ is required for the load to be dissipated, where τ is related to the period of the apparent specimen oscillations and can be predicted empirically for a span-to-width ratio of 4 by:

$$\tau = 3.36 \left(\frac{W}{S_o} \right) (EBC_s)^{1/2} \quad (\text{Eq 4})$$

where W is the specimen width, B is the specimen thickness, C_s is the specimen compliance, E is the Young's modulus, S_o is the speed of sound in the specimen, and τ is typically $30 \mu\text{s}$ for standard Charpy steel specimens. When any time, t , is less than 2τ , it is not possible to use the striker signal to measure the portion of the specimen load caused by inertial effects. An empirical specification for reliable load and time evaluation is:

$$t \geq 3\tau \quad (\text{Eq 5})$$

Control of t is obtained by control of the initial impact velocity. The constant 3 in Eq 5 may be as low as 2.3 without adversely affecting the test results, if the curve-fitting technique described below is followed. A value of 3 was chosen for the case of “unlimited” frequency response. The original EPRI procedures corresponded to the 2.3 factor and included the selective filtering for curve fitting (Ref 28). Computer simulations of the Charpy test have approximately verified the value of τ and the 3τ criterion (Ref 44).

The potential problem of limited frequency response of the transducer amplifier is avoided by specifying:

$$t \geq 1.1t_R \quad (\text{Eq 6})$$

where t_R is defined as the 0.915 dB response time of the instrumentation, as indicated in Eq 3. Inadequate response results in a distorted signal response. It is important to note that the electronic attenuation must be representative of a resistance-capacitance circuit for Eq 6 to apply.

The curve fitting of the oscillations is achieved by specifying a minimum t_R . The amplitude of the observed oscillations is therefore reduced such that the disparity between tup contact load and effective deformation load is minimal. For the best test, it has been empirically found for resistance-capacitance circuit systems that:

$$t_R \geq 1.4t \quad (\text{Eq 7})$$

is adequate for the electronic curve fitting without altering the overall curve, when $t \geq 2.3\tau$. When $t \geq 3\tau$, it is not necessary to electronically curve fit because the disparity between the contact load and the specimen deformation load is less than approximately 5%.

The requirements for obtaining acceptable load-time records (in particular, Eq 5) result in the need to control V_o . By controlling the impact velocity, a corresponding control of kinetic energy (E_o) is inherent. The reduction in striker velocity during the impact loading of the specimen should therefore be minimized. A conservative requirement is:

$$E_o \geq 3W_M \quad (\text{Eq 8})$$

where W_M is the system energy dissipated to maximum load P_M . This requirement ensures that the tup velocity is not reduced by more than 20% up to maximum load. This requirement is seldom a problem for full-impact Charpy V-notch tests; Eq 8 may not be met, however, when precracked Charpy tests are conducted for very tough materials. The test requirements for reliable load measurement are summarized as follows:

Inertial effects	$t \geq 3\tau$
Limited frequency response	$t \geq 1.1t_R$, required only if $2.3\tau \leq t < 3\tau$
Electronic curve fitting	$t_R \geq 1.4\tau$
Energy criterion	$E_o \geq 3W_M$

The time t corresponds to the shortest time required for measurement after the specimen has been impacted; that is, t is the time to maximum load t_M for the elastic fracture, and t is the time to general yield, t_{GY} , in the postgeneral yield fracture (See Fig. 11). The specification for electronic curve fitting is only required if $2.3\tau \leq t < 3\tau$. Because it is often difficult to ensure that $t \geq 3\tau$ and because the filtering has no adverse effect when $t \geq 2.3\tau$ filtering at $t_R \geq 1.4\tau$ is always possible, assuming that $t \geq 1.1t_R$.

Limitations on Testing. Violation of any of the general test requirements presented above will invalidate the data obtained from instrumented Charpy V-notch tests. Limitations of this testing technique are the same as those for standard Charpy testing. The effects of small size relative to typical component size, the rounded machine notch, and shallow notch depth restrict general applicability and usefulness of the Charpy test. Note that the notch depth for the Charpy V-notch specimen is too shallow to prevent yielding across the gross section of the specimen.

Instrumentation has allowed separation of energy components and measurement of applied loads throughout the fracture event, but direct determination of the initiation component is not directly possible for ductile (microvoid coalescence) initiation from the instrumented test record. Some of these limitations have been addressed by fatigue precracking the Charpy specimen, which eliminates the notch effects and makes it a small fracture-mechanics-type specimen.

References cited in this section

23. W. Schmitt, W. Böhme, and D.-Z. Sun, New Developments in Fracture Toughness Evaluation, *Structural Integrity: Experiments, Models, Applications—European Conference of Fracture (ECF) 10*, Vol 1, Engineering Materials Advisory Service, 1990, p 159–170
24. P.R. Sreenivasan, Instrumented Impact Testing—Accuracy, Reliability, and Predictability of Data, *Trans. Indian Inst. Met.*, Vol 49 (No. 5), Oct 1996, p 677–696
25. B. Augland, Fracture Toughness and the Charpy V-Notch Test, *Br. Weld. J.*, Vol 9 (No. 7), 1962, p 434
26. G.D. Fearnough and C.J. Hoy, Mechanism of Deformation and Fracture in the Charpy Test as Revealed by Dynamic Recording of Impact Loads, *J. Iron Steel Inst. Jpn.*, Vol 202, 1964, p 912
27. R.A. Wullaert, Application of the Instrumented Charpy Impact Test, *Impact Testing of Metals*, STP 466, ASTM, 1970, p 148–164
28. D.R. Ireland, W.L. Server, and R.A. Wullaert, “Procedures for Testing and Data Analysis,” ETI Report TR-75-43, Effects Technology, Inc., Santa Barbara, CA, Oct 1975
29. D.R. Ireland, Procedures and Problems Associated with Reliable Control of the Instrumented Impact Test, *Instrumented Impact Testing*, STP 563, ASTM, 1974, p 3–29
30. L.E. Steele, Ed., *Radiation Embrittlement of Nuclear Pressure Vessel Steels: An International Review*, STP 1011, ASTM, 1989
31. S. Kessler, G.C. Adams, S.B. Driscoll, and D.R. Ireland, *Instrumented Impact Testing of Plastics and Composites Materials*, STP 936, ASTM, 1986

32. "Plastic—Determination Of Charpy Impact Properties: Part 2—Instrumented Impact Test," ISO-179-2, International Organization for Standardization
33. *Impact Testing of Metals*, STP 466, ASTM, 1970
34. *Instrumented Impact Testing*, STP 563, ASTM, 1974
35. C.E. Turner, in *Advanced Seminar on Fracture Mechanics*, EURA-TOM-ISPRA Courses, 1975
36. *Dynamic Fracture Toughness*, The Welding Institute and The American Society for Metals, 1976
37. E.C.J. Buys and A. Cowan, Interpretation of the Instrumented Impact Test, *Weld. World*, Vol 8 (No. 1), 1970, p 70–76
38. Pressure Vessel Research Committee/Metal Properties Council Working Group on Instrumented Precracked Charpy Testing, "Instrumented Precracked Charpy Testing: Report I—Recommended Testing Procedure, Report II—Associated Test Program," Westinghouse Research Laboratory, Pittsburgh, PA, 1974
39. R.A. Wullaert, Ed., *CSNI Specialist Meeting on Instrumented Precracked Charpy Testing*, Nov 1980, EPRI NP-2102-LD, Electric Power Research Institute, 1981
40. "ESIS Instrumented Charpy V-Notch Standard," Proposed Standard Method for the Instrumented Charpy-V Impact Tests on Metallic Materials, Draft 10, ESIS, Jan 14, 1994
41. E. Lucon, Instrumented Impact Testing of Sub-Size Charpy-V Specimens: The Activity of the ESIS TC5 Working Party, *ECF 11—Mechanisms and Mechanics of Damage and Failure*, Vol 1, Elsevier, 1996, p 621
42. T. Kobayashi and I. Yamamoto, Progress and Development in the Instrumented Charpy Impact Testing Method, *Bull. Jpn. Inst. Met.*, Vol 32 (No. 3), 1993, p 151–159 (in Japanese)
43. W.L. Server, Impact Three-Point Bend Testing for Notches and Precracked Specimens, *J. Test. Eval.*, Vol 6 (No. 1), 1978, p 29–34
44. D.M. Norris, D. Quiñones, and B. Moran, Computer Simulation of Plastic Deformation in the Charpy V-Notch Impact Test, *What Does the Charpy Test Really Tell Us?: Proceedings of the American Institute of Mining, Metallurgical and Petroleum Engineers*, American Society for Metals, 1978, p 22–32

Impact Toughness Testing

Precracked Charpy Test

By inducing a fatigue precrack in the Charpy specimen, the notch acuity and depth restrictions are eliminated. Early work concentrated on correlations with fracture toughness using only the total absorbed energy (i.e., uninstrumented testing). These energy values usually are normalized per unit area (A) below the fatigue crack; the normalized energy values are designated as W/A .

Most of the correlations of W/A with fracture toughness have been conducted using slow-bend specimens. The basic problem in reaching an impact correlation is the difference in loading rates between the Charpy impact

and the static K_{Ic} tests, particularly for loading-rate sensitive materials (Ref 45). A general trend exists for a correlation between K_{Ic}^2/E and W/A , but the limited data and scatter make this difficult to utilize (Ref 16). A better correlation with K_{Id} may be possible. The reason for using K_{Ic}^2/E as the basis is the approximate proportionality between K_{Ic}^2/E and W/A , based on a presumed fracture mechanics relationship (Ref 45). The precracked Charpy W/A values can also be used to estimate the nil-ductility transition temperature. The typical technique defines an inflation point between lower shelf and transition region behavior as the estimated nil-ductility transition temperature (Ref 46). Some exceptions have been noted to this approach (Ref 47).

Instrumented Data

The types of data and test techniques used for instrumented precracked Charpy testing are the same as those discussed earlier for instrumented Charpy impact testing. The 3τ criterion, which limits the impact velocity, becomes more important for deeply cracked, brittle materials. The greatest advantage of precracking is the transformation of the Charpy V-notch specimen into a dynamic fracture mechanics test piece. The direct calculation of fracture toughness (within certain limitations) is now possible using the instrumented load-time information. The following discussion presents the calculational aspects of these fracture toughness parameters. If fracture is known to initiate at maximum load (as it usually does for cleavage initiation), the energy value of W_M (see Fig. 11) can be considered an initiation energy. However, W_M includes contributions other than that caused by the deflection of the specimen. Therefore, a compliance energy correction is needed to determine the true specimen energy, E_M (Ref 48). When the fracture is linear elastic (fracture before general yield; see the first two load-time records in Fig. 11), the value of E_M can be calculated directly:

$$E_M = \frac{C_{ND}(P_M^2)}{2EB} \quad (\text{Eq 9})$$

where C_{ND} is the nondimensional specimen compliance (Ref 49). For a fracture occurring after general yield (see Fig. 11), E_M is obtained by correcting W_M :

$$E_M = W_M - \left\{ \left[\frac{P_M^2}{2} \right] \left[C_T - \left(\frac{C_{ND}}{EB} \right) \right] \right\} \quad (\text{Eq 10})$$

where C_T is the total system compliance calculated at general yield and corrected for the decrease in velocity through general yield:

$$C_T = \left(\frac{V_o t_{GY}}{P_{GY}} \right) - \left(\frac{V_o^2 t_{GY}^2}{8E_o} \right) \quad (\text{Eq 11})$$

This compliance correction is assumed to be linear with load, but the actual correction is not so simple. However, the error in assuming a linear relationship results in a slightly smaller (conservative) value of E_M (Ref 43).

It is often desirable to partition the total fracture energy into initiation and postinitiation (propagation) components. Assuming initiation occurs at maximum load, the propagation energy, E_P , is:

$$E_P = E_T - E_M \quad (\text{Eq 12})$$

where E_T is the total fracture energy, as determined from a dial indicator, kinetic energy change (initial and final velocity measurements), or ΔE_o .

Linear Elastic Fracture Toughness. When the fracture is elastic (fracture occurs before general yield), the stress-intensity factor, K_{Ic} , can be calculated by applying linear elastic fracture mechanics:

$$\begin{aligned}
K_{Ic} &= \frac{4P_M}{BW^{1/2}} \\
&\times \left\{ 3 \left(\frac{a}{W} \right)^{1/2} \left[1.99 - \left(\frac{a}{W} \right) \left(1 - \frac{a}{W} \right) \right] \right. \\
&\times \left(2.15 - 3.93 \frac{a}{W} + 2.7 \frac{a^2}{W^2} \right) \left. \right\} \\
&+ \left[2 \left(1 + \frac{2a}{W} \right) \left(1 - \frac{a}{W} \right)^{3/2} \right]
\end{aligned} \tag{Eq 13}$$

where a is the crack length.

The ASTM size requirements for a valid K_{Ic} are quite limiting, even if a dynamic yield strength is used. However, the general specimen size requirements of ASTM E 399 may be too conservative for dynamic testing of ferritic medium-strength steels (Ref 50). Therefore, if general yielding has not occurred, a linear-elastic value of fracture toughness, K_{Ic} , generally is calculated. The stress intensification rate \dot{K} is calculated as:

$$\dot{K} = \frac{K_{Ic}}{t_M} \tag{Eq 14}$$

This loading rate reflects the dynamic aspect of the loading, because the lowest \dot{K} for impact loading of precracked Charpy specimens is on the order of $11 \times 10^4 \text{ MPa}\sqrt{\text{m}} \cdot \text{s}^{-1} \times (1 \times 10^5 \text{ ksi}\sqrt{\text{in.}} \cdot \text{s}^{-1})$.

Postgeneral Yield Fracture Toughness. When general yielding occurs, an energy-based value of the J -integral can be used to obtain a measure of fracture toughness. The calculation of ductile fracture toughness, J_{Ic} , is contingent upon knowing the initiation point of fracture on the load-time record. For cleavage-initiated fracture, this point generally corresponds to maximum load. However, for fibrous (ductile) initiation, maximum load is generally a nonconservative assumption. When the initiation point is known or has been determined experimentally (Ref 51) and when $a/W \geq 0.5$ (Ref 52), then:

$$J_{Ic} = \frac{2E_M}{Bb} \tag{Eq 15}$$

where b is the remaining ligament depth ($W - a$). A stress-intensity factor K_{Ic} can be obtained from the J_{Ic} value as:

$$K_{Ic} = (EJ_{Ic})^{1/2} \tag{Eq 16}$$

An average K can also be computed, as in Eq 16, by using a K_{Ic} value. Validity criteria related to specimen dimensions appear to be (Ref 43):

$$a, b, B \geq 25 \left(\frac{J_{Ic}}{\sigma_f} \right) \text{ (fibrous initiation)} \tag{Eq 17}$$

and

$$a, b, B \geq 50 \left(\frac{J_{Ic}}{\sigma_f} \right) \text{ (cleavage initiation)} \tag{Eq 18}$$

where σ_f is the flow stress, defined as the average of the yield stress and the ultimate stress. For dynamic loading, the yield stress, σ_y , and flow stress, σ_f , of standard Charpy V-notch specimens can be estimated for postgeneral yield behavior as:

$$\sigma_y = 2.99 P_{GY} \frac{W}{Bb^2} \tag{Eq 19}$$

and

$$\sigma_f = \frac{[2.99(P_{GY} + P_M)W]}{2Bb^2} \quad (\text{Eq 20})$$

The general form of the equation results from slip-line field solutions for blunt-notch specimens, and the constant 2.99 has been obtained from extrapolation of results from a slip-line field solution that included the tup indentation at the center loading point (Ref 53). The constant of 2.99 reduces to 2.85 for sharp-notch specimens with a fatigue precrack. The stress values obtained using this approach agree favorably with high rate tensile test results (Ref 54).

Limitations. The test requirements and data analysis procedures described in this article were developed for ferritic pressure vessel steels. A review of instrumented precracked Charpy testing can be found in Ref 55, which discusses the theory and applicability of instrumented precracked Charpy testing. Not all of the relationships and approaches presented in Ref 55 are universally accepted because standards or recommended practices do not currently exist.

Related Test Techniques

Several attempts have been made to use the precracked Charpy specimen at loading rates beyond the limits applicable to quasi-static analysis. The procedures described above assume a quasi-static situation for times greater than the limiting values near 3τ . One such attempt for larger than Charpy-size specimens is described in Ref 56, in which strain gages were mounted near the crack tip to avoid many of the spurious wave effects. Other studies have been conducted using Hopkinson bar techniques (Ref 57) and the shadow optic method of caustics (Ref 58). These studies indicate the need for dynamic analysis when using the instrumented Charpy striker approach at high loading rates.

References cited in this section

16. "Rapid Inexpensive Tests for Determining Fracture Toughness," National Materials Advisory Board, National Academy of Sciences, Washington, D.C., 1976
43. W.L. Server, Impact Three-Point Bend Testing for Notches and Precracked Specimens, *J. Test. Eval.*, Vol 6 (No. 1), 1978, p 29–34
45. T.M.F. Ronald, J.A. Hall, and C.M. Pierce, Usefulness of Precracked Charpy Specimens for Fracture Toughness Screening Tests of Titanium Alloys, *Metall. Trans.*, Vol 3, April 1972, p 813–818
46. G.M. Orner and C.E. Hartbower, Transition-Temperature Correlations in Construction Alloy Steels, *Weld. J.*, Vol 40 (No. 9), Oct 1961, p 459s
47. J.H. Gross, The Effect of Strength and Thickness on Notch Ductility, *Weld. J.*, Vol 48 (No. 10), Oct 1969, p 441s
48. W.L. Server, D.R. Ireland, and R.A. Wullaert, "Strength and Toughness Evaluations from an Instrumented Impact Test," ETI TR-74-29R, Effects Technology, Inc., Santa Barbara, CA, Nov 1974
49. H.J. Saxton et al., Load Point Compliance of the Charpy Impact Specimen, *Instrumented Impact Testing*, STP 563, ASTM, 1974, p 30–49
50. W.L. Server, R.A. Wullaert, and J.W. Sheckherd, "Verification of the EPRI Dynamic Fracture Toughness Testing Procedures," ETI TR 75–42, Effects Technology, Inc. Santa Barbara, CA, Oct 1975
51. W.L. Server, W. Oldfield, and R.A. Wullaert, "Experimental and Statistical Requirements for Developing a Well-Defined KIR Curve," EPRI NP-372, Electric Power Research Institute, Palo Alto, CA, May 1977

52. J.D.G. Sumpter and C.E. Turner, Method for Laboratory Determination of J_c , *Cracks and Fracture*, STP 601, ASTM, 1976, p 3–18
53. D.J.F. Ewing, Calculations on the Bending of Rigid/Plastic Notched Bars, *J. Mech. Phys. Solids*, Vol 16, 1968, p 205–213
54. W.L. Server, General Yielding of Charpy V-Notch and Precracked Charpy Specimens, *J. Eng. Mater. Technol. (Trans. ASME)*, Vol 100, April 1978, p 183–188
55. Committee on Safety of Nuclear Installations Specialist Meeting on Instrumented Precracked Charpy Testing, EPRI NP-2102-LD, Electric Power Research Institute, Palo Alto, CA, Nov 1981
56. F.J. Loss, Ed., “Structural Integrity of Water Reactor Pressure Boundary Components,” Progress Report Ending Feb 1976, NRL Report 8006, Naval Research Laboratory, Washington, D.C., Aug 1976
57. T. Nicholas, “Instrumented Impact Testing Using a Hopkinson Bar Apparatus,” AFML-TR-75-54, Air Force Materials Laboratory, Wright-Patterson Air Force Base, Dayton, OH, July 1975
58. J.F. Kalthoff et al., “Measurements of Dynamic Stress Intensity Factors in Impacted Bend Specimens,” Committee on Safety of Nuclear Installations Specialist Meeting on Instrumented Precracked Charpy Testing, EPRI NP-2102-LD, Electric Power Research Institute, Palo Alto, CA, Nov 1981

Impact Toughness Testing

Drop Weight Testing

Because Charpy V-notch testing does not necessarily reveal the same transition temperature as that observed for full-size parts, many other tests have been devised. Two such tests have achieved some degree of popularity. These are the drop-weight test (DWT) and the drop-weight tear test (DWTT). Both of these tests were developed at the United States Naval Research Laboratory. Both tests yield a transition temperature that more nearly coincides with that of full-size parts. This has been described as the nil-ductility temperature (NDT). Both tests have limited usage because of the required specimen sizes. There are three types of DWT specimens, as shown in Table 4. The smallest of these measures $16 \times 51 \times 127 \text{ mm}$ ($\frac{5}{8} \times 2 \times 5 \text{ in.}$), and thus, when four to eight specimens are required, a considerable amount of material is expended. Often parts are not of sufficient size or are not shaped in such a manner to allow preparation of such specimens. A provision is made for remelting and casting material to specimen size. Most DWT tests are made on plate that is 9.5 mm ($\frac{3}{8} \text{ in.}$) thick or thicker. The DWTT is also a plate testing specification. This test requires a specimen $76 \times 305 \text{ mm}$ ($3 \times 12 \text{ in.}$) by full plate size.

Table 4 Standard drop-weight test (DWT) conditions

Type of specimen	Specimen size, mm (in.)	Span, mm (in.)	Deflection stop, mm (in.)	Yield strength level, MPa (ksi)	Drop-weight energy for given yield strength level ^(a)	
					J	ft · lbf
P-1	25.4 × 89 × 356 (1 × 3½ × 14)	305 (12.0)	7.6 (0.3)	210–340 (30–50)	800	600
				340–480 (50–70)	1100	800
				480–620 (70–90)	1350	1000
				620–760 (90–)	1650	1200

				110)		
P-2	19 × 51 × 127 ($\frac{3}{4}$ × 2 × 5)	102 (4.0)	1.5 (0.06)	210–410 (30–60)	350	250
				410–620 (60–90)	400	300
				620–830 (90–120)	450	350
				830–1030 (120–150)	550	400
P-3	15.9 × 51 × 127 ($\frac{5}{8}$ × 2 × 5)	102 (4.0)	1.9 (0.075)	210–410 (30–60)	350	250
				410–620 (60–90)	400	300
				620–830 (90–120)	450	350
				830–1030 (120–150)	550	400

(a) Initial test of a steel with a given strength level should be conducted with the drop-weight energy stated in this column. In the event that insufficient deflection is developed (no-test performance), an increased drop-weight energy should be employed for other specimens of the given steel.

The same piece of test equipment is used for both the drop-weight test and the drop-weight tear test. The difference lies in the anvil that holds the specimen. The principal requirement is that sufficient impact can be generated to produce cracking. This is commonly provided by a vertical structure on which weights can be attached using guides. The weights are raised to a measured height, quickly released, and guided to strike the specimen properly.

The Drop-Weight Test

The DWT specimen and procedure are shown in Fig. 13 and are described in ASTM E 208. The crack inducer is a bead of hard-facing metal approximately 76 mm (3 in.) long. The specimen, 89 × 356 × 19 mm ($3\frac{1}{2}$ × 14 × $\frac{3}{4}$ in.), is placed, weld down, on rounded end supports and is struck by a 27 kg (60 lb) falling weight with sufficient energy to bend the specimen about 5°. A cleavage crack forms in the bead as soon as incipient yield occurs (at about 3° deflection), thus forming the sharpest possible notch, a cleavage crack in the test specimen. A series of specimens is tested over a range of temperatures to find the nil-ductility transition temperature.

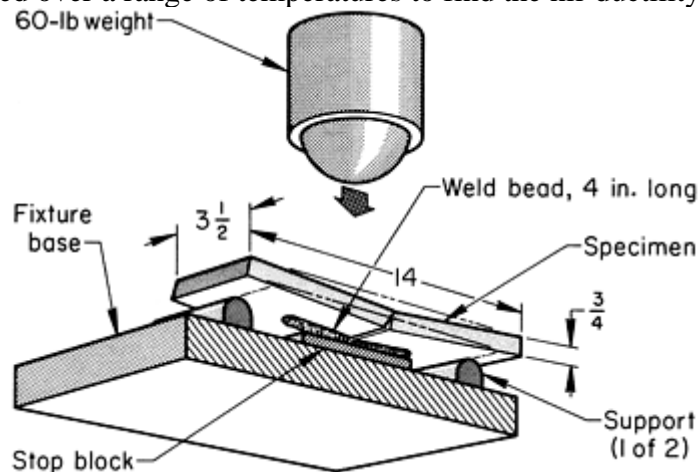


Fig. 13 Drop-weight test method

The weld bead is deposited on one side of the specimen at the center using a copper template. The weld bead is purposely a hard, brittle deposit (the Murex-Hardex N electrode is recommended). A notch is made in the weld bead, but not in the specimen itself. The specimen, after being cooled to the desired temperature, is placed in the anvil with the notched weld deposit facing downward. The weight is dropped, striking the back side of the specimen (the amounts of weight and height depend on the strength of the material being tested; see Table 4). The specimen is allowed to deflect slightly under the impact load, controlled by deflection stops. This initiates a crack at the notch in the weld bead. When the crack reaches the specimen material it will be either propagated or arrested. The specimen is then examined to see whether or not it has fractured. A specimen is considered to

be broken if the crack extends to one or both sides of the specimen surface with the weld bead. If the crack does not propagate to the edge it is considered a “no break.” If the weld notch is not visibly cracked, or if complete deflection does not occur (determined by mark transfer on the deflection stops), it is considered a “no test.” The nil-ductility transition temperature (NDTT) is the maximum temperature at which the specimen breaks. When minimum temperatures are set in material specifications, at least two specimens must be tested at the specified temperature. All specimens tested shall show a “no-break” performance.

Drop-Weight Tear Test Procedure

The drop-weight tear test (ASTM E 436) is similar in some ways to the drop-weight test. The transition fracture appearance occurs at the same temperature as for full-size parts. It has the same sudden change from shear to cleavage as that observed in full-scale pieces of equipment. The test is relatively simple in terms of both specimen preparation and lack of sensitivity to specimen-preparation techniques. The results vary with specimen thickness in the same manner as actual parts do. The principal short coming, as in the drop-weight test, is that testing is confined to plate material between 3 and 19 mm (0.125 and 0.750 in.) thick. The test specimen is even larger than the DWT specimen: it is 76 mm (3 in.) wide by 305 mm (12 in.) long. Tests are made with the same apparatus used for the drop-weight test, but the test fixture for holding the specimen is altogether different. A large pendulum-type machine can also be used, but the vertical weight-dropping apparatus is more commonly used. Up to 2700 J (2000 ft · lbf) of energy may be required.

Test-Specimen Anvil. The holder for the test specimen must support the specimen on edge (305 mm, or 12 in., long edge) in such a manner that rotation will not occur when the specimen is struck. This usually requires adjustable supports for differing specimen thicknesses. Hardened supports at each end suspend the specimen, and a centering guide at one end centers the specimen. A slot in the center of the anvil allows downward clearance for the breaking specimen (Fig. 14).

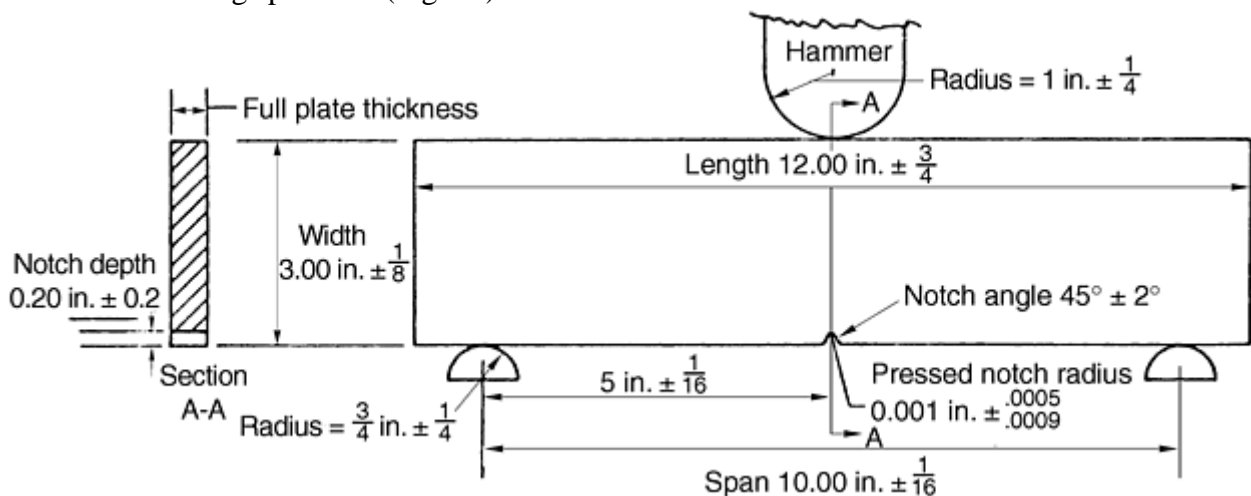


Fig. 14 Drop-weight tear test specimen and support dimensions

Specimen Preparation. Test specimens can be removed by sawing, shearing, or flame cutting. Specimen dimensions and tolerances are shown in Fig. 14. A notch is impressed at the center of one of the 305 mm (12 in.) edges. This is accomplished by using a sharp tool-steel chisel that is hardened. The sharp edge should have an angle of 45 ± 1 or 2° . The depth of the notch is 0.5 ± 0.05 mm (0.020 ± 0.002 in.). The combination of the sharpness of the notch (radius of about 0.013 mm, or 0.0005 in.) and the cold working that occurs as the result of impressing it produces cleavage fractures under the notch.

Test Procedure. Specimens are tested at various temperatures. They are brought to the desired temperature by immersing them in a cooled solution and holding for at least 15 min at temperature. The bath should be agitated, and if several specimens are cooled simultaneously they should be separated by several specimen thicknesses. Specimens should be broken within 10 s after they are removed from the bath. The cooled specimen is inserted in the anvil so that the notch is directly beneath the point of load application, and the test load, which must be only of sufficient magnitude to produce a fracture, is suddenly applied. If the specimen buckles under the test load, the test is considered to be invalid. Otherwise, the specimen fractures and separates as it moves into the slotted anvil without the two pieces being jammed against one another.

Test Results. The test is evaluated by examining the broken pieces. The idea is to determine the percentages of the fracture surface that exhibit ductile shear and brittle cleavage. The two regions are very different in appearance, and the transition from one to the other is abrupt. There are two methods of making this evaluation. One is for percentages of shear from 45 to 100% (Fig. 15), and the other for percentages from 0 to 45% (Fig. 16). The acceptance criterion is percentage of shear at a specific temperature. The temperature at which 50% shear occurs is sometimes considered the ductile-to-brittle transition temperature. Such tests have often been used for evaluation of line-pipe material for natural-gas transmission lines. The specimens from the curved pipe may be flattened prior to testing.

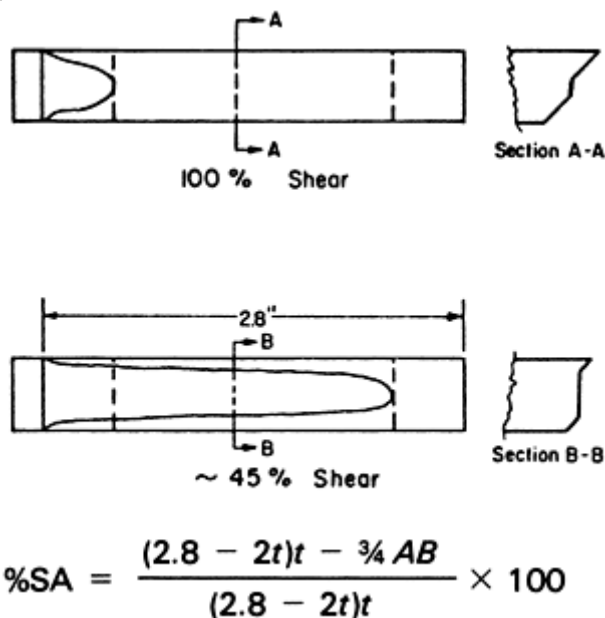


Fig. 15 Method of calculating percent shear for drop-weight tear testing by examination and measurements made of the fractures. This method applies when the percent shear is between 45% and 100%. %SA is percent shear area; A is the width of the cleavage fracture at the one “ t ” line beneath the notch, in.; and B is the length of the cleavage fracture in between the two “ t ” lines, in.

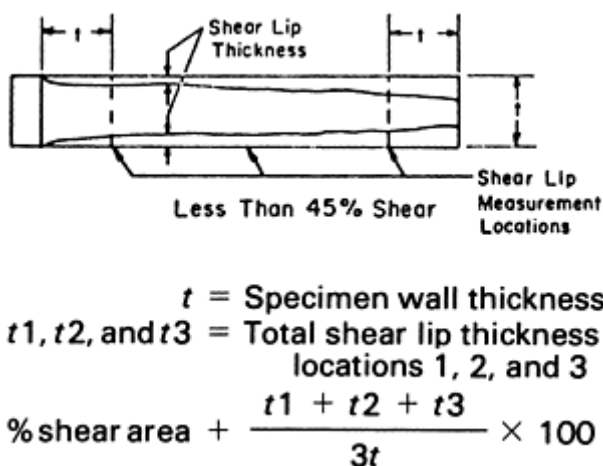


Fig. 16 Method of shear calculation for drop-weight tear testing when the percent shear is less than 45%

Impact Toughness Testing

Other Impact Tests

Izod impact testing uses a specimen with a V-notch (Fig. 17) that is similar to the Charpy V-notch specimen. The principal difference is that the specimen is gripped at one end only, allowing the cantilevered end to be struck by the pendulum (Fig. 18). An advantage of this method is that several notches can be made in a single specimen and the ends broken off one at a time. The disadvantage that has caused it to lose popularity is that the required time for and method of clamping the specimen in an anvil preclude low-temperature testing. Izod specimens can also be round. Many testing machines can be used for both Charpy and Izod testing.

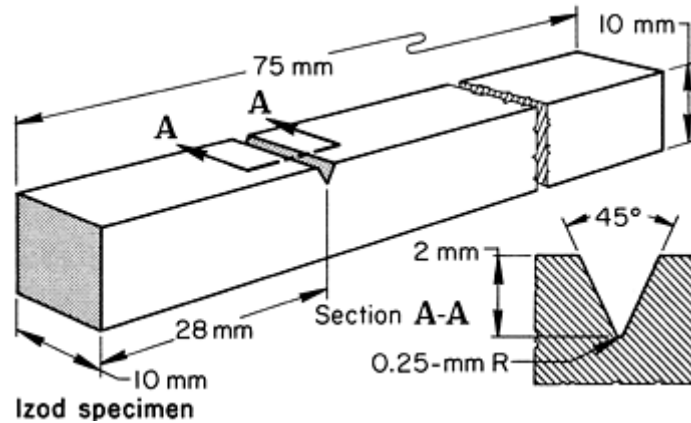


Fig. 17 Izod specimen

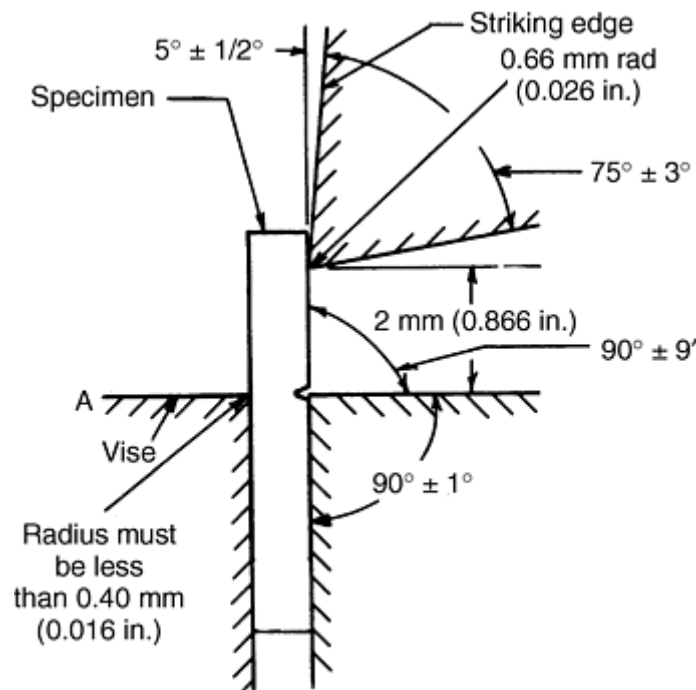


Fig. 18 Cross section depicting clamped specimen and contact point for testing. All dimensional tolerances are ± 0.05 mm (0.002 in.) unless otherwise specified. The clamping surfaces of A and B are flat and parallel within 0.025 mm (0.001 in.). Finish on unmarked parts is 2 μ m (63 μ in.). Striker width must be greater than that of the specimen being tested.

Impact toughness values from the British Standard Izod test are compared with various other methods of testing in Fig. 19. These graphs, derived from a large number of test results on carbon and low-alloy steels, are only intended to show comparative trends. The curves in Fig. 19 should not be used for comparing or compiling specifications (Ref 59).

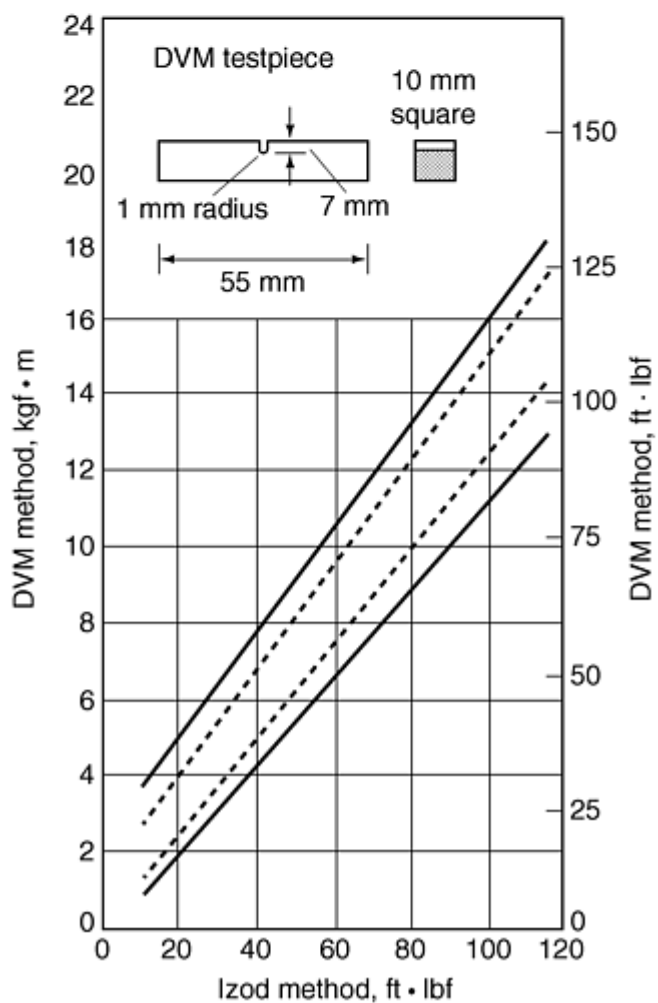
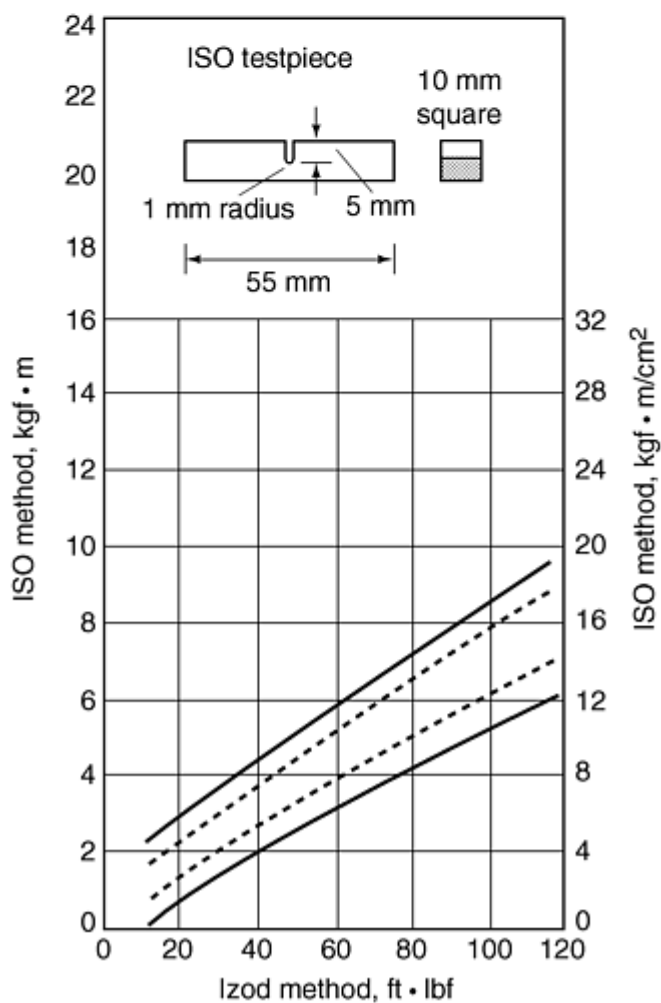
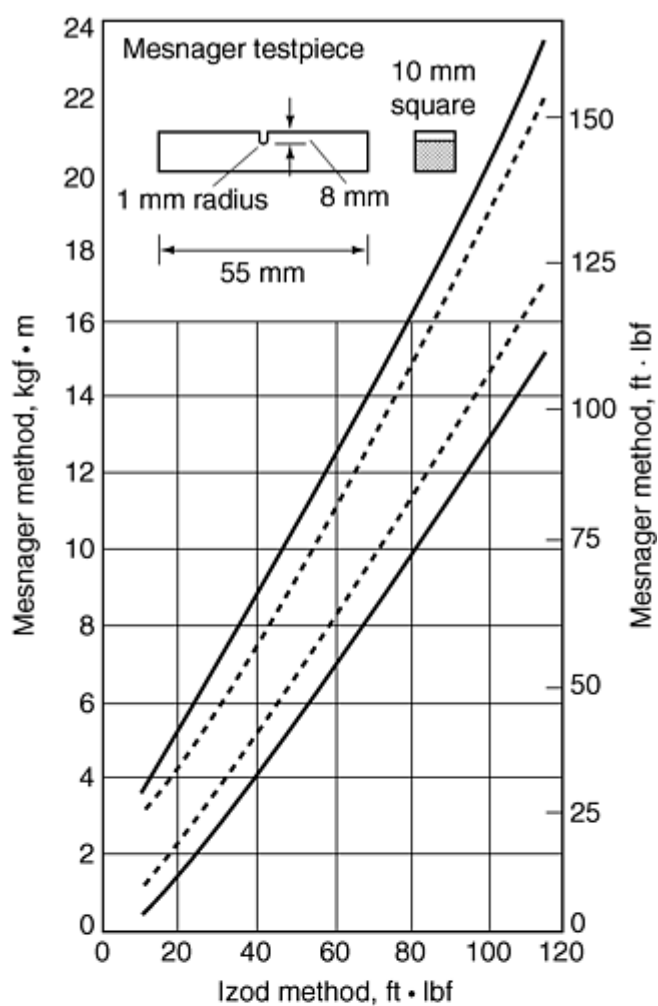
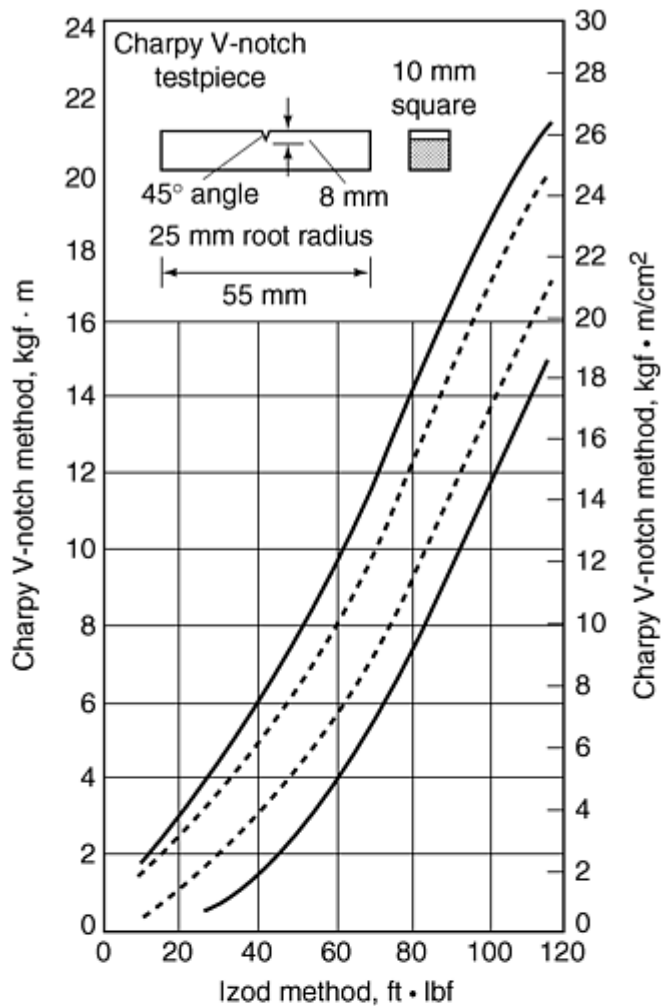


Fig. 19 Impact values obtained with the British Standard Izod test and other test methods. The inner dotted band represents the area within which 50% of the results may be expected to fall, while the wider full band covers approximately 80% of results. Source: Ref 59

The one-point bend test uses a single-edge cracked specimen and the same testing arrangement as a conventional three-point bend test, except that the end supports are removed (Fig. 20). The specimen holder used in a Charpy or Izod test is replaced by a simple frame that supports the specimen, while allowing it to move freely in the horizontal plane. Depending on the design of the original pendulum and hammer, the impact tester may require retrofitting with a new hammer and striker that will not interfere with the specimen edges or the support frame. When the hammer strikes the specimen, the center portion of the specimen is accelerated away from the hammer; the end portions of the specimen lag behind because of inertia. This causes the specimen to bend and to load the crack tip.

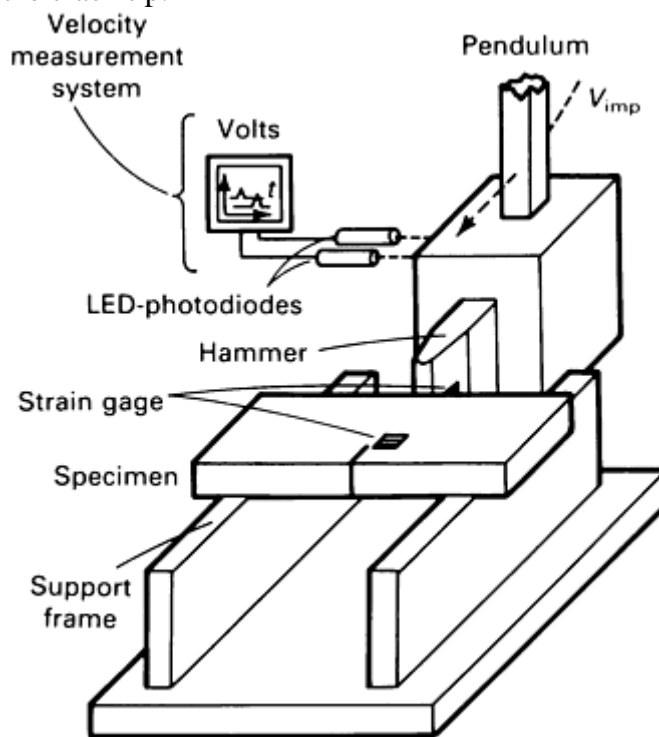


Fig. 20 Experimental setup used to perform the one-point bend test

The primary advantage of the one-point bend test is that the measured stress-intensity history incorporates dynamic effects completely. Therefore, no limits need to be imposed on the impact velocity and the test duration to fracture. Use of the one-point bend test currently is restricted to small-scale yielding conditions (Ref 60).

Dynamic Notched Round Bar Testing. The dynamic notched round bar specimen is a long cylindrical bar with a fatigue precrack (Fig. 21). During the test, the specimen is loaded in tension at one end by an impact of sufficiently large magnitude that the resulting stress pulse produces a fracture at the notch. In principle, therefore, the dynamic notched round bar test is more amenable to analysis than the Charpy test because the fracture process is completed before the stress pulse has sufficient time to be reflected from the farthest end of the bar.

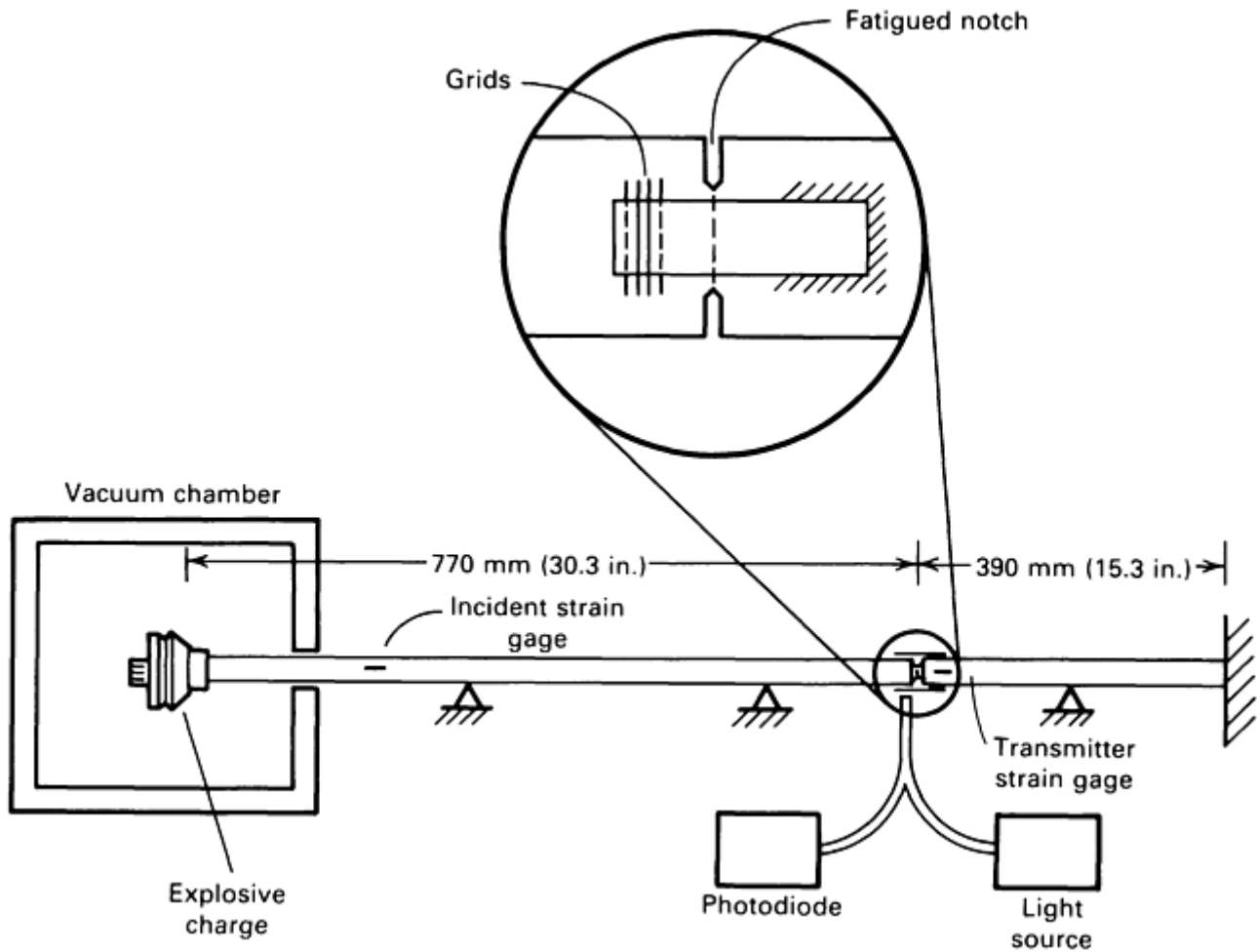


Fig. 21 Typical apparatus for dynamic fracture initiation experiment. Source: Ref 61

The Charpy test is a simple, low-cost test that rapidly detects changes in ductility. However, the Charpy test does have certain disadvantages for quantitative assessments. Fracture in the Charpy specimen does not occur under plane-strain conditions. Furthermore, the state of stress at the fracture site is unknown and quite complex due to multiple pulse reflections from its various surfaces. For these reasons, it is difficult to interpret Charpy results in terms of elastic or elastic-plastic fracture toughness parameters, although, as previously described, instrumented impact testing of precracked Charpy V-notch specimens provides useful results for evaluations of dynamic fracture toughness, as described in more detail in Ref 62.

Dynamic notched round bar testing yields data from which a reliable value of the dynamic critical stress-intensity factor K_{Id} can be calculated easily. Hence, results are immediately related on a quantitative basis to fracture mechanics parameters. However, the test setup is rather elaborate, and more material is required for each specimen compared to Charpy testing. As a result, the technique is not suitable for routine testing. It may be used, however, when a precise evaluation of the fracture initiation properties of a particular material is required, perhaps as a function of temperature as well as of loading rate.

In this test, measurements of the average stress across the fracture plane and of crack-opening displacement, both as functions of time, are easily obtained. Various methods can be used to measure crack-opening displacement, but the stress across the fracture plane is most easily determined by using electric resistance strain gages applied to the surface of the bar downstream from the fracture site. In this respect, and several others, the dynamic notched round bar test resembles the Kolsky (or split-Hopkinson) bar used in dynamic plasticity. Another example of using a notched round bar in evaluation of dynamic fracture toughness is given in Ref 63, where the K_{Id} toughness of A533-B reactor-grade steel was determined over the temperature range from 3 to 50 °C (37–122 °F), by dynamic loading of notched round bar specimens with axial precompression of the notch.

The Schnadt specimen, details of which are shown in Fig. 22, has been used primarily in Europe for testing ship plate. In the Schnadt test, five test pieces are used with different notch radii, ranging from no notch to a severe notch made by pressing a sharp knife into the bottom of a milled groove. A hardened steel pin is inserted in a

hole parallel to and behind the notch, replacing the material normally under compression in the Charpy or Izod tests. The specimen is broken by impact as a three-point-loaded beam.

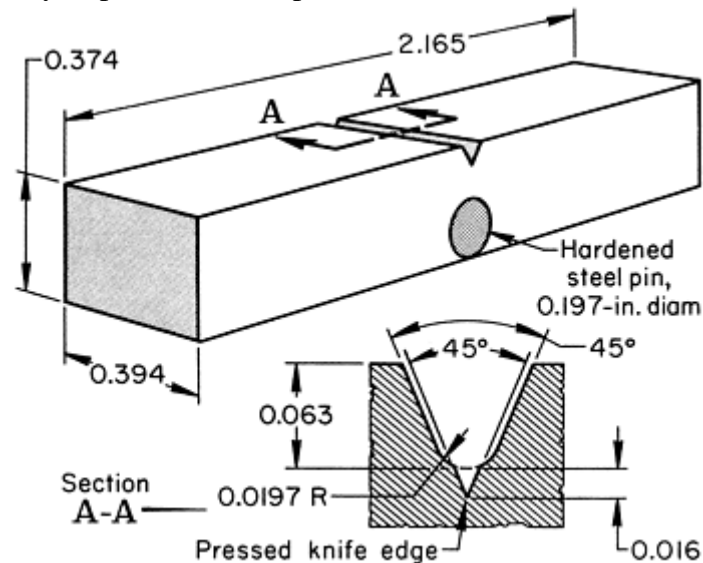


Fig. 22 Details of the Schnadt notched-bar impact-test specimen

References cited in this section

59. J. Woolman and R.A. Mottram, *The Mechanical and Physical Properties of the British Standard DN Steels*, Vol 1, Appendix UI, The British Iron and Steel Research Association, 1964, p 442
60. J.H.J. Giovanola, One-Point Bend Test, *Mechanical Testing*, Vol 8, *ASM Handbook*, 1985, ASM International, p 271–275
61. L.S. Costin, J. Duffy, and L.B. Freund, Fracture Initiation in Metals Under Stress Wave Loading Conditions, *Fast Fracture and Crack Arrest*, STP 627, G.T. Hahn and M.F. Kanninen, Ed., ASTM, 1977, p 301–318
62. R.H. Hawley, J. Duffy, C.F. Shih, Dynamic Notched Round Bar Testing, *Mechanical Testing*, Vol 8, *ASM Handbook*, 1985, ASM International, p 275–284
63. G.R. Irwin, J.W. Dally, X.-J. Zhang, and R.J. Bonenberger, Lower-Bound Initiation Toughness of A533-B Reactor-Grade Steel, *Rapid Load Fracture Testing*, STP 1130, ASTM, 1991, p 9–23

Impact Toughness Testing

Acknowledgments

Contents of this article were adapted from the following:

- Impact Testing, by R.C. Anderson, in *Inspection of Metals: Destructive Testing*, ASM International, 1988, p 121–170
- Charpy Impact Testing, by William Seaver, in *Mechanical Testing*, Vol 8, *ASM Handbook*, 1985, p 261–269

References

1. Use of Precracked Charpy Specimens, *Fracture Control and Prevention*, American Society for Metals, 1974, p 255–282
2. C.E. Turner, *Impact Testing of Metals*, STP 466, ASTM, 1970, p 93
3. O.L. Towers, Effects of Striker Geometry on Charpy Results, *Met. Constr.*, Nov 1983, p 682–685
4. J.M. Holt, Ed., *Charpy Impact Test: Factors and Variables*, STP 1072, ASTM, 1990
5. T.A. Siewert and A.K. Schmieder, Ed., *Pendulum Impact Machines: Procedures and Specimens for Verification*, STP 1248, ASTM, 1995
6. B.F. Dixon, Reliability of Fracture Appearance Measurement in the Charpy Test, *Weld. J.*, Vol 73 (No. 8), Aug 1994, p 39–46
7. “Rules for Construction of Nuclear Power Plant Components,” ASME Boiler and Pressure Vessel Code, Section III, Division 1³₄, Appendices, Nonmandatory Appendix G, American Society for Mechanical Engineers, 1983
8. Energy (Title 10), Domestic Licensing of Production and Utilization Facilities (Part 50), *Code of Federal Regulations*, U.S. Government Printing Office, 1981
9. J.M. Barsom, The Development of AASHTO Fracture Toughness Requirements for Bridge Steels, *Eng. Fract. Mech.*, Vol 7 (No. 3), Sept 1975, p 605–618
10. J.M. Barsom and S.T. Rolfe, Correlations Between K_{Ic} and Charpy V-Notch Test Results in the Transition Temperature Range, *Impact Testing of Materials*, STP 466, ASTM, 1979, p 281–302
11. R.H. Sailors and H.T. Corten, Relationship Between Material Fracture Toughness Using Fracture Mechanics and Transition Temperature Tests, *Fracture Toughness, Proceedings of the 1971 National Symposium on Fracture Mechanics—Part II*, STP 514, ASTM, 1972, p 164–191
12. J.A. Begley and W.A. Logsdon, “Correlation of Fracture Toughness and Charpy Properties for Rotor Steels,” WRL Scientific Paper 71-1E7-MSLRF-P1, Westinghouse Research Laboratory, Pittsburgh, PA, July 1971
13. B. Marandet and G. Sanz, Evaluation of the Toughness of Thick Medium-Strength Steels by Using Linear Elastic Fracture Mechanics and Correlations Between K_{Ic} and Charpy V-Notch, *Flaw Growth and Fracture*, STP 631, ASTM, 1977, p 72–95
14. R.A. Wullaert, Fracture Toughness Predictions from Charpy V-Notch Data, *What Does the Charpy Test Really Tell Us?: Proceedings of the American Institute of Mining, Metallurgical and Petroleum Engineers*, American Society for Metals, 1978

15. S.T. Rolfe and S.R. Novak, Slow-Bend K_{Ic} Testing of Medium-Strength High-Toughness Steels, *Review of Developments in Plane-Strain Fracture Toughness Testing*, STP 463, ASTM, 1970, p 124–159
16. “Rapid Inexpensive Tests for Determining Fracture Toughness,” National Materials Advisory Board, National Academy of Sciences, Washington, D.C., 1976
17. *What Does the Charpy Test Really Tell Us?: Proceedings of the American Institute of Mining, Metallurgical and Petroleum Engineers*, American Society for Metals, 1978
18. D.M. Norris, J.E. Reaugh, and W.L. Server, A Fracture-Toughness Correlation Based on Charpy Initiation Energy, *Fracture Mechanics: Thirteenth Conference*, STP 743, ASTM, 1981, p 207–217
19. W.L. Server et al., “Analysis of Radiation Embrittlement Reference Toughness Curves,” EPRI NP-1661, Electric Power Research Institute, Palo Alto, CA, Jan 1981
20. Metal Properties Council MPC-24, Reference Fracture Toughness Procedures Applied to Pressure Vessel Materials, *Proceedings of the Winter Annual Meeting of the American Society for Mechanical Engineers*, American Society of Mechanical Engineers, New York, 1984
21. J.A. Joyce, Predicting the Ductile-to-Brittle Transition in Nuclear Pressure Vessel Steels from Charpy Surveillance Specimens, *Recent Advances in Fracture*, Minerals, Metals and Materials Society/AIME, 1997, p 65–75
22. T. Iwadate, Y. Tanaka, and H. Takemata, Prediction of Fracture Toughness K_{Ic} Transition Curves of Pressure Vessel Steels from Charpy V-Notch Impact Test Results, *J. Pressure Vessel Technol. (Trans. ASME)*, Vol 116 (No. 4), p 353–358
23. W. Schmitt, W. Böhme, and D.-Z. Sun, New Developments in Fracture Toughness Evaluation, *Structural Integrity: Experiments, Models, Applications—European Conference of Fracture (ECF) 10*, Vol 1, Engineering Materials Advisory Service, 1990, p 159–170
24. P.R. Sreenivasan, Instrumented Impact Testing—Accuracy, Reliability, and Predictability of Data, *Trans. Indian Inst. Met.*, Vol 49 (No. 5), Oct 1996, p 677–696
25. B. Augland, Fracture Toughness and the Charpy V-Notch Test, *Br. Weld. J.*, Vol 9 (No. 7), 1962, p 434
26. G.D. Fearnehough and C.J. Hoy, Mechanism of Deformation and Fracture in the Charpy Test as Revealed by Dynamic Recording of Impact Loads, *J. Iron Steel Inst. Jpn.*, Vol 202, 1964, p 912
27. R.A. Wullaert, Application of the Instrumented Charpy Impact Test, *Impact Testing of Metals*, STP 466, ASTM, 1970, p 148–164
28. D.R. Ireland, W.L. Server, and R.A. Wullaert, “Procedures for Testing and Data Analysis,” ETI Report TR-75-43, Effects Technology, Inc., Santa Barbara, CA, Oct 1975
29. D.R. Ireland, Procedures and Problems Associated with Reliable Control of the Instrumented Impact Test, *Instrumented Impact Testing*, STP 563, ASTM, 1974, p 3–29
30. L.E. Steele, Ed., *Radiation Embrittlement of Nuclear Pressure Vessel Steels: An International Review*, STP 1011, ASTM, 1989
31. S. Kessler, G.C. Adams, S.B. Driscoll, and D.R. Ireland, *Instrumented Impact Testing of Plastics and Composites Materials*, STP 936, ASTM, 1986

32. "Plastic—Determination Of Charpy Impact Properties: Part 2—Instrumented Impact Test," ISO-179-2, International Organization for Standardization
33. *Impact Testing of Metals*, STP 466, ASTM, 1970
34. *Instrumented Impact Testing*, STP 563, ASTM, 1974
35. C.E. Turner, in *Advanced Seminar on Fracture Mechanics*, EURA-TOM-ISPRA Courses, 1975
36. *Dynamic Fracture Toughness*, The Welding Institute and The American Society for Metals, 1976
37. E.C.J. Buys and A. Cowan, Interpretation of the Instrumented Impact Test, *Weld. World*, Vol 8 (No. 1), 1970, p 70–76
38. Pressure Vessel Research Committee/Metal Properties Council Working Group on Instrumented Precracked Charpy Testing, "Instrumented Precracked Charpy Testing: Report I—Recommended Testing Procedure, Report II—Associated Test Program," Westinghouse Research Laboratory, Pittsburgh, PA, 1974
39. R.A. Wullaert, Ed., *CSNI Specialist Meeting on Instrumented Precracked Charpy Testing*, Nov 1980, EPRI NP-2102-LD, Electric Power Research Institute, 1981
40. "ESIS Instrumented Charpy V-Notch Standard," Proposed Standard Method for the Instrumented Charpy-V Impact Tests on Metallic Materials, Draft 10, ESIS, Jan 14, 1994
41. E. Lucon, Instrumented Impact Testing of Sub-Size Charpy-V Specimens: The Activity of the ESIS TC5 Working Party, *ECF 11—Mechanisms and Mechanics of Damage and Failure*, Vol 1, Elsevier, 1996, p 621
42. T. Kobayashi and I. Yamamoto, Progress and Development in the Instrumented Charpy Impact Testing Method, *Bull. Jpn. Inst. Met.*, Vol 32 (No. 3), 1993, p 151–159 (in Japanese)
43. W.L. Server, Impact Three-Point Bend Testing for Notches and Precracked Specimens, *J. Test. Eval.*, Vol 6 (No. 1), 1978, p 29–34
44. D.M. Norris, D. Quiñones, and B. Moran, Computer Simulation of Plastic Deformation in the Charpy V-Notch Impact Test, *What Does the Charpy Test Really Tell Us?: Proceedings of the American Institute of Mining, Metallurgical and Petroleum Engineers*, American Society for Metals, 1978, p 22–32
45. T.M.F. Ronald, J.A. Hall, and C.M. Pierce, Usefulness of Precracked Charpy Specimens for Fracture Toughness Screening Tests of Titanium Alloys, *Metall. Trans.*, Vol 3, April 1972, p 813–818
46. G.M. Orner and C.E. Hartbower, Transition-Temperature Correlations in Construction Alloy Steels, *Weld. J.*, Vol 40 (No. 9), Oct 1961, p 459s
47. J.H. Gross, The Effect of Strength and Thickness on Notch Ductility, *Weld. J.*, Vol 48 (No. 10), Oct 1969, p 441s
48. W.L. Server, D.R. Ireland, and R.A. Wullaert, "Strength and Toughness Evaluations from an Instrumented Impact Test," ETI TR-74-29R, Effects Technology, Inc., Santa Barbara, CA, Nov 1974
49. H.J. Saxton et al., Load Point Compliance of the Charpy Impact Specimen, *Instrumented Impact Testing*, STP 563, ASTM, 1974, p 30–49

50. W.L. Server, R.A. Wullaert, and J.W. Sheckherd, "Verification of the EPRI Dynamic Fracture Toughness Testing Procedures," ETI TR 75-42, Effects Technology, Inc. Santa Barbara, CA, Oct 1975
51. W.L. Server, W. Oldfield, and R.A. Wullaert, "Experimental and Statistical Requirements for Developing a Well-Defined KIR Curve," EPRI NP-372, Electric Power Research Institute, Palo Alto, CA, May 1977
52. J.D.G. Sumpter and C.E. Turner, Method for Laboratory Determination of J_c , *Cracks and Fracture*, STP 601, ASTM, 1976, p 3-18
53. D.J.F. Ewing, Calculations on the Bending of Rigid/Plastic Notched Bars, *J. Mech. Phys. Solids*, Vol 16, 1968, p 205-213
54. W.L. Server, General Yielding of Charpy V-Notch and Precracked Charpy Specimens, *J. Eng. Mater. Technol. (Trans. ASME)*, Vol 100, April 1978, p 183-188
55. Committee on Safety of Nuclear Installations Specialist Meeting on Instrumented Precracked Charpy Testing, EPRI NP-2102-LD, Electric Power Research Institute, Palo Alto, CA, Nov 1981
56. F.J. Loss, Ed., "Structural Integrity of Water Reactor Pressure Boundary Components," Progress Report Ending Feb 1976, NRL Report 8006, Naval Research Laboratory, Washington, D.C., Aug 1976
57. T. Nicholas, "Instrumented Impact Testing Using a Hopkinson Bar Apparatus," AFML-TR-75-54, Air Force Materials Laboratory, Wright-Patterson Air Force Base, Dayton, OH, July 1975
58. J.F. Kalthoff et al., "Measurements of Dynamic Stress Intensity Factors in Impacted Bend Specimens," Committee on Safety of Nuclear Installations Specialist Meeting on Instrumented Precracked Charpy Testing, EPRI NP-2102-LD, Electric Power Research Institute, Palo Alto, CA, Nov 1981
59. J. Woolman and R.A. Mottram, *The Mechanical and Physical Properties of the British Standard DN Steels*, Vol 1, Appendix UI, The British Iron and Steel Research Association, 1964, p 442
60. J.H.J. Giovanola, One-Point Bend Test, *Mechanical Testing*, Vol 8, *ASM Handbook*, 1985, ASM International, p 271-275
61. L.S. Costin, J. Duffy, and L.B. Freund, Fracture Initiation in Metals Under Stress Wave Loading Conditions, *Fast Fracture and Crack Arrest*, STP 627, G.T. Hahn and M.F. Kanninen, Ed., ASTM, 1977, p 301-318
62. R.H. Hawley, J. Duffy, C.F. Shih, Dynamic Notched Round Bar Testing, *Mechanical Testing*, Vol 8, *ASM Handbook*, 1985, ASM International, p 275-284
63. G.R. Irwin, J.W. Dally, X.-J. Zhang, and R.J. Bonenberger, Lower-Bound Initiation Toughness of A533-B Reactor-Grade Steel, *Rapid Load Fracture Testing*, STP 1130, ASTM, 1991, p 9-23

Evaluation of Environmentally Assisted Crack Growth

Y. Katz, N. Tymiak, and W.W. Gerberich, University of Minnesota

Introduction

ENVIRONMENTALLY ASSISTED CRACK GROWTH is a special form of mechanical degradation that occurs when the combined effect (or interaction) of environment and applied or residual stresses causes subcritical crack growth or fracture. Materials ranging from metals and alloys to glasses, plastics, composites, and ceramics can be susceptible. Even materials such as very pure metals, which were once considered not susceptible to environmentally assisted cracking, have usually, on more detailed investigation, proven to be so. Relevant crack propagation rates from environmentally assisted cracking can range from more than 10 to less than 10^{-10} mm/s depending on the environment, load condition, and material.

In broad terms, environmentally assisted cracking includes stress-corrosion cracking, hydrogen embrittlement, and corrosion fatigue. Although these phenomena represent distinct forms of cracking, they also overlap to some degree, as the interaction of mechanical loads and environmental conditions has common mechanisms of degradation across a spectrum of loading conditions and materials. Thus, the choice between the term stress-corrosion cracking and corrosion fatigue may be somewhat arbitrary, as they may both refer to the same underlying degradation phenomenon. However, not all aspects of environmentally assisted crack advance are identical in all cracking systems. Therefore, phenomenological categories are still useful divisions in the evaluation of environmentally assisted crack growth.

This article briefly describes the typical test methods for the evaluation of hydrogen embrittlement, stress-corrosion cracking, and corrosion fatigue with an emphasis on fracture mechanics methodologies for metals. A brief overview on the environmentally assisted crack growth of nonmetallic materials is also included. In general, the test results of environmentally assisted cracking can be influenced by a wide range of variables, such as those listed in Table 1. In addition, because of the large contribution of environment to crack advance, attention to experimental detail is often critical. Unless the multidisciplinary nature of these studies is recognized, most efforts will produce seriously misleading results or outright confusion, which is perhaps most responsible for the slow progress in quantifying and understanding environmental cracking. Familiarity with chemical and physical metallurgy, mechanics, chemistry, electrochemistry, and corrosion also is generally considered essential.

Table 1 Material, environmental, and mechanical variables of environmentally assisted cracking

Metallurgical variables

- **Alloy composition**
- **Distribution of alloying elements and impurities**
- **Microstructure and crystal structure**
- **Heat treatment**
- **Mechanical working**
- **Preferred orientation of grains and grain boundaries (texture)**
- **Mechanical properties (strength, fracture toughness, etc.)**

Environmental variables

- **Temperature**
- **Types of environments: gaseous, liquid, liquid metal, etc.**
- **Partial pressure of damaging species in gaseous environments**

- Concentration of damaging species in aqueous or other liquid environments
- Electrical potential
- pH
- Viscosity of the environment
- Coatings, inhibitors, etc.

Mechanical variables

- Maximum stress or stress-intensity factor, σ_{\max} or K_{\max}
- Cyclic stress or stress-intensity range, $\Delta\sigma$ or ΔK
- Stress ratio (R)
- Cyclic loading frequency
- Cyclic load waveform (constant-amplitude loading)
- Load interactions in variable-amplitude loading
- State of stress
- Residual stress
- Crack size and shape, and their relation to component size and geometry

Evaluation of Environmentally Assisted Crack Growth

Y. Katz, N. Tymiak, and W.W. Gerberich, University of Minnesota

Evaluation of Hydrogen Embrittlement

Hydrogen embrittlement is a time-dependent fracture process caused by the absorption and diffusion of atomic hydrogen into a metal, which results in a loss in ductility and tensile strength. Hydrogen embrittlement is distinguished from stress-corrosion cracking generally by the interactions of the specimens with applied currents (Ref 1). Cases where the applied current makes the specimen more anodic and accelerates cracking are considered to be stress-corrosion cracking, with the anodic-dissolution process contributing to the progress of cracking. On the other hand, when cracking is accentuated by current in the opposite direction, the hydrogen-evolution reactions are accelerated, and the cracking process is considered to be dominated by hydrogen embrittlement. These two basic types of environmental conditions have different phenomenological effects on cracking mechanisms, as briefly summarized in Table 2 for anodic and cathodic reactions.

Table 2 Corrosion/deformation cracking mechanisms including hydrogen embrittlement

Mechanism	Phenomenological implications
Anodic dissolution	Crack-tip blunting
Anodic-dissolution-formed film (oxide or dealloyed)	Film fracture or film-induced cleavage
Passivating film removal or breakdown	Promotion of plasticity (e.g., slip reversal in fatigue)
Cathodic reaction	Hydrogen enhanced crack-tip decohesion, or HEDE (brittle fracture)
	Hydrogen enhanced localized plasticity, or HELP (ductile fracture)
	Hydrogen phase forms and fractures

In a broad sense, the key phenomenological consequence of hydrogen embrittlement is subcritical crack growth that often produces a time-delayed fracture in production parts, sometimes even with no externally applied stress. However, the mechanisms of hydrogen embrittlement are not entirely understood, even though hydrogen

embrittlement of metals is an old, frequently encountered, phenomenon. There are many different sources of hydrogen, several types of embrittlement, and various theories for explaining the observed effects. These factors make evaluation more difficult. Hydrogen embrittlement is also a complex phenomenon that probably cannot be described by a single dominant mechanism.

Reference cited in this section

1. M.G. Fontana and N.D. Greene, *Corrosion Engineering*, McGraw-Hill, 1978, p 113

Evaluation of Environmentally Assisted Crack Growth

Y. Katz, N. Tymiak, and W.W. Gerberich, University of Minnesota

Types of Hydrogen Embrittlement (Ref 2 and 3)

The metals processing, chemical, and petroleum industries have experienced various types of hydrogen-induced cracking for many years. Examples include hydrogen-induced failures of parts that have been forged, heat treated, welded, chemically milled, pickled, or exposed to paint removers. Hydrogen embrittlement is a problem in welding, due to the complex nature of welds and the various sources of hydrogen. Hydrogen sulfide stress cracking is also a major concern in the petroleum industry, and the aerospace industry has experienced unexpected hydrogen embrittlement problems, principally in dealing with high-strength steels. Other examples include hydrogen embrittlement of parts installed in boilers, pressurized-water reactors, high-pressure hydrogenation units, and parts with cathodic protection. Hydrogen cracking has also been a serious concern when hydrogen is used as the liquid fuel in engines.

There are three basic types of hydrogen embrittlement observed in metals:

- Internal reversible hydrogen embrittlement
- Hydrogen environment embrittlement
- Hydrogen reaction embrittlement

If specimens have been precharged with hydrogen from any source or in any manner and embrittlement is observed during mechanical testing, then embrittlement is caused by either internal reversible embrittlement or hydrogen reaction embrittlement. If hydrides or other new phases containing hydrogen form during testing in gaseous hydrogen, then embrittlement is attributed to hydrogen reaction embrittlement. For all embrittlement determined during mechanical testing in gaseous hydrogen other than internal reversible and hydrogen reaction embrittlement, hydrogen environment embrittlement is assumed to be responsible.

Internal reversible hydrogen embrittlement has also been termed slow-strain-rate embrittlement and delayed failure. This is the classical type of hydrogen embrittlement that has been studied quite extensively. Widespread attention has been focused on the problem resulting from electroplating, particularly of cadmium in high-strength steel components. Other sources of hydrogen are processing treatments, such as melting and pickling. More recently, the embrittling effects of many stress-corrosion processes have been attributed to corrosion-produced hydrogen. Hydrogen that is absorbed from any source is diffusible within the metal lattice. To be fully reversible, embrittlement must occur without the hydrogen undergoing any type of chemical reaction after it has been absorbed within the lattice.

Internal reversible hydrogen embrittlement can occur after a very small average concentration of hydrogen has been absorbed from the environment. However, local concentrations of hydrogen are substantially greater than average bulk values. For steels, embrittlement is usually most severe at room temperature during either delayed failure or slow-strain-rate tension testing. This time-dependent nature (incubation period) of embrittlement suggests that diffusion of hydrogen within the lattice controls this type of embrittlement. Cracks initiate internally, usually below the root of a notch at the region of maximum triaxiality. Embrittlement in steel is

reversible (ductility can be stored) by relieving the applied stress and aging at room temperature, provided microscopic cracks have not yet initiated. Internal reversible hydrogen embrittlement has also been observed in a wide variety of other materials, including nickel-base alloys and austenitic stainless steels, provided they are severely charged with hydrogen.

Hydrogen environment embrittlement was recognized as a serious problem in the mid-1960s when the National Aeronautics and Space Administration (NASA) and its contractors experienced failure of ground-based hydrogen storage tanks. These tanks were rated for hydrogen at pressures of 35 to 70 MPa (5–10 ksi). Consequently, the failures were attributed to high-pressure hydrogen embrittlement. Because of these failures and the anticipated use of hydrogen in advanced rocket and gas turbine engines and auxiliary power units, NASA initiated both in-house and contractual research. The contractual effort generally has been to define the relative susceptibility of structural alloys to hydrogen environment embrittlement. A substantial amount of research has concerned the mechanism of the embrittlement process. There is marked disagreement as to whether hydrogen environment embrittlement is a form of internal reversible hydrogen embrittlement or is truly a distinct type of embrittlement.

Hydrogen Reaction Embrittlement. Although the sources of hydrogen may be any of those mentioned previously, this type of embrittlement is quite distinct from hydrogen environment embrittlement. Once hydrogen is absorbed, it may react near the surface of diffuse substantial distances before it reacts. Hydrogen can react with itself, with the matrix, or with a foreign element in the matrix. The chemical reactions that comprise this type of embrittlement or attack are well known and are encountered frequently. The new phases formed by these reactions are usually quite stable, and embrittlement is not reversible during room-temperature aging treatments.

Atomic hydrogen (H) can react with the matrix or with an alloying element to form a hydride (MH_x). Hydride phase formation can be either spontaneous or strain induced. Atomic hydrogen can react with itself to form molecular hydrogen (H_2). This problem is frequently encountered after steel processing and welding; it has been termed flaking or “fisheyes.” Atomic hydrogen can also react with a foreign element in the matrix to form a gas. A principal example is the reaction with carbon in low-alloy steels to form methane (CH_4) bubbles. Another example is the reaction of atomic hydrogen with oxygen in copper to form steam (H_2O), resulting in blistering and a porous metal component.

Although hydrogen reaction embrittlement is not a major topic in this article, its definition is included for the sake of completeness and in the hope of establishing a single definition for each of the various hydrogen embrittlement phenomena to avoid problems with semantics.

Further confusion results from the relation of stress-corrosion cracking (SCC) to hydrogen embrittlement, because the crack growth mechanism is often found to be the same. On the surface, the active corrosion process produces the hydrogen that is the cause of the failure. In SCC, the pits or crevices (polarized anodically) are initiation sites, and, therefore, although the growth mechanisms are the same, the method of prevention based on initiation can be different.

References cited in this section

2. L. Raymond, Ed., *Hydrogen Embrittlement Testing*, STP 543, ASTM, 1972
3. L. Raymond, Evaluation of Hydrogen Embrittlement, *Corrosion*, Volume 13, *ASM Handbook*, ASM International, 1987, p 283–284

Mechanisms and Models

Although the micromechanisms of hydrogen-related fracture have been the subject of intense interest and review in the literature (Ref 4, 5, 6, 7, and 8), many facets of hydrogen embrittlement are still not entirely understood. This is due, in part, to the ad hoc nature of many test methods and the large number of variables (Fig. 1) that influence test results. Several different types of mechanisms, rather than just one dominant mechanism, may also occur.

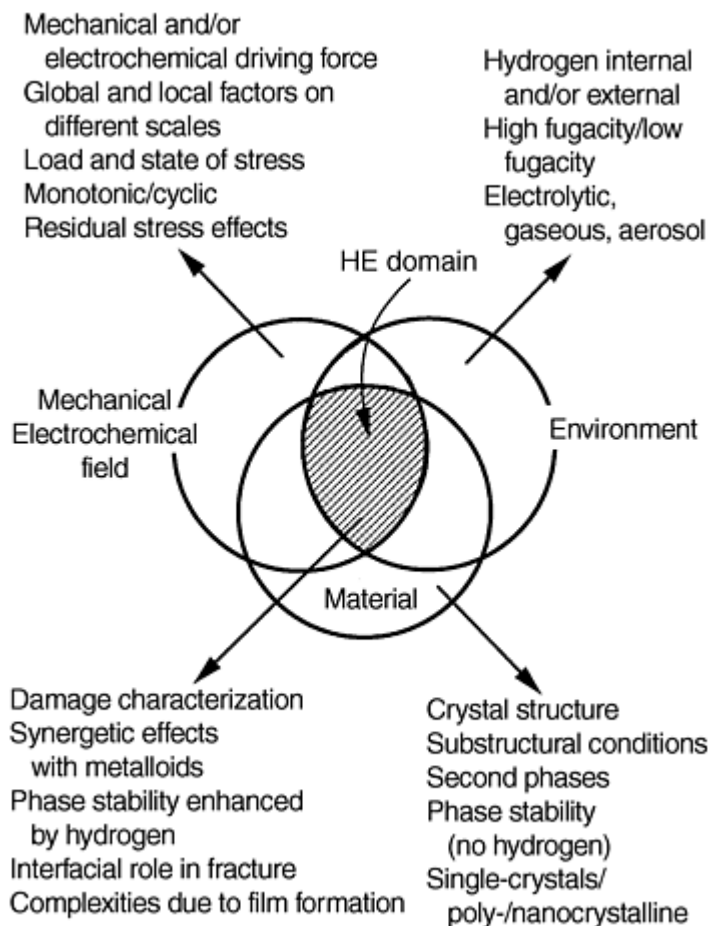


Fig. 1 Interaction variables in hydrogen embrittlement

Although numerous mechanisms have been proposed, there appear to be at least three distinct mechanisms of hydrogen embrittlement in metals (Table 2):

- Hydrogen-enhanced decohesion (HEDE) mechanism, which is characterized by hydrogen decreasing either grain boundary or cleavage plane cohesion (Ref 6, 9, 10, 11, 12, and 13)
- Hydrogen-enhanced local plasticity (HELP) mechanism, which proposes that solid-solution free hydrogen causes dislocation unpinning, which may increase dislocation mobility and allow highly localized deformation (Ref 7 and 8)
- Hydride formation (as previously noted, included here only for the sake of completeness)

In terms of mechanical testing and the use of fracture mechanics, the following sections describe the HEDE and HELP mechanisms in more detail. These damage models are conceptually related to the fracture-mechanics concepts of failure by brittle fracture or plastic collapse. In general, fracture occurs under one of three

conditions: plastic collapse, brittle fracture, or elastic-plastic fracture. These three fracture criteria are roughly defined in the failure assessment diagram (Fig. 2) of the R-6 Method (Ref 14), where the envelope of safe operation in the elastic-plastic region converges to either a brittle fracture condition ($K/K_c = 1$) or plastic collapse ($\sigma/\sigma_c = 1$). The HEDE and HELP mechanisms are conceptually related to these basic concepts of fracture mechanics, as illustrated in Fig. 2.

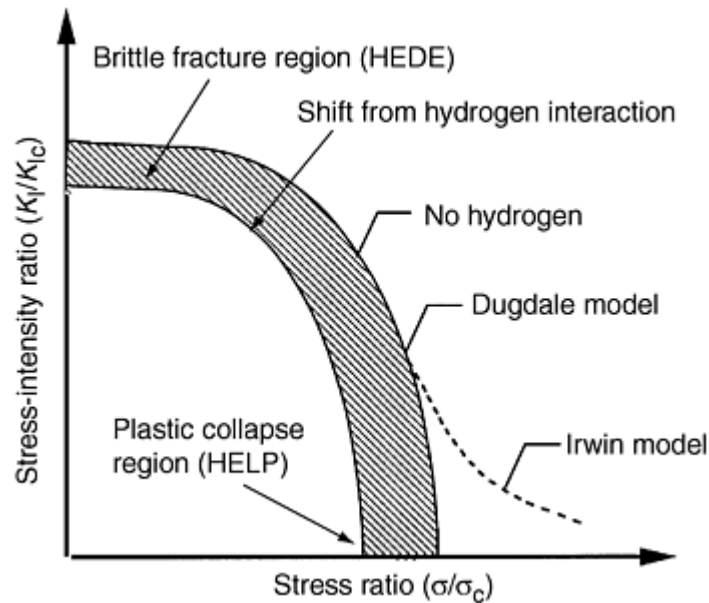


Fig. 2 Failure assessment diagram showing operative region of HEDE and HELP hydrogen degradation

Hydrogen-enhanced decohesion (HEDE) is based on brittle fracture associated with “embrittlement.” The HEDE model has allowed considerable progress to be achieved particularly regarding fracture criteria, including subcritical crack growth, threshold values, damage dependency on the hydrogen partial pressure, temperature, kinetic considerations, and delayed fracture analysis.

The HEDE model actually goes back to the original hydrogen embrittlement study by Troiano (Ref 15 and 16), which later developed in different stages. Following a comprehensive series of research activities (Ref 11 and 12), as related to brittle fracture concepts in general, further developments resulted also in the HEDE hydrogen embrittlement model (Ref 9 and 17). Basically the initial considerations are:

- Can the near-crack-tip mechanical field be better established?
- How can far-field stresses from fracture mechanics be related to theoretical calculations that established that hydrogen does decrease the cohesive strength of cleavage planes and grain boundaries?

The latter finding emerged from embedded-atom (Ref 18 and 19) and full-energy (Ref 20) calculations.

Following these developments, the connection between the local stress intensity, k_{tip} , and the far field, K_I , has been found (Ref 17 and 21). This was then coupled to the decrease in resistance associated with localized hydrogen concentrations. Moreover, this approach turned out to be very consistent experimentally with the ability to accommodate the principal common features related to the decrease of the threshold value, K_{Ith} , and the substantial increase of the crack growth rate with increasing K_I . Note that the high sensitivity of high-strength materials to hydrogen embrittlement becomes the dominant process in the more general framework of SCC.

Hydrogen-enhanced local plasticity (HELP) is based on the localized loss of load-bearing capacity from “shear” decohesion. The HELP model proposes the notion that solid-solution free hydrogen in metals causes dislocation underpinning, which increases dislocation mobility and allows highly localized deformation. Moreover, such enhanced plasticity has been claimed to result in localized softening, which enhances plastic failure in contrast to the usual sense of embrittlement. Enhanced ductile processes due to hydrogen interaction had first been suggested by Beachem (Ref 22), later joined by others (Ref 7 and 23). In fact, the direct relation between H solute causing enhanced dislocation mobility and fracture has been shown using in situ environmental cell transmission electron microscopy (TEM) measurements (Ref 24, 25, and 26). Nevertheless, observations of

deformation behavior and fracture under such plane-stress conditions leave significant issues unresolved. At least two major questions still remain:

- What is the exact sequence of events causing fracture in the bulk?
- Even observed, how do hydrogen solutes result in slip localization? Is this related to hydrogen-induced slip localization or to low-energy dislocation structures? Can local internal strains be separated from the role of any concurrent internal stress field?

Thus, in contrast to the HEDE model, the localized plasticity part of the HELP mechanism suggests alternatively that hydrogen promotes “shear” decohesion along slip planes. The HELP model still has limited predictive capability that needs to be developed.

References cited in this section

4. K. Sieradzki, Atomistic and Micromechanical Modeling Aspects of Environment-Induced Cracking of Metals, *EICM Proc.*, R.P. Gangloff and M.B. Ives, Ed., National Association of Corrosion Engineers, 1990, p 125
5. W.W. Gerberich and S.-H. Chen, Environment-Induced Cracking of Metals, Fundamental Processes: Micromechanics, *Int. Conf. Environmentally Induced Cracking*, Oct 1988, National Association of Corrosion Engineers, 1990, p 167–187
6. W.W. Gerberich, P. Marsh, J. Hoehn, S. Venkataraman, and H. Huang, Hydrogen/Plasticity Interactions in Stress Corrosion Cracking, *Corrosion-Deformation Interactions*, CD1 '92, *Les Editions de Physique les Ulis*, T. Magnin, Ed., 1993, p 325–343
7. H.K. Birnbaum, Mechanism of Hydrogen-Related Fracture of Metals, *EICM Proc.*, R.P. Gangloff and M.B. Ives, Ed., National Association of Corrosion Engineers, 1990, p 21
8. H.K. Birnbaum, I.M. Robertson, D. Sofronis, and D. Teter, Mechanism of Hydrogen-Related Fracture—A Review, *CDI '96*, T. Magnin, Ed., The Institute of Materials, 1997, p 172
9. M.-J. Lii, X.-F. Chen, Y. Katz, and W.W. Gerberich, Dislocation Modeling and Acoustic Emission Observation of Alternating Ductile/Brittle Events in Fe-3wt%Si Crystals, *Acta Metall.*, Vol 38, 1990, p 2435–2452
10. S.-H. Chen, Y. Katz, and W.W. Gerberich, Crack Tip Strain Fields and Fracture Microplasticity in Hydrogen Induced Cracking of Fe-3wt%Si Single Crystals, *Philos. Mag. A*, Vol 63 (No. 1), 1990, p 131–155
11. W. Zielinski and W.W. Gerberich, Crack-Tip Dislocation Emission Arrangements for Equilibrium: Part I—In situ TEM Observations of Fe-2wt%Si, *Acta Metall. Mater.*, Vol 40, 1992, p 2861–2871
12. H. Huang and W.W. Gerberich, Crack-Tip Dislocation Emission Arrangements for Equilibrium: Part II—Comparisons to Analytical and Computer Simulation Models, *Acta Metall. Mater.*, Vol 40, 1992, p 2873–2881
13. P. Marsh, W. Zielinski, H. Huang, and W.W. Gerberich, Crack-Tip Dislocation Emission Arrangements for Equilibrium: Part III—Applications to Large Applied Stress Intensities, *Acta Metall. Mater.*, Vol 40, 1992, p 2883–2894
14. R.P. Harrison, K. Loosemore, I. Milne, and A.R. Dowling, CEGB R/H/R6 Rev 2, General Electricity Generating Board, United Kingdom, 1986

15. E.A. Steigewald, F.W. Schaller, and A.R. Troiano, *Trans. Metall. Soc. AIME*, Vol 218, 1960, p 832
16. A.R. Troiano, *Trans. ASM*, Vol 52, 1960, p 54
17. H. Huang and W.W. Gerberich, Quasi-Equilibrium Modeling of the Toughness Transition During Semibrittle Cleavage, *Acta Metall. Mater.*, Vol 42 (No. 3), 1994, p 639–647
18. M.S. Daw and M.I. Baskes, *Phys. Rev. B*, Vol 29, 1984, p 6443
19. N.R. Moody, J.E. Angelo, S.M. Foiles, M.I. Baskes, and W.W. Gerberich, Atomistic Simulation of the Hydrogen-Induced Fracture Process in an Ion-Based Superalloy, *Sixth Israel Materials and Engineering Conf.*, D. Itshak, D. Iliezer, and J. Haddad, E., Ben-Gurion University of the Negev, 1993, p 444
20. C.L. Fu and G.S. Painter, *J. Mater. Res.*, Vol 6, 1991, p 719
21. X. Chen, T. Foecke, M. Lii, Y. Katz, and W.W. Gerberich, The Role of Stress State on Hydrogen-Induced Cracking in Fe-Si Single Crystals, *Eng. Fract. Mech.*, Vol 35 (No. 6), 1989, p 997–1017
22. C.D. Beachem, *Metall. Trans.*, Vol 3, 1972, p 437
23. S.P. Lynch, Environmentally Assisted Cracking, Overview of Evidence for an Adsorption Induced Localized Slip Process, *Acta Metall.*, Vol 20, 1988, p 2639
24. G. Bond, I.M. Robertson, and H.K. Birnbaum, The Influence of Hydrogen on Deformation and Fracture Processes in High Strength Aluminum, *Acta Metall.*, Vol 35, 1987, p 2289
25. T. Matsumoto, J. Eastman, and H.K. Birnbaum, Direct Observations of Enhanced Dislocation Mobility Due to Hydrogen, *Scr. Metall.*, Vol 15, 1981, p 1033
26. T. Tabata and H.K. Birnbaum, Direct Observations of the Effects of Hydrogen on the Behavior of Dislocations in Iron, *Scr. Metall.*, Vol 17, 1993, p 947

Evaluation of Environmentally Assisted Crack Growth

Y. Katz, N. Tymiak, and W.W. Gerberich, University of Minnesota

Hydrogen Embrittlement Tests

Hydrogen embrittlement testing includes a wide variety of industrial and research methods. Industrial methods are often directed toward the prevention and control of hydrogen embrittlement from processing operations (such as plating) process and maintenance chemicals. These procedures are covered in ASTM F 519, “Standard Method for Mechanical Hydrogen Embrittlement Testing of Plating Processes and Aircraft Maintenance Chemicals.” Other industrial methods include sustained or step-load stress tests to evaluate the effectiveness of the hydrogen embrittlement relief treatments on hardware such as springs or structural fasteners.

With the development of fracture mechanics, conventional test methods have been modified for measurements in terms of crack nucleation, crack growth rate, and threshold stress-intensity values. Many research techniques have also been developed in order to obtain a more fundamental understanding of hydrogen embrittlement. Examples of research methods include:

- Measurement of threshold values under monotonic/cyclic loads (Ref 6, 27, 28, 29, 30, and 31)

- Electron microscopy, x-ray, and Mössbauer methods (Ref 6, 9, 27, 28, 32, 33, and 34)
- Fracture mechanics methodology (Ref 5, 6, 9, 31, and 35) with sustained loads or overloads
- Subcritical crack kinetics (Ref 9 and 35)
- Interfacial strength (Ref 36)
- Slow-strain-rate tests (Ref 5, 9, 10, 37, 38 and 39)
- Time-dependent tests (Ref 40)
- Internal friction, acoustic emission, and phonon dispersion (Ref 5, 9, 41, and 42)
- Elastic moduli measurements (Ref 43)
- Microautoradiography (Ref 44, 45, and 46)
- Infrared spectroscopy (Ref 47)

Research methods are directed toward improved understanding of the hydrogen embrittlement process and its fundamental characterization in terms of atomistic models (Ref 18 and 19), cohesive energy (Ref 15 and 48), discretized dislocation model (Ref 5, 6, 9 and 49), thermodynamically based computations (Ref 50 and 51), hydrogen/metal interaction (Ref 20 and 52), critical-concentration sites (Ref 17, 21, 53, and 54), and strain-energy models (Ref 8).

The main focus of this section is on accelerated small-specimen test methods for failure analysis and production control of hydrogen embrittlement. Because hydrogen embrittlement is a time-dependent process, accelerated testing has economic benefit for testing.

Standardized Tests

The evaluation of hydrogen embrittlement for particular materials and products forms are published in several standards that include:

Designation	Title
ASTM A 143	Practice for Safeguarding against Embrittlement of Hot-Dip Galvanized Steel Products and Procedure for Detecting Embrittlement
ASTM B 577	Standard Test for Detection of Cuprous Oxide (Hydrogen Embrittlement Susceptibility) in Copper
ASTM F 326	Standard Test for Electronic Hydrogen Embrittlement Test for Cadmium-Electroplating Processes
ASTM F 519	Mechanical Hydrogen Embrittlement Evaluation of Plating Processes and Service Environments
ASTM F 1459	Determination of the Susceptibility of Metallic Materials to Gaseous Hydrogen Embrittlement
ASTM F 1624	Standard Test Method for Measurement of Hydrogen Embrittlement Threshold in Steel by the Incremental Step Loading Technique
ASTM G 142	Determination of Susceptibility of Metals to Embrittlement in Hydrogen-Containing Environments
ASTM G 129	Slow Strain Rate Testing to Evaluate the Susceptibility of Metallic Materials to Environments
BS 5899	Method for Hydrogen Embrittlement Test for Copper
BS-EN 2831	Hydrogen Embrittlement of Steels, Test by Slow Bending
BS-EN 2832	Hydrogen Embrittlement of Steels, Notched Specimen Test
BS-EN-ISO 2626	Copper—Hydrogen Embrittlement Test
ISO 2626	Copper—Hydrogen Embrittlement Test
ISO 15330	Fasteners—Preloading Test for the Detection of Hydrogen Embrittlement Parallel Bearing

The major application area for some of these standard tests are briefly described in this section, followed by descriptions of test methods and specimen types.

There are also numerous standards related to the prevention of hydrogen embrittlement, such as:

Designation	Title
AMS 2759/9	Hydrogen Embrittlement Relief (Baking) of Steel Parts
ASTM B 839	Residual Embrittlement in Metallic Coated, Externally Threaded Articles, Fasteners, and Rod
ASTM B 850	Standard Guide for Post-Coating Treatments of Steel for Reducing Risk of Hydrogen Embrittlement
ASTM B 849	Standard Spec Pre-Treatments of Iron or Steel for Reducing Risk of Hydrogen Embrittlement
ASTM F 1940	Process Control Verification to Prevent Hydrogen Embrittlement in Plated or Coated Fasteners
IFI 142	Hydrogen Embrittlement Risk Assessment

From a prevention standpoint, hydrogen embrittlement failures are reduced or eliminated by controlling the amount of hydrogen introduced during manufacture, processing, and in-service environment (including the use of cleaners and paint strippers) of materials. Test methods and the necessary prevention controls are covered in standards such as ASTM F 519 and ASTM F 326, as described below.

Another concern in the evaluation of hydrogen embrittlement appears to involve the identification of residual stresses that result from manufacturing operations such as heat treatment and, especially, welding. Much more attention must be given to evaluating the potential for hydrogen embrittlement failures in the presence of residual stresses. The occurrence and measurement of residual stresses are discussed in more detail in the article “Residual Stress Measurements” in this Volume.

ASTM F 519 and ASTM F 326. As previously noted, ASTM F 519 and ASTM F 326 describe the testing, evaluation, and prevention of hydrogen embrittlement. These standards are based on (1) not putting hydrogen into the steel by keeping the hydrogen in the plating bath at acceptably low levels (ASTM F 326) and (2) using mechanical tests to ensure that the amount of residual hydrogen after baking is under acceptably low levels (ASTM F 519).

ASTM F 326. This standard method covers an electronic hydrogen detection instrument procedure for the measurement of plating permeability to hydrogen, a variable that is related to hydrogen absorbed by steel during plating and to the hydrogen permeability of the plate during post-plate baking. A specific application of this method involves controlling cadmium-plating processes in which the plate porosity relative to hydrogen is critical, such as with cadmium plating of high-strength steel.

This method uses a metal-shelled vacuum probe as an ion gage. A section of the probe shell is cadmium plated at the lowest current density encountered during the electroplating process. During subsequent baking, the probe ion current that is proportional to hydrogen pressure is recorded as a function of time. The slope of this curve has an empirical relationship to failure data, such as those discussed in ASTM F 519.

ASTM F 519. This method covers the evaluation of the hydrogen-generating potential of fluids (aircraft maintenance chemicals) and the hydrogen embrittlement control of electroplating processes. Test specimens are installed into the plating bath during the plating of hardware to monitor indirectly the amount of hydrogen in the plating bath. The acceptable level of hydrogen is determined by a go/no-go situation established by the failure of a sustained loaded, stressed specimen that has been baked at 190 ± 14 °C (375 ± 25 °F) for a minimum of 23 h. The procedures and requirements are specified for the following five types of AISI 4340 steel test specimens:

- Type 1a: notched round bars, stressed in tension, under constant load
- Type 1b: notched round bars loaded in tension with stressed O-rings
- Type 1c: notched round bars loaded in bending with loading bars
- Type 1d: notched C-rings loaded in bending with loading bolt
- Type 2a: unnotched ring specimens loaded in bending with displacement bars

For platings, no stress is applied until the parts have been baked; baking is specified to occur within 1 h after plating. For maintenance chemicals and cleaners, stress is applied before the test specimens are exposed to the environment. The latter condition is obviously much more severe and discriminates against much lower levels of hydrogen but is more representative of their end use.

Hydrogen Embrittlement of Copper and Copper Alloys. Hydrogen embrittlement is observed when tough pitch coppers, which are alloys containing cuprous oxide, are exposed to a reducing atmosphere. Most copper alloys

are deoxidized and thus are not subject to hydrogen embrittlement. Nonetheless, several standards test methods for copper include:

Designation	Title
ASTM B 577	Standard Test for Detection of Cuprous Oxide (Hydrogen Embrittlement Susceptibility) in Copper
BS 5899	Method for Hydrogen Embrittlement Test for Copper
BS-EN-ISO 2626	Copper—Hydrogen Embrittlement Test
ISO 2626	Copper—Hydrogen Embrittlement Test

Hydrogen can be involved in copper-zinc or copper-aluminum alloys where hydrogen is more likely to be produced during cathodic reactions. For copper, minor bulk effects in terms of hydrogen embrittlement may relate to the limited range of hydrogen solubility in pure copper. This is not the case in the many copper alloys, such as β brass, that have the ordered *B2* crystal structure.

Fasteners and Bolts. ASTM F 1940 is a test method for process control verification to prevent hydrogen embrittlement in plated or coated fasteners. The test method uses a notched square bar specimen that conforms to ASTM F 519. ASTM F 1940 is a production-control method for the evaluation and control of the potential for hydrogen embrittlement that may arise from various sources of hydrogen in a plating or coating process. It does not address hydrogen embrittlement from environmental exposure (as in the case of ASTM F 1624, “Standard Test Method for Measurement of Hydrogen Embrittlement Threshold in Steel by the Incremental Step Loading Technique”). It is also not intended to measure the relative susceptibility of steels to either process-induced or environmentally induced hydrogen embrittlement.

ASTM F 606, “Standard Method for Conducting Tests to Determine the Mechanical Properties of Externally and Internally Threaded Fasteners, Washers, and Rivets” also describes a hydrogen embrittlement test for a metallic-coated externally threaded fastener. This test requires the use of a wedge to produce a sustained combined tension and bending load. The tension load is specified as 75% of the minimum ultimate tensile strength. The time specified is 48 h, after which the test fastener is visually and microscopically examined for hydrogen-embrittlement-induced failure. The torque is then reapplied to attain at least 90% of the initial tightening torque. The fastener should show no evidence of hydrogen-induced cracking when visually examined, and the retightening torque should not be less than 90% of the initial tightening torque to indicate successful testing.

In addition to standard ASTM tests, there are also other examples of nonstandardized tests for special product forms or evaluation of susceptibility to hydrogen embrittlement. Two examples are described below.

Hydrogen Embrittlement Testing of Steel Screws. Testing for hydrogen embrittlement of steel self-drilling tapping screws consists of inserting the self-drilling tapping screw against a type B standard plane washer and tightening to a prescribed torque. This stress is maintained for 24 h; the prescribed torque is then reapplied, and the screw is removed by the application of a removal torque. The fastener has failed the test if the reapplication of the torque cannot be obtained, or if the screw cannot be removed without shearing the fastener.

Modified Charpy V-Notch Testing of Bolts. Plated fasteners have been evaluated using a modified Charpy specimen configuration. Fixture adapters are screwed onto the shank of the fastener and tightened to a total length of 55 mm (2.16 in.), which is the length of a standard Charpy V-notch specimen. The assembly is inserted in a four-point bend test fixture meeting ASTM F 519 requirements. The rising-step-load test technique is used, and the specimen is loaded directly to failure. Overload fracture is measured and observed with scanning electron microscopy (SEM), and the maximum fracture load is thus established.

A second sample is then step loaded at 1 h intervals at each step until crack initiation begins, usually within 8 h. Crack extension continues, and the decreasing load is recorded. Scanning electron microscopy can be used to verify the presence of brittle cracking typical of hydrogen-embrittlement-type failures (i.e., flat facets instead of dimpled rupture).

Test Configurations

Conventional test methods include the cantilever beam, wedge-opening load, contoured double-cantilever beam tests, three-point and four-point bending, disk-pressure tests, and slow-strain-rate tension tests. Disk-pressure tests are used for testing in hydrogen atmosphere. The cantilever beam, wedge-opening load, and contoured

double-cantilever beam tests have also been adapted for testing in high-pressure gaseous hydrogen environments.

The cantilever beam test is a constant-load test in which a V-notched specimen is inserted along a portion of the beam and enclosed by an environmental chamber (Fig. 3). A crack at the root of the V-notch is initiated and extended by fatigue before testing. The notch-root thickness is prescribed by the requirement of $K_{\max}^2 < 0.4 B/YS^2$ (where B is the thickness and YS is the yield strength of the specimen), although this is often excessive for high-toughness steels. The specimen is subjected to a constant load over a predetermined time period. As the crack grows, the stress intensity increases. Time to failure is plotted versus applied stress intensity. The lower limit of the resultant curve is a threshold stress intensity for hydrogen embrittlement, K_{IHE} , as shown in Fig. 4.

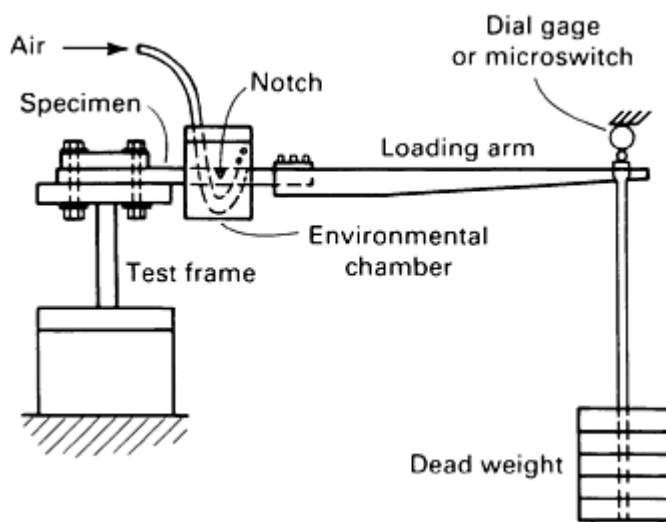


Fig. 3 Fatigue-cracked cantilever beam test specimen and fixtures. Source: Ref 55

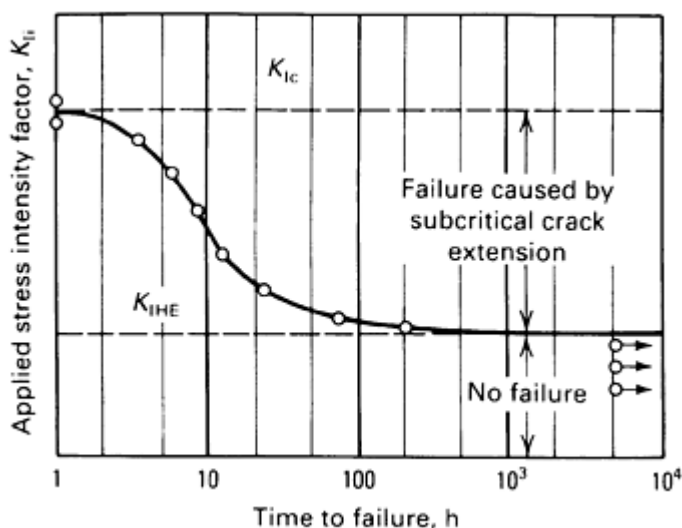


Fig. 4 Procedure to obtain K_{IHE} with precracked cantilever beam test specimen. Source: Ref 55

The K_{IHE} results of a cantilever beam test depend on how much time elapses before the test is terminated. Recommended test periods for establishing the true stress-intensity threshold range from 200 h, which is typical for hydrogen embrittlement testing, to as long as 5000 h (Ref 56). Another limitation of this test method is that it can be expensive in terms of materials and machining. As many as 12 specimens, placed under different loads in separate test machines, are needed for each test in order to obtain valid K_{IHE} values.

The wedge-opening load test applies a constant wedge- or crack-opening displacement; as the crack extends, stress intensity decreases until crack arrest occurs (Fig. 5). The initial load is assumed to be slightly above K_{IHE} . The specimen is maintained under these conditions for about 5000 h to establish the threshold. The crack grows

to a point after which further growth is not measured (K_{IHE}). However, it is difficult to determine precisely when the no-growth criterion is met. Crack-tip opening displacement should also be monitored.

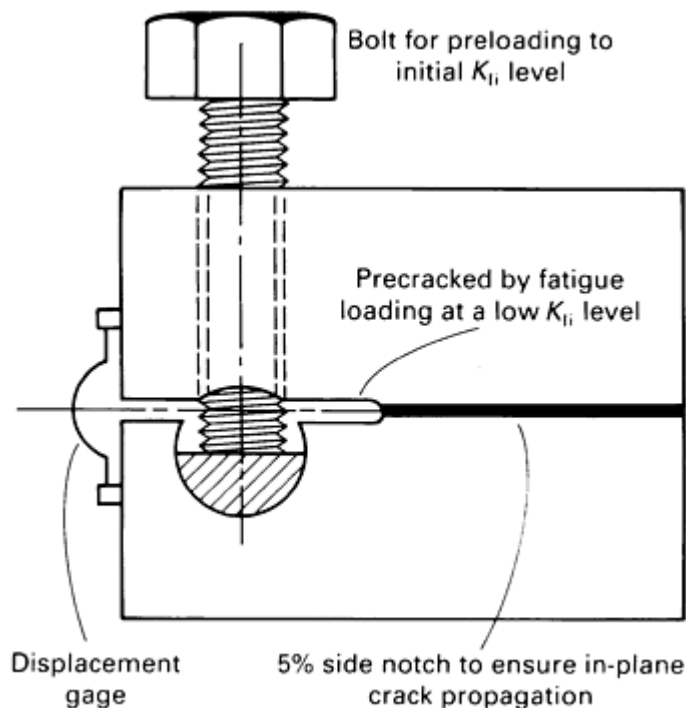


Fig. 5 Schematic showing basic principle of modified wedge-opening load test specimen

The wedge-opening load test and the cantilever beam test both require costly and time-consuming steps and result in a parameter, K_{IHE} , whose design significance is questionable. However, the parameter does provide a relative ranking of susceptibility to hydrogen embrittlement or, more generally, SCC. The advantage of the wedge-opening load test is that only one specimen is required to measure K_{IHE} .

Generally, the threshold stress intensity measured with the wedge-opening load test is lower than that measured with the cantilever beam test. For example, Fig. 6 shows the results of wedge-opening load and cantilever beam tests on 25.4 mm (1 in.) thick iron-nickel-cobalt alloy steel specimens. The data imply that the crack arrest K_{IHE} values from the wedge-opening load test is the lower than the limit for the cantilever beam K_{IHE} threshold.

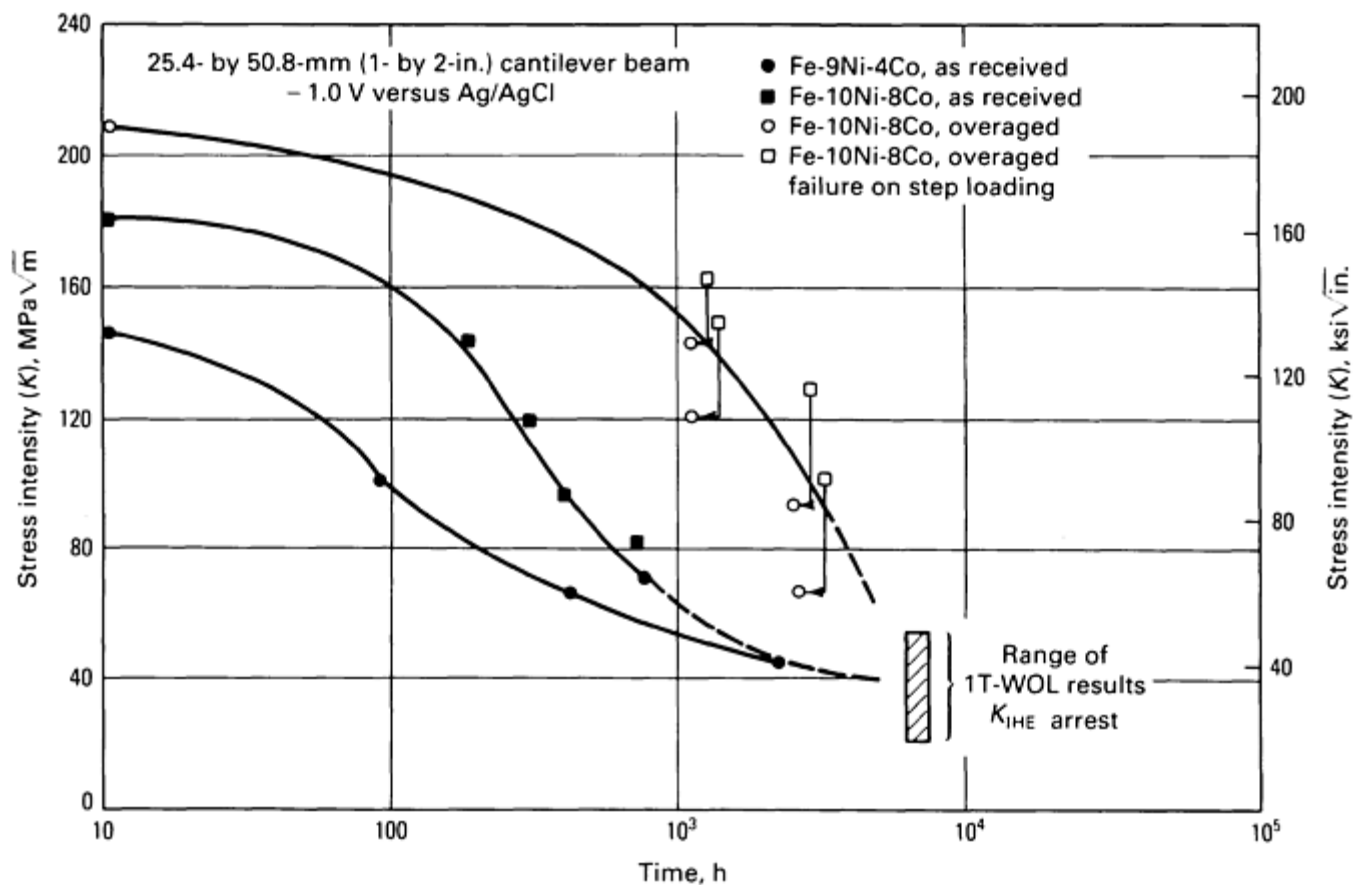


Fig. 6 Comparison of single-edge-notched cantilever beam and wedge-opening load (WOL) test results for hydrogen embrittlement cracking of iron-nickel-cobalt steels. The open circles represent “no fracture” at various exposure times for an overaged Fe-10Ni-8Co alloy in a cantilever beam test. The open squares indicate failure at increased stress intensities, following step loading at various exposure times at the lower stress intensity. Source: Ref 57

Corrosion reactions, accompanied by expansion in volume, may occur at the crack tip. This changes the opening displacement and increases the load, thus altering the desired testing conditions. In long-term tests, it is essential to ensure that the concentration and the composition of the environmental solution do not change over time. For example, evaporation may cause the solution level to drop the crack line of the specimen; this would render the test invalid. The data plots in Fig. 6 also suggest that load increases during the test produce more aggressive hydrogen embrittlement conditions. This may be due to the possible formation of an oxide film on the surface. When the load is increased, the oxide film is broken, exposing fresh metal, and more hydrogen is produced at the crack tip. For this reason, the test should use a rising load, because the constant-load cantilever-beam test does not provide worst-case (fresh metal exposed) loading conditions.

The data also suggest that the cantilever beam test can generate an artificially high K_{IHE} threshold, depending on the time limit selected. If the test had been terminated at 200 h rather than at 5000 h, the reported K_{IHE} values from the cantilever beam test (Fig. 6) would have been four times higher than those measured after the longer time period. Similarly, if insufficient time is allowed in the wedge-opening load test, the incubation period may not be exceeded, and no crack growth will result.

The contoured double-cantilever beam test is used to measure crack growth rate at a constant stress-intensity factor. This test simplifies the calculation of stress intensity by using a contoured specimen so that stress intensity is proportional to the applied load and is independent of the crack length. Under a constant load, stress intensity also remains constant with crack extension. For the test geometry shown in Fig. 7, the stress-intensity factor equals 20 times the load ($K = 20P$).

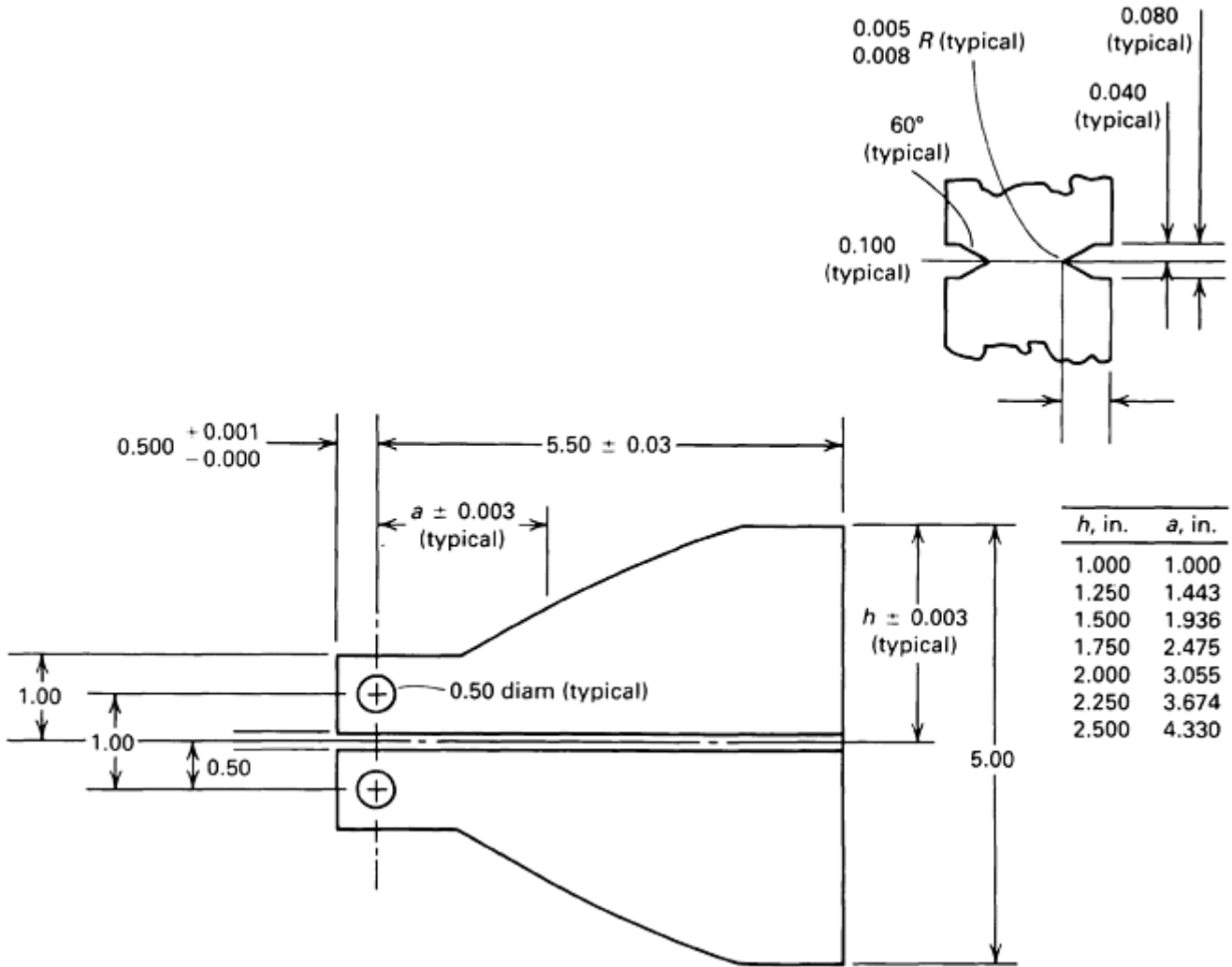


Fig. 7 Dimensions and configuration for double-cantilever beam test specimen. Specimen contoured to $3a^2/h^3 + 1/h = C$, where C is a constant. All values given in inches

Data on hydrogen embrittlement can be obtained with specimens below the thickness requirement of $K_{\max}^2 < 0.4 B/Y_S^2$ by using side grooves (Ref 58). Side grooves provide additional constraint on the material being tested. They also enable the maintenance of a plane-strain condition in a thin specimen by enhancing stress triaxiality. This method has been extensively used to study the effect of heat treatment (hardness) and environment on the hydrogen stress cracking of AISI 4340 steels (Fig. 8). The contoured double-cantilever beam test has also been used to study the stress history effect that produces an incubation time before hydrogen stress cracking (Ref 59).

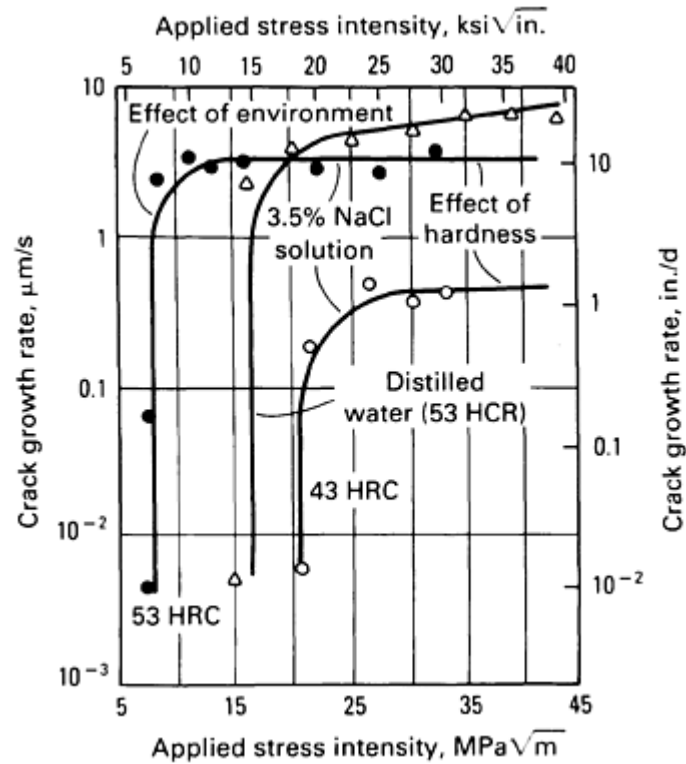


Fig. 8 Hydrogen embrittlement crack growth rate as a function of applied stress intensity for two different hardnesses and environments for an AISI 4340 steel contoured double-cantilever beam test specimen

A new method for accelerating the collection of near-threshold corrosion fatigue crack propagation data, using local hydrogen embrittlement in the crack-tip region, has been investigated for ASTM A 710 HSLA steel with the “constant- K ” contoured double-cantilever beam (CDCB) specimens (Ref 60). Near-threshold fatigue crack growth rates were found to be 100 times faster in the locally hydrogen-charged specimens than in the uncharged material. Fatigue thresholds, ΔK_{th} , were also defined in less than one-fifth the time required for load shedding tests in air at 0.2 Hz. Although demonstrated for HSLA steels, the technique is applicable to any material that can be embrittled by hydrogen.

Three-Point and Four-Point Bend Tests. The contoured double-cantilever beam test uses a constant load to maintain a constant stress-intensity factor with crack extension. The same effect can be produced by using a three- or four-point bend test under displacement control. These tests use heavily side-grooved Charpy V-notch specimens (Fig. 9). Because crack-opening displacement is constant as the crack extends, the load decreases; therefore, there is a slight initial increase in stress intensity to a maximum value that drops slightly as the ratio of crack depth to specimen width exceeds 0.5. Typically, stress intensity is constant within a small range. Figure 10 compares the change in stress-intensity factor with crack extension as a function of load control to that of displacement control for a three-point bend specimen.

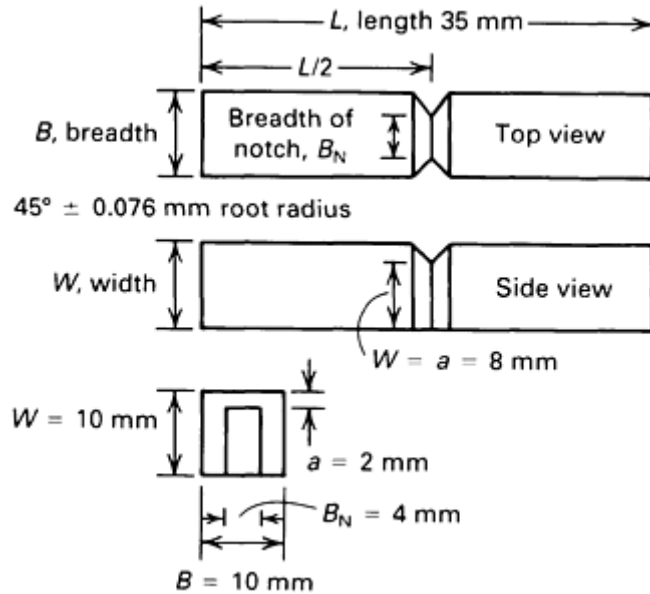


Fig. 9 Side-grooved Charpy V-notch test specimen used for three- and four-point bend tests

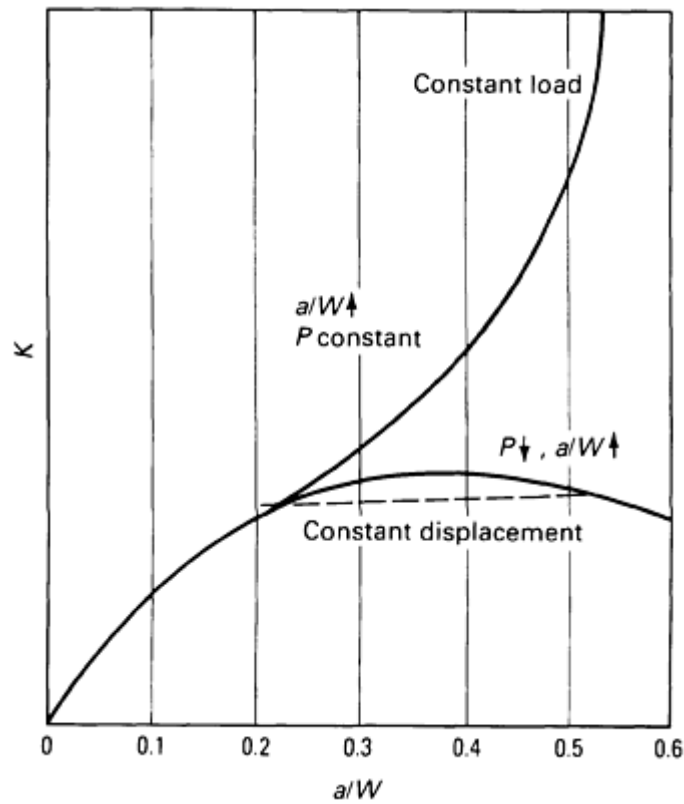


Fig. 10 Change in stress-intensity factor with crack extension as a function of load control and displacement control for a three-point bend specimen

The constraint effect and thickening action of the side-groove on a Charpy-size specimen in three-point bending are discussed in Ref 61. Evaluation of hydrogen embrittlement under three-point or four-point bending is also tested with other types of besides side-grooved Charpy specimens. For example, fracture tests using blunt-notched specimens tested in four-point bending have been used in the investigation of hydrogen damage mechanisms in a commercially produced 9Cr1Mo (Ref 62) and AISI 1080 steel (Ref 63). A nonstandard double-beam (DB) specimen in four-point bending was also used in the evaluation of cracking in wet H₂S environments for two commonly used pressure vessel steels (ASTM A 516-70 and A 285C) (Ref 64). The four-point test on these two pressure vessel steels was done in conjunction with several other test methods including:

- NACE TM0177-90A tensile tests
- NACE TM0177-90A tensile test with one-side (OS) exposure
- NACE TMO284
- NACE TM0284 with TM0177 solution
- TM0184 with OS exposure
- Nonstandard DB specimen in four-point bending with both immersion (IMM) and OS exposure

All the test methods showed a higher susceptibility to hydrogen-induced cracking in the A516-70 steel than in the A285C steel (Ref 64).

The rising-step-load test provides a stress intensity that is different at each load but that remains constant with crack extension as each load level is sustained. Crack initiation is signaled by a drop in load (Fig. 11). The rising step-load test was developed as an accelerated low-cost test for measuring the resistance of steels (particularly weldments) to hydrogen embrittlement (Ref 57, 66). The threshold obtained by this method could be slightly higher if the test duration of each load is too short, but the test duration can be extended near the initiation loads in duplicate tests in order to obtain a more accurate measurement.

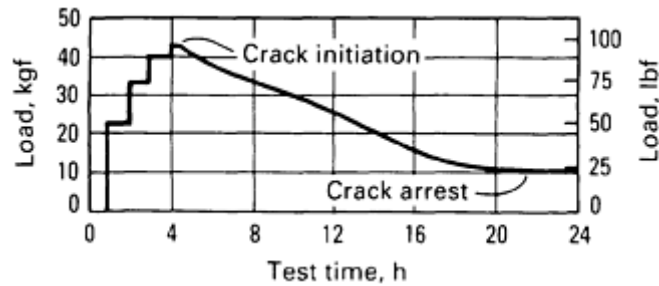


Fig. 11 Typical load-time record for four-point rising step-load test. Source: Ref 65

To index susceptibility to hydrogen-assisted cracking, the test should last no longer than 24 h, and the hydrogen source should reflect the most aggressive environment (Ref 3). In one experiment, a 3.5% sodium chloride solution was selected to simulate seawater, and a cathodic potential of -1.2 V versus saturated calomel electrode (SCE) was used to generate hydrogen in order to reproduce the extreme conditions of sacrificial anodic protection generally found on a ship hull.

A Charpy specimen is used because such specimens are small and easy to machine and handle. Instead of using fatigue precrack, a machined notch-root is sometimes done to lower the cost and to give less ambiguous environmental conditions at the crack tip. A common practice used in crack growth rate tests to prevent the crack from branching is to use specimens with deep side grooves. Side grooves are also used in crack-opening displacement or J -integral testing in order to cause load displacement curves to increase monotonically to fracture by inducing a highly triaxial stress field at the crack tip. Because a Charpy specimen is small, deep side grooves produce a triaxial stress field at the notch and thus promote crack initiation. The extent of the side grooving is such that the remaining ligament is only 40% of the original thickness. The modified Charpy specimen dimensions are shown in Fig. 9.

Specimen loading under four-point bending can be accomplished by means of beams and an instrumented bolt as shown in Fig. 12. Bending is done under constant displacement control and stress intensity to produce crack growth. The specimen is enclosed in an environmental chamber with a potentiostat to produce hydrogen while under stress.

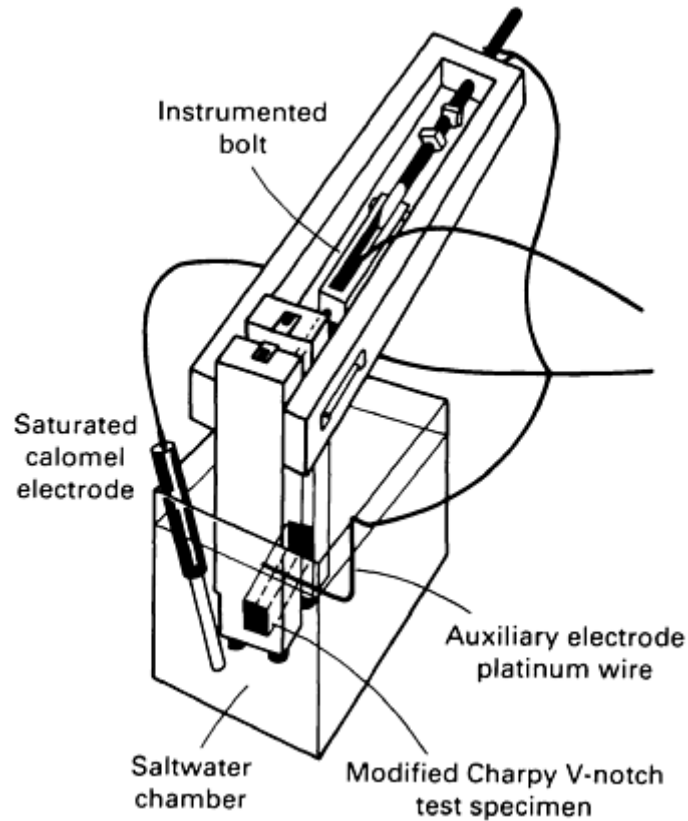


Fig. 12 Loading frame used for rising step-load test

The rising step-load test was used to evaluate high-strength HY ship steels and weldments in an environment simulating seawater under conditions of cathodic protection commonly used to protect ship hulls (Ref 66). Samples from the heat-affected zone (HAZ) and other locations in the weld metal were tested. Interlayer gas tungsten arc heating was evaluated as a means of providing a refined, homogeneous, tempered microstructure with improved resistance to hydrogen stress cracking. Test results showed that HY-180 is more susceptible to hydrogen stress cracking than HY-130 and that the resistance to hydrogen embrittlement of specimens taken from the HAZ and the fusion line is consistently higher than that of weld metal specimens (Ref 66).

Another application example of the rising step-load bend technique is the evaluation of potential-step polarization and hydrogen over-potential on crack propagation and crack arrest of T-250 maraging steel and PH-13-8Mo (UNS S13800) steel (Ref 67). In this case, the critical stress-intensity threshold for hydrogen-assisted cracking was measured as a function of potential. A fractographic examination of specimens tested at different potentials revealed distinct changes in the fracture mechanism as a function of potential. These changes are explained in terms of the decohesion model for hydrogen-assisted cracking. The crack arrest and propagation results reveal that the crack tip responds instantly to changes in the hydrogen activity from step polarization. The ability to arrest and restart crack propagation by stepping the applied potential at a constant applied stress intensity is demonstrated, proving that stress-intensity threshold is a direct function of hydrogen.

The disk-pressure test method measures the susceptibility to hydrogen embrittlement of metallic materials under a high-pressure gaseous environment (Ref 68). In this test, a thin disk of the metallic material to be tested is placed as a membrane in a test cell and subjected to helium pressure until it bursts. Because helium is inert, the fracture is caused by mechanical overload; no secondary physical or chemical action is involved. An identical disk is placed in the same test cell and subjected to hydrogen pressure until it bursts. Metallic materials that are susceptible to environmental hydrogen embrittlement fracture under a pressure that is lower than the helium-burst pressure; materials that are not susceptible fracture under the same pressure for both hydrogen and helium.

The test is used for the selection and quality control of materials, protective coatings, surface finishes, and other processing variables. The ratio, S_{H_2} , between the helium-burst pressure, P_{He} , and the hydrogen-burst pressure, P_{H_2} , indicates the susceptibility of the material to environmental hydrogen embrittlement. If S_{H_2} is equal to or less than 1, the material is not susceptible to environmental hydrogen embrittlement. When S_{H_2} is greater than 2, the material is considered to be highly susceptible. At values between 1 and 2, the material is moderately

susceptible, with failure expected after long exposure to hydrogen; therefore, the material must be protected against exposure.

A compilation of test results (Ref 3 and 68) indicate:

- Alloys having little or no sensitivity: 7075-T6 aluminum; Haynes 188 (cobalt base); beryllium copper (copper base); types 304, 316, and 310 austenitic stainless steel; type 430 ferritic steel; and age-hardened austenitic A 286 steel
- Alloys with high sensitivity: Cobalt- and iron-base alloys, including Haynes 25 and medium- and high-strength steels

Finite element models of the specimen have also been used for interpreting experimental results and to achieve a more general understanding of the capabilities of the disk pressure test for the characterization of hydrogen embrittlement effects (Ref 69).

Slow-strain-rate tensile tests can be used to evaluate many product forms, including plate, rod, wire, sheet, and tubing, as well as welded parts. Smooth, notched, or precracked specimens can be used. The principal advantage of this standardized test is that the susceptibility to hydrogen stress cracking for a particular metal/environment combination can be rapidly assessed. A variety of specimen shapes and sizes can be used; the most common is a smooth bar tensile coupon, as described in ASTM E 8. The specimen is exposed to the environment and is stressed under displacement control. For stainless steel in chloride solution, the strain rate is 10^{-6} s^{-1} . One or more of the following parameters are applied to the tensile test at the same initial strain rate:

- Time to failure
- Ductility, as assessed, for example, by reduction of area or elongation to fracture
- Maximum load achieved or reduction in ultimate and yield tensile stress
- Area bounded by a nominal stress-elongation curve or a true-stress/true-strain curve
- Presence of secondary cracking on the specimen gage section
- Appearance of the fracture surface

Slow-strain-rate tension testing is used extensively in the evaluation of environmentally assisted crack growth, and several standards have been published including:

Designation	Title
ISO 7539 (Part 7)	Slow Strain Rate Testing
ASTM G 129	Slow Strain Rate Testing to Evaluate the Susceptibility of Metallic Materials to Environment

Slow-strain-rate testing is used extensively in materials research, as described in more detail in Ref 70. The decreasing of fracture ductility from testing at a lowered strain rate in tension has been useful in establishing the threshold stress-intensity factor K_{th} of high-strength steel (Ref 71) consistent with the model of K_{th} behavior of high-strength steel suggested by Gerberich (Ref 72). The slow-strain-rate tension test has also confirmed that initiation of cracks with low concentration of hydrogen is a mainly strain-controlled process in steels (Ref 73).

References cited in this section

3. L. Raymond, Evaluation of Hydrogen Embrittlement, *Corrosion*, Volume 13, *ASM Handbook*, ASM International, 1987, p 283–284
5. W.W. Gerberich and S.-H. Chen, Environment-Induced Cracking of Metals, Fundamental Processes: Micromechanics, *Int. Conf. Environmentally Induced Cracking*, Oct 1988, National Association of Corrosion Engineers, 1990, p 167–187
6. W.W. Gerberich, P. Marsh, J. Hoehn, S. Venkataraman, and H. Huang, Hydrogen/Plasticity Interactions in Stress Corrosion Cracking, *Corrosion-Deformation Interactions*, CD1 '92, *Les Editions de Physique les Ulis*, T. Magnin, Ed., 1993, p 325–343

8. H.K. Birnbaum, I.M. Robertson, D. Sofronis, and D. Teter, Mechanism of Hydrogen-Related Fracture—A Review, *CDI '96*, T. Magnin, Ed., The Institute of Materials, 1997, p 172
9. M.-J. Lii, X.-F. Chen, Y. Katz, and W.W. Gerberich, Dislocation Modeling and Acoustic Emission Observation of Alternating Ductile/Brittle Events in Fe-3wt%Si Crystals, *Acta Metall.*, Vol 38, 1990, p 2435–2452
10. S.-H. Chen, Y. Katz, and W.W. Gerberich, Crack Tip Strain Fields and Fracture Microplasticity in Hydrogen Induced Cracking of Fe-3wt%Si Single Crystals, *Philos. Mag. A*, Vol 63 (No. 1), 1990, p 131–155
15. E.A. Steigewald, F.W. Schaller, and A.R. Troiano, *Trans. Metall. Soc. AIME*, Vol 218, 1960, p 832
17. H. Huang and W.W. Gerberich, Quasi-Equilibrium Modeling of the Toughness Transition During Semibrittle Cleavage, *Acta Metall. Mater.*, Vol 42 (No. 3), 1994, p 639–647
18. M.S. Daw and M.I. Baskes, *Phys. Rev. B*, Vol 29, 1984, p 6443
19. N.R. Moody, J.E. Angelo, S.M. Foiles, M.I. Baskes, and W.W. Gerberich, Atomistic Simulation of the Hydrogen-Induced Fracture Process in an Ion-Based Superalloy, *Sixth Israel Materials and Engineering Conf.*, D. Itshak, D. Iliezer, and J. Haddad, E., Ben-Gurion University of the Negev, 1993, p 444
20. C.L. Fu and G.S. Painter, *J. Mater. Res.*, Vol 6, 1991, p 719
21. X. Chen, T. Foecke, M. Lii, Y. Katz, and W.W. Gerberich, The Role of Stress State on Hydrogen-Induced Cracking in Fe-Si Single Crystals, *Eng. Fract. Mech.*, Vol 35 (No. 6), 1989, p 997–1017
27. D.G. Ulmer and C.J. Alstetter, Hydrogen Induced Strain Localization and Failure of Austenitic Stainless Steels at High Hydrogen Concentrations, *Acta Metall. Mater.*, Vol 39, 1991, p 1237
28. P.D. Hicks and C.J. Alstetter, *Metall. Trans. A*, Vol 23A, 1992, p 237
29. H. Vehoff and P. Neumann, *Acta Metall.*, Vol 28, 1980, p 265
30. W.W. Gerberich, H. Huang, and P.G. Marsh, Macroscopic and Microscopic Modeling of Hydrogen Embrittlement Thresholds, *Second Workshop on Hydrogen Effects on Materials in Propulsion Systems*, NASA Conf. 3182, Marshall Flight Center, 1992, p 196–203
31. J.J. Lewandowski and A.W. Thompson, *Hydrogen Effects on Material Behavior*, N.R. Moody and A.W. Thompson, Ed., TMS, 1990, p 817
32. D.S. Shih, I.M. Robertson, and H.K. Birnbaum, Hydrogen Embrittlement of α Titanium in situ TEM Studies, *Acta Metall.*, Vol 36, 1988, p 111
33. I.M. Robertson and H.K. Birnbaum, An HVEM Study of Hydrogen Effects on Deformation and Fracture of Nickel, *Acta Metall.*, Vol 34, 1986, p 353
34. H. Mathias, Y. Katz, and S. Nadiv, Hydrogenation/Gas Release Effects in Austenitic Steels: Quantitative Study, *Metal-Hydrogen Systems*, T.N. Vezirogen, Ed., Pergamon Press, 1982, p 225
35. Y. Katz, X. Chan, M.J. Lii, M. Lanxner, and W.W. Gerberich, The Anisotropic Nature of Local Crack Stability in BCC Crystals, *Eng. Fract. Mech.*, Vol 41 (No. 4), 1991, p 541–567

36. N.R. Moody, S.K. Venkataraman, R.Q. Hwang, J.E. Angelo, and W.W. Gerberich, Hydrogen Effects on the Fracture of Thin Tantalum Nitride Films, *Symp. Corrosion/Deformation Interactions*, 2, Vol 21, T. Magnin, Ed., Eur. Fed. Corrosion, 1997, p 227–237
37. W.W. Gerberich, R.A. Oriani, M.-J. Lii, X. Chen, and T. Foecke, The Necessity of Both Plasticity and Brittleness in the Fracture Thresholds of Iron, *Philos. Mag. A*, Vol 63 (No. 2), 1991, p 363–376
38. R.N. Parkins, Stress Corrosion Cracking, *EICM Proc.*, R.P. Gangloff and M.B. Ives, Ed., National Association of Corrosion Engineers, 1990, p 1
39. Y. Katz, A. Bussiba, and H. Mathias, The Influence of Austenitic Stability on Fatigue Crack Growth Retardation, *Material Experimentation and Design in Fatigue*, F. Sheratt, J.B. Sturgeon, and R.A.F. Farnborough, Ed., IPC Science and Tech. Press, Guildford, Surrey, 1981, p 147
40. C.W. Tien and C.J. Alstetter, Hydrogen-Enhanced Plasticity of 310S Stainless Steel, CDI '92, *Les Editions de Physique les Ulis*, T. Magnin, Ed., 1993, p 355
41. V.G. Gavriljuk, H. Hänninen, S.Yu. Smouk, A.V. Tarasenko, A.S. Tereschenko, and K. Ullakko, Phase Transformation and Relaxation Phenomena in Hydrogen Charged CrNiMn and CrNi Stable Austenitic Stainless Steel, *Hydrogen Effects in Materials*, A.W. Thompson and N.R. Moody, Ed., The Minerals, Metals, Materials Society, 1996, p 893
42. V.G. Gavriljuk, H. Hanninen, A.S. Tereschenko, and K. Ullakko, Effects of Nitrogen on Hydrogen-Induced Phase Transformation in Stable Austenitic Stainless Steel, *Scr. Metall. Mater.*, Vol 28, 1993, p 247
43. P. Sofronis and H.K. Birnbaum, Mechanism of Hydrogen-Dislocation-Impurity Interactions—I. Increasing Shear Modulus, *J. Mech. Phys. Solids*, Vol 43, 1995, p 49
44. H. Mathias, Y. Katz, and S. Nadiv, High Resolution Micro-Autoradiography as Complementary Research Technique, *Proc. Sixth Congress on Electron Microscopy*, D.C. Brandon, Ed., Tal. International, Jerusalem, 1976, p 399
45. P. Lacombe, M. Aucouturier, and J. Chene, Hydrogen Trapping and Hydrogen Embrittlement, *Hydrogen Embrittlement and Stress Corrosion Cracking*, R. Gibala and R.F. Hehemann, Ed., American Society for Metals, 1984
46. A.M. Brass and J. Chene, Hydrogen-Deformation Interactions in Iron and Nickel Base Alloys, *CDI '96*, T. Magnin, Ed., The Institute of Metals, 1997, p 197
47. A. Bussiba, H. Alush, and Y. Katz, Corrosion/Deformation Interactions in U/Water Systems, *Mater. Sci. Res. Int.*, Vol 3, 1997, p 244
48. R.A. Oriani and P.H. Josephic, *Acta Metall.*, Vol 22, 1977, p 979
49. H. Kobayashi and K. Ema, *Physics and Technology of Amorphous SiO₂*, R.A.B. Devine, Ed., 1987, Plenum Press, p 71
50. E.A. Clark, R. Yeske, and H.K. Birnbaum, The Effect of Hydrogen on the Surface Energy of Nickel, *Metall. Trans. A*, Vol 11, 1980, p 1903
51. J.P. Hirth, *Philos. Trans. R. Soc. London Ser.*, Vol 295, 1980, p 139
52. J.P. Hirth and J.R. Rise, *Metall. Trans. A*, Vol 11A, 1984, p 1501

53. T.Y. Zhang and J.E. Hack *Metall. Mater. Trans. A*, Vol 30, 1999, p 155
54. W.W. Gerberich, P. Marsh, and H. Huang, The Effect of Local Dislocation Arrangements on Hydrogen-Induced Cleavage, *Parkins Symposium on Fundamental Aspects of Stress Corrosion Cracking*, S. Breummer and W.W. Gerberich, Ed., TMS-AIME, 1992, p 191–204
55. S.T. Rolfe and I.M. Barsom, *Fracture and Fatigue Control in Structures*, Prentice-Hall, 1977
56. R.P. Wei, S.R. Novak, and D.R. Williams, Some Important Considerations in the Development of Stress Corrosion Cracking Test Methods, *Mater. Res. Stand.*, Vol 12 (No. 9), Sept 1972, p 25
57. C.A. Zanis, P.W. Holsberg, and E.C. Dunn, Jr., Seawater Subcritical Cracking of HY-Steel Weldments, *Weld. J. Res. Suppl.*, Vol 59, Dec 1980
58. “Rapid Inexpensive Tests for Determining Fracture Toughness,” NMAB-328, National Academy of Sciences, 1976
59. D.L. Dull and L. Raymond, Stress History Effect on Incubation Time for Stress Corrosion Crack Growth in AISI 4340 Steel, *Metall. Trans.*, Vol 3, Nov 1972, p 2943–2947
60. G. Liu-Nash, J.A. Todd, and S. Mostovoy, An Accelerated Test Method for Determining Near-Threshold Stress Intensity Values in HSLA Steels, *Fatigue and Fracture of Engineering Materials and Structures*, Vol 20 (No. 12), 1997, p 1657–1664
61. X.P. Zhang and Y.W. Shi, The Reasonable Design of Charpy-Size Specimen for Fracture Toughness Test in Nuclear Surveillance, *Int. J. Pressure Vessels Piping*, Vol 62 (No. 3), 1995, p 219–225
62. M. Wall, C.E. Lane, and C.A. Hipsley, Fracture Criteria for Hydrogen and Temper Embrittlement in 9Cr1Mo Steel, *Acta Metall. Mater.*, Vol 42 (No 4), April 1994, p 1295–1309
63. J.J. Lewandowski and A.W. Thompson, Hydrogen Effects on Cleavage Fracture in Fully Pearlitic Eutectoid Steel, *Hydrogen Effects on Material Behavior*, TMS, 1990, p 861–870
64. R.D. Kane, M.S. Cayard, and M. Prager, “Test Procedures for Evaluation of Resistance of Steels to Cracking in Wet H₂S Environments,” Paper No. 519, NACE International, 1994, p 22
65. D.L. Dull and L. Raymond, Electrochemical Techniques, *Hydrogen Embrittlement and Testing*, STP 543, ASTM, 1974, p 20–33
66. P.J. Fast, C.S. Susskind, and L. Raymond, “Charpy V-Notched Specimens for Indexing Stress Corrosion Cracking in HY Ship Steels and Weld Metals,” Final report, Contract F04701-78-C-0079, The Aerospace Corporation, Aug 1979
67. P.S. Tyler, M. Levy, and L. Raymond, Investigation of the Conditions for Crack Propagation and Arrest under Cathodic Polarization by Rising Step Load Bend Testing, *Corrosion*, Vol 47 (No. 2), 1991, p 82–87
68. J.P. Fiddle, R. Bernardi, R. Broudeur, C. Roux, and M. Rapin, Disk Pressure Testing of Hydrogen Environment Embrittlement, *Hydrogen Embrittlement Testing*, STP 543, ASTM, 1974, p 221–253
69. M. Beghini, G. Benamati, and L. Bertini, Hydrogen Embrittlement Characterization by Disk Pressure Tests: Test Analysis and Application to High Chromium Martensitic Steels, *J. Eng. Mater. Technol. (Trans. ASME)*, Vol 118 (No. 2), 1996, p 179–185

70. *Slow Strain Rate Testing for the Evaluation of Environmentally Induced Cracking: Research*, STP 1210, ASTM, 1993
71. B. Ule, F. Vodopivec, and L. Vehovar, The Application of Slow Strain Rate Tension Test for Quantitative Evaluation of Hydrogen-Induced Cracking Susceptibility of High Strength Steels, *ECF 8—Fracture Behaviour and Design of Materials and Structures*, Vol I, Engineering Materials Advisory Services Ltd., 1990, p 461–468
72. W.W. Gerberich, Effect of Hydrogen in High-Strength and Martensitic Steels, *Hydrogen in Metals*, American Society for Metals, 1976, p 115
73. B. Ule, F. Vodopivec, and L. Vehovar, The Application of Critical Strain Fracture Criteria for the Quantitative Evaluation of Hydrogen Embrittlement of High-Strength Steels, Conference: Use of Special Steels, Alloys and New Materials in Chemical Process Industries (Lyon, France, 22–23 May 1991), *Bull. Cercle D'Etudes Met.*, Vol 16 (No. 1), May 1991, p 28.1–28.11

Evaluation of Environmentally Assisted Crack Growth

Y. Katz, N. Tymiak, and W.W. Gerberich, University of Minnesota

Evaluation of Stress-Corrosion Cracking

Stress-corrosion cracking (SCC) can be influenced by a combination of anodic and/or cathodic reactions that influence crack growth mechanisms, as briefly summarized in Table 2. Thus, SCC can be a more complex process than hydrogen embrittlement, although many of the test methods are similar. Nonetheless, this section briefly describes the key features of SCC testing, as recently published in Ref 74. More detailed information on SCC testing is also contained in Ref 75 and 76.

Detailed information on SCC mechanisms and models is also beyond the scope of this article. Alloy design against SCC is an ongoing mission coupled with environmental control efforts. Generalized statements concerning interactive problems are not recommended, as they can be misleading. Table 3 summarizes typical SCC behavior for various alloy systems. In most cases, the scope of a comprehensive analysis must be designed to fit a given application.

Table 3 Stress-corrosion cracking of selected material systems

Material	Environment ^(a)	Applications	Remarks
Ferrous alloys			
Carbon steels, ferritic, pearlitic, or tempered martensitic (normally low carbon)	NaOH and nitrate solution H ₂ S, ammonia, carbonate/bicarbonate, aqueous solutions chlorides, seawater	Oil/gas production and transmission, oil refining, pulp and paper processing, power generation, marine and general application, wire products, strands, and wire ropes	Alloying has significant effects on SCC Crack propagation rate increases with water vapor lowering chloride concentration is beneficial.
High-strength steels (low or high alloy) normally tempered	Water and water vapor, aqueous electrolytes including phosphate ions, NaCl solutions, H ₂ S, strong acids, various organic	Aerospace, construction tools, dies, fasteners, landing gears, and general applications	Mutual considerations and compromises regarding alloying elements Trade-offs in mechanical

martensite	compounds		properties like yield strength, toughness, and SCC are controlled by alloying.
Ferritic stainless steels	Chloride ions aqueous solutions	Housewares, food industry (vessels, pipeline transmission, and general applications)	Highly sensitive to alloying elements with synergistic effects
Austenitic stainless steels	Chloride ion in solutions or steam, NaOH solutions, NaCl + H ₂ O ₂ solutions, seawater	Food industry (e.g., transmission) houseware, nuclear and chemical industry, biomedical instruments	Phase-stability aspects Attention also to carbon concentration and elements affecting sensitization
Duplex structure (combination of austenite and ferrite phases) stainless steels	Chloride ions (higher resistance than other stainless steel in some situations) aqueous solutions	Chemical and nuclear industry or more specific applications	Duplex stainless steel is picked to preserve a specific microstructure, thereby requiring particular attention to welding.
Martensitic and precipitation-hardening stainless steels	NaCl + H ₂ O ₂ , seawater, NaOH + H ₂ S, NaOH solutions, other sulfur compounds, marine environments	Aerospace, aeronautical, houseware, surgical tools	Used for applications that require high strength. This material group allows yield strength values to exceed 1100 MPa, calling for stress-intensity threshold evaluation.
Nonferrous alloys			
Low- and high-strength aluminum alloys	NaCl solutions, seawater, water vapor, aqueous solutions, halide ions, Cl, Br, and I solutions (synergistic effects)	General building construction elements, aerospace, aeronautic transportation, naval vessels	Attention to material selection in terms of alloy composition and strength Commercial aluminum alloys are well specified in material groups (composition and processing parameters). Combined environment and material group interaction differ regarding severity.
Nickel alloys	Pure steam, NaOH or KOH solutions, fused caustic sulfur compounds, various aqueous halide solutions, aqueous solutions, and cupric acid	Heat exchangers, higher-temperature applications in nuclear and chemical industry. Superalloys for jet engine components	Sensitive to microstructure and phases like γ, γ', and carbides
Copper alloys (including α or β brass)	Ammonia solutions, amines, water, mercury salt solutions, distilled water	General applications, munitions, marine components	...
Nickel-copper alloy (Monel)	HF or H ₂ SiFe ₆ solutions Mercury salt solutions	Specific corrosion-resistant applications	...
Titanium alloys	Seawater, organic liquids, N ₂ O ₄ , aqueous Cl, B, and I solutions, HCl + methanol solutions, HNO ₃ ,	Space, aircraft, biomedical prostheses, deep sea, and other specific applications	Microstructure and phase optimization for specific environment. Normally alloy types consider the α

	chlorinated hydrocarbons		(hexagonal closed packed) and the β (body-centered phase volume fraction). β at ambient temperatures is stabilized by alloying with Cr, Mo, V, Ta, and W.
Magnesium alloys	NaCl + K ₂ CrO ₄ solutions, marine atmosphere, distilled water, and other Cl ⁻ solutions	Specific applications relating to transportation	Highly reactive material group with intensive efforts for development in alloy design, i.e., ratio of strength to weight with acceptable properties
Zr alloys	Organic liquids Cl ⁻ solution I ² at elevated temperature	Nuclear applications for cladding and others based on beneficial nuclear properties	Attention to SCC susceptibility to iodine embrittlement
α -uranium alloys or stabilized γ -uranium	Cl solutions Water and wafer vapor Oxygen and hydrogen gas	Nuclear industry application for heavy metal specific applications	...
Thin-film aluminum and copper metallization	Hydrogen produced by thin-film processing or chemomechanical polishing; relative humidity attack of galvanic couples	Conductors, interconnects for microelectronics, optoelectronics, microelectromechanical systems, flexible circuits	Small volume effects on adhesion, strength, environmental susceptibility

(a) Environment here is used in the context of those known to produce SCC or hydrogen embrittlement, but those listed are not meant to be all-inclusive.

Besides common structural materials, there are special applications involving small-volume devices and multilayer or composite systems. To evaluate such materials, all the microstructural aspects and processing history must be provided (e.g., specific heat treatments and textures for structural components or sputtering temperatures and pressures for thin films).

Similar attention to detail applies to the environmental conditions where synergism is one of the major considerations. For example, in nuclear power stations, neutron or gamma radiation affects materials in terms of enhanced precipitation kinetics or reduced fracture resistance. Additionally, radiation affects the environment, for example, through radiolytic decay products. Informative background on such complexities has been published (Ref 38, 77, and 78). On the conceptual level, it is emphasized to the designer that design criteria can be established only when combined with experimental SCC evaluations.

Additional considerations include:

- High resistance to general corrosion is frequently a cause of major confusion when considering localized processes. General corrosion resistance of aluminum alloys, titanium alloys, or even nickel alloys does not imply resistance to local SCC under specific conditions.
- Attention should be given to processing variables. In many cases, alloy design is aimed at achieving some optimized conditions. This might necessitate sacrificing mechanical properties to minimize time-dependent damaging effects.
- Many applications, such as those associated with the power industry and others, follow restricted codes related to detrimental combinations of alloy concentration and impurities. Familiarity with the physical/chemical bases of such codes or standards for analogous applications are always beneficial.
- Although in many cases SCC arises from an ill-advised material selection, many also stem from poor assessment of the local mechanical/chemical loading factors.
- The distinction between long and small crack behavior is also a factor. Observations have confirmed that higher crack growth rates occur for small cracks compared to long cracks under identical applied stress-intensity conditions.

Considering the last point, the issue of crack size becomes particularly apparent regarding the initiation stage. During slow-strain-rate testing on smooth specimens, multicracking phenomena can also occur with different damage characteristics. At least intuitively, such behavior calls for a statistical approach, which potentially implies insight as to how one might approach design. Questions that might be included are:

- Is the attention only to the longest crack justified and at what stage of damage evolution?
- What about small crack coalescence that might evolve into a long-crack situation?

The latter is even more understandable in initiation-controlled processes. Critical crack growth does not necessarily involve a very long crack. Small cracks increasing by a factor of 2 to 3 can consume 80% of the total life (Ref 79).

Accordingly, other approaches, such as the one addressed by Parkins (Ref 80), have incorporated the aforementioned aspects. As indicated in Ref 80, the crack propagation rate is related to the crack density. Along with this, statistical models can be established for crack density and size with particular implication to the initiation stage and small crack growth. Interrupted tests as a function of time can establish crack-distribution functions incorporated in engineering models. Activities along such phenomenological lines have been conducted without using any mechanistic hypothesis (Ref 81). At this stage, a well-established methodology for design is not yet available, but the practical potential is self-evident. Although such a phenomenological approach is essential, the combination with mechanistic analysis would be more comprehensive. For such an analysis to be successful, a crack-distribution assessment should be assisted by high-resolution direct observation and not only by indirect methods such as acoustic emission.

References cited in this section

38. R.N. Parkins, Stress Corrosion Cracking, *EICM Proc.*, R.P. Gangloff and M.B. Ives, Ed., National Association of Corrosion Engineers, 1990, p 1
74. G. Koch, Stress Corrosion Cracking and Hydrogen Embrittlement, *Fatigue and Fracture*, Vol 19, *ASM Handbook*, ASM International, 1996, p 481–506
75. D. Sprowls, Evaluation of Stress-Corrosion Cracking, *Corrosion*, Vol 13, *ASM Handbook*, 1987, p 245–282
76. D. Sprowls, Evaluation of Stress Corrosion Cracking, *Stress Corrosion Cracking, Materials Performance and Evaluation*, ASM International, 1992, p 363–416
77. R.H. Jones and R.E. Ricker, Stress Corrosion Cracking Mechanisms, *Stress Corrosion Cracking, Materials Performance and Evaluation*, ASM International, 1992, p 1–41
78. R.W. Staehle, Understanding “Situation-Dependent Strength,” a Fundamental Objective in Assessing the History of Stress Corrosion Cracking, *EICM Proc.*, R.P. Gangloff and M.B. Ives, Ed., National Association of Corrosion Engineers, 1990, p 561
79. M.A. Gaudett and J. R. Scully, The Effects of Pre-Dissolved Hydrogen on Cleavage and Grain-Boundary Fracture Initiation in Metastable Beta Ti-3Al-8V-4Cr-4Mo-4Zr, *Met. Mater. Trans. A*, Vol 30A, 1999, p 65
80. R.N. Parkins, *Corros. Sci.*, Vol 29, 1989, p 1019
81. G. Santarini, A Morphological Model for Quantitative Characterization of Stress Corrosion Cracking, *CDI '96*, T. Magnin, Ed., The Institute of Metals, p 55

Evaluation of Environmentally Assisted Crack Growth

Y. Katz, N. Tymiak, and W.W. Gerberich, University of Minnesota

SCC Testing

In order to determine the susceptibility of alloys to SCC, several types of testing are available that are covered in ASTM standards:

ASTM No.	Title
G 30	Standard Practice for Making and Using U-Bend Stress-Corrosion Test Specimens
G 35	Standard Practice for Determining the Susceptibility of Stainless Steels and Related Nickel-Chromium-Iron Alloys to Stress-Corrosion Cracking in Polythionic Acids
G 36	Standard Practice for Evaluating Stress-Corrosion-Cracking Resistance of Metals and Alloys in a Boiling Magnesium Chloride Solution
G 37	Standard Practice for Use of Mattsson's Solution of pH 7.2 to Evaluate the Stress-Corrosion Cracking Susceptibility of Copper-Zinc Alloys
G 38	Standard Practice for Making and Using C-Ring Stress-Corrosion Test Specimens
G 39	Standard Practice for Preparation and Use of Bent-Beam Stress-Corrosion Test Specimens
G 41	Standard Practice for Determining Cracking Susceptibility of Metals Exposed under Stress to a Hot Salt Environment
G 44	Standard Practice for Exposure of Metals and Alloys by Alternate Immersion in Neutral 3.5% Sodium Chloride Solution
G 47	Standard Test Method for Determining Susceptibility to Stress-Corrosion Cracking of 2xxx and 7xxx Aluminum Alloy Products
G 58	Standard Practice for Preparation of Stress-Corrosion Test Specimens for Weldments
G 64	Standard Classification of Resistance to Stress-Corrosion Cracking of Heat Treatable Aluminum Alloys
G 103	Standard Test Method for Performing a Stress-Corrosion Cracking Resistance of Low Copper 7xxx Series Al-Zn-Mg-Cu Alloys in Boiling 6% Sodium Chloride Solution

In addition, other standards include:

Designation	Title
ISO 7539	Metals and Alloys—Stress-Corrosion Testing
DIN 50915	Testing the Resistance of Unalloyed and Low-Alloy Steels to Intergranular Stress-Corrosion Cracking
NACE TM0284	Evaluation of Pipeline Steels for Resistance to Stepwise Cracking
NACE TM0177	Laboratory Testing of Metals for Resistance to Specific Forms of Environmental Cracking

The general test methods and the type of information derived from testing are illustrated in Fig. 13. These test concepts apply to both SCC and hydrogen embrittlement. Tests for corrosion fatigue tests are also illustrated.

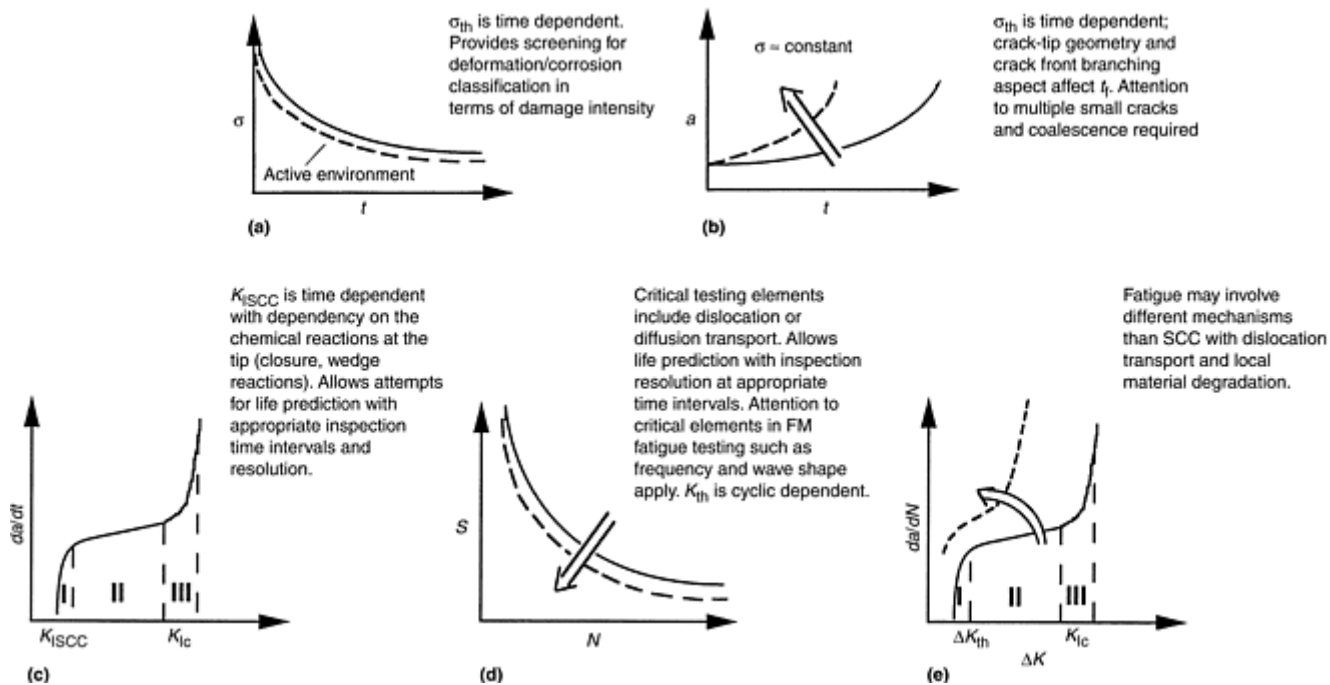


Fig. 13 General types of tests related to stress-corrosion cracking (SCC), hydrogen embrittlement, and corrosion fatigue. (a) Smooth specimen SCC testing for determination of a stress threshold, σ_{th} . (b) Slow-strain-rate (SSR) testing for strain-rate controlled evaluation of σ_{th} and time to failure, t_f . (c) Fracture mechanics evaluation with a notched or precracked specimen for determination of crack growth rate (da/dt) or crack growth threshold (K_{ISCC}). (d) Corrosion fatigue life ($S-N$) testing. (e) Corrosion fatigue crack growth testing for determination of crack growth rates of fatigue cracking threshold (ΔK_{th})

If the objective of testing is to predict the service behavior or to screen alloys for service in a specific environment, it is often necessary to obtain SCC information in a relatively short time. This requires acceleration of testing by increasing the severity of the environment or the critical test parameters. The former can be accomplished by increasing the test temperature or the concentration of corrosive species in the test solution and by electrochemical stimulation. Test parameters that can be changed to reduce the testing time include the application of higher stresses, continuous straining, and precracking, which allows bypassing the crack nucleation phase of the SCC process.

Stress-corrosion specimens can be divided into two main categories, namely smooth, and precracked or notched specimens. Further distinction can be made in the loading mode, such as constant deflection, constant load, and constant extension or strain rate. These different loading modes are briefly reviewed in the following sections. More detailed information is in Ref 76.

Important parameters during SCC testing include the orientation grain flow direction relative to stressing direction, surface condition, and residual stress. The nucleation of stress-corrosion cracks strongly depends on initial surface reactions, and thus the surface condition of the test specimens, particularly smooth specimens, has a significant effect on the test results. Smooth test specimens are often tested with a mechanically (machined or abraded) or (electro) chemically treated surface. It is very important to avoid or to remove machining marks or scratches perpendicular to the loading direction (per ASTM G 1, "Standard Practice for Preparing, Cleaning, and Evaluating Corrosion Test Specimens").

Reference cited in this section

76. D. Spowls, Evaluation of Stress Corrosion Cracking, *Stress Corrosion Cracking, Materials Performance and Evaluation*, ASM International, 1992, p 363–416

Smooth Specimen SCC Testing

Smooth SCC specimens allow for the evaluation of the total SCC life, which includes crack nucleation and propagation. Testing can be conducted under constant extension or strain, constant load, and constant extension or strain rate. The selection of a specific test method for SCC strongly depends on the particular service application and the time allowed for testing.

Constant Extension Testing

Constant extension or constant strain tests on smooth specimens are widely used and do not require elaborate testing fixtures. Depending on the specific configuration of the test articles, different types of constant extension tests are being used, the most common being bent-beam, U-bend, C-ring, and tensile type specimens. The simplest method of providing a constant load consists of a deadweight hung on one end of the specimen. This method is particularly useful for wire specimens. For specimens of larger cross section, however, lever systems such as those used in creep-testing machines are more practical. The primary advantage of any deadweight loading device is the constancy of the applied load.

Constant-strain SCC tests are performed in low-compliance tension-testing machines. The specimen is loaded to the required stress level, and the moving beam is then locked in position. Other laboratory stressing frames have been used, generally for testing specimens of smaller cross section.

Bent-Beam Specimens. The different types of bent-beam specimens are illustrated in Fig. 14. These specimens may be used to test sheet plate and flat extruded material, or wires and extrusions with a circular cross section. The figure shows that bending can be accomplished in several ways depending on the dimensions of the specimen. Stressing of the specimen is accomplished by bending the specimen in a stressing device, while restraining the ends. During stress-corrosion testing, both specimen and stressing device are exposed to the test environment. The most simple loading arrangement is the two-point loaded bent beam, which can only be used on relatively thin sheet or wire material. The elastic stress at the mid-point of the specimen can be estimated from the following equation:

$$L = (ktE/\sigma) \sin^{-1} (H/HktE)$$

where L is the specimen length, σ is the maximum stress, E is the elastic modulus, H is the length of holder, t is the specimen thickness, and k is the empirical constant (1.280).

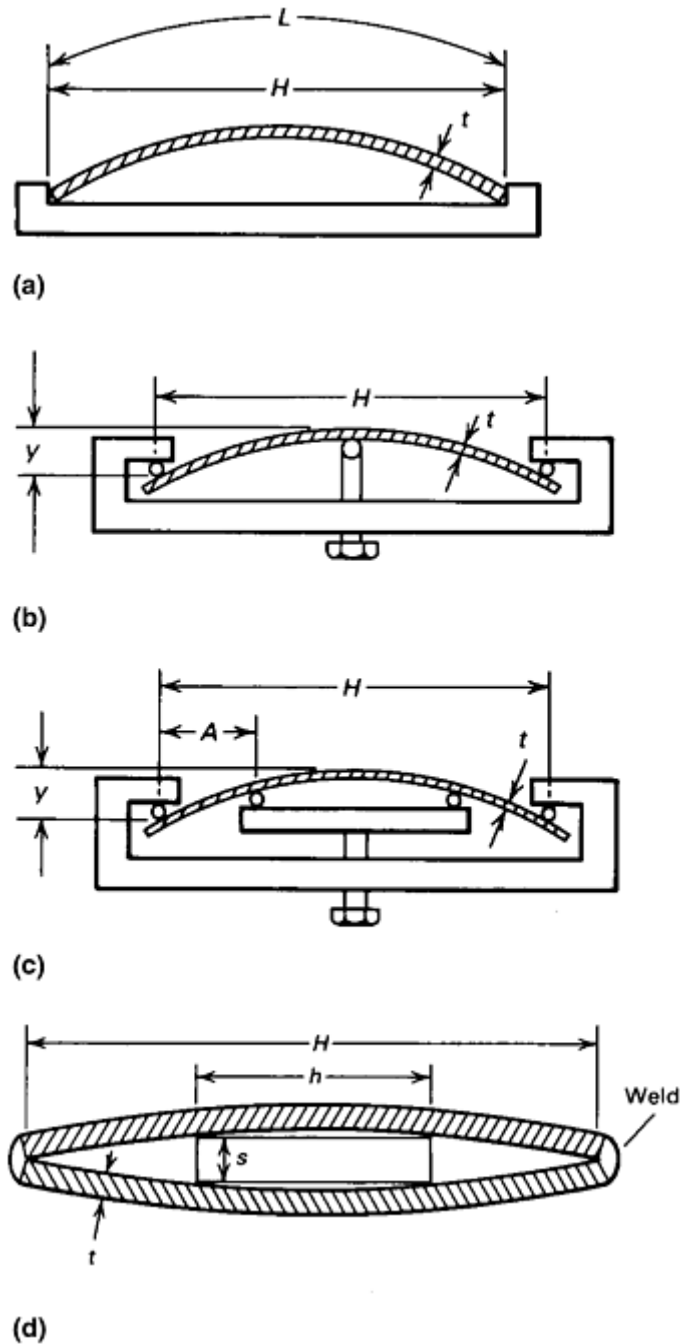


Fig. 14 Schematic specimen and holder configurations for bent-beam specimens. (a) Two-point loaded specimen. (b) Three-point loaded specimen. (c) Four-point loaded specimen. (d) Welded double-beam specimen. Source: ASTM G 9

Three-Point Bend Specimens. Three-point bend tests are commonly used because of the ease of load application and the ability to use the same loading rigs for different stresses. The load is applied by turning a bolt in the rig, deflecting the specimen. The elastic stress at the mid-point of the specimen is calculated from the following equation:

$$\sigma = 6Et y / H^2$$

where σ is the maximum tensile stress, E is the elastic modulus, t is the specimen thickness, y is the maximum deflection, and H is the length of holder.

This test has a number of disadvantages. First, dissimilar metal corrosion and/or crevice corrosion can occur under the bolt. Secondly, once the crack has formed, the stress condition changes such that the outer layer of the specimen is not subject to a tensile stress only, but to a complex combination at tensile and bending stresses. The propagating crack will then deviate from the centerline. Thus, the three-point bend test can only be used as

a qualitative test to assess the susceptibility to stress-corrosion cracking. With the four-point bend test, described in the next paragraph, tensile stresses can be maintained during the growth of the crack.

Four-Point Bend Specimens. Four-point bend testing provides a uniform tensile stress over a relatively large area of the specimen. The elastic stress in the outer layer of the specimen between the two inner supports can be calculated from the following equation:

$$\sigma = 12Ety/(3H^2 - 4A^2)$$

where σ is the maximum tensile stress, E is the elastic modulus, t is the specimen thickness, y is the maximum deflection, H is the distance between outer supports, and A is the distance between outer and inner supports.

U-bend specimens are prepared by bending a strip 180° around a mandrel with a predetermined radius (Fig. 15). The figure shows that bends less than 180° degrees are also used. Standardized test methods are described in ASTM G 30. Because of the ease of fabrication, a large amount of specimens can be fabricated, and this test is therefore widely used to qualitatively evaluate the susceptibility of alloy and heat treatment to stress-corrosion cracking.

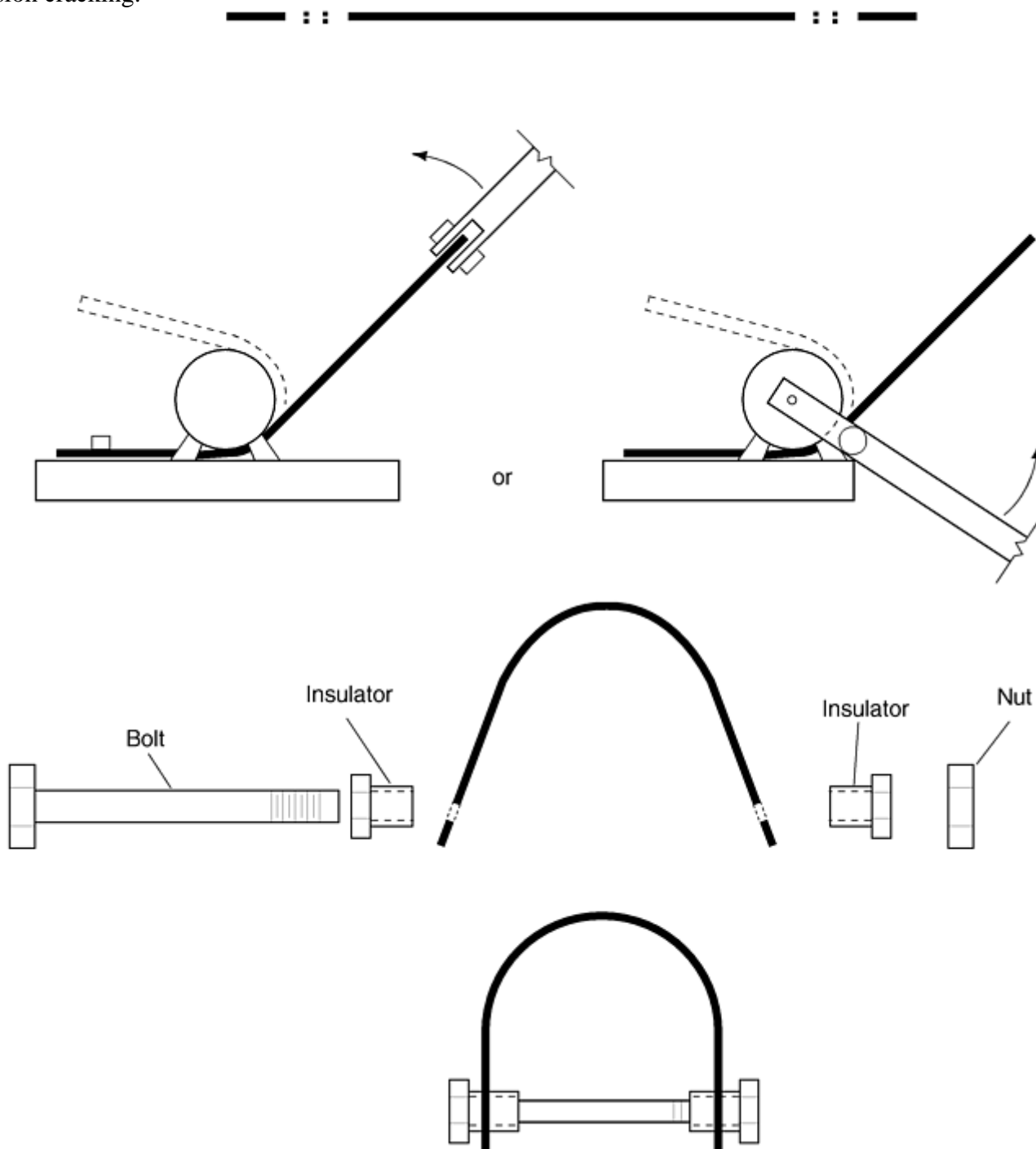


Fig. 15 Schematic two-stage stressing of a U-bend specimen. Source: ASTM G 30

A good approximation of the strain at the apex of the U-bend is:

$$\varepsilon = t/2R, \text{ when } t < R$$

where t is the specimen thickness and R is the radius of the bend. Then, an appropriate value for the maximum stress can be obtained from the stress-strain curve of the test material.

C-ring specimens are commonly used to determine the susceptibility to stress-corrosion cracking of alloys in different product forms. This test is particularly useful for testing of tubing, rod, and bar in the short-transverse direction, as illustrated in Fig. 16. The specimens are typically bolt loaded to a constant strain or constant load per ASTM G 338. If the stresses in the outer layers of the apex of the C-rings are in the elastic region, the stresses can be accurately calculated using the following equations:

$$D_f = D - \Delta$$

where

$$\Delta = \sigma d^2 / 4EtZ$$

and where D is the outer diameter of the C-ring before stressing, D_f is the outer diameter of stressed C-ring, σ is the elastic stress, Δ is the change of D at the desired stress, d is the mean diameter ($D - t$), t is the wall thickness, E is the elastic modulus, and Z is the correction factor for curved beam.

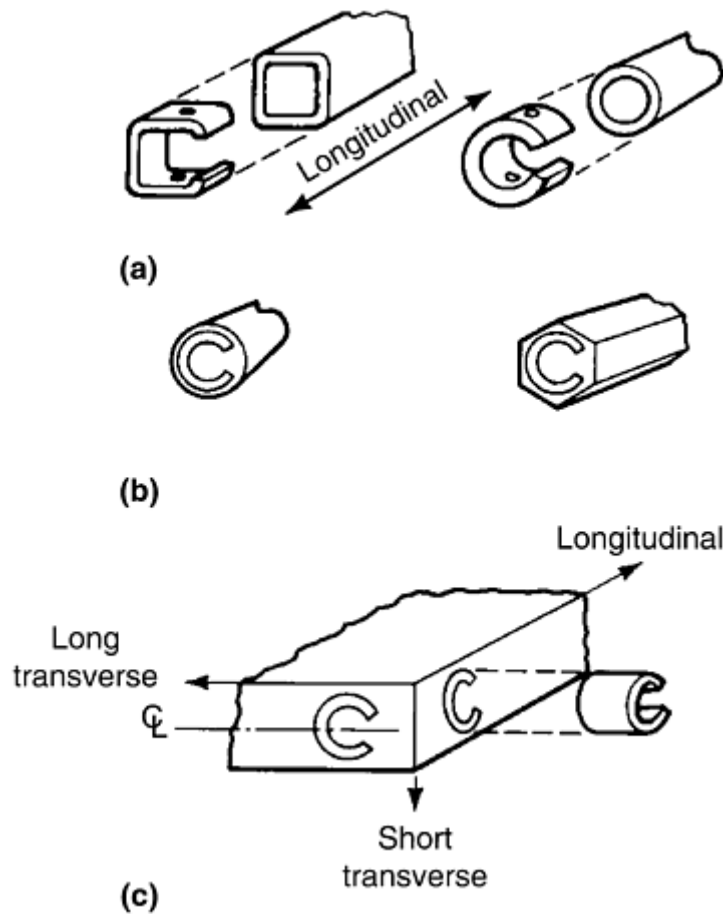


Fig. 16 Sampling procedure for testing various products with C-rings. (a) Tube. (b) Rod and bar. (c) Plate. Source: ASTM G 338

The stress on C-ring specimens can be more accurately determined by attaching circumferential and transverse strain gages to the stressed surface. The circumferential (σ_C) and transverse (σ_T) elastic stresses can be calculated with (Ref 82 and 83):

$$\sigma_C = E / (1 - \mu^2) \times (\varepsilon_C + \mu \varepsilon_T)$$

$$\sigma_T = E / (1 - \mu^2) \times (\varepsilon_T + \mu \varepsilon_C)$$

where E is the elastic modulus, μ is the Poisson's ratio, ε_C is the circumferential strain, and ε_T is the transverse strain.

Tensile Specimens. For specific purposes, such as alloy development, a large number of stress-corrosion specimens need to be evaluated. Tensile specimens have been used for this purpose where specimens used to determine tensile properties in air are adapted to SCC, as discussed in ASTM G 49. When uniaxially loaded in tension, the stress pattern is simple and uniform, and the magnitude of the applied stress can be accurately determined. Specimens can be quantitatively stressed by using equipment for application of either a constant load, a constant strain, or an increasing load or strain.

This type of test is one of the most versatile methods of SCC testing because of the flexibility permitted in the type and size of the test specimen, the stressing procedures, and the range of stress level. It allows the simultaneous exposure of unstressed specimens (no applied load) with stressed specimens and subsequent tension testing to distinguish between the effects of true SCC and mechanical overload.

A wide range of test specimen sizes can be used, depending primarily on the dimensions of the product to be tested. Stress-corrosion test results can be significantly influenced by the cross section of the test specimen. Although large specimens may be more representative of most structures, they often cannot be prepared from the available product forms being evaluated. They also present more difficulties in stressing and handling in laboratory testing.

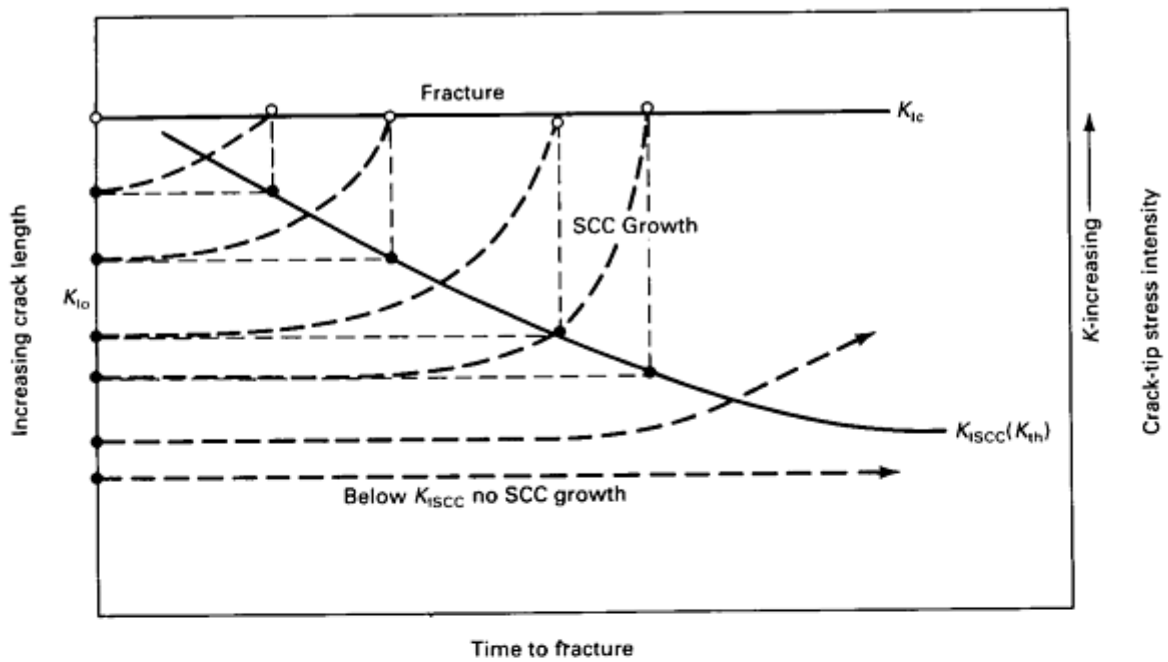
Smaller cross-sectional specimens are widely used. They have a greater sensitivity to SCC initiation, usually yield test results rapidly, and permit greater convenience in testing. However, the smaller specimens are more difficult to machine, and test results are more likely to be influenced by extraneous stress concentrations resulting from nonaxial loading, corrosion pits, and so on. Therefore, use of specimens less than about 10 mm (0.4 in.) in gage length and 3 mm (0.12 in.) in diameter is not recommended, except when testing wire specimens.

Tension specimens containing machined notches can be used to study SCC and hydrogen embrittlement. The presence of a notch induces a triaxial stress state at the root of the notch, in which the actual stress will be greater by a concentration factor that is dependent on the notch geometry. The advantages of such specimens include the localization of cracking to the notch region and acceleration of failure. However, unless directly related to practical service conditions, the results may not be relevant.

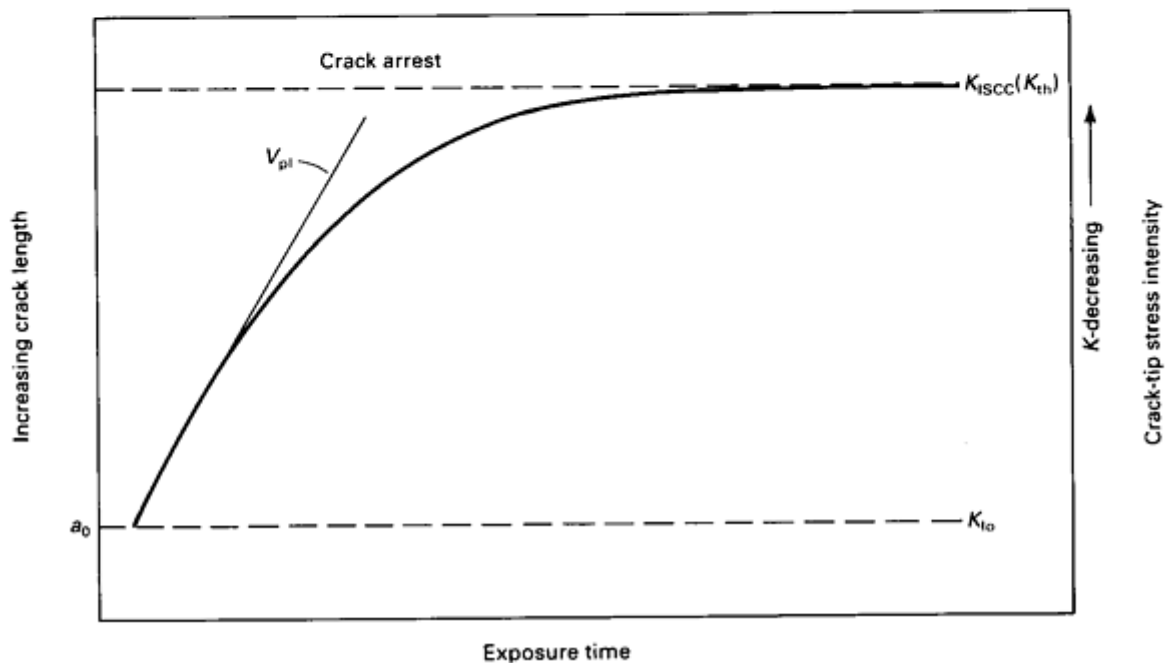
Tension specimens can be subjected to a wide range of stress levels associated with either elastic or plastic strain. Because the stress system is intended to be essentially uniaxial (except in the case of notched specimens), great care must be exercised in the construction of stressing frames to prevent or minimize bending or torsional stresses.

Constant Load Testing

Although the constant extension tests are widely used for evaluating the susceptibility of alloys to stress-corrosion cracking because of the ease of specimen preparation and the ability to test a large number of specimens at one time, there is one major drawback. Once stress-corrosion cracks have formed, the gross cross section stress decreases, which will eventually cause the crack to stop. Application of a constant or a static load provides an alternative test method that represents some actual field conditions that can provide threshold values. It should be cautioned, however, that such threshold values are strongly dependent on the method of loading (i.e., deadweight or spring) and the specimen size and cannot be considered a material property. Moreover, Fig. 17 and (Ref 84) shows that as a crack develops, the stress at the crack tip increases, possibly decreasing the time to failure.



(a)



(b)

Fig. 17 Schematic comparison of determination of threshold stress integrity factor (K_{ISCC} or K_{th}). (a) Constant-load (K -increasing) test. (b) Constant crack opening displacement (K -decreasing) test. Source: Ref 84

Constant Strain Rate Testing

Constant or slow-strain-rate testing is a very useful technique to evaluate the susceptibility of materials to SCC in a relatively short period of time (Ref 84 and 85). Typical strain rates range between 10^{-5} s^{-1} and 10^{-7} s^{-1} , but for most materials the typical strain rate is at 10^{-6} s^{-1} . The strain sensitivity to SCC can change for different alloys, even of the same metal. Figure 18 (Ref 85) shows that for the 2000 series aluminum alloys, the critical strain rate for the highest susceptibility to cracking is 10^{-6} s^{-1} , whereas no such critical strain rate exists for the

7000 series aluminum alloys. This difference in slow-strain-rate behavior of the two alloys may indicate different mechanisms for SCC. The slow-strain-rate behavior indicates that the principal mechanism for cracking of the 2000 series alloys is film rupture—anodic dissolution model, while the predominant mechanism for cracking of the 7000 series alloys is hydrogen embrittlement.

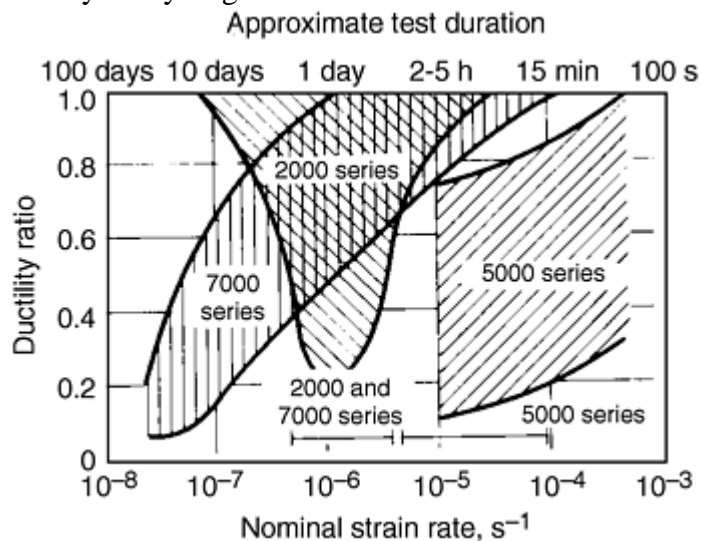


Fig. 18 Strain rate regimes for SCC of 2000, 5000, and 7000 series aluminum alloys in a 3% aqueous NaCl solution plus 0.3% H₂O₂. Source: Ref 85

The parameters that are typically measured in slow-strain-rate testing to determine the susceptibility to SCC are:

- Time to failure
- Percent elongation
- Percent reduction in cross-sectional area at the fracture surface
- Reduction in ultimate and yield tensile stress
- Presence of secondary cracking on the specimen gage section
- Appearance of the fracture surface

In order to assess the susceptibility of a material to SCC, the results of the slow-strain-rate test in a particular environment must be compared with those in an inert environment, such as dry nitrogen gas.

References cited in this section

82. *Stress Corrosion Testing*, STP 425, ASTM, 1967, p 3
83. H.L. Craig, D.O. Sprowls, and D.E. Piper, *Handbook on Corrosion Testing and Evaluation*, W.H. Ails, Ed., John Wiley and Sons, 1976, p 213
84. G. Vogt, *Werkstoff. Korros.*, Vol 29, 1978, p 721
85. N.J.H. Holroyd and G.M. Scamans, *Slow-Strain Rate Stress Corrosion Testing of Aluminum Alloys, Environment-Sensitive Fracture*, STP 821, S.V. Dean, E.N. Pugh, and G.M. Ugianski, Ed., ASTM, 1984, p 202

Precracked Specimen Testing

The use of precracked specimens in the evaluation of SCC is based on the engineering concept that all structures contain cracklike flaws. Moreover, precracking can contribute to the susceptibility to SCC of alloys such as titanium alloys, and this susceptibility may not always be evident from smooth specimens.

Precracking eliminates the uncertainties that are associated with crack nucleation and can provide a flaw geometry for which a stress analysis is available through fracture mechanics. Expressing stress-corrosion characteristics in terms of fracture mechanics provides a relationship between applied stress, crack length, and crack growth in a corrosive environment. When the plasticity can be ignored, or in other words, when the plastic zone ahead of the propagating crack is below a certain value and a triaxial or plane strain stress state exists at the crack tip, linear elastic fracture mechanics (LEFM) can be applied to describe the relationship between crack length (a) and the applied stress (σ) by the stress-intensity factor K :

$$K = F\sigma \cdot \sqrt{a}$$

where F is a polynomial factor that accounts for the specimen geometry. Linear elastic fracture mechanics, and thus the K factor, cannot be used to describe the relationship between applied stress and the crack length when there is significant plasticity or when the stress state at the crack tip is plane stress. Then, a more fundamental parameter, the J integral, is used.

Almost all standard plane strain fracture mechanics test specimens can be adapted to SCC testing. Several examples are illustrated schematically in Fig. 19 (Ref 76). ASTM E 399 describes the allowable specimen dimensions and test procedures for precracked specimens.

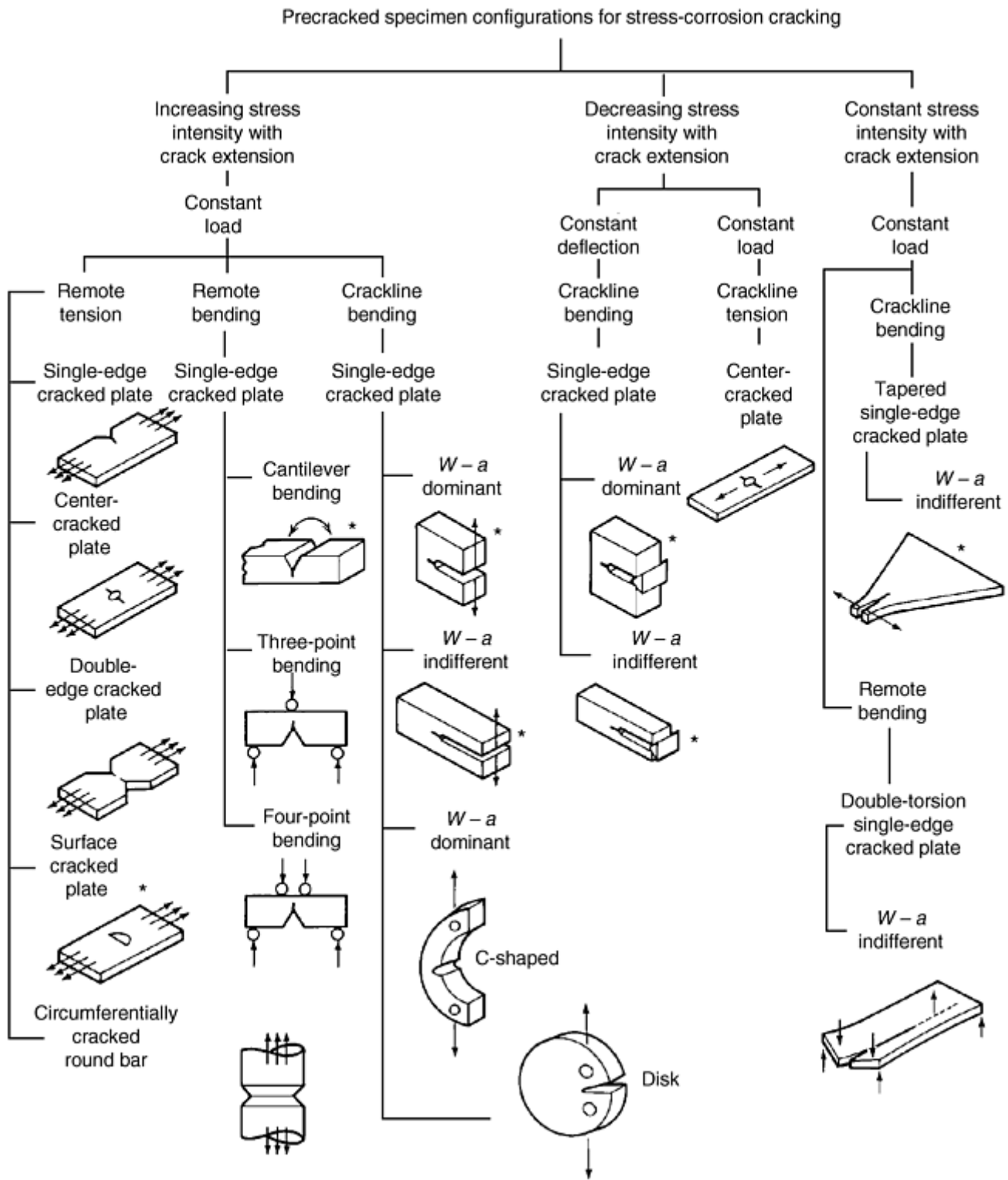


Fig. 19 Classification of precracked specimens for SCC testing. Source: Ref 76

Specimen Preparation. When using precracked fracture mechanics specimens, specific dimensional requirements need to be considered, as well as crack configuration and orientation. The basic dimensional requirement for application of LEFM is that dimensions are such that plane strain condition can be maintained. In general, for a valid K measurement, neither that crack length nor the specimen thickness should be less than $2.5 (K_{Ic}/\sigma_Y)^2$.

Several designs of initial crack configuration are available. ASTM E 399 recommends that the notch root radius is not greater than 0.127 mm (0.005 in.), unless a chevron notch is used, in which case it may be 0.25 mm (0.01 in.). In order to start out with a crack as sharp as possible, ASTM E 399 describes procedures for precracking.

The K level used for precracking should not exceed about two-thirds of the intended initial K value. This procedure prevents the forming of compressive stresses at the crack tip, which may alter the SCC behavior of the alloys.

Aluminum alloys can also be precracked by the pop-in method, where the wedge-opening method is used to the point of tensile overload. This method cannot be used for steels and titanium alloys, because of the strength of these alloys.

Loading Procedures. Stress-corrosion crack growth in precracked specimens can be studied in K -increasing and K -decreasing tests (Ref 84). In constant load or K -increasing tests, crack growth results in increased crack opening, which keeps the environment at the crack tip and corrosion products from interfering with crack growth. One of the problems with this mode of loading is that with increasing K , the plastic zone ahead of the crack tip may increase and at some point interfere with crack propagation. Moreover, for this type of testing bulky and relatively expensive equipment is required.

Constant displacement (K -decreasing) tests do not have the problems of the K -increasing tests indicated above. The plastic zone ahead of the crack tip does not increase with increasing crack size, so that the stress condition always remains in the plane strain mode. Also, the constant displacement tests can be self-loaded, and thus external testing equipment is not needed. Because in these tests the stress-intensity factor decreases with increasing crack growth, the stress-corrosion threshold stress-intensity factor (K_{Isc}) can be easily determined by exposing a number of specimens loaded to different initial K_I values. This can even be accomplished by crack arrest in one specimen.

A major problem with this test method occurs when corrosion products form in the crack, blocking the crack mouth and interfering with the environment at this crack tip. Moreover, the oxide can wedge open the crack and change the originally applied displacement and load.

Measurement of Crack Growth. In order to quantify the crack growth behavior in precracked stress-corrosion specimens, the crack length needs to be monitored, so that the crack velocity (da/dt) can be calculated, and the relationship between the increasing K and the crack velocity can be determined. There are basically three methods to monitor the growth of stress-corrosion cracks:

- Visual/optical measurements
- Measurement of the crack-opening displacement using clip gages
- The potential drop measurement, which monitors the increase in resistance across two points on either side of the propagating crack

These methods are described further in ASTM E 647, “Standard Test Method for Measurement of Fatigue Crack Growth Rates.”

References cited in this section

76. D. Sprowls, Evaluation of Stress Corrosion Cracking, *Stress Corrosion Cracking, Materials Performance and Evaluation*, ASM International, 1992, p 363–416

84. G. Vogt, *Werkstoff. Korros.*, Vol 29, 1978, p 721

Evaluation of Environmentally Assisted Crack Growth

Y. Katz, N. Tymiak, and W.W. Gerberich, University of Minnesota

Corrosion Fatigue

Similar to SCC and/or hydrogen embrittlement under monotonic loads, environmentally assisted crack growth occurs under fatigue conditions as well. Several mechanistic aspects are similar for these forms of

environmentally assisted crack growth, although several areas of corrosion fatigue are not fully clarified, particularly with respect to the numerous variables and complex interactions that may cause crack initiation. However, very useful information is available in the literature regarding computational mechanics and advanced experimental techniques for corrosion fatigue (e.g., Ref 86 and 87). General reviews on SCC and corrosion fatigue are also contained in Ref 88 and 89. This section is a brief overview on the key variables and test methods of corrosion fatigue testing from Ref 90.

References cited in this section

86. R.P. Gangloff, Corrosion Fatigue Crack Propagation in Metals, *EICM Proc.*, R.P. Gangloff and M.B. Ives, Ed., National Association of Corrosion Engineers, 1990, p 55
87. D.J. Duquett, Corrosion Fatigue Crack Initiation Processes—A State of the Art Review, *EICM Proc.*, R.P. Gangloff and M.B. Ives, Ed., National Association of Corrosion Engineers, 1990, p 45
88. R.W. Revie, *Uhlig's Corrosion Handbook*, 2nd ed., John Wiley & Sons, 2000
89. R. Baboian, Ed., *Corrosion Tests and Standards: Application and Interpretation*, ASTM, 1995
90. P.L. Andresen, Corrosion Fatigue Testing, *Fatigue and Fracture*, Vol 19, *ASM Handbook*, 1996, p 193–209

Evaluation of Environmentally Assisted Crack Growth

Y. Katz, N. Tymiak, and W.W. Gerberich, University of Minnesota

Key Test Variables (Ref 90)

The specific types and influence rankings of experimental variables in corrosion fatigue can vary markedly with specific alloy/environment systems. However, the following factors are crucial in most investigations of corrosion fatigue:

- Stress-intensity amplitude (ΔK) or stress amplitude ($\Delta\sigma$)
- Loading frequency (ν)
- Load ratio ($R = P_{\min}/P_{\max}$ or K_{\min}/K_{\max})
- Chemical concentration and contaminants (e.g., for aqueous environments: ionic species, pH, and dissolved species/gases, such as oxygen, hydrogen, and copper ion, that influence the corrosion potential)
- Alloy microstructure, yield strength, and often inhomogeneities, such as MnS and other inclusions and second phases, grain-boundary enrichment or depletion, and so forth

Other variables, such as load waveform, load history, and test temperature may also contribute, but they vary substantially in importance from system to system. Electrode potential should be monitored and, if appropriate, maintained constant during corrosion fatigue experimentation. Often, apparent effects of variables such as solution dissolved oxygen content, flow rate, ion concentration, and alloy composition on corrosion fatigue are traceable to changing electrode potential.

Stress-Intensity Amplitude (ΔK). While environmental crack growth rates increase with increasing ΔK , the specific dependency varies greatly. In some environments, the effect of environment is merely to offset the observed crack growth rate by some fixed factor above the inert rate. However, there is often a profound shift in the dependence of ΔK , typically producing a reduced ΔK dependence in aggressive environments, at least in the

intermediate region where power-law behavior is observed. It is always important to examine the entire relevant ΔK regime, not assuming the observed enhancement at a specific ΔK .

Environments do not always enhance the crack growth rate. The most common origins of crack retardation are associated with increased crack closure and crack blunting. Crack closure is most often increased by thicker oxides and perhaps the rougher (i.e., intergranular, with secondary cracks) fracture surface (Ref 91 and 92). Crack blunting results from aggressive environments that result in inadequate passivity. If the flanks of the crack are not adequately passive, then the crack tip will not remain sharp. This has been observed in low-alloy and carbon steels in hot water (Ref 93) and in other systems.

Shifts in ΔK , K_{max} , or load ratio during testing should be made very gradually, preferably continuously (e.g., under computer control). Changes in K should be limited to less than 10%, preferably much less. Any large change in growth rate should be confirmed using increments of <1%. Data may differ for rising K versus K -shedding conditions. Crack increments should be sufficient to provide statistically significant crack growth rates (e.g., >10 times above the crack length resolution) and should account for effects of plastic zone size under prior conditions during K -shedding. Shifts in frequency and hold time are not as restrictive, although changes greater than 3 to 10 times can lead to anomalous results.

The presence of an environment can also shift the dependence on stress amplitude ($\Delta\sigma$) or plastic strain amplitude ($\Delta\varepsilon$), not only by decreasing the stress at which a certain cyclic life can be attained, but also by eliminating the stress amplitude threshold altogether (Fig. 20). This, and increased scatter in the data, can lead to differences in estimating environmental effects at different stress amplitudes (Fig. 21). Note also that there is a consistent trend versus time in which the “bounding” curves are periodically shifted lower and to the left in Fig. 21.

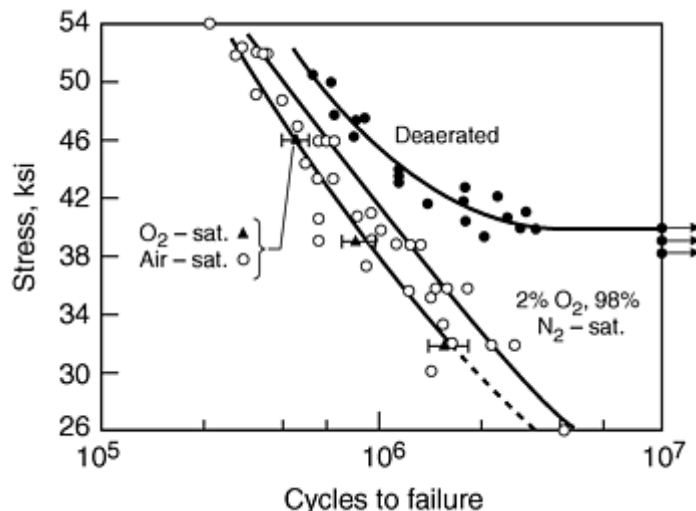


Fig. 20 Stress amplitude versus cycle to failure for corrosion fatigue of 0.18% C steel in 3% NaCl at 25 °C, showing the strong effect of dissolved oxygen in accelerating cracking and eliminating the stress threshold. Source: Ref 94

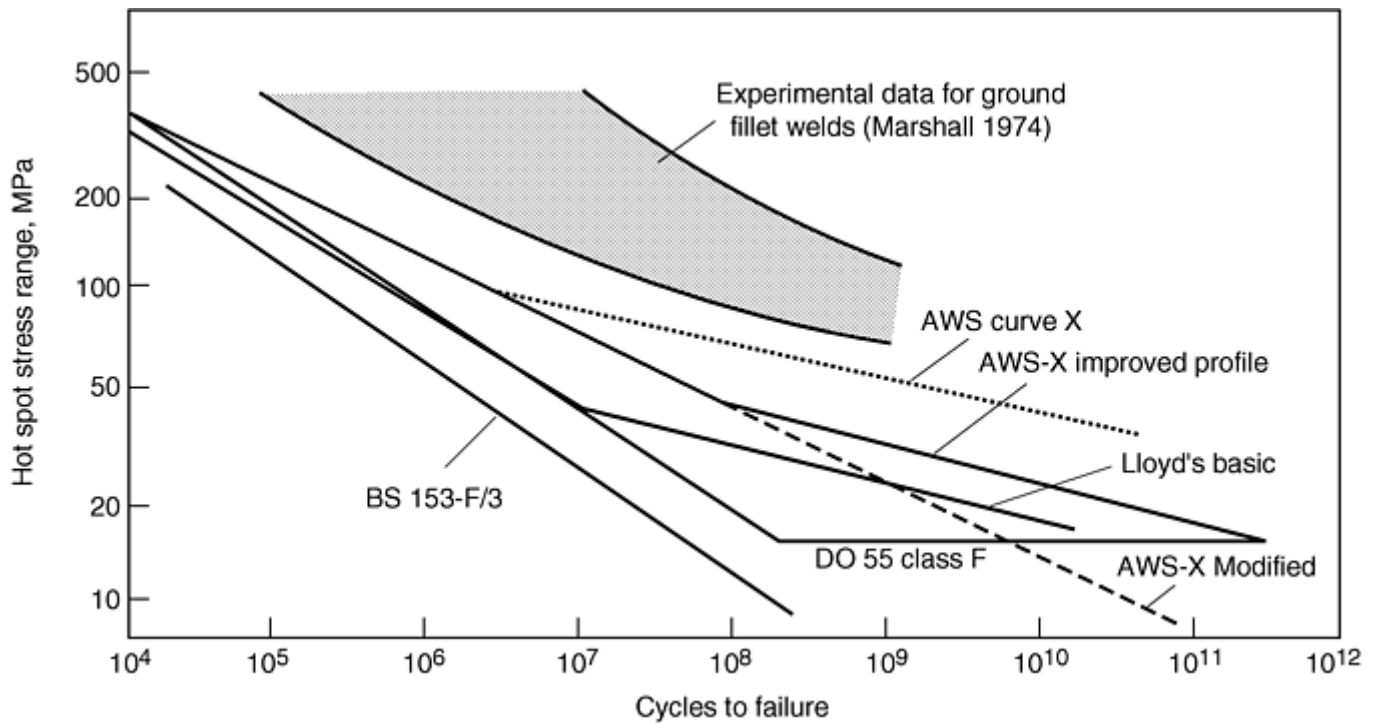


Fig. 21 Empirically derived design codes for corrosion fatigue of offshore welded tube structures, illustrating their invalidity under specific test conditions and their constantly changing formulation. Hot spot stress range refers to local peak stress amplitudes at specific locations of the structure. Source: Ref 95

Loading Frequency (ν). Because the environment induces a significant time-dependent response, environment enhancement can vary markedly with loading frequency. At high frequency, it is common for the environmental enhancement to be substantially eliminated because of inadequate time available for associated chemical reaction and mass transport kinetics. Transitions in significant environmental enhancement are often apparent when plotting crack growth rate versus frequency or hold time. Predictive modeling has been quite successful in accounting for the transition between cycle- and time-dependent behavior as a function of corrosion potential, water purity, and degree of sensitization of the stainless steel (Ref 96 and 97).

Load Ratio (R). At higher load ratios (P_{\min}/P_{\max}), corrosion fatigue crack growth rates are usually higher than in inert environments. This can be viewed as a mean stress effect, and the greater environmental enhancement can be considered to result from the expected increase in contribution of time-dependent crack advance that would occur even under static load conditions.

Test Environment and Chemical Contaminants. Besides the obvious concern of primary species (such as NaCl concentration for salt water) in corrosion fatigue, small amounts of contaminants are also a key variable. A striking example (Ref 98) of an environmental-purity effect is illustrated in Fig. 22 for gaseous hydrogen embrittlement of a low-strength carbon steel. Relative to vacuum, crack growth is accelerated by factors of 3 and 25 for moist air and highly purified low-pressure hydrogen gas, respectively. Small additions of oxygen to the hydrogen environment essentially eliminate the brittle corrosion fatigue component to crack growth, consistent with a trend first reported by Johnson (Ref 99). Similar effects have been reported for carbon monoxide and unsaturated hydrocarbon contamination of otherwise pure hydrogen environments. In aqueous environments, the effects of bulk ionic concentration and pH are often quite pronounced (especially in unbuffered systems), although dissolved oxidants are often of greater consequence (e.g., dissolved oxygen, hydrogen peroxide, and copper and iron ions), as are contaminants (e.g., dissolved sulfur, chloride, lead, mercury).

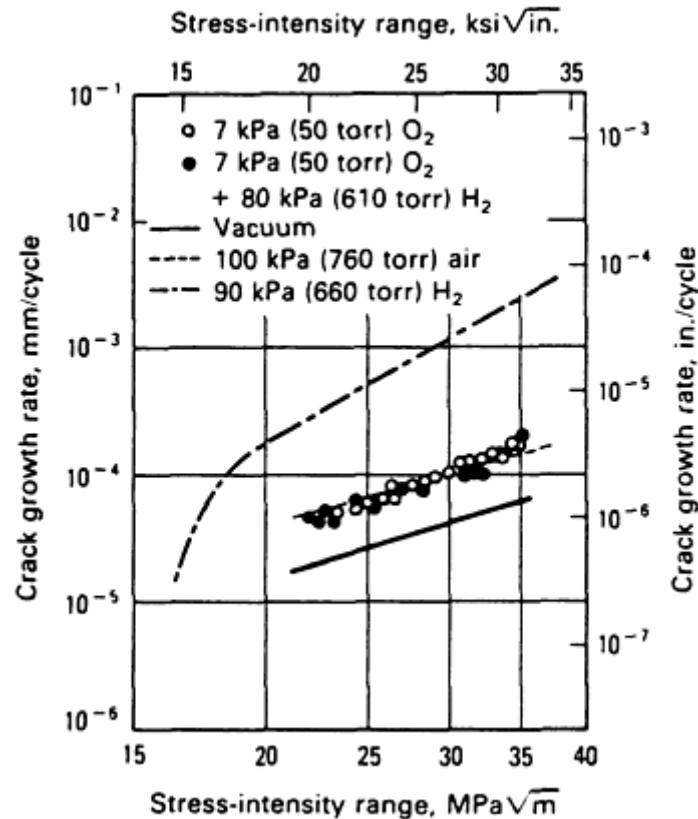


Fig. 22 Effect of oxygen (O₂) contamination on gaseous hydrogen embrittlement of a low-strength AISI/SAE 1020 carbon steel. Frequency: 1 Hz. Source: Ref 98

The primary role of oxidizing and reducing species, especially dissolved oxygen and hydrogen, is in shifting the corrosion potential. Some species, such as nitrate, may also directly influence crack chemistry and, if reduced to ammonia, can be directly responsible for environmental enhancement (e.g., of brasses). In many cracking systems, the role of oxidants (elevated corrosion potential) is an indirect one, because inside the crack the oxidants are generally fully consumed and the corrosion potential is low. In such systems, the role of oxidants is to create a potential gradient, usually near the crack mouth, that causes anions (e.g., Cl⁻) to concentrate in the crack and causes the pH to shift.

Oxidants increase the corrosion potential in aqueous environments, which can have very pronounced effects on environmental enhancement. This can occur at exceedingly low concentrations; in high-temperature water, crack growth rates can increase by orders of magnitude merely from the presence of parts-per-billion levels of dissolved oxygen in water. Similar enhancements are observed for small concentrations of aqueous impurities (e.g., <10 ppb of sulfate or chloride) or MnS inclusions in low-alloy and carbon steels, which dissolve within the crack to form sulfides. This usually is associated with the formation of a differential aeration cell by complete oxygen consumption within the crack (Fig. 23). Thus, even very small cracks usually advance under deaerated conditions, and the gradient in corrosion potential that is formed from crack mouth to crack tip causes an increase in anion concentration and a shift in pH in the crack. The shift is often acidic, but not necessarily so, because it requires the presence of non-OH⁻ anions to balance the acidity (H⁺). Thus, if only OH⁻ is present (e.g., from NaOH), the pH shift can only be in the alkaline direction.

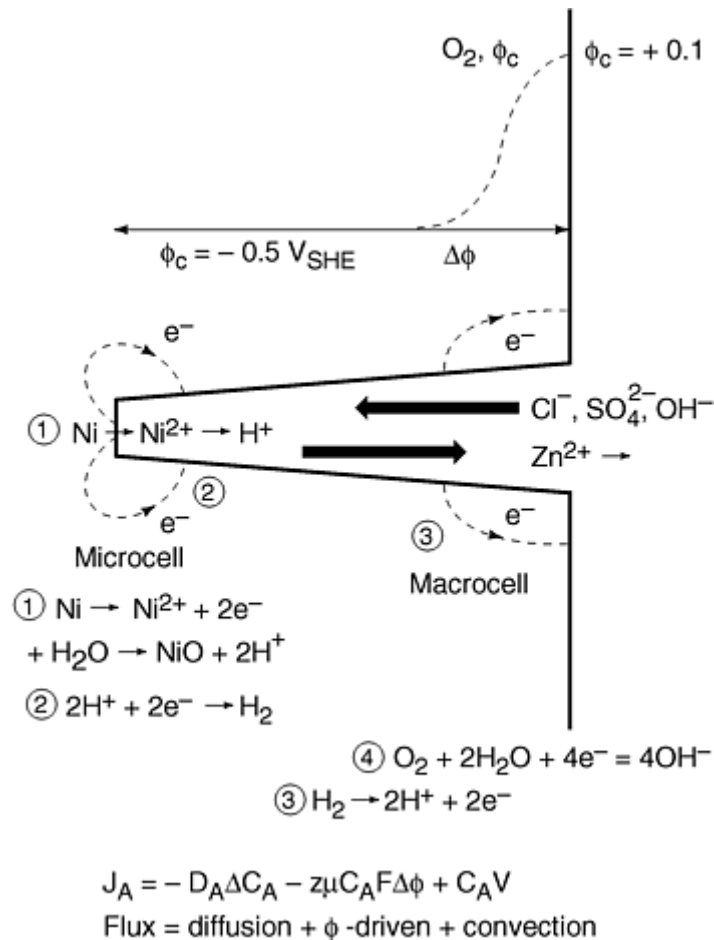


Fig. 23 Schematic of crack showing the differential aeration macrocell that establishes the crack-tip chemistry and the local microcell that is associated with metal dissolution and crack advance. Because the differential aeration macrocell is not essential to elevated crack growth rates, some coupling of the currents associated with these two cells may occur, but this is unnecessary. Source: Ref 100

Potentiostats can be used to control the specimen potential, although their use (which rarely directly simulates the real situation) can provide misleading data. Primary concerns are associated with:

- *Voltage drop in solution:* The reference electrode reading may be biased by the potential distribution in the solution associated with passage of ionic current.
- *Failure to polarize the crack tip:* Even in highly conductive solutions, the crack-tip potential is rarely significantly affected by external polarization, and therefore crack advance does not occur at the potential that is controlled on the specimen surface.
- *A reversal of surface reactions and shifts in local pH:* In solutions containing oxygen, the reaction on the external surface is cathodic, and inside the crack, anodic reactions occur. With a potentiostat, as the specimen is polarized to more positive potentials, it becomes more anodic and causes oxidation reactions to take place predominantly on the metal surface, which can alter the local pH. Cathodic reactions occur predominantly on the relatively remote counterelectrode.

To accurately measure potentials, commercial or custom-built reference electrodes are used. Both to measure potentials accurately and to prevent galvanic coupling, it is desirable to electrically isolate the specimen from the linkage and surrounding metal surfaces. If the environment is not very conducting or the potentials of surrounding metal surfaces are not too different from the specimen, electrical isolation may not be critical. However, it is then necessary to place the reference electrode much closer to the test specimen than to other (electrically connected) metal surfaces.

Other concerns for the environment include:

- Specimen and grip design (e.g., to avoid failure at crevices by minimizing stress in creviced regions)

- Proper design of environmental cells (e.g., to avoid contamination from leachants from or diffusion of oxygen through plastics)
- Maintenance of proper chemistry, which often requires refreshed/flowing systems for controlling the chemistry in gases or liquids
- Proper stability and measurement of temperature (near the specimen)
- Proper and thorough monitoring/recording of all relevant chemical and electrochemical parameters

Metallurgical Variables. Microstructure and alloy strength influence fatigue crack propagation in embrittling gases and liquids. In general, brittle corrosion fatigue cracking is accentuated by:

- Impurity (e.g., phosphorus or sulfur) segregation at grain boundaries
- Solute depletion or sensitization (e.g., chromium) about grain boundaries
- Planar deformation associated with ordering or peak-aged coherent precipitates
- Increased yield strength or hardness
- Large inclusions (e.g., MnS)

The effects of alloy composition, grain size, and microstructure (e.g., bainitic versus martensitic steel) vary with environment and brittle cracking mechanism. Laboratory experiments are necessary to establish specific trends. Yield strength plays a large role in environmental cracking, which has been attributed both to enhanced crack-tip strain rate as well as to complete shifts in the crack advance mechanism. The importance of hydrogen embrittlement in higher-strength materials has been confirmed by experiments in gaseous hydrogen. Its direct role in environmental crack advance is considered to be limited to about 150 °C (300 °F) in iron- and nickel-base alloys, although it may have an indirect role at higher temperatures.

Similar effects have been observed for bulk or surface cold work, which raises the yield strength. Thus, machining and surface treatments such as shot peening can significantly affect cracking. Shot peening and related treatments that produce surface compressive stresses can be very beneficial, provided that cracks do not exist (or form) and that tensile stresses do not exceed them. If sufficient strain occurs, transgranular cracks often nucleate in the surface-hardened region.

Other important microstructure factors include γ' or δ phases on grain boundaries of nickel alloys, martensite formation in steels, carbide formation (sensitization) in stainless steel and nickel alloys, and inhomogeneities (e.g., MnS and nonmetallic inclusions). These often have an even larger role in corrosion fatigue than under inert conditions, and a uniform microstructure or distribution of inhomogeneities can rarely be assumed.

Crack Closure Effects. Premature crack surface contact during unloading, or “crack closure,” can greatly reduce rates of fatigue crack propagation. The true (or effective) crack-tip driving force is reduced below the applied ΔK because of the reduced crack-tip displacement range. Closure phenomena are produced by a variety of mechanisms and are particularly relevant to fatigue crack propagation in the near-threshold regime, after large load excursions, or for corrosive environments.

Two mechanisms of crack closure are relevant to corrosion fatigue. Rough intergranular crack surfaces (typical of environmental embrittlement) promote crack closure, because uniaxially loaded cracks open in a complex three-dimensional mode, thus allowing for surface interactions and load transfer. Roughness-induced closure is most relevant to corrosion fatigue at low ΔK and at stress-ratio levels where absolute crack opening displacements (0.5–3 mm, or 0.02–0.12 in.) are less than fractured grain heights (5–50 mm, or 0.20–2 in.).

Alternately, crack closure is impeded by dense corrosion products within the fatigue crack. For mildly oxidizing environments, such as moist air, this closure mechanism is relevant at low stress-intensity levels and contributes to the formation of a “threshold,” as described in Ref 101.

For corrosive bulk environments or localized crack solutions, cracking at high ΔK values may be retarded below the growth rates observed for air or vacuum due to corrosion product formation within the crack. The engineering significance of beneficial crack closure influences depends on the stability of the corrosion product during complex tension-compression loading and fluid conditions.

References cited in this section

90. P.L. Andresen, Corrosion Fatigue Testing, *Fatigue and Fracture*, Vol 19, *ASM Handbook*, 1996, p 193–209

91. J.C. Newman, Jr. and W. Elber, Ed., *Mechanics of Fatigue Crack Closure*, STP 982, ASTM, 1988
92. P.L. Andresen and P.G. Campbell, The Effects of Crack Closure in High Temperature Water and Its Role in Influencing Crack Growth Data, *Proc. Fourth International Symp. on Environmental Degradation of Materials in Nuclear Power Systems—Water Reactors*, National Association of Corrosion Engineers, 1990, p 4-86 to 4-110
93. F.P. Ford, “Mechanisms of Environmental Cracking in Systems Peculiar to the Power Generation Industry,” Final Report NP-2589, Electric Power Research Institute, 1982
94. D.J. Duquette and H.H. Uhlig, *Trans. Am. Soc. Met.*, Vol 61, 1968, p 449
95. P.L. Andresen, R.P. Gangloff, L.F. Coffin, and F.P. Ford, Overview—Applications of Fatigue Analysis: Energy Systems, *Proc. Fatigue/87*, EMACS, 1987
96. F.P. Ford, D.F. Taylor, P.L. Andresen, and R.G. Ballinger, “Corrosion Assisted Cracking of Stainless and Low Alloy Steels in LWR Environments,” Final Report NP-5064-S, Electric Power Research Institute, 1987
97. P.L. Andresen and F.P. Ford, Use of Fundamental Modeling of Environmental Cracking for Improved Design and Lifetime Evaluation, *J. Pressure Vessel Technol. (Trans. ASME)*, Vol 115 (No. 4), 1993, p 353–358
98. H.G. Nelson, Hydrogen Induced Slow Crack Growth of a Plain Carbon Pipeline Steel under Conditions of Cyclic Loading, *Effect of Hydrogen on the Behavior of Materials*, A.W. Thompson and I.M. Bernstein, Ed., The Metals Society—American Institute of Mining, Metallurgical, and Petroleum Engineers, 1976, p 602–611
99. H.H. Johnson, Hydrogen Brittleness in Hydrogen and Hydrogen-Oxygen Gas Mixtures, *Stress Corrosion Cracking and Hydrogen Embrittlement of Iron Based Alloys*, J. Hochmann, J. Slater, R.D. McCright, and R.W. Staehle, Ed., National Association of Corrosion Engineers, 1976, p 382–389
100. P.L. Andresen and L.M. Young, Characterization of the Roles of Electrochemistry, Convection and Crack Chemistry in Stress Corrosion Cracking, *Proc. Seventh International Symposium on Environmental Degradation of Materials in Nuclear Power Systems—Water Reactors*, National Association of Corrosion Engineers, 1995, p 579–596
101. S. Suresh and R.O. Ritchie, *Int. Metals Rev.*, Vol 29, 1984, p 445–476

Evaluation of Environmentally Assisted Crack Growth

Y. Katz, N. Tymiak, and W.W. Gerberich, University of Minnesota

Corrosion Fatigue Crack Growth Test Methods (Ref 90)

Standard methods of fatigue crack growth (as defined in ASTM E 647 and described in the article “Fatigue Crack Growth Testing” in this Volume) are generally applicable to corrosion fatigue crack growth tests. ASTM E 647 also contains an appendix specific to crack growth in marine environments. Procedures for other corrosion fatigue environments are not standardized, but various methods have evolved. Some general aspects of corrosion fatigue crack growth are described below, and additional background is provided in Ref 102.

Three problem areas are relevant to corrosion fatigue experimentation. First, the environment must be contained about the cracked specimen without affecting loading, crack monitoring, or specimen-environment composition. Parameters such as environmental purity, composition, temperature, and electrode potential must be monitored and controlled frequently.

Second, the deleterious effect of low cyclic frequency dictates that crack growth rates must be measured at low (often <0.2 Hz) frequencies, which lead to long test times, often from several days to weeks. Load-control and crack-monitoring electronics and environment composition must be stable throughout long-term testing.

Third, crack length must also be measured for calculations of stress intensity and crack growth rate. Optical methods are often precluded by the environment and test chamber. Indirect methods, based on specimen compliance or electrical potential difference, have been applied successfully to monitor crack growth in a wide variety of hostile environments and are described in more detail below. Experimental and analytical requirements, however, are complex for indirect crack monitoring.

Finally, specimen thickness, as it influences the degree of plane-strain constraint, and crack size, as it influences the chemical driving force, may affect corrosion fatigue crack speeds. Currently, such effects are unpredictable; specimen thickness and crack geometry must be treated as variables. In corrosion fatigue, the electrochemistry within the crack is mass transport dependent and can vary with crack depth, and possibly also with specimen geometry and with accessibility of solution in the through-thickness direction via the crack sides. These factors can influence crack growth rates despite the constancy of the range of the stress-intensity factor.

Because corrosion fatigue testing is often performed at low cyclic frequencies, multiple test stations are desirable. For this reason and for general economy, compact tension specimens are frequently used. Such specimens minimize the applied load required to achieve a given crack-tip stress intensity, thus permitting the use of low-load capacity and less expensive test machines. In applying load to specimens in a test cell, cell friction must not affect load in sealed systems. This is generally not a significant factor in most ambient-temperature applications, however. Insulation between specimens and grips, pin assemblies, and so forth is essential to avoid galvanic effects, but greases should not be used.

Electrode Potential

Monitoring and reporting the electrode potential during corrosion fatigue experiments is important. The potential should be measured using a reference electrode located in the bulk solution adjacent to the specimen. When impressed currents are applied to the specimen, measurement should be made adjacent to the surface using a Luggin capillary to minimize the potential drop between the reference electrode and the metal surface, the magnitude of which will depend on the solution conductivity and flow of current.

Selection of a reference electrode depends on the particular application, but those most commonly used in laboratory room-temperature tests are the SCE and the silver/silver chloride electrode. For some solutions in which contamination with chloride is undesirable, use of a mercury/mercurous sulfate reference electrode is an option. Contamination can be reduced by using commercially available double-junction electrodes, in which the outer jacket is filled with test solution.

In quoting measured potentials, the potential should be referred to a standard scale such as the standard hydrogen electrode (SHE) or the SCE at $25\text{ }^{\circ}\text{C}$ ($75\text{ }^{\circ}\text{F}$). In tests remote from $25\text{ }^{\circ}\text{C}$ ($75\text{ }^{\circ}\text{F}$), allowance must be made for the fact that the half-cell potential of the reference electrode varies with temperature. A high-impedance meter ($>10^{12}$ W), such as an electrometer or a pH meter, should be used for monitoring potential, although periodic (short-term) measurements can usually be successfully performed using digital voltmeters whose input impedance is $\geq 10^9\ \Omega$ (usually limited ≤ 2 V full-scale direct-current, dc, ranges).

Near room temperature, it generally is possible to use commercial reference electrodes such as calomel and silver chloride electrodes; some electrode designs permit use near boiling. Designs that place the reference electrode in a separate chamber at a different temperature than the test solution are complicated by formation of a thermal junction potential in the electrolyte, the magnitude of which may be large (above 0.1 V).

At temperatures above boiling, a custom reference electrode generally is necessary. Most investigators use internal or external silver/silver chloride reference electrodes. For internal electrodes, the silver chloride reaction occurs at the test temperature. For external electrodes, the silver chloride reaction occurs at room temperature, but system pressure is applied (so no streaming potentials form), with a temperature gradient occurring in the potassium chloride electrolyte as it enters the autoclave. A porous junction in the autoclave

isolates the potassium chloride electrolyte from the autoclave solution. This thermal junction potential has been well characterized over a range of temperatures and potassium chloride concentrations (Ref 103).

Potentials should be reported on the SHE scale, particularly for elevated-temperature tests, for which the conversion factors to V(SHE) are not widely known. However, when comparing results as a function of temperature, it may be helpful to eliminate the contribution of the standard hydrogen cell, because as in other reactions, it has a potential that varies with temperature. It is by convention that the standard hydrogen cell is 0 V at any temperature; relative to the standard hydrogen reaction at 25 °C (75 °F), the potential of the standard hydrogen reaction is about 0.021 V at 50 °C (120 °F), 0.057 V at 100 °C (212 °F), 0.086 V at 150 °C (300 °F), and about 0.105 V between 210 and 300 °C (410 and 570 °F).

Application of imposed potential using a potentiostat requires electrical isolation of the specimen. In some cases, it may be difficult to insulate the specimen from the loading linkage; instead, the linkage must be insulated from the autoclave, and the measured current flow cannot be attributed only to reactions at the specimen. Ground loops present perpetual problems, because most potentiostats are designed to hold the specimen at ground (or virtual ground). With necessary mechanical and plumbing connections, the autoclave is usually connected to ground; thus, the specimen is effectively connected to the autoclave. The problem is compounded if the autoclave is used as the counterelectrode, because the ground loop shorts out the potentiostat. Options include thorough electrical isolation of the autoclave from ground and use of a fully floating potentiostat.

Attachment of a lead to the specimen to permit measurement or application of potential can be a challenge in aggressive environments. Recommendations include use of wire that is either identical to the specimen or a very noble metal, such as platinum. Attachment using a weld bead (e.g., by gas-tungsten arc welding) usually is superior to spot welding. Covering the lead wire with heat-shrink Teflon and, at low test temperatures, covering the weld with an organic “stop-off” coating helps maintain a good connection and minimizes the effects of the wire (via galvanic coupling or its contribution to the measured current). Another technique involves the use of a commercially available plasma sprayed insulating coating, which can also be used in high-temperature water.

Errors in the potential applied by a potentiostat can occur in solutions of low conductivity. These iR drops, which result from current flow between the counterelectrode and working electrode in the high-resistance solution, are detected by the reference electrode and summed with the electrode potential of the specimen. Electronic compensation is possible, but not straightforward in most high-resistivity media. Partial compensation is possible by placing the reference electrode near the specimen, although for small specimens the measured potential becomes very sensitive to electrode positioning. A rough estimate of the possible error can be made by multiplying the resistivity of the solution (preferably determined by measuring the alternating current, ac, flowing between the counterelectrode and working electrode when a known 1000 Hz ac voltage is applied) by the potentiostat current that flows during a test.

Monitoring Crack Length

The electrical potential technique and the compliance method are frequently used to monitor fatigue crack growth in solution and in gaseous environments. Visual methods generally are not practical; often, the crack and the test specimen are obscured by the test chamber, or a microscope with a long focal length is needed.

The electrical potential technique is preferred over the compliance method for use inside an environmental test chamber, because the compliance gage may outgas and is a potential source of test environment contamination. Its use in a corrosive environment is also unsuitable. The electric potential technique, however, is noncontaminating and can be used in most environments.

Use of the compliance method is generally limited to compact tension (CT, or compact type) and wedge-opening load specimens. It is not used for center-cracked tension specimens because of limitations in sensitivity and accuracy. The electrical potential technique can be readily applied to all three specimen types. The principal drawback of the electrical potential technique is that the specimen must be electrically conductive; thus, it cannot be applied directly to specimens made of nonelectrically conducting materials, such as polymer-based composites and ceramics. In addition, electrical shorting across the crack surfaces may affect its measurement accuracy, particularly for tests in vacuum. Both the electrical potential and compliance techniques can be readily interfaced with a computer for real-time control of the experiment and for online data acquisition and reduction.

Potential Drop Method. The most common and sensitive in situ crack monitoring technique is reversing dc potential drop, which typically applies a constant current to a specimen and measures the changes in potential across the specimen as the crack grows. High-quality implementations of dc potential drop are consistently able to achieve a crack length resolution on 1T compact-type specimens of about 1 mm (0.04 in.), and an overall accuracy of <5% on the overall increment in crack advance. Current and potential leads can be insulated using Teflon tubing for test temperatures up to 300 °C (570 °F); above 300 °C, zirconia is generally used.

During environmental testing, there are several special considerations. Solution conductivity can be a major issue; an extreme example is the inability to use potential drop in liquid metal environments. Some deviations in crack length versus measured potential response can also occur in highly conducting environments (e.g., aqueous solutions), and it must be recognized that the crack chemistry can be substantially more conductive and at different pH than the bulk solution. However, despite the small distance between the upper and lower crack flanks, the role of ionic (e.g., aqueous) conductivity is not large compared to that of metal conductivity, because aqueous conductivities are typically measured in 10^{-1} to 10^{-6} S/cm (S, or Siemen, is W^{-1}), whereas metal conductivities are typically between 10^5 and 10^6 S/cm. Thus, errors associated with aqueous environments are relatively small, although not always ignorable.

Another concern relates to inaccuracies in indicated crack length because of a nonuniform crack front or because of metal contact along the crack flank during the fatigue cycle. In both cases, an abnormal fraction of the dc current “shorts” through the uncracked metal ligament in the wake of the nominal crack front, and the measured potential and indicated crack length is strongly affected. For example, if the crack front moves forward in a 25 mm (1 in.) compact-type specimen by 3 mm (0.12 in.) in all locations except along one narrow, rectangular ligament that is only 1 mm (0.04 in.) wide, the indicated crack advance by potential drop can be very small (i.e., dramatically less than the area average of crack advance). Nonuniform crack fronts are much more common when the environmental contribution to crack advance is high, and static loading (stress-corrosion cracking) is generally much worse than dynamic loading (e.g., corrosion fatigue). Certain microstructures, such as weld metal, can be quite susceptible to accelerated or retarded crack advance in localized regions (i.e., along certain weld dendrites). The “unzipping” of the final metal ligament can lead to anomalously high “apparent” crack growth rates over certain testing periods.

Other concerns for dc potential drop include electrochemical effects, particularly polarization. If a well-designed, ground isolated power supply is used, then all of the dc current that leaves the “+” terminal must return on the “-” terminal, and direct polarization of the specimen is not possible. In most cases, there is little basis for concern for the electrochemical effects of using dc potential drop, although, for example, the small potential difference between the crack flanks could have some influence in tight cracks in conductive solutions. This potential difference is very small near the crack tip, so it is more likely to influence, for example, dissolution of MnS inclusions at some distance toward the crack mouth, where the potential difference across the crack flanks is higher. While the potential difference between the upper and lower surfaces of the crack is small (typically 100 mV in many potential drop implementations), the gradient can be relatively large because of the small separation of the crack faces. The importance of this issue can be quantified by establishing a steady-state crack growth rate and disconnecting the potential drop system for a period of time, then reconnecting it to evaluate its effect (or by comparing a duplicate experiment using an extensometer to monitor the crack growth rate).

Electrochemical effects can also result from improperly insulated dc current leads. Because significant current is passed through leads that are often relatively small, the potential drop in the current leads can be large (e.g., >1 V). If the current leads are not continuously insulated through the entire solution right up to the location where they are spot welded onto the specimen, there is an opportunity for crosstalk with closely adjacent potential leads (where the signal is typically 100 mV). Additionally, biasing of the specimen can occur if the current leads are not continuously insulated through the system seals. Any ionic communication in the tight-fitting seal area permits leakage to the metal (e.g., autoclave), and a circuit is established. The current leads act like a 1 V battery that is shared across two resistors, one representing the water resistivity in the seal and one representing the water resistivity between the specimen and the autoclave. This can cause some polarization of the specimen in conductive solutions, or voltage (iR) drop in low-conductivity solutions. In the latter case, even though no substantial polarization occurs, reference electrodes that are located between the specimen and the autoclave “see” the voltage drop, and the apparent (measured) corrosion potential can be observed to fluctuate as the direction of the dc current is reversed. This represents a good check of the integrity of the dc potential drop system and wire insulation.

Finally, there is a potential concern for self-heating of the specimen by the applied dc current. While this is not a problem in aqueous environments or at common current densities, there have been cases where high current densities coupled with air or vacuum exposure resulted in significant self-heating.

Compliance Method and Other Cracking Monitoring Methods. The next most common crack monitoring technique is mechanical compliance, which relies on the relationship between crack mouth opening displacement and load during an unload/reload cycle). Resolution is typically limited by the strain gage or proximity sensors (e.g., eddy current or capacitance) that must monitor crack opening displacement in the (high-temperature water) environment. See the article “Fatigue Crack Growth Testing” in this Volume.

Another method is the ac potential drop technique, which relies on the “skin” (surface) effect of high-frequency current in metals. The advantage of the skin effect for detecting crack nucleation is generally more than offset by the higher noise (poorer noise rejection) of the ac measurement, even with sophisticated lock-in amplifiers, although improved instrumentation is closing the gap. Other crack-following techniques include burst detection by monitoring pressurized tubes, periodic ultrasonic or eddy current scans to detect small cracks, and periodic interruption and inspection.

In aqueous environments, electrochemical noise can be used as a semiquantitative crack monitoring technique. This technique measures the small variations in corrosion potential and/or corrosion current as cracks (or other corrosion phenomena, such as pitting) nucleate and grow. This technique is good at discriminating the early stages of crack initiation. However, the correlation between crack depth (or number of cracks) and the electrochemical noise signal is at best semiquantitative, because: (a) the noise signal intensity decreases with increasing crack depth, increasing distance between sensors, and the location of cracking on the specimen surface (especially in low-conductivity solutions); and (b) noise from multiple small cracks cannot be distinguished from noise from longer cracks.

References cited in this section

90. P.L. Andresen, Corrosion Fatigue Testing, *Fatigue and Fracture*, Vol 19, *ASM Handbook*, 1996, p 193–209
102. R. Gangloff, Corrosion Fatigue, *Corrosion Tests and Standards: Application and Interpretation*, R. Baboian, Ed., ASTM, 1995
103. *Electrochem. Soc.*, Vol 126, 1979, p 908

Evaluation of Environmentally Assisted Crack Growth

Y. Katz, N. Tymiak, and W.W. Gerberich, University of Minnesota

Vacuum and Gases at Room Temperature (Ref 90)

One of the most critical considerations for fatigue tests in vacuum and gaseous environments is the maintenance of the purity of (and the reduction and measurement of the impurity level in) the test environment. As mentioned above, small amounts of contaminants (impurities) in the test environment can lead to fatigue crack growth rates that are not representative of the resistance of the material to fatigue crack growth in that environment.

A clean environmental test chamber that provides a very low background pressure and quantifiable impurity levels (below 10^{-7} to 10^{-6} Pa, or 7.5×10^{-10} to 7.5×10^{-9} torr) is essential, even if the tests are to be carried out in gaseous environments at relatively high pressures (i.e., above the background).

Environment Containment. An all-metal environmental test chamber with mechanical-force feedthroughs is preferred for the study of environmentally assisted fatigue crack growth in vacuum and gaseous environments. Stainless steels are suitable materials for the environmental test chamber, with copper used as the gasketing

material. The test chamber usually is equipped with a glass viewport that enables the operator to visually monitor the progress of the experiment.

With adequate pumping, the background pressure in the clean test chamber is usually below 10^{-6} Pa (7.5×10^{-9} torr). Maintaining an ultraclean test system is important, because a small amount of impurities can either significantly reduce or accelerate the fatigue crack growth rate, depending on the material and the types of impurities.

To achieve a low background pressure, the test chamber frequently is baked out (with the test specimen in place) at a temperature above ambient (60–400 °C, or 140–750 °F) to remove adsorbed and absorbed gases on the chamber wall. The bakeout temperature should be considerably below the tempering or aging temperature of the test material to ensure that the microstructure and the mechanical properties of the test material are not altered by the bakeout process. For example, the first-step artificial aging temperature for high-strength 7050-T7451 aluminum alloy is 121 °C (250 °F). The bakeout temperature for the test chamber is thus normally kept below 80 °C (175 °F).

Environment. Only high-purity, laboratory-grade gases should be used. Additional purification and dehumidification of the gas is recommended by passing it through a molecular-sieve purifier and a cold trap (-196 °C, or -320 °F) before allowing the gas to enter the test chamber. Gas pressure in the environmental test chamber is usually controlled by admitting the gas through a variable-leak valve.

If the test environment contains a toxic gas (such as hydrogen sulfide) or a combustible gas (such as hydrogen or methane), a protective hood with negative suction pressure should be used to enclose the test chamber or the entire test system. The test chamber should be purged thoroughly with an inert gas, such as argon or nitrogen, before it is reopened to the atmosphere.

If water vapor is used as the test environment, it can be drawn through the variable-leak valve from a high-purity reservoir that is attached to the test chamber. Deionized distilled water in the reservoir should be purified further by subjecting it to repeated freezing/pumping/thawing cycles to remove residual dissolved gases in the water (Ref 104).

Certain gases can decompose or react with containment vessels over time. For example, hydrogen sulfide can react with a stainless steel container to produce hydrogen. Provision must be made to remove the product gases before the test gas is admitted into the test chamber.

Finally, if the environment consists of mixed gases, the gas at the lowest partial pressure should be admitted first. If premixed gases are used, they must be thoroughly mixed in the supply reservoir to minimize stratification.

If test conditions such as gas pressure, test frequency, or applied load are changed during fatigue testing, a transient period may occur before the material assumes the steady-state fatigue crack growth rate that corresponds to the new test condition. The duration of this transient period depends on several variables, including the type of material, the test environment, and the magnitude of the change in test conditions.

References cited in this section

90. P.L. Andresen, Corrosion Fatigue Testing, *Fatigue and Fracture*, Vol 19, *ASM Handbook*, 1996, p 193–209

104. *Surf. Sci.*, Vol 64, 1977, p 617

Evaluation of Environmentally Assisted Crack Growth

Y. Katz, N. Tymiak, and W.W. Gerberich, University of Minnesota

High-Temperature Vacuum and Oxidizing Gases

Fatigue testing in elevated-temperature vacuum and oxidizing environments requires a carefully designed vacuum test chamber. The chamber must keep the test specimen in a vacuum or oxidizing gas environment, allowing forces to be applied to the specimen, a means to measure crack length, and a method of applying and controlling the specimen temperature.

Variables that can affect fatigue crack growth rate at high temperature are time and rate dependent or structure dependent. Examples of time- and rate-dependent variables are oxidation and creep. Structure-dependent variables include phase transformations, nucleation and growth of new and existing phases, and grain growth. When fatigue crack growth rate test data are reported for these environments, test temperature, vacuum pressure, partial pressure of oxidizing gas, waveform type, waveform frequency, and stress ratio must be reported. Additional information on high-temperature fatigue crack growth testing is given in the article "Fatigue Crack Growth Testing" in this Volume.

Environment Chambers. Materials used in the test chamber should be selected to minimize outgassing in vacuum. For example, many plastic materials contain plasticizers, which slowly outgas in vacuum. These types of materials limit the ultimate vacuum obtainable. Stainless steel is suitable for the manufacture of the main test chamber. Components in the chamber should be designed for fast outgassing. When threaded components are used in the test chamber, channels should be machined in the threads to allow paths for fast outgassing.

For vacuum levels of 6.5×10^{-5} Pa (5×10^{-7} torr), O-rings provide sufficient sealing; for higher vacuum levels, copper gaskets should be used. Electricity, water, radiofrequency, and the thermocouple can be input into the chamber using standard vacuum feedthroughs.

Specimen Heating and Temperature Control. Induction heating is the only suitable method to heat test specimens in vacuum and oxidizing environments. Radiofrequency generators with frequencies of 200 to 500 kHz are used for induction heating of test specimens. The induction coils should be made of copper and have no insulating coating. When oxidizing gases are introduced into the test chamber, a certain pressure range exists at which the gases will be ionized between the specimen and induction coils. In this pressure range, it is impossible to heat the specimen, because the radiofrequency field arcs and shuts off the radiofrequency generator. To continue testing, the gas pressure must be either increased or decreased.

Two types of temperature controllers that are suitable for induction heating are thermocouple and infrared controllers. Each controller type has advantages and disadvantages. Infrared temperature controllers measure and control temperature from the spectral energy density emitted from the test specimen over a certain wavelength range. These measurements are noncontacting, but require a clear optical path from the sensor head to the test specimen. Infrared temperature controllers have a minimum temperature measurement capability of approximately 350 °C (660 °F). Two-color infrared controllers eliminate errors due to transmission loss and emissivity changes, but they have a minimum temperature measuring capability of 700 °C (1290 °F).

Thermocouple temperature controllers are also used in vacuum test chambers. A variety of thermocouple types can be used, depending on the temperature range and the required durability of the thermocouple. For example, American National Standards Institute type S and type K thermocouple temperature ranges overlap, but for long-term tests of more than one week, type S thermocouples are preferred because they are more oxidation resistant. This would not be a consideration in a high-vacuum environment. Thin thermocouple wire less than 0.25 mm (0.01 in.) in diameter must be used to eliminate inductive heating of the thermocouple wire. With some temperature controllers, it is necessary to filter out radiofrequency noise in the thermocouple with a passive inductor/capacitor-type filter.

Test Specimens. Because high-temperature vacuum requires specimen heating by induction, many of the standard fracture mechanics test specimens cannot be used. Center-cracked tension and single-edge notched specimens are commonly used, because it is relatively easy to maintain the specimen gage section at uniform temperature with induction heating. When tests are conducted at high vacuum levels or low oxidizing gas partial pressures, specimen thickness may affect crack growth rate, because transport of the oxidizing gas to the crack tip may be the rate-limiting factor.

Aqueous Solutions at Ambient Temperature (Ref 90)

Fatigue studies in aqueous solutions at ambient temperatures present fewer problems experimentally than many of the other environments considered in this article. Nevertheless, it is often the case that the most frequent problem in determining the validity of corrosion fatigue data lies with the control and monitoring of the bulk water chemistry and the monitoring and recording of the electrochemical potential.

Environment Containment. Glass and plastics are suitable materials for environmental test chambers and ancillary pipework for aqueous solutions at ambient temperatures. At elevated temperatures (>60 °C, or 140 °F), however, dissolution of silicates from glassware can inhibit corrosion. Dissolution of plasticizers from certain plastics (e.g., polypropylene) is also a concern. Flexible plastics, such as twin-pack casting silicone rubber, have proved to be useful in the vicinity of the fatigue specimen.

A corrosion fatigue test cell that avoids the need for a water-tight seal at the specimen is shown in Fig. 24. Normal specimen movement and any sudden fracture event can be accommodated without catastrophic consequences. Highly effective seals between plastic and metal surfaces can be made with silicone rubber caulking compounds, if necessary, although sufficient time must be allowed for escape of the acetic acid solvent base.

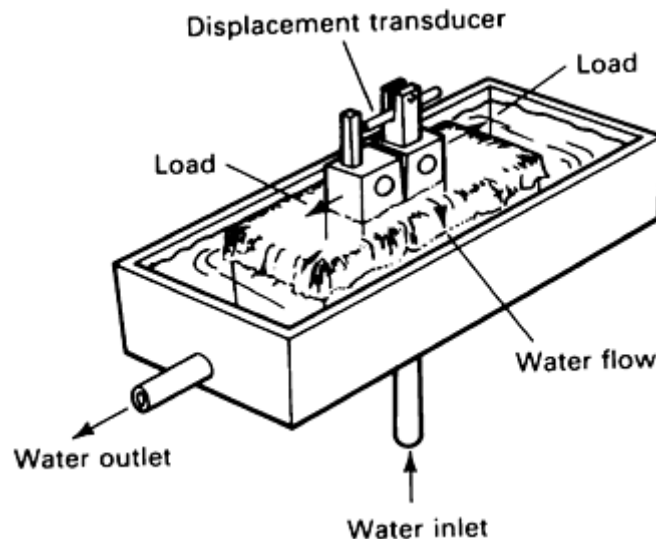


Fig. 24 Typical corrosion fatigue test cell. Maintenance of the equilibrium oxygen concentration is ensured by cascading the solution in the circulation rig.

Fatigue specimens of passive metals such as aluminum, titanium, and stainless steel may be subject to crevice corrosion under the caulking compound unless a primer and epoxy paint coat are applied initially to the metal surface. Gasket seals using O-rings, for example, can also form a satisfactory seal, but generally are more expensive to engineer and can also be subject to crevice corrosion in some configurations. The decision to circulate the environment depends on the application and the extent of any problems in controlling water chemistry.

Water Chemistry. The prevailing water chemistry and the electrode potential of the material in its environment in the field are essential factors in any simulation experiment. Accelerated fatigue cracking can occur in a number of environments, including seawater, salt water/salt spray, and body fluids. These must be reproduced as closely as possible in the laboratory, although limitations are necessarily imposed in simulating aspects of complex environments, such as the biological activity of seawater.

The importance of reproducing the service environment as closely as possible is illustrated by comparing the behavior of metals in sodium chloride and in seawater. The buffering action of seawater associated with dissolved bicarbonate/carbonate can result in the formation of calcareous scale under cathodic protection, which

can precipitate in cracks and influence the cyclic crack opening and closing, thus affecting crack growth rates. Substitute ocean water, as described in ASTM D 1141, usually is a satisfactory substitute for seawater, but some differences have been observed in relation to the rate of calcareous scale formation and the rate of corrosion fatigue growth.

Laboratory solutions should be prepared using the purest chemicals available in distilled or deionized water. Concentrations at the level of parts per million can have profound effects on electrochemistry and corrosion. Several variables must be measured and controlled when simulating an aqueous environment: solution purity, composition, temperature, pH, dissolved oxygen content, and the flow (circulation) rate of the solution.

Reference cited in this section

90. P.L. Andresen, Corrosion Fatigue Testing, *Fatigue and Fracture*, Vol 19, *ASM Handbook*, 1996, p 193–209

Evaluation of Environmentally Assisted Crack Growth

Y. Katz, N. Tymiak, and W.W. Gerberich, University of Minnesota

Acidified Chloride (Ref 90)

Investigations performed in acidified chloride, particularly at high temperature, pose unique problems. These include not only experimental barriers, such as suitable containment and seal materials and sensitivity to low-level oxidizing species, but also interpretational complexities, such as the effects of pitting and crevice processes on enhancement or retardation (by blunting) of crack initiation and growth. Care must be exercised in designing and conducting experiments to ensure personnel and equipment safety and to ensure proper simulation, control, and monitoring of environmental parameters.

Below 100 °C (212 °F). Materials and techniques for solution containment depend on the test-temperature regime. Below the boiling point in solutions containing dissolved oxygen, a primary design concern is to prevent leaks that can damage equipment. A horizontal loading frame helps ensure that sensitive components are not readily damaged by leaks. Additionally, some specimen configurations (such as compact tension) permit the loading linkage to be placed above the solution, simplifying the choice of materials and seal designs.

Testing in deaerated solutions may require careful selection of materials, depending on the sensitivity of the test to low oxygen concentration. For example, the clear, flexible tubing often used in laboratories is very permeable to oxygen. Additionally, some plastics degrade in acidic environments.

Above 100 °C (212 °F), the propensity for pitting and crevice attack increases, the internal pressure rises, the design strength of some materials (e.g., titanium) begins to decrease, and good seal design (particularly for sliding seals) is crucial. Pitting and crevice potential studies show that the resistance of iron- and nickel-base alloys in environments containing chloride decrease from room temperature to about 200 °C (390 °F).

The best approach for selecting pressure boundary materials is to combine published data with recommendations from autoclave manufacturers and metals producers. No assumptions should be made regarding the performance of materials with varying environment. For example, commercial-purity titanium, which is often used in neutral and acidified chloride environments, performs very poorly in acidified chloride under reducing conditions, in acidified environments containing sulfate, and in caustic environments at high temperature. Addition of a small amount (0.2%) of palladium (grade 7) greatly improves resistance in acidified environments that contain sulfate.

Above 200 °C (390 °F), materials selection is particularly difficult. In general, for acidified chlorides, commercial-purity titanium is favored under oxidizing conditions (containing oxygen, iron ion, or copper ion), while zirconium (for example, UNS R60702) is favored for reducing environments. Zirconium alloys are highly intolerant of fluoride. In some cases, high-strength materials, such as Ti-6Al-4V or the Hastelloy C series

alloys, are required, although there is generally a loss in corrosion resistance. Liners of Teflon or tantalum are options in some instances.

Because of its effect on the autoclave and test results, control of the oxidizing nature of the environment is often critical. In addition to oxidizing species, such as oxygen, iron ions, and copper ions, care in the use of externally applied potential is required. The autoclave may be polarized into a harmful regime if ground loops exist, or if it is used as the counterelectrode. A similar result can occur if the autoclave contacts a dissimilar metal.

Because of the rate and extent of expansion on leakage, hot pressurized water poses a serious safety hazard. Each autoclave must have a pressure-relief device attached to it, preferably in a fashion that does not permit bypassing or isolation. Selection of the pressure-relief device must account for the pressure, environment (often gold-coated elements are used in rupture disks), and temperature at which the device actually operates. Additionally, autoclaves, particularly when used in aggressive environments, must be examined regularly for damage resulting from pitting, crevice attack, general corrosion, hydriding, and so forth.

Pressure testing coupled with dimensional checks must also be performed. Manufacturers offer this service and will usually provide the test details. Test pressure and dimensional tolerances are a function of autoclave design, material, and temperature of use. Leaks may also occur in tubing and in valves, which are often difficult to inspect or test. Leaks almost always develop slowly. Nevertheless, a relatively rapid, controlled method for depressurizing the system should be included in the system design.

For some applications, inexpensive miniature autoclaves can be custom fabricated. The small internal volume of these devices is an advantage if a leak occurs in the system.

Reference cited in this section

90. P.L. Andresen, Corrosion Fatigue Testing, *Fatigue and Fracture*, Vol 19, *ASM Handbook*, 1996, p 193–209

Evaluation of Environmentally Assisted Crack Growth

Y. Katz, N. Tymiak, and W.W. Gerberich, University of Minnesota

Liquid Metal Environments (Ref 90)

Liquid metals (sodium, potassium, and lithium, for example) are frequently used in heat-transport applications at elevated temperatures. Such applications include liquid-metal-cooled nuclear reactors, first-wall coolant for fusion devices, and heat-transport systems in solar collectors. These applications often involve cyclic temperature and/or pressure fluctuations, as well as other sources of cyclic stresses. For this reason, knowledge of the fatigue crack propagation behavior of structural alloys in the liquid metal environments is sometimes necessary.

Generally, liquid metals react (in some cases, quite violently) with air and/or water vapor; therefore, testing systems must be designed to exclude both air and water. Three basic designs have been developed to expose the specimen (or crack region of a specimen) to the liquid metal environment, while excluding air, water, and other contaminants.

The simplest method uses a sealed environmental chamber attached to the specimen that completely surrounds the notch and crack extension plane in a compact-type specimen. The small environmental chamber contains the liquid metal, but does not extend to the region of the loading holes; hence, the loading pins, clevis grips, and remainder of the load train are not subjected to the liquid metal environment.

Relative motion across the notch and crack area is accommodated by bellows. This type of system has the advantages of simplicity and low cost. The main disadvantage is that the liquid metal is static; hence, the characteristics of large heat transport systems (e.g., mass transport due to nonisothermal operation) cannot be studied.

The second type of system, a circulating loop, is much more costly to build and operate, but it can be used to study potential effects on fatigue crack propagation such as mass transport, which occurs during carburizing, decarburizing, and dissolution of alloying elements. A third type of system consists of an open crucible (containing the test specimen immersed in static liquid metal) that is located within an inert gas cell or glovebox. This type of system is relatively inexpensive to build and operate, but it has the greatest potential for exposure to air and other contaminants.

Austenitic stainless steels generally have been used in the construction of current systems, and their use has been satisfactory. System designers should consider, however, that under some conditions mechanical properties (tensile, stress rupture, etc.) can be influenced by long-term exposure to liquid metals.

In most cases, fatigue crack propagation rates are lower in sodium environments than in elevated-temperature air environments. The relatively benign nature of sodium environments also leaves the fracture faces in excellent condition for viewing with optical microscopes, scanning electron microscopes, or transmission electron microscopes.

Reference cited in this section

90. P.L. Andresen, Corrosion Fatigue Testing, *Fatigue and Fracture*, Vol 19, *ASM Handbook*, 1996, p 193–209

Evaluation of Environmentally Assisted Crack Growth

Y. Katz, N. Tymiak, and W.W. Gerberich, University of Minnesota

Steam or Boiling Water with Contaminants (Ref 90)

Corrosive environments, such as steam or boiling water with contaminants, come in contact with many structural components. To assess the structural integrity of machine hardware, testing in the environments of concern is essential. Fatigue crack growth testing in corrosive environments requires special care because of the presence of corrosive media and testing complexity.

Environment Containment. Special designs are required to accommodate fatigue crack growth testing in steam or boiling water with contaminants. If the environmental pressure and temperature are moderate, for example at a pressure of 500 kPa (72.5 psi) and a temperature of 100 °C (212 °F), simple stainless steel O-ring sealed chambers can be clamped to each side of the specimen in which cracking will occur. If necessary, the test environment can be circulated through the chamber at a controlled flow rate.

If the environmental pressure and temperature are high, for example in steam at a pressure of 7.2 MPa (1040 psi) and a temperature of 288 °C (550 °F), a chamber that encloses the test specimens must be constructed. Composition of the test environment must be carefully analyzed before and after the experiment, given the variety of possible chemical effects on crack growth rates.

Dissolved Oxygen. Control and measurement of dissolved oxygen levels in the steam environment are of prime importance, because oxygen can affect fatigue crack propagation rate properties. Oxygen content can be controlled by bubbling argon or nitrogen through the water reservoir, or by maintaining a hydrogen overpressure. Oxygen content can be measured by using a colorimetric technique or by using oxygen analyzers that continuously monitor oxygen in the parts per billion range.

Reference cited in this section

90. P.L. Andresen, Corrosion Fatigue Testing, *Fatigue and Fracture*, Vol 19, *ASM Handbook*, 1996, p 193–209

Environmentally Assisted Cracking of Nonmetallic Materials

This section briefly reviews the evaluation of environmentally assisted crack growth in ceramics and plastics. However, another important manifestation of environmentally assisted cracking is the interfacial failures between two materials such as metal-polymer (Ref 105 and 106), ceramic-polymer (Ref 107), or metal-ceramic (Ref 108 and 109) interfaces. Evaluating interfacial failures from environmental degradation requires an understanding of adhesion; and further information on this topic is contained in the article “Adhesion Testing” in this Volume.

References cited in this section

105. A. Carre and J. Shultz, Polymer-Aluminum Adhesion. III. Effect of a Liquid Environment, *J. Adhes.*, Vol 18, 1984, p 171–184
106. J.D. Venables, Review: Adhesion and Durability of Metal-Polymer Bonds, *J. Mater. Sci.*, Vol 19, 1984, p 2431–2453
107. H. Wu, J.T. Dickinson, and S.C. Langford, Dynamic Measurements, of Humidity Attack on Polymer/Glass Interfaces Under Stress, *J. Adhes. Sci.*, Vol 11, 1997, p 695–717
108. S.X. Mao and A.G. Evans, The Influence of Blunting on Crack Growth at Oxide/Metal Interfaces, *Acta Mater.*, Vol 45, 1997, p 4263–4270
109. T.S. Oh, J. Rodel, R.M. Cannon, and R.O. Ritchie, Ceramic/Metal Interfacial Crack Growth Toughening by Controlled Microcracks and Interfacial Geometries, *Acta Metall.*, Vol 36, 1988, p 2083–2093

Environmentally Assisted Cracking in Ceramics

Ceramics are increasingly being used as either dielectrics or protective barriers where stress and environment interact to pose severe conditions. Being very brittle, ceramics in general exhibit very limited toughness compared to materials capable of substantial plastic deformation such as metals and polymers. Moreover, some classes of ceramic materials are extremely susceptible to environmental stress cracking. In glasses, this is manifested by stable slow crack growth at stress intensities substantially lower than fracture toughness determined from fast fracture or in an inert media. This phenomenon, frequently referred to as static fatigue, SCC, or subcritical crack growth, may be observed in almost every ceramic material providing an appropriate environment. Crack-growth kinetics curves for ceramics generally exhibit three distinctive regions as shown in Fig. 25. Region I is controlled by environment crack-tip reactions and may be described with a power-law relationship:

$$v = AK^N \quad (\text{Eq 1})$$

where v is crack velocity and A and N are constants. Equation 1 may be rewritten in a slightly different form:

$$v = v^* \left(\frac{K}{K_c} \right)^N \quad (\text{Eq 2})$$

where v^* is an empirical constant; the smaller N is, the higher the susceptibility to a static fatigue. Region I is of primary importance for design considerations. A linear region II is governed by transport of reactive species toward a crack tip. Finally, region III is determined by an “inert” fracture toughness with possible effects of electrostatic interactions (Ref 110). Controlling mechanisms of crack growth processes in these regions in different ceramic/environment systems are discussed here followed by a review of testing methods and a summary of crack growth data for selected systems.

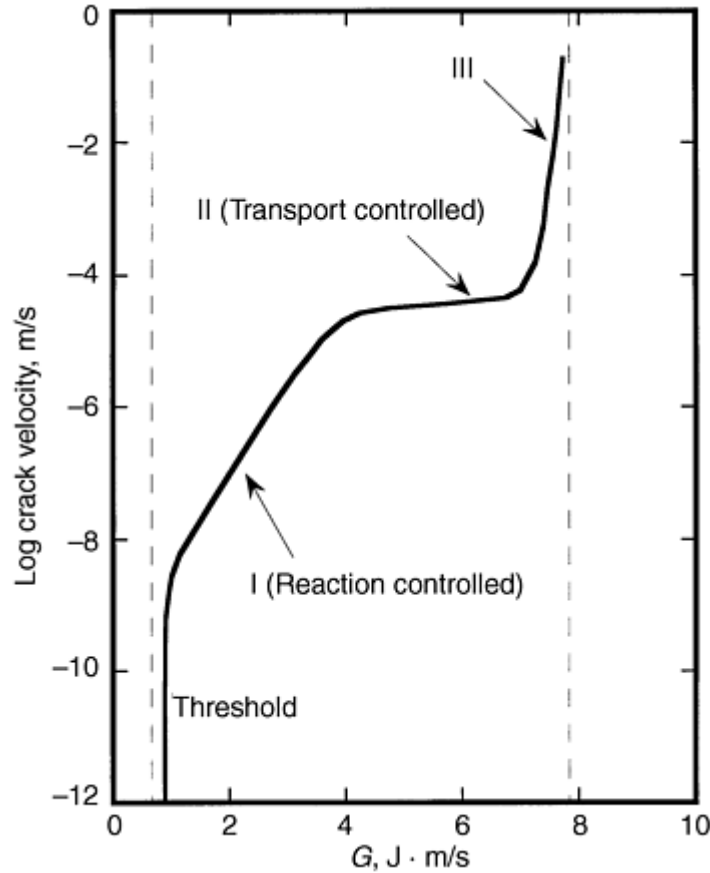


Fig. 25 Crack growth kinetics curve showing three characteristic regions

Environment/Ceramic Interactions with No Stress

Although frequently regarded as inert, most ceramic materials are reactive when exposed to appropriate environment/temperature combination. Several examples are discussed here with the consideration for governing mechanisms.

Glasses. Glass dissolves slowly in aqueous solutions under ambient temperature. Here, different mechanisms dominate at different pH levels. In acidic solutions, ion exchange between the alkali ions in the glass and hydrogen atoms in the solution occurs (Ref 111). Generally, the exchange rate increases with increasing concentration of alkali ions in the glass composition. An exchange process produces more basic solution near the glass surface. Similarly, the presence of alkaline earth elements such as calcium and magnesium would also result in increase of a local pH. In contrast, for a pure silica glass, hydrolysis of silanol groups adds hydrogen ions to produce a slight acidification (Ref 112).

In basic environments, hydroxyl ions react with the bonds of the network (Ref 113). In general, dissolution rates increase with increasing pH. The increase is particularly steep for $\text{pH} > 9$, where a direct attack on the

silicate network becomes possible (Ref 114). With the network dissolution, atoms of modifiers such as phosphorus and boron may enter the solution, producing a more acidic local environment.

Depending on the exchange rates between a restricted volume such as a crack and a bulk solution, local environment composition inside this volume will be determined by an external environment (sufficient exchange), glass composition (insufficient exchange), or both.

Crystalline Ceramics. It should be noted that environmental reactions for single crystals may depend on the crystallographic orientation of an exposed surface. For the same environment/ceramic system, interaction may be strongly dependent on the structure of a material. A situation is even more complicated for composites where presence of second-phase particles may change susceptibility to an environmental attack.

Oxides. Environmental degradation of metal oxides such as alumina and titania has been observed in some aqueous solutions (Ref 115).

Nonoxide Ceramics. Susceptibility to SCC for a variety of ceramics may be attributed to oxide removal by an active environment. For example, silicon exhibits SCC when exposed to HF acid as revealed by indentation induced cracking (Ref 116). For silicon-base ceramics, integrity and protective properties of silicon oxide may also be critical in determining their environmental susceptibility. For example, SiC is sensitive to environmental attack under a combination of elevated temperatures and vapors containing metal halides (Ref 117) or Na₂SO₄ in oxidizing atmospheres (Ref 118). With the Na₂SO₄ environment, corrosion was attributed to chemical alteration of the normally protective SiO₂. In aqueous acid solutions at ambient temperatures, susceptibility to environmental attack may also depend critically on the formation of silica layers as demonstrated, for example, by Cook et al. (Ref 119) in their study on sintered and reaction-bonded SiC. Here, both materials were passive in aqueous solutions of HCl, HNO₃, and H₂SO₄, but reactive in HF solution. Here, reaction-bonded SiC exhibited a higher degree of degradation. With the above, structural differences may be very important in determining reactivity of a polycrystalline material. Grain-boundary chemistry would be very important notably for nanocrystalline materials where the fraction of grain-boundary material increases substantially.

Environment/Fracture Zone Interactions

The crack-tip environment interactions may be divided into four categories that were originally suggested for glasses (Ref 120), but may be extended to a broader range of ceramic materials.

Bond rupture reactions involve environmental assistance in breaking strained bonds at a near-tip region. With all the complexity of mechanisms that may be involved in subcritical crack growth in ceramics (diffusion, Ref 121, surface relaxation, Ref 122, or plasticity, Ref 123), molecular reactions at the crack tip appear to be a major driving force for subcritical crack growth. Michalske et al. (Ref 124) proposed a model of a reaction between water and highly strained silica bonds in the near-tip region. Here, the ability of water to donate both electrons and protons appears to be critical as shown in Fig. 26 (Ref 125). In excellent agreement with the above model, similar crack velocity versus stress intensity (v/K) curves result from testing in water and other species with the same structure and bonding characteristics as shown in Fig. 27 (Ref 125). Note that with the nearly equal molecular sizes of water and ammonia, kinetic diagrams for these liquids are indistinguishable.

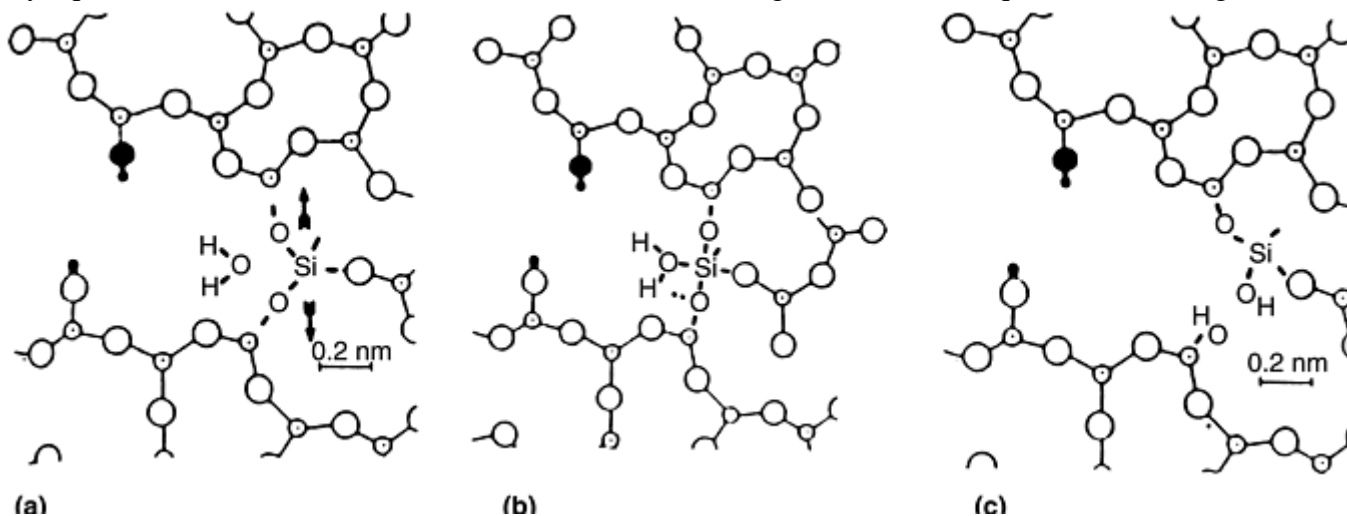


Fig. 26 Dissociative chemisorption reaction on crack-tip bond. (a) Physisorption on strained crack-tip bond. (b) Concerted reaction resulting in crack-tip bond rupture. (c) Formation of silanol covered fracture surface. Source: Ref 125

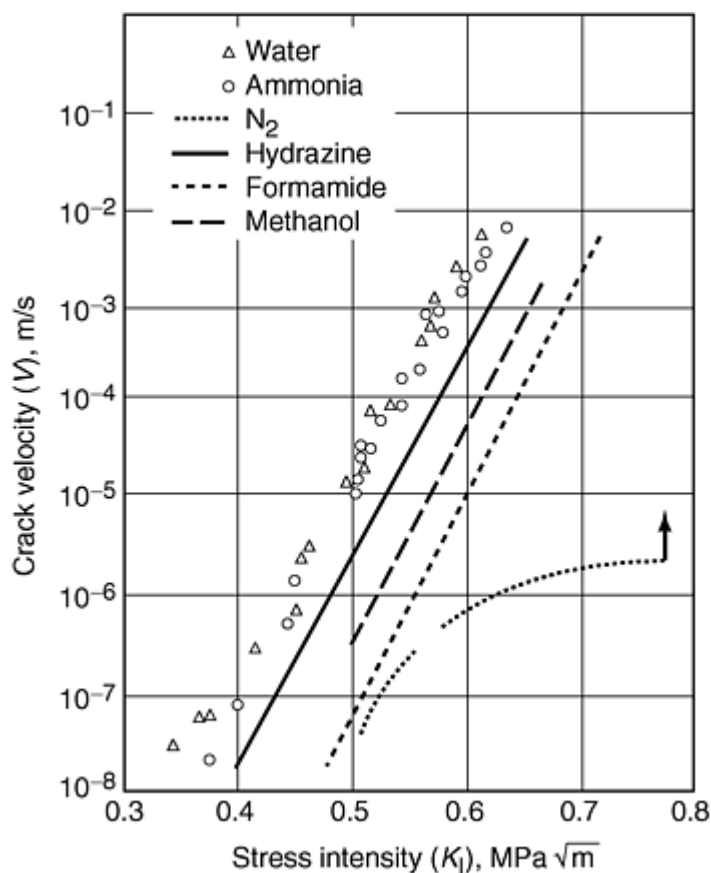


Fig. 27 Crack velocity versus stress-intensity diagram for vitreous silica at room temperature, showing that water, hydrazine, ammonia, methanol, and formamide all have the effect of increasing the rate of slow crack growth. Source: Ref 125

With crack growth rates dependent on the relative humidity rather than concentration of water in an environment (Ref 126), it is implicit that there cannot be an absolutely inert liquid given even a small quantity of water present. The above may be evident from comparison of kinetic curves for water and “dry” nitrogen as shown in Fig. 27. Nearly equal initial slopes indicate similar mechanisms, while a difference between intercepts comes from a difference in activities of water in different environments. In acidic aqueous solutions, the water molecule is also suggested to be the key participant with the resulting mechanisms the same as in water. Analogous mechanisms of water-assisted bond rupture may occur for crystalline materials such as alumina having an ionic/covalent interatomic bond structure similar to silica (Ref 124). In basic solutions, the attack of the OH ion appears to control crack growth rates.

Surface layer formation involves reactions changing the chemical composition and physical properties of a ceramic surface. Surface layers with tensile (Ref 127) stresses may develop facilitating crack growth. Tensile surface stresses may be responsible for a horizontal v/K dependence in the low K region for soda silica glass as shown in Fig. 28. Note that absence of a static fatigue limit in this case may be quite disadvantageous for some practical applications.

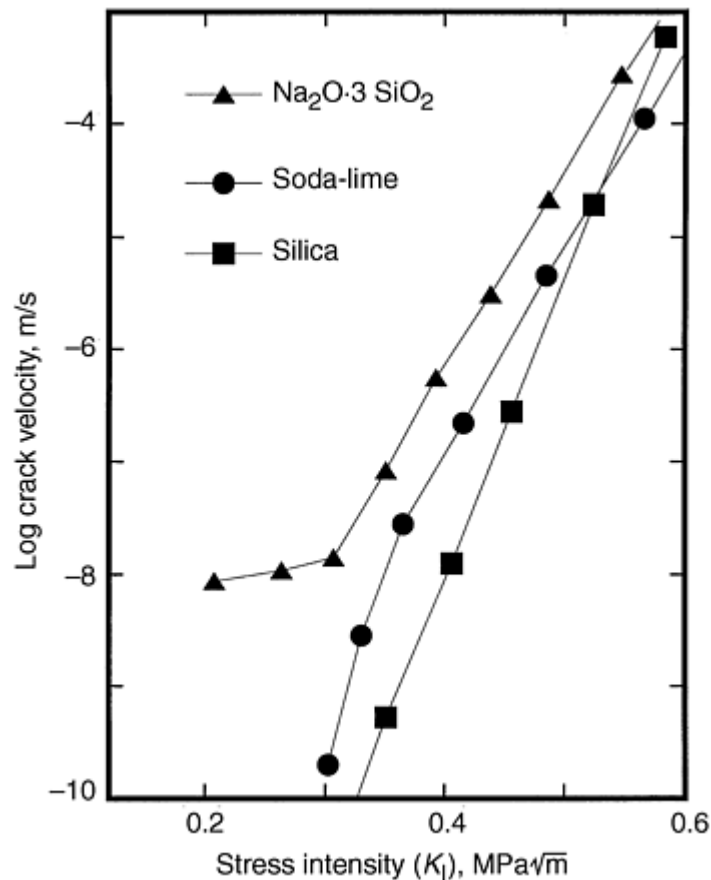


Fig. 28 Crack velocity versus stress-intensity diagram showing the stress-corrosion behavior of three different silicate glasses in water. Source: Ref 127

Surface deposition involves preferential deposition of a reaction product in the crack-tip vicinity. For silica-aqueous systems, dissolution-precipitation processes may lead to silica deposits at the crack tip resulting in crack-tip blunting (Ref 127). On the other hand, in some cases, wedging associated with the reaction product inside of a crack may add to the driving force for crack extension (Ref 128).

Intermolecular or Interatomic Surface Forces. Environmental effects may decrease interatomic forces or produce surface bonds. Formation of hydrogen-bond linkages of surface adsorbed water molecules and electrostatic bonds between anionic surface groups (Ref 127) may oppose crack propagation. In contrast, an environment acting as a dielectric would decrease van der Waals dispersion forces (Ref 129). For highly ionic solids such as MgF_2 , ion solvation, a mechanism involving neutralization of the electrostatic attraction between ions may be a dominant mechanism (Ref 130) of static fatigue. Here, media with the high dielectric constants such as water or methanol would be effective in facilitating subcritical crack growth.

Crack Growth Kinetics

Thresholds. In an ideal system with no additional shielding mechanisms, threshold corresponds to an equilibrium where $G = 2\gamma$ and frequencies of bond fracture and bond healing events are equal resulting in zero crack velocity (Ref 131). Local processes in the crack-tip vicinity may affect local crack-tip stress, thus changing local strain-energy release rates. For example, crack blunting due to selective silica deposition would lower the local stress intensity. In contrast, tensile stresses in the near-surface region would increase the local stress intensity. This mechanism results in the absence of a threshold for soda silica glass in water, as mentioned earlier.

Reaction-Controlled Region. This part of the kinetic diagram is determined by environment, material composition, and temperature.

Environment and Material Composition. In general, increasing pH results in decreasing the exponent N of Eq 1, indicating greater susceptibility to SCC as shown in Fig. 29 for a pure silica glass (Ref 132). In this case, the glass did not contain elements that might have affected local crack-tip environment via dissolution reactions.

With the more complex glass composition, the effect is more intricate since crack-tip environment could be strongly affected by the glass composition. This effect may become prevalent at high crack velocities where there is insufficient exchange with an external environment (Ref 133).

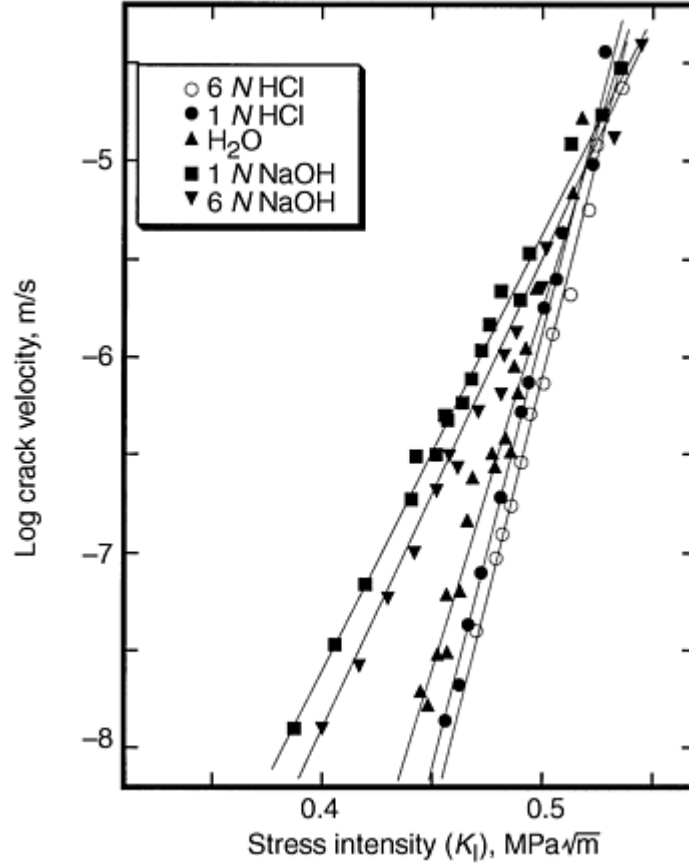


Fig. 29 Crack velocity as a function of pH for silica glass. Source: Ref 132

With moisture-containing “inert” media, the activity of water in a given medium will determine a horizontal shift of the v/K curve with respect to that for water as shown in Fig. 27. As already mentioned in the previous section and shown in Fig. 27, bonding and structure of the environmental molecule are very important in determining SCC. Here, identical slopes of v/K curves for reactive media such as water, ammonia, hydrazine, methanol, and formamide indicate similar mechanisms. It should be noted that intercepts of kinetic curves increase with the increasing molecule sizes. The latter effect may possibly be related to crack-tip opening limitations (Ref 125).

Temperature. With the thermally activated governing reaction, there is a strong temperature dependence on crack growth rates as shown in Fig. 30 (Ref 131 and 134). Crack growth kinetics in the reaction controlled region may be described with a recently developed reaction rate model (Ref 131).

$$v = (a \, dc/dA) v_0 \sinh[(G - 2\gamma)/\eta] \quad (\text{Eq 3})$$

Here, a is a characteristic length in the bond rupture process, G is strain-energy release rate, γ is surface energy as affected by an environment, $\eta = 2kT/a^2$, and v_0 is a parameter determined by material properties. This parameter is crack-geometry independent and increases with increasing temperature. It is assumed that a crack may be characterized by a single geometrical crack length parameter c , and this crack length parameter is related to crack area by an expression: $A \propto c^\alpha$. Here, a parameter $\alpha = 1, 2, \text{ or } 3$ depends on the number of dimensions for crack growth. For example, $A = \pi c^2$ for a circular crack geometry. As follows from Eq 3, a parameter 2γ determines the horizontal position of the v/G curve, and $1/\eta$ characterizes the slope and v_0 , its vertical position. For a given material/environment combination, increasing temperature would cause an upward vertical displacement and decrease of the slope of the v/G curve. These trends correspond to experimentally observed temperature effects as shown in Fig. 30. A horizontal shift of the v/G curves increasing with increasing molecule size would also be predicted by Eq 3. Here, increasing molecule size would require higher crack opening displacement and, consequently, an increasing G value.

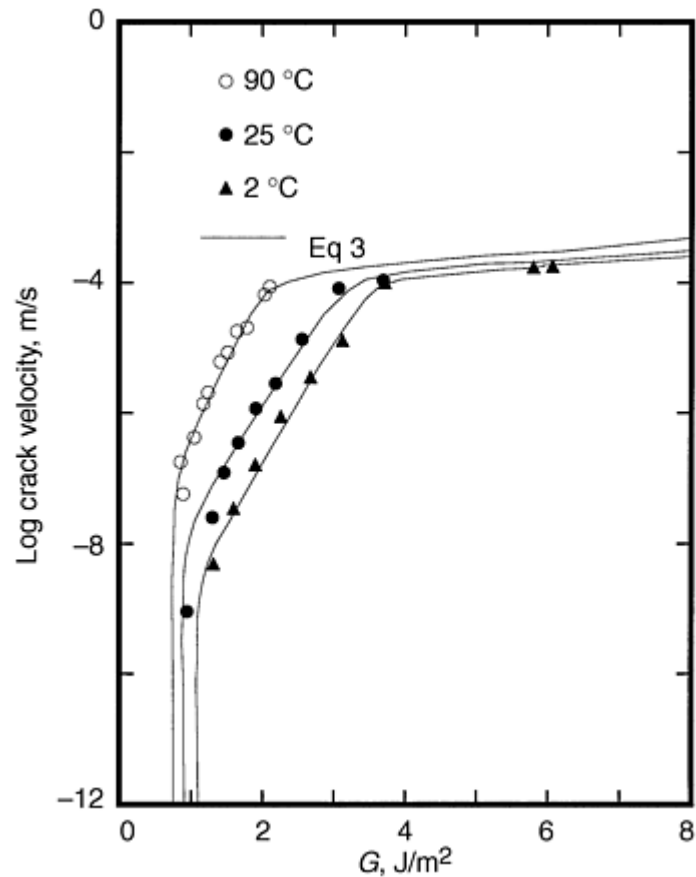


Fig. 30 Crack growth rates for soda lime glass. Experimental data (Ref 134) are presented with the best fit with the theoretical dependence given in Eq 3 (Ref 131)

Transport-Controlled Region. This region may depend on the activity of reactive species, for example, on a relative humidity as shown in Fig. 31 (Ref 135). Crack geometry and pressure gradients along a crack may also be important in determining transport towards a crack tip.

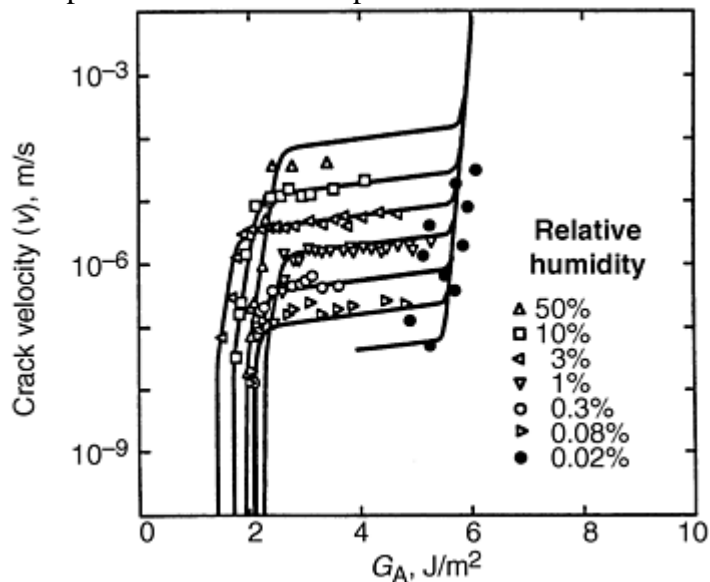


Fig. 31 Crack velocity curves for sapphire in moist air at different relative humidities. Double-cantilever beam data (constant load) at 25 °C (77 °F). Solid curves are theoretical fits to experimental data. Source: Ref 135

A transport model (Ref 131) describes crack velocity during stage II with the following expression:

$$v = \frac{(p_A^0 - p_A)kG}{(2\pi mkT)^{1/2} E} \quad (\text{Eq 4})$$

where p_A^0 and p_A are the partial pressures of the reactive species in the external environment and at the crack tip, respectively, m is the mass of the reactive species, and k is a dimensionless attenuation coefficient. This parameter characterizes the constraining profile of the crack over which the pressure gradient acts.

Polycrystalline Materials. In addition to structure effects affecting ceramic/environment reactions, as discussed earlier, presence of grain boundaries increase the level of complexity. Variation of grain-boundary chemistry was correlated to the change of crack growth exponents for polycrystalline alumina as determined with dynamic fatigue testing (Ref 136). Occurrence of transgranular versus intergranular fracture would depend on variety of factors. These include crack velocity and chemical composition of grains and grain boundaries (Ref 137).

Testing Methods

Linear elastic fracture mechanics developed for metallic systems are generally applicable to ceramics, as described in more detail in the article "Fracture Toughness of Ceramics and Ceramic Matrix Composites" in this Volume. Classical fracture mechanics techniques for brittle materials are also discussed in Ref 138. Based on the crack extension data, A and N can be determined by curve fitting Eq 1 to a power-law dependence. Among disadvantages in the above method would be a large amount of material necessary to produce a specimen of proper dimensions. A high scatter in experimental data, especially for polycrystalline ceramics, is a disadvantage here.

Dynamic fatigue techniques involve measurement of strength as a function of stressing rate. Both of these methods may be correlated with the following expression (Ref 139):

$$\sigma^{N+1} = [2(N+1)\sigma_{Ic}^N / AY^2 K_{Ic}^N (N-2)\dot{\sigma}] \quad (\text{Eq 5})$$

Here A and N correspond to the same coefficient and exponent in Eq 1, Y is a constant, σ_{Ic} is inert fracture strength, $\dot{\sigma}$ is stressing rate, K_{Ic} is critical stress-intensity factor. Alternatively, Eq 3 may be applied for the analysis of dynamic fatigue results as described in (Ref 127). With this approach, parameters γ , η , and v_0 determined from the best fit to experimental data may be used to predict crack growth kinetics for a specific geometry of interest.

In general, there is a satisfactory correlation between crack growth parameters determined with classical fracture mechanics and dynamic fatigue approaches. However, the role of surface state should be carefully evaluated when interpreting experimental results obtained with the dynamic fatigue data (Ref 140). Also, for reliable results, strength should be measured over at least three orders of magnitude in stressing rates (Ref 141). Introducing a controlled-size flaw for dynamic fatigue testing would be advantageous especially with the flaw size/geometry similar to those expected in service.

References cited in this section

110. S.M. Wiederhorn, S.W. Freimann, and E.R. Fuller, Jr., Effect of Water and Other Dielectrics on Crack Growth, *J. Mater. Sci.*, Vol 17, 1982, p 3460–3478
111. R.W. Douglas and T.M.M. El-Shamy, *J. Am. Ceram. Soc.*, Vol 50, 1967
112. M.L. Hair, Hydroxyl Groups in Silica Surface, *J. Non-Cryst. Solids*, Vol 19, 1975, p 299–309
113. R.J. Charles, Glass Surface Analysis by Auger Electron Spectroscopy, *J. Appl. Phys.*, Vol 2, 1958
114. C.G. Pantano, D.B. Dove, and G.Y. Onoda, *J. Noncryst Solids*, Vol 19, 1975, p 41–53

115. J.D. VENABLES, Review, Adhesion and Durability of Metal-Polymer Bonds, *J. Mater. Sci.*, Vol 19, 1984, p 2431–2453
116. M.D. THOULESS and R.F. COOK, Stress Corrosion Cracking in Silicon, *Appl. Phys. Lett.*, Vol 56, 1990, p 1962–1964
117. J.I. FEDERER, Stress-Corrosion of SiC in an Oxidizing Atmosphere Containing NaCl, *Adv. Ceram. Mater.*, Vol 3, 1988, p 293–295
118. J.I. FEDERER, Corrosion of SiC Ceramic by Na₂SO₄, *Adv. Ceram. Mater.*, Vol 3, 1988, p 56–61
119. S.G. COOK, J.A. LITTLE, and J E. KING, Corrosion of Silicon Carbide Ceramics Using Conventional and Electrochemical Methods, *Br. Corros. J.*, Vol 29, 1994, p 183–189
120. B.C. BURKNER and T.A. MICHALSKE, Effect of Surface Corrosion on Glass Fracture, *Fracture Mechanics of Ceramics*, Vol 8, R.C. BRADT, Ed., Plenum Press, New York, 1986, p 391
121. D.P.H. HASSELMAN, *Ultrafine Grain Ceramics*, J.J. BURKE, N.L. REED, and V. WEISS, Ed., Syracuse University Press, 1970, p 297–315
122. M. TOMOZAWA and Y.-L. PENG, Surface Relaxation as a Mechanism of Static Fatigue of Pristine Silica Glass Fibers, *J. Non-Cryst. Solids*, Vol 240, 1998, p 104–109
123. D.M. MARSH, *Proc. R. Soc. (London) A*, Vol 270, 1964
124. T.A. MICHALSKE and S.W. FREIMAN, A Molecular Mechanism for Stress Corrosion in Vitreous Silica, *J. Am. Ceram. Soc.*, Vol 66, 1983, p 284–288
125. T.A. MICHALSKE and B.C. BUNKER, Steric Effects in Stress Corrosion Fracture of Glass, *J. Am. Ceram. Soc.*, Vol 70, 1987, p 780–784
126. S.W. FREIMAN, Effects of Chemical Environments on Slow Crack Growth in Glasses and Ceramics, *J. Geophys. Res.*, Vol 89, 1984, p 4072–4076
127. B.C. BUNKER and T.A. MICHALSKE, Effect of Surface Corrosion on Glass Fracture, *Fracture Mechanics of Ceramics*, Vol 8, R.C. BRADT, Ed., Plenum Press, 1986, p 391
128. C.J. SIMMONS and S.W. FREIMAN, Effect of Corrosion Processes on Subcritical Crack Growth in Glass, *J. Am. Ceram. Soc.*, Vol 64, 1981, p 683–686
129. D.R. CLARKE, B.R. LAWN, and D.H. ROACH, The Role of Surface Forces in Fracture, *Fracture Mechanics of Ceramics*, Vol 8, R.C. BRADT, et al., Ed., Plenum Press, 1986
130. T.A. MICHALSKE, B.C. BUNKER, and S.J. FRIEMAN, Stress Corrosion of Ionic and Mixed Ionic/Covalent Solids, *J. Am. Ceram. Soc.*, Vol 69, 1986, p 721–724
131. R.F. COOK, Environmentally Controlled Nonequilibrium Crack Propagation in Ceramics, *Mater. Sci. Eng. A*, Vol 260, 1999, p 29–40
132. S.M. WIEDERHORN and H. JOHNSON, Effect of pH on Crack Propagation in Glass, *J. Am. Ceram. Soc.*, Vol 56, 1973, p 192–197
133. S.M. WIEDERHORN, Mechanisms of Subcritical Crack Growth in Glass, *Fracture Mechanics of Ceramics*, p 549–581

134. S.M. Wiederhorn and I.H. Boltz, Stress Corrosion and Static Fatigue of Glass, *J. Am. Ceram. Soc.*, Vol 53, 1970, p 543–548
135. B.R. Lawn, *Fracture of Brittle Solids*, 2nd ed., Cambridge University Press, 1993, 378 pages
136. J.R. Hellmann, J. Matsko, S.W. Freiman, and T.L. Baker, Microstructure-Mechanical Property Relationships in 94% Alumina Ceramics, *Tailoring Multiphase and Composite Ceramics*, R.E. Tressler, G.L. Messing, C.G. Pantano, and R.E. Newnham, Ed., Plenum Press, 1986, p 367–380
137. J.J. Mechlosky and S.W. Freiman, Fractographic Analysis of Delayed Failure in Ceramics, *Fractography and Materials Science*, STP 733, ASTM, 1981, p 246–258
138. M. Sakai and R.C. Bradt, Fracture Toughness Testing of Brittle Materials, *Int. Mater. Rev.*, Vol 38, 1993, p 53–79
139. S.M. Wiederhorn, *Fracture Mechanics of Ceramics*, Vol 2, R.C. Bradt, D.P.H. Hasselmann, and F.F. Lange, Ed., Plenum Press, 1974, p 613–646
140. J.E. Ritter, and R.P. LaPorte, Effect of Test Environment on Stress-Corrosion Susceptibility of Glass, *J. Am. Ceram. Soc.*, Vol 58, 1975, p 265–267
141. S.W. Freiman, Stress-Corrosion Cracking of Glasses and Ceramics, *Stress-Corrosion Cracking, Materials Performance and Evaluation*, R.H. Jones, Ed., ASM International, 1992, p 337–344

Evaluation of Environmentally Assisted Crack Growth

Y. Katz, N. Tymiak, and W.W. Gerberich, University of Minnesota

Environmental Stress Cracking and Crazeing in Polymers

Environmental stability of a polymer or an interface involving a polymeric material is of critical importance for a variety of applications. Ranging from nanoscale films to pipelines, these include biomedical and microelectronic devices, vessels, cladding, and composite materials. A variety of environments interacting with polymers during processing/service conditions include organic and inorganic liquids, pressurized gases, living tissues, and soils as well as irradiation exposure. In many cases, polymers are utilized to decrease the severity of environmental attack on metallic components. For example, polymer films, coatings, and finishes are designed to prevent environmental degradation of metallic surfaces. Polymer washers are frequently utilized in pipelines in order to eliminate galvanic contacts. Similarly, polymer fillers serve to reduce crevice corrosion effects at joint sites. For any of the above, the preventive effect is determined by the structural integrity of a polymeric component under exposure to an aggressive environment (with or without mechanical stresses). Design considerations for a polymer as a prospective material for a given application should account for:

- How interaction with a given environment affects the polymer microstructure on the molecular scale
- How stress-strain conditions particular to a given application influence these interactions
- How resulting microstructural changes affect plasticity and fracture behavior of a polymer

Note that consideration should be given to the highly time-dependent and temperature-dependent mechanical behavior of polymers as viscoelastic-plastic solids. This introduces an additional challenge if combined with the time-dependent nature of deformation/environment interactions.

Deformation and Fracture with No Environment

Factors determining mechanical behavior of polymers include structure, applied stress-state, testing time, and temperature with respect to T_g , the glass-transition temperature. With an increasing degree of crystallinity and a temperature sufficiently below a glass transition, polymers experience a ductile-brittle transition. Plastic deformation in polymers occurs either via shear yielding, crazing, or plastic instability (necking). Conditions essential for craze formation are temperature above T_g and a dilatational hydrostatic stress-state component. Dilatational stress results in formation of highly voided regions with so-called fibrils. These are fiberlike semicohesive structures capable of sustaining significant stress levels. In many cases, craze zone evolution at the vicinity of a nucleating or advancing crack plays an essential role in the fracture process in amorphous (Ref 142) and crystalline (Ref 143) polymers.

Polymer/Environment Interactions with No Stress

The main issues dealing with solid polymer/environment interactions are the penetration mechanism (diffusion) and change in polymer properties determining its mechanical behavior. Possible environmentally related changes include change in degree of crystallinity, polymer surface energy reduction (Ref 144), decrease of T_g (plasticizing), and dimensional change of a polymer (swelling). The latter change can be expressed in terms of the coefficient of hydroelasticity. This parameter is sensitive to both the chemical composition and the physical structure of a polymer (Ref 145). Finally, dissolution of a polymer may occur.

Environmentally Assisted Cracking and Crazing

Several important points need to be emphasized here, as shown in Fig. 32. First of all, environmentally enhanced cracking and/or crazing may occur even in “inert” media that does not affect a given polymer under no applied stress (Ref 146). Moreover, with the absence of environmental effects under simple tension, environmental stress crazing and/or cracking may occur under more complex stress states (Ref 147). For active media, stress may enhance environmental effects such as plasticization and swelling. This may become critically important at the highly stressed crack-tip region. In addition, for fast-moving cracks (200–650 m/s, or 650–2130 ft/s), a crack-tip temperature increase up to 500 K is possible (Ref 148). Thus, even for medium growth rates with a small environmentally induced decrease in T_g and/or a small temperature increase, local effects at the crack tip may be significant. Organic plasticizers or even inorganic salt solutions (Ref 149) are known to affect tensile properties of some polymers, for example, nylon. Local stress-enhanced crack-tip environmental interactions may induce a substantial decrease in the Young's modulus, thus easing local deformation. With the above examples, it becomes evident that predictions for environmental crazing or cracking for a given polymer/environment system may not be based exclusively on the interactions with no stress applied. Also, local crack-tip conditions need to be accounted for. It should also be noted that both cracking and crazing kinetics must be considered in assessing environmental effects. For example, high craze rates but more stable craze structure may result in longer time to complete failure. A brief consideration of the mechanisms of environmental stress crazing and cracking is given here as well as references for most commonly used experimental procedures. Examples for selected polymer/environment systems are included with consideration for dominating mechanisms and critical parameters.

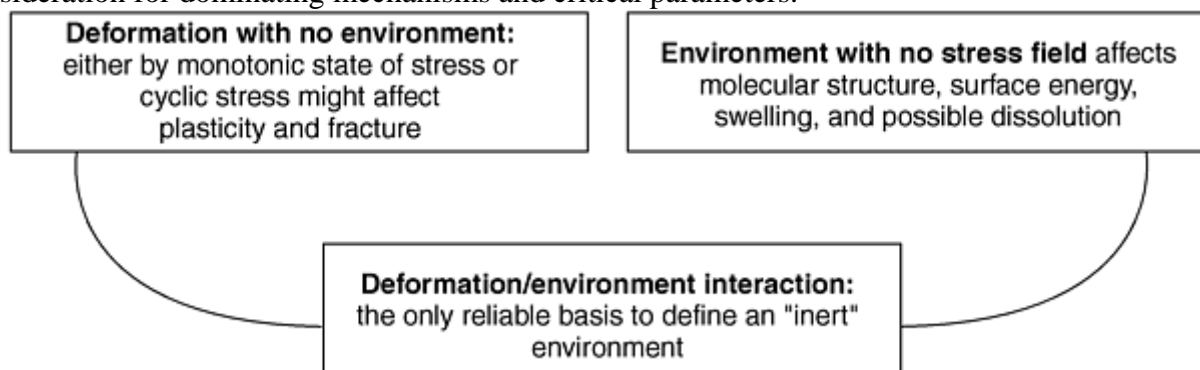


Fig. 32 Polymer/environment/stress interactions

Mechanisms in Liquid Media

Liquid Transport through a Porous Craze Zone or a Crack. Suggested driving forces are: (a) atmospheric pressure as the craze voids are under a vacuum, (b) capillary pressure in the craze or a crack, and (c) superimposed hydrostatic pressure (Ref 150). Viscosity of the liquid and a spreading coefficient with respect to a polymer are critical parameters controlling liquid transport through a crack and/or a craze zone. Specific liquid/polymer interactions may also be involved here.

Liquid Fracture Zone Interactions. An active media absorption at the fracture zone surface is followed by local changes in polymer properties. For some polymers, for example, polyethylene, stress enhances liquid absorption. Thus, under exposure to a solvent, enhanced swelling is expected in the highly stressed near-tip regions. It seems that solvent swells and plasticizes both the craze fibrils and the layer of bulk polymer contiguous to the craze surface. One of the consequences is believed to be a stress relaxation in a fibril. As the stress relaxes in a fibril, new fibrils need to be generated to balance the stress concentration at the crack tip. Thus, the craze tip advances. There is some evidence that inorganic media such as metal salt solutions can also diffuse into polymer and cause stress relaxation in a fibril (Ref 149). It is suggested that for media resistant to swelling, local plasticization may increase the effective radius of curvature at the crack tip, thus reducing the stress concentration (Ref 151).

Craze and/or Crack Growth Kinetics. For a variety of glassy polymer/liquid systems, crack growth rate versus stress-intensity dependencies exhibit three characteristic regions (Ref 147). In region I, crack growth rate increases rapidly with the stress-intensity factor once a threshold value is exceeded. This region is believed to be controlled by environment/polymer interactions. In region II, crack growth rate is controlled either by hydrodynamic flow properties of the environment (Ref 152), or by velocity of adsorption at the fracture process zone (Ref 153). For some systems, a region III exists where the fracture process is controlled by the mechanical properties of a material in air (Ref 154). However, in some cases, K_{Ic} in the presence of an environment may be either decreased or increased. For example, environmentally enhanced crazing results in an increased K_{Ic} for polymethylmethacrylate (PMMA) exposed to organic solvents (Ref 147). In this case, K_{Ic} may also depend on crosshead speed since the amount of crazing formed at the tip can vary with crack velocity (Ref 155). At the same time, the reader is cautioned to be aware that such solvents could enhance crack growth kinetics well below K_{Ic} . If a solvent causes dissolution and not crazing, K_{Ic} can be reduced (Ref 147). In some cases, crack deceleration due to crack-tip blunting is observed following region II (Ref 156). It should become clear that different solvent/polymer interactions may produce enhanced or decreased crack growth rates or final fracture, requiring case-by-case evaluation. A level of complexity increases substantially if a polymer is subjected to a cyclic rather than monotonic load. Here, crack growth may be highly dependent on the test frequency and loading amplitude as well as the stress-intensity factor range (Ref 157).

Mechanisms in Gaseous Media

Gas Fracture Zone Interactions. In general, hydrostatic pressure will increase T_g . However, if the pressurizing environment is soluble in the polymer, one might expect an initial decrease in T_g as a polymer is plasticized by an environment (Ref 158). An effect of gases such as argon, oxygen, and carbon dioxide close to their condensation point (high thermodynamic activity) is to reduce the surface energy of a crystalline polymer, facilitating the creation of a new surface in the holes and voids of the craze (Ref 159). On the other hand, high dilatational stress at the tip of an incidental flaw or an existing craze promotes enhanced absorption of a gas.

Craze Growth. The locally absorbed gas acts as a plasticizer, easing the flow involved in the craze nucleation and growth. The above effects are suggested to explain the ductile behavior of crystalline polymers between liquid nitrogen and room temperature. In the absence of a gas or at temperatures sufficiently above a gas condensation point, the crystalline material is rather brittle with a very limited extent of crazing. Craze velocity is directly related to the diffusion coefficient of a gas in a polymer (Ref 160).

Testing

Smooth specimens are commonly used when craze initiation and growth are investigated (Ref 150). If diffusivity of an environment is high, a constant strain rate tensile test may be utilized (Ref 150, 156). For low-diffusivity liquids, a creep test may be a better option (Ref 156). Note that for some inert liquids, no crazing

occurs under tensile load. However, for the same polymer/environment, crazing may occur readily under torsion (Ref 161) or tension with superimposed hydrostatic compression (Ref 162). Thus, evaluation of a polymer for a given application requires testing under loading conditions corresponding to those expected during service. An apparatus for tension or compression superimposed with the hydrostatic pressure and an environmental chamber may be obtained from Ref 163 and 164.

Environmentally assisted crack/craze propagation can be evaluated with double-edge (Ref 149) or single-edge notched (Ref 153) specimens. Razor-blade cutting is a common precracking technique. A procedure for obtaining sharp reproducible cracks of controlled length is detailed in Ref 165. Good results may also be accomplished with fatigue (Ref 166) or controlled impact (Ref 167). With a sustained load apparatus and an environmental chamber, as described in Ref 168, environmentally assisted craze and crack growth kinetics may be evaluated under constant load conditions (Ref 149, 153, and 169).

To summarize this section on environmentally induced degradation of polymeric systems, a number of the important chemomechanical factors are given in Table 4, and few examples of environmental interactions are summarized in Table 5.

Table 4 Summary of chemomechanical factors influencing environmental cracking and crazing in polymers

Factor	Considerations
Polymer	Degree of crystallinity
	Molecular weight
	Glass transition temperature
	Coefficient of hydroelasticity
	Solubility
Medium	Viscosity
	Spreading coefficient on a polymer
	Type: active or inert
	For active media: solubility as compared to that for a polymer; frequently, crack growth rates increase with the decreasing difference between solubility of a polymer and that of a liquid ($\delta_1 - \delta_P$) (Ref 149). Also, how much does it change T_g of a polymer; Q/R, a ratio of ionic charge to the ionic radius, is a critical parameter for several salt solutions (Ref 149).
Temperature	Testing temperature and a local crack-tip temperature (as increased locally at a tip of a rapidly growing crack of a) with respect to T_g (as decreased by an environment)
Loading Stress state	Dilatational component (necessary for crazing)
	Hydrostatic compression (suppresses crazing; facilitates liquid flow towards a tip of a moving crack) (Ref 150)
Strain rate	Affects craze and crack growth rate
Crack growth rate	Influences craze growth
	For high crack-growth rates: local temperature elevation at the crack tip (Ref 148), liquid transport (Ref 152), or absorption-controlled mechanisms (Ref 153)

Table 5 Examples of environmental interactions for selected systems

Material	Environment	Sample geometry	Loading	Environmental effects measured in terms of:	Suggested mechanism	Critical parameters
Low-density polyethylene (Ref 153)	Methanol, ethanol, ethyleneglycol, diethylene triamine DETA-NaOH	Single notched (sharp crack)	Sustained load 0.13 MPa applied stress (yield stress 11.3 MPa)	Crack velocity versus applied stress intensity	Micelles absorption on the fibril surface with the subsequent	Highest crack-growth rates with the lowest ($\delta_1 - \delta_P$) crack-growth rates

	(detergent)				fibril fracture	increasing with the increasing detergent concentration
Nylon (Ref 149)	Aqueous salt solutions: CaCl, LiCl, MgCl	Precracked tensile bars	Constant applied stress intensity	Craze growth velocity	Environment-induced decrease in T_g . Relaxation-controlled craze growth	The higher Q/R ratio, the more significant T_g reduction, the more enhanced craze growth
Polystyrene (Ref 150)	Silicon oil	Smooth cylindrical	Tension or tension with superimposed hydrostatic compression	Change in crazing behavior	Liquid flow controlled as affected by a stress-state hydrostatic compression facilitates liquid flow toward a crack tip	Type of a stress state

References cited in this section

142. G.H. Michler, Correlation Between Craze Formation and Mechanical Behaviour of Amorphous Polymers, *J. Mater. Sci.*, Vol 25, 1990, p 2321–2334
143. A.S. Argon, Sources of Toughness in Polymers, *Advances in Fracture Research*, Proc. Seventh Int. Conf. on Fracture (ICF), Vol 4, Pergamon, 1989, p 2661–2681
144. A. Carre and J. Shultz, Polymer-Aluminum Adhesion III. Effect of a Liquid Environment, *J. Adhes.*, Vol 15, 1983 p 151–162
145. G. Marom and D. Cohn, Deformations of Polymers and Composite under Swelling Conditions, *Plastics & Rubber: Materials & Applications*, Vol 5, 1980, p 165–168
146. S.V. Hoa, Relative Influence of the Mobility and the Solubility Parameters of Fluids on the Mechanical Behavior of High Impact Polystyrene, *Polym. Eng. Sci.*, Vol 20, 1980, p 1157–1160
147. A.G. Atkins and Y.W. Mai, *Elastic and Plastic Fracture: Metals, Polymers, Ceramics, Composites, Biological Materials*, Halsted Press, 1985, p 817
148. K.N.G. Fuller and P.G. Fox, The Temperature Rise at the Tip of Fast-Moving Cracks in Glassy Polymers. *Proc. R. Soc. (London) A*, Vol 341, 1974, p 537–557
149. M.G. Wyzgoski and G.E. Novak, Stress Cracking of Nylon in Aqueous Salt Solutions. Part 3 Craze-Growth Kinetics, *J. Mater. Sci.*, Vol 22, 1987, p 2615–2623
150. A. Moet and E. Baer, On the Mechanism of Pressure Induced Environmental Stress Cracking in Polystyrene, *J. Mater. Sci.*, Vol 15, 1980, p 31–41

151. M.E.R. Shanahan, M Debski, F. Bomo, and J. Shultz, *J. Polym. Sci.*, Polymer Physics Edition, Vol 21, 1983, p 1103–1109
152. J.G. Williams and G.P. Marshall, Environmental Crack and Craze Growth Phenomena in Polymers, *Proc. R. Soc. (London) A*, Vol 342, 1975, p 55–77
153. K. Tonyali and C.E. Rogers, Stress-Cracking of Polyethylene in Organic Liquids, *Polymer*, Vol 28, 1987, p 1472–1477
154. M.E.R. Shanahan and J. Shultz, Environmental Stress Cracking of Polyethylene: Analysis of the Three Zones of Behavior and Determination of Crack-Front Dimensions, *J. Polym. Sci.*, Polymer Physics Edition, Vol 18, 1980, p 1747–1752
155. Y.W. Mai and A.G. Atkins, On the Velocity-Dependent Fracture Toughness of Epoxy Resins, *J. Mater. Sci.*, Vol 10, 1975, p 2000–2003
156. J.C. Arnold, The Influence of Liquid Uptake on Environmental Stress Cracking of Glassy Polymers, *Mater. Sci. Eng. A*, Vol 197, 1995, p 119–124
157. H.M. El-Hakeem and L.E. Culver, Environmental Dynamic Fatigue Crack Propagation in High Density Polyethylene: An Empirical Modelling Approach, *Int. J. Fat.*, Vol 3, 1981, p 3–8
158. W.-Ch.V. Wang, E.J. Kramer, and W.H. Sachse, Effects of High-Pressure CO₂ on the Glass Transition Temperature and Mechanical Properties of Polystyrene, *J. Polym. Sci.*, Vol 20, 1982, p 1371–1384
159. A. Peterlin and H.G. Olf, Crazing and Fracture in Crystalline, Isotactic Polypropylene and the Effect of Morphology, Gaseous Environments, and Temperature, *J. Polym. Sci.*, 1975, p 243–264
160. N. Brown and S. Fischer, Nucleation and Growth of Crazes in Amorphous Polychlorotrifluoroethylene in Liquid Nitrogen, *J. Polym. Sci.*, Polymer Physics Edition, Vol 13, 1975, p 1979–1982
161. R.A. Duckett, B.C. Goswami, L. Stewart, I.M. Ward, and A.M. Zihlif, The Yielding and Crazing Behaviour of Polycarbonate in Torsion under Superposed Hydrostatic Pressure, *Br. Polym. J.*, Vol 10, 1978, p 11–16
162. K. Matsushige, S. Radcliffe, and E. Baer, The Environmental Stress-Crazing and Cracking in Polystyrene under High Pressure, *J. Macromol. Sci. Phys.*, Vol B11, 1975, p 565–592
163. H.Li. Pugh, Ed., *High Pressure Engineering*, Mechanical Engineering Publications, 1975, p 41
164. D.R. Mears, K.D. Pae, and J.A. Sauer, Effects of Hydrostatic Pressure on the Mechanical Behavior of Polyethylene and Polypropylene, *J. Appl. Phys.*, Vol 40, 1969, p 4229–4237
165. E.H. Andrews and L. Bevan, Mechanics and Mechanism of Environmental Crazing in a Polymeric Glass, *Polymer*, Vol 13, 1972, p 337–347
166. J.R. Atkinson and P.G. Faulker, *J. Appl. Polym. Sci.*, Vol 15, 1971, p 209
167. G.P. Marshall, G.P. Culver, and J.G. Williams, Craze Growth in Polymethylmethacrylate: A Fracture Mechanics Approach, *Proc. R. Soc. (London) A*, Vol 319, 1970, p 165–187

168. M.G. Wyzgoski and G.E. Novak, Stress Cracking of Nylon Polymers in Aqueous Salt Solutions. I. Stress-Rupture Behaviour, *J. Mater. Sci.*, Vol 22, 1987, p 1707–1714
169. M.C. Kenney, J.F. Mandell, and F.J. McGarry, The Effects of Sea Water and Concentrated Salt Solutions on the Fatigue of Nylon 6,6 Fibres, *J. Mater. Sci.*, Vol 20, 1985, p 2060–2070

Evaluation of Environmentally Assisted Crack Growth

Y. Katz, N. Tymiak, and W.W. Gerberich, University of Minnesota

Nanomechanical Testing

Nanomechanical techniques such as nanoindentation and nanoscratch methods have emerged from conventional hardness testing as described in more detail in the article “Instrumented Indentation Testing” in this Volume. Nanoscaled depth and load resolution available with the commercial nanoindenters allows probing of material properties at very shallow penetration depth. During a typical indentation test, an indenter is driven in and out of a surface under investigation. Resulting load-displacement curves serve as a basis for the mechanical behavior evaluation (Ref 170). Indentation curve discontinuities may be indicative of plasticity onset or various fracture events. Additional insight can be gained by examining a residual indentation cavity (Ref 171, 172, and 173). Here, features of plastic deformation and fracture would be of primary interest. One instrument, the Hysitron Triboscope, attached to an atomic force microscope (AFM), combines nanoindentation with the imaging of an indented area. This becomes especially advantageous for the evaluation of time-dependent phenomena. With nanoindentation, basic elastic-plastic properties such as Young's modulus (Ref 170) and yield stress (Ref 173) can be determined. Indentation-induced cracks allow evaluation of fracture behavior for bulk materials and thin films (Ref 174, 175, and 176).

During a continuous microscratch test, controlled vertical displacement alongside with the normal and tangential loads are recorded while an indenter is being moved across a surface under applied load. Examination of a residual scratch groove provides insight into evolution of plastic deformation and fracture with increasing load.

Note that for the systems where controlling flaws have a contact origin, nanoindentation and nanoscratch appear to be the most appropriate evaluation techniques. That is, they account for a specific stress-strain state around cracks initiated with normal or sliding contact such as environmentally enhanced fretting fatigue.

References cited in this section

170. W.C. Oliver and G.M. Pharr, An Improved Technique for Determining Hardness and Elastic Modulus Using Load and Displacement Sensing Indentation Experiments, *J. Mater. Res.*, Vol 7, 1992, p 1564–1583
171. T.F. Page, L. Riester, and S.V. Hainsworth, The Plasticity Response of 6H-SiC and Related Isostructural Materials to Nanoindentation, *Mater. Res. Soc. Symp. Proc.*, Vol 522, 1998, p 113–118
172. W. Zielinski, H. Huang, S. Venkataraman, and W.W. Gerberich, Dislocation Distribution under a Microindentation into an Iron-Silicon Single Crystal, *Philos. Mag. A*, Vol 72, 1995, p 1221–1237
173. D. Kramer, H. Huang, M. Kriese, J. Robach, J. Nelson, J.N.A Wright, D. Bahr, and W.W. Gerberich, Yield Strength Predictions from the Plastic Zone around Nanocontacts, *Acta Mater.*, Vol 47, 1998, p 333–343

174. D.S. Harding, W.C. Oliver, and G.M. Pharr, Cracking During Nanoindentation and Its Use in the Measurement of Fracture Toughness, *Thin Films: Stresses and Mechanical Properties V*, Symposium, Materials Research Society, 1995, p 663–668
175. X. Li and B. Bhushan, Micro/Nanomechanical Characterization of Ceramic Films for Microdevices, *Thin Solid Films*, Vol 340, 1999, p 210–217
176. M.R. Begley, A.G. Evans, and J.W. Hutchinson, Spherical Impression of Thin Elastic Films on Elastic-Plastic Substrates, *Int. J. Solid. Struct.*, Vol 36, 1999, p 2773–2788

Evaluation of Environmentally Assisted Crack Growth

Y. Katz, N. Tymiak, and W.W. Gerberich, University of Minnesota

Evaluation of Nanoscale Environmental Effects

Here, indentation curve analysis may be combined with the imaging of a residual indentation cavity or a scratch groove. While both AFM and scanning electron microscopy (SEM) may provide high resolution images, AFM gives the advantage of quantitative evaluation of nanoscale fracture and plasticity features as discussed in detail in the section “Scanning Probe Microscopy.”

Environmentally Affected Plastic Deformation. For indentation into dislocation-free single-crystal materials, a characteristic discontinuity of a load-displacement curve may be indicative of plasticity initiation. Similar effects may be observed for coarse-grained polycrystalline materials where indentation size is small compared with the grain size.

With the *ex situ* testing of sapphire surfaces aged in different environments, clear evidence of chemomechanical effects was obtained by Hainsworth et al. (Ref 177). Here, presence of a damaged surface layer was suggested to explain decreased plasticity initiation loads after environmental exposure.

Several researchers have investigated the role of chemical or electrochemical oxide film removal on crystal plasticity (Ref 178, 179, and 180). With the potentiostatic control (Ref 178 and 180), it is possible to promote either oxide dissolution or growth by application of appropriate potential steps. It was discovered that electrochemical oxide film removal resulted in a dramatic decrease of the materials strength. With the electrochemical repassivation, an ability to support near theoretical strength was returned to the material. An example is shown in Fig. 33 (Ref 181), where indentation curves correspond to tests under different surface conditions controlled via applied potential. The yield point is influenced strongly by the presence of a passive film on titanium (Ref 181). A grade II titanium was vacuum annealed producing alpha grains of approximately 50 μm in diameter. Using the Hysitron Triboscope in conjunction with a Park Scientific Autoprobe CP scanning probe microscope, individual grains were imaged in a 0.01 *N* sulfuric acid solution, and a grain large enough to perform multiple indentations with no overlap was selected for indentation. This sample was then electrochemically polarized using a three-electrode system, with the titanium acting as the working electrode, a Ag/AgCl reference electrode, and a platinum counterelectrode. After identifying an appropriate grain, indentations were made using a Berkovich indenter tip after stepping the potential to 0.68 V above open circuit, showing reproducible yield points. The tip was then withdrawn 100 μm from the surface, and the passive film was removed by holding the specimen at 0.03 V above open circuit until the current began to increase (signifying the removal of the passive film). Indentations at this point show no significant yield point. However, after stepping the voltage back to the passive regime (0.77 V above open circuit) the yield point is recovered, and after 5 min the initial and newly passivated surface show almost identical indentation curves.

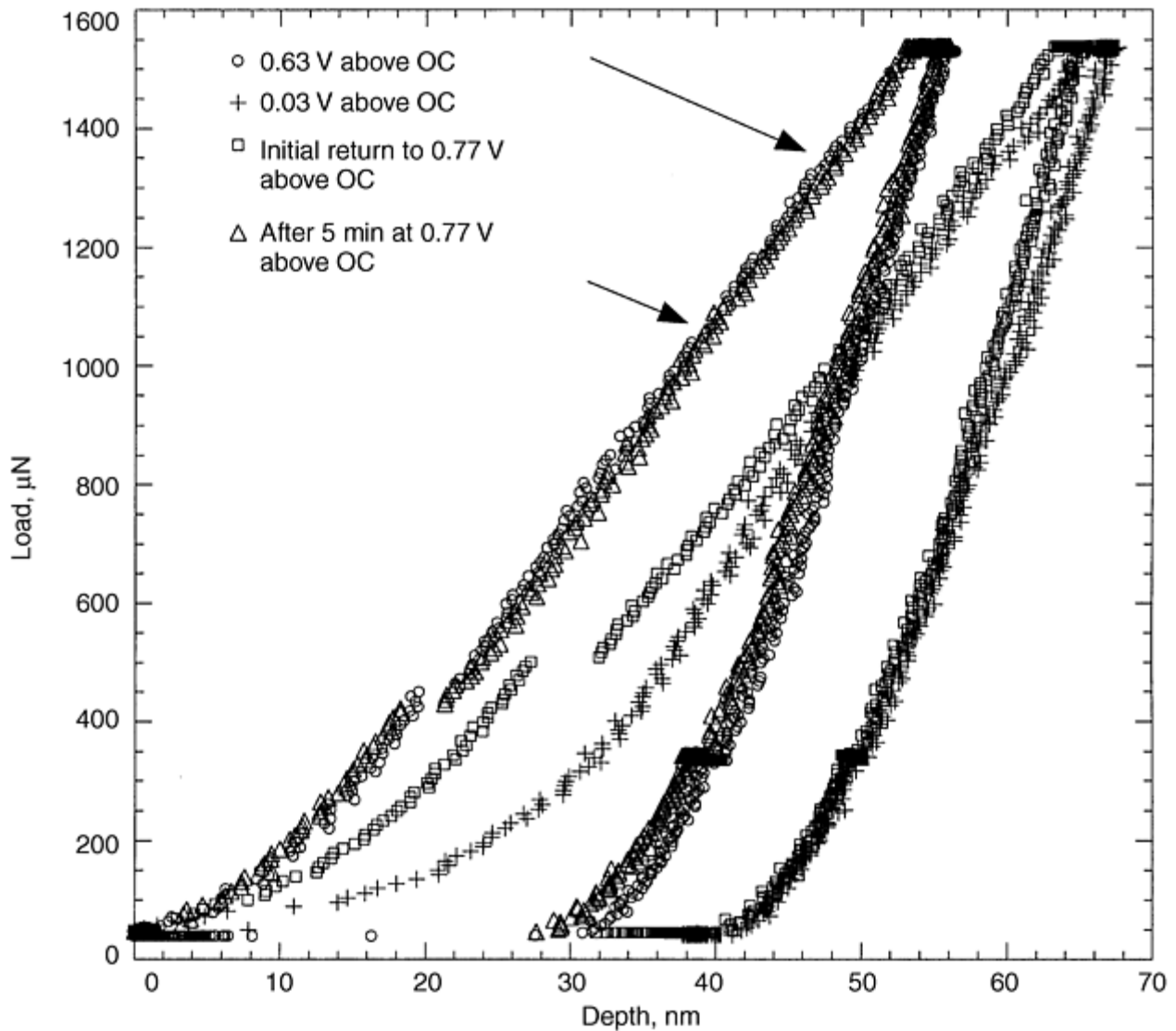


Fig. 33 Four indentations into grade II titanium in 0.01 N sulfuric acid during electrochemical polarization. The first indentation was made in the passive regime, at 0.63 V above open circuit (OC) by stepping to that potential from open circuit. The second was after removing the passive film by holding at potential 0.03 V above open circuit for about 10 min. The potential was then stepped to 0.77 V above open circuit, and indentations were made immediately after stepping and after 5 min at that potential. Source: Ref 181

To investigate hydrogen effects on yield initiation in 316 stainless steel, hydrogen charged and noncharged samples have been evaluated under indentation load (Ref 182). Reproducible load excursions at an average load of 200 μN were observed for noncharged samples as shown in Fig. 34(a) (Ref 182). These were attributed to the plasticity initiation as unloading just prior to an excursion load yielded no residual deformation. For comparison, indentation testing was carried immediately after hydrogen charging. Here, two samples charged at different conditions have been evaluated. Sample C1 was charged at 500 mA/m^2 for 6 h, and sample C2 was exposed to charging at 10 mA for 6 h. Figure 34(b) (Ref 182) shows indentation testing results for sample C1. As shown in this figure, yield initiation occurred at 650 to 700 μN immediately after charging. With increasing time, the load for plasticity initiation decreased down to 300 μN . For sample C2, yield initiation was observed at 350 μN instantly after charging. Then, the excursion load decreased approaching 200 μN . It became evident that the yield initiation load increases with increasing initial hydrogen concentrations. Hydrogen outgasses with time, causing the yield points to decrease back to its initial value. The above would agree with the notion that hydrogen suppresses dislocation nucleation and/or kinetics.

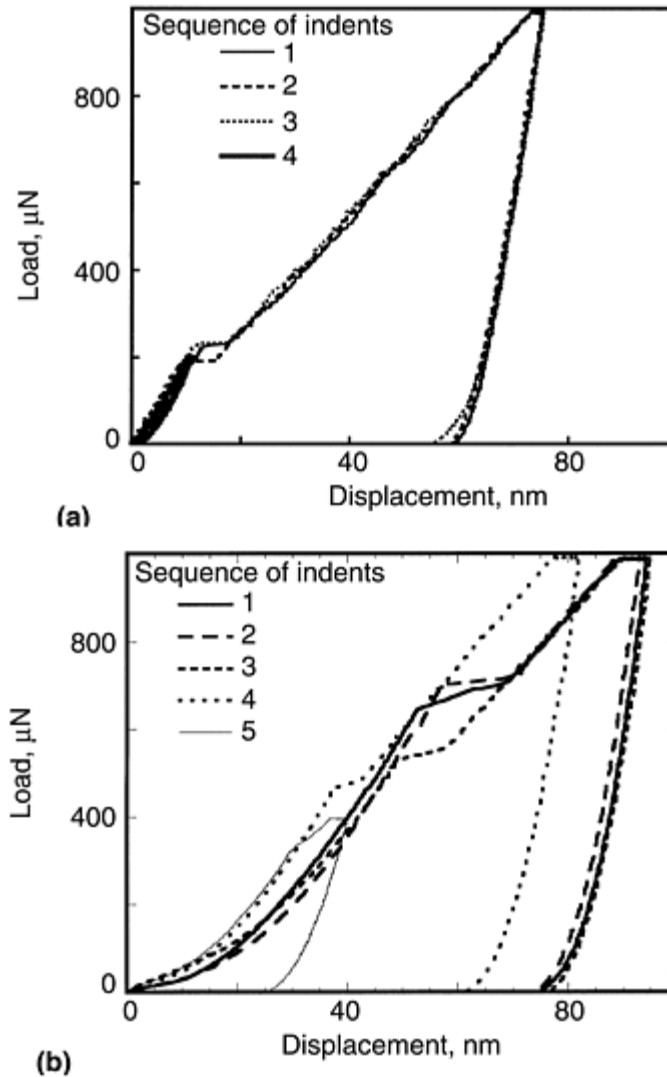


Fig. 34 Hydrogen effects on yield initiation in 316 stainless steel. (a) Noncharged sample. Curves 1 to 4 represent a sequence of indents over a 35 min time frame. (b) Indentation immediately after charging. Sample C1 at high hydrogen concentration. Time increases for curves 1 to 5 over a 35 min time frame. Source: Ref 182

Hydrogen/plasticity interactions were further explored with continuous scratch testing (Ref 181 and 183). Evaluation in a low-load regime allowed probing of near-surface hydrogen-saturated regions. A marked difference in both localized plastic deformation and microfracture has been observed as shown in Fig. 35 and 36. Here, both scratch grooves correspond to the same level of applied load. Atomic force microscopy enabled a quantitative analysis of environmental effects on plasticity and fracture. A comparison of plastic deformation characteristics for hydrogen-charged and noncharged surfaces as obtained from AFM measurements is shown in Table 6 (Ref 182 and 183).

Table 6 Hydrogen-charging effects on plastic deformation characteristics

Surface features	Noncharged	Charged
Along the pileup		
Slip-step spacing (s), nm	100	290
Slip-step height (h), nm	15	95
Perpendicular to the pileup		
Slip-step spacing (s), nm	105	260
Slip-step height (h), nm	13	16

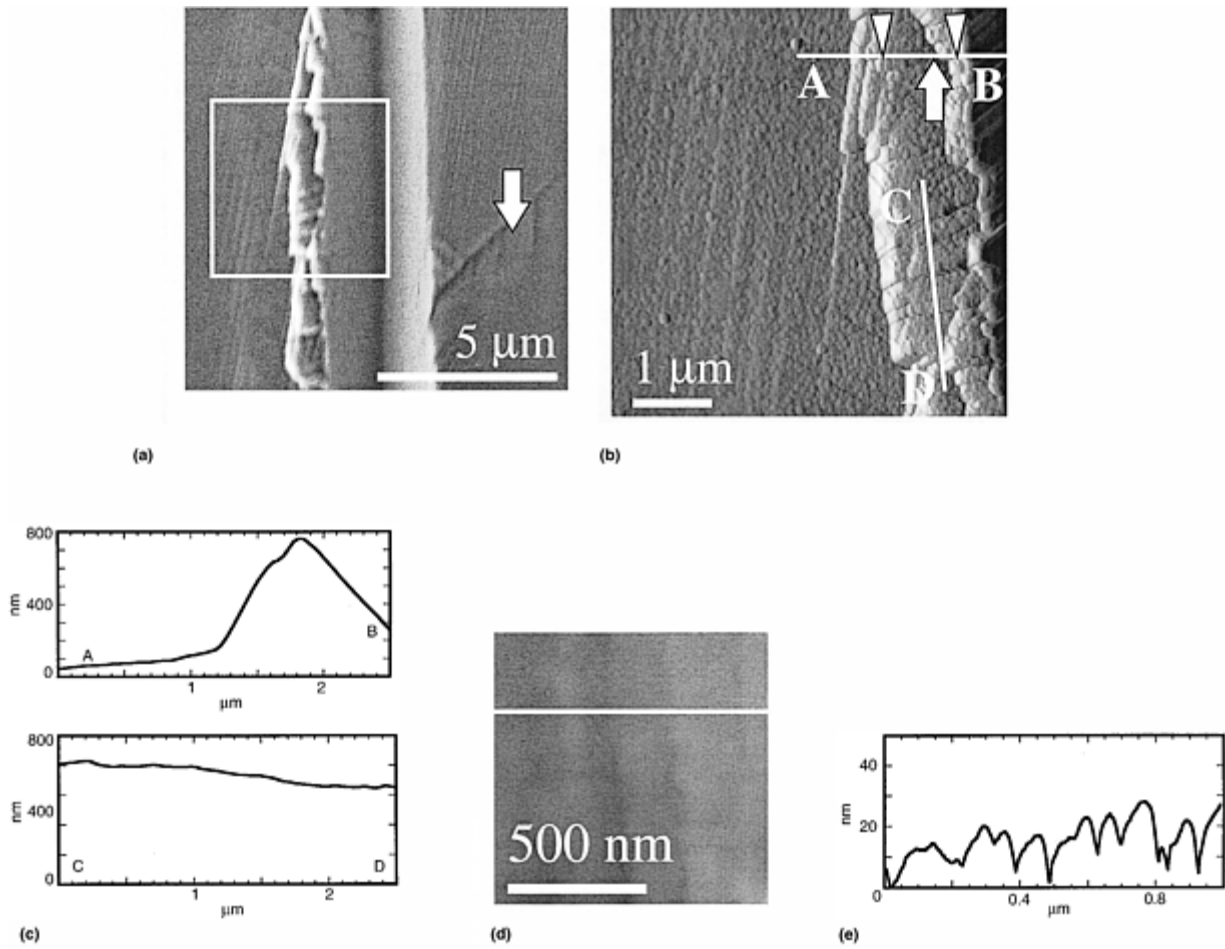


Fig. 35 Plastic deformation features typical for a noncharged sample (see also Fig. 36.) (a) SEM micrograph. (b) AFM deflection image corresponding to a square area in (a). (c) Cross sections corresponding to line traces in (b). (d) AFM micrograph showing a magnified view of slip steps. (e) Cross section corresponding to (d). Source: Ref 182

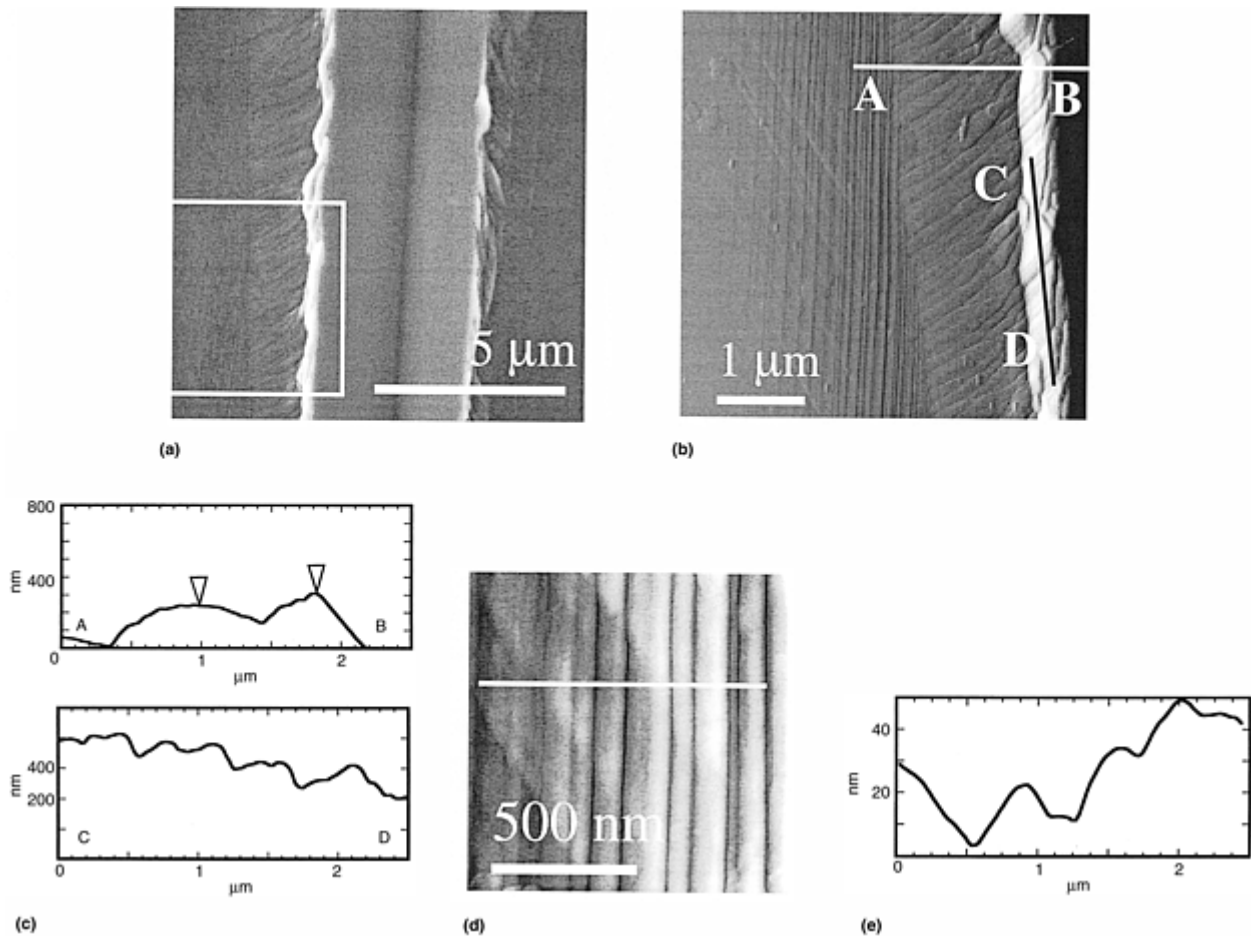


Fig. 36 Plastic deformation and fracture features typical for a hydrogen charged sample. (a) SEM micrograph. (b) AFM deflection image corresponding to a square area in (a). (c) Cross sections corresponding to line traces in (b). (d) AFM micrograph showing a magnified view of slip steps. (e) Cross section corresponding to (d). Arrows point toward cracks. Source: Ref 182

Crack Initiation. Examples where nanomechanical testing in conjunction with the imaging techniques has been applied for crack initiation studies in different types of materials are provided in this section.

Metals. With the continuous microscratch under increasing load, crack initiation onset can be determined by analyzing a cracking pattern along a scratch groove. Location of the first crack is correlated to the magnitude of the applied load as determined based on the known loading and horizontal indenter motion rates. For the same load level, microcracking was evident for a hydrogen-charged sample, while there no cracks were seen for a noncharged sample, as shown in Fig. 35 and 36 (Ref 182). This suggests decreased stress for crack initiation in hydrogen-charged material.

Ceramics. The initiation of radial cracking in Vickers indentation of soda-lime glass was found to be strongly rate and environment dependent (Ref 184). With sufficiently long contact times, radial cracking initiated during unloading. For short contacts, crack initiation occurred after a complete load removal with significant scatter in delay times. These decreased with increasing peak load and increasing water content in an environment. Observed phenomena were interpreted in terms of incubation times necessary to develop a critical nucleus for crack initiation. With SEM, constrained shear fault were identified as possible crack precursors. A proposed theoretical model considers a two-step process with precursor faulting followed by crack growth to an instability. Moisture may influence both of these steps: first by enhancing the initiation of decohesion and second by slow crack growth. A stress-intensity factor analysis for the microcrack extension in residual-contact and applied-stress fields was used in conjunction with appropriate fracture conditions to determine critical instability configurations (Ref 185).

Polymers. Indentation-induced cracking in polystyrene (Ref 186) originated at the tip of a yielded zone where a characteristic shear band pattern has been observed. Based on a slip-line field analysis for the stress distribution within a plastic zone and elastic analysis for a surrounding material, the principal stresses corresponding to crack initiation were estimated. These were found to be similar to crazing initiation stresses for this material.

An approach may possibly be extended to evaluate environmental effects on cracking and crazing initiation in polymers.

References cited in this section

177. S.V. Hainsworth and T.F. Page, Nanoindentation Studies of the Chemomechanical Effect in Sapphire, *J. Mater. Sci.*, Vol 29, 1994, p 5529–5540
178. S.K. Venkataraman, D.L. Kohlstedt, and W.W. Gerberich, Continuous Microindentation of Passivating Surfaces, *J. Mater. Res.*, Vol 8, 1993, p 685–688
179. D.F. Bahr, J.C. Nelson, N.I. Tymiak, and W.W. Gerberich, The Mechanical Behaviour of a Passivating Surface under Potentiostatic Control, *J. Mater. Res.*, Vol 12, 1997, p 3345–3353
180. S.G. Corcoran, S.R. Brankovic, N. Dimitrov, and K. Sieradzki, Nanoindentation of Atomically Modified Surfaces, *Thin-Films—Stresses and Mechanical Properties VII*, R.C. Cammarata, M. Nastasi, E.P. Busso, and W.C. Oliver, Ed., Symposium Materials Research Society, 1998, p 77–84
181. M. Pang, D.E. Wilson, and D.F. Bahr, The Strength and Fracture of Passive Oxide Films on Metals, submitted to Proc. Materials Research Society, *Thin Films: Stresses and Mechanical Properties VIII*, 1999
182. Y. Katz, N.I. Tymiak, and W.W. Gerberich, Nano-mechanical Probes as New Approaches to Hydrogen/Deformation Interaction Studies, An invited paper for *Recent Advances in the Engineering Aspects of Hydrogen Embrittlement of the Engineering Fracture Mechanics*, 1999
183. N.I. Tymiak, S. Gabric-Miskulin, Y. Katz, and W.W. Gerberich, Nanoindentation Evaluation of Hydrogen Affected Yield and Fracture in 316 Stainless Steel, *Int. Conf. Environmental Degradation of Engineering Materials*, Gdansk, Poland, 1999
184. B.R. Lawn, T.P. Dabbs, and C.J. Fairbanks, Kinetics of Shear-Activated Indentation Crack Initiation in Soda-Lime Glass, *J. Mater. Sci.*, Vol 18, 1983, p 2785–2797
185. S. Lathabai, J. Rodel, T. Dabbs, and B.R. Lawn, Fracture Mechanics Model for Subthreshold Indentation Flaws. I. Equilibrium Fracture, *J. Mater. Sci.*, Vol 26, 1991, p 2157–2168
186. D. Kells and N.J. Mills, The Initiation of Indentation Fracture in Polystyrene, *Philos. Mag. A*, Vol 44, 1981, p 1149–1163

Evaluation of Environmentally Assisted Crack Growth

Y. Katz, N. Tymiak, and W.W. Gerberich, University of Minnesota

Methods for Small-Volume Testing

Indentation and Continuous Scratch-Induced Cracking. Both cohesive and adhesive fracture are considered here.

Indentation-Induced Cohesive Cracking. Different systems of cracks may form during loading and unloading parts of an indentation process. These systems include cone, median, radial, half-penny, and lateral as discussed in a recent review (Ref 187). Sequential occurrence of different cracking patterns is determined by combination

of the evaluated material and an indenter geometry (Ref 188). With the blunt indenters, such as large radii spheres, cracking initiation would normally precede plasticity onset (Ref 187). In contrast, sharp pyramidal or conical indenters would initiate plastic deformation prior to cracking (Ref 187). Once yielding takes place during an indentation test, residual plastic deformation exists after load removal. Accommodation of this plastically deformed volume by surrounding elastic material results in a residual stress field. These stresses act to open an indentation crack in a similar way as a center-loaded point force. The stress intensity in this case can be approximated with (Ref 189, 190):

$$K_{\text{residual}} = \chi P/c^{3/2} \quad (\text{Eq 6})$$

where P is an indentation load, c is crack length, and χ is a characteristic constant for a given combination of material and indenter. It should be noted that with the absence of an additional external load, an indentation-induced crack is stable as the stress intensity decreases with increasing crack length. With the applied external load, the total stress intensity becomes (Ref 189, 191):

$$K_{\text{tot}} = K_{\text{app}} + K_{\text{res}} = \psi \sigma_{\text{app}} \sqrt{c} + \chi \frac{P}{c^{3/2}} \quad (\text{Eq 7})$$

where ψ is a geometrical factor, and σ_{ap} is applied stress.

Indentation-Induced Adhesive Fracture. For ductile films on brittle substrates, indentation-induced plastic deformation in a film provides a driving force for delamination (Ref 192, 193, and 194). With brittle films on ductile substrates, the delamination driving force more often comes from plastic deformation of the substrate (Ref 195, 196).

Continuous Scratch. Scratches are produced by traversing a surface at constant or continuously increasing vertical displacement. While the pattern of indentation cracking is defined by elastic-plastic properties of an indented material, indenter geometry, and load range, scratch-induced cracking depends on all of the above parameters plus several others. These factors include scratch velocity, indenter/surface adhesion, and a friction coefficient. With much more complicated stress/strain state and possible involvement of material time-dependent behavior, mechanisms of scratch-induced deformation and cracking are not well understood yet. Given the complexity of the problem, quantitative information gained from a scratch test should be interpreted very cautiously. To compare two materials, it is preferable to test them both using the same loading conditions. These would include indenter geometry, loading, and horizontal drive velocity. Similarly, such evaluations would require testing of both environmentally exposed and nonexposed samples under the same loading conditions. Theoretical analyses for scratch-induced cohesive and adhesive fracture may be obtained from Ref 197, 198, 199, 200, and 201, respectively.

Indentation or scratch “precracking” followed by application of an external load under exposure to an environment may be used. Possible geometries include a disk (Ref 202, 203) or cantilever beam specimen (Ref 204). Most commonly used is four-point bending test (Ref 205). Attention should be paid to possible effects of elastic anisotropy and asymmetry of indentation-induced plastic deformation and fracture (Ref 190). Crack extension can be monitored with optical microscopy (Ref 206). Crack arrest marking can be generated on the fracture surfaces by temporary unloading during subcritical crack growth (Ref 207).

Crack extension is driven by a combined action of applied load and residual indentation induced tensile stresses as given by Eq 7. Analysis of this equation implies stable crack growth providing $K \geq K_c$ and $dK/dc < 0$. Instability will occur as $dK/dc = 0$ and $K = K_c$. From these instability conditions, fracture strength, and critical crack length under inert conditions may be obtained:

$$\sigma_m = \frac{3K_{\text{Ic}}}{4\psi c_m^{1/2}} \quad (\text{Eq 8})$$

$$c_m = \left(\frac{4\chi P}{K_{\text{Ic}}} \right) \quad (\text{Eq 9})$$

Fatigue strength of an indented specimen may be expressed by the following function of stressing rate (Ref 208):

$$\sigma_f = (\beta' \dot{\sigma}_a)^{1/(n'+1)} \quad (\text{Eq 10})$$

where $n' = 0.75N + 0.5$ and

$$\beta = \frac{(2\pi n')^{1/2} \sigma_m^{n'}}{v^*}$$

with N and v^* being parameters used in Eq 2.

Values of n' and β' may be determined from the slope and the intercept of the dynamic fatigue curve, respectively. Examples of dynamic curves for soda-lime glass in various environments are shown in Fig. 37 (Ref 209). Here, low susceptibility to environmental crack growth in silicon and motor oils is evident from large values of n' exponents.

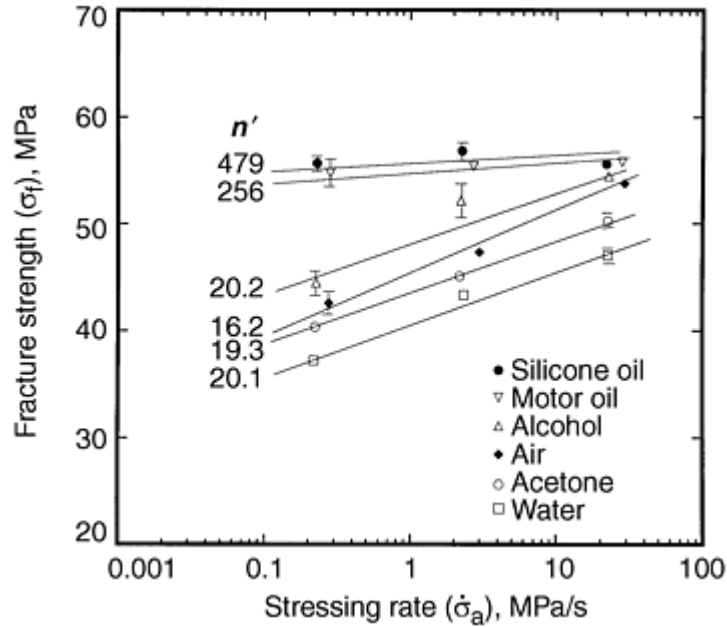


Fig. 37 Dynamic fatigue results of indented soda-lime glass specimens. Indent load, 19.6 N. Error bars represent ± 1.0 standard deviation. Source: Ref 209

Annealing or surface layer removal may be utilized to remove residual stresses prior to testing. Neglecting residual stress would result in a significant strength underestimate as shown in Fig. 38 (Ref 210). This in turn would give an overestimate of environmental susceptibility as determined via crack growth kinetics parameters from Eq 10.

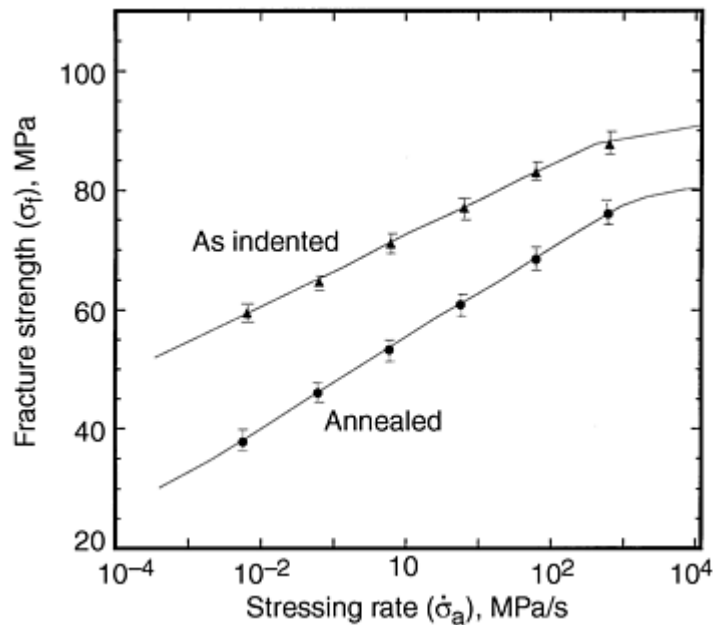


Fig. 38 Dynamic fatigue response for indented soda-lime glass disks broken in water. Vickers indent load, 5 N. Source: Ref 210

It should also be stressed that in general, parameters χ and ψ are not constant but may be affected by changing crack geometry and interference between different crack systems (Ref 211). An example of changes in these parameters during different crack evolution stages is shown in Fig. 39.

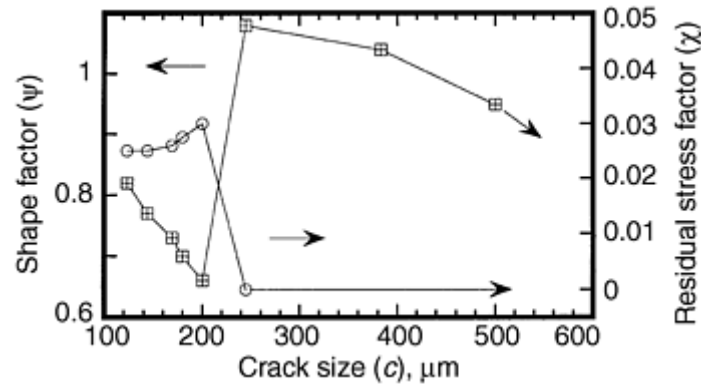


Fig. 39 Complete trends of the shape factor (ψ) and of the residual stress factor (χ) as a function of the crack size (c). Source: Ref 211

Contact Mechanics Testing under or Following Exposure to an Environment. Environmental effects may be assessed by measuring an extent of indentation or scratch-induced cracking with and without an environment. A driving force here would be indentation-induced residual stresses as given by Eq 6. Based on the dynamic fatigue data, an analytical expression for a time dependent crack extent, $c(t)$ may be obtained (Ref 210). Fatigue parameters may be determined from plotting c versus t in double-log coordinates. However, values of crack growth exponents obtained from residual indentation stress driven slow crack growth were significantly different from these obtained in the same environments with dynamic fatigue (Ref 210). Moreover, postindentation crack growth in motor oil exhibited a significant environmental susceptibility in contrast to static fatigue testing. It was suggested that presence of the limited amount of water present in the oil would only be effective in the small crack regime corresponding to a residual stress driven crack extension. Whatever the reason, for the observed discrepancy design considerations would require using testing conditions most closely approximating service conditions. Special considerations required for cohesive and adhesive fracture in thin films are mentioned below.

Environmentally Assisted Crack Growth in Thin Films. Sensitivity to environmentally assisted cracking for small volumes often differs from that for bulk materials. Possible reasons include microstructural differences, one of the most important being nanoscale grain sizes for submicron thick films. With a nanoscale grain size, the fraction of grain-boundary material increases dramatically. With grain boundaries being the preferred pathway for diffusion, diffusivity increases with the grain size reduced to the nanoscale. Also, with the grain boundaries being more prone to preferential dissolution, susceptibility to environmental attack is enhanced for nanocrystalline materials. In addition, increasing fraction of grain boundaries results in elevated internal stresses in a film. These stresses combined with the ones produced by substrate constraint may affect resistance to crack propagation. Similarly, when indentation depth scales with the depth of any surface affected layer, stresses in this layer may affect indentation-induced crack growth. Tensile stresses would favor indentation crack propagation as opposed to compressive ones. In addition, stress relaxation could be promoted by either sign residual stress at higher temperatures. While the initial residual stress would tend to promote slow crack growth, any relaxation with time would diminish the driving force.

Environmentally Affected Thin-Film Adhesion. Contact mechanics methods provide the following advantages for thin-film adhesion testing:

- There is no possibility for interfacial property changes.
- Very small amount of material is required for testing.
- Testing can be carried under temperature, potentiostatic, or environmental control.
- Very simple sample preparation and testing procedure.

Indentation-induced blister for charged and noncharged samples are shown in Fig. 40 (Ref 182). Here, the larger size of an indentation-induced delamination for hydrogen-charged sample indicates hydrogen charging induced adhesion degradation.

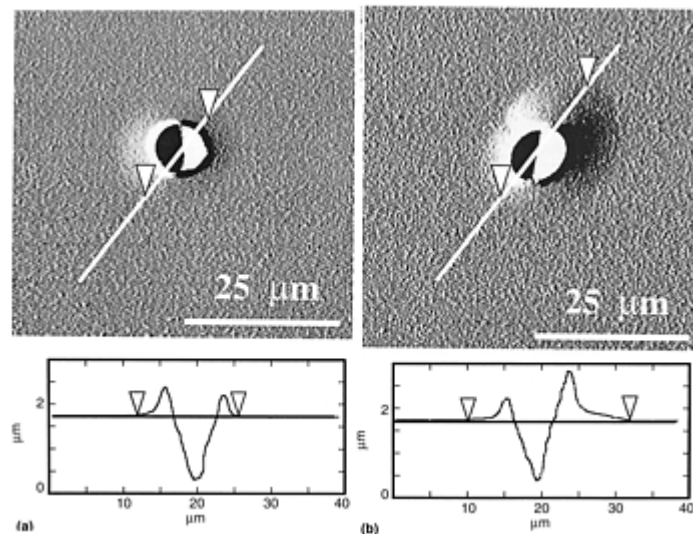


Fig. 40 Indentation-induced delaminations in 500 nm titanium-copper film. (a) Noncharged sample. (b) Hydrogen-charged sample. Source: Ref 182

References cited in this section

182. Y. Katz, N.I. Tymiak, and W.W. Gerberich, Nano-mechanical Probes as New Approaches to Hydrogen/Deformation Interaction Studies, An invited paper for *Recent Advances in the Engineering Aspects of Hydrogen Embrittlement of the Engineering Fracture Mechanics*, 1999
187. P. Ostojsic and R. McPherson, A Review of Indentation Fracture Theory: Its Development, Principles and Limitations, *Int. J. Fract.*, Vol 33, 1987, p 297–312
188. R.F. Cook and G.M. Pharr, Direct Observation and Analysis of Indentation Cracking in Glasses and Ceramics, *J. Am. Ceram. Soc.*, Vol 73, 1990, p 787–817
189. G.R. Anstis, P. Chantikul, B.R. Lawn, and D.B. Marshall, A Critical Evaluation of Indentation Techniques for Measuring Fracture Toughness, *J. Am. Ceram. Soc.*, Vol 64, 1981, p 533–538
190. D.B. Marshall and R.B. Lawn, Residual Stress Effect in Sharp Contact Cracking, *J. Mater. Sci.*, Vol 14, 1979, p 2001–2012
191. D.B. Marshall, R.B. Lawn, and P. Chantikul, Residual Stress Effects in Sharp Contact Cracking. Part 2. Strength Degradation, *J. Mater. Sci.*, Vol 14, 1979, p 2225–2235
192. D.B. Marshall and A.G. Evans, Measurement of Adherence of Residually Stressed Thin Film by Indentation. I. Mechanics of Interface Delamination, *J. Appl. Phys.*, Vol 56, 1984, p 2632–2638
193. M. J. Matthewson, Axi-Symmetric Contact on Thin Compliant Coatings, *J. Mech. Phys. Solids*, Vol 29, 1981, p 89–113
194. L.G. Rosenfeld, J.E. Ritter, T.J. Larner, and M.R. Lin, Use of the Microindentation Technique for Determining Interfacial Fracture Energy, *J. Appl. Phys.*, Vol 67, 1990, p 3291–3296
195. J.J. Vlassak, M.D. Drory, and W.D. Nix, A Simple Technique for Measuring the Adhesion of Brittle Films to Ductile Substrates with Applications to Diamond-Coated Titanium, *J. Mater. Res.*, Vol 12, 1997, p 1990–1910
196. M.D. Drory and J.W. Hutchinson, Measurement of Brittle-Film Adhesion on a Ductile Substrate by Indentation, *Proc. Roy. Soc. (London) A*, 1996, p 2319–2341

197. J.W. Hoehn, S.K. Venkataraman, H. Huang, and W.W. Gerberich, Micromechanical Test Applied to NiAl, *Mater. Sci. Eng. A*, Vol A192/193, 1995, p 301–308
198. P.R. Chalker, S.J. Bull, and D.S. Rickerby, A Review of the Methods for the Evaluation of Coating-Substrate Adhesion, *Mater. Sci. Eng. A*, Vol A140, 1991, p 583–592
199. S.V. Hainsworth, S.J. Bull, and T.F. Page, Scratch Deformation Response of Thin CN_x Coatings at Ultra-Low Loads, *Fundamentals of Nanoindentation and Nanotribology*, Symposium. Materials Research Society, 1998, p 433–438
200. T.W. Wu, Microscratch and Load Relaxation Tests for Ultra-Thin Films, *J. Mater. Res.*, Vol 6, 1991, p 407–426
201. S. Venkataraman, D.L. Kohlstedt, and W.W. Gerberich, Continuous Microscratch Measurements of the Practical and True Works of Adhesion for Metal/Ceramic Systems, *J. Mater. Res.*, Vol 11, 1996, p 3133–3145
202. D.B. Marshall and B.R. Lawn, Flaw Characteristics in Dynamic Fatigue: The Influence of Residual Contact Stresses, *J. Am. Ceram. Soc.*, Vol 63, 1980, p 532–536
203. J. Zhang and A.J. Ardell, Measurement of the Fracture Toughness of Ceramic Materials Using a Miniaturized Disk-Bend Test, *J. Am. Ceram. Soc.*, Vol 76, 1993, p 1340–1344
204. R.W. Rice, C.C Wu, and K.R. McKinney, Fracture and Fracture Toughness of Stoichiometric MgAl₂O₄ Crystals at Room Temperature, *J. Mater. Sci.*, Vol 31, 1996, p 1353–1560
205. Y. Kimura, T. Yagasaki, and T. Kunio, On the Delayed Fracture Characteristics of Vickers Indented Glass in Deionized Water, *Eng. Fract. Mech.*, Vol 19, 1984, p 1025–1033
206. H. Matzke, Hertzian Indentation of Thorium Dioxide, ThO₂, *J. Mater. Sci.*, Vol 15, 1980, p 739–746
207. P.J. Dwivedi and D.J. Green, Determination of Subcritical Crack Growth Parameters by in Situ Observation of Indentation Cracks, *J. Am. Ceram. Soc.*, Vol 78, 1995, p 2122–2128
208. E.R. Fuller, B.R. Lawn, and R.F. Cook, Theory of Fatigue for Brittle Flaws Originating from Residual Stress Concentration, *J. Am. Ceram. Soc.*, Vol 66, 1983, p 314–321
209. S.R. Choi and J.A. Salem, Slow Crack Growth of Indent Cracks in Glass with and without Applied Stress, *Mater. Sci. Eng. A*, Vol A149, 1992, p 259–264
210. D.B. Marshall and B.R. Lawn, Flaw Characteristics in Dynamic Fatigue: The Influence of Residual Contact Stresses, *J. Am. Ceram. Soc.*, Vol 63, 1980, p 532–536
211. V.M. Sglavo and D.J. Green, The Sub-Critical Indentation Fracture Process in Soda-Lime-Silica Glass, *Eng. Fract. Mech.*, Vol 55, 1996, p 35–46

Scanning Probe Microscopy

Scanning probe microscopes (SPM) such as the scanning tunneling microscope (STM) (Ref 212), AFM (Ref 213, 214, 215), and their modifications provide imaging and *quantitative* evaluation of atomic level surface features. One important feature is that atomic-scale resolution can be gained without an extensive sample modification such as thinning and/or polishing. Thus, small-scale aspects of plastic deformation and fracture can be observed without influence of sample preparation. Also, quantitative information can be obtained from *direct* three-dimensional topography measurements. An advantage of SPM is evident when three-dimensional strain (Ref 216) and stress (Ref 217) fields near a tip of a brittle crack can be obtained directly as compared to a rather complicated procedure based on digitizing of SEM images (Ref 218). Another example could be resolving nanoscale plasticity features associated with a brittle crack (Ref 216). Both STM and AFM can be easily operated in a variety of environments (Ref 219, 220). While the STM cannot be utilized for insulators, AFM works equally well on conducting, semiconducting, or insulating surfaces such as polymers and ceramics. With the controlled potential applied to the metallic (Ref 221) or semiconductor (Ref 222) surface, various solid/electrolyte interactions such as metal dissolution/electrodeposition or passive film evolution can be visualized and evaluated quantitatively. Here, surface topography mapping provides an accurate spatial distribution of material removal or deposition rates. Examples include localized dissolution enhanced by indentation-induced plastic deformation (Ref 223) and grain-boundary sensitization (Ref 224, 225). In the latter, selectively placed indents have been utilized to reveal preferential dissolution along chromium-depleted near-boundary regions (Ref 225). With the alternating periods of loading and SPM observations, an insight into crack initiation and growth can be gained. The above approach has been successively applied to initial stages of environmentally assisted fatigue (Ref 226, 227). In the latter, number of cycles for crack initiation was correlated to a damage parameter accounting for *global* plastic strain alongside with the corresponding *local* plasticity characteristics. These include persistent slip band (PSB) spacings and heights as measured with the SPM. Environmental effects on the fracture onset under increasing monotonic load can be evaluated from nanoscratch testing combined with the AFM imaging as described in more detail in the preceding section. Invention of loading devices operated in conjunction with the SPM (Ref 224, 228) enabled a continuous monitoring of crack initiation and propagation. In situ observations of loaded cracks in vacuo and laboratory air (Ref 224) show a clear environmental effect apparent from the sharpness of an air-exposed crack as opposed to blunting occurring at a crack tip in vacuo. Additional advantages come from indentation combined with the AFM pretest and posttest imaging of an indented area as detailed in the previous section.

References cited in this section

212. G. Binnig, H. Rohrer, C. Gerber, and E. Weibell, Tunneling Through a Controllable Vacuum Gap, *Appl. Phys. Lett.*, Vol 40, 1982, p 178–180
213. G. Binnig, C.F. Quate, and C. Gerber, *Phys. Rev. Lett.*, Vol 56, 1982, p 930
214. D. Rugar and P.K. Hansma, Atomic Force Microscopy, *Phys. Today*, Vol 43, 1990, p 23–28
215. D. Sarid, *Scanning Force Microscopy*, Oxford University, 1991
216. T. Foecke, R.M. King, A.F. Dale, and W.W. Gerberich, Imaging of Cracks in Semiconductors Using Scanning Tunneling Microscopy, *J. Vac. Sci. Technol.*, Vol B9, 1991, p 673–676
217. T. Kinoshita, Stress Singularity Near the Crack-Tip in Silicon Carbide: Investigation by Atomic Force Microscopy, *Acta Mater.*, Vol 46, 1998, p 3963–3974

218. K. Jakus, S. Michael, and J.E. Ritter, Measurement of Crack Tip Inelastic Deformations Using Digital Image Correlation, *Adv. Ceram. Mater.*, Vol 3, 1988, p 268–272
219. S. Manne, J. Massie, V.B. Elings, P.K. Hansma, and A.A. Gewirth, Electrochemistry on a Gold Surface Observed with the Atomic Force Microscope, *J. Vac. Sci. Technol. B*, Vol 9, 1991, p 950–954
220. P.K. Hansma and J. Tersoff, Scanning Tunnelling Microscopy, *J. Appl. Phys.*, Vol 61, 1987, p R1–23
221. P. Mrozek, Y.-E. Sung, and A. Wieckowski, Silver Deposition on the Au(111) Electrode without Interference by Specifically Adsorbed Anions, *Surf. Sci.*, Vol 335, 1995, p 44–51
222. S.-L. Yau, F.-R.F. Fan, and A.J. Bard, In situ STM Imaging of Silicon(111) in HF under Potential Control, *J. Electrochem. Soc.*, Vol 139, 1992, p 2825–2829
223. K. Komai, K. Minoshima, and M. Itoh, *J. Soc. Matter. Sci. Jpn.*, 1994, p 336
224. K. Komai and K. Minoshima, Nanometric Visualization of Localized Damage by Scanning Probe Microscopy, *Mater. Sci. Res. Int.*, Vol 2, 1996, p 209–219
225. N.I. Tymiak, D.F. Bahr, J.C. Nelson, and W.W. Gerberich, “Micromechanical Probes of a Sensitized Stainless Steel in Corrosive Environments,” Presented at TMS Fall Conference, Symposium on Welding of Stainless Steel Alloys (Indianapolis, IN), Sept 1997
226. G. Venkataraman, T.S. Sriram, M.E. Fine, and Y.W. Chung, STM and Surface Analytical Study of the Effect of Environment on Fatigue Crack Initiation in Silver Single Crystals I, Surface Chemical Effects, *Scr. Metall.*, Vol 24, 1990, p 273–278
227. P.G. Marsh, S.E. Harvey, M.D. Kriese, and W.W. Gerberich, Environmental Effects on Fatigue Crack Development in HSLA Steel and Fine Grain α -Titanium, *Scr. Metall.*, Vol 33, 1995, p 825–829
228. M. Goken, H. Vehoff, and P. Neumann, *J. Vac. Sci. Technol. B*, Vol 14, 1996, p 1157

Evaluation of Environmentally Assisted Crack Growth

Y. Katz, N. Tymiak, and W.W. Gerberich, University of Minnesota

Acknowledgments

Portions of this article are adapted from the following:

- L. Raymond, Evaluation of Hydrogen Embrittlement, *Corrosion*, Vol 13, *ASM Handbook*, ASM International, 1987, p 283–290
- P.L. Andresen, Corrosion Fatigue Testing, *Fatigue and Fracture*, Vol 19, *ASM Handbook*, ASM International, 1996, p 193–209
- G. H. Koch, Stress-Corrosion Cracking and Hydrogen Embrittlement, *Fatigue and Fracture*, Vol 19, *ASM Handbook*, ASM International, 1996, p 483–506

References

1. M.G. Fontana and N.D. Greene, *Corrosion Engineering*, McGraw-Hill, 1978, p 113
2. L. Raymond, Ed., *Hydrogen Embrittlement Testing*, STP 543, ASTM, 1972
3. L. Raymond, Evaluation of Hydrogen Embrittlement, *Corrosion*, Volume 13, *ASM Handbook*, ASM International, 1987, p 283–284
4. K. Sieradzki, Atomistic and Micromechanical Modeling Aspects of Environment-Induced Cracking of Metals, *EICM Proc.*, R.P. Gangloff and M.B. Ives, Ed., National Association of Corrosion Engineers, 1990, p 125
5. W.W. Gerberich and S.-H. Chen, Environment-Induced Cracking of Metals, Fundamental Processes: Micromechanics, *Int. Conf. Environmentally Induced Cracking*, Oct 1988, National Association of Corrosion Engineers, 1990, p 167–187
6. W.W. Gerberich, P. Marsh, J. Hoehn, S. Venkataraman, and H. Huang, Hydrogen/Plasticity Interactions in Stress Corrosion Cracking, *Corrosion-Deformation Interactions*, CD1 '92, *Les Editions de Physique les Ulis*, T. Magnin, Ed., 1993, p 325–343
7. H.K. Birnbaum, Mechanism of Hydrogen-Related Fracture of Metals, *EICM Proc.*, R.P. Gangloff and M.B. Ives, Ed., National Association of Corrosion Engineers, 1990, p 21
8. H.K. Birnbaum, I.M. Robertson, D. Sofronis, and D. Teter, Mechanism of Hydrogen-Related Fracture—A Review, *CDI '96*, T. Magnin, Ed., The Institute of Materials, 1997, p 172
9. M.-J. Lii, X.-F. Chen, Y. Katz, and W.W. Gerberich, Dislocation Modeling and Acoustic Emission Observation of Alternating Ductile/Brittle Events in Fe-3wt%Si Crystals, *Acta Metall.*, Vol 38, 1990, p 2435–2452
10. S.-H. Chen, Y. Katz, and W.W. Gerberich, Crack Tip Strain Fields and Fracture Microplasticity in Hydrogen Induced Cracking of Fe-3wt%Si Single Crystals, *Philos. Mag. A*, Vol 63 (No. 1), 1990, p 131–155
11. W. Zielinski and W.W. Gerberich, Crack-Tip Dislocation Emission Arrangements for Equilibrium: Part I—In situ TEM Observations of Fe-2wt%Si, *Acta Metall. Mater.*, Vol 40, 1992, p 2861–2871
12. H. Huang and W.W. Gerberich, Crack-Tip Dislocation Emission Arrangements for Equilibrium: Part II—Comparisons to Analytical and Computer Simulation Models, *Acta Metall. Mater.*, Vol 40, 1992, p 2873–2881
13. P. Marsh, W. Zielinski, H. Huang, and W.W. Gerberich, Crack-Tip Dislocation Emission Arrangements for Equilibrium: Part III—Applications to Large Applied Stress Intensities, *Acta Metall. Mater.*, Vol 40, 1992, p 2883–2894
14. R.P. Harrison, K. Loosemore, I. Milne, and A.R. Dowling, CEGB R/H/R6 Rev 2, General Electricity Generating Board, United Kingdom, 1986

15. E.A. Steigewald, F.W. Schaller, and A.R. Troiano, *Trans. Metall. Soc. AIME*, Vol 218, 1960, p 832
16. A.R. Troiano, *Trans. ASM*, Vol 52, 1960, p 54
17. H. Huang and W.W. Gerberich, Quasi-Equilibrium Modeling of the Toughness Transition During Semibrittle Cleavage, *Acta Metall. Mater.*, Vol 42 (No. 3), 1994, p 639–647
18. M.S. Daw and M.I. Baskes, *Phys. Rev. B*, Vol 29, 1984, p 6443
19. N.R. Moody, J.E. Angelo, S.M. Foiles, M.I. Baskes, and W.W. Gerberich, Atomistic Simulation of the Hydrogen-Induced Fracture Process in an Ion-Based Superalloy, *Sixth Israel Materials and Engineering Conf.*, D. Itshak, D. Iliezer, and J. Haddad, Ed., Ben-Gurion University of the Negev, 1993, p 444
20. C.L. Fu and G.S. Painter, *J. Mater. Res.*, Vol 6, 1991, p 719
21. X. Chen, T. Foecke, M. Lii, Y. Katz, and W.W. Gerberich, The Role of Stress State on Hydrogen-Induced Cracking in Fe-Si Single Crystals, *Eng. Fract. Mech.*, Vol 35 (No. 6), 1989, p 997–1017
22. C.D. Beachem, *Metall. Trans.*, Vol 3, 1972, p 437
23. S.P. Lynch, Environmentally Assisted Cracking, Overview of Evidence for an Adsorption Induced Localized Slip Process, *Acta Metall.*, Vol 20, 1988, p 2639
24. G. Bond, I.M. Robertson, and H.K. Birnbaum, The Influence of Hydrogen on Deformation and Fracture Processes in High Strength Aluminum, *Acta Metall.*, Vol 35, 1987, p 2289
25. T. Matsumoto, J. Eastman, and H.K. Birnbaum, Direct Observations of Enhanced Dislocation Mobility Due to Hydrogen, *Scr. Metall.*, Vol 15, 1981, p 1033
26. T. Tabata and H.K. Birnbaum, Direct Observations of the Effects of Hydrogen on the Behavior of Dislocations in Iron, *Scr. Metall.*, Vol 17, 1993, p 947
27. D.G. Ulmer and C.J. Alstetter, Hydrogen Induced Strain Localization and Failure of Austenitic Stainless Steels at High Hydrogen Concentrations, *Acta Metall. Mater.*, Vol 39, 1991, p 1237
28. P.D. Hicks and C.J. Alstetter, *Metall. Trans. A*, Vol 23A, 1992, p 237
29. H. Vehoff and P. Neumann, *Acta Metall.*, Vol 28, 1980, p 265
30. W.W. Gerberich, H. Huang, and P.G. Marsh, Macroscopic and Microscopic Modeling of Hydrogen Embrittlement Thresholds, *Second Workshop on Hydrogen Effects on Materials in Propulsion Systems*, NASA Conf. 3182, Marshall Flight Center, 1992, p 196–203
31. J.J. Lewandowski and A.W. Thompson, *Hydrogen Effects on Material Behavior*, N.R. Moody and A.W. Thompson, Ed., TMS, 1990, p 817
32. D.S. Shih, I.M. Robertson, and H.K. Birnbaum, Hydrogen Embrittlement of α Titanium in situ TEM Studies, *Acta Metall.*, Vol 36, 1988, p 111
33. I.M. Robertson and H.K. Birnbaum, An HVEM Study of Hydrogen Effects on Deformation and Fracture of Nickel, *Acta Metall.*, Vol 34, 1986, p 353
34. H. Mathias, Y. Katz, and S. Nadiv, Hydrogenation/Gas Release Effects in Austenitic Steels: Quantitative Study, *Metal-Hydrogen Systems*, T.N. Vezirogen, Ed., Pergamon Press, 1982, p 225

35. Y. Katz, X. Chan, M.J. Lii, M. Lanxner, and W.W. Gerberich, The Anisotropic Nature of Local Crack Stability in BCC Crystals, *Eng. Fract. Mech.*, Vol 41 (No. 4), 1991, p 541–567
36. N.R. Moody, S.K. Venkataraman, R.Q. Hwang, J.E. Angelo, and W.W. Gerberich, Hydrogen Effects on the Fracture of Thin Tantalum Nitride Films, *Symp. Corrosion/Deformation Interactions, 2*, Vol 21, T. Magnin, Ed., Eur. Fed. Corrosion, 1997, p 227–237
37. W.W. Gerberich, R.A. Oriani, M.-J. Lii, X. Chen, and T. Foecke, The Necessity of Both Plasticity and Brittleness in the Fracture Thresholds of Iron, *Philos. Mag. A*, Vol 63 (No. 2), 1991, p 363–376
38. R.N. Parkins, Stress Corrosion Cracking, *EICM Proc.*, R.P. Gangloff and M.B. Ives, Ed., National Association of Corrosion Engineers, 1990, p 1
39. Y. Katz, A. Bussiba, and H. Mathias, The Influence of Austenitic Stability on Fatigue Crack Growth Retardation, *Material Experimentation and Design in Fatigue*, F. Sheratt, J.B. Sturgeon, and R.A.F. Farnborough, Ed., IPC Science and Tech. Press, Guildford, Surrey, 1981, p 147
40. C.W. Tien and C.J. Alstetter, Hydrogen-Enhanced Plasticity of 310S Stainless Steel, CDI '92, *Les Editions de Physique les Ulis*, T. Magnin, Ed., 1993, p 355
41. V.G. Gavriljuk, H. Hänninen, S.Yu. Smouk, A.V. Tarasenko, A.S. Tereschenko, and K. Ullakko, Phase Transformation and Relaxation Phenomena in Hydrogen Charged CrNiMn and CrNi Stable Austenitic Stainless Steel, *Hydrogen Effects in Materials*, A.W. Thompson and N.R. Moody, Ed., The Minerals, Metals, Materials Society, 1996, p 893
42. V.G. Gavriljuk, H. Hanninen, A.S. Tereschenko, and K. Ullakko, Effects of Nitrogen on Hydrogen-Induced Phase Transformation in Stable Austenitic Stainless Steel, *Scr. Metall. Mater.*, Vol 28, 1993, p 247
43. P. Sofronis and H.K. Birnbaum, Mechanism of Hydrogen-Dislocation-Impurity Interactions—I. Increasing Shear Modulus, *J. Mech. Phys. Solids*, Vol 43, 1995, p 49
44. H. Mathias, Y. Katz, and S. Nadiv, High Resolution Micro-Autoradiography as Complementary Research Technique, *Proc. Sixth Congress on Electron Microscopy*, D.C. Brandon, Ed., Tal. International, Jerusalem, 1976, p 399
45. P. Lacombe, M. Aucouturier, and J. Chene, Hydrogen Trapping and Hydrogen Embrittlement, *Hydrogen Embrittlement and Stress Corrosion Cracking*, R. Gibala and R.F. Hehemann, Ed., American Society for Metals, 1984
46. A.M. Brass and J. Chene, Hydrogen-Deformation Interactions in Iron and Nickel Base Alloys, *CDI '96*, T. Magnin, Ed., The Institute of Metals, 1997, p 197
47. A. Bussiba, H. Alush, and Y. Katz, Corrosion/Deformation Interactions in U/Water Systems, *Mater. Sci. Res. Int.*, Vol 3, 1997, p 244
48. R.A. Oriani and P.H. Josephic, *Acta Metall.*, Vol 22, 1977, p 979
49. H. Kobayashi and K. Ema, *Physics and Technology of Amorphous SiO₂*, R.A.B. Devine, Ed., 1987, Plenum Press, p 71
50. E.A. Clark, R. Yeske, and H.K. Birnbaum, The Effect of Hydrogen on the Surface Energy of Nickel, *Metall. Trans. A*, Vol 11, 1980, p 1903

51. J.P. Hirth, *Philos. Trans. R. Soc. London Ser.*, Vol 295, 1980, p 139
52. J.P. Hirth and J.R. Rise, *Metall. Trans. A*, Vol 11A, 1984, p 1501
53. T.Y. Zhang and J.E. Hack *Metall. Mater. Trans. A*, Vol 30, 1999, p 155
54. W.W. Gerberich, P. Marsh, and H. Huang, The Effect of Local Dislocation Arrangements on Hydrogen-Induced Cleavage, *Parkins Symposium on Fundamental Aspects of Stress Corrosion Cracking*, S. Breummer and W.W. Gerberich, Ed., TMS-AIME, 1992, p 191–204
55. S.T. Rolfe and I.M. Barsom, *Fracture and Fatigue Control in Structures*, Prentice-Hall, 1977
56. R.P. Wei, S.R. Novak, and D.R. Williams, Some Important Considerations in the Development of Stress Corrosion Cracking Test Methods, *Mater. Res. Stand.*, Vol 12 (No. 9), Sept 1972, p 25
57. C.A. Zanis, P.W. Holsberg, and E.C. Dunn, Jr., Seawater Subcritical Cracking of HY-Steel Weldments, *Weld. J. Res. Suppl.*, Vol 59, Dec 1980
58. “Rapid Inexpensive Tests for Determining Fracture Toughness,” NMAB-328, National Academy of Sciences, 1976
59. D.L. Dull and L. Raymond, Stress History Effect on Incubation Time for Stress Corrosion Crack Growth in AISI 4340 Steel, *Metall. Trans.*, Vol 3, Nov 1972, p 2943–2947
60. G. Liu-Nash, J.A. Todd, and S. Mostovoy, An Accelerated Test Method for Determining Near-Threshold Stress Intensity Values in HSLA Steels, *Fatigue and Fracture of Engineering Materials and Structures*, Vol 20 (No. 12), 1997, p 1657–1664
61. X.P. Zhang and Y.W. Shi, The Reasonable Design of Charpy-Size Specimen for Fracture Toughness Test in Nuclear Surveillance, *Int. J. Pressure Vessels Piping*, Vol 62 (No. 3), 1995, p 219–225
62. M. Wall, C.E. Lane, and C.A. Hipsley, Fracture Criteria for Hydrogen and Temper Embrittlement in 9Cr1Mo Steel, *Acta Metall. Mater.*, Vol 42 (No 4), April 1994, p 1295–1309
63. J.J. Lewandowski and A.W. Thompson, Hydrogen Effects on Cleavage Fracture in Fully Pearlitic Eutectoid Steel, *Hydrogen Effects on Material Behavior*, TMS, 1990, p 861–870
64. R.D. Kane, M.S. Cayard, and M. Prager, “Test Procedures for Evaluation of Resistance of Steels to Cracking in Wet H₂S Environments,” Paper No. 519, NACE International, 1994, p 22
65. D.L. Dull and L. Raymond, Electrochemical Techniques, *Hydrogen Embrittlement and Testing*, STP 543, ASTM, 1974, p 20–33
66. P.J. Fast, C.S. Susskind, and L. Raymond, “Charpy V-Notched Specimens for Indexing Stress Corrosion Cracking in HY Ship Steels and Weld Metals,” Final report, Contract F04701-78-C-0079, The Aerospace Corporation, Aug 1979
67. P.S. Tyler, M. Levy, and L. Raymond, Investigation of the Conditions for Crack Propagation and Arrest under Cathodic Polarization by Rising Step Load Bend Testing, *Corrosion*, Vol 47 (No. 2), 1991, p 82–87
68. J.P. Fiddle, R. Bernardi, R. Broudeur, C. Roux, and M. Rapin, Disk Pressure Testing of Hydrogen Environment Embrittlement, *Hydrogen Embrittlement Testing*, STP 543, ASTM, 1974, p 221–253

69. M. Beghini, G. Benamati, and L. Bertini, Hydrogen Embrittlement Characterization by Disk Pressure Tests: Test Analysis and Application to High Chromium Martensitic Steels, *J. Eng. Mater. Technol. (Trans. ASME)*, Vol 118 (No. 2), 1996, p 179–185
70. *Slow Strain Rate Testing for the Evaluation of Environmentally Induced Cracking: Research*, STP 1210, ASTM, 1993
71. B. Ule, F. Vodopivec, and L. Vehovar, The Application of Slow Strain Rate Tension Test for Quantitative Evaluation of Hydrogen-Induced Cracking Susceptibility of High Strength Steels, *ECF 8—Fracture Behaviour and Design of Materials and Structures*, Vol I, Engineering Materials Advisory Services Ltd., 1990, p 461–468
72. W.W. Gerberich, Effect of Hydrogen in High-Strength and Martensitic Steels, *Hydrogen in Metals*, American Society for Metals, 1976, p 115
73. B. Ule, F. Vodopivec, and L. Vehovar, The Application of Critical Strain Fracture Criteria for the Quantitative Evaluation of Hydrogen Embrittlement of High-Strength Steels, Conference: Use of Special Steels, Alloys and New Materials in Chemical Process Industries (Lyon, France, 22–23 May 1991), *Bull. Cercle D'Etudes Met.*, Vol 16 (No. 1), May 1991, p 28.1–28.11
74. G. Koch, Stress Corrosion Cracking and Hydrogen Embrittlement, *Fatigue and Fracture*, Vol 19, *ASM Handbook*, ASM International, 1996, p 481–506
75. D. Sprowls, Evaluation of Stress-Corrosion Cracking, *Corrosion*, Vol 13, *ASM Handbook*, 1987, p 245–282
76. D. Sprowls, Evaluation of Stress Corrosion Cracking, *Stress Corrosion Cracking, Materials Performance and Evaluation*, ASM International, 1992, p 363–416
77. R.H. Jones and R.E. Ricker, Stress Corrosion Cracking Mechanisms, *Stress Corrosion Cracking, Materials Performance and Evaluation*, ASM International, 1992, p 1–41
78. R.W. Staehle, Understanding “Situation-Dependent Strength,” a Fundamental Objective in Assessing the History of Stress Corrosion Cracking, *EICM Proc.*, R.P. Gangloff and M.B. Ives, Ed., National Association of Corrosion Engineers, 1990, p 561
79. M.A. Gaudett and J. R. Scully, The Effects of Pre-Dissolved Hydrogen on Cleavage and Grain-Boundary Fracture Initiation in Metastable Beta Ti-3Al-8V-4Cr-4Mo-4Zr, *Met. Mater. Trans. A*, Vol 30A, 1999, p 65
80. R.N. Parkins, *Corros. Sci.*, Vol 29, 1989, p 1019
81. G. Santarini, A Morphological Model for Quantitative Characterization of Stress Corrosion Cracking, *CDI '96*, T. Magnin, Ed., The Institute of Metals, p 55
82. *Stress Corrosion Testing*, STP 425, ASTM, 1967, p 3
83. H.L. Craig, D.O. Sprowls, and D.E. Piper, *Handbook on Corrosion Testing and Evaluation*, W.H. Ails, Ed., John Wiley and Sons, 1976, p 213
84. G. Vogt, *Werkstoff. Korros.*, Vol 29, 1978, p 721

85. N.J.H. Holroyd and G.M. Scamans, *Slow-Strain Rate Stress Corrosion Testing of Aluminum Alloys, Environment-Sensitive Fracture*, STP 821, S.V. Dean, E.N. Pugh, and G.M. Ugianski, Ed., ASTM, 1984, p 202
86. R.P. Gangloff, Corrosion Fatigue Crack Propagation in Metals, *EICM Proc.*, R.P. Gangloff and M.B. Ives, Ed., National Association of Corrosion Engineers, 1990, p 55
87. D.J. Duquett, Corrosion Fatigue Crack Initiation Processes—A State of the Art Review, *EICM Proc.*, R.P. Gangloff and M.B. Ives, Ed., National Association of Corrosion Engineers, 1990, p 45
88. R.W. Revie, *Uhlig's Corrosion Handbook*, 2nd ed., John Wiley & Sons, 2000
89. R. Baboian, Ed., *Corrosion Tests and Standards: Application and Interpretation*, ASTM, 1995
90. P.L. Andresen, Corrosion Fatigue Testing, *Fatigue and Fracture*, Vol 19, *ASM Handbook*, 1996, p 193–209
91. J.C. Newman, Jr. and W. Elber, Ed., *Mechanics of Fatigue Crack Closure*, STP 982, ASTM, 1988
92. P.L. Andresen and P.G. Campbell, The Effects of Crack Closure in High Temperature Water and Its Role in Influencing Crack Growth Data, *Proc. Fourth International Symp. on Environmental Degradation of Materials in Nuclear Power Systems—Water Reactors*, National Association of Corrosion Engineers, 1990, p 4-86 to 4-110
93. F.P. Ford, “Mechanisms of Environmental Cracking in Systems Peculiar to the Power Generation Industry,” Final Report NP-2589, Electric Power Research Institute, 1982
94. D.J. Duquette and H.H. Uhlig, *Trans. Am. Soc. Met.*, Vol 61, 1968, p 449
95. P.L. Andresen, R.P. Gangloff, L.F. Coffin, and F.P. Ford, Overview—Applications of Fatigue Analysis: Energy Systems, *Proc. Fatigue/87*, EMACS, 1987
96. F.P. Ford, D.F. Taylor, P.L. Andresen, and R.G. Ballinger, “Corrosion Assisted Cracking of Stainless and Low Alloy Steels in LWR Environments,” Final Report NP-5064-S, Electric Power Research Institute, 1987
97. P.L. Andresen and F.P. Ford, Use of Fundamental Modeling of Environmental Cracking for Improved Design and Lifetime Evaluation, *J. Pressure Vessel Technol. (Trans. ASME)*, Vol 115 (No. 4), 1993, p 353–358
98. H.G. Nelson, Hydrogen Induced Slow Crack Growth of a Plain Carbon Pipeline Steel under Conditions of Cyclic Loading, *Effect of Hydrogen on the Behavior of Materials*, A.W. Thompson and I.M. Bernstein, Ed., The Metals Society—American Institute of Mining, Metallurgical, and Petroleum Engineers, 1976, p 602–611
99. H.H. Johnson, Hydrogen Brittleness in Hydrogen and Hydrogen-Oxygen Gas Mixtures, *Stress Corrosion Cracking and Hydrogen Embrittlement of Iron Based Alloys*, J. Hochmann, J. Slater, R.D. McCright, and R.W. Staehle, Ed., National Association of Corrosion Engineers, 1976, p 382–389
100. P.L. Andresen and L.M. Young, Characterization of the Roles of Electrochemistry, Convection and Crack Chemistry in Stress Corrosion Cracking, *Proc. Seventh International Symposium on Environmental Degradation of Materials in Nuclear Power Systems—Water Reactors*, National Association of Corrosion Engineers, 1995, p 579–596

101. S. Suresh and R.O. Ritchie, *Int. Metals Rev.*, Vol 29, 1984, p 445–476
102. R. Gangloff, Corrosion Fatigue, *Corrosion Tests and Standards: Application and Interpretation*, R. Baboian, Ed., ASTM, 1995
103. *Electrochem. Soc.*, Vol 126, 1979, p 908
104. *Surf. Sci.*, Vol 64, 1977, p 617
105. A. Carre and J. Shultz, Polymer-Aluminum Adhesion. III. Effect of a Liquid Environment, *J. Adhes.*, Vol 18, 1984, p 171–184
106. J.D. Venable, Review: Adhesion and Durability of Metal-Polymer Bonds, *J. Mater. Sci.*, Vol 19, 1984, p 2431–2453
107. H. Wu, J.T. Dickinson, and S.C. Langford, Dynamic Measurements, of Humidity Attack on Polymer/Glass Interfaces Under Stress, *J. Adhes. Sci*, Vol 11, 1997, p 695–717
108. S.X. Mao and A.G. Evans, The Influence of Blunting on Crack Growth at Oxide/Metal Interfaces, *Acta Mater.*, Vol 45, 1997, p 4263–4270
109. T.S. Oh, J. Rodel, R.M. Cannon, and R.O. Ritchie, Ceramic/Metal Interfacial Crack Growth Toughening by Controlled Microcracks and Interfacial Geometries, *Acta Metall.*, Vol 36, 1988, p 2083–2093
110. S.M. Wiederhorn, S.W. Freimann, and E.R. Fuller, Jr., Effect of Water and Other Dielectrics on Crack Growth, *J. Mater. Sci.*, Vol 17, 1982, p 3460–3478
111. R.W. Douglas and T.M.M. El-Shamy, *J. Am. Ceram. Soc.*, Vol 50, 1967
112. M.L. Hair, Hydroxyl Groups in Silica Surface, *J. Non-Cryst. Solids*, Vol 19, 1975, p 299–309
113. R.J. Charles, Glass Surface Analysis by Auger Electron Spectroscopy, *J. Appl. Phys.*, Vol 2, 1958
114. C.G. Pantano, D.B. Dove, and G.Y. Onoda, *J. Noncryst Solids*, Vol 19, 1975, p 41–53
115. J.D. Venable, Review, Adhesion and Durability of Metal-Polymer Bonds, *J. Mater. Sci.*, Vol 19, 1984, p 2431–2453
116. M.D. Thouless and R.F. Cook, Stress Corrosion Cracking in Silicon, *Appl. Phys. Lett.*, Vol 56, 1990, p 1962–1964
117. J.I. Federer, Stress-Corrosion of SiC in an Oxidizing Atmosphere Containing NaCl, *Adv. Ceram. Mater.*, Vol 3, 1988, p 293–295
118. J.I. Federer, Corrosion of SiC Ceramic by Na₂SO₄, *Adv. Ceram. Mater.*, Vol 3, 1988, p 56–61
119. S.G. Cook, J.A. Little, and J E. King, Corrosion of Silicon Carbide Ceramics Using Conventional and Electrochemical Methods, *Br. Corros. J.*, Vol 29, 1994, p 183–189
120. B.C. Burkner and T.A. Michalske, Effect of Surface Corrosion on Glass Fracture, *Fracture Mechanics of Ceramics*, Vol 8, R.C. Bradt, Ed., Plenum Press, New York, 1986, p 391

121. D.P.H. Hasselman, *Ultrafine Grain Ceramics*, J.J. Burke, N.L. Reed, and V. Weiss, Ed., Syracuse University Press, 1970, p 297–315
122. M. Tomozawa and Y.-L. Peng, Surface Relaxation as a Mechanism of Static Fatigue of Pristine Silica Glass Fibers, *J. Non-Cryst. Solids*, Vol 240, 1998, p 104–109
123. D.M. Marsh, *Proc. R. Soc. (London) A*, Vol 270, 1964
124. T.A. Michalske and S.W. Freiman, A Molecular Mechanism for Stress Corrosion in Vitreous Silica, *J. Am. Ceram. Soc.*, Vol 66, 1983, p 284–288
125. T.A. Michalske and B.C. Bunker, Steric Effects in Stress Corrosion Fracture of Glass, *J. Am. Ceram. Soc.*, Vol 70, 1987, p 780–784
126. S.W. Freiman, Effects of Chemical Environments on Slow Crack Growth in Glasses and Ceramics, *J. Geophys. Res.*, Vol 89, 1984, p 4072–4076
127. B.C. Bunker and T.A. Michalske, Effect of Surface Corrosion on Glass Fracture, *Fracture Mechanics of Ceramics*, Vol 8, R.C. Bradt, Ed., Plenum Press, 1986, p 391
128. C.J. Simmons and S.W. Freiman, Effect of Corrosion Processes on Subcritical Crack Growth in Glass, *J. Am. Ceram. Soc.*, Vol 64, 1981, p 683–686
129. D.R. Clarke, B.R. Lawn, and D.H. Roach, The Role of Surface Forces in Fracture, *Fracture Mechanics of Ceramics*, Vol 8, R.C. Bradt, et al., Ed., Plenum Press, 1986
130. T.A. Michalske, B.C. Bunker, and S.J. Frieman, Stress Corrosion of Ionic and Mixed Ionic/Covalent Solids, *J. Am. Ceram. Soc.*, Vol 69, 1986, p 721–724
131. R.F. Cook, Environmentally Controlled Nonequilibrium Crack Propagation in Ceramics, *Mater. Sci. Eng. A*, Vol 260, 1999, p 29–40
132. S.M. Wiederhorn and H. Johnson, Effect of pH on Crack Propagation in Glass, *J. Am. Ceram. Soc.*, Vol 56, 1973, p 192–197
133. S.M. Wiederhorn, Mechanisms of Subcritical Crack Growth in Glass, *Fracture Mechanics of Ceramics*, p 549–581
134. S.M. Wiederhorn and I.H. Boltz, Stress Corrosion and Static Fatigue of Glass, *J. Am. Ceram. Soc.*, Vol 53, 1970, p 543–548
135. B.R. Lawn, *Fracture of Brittle Solids*, 2nd ed., Cambridge University Press, 1993, 378 pages
136. J.R. Hellmann, J. Matsko, S.W. Freiman, and T.L. Baker, Microstructure-Mechanical Property Relationships in 94% Alumina Ceramics, *Tailoring Multiphase and Composite Ceramics*, R.E. Tressler, G.L. Messing, C.G. Pantano, and R.E. Newnham, Ed., Plenum Press, 1986, p 367–380
137. J.J. Mechlosky and S.W. Freiman, Fractographic Analysis of Delayed Failure in Ceramics, *Fractography and Materials Science*, STP 733, ASTM, 1981, p 246–258
138. M. Sakai and R.C. Bradt, Fracture Toughness Testing of Brittle Materials, *Int. Mater. Rev.*, Vol 38, 1993, p 53–79

139. S.M. Wiederhorn, *Fracture Mechanics of Ceramics*, Vol 2, R.C. Bradt, D.P.H. Hasselmann, and F.F. Lange, Ed., Plenum Press, 1974, p 613–646
140. J.E. Ritter, and R.P. LaPorte, Effect of Test Environment on Stress-Corrosion Susceptibility of Glass, *J. Am. Ceram. Soc.*, Vol 58, 1975, p 265–267
141. S.W. Freiman, Stress-Corrosion Cracking of Glasses and Ceramics, *Stress-Corrosion Cracking, Materials Performance and Evaluation*, R.H. Jones, Ed., ASM International, 1992, p 337–344
142. G.H. Michler, Correlation Between Craze Formation and Mechanical Behaviour of Amorphous Polymers, *J. Mater. Sci.*, Vol 25, 1990, p 2321–2334
143. A.S. Argon, Sources of Toughness in Polymers, *Advances in Fracture Research*, Proc. Seventh Int. Conf. on Fracture (ICF), Vol 4, Pergamon, 1989, p 2661–2681
144. A. Carre and J. Shultz, Polymer-Aluminum Adhesion III. Effect of a Liquid Environment, *J. Adhes.*, Vol 15, 1983 p 151–162
145. G. Marom and D. Cohn, Deformations of Polymers and Composite under Swelling Conditions, *Plastics & Rubber: Materials & Applications*, Vol 5, 1980, p 165–168
146. S.V. Hoa, Relative Influence of the Mobility and the Solubility Parameters of Fluids on the Mechanical Behavior of High Impact Polystyrene, *Polym. Eng. Sci.*, Vol 20, 1980, p 1157–1160
147. A.G. Atkins and Y.W. Mai, *Elastic and Plastic Fracture: Metals, Polymers, Ceramics, Composites, Biological Materials*, Halsted Press, 1985, p 817
148. K.N.G. Fuller and P.G. Fox, The Temperature Rise at the Tip of Fast-Moving Cracks in Glassy Polymers. *Proc. R. Soc. (London) A*, Vol 341, 1974, p 537–557
149. M.G. Wyzgoski and G.E. Novak, Stress Cracking of Nylon in Aqueous Salt Solutions. Part 3 Craze-Growth Kinetics, *J. Mater. Sci.*, Vol 22, 1987, p 2615–2623
150. A. Moet and E. Baer, On the Mechanism of Pressure Induced Environmental Stress Cracking in Polystyrene, *J. Mater. Sci.*, Vol 15, 1980, p 31–41
151. M.E.R. Shanahan, M Debski, F. Bomo, and J. Shultz, *J. Polym. Sci.*, Polymer Physics Edition, Vol 21, 1983, p 1103–1109
152. J.G. Williams and G.P. Marshall, Environmental Crack and Craze Growth Phenomena in Polymers, *Proc. R. Soc. (London) A*, Vol 342, 1975, p 55–77
153. K. Tonyali and C.E. Rogers, Stress-Cracking of Polyethylene in Organic Liquids, *Polymer*, Vol 28, 1987, p 1472–1477
154. M.E.R. Shanahan and J. Shultz, Environmental Stress Cracking of Polyethylene: Analysis of the Three Zones of Behavior and Determination of Crack-Front Dimensions, *J. Polym. Sci.*, Polymer Physics Edition, Vol 18, 1980, p 1747–1752
155. Y.W. Mai and A.G. Atkins, On the Velocity-Dependent Fracture Toughness of Epoxy Resins, *J. Mater. Sci.*, Vol 10, 1975, p 2000–2003
156. J.C. Arnold, The Influence of Liquid Uptake on Environmental Stress Cracking of Glassy Polymers, *Mater. Sci. Eng. A*, Vol 197, 1995, p 119–124

157. H.M. El-Hakeem and L.E. Culver, Environmental Dynamic Fatigue Crack Propagation in High Density Polyethylene: An Empirical Modelling Approach, *Int. J. Fat.*, Vol 3, 1981, p 3–8
158. W.-Ch.V. Wang, E.J. Kramer, and W.H. Sachse, Effects of High-Pressure CO₂ on the Glass Transition Temperature and Mechanical Properties of Polystyrene, *J. Polym. Sci.*, Vol 20, 1982, p 1371–1384
159. A. Peterlin and H.G. Olf, Crazing and Fracture in Crystalline, Isotactic Polypropylene and the Effect of Morphology, Gaseous Environments, and Temperature, *J. Polym. Sci.*, 1975, p 243–264
160. N. Brown and S. Fischer, Nucleation and Growth of Crazes in Amorphous Polychlorotrifluoroethylene in Liquid Nitrogen, *J. Polym. Sci.*, Polymer Physics Edition, Vol 13, 1975, p 1979–1982
161. R.A. Duckett, B.C. Goswami, L. Stewart, I.M. Ward, and A.M. Zihlif, The Yielding and Crazing Behaviour of Polycarbonate in Torsion under Superposed Hydrostatic Pressure, *Br. Polym. J.*, Vol 10, 1978, p 11–16
162. K. Matsushige, S. Radcliffe, and E. Baer, The Environmental Stress-Crazing and Cracking in Polystyrene under High Pressure, *J. Macromol. Sci. Phys.*, Vol B11, 1975, p 565–592
163. H.Li. Pugh, Ed., *High Pressure Engineering*, Mechanical Engineering Publications, 1975, p 41
164. D.R. Mears, K.D. Pae, and J.A. Sauer, Effects of Hydrostatic Pressure on the Mechanical Behavior of Polyethylene and Polypropylene, *J. Appl. Phys.*, Vol 40, 1969, p 4229–4237
165. E.H. Andrews and L. Bevan, Mechanics and Mechanism of Environmental Crazing in a Polymeric Glass, *Polymer*, Vol 13, 1972, p 337–347
166. J.R. Atkinson and P.G. Faulker, *J. Appl. Polym. Sci.*, Vol 15, 1971, p 209
167. G.P. Marshall, G.P. Culver, and J.G. Williams, Craze Growth in Polymethylmethacrylate: A Fracture Mechanics Approach, *Proc. R. Soc. (London) A*, Vol 319, 1970, p 165–187
168. M.G. Wyzgoski and G.E. Novak, Stress Cracking of Nylon Polymers in Aqueous Salt Solutions. I. Stress-Rupture Behaviour, *J. Mater. Sci.*, Vol 22, 1987, p 1707–1714
169. M.C. Kenney, J.F. Mandell, and F.J. McGarry, The Effects of Sea Water and Concentrated Salt Solutions on the Fatigue of Nylon 6,6 Fibres, *J. Mater. Sci.*, Vol 20, 1985, p 2060–2070
170. W.C. Oliver and G.M. Pharr, An Improved Technique for Determining Hardness and Elastic Modulus Using Load and Displacement Sensing Indentation Experiments, *J. Mater. Res.*, Vol 7, 1992, p 1564–1583
171. T.F. Page, L. Riester, and S.V. Hainsworth, The Plasticity Response of 6H-SiC and Related Isostructural Materials to Nanoindentation, *Mater. Res. Soc. Symp. Proc.*, Vol 522, 1998, p 113–118
172. W. Zielinski, H. Huang, S. Venkataraman, and W.W. Gerberich, Dislocation Distribution under a Microindentation into an Iron-Silicon Single Crystal, *Philos. Mag. A*, Vol 72, 1995, p 1221–1237
173. D. Kramer, H. Huang, M. Kriese, J. Robach, J. Nelson, J.N.A Wright, D. Bahr, and W.W. Gerberich, Yield Strength Predictions from the Plastic Zone around Nanocontacts, *Acta Mater.*, Vol 47, 1998, p 333–343

174. D.S. Harding, W.C. Oliver, and G.M. Pharr, Cracking During Nanoindentation and Its Use in the Measurement of Fracture Toughness, *Thin Films: Stresses and Mechanical Properties V*, Symposium, Materials Research Society, 1995, p 663–668
175. X. Li and B. Bhushan, Micro/Nanomechanical Characterization of Ceramic Films for Microdevices, *Thin Solid Films*, Vol 340, 1999, p 210–217
176. M.R. Begley, A.G. Evans, and J.W. Hutchinson, Spherical Impression of Thin Elastic Films on Elastic-Plastic Substrates, *Int. J. Solid. Struct.*, Vol 36, 1999, p 2773–2788
177. S.V. Hainsworth and T.F. Page, Nanoindentation Studies of the Chemomechanical Effect in Sapphire, *J. Mater. Sci.*, Vol 29, 1994, p 5529–5540
178. S.K. Venkataraman, D.L. Kohlstedt, and W.W. Gerberich, Continuous Microindentation of Passivating Surfaces, *J. Mater. Res.*, Vol 8, 1993, p 685–688
179. D.F. Bahr, J.C. Nelson, N.I. Tymiak, and W.W. Gerberich, The Mechanical Behaviour of a Passivating Surface under Potentiostatic Control, *J. Mater. Res.*, Vol 12, 1997, p 3345–3353
180. S.G. Corcoran, S.R. Brankovic, N. Dimitrov, and K. Sieradzki, Nanoindentation of Atomically Modified Surfaces, *Thin-Films—Stresses and Mechanical Properties VII*, R.C. Cammarata, M. Nastasi, E.P. Busso, and W.C. Oliver, Ed., Symposium Materials Research Society, 1998, p 77–84
181. M. Pang, D.E. Wilson, and D.F. Bahr, The Strength and Fracture of Passive Oxide Films on Metals, submitted to Proc. Materials Research Society, *Thin Films: Stresses and Mechanical Properties VIII*, 1999
182. Y. Katz, N.I. Tymiak, and W.W. Gerberich, Nano-mechanical Probes as New Approaches to Hydrogen/Deformation Interaction Studies, An invited paper for *Recent Advances in the Engineering Aspects of Hydrogen Embrittlement of the Engineering Fracture Mechanics*, 1999
183. N.I. Tymiak, S. Gabric-Miskulin, Y. Katz, and W.W. Gerberich, Nanoindentation Evaluation of Hydrogen Affected Yield and Fracture in 316 Stainless Steel, *Int. Conf. Environmental Degradation of Engineering Materials*, Gdansk, Poland, 1999
184. B.R. Lawn, T.P. Dabbs, and C.J. Fairbanks, Kinetics of Shear-Activated Indentation Crack Initiation in Soda-Lime Glass, *J. Mater. Sci.*, Vol 18, 1983, p 2785–2797
185. S. Lathabai, J. Rodel, T. Dabbs, and B.R. Lawn, Fracture Mechanics Model for Subthreshold Indentation Flaws. I. Equilibrium Fracture, *J. Mater. Sci.*, Vol 26, 1991, p 2157–2168
186. D. Kells and N.J. Mills, The Initiation of Indentation Fracture in Polystyrene, *Philos. Mag. A*, Vol 44, 1981, p 1149–1163
187. P. Ostojic and R. McPherson, A Review of Indentation Fracture Theory: Its Development, Principles and Limitations, *Int. J. Fract.*, Vol 33, 1987, p 297–312
188. R.F. Cook and G.M. Pharr, Direct Observation and Analysis of Indentation Cracking in Glasses and Ceramics, *J. Am. Ceram. Soc.*, Vol 73, 1990, p 787–817
189. G.R. Anstis, P. Chantikul, B.R. Lawn, and D.B. Marshall, A Critical Evaluation of Indentation Techniques for Measuring Fracture Toughness, *J. Am. Ceram. Soc.*, Vol 64, 1981, p 533–538

190. D.B. Marshall and R.B. Lawn, Residual Stress Effect in Sharp Contact Cracking, *J. Mater. Sci.*, Vol 14, 1979, p 2001–2012
191. D.B. Marshall, R.B. Lawn, and P. Chantikul, Residual Stress Effects in Sharp Contact Cracking. Part 2. Strength Degradation, *J. Mater. Sci.*, Vol 14, 1979, p 2225–2235
192. D.B. Marshall and A.G. Evans, Measurement of Adherence of Residually Stressed Thin Film by Indentation. I. Mechanics of Interface Delamination, *J. Appl. Phys.*, Vol 56, 1984, p 2632–2638
193. M. J. Matthewson, Axi-Symmetric Contact on Thin Compliant Coatings, *J. Mech. Phys. Solids*, Vol 29, 1981, p 89–113
194. L.G. Rosenfeld, J.E. Ritter, T.J. Larner, and M.R. Lin, Use of the Microindentation Technique for Determining Interfacial Fracture Energy, *J. Appl. Phys.*, Vol 67, 1990, p 3291–3296
195. J.J. Vlassak, M.D. Drory, and W.D. Nix, A Simple Technique for Measuring the Adhesion of Brittle Films to Ductile Substrates with Applications to Diamond-Coated Titanium, *J. Mater. Res.*, Vol 12, 1997, p 1990–1910
196. M.D. Drory and J.W. Hutchinson, Measurement of Brittle-Film Adhesion on a Ductile Substrate by Indentation, *Proc. Roy. Soc. (London) A*, 1996, p 2319–2341
197. J.W. Hoehn, S.K. Venkataraman, H. Huang, and W.W. Gerberich, Micromechanical Test Applied to NiAl, *Mater. Sci. Eng. A*, Vol A192/193, 1995, p 301–308
198. P.R. Chalker, S.J. Bull, and D.S. Rickerby, A Review of the Methods for the Evaluation of Coating-Substrate Adhesion, *Mater. Sci. Eng. A*, Vol A140, 1991, p 583–592
199. S.V. Hainsworth, S.J. Bull, and T.F. Page, Scratch Deformation Response of Thin CN_x Coatings at Ultra-Low Loads, *Fundamentals of Nanoindentation and Nanotribology*, Symposium. Materials Research Society, 1998, p 433–438
200. T.W. Wu, Microscratch and Load Relaxation Tests for Ultra-Thin Films, *J. Mater. Res.*, Vol 6, 1991, p 407–426
201. S. Venkataraman, D.L. Kohlstedt, and W.W. Gerberich, Continuous Microscratch Measurements of the Practical and True Works of Adhesion for Metal/Ceramic Systems, *J. Mater. Res.*, Vol 11, 1996, p 3133–3145
202. D.B. Marshall and B.R. Lawn, Flaw Characteristics in Dynamic Fatigue: The Influence of Residual Contact Stresses, *J. Am. Ceram. Soc.*, Vol 63, 1980, p 532–536
203. J. Zhang and A.J. Ardell, Measurement of the Fracture Toughness of Ceramic Materials Using a Miniaturized Disk-Bend Test, *J. Am. Ceram. Soc.*, Vol 76, 1993, p 1340–1344
204. R.W. Rice, C.C. Wu, and K.R. McKinney, Fracture and Fracture Toughness of Stoichiometric MgAl₂O₄ Crystals at Room Temperature, *J. Mater. Sci.*, Vol 31, 1996, p 1353–1560
205. Y. Kimura, T. Yagasaki, and T. Kunio, On the Delayed Fracture Characteristics of Vickers Indented Glass in Deionized Water, *Eng. Fract. Mech.*, Vol 19, 1984, p 1025–1033
206. H. Matzke, Hertzian Indentation of Thorium Dioxide, ThO₂, *J. Mater. Sci.*, Vol 15, 1980, p 739–746

207. P.J. Dwivedi and D.J. Green, Determination of Subcritical Crack Growth Parameters by in Situ Observation of Indentation Cracks, *J. Am. Ceram. Soc.*, Vol 78, 1995, p 2122–2128
208. E.R. Fuller, B.R. Lawn, and R.F. Cook, Theory of Fatigue for Brittle Flaws Originating from Residual Stress Concentration, *J. Am. Ceram. Soc.*, Vol 66, 1983, p 314–321
209. S.R. Choi and J.A. Salem, Slow Crack Growth of Indent Cracks in Glass with and without Applied Stress, *Mater. Sci. Eng. A*, Vol A149, 1992, p 259–264
210. D.B. Marshall and B.R. Lawn, Flaw Characteristics in Dynamic Fatigue: The Influence of Residual Contact Stresses, *J. Am. Ceram. Soc.*, Vol 63, 1980, p 532–536
211. V.M. Sglavo and D.J. Green, The Sub-Critical Indentation Fracture Process in Soda-Lime-Silica Glass, *Eng. Fract. Mech.*, Vol 55, 1996, p 35–46
212. G. Binnig, H. Rohrer, C. Gerber, and E. Weibell, Tunneling Through a Controllable Vacuum Gap, *Appl. Phys. Lett.*, Vol 40, 1982, p 178–180
213. G. Binnig, C.F. Quate, and C. Gerber, *Phys. Rev. Lett.*, Vol 56, 1982, p 930
214. D. Rugar and P.K. Hansma, Atomic Force Microscopy, *Phys. Today*, Vol 43, 1990, p 23–28
215. D. Sarid, *Scanning Force Microscopy*, Oxford University, 1991
216. T. Foecke, R.M. King, A.F. Dale, and W.W. Gerberich, Imaging of Cracks in Semiconductors Using Scanning Tunneling Microscopy, *J. Vac. Sci. Technol.*, Vol B9, 1991, p 673–676
217. T. Kinoshita, Stress Singularity Near the Crack-Tip in Silicon Carbide: Investigation by Atomic Force Microscopy, *Acta Mater.*, Vol 46, 1998, p 3963–3974
218. K. Jakus, S. Michael, and J.E. Ritter, Measurement of Crack Tip Inelastic Deformations Using Digital Image Correlation, *Adv. Ceram. Mater.*, Vol 3, 1988, p 268–272
219. S. Manne, J. Massie, V.B. Elings, P.K. Hansma, and A.A. Gewirth, Electrochemistry on a Gold Surface Observed with the Atomic Force Microscope, *J. Vac. Sci. Technol. B*, Vol 9, 1991, p 950–954
220. P.K. Hansma and J. Tersoff, Scanning Tunnelling Microscopy, *J. Appl. Phys.*, Vol 61, 1987, p R1–23
221. P. Mrozek, Y.-E. Sung, and A. Wieckowski, Silver Deposition on the Au(111) Electrode without Interference by Specifically Adsorbed Anions, *Surf. Sci.*, Vol 335, 1995, p 44–51
222. S.-L. Yau, F.-R.F. Fan, and A.J. Bard, In situ STM Imaging of Silicon(111) in HF under Potential Control, *J. Electrochem. Soc.*, Vol 139, 1992, p 2825–2829
223. K. Komai, K. Minoshima, and M. Itoh, *J. Soc. Matter. Sci. Jpn.*, 1994, p 336
224. K. Komai and K. Minoshima, Nanometric Visualization of Localized Damage by Scanning Probe Microscopy, *Mater. Sci. Res. Int.*, Vol 2, 1996, p 209–219
225. N.I. Tymiak, D.F. Bahr, J.C. Nelson, and W.W. Gerberich, “Micromechanical Probes of a Sensitized Stainless Steel in Corrosive Environments,” Presented at TMS Fall Conference, Symposium on Welding of Stainless Steel Alloys (Indianapolis, IN), Sept 1997

226. G. Venkataraman, T.S. Sriram, M.E. Fine, and Y.W. Chung, STM and Surface Analytical Study of the Effect of Environment on Fatigue Crack Initiation in Silver Single Crystals I, *Surface Chemical Effects*, *Scr. Metall.*, Vol 24, 1990, p 273–278
227. P.G. Marsh, S.E. Harvey, M.D. Kriese, and W.W. Gerberich, Environmental Effects on Fatigue Crack Development in HSLA Steel and Fine Grain α -Titanium, *Scr. Metall.*, Vol 33, 1995, p 825–829
228. M. Goken, H. Vehoff, and P. Neumann, *J. Vac. Sci. Technol. B*, Vol 14, 1996, p 1157

Fracture Resistance Testing of Plastics

Kevin M. Kit and Paul J. Phillips, University of Tennessee, Knoxville

Introduction

POLYMERIC MATERIALS are many and varied, ranging from pure glasses to blends to semicrystalline solids. Their mechanical properties range from pure elasticity with very high strains to fracture (rubbers or elastomers) to almost pure Hookian elasticity with low strains to fracture (glasses); the majority of polymers have properties somewhere between these two extremes. Virtually all polymeric materials show some form of inelastic behavior (Ref 1, 2). The elastomers show hysteresis, and the glasses show some form of yielding. The inelastic behavior is not restricted to the tip of a crack, but is present in some form or another throughout the material. The inelasticity is a direct result of the time dependence of the motions of the polymer chains. With the exceptions of certain untoughened epoxy resins and related thermosets, inelasticity is the norm. Hence, the expectation of many theories of fracture mechanics that Hookian behavior can be assumed is not to be realized. Even theories that assume elastic-plastic criteria are inadequate because they assume plastic behavior at the crack tip and elastic behavior throughout the remainder of the specimen, whereas in the real materials, there is viscoelastic deformation of some form or other occurring in the bulk of the specimen.

The presence of inelasticity in the entire specimen, as well as at the crack tip, results in additional energy being required for crack propagation. Hence, in any mechanical test the energy measured to propagate a crack consists of the surface energy of the crack, energy of plastic deformation at the crack tip, and energy of inelastic deformation of the entire specimen (Ref 3). Because the latter two forms of energy absorption are a direct result of the time-dependent behavior of the polymer chains, the energy absorbed displays a strong dependence on the rate at which stress is applied. The crack opening displacements in polymeric materials can be quite large and, hence, the microstrain at a crack tip will be similarly large. In polymeric materials displaying minimal levels of plasticity and/or inelasticity, such as untoughened epoxies, the crack opening displacement is quite small. At the other extreme is the elastomer, or rubber, where the crack opening displacement is so large that the process is usually referred to as tearing. The crack opening displacement can reflect two extremes in deformation behavior: shear yielding or crazing (Ref 3). Both reflect large amounts of plastic deformation at the crack tip. In the case of some polymers, for example, polycarbonate, a large yield zone is observed. In others, the phenomenon is referred to as crazing, where the apparent crack is really a zone of fibrous material produced by the stress field ahead of the crack. This phenomenon can be present in glassy materials as well as semicrystalline materials, and it corresponds to microyielding to levels of several hundred percent strain. A similar phenomenon can also be observed in unnotched specimens where regions in the bulk of the specimen display what is usually described as stress whitening.

In addition to the behavior described above, polymers are also sensitive to the environment, both gaseous and liquid (Ref 3). An example of the effects of gaseous environments is the effect of atmospheric ozone on crack propagation rates in natural rubber (Ref 4). In the case of a liquid the behavior can be caused by several different effects (Ref 5, 6). First, there is always the possibility that the liquid may be a solvent and be absorbed by the polymer; the absorption process may occur more rapidly at the tip of a crack. In this case the liquid will

plasticize the polymer, lowering its glass transition temperature and thereby altering all of its fundamental properties. Second, the liquid may react chemically with the polymer, changing its fundamental structure and properties on a microscopic or macroscopic scale. Third, the liquid may simply wet the polymer, lowering the surface energy and making crack or craze propagation much easier. A well-known example of such behavior is the effect of carbon tetrachloride on polycarbonate.

References cited in this section

1. N.G. McCrum, B.E. Read, and G. Williams, *Anelastic and Dielectric Effects in Polymeric Solids*, Wiley, 1967
2. I.M. Ward, *Mechanical Properties of Solid Polymers*, Wiley, 1983, p 15
3. E.H. Andrews, Cracking and Crazing in Polymeric Glasses, *The Physics of Glassy Polymers*, R.N. Haward, Ed., Wiley, 1973, p 394
4. R. Natarajan and P.E. Reed, *J. Polym. Sci. A, Polym. Chem.*, Vol 2 (No. 10), 1972, p 585
5. G.A. Bernier and R.P. Kambour, *Macromolecules*, Vol 1, 1968, p 393
6. E.H. Andrews, G.M. Levy and J. Willis, *J. Mater. Sci.*, Vol 8, 1973, p 1000

Fracture Resistance Testing of Plastics

Kevin M. Kit and Paul J. Phillips, University of Tennessee, Knoxville

Historical Development

Fracture in polymers was first studied intensively for rubber, and tests were developed logistically in the early 1900s (Ref 7, 8). Standard test methods included tensile testing with “dog-bone” specimens where the breaking strength was obtained. By the 1920s, standard tests for tear strength, using “trouser-type” specimens, were in use. Such methods are still in common use, the tensile test to failure using a dog-bone specimen being one of the most popular for the characterization of all kinds of polymers (Ref 8). As new polymers are developed and testing is needed, tensile testing on sheets or thin films as a method of characterization still tends to be preferred over the standardized ASTM tests for fracture strength. This may occur sometimes due to the amount of specimen available and at other times due to the simplicity of specimen preparation and characterization.

Fracture testing using standardized linear fracture mechanics approaches, such as K_{Ic}/G_{Ic} methods, has been used for decades as a means of carrying out fracture testing (Ref 3, 9). However, because of the previously mentioned inelasticity problems, polymers have stress distributions at the tip of a crack that cannot be calculated or described adequately by the assumptions of classical elasticity theory. Such approaches clearly cannot describe adequately the behavior of even the most well-behaved systems. Early attempts at describing the fracture phenomenon in a more realistic manner recognized that the most important parameter describing the phenomenon was the energy absorbed by the fracture process (Ref 10). The energy balance approach was suggested very early by Griffith (Ref 11) but was used for rubber by Rivlin and Thomas (Ref 12) who used a \mathcal{G} to describe the total work needed to create a unit area of surface (or the tearing energy in the case of rubber). Attempts at applying this approach were made successfully by Andrews and coworkers (Ref 3), Kambour (Ref 13), and Berry (Ref 14). The beginning of a generalized theory of fracture mechanics, not requiring linear fracture assumptions, was developed by Andrews (Ref 15). Study of fracture then concentrated for several years on the development and understanding of the mechanisms of craze formation because, clearly, the formation of crazes ahead of the crack is the major contributor to the energy absorbed in fracture in most

polymers (Ref 15). Indeed, because crazing is the precursor to fracture itself, it justifies attention on that ground alone.

A concurrent development, which now is used in the testing of polymers, is the J -integral method; it is essentially the equivalent of G_I for a nonlinear system. Discovered by Rice (Ref 16, 17), and developed independently by Begley and Landes (Ref 18, 19), the J -integral method has been applied successfully to polymers by the Williams group and others (Ref 20, 21, and 22). The disadvantage of the method is that it requires multiple specimens in its strict form, discouraging widespread use. A single specimen method was developed and used successfully on polypropylene by Ouederni and Phillips (Ref 23), but it has not yet been converted into a standard ASTM method.

References cited in this section

3. E.H. Andrews, Cracking and Crazing in Polymeric Glasses, *The Physics of Glassy Polymers*, R.N. Haward, Ed., Wiley, 1973, p 394
7. L.E. Weber, *The Chemistry of Rubber Manufacture*, Griffin, London, 1926, p 336
8. K. Memmler, *The Science of Rubber*, R.F. Dunbrook and V.N. Morris, Ed., Reinhold, 1934, p 523
9. G.R. Irwin, in *Encyclopaedia of Physics*, Vol 6, Springer Verlag, 1958
10. N.G. McCrum, C.P. Buckley, and C.B. Bucknall, *Principles of Polymer Engineering*, Oxford University Press, 1997, p 201
11. A.A. Griffith, *Phil. Trans. R. Soc. (London) A*, Vol 221, 1921, p 163
12. R.S. Rivlin and A.G. Thomas, *J. Polym. Sci.*, Vol 10, 1953, p 291
13. R.P. Kambour, *Appl. Polym. Symp.*, Vol 7, John Wiley & Sons, 1968, p 215
14. J.P. Berry, *J. Polym. Sci. A, Polym. Chem.*, Vol 2, 1964, p 4069
15. E.H. Andrews, *J. Mater. Sci.*, Vol 9, 1974, p 887
16. J.R. Rice, *J. Appl. Mech. (Trans. ASME)*, Vol 35, 1968, p 379
17. J.R. Rice, *Fracture*, Vol 2, 1968, p 191
18. J.A. Begley and J.D. Landes, in *Fracture Toughness*, ASTM STP 514, 1972, p 1
19. J.D. Landes and J.E. Begley, in *Fracture Toughness*, ASTM STP 514, 1972, p 24
20. J.M. Hodgkinson and J.G. Williams, *J. Mater. Sci.*, Vol 16, 1981, p 50
21. S. Hashemi and J.D. Williams, *Polym. Eng. Sci.*, Vol 26, 1986, p 760
22. Y.W. Mai and P. Powell, *J. Polym. Sci. B, Polym. Phys.*, Vol 29, 1991, p 785
23. M. Ouederni and P.J. Phillips, *J. Polym. Sci. B., Polym. Phys.*, Vol 33, 1995, p 1313

Fracture Test Methods for Polymers

Several methods have been developed specifically for determining the fracture toughness of polymeric materials. ASTM D 5045 (Ref 24) describes a method for determining the linear elastic fracture toughness (K_{Ic} and G_{Ic}) of polymers. This methodology is appropriate for highly crosslinked thermosets (e.g., epoxy) or glassy thermoplastics incapable of significant plastic deformation (e.g., polystyrene). ASTM D 6068 (Ref 25) describes a method for measuring J - R curves (a measure of elastic-plastic fracture toughness) for polymer specimens that are not large enough to experience conditions of plane strain during loading. However, methods originally developed to characterize the elastic-plastic fracture of ductile metallic materials are most commonly used (with slight modifications) to characterize ductile polymers. These methods are based on the concept of the J -integral to determine plane strain fracture toughness values. To date, the most commonly used method is that of ASTM E 813 (Ref 26). This method was discontinued in 1989 and replaced by ASTM E 1737 (Ref 27). The differences between the two are minor, but the methods for data analysis and reporting described in ASTM E 1737 should now be followed.

J-Integral Testing

ASTM E 1737 is more general than ASTM E 813 and describes the method for determining either J_{Ic} or J_c under plane stress conditions. J_{Ic} is the critical value of the J -integral at which onset of stable crack growth occurs. If stable crack growth is not observed, then J_c is defined as the value of the J -integral at which unstable crack growth (i.e., failure) occurs. The J -integral is a measure of the amount of energy absorbed (due to both elastic and plastic responses) during the growth of a crack through the material of interest.

Experimentally, J is determined as a function of crack extension, Δa , in a notched specimen loaded in tension. J is calculated according to (Ref 28):

$$J = \frac{2U}{bB} \quad (\text{Eq 1})$$

where U is the area under the load-displacement curve and B and b are the dimensions of the specimen in the plane of the crack. Testing is most commonly performed on single-edge notched bend or on compact tension specimens containing machined notches (see Fig. 2 in the article “Fracture Toughness Testing” in this Volume). ASTM E 1737 specifies that the specimen be fatigued so that a sharp “precrack” is formed at the base of the notch. However, this is not a viable technique for most thermoplastic polymers. The accepted method for creating a precrack in polymer samples is to tap a fresh, unused razor blade into the notch immediately preceding the test, as specified in ASTM D 6068 and D 5045.

To ensure the existence of plane strain conditions at the crack tip, specimen thickness, B , and the original uncracked ligament, b_o (i.e., the distance the crack would have to extend to separate the specimen into two pieces), must be greater than $25J_{Ic}/\sigma_y$ where J_{Ic} is the elastic-plastic fracture toughness and σ_y is the yield strength. Because J_{Ic} is generally not known a priori, specimen dimensions must be based on an estimated value of J_{Ic} and then verified after testing. It has been shown (Ref 29) that the specimen size requirements specified by ASTM E 1737 can be relaxed for some polymers, such as low-density polyethylene and a polypropylene copolymer, to $B, b_o > 17 J_{Ic}/\sigma_y$.

In order to arrive at a value of J_{Ic} , J -integral values are plotted as a function of crack extension, Δa , to form a so-called R -curve. This data may be collected using single specimen or multiple specimen techniques. The multiple specimen technique is widely accepted as a valid measure of the elastic-plastic fracture toughness of polymers and is commonly employed. However, results from the much simpler single specimen technique have also been shown to be valid, and the implementation of this technique is increasing. These techniques differ only in the determination of the R -curve; specimen requirements and data analysis to determine J_{Ic} are identical. Both are summarized in the following sections.

Multiple Specimen Technique. In both techniques, it is desirable to determine J at a minimum of ten equally spaced Δa points. In the multiple specimen technique, each J - Δa point on the R -curve is generated with a different specimen. Each specimen is loaded to a level judged to produce a desired, stable crack growth extension, Δa , and is then unloaded. Polymer specimens are then removed from the test frame and fractured in liquid nitrogen. (This last step deviates from ASTM E 1737, which specifies that the specimens be fatigued first.) The precrack, stable crack growth and freeze-fracture regions of the fracture surface are usually easily identifiable (Ref 25), and an optical microscope is used to measure Δa (the length of the stable crack growth region) at nine points equally spaced across the thickness of the specimen. These nine values are averaged as described by ASTM E 1737. J is then calculated according to:

$$J = J_{el} + J_{pl} \quad (\text{Eq 2})$$

where J_{el} and J_{pl} are the elastic and plastic components of J , calculated as:

$$J_{el} = \frac{K^2 (1 - \nu^2)}{E} \quad (\text{Eq 3})$$

$$J_{pl} = \frac{\eta A_{pl}}{B_N b_o} \quad (\text{Eq 4})$$

K is a function of maximum load and specimen geometry, ν is Poisson's ratio, E is Young's modulus, A_{pl} is the area under the load-displacement curve for the entire loading-unloading cycle, and B_N is specimen thickness. For single-edge notch and compact tension specimens, $\eta = 2$, while for the disk-shape compact tension specimen, η is a function of geometry. Equations for K for each specimen type are given in Annex 4 of ASTM E 1737.

Single Specimen Technique. The single specimen technique relies on the ability to determine the extent of crack growth, Δa , while the specimen is loaded in the test frame. If this can be done, then many J - Δa data pairs can be collected from one specimen. Crack growth is usually determined by an elastic compliance method or by an electrical resistance method. In the elastic compliance method, the specimen is unloaded periodically during the test. At each unloading point, Δa is calculated as a function of the slope of the unload line, Young's modulus, and specimen geometry. However, due to the viscoelastic behavior of polymers, accurate determination of crack lengths by this method is suspect (Ref 30, 31).

Another method determines the crack length by measuring the voltage drop across the uncracked ligament through which a constant direct current is passed. This method is also not generally applicable to polymers because most are poor conductors. However, Ouederni and Phillips (Ref 23) have developed a method that involves measuring crack extension directly with a video camera. A thin copper grid deposited on the surface of the specimen serves as a scale reference. Another J -integral technique that has been successfully applied to polymers is the normalization method (Ref 31). This method does not require specimen unloading or in situ measurements of crack growth. The crack length is calculated by separating total displacement into elastic and plastic components, each of which is a function of crack length. After a fitting procedure is used to establish a relationship between plastic displacement and crack length, the actual crack length can be calculated at any point on the load-displacement curve. Zhou et al. (Ref 31) used this technique to determine J_{Ic} for two rubber-toughened nylons and found their results very close to values obtained by the standard multiple specimen method.

Determination of J_{Ic} . Before the data can be analyzed, it must be checked to verify that it spans a sufficiently large range of Δa . This procedure to determine qualifying data is detailed in ASTM E 1737. Qualifying J data must also be less than the smaller of $b_o \sigma_y / 20$ and $B \sigma_y / 20$ to ensure that all data points are measured under plane strain conditions. Qualified data are fit by the method of least squares to the curve described by:

$$\ln J = \ln C_1 + C_2 \ln \left(\frac{\Delta a}{k} \right) \quad (\text{Eq 5})$$

where C_1 and C_2 are fitting parameters and $k = 1 \text{ mm}$ (0.04 in.). A linear blunting line must also be constructed along the line defined by:

$$J = 2\sigma_y \Delta a \quad (\text{Eq 6})$$

where σ_y is the average of the 0.2% offset yield strength and the ultimate tensile strength. The blunting line accounts for deflection that occurs due to plastic deformation near the crack tip prior to the onset of stable crack

growth. ASTM E 1737 specifies that the J value at the intersection of the fit data and a line offset 0.2 mm (0.008 in.) from the blunting line defines an interim value, J_0 , which is used to verify the existence of plane strain conditions. If both B and b_0 are indeed greater than $25J_{Ic}/\sigma_y$, and some additional data qualifications are met, then the value of J_0 is taken to be equal to J_{Ic} . Experimental and fit R -curves for an acrylonitrile-butadiene-styrene (ABS) copolymer are shown in Fig. 1 along with the blunting and 0.2 mm offset lines. The intersection of the fit R -curve and the 0.2 mm offset line indicates a J_{Ic} of 5.31 kJ/m^2 .

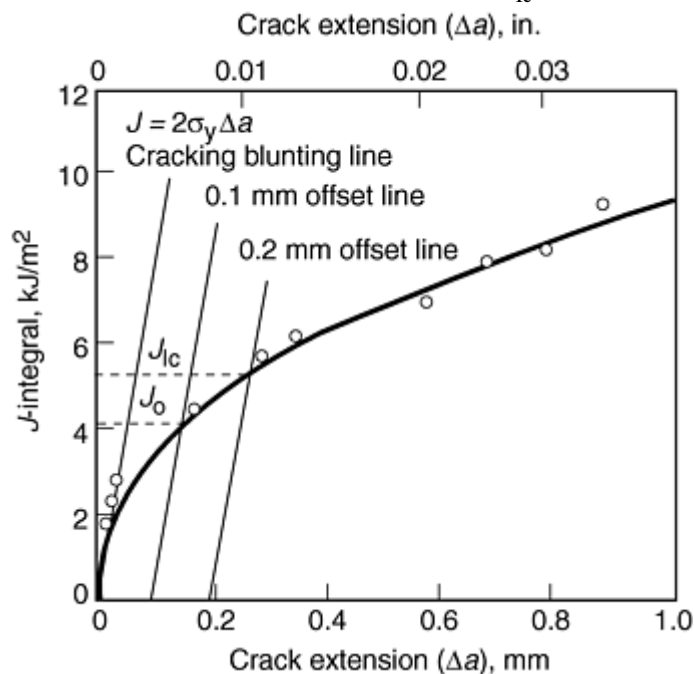


Fig. 1 Experimental R -curve for an ABS copolymer showing power-law fit, blunting line, and 0.2 mm offset line. Source: Ref 32

Modifications for Polymeric Materials. Due to the unique properties of polymers, several modifications to the J -integral method have been proposed and used. Some of these modifications that affect the collection of J - Δa data have already been mentioned, and these are quite widely accepted as standard.

In some cases, crack tip blunting may not occur before or during stable crack growth in polymers. Crack tip blunting can be verified by direct microscopic observation or if J data follows the blunting line ($J = 2\sigma_y\Delta a$) for small amounts of crack growth. Some of the data in Fig. 1 lie on the blunting line, indicating that blunting does occur (Ref 32). If blunting is not known to occur, J_{Ic} should be determined by extrapolating a linear fit to the J - Δa data to zero crack growth ($\Delta a = 0$). It has been argued in Ref 33 that J - Δa data should, under conditions of plane strain, follow:

$$J = J_{Ic} + \frac{dJ}{d\Delta a} \Delta a \quad (\text{Eq 7})$$

For small crack growth, J should vary linearly with Δa , and the value of J_{Ic} should be determined as previously explained. Optical microscopy (Ref 34, 35) has shown that crack blunting does not occur in certain grades of high-density polyethylene, toughened nylon 6/6, ABS, and toughened polycarbonate. As further evidence, the J data collected from the high-density polyethylene (Ref 35) does not follow the blunting line for small Δa , as shown in Fig. 2.

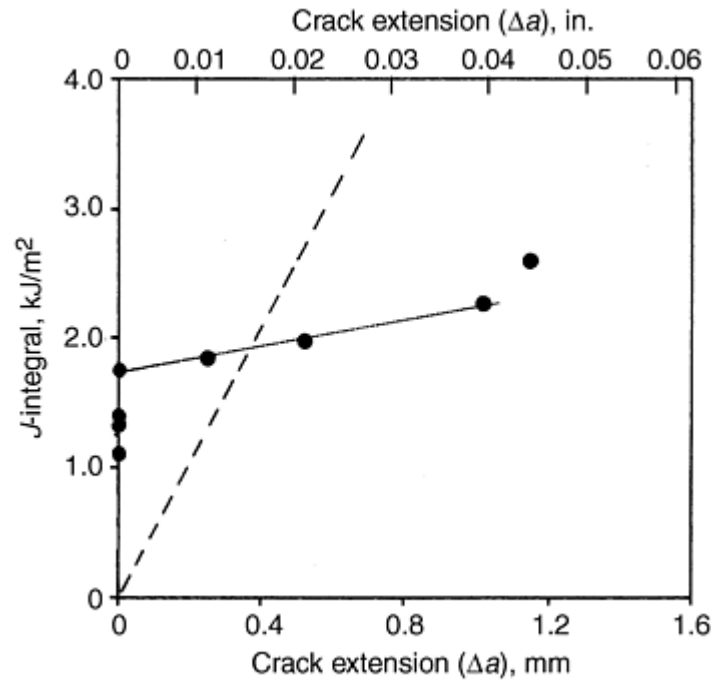


Fig. 2 Experimental R -curve for a high-density polyethylene showing the dashed blunting line and the absence of blunting behavior. Source: Ref 35

If crack tip blunting does occur, the procedure described will yield conservative values of J_{Ic} . If blunting is known to occur, then J_{Ic} should be determined by the methods of ASTM E 1737 or ASTM E 813. The determination of J_{Ic} by ASTM E 813 differs in that J_{Ic} is taken at the intersection of a *linearly* fit R -curve and the blunting line. This construction is shown in Fig. 3 for the same data used in Fig. 1. The intersection of the linear R fit and the blunting line indicates a J_{Ic} of 3.95 kJ/m² (compare to the ASTM E 1737 value of 5.31 kJ/m²). The method in ASTM E 813 usually gives more conservative values than that in ASTM E 1737. Chang et al. (Ref 29, 31, 35, and 36) have analyzed J data of high-impact polystyrene (HIPS), ABS, a polycarbonate (PC)/ABS blend, and a polycarbonate/polybutylene terephthalate (PBT) blend by three methods (ASTM E 1737, ASTM E 813, and the no-blunting method described previously). As can be seen in Table 1, the no-blunting method is the most conservative, while ASTM E 1737 is the least conservative. If no direct evidence of crack tip blunting exists, the most conservative method for calculating J_{Ic} should be used.

Table 1 Comparison of J_{Ic} data for several polymers determined by different methods

Method	J_{Ic} , kJ/m ²			
	HIPS	ABS	PC/ABS	PC/PBT
No blunting	3.24	3.57	3.00	5.47
ASTM E 813	3.60	3.95	3.55	7.17
ASTM E 1737	4.30	5.31	7.85	13.41

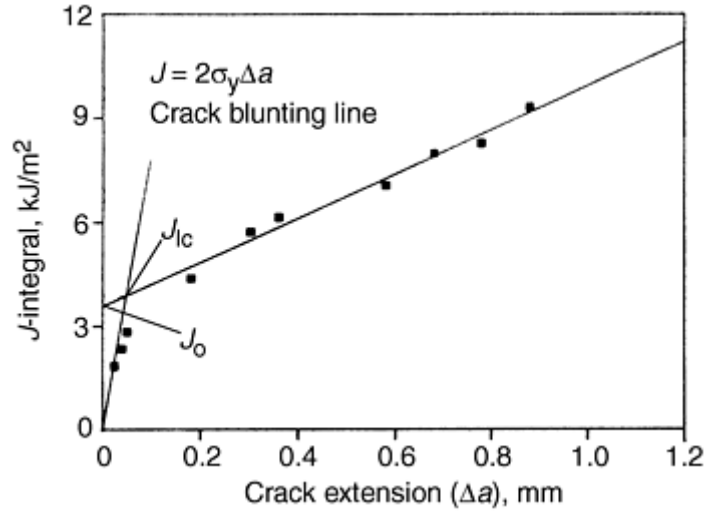


Fig. 3 Experimental R-curve for an ABS copolymer showing linear fit and blunting line. Source: Ref 32

Several workers have shown that the plane strain thickness requirements specified by ASTM E 813 and ASTM E 1737 are too conservative in certain cases, while not conservative enough in others. Rimnac et al. (Ref 38) and Huang (Ref 39) have shown that the requirement is too conservative for tough thermoplastics, ultrahigh-molecular-weight polyethylene ($J_{Ic} = 95 \text{ kJ/m}^2$), and rubber-toughened nylon 6/6 ($J_{Ic} = 30 \text{ kJ/m}^2$). Both studies found that size-independent values of J_{Ic} were obtained for specimen thicknesses greater than $6J_{Ic}/\sigma_y$, which is approximately 25% of the recommended minimum thickness. Conversely, Lu et al. (Ref 40) found that size-independent values of J_{Ic} for a relatively brittle PC/ABS blend ($J_{Ic} = 4 \text{ kJ/m}^2$) were not obtained until the thickness was greater than $64J_{Ic}/\sigma_y$, which is more than twice the recommended minimum thickness. In light of these results, it is recommended that J_{Ic} be determined for various thicknesses to ensure that the true plane strain value is obtained.

Linear Elastic Fracture Toughness

Other methods also exist to determine the plane strain fracture toughness of polymers. ASTM D 5045 specifies a procedure for determining the critical strain energy release rate, G_{Ic} , of polymers. This parameter is equivalent to J_{Ic} for materials that exhibit linear (or nearly linear) elastic behavior (Ref 41). ASTM D 5045 specifies the use of single-edge notch bend or compact tension specimens. Precracks are created by tapping a fresh, unused razor blade into the machined notch immediately preceding the test. The samples are then loaded to a level that causes a 2.5% apparent crack extension. However, significant deviation from linear elastic behavior must not occur at this load level. The procedure for testing this requirement is detailed in ASTM D 5045. An interim value of the critical strain energy release rate, G_Q is determined by:

$$G_Q = \frac{U}{Bb\phi} \quad (\text{Eq 8})$$

where ϕ is a function of b and the original crack length, a . This interim value can be qualified as the plane strain critical strain energy release rate if plane strain conditions are verified. The standard specifies that B , b , and a must be greater than $2.5 (K_{Ic}/\sigma_y)^2$ where K_{Ic} is the plane strain fracture toughness and is related to G_{Ic} by:

$$K_{Ic} = \frac{E}{1 - \nu^2} G_{Ic} \quad (\text{Eq 9})$$

Using this relation, the size requirement for plane strain conditions can be written as:

$$B, b, a > \frac{2.5E}{\sigma_y(1 - \nu^2)} \frac{G_{Ic}}{\sigma_y} \quad (\text{Eq 10})$$

Using typical values for E (1 GPa, or 145 ksi), σ_y (60 MPa, or 8.7 ksi), and ν (0.4), the size requirement is $B, a > 50G_{Ic}/\sigma_y$, which is twice the size requirement for determining plane strain J_{Ic} .

Due to the viscoelastic properties of polymers, test temperature and strain rate should be well controlled and reported. The standard recommends 23 °C (73 °F) and a crosshead speed of 10 mm/min (0.4 in./min). The orientation of the specimen with respect to processing direction (e.g., extrusion direction and mold flow direction) should also be reported because of the strong dependence of mechanical properties on molecular orientation that often develops during processing.

Testing of Thin Sheets and Films

In order to ensure the existence of plane strain state, the dimensions of the sample normal to the applied stress are usually required to be greater than $25J_{Ic}/\sigma_y$, where J_{Ic} is the elastic-plastic fracture toughness and σ_y is the yield strength. Both J_{Ic} and σ_y are generally considerably lower than the corresponding values for metallic materials, but the ratio J_{Ic}/σ_y is usually much larger for polymeric materials. Therefore, the plane strain size requirements for polymeric fracture specimens are often unrealistic (on the order of 5 cm or 2 in.). In many applications, the properties of polymeric materials are strongly dependent on the level of molecular orientation and crystallinity. These levels, in turn, are strongly dependent on the thermal and mechanical histories experienced during processing. Specimens that are produced to fulfill the plane strain condition are likely to have quite different thermal and mechanical histories than polymer materials processed into sheet or film. Therefore, the thicker test specimens do not reflect the actual properties of the polymer for the intended application. For these reasons, ASTM D 6068 is often a more desirable method than the plane strain method of ASTM E 813 or E 1737. This method was developed specifically for the determination of R -curves from thin sheets or films. However, this is not a valid method for determining J_{Ic} , and results should not be reported as such. When using this method, specimen size and the values of C_1 and C_2 (which characterize the power-law fit of the R -curve) should be reported.

Other Methods

Alternative methods for determining the fracture toughness of polymer materials have recently been proposed. Most notable are the normalization and hysteresis methods, which are both single specimen techniques. The normalization method does not require unloading cycles or online crack measurement and has been used successfully for metallic materials (Ref 31). The method is based on the assumption that the load, P , on the specimen can be represented by:

$$P = G(a)H(v_{pl}) \quad (\text{Eq 11})$$

where $G(a)$ is a known function of crack length and specimen geometry, and $H(v_{pl})$ is a function of plastic displacement, v_{pl} . After the form of $H(v_{pl})$ is fit to experimental data, values of a (and hence J) can be determined at any point on the load-displacement curve. J_{Ic} can then be determined from the R -curve using the methods described above. Zhou et al. (Ref 31) found that the results of this method are slightly less conservative than those determined by ASTM E 813 and more conservative than ASTM E 1737 for two rubber-toughened nylons (nylon 6/6 and an amorphous nylon).

The hysteresis method requires the application of multiple load-unload cycles to successively larger displacements (Ref 30, 32, and 37), as shown in Fig. 4. The area between the loading and unloading lines on the load-displacement curve is defined as the hysteresis energy, and this is plotted against maximum displacement for each loading cycle, as shown in Fig. 5. For small displacements, crack growth does not occur, and the hysteresis energy varies linearly with displacement. This data is fit with a linear blunting line. After crack growth commences, the hysteresis energy varies nonlinearly with displacement and can be fit with a power law. The displacement at which the linear blunting line intersects with the power-law curve is taken as the critical displacement to initiate crack growth, and the value of J at this displacement is taken as J_{Ic} . It has been found that the results of this method are slightly less conservative than those determined by ASTM E 813 and more conservative than ASTM E 1737 for several polymers (ABS, PC/ABS, HIPS, and PC/PBT) (Ref 32, 36, 37, and 42).

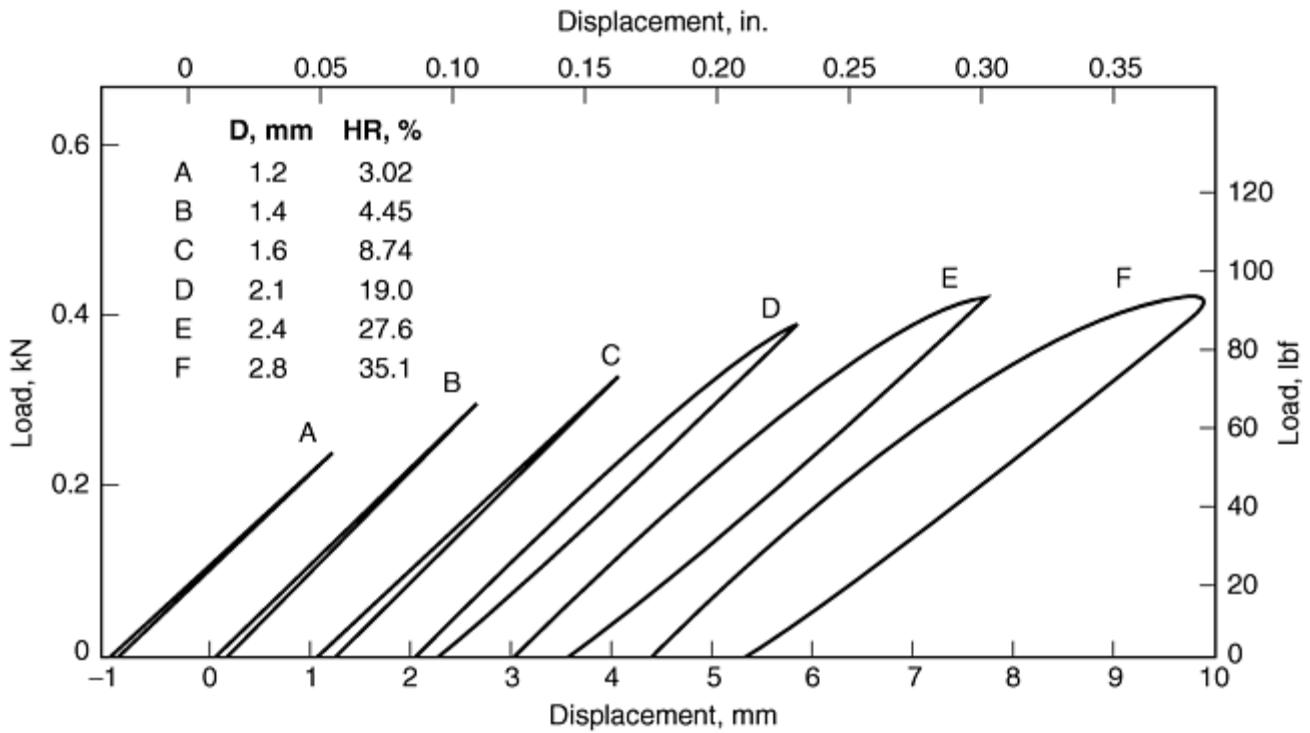


Fig. 4 Hysteresis loops for several loading-unloading cycles for a PC/PBT blend. D, specimen displacement; HR, ratio of hysteresis energy to total strain energy. Source: Ref 37

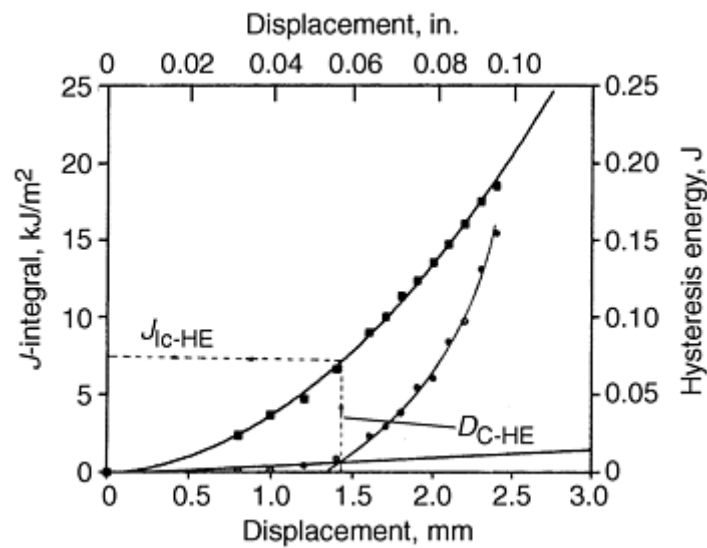


Fig. 5 J -integral and hysteresis energy vs. displacement for a PC/PBT blend. Test rate, 2 mm/min (0.08 in./min). J_{IC-HE} and D_{C-HE} are critical values of J and D for initiation of crack propagation. Source: Ref 37

References cited in this section

23. M. Ouederni and P.J. Phillips, *J. Polym. Sci. B., Polym. Phys.*, Vol 33, 1995, p 1313
24. "Standard Test Methods for Plane Strain Fracture Toughness and Strain Energy Release Rate of Plastic Materials," ASTM D 5045, *Annual Book of Standards*, Vol 08.03, ASTM, 1996
25. "Standard Test Method for Determining J-R Curves of Plastic Materials," ASTM D 6068, *Annual Book of Standards*, Vol 08.03, ASTM, 1996
26. "Standard Test Method for J_{IC} , A Measure of Fracture Toughness," ASTM E 813, *Annual Book of Standards*, Vol 03.01, ASTM, 1989

27. "Standard Test Method for J-Integral Characterization of Fracture Toughness," ASTM E 1737, *Annual Book of Standards*, Vol 03.01, ASTM, 1996
28. J.D. Landes and J.A. Begley, in *Fracture Toughness*, ASTM STP 560, 1974, p 170
29. S. Hashemi and J.G. Williams, *Plast. Rubber Process. Appl.*, Vol 6, 1986, p 363
30. M.-L. Lu and F.-C. Chang, *Polymer*, Vol 36, 1995, p 2541
31. Z. Zhou, J.D. Landes, and D.D. Huang, *Polym. Eng. Sci.*, Vol 34, 1994, p 128
32. M.-L. Lu, C.-B. Lee, and F.-C. Chang, *Polym. Eng. Sci.*, Vol 35, 1995, p 1433
33. J.W. Hutchinson and P.C. Paris, in *Elastic-Plastic Fracture*, ASTM STP 668, 1979, p 37
34. I. Narisawa and M.T. Takemori, *Polym. Eng. Sci.*, Vol 29, 1989, p 671
35. H. Swei, B. Crist, and S.H. Carr, *Polymer*, Vol 32, 1991, p 1440
36. C.-B. Lee, M.-L. Lu, and F.-C. Chang, *J. Appl. Polym. Sci.*, Vol 47, 1993, p 1867
37. M.-L. Lu and F.-C. Chang, *J. Appl. Polym. Sci.*, Vol 56, 1995, p 1065
38. B.M. Rimmac, T.W. Wright, and R.W. Klein, *Polym. Eng. Sci.*, Vol 28, 1988, p 1586
39. B.D. Huang, in *Toughened Plastics I: Science and Engineering*, C.K. Riew and A.J. Kinloch, Ed., Vol 233, p 39, *ACS Advances in Chemistry Series*, American Chemical Society, 1993
40. M.-L. Lu, K.-C. Chiou, and F.-C. Chang, *Polymer*, Vol 37, 1996, p 4289
41. K.J. Pascoe, in *Failure of Plastics*, W. Brostow and R.D. Corneliussen, Ed., Hanser Publishers, 1989, p 119
42. M.-L. Lu, K.-C. Chiou, and F.-C. Chang, *Polym. Eng. Sci.*, Vol 36, 1996, p 2289

Fracture Resistance Testing of Plastics

Kevin M. Kit and Paul J. Phillips, University of Tennessee, Knoxville

References

1. N.G. McCrum, B.E. Read, and G. Williams, *Anelastic and Dielectric Effects in Polymeric Solids*, Wiley, 1967
2. I.M. Ward, *Mechanical Properties of Solid Polymers*, Wiley, 1983, p 15
3. E.H. Andrews, Cracking and Crazing in Polymeric Glasses, *The Physics of Glassy Polymers*, R.N. Haward, Ed., Wiley, 1973, p 394
4. R. Natarajan and P.E. Reed, *J. Polym. Sci. A, Polym. Chem.*, Vol 2 (No. 10), 1972, p 585

5. G.A. Bernier and R.P. Kambour, *Macromolecules*, Vol 1, 1968, p 393
6. E.H. Andrews, G.M. Levy and J. Willis, *J. Mater. Sci.*, Vol 8, 1973, p 1000
7. L.E. Weber, *The Chemistry of Rubber Manufacture*, Griffin, London, 1926, p 336
8. K. Memmler, *The Science of Rubber*, R.F. Dunbrook and V.N. Morris, Ed., Reinhold, 1934, p 523
9. G.R. Irwin, in *Encyclopaedia of Physics*, Vol 6, Springer Verlag, 1958
10. N.G. McCrum, C.P. Buckley, and C.B. Bucknall, *Principles of Polymer Engineering*, Oxford University Press, 1997, p 201
11. A.A. Griffith, *Phil. Trans. R. Soc. (London) A*, Vol 221, 1921, p 163
12. R.S. Rivlin and A.G. Thomas, *J. Polym. Sci.*, Vol 10, 1953, p 291
13. R.P. Kambour, *Appl. Polym. Symp.*, Vol 7, John Wiley & Sons, 1968, p 215
14. J.P. Berry, *J. Polym. Sci. A, Polym. Chem.*, Vol 2, 1964, p 4069
15. E.H. Andrews, *J. Mater. Sci.*, Vol 9, 1974, p 887
16. J.R. Rice, *J. Appl. Mech. (Trans. ASME)*, Vol 35, 1968, p 379
17. J.R. Rice, *Fracture*, Vol 2, 1968, p 191
18. J.A. Begley and J.D. Landes, in *Fracture Toughness*, ASTM STP 514, 1972, p 1
19. J.D. Landes and J.E. Begley, in *Fracture Toughness*, ASTM STP 514, 1972, p 24
20. J.M. Hodgkinson and J.G. Williams, *J. Mater. Sci.*, Vol 16, 1981, p 50
21. S. Hashemi and J.D. Williams, *Polym. Eng. Sci.*, Vol 26, 1986, p 760
22. Y.W. Mai and P. Powell, *J. Polym. Sci. B, Polym. Phys.*, Vol 29, 1991, p 785
23. M. Ouederni and P.J. Phillips, *J. Polym. Sci. B., Polym. Phys.*, Vol 33, 1995, p 1313
24. "Standard Test Methods for Plane Strain Fracture Toughness and Strain Energy Release Rate of Plastic Materials," ASTM D 5045, *Annual Book of Standards*, Vol 08.03, ASTM, 1996
25. "Standard Test Method for Determining J-R Curves of Plastic Materials," ASTM D 6068, *Annual Book of Standards*, Vol 08.03, ASTM, 1996
26. "Standard Test Method for J_{Ic} , A Measure of Fracture Toughness," ASTM E 813, *Annual Book of Standards*, Vol 03.01, ASTM, 1989
27. "Standard Test Method for J-Integral Characterization of Fracture Toughness," ASTM E 1737, *Annual Book of Standards*, Vol 03.01, ASTM, 1996
28. J.D. Landes and J.A. Begley, in *Fracture Toughness*, ASTM STP 560, 1974, p 170
29. S. Hashemi and J.G. Williams, *Plast. Rubber Process. Appl.*, Vol 6, 1986, p 363

30. M.-L. Lu and F.-C. Chang, *Polymer*, Vol 36, 1995, p 2541
31. Z. Zhou, J.D. Landes, and D.D. Huang, *Polym. Eng. Sci.*, Vol 34, 1994, p 128
32. M.-L. Lu, C.-B. Lee, and F.-C. Chang, *Polym. Eng. Sci.*, Vol 35, 1995, p 1433
33. J.W. Hutchinson and P.C. Paris, in *Elastic-Plastic Fracture*, ASTM STP 668, 1979, p 37
34. I. Narisawa and M.T. Takemori, *Polym. Eng. Sci.*, Vol 29, 1989, p 671
35. H. Swei, B. Crist, and S.H. Carr, *Polymer*, Vol 32, 1991, p 1440
36. C.-B. Lee, M.-L. Lu, and F.-C. Chang, *J. Appl. Polym. Sci.*, Vol 47, 1993, p 1867
37. M.-L. Lu and F.-C. Chang, *J. Appl. Polym. Sci.*, Vol 56, 1995, p 1065
38. B.M. Rimmac, T.W. Wright, and R.W. Klein, *Polym. Eng. Sci.*, Vol 28, 1988, p 1586
39. B.D. Huang, in *Toughened Plastics I: Science and Engineering*, C.K. Riew and A.J. Kinloch, Ed., Vol 233, p 39, *ACS Advances in Chemistry Series*, American Chemical Society, 1993
40. M.-L. Lu, K.-C. Chiou, and F.-C. Chang, *Polymer*, Vol 37, 1996, p 4289
41. K.J. Pascoe, in *Failure of Plastics*, W. Brostow and R.D. Corneliussen, Ed., Hanser Publishers, 1989, p 119
42. M.-L. Lu, K.-C. Chiou, and F.-C. Chang, *Polym. Eng. Sci.*, Vol 36, 1996, p 2289

Fracture Toughness of Ceramics and Ceramic Matrix Composites

J.H. Miller, Oak Ridge National Laboratory P.K. Liaw, The University of Tennessee, Knoxville

Introduction

CERAMICS are lightweight structural materials with much higher resistance to high temperatures and aggressive environments than other conventional engineering materials. These characteristics of ceramics hold promise in various applications for gas turbines, heat exchangers, combustors and boiler components in the power generation systems, first-wall and high-heat-flux surfaces in fusion reactors, and structural components in the aerospace industry (Ref 1, 2, 3, 4, 5, 6, 7, 8, 9, 10, 11, 12, 13, 14, 15, 16, 17, 18, 19, 20, 21, 22, 23, 24, and 25). However, most of these engineering applications require high reliability and the improvement of ceramic fracture toughness.

Monolithic ceramics are inherently brittle, making them highly sensitive to process- and service-related flaws. Due to their low toughness, monolithic ceramics are prone to catastrophic failure and, thus, may be unsuitable for engineering applications that require high reliability. Ceramic matrix composites (CMCs), however, can provide significant improvement in fracture toughness and the avoidance of catastrophic failure (Ref 1, 2, 3, 4, 5, 6, 7, 8, 9, 10, 11, 12, 13, 14, 15, 16, 17, 18, 19, 20, 21, 22, 23, 24, 25, 26, 27, 28, 29, 30, 31, 32, 33, 34, 35, 36, 37, 38, 39, 40, and 41). The fracture mechanisms in CMCs are identical to those found in monolithic

ceramics (brittle), but “plastic-like” behavior occurs in CMCs because of the toughening mechanisms of crack bridging, branching, and deflection. The reinforcing particles, whiskers, or fibers that are present in the ceramic matrix allow the bulk composite material to avoid unstable crack growth and the resulting catastrophic failure. The toughness of CMCs comes from the fact that the reinforcement can provide crack bridges and cause cracks to branch, deflect, or arrest. These issues are quite complicated, and they demonstrate the critical need for the understanding of the fracture properties of ceramics and CMCs.

Much work has been done to develop methods for evaluating the fracture toughness of ceramic materials (Ref 42, 43, 44, 45, 46, 47, 48, 49, and 50). The concepts of both linear-elastic fracture mechanics (LEFM) and elastic-plastic fracture mechanics (EPFM) are both of interest in regard to ceramic materials. Monolithic ceramics, due to their brittle nature, behave in a linear-elastic manner. This fact has led to the successful use of LEFM methods for monolithic ceramics. Many CMCs, on the other hand, have an elastic-plastic fracture behavior. This fact has led researchers to attempt to use EPFM methods to evaluate the fracture toughness of CMCs.

This article briefly introduces LEFM and EPFM concepts and methods that have been developed or adapted for the evaluation of the fracture behavior of monolithic ceramics and CMCs. The general concepts of LEFM and EPFM are briefly reviewed, and test methods are described for fracture toughness testing of monolithic ceramics and CMCs. More detailed information on the fracture resistance testing of monolithic ceramics is also contained in the article “Fracture Resistance Testing of Brittle Solids” in this Volume, while this article places emphasis on the fracture toughness testing of cmcs. Measuring the fracture toughness of CMCs is not as developed as toughness testing of monolithic ceramics. The toughening mechanisms of microcracking, crack bridging, and crack branching cause CMCs to behave in an elastic-plastic-like manner, which makes EPFM methods attractive. LEFM and EPFM methods have both been used to evaluate the toughness of CMCs, but because the level of understanding of the complex fracture mechanisms present in CMCs is not well developed, no connection has been made between the macroscopic toughness, either elastic or elastic-plastic, and the fracture mechanisms. As a result, evaluation of the fracture toughness of CMCs has been limited. However, as the cracking mechanisms become better understood, LEFM and EPFM methods will become better adapted for use in the evaluation of CMC fracture toughness behavior.

References cited in this section

1. T.M. Besmann, B.W. Sheldon, R.A. Lowden, and D.P. Stinton, Vapor Phase Fabrication and Properties of Continuous-Filament Ceramic Composites, *Science*, Vol 253, 1991, p 1104
2. M. Bouquet, J.M. Bribis, and J.M. Quenisset, Toughness Assessment of Ceramic Matrix Composites, *Compos. Sci. Technol.*, Vol 37, 1990, p 223–248
3. C.H. Hsueh, P.F. Becher, and P. Angelini, Effects of Interfacial Films on Thermal Stresses in Whisker-Reinforced Ceramics, *J. Am. Ceram. Soc.*, Vol 71 (No. 11), 1988, p 929–933
4. D.P. Stinton, A.J. Caputo, and R.A. Lowden, Synthesis of Fiber-Reinforced SiC Composites by Chemical Vapor Infiltration, *Am. Ceram. Soc. Bull.*, Vol 65 (No. 2), 1986, p 347–350
5. D.P. Stinton, W.J. Lackey, R.J. Lauf, and T.M. Besmann, Fabrication of Ceramic-Ceramic Composites by Chemical Vapor Deposition, *Ceram. Eng. Sci. Proc.*, Vol 5, 1984, p 668–676
6. J.H. Miller, R.A. Lowden, and P.K. Liaw, Fiber Coatings and the Fracture Behavior of a Continuous Fiber Ceramic Composite, *Symposium on Ceramic Matrix Composites—Advanced High-Temperature Structural Materials*, R.A. Lowden, M.K. Ferber, J.R. Hellmann, K.K. Chawla, and S.G. DiPietro, Ed., Vol 365, Materials Research Society, 1995, p 403–410
7. M.A. Borst, W.Y. Lee, Y. Zhang, and P.K. Liaw, Preparation and Characterization of Chemically Vapor Deposited ZrO₂ Coating on Nickel and Ceramic Fiber Substrates, *J. Am. Ceram. Soc.*, Vol 80 (No. 6), 1997, p 1591–1594

8. N. Miriyala, P.K. Liaw, C.J. McHargue, L.L. Snead, and J.A. Morrison, The Monotonic and Fatigue Behavior of a Nicalon/Alumina Composite at Ambient and Elevated Temperatures, American Ceramic Society Meeting, *Ceram. Eng. Sci. Proc.*, Vol 18 (No. 3), 1997, p 747–756
9. W. Zhao, P.K. Liaw, and N. Yu, Effects of Lamina Stacking Sequence on the In-Plane Elastic Stress Distribution of a Plain-Weave Nicalon Fiber-Reinforced SiC Laminated Composite with a Lay-Up of [0/30/60], American Ceramic Society Meeting, *Ceram. Eng. Sci. Proc.*, Vol 18 (No. 3), 1997, p 401–408
10. W. Zhao, P.K. Liaw, and D.C. Joy, Microstructural Characterization of a 2-D Woven Nicalon/SiC Ceramic Composite by Scanning Electron Microscopy Line-Scan Technique, American Ceramic Society Meeting, *Ceram. Eng. Sci. Proc.*, Vol 18 (No. 3), 1997, p 295–302
11. J.G. Kim, P.K. Liaw, D.K. Hsu, and D.J. McGuire, Nondestructive Evaluation of Continuous Nicalon Fiber Reinforced SiC Composites, American Ceramic Society Meeting, *Ceram. Eng. Sci. Proc.*, Vol 18 (No. 4), 1997, p 287–296
12. N. Miriyala, P.K. Liaw, C.J. McHargue, and L.L. Snead, The Monotonic and Fatigue Behavior of a Nicalon/Alumina Composite at Ambient and Elevated Temperatures, *Ceram. Eng. Sci. Proc.*, Vol 18 (No. 3), 1997, p 747–756
13. W. Zhao, P.K. Liaw, N. Yu, E.R. Kupp, D.P. Stinton, and T.M. Besmann, Computation of the Lamina Stacking Sequence Effect on the Elastic Moduli of a Plain-Weave Nicalon Fiber Reinforced SiC Laminated Composite with a Lay-Up of [0/30/60], *J. Nucl. Mater.*, Vol 253, 1998, p 10–19
14. N. Miriyala, P.K. Liaw, C.J. McHargue, and L.L. Snead, “The Mechanical Behavior of A Nicalon/SiC Composite at Ambient Temperature and 1000 °C”, *J. Nucl. Mater.*, Vol 253, 1998, p 1–9
15. W.Y. Lee, Y. Zhang, I.G. Wright, B.A. Pint, and P.K. Liaw, Effects of Sulfur Impurity on the Scale Adhesion Behavior of a Desulfurized Ni-Based Superalloy Aluminized by Chemical Vapor Deposition, *Metall. Mater. Trans. A*, Vol 29, 1998, p 833
16. P.K. Liaw, Understanding Fatigue Failure in Structural Materials, *JOM*, Vol 49 (No. 7), 1997, p 42
17. N. Miriyala and P.K. Liaw, CFCC (Continuous-Fiber-Reinforced Ceramic Matrix Composites) Fatigue: A Literature Review, *JOM*, Vol 49 (No. 7), 1997, p 59–66, 82
18. N. Miriyala and P.K. Liaw, Specimen Size Effects on the Flexural Strength of CFCCs, American Ceramic Society Meeting, *Ceram. Eng. Sci. Proc.*, Vol 19, 1998
19. W. Zhao, P.K. Liaw, and N. Yu, Computer-Aided Prediction of the First Matrix Cracking Stress for a Plain-Weave Nicalon/SiC Composite with Lay-Ups of [0/20/60] and [0/40/60], *Ceram. Eng. Sci. Proc.*, Vol 19, 1998, p 3
20. W. Zhao, P.K. Liaw, and N. Yu, Computer-Aided Prediction of the Effective Moduli for a Plain-Weave Nicalon/SiC Composite with Lay-Ups of [0/20/60] and [0/40/60], *Ceram. Eng. Sci. Proc.*, Vol 19, 1998
21. N. Miriyala, P.K. Liaw, C.J. McHargue, A. Selvarathinam, and L.L. Snead, The Effect of Fabric Orientation on the Flexural Behavior of CFCCs: Experiment and Theory, The 100th Annual American Ceramic Society Meeting, 3–6 May 1998 (Cincinnati), in press
22. N. Miriyala, P.K. Liaw, C.J. McHargue, and L.L. Snead, Fatigue Behavior of Continuous Fiber-Reinforced Ceramic-Matrix Composites (CFCCs) at Ambient and Elevated Temperatures, invited paper presented at symposium proceedings in honor of Professor Paul C. Paris, *High Cycle Fatigue of*

Structural Materials, W.O. Soboyejo and T.S. Srivatsan, Ed., The Minerals, Metals, and Materials Society, 1997, p 533–552

23. W. Zhao, P.K. Liaw, and N. Yu, The Reliability of Evaluating the Mechanical Performance of Continuous Fiber-Reinforced Ceramic Composites by Flexural Testing, *Int. Conf. on Maintenance and Reliability*, 1997, p 6-1 to 6-15
24. P.K. Liaw, J. Kim, N. Miriyala, D.K. Hsu, N. Yu, D.J. McGuire, and W.A. Simpson, Jr., Nondestructive Evaluation of Woven Fabric Reinforced Ceramic Composites, *Symposium on Nondestructive Evaluation of Ceramics*, C. Schilling, J.N. Gray, R. Gerhardt, and T. Watkins, Ed., Vol 89, 1998, p 121–135
25. M.E. Fine and P.K. Liaw, Commentary on the Paris Equation, invited paper presented at symposium proceedings in honor of Professor Paul C. Paris, *High Cycle Fatigue of Structural Materials, High Cycle Fatigue of Structural Materials*, W.O. Soboyejo and T.S. Srivatsan, Ed., The Minerals, Metals, and Materials Society, 1997, p 25–40
26. W. Zhao, P.K. Liaw, D.C. Joy, and C.R. Brooks, Effects of Oxidation, Porosity and Fabric Stacking Sequence on Flexural Strength of a SiC/SiC Ceramic Composite, *Processing and Properties of Advanced Materials: Modeling, Design and Properties*, B.Q. Li, Ed., The Minerals, Metals, and Materials Society, 1998, p 283–294
27. W. Zhao, P.K. Liaw, and N. Yu, Computer Modeling of the Fabric Stacking Sequence Effects on Mechanical Properties of a Plain-Weave SiC/SiC Ceramic Composite, *Proc. on Processing and Properties of Advanced Materials: Modeling, Design and Properties*, B.Q. Li, Ed., The Minerals, Metals, and Materials Society, 1998, p 149–160
28. J. Kim and P.K. Liaw, The Nondestructive Evaluation of Advanced Ceramics and Ceramic-Matrix Composites, *JOM*, Vol 50 (No. 11), 1998
29. N. Yu and P.K. Liaw, Ceramic-Matrix Composites: An Integrated Interdisciplinary Curriculum, *J. Eng. Ed.*, supplement, 1998, p 539–544
30. P.K. Liaw, Continuous Fiber Reinforced Ceramic Composites, *J. Chin. Inst. Eng.*, Vol 21 (No. 6), 1998, p 701–718
31. N. Yu and P.K. Liaw, “Ceramic-Matrix Composites: Web-Based Courseware and More,” paper presented at the 1998 ASEE annual conference and exposition, June 28–July 1, 1998 (Seattle)
32. N. Yu and P.K. Liaw, “Ceramic-Matrix Composites,” <http://www.engr.utk.edu/~cmc>
33. P.K. Liaw, O. Buck, R.J. Arsenault, and R.E. Green, Jr., Ed., *Nondestructive Evaluation and Materials Properties III*, The Minerals, Metals, and Materials Society, 1997
34. W.M. Matlin, T.M. Besmann, and P.K. Liaw, Optimization of Bundle Infiltration in the Forced Chemical Vapor Infiltration (FCVI) Process, *Symposium on Ceramic Matrix Composites—Advanced High-Temperature Structural Materials*, R.A. Lowden, M.K. Ferber, J.R. Hellmann, K.K. Chawla, and S.G. DiPietro, Ed., Vol 365, Materials Research Society, 1995, p 309–315
35. P.K. Liaw, D.K. Hsu, N. Yu, N. Miriyala, V. Saini, and H. Jeong, Measurement and Prediction of Composite Stiffness Moduli, *Symposium on High Performance Composites: Commonalty of Phenomena*, K.K. Chawla, P.K. Liaw, and S.G. Fishman, Ed., The Minerals, Metals, and Materials Society, 1994, p 377–395

36. N. Chawla, P.K. Liaw, E. Lara-Curzio, R.A. Lowden, and M.K. Ferber, Effect of Fiber Fabric Orientation on the Monotonic and Fatigue Behavior of a Continuous Fiber Ceramic Composite, *Symposium on High Performance Composites*, K.K. Chawla, P.K. Liaw, and S.G. Fishman, Ed., The Minerals, Metals and Materials Society, 1994, p 291–304
37. P.K. Liaw, D.K. Hsu, N. Yu, N. Miriyala, V. Saini, and H. Jeong, Modulus Investigation of Metal and Ceramic Matrix Composites: Experiment and Theory, *Acta Metall. Mater.*, Vol 44 (No. 5), 1996, p 2101–2113
38. P.K. Liaw, N. Yu, D.K. Hsu, N. Miriyala, V. Saini, L.L. Snead, C.J. McHargue, and R.A. Lowden, Moduli Determination of Continuous Fiber Ceramic Composites (CFCCs), *J. Nucl. Mater.*, Vol 219, 1995, p 93–100
39. P.K. Liaw, book review on *Ceramic Matrix Composites* by K.K. Chawla, *MRS Bull.*, Vol 19, 1994, p 78
40. D.K. Hsu, P.K. Liaw, N. Yu, V. Saini, N. Miriyala, L.L. Snead, R.A. Lowden, and C.J. McHargue, Nondestructive Characterization of Woven Fabric Ceramic Composites, *Symposium on Ceramic Matrix Composites—Advanced High-Temperature Structural Materials*, R.A. Lowden, M.K. Ferber, J.R. Hellmann, K.K. Chawla, and S.G. DiPietro, Ed., Vol 365, Materials Research Society, 1995, 203–208
41. S. Shanmugham, D.P. Stinton, F. Rebillat, A. Bleier, E. Lara-Curzio, T.M. Besmann, and P.K. Liaw, Oxidation-Resistant Interfacial Coatings for Continuous Fiber Ceramic Composites, S. Shanmugham, D.P. Stinton, F. Rebillat, A. Bleier, T.M. Besmann, E. Lara-Curzio, and P.K. Liaw, *Ceram. Eng. Sci. Proc.*, Vol 16 (No. 4), 1995, p 389–399
42. C.B. Thomas, “Processing, Mechanical Behavior, and Microstructural Characterization of Liquid Phase Sintered Intermetallic-Bonded Ceramic Composites,” M.S. Thesis, The University of Tennessee, Knoxville, 1996
43. J.H. Miller, “Fiber Coatings and The Fracture Behavior of a Woven Continuous Fiber Fabric-Reinforced Ceramic Composite,” M.S. Thesis, The University of Tennessee, Knoxville, 1995
44. I.E. Reimonds, A Review of Issues in the Fracture of Interfacial Ceramics and Ceramic Composites, *Materials Science and Engineering A*, Vol 237 (No. 2), 1997, p 159–167
45. D.L. Davidson, Ceramic Matrix Composites Fatigue and Fracture, *JOM*, Vol 47 (No. 10), 1995, p 46–50, 81, 82
46. J.C. McNulty and F.W. Zok, Application of Weakest-Link Fracture Statistics to Fiber-Reinforced Ceramic-Matrix Composites, *J. Am. Ceram. Soc.*, Vol 80 (No. 6), 1997, p 1535–1543
47. Z.G. Li, M. Taya, M.L. Dunn, and R. Watanabe, Experimental-Study of the Fracture-Toughness of a Ceramic/Ceramic-Matrix Composite Sandwich Structure, *J. Am. Ceram. Soc.*, Vol 78 (No. 6), 1995, p 1633–1639
48. A. Ishida, M. Miyayama, and H. Yanagida, Prediction of Fracture and Detection of Fatigue in Ceramic Composites from Electrical-Resistivity Measurements, *J. Am. Ceram. Soc.*, Vol 77 (No. 4), 1994, p 1057–1061
49. M. Sakai and H. Ichikawa, Work of Fracture of Brittle Materials with Microcracking and Crack Bridging, *Int. J. Fract.*, Vol 55 (No. 1), 1992, p 65–79
50. J.B. Quinn and G.D. Quinn, “Indentation Brittleness of Ceramics: A Fresh Approach,” *J. Mater. Sci.*, Vol 32 (No. 16), 1997, p 4331–4346

An Overview of Fracture Mechanics

Fracture mechanics involves the stress analysis of cracking in structures or bodies with cracks or flaws. Most of the work in this field has concentrated on the cracking behavior of metals, so this brief overview introduces the concepts and ideas of LEFM and EPFM for metals (Ref 51, 52, and 53). This is followed by a description of the use of LEFM and EPFM methods in the evaluation of monolithic ceramic and CMCs, respectively.

Linear-Elastic Fracture Mechanics

The use of LEFM is applicable under two conditions:

- The applied load deforms a cracked body in a linear-elastic manner.
- The flaw or crack is assumed to be a sharp crack with a tip radius near zero.

The stresses required for cracking under these two conditions can be analyzed according to LEFM by two parameters: the energy release rate and the stress intensity factor.

The energy release rate, G , is the amount of stored energy that is available for an increment of crack extension:

$$G = \frac{d\Pi}{dA} \quad (\text{Eq 1})$$

where Π is the stored potential energy and A is the crack surface area that is created as the crack grows. In other words, G is the amount of stored elastic energy that is converted to surface energy as the crack grows. Because the body behaves in an elastic manner, all of the energy available is used to create the crack surfaces (Ref 51, 52, and 53).

Expressions for the energy release rate can be derived based on the geometry of the crack and the loading conditions. Two basic types of configurations are shown in Fig. 1 and 2 for an edge crack and a central through-thickness crack, respectively, for Mode I (tensile opening) loads. In this case, crack length is defined by typical convention as a for an edge crack (Fig. 1) and as a $2a$ for a central through-thickness crack (Fig. 2). With this convention, then the value of G for a wide plate (plate width $\gg a$) in plane stress is as follows (Ref 51, 52, and 53):

$$G = \frac{\pi\sigma^2 a}{E} \quad (\text{Eq 2})$$

where σ is the applied stress, E is Young's modulus, and a is either the total length of an edge crack (Fig. 1) or half the length of center crack ($2a$ in Fig. 2). Equation 2 thus applies to both of these basic configurations in Fig. 1 and 2 with the appropriate definition for a as shown.

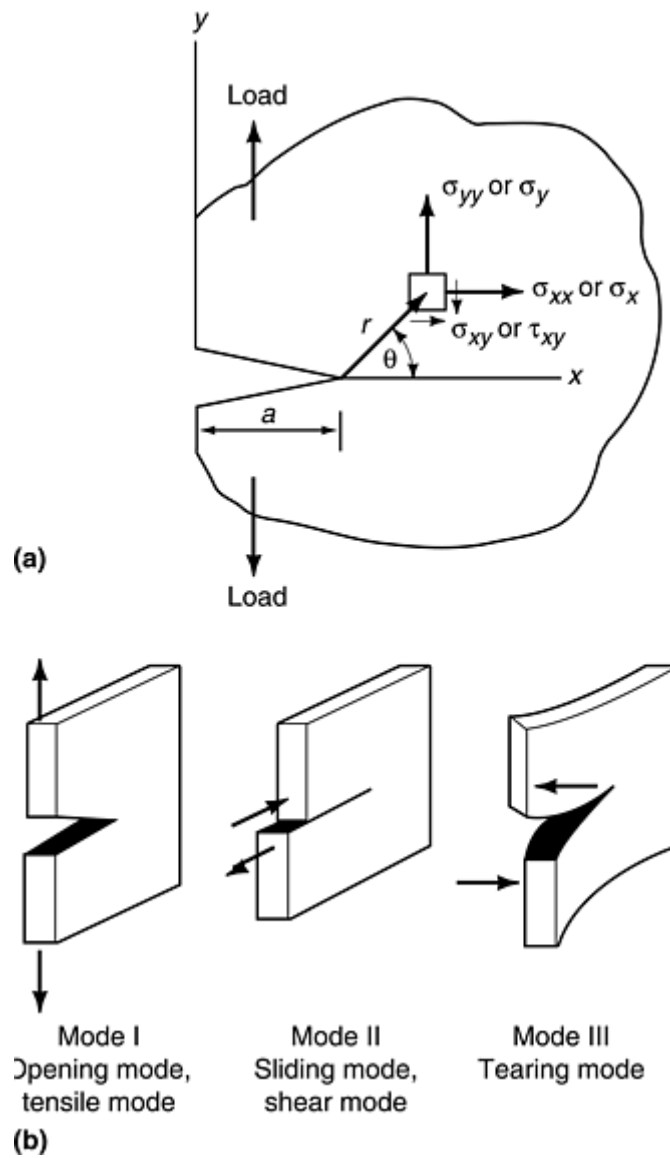


Fig. 1 Schematic illustration of an edge-notched specimen. (a) Crack length, a , and general coordinate system for crack tip stresses in Mode I loading.

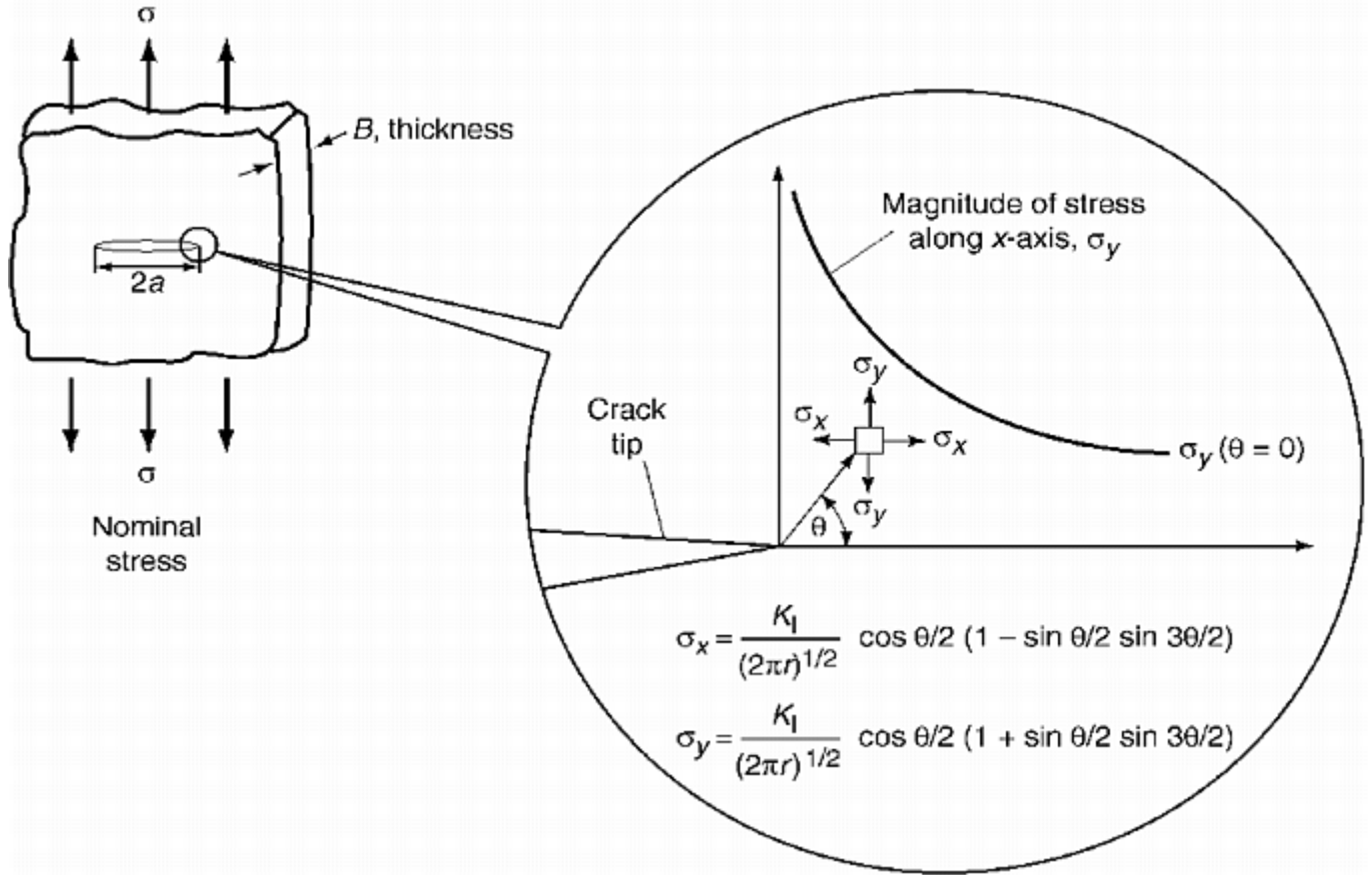


Fig. 2 Schematic illustration stress distributions near the tip of a through-thickness crack an infinitely wide plate (plate width \gg than the crack length, $2a$)

The stress intensity factor, K , is a measure of stress intensity in the entire elastic stress field around the crack tip. It is derived based on the analysis of the stress field near the tip of a sharp crack, rather than an energy consideration, as in the case of the energy release rate. The stress intensity factor can be related to the local stress at the crack tip as:

$$\sigma_{YY} = \frac{K_I}{\sqrt{2\pi r}} \quad (\text{Eq 3})$$

where σ_{YY} is the local stress near the tip of the crack, K_I is the stress intensity factor with a Mode I (tensile opening) load, and r is the distance in front of the crack tip (with $\theta = 0$) (Fig. 1). The stress intensity factor in Mode I loading can also be related to the applied or nominal stress as (Ref 51, 52, 53):

$$K_I = \sigma_{\text{nom}} Y \sqrt{\pi a} \quad (\text{Eq 4})$$

where σ_{nom} is the nominal or applied stress and Y is a geometrical factor that is specific to a particular loading condition and crack configuration. As in the case of Eq 2, the crack length, a , in Eq 4 is defined either as the length of an edge crack (a in Fig. 1) or as one-half the length of a through-thickness crack ($2a$ in Fig. 2). With these definitions for a , Eq 4 applies for both an edge crack and a center crack configuration.

Figure 3 shows a schematic plot of the stress normal to the crack plane as a function of the distance, r , from the crack tip for both σ_{YY} and σ_{nom} (Ref 51, 52, and 53). According to Eq 3 and Fig. 3, there is a singularity in the stress field at the tip of the crack. This fact is the reason why elastic action is an important assumption in LEFM. If significant plasticity occurred, the crack would be blunted by the plastic flow, and the stress intensity solution would no longer be valid.

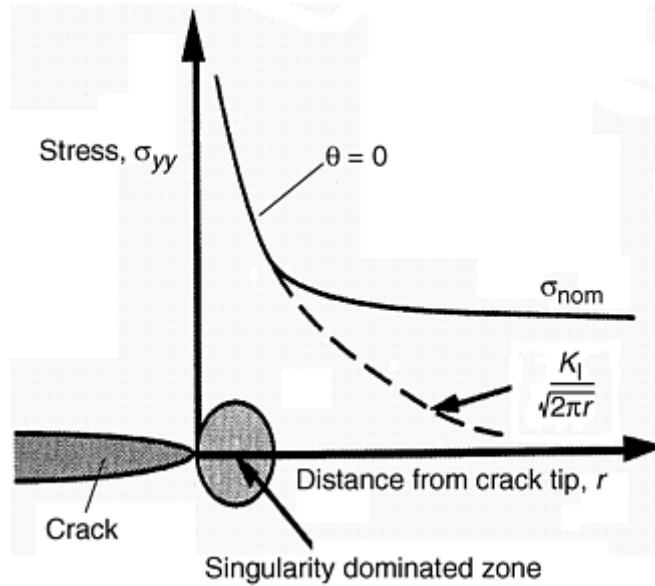


Fig. 3 Schematic plot of the stress field around a crack. Source: Ref 52

With Eq 4, it is possible to relate the magnitude of the single parameter, K , to the applied stress and crack size. This is the basis for most common applications of LEFM. Through the use of published expressions for the geometry factor, Y , many common loading conditions and structures can be analyzed. The published expressions for K_I that include the proper Y for specific loading and cracking conditions are commonly called K -calibrations. The calculated stress intensity factor from the K -calibration and the loading level can be compared to a critical stress intensity value to determine the safety of the structure (Ref 51, 52, and 53). The energy release rate is related to the stress intensity factor by the equation:

$$G = \frac{K_I^2}{E'} \quad (\text{Eq 5})$$

where $E' = E$ (Young's modulus) for plane stress conditions, or where:

$$E' = \frac{E}{1 - \nu^2} \quad (\text{Eq 6})$$

where ν is Poisson's ratio for plane strain conditions.

Critical Crack Growth. Crack extension can either be stable or unstable depending on material properties and specimen geometry. Therefore, an important issue in LEFM is the definition of critical conditions that lead to unstable crack growth. Critical conditions for unstable crack growth can be expressed as either a critical energy release rate or a critical stress intensity factor. The critical value is the value of G or K at the instant when unstable crack extension occurs, that is, when the crack propagates through the specimen and thus causes the specimen to break in two. The critical energy release rate, G_c , or the critical stress intensity factor, K_c , are thus defined as the values of G and K at the instant of unstable crack extension that leads to fracture. Under these conditions, either parameter can be defined as the fracture toughness of the material. Usually K_c is the chosen parameter to express the fracture toughness. If the fracture toughness is not a function of specimen size or geometry then this fracture toughness value can be considered a material property. Otherwise, the fracture toughness result is only valid under the conditions it was measured (Ref 51, 52, 53, and 54).

Crack Growth Resistance and R -Curves. If stable crack growth occurs, a single value for fracture toughness is difficult to define. In the case of stable crack growth, a plot of the experimentally measured fracture parameter, in terms of either G or K , versus crack length is developed. This plot can be generated from the load and crack length data taken from a material test. The stress intensity or the energy release rate is calculated from the measured load and crack length data using expressions similar to those shown in Eq 2 and 4 (the correct expression must be used for the conditions of the test). Fracture parameters calculated in this way are defined as the resistance to crack growth parameters because they are calculated from a crack growing in a stable manner. The resistance to crack growth, expressed in terms of the energy release rate, is given the symbol R , and the resistance to crack growth, expressed in terms of the stress intensity factor, is given the symbol K_R . The plot of resistance to crack growth, either R or K_R , versus crack length is called a crack growth resistance curve, or R -

curve, and the entire curve becomes the measure of fracture toughness. Schematic examples of R -curves plotted in terms of G and K are shown in Fig. 4 and 5, respectively (Ref 51, 52, and 53).

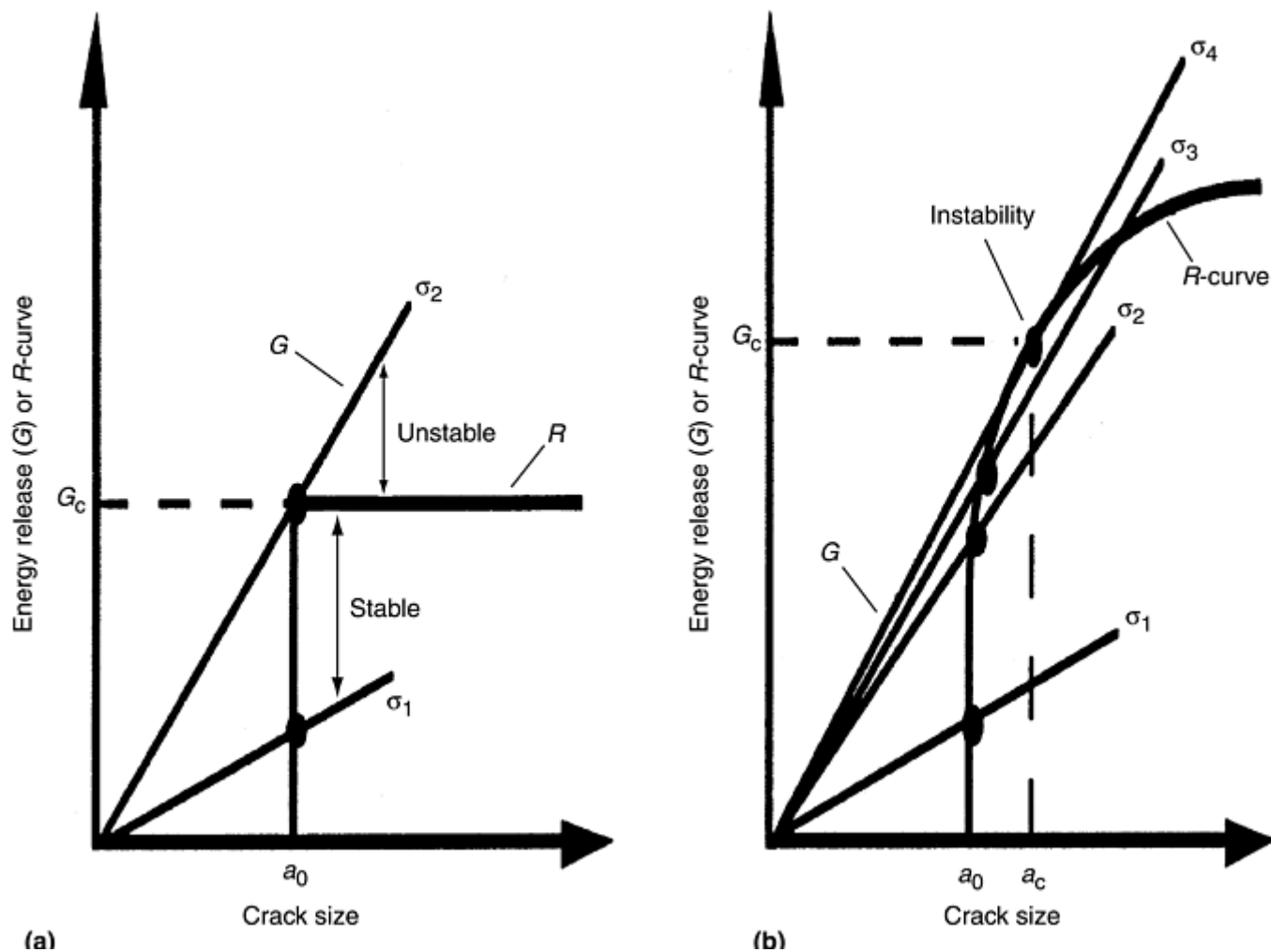


Fig. 4 Schematic crack growth resistance curves and crack driving force curves, in terms of the energy release rate, G . (a) Single-valued fracture toughness. (b) Rising R -curve behavior. Adapted from Ref 52

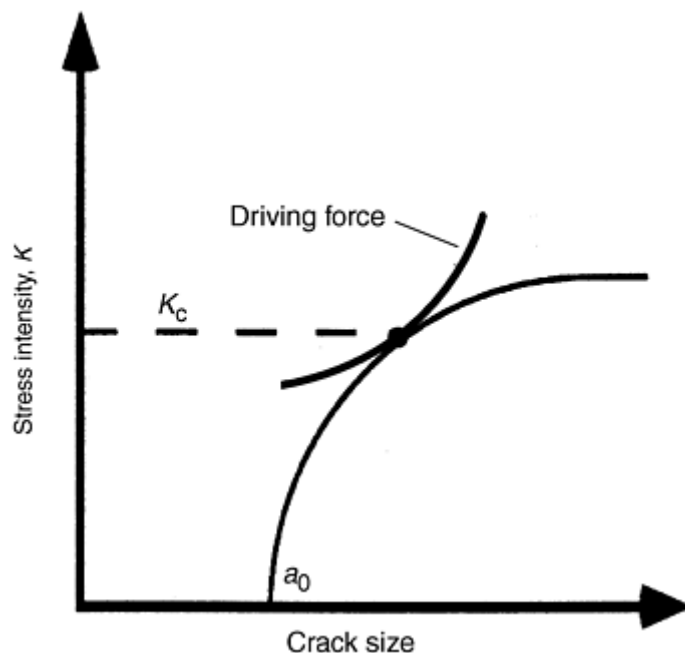


Fig. 5 Schematic crack growth resistance curve and crack driving force curve in terms of the stress intensity factor, K . Adapted from Ref 52

Figure 5(a) shows a flat R -curve, which is the result of unstable crack growth. The flat R -curve presents the ease of defining fracture toughness as a critical value for unstable crack growth, in this case G_c . Figure 5(b) is an example of an R -curve that demonstrates stable crack growth prior to instability. Stable crack growth occurs because the crack growth resistance increases with increasing crack length. This trend is called the rising R -curve behavior. An R -curve plotted in terms of K rather than G is shown in Fig. 5 (Ref 51, 52, and 53).

The R -curve can be used to predict the conditions that will cause crack extension. To do this, it is necessary to plot the crack driving force on the same axes as the crack growth resistance curve. The curve for crack driving force is calculated using the same expressions of K and G that relate the geometry and loading conditions to fracture. However, instead of using the data from a crack propagation test, the procedure is to calculate crack driving force curves by holding the stress, or load, constant and increasing the crack length incrementally. The point where the crack driving force curve crosses the resistance curve represents the condition under which critical crack growth occurs (Ref 51, 52, and 53). The expected in-service stress levels of a cracked body can be evaluated from this.

In summary, crack growth can either be stable or unstable. If the driving force curve crosses the resistance curve at the tangency point, the crack growth will be unstable. If it crosses below this point, the crack growth will be stable. To determine the point where the unstable crack growth occurs it is necessary to establish an iterative scheme of generating driving force curves for different stress levels until tangency is achieved. Schematic examples of driving force curves plotted with resistance to crack growth curves are also shown in Fig. 4 and 5. Also evident in the figures are definitions of the critical energy release rate, G_c Fig. (4) and critical stress intensity factor K_c (Fig. 5). These critical values are defined at the point of instability (Ref 51, 52, and 53).

Elastic-Plastic Fracture Mechanics

EPFM does not have the requirement that the material behave in a linear-elastic manner. Instead, nonlinear or plastic deformation is allowed in EPFM methods to a much greater extent than in LEFM methods. The primary fracture parameter for EPFM is the J -integral. The J -integral, or more simply J , can be defined in two ways (Ref 56, 57). The first is defined by a path-independent line integral around the crack tip. The second is an energy definition similar to G , except that linear behavior is not required.

The energy definition of J states that J is a more general form of the energy release rate, G , where:

$$J = - \frac{d\Pi}{dA} \quad (\text{Eq 7})$$

When permanent deformation occurs (as in the case of plastic deformation of metals), some of the stored potential energy, Π , is dissipated and is therefore unavailable for crack extension. In this context, J can be thought of as the potential energy absorbed by a cracked body prior to crack growth. In other words, J is a measure of the intensity of the entire elastic-plastic stress-strain field around the crack tip, and J reaches a critical value just prior to crack extension.

A special case of the energy definition of J is the value for G (when the energy is released as a crack grows in a linear-elastic material). For the special case of linear-elastic behavior, there is little or no energy absorbed by permanent deformation, and the only energy dissipation is due to the crack surface creation. Hence, under linear-elastic conditions $J = G$:

$$J = G = \frac{K^2}{E'} \quad (\text{Eq 8})$$

where E' is equal to E or is related to the elastic modulus per Eq 6.

Under nonlinear conditions beyond the elastic regime, calculating J can be much more difficult. Unlike the K solutions or K -calibrations (which exist for many different crack and load configurations with K values for many situations), expressions that relate J values to the applied load and crack configuration are very few. For the simple situation of an edge-cracked specimen under elastic-plastic loading conditions, the energy definition of J is as follows:

$$J = - \frac{1}{B} \left(\frac{\partial U}{\partial a} \right)_{\Delta} \quad (\text{Eq 9})$$

where B is the specimen thickness, Δ is the load-line displacement, and U is the area under the P - Δ curve up to the initiation of crack growth (Ref 51, 52, and 53) where P is the applied load. Because a certain amount of the deformation must always be elastic, the expression for J in Eq 9 can be separated into elastic and plastic components and be rewritten as follows:

$$J = \frac{K_I^2}{E'} + \frac{\eta_{PL} U_{PL}}{Bb} \quad (\text{Eq 10})$$

where η_{PL} is a dimensionless constant that depends on the specimen and loading configuration, U_{PL} is the plastic area under the P - Δ curve, and b is the remaining ligament ($W-a$, where W is the specimen width). Equation 11 is used in experimentally measuring J (Ref 51, 52, 53, and 57).

In the elastic-plastic regime, there is typically some amount of stable crack growth prior to an unstable crack extension. The stable crack growth occurs because of energy dissipation and the crack blunting induced by plastic deformation. As a result, when J is experimentally measured, an R -curve based on the J parameter is generated. This J -based R -curve is a plot of the resistance to crack growth, J_R , as a function of crack length or extension (Fig. 4). The critical J , J_{Ic} in the opening mode, is then taken from the J_R curve at a point near the initiation of crack growth (Ref 51, 52, 53, 54, 55, 56, and 57).

The basic procedure for experimentally measuring J involves testing a bend specimen or a compact tension specimen with a deep crack and using the load, displacement, and crack length data to calculate J with Eq 11. J is calculated for several different crack lengths, and the J_R curve is generated. From the J_R curve, the J_{Ic} is taken at the point where initial crack extension occurred, as shown in Fig. 6. The test can be done with one of two goals. If the point of the test is to determine J_{Ic} , J is calculated with less attention to the fact that some crack extension occurred during the test. Ignoring the crack extension does not present much error because the crack growth initiation is the important feature in the test. If the development of the full J_R curve is the goal of the test, more care is taken in the data analysis to take into account the growing crack (Ref 51, 52, 53, 54, and 57).

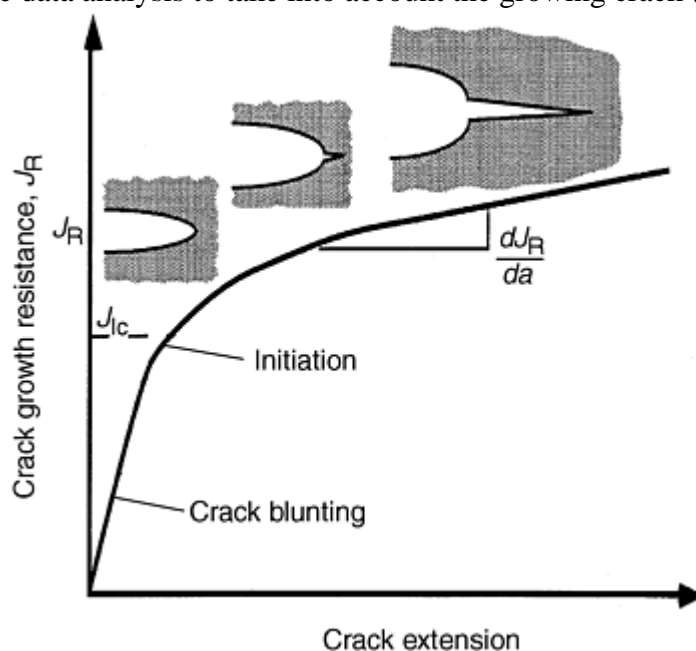


Fig. 6 Schematic crack growth resistance curve in terms of J_R . Adapted from Ref 52

References cited in this section

51. R.W. Hertzberg, *Deformation and Fracture Mechanics of Engineering Materials*, 3rd ed., John Wiley & Sons, 1989
52. T.L. Anderson, *Fracture Mechanics*, 2nd ed., CRC Press, 1995
53. J.M. Barsom and S.T. Rolfe, *Fracture and Fatigue Control in Structures*, Prentice-Hall, Inc., 1987

54. "Standard Test Method for Plane-Strain Fracture Toughness of Metallic Materials," ASTM Standard E 399-90, *ASTM Book of Standards*, Vol 03.01, American Society for Testing and Materials, 1995
55. J.R. Rice, *Journal of Applied Mechanics*, Vol 35, 1968, p 379-386
56. J.A. Begley, G.A. Clark, and J.D. Landes, Results of an ASTM Cooperative Testing Procedure by Round Robin Tests of HY130 Steel, *JTEVA*, Vol 10 (No. 5), 1980
57. "Standard Test Method for J_{IC} , A Measurement of Fracture," ASTM Standard E 813-87, *ASTM Book of Standards*, Vol 03.01, American Society for Testing and Materials, 1995

Fracture Toughness of Ceramics and Ceramic Matrix Composites

J.H. Miller, Oak Ridge National Laboratory P.K. Liaw, The University of Tennessee, Knoxville

Fracture Mechanics of Ceramics and CMCs

The concepts of both LEFM and EPFM methods, as previously described in the context of metallic materials, provides a general basis for the fracture mechanics of monolithic ceramics and ceramic matrix composites. Generally LEFM methods are applicable for monolithic ceramics while EPFM methods may be suitable for CMCs.

Monolithic ceramics are inherently brittle due to their strong bonding and more complicated (less symmetric) crystal structures. Compared to metallic materials, the mixed ionic and covalent atomic bonding and low-symmetry crystal structure of ceramics severely limit the opportunity for plastic deformation mechanisms from dislocation formation, movement, and slip. Monolithic ceramics thus have high strength and stiffness with much less plastic deformation than metals. As a result, their behavior is primarily linear-elastic, which is one of the required conditions for LEFM methods.

The other condition for LEFM analysis is the presence of a sharp crack or flaw with a crack tip radius approaching zero. Monolithic ceramics meet this condition as well, and LEFM has been used successfully to evaluate monolithic ceramic fracture behavior. Some additional work was necessary to augment LEFM techniques to handle the difficulties of obtaining sharp starter cracks and maintaining stable crack growth that occur in brittle ceramics. Nonetheless, the result of the application of LEFM to monolithic ceramics is a relatively mature state of the art. Techniques exist to determine the single-valued critical fracture toughness and to measure crack growth resistance behavior of monolithic ceramic materials. Current research is centered on the further refinement of these techniques (see also the article "Fracture Resistance Testing of Brittle Solids" in this Volume).

Ceramic matrix composites are being developed in an attempt to increase the toughness and damage tolerance of ceramic materials. The toughness of CMCs is greater than the monolithic ceramics due to the toughening (energy-absorbing) mechanisms of microcracking, crack bridging, and crack branching. These toughening mechanisms enable the CMC to behave in a manner that closely resembles the elastic-plastic behavior of metals. Although this fact may suggest EPFM as appropriate for the study of CMCs, there are differences in the deformation mechanism of ductile metals and CMCs that can bring into question the appropriateness of metal-based EPFM methods for use with CMCs.

Metals dissipate crack-tip energy by the plastic deformation mechanisms of slip, dislocation generation, and dislocation movement. CMCs, on the other hand, dissipate crack tip energy through crack branching, fiber bridging, and microcracking. In both cases, energy is dissipated by nonlinear deformation of the body prior to crack extension. Fortunately, EPFM theory does not depend on the mechanism through which the energy is dissipated during nonlinear deformation, only on the fact that it does occur. As a result, even though the deformation mechanisms are very different, EPFM theory is valid for both metals and CMCs. Unfortunately, the complex nature of the processes that cause the nonlinear fracture behavior in CMCs complicates the

experimental application of EPFM methods to CMCs. The following section describes toughness tests that are used on monolithic ceramics and CMCs.

Fracture Toughness of Ceramics and Ceramic Matrix Composites

J.H. Miller, Oak Ridge National Laboratory P.K. Liaw, The University of Tennessee, Knoxville

Fracture Toughness Evaluation

This section describes some fracture toughness measurement techniques that are being used on ceramics and CMCs. The descriptions are organized by specimen type, and they include advantages and disadvantages of each specimen type as well as experimental control schemes that have been employed on each specimen type. More detailed information on the fracture toughness testing of monolithic ceramics is also provide in the article "Fracture Resistance Testing of Brittle Solids" in this Volume.

Single Edge Notch Bending (SENB). The SENB specimen, shown in Fig. 7(a) has a rectangular cross section with a straight-through saw notch. It is loaded in either three- or four-point bending. The advantages of the SENB include ease of machining due to simple geometry and ease of use due to simple three- or four-point bend loading, which uses a fixture loaded in simple compression. The SENB, while easy to machine and test, is not very stiff. This leads to problems in starting a sharp crack at the end of the saw notch and in achieving stable crack extension (Ref 58).

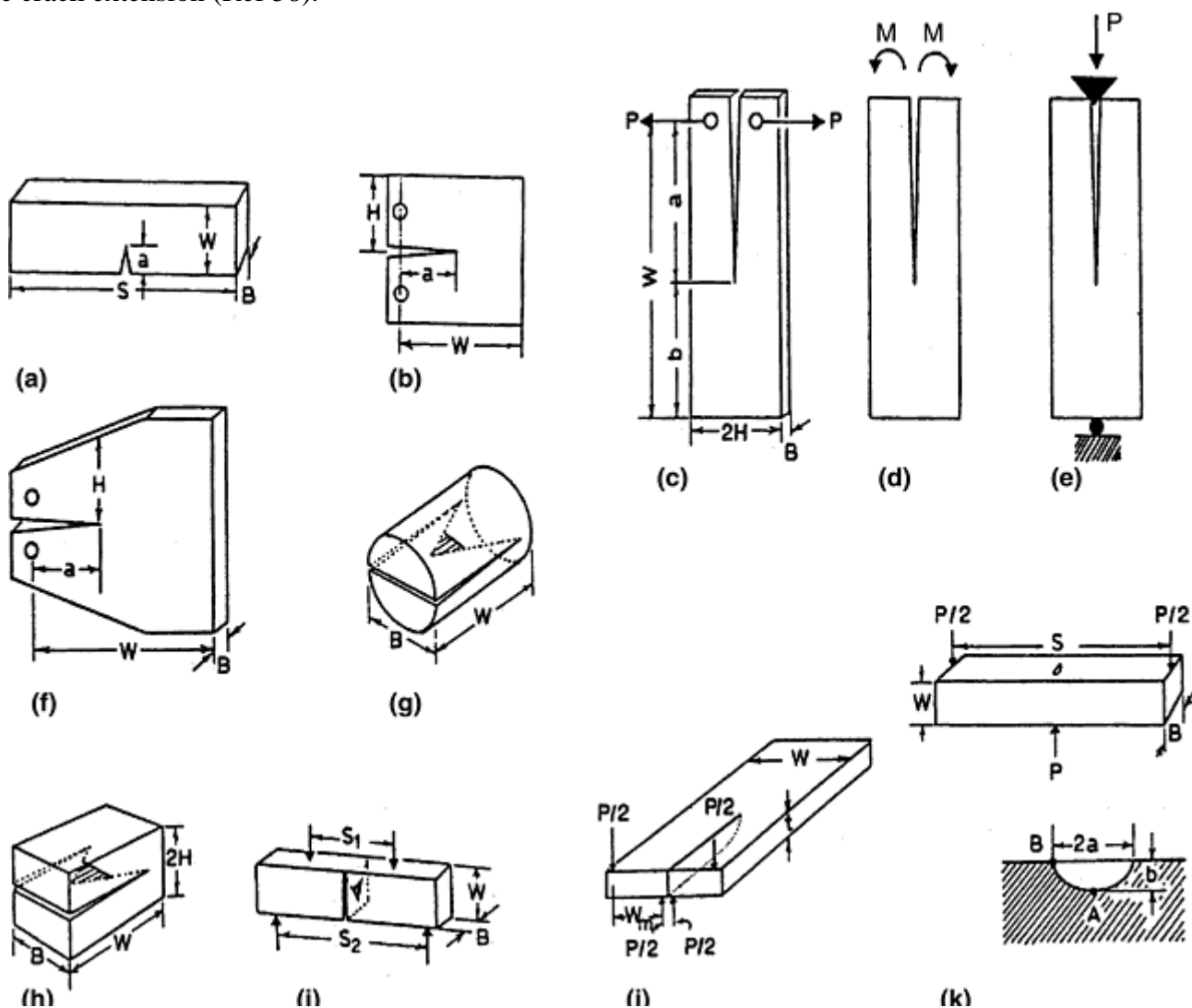


Fig. 7 Fracture toughness specimens. (a) Single edge notch bending (SENB). (b) Compact tension (CT) or wedge open loaded (WOL). (c) Double cantilever beam (DCB) tensile loading. (d) DCB constant bending moment loading. (e) DCB wedge loading. (f) Tapered DCB. (g) Chevron notch short rod. (h) Chevron notch short bar. (i) Chevron notch bending. (j) Double torsion (DT). (k) Three-point bending with controlled surface flaw (CSF). P , load. Adapted from Ref 58

One method of producing a sharp starter crack in a SENB specimen involves using a hardness indenter to introduce a surface flaw and forcing the surface flaw to propagate to the outer edges and become a sharp edge crack. This can be done by loading the indented specimen in compression between two rigid plates. One of the plates has a single groove, and the indentation crack is positioned over the groove. During the compressive loading, the surface flaw is subjected to tensile opening stresses due to the groove, while the bulk of the material is in compression. This tension allows the crack to grow to become an edge crack, while the compression prevents the crack from propagating in an unstable manner through the specimen (Ref 59).

SENB specimens have been used to measure the fracture toughness of a yttria-partially stabilized zirconia (Y-PSZ) ceramic at ambient and elevated temperatures (Ref 59). The point of this work was to demonstrate the use of a new technique of controlling the fracture test in such a way as to promote stable crack growth so that the R -curve behavior of the ceramic could be measured. Crack mouth opening displacement (CMOD) was monitored using a laser extensometer, and the CMOD signal was used in the control of the servohydraulic testing machine in real time. The results of this type of control were positive, and stable crack growth was achieved (Ref 59).

The SENB method has also been improved by a scheme that employs both a method to provide for stable crack growth and better real-time computer-aided data acquisition (Ref 60). The crack growth stability was augmented by adjusting the stiffness of the test frame in such a way as to promote stable crack growth. The test machine stiffness, or compliance, was adjusted by placing a “parallel elastic element” (PEL) supporting structure between the crosshead and the top of the three-point bend loading fixture (Fig. 8). The optimum compliance for stable crack growth was determined by theoretical analysis and experimentation. During testing, the compliance of the specimen and the test frame were continuously monitored in real time through the use of a computer. The real-time load and displacement data from various points in the test system, as presented in Fig. 8. After the optimum PEL compliance was determined, and stable crack growth was achieved, the R -curves of the test materials were measured. The real-time load and displacement (and, therefore, compliance) monitoring, along with compliance versus crack length calibrations and the stress intensity calibrations, allowed the crack length, crack velocity, and stress intensity level to be calculated in real time during the test (Ref 60).

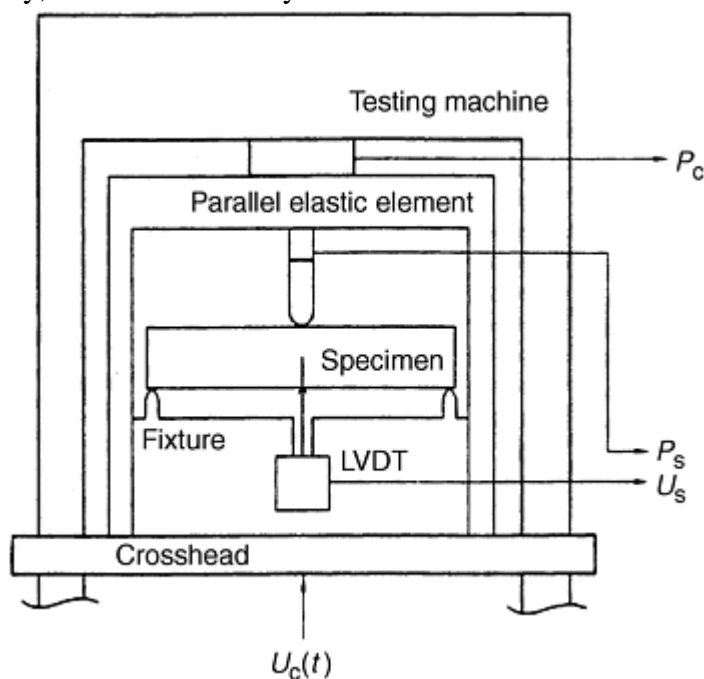


Fig. 8 Schematic of the compliance-controlled three-point bending test with a parallel elastic element (PEL). Adapted from Ref 60

Compact Tension (CT). The CT sample is a common specimen in fracture mechanics tests. It is loaded in tension, but the primary stress is due to bending because the load line is offset from the crack front (Fig. 7b). Relatively stable crack propagation is possible with the CT specimen if a stiff testing machine is used. Also, a variant of the CT can be used in a wedge-opening mode to increase the stable crack growth capability (Ref 49). The stable crack growth capability allows for the generation of R -curves using the CT specimen (Ref 61). The CT specimen is complicated to machine in ceramic materials, and precracking the can be difficult (Ref 58). In addition to R -curve measurements of monolithic ceramics (Ref 61), R -curves have been measured in CMCs using the CT specimen. CT specimens have been employed to generate R -curves for CMCs in an attempt to analyze the crack-face fiber-bridging stress field (the stress field in the wake of the crack that is due to fiber bridging). The crack-face fiber-bridging stress is evaluated by comparing the experimentally measured compliance versus crack length, which includes the contribution of the fiber bridging, to the compliance versus crack length data calculated from the elastic properties of the CMC, assuming no fiber bridges are present (Ref 62).

The J -parameter toughness has also been measured using a CT specimen (Ref 63). A J -based testing technique has been developed for CMCs using the CT specimen geometry. The concept of the J -parameter is used to determine the contribution of the process zone (the contribution of, for instance, fiber bridging and crack branching, analogous to the plastic zone in metals) to the toughness of the CMC. The J -parameter contribution of the process zone is determined using Eq 12 (Ref 63):

$$J_{\infty} + J_b + J_{\text{tip}} = 0 \quad (\text{Eq 11})$$

where J_{∞} is the far field J , J_b is the process zone J (analogous to J_{plastic}), and J_{tip} is the crack tip J . Also, it is assumed that elastic action takes place at the crack tip, so J_{tip} can be calculated from K_{tip} using Eq 9. The value of J_{∞} was experimentally calculated from measurements using CT specimens with two different crack lengths, a_1 and a_2 . The value J_{∞} is the far-field J , as the crack grows from a_1 to a_2 . Therefore, J_b was calculated from Eq 12 (Ref 63).

The J -parameter toughness has also been measured with CT specimens in a study conducted to compare the toughness values of woven fabric-reinforced CMCs with different interphases (Ref 64). The value of J , calculated from the experimental load-displacement curves at the point of maximum load, corresponds to macrocrack initiation in the process zone (Ref 64).

Double Cantilever Beam (DCB) Testing. The DCB specimen looks like a long CT specimen. It can be loaded in three different configurations: direct tension, constant bending moment, and wedge opening. The tensile-loaded DCB is very similar to the CT in all respects (Fig. 7c), but the DCB geometry is better than the CT for growing stable cracks. The tapered DCB, shown in Fig. 7(f), provides a constant K_I level with crack growth. Another DCB variant that provides a constant K_I level with crack growth is the moment-loaded DCB (Fig. 7d). Unfortunately, the fixturing that applies the moment to the arms of the DCB can be difficult to deal with. The final DCB variant is the wedge-loaded DCB (Fig. 7e). The wedge loading allows the specimen to be tested in simple compression. The wedge-loaded DCB specimen was first used in ASTM method E 561. All the DCB variants may need side grooves to keep the crack moving down the center of the specimen. The grooves complicate the K -calibration, and machining damage in the groove can affect the crack extension (Ref 58).

Specimens very similar to the constant bending moment DCB, called the Browne/Chandler test specimen, have been employed in the determination of R -curves for monolithic ceramics (Ref 65). The Browne/Chandler specimen geometry, shown in Fig. 9, applies loads to the outside corners of a specimen, supported by a stiff solid base, that has a rectangular cross section and a vertical edge crack. This loading induces a bending moment around the center of the specimen, which causes the crack to open and extend. If the applied load were held constant, the stress intensity at the crack tip would decrease as the crack grew. Therefore, the load must increase in order for crack growth to continue, which prevents unstable fracture. Also, crack-guiding side grooves are not necessary because the compressive stress parallel to the crack keeps the crack growing down the center of the specimen. Unfortunately, the Browne/Chandler test geometry does not lend itself to an analytical solution of K -calibrations for all crack lengths. As a result, stress intensities have to be estimated using numerical methods at both very short and very long crack lengths (Ref 65).

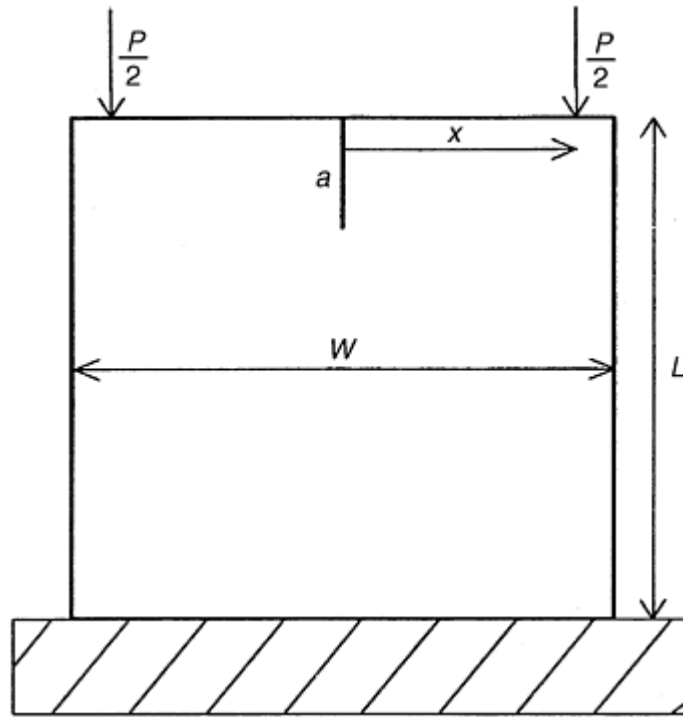


Fig. 9 Schematic sketch of the Browne/Chandler test geometry. Adapted from Ref 65

Chevron Notch Methods (CHV). The chevron notch is used in three specimens (Ref 58, 66). There is a short rod CHV (Fig. 7g), a short rectangular bar CHV (Fig. 7h), and a bend bar with a rectangular cross section and a chevron notch (Fig. 7i). The chevron notch geometry, due to the increase in the width of the crack surface during crack extension, forces rising *R*-curve behavior in ideally brittle materials. This means that after crack initiation, the crack front is stable and is always ideally sharp. Stable crack growth is not always found in practice due to the fact that excess stored energy in the specimen can overcome the geometrical tendency to force rising *R*-curve behavior. In these cases, the excess stored energy can cause catastrophic failure in the specimen. As a result, a stiff specimen geometry and test machine are important (Ref 58, 66).

One of the main advantages of the chevron notch geometry is the fact that it is possible to calculate the fracture toughness based on the maximum load and the specimen dimensions alone for ideally brittle materials. Due to the shape of the growing crack, the geometry factor, *Y*, goes through a minimum as crack growth occurs. The minimum in the geometry factor corresponds to the maximum load in the test. This unique fact allows the fracture toughness to be calculated without knowledge of the crack length (Ref 58). However, calculation of fracture toughness from the maximum load and specimen dimensions does not work for materials that exhibit natural rising *R*-curve behavior. In these cases, the minimum in the geometry factor versus crack length does not correspond with the maximum load, and the crack length must be known to calculate the fracture toughness (Ref 58).

The chevron notch specimen has become almost a standard for measuring fracture toughness in ceramic materials (Ref 58, 67, 68, and 69). In fact, the only ASTM standard test method for determining the fracture toughness of ceramics, B 771-87, uses the short rod and short bar chevron notch specimen (Ref 69). In addition, chevron notch samples are used in ASTM PS70, "Provisional Test Method For Determining The Fracture Toughness of Advanced Ceramics at Ambient Temperatures" (Ref 66). Also, researchers with new fracture tests use chevron notch results to benchmark the results of the new tests (Ref 61, 70, and 71).

Double Torsion (DT). The DT specimen, shown in Fig. 7(j), is a flat plate with a longitudinal through crack that is loaded in torsion. The torsional loading applies a bending moment that opens the crack on the tensile surface and closes the crack on the compressive surface. The applied moment causes the K_I level to be constant over a wide range of crack length. It also causes the crack front to be significantly curved between the top and bottom surfaces. This curvature of the crack front opposes the straight-through crack assumptions used in the stress intensity calculation, and causes errors in the toughness calculation (Ref 58).

Indentation Techniques. Indentation fracture toughness techniques utilize a sharp crack introduced in the material by a Knoop or a Vickers indenter. The Knoop indenter causes a single crack, which makes it attractive for use in fracture mechanics methods involving a surface flaw. The Vickers indenter creates two cracks that

are mutually perpendicular to each other. Both indentation methods can produce reproducible surface cracks, but the residual stress field from the indentation is complicated and must be removed or accounted for in the analysis (Ref 58, 72, 73, and 74)

Indentation creates subsurface cracks, due to tensile stress formation, just below the contact point of the indenter. These subsurface cracks are called median cracks. As the indenter is removed, the median cracks become unstable and grow to the indented surface. The resulting crack is called a radial crack. In some high-toughness brittle systems, small radial surface cracks can form prior to subsurface median crack formation. These shallow surface cracks are called Palmqvist cracks. Schematic drawings of median, radial, and Palmqvist cracks are shown in Fig. 10 (Ref 58, 72, 73, 74).

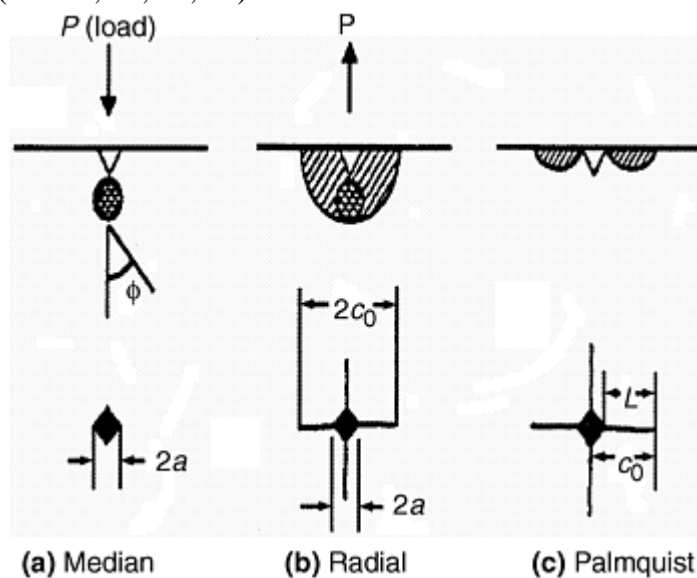


Fig. 10 Schematic diagram illustrating types of crack systems formed around an indentation. Adapted from Ref 42, 71

There are three indentation-induced crack techniques for measuring fracture toughness in ceramics: the controlled surface flaw (CSF) technique, the indentation microfracture (IM) technique, and the indentation strength in bending (ISB) technique. The CSF method can provide a quantitative measure of the fracture toughness because the stress intensity around the surface flaw is well known, but the IM and ISB provide only estimates based on empirical expressions (Ref 58, 72, 73, and 74).

The CSF method involves testing a bending specimen with an elliptical surface crack induced by a Knoop indenter (see Fig. 7k). The Knoop indenter is used to create a subsurface median crack. Then, the surface is carefully polished to remove the indent and the associated residual stresses. The polishing also reveals the median crack to the surface, and an elliptical surface flaw with no residual stress is the result. When the specimen is tested, the surface flaw causes the initiation of fracture, and K_{Ic} can be calculated based on the applied loads and the crack size (Ref 58, 73).

The ISB is similar to the CSF technique (Ref 73). The ISB approach uses the Vickers indenter to induce median-radial cracks on the tensile surface of a bending specimen. Through manipulation of the K -calibrations for the crack system, which account for both the applied and residual stresses, it is possible to develop an expression that relates the fracture stress in bending and the indentation load to the fracture toughness. Therefore, the ISB method involves calculating the fracture toughness based on the indentation load and the experimental fracture stress from a bending test. This method has the advantage of being relatively simple to conduct, and there is no need to measure crack size. The disadvantage comes from the use of empirical factors in the manipulation of the K -calibrations that are used to develop the expression relating the indentation load and fracture stress to the fracture toughness. This causes the fracture toughness measured by this method to be only an estimate (Ref 58, 73).

Another fracture toughness specimen that uses a Vickers hardness indenter to introduce sharp cracks into a ceramic material is the miniature disk bend test (MDBT) specimen (Ref 70, 75). These specimens are 3 mm (0.1 in.) in diameter and range in thickness from 200 to 700 μm . Vickers indentation cracks are introduced into the center of the tensile side of the specimen. The disk specimen is loaded in a ring-on-ring bending mode, schematically shown in Fig. 11. The MDBT is similar to the ISB test. In both experiments, the fracture stress

and indentation load are related to the fracture toughness. Therefore, the fracture toughness is calculated from the indentation load and the fracture stress from the MDBT. The advantages of the MDBT are the small amount of material that is needed to conduct the test and the fact that the crack length need not be measured (Ref 70, 75).

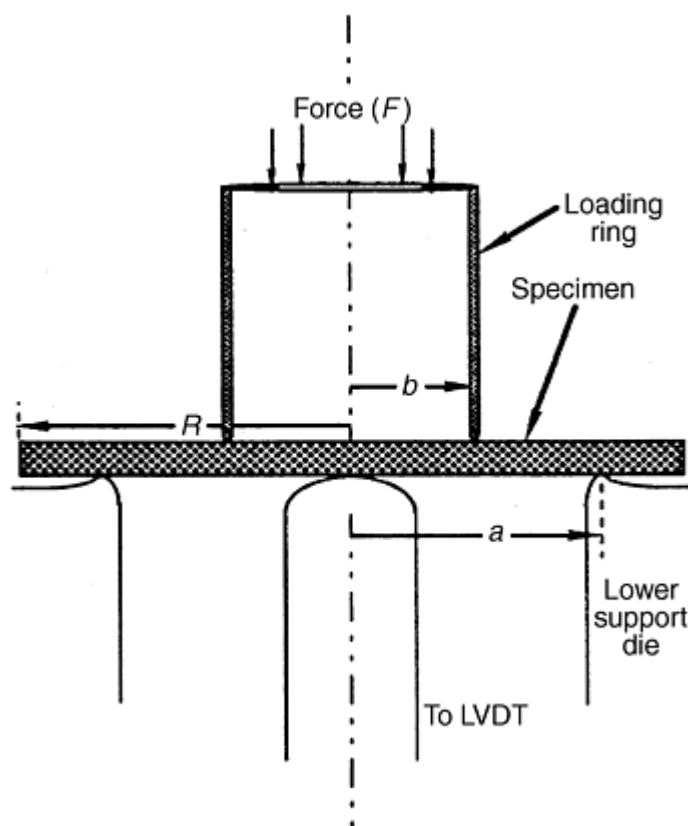


Fig. 11 Schematic sketch of the miniature disk bend test (MDBT) geometry. Adapted from Ref 70

The indentation microfracture (IM) method introduces cracks into the surface of a sample with a Vickers indenter and uses the length of those cracks to estimate the fracture toughness (Ref 58, 72). This method is very attractive because it is so easy to conduct the test. As a result, many good empirical toughness relations have been generated for specific crack geometries. It is important in this method to ensure that median-radial cracks are analyzed rather than Palmqvist cracks. The shallow Palmqvist cracks are hard to measure, and, consequently, significant error and scatter are introduced in the data (Ref 58, 71).

Typical Fracture Toughness Properties of Ceramics and CMCs. The critical fracture toughness, K_{Ic} , of monolithic ceramics is low, on the order of 1 to 4 $\text{MPa}\sqrt{m}$ (0.9 to 3.5 $\text{ksi}\sqrt{\text{in.}}$), while CMCs can have toughness values near 20 $\text{MPa}\sqrt{m}$ (18 $\text{ksi}\sqrt{\text{in.}}$). The K_{Ic} values for several ceramics and a few CMCs are shown in Table 1. Where possible, the values of K_{Ic} measured by different methods on the same material are included for comparison. From the table, it is evident that the many methods agree well.

Table 1 Typical ceramic and CMC properties

Material	K_{Ic} ($\text{MPa}\sqrt{m}$)	Method	Reference
Glass ceramic pyroceram (Corning)	2.7	CSF	72
	2.5	DCB	72
	2.9	ISB	73
	2.4	CMDCB	50
	2.2	MDBT	70
Al_2O_3 AD999 (Coors)	2.6	CSF	72
	3.9	DCB	72
	3.1	ISB	73

	4	CSF	50
Al ₂ O ₃ AD90 (Coors)	2.1	CSF	72
	2.9	DCB	72
	2.8	ISB	73
Al ₂ O ₃ sapphire (Coors)	1.6	CSF	72
	2.1	DCB	72
	3	ISB	73
Si ₃ N ₄ NC132 (Norton)	4	CSF	72
	4	DCB	72
	5	ISB	73
	4.6	CSF	50
Si ₃ N ₄ NC350 (Norton)	2.1	CSF	72
	2	DCB	72
	2.1	ISB	75
Si ₃ N ₄ NBD200 (Norton)	5.4	CSF	50
Si ₃ N ₄ NT154 (Norton)	5.8	CSF	50
Si ₃ N ₄	5	MDBT	70
SiC NC203 (Norton)	3.5	CSF	72
	4	DCB	72
	4.5	ISB	73
α -SiC (Carborundum)	3	CN, CSF	50
	3.3	SENB	68
	2.7	CN	68
NiAl polycrystalline	1.75	MDBT	75
Y-PSZ	3.6	SENB	59
SiC/TiB ₂ composite	6.8	SENB	68
	4.1	CN	68

CMDCB, constant moment double cantilever beam; CN, chevron notch; CSF, controlled surface flaw; DCB, double cantilever beam; ISB, indentation strength in bending; MDBT, miniature disk bend test; SENB, single edge notch bend

Ceramics can exhibit either flat or rising *R*-curve behavior, depending on processing-derived microstructure (Ref 67). Figure 12 shows *R*-curves for three different silicon nitride (Si₃N₄) materials, A, B, and C. The *R*-curves were measured using short bar chevron notch methods. Material A is a hot pressed commercial Si₃N₄ (SN-84H by NGK Technical Ceramics) with low fracture toughness; it results in flat *R*-curve behavior. Materials B and C, which have relatively higher fracture toughness, are monolithic Si₃N₄ (AS700 by Allied Signal Inc.) prepared by gas pressure sintering green billets, which were formed by cold isostatic pressing. These two Si₃N₄ materials exhibit rising *R*-curve behavior (Ref 67).

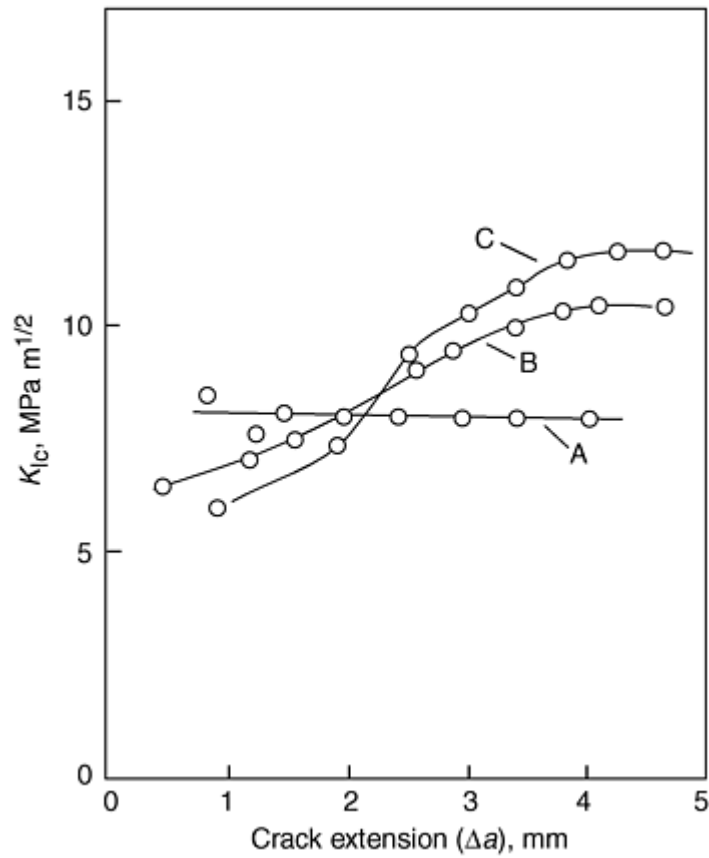


Fig. 12 *R*-curves of three Si_3N_4 ceramic materials measured by the short rod chevron notch technique. Adapted from Ref 67

An *R*-curve from short bar chevron notch tests on a SiC-whisker-reinforced alumina matrix composite is presented in Fig. 13 (Ref 67). The whisker-reinforced alumina composite also exhibits rising *R*-curve behavior.

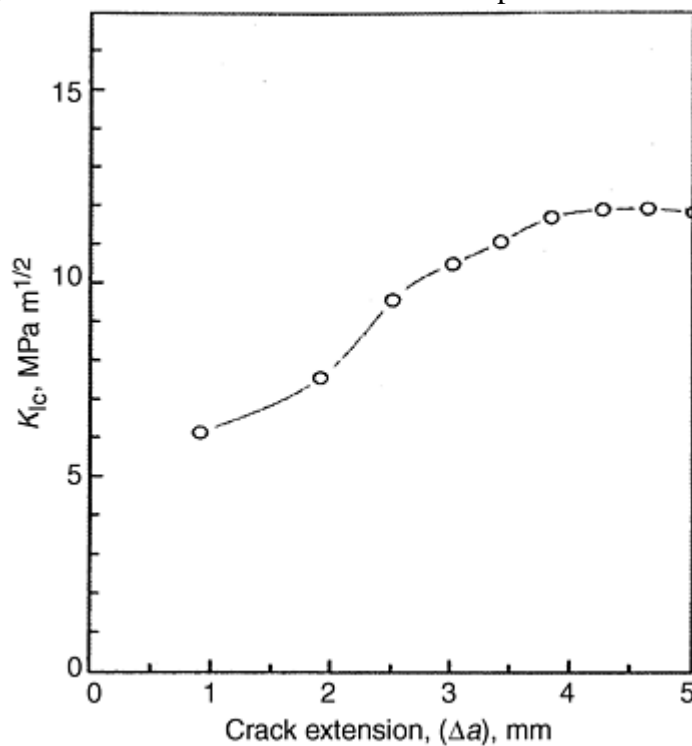


Fig. 13 Rising *R*-curve of a SiC whisker reinforced alumina ceramic matrix composite (CMC), measured by the double cantilever beam technique. Adapted from Ref 67

The rising R -curve behavior of an isostatically pressed and sintered ceria-partially stabilized zirconia (Ce-PSZ) ceramic is given in Fig. 14 (Ref 61). This R -curve was measured using a crack line wedge-loaded (CLWL) technique, which is a wedge-loaded variant of the compact tension specimen.

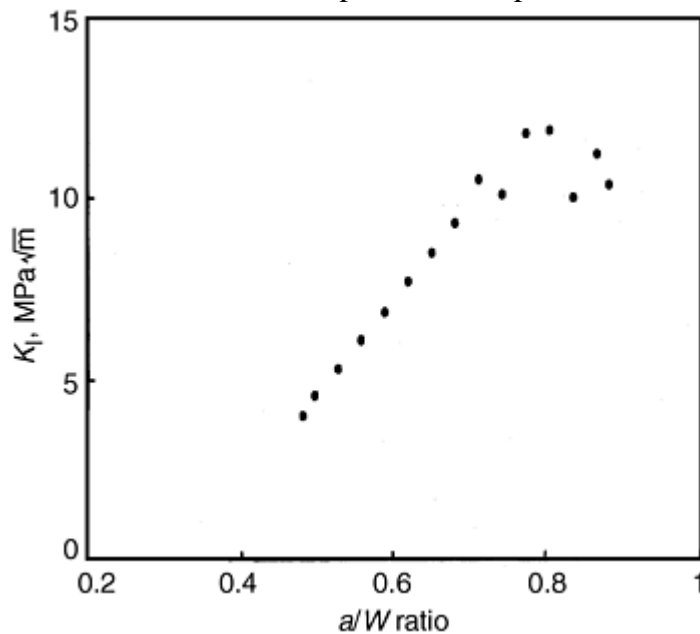


Fig. 14 Rising R -curve of a Ce-PSZ ceramic measured by the crack line wedge loaded technique. a and w refer to dimensions defined in Fig. 7(c). Adapted from Ref 61

Table 2 presents critical toughness expressed in terms of the J -integral, J_c , for short Nicalon fiber-reinforced foam glass matrix composites (Ref 63). Values for J_c range from 3.5 to 241.8 N/m, depending on fiber length and fiber volume fraction. The interface condition also strongly affects the value of J_c (Ref 64). Table 3 shows a wide range of J_c values for continuous woven Nicalon fiber fabric-reinforced SiC matrix composites produced by chemical vapor infiltration. In Table 3, the interface condition is given an arbitrary designation of numbers from one to ten. The interfaces of these composites were modified by applying various multilayered carbon and SiC fiber coatings, the details of which are can be found in Ref 64. Table 3 clearly shows that the interface condition causes the value of J_c to vary over a wide range from 11800 to 28520 N/m. Also notice that the values of J_c for the materials of Tables 2 and 3 are quite different. This fact indicates that composite constituent materials, volume fractions, and interfacial properties all have a very pronounced effect on the toughness of CMCs.

Table 2 J_c values for short Nicalon fiber reinforced foam glass matrix composites

Fiber length, mm	Fiber volume fraction, %	J_c , N/m
3	1.0	61.6
6	1.0	147.5
13	0.1	3.5
13	0.2	14.8
13	0.8	210.0
13	1.0	241.8

Source: Ref 63

Table 3 J_c values for continuous Nicalon fiber fabric reinforced SiC composites

Interface condition	J_c , N/m
1	11,800
2	19,200
3	19,400

4	24,700
5	10,700
6	18,900
7	15,650
8	19,340
9	14,400
10	28,520

Source: Ref 64

References cited in this section

42. C.B. Thomas, "Processing, Mechanical Behavior, and Microstructural Characterization of Liquid Phase Sintered Intermetallic-Bonded Ceramic Composites," M.S. Thesis, The University of Tennessee, Knoxville, 1996
49. M. Sakai and H. Ichikawa, Work of Fracture of Brittle Materials with Microcracking and Crack Bridging, *Int. J. Fract.*, Vol 55 (No. 1), 1992, p 65–79
50. J.B. Quinn and G.D. Quinn, "Indentation Brittleness of Ceramics: A Fresh Approach," *J. Mater. Sci.*, Vol 32 (No. 16), 1997, p 4331–4346
58. M. Sakai and R.C. Bradt, Fracture Toughness Testing of Brittle Materials, *Int. Mater. Rev.*, Vol 38 (No. 2), 1993, p 53–78
59. J.Y. Pastor, J. Llorca, J. Planas, and M. Elices, Stable Crack-Growth in Ceramics at Ambient and Elevated-Temperatures, *J. Eng. Mater. Technol. (Trans. ASME)*, Vol 115 (No. 3), 1993, 281–285
60. V.G. Borovik, V.M. Chushko, and S.P. Kovalev, Computer-Aided, Single-Specimen Controlled Bending Test for Fracture-Kinetics Measurements in Ceramics, *J. Am. Ceram. Soc.*, Vol 78 (No. 5), 1995, p 1305–1312
61. J.C. Descamps, A. Poulet, P. Descamps, and F. Cambier, A Novel Method to Determine the R-Curve Behavior of Ceramic Materials—Application to a Ceria-Partially Stabilized Zirconia, *J. Eur. Ceram. Soc.*, Vol 12 (No. 1), 1993, p 71–77
62. V. Kostopoulos and Y.P. Markopoulos, On the Fracture Toughness of Ceramic Matrix Composites, *Mater. Sci. Eng. A*, Vol 250 (No. 2), 1998, p 303–312
63. T. Hashida, V.C. Li, and H. Takahashi, New Development of the J-Based Fracture Testing Technique for Ceramic-Matrix Composites, *J. Am. Ceram. Soc.*, Vol 77 (No. 6), 1994, p 1553–1561
64. C. Droillard and J. Lamon, Fracture Toughness of 2-D Woven SiC/SiC CVI-Composites with Multilayered Interphases, *J. Am. Ceram. Soc.*, Vol 79 (No. 4), 1996, p 849–858
65. H.W. Chandler, R.J. Henderson, M.N. Al Zubaidy, M. Saribiyik, and A. Muhaidi, A Fracture Test for Brittle Materials, *J. Eur. Ceram. Soc.*, Vol 17 (No. 6), 1997, p 759–763
66. "Provisional Test Method For Determining The Fracture Toughness Of Advanced Ceramics At Ambient Temperatures," ASTM PS70, *Annual Book of Standards*, Vol 15.01, American Society for Testing and Materials, 1996
67. D.J. Lee, Simple Method to Measure the Crack Resistance of Ceramic Materials, *J. Mater. Sci.*, Vol 30 (No. 8), 1995, p 4617–4622

68. P.A. Withey, R.L. Brett, and P. Bowen, Use of Chevron Notches for Fracture-Toughness Determination in Brittle Solids, *Mater. Sci. Technol.*, Vol 8 (No. 9), 1992, p 805–809
69. “Standard Test Method for Short Rod Fracture Toughness of Cemented Carbides,” ASTM Standard B 771-87, *ASTM Book of Standards*, Vol 02.05, American Society for Testing and Materials, 1995
70. J.M. Zhang and A.J. Ardell, Measurement of the Fracture-Toughness of Ceramic Materials Using a Miniaturized Disk-Bend Test, *J. Am. Ceram. Soc.*, Vol 76 (No. 5), 1993, p 1340–1344
71. S. Danchaivijit, D.K. Shetty, and J. Eldridge, Critical Stresses for Extension of Filament-Bridged Matrix Cracks in Ceramic-Matrix Composites—An Assessment with a Model Composite with Tailored Interfaces, *J. Am. Ceram. Soc.*, Vol 78 (No. 5), 1995, p 1139–1146
72. G.R. Anstis, P. Chantikul, B.R. Lawn, and D.B. Marshall, A Critical Evaluation of Indentation Techniques for Measuring Fracture Toughness: I, Direct Crack Measurements, *J. Am. Ceram. Soc.*, Vol 64 (No. 9), 1981, p 533–538
73. P. Chantikul, G.R. Anstis, B.R. Lawn, and D.B. Marshall, A Critical Evaluation of Indentation Techniques for Measuring Fracture Toughness: II, Strength Method, *J. Am. Ceram. Soc.*, Vol 64 (No. 9), 1981, p 539–543
74. B.R. Lawn, A.G. Evans, and D.B. Marshall, Elastic/Plastic Indentation Damage in Ceramics: The Median Radial Crack System, *J. Am. Ceram. Soc.*, Vol 63 (No. 9/10), 1980, p 574–581
75. S.J. Eck and A.J. Ardell, Fracture Toughness of Polycrystalline NiAl from Finite-Element Analysis of Miniaturized Disk-Bend Test Results, *Metall. Mater. Trans. A*, Vol 28 (No. 4), 1997, p 991–996

Fracture Toughness of Ceramics and Ceramic Matrix Composites

J.H. Miller, Oak Ridge National Laboratory P.K. Liaw, The University of Tennessee, Knoxville

Summary

As described in this article (and the article “Fracture Resistance Testing of Brittle Solids” in this Volume), several test methods are used for the determination of the fracture behavior of ceramics. Many of these methods include several variations of their own, suggesting the need for more standardization of test methods.

From the preceding discussions, fracture toughness determination of monolithic ceramics appears to be mature. The fact that most monolithic ceramics behave in a linear-elastic manner has allowed the direct transition of theory from LEFM developed for metals to use on ceramics. Current fracture toughness research on monolithic ceramics is centered on refining test methods, data acquisition techniques, and theoretical and numerical analyses (Ref 48, 60, 67, and 70). Methods have been developed to overcome the difficulties in initiating sharp starter cracks (Ref 58, 59), providing stable crack growth (Ref 61, 65, and 67), and minimizing the amount of expensive test materials required for fracture testing (Ref 59, 70).

Fracture toughness evaluation for CMCs is much less developed than for monolithic ceramics. The elastic-plastic-like failure behavior of CMCs makes EPFM look like an attractive method for evaluating their fracture behavior. Some, but not much, research based on EPFM methods has been used in attempts to quantify the contribution of plastic-like mechanisms in CMCs (Ref 63, 64). Unfortunately, the low level of understanding of the very complicated toughening mechanisms of microcracking, fiber bridging, and crack branching precludes a direct transition of the EPFM theory that exists for metals to CMCs.

The permanent or plastic deformation that EPFM was developed to handle in metals is due to the dislocation creation, movement, and slip. These metallic plasticity concepts were well understood prior to the development of EPFM, and were, therefore, available to influence the development of EPFM. In contrast, the plastic-like mechanisms in CMCs are microcracking, crack bridging, and crack branching. A significant amount of work still needs to be done before these complicated mechanisms are well understood. As a result, the development of EPFM methods for CMCs is, and will continue to be, slow.

The bulk of the current research on CMC behavior centers on increasing the understanding of the CMC toughening mechanisms. Researchers continue to work on understanding the fracture mechanisms in CMCs at many levels (Ref 71, 76, 77, 78, and 79). Much research is still being done to evaluate the forces and stresses involved in the fiber bridging that occurs in the wake of cracks (Ref 71, 76, 77, 78, and 79). The ultimate goal of the research is to develop theories that will connect the results of LEFM and EPFM tests to the complex mechanisms of microcracking, crack bridging, and crack branching. As this goal is achieved, mature fracture mechanics technology will be realized for CMCs.

References cited in this section

48. A. Ishida, M. Miyayama, and H. Yanagida, Prediction of Fracture and Detection of Fatigue in Ceramic Composites from Electrical-Resistivity Measurements, *J. Am. Ceram. Soc.*, Vol 77 (No. 4), 1994, p 1057–1061
58. M. Sakai and R.C. Bradt, Fracture Toughness Testing of Brittle Materials, *Int. Mater. Rev.*, Vol 38 (No. 2), 1993, p 53–78
59. J.Y. Pastor, J. Llorca, J. Planas, and M. Elices, Stable Crack-Growth in Ceramics at Ambient and Elevated-Temperatures, *J. Eng. Mater. Technol. (Trans. ASME)*, Vol 115 (No. 3), 1993, 281–285
60. V.G. Borovik, V.M. Chushko, and S.P. Kovalev, Computer-Aided, Single-Specimen Controlled Bending Test for Fracture-Kinetics Measurements in Ceramics, *J. Am. Ceram. Soc.*, Vol 78 (No. 5), 1995, p 1305–1312
61. J.C. Descamps, A. Poulet, P. Descamps, and F. Cambier, A Novel Method to Determine the R-Curve Behavior of Ceramic Materials—Application to a Ceria-Partially Stabilized Zirconia, *J. Eur. Ceram. Soc.*, Vol 12 (No. 1), 1993, p 71–77
63. T. Hashida, V.C. Li, and H. Takahashi, New Development of the J-Based Fracture Testing Technique for Ceramic-Matrix Composites, *J. Am. Ceram. Soc.*, Vol 77 (No. 6), 1994, p 1553–1561
64. C. Droillard and J. Lamon, Fracture Toughness of 2-D Woven SiC/SiC CVI-Composites with Multilayered Interphases, *J. Am. Ceram. Soc.*, Vol 79 (No. 4), 1996, p 849–858
65. H.W. Chandler, R.J. Henderson, M.N. Al Zubaidy, M. Saribiyik, and A. Muhaidi, A Fracture Test for Brittle Materials, *J. Eur. Ceram. Soc.*, Vol 17 (No. 6), 1997, p 759–763
67. D.J. Lee, Simple Method to Measure the Crack Resistance of Ceramic Materials, *J. Mater. Sci.*, Vol 30 (No. 8), 1995, p 4617–4622
70. J.M. Zhang and A.J. Ardell, Measurement of the Fracture-Toughness of Ceramic Materials Using a Miniaturized Disk-Bend Test, *J. Am. Ceram. Soc.*, Vol 76 (No. 5), 1993, p 1340–1344
71. S. Danchaivijit, D.K. Shetty, and J. Eldridge, Critical Stresses for Extension of Filament-Bridged Matrix Cracks in Ceramic-Matrix Composites—An Assessment with a Model Composite with Tailored Interfaces, *J. Am. Ceram. Soc.*, Vol 78 (No. 5), 1995, p 1139–1146

76. P. Brenet, F. Conchin, G. Fantozzi, P. Reynaud, D. Rouby, and C. Tallaron, Direct Measurement of Crack-Bridging Traction: A New Approach to the Fracture Behavior of Ceramic/Ceramic Composites, *Compos. Sci. Technol.*, Vol 56 (No. 7), 1996, p 817–823
 77. C.H. Hsueh, Crack-Wake Interfacial Debonding Criteria for Fiber-Reinforced Ceramic Composites, *Acta Metall.*, Vol 44 (No. 6), 1996, p 2211–2216
 78. D.R. Mumm and K.T. Faber, Interfacial Debonding and Sliding in Brittle-Matrix Composites Measured Using an Improved Fiber Pullout Technique, *Acta Metall.*, Vol 43 (No. 3), 1995, p 1259–1270
 79. A. Domnanovich, H. Peterlik, and K. Kromp, Determination of Interface Parameters for Carbon/Carbon Composites by the Fibre-Bundle Pull-Out Test, *Compos. Sci. Technol.*, Vol 56, 1996, p 1017–1029
-

Fracture Toughness of Ceramics and Ceramic Matrix Composites

J.H. Miller, Oak Ridge National Laboratory P.K. Liaw, The University of Tennessee, Knoxville

Acknowledgments

Professor P.K. Liaw is kindly and greatly supported by the NSF Division of Design, Manufacture, and Industrial Innovation, under Grant No. DMI-9724476, and the Combined Research-Curriculum Development (CRCD) Program under EEC-9527527 to the University of Tennessee, Knoxville (UTK), with Dr. Delcie R. Durham and Ms. Mary Poats as program managers, respectively. We would like to acknowledge the financial support of the Office of Research and the Center for Materials Processing at UTK. We would also like to express our appreciation to Dr. John Landes, Dr. Allen Yu, and Dr. Ray Buchanan, all from UTK, for their comments and help during the preparation of this article.

This research was performed in cooperation with the UTK under contract 11X-SN191V with the Lockheed-Martin Energy Research Corporation and is sponsored by the US Department of Energy, Assistant Secretary for Conservation and Renewable Energy, Office of Industrial Technology, Industrial Energy Division, under contract DE-AC05-84OR21400 with the Lockheed-Martin Energy Research Corporation.

Fracture Toughness of Ceramics and Ceramic Matrix Composites

J.H. Miller, Oak Ridge National Laboratory P.K. Liaw, The University of Tennessee, Knoxville

References

1. T.M. Besmann, B.W. Sheldon, R.A. Lowden, and D.P. Stinton, Vapor Phase Fabrication and Properties of Continuous-Filament Ceramic Composites, *Science*, Vol 253, 1991, p 1104
2. M. Bouquet, J.M. Bribis, and J.M. Quenisset, Toughness Assessment of Ceramic Matrix Composites, *Compos. Sci. Technol.*, Vol 37, 1990, p 223–248
3. C.H. Hsueh, P.F. Becher, and P. Angelini, Effects of Interfacial Films on Thermal Stresses in Whisker-Reinforced Ceramics, *J. Am. Ceram. Soc.*, Vol 71 (No. 11), 1988, p 929–933

4. D.P. Stinton, A.J. Caputo, and R.A. Lowden, Synthesis of Fiber-Reinforced SiC Composites by Chemical Vapor Infiltration, *Am. Ceram. Soc. Bull.*, Vol 65 (No. 2), 1986, p 347–350
5. D.P. Stinton, W.J. Lackey, R.J. Lauf, and T.M. Besmann, Fabrication of Ceramic-Ceramic Composites by Chemical Vapor Deposition, *Ceram. Eng. Sci. Proc.*, Vol 5, 1984, p 668–676
6. J.H. Miller, R.A. Lowden, and P.K. Liaw, Fiber Coatings and the Fracture Behavior of a Continuous Fiber Ceramic Composite, *Symposium on Ceramic Matrix Composites—Advanced High-Temperature Structural Materials*, R.A. Lowden, M.K. Ferber, J.R. Hellmann, K.K. Chawla, and S.G. DiPietro, Ed., Vol 365, Materials Research Society, 1995, p 403–410
7. M.A. Borst, W.Y. Lee, Y. Zhang, and P.K. Liaw, Preparation and Characterization of Chemically Vapor Deposited ZrO₂ Coating on Nickel and Ceramic Fiber Substrates, *J. Am. Ceram. Soc.*, Vol 80 (No. 6), 1997, p 1591–1594
8. N. Miriyala, P.K. Liaw, C.J. McHargue, L.L. Snead, and J.A. Morrison, The Monotonic and Fatigue Behavior of a Nicalon/Alumina Composite at Ambient and Elevated Temperatures, American Ceramic Society Meeting, *Ceram. Eng. Sci. Proc.*, Vol 18 (No. 3), 1997, p 747–756
9. W. Zhao, P.K. Liaw, and N. Yu, Effects of Lamina Stacking Sequence on the In-Plane Elastic Stress Distribution of a Plain-Weave Nicalon Fiber-Reinforced SiC Laminated Composite with a Lay-Up of [0/30/60], American Ceramic Society Meeting, *Ceram. Eng. Sci. Proc.*, Vol 18 (No. 3), 1997, p 401–408
10. W. Zhao, P.K. Liaw, and D.C. Joy, Microstructural Characterization of a 2-D Woven Nicalon/SiC Ceramic Composite by Scanning Electron Microscopy Line-Scan Technique, American Ceramic Society Meeting, *Ceram. Eng. Sci. Proc.*, Vol 18 (No. 3), 1997, p 295–302
11. J.G. Kim, P.K. Liaw, D.K. Hsu, and D.J. McGuire, Nondestructive Evaluation of Continuous Nicalon Fiber Reinforced SiC Composites, American Ceramic Society Meeting, *Ceram. Eng. Sci. Proc.*, Vol 18 (No. 4), 1997, p 287–296
12. N. Miriyala, P.K. Liaw, C.J. McHargue, and L.L. Snead, The Monotonic and Fatigue Behavior of a Nicalon/Alumina Composite at Ambient and Elevated Temperatures, *Ceram. Eng. Sci. Proc.*, Vol 18 (No. 3), 1997, p 747–756
13. W. Zhao, P.K. Liaw, N. Yu, E.R. Kupp, D.P. Stinton, and T.M. Besmann, Computation of the Lamina Stacking Sequence Effect on the Elastic Moduli of a Plain-Weave Nicalon Fiber Reinforced SiC Laminated Composite with a Lay-Up of [0/30/60], *J. Nucl. Mater.*, Vol 253, 1998, p 10–19
14. N. Miriyala, P.K. Liaw, C.J. McHargue, and L.L. Snead, “The Mechanical Behavior of A Nicalon/SiC Composite at Ambient Temperature and 1000 °C”, *J. Nucl. Mater.*, Vol 253, 1998, p 1–9
15. W.Y. Lee, Y. Zhang, I.G. Wright, B.A. Pint, and P.K. Liaw, Effects of Sulfur Impurity on the Scale Adhesion Behavior of a Desulfurized Ni-Based Superalloy Aluminized by Chemical Vapor Deposition, *Metall. Mater. Trans. A*, Vol 29, 1998, p 833
16. P.K. Liaw, Understanding Fatigue Failure in Structural Materials, *JOM*, Vol 49 (No. 7), 1997, p 42
17. N. Miriyala and P.K. Liaw, CFCC (Continuous-Fiber-Reinforced Ceramic Matrix Composites) Fatigue: A Literature Review, *JOM*, Vol 49 (No. 7), 1997, p 59–66, 82
18. N. Miriyala and P.K. Liaw, Specimen Size Effects on the Flexural Strength of CFCCs, American Ceramic Society Meeting, *Ceram. Eng. Sci. Proc.*, Vol 19, 1998

19. W. Zhao, P.K. Liaw, and N. Yu, Computer-Aided Prediction of the First Matrix Cracking Stress for a Plain-Weave Nicalon/SiC Composite with Lay-Ups of [0/20/60] and [0/40/60], *Ceram. Eng. Sci. Proc.*, Vol 19, 1998, p 3
20. W. Zhao, P.K. Liaw, and N. Yu, Computer-Aided Prediction of the Effective Moduli for a Plain-Weave Nicalon/SiC Composite with Lay-Ups of [0/20/60] and [0/40/60], *Ceram. Eng. Sci. Proc.*, Vol 19, 1998
21. N. Miriyala, P.K. Liaw, C.J. McHargue, A. Selvarathinam, and L.L. Snead, The Effect of Fabric Orientation on the Flexural Behavior of CFCCs: Experiment and Theory, The 100th Annual American Ceramic Society Meeting, 3–6 May 1998 (Cincinnati), in press
22. N. Miriyala, P.K. Liaw, C.J. McHargue, and L.L. Snead, Fatigue Behavior of Continuous Fiber-Reinforced Ceramic-Matrix Composites (CFCCs) at Ambient and Elevated Temperatures, invited paper presented at symposium proceedings in honor of Professor Paul C. Paris, *High Cycle Fatigue of Structural Materials*, W.O. Soboyejo and T.S. Srivatsan, Ed., The Minerals, Metals, and Materials Society, 1997, p 533–552
23. W. Zhao, P.K. Liaw, and N. Yu, The Reliability of Evaluating the Mechanical Performance of Continuous Fiber-Reinforced Ceramic Composites by Flexural Testing, *Int. Conf. on Maintenance and Reliability*, 1997, p 6-1 to 6-15
24. P.K. Liaw, J. Kim, N. Miriyala, D.K. Hsu, N. Yu, D.J. McGuire, and W.A. Simpson, Jr., Nondestructive Evaluation of Woven Fabric Reinforced Ceramic Composites, *Symposium on Nondestructive Evaluation of Ceramics*, C. Schilling, J.N. Gray, R. Gerhardt, and T. Watkins, Ed., Vol 89, 1998, p 121–135
25. M.E. Fine and P.K. Liaw, Commentary on the Paris Equation, invited paper presented at symposium proceedings in honor of Professor Paul C. Paris, *High Cycle Fatigue of Structural Materials, High Cycle Fatigue of Structural Materials*, W.O. Soboyejo and T.S. Srivatsan, Ed., The Minerals, Metals, and Materials Society, 1997, p 25–40
26. W. Zhao, P.K. Liaw, D.C. Joy, and C.R. Brooks, Effects of Oxidation, Porosity and Fabric Stacking Sequence on Flexural Strength of a SiC/SiC Ceramic Composite, *Processing and Properties of Advanced Materials: Modeling, Design and Properties*, B.Q. Li, Ed., The Minerals, Metals, and Materials Society, 1998, p 283–294
27. W. Zhao, P.K. Liaw, and N. Yu, Computer Modeling of the Fabric Stacking Sequence Effects on Mechanical Properties of a Plain-Weave SiC/SiC Ceramic Composite, *Proc. on Processing and Properties of Advanced Materials: Modeling, Design and Properties*, B.Q. Li, Ed., The Minerals, Metals, and Materials Society, 1998, p 149–160
28. J. Kim and P.K. Liaw, The Nondestructive Evaluation of Advanced Ceramics and Ceramic-Matrix Composites, *JOM*, Vol 50 (No. 11), 1998
29. N. Yu and P.K. Liaw, Ceramic-Matrix Composites: An Integrated Interdisciplinary Curriculum, *J. Eng. Ed.*, supplement, 1998, p 539–544
30. P.K. Liaw, Continuous Fiber Reinforced Ceramic Composites, *J. Chin. Inst. Eng.*, Vol 21 (No. 6), 1998, p 701–718
31. N. Yu and P.K. Liaw, “Ceramic-Matrix Composites: Web-Based Courseware and More,” paper presented at the 1998 ASEE annual conference and exposition, June 28–July 1, 1998 (Seattle)
32. N. Yu and P.K. Liaw, “Ceramic-Matrix Composites,” <http://www.engr.utk.edu/~cmc>

33. P.K. Liaw, O. Buck, R.J. Arsenault, and R.E. Green, Jr., Ed., *Nondestructive Evaluation and Materials Properties III*, The Minerals, Metals, and Materials Society, 1997
34. W.M. Matlin, T.M. Besmann, and P.K. Liaw, Optimization of Bundle Infiltration in the Forced Chemical Vapor Infiltration (FCVI) Process, *Symposium on Ceramic Matrix Composites—Advanced High-Temperature Structural Materials*, R.A. Lowden, M.K. Ferber, J.R. Hellmann, K.K. Chawla, and S.G. DiPietro, Ed., Vol 365, Materials Research Society, 1995, p 309–315
35. P.K. Liaw, D.K. Hsu, N. Yu, N. Miriyala, V. Saini, and H. Jeong, Measurement and Prediction of Composite Stiffness Moduli, *Symposium on High Performance Composites: Commonality of Phenomena*, K.K. Chawla, P.K. Liaw, and S.G. Fishman, Ed., The Minerals, Metals, and Materials Society, 1994, p 377–395
36. N. Chawla, P.K. Liaw, E. Lara-Curzio, R.A. Lowden, and M.K. Ferber, Effect of Fiber Fabric Orientation on the Monotonic and Fatigue Behavior of a Continuous Fiber Ceramic Composite, *Symposium on High Performance Composites*, K.K. Chawla, P.K. Liaw, and S.G. Fishman, Ed., The Minerals, Metals and Materials Society, 1994, p 291–304
37. P.K. Liaw, D.K. Hsu, N. Yu, N. Miriyala, V. Saini, and H. Jeong, Modulus Investigation of Metal and Ceramic Matrix Composites: Experiment and Theory, *Acta Metall. Mater.*, Vol 44 (No. 5), 1996, p 2101–2113
38. P.K. Liaw, N. Yu, D.K. Hsu, N. Miriyala, V. Saini, L.L. Snead, C.J. McHargue, and R.A. Lowden, Moduli Determination of Continuous Fiber Ceramic Composites (CFCCs), *J. Nucl. Mater.*, Vol 219, 1995, p 93–100
39. P.K. Liaw, book review on *Ceramic Matrix Composites* by K.K. Chawla, *MRS Bull.*, Vol 19, 1994, p 78
40. D.K. Hsu, P.K. Liaw, N. Yu, V. Saini, N. Miriyala, L.L. Snead, R.A. Lowden, and C.J. McHargue, Nondestructive Characterization of Woven Fabric Ceramic Composites, *Symposium on Ceramic Matrix Composites—Advanced High-Temperature Structural Materials*, R.A. Lowden, M.K. Ferber, J.R. Hellmann, K.K. Chawla, and S.G. DiPietro, Ed., Vol 365, Materials Research Society, 1995, 203–208
41. S. Shanmugham, D.P. Stinton, F. Rebillat, A. Bleier, E. Lara-Curzio, T.M. Besmann, and P.K. Liaw, Oxidation-Resistant Interfacial Coatings for Continuous Fiber Ceramic Composites, S. Shanmugham, D.P. Stinton, F. Rebillat, A. Bleier, T.M. Besmann, E. Lara-Curzio, and P.K. Liaw, *Ceram. Eng. Sci. Proc.*, Vol 16 (No. 4), 1995, p 389–399
42. C.B. Thomas, “Processing, Mechanical Behavior, and Microstructural Characterization of Liquid Phase Sintered Intermetallic-Bonded Ceramic Composites,” M.S. Thesis, The University of Tennessee, Knoxville, 1996
43. J.H. Miller, “Fiber Coatings and The Fracture Behavior of a Woven Continuous Fiber Fabric-Reinforced Ceramic Composite,” M.S. Thesis, The University of Tennessee, Knoxville, 1995
44. I.E. Reimonds, A Review of Issues in the Fracture of Interfacial Ceramics and Ceramic Composites, *Materials Science and Engineering A*, Vol 237 (No. 2), 1997, p 159–167
45. D.L. Davidson, Ceramic Matrix Composites Fatigue and Fracture, *JOM*, Vol 47 (No. 10), 1995, p 46–50, 81, 82
46. J.C. McNulty and F.W. Zok, Application of Weakest-Link Fracture Statistics to Fiber-Reinforced Ceramic-Matrix Composites, *J. Am. Ceram. Soc.*, Vol 80 (No. 6), 1997, p 1535–1543

47. Z.G. Li, M. Taya, M.L. Dunn, and R. Watanbe, Experimental-Study of the Fracture-Toughness of a Ceramic/Ceramic-Matrix Composite Sandwich Structure, *J. Am. Ceram. Soc.*, Vol 78 (No. 6), 1995, p 1633–1639
48. A. Ishida, M. Miyayama, and H. Yanagida, Prediction of Fracture and Detection of Fatigue in Ceramic Composites from Electrical-Resistivity Measurements, *J. Am. Ceram. Soc.*, Vol 77 (No. 4), 1994, p 1057–1061
49. M. Sakai and H. Ichikawa, Work of Fracture of Brittle Materials with Microcracking and Crack Bridging, *Int. J. Fract.*, Vol 55 (No. 1), 1992, p 65–79
50. J.B. Quinn and G.D. Quinn, “Indentation Brittleness of Ceramics: A Fresh Approach,” *J. Mater. Sci.*, Vol 32 (No. 16), 1997, p 4331–4346
51. R.W. Hertzberg, *Deformation and Fracture Mechanics of Engineering Materials*, 3rd ed., John Wiley & Sons, 1989
52. T.L. Anderson, *Fracture Mechanics*, 2nd ed., CRC Press, 1995
53. J.M. Barsom and S.T. Rolfe, *Fracture and Fatigue Control in Structures*, Prentice-Hall, Inc., 1987
54. “Standard Test Method for Plane-Strain Fracture Toughness of Metallic Materials,” ASTM Standard E 399–90, *ASTM Book of Standards*, Vol 03.01, American Society for Testing and Materials, 1995
55. J.R. Rice, *Journal of Applied Mechanics*, Vol 35, 1968, p 379–386
56. J.A. Begley, G.A. Clark, and J.D. Landes, Results of an ASTM Cooperative Testing Procedure by Round Robin Tests of HY130 Steel, *JTEVA*, Vol 10 (No. 5), 1980
57. “Standard Test Method for J_{IC} , A Measurement of Fracture,” ASTM Standard E 813-87, *ASTM Book of Standards*, Vol 03.01, American Society for Testing and Materials, 1995
58. M. Sakai and R.C. Bradt, Fracture Toughness Testing of Brittle Materials, *Int. Mater. Rev.*, Vol 38 (No. 2), 1993, p 53–78
59. J.Y. Pastor, J. Llorca, J. Planas, and M. Elices, Stable Crack-Growth in Ceramics at Ambient and Elevated-Temperatures, *J. Eng. Mater. Technol. (Trans. ASME)*, Vol 115 (No. 3), 1993, 281–285
60. V.G. Borovik, V.M. Chushko, and S.P. Kovalev, Computer-Aided, Single-Specimen Controlled Bending Test for Fracture-Kinetics Measurements in Ceramics, *J. Am. Ceram. Soc.*, Vol 78 (No. 5), 1995, p 1305–1312
61. J.C. Descamps, A. Poulet, P. Descamps, and F. Cambier, A Novel Method to Determine the R-Curve Behavior of Ceramic Materials—Application to a Ceria-Partially Stabilized Zirconia, *J. Eur. Ceram. Soc.*, Vol 12 (No. 1), 1993, p 71–77
62. V. Kostopoulos and Y.P. Markopoulos, On the Fracture Toughness of Ceramic Matrix Composites, *Mater. Sci. Eng. A*, Vol 250 (No. 2), 1998, p 303–312
63. T. Hashida, V.C. Li, and H. Takahashi, New Development of the J-Based Fracture Testing Technique for Ceramic-Matrix Composites, *J. Am. Ceram. Soc.*, Vol 77 (No. 6), 1994, p 1553–1561
64. C. Droillard and J. Lamon, Fracture Toughness of 2-D Woven SiC/SiC CVI-Composites with Multilayered Interphases, *J. Am. Ceram. Soc.*, Vol 79 (No. 4), 1996, p 849–858

65. H.W. Chandler, R.J. Henderson, M.N. Al Zubaidy, M. Saribiyik, and A. Muhaidi, A Fracture Test for Brittle Materials, *J. Eur. Ceram. Soc.*, Vol 17 (No. 6), 1997, p 759–763
 66. “Provisional Test Method For Determining The Fracture Toughness Of Advanced Ceramics At Ambient Temperatures,” ASTM PS70, *Annual Book of Standards*, Vol 15.01, American Society for Testing and Materials, 1996
 67. D.J. Lee, Simple Method to Measure the Crack Resistance of Ceramic Materials, *J. Mater. Sci.*, Vol 30 (No. 8), 1995, p 4617–4622
 68. P.A. Withey, R.L. Brett, and P. Bowen, Use of Chevron Notches for Fracture-Toughness Determination in Brittle Solids, *Mater. Sci. Technol.*, Vol 8 (No. 9), 1992, p 805–809
 69. “Standard Test Method for Short Rod Fracture Toughness of Cemented Carbides,” ASTM Standard B 771-87, *ASTM Book of Standards*, Vol 02.05, American Society for Testing and Materials, 1995
 70. J.M. Zhang and A.J. Ardell, Measurement of the Fracture-Toughness of Ceramic Materials Using a Miniaturized Disk-Bend Test, *J. Am. Ceram. Soc.*, Vol 76 (No. 5), 1993, p 1340–1344
 71. S. Danchaivijit, D.K. Shetty, and J. Eldridge, Critical Stresses for Extension of Filament-Bridged Matrix Cracks in Ceramic-Matrix Composites—An Assessment with a Model Composite with Tailored Interfaces, *J. Am. Ceram. Soc.*, Vol 78 (No. 5), 1995, p 1139–1146
 72. G.R. Anstis, P. Chantikul, B.R. Lawn, and D.B. Marshall, A Critical Evaluation of Indentation Techniques for Measuring Fracture Toughness: I, Direct Crack Measurements, *J. Am. Ceram. Soc.*, Vol 64 (No. 9), 1981, p 533–538
 73. P. Chantikul, G.R. Anstis, B.R. Lawn, and D.B. Marshall, A Critical Evaluation of Indentation Techniques for Measuring Fracture Toughness: II, Strength Method, *J. Am. Ceram. Soc.*, Vol 64 (No. 9), 1981, p 539–543
 74. B.R. Lawn, A.G. Evans, and D.B. Marshall, Elastic/Plastic Indentation Damage in Ceramics: The Median Radial Crack System, *J. Am. Ceram. Soc.*, Vol 63 (No. 9/10), 1980, p 574–581
 75. S.J. Eck and A.J. Ardell, Fracture Toughness of Polycrystalline NiAl from Finite-Element Analysis of Miniaturized Disk-Bend Test Results, *Metall. Mater. Trans. A*, Vol 28 (No. 4), 1997, p 991–996
 76. P. Brenet, F. Conchin, G. Fantozzi, P. Reynaud, D. Rouby, and C. Tallaron, Direct Measurement of Crack-Bridging Traction: A New Approach to the Fracture Behavior of Ceramic/Ceramic Composites, *Compos. Sci. Technol.*, Vol 56 (No. 7), 1996, p 817–823
 77. C.H. Hsueh, Crack-Wake Interfacial Debonding Criteria for Fiber-Reinforced Ceramic Composites, *Acta Metall.*, Vol 44 (No. 6), 1996, p 2211–2216
 78. D.R. Mumm and K.T. Faber, Interfacial Debonding and Sliding in Brittle-Matrix Composites Measured Using an Improved Fiber Pullout Technique, *Acta Metall.*, Vol 43 (No. 3), 1995, p 1259–1270
 79. A. Domnanovich, H. Peterlik, and K. Kromp, Determination of Interface Parameters for Carbon/Carbon Composites by the Fibre-Bundle Pull-Out Test, *Compos. Sci. Technol.*, Vol 56, 1996, p 1017–1029
-

Fracture Resistance Testing of Brittle Solids

Michael Jenkins, University of Washington; Johnathan Salem, NASA-Glenn Research Center

Introduction

CATASTROPHIC FAILURE best typifies the characteristic behavior of brittle solids in the presence of cracks or crack-like flaws under ambient conditions. Examples of engineering materials that behave as brittle solids include glasses, ceramics, and hardened metal alloys, such as bearing or brake steels. Figure 1 shows the linear-elastic stress-strain curves and abrupt failures of a glass and a ceramic. This behavior is contrasted with the linear/nonlinear stress-strain curves and “graceful” failure of a ductile-like material, such as a metal, or in this case, a continuous fiber-reinforced composite.

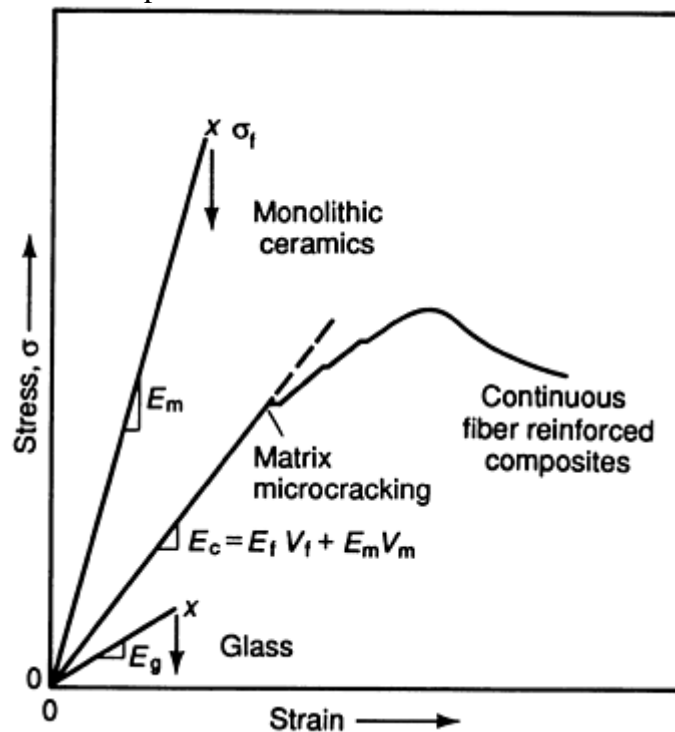


Fig. 1 Comparison of stress-strain curves for ceramics and glasses (as examples of brittle solids) and fiber-reinforced composites (as examples of nonbrittle solids). Source: Ref 1

Sometimes under nonambient conditions, materials that normally fail in a ductile manner may fail in a brittle manner (e.g., carbon steel at temperatures less than their nil-ductility) and those materials that normally fail in a brittle manner may exhibit pseudo-plasticity and failure in a ductile manner (e.g., ceramics containing glassy secondary phases at temperatures greater than the glass-softening temperature).

Because catastrophic failure occurs without warning and can occur in any engineering material under the “suitably wrong” conditions, it is important to characterize the fracture behavior of materials in order to produce engineering designs that can accommodate this phenomenon. This article reviews the fracture behavior of brittle solids and the various methods that have been developed to characterize this behavior.

Reference cited in this section

1. G.D. Quinn, Strength and Proof Testing, *Ceramics and Glasses*, Vol 4, *Engineering Materials Handbook*, ASM International, 1991, p 585–598
-

Concepts of Fracture Mechanics as Applied to Brittle Materials

Many assumptions accompany engineering analyses. For example, in fundamental mechanics of materials it is often assumed that materials are linear elastic, homogeneous, uniform, and isotropic from a macroscopic view. These assumptions are more or less appropriate for polycrystalline materials without any crystallographic ordering. Microscopically, of course, these assumptions become tenuous at best, especially for dimensional scales on the order of grain sizes.

In the study of crack and material interactions, fundamental engineering fracture mechanics also makes several assumptions. These include the linear elastic, homogeneous, uniform, and isotropic assumptions of material response. In addition, it is assumed that the change in stored elastic strain energy is used entirely by the fracture process in creating new fracture surfaces and that the crack itself exists in an infinite body and is not influenced by any boundary conditions. Using these assumptions, it is possible to write the original Griffith criterion for fracture in terms of an applied fracture stress (Ref 1, 2, and 3):

$$\sigma_f = \sqrt{\frac{4\gamma_f E}{\pi(1-\nu^2)c}} \quad (\text{Eq 1})$$

where σ_f is the applied stress at fracture, γ_f is the energy required to create a unit of fractured surface area (i.e., fracture surface energy), E is the elastic modulus, ν is Poisson's ratio, and c is the flaw (i.e., crack) dimension (in the case of an internal flaw, the radius). The observed fracture strengths, S_f , of brittle solids (i.e., the applied stress at fracture given by Eq 1 where $S_f = \sigma_f$) are related to the size and distributions of the strength-limiting flaws, c , in the material (assuming γ_f , E , and ν are deterministic material properties). Strength distributions are therefore related to the distributions of these flaws: intrinsic flaws (e.g., those due to processing) are those that can be treated as microcracks (short cracks) and are on the order of the microstructure; extrinsic or induced flaws (e.g., those due to service) are those that can be treated as macrocracks (long cracks) and are on the order of component dimensions. Note that sometimes extrinsic flaws may be of the same dimensional order as intrinsic flaws.

The microcrack-like flaws are randomly distributed in size, location, orientation, and shape (scattered) throughout brittle materials, causing a range of fracture strengths in otherwise identical components or parts. This inherent scatter leads to fracture strengths that are related to the geometric size (i.e., surface area or volume) of the component. In other words, the larger the component is, the greater the probability of a larger (or properly oriented, or properly shaped, etc.) flaw to occur and, hence, the lower the fracture strength is. Therefore, fracture strength is not a deterministic property in brittle materials unless the flaws are extremely uniform and consistent. Factors of safety in the conventional sense cannot be used. Strength values vary significantly with size and shape of the component (or test specimen) and with processing conditions. There may even be batch-to-batch differences as a consequence of material inconsistencies. These factors, coupled with the "inherent" brittleness of the materials, mean that either extremely conservative stress/strength-based deterministic design philosophies or probabilistic reliability methods must be used for components fabricated from brittle materials.

The concepts of engineering fracture mechanics can be applied when a flaw has a measurable crack size. In this case, the stress field at the crack tip is described in terms of stress intensity factor, which can be written as (Ref 4, 5):

$$K = Y\sigma\sqrt{\pi a} \quad (\text{Eq 2})$$

where K is the stress intensity factor, σ is an applied stress, Y is a geometry correction factor, and a is the macrocrack dimension. Three "modes" of fracture are related to the "mode" of loading (Fig. 2). Mode I, the "opening mode," is considered to be the limiting case for the tendency to fracture because a tensile normal stress "opens" the crack with the resulting stresses in the material "carried" at the crack tip (as opposed to partially distribute through interaction of the crack faces as in modes II and III).

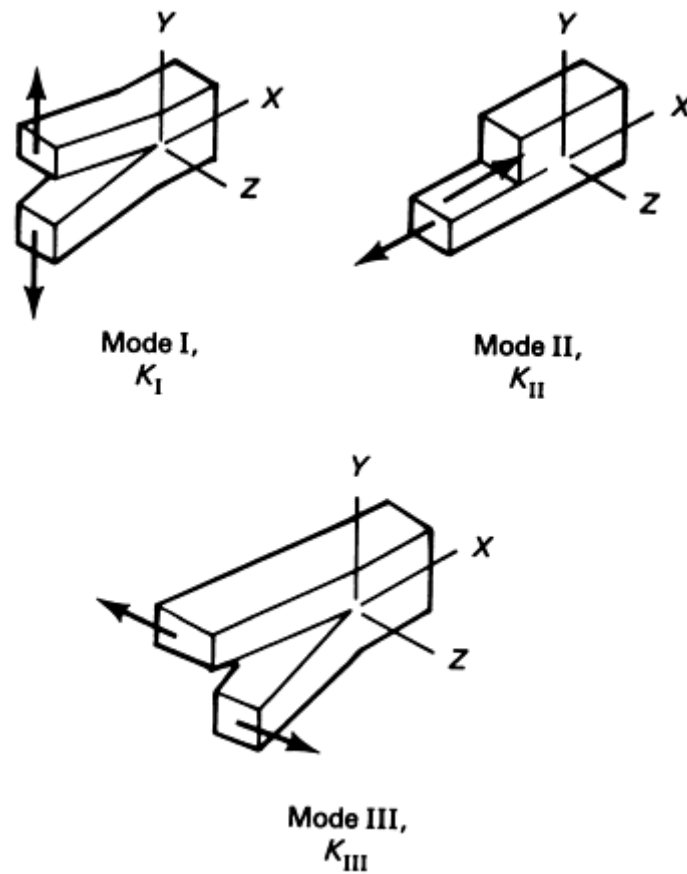


Fig. 2 Modes of fracture. Mode I (opening), mode II (sliding), and mode III (tearing). Source: Ref 4

The critical mode I condition for brittle fracture in a component with a crack-like flaw is reached at a combination of the crack/component geometry correction factor, Y ; a sufficiently high tensile, normal stress, σ ; and a sufficiently long, sharp crack, a . If the fracture resistance of the material is not a function of crack length then catastrophic fracture will occur in the component when the stress intensity factor is equal to the critical stress intensity factor at fracture in the component:

$$\text{Brittle fracture if } K_I = K_{Ic} \tag{Eq 3}$$

where K_I is the mode I stress intensity factor and K_{Ic} is the fracture toughness* of the material (i.e., resistance to fracture), which can be related to fundamental fracture behavior of the material through the Griffith approach (Ref 1, 4):

$$K_{Ic} = \sqrt{\frac{2\gamma_f E}{(1-\nu^2)}} \tag{Eq 4}$$

From a practical view, materials scientists often prefer to use the Griffith approach and γ_f (Eq 1) to describe the fracture characteristics of materials and their relation to the fundamental aspects of the material. However, designers and engineers prefer the fracture-mechanics approach and K_{Ic} (Eq 2 and 3) because fracture characteristics of the component can be related to the applied stress and the crack size.

Note that Eq 3 is a necessary, but not sufficient, condition for fracture. From the Griffith fracture criterion, fracture does not occur at the extreme value of the energy balance as a function of crack length, $U = f(c)$, but rather when the derivative of this energy with respect to the crack length, dU/dc , is equal to zero (Ref 3).

If the resistance of the material to fracture is denoted as R , then, according to Ref 3, the conditions for unstable (brittle catastrophic) fracture can be written as:

$$K_I = R \text{ and } \frac{dK}{dc} \geq \frac{dR}{dc} \tag{Eq 5a}$$

Stable (noncatastrophic) fracture is represented as:

$$K_I \leq R \text{ and /or } \frac{dK}{dc} < \frac{dR}{dc} \quad (\text{Eq 5b})$$

where dK/dc and dR/dc are the derivatives of the stress intensity factor, K , and the fracture resistance of the material, R , with respect to the crack length, c , respectively. Equations 5a(a) and 5b(b) can be illustrated as a fracture resistance or R -curve, as shown in Fig. 3. Note that the R term can be further described in parts such that (Ref 3):

$$R = R_0 + R(c) \quad (\text{Eq 6})$$

where R_0 can be considered the intrinsic fracture resistance, and $R(c)$ is the R -curve component. Note that at some finite length of crack extension, R becomes constant and $R(c)$ is no longer a function of c . This “steady-state” value of fracture resistance [$R_\infty \neq f(c)$] corresponds to fully developed “toughening mechanisms” (Ref 1, 3). R -curve behavior in brittle materials typically develops because of microstructural effects, as shown in Fig. 4. R -curve effects often confuse and frustrate attempts to experimentally measure R_0 (or K_{Ic}) because the effects of crack growth history add to experimental scatter if R (or K_{Ic}) is measured and reported outside the context of the crack extension.

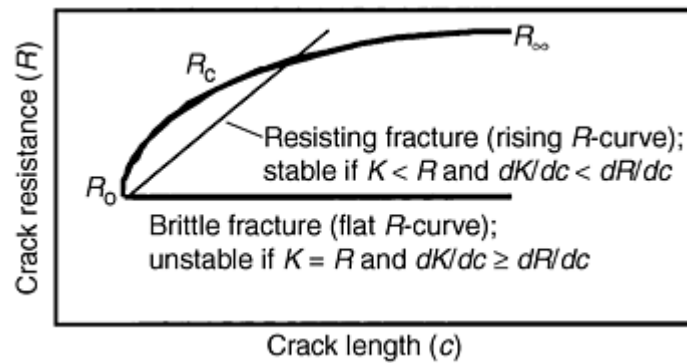


Fig. 3 Schematic representation of R -curve behavior

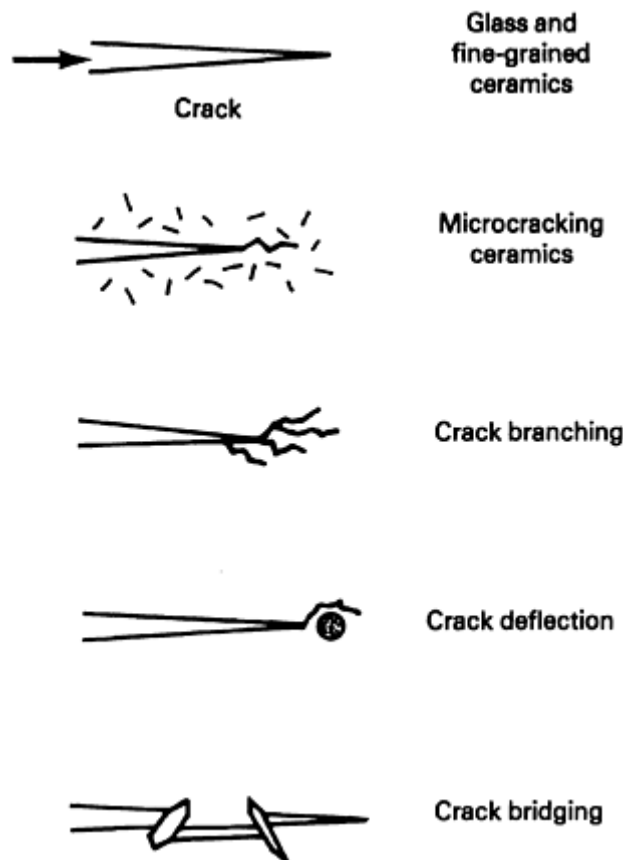


Fig. 4 Microstructural features responsible for fracture resistance as a function of crack length (R -curve effects). Source: Ref 1

Part of the debate surrounding the development of standardized test methods (Ref 7, 8, 9, and 10) for determining the fracture resistance of brittle ceramics has been whether the test method should measure the intrinsic fracture resistance, R_o , or the fully developed fracture resistance, R_∞ . To address this question, the operational aspects of the test method must take into account intrinsic versus extrinsic flaws (or cracks), the degree of crack extension prior to measurement of the fracture resistance, the resulting linearity (or nonlinearity) of the loading curve, features on the fracture surfaces, and other “clues” indicating brittle or nonbrittle fracture.

Typically, brittle materials exhibit low values of fracture toughness ($K_{Ic} = R_o$) ($<1 \text{ MPa}\sqrt{m}$ for many glasses, $<10 \text{ MPa}\sqrt{m}$ for many monolithic ceramics, and $<20 \text{ MPa}\sqrt{m}$ for cast irons and hardened steel alloys). These low fracture toughnesses combined with moderate strengths mean that from a Griffith approach, intrinsic flaw sizes may only be on the order of 1 to 50 μm , which often lead to low, broad strength distributions. From a fracture-mechanics approach, lower fracture toughness combined with detectable macrocrack sizes severely limit the design stresses allowable in components comprised of brittle materials.

Thus, the real utility of measuring the fracture resistance of brittle materials may not be in its direct application to crack- or flaw-based design (e.g., when does $K_I = K_{Ic}$?) through either Griffith or fracture-mechanics approaches. Instead, measures of fracture resistance (e.g., K_{Ic}) may find their greatest utility when combined with other material properties in relative comparison indices, such as those that describe wear or brittleness.

One possible proposed abrasive wear model for ceramics is (Ref 11, 12):

$$\dot{V} \propto P^{1.5} K_c^{-0.5} H^{-0.625} \left(\frac{E}{H} \right)^{0.8} \quad (\text{Eq 7})$$

where \dot{V} is the volume-loss rate of material, P is the applied load, K_c is the fracture resistance, and H is the hardness. Although the exponents in Eq 7 are specific to the application and material, it is apparent from the model that to minimize abrasive wear at high loads, P , the material must possess high K_c , high H , and low E .

A possible proposed erosive wear model for ceramics has the form (Ref 12, 13):

$$\varepsilon_v \propto v^2 \frac{\pi d^4}{12} (E\rho/K_c^2) \quad (\text{Eq 8})$$

where ε_v is the volume of material removed, v is the impact velocity of the particle with diameter d , and ρ is the density of the particle. Again, note that for high velocities of impacting particles, the erosive wear of the material can be minimized by a high K_c , low E , and low ρ .

Finally, the susceptibility of a material to cracking rather than deformation under the action of a concentrated stress can be defined in terms of its brittleness (Ref 14, 15):

$$B = \left(\frac{HE}{K_{Ic}^2} \right) \quad (\text{Eq 9})$$

where B is the brittleness. In this case, in order to decrease the tendency toward brittle behavior (i.e., cracking rather than plastic deformation), B needs to be decreased by decreasing H and E and increasing K_{Ic} .

These examples of relative comparison indices show that quantifying the fracture resistance of brittle solids has direct and important applications other than those conventionally thought of from a fracture-mechanics viewpoint. In addition, as indicated in Eq 7, 8, and 9, depending on the application, the exponent on the fracture-resistance term can have a significant influence on the resulting value of the index being calculated. Thus, accurate and precise measures of the fracture resistance of brittle materials are of paramount importance for making sensible predictions of material behavior using relative comparison indices.

Footnote

* ASTM Committee E08 denotes the symbol K_{Ic} to represent the “plane strain fracture toughness” of a material. Plane strain fracture toughness is defined as: “the crack extension resistance under conditions of crack-tip plane strain... (and)... the value of stress intensity factor designated as K_{Ic} as measured using the operational procedure (and satisfying all validity requirements) specified in ...(ASTM E399)... which provides for the measurement of crack-extension resistance at the start of crack extension and provides operational definitions

of crack-tip sharpness, start of crack extension and crack-tip plane strain” (Ref 6).

References cited in this section

1. G.D. Quinn, Strength and Proof Testing, *Ceramics and Glasses*, Vol 4, *Engineering Materials Handbook*, ASM International, 1991, p 585–598
 2. A.A. Griffith, The Phenomena of Rupture and Flow in Solids, *Philos. Trans. R. Soc. (London) A*, Vol 221, 1920, p 163–198
 3. B. Lawn, *Fracture of Brittle Solids*, Cambridge University Press, 1993
 4. K.E. Amin, Toughness, Hardness, and Wear, *Ceramics and Glasses*, Vol 4, *Engineered Materials Handbook*, S.J. Schneider, J., Ed., ASM International, 1991, p 599–609
 5. G.R. Irwin, Fracture I, *Handbuch der Physik*, Vol 6, Springer-Verlag, Berlin, Germany, 1958, p 558–590
 6. “Standard Test Method for Plane Strain Fracture Toughness of Metallic Materials,” E 399-90, *Annual Book of ASTM Standards*, Vol 03.01, ASTM, 1998
 7. STP 678, *Fracture Mechanics Applied to Brittle Materials*, S.W. Freiman, Ed., ASTM, 1979
 8. T. Fujii and T. Nose, Evaluation of Fracture Toughness of Ceramic Materials, *IJIS Int.*, Vol 29 (No. 9), 1989, p 717–725
 9. G.D. Quinn, M.G. Jenkins, J.A. Salem, and I. Bar-On, Standardization of Fracture Toughness Testing of Ceramics in the United States, *Kor J. Ceram.*, Vol 4 (No. 4), 1998, p 311–322
 10. M. Sakai and R.C. Bradt, Fracture Toughness Testing of Brittle Materials, *Int. Mater. Rev.*, Vol 38 (No. 2), 1993, p 53–58
 11. J. Larsen-Basse, Abrasive Wear of Ceramics, *Friction and Wear of Ceramics*, S. Jahanmir, Ed., Marcel Dekker, Inc., New York, 1994, p 99–118
 12. A. Evans and D. Marshall, Wear Mechanisms in Ceramics, *Fundamentals of Friction and Wear of Materials*, D. Rigney, Ed., American Society for Metals, 1981, p 439–452
 13. J. Ritter, Erosion Damage in Structural Ceramics, *Material Sci. Eng.* Vol 71, 1985, p 195–201
 14. J.B. Quinn and G.D. Quinn, Hardness and Brittleness of Ceramics, *Ceram. Eng. Sci. Proc.*, Vol 17 (No. 3), 1996, p 59–68
 15. J.B. Quinn and G.D. Quinn, Indentation Brittleness of Ceramics: A Fresh Approach, *J. Mater. Sci.*, Vol 32, 1997, p 4331–4346
-

Fracture Toughness and *R*-Curve Testing at Ambient Temperature

In 1970, the fracture-mechanics and metals communities developed the premiere fracture—toughness testing standard for determining plane strain fracture toughness of metals: ASTM E 399, “Standard Test Method for Plane Strain Fracture Toughness of Metallic Materials” (Ref 6). ASTM Committee E-8 on “Fatigue and Fracture” has defined the term *fracture toughness* and the symbol, K_{IC} , based on the operational methods of ASTM E 399. This test method includes several necessary aspects for an acceptable fracture test method:

- All test specimens must have atomistically sharp precracks at the onset of fracture
- Precracks must be well characterized and measurable at the conclusion of the fracture measurement
- Crack geometry must have a valid stress intensity factor
- Plane strain conditions must exist at the crack tip for the measurement of plane strain fracture toughness.

ASTM E 399 was developed and is appropriate for measuring plane strain fracture toughness in ductile metals but does not necessarily address the unique aspects of brittle solids (e.g., cyclic fatigue precracking is not easily accomplished in brittle materials). In addition, test specimens are rather large, as are the notches, cracks, and precracks, presumably for ease of implementation as well as to minimize the influence of dimensional variations on the repeatability and reproducibility of the fracture-resistance measurement. In recent years, ASTM committees have developed numerous standard test methods for metals; recently, a “unified” standard test method for fracture testing was introduced (ASTM E 1820, “Standard Test Method for Measurement of Fracture Toughness”) (Ref 16). Although a variety of precracking, crack length, fracture parameter (e.g., fracture toughness, *R*-curve, etc.), gripping, and test-specimen preparation techniques are detailed in these standards, many aspects may not be directly applicable to brittle materials.

Since the introduction of ASTM E 399, standards-writing bodies worldwide have labored to develop similar robust and well-accepted test methods for brittle solids, particularly advanced ceramics (Ref 7, 8, 9, and 10). The following sections, where applicable, discuss general aspects of these test methods for extrinsic flaws (macrocracks) and intrinsic flaws (microcracks) in test specimens. The reader is referred to the standards themselves for specific details when such standards exist and to appropriate references when a useful technique is described.

Standard Test Methods for Fracture Toughness at Ambient Temperature

ASTM Standard for Fracture Toughness of Ceramics. After nearly eight years of focused effort, which included downselecting from five to three operational procedures and the introduction of an interim limited-life (two years) provisional standard (Ref 17), ASTM C 1421 “Standard Test Methods for the Determination of Fracture Toughness of Advanced Ceramics at Ambient Temperature” (Ref 18) was approved as a full consensus standard in early 1999. A technical and historical overview of the evolution of these test methods has been published (Ref 9). Only a summary of the test methods is discussed here.

Generally, the test methods involve the flexural testing of extrinsically flawed bend bars, as shown in Fig. 5. Regardless of test method, a minimum of four valid tests is required to complete a test series.

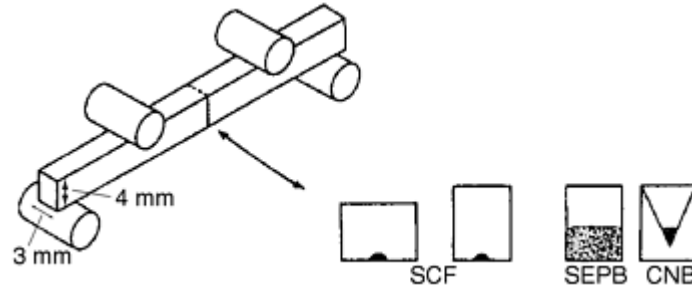


Fig. 5 Three test-method configurations for fracture-toughness testing of ceramics included in ASTM C 1421. SCF, surface crack in flexure; SEPB, single-edge precracked beam; CNB, chevron notched beam

In the case of the single-edge precracked beam (SEPB) test specimen, prior to fracture testing, a compression bridge anvil is used with the 3 by 4 mm (0.12 × 0.16 in.) cross section “bend bar” test specimen to produce precracks from either a saw notch or a series of Vickers indentations. The precracked test specimen is then fracture tested in either three- or four-point flexure (20 by 40 mm, or 0.8 × 1.6 in., inner/outer spans in four-point flexure is recommended, although outer spans as short as 16 mm, or 0.6 in., in three-point flexure are permissible). Various methods are suggested for determining conditions of instability, stable crack extension, and other anomalies that can affect the test results.

Requirements for the precrack include the following:

- Inclination of the precrack front must be $a_{av} - a_{min} < 0.1 a_{av}$, where a_{av} and a_{min} are the average and minimum precrack lengths, respectively.
- The inclination of the propagation direction on the bottom surface and both sides of the specimen is $\leq 5^\circ$.
- The precrack length is between $0.35W$ and $0.60W$, where W is the test specimen height.

For three-point flexure, the fracture toughness by the SEPB method is calculated as:

$$K_{Ipb} = g \left(\frac{P_{max} S_o 10^{-6}}{BW^{3/2}} \right)^{1/2} \times \left(\frac{3(a/W)^{1/2}}{2(1-a/W)^{3/2}} \right) \quad (\text{Eq 10})$$

where K_{Ipb} is the fracture toughness (in $\text{MPa}\sqrt{m}$) using the SEPB method, P_{max} is the maximum force (in newtons) at fracture, S_o is the outer support span (in meters), B is the test specimen breadth (in meters), W is the test specimen height (in meters), a is the precrack length (in meters), and g is the geometry correction factor that depends on the three-point flexure geometry (Ref 17, 18).

For four-point flexure, the fracture toughness by the SEPB method is calculated as:

$$K_{Ipb} = f \left(\frac{P_{max} (S_o - S_i) 10^{-6}}{BW^{3/2}} \right)^{1/2} \times \left(\frac{3(a/W)^{1/2}}{2(1-a/W)^{3/2}} \right) \quad (\text{Eq 11})$$

where S_i is the inner support span (in meters) and f is the geometry correction factor that depends on the four-point flexure geometry (Ref 17, 18).

In the case of the surface crack in flexure (SCF) test specimen, a Knoop indenter is used to create a semielliptical surface precrack. An essential step in this method is the removal of residual stresses induced by the indenter. Grinding and polishing are recommended whereas annealing is not because it can lead to crack healing and crack tip blunting. The precracked test specimen is then fracture tested only in four-point flexure (20 and 40 mm, or 0.8 and 1.6 in., inner and outer spans, respectively). Post-test fractography is necessary to determine the precrack size for the calculation of the fracture toughness. It has been argued that the SCF

method may give results representative of the intrinsic fracture resistance of the material because the induced flaw can be on the order of the intrinsic flaws (Ref 9).

The fracture toughness by the SCF method is calculated as:

$$K_{Isc} = Y \left(\frac{3P_{\max}(S_o - S_i)10^{-6}}{2BW^2} \right)^{1/2} \quad (\text{Eq 12})$$

where K_{Isc} is the fracture toughness (in MPa \sqrt{m}) using the SCF method and Y is the greater of two possible geometry correction factors:

$$Y_d = \frac{(\sqrt{\pi}MH_2)}{\sqrt{Q}} \quad (\text{Eq 13a})$$

$$Y_s = \frac{(\sqrt{\pi}MH_1S)}{\sqrt{Q}} \quad (\text{Eq 13b})$$

where M , H_1 , H_2 , Q , and S are dimensionless functions based on an assumed half semiellipsed precrack shape (Ref 17, 18).

In the chevron notched beam (CNB) test specimen, a V-shaped notch is cut in the “bend bar” with the tip of the V oriented to the tensile stress during fracture testing. The advantage of the CNB test is that no prior precracking is required. Instead, the crack initiates at the tip of the chevron during testing. The crack then propagates through the chevron in a stable manner because the chevron presents an ever-widening crack front to the propagating crack. Examination of the loading curves provides an indication of stable fracture (e.g., smooth, nonlinear rollover), a necessary requirement for a valid CNB test. Either three- or four-point flexure is allowed for the CNB with allowable test geometry parameters (L , W , S_o , and S_i) dependent on the test configuration chosen (A, B, C, or D) (Ref 18). Valid tests must have chevron notch planes that meet within three notch thicknesses; the tip of the chevron must be less than 2% of the test specimen breadth, B , from the centerline; and the difference between the two chevron length measurements and the average of the chevron length must be less than 2% of the test specimen height, W .

The fracture toughness by the CNB method is calculated as:

$$K_{Ivb} = Y_{\min}^* \left(\frac{P_{\max}(S_o - S_i)10^{-6}}{BW^{3/2}} \right)^{1/2} \quad (\text{Eq 14})$$

where K_{Ivb} is the fracture toughness (in MPa \sqrt{m}) using the CNB method and Y_{\min}^* is the minimum stress intensity factor coefficient for the relevant geometry (Ref 17, 18).

Interferences addressed in ASTM C 1421 include slow crack growth (i.e., environmentally assisted crack growth), R -curve effects, and stability. Other methods considered but not addressed in the standard include indentation strength in bending (ISB), indentation fracture (IF), double cantilever beam (DCB), and single-edge notched beam (SENB). Discussions of why these methods were not included in the ASTM standard are provided elsewhere (Ref 9).

JIS Standard for Fracture Toughness of Ceramics. In 1990, the Japanese Industrial Standards Committee (JISC) adopted the Japanese Industrial Standard (JIS) R1607 “Testing Methods for the Fracture Toughness of High Performance Ceramics” (Ref 19). This standard contains two test methods for the determination of the fracture toughness of ceramics: SEPB and IF.

Similar to the ASTM SEPB method, either Vickers indentations or a straight notch can be used as “starters” in the 3 by 4 mm (0.12 × 0.16 in.) cross section bar prior to the use of the compression bridge anvil. Unlike the ASTM SEPB method, after introducing the precrack, the fracture test is conducted only in three-point flexure using either 16 or 30 mm (0.63 or 1.18 in.) outer spans. Requirements for the precrack include the following:

- The length variation and inclination of the precrack front must be $(a_{\max} - a_{\min})/2 < 0.1$, where a_{\max} and a_{\min} are the maximum and minimum precrack lengths, respectively.
- The inclination of the propagation direction on the bottom surface and both sides of the specimen is $\leq 10^\circ$.

- The precrack length is between 1.2 and 2.4 mm (0.05 and 0.09 in.).

The fracture toughness by the SEPB method is calculated as:

$$K_{Isepb} = \left(\frac{PS}{BW^{3/2}} \right)^{1/2} \left(\frac{3(a/W)^{1/2} Y}{2} \right) \quad (\text{Eq 15})$$

where K_{Isepb} is the fracture toughness (in $\text{MPa}\sqrt{\text{m}}$) using the SEPB method (Ref 19). The average of five valid tests is reported.

For the IF method, a Vickers hardness tester “at a large load” is used to create the impression (cracked from corners), as shown in Fig. 6. Within 10 minutes after the creation of the indentation, both diagonal dimensions (two corner crack lengths combined with the indentation diagonal length) are measured. The corner cracks must satisfy the following conditions:

- Cracks start at the corner of the indentation and propagate in the diagonal direction.
- Lengths of any two cracks normal to each other differ by less than 10% of the average crack length.
- Any crack length is at least 2.5 times the diagonal length of the indentation.

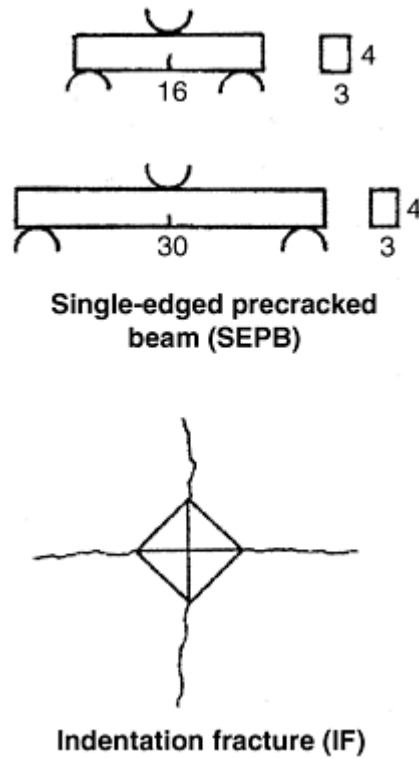


Fig. 6 Two methods for fracture-toughness testing of ceramics contained in JIS R1607-90. Dimensions in millimeters. Source: Ref 19

The quasi-fracture toughness is calculated as:

$$K_c = 0.018 \left(\frac{E}{H_v} \right)^{1/2} \left(\frac{P}{C^{3/2}} \right) \quad (\text{Eq 16})$$

$$= 0.026 \frac{E^{1/2} P^{1/2} a}{C^{3/2}}$$

where K_c is the quasi fracture toughness (in $\text{Pa}\sqrt{\text{m}}$) using the IF method, H_v is the Vickers hardness (in pascals), C is half the average crack length (in meters), and a is half the average diagonal length of the indentation (in meters). There is considerable controversy surrounding the result of the IF for accurate and precise measurements of fracture toughness. Two obvious concerns are the choice of the “calibration constant,”

which is 0.018 in Eq 18 but could be one of over 19 different values (Ref 20, 21) and the highly subjective estimate of the final crack tip. Even JIS R1607 states that the result of the IF method cannot be strictly considered a fracture toughness.

ISO Standard for Fracture Toughness of Ceramics. The International Organization for Standardization (ISO) made significant progress in 1999 when ISO DIS15732, “Fine Ceramics (Advanced Ceramics, Advanced Technical Ceramics)—Test Method for Fracture Toughness of Monolithic Ceramics at Room Temperature by Single Edge Pre-Cracked Beam (SEPB) Method” (Ref 22) was approved. In addition, a new working group has introduced an advanced draft of an SCF fracture testing method (Ref 23). ISO Technical Committee (TC) 206 has oversight of both these efforts, although in this article only ISO DIS15732 is discussed in detail because many of the essential aspects of the current draft of the SCF test method are similar to the SCF test method contained within ASTM C 1421. “Harmonization” of existing national and regional standards, not development of completely new standards, is one of the charter goals of ISO TC206.

ISO DIS15732 is a combination of the two existing national standards containing the SEPB fracture test method: ASTM C 1421 and JIS R1607. Because the proper introduction of the precrack is critical to the success of the SEPB method for both ASTM and JIS standards, explicit directions and illustrations are provided in an annex (Fig. 7). Both three- and four-point flexure are allowed in certain outer and inner support spans, again, as contained in both the ASTM and JIS standards (Fig. 8). Also, as contained in the ASTM and JIS standards, either a row of Vickers (or Knoop) indentations or a saw notch are allowed for the precrack starter. Similarly, the cross section of the beam is 3 by 4 mm (0.12×0.16 in.) with minimum lengths ranging from 18 to 45 mm (0.7–1.8 in.) depending on the testing configuration.

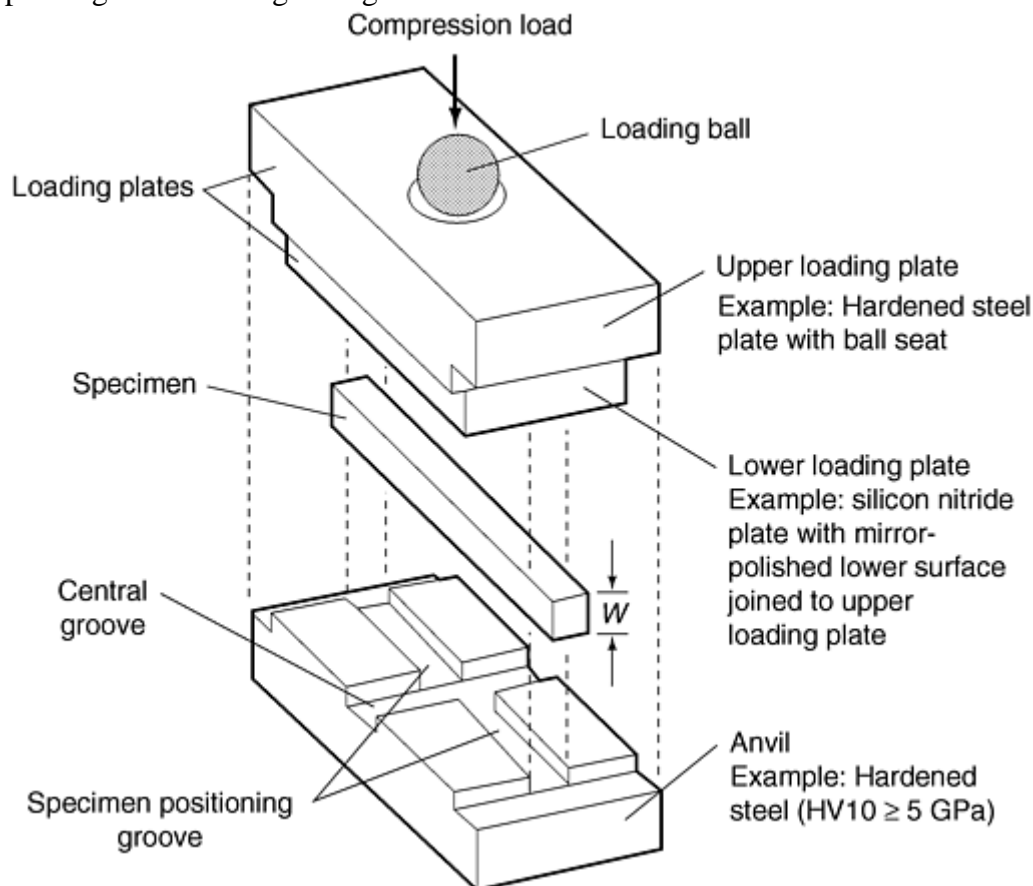


Fig. 7 Illustration of compression bridge anvil for fracture-toughness testing of ceramics in ISO DIS 15732. Source: Ref 22

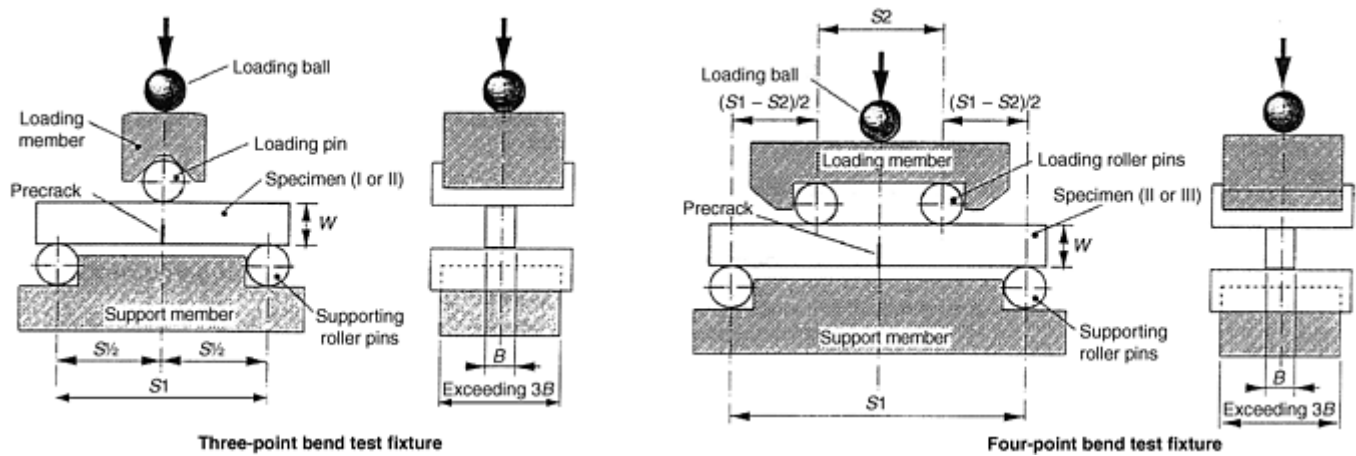


Fig. 8 Test configurations for ISO DIS 15732. For three-point bend (flexure), S_1 can be 16 or 30 mm (0.63 or 1.18 in.). For four-point bend (flexure), S_1 can be 30 mm (1.18 in.) with S_2 at 10 mm (0.39 in.), or S_1 can be 40 mm (1.57 in.) with S_2 at 20 mm (0.79 in.). Source: Ref 22

Notable additions to ISO DIS15732 not contained in either the ASTM or the JIS standards are sections on determining precrack length and stable crack growth using compliance changes and fractography. Additional sections deal with permissible range of stable crack growth ($\leq 2\%$ of the average precrack length) and permissible relative compliance change ($\leq 10\%$ of the ratio of precrack length to test specimen height). Requirements for the precrack include the following:

- Length variation and inclination of the precrack front must be (similar to JIS R1607) $(a_{\max} - a_{\min})/2 < 0.1$, where a_{\max} and a_{\min} are the maximum and minimum precrack lengths, respectively.
- The inclination of the propagation direction on the bottom surface and both sides of the specimen is $\leq 5^\circ$ for the three-point flexure geometries and $\leq 10^\circ$ for the four-point flexure geometries (mixture of JIS R1607 and ASTM C1421).
- The precrack length is between $0.35W$ and $0.60W$, where W is the test specimen height (similar to ASTM C1421).

Notes are provided regarding R -curve effects (the measured fracture toughness may be “artificially high” if stable crack growth occurs after pop-in of the precrack) and slow crack growth effects (the measured fracture toughness may be reduced because of environmentally assisted crack propagation).

The fracture toughness by the SEPB method is calculated using Eq 15 for the three-point flexure geometries and Eq 11 for the four-point flexure geometries. Five or more valid test results are used in calculating an average fracture toughness value.

CEN Standard for Fracture Toughness of Ceramics. Comité Européen de Normalisation (CEN) is the de facto standards-writing body for the European Union. As of 1999, a pre-Euro Norm Voluntaire (preENV) had been drafted indicating the intent to develop a seven-part fracture-toughness testing standard within CEN Technical Committee (TC) 184 on Advanced Technical Ceramics. The first part of this standard is currently in draft form and provides summaries of the six test methods contained in each of the following six sections, as well as guidance to the user as to choice and application of a particular test method (Ref 24).

A pictorial summary of the six test methods is shown in Fig. 9; a summary and comparison are provided in Tables 1 and 2, respectively. Note that with the exception of the IF method, all six methods use “bend-bar” test specimen geometries. Of the six, the SEPB method is contained in the current ASTM, JIS, and ISO standards. The CNB method is contained in the ASTM standard, as is the SCF method. The IF method is contained in the JIS standard. Two methods not yet standardized are the single-edge V-notch beam (SEVNB) and the indentation strength (IS) methods. These two methods are discussed briefly here.

Table 1 Methods for determining apparent fracture toughness using small test specimens

Method	Description	Calibrations	Uncertainties or difficulties
Single-edge precracked beam (SEPB)	A flexural test in a beam into the tensile side of which a short straight crack has been introduced	Accurate calibrations available for wide range of precrack lengths. Fracture toughness is determined at a defined crack length.	Precracking requires some skill to obtain straight-fronted cracks. Results are influenced by rising fracture-resistance behavior.
Chevron notched beam (CNB)	A flexural test in a beam into the tensile side of which a short straight crack has been introduced	Accurate calibrations	Fracture toughness is calculated at assumed crack length. Crack initiation may be difficult in some materials due to machining residual stresses. Result may be influenced by rising fracture resistance behavior.
Surface crack in flexure (SCF)	A flexural test in a beam into the tensile side of which a short straight crack has been introduced	Accurate calibrations assuming the precrack shape approximates to an ellipse after removal of surface damage region	Requires observation and measurements of precrack dimensions, which may not be clearly visible. Limited to materials in which indentation produces good-quality cracks. Result typical for small cracks
Single-edge V-notch beam (SEVNB)	A flexural test in a beam into the tensile side of which a short straight crack has been introduced	Accurate calibrations assuming sharp crack (same as SEPB)	Assumes that if the tip radius of the sharp notch is of the order of the grain size, then the notch is equivalent to a sharp crack and the SEPB calibration can be used
Indentation fracture (IF)	A flexural test in a beam into the tensile side of which a short straight crack has been introduced	Poor calibrations owing to uncertainties in stress fields developed by indentation methods of cracking. Wide variety of different calibrations available	Effective only in materials that do not chip or flake when indented. Inappropriate for tough or porous materials. Result typical for small cracks
Indentation strength (IS)	A flexural test on a beam into the tensile side of which has been placed an indentation	Poor calibrations owing to uncertainties in residual stress fields developed by indentations that are not removed	Reproducible test if well-defined cracks are developed by indentation. Result typical for small cracks, but may not be indentation-force dependent. Inappropriate for porous materials

Adapted from Ref 24

Table 2 Comparison of fracture-toughness test methods

Criterion	Test method					
	SEPB	CNB	SCF	SEVNB ^(a)	IF	IS
Confidence in calibration ^(b)	Good	Good	Good	Good	Poor	Poor
Relative ranking of materials	Yes	Yes	Yes	Yes	Possible for similar materials	Yes
Long-crack fracture toughness	Yes	Yes	No	No	No	No
Determine <i>R</i> -curve	Yes	No	No	No ^(c)	No	No

effects						
Short-crack fracture toughness	No	No	Yes	Yes ^(d)	Yes	Yes
Fast-fracture fracture toughness	Yes	No	Yes	Yes	Yes	Yes
Controlled-crack-growth fracture toughness	Possible	Yes	No	No	No	No
Low scatter results	Possible	Possible	Yes	Yes	No	Yes
Fine-grained materials	Yes	Yes	Yes	Yes	Yes	Yes
Coarse-grained materials	Yes	Yes	Unlikely	Yes	Unlikely	Unlikely
OK if $K_{Ic} < 6$ MPa \sqrt{m}	Yes	Yes	Yes	Yes	Yes	Yes
OK if $K_{Ic} > 6$ MPa \sqrt{m}	Yes	Yes	Possible ^(e)	Yes	No	No
Sensitive to crack growth before fracture	Yes	Uses a moving crack front	Yes	Possible	Yes	Yes
Sensitive to notch/precrack geometry	Possible	Probable	Yes	Possible for fine-grained materials	Not appropriate	Not appropriate
Suitable for elevated temperature	Yes ^(f)	Yes	Yes ^(f)	Yes	No	Possible^(f)
Cost of effort to do tests	High	Medium	High	Medium	Low	Medium
Cost of facilities to do tests	Medium	Medium	High	Medium	Low	Medium

(a) Attributes given are for notch root radii of $\leq 5 \mu\text{m}$.

(b) On a fracture mechanics basis alone, the quality of the experimental result is influenced by the nature of the material.

(c) Unless used initially to grow a crack from a notch.

(d) If the notch is considered to have a short flaw at its tip, R -curve effects are avoided.

(e) Increasing likelihood of poor precrack generation with increasing fracture toughness.

(f) Upper temperature limit is crack-tip blunting, crack healing, and/or oxidation. Adapted from Ref 24

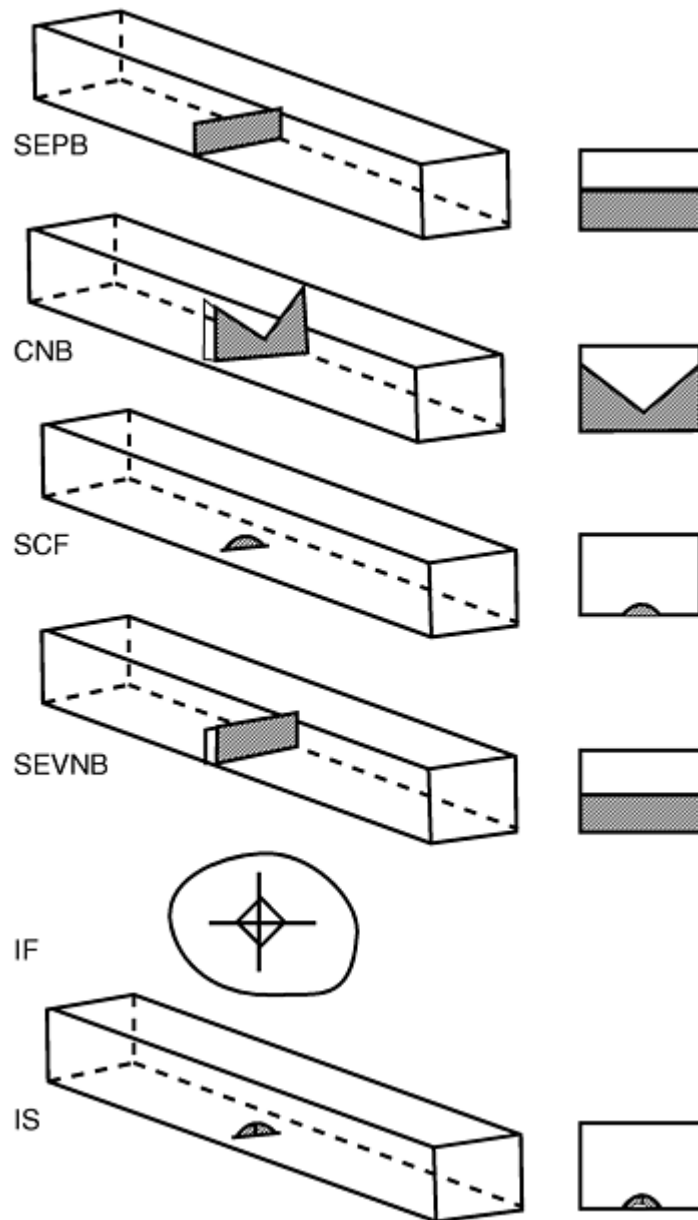


Fig. 9 Pictorial summary of test methods contained in CEN TC184 draft fracture toughness standard (Ref 24). SEPB, single-edge precracked beam; CNB, chevron notched beam; SCF, surface crack in flexure; SEVNB, single-edge V-notched beam; If, indentation fracture; IS, indentation strength

The SEVNB method is a variation of the single-edge notch beam (SENB) method, which has been a mainstay of the fracture testing community since before the introduction ASTM E 399. However, in brittle materials, the SEVNB addresses a problem that had long plagued the SENB method: how should a sharp crack at the tip or root of the saw notch be introduced? No matter how thin the diamond saw blade (even 50–100 μm thick), a blunt notch is still not an atomistically sharp crack, and, hence, without the introduction of a precrack at the notch tip (e.g., fatigue precracking or SEPB compression bridge loading), the SENB test does not meet one of the basic requirements for a fracture toughness test: a well-defined, atomistically sharp crack. When compared to sharp-crack methods, blunt-notch methods tend to “overestimate” fracture toughness with results that are often a function of notch thickness (e.g., see Ref 25 for a comparison of results for sharp-crack and blunt-notch techniques for alpha silicon carbide).

What sets the SEVNB method apart from the usual SENB method is that after the initial notch is sawed into the beam, the notch tip is “sharpened” (Ref 26, 27). In the latest rendition of the SEVNB method, a reciprocating (either manual or mechanized) conventional razor blade is used, along with various grits of diamond paste, to create the V at the tip of the saw notch (Ref 27). This V-notching technique tends to create notch root radii (or damage zone) less than those that would make the measured fracture toughness a function of the notch width or geometry. The SEVNB method produces precise and accurate results similar to sharp-crack methods (e.g.,

SEPB and SCF) without the need to precrack the test specimen (Ref 27). In addition, measurement of the notch depth at fracture allows the use of the same well-established equations, such as those used for SEPB method (e.g., Eq 11, 12, and 15) for calculating fracture toughness.

The IS method is based on the applications of Eq 1 and 4 to the flexural strength testing of flexural test specimens that have been indented (either Knoop or Vickers) with ever-increasing indentation forces. The size of the controlled indentation flaw increases with increasing indentation force. Therefore, for a material with a deterministic fracture resistance, the measured flexural strength will decrease with increasing flaw size (or increasing indentation force). The mathematics have been worked out relating fracture resistance, flexural strength, and flaw size for sharp indenters producing median cracks (Ref 3).

The actual mechanics of the conducting test involve first placing one indentation each in a series of standard flexure test specimens (each test specimen receives one indentation at one indentation force), such as those specified in ASTM C 1161 (Ref 28) at ever-increasing indentation forces using either a Knoop or Vickers indenter. A standard flexural strength test is then conducted, preferably in four-point flexure to avoid the necessity of trying to align the small indentation with the nose of the loading support in three-point flexure. For four-point flexure, the flexural strength is calculated as:

$$S_f = \frac{3P_f(S_o - S_i)}{2BW^2} \quad (\text{Eq 17})$$

where S_f is the flexural strength and P_f is the force at fracture (typically maximum force for a brittle material). The fracture toughness using the indentation strength method for the particular test can then be calculated using the relation (Ref 29):

$$K_{\text{IIS}} = 0.59 \left(\frac{E}{H_v} \right)^{1/8} (S_f P^{1/3})^{3/4} \quad (\text{Eq 18})$$

where P is the indentation force.

Obvious advantages of the IS method are that it involves readily available flexure test specimens and test standards for both flexure strength and indentations. In addition, the IS method does not require a subjective measure of crack size (from the viewpoint of the fracture-mechanics community, this is also an obvious weakness) (Ref 2). Another weakness is that hardness and elastic modulus need to be measured separately. A final point is that the constant 0.59 in Eq 18 as determined from logarithmic regression analysis (Ref 2) has an estimated standard deviation of 0.12 (a somewhat large source of variability for a “constant”). While the IS method is attractively simple, relative measurements on a given material “are typically reliable to much better than 20%” (Ref 3), making the results of limited value compared to some of the other methods discussed up to this point.

Other Test Methods for Fracture Toughness at Ambient Temperature

Many other successful methods for determining fracture toughness of brittle materials (not yet standardized) have been introduced and refined over the past several years. Some of the more popular methods are discussed in the following sections. Note that these discussions are limited to sharp-crack methods because of the limitation of methods using blunt notches.

The double torsion (DT) method was once seen as a strong contender for a standard test method (Ref 4, 7, 8, 9, and 10). This method (Fig. 10) allows the use of a variety of basic specimen shapes and test geometries, although the most common is a long, thin plate with a side groove cut along its length to guide and crack (although there is evidence that with good alignment, better results are obtained without the groove (Ref 31). Ball-bearing supports tend to minimize friction and help alignment. Various analyses have shown that the applied stress intensity factor is independent of crack length over the dimensionless crack length range of 0.55 to 0.65 a/W (Ref 4). One formulation for stress intensity factor for determining fracture toughness using the DT method is (Ref 30):

$$K_{\text{Idt}} = PW_m \sqrt{\frac{3}{Wd^3 d_n(1-\nu)\xi}} \quad (\text{Eq 19})$$

where W_m is half the test specimen width minus half the notch width, d is the total thickness, d_n is the notch depth, and ξ is a correction factor for thick test specimens such that $\xi = 1 - 0.6302t + 1.20t \exp(-\pi/\tau)$ where $t =$

$2d/W$ and W is the total width of the test specimen. Although the three-dimensionality of the crack front in the DT test specimen has led to some controversy about whether Eq 19 really represents a mode I stress intensity factor, evidence exists that $K_{I_{dt}}$ for various brittle materials compares well to other sharp-crack mode I methods (Ref 25, 30). Obvious advantages of the DT method include the simple loading configuration, its constant stress intensity factor geometry, simple test specimen geometry, and stable crack propagation configuration. Some disadvantages include the relatively large volume of test material (compared to a simple flexure bar) required for a single test, the more complicated arrangement of ball bearings and other components for supports, the curved crack front, and concerns about the three-dimensionality of the crack tip.

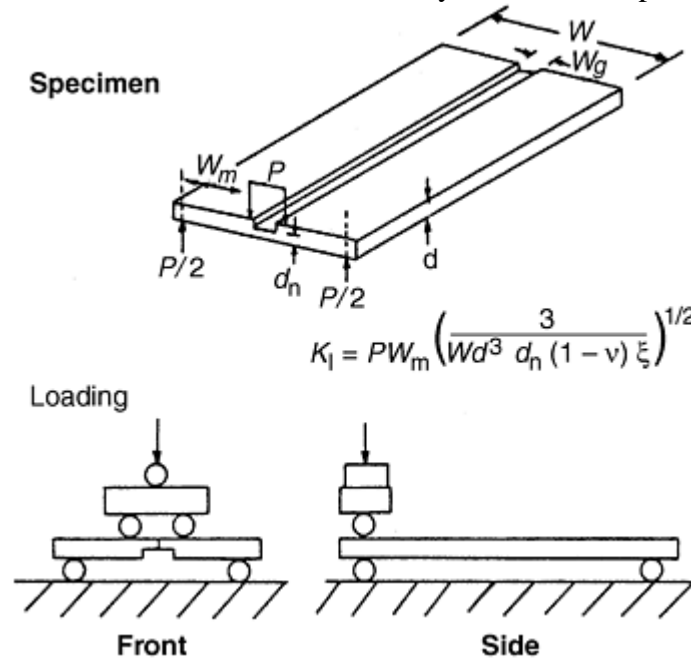


Fig. 10 Schematic illustration and nomenclature for double torsion (DT) fracture-toughness test methods. Source: Ref 30

The double cantilever beam (DCB) test method has been part of fracture mechanics in various forms since the inception of the discipline. Indeed, variations of the DCB method even appear in ASTM E 399 for fracture toughness testing of metals. A unique aspect of the DCB test method applied to brittle materials is the method of load application that can have a variety of forms, as shown in Fig. 11. The applied-load method can be particularly troublesome in brittle materials that are susceptible to tensile forces. However, the compressively loaded wedge-loading method and the compressively loaded applied-moment method are suited to testing brittle materials. Often side grooves are used to guide the crack longitudinally. For the applied-load geometry, the stress intensity factor and subsequent fracture toughness have been formulated as (Ref 4):

$$K_{I_{dcb}} = 3.45 \frac{Pa}{bh^{3/2}} \left[1 + 0.7 \left(\frac{h}{a} \right) \right] \quad (\text{Eq 20})$$

where h is half height of the test specimen, b is thickness of the test specimen, and a is the crack length. Some advantages of this geometry are that for some cases the stress intensity factor is independent of crack length (e.g., tapered DCB or applied moment DCB), test specimen preparation can be simple, material usage is efficient, and the loading configuration can be simple. The primary disadvantage is that a sharp crack needs to be introduced to avoid problems of initiation and propagation of a crack from the blunt notch.

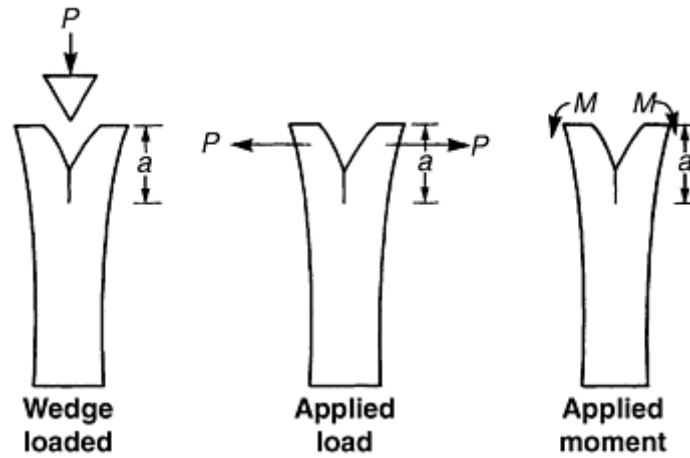


Fig. 11 Double cantilever beam (DCB) fracture test methods

Chevron notched short-rod and short-bar (CNSR and CNSB) test methods (Fig. 12) have many of the advantages of the CNB test method: simple notch preparation, in situ (automatic) crack initiation at the tip of the chevron, and inherent stable crack propagation in the chevron. However, an additional advantage of the CNSR and CNSB geometries is the efficient use of material because the volume of material needed to support a flexural test specimen is avoided. For the CNSB geometry, a suggested formulation for the stress intensity factor and subsequent fracture toughness can be determined as (Ref 4, 32):

$$K_{Icnsb} = \frac{P}{B\sqrt{W}} Y_{min}^* \quad (\text{Eq 21})$$

where P is the applied force, W is length of the test specimen, B is thickness of the test specimen, and Y_{min}^* is the minimum geometry correction factor for the chevron notch geometry. A disadvantage of the CNSR and CNSB test method is the tensile loading required for the fracture test, as shown in Fig. 12.

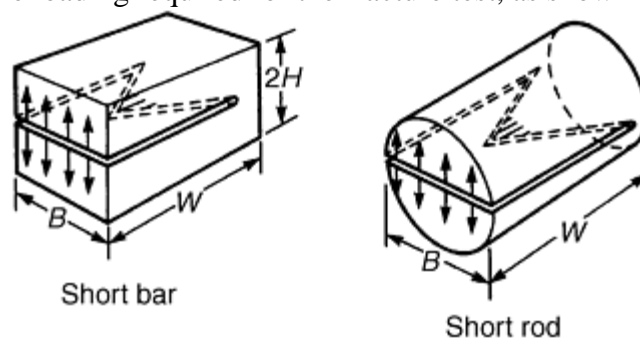


Fig. 12 Examples of chevron notched short bar (CNSB) and chevron notched short rod (CNSR) test specimens. Source: Ref 4, 32

Fractographic methods (Ref 33, 34) applied to strength tests of intrinsically flawed test specimens involve interpretation of fracture features, quantification of the type and size of the strength-limiting flaws, determination of the applied stress at the flaw suite, and, finally, the calculation of the fracture toughness of the material. It is important to realize that it is usually difficult to directly measure flaws initiating at fracture sites (Ref 35 contains information on fractographic aspects of brittle materials). However, as a consequence of the rapid crack propagation during brittle fracture, the fractured region around flaws often exhibits distinct regions (Fig. 13): flaw origin, fracture mirror (smooth region surrounding the origin), mirror (radial ridges surround the mirror), and hackle (rough ridges surrounding the mirror). Crack branching can exist outside the hackle region as well. A quantitative relationship exists between the stress at the fracture and the distance from the flaw to each of the boundaries of this fracture region such that (Ref 33):

$$\sigma r_j^{1/2} = A_j \quad (\text{Eq 22})$$

where σ is the stress at fracture, r_j is the distance to a particular boundary, and A_j is the corresponding mirror constant such that

$$A_j = \frac{\sqrt{a_{cr} b_{cr}}}{r_j} \quad (\text{Eq 23})$$

where a_{cr} is the failure-initiating flaw depth, b_{cr} is its half depth, and r_j is the relation of fracture mechanics to fractography is given as (Ref 32):

$$K_{If} = \frac{\sqrt{1.2 \pi} \left(\frac{c}{r_j} \right)^{1/2}}{\phi} A_j \quad (\text{Eq 24})$$

where K_{If} is the fracture toughness determined from fractography, $c = \sqrt{a_{cr} b_{cr}}$, as illustrated in Fig. 14, and ϕ is an elliptical integral of the second kind that accounts for degree of ellipticity of the flaw.

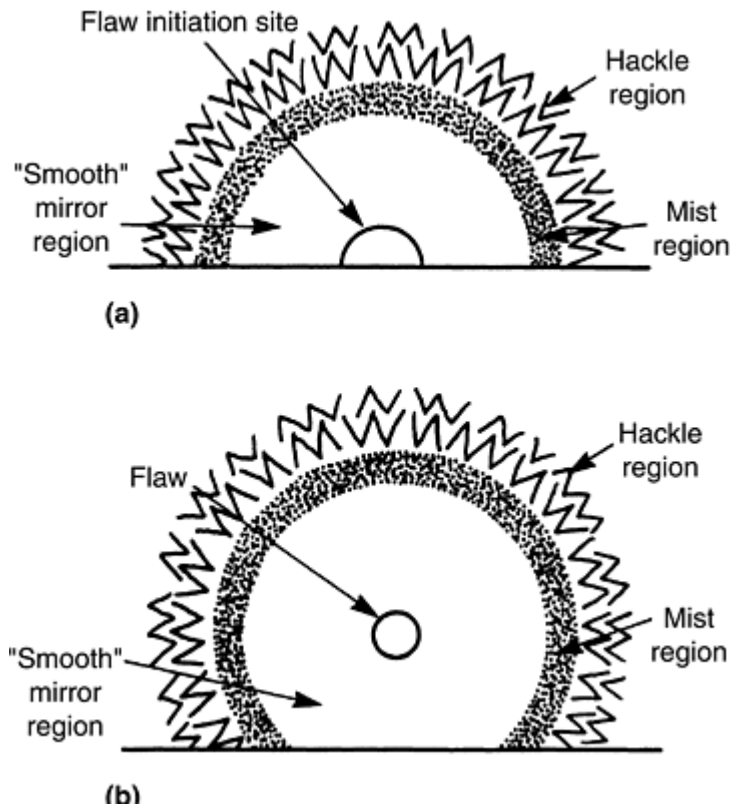


Fig. 13 Nomenclature for fracture features. (a) Surface flaws. (b) Volume flaws. Source: Ref 4, 34

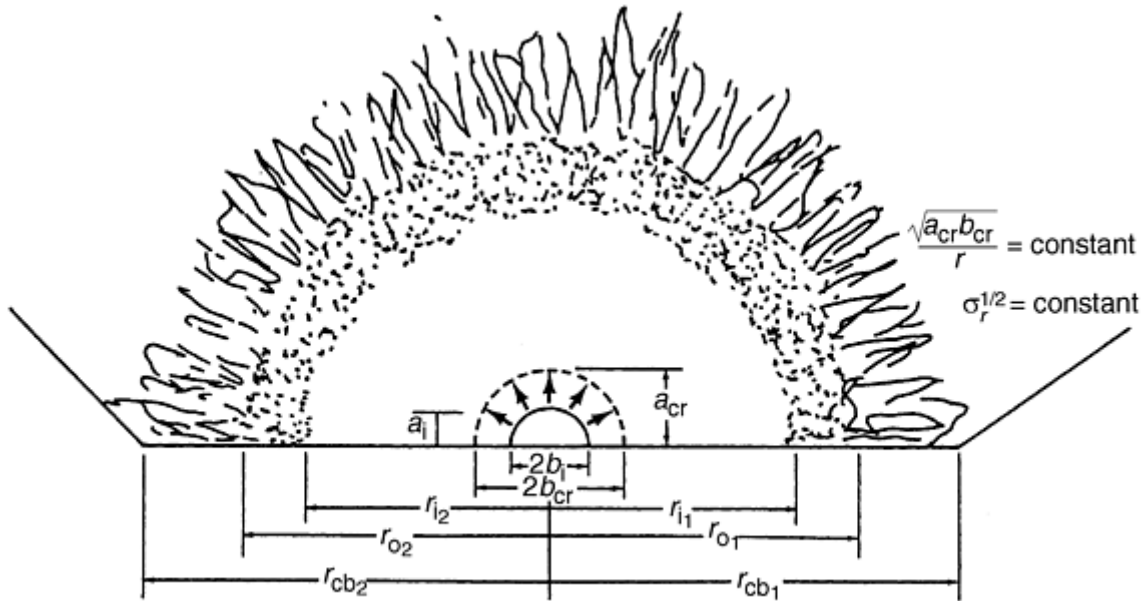


Fig. 14 Schematic of fracture surface of brittle materials showing the idealized preexisting flaw of depth a_i and half-width b_i and the failure-initiating critical flaw of depth a_{cr} and half-width b_{cr} . For rapid loading, a_i and b_i should be nearly coincident with a_{cr} and b_{cr} . The fracture-mirror radii boundaries are also shown in the figure: r_i , mirror-mist; r_o , mist-hackle; and r_{cb} , macroscopic crack branching. For some conditions, r_o and r_{cb} cannot be distinguished. σ is the fracture stress. Source: Ref 33

Evaluation of Fracture-Toughness Test Results

Although many examples exist in the literature of small batches of fracture toughness results for fracture resistance testing using a wide variety of methods applied to brittle solids, it is only recently that results are beginning to appear combining statistically significant sample sets of results for well-documented materials fracture tested using accepted and/or approved standardized test methods. For example, ASTM C 1421 (Ref 18) contains a precision and bias section that compares extensive results from various sources (including two round-robin programs sanctioned by the Versailles Advanced Materials and Standards, or VAMAS, organization) (Ref 36, 37) obtained using the test methods SEPB, SCF, and CNB detailed in ASTM C 1421 (although not necessarily the exact procedures). Two materials are highlighted: a sintered silicon carbide [Hexoloy SA, Carborundum (now Ste. Gobain), Niagara Falls, New York] and a hot-pressed silicon nitride [NC132, Norton Co. (now Ste. Gobain), Worcester, Massachusetts]. Each of these materials has a “flat” R -curve and displays little environmental susceptibility at room temperature. The results, graphically illustrated in Fig. 15 and 16, generally show the consistency of the fracture toughness measurements for two brittle materials regardless of sharp-crack technique.

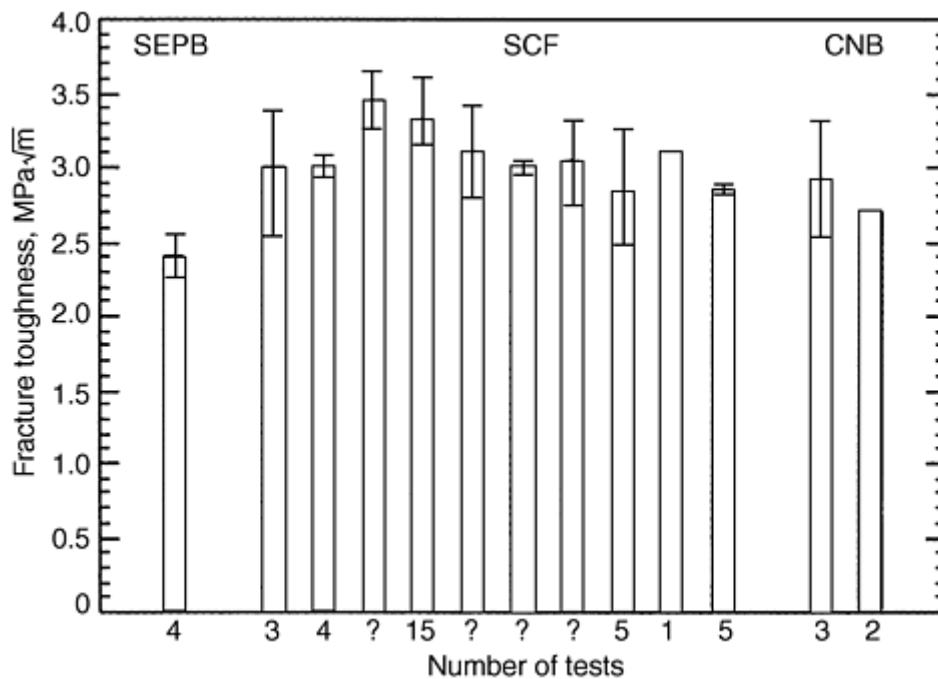


Fig. 15 Comparison of fracture-toughness test results from multiple sources for Hexoloy SA (sintered alpha silicon carbide) using three test methods described in ASTM C 1421. Each bar represents the mean plus or minus one standard deviation. SEPB, single-edge precracked beam; SCF, surface crack in flexure; CNB, chevron notched beam. Adapted from Ref 18

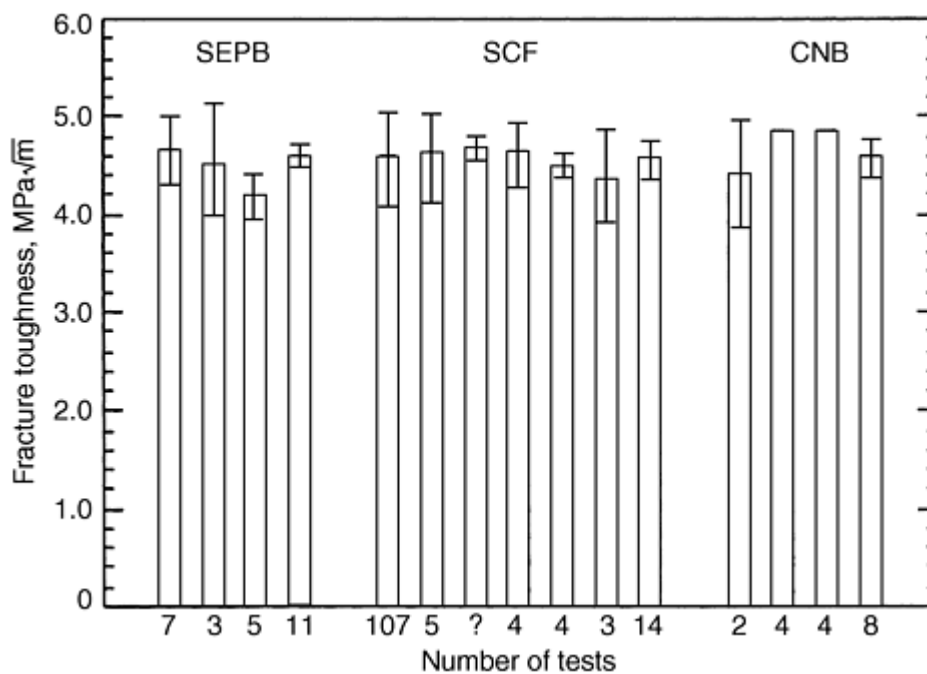


Fig. 16 Comparison of fracture-toughness test results from multiple sources for NC 132 (hot-pressed beta silicon nitride) using three test methods described in ASTM C 1421. Each bar represents the mean plus or minus one standard deviation. SEPB, single-edge precracked beam; SCF, surface crack in flexure; CNB, chevron notched beam. Adapted from Ref 18

A noteworthy use of ASTM C 1421 is to evaluate multiple billets of a standard reference material (SRM 2100, National Institute Standards and Technology, Gaithersburg, Maryland, 1999) known as SRM2100, the same hot-pressed silicon nitride as used in the VAMAS round robin and as shown in Fig. 16. For example, for billet C of the SRM at room temperature, the results were:

Method	Fracture toughness,	No. of valid tests
--------	---------------------	--------------------

	$\text{MPa}\sqrt{m}$	
SCF	$K_{\text{Isc}} = 4.58 \pm 0.16^{(a)}$	26
CNB	$K_{\text{Ivb}} = 4.60 \pm 0.13^{(a)}$	26
SEPB	$K_{\text{Ipb}} = 4.58 \pm 0.10^{(a)}$	19

(a) Mean \pm one standard deviation

This remarkable consistency of fracture toughness results for a single material confirms that the sharp-crack methods contained within ASTM C 1421 have been “optimized” (Ref 9) such that genuine material variability (e.g., billet-to-billet or batch-to-batch) can be discerned and quantified.

R-Curve Behavior at Ambient Temperature

R -curve behavior (i.e., increasing fracture resistance with crack extension, Fig. 3) for brittle materials, as discussed briefly in the introduction, is often a result of interactions of the crack and microstructure. For example, fracture process mechanisms as shown in Fig. 4 can be roughly divided into frontal and wake mechanisms. But why measure *R*-curve behavior in brittle materials? The need to measure *R*-curve behavior can include establishing the unequivocal starting point of the *R*-curve (i.e., intrinsic fracture resistance), R_0 , or it can include determining the final steady-state fracture resistance, R_∞ , or it may include defining the behavior between the extremes of the intrinsic and steady-state fracture resistance, $R(c)$ which may also be a function of crack shape, test specimen geometry, and testing parameters.

In metals, frontal mechanisms—specifically, plastic deformations in a region ahead of and near the crack tip—are responsible for crack closure effects (Ref 38). For engineering analysis, elastic-plastic fracture-mechanics concepts are usually applied, typically using K with a crack-size plasticity adjustment or the J -integral. It is important to realize that *R*-curves are not material properties (unlike fracture toughness), but are instead related to the testing conditions, including test rate and test specimen geometry (e.g., material thickness). Recently, ASTM E 1820 “Standard Test Method for Measurement of Fracture Toughness” (Ref 16) was introduced as a “unified” test method for fracture testing metals at room temperature. The test procedures of five other test methods are contained in ASTM E 1820 to allow extraction of fracture resistance in terms of K , J , and crack-tip opening displacement (CTOD) from a single test at room temperature. Three test specimens (similar to those used in ASTM E 399) are described: SENB, compact tension (CT), and a disk-shaped compact tension (DSCT). All require precracking, usually with cyclic loading, to promote fatigue crack initiation and propagation. Test conditions and procedures are specific to the fracture parameter being measured. However, a compliance method is described to establish in situ crack length during stable crack propagation.

ASTM E 1820 (Ref 16) was developed, and is appropriate, for measuring plane strain fracture toughness in ductile metals but does not necessarily address the unique aspects of brittle solids. In addition, test specimens are rather large, as are the notches, cracks, and precracks, presumably for ease of implementation as well as to minimize the influence of dimensional variations on the repeatability and reproducibility of the fracture resistance measurement.

Since the introduction of ASTM E 1820, standards-writing bodies worldwide have done little to introduce standard *R*-curve test methods for brittle solids, particularly for advanced ceramics. Several possible explanations exist for this:

- No single method for establishing *R*-curve behavior in brittle materials has stood out.
- No methodology has been established on how to use the measured *R*-curve behavior of brittle materials (in engineering or materials design).
- It is not clear if current fracture toughness techniques really can establish the starting point of *R*-curve behavior.
- *R*-curve behavior is not a material property because it is dependent on factors such as test specimen geometry, crack history, test mode, and rate.

However, although no standardized test methods exist for *R*-curve behavior in brittle materials, many unique and novel test methods have been reported. Often these methods focus on quantifying specific mechanisms giving rise to *R*-curve behavior rather than measuring the *R*-curve itself. The following sections, while not

intended to be an exhaustive listing of reported methods, discuss general aspects of these test methods for extrinsic flaws (macrocracks) and intrinsic flaws (microcracks) in test specimens.

Test Methods for *R*-Curve at Ambient Temperature. Regardless of the organization (ASTM, ISO, CEN, or JISC), no standardized test method for *R*-curve behavior of brittle materials has been proposed or approved. In the future, if the need for such standards are established, it will be useful to build on existing standards for fracture toughness testing of brittle materials such as ASTM did in developing E 1820.

Direct adaptation of *R*-curve test methods for metals is one approach that has been successfully used in determining the *R*-curve behavior in brittle materials. As shown in Fig. 17, an SENB test specimen in three-point flexure was used to test Westerly granite (Ref 39). Single fatigue cracks were introduced at the root of the notch by cyclic “loading” at 2.2 Hz under crack-mouth displacement (CMD) control mode with an initial force up to 90% of the breaking force. Both compliance and dye penetration methods were used to determine crack length during the stable crack-extension part of the fracture test. Apparent fracture toughness (K_R) and the *J*-integral (J_R) as functions of crack length were established.

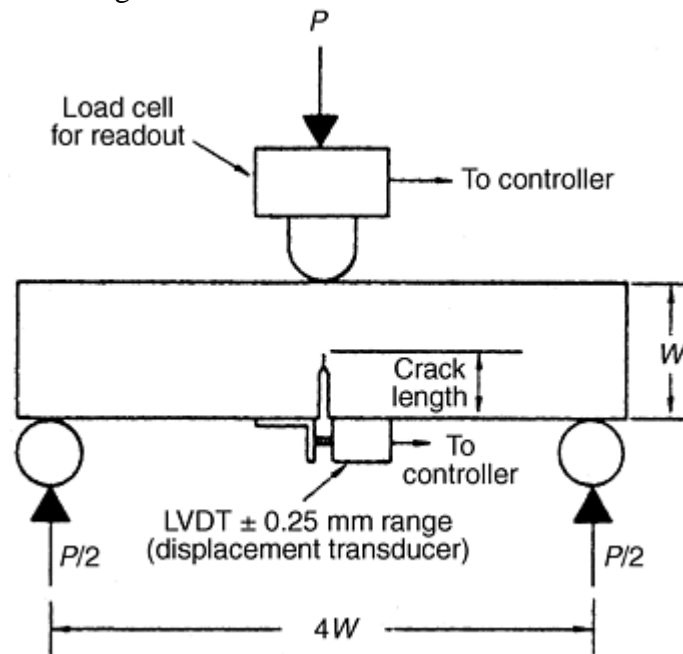


Fig. 17 Single-edge notch beam (SENB) fracture test specimen of Westerly granite used to determine *R*-curve behavior. LVDT, linear variable differential transformer. Source: Ref 39

Using SENB test specimens, but with a slightly different approach for stable crack propagation, the *R*-curve behavior of aluminum oxide ceramics was measured (Ref 40). Although no precrack was initiated at the tip of the notch root, it was reported that the three-point flexure test system was sufficiently stiff to allow stable crack propagation. Different initial notch depths led to the determination of a notch-depth independent intrinsic fracture resistance, while a notch-depth dependent fracture resistance as a function of crack length, $R(c)$, was determined. Both shape and magnitude of the *R*-curve were dependent on test parameters (i.e., test mode, test rate, and test specimen geometry).

A variation of the SENB was used to determine the grain-bridging contributions during *R*-curve testing of aluminum oxide and magnesium aluminate spinel (Ref 41, 42). A “back-notched” SENB test specimen (Fig. 18) was tested in four-point flexure. An aluminum oxide wedge was inserted into the back notch for load support throughout the fracture test. The fracture test was conducted until complete propagation of the crack across the unnotched section of the test specimen. The cracked (but not separated) SENB test specimens were then longitudinally tested in tension to determine the tensile stress-strain response of the fracture process zone. The *R*-curve was inferred from the postfracture tensile test results (Ref 42).

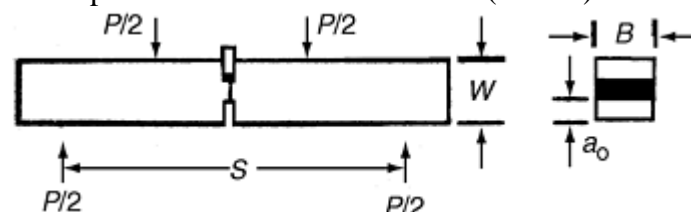


Fig. 18 Single-edge notch beam (SENB) fracture test specimen with back notch and wedge used to determine R -curve parameters from postfracture tensile tests. Source: Ref 41

A further study of R -curve effects in aluminum oxide was carried out using CNSB test specimens (Ref 43) (Fig. 12). The inherently stable crack propagation in the chevron notch geometry was used to incrementally extend the crack before unloading slightly to determine the compliance for calculating the instantaneous crack length. R -curves were plotted as stress intensity factor versus crack extension. A bearing steel was also evaluated using this technique (Ref 44).

R -curves for two brittle materials were determined (Ref 45) using one of the test specimen geometries (CNB) contained in the ASTM standardized fracture toughness method for brittle materials (ASTM C 1421). In this study, three-point flexure was used with square-cross section test specimens (Fig. 19). The tests were conducted monotonically, and the instantaneous compliance (not unloading compliance) was used to determine the instantaneous crack length. Crack mouth opening displacement (CMOD) was measured using a laser interferometric displacement gage.

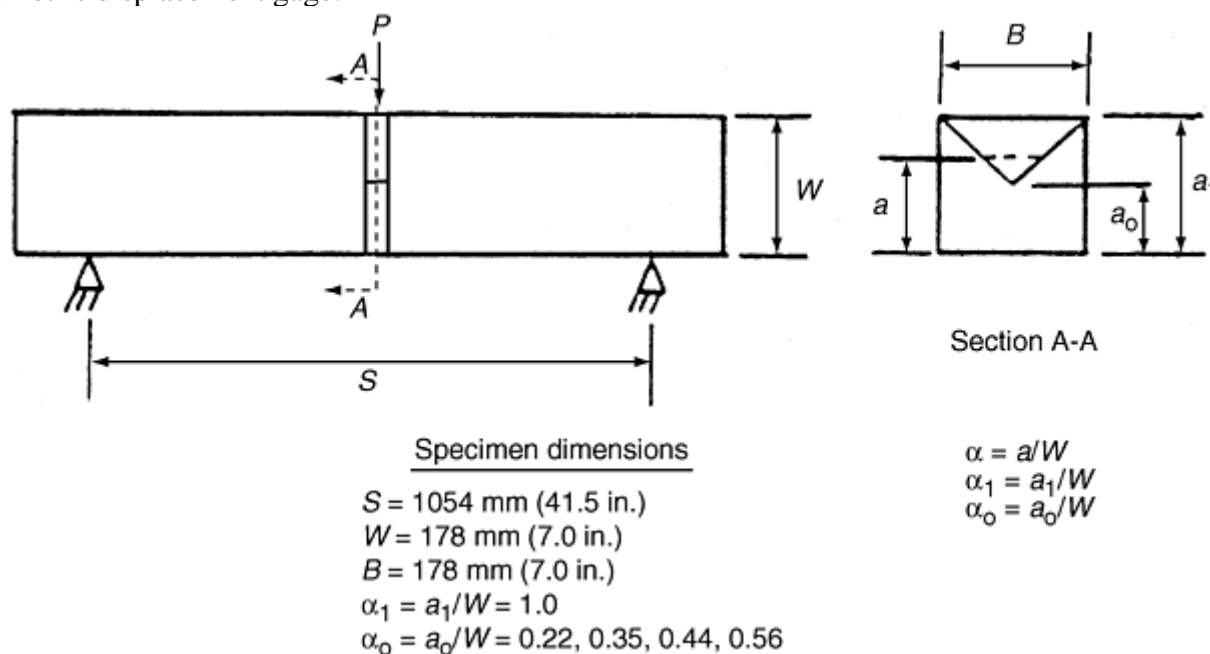


Fig. 19 Chevron notched beam (CNB) test specimen in three-point flexure for R -curve effects. Four normalized depth ratios (α_0) were included. Source: Ref 45

R -curve evaluation also was performed using the IS method (Ref 46). When the IS method is used to evaluate fracture strength/resistance in Eq 17 and 18, fracture toughness is related to the indentation force as well as the hardness and elastic modulus of the material. This fracture toughness is calculated for each strength test of the indented flexure test specimens (in these cases, the relationship between the flexural strength, S_f , and the indentation force, P , was assumed to be the theoretical: $S_f \propto P^{-1/3}$). However, for determining R -curve behavior and when all the data are fitted [i.e., $S_f = f(P)$], the exponent on P will only be $-\frac{1}{3}$ for materials with flat R -curves. Furthermore, if the R -curve is described as a power-law function of crack length, the result is (Ref 46):

$$K_{IR} = k(\Delta a)^\tau \quad (\text{Eq 25})$$

where k and τ are constants and Δa is the crack extension, then $\tau = 0$ if the R -curve is flat.

If the R -curve is not flat, then the relationship between flexural strength and indentation force is:

$$S_f \propto \alpha P^{-\beta} \quad (\text{Eq 26})$$

where the exponents β can be defined as $\tau = (1 - 3\beta)/(2 + 2\beta)$, and the coefficient α is defined as $K = Y\alpha(\beta\gamma)^{-\beta}(1 + \beta)^{(1 + \beta)}$ where Y and γ are related to the indentation crack geometry. Note that limiting values on τ are 0 for flat R -curve materials and 0.5 for the steepest rising R -curve material that still fractures catastrophically. This technique is illustrated in Fig. 20 where the assumption of flat R -curve ($\beta = -\frac{1}{3}$) obviously does not work. Note

that annealing to relieve the residual stress (*A* and *B* in Fig. 20) caused by the deformation of the indenter can significantly affect the fracture results.

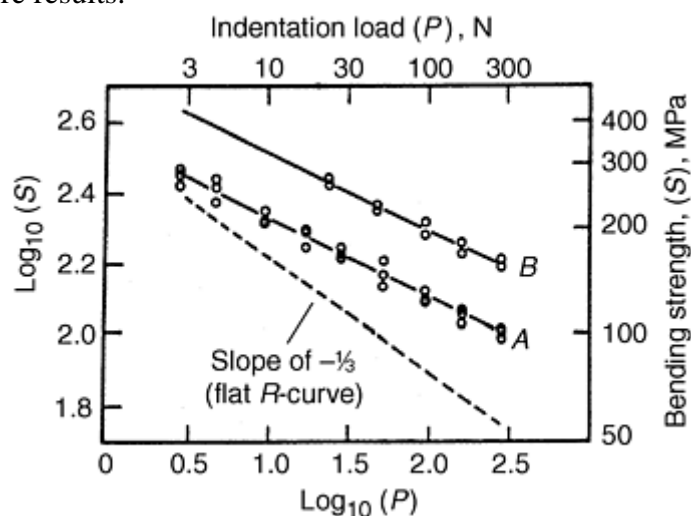


Fig. 20 Indentation strength (IS) fracture test method for *R*-curve behavior where observed flexural strength is a function of indentation force in a series of two experiments. Specimens for *A* included residual stress of indentation; specimens for *B* had the residual stress annealed out at elevated temperature. Source: Ref 46

For design purposes, the utility of this IS fracture test method is not in fracture mechanics-related analyses. Rather, its greater utility is its application to strength-rated analyses. If the strength distribution is described as Weibull (weakest link), then the Weibull shape parameter, m (i.e., Weibull modulus), can be related to the degree of the *R*-curve by (Ref 47):

$$m = \frac{m_o}{(1 - 2\tau)} \quad (\text{Eq 27})$$

where m_o is the Weibull modulus for $\tau = 0$. Equation 27 holds for a range of flaw sizes related to the indentations of the IS method. Equation 27 also shows that as the slope of the *R*-curve increases, so does the Weibull modulus, thus decreasing the scatter in the strength distribution. Note that m can potentially be equal to ∞ for a deterministic strength (i.e., $\tau \rightarrow \frac{1}{2}$).

Examples of *R*-Curve Test Data. Various types and levels of *R*-curves exist for brittle materials. For example, an *R*-curve for Westerly granite is shown in Fig. 21. Note in this case that the *J*-integral is plotted as a function of crack extension. Extrapolation of the *R*-curves to zero crack extension results in determination of J_{Ic} , which, when related to K_{Ic} , gives an agreement within 4% of K_{Ic} determined directly (Ref 39).

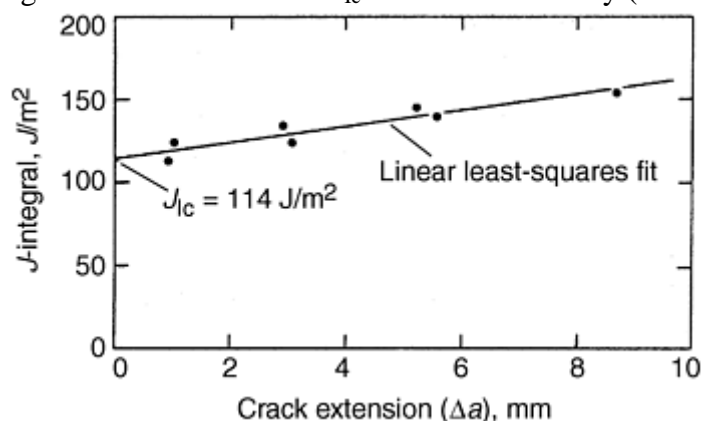


Fig. 21 *J*-integral *R*-curve determined from single-edge notch beam (SENB) fracture test specimens of Westerly granite. Source: Ref 39

R -curves in terms of an energy parameter (K_I^2 / E) are plotted in Fig. 22 for an aluminum oxide. Note that both the slopes and the shapes of the R-curves vary with notch depth, although the initial values of the R-curves appear to be independent of notch depth (Ref 40).

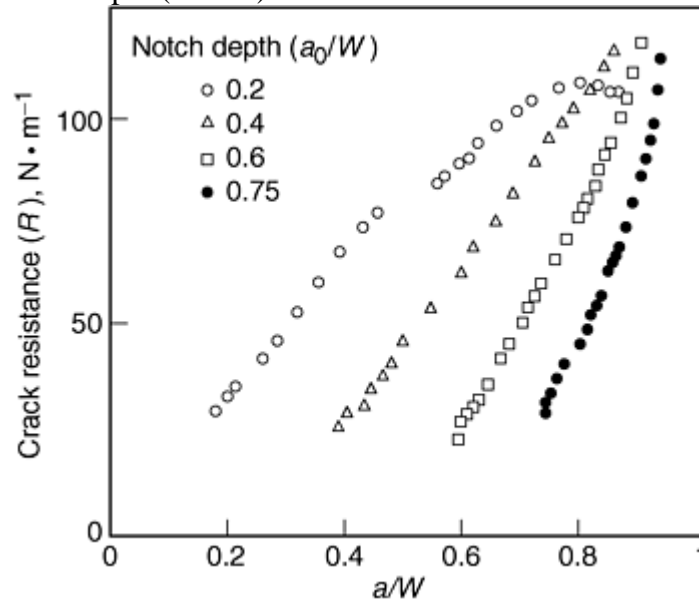


Fig. 22 R-curves as a function of crack depth for aluminum oxide. Source: Ref 40

R -curves determined from CNSB test specimens and in terms of stress intensity factors are shown in Fig. 23. Also shown in Fig. 23 is an R-curve determined from the IS method for the same material. Note that the R-curves are dependent on geometry, test method, and type of crack (intrinsic versus extrinsic) (Ref 44), although they do band the same K_I range.

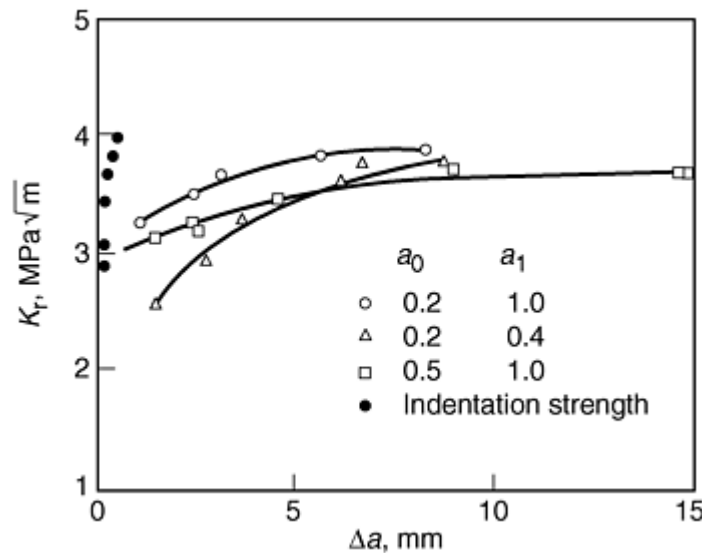


Fig. 23 Comparison of R-curves for aluminum oxide determined from the chevron notched short bar (CNSB) and indentation strength (IS) methods. Source: Ref 44

With the proper testing configuration, even flat R-curves can be measured using the CNB test specimen, as shown in Fig. 24 (Ref 45). These R-curves are not only flat, but the fracture toughness for one of the materials (silicon carbide) is only in the range of $3 \text{ MPa}\sqrt{m}$.

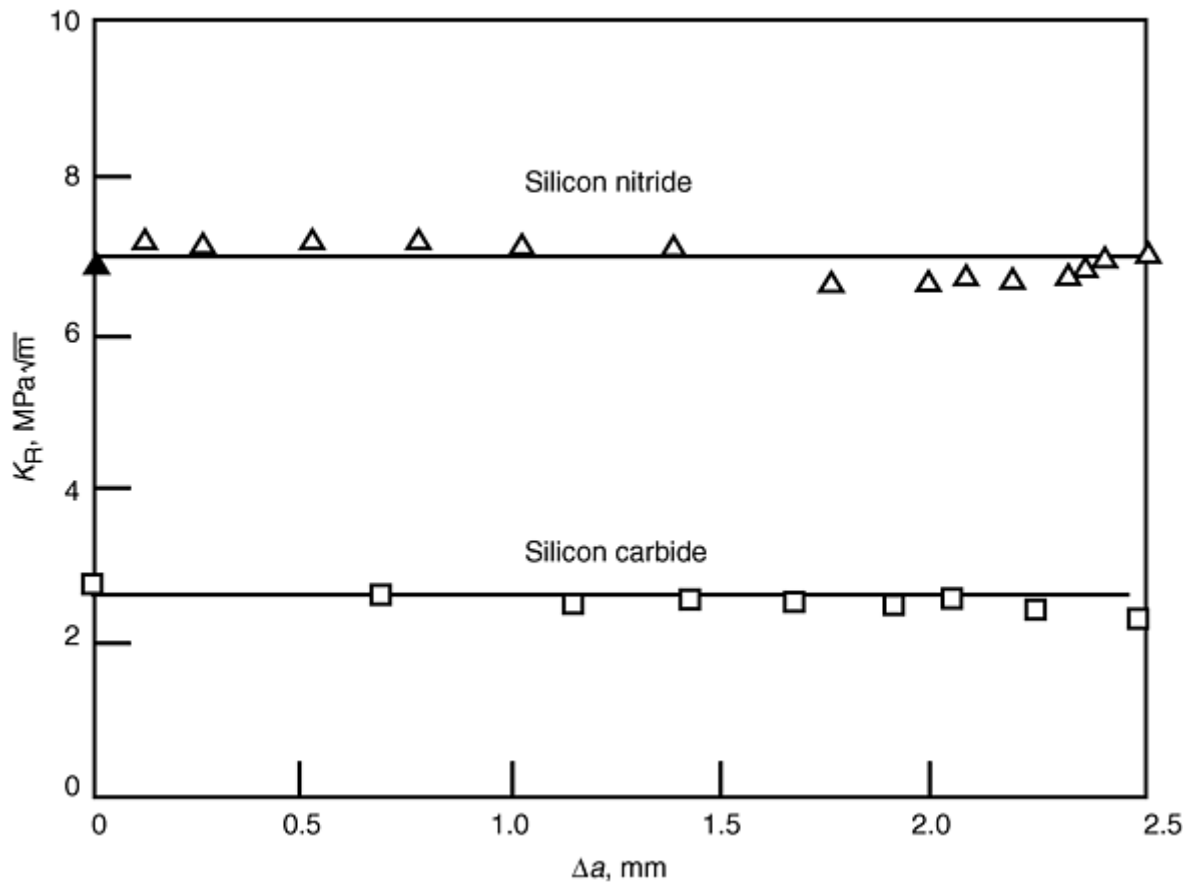


Fig. 24 Flat R -curves for silicon nitride and silicon carbide chevron notched, three-point bend (CNB) specimens at room temperature. Source: Ref 45

References cited in this section

2. A.A. Griffith, The Phenomena of Rupture and Flow in Solids, *Philos. Trans. R. Soc. (London) A*, Vol 221, 1920, p 163–198
3. B. Lawn, *Fracture of Brittle Solids*, Cambridge University Press, 1993
4. K.E. Amin, Toughness, Hardness, and Wear, *Ceramics and Glasses*, Vol 4, *Engineered Materials Handbook*, S.J. Schneider, J., Ed., ASM International, 1991, p 599–609
6. “Standard Test Method for Plane Strain Fracture Toughness of Metallic Materials,” E 399-90, *Annual Book of ASTM Standards*, Vol 03.01, ASTM, 1998
7. STP 678, *Fracture Mechanics Applied to Brittle Materials*, S.W. Freiman, Ed., ASTM, 1979
8. T. Fujii and T. Nose, Evaluation of Fracture Toughness of Ceramic Materials, *IJIS Int.*, Vol 29 (No. 9), 1989, p 717–725
9. G.D. Quinn, M.G. Jenkins, J.A. Salem, and I. Bar-On, Standardization of Fracture Toughness Testing of Ceramics in the United States, *Kor J. Ceram.*, Vol 4 (No. 4), 1998, p 311–322
10. M. Sakai and R.C. Bradt, Fracture Toughness Testing of Brittle Materials, *Int. Mater. Rev.*, Vol 38 (No. 2), 1993, p 53–58
16. “Standard Test Method for Measurement of Fracture Toughness,” C 1820-96, *Annual Book of ASTM Standards*, Vol 3.01, ASTM, 1999

17. "Standard Test Methods for the Determination of Fracture Toughness of Advanced Ceramics at Ambient Temperature," PS 070-97, *Annual Book of ASTM Standards*, Vol 15.01, ASTM, 1998
18. "Standard Test Methods for the Determination of Fracture Toughness of Advanced Ceramics at Ambient Temperature," C 1421-99, *Annual Book of ASTM Standards*, Vol 15.01, ASTM, 1999
19. "Testing Methods for the Fracture Toughness of High Performance Ceramics," JIS R1607-90, Japanese Industrial Standards Committee, Tokyo, Japan, 1990
20. G. Anstis, P. Chantikul, B. Lawn, and D. Marshall, A Critical Evaluation of Indentation Techniques for Measuring Fracture Toughness I: Direct Crack Measurements," *J. Am. Ceram. Soc.*, Vol 64 (No. 9), 1981, p 533–538
21. C.B. Ponton and R.D. Rawlings, Dependence of the Vickers Indentation Fracture Toughness on the Surface Crack Length, *Br. Ceram. Trans. J.*, Vol 88, 1989, p 83–99
22. "Fine Ceramics (Advanced Ceramics, Advanced Technical Ceramics)—Test Method for Fracture Toughness of Monolithic Ceramics at Room Temperature by Single Edge Pre-Cracked Beam (SEPB) Method," ISO DIS15732, Geneva, Switzerland, 1999
23. "Fine Ceramics (Advanced Ceramics, Advanced Technical Ceramics)—Test Method for Fracture Toughness of Monolithic Ceramics at Room Temperature by Surface Crack in Flexure (SCF) Method," ISO TC206/WG16, Geneva, Switzerland, 1999
24. "Advanced Technical Ceramics—Monolithic Ceramics—Test Methods for Determination of Apparent Fracture Toughness," CEN TC184, Brussels, Belgium, 1999 (draft, prENV)
25. A. Ghosh, M.G. Jenkins, A.S. Kobayashi, K.W. White, and R.C. Bradt, The Fracture Resistance of a Sintered Silicon Carbide Using the Chevron-Notch Bend Bar, *Silicon Carbide '87, Ceramic Transactions*, Vol 2, J.D. Crawley and C.E. Semler, Ed., The American Ceramic Society, Inc., Westerville, Ohio, 1989, p 241–251
26. H. Awaji and Y. Sakaida, V-Notch Technique for Single-Edge Notched Beam and Chevron Notch Methods, *J. Am. Ceram. Soc.*, Vol 73 (No. 11), 1990, p 3522–3523
27. J. Kübler, Fracture Toughness of Ceramics Using the SEVNB Method, *Ceram. Eng. Sci. Proc.*, Vol 20 (No. 4), 1999
28. "Standard Test Method for Flexural Strength of Advanced Ceramics at Ambient Temperatures," C 1161-94, *Annual Book of ASTM Standards*, Vol 15.01, ASTM, 1999
29. P. Chantikul, G. Anstis, B. Lawn, and D. Marshall, A Critical Evaluation of Indentation, Techniques for Measuring Fracture Toughness II: Strength Methods, *J. Am. Ceram. Soc.*, Vol 64 (No. 9), 1981, p 539–543
30. B.J. Pletka, E.R. Fuller, Jr., and B.G. Koepke, An Evaluation of Double Torsion Testing: Experimental, STP 678, *Fracture Mechanics Applied to Brittle Materials*, S.W. Frieman, Ed., ASTM, 1979, p 19–37
31. E.R. Fuller, Jr., An Evaluation of Double Torsion Testing: Analysis, STP 678, *Fracture Mechanics Applied to Brittle Materials*, S. Frieman, Ed., ASTM, 1979, p 3–18
32. J.A. Salem and J.L. Shannon, Jr., Fracture Toughness of Si₃N₄ Measured with Short Bar Chevron Notched Specimens, *J. Mater. Sci.*, Vol 22 (No. 1), 1987, p 321–324

33. J.J. Mecholsky and S.W. Frieman, Determination of Fracture Mechanics Parameters Through Fractographic Analysis of Ceramics, STP 678, *Fracture Mechanics Applied to Brittle Materials*, S.W. Frieman, Ed., ASTM, 1979, p 136–150
 34. R.W. Rice, Fractographic Determination of K_{Ic} and Effects of Microstructural Stresses in Ceramics, *Fractography of Glasses and Ceramics*, V. Frechette and J. Varner, Ed., Vol 17, *Ceramic Transactions*, American Ceramic Society, 1991
 35. “Standard Practice for Fractography and Characterization of Fracture Origins in Advanced Ceramics,” C 1322-96, *Annual Book of ASTM Standards*, Vol 15.01, ASTM, 1999
 36. H. Awaji, J. Kon, and H. Okuda, “The VAMAS Fracture Toughness Round Robin on Ceramics,” VAMAS report 9, JFCC, Nagoya, Japan, 1990
 37. G.D. Quinn, R.J. Gettings, and J.J. Kübler, “Fracture Toughness of Ceramics by the Surface Crack in Flexure (SCF) Method, A VAMAS Round Robin,” VAMAS report 17, NIST, Gaithersburg, Maryland, 1994
 38. G.R. Irwin, Fracture Mechanics, *Mechanical Testing*, Vol 8, *ASM Handbook*, ASM International, 1985, p 439–464
 39. R.A. Schmidt and T.J. Lutz, K_{Ic} and J_{Ic} of Westerly Granite-Effects of Thickness and In-Plane Dimensions, STP 678, *Fracture Mechanics Applied to Brittle Materials*, S.W. Frieman, Ed., ASTM, 1979
 40. R. Steinbruch, R. Kehands, and W. Schaarnwächter, Increase of Crack Resistance during Slow Crack Growth in Al_2O_3 Bend Specimens, *J. Mater. Sci.*, Vol 18, 1983, p 265–270
 41. J.C. Hay and K.W. White, Grain-Bridging Mechanisms in Monolithic Alumina and Spinel, *J. Am. Ceram. Soc.*, Vol 76 (No. 7), 1993, p 1849–1854
 42. J.C. Hay and K.W. White, Crack Face Bridging Mechanisms in Monolithic $MgAl_2O_3$ Spinel Microstructures, *Acta Metall. Mater.*, Vol 40 (No. 11), 1992, p 3017–3025
 43. J.A. Salem, J.L. Shannon, Jr., and R.C. Bradt, Crack Growth Resistance of Textured Alumina, *J. Am. Ceram. Soc.*, Vol 72 (No. 1), 1989, p 20–27
 44. J.A. Salem, J.L. Shannon, Jr., and M.G. Jenkins, Some Observation on Fracture Toughness and Fatigue Testing with Chevron-Notched Specimens, STP 1172, *Chevron-Notch Fracture Test Experience: Metals and Non-Metals*, K.R. Brown and F.I. Baratta, Ed., ASTM, 1992, p 9–25
 45. M.G. Jenkins, A.S. Kobayashi, K.W. White, and R.C. Bradt, A 3-D Finite Element Analysis of a Chevron-Notched, Three-Point Bend Fracture Specimen for Ceramic Materials, *Int. J. Fract.*, Vol 34, 1987, p 281–295
 46. R.F. Krause, Jr., Rising Fracture Toughness from the Bending Strength of Indented Alumina Beams, *J. Am. Ceram. Soc.*, Vol 71 (No. 5), 1988, p 338–343
 47. J.E. Ritter, Crack Propagation in Ceramics, *Ceramics and Glasses*, Vol 4, *Engineering Materials Handbook*, ASM International, 1991, p 694–699
-

Fracture Toughness and *R*-Curve Testing at Elevated Temperature

Decreasing mechanical properties and performance with increasing temperature are consistently observed for most materials. Complications of tests at elevated temperature include temperature control, environmental effects (both material and test apparatuses), and time-dependent behavior (e.g., creep or oxidation).

In fracture testing, a particularly troubling complication is the effect of material and/or environmental interactions on the crack-tip conditions. A good example of this is crack-tip blunting, which may more easily occur after the trouble of introducing an atomistically sharp precrack in fracture testing specimens.

At this time, no standardized test methods exist for fracture testing at elevated temperature (for metals or nonmetals). As the need increases for such standards, they will no doubt be introduced, not without much controversy and complication.

Test Methods for Fracture Toughness at Elevated Temperature

At this time there are no specific elevated-temperature standards for fracture toughness testing. Apparently, it is assumed that ambient temperature standards will be implemented with due care taken to ensure proper use at elevated temperatures. In most cases, this is a reasonable approach. However, complications that have been noted are crack healing and blunting in those methods that rely on precracking prior to fracture testing.

An early report of this “flaw healing” in SCF tests showed that fracture strength of indented flexure bars made of a silicon carbide increased by a factor of three after annealing in air. This implies that the increase in strength is due to the reduction in the effect of the SCF precrack on the susceptibility to fracture. Annealing in a vacuum caused a similar, but somewhat reduced, effect (Ref 48).

Special caution is advised in extending methods that start with a sharp crack introduced at ambient temperature. These methods include SEPB, SCF, IS, and precracked methods such as SENB and DCB. Methods that form cracks in situ will probably not experience the “flaw healing” phenomenon. These methods include all the chevron notched test specimens (CNB, CNSB, CNSR), SEVNB, and DT. Given the difficulties of properly performing and analyzing the IF method at ambient temperature, it appears doubtful that it could be successful at elevated temperatures.

Examples of Elevated-Temperature Fracture Toughness Test Data

“Flaw healing” can be a particular problem at elevated temperatures for precracked fracture test methods. However, even methods such as the CNB may exhibit difficulties in initiating and propagating cracks under certain conditions (e.g., very high temperatures). An in situ toughened silicon nitride (SN251, Kyocera Corporation, Kyoto, Japan 1990 vintage) was fracture tested using CNB, SEPB, and fine notched (50 μm thickness) SENB (Ref 44). The load-displacement curves for the CNB tests are shown in Fig. 25. The stable curves at 25 and 1200 °C (77 and 2200 °F) provide valid test results according to ASTM C 1421. However, the highly nonlinear behavior at 1371 °C (2500 °F), although stable and valid according to the standard, was ruled an invalid test because a crack initiated and grew only part way before stopping at the tip of the chevron. Instead, the highly nonlinear behavior shown in Fig. 25 was attributed to “plastic hinging” (Ref 44).

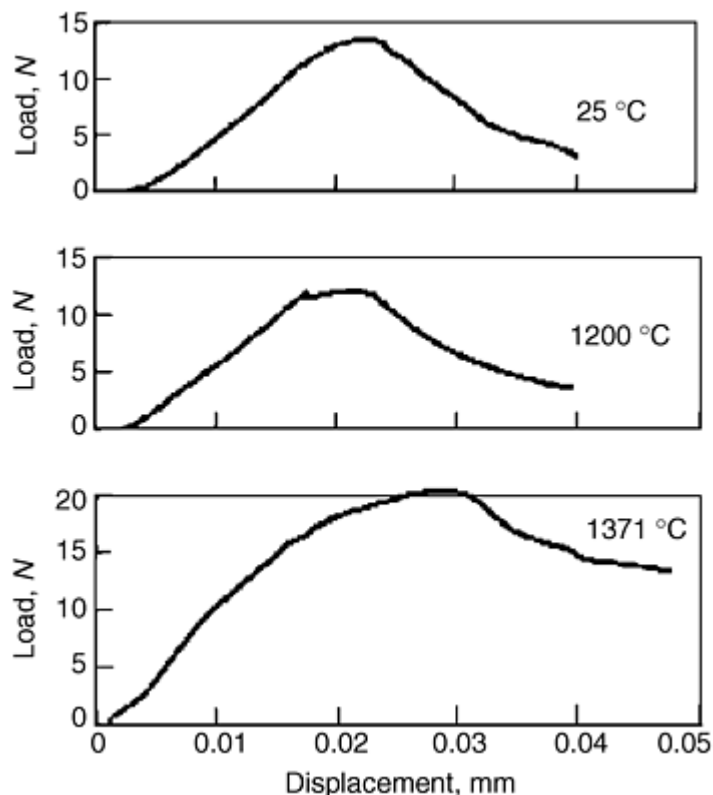


Fig. 25 Load displacement curves for stable fracture in chevron notched beam (CNB) fracture tests of an in situ toughened silicon nitride. The test at 1370 °C is an invalid test because a crack never initiated at the tip of the chevron, and plastic hinging occurred. Source: Ref 44

Comparison of fracture toughness results from CNB, SEPB, and sharp notch SENB are presented in Fig. 26. Note that under the proper conditions at 1371 °C (2500 °F) (fast heat up and short hold times), the SEPB method, despite the sharp precrack, gives results similar to the sharp notch SENB method. The CNB method at 1371 °C (2500 °F) under these test conditions tends to overestimate fracture toughness as expected from the nonlinear loading curve shown in Fig. 25.

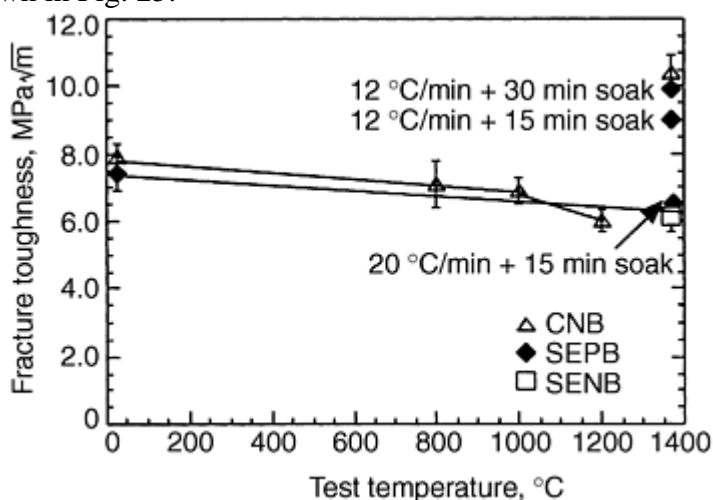


Fig. 26 Comparison of fracture toughness for in situ toughened silicon nitride (SN251) as functions of temperature for chevron notched beam (CNB), single-edge precracked beam (SEPB), and single-edge V-notch beam (SEVNB) fracture test methods

In a demonstration of the diversity of application of the CNB method, fracture toughness for seven advanced ceramics (from aluminum oxide to silicon carbide to silicon nitride) and eight temperatures (from 20–1400 °C or 68–2600 °F) in ambient air are plotted with error bars in Fig. 27. With the exception of the nonlinear behavior of the in situ toughened silicon nitride, all results are predictable and consistent (Ref 49).

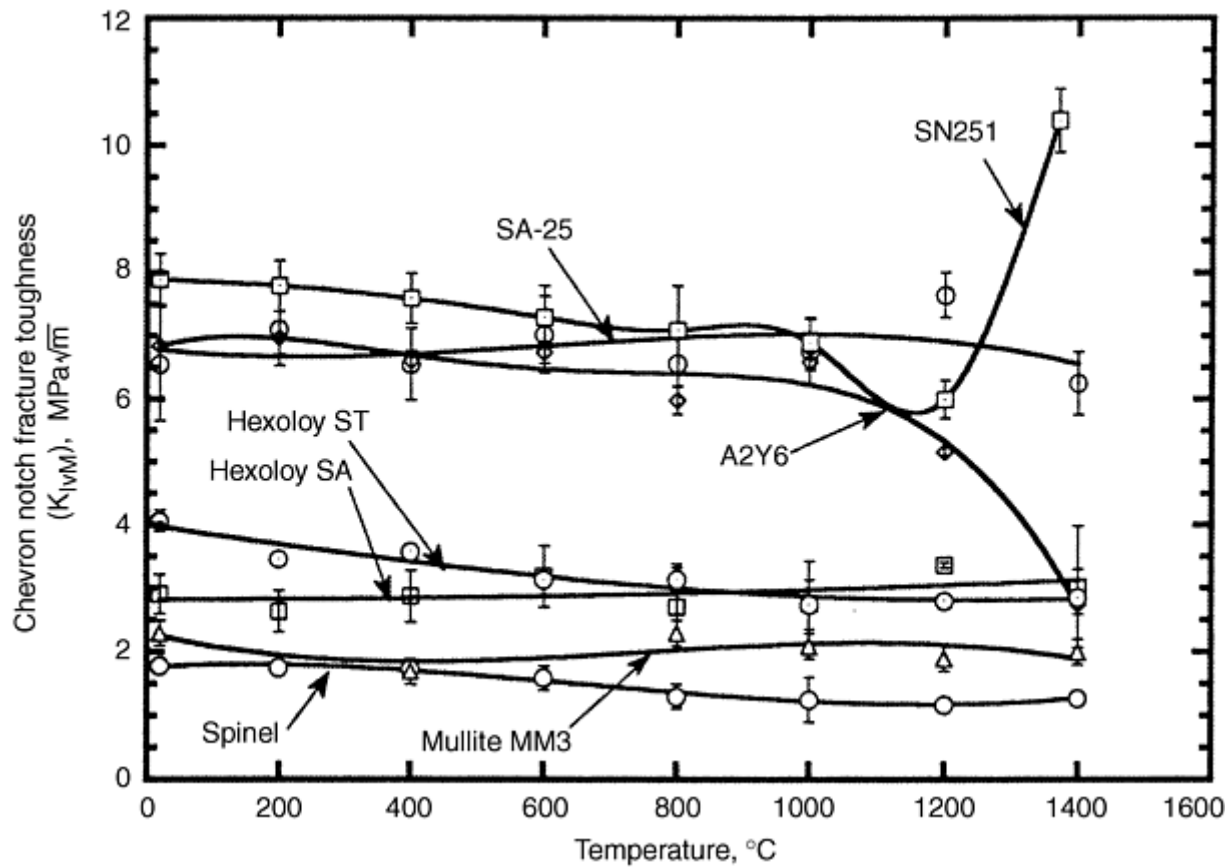


Fig. 27 Fracture toughness results as functions for temperature for seven advanced ceramic materials. Source: Ref 49

R-Curve Testing at Elevated Temperature

Temperature-dependent mechanical properties and performance are consistently observed for most materials. At elevated temperatures complications of fracture testing include temperature control, environmental effects (both material and test apparatuses), and time-dependent behavior.

In *R*-curve fracture testing, the complication of materials and/or environmental interactions on the crack-tip conditions is of concern. For example, crack-tip blunting can occur after an atomistically sharp precrack is introduced in fracture test specimens. Even methods that are successful at in situ crack initiation can exhibit problems with “flaw healing” as the crack propagates through the material during *R*-curve testing.

At this time, no dominant test methods exist for *R*-curve testing at elevated temperature (for metals or nonmetals). If the need develops for such test methods, they will no doubt be introduced, but not without much controversy and complication.

Test Methods for *R*-Curve Testing at Elevated Temperature. Currently, there are no specific elevated temperature standards for *R*-curve testing. Apparently, it is assumed that ambient temperature standards will be implemented with due care taken to ensure proper use at elevated temperatures. In most cases, this is a reasonable approach. However, complications that have been noted are crack healing and blunting in those methods that rely on precracking prior to fracture testing.

One successful method promoted as characterizing the complete fracture history (crack initiation to stable crack propagation to final fracture) of a brittle material in a single test used to CNB test specimen (Ref 49). This method used a monotonic load history combined with a laser-based apparatus to measure CMOD, and it used a compliance method to determine crack length, fracture toughness, *R*-curve, and work of fracture for a range of monolithic and composite advanced ceramics.

Special caution is advised in extending methods that start with a sharp crack introduced at ambient temperature. These methods include SEPB, SCF, IS, and precracked methods such as SENB and DCB. Methods that form cracks in situ will probably not experience the “flaw healing” phenomenon. These methods include other chevron notched test specimens (CNB, CNSB, CNSR), SEVNB, and DT. Given the difficulties of properly

performing and analyzing the IF method at ambient temperature, it appears doubtful that it could be successful at elevated temperatures.

Examples of Elevated-Temperature *R*-Curve Test Data. The use of the CNB method to characterize the complete fracture history of a single test specimen (Ref 45) is an excellent demonstration of the information available to characterize fracture behavior of brittle materials. For example, flat *R*-curves for three materials are shown at two temperatures (20 and 1200 °C, or 68 and 2200 °F) in Fig. 28(a). Nonlinear *R*-curves are shown for four materials in Fig. 28(b). Keep in mind that it has been shown that *R*-curves are not material properties and are highly dependent on test conditions, including test specimen geometry. Thus, the *R*-curves shown in Fig. 28 indicate material response and “toughening mechanisms” in the presence of cracks. However, the information is of questionable use for design purposes.

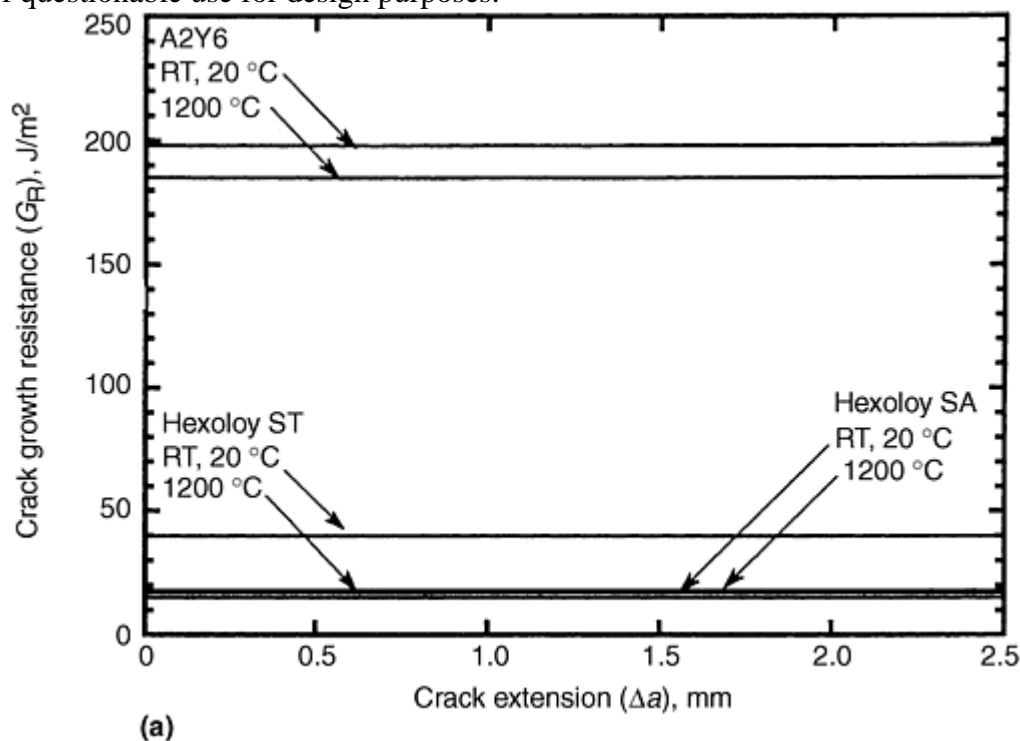


Fig. 28 *R*-curves for materials tested at room and elevated temperature using the chevron notch beam (CNB) method. (a) Flat *R*-curves. (b) Nonlinear *R*-curves. Source: Ref 49

References cited in this section

44. J.A. Salem, J.L. Shannon, Jr., and M.G. Jenkins, Some Observation on Fracture Toughness and Fatigue Testing with Chevron-Notched Specimens, STP 1172, *Chevron-Notch Fracture Test Experience: Metals and Non-Metals*, K.R. Brown and F.I. Baratta, Ed., ASTM, 1992, p 9–25
45. M.G. Jenkins, A.S. Kobayashi, K.W. White, and R.C. Bradt, A 3-D Finite Element Analysis of a Chevron-Notched, Three-Point Bend Fracture Specimen for Ceramic Materials, *Int. J. Fract.*, Vol 34, 1987, p 281–295
48. J.J. Petrovic and M.C. Mendiratta, Fracture from Controlled Surfaces Flows, *Fracture Mechanics Applied to Brittle Materials*, STP 678, S.W. Frieman, Ed., ASTM, 1992, p 83–102
49. M.G. Jenkins, M.K. Ferber, A. Ghosh, J.T. Peussa, and J.A. Salem, Chevron-Notched, Flexure Tests for Measuring the Elevated Temperature Fracture Resistance of Structural Ceramics, STP 1172, *Chevron-Notch Fracture Test Experience: Metals and Non-Metals*, K.R. Brown and F.I. Baratta, Ed., ASTM, 1992, p 159–177

Fracture Resistance Testing of Brittle Solids

Michael Jenkins, University of Washington; Johnathan Salem, NASA-Glenn Research Center

Summary

The fracture of theoretical brittle solids, while conceptually (and mathematically) rather simple and straightforward, is far from simple in practice. “Real” materials often contain residual stresses, microstructures, and geometric features that can complicate test methods intended to extract what appears to be a fundamental material property: fracture resistance in the form of fracture toughness. Further complicating test methods are differences in fracture behavior because of the type of flaw: intrinsic flaws (i.e., microcracks) often provide information on intrinsic fracture resistance behavior; that is, fundamental behavior without influence of microstructure or history of crack propagation (i.e., *R*-curve) fracture resistance. In contrast, extrinsic flaws (i.e., induced cracks) can be used to measure either the intrinsic or the steady-state fracture resistance, but can also lead to apparently large scatter (actually, differences) in the results if the influence of the microstructure and history of crack propagation are not accounted for.

Standardized test methods for fracture of brittle solids (specifically, advanced ceramics) developed to date (e.g., ASTM C 1421, JIS R1607, and ISO DIS15732) have concentrated on maximizing repeatability and reproducibility of the fracture resistance measurements at the onset of brittle fracture. Minimizing the effects of *R*-curve behavior, environmentally assisted crack growth and variability in testing are primary concerns.

Although *R*-curve behavior is recognized as having a strong influence on the fracture behavior of polycrystalline brittle solids, no standardization activities are currently underway to develop standard test methods. Several reasons may be responsible for this lack of activity:

- Research in this area is still quite active and no dominant methods have emerged.
- It is not clear how to deal with the issue of intrinsic fracture resistance versus steady-state fracture resistance and how this relates to the design methodologies that include probabilistic methods and statistical strength distributions.
- *R*-curve behavior is not a material property because it is dependent on component (i.e., test specimen) geometry, crack shape, crack propagation history, stress levels, and test parameters.

At elevated temperature, methods that involve the creation of sharp precracks at room temperature may become unusable at certain elevated temperatures as crack healing and crack-tip blunting negate the effects of precracks. Methods that use either in situ crack formation or very sharp notches seem to provide better ways to measure either fracture toughness or *R*-curve behavior at elevated temperatures.

For brittle solids, it is clear that the driver behind methods to determine fracture resistance is not necessarily for its use in determining the resistance of the material or design to extrinsic flaws. Instead, the need is to accurately and precisely determine the fracture resistance of brittle solids for use in relative comparison indices for evaluation of material performance in fracture-resistance related (but not fracture-resistance driven) applications.

Fracture Resistance Testing of Brittle Solids

Michael Jenkins, University of Washington; Johnathan Salem, NASA-Glenn Research Center

References

1. G.D. Quinn, Strength and Proof Testing, *Ceramics and Glasses*, Vol 4, *Engineering Materials Handbook*, ASM International, 1991, p 585–598
2. A.A. Griffith, The Phenomena of Rupture and Flow in Solids, *Philos. Trans. R. Soc. (London) A*, Vol 221, 1920, p 163–198
3. B. Lawn, *Fracture of Brittle Solids*, Cambridge University Press, 1993
4. K.E. Amin, Toughness, Hardness, and Wear, *Ceramics and Glasses*, Vol 4, *Engineered Materials Handbook*, S.J. Schneider, J., Ed., ASM International, 1991, p 599–609
5. G.R. Irwin, Fracture I, *Handbuch der Physik*, Vol 6, Springer-Verlag, Berlin, Germany, 1958, p 558–590
6. “Standard Test Method for Plane Strain Fracture Toughness of Metallic Materials,” E 399-90, *Annual Book of ASTM Standards*, Vol 03.01, ASTM, 1998
7. STP 678, *Fracture Mechanics Applied to Brittle Materials*, S.W. Freiman, Ed., ASTM, 1979
8. T. Fujii and T. Nose, Evaluation of Fracture Toughness of Ceramic Materials, *IJIS Int.*, Vol 29 (No. 9), 1989, p 717–725
9. G.D. Quinn, M.G. Jenkins, J.A. Salem, and I. Bar-On, Standardization of Fracture Toughness Testing of Ceramics in the United States, *Kor J. Ceram.*, Vol 4 (No. 4), 1998, p 311–322
10. M. Sakai and R.C. Bradt, Fracture Toughness Testing of Brittle Materials, *Int. Mater. Rev.*, Vol 38 (No. 2), 1993, p 53–58
11. J. Larsen-Basse, Abrasive Wear of Ceramics, *Friction and Wear of Ceramics*, S. Jahanmir, Ed., Marcel Dekker, Inc., New York, 1994, p 99–118
12. A. Evans and D. Marshall, Wear Mechanisms in Ceramics, *Fundamentals of Friction and Wear of Materials*, D. Rigney, Ed., American Society for Metals, 1981, p 439–452
13. J. Ritter, Erosion Damage in Structural Ceramics, *Material Sci. Eng.* Vol 71, 1985, p 195–201
14. J.B. Quinn and G.D. Quinn, Hardness and Brittleness of Ceramics, *Ceram. Eng. Sci. Proc.*, Vol 17 (No. 3), 1996, p 59–68
15. J.B. Quinn and G.D. Quinn, Indentation Brittleness of Ceramics: A Fresh Approach, *J. Mater. Sci.*, Vol 32, 1997, p 4331–4346
16. “Standard Test Method for Measurement of Fracture Toughness,” C 1820-96, *Annual Book of ASTM Standards*, Vol 3.01, ASTM, 1999
17. “Standard Test Methods for the Determination of Fracture Toughness of Advanced Ceramics at Ambient Temperature,” PS 070-97, *Annual Book of ASTM Standards*, Vol 15.01, ASTM, 1998
18. “Standard Test Methods for the Determination of Fracture Toughness of Advanced Ceramics at Ambient Temperature,” C 1421-99, *Annual Book of ASTM Standards*, Vol 15.01, ASTM, 1999
19. “Testing Methods for the Fracture Toughness of High Performance Ceramics,” JIS R1607-90, Japanese Industrial Standards Committee, Tokyo, Japan, 1990

20. G. Anstis, P. Chantikul, B. Lawn, and D. Marshall, A Critical Evaluation of Indentation Techniques for Measuring Fracture Toughness I: Direct Crack Measurements,” *J. Am. Ceram. Soc.*, Vol 64 (No. 9), 1981, p 533–538
21. C.B. Ponton and R.D. Rawlings, Dependence of the Vickers Indentation Fracture Toughness on the Surface Crack Length, *Br. Ceram. Trans. J.*, Vol 88, 1989, p 83–99
22. “Fine Ceramics (Advanced Ceramics, Advanced Technical Ceramics)—Test Method for Fracture Toughness of Monolithic Ceramics at Room Temperature by Single Edge Pre-Cracked Beam (SEPB) Method,” ISO DIS15732, Geneva, Switzerland, 1999
23. “Fine Ceramics (Advanced Ceramics, Advanced Technical Ceramics)—Test Method for Fracture Toughness of Monolithic Ceramics at Room Temperature by Surface Crack in Flexure (SCF) Method,” ISO TC206/WG16, Geneva, Switzerland, 1999
24. “Advanced Technical Ceramics—Monolithic Ceramics—Test Methods for Determination of Apparent Fracture Toughness,” CEN TC184, Brussels, Belgium, 1999 (draft, prENV)
25. A. Ghosh, M.G. Jenkins, A.S. Kobayashi, K.W. White, and R.C. Bradt, The Fracture Resistance of a Sintered Silicon Carbide Using the Chevron-Notch Bend Bar, *Silicon Carbide '87, Ceramic Transactions*, Vol 2, J.D. Crawley and C.E. Semler, Ed., The American Ceramic Society, Inc., Westerville, Ohio, 1989, p 241–251
26. H. Awaji and Y. Sakaida, V-Notch Technique for Single-Edge Notched Beam and Chevron Notch Methods, *J. Am. Ceram. Soc.*, Vol 73 (No. 11), 1990, p 3522–3523
27. J. Kübler, Fracture Toughness of Ceramics Using the SEVNB Method, *Ceram. Eng. Sci. Proc.*, Vol 20 (No. 4), 1999
28. “Standard Test Method for Flexural Strength of Advanced Ceramics at Ambient Temperatures,” C 1161-94, *Annual Book of ASTM Standards*, Vol 15.01, ASTM, 1999
29. P. Chantikul, G. Anstis, B. Lawn, and D. Marshall, A Critical Evaluation of Indentation, Techniques for Measuring Fracture Toughness II: Strength Methods, *J. Am. Ceram. Soc.*, Vol 64 (No. 9), 1981, p 539–543
30. B.J. Pletka, E.R. Fuller, Jr., and B.G. Koepke, An Evaluation of Double Torsion Testing: Experimental, STP 678, *Fracture Mechanics Applied to Brittle Materials*, S.W. Frieman, Ed., ASTM, 1979, p 19–37
31. E.R. Fuller, Jr., An Evaluation of Double Torsion Testing: Analysis, STP 678, *Fracture Mechanics Applied to Brittle Materials*, S. Frieman, Ed., ASTM, 1979, p 3–18
32. J.A. Salem and J.L. Shannon, Jr., Fracture Toughness of Si_3N_4 Measured with Short Bar Chevron Notched Specimens, *J. Mater. Sci.*, Vol 22 (No. 1), 1987, p 321–324
33. J.J. Mecholsky and S.W. Frieman, Determination of Fracture Mechanics Parameters Through Fractographic Analysis of Ceramics, STP 678, *Fracture Mechanics Applied to Brittle Materials*, S.W. Frieman, Ed., ASTM, 1979, p 136–150
34. R.W. Rice, Fractographic Determination of K_{Ic} and Effects of Microstructural Stresses in Ceramics, *Fractography of Glasses and Ceramics*, V. Frechette and J. Varner, Ed., Vol 17, *Ceramic Transactions*, American Ceramic Society, 1991

35. "Standard Practice for Fractography and Characterization of Fracture Origins in Advanced Ceramics," C 1322-96, *Annual Book of ASTM Standards*, Vol 15.01, ASTM, 1999
36. H. Awaji, J. Kon, and H. Okuda, "The VAMAS Fracture Toughness Round Robin on Ceramics," VAMAS report 9, JFCC, Nagoya, Japan, 1990
37. G.D. Quinn, R.J. Gettings, and J.J. Kübler, "Fracture Toughness of Ceramics by the Surface Crack in Flexure (SCF) Method, A VAMAS Round Robin," VAMAS report 17, NIST, Gaithersburg, Maryland, 1994
38. G.R. Irwin, Fracture Mechanics, *Mechanical Testing*, Vol 8, *ASM Handbook*, ASM International, 1985, p 439–464
39. R.A. Schmidt and T.J. Lutz, K_{Ic} and J_{Ic} of Westerly Granite-Effects of Thickness and In-Plane Dimensions, STP 678, *Fracture Mechanics Applied to Brittle Materials*, S.W. Frieman, Ed., ASTM, 1979
40. R. Steinbruch, R. Kehands, and W. Schaarnwächter, Increase of Crack Resistance during Slow Crack Growth in Al_2O_3 Bend Specimens, *J. Mater. Sci.*, Vol 18, 1983, p 265–270
41. J.C. Hay and K.W. White, Grain-Bridging Mechanisms in Monolithic Alumina and Spinel, *J. Am. Ceram. Soc.*, Vol 76 (No. 7), 1993, p 1849–1854
42. J.C. Hay and K.W. White, Crack Face Bridging Mechanisms in Monolithic $MgAl_2O_3$ Spinel Microstructures, *Acta Metall. Mater.*, Vol 40 (No. 11), 1992, p 3017–3025
43. J.A. Salem, J.L. Shannon, Jr., and R.C. Bradt, Crack Growth Resistance of Textured Alumina, *J. Am. Ceram. Soc.*, Vol 72 (No. 1), 1989, p 20–27
44. J.A. Salem, J.L. Shannon, Jr., and M.G. Jenkins, Some Observation on Fracture Toughness and Fatigue Testing with Chevron-Notched Specimens, STP 1172, *Chevron-Notch Fracture Test Experience: Metals and Non-Metals*, K.R. Brown and F.I. Baratta, Ed., ASTM, 1992, p 9–25
45. M.G. Jenkins, A.S. Kobayashi, K.W. White, and R.C. Bradt, A 3-D Finite Element Analysis of a Chevron-Notched, Three-Point Bend Fracture Specimen for Ceramic Materials, *Int. J. Fract.*, Vol 34, 1987, p 281–295
46. R.F. Krause, Jr., Rising Fracture Toughness from the Bending Strength of Indented Alumina Beams, *J. Am. Ceram. Soc.*, Vol 71 (No. 5), 1988, p 338–343
47. J.E. Ritter, Crack Propagation in Ceramics, *Ceramics and Glasses*, Vol 4, *Engineering Materials Handbook*, ASM International, 1991, p 694–699
48. J.J. Petrovic and M.C. Mendiratta, Fracture from Controlled Surfaces Flaws, *Fracture Mechanics Applied to Brittle Materials*, STP 678, S.W. Frieman, Ed., ASTM, 1992, p 83–102
49. M.G. Jenkins, M.K. Ferber, A. Ghosh, J.T. Peussa, and J.A. Salem, Chevron-Notched, Flexure Tests for Measuring the Elevated Temperature Fracture Resistance of Structural Ceramics, STP 1172, *Chevron-Notch Fracture Test Experience: Metals and Non-Metals*, K.R. Brown and F.I. Baratta, Ed., ASTM, 1992, p 159–177

Fatigue and Fracture Mechanics

Introduction

FATIGUE is the progressive, localized, and permanent structural damage that occurs when a material is subjected to cyclic or fluctuating strains at nominal stresses that have maximum values less than (and often much less than) the static yield strength of the material (Ref 1). This process of fatigue failure can be divided into different stages, which, from the standpoint of metallurgical processes, can be divided into five stages (Ref 1):

1. Cyclic plastic deformation prior to fatigue crack initiation
2. Initiation of one or more microcracks
3. Propagation or coalescence of microcracks to form one or more microcracks
4. Propagation of one or more macrocracks
5. Final failure

This division is defined by the characterization of the underlying fatigue damage of a material. It also clearly defines the requirement of plastic deformation for the onset of crack initiation. In general, three simultaneous conditions are required for the occurrence of fatigue damage: cyclic stress, tensile stress, and plastic strain. If any one of these three conditions is not present, a fatigue crack will not initiate and propagate. The plastic strain resulting from cyclic stress initiates the crack; and the tensile stress (which may be localized tensile stresses caused by compressive loads) promotes crack propagation (Ref 1).

The stages of fatigue can also be defined in more general terms from the perspective of mechanical behavior of crack growth. For example, another division of the fatigue process is defined as follows (Ref 2):

- Nucleation (initiation of fatigue cracks)
- Structurally dependent crack growth rates (often called the “short crack” or “small crack” phase)
- Crack growth rates that can be characterized by either linear elastic fracture mechanics, elastic-plastic fracture mechanics, or fully plastic fracture mechanics
- Final instability

This definition of the stages in the fatigue process is roughly equivalent to the first, except that crack propagation is expressed in terms of crack growth rates, and nucleation is meant to include all processes leading up to crack initiation.

In general, the fatigue process consists of a crack initiation and a crack propagation phase. There is, however, no general agreement when (or at what crack size) the crack initiation process ends, and when the crack growth process begins (Ref 3). Nonetheless, the separation of the fatigue process into initiation and propagation phases has been an important and useful advance in engineering.

Another important engineering advance is the transfer of the multistage fatigue process from the field to the laboratory. In order to study, explain, and qualify component designs, or to conduct failure analyses, a key engineering step is often the simulation of the problem in the laboratory. Any simulation is, of course, a compromise of what is practical to quantify, but the study of the multistage fatigue process has been greatly advanced by the combined methods of strain-control testing and the development fracture mechanics of fatigue crack growth rates. This combined approach (Fig. 1) is a key advance that allows better understanding and simulation of both crack nucleation in regions of localized strain and the subsequent crack growth mechanisms outside the plastic zone. This integration of fatigue and fracture mechanics has had important implications in many industrial applications for mechanical and materials engineering.

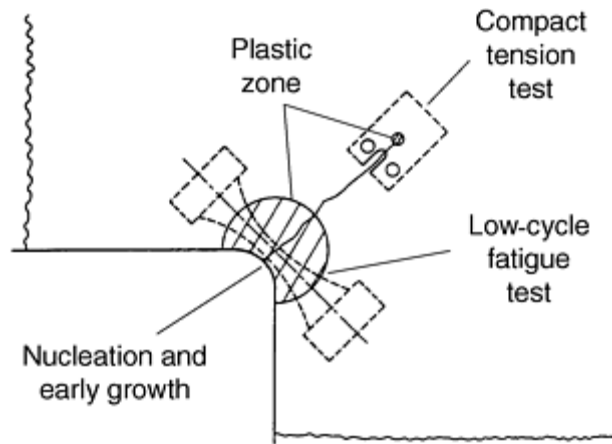


Fig. 1 Laboratory simulation of the multistage fatigue process. Source: Ref 2

This introductory article briefly reviews the three basic types of fatigue properties, which are:

- Stress-life ($S-N$)
- Strain life ($\epsilon-N$)
- Fracture mechanic crack growth ($da/dN-\Delta K$)

These three types of fatigue properties each play a role in engineering, and each property is used in the context of an underlying fatigue design philosophy as follows:

Design philosophy	Design methodology	Principal testing data description
Safe-life, infinite-life	Stress-life	$S-N$
Safe-life, finite-life	Strain-life	$\epsilon-N$
Damage tolerant	Fracture mechanics	$da/dN-\Delta K$

The $S-N$ and $\epsilon-N$ techniques are usually appropriate for situations where a component or structure can be considered a continuum (i.e., those meeting the “no cracks” assumption). In the event of a crack-like discontinuity, the $S-N$ or $\epsilon-N$ methods (except through residual life testing) offer little or quantitative basis for assessment of fatigue life.

Another limitation of the $S-N$ and $\epsilon-N$ methods is the inability of the controlling quantities to make sense of the presence of a crack. A brief review of basic elasticity calculations shows that both stress and strain become astronomical at a discontinuity such as a crack, far exceeding any recognized property levels that might offer some sort of limitation. Even invoking plasticity still leaves inordinately large numbers or, conversely, extremely low tolerable loads.

The solution to this situation is the characterization and quantification of the stress field at the crack tip in terms of stress intensity in linear elastic fracture mechanics. It recognizes the singularity of stress at the tip and provides a tractable controlling quantity and measurable material property. The use of the stress intensity as a controlling quantity for crack extension under cyclic loading thus enhances the engineering analysis of the fatigue process.

More detailed information on fatigue and fracture mechanics can be found in *Fatigue and Fracture*, Volume 19 of *ASM Handbook*.

References cited in this section

1. M.E. Fine and Y.-W. Chung, Fatigue Failure in Metals, *Fatigue and Fracture*, Volume 19, *ASM Handbook*, ASM International, 1996, p 63–72
2. D.W. Hoepfner, Industrial Significance of Fatigue Problems, *Fatigue and Fracture*, Vol 19, *ASM Handbook*, ASM International, 1996, p 3–4

3. E. Krempl, Design for Fatigue Resistance, *Materials Selection and Design*, Vol 20, *ASM Handbook*, ASM International, 1997, p 516–532

Fatigue and Fracture Mechanics

Infinite-Life Criterion (S - N Curves) (Ref 4)

The safe-life, infinite-life philosophy is the oldest of the approaches to fatigue. Examples of attempts to understand fatigue by means of properties, determinations, and representations that relate to this method include August Wöhler's work on railroad axles in Germany in the mid-1800s. The design method is stress-life, and a general property representation would be S - N (stress versus log number of cycles to failure). Failure in S - N testing is typically defined by total separation of the sample.

General applicability of the stress-life method is restricted to circumstances where continuum, “no cracks” assumptions can be applied. However, some design guidelines for weldments (which inherently contain discontinuities) offer what amount to residual life and runout determinations for a variety of process and joint types that generally follow the safe-life, infinite-life approach. The advantages of this method are simplicity and ease of application, and it can offer some initial perspective on a given situation. It is best applied in or near the elastic range, addressing constant-amplitude loading situations in what has been called the long-life (hence, infinite-life) regime.

The stress-life approach seems best applied to components that look like the test samples and are approximately the same size (this satisfies the similitude associated with the use of total separation as a failure criterion). Much of the technology in application of this approach is based on ferrous metals, especially steels. Steels are predominant as a structural material, but steels also display a fatigue limit or endurance limit at a high number of cycles (typically $>10^6$) under benign environmental conditions. The infinite-life asymptotic behavior of steel fatigue life, thus, provides a useful and beneficial result of S - N testing. However, most other materials do not exhibit this infinite life response. Instead, many materials display a continuously decreasing stress-life response, even at a great number of cycles (10^6 - 10^9), which is more correctly described by a fatigue strength at a given number of cycles.

Assessing Fatigue S - N Properties. Given the extensive history of the stress-life method, substantial property data are available, but beware of the testing conditions employed in producing older data. The usefulness of property data is a critical point due to the numerous variables that influence fatigue results. For example, if a series of tests are conducted at a constant stress ratio ($R = S_{\min}/S_{\max}$), and the alternating stress amplitude (S_a) is used as the other independent dynamic variable, an S - N curve for that situation can be produced, and all dynamic variables can be determined. However, if only one variable is given (e.g., S_a or S_{\max}), there is insufficient information to tell what the test conditions were and the data are virtually useless.

In many cases, insufficient information is available for the effective use of S - N data. Many necessary pieces of data are simply missing. A partial list of important questions might be as follows:

- What were the coupon size and geometry?
- Was there a stress concentration?
- What was the temperature?
- Was an environment other than lab air employed?
- What was the specimen orientation in the original material?
- Does the line represent minimum, mean, or median response?
- How many samples were tested?
- What was the scatter?
- If the plot is based on constant-amplitude data, what were the frequency and waveform?
- Was testing performed using variable-amplitude loading? What was the spectrum?
- What was the failure criterion?
- If there were runouts, how were they handled and represented?

If the data found describe a thin sheet response, it is the wrong data. If the product form is correct, but the plot represents testing done at $R = 0.3$ and fully reversed data are required, the plot may be helpful, but it is not what is desired.

An example of what should be considered important as supporting facts can be found in ASTM E 468, "Presentation of Constant Amplitude Fatigue Test Results for Metallic Materials." It provides guidelines for presenting information other than just final data.

S-N Data Presentation. Stress is the controlling quantity in this method. The most typical formats for the data are plots of the log number of cycles to failure (sample separation) versus either stress amplitude (S_a), maximum stress (S_{max}), or perhaps stress range (ΔS).

Mean stress influences are also very important, and each design approach must consider them. According to Bannantine et al. (Ref 5), the archetypal mean (S_m) versus amplitude (S_a) presentation format for displaying mean stress effects in the safe-life, infinite-life regime was originally proposed by Haigh. The Haigh diagram can be a plot of real data, but it requires an enormous amount of information for substantiation. A slightly more involved, but also more useful, means of showing the same information incorporates the Haigh diagram with S_{max} and S_{min} axes to produce a constant-life diagram. Examples of these are provided subsequently.

For general consideration of mean stress effects, various models of the mean-amplitude response have been proposed. A commonly encountered representation is the Goodman line, although several other models are possible (e.g., Gerber and Soderberg). The conventional plot associated with this problem is produced using the Haigh diagram, with the Goodman line connecting the ultimate strength on S_m , and the fatigue limit, corrected fatigue limit, or fatigue strength on S_a . This line then defines the boundary of combined mean-amplitude pairs for anticipated safe-life response. The Goodman relation is linear and can be readily adapted to a variety of manipulations.

In many cases Haigh or constant-life diagrams are simply constructs, using the Goodman representation as a means of approximating actual response through the model of the behavior. For materials that do not have a fatigue limit, or for finite-life estimates of materials that do, the fatigue strength at a given number of cycles can be substituted for the intercept on the stress-amplitude axis. Examples of the Haigh and constant-life diagrams are provided in Fig. 2 and 3. Figure 3 is of interest also because of its construction in terms of a percentage of ultimate tensile strength for the strength ranges included.

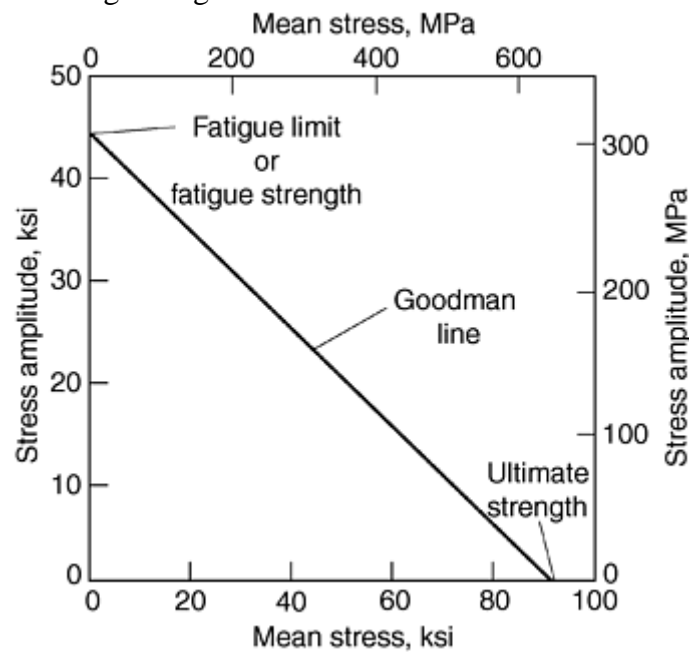


Fig. 2 A synthetically generated Haigh diagram for an alloy steel (620 MPa, or 90 ksi, ultimate tensile strength) based on typically employed approximations for the axes intercepts and using the Goodman line to establish the acceptable envelope for safe-life, infinite-life combinations. The Goodman line represents an unconnected 10^6 estimate at 50% failure (criterion: separation).

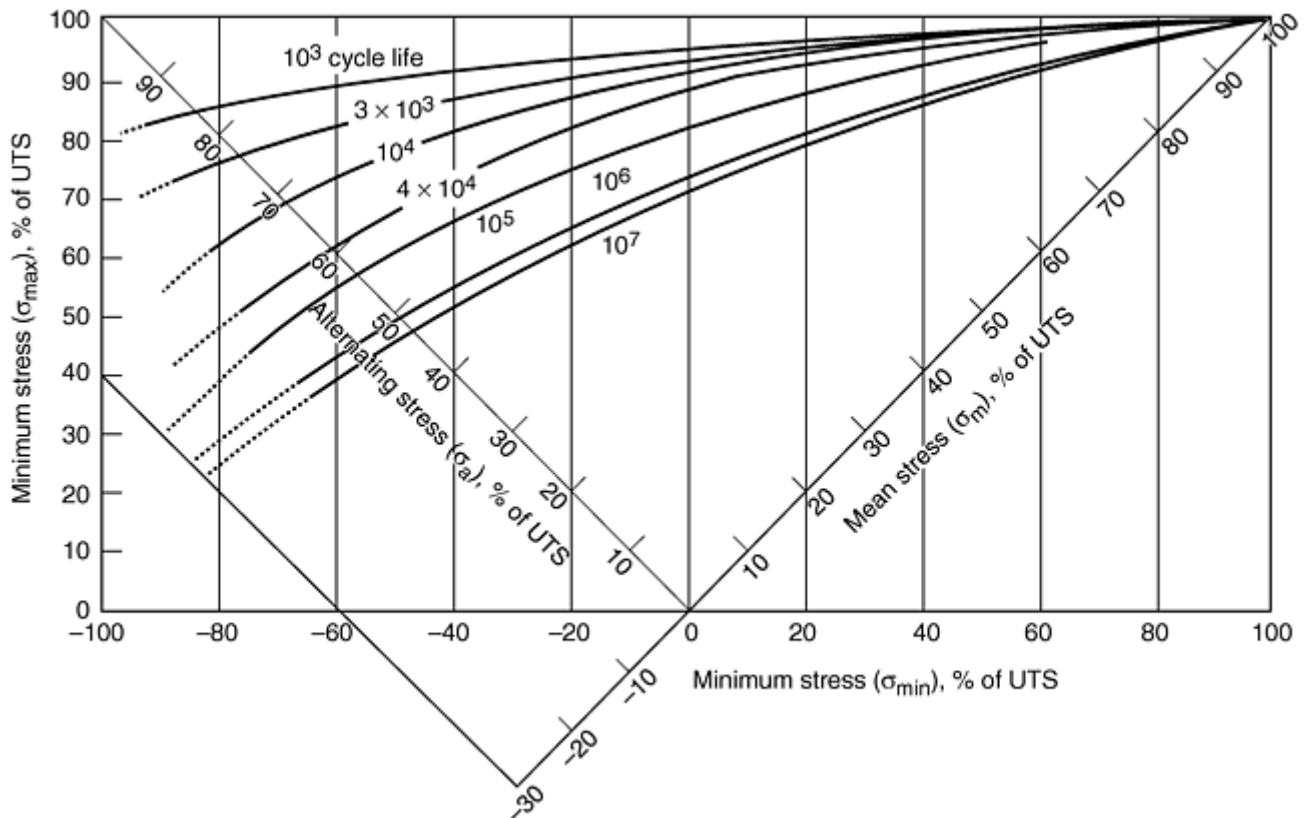


Fig. 3 A constant-life diagram for alloy steels that provides combined axes for more ready interpretation. Note the presence of safe-life, finite-life lines on this plot. This diagram is for average test data for axial loading of polished specimens of AISI 4340 steel (ultimate tensile strength, UTS, 860 to 1240 MPa, or 125 to 180 ksi) and is applicable to other steels (e.g., AISI 2330, 4130, 8630). Source: Ref 6

References cited in this section

4. D.W. Cameron and D.W. Hoepfner, *Fatigue Properties in Engineering, Fatigue and Fracture*, Vol 19, *ASM Handbook*, ASM International, 1996, p 15–26
5. J.A. Bannantine, J.J. Comer, and J.L. Handrock, *Fundamentals of Metal Fatigue Analysis*, Prentice-Hall, 1990
6. R.C. Juvinall, *Engineering Considerations of Stress, Strain, and Strength*, McGraw-Hill, 1967, p 274

Fatigue and Fracture Mechanics

Finite-Life Criterion (ϵ - N Curves) (Ref 4)

Strain life is the general approach employed for continuum response in the safe-life, finite-life regime. It is primarily intended to address the low-cycle fatigue area (e.g., from approximately 10^2 to 10^6 cycles). The ϵ - N method can also be used to characterize the “long-life” fatigue behavior of materials that do not show a fatigue limit.

From a properties standpoint, the representations of strain-life data are similar to those for stress-life data. However, because plastic strain is a required condition for fatigue, strain-controlled testing offers advantages in the characterization of fatigue crack initiation (prior to subsequent crack growth and final failure). The S - N method is based on just one failure criterion—the total separation of the test coupon. In contrast, any of the following may be used as the failure criterion in strain-controlled fatigue testing (per ASTM E 606): separation,

modulus ratio, microcracking (initiation), or percentage of maximum load drop. This flexibility can provide better characterization of fatigue behavior.

Testing for strain-life data is not as straightforward as the simple load-controlled (stress-controlled) $S-N$ testing. Monitoring and controlling using strain requires continuous extensometer capability. In addition, the developments of the technique may make it necessary to determine certain other characteristics associated with either monotonic or cyclic behavior. Further details on testing are given in the article “Fatigue, Creep Fatigue, and Thermomechanical Fatigue Life Testing” in this Volume.

Reference cited in this section

4. D.W. Cameron and D.W. Hoepfner, Fatigue Properties in Engineering, *Fatigue and Fracture*, Vol 19, *ASM Handbook*, ASM International, 1996, p 15–26

Fatigue and Fracture Mechanics

Fracture Mechanics Approach (Ref 7)

Fracture of structural and equipment components as a result of cyclic loading has long been a major design problem and the subject of numerous investigations. Although a considerable amount of fatigue data are available, the majority have been concerned with the nominal stress required to cause failure in a given number of cycles—namely, $S-N$ curves. Usually, such data are obtained by testing smooth specimens which, although of some qualitative use for guiding material selection, are subject to limitations caused primarily by the failure to adequately distinguish between fatigue-crack-initiation life and fatigue-crack-propagation life. The existence of surface irregularities and cracklike imperfections reduces and may eliminate the crack-initiation portion of the fatigue life of the component. Fracture-mechanics methodology offers considerable promise for improved understanding of the initiation and propagation of fatigue cracks and problem resolution in designing to prevent failures by fatigue.

Fatigue-Crack Initiation. Initiation of fatigue cracks in structural and equipment components occurs in regions of stress concentrations, such as notches, as a result of stress fluctuation. The material element at the tip of a notch in a cyclically loaded component is subjected to the maximum stress range, $\Delta\sigma_{\max}$. Consequently, this material element is most susceptible to fatigue damage and is, in general, the origin of fatigue-crack initiation. It can be shown that, for sharp notches, the maximum-stress range on this element can be related to the stress-intensity-factor range, ΔK_I , as follows (Ref 8):

$$\Delta\sigma_{\max} = \frac{2}{\sqrt{\pi}} \frac{\Delta K_I}{\sqrt{\rho}} = \Delta\sigma(k_t) \quad (\text{Eq 1})$$

where ρ is the notch-tip radius, $\Delta\sigma$ is the range of applied nominal stress, and k_t is the stress-concentration factor.

Fatigue-crack-initiation behavior of various steels is presented in Fig. 4 (Ref 8) for specimens subjected to zero-to-tension bending stress and containing a smooth notch that resulted in a stress-concentration factor of about 2.5. The data show that $\Delta K_I/\sqrt{\rho}$, and, therefore, $\Delta\sigma_{\max}$ is the primary parameter that governs fatigue-crack-initiation behavior in regions of stress concentration for a given steel tested in a benign environment. The data also indicate the existence of a fatigue-crack-initiation threshold, $\Delta K_I/\sqrt{\rho}_{\text{th}}$, below which fatigue cracks would not initiate at the roots of the tested notches. The value of this threshold is characteristic of the steel and increases with increasing yield or tensile strength of the steel. The data show that the fatigue-crack-initiation life of a component subjected to a given nominal-stress range increases with increasing strength. However, this difference in fatigue-crack-initiation life among various steels decreases with increasing stress-concentration factor (Ref 8).

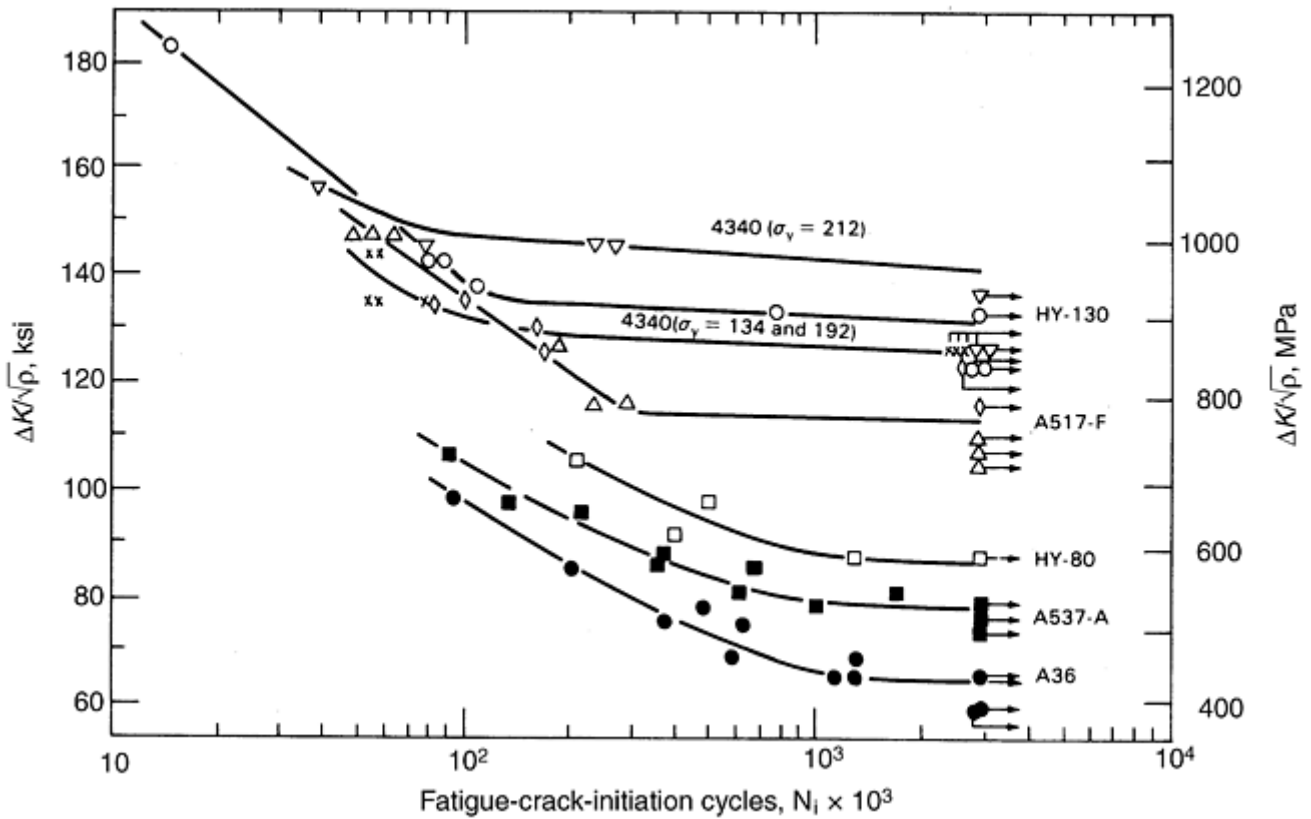


Fig. 4 Fatigue-crack-initiation behavior of various steels at a stress ratio of +0.1. Source: Ref 8

Finally, fatigue-crack-initiation data for various steels subjected to stress ratios (ratio of nominal minimum applied stress to nominal maximum applied stress) ranging from -1.0 to +0.5 indicate that fatigue-crack-initiation life is governed by the total maximum stress (tension plus compression) range at the tip of the notch (Ref 9). The data presented in Fig. 5 (Ref 10) indicate that the fatigue-crack-initiation threshold, $\Delta K_I/\sqrt{\rho}_{th}$, for various steels subjected to stress ratios ranging from -1.0 to +0.5 can be estimated from

$$\frac{\Delta K_{total}}{\sqrt{\rho}} = 10\sqrt{\sigma_{ys}} \quad (\text{Eq 2})$$

where ΔK_{total} is the stress-intensity-factor range calculated by using the tension-plus-compression stress range, and σ_{ys} is the yield strength of the material.

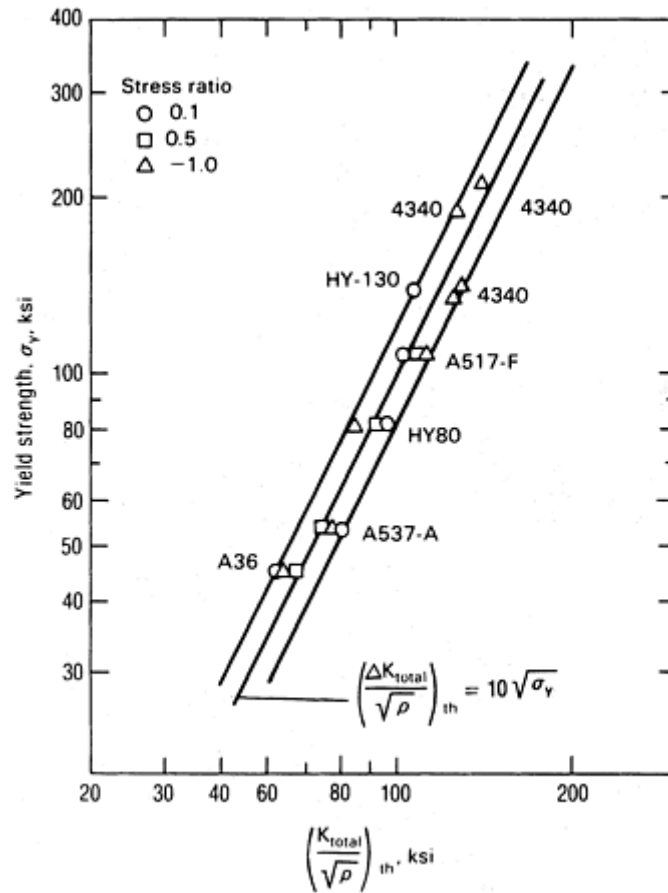


Fig. 5 Dependence of fatigue-crack-initiation threshold on yield strength

Fatigue-Crack Propagation. Extensive data have shown that the fatigue-crack-propagation behavior of metals is controlled primarily by the stress-intensity-factor range, ΔK_I . The fatigue-crack-propagation behavior of metals can be divided into three regions, as shown in Fig. 6 (Ref 11). The behavior in region 1 exhibits a fatigue-crack-propagation threshold, ΔK_{th} , which corresponds to the stress-intensity-factor range, below which cracks do not propagate under cyclic-stress fluctuations. An analysis of experimental results published on nonpropagating fatigue cracks shows that conservative estimates of ΔK_{th} for various steels subjected to different stress ratios, R , can be predicted (Ref 8) from:

$$\Delta K_{th} = 6.4(1 - 0.85R)$$

for

$$R \geq +0.1 \tag{Eq 3a}$$

and

$$\Delta K_{th} = 5.5 \text{ for } R < +0.1 \tag{Eq 3b}$$

where ΔK_{th} is in $\text{ksi}\sqrt{\text{in}}$.

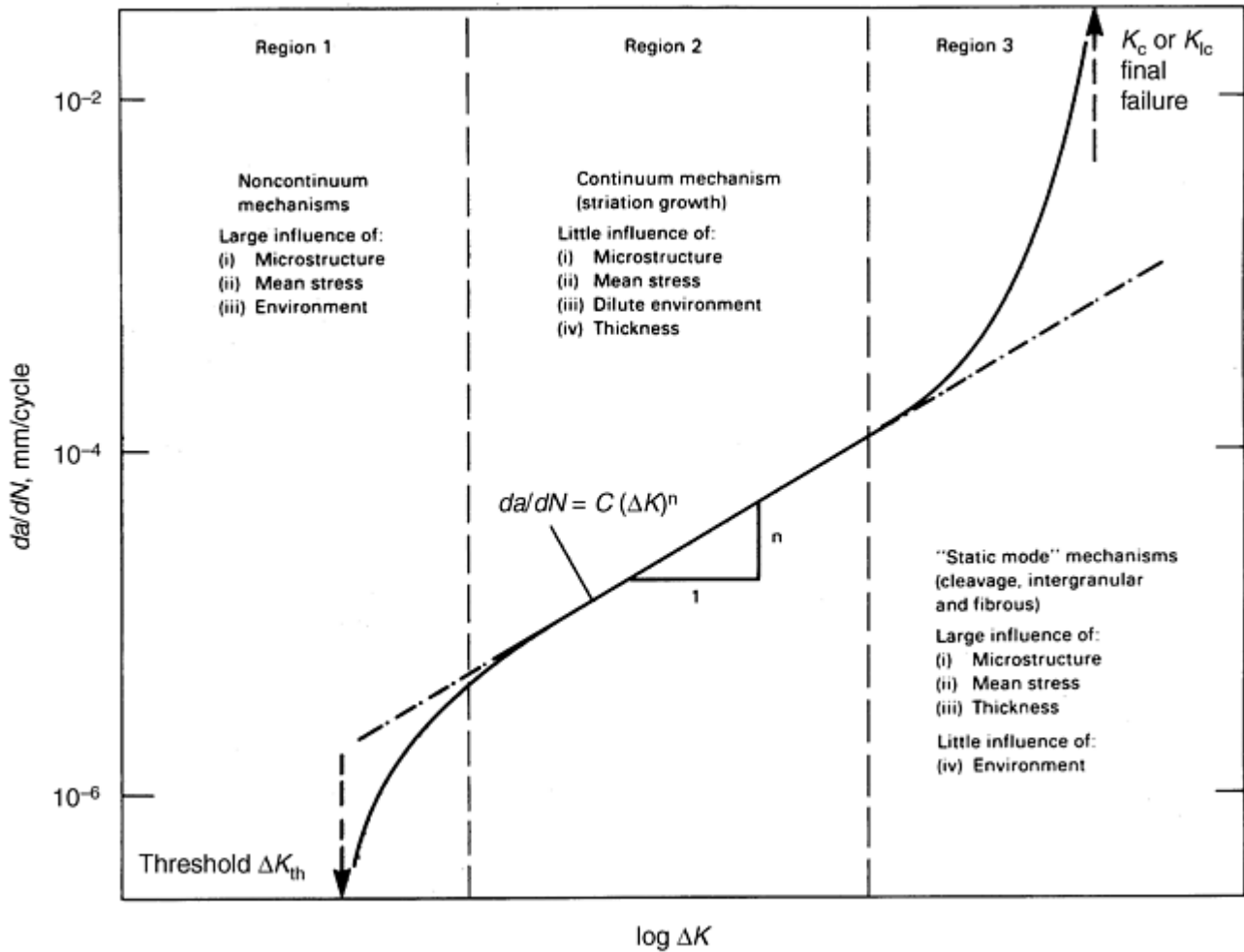


Fig. 6 Schematic illustration of variation of fatigue-crack-growth rate, da/dN , with alternating stress intensity, ΔK , in steels, showing regions of primary crack-growth mechanisms. Source: Ref 11

Equation 3a and 3b indicates that the fatigue-crack-propagation threshold for steels is primarily a function of the stress ratio and is essentially independent of chemical or mechanical properties.

The behavior in region 2 (Fig. 6) represents the fatigue-crack-propagation behavior above ΔK_{th} , which can be represented by the power-law relationship:

$$\frac{da}{dN} = A(\Delta K_1)^n \quad (\text{Eq 4})$$

where a is crack length, N is number of cycles, and A and n are constants.

Extensive fatigue-crack-growth-rate data for various steels show that the primary parameter affecting growth rate in region 2 is the stress-intensity-factor range, and that the mechanical and metallurgical properties of these steels have negligible effects on the fatigue-crack-growth rate in a room-temperature air environment. The data for martensitic steels fall within a single band, as shown in Fig. 7 (Ref 8), and the upper bound of scatter can be obtained (Ref 8) from:

$$\frac{da}{dN} = 0.66 \times 10^{-8} (\Delta K_1)^{2.25} \quad (\text{Eq 5})$$

where a is in inches and ΔK_1 is in $\text{ksi}\sqrt{\text{in}}$. Similarly, as shown in Fig. 8 (Ref 8), data for ferrite-pearlite steels fall within a single band (different from the band for martensitic steels), and the upper bound of scatter can be calculated from:

$$\frac{da}{dN} = 3.6 \times 10^{-10} (\Delta K_1)^{3.0} \quad (\text{Eq 6})$$

where a is in inches and ΔK_1 is in $\text{ksi}\sqrt{\text{in}}$.

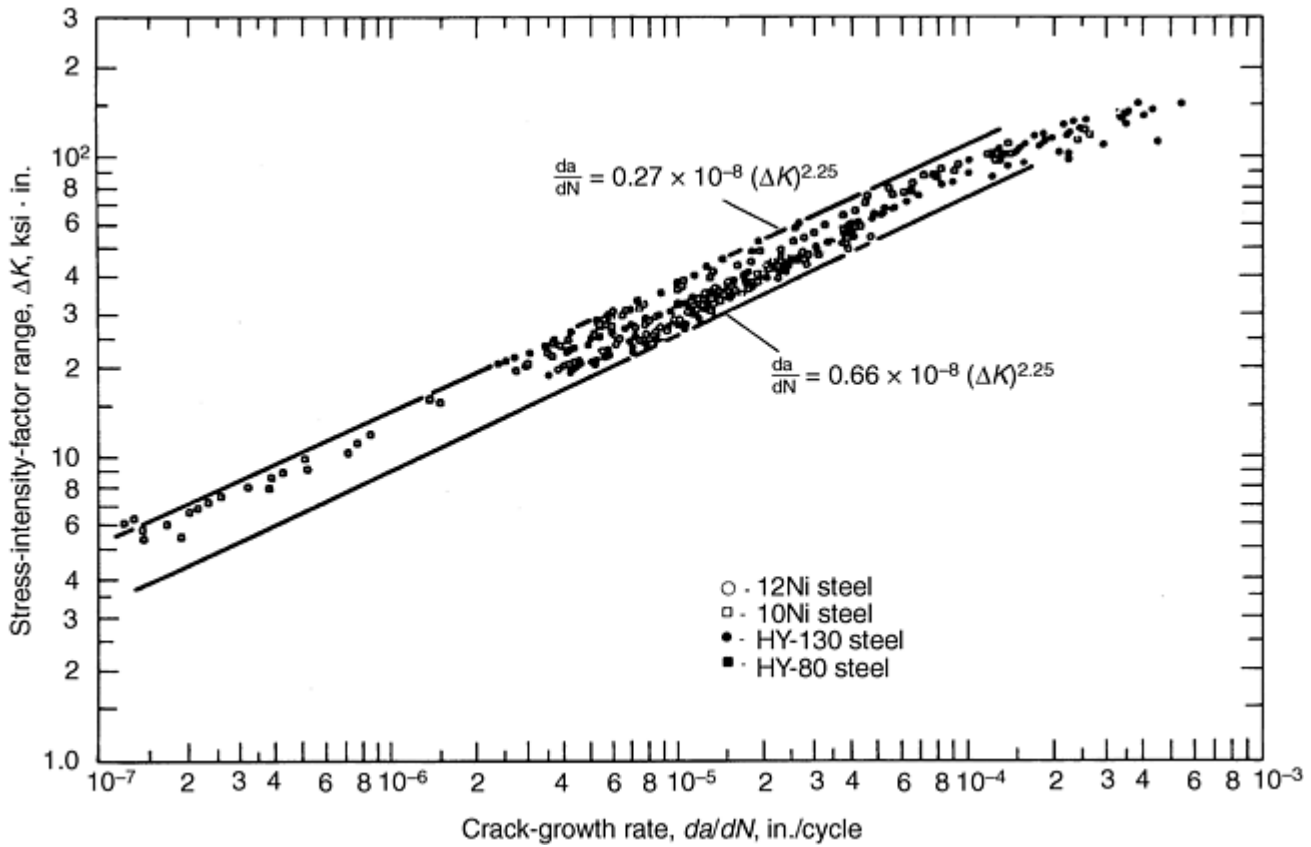


Fig. 7 Summary of fatigue-crack-growth data for martensitic steels. Source: Ref 8

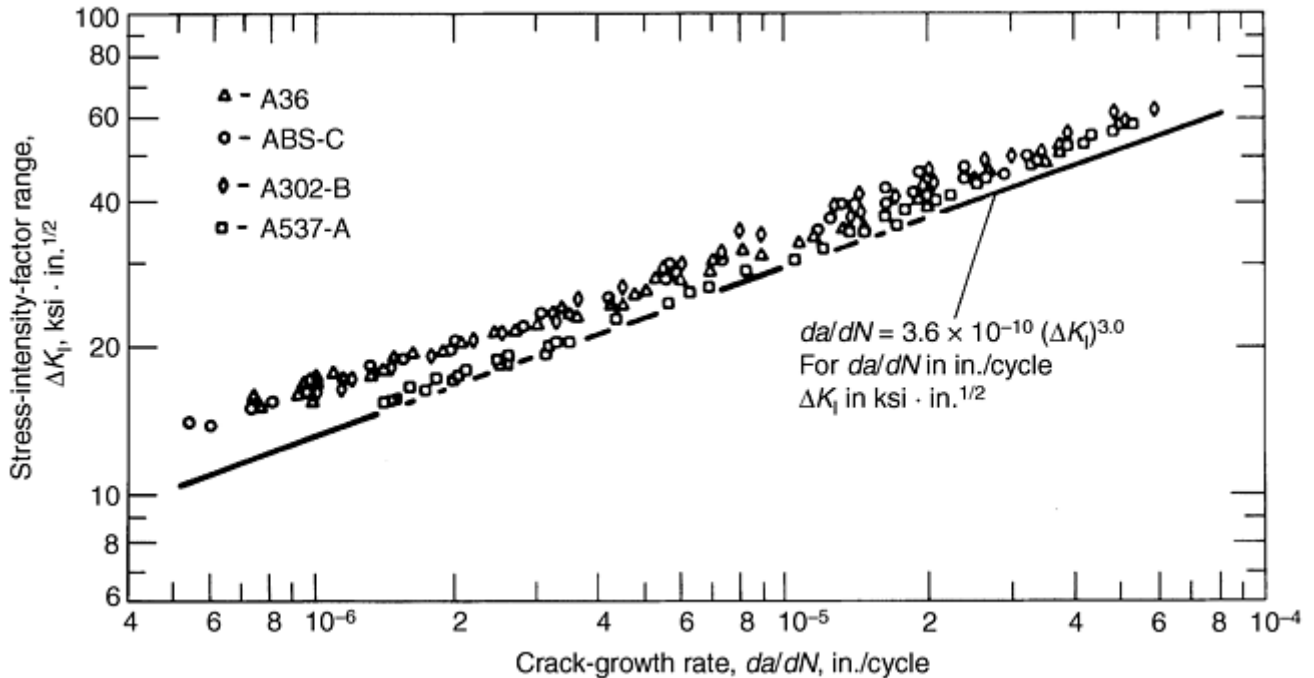


Fig. 8 Summary of fatigue-crack-growth data for ferrite-pearlite steels. Source: Ref 8

The stress ratio and mean stress have negligible effects on the rate of crack growth in region 2. Also, the frequency of cyclic loading and the wave form (sinusoidal, triangular, square, or trapezoidal) do not affect the rate of crack propagation per cycle of load for steels in benign environments (Ref 8).

The acceleration of fatigue-crack-growth rates that determines the transition from region 2 to region 3 appears to be caused by the superposition of a brittle or a ductile-tearing mechanism onto the mechanism of cyclic subcritical crack extension, which leaves fatigue striations on the fracture surface. These mechanisms occur when the strain at the tip of the crack reaches a critical value (Ref 8). Thus, the fatigue-rate transition from

region 2 to region 3 depends on the maximum stress-intensity factor, on the stress ratio, and on the fracture properties of the material (Ref 8).

References cited in this section

7. J.M. Barsom, Fracture Mechanics—Fatigue and Fracture, *Metals Handbook Desk Edition*, 1985, p 32-2 to 32-7
8. S.T. Rolfe and J.M. Barsom, *Fracture and Fatigue Control in Structures—Applications of Fracture Mechanics*, 3rd ed., ASTM, 1999
9. M.E. Taylor and J.M. Barsom, Effect of Cyclic Frequency on the Corrosion-Fatigue Crack-Initiation Behavior of ASTM A 517 Grade F Steel, *Fracture Mechanics: Thirteenth Conf.*, STP 743, ASTM, 1981
10. R. Roberts, J.M. Barsom, J.W. Fisher, and S.T. Rolfe, “Fracture Mechanics for Bridge Design,” FHWA-RD-78-69, Federal Highway Administration, Office of Research and Development, July 1977
11. R.O. Ritchie, Near-Threshold Fatigue-Crack Propagation in Steels, *Int. Met. Rev.*, Vol 24 (No. 5, 6), 1979

Fatigue and Fracture Mechanics

Acknowledgments

Sections of this article were adapted from several *ASM Handbook* articles, in particular those cited as Ref 1, 2, 3, 4 and 7.

References cited in this section

1. M.E. Fine and Y.-W. Chung, Fatigue Failure in Metals, *Fatigue and Fracture*, Volume 19, *ASM Handbook*, ASM International, 1996, p 63–72
2. D.W. Hoepfner, Industrial Significance of Fatigue Problems, *Fatigue and Fracture*, Vol 19, *ASM Handbook*, ASM International, 1996, p 3–4
3. E. Krempl, Design for Fatigue Resistance, *Materials Selection and Design*, Vol 20, *ASM Handbook*, ASM International, 1997, p 516–532
4. D.W. Cameron and D.W. Hoepfner, Fatigue Properties in Engineering, *Fatigue and Fracture*, Vol 19, *ASM Handbook*, ASM International, 1996, p 15–26
7. J.M. Barsom, Fracture Mechanics—Fatigue and Fracture, *Metals Handbook Desk Edition*, 1985, p 32-2 to 32-7

Fatigue and Fracture Mechanics

References

1. M.E. Fine and Y.-W. Chung, Fatigue Failure in Metals, *Fatigue and Fracture*, Volume 19, *ASM Handbook*, ASM International, 1996, p 63–72
2. D.W. Hoepfner, Industrial Significance of Fatigue Problems, *Fatigue and Fracture*, Vol 19, *ASM Handbook*, ASM International, 1996, p 3–4
3. E. Krempl, Design for Fatigue Resistance, *Materials Selection and Design*, Vol 20, *ASM Handbook*, ASM International, 1997, p 516–532
4. D.W. Cameron and D.W. Hoepfner, Fatigue Properties in Engineering, *Fatigue and Fracture*, Vol 19, *ASM Handbook*, ASM International, 1996, p 15–26
5. J.A. Bannantine, J.J. Comer, and J.L. Handrock, *Fundamentals of Metal Fatigue Analysis*, Prentice-Hall, 1990
6. R.C. Juvinall, *Engineering Considerations of Stress, Strain, and Strength*, McGraw-Hill, 1967, p 274
7. J.M. Barsom, Fracture Mechanics—Fatigue and Fracture, *Metals Handbook Desk Edition*, 1985, p 32-2 to 32-7
8. S.T. Rolfe and J.M. Barsom, *Fracture and Fatigue Control in Structures—Applications of Fracture Mechanics*, 3rd ed., ASTM, 1999
9. M.E. Taylor and J.M. Barsom, Effect of Cyclic Frequency on the Corrosion-Fatigue Crack-Initiation Behavior of ASTM A 517 Grade F Steel, *Fracture Mechanics: Thirteenth Conf.*, STP 743, ASTM, 1981
10. R. Roberts, J.M. Barsom, J.W. Fisher, and S.T. Rolfe, “Fracture Mechanics for Bridge Design,” FHWA-RD-78-69, Federal Highway Administration, Office of Research and Development, July 1977
11. R.O. Ritchie, Near-Threshold Fatigue-Crack Propagation in Steels, *Int. Met. Rev.*, Vol 24 (No. 5, 6), 1979

Fatigue, Creep Fatigue, and Thermomechanical Fatigue Life Testing

Gary R. Halford and Bradley A. Lerch, Glenn Research Center at Lewis Field, National Aeronautics and Space Administration; Michael A. McGaw, McGaw Technology, Inc.

Introduction

THE FATIGUE CRACK INITIATION RESISTANCE of an alloy is determined by conducting a series of tests over a range of values of stress amplitude or strain range. The observed number of cycles to failure is plotted against the stress amplitude or strain range to obtain a fatigue curve. The fatigue properties quoted for an alloy are typically the constants used in the equation(s) that describe the fatigue curve. Fatigue lives of interest may be as low as 10^2 or higher than 10^9 cycles. Because of the enormous scatter associated with fatigue, dozens of tests may be needed to confidently establish a fatigue curve, and the cost may run into several thousands of dollars. To further establish the effects on fatigue life of, for example, the test temperature, environment, alloy condition, mean stress effects, creep-fatigue effects, and thermomechanical cycling, requires an extraordinarily

large and usually very costly test matrix. The total effort required to establish the fatigue resistance of an alloy should not be taken lightly.

Fatigue crack initiation tests are conducted on relatively small—and presumed to be initially crack-free—samples of an alloy that are intended to be representative of the metallurgical and physical condition of the alloy. Generally, samples are smooth and have uniformly polished surfaces within the test section. Some may have intentionally machined notches of well-controlled geometry, but the surface at the root of the notch is usually not polished. The purpose of polishing is to attain a reproducible surface finish. This is to eliminate surface finish as an uncontrolled variable. Test specimens are cyclically loaded until macroscopically observable cracks initiate and eventually grow to failure. Normally, the fatigue failure life of a specimen is defined as the number of cycles to separation of the specimen into two pieces. Alternative definitions are becoming more common, particularly for low-cycle fatigue testing, wherein some prescribed indication of impending failure due to cracking is adopted. Specific criteria will be described later. As a rule, cracks that develop during testing are not measured, nor are the test parameters intentionally altered owing to the presence of cracking. The topic of fatigue crack propagation testing of alloys is discussed in the articles “Fatigue Crack Growth Testing” and “Creep Crack Growth Testing” in this Volume.

Microscopic-sized fatigue cracks tend to nucleate quite early in cyclic life (in the first 1–10%) in the high-strain, plasticity-dominated, low-cycle life regime. In this regime, cyclic plasticity is widespread throughout the specimen test section, and the range of plastic strain is used as a measure of the severity of fatigue “loading.” On the other hand, cracks begin to appear quite late in cyclic life (90–99%) in the very low-strain, elastically dominated, high-cycle life regime. There is a gradual transition between these two extremes of behavior for intermediate strain ranges and cyclic lifetimes. In the high-cycle life regime, the cyclic behavior at the macroscopic, phenomenological level is usually considered by design engineers to be linearly elastic and thermodynamically reversible. It is important to recognize, however, that the micromechanisms of fatigue crack nucleation and growth in metals and alloys are linked directly to the occurrence of reversed cyclic plasticity. Fatigue will not occur without it. Even fatigue cracking that occurs in the range of a billion cycles to failure or more *must involve* reversed plasticity. It is also important to recognize that the fatigue process is a progressively degenerative one. For any given condition of cyclic loading that eventually leads to a fatigue failure, there is some, though minute, permanent change from one cycle to the next. While the macroscopic behavior may appear to be, for instance, linear, reversible, and elastic at the microstructural level, irreversible, nonlinear, inelastic deformations occur in highly localized regions that accumulate until macroscopically observable cracking occurs.

Although the results of crack initiation tests conducted on small specimens do not precisely establish the fatigue life of a large part, such tests do provide useful information on the intrinsic fatigue crack initiation behavior of a metal or alloy. As a result, such data can be utilized to develop engineering design criteria to prevent initiation of fatigue cracks in structural components. The use of small-specimen fatigue test data is the basis of fatigue design codes for pressure vessels; piping components; nuclear reactors; turbine blades; wheels; shafts; complex welded, riveted, or bolted structures; automotive and off-highway equipment; exotic aerospace components; and even soldered joints of lead-free electronic chips.

All alloys and metals in structural elements are susceptible to fatigue crack initiation if the structure is subjected to sufficiently large and numerous amplitudes of cyclic loading.

Following a brief description of the phenomena of crack initiation and early growth, this article examines specimen design and preparation as well as the apparatus used in crack initiation testing. Variables that influence the resistance of alloys to fatigue crack initiation, such as the effect of mean and residual stress, stress concentrations, stress amplitude, and surface properties, are briefly reviewed. The initial portion of this article deals with fatigue testing of alloys in the regime wherein the isothermal temperature of testing is below the range wherein behavior is significantly influenced by time-dependent mechanisms, such as creep, oxidation, and metallurgical transformations. The testing procedures, instrumentation, and hardware must be altered to accommodate creep-fatigue testing and thermomechanical fatigue testing, and these items will be addressed as required throughout this article. Applicable ASTM standards for baseline fatigue testing are listed in Table 1.

Table 1 Applicable ASTM standards for baseline fatigue testing

Specification No.	Title	Comments
-------------------	-------	----------

ASTM standards on fatigue testing methods		
B 593	Bending Fatigue Testing for Copper-Alloy Spring Materials	Cantilever bend testing methods
E 466	Conducting Force Controlled Constant Amplitude Axial Fatigue Tests of Metallic Materials	Load controlled fatigue; no measurement of strain
E 467	Verification of Constant Amplitude Dynamic Loads on Displacements in an Axial Load Fatigue Testing System	Calibration of dynamic loads under HCF
E 468	Presentation of Constant Amplitude Fatigue Test Results for Metallic Materials	Reporting of load controlled fatigue data
E 606	Strain-Controlled Fatigue Testing	Fatigue testing using strain measurement
E 739	Statistical Analysis of Linear or Linearized Stress-Life (<i>S-N</i>) and Strain-Life (ϵ - <i>N</i>) Fatigue Data	Statistical analysis of fatigue life curves
E 1049	Cycle Counting in Fatigue Analysis	Cycle counting procedures for spectrum loads
E 1823	Terminology Relating to Fatigue and Fracture Testing	Definitions used in fatigue testing
ASTM standards with equipments requirements		
B 557	Tension Testing of Wrought and Cast Aluminum-and Magnesium-Alloy Products	Lists specimen and grip designs
E 4	Force Verification of Testing Machines	Calibration of load cells for test frames
E 8	Tension Testing of Metallic Materials	Lists specimen and grip designs
E 21	Elevated Temperature Tension Tests of Metallic Materials	Guidance for elevated temperature testing
E 74	Calibration of Force-Measuring Instruments for Verifying the Force Indication of Testing Machines	Calibration of force standards
E 83	Verification and Classification of Extensometers	Calibration and classes of extensometers
E 1012	Verification of Specimen Alignment under Tensile Loading	Load frame alignment and measurement of bending strains
E 1237	Installing Bonded Resistance Strain Gages	Installation of strain gages
E 1319	High-temperature Strain Measurement	Use of high-temperature strain gages
E 1856	Evaluating Computerized Data Acquisition Systems Used to Acquire Data from Universal Testing Machines	Use and accuracy of computerized data acquisition systems
International and other national standards^(a)		
ISO/DIS 12106, 1998	Metallic Materials—Fatigue Testing—Axial Strain-Controlled Method	
ISO 1099, 1975	Metals—Axial Load Fatigue Testing	
ISO 1143, 1975	Rotating Bar Bending Fatigue Testing	
ISO 1352, 1977	Steel—Torsional Stress Fatigue Testing	
JIS Z 2279, 1992	Method of High Temperature Low Cycle Fatigue Testing for Metallic Materials	
DIN 51228, 1993	Fatigue Testing Machines—General Requirements	
DIN 50113, 1982	Testing of Metals—Rotating Bending Fatigue Test	

(a) Available in the US through Global Engineering Documents, Clayton, MO

Process of Fatigue Crack Initiation and Early Growth

Fatigue crack initiation and early growth require cyclic inelastic deformation. For alloys and metals tested at subcreep temperatures, the nonlinear inelastic behavior is invariably plasticity, that is, the slip associated with dislocation motion along the most densely packed crystallographic planes aligned favorably with the maximum resolved shear stress. In low-cycle fatigue testing, the cyclic plasticity is widely spread throughout the gage portion of the specimen and is readily measured with commercially available strain measuring devices. In this regime, the cyclic stresses will be near or above the conventional offset yield strength of the alloy. Cyclic strain hardening or softening typically also occurs. On the other hand, at very long cyclic lives, cyclic plasticity is still present, although certainly not detectable with conventional strain measurement techniques. Reversed crystallographic slip is highly localized within a few of the most favorably oriented grains or near highly localized stress concentrations. Stress-strain response appears to be totally elastic in this life regime. Because of the extreme localization at the smallest cyclic stresses and strains and, hence, longest lives, the tendency is for only one major crack to initiate and grow to failure in this regime. In the high-strain regime, corresponding to low-cycle fatigue lives, there is a tendency for the material to develop multiple crack initiations and early growth followed by eventual link-up of independent cracks into a single fatal fatigue crack. The transition between low-cycle fatigue and high-cycle fatigue is essentially a gradual one with mechanisms varying more in degree than in kind. The region between low- and high-cycle fatigue is referred to as intermediate-cycle fatigue. With few exceptions, such as rolling-contact fatigue and influences of mechanical or metallurgical surface treatments, cracks initiate at a free surface. Usually the surface is the external surface of the specimen, although it could be an internal surface associated with a void or a debonded internal particle. Cyclic plasticity is less constrained at a free surface due to the fewer nearest neighbors and, hence, fewer atomic bonds available to inhibit dislocation motion. Dislocations also exit and disappear at free surfaces, leaving one atomic-sized step for each dislocation that exists on a particular slip plane. Typically, more than one slip plane is involved. Any given slip plane experiences nonreversed slip, that is, the amount of slip in the slip direction of the plane during one direction of loading is not recovered in the opposite direction when the direction of loading is reversed. Rather, the overall deformation is recovered, but some of it may be on parallel slip planes. The active parallel slip planes are separated by numerous atomic distances and form what are known as slip bands. Within a band the to-and-fro slip is not uniform, resulting in considerable disarray beneath the surface and outcroppings that are highly irregular. These are referred to as persistent slip bands, that is, those deeper than several microns below the free surface. Persistent slip bands remain active throughout the bulk of the cyclic life.

As the number of applied fatigue cycles of cyclic plasticity increase, the severity of the irregularity increases until such time as the outcroppings form extrusion-intrusion pairs within the slip bands. Intrusions are the nuclei or formative stages of atomic-sized fatigue cracks known as stage I cracks (defined as cracking along the crystallographic slip plane). The intrusion grows slowly with continued cycling. Once the depth of the intrusion is great enough, the surrounding material perceives it as a crack that exerts its own highly localized stress-strain field. At this stage of the evolving fatigue process, the stress-strain field of the nucleated crack, which superimposes itself on the applied stress-strain field, becomes the dominant field. The cracking response changes accordingly, and the global crack direction turns to become perpendicular to the maximum principal stress direction immediately in front of the crack. This signals the onset of stage II fatigue cracking, which generally prevails until fatigue failure occurs. Inspection of a fatigue fracture surface with the naked eye generally reveals primarily stage II cracking because stage I cracks are seldom greater than a grain size or two in depth. Cracks may also start at the location of surface irregularities due to grain boundaries, chemical attack, and casting or machining imperfections. Nevertheless, cyclic plasticity is always a necessary ingredient for the nucleation process.

Although the scenario described above is simplified, it provides phenomenological insight into the gradual, progressive nature of the fatigue process that is useful in understanding cyclic testing in the low-, intermediate-, and high-cycle fatigue regimes. There are no sharp demarcations between the three regions when described by

the number of cycles to failure. In fact, the distinction is better founded in terms of the magnitude of the range of cyclic plastic strain than in terms of number of cycles due to the overwhelming influence of the plasticity. As an example, high-ductility, low-strength metals such as copper behave in a low-cycle fatigue manner even at 10^6 cycles to failure, because the cyclic strain range may be half plastic and half elastic even at this life level. By contrast, a low-ductility, high-strength hardened ball-bearing steel exhibits high-cycle-type fatigue behavior at cyclic lives of only 10^3 , owing to the minuscule amount of plasticity that is overwhelmed by the large elastic component of cyclic strain.

Fatigue, Creep Fatigue, and Thermomechanical Fatigue Life Testing

Gary R. Halford and Bradley A. Lerch, Glenn Research Center at Lewis Field, National Aeronautics and Space Administration; Michael A. McGaw, McGaw Technology, Inc.

Fatigue Testing Machines

Numerous types of testing machines have been developed for fatigue crack initiation testing. Fatigue testing machines covered in this article deal with nominally uniaxial normal-stress applications. Multiaxial fatigue loading, including torsional and contact fatigue (e.g., rolling elements, gears, and impact) is covered in the article “Multiaxial Fatigue Testing” in this Volume. Most fatigue testing machines have been developed to a high degree and are marketed commercially to laboratories for conducting a wide variety of fatigue testing. Machines have been developed for various modes of loading that, in turn, dictate the configuration of the test specimen. Considerable variation of specimen geometry can be accommodated by each of the modes as discussed in the following paragraph.

Fatigue Loading Modes

Three basic modes of loading are used: direct axial loading, plane-bending, and rotating-beam loading. Specimens for direct axial stress machines may have a wide range of cross-sectional geometries (solid or hollow) and have a uniform gage length with axial cross sections that are round, elliptical, square, rectangular, or thin sheet. Specimens of nonuniform cross section include sharp notches and low stress concentration, hourglass-shaped specimens for diametral strain control. Bending specimens may have cross sections of uniform width and thickness for three- or four-point loading, or tapered cross sections (designed for constant stress along the length) for cantilevered plane-bending or rotating-beam testing. All bending specimens could be machined with stress concentrations in the form of notches. Examples of standardized fatigue test specimens are presented in the section “Ancillary Equipment and Specimens” in this article.

Classifications of Fatigue Testing Machines

In addition to the loading mode, fatigue testing machines are further classified by their basic drive mechanism and by the test parameter to be controlled. The basic drive system is most often electrical. An electric motor directly drives rotating-beam testing machines. An eccentric cam attached to a drive motor deflects the cantilevered end of a plane-bending fatigue specimen. Eccentric cams coupled with flexure-plate, parallel-motion pivoted lever arms can also drive axially loaded specimens in a direct-stress machine. Direct-stress machines can also be modified with fixturing to perform plane-bending fatigue tests, either in three-point or four-point bending. The rotary motion of an eccentric cam on an electric drive motor can be used to excite a linear oscillating spring-mass system at its resonance point to provide direct-stress loading of a fatigue specimen. Electromagnetic excitation can be used to excite a mass or inertial system to load a specimen in direct stress or plane bending. Ultrasonic fatigue testing is possible at frequencies up to 20 kHz using electromagnetic excitation of a specimen gripped at one end and excited at its natural frequency in the axial direction. Even piezoelectric devices have been used to create small high-frequency displacement excitations for specialized fatigue testing. Electric motors also turn the pumps to pressurize the fluids used in modern

servohydraulic testing machines. The greatest versatility comes with closed-loop, servohydraulic testing systems that offer capability to control any of the primary fatigue variables, provided that that variable can be sensed electronically.

Test parameter control is usually fixed for the simplest and least costly fatigue machines. Rotating-beam testing is generally done under constant bending moment control. Provided the maximum bending stress remains linearly elastic, the elastically calculated stress or strain is presumed to be a controlled constant. However, should a small amount of inelasticity occur at the peak stress of the cycle, the maximum stress will drop due to stress redistribution. This action results in neither a constant pure stress nor strain control, although the strain or displacement will tend to be controlled more consistently than the stress might be. For plane bending, if the loading is performed through a rotating eccentric cam, the control condition is closest to a constant displacement control. If the loading is done with a bending fixture attached to a direct-stress machine that is under load control, then the control mode for the bending specimen is constant bending moment. Servohydraulic direct-stress machines can be operated in constant load, strain, or displacement control depending upon which variable signal is being sensed and fed back into the servocontrolled loop. While the most versatile, such machines typically require higher initial, operating, and maintenance costs.

All fatigue testing machines have a basic loading frame that resists the loads imposed on the test specimen. This frame also supports a number of other components, including the drive mechanism that transmits loading to the specimen through grips, load cells, extensometry, and other measurement devices. If heating, cooling, or environmental chambers are involved, they too have to be supported by the loading frame. Key attributes of the loading frame are to provide accessible space for installing and removing test specimens; once installed, they have very high stiffness relative to the stiffness of the specimen. In other words, the testing machine should undergo as little elastic loading displacement as possible. Ideally, the bulk of the displacement should be absorbed by the specimen. The loading train within the testing machine should also have excellent alignment of the load line with the specimen to prevent premature specimen warping or buckling under high loads. Typical load train components in a modern servohydraulic axial fatigue machine are shown in Fig. 1. Schematic diagrams of the load train components for other common fatigue testing machines are shown in Fig. 2 3 4 5 6 7. Brief descriptions of the various commercially available fatigue testing machines are given in the following sections.

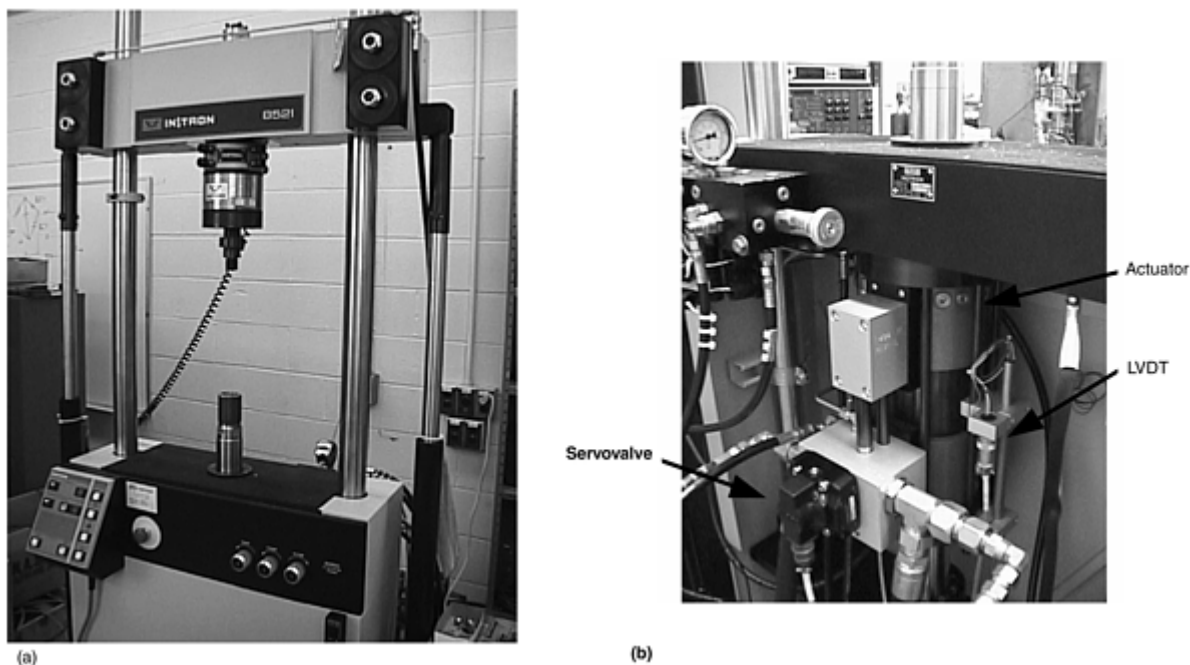


Fig. 1 Modern servohydraulic axial fatigue testing machine. (a) Basic load train. (b) Hydraulic actuator, servovalve, and displacement sensor (LVDT)

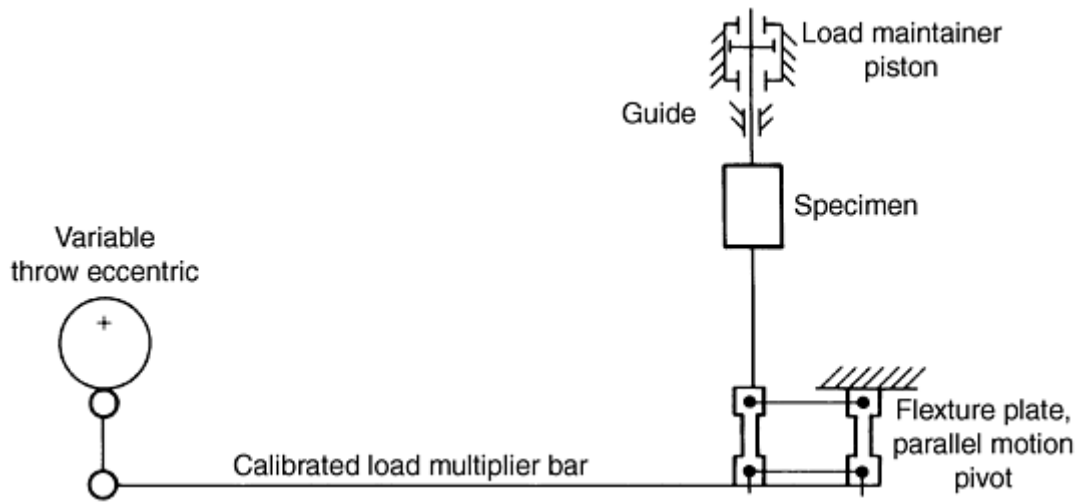


Fig. 2 Schematic of a rotating eccentric crank and lever fatigue testing machine for axial (direct-stress) loading

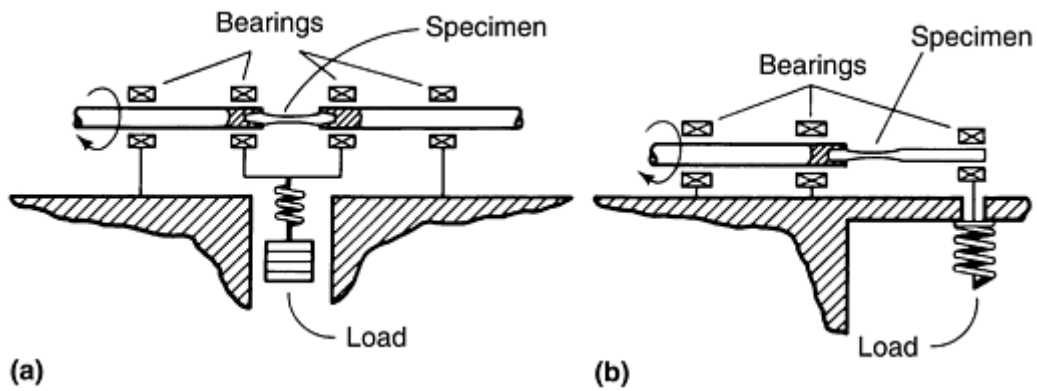


Fig. 3 Schematics of rotating-beam fatigue testing machines. (a) Four-point loading R.R. Moore testing machine. (b) Cantilever loading rotating-beam machine

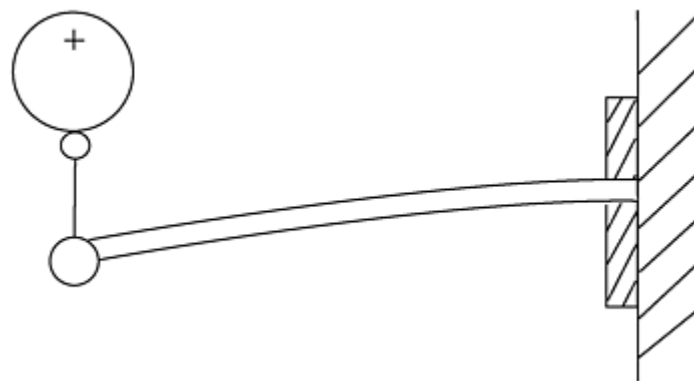


Fig. 4 Schematic of a cantilever plane-bending fatigue testing machine

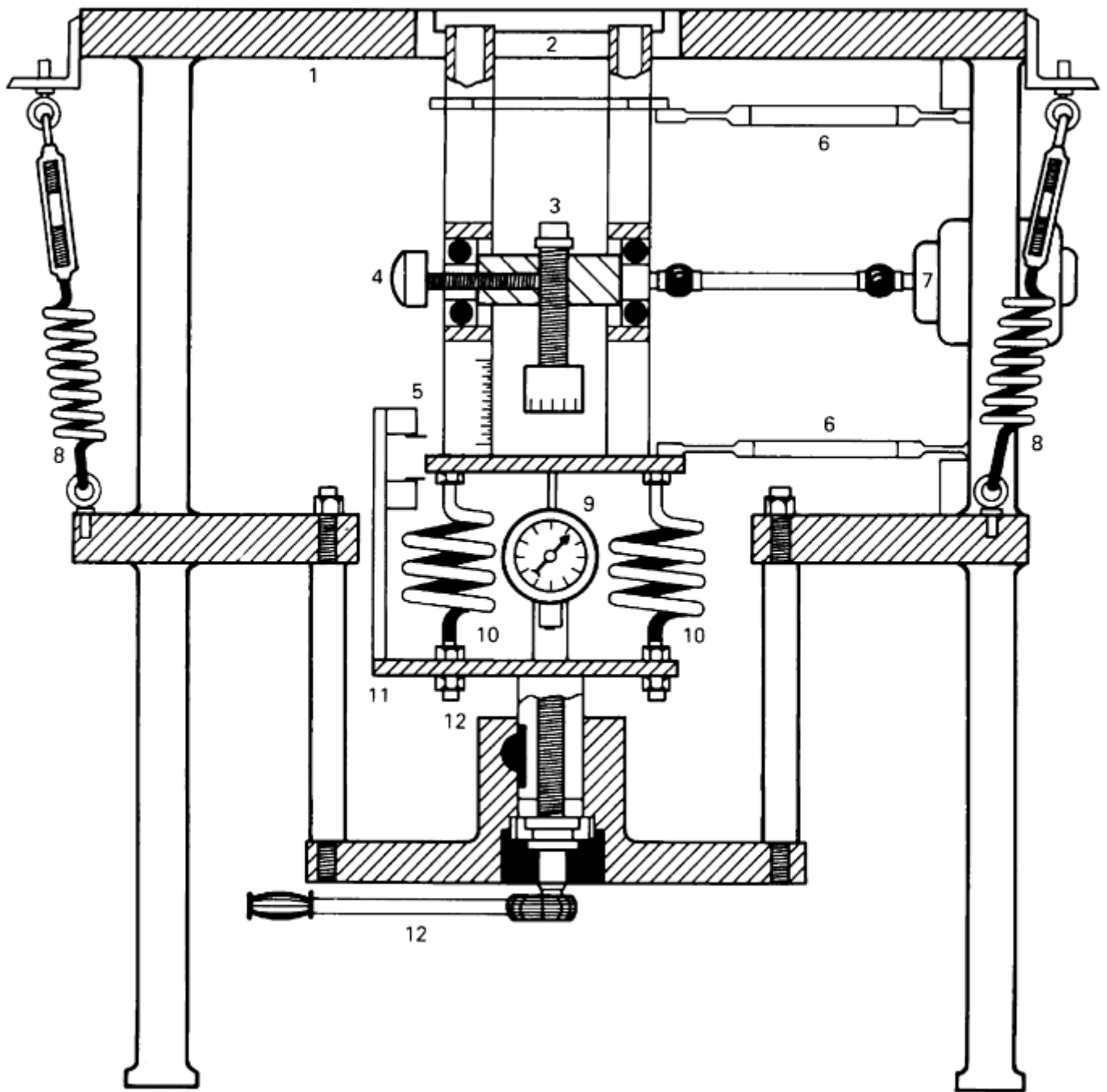


Fig. 5 Schematic of a forced-vibration rotating eccentric mass fatigue testing machine. 1, stationary frame with large top providing ample work space; 2, reciprocating platen; 3, rotating eccentric mass is source of dynamic force, which is varied by screwing threaded rod in or out; 4, thread screw locks threaded rod in position; 5, scale reads in pounds of vibratory force; 6, flexure plates absorb horizontal centrifugal force so that only vertical force is transmitted to platen; 7, synchronous motor drives eccentric mass at constant 1800 cycles/min; 8, springs provide seismic mounting so that no vibration is transmitted to or from surroundings; 9, dial indicates preload; 10, compensator springs absorb all inertia forces produced by reciprocating masses, preventing transmission to the specimen; 11, plate holds one end of compensator springs firmly to stationary frame; 12, preload mechanism

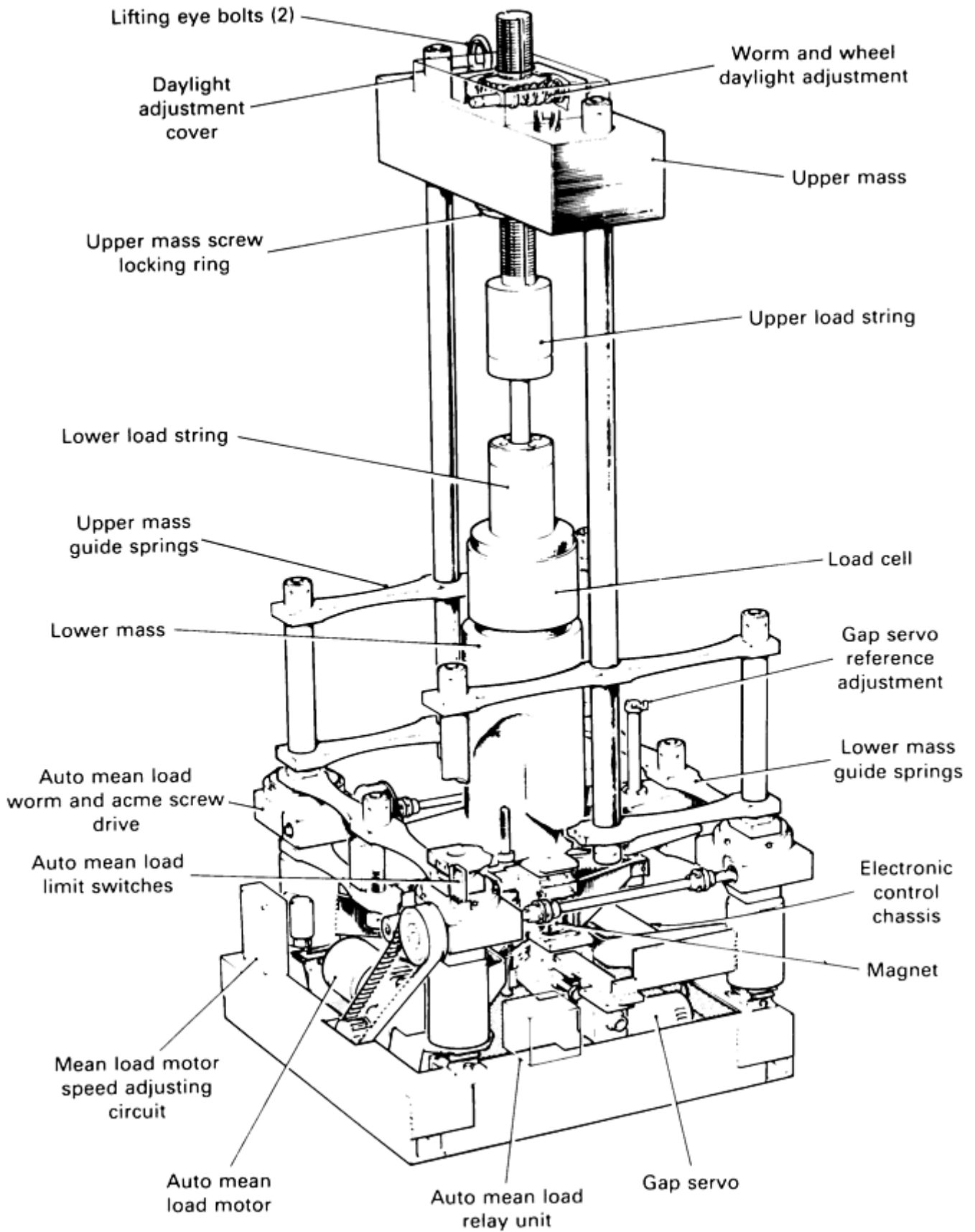


Fig. 6 Schematic of a closed-loop resonant fatigue testing machine

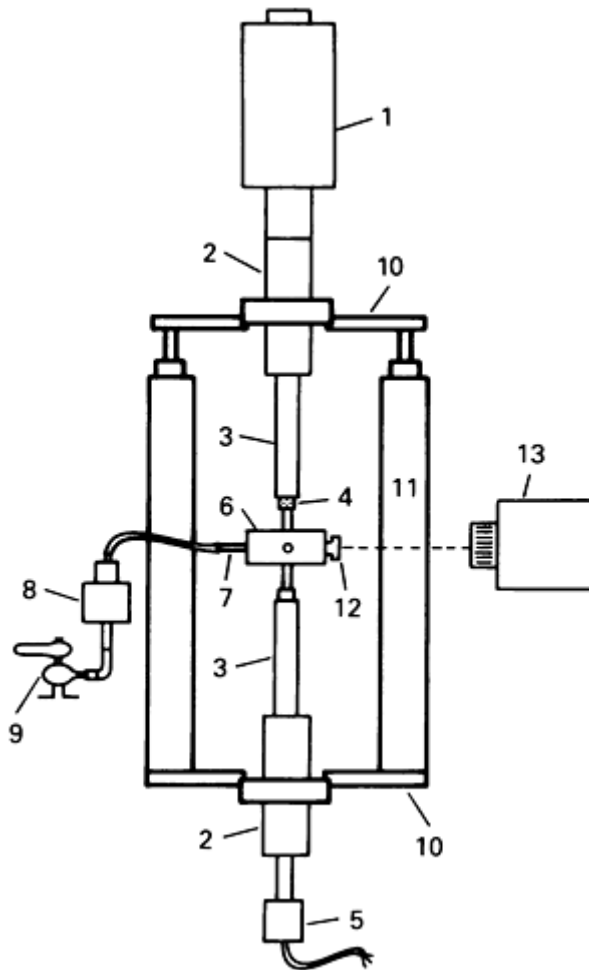


Fig. 7 Schematic of an ultrasonic (920 kHz) fatigue testing machine with mean load capability. 1, converter; 2, booster horn; 3, connecting horn; 4, specimen; 5, capacitance gage; 6, cooling ring; 7, four air inlets; 8, venturi air cooler; 9, air supply; 10, upper and lower support plates; 11, hydraulic pistons; 12, window; 13, infrared camera

Axial (Direct-Stress) Fatigue Testing Machines. The direct-stress fatigue testing machine subjects a test specimen to a uniform stress or strain through its cross section. For the same cross section, an axial fatigue testing machine must be able to apply a greater force than a static bending machine to achieve the same stress. Axial machines are used to obtain fatigue data for most applications and offer the best method of establishing, by closed-loop control, a controlled strain range in the plastic strain regime (low-cycle fatigue).

Servo-hydraulic closed-loop systems offer optimum control, monitoring, and versatility. These can be obtained as component systems and can be upgraded as required. A hydraulically actuated cylinder typically is used to apply the load in axial fatigue testing. A servovalve governs the flow of hydraulic fluid to the cylinder. The direction and rate of flow is dictated by the electronic control signal to the servovalve through a feedback control loop. Due to the versatility provided by the servo-hydraulic system in control modes (load, strain, displacement, related variables, or computed combinations of these variables such as plastic strain), the same machine can be used for both high-cycle fatigue and low-cycle (stress- or strain-controlled) fatigue testing. A wide variety of grips, including self-aligning (typically tension-tension only) types, are available for these machines.

Electromechanical systems have been developed for axial fatigue studies. The crank and lever machine of Fig. 2(a) is an example of one of the testing systems using this drive mechanism. Forced vibration and resonant systems have also been used extensively. Older machine designs were open-loop systems, but newer machines have closed-loop features to continuously maintain loading levels. An older-style forced-vibration rotating eccentric mass machine with a direct-stress fixture is shown in Fig. 5, and a closed-loop resonant machine is shown in Fig. 6.

In crank and lever machines, a cyclic load is applied to one end of the test specimen through a deflection-calibrated lever that is driven by a variable-throw crank. The load is transmitted to the specimen through a

flexure system, which provides straight-line motion to the specimen. The other end of the specimen is connected to the loading frame. Some machines have a hydraulic piston that is part of an electrohydraulically controlled load-maintaining system that senses specimen yielding. This system automatically restores the preset load through the hydraulic piston. Thus, the static and dynamic loads are applied to opposite ends of the specimen, making it possible to maintain a constant load on the specimen regardless of dimensional changes caused by specimen fatigue.

Electromagnetic or magnetostrictive excitation may be used for axial fatigue testing machine drive systems when low-load amplitudes and high-cycle fatigue lives are desired in short test durations. The ultrahigh-cycle frequency of operation of these types of machines (on the order of 10–25 kHz) enables testing to long fatigue lives ($>10^8$ cycles) within weeks. An example of one of these types of machines is illustrated in Fig. 7. A comprehensive review on all aspects of ultrasonic fatigue testing is given in the article “Ultrasonic Fatigue Testing” in this Volume.

Bending Fatigue Machines. The most highly used type of fatigue machine has probably been the bending fatigue machine. These simple, inexpensive systems have allowed laboratories to conduct extensive test programs with a low investment in equipment. The most common general-purpose bending fatigue machines are cantilever-beam plane-bending (repeated-flexure) and rotating-beam machines.

Cantilever-beam plane-bending machines use flat test specimens that have a tapered width and uniform thickness. This configuration results in a sizable portion of the test specimen volume having a uniform bending stress. Substantially smaller loads are required than for axial fatigue of the same section size. In bending, the stress is highest at the surface, making this test mode advantageous for studying the effects of surface treatments or coatings.

Because of their large displacement, the cam or eccentric principles used in cantilever-beam plane-bending machines typically have a limited cyclic frequency compared to rotating-beam types. Both deflection-controlled and load-controlled types are available and are in use today.

Rotating-beam machines are the earliest type of fatigue testing machine, and they remain in occasional use today. The specimen has a round cross section and is subjected to dead-weight loading while swivel bearings permit rotation. A given point on the circular test-section surface, during each rotation, is subjected to sinusoidal stress variation from tension on the top to compression on the bottom. It is not possible to run mean-stress effects tests with this machine.

Typical rotating-beam machine types are shown in Fig. 3. The R.R. Moore-type machines (Fig. 3a) typically operate at 167 Hz. In all bending-type tests, only the material near the surface is subjected to the maximum stress; therefore, in a small-diameter specimen, only a very small volume of material is under testing. Thus the fatigue strength and lives obtained from small rotating-beam fatigue tests typically are higher than those obtained from axial fatigue tests for specimens with the same cross-sectional area.

Regimes of Operation

The choice of the fatigue testing machine will depend strongly on the fatigue-life regime to be investigated and upon the type of fatigue data desired.

High-Cycle Fatigue. At the high-cycle fatigue (HCF) end of the fatigue spectrum (10^5 to 10^8 and higher), high-frequency cycling is an absolute must. It requires nearly 12 days of cycling at 1000 Hz to reach 10^8 cycles to failure. Even ultrasonic fatigue testing at 20,000 Hz would require 14 hours to reach this life level. Fortunately, in the HCF regime, the cyclic plasticity is so minuscule that specimen heating, while ever present, does not restrict testing. Rise-in-temperature measurements made during high-frequency cycling have, however, been used successfully to help identify high-cycle fatigue endurance strengths (Ref 1). On the macroscopic phenomenological level, specimen behavior is considered to be linearly elastic. Hence, load-controlled testing is entirely adequate and, in practical fact, is virtually dictated. Any conventional fatigue extensometer would be of no added value to testing even if means were found to keep it from being shaken off at higher frequencies.

In the high-cycle fatigue regime, statistical variation in fatigue life is quite large (see the section on statistical aspects of fatigue data). This dictates multiple test results to provide a sufficient database to establish the fatigue resistance of the material. The exceptionally large amount of total testing time in turn requires multiple fatigue testing machines. Consequently, the cost per machine must be relatively low. The simpler fatigue testing machines based on constant loading or displacement in plane bending, rotating bending, and direct stress are used almost exclusively for evaluation of very-high-cycle fatigue resistance of materials. Ultrasonic fatigue

testing is rarely used because the cyclic strain rates are much higher than found in service. This large difference in strain rate may result in different micromechanisms of straining and, hence, fatigue crack initiation mechanisms.

Low-Cycle Fatigue. Conventional low-cycle fatigue (LCF) crack initiation data in the regime of 10 to 10^5 cycles to failure are best obtained under strain cycling conditions, leaving little choice but to use an electrohydraulic direct-stress fatigue machine with an extensometer and servostrain control. The cyclic frequency need not be high. Even at 1 Hz, 10^5 cycles can be reached in just over a day. In fact, higher frequencies would not be desirable at lower life levels where cyclic plasticity could be significant. Energy dissipation due to rapid cyclic plasticity would cause considerable, and highly undesired, specimen heating, assuming the specimen is not already being heated to an elevated test temperature. (If cyclically generated heat is not dissipated, the resultant thermal expansion of the specimen test section creates an “apparent” mechanical strain. Under servocontrolled cyclic straining, thermal expansion would be offset by enforced compression and, hence, compressive mean stress, destroying the original purpose of the test.)

Elevated-temperature fatigue testing, especially low-cycle isothermal creep-fatigue (ICF) and thermomechanical fatigue (TMF), invariably requires servocontrolled, strain-cycling capabilities to avoid undesirable creep or plasticity ratcheting strains. The maximum cyclic rates during TMF cycling are typically quite low due to the relatively low rate at which temperatures of test samples can be changed in a controlled manner. Due to the relatively long testing time per cycle for ICF and TMF tests, and due to the high costs per test and high machine acquisition and maintenance costs, there have been few published investigations of the statistical nature of ICF and TMF; however, proprietary databases exist in some large corporations for certain critical materials applications. High-temperature fatigue testing will be discussed in greater detail in following sections of this article.

Reference cited in this section

1. W.J. Putnam and J.W. Harsch, “Rise of Temperature” Method of Determining Endurance Limit, *An Investigation of the Fatigue of Metals*, H.F. Moore and J.B. Koppers, Ed., Engineering Experiment Station Bulletin 124, University of Illinois, Oct 1921, p 119–127

Fatigue, Creep Fatigue, and Thermomechanical Fatigue Life Testing

Gary R. Halford and Bradley A. Lerch, Glenn Research Center at Lewis Field, National Aeronautics and Space Administration; Michael A. McGaw, McGaw Technology, Inc.

Ancillary Equipment and Specimens

A fatigue testing machine typically will have a number of components or accessories added to the basic loading frame. The most common are shown in Fig. 8. Ancillary equipment performs various functions, such as load and strain detection and specimen gripping and alignment, and provides a controlled environment for the specimen. Load cells, grips and alignment devices, extensometry, environmental chambers, furnaces and other methods of heating are briefly discussed below.

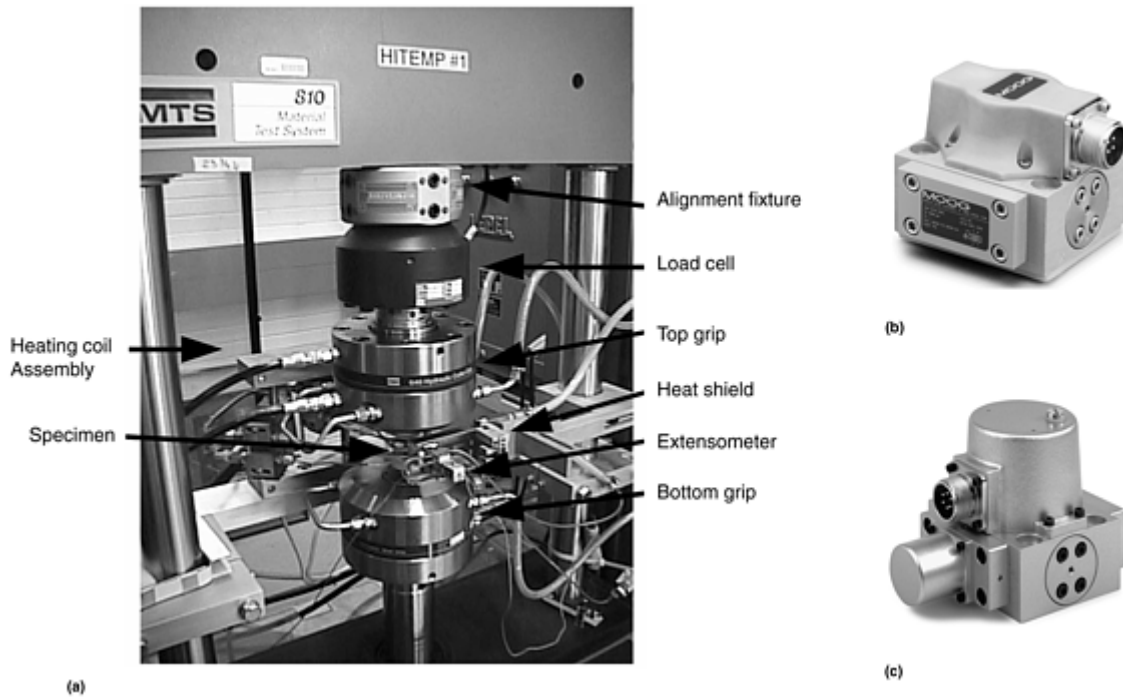


Fig. 8 Ancillary equipment installed on an axial servohydraulic fatigue machine. (a) General view. (b) Conventional servovalve. (c) High-frequency servovalve

Load Application, Measurement, and Control

Hydraulic Cylinder. The forces and displacements in servohydraulic materials testing systems are produced by a hydraulic actuator (Fig. 1b). Many types of hydraulic actuators (cylinders) are in common use in industrial equipment; however, hydraulic cylinders used in materials testing machines are differentiated from others in the following ways: they are fatigue rated so that they may be reliably used in fatigue testing where the duty cycles will be substantial, and they feature specialized seal designs to enable high lateral stiffness to be obtained, which is important in maintaining alignment during testing.

Load Cell. The force-measuring device in a fatigue machine is called a load cell. It typically consists of resistance strain gages bonded to a linear elastic spring element, which carries the same load as the specimen. The gages make up an electrical resistance bridge circuit. Applied load creates a bridge out of balance that is linearly proportional to the load. Load cell design is sophisticated and has evolved over several decades. Load cells must be accurate to within 1% of the applied load (ASTM E 4) and be insensitive to side loads. Load cells should be stiff and stable and have minimal amounts of hysteresis and nonlinearity. Commercially available load cells are insensitive to small thermal fluctuations. However, care must still be taken to ensure that the cell is thermally protected during testing at elevated temperature. In addition, the load cell and cabling should have shielding to prevent electronic noise, particularly as induced from specimen heating systems. Load cells are designed with overload protection, which prevents damage of the cell due to misuse, and must be rated for fatigue testing.

This description applies to load cells used in axial loading as well as some plane-bending loading (three- and four-point loading not discussed herein) wherein the bending loads are imposed by loading in an axial loading frame. Cantilever plane-bending fatigue testing is done in smaller, simpler testing machines, and the load cell used to measure the bending load may differ in detail. For plane cantilever bending using an eccentric drive mechanism, the bending load cell can be built into the grips. Some rotating-bending test machines do not use a load cell, but rather rely on deadweight loading and knowledge of the lever arm distance to determine the applied bending moment. All force-measuring systems require periodic calibration to ensure accuracy. Methods of calibration and the intervals at which they are performed are specified in standards such as ASTM E 4. An excellent review of load cell design can be found in Ref 2.

Most often, the forces and displacements imparted on a test specimen by a testing machine originate from a hydraulic cylinder, the ram displacement of which is controlled by a servovalve (Fig. 1b).

Servo valves (Fig. 8b and 8c) are electromechanical devices that provide a means of controlling the flow of (hydraulic) fluid supplied to a hydraulic cylinder. This is generally accomplished by an electrically actuated element connected to a spool, where the spool is machined in such a manner so as to permit fluid flow to occur in proportion to its position relative to fluid inlet and outlet ports. These devices generally have a transfer function expressed in terms of the current (in milliamperes) required to develop a specific rate of flow. Conventional servo valves (Fig. 8b), as described above, are the most common design in use with servohydraulic materials testing equipment and provide acceptable frequency response for most fatigue testing applications. However, high-frequency servo valves are often used in the economical production of high-cycle fatigue data in excess of 10^6 cycles. One type of high-frequency servo valve used in materials testing applications uses a voice coil to actuate a pilot spool, which in turn ports fluid to a main stage spool, which in turn is used to port fluid to the actuator. This arrangement—in which the pilot spool position, obtained with a linear variable differential transformer sensor, is used in a control loop—provides very-high-frequency capability for materials testing. Other types of high-frequency servo valves, such as the one shown in Fig. 8c, do not use a voice coil to actuate a pilot spool.

Gripping Systems

Well-designed fixturing is required to transmit the applied load through the specimen to the load cell. The grip system must be versatile enough to allow easy installation of the specimen, but must not cause damage to the specimen test section during installation and testing. In addition, the grips must ensure good alignment and be able to withstand the environment associated with the test. The gripping system should have high lateral stiffness to maintain good alignment (more information about alignment can be found in the section “Alignment Considerations” in this article). For uniaxial, tension-compression testing, the specimen and grips must be designed such that there is no backlash while passing through zero load. Modern gripping systems usually consist of a block of high-stiffness metal (typically steel) that attaches to the load train. The body of the grip may be water-cooled to prevent overheating during tests at elevated temperatures. The grip body has some type of insert that aids in specimen installation and accommodates the geometry of the specimen grip ends (Fig. 9). The inserts are typically made of a material with high hardness (such as tool steel) to minimize wear and distortion due to repeated clamping. For elevated-temperature operations, a high-temperature alloy is often chosen.

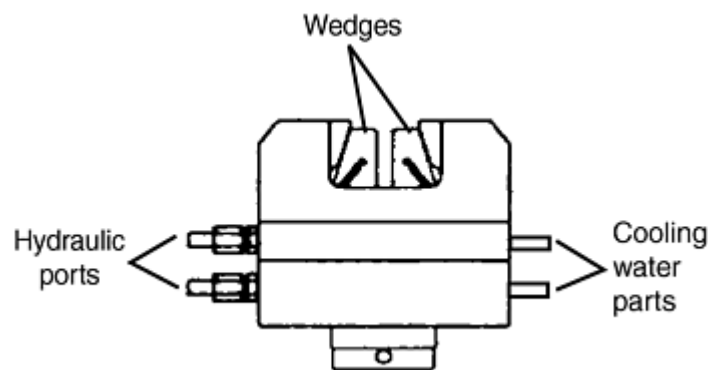


Fig. 9 Schematic of typical hydraulic wedge grip

To properly grip the specimen, inserts are used in the grip body or directly on the pull rods. These are generally of the collet or wedge type. Some of the more common types of inserts are shown in Fig. 10. Collets can be used for flat and round specimens and are most often used for tension-compression testing. Wedge inserts are used for flat specimens, primarily tested in tension. Both collets and wedges generally operate in a grip, such as the one shown in Fig. 9. The specimen is held in place with friction that is regulated by squeezing the sample within the inserts using hydraulic pressure. This system provides easy specimen installation and maintains excellent alignment. The gripping surfaces of the insert often have a knurled surface or are treated with an abrasive coating to enhance the friction and allow higher axial loads to be applied without the specimen slipping in the grips. Grip surfaces that are too coarse can cause unwanted grip failures.

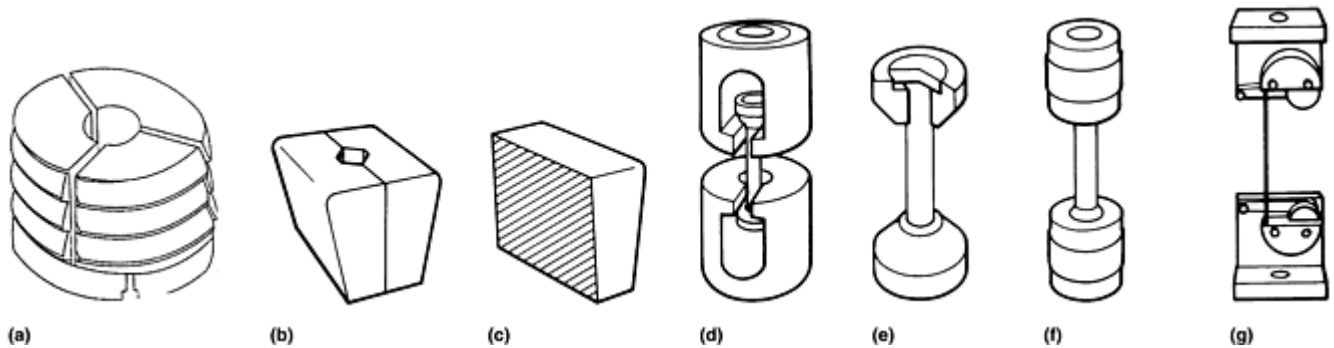


Fig. 10 Grip insert designs used for axial fatigue testing. (a) Three-piece collet grip for cylindrical specimens. (b) V-grips for rounds for use in wedge grip body. (c) Wedges for flat specimens. (d) Universal open-front holders. (e) Adapters for special samples (e.g., screws, bolts, and studs) for use with open-front holders. (f) Holders for threaded samples. (g) Snubber-type wire grips for flexible wire or cable

When testing at elevated temperatures, the grips must be able to maintain their operating capabilities. There are two basic methods for gripping at high temperatures. The first is to keep the grips out of the hot zone and water cool them to prevent overheating. This is most effective with heating systems where only localized heating (in the gage section) occurs, such as with induction, radiant heaters, and small furnaces. The drawback to cooled grips is that the grips act as a large heat sink, pulling the heat out of the specimen. This can make it difficult to achieve an acceptably low thermal gradient along the length of the specimen test section.

The second method is to employ hot grips. With this gripping system, the grips reside in or near the hot zone. This is commonly used with large muffle-type furnaces. Negligibly low thermal gradients along the specimen test section are easily achieved with hot grips because the grip temperature is similar to that of the test section. The grip material must be of a high-temperature alloy, typically a nickel- or cobalt-base alloy. Care must be taken to ensure that the specimen does not permanently affix itself to the grips. A high-temperature lubricant, such as MoSi_2 or Al_2O_3 , is typically used to prevent this permanent affixation from happening. Hot grips are generally replaced at a greater frequency than cooled grips due to long term deformation (creep) of the grips and oxidation and microstructural instabilities that may weaken and distort the grip material.

Another type of fixture is commonly used for threaded samples. These fixtures consist of a block of material with internal threads to accommodate the specimen. To lock the specimen to the grips, jamb nuts are tightened to preload the specimen grip ends within the grips and eliminate backlash. Care must be taken to avoid applying a torque across the specimen test section during installation. This fixture has an advantage that very small specimens can be used, thus minimizing material mainly due to the relatively short grip section needed compared to wedge or collet grips. The disadvantage of such grips is that alignment can be poor and can vary from set-up to set-up for a given specimen, as well as from specimen to specimen. Also, notch-sensitive materials may tend to break in the threads rather than the test section if the thread diameter is too small compared to the gage section diameter.

Grips for three- and four-point bending carried out in an axial loading frame often take the form of simple rollers that transmit normal forces, but negligible shear forces, to the surface of bending specimens. Care is taken to maintain the orientation and location of the rollers and the specimen relative to the loading frame. Consideration should also be given to surface-initiated cracking from the contact line of the rollers, although this is offset by the compressive Hertzian stresses imposed by the rollers. For bending in both directions, symmetric sets of rollers must be located on the opposite faces of the bend specimen and preloaded to prevent backlash. Three- and four-point bending fatigue tests are used often to test notched geometries or to grow cracks for subsequent fracture toughness testing.

Grips are considerably simpler, and alignment, while still important, is not as critical for cantilever plane bending using an eccentric drive as it is for axial loading. The larger, fixed end of the specimen is typically bolted to a rigid plate on the test frame. The flat plane of the specimen must remain plane and be aligned with respect to the bending axis. Clamping forces must be high enough to prevent relative motion in the grips, but not so high as to introduce clamping stresses that would cause changes to the reduced width and thickness of the test section. Gripping of the cantilevered end of the specimen is relatively unimportant because of the low bending stresses present. However, the gripping and means of force transmittal must freely accommodate the

forced displacement of the end of the specimen that traces the arc of a circle. The specimen must be free of loading along its longitudinal axis and free of all extraneous bending moments. Collet, or lathe, grips are commonly used for rotating-beam specimens and must be designed so that fretting does not occur in the grip. Also, the grip design must prohibit seizure of the specimen, allowing easy specimen removal without damage. Care must be taken that the tightening of the grips does not induce misalignment and, hence, unwanted stresses in the specimen test section.

Extensometry and Strain Measuring Devices

Because fatigue damage occurs as a result of plasticity, it is desirable to measure the deformation occurring within the gage section during a test. The deformation or displacements can be easily tracked using a number of devices. The most accurate methods involve measurement of the strain in the gage section of the specimen. Measurements over larger sections, such as displacement between the crosshead (stroke), should not be used because they include displacement components from the load train as well as the deformation that occurs in the specimen. A number of studies have been conducted in which strain has been measured on specimen ridges outside the gage section (Ref 3, 4), an approach that involves analysis of the deformation in the radius section to determine only the contribution to displacement coming from the gage section. The relative contributions depend on the degree of plastic strain, therefore, a variable calibration is required.

Direct measurements on the gage section are more straightforward and can be performed with a number of devices, such as strain gages, extensometers, and optical devices. The key to any of these devices is that, in addition to taking accurate strain readings, the device cannot affect the fatigue life of the sample. In addition, these devices should not only be able to record displacement, but also be stable enough to be used to close a feedback loop in a strain-controlled mode. Resistance strain gages are very accurate and can be used to both measure strains in any direction and control strain during the test. They are best suited for nominally elastic straining tests. Sustained cyclic strains larger than about 0.75% amplitude may be inappropriate for use of resistance strain gages (Ref 5). Strain gages can be very small in size, and, therefore, many can be applied to a standard test specimen and used to measure bending strains, Poisson's ratio, and strains in various axes. Commercially available gages provide resolutions and accuracies suitable for fatigue testing. Standard texts on strain gage usage (see, for example, Ref 6) can guide the user in this area. The gages should be rated for cyclic use over the range of strains needed for the test. Care must be taken to ensure that specimen surface preparation for gage installation does not induce premature fatigue cracking of the specimen.

Resistance strain gages are used principally at room temperature. However, resistance strain gages are available that have limited use at temperatures as high as 800 °C (1500 °F) (Ref 7, 8). These gages are used where measuring strains in various directions on the specimen is desirable, or where easy access to the specimen by an extensometer is not possible (e.g., in a furnace). However, they are difficult to use, often suffer from long-term drift, and must be individually compensated for each temperature range. More information on these gages can be found in ASTM E 1319.

The most common method of measuring strains in fatigue tests is through the use of a mechanical extensometer. Extensometers employ some method of contact with the specimen that relays the displacement through a lever system to an electronic sensing element. The sensor is generally a strain gage bridge, a capacitance transducer, or a linear variable differential transformer (LVDT). Generally LVDTs are larger and heavier than the other two types.

Extensometers are rated according to their accuracy (ASTM E 83). Like load cells, extensometers should have a linear response and have minimal hysteresis (ASTM E 606). Extensometers require periodic calibration (ASTM E 83) to ensure their accuracy (Ref 5).

Axial Extensometers. For tests at room temperature, clip-on extensometers are generally used, attaching to the specimen using breakaway features, such as springs, sheet metal clamps, and other low-pressure clamping arrangements. Metallic knife-edge probes provide a sharp point of contact and are mechanically set to the exact gage length. Often, small strips of tape are adhered to the specimen to give the knife edges something to “bite into” without damaging the specimen.

When testing at elevated temperatures, the sensing element of the extensometer must be protected from the heat. Moving the sensor away from the heat source by the use of longer probes can accomplish this. However, metal probes are no longer suitable and are replaced with a ceramic material. The probes are rods with a suitable specimen contact geometry, such as knife-edge, V-notch, or conical point geometry, depending on the

specimen material and gage section geometry. The probes must not damage the surface of the specimen, must not be reactive with the specimen material, must remain in stationary contact with the specimen surface, and must not deform (particularly creep) during the test.

The extensometer probes are mechanically preloaded (typically using springs) to hold them in direct contact with the specimen surface. The force must be sufficient to prevent slippage of the probes, but not so high as to deform the specimen (particularly due to creep) or to otherwise influence specimen failure. Commercial extensometers are available with a wide range of contact forces. The extensometer is mounted to a fixture that may also act as a heat shield, further protecting the sensing element. The extensometer-sensing element is usually air or water cooled to maintain temperature equilibrium during the test so that there is no temperature-induced drift in the strain reading.

Where a large furnace is used (generally with hot grips), the sensing element must be moved even further from the specimen, and long probes or rods must be used to transfer the specimen displacement out of the furnace to the sensing device. Systems of this type can be found in Ref 9, 10, and 11.

Optical extensometers are also available. Most are based on lasers. Their major advantage is the zero mass of a laser beam that offers potentially high response to specimen straining. Another advantage, depending on the type of laser detection employed, is elimination of direct attachment of an extensometer to the specimen. This is particularly important for brittle and notch-sensitive materials. Of course, an optical path must be available between the specimen and the laser/detector. This type of extensometer, however, can be expensive to purchase, set up, and maintain. While speckle-pattern and interferometric systems are available, their adaptation for closed-loop servostrain control is quite difficult. For that reason, only the optical target (flag) system will be discussed here. This system uses a laser beam and detector array to scan the displacement of flags that define a gage length. Typically, the laser scans multiple times per second and averages the distance between two flags attached to the specimen. Unfortunately, current scanning rates are too low to achieve high-strain-rate response. Another problem is that the flags have to be specially designed to maintain a sharp edge at temperature, must adhere to the specimen without inducing damage, and must remain on the specimen throughout the duration of the test. A good comparison of the capabilities of a laser/target extensometer with various other types of strain measuring devices can be found in Ref 12.

Diametral extensometers are used to measure the change in diameter of a specimen due to Poisson's contraction. They are used primarily with axially loaded, hourglass fatigue specimens and at large strain ranges where premature cyclic plastic buckling would rule out use of straight gage length specimens. Generally, the design is a hinge and transducer with the extensometer mass supported by wires or self-centering springs, such that very low contact forces are needed. This design avoids some of the problems associated with use of axial extensometers. Diametral strain can be converted into axial strain using equations found in Ref 10, 13, and 14. However, if the load is not constant (a result, for example, of cyclic strain hardening or softening) during a constant diametral strain-range-controlled test, then the longitudinal strain range will vary. However, computer-controlled testing could be used to compensate so as to maintain a constant total axial strain range. Another drawback to the diametral extensometer is that the change in diameter of the specimen during a fatigue test is very small, and high resolution is required for the sensing device. However, this extensometer is typically used for large strain ranges and therefore sensitivity is not critical. Only a small volume of material experiences the full loads and strains during the test, which limits the size of microstructural features that can be effectively sampled. Information on a number of diametral extensometer designs can be found in Ref 13. Diametral extensometers were used extensively prior to the development of the current generation of axial extensometers.

Heating Systems

When fatigue testing is conducted at elevated temperatures, any method that can heat the specimen to the desired temperature and be adaptable to the existing test equipment might be used. The key to choosing the appropriate heating method depends primarily on ease of use and the ability to obtain the desired temperatures and thermal gradients. According to ASTM E 606, the thermal gradient within the gage section must be within 2 °C (3.6 °F) or 1% of the test temperature, whichever is larger. Also, the nominal temperature should not vary during the test by more than ± 2 °C (± 3.6 °F). These requirements are not overly restrictive, but do require some consideration and effort to achieve. There are various heating methods that can easily attain these limits and have proven themselves for use with fatigue testing; these methods are discussed in this section. Test results not meeting ASTM standards should be so indicated and the deviation quantified.

Induction Heating. One of the most versatile methods of heating and probably the most widely used for low-cycle fatigue of metallic materials is direct induction heating. Induction heaters generate either audio or radio frequency electromagnetic fields to induce eddy currents in the near surface of a test specimen. The current is passed from the induction generator into water-cooled copper tubing wrapped into coils, which surround the specimen. These coils can be made to fit any size or shape of specimen, making this system of heating highly versatile. The tubing is normally covered with a high-temperature insulating material to prevent accidental shorting between coils. There is generally no limitation on the maximum temperature that can be obtained using induction heating, provided that the induction generator has sufficient capacity and that adequate cooling is available for the working coils. For the majority of test specimens and materials, a 5 kW induction heater will suffice. These types of heaters have very low thermal mass and are ideal for rapid thermal cycling, such as would be needed for TMF testing. The major disadvantage of induction heating is the difficulty in establishing the required thermal gradient. Localized heating can readily occur with temperatures varying by as much as 20 °C (36 °F) over short distances (e.g., 6 mm, or 0.25 in.). Manipulating the position and proximity of the induction coils can bring these gradients into compliance with requirements. Unfortunately, this process is more art than science. At least one method has been developed (see Fig. 11) that separates the coil into three independent segments (Ref 15). Each segment can be moved while the specimen is at temperature, thereby greatly reducing the time required to establish an acceptable thermal gradient.

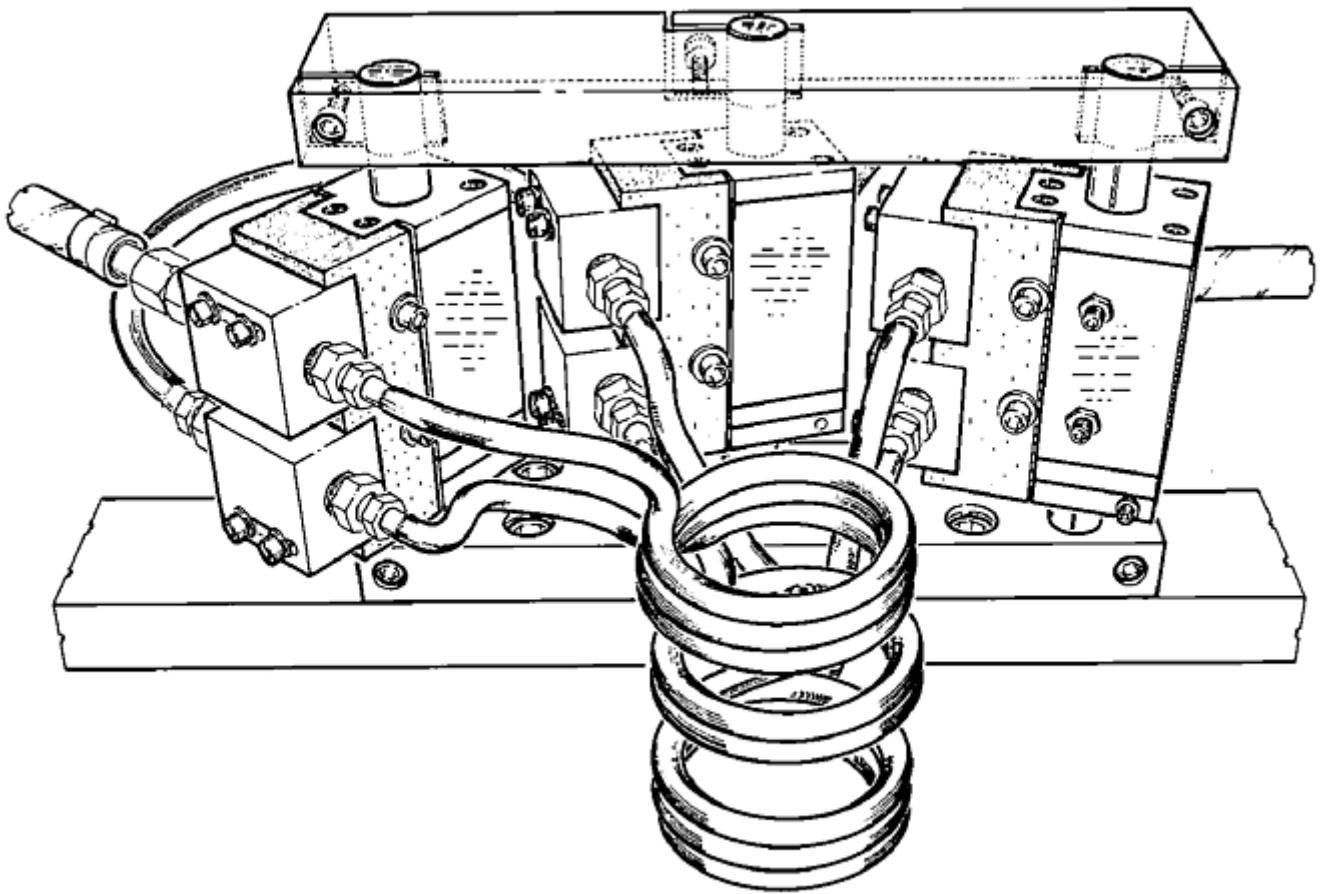


Fig. 11 Adjustable work coil fixture for direct induction heating in elevated-temperature fatigue testing

Another disadvantage to direct induction heating is that temperature measurement requires thermocouples to be bonded to the specimen (i.e., welded). If there is poor contact between the specimen and the thermocouple, the thermocouple will be independently heated by the induction field and give erroneous readings. Unfortunately, welding thermocouples onto the gage of the sample may initiate premature cracking. There are at least three ways to work around the thermocouple attachment problem. First, one can weld the control thermocouple to a place other than the gage section, such as the grip. The temperature relation between the gage section and the grip would have to be determined with a calibration specimen and shown to be constant from one specimen to

the next. Second, one can use a noncontacting temperature-measurement device (e.g., optical pyrometer). Third, one can use susceptor heating. In this method, a susceptor material—usually SiC, graphite, or metal—is placed within the induction coil. The induction field heats the susceptor, which in turn radiates heat to the specimen. This method is commonly used for materials that are poor electrical conductors. Even though a susceptor is used, some amount of coupling between the induction field and the specimen can still occur. Also, a susceptor has a larger thermal mass, and the temperature of the specimen cannot be changed as quickly as by direct induction. Therefore, this type of heating may have limited use for TMF testing.

Radiant Heating. Another type of heating, quartz-lamp radiant heating, works particularly well with flat specimens (but has also been used successfully with cylindrical specimens). With this method, radiant energy is focused onto the specimen by means of a parabolic reflector. Because the lamps are designed for a specific focal length, which ensures a certain area of constant temperature, they are not readily adaptable to specimens and test set-ups other than for the purpose for which they were originally designed. The lamps have very fast heating rates and are suited for moderately rapid thermal cycling. Care must be taken to ensure that the specimen is not shadowed by instrumentation.

Radiant heating using wire resistance coils in a hollow furnace is also a common heating method. Muffle furnaces, either split or in one piece, can be used, but these are typically large. Smaller furnaces can be constructed out of banks of individual heating elements or of continuous windings of Nichrome wire for specific applications. Both furnace types can be manufactured in single- or multi-zone configurations. These furnaces provide uniform and constant temperatures with very low thermal gradients and are ideally suited for long-term exposures. Because the area within the furnace is essentially at the same temperature, thermocouples need not be in intimate contact with the specimen. This permits the use of wrap-around and probe-type thermocouples. However, the furnaces are generally large, which increases the distance between the load platens resulting in a less-stiff load train. Also, access to the specimen with instrumentation is difficult and must be considered before the furnace is constructed in order to include a sufficient number of properly sized ports. Finally, the very large thermal mass of these systems makes them poorly suited for rapid thermal cycling. A highly specialized radiant heating system consists of a silicon carbide heating element that is inserted inside a tubular specimen and radiates heat to the inside surface of the specimen. The presence of thermal gradients throughout the wall and along the length is a disadvantage, but this disadvantage is offset by entirely freeing up the external-surface outer diameter of the specimen for any extensometry or other measurement paraphernalia (Ref 14).

Direct resistance heating is another specialty heating technique that has been used to advantage for elevated-temperature fatigue tests including TMF (Ref 16, 17, and 18). The specimen itself becomes the heating element. Although a metallic specimen possesses a low electrical resistance, passing a very high current (on the order of a kiloampere) directly through the specimen will produce heat within the specimen that is proportional to the product of the current times the voltage drop across the length of the specimen. Extraordinarily high rates of heating are attainable. Transverse temperature gradients are inherently small compared to other heating techniques because the heat is generated uniformly within the material. Heat transfer is not necessary to heat the interior, because heat is being generated uniformly throughout the volume of a uniform test section at the same rate as at the surface. Actually, the center of the specimen may be ever so slightly hotter than the surface because of radiation losses and the slightly higher heat flow rate of surface material. Extensive water cooling is necessary to prevent oxidation and contact resistance of all high-current connections, including those of the specimen to its grips. Water cooling assists rapid specimen cooling when TMF tests are conducted. Disadvantages of direct resistance heating include safety concerns regarding large currents and the potential for inadvertent short circuit arcs that could produce instant molten metal and severe burns. Large currents also introduce control difficulties and high magnetic fields, causing interference with sensitive electronic control equipment indigenous to modern fatigue testing systems.

Temperature Control. With all heating methods, temperature is commonly controlled using commercially available, solid-state temperature controllers. These controllers can be purchased with resolutions far superior to what is needed for fatigue testing. Proportional-integral-derivative (PID) control settings can be adjusted to maintain the control temperature to within 0.1 °C of the desired temperature. These controllers can be operated manually or programmed to follow a signal generator output. Hence, temperature cycling can be phased with mechanical strain cycling during a TMF test.

To minimize temperature variations during testing due to air currents in the laboratory, it is recommended that an enclosure be installed around the zone of the specimen. Another important concern for all methods of

specimen heating is unwanted electronic interference created by the temperature controllers. Unless an off-the-shelf engineered testing system is purchased, care is required to shield or filter troublesome signals.

Environmental Chambers

When environments other than still laboratory air are desired, an environmental chamber must be used (Fig. 12). Examples include a vacuum or inert gases (argon, helium) to eliminate effects of oxidation at high temperatures; high pressure; high-temperature gases, such as oxygen or hydrogen to simulate liquid rocket engine environments; radiation from radioactive sources for the study of nuclear reactor components; cryogenic environments for the study of alloys used in super-cold applications; or even corrosive environments that can degrade the fatigue properties of a material. Each environment poses its own set of concerns for the protection of grips, extensometry, and load cells. If, for example, a vacuum or pressurized chamber is required, any parasitic loads transmitted through the structural components required to maintain the environment (e.g., seals, baffles, or bellows) must be eliminated from the load cell signal.

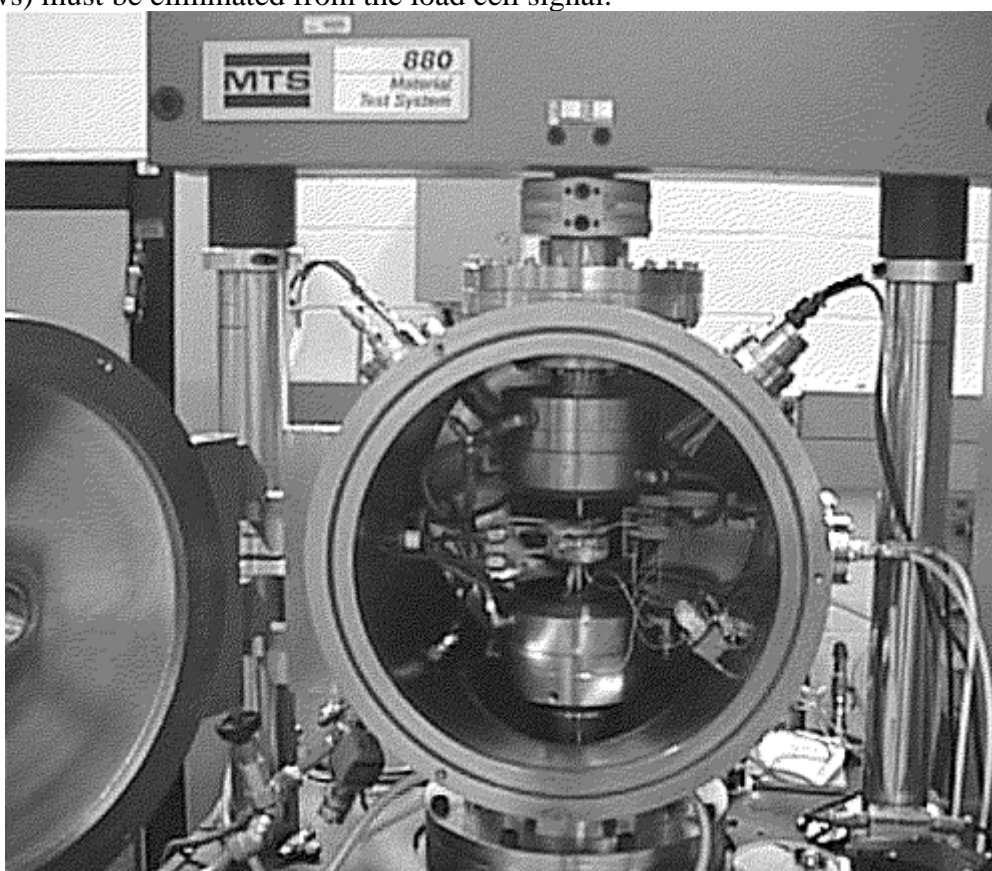


Fig. 12 Environmental chamber for fatigue testing

Careful attention must be given to gaining access to the specimen and grips for installation and removal of specimens, and the attachment and support of extensometry. Viewing ports are also highly desirable. For sealed systems, insulated electrical feed-through connectors are required for transducer signals (e.g., strain, pressure, and temperature).

Representation of Material and Specimen Configurations

A specimen is a representative sample of an alloy and is used to determine and compare the basic fatigue characteristics of a material. In addition to this primary use, specimens can be designed to study the effects on fatigue resistance of several important factors. These factors can be categorized as:

- *Geometric features*, such as stress concentrations including intentional notches, holes, fillet radii, and attachment configurations; unintentional voids or flaws; and damage due to handling or service use

- *Bulk properties*, such as those influenced by degree and orientation of cold working, temperature of testing, thermal exposure, heat treatment, and radiation
- *Surface-related effects*, including mechanical surface finish, shot peening, burnishing, laser shock treatment, residual stresses, environmental interactions, fretting, galling, and coatings
- *Loading-related factors*, such as mean stress, multiaxiality, cumulative damage, temperature of testing, thermal cycling, and creep-fatigue interaction that might occur at low testing frequency and hold times

Nomenclature for a typical fatigue specimen is given in Fig. 13. A test specimen has three sections: the test section, a transition zone, and the two grip ends. The test section is where the quoted stresses, strains, temperature, and environment are measured or controlled and where fatigue cracking and failure are designed to occur. The majority of the specimen deformation occurs in this section. The grip ends are designed to transfer load from the test machine grips to the test section and may be identical at either end, particularly for axial fatigue tests. The transition from the grip ends to the test area is designed with large, smoothly blended radii to minimize stress concentration in the transition, which could otherwise initiate undesired fatigue cracking.

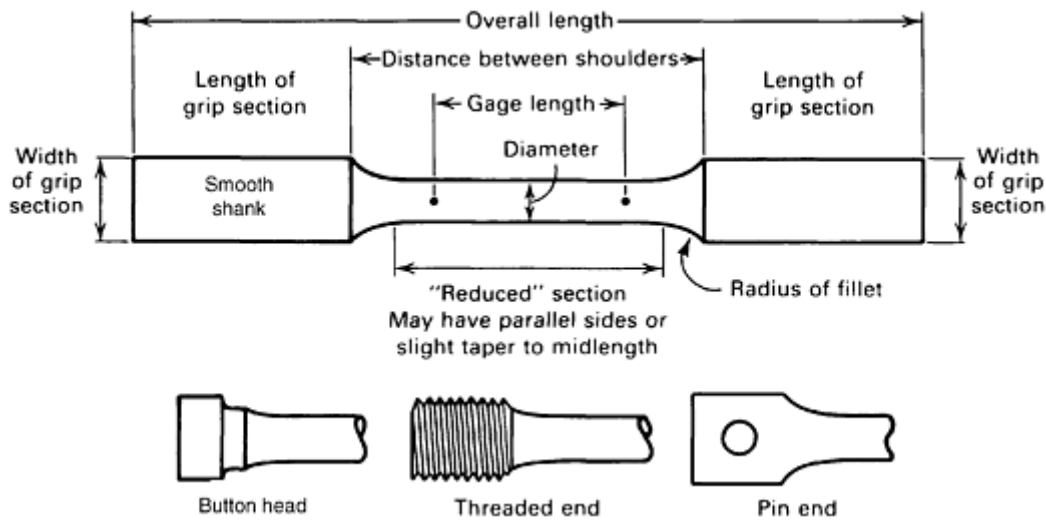


Fig. 13 Nomenclature for a typical fatigue specimen. Ends of round specimens may have smooth shanks, button heads, or threads. Smooth shanks should be long enough to accommodate some type of wedge grip. Rectangular specimens are generally made with smooth shanks, but may be shouldered to contain a hole for a pin bearing.

The design and type of specimen used depends on the fatigue testing machine and the objective of the fatigue study. The test section in the specimen is reduced in cross section to increase the stresses and strains there and, hence, avoid failure in the transition region and in the grip ends. The test section should be proportioned to properly test the material, accounting for adequate sampling of specific microstructural features (e.g., defects and grain size), yet still be small enough that the load capacity of the load frame is not exceeded.

The location from which a test specimen is taken from the initial product form is important because the manner in which a material is processed influences the uniformity of microstructure along the length of the product as well as through its thickness. For example, the properties of metal cut from castings are influenced by the rate of cooling and by shrinkage stresses at changes in section. Generally, specimens taken from the surface of castings are stronger. Many ASTM standards, such as E 8 and B 557, provide guidance in the selection of test specimen orientation relative to the rolling direction of the plate or the major forming axes of other types of products, and in the selection of test specimen location relative to the surface of the product.

Orientation is also important to standardize test results relative to the directionality of properties that often develops in the microstructure of materials during processing. Some causes of directionality include the fibering of inclusions in steels, the formation of crystallographic textures in most metals and alloys, and preferred growth directions in directionally solidified and single-crystal materials.

Specimen Machining and Surface Preparation

Because fatigue crack initiation typically is surface dependent, proper machining and surface preparation of test specimens are critical. Unless care is taken, scatter caused by variable surface conditions will overwhelm the inherent scatter of the material being studied.

Because a primary aim of fatigue testing is comparison of materials, uniform preparation procedures must be established. Machining operations must not alter the surface structure of the metal; thus, heat generation, heavy cutting, and severe grinding are prohibited. Final machining should be parallel to the direction of applied stress. Transition fillets must be blended into the test area without steps or undercutting. Surface polishing using metallographic techniques is preferred for smooth specimens, where machining marks are removed by a sequence of grinding steps. Example procedures for machining of specimens are given in ASTM E 466 and Ref 19.

The final polishing is not a buffing operation, but a cutting operation that uses lapping compounds or aluminum oxide powder in a liquid medium to remove grinding scratches. For flat sheet or plate specimens, edges should be slightly rounded and ground to eliminate nicks, dents, cuts, and sharp edges, which can lead to premature crack initiation. The relationship between surface characteristics and fatigue properties is discussed later in this article.

Test specimens received from a machine shop are expected to meet size specifications provided to the shop. To ensure dimensional accuracy, however, each test specimen should be measured prior to testing. Gage length, fillet radius, and cross-sectional dimensions are easily measured. Cylindrical test specimens should be measured for concentricity. Maintaining acceptable concentricity is extremely important in minimizing unintended bending stresses.

In general, flat specimens are difficult to manufacture without twisting or bending; especially if they are taken from rolled products. The potential warping of thin specimens and their inadequate section modulus lead to ready elastic buckling under compressive loads. Therefore, these types of specimens are usually only tested in tension. Lateral antibuckling guides can be used to prevent buckling of compressively loaded thin flat specimens (Ref 20). However, the buckling guides introduce other problems (surface contact and small amounts of rubbing action at points of contact) that can affect the fatigue properties.

The product form from which the specimen is taken often influences the geometry of a test specimen. Obviously, only flat specimens can be obtained from sheet products. Test specimens taken from thick plates or bar stock may be either round or flat. Occasionally, subscale specimens must be employed if the product form is too small for standard specimen dimensions.

Cylindrical Specimens. Three types of specimens with circular cross sections are commonly used:

- Specimens with tangentially blending fillets between the test section and the grip ends (Fig. 14a and b)
- Specimens with a continuous radius between the grip ends with the minimum diameter at the center (Fig. 14b and d and 15a). These are referred to as hourglass specimens and are commonly used when strain ranges are larger than 2%.
- Specimens for use in cantilever-beam loading with tapered diameters proportioned to produce nominally constant stress along the test section

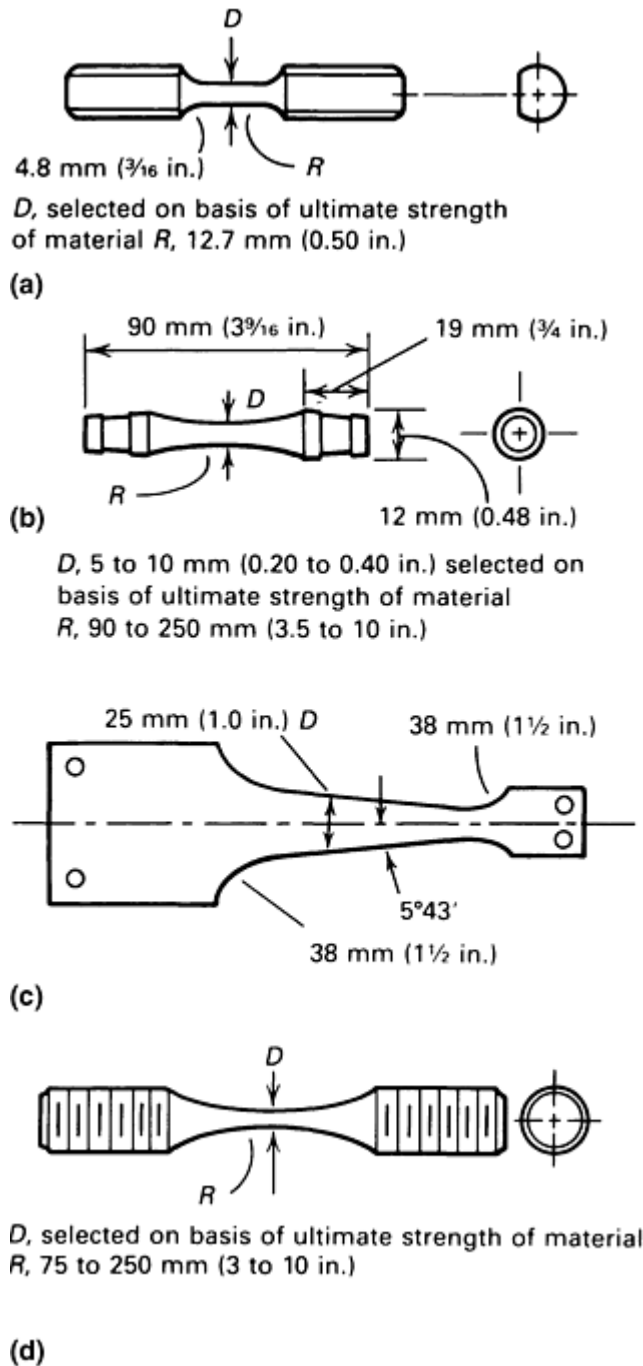


Fig. 14 Typical fatigue test specimens. (a) Torsional specimen. (b) Rotating-beam specimen. (c) Plate specimen for cantilever reverse bending. (d) Axial loading specimen

The design of the grip ends depends on the machine design and the gripping devices used. Round specimens for axial fatigue machines using grip inserts like those shown in Fig. 10 may be threaded, button-head, or smooth-shank types. For rotating-beam machines, short tapered grip ends with internal threads are used, and the specimen is pulled into the grip by a draw bar. A long, smooth shank end is used on machines with lathe-type collets.

Flat Sheet and Plate Specimens. Generally, flat specimens for either axial or bending fatigue tests are reduced in width in the test section but may have small thickness reductions as well. The most commonly used types include:

- Specimens with tangentially blending fillets between the test section and the grip ends (Fig. 15c). This specimen has a straight gage section and is used in both axial and bending fatigue.

- Specimens with a continuous radius between the grip ends, giving a flat hourglass design (Fig. 15d). These are also used in both axial and bending fatigue test.
- Specimens for use in cantilever reverse-bending tests with tapered widths (Fig. 14c)

Flat specimens generally are clamped in flat wedge-type grips or may be held with a stiff bolted clamp/joint friction grip for reversed axial loading. Pin loading can be used when only tensile loads are encountered. When pin loading is utilized, the holes drilled in the grip end must be designed to avoid shear or bearing failures at the holes, tensile failure between the holes at maximum load, and fatigue cracking at the holes in the grip end. In axial fatigue testing of flat sheet specimens, the test length and cross section must be designed to prevent premature buckling of the specimen.

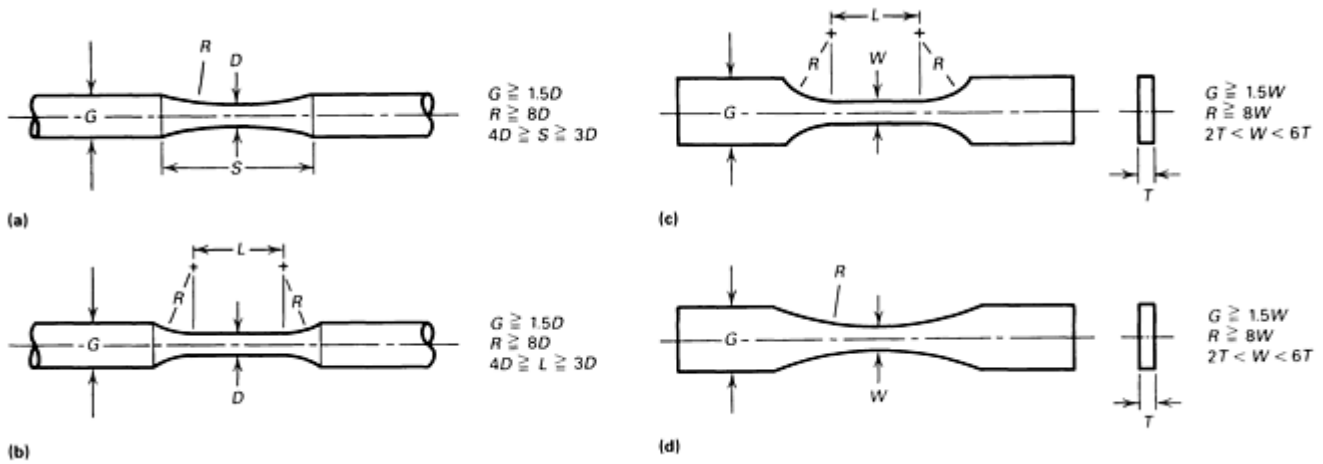


Fig. 15 Typical round and flat fatigue test-specimen configurations. (a) Hourglass specimen with continuous radius between grip ends. (b) Round specimen with tangentially blended fillets between test section and grip ends. (c) Flat specimen with tangentially blended fillets between test section and grip ends. (d) Flat specimen with continuous radius between the grip ends

Alignment Considerations

The keys to achieving accurate fatigue data include ensuring that applied loading is aligned with the specimen axis. This is particularly important in axially loaded specimens. Poor and nonreproducible alignment produces bending strains that reduce the fatigue life and increase the scatter in the data. In fact, it has been calculated that the largest contributing factor to scatter in LCF data is due to bending (Ref 21). Bending strains arise when there is a misalignment somewhere in the load train. The axially and concentricity of the actuator, grips, test specimen, and load cell should be verified and corrected if there is a problem. Coarse adjustments can be made by removing the preload and loosening the load train. These components can then be shifted and/or shimmed to gain proper alignment. Once the load train has been retightened, the small bending strains, *which always exist*, must be measured and minimized. This is typically done by using a strain-gaged trial test specimen, which allows bending strains to be calculated as a function of position along the test specimen, using the same material and test set-up as used in the actual test program. This process can be somewhat involved, and ASTM E 1020 describes it, along with many articles (Ref 22, 23, 24, and 25).

During axial loading, the bending strains should be kept below a specified amount, as described in various fatigue testing standards. For example, ASTM E 606 recommends that the maximum bending strain should not exceed 5% of the minimum axial strain range used during the test. If the bending strains exceed these amounts, the test rig must be further aligned. In past years, this was done by a trial and error method similar to the coarse adjustment procedure described above. This process could take days of effort to achieve moderate bending results. Recently, a new device has been developed (Fig. 16), which fits into one end of the load train (Fig. 8) and allows adjustment of both angular and concentric components of bending while the load train is under preload. This reduces the time needed for achieving proper alignment to within a few hours.

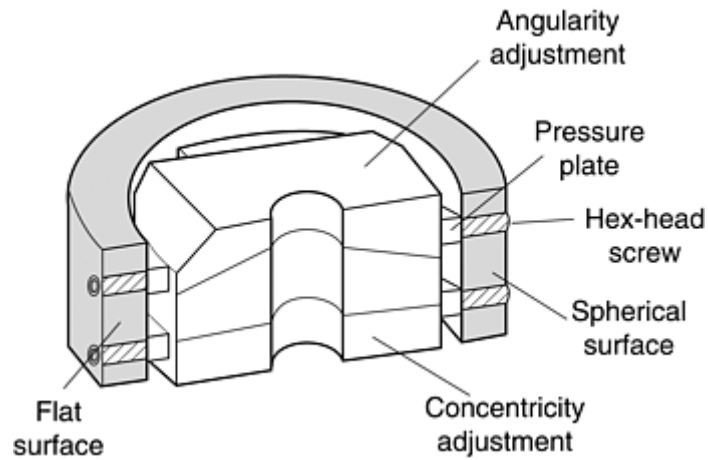


Fig. 16 Alignment fixture for minimizing bending strains in axial fatigue testing

The amount of bending strain in the specimen is affected by gripping methods and specimen design. Better alignment can be achieved using collet, wedge, and button-head grips. Threaded specimens generally give poorer alignment with equally poor reproducibility. Likewise, wear and oxidation of the grips can lead to poor alignment.

Graphic Recorders

In addition to software-based digital recording methods, analog recording devices are also commonly employed for materials testing applications. Strip-chart recorders, enabling time-based paper chart records of various control and response variables, are used. Generally, the strip chart record is used to provide a means to diagnose why a test went off-line, if it does so prior to failure, and to record the gross response variable behavior (e.g., load response) at the point of incipient failure under strain control conditions. Most pen-based strip chart recorders are useful for lower-frequency testing applications (e.g., <1 Hz), because their limited frequency response precludes use to higher frequencies. XY recorders are also commonly employed to record material stress-strain (load-displacement) response or hysteresis loop response in fatigue tests. XY and strip-chart recorders often feature a selection of preset gain ranges (e.g., 0.1 V, 1 V, 10 V or 1 V, 2 V, 5 V, 10 V) for use in plotting signals from the test system. For materials testing applications, it is most desirable that the preset gain controls offer ranges that approximately double the value of the previous setting with each subsequent setting (e.g., 1 V, 2 V, 5 V, 10 V). Analog recorders of these types are often used in conjunction with digital controllers and associated software due to the additional flexibility offered.

References cited in this section

2. *Strain Gage Based Transducers, Their Design and Construction*, Measurements Group, Inc., Raleigh, NC, 1988
3. M.F. Day and G.F. Harrison, Design and Calibration of Extensometers and Transducers, *Measurement of High Temperature Mechanical Properties*, M.S. Loveday et al., Ed., National Physical Laboratory, London, 1982, p 225–240
4. G.B. Thomas, Axial Extensometry for Ridged Specimens, *Techniques for High Temperature Fatigue Testing*, G. Sumner and V.B. Livesey, Ed., Elsevier Applied Science, 1985, p 45–56
5. J.W. Dally and W.F. Riley, *Experimental Stress Analysis*, McGraw-Hill, 1978, p 179–179
6. R.L. Hannah and S.E. Reed, Ed., *Strain Gage Users' Handbook*, Elsevier Applied Science, New York, 1992

7. J.-F. Lei and W.D. Williams, PdCr Based High Temperature Static Strain Gage, *AIAA 2nd Int. National Aerospace Planes Conf. Publication*, AIAA-90-5236, 1990
8. J.-F. Lei, M.G. Castelli, D. Androjna, C. Blue, R. Blue, and R.Y. Lin, Comparison Testings Between Two High-Temperature Strain Measurement Systems, *Exp. Mech.*, Vol 36 (No. 4), 1996, p 430–435
9. E.G. Ellison, Thermal-Mechanical Strain Cycling and Testing at Higher Temperatures, *Measurement of High Temperature Mechanical Properties*, M.S. Loveday et al., Ed., National Physical Laboratory, London, 1982, p 204–224
10. E.G. Ellison and R.D. Lohr, The Extensometer-Specimen Interface, *Techniques for High Temperature Fatigue Testing*, G. Sumner and V.B. Livesey, Ed., Elsevier Applied Science, 1985, p 1–28
11. Creep, Stress-Rupture, and Stress-Relaxation Testing, *Mechanical Testing*, Vol 8, *Metals Handbook*, ASM International, 1985, p 313
12. J.Z. Gyekenyesi and P.A. Bartolotta, “An Evaluation of Strain Measuring Devices for Ceramic Composites,” NASA TM 105337, National Aeronautics and Space Administration, Nov 1991
13. R. Hales and D.J. Walters, Measurement of Strain in High Temperature Fatigue, *Measurement of High Temperature Mechanical Properties*, M.S. Loveday et al., Ed., National Physical Laboratory, London, 1982, p 241–254
14. ASTM STP 465, *Manual of Low Cycle Fatigue Testing*, R.M. Wetzel and L.F. Coffin, Ed., American Society for Testing and Materials, 1969
15. M.G. Castelli and J.R. Ellis, “Improved Techniques for Thermomechanical Testing in Support of Deformation Modeling,” ASTM STP 1186, *Thermomechanical Fatigue Behavior of Materials*, H. Sehitoglu, Ed., American Society for Testing and Materials, 1993, p 195–211
16. S.S. Manson, G.R. Halford, and M.H. Hirschberg, Creep-Fatigue Analysis by Strain-Range Partitioning, *Design for Elevated Temperature Environment*, American Society of Mechanical Engineers, 1971, p 12–28
17. K.D. Sheffler and G.S. Doble, “Influence of Creep Damage on the Low-Cycle Thermal-Mechanical Fatigue Behavior of Two Tantalum Base Alloys,” NASA CR-121001, National Aeronautics and Space Administration, 1972
18. M.H. Hirschberg, D.A. Spera, and S.J. Klima, “Cyclic Creep and Fatigue of TD-NiCr (Thoria-Dispersion-Strengthened Nickel-Chromium), TD-Ni, and NiCr Sheet at 1200 °C,” NASA TN D-6649, National Aeronautics and Space Administration, 1972
19. P.R. Breakwell, J.R. Boxall and G.A. Webster, Specimen Manufacture, *Measurement of High Temperature Mechanical Properties*, M.S. Loveday et al., Ed., National Physical Laboratory, London, 1982, p 322–340
20. E.T. Camponeschi, Jr., “Compression of Composite Materials: A Review,” ASTM STP 1110, *Composite Materials: Fatigue and Fracture (Third Volume)*, T.K. O'Brien, Ed., American Society for Testing and Materials, 1991, p 550–578
21. F.A. Kandil and B.F. Dyson, Influence of Load Misalignment During Fatigue Testing I and II, *Fatigue and Fracture of Engineering Materials and Structures*, Vol 16 (No. 5), 1993, p 509–537

22. J. Bressers, Axiality of Loading, *Measurement of High Temperature Mechanical Properties*, M.S. Loveday et al., Ed., National Physical Laboratory, London, 1982, p 278–295
23. J. Bressers, Ed., *A Code of Practice for the Measurement of Misalignment Induced Bending in Uniaxially Loaded Tension-Compression Test Pieces* (Institute for Advanced Materials, Joint Research Centre, Netherlands, and the High Temperature Mechanical Testing Committee), the Directorate-General of the European Commission, Luxembourg, 1995, 52 pages
24. F.A. Kandil, *Measurement of Bending in Uniaxial Low Cycle Fatigue Testing*, National Physical Laboratory, Teddington, England, 1998
25. A.K. Schmieder, “Measuring the Apparatus Contribution to Bending in Tension Specimens,” ASTM STP 488, *Elevated Temperature Testing Problem Areas*, American Society for Testing and Materials, 1971, p 15–42

Fatigue, Creep Fatigue, and Thermomechanical Fatigue Life Testing

Gary R. Halford and Bradley A. Lerch, Glenn Research Center at Lewis Field, National Aeronautics and Space Administration; Michael A. McGaw, McGaw Technology, Inc.

Electronic Test Controls

Electronic test controls (controllers) are used to adjust and maintain the desired control parameter(s) for a given fatigue test. Controllers also provide test termination capabilities for many criteria, for example, failure, load drop-off, deflection, or extension limit excellence. Modern fatigue testing is generally performed using closed-loop servocontrollers, wherein the controlled parameter is continually sensed and compared to the desired command, and the result of this comparison, the error signal, is used to drive the actuator (which may be hydraulic or electromechanical in nature). Sensors for measuring the relevant mechanical quantities (e.g., load cells and extensometers, as discussed elsewhere in this article) provide the feedback, and the control mode of the test is defined by the sensor being used for feedback control. Control is typically effected through a PID strategy wherein the error signal is amplified by gain terms that can be independent of time (proportional gain), as well as dependent on time (integral and derivative gain). A typical closed-loop control system is shown in Fig. 17.

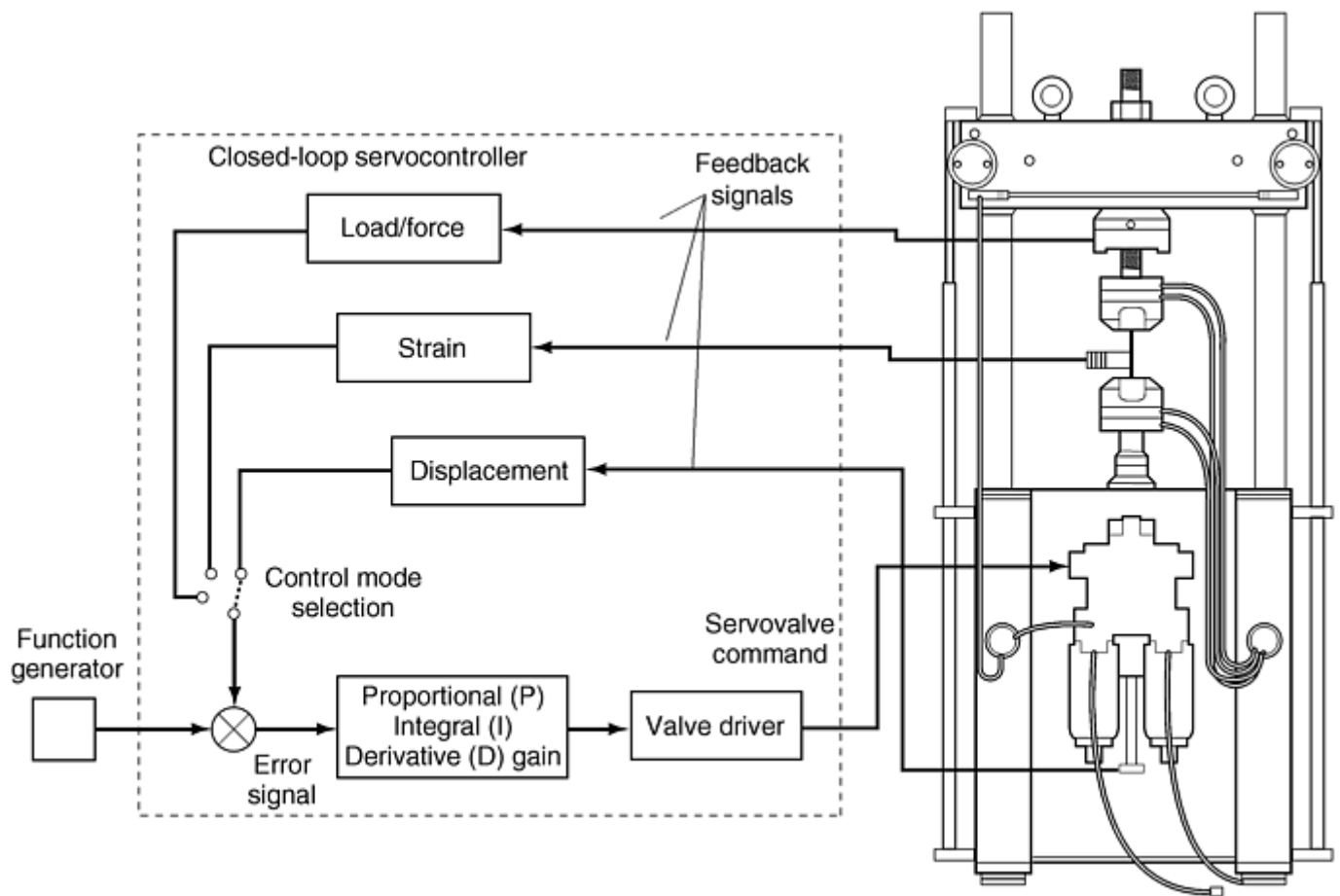


Fig. 17 Typical closed-loop servocontroller system for fatigue testing

A functional fatigue testing machine requires the ability to flexibly define test needs with regard to command waveform generation and data acquisition. A variety of technologies are available to accomplish closed loop control of materials testing systems, in performing standard materials tests, and for the development of custom testing applications. This section discusses these technologies and particularly focuses on the state of the art of software tools for materials testing.

Load Frames: Analog and Digital Controls

Analog controllers are the most commonly used test controllers in fatigue testing laboratories today. Analog controllers have been brought to a high level of refinement, and the latest examples exhibit relatively low noise and reasonably wide-frequency bandwidth. Analog controllers typically provide numerous inputs and outputs that can be used to flexibly adapt to nearly any testing requirement. In addition, materials testing applications software that is designed for analog controllers can be used broadly on many different controller models. The disadvantages of analog controls include the fact that many models do not provide the ability to switch control modes while the test system is energized (under hydraulic pressure), and that calibration of the sensors and the test controller is typically done through trim pot adjustments, a process that can be time consuming.

Digital controllers have been available for the past several years, and the usability of these controllers continues to improve with each new generation. The fundamental difference between an analog controller and a digital controller centers on the summing junction (Fig. 17). A digital controller closes the control loop using a microprocessor instead of continuous-signal analog amplifiers. In a digital controller, the loop closure rate (the rate at which the microprocessor must update the control loop) is directly related to the maximum test frequency performance (i.e., bandwidth) that can be attained. The loop closure rates required for servohydraulic systems demand very-high-performance digital systems. One of the factors driving the development of digital controls is that control mode switching is simpler, as the loop is digital, and many of the problems relating to offset error in analog systems are not present in their digital counterparts. In addition, from a manufacturer's viewpoint, the cost of digital technology continues to drop (for a given level of performance), and the

manufacturing of digitally based products is inherently simpler, owing to fewer required circuit trim adjustments. The chief disadvantages of digital controllers are that changes to the controller organization cannot be done except through software modification of the controller, effectively isolating the user from making any change, and digital controllers generally require software graphical user interfaces. Most digital controller operator interfaces can be labyrinthine to navigate and use, complicating their use and increasing the probability of user mistakes.

Comparison of Analog and Digital Controllers. Both analog and digital control technologies are available for use in performing materials tests, and it is not possible to make definitive statements regarding the superiority of either technology for materials testing needs. The decision as to which controller technology to use may be more prosaic as well: life cycle costs and training costs, among others, must be carefully considered before a choice is rendered. Because analog controllers provide a nearly universal interface for admitting external program command signals, as well as provide high-level conditioned transducer signals for data acquisition, they are easily interfaced to computers for test control purposes. The software created can be generally applied to testing needs regardless of the specific manufacturer's model of the analog servocontroller. Digital controllers, on the other hand, feature software that is based on the "command set" for the specific controller. Thus, materials testing needs that cannot be realized from off-the-shelf software must be custom developed, and any such software is uniquely tied to that specific digital controller model. Finally, analog controllers have a demonstrated longevity, whereas the digital controller will likely have a much more rapid obsolescence, owing to the rapid evolution of digital components.

Furnace Controls

The control of furnaces used in materials testing is largely accomplished using closed-loop temperature controls. Because thermal processes inherently vary slowly (therefore the control loop update rate requirements are relatively modest), and because the costs of microprocessor technology continue to drop, nearly all temperature controllers available today are digitally based. Care must be exercised when selecting a given temperature controller to ensure that it is compatible with the control input requirements of the heating system that is being used. If thermomechanical tests are contemplated, or other nonisothermal temperature requirements are being contemplated, the temperature controller must have facilities for varying the temperature set point, either by means of an external command signal or with a controller command set. Of the two, facilities for accepting an external command signal are preferred, because this provides the greatest flexibility and simplicity in the test apparatus.

Test Program Development and Software

Software systems for performing materials tests have been in use for approximately 25 years (Ref 26). During this period, computer technology has changed dramatically, but, ironically, testing needs have not. Scientists and engineers have a continuing need for flexible and powerful tools to design and conduct materials tests, be they standard tests or unique experiments representative of research and development efforts. Software systems developed to satisfy testing needs have typically been developed along three lines: single application software created uniquely to meet a specific testing requirement (e.g., ASTM E 606), general-purpose testing software designed to provide a flexible set of tools that can be used to implement a broad spectrum of testing requirements, and lastly, custom-written test application software.

Single-Purpose Software. Software for performing standardized tests is widely available from several vendors, operating for both analog and digital servocontrollers. Materials testing engineers charged with conducting standardized materials tests are strongly encouraged to review commercially available offerings before considering custom-application software development. Most specific test requirements (e.g., high-cycle fatigue, low-cycle fatigue, and fatigue crack growth) are well represented by commercially available application software. While the cost of commercial materials testing software is significant, custom-application development is not trivial and is time consuming.

General-Purpose Software. Several examples of general-purpose testing software are readily available from a variety of vendors. Generally, these applications operate on a PC interfaced (in varying degrees of complexity) to a servocontroller, either digital (Ref 27, 28, and 29) or analog and/or digital (Ref 30, 31, 32, 33, and 34). These tools permit the construction of reasonably complicated test sequences and provide for data acquisition

needs. Some systems provide the ability to build test sequences that are limit programmed (e.g., a load-controlled, strain-limited waveform), can offer multimode test control (e.g., dynamically switching control modes during the test), and can provide the ability to perform calculated control of either or both the control variable, as well as the significant waveform parameters (e.g., amplitude, rate, and frequency) (Fig. 18). Examples of the testing applications that can be accomplished with this class of testing software include TMF, biaxial and multiaxial fatigue, creep-fatigue, and bithermal fatigue. These general-purpose systems have grown in sophistication to the point where one must carefully consider one's testing needs before embarking on a custom-application programming project; often, the general-purpose system can provide the quicker solution and at a much more attractive cost.

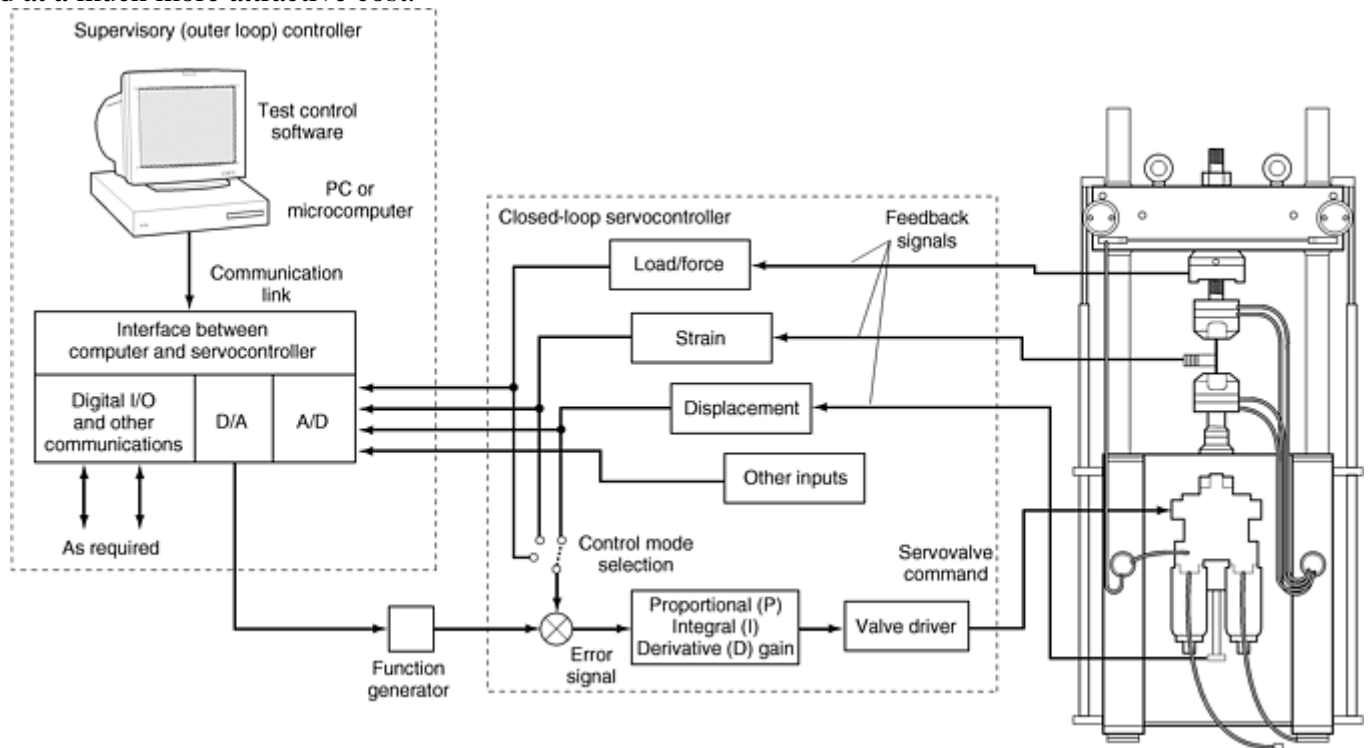


Fig. 18 Typical supervisory (outer loop) calculated-variable controller system for fatigue testing

Custom-Application Software. When testing requirements are very specific and unique, materials testing engineers must often develop their own materials testing application software. The approach taken can vary widely depending on the nature of the test controller and the needs of the application.

Data Acquisition Requirements. Regardless of the approach taken with respect to testing software, certain data acquisition requirements must be met with regard to the amount of data collected, the rate of collection, and the overall accuracy of the data collected. Fatigue tests involving the use of sinusoidal waveforms (commonly used for high-cycle fatigue testing), for example, typically require a data collection rate of fifty points per cycle to enable the cycle to be accurately rendered. A triangular waveform is most often used for low-cycle fatigue testing. Accurately rendering a hysteresis loop in this case requires a data collection rate of up to four hundred points per cycle. When selecting or evaluating data acquisition capabilities for fatigue testing, consideration must also be given to the specific properties of the analog/digital (A/D) system: important characteristics include resolution, accuracy, and noise level. Another important characteristic concerns how the A/D system handles multichannel signal input. Typically, two approaches are taken. The first and most common approach is to simply multiplex the input signals to the A/D system. A concern here is the potential for channel-to-channel data skew: each channel scanned is obtained at a different time than the others. Depending on the conversion rate of the A/D system and the testing frequency being employed, the channel skew can be significant. A second approach for handling multichannel inputs is to use a simultaneous sample and hold amplifier for each channel. In this approach, all channels are sampled and held at the same time and are then multiplexed to the A/D for conversion. Yet other data acquisition systems employ individual A/D converters for each input channel (see ASTM E 1856 for a more detailed discussion of this topic).

Data Analysis. The software available for data analysis largely mirrors that available for testing applications; the standardized test applications generally have built-in data analysis and reporting capabilities, optimized to

report test results in standardized formats. However, test data obtained from general-purpose testing software, and especially data obtained from custom-application programs, must generally be imported into a data analysis program. The most common data analysis programs are the scientific data analysis and plotting applications widely available from many vendors. Another popular method is to import test data into spreadsheet programs. Many of the scientific analysis packages (as well as the spreadsheet programs) provide the ability to develop reasonably sophisticated analysis algorithms (“macros” in spreadsheets, for example), thus providing a convenient and powerful means of data analysis and presentation.

References cited in this section

26. A.A. Braun, “A Historical Overview and Discussion of Computer-Aided Materials Testing,” ASTM STP 1231, *Automation in Fatigue and Fracture: Testing and Analysis*, C. Amzallag, Ed., American Society for Testing and Materials, 1994, p 5–17
27. S. Dharmavasan, D.R. Broome, M.C. Lugg, and W.D. Dover, FLAPS—A Fatigue Laboratory Applications Package, *Proc. 4th Int. Conf. on Engineering Software*, R.A. Adey, Ed., Springer-Verlag, London, 1985
28. A.A. Braun, The Development of a Digital Control System Architecture for Materials Testing Applications, *Proc. 17th Int. Symposium for Testing and Failure Analysis*, ASM International, 1991, p 437–444
29. S. Dharmavasan and S.M.C. Peers, “General Purpose Software for Fatigue Testing,” ASTM STP 1231, *Automation in Fatigue and Fracture: Testing and Analysis*, C. Amzallag, Ed., American Society for Testing and Materials, 1994, p 18–35
30. M.A. McGaw and P.J. Bonacuse, Automation Software for a Materials Testing Laboratory, *Proc. Turbine Engine Hot Section Technology (HOST)*, NASA CP-2444, National Aeronautics and Space Administration, 1986, p 399–406
31. M.A. McGaw and P.J. Bonacuse, “Automation Software for a Materials Testing Laboratory,” ASTM STP 1092, *Applications of Automation Technology to Fatigue and Fracture Testing*, A.A. Braun et al., Ed., American Society for Testing and Materials, 1990, p 211–231
32. M.A. McGaw and P.A. Bartolotta, The NASA Lewis Research Center High Temperature Fatigue and Structures Laboratory, *Proc. 4th Annual Hostile Environments and High Temperature Measurement Conf.*, Society for Experimental Mechanics, 1987, p 12–29
33. M.A. McGaw, materials testing software LEW-16160, COSMIC, 1995
34. J. Christiansen, R.L.T. Oehmke, and E.A. Schwarzkopf, “Materials Characterization Using Calculated Control,” ASTM STP 1303, *Applications of Automation Technology to Fatigue and Fracture Testing*, A.A. Brown and L.N. Gilbertson, Ed., American Society for Testing and Materials, 1997

Fatigue, Creep Fatigue, and Thermomechanical Fatigue Life Testing

Gary R. Halford and Bradley A. Lerch, Glenn Research Center at Lewis Field, National Aeronautics and Space Administration; Michael A. McGaw, McGaw Technology, Inc.

Baseline Isothermal Fatigue Testing

It is important to understand the underlying purposes of the testing to be performed. This understanding will aid in selecting a fatigue testing machine and specimen design. Normally, a baseline condition is established from which effects on fatigue life of a wide variety of variables might be assessed. Laboratory ambient conditions of room temperature, atmospheric pressure, and humidity are a commonly accepted condition for baseline testing; however, other choices of, for instance, temperature may be more appropriate. Baseline testing is usually performed with the numerous fatigue life-influencing variables held constant at what would be considered “default” conditions. For example, completely reversed loading (zero mean stress) may be used, or perhaps zero-to-maximum loading is preferred owing to the nominal zero-to-maximum loadings expected in service. Note that rotating-beam machines are incapable of mechanically imposing mean stresses. If mean stress assessment is contemplated for testing beyond the baseline, a different type fatigue machine is required. The acquired baseline database may have value in serving any of several diverse purposes:

- Ranking fatigue resistance of alloys
- Performing micromechanistic studies
- Guiding development of fatigue-life prediction models
- Collecting statistical documentation
- Establishing fatigue design curves
- Conducting failure analysis

Testing Regime. Of additional importance is the fatigue-life regime of interest—low-cycle or high-cycle fatigue. As discussed earlier, the amount of time available for testing, along with the number of companion machines and their cyclic frequency capability, will dictate which type of machine is best suited for the task at hand. For fatigue lives far beyond 10^5 , a high frequency of testing is a necessity. However, at lives well below 10^5 , high frequency is a liability, not an asset. With the exception of very high cyclic lives, servohydraulic direct-stress testing machines offer the greatest possible versatility in testing machines today. Specially designed, and hence costly, commercially available servohydraulic machines can achieve 1000 Hz.

Calibration and Standard Test Procedures. Once equipped with an appropriate fatigue testing machine and a specimen design, it is important to follow applicable standards for testing (e.g., ASTM and ISO standards). The major items covered by ASTM standards include calibration of, for example, load cells, extensometers, other sensors, read-out equipment, and recorders for data storage; alignment of the loading axis of the testing machine with grips and with the test specimen; specimen design, including alignment of the test section with grip ends; surface finish; material quality control from specimen to specimen; and purity of loading command signals. Table 1 lists the currently applicable ASTM standards for baseline (and associated) fatigue testing.

Adhering to testing standards is particularly important in fatigue testing due to the inherently high degree of scatter in fatigue resistance. In creating the standards, efforts were made to ensure uniformity of specimen geometry, surface finish, loading alignment and gripping, temperature and humidity (for alloys sensitive to moisture level), and uniformity in all aspects of the testing machine frame and loading train, its ancillary equipment, controllers, recorders, data storage, and data manipulation.

Generating Fatigue Crack Initiation Data. The loading mode, life regime, test temperature and environmental conditions, mean stress, surface finish, and heat treatment condition, among others, dictate the testing machine and ancillary equipment required. Once these are in place and calibrated and the representative test specimens have been prepared, a baseline fatigue testing program can be conducted. If the program involves several variables, it is wise to first perform a design-of-experiments study to maximize the information to be obtained while minimizing the number of tests and attendant costs. In any event, it should be noted that the cost of specimen preparation is usually not the dominant cost in a fatigue testing program. It is wise to ensure that a sufficient excess of specimens is made to more than adequately cover the initial number required in the program. Having specimens left over from a baseline study is often beneficial, particularly if additional factors are to be studied and if scatter in fatigue lives has been great enough to warrant additional tests to better establish the statistical results. It is generally not possible to duplicate the specimen consistency at a much later date, so it is better to have extra, rather than not enough, specimens to begin a test program.

It is advisable to estimate the expected fatigue life of any test prior to starting the test to avoid excessively long or short test times. Past testing experience with similar materials is valuable in making life estimates. Empirical equations have been published for estimating fatigue resistance based on conventional tensile test data for the material, temperature, and environment of interest. The equations of Manson (Ref 35) and Morrow (Ref 36)

have proven invaluable in this regard (see Eq 1, which follows). In fact, the method of universal slopes (MUS) has been used to bypass fatigue testing (Ref 35). With appropriate factors of safety, the MUS has been used in the establishment of low-cycle fatigue design curves for many of the alloys used in the main engines of the US space shuttle (Ref 37). The fatigue resistance of a large number of alloys in a variety of heat-treated conditions over a range of temperatures and aggressive environments has been established in this manner.

If a broad range of testing times are to be involved, it is also advisable to conduct the shortest-time tests first, then take advantage of these results to govern the loading levels applied for the longest-life tests. One should avoid running tests that must be discontinued. Considerably less information is gained from such “run-outs.”

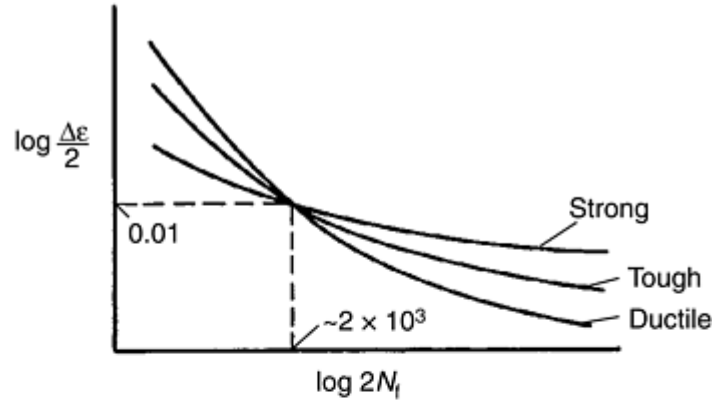
Sufficient tests should be run to failure over the range of variables studied to permit a statistical assessment of the results. This is particularly true for the baseline results from which other fatigue test results are to be compared.

The extent to which the test data are recorded *during testing* depends on the end use of the fatigue data. In high-cycle fatigue, most alloys behave nominally elastically, and there is little reason to monitor test parameters during the test, as there will be little (if any) change to observe until fatigue failure is imminent. However, in strain-controlled low-cycle fatigue with observable amounts of plasticity, significant changes might occur that warrant recording, for example, cyclic strain hardening or softening, relaxation of mean stress, and even cyclic stress-strain response changes due to crack nucleation. It is quite important to be able to monitor these changes during testing. For example, the hysteresis loop at “half-life” is usually chosen to be the representative loop of the entire fatigue test. This loop provides the values of the stress amplitude, stress range, mean stress, total strain range, inelastic (plastic) strain range, and the elastic strain range that are tabulated along with the number of cycles to failure. Since the number of cycles to failure is not known until after the test has passed the half-life point, it is necessary to monitor and record this information either continuously or at intervals close enough to be able to interpolate to the half-life condition once the test has failed.

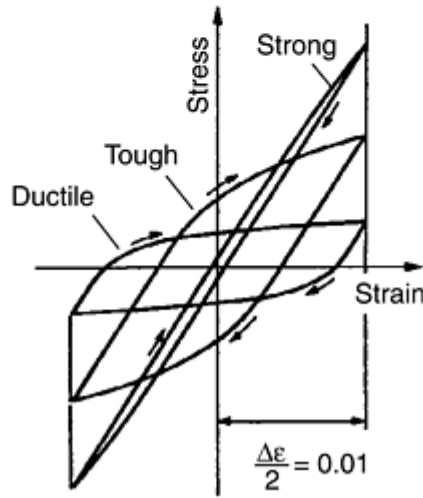
Baseline fatigue data are generally tabulated and plotted. Schematic fatigue curves (Ref 38) are shown in Fig. 19(a) for strong, tough, and ductile alloys. The corresponding stress-strain hysteresis loops are depicted in Fig. 19(b). This figure illustrates the common observation that the number of cycles to failure for a 1.0% total strain range is approximately 1000 cycles, regardless of the strength or ductility level of an alloy when there is a trade-off between strength and ductility due to different alloy processing. Presuming an equation form, fatigue data can be analyzed using least-squares curve-fitting analyses. The most common equation form for low-cycle fatigue and for lives to about 10^6 cycles is:

$$\Delta\varepsilon_{\text{total}} = \Delta\varepsilon_{\text{elastic}} + \Delta\varepsilon_{\text{plastic}} = B(N_f)^b + C(N_f)^c \quad (\text{Eq 1})$$

where, $\Delta\varepsilon_{\text{total}}$ is the total mechanical strain range at half-life, $\Delta\varepsilon_{\text{elastic}}$ is the elastic strain range (equal to $\Delta\sigma/E$) at half-life, $\Delta\varepsilon_{\text{plastic}}$ is the plastic (inelastic) strain range at half-life, N_f is the number of cycles to failure, b is the slope of elastic strain-range life line on log-log coordinates, B is the intercept of elastic strain-range life line at $N_f = 1$, c is the slope of plastic strain-range life line on log-log coordinates, C is the intercept of plastic strain range life line at $N_f = 1$, $\Delta\sigma$ is the stress range at half-life, and E is the modulus of elasticity. The method of universal slopes that is used to estimate fatigue curves has the same form as Eq 1. The values of the “universalized slopes” are given by $b = -0.12$ and $c = -0.60$.



(a)



(b)

Fig. 19 Representation of the cyclic strain resistance of idealized alloys (strong, tough, ductile). (a) Fatigue curves. (b) Stress-strain hysteresis loops. After Ref 38

The corresponding values of the intercepts are determined from conventional tensile test results for the alloy at the temperature and environmental conditions of interest: $B = 3.5\sigma_{ult}/E$ and σ_{ult} is the ultimate tensile strength, and $C = D^{0.6}$. True ductility (also true fracture strain) is abbreviated D ; reduction of area in the tensile test is abbreviated RA.

$$D = \ln[(100)/(100 - \%RA)]$$

Morrow's formulation is similar and has seen widespread use in the automotive and off-highway equipment industries. It takes the following specific form:

$$\begin{aligned} (\Delta\varepsilon_{total}/2) &= (\Delta\varepsilon_{elastic}/2) + (\Delta\varepsilon_{plastic}/2) \\ &= (\sigma'_f/E)(2N_f)^b + \varepsilon'_f(2N_f)^c \end{aligned} \tag{Eq 2}$$

where $\Delta\varepsilon_{total}/2$ is the total mechanical strain amplitude at half-life, $\Delta\varepsilon_{elastic}/2$ is the elastic strain amplitude ($\Delta\sigma/2E$) at half-life, $\Delta\varepsilon_{plastic}/2$ is the plastic (inelastic) strain amplitude at half-life, $2N_f$ is the number of reversals to failure ($2 \times N_f$), b is the slope of the elastic strain-amplitude life line on log-log coordinates, σ'_f/E is the intercept of elastic strain amplitude life line at $2N_f = 1$, c is the slope of the plastic strain-amplitude life line on log-log coordinates, ε'_f is the intercept of plastic strain amplitude life line at $2N_f = 1$, and $\Delta\sigma/2$ is the stress amplitude at half-life.

Morrow's fatigue-life equation in its predictive form assumes the slopes and intercepts can be approximated from tensile test properties by $b = n/(5 + n)$, where n is the strain hardening exponent (the cyclic strain hardening exponent, n' , may give better predictions; $n' = b/c$; $c = 1/(5 + n)$); and $\sigma'_f/E = \sigma_f/E$ where σ_f is the true fracture stress (fracture load divided by fracture area). The true fracture strain is equal to the true ductility, D , is equal to ε'_f is equal to ε_f .

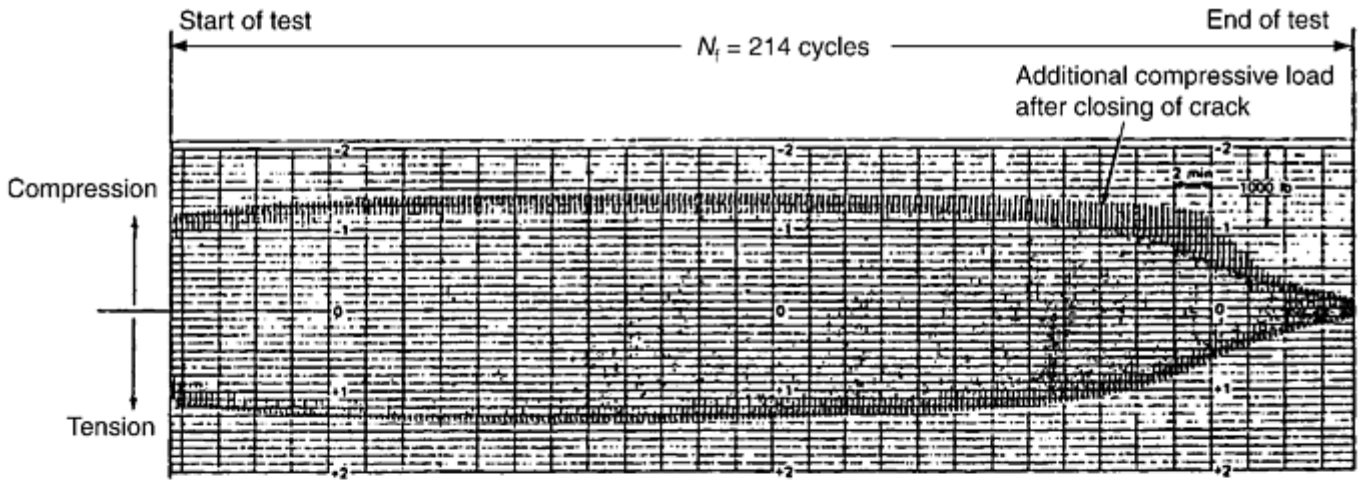
The slopes and intercepts from the equations above are referred to as the basic fatigue properties. Reference 39 contains an extensive listing of these fatigue properties, along with corresponding tensile properties, for a wide variety of steels, stainless steels, nickel-base superalloys, titanium alloys, aluminum alloys, weldments, and castings. How the fatigue properties might be affected by factors that influence fatigue behavior is discussed in the section “Testing for Effects of Variables on Fatigue Resistance” in this article.

In the high-cycle fatigue regime, that is, beyond approximately 10^6 cycles to failure, the log-log slopes of the fatigue curves tend to become shallower than at lower life levels. For certain steels and selected body-centered cubic (bcc) alloys, a fatigue or endurance limit of “infinite” life for cyclic stresses below the limit may be observed in laboratory fatigue test results. Such limits may be erased by interspersed low-cycle fatigue loadings that can break up the dislocation pinning by small interstitial atoms in the bcc structure. Under these circumstances, the fatigue curve continues to drop in strength level below the original fatigue limit. Slopes of the fatigue curve in the very-high-cycle fatigue regime may drop to -0.04 or less. Manson (Ref 40) has reported ultrahigh-cycle fatigue life extrapolation procedures.

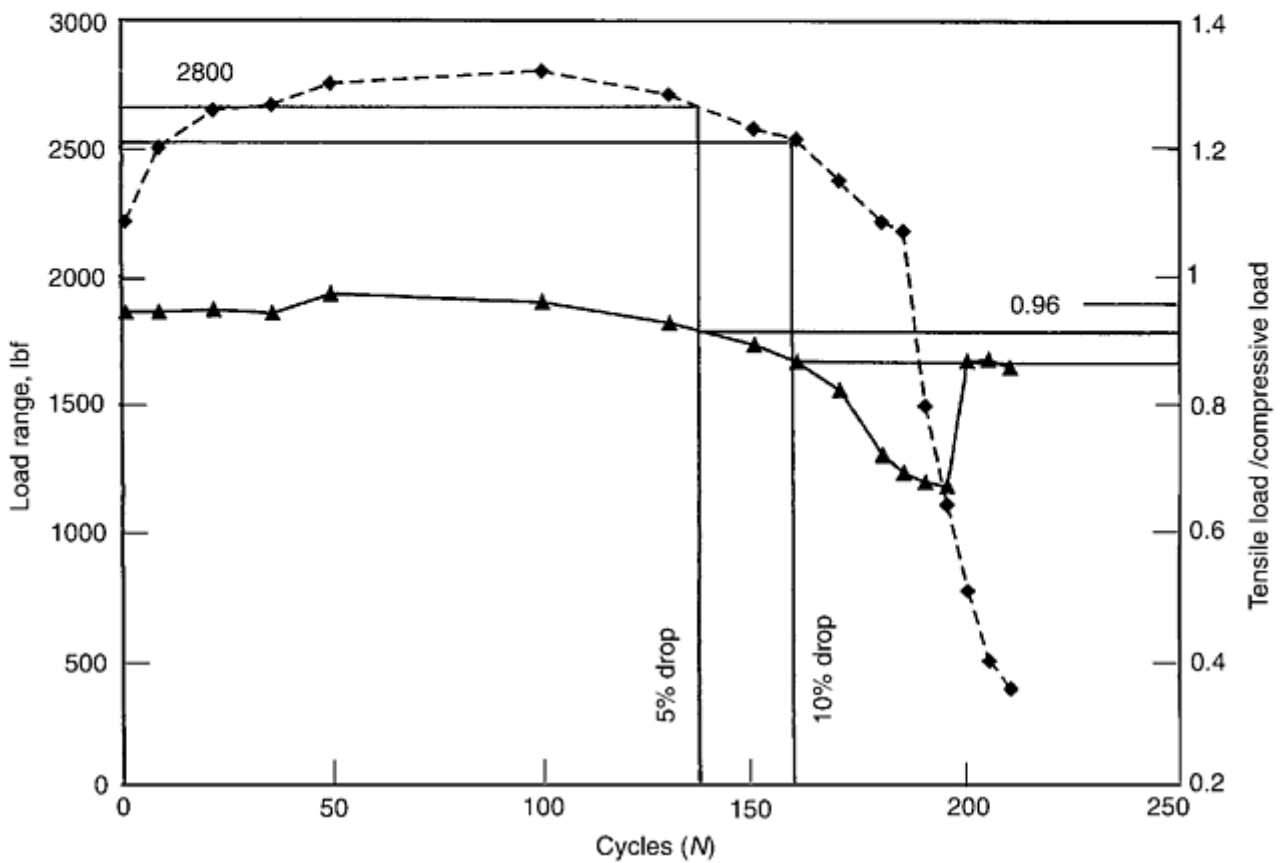
Criteria for Defining Fatigue Life. The first and most common definition of fatigue life for alloy testing is the number of cycles of loading required for complete fracture of the specimen into two pieces. This definition is unequivocal. It is easy to identify this terminal event in most fatigue tests. (During strain-controlled tests at low strain amplitudes, cracking may reduce the stress level sufficiently so that the specimen never separates; in this case, some other definition of failure must be used.) At fracture, the specimen grips are free to move apart, allowing a mechanically activated switch to be tripped that stops the cyclic drive mechanism and the cycle counter. Electrical continuity of the specimen is also broken permitting direct electrical switching of circuits controlling the machine. Complete specimen separation is typically an acceptable measure of the crack initiation fatigue life for high-cycle fatigue wherein the fatigue crack nucleation portion dominates the total life (perhaps 90–99%). However, because the separation life does include a portion of cyclic crack growth, this quoted life is somewhat larger than the number of cycles to physically initiate a crack. As the fatigue loading levels increase and the cyclic lifetime decreases into the low-cycle fatigue regime, less and less of the life is spent nucleating a crack, and more and more life is spent growing the crack(s) to the critical length for sudden fracture into two pieces. To accurately define the cyclic crack initiation life, particularly in low-cycle fatigue, one ideally would measure the actual crack size (depth and length) as cycling progressed. When a predetermined crack size was reached, the number of cycles to “failure” would be noted and testing stopped. Unfortunately, this is highly impractical for most testing because it cannot be implemented on an automated basis for the large numbers of fatigue tests conducted annually.

The only practical definitions available are those based on measurements that are readily available from the test instrumentation. This is usually in the form of changes in specimen elastic or plastic “stiffness” as determined from stress-strain or load-deflection measurements. As a specimen develops a fatigue crack under completely reversed strain control, its growth causes the load carrying response of the specimen to decrease. Different degrees of drop in the cyclic load range for a fixed strain range have been used to define crack initiation failure for low-cycle fatigue testing. The most commonly used criteria have been the very first indications of an impending drop in the load range (i.e., impending cracking) and a 5% drop in the load range. Obviously other percentage drops (10, 20, and 50) could be defined and used. Unfortunately, it may be difficult to distinguish between load range drop due to cracking and load range drop due to cyclic strain softening of initially work hardened materials. Even cyclic strain hardening could confound the measurement by offsetting the drop due to cracking.

A logical way to separate the effects on load response of cyclic strain hardening or softening from cracking is to track the ratio of the peak tensile load to the peak compressive load (Ref 41). If only hardening or softening occurs, the load range will change, but the tensile/compressive load ratio will be affected very little. As fatigue cracking progresses, the decrease in the tensile load amplitude exceeds that of the decrease of the compressive load amplitude. This is observable in Fig. 20(a) from a load-versus-time trace for a low-cycle, completely reversed, strain-controlled test (Ref 42). As cracking occurs, the change of the load ratio is almost twice as much as the change in the load range, thus making it a more sensitive, as well as a more physically based, measure of cracking. The load response would also be observable in a stress-strain hysteresis loop. In compression, the crack faces close and carry load. This results in a cusp on the hysteresis loop near the compressive peak. In tension, the peak load is carried only by the smaller, uncracked area.



(a)



(b)

Fig. 20 Cyclic load response during strain-controlled low-cycle fatigue test of annealed AISI 304 stainless steel in air at 816 °C (1500 °F). Total strain range, 3.26%, 0.056 Hz. (a) Cyclic load response for defining cyclic life to crack initiation. (b) Cyclic load range and ratio of tensile to compressive peak load versus applied cycles. Source: Ref 42

To apply these criteria for defining fatigue crack initiation life, the load ratio must be measured during the precrack nucleation period. Note that the load ratio during this interval may not equal 1.00. It has been observed to vary from as low as 0.9 to about 1.05 depending on material. The ratio, however, is nominally independent of the amount of cyclic hardening or softening that occurs, and, hence, a greater duration of cyclic loading can be used to establish the average value of the ratio before cracking commences. A graphic quantitative example is given by Fig. 20(b) based on the data from Fig. 20(a). Both load ratio and load range are plotted versus applied cycles. The load ratio is relatively constant at 0.96 for the first half of the test, but, by about 100 cycles, it begins to drop steadily. At about 200 cycles, the ratio suddenly and inexplicably rises. This rise signals the end

of useful information from the test. Even though the specimen is still in one piece, the computed stresses and strains are no longer representative of what is going on in the gage length of the specimen. At this point, the dominant crack has grown to a large fraction of the specimen diameter, and the extensometer is subjected to large amounts of bending in addition to axial deformation. The specimen may not have failed completely, but the test has. The corresponding load range is also shown. After considerable initial hardening of 25%, a half-life (“stabilized”) value of 2800 lbf (12.5 kN) is reached. This is followed by an accelerating drop until complete fracture of the specimen occurs at greater than 214 cycles. For the particular test data shown, the load ratio and the load range follow approximately parallel behavior. For this example, a 5% drop in load range and load ratio corresponds to the same number of cycles (~138 cycles). Similarly, a 10% drop in both gives approximately 158 cycles. In this case, either the load range or the load ratio drop criteria would give acceptable definitions of fatigue crack initiation life. This is not expected to be the general case for the following reasons.

For a cyclically stable material with very little strain hardening within a hysteresis loop, a 5% load range drop would correspond to approximately a 10% drop in the load ratio if the only reason for load drop were the presence of a crack. This in turn would imply a 10% loss in specimen cross-sectional area if there were no concentration of stress surrounding the crack tip. However, since there is a concentration of stress in front of the crack, higher stresses are encountered there, thus increasing the tensile load-carrying capacity. Hence, a 10% loss of area would actually correspond to less than a 10% loss of load ratio. Load ratios in the neighborhood of 5 to 8% have been noted.

With modern automated data recording and reduction, it is possible to determine the fatigue life by all of these definitions, including complete fracture into two pieces. In this way, any definition of fatigue crack initiation life can be selected for the purposes at hand. References 41 and 42 contain tabulated fatigue crack initiation lives for several engineering alloys for the four criteria, as discussed above:

N_0	First indication of impending cracking
N_5	5% drop in load range from stabilized range (or at half-life value if stabilization does not occur)
N_i	10% drop in ratio of tensile to compressive load from stabilized range (or at half-life if stabilization does not occur)
N_f	Complete separation of specimen

Similar criteria based on the same concepts could be established for completely reversed, load-controlled tests. Instead of a decrease in load response due to cracking, an increase in strain or deflection response would be measured to define fatigue crack initiation.

Care should be exercised in applying these criteria when multiple cracks initiate parallel to one another. Many shallow cracks will have the same integrated effect on specimen gage length compliance as one deeper crack. In addition, the exact location of the crack(s) relative to the contact points (defining the gage length) of the extensometer can have an appreciable influence on the apparent (measured) compliance. For example, should cracking initiate outside the gage section, the extensometer would not detect a change in compliance. Should cracking initiate within the gage section, the load path would not necessarily remain along the centerline of the specimen, and bending would occur. This, in turn, can cause the extensometer to register different outputs depending on the plane of bending relative to orientation of the extensometer. These confounding influences also affect the load range drop criteria for crack initiation.

Information to be Documented for Baseline Fatigue Tests. Guidelines are presented for what baseline fatigue test information should be documented. Tables 2 and 3, respectively, provide comprehensive listings of pertinent pretest and in-test/post-test information to be considered for inclusion. In preparing Table 3, it was assumed that closed-loop; servostrain-controlled axial fatigue testing was the mode of operation. If other modes of testing are used, the guidelines may have to be altered accordingly. Obviously, the information gleaned from a fatigue test in progress will depend on the extent of instrumentation available, the type of testing machine, and the mode of testing.

Table 2 Pretest information guidelines for baseline fatigue tests including studies of preexisting effects on fatigue

Alloy designation and description	Heat number and composition, forming processes, degree of anisotropy, heat treatment and environmental preexposure conditions, final machining parameters, photomicrographs, hardness, tensile properties
Specimen	Drawing and specifications, orientation of axis to product form, accurately measured

configuration	specimens dimensions (including notch description) and area of cross section (diameter and area for direct stress mode of loading), surface finish and method of preparation, final heat treatment, individual specimen identification number, description of any coating including any processing affecting the surface layer (preoxidation, prefretting, galling, wear erosion, corrosion, carburizing, nitriding, anodizing, shot peening, laser-shock peening, burnishing, and other means of introducing residual stresses, magnitude, and sign of residual stresses, etc.), thickness, orientation of gripped specimen to testing machine
Testing machine	Designation of machine, type of grips, dates of last alignment and calibration of load cell, types of heating and environmental control, type of extensometer, and date of last calibration
Test engineer and operator	Names and dates of set-up and start of test
Test mode, control details, and test conditions	Model of control (e.g., strain, load or deflection), cyclic frequency and waveform including description of mean and alternating components, test temperature and mean of measurement and control, relative humidity and nature of environment, starting date and time error detector limits for shut-down, estimate of test duration and basis for estimate

Table 3 In-test and post-test information guidelines for baseline fatigue tests including studies of preexisting effects on fatigue

Cyclically varying parameters	Value of fixed test control parameters (e.g., stress, strain, or displacement); continuous recording of variations of maximum, minimum, amplitude, range, and mean values of stress and strain as a function of applied cycles; cycles variation of load range variation and ratio of tensile to compressive peak loads to help define failure life and help-life; continuous or periodic recording of variations of stress-strain hysteresis loops
Lifetime information	Cyclic failure lives based on various cyclic failure criteria; failure life (cycles and corresponding time) for criterion adopted; half-life cycles; total, inelastic, and elastic strain ranges at half-life; maximum, minimum, stress amplitude, stress range, mean stress, and mean stress ratio at half-life; degree of cyclic hardening and/or softening from first cycle to half-life (or cycles at stabilization of stress-strain response); description of fracture surface including initiation site(s); location of fracture relative to extensometer probes
Deviations from original test plans	Details of stress and strain history immediately prior to controlled or uncontrolled shut-downs prior to test completion
Data analysis from multiple specimens	Cyclic stress-strain curve and equation constants at half-life (or cycles at stabilization), fatigue curves and equation constants (i.e., fatigue properties)

Example Crack Initiation Fatigue-Life Curves. Fatigue curves are displayed in a variety of forms, although fatigue life is generally plotted on a logarithmic scale. The fatigue loading parameter is usually stress or strain. Stress is most commonly plotted as stress amplitude, stress range, or maximum stress, and the scale may be arithmetic or logarithmic. Examples are given in Fig. 21. These are referred to as *S-N* curves, and an indication of the mean stress ratio should always be given. When strain is the fatigue loading parameter, the total (elastic plus plastic), plastic, or the elastic strain ranges may be plotted. These are usually plotted on logarithmic scales, as shown in Fig. 22, and are referred to as strain-life curves. Unless the fatigue strain cycling ratio is given, it is understood that the curves represent completely reversed loading. The plastic strain-versus-life curve is known as the Manson-Coffin (or Coffin-Manson) low-cycle fatigue curve. The elastic strain range-versus-life curve has come to be known as the Basquin curve (Ref 43). The total strain range-versus-life representation of fatigue data has its origins in the late 1950s and early 1960s. Coffin (Ref 44) originally represented the elastic strain range-versus-life component of the total strain range-versus-life curve as a horizontal line with a strain range value equal to twice the 0.2% offset yield strength divided by the elastic modulus. Langer (Ref 45) used the same basic idea, but replaced the yield strength with the endurance limit strength. He went on to multiply the total strain amplitude by the modulus of elasticity to compute the pseudo-stress amplitude. The resultant fatigue

(*S-N*) curve could then be used in direct conjunction with elastic stress analyses. This representation was adopted by the ASME Code, Section III, for Boiler and Pressure Vessel components.

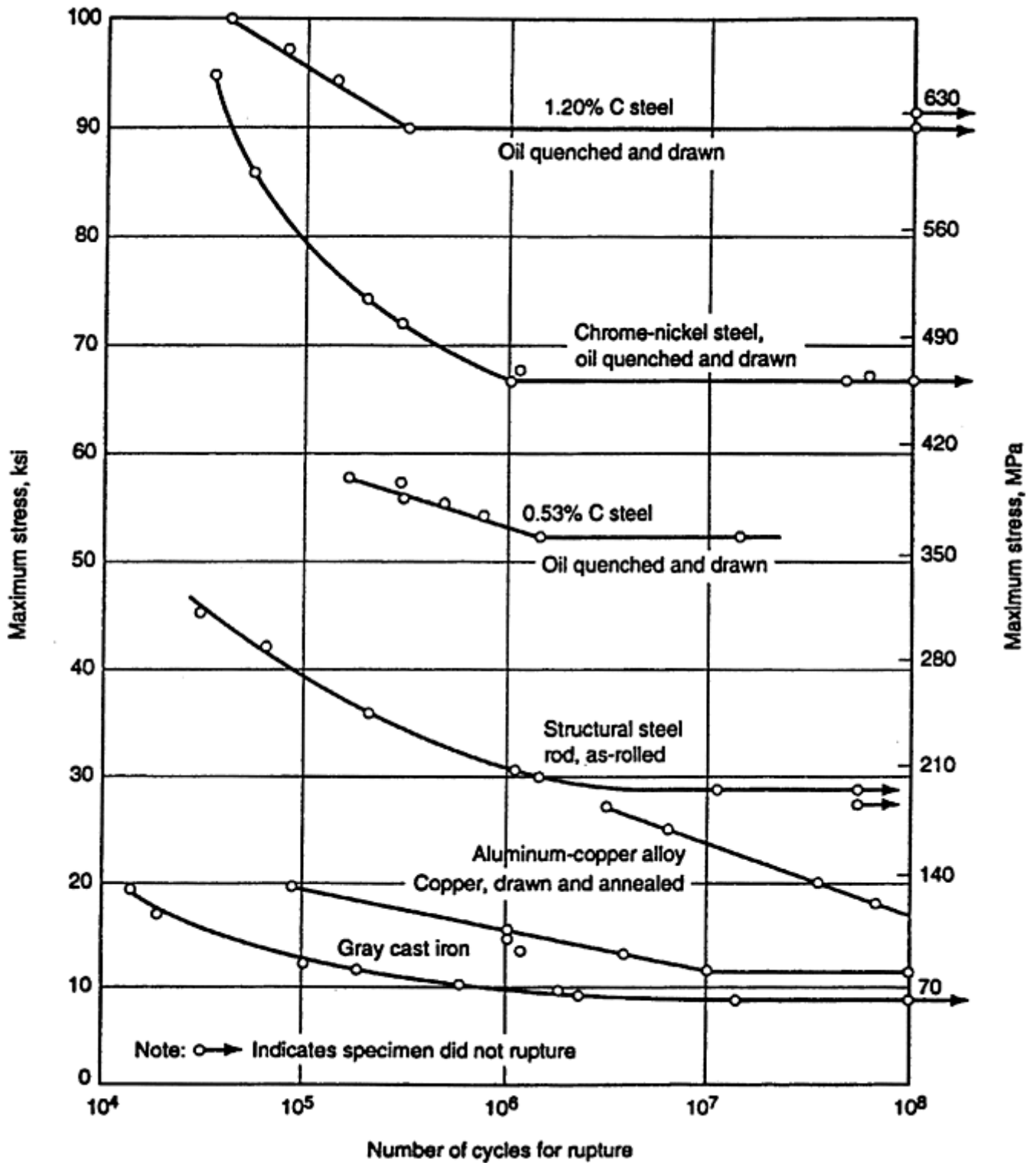


Fig. 21 Typical *S-N* diagrams for various alloys subjected to completely reversed loading at ambient temperature

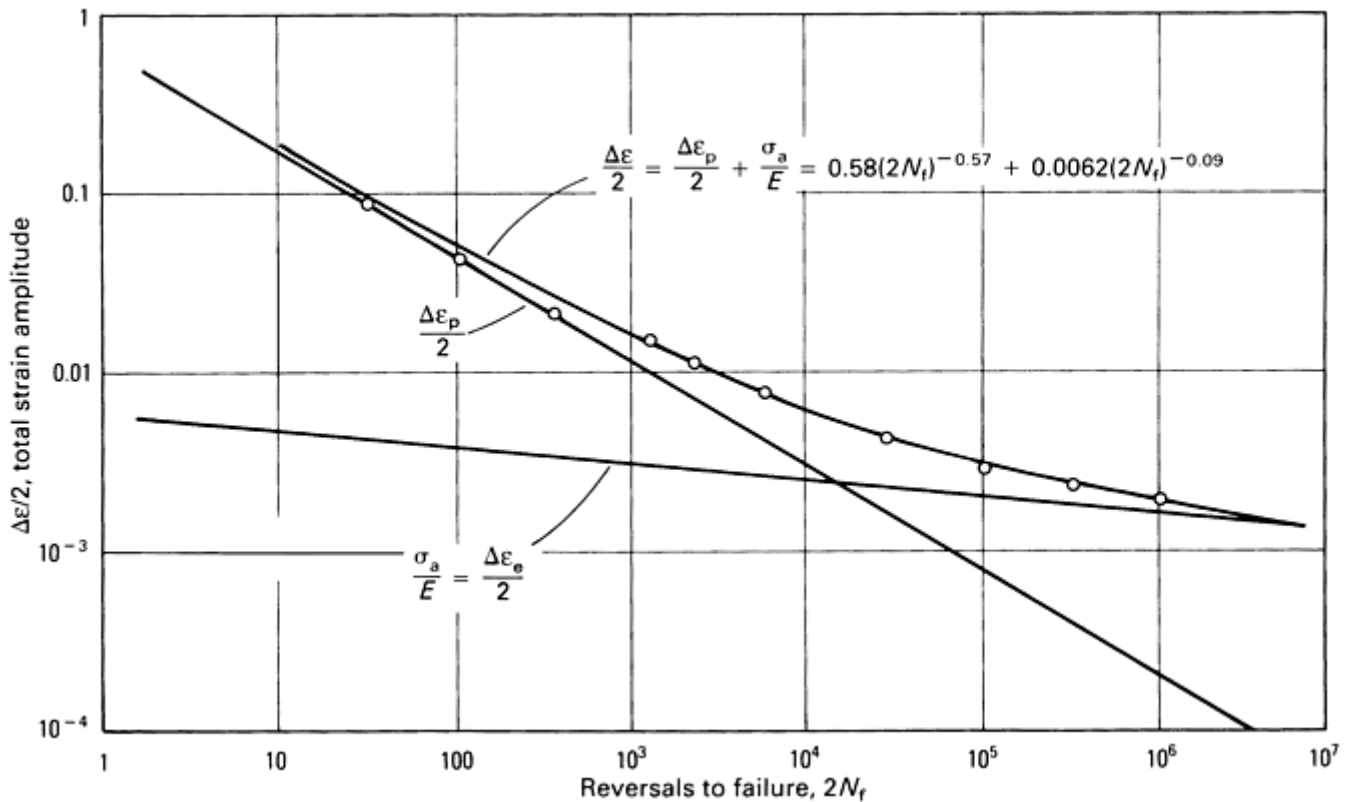


Fig. 22 Typical strain-life fatigue curve showing elastic and plastic components, annealed 4340 steel

Manson (Ref 46) and Morrow (Ref 36) carried the fatigue curve representation a step further by recognizing that the elastic strain range-versus-life curve had a negative slope such as first observed by Basquin a half century earlier.

Out of the total strain range-versus-life representation of fatigue resistance comes an important observation and useful concept (e.g., see Ref 40). At some point along the fatigue curve, the elastic strain range and the plastic strain range will be equal. This point defines what is known as the transition fatigue life, $N_{f,trans}$, and the corresponding transition total strain range, $\Delta\epsilon_{total,trans}$, is equal to $2\Delta\epsilon_{plastic}$, which is equal to $2\Delta\epsilon_{elastic}$. Below the transition fatigue life, the behavior is clearly low-cycle fatigue as the plastic strain range dominates over the elastic strain range. Low cycle fatigue actually continues to higher lives beyond the transition life. High-cycle fatigue behavior, in which the elastic strain range overwhelmingly dominates over the plastic strain range, does not begin until at least one order of magnitude in life beyond the transition life.

References cited in this section

35. S.S. Manson, Fatigue—A Complex Subject, *Exp. Mech.*, Vol 5 (No. 7), 1965, p 193–226
36. J. Morrow, “Cyclic Plastic Strain Energy and Fatigue of Metals,” ASTM STP 378, *Internal Friction, Damping, and Cyclic Plasticity*, American Society for Testing and Materials, 1965, p 45–84
37. J.F. Newell, A Note of Appreciation for the MUS, *Material Durability/Life Prediction Modeling: Materials for the 21st Century*, S.Y. Zamrik and G.R. Halford, Ed., Pressure Vessel and Piping Conference, PVP Vol 290, American Society of Mechanical Engineers, 1994, p 57–58
38. R.W. Landgraf, “The Resistance of Metals to Cyclic Deformation,” ASTM STP 467, *Achievement of High Fatigue Resistance in Metals and Alloys*, American Society for Testing and Materials, 1970, p 3–36

39. Parameters for Estimating Fatigue Life, *Fatigue and Fracture*, Vol 19, *ASM Handbook*, ASM International, 1996, p 963–979
40. S.S. Manson, Predictive Analysis of Metal Fatigue in the High Cyclic Life Range, *Methods for Predicting Material Life in Fatigue*, W.J. Ostergren and J.R. Whitehead, Ed., American Society of Mechanical Engineers, 1979, p 145–183
41. Characterization of Low Cycle High Temperature Fatigue by the Strain-Range Partitioning Method, *AGARD Conf. Proc.*, No. 243, NATO, 1978
42. J.B. Conway, R.H. Stentz, and J.T. Berling, *Fatigue, Tensile, and Relaxation Behavior of Stainless Steels*, United States Atomic Energy Commission, 1975, p 11
43. O.H. Basquin, The Exponential Law of Endurance Tests, *Proc. ASTM*, Vol 10 (Part II), 1910, p 625–630
44. L.F. Coffin, Jr., Thermal Stress Fatigue, *Prod. Eng.*, June 1957
45. B.F. Langer, Design of Pressure Vessels for Low Cycle Fatigue, *J. Basic Eng. (Trans. ASME)*, Vol 84 (No. 4), 1962, p 389
46. S.S. Manson, discussion of ASME paper 61-WA-199 by J.F. Tavernelli and L.F. Coffin, Jr., *J. Basic Eng. (Trans. ASME)*, Vol 85 (No. 4), 1962, p 537–541

Fatigue, Creep Fatigue, and Thermomechanical Fatigue Life Testing

Gary R. Halford and Bradley A. Lerch, Glenn Research Center at Lewis Field, National Aeronautics and Space Administration; Michael A. McGaw, McGaw Technology, Inc.

Testing for Effects of Variables on Fatigue Resistance

The fatigue resistance of an alloy is sensitive to a large number of variables. There are too many variables to investigate them all. To do so would require an enormous test matrix, a large number of fatigue testing machines, and a huge budget. Fortunately, similar behavior trends are observed by various classes of alloys. This allows engineers to experimentally document the behavior of many of the more commonly encountered variables using only a limited number of tests. As a prime example, several different models can describe the effects of mean stress on fatigue life. All predict lowered fatigue resistance to tensile mean stress and enhanced life with compressive mean stress. Another example is the correlation between tensile test properties and baseline fatigue resistance as given by Eq 1 and 2, that is, increases in the ductility of an alloy generally enhance low-cycle fatigue life, whereas increases in tensile strength produce greater high-cycle fatigue resistance. These correlations have proven quite valuable. If more accurate assessments of the effects of variables on fatigue are required, they can be determined experimentally. This section discusses the more commonly investigated variables.

The variables affecting fatigue can be categorized into four types: bulk and geometric factors, and surface- and active loading-related factors. Common examples of each type are listed in Table 4. Synergistic interactions may occur among these influences. For example, the loading-related factor of high-temperature testing in air would induce the surface related factor of oxidation. Seldom are surface-related effects of this nature beneficial to fatigue resistance.

Table 4 Significant variables affecting fatigue resistance

Bulk property effects

- **Degree of cold working and/or annealing**
- **Heat treatment**
- **Anisotropy (forming, directional solidification, or single crystal)**
- **Alloy composition**
- **Nuclear radiation**

Surface-related effects

- **Mechanical surface finish (e.g., as-cast, forged, machined, or ground)**
- **Residual stresses**
- **Mechanically induced (e.g., shot peening, burnishing, laser shock peening; machining, or grinding)**
- **Thermally assisted (e.g., rapid surface solidification, welding electrodischarge machining, carburizing, or nitriding)**
- **Environment (oxidation, sulfidation, corrosion, ion transport, or hydrogen embrittlement)**
- **Cavitation**
- **Fretting and galling**
- **Wear and erosion**
- **Coatings (plating, anodizing, ion implantation, oxidation protective, or thermal barriers)**

Geometric effects

- **Notches**
- **Edges and thin sections**
- **Size effects and highly stressed volume**

Active loading-related effects

- **Actively imposed mean stresses and strains**
- **Multiaxiality of stress and strain (proportional and nonproportional)**
- **Cumulative damage (variable levels and types of loading)**
- **Temperature of testing (from cryogenic to high)**
- **Creep-fatigue interaction (low frequency, low strain rate, stress hold times, strain hold, and tensile-versus-compressive hold times)**
- **Thermal fatigue, TMF (continuous temperature strain cycling and bithermal cycling)**

Bulk and surface-related property effects could be further classified as preexisting or concurrent. Geometric effects are generally preexisting with respect to laboratory specimen fatigue testing. Examples of preexisting bulk effects are cold working introduced during the forming process and metallurgical heat treatment of the alloy. Either could significantly alter the strength of an alloy and, hence, alter its fatigue resistance. Concurrent effects can include time-dependent creep, oxidation, or solid-state metallurgical changes, all resulting from exposure of the alloy to high temperature during operational use or specimen testing. Effects on fatigue resistance of preexisting factors can be dealt with by simply considering the alloy as a new material to be evaluated.

Concurrent influences, however, require additional consideration to ensure testing adequately reflects the influences encountered in service. For example, high-temperature service may involve more than an order of magnitude greater exposure time than can be afforded during fatigue testing. Consequently, the testing program must be designed to provide data that can be extrapolated with confidence into the time regime of practical interest. This is a particularly vexing problem in the area of high-temperature fatigue, creep-fatigue, and TMF testing of alloys.

Invariably, engineering models of fatigue behavior are created to allow confident interpolation and extrapolation, particularly for structural applications. Models are calibrated to reflect the influences of a multitude of variables. Many models have been proposed over the past century. Those of greatest value for

engineering design are the ones that are relatively simple, logical, and clearly reflect a cause-and-effect relationship. They are the easiest to remember and use. Those models that reflect a high degree of mechanistic fidelity are naturally of greatest benefit to the material science and failure analysis community. If such models can also be expressed in tractable terms, engineers will also use them for designing in structural durability of machine components. Understanding the root causes of fatigue permits engineers to better guard against this insidious failure mode.

Preexisting Variables

Because of the similarities of testing for preexisting bulk or surface-related effects on fatigue resistance, they will be discussed together. Guidelines for information to be documented from fatigue tests of preexisting variables are contained in Tables 2 and 3.

Bulk Property and Surface-Related Effects. Material with preexisting effects can be evaluated by conducting fatigue tests using the same techniques and procedures as for baseline fatigue testing. The affected material is considered as a new material, but one for which some background knowledge exists. It is not uncommon to see a series of fatigue curves for the same alloy composition wherein each curve reflects differing degrees of cold working, heat treatment, or surface finish. The fatigue results are typically used to select an optimum fabrication method or to indicate material conditions to be avoided. In general, fewer fatigue tests are required, *provided the baseline results are well behaved and well defined*. However, if there were more scatter in the property-affected results, more tests would be required to adequately define the new fatigue curve.

Geometric Effects. The most commonly investigated geometric effects are those of notches and the degree of the theoretical stress concentration, K_t , they impose. Invariably, the fatigue resistance decreases with higher stress concentration factors. The extent of fatigue strength loss for a given fatigue life, however, is never as great as might be suggested by the value of the stress concentration factor. Furthermore, the effectiveness of the stress concentration factor decreases as the root radius decreases and the overall size of the notch decreases. There are several reasons for this behavior that are adequately explained in most textbooks covering fatigue. As discussed earlier, it is of great importance to fatigue testing that uniformity of the notched specimens be maintained to reduce confounding scatter issues. Particular care is required to achieve this goal when dealing with very small notch root radii.

The testing of notched specimens in the high-strain, low-cycle fatigue regime may introduce yielding at the root of the notch. If the cyclic loads are great enough, the yielding will occur on each cycle, despite the fact that the overall specimen appears to behave nearly elastically. The cyclic strain range at the notch root will be larger than indicated by the theoretical stress concentration factor, and the cyclic stress range will be smaller. Analytic approaches are available to describe the stress-strain behavior at the notch root in terms of the applied loading and the cyclic stress-strain curve of the material. See, for example, applications (Ref 47, 48) of Neuber's (Ref 49) and Glinka's (Ref 50) notch analysis approaches. Also of great importance to the fatigue testing of notched specimens is the cyclic relaxation of initial mean stresses at the notch root. For example, for zero to maximum load-controlled cycling, the local notch root stress can relax from an initial zero to maximum condition on the first cycle to a completely reversed condition as cycling progresses. Such changes in the local stress-strain response have a profound influence on the fatigue life of notched specimens. As the cyclic loading level is decreased and longer lives are achieved, there is less and less of a chance for relaxation of the initial cycle mean stress. Consequently, the resultant fatigue curve will exhibit a very low mean stress effect in the low-cycle regime, but will exhibit the full effect of mean stress in the high-cycle regime. Without performing a local stress-strain analysis at the root of the notch, it is nearly impossible to ascertain whether or not a mean stress will relax, and to what extent. The issue of mean stress relaxation becomes critically important in performing cumulative fatigue damage experiments with notched specimens.

Other specimen geometric effects include thin sections and sharp edges. Both can result in fatigue-life reductions due to the fact that there is far less constraint to the motion of dislocations due to the high ratio of surface area to volume. This effect is accentuated at high temperatures wherein creep can occur more readily by grain boundary sliding. Reducing a section thickness to only one or two grain diameters can greatly reduce the normal constraint offered by surrounding grains, thus enhancing creep deformation and increasing the degree of creep-fatigue interaction. When performing fatigue, creep-fatigue, and TMF tests of thin sections, one should caution against having too few grains through the thickness.

Yet another preexisting geometric aspect is the so-called size effect. The smaller the volume and related surface area are for the fatigue-affected zone of a test specimen, the less probability there is of encountering a microscopic flaw leading to early crack initiation. Large specimens with relatively large volumes and high surface areas will invariably exhibit lower fatigue lives than small specimens with relatively small volumes of highly stressed material. While this effect is not an overwhelming one, it should be considered when selecting a particular fatigue specimen for a testing program. In general, the highly stressed volume should be as large as can be tolerated, because many practical machine components have much larger highly stressed volumes than can be accommodated in a corresponding fatigue test specimen.

Concurrent Variables

Concurrent changes of the variables affecting the fatigue resistance are obviously more complex to evaluate. The fatigue resistance being measured is a moving target and quantitatively depends on how much change has accrued over the period of testing. Concurrent changes are due to bulk and surface-related factors, as well as active load-related effects due to mechanical loading and temperature changes during testing. Obviously, the information to be documented for fatigue tests involving concurrent variables is more extensive than shown in Tables 2 and 3.

Bulk Property and Surface-Related Effects. Keep in mind that the laboratory fatigue results are being measured to help assess the structural durability of hardware with specific missions of exposure, loading, temperature, and time, among other factors. Mission loadings often have total durations lasting into years of exposure that cannot be affordably duplicated in laboratory tests. The laboratory coupon results must, therefore, capture the concurrent influences in such a way that they can be generalized and then brought to bear on specific applications. To do so usually requires a physically based model or equation that can relate the laboratory conditions to the mission loading and exposure conditions. An analogy can be made to time-temperature parameters that relate higher-temperature, shorter-time laboratory stress rupture results to longer-time, lower-temperature mission loading exposure. Available time-temperature parameters are generally consistent with the concepts of activation energy for thermally governed time-dependent creep processes. If models are not available for a smooth transition between laboratory and service conditions, extreme or bounding approaches may be necessary.

As an example, suppose the concurrent degradation in service is fretting. Alloy coupons could be prepared with surfaces that have been independently fretted to varying degrees. Subjecting these coupons to subsequent fatigue tests will demonstrate the effects of fretting as though it were a preexisting influence. Testing in this step-wise sequence imposes all of the fretting damage at the beginning of the test, and it could be expected to cause the maximum damage and, hence, a lower-bound fatigue life. This testing philosophy assumes no concurrent synergy between accumulation of fretting damage and accumulation of fatigue damage. Similar evaluations are possible for effects of nuclear radiation on bulk properties (causing, for example, increased strength and decreased ductility) or oxidation on surface-related effects (decreasing surface resistance to cracking). One should not discount the option of testing with a few multiple steps, for example:

- Apply static oxidation to a specimen in a furnace for a time interval.
- Follow this with rapid fatigue cycling for a predetermined block of cycles.
- Remove the specimen from the fatigue machine.
- Reinsert the specimen into the furnace for an additional time interval.
- Reinstall the specimen in the fatigue machine for an additional block of cycles.
- Repeat this process until the specimen fails due to oxidation-accelerated fatigue.

While this procedure is manpower intensive, total testing time in a fatigue machine could be greatly reduced while developing data that are far more relevant to the missions.

Active Loading-Related Effects. A number of active loading variables also fall into the category of concurrent variables. Prime examples of active loading variables are applied mean stresses, multiaxial stress-strain states, cumulative fatigue damage (not constant) loadings, and temperature-related effects such as creep fatigue and TMF. Creep fatigue and TMF are of such significance and require so many changes to conventional fatigue testing procedures that they merit separate discussion.

Mean Stresses. Perhaps the most commonly considered variable for fatigue testing is the mean stress. Mean stress effects on fatigue were recognized by Gerber (Ref 51) as early as the 1870s and have been a source of concern since. One of the most recent thorough reviews of the subject is given by Conway and Sjødahl (Ref 52).

A typical mean stress evaluation test would be conducted under load control of axial or plane bending in the nominally elastic high-cycle fatigue regime. Under plane bending, one surface has a tensile mean stress whereas the opposite surface has a compressive mean stress of equal magnitude. It is not possible to run independent tensile or compressive mean stress bending fatigue tests. Because tensile mean stresses are typically more damaging than compressive mean stresses, the bending specimen would always initiate fatigue cracks from the tensile mean stress surface. The plane-bending fatigue test is inappropriate for studying mean stress effects in the lower cycle-to-failure regime. Once small amounts of inelasticity occur at the outer surfaces, stress relaxation and redistribution occur and the local mean stresses are no longer directly proportional to the imposed mean loads. In fact, the load amplitude and mean will not change as a result of the local changes in stress, and the test engineer will be unaware of any changes to the stresses. Note that it is not possible to conduct mean stress studies under rotating-bending fatigue.

To avoid the problems of bending, axial loading is the recommended mode of testing for mean stress effects. Figure 23 schematically illustrates the decrease in alternating-stress fatigue resistance as the tensile mean stress increases. Frequently, the fatigue curve is displayed in terms of the maximum applied stress in the cycle. Figure 24 shows typical results of the effect of the stress ratio, R (algebraic minimum/algebraic maximum), on the axial fatigue resistance of 2024-T3 aluminum alloy at room temperature over the life range of 10^4 to 10^7 cycles to failure (Ref 52). Care should be taken when mean stresses are applied under load control at very high maximum tensile or compressive stresses. Too high a stress can cause yielding and, hence, cyclic ratcheting in the direction of the mean stress. If in tension, this can lead to eventual excessive tensile strain, subsequent tensile necking (as in a tensile test), and failure long before fatigue cracks have an opportunity to form and grow. Unless an extensometer is employed, small but damaging amounts of ratcheting may escape detection.

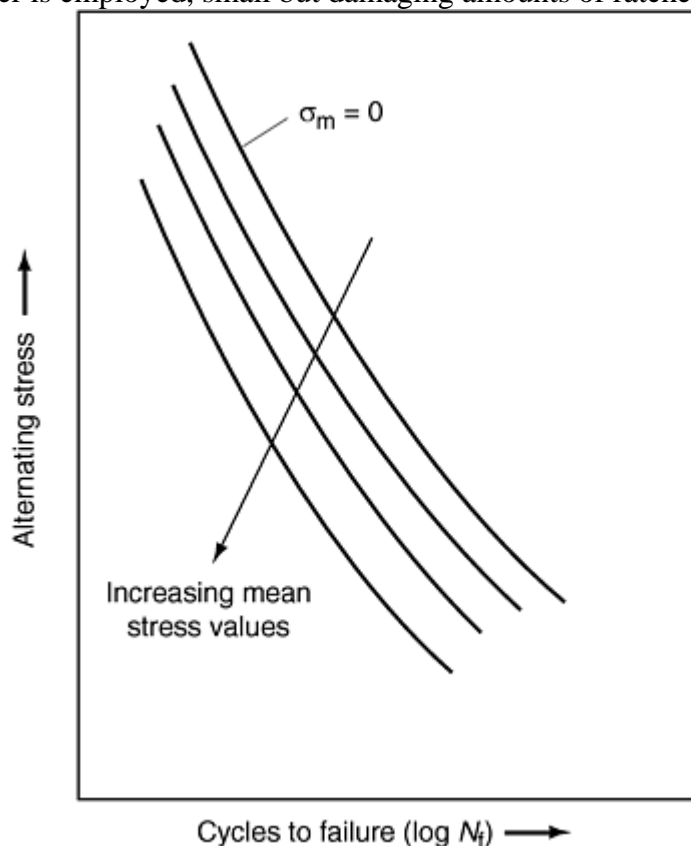


Fig. 23 Schematic axial fatigue curve illustrating the effect of tensile mean stress. After Ref 52

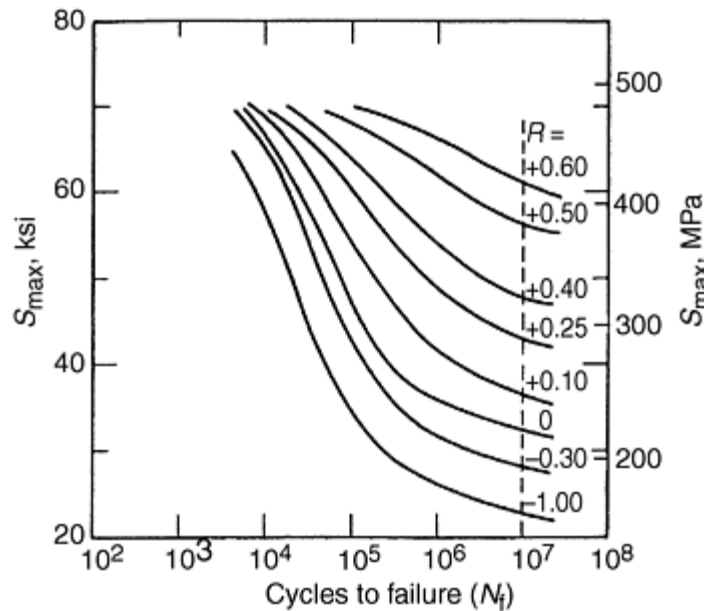


Fig. 24 Effect of tensile mean stresses on axial fatigue resistance of 2024-T3 aluminum alloy at room temperature. After Ref 52

Mean loading effects in the low-cycle fatigue regime are best dealt with under strain control. The strain control mode rules out ratcheting, although initial mean stresses imposed by mean straining do have an opportunity to cyclically relax. When imposed strain ranges are large enough that the inelastic strain range is on the order of a tenth of the total or elastic strain range, it is very probable that any initial mean stress will cyclically relax to zero, that is, become completely reversed, even though the straining is not completely reversed (Ref 53). In the high-strain, low-cycle fatigue regime, there is little, if any, effect of mean strain on fatigue life for ductile alloys. However, as the strain range is decreased and the life increases, a nominally elastic condition is reached. Then, a tensile mean strain will be accompanied by a directly proportional tensile mean stress, and the fatigue life will decrease compared to a completely reversed strain cycle. The end result is shown schematically in Fig. 25. Typical data of this nature have been reported for a high-temperature gas turbine engine alloy in (Ref 54).

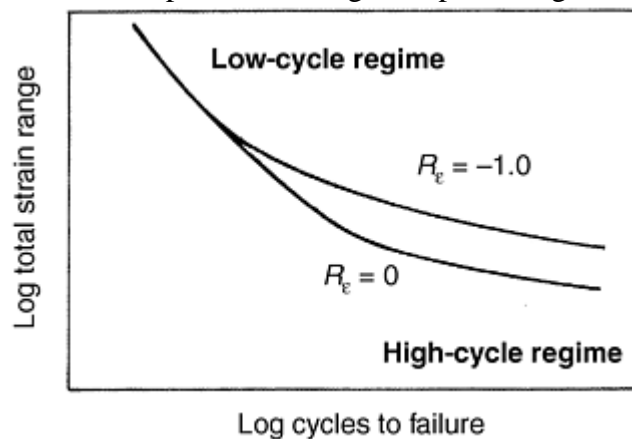


Fig. 25 Schematic illustration of mean-strain cycling effects on low-cycle fatigue resistance. Mean stresses relax to zero at large strain ranges but remain at low strain ranges, thus reducing life.

Multiaxiality. Investigation of multiaxial stress and strain states on fatigue resistance is a perennial issue because the cyclic stress-strain states at critical locations in machinery components are rarely uniaxial. However, the vast majority of fatigue tests are performed using uniaxial loading. The issues involved are so extensive that the subject has merited a separate article (“Multiaxial Fatigue Testing”) in this Volume and will not be discussed further in this article.

Cumulative Fatigue Damage. Commonly employed cumulative fatigue damage tests involve random, or nonsteady, loading wherein both the amplitude and mean value of the loading vary continuously (Fig. 26a). Such tests are attempts to simulate in the laboratory the detailed loadings encountered in service. The sequence

of loading is commonly referred to as spectrum loading. Also common are simplified, or compressed, loading patterns that have been shown analytically to account for the equivalent amount of fatigue damage that existed in the more complex spectrum loading. These compressed loading patterns capture the basic profile of loading. An illustrative schematic example is shown in Fig. 26(b). In this instance, the simplified loading pattern is arrived at by an equivalent rainflow cycle counting technique (Ref 55). Obviously, reducing the number of loading levels permits simplification of testing. Because a loading pattern may repeat itself, the fatigue loading can be applied in the form of repetitive blocks. Terrestrial-based vehicles, aerospace airframes, and civil engineering structures such as bridges typically experience random loadings during their fatigue crack initiation lifetimes. Greater details on how to approach complex cumulative fatigue damage assessment and testing can be found in Ref 56.

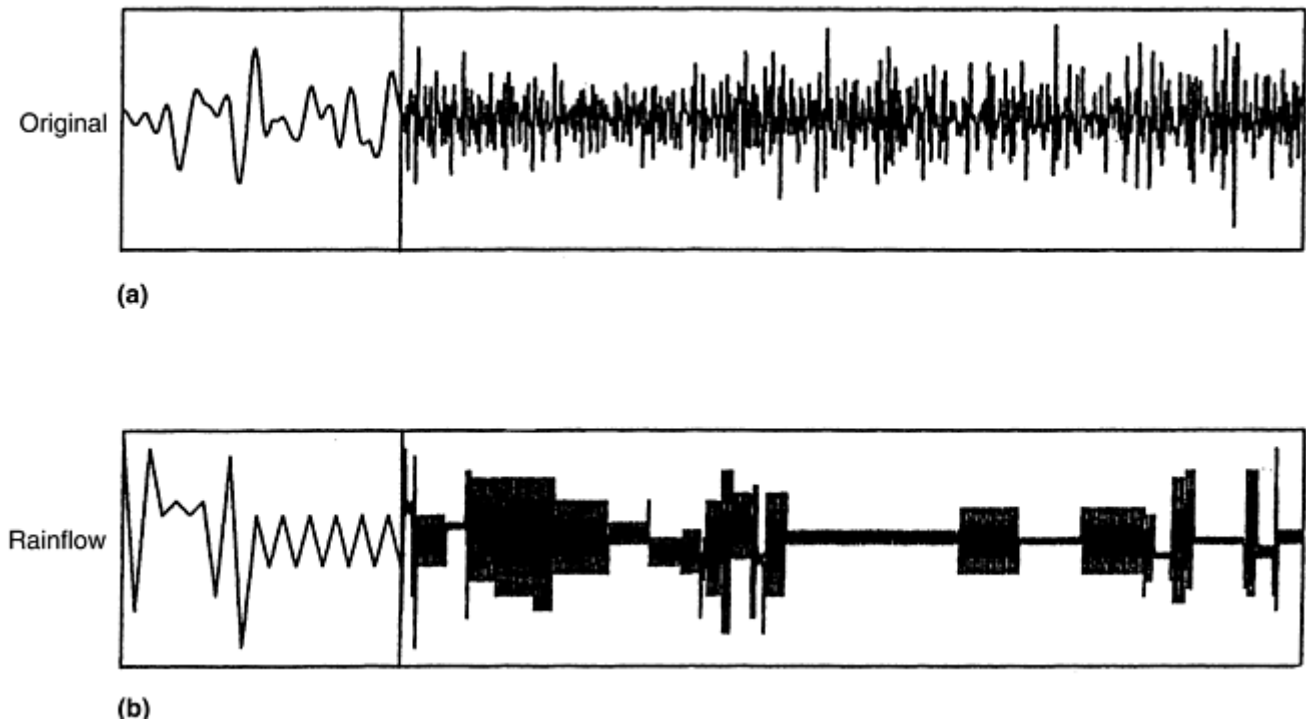


Fig. 26 Nonsteady fatigue loading. (a) Random-appearing original loading pattern. (b) Loading pattern reconstructed by rainflow method of cycle counting. After Ref 55

In the extreme are cumulative fatigue damage tests that involve only two loading levels, one in the low-cycle fatigue (LCF) regime, the other in the high-cycle fatigue (HCF) regime. Using this highly simplified testing pattern, it has typically been observed that LCF cycling (to a fraction of the expected life) followed by HCF cycling to failure reduces overall life, and the reverse loading order increases overall life. This is referred to commonly as the classic loading order effect (Ref 57, 58) and is illustrated in Fig. 27. This effect is not captured by linear damage assessment. Consequently, nonlinear cumulative fatigue damage models have proliferated (Ref 58) since Miner's linear damage rule was published in 1945 (Ref 59). The accuracy and viability of any cumulative fatigue damage rule hinges on the assumption that the physical mechanism of damage does not change as loading levels are changed. Clearly, understanding the damage mechanisms is an important and necessary step in the development of accurate models.

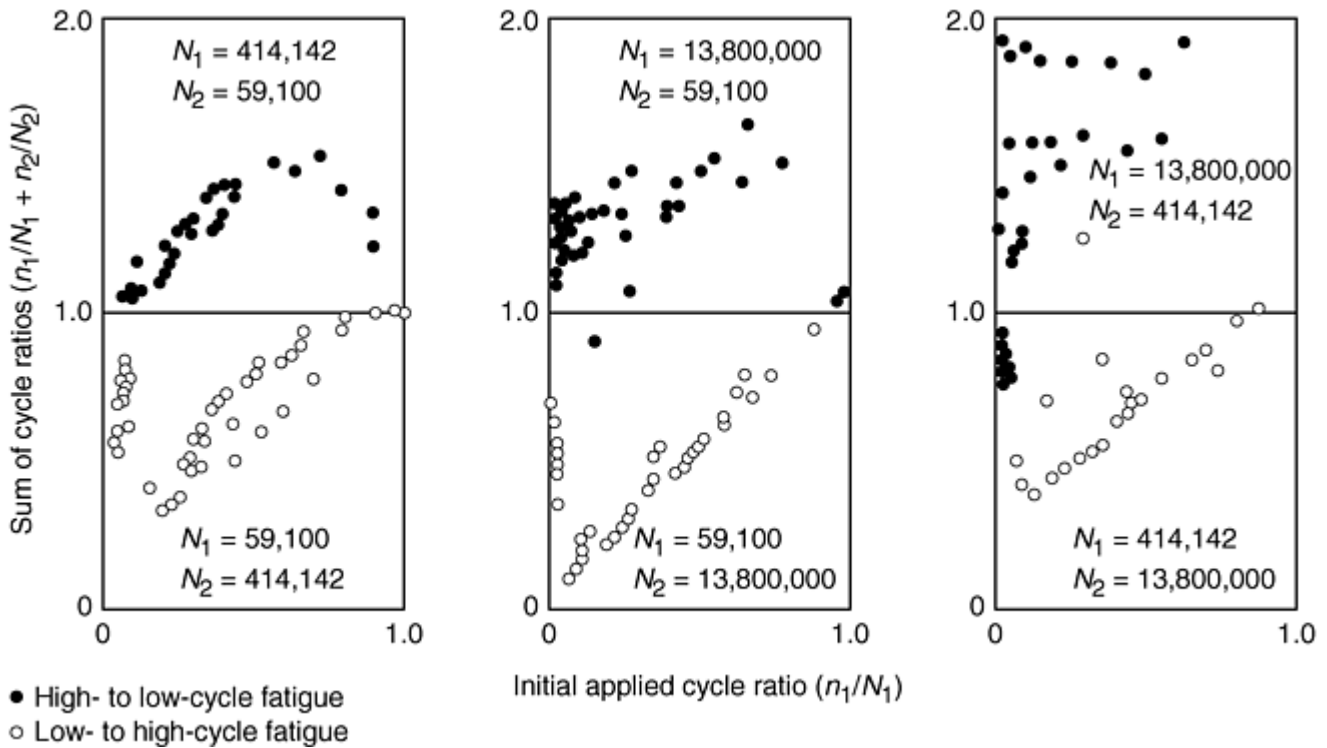


Fig. 27 Examples of classic loading order effect in two load level tests of British aluminum alloy D.T.D. 683. Source: Ref 57

Cumulative fatigue damage testing can also involve more than just loading level variations. Changes in the type of loading—for example, thermomechanical and isothermal (Ref 60), axial and torsion (Ref 61), and fatigue and creep-fatigue (Ref 62)—during testing may also be of importance. Temperature-related effects such as creep-fatigue and TMF are of such significance, and require so many changes to conventional fatigue testing procedures, that they merit separate discussion in the following sections.

References cited in this section

47. D.F. Socie, N.E. Dowling, and P. Kurath, "Fatigue Life Estimation of Notched Members," ASTM STP 833, *Fracture Mechanics: Fifteenth Symposium*, R.J. Sanford, Ed., American Society for Testing and Materials, 1984, p 284–299
48. S.M. Tipton and D.V. Nelson, Developments in Life Prediction of Notched Components Experiencing Multiaxial Fatigue, *Material Durability/Life Prediction Modeling—Materials for the 21st Century*, S.Y. Zamrik and G.R. Halford, Ed., Pressure Vessel and Piping Conference, PVP Vol 290, American Society of Mechanical Engineers, 1994, p 35–48
49. H. Neuber, Theory of Stress Concentration for Shear Strained Prismatical Bodies with Arbitrary Nonlinear Stress-Strain Law, *J. Appl. Mech. (Trans. ASME)*, Vol 28, 1961, p 544–550
50. G. Glinka, Energy Density Approach to Calculation of Inelastic Stress-Strain near Notches and Cracks, *Eng. Fract. Mech.*, Vol 22, 1985, p 485–508
51. W.Z. Gerber, Bestimmung der Zulossigne Sannugen in Eisen Construction, *Bayer. Arch. Ing. Ver.*, Vol 6, 1974, p 101 (in German)
52. J.B. Conway and L.H. Sjoedahl, *Analysis and Representation of Fatigue Data*, ASM International, 1991, p 21, 145–178

53. G.R. Halford and A.J. Nachtigall, The Strain-Range Partitioning Behavior of an Advanced Gas Turbine Disk Alloy, AF2-1DA, *J. Aircr.*, Vol 17, 1980, p 598–604
54. M. Doner, K.R. Bain, and J.H. Adams, Evaluation of Methods for Treatment of Mean Stress Effects on Low-Cycle Fatigue, *J. Eng. Power (Trans. ASME)*, Vol 104, 1982, p 403–411
55. Y. Murakami, Ed., *The Rainflow Method in Fatigue*, Butterworth Heinemann Ltd., Oxford, 1992
56. M.R. Mitchell, Fundamentals of Modern Fatigue Analysis for Design, *Fatigue and Fracture*, Vol 19, *ASM Handbook*, ASM International, 1996, p 227–249
57. S.S. Manson and G.R. Halford, Re-Examination of Cumulative Fatigue Damage Analysis—An Engineering Perspective, *Eng. Fract. Mech.*, Vol 25, 1986, p 539–571
58. G.R. Halford, Cumulative Fatigue Damage Modeling—Crack Nucleation and Early Growth, *Int. J. Fatigue*, Vol 19 (No. 1) supplement, 1997, p S253–S260
59. M.A. Miner, Cumulative Damage in Fatigue, *J. Appl. Mech.*, Vol 12 (No. 3), 1945, p A159–A164
60. P.T. Bizon, D.J. Thoma, and G.R. Halford, Interaction of High Cycle and Low Cycle Fatigue of Haynes 188 at 1400 °F, *Structural Integrity and Durability of Reusable Space Propulsion Systems*, NASA CP-2381, 1985, p 129–138
61. S. Kalluri and P.J. Bonacuse, “Cumulative Axial and Torsional Fatigue: An Investigation of Load-Type Sequencing Effects,” ASTM STP 1387, *Symposium on Multiaxial Fatigue and Deformation: Testing and Prediction*, S. Kalluri and P.J. Bonacuse, Ed., American Society for Testing and Materials, 2000 (in press)
62. R.M. Curran and B.M. Wundt, Continuation of a Study of Low-Cycle Fatigue and Creep Interaction in Steels at Elevated Temperatures, *1976 ASME-MPC Symposium on Creep-Fatigue Interaction*, Materials Property Council MPC-3, American Society of Mechanical Engineers, 1976, p 203–282

Fatigue, Creep Fatigue, and Thermomechanical Fatigue Life Testing

Gary R. Halford and Bradley A. Lerch, Glenn Research Center at Lewis Field, National Aeronautics and Space Administration; Michael A. McGaw, McGaw Technology, Inc.

Creep-Fatigue Interaction

Creep-fatigue interaction testing and modeling have been intense activities since the late 1950s. Interest was spawned by the introduction, and seemingly premature failures, of components in structural equipment operating at elevated temperatures. Examples include aeronautical gas turbine engines; steam turbines; nuclear reactors and pressure vessel and piping components for electric power generation and chemical processing plants; casting and forging dies; railroad wheels subjected to brake-shoe application; automotive cylinder heads, exhaust valves, manifolds, and exhaust piping systems; and reusable rocket engines. In many cases, the elevated temperature of operation is reasonably constant (isothermal) over a period of time while components are under load and can suffer creep or stress-relaxation processes that hasten crack initiation and early growth. The modes of cracking have frequently exhibited creep-like fractures intermixed with cycle-dependent fatigue-type cracking. Hence the descriptive name, creep-fatigue interaction.

Extensive reviews of creep-fatigue interaction were prepared in the early 1980s (Ref 63, 64, 65). Over the intervening decades, more than 100 models or their variations have been proposed to describe creep-fatigue

interaction (Ref 66, 67). As many as a dozen of the models have survived and have been applied to practical situations. The three most widely used are the time- and cycle-fraction rule from the ASME Code Case N-47-23 (Ref 68), strain-range partitioning (SRP) (Ref 69) and its total strain version (Ref 70), and continuous damage mechanics (Ref 71).

The fatigue machines and associated equipment normally used for creep-fatigue experiments are essentially the same as those used for baseline fatigue tests. Current practice calls for axial loading of a uniform-gage length specimen mounted in a closed-loop servocontrolled fatigue testing machine with provisions for heating the sample to elevated temperatures. Closed-loop strain-controlled testing is most commonly used; when it is not used, strain limit control is imposed to prevent creep ratcheting. The major difference between creep-fatigue and baseline isothermal fatigue testing is in the time per cycle. To introduce creep into the cycle, the frequency is reduced by cycling at a lower strain rate or by introducing a hold period at some selected point within each cycle. Most commonly, a hold period is inserted at the peak strains in a cycle, that is, at maximum or minimum algebraic strains, or at both peaks.

Creep-fatigue interaction testing is conducted at a high enough isothermal temperature that thermally activated, diffusion-controlled creep deformation mechanisms can operate under stress as a function of both time and temperature. As a rough rule of thumb, the transition temperature for creep is on the order of half the absolute melting temperature of an alloy. In earlier years, creep-fatigue testing was conducted to simply ascertain the extent of the damaging effect of creep on cyclic (fatigue) life. Today, tests are still run for that purpose, but more often than not, creep-fatigue testing is designed also to evaluate and calibrate the constants in a viable creep-fatigue life prediction model.

The addition of creep to a cycle of normal fatigue loading will invariably reduce the cyclic life, although the clock time to failure may remain constant or actually increase. Conversely, the superposition of fatigue cycling and conventional monotonic creep will also alter the rate of creeping and the time to rupture. Because of the importance placed on knowing the values of stress and time-dependent deformation, it is generally regarded that creep-fatigue testing be done with axially loaded specimens equipped with extensometry. While some interspersed creep-fatigue testing, that is, repeated blocks of brief periods of creep followed by brief periods of fatiguing, has been reported (Ref 62), the most common tests involve repeating cycles of straining with hold periods imposed in tension or compression alone or in combination. The hold periods may be under constant strain or constant stress. If under constant stress, strain limits are generally imposed to preclude ratcheting. Alternatively, creep could be introduced by controlled slow straining rates in tension, compression, or both.

Figures 28 illustrates the various isothermal hysteresis loops that are commonly encountered in fatigue and creep-fatigue testing. Figures 28(a), 28(e), 28(f), and 28(g) were used to generate the data shown in Fig. 29 for AISI type 304 stainless steel (Ref 67). Here the inelastic strain range is plotted against cycles to failure on log-log coordinates. As can be seen, significant cyclic life losses (a factor of 10 or more) are possible with strain hold periods of just 30 minutes per cycle in tension only. Hold periods of up to 180 minutes per cycle do not necessarily further reduce the cyclic life, implying a saturation condition beyond a certain hold period for strain hold (stress relaxation) creep-fatigue cycles. Those cycles that are balanced in nature, that is, the tensile and compressive halves experience the same strain rates or hold times, will not exhibit an algebraic mean stress, whereas the unbalanced cycles will. The mean stress is tensile if the hold period or slow straining rate is in compression and vice versa. Evidence suggests that these mean stresses do not exhibit the classical mean stress effect on cyclic life in the high-strain range, low-cycle fatigue regime (Ref 54), and hence can be ignored. Similar creep-fatigue cycling results for AISI type 304 stainless steel and Incoloy 800 have been reported in Ref 72. These results were analyzed in Ref 73 by both the time- and cycle-fraction rule and the method of strain-range partitioning based on information provided in Ref 72.

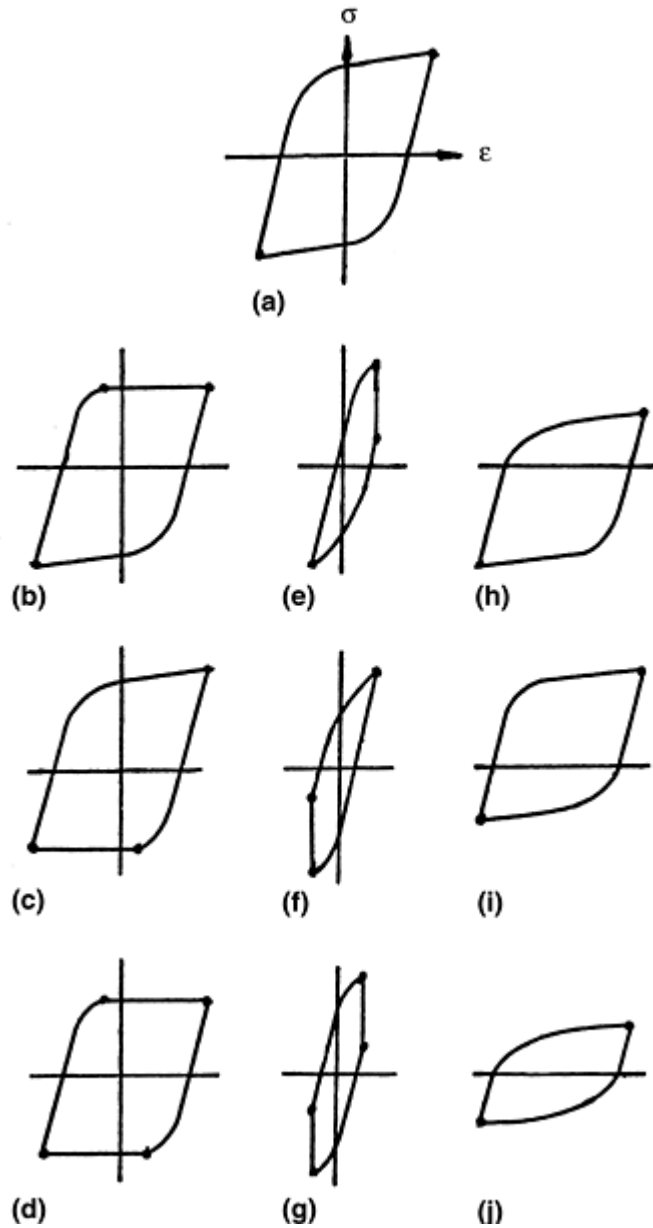


Fig. 28 Schematic hysteresis loops encountered in isothermal creep-fatigue testing. (a) Pure fatigue, no creep. (b) Tensile stress hold, strain limited. (c) Compressive stress hold, strain limited. (d) Tensile and compressive stress hold, strain limited. (e) Tensile strain hold, stress relaxation. (f) Compressive strain hold, stress relaxation. (g) Tensile and compressive strain hold, stress relaxation. (h) Slow tensile straining rate. (i) Slow compressive straining rate. (j) Slow tensile and compressive straining rate

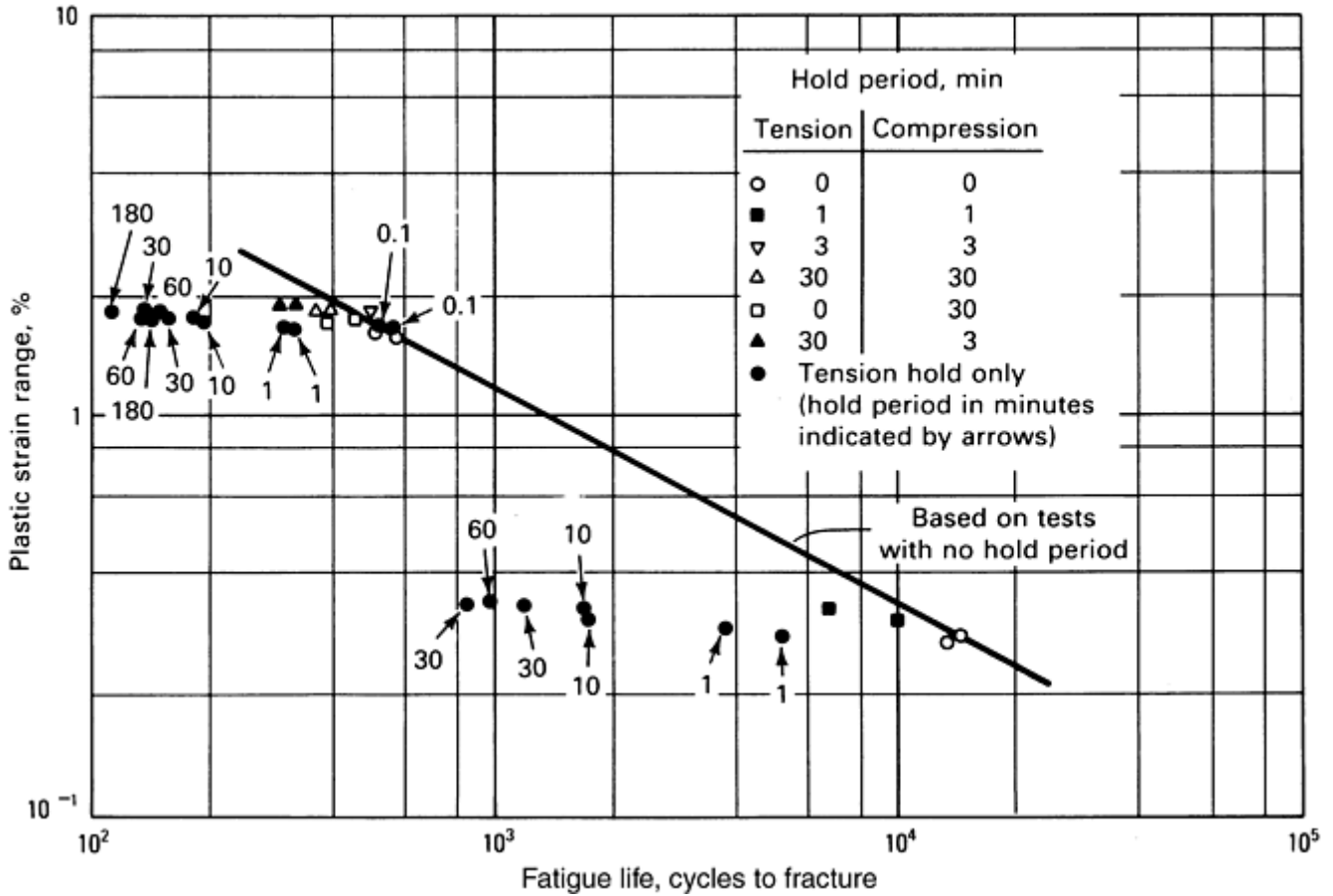


Fig. 29 Creep-fatigue interaction effects on isothermal cyclic life of AISI type 304 stainless steel tested in air at 650 °C (1200 °F), normal straining rate of $4 \times 10^{-3} \text{ s}^{-1}$. After Ref 65

Comparison of the two creep-fatigue life prediction models is given in Fig. 30. In this instance, the time- and cycle-fraction rule, which utilizes a stress-based approach to assessing creep damage, does not do an acceptable job of predicting the laboratory results. Cyclic lives can be over-predicted by as much as a factor of 5 and under-predicted by a factor of 20, thus creating a band of uncertainty in predicted life of two orders of magnitude. The method of strain-range partitioning is a strain-based approach and assigns creep damage according to the magnitudes of the creep strains encountered in a cycle. The figure indicates a strain-based approach is superior in this case.

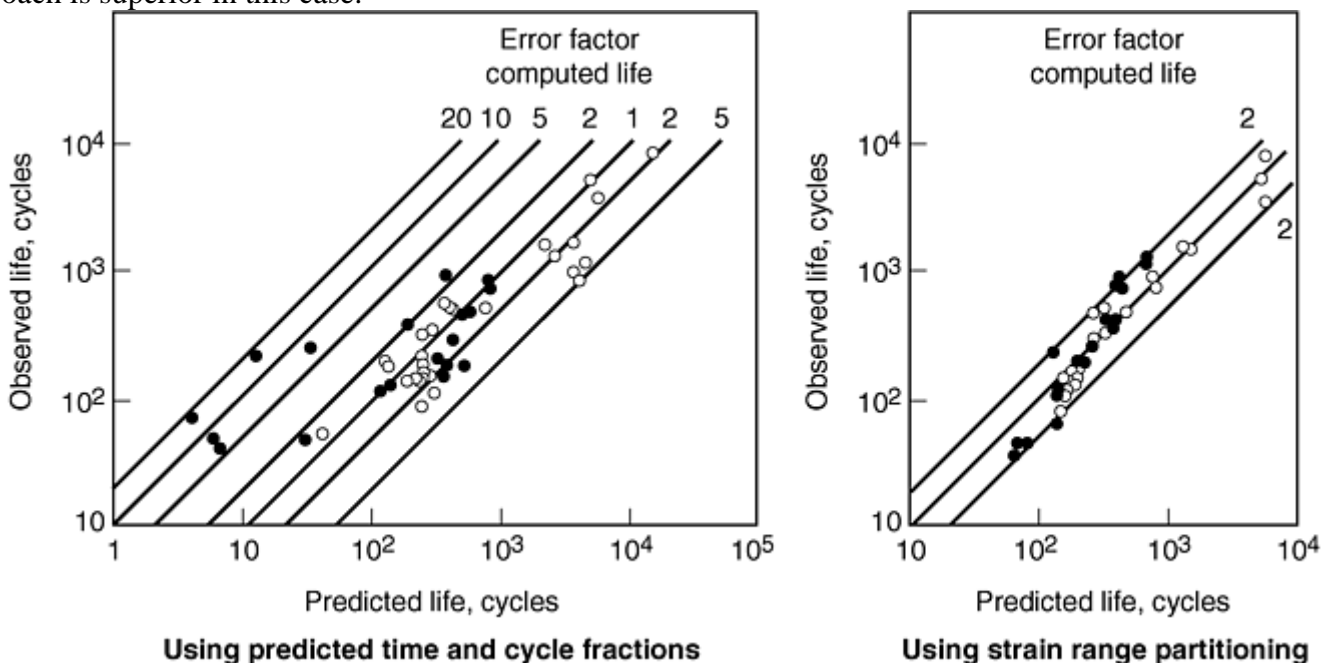


Fig. 30 Predictability of creep-fatigue lives for tensile strain hold time cycles for Incoloy 800 and AISI type 304 stainless steel at elevated temperatures. Source: Ref 70, 71

A viable creep-fatigue model is of great importance to be able to design equipment to operate for long periods of time at elevated temperature. Services lifetimes are typically much greater than the longest affordable creep-fatigue testing lifetimes of laboratory specimens. What a viable model has to offer is increased confidence in the extrapolations to longer times to failure than were used in the model calibration. A physically based model is expected to hold greater promise than simple empirical extrapolation of noncorrelated laboratory data. Because laboratory creep-fatigue measurements are the basic ingredients of the foundation for assessing extrapolated long-time structural durability, it is imperative that accurate measurements and control of the testing variables be maintained. The problem is a much more stringent one than for lower-temperature, fatigue-life extrapolation because of the influence of time and temperature. Creep is sensitive to temperature in a highly nonlinear exponential dependency and sensitive to stress and time of exposure in nonlinear power-law dependencies. The temperature and time dependencies also include the effects of interaction with the environment. Typically, oxygen is the surrounding environment and surface oxidation can greatly influence the susceptibility of exposed surfaces to premature crack initiation and early growth. Most creep-fatigue models are calibrated and used without the benefit of separating the effects of oxidation from the creep effects. A listing of models with the potential for accounting specifically for oxidation or other environmental interaction effects is found in (Ref 67).

Creep-fatigue test results are generally more extensive than simpler fatigue results. Table 5 lists, among other items to be discussed, the additional information that should typically be reported for each creep-fatigue test conducted.

Table 5 In-test and post-test information guidelines for creep fatigue and thermomechanical fatigue

Cyclically varying parameters	Value of fixed test control parameters (stress, strain, temperature, temperature and straining rates, hold times, phasing relation between temperature and strain, as applicable); continuous recording of variations of maximum, minimum, amplitude, range, and mean values of stress, strain, and temperature as a function of applied cycles (or sufficient information for calculation of these parameters); cyclic variation of load range ratio of tensile to compressive peak loads (under strain control) and cyclic variation of strain range and ratio of maximum to minimum strain peaks (under load control) to help define failure life and hence half-life; continuous or periodic recording of variations of stress-strain hysteresis loops and stress versus time and strain versus time; any parameter deemed necessary for evaluation of a particular creep-fatigue or thermomechanical fatigue model (e.g., for strain range partitioning, the amounts of tensile and compressive creep and plastic strains)
Lifetime information	Cyclic failure lives based on various cyclic failure criteria; failure life (cycles and corresponding time) for criterion adopted; half-life cycles; total, inelastic (partitioned strain ranges and method of partitioning if using strain range partitioning), and elastic strain ranges at half-life; maximum, minimum, stress amplitude, stress range, mean stress, and mean stress ratio at half-life; degree of cyclic hardening and/or softening from first cycle to half-life (or cycles at stabilization of stress-strain response); description of fracture surface including initiation site(s); degree of transgranular and intergranular cracking; location of fracture relative to extensometer probes
Deviations from original test plans	Details of stress and strain history and temperature immediately prior to controlled or uncontrolled shut-downs prior to test completion
Data analysis from multiple specimens	Cyclic stress-strain curve and how it varies with strain rate, frequency, cycle time, hold time, and temperature; equation constants at half-life (or cycles at stabilization), that is, the cyclic flow properties; fatigue curves, creep-fatigue curves, and thermomechanical fatigue curves expressed in terms of inelastic strain range, total range, and elastic strain range versus cyclic life; equation constants and how they vary with temperature and some measure of testing time, that is, the cyclic failure

References cited in this section

54. M. Doner, K.R. Bain, and J.H. Adams, Evaluation of Methods for Treatment of Mean Stress Effects on Low-Cycle Fatigue, *J. Eng. Power (Trans. ASME)*, Vol 104, 1982, p 403–411
62. R.M. Curran and B.M. Wundt, Continuation of a Study of Low-Cycle Fatigue and Creep Interaction in Steels at Elevated Temperatures, *1976 ASME-MPC Symposium on Creep-Fatigue Interaction*, Materials Property Council MPC-3, American Society of Mechanical Engineers, 1976, p 203–282
63. S.S. Manson, Critical Review of Predictive Methods for Treatment of Time-Dependent Metal Fatigue at High Temperatures, *Pressure Vessels and Piping: Design Technology—1982—A Decade of Progress*, American Society of Mechanical Engineers, 1982, p 203–225
64. D.A. Miller, R.H. Priest, and E.G. Ellison, A Review of Material Response and Life Prediction Techniques under Fatigue-Creep Loading Conditions, *High Temp. Mater. Process.*, Vol 6, 1984, p 155–194
65. V.M. Radhakrishnan, Life Prediction in Time Dependent Fatigue, *Advances in Life Prediction Methods*, American Society of Mechanical Engineers, 1983, p 143–150
66. G.R. Halford, Evolution of Creep-Fatigue Life Prediction Models, *Creep-Fatigue Interaction at High Temperature*, G.K. Haritos and O.O. Ochoa, Ed., Vol 21, American Society of Mechanical Engineers, 1991, p 43–57
67. G.R. Halford, Creep-Fatigue Interaction, *Heat Resistant Materials*, ASM International, 1997, p 499–517
68. Code Case N-47-23, American Society of Mechanical Engineers, 1986
69. S.S. Manson, G.R. Halford, and M.H. Hirschberg, Creep-Fatigue Analysis by Strain-Range Partitioning, *Symposium on Design for Elevated Temperature Environment*, American Society of Mechanical Engineers, 1971, p 12–28
70. J.F. Saltsman and G.R. Halford, “An Update on the Total Strain Version of SRP,” ASTM STP 942, *Low Cycle Fatigue—Directions for the Future*, H.D. Solomon, G.R. Halford, L.R. Kaisand, and B.N. Leis, Ed., American Society for Testing and Materials, 1988, p 329–341
71. J.-L. Chaboche, Continuous Damage Mechanics: A Tool to Describe Phenomena before Crack Initiation, *Nucl. Eng. Des.*, Vol 64, 1981, p 233–247
72. C.E. Jaske, H. Mindlin, and J.S. Perrin, “Combined Low-Cycle Fatigue and Stress Relaxation Behavior of Alloy 800 and Type 304 Stainless Steel at Elevated Temperatures,” ASTM STP 520, *Fatigue at Elevated Temperature*, American Society for Testing and Materials, 1973, p 365–376
73. S.S. Manson, “The Challenge to Unify Treatment of High Temperature Fatigue— A Partisan Proposal Based on Strain-Range Partitioning,” ASTM STP 520, *Fatigue at Elevated Temperature*, American Society for Testing and Materials, 1973, p 744–782

Thermomechanical Fatigue

Thermal fatigue is a structural failure mode in many high-temperature components. Thermal fatigue loading is induced by temperature gradients during transient heating or cooling from one high temperature of operation to another. Thermal fatigue loading can also occur when heating and cooling are present simultaneously and thermal gradients are maintained during steady-state operation. Internally air-cooled high-temperature turbine blades are examples. Thermal gradients produce differential expansion as the hottest material wants to expand more than the cooler, but is constrained from doing so by the cooler and stronger material. The constraint is perceived by the hottest material as a compressive thermal strain that is no different in its effect on the material than would be a mechanically induced strain of equal magnitude. Similarly, the coldest material is forced by the hottest to expand more than normal. The thermally induced strain in the colder material is tensile. Conditions of strain compatibility will be maintained. The corresponding thermal stresses result directly from the thermal strains according to the current stress-strain relation and the necessity to obey the laws of equilibrium. The integrated sum of the internal stresses into forces must always equal zero. Because of the gradients of the primary variables, it is impossible to measure the thermal fatigue properties of a material in the same way that isothermal fatigue or creep-fatigue properties are measured, that is, in terms of holding certain variables constant while the response of the others are measured. To overcome this basic difficulty, TMF tests have been devised.

Thermomechanical Fatigue Testing. The testing machine and specimen set up for TMF testing are essentially the same as used for creep-fatigue testing or baseline high-temperature isothermal fatigue testing. The major distinction is that the temperature of the specimen, instead of remaining constant, must be programmed to vary in a precisely defined manner. Furthermore, the cycling rate must, at times, be rather high, requiring the ability to heat and cool the test specimen as rapidly as possible without creating undue thermal gradients. This requirement virtually rules out the use of conventional clamshell radiation furnaces because of their large thermal inertia. Most commonly, induction heating is used. This is because of the reasonably high rates of heating possible, and because the temperature gradient along the specimen gage length can be controlled better with a three-zone induction heating coil arrangement, as shown in Fig. 11. Induction coils are also more conducive for use of extensometers. Direct resistance heating, although not commonly used, has the capability of heating a sample so rapidly that it could be melted in a matter of seconds. Heating is usually not the limiting factor in governing the cycling rate, rather, cooling is. Forced air cooling has been used successfully. Jets of air are impinged on the specimen surface along the gage length and around the circumference. Excessive cooling induces thermal gradients and, hence, unwanted thermal stress and strains. A balance must be achieved between cooling (as well as heating) rate and the extent of undesired thermally induced stresses and strains. Thermal cycling rates as fast as 3 minutes per cycle are employed on a routine basis. A test run to 12,000 cycles requires 36,000 minutes or 600 hours. This is without consideration of a hold period at the peak temperature. A testing program involving dozens of specimens could thus become extremely expensive and time consuming. Cycling rates as high as 20 seconds per cycle have been achieved through diligence. However, the thermal gradients are quite high and control of the temperature and strain is poor, although reproducible.

Raising the minimum temperature in the laboratory TMF cycle is a commonly used approach to help speed up TMF testing frequency. This can considerably reduce the time needed to cool because cooling follows an exponential decay curve. Removing the last portion of that curve can significantly decrease the cooling time per cycle. However, the range of temperature is reduced in the process, and the measured TMF characteristics are removed further from what occurs in most applications. For most industrial equipment, the minimum temperature in a thermal fatigue cycle is ambient, and is considerably below the minimum temperature usually selected for TMF testing. Normally, the testing conditions of temperature range, minimum temperature, and cycling rate are determined by compromise. Regardless of the minimum temperature selected for testing, there remains the desire to shorten the time per cycle; this leads to higher thermal gradients throughout the test specimen.

Of course, one of the purposes of TMF testing is to intentionally keep thermal gradients negligibly small while the overall temperature of the test volume of the specimen is raised and lowered cyclically. Simultaneously, the magnitude of the uniformly distributed strains (stresses) in the specimen is controlled independently of the temperature change, although a fixed phasing is usually maintained between them. As a consequence, the test specimen could be programmed to experience cyclic thermal and mechanical strains just as the material might at a critical point were it undergoing thermal fatigue in a structural element. In this way, the resistance of a material to thermal fatigue can be experimentally evaluated for a range of phasings and amplitudes of strain (stress) and temperature. Figure 31 illustrates a series of basic TMF strain cycles for the most rudimentary of TMF situations in which mechanical strain and temperature vary in lock step with one another. A triangular waveform is used for the example cycles, although sinusoidal, is also in vogue. When the same waveform is used for both strain and temperature, their time phase shift can be described by a single parameter, the phase angle. In-phase cycling (0° phase shift) is defined as having the maximum algebraic strain occur at the same instant as the maximum temperature and having the minimum algebraic strain occur at the minimum temperature. Out-of-phase TMF cycling (180° phase shift) is just the reverse of in-phase cycling. A phase angle of 90° or 270° corresponds to a diamond-shaped (sometimes referred to as baseball) pattern of mechanical strain versus temperature. The resultant stress-strain hysteresis loop for a diamond cycle will appear as unusual because the maximum and minimum temperatures do not occur at the maximum or minimum mechanical strain. These and other basic cycles (bithermal) to be introduced later serve as excellent uniform types of cycles for characterizing the TMF fatigue resistance of materials.

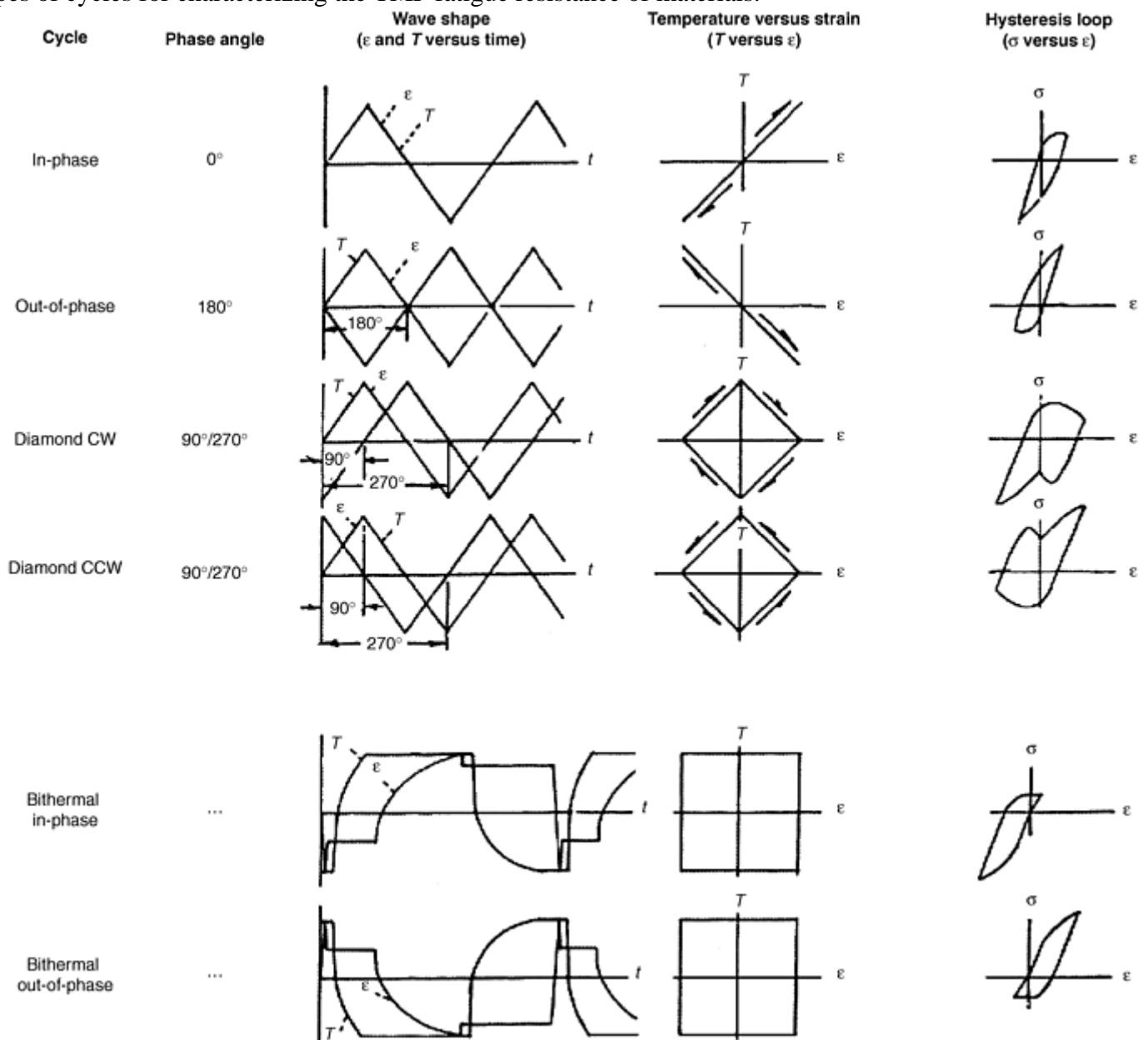


Fig. 31 Basic thermomechanical fatigue strain cycles

Rarely, however, are the simple cycles discussed above encountered exactly in service. Because TMF fatigue life is generally wave-shape dependent, means are required to generalize laboratory characterizations so they may be applied to any unique thermal fatigue cycle encountered in service. This is usually accomplished with a life prediction model. Again, physically based models will have the greatest potential for proper interpolation and extrapolation of results generated. There are spectra of TMF tests of any given type of cycle that could be conducted in a laboratory: phasings could cover the range from in phase to out of phase and all points between, as well as for TMF cycles that are not describable, by quoting a simple measure of phasing; temperature ranges could be very narrow or very wide; the maximum and minimum temperatures could also cover a broad range, as could the mechanical strain range. The frequency (or other measure of the cycling rate and hold periods) is yet another critical variable to be investigated if one is to document the broad range of the thermal fatigue resistance of a material. A complete test matrix that could capture all of the pertinent variables is too large to be practical. Judicious selection of the variables and their combinations and ranges is usually required based on the potential application of the results. ASTM committee E-08 on fatigue is currently crafting a standard for basic TMF fatigue testing (Ref 74) involving simple waveforms (e.g., triangular, sinusoidal) of phased strain and temperature cycling. Once approved and published, the standard will be a valuable document to consult before conducting TMF tests. Table 5 lists in-test and post-test information that should be documented for each TMF test conducted.

As discussed in the reviews of Ref 75, 76, and 77, the thermal fatigue resistance of a material is not necessarily derivable from isothermal fatigue resistance, and it is frequently lower than isothermal fatigue resistance. This is generally observed despite comparisons made to isothermal fatigue resistance measured at the maximum TMF test temperature (i.e., usually thought to be the lowest isothermal fatigue resistance within the span of the TMF temperature range). The basis for comparison of isothermal and TMF fatigue resistance of a material is also important. For example, the TMF resistance may be poorer if the inelastic strain range is used as the basis of comparison, but could be better if the total strain range is used. This apparent dichotomy is a direct result of the differences in the cyclic stress-strain behavior between isothermal and TMF cycling. Comparisons of isothermal and TMF fatigue resistance to inelastic strain for two example alloys (Ref 78, 79) are shown in Fig. 32 and 33.

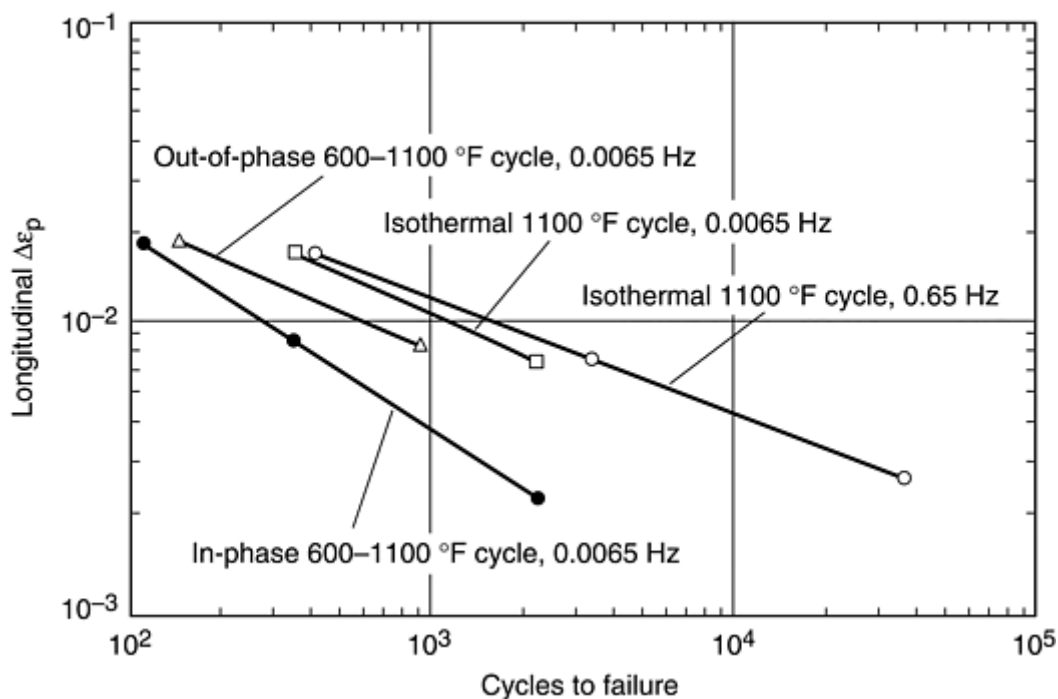


Fig. 32 Comparison of isothermal and thermomechanical fatigue resistance of A 286 precipitation-hardening stainless steel. Source: Ref 76, 77, 78

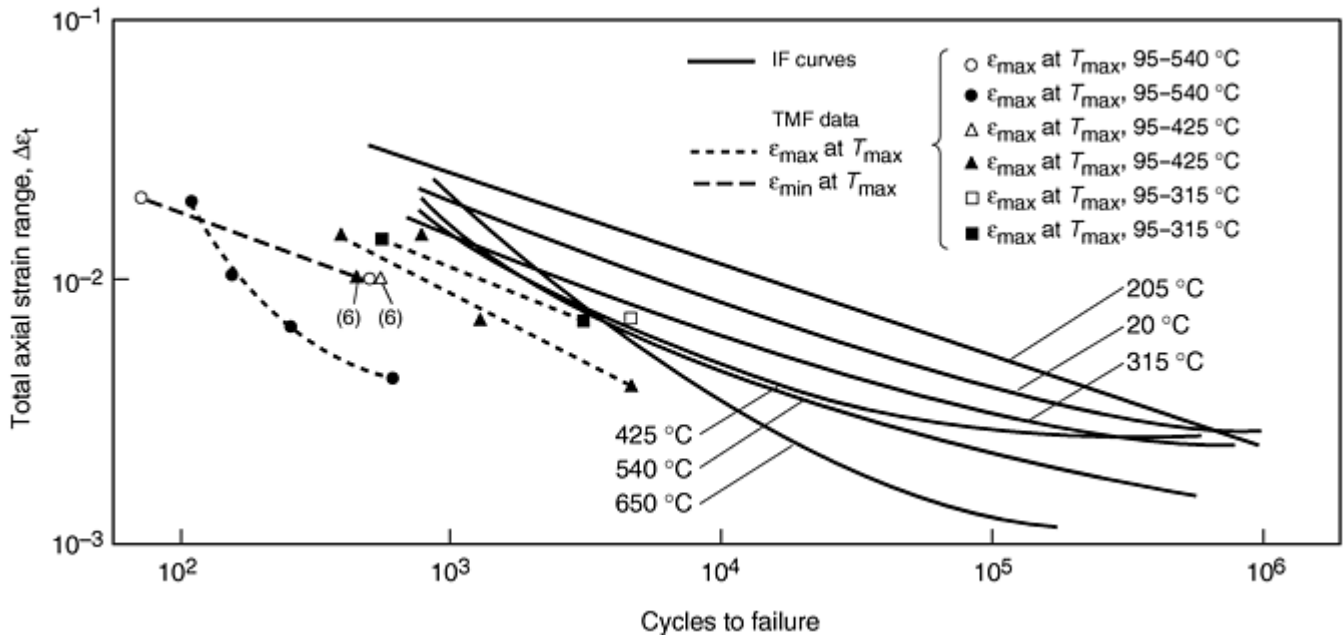


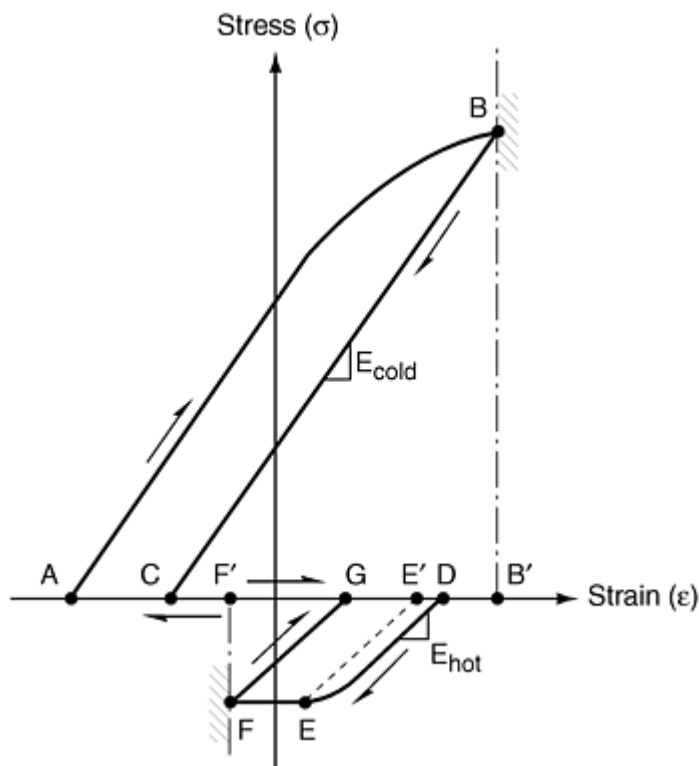
Fig. 33 Comparison of isothermal and thermomechanical fatigue resistance of AISI 1010 carbon steel.
Source: Ref 76, 77, 79

Thermomechanical Fatigue-Life Modeling. Because of the large number of variables and the inherent problem of not being able to afford to test for all possible combinations of variables, alternate approaches are desirable. One attractive approach is to adopt a TMF life prediction method. By calibrating the constants in equations representing the model, the means are available to calculate behavior under other conditions by interpolation and extrapolation. A variety of TMF life prediction models are discussed in Ref 67, 73, 76, and 77. Among the more frequently used models are the ASME time- and cycle-fraction rule (Ref 68), the continuum damage model of ONERA (the French space agency) (Ref 71), the University of Illinois creep-fatigue-oxidation model (Ref 80, 81), and the NASA Glenn (formerly Lewis) method of strain-range partitioning (SRP) (Ref 82).

The SRP approach for creep-fatigue and TMF life prediction takes advantage of bithermal fatigue testing (Ref 83). As the name implies, bithermal cycling is conducted using two isothermal temperatures within each cycle. The high isothermal temperature represents the maximum temperature of a more complex TMF cycle, while the low isothermal temperature represents the minimum. The impetus for developing bithermal testing was to permit direct measurement of both thermal expansion strain and mechanical strain without them being intermixed. Visual observation of a bithermal hysteresis loop unequivocally identifies these two types of strain. During conventional TMF cycling, thermal and mechanical strains are applied simultaneously and can only be separated by calculation. During bithermal cycling, mechanical straining (and stress) is applied only during the two isothermal halves and not when the temperature is being changed. The stress on the specimen is controlled at zero during any change in temperature, thus providing a clear separation of thermal expansion and mechanical strains.

A schematic bithermal hysteresis loop is shown in Fig. 34. An out-of-phase cycle is shown. All tensile mechanical straining is done at the low temperature, and compressive mechanical straining is done at the high temperature. The loading sequence in traversing a cycle is noted in the table to Fig. 34. The tensile loading from point A to B and unloading from B to C is done at the cold temperature where the elastic modulus is E_{cold} . It is presumed the temperature is low enough and the straining rate is high enough that time-dependent creep is precluded and only plasticity occurs. Hence, the tensile inelastic (plastic) strain is AC and the corresponding elastic strain is CB' , that is, stress at B divided by E_{cold} . At point C the load is held at zero and the specimen temperature raised to the hottest temperature where the elastic modulus is E_{hot} . The specimen expands freely from C to D, a direct measure of the thermal expansion strain over the temperature range. Once thermal stability has been attained, the specimen is strained rapidly into compression until a predetermined stress is reached at point E. The inelastic strain DE'' is time-independent plastic strain. Under the stress at E, compressive creep occurs until the strain limit at point F is reached and the specimen is rapidly unloaded to point G. The amount of compressive creep strain is EF, and the compressive inelastic strain is $DG = DE'' + EF$ (or $E''G$). The corresponding compressive elastic strain is the creep stress (along EF) divided by E_{hot} . Cooling

from point G to point A completes the bithermal loop. The thermal contraction GA should be equal to the expansion CD.



Strain	Type of strain	Temperature	Action
AB	Elastic + plastic	Low	Rapid straining
BC	Elastic unloading	Low	Rapid straining
CD	Thermal expansion	Low-high	Zero stress
DE	Elastic + plastic	High	Rapid straining
EF	Creep	High	Constant stress
FG	Elastic unloading	High	Rapid straining
GA	Thermal constraction	High-low	Zero stress

Fig. 34 Schematic bithermal hysteresis loop (out-of-phase cycle)

It is simple to interpret directly from the hysteresis loop of Fig. 31 the magnitudes of the elastic strains, the inelastic strains, the total strains, and the thermal expansion strains. It is much more difficult to determine these parameters from a continuously varying TMF hysteresis loop. The elastic strain range for the bithermal loop is the sum of the absolute values of the tensile and compressive elastic strains. The corresponding inelastic strain range is the width of the hysteresis loop at zero stress. There are two measures of this strain range, AC or DG. Theoretically, they must be equal; otherwise, cyclic ratcheting takes place. However, the fixed strain limits prevent ratcheting. Since every experimental measurement has some scatter, it is recommended that AC and DG be averaged to determine the value of the inelastic strain range. The total strain range of the bithermal loop is the sum of the elastic and inelastic strain ranges. The loop also reveals the partitioning of the inelastic strains into its creep and plasticity components for use in the strain-range partitioning method for life prediction. An in-phase bithermal hysteresis loop would look just like the out-of-phase loop, except that the loop would be mirror imaged about the strain axis. Thermal fatigue cycles experienced in service rarely have high enough temperatures in both the tensile and compressive halves to suffer creep strains in both directions. Even the 90° or 270° diamond-type cycles tend to experience creep strains predominately in tension or compression only. If, however, the total strain range is very large, all TMF cycles will experience reversed creep. Such cycles rarely, if ever, occur in service situations and are an artifact of TMF testing in the laboratory. By contrast, bithermal tests, for any magnitude of strain range, can be devised that do not experience reversed creep. Commercially available software is available to conduct bithermal tests on a routine basis using computer control.

Laboratory TMF testing is comparatively expensive. Obtaining data from tests of more than a couple of weeks duration (~10,000 cycles) is prohibitively expensive. Accelerated TMF testing is generally not feasible. Hence, application of TMF life prediction methods to long-life structures requires considerable extrapolation of laboratory results. Three primary variables in the laboratory results must be extrapolated: cycles to failure, time to failure, and the mechanical component of the total strain range. Because of the complexity of TMF cycling, it is essential to capitalize on calibrated models for both the failure and the flow (cyclic stress-strain) behavior. Failure behavior can only be calibrated with the longest-life data available, but the flow behavior can be calibrated without carrying tests to the point of failure. Affordable yet realistically long hold times per cycle and small mechanical strain ranges can be applied for just a few cycles to capture the desired flow behavior under anticipated service conditions. Measured flow behavior can then be used to calibrate sophisticated cyclic viscoplastic models (see, for example, Ref 76, 77, and 84) or simpler empirical relations (Ref 82). The latter have been utilized recently for the development of life prediction modeling for long-life automotive exhaust systems (Ref 85). Because cyclic response behavior is so highly dependent on the two major variables of time and temperature, it is imperative that modeling play a vital role in describing practical thermal fatigue cycles and, hence, in extending the direct usefulness of failure data generated at shorter and more affordable lifetimes.

References cited in this section

67. G.R. Halford, Creep-Fatigue Interaction, *Heat Resistant Materials*, ASM International, 1997, p 499–517
68. Code Case N-47-23, American Society of Mechanical Engineers, 1986
71. J.-L. Chaboche, Continuous Damage Mechanics: A Tool to Describe Phenomena before Crack Initiation, *Nucl. Eng. Des.*, Vol 64, 1981, p 233–247
73. S.S. Manson, “The Challenge to Unify Treatment of High Temperature Fatigue— A Partisan Proposal Based on Strain-Range Partitioning,” ASTM STP 520, *Fatigue at Elevated Temperature*, American Society for Testing and Materials, 1973, p 744–782
74. “Proposed Standard Test Method for Strain Controlled Thermomechanical Fatigue Testing,” draft/working document prepared by the ASTM Thermomechanical Fatigue Task Group, E08.05.07, American Society for Testing and Materials, 1999
75. G.R. Halford, Low-Cycle Thermal Fatigue, *Thermal Stresses II*, R.B. Hetnarski, Ed., Elsevier Science Publishers, Amsterdam, 1987, p 329–428
76. H. Sehitoglu, Thermal and Thermomechanical Fatigue of Structural Alloys, *Fatigue and Fracture*, Vol 19, *ASM Handbook*, 1996, p 527–556
77. *Heat-Resistant Materials*, ASM International, 1997, p 454–485
78. K.D. Sheffler, “Vacuum Thermal-Mechanical Fatigue Testing of Two Iron-Base High Temperature Alloys,” ASTM STP 612, *Thermal Fatigue Resistance of Materials and Components*, D.A. Spera and D.F. Mowbray, Ed., American Society for Testing and Materials, 1976, p 214–226
79. C.E. Jaske, “Thermal-Mechanical, Low-Cycle Fatigue of AISI 1010 Steel,” ASTM STP 612, *Thermal Fatigue Resistance of Materials and Components*, D.A. Spera and D.F. Mowbray, Ed., American Society for Testing and Materials, 1976, p 170–198
80. R. Neu and H. Sehitoglu, Thermo-Mechanical Fatigue Oxidation, Creep, Part I: Experiments, *Metall. Trans. A*, Vol 20, 1989, p 1755–1767
81. R. Neu and H. Sehitoglu, Thermo-Mechanical Fatigue Oxidation, Creep, Part II: Life Prediction, *Metall. Trans. A*, Vol 20, 1989, p 1769–1783

82. J.F. Saltsman and G.R. Halford, "Life Prediction of Thermomechanical Fatigue Using The Total Strain Version of Strain-Range Partitioning (SRP)—A Proposal," NASA TP-2779, Feb 1988
83. G.R. Halford, M.A. McGaw, R.C. Bill, and P.D. Fanti, "Bithermal Fatigue: A Link Between Isothermal and Thermomechanical Fatigue," ASTM STP 942, *Low Cycle Fatigue*, H.D. Solomon, G.R. Halford, L.R. Kaisand, and B.N. Leis, Ed., American Society for Testing and Materials, 1988, p 625–637
84. D.N. Robinson and R.W. Swindeman, Unified Creep-Plasticity Constitutive Equations for $2\frac{1}{4}$ Cr-1Mo Steel at Elevated Temperature, ORNL/TM-8444, 1982
85. G.-Y. Lui, M.B. Behling, and G.R. Halford, "Bithermal Low-Cycle Fatigue Characterization of the High Temperature Exhaust System Alloy SS409 Using the Strain-Range Partitioning (SRP) Approach," paper presented at *The Complete Metals & Materials Experience*, ASM International, Cincinnati, Nov 1999

Fatigue, Creep Fatigue, and Thermomechanical Fatigue Life Testing

Gary R. Halford and Bradley A. Lerch, Glenn Research Center at Lewis Field, National Aeronautics and Space Administration; Michael A. McGaw, McGaw Technology, Inc.

Helpful Guidelines for Fatigue Testing

Both novice and experienced fatigue test engineers should find the following operational guidelines valuable. It should also be pointed out that there are a considerable number of commercial fatigue testing laboratories located throughout the world. These laboratories may be equipped to perform certain tests more economically and in a more timely fashion than could be done in a smaller, less-equipped laboratory.

Overall laboratory operation, safety, and training guidelines include the following considerations:

- Operation of modern fatigue testing laboratories has become sophisticated. Hardware and software are complex and require considerable training for safe, accurate, and reliable operation.
- Carelessness is intolerable because serious, maiming accidents can occur in split seconds with fast-responding, high-pressure hydraulic equipment. Noise from hydraulic pumps, valves, and vibrating lines must be attenuated to prevent hearing damage to operators. High-temperature testing also poses a potential burn hazard. Shields, guards, and hazard warning signs are helpful in preventing accidents to laboratory visitors. OSHA regulations, along with other related safety regulations and procedures, should be observed.
- Cleanliness of hydraulic fluid is crucial, and systematic replacement of micron-level filters should be scheduled. Room air cleanliness is also important for reliable operation of all computers and electronic equipment.
- Calibration of all measuring devices, electronics, and computer software should be checked on a regular basis, and a frequency of calibration policy should be established. See ASTM and ISO 9000 standards for maintaining quality systems.
- Basic and advanced training courses for use of testing machines and ancillary equipment are generally available through the respective manufacturers. Skills may be required in several areas, including mechanical and hydraulic systems, electronics and instrumentation, computers and software, thermal management, and environmental control.
- In addition, it is necessary to keep abreast of the latest developments in fatigue behavior and fatigue-life prediction technologies. Short courses are offered by a variety of educational institutions.

Overall Control of Materials to be Tested. A record-keeping system should be set up to keep track of all of the materials being tested. Information on each might include:

- Commercial name or designation
- Nominal (and actual) chemical composition
- Commercial source and dates of production and acquisition
- Product form (e.g., billet, plate, sheet, or bar)
- Method of production (e.g., casting, forging, rolling, or heat treatment)
- AMS, ASM, ASTM, or other specifications
- X-rays and/or NDE results
- Representative micrographs and documentation of anisotropy on material stock
- Proper storage of material stock to avoid any possible contamination
- Reference to mechanical and pertinent physical, thermal, and electrical properties
- Tensile test properties (elastic modulus, Poisson's ratio, yield and ultimate strength, ductility as percent reduction of area and percent elongation)
- Clear designation of material stock (e.g., stamped identification number and color coding)

Overall Control of Specimens. A record-keeping system should be set up to track all specimens made of the above materials. Specimen information might include:

- Diagram of specimen location and orientation relative to material stock
- Specimen drawing(s), dimensions, and specifications for machining
- Specimen final preparation (e.g., heat treatment or surface treatment)
- Specimen dimensions and means of measurement
- Specimen material and individual identification scheme (stamped alphanumeric in visible area near both ends and visible once installed in machine)
- Accessible yet protective specimen storage to prevent damage prior to test
- Document thermocouple attachment techniques and calibration (temp gradients)
- Care exercised in gripping specimens in testing machine
- Orientation of specimen in grips in fatigue machine
- Care to not damage fracture surface prior to machine automatic shut-down
- Care exercised in removing fatigued specimens from testing machine
- Accessible storage system for tested specimens (do not store with fracture surfaces of mating pieces touching)
- Maintain records of metallographic mounts taken from broken specimens

Laboratory Documentation of Set-Ups, Procedures, Calibrations, and Maintenance. One should maintain continuous laboratory documentation books for recording particulars of each new set-up and each new program. Books should be kept, along with fatigued specimens and raw data records, for as long as is practical (then a little longer). Resurrecting old data is far less costly than having to generate new data, and old data are invaluable if untested material specimens are no longer available at a much later date. Data books should be signed and dated by the test engineer(s) and technician(s).

Pretest Checklist. Maintain a checklist to go over prior to the start of each new test. Checklists may consider the following:

- Always predict the cyclic and clock lifetime of each specimen prior to testing.
- All pertinent test information is entered onto any data sheets, paper recorders, computerized data taking and manipulating systems. This information includes fatigue machine number, material, specimen identification number, type of test, temperature, frequency, hold periods, control parameter(s), parameters to be recorded, equipment being used, test engineer, extensometer and load cell ranges of scales employed, ranges of analog recorders, strip chart speeds, computer control programs and data processors utilized, date, time, and any other unique test information.
- An analog X-Y recorder for load cell and extensometer output (stress and strain) is highly recommended even though results can also be recorded electronically. In case of a mishap, the X-Y recording provides

a better vision of what might have gone wrong and how to correct it than do individual load or extensometer signals as a function of time.

- Ensure that each piece of equipment is turned on and functioning properly (e.g., pens of recorders are ready to write and timers and cycle counters are working).
- Ensure that safety limits are set to prevent overload of the specimen and damage of equipment in case of an accident.
- Before actually starting a test, trace a low-amplitude stress-strain hysteresis loop on the X-Y recorder as a check that the recorder is functioning and to check that the modulus of elasticity is close to its expected value. If not, one or more bits of information may be erroneous (e.g., load or extensometer scales, X-Y recorder scales, or specimen dimensions).
- Decide, up front, how to abort a test that is not following the expected response (e.g., abrupt shut down or gradual shut down). During the early stages of a test, be prepared to switch scales of recorders or signal conditioners to better record response signals. For example, large amounts of cyclic strain hardening under strain control may require a switch to a coarser load scale in order to avoid missing measurement of off-scale signals. Do not switch ranges of the control signal during the test.

During the fatigue test the following should be considered:

- As a test progresses, make note of any changes in specimen response (e.g., cyclic strain hardening, softening, relaxation of initial mean stresses under strain control, any strain ratcheting occurring under load control, or any changes in specimen).
- Pay particularly close attention to the progression of failure of the test specimen, marking notes of anything out of the ordinary.
- After specimen failure, and after the machine has been stopped, record the orientation (relative to the specimen and its mounting in the grips and machine) of the initiation location(s) of cracking
- Shut down and rezero all equipment that will not be needed immediately for the next test.
- Record observations of the fracture surface (e.g., single or multiple cracks, multiple planes of cracking, secondary cracking, or angular orientation of cracks to specimen axis).
- Ascertain cyclic lifetime (and, hence, half-life values) at various points along the process of cracking and final fracture using criteria contained in the next of this Section.
- Reduce and tabulate the figure characterization data (e.g., half-life values of total, elastic, and inelastic strain ranges; stress range or amplitude; and mean stress), and compare observed lives with lives predicted prior to testing.
- Add each fatigue data point to the evolving fatigue curve to maintain a current view of the extent of the figure curve. This knowledge may dictate the conditions to be imposed on the next fatigue test

Fatigue, Creep Fatigue, and Thermomechanical Fatigue Life Testing

Gary R. Halford and Bradley A. Lerch, Glenn Research Center at Lewis Field, National Aeronautics and Space Administration; Michael A. McGaw, McGaw Technology, Inc.

Acknowledgments

The authors gratefully acknowledge the help of Peter J. Bonacuse, Army's Vehicle Technology Center, NASA Glenn Research Center, for his valuable technical peer review of the manuscript.

References

1. W.J. Putnam and J.W. Harsch, "Rise of Temperature" Method of Determining Endurance Limit, *An Investigation of the Fatigue of Metals*, H.F. Moore and J.B. Kommers, Ed., Engineering Experiment Station Bulletin 124, University of Illinois, Oct 1921, p 119–127
2. *Strain Gage Based Transducers, Their Design and Construction*, Measurements Group, Inc., Raleigh, NC, 1988
3. M.F. Day and G.F. Harrison, Design and Calibration of Extensometers and Transducers, *Measurement of High Temperature Mechanical Properties*, M.S. Loveday et al., Ed., National Physical Laboratory, London, 1982, p 225–240
4. G.B. Thomas, Axial Extensometry for Ridged Specimens, *Techniques for High Temperature Fatigue Testing*, G. Sumner and V.B. Livesey, Ed., Elsevier Applied Science, 1985, p 45–56
5. J.W. Dally and W.F. Riley, *Experimental Stress Analysis*, McGraw-Hill, 1978, p 179–179
6. R.L. Hannah and S.E. Reed, Ed., *Strain Gage Users' Handbook*, Elsevier Applied Science, New York, 1992
7. J.-F. Lei and W.D. Williams, PdCr Based High Temperature Static Strain Gage, *AIAA 2nd Int. National Aerospace Planes Conf. Publication*, AIAA-90-5236, 1990
8. J.-F. Lei, M.G. Castelli, D. Androjna, C. Blue, R. Blue, and R.Y. Lin, Comparison Testings Between Two High-Temperature Strain Measurement Systems, *Exp. Mech.*, Vol 36 (No. 4), 1996, p 430–435
9. E.G. Ellison, Thermal-Mechanical Strain Cycling and Testing at Higher Temperatures, *Measurement of High Temperature Mechanical Properties*, M.S. Loveday et al., Ed., National Physical Laboratory, London, 1982, p 204–224
10. E.G. Ellison and R.D. Lohr, The Extensometer-Specimen Interface, *Techniques for High Temperature Fatigue Testing*, G. Sumner and V.B. Livesey, Ed., Elsevier Applied Science, 1985, p 1–28
11. Creep, Stress-Rupture, and Stress-Relaxation Testing, *Mechanical Testing*, Vol 8, *Metals Handbook*, ASM International, 1985, p 313
12. J.Z. Gyekenyesi and P.A. Bartolotta, "An Evaluation of Strain Measuring Devices for Ceramic Composites," NASA TM 105337, National Aeronautics and Space Administration, Nov 1991
13. R. Hales and D.J. Walters, Measurement of Strain in High Temperature Fatigue, *Measurement of High Temperature Mechanical Properties*, M.S. Loveday et al., Ed., National Physical Laboratory, London, 1982, p 241–254
14. ASTM STP 465, *Manual of Low Cycle Fatigue Testing*, R.M. Wetzel and L.F. Coffin, Ed., American Society for Testing and Materials, 1969

15. M.G. Castelli and J.R. Ellis, "Improved Techniques for Thermomechanical Testing in Support of Deformation Modeling," ASTM STP 1186, *Thermomechanical Fatigue Behavior of Materials*, H. Sehitoglu, Ed., American Society for Testing and Materials, 1993, p 195–211
16. S.S. Manson, G.R. Halford, and M.H. Hirschberg, Creep-Fatigue Analysis by Strain-Range Partitioning, *Design for Elevated Temperature Environment*, American Society of Mechanical Engineers, 1971, p 12–28
17. K.D. Sheffler and G.S. Doble, "Influence of Creep Damage on the Low-Cycle Thermal-Mechanical Fatigue Behavior of Two Tantalum Base Alloys," NASA CR-121001, National Aeronautics and Space Administration, 1972
18. M.H. Hirschberg, D.A. Spera, and S.J. Klima, "Cyclic Creep and Fatigue of TD-NiCr (Thoria-Dispersion-Strengthened Nickel-Chromium), TD-Ni, and NiCr Sheet at 1200 °C," NASA TN D-6649, National Aeronautics and Space Administration, 1972
19. P.R. Breakwell, J.R. Boxall and G.A. Webster, Specimen Manufacture, *Measurement of High Temperature Mechanical Properties*, M.S. Loveday et al., Ed., National Physical Laboratory, London, 1982, p 322–340
20. E.T. Camponeschi, Jr., "Compression of Composite Materials: A Review," ASTM STP 1110, *Composite Materials: Fatigue and Fracture (Third Volume)*, T.K. O'Brien, Ed., American Society for Testing and Materials, 1991, p 550–578
21. F.A. Kandil and B.F. Dyson, Influence of Load Misalignment During Fatigue Testing I and II, *Fatigue and Fracture of Engineering Materials and Structures*, Vol 16 (No. 5), 1993, p 509–537
22. J. Bressers, Axiality of Loading, *Measurement of High Temperature Mechanical Properties*, M.S. Loveday et al., Ed., National Physical Laboratory, London, 1982, p 278–295
23. J. Bressers, Ed., *A Code of Practice for the Measurement of Misalignment Induced Bending in Uniaxially Loaded Tension-Compression Test Pieces* (Institute for Advanced Materials, Joint Research Centre, Netherlands, and the High Temperature Mechanical Testing Committee), the Directorate-General of the European Commission, Luxembourg, 1995, 52 pages
24. F.A. Kandil, *Measurement of Bending in Uniaxial Low Cycle Fatigue Testing*, National Physical Laboratory, Teddington, England, 1998
25. A.K. Schmieder, "Measuring the Apparatus Contribution to Bending in Tension Specimens," ASTM STP 488, *Elevated Temperature Testing Problem Areas*, American Society for Testing and Materials, 1971, p 15–42
26. A.A. Braun, "A Historical Overview and Discussion of Computer-Aided Materials Testing," ASTM STP 1231, *Automation in Fatigue and Fracture: Testing and Analysis*, C. Amzallag, Ed., American Society for Testing and Materials, 1994, p 5–17
27. S. Dharmavasan, D.R. Broome, M.C. Lugg, and W.D. Dover, FLAPS—A Fatigue Laboratory Applications Package, *Proc. 4th Int. Conf. on Engineering Software*, R.A. Adey, Ed., Springer-Verlag, London, 1985
28. A.A. Braun, The Development of a Digital Control System Architecture for Materials Testing Applications, *Proc. 17th Int. Symposium for Testing and Failure Analysis*, ASM International, 1991, p 437–444

29. S. Dharmavasan and S.M.C. Peers, "General Purpose Software for Fatigue Testing," ASTM STP 1231, *Automation in Fatigue and Fracture: Testing and Analysis*, C. Amzallag, Ed., American Society for Testing and Materials, 1994, p 18–35
30. M.A. McGaw and P.J. Bonacuse, Automation Software for a Materials Testing Laboratory, *Proc. Turbine Engine Hot Section Technology (HOST)*, NASA CP-2444, National Aeronautics and Space Administration, 1986, p 399–406
31. M.A. McGaw and P.J. Bonacuse, "Automation Software for a Materials Testing Laboratory," ASTM STP 1092, *Applications of Automation Technology to Fatigue and Fracture Testing*, A.A. Braun et al., Ed., American Society for Testing and Materials, 1990, p 211–231
32. M.A. McGaw and P.A. Bartolotta, The NASA Lewis Research Center High Temperature Fatigue and Structures Laboratory, *Proc. 4th Annual Hostile Environments and High Temperature Measurement Conf.*, Society for Experimental Mechanics, 1987, p 12–29
33. M.A. McGaw, materials testing software LEW-16160, COSMIC, 1995
34. J. Christiansen, R.L.T. Oehmke, and E.A. Schwarzkopf, "Materials Characterization Using Calculated Control," ASTM STP 1303, *Applications of Automation Technology to Fatigue and Fracture Testing*, A.A. Brown and L.N. Gilbertson, Ed., American Society for Testing and Materials, 1997
35. S.S. Manson, Fatigue—A Complex Subject, *Exp. Mech.*, Vol 5 (No. 7), 1965, p 193–226
36. J. Morrow, "Cyclic Plastic Strain Energy and Fatigue of Metals," ASTM STP 378, *Internal Friction, Damping, and Cyclic Plasticity*, American Society for Testing and Materials, 1965, p 45–84
37. J.F. Newell, A Note of Appreciation for the MUS, *Material Durability/Life Prediction Modeling: Materials for the 21st Century*, S.Y. Zamrik and G.R. Halford, Ed., Pressure Vessel and Piping Conference, PVP Vol 290, American Society of Mechanical Engineers, 1994, p 57–58
38. R.W. Landgraf, "The Resistance of Metals to Cyclic Deformation," ASTM STP 467, *Achievement of High Fatigue Resistance in Metals and Alloys*, American Society for Testing and Materials, 1970, p 3–36
39. Parameters for Estimating Fatigue Life, *Fatigue and Fracture*, Vol 19, *ASM Handbook*, ASM International, 1996, p 963–979
40. S.S. Manson, Predictive Analysis of Metal Fatigue in the High Cyclic Life Range, *Methods for Predicting Material Life in Fatigue*, W.J. Ostergren and J.R. Whitehead, Ed., American Society of Mechanical Engineers, 1979, p 145–183
41. Characterization of Low Cycle High Temperature Fatigue by the Strain-Range Partitioning Method, *AGARD Conf. Proc.*, No. 243, NATO, 1978
42. J.B. Conway, R.H. Stentz, and J.T. Berling, *Fatigue, Tensile, and Relaxation Behavior of Stainless Steels*, United States Atomic Energy Commission, 1975, p 11
43. O.H. Basquin, The Exponential Law of Endurance Tests, *Proc. ASTM*, Vol 10 (Part II), 1910, p 625–630
44. L.F. Coffin, Jr., Thermal Stress Fatigue, *Prod. Eng.*, June 1957

45. B.F. Langer, Design of Pressure Vessels for Low Cycle Fatigue, *J. Basic Eng. (Trans. ASME)*, Vol 84 (No. 4), 1962, p 389
46. S.S. Manson, discussion of ASME paper 61-WA-199 by J.F. Tavernelli and L.F. Coffin, Jr., *J. Basic Eng. (Trans. ASME)*, Vol 85 (No. 4), 1962, p 537–541
47. D.F. Socie, N.E. Dowling, and P. Kurath, “Fatigue Life Estimation of Notched Members,” ASTM STP 833, *Fracture Mechanics: Fifteenth Symposium*, R.J. Sanford, Ed., American Society for Testing and Materials, 1984, p 284–299
48. S.M. Tipton and D.V. Nelson, Developments in Life Prediction of Notched Components Experiencing Multiaxial Fatigue, *Material Durability/Life Prediction Modeling—Materials for the 21st Century*, S.Y. Zamrik and G.R. Halford, Ed., Pressure Vessel and Piping Conference, PVP Vol 290, American Society of Mechanical Engineers, 1994, p 35–48
49. H. Neuber, Theory of Stress Concentration for Shear Strained Prismatical Bodies with Arbitrary Nonlinear Stress-Strain Law, *J. Appl. Mech. (Trans. ASME)*, Vol 28, 1961, p 544–550
50. G. Glinka, Energy Density Approach to Calculation of Inelastic Stress-Strain near Notches and Cracks, *Eng. Fract. Mech.*, Vol 22, 1985, p 485–508
51. W.Z. Gerber, Bestimmung der Zulossigne Sannugen in Eisen Construction, *Bayer. Arch. Ing. Ver.*, Vol 6, 1974, p 101 (in German)
52. J.B. Conway and L.H. Sjoedahl, *Analysis and Representation of Fatigue Data*, ASM International, 1991, p 21, 145–178
53. G.R. Halford and A.J. Nachtigall, The Strain-Range Partitioning Behavior of an Advanced Gas Turbine Disk Alloy, AF2-1DA, *J. Aircr.*, Vol 17, 1980, p 598–604
54. M. Doner, K.R. Bain, and J.H. Adams, Evaluation of Methods for Treatment of Mean Stress Effects on Low-Cycle Fatigue, *J. Eng. Power (Trans. ASME)*, Vol 104, 1982, p 403–411
55. Y. Murakami, Ed., *The Rainflow Method in Fatigue*, Butterworth Heinemann Ltd., Oxford, 1992
56. M.R. Mitchell, Fundamentals of Modern Fatigue Analysis for Design, *Fatigue and Fracture*, Vol 19, *ASM Handbook*, ASM International, 1996, p 227–249
57. S.S. Manson and G.R. Halford, Re-Examination of Cumulative Fatigue Damage Analysis—An Engineering Perspective, *Eng. Fract. Mech.*, Vol 25, 1986, p 539–571
58. G.R. Halford, Cumulative Fatigue Damage Modeling—Crack Nucleation and Early Growth, *Int. J. Fatigue*, Vol 19 (No. 1) supplement, 1997, p S253–S260
59. M.A. Miner, Cumulative Damage in Fatigue, *J. Appl. Mech.*, Vol 12 (No. 3), 1945, p A159–A164
60. P.T. Bizon, D.J. Thoma, and G.R. Halford, Interaction of High Cycle and Low Cycle Fatigue of Haynes 188 at 1400 °F, *Structural Integrity and Durability of Reusable Space Propulsion Systems*, NASA CP-2381, 1985, p 129–138
61. S. Kalluri and P.J. Bonacuse, “Cumulative Axial and Torsional Fatigue: An Investigation of Load-Type Sequencing Effects,” ASTM STP 1387, *Symposium on Multiaxial Fatigue and Deformation: Testing and Prediction*, S. Kalluri and P.J. Bonacuse, Ed., American Society for Testing and Materials, 2000 (in press)

62. R.M. Curran and B.M. Wundt, Continuation of a Study of Low-Cycle Fatigue and Creep Interaction in Steels at Elevated Temperatures, *1976 ASME-MPC Symposium on Creep-Fatigue Interaction*, Materials Property Council MPC-3, American Society of Mechanical Engineers, 1976, p 203–282
63. S.S. Manson, Critical Review of Predictive Methods for Treatment of Time-Dependent Metal Fatigue at High Temperatures, *Pressure Vessels and Piping: Design Technology—1982—A Decade of Progress*, American Society of Mechanical Engineers, 1982, p 203–225
64. D.A. Miller, R.H. Priest, and E.G. Ellison, A Review of Material Response and Life Prediction Techniques under Fatigue-Creep Loading Conditions, *High Temp. Mater. Process.*, Vol 6, 1984, p 155–194
65. V.M. Radhakrishnan, Life Prediction in Time Dependent Fatigue, *Advances in Life Prediction Methods*, American Society of Mechanical Engineers, 1983, p 143–150
66. G.R. Halford, Evolution of Creep-Fatigue Life Prediction Models, *Creep-Fatigue Interaction at High Temperature*, G.K. Haritos and O.O. Ochoa, Ed., Vol 21, American Society of Mechanical Engineers, 1991, p 43–57
67. G.R. Halford, Creep-Fatigue Interaction, *Heat Resistant Materials*, ASM International, 1997, p 499–517
68. Code Case N-47-23, American Society of Mechanical Engineers, 1986
69. S.S. Manson, G.R. Halford, and M.H. Hirschberg, Creep-Fatigue Analysis by Strain-Range Partitioning, *Symposium on Design for Elevated Temperature Environment*, American Society of Mechanical Engineers, 1971, p 12–28
70. J.F. Saltsman and G.R. Halford, “An Update on the Total Strain Version of SRP,” ASTM STP 942, *Low Cycle Fatigue—Directions for the Future*, H.D. Solomon, G.R. Halford, L.R. Kaisand, and B.N. Leis, Ed., American Society for Testing and Materials, 1988, p 329–341
71. J.-L. Chaboche, Continuous Damage Mechanics: A Tool to Describe Phenomena before Crack Initiation, *Nucl. Eng. Des.*, Vol 64, 1981, p 233–247
72. C.E. Jaske, H. Mindlin, and J.S. Perrin, “Combined Low-Cycle Fatigue and Stress Relaxation Behavior of Alloy 800 and Type 304 Stainless Steel at Elevated Temperatures,” ASTM STP 520, *Fatigue at Elevated Temperature*, American Society for Testing and Materials, 1973, p 365–376
73. S.S. Manson, “The Challenge to Unify Treatment of High Temperature Fatigue— A Partisan Proposal Based on Strain-Range Partitioning,” ASTM STP 520, *Fatigue at Elevated Temperature*, American Society for Testing and Materials, 1973, p 744–782
74. “Proposed Standard Test Method for Strain Controlled Thermomechanical Fatigue Testing,” draft/working document prepared by the ASTM Thermomechanical Fatigue Task Group, E08.05.07, American Society for Testing and Materials, 1999
75. G.R. Halford, Low-Cycle Thermal Fatigue, *Thermal Stresses II*, R.B. Hetnarski, Ed., Elsevier Science Publishers, Amsterdam, 1987, p 329–428
76. H. Sehitoglu, Thermal and Thermomechanical Fatigue of Structural Alloys, *Fatigue and Fracture*, Vol 19, *ASM Handbook*, 1996, p 527–556
77. *Heat-Resistant Materials*, ASM International, 1997, p 454–485

78. K.D. Sheffler, "Vacuum Thermal-Mechanical Fatigue Testing of Two Iron-Base High Temperature Alloys," ASTM STP 612, *Thermal Fatigue Resistance of Materials and Components*, D.A. Spera and D.F. Mowbray, Ed., American Society for Testing and Materials, 1976, p 214–226
79. C.E. Jaske, "Thermal-Mechanical, Low-Cycle Fatigue of AISI 1010 Steel," ASTM STP 612, *Thermal Fatigue Resistance of Materials and Components*, D.A. Spera and D.F. Mowbray, Ed., American Society for Testing and Materials, 1976, p 170–198
80. R. Neu and H. Sehitoglu, Thermo-Mechanical Fatigue Oxidation, Creep, Part I: Experiments, *Metall. Trans. A*, Vol 20, 1989, p 1755–1767
81. R. Neu and H. Sehitoglu, Thermo-Mechanical Fatigue Oxidation, Creep, Part II: Life Prediction, *Metall. Trans. A*, Vol 20, 1989, p 1769–1783
82. J.F. Saltsman and G.R. Halford, "Life Prediction of Thermomechanical Fatigue Using The Total Strain Version of Strain-Range Partitioning (SRP)—A Proposal," NASA TP-2779, Feb 1988
83. G.R. Halford, M.A. McGaw, R.C. Bill, and P.D. Fanti, "Bithermal Fatigue: A Link Between Isothermal and Thermomechanical Fatigue," ASTM STP 942, *Low Cycle Fatigue*, H.D. Solomon, G.R. Halford, L.R. Kaisand, and B.N. Leis, Ed., American Society for Testing and Materials, 1988, p 625–637
84. D.N. Robinson and R.W. Swindeman, Unified Creep-Plasticity Constitutive Equations for $\frac{1}{24}\text{Cr-1Mo}$ Steel at Elevated Temperature, ORNL/TM-8444, 1982
85. G.-Y. Lui, M.B. Behling, and G.R. Halford, "Bithermal Low-Cycle Fatigue Characterization of the High Temperature Exhaust System Alloy SS409 Using the Strain-Range Partitioning (SRP) Approach," paper presented at *The Complete Metals & Materials Experience*, ASM International, Cincinnati, Nov 1999

Ultrasonic Fatigue Testing

Introduction

ULTRASONIC FATIGUE TESTING involves cyclic stressing of material at frequencies typically in the range of 15 to 25 kHz. The major advantage of using ultrasonic fatigue is its ability to provide fatigue-limit and near-threshold data within a reasonable length of time. High-frequency testing provides rapid evaluation of the high-cycle fatigue limit of engineering materials. Fatigue crack growth at extremely slow crack propagation rates is also possible with ultrasonic frequency testing.

Ultrasonic fatigue testing is applicable to most engineering materials, including metals, ceramics, glasses, plastics, and composites. Test data can be used for screening of high-cycle fatigue properties or extending the fatigue data already available from conventional frequency fatigue testing.

This article reviews underlying concepts and basic techniques for performing ultrasonic fatigue tests. It describes test equipment design, specimen design, and effective control over test variables. Results obtained with ultrasonic fatigue test methods are discussed with respect to strain-rate-dependent material behavior. Standardized procedures and test machinery for performing ultrasonic fatigue tests currently are not available.

Historical Perspective

Development of higher-frequency testing machines began early in the 20th century. Prior to 1911, the highest fatigue testing frequency was on the order of 33 Hz, using mechanically driven systems. Electrodynamical resonance systems appeared in 1911 when Hopkinson (Ref 1) introduced a machine capable of 116 Hz. In 1925, Jenkin (Ref 2) tested wires of copper, iron, and steel at 2 kHz, using similar techniques. In 1929, Jenkin and Lehmann (Ref 3) were able to test materials up to 10 kHz using a pulsating air resonance system.

Mason (Ref 4) achieved ultrasonic frequency (20 kHz) in 1950 with the adaptation of magnetostrictive and piezoelectric-type transducers to fatigue testing. This method translated 20 kHz electrical voltage signals into 20 kHz mechanical displacements. A displacement-amplifying acoustical horn and the test specimen were driven into resonance by the transducer. This concept has remained basically unchanged and is the foundation of the practices used in modern ultrasonic fatigue test technology.

In the early 1960s, frequencies as high as 92 and 199 kHz were employed for fatigue tests using Mason's techniques (Ref 5, 6) These extremely high frequencies surpass the upper limits of practicality because of the constraints of specimen size (frequency is inversely proportional to specimen length), machining tolerances, strain amplitude measurements, and energy considerations. A review of the ultrasonic fatigue testing in the 1970s and 1980s shows that the majority of test stands operate at frequencies between 17 and 25 kHz.

This unofficial standard is primarily dictated by the availability of commercial high-power ultrasonic transducers and power supplies. These frequencies are also desirable from a safety viewpoint because they are above the range of normal human hearing. Fatigue testing at 20 kHz proceeds quietly in comparison to testing at 1 to 10 kHz.

References cited in this section

1. B. Hopkinson, *Proc. R. Soc. (London) A*, Vol 86, 1911, p 101
2. C.F. Jenkin, *Proc. R. Soc. (London) A*, Vol 109, 1925, p 119.
3. C.F. Jenkin and G.D. Lehmann, *Proc. R. Soc. (London) A*, Vol 125, 1929, p 83
4. W.P. Mason, *Piezoelectric Crystals and Their Application in Ultrasonics*, Van Nostrand, New York, 1950, p 161
5. F. Girard and G. Vidal, *Rev. Metall.*, Vol 56, 1959, p 25.
6. M. Kikukawa, K. Ohji, and K. Ogura, *J. Basic. Eng. (Trans. ASME D)*, Vol 87, 1965, p 857

Strain Rates, Frequency, and Time Compression

Ultrasonic fatigue testing increases the frequency of stress cycling to reduce the time necessary to accumulate a large number of cycles. Consequently, the strain rate at these frequencies for a given strain amplitude is also increased. In Table 1, strain rate is calculated as a function of frequency and strain amplitude. For typical fatigue strain amplitudes in the range of 10^{-4} to 10^{-3} , the strain rate at 20 kHz ranges from 2 to 20 s^{-1} .

Table 1 Strain rate as a function of test frequency and strain range

Frequency, Hz	Strain rate ($\dot{\epsilon}$), s^{-1} , at strain (ϵ) of:			
	$\epsilon = 10^{-5}$, m/m	$\epsilon = 10^{-4}$, m/m	$\epsilon = 10^{-3}$, m/m	$\epsilon = 10^{-2}$, m/m
10	10^{-4}	10^{-3}	10^{-2}	10^{-1}
100	10^{-3}	10^{-2}	10^{-1}	1
1,000	10^{-2}	10^{-1}	1	10
10,000	10^{-1}	1	10	10^2
100,000	1	10	10^2	10^3

Ultrasonic fatigue techniques are particularly useful for providing fatigue data in applications where strains are being applied and removed at kilohertz frequencies; (e.g., high-frequency loading of turbine blades). In fact, ultrasonic fatigue testing may provide a better simulation of the higher frequency vibrations encountered in service than conventional testing does in these cases. The test method is most applicable when the test material ultimately will be applied in service at frequencies at or near the test frequency. For applications with lower frequency vibrations, the effect of frequency and strain rate on test results must be interpreted.

The time compression per cycle obtained with ultrasonic fatigue is pronounced. For example, a conventional fatigue test at 1 Hz would take 320 years for a 10^{10} cycle test. At 100 Hz, the test would take 3.2 years. At an ultrasonic frequency of 20 kHz, this test would be completed in less than 6 days. The time required to complete fatigue tests at different frequencies is shown in Fig. 1. This time compression is extremely attractive for situations that require high-cycle data.

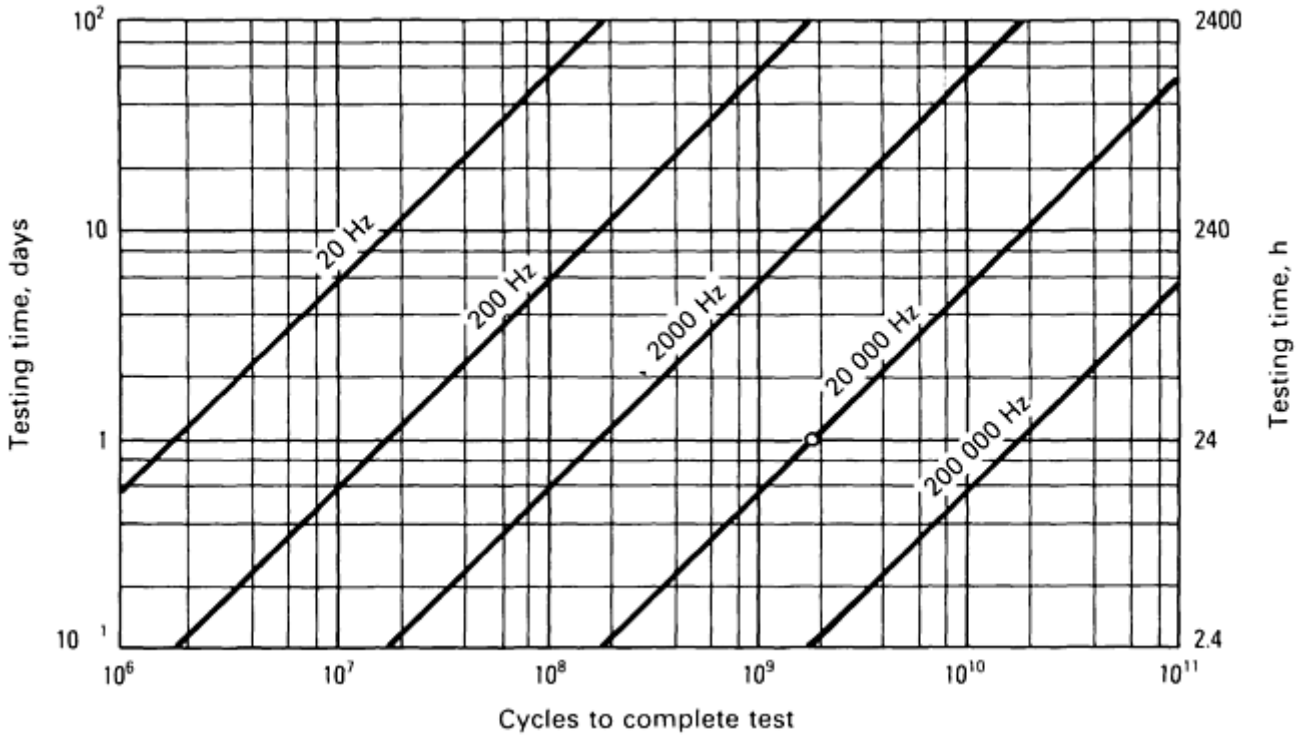


Fig. 1 Testing time versus number of cycles to complete test as a function of frequency

In comparison to conventional frequency testing, more test conditions and/or replicate tests can be performed in a given period of time at ultrasonic frequency. This provides results and conclusions that are statistically more meaningful for planning and design. On the other hand, the minimum number of cycles that can be measured practically is limited by kilohertz cycling. This limit is 10^5 cycles for open-loop testing, with a testing time of 5 s. Shorter times (~ 1 s) are possible with closed-loop computer control of the test and data acquisition systems. Similar time compression is possible in fatigue crack growth rate testing using ultrasonic fatigue. Figure 2 is a schematic of a typical crack growth rate, da/dN , versus stress intensity curve. The time necessary to measure a crack advance of 0.1 mm (0.004 in.) while testing at 1 Hz or 20 kHz is compared on the right side of the figure. It is obvious that ultrasonic testing is the only practical approach to observe the extremely slow crack growth rates that are characteristic of the threshold regime. Crack growth rate measurements as low as 10^{-11} mm ($4 \times$

10^{-13} in.) have been reported. Again, the practical upper bound of measurable fatigue crack growth rate at 20 kHz is on the order of 10^{-5} mm (4×10^{-7} in.) per cycle due to the rapid cycle accumulation.

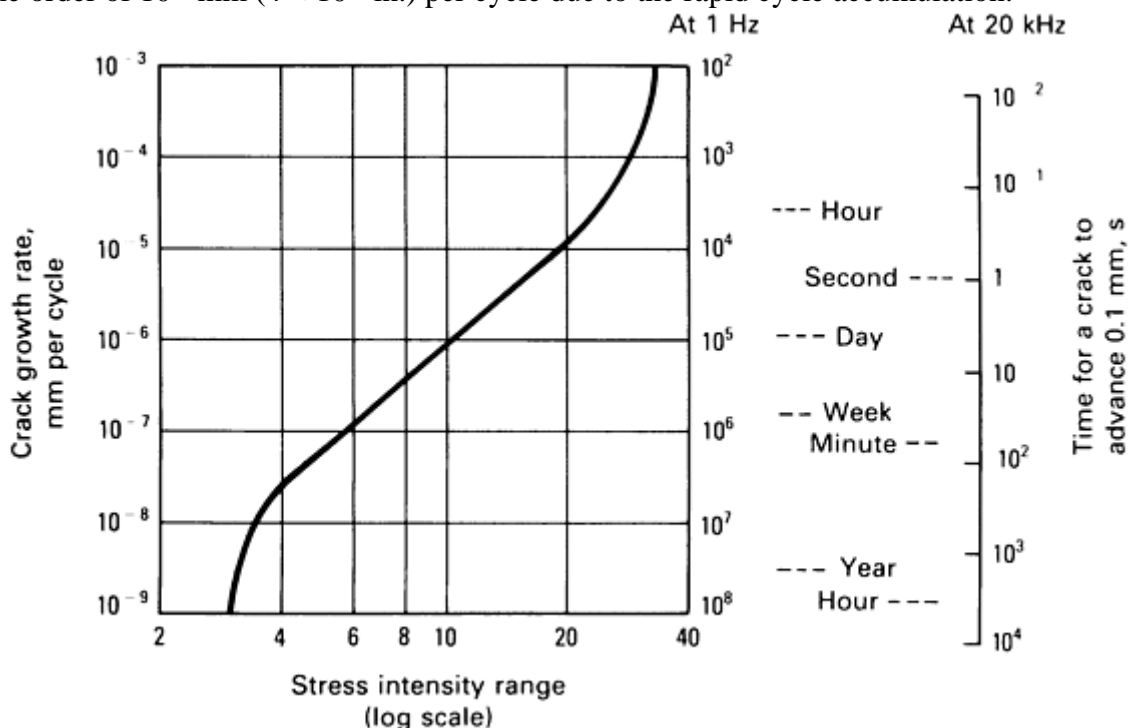


Fig. 2 Typical crack growth rate versus stress intensity curve. Difference in time to observe a finite crack growth increment at ultrasonic (20 kHz) and conventional (1 Hz) frequencies is shown.

The testing time compression possible with ultrasonic fatigue is an incentive for applying the technology in a more generic sense, that is, to extend fatigue information obtained at conventional frequencies and lower numbers of cycles to higher-cycle fatigue limits and threshold fatigue crack growth rates. Because this accelerated test method alters testing conditions to produce fatigue in a shorter period of time, the influence of frequency and strain rate on cyclic material behavior must be well understood.

General acceptance of ultrasonic fatigue testing also requires an understanding of how to obtain data free of testing-induced artifacts. Improper execution can have a marked effect on the property data obtained. Much of the skepticism that endures about the use of ultrasonic fatigue stems from earlier testing where questionable techniques were used to measure cyclic strain amplitude and provide adequate cooling of the specimen. Accordingly, the effects of strain rate, frequency, and test technique are the subject of most research on ultrasonic fatigue (Ref 7, 8)

In general, testing by ultrasonic fatigue produces fatigue data that differ only slightly from those observed at more conventional frequencies. Some data reveal a shift in the ultrasonic fatigue stress-life data ($S-N$) for a given stress level toward increased lifetimes relative to conventional-frequency results (Ref 9, 10, and 11) Other reports indicate no shift in the $S-N$ behavior (Ref 12, 13). Most reports indicate that fatigue degradation at ultrasonic frequency occurs by the same sequence of events as at conventional frequencies, namely, saturation of rapid hardening, formation of persistent slip bands, formation and growth of intrusions, and crack propagation.

Materials that exhibit clearly defined endurance limits at conventional frequencies usually exhibit endurance limits at similar cyclic stress amplitudes at ultrasonic frequencies. Similarly, materials that exhibit threshold stress intensities for fatigue crack growth at conventional frequencies also exhibit this behavior at ultrasonic frequencies. Shifts in $S-N$ fatigue behavior to higher stress levels and longer lifetimes or da/dN behavior to slower crack growth rates do not occur for all materials tested at high frequency. Recent testing shows that the effect of frequency on $S-N$ and da/dN performance is primarily a function of the microplasticity and slip character of the material system under test.

It might also be inferred that corrosion fatigue interactions should be negligible at ultrasonic frequency due to the short cyclic period. Again, experimental results illustrate that corrosion fatigue interactions are indeed

observed at ultrasonic frequencies. Recent testing shows that ultrasonic fatigue is an effective method for the evaluation of the degradation of fatigue properties produced by environmental interactions.

Ultrasonic fatigue testing is applicable to most situations in which conventional-frequency fatigue testing has been employed. Examples of a variety of results from ultrasonic fatigue are presented later in this article. As the technique continues to develop, the precise limits of applicability will become more clearly defined.

References cited in this section

7. L.E. Willertz, *Int. Met. Rev.*, No. 2, 1980, p 65, rev 250
8. J.M. Wells, O. Buck, L.D. Roth, and J.K. Tien, Ed., *Ultrasonic Fatigue*, TMS-AIME, Warrendale, PA, 1982
9. B.S. Hockenhull, in *Physics and Non Destructive Testing*, Gordon Breach, New York, 1967, p 195
10. H. Koganei, S. Tanaka, and T. Sakurai, *Trans. Iron Steel Inst. Jpn.*, Vol 17, 1977, p 1979
11. J. Awatani and K. Katagiri, *Bull. Jpn. Soc. Mech. Eng.*, Vol 12, 1969, p 10
12. W. Hoffelner, in *High Temperature Alloys for Gas Turbines: 1982*, R. Brunetaud, D. Coutsouradis, T.B. Gibbons, Y. Lindblum, D.B. Meadowcraft, and R. Stickler, Ed., R. Reidal Publishing, Boston, 1982, p 645
13. L.D. Roth and L.E. Willertz, in *Environment Sensitive Fracture: Evaluation and Comparison of Test Methods*, ASTM STP 821, E.N. Pugh and G.M. Ugiansky, Ed., ASTM, Philadelphia, 1984, p 497

Ultrasonic Fatigue Testing

Testing Principles

The principles of ultrasonic fatigue testing are quite simple. Ultrasonic fatigue is a resonant test method, in which a large-amplitude displacement wave must be established in a resonant specimen. This wave is generated by a relatively small periodic stimulus at the same frequency as the natural frequency of the test specimen. Resonance is required to achieve the strain amplitude needed to produce fatigue in materials.

Displacement and strain are developed in a bar of material subjected to resonant acoustic loading. Consider a straight bar of material having a uniform diameter and length L (Fig. 3). A sound wave injected longitudinally into one end of the bar travels at a certain velocity through the bar, is reflected from the opposite end, and returns to the point of entrance. The wave velocity, C , is determined by the material properties, the Young's modulus, E , and the density (mass/volume), ρ , by:

$$C = \left(\frac{E}{\rho} \right)^{1/2} \quad (\text{Eq 1})$$

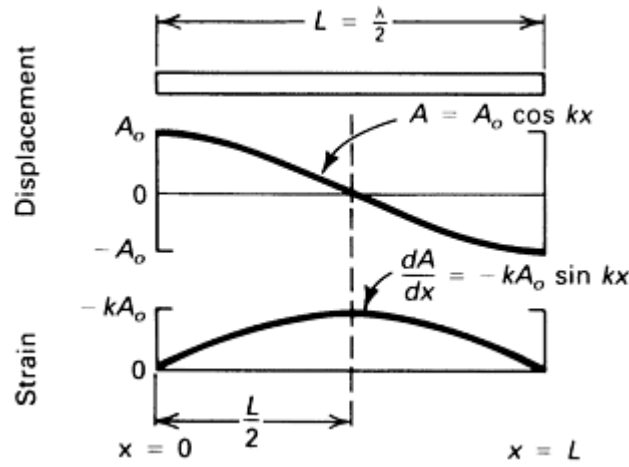


Fig. 3 Distribution of oscillatory displacement amplitude and strain amplitude over the length of a resonant bar of uniform cross section

This velocity is the speed of sound through the material. The time required to travel the length of the bar and return is $2L/C$. If this time is equal to the period of the injected sound wave, the reflected wave will be exactly in phase with the injected wave, standing wave conditions will be established, and the bar will be in resonance. The length, L , of the bar is then exactly equal to the half wavelength of the sound wave. The variation of displacement amplitude of oscillation at a point x along the length of the bar will be:

$$A(x) = A_0 \cos(kx) \quad (\text{Eq 2})$$

where A_0 is the displacement amplitude at the end of the bar, k is $2\pi/\lambda$, and λ is the wavelength of sound at the resonant frequency.

The strain distribution along the bar will be the derivative of the displacement amplitude with respect to distance or:

$$\epsilon(x) = \frac{dA(x)}{dx} = -kA_0 \sin(kx) \quad (\text{Eq 3})$$

Thus, the maximum strain occurs when $\sin(kx) = 1$, or $x = \lambda/4$. The maximum strain varies between $\pm kA_0$ during each cycle. Figure 3 shows the distribution of longitudinal displacement amplitude and strain amplitude along the length of a bar in resonance. The minimum displacement (displacement node) and maximum strain (strain antinode) occur at the center of the bar. Similarly, the maximum displacement (displacement antinode) and minimum strain (strain node) occur at the ends of the bar.

The stress distribution for each point along the bar is obtained by an elastic conversion of the strain distribution:

$$\sigma(x) = E \cdot \epsilon(x) \quad (\text{Eq 4})$$

where E is the dynamic Young's modulus of the material. The dynamic modulus of elasticity must be determined for the appropriate test frequency. Because of the elastic conversion, the stress maximum physically coincides with the strain maximum. Stresses cannot be obtained independent of strains in ultrasonic fatigue testing. Therefore, strict stress-controlled tests cannot be performed. Without independent per-cycle stress and strain information, plastic strain-controlled tests also are not possible at this time. For more information on plastic strain-controlled ultrasonic fatigue testing, see Ref 14.

The example of the uniform resonant bar embodies the basic concepts of ultrasonic fatigue testing. With appropriate geometric modification, these concepts can be used to design the mechanical portion of the converter, the acoustic horns, and the test specimen.

The major difference between a conventional fatigue test specimen and a high-frequency resonant specimen is that the cyclic strain amplitude varies from zero at the ends to a maximum at the center, rather than being constant over its entire length. This confines fatigue damage and, hence, fatigue crack initiation and propagation to the center of the specimen. Because there is minimal strain at the ends of a resonant bar, the requirements for attachment of one resonant bar to another and for gripping the specimen also are minimal.

To produce strain in a bar, only one end of a resonant bar specimen must be in acoustic contact with the source of the sound waves. This permits the testing of thin materials under reversed tension-compression loading without risk of buckling the specimen. Consequently, sheet, tubing, and wire specimens may be subjected to

fully reversed loading during ultrasonic fatigue, whereas more complex gripping and alignment techniques are required to accomplish similar tests at conventional frequencies. The large and cumbersome arrangements for gripping the specimen that often are required in conventional fatigue testing are not needed in ultrasonic fatigue.

A specimen with a free end also provides the ultrasonic fatigue system with a degree of portability that is not easily obtained with conventional-frequency test methods. Fatigue testing can be performed with the specimen in an operating environment by feeding the free end of the wave train through an access port to the environment. Similarly, testing can be performed under the view of an optical or electron microscope without the need of complex load-transmitting stages.

Cyclic straining can be achieved in a bar at any desired resonance frequency by appropriately choosing (tuning) the length of the bar. For a bar with a uniform cross section, the required length for fatigue testing will be $\lambda/2$ at the resonance frequency. For bars with variable cross sections or dumbbell specimen geometries, the resonant length generally is shorter than the resonant length of a uniform bar at the given test frequency. Thus, each component in a resonant testing system must be designed (tuned) to the resonance frequency to transmit the acoustic energy efficiently into the test specimen. The equations developed by Neppiras (Ref 15) are helpful in calculating the appropriate resonant lengths for variable specimen section geometries. These equations are presented later in this article in a section on specimen design.

References cited in this section

14. P. Bajons, in *Ultrasonic Fatigue*, J.M. Wells, O. Buck, L.D. Roth, and J.K. Tien, Ed., TMS-AIME, Warrendale, PA, 1982, p 15
15. E.A. Neppiras, *Proc. ASTM*, Vol 59, 1959, p 691

Testing Equipment and Methods

Packaged ultrasonic fatigue test systems, with one exception, are not commercially available. However, an ultrasonic fatigue test system may be constructed easily from commercially available parts. Tien et al. (Ref 16) describe the construction of a test machine using ultrasonic components normally used in ultrasonic joining processes. This machine, an open-loop test stand, contains the basic equipment needed for testing. Information on test stands with additional capabilities—including double converters, mean loading, electrochemical cells, and computerized control systems—can be found in Ref 17, 18, and 19, and 20. A portable test machine including ultrasonics, external loading frame, environmental system, and test chamber is shown in Fig. 4.



Fig. 4 Portable 20 kHz corrosion-fatigue machine with mean load capability

Figure 5 is a schematic of a typical ultrasonic fatigue test machine. The machine is centered around an acoustic wave train composed of a sonic energy converter, a series of acoustic amplifying horns, and the test specimen. A typical wave train is shown in Fig. 6. The acoustic energy is supplied by a high-frequency power supply. An amplitude-measuring device and a means of dissipating the heat generated by the deformation process are also necessary. This basic equipment is appropriate for stress-life ($S-N$) or fatigue-crack-growth rate (da/dN) testing. A frequency display, cycle counter, and temperature-measuring equipment are used to monitor the test. Additional monitoring equipment is necessary to measure crack length in da/dN testing.

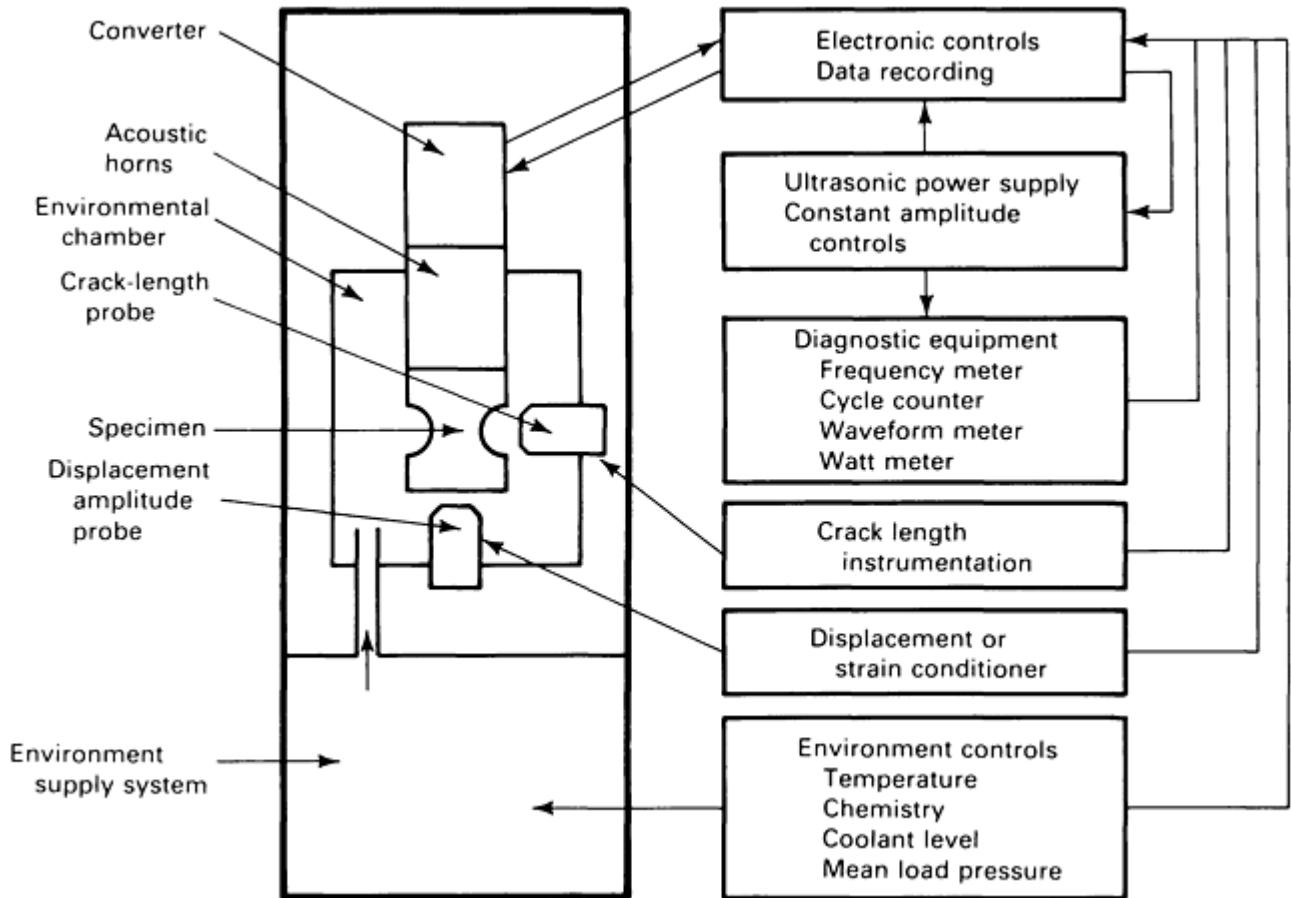


Fig. 5 Schematic of an ultrasonic fatigue test system



Fig. 6 Typical 20 kHz acoustic wave train

Power supplies for ultrasonic fatigue testing typically range from 500 to 4000 W of electrical power. The actual output to the specimen is lower than this during normal resonant operation. Most power supplies have built-in feedback circuits, which produce a constant-amplitude oscillation in the converter. Some power supplies have circuits for automatic shutoff when the specimen or any part of the wave train goes out of resonance. This is useful for *S-N* testing. The fatigue crack at failure will be some fraction of the cross-sectional area when the power supply shuts off. This fraction can range from a few percent to 50% of the cross-sectional area, depending on the automatic shut-off controls.

Sonic Converters. Acoustic resonance is developed in the converter by application of the electrical excitation provided by the power supply. The converter generates a standing acoustic wave that produces a cyclic displacement at the end of the converter. The acoustic wave proceeds down the rest of the resonant wave train to the specimen. Variation of the displacement and strain amplitudes along the wave train is shown in Fig. 7.

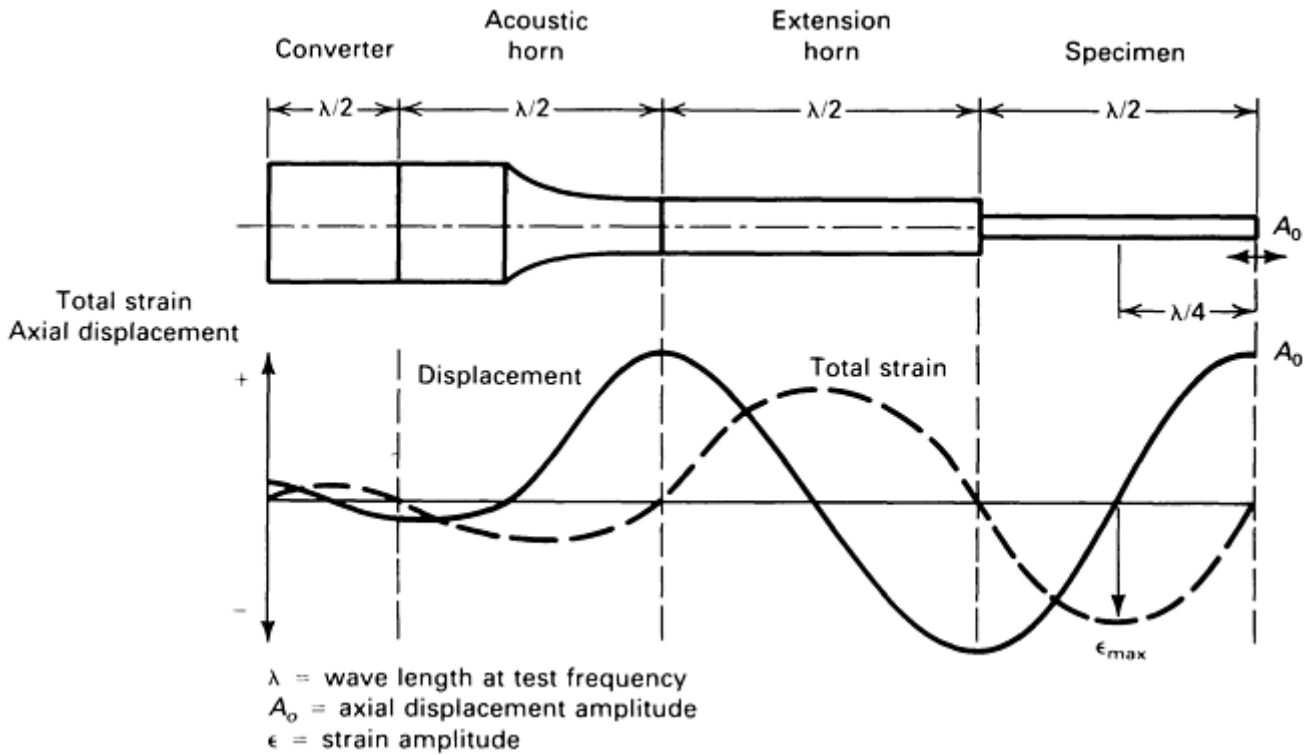


Fig. 7 Variation of the displacement and strain amplitudes along the acoustic wave train

Several cycles of application of the electronic stimulus of the power supply are required to achieve the maximum resonant amplitude in the converter and the rest of the wave train. The rise time of the converter should be known when considering a pulsed mode versus continuous-cycling mode of an ultrasonic fatigue system. In a pulsed-mode operation, the specimen is subjected to a series of pulses (~ 1 s) of high-amplitude cycles followed by a cooling period without cycling. Rise time of ultrasonic equipment varies among manufacturers. If rise time is longer than pulse time, variable-amplitude test conditions exist. Pulsed-mode operation has been suggested by some investigators to overcome the rapid heating manifested by high-damping materials upon cycling. Ultrasonic fatigue systems take several cycles for the maximum resonant amplitude to be developed. Hence the tendency to overshoot the desired amplitude setpoint on the first cycle is small.

Converters for generating ultrasonic displacement waves generally are magnetostrictive or piezoelectric devices. Most modern converters use piezoelectric materials for conversion efficiency. Magnetostrictive devices have a low (20%) conversion efficiency. Piezoelectric converters with efficiencies greater than 90% are readily available.

Converter types and designs vary among manufacturers. Some piezoelectric devices use lead-zirconium-titanate (PZT) for the converter material. The end displacement amplitude developed by a 20 kHz PZT converter ranges from 0.010 to 0.020 mm (0.0004 to 0.0008 in.). Piezoelectric plastic materials are being considered for higher-amplitude ultrasonic converters.

A single- or double-converter arrangement can be used to drive the specimen into resonance. In a single-transducer system, one end of the specimen is coupled to the converter and the other end remains free. In a double-converter system, both ends of the specimen are coupled to two coaxial antiphase-driven ultrasonic converters (Ref 17). The advantage of a double-converter system is its symmetry.

A comparison of the displacement, strain, and specific energy parameters for a high-damping perspex (Lucite) test specimen tested with a single- and double-converter system is shown in Fig. 8 (Ref 21). The symmetry of the converters is reflected in the greater symmetry of the displacement and strain distributions produced in a resonant specimen. While equivalent testing conditions can be produced with either single- or double-converter systems through precise design of the acoustic elements, the double converter is less sensitive to small differences between the resonance frequency of the specimen and the driving frequency of the converter. Data also show that the double-converter arrangement is less sensitive to detuning of the specimen due to changes in elastic properties or the growth of a fatigue crack. Fatigue crack growth testing benefits from the longer crack length attainable with a double-converter system before significant frequency degradation occurs.

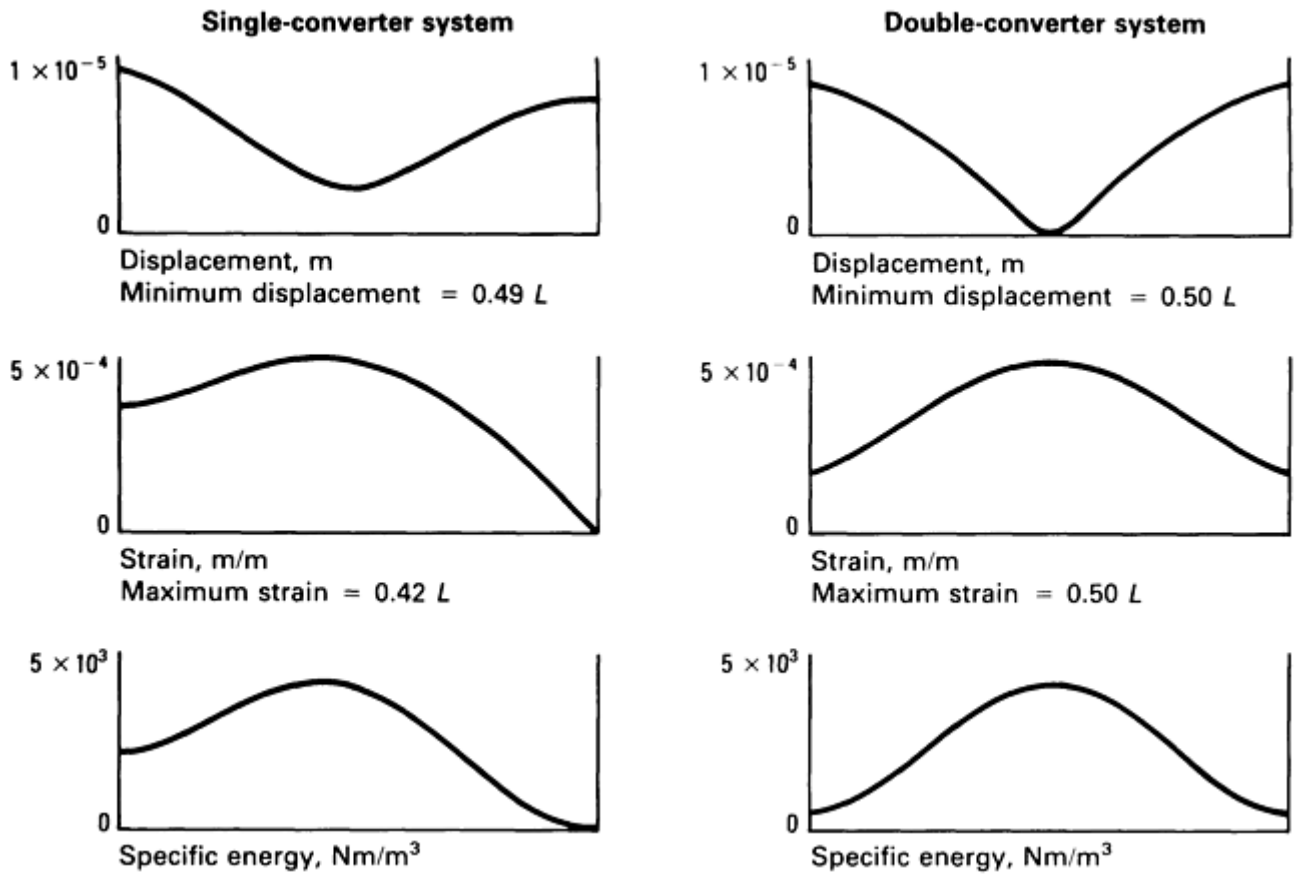


Fig. 8 Comparison of single- and double-converter systems. Calculated displacement, strain, and specific energy parameters for a highly damped perspex specimen ($L = \lambda/2$) are shown. The single-converter system was excited from the left side. Assumed values for the specimen: $E = 48 \text{ GPa}$ ($6.9 \text{ psi} \times 10^6$); $\rho = 1.2 \text{ g/cm}^3$; frequency = 20 kHz. Source: Ref 21

Acoustic horns transmit the resonance developed by the converter to the specimen. One or more acoustic amplifying horns generally are placed in the wave train to raise the strain amplitude in the specimen to the level required for fatigue. Design of these horns was developed by Mason (Ref 22) and Neppiras (Ref 15).

Acoustic horns are bars of resonant length with cross-sectional areas that change either continuously or discontinuously as distance from the input end varies. To maintain the requirement of continuity of particle velocity along the horn length, the vibrational amplitude must increase in areas of reduced cross-sectional area. This produces displacement and strain amplification. For the simple stepped-down horn shown in Fig. 9(a), displacement and, hence, strains are amplified by the ratio of the cross-sectional areas of the horn:

$$A_o = \frac{\text{Area}_{\text{input}}}{\text{Area}_{\text{output}}} \cdot A_i \quad (\text{Eq 5})$$

where A_o is the displacement amplitude on the output end of the horn, and A_i is the displacement amplitude on the input end of the horn. Conversely, an increase in cross-sectional area causes deamplification. A number of different horn shapes have been designed by detailed mathematical analysis (Ref 23, 24, 25, and 26); typical examples are shown in Fig. 9 along with the particle velocity and stress distribution along their length.

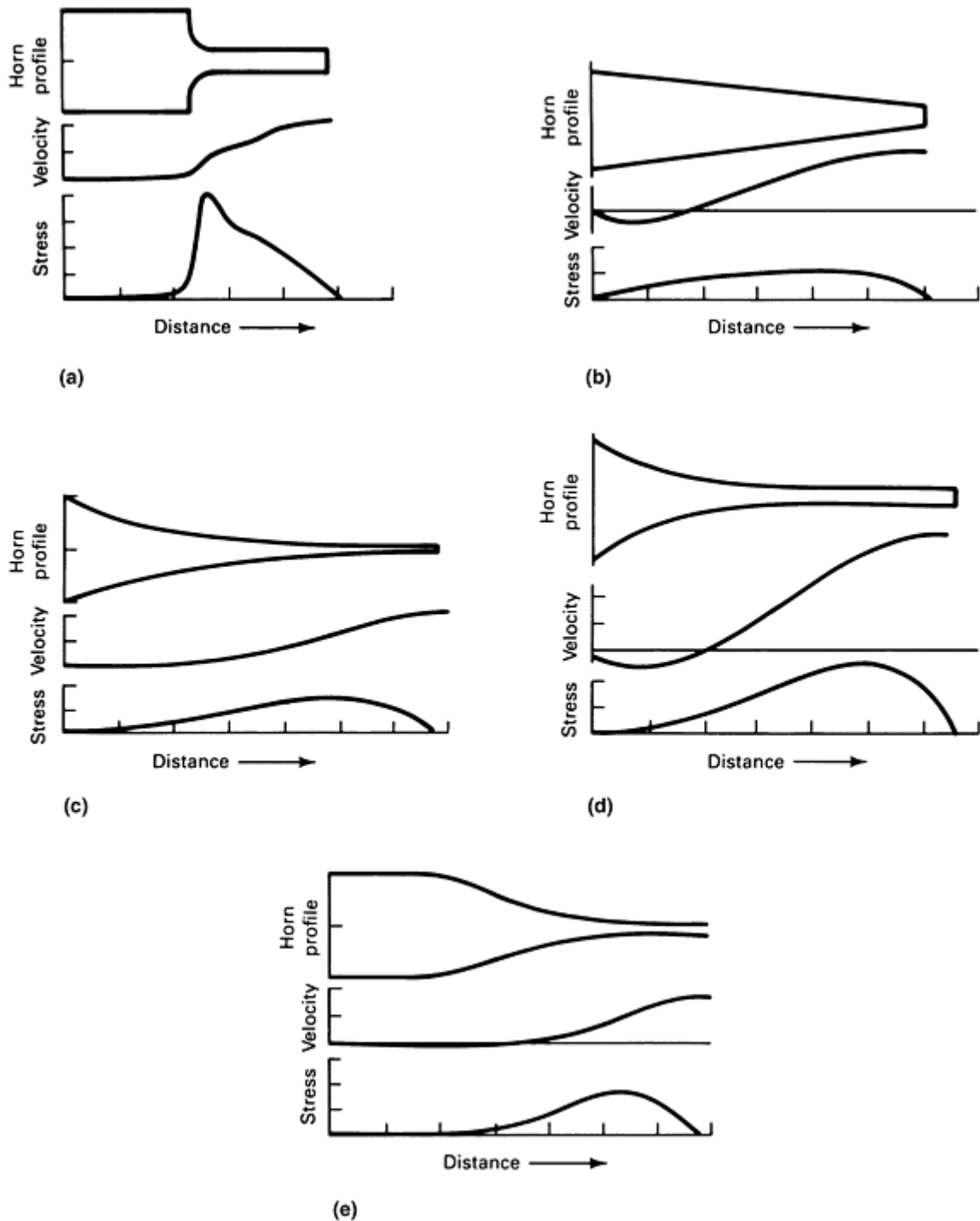


Fig. 9 Profiles of acoustic horns for amplifying converter output. Variations in particle velocity and stress along horns are shown below each profile. (a) Stepped. (b) Conical. (c) Exponential. (d) Catenoidal. (e) Fourier. Source: Ref 23

An obvious problem with the stepped horn is the manifestation of very-high-stress amplitudes at the step. This eventually causes the horn to fail by fatigue at the step. The Fourier horn (Fig. 9e) is the best overall horn design for achieving the highest amplification with the greatest strength and stiffness. Ultrasonic converter suppliers typically carry a variety of acoustic horn designs with amplifications ranging from 1 to 10 to 1. Some manufacturers will design acoustic horns for custom applications, including very high amplifications, special frequencies, or sealing the entrance of an environmental chamber.

Extension Acoustic Horns. The need for extension horns generally arises when the test specimen must be isolated in a controlled environmental chamber, furnace, or external load frame. Typically, a 1 to 1 extension horn is used—that is, a uniform bar of length $\lambda/2$, having been modified with a flange for seating an environmental seal or for attaching the wave train to the external load frame.

It is important to select materials that will not affect the test. Extension horn material should be low damping whenever possible to avoid losses and excessive heating. For corrosive environments, the horn material should be such that a galvanic couple is not set up between the specimen and horn. If high temperatures are to be encountered, the horn material must possess appropriate high-temperature strength. The elastic properties of the material should be determined for the temperature of the desired test. Some properties of materials used for acoustic extension horns are presented in Table 2.

Table 2 Typical 20 kHz resonance properties for acoustic extension horn materials

Material	Density (ρ), g/cm ³	Wavelength of sound at the resonant frequency (λ)		Young's modulus (E)	
		mm	in.	MPa	psi $\times 10^6$
Ra-333	8.3	244	9.61	199,300	28.9
Udimet 710	8.1	264	10.40	224,090	32.5
Udimet 720	8.1	264	10.40	226,160	32.8
MP35N	8.5	246	9.68	206,160	22.9
Ti-6Al-4V	4.4	249	9.80	108,940	15.8
AISI 403	7.7	262	10.31	210,960	30.6
17-4PH	7.8	250	9.84	199,960	28.9

Amplitude Detection. The accuracy of determining specimen strain depends to a great extent on the accuracy of the measurement of the displacement amplitude at the end of the specimen. Much research has been directed toward the development of sensitive methods for measuring displacement amplitude at ultrasonic frequencies. The simplest, most reliable method is observation of the trajectory of a feature on the specimen surface with a dark-field optical microscope having coaxial lighting and a filar eyepiece.

At magnifications of 500 \times and a reticle scale in hundredths of a millimeter, displacements on the order of 2 to 3 μm can be detected. The trajectory of a point on the specimen surface appears as a bright streak whose length will be the peak-to-peak displacement amplitude. Visual observation of displacement amplitude with a microscope does not lend itself to automated recording of the displacement. However, it is the preferred method for calibrating more automated amplitude detection equipment, because secondary modes of vibration are easily detected. Secondary modes cause the normally linear trajectory of a point to skew or appear to orbit about another point.

Other amplitude detection devices more suitable for automated data acquisition or feedback to a closed-loop fatigue apparatus have also been used. These generally are displacement-measuring devices, which come in many forms, including capacitance gages (Ref 16, 27), permanent magnet-coil arrangements that use eddy currents (Ref 17, 28), a microphone pickup (Ref 29), a photodiode arrangement (Ref 30), and closed-circuit television (Ref 31).

Noncontacting capacitance-type detectors to measure displacement amplitudes at ultrasonic frequency are commercially available with sensitivities on the order of $3 \times 10^2 \mu\text{m}$ and linear frequency response up to 50 kHz. Eddy current probes also are commercially available and are frequently used to measure displacement. Because eddy currents are sensitive to composition and microstructure, eddy current probes require calibration of the output signal versus displacement for each new material that is tested. These devices generally are not useful for measuring displacement of nonconducting or low-permeability materials. When the end of the specimen is inaccessible due to an environment chamber or extension horns, the displacement must be calibrated from the specimen to some other point on the wave train.

Strain can be measured by directly applying strain gages to the specimen and reading the value from a strain conditioner that has a frequency response equivalent to the test frequency. Several problems are associated with strain gages applied directly to the specimen. Strain gages, strain gage leads and the adhesive that holds a strain gage onto the specimen are subject to fatigue loading and have finite cyclic lifetimes. If they are placed at the point of maximum strain on the specimen they generally will fail before the specimen does. Attachment of the gage to the specimen may modify the specimen surface and lower its fatigue properties. The presence of a gage on the specimen can cause additional heating to occur under the gage. These problems can be avoided by placing the gage on an adjacent extension horn where the maximum strains are lower than those on the specimen. The strain in the specimen then can be calibrated to the strain in the extension horn.

It is best to use amplitude detectors that can be located at, or as close as possible to, the specimen. Consideration should be given as to whether the environment that is used will interfere with operation of the device. Some devices give outputs that vary when they are positioned away from the specimen and require calibration for each material; electrodynamic devices operating on eddy currents induced in the vibrating specimen fall into this category. These devices are more difficult to use than capacitance gages, whose output is linear over a known range and does not depend on the properties of the test material. Capacitance gages also need to be calibrated if the working environment changes the dielectric constant.

Crack growth measuring systems for ultrasonic fatigue tests are similar to those used at conventional frequencies. Optical methods can be used because the fatigue crack grows in the plane of maximum strain, which is a displacement node. As a result, the crack will not appear to be vibrating. Optical methods using microscopes on traveling stages can be operated manually or automatically. Automated systems for video monitoring of the crack length are described in Ref 19. Foil-type crack growth gages can be attached to the specimen in the path of the growing crack. These gages develop a linearly varying potential as the crack tears the foil and have been shown to operate linearly under 20 kHz cycling. The usual requirements for monitoring the symmetry of fatigue crack length in double-edge-cracked or center-cracked specimens at conventional frequency also apply for ultrasonic frequency testing.

Cooling Systems. As in conventional fatigue testing, the components of fatigue deformation generate heat within the specimen in an amount equal to the area enclosed by the stress-strain hysteresis loop in each cycle. At 20 kHz, the specific energy input at high stresses can be as high as several hundred watts per cubic centimeter for high damping materials. Large temperature excursions can result if the heat is not removed. These temperature excursions not only change the properties of the test material, but can introduce mean tensile stresses on the surface of solid specimens because of the differential thermal expansion between the core and surface of the specimen.

In most cases, the heat generated can be dissipated by forced cooling if the heat transfer path is not too lengthy. In some cases, the heat generated cannot be eliminated by forced-air cooling, and more efficient external and internal cooling may be necessary. A hollow specimen can be used to decrease the heat-transfer path through the metal.

In specimens of materials with high damping and large cross sections, this heat rise can be extreme. Figure 10(a) shows the temperature contour of a 12 mm (0.48 in.) diam resonant steel bar without cooling (Ref 32). The strain antinode heated to almost 400 °C (750 °F) during ultrasonic-frequency cycling at a stress level of 150 MPa (22 ksi). The highest temperatures are observed at the strain antinode. Efficient cooling of a test specimen would obviously require the greatest volume of coolant to flow over the strain antinode. Large temperature excursions can usually be minimized in practice by the choice of a hollow dumbbell specimen design.

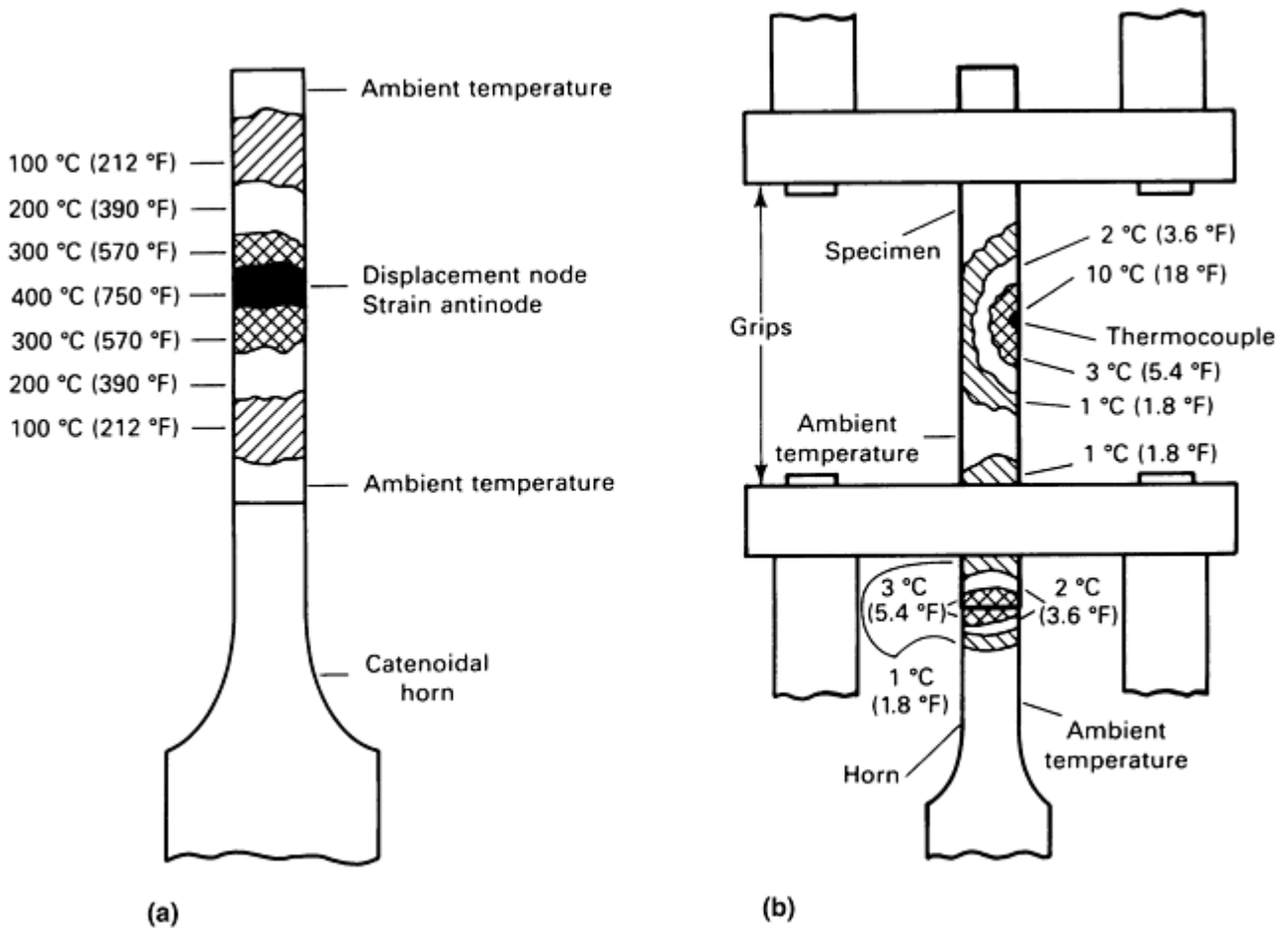


Fig. 10 Infrared thermogram of specimen under 20 kHz excitation without cooling. (a) Resonant specimen exhibiting nodal heating. (b) Localized heating due to thermocouple epoxied to surface of nonresonant specimen. Source: Ref 32

The damping characteristic of the material and the efficiency of the coolant determine the choice of a solid or hollow specimen design for testing. In general, cooling a material with high damping (such as pure copper) with forced-air heat transfer requires a thin-walled hollow specimen to ensure that the temperature rise is acceptably low. At the other end of the damping spectrum, titanium alloys generate so little heat at 20 kHz at modest stress levels that virtually any specimen geometry is compatible with the temperature rise limitations.

Martensitic steel lies somewhere between copper and titanium, and hollow or solid specimens may be selected depending on whether the coolant is forced air or water. Measurement of the temperature rise at the uncooled interior of a hollow type 403 stainless steel specimen (1.25 mm, or 0.05 in., wall thickness, with water cooling at the external surface) revealed a temperature rise of less than 10 °C (18 °F) even during fatigue at stresses high enough to cause failure in 10^7 cycles.

Monitoring the temperature rise is essential to obtaining reliable data, particularly when testing in air. Attaching a thermocouple to the specimen at the maximum strain point presents two basic problems. First, the specimen could be damaged and premature fatigue failure could occur. Second, infrared data show that attachment of the thermocouple to a nonresonant bar causes localized heating in the vicinity of the thermocouple (Fig. 10b).

The localized heating implies that thermocouples may not be reliable for measuring the specimen temperature during ultrasonic vibration. It has been proposed that the localized heating could be caused by vibration of the leads of the thermocouple due to active displacement at all positions of a nonresonant specimen. Hence, placing the thermocouple at the displacement node of a resonant specimen might minimize this local heating. This viewpoint has not yet been verified.

Two alternate temperature-sensing methods that work well in air environments are infrared imaging of the specimen and application of temperature-sensitive paint to the specimen surface. These methods provide only surface temperature information. The subsurface temperature is hotter. In liquid environments, the alternate temperature measurements will not work, and thermocouple data may be the only possible method. In liquid environments, particularly water, temperature control is somewhat easier because the liquid acts as a coolant

and moderates the temperature excursion. Generally, the liquid is controlled to some temperature below the desired temperature so that the excess heat generated from testing will be dissipated in the liquid. For elevated-temperature testing, the furnace temperature must be controlled so that the heat generated in the specimen helps achieve the desired temperature.

A forced-air cooling system with an infrared temperature monitoring system is shown in Fig. 11. Air jets are aimed at the strain antinode. With an air line pressure of 0.5 MPa (72.5 psi) and a venturi-type air cooler in the line, an air jet exit temperature of 0 °C (32 °F) can be obtained. A liquid cooling system requires that the liquid flow over the surface of the specimen.

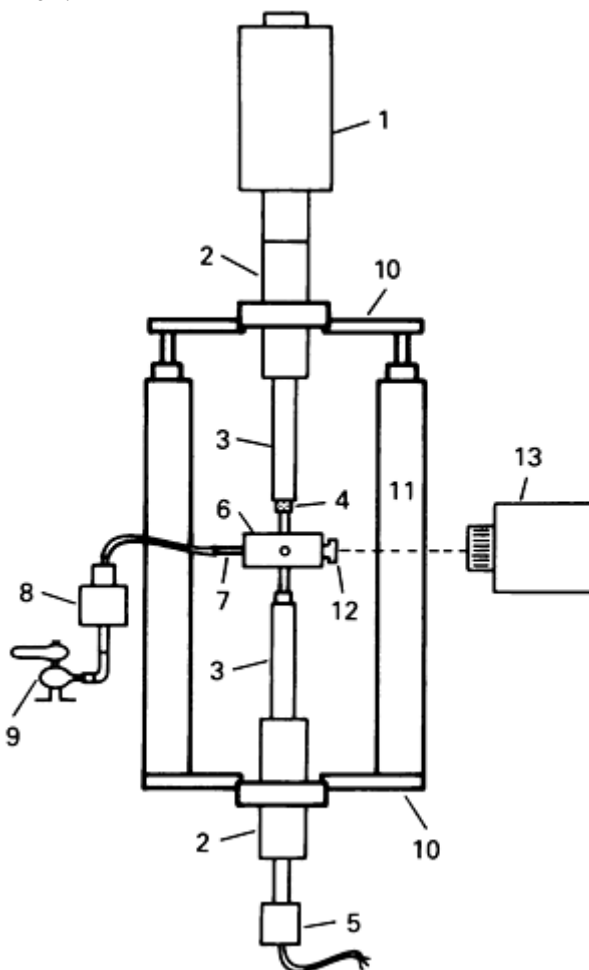


Fig. 11 Test facility (20 kHz) showing positioning of forced-air cooling, infrared temperature monitor, and external load frame for mean load. 1, converter; 2, booster horn; 3, connecting horn; 4, specimen; 5, capacitance gage; 6, cooling ring; 7, four air inlets; 8, venturi air cooler; 9, air supply; 10, upper and lower support plates; 11, hydraulic pistons; 12, window; 13, infrared camera

The major difference in ultrasonic fatigue testing compared to conventional fatigue testing is that the specimen should not be totally immersed in a bath of coolant. Immersing the specimen could prevent the system from obtaining constant-amplitude resonance. If resonance can be obtained while immersed, cavitation erosion damage may occur at fillets and ends of the specimen. This can be prevented by the application of a thin film of rubber compound, such as carboline neoprene adhesive, to these areas of the specimen. A typical liquid cooling system is shown in Fig. 12. In this system, the liquid flows onto the specimen and drains off to be recirculated. This system can also be used for environmental testing.

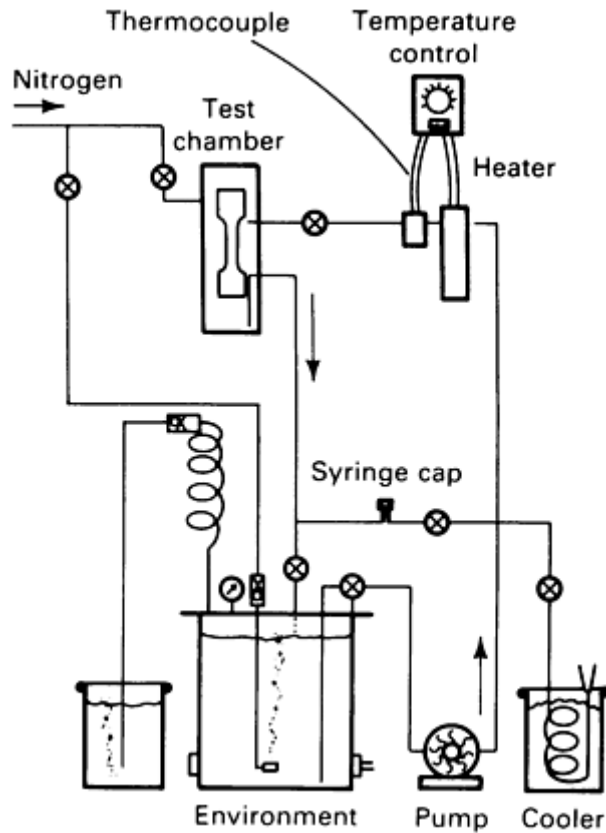


Fig. 12 Environment supply system for liquid cooling or corrosion-fatigue testing

In a liquid cooling system, an inert coolant is necessary to achieve baseline fatigue property data approaching those of air tests. The coolant must not be corrosive to the material and must have a heat capacity large enough to remove the heat from the specimen. Deionized, low-oxygen-content water is a very high-heat-capacity, minimally corrosive coolant for most materials. It is a little more difficult to use low-oxygen deionized water as a coolant because an environmental system is necessary to control the gaseous traces in the water. Acid-free transformer oil is another coolant frequently used for ultrasonic fatigue tests. Liquid cryogen coolants, such as liquid nitrogen, generally are less effective due to their tendency to vaporize on contact with the specimen. The vapor forms a boundary layer at the specimen surface, which reduces effective cooling instead of increasing it. Fatigue property data obtained with a nonaggressive coolant generally are slightly lower than data obtained with air cooling. Baseline data obtained with an inert coolant are usually necessary for the interpretation of corrosion fatigue data.

External Load Frame. The wave train arrangement can be used without further attachment for completely reversed tension-compression testing. The wave train can also be placed in an external load frame, such as a tensile test machine, to provide static mean loading or superposition of large-amplitude low-frequency cycling on top of the high-frequency cycling (Ref 18, 32). The external load frame is attached to the wave train at the displacement nodes on acoustic horns on either side of the specimen, as shown in Fig. 11.

Design of specimens to be subject to superimposed external loads must take two additional factors into account. First, the elongation of the specimen due to external straining must be considered to stay within the bounds of the resonance conditions. Second, there have been observations of softening of metals during simultaneous tensile or compressive mechanical deformation and high-frequency straining, which is known as the Blaha effect (Ref 33). These mechanisms are discussed in more detail in Ref 32. Test engineers should be aware of this effect because it can result in additional plastic deformation of the material during testing.

Environmental Fatigue. Ultrasonic fatigue testing can be performed under most environmental conditions. One possible exception is vacuum, in which testing is narrowed to a few very-low-damping materials at low stress levels. Environmental testing requires the normal ultrasonic fatigue testing apparatus with the addition of an environmental chamber around the test specimen and an environmental supply system.

Elevated Temperatures. For high-temperature testing, the furnace serves as the environmental chamber and supply system. A high-temperature test stand with mean load capability can be constructed by placing a furnace around the specimen in the test system shown in Fig. 11. Some tuning generally is required to design extension

horns that will be resonant in the temperature gradient from the furnace midpoint to the ambient temperature outside the furnace, because the resonant frequency is temperature dependent. For high-temperature fatigue, the specimen displacement amplitude usually will have to be calibrated to a displacement antinode outside the furnace (Ref 34).

Aggressive Liquid Environments. Testing in corrosive liquid environments requires both an environmental chamber and an environmental recirculation system. This is essentially the same equipment needed for inert liquid cooling, as shown in Fig. 12. Additional features are incorporated into the environmental recirculation system to provide control of the solution composition, purity, and temperature. Ports are incorporated so that environment composition samples can be taken for documentation and solution pH can be adjusted. An inert gas overpressure is usually maintained throughout the system to control the dissolved oxygen content of the test solution. Appropriate plumbing and seals are incorporated so that the specimen chamber can be purged of air prior to circulation of the environment.

A controlled-corrosion fatigue chamber is shown in Fig. 13. This chamber exhibits features needed for electrochemical corrosion fatigue study (Ref 20). The chamber is composed of an outer chamber and an inner chamber constructed of Teflon. The inner chamber contains a finite volume of liquid around the gage section of the specimen. A platinum electrode is fitted into the inner chamber for anodic or cathodic polarization of the specimen. A window is placed at the side of the inner chamber to enable viewing of the amount of liquid in the inner chamber. A port is placed in the front of the inner chamber so that a standard reference electrode can be inserted to measure the electrochemical potential of the specimen. The electrodes can be removed for normal corrosion fatigue testing.

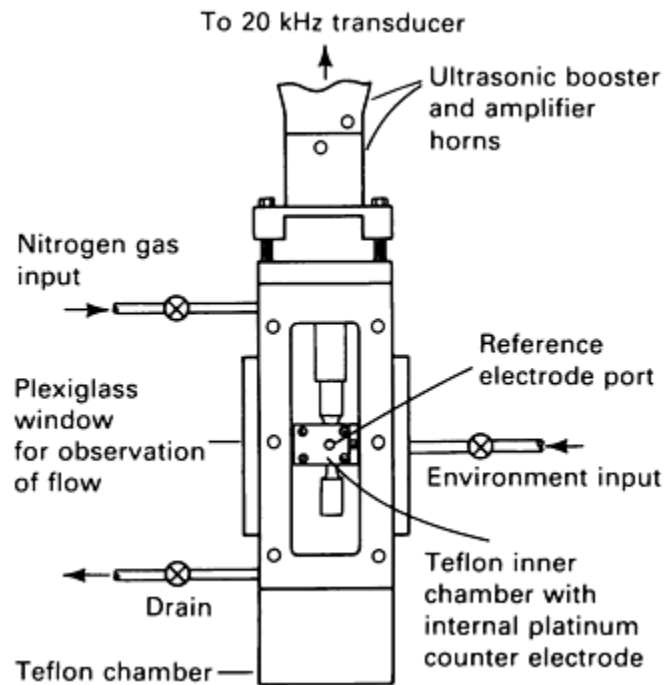


Fig. 13 Environmental fatigue test chamber for electrochemical 20 kHz testing

Proper selection of horn material is important in corrosion fatigue testing, because a mismatched specimen and horn material combination may set up a galvanic couple when the joint is wetted with a conductive solution. Depending on the galvanic couple, the horn material may cause the gage of the specimen to be electrochemically more active or passive than normal. This could have a pronounced effect on the corrosion fatigue properties that are being determined. It is advisable to make the specimen and the extension horn out of the same material. If the horn and specimen must be made out of dissimilar metals, care must be taken to ensure that the joint is not exposed to the conductive test solution.

In fatigue crack growth testing in liquid environments, the effect of the liquid inside the growing fatigue crack also must be considered. The effect of the liquid fatigue crack growth rate is currently being investigated. Depending on the fluid properties, the fatigue crack may be wedged open, causing errors in the da/dN and threshold stress intensity range, ΔK_{th} question is whether the environment ever extends to the crack tip. It has been suggested that at high crack growth rates, the environment has little influence on rapid crack growth, and the crack tip behaves as if it were in vacuum (Ref 35).

References cited in this section

15. E.A. Neppiras, *Proc. ASTM*, Vol 59, 1959, p 691
16. J.K. Tien, S. Purushothoman, R.M. Arons, J.P. Wallace, O. Buck, H.L. Marcus, R.V. Inman, and G.J. Crandall, *Rev. Sci. Instrum.*, Vol 46, 1975, p 840
17. W. Kromp, K. Kromp, H. Bitt, H. Langer, and B. Weiss, *Ultrasonics International 1973 Conference Proceedings*, IPC Science and Technology Publications, Guildford, Surrey, U.K., 1973, p 238
18. I. Hansson and A. Tholen, *Ultrasonics*, March 1978, p 57
19. S. Stanzl and E. Tschegg, *Met. Sci.*, April 1980, p 137
20. R.A. Yeske and L.D. Roth, in *Ultrasonic Fatigue*, J.M. Wells, O. Buck, L.D. Roth, and J.K. Tien, Ed., TMS-AIME, Warrendale, PA, 1982, p 365
21. P. Trimmel and W. Kromp, in *Ultrasonic Fatigue*, J.M. Wells, O. Buck, L.D. Roth, and J.K. Tien, Ed., TMS-AIME, Warrendale, PA, 1982, p 37
22. W.P. Mason, *J. Acoust. Soc. Am.*, Vol 28, 1956, p 1207
23. J.R. Frederick, *Ultrasonic Engineering*, John Wiley & Sons, New York, 1970
24. G. Amza and D. Drimer, *Ultrasonics*, Vol 14, 1976, p 223
25. E. Eisner, *J. Acoust. Soc. Am.*, Vol 35, 1963, p 1367
26. L. Balamuth, *Trans. IRE (Ultrasonic Eng.)*, Vol 2, 1954, p 23
27. B.S. Hockenhull, C.N. Owston, and R.G. Hacking, *Ultrasonics*, Vol 9, 1971, p 26
28. A. Thiruvengadam, *J. Eng. Ind. (Trans. ASME)*, Vol 11, 1966, p 332
29. H. Konagai, S. Tanaka, and T. Sakurai, *J. Soc. Mater. Sci., Jpn.*, Vol 24, 1975, p 753
30. G.C. George, *Corrosion Fatigue: Chemistry, Mechanics and Microstructure*, O. Devereux et al., Ed., National Association of Corrosion Engineers, Houston, 1972, p 459
31. V.A. Kuz'menko, G.G. Pisarenko, and A.K. Gerikhanov, *Probl. Prochn.*, Vol 4, 1977, p 120
32. R.B. Mignogna and R.E. Green, Jr., in *Ultrasonic Fatigue*, J.M. Wells, O. Buck, L.D. Roth, and J.K. Tien, Ed., TMS-AIME, Warrendale, PA, 1982, p 63
33. F. Blaha and B. Langenecker, *Die Naturwiss.*, Vol 42, 1955, p 556
34. G. Whitlow, L.E. Willertz, and J.K. Tien, in *Ultrasonic Fatigue*, J.M. Wells, O. Buck, L.D. Roth, and J.K. Tien, Ed., TMS-AIME, Warrendale, PA, 1982, p 321
35. J.K. Tien and R.P. Gamble, *Met. Trans.*, Vol 2, 1971, p 1933

Test Specimens

Ultrasonic fatigue test specimens must be designed to resonate at the desired test frequency. The first step in designing an ultrasonic fatigue test specimen, acoustic horn, or resonant bar is to obtain the appropriate properties and constants of the materials. The material density, dynamic modulus of elasticity, and the half wavelength of sound in the material at the desired testing frequency must be determined.

Frequency, Wavelength, and Speed of Sound. The longitudinal resonance frequency of a bar test material is measured experimentally, as shown in Fig. 14. A uniform bar of test material is excited by a small converter coupled to a variable-frequency oscillator. The converter can be an electrodynamic vibrator or any other vibrator capable of ultrasonic frequencies. A piezoelectric pickup is placed against the opposite end of the bar to monitor the amplitude of vibration. For most pure metals and alloys, the bar should be about 100 to 150 mm (4 to 6 in.) long and 4 to 10 mm (0.16 to 0.4 in.) in diameter. This diameter is comparable to the diameters of most test specimen gages.

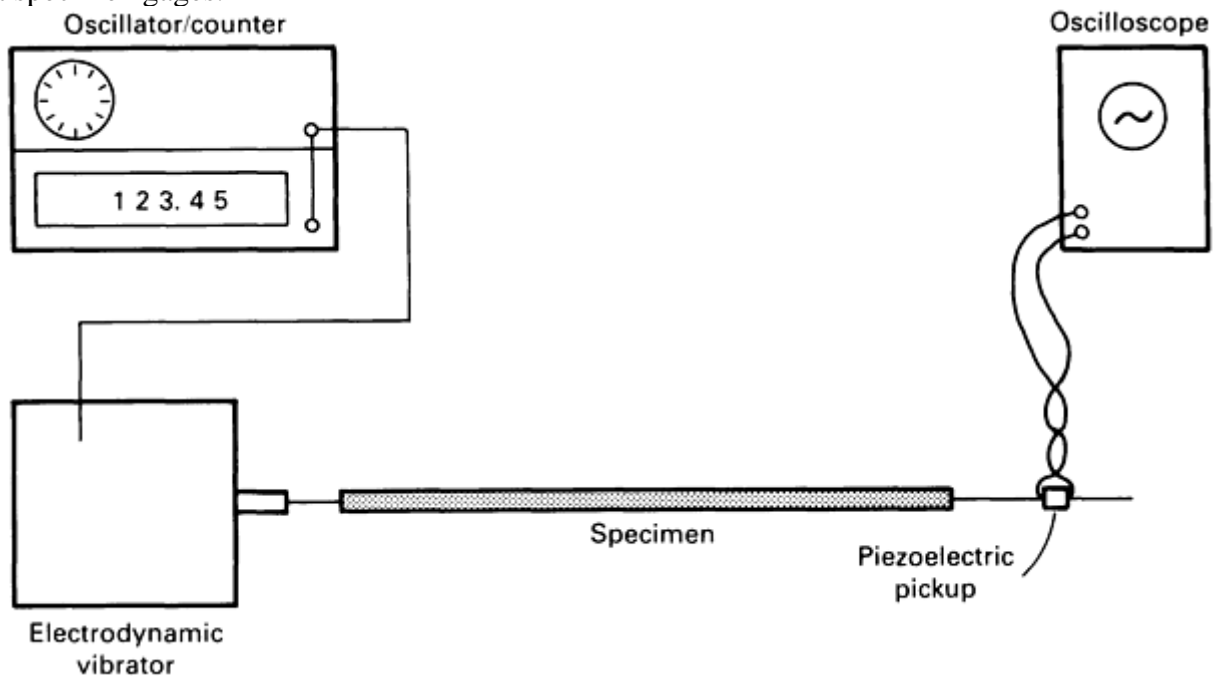


Fig. 14 Experimental measurement of the longitudinal resonance frequency of specimens

The bar should be similar in size to the eventual specimen gage diameter, because measured resonant frequencies vary with large-diameter bars. This directly affects calculation of the dynamic elastic modulus, and ultimately affects calculation of the fatigue stress amplitude. Frequencies on the order of tens of kilohertz should be measured for a bar length in this given range. Sweeping the oscillator through the frequency spectrum produces a large increase in output for some frequency; this is the resonance frequency. The length of the bar is $\lambda/2$ for the experimentally determined resonance frequency. Resonant wavelengths for several pure metals at test frequencies of 20 kHz and 2 MHz are given in Table 3. The resonant wavelength is inversely proportional to frequency. The need for a macroscopic test specimen frequently precludes high-frequency testing in the 2 MHz range. The speed of sound through the material can be calculated by relating the speed of sound, C , to frequency, f , and wavelength, λ :

$$C = \lambda_1 f_1 = \lambda_2 f_2 \quad (\text{Eq 6})$$

Table 3 Resonant specimen lengths for several pure metals

Metal	Young's modulus		Resonant specimen length ($\lambda/2$) at:			
			20 kHz		2 MHz	
	GPa	psi $\times 10^6$	mm	in.	mm	in.
Al	62	9.0	120	4.7	1.20	0.047
Cu	110	15.9	88	3.5	0.88	0.035
Ti	116	16.8	127	5.0	1.27	0.050
Fe	196	28.4	124	4.9	1.24	0.049
Ni	207	30.0	121	4.7	1.21	0.047

The resonance frequency of a bar of arbitrary length, as determined in the previously described experiment, may not be the driving frequency of the converter that will be used for testing. The appropriate wavelength for testing frequency is calculated by assuming that the speed of sound through the material remains constant for a given material and temperature.

The dynamic modulus of elasticity, or dynamic Young's modulus, E , can be determined by combining Eq 1 and 6 to obtain:

$$E = \rho(\lambda f)^2 \quad (\text{Eq 7})$$

The dynamic modulus differs from the static modulus (relaxed modulus) obtained from a tensile test. The static modulus is inadequate for converting the strain amplitude to stress amplitude because it will include anelastic contributions to strain that are absent at ultrasonic frequency. Use of the static modulus gives stress estimates that are too low because the static modulus is typically less than the dynamic modulus.

Stress-Life Specimen Design. Several specimen designs for ultrasonic fatigue stress-life testing are shown in Fig. 15. Although the uniform bar is the most easily produced specimen, it generally is not employed in testing. The stress concentration due to the screw threads used for gripping causes the local stress in the thread to exceed the maximum stress produced at the center of the specimen. Failure in the screw threads rather than in the center of the specimen would result.

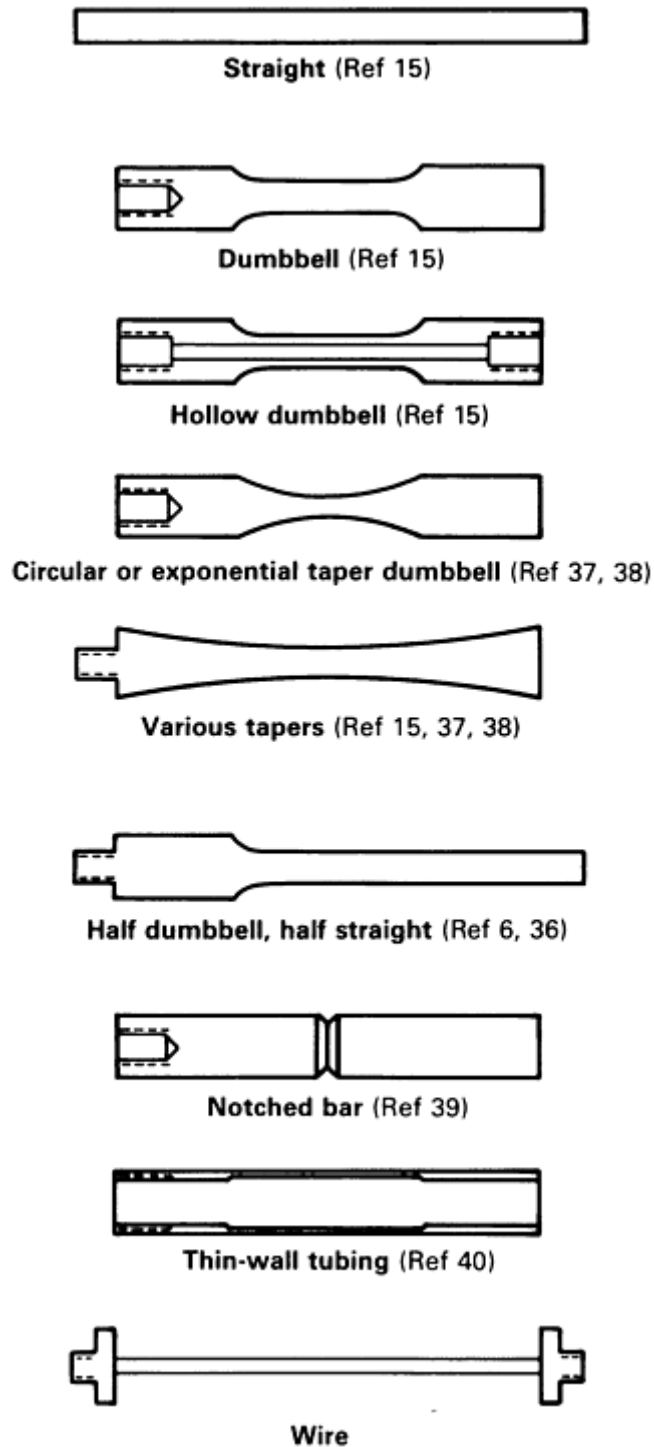


Fig. 15 Profiles of specimen designs for ultrasonic fatigue. References cited provide mathematical analyses required to compute stress and strains.

Strain amplification is desirable at the center of the specimen. This is accomplished by reducing the cross-sectional area of the gage section to produce a dumbbell-shaped specimen. By reducing the cross-sectional area, the total power needed to drive the specimen into resonance is reduced. Consequently, the amount of heat produced in the specimen is reduced, which also reduces the cooling requirements.

The choice of specimen design for a particular test depends on many factors, including the amount of material available, maximum amplitude of the wave train, amount and type of cooling available or allowable, minimum diameter to ensure stiffness and eliminate flexural modes, and desired strain level in the gage section. The calculation of the appropriate resonant specimen geometry is the primary task in designing an ultrasonic fatigue specimen. Other considerations for ultrasonic fatigue specimens are the same as those encountered in conventional fatigue testing, including surface finish, minimization of residual stresses, capabilities of the machine shop, and costs of producing the specimen.

Complex Specimen Geometries. More complicated expressions are needed to determine the dimensions and strain amplitude at the point of maximum strain for specimens with nonuniform geometries. A dumbbell-type specimen is resonant at frequency f if Eq 7 and the following equation are satisfied simultaneously (Ref 15):

$$\left(\frac{d_1}{d_2}\right)^2 = \cot\left(\frac{2\pi L_1}{\lambda}\right) \cdot \cot\left(\frac{2\pi L_2}{\lambda}\right) \quad (\text{Eq 8})$$

The variable dimensions L_1 , L_2 , d_1 , and d_2 are shown in Fig. 16. Equations 7 and 8 are the basic design equations for an ideal dumbbell specimen. Using this representation, any three dimensions can be selected; the fourth can be calculated for a given wavelength. The maximum elastic strain on the gage length of the dumbbell specimen shown in Fig. 16 is given by (Ref 15):

$$\epsilon_{\max} = kA_0 \cdot \left[\frac{\cos(kL_1)}{\sin(kL_2)} \right] \quad (\text{Eq 9})$$

where k is $2\pi/\lambda$ and A_0 is displacement amplitude at the end of the dumbbell. Comparing Eq 9 with the maximum strain obtained in a uniform bar shows that the term in square brackets is the magnitude of the amplification of strain amplitude produced by the dumbbell shape. The term in square brackets is often referred to as the strain amplification factor.

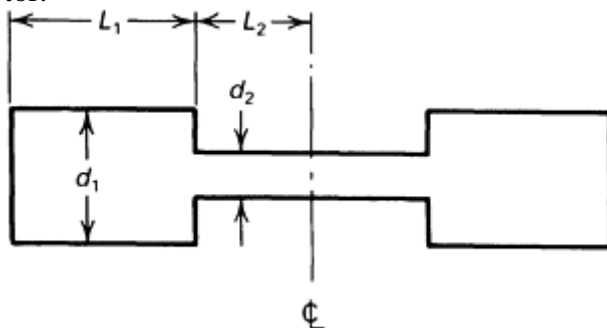


Fig. 16 Ideal dumbbell specimen dimensions

Direct measurement of the strain profile from a test specimen has been reported (Ref 41). A contacting probe aids in measuring the displacement and strain distribution for specimens with complex geometries. The displacement and strain amplitudes along the length of a circular, tapered dumbbell specimen are shown in Fig. 17. The amplification of the strain amplitude due to the dumbbell shape is clearly indicated.

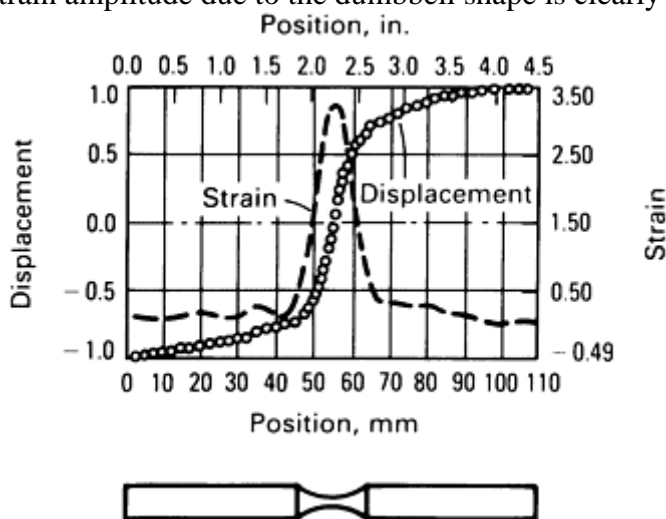


Fig. 17 Distribution of displacement and strain amplitudes obtained from a dumbbell-shaped Ti-6Al-4V specimen at 14.2 kHz. Source: Ref 41

If the ideal dumbbell calculations are used, small adjustments to the overall length of the specimen may be necessary during specimen design to achieve the desired test frequency. For example, if a hole is tapped in one

end of the specimen to attach the specimen to the horn, the equivalent mass of material removed for the hole must be replaced in the form of extra length of that dumbbell head. If the attachment stud is the same density as the specimen, then no adjustments are required. However, if a steel stud is used to hold an aluminum specimen, a mass adjustment to the length of the dumbbell head will be needed. Similar tuning considerations should be made when placing fillets between the dumbbell heads and the gage section.

Fillets and Radii. Efficient propagation of acoustic energy along the length of a dumbbell specimen requires that a smooth transition be provided between the heads and the gage section of the specimen. For some specimen designs such as a circular or exponential tapered dumbbell, this smooth transition is the major design element. Specimen designs that use the Neppiras formula (Eq 7 and 8) for an ideal dumbbell must provide a fillet at the transition from head to gage section. Constant-radius fillets are easily machined and can be used if other alternatives are not feasible.

Depending on the choice of radius, some heat will be generated at the fillet because a constant radius fillet does not provide optimal transition in particle velocity. The recommended fillet design is the baud streamline fillet (Ref 42). This design has a continuously varying fillet radius. Its shape is like that of a nonturbulent stream of water as it drains out of a tank with a circular hole. It is highly efficient in providing a smooth transition of particle velocity. This is quite useful for testing high-damping or precipitation-hardened materials. One disadvantage of the baud streamline design is that it requires a tape- or computer-controlled lathe to produce the desired profile.

Notched Bar Specimens. A notched specimen is a special condition of a dumbbell specimen, where L_2 is very small and L_1 is close to $\lambda/4$ to maintain resonance. For a bar containing a narrow notch, the maximum strain in the notch (exclusive of stress concentration factors) is the product of the maximum strain at $\lambda/4$ of a uniform bar without the notch multiplied by the area ratio $(d_1/d_2)^2$ (Ref 39). The L and d dimensions are defined in the ideal dumbbell specimen shown in Fig. 16.

Finite element analysis of the notched bar specimen design shows that, despite differences in the stress distribution along the specimen length between static- and dynamic-loaded specimens, the stress distribution and configuration in the notch region are the same. The complete equation for the maximum stress, σ_{\max} , in a notched resonant member can be calculated by multiplying the maximum strain, $kA_0 \cdot (d_1/d_2)^2$, by the dynamic modulus, E , and the stress concentration factor, K'_t , as:

$$\sigma_{\max} = EkA_0 \cdot \left(\frac{d_1}{d_2} \right)^2 \cdot K'_t \quad (\text{Eq 10})$$

where K'_t is the von Mises stress concentration factor. The von Mises stress concentration factor is used instead of K_t for analyzing high-cycle fatigue results (Ref 43). This is based on the findings that high-cycle fatigue failure is dictated by the alternating von Mises stress, where K'_t is approximately 10% less than K_t . Definition of additional parameters relating to notch fatigue, including notch bar fatigue strength and notch sensitivity, are found in Ref 39.

Design of resonant fatigue crack growth rate specimens is based on physical concepts similar to stress-life specimen design. The major difference is that a sharp crack is introduced into the design at the point of maximum strain. Therefore, the relationships developed for purely elastic deformation are not exactly fulfilled when appreciable plastic deformation occurs at the crack tip, when changes occur in Young's modulus due to localized plastic deformation, or when the specimen is detuned by the growing crack. Discussion of these issues can be found in Ref 44.

The first ultrasonic fatigue crack growth test specimen was a simple resonant bar with an electrodischarge machined slot cut into one side of the bar (Ref 45). Typical geometries of fatigue crack growth specimens are shown in Fig. 18, including single-edge-cracked specimens (Ref 19), double-edge-cracked specimens (Ref 46) with axial loading, center-cracked specimens with axial loading (Ref 47, 48), and single-edge-cracked specimens with transverse loading (Ref 49). Crack length, a , is shown.

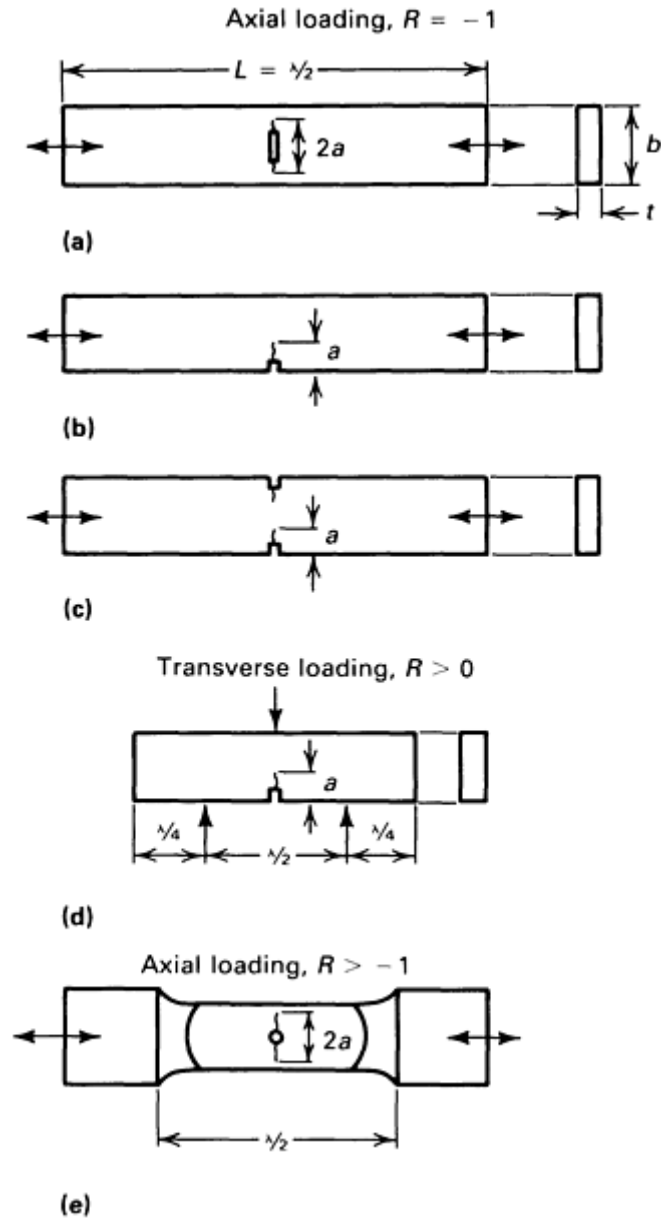


Fig. 18 Specimen geometries for crack growth measurements under high-frequency resonance excitation. (a) Center-cracked specimen. (b) Single-edge-cracked specimen. (c) Double-edge-cracked specimen. (d) Single-edge-cracked specimen. (e) Center-cracked specimen. R , fatigue stress ratio; a , crack length; b , specimen width; t , specimen thickness. Source: Ref 44

Fatigue crack growth test specimen length is controlled by the test frequency, as in the stress-life case. However, the cross-sectional dimensions selected can vary considerably. The current trend in specimen design is to incorporate the relevant criteria of conventional-frequency fatigue crack growth and fracture mechanics into the design. One factor pertains to specimen thickness, d , which should be large in comparison to the plastic zone size at the applied stress intensity range. This is consistent with the pertinent ASTM recommendation:

$$d \geq 2.5 \left(\frac{\Delta K_{\max}}{\sigma_y} \right)^2 \quad (\text{Eq 11})$$

ΔK_{\max} is the maximum stress intensity range, and σ_y is the yield strength of the material. The exception to this rule arises when materials have high damping and produce large quantities of heat. In this case, the specimen must be thin enough to ensure adequate cooling. The specimen also must be thick enough to suppress other modes of vibration, such as flexural oscillations.

The dimension of the starting notch and the permissible fractional length of fatigue crack extension also influences the design of the specimen width, b . For center-cracked specimens, the crack advance should be

limited to a/b ratios of less than 0.4 (Ref 48). For specimens that are wide in comparison to the crack length, flexural contributions due to lateral displacement become significant.

Specimens tested under superimposed static loads (higher R ratios) require regions with cross sections larger than the gage section in order to transmit the required tensile load. The specimen shown in Fig. 18(e) is similar to that specified for conventional fatigue crack growth tests (Ref 50). Currently, specimen choice is equivocal. Standardization of a test specimen will be determined by the ability of a specimen to provide the necessary da/dN and ΔK data. Research is focusing on providing accurate stress intensity values under resonant conditions.

Stress Intensity Concepts. Design of fatigue crack growth rate specimens is useful only if the stress intensity at the crack tip can be calculated. In the simplest method of computing stress intensity range, the nominal stress amplitude is obtained from the displacement amplitude, and the ΔK value is calculated as:

$$\Delta K = \Delta\sigma \sqrt{a\pi} \cdot F_1\left(\frac{a}{b}\right) \quad (\text{Eq 12})$$

where $F_1(a/b)$ is a correction factor to account for the presence of a crack in the finite width of the specimen. This method does not account for the effects of a growing crack on the resonance behavior of the system. It assumes that the relationship between displacement and strain amplitude remains constant with detuning of the specimen due to crack growth. This problem can be avoided by measuring the strain directly with strain gages placed in the crack plane. Additional correction factors to the stress intensity formulism mentioned previously (Eq 12) have been added to account for the growth of the crack by normalizing the measured effective stress to the initial cross section (Ref 51).

A dynamic correction factor for ΔK also has been determined with finite element analysis. This results in a factor that is a function of the ratio of crack length (a) to specimen width (w), specimen width to length (W/L), and the instantaneous frequency (v).

A summary of frequently used correction formulas to calculate ΔK is given in Table 4. Further study must be undertaken to develop a standardized computation procedure for ΔK in resonant specimens.

Table 4 Computation of stress intensity ranges

Specimen geometry (loading mode)	Equation	Ref
Side notch in octagonal bar (longitudinal)	$\Delta K = 1.95 \cdot \Delta\sigma \cdot f\left(\frac{a}{b}\right) \cdot \sqrt{\frac{a}{Q}}$	52
Center-notch flat bar (longitudinal) ^(a)	$\Delta K = \frac{U_o}{W} \cdot E\sqrt{a} \cdot \sqrt{3} \left(\frac{a}{W}, \frac{W}{L}, v\right)$	48
Center-notch flat bar (longitudinal), $a/w < 0.5$	$\Delta K = \epsilon_t \cdot E\sqrt{a}\sqrt{\pi} \cdot f\left(\frac{a}{b}\right) \cdot f\left(\frac{b-a}{b}\right)$	51
Double-side-notch flat bar (longitudinal), $a/w < 0.4$	$\Delta K = \epsilon_t \cdot E\sqrt{a}\sqrt{\pi} \cdot f\left(\frac{a}{b}\right) \cdot f\left(\frac{b-a}{b}\right)$	46
Single-edge-notch thin, flat strip (longitudinal), $a/w < 0.6$	$\Delta K = \Delta\sigma \cdot \sqrt{a}\sqrt{\pi} \cdot f\left(\frac{a}{b}\right)$	19
Single-edge-notch rectangular bar (transverse)^(a)	$\Delta K = \frac{U_o \cdot E}{W} \sqrt{a} \cdot f_2\left(\frac{a}{W}, \frac{W}{L}, v\right)$	48

Note: E , elastic modulus, U_o displacement in the load line.

(a) By finite element analysis.

Source: Ref 14

Specimen Grips. The requirements for gripping an ultrasonic fatigue specimen are minimal. The only gripping requirements in ultrasonic fatigue are maintenance of intimate contact between the specimen and horn to allow good acoustic coupling and the absence of external forces that would disturb the resonance of the remainder of the wave train. Consequently, a fatigue specimen with a 5 mm (0.2 in.) gage can be held in place by a single 6.4 mm (0.25 in.) stud while being fatigued to failure at a stress amplitude of 485 MPa (70 ksi) or more.

Generally, gripping is accomplished by an internal thread arrangement. This arrangement is adequate, even with a specimen that is difficult to grip, such as thin-walled tubing. Gripping can be accomplished by an external screw-down collar, which grips the specimen to an extension horn. This is particularly useful for tests at high mean loads. Gripping can also be accomplished by brazing or welding the specimen to a threaded adapter or directly to an acoustic horn. A holder for wire specimens has been developed that allows multiple specimens to be tested in a batch mode (Ref 53). An interference fit of the specimen with the horn also is satisfactory, as long as good acoustic coupling with the horn is obtained. Attachment of the specimen to the acoustic horn may be accomplished using an adhesive. This is appropriate for fatigue testing of brittle materials, such as glass and ceramics.

Most ultrasonic converter cases are grounded. If metal-to-metal contact is maintained throughout the wave train, the specimen will be grounded also. An electrically floating specimen is needed if electrochemical potential or corrosion current is to be measured during testing. The specimen can be isolated from the horn by using an extension horn made of a nonconducting material, such as Lucite, to grip the specimen. Such grips limit the magnitude of the stress amplitude that can be transmitted to the specimen because of high dissipation of energy or low fatigue strength of these materials.

References cited in this section

14. P. Bajons, in *Ultrasonic Fatigue*, J.M. Wells, O. Buck, L.D. Roth, and J.K. Tien, Ed., TMS-AIME, Warrendale, PA, 1982, p 15
15. E.A. Neppiras, *Proc. ASTM*, Vol 59, 1959, p 691
19. S. Stanzl and E. Tschegg, *Met. Sci.*, April 1980, p 137
39. L.E. Willertz and L. Patterson, in *Ultrasonic Fatigue*, J.M. Wells, O. Buck, L.D. Roth, and J.K. Tien, Ed., TMS-AIME, Warrendale, PA, 1982, p 119
41. C.R. Sirian, A.F. Conn, R.B. Mignogna, and R.E. Green, Jr., in *Ultrasonic Fatigue*, J.M. Wells, O. Buck, L.D. Roth, and J.K. Tien, Ed., TMS-AIME, Warrendale, PA, 1982, p 87
42. R.E. Petersen, *Stress Concentration Factors*, John Wiley & Sons, New York, 1973
43. R.E. Petersen, *Trans. ASME (Appl. Mech. Sect.)*, Vol 58, 1936, p A-149
44. R. Stickler and B. Weiss, in *Ultrasonic Fatigue*, J.M. Wells, O. Buck, L.D. Roth, and J.K. Tien, Ed., TMS-AIME, Warrendale, PA, 1982, p 135
45. S. Purushothoman, J.P. Wallace, and J.K. Tien, *Ultrasonics International 1973 Conference Proceedings*, IPC Science and Technology Publications, Guildford, Surrey, U.K., 1973, p 244
46. W. Hessler, H. Mullner, and B. Weiss, *Met. Sci.*, May 1981, p 225
47. B. Weiss, R. Stickler, J. Fembock, and K. Pffafinger, *Fatigue Eng. Mater. Struct.*, Vol 2, 1979, p 73
48. W. Hoffelner and P. Gudmundson, *Eng. Fract. Mech.*, Vol 16, 1982, p 365
49. W. Hoffelner, *J. Phys. E, Sci. Instrum.*, Vol 13, 1980, p 617
50. N. Dowling, *Cyclic Stress-Strain and Plastic Deformation Aspects of Fatigue Growth*, STP 637, ASTM, Philadelphia, 1976, p 97
51. B. Weiss, Determination of The Threshold Stress Intensity Value of Mo and Mo-Alloys using a 20 kHz method (German), *Metall*, Vol 34, 1980, p 636

52. S. Purushothoman and J.K. Tien, *Metall. Trans. A*, Vol 9, 1975, p 367

53. J. Babouk, K. Kromp, W. Kromp, and P. Bajons, in *Ultrasonic Fatigue*, J.M. Wells, O. Buck, L.D. Roth, and J.K. Tien, Ed., TMS-AIME, Warrendale, PA, 1982, p 51

Ultrasonic Fatigue Testing

Applications

Ultrasonic fatigue testing has been applied successfully to many situations that require fatigue initiation and crack growth data. Testing has been performed under a variety of loading conditions, specimen geometries, and environmental constraints. With perhaps the exception of plastic strain-controlled testing and single-cycle hysteresis testing, ultrasonic fatigue techniques can be readily applied to the problems of fatigue that traditionally have been confronted at lower frequencies.

Plastic strain rate is a function of strain amplitude and waveform as well as cyclic frequency. In ultrasonic fatigue testing, there is some question as to the effect of increased strain rate from testing at ultrasonic frequencies. Experimentation generally is required, but it is also clear that body-centered cubic (bcc) materials exhibit a much larger strain-rate dependence than face-centered cubic (fcc) materials.

The cyclic deformation of bcc materials is quite different from that of fcc materials and can be quite complex. The athermal portion of the flow stress is due primarily to dislocation interactions leading to work hardening. The effective stress is dominated by the lattice friction stress. Thus, strain rate and effect of impurities are extremely important in the deformation behavior of bcc materials.

In general, the strain-rate sensitivity of engineering alloys and materials often requires experimental verification because of the many possible combinations of alloy compositions, properties, and operating environments. Changes in alloy composition affect the activation barriers to deformation, and the high-frequency behavior might be moderated between the paradigms of bcc and fcc materials. Testing in aggressive environments can offset the expected behavior. Additional information on strain-rate-dependent fatigue behavior can be found in Ref 54, 55, 56.

References cited in this section

54. C. Laird and P. Charlsey, in *Ultrasonic Fatigue*, J.M. Wells, O. Buck, L.D. Roth, and J.K. Tien, Ed., TMS-AIME, Warrendale, PA, 1982, p 183

55. J.K. Tien, in *Ultrasonic Fatigue*, J.M. Wells, O. Buck, L.D. Roth, and J.K. Tien, Ed., TMS-AIME, Warrendale, PA, 1982, p 1

56. L.E. Coffin, in *Ultrasonic Fatigue*, J.M. Wells, O. Buck, L.D. Roth, and J.K. Tien, Ed., TMS-AIME, Warrendale, PA, 1982, p 423

Ultrasonic Fatigue Testing

Acknowledgments

Adapted from the article “Ultrasonic Fatigue Testing” by L.D. Roth (with contributions from participants of the First International Conference on Ultrasonic Fatigue Testing) published in *Mechanical Testing*, Volume 8 of the 9th Edition *Metals Handbook*.

Ultrasonic Fatigue Testing

References

1. B. Hopkinson, *Proc. R. Soc. (London) A*, Vol 86, 1911, p 101
2. C.F. Jenkin, *Proc. R. Soc. (London) A*, Vol 109, 1925, p 119.
3. C.F. Jenkin and G.D. Lehmann, *Proc. R. Soc. (London) A*, Vol 125, 1929, p 83
4. W.P. Mason, *Piezoelectric Crystals and Their Application in Ultrasonics*, Van Nostrand, New York, 1950, p 161
5. F. Girard and G. Vidal, *Rev. Metall.*, Vol 56, 1959, p 25.
6. M. Kikukawa, K. Ohji, and K. Ogura, *J. Basic. Eng. (Trans. ASME D)*, Vol 87, 1965, p 857
7. L.E. Willertz, *Int. Met. Rev.*, No. 2, 1980, p 65, rev 250
8. J.M. Wells, O. Buck, L.D. Roth, and J.K. Tien, Ed., *Ultrasonic Fatigue*, TMS-AIME, Warrendale, PA, 1982
9. B.S. Hockenhull, in *Physics and Non Destructive Testing*, Gordon Breach, New York, 1967, p 195
10. H. Koganei, S. Tanaka, and T. Sakurai, *Trans. Iron Steel Inst. Jpn.*, Vol 17, 1977, p 1979
11. J. Awatani and K. Katagiri, *Bull. Jpn. Soc. Mech. Eng.*, Vol 12, 1969, p 10
12. W. Hoffelner, in *High Temperature Alloys for Gas Turbines: 1982*, R. Brunetaud, D. Coutsouradis, T.B. Gibbons, Y. Lindblum, D.B. Meadowcraft, and R. Stickler, Ed., R. Reidal Publishing, Boston, 1982, p 645
13. L.D. Roth and L.E. Willertz, in *Environment Sensitive Fracture: Evaluation and Comparison of Test Methods*, ASTM STP 821, E.N. Pugh and G.M. Ugiansky, Ed., ASTM, Philadelphia, 1984, p 497
14. P. Bajons, in *Ultrasonic Fatigue*, J.M. Wells, O. Buck, L.D. Roth, and J.K. Tien, Ed., TMS-AIME, Warrendale, PA, 1982, p 15
15. E.A. Neppiras, *Proc. ASTM*, Vol 59, 1959, p 691
16. J.K. Tien, S. Purushothoman, R.M. Arons, J.P. Wallace, O. Buck, H.L. Marcus, R.V. Inman, and G.J. Crandall, *Rev. Sci. Instrum.*, Vol 46, 1975, p 840
17. W. Kromp, K. Kromp, H. Bitt, H. Langer, and B. Weiss, *Ultrasonics International 1973 Conference Proceedings*, IPC Science and Technology Publications, Guildford, Surrey, U.K., 1973, p 238
18. I. Hansson and A. Tholen, *Ultrasonics*, March 1978, p 57

19. S. Stanzl and E. Tschegg, *Met. Sci.*, April 1980, p 137
20. R.A. Yeske and L.D. Roth, in *Ultrasonic Fatigue*, J.M. Wells, O. Buck, L.D. Roth, and J.K. Tien, Ed., TMS-AIME, Warrendale, PA, 1982, p 365
21. P. Trimmel and W. Kromp, in *Ultrasonic Fatigue*, J.M. Wells, O. Buck, L.D. Roth, and J.K. Tien, Ed., TMS-AIME, Warrendale, PA, 1982, p 37
22. W.P. Mason, *J. Acoust. Soc. Am.*, Vol 28, 1956, p 1207
23. J.R. Frederick, *Ultrasonic Engineering*, John Wiley & Sons, New York, 1970
24. G. Amza and D. Drimer, *Ultrasonics*, Vol 14, 1976, p 223
25. E. Eisner, *J. Acoust. Soc. Am.*, Vol 35, 1963, p 1367
26. L. Balamuth, *Trans. IRE (Ultrasonic Eng.)*, Vol 2, 1954, p 23
27. B.S. Hockenhull, C.N. Owston, and R.G. Hacking, *Ultrasonics*, Vol 9, 1971, p 26
28. A. Thiruvengadam, *J. Eng. Ind. (Trans. ASME)*, Vol 11, 1966, p 332
29. H. Konagai, S. Tanaka, and T. Sakurai, *J. Soc. Mater. Sci., Jpn.*, Vol 24, 1975, p 753
30. G.C. George, *Corrosion Fatigue: Chemistry, Mechanics and Microstructure*, O. Devereux et al., Ed., National Association of Corrosion Engineers, Houston, 1972, p 459
31. V.A. Kuz'menko, G.G. Pisarenko, and A.K. Gerikhanov, *Probl. Prochn.*, Vol 4, 1977, p 120
32. R.B. Mignogna and R.E. Green, Jr., in *Ultrasonic Fatigue*, J.M. Wells, O. Buck, L.D. Roth, and J.K. Tien, Ed., TMS-AIME, Warrendale, PA, 1982, p 63
33. F. Blaha and B. Langenecker, *Die Naturwiss.*, Vol 42, 1955, p 556
34. G. Whitlow, L.E. Willertz, and J.K. Tien, in *Ultrasonic Fatigue*, J.M. Wells, O. Buck, L.D. Roth, and J.K. Tien, Ed., TMS-AIME, Warrendale, PA, 1982, p 321
35. J.K. Tien and R.P. Gamble, *Met. Trans.*, Vol 2, 1971, p 1933
36. C.H. Green and F. Guiu, *J. Phys. D., Appl. Phys.*, Vol 9, 1976, p 1071
37. J. Awatani, *Bull. Jpn. Soc. Mech. Eng.*, Vol 4, 1961, p 466
38. P. Bajons and W. Kromp, *Ultrasonics*, Vol 16, 1978, p 213
39. L.E. Willertz and L. Patterson, in *Ultrasonic Fatigue*, J.M. Wells, O. Buck, L.D. Roth, and J.K. Tien, Ed., TMS-AIME, Warrendale, PA, 1982, p 119
40. Westinghouse Electric Co., EPRI technical report NP-2957, Electric Power Research Institute, Palo Alto, CA, March 1983
41. C.R. Sirian, A.F. Conn, R.B. Mignogna, and R.E. Green, Jr., in *Ultrasonic Fatigue*, J.M. Wells, O. Buck, L.D. Roth, and J.K. Tien, Ed., TMS-AIME, Warrendale, PA, 1982, p 87

42. R.E. Petersen, *Stress Concentration Factors*, John Wiley & Sons, New York, 1973
43. R.E. Petersen, *Trans. ASME (Appl. Mech. Sect.)*, Vol 58, 1936, p A-149
44. R. Stickler and B. Weiss, in *Ultrasonic Fatigue*, J.M. Wells, O. Buck, L.D. Roth, and J.K. Tien, Ed., TMS-AIME, Warrendale, PA, 1982, p 135
45. S. Purushothoman, J.P. Wallace, and J.K. Tien, *Ultrasonics International 1973 Conference Proceedings*, IPC Science and Technology Publications, Guildford, Surrey, U.K., 1973, p 244
46. W. Hessler, H. Mullner, and B. Weiss, *Met. Sci.*, May 1981, p 225
47. B. Weiss, R. Stickler, J. Fembock, and K. Pffafinger, *Fatigue Eng. Mater. Struct.*, Vol 2, 1979, p 73
48. W. Hoffelner and P. Gudmundson, *Eng. Fract. Mech.*, Vol 16, 1982, p 365
49. W. Hoffelner, *J. Phys. E, Sci. Instrum.*, Vol 13, 1980, p 617
50. N. Dowling, *Cyclic Stress-Strain and Plastic Deformation Aspects of Fatigue Growth*, STP 637, ASTM, Philadelphia, 1976, p 97
51. B. Weiss, Determination of The Threshold Stress Intensity Value of Mo and Mo-Alloys using a 20 kHz method (German), *Metall*, Vol 34, 1980, p 636
52. S. Purushothoman and J.K. Tien, *Metall. Trans. A*, Vol 9, 1975, p 367
53. J. Babouk, K. Kromp, W. Kromp, and P. Bajons, in *Ultrasonic Fatigue*, J.M. Wells, O. Buck, L.D. Roth, and J.K. Tien, Ed., TMS-AIME, Warrendale, PA, 1982, p 51
54. C. Laird and P. Charlseay, in *Ultrasonic Fatigue*, J.M. Wells, O. Buck, L.D. Roth, and J.K. Tien, Ed., TMS-AIME, Warrendale, PA, 1982, p 183
55. J.K. Tien, in *Ultrasonic Fatigue*, J.M. Wells, O. Buck, L.D. Roth, and J.K. Tien, Ed., TMS-AIME, Warrendale, PA, 1982, p 1
56. L.E. Coffin, in *Ultrasonic Fatigue*, J.M. Wells, O. Buck, L.D. Roth, and J.K. Tien, Ed., TMS-AIME, Warrendale, PA, 1982, p 423

Fretting Fatigue Testing

S.J. Shaffer and W.A. Glaeser, Battelle Memorial Institute

Introduction

FRETTING is a special wear process that occurs at the contact area between two materials under load and subject to slight relative movement by vibration or some other force. Damage begins with local adhesion between mating surfaces and progresses when adhered particles are removed from a surface. When adhered particles are removed from the surface, they may react with air or other corrosive environments. Affected surfaces show pits or grooves with surrounding corrosion products. On ferrous metals, corrosion product is

usually a very fine, reddish iron oxide; on aluminum, it is usually black. The debris from fretting of noble metals does not oxidize.

Under fretting conditions, fatigue strength or endurance limits can be reduced by as much as 50 to 70% during fatigue testing (e.g., see Fig. 1a). During fretting fatigue, cracks can initiate at very low stresses, well below the fatigue limit of nonfretted specimens. In fatigue without fretting, the initiation of small cracks can represent 90% of the total component life. The wear mode known as fretting can cause surface microcrack initiation within the first several thousand cycles, significantly reducing the component life. Additionally, cracks due to fretting are usually hidden by the contacting components and are not easily detected. If conditions are favorable for continued propagation of cracks initiated by fretting, catastrophic failure can occur (Fig. 1b). As such, prevention of fretting fatigue is essential in the design process by eliminating or reducing slip between mated surfaces.

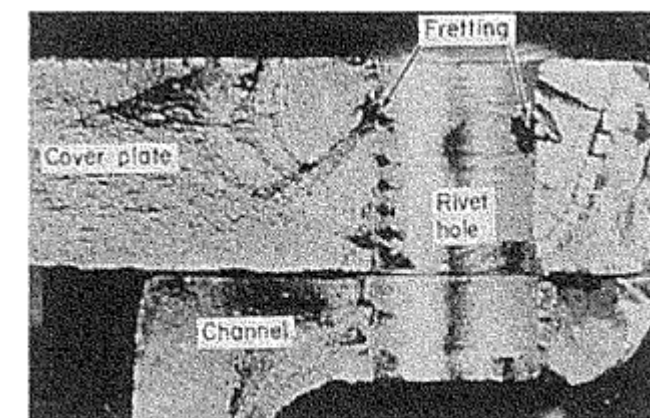
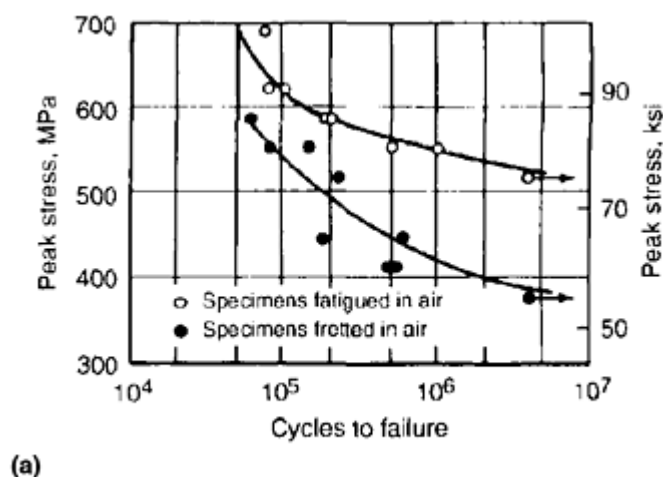


Fig. 1 Effects of fretting. (a) Comparison of fatigue life for 4130 steel under fretting and nonfretting conditions. Specimens were water quenched from 900 °C (1650 °F), tempered 1 h at 450 °C (840 °F), and tested in tension-tension fatigue. Normal stress was 48.3 MPa (7 ksi); slip amplitude was 30–40 μm. (b) Example of catastrophic fatigue due to fretting of a flanged joint

The initiation of fatigue cracks in fretted regions depends mainly on the state of stress in the surface, particularly stresses caused by high friction. The direction of growth of the fatigue cracks is associated with the direction of contact stresses and takes place in a direction perpendicular to the maximum principal stress in the fretting area. After formation due to fretting, cracks propagate initially under shear (mode II) conditions under the influence of the near-surface shear-stress field due to friction of fretting. Beyond that, tensile (mode I) crack propagation under bulk cyclic stresses controls further propagation.

The topics covered in this article are:

- Mechanisms of fretting and fretting fatigue

- Typical occurrences of fretting fatigue
- Fretting fatigue testing
- Prevention methods

Many investigators have contributed to the theoretical and practical research in the field of fretting and fretting fatigue, and the information in this section is derived from their work. Several general texts are available (Ref 1, 2, 3, 4). Reference 5 is another key source for information and illustrations of fretting fatigue failures. In addition, more current discussions and background are provided in the book *Fretting Fatigue* edited by R.B. Waterhouse and T.C. Lindley. The article “On Fretting Maps” by O. Vingsbo and S. Söderberg is another useful general reference on fretting. (See the Selected References for complete bibliographic information.)

As yet, general techniques or models permitting prediction of crack initiation due to fretting are limited. However, an understanding of the factors contributing to fretting fatigue can help minimize the risk and extent of damage. The examples presented in this article from case studies, theoretical work, and laboratory investigations are intended to assist the reader in recognizing the potential for fretting fatigue in design and materials selection. General principles and practical methods for the abatement or elimination of fretting fatigue are summarized in Table 1. More recent information on fretting fatigue testing can be found in ASTM STP 1367 (listed under “Selected References” at the end of this article).

Table 1 Reduction or elimination of fretting fatigue

Principle of abatement or mitigation	Practical method
Reduction in surface shear forces	<ul style="list-style-type: none"> • Reduction in surface normal forces • Reduction in coefficient of friction with coating or lubricants
Reduction/elimination of stress concentrations	<ul style="list-style-type: none"> • Large radii • Material removal (grooving) • Compliant spacers
Introduction of surface compressive stress	<ul style="list-style-type: none"> • Shot or bead blasting • Interference fit • Nitriding/heat treatment
Elimination of relative motion	<ul style="list-style-type: none"> • Increase in surface normal load • Increase in coefficient of friction
Separation of surfaces	<ul style="list-style-type: none"> • Rigid spacers • Coatings • Compliant spacers
Elimination of fretting condition	<ul style="list-style-type: none"> • Drive oscillatory bearing • Remove material from fretting contact (pin joints) • Separation of surfaces (compliant spacers)
Improved wear resistance	<ul style="list-style-type: none"> • Surface hardening • Ion implantation • Soft coatings • Slippery coatings
Reduction of corrosion	<ul style="list-style-type: none"> • Anaerobic sealants • Soft or anodic coatings

References cited in this section

1. R.B. Waterhouse, Ed., *Fretting Fatigue*, Applied Science, 1981
2. M.H. Attia and R.B. Waterhouse, Ed., *Standardization of Fretting Fatigue Test Methods and Equipment*, STP 1159, ASTM, 1992
3. D.A. Hills and D. Nowell, *Mechanics of Fretting Fatigue*, Kluwer Academic Publishers, 1994
4. R.B. Waterhouse, Fretting Corrosion, *Fretting Fatigue*, Pergamon Press, 1972
5. *Proc. Specialists Meeting on Fretting in Aircraft Systems*, AGARD-CP-161, Advisory Group for Aerospace Research and Development, 1974

Fretting Fatigue Testing

S.J. Shaffer and W.A. Glaeser, Battelle Memorial Institute

Fretting and Fretting Fatigue Mechanisms

In general, fretting occurs between two tight-fitting surfaces that are subjected to a cyclic, relative motion of extremely small amplitude. Although certain aspects of the mechanism of fretting are still not thoroughly understood, the fretting process is generally divided into the following three parts: initial conditions of surface adhesion, oscillation accompanied by the generation of debris, and fatigue and wear in the region of contact. Fretting wear occurs from repeated shear stresses that are generated by friction during small-amplitude oscillatory motion or sliding between two surfaces pressed together in intimate contact. Surface cracks initiate in the fretting wear region. The relative slip amplitude is typically less than 50 μm (0.002 in.), and displacements as small as 10^{-4} μm have produced fretting. Generation of fine wear debris that usually oxidizes is an indication of fretting wear (Fig. 2). The following factors are known to influence the severity of fretting:

- *Contact load*. As long as fretting amplitude is not reduced, fretting wear will increase linearly with increasing load.
- *Amplitude*. There appears to be no measurable amplitude below which fretting does not occur. However if the contact conditions are such that deflection is only elastic, it is not likely that fretting damage will occur. Fretting wear loss increases with amplitude. The effect of amplitude can be linear, or there can be a threshold amplitude above which a rapid increase in wear occurs (Ref 4). The transition is not well established and probably depends on the geometry of the contact.
- *Frequency*. When fretting is measured in volume of material removed per unit sliding distance, there does not appear to be a frequency effect.
- *Number of cycles*. An incubation period occurs during which fretting wear is negligible. After the incubation period, a steady-state wear rate is observed, and a more general surface roughening occurs as fretting continues.
- *Relative humidity*. For materials that rust in air, fretting wear is higher in dry air than in saturated air.
- *Temperature*. The effect of elevated temperature on fretting depends on the oxidation characteristics of the material.

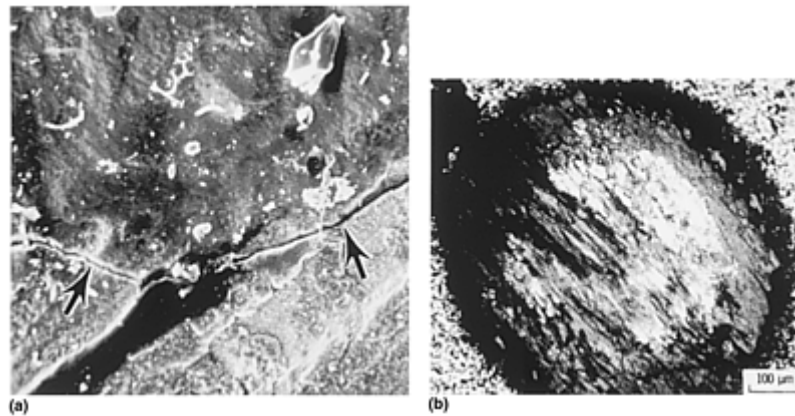


Fig. 2 Fretting wear scars. (a) On steel (arrows indicate fatigue crack). Courtesy of R.B. Waterhouse, University of Nottingham. (b) On high-purity nickel. Courtesy of R.C. Bill, NASA Lewis Research Center

In terms of fatigue, the following three primary variables contribute to shear stresses at the surface and, hence, are important for crack initiation and initial propagation of fretting fatigue cracks:

- Normal load (e.g., contact pressure)
- Relative displacement (slip amplitude)
- Coefficient of friction

The other primary variable is the bulk tensile stresses that control crack propagation beyond the limit of the surface-induced stress field. Secondary factors, including surface roughness, surface contaminants, contact size, debris accumulation, and environment affect fretting fatigue through their influence on the primary variables. Effective lubrication will reduce friction stresses and wear-particle accumulation.

Fretting Modes and Contact Conditions. The oscillatory motion responsible for fretting can be induced by system vibrations or by cyclic loading of one of the components. The relative displacement can be either amplitude controlled or load controlled, or a combination of both. Methods to control fretting fatigue depend on which of these two modes dominates the contact conditions.

Stress Conditions. The nominal macroscopic normal stress between the two surfaces is defined by the normal force divided by the nominal area of contact. Subsurface stress distributions can be computed using Hertzian calculations and the macroscopic contact geometry. The normal stress is also influenced by geometric stress concentrations. The real area of contact is limited to the contacting tips of the microscopic asperities on each of the surfaces, and the local (microscopic) normal stress is dictated by the yield strength of the softer of the two materials. Superimposed on the local normal stresses are shear stresses resulting from the friction of relative displacement of the two contacting members. The magnitude of the shear stresses induced by asperity contact depends on the coefficient of friction (due to adhesive forces between, and interpenetration of, asperities), the local load, asperity geometry, the elastic moduli of the two surfaces, and the amplitude of relative displacement.

Strain Conditions. If the amplitude of oscillation is small, the shear strains are elastic, and the contact condition is one of sticking or *no slip*. Even under microelastic displacements, fatigue cracks can form due to reverse bending at the bases of the contacting asperities. If the amplitude of oscillation is large, depending on the strength and ductility of the asperities in contact, and on the adhesive forces acting between them, the asperities will be forced to pass over one another and *slip* occurs.* With slip, the possibility of wear exists from either adhesion, abrasion, or delamination. All of these material-removal mechanisms lead to a roughening of the surface, the creation of sites for crack initiation, and the generation of wear debris. Cracks can also be initiated by pitting that occurs during fretting.

Conditions for Slip. The local contact conditions may be predominantly displacement controlled or load controlled. In displacement-controlled fretting contacts undergoing full slip, the amplitude of motion is controlled by the external displacements, an example being the relative displacement imposed on adjoining strands of a wire rope passing over a pulley. For force-controlled fretting contacts, the displacement depends on the macroscopic shear force, the normal force, and the coefficient of friction; for example, the mating forces of

a bolted flange or a hub/shaft press fit interface. No slip occurs until the shear stress exceeds the product of the normal force and local coefficient of friction. The condition for slip is met when

$$\tau > \mu\sigma_n \quad (\text{Eq 1})$$

where τ is the local shear stress, μ is the coefficient of friction between contacting surfaces, and σ_n is the local normal stress.

Regions of both slip and no-slip can occur at an interface of contacting solids. This is most easily seen for convex contacts using the elastic stress analysis of a sphere pressed into a plate, as shown in Fig. 3 (Ref 6). The normal (Hertzian) stress field is an elliptical distribution with the maximum stress occurring under the center of the contact. The shear stresses, which promote relative slip, are a maximum at the edges of the contact (limited by yielding) and a minimum in the center. The forces resisting sliding due to the shear stress are given by μN . The condition pictured is known as *partial slip*. As μN is increased, the region of sticking expands, and vice versa. When the shear forces of fretting are superimposed on this stress field, the result is a smaller “stick” area. This analysis can also apply to a cylindrical contact or can be adapted to microscopic asperity contacts.

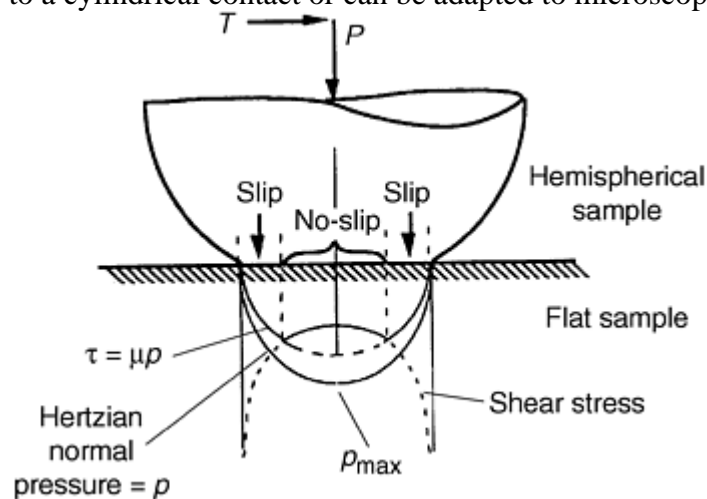


Fig. 3 Stress distribution for hemispherical contact pressed into flat plate. Source: Ref 6

For contact between nominally flat surfaces, the stress state is different, though the slip condition is still defined by Eq 1. The macroscopic stress concentrations for well-defined geometries can be computed using finite-element modeling (FEM) analysis, although wear will change the assumed contact geometry. A general treatment of the subject can be found in Ref 3.

Fatigue-Crack Nucleation from Fretting. Crack nucleation due to fretting must involve a stress concentration or discontinuity. At the microscopic level, examples include: microcracks formed at the base of asperities due to reverse-bending fatigue of the asperities, stress concentrations in the pits left by sheared adhering “cold-welded” asperity junctions, corrosion pits that form due to removal of protective oxides by fretting, grooves due to abrasion, or delamination of a thin surface region whose work-hardening capacity has been exhausted. At the macroscopic level, cracks are proposed to form solely as a result of geometric stress concentrations, usually at the edges of the fretting contact region, where shear stresses are predicted to be highest, at some microscopic inhomogeneity. The two views are not significantly different. The second view is more amenable to modeling and FEM analysis.

The location of crack nucleation depends on the contact conditions. Under *full-slip conditions*, in the absence of stress concentrations at the edge of the contact, cracks can nucleate anywhere in the contact region. The number of asperity interactions per cycle depends on the asperity distribution (surface roughness) and the amplitude of relative motion. Several cracks may be formed. Their stress fields can interact and lead to a decrease in the stress field associated with a single crack. This may explain why multiple nonpropagating cracks are often found in association with fretting. Under *partial-slip conditions*, the cracks always form at the border between the slip and the no-slip regions. In this case, multiple cracks are proposed to result from the movement of the slip/no-slip boundary due to the generation of debris (Ref 7). Though less likely, cracks can also form in the region of *no slip* (full sticking) due to reciprocating subsurface shear stresses associated with reversing elastic deformation of the contacting asperities and stress concentrations at their bases leading to local microplastic deformation and fatigue.

Fatigue-Crack Propagation during Fretting Fatigue. Crack propagation is initially driven by the stress state dominated by the surface shearing. As such, when viewed in cross section, the crack direction initially appears at an angle to the surface of between 35 and 55°. Mode II crack propagation dominates this region. The mode II propagation may depend on material parameters such as grain size, texture, and phase morphology. Because the surface shear stresses fall off rapidly with depth, the crack will either arrest, or, if static or alternating tensile stresses exist in the bulk material, will change direction and run perpendicular to the surface as the driving forces come under the control of the bulk tensile forces (Fig. 4). The depth at which this occurs depends on the magnitude of the surface shear stresses, which depend on the coefficient of friction and normal contact stress. For Hertzian stresses of convex contacts, this depth is on the order of the half-width of the contact area. Beyond this depth, mode I crack propagation analysis can be used to predict the growth rate under the bulk stress state.

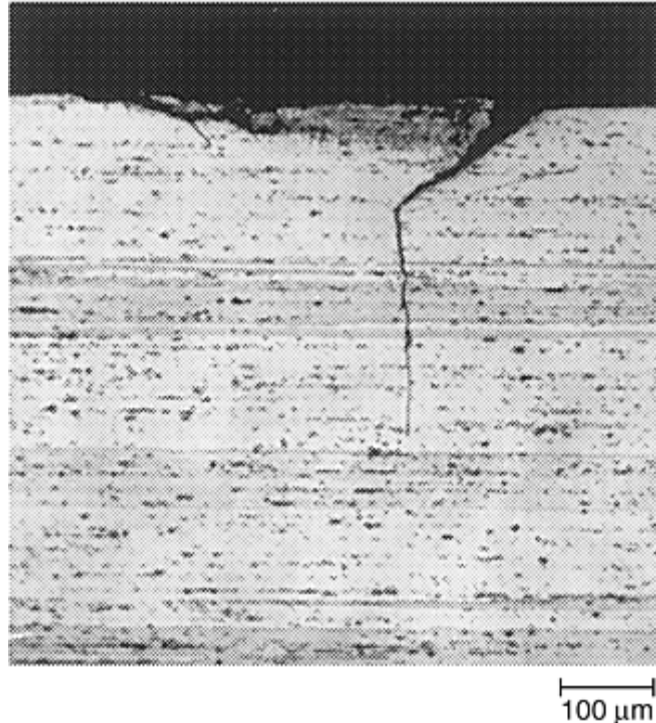


Fig. 4 Example of fretting fatigue crack viewed in cross section. Courtesy of R.B. Waterhouse, University of Nottingham

A phenomenon peculiar to fretting is that some of the fatigue cracks do not propagate because the effect of contact stress extends only to a very shallow depth below the fretted surface. At this point, favorable compressive residual stresses retard or completely halt crack propagation. Under full-slip conditions, the wear rate caused by fretting occasionally outpaces the growth rate of surface-initiated fatigue cracks. In this situation, fretting wear preempts fretting fatigue.

Footnote

* In fretting, the term *slip* is used to denote small-amplitude surface displacements. In contrast to *sliding*, which denotes macroscopic displacements. Additionally, in this article *slip* does not refer to the mechanism of fatigue resulting as a consequence of dislocation motion.

References cited in this section

3. D.A. Hills and D. Nowell, *Mechanics of Fretting Fatigue*, Kluwer Academic Publishers, 1994
4. R.B. Waterhouse, Fretting Corrosion, *Fretting Fatigue*, Pergamon Press, 1972
6. R.D. Mindlin, Compliance of Elastic Bodies in Contact, *J. Appl. Mech.*, Vol 16, 1949, p 259–268

Fretting Fatigue Testing

S.J. Shaffer and W.A. Glaeser, Battelle Memorial Institute

Typical Systems and Specific Remedies

Fretting generally occurs at contacting surfaces that are intended to be fixed in relation to each other but that actually undergo minute alternating relative motion that is usually produced by vibration. Fretting generally does not occur on contacting surfaces in continuous motion, such as ball or sleeve bearings. There are exceptions, however, such as contact between balls and raceways in bearings and between mating surfaces in oscillating bearings and flexible couplings. Common sites for fretting are in joints that are bolted, keyed, pinned, press fitted, or riveted; in oscillating bearings, splines, couplings, clutches, spindles, and seals; in press fits on shafts; and in universal joints, baseplates, shackles, and orthopedic implants.

Three general geometries and loading conditions for fretting fatigue are considered in this section:

- Parallel surfaces clamped together with some type of fastener, such as a bolted flange or riveted lap joint
- Parallel surfaces loaded by means of a press or interference fit, such as a gear or wheel on a shaft
- Convex contacts, as found beneath a convex washer, between crossed cylinders such as wire rope strands, or a sphere or a cylinder in a bearing race

Specific remedies to reduce fretting are given for these common examples. When fretting occurs, it often cannot be eliminated but can be reduced in severity.

Parallel Contact with External Loading (Fastened Joints). Bolted flanges in pipe systems are common locations for fretting fatigue. Cracks can occur in the plate either under a bolt head or washer (load controlled), on the inside diameter of the bolt through-hole (displacement controlled), or on the surface of one plate at the point of contact with the end of the other plate (load controlled) (Fig. 5a). Lap joints are found in both heavy plates and thin sheets such as aircraft skins. Fretting can occur in the joint or under the head of a countersunk screw, bolt, or rivet (Fig. 5b).

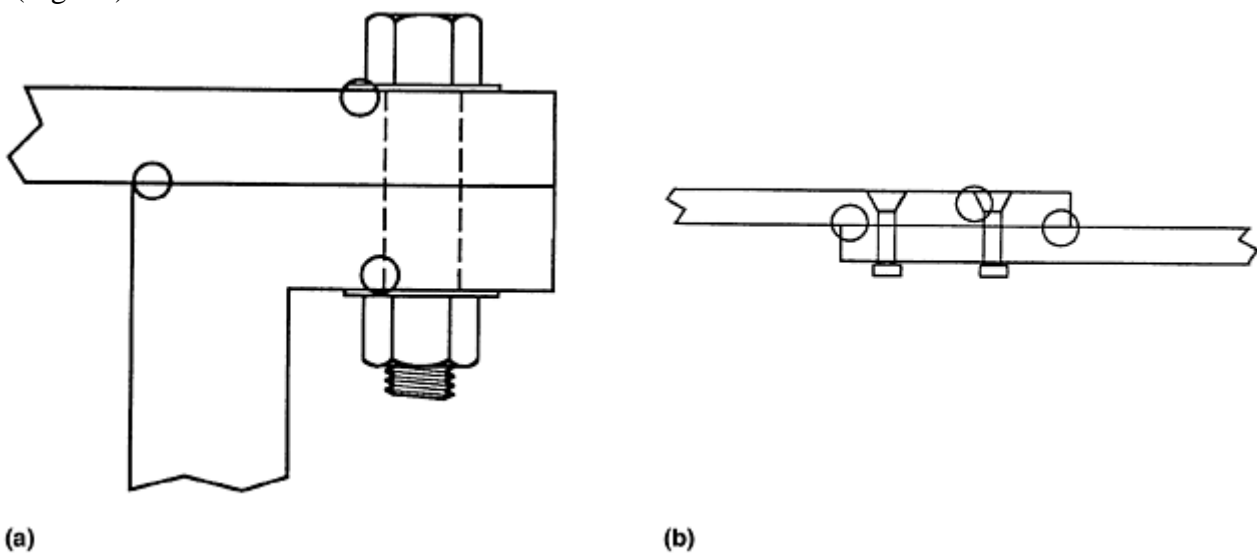


Fig. 5 Typical location of fretting fatigue cracks in (a) a bolted flange, and (b) a lap joint

For both these geometries, the reduction or abatement of fretting severity depends on whether the motion is load controlled or displacement controlled. If it is displacement controlled, then reducing the contact stress and

minimizing the coefficient of friction at the interface is recommended. For lap joints, however, a reduction in the coefficient of friction may result in insufficient load transmitted by the interface, transferring the load to the fasteners and leading to their failure. For load-controlled motions, it may be possible to increase either the clamping force or the coefficient of friction to completely eliminate relative motion between the two contacting members. While adhesives can be used to eliminate the relative motion, their use complicates future disassembly. If motion cannot be completely eliminated, then minimizing the coefficient of friction may help, although this will likely lead to an increased slip amplitude. Alternatively, a thin compliant layer, such as rubber or other polymer, may be able to absorb the deflection and prevent contact between the two members. For pin joints, fretting can occur on diagonally opposite sides of the pin at the points of contact with the hole due to vibrations or reversing loads. In these cases, White (Ref 8) showed that an increase in fatigue strength can be achieved by machining flats on the sides of the pins to prevent contact at the position of maximum stress, thus removing the region where fretting occurs (Fig. 6).

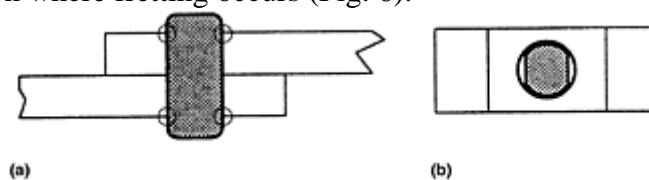


Fig. 6 Pin joint. (a) Fretting locations. (b) Material removal to eliminate region of highest stress

Parallel Surfaces without External Loading. Hubs, flywheels, gears, and other types of press-fit wheels, pulleys, or disks on shafts are subject to fretting fatigue caused by reverse bending strains compounded by the stress concentration where the shaft meets the disk (Fig. 7a). The introduction of lubricant in the interface can make matters worse by increasing the relative slip. In this case, it is best to attempt a strong interference fit. This can be achieved through cooling the shaft and heating the bore of the hole during assembly in order to produce sufficiently high normal stresses to completely eliminate slip within the interface. After assembly, both surfaces will also be in a state of compressive stress, providing further resistance to fatigue-crack propagation. Finally, if possible, a stress-relieving groove or large radius on the shaft (Fig. 7b) should be incorporated into the design.

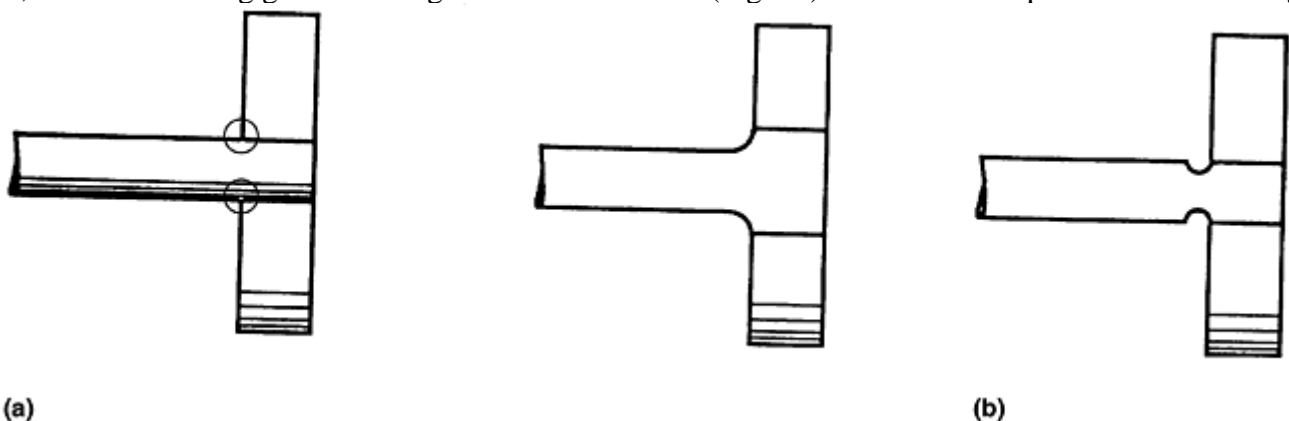


Fig. 7 Wheel on shaft. (a) Location of fretting fatigue cracks. (b) Stress-reduction grooves

Gas-turbine rotor-blade roots and other dovetail joints are potential locations of fretting fatigue failures (Fig. 8a). In this case, the loading conditions are variable and depend on the rotational speed. For these situations, stress-relieving grooves can be incorporated into the design (Fig. 8b). Coatings to reduce the coefficient of friction (and hence the surface shear forces) can also help. Experiments by Ruiz and Chen on simulated blade/disk dovetail joints at 600 °C (1112 °F) indicated that shot peening followed by electroplating with a 10 μm (394 μin.) thick Co/C surface layer was effective (Ref 9). Another example is provided in the article by Johnson in Ref 5.

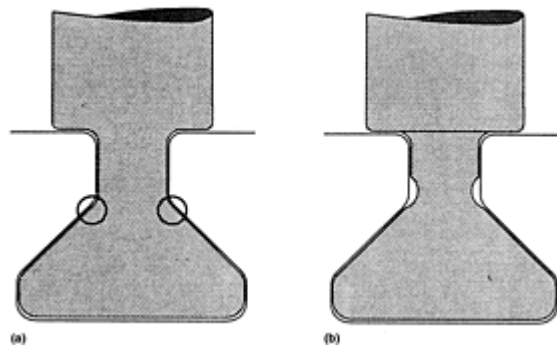


Fig. 8 Dovetail joint. (a) Location of fretting fatigue cracks. (b) Stress-reduction grooves

Convex Surfaces. Fretting fatigue in control cables or wire ropes is caused by small relative displacements between the individual strands as the cable flexes in passing over pulleys, or by varying stresses from wind or water currents (Fig. 9). Stainless steel control cables are particularly susceptible because of the high friction and galling propensity between the strands. Fatigue fractures of the inner strands of the cables make detection by visual inspection virtually impossible until the ends of the fractured strands pop out through the outer strands. Wire rope fretting fatigue in control cables is an example of displacement-controlled contact. As such, large pulley diameters as a function of cable cross section can be specified in the design in order to decrease the displacement and minimize fretting fatigue. Incorporation of lubricant in the cable will reduce strand-to-strand shear forces, but only as long as the lubricant is contained within the rope interior by the outer strands. Takeuchi and Waterhouse report that electrodeposited zinc coatings helped prevent fretting fatigue of wire rope in sea water (Ref 10). The zinc provides both a reduction in the effects of corrosion and a low-shear-strength surface film that reduces friction.

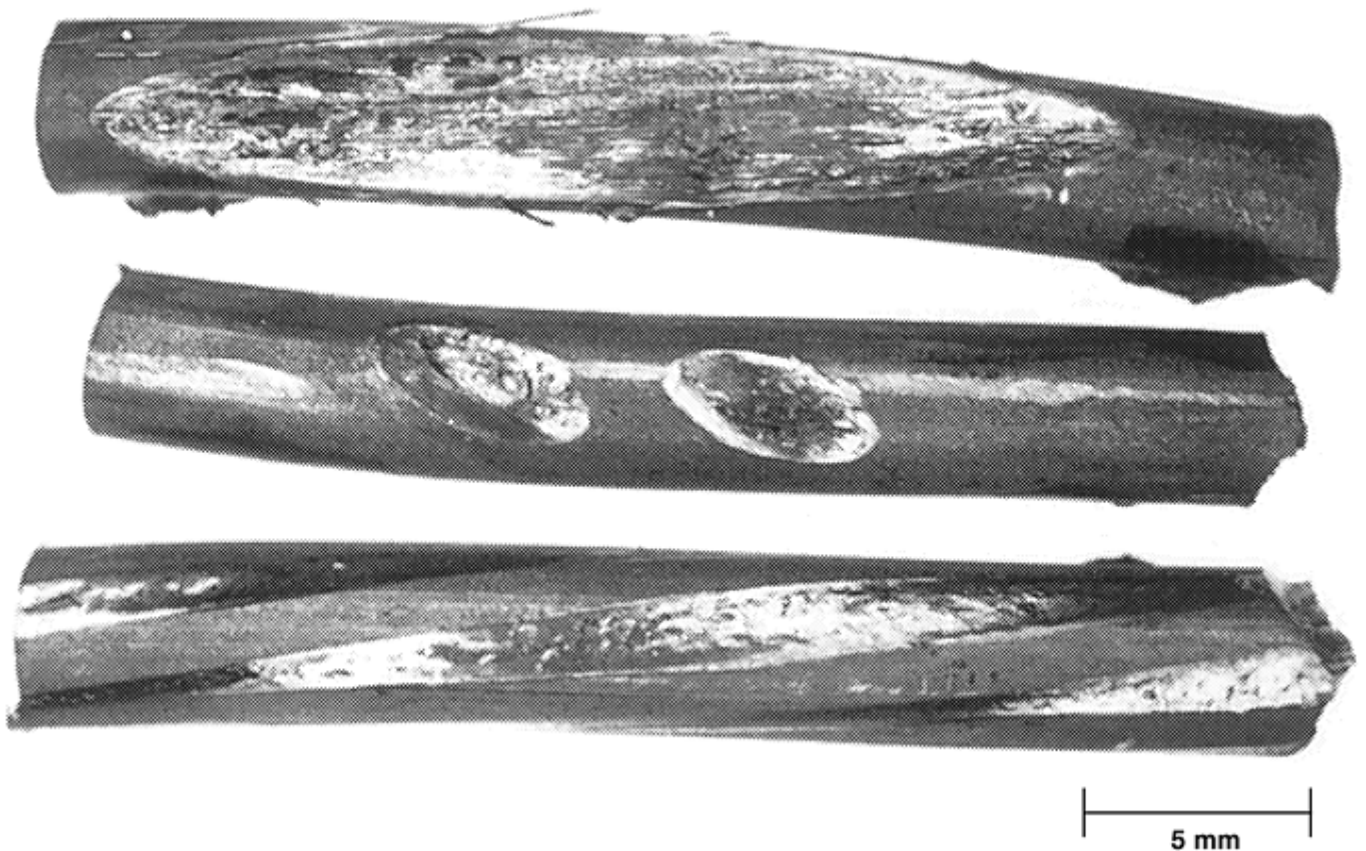


Fig. 9 Examples of fretting on inner strands of drag-line wire rope

In rolling-element bearings, high Hertzian normal stresses occur beneath the contact of bearing balls in their races. Control-system or oscillatory-pivot bearings are often subjected to a low-amplitude, but high-frequency, dithering motion leading to fretting or false brinelling between the balls and the race. (The difference between false brinelling and fretting is discussed in the article “Fretting Wear” in *Friction, Lubrication, and Wear*

Technology, Volume 18 of *ASM Handbook*.) Continuous rotation of one of the races can help prevent fretting under these circumstances (Ref 11).

For convex washers and other convex contacts, a coating, nonmetallic shim, or lubricating film can help reduce the surface shear forces.

References cited in this section

5. *Proc. Specialists Meeting on Fretting in Aircraft Systems*, AGARD-CP-161, Advisory Group for Aerospace Research and Development, 1974
8. D.J. White, *Proc. Inst. Mech. Eng.*, Vol 185, 1970–1971, p 709–716
9. C. Ruiz and K.C. Chen, Life Assessment of Dovetail Joints between Blades and Disks in Aero-Engines, paper C241/86, *Proc. Conf. Fatigue of Engineering Materials and Structures*, Institute of Mechanical Engineers, 1986, p 187–194
10. M. Takeuchi and R.B. Waterhouse, Fretting-Corrosion-Fatigue of High Strength Steel Roping Wire and Some Protective Measures, *Proc. Int. Conf. Evaluation of Materials Performance in Severe Environments*, EVALMAT 89, Iron and Steel Institute of Japan, 1989, p 453–460
11. J.A. Collins, Fretting, Fretting Fatigue, and Fretting Wear, *Failure of Materials in Mechanical Design—Analysis, Prediction, Prevention*, 2nd ed., John Wiley & Sons, 1992, p 504–524

Fretting Fatigue Testing

S.J. Shaffer and W.A. Glaeser, Battelle Memorial Institute

Testing, Modeling, and Analysis

When fretting fatigue is encountered or anticipated, laboratory tests are usually required to find a solution. Test results can also be used to develop an empirical model and are required for validation if a model is to be used for design changes. This section presents types of fretting fatigue tests, the forms of results found in the literature, and the effect of variables on fretting fatigue from different research test programs.

Types of Fretting Fatigue Tests. Fretting fatigue tests are designed to accomplish one of three goals. The first is a test to predict or duplicate field failures and evaluate the effect of design changes or treatments based on replication or simulation of service components and conditions. This is most useful if all the service conditions are known and can be replicated or appropriately scaled, but the results will have limited applicability. A second type of test uses a simple geometry and setup. The contact conditions may not be well defined or directly applicable to a specific application, but they are assumed to be the same for every specimen set and many tests can be conducted at a reasonable cost for screening new material combinations. In the third type of fretting fatigue test, well-defined geometries and controlled and/or monitored loads and displacements are used. These more fundamental tests are intended to evaluate the effect of specific variables such as amplitude, clamping loads, reciprocating stresses, environments, or palliative methods, and to develop and validate fretting fatigue models. In order to apply published test results to a specific component, the test parameters must be well defined and understood for each engineering application. At present, work is under way to standardize test methods in order to assist with this endeavor (Ref 2).

For most fretting fatigue testing, fretting pads are positioned on opposite faces of the sample and can be either single or double footprints of flat or convex contact geometry. The relative displacement between the pads and the sample can be driven independently or can be controlled by the loads and motion of the system (Fig. 10). Of the four methods for cyclic loading of fretting fatigue specimens, general trends indicate that torsional

specimens have the smallest drop in fatigue strength, while the largest drop is for tests carried out under rotating-bending or plane-reverse-bending conditions, with plane push-pull testing falling in between (Ref 7).

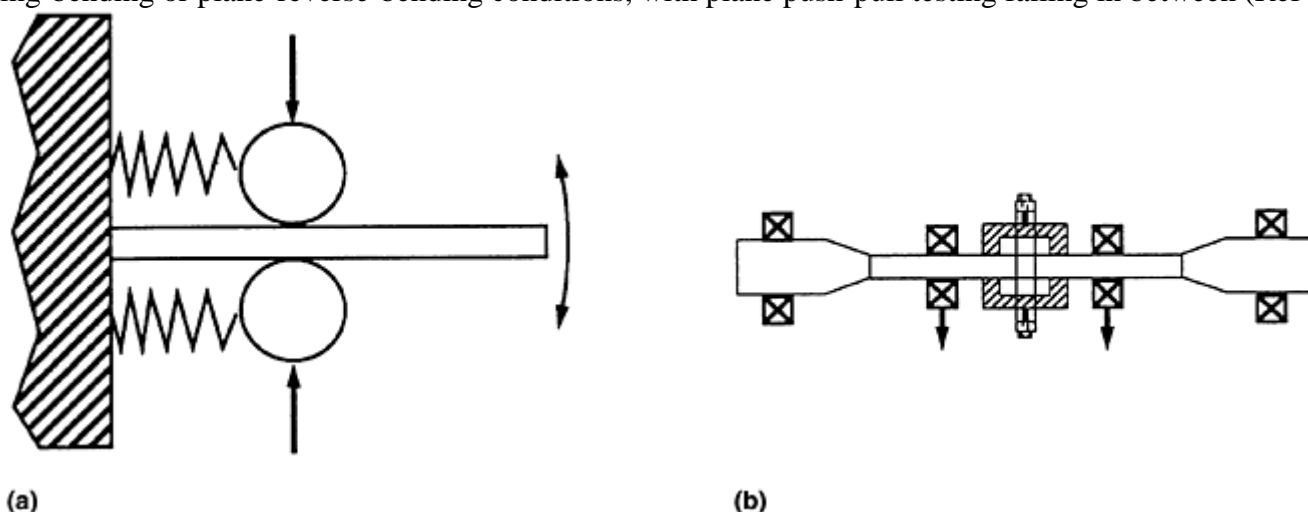


Fig. 10 Examples of fretting fatigue test configurations. (a) Cantilever beam reverse bending with single pads. (b) Rotating fully reversing bending with double foot-pad bridges and proving ring

The influence of fretting on fatigue strength can be determined by two basic methods. In one method, a sample is subjected to a certain number of cycles of fretting, followed by standard fatigue testing to failure without fretting. Plots of fretting cycles versus total cycles are recorded. This method has been used to determine the number of cycles for fatigue-crack detection under the given geometry, material, normal stress, applied reversing stress, and relative slip amplitude (Ref 12).

Influence of Fretting on $S-N$ Plot. In the second method, the sample is subjected to fretting for the entire test. The fretting fatigue life or strength is determined by plotting the number of cycles to failure on an $S-\log N$ curve where $\pm S$ is the alternating stress. The strength-reduction factor (SRF) is defined by the ratio of the plain fatigue strength to the fretting fatigue strength as shown in Fig. 11 and is attributed to a decrease in crack nucleation time. A shift in cycles to failure at a given strength level is attributed to an increase in crack propagation rate and is often observed under corrosive environments.

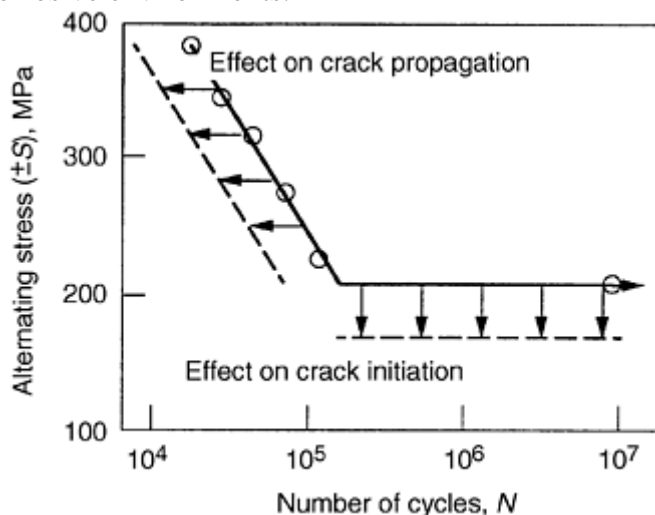


Fig. 11 Effect of fretting on fatigue strength reduction through crack initiation. Fatigue strength reduction is equal to the difference between the solid and dashed lines.

The number of cycles to failure can be defined either as full specimen rupture or by initiation of a propagating (into the bulk stress region) crack. Crack length can be determined either from cross-sectional metallography or by specimen compliance methods.

Stress Analysis, Modeling, and Prediction of Fretting Fatigue. Testing, stress analysis, and modeling are complementary techniques required for understanding and predicting fretting fatigue behavior. For well-defined conditions, test results provide input to models. These models aim to predict crack-initiation location, time,

propagation rate, and the effect of changes in variables on these factors. At present, prediction of fretting fatigue is less developed than for plain (unnotched) fatigue. The main limitation is that continuum-mechanics approaches do not consider microstructural inhomogeneities, and crack nucleation is controlled by such factors as well as “short” fatigue-crack propagation.

Most of the early work in stress-field modeling for fretting fatigue uses, as a starting point, analysis similar to that used by Mindlin (Ref 6) of a sphere pressed into a half plane and expands this to consider other geometries and imposed shear loads. If stress fields are computed using FEM analysis, an assumed contact geometry and coefficient of friction are used, and loads are imposed at various mesh locations in order to compute stresses and subsequent strains. Alternatively, displacements can be imposed and strains and stresses computed. To facilitate modeling, the stress singularity associated with an abrupt contact geometry change, such as at the edge of a bolted flange or a hub/shaft interface, is accommodated by plastic deformation, and a limiting stress is assumed. Current models are limited in that changes in contact geometry due to wear and variations in coefficient of friction due to lubrication or debris accumulation are difficult to take into account.

Experiments have been undertaken and models have been proposed for both the full- and partial-slip regimes and are based on empirical observations. Full-slip and partial-slip conditions can be achieved by varying the test configurations.

In addition, while most fretting contacts are some combination of load- and displacement-controlled conditions, laboratory experiments can be designed either to drive the fretting pads independently (displacement controlled) or to allow them to move as a consequence of the clamping force and displacement of the “beam” sample (load controlled).

For fretting under conditions of full slip, two early models predict the SRF due to fretting. Nishioka and Hirakawa (Ref 13) derived the following equation to describe the fretting fatigue strength limit determined using their displacement-controlled experiment setup with full-slip conditions under the fretting pads (Fig. 10).

$$\sigma_{fw1} = \sigma_{w1} - \mu p_o \{1 - e^{(-\delta/K)}\} \quad (\text{Eq 2})$$

where σ_{fw1} is the fretting fatigue strength, σ_{w1} is the plain fatigue strength, p_o is the clamping pressure, δ is the slip amplitude (in mm), and K is a constant dependent on the material and surface condition (on the order of 3.4×10^{-3} mm, or 1.34×10^{-4} in., in Ref 13).

In later work of Wharton et al. (Ref 14), a similar form was developed in which notch sensitivity of the base material was taken into account. The reduction in fatigue strength due to fretting was then proposed to also be proportional to the shear stress resulting from the contact pressure of the cylindrical fretting pads, inversely proportional to the contact width, and given by the equation:

$$\sigma_{wf} = \sigma_{wo} - q(8\mu P/\pi b) \quad (\text{Eq 3})$$

where σ_{wf} is the fatigue strength with fretting, σ_{wo} is the fatigue strength without fretting, q is the notch sensitivity factor, P is the load per unit length, and b is the contact width under the fretting pads (mm). Note that both these predictions show that SRF is worse as μP or μP_o is increased.

For probable location of fretting fatigue crack nucleation in the partial-slip regime, the approach of Ruiz and Chen (Ref 9) can be used. In their analysis of a dovetail interface, a fretting parameter representing the energy available for causing fretting damage, and given by the product of the slip amplitude, δ , and shear stress, τ , at points under the interface, was computed. Next, the product $\sigma\tau\delta$, called the fretting fatigue parameter, is computed, where σ is the maximum surface tensile stress (resulting from the bulk cyclic loading). A fretting fatigue crack is predicted to occur where the local value of $\sigma\tau\delta$ in the interface exceeds an empirically determined critical value, or, fretting occurs when:

$$\sigma\tau\delta \geq \sigma\tau\delta_{crit} \quad (\text{Eq 4})$$

If $\sigma\tau\delta$ and $\sigma\tau\delta_{crit}$ can be experimentally determined, then the designer can use this value as a design guide. Note that both the slip amplitude and the shear stress depend on the coefficient of friction (with opposite responses) and the imposed loading. Analysis by Nowell and Hills (Ref 15) of this work provided a theoretical justification and a possible method for predicting “initiation” (or nucleation) time based on the total accumulated incremental strain. With further effort, it appears that the composite parameter approach can be applied to fretting fatigue in the full-slip regime and can be expanded to include plasticity.

Other models may be used to determine whether the conditions at the interface will be of full or partial slip and to predict the location of the partial slip. These are generally FEM studies and make use of assumed macroscopic contact conditions and bulk material properties. The text by Hills and Nowell covers this area; yet

it is claimed that no current models exist that can predict crack-initiation times strictly from the knowledge of the states of stress, strain, and displacement on a macroscopic scale (Ref 16). Though experiments are required to determine $\sigma\tau\delta_{crit}$, the most probable location of cracking may be predicted using FEM analysis and the criteria of Ruiz and Chen (Ref 9). If conditions are sufficiently well defined, the slip characteristics of the interfaces may also be predicted. Whether the interface is in full slip or the extent of partial slip will help guide the choice of palliative. This article presents some palliatives that have been applied successfully in the past for fretting abatement. However, the designer is advised to apply discretion in applying techniques listed because results depend on the particular condition. In their review, Gordelier and Chivers (Ref 17) attribute contradictory effects of similar treatments on fretting fatigue to the differing effects on the base materials and to the different contact conditions.

References cited in this section

2. M.H. Attia and R.B. Waterhouse, Ed., *Standardization of Fretting Fatigue Test Methods and Equipment*, STP 1159, ASTM, 1992
6. R.D. Mindlin, Compliance of Elastic Bodies in Contact, *J. Appl. Mech.*, Vol 16, 1949, p 259–268
7. R.B. Waterhouse, Theories of Fretting Processes, *Fretting Fatigue*, Applied Science, 1981, p 203–220
9. C. Ruiz and K.C. Chen, Life Assessment of Dovetail Joints between Blades and Disks in Aero-Engines, paper C241/86, *Proc. Conf. Fatigue of Engineering Materials and Structures*, Institute of Mechanical Engineers, 1986, p 187–194
12. K. Nishioka and K. Hirakawa, Fundamental Investigations of Fretting Fatigue, Part 3, Some Phenomena and Mechanisms of Surface Cracks, *Bull. Jpn. Soc. Mech. Eng.*, Vol 12 (No. 51), 1969, p 397–407
13. K. Nishioka and K. Hirakawa, Fundamental Investigations of Fretting Fatigue, Part 5: The Effect of Relative Slip Amplitude, *Bull. Jpn. Soc. Mech. Eng.*, Vol 12 (No. 52), 1969, p 692–697
14. M.H. Wharton, R.B. Waterhouse, K. Hirakawa, and K. Nishioka, The Effect of Different Contact Materials on the Fretting Fatigue Strength of an Aluminum Alloy, *Wear*, Vol 26, 1973, p 253–260
15. D. Nowell and D.A. Hills, Crack Initiation Criteria in Fretting Fatigue, *Wear*, Vol 136, 1990, p 329–343
16. D.A. Hills and D. Nowell, *Mechanics of Fretting Fatigue*, Kluwer Academic Publishers, 1994, p 210
17. S.C. Gordelier and T.C. Chivers, A Literature Review of the Palliatives for Fretting Fatigue, *Wear*, Vol 56, 1979, p 177–190

Fretting Fatigue Testing

S.J. Shaffer and W.A. Glaeser, Battelle Memorial Institute

Variables Investigated during Fretting Fatigue Tests

Of the dozens of variables that can potentially affect fretting (Ref 18), the three primary variables that control fatigue-crack initiation are surface contact stress, slip amplitude, and coefficient of friction. All other variables are secondary and affect fretting and fretting fatigue through their influence on the primary variables. Unfortunately, many contradictory data appear in the literature (Ref 17). The contradictions concern whether

the fretting conditions were displacement controlled or load controlled and the interactions of the secondary variables between each other and the primary variables. This section presents the results of various investigations into the effect of variables on fretting fatigue.

Contact Stress and Alternating Stress. Contact stresses include both normal and shear stresses imposed at the sample surface. The cyclic shear stresses at the surface are the cause of crack nucleation (where the propensity to cracking from the stress state is also affected by pits, corrosion, and other forms of surface degradation). The magnitude of shear stresses depend on the imposed forces and displacements, the coefficient of friction, macroscopic stress concentrations, and local asperity geometries and distribution. Nishioka and Hirakawa (Ref 19) reported that fretting fatigue strength based on fatigue-crack initiation (or nucleation) was found to decrease linearly with increasing normal force. For fretting fatigue strength based on fracture, they found a critical contact pressure, above which no further degradation occurred. Although their experiments did not reach this level, a sufficiently high normal force can sometimes result in the closure of cracks initiated by fretting through the superposition of a compressive stress.

Alternating stress is the stress imposed on the bulk sample, characterized by an amplitude and a mean stress. For fully reversing bending (which occurs on a rotating shaft), the mean stress is zero. Nishioka and Hirakawa performed experiments in reverse bending on annealed and induction-hardened medium-carbon steel under displacement-controlled conditions (full slip). They found that the mean stress did not affect the range of alternating stress amplitude for fatigue-crack initiation due to fretting, but that it did affect crack propagation (Ref 19).

Wharton et al. also found that the percentage of fatigue life reduction due to fretting, defined by crack propagation to failure, was independent of applied alternating stress level for 70/30 brass and for a 0.7% carbon steel (Ref 20). These experiments were performed in rotating bending using flat fretting pad contacts (Ref 21, 22). Ruiz and Chen found that peak contact stress was important at 600 °C (1112 °F), but at room temperature the fretting parameter, $\tau\delta$, dominated (Ref 9). This was attributed to the nature of the oxide and the influence of the wear debris.

Displacement (Slip Amplitude) and Direction. For conditions of full slip, there is general agreement in the literature that the effect is most severe for slip amplitudes of 20 to 25 μm (787–984 $\mu\text{in.}$). In work on 4130 steel, Gaul and Duquette (Ref 23) found that for clamping pressures of 20 to 41 MPa (3–6 ksi), a minimum in the fatigue life at a given alternating stress occurred at a slip amplitude of 20 μm (787 $\mu\text{in.}$). At amplitudes higher than this, the wear rate due to fretting exceeded the rate of crack growth rate just after initiation and the fretting fatigue strength increased. A similar critical amplitude of relative slip, on the order of 15 to 20 μm (590–787 $\mu\text{in.}$), was found by Nishioka and Hirakawa (Ref 13) for both induction-hardened and quenched-and-tempered medium-carbon steel samples. Clamping pressures of 120 MPa (17 ksi) were used in their work. They also concluded that the fatigue strength-reduction factor due to fretting can be minimized if the fretting amplitude (relative slip) can be kept below 5 μm (197 $\mu\text{in.}$).

An effect related to slip amplitude is that of contact width. Experiments showed that larger-diameter cylinders had a greater detrimental effect on fretting fatigue life for the same line contact stress than small-diameter cylinders (Ref 24). This may be caused by increased partial slip or more asperity contacts per stress cycle.

Nowell and Hills (Ref 15) looked at the effect of slip amplitude through elastic modeling of fretting fatigue in the partial-slip regime. In low-amplitude fretting experiments using cylindrical-radii fretting pads pressed against an in-plane tension/compression loaded Al-4Cu alloy sample, they found a critical contact width for fretting fatigue damage. They also found that a transition between long and short fatigue lives occurred for microslip amplitudes of 0.9 to 1.2 μm (35–47 $\mu\text{in.}$) in the slip zones. This is considerably smaller than the maximum damage displacement of 20 to 30 μm (787–1181 $\mu\text{in.}$) found by Nishioka and Hirakawa and others in their full-slip experiments on steel samples.

The results of work by Collins and Tovey (Ref 25) indicate that fretting motion in the same direction as the cyclic stress has a greater effect than fretting in the perpendicular direction. They used this result to conclude that cracks are nucleated by adhesive wear rather than by abrasive plowing via the expected orientation from each mode.

Coefficient of Friction. The coefficient of friction probably has the greatest influence on fretting fatigue. It influences both slip amplitude and shear stress, though in opposite ways. The influence of different material combinations on fretting fatigue life has been reported to be due to the coefficient of friction (Ref 14). For load-controlled fretting, an increase in coefficient of friction can prevent slip over the whole contact region and reduce or eliminate fretting fatigue. For amplitude-controlled fretting, the opposite effect can be expected, and a

reduction in the coefficient of friction is desired because the surface shear stresses are reduced. Reduction in the coefficient of friction for clamped (bolted or riveted) joints has been shown to be detrimental in some cases because the lower coefficient of friction between the overlapping plates increases the load-carrying requirements of the bolts or rivets leading to failures initiating at the hole edges (Ref 17).

High Temperature. Fretting fatigue strength decreases with increasing temperature for titanium alloys (Ref 26), but was found to increase for the nickel-base alloy Inconel 718 (Ref 27) due to the formation of a protective oxide glaze. Such glazes typically lower the coefficient of friction. For iron-base alloys, both hard and soft flame-sprayed coatings based on molybdenum have shown success in improving the fretting fatigue strength at 300 °C (572 °F). Overs et al. (Ref 28) attribute the improvement to MoO₂ glaze formation.

Environment and Corrosive Media. The effect of environment on fretting fatigue depends on the material and its corrodibility. Fretting action readily destroys passivating films on materials that are normally corrosion resistant. Poon and Hoepfner found that when fretting and corrosion occur simultaneously, the effect of corrosion on fatigue is dominant (Ref 29). As such, many palliatives or remedies for fretting fatigue can be viewed in terms of their effectiveness on corrosion fatigue.

In mildly corrosive aqueous environments, such as weak sodium-chloride solutions representative of human body fluids, the fretting fatigue strength of materials not resistant to corrosion is reduced compared with fretting fatigue in air. Corrosion-resistant materials, such as austenitic stainless steel and titanium, have reduced fretting fatigue strengths in both environments due to the disruption by fretting of the otherwise protective oxide (Ref 30).

Endo found that ductile carbon steels are not affected by water vapor in fretting fatigue (Ref 31). Nishioka and Hirakawa found corrosion to be a secondary factor in fretting fatigue in their work on medium-carbon steels by comparing test data from argon and air experiments (Ref 32). Somewhat in contrast, Endo found that the fretting fatigue strength of carbon steel was higher in argon than in air, explaining that while the crack initiation rate is almost the same, the crack propagation rate is lower in argon (Ref 31).

Aluminum alloys are known to be very sensitive to water corrosion under dynamic conditions. Endo found that both crack initiation and propagation are accelerated by traces of water vapor due to corrosive attack, but not by oxygen. In the case of argon versus air experiments, the removal of oxygen was found to decrease the tangential stress due to soft aluminum wear debris accumulating between the mating surfaces (Ref 31). The alumina formed on aluminum would, if broken, be expected to be more abrasive and give rise to higher shear stresses than soft metallic wear debris.

Compared with tests in air, Ti-6Al-4V alloy was found to be adversely affected by corrosive atmospheres of humid argon and 1% NaCl at alternating stress levels above 120 MPa (17 ksi), but improved fatigue life was observed below 90 MPa (13 ksi) (Ref 33). The nature of the corrosion product was proposed to play a major role, in some cases forming a compacted layer that shielded the metal against crack initiation. Hoepfner reports that steel does not exhibit such a strong dependence on corrosion product (Ref 34).

Corrosion or oxidation are not required in the fretting process. Metallic fretting debris will form with gold or platinum contacts or other nonoxidizable materials (Ref 35).

Microstructure and Material. If the design requirements permit their use, annealed materials were found to be less susceptible to fretting fatigue than materials in the work-hardened state (Ref 20). Similarly, cast structures were less susceptible than forged structures (Ref 36). These results imply that if fatigue-crack nucleation takes place through a wear mode involving exhaustion of work hardening, then prior-worked materials have a significantly shorter nucleation period.

Reeves and Hoepfner (Ref 37) found that carbon steel in the martensitic condition is more resistant to fretting fatigue than in the normalized (ferrite-plus-pearlite) steel due to the higher hardness and wear resistance of the martensitic steel. Nishioka and Hirakawa also found the fatigue limit to be higher on induction-hardened versus annealed steel (Ref 19). These results imply that more wear-resistant materials have better fretting fatigue properties.

Copper-Base Alloys. Wharton et al. (Ref 20) found that 70/30 brass does not show a strength limit in either plain fatigue or fretting fatigue. However, they found that the fretting fatigue strength at a given number of cycles is reduced by a fixed proportion over the plain fatigue strength for two microstructural conditions, independent of applied stress. The reduction was 61 and 74%, for annealed and work-hardened brass, respectively.

Ferritic Alloys. Endo and Goto (Ref 38) found that fatigue cracks generally initiate in ferrite grains, and propagate perpendicular to the sliding direction through a pearlitic region, irrespective of the orientation of the

pearlite plates. Their experiments were performed under reverse bending. They also reported that for two-stage tests on a medium-carbon steel (ferrite-plus-pearlite microstructure), no further reduction in fatigue life occurred if the fretting was continued for the entire test or was stopped after one-quarter of the total life. They concluded that the saturation point in the curve representing fretting cycles versus total fatigue cycles corresponds to the point at which cracks that were initiated during fretting had grown to a depth where they propagated solely due to the macroscopic repeated stress (Ref 38).

Titanium Alloys. For three alpha + beta titanium microstructures, a fine or acicular microstructure was found to be more resistant to damage, defined by the number of propagating cracks found after a given number of cycles at a fixed stress, than a coarser-annealed structure (Ref 7). The finer alloy structure also had a lower SRF.

References cited in this section

7. R.B. Waterhouse, Theories of Fretting Processes, *Fretting Fatigue*, Applied Science, 1981, p 203–220
9. C. Ruiz and K.C. Chen, Life Assessment of Dovetail Joints between Blades and Disks in Aero-Engines, paper C241/86, *Proc. Conf. Fatigue of Engineering Materials and Structures*, Institute of Mechanical Engineers, 1986, p 187–194
13. K. Nishioka and K. Hirakawa, Fundamental Investigations of Fretting Fatigue, Part 5: The Effect of Relative Slip Amplitude, *Bull. Jpn. Soc. Mech. Eng.*, Vol 12 (No. 52), 1969, p 692–697
14. M.H. Wharton, R.B. Waterhouse, K. Hirakawa, and K. Nishioka, The Effect of Different Contact Materials on the Fretting Fatigue Strength of an Aluminum Alloy, *Wear*, Vol 26, 1973, p 253–260
15. D. Nowell and D.A. Hills, Crack Initiation Criteria in Fretting Fatigue, *Wear*, Vol 136, 1990, p 329–343
17. S.C. Gordelier and T.C. Chivers, A Literature Review of the Palliatives for Fretting Fatigue, *Wear*, Vol 56, 1979, p 177–190
18. J.A. Collins and S.M. Marco, The Effect of Stress Direction during Fretting on Subsequent Fatigue Life, *Proc. ASTM*, Vol 64, 1964, p 547–560
19. K. Nishioka and K. Hirakawa, Fundamental Investigations of Fretting Fatigue, Part 4: The Effect of Mean Stress, *Bull. Jpn. Soc. Mech. Eng.*, Vol 12 (No. 51), 1969, p 408–414
20. M.H. Wharton, D.E. Taylor, and R.B. Waterhouse, Metallurgical Factors in the Fretting Fatigue Behaviour of 70/30 Brass and 0.7% Carbon Steel, *Wear*, Vol 23, 1973, p 251–260
21. R.B. Waterhouse and D.E. Taylor, The Initiation of Fatigue Cracks in a 0.7% Carbon Steel by Fretting, *Wear*, Vol 17, 1971, p 139–147
22. R.B. Waterhouse and M. Allery, The Effect of Powders in Petrolatum on the Adhesion between Fretted Surfaces, *Trans. ASLE*, Vol 9, 1966, p 179
23. D.J. Gaul and D.J. Duquette, The Effect of Fretting and Environment on Fatigue Crack Initiation and Early Propagation in a Quenched and Tempered 4130 Steel, *Metall. Trans. A*, Vol 11, Sept 1980, p 1555–1561
24. R.B. Waterhouse, Fretting Fatigue, *Int. Mater. Rev.*, Vol 37 (No. 2), 1992, p 77–97
25. J.A. Collins and F.M. Tovey, Fretting-Fatigue Mechanisms and the Effect of Motion on Fatigue Strength, *J. Mater.*, Vol 7 (No. 4), 1972, p 460–464

26. M.M. Hamdy and R.B. Waterhouse, The Fretting Fatigue Behavior of Ti-6Al-4V at Elevated Temperatures, *Wear*, Vol 56, 1979, p 1–8
27. M.M. Hamdy and R.B. Waterhouse, The Fretting Fatigue Behavior of a Nickel-Based Alloy (Inconel 718) at Elevated Temperatures, *Wear of Materials*, American Society of Mechanical Engineers, 1979, p 351–355
28. M.P. Overs, S.J. Harris, and R.B. Waterhouse, in *Wear of Materials*, American Society of Mechanical Engineers, 1979, p 379–387
29. C. Poon and D.W. Hoepfner, The Effect of Environment on the Mechanism of Fretting Fatigue, *Wear*, Vol 52, 1979, p 175–191
30. R.B. Waterhouse, Fretting Fatigue in Aqueous Electrolytes, *Fretting Fatigue*, R.B. Waterhouse, Ed., Applied Science, 1981, p 159–177
31. K. Endo, Practical Observations of Initiation and Propagation of Fretting Fatigue Cracks, *Fretting Fatigue*, R.B. Waterhouse, Ed., Applied Science, 1981, p 127–141
32. K. Nishioka and K. Hirakawa, Some Further Experiments on the Fatigue Strength of Medium Carbon Steel, *Proc. Mech. Behav. Mater.*, Vol 3, 1971, p 308–318
33. M.H. Wharton and R.B. Waterhouse, Environmental Effects in the Fretting Fatigue of Ti-6Al-4V, *Wear*, Vol 62, 1980, p 287–297
34. D.W. Hoepfner, Environmental Effects in Fretting Fatigue, *Fretting Fatigue*, R.B. Waterhouse, Ed., Applied Science, 1981, p 143–158
35. D. Godfrey and J. Bailey, Early Stages of Fretting of Copper, Iron and Steels, *Lub. Eng.*, Vol 10, 1954, p 155–159
36. G. Sachs and P. Stefan, Chafing Fatigue Strength of Some Metals and Alloys, *Trans. ASM*, Vol 29, 1941, p 373–401
37. R.K. Reeves and D.W. Hoepfner, Microstructural and Environmental Effects on Fretting Fatigue, *Wear*, Vol 47, 1978, p 221–229
38. K. Endo and H. Goto, Initiation and Propagation of Fretting Fatigue Cracks, *Wear*, Vol 38, 1976, p 311–324

Fretting Fatigue Testing

S.J. Shaffer and W.A. Glaeser, Battelle Memorial Institute

Prevention or Improvement

Fretting can be minimized or eliminated in many cases by one or more of the methods outlined in Table 1. Additional techniques in the design stages to diminish the effect of fretting on fatigue are discussed in more detail in this article in terms of:

- *Modification of the surface stress state* by introduction of compressive stresses, reduction of surface shear stresses, or elimination or reduction of relative motion

- *Application of principles for wear and fracture toughness* in selection of materials, coatings, and lubricants

Surface Stress Modification

Design for Introduction of Residual Compressive Stress. The only treatment or remedy that has been shown to be universally effective in improving fretting fatigue is the introduction of residual compressive stresses. The compressive stress will reduce the driving force for both crack initiation and propagation. Residual compressive stresses can be imparted through high and uniform clamping forces or interference fits, plastic deformation of the surfaces, phase changes, and precipitation or diffusion/thermal treatments. If sufficiently deep, superposition of the compressive stress can also decrease the tensile stress field on the propagating crack in the base material.

Plastic deformation by means of shot peening, surface rolling, or ballizing the inside diameter of through-holes has the secondary effect of work hardening of the surface. In some cases, this work hardening leads to higher resistance to fretting wear. Waterhouse and Saunders (Ref 39) have attributed the increase in fretting fatigue strength of austenitic stainless steels by shot peening to an increase in surface hardness to 400 HV, compared to 150 HV for the bulk material, resulting in an increase in the fretting fatigue strength to that of the plain fatigue strength without fretting. In contrast, Leadbeater et al. (Ref 40) found that the improved fretting fatigue life in an aluminum 2014A alloy by shot peening was most likely due only to residual compressive stresses. They determined that while increasing surface roughness had a small beneficial effect, work hardening did not influence fretting fatigue properties.

Cold-working methods are not effective in applications where temperatures during service, or those generated locally due to fretting, would lead to annealing of the previously work-hardened surface.

Nitriding is a very effective palliative for steels. It introduces residual compressive stresses in the surface, and local hardening through solid solution strengthening can decrease the areas of real contact of self-mated ferrous material couples. Both chemical and ion implantation nitriding methods can be used. The effectiveness of carburizing will vary. Although the strength and hardness of the surface will be increased, the heat treatment required to create the martensitic transformation, carburizing, can produce either compressive or tensile residual stresses depending on the section size and shape. Tensile stresses, of course, would be detrimental.

Avoidance of Stress Raisers. Reducing geometric stress raisers in the vicinity of the contact will help prevent fretting fatigue-crack nucleation. Examples were presented in the section “Parallel Surfaces without External Loading” and in Fig. 7 and 8. Local stress raisers due to pitting by wear or pits caused by corrosion can be prevented by corrosion-resistant coatings, such as zinc, or by cathodic protection.

Spacers or Shims. If the amplitude of relative displacement is small, it may be possible to absorb all of the transmitted shear stresses through the elasticity of a thin, flexible layer such as rubber. The effectiveness of this method depends on the modulus of the layer, its thickness, the severity of the normal load, and whether the relative motion is displacement controlled. For aluminum alloys used for aircraft skins at temperatures up to 150 °C (302 °F), Taylor reports in work by Harris (Ref 41) that several investigations have shown the success against fretting fatigue of a joint bonded with isocyanate epoxy resin loaded with MoS₂. It is likely that the solid lubricant lowered the transmitted shear stresses while the resin prevented metal-to-metal contact. It has also been reported that both pure aluminum and copper are effective shim materials to be used against steel for reducing the transmitted shear stresses (Ref 24).

Lubricants. By using lubricants to lower the coefficient of friction, shear stresses resulting from the normal load will be decreased. Again, the amplitude of displacement may be increased. Oils and greases tend to be forced from the interface. Rough surfaces, such as those left by a shot-peening operation, can help retain liquid lubricants. Surface finishes that deliver oil to the fretting site are beneficial. Liquid lubricants can be effective on wire rope, where there is some containment of the lubricant due to the outer strands. Solid lubricants tend to be worn away over time and therefore have limited effectiveness.

Relative Motion. If the relative motion of the two members can be eliminated, the fatigue life can then be computed using standard methods found elsewhere in this Volume. The design concern then shifts to minimizing the stress concentration at the edges of the contact. Methods for eliminating motion include increasing the normal load and/or increasing the coefficient of friction of the interface to expand the region of no slip to the entire contact.

Surface Roughness. Surprisingly, a deliberately rough surface finish may be the best for minimizing fretting fatigue damage. Waterhouse suggests machining grooves in the surface of one of the two contacting members, preferably the one that is not subjected to the major cyclic stresses (Ref 42). It was suggested that the benefit found in this work on aluminum was due to a minimization of the extent of any one contact area. An alternative explanation is that the debris generated during fretting may be more readily trapped in the grooves, thus promoting both a lubricating effect and a reduction in the local stresses due to support by the compacted debris.

Wear and Cracking Resistance

Material Selection for Fretting Fatigue Resistance. Two guides for materials selection choices should be used. The first is based on materials and treatments selected for avoidance of fretting damage, hence minimizing crack nucleation (see Table 2). Materials with low propensity for adhesion are described by Rabinowicz (Ref 44) in terms of the inverse of metallurgical compatibility. Typically, dissimilar couples are preferred. Self-lubricating components, such as porous metal washers impregnated with lubricant, can be used. Materials with high work-hardening capacity or dynamic recrystallization characteristics can also minimize fatigue-crack initiation.

Table 2 Relative fretting resistance of various material combinations

Combination	Fretting resistance
Aluminum on cast iron	Poor
Aluminum on stainless steel	Poor
Bakelite on cast iron	Poor
Cast iron on cast iron, with shellac coating	Poor
Cast iron on chromium plating	Poor
Cast iron on tin plating	Poor
Chromium plating on chromium plating	Poor
Hard tool steel on stainless steel	Poor
Laminated plastic on cast iron	Poor
Magnesium on cast iron	Poor
Brass on cast iron	Average
Cast iron on amalgamated copper plate	Average
Cast iron on cast iron	Average
Cast iron on cast iron, rough surface	Average
Cast iron on copper plating	Average
Cast iron on silver plating	Average
Copper on cast iron	Average
Magnesium on copper plating	Average
Zinc on cast iron	Average
Zirconium on zirconium	Average
Cast iron on cast iron with coating of rubber cement	Good
Cast iron on cast iron with Molykote lubricant	Good
Cast iron on cast iron with phosphate conversion coating	Good
Cast iron on cast iron with rubber gasket	Good
Cast iron on cast iron with tungsten sulfide coating	Good
Cast iron on stainless steel with Molykote lubricant	Good
Cold-rolled steel on cold-rolled steel	Good
Hard tool steel on tool steel	Good
Laminated plastic on gold plating	Good

Source: Ref 43

The second materials selection guide is the use of alloy compositions and thermomechanical treatments for existing alloys that improve their fatigue-crack propagation resistance, as described elsewhere in this Volume and in a variety of mechanical properties handbooks (Ref 45, 46, and 47).

Soft coatings provide a “sacrificial,” low-shear strength layer that reduces the magnitude of the oscillatory shear stresses transmitted into the substrate. Both a lower coefficient of friction and a lower shear strength contribute. A coating that dynamically recrystallizes under service conditions would be expected to be effective. Situations that result in creep of the soft coating must be avoided, as the introduction of excessive clearance or a decrease in preload on bolts or washers can occur. In addition, low friction of soft coatings can lead to larger relative displacements for load-controlled fretting.

Diffusion treatments, such as sulfidized coatings on steel, were shown to be effective in delaying the initiation of a propagating fatigue crack in carbon steels in the laboratory when impregnated with a suitable oil-in-water emulsion (Ref 48) and subsequently applied successfully to compressor-blade roots (Ref 42).

Hard coatings minimize the areas of real contact and penetration by opposing asperities and are less prone to adhesive wear. However, hard coatings have high friction coefficients. As such, high shear stresses are transmitted into the coating, which can limit their effectiveness. Care must be taken in design of coating thickness to avoid high shear stresses at the depth of the coating/substrate interface, which is typically a plane of weakness.

Additionally, hard coatings, such as chromium platings, are often filled with cracks; sprayed molybdenum coatings usually contain pores. These defects in the coatings can serve as initial sites for fatigue cracks to develop and propagate into the substrate. Postcoating shot peening is recommended. Improvement in both electrodeposited chromium and nickel coatings was achieved by thermal diffusion processing followed by shot peening (Ref 42).

While hard coatings can reduce the overall fatigue strength compared with that of samples tested without prior fretting, under fretting fatigue conditions they typically show an improvement over uncoated materials. A pretreatment, such as shot peening or vapor blasting, may be required to compensate for the reduction in normal fatigue strength due to the hard coating. In the case of carbon steel, sprayed molybdenum coatings were found to increase the fretting fatigue strength from 33 to 72% of the normal fatigue strength compared with uncoated samples (Ref 49).

Nonmetallic coatings offer improvement in fretting fatigue resistance by lowering the coefficient of friction and preventing metal-to-metal welding at asperity contacts. The same types of substances that are considered solid “boundary” lubricants for wear control can be used. Conversion coatings produced by phosphating and anodizing, polymer sheets of nylon or polytetrafluoroethylene, and polymerized epoxy resins can all be used. In the case of porous coatings, impregnation with oils or greases can provide effective means of reducing or eliminating the occurrence of fretting fatigue when operating in the full-slip regime over the supply life of the lubricant.

References cited in this section

24. R.B. Waterhouse, Fretting Fatigue, *Int. Mater. Rev.*, Vol 37 (No. 2), 1992, p 77–97
39. R.B. Waterhouse and D.A. Saunders, The Effect of Shot-Peening on the Fretting Fatigue Behaviour of an Austenitic Stainless Steel and a Mild Steel, *Wear*, Vol 53, 1979, p 381–386
40. G. Leadbeater, B. Noble, and R.B. Waterhouse, The Fatigue of an Aluminum Alloy Produced by Fretting on a Shot Peened Surface, *Advances in Fracture Research*, Vol 3 (Fracture 84), 4–10 Dec 1984, Pergmon Press
41. D.E. Taylor, Fretting Fatigue in High Temperature Oxidising Gases, *Fretting Fatigue*, R.B. Waterhouse, Ed., Applied Science, 1981, p 177–202
42. R.B. Waterhouse, Avoidance of Fretting Fatigue, *Fretting Fatigue*, R.B. Waterhouse, Ed., Applied Science, 1981, p 221–240
43. J.R. McDowell, in *Symposium on Fretting Corrosion*, STP 144, ASTM, 1952

44. E. Rabinowicz, Wear Coefficients—Metals, *Wear Control Handbook*, American Society of Mechanical Engineers, 1980, p 475–501
45. AFML-TR-68-115, *Aerospace Structural Metals Handbook*, Materials and Ceramics Information Center, Battelle Columbus Laboratories, 1991
46. MCIC-HB-OIR, *Damage Tolerant Design Handbook*, Materials and Ceramics Information Center, Battelle Columbus Laboratories, 1983
47. MIL-HDBK-5F, *Military Handbook for Metallic Materials and Elements for Aerospace Vehicle Structures*, U.S. Department of Defense, 1990
48. R.B. Waterhouse and M. Allery, The Effect of Non-Metallic Coatings on the Fretting Corrosion of Mild Steel, *Wear*, Vol 8, 1965, p 112–120
49. D.E. Taylor and R.B. Waterhouse, Sprayed Molybdenum Coatings as a Protection Against Fretting Fatigue, *Wear*, Vol 20, 1972, p 401–407

Fretting Fatigue Testing

S.J. Shaffer and W.A. Glaeser, Battelle Memorial Institute

Acknowledgments

This article was adapted from S.J. Shaffer and W.A. Glaeser, Fretting Fatigue, *Fatigue and Fracture*, Vol 19, *ASM Handbook*, ASM International, 1996, p 314–320.

Fretting Fatigue Testing

S.J. Shaffer and W.A. Glaeser, Battelle Memorial Institute

References

1. R.B. Waterhouse, Ed., *Fretting Fatigue*, Applied Science, 1981
2. M.H. Attia and R.B. Waterhouse, Ed., *Standardization of Fretting Fatigue Test Methods and Equipment*, STP 1159, ASTM, 1992
3. D.A. Hills and D. Nowell, *Mechanics of Fretting Fatigue*, Kluwer Academic Publishers, 1994
4. R.B. Waterhouse, Fretting Corrosion, *Fretting Fatigue*, Pergamon Press, 1972
5. *Proc. Specialists Meeting on Fretting in Aircraft Systems*, AGARD-CP-161, Advisory Group for Aerospace Research and Development, 1974
6. R.D. Mindlin, Compliance of Elastic Bodies in Contact, *J. Appl. Mech.*, Vol 16, 1949, p 259–268

7. R.B. Waterhouse, Theories of Fretting Processes, *Fretting Fatigue*, Applied Science, 1981, p 203–220
8. D.J. White, *Proc. Inst. Mech. Eng.*, Vol 185, 1970–1971, p 709–716
9. C. Ruiz and K.C. Chen, Life Assessment of Dovetail Joints between Blades and Disks in Aero-Engines, paper C241/86, *Proc. Conf. Fatigue of Engineering Materials and Structures*, Institute of Mechanical Engineers, 1986, p 187–194
10. M. Takeuchi and R.B. Waterhouse, Fretting-Corrosion-Fatigue of High Strength Steel Roping Wire and Some Protective Measures, *Proc. Int. Conf. Evaluation of Materials Performance in Severe Environments*, EVALMAT 89, Iron and Steel Institute of Japan, 1989, p 453–460
11. J.A. Collins, Fretting, Fretting Fatigue, and Fretting Wear, *Failure of Materials in Mechanical Design—Analysis, Prediction, Prevention*, 2nd ed., John Wiley & Sons, 1992, p 504–524
12. K. Nishioka and K. Hirakawa, Fundamental Investigations of Fretting Fatigue, Part 3, Some Phenomena and Mechanisms of Surface Cracks, *Bull. Jpn. Soc. Mech. Eng.*, Vol 12 (No. 51), 1969, p 397–407
13. K. Nishioka and K. Hirakawa, Fundamental Investigations of Fretting Fatigue, Part 5: The Effect of Relative Slip Amplitude, *Bull. Jpn. Soc. Mech. Eng.*, Vol 12 (No. 52), 1969, p 692–697
14. M.H. Wharton, R.B. Waterhouse, K. Hirakawa, and K. Nishioka, The Effect of Different Contact Materials on the Fretting Fatigue Strength of an Aluminum Alloy, *Wear*, Vol 26, 1973, p 253–260
15. D. Nowell and D.A. Hills, Crack Initiation Criteria in Fretting Fatigue, *Wear*, Vol 136, 1990, p 329–343
16. D.A. Hills and D. Nowell, *Mechanics of Fretting Fatigue*, Kluwer Academic Publishers, 1994, p 210
17. S.C. Gordelier and T.C. Chivers, A Literature Review of the Palliatives for Fretting Fatigue, *Wear*, Vol 56, 1979, p 177–190
18. J.A. Collins and S.M. Marco, The Effect of Stress Direction during Fretting on Subsequent Fatigue Life, *Proc. ASTM*, Vol 64, 1964, p 547–560
19. K. Nishioka and K. Hirakawa, Fundamental Investigations of Fretting Fatigue, Part 4: The Effect of Mean Stress, *Bull. Jpn. Soc. Mech. Eng.*, Vol 12 (No. 51), 1969, p 408–414
20. M.H. Wharton, D.E. Taylor, and R.B. Waterhouse, Metallurgical Factors in the Fretting Fatigue Behaviour of 70/30 Brass and 0.7% Carbon Steel, *Wear*, Vol 23, 1973, p 251–260
21. R.B. Waterhouse and D.E. Taylor, The Initiation of Fatigue Cracks in a 0.7% Carbon Steel by Fretting, *Wear*, Vol 17, 1971, p 139–147
22. R.B. Waterhouse and M. Allery, The Effect of Powders in Petrolatum on the Adhesion between Fretted Surfaces, *Trans. ASLE*, Vol 9, 1966, p 179
23. D.J. Gaul and D.J. Duquette, The Effect of Fretting and Environment on Fatigue Crack Initiation and Early Propagation in a Quenched and Tempered 4130 Steel, *Metall. Trans. A*, Vol 11, Sept 1980, p 1555–1561
24. R.B. Waterhouse, Fretting Fatigue, *Int. Mater. Rev.*, Vol 37 (No. 2), 1992, p 77–97
25. J.A. Collins and F.M. Tovey, Fretting-Fatigue Mechanisms and the Effect of Motion on Fatigue Strength, *J. Mater.*, Vol 7 (No. 4), 1972, p 460–464

26. M.M. Hamdy and R.B. Waterhouse, The Fretting Fatigue Behavior of Ti-6Al-4V at Elevated Temperatures, *Wear*, Vol 56, 1979, p 1–8
27. M.M. Hamdy and R.B. Waterhouse, The Fretting Fatigue Behavior of a Nickel-Based Alloy (Inconel 718) at Elevated Temperatures, *Wear of Materials*, American Society of Mechanical Engineers, 1979, p 351–355
28. M.P. Overs, S.J. Harris, and R.B. Waterhouse, in *Wear of Materials*, American Society of Mechanical Engineers, 1979, p 379–387
29. C. Poon and D.W. Hoepfner, The Effect of Environment on the Mechanism of Fretting Fatigue, *Wear*, Vol 52, 1979, p 175–191
30. R.B. Waterhouse, Fretting Fatigue in Aqueous Electrolytes, *Fretting Fatigue*, R.B. Waterhouse, Ed., Applied Science, 1981, p 159–177
31. K. Endo, Practical Observations of Initiation and Propagation of Fretting Fatigue Cracks, *Fretting Fatigue*, R.B. Waterhouse, Ed., Applied Science, 1981, p 127–141
32. K. Nishioka and K. Hirakawa, Some Further Experiments on the Fatigue Strength of Medium Carbon Steel, *Proc. Mech. Behav. Mater.*, Vol 3, 1971, p 308–318
33. M.H. Wharton and R.B. Waterhouse, Environmental Effects in the Fretting Fatigue of Ti-6Al-4V, *Wear*, Vol 62, 1980, p 287–297
34. D.W. Hoepfner, Environmental Effects in Fretting Fatigue, *Fretting Fatigue*, R.B. Waterhouse, Ed., Applied Science, 1981, p 143–158
35. D. Godfrey and J. Bailey, Early Stages of Fretting of Copper, Iron and Steels, *Lub. Eng.*, Vol 10, 1954, p 155–159
36. G. Sachs and P. Stefan, Chafing Fatigue Strength of Some Metals and Alloys, *Trans. ASM*, Vol 29, 1941, p 373–401
37. R.K. Reeves and D.W. Hoepfner, Microstructural and Environmental Effects on Fretting Fatigue, *Wear*, Vol 47, 1978, p 221–229
38. K. Endo and H. Goto, Initiation and Propagation of Fretting Fatigue Cracks, *Wear*, Vol 38, 1976, p 311–324
39. R.B. Waterhouse and D.A. Saunders, The Effect of Shot-Peening on the Fretting Fatigue Behaviour of an Austenitic Stainless Steel and a Mild Steel, *Wear*, Vol 53, 1979, p 381–386
40. G. Leadbeater, B. Noble, and R.B. Waterhouse, The Fatigue of an Aluminum Alloy Produced by Fretting on a Shot Peened Surface, *Advances in Fracture Research*, Vol 3 (Fracture 84), 4–10 Dec 1984, Pergmon Press
41. D.E. Taylor, Fretting Fatigue in High Temperature Oxidising Gases, *Fretting Fatigue*, R.B. Waterhouse, Ed., Applied Science, 1981, p 177–202
42. R.B. Waterhouse, Avoidance of Fretting Fatigue, *Fretting Fatigue*, R.B. Waterhouse, Ed., Applied Science, 1981, p 221–240
43. J.R. McDowell, in *Symposium on Fretting Corrosion*, STP 144, ASTM, 1952

44. E. Rabinowicz, Wear Coefficients—Metals, *Wear Control Handbook*, American Society of Mechanical Engineers, 1980, p 475–501
45. AFML-TR-68-115, *Aerospace Structural Metals Handbook*, Materials and Ceramics Information Center, Battelle Columbus Laboratories, 1991
46. MCIC-HB-OIR, *Damage Tolerant Design Handbook*, Materials and Ceramics Information Center, Battelle Columbus Laboratories, 1983
47. MIL-HDBK-5F, *Military Handbook for Metallic Materials and Elements for Aerospace Vehicle Structures*, U.S. Department of Defense, 1990
48. R.B. Waterhouse and M. Allery, The Effect of Non-Metallic Coatings on the Fretting Corrosion of Mild Steel, *Wear*, Vol 8, 1965, p 112–120
49. D.E. Taylor and R.B. Waterhouse, Sprayed Molybdenum Coatings as a Protection Against Fretting Fatigue, *Wear*, Vol 20, 1972, p 401–407

Fretting Fatigue Testing

S.J. Shaffer and W.A. Glaeser, Battelle Memorial Institute

Selected References

- R.B. Waterhouse, Fretting Wear, *Friction Lubrication and Wear Technology*, Vol 18, *ASM Handbook*, ASM International, 1992, p 242–256
- R.B. Waterhouse and T.C. Lindley, *Fretting Fatigue*, ESIS 18, Mechanical Engineering Publications, 1994
- O. Vingsbo and S. Söderberg, On Fretting Maps, *Wear*, Vol 126, 1988, p 131–147
- D.W. Hoepfner et al., *Fretting Fatigue: Current Technologies and Practices*, STP 1367, ASTM, 2000

Fatigue Crack Growth Testing

Ashok Saxena, Georgia Institute of Technology; Christopher L. Muhlstein, University of California, Berkeley

Introduction

FATIGUE is generally understood to be a process dominated by cyclic plastic deformation, such that fatigue damage can occur at stresses below the monotonic yield strength. The process of fatigue cracking generally begins from locations where discontinuities exist or where plastic strain accumulates preferentially in the form of slip bands. In most situations, fatigue failures initiate in regions of stress concentration, such as sharp notches, nonmetallic inclusions, or at preexisting cracklike defects. Where failures occur at sharp notches or other stress raisers, cracks first initiate and then propagate to critical size, at which time sudden failure occurs. The fatigue life consists of crack initiation as well as crack propagation. On the other hand, when fatigue failures are caused by large inclusions or preexisting cracklike defects, the entire life consists of crack

propagation. Such situations are commonly encountered in service failures. A typical example of such a failure in a railroad track is shown in Fig. 1. The light area in the photograph is the region of fatigue crack growth, and the surrounding darker area is the region of fast fracture. The dark spot within the light area is the origin of the failure, which is a preexisting defect due to a hydrogen flake.

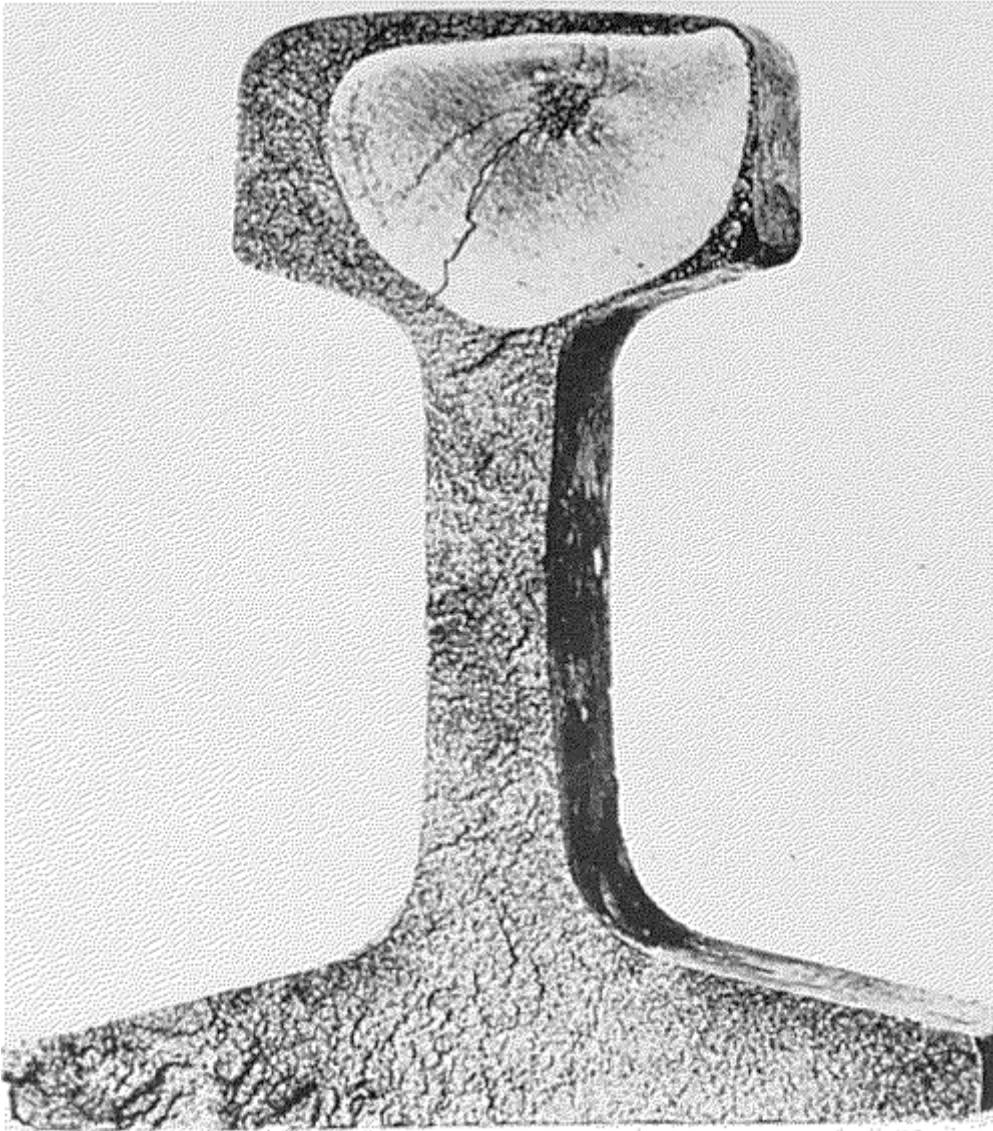


Fig. 1 Fatigue failure of a railroad track

Testing of smooth or notched specimens generally characterizes the overall fatigue life of a specimen material. This type of testing, however, does not distinguish between fatigue crack initiation life and fatigue crack propagation life. With this approach, preexisting flaws or cracklike defects, which would reduce or eliminate the crack initiation portion of the fatigue life, cannot be adequately addressed. Therefore, testing and characterization of fatigue crack growth is used extensively to predict the rate at which subcritical cracks grow due to fatigue loading. For components subjected to cyclic loading, this capability is essential for life prediction, recommendation of a definite accept/reject criterion during nondestructive inspection, and calculation of in-service inspection intervals for continued safe operation.

Fatigue Crack Growth Testing

Ashok Saxena, Georgia Institute of Technology; Christopher L. Muhlstein, University of California, Berkeley

Linear elastic fracture mechanics (LEFM) is an analytical framework that relates the magnitude and distribution of stress in the vicinity of a crack tip to the nominal stress applied to the structure; to the size, shape, and orientation of the crack or cracklike imperfection; and to the crack growth and fracture resistance of the material. The approach is based on the analysis of stress-field equations, which show that the elastic stress field in the region of a crack tip can be described by a single parameter, K called the stress-intensity factor. This same approach is also used to characterize fatigue crack growth rates (da/dN) in terms of the cyclic stress-intensity range parameter (ΔK).

When a component or specimen containing a crack is subjected to cyclic loading, the crack length (a) increases with the number of fatigue cycles (N) if the load amplitude (ΔP), load ratio (R), and cyclic frequency (ν), are held constant. The da/dN increases as the crack length increases during a given test. The da/dN is also higher at any given crack length for tests conducted at higher load amplitudes. Thus, the following functional relationship can be derived from these observations:

$$\left(\frac{da}{dN}\right)_{R, \nu} = f(\Delta P, a) \quad (\text{Eq 1})$$

where the function f is dependent on the geometry of the specimen, the crack length, the loading configuration, and the cyclic load range. This general relation is simplified with the use of the ΔK parameter as summarized below.

Correlation between da/dN and ΔK . In 1963, Paris and Erdogan (Ref 1) published an analysis with considerable fatigue crack growth rate (FCGR) data and demonstrated that a correlation exists between da/dN and the cyclic stress intensity parameter, ΔK . They argued that ΔK characterizes the magnitude of the fatigue stresses in the crack-tip region; hence, it should characterize the crack growth rate. Such a proposition is in obvious agreement with the functional relationships of Eq 1. The parameter ΔK accounts for the magnitude of the load range (ΔP) as well as the crack length and geometry. A number of later studies (Ref 2) have confirmed the findings of Paris and Erdogan. The data for intermediate FCGR values can be represented by the following simple mathematical relationship, commonly known as the Paris equation:

$$\frac{da}{dN} = C (\Delta K)^n \quad (\text{Eq 2})$$

where C and n are constants that can be obtained from the intercept and slope, respectively, of the linear $\log da/dN$ versus $\log \Delta K$ plot. This representation of FCGR is a useful model for midrange FCGR values (Fig. 2).

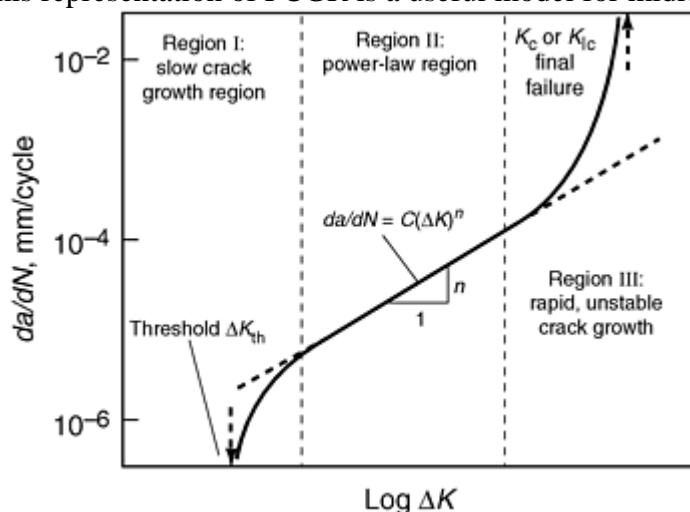


Fig. 2 Fatigue crack growth regimes versus ΔK

It has been shown and it is generally believed that specimen thickness has no significant effect on the FCGR behavior (Ref 3). The ability of ΔK to account for so many variables has tremendous significance in the application of the data. Thus, the FCGR behavior expressed as da/dN versus ΔK can be regarded as a fundamental material property analogous to the yield and ultimate tensile strengths and plane strain fracture toughness, K_{Ic} . From the knowledge of this property, prediction of the crack length versus cycles behavior of any component using that material and containing a preexisting crack or cracklike defect can be obtained, as

long as the fatigue stresses in the component are known and a K expression for the crack/load configuration is available.

Crack-Tip Plasticity during Fatigue. The cyclic stress-intensity parameter, ΔK , is based on LEFM, and it characterizes only the elastic stress field beyond the plastic zone. However, fatigue is a process dominated by cyclic plastic deformation. Even when fatigue damage occurs at stresses below the monotonic yield strength, the process of fatigue cracking begins from locations where there are discontinuities, such as nonmetallic inclusions, or from surfaces where plastic strain accumulates preferentially in the form of slip bands (Ref 4). Therefore, a brief explanation is given for why ΔK can characterize fatigue crack growth behavior.

When a cracked body is subjected to cyclic loading, a monotonic plastic zone develops at the crack tip during the first loading cycle. If predominantly linear elastic conditions are maintained during loading, as are necessary for ΔK to be a valid crack-tip parameter, compressive stress develops within this plastic zone during unloading. Compressive stress develops, because the elastic forces in the overall body tend to restore the original shape (Ref 2). The magnitude of the maximum compressive stress increases as the crack tip is approached. In a small region within the monotonic plastic zone, the maximum compressive stress exceeds the yield strength, resulting in plastic flow in compression. This small region of reversing plastic flow is called the cyclic plastic zone. A simple estimate of the size of this zone was made by Paris (Ref 2) and Rice (Ref 5) for nonhardening materials by substituting $2\sigma_{ys}$ in place of σ_{ys} in the expression for monotonic plastic zone size and by replacing K with ΔK :

$$r_{cp} = \frac{1}{\pi} \left(\frac{\Delta K}{2\sigma_{ys}} \right)^2 \quad (\text{Eq 3})$$

where r_{cp} is the cyclic plastic zone size under plane-stress conditions. For materials that undergo cyclic hardening or softening, a first-order estimate of the fatigue plastic zone size can be obtained by replacing σ_{ys} with the cyclic yield strength (σ_{cys}) in Eq 3.

General Crack Growth Behavior. When crack growth rates over six to seven decades are plotted against ΔK , the behavior is no longer a straight line on a log-log plot. Results of FCGR tests for nearly all metallic structural materials have shown that the da/dN versus ΔK curves have three distinct regions. The behavior in region I (Fig. 2) exhibits a fatigue crack growth threshold, ΔK_{th} , which corresponds to the stress-intensity factor range below which cracks do not propagate. Equation 2 is applicable in the midrange of da/dN values for FCGR (region II, Fig. 2). Typically, the validity of Eq 2 is limited over a range of two to four decades for midrange crack growth rates.

At high ΔK values (region III, Fig. 2), the K_{max} approaches the critical K for instability, K_c , and the crack growth rate accelerates. In some instances, K_c may be equal to K_{Ic} , but this situation cannot be generalized because the FCGR specimens or even actual components may not always satisfy size requirements for valid linear elastic plane-strain conditions. In some materials, there is also an effect of prior fatiguing on the K value at which instability occurs (Ref 6). In such situations, K_c will not be equal to the K_{Ic} of the material.

At low ΔK values (region I, Fig. 2), the crack growth rate decreases rapidly with decreasing ΔK , and ultimately ΔK approaches a threshold value, ΔK_{th} , when the crack growth rate approaches zero. In high-cycle fatigue applications, ΔK_{th} is an important design parameter. The above definition of ΔK_{th} is an idealized definition; for practical usage, it is important to define its value unambiguously. An operational value of ΔK_{th} is frequently defined as the ΔK value at a da/dN of 10^{-10} m/cycle (Ref 7).

FCGR under Elastic-Plastic Conditions. There are applications when fatigue crack growth occurs under conditions of gross plastic deformation, or at least under conditions for which dominant linear elasticity cannot be ensured. As a crack tip parameter, ΔK breaks down under these conditions and can no longer be expected to uniquely characterize FCGR behavior. Dowling and Begley have defined a cyclic J -integral, ΔJ , which is determined utilizing the loading portion of the load-displacement diagram during cyclic loading (Ref 8, 9).

Metals and alloys can be assumed to deform according to the cyclic stress-strain law given by:

$$\Delta \epsilon = \frac{\Delta \sigma}{E} + D' \left(\frac{\Delta \sigma}{2\sigma_{cys}} \right)^{m'} \quad (\text{Eq 4})$$

where $\Delta \epsilon$ is the cyclic strain range, $\Delta \sigma$ is the cyclic stress range, E is the elastic modulus, and D' and m' are empirically determined material constants. The value of ΔJ for such materials can be defined (Ref 10):

$$\Delta J = \int_{\Gamma} (\Delta W) dy - \Delta T_i \left(\frac{\partial \Delta u_i}{\partial x} \right) ds \quad (\text{Eq 5})$$

The term ΔJ in Eq 5 is a path-independent integral along any given path Γ that originates at the lower crack surface and ends on the upper crack surface traversing along the contour in a counterclockwise direction. The definition of ΔJ is written as a direct analogy to Rice's J -integral (Ref 11), used extensively in characterizing fracture under monotonic loading conditions. The term ΔW in Eq 5 is defined as follows:

$$\Delta W = \int \Delta \epsilon_{ij} \sigma_{ij} d(\Delta \epsilon_{ij}) \quad (\text{Eq 6})$$

Other terms in Eq 5 and 6 are:

- ΔT_i is the range of the traction vector
- Δu_i is the range of displacement
- ds is an element along the contour Γ
- $\Delta \sigma_{ij}$ and $\Delta \epsilon_{ij}$ are the ranges of the stress and strain, respectively

All range quantities are calculated by subtracting the values at minimum load from the corresponding values at maximum load. When ΔJ is defined in the above manner, its value characterizes the crack-tip stress and strain ranges according to the Hutchinson (Ref 12) and Rice and Rosengren (Ref 13) relationships. It must also be noted that for linear elastic conditions, Eq 5 will yield the following relationship:

$$\Delta J = \frac{\Delta K^2}{E} \quad (\text{Eq 7})$$

From the above relationship, the data from linear elastic tests and elastic-plastic or fully plastic tests can be combined into a single plot of da/dN with ΔK or $\sqrt{E\Delta J}$. Similarly, the data can be correlated with $\Delta K^2/E$ or ΔJ . Figure 3 shows the FCGR data for A533 and for 304 stainless steel in this manner (Ref 9, 14). These data were developed on specimens of two geometries and, more notably, with varying sizes within those geometries. Thus, small specimens exhibited considerable plasticity, and the large specimens were under dominantly elastic conditions. Despite the enormous differences in the scales of plasticity among the various tests, the FCGR data lay in a single scatter band.

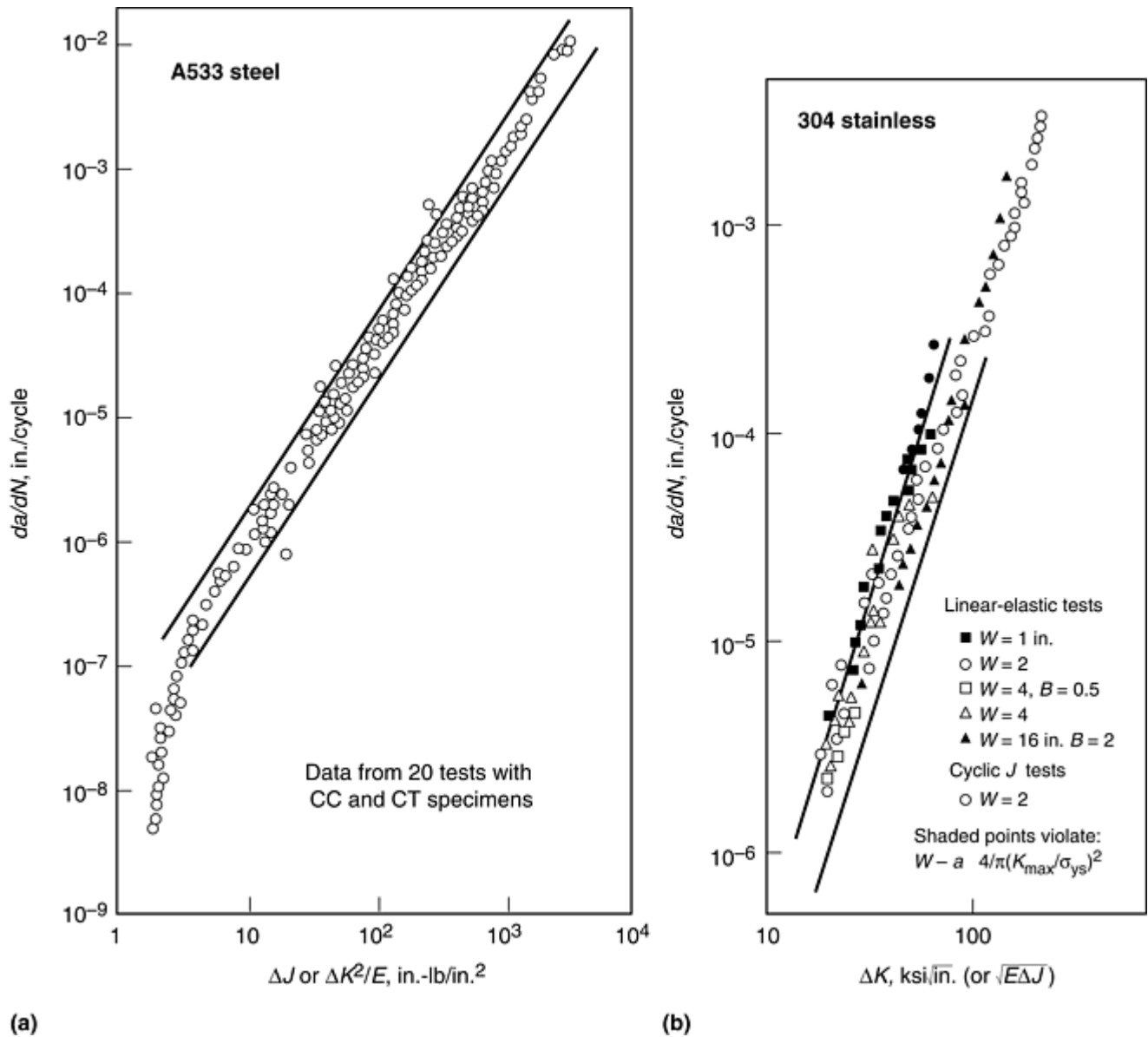


Fig. 3 Fatigue crack growth rate obtained under linear elastic and elastic-plastic conditions in (a) A533 steel and (b) 304 stainless steel. CC, center-cracked specimen; CT, compact-type specimen. Source: Ref 9, 14

Crack Closure. The concept of crack closure was first introduced by Elber (Ref 15, 16) as an effect from a zone of residual deformation left in the wake of a growing fatigue crack. According to this concept, crack surfaces at the crack tip might stay closed during a portion of the fatigue cycle due to compressive residual stress acting at the crack tip. Elber further postulated that this portion of the loading cycle is ineffective in growing the fatigue crack; thus, the corresponding load should be subtracted from the applied ΔP to determine the effective value of ΔK .

Figure 4 presents a series of schematic sketches that show the stress and strain distributions at the crack tip at maximum and minimum load. At the maximum load, *A*, all the load is borne by the uncracked ligament, because cracks are unable to transmit the load. At the minimum load, *B*, there are compressive stresses to the left of the crack tip, because there is contact between opposing crack surfaces within the zone of residual plastic deformation. This contact causes the effective stiffness of the cracked body to change, which manifests itself in the load-displacement diagram. Thus, the crack closure load can be defined as the load at which this change in stiffness occurs.

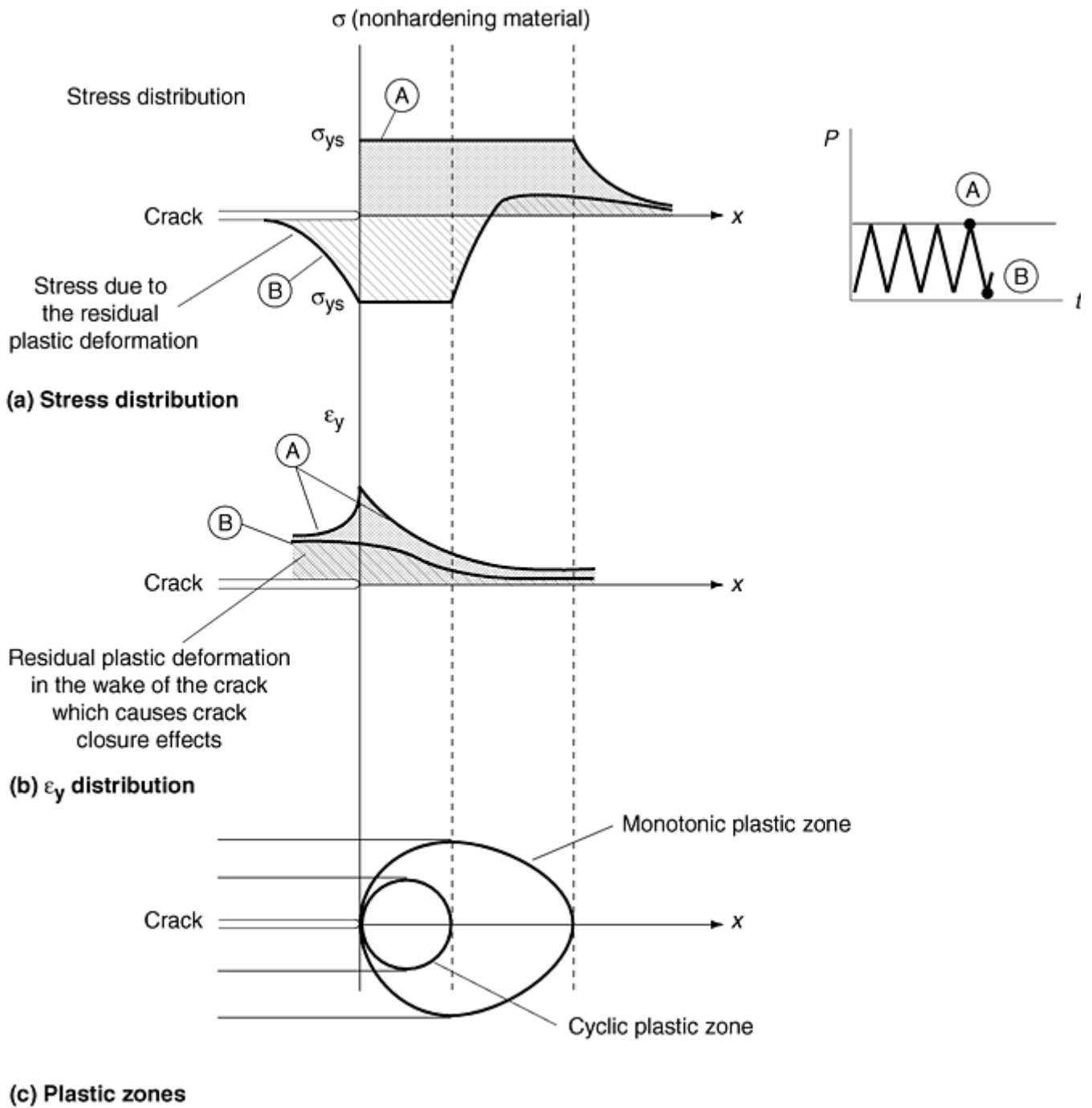


Fig. 4 Schematic of crack-tip conditions during crack closure

Figure 5(a) shows a schematic load-deflection diagram and the crack closure point. Figure 5(b) plots only the deviation between the total deflection and the linearly predicted deflection, thus highlighting the crack closure point.

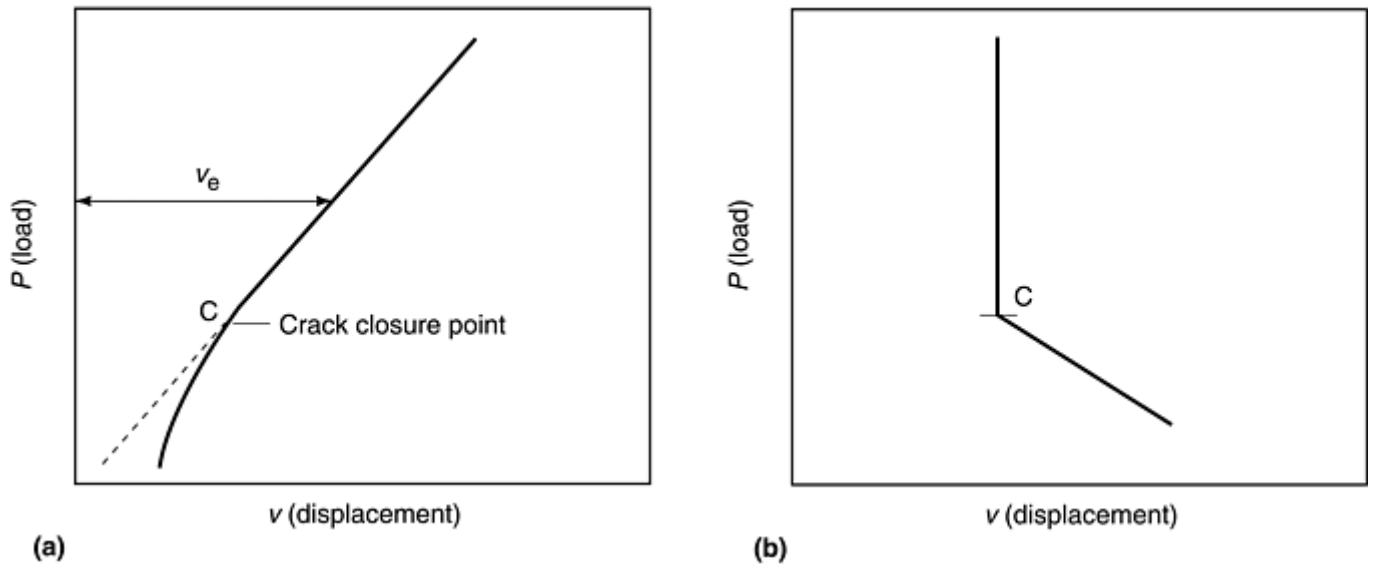


Fig. 5 Load versus displacement diagrams. (a) Diagram showing a change in stiffness at the crack closure point. (b) A plot of total deflection minus the elasticity calculated deflection amplified to highlight crack closure. v_e , elastic displacement

The importance of crack closure varies with the crack growth regime, crack tip material-microstructure interactions, and the extent of plasticity. Crack closure is more significant in the near-threshold regime (region I, Fig. 2) than in region II (Fig. 2). Materials in which the crack path is such that rougher crack surfaces are produced usually exhibit enhanced crack closure levels. The crack closure levels can also increase with plasticity. For example, during fatigue crack growth in the elastic-plastic regime, crack closure levels take on added significance (Ref 8, 9).

References cited in this section

1. P.C. Paris and F. Erdogan, *J. Basic Eng. (Trans. ASME)*, Series D, Vol 85, 1963, p 528–534
2. P.C. Paris, *Proc. 10th Sagamore Conf.*, Syracuse University Press, 1965, p 107–132
3. J.R. Griffiths and C.E. Richards, *Mater. Sci. Eng.*, Vol 11, 1973, p 305–315
4. J.C. Grosskrutz, Strengthening in Fracture and Fatigue, *Metall. Trans.*, Vol 3, 1972, p 1255–1262
5. J.R. Rice, in *Fatigue Crack Propagation*, STP 415, ASTM, 1967, p 247–311
6. N.E. Dowling, in *Flaw Growth and Fracture*, STP 631, ASTM, 1977, p 139–158
7. Standard Test Method for Measurement of Fatigue Crack Growth Rates, E 647-91, *Annual Book of ASTM Standards*, Vol 03.01, 1992, ASTM, p 674–701
8. N.E. Dowling and J.A. Begley, in *Mechanics of Crack Growth*, STP 590, ASTM, 1976, p 82–103
9. N.E. Dowling, in *Cracks and Fracture*, STP 601, ASTM, 1977, p 131–158
10. H.S. Lamba, The J-Integral Applied to Cyclic Loading, *Eng. Fract. Mech.*, Vol 7, 1975, p 693–696
11. J.R. Rice, *J. Appl. Mech. (Trans. ASME)*, Vol 35, 1968, p 379–386
12. J.W. Hutchinson, *J. Mech. Phys. Solids*, Vol 16, 1968, p 337–347

13. J.R. Rice and G.F. Rosengren, *J. Mech. Phys. Solids*, Vol 16, 1968, p 1–12
14. W.R. Brose and N.E. Dowling, in *Elastic-Plastic Fracture*, STP 668, ASTM, 1979, p 720–735
15. W. Elber, Fatigue Crack Closure under Cyclic Tension, *Eng. Fract. Mech.*, Vol 2, 1970, p 37–45
16. W. Elber, *The Significance of Fatigue Crack Closure*, STP 486, ASTM, 1971, p 230–242

Fatigue Crack Growth Testing

Ashok Saxena, Georgia Institute of Technology; Christopher L. Muhlstein, University of California, Berkeley

Test Methods and Procedures

ASTM standard E 647 (Ref 7) is the accepted guideline for fatigue crack growth testing and is applicable to a wide variety of materials and growth rates.

FCGR testing consists of several steps, beginning with selecting the specimen size, geometry, and crack-length measurement technique. When planning the tests, the investigator must have an understanding of the application of FCGR data. Testing is often performed in laboratory air at room temperature; however, any gaseous or liquid environment and temperature of interest may be used to determine the effect of temperature, corrosion, or other chemical reaction on cyclic loading (see the appendix “High-Temperature Fatigue Crack Growth Testing” at the end of this article). Cyclic loading also may involve various waveforms for constant-amplitude loading, spectrum loading, or random loading.

In addition, many of the conventions used in plane-strain fracture toughness testing (ASTM E 399, Ref 17) are also used in FCGR testing. For tension-tension fatigue loading, K_{Ic} loading fixtures frequently can be used. For this type of loading, both the maximum and minimum loads are tensile, and the load ratio, $R = P_{\min}/P_{\max}$, is in the range $0 < R < 1$. A ratio of $R = 0.1$ is commonly used for developing data for comparative purposes.

Cyclic crack growth rate testing in the threshold regime (region I, Fig. 2) complicates acquisition of valid and consistent data, because the crack growth behavior becomes more sensitive to the material, environment, and testing procedures. Within this regime, the fatigue mechanisms of the material that slow the crack growth rates are more significant.

It is extremely expensive to obtain a true definition of ΔK_{th} , and in some materials a true threshold may be nonexistent. Generally, designers are more interested in the FCGR in the near-threshold regime, such as the ΔK that corresponds to a FCGR of 10^{-8} to 10^{-10} m/cycle (3.9×10^{-7} to 10^{-9} in./cycle). Because the duration of the tests increases greatly for each additional decade of near-threshold data (e.g., 10^{-8} to 10^{-9} to 10^{-10} m/cycle), the precise design requirements should be determined in advance of the test. Although the methods of conducting fatigue crack threshold testing may differ, ASTM E 647 addresses these requirements.

In all areas of crack growth rate testing, the resolution capability of the crack measuring technique should be known; however, this knowledge becomes considerably more important in the threshold regime. The smallest amount of crack-length resolution is desired, because the rate of decreasing applied loads (load shedding) is dependent on how easily the crack length can be measured. The minimum amount of change in measured crack growth should be ten times the crack-length measurement precision. It is also recommended that for noncontinuous load shedding testing, where, $[(P_{\max 1} - P_{\max 2})/P_{\max 1}] > 0.02$, the reduction in the maximum load should not exceed 10% of the previous maximum load, and the minimum crack extension between load sheds should be at least 0.50 mm (0.02 in.)

In selecting a specimen, the resolution capability of the crack measuring device and the K -gradient (the rate at which K is increased or decreased) in the specimen should be known to ensure that the test can be conducted appropriately. If the measuring device is not sufficient, the threshold crack growth rate may not be achieved before the specimen is separated in two. To avoid such problems, a plot of the control of the stress intensity (K versus a) should be generated before selection of the specimen.

When a new crack-length measuring device is introduced, a new type of material is used, or any other factor is different from that used in previous testing, the K -decreasing portion of the test should be followed with a constant load amplitude (K -increasing) to provide a comparison between the two methods. Once a consistency is demonstrated, constant-load amplitude testing in the low crack growth rate regime is not necessary under similar conditions.

References cited in this section

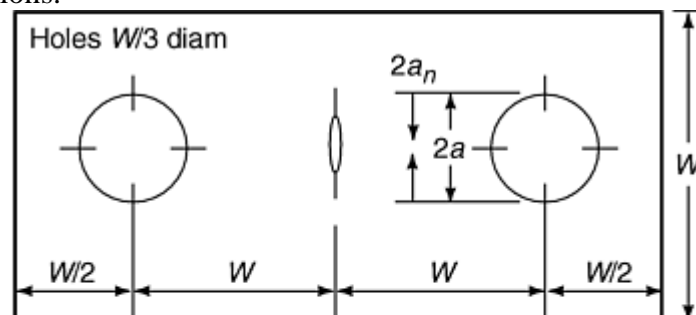
7. Standard Test Method for Measurement of Fatigue Crack Growth Rates, E 647-91, *Annual Book of ASTM Standards*, Vol 03.01, 1992, ASTM, p 674–701
17. Standard Method for Plane-Strain Fracture Toughness of Metallic Materials, E 399-90, *Annual Book of ASTM Standards*, Vol 3.01, 1992, ASTM, p 569–596

Fatigue Crack Growth Testing

Ashok Saxena, Georgia Institute of Technology; Christopher L. Muhlstein, University of California, Berkeley

Specimen Selection and Preparation

The two most widely used types of specimens are the middle-crack tension, MT, and the compact-type specimen, CT (Fig. 6, 7). However, any specimen configuration with a known stress-intensity factor solution can be used in FCGR testing, assuming that the appropriate equipment is available for controlling the test and measuring the crack dimensions.

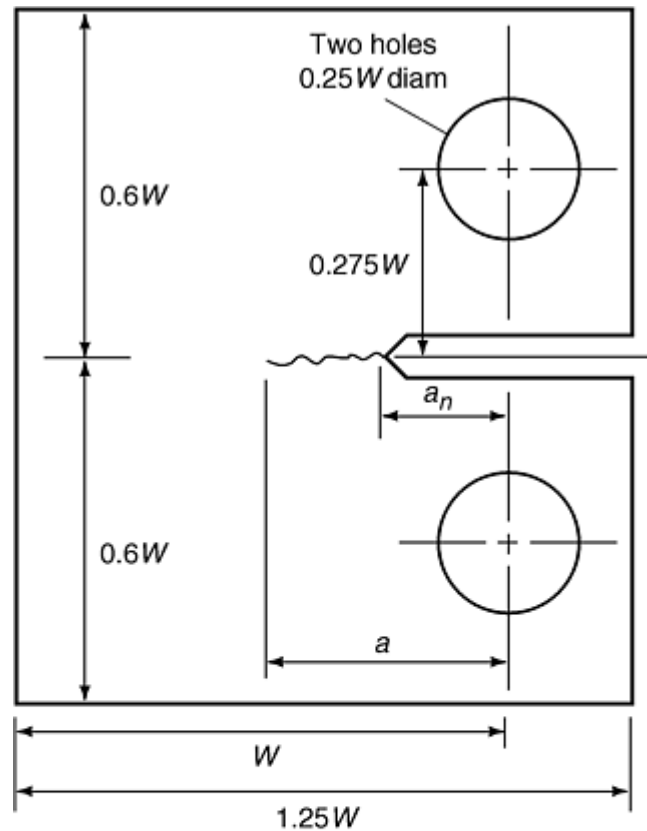


Center-cracked tension specimens ΔK :

$$\Delta K = \frac{\Delta P}{B} \sqrt{\frac{\pi \alpha}{2W}} \sec \frac{\pi \alpha}{2}$$

$$\text{where } \alpha = \frac{2a}{W}; \text{ expression valid for } \frac{2a}{W} < 0.95$$

Fig. 6 Standard center-cracked tension (middle-tension) specimen and ΔK solution. Specimen width (W) ≤ 75 mm (3 in.). $2a_n$ machined notch; a , crack length; B , specimen thickness



Compact-type specimens ΔK value:

$$\Delta K = \frac{\Delta P (2 + \alpha)}{B \sqrt{W} (1 - \alpha)^{3/2}} (0.886 +$$

$$4.64\alpha - 13.32\alpha^2 + 14.72\alpha^3 - 5.6\alpha^4), \text{ where}$$

$$\alpha = \frac{a}{W}; \text{ expression valid for } \frac{a}{W} \leq 0.2$$

Fig. 7 Standard compact-type specimen and ΔK value (per ASTM E 674). Allowable thickness: $W/20 \leq B \leq W/4$. Minimum dimensions: $W = 25 \text{ mm (1.0 in.)}$; machined notch size (a_n) = $0.20W$

Specimens used in FCGR testing may be grouped into three categories: pin-loaded (Fig. 6, 7), bend-loaded (Fig. 8a) and wedge-gripped specimens (Fig. 8b – d). Precisely machined specimens are essential, and ASTM E 647 specifies the recommended tolerances and K -calibrations for CT and MT geometries. Single-edge bend, arc-shaped, and disk-shaped compact specimen geometries and the corresponding K -calibrations are discussed in ASTM E 399. Comparable tolerances should be specified for “nonstandard” specimens. The selection of an appropriate geometry requires consideration of material availability and raw form, desired loading condition, and equipment limitations.

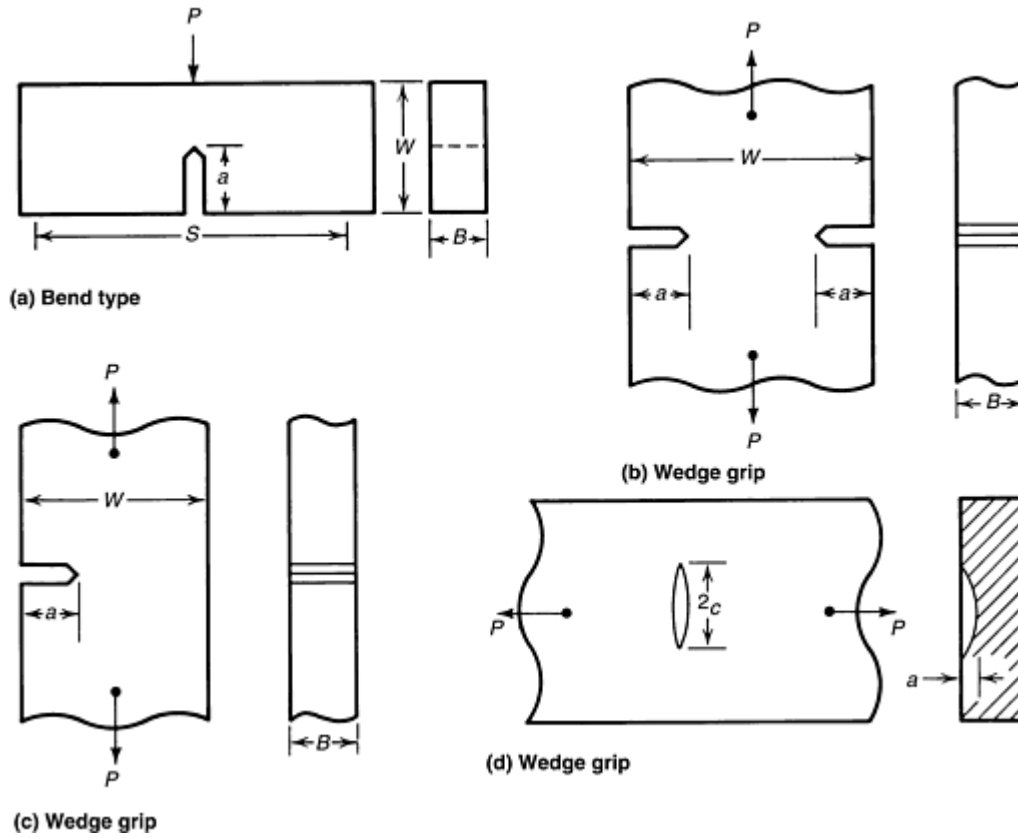


Fig. 8 Alternative crack growth specimen geometries. (a) Single-edge-crack bending specimen. (b) Double-edge-crack tension specimen. (c) Single-edge-crack tension specimen. (d) Surface-crack tension specimen

Crack Length and Specimen Size. The applicable range of the stress-intensity solution of a specimen configuration is very important. Many stress-intensity expressions are valid only over a range of the ratio of crack length to specimen width (a/W). For example, the expression given in Fig. 7 for the CT specimen is valid for $a/W > 0.2$; the expression for the middle-tension (MT) specimen (Fig. 6) is valid for $2a/W < 0.95$. The use of stress-intensity expressions outside the applicable crack-length region can produce significant errors in data. The size of the specimen must also be appropriate. To follow the rules of LEFM, the specimen must be predominantly elastic. However, unlike the requirements for plane-strain fracture toughness testing, there are no specific requirements of minimum specimen thickness. The thickness is considered to be a controlled test variable and depends on the application. The material characteristics, specimen size, crack length, and applied load will dictate whether the specimen is predominantly elastic. Because the loading modes of different specimens vary significantly, each specimen geometry must be considered separately.

For the MT specimen, the following is required:

$$W - 2a \geq \frac{1.25P_{\max}}{B\sigma_{ys}} \quad (\text{Eq 8})$$

where $W - 2a$ is the uncracked ligament of the specimen (see Fig. 6) and σ_{ys} is the 0.2% offset yield strength at the temperature corresponding to the FCGR data.

For the CT specimen, the following is required:

$$W - a \geq \frac{4}{\pi} \left(\frac{K_{\max}}{\sigma_{ys}} \right)^2 \quad (\text{Eq 9})$$

where $W - a$ is the uncracked ligament (Fig. 7). For the CT specimen, the size requirement in Eq 9 limits the monotonic plastic zone in a plane-stress state to approximately 25% of the uncracked ligament. For both Eq 8 and 9, ASTM E 647 recommends the use of the monotonic yield strength. The size requirements in Eq 8 and 9 are appropriate for low-strain hardening materials ($\sigma_{\text{uts}}/\sigma_{ys} \leq 1.3$), where σ_{uts} is the ultimate tensile strength of

the material. For higher-strain-hardening materials, Eq 8 and 9 may be too restrictive. In such situations, the criteria may be relaxed by replacing the yield strength, σ_{ys} , with the effective yield strength, σ_F :

$$\sigma_F = \frac{(\sigma_{ys} + \sigma_u)}{2} \quad (\text{Eq 10})$$

Specimen Thickness. While fatigue crack growth rates have been shown to be relatively insensitive to stress state (i.e., plane-stress versus plane-strain, Ref 3), there are some practical limitations on specimen thickness. ASTM E 647 recommends that generally CT specimen thickness (B) range between 5 and 25% of width ($W/20 \leq B \leq W/4$). Middle-tension specimens may have thicknesses up to 12% of width ($\leq W/8$). When other specimen geometries are used, similar ranges for thickness should be employed.

Although a wide variety of specimen thicknesses are permitted, the amount of crack curvature in the specimen will increase as the thickness increases. Because stress-intensity solutions are based on a straight through-crack, a significant amount of curvature, if not properly considered, can lead to an error in the data. Crack-curvature correction calculations are detailed in ASTM E 647. The minimum allowable thickness depends on the gripping method used; however, the bending strains should not exceed 5% of the nominal strain in the specimen.

Material Form and Microstructure Considerations. The material and its microstructure play an important role in the selection of an appropriate specimen geometry. Materials with anisotropic microstructures due to processing, such as rolling or forging, may show large variations in FCGR in different directions (Ref 18). If the experimental crack growth rate data are to be used for life estimates, the orientation of the specimen should be selected to represent loading orientations expected in service.

In order to eliminate grain size effects, it is usually recommended that the specimen thickness (B) be greater than 30 grain diameters (Ref 19, 20). In some instances, such as in large-grain (~ 3 mm) lamellar γ - α_2 Ti-Al intermetallic or α - β titanium alloys, the required specimen sizes would be prohibitively expensive, test loads would be very high, and the component dimensions would probably be less than 30 times the grain size. In such instances, testing should be performed on thicknesses representative of the component. Curvature of the crack front and side-to-side variation in crack length due to excessive thickness can also be a problem in thick specimens, as discussed below.

Loading Considerations. The desired loading conditions play an important role in the specimen geometry and size selection process. Loading considerations include load ratio, R , residual stresses, K -gradients, and maintaining small-scale yielding. All specimen geometries are well suited for tension-tension ($R > 0$) testing. However, tests that call for negative R (i.e., those with minimum loads less than 0) are restricted to symmetric, wedge-grip loaded specimens, such as the MT specimens. This limitation is due to questions about the crack-tip stress field under compressive loads (Ref 7) and difficulties moving through zero load with pin-loaded specimens.

Residual stresses in the material also have a marked effect on FCGR. Depending on the orientation of the residual stresses, specimen dimensions or geometries should be altered. Residual stresses through the thickness of the specimen (i.e., perpendicular to the direction of crack growth) may accelerate or retard crack growth. When these stresses are not uniform, ASTM E 647 recommends a reduction of the thickness-to-width ratio (B/W).

The rate at which K increases as the crack extends at a constant-load amplitude is given by the geometry function $f(a/W)$ and may be a consideration when selecting the most appropriate specimen geometry. Figure 9 shows the effect of geometry on the K -gradient through a variety of specimen geometries. Specimens with shallower K -gradients are preferable for brittle materials, while the opposite is true for ductile materials.

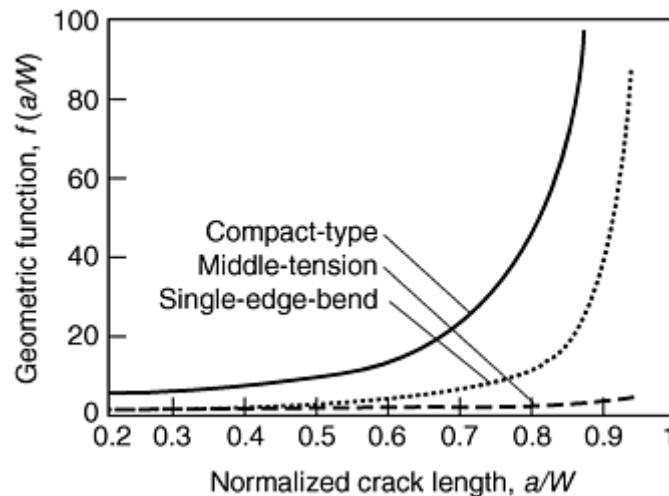


Fig. 9 K -gradients for a number of fatigue crack growth specimens. Source: Ref 7, 17

Equipment Considerations. Specimen size and geometry also can be influenced by laboratory equipment, such as the loadframe, loadcell, existing loading fixtures, testing environment, and even the crack-length measurement apparatus. To minimize cost, specimen sizes and geometries should be selected to use existing clevises, pins, and other hardware.

Most modern mechanical testing laboratories exclusively use electroservohydraulic loadframes for FCGR investigations. Current controls and data acquisition technology have hydraulic loadframes more versatile than the electromechanical systems used previously. When selecting a specimen geometry and size, it is important to be aware of the load capacity of the actuator and loadframe. Loads that are too high cannot be applied, and those loads that are too low cannot be controlled with the required accuracy ($\pm 2\%$). In addition, the load cell to be used during testing must be able to measure the maximum applied load and resolve the lowest expected amplitudes, as specified in ASTM E 4.

When testing in environments, specimens fit inside ovens, furnaces, or other chambers with ample space left for clevises, cantilever beam clip gages, and other hardware. Special notch geometries or knife-edge attachment locations are often necessary for attaching clip gages or other types of extensometers for nonvisual crack-length measurements using compliance techniques.

Notch and Specimen Preparation. The method by which a notch is machined depends on the specimen material and the desired notch root radius (ρ). Sawcutting is the easiest method but is generally acceptable only for aluminum alloys. For a notch root radius of $\rho \leq 0.25$ mm (0.010 in.) in aluminum alloys, milling or broaching is required. A similar notch root radius in low- and medium-strength steels can be produced by grinding. For high-strength steel alloys, nickel-base superalloys, and titanium alloys, electrical discharge machining may be necessary to produce a notch root radius of $\rho \leq 0.25$ mm (0.010 in.).

The specimen is polished to allow measurement of the crack during the precracking and testing phases of the experiment. Many specimens can be polished using standard metallography practices. In some instances, etching of the polished surface may provide better contrast for viewing of the crack. If the specimen is too large or small to be handled, then hand grinders, finishing sanders, or handheld drills can be used with pieces of polishing cloth to locally apply the abrasive and create a satisfactory viewing surface. These techniques are quick and easy to apply, and they are often used when visual measurements are made only during precracking and subsequent measurements are made by automated techniques, such as electric potential or compliance.

Precracking. The K -calibration functions found in ASTM E 647 and E 399 are valid for sharp cracks within the range of crack length specified. Consequently, before testing begins, a sharp fatigue crack that is long enough to avoid the effects of the machined notch must be present in the specimen ($0.1B$, or $0.1H$, or 1 mm [0.040 in.], whichever is greatest). The process that generates this crack is termed precracking. In general, loads for precracking should be selected such that the K_{\max} at the end of precracking does not exceed levels expected at the start of a test.

For most metals, precracking is a relatively simple process that can be performed under load or displacement control conditions. Moderate growth rates (1×10^{-5} m/cycle) can be selected by estimating the necessary ΔK from growth curves in the literature. Precracking of a specimen prior to testing is conducted at stress intensities sufficient to cause a crack to initiate from the starter notch and propagate to a length that will eliminate the

effect of the notch. To decrease the amount of time needed for precracking to occur, common practice is to initiate the precracking at a load above that used during testing and to subsequently reduce the load.

Load generally is reduced uniformly to avoid transient (load-sequence) effects. Crack growth can be arrested above the threshold stress-intensity value due to formation of the increased plastic zone ahead of the tip of the advancing crack. Therefore, the step size of the load during precracking should be minimized. Under these circumstances, the loads should be shed no faster than 20% (per increment of crack extension, as discussed below) from the previous load increment (Ref 7), which eliminates load-sequence effects on growth rates. As the crack approaches the final desired size, the percentage can be decreased.

The amount of crack extension between each load decrease must also be controlled. If the step is too small, the influence of the plastic zone ahead of the crack may still be present. To avoid transient (load-sequence) effects in the test data, the load range in each step should be applied over a crack-length increment of at least $(3\pi)(K'_{\max}/\sigma_{ys})^2$, where K'_{\max} is the terminal value of K_{\max} from the previous load step. This requirement ensures that the crack extension between load sheds is at least three plastic zone diameters.

The influence of the machined starter notch must be eliminated so that the crack tip conditions are stable. For CT and MT specimens, this condition requires that the final precrack be at least 10% of the thickness of the specimen or equivalent to the height of the starter notch, whichever is greater (Ref 7).

Two additional considerations regarding crack shape are the amount of crack variation from the front and back sides of the specimen and the amount of out-of-plane cracking. Due to microstructural changes through the specimen thickness, residual stresses (particularly in weldments), or misalignment of the specimen in the grips, the crack may grow unevenly on the two surfaces. If any two crack-length measurements vary by more than $0.025W$ or by more than $0.25B$ (whichever is less), the precracking operation is not suitable, and test results will not be valid. If a fatigue precrack departs more than $\pm 5^\circ$ from the plane of symmetry, the specimen is not suitable for subsequent testing.

Precracking of Brittle Materials. Brittle materials, such as intermetallics and ceramics, can be very difficult to precrack. It is not uncommon to initiate a flaw that immediately propagates to failure. This transformation is due, in part, to the increasing K -gradient found in FCGR specimens and the relatively narrow range of ΔK for stable crack growth.

To improve the chances of successful precracking of brittle materials, chevron notches are advised. Chevron-notched specimens (Fig. 10) are used for determining the fracture toughness of brittle materials that are difficult to fatigue precrack. Chevron notches generate decreasing K -gradients at the start of precracking and may be machined as part of the specimen, or they may be added just prior to testing using a thin diamond wafering blade. The maximum slope of the chevron notch should be 45° . Precracking of brittle materials should be performed under displacement control conditions, so that as the crack extends, the load and the applied K decrease. Lastly, the loads should be increased slowly from low levels due to the stochastic nature of crack initiation in these materials. If initiation is especially difficult, compressive overloads may assist the process. It is also helpful to monitor the initiation process with a method other than optical observation. Electric potential techniques (bulk and foil) and back face strain (BFS) compliance techniques are very effective.

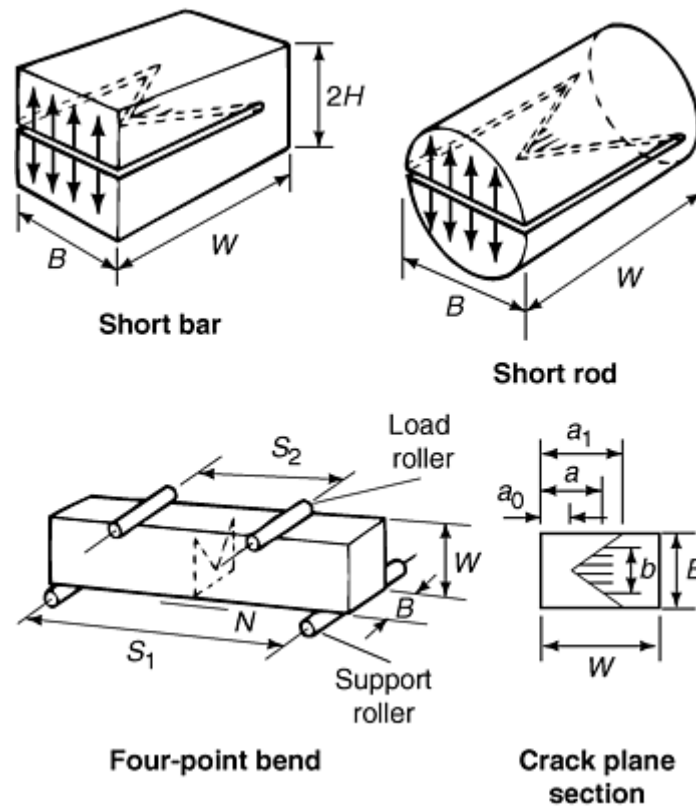


Fig. 10 Schematic of chevron notches in fracture mechanics specimens. Area b is the crack area.

Once precracking has been completed, an accurate optical measurement of the initial crack length, a_0 , must be made on both sides of the specimen to within 0.10 mm (0.004 in.) or $0.002W$ (whichever is greatest), or to within 0.25 mm (0.01 in.) for specimens where $W > 127$ mm (5 in.). If the crack lengths on the two surfaces differ by more than $0.25B$, then the test will not be valid, because K -calibration functions presume the existence of a straight crack front. Middle-tension specimens further require that both halves of the precrack be the same length to within $0.025W$. In addition, ASTM E 647 requires that cracks lie on the centerline such that the crack is no more than $\pm 20^\circ$ from a centerline over a distance $0.1W$. Once the precrack has been measured and side-to-side variation and distance from centerline have been established, testing may begin.

Gripping of the specimen must be done in a manner that does not violate the stress-intensity solution requirements. For example, in a single-edge notched specimen, it is possible to produce a grip that permits rotation in the loading of the specimen, or it is possible to produce a rigid grip. Each of these grips requires a different stress-intensity solution. In grips that are permitted to rotate, such as the CT specimen grip, the pin and hole clearances must be designed to minimize friction. It is also advisable to consider lateral movement above and below the grips.

When appropriate, the use of a lubricant is recommended to reduce friction. In thick samples, the amount of bending in the pins should be minimized. Finally, the alignment of the system should be checked carefully to avoid undesirable bending stresses, which generally cause uneven cracking. Alignment can be easily checked using a strain gage specimen of a geometry similar to that used in the test program. Generally, bending strains should not exceed 5% of the nominal strain to be used in the test program.

Gripping arrangements for CT and CCT specimens are described in ASTM E 647 (Ref 7). For a CCT specimen less than 75 mm (3 in.) in width, a single pin grip is generally suitable. Wider specimens generally require additional pins, friction gripping, or some other method to provide sufficient strength in the specimen and grip to prohibit failure at undesirable locations, such as in the grips.

References cited in this section

3. J.R. Griffiths and C.E. Richards, *Mater. Sci. Eng.*, Vol 11, 1973, p 305–315

7. Standard Test Method for Measurement of Fatigue Crack Growth Rates, E 647-91, *Annual Book of ASTM Standards*, Vol 03.01, 1992, ASTM, p 674–701
17. Standard Method for Plane-Strain Fracture Toughness of Metallic Materials, E 399-90, *Annual Book of ASTM Standards*, Vol 3.01, 1992, ASTM, p 569–596
18. K.T. Venkateswara Rao, W. Yu, and R.O. Ritchie, *Metall. Trans. A*, Vol 19 (No. 3), March 1988, p 549–561
19. A.W. Thompson and R.J. Bucci, *Metall. Trans.*, Vol 4, April 1973, p 1173–1175
20. G.R. Yoder and D. Eylon, *Metall. Trans. A*, Vol 10, Nov 1979, p 1808–1810

Fatigue Crack Growth Testing

Ashok Saxena, Georgia Institute of Technology; Christopher L. Muhlstein, University of California, Berkeley

Crack-Length Measurement

Precise measurements of fatigue crack extension are crucial for the determination of reliable crack growth rates. ASTM E 647 requires a minimum resolution of 0.1 mm (0.004 in.) in crack-length measurement. Crack extension measurements are recommended at intervals 10 times the minimum required resolution.

Various crack measurement techniques have been applied, including optical (visual and photographic), ultrasonic, acoustic emission, electrical (eddy current and resistance), and compliance (displacement and BFS gages) methods. Optical, compliance, and electric potential difference are the most common laboratory techniques, and merits and limitations are reviewed in detail in the following sections. Other references are listed in “Selected References” at the end of this article.

Optical Crack Measurement

Monitoring of fatigue crack length as a function of cycles is most commonly conducted visually by observing the crack at the specimen surfaces with a traveling low-power microscope at a magnification of 20 to 50 \times . Crack-length measurements are made at intervals such that a nearly even distribution of da/dN versus ΔK is achieved. The minimum amount of extension between readings is commonly about 0.25 mm (0.010 in.).

For planar specimens, the crack length is measured on one or both surfaces, depending on the section thickness. For example, ASTM E 647 (Ref 7) specifies a B/W value of 0.15 as the limit; measurements on only one side are sufficient if $B/W < 0.15$.

Through-thickness variations in crack length must be considered and corrected if too severe. Typical behavior is for the crack length to lead at the midplane (crack tunneling). Because this situation cannot be observed in situ by visual monitoring, posttest observations must be made. Rough alignment of the traveling microscope can be easily achieved by shining a pen light through the eyepiece on the crack-tip region. To ensure accurate crack measurements, obliquely incident light on a well-polished specimen surface is an effective means of highlighting fine cracks. High-intensity strobe lights with adjustable function generators are used to allow “motion free” viewing of cracks during high-frequency tests. The development of extra-long focal length optics has added new functionality to optical techniques. These microscopes allow the in situ observation and image analysis of crack-tip processes while keeping the instruments a reasonable distance (>381 mm, or 15 in.) from the specimen and other testing hardware.

To account for through-thickness crack-length variation, ASTM E 647 recommends measuring the crack length at five points along the crack front contour and averaging the five readings. If the average of the five points exceeds the surface length by more than 5%, the average length is used in computing the growth rate and K .

The optical technique is straightforward and, if the specimen is carefully polished and does not oxidize during the test, produces accurate results. However, the process is time consuming, subjective, and can be automated only with complicated and expensive video-digitizing equipment. In addition, many FCGR tests are conducted in simulated-service environments that obscure direct observation of the crack. The trend toward laboratory automation has resulted in the development of indirect methods of determining crack extension, such as specimen compliance and electric potential monitoring.

Compliance Method

Under linear elastic conditions for a given crack size, the displacement, v , across the load points or at any other locations across the crack surfaces is directly proportional to the applied load (P). The compliance, C , of the specimen is defined:

$$C = \frac{v}{P} \quad (\text{Eq 11})$$

The relationship between dimensionless compliance, BEC , where B is the thickness and E is the elastic modulus, and the dimensionless crack size, a/W , where W is the specimen width, is unique for a given specimen geometry (Ref 21). Thus:

$$BEC = f\left(\frac{a}{W}\right) \quad (\text{Eq 12})$$

The inverse relationship (Ref 21) between crack size and compliance can be written as $a/W = q(u)$, where $u = [1 + BEC]^{-0.5}$. This relationship may be determined numerically using finite element techniques or by experiment. ASTM E 647 also specifies these relationships for CT and MT specimens.

The compliance of an elastically strained specimen (expressed as the quotient of the displacement, v , and the tensile load, P , per Eq 11) is determined by measuring the displacement along, or parallel to, the load line. Figure 11 illustrates that the more deeply a specimen is cracked, the greater the amount of v will be measured for a specific value of tensile load. Additional information on the method and calculation of compliance can be found in the "Selected References" at the end of this article.

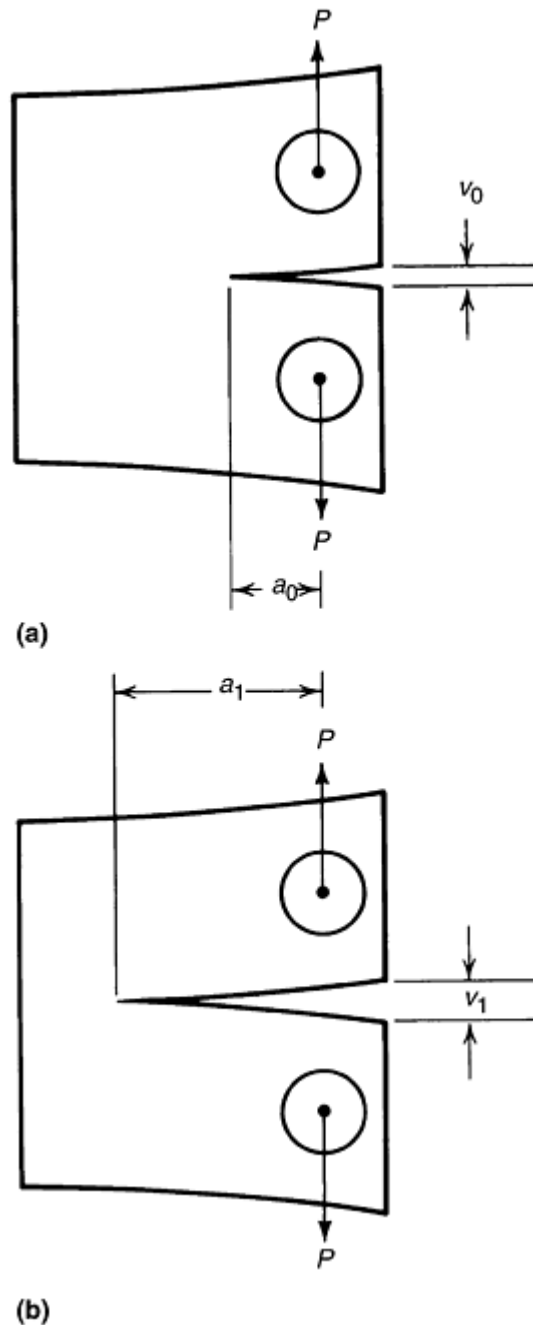


Fig. 11 Schematic of the relationship between compliance and crack length. (a) $C(a_0) = v_0/P$. (b) $C(a_1) = v_1/P$

Instrumentation. The displacement usually is measured across the crack mouth opening using cantilever beam clip gages, optical (laser and white light) extensometry, or BFS gages. Linear variable differential transducers have been used, but hysteresis in the response can sometimes be a problem. Each technique has its own advantages and may be used to continuously monitor crack length. An additional benefit of compliance techniques is that the same signal can be used for determining crack closure, as discussed below.

Cantilever beam clip gages, based on resistive and capacitance strain gage technology, are well suited for elevated (<370 °C) and high-temperature tests (up to 1200 °C), respectively. Deflection of the arms is measured by the output of the strain gages mounted on the clip gage arms. Extensometer and transducer design theory is well established in the literature (Ref 17, 22). Attachment of clip gages to the specimen is achieved through integral, machined knife edges or by knife-edge blocks bolted to the front face of the specimen across the crack plane.

Optical extensometry techniques include those based on fiber optics and laser technology. There are two main types of optical extensometry used in compliance measurement. The first type is an advanced laser system that tracks the motion of spots projected on the specimen. In this instance, the transmitter and receiver are located

on the same side of the specimen. A second group of extensometers measure the width of the notch using a transmitter and receiver on opposite sides of the specimen. Laser and white light systems based on these principles are available commercially. Optical systems may have restrictions on frequency response. Like optical crack-length measurement techniques, most optical extensometry techniques are difficult to use when testing at elevated temperatures or in environmental chambers.

An electrical resistance strain gage mounted opposite the notch on the back face of the fatigue specimen is termed a back face strain (BFS) gage. Just as with the clip gage, the load-strain signal from the BFS gage may be used to determine the crack length in the specimen. While conventional strain gages are limited to elevated temperatures (<370 °C) in gaseous or aqueous environments, they have the advantage of directly measuring strain without the application of force. The direct measurement of strain eliminates frequency limitations associated with clip gages at the expense of having no geometric amplification of the strains or the sensitivity benefits of a four active leg Wheatstone bridge (Ref 22). A BFS gage is especially useful for nonmetallic materials where integral knife edges and tapped holes for knife-edge blocks are difficult to machine.

The required sensitivity of the system depends on specimen geometry and sizes. In general, noise-free, amplified output of about 1 V direct current (dc) per 1 mm (0.04 in.) of deflection is satisfactory. Similarly, for the load range applied to the specimen, an approximately 1 V dc change in signal from the load cell is required for accurate calculation of the compliance.

Attachment of Displacement Measurement Hardware. One of the most important factors affecting the accuracy of crack-opening displacement measurements is the manner in which the displacement transducer is attached to the test sample. Transducers for measuring the crack-opening displacement commonly consist of cantilevered arms affixed across the crack. When the crack is opened, deflections either in the arms, or in a flexure attached to the arms, induces measurable strains, which are ultimately converted to displacements.

To prevent slipping of the gage during testing, the gage must have an adequate, well-documented clamping force (~2500 g). This force must be added to the mean tensile load applied to the specimen by the gage during data analysis. For thin or small specimens, the gage-induced mean load may be high enough to preclude testing at the desired load levels. Even with high clamping forces, there will be a limitation on the maximum testing frequency for the gage due to the excitation of resonant modes in the gage or inadequate clamping force. If necessary, higher frequencies can be achieved by bolting the clip gage to the specimen.

The transducer can be bolted across the crack opening at the point of testing, or it can be attached to the specimen through hardened knife-edge pivots that are mechanically or adhesively affixed to the specimen. The transducer can also be affixed via knife-edge contacts machined into the test sample. For elevated-temperature testing, feed-rod systems are frequently used.

The bolt-on system of attaching the transducer to the test specimen (Fig. 12) is capable of reacting to high acceleration loads. These loads result from higher-frequency dynamic testing when the rocking movement generated by the mass of the transducer is carried to the bolt-on attachment through the transducer frame. This attachment system is preferred when a transducer has high mass or an effective mass center located a great distance from the specimen contact pads.

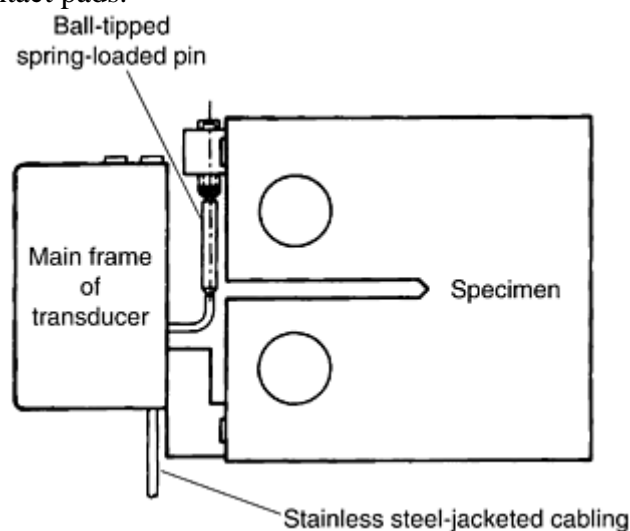


Fig. 12 Bolt-on attachment of crack-opening displacement transducer to fatigue test specimen

The bolt-on system also provides accurate crack-opening displacement measurements on specimens tested under environments not conducive to the use of knife edges, such as elevated-temperature or corrosive environments. In addition, the bolt-on attachment system allows the use of stiffer cabling without disturbing the measurement. For example, a displacement transducer with relatively rigid stainless steel-jacketed cabling can be used to make measurements in pressurized high-temperature water/steam environments.

Hardened knife-edge pivot contacts (Fig. 13) provide a measurement system with minimal sliding action; the knife-edge rocks in a hardened seat in the transducer arm. This condition allows measurements to be made with very low hysteresis levels. Contact and seat-ramp angles can be designed for optimal tradeoffs between static and dynamic measurement accuracy, dynamic stability, and contact durability. Male knife-edge contact replacements are relatively low in cost, and various configurations are available, such as three-point contact, line contact, large radius, and small radius.

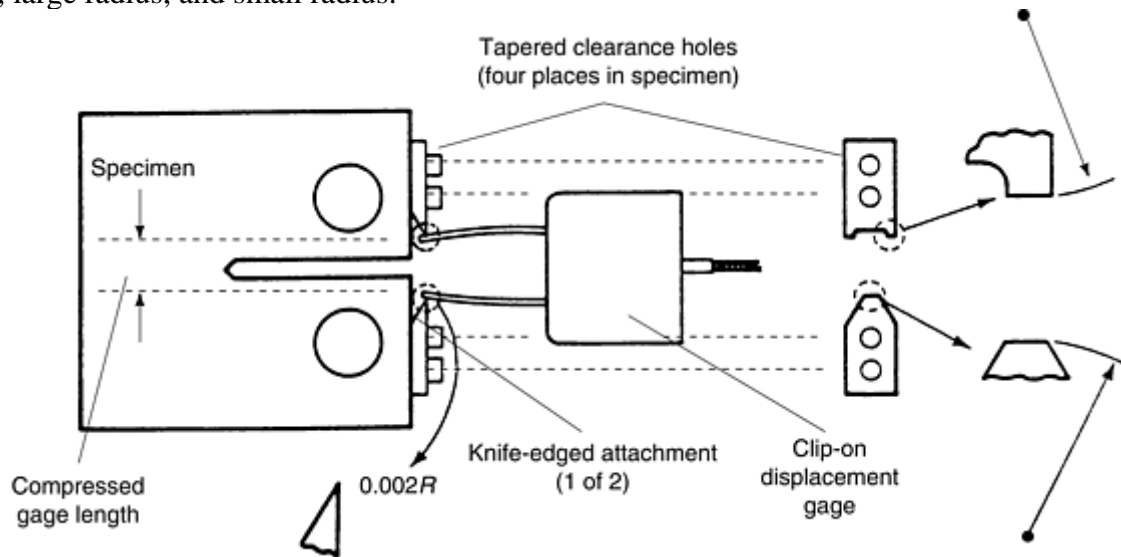


Fig. 13 Bolt-on hardened knife-edge attachment of crack-opening displacement transducer to fatigue test specimen

Knife-edge contacts machined into the test sample (Fig. 14) eliminate the possibility of knife-edge screws loosening, resulting in slippage and hysteresis. The compressed initial gage length can be machined to the required tolerance.

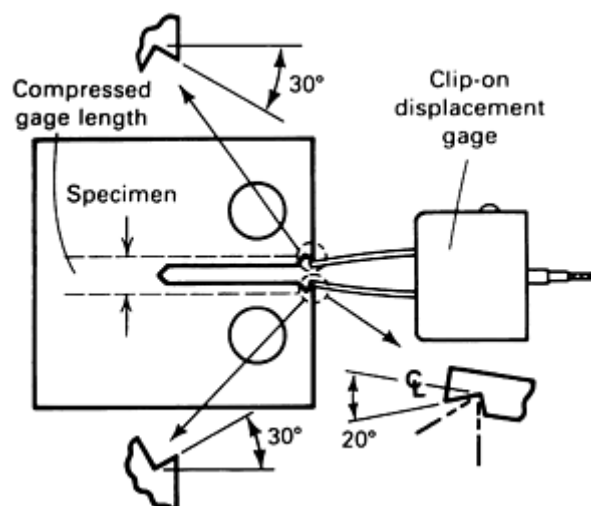


Fig. 14 Attachment of crack-opening displacement transducer to specimen by machined knife-edge contacts

Computing Normalized Compliance. When measuring the compliance of a fatigue specimen, the usual practice is to compute a normalized compliance ($EB\delta/P$). This normalized compliance is plotted against a normalized crack length, a/W . For standard geometries, such as a CT specimen, this relationship has the form shown in Fig. 15. Thus, from the measured compliance, a crack length can be obtained from the known analytical

relationships, as shown in Fig. 15 (Ref 21). Note that when the crack is short ($a/W \sim 0.2$ to 0.4), the compliance is less sensitive to changes in crack length than when the crack length is long ($a/W > 0.5$). Thus, the sensitivity of the compliance method is significantly improved for the longer crack lengths, both because of this relationship and because the amount of crack mouth opening and the resulting displacement gage signal are larger. The amount of displacement or measured crack mouth opening is a strong function of the location of the line of measurement of the gage with respect to the load line, which is the reference point for crack extension. The farther away from the crack tip the measurement can be made, the more displacement that will be incurred, and the sensitivity of the method will be improved proportionately.

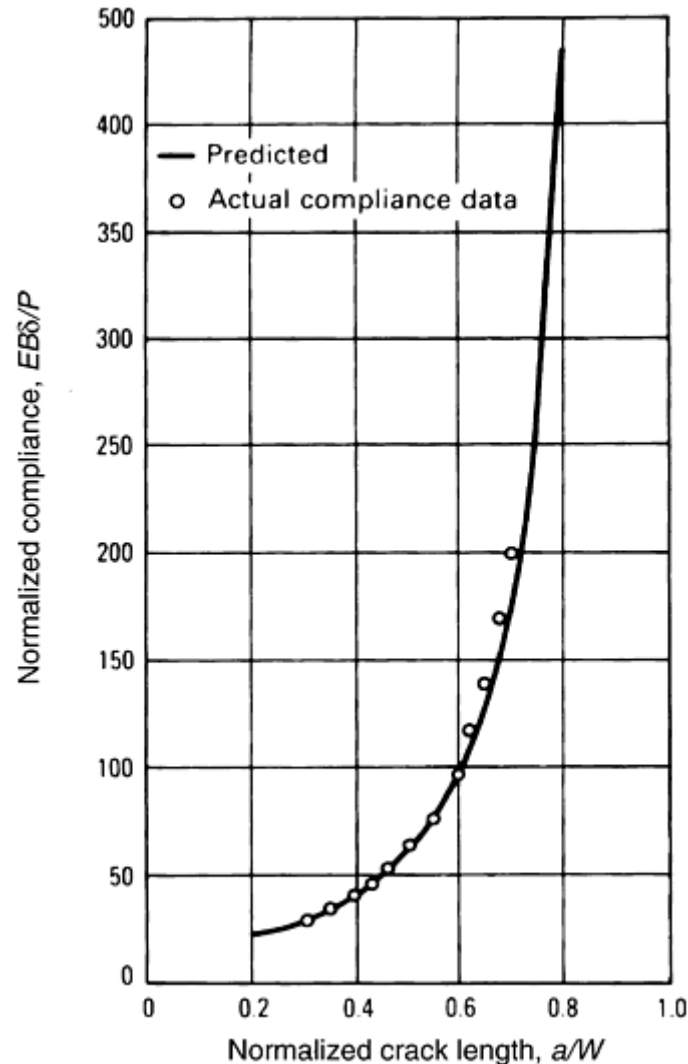


Fig. 15 Comparison of predicted and experimental compliance for a compact-type fatigue specimen

Data Acquisition and Processing. The signals from the load cell and displacement gage must be obtained simultaneously in order for this method to work to its best advantage. In the most direct instance, the two signals can be fed to an x - y recorder, with the load applied to the y -axis and displacement to the x -axis. At various intervals during the test, a trace of the two signals can be made. If the test is being conducted at a reasonably high frequency (>1 Hz), then the frequency will have to be reduced so that the slow rate of the recorder can keep up with the changing voltage. This maintenance is not a problem if a transient recorder is used and the results from the two channels (load and displacement) are co-plotted. The slopes of the recorder traces can be measured, multiplied by suitable calibration factors, and used in the compliance to crack-length relationship.

A more sophisticated method uses a computerized data acquisition system to obtain load displacement data. These systems are usually faster and, thus, can accept data from rather high-frequency waveforms. In addition, software can be developed to perform the calculations involved in processing the compliance data to crack length. Software to perform FCGR measurements is generally available from manufacturers, but most

researchers write their own data acquisition packages, perhaps using some of the manufacturer-supplied subroutines specific to the hardware involved.

Additionally, data should be taken between about 10 and 90% of the load range. Eliminating the top and bottom fractions of the load range avoids problems of crack closure (at loads approaching zero) or incipient plasticity (near the load maximum, at longer crack lengths). The sets of load-displacement pairs are fitted to a straight line; the slope of which is used in the compliance expression.

Electric Potential Difference Method

The electrical potential, or potential drop, technique has gained increasingly wide acceptance in fracture research as one of the most accurate and efficient methods for monitoring the initiation and propagation of cracks. This method relies on a disturbance in the electrical potential field about any discontinuity in a current-carrying body, and the magnitude of the disturbance depends on the size and shape of the discontinuity.

For the application of crack growth monitoring, the electrical potential method entails passing a constant current (maintained constant by external means) through a cracked test specimen and measuring the change in electrical potential across the crack as it propagates. With increasing crack length, the uncracked cross-sectional area of the test piece decreases, its electrical resistance increases, and the potential difference between two points spanning the crack rises. By monitoring this potential increase, V_a , and comparing it with some referencing potential, V_0 , the ratio of crack length to width, a/W , can be determined through the use of the relevant calibration curve for the particular test piece geometry concerned. The crack length is expressed as a function of the normalized potential (V/V_0) and the initial crack length (a_0), as shown in Fig. 16.

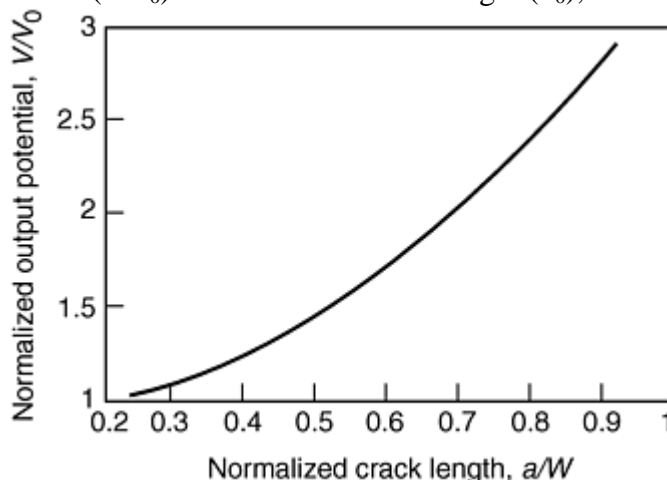


Fig. 16 Potential response for a compact-type specimen

Accuracy of electrical potential measurements of crack length may be limited by a number of factors, including the electrical stability and resolution of the potential measurement system, electrical contact between crack surfaces where the fracture morphology is rough or where significant crack closure effects are present, and changes in electrical resistivity with plastic deformation. Another key factor is the determination of calibration curves relating changes in potential across the crack (V_a) to crack length (a). In most instances, experimental calibration curves have been obtained by measuring the electrical potential difference across the machined slots of increasing length in a single test piece; across a growing fatigue crack, where the length of the crack at each point of measurement is marked on the fracture surface by a single overhead cycle or by a change in mean stress; across a growing fatigue crack in thin specimens, where the length of the crack is measured by surface observation.

Other experimental calibrations have been achieved using an electrical analog of the test piece, where the specimen design is duplicated, usually with increased dimensions for better accuracy, using graphitized analog paper or thin aluminum foil, and where the crack length can be increased simply by cutting with a razor blade. Such calibration procedures, however, are relatively inaccurate, particularly at short crack lengths, and are tedious to perform. Furthermore, where measurements of crack initiation and early growth are required ahead of short cracks or notches of varying acuity, such procedures demand a new experimental calibration to be obtained for each notch geometry.

Electric potential response may be determined empirically (Ref 23, 24, and 25) or using numerical methods, such as finite element or conformal mapping techniques (Ref 26, 27, 28, 29, and 30). Johnson's analytical solution of the MT geometry is widely used in experimental work due to its flexibility (Ref 28):

$$a = \frac{W}{\pi} \cos^{-1} \left[\frac{\cosh[(\pi/W) \times Y_0]}{\cosh \left[\frac{V}{V_0} \times \cosh^{-1} \left[\frac{\cosh[(\pi/W) \times Y_0]}{\cosh[(\pi/W) \times a_r]} \right] \right]} \right] \quad (\text{Eq 13})$$

$$\text{for } 0 \leq 2 \frac{a}{W} \leq 1$$

where a is the crack size, a_r is the reference crack size from another method, W is the specimen width, Y_0 is the voltage measurement lead spacing from crack plane, V is the measured electric potential difference, and V_r is the measured voltage corresponding to a_r . With minor modifications, Eq 13 can be applied to edge-cracked geometries by treating them as half of a MT geometry. Third- or higher-order polynomial expressions with coefficients obtained from regression analysis can be used to describe the potential response of the specimens when simplified expressions are required or Eq 13 does not apply.

A schematic diagram of a typical experimental setup for electrical potential crack monitoring measurements is shown in Fig. 17. The technique can be used with alternating current (ac) or dc power supplies. Alternating current systems have lower power requirements and do not suffer from the thermally induced potentials that plague dc systems. On the other hand, dc systems are widely used because of the relative simplicity. Consequently, this discussion of typical experimental setups is restricted to dc systems.

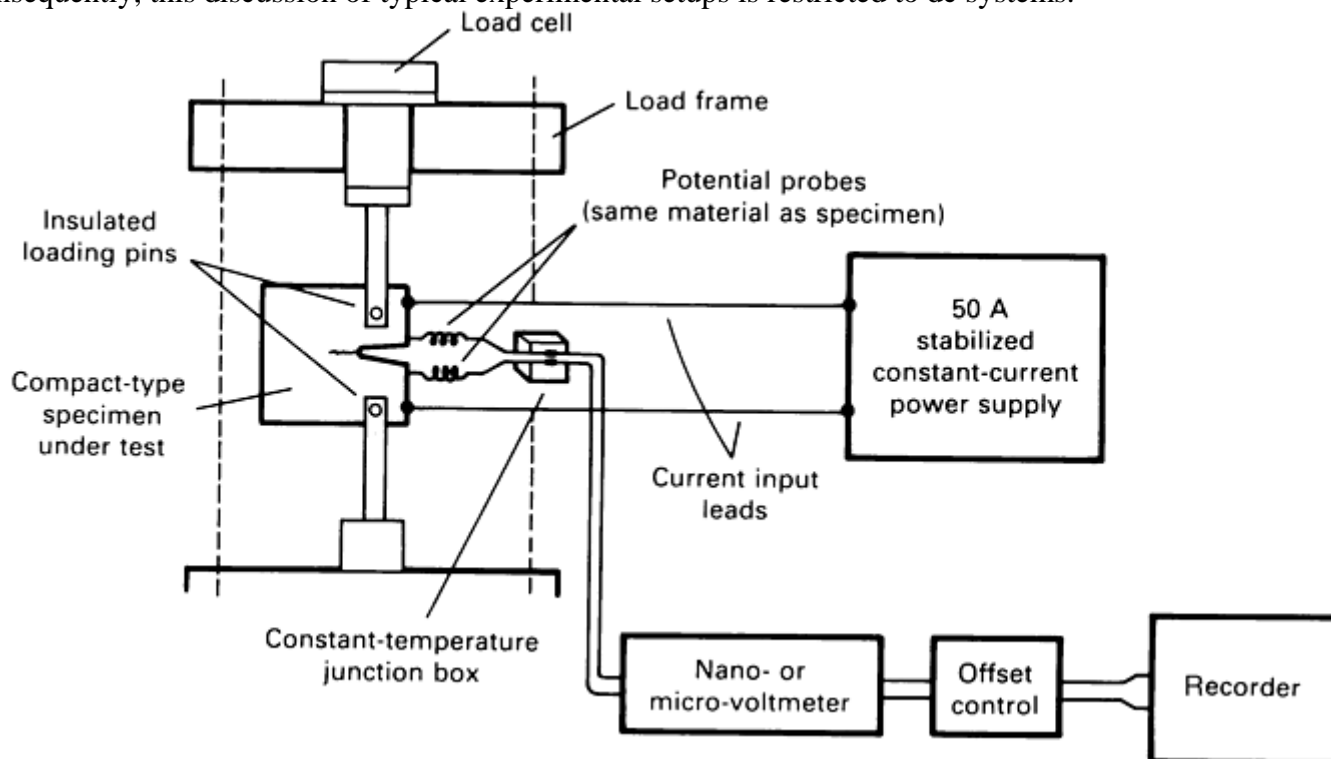


Fig. 17 Schematic of the direct current electrical potential crack monitoring system

The main component of a dc electric potential system is a power supply capable of producing a large, stabilized constant current. Applied currents range from 5 to 50 A with output voltages from 0.1 to 50 mV. Power supplies must be stable to 1 part in 10^4 or better, and nano- or microvoltmeters with a resolution of 0.05 to 0.5 μV are used (Ref 7). It is crucial that all dc potential measurement equipment (power supplies, voltage meters, etc.) and the loadframe itself be properly grounded. Before a power supply or nearby electromagnetic field

(EMF) source (e.g., induction heater) is faulted for poor performance of the electric potential technique, researchers are reminded to check that all equipment is properly grounded. In some instances, EMF shielding may be required.

High-resolution, stable, properly grounded equipment does not guarantee reliable performance and high resolution for the dc potential difference technique. Proper selection and use of current and potential leads are essential. High-current (welding) cable is ideal for current input leads, which are usually bolted to the specimen. To reduce noise, the potential leads should be firmly attached to the specimen, shielded, and twisted together. To ensure that current will pass through the specimen, the ratio of the loadtrain resistance to that of the specimen must be on the order of 10^4 . If this ratio cannot be achieved, the specimen must be electrically isolated using nonconducting (e.g., alumina) pins and washers or sleeves. The current applied to the specimen should be large enough to produce a measurable potential. Table 1 lists typical current and output voltages for CT specimens of aluminum, steel, and titanium. Excessive current (>10 A) can cause heating of the specimen and should be avoided. Potential leads should be made from fine wire of the same material as the specimen to reduce thermally induced EMF. Potential measurement leads and equipment should be kept away from EMF sources, such as transformers, to further reduce noise.

Table 1 Typical electric potential difference (EPD) voltages as measured on a standard compact-type specimen

Material	Approximate EPD, mV	Approximate change in crack length for 1 μ V change in EPD, μ m
Aluminum	0.1	300
Steel	0.6	50
Titanium	3.5	9

Based on $a/W = 0.22$, $B = 7.7$ mm, and $W = 50$ mm. Lead geometry per Ref 7 and direct current of 10 A. Crack tip processes, such as fatigue crack closure (see the section “Crack Closure” in this article), can reduce the potential of the specimen as the crack faces come together, effectively shortening the crack. This situation is especially a problem when testing materials that do not form protective, nonconducting oxide layers in the environment of interest. The solution to this problem is to measure the potential output at the peak load. In addition to crack closure, crack-tip plasticity and distributed damage, such as microcracking, must be considered. Large plastic zones, such as those encountered under elastic-plastic conditions, disturb the equipotential lines much like the crack (Ref 31). Distributed damage processes can also complicate measurements by making it difficult to define a continuous crack. Hence, optical measurements of the crack should be made to ensure that the electric potential difference technique provides a realistic representation of crack length. Changes in the electrical properties of the material can also limit the effectiveness of dc potential systems.

Changes in conductivity can complicate electric potential measurements. When high-conductivity materials, such as aluminum, are tested, temperature fluctuations of ± 1 °C will cause a change in potential on the order of a few μ V due to the temperature dependence of conductivity, and this change may vary with time. This condition can limit the crack extension resolution. Environmental chambers are useful with high-conductivity materials, even when testing at room temperature.

The primary difficulty with the dc electric potential technique is the junction potentials created at points of current and potential lead attachment. When dissimilar materials are in contact, a potential is generated due to the thermocouple effect, and it may be of the same order of magnitude as the potential generated by the specimen. This thermally induced potential, also known as the thermal voltage, may not be constant. Consequently, care must be taken to separate changes in potential due to fluctuations in thermal voltage from changes due to crack extension. This concern is especially important when measuring the slow growth rates found in the near-threshold regime (region I, Fig. 2).

There are three common approaches to account for the thermal voltage. The first method is to periodically turn off the power supply, note the value of thermal voltage, and subtract it from the output of the specimen with the current applied. This approach is acceptable for manually run tests, but it is not very useful when a continuous signal is required for computer-controlled tests. One alternative to manual measurement of the thermal voltage

is to apply a current to an uncracked specimen with no applied load in the same environment as the test specimen in the “reference potential” technique. The tendency of the thermal voltage to drift should be the same in both the cracked and uncracked specimens. The drift can then be monitored, and the thermal voltage simply becomes an offset. Attempts have been made to apply the reference potential technique to a single specimen by measuring potentials in areas of the specimen that are “insensitive” to crack extension. The development of high-current-capacity solid-state switches has made the use of fully reversed electric potential drop systems a third method for dealing with thermal voltages. If the direction of current flow is periodically reversed, the thermal voltage, which has a fixed polarity, will shift the maximum and minimum output potentials but will not influence the range or amplitude of the signal. Thus, the amplitude of the output potential can be used to determine the length of the crack.

The electric potential technique may also be applied to nonconducting specimens with the use of conducting thin foils. The foils, applied prior to testing, crack with the underlying specimen. Current is applied to the foil instead of to the specimen, and the calibrated response of the foil may be used to monitor the growth of the crack. This technique may be used for room- and elevated-temperature tests, provided that the foil accurately reflects the growth of the crack. Polymer-backed gages sold under the trade name KrakGage (Hartrun Corp., St. Augustine, FL) require special hardware for mounting and use and may be used with conducting or nonconducting specimens. It is also possible to vapor deposit gages directly to nonconducting specimens or to nonconducting oxide films on conducting or nonconducting (e.g., SiC) materials. The drawback of electric potential foils is the tendency for cracks with small opening displacements to “tunnel” under the gage. This crack extension without breaking the foil will lead to inaccurate growth rates.

Optimization Parameters. In any specimen geometry, there are numerous locations for both the current input leads and the potential measurement probes. Optimization of the technique involves finding the best locations, considering accuracy, sensitivity, reproducibility, and magnitude of output (measurability).

In practice, the accuracy of the electrical potential technique may be limited by several factors:

- Electrical stability and resolution of the potential measurement system
- Crack front curvature
- Electrical contact between crack surfaces where the fracture morphology is particularly rough
- Electrical contact between crack surfaces where significant crack closure effects are present
- Changes in electrical resistivity with plastic deformation, temperature variations, or both

Reproducibility refers to inaccuracies produced by small errors in positioning the potential measurement leads. Such leads are generally fine wires spot welded or screwed to the specimen, and accurate positioning is typically no better than within 0.5 mm (0.02 in.). To maximize reproducibility, these leads should be placed in an area where the calibration curve is relatively insensitive to small changes in position—that is, where dV/dx and dV/dy are small, where x and y are position coordinates—with the origin at the midpoint of the specimens. This position is often at variance with sensitivity considerations for measuring small changes in crack length.

To optimize measurability (i.e., signal-to-noise ratios), current input and potential measurement lead locations are chosen to maximize the absolute magnitude of the output voltage signal, V_a . As output, voltages are generally at the microvolt level and because of the high electrical conductivity of metals, a practical means of achieving measurability is simply to increase the input current. However, there is a limit to this increase, because when the current is too large (typically exceeding 30 A in a 12.7 mm, or 0.5 in., thick 1T steel CT specimen), appreciable specimen heating can result from contact resistance at current input positions.

Studies have shown that there must be a compromise between the sensitivity, reproducibility, and magnitude of the output signal when using electric potential techniques. In the instance of CT specimens, it has been shown that potential leads are best placed on the notched side of the specimen, as close to the mouth as possible, as recommended by the ASTM E 647. When using nonstandard geometries, the above references should ensure a sound basis for lead placement.

References cited in this section

7. Standard Test Method for Measurement of Fatigue Crack Growth Rates, E 647-91, *Annual Book of ASTM Standards*, Vol 03.01, 1992, ASTM, p 674–701

17. Standard Method for Plane-Strain Fracture Toughness of Metallic Materials, E 399-90, *Annual Book of ASTM Standards*, Vol 3.01, 1992, ASTM, p 569–596
21. A. Saxena and S.J. Hudak, Review and Extension of Compliance Information for Common Crack Growth Specimens, *Int. J. Fract.*, Vol 14 (No. 5), 1978, p 453–468
22. J.W. Dally and W.F. Riley, *Experimental Stress Analysis*, 3rd ed., McGraw-Hill, 1991
23. R.O. Ritchie, G.C. Garrett, and J.F. Knott, *Int. J. Fract. Mech.*, Vol 7, 1971, p 462–467
24. C.Y. Li and R.P. Wei, *Mater. Res. Stand.*, Vol 6, 1966, p 392–445
25. R.O. Ritchie and J.F. Knott, *Acta Metall.*, Vol 21, 1973, p 639–648
26. R.O. Ritchie and K.J. Bathe, *Int. J. Fract.*, Vol 15, 1979, p 47–55
27. G. Clark and J.F. Knott, *J. Mech. Phys. Solids*, Vol 23, 1975, p 265–276
28. H.H. Johnson, *Mater. Res. Stand.*, Vol 5, 1965, p 442–445
29. G.H. Aronson and R.O. Ritchie, *J. Test. Eval.*, Vol 7, 1979, p 208–215
30. M.A. Ritter and R.O. Ritchie, *Fat. Eng. Mater. Struct.*, Vol 5, 1982, p 91–99
31. G.M. Wilkowski and W.A. Maxey, *Fracture Mechanics: 14th Symposium—Vol II: Testing and Applications*, STP 791, J.C. Lewis and G. Sines, Ed., ASTM, 1983, p II-266 to II-294

Fatigue Crack Growth Testing

Ashok Saxena, Georgia Institute of Technology; Christopher L. Muhlstein, University of California, Berkeley

Loading Methods

The goal of a FCGR test is to generate a record of a versus N under specified loading conditions. This information can be generated by applying cyclic varying loads of specified amplitude and frequency.

The frequency of the test should, when possible, be kept constant; however, it may be necessary to reduce the frequency of a test in order to make crack-length measurements. Frequency effects are usually not observed in metals in laboratory air at room temperature over the range of typical testing frequencies (1 to 100 Hz). Although higher-frequency tests finish more quickly, specimen and loadtrain stiffness, as well as load range, impose a practical limit on the maximum testing frequency. Steel specimens 50 mm wide can be run on a typical 90 kN (1 tonf) capacity loadframe at 25 to 50 Hz. If compliance methods are being used to control the test or monitor crack extensions, the frequency response of the clip gage and recording instruments may limit the maximum frequency for testing.

The waveform to be used during a test is usually a sine or sawtooth (ramp) shape. Both waveforms will generate similar data at room temperature in benign environments. However, sine waveforms are easier for servohydraulic systems to control. Ramp waveforms should be used when elevated-temperature FCGR and creep-fatigue interaction are of interest (see appendix to this article, “High-Temperature Fatigue Crack Growth Testing”) or when testing in aqueous environments (Ref 32).

Five types of FCGR tests are used in laboratories today. How the specimen is loaded defines the type of growth rate test. Different types of tests are often conducted in series to confirm growth rates and to use as much of the

specimen as possible. To avoid load sequence effects, tests conducted in series should adhere to the same guidelines specified for precracking.

The simplest test type is one in which the load amplitude is kept constant and the applied ΔK increases as the crack extends. The simplicity of the test is its advantage. However, this test is essentially impractical for crack growth rates below 1×10^{-8} m/cycle. In a second type of test, loads are shed manually at increments of 10% or less. Although cumbersome because they require constant attention, these tests allow the generation of data for slower crack growth in a more time-efficient manner than the constant-load-amplitude test. The prevalence of personal computers and modern controls technology in current laboratories has popularized the remaining three types of so-called “continuous loadshedding” or “ K -controlled” experiments.

Continuous loadshedding tests are those in which loads are shed at steps of 2% or less for a predetermined increment of crack extension. During these tests, the crack length is continuously monitored by electric potential, compliance, or another suitable technique. Loads are shed or increased according to the following relation proposed by Saxena et al. (Ref 33):

$$\Delta K = \Delta K_0 \exp[c(a - a_0)] \quad (\text{Eq 14})$$

where ΔK is the applied range of ΔK , ΔK_0 is the initial range of ΔK , c is the normalized K -gradient, a is the current crack length, and a_0 is the initial crack length. The normalized K -gradient is defined as:

$$c = \frac{1}{K} \left(\frac{dK}{da} \right) [L^{-1}] \quad (\text{Eq 15})$$

The use of Eq 14 for changing fatigue loads is ideally suited for personal computers, and it allows testing under K -controlled conditions. If the normalized K -gradient is less than zero, the applied ΔK will be decreased as the crack extends. These tests are termed K -decreasing tests. Conversely, $c \geq 0$ will lead to increasing ΔK as the crack extends.

The appropriate value of c for a decreasing ΔK test is that which avoids the anomalous growth rates caused by shedding loads too quickly. Investigators have determined that $c = 0.08 \text{ mm}^{-1}$ (-2 in.^{-1}) is an appropriate value for decreasing ΔK tests on most metals (Ref 34). This value of c was derived to eliminate load-interaction effects caused by crack-tip plasticity in metals. The same value of c for a K -decreasing test in intermetallics and ceramics is recommended. This value ensures that sufficient data can be obtained over the narrow range of stable crack growth, even though plastic zones are considerably smaller or nonexistent in these materials (Ref 35, 36).

Increasing ΔK tests (i.e., $c > 0$) are usually conducted to confirm the growth rates measured during the previous K -decreasing portion of the test. Increasing ΔK tests may, if necessary, be conducted with larger normalized K -gradients. It is important to note that during an increasing ΔK test, loads may have to be decreased as the crack extends, which could lead to difficulties with control. Hence, it is preferable to use the simple constant-amplitude test instead of a controlled increasing ΔK test.

The first type of continuous loadshedding test is where the load ratio (R) is held constant. Constant- R tests generate the same type of information as constant-amplitude tests. Low- and high- R ($R = 0.1$ and 0.5 , respectively) tests are usually conducted for comparison purposes.

Another type of K -controlled test is a constant- K_{\max} test, which is essentially a variable- R test. When K_{\max} is held constant as the crack extends, R will vary as shown schematically in Fig. 18. Once again, the value of ΔK to be applied to the specimens is dictated by Eq 14. The advantage of this test is that it quickly establishes the role of R on crack growth rate. For decreasing ΔK in constant- K_{\max} tests with negative c , the lower crack growth rates are at very high values of R . The behavior of threshold cracks under these conditions has been used as a measure of “closure free” fatigue crack growth, reflecting the “intrinsic resistance” of the material to fatigue (Ref 37).

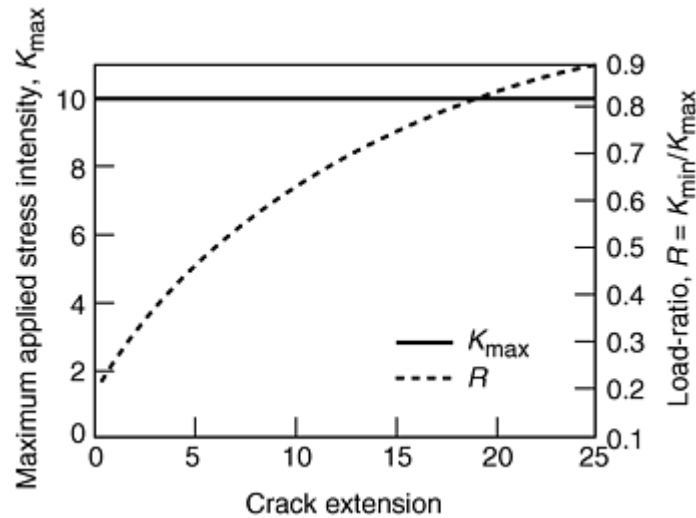


Fig. 18 Constant K_{max} test load ratio

The last type of continuous loadshedding fatigue test is a constant- K_{mean} test. Much like the constant- K_{max} test, a constant- K_{mean} test can be used as a comparison with constant K_{max} to help establish the role of K_{mean} versus K_{max} on fatigue crack growth rates. Constant- K_{max} and - K_{mean} tests have been popular in the testing of brittle materials where definitive mechanisms for crack advance have yet to be established.

Once testing is complete, the final crack in the specimen should be measured optically on both sides of the specimen. This measurement will be compared to the terminal crack length predicted by other measurement techniques in the analysis of the investigation.

Electromechanical Fatigue Testing Systems. The primary function of electromechanical fatigue testers is to apply millions of cycles to a test piece at oscillating loads up to 220 kN (2.5 tonf) to investigate fatigue life, or the number of cycles to failure under controlled cyclic loading conditions. Variables associated with fatigue-life tests are frequency of loading and unloading, amplitude of loading (maximum and minimum loads), and control capabilities. The fundamental data output requirement is the number of cycles to failure, as defined by the application.

A variety of electromechanical fatigue testers have been developed for different applications. Forced-displacement, forced-vibration, rotational-bending, resonance, and servomechanical systems are discussed in this article and are compared in Table 2. Other specialized electromechanical systems are available to perform specific tasks.

Table 2 Comparison of electromechanical fatigue systems

Parameter	Forced displacement	Forced vibration	Rotational bending	Resonance	Servomechanical
Tension	Yes	Yes	No	Yes	Yes
Compression	Yes	Yes	No	Yes	Yes
Reverse stress	Yes	Yes	Yes	Yes	Yes
Bending	Yes	Yes	Yes	Yes	Yes
Frequency range	Fixed	Fixed, 1800 rpm	0–10,000 rpm	40–300 Hz	0–1 Hz
Load range	Typically <450 N (<100 lbf)	Up to 220 kN (50,000 lbf)	...	Up to 180 kN (40,000 lbf)	Up to 90 kN (20,000 lbf)
Type Control	Open-loop	Open-loop	Open-loop	Closed-loop	Closed-loop
Mode	Displacement	Load	Rotation/bending	Load	Load, displacement, strain
Maximum	...	25.4 mm	...	1.0 mm (0.040)	100 mm (4 in.)

deflection		(1.00 in.)		in.)	
Advantages	Simple, straightforward	Versatile, efficient, durable	Efficient, durable, simple	Fully closed-loop, extremely efficient	Fully closed-loop, high precision
Disadvantages	No load control, very limited applications (soft samples)	Fixed frequency, limited control (open-loop)	Rotational bending only, limited applications	Operating frequency directly proportional to sample stiffness	Low frequency only

Servohydraulic testing machines are particularly well suited to provide the control capabilities required for fatigue testing. Extreme demands for sensitivity, resolution, stability, and reliability are imposed by fatigue evaluations. Displacements may have to be controlled (often for many days) to within a few microns, and forces can range from 100 kN (1 tonf) to just a few newtons. This wide range of performance can be obtained with servomechanisms in general and, in particular, with the modular concept of servohydraulic systems.

Usually, the problem of selecting the appropriate system is simply a matter of optimizing the various components to form a system best suited to the given testing application. With any type of control system, the objective is to obtain an output that relates as closely as possible to the programmed input. In a fatigue testing system, it may be desired to vary the force on a specimen in a sinusoidal manner, at a frequency of 1 Hz over a force range of 0 to 100 kN (0 to 1 tonf). The only practical means of precision accomplishment is through the use of a negative-feedback closed-loop system.

References cited in this section

32. R.J. Selines and R.M. Pelloux, Effect of Cyclic Stress Waveform on Corrosion Fatigue Crack Propagation in Al-Zn-Mn Alloys, *Metall. Trans.*, Vol 13, 1972, p 2525–2531
33. A. Saxena, S.J. Hudak, Jr., J.K. Donald, and D.W. Schmidt, *J. Test. Eval.*, Vol 6 (No. 3), May 1978, p 167–174
34. R.J. Bucci, Development of a Proposed ASTM Standard Test Method for Near-Threshold Fatigue Crack Growth Rate Measurement, *Fatigue Crack Growth Measurement and Data Analysis*, S.J. Hudak, Jr. and R.J. Bucci, Ed., STP 738, ASTM, 1981, p 5–28
35. K.T. Venkateswara Rao, Y.W. Kim, C.L. Muhlstein, and R.O. Ritchie, *Mater. Sci. Eng. A*, Vol 192/193, 1995, p 474–487
36. R.J. Dauskardt, W. Yu, and R.O. Ritchie, *J. Am. Ceram. Soc.*, Vol 70 (No. 10), Oct 1987, p C248–C252
37. R.W. Hertzberg, W.A. Herman, and R.O. Ritchie, *Scr. Metall.*, Vol 21, 1987, p 1541

Fatigue Crack Growth Testing

Ashok Saxena, Georgia Institute of Technology; Christopher L. Muhlstein, University of California, Berkeley

Analysis of Crack Growth Data

The two major aspects of FCGR test analysis are to ensure suitability of the test data and to calculate growth rates from the data. In addition to growth rate calculations, analysis also may require the calculation of fatigue crack closure levels and the characterization of fracture surface and metallographic features, as discussed in this

section. Combining the results from all of these areas is necessary to develop an understanding of the FCGR behavior of the material. Finally, the reliability of “real time” analysis by personal computers must be verified, and the sophisticated tests performed in modern laboratories must undergo some degree of analysis. Hence, it is essential that computer-controlled tests generate records of a versus N as well as FCGR.

Validity of the Test Data. The first step is to ensure the validity of the test data and make corrections to the crack length, if necessary. Crack measurement intervals are recommended in ASTM E 647 according to specimen type. For CT specimens:

$$\Delta a \leq 0.04W \text{ for } 0.25 \leq \frac{a}{W} \leq 0.40$$

$$\Delta a \leq 0.02W \text{ for } 0.40 \leq \frac{a}{W} \leq 0.60$$

$$\Delta a \leq 0.01W \text{ for } \frac{a}{W} \geq 0.60$$

For MT specimens:

$$\Delta a \leq 0.03W \text{ for } \frac{a}{W} < 0.60$$

$$\Delta a \leq 0.03W \text{ for } \frac{a}{W} > 0.60$$

At the end of the test, the final crack length is measured on both sides of the specimen. A comparison should be made between optical measurements and the final predicted crack length by any nonoptical techniques used. Differences between the measured crack lengths should be corrected using a linear relationship. In other words, the error between the final measured and predicted crack size is linearly distributed over the crack extension range. If periodic optical measurements were made during the test, other more appropriate correction procedures can be used.

Thicker specimens should be fractured after testing to determine the degree of crack front curvature. Cooling the specimen to liquid nitrogen temperatures allows the brittle fracture of most metallic materials and reveals a clear demarcation between the fatigued and fractured portions of the specimen. Five evenly spaced measurements of crack length should be made across the crack front. The average length should then be used as the final crack length, and the corrections should be applied using this value instead of the surface measurements.

Crack Growth Rate Calculation. A number of different numerical techniques have been used to calculate crack growth rates from the set of (a_i, N_i) data points of a given crack growth rate test (Table 3). The secant and incremental polynomial methods are the most widely used. When the data are processed to a final smoothed $da/dN = f(\Delta K)$ format, these methods provide approximately equivalent results. However, the scatter of individual da/dN values about the average depends greatly on the data reduction method.

Table 3 Methods for calculating crack growth rates

Incremental polynomial method:

A least-squares, second-order polynomial is obtained for successive sets of $(2k + 1)$ data points:

$$\hat{a}_i = b_0 + b_1 \left(\frac{N_i - C_1}{C_2} \right) + b_2 \left(\frac{N_i - C_1}{C_2} \right)^2$$

where $C_1 = (N_{i+k} + N_{i-k})/2$ and $C_2 = (N_{i+k} - N_{i-k})/2$ are centering and scaling constants, respectively, that are introduced to prevent numerical problems in obtaining the least squares fit. The crack growth rate at a_i , the predicted central crack length at N_i , is given by the derivative:

$$\left. \frac{da}{dN} \right|_{\hat{a}_i} = \frac{b_1}{C_2} + 2b_2 \frac{(N_i - C_1)^2}{C_2}$$

Typical values of k are 1, 2, or 3, resulting in the second-order polynomial being estimated on the basis of 3, 5, or 7 successive data points. The estimated crack growth rate function loses k data points at each end.

Less apparent scatter is obtained for larger k values.

Secant method:

In the secant method for differentiating the a versus N data, the average crack extension per cycle is calculated for each pair of data points, and ΔK is calculated at the midpoint of the crack lengths:

$$\left. \frac{da}{dN} \right|_{\hat{a}_i} = \frac{a_{i+1} - a_i}{N_{i+1} - N_i}$$
$$\hat{a}_i = \frac{a_{i+1} + a_i}{2}$$

This method is simple but exhibits the most scatter in da/dN values.

Modified difference methods:

These methods are finite difference techniques for estimating the derivative at the midpoint of a data set. These methods use numerical derivatives. The formula for estimating the derivative at the midpoint a_i of three successive data points is given by:

$$\left. \frac{da}{dN} \right|_{a_i} = \frac{a_i - a_{i-1}}{N_i - N_{i-1}} + \left[\frac{N_i - N_{i-1}}{N_{i+1} - N_{i-1}} \right] \left[\frac{a_{i+1} - a_i}{N_{i+1} - N_i} - \frac{a_i - a_{i-1}}{N_i - N_{i-1}} \right]$$

The secant method fits a line between adjacent data points. The slope of the line is the crack growth rate, da/dN . The load at the average crack length of the interval is used to calculate the corresponding ΔK . It is not uncommon to collect data points more closely spaced than the 0.25 mm (0.010 in.) minimum crack extension for growth rate calculations. When more data are available, a straight line through the multiple data points can be fitted by regression analysis to calculate crack growth rates. A 50% overlap between data sets used for calculating successive crack growth rates can considerably reduce scatter in the processed data. This method is termed the modified secant method.

The polynomial method uses the derivative of a second-order polynomial fitted to a fixed number of data points (often five or seven). The growth rate and ΔK level are calculated for the average value of crack length in the interval. This method tends to provide data with less scatter than the secant method. In practice, there are no systematic differences in the da/dN versus ΔK trends if the same data are processed by these different techniques (Ref 38). In fact, little difference is observed between the data processed by the modified secant method and the polynomial method.

Variability. Although the apparent variability in the resulting da/dN value depends on the calculation method, none of the methods introduces a significant bias to an overall mean trend curve. Figure 19(b) plots da/dN versus ΔK , as calculated from the data of Fig. 19(a), using the secant, incremental polynomial, and five-point modified difference methods. Because methods of analyzing and interpreting the scatter in da/dN are not currently available, the simpler techniques—the secant and incremental polynomial methods—are often chosen.

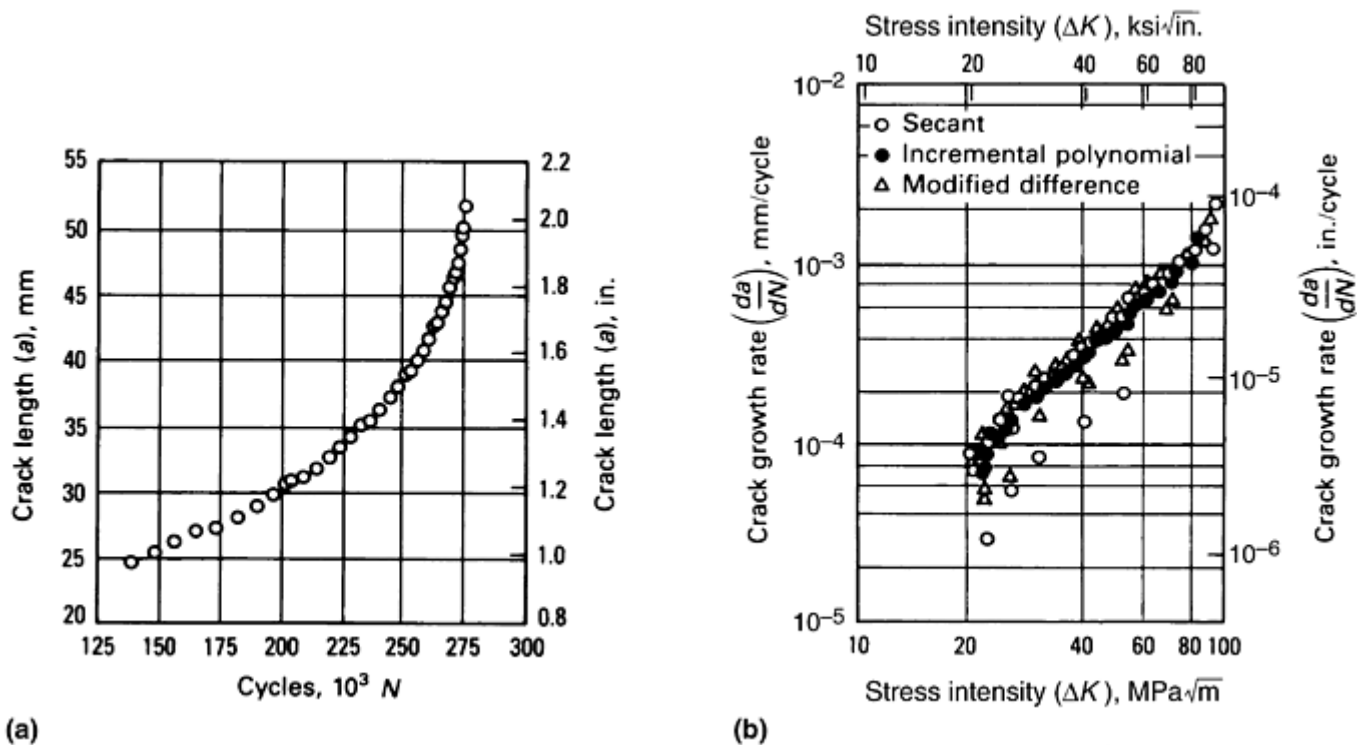


Fig. 19 Comparison of da/dN calculation methods. (a) Crack length test data. (b) Plot of calculated da/dN rates from the data in (a)

Crack Closure Analysis. The determination of the fatigue crack closure load is a subject of vigorous debate. Visual inspection of compliance curves can be used to estimate closure levels. However, the method is subjective and not well suited for large amounts of data. ASTM task groups have explored the use of the compliance offset and correlation method for closure analysis (Ref 39). In the compliance offset method, crack closure levels are determined by finding the point that deviates from the linear portion (i.e., is offset) by a set amount (usually 1, 2, 4, or 8%). The correlation method determines the closure level by mathematically representing the “strength” of the linear relationship between load and displacement/strain along the curve. To confirm that the methods are applied correctly, algorithms should be tested with hypothetical, bilinear compliance curves, for which both methods should yield identical results.

The compliance offset method is generally applied using a computer, because the calculations do not lend themselves to the use of spreadsheets. The procedure is as follows:

1. Collect digitized strain/displacement and load data for a complete load cycle. The data sampling rate should be high enough to ensure that at least one data pair (displacement and load) is taken in every 2% interval of the cyclic load range.
2. Starting with the first data sample below maximum load on the unloading curve, fit a least-squares straight line to a segment of the curve spanning approximately the uppermost 25% of the cyclic load range. The slope of this line is the compliance value that corresponds to the fully open crack configuration.
3. Starting with the first data sample below maximum load on the loading curve, fit least-squares straight lines to segments of the curve that span approximately 10% of the cyclic load range and that overlap each other by approximately 5% of the range. Store the compliance (slope) and the corresponding mean load for each segment in a vertical array with the highest load location at the top.
4. Replace the compliance stored in each location in the array with the corresponding compliance offset, which is computed as a percentage of the “open crack” compliance and is given by:

$$\text{Compliance offset} = \frac{(\text{"Open crack compliance"} - \text{compliance})(100)}{\text{"Open crack" compliance}} \quad (\text{Eq 16})$$

5. Identify the highest load location in the array that has a compliance offset greater than the selected offset criterion, and for which all array locations below have compliance offsets greater than the offset criterion.
6. Starting at the array location identified in step 5, identify the nearest, higher load location that has a compliance offset less than the selected offset criterion, and for which all array locations above it have compliance offsets less than the offset criterion.
7. Determine the opening load corresponding to the selected offset criterion by linear interpolation between the two (compliance offset, load) points identified in steps 5 and 6 (Ref 39).

An alternative to the offset method is the correlation coefficient method. The correlation coefficient, r , is defined as (Ref 39):

$$r = \frac{n\sum(x_i y_i) - \sum x_i \sum y_i}{[(n\sum x_i^2 - (\sum x_i)^2)(n\sum y_i^2 - (\sum y_i)^2)]^{1/2}} \quad (\text{Eq 17})$$

where n is the number of data pairs, Σ denotes the summation from $i = 1$ to n , x_i are individual load data samples, and y_i are individual displacement data samples. The closure level is defined as the load at which the correlation coefficient has the highest value. In contrast to the offset method, in which different levels of offset can be selected, there is only one criterion in this method. Both methods generate similar closure levels for the same data. However, issues of data quality are currently the biggest problem for consistent experimental closure analysis. Methods to characterize data quality are presently being explored.

Fracture Surface Characterizations. Cracked specimens are also useful for establishing modes of crack advance and other interactions of the crack with the microstructure. Scanning electron microscopy is used to characterize the fracture surface. Care should be taken to establish the level of ΔK associated with the image of the fracture surface. This relationship is especially important when working with brittle materials where inspection of the surface does not reveal an obvious difference in fracture surface morphology between the fatigued material and posttest fracture.

Portions are often removed from the interior of the specimen and mounted for metallographic preparation. "Crack profiles" can be useful for demonstrating the interaction of the crack with the microstructure. There can be marked differences in how cracks interact with microstructures, especially in instances where crack closure and distributed damage are important.

References cited in this section

38. W.G. Clark and S.J. Hudak, The Analysis of Fatigue Crack Rate Data, *Application of Fracture Mechanics to Design*, J.J. Burke and V. Weiss, Ed., Vol 22, Plenum, 1979, p 67–81
39. E.P. Phillips, "Results of the Second Round Robin on Opening Load Measurement Conducted by ASTM Task Group E24.04.04 on Crack Closure Measurement and Analysis," Technical Memorandum 109032, National Aeronautics and Space Administration, Nov 1993

Appendix: High-Temperature Fatigue Crack Growth Testing

David C. Maxwell, University of Dayton; Theodore Nicholas, Wright-Patterson Air Force Base

Introduction

The concepts and procedures for fatigue crack growth testing at room or ambient temperature described in this article are generally applicable to elevated-temperature conditions. In this appendix, some of the features unique to testing and measurement at high temperatures are reviewed. In particular, methods for heating and controlling temperature are discussed briefly. Other aspects related to instrumentation, measurement, and test techniques are also highlighted. While there are no well-established standards for elevated-temperature crack growth testing, one standard testing procedure has been recommended recently based on a cooperative study using 304 stainless steel (Ref 40). While documentation on methods employed in elevated-temperature crack growth testing are scattered widely in the open literature, conferences devoted to this particular subject include many papers that provide details of individual investigations (e.g., Ref 41).

Specimen Design. In general, the specimens used in room-temperature testing are equally applicable for high-temperature testing. In fact, in making comparisons of crack growth rates as a function of temperature, it is considered good practice to retain the same test specimen geometry at all temperatures tested.

An exception to this practice is the specialized instance of testing under thermomechanical fatigue (TMF) crack growth conditions. Here, the temperature as well as the load is cycled. In order to control the cyclic temperature on the specimen, effective means of both heating and cooling the specimen must be employed. This procedure usually requires either a thin planar specimen or a thin-walled tube, both of which minimize the thermal mass and allow for more rapid heating or cooling and better control of temperature gradients. Information on some of the techniques that have been employed for TMF can be found in conference proceedings, such as those of ASTM (Ref 42, 43), American Society of Mechanical Engineers (ASME) (Ref 44), or the International Conferences on Fatigue and Fatigue Thresholds (Ref 45, 46).

Another aspect of TMF crack growth almost unique to this type of test is the use of strain control as the mode of load application, similar to that used in low-cycle fatigue. A brief discussion of the problems and limitations of the use of strain control in elevated-temperature or TMF crack growth testing can be found in Ref 47.

The final consideration in TMF crack growth testing is the ability to heat and cool the specimen, or the access of heat and cooling air to the specimen. For example, clevises used on CT specimens tend to shield the specimen from the heating or cooling source and make it difficult to control the temperature cycle. Therefore, other geometries, such as MT geometries, are generally used for this type of test.

Specimen Gripping. There are two main considerations in gripping specimens at high temperature. The first consideration is the possible introduction of friction at any type of pin joint. Whereas friction can be minimized at room temperature through lubrication or careful surface finishing, these methods are less effective at elevated temperatures. Special high-temperature lubricants or oxidation-resistant materials for pins and clevises are methods for minimizing the development of friction in pin joints. Rigid fixtures and grips, on the other hand, do not require such considerations.

The second aspect of gripping at high temperatures is the possible loss of friction due to mismatches in the coefficient of thermal expansion of grips and specimens. Calculations or experimental evaluations should be made to ensure that the load-carrying capacity of the gripping system does not degrade due to differential thermal expansions so that slippage might occur.

Further, it should be demonstrated that excessive clamping stresses do not develop such that the specimen is crushed or the grips fail. This aspect of high-temperature testing is only applicable to instances where “hot” grips are used, such as when the grips and specimens are both contained within a furnace. Cold grips, on the other hand, produce high-temperature gradients along the length of the specimen and make it more difficult to maintain a constant temperature over the gage length or the crack growth region of the specimen.

Heating Methods. There are several methods available for heating specimens and maintaining a constant and uniform temperature during elevated-temperature crack growth testing. One of the more common methods is to use a commercially available or homemade furnace and power controllers that produce one or more zones of uniform, controlled temperature. Temperature control is achieved from thermocouple feedback, either from within the chamber, where the air temperature is being controlled, or from thermocouples directly attached to the specimen at one or more locations. In either situation, temperature control with commercial units is generally accurate and reliable and can be considered a mature, state-of-the-art technology.

A second method of heating specimens is through the use of induction heaters, where the specimen is heated by alternating currents produced by an EMF generated by the inductance coil surrounding the test specimen. Shielding of the specimen by grips may cause nonuniform temperature distribution. Therefore, single-edge-tension specimen geometries are generally preferred. The number and spacing of the coils, though calculated from formulas provided with such apparatus, is determined most often from trial and error and usually requires a certain amount of experience for optimal performance. Feedback is provided from one or more thermocouples attached to the specimen, and uniformity of temperature must be checked with some type of temperature mapping system, such as multiple thermocouples on a dummy specimen.

Another method of heating used in several laboratories is the use of radiant energy from quartz lamps mounted in reflective and cooled housings. Each lamp focuses energy over a limited portion of the test specimen, so multiple lamps, multiple thermocouples, and good thermal conductivity across the specimen all lead to more uniform temperature fields. A description of the technique of quartz lamp heating can be found in Ref 48.

The last common method of specimen heating is direct resistance heating. Here, a current is passed directly through the specimen from one end to another. The test apparatus must be electrically insulated from the input and output leads. Uniform gage length specimens are better adapted to this method of heating than highly nonuniform ones; therefore, a MT specimen would be a much better candidate than a CT specimen. Because the high current passes through the specimen, no conducting leads can be attached to the specimen that would provide an alternative path for the current. Thus, temperature measurement from thermocouples attached directly to the specimen and electric potential crack growth measurements cannot be made with this type of heating. Similarly, extensometry that attaches directly to the specimen must use nonconducting elements.

Temperature Measurement. The science of the measurement of temperature, known as pyrometry, dates back before World War II. Books on the subject of pyrometry in general (Ref 49), or optical pyrometry in particular (Ref 50), were published in 1941 and provide detailed descriptions of the theory and the methods used in that era. The basic principles have not changed. The most common method for temperature measurement is through the use of thermocouples, or thermoelectric pyrometer, directly attached to the specimen. A thermocouple is made by welding two dissimilar wires together at one end. A change in temperature will generate an EMF that can be recorded on an instrument attached to the other end of the wires. These readings provide a real-time, continuous record of temperatures at a given point on a specimen, and they are commonly used for temperature control feedback as well as direct temperature measurement.

Another commonly used method of measuring temperature is through the use of commercially available infrared detectors, which sense the radiation emitted from a sample and convert the frequency of the radiation to temperature after appropriate calibration. The theory and methods of optical pyrometry are documented in numerous places (e.g., Ref 51, 52). The emissivity of the test material whose temperature is being measured is the quantity used as the basis of the measurement. Emissivity is the ratio between total radiant energy per square centimeter per second between the specimen being measured and a black body at the same temperature. Thus, as the emissivity of a material decreases from 1, the apparent temperature as measured by an optical pyrometer will deviate from the actual temperature by a greater amount.

The emissivity of a heated specimen will always be less than 1, and the apparent temperature will, therefore, be less than the desired test temperature. Emissivity can be influenced by surface roughness, the spectral transmission of any windows between the test specimen and the measuring instrument, and the chemical changes of the specimen surface due to oxidation or other environmental degradation. All these issues should

be addressed when using optical pyrometry. Commercial units are widely available for this type of measurement and usually come with detailed instructions.

Crack-Length Measurement. Electric potential drop is a common method of crack-length determination, both at room temperature and at elevated temperatures. The major consideration for elevated-temperature testing is to ensure that temperature fields are uniform and constant between the potential drop leads. Changes in temperature can result in a false indication of crack-length changes. The error is due to the resistivity change in the material caused by a change in temperature, and this change, in turn, is dependent on the resistivity characteristics of the material. For the direct current potential drop (DCPD) method, a 3 °C (5.5 °F) change in temperature in an aluminum alloy can result in a 1% change in the DCPD signal, whereas for the same change in resistivity, Inconel 718 requires a 100 °C (180 °F) change in temperature (Ref 53). The electric potential drop method of crack-length measurement, used commonly in both room- and elevated-temperature isothermal crack growth testing, has also been applied to TMF testing (Ref 54). As with any other technique, modifications and improvements are continually being developed and documented in the literature, as in the work of Shin et al. (Ref 55), where modification to the dc potential drop system is reported.

Compliance methods are equally valid at elevated temperatures as at room temperature, provided that some simple considerations are addressed. Nonconstant thermal gradients must be avoided, because any change in the dimensions of any part of a mechanical extensometer can result in a change in electrical output. The gage portion, which is normally attached to the specimen through special high-temperature extension arms or feed rods, is usually shielded from the specimen (Fig. 20) and cooled with either blowing air or circulating water. Whatever the setup, the gage should reach thermal equilibrium and stability before measurements are made, in order to avoid false indications due to thermal transients.

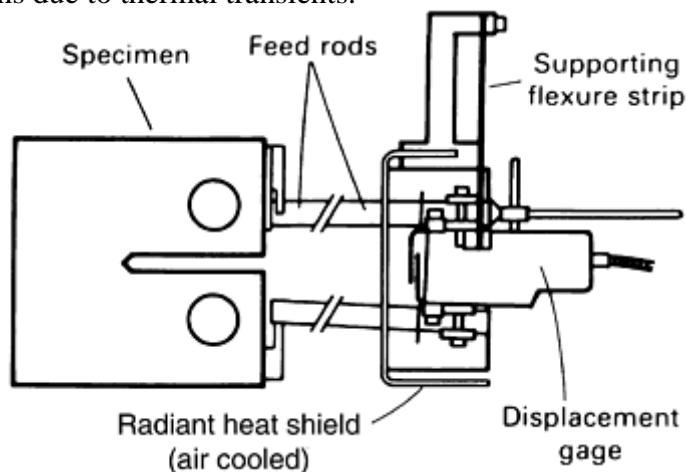


Fig. 20 Feed-rod attachment for high-temperature tests. Feed rods are made of quartz for tests up to 1000 °C or ceramics for tests at higher temperatures.

Optical methods are less widely used today than previously because of the availability of automated methods for crack-length measurement. Optical methods, such as use of a traveling microscope, are useful for reference measurements and are equally valid at room or elevated temperature. At elevated temperature, however, the resolution of crack length may be reduced because of deterioration of the specimen surface through oxidation. When specialized optical methods such as laser interferometry are used, the deterioration of the specimen surface over time should be considered so that the optical information is still available with sufficient resolution.

Special Methods. Other specialized techniques see occasional application in high-temperature crack growth testing. For example, crack growth over prolonged periods of time has been measured using real-time holographic interferometry (Ref 56). Compact-tension specimens were tested under sustained load at 120 °C (250 °F) for 860 h, and crack-opening displacement (COD) was monitored. The COD measurements had to be converted to crack lengths using an elastic-plastic finite-element analysis code and clip gage COD measurements on a reference sample.

Validity of K Solutions. The reduction of crack length versus N data to a $da/dN-\Delta K$ curve depends on having a K solution for the specimen geometry being used. Stress-intensity solutions are widely available, or can be easily generated, for almost any specimen geometry used in laboratory testing. These solutions, however, are based on the assumption of a homogeneous material and do not take into account any thermal gradients or

thermal stresses that may arise in elevated-temperature crack growth testing. For situations where the specimen and grips are at a uniformly high temperature, such as within a furnace, there is no problem. For situations where the temperature is nonuniform, such as with inductance or quartz lamp heating with cooled grips, temperature gradients are developed along the axis of the specimen. These gradients, in turn, may result in thermal stresses that produce thermal K -values that alter the isothermal K solution for a given specimen. These thermal K -values, therefore, must be taken into account in the K analysis of the particular crack geometry.

Ohta et al. (Ref 57) found that crack growth rate data at 300 °C (570 °F) in a MT specimen only matched room-temperature data in a low-alloy ferritic steel (SB46) when the parabolic temperature gradient that existed along the specimen was taken into account using finite element analysis, which was confirmed with experimental measurements. Coker et al. (Ref 58) conducted a finite element analysis of a single-edge-crack specimen with thermal gradients between the plane of the crack and the room-temperature grips. For the specific geometry and temperature profile, stress-intensity factors due to thermal stresses were below $2 \text{ MPa}\sqrt{m}$ for $a/W \leq 0.8$. While these values are small, near-threshold tests involving very small values of ΔK could be substantially influenced by thermal stresses. It is important, therefore, to have calculations or estimates of thermal-stress-induced values that have nonuniform temperature profiles. Unfortunately, there are very few papers in the literature where this particular problem is addressed. Nonetheless, this consideration can be important in high-temperature testing, particularly when testing in the near-threshold regime or when thermal gradients are severe.

Thermal gradients and effective K -values resulting from direct resistance heating are discussed by Cunningham and Griffin (Ref 59). The analysis shows when direct resistance heating becomes important during the cyclic conditions of thermal fatigue. The results indicate that stress intensities resulting from thermal gradients due to direct resistance heating are generally small except when thermal cycling frequencies are high. The thermal gradients and K -values resulting from thermal cycling are reported in a subsequent publication (Ref 60). There, for high thermal frequencies, significant magnitudes of K can be developed at the crack tip due to the thermal transients. For those involved in TMF crack growth testing, this information should be considered when determining the stress intensity at the crack tip.

References cited in this section

40. Y. Asada, M. Kitagawa, N. Shimakawa, T. Kodaira, T. Asayama, and Y. Wada, Standardization of Procedures for the High-Temperature Crack Growth Testing for FBR Materials in Japan, *Nucl. Eng. Des.*, Vol 133, 1992, p 465–473
41. S. Mall and T. Nicholas, Ed., *Elevated Temperature Crack Growth*, MD-Vol 18, ASME, 1990
42. H. Sehitoglu, Ed., *Thermomechanical Fatigue Behavior of Materials*, STP 1186, ASTM, 1993
43. M.J. Verrilli and M.G. Castelli, Ed., *Thermomechanical Fatigue Behavior of Materials*, STP 1263, ASTM, 1995
44. W.J. Jones, Ed., *Thermomechanical Behavior of Advanced Structural Materials*, AD-Vol 34/AMD-Vol 173, ASME, 1993
45. H. Kitagawa and T. Tanaka, Ed., *Fatigue 90*, Materials and Components Engineering Publications, Ltd., Birmingham, UK, 1990
46. J.-P. Bailon and J.I. Dickson, *Fatigue 93*, Engineering Materials Advisory Services, Ltd., West Midlands, UK, 1993
47. T. Nicholas, M.L. Heil, and G.K. Haritos, Predicting Crack Growth under Thermo-Mechanical Cycling, *Int. J. Fract.*, Vol 41, 1989, p 157–176
48. G.A. Hartman, A Thermal Control System for Thermal/Mechanical Cycling, *J. Test. Eval.*, Vol 13, 1985, p 363–366

49. W.P. Wood and J.M. Cork, *Pyrometry*, McGraw-Hill, 1941
50. W.E. Forsythe, *Optical Pyrometry: Temperature—Its Measurement and Control in Science and Industry*, Reinhold Publishing, 1941
51. H.J. Kostkowski and R.D. Lee, “Theory and Methods of Optical Pyrometry,” Monograph 41, National Bureau of Standards, 1962
52. J.C. Richmond and D.P. DeWitt, Ed., *Applications of Radiation Thermometry*, STP 895, ASTM, 1985
53. J.K. Donald and J. Ruschau, Direct Current Potential Difference Fatigue Crack Measurement Techniques, *Fatigue Crack Measurement: Techniques and Applications*, K.J. Marsh, R.A. Smith, and R.O. Ritchie, Ed., EMAS, West Midlands, UK, 1991, p 11–37
54. G.A. Hartman and D.A. Johnson, DC Electric Potential Method Applied to Thermal/Mechanical Fatigue Crack Growth Testing, *Exp. Mech.*, Vol 11, 1987, p 106–112
55. C.-S. Shin, W.H. Huang, and H.-Y. Chen, An Improved DC Potential Drop System for Crack Length Measurement, *J. Chinese Inst. Eng.*, Vol 16, 1993, p 29–40
56. T.R. Hsu, R. Lewak, and B.J.S. Wilkins, Measurements of Crack Growth in a Solid at Elevated Temperature by Holographic Interferometry, *Exp. Mech.*, Vol 18, 1978, p 297–302
57. A. Ohta, M. Kosuge, S. Matsuoka, E. Takeuchi, Y. Muramatsu, and S. Nishijima, Significant Effect of Thermal Stresses on Fatigue Crack Propagation Properties, *Int. J. Fract.*, Vol 38, 1988, p 207–216
58. D. Coker, B.K. Parida, and N.E. Ashbaugh, “Thermal Stresses due to a Temperature Gradient on a Single Edge Notch Specimen,” Report UDR-TM-93-07, University of Dayton Research Institute, 1993
59. S.E. Cunningham and J.H. Griffin, On the Importance of Direct Resistance Heating in Thermo-Mechanical Fatigue, *Int. J. Fract.*, Vol 46, 1990, p 257–270
60. S.E. Cunningham and J.H. Griffin, Estimating the Importance of Cyclic Thermal Loads in Thermo-Mechanical Fatigue, *Int. J. Fract.*, Vol 47, 1991, p 161–180

Fatigue Crack Growth Testing

Ashok Saxena, Georgia Institute of Technology; Christopher L. Muhlstein, University of California, Berkeley

References

1. P.C. Paris and F. Erdogan, *J. Basic Eng. (Trans. ASME)*, Series D, Vol 85, 1963, p 528–534
2. P.C. Paris, *Proc. 10th Sagamore Conf.*, Syracuse University Press, 1965, p 107–132
3. J.R. Griffiths and C.E. Richards, *Mater. Sci. Eng.*, Vol 11, 1973, p 305–315
4. J.C. Grosskrutz, Strengthening in Fracture and Fatigue, *Metall. Trans.*, Vol 3, 1972, p 1255–1262
5. J.R. Rice, in *Fatigue Crack Propagation*, STP 415, ASTM, 1967, p 247–311

6. N.E. Dowling, in *Flaw Growth and Fracture*, STP 631, ASTM, 1977, p 139–158
7. Standard Test Method for Measurement of Fatigue Crack Growth Rates, E 647-91, *Annual Book of ASTM Standards*, Vol 03.01, 1992, ASTM, p 674–701
8. N.E. Dowling and J.A. Begley, in *Mechanics of Crack Growth*, STP 590, ASTM, 1976, p 82–103
9. N.E. Dowling, in *Cracks and Fracture*, STP 601, ASTM, 1977, p 131–158
10. H.S. Lamba, The J-Integral Applied to Cyclic Loading, *Eng. Fract. Mech.*, Vol 7, 1975, p 693–696
11. J.R. Rice, *J. Appl. Mech. (Trans. ASME)*, Vol 35, 1968, p 379–386
12. J.W. Hutchinson, *J. Mech. Phys. Solids*, Vol 16, 1968, p 337–347
13. J.R. Rice and G.F. Rosengren, *J. Mech. Phys. Solids*, Vol 16, 1968, p 1–12
14. W.R. Brose and N.E. Dowling, in *Elastic-Plastic Fracture*, STP 668, ASTM, 1979, p 720–735
15. W. Elber, Fatigue Crack Closure under Cyclic Tension, *Eng. Fract. Mech.*, Vol 2, 1970, p 37–45
16. W. Elber, *The Significance of Fatigue Crack Closure*, STP 486, ASTM, 1971, p 230–242
17. Standard Method for Plane-Strain Fracture Toughness of Metallic Materials, E 399-90, *Annual Book of ASTM Standards*, Vol 3.01, 1992, ASTM, p 569–596
18. K.T. Venkateswara Rao, W. Yu, and R.O. Ritchie, *Metall. Trans. A*, Vol 19 (No. 3), March 1988, p 549–561
19. A.W. Thompson and R.J. Bucci, *Metall. Trans.*, Vol 4, April 1973, p 1173–1175
20. G.R. Yoder and D. Eylon, *Metall. Trans. A*, Vol 10, Nov 1979, p 1808–1810
21. A. Saxena and S.J. Hudak, Review and Extension of Compliance Information for Common Crack Growth Specimens, *Int. J. Fract.*, Vol 14 (No. 5), 1978, p 453–468
22. J.W. Dally and W.F. Riley, *Experimental Stress Analysis*, 3rd ed., McGraw-Hill, 1991
23. R.O. Ritchie, G.C. Garrett, and J.F. Knott, *Int. J. Fract. Mech.*, Vol 7, 1971, p 462–467
24. C.Y. Li and R.P. Wei, *Mater. Res. Stand.*, Vol 6, 1966, p 392–445
25. R.O. Ritchie and J.F. Knott, *Acta Metall.*, Vol 21, 1973, p 639–648
26. R.O. Ritchie and K.J. Bathe, *Int. J. Fract.*, Vol 15, 1979, p 47–55
27. G. Clark and J.F. Knott, *J. Mech. Phys. Solids*, Vol 23, 1975, p 265–276
28. H.H. Johnson, *Mater. Res. Stand.*, Vol 5, 1965, p 442–445
29. G.H. Aronson and R.O. Ritchie, *J. Test. Eval.*, Vol 7, 1979, p 208–215
30. M.A. Ritter and R.O. Ritchie, *Fat. Eng. Mater. Struct.*, Vol 5, 1982, p 91–99

31. G.M. Wilkowski and W.A. Maxey, *Fracture Mechanics: 14th Symposium—Vol II: Testing and Applications*, STP 791, J.C. Lewis and G. Sines, Ed., ASTM, 1983, p II-266 to II-294
32. R.J. Selines and R.M. Pelloux, Effect of Cyclic Stress Waveform on Corrosion Fatigue Crack Propagation in Al-Zn-Mn Alloys, *Metall. Trans.*, Vol 13, 1972, p 2525–2531
33. A. Saxena, S.J. Hudak, Jr., J.K. Donald, and D.W. Schmidt, *J. Test. Eval.*, Vol 6 (No. 3), May 1978, p 167–174
34. R.J. Bucci, Development of a Proposed ASTM Standard Test Method for Near-Threshold Fatigue Crack Growth Rate Measurement, *Fatigue Crack Growth Measurement and Data Analysis*, S.J. Hudak, Jr. and R.J. Bucci, Ed., STP 738, ASTM, 1981, p 5–28
35. K.T. Venkateswara Rao, Y.W. Kim, C.L. Muhlstein, and R.O. Ritchie, *Mater. Sci. Eng. A*, Vol 192/193, 1995, p 474–487
36. R.J. Dauskardt, W. Yu, and R.O. Ritchie, *J. Am. Ceram. Soc.*, Vol 70 (No. 10), Oct 1987, p C248–C252
37. R.W. Hertzberg, W.A. Herman, and R.O. Ritchie, *Scr. Metall.*, Vol 21, 1987, p 1541
38. W.G. Clark and S.J. Hudak, The Analysis of Fatigue Crack Rate Data, *Application of Fracture Mechanics to Design*, J.J. Burke and V. Weiss, Ed., Vol 22, Plenum, 1979, p 67–81
39. E.P. Phillips, “Results of the Second Round Robin on Opening Load Measurement Conducted by ASTM Task Group E24.04.04 on Crack Closure Measurement and Analysis,” Technical Memorandum 109032, National Aeronautics and Space Administration, Nov 1993
40. Y. Asada, M. Kitagawa, N. Shimakawa, T. Kodaira, T. Asayama, and Y. Wada, Standardization of Procedures for the High-Temperature Crack Growth Testing for FBR Materials in Japan, *Nucl. Eng. Des.*, Vol 133, 1992, p 465–473
41. S. Mall and T. Nicholas, Ed., *Elevated Temperature Crack Growth*, MD-Vol 18, ASME, 1990
42. H. Sehitoglu, Ed., *Thermomechanical Fatigue Behavior of Materials*, STP 1186, ASTM, 1993
43. M.J. Verrilli and M.G. Castelli, Ed., *Thermomechanical Fatigue Behavior of Materials*, STP 1263, ASTM, 1995
44. W.J. Jones, Ed., *Thermomechanical Behavior of Advanced Structural Materials*, AD-Vol 34/AMD-Vol 173, ASME, 1993
45. H. Kitagawa and T. Tanaka, Ed., *Fatigue 90*, Materials and Components Engineering Publications, Ltd., Birmingham, UK, 1990
46. J.-P. Bailon and J.I. Dickson, *Fatigue 93*, Engineering Materials Advisory Services, Ltd., West Midlands, UK, 1993
47. T. Nicholas, M.L. Heil, and G.K. Haritos, Predicting Crack Growth under Thermo-Mechanical Cycling, *Int. J. Fract.*, Vol 41, 1989, p 157–176
48. G.A. Hartman, A Thermal Control System for Thermal/Mechanical Cycling, *J. Test. Eval.*, Vol 13, 1985, p 363–366
49. W.P. Wood and J.M. Cork, *Pyrometry*, McGraw-Hill, 1941

50. W.E. Forsythe, *Optical Pyrometry: Temperature—Its Measurement and Control in Science and Industry*, Reinhold Publishing, 1941
51. H.J. Kostkowski and R.D. Lee, “Theory and Methods of Optical Pyrometry,” Monograph 41, National Bureau of Standards, 1962
52. J.C. Richmond and D.P. DeWitt, Ed., *Applications of Radiation Thermometry*, STP 895, ASTM, 1985
53. J.K. Donald and J. Ruschau, Direct Current Potential Difference Fatigue Crack Measurement Techniques, *Fatigue Crack Measurement: Techniques and Applications*, K.J. Marsh, R.A. Smith, and R.O. Ritchie, Ed., EMAS, West Midlands, UK, 1991, p 11–37
54. G.A. Hartman and D.A. Johnson, DC Electric Potential Method Applied to Thermal/Mechanical Fatigue Crack Growth Testing, *Exp. Mech.*, Vol 11, 1987, p 106–112
55. C.-S. Shin, W.H. Huang, and H.-Y. Chen, An Improved DC Potential Drop System for Crack Length Measurement, *J. Chinese Inst. Eng.*, Vol 16, 1993, p 29–40
56. T.R. Hsu, R. Lewak, and B.J.S. Wilkins, Measurements of Crack Growth in a Solid at Elevated Temperature by Holographic Interferometry, *Exp. Mech.*, Vol 18, 1978, p 297–302
57. A. Ohta, M. Kosuge, S. Matsuoka, E. Takeuchi, Y. Muramatsu, and S. Nishijima, Significant Effect of Thermal Stresses on Fatigue Crack Propagation Properties, *Int. J. Fract.*, Vol 38, 1988, p 207–216
58. D. Coker, B.K. Parida, and N.E. Ashbaugh, “Thermal Stresses due to a Temperature Gradient on a Single Edge Notch Specimen,” Report UDR-TM-93-07, University of Dayton Research Institute, 1993
59. S.E. Cunningham and J.H. Griffin, On the Importance of Direct Resistance Heating in Thermo-Mechanical Fatigue, *Int. J. Fract.*, Vol 46, 1990, p 257–270
60. S.E. Cunningham and J.H. Griffin, Estimating the Importance of Cyclic Thermal Loads in Thermo-Mechanical Fatigue, *Int. J. Fract.*, Vol 47, 1991, p 161–180

Fatigue Crack Growth Testing

Ashok Saxena, Georgia Institute of Technology; Christopher L. Muhlstein, University of California, Berkeley

Selected References

Fatigue Crack Growth Rate Testing

- D. Blatt, R. John, and D. Coker, Single Edge Notched Specimens with Clamped Ends for Automated Crack Growth Testing, *Proc. SEM Spring Conf. on Experimental Mechanics*, Society for Experimental Mechanics, 1993
- D. Blatt, R. John, and D. Coker, Stress Intensity Factor and Compliance Solutions for a Single Edge Notched Specimen with Clamped Ends, *Eng. Fract. Mech.*, Vol 47 (No. 4), March 1994
- D.C. Freeman and M.J. Strum, Near Threshold Fatigue Testing, Report DE93009069/XAB, *Gov. Res. Announc. Index*, 1993

- J.C.P. Kam and W.D. Dover, The Recent Development of Advanced Fatigue Crack Growth Testing Technology for Large Scale Offshore Tubular Joints, *Conf. Proc. Engineering Integrity through Testing*, Engineering Materials Advisory Services Ltd., West Midlands, UK, 1990
- R.K. Nanstad et al., A Computer-Controlled Automated Test System for Fatigue and Fracture Testing, *Conf. Proc. Applications of Automation Technology to Fatigue and Fracture Testing*, STP 1092, ASTM, 1990
- S. Nishijima, S. Matsuoka, and E. Takeuchi, Environmentally Affected Fatigue Crack Growth, *Fatigue 90*, Materials and Component Engineering Publications, Birmingham, UK, 1990
- H.-H. Over and B. Buchmayr, Collection and Evaluation of Fatigue and Fracture Mechanics Data According to the European High Temperature Materials Databank (Petten) Standard, *Conf. Proc. Applications of Automation Technology to Fatigue and Fracture Testing*, STP 1092, ASTM, 1990
- S. Saki, T. Asakawa, and H. Okamura, Automatic Data Acquisition System for Fatigue Crack Growth in the Range from SSY to LGSY Region, *Proc. Asian Pacific Conf. on Fracture and Strength '93*, Japan Society of Mechanical Engineers, 1993
- J. Solin and J. Hayrynen, Simulation of Mechanical and Environmental Conditions in Fatigue Crack Growth Testing, *Conf. Proc. Applications of Automation Technology to Fatigue and Fracture Testing*, STP 1092, ASTM, 1990

Crack Measurement

- C.J. Beevers, *Advances in Crack Length Measurement*, Engineering Materials Advisory Services Ltd., West Midlands, UK, 1983
- C.J. Beevers, *The Measurement of Crack Length and Shape during Fracture and Fatigue*, Engineering Materials Advisory Services Ltd., West Midlands, UK, 1980
- M.S. Domack, Evaluation of K_{ISCC} and da/dt Measurements for Aluminum Alloys Using Precracked Specimens, *Conf. Proc. Environmentally Assisted Cracking: Science and Engineering*, STP 1049, ASTM, 1990
- R.L. Hewitt, Accuracy and Precision of Crack Length Measurement Using a Compliance Technique, *J. Test. Eval.*, Vol 11, 1983, p 150–155
- H.H. Johnson, Calibrating the Electrical Potential Method for Studying Slow Crack Growth, *Mat. Res. Stand.*, Vol 5, 1965, p 442–445
- J.A. Kapp, G.S. Leger, and B. Gross, “Wide Range Displacement Expressions for Standard Fracture Mechanics Specimens,” Report ARLCB-TR-84025, Army Armament Research and Development Center, 1984
- C.Y. Li and R.P. Wei, Calibrating the Electrical Potential Method for Studying Slow Crack Growth, *Mat. Res. Stand.*, Vol 6, 1966, p 392–394
- D.C. Maxwell, J.P. Gallagher, and N.E. Ashbaugh, “Evaluation of COD Compliance Determined Crack Growth Rates,” Report AFWAL-TR-84-4062, Wright-Patterson Air Force Base
- A.C. Pickard, R.A. Venables, and S.I. Vukelich, Crack Detection and Crack Length Measurement in the Gas Turbine Industry, *Fatigue Crack Measurement: Techniques and Applications*, Engineering Materials Advisory Services Ltd., West Midlands, UK, 1991

Fatigue Testing and Behavior of Plastics

Lisa A. Pruitt, University of California at Berkeley

Introduction

FATIGUE FRACTURE OF ENGINEERING PLASTICS due to cyclic loading conditions is of critical concern when designing polymeric components for structural employment. Like all engineering materials, failure often ensues in the plastic as a consequence of accumulated irreversible damage or growth of a fatigue flaw to a critical dimension. The fatigue life of a polymeric component is controlled by a number of factors; in general, polymers are more sensitive to the testing environment than metal or ceramic counterparts. These variables include the stress or strain amplitude of the loading cycle; the mean stress of the cycle; the presence of stress concentrations or initial defects in the component; the frequency, temperature, and environment of the test; and the molecular properties of the polymer. These factors are of considerable interest and practicality for the safe design of structural polymeric components subjected to repetitive loading.

When designing for the fatigue life of an engineering plastic, one of two distinct philosophies is generally practiced. The total life approach is utilized with unnotched specimens that are assumed to be defect free, and this methodology is predicated on the notion that fatigue failure is a consequence of both crack nucleation and subsequent growth. Conversely, the defect tolerant approach bases the fatigue life of a component on the number of loading cycles needed to propagate a crack of an initial size to a critical dimension. Over the last few decades, numerous researchers have provided detailed reviews (Ref 1, 2, 3, 4, 5, 6, 7, and 8) of fatigue behavior in polymers based on both total life and fracture mechanics approaches.

This article provides a review of fatigue test methodologies and an overview of general fatigue behavior in engineering plastics. Many factors affect the fatigue performance of engineering materials, including molecular and mechanical variables as well as the design of the fatigue test. The appropriate test conditions should be used when evaluating the life of the polymer. If a structural component is likely to be free of defects and stress concentrations or if the component is likely to spend the majority of its lifetime in the initiation stage of crack growth, then the total life philosophy is preferred. On the other hand, fracture mechanics should be used for safety critical fatigue designs and in flawed structural components likely to sustain a high degree of stable crack growth prior to fracture.

References cited in this section

1. E.H. Andrews, *Testing of Polymers*, W. Brown, Ed., Wiley, 1969, p 237
2. P. Beardmore and S. Rabinowitz, *Treat. Mater. Sci. Technol.*, Vol 6, 1975, p 267
3. J.A. Sauer and G.C. Richardson, *Int. J. Fract.*, Vol 16, 1980, p 499
4. R.W. Hertzberg, M.D. Skibo, and J.A. Manson, *Fatigue Mechanisms*, ASTM STP 675, ASTM, 1979, p 471
5. R.W. Hertzberg and J.A. Manson, *Fatigue of Engineering Plastics*, Academic Press, 1980
6. R.W. Hertzberg and J.A. Manson, in *Encyclopedia of Polymer Science and Engineering*, Wiley, 1986, p 378
7. H.H. Kausch and J.G. Williams, in *Encyclopedia of Polymer Science and Engineering*, Wiley, 1986, p 341

8. J.A. Sauer and M. Hara, *Advances in Polymer Science 91/92*, H.H. Kausch, Ed., Springer-Verlag, 1990, p 71

Fatigue Testing and Behavior of Plastics

Lisa A. Pruitt, University of California at Berkeley

Fatigue Crack Initiation

Stress-Based Loading. The traditional total life philosophy for fatigue life prediction is based on an endurance limit established from stress-log cycle plots, also known as *S-N* curves. In these tests, uncracked specimens are subjected to a constant amplitude load cycle until failure occurs. Often fatigue tests are performed on closed-loop servohydraulic universal test machines, which enable fatigue tests to be performed under a variety of waveforms over a range of test frequencies (including spectrum loadings). The stress amplitude can be applied through torsion, rotation, beam bending, or axial loads. Specimens (Fig. 1) are chosen according to the loading method employed. For example, the standard fatigue test for plastics in ASTM D 671 specifies repeat flexural stress as a standard fatigue test. In this test, a triangulated specimen geometry (Fig. 1d) provides a uniform flexural stress across the entire gauge section.

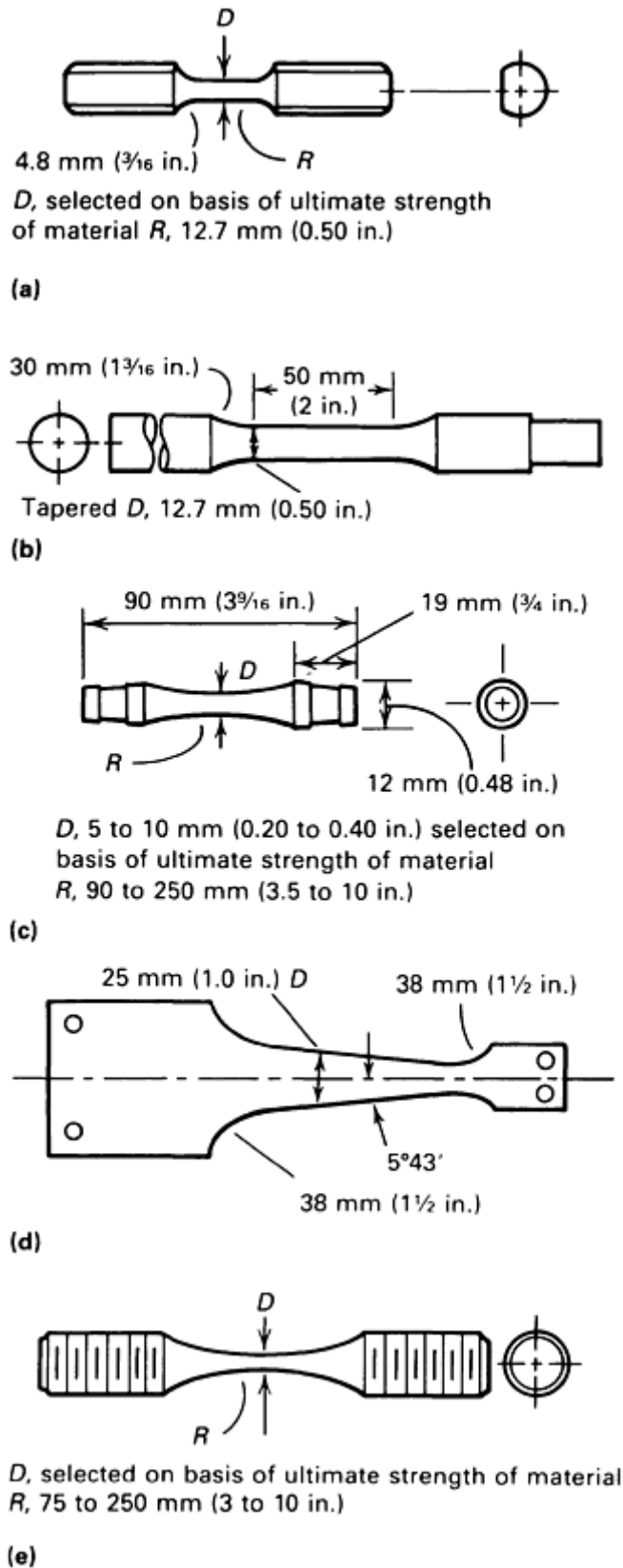


Fig. 1 Schematic of specimens used for total life fatigue analysis. Tests can be done (a) in torsion, (b) with a rotating cantilever, (c) with a rotating beam, (d) with cantilever reverse bending, or (e) under axial loading

In fatigue testing, the applied stress, σ_a , is typically described by the stress amplitude of the loading cycle:

$$\sigma_a = \frac{\sigma_{\max} - \sigma_{\min}}{2} \quad (\text{Eq 1})$$

where σ_{\max} is the maximum stress and σ_{\min} is the minimum stress of the fatigue cycle. The stress amplitude, also denoted as S , is generally plotted against the number of cycles to failure, N , on a linear-log scale, which is called an $S-N$ plot. A general trait of these plots is that the number of cycles to failure increases as the stress amplitude is reduced. In some polymers, there is a critical stress level, often referred to as the *endurance limit* of the material, below which the specimen does not fail in less than 10^7 cycles.

Figure 2 shows the $S-N$ behavior of several commodity plastics. It should be noted that nylon and polyethylene terephthalate (PET) do not exhibit an endurance limit. Other plastics—including polyethylene (PE), polypropylene oxide (PPO), polystyrene (PS), polytetrafluoro-ethylene (PTFE), polypropylene (PP), polymethyl-methacrylate (PMMA), and epoxy (EP)—exhibit a stress limit below which failure does not occur in less than 10^7 cycles for these testing conditions. Because plastics are sensitive to many factors including frequency, temperature, mean stress, and molecular structure, the fatigue test conditions must closely mimic the service conditions of the polymeric component. Despite the simple nature of these experimental tests, the $S-N$ approach is widely accepted in the engineering plastics community for design applications where stress concentrations are expected to be minimal or where the fatigue life of the component is likely to be dominated by the nucleation of a crack.

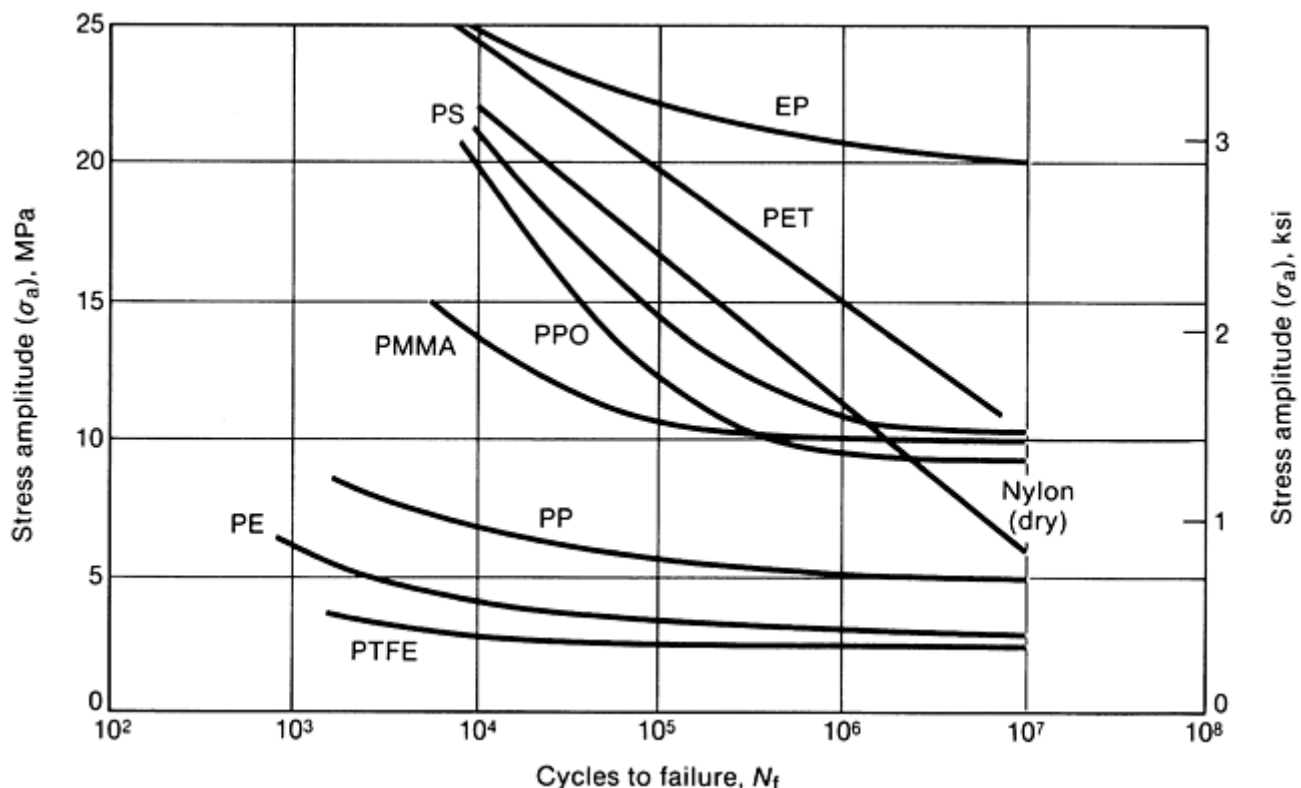


Fig. 2 Stress amplitude versus cycles to failure, or $S-N$ behavior, of several commodity plastics

Displacement and Strain-Based Loading. While stress-based tests are appropriate for the evaluation of plastics chosen for load-controlled applications, these tests might not be suitable for circumstances where the structural component is likely to experience fluctuations in displacement or strain. In such instances, strain- or displacement-based tests might be more appropriate. In such tests, the configuration typically is based on a fixed cantilever subjected to repeated constant deflection. The initial stress range will typically decay under cyclic loading (much like a stress relaxation experiment) and is caused by plastic deformation or softening of the polymer. Hysteretic heating from deformation can further result in an inaccurate prediction of the cyclic stress amplitude (Ref 9). However, because stresses generally decay in this type of test, thermal failures are rarely encountered (Ref 5).

Strain-based tests are often utilized for components with accumulated strain or blunt notches (Ref 5). The majority of strain-based fatigue tests are performed using fully reversed loading conditions, generally accompanied by a cyclic softening phenomena in plastics (Ref 2, 9). Under cyclic strain conditions, the fatigue response is best characterized by the cyclic stress-strain curve. This curve is created by testing several specimens subjected to a range of controlled cyclic strain limits. Tests are continued for each specimen until the hysteresis loops become saturated. A curve is fit through the amplitude of these saturated hysteresis loops in

order to establish a cyclic stress-strain curve. Figure 3 shows a comparison of the cyclic and monotonic stress-strain curves for several polymers. An interesting feature of these polymers is that they all soften and exhibit lower yield points under cyclic strain than under monotonic conditions (as opposed to metals, which can exhibit either cyclic softening or cyclic hardening).

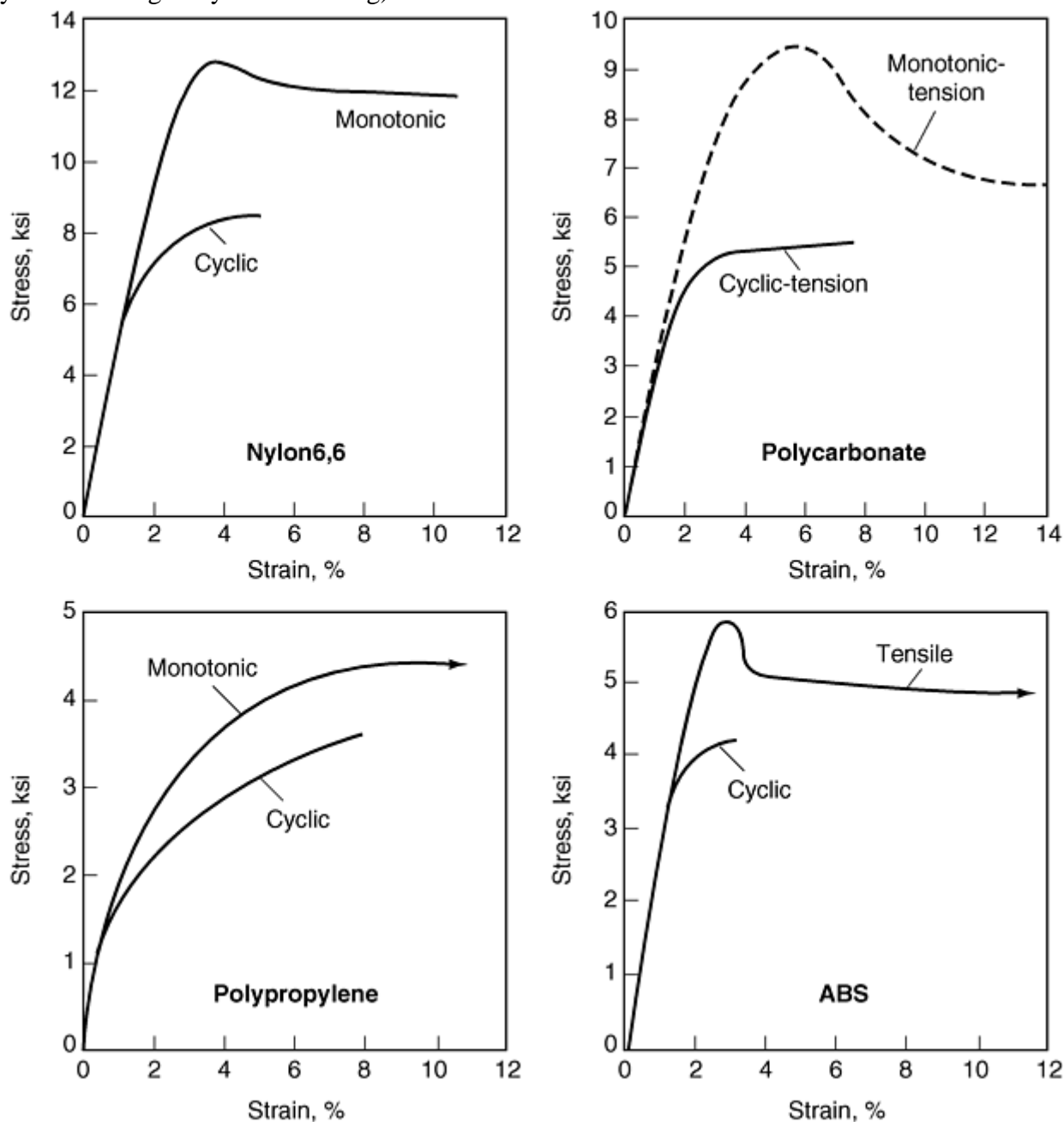


Fig. 3 Comparison of the cyclic and monotonic stress-strain curves for several polymers. Source: Ref 2

The cyclic strain life data can also be portrayed in a manner analogous to the $S-N$ approach. The total strain amplitude can be divided into elastic and plastic strain amplitude components. The strain amplitude of the fatigue cycle is plotted against the number of cycles or load reversals to failure, which provides an empirical relationship between the strain amplitude of the fatigue cycle and the number of cycles to specimen failure (Ref 6):

$$\epsilon_a = \frac{\sigma'_f}{E} (2N_f)^b + \epsilon'_f (2N_f)^c \quad (\text{Eq 2})$$

Here, ϵ_a is the strain amplitude, σ'_f is the strength coefficient, $2N_f$ is the number of load reversals to failure, ϵ'_f is the ductility coefficient, and b and c are material constants. The first term on the right side of Eq 2 is the elastic component of the strain amplitude, and the second term is the plastic component of the strain amplitude. Tests dominated by the elastic component of strain are considered high-cycle fatigue with little plastic strain. Low-

cycle fatigue tests are identified by the relatively small number of cycles or reversals to failure and the large degree of plastic strain.

An important concern in the testing of polymers is that the attributes of the fatigue test are crucial to the relative ranking of fatigue resistance among various polymers. For example, polymers with higher damping capacities can be less resistant to fatigue. These polymers experience thermal heating when tested under constant stress amplitude. Conversely, these same polymers can have enhanced fatigue resistance if tested under constant deflection conditions. Moreover, the relative placement of fatigue resistance in polymers correlates strongly to whether the tests are performed under adiabatic or isothermal conditions (Ref 5).

Thermal Fatigue and Hysteretic Heating. Due to the viscoelastic nature of polymeric solids, a portion of the strain energy dissipates under cyclic loading conditions. This heat generation results in an increase in specimen temperature until the heat generated per cycle is equal to the heat dissipated through conduction, convection, and radiation. The temperature of the specimen depends strongly on the frequency of the test, the amplitude of the applied stress or strain, and the damping properties of the polymer. In some instances, especially in unnotched specimens, the temperature of the polymer specimen can locally surpass the glass transition or flow temperature of the polymer. Ferry (Ref 9) has found that the energy dissipated per second, \dot{E} , is given by:

$$\dot{E} = \pi \nu J''(\nu, T, \sigma) \sigma^2 \quad (\text{Eq 3})$$

where ν is the frequency, J'' is the loss compliance, T is temperature, and σ is the peak stress of the fatigue cycle. The rate of change of temperature for adiabatic heating conditions in which the heat generated is transferred into temperature rise is given as:

$$\frac{dT}{dt} = \frac{\dot{E}}{\rho C_p} \quad (\text{Eq 4})$$

where ρ is the mass density and C_p is the heat capacity of the polymer. In general, the increase in temperature will scale with increase in frequency, stress amplitude, and internal friction of the polymer. Figure 4 shows the thermal fatigue behavior of polyacetal and its dependence on test frequency. The temperature rise in the specimen can be monitored with a thermal couple or an infrared sensor. In many polymer systems, the thermal work influenced by high damping and low thermal conductivity contributes to micromechanisms of permanent deformation including craze formation, shear bands, voids, or even microcracks (Ref 8).

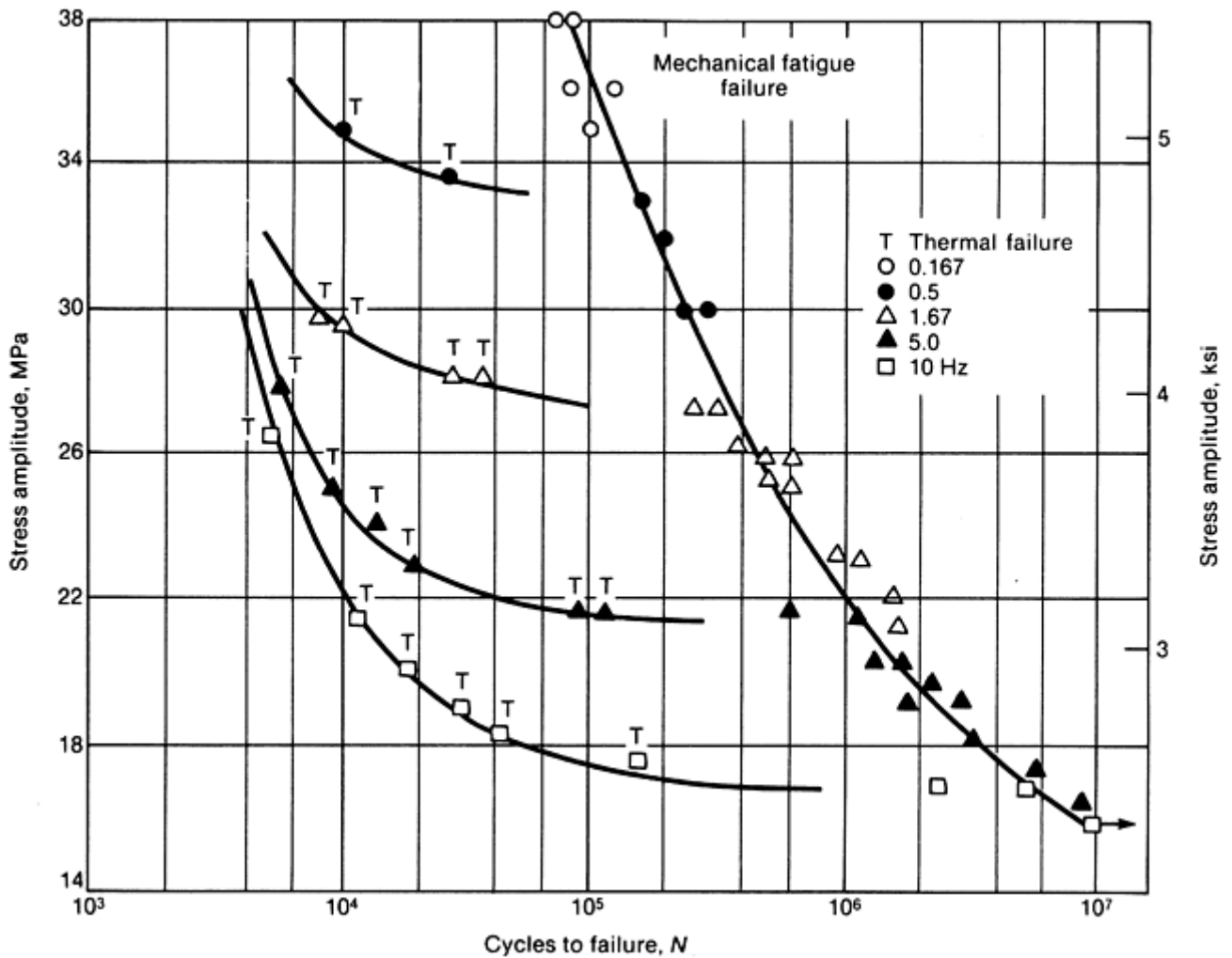


Fig. 4 Plot showing the effect of increasing test frequency and stress amplitude on the fatigue failure of polyacetal

The hysteresis loops observed under cyclic loading conditions can provide useful insight into micromechanisms of fatigue damage. Figure 5 shows the hysteresis loops after various numbers of fatigue cycles in both high impact polystyrene (HIPS) and acrylonitrile butadiene-styrene (ABS). An interesting observation is that the hysteresis loops are symmetric for ABS, while the hysteresis loops become much larger for the tensile portion of the fatigue cycle in HIPS as the fatigue test progresses. These events are understandable considering ABS undergoes shear yielding mechanisms and the HIPS undergoes crazing that requires a tensile component of stress. Crazing results from fibrillation or polymeric drawing ahead of the fatigue flaw. The advancement of the craze zone is associated with damage accumulation in the leading fibrils; thus, the tensile portion of the hysteresis loop grows as damage accumulates in the specimen.

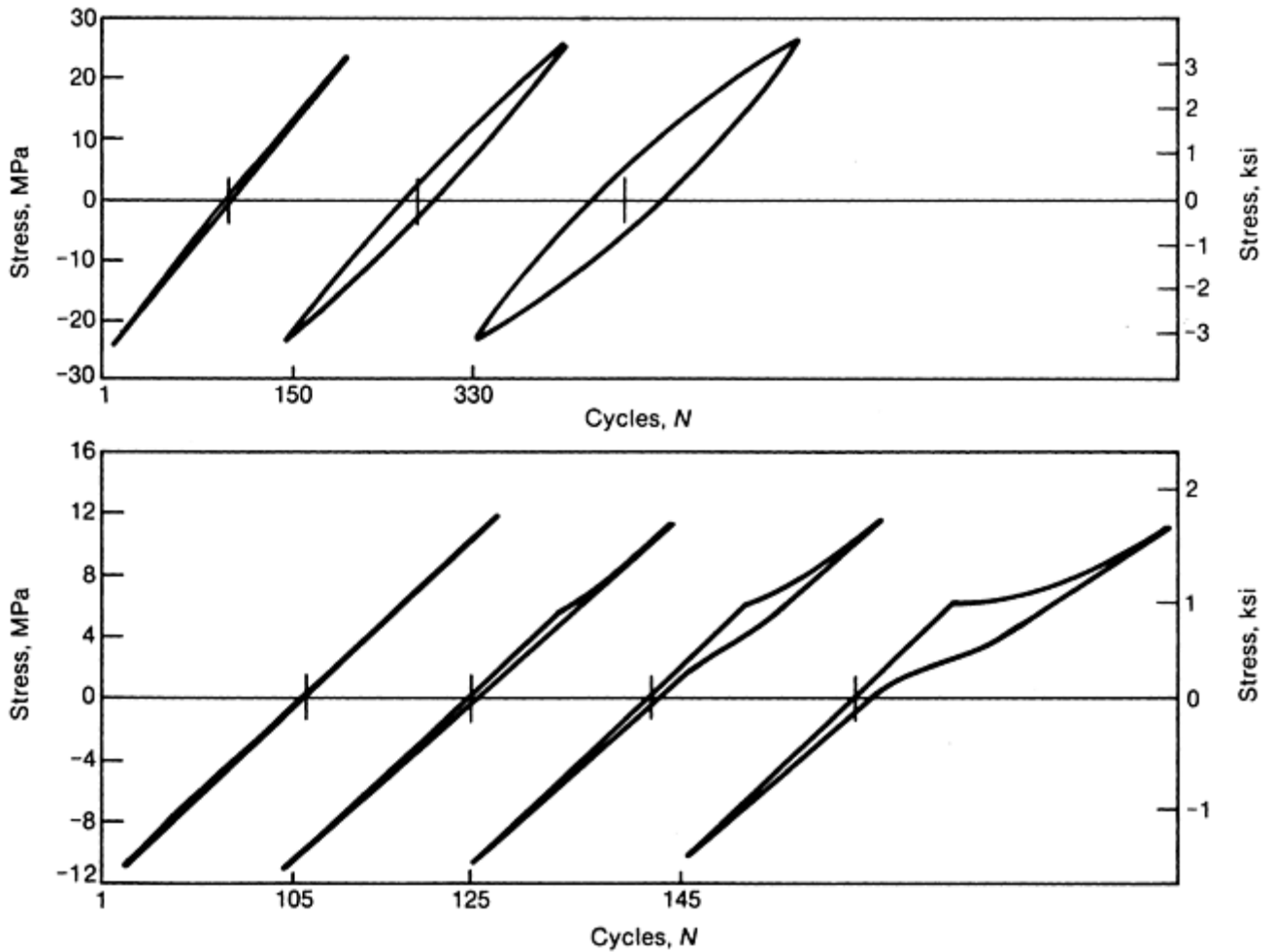


Fig. 5 Hysteresis loops after various numbers of fatigue cycles in both high impact polystyrene (HIPS) (bottom) and acrylonitrile butadiene styrene (ABS) (top). Note the lack of symmetry in the HIPS due to crazing mechanisms. See text for discussion.

References cited in this section

2. P. Beardmore and S. Rabinowitz, *Treat. Mater. Sci. Technol.*, Vol 6, 1975, p 267
5. R.W. Hertzberg and J.A. Manson, *Fatigue of Engineering Plastics*, Academic Press, 1980
6. R.W. Hertzberg and J.A. Manson, in *Encyclopedia of Polymer Science and Engineering*, Wiley, 1986, p 378
8. J.A. Sauer and M. Hara, *Advances in Polymer Science 91/92*, H.H. Kausch, Ed., Springer-Verlag, 1990, p 71
9. J.D. Ferry, *Viscoelastic Properties of Polymers*, Wiley, 1961

Fatigue Testing and Behavior of Plastics

Lisa A. Pruitt, University of California at Berkeley

Fatigue Crack Propagation

Fracture Mechanics Concepts and the Defect-Tolerant Philosophy. The use of fracture mechanics for fatigue design is based on the tacit assumption that structural components are intrinsically flawed and capable of sustaining a considerable amount of stable crack growth before failure. The fatigue life of a component based on this defect-tolerant approach is dictated by the number of loading cycles needed to propagate a crack of an initial size to a critical dimension. Fracture mechanics is used widely in the characterization of fatigue crack propagation behavior of advanced engineering plastics capable of sustaining a substantial subcritical crack growth prior to fracture. Fracture mechanics is also used in safety-critical applications where defect-tolerant life estimates are essential. Characterizing crack growth behavior in polymers can be complicated by fatigue cracks known to propagate at different rates depending on the near-tip damage micromechanisms, mean stress, frequency, or test environment. These factors are of significant interest and practicality for the safe design of structural polymeric components subjected to repetitive loading.

The stress intensity factor, K , derived from linear elastic fracture mechanics, is the parameter used to describe the magnitude of the stresses, strains, and displacements in the region ahead of the crack tip. The linear elastic solution (Fig. 6) for the normal stress, σ_{yy} , in the opening mode of loading is written as a function of distance, r , and angle, θ , away from the crack tip (Ref 10):

$$\sigma_{yy} = \frac{K_I}{\sqrt{2\pi r}} \cdot \cos \frac{\theta}{2} \left(1 + \sin \frac{\theta}{2} \sin \frac{3\theta}{2} \right) \quad (\text{Eq 5})$$

where K_I is the mode I (opening mode) stress intensity factor. This parameter incorporates the boundary conditions of the cracked body and is a function of loading, crack length, and geometry. The stress intensity factor can be found for a wide range of specimen types and is used to scale the effect of the far-field load, crack length, and geometry of the flawed component. Standard specimens employed in fatigue crack propagation studies are the single-edge-notch specimen (Fig. 7a) and the compact-tension specimen (Fig. 7b). The form of the stress intensity factor for the compact-tension geometry is given as (Ref 10):

$$K_I = \frac{P}{B\sqrt{W}} \cdot f(\alpha) \quad (\text{Eq 6})$$

$$f(\alpha) = \frac{(2 + \alpha)}{(1 - \alpha)^{3/2}} [0.886 + 4.64\alpha - 13.32\alpha^2 + 14.72\alpha^3 - 5.6\alpha^4]$$

where P is the remote far-field load, B is the specimen thickness, W is the width, and α is the ratio a/W that increases as the fatigue crack, a , advances in length.

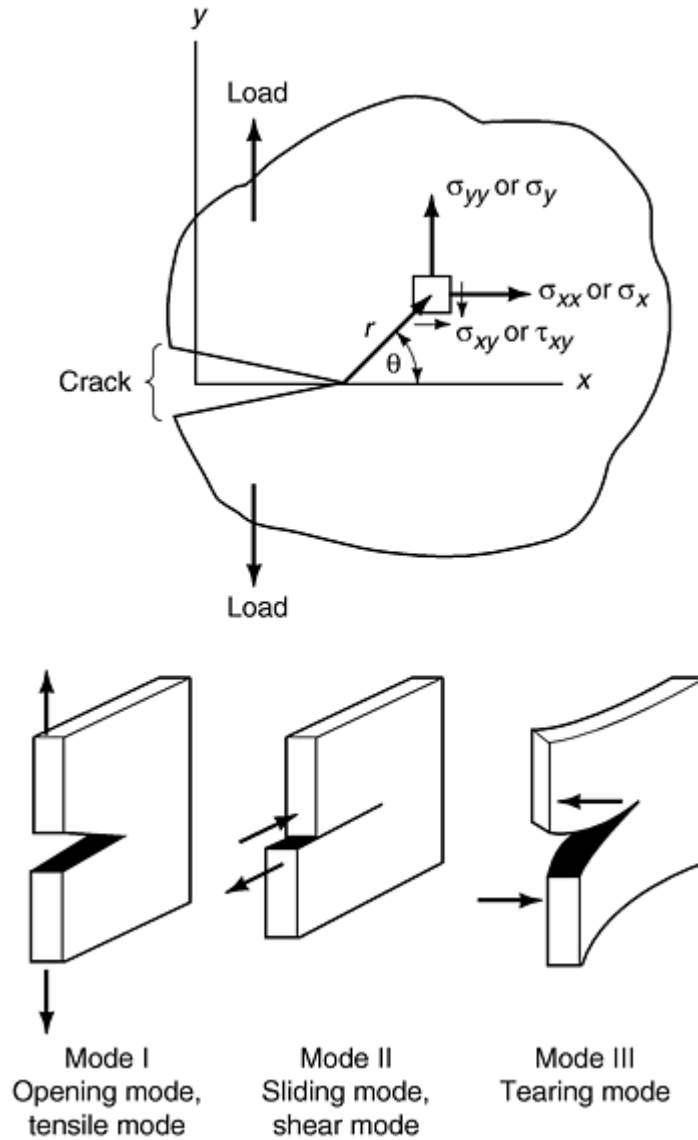


Fig. 6 Coordinate system for crack-tip stresses in mode I loading (see Eq 5)

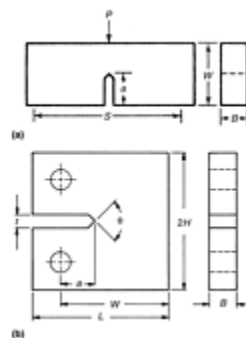


Fig. 7 Specimens employed in fatigue crack propagation studies. (a) Single-edge-notch specimen. (b) Compact-tension specimen

Regimes of Fatigue Crack Propagation. Fracture mechanics provides a design approach for predicting the life of a cracked structural component under cyclic loading conditions. While the micromechanisms of deformation differ for metals, polymers, and ceramics, the fatigue crack propagation behavior of these materials share many macroscopic similarities. As with crystalline materials, there are three distinct regimes of crack propagation for polymers under constant amplitude cyclic loading conditions. These regimes include the slow crack growth or threshold regime, the intermediate crack growth or Paris regime, and the rapid crack growth or fast fracture regime (Fig. 8). The velocity of an advancing fatigue crack subjected to a constant stress amplitude loading is

determined from the change in crack length, a , as a function of the number of loading cycles, N . The fatigue crack propagation rate per cycle, da/dN , is found from experimentally generated curves, in which a is plotted as a function of N . For constant amplitude loading, the rate of crack growth increases as the crack grows longer. Paris et al. (Ref 11) suggested that the stress intensity factor range, $\Delta K = K_{\max} - K_{\min}$, which captures the far-field cyclic stress, crack length, and geometry, should be the characteristic driving parameter for fatigue crack propagation. This basis of the Paris relationship states that da/dN scales with ΔK through the power law relationship:

$$\frac{da}{dN} = C \cdot \Delta K^m \quad (\text{Eq 7})$$

where C and m are empirical constants. These constants can be strongly affected by polymer morphology, test frequency, stress ratio (the stress ratio, R , is defined as the ratio of the minimum stress to the maximum stress of the fatigue cycle) of the fatigue cycle, as well as by test temperature and environment. Figure 8 shows that the Paris equation is valid for intermediate ΔK levels spanning crack propagation rates from approximately 10^{-6} to 10^{-4} mm/cycle.

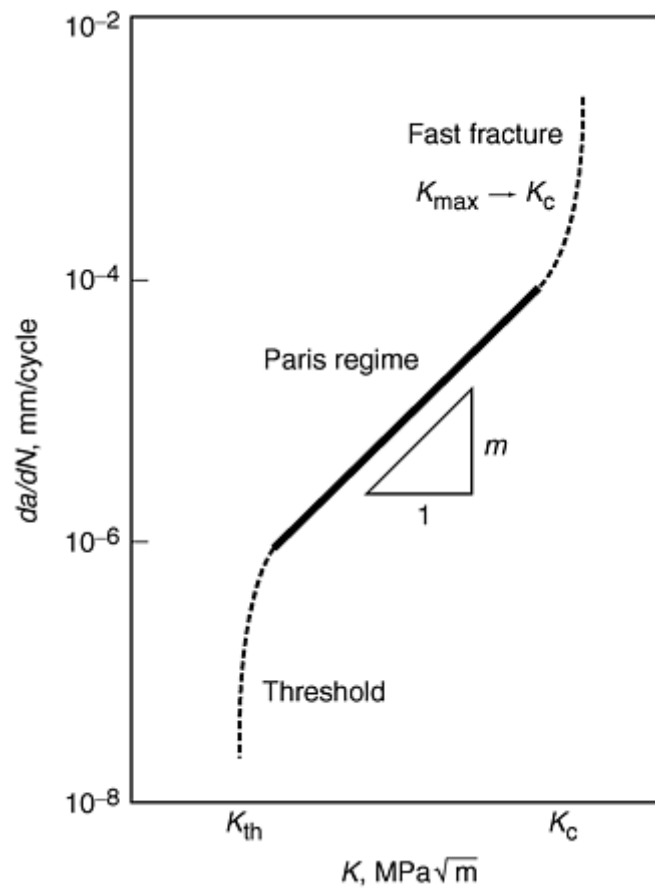


Fig. 8 Schematic illustration of the three distinct regimes of crack propagation rate observed in fatigue testing under constant amplitude loading conditions. For polymers, typical values of m range from 3 to 50 depending on the polymer system.

The Paris relationship is a useful tool for fatigue life prediction. It is implied in this defect-tolerant approach that all structural components are intrinsically flawed with an initial crack size, a_i . Assuming the fatigue loading is performed under constant stress amplitude conditions, the geometric factor, $f(a)$, does not change within the limits of integration. Fracture occurs when the crack reaches a critical value, a_c , the Paris equation can be integrated to predict the fatigue life of the component:

$$N_f = \frac{2}{(m-2)Cf(\alpha)^m(\Delta\sigma)^m \pi m/2} \cdot \left[\frac{1}{a_i^{(m-2)/2}} - \frac{1}{a_c^{(m-2)/2}} \right] \text{ for } m \neq 2 \quad (\text{Eq 8})$$

Crack Shielding Mechanisms in Polymers. The crack driving force near a fatigue crack tip, ΔK_{tip} , will be lower than the “applied” crack driving force, ΔK_a , when extrinsic toughening mechanisms are present. The presence of extrinsic toughening mechanisms shields the crack tip, thereby decreasing the crack driving force and the crack growth rate. Ritchie (Ref 12) has expressed the extrinsic crack-tip shielding effect:

$$\Delta K_{tip} = \Delta K_a - K_s \quad (\text{Eq 9})$$

where K_s is the stress intensity factor due to shielding. Under cyclic loading conditions, there are three general types of shielding mechanisms: crack deflection, process zone shielding, and contact shielding (Fig. 9). Shielding due to crack path deflection results in improvements in the fatigue crack propagation behavior over all ranges of ΔK . By contrast, process zone shielding mechanisms operate more effectively at high ΔK levels, whereas contact shielding mechanisms are more effective at low ΔK levels.

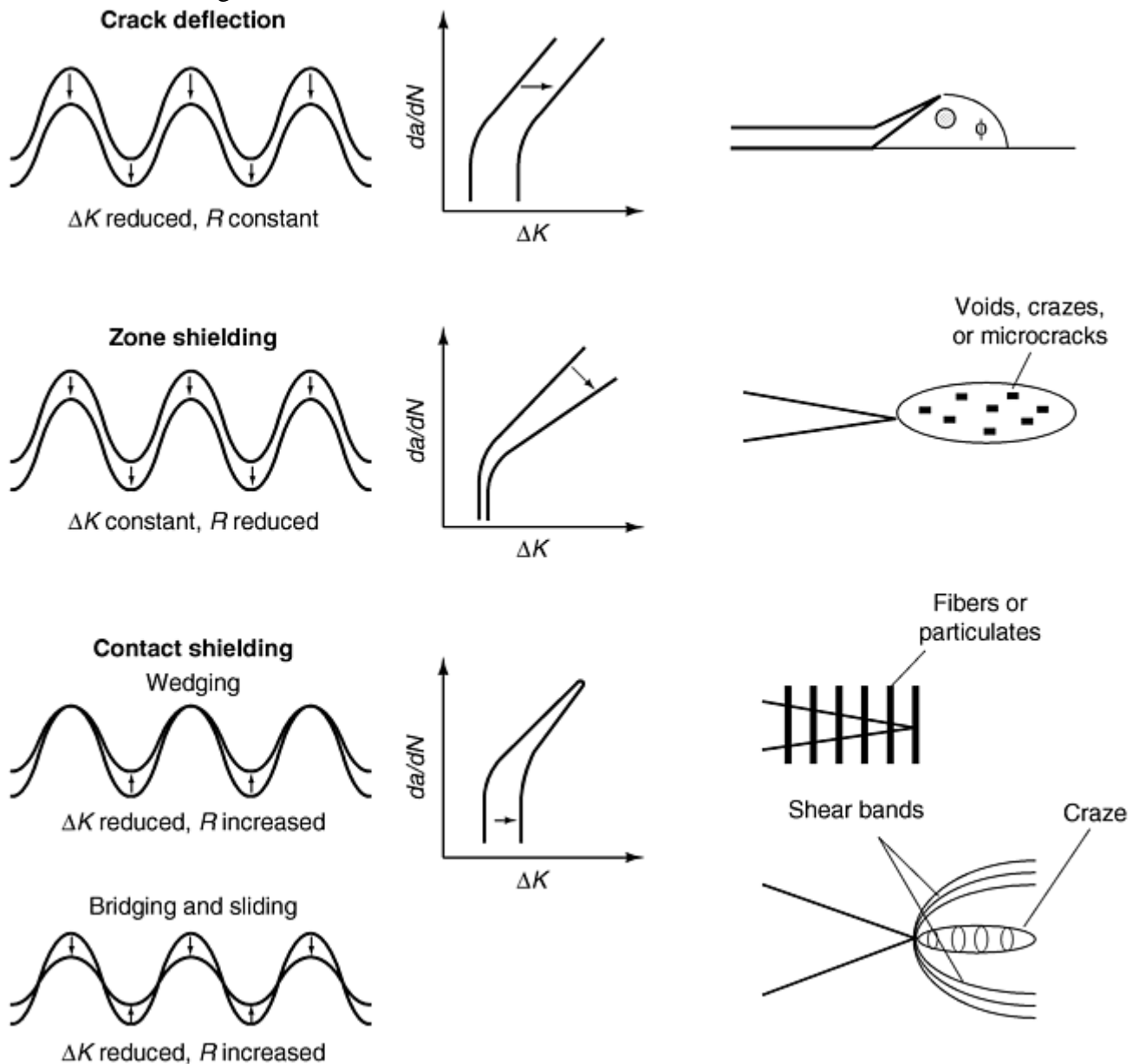


Fig. 9 Schematic illustration of the three types of shielding mechanisms: crack deflection, zone shielding, and contact shielding

The amount of shielding due to crack path deflection has been modeled by Suresh (Ref 13). Suresh derived the effective fatigue crack driving force and subsequent crack growth rates by analyzing a small segment of the crack with an out-of-plane deflection:

$$\Delta K_{tip} = \frac{b \cos^2(\theta/2) + c}{b + c} \Delta K_a \quad (\text{Eq 10})$$

$$\frac{da}{dN} = \frac{b \cos \theta + c}{b + c} \cdot \left(\frac{da}{dN} \right)_n \quad (\text{Eq 11})$$

where θ is the deflection angle, b is the deflected distance, and c is the undeflected distance.

The amount of shielding caused by process zone mechanisms depends on the nature of the plastic deformation of the crack tip, such as massive crazing or shear banding (Ref 14, 15, 16, 17, and 18). The yielding in front of the crack caused by far-field tensile loading results in the formation of a plastic or permanent deformation zone. For a crazeable polymer (Fig. 10), a Dugdale (Ref 13), or strip yield, approximation is used to estimate the size of this plastic zone, r_d :

$$r_d = \frac{\pi}{8} \left(\frac{K_I}{\sigma_y} \right)^2 \quad (\text{Eq 12})$$

where σ_y is the craze stress. For an elastic, perfectly plastic material behavior, the plane-stress plastic zone (Ref 13), r_p , can be estimated:

$$r_p \approx \frac{1}{\pi} \left(\frac{K_I}{\sigma_y} \right)^2 \quad (\text{Eq 13})$$

where σ_y is the yield stress.

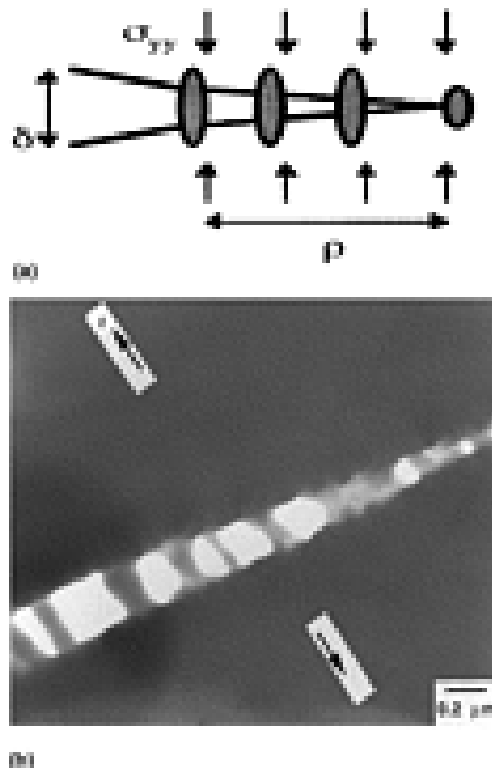


Fig. 10 Crazing. (a) Schematic of a craze zone preceding the crack. Note the craze consists of load bearing fibrils and void space. (b) Transmission electron micrograph of a craze preceding a fatigue crack in polycarbonate

Under cyclic loading, a reversed cyclic plastic zone will be generated within the monotonic plastic zone. For an elastic, perfectly plastic material, this region of residual tensile stress is one fourth the size of the monotonic

plastic zone described in Eq 13. Cyclic plastic zones have been observed in several amorphous polymer systems and are important in the inception of cracks under cyclic compression loading (Ref 13). Qualitatively, it is easy to see that the size of the plastic zone increases with ΔK ; therefore, process zone shielding mechanisms are effective at high ΔK levels.

Contact shielding involves physical contact between mating crack surfaces because of the presence of asperities, second-phase particles, and/or fibers. Premature contact between the crack surfaces occurs during unloading at a stress intensity level known as K_{cl} , which is the closure stress intensity. The degree of shielding caused by closure effects can be calculated:

$$\Delta K_{tip} = K_{max} - K_{cl} \quad (\text{Eq 14})$$

where K_{max} is the maximum stress intensity of the fatigue cycle. It should be noted from Eq 14 that the ΔK_{tip} is less than ΔK_a , thus effectively lowering the stress intensity felt at the crack tip. Mechanisms such as contact shielding and fiber bridging can contribute to this phenomenon. Contact shielding can arise from contact between asperities or from fiber bridging in reinforced or blended polymers. Fiber bridging has been shown to be a viable shielding mechanism in short fiber composites by Lang and his coworkers (Ref 19). In summary, extrinsic shielding mechanisms can be utilized to improve resistance to fatigue crack propagation in engineering polymers.

References cited in this section

10. G.C. Sih, *Handbook of Stress Intensity Factors*, Lehigh University Press, 1973
11. P.C. Paris, M.P. Gomez, and W.P. Anderson, *Trends Eng.*, Vol 13, 1961, p 9
12. R.O. Ritchie, *Proc. of the 5th Int. Conf.*, M.G. Yan, S.H. Zhang, and Z.M. Zheng, Ed., Pergamon Press, 1988, p 5
13. S. Suresh, *Fatigue of Materials*, 2nd ed., Cambridge University Press, 1998
14. A.G. Evans, Z.B. Ahmad, D.G. Gilbert, and P.W.R. Beaumont, *Acta Metall.*, Vol 34, 1986, p 79
15. C.B. Bucknall and W.W. Stevens, in *Toughening of Plastics*, Plastics and Rubber Institute, London, 1978, p 24
16. R.W. Hertzberg, *Deformation and Fracture Mechanics of Engineering Materials*, 4th ed., Wiley, 1996
17. T.L. Anderson, *Fracture Mechanics: Fundamentals and Applications*, CRC Press, 1995
18. A.S. Argon, *Proc. of 7th Int. Conf. on Advances in Fracture Research*, K. Samala, K. Ravi-Chander, D.M.R. Taplin, and P. Rama Rao, Ed., Pergamon Press, 1989
19. R.W. Lang, J.A. Manson, R.W. Hertzberg, and R. Schirrer, *Polym. Eng. Sci.*, Vol 24, 1984, p 833

Fatigue Testing and Behavior of Plastics

Lisa A. Pruitt, University of California at Berkeley

Factors Affecting Fatigue Performance of Polymers

Molecular Variables. Polymers are sensitive to a number of molecular variables including molecular weight, molecular weight distribution, crystallinity, chain entanglement density, and crosslinking (Ref 3, 5, 20, and 21). In general, as the molecular weight of the polymer is increased, the fatigue resistance of the polymer is

enhanced. Some polymers (as mentioned earlier) are susceptible to craze nucleation that leads to subsequent crack growth and fatigue failure. Figure 10(a) schematically illustrates the load bearing fibrils that comprise the craze zone. Figure 10(b) shows a transmission electron micrograph of a craze preceding a fatigue crack in polycarbonate (PC).

When a critical amount of damage has accumulated, the crack advances through the load bearing fibrils of the craze zone. This advancement can occur by a void growth mechanism potentially enhanced by temperature, chemical environment, or rupture of the highly stressed fibrils. The craze often advances in a discontinuous manner and results in discontinuous crack growth in certain stress regimes (Ref 5). Kramer (Ref 22) has shown that craze stability depends on numerous factors including the molecular weight and chain entanglement density of the polymer. The stability or strength of the craze can be improved by increasing the molecular weight of the polymer. Numerous studies indicate that increasing the molecular weight of the polymer increases craze strength, creep rupture strength, and endurance limit under cyclic loading conditions (Ref 3, 5, 18, and 22).

Semicrystalline polymers provide improved fatigue resistance over glassy amorphous polymers. One explanation is that the composite, two-phase structure, offers enhanced toughness. Improved strength is provided by the more rigid crystalline phase, and ductility is provided by the more compliant amorphous phase. Semicrystalline polymers provide higher fracture energies and can accommodate both amorphous and crystalline modes of plasticity.

The arrangement of the crystallites within the amorphous phase or the polymer morphology is also important to the resistance of fatigue. For example, branched versions of polyethylene offer decreased resistance, while very high molecular weight versions of polyethylene with an enhanced level of tie molecules provide superior resistance to fatigue crack propagation in comparison to generic linear polyethylene (Ref 3). In general, semicrystalline polymers, such as nylon, polyacetal, and polyethylene, offer excellent resistance to fatigue crack propagation and provide high *S-N* endurance limits (Ref 5). In comparison, amorphous glassy polymers often suffer inferior fatigue strength due to a lack of shielding or toughening modes, because many amorphous polymers are used below the glass transition temperature and are incapable of large amounts of ductile or viscous deformation. Figure 11 shows a comparison of fatigue crack propagation behavior in the Paris regime for several amorphous and semicrystalline polymers, and it is evident that the semicrystalline polymers offer improved fatigue crack growth resistance.

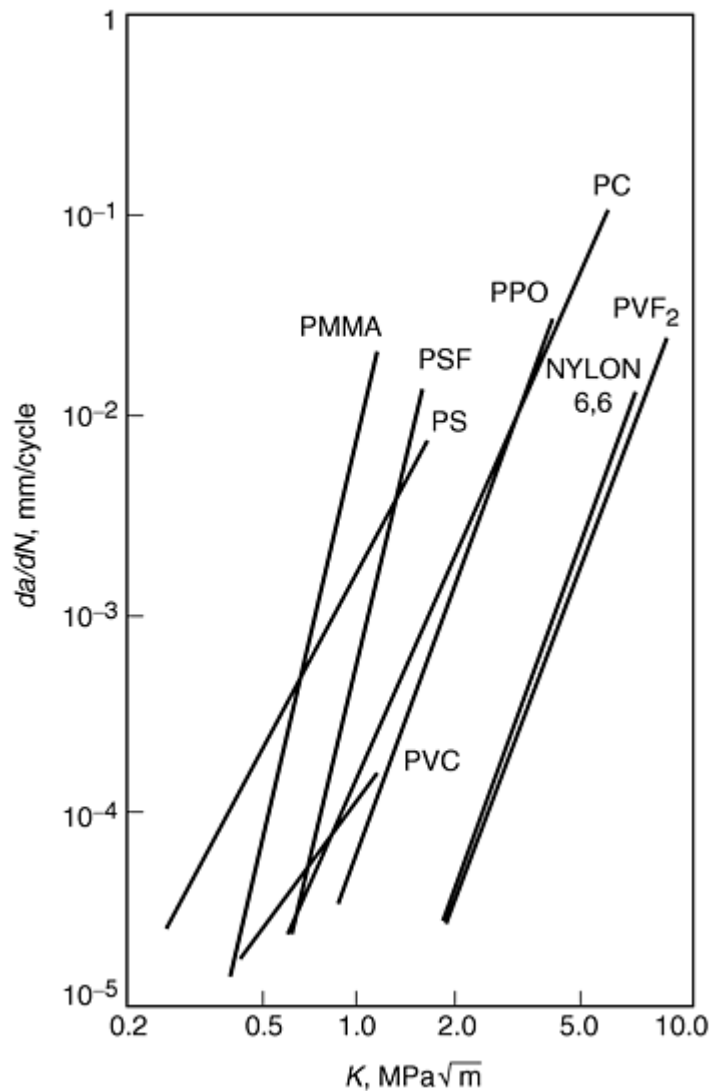


Fig. 11 Comparison of fatigue crack propagation behavior in the Paris regime for several amorphous and semicrystalline polymers. Note enhanced fatigue resistance of the semicrystalline polymers. Source: Ref 5

Effect of Reinforcements. The addition of rubber particles to a ductile or brittle polymer provides a process zone shielding mechanism involving massive shear banding of the matrix, which leads to improved fatigue crack propagation resistance. The role of crack-tip shielding mechanisms on the crack growth rate regime has been modeled by Ritchie (Ref 12). According to Ref 12, the occurrence of a process zone shielding mechanism should change the slope (m) in the Paris regime but should not change the crack growth behavior at low crack growth or near-threshold regime. Experimental support of this model has been given by Azimi et al. (Ref 23). Figure 12 shows that the addition of rubber decreases the slope, m , and retards crack growth at high crack growth rates due to toughening mechanisms. At low values of stress intensity range (ΔK), however, the crack growth rates for the rubber-toughened epoxies are nearly identical to those of the unmodified (neat) resin. At low ΔK levels, the process zone in front of the crack tip is small; the rubber reinforcements are not highly stressed; hence, the crack grows with minimal plasticity in this regime. Conversely, at high ΔK levels, the process zone is much larger than the size of the particles, and the rubber additions within this region are highly stressed. The subsequent rubber particle cavitation causes significant additional plasticity in the matrix, and the crack propagation rate is reduced.

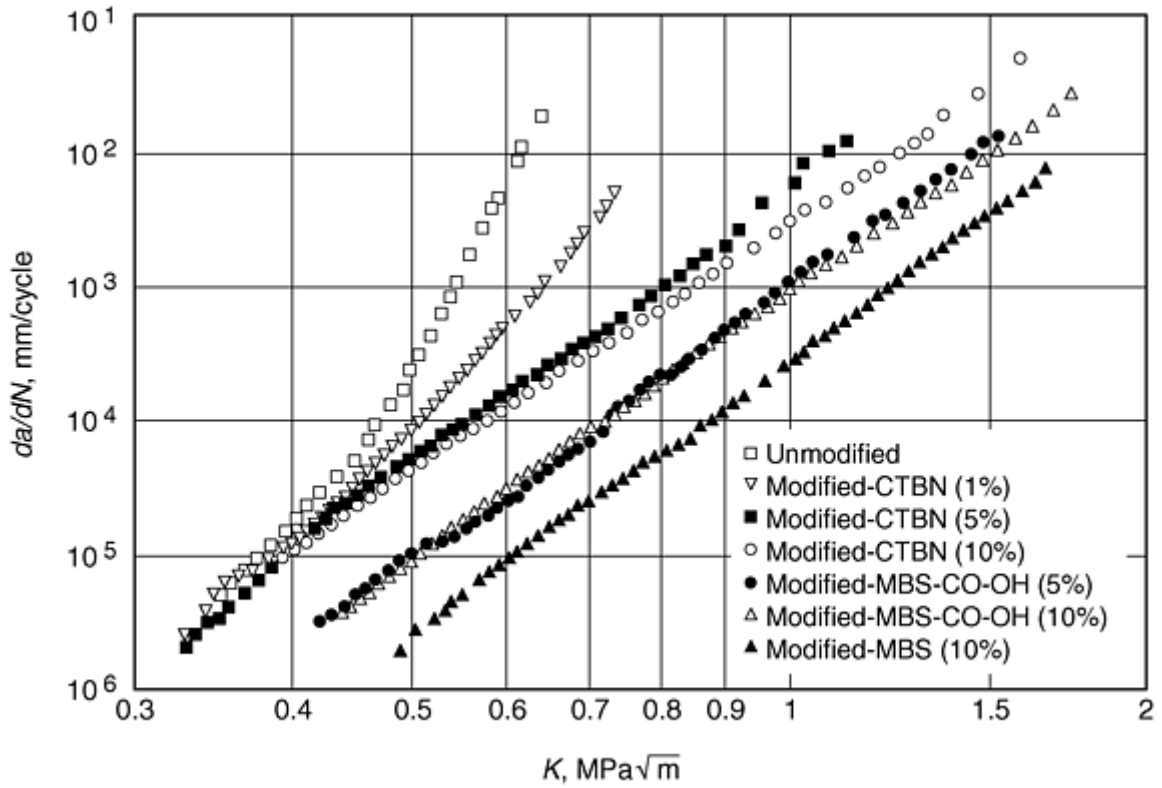


Fig. 12 Fatigue crack propagation behavior for a rubber-toughened epoxy. The addition of rubber decreases the slope, m , at high crack growth rates due toughening mechanisms and retarded crack growth. CTBN, carboxy-terminated polybutadiene acrylonitrile rubber; MBS, methacrylate-butadiene-styrene

Blending rubber-toughened polymers with a small amount of inorganic filler can also improve fatigue crack propagation resistance. Azimi et al. (Ref 23) have studied several glass-filled, rubber-toughened blends, and they believe the improved fatigue crack propagation resistance is the result of a synergistic interaction between the hollow glass filler at the crack tip and the plastic zone triggered by the rubber particles. The synergistic effect occurs by crack bridging via the glass phase and enhanced plasticity due to the presence of the rubber particles.

An interesting distinction must be made between fatigue crack initiation and propagation studies. The addition of rubber particles or reinforcements results in an increased resistance to crack propagation. However, this same material often exhibits a *decreased resistance* to fatigue crack initiation or flaw inception. The second phase addition serves as a nucleation site for crazes, voids, or shear bands and results in a decreased threshold for crack inception. For example, high impact polystyrene studies (Ref 5) have shown an increased resistance to crack propagation but a degraded resistance to crack inception when compared to the neat polystyrene resin. Thus, designers need to have a clear understanding of the component design and loading environment when making their material selection.

Mean Stress Effects. The fatigue response of a polymeric material is highly sensitive to the mean stress, σ_m , of the fatigue cycle:

$$\sigma_m = \frac{\sigma_{\max} + \sigma_{\min}}{2} \quad (\text{Eq 15})$$

Depending on the structure of the polymer and the micromechanisms of deformation, there are two distinct responses to an increase in mean stress. For a nominal stress intensity range, some polymers exhibit an increase in crack propagation rate while others show a decrease in crack growth rate. The published research on the effects of mean stress and R -ratio covers a broad range of polymer classes including amorphous, semicrystalline, crosslinked, and rubber-modified polymers (Ref 24, 25, 26, 27, 28, 29, 30, 31, 32, 33, and 34). Table 1 provides a summary of the effect of increased mean stress for several advanced polymer systems.

Table 1 Effect of increasing mean stress on polymer fatigue crack propagation

Polymer	Reference
Increasing crack propagation rate with increasing mean stress	
High density polyethylene	15
Nylon	5
High molecular weight PMMA	21, 25
Polystyrene	30, 35
Epoxy	24
Polyethylene copolymer	26
Decreasing crack propagation rate with increasing mean stress	
Low density polyethylene	5
Polyvinyl chloride	34
Low molecular weight PMMA	21
Rubber-toughened PMMA	15
High impact polystyrene	15, 35
Acrylonitrile-butadiene-styrene	15
Polycarbonate	24, 32, 33, 44
Toughened polycarbonate copolyester	27

Increasing crack growth rates associated with an increased stress ratio or mean stress are observed in epoxy resins, PMMA, HDPE copolymers, PS, PVC, and nylon. A number of different explanations and relationships have been proposed to rationalize the effect of mean stress on fatigue crack propagation. Arad et al. (Ref 28) suggested that the fatigue crack growth rates could be scaled to the stress intensity factor with the following relationship:

$$\frac{da}{dN} = \beta \cdot \lambda^n = \beta \cdot (K_{\max}^2 - K_{\min}^2)^n \quad (\text{Eq 16})$$

where β depends on the loading environment, frequency, and material properties, and n is a material constant. A micromechanistic explanation for this response to an increase in stress ratio or mean stress is also possible. Polymers that become more prone to fracture with increasing mean stress are most likely affected by the monotonic fracture process associated with the maximum portion of the loading cycle as it approaches a critical stress intensity level. In general, these polymers are susceptible to crazing, chain scission, or crosslink rupture. For these polymer types, an increase in mean stress results in faster crack propagation rates.

Remarkably, several polymer blends offer improved resistance to crack propagation as the mean stress is increased (Ref 5). These polymers include ABS, HIPS, PC, low density or branched polyethylene, low molecular weight PMMA, and rubber-toughened PMMA (Table 1). Hertzberg postulated that the strain energy normally available for crack extension is consumed through deformation or structural reorganization ahead of the crack tip. The use of strain energetics to describe fracture processes in polymers (Ref 1, 36) is formulated:

$$E = E_0 \cdot \left[\frac{C}{C - f(\psi)} \right] \quad (\text{Eq 17})$$

Here E is the total energy used by the solid to create a new unit area of surface through crack advance, E_0 is the energy expended for an ideal elastic solid, C is a material constant that depends on the strain state of the polymer, and ψ is the hysteresis ratio. The energy lost due to inelastic energy expenditure is captured by ψ . If the energy loss is large, the amount of energy needed to cause fracture increases; hence, it is expected that the crack growth rate will be reduced as ψ increases. Hertzberg and Manson (Ref 5) proposed that the effect of mean stress on the fatigue crack propagation resistance of polymeric materials is directly linked to the parameter, ψ . Thus, polymeric materials with a molecular structure susceptible to hysteretic losses or polymers capable of structural reorganization are likely to be more resistant to fatigue crack propagation as the mean stress is increased. These polymers have near tip processes that dissipate elastic energy ahead of the crack tip: rubber toughening, orientation hardening, chain slip, and shear banding.

Variable amplitude fatigue plays an important role in the design of polymeric components subjected to variations in the load cycle. Further, variable amplitude fatigue is a concern for components likely to experience periodic or unanticipated tensile or compressive overloads. It is conventional to model the effect of variable amplitude loading using the concept of cumulative damage (e.g., Palmgren-Miner mean accumulation rule).

While this concept has strength in crack initiation models, it does not capture the role of overload type or order in the loading sequence and the subsequent effect on a propagating crack.

Application of a single tensile overload can extend the life of a cracked component by retarding the rate of crack advance (Ref 13). This transient crack propagation behavior is often controlled by several mechanisms including crack closure (Ref 37), residual compressive stresses upon unloading (Ref 31, 38, and 39), and crack-tip blunting (Ref 40). The closure concept justifies the retardation of crack velocity in terms of residual compressive stresses left in the plastically deformed wake of the advancing crack. The result is premature contact between the crack faces while the specimen is still in the tensile portion of the fatigue cycle, and it effectively reduces the stress intensity range driving the crack advance. This crack closure mechanism has been proposed by Pitoniak et al. (Ref 41) to describe crack retardation in PMMA and by Murakami (Ref 42) for PC. Blunting has been proposed to describe the reduced crack velocity following tensile overloads (Ref 43). Although crack-tip blunting can temporarily affect the crack velocity subsequent to the overload, it does not explain a prolonged regime of crack retardation. Pruitt et al. (Ref 44) have shown that the zone of residual compressive stresses sustained at the crack tip upon unloading in amorphous polymers increases in size and magnitude as the far-field tensile load is increased. These residual compressive stresses sustained at the crack tip are believed to decrease the crack propagation rate following the tensile overload. The crack has to grow through this zone of residual compression before it can return to its initial crack propagation rate for the ΔK sustained prior to overload. This trend has been observed in numerous polymer systems (Ref 35, 44). Many current life prediction models are formulated on the basis of residual compressive stresses for the rationalization of crack retardation.

Compressive overloads can also be detrimental to the life of a structural component as the overload can result in an enhanced rate of crack propagation. The application of fully compressive cyclic loads results in the inception and growth of fatigue cracks ahead of stress concentrations and notches in polymers (Ref 39, 44). Figure 13 shows the nucleation and growth of a mode I fatigue crack in the plane of the notch as a result of cyclic compression loading in HIPS. The source of this crack growth is the generation of a zone of residual tensile stresses upon unloading from far-field compression. Permanent deformation ahead of the notch tip in polymers can be induced by crazing, shear flow, chain reorientation, or a combination thereof (Fig. 14). In summary, the application of compressive overloads to polymers with stress concentrations can result in the generation of residual tensile stresses and concomitant enhancement of crack velocity resulting in shortened component life.

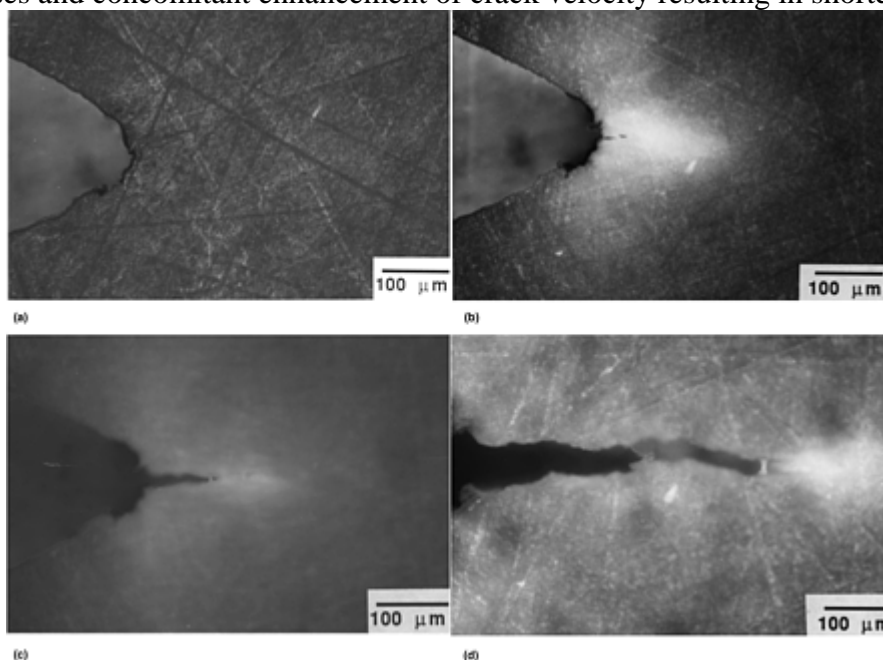


Fig. 13 Optical micrographs showing the nucleation and growth of a mode I fatigue crack in the plane of the notch as a result of cyclic compression loading in HIPS. (a) Crazing before fatigue cycling. (b) Nucleation of fatigue crack after 15,000 cycles. (c) Crack growth after 20,000 cycles. (d) Crack growth after 50,000 cycles. Source: Ref 43

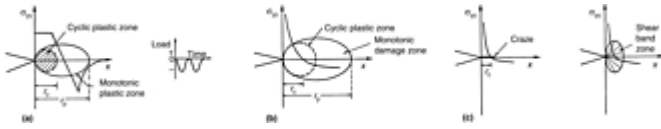


Fig. 14 Schematic illustrating the possible mechanisms of permanent deformation ahead of the notch tip. (a) Cyclic plastic zone typical of metals. (b) Cyclic damage zone typical of ceramics. (c) Craze or shear-band zones typical of polymer. Source: Ref 43

Waveform and Frequency Effects. Many polymers, due to the viscoelastic nature, are highly sensitive to the waveform or frequency of a fatigue test. Some crazeable polymers, such as PS, PMMA, and HIPS, exhibit decreased crack propagation as the test frequency is increased, while materials such as PC, nylon, and polysulfone exhibit no sensitivity (Ref 5). In crazeable polymers, the increased test frequency can diminish chain disentanglement effects at the crack tip and result in a decreased rate of crack propagation. Wnuk (Ref 45) proposed that the crack propagation in a polymer could be described as the sum of the elastic and viscoelastic contributions:

$$\frac{da}{dN} = C_1 \left(\frac{\Delta K}{K_{Ic}} \right)^{n_1} + C_2 \left(\frac{\Delta K}{K_{Ic}} \right)^{n_2} \cdot \frac{1}{\nu} \quad (\text{Eq 18})$$

where K_{Ic} is plane-strain fracture toughness, and the first term is the elastic contribution, which includes an elastic compliance term, C_1 . The second term is the time-dependent contribution, which includes a creep compliance term, C_2 , and the test frequency, ν .

Strain rate can also play a critical role in the fatigue response of time-dependent polymers. Hertzberg et al. (Ref 46) found strong sensitivity to waveform in PVC, PS, PMMA, and especially vinyl urethane. The square wave provides a high strain rate in ramp-up, then it subjects the specimen to a longer period of peak load than a triangular waveform with the same stress amplitude. This difference in load function can cause major differences in fatigue crack propagation. For example, in vinyl urethane (VUR), the fatigue crack propagation rate is reduced by a factor of 6 when switching from a triangular to a square wave loading function (Ref 47). This behavior is attributed to the higher strain rate that dominates for very flexible polymers, such as VUR. Another important factor is the amount of creep sustained at the peak load of the fatigue cycle. Polymers, such as PMMA, that are susceptible to creep damage will generally perform poorly when tested under the square waveform loading due to creep at peak load (Ref 46).

Environmental factors can play a critical role in the fatigue performance of engineering polymers. Many amorphous polymers are known to be susceptible to chemically induced crazing (Ref 5). In such instances, the crack inception values can be substantially reduced in the presence of aggressive media (Ref 5). For example, PC is known to nucleate surface crazes in the presence of acetone vapor. Many rubbers are susceptible to oxidation-induced embrittlement (Ref 48). Many medical polymers, such as orthopedic grade ultrahigh molecular weight polyethylene (UHMWPE) or bone cement (PMMA), degrade due to oxidation embrittlement and chain scission. These mechanisms are induced by ionizing modes of sterilization and subsequent aging (Ref 49, 50, 51, 52, 53, 54, 55, 56, 57, and 58). An example of the embrittling effect of gamma radiation sterilization on the fatigue crack propagation resistance of medical grade UHMWPE used for total joint replacements is provided in Fig. 15. While not all aggressive environments and effects on polymers are discussed here, it is clear that care should be taken to conduct fatigue tests that mimic not only the mechanical loads but also the chemical and aging environments that are most likely to be encountered in the lifetime of the device.

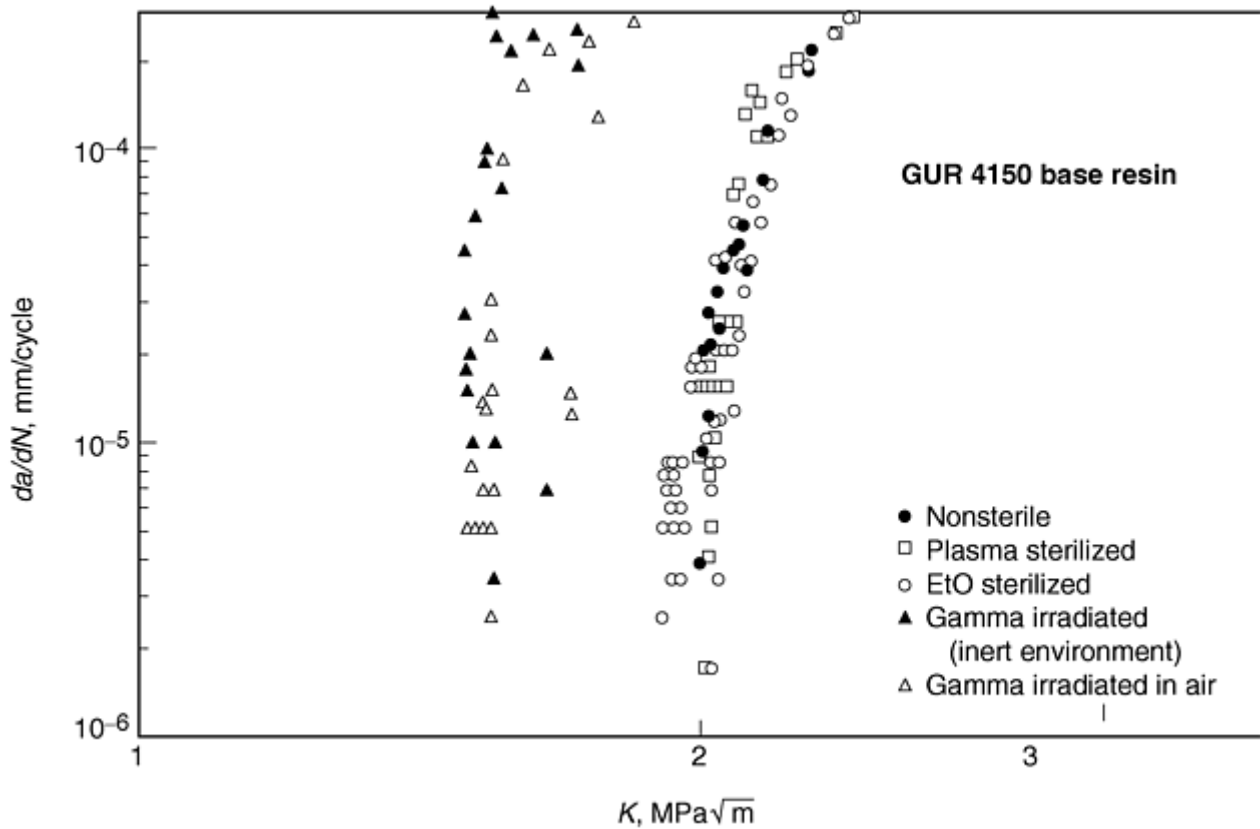


Fig. 15 Fatigue plot illustrating the devastating effect of gamma radiation sterilization on the fatigue resistance of orthopedic grade ultrahigh molecular weight polyethylene used for total joint replacements

References cited in this section

1. E.H. Andrews, *Testing of Polymers*, W. Brown, Ed., Wiley, 1969, p 237
3. J.A. Sauer and G.C. Richardson, *Int. J. Fract.*, Vol 16, 1980, p 499
5. R.W. Hertzberg and J.A. Manson, *Fatigue of Engineering Plastics*, Academic Press, 1980
12. R.O. Ritchie, *Proc. of the 5th Int. Conf.*, M.G. Yan, S.H. Zhang, and Z.M. Zheng, Ed., Pergamon Press, 1988, p 5
13. S. Suresh, *Fatigue of Materials*, 2nd ed., Cambridge University Press, 1998
15. C.B. Bucknall and W.W. Stevens, in *Toughening of Plastics*, Plastics and Rubber Institute, London, 1978, p 24
18. A.S. Argon, *Proc. of 7th Int. Conf. on Advances in Fracture Research*, K. Samala, K. Ravi-Chander, D.M.R. Taplin, and P. Rama Rao, Ed., Pergamon Press, 1989
20. A.J. Kinloch and F.J. Guild, in *Advances in Chemistry Series 252: Toughened Plastics II: Novel Approaches in Science and Engineering*, American Chemical Society, Washington, D.C., 1996, p 1
21. T.R. Clark, R.W. Hertzberg, and N. Nohammadi, in *8th Int. Conf. Deformation, Yield and Fracture of Polymers*, Plastics and Rubber Institute, London, 1991, p 31/1
22. E.J. Kramer and L.L. Berger, *Advances in Polymer Science 91/92*, H.H. Kausch, Ed., Springer-Verlag, 1990, p 1

23. H.R. Azimi, R.A. Pearson, and R.W. Hertzberg, *J. Mater. Sci.*, Vol 31, 1996, p 3777
24. S.A. Sutton, *Eng. Fract. Mech.*, Vol 6, 1974, p 587
25. B. Mukherjee and D.J. Burns, *Mech. Eng. Sci.*, Vol 11, 1971, p 433
26. Y.-Q. Zhou and N. Brown, *J. Poly. Sci. B, Polym. Phys.*, Vol 30, 1992, p 477
27. E.J. Moskala, in *8th Int. Conf. Deformation, Yield and Fracture of Polymers*, Plastics and Rubber Institute, London, 1991, p 51/1
28. S. Arad, J.C. Radon, and L.E. Culver, *J. Mech. Eng. Sci.*, Vol 13, 1971, p 75
29. A.S. Argon and R.E. Cohen, *Advances in Polymer Science 91/92*, H.H. Kausch, Ed., Springer-Verlag, 1990, p 300
30. J.A. Manson, R.W. Hertzberg, and P.E. Bretz, *Advances in Fracture Research*, D. Francois, Ed., Pergamon Press, 1981, p 443
31. L. Pruitt and S. Suresh, *Polymer*, Vol 35, 1994, p 3221
32. L. Pruitt and D. Rondinone, *Polym. Eng. Sci.*, Vol 36, 1996, p 1300
33. M.T. Takemori, *Polym. Eng. Sci.*, Vol 22, 1982, p 937
34. N.J. Mills and N. Walker, *Polymer*, Vol 17, 1976, p 335
35. L. Pruitt, Ph.D. Dissertation, Brown University, 1993
36. S.M. Cadwell, R.A. Merrill, C.M. Sloman, and F.L. Yost, *Ind. Eng. Chem. Anal. Ed.*, Vol 12, 1940, p 19
37. W. Elber, *Eng. Fract. Mech.*, Vol 2, 1970, p 37
38. S. Suresh, *Eng. Fract. Mech.*, Vol 18, 1983, p 577
39. L. Pruitt and S. Suresh, *Philos. Mag. A*, Vol 67, 1993, p 1219
40. J.R. Rice, in *Fatigue Crack Propagation*, ASTM STP 415, ASTM, 1967, p 247
41. F.J. Pitoniak, A.F. Grandt, L.T. Montulli, and P.F. Packman, *Eng. Fract. Mech.*, Vol 6, 1974, p 663
42. R. Murakami, S. Noguchi, K. Akizono, and W.G. Ferguson, *J. Fract. Eng. Mater. Struct.*, Vol 6, 1987, p 461
43. D.H. Banasiak, A.F. Grandt, and L.T. Montulli, *J. Appl. Polym. Sci.*, Vol 21, 1977, p 1297
44. L. Pruitt, R. Herman, and S. Suresh, *J. Mater. Sci.*, Vol 27, 1992, p 1608
45. M.P. Wnuk, *J. Appl. Mech.*, Vol 41 (No. 1), 1974, p 234
46. R.W. Hertzberg, J.A. Manson, and M.D. Skibo, *Polym. Eng. Sci.*, Vol 15, 1975, p 252
47. J.S. Harris and I.M. Ward, *J. Mater. Sci.*, Vol 8, 1973, p 1655

48. K. Dawes and L.C. Glover, *Physical Properties of Polymers Handbook*, J.E. Mark, Ed., AIP Press, 1966, p 557
49. S.M. Kurtz, D.L. Bartel, and C.M. Rimnac, *Trans. 40th Annual Meeting of the Orthopedic Research Society* (San Francisco), Orthopedic Research Society, 1994, p 584
50. G.M. Connelly, C.M. Rimnac, T.M. Wright, R.W. Hertzberg, and J.A. Manson, *J. Orth. Res.*, Vol 2, 1984, p 119
51. T.M. Wright, C.M. Rimnac, S.D. Stulberg, L. Mintz, A.K. Tsao, R.W. Klein, and C. McCrae, *Clin. Orth.*, Vol 276, 1992, p 126
52. M. Goldman and L. Pruitt, *J. Biomed. Mater. Res.*, Vol 40 (No. 3), 1998, p 378–384
53. M. Goldman, R. Gronsky, and L. Pruitt, *J. Mater. Sci.: Mater. Med.*, Vol 9, 1998, p 207–212
54. C.M. Rimnac, T.M. Wright, and R.W. Klein, *Polym. Eng. Sci.*, Vol 28, 1988, p 1586
55. M. Goldman, R. Ranganathan, R. Gronsky, and L. Pruitt, *Polymer.*, Vol 37 (No. 14), 1996, p 2909–2913
56. D. Baker, R. Hastings, and L. Pruitt, *Polymer*, 1999, in press
57. L. Pruitt and R. Ranganathan, *Mater. Sci. Eng. C: Biomimetic Mater., Sens. Syst.*, Vol 3, 1995, p 91–93
58. L. Pruitt, J. Koo, C. Rimnac, S. Suresh, and T. Wright, *J. Orth. Res.*, Vol 13, 1995, p 143–146

Fatigue Testing and Behavior of Plastics

Lisa A. Pruitt, University of California at Berkeley

Fractography

One of the most useful tools in failure analysis is fractography, the study of fracture surfaces. Scanning electron microscopy (SEM) can provide vast insight into failure mechanisms of polymers subjected to cyclic loading. Analysis of the surface with SEM provides the site of crack inception. Discontinuous growth bands are often encountered with polymers that undergo crazing. In such instances, the damage must accumulate before the leading fiber can fail and the crack can advance. This results in discontinuous growth bands or markings that are observed in fractography (Ref 5). Fractographic examination can also provide information on the formation of discontinuous or continuous crack growth bands. Figure 16(a) shows the typical ductile mechanisms observed in pristine UHMWPE, while Fig. 16(b) shows a typical brittle failure in acrylic-based bone cement. Fractography can provide useful insight into the nature of fracture processes acting at the crack tip and is a valid supplement for thorough fatigue characterization of engineering polymers (Ref 59).

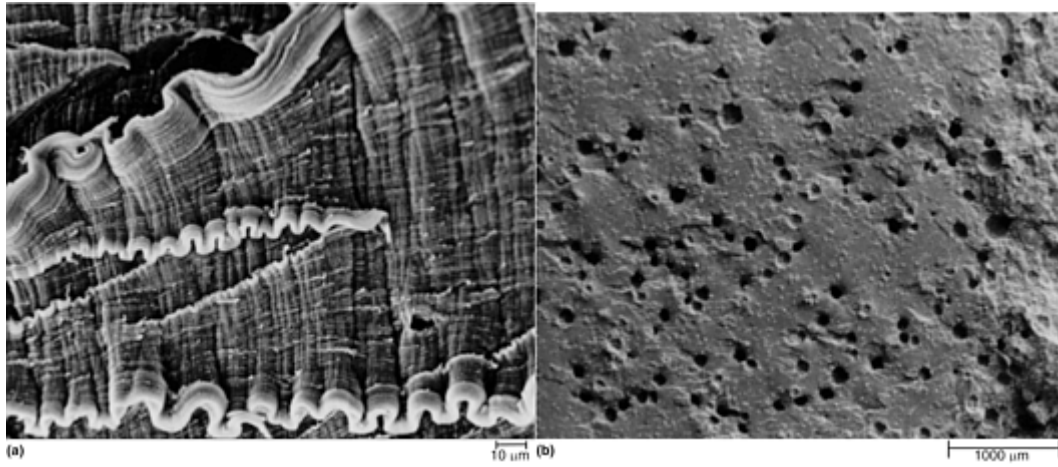


Fig. 16 Scanning electron micrographs depicting (a) the ductile mechanisms observed in pristine UHMWPE and (b) the brittle mechanisms found in acrylic bone cement

References cited in this section

5. R.W. Hertzberg and J.A. Manson, *Fatigue of Engineering Plastics*, Academic Press, 1980
59. L. Engel, H. Klingele, G.W. Ehrenstein, and H. Schaper, *An Atlas of Polymer Damage*, Wolfe Science Books, Vienna, 1981

Fatigue Testing and Behavior of Plastics

Lisa A. Pruitt, University of California at Berkeley

References

1. E.H. Andrews, *Testing of Polymers*, W. Brown, Ed., Wiley, 1969, p 237
2. P. Beardmore and S. Rabinowitz, *Treat. Mater. Sci. Technol.*, Vol 6, 1975, p 267
3. J.A. Sauer and G.C. Richardson, *Int. J. Fract.*, Vol 16, 1980, p 499
4. R.W. Hertzberg, M.D. Skibo, and J.A. Manson, *Fatigue Mechanisms*, ASTM STP 675, ASTM, 1979, p 471
5. R.W. Hertzberg and J.A. Manson, *Fatigue of Engineering Plastics*, Academic Press, 1980
6. R.W. Hertzberg and J.A. Manson, in *Encyclopedia of Polymer Science and Engineering*, Wiley, 1986, p 378
7. H.H. Kausch and J.G. Williams, in *Encyclopedia of Polymer Science and Engineering*, Wiley, 1986, p 341
8. J.A. Sauer and M. Hara, *Advances in Polymer Science 91/92*, H.H. Kausch, Ed., Springer-Verlag, 1990, p 71

9. J.D. Ferry, *Viscoelastic Properties of Polymers*, Wiley, 1961
10. G.C. Sih, *Handbook of Stress Intensity Factors*, Lehigh University Press, 1973
11. P.C. Paris, M.P. Gomez, and W.P. Anderson, *Trends Eng.*, Vol 13, 1961, p 9
12. R.O. Ritchie, *Proc. of the 5th Int. Conf.*, M.G. Yan, S.H. Zhang, and Z.M. Zheng, Ed., Pergamon Press, 1988, p 5
13. S. Suresh, *Fatigue of Materials*, 2nd ed., Cambridge University Press, 1998
14. A.G. Evans, Z.B. Ahmad, D.G. Gilbert, and P.W.R. Beaumont, *Acta Metall.*, Vol 34, 1986, p 79
15. C.B. Bucknall and W.W. Stevens, in *Toughening of Plastics*, Plastics and Rubber Institute, London, 1978, p 24
16. R.W. Hertzberg, *Deformation and Fracture Mechanics of Engineering Materials*, 4th ed., Wiley, 1996
17. T.L. Anderson, *Fracture Mechanics: Fundamentals and Applications*, CRC Press, 1995
18. A.S. Argon, *Proc. of 7th Int. Conf. on Advances in Fracture Research*, K. Samala, K. Ravi-Chander, D.M.R. Taplin, and P. Rama Rao, Ed., Pergamon Press, 1989
19. R.W. Lang, J.A. Manson, R.W. Hertzberg, and R. Schirrer, *Polym. Eng. Sci.*, Vol 24, 1984, p 833
20. A.J. Kinloch and F.J. Guild, in *Advances in Chemistry Series 252: Toughened Plastics II: Novel Approaches in Science and Engineering*, American Chemical Society, Washington, D.C., 1996, p 1
21. T.R. Clark, R.W. Hertzberg, and N. Nohammadi, in *8th Int. Conf. Deformation, Yield and Fracture of Polymers*, Plastics and Rubber Institute, London, 1991, p 31/1
22. E.J. Kramer and L.L. Berger, *Advances in Polymer Science 91/92*, H.H. Kausch, Ed., Springer-Verlag, 1990, p 1
23. H.R. Azimi, R.A. Pearson, and R.W. Hertzberg, *J. Mater. Sci.*, Vol 31, 1996, p 3777
24. S.A. Sutton, *Eng. Fract. Mech.*, Vol 6, 1974, p 587
25. B. Mukherjee and D.J. Burns, *Mech. Eng. Sci.*, Vol 11, 1971, p 433
26. Y.-Q. Zhou and N. Brown, *J. Poly. Sci. B, Polym. Phys.*, Vol 30, 1992, p 477
27. E.J. Moskala, in *8th Int. Conf. Deformation, Yield and Fracture of Polymers*, Plastics and Rubber Institute, London, 1991, p 51/1
28. S. Arad, J.C. Radon, and L.E. Culver, *J. Mech. Eng. Sci.*, Vol 13, 1971, p 75
29. A.S. Argon and R.E. Cohen, *Advances in Polymer Science 91/92*, H.H. Kausch, Ed., Springer-Verlag, 1990, p 300
30. J.A. Manson, R.W. Hertzberg, and P.E. Bretz, *Advances in Fracture Research*, D. Francois, Ed., Pergamon Press, 1981, p 443
31. L. Pruitt and S. Suresh, *Polymer*, Vol 35, 1994, p 3221

32. L. Pruitt and D. Rondinone, *Polym. Eng. Sci.*, Vol 36, 1996, p 1300
33. M.T. Takemori, *Polym. Eng. Sci.*, Vol 22, 1982, p 937
34. N.J. Mills and N. Walker, *Polymer*, Vol 17, 1976, p 335
35. L. Pruitt, Ph.D. Dissertation, Brown University, 1993
36. S.M. Cadwell, R.A. Merrill, C.M. Sloman, and F.L. Yost, *Ind. Eng. Chem. Anal. Ed.*, Vol 12, 1940, p 19
37. W. Elber, *Eng. Fract. Mech.*, Vol 2, 1970, p 37
38. S. Suresh, *Eng. Fract. Mech.*, Vol 18, 1983, p 577
39. L. Pruitt and S. Suresh, *Philos. Mag. A*, Vol 67, 1993, p 1219
40. J.R. Rice, in *Fatigue Crack Propagation*, ASTM STP 415, ASTM, 1967, p 247
41. F.J. Pitoniak, A.F. Grandt, L.T. Montulli, and P.F. Packman, *Eng. Fract. Mech.*, Vol 6, 1974, p 663
42. R. Murakami, S. Noguchi, K. Akizono, and W.G. Ferguson, *J. Fract. Eng. Mater. Struct.*, Vol 6, 1987, p 461
43. D.H. Banasiak, A.F. Grandt, and L.T. Montulli, *J. Appl. Polym. Sci.*, Vol 21, 1977, p 1297
44. L. Pruitt, R. Herman, and S. Suresh, *J. Mater. Sci.*, Vol 27, 1992, p 1608
45. M.P. Wnuk, *J. Appl. Mech.*, Vol 41 (No. 1), 1974, p 234
46. R.W. Hertzberg, J.A. Manson, and M.D. Skibo, *Polym. Eng. Sci.*, Vol 15, 1975, p 252
47. J.S. Harris and I.M. Ward, *J. Mater. Sci.*, Vol 8, 1973, p 1655
48. K. Dawes and L.C. Glover, *Physical Properties of Polymers Handbook*, J.E. Mark, Ed., AIP Press, 1966, p 557
49. S.M. Kurtz, D.L. Bartel, and C.M. Rimnac, *Trans. 40th Annual Meeting of the Orthopedic Research Society* (San Francisco), Orthopedic Research Society, 1994, p 584
50. G.M. Connelly, C.M. Rimnac, T.M. Wright, R.W. Hertzberg, and J.A. Manson, *J. Orth. Res.*, Vol 2, 1984, p 119
51. T.M. Wright, C.M. Rimnac, S.D. Stulberg, L. Mintz, A.K. Tsao, R.W. Klein, and C. McCrae, *Clin. Orth.*, Vol 276, 1992, p 126
52. M. Goldman and L. Pruitt, *J. Biomed. Mater. Res.*, Vol 40 (No. 3), 1998, p 378–384
53. M. Goldman, R. Gronskey, and L. Pruitt, *J. Mater. Sci.: Mater. Med.*, Vol 9, 1998, p 207–212
54. C.M. Rimnac, T.M. Wright, and R.W. Klein, *Polym. Eng. Sci.*, Vol 28, 1988, p 1586
55. M. Goldman, R. Ranganathan, R. Gronskey, and L. Pruitt, *Polymer.*, Vol 37 (No. 14), 1996, p 2909–2913

56. D. Baker, R. Hastings, and L. Pruitt, *Polymer*, 1999, in press
57. L. Pruitt and R. Ranganathan, *Mater. Sci. Eng. C: Biomimetic Mater., Sens. Syst.*, Vol 3, 1995, p 91–93
58. L. Pruitt, J. Koo, C. Rimnac, S. Suresh, and T. Wright, *J. Orth. Res.*, Vol 13, 1995, p 143–146
59. L. Engel, H. Klingele, G.W. Ehrenstein, and H. Schaper, *An Atlas of Polymer Damage*, Wolfe Science Books, Vienna, 1981

Fatigue Testing of Brittle Solids

J.A. Salem, Glenn Research Center at Lewis Field; M.G. Jenkins, University of Washington

Introduction

CERAMICS AND GLASSES subjected to static or cyclic loads exhibit time-dependent failure due to the growth in inherent and induced flaws to a critical size (Ref 1, 2, 3, 4, 5, 6, and 7). Cyclic loading is not required to generate crack extension. Hence, the phenomenon is referred to as “static fatigue.” The phenomenon is also referred to as subcritical crack growth, stress corrosion, delayed failure, slow crack growth, or environmentally induced fatigue.

This phenomenon depends on the chemical makeup and temperature of the environment and the applied stress-intensity factor. For relatively low stress-intensity factors, a fatigue limit below which crack growth arrests has been measured for static loading (Ref 8, 9, 10, and 11). However, the threshold occurs at low velocities, and the threshold is generally ignored in engineering applications.

Although slow crack growth is more severe for glass and glassy polycrystalline ceramics, single crystals such as sapphire and magnesium fluoride also exhibit time-dependent failure under static loads (Ref 12, 13, and 14). Thus, the structural application of glasses and ceramics requires consideration of static fatigue or slow crack growth behavior, and testing standards (Ref 15, 16, 17, 18, and 19) have been developed to generate data and determine fatigue parameters for materials screening and life prediction. Two types of flaws are generally used in the determination of the slow crack properties of ceramics: short, inherent flaws or long, induced cracks. Although machining processes such as surface grinding can introduce flaws, such flaws are generally short enough to be treated as inherent flaws. In some cases, the material can be heat treated (Ref 20) or etched (Ref 21) to minimize the presence of such populations. The testing standards focus on preexisting flaws within the material and allow those flaws to grow until catastrophic failure occurs. The fatigue parameters are inferred from strength data instead of by direct measurement of the crack growth.

In addition to the crack growth due to an environmentally induced stress corrosion mechanism, many ceramics materials exhibit enhanced fatigue crack growth during cyclic loading, and cyclically induced fatigue crack growth has been measured in vacuum (Ref 22, 23, 24, 25, 26, 27, 28, 29, 30, 31, and 32). This behavior is somewhat akin to that exhibited by metals, and measurements with short cracks can be considerably different from those measured with long cracks. This sensitivity to crack length is a consequence of the mechanisms used to toughen ceramics (e.g., grain bridging in the crack wake), which are extrinsic in nature. Fatigue crack growth of long cracks in toughened ceramics results as the toughening mechanism breaks down during load reversals, whereas for short cracks or ceramics without the presence of a toughening mechanism, crack growth is dominated by environmental factors and intrinsic fatigue mechanisms. Factors such as grain size and grain boundary phase, which generally relate to the toughening or environmental sensitivity, influence the sensitivity to cyclic loading (Ref 29, 30, 31, 32, and 33).

The distinction between environmentally induced fatigue and cyclically induced fatigue is not always clear, and some ceramics will exhibit a combination of both mechanisms.

Structural components made from ceramics materials that are expected to have long lives will fail from small cracks developed over long times. Thus, the development of standardized cyclic fatigue test methods has also revolved around the use of small, inherent flaws.

References cited in this section

1. C. Gurney and S. Pearson, Fatigue of Mineral Glass under Static and Cyclic Loading, *Proc. R. Soc. A.*, Vol 192, 1948, p 537–543
2. E.B. Shand, Experimental Study of Fracture of Glass, Part I: The Fracture Process, *J. Ceram. Soc.*, Vol 37, 1954, p 52–60
3. S. Pearson, Delayed Fracture of Sintered Alumina, *Proc. Physiol Soc.*, Vol 69, Part 12, Section B, Dec 1956, p 1293–1296
4. R.E. Mould and R.D. Southwick, Strength and Static Fatigue of Abraded Glass under Controlled Ambient Conditions, Part II: Effect of Various Abrasions and the Universal Fatigue Curve, *J. Am. Ceram. Soc.*, Vol 42, 1959, p 582–592
5. S.M. Wiederhorn, Influence of Water Vapor on Crack Propagation in Soda-Lime Glass, *J. Am. Ceram. Soc.*, Vol 50, 1967, p 407–414
6. A.G. Evans and F.F. Lange, Crack Propagation and Fracture in Silicon Carbide, *J. Mater. Sci.*, Vol 10 (No. 10), 1975, p 1659–1664
7. J.E. Ritter and J.N. Humenik, Static and Dynamic Fatigue of Polycrystalline Alumina, *J. Mater. Sci.*, Vol 14 (No. 3), 1979, P 626–632
8. S.M. Wiederhorn and L.H. Boltz, Stress Corrosion and Static Fatigue of Glass, *J. Am. Ceram. Soc.*, Vol 62 (No. 7–8), 1970, p 547–548
9. B.J.S. Wilkins and E. Dutton, Static Fatigue Limit with Particular Reference to Glass, *J. Am. Ceram. Soc.*, Vol 59 (No. 3–4), 1976, p 108–112
10. T.A. Michalske, The Stress Corrosion Limit: Its Measurement and Implications, *Fracture Mechanics of Ceramics*, Vol 5, R.C. Bradt, A.G. Evans, D.P.H. Hasselman, and F.F. Lange, Ed., Plenum Publishing Corp., 1983
11. T. Fett, K. Germerdonk, A. Grossmuller, K. Keller, and D. Munz, Subcritical Crack Growth and Threshold in Borosilicate Glass, *J. Mater. Sci.*, Vol 26, 1991, p 253–257
12. S.M. Wiederhorn, Moisture Assisted Crack Growth in Ceramics, *Int. J. Fract. Mech.*, Vol 4 (No. 2), 1968, p 171–177
13. S.M. Wiederhorn, B.J. Hockey, and D.E. Roberts, Effect of Temperature on the Fracture of Sapphire, *Philos. Mag.*, Vol 28 (No. 4), 1973, p 783–796
14. T.A. Michalske, B.C. Bunker, and S.W. Freiman, Stress Corrosion of Ionic and Mixed Ionic/Covalent Solids, *J. Am. Ceram. Soc.*, Vol 69 (No. 10), 1986, p 721–724
15. DD ENV 843-3 Advanced Technical Ceramics—Monolithic Ceramics—Mechanical Properties at Room Temperature, Part 3: Determination of Subcritical Crack Growth Parameters from Constant Stressing Rate Flexural Strength Tests, British Standards Institution, London, 1997

16. "Testing Method for Bending Fatigue of Fine Ceramics," JIS R 1621, Japanese Standards Association, Tokyo, Japan, 1996
17. "Standard Test Method for Determination of Slow Crack Growth Parameters of Advanced Ceramics by Constant Stress-Rate Flexural Testing at Ambient Temperature," C 1368, *Annual Book of ASTM Standards*, ASTM, Vol 15.01, 1999, p 706–714
18. "Test Methods for Static Bending Fatigue of Fine Ceramics," JIS R 1632, Japanese Standards Association, Tokyo, Japan, Dec 1998
19. Standard Practice for Constant-Amplitude, Axial Tension-Tension Cyclic Fatigue of Advanced Ceramics at Ambient Temperatures," C1361, *Annual Book of ASTM Standards*, ASTM
20. J.A. Salem, N.N. Nemeth, L.M. Powers, and S.R. Choi, Reliability Analysis of Uniaxially Ground Brittle Materials, *J. Eng. Gas Turbines Power (Trans. ASME)*, Vol 118, 1996, p 863–871
21. D.H. Roach and A.R. Cooper, "Etching of Soda Lime Glass-Another Look," in the third proceedings of a symposium sponsored by the Etel Institute for Silicate Research/The University of Toledo and the Northwestern Ohio Section of the Am. Ceram. Soc., W. Kneller, Ed., March 1983, p 1–7
22. F. Gigu, Cyclic Fatigue of Polycrystalline Alumina in Direct Push-Pull, *J. Mater. Sci. Lett.*, Vol 13 (No. 6), 1978, p 1357–1361
23. M.V. Swain, Lifetime Prediction of Ceramic Materials, *Mater. Forum*, Vol 9 (No. 1–2), 1st and 2nd Quarter 1986, p 34–44
24. H. Kawakubo and K. Komeya, Static and Cyclic Fatigue Behavior of a Sintered Silicon Nitride at Room Temperature, *J. Am. Ceram. Soc.*, Vol 70 (No. 6), 1987, p 400–405
25. R.H. Dauskardt, W. Yu, and R.O. Ritchie, Fatigue Crack Propagation in Transformation Toughened Zirconia, *J. Am. Ceram. Soc.*, Vol 70 (No. 10), 1987, p C-248–C-252
26. G. Grathwohl, Fatigue of Ceramics under Cyclic Loading, *Mater. Sci. Technol.*, Vol 19 (No. 4), April 1988, p 113–124 (in German)
27. M.J. Reece, F. Guiu, and M.F.R. Sammur, Cyclic Fatigue Crack Propagation in Alumina under Direct Tension-compression Loading, *J. Am. Ceram. Soc.*, Vol 72 (No. 2), 1989, p 348–352
28. Y. Mutoh, M. Takahashi, T. Oikawa, and H. Okamoto, Fatigue Crack Growth of Long and Short Cracks in Silicon Nitride, *Fatigue of Advanced Materials*, R.O. Ritchie, R.H. Dauskardt, and B.N. Cox, Ed., Material and Component Engineering Publications, Ltd., Edgbaston, U.K., 1991, p 211–225
29. S. Horibe and H. Hirahara, Cyclic Fatigue of Ceramics Materials: Influence of Crack Path and Fatigue Mechanisms, *Acta Metall. Mater.*, Vol 39 (No. 6), 1991, p 1309–1317
30. M. Okazaki, A.J. McEvily, and T. Tanaka, On the Mechanism of Fatigue Crack Growth in Silicon Nitride, *Metall. Trans. A*, Vol 22A, 1991, p 1425–1434
31. T. Tanaka, N. Okabe, H. Nakayama, and Y. Ishimaru, Fatigue Crack Growth of Silicon Nitride with Crack Wedging by Fine Fragments, *Fatigue Fract. Eng. Mater. Struct.*, Vol 17 (No. 7), 1992, p 643–653
32. R.O. Ritchie, C.J. Gilbert, and J.M. McNaney, Mechanics and Mechanisms of Fatigue Damage and Crack Growth in Advanced Materials, *Int. J. Solids Struct.*, Vol 37, 2000, p 311–329

33. R. Dauskardt, Cyclic Fatigue-Crack Growth in Grain Bridging Ceramics, *J. Eng. Mater. Technol. (Trans. ASME)*, Vol 115, 1993, p 115–251

Fatigue Testing of Brittle Solids

J.A. Salem, Glenn Research Center at Lewis Field; M.G. Jenkins, University of Washington

Fatigue Mechanism

Fatigue mechanisms in brittle solids can be classified as environmentally induced fatigue or as cyclic fatigue. Environmentally Induced Fatigue. Environmentally induced, or static, fatigue in ceramics and glasses is a chemically activated atomic reaction that is enhanced by stress and temperature. Crack growth occurs by breakage of the bonds at the crack tip. In particular, the introduction of water to the environment can have a severe effect on the fatigue parameters, and the moisture in air is sufficient to cause crack growth in ceramics and glasses subjected to stress.

For aqueous solutions, the rate of crack growth is increased with the increasing concentration of OH⁻ ions, which break the metal-oxygen-metal bonds in silicate glass and oxide ceramics. For nonoxide ceramics that do not contain a glassy phase (e.g., SiC), the presence of room temperature water vapor may have little effect on crack growth rates. Acid base pairs have the strongest influence on crack growth (Ref 14, 34). Michalske et al. (Ref 34) developed an atomistic model addressing the role of mechanical strain in accelerating chemical reactions between crack tip bonds in silica and environmental molecules. The strain field at the crack tip deforms the Si-O bond angle, thereby resulting in bond defects that increase the chemical activity of the bonds. Chemisorption of the attacking species results in bond breakage. The absolute rate of crack extension depends on the combined rates of active bond formation and chemical attack at strain-induced defects.

Additional studies on the {1012} of sapphire in water, ammonia, hydrazine, and acetonitrile indicated the same mechanism—dissociative chemisorption—but with different details that make the fatigue parameter more sensitive to the specific environment (Ref 14).

In contrast to the slow crack growth mechanism in sapphire, that in magnesium fluoride, which is ionically bonded, appeared to be ionic solvation of strained ions at the crack tip. The actively corrosive environments, in this case, water, methanol, and acetonitrile, reduced the electrostatic attraction between oppositely charged ion pairs at the crack tip.

For corrosive environments such as elevated temperature water or pressurized steam, silicon nitrides undergo severe pitting or grain loss, depending on the oxide additives and grain morphology (Ref 35, 36). For silicon nitride with amorphous silica at the grain boundaries, intergranular corrosion results in the Si₃N₄ grains falling out. However, for silicon nitrides with even small amounts of oxide additives, the leachability of the grain boundary is substantially changed. Depending on the additives, pits form under either a protective or nonprotective corrosion layer (Ref 35). The implication for environmentally induced crack growth is that harsh environments involving elevated temperature steam, such as turbines, will result in substantially accelerated crack growth.

Cyclic Fatigue. A variety of mechanisms have been proposed to result in cyclically induced fatigue in ceramics (Ref 26, 29, 30, 31, 32, 33, 37, 38, and 39). Generally, the fatigue mechanism is related to the crack growth resistance mechanism of the particular material. For example, the breakdown of bridging grains or transformation zones that produce *R*-curve effects in silicon nitrides and transformation-toughened zirconia. Also, mechanisms such as the coalescence of microcrack clusters at grain boundaries have been proposed (Ref 39). As the material is cycled, the toughening mechanism is broken down, thereby increasing the crack tip stress-intensity factor, allowing crack extension until the crack growth resistance redevelops.

One of the most critical aspects of cyclic fatigue testing is the size of the crack used. Results generated with long cracks can be substantially different from those generated with short cracks (Ref 28, 40).

References cited in this section

14. T.A. Michalske, B.C. Bunker, and S.W. Freiman, Stress Corrosion of Ionic and Mixed Ionic/Covalent Solids, *J. Am. Ceram. Soc.*, Vol 69 (No. 10), 1986, p 721–724
26. G. Grathwohl, Fatigue of Ceramics under Cyclic Loading, *Mater. Sci. Technol.*, Vol 19 (No. 4), April 1988, p 113–124 (in German)
28. Y. Mutoh, M. Takahashi, T. Oikawa, and H. Okamoto, Fatigue Crack Growth of Long and Short Cracks in Silicon Nitride, *Fatigue of Advanced Materials*, R.O. Ritchie, R.H. Dauskardt, and B.N. Cox, Ed., Material and Component Engineering Publications, Ltd., Edgbaston, U.K., 1991, p 211–225
29. S. Horibe and H. Hirahara, Cyclic Fatigue of Ceramics Materials: Influence of Crack Path and Fatigue Mechanisms, *Acta Metall. Mater.*, Vol 39 (No. 6), 1991, p 1309–1317
30. M. Okazaki, A.J. McEvily, and T. Tanaka, On the Mechanism of Fatigue Crack Growth in Silicon Nitride, *Metall. Trans. A*, Vol 22A, 1991, p 1425–1434
31. T. Tanaka, N. Okabe, H. Nakayama, and Y. Ishimaru, Fatigue Crack Growth of Silicon Nitride with Crack Wedging by Fine Fragments, *Fatigue Fract. Eng. Mater. Struct.*, Vol 17 (No. 7), 1992, p 643–653
32. R.O. Ritchie, C.J. Gilbert, and J.M. McNaney, Mechanics and Mechanisms of Fatigue Damage and Crack Growth in Advanced Materials, *Int. J. Solids Struct.*, Vol 37, 2000, p 311–329
33. R. Dauskardt, Cyclic Fatigue-Crack Growth in Grain Bridging Ceramics, *J. Eng. Mater. Technol. (Trans. ASME)*, Vol 115, 1993, p 115–251
34. T.A. Michalske and B.C. Bunker, Slow Fracture Based on Strained Silicate Structures, *J. Appl. Phys.*, Vol 56 (No. 10), 1984, p 2686–2694
35. T. Yishio and K. Oda, Aqueous Corrosion and Pit Formation of Si_3N_4 under Hydrothermal Conditions, *Ceram. Trans.*, Vol 10, 1990, p 367–386
36. M.K. Ferber, H.T. Lin, and J. Keiser, Oxidation Behavior of Non-Oxide Ceramics in a High-Pressure, High-Temperature Steam Environment, *Mechanical, Thermal and Environmental Testing and Performance of Ceramic Composites and Components*, STP 1392, M.G. Jenkins, E. Lara-Curzio, and S. Gonczy, Ed., ASTM, 2000
37. G. Vekinis, M.F. Ashby, and P.W. Beaumont, R-Curve Behaviour of Al_2O_3 Ceramics, *Acta Metall. Mater.*, Vol 38 (No. 6), 1990, p 1151–1162
38. D.A. Krohn and D.P.H. Hasselman, Static and Cyclic Fatigue Behavior of a Polycrystalline Alumina, *J. Am. Ceram. Soc.*, Vol 55 (No. 4), 1972, p 208–211
39. M. Masuda, T. Soma, M. Matsui, and I. Oda, Fatigue of Ceramics, Part 1: Fatigue Behavior of Sintered Silicon Nitride under Tension-Compression Cyclic Stress, *J. Ceram. Soc. Jpn. Int. Ed.*, Vol 96, 1988, p 275–280
40. A. Steffen, R.H. Dauskardt, and R.O. Ritchie, Cyclic Fatigue Life and Crack Growth Behavior of Microstructural Small Cracks in Magnesia-Partially-Stabilized Zirconia Ceramics, *J. Am. Ceram. Soc.*, Vol 74 (No. 6), 1991, p 1259–1268

Fatigue Mechanism

Fatigue mechanisms in brittle solids can be classified as environmentally induced fatigue or as cyclic fatigue. Environmentally Induced Fatigue. Environmentally induced, or static, fatigue in ceramics and glasses is a chemically activated atomic reaction that is enhanced by stress and temperature. Crack growth occurs by breakage of the bonds at the crack tip. In particular, the introduction of water to the environment can have a severe effect on the fatigue parameters, and the moisture in air is sufficient to cause crack growth in ceramics and glasses subjected to stress.

For aqueous solutions, the rate of crack growth is increased with the increasing concentration of OH⁻ ions, which break the metal-oxygen-metal bonds in silicate glass and oxide ceramics. For nonoxide ceramics that do not contain a glassy phase (e.g., SiC), the presence of room temperature water vapor may have little effect on crack growth rates. Acid base pairs have the strongest influence on crack growth (Ref 14, 34). Michalske et al. (Ref 34) developed an atomistic model addressing the role of mechanical strain in accelerating chemical reactions between crack tip bonds in silica and environmental molecules. The strain field at the crack tip deforms the Si-O bond angle, thereby resulting in bond defects that increase the chemical activity of the bonds. Chemisorption of the attacking species results in bond breakage. The absolute rate of crack extension depends on the combined rates of active bond formation and chemical attack at strain-induced defects.

Additional studies on the {1012} of sapphire in water, ammonia, hydrazine, and acetonitrile indicated the same mechanism—dissociative chemisorption—but with different details that make the fatigue parameter more sensitive to the specific environment (Ref 14).

In contrast to the slow crack growth mechanism in sapphire, that in magnesium fluoride, which is ionically bonded, appeared to be ionic solvation of strained ions at the crack tip. The actively corrosive environments, in this case, water, methanol, and acetonitrile, reduced the electrostatic attraction between oppositely charged ion pairs at the crack tip.

For corrosive environments such as elevated temperature water or pressurized steam, silicon nitrides undergo severe pitting or grain loss, depending on the oxide additives and grain morphology (Ref 35, 36). For silicon nitride with amorphous silica at the grain boundaries, intergranular corrosion results in the Si₃N₄ grains falling out. However, for silicon nitrides with even small amounts of oxide additives, the leachability of the grain boundary is substantially changed. Depending on the additives, pits form under either a protective or nonprotective corrosion layer (Ref 35). The implication for environmentally induced crack growth is that harsh environments involving elevated temperature steam, such as turbines, will result in substantially accelerated crack growth.

Cyclic Fatigue. A variety of mechanisms have been proposed to result in cyclically induced fatigue in ceramics (Ref 26, 29, 30, 31, 32, 33, 37, 38, and 39). Generally, the fatigue mechanism is related to the crack growth resistance mechanism of the particular material. For example, the breakdown of bridging grains or transformation zones that produce *R*-curve effects in silicon nitrides and transformation-toughened zirconia. Also, mechanisms such as the coalescence of microcrack clusters at grain boundaries have been proposed (Ref 39). As the material is cycled, the toughening mechanism is broken down, thereby increasing the crack tip stress-intensity factor, allowing crack extension until the crack growth resistance redevelops.

One of the most critical aspects of cyclic fatigue testing is the size of the crack used. Results generated with long cracks can be substantially different from those generated with short cracks (Ref 28, 40).

References cited in this section

14. T.A. Michalske, B.C. Bunker, and S.W. Freiman, Stress Corrosion of Ionic and Mixed Ionic/Covalent Solids, *J. Am. Ceram. Soc.*, Vol 69 (No. 10), 1986, p 721–724

26. G. Grathwohl, Fatigue of Ceramics under Cyclic Loading, *Mater. Sci. Technol.*, Vol 19 (No. 4), April 1988, p 113–124 (in German)
28. Y. Mutoh, M. Takahashi, T. Oikawa, and H. Okamoto, Fatigue Crack Growth of Long and Short Cracks in Silicon Nitride, *Fatigue of Advanced Materials*, R.O. Ritchie, R.H. Dauskardt, and B.N. Cox, Ed., Material and Component Engineering Publications, Ltd., Edgbaston, U.K., 1991, p 211–225
29. S. Horibe and H. Hirahara, Cyclic Fatigue of Ceramics Materials: Influence of Crack Path and Fatigue Mechanisms, *Acta Metall. Mater.*, Vol 39 (No. 6), 1991, p 1309–1317
30. M. Okazaki, A.J. McEvily, and T. Tanaka, On the Mechanism of Fatigue Crack Growth in Silicon Nitride, *Metall. Trans. A*, Vol 22A, 1991, p 1425–1434
31. T. Tanaka, N. Okabe, H. Nakayama, and Y. Ishimaru, Fatigue Crack Growth of Silicon Nitride with Crack Wedging by Fine Fragments, *Fatigue Fract. Eng. Mater. Struct.*, Vol 17 (No. 7), 1992, p 643–653
32. R.O. Ritchie, C.J. Gilbert, and J.M. McNaney, Mechanics and Mechanisms of Fatigue Damage and Crack Growth in Advanced Materials, *Int. J. Solids Struct.*, Vol 37, 2000, p 311–329
33. R. Dauskardt, Cyclic Fatigue–Crack Growth in Grain Bridging Ceramics, *J. Eng. Mater. Technol. (Trans. ASME)*, Vol 115, 1993, p 115–251
34. T.A. Michalske and B.C. Bunker, Slow Fracture Based on Strained Silicate Structures, *J. Appl. Phys.*, Vol 56 (No. 10), 1984, p 2686–2694
35. T. Yishio and K. Oda, Aqueous Corrosion and Pit Formation of Si_3N_4 under Hydrothermal Conditions, *Ceram. Trans.*, Vol 10, 1990, p 367–386
36. M.K. Ferber, H.T. Lin, and J. Keiser, Oxidation Behavior of Non-Oxide Ceramics in a High-Pressure, High-Temperature Steam Environment, *Mechanical, Thermal and Environmental Testing and Performance of Ceramic Composites and Components*, STP 1392, M.G. Jenkins, E. Lara-Curzio, and S. Gonczy, Ed., ASTM, 2000
37. G. Vekinis, M.F. Ashby, and P.W. Beaumont, R-Curve Behaviour of AP_2O_3 Ceramics, *Acta Metall. Mater.*, Vol 38 (No. 6), 1990, p 1151–1162
38. D.A. Krohn and D.P.H. Hasselman, Static and Cyclic Fatigue Behavior of a Polycrystalline Alumina, *J. Am. Ceram. Soc.*, Vol 55 (No. 4), 1972, p 208–211
39. M. Masuda, T. Soma, M. Matsui, and I. Oda, Fatigue of Ceramics, Part 1: Fatigue Behavior of Sintered Silicon Nitride under Tension-Compression Cyclic Stress, *J. Ceram. Soc. Jpn. Int. Ed.*, Vol 96, 1988, p 275–280
40. A. Steffen, R.H. Dauskardt, and R.O. Ritchie, Cyclic Fatigue Life and Crack Growth Behavior of Microstructural Small Cracks in Magnesia-Partially-Stabilized Zirconia Ceramics, *J. Am. Ceram. Soc.*, Vol 74 (No. 6), 1991, p 1259–1268

Strength-Based Test Methods

Strength-based methods or “indirect” methods employ smooth test specimens, such as flexural beams or tensile specimens, and estimate fatigue properties from strengths measured over different time intervals. Strength-based methods directly sample the flaw distribution within or on the surface of the test specimens. The cracks thus develop from at least some of the same sources as in a component of the same material. However, the results are subject to the scatter inherent in the strength distribution of the material, and thus a relative large number of tests are required. Further, strength-based methods do not measure the actual crack size but infer it from the measured strength.

Three basic strength test methods and accompanying analytical relations have been developed for determining the fatigue parameters and behavior of ceramics and glasses: static loading, dynamic loading, and cyclic loading.

Static Loading. Typically, tensile specimens or flexure specimens (e.g., beams or plates) are subjected to a constant load in the environment of interest. The time-to-failure and the applied stress are recorded and used to determine the fatigue parameters according to any of the Eq 1, 2, 3, 4, and 5. The generalized slow crack growth behavior for static loading is shown in Fig. 2.

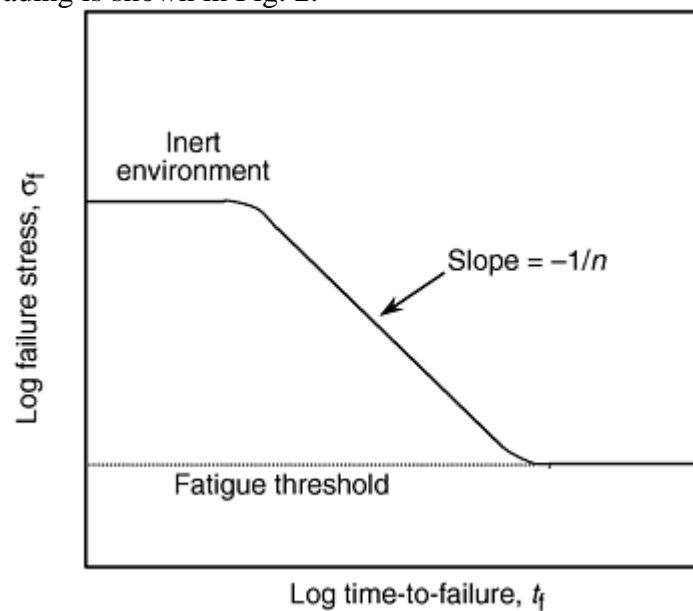


Fig. 2 Generalized failure stress as a function of time-to-failure on a logarithmic scale for ceramics and glasses exhibiting environmentally induced slow crack growth

One test method, Japanese Industrial Standard (JIS) 1632 “Test Methods for Static Bending Fatigue of Fine Ceramics,” has been standardized for the determination of fatigue strength by static loading (Ref 18) at room or elevated temperatures. The standard gives guidance on the test method but not in the calculation of fatigue parameters such as A and n .

Uniaxial flexural test specimens are manufactured and tested in three- or four-point loading in accordance with JIS R 1601, “Test Method for Flexural Strength (Modulus of Rupture) of Fine Ceramics” (Ref 56). The use of at least three stress levels is recommended, and the breaking times at one of the stress levels must be distributed between 0 and 100 h, minimum. No requirement on the number of test pieces is specified; however, three tests per stress level are recommended. Tests may be stopped after 100 h if failure has not occurred. An initial fatigue stress equal to 75% of the fracture strength is used. Subsequent stresses differing by 5 to 10% from the initial fatigue load are applied, depending on the initial time-to-failure and scatter in the data. An example of failure stress data as a function of the failure time is shown in Fig. 3 (Ref 18).

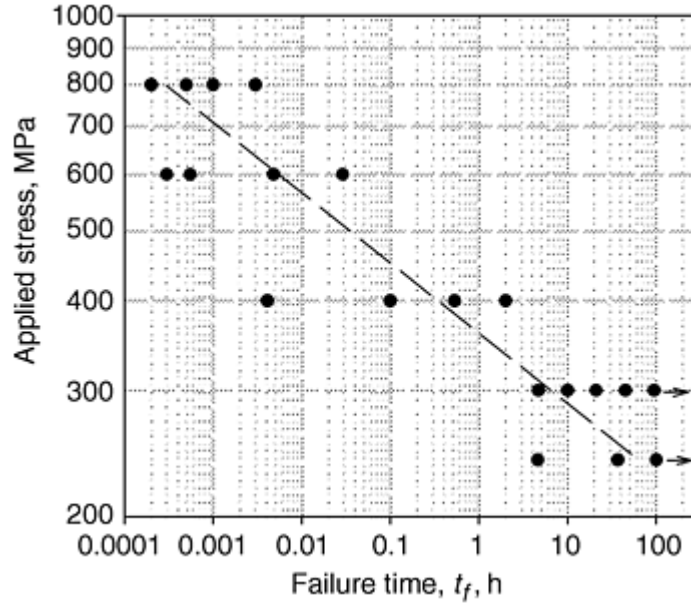


Fig. 3 Example of failure stress as a function of time-to-failure on a logarithmic scale for ceramics and glasses exhibiting environmentally induced slow crack growth. Adapted from Ref 18

The stress at fracture or fatigue strength σ_f , is related to the time-to-failure, t_f , by (Ref 43, 57, and 58):

$$t_f = \frac{B}{\sigma_f^2} \left[\left(\frac{\sigma_i}{\sigma_f} \right)^{n-2} - 1 \right] \quad (\text{Eq 7})$$

where B is a parameter associated with A , n , fracture toughness, crack geometry, and loading configuration, and σ_i is the “inert” strength or the strength under noncorrosive conditions for which no crack extension occurs. For most ceramics and glass, $n > 10$ so that Eq 7 can generally be simplified to:

$$t_f = B \sigma_i^n \sigma_f^{-n} \quad (\text{Eq 8})$$

The fatigue parameter n can be determined from the slope of a $\log t_f$ versus $\log \sigma_f$ plot by writing Eq 8 as:

$$\log t_f = -n \log \sigma_f + \log D \quad (\text{Eq 9})$$

where

$$\log D = \log(B \sigma_i^n) \quad (\text{Eq 10})$$

Once the slope and intercept of Eq 9 are estimated, the parameters n and D and the standard deviation SD_n and SD_D can be estimated by a Taylor series expansion of the random variable of interest (Ref 59):

$$n = -\alpha \quad (\text{Eq 11})$$

$$SD_n \approx SD_\alpha \quad (\text{Eq 12})$$

$$D = 10^\beta \quad (\text{Eq 13})$$

$$SD_D \approx (\ln 10)(SD_\beta)(10^\beta) \quad (\text{Eq 14})$$

where α is the slope and β is the intercept estimated by linear regression of Eq 9. For some design codes, the fatigue parameters B and A are necessary (Ref 60, 61, 62). The parameter B and the standard deviation can be estimated from:

$$B = 10^\beta \sigma_i^{\alpha+2} \quad (\text{Eq 15})$$

$$SD_B \approx 10^\beta \sigma_i^{\alpha+2} \sqrt{2 \ln(10) SD_\beta^2 - \frac{\alpha+2}{\sigma_i^2} SD_{\sigma_i}^2 + \ln(\sigma_i)^2 SD_\alpha^2} \quad (\text{Eq 16})$$

The parameter A in Eq 2 can be calculated from:

$$A = \frac{2 K_{lc}^2}{BY^2(n-2)} \quad (\text{Eq 17a})$$

or

$$A = \frac{-2 K_{lc}^2}{10^\beta \sigma_i^{\alpha+2} (\alpha+2) Y^2} \quad (\text{Eq 17b})$$

with

$$SD_A \approx A \sqrt{(\ln 10)^2 SD_\beta^2 + \frac{(\alpha+2)^2}{\sigma_i^2} SD_{\sigma_i}^2 + \left(\ln \sigma_i + \frac{1}{\alpha+2} \right)^2 SD_\alpha^2} \quad (\text{Eq 18})$$

where Y is the stress-intensity factor coefficient and treated as a constant.

Note that plots of static fatigue data (e.g., Fig. 3) are usually made with the applied stress appearing as the dependent variable; however, the dependent variable actually is the time-to-failure, and it must be minimized in the regression analysis.

Dynamic Loading. Typically, tensile or flexure test specimens (e.g., beams or plates) are subjected to a constant stress rate in the environment of interest. The failure stress and the applied stress rate are recorded and used to determine the fatigue parameters according to any of the Eq 1, 2, 3, 4, and 5. Figure 4 illustrates the observed strength as a function of stress rate for dynamic loading. A detailed error analysis has been conducted for dynamic loading (Ref 63).

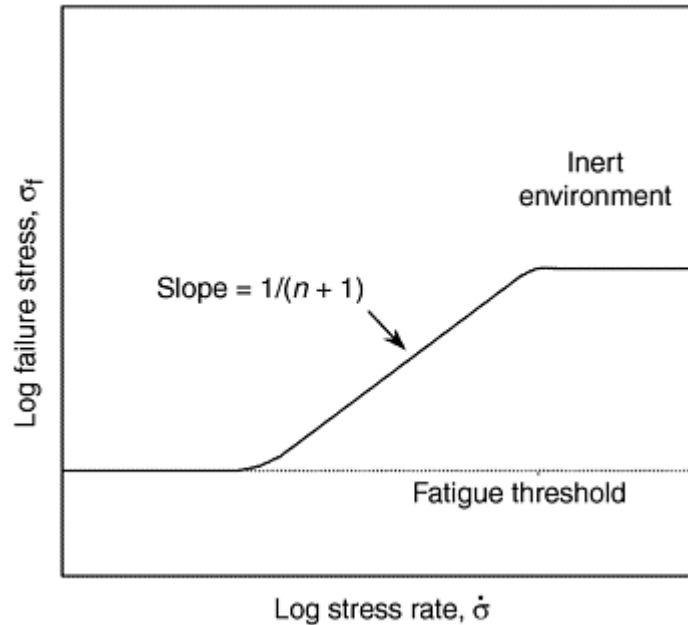


Fig. 4 Generalized fracture strength as a function of stress rate on a logarithmic scale for ceramics and glasses exhibiting environmentally induced slow crack growth

Two test methods have been standardized for the determination of fatigue strength by dynamic loading (Ref 15, 17). One standard (Ref 17), ASTM C 1368 “Standard Test Method for Determination of Slow Crack Growth Parameters of Advanced Ceramics by Constant Stress-Rate Flexural Testing at Ambient Temperature” also

gives detailed guidance in the calculation of the fatigue parameter n , based on Eq 2. The standard uses uniaxial flexural test specimens that are manufactured in accordance with ASTM C 1161 “Standard Test Method for Flexural Strength of Advanced Ceramics at Ambient Temperature” (Ref 64) and tested in four-point flexure. A total of 40 test specimen loaded at four stress rates that cover at least three orders of magnitude are required, with a minimum of four tests at any of the rates. An example of failure stress data as a function of the stress rate is shown in Fig. 5. The stress at fracture or fatigue strength, σ_f , is related to the stress-rate, $\dot{\sigma}$, by (Ref 57, 58):

$$\sigma_f = [B(n+1)\sigma_i^n \dot{\sigma}]^{1/n+1} \quad (\text{Eq 19})$$

where B is a parameter associated with A , n , fracture toughness, crack geometry, and loading configuration, and σ_i is the inert strength. The fatigue parameter n can be determined from the slope of a $\log \sigma_f$ versus $\log \dot{\sigma}$ plot by writing Eq 19 as:

$$\log \sigma_f = \frac{1}{n+1} \log \dot{\sigma} + \log D \quad (\text{Eq 20})$$

where

$$\log D = \frac{1}{n+1} \log [B(n+1)\sigma_i^{n-2}] \quad (\text{Eq 21})$$

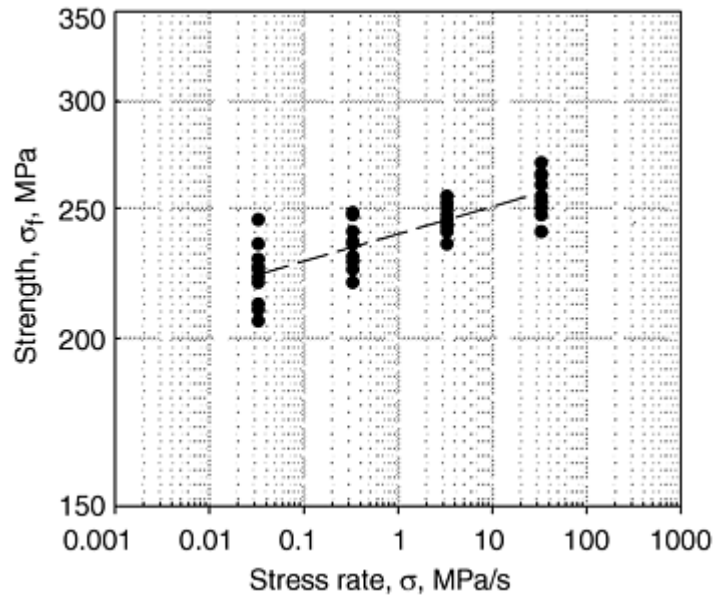


Fig. 5 Example of failure stress as a function of stress rate on a logarithmic scale for ceramics and glasses exhibiting environmentally induced slow crack growth. Adapted from Ref 17

The dependent variable is the fracture stress, and regression is performed to minimize fracture stress variation. Once the slope and intercept of Eq 20 are estimated, the parameters n and D and the standard deviation SD_n and SD_D are estimated from:

$$n = \frac{1}{\alpha} - 1 \quad (\text{Eq 22})$$

$$SD_n \approx \frac{SD_\alpha}{\alpha^2} \quad (\text{Eq 23})$$

$$D = 10^\beta \quad (\text{Eq 24})$$

$$SD_D \approx (\ln 10)(SD_\beta)(10^\beta) \quad (\text{Eq 25})$$

where α and β are the slope and the intercept, respectively, estimated by linear regression of Eq 20. These formulation follow a recently published standard (Ref 17) and provided values of n and D . For some design codes, however, the parameters B and A are necessary (Ref 60, 61, and 62). The parameter B and the standard deviation can be estimated from:

$$B = \frac{\alpha 10^{\beta/\alpha}}{\sigma_i^{-3+(1/\alpha)}} \quad (\text{Eq 26})$$

and

$$SD_B \approx \frac{10^{\beta/\alpha}}{\sigma_i^{-3+(1/\alpha)}} \left\{ \ln 10^2 SD_\beta^2 + (\alpha - \beta \ln 10 + \ln \sigma_i)^2 \times \frac{SD_\alpha^2}{\alpha^2} + \frac{(1 - 3\alpha)^2}{\sigma_i^2} \right\}^{-0.5} SD_{\sigma_i}^2 \quad (\text{Eq 27})$$

The parameter A corresponding to Eq 2 can be calculated from Eq 17aa or with the standard deviation of A from:

$$A = \frac{2K_{Ic}^2 (\hat{\sigma}_i)^{-3+(1/\alpha)}}{10^{\beta/\alpha} (1 - 3\alpha) Y^2} \quad (\text{Eq 28})$$

$$SD_A \approx A \left\{ 4 \frac{SD_{K_{Ic}}^2}{K_{Ic}^2} + \frac{(\ln 10)^2}{\alpha^2} SD_\beta^2 + \left(\frac{1}{\alpha} - 3 \right)^2 \times \frac{SD_{\sigma_i}^2}{\sigma_i^2} + \left[\alpha - \beta \ln 10 + \ln \sigma_i - \left(\frac{1}{\alpha} - 3 \right)^{-1} \right]^2 \times \frac{SD_\alpha^2}{\alpha^4} \right\}^{-0.5} \quad (\text{Eq 29})$$

In order to verify that the dynamic fatigue methodology is sufficiently robust for industrial use in the development of design data, several round-robin test programs have been performed (Ref 65, 66, 67, and 68). One round-robin involved dynamic fatigue testing of eight ceramic materials (Ref 65), with a given material being tested by only one research institute and one manufacturer. A total of 30 specimens were tested in distilled water at three to four stress rates ranging from 10^{-2} to 10 MPa/s. In addition, the inert strength and Weibull modulus were measured at 100 MPa/s. As Fig. 6 illustrates, good agreement occurred between the research and industrial laboratories for materials with a low fatigue parameter, n , but poor agreement for materials with a high fatigue parameter. It was believed that increasing the number of test specimens would improve the results, as a single data point tended to have an unduly large effect on the slope for materials with high n values.

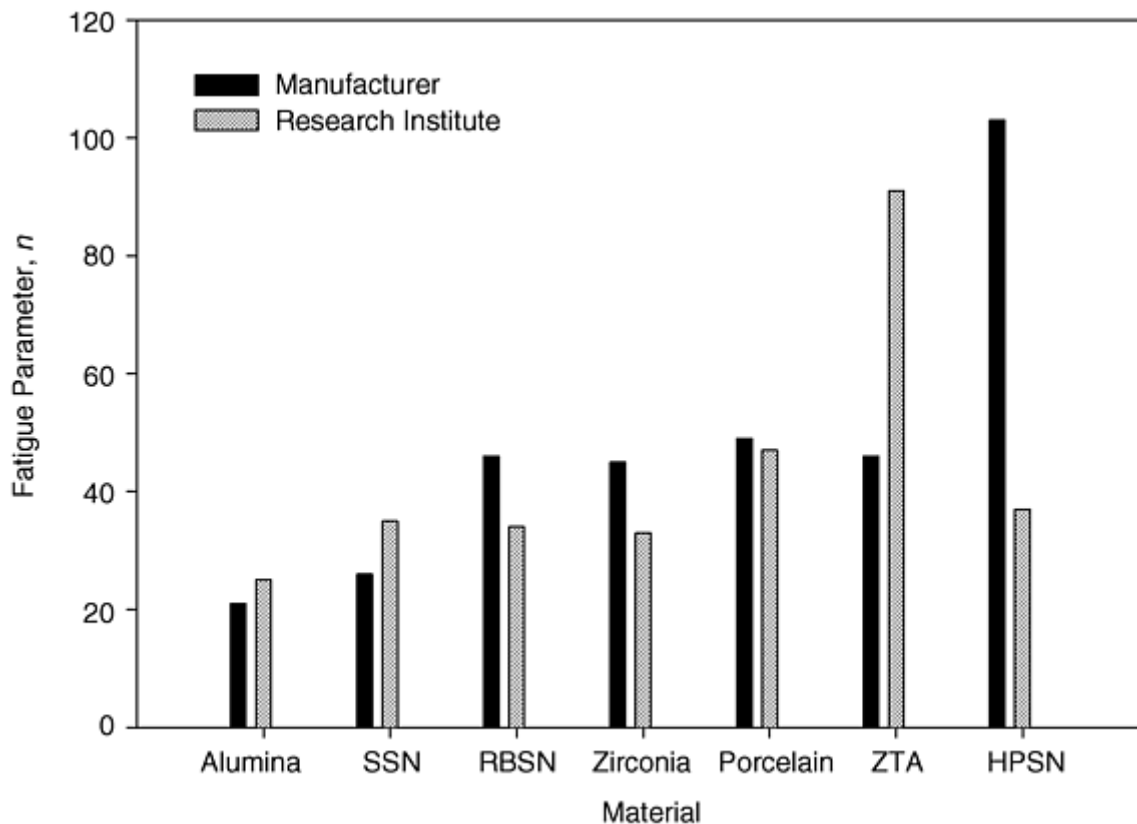


Fig. 6 Round-robin results comparing fatigue parameters of various ceramics determined by using dynamic loading. SSN, sintered silicon nitride; RBSN, reaction-bonded silicon nitride; ZTA, zirconia-toughened alumina; HPSN, hot pressed silicon nitride. Source: Ref 66

A second round-robin tested alumina flexure specimens in distilled water (Ref 66, 67). The participants were instructed to test 15 specimens in the as-received condition and 15 specimens with a 5 kg indentation. Most participants covered less than two orders of magnitude in the stress rate, and the combined participant data covered nearly five orders of magnitude. Figure 7 summarizes the fatigue parameters generated by the participants for the as-received condition. Generally, the results improve as the number of specimens increases from 15 to 33. However, even 33 test specimens can be inadequate. Most troublesome is the fact that the fatigue parameter has been overestimated two out of three times. If the data points that appear to be outliers are removed, a slight improvement results, as shown in Fig. 8. Although the final recommendations from the round-robin were not published, the initial recommendations were that at least three orders of magnitude be covered. Also, for testing at rates greater than 100 MPa/s, a piezoelectric load cell was recommended.

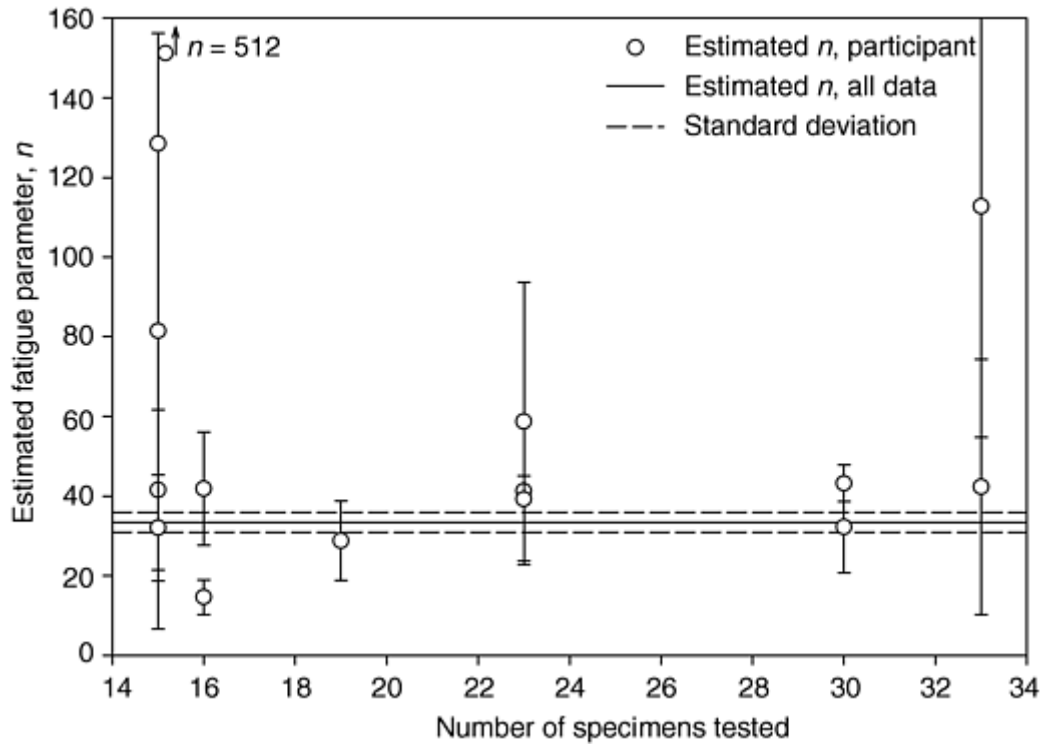


Fig. 7 Round-robin results comparing estimated fatigue parameters measured by dynamic loading of an alumina in distilled water

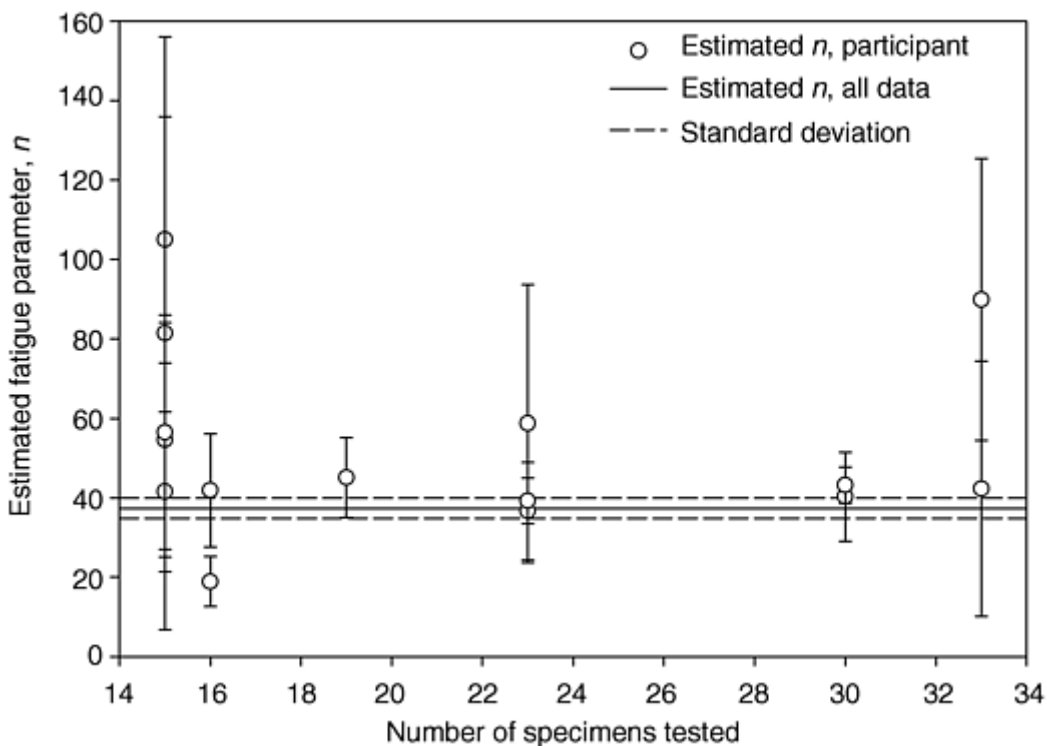


Fig. 8 Round-robin results comparing estimated fatigue parameters for an alumina in distilled water. Outlying data were censored.

The effect of the range of the stress rate can be seen in Fig. 9. If three orders of magnitude are covered, the estimated value of n improves somewhat; however, more data are needed. It is not effective to increase the number of tests without increasing the stress range. For example, one data set consisting of 33 tests measured over 2.4 orders of magnitude still resulted in an estimated fatigue parameter three times greater than that for all the data. Based on these results, it appears that at least 30 specimens and three orders-of-magnitude separation

are required. Better results from a statistical viewpoint could be attained by testing $\frac{1}{2}$ of the specimens at the lowest rate and $\frac{1}{2}$ at the highest rate (Ref 63).

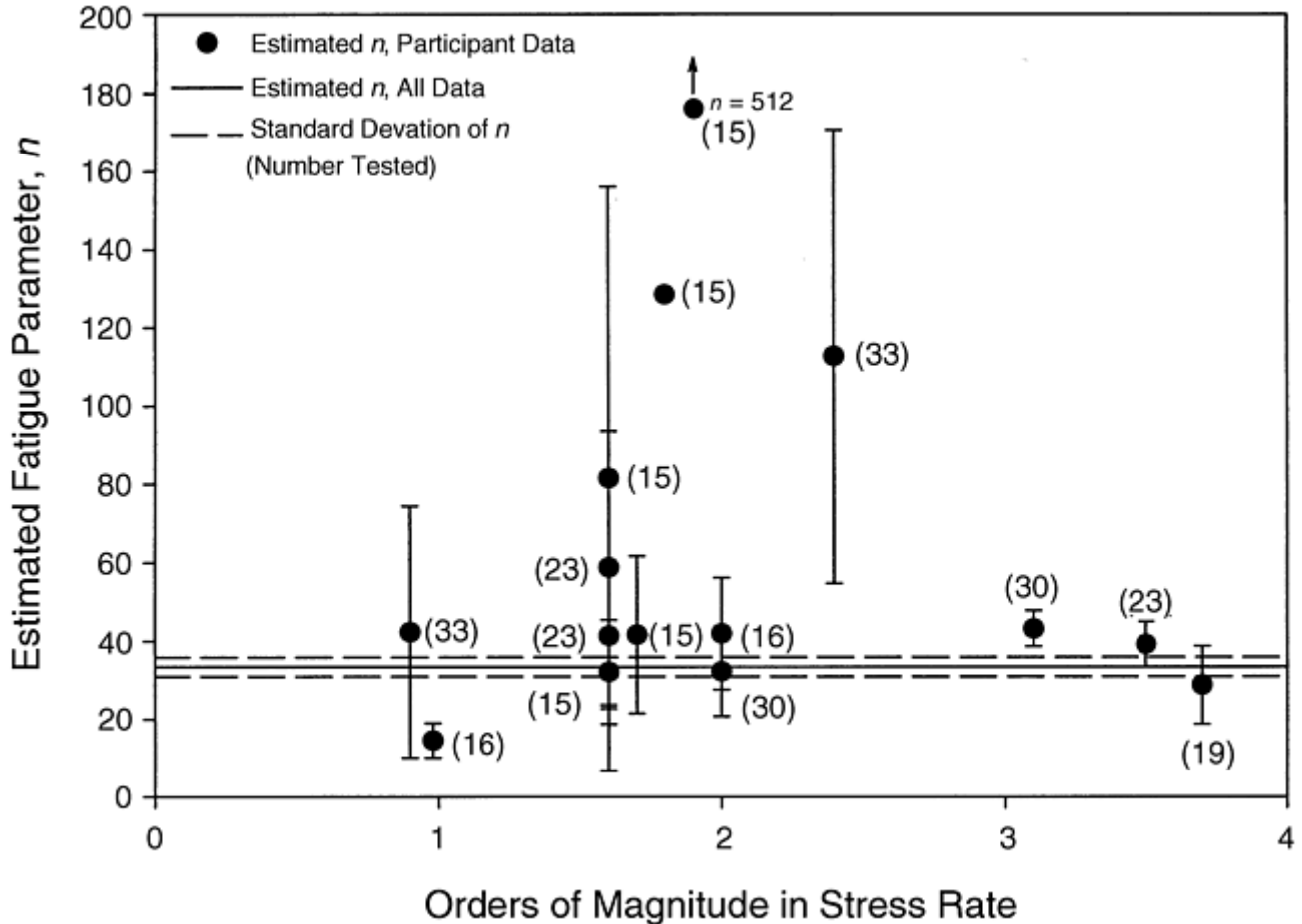


Fig. 9 Round-robin results comparing estimated fatigue parameters for an alumina tested in distilled water. Numbers in parentheses represent the number of specimens tested.

The round-robin results prompted the National Physical Laboratory to sponsor a follow-up, United Kingdom only, round-robin (Ref 68). This led to another testing standard, ENV 843-3 “Determination of Subcritical Crack Growth Parameters from Constant Stressing Rate Flexural Strength Tests” (Ref 15).

Cyclic Loading. Cyclic loading of ceramics and glasses has been performed for quite some time (e.g., Ref 1). Initial results on glasses and materials with glass boundaries indicated little synergy of cycling on the life. Thus, simpler test methods such as static and dynamic loading have generally been used, and the analysis adjusted to account for load variation (Ref 45). However, as ceramics materials have been made less glasslike by devitrification treatments and have been toughened by elongating the grain structure, transformation toughening, or adding second phase particles, cyclic loading has been recognized as a significant issue (Ref 22, 23, 24, 25, 26, 27, 28, 29, 30, 31, and 32), and fatigue effects independent of the environment have been measured.

Two testing methods have been standardized for the determination of cyclic fatigue strength of ceramics (Ref 16, 19). The standards focus on the method of data generation and give no guidance on how the data are to be used. The two standards are somewhat complementary because one uses flexure of rectangular beam (Ref 16), while the other uses uniaxial tension (Ref 19).

Test method JIS R 1621 “Testing Method for Bending Fatigue of Fine Ceramics” (Ref 16) recommends applying a 20 Hz sinusoidal wave with an R -ratio of 0.1 to standard three- or four-point flexure configurations (Ref 56). Other waveforms and frequencies are allowed. Three tests at three different maximum stress levels that result in specimen fracture before 10^7 cycles are recommended. If three tests in a row result in lives greater than 10^7 cycles, the remaining tests are conducted at a higher stress. The initial stress level is based on the monotonic strength of the materials as measured with the same specimen and testing configuration. Testing can

be halted after 10^7 cycles. An example of failure stress data as a function of the applied cycles is shown in Fig. 10.

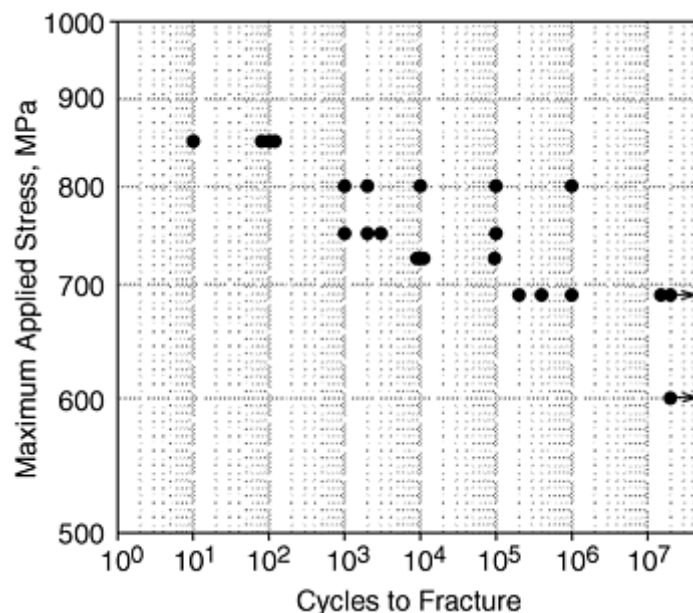


Fig. 10 Example of the cycles to fracture for a ceramic material subjected to cyclic loading. Adapted from Ref 16

Axial cyclic tensile fatigue testing can be performed with ASTM C 1361 “Standard Practice for Constant-Amplitude, Axial Tension-Tension Cyclic Fatigue of Advanced Ceramics at Ambient Temperatures” (Ref 19). Any of the tensile test specimens specified in ASTM C 1273 “Standard Test Method for Tensile Strength of Monolithic Advanced Ceramics at Ambient Temperatures” (Ref 69) are allowed. These include a variety of cylindrical button-head specimens, pin-loaded dog-bone specimens, and shoulder-loaded dog-bone specimens. The standard allows any frequency, waveform, and R ratio as needed for a particular application. A test may be terminated for any of four reasons: specimen fracture, reaching a predetermined number of run-out cycles, reaching a predetermined specimen compliance or material elastic modulus, or reaching a predetermined phase lag between control mode and response.

Tension-compression cyclic fatigue has been attained by use of the button-head tensile specimen and a clamping and alignment fixture (Ref 39). Fully reversed bending fatigue can also be attained with flexure specimens by use of two symmetric sets of load and support pins (Ref 70).

Another cyclic fatigue test method that has been applied to ceramics is rotary bending (Ref 71, 72). This approach is particularly relevant to applications involving shafts, such as ceramic turbocharger rotors. The method avoids problems associated with edge finish by using cylindrical specimens, and a wide range of frequencies is easily attained. Tests run on alumina and silicon nitride at 57 Hz indicate a linear $S-N$ curve to 10^7 cycles at which an indistinct knee occurs, implying a fatigue limit at $\sim 10^8$ cycles. The endurance stress corresponded to about $\frac{1}{4}$ of the strength of the alumina and about $\frac{1}{2}$ that of the silicon nitride. The fatigue parameter n was 13 for the alumina and 25 for the silicon nitride, respectively, which is lower than those typically determined for aluminas and silicon nitrides by static or dynamic techniques. The differences in the fatigue parameters were attributed to the effect of reversed bending.

Cyclic fatigue of ceramics has also been performed by using cantilever bending of rectangular, dog-bone, and tapered-beam test specimens at a variety of frequencies. Tapered beams and dog-bone specimens reduce the probability that failure will occur at the support where the stress is a maximum. Figure 11 illustrates a tapered-cantilever beam used to obtain 3000 Hz accelerated fatigue data on silicon nitride (Ref 39).

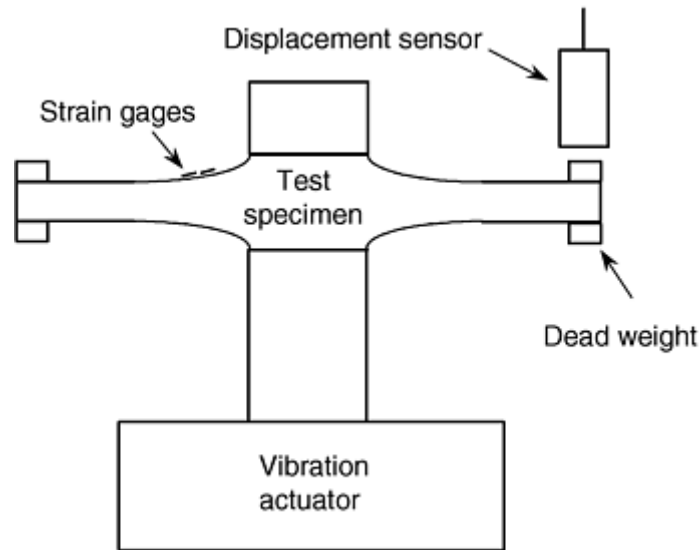


Fig. 11 Schematic of a high-frequency, tapered-cantilever beam test apparatus. Source: Ref 39

Testing of silicon nitride using tapered-cantilever beams at frequencies as high as 3000 Hz indicated a fatigue limit at 40% of the monotonic strength (Ref 39). Interestingly, the life depended on the number of cycles rather than the time and was well described by the modified Goodman diagram used to describe metallic fatigue. The probability of failure was well described by the Weibull model. Axial tension-compression testing of the same sintered silicon nitride indicated a fatigue limit around 10^7 cycles at a stress of 60% of the strength and an increase in fatigue strength with increasing R ratio. The implication for this particular silicon nitride is that a cyclic effect, rather than environmentally induced stress corrosion, dominated crack growth.

Tests using dog-bone specimens at 30 Hz (Ref 73) indicated no effect of cycling on the strength of two different silicon nitrides for less than 10^7 cycles; however, relatively few specimens were tested. At temperatures of 1200 and 1300 °C (2190 and 2370 °F), the effects of fatigue were more pronounced.

In contrast to the reversed fatigue results, tension-tension flexure fatigue of reaction-bonded, hot pressed, and sintered silicon nitrides indicated environmentally related crack growth to be the failure-controlling mechanism (Ref 74).

Fatigue testing of magnesia-partially-stabilized zirconia by using straight cantilever beams indicated a fatigue limit around 10^8 cycles at a stress of 50% of the tensile strength (Ref 40). Reversed loading significantly shortened the life of the material as compared with tension-tension loading.

Generally, servohydraulic actuators are used to generate cyclic fatigue loading of test specimens. However, piezoelectric actuators in the form of stacks and cantilever spring plates also have been used (Ref 75, 76). These systems allow relatively high frequencies (30 to 550 Hz) and compact test frames that do not require a hydraulic pressure source. Figure 12 illustrates the test apparatuses.

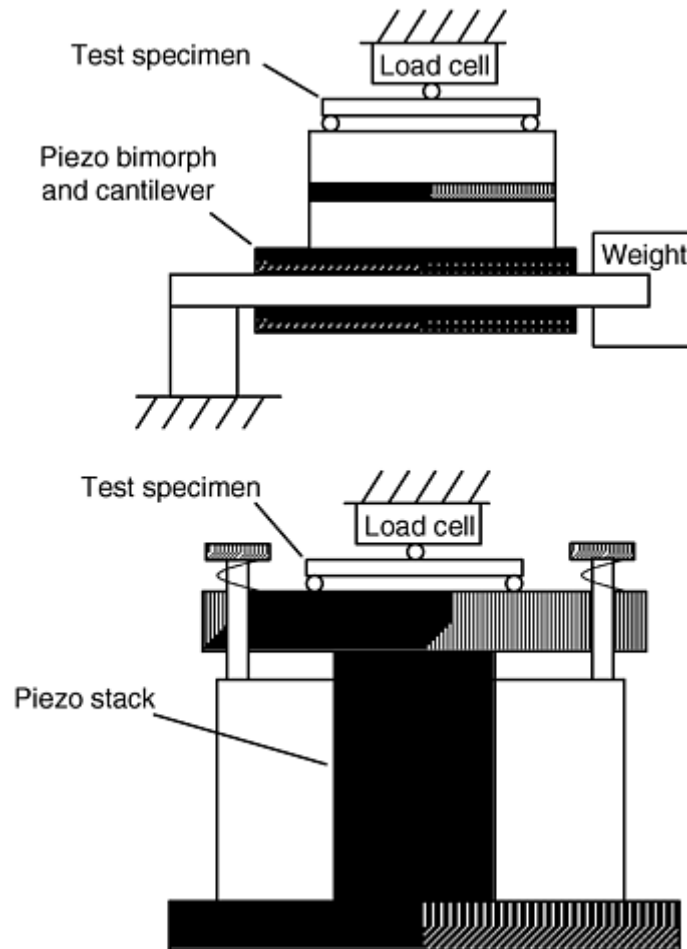


Fig. 12 Schematics of test apparatuses using piezo-electric ceramics to generate fatigue loading of ceramic beam specimens. Source: Ref 75, 76

Cyclic fatigue test results indicate substantial changes in the mechanism controlling crack growth (i.e., cyclically induced versus environmentally induced) for different materials. Fatigue behavior for a given ceramic (e.g., silicon nitride) depends on factors such as the grain boundary phase, grain size, and the fracture mode (transgranular versus intergranular). Thus, fatigue testing needs to consider both environmentally induced and cyclically induced crack growth.

References cited in this section

1. C. Gurney and S. Pearson, Fatigue of Mineral Glass under Static and Cyclic Loading, *Proc. R. Soc. A.*, Vol 192, 1948, p 537–543
15. DD ENV 843-3 Advanced Technical Ceramics—Monolithic Ceramics—Mechanical Properties at Room Temperature, Part 3: Determination of Subcritical Crack Growth Parameters from Constant Stressing Rate Flexural Strength Tests, British Standards Institution, London, 1997
16. “Testing Method for Bending Fatigue of Fine Ceramics,” JIS R 1621, Japanese Standards Association, Tokyo, Japan, 1996
17. “Standard Test Method for Determination of Slow Crack Growth Parameters of Advanced Ceramics by Constant Stress-Rate Flexural Testing at Ambient Temperature,” C 1368, *Annual Book of ASTM Standards*, ASTM, Vol 15.01, 1999, p 706–714
18. “Test Methods for Static Bending Fatigue of Fine Ceramics,” JIS R 1632, Japanese Standards Association, Tokyo, Japan, Dec 1998

19. Standard Practice for Constant-Amplitude, Axial Tension-Tension Cyclic Fatigue of Advanced Ceramics at Ambient Temperatures,” C1361, *Annual Book of ASTM Standards*, ASTM
22. F. Gigu, Cyclic Fatigue of Polycrystalline Alumina in Direct Push-Pull, *J. Mater. Sci. Lett.*, Vol 13 (No. 6), 1978, p 1357–1361
23. M.V. Swain, Lifetime Prediction of Ceramic Materials, *Mater. Forum*, Vol 9 (No. 1–2), 1st and 2nd Quarter 1986, p 34–44
24. H. Kawakubo and K. Komeya, Static and Cyclic Fatigue Behavior of a Sintered Silicon Nitride at Room Temperature, *J. Am. Ceram. Soc.*, Vol 70 (No. 6), 1987, p 400–405
25. R.H. Dauskardt, W. Yu, and R.O. Ritchie, Fatigue Crack Propagation in Transformation Toughened Zirconia, *J. Am. Ceram. Soc.*, Vol 70 (No. 10), 1987, p C-248–C-252
26. G. Grathwohl, Fatigue of Ceramics under Cyclic Loading, *Mater. Sci. Technol.*, Vol 19 (No. 4), April 1988, p 113–124 (in German)
27. M.J. Reece, F. Guiu, and M.F.R. Sammur, Cyclic Fatigue Crack Propagation in Alumina under Direct Tension-compression Loading, *J. Am. Ceram. Soc.*, Vol 72 (No. 2), 1989, p 348–352
28. Y. Mutoh, M. Takahashi, T. Oikawa, and H. Okamoto, Fatigue Crack Growth of Long and Short Cracks in Silicon Nitride, *Fatigue of Advanced Materials*, R.O. Ritchie, R.H. Dauskardt, and B.N. Cox, Ed., Material and Component Engineering Publications, Ltd., Edgbaston, U.K., 1991, p 211–225
29. S. Horibe and H. Hirahara, Cyclic Fatigue of Ceramics Materials: Influence of Crack Path and Fatigue Mechanisms, *Acta Metall. Mater.*, Vol 39 (No. 6), 1991, p 1309–1317
30. M. Okazaki, A.J. McEvily, and T. Tanaka, On the Mechanism of Fatigue Crack Growth in Silicon Nitride, *Metall. Trans. A*, Vol 22A, 1991, p 1425–1434
31. T. Tanaka, N. Okabe, H. Nakayama, and Y. Ishimaru, Fatigue Crack Growth of Silicon Nitride with Crack Wedging by Fine Fragments, *Fatigue Fract. Eng. Mater. Struct.*, Vol 17 (No. 7), 1992, p 643–653
32. R.O. Ritchie, C.J. Gilbert, and J.M. McNaney, Mechanics and Mechanisms of Fatigue Damage and Crack Growth in Advanced Materials, *Int. J. Solids Struct.*, Vol 37, 2000, p 311–329
39. M. Masuda, T. Soma, M. Matsui, and I. Oda, Fatigue of Ceramics, Part 1: Fatigue Behavior of Sintered Silicon Nitride under Tension-Compression Cyclic Stress, *J. Ceram. Soc. Jpn. Int. Ed.*, Vol 96, 1988, p 275–280
40. A. Steffen, R.H. Dauskardt, and R.O. Ritchie, Cyclic Fatigue Life and Crack Growth Behavior of Microstructural Small Cracks in Magnesia-Partially-Stabilized Zirconia Ceramics, *J. Am. Ceram. Soc.*, Vol 74 (No. 6), 1991, p 1259–1268
43. S.M. Weiderhorn, Prevention of Failure in Glass by Proof-Testing, *J. Am. Ceram. Soc.*, Vol 56 (No. 4), 1973, p 227–228
45. A.G. Evans and E.R. Fuller, Crack Propagation in Ceramic Materials under Cyclic Loading Conditions, *Metall. Trans. A*, Vol 5 (No. 1), 1974, p 27–33
56. “Test Method for Flexural Strength (Modulus of Rupture) of Fine Ceramics,” JIS R 1601, Japanese Standards Association, Tokyo, Japan, 1995

57. J.E. Ritter, Jr., Assessment of Reliability of Ceramic Materials, *Fracture Mechanics of Ceramics*, Vol 6, R.C. Bradt et al., Ed., Plenum Press, 1983, p 227–251
58. J.E. Ritter, Jr., Engineering Design and Fatigue Failure of Brittle Materials, *Fracture Mechanics of Ceramics*, Vol 4, R.C. Bradt et al., Ed., Plenum Press, 1978, p 667–685
59. E.B. Haugen, *Probabilistic Mechanical Design*, John Wiley & Sons, 1980
60. N.N. Nemeth, L.M. Powers, L.A. Janosik, and J.P. Gyekenyesi, “Durability Evaluation of Ceramic Components Using CARES/LIFE,” ASME Paper 94-GT-362 and NASA-TM 106475, ASME/IGTI Gas Turbine Conference, June 1994
61. A.D. Peralta, D.C. Wu, P.J. Brehm, J.C. Cuccio, and M.N. Menon, Strength Prediction of Ceramic Components under Complex Stress States, *Proceedings of the International Gas Turbine and Aeroengine Congress and Exposition*, 5–8 June 1995 (Houston, TX), American Society of Mechanical Engineers, 1995; Allied Signal Document 31-12637, 1995
62. “Fatigue Crack Growth Program NASA/Flagro 2.0,” JSC 22267A, NASA Johnson Space Flight Center, May 1994
63. J.E. Ritter, N. Bandyopadhyay, and K. Jakus, *Am. Ceram. Soc. Bull.*, Vol 60, 1981, p 798
64. “Standard Test method for Flexural Strength of Advanced Ceramics at Ambient Temperature,” C 1161, *Annual Book of ASTM Standards*, ASTM, Vol 15.01, 1999, p 309–315
65. H.A. Linders and B. Caspers, Method for Determining Life Diagrams of Mechanoceramic Materials DKG/DKM-Joint Experiment, *Ceramics in Science and Practice, Mechanical Properties of Ceramic Construction Materials*, G. Grathwohl, Ed., DGM Information Association, Verlag, Germany, 1993, p 191–195 (in German)
66. S. Freiman, “Pre-Standardization and Standardization Activities in the USA in Mechanical Property Testing of Advanced Structural Ceramics,” presentation at the 7th CIMTEC World Ceramics Congress, Montecatini Terme, Italy, 23 June 1990
67. S.W. Freiman and E.R. Fuller, Versailles Project on Advanced Materials and Standards, VAMAS TWA 3 Bulletin 8, July 1988
68. W.P. Byrn and R. Morrell, “Results of the UK Interlaboratory Strength Test Exercise,” NPL Report DMM (D) 72, National Physical Laboratory, Teddington, Middlessex, U.K., Crown Copyright, Dec 1990
69. “Standard Test Method for Tensile Strength of Monolithic Advanced Ceramics at Ambient Temperatures,” C 1273, *Annual Book of ASTM Standards*, Vol 15.01, ASTM, 1999, p 671–678
70. Cyclic Fatigue Testing of Silicon Nitride, *Ceramics* (newsletter), Ceramics Division of IIT Research Institute, Chicago, IL, 42, March 1978; *Ceram. Eng. and Sci. Proc. of the 18th Annual Conference on Composites and Advanced Ceram. Mater.-A*, Part 1 of 2, 9–14 Jan 1994, Vol 15 (No. 4), July–Aug 1994 (Cocoa Beach, FL), *Am. Ceram. Soc.*, Westerville, OH, 1994, p 32–39
71. H.N. Ko, Cyclic Fatigue Behavior of Ceramics under Rotary Bending, *Materials Research Society International Meeting on Advanced Materials*, Materials Research Society, Vol 5, 1989, p 43–48
72. H.N. Ko, Cyclic Fatigue Behavior of Sintered Al₂O₃ under Rotary Bending, *J. Mater. Sci. Lett.*, Vol 6, 1987, p 801–805

73. R. Kossowsky, "Cyclic Fatigue of Hot Pressed Silicon Nitride," *J. Am. Ceram. Soc.*, Vol 56, 1973, p 10, 531–535
74. Y. Matsuo, Y. Hattori, Y. Katayama, and I. Fukuura, Cyclic Fatigue Behavior of Ceramics, *Progress in Nitrogen Ceramics*, F.L. Riley, Ed., Martinus Nijhoff, 1983, p 515–522
75. K. Ohya, K. Ogura, and M. Takatsu, Effect of Loading Waveform on Cyclic Fatigue Behavior of PSZ, *J. Soc. Mater. Sci., Jpn.*, Vol 38 (No. 425), 1989, p 144–148
76. K. Ohya, K. Ogura, and M. Takatsu, Cyclic Fatigue Testing Device for Fine Ceramics by Using Piezo-Electric Bimorph Actuator, *J. Soc. Mater. Sci., Jpn.*, Vol 38 (No. 424), 1989, p 44–48

Fatigue Testing of Brittle Solids

J.A. Salem, Glenn Research Center at Lewis Field; M.G. Jenkins, University of Washington

Fracture Mechanics Methods

Fracture mechanics methods or "direct" methods generally employ test specimens with relatively large, induced cracks. Crack growth data is typically determined directly by observation of the crack or by devices that monitor test specimen compliance, such as clip gages and strain gages (Ref 77, 78). One exception to this is the double torsion specimen, which has a relatively constant stress-intensity factor, K_I , over a wide range of crack length. Thus, the K_I can be calculated without observation of the crack length. When used in this fashion, the method is effectively an indirect, long crack method.

Two general types of fracture mechanics specimen are employed: line loaded or flexural specimens. Line-loaded specimens such as the double torsion (DT), double-cantilever beam (DCB), or compact tension (CT) allow cracks to be extended over large distances. Flexural specimens such as notched and precracked beams can be scaled so that crack length is comparatively small or large.

The main advantage of fracture mechanics specimens is that large amounts of data can be derived from a single test specimen, and the results are not subject to the scatter associated with the natural flaw distribution that is sampled by strength techniques. However, as the cracks are large in comparison with those developed naturally in smooth specimens, the fatigue behavior may be different. In particular, for materials that exhibit transformation toughening or for materials with a coarse or elongated grain structure, a strong effect of crack length on crack growth resistance is exhibited. Figure 13 shows the effect of crack growth resistance on the stress-intensity factor for both long and short crack lengths. Although the same range of stress-intensity factors is measured, the rates at which resistance develops, and possibly the rate at which fatigue damages the resistance, are very different. Thus, techniques that use different crack length scales may result in different fatigue parameters.

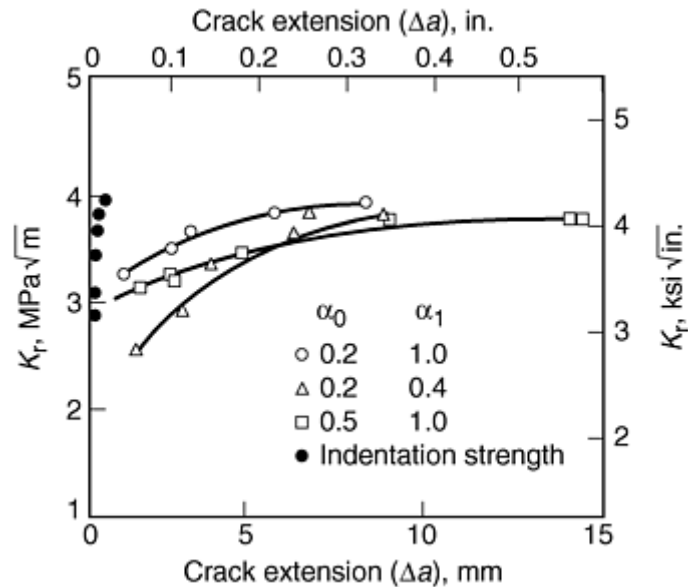


Fig. 13 Crack growth resistance as a function of crack extension for alumina

The Double Torsion Method. The double torsion method, which was developed by Outwater and Gerry (Ref 79, 80) and developed further by other researchers (Ref 81, 82, 83, 84, 85, 86, 87, 88, and 89) is illustrated in Fig. 14. Detailed experimental and analytical analyses of the specimen have been given by Fuller (Ref 88) and Pletka et al. (Ref 89). Tests can be performed with or without a guide groove on one or both sides of the specimen. However, the use of a guide groove can lead to errors (Ref 90, 91), and elimination of the groove can be achieved by using thin, carefully aligned specimens. If side grooves must be used, wide grooves and thinner specimens help to avoid interaction between the groove wall and the crack.

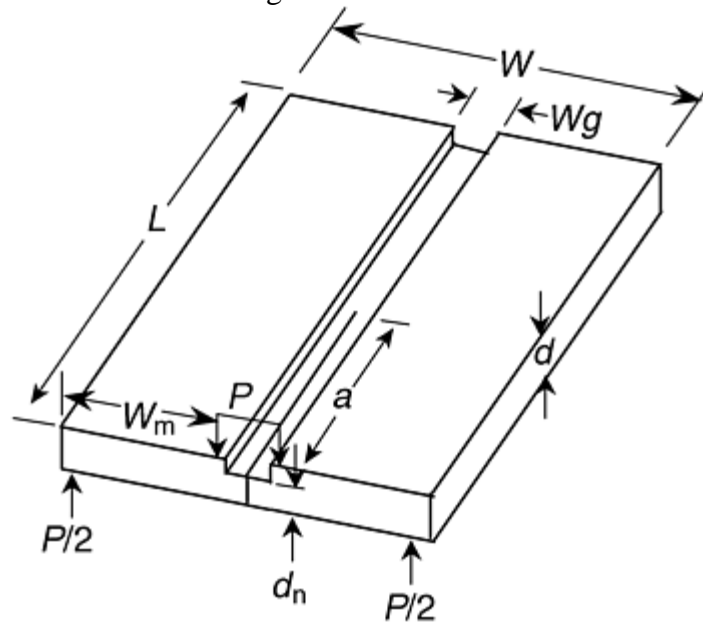


Fig. 14 Schematic of the double torsion test specimen. Source: Ref 88

A variety of complications associated with the test specimen have been discussed and analyzed to varying degrees. These include crack front curvature leading to a variation in the stress-intensity factor along the crack front; variation in the stress-intensity factor with crack length; and poor reproducibility of data for certain conditions, particularly for polycrystalline ceramics when multiple load relaxations are performed with the same specimens.

Most noteworthy is the last of the problems just noted, as opposite trends have been observed for different materials. It seems that the crack-microstructure interactions, which are more prevalent for long cracks, may be the source of discrepancy.

Despite the complication associated with the DT, it does provide a simple geometry that is easy to load and crack. Further, for testing of opaque materials or for hostile environments, the constant stress-intensity factor is advantageous.

The stress-intensity factor for the DT method is (Ref 89):

$$K_{I dt} = PW_m \sqrt{\frac{3}{Wd^3 d_n (1 - \nu) \xi}} \quad (\text{Eq 30})$$

with:

$$\xi = 1 - 0.6302t + 1.20t \exp(-\pi/t)$$

where P is the applied force, W_m is half the test specimen width minus half the notch width, d is the total thickness, d_n is the notch depth, W is the total width, ν is Poisson's ratio, and ξ is a correction factor for thick test specimens where $t = 2d/W$. It has been recommended that the crack length be maintained between $W < a < L - W$, where a is the crack length and L is the length, to ensure that the crack is in the constant K_I region (Ref 88).

Three methods of loading DT specimens have been developed: constant load, constant displacement (Ref 83, 84) and load relaxation. The load relaxation technique has the advantage that less crack extension is required to obtain an accurate measure of crack velocity and stress intensity factor (Ref 88).

In the load relaxation technique, a precracked specimen is loaded rapidly in a displacement control mode (~ 0.2 to 0.5 mm/min, or ~ 0.01 to 0.02 in./min) to nearly the load required to cause specimen fracture. If the crack begins to move rapidly, the displacement is halted and the load is recorded as a function of time. Once the crack has stopped apparent movement, the test specimen is removed and the final crack length measured. The stress-intensity factor at any load is calculated from Eq 30, and the crack velocity from the slope of the load-time curve and either the specimen displacement or the crack length and load before or after the test (Ref 91):

$$v = \frac{da}{dt} = - \frac{Wt^3 Ey}{6W_m P^2 (1 + \nu)} \left(\frac{dP}{dt} \right)_y \quad (\text{Eq 31})$$

$$v = \frac{da}{dt} = - \frac{P_{i,f} a_{i,f}}{P^2} \left(\frac{dP}{dt} \right)_y \quad (\text{Eq 32})$$

where E is Young's modulus, P_i and a_i are the initial load and crack length values, respectively, and P_f and a_f are the values at the end of the relaxation.

The DCB Method. The double-cantilever beam (DCB) specimen has been used to test glass, sapphire, magnesium fluoride, and various polycrystalline ceramics (Ref 8, 14, 91, 92, and 93). Also, a form of the DCB specimen referred to as the *compact tension* has been standardized for fracture toughness testing of metals (Ref 52). A variety of methods can be used to apply load to the DCB specimen. These include wedge loading and the application of a constant moment (Ref 94). If a constant K_I is desired, the specimen can be tapered (Ref 95). Often, side grooves are used to guide the crack longitudinally. For the geometry shown in Fig. 15, the stress-intensity factor and fracture toughness can be determined from:

$$K_I = \frac{Pa}{h^{3/2} \sqrt{Bb}} \left(3.47 + 2.32 \frac{h}{a} \right) \quad (\text{Eq 33})$$

where P is the applied force, h is half height of the test specimen, B is the thickness of the test specimen, b is the Web thickness, and a is the crack length. Some advantages of this geometry are the constant stress-intensity factor for some configurations (e.g., tapered DCB or applied moment DCB), simple test specimen preparation, efficient material usage, and the simple loading configuration. The primary disadvantages are effects associated with the side groove and the difficulty of introducing a sharp crack.

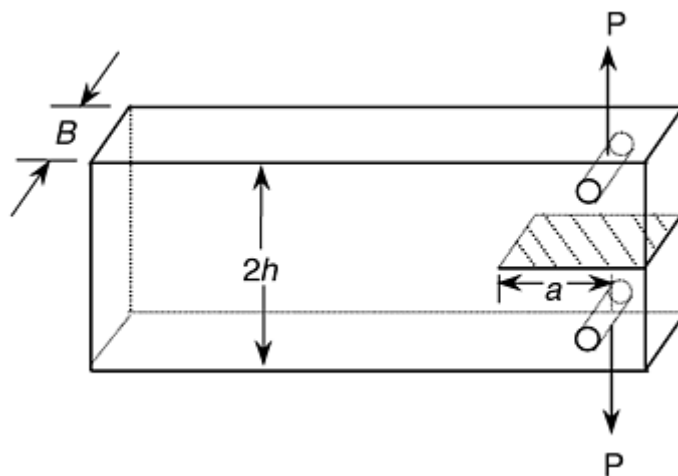


Fig. 15 Double-cantilever beam (DCB) test specimen (Ref 8). Slots on both sides of the specimen for restraining the crack to the midplane are not shown.

Generally, crack growth measurements are made by optical observation of the crack on the side of the specimens while a constant load is applied. For glass, good agreement between DCB and strength measurements (Ref 8, 91) and between DCB and DT measurements have been obtained (Ref 86, 96).

Cyclic Fatigue by Other Fracture Mechanics Methods. Cyclic fatigue measurement using the direct or fracture mechanics approach can be classified into two crack-length regimes: long cracks made by using large specimens that are typically applied in metals testing (e.g., compact tension) or shorter cracks generated by indentation with Knoop or Vickers hardness indenters (Fig. 16). Both the DT and DCB, however, can be loaded cyclically.

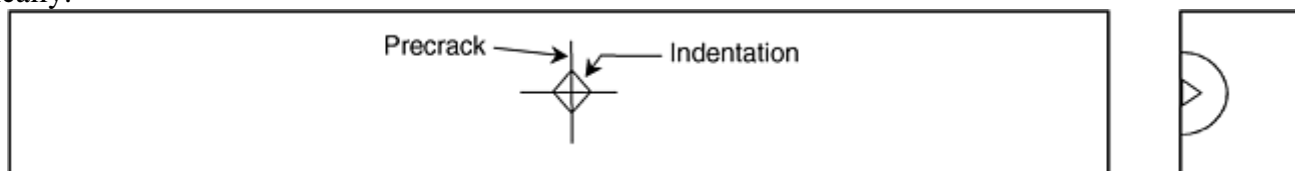


Fig. 16 Flexure test specimen with a precrack formed by Vickers indentation

Both crack-length regimes have advantages and disadvantages. The core issue for both approaches is whether the behavior in real applications is represented. For long cracks this is basically an issue of scale, while for the short, indentation cracks, the residual stress field about the indentation and its changes during fatigue are an issue.

Probably the simplest method of long crack testing is the use of the single-edge-precracked-beam (SEPB) specimen. A precrack is formed by bridge indentation (Ref 97) and loaded in three- or four-point flexure. The crack extension can be monitored directly on the specimen sides, or by compliance measurements via extensometers, clip gages, strain gages (Ref 77, 78), or electrical grids (Ref 98, 99).

This method has been used to generate long crack fatigue data for silicon nitride in vacuum and air (Ref 30). The results indicate lower threshold stress-intensity factors for cyclic loading or air as compared with static loading or vacuum. The threshold is also a function of crack length and thus related to the crack growth resistance mechanism. No dependence on frequency was found between 0.5 and 20 Hz, however, and an effect of R -ratio was found.

The compact tension specimen has been used frequently to test ceramics (Ref 25, 33, 100, and 101), and long-crack data have been generated for comparison with short-crack data for materials such as SiC-whisker-reinforced alumina, pyrolytic carbon, and magnesia-partially-stabilized zirconia.

For magnesia-partially-stabilized zirconia, fatigue measurements with long cracks indicate a threshold at ~50% of the fracture toughness and the slowest growth rates for the materials with the most transformation toughening. However, for short, naturally developing cracks, growth occurs below the long-crack threshold, and, as with metals, a negative dependency of growth rate on stress intensity is exhibited.

Short fatigue crack testing of many ceramics is complicated by the infrequent development of natural cracks and the difficulty of detecting such cracks. This difficulty can be circumvented by precracking the polished

surface of a beam with a Vickers or Knoop indenter. The crack size during static or cyclic loading in four-point or cantilever flexure is monitored optically or via electron microscopy (Ref 29, 100, and 101). Multiple cracks can be placed on a single specimen.

Ideally, short cracks without the residual stress should be used, as is done in standardized fracture toughness testing (Ref 102). This can be accomplished by polishing the specimen until a sufficient amount of the indentation and crack has been removed.

A number of more exotic methods, such as compressive cyclic fatigue of notched specimens, have also been used to demonstrate cyclically induced fatigue in ceramics (Ref 103, 104).

References cited in this section

8. S.M. Weiderhorn and L.H. Boltz, Stress Corrosion and Static Fatigue of Glass, *J. Am. Ceram. Soc.*, Vol 62 (No. 7–8), 1970, p 547–548
14. T.A. Michalske, B.C. Bunker, and S.W. Freiman, Stress Corrosion of Ionic and Mixed Ionic/Covalent Solids, *J. Am. Ceram. Soc.*, Vol 69 (No. 10), 1986, p 721–724
25. R.H. Dauskardt, W. Yu, and R.O. Ritchie, Fatigue Crack Propagation in Transformation Toughened Zirconia, *J. Am. Ceram. Soc.*, Vol 70 (No. 10), 1987, p C-248–C-252
29. S. Horibe and H. Hirahara, Cyclic Fatigue of Ceramics Materials: Influence of Crack Path and Fatigue Mechanisms, *Acta Metall. Mater.*, Vol 39 (No. 6), 1991, p 1309–1317
30. M. Okazaki, A.J. McEvily, and T. Tanaka, On the Mechanism of Fatigue Crack Growth in Silicon Nitride, *Metall. Trans. A*, Vol 22A, 1991, p 1425–1434
33. R. Dauskardt, Cyclic Fatigue-Crack Growth in Grain Bridging Ceramics, *J. Eng. Mater. Technol. (Trans. ASME)*, Vol 115, 1993, p 115–251
52. “Standard Test Method for Plane Strain Fracture Toughness of Metallic Materials,” E 399, *Annual Book of ASTM Standards*, Vol 03.01, ASTM, 1998
77. J.A. Salem, L.J. Ghosn, and M.G. Jenkins, A Strain Gage Technique to Measure Stable Crack Extension in Ceramics, *Post Conference Proceedings of the 1997 SEM Spring Conference on Experimental Mechanics*, Society for Experimental Mechanics, Bethel, CT, 1997, p 1–8
78. J.A. Salem, L.J. Ghosn, and M.G. Jenkins, Back-Face Strain as a Method for Monitoring Stable Crack Extension in Ceramics, *Ceram. Eng. Sci. Proc.*, Vol 19 (No. 3), 1998, p 587–594
79. J.O. Outwater and D.J. Gerry, “On the Fracture Energy of Glass,” NRL Interim Contract Report, Contract NONR 3219(01)(x), AD 640848, University of Vermont, Burlington, VT, Aug 1966
80. J.O. Outwater and D.J. Gerry, “On the Fracture Energy, Rehealing Velocity and Fracture Energy of Cast Epoxy Resin,” Paper 13-D, presented at the 22nd Society of Plastic Industry Conference, 1967; also, *J. Adhes.*, Vol 1, 1969, p 290–298
81. G.W. Weidmann and D.G. Holloway, Slow Crack Propagation in Glass, *Phys. Chem. Glasses*, Vol 15 (No. 5), Oct 1974, p 116–122
82. C.D. Beacham, J.A. Kies, and B.F. Brown, A Constant K Specimen for Stress Corrosion Cracking Testing, *Mater. Res. Standards*, Vol 11, 1970, p 30
83. A.G. Evans, Method For Evaluating the Time-Dependent Failure Characteristics of Brittle Material and Its Application to Polycrystalline Alumina, *J. Mater. Sci.*, Vol 7 (No. 10), 1972, p 1137–1146

84. A.G. Evans and S.M. Wiederhorn, Crack Propagation and Failure Prediction in Silicon Nitride at Elevated Temperatures, *J. Mater. Sci.*, Vol 9, 1974, p 270–278
85. A.G. Evans, L.R. Russel, and D.W. Richerson, Slow Crack Growth in Ceramic Materials at Elevated Temperatures, *Metall. Trans. A*, Vol 6A (No. 14), 1975, p 707–716
86. K.R. McKinney and H.L. Smith, Method of Studying Subcritical Cracking of Opaque Materials, *J. Am. Ceram. Soc.*, Vol 56 (No. 1), 1973, p 30–32
87. P.N. Thornby, Experimental Errors in Estimating Times to Failures, *J. Am. Ceram. Soc.*, Vol 59 (No. 11–12), 1976, p 514–517
88. E.R. Fuller, Jr., an Evaluation of Double Torsion Testing: Analysis, *Fracture Mechanics Applied to Brittle Materials*, STP 678, S.W. Frieman, Ed., ASTM, 1979, p 3–18
89. B.J. Pletka, E.R. Fuller, Jr., and B.G. Koepke, An Evaluation of Double Torsion Testing: Experimental, *Fracture Mechanics Applied to Brittle Materials*, STP 678, S.W. Frieman, Ed., ASTM, 1979, p 19–37
90. C.G. Annis and J.S. Cargill, Modified Double Torsion Method for Measuring Crack Velocity in NC-132 Si_3N_4 , *Fracture Mechanics of Ceramics*, Vol 4, R.C. Bradt et al., Ed., Plenum Press, 1978, p 737–744
91. D.P. Williams and A.G. Evans, A Simple Method for Studying Slow Crack Growth, *J. Test. Eval.*, Vol 1 (No. 4), 1973, p 264–270
92. K.R. Linger and D.G. Holloway, Fracture Energy of Glass, *Philos. Mag.*, Vol 18 (No. 156), 1968, p 1269–1280
93. J.A. Salem, M.G. Jenkins, M.K. Ferber, and J.L. Shannon, Jr., Effects of Pre-Cracking Method on Fracture Properties of Alumina, *Proceedings of Society of Experimental Mechanics Conference on Experimental Mechanics*, 10–13 June 1991 (Milwaukee, WI), Society for Experimental Mechanics, Bethel, CT, 1991, p 762–769
94. S.W. Freiman, D.R. Mulville, and P.W. Mast, *J. Mater. Sci.*, Vol 8 (No. 11), 1973, p 1527–1533
95. S. Mostovoy, P.B. Crosley, and E.J. Ripling, Use of Crack-Line-Loaded Specimens for Measuring Plane-Strain Fracture Toughness, *J. Mat.*, Vol 2 (No. 3), Sept 1967, p 661–681
96. A.G. Evans and H. Johnson, The Fracture Stress and Its Dependence on Slow Crack Growth, *J. Mater. Sci.*, Vol 10, 1975, p 214–222
97. T. Sadahiro, Transverses Rupture Strength and Fracture Toughness of WC-Co Alloys, *J. Jpn. Inst. Met.*, Vol 45, 1981, p 291–295
98. D.J. Martin, K.W. Davido, and W.D. Scott, Slow Crack Growth Measurement Using an Electric Grid, *Am. Ceram. Soc. Bull.*, Vol 65 (No. 7), 1986, p 1052–1156
99. P.K. Liaw, H.R. Hartmann, and W.A. Lodgson, A New Transducer to Monitor Fatigue Crack Propagation, *J. Test Eval.*, Vol 11 (No. 3), 1983, p 202–207
100. R.H. Dauskardt, R.O. Ritchie, J.K. Takemoto, and A.M. Brendzel, Cyclic Fatigue in Pyrolytic Carbon-Coated Graphite Mechanical Heart-Valve Prostheses: Role of Small Cracks in Life Prediction, *J. Biomed. Mater. Res.*, Vole 28, 1994, p 791–804

101. R.H. Dauskardt, M.R. James, J.R. Porter, and R.O. Ritchie, Cyclic Fatigue-Crack Growth in a SiC-Whisker-Reinforced Alumina Ceramic Composite: Long- and Small-Crack Behavior, *J. Am. Ceram. Soc.*, Vol 75 (No. 4), 1992, p 759–771
102. “Standard Test Methods for Fracture Toughness of Advanced Ceramics,” C 1421, *Annual Book of ASTM Standards*, ASTM, Vol 15.01, 2000, p 631–662
103. L. Ewart and S. Suresh, Dynamic Fatigue Crack Growth in Polycrystalline Alumina under Cyclic Compressive Loads, *J. Mater. Sci.*, Vol 5, 1986, p 774–778
104. L. Ewart and S. Suresh, Crack Propagation in Ceramics under Cyclic Loads, *J. Mater. Sci.*, Vol 22, 1987, p 1173–1192

Fatigue Testing of Brittle Solids

J.A. Salem, Glenn Research Center at Lewis Field; M.G. Jenkins, University of Washington

Comparison of Indirect and Direct Methods

Several researchers (Ref 105, 106, and 107) have noted that indirect techniques, such as dynamic fatigue, can result in large errors in the estimated fatigue parameters of polycrystalline ceramics exhibiting environmentally induced crack growth when the failure times are relatively short. Further, such methods cannot be used to accurately predict the life of components unless some precautions are taken. For example, for a mullite with a region I fatigue parameter of $n = 41$ as measured with the double-torsion method, the use of stress rates greater than 1 MPa/s resulted in an estimated value of $n = 19$ (Ref 105). For a silicon nitride with a parameter of $n = 66$, the values estimated from dynamic fatigue was $n = 100$. Similar differences were shown to exist between flexural data and double torsion data for magnesium alumina silicate ($n = 51$ versus 84) (Ref 89, 107).

This is a result of the fact that indirect methods average all three regions of the fatigue curves into a single region, and for short duration tests, all the regions are significant. However, in a component with a long life, region I is dominant.

One exception to this is static fatigue tests, in which the failure times tend to be long and the crack growth dominated by region I. The dynamic fatigue test might be made more applicable to the generation of design data for long-term applications by using stress rates that are sufficiently slow.

References cited in this section

89. B.J. Pletka, E.R. Fuller, Jr., and B.G. Koepke, An Evaluation of Double Torsion Testing: Experimental, *Fracture Mechanics Applied to Brittle Materials*, STP 678, S.W. Frieman, Ed., ASTM, 1979, p 19–37
105. F. Sudreau, C. Olagnon, and G. Fantozzi, Lifetime Prediction of Ceramics: Importance of Test Method, *Ceram. Int.*, Vol 10, 1994, p 125–135
106. E.M. Rockar and B.J. Pletka, Fracture Mechanics of Alumina in a Simulated Biological Environment, *Fracture Mechanics of Ceramics*, Vol 4, R.C. Bradt et al., Ed., Plenum Press, 1978, p 725–735
107. Pletka and Wiederhorn, Subcritical Crack Growth in Glass-Ceramics, *Fracture Mechanics of Ceramics*, Vol 4, R.C. Bradt et al., Ed., Plenum Press, 1978, p 745–759

Fatigue Testing of Brittle Solids

J.A. Salem, Glenn Research Center at Lewis Field; M.G. Jenkins, University of Washington

Summary

Fatigue testing of ceramics and glasses is performed by either indirect or direct methods. Indirect or strength methods employ smooth tensile or flexure specimens and infer the fatigue parameters from strength measurements without crack length measurements. Direct methods employ either long cracks or short cracks, and the crack length is measured by observation of the crack or by inference from devices such as strain gages and electrical resistance grids. Long crack test specimens include fracture mechanics specimens such as the DT, DCB, CT, and SEPB. Short crack methods employ surface cracks formed by indentation, or surface cracks that develop naturally on the surface of a smooth test specimen. Structural ceramic and glass components that are designed to have long lives will fail from small cracks developed over long periods of time. The cracks will develop from either inherent processing flaws or from damage generated in component machining and handling (e.g., machining cracks). Cyclic loading, though not required to induce growth in glasses and many ceramics, tends to accelerate fatigue crack growth. Thus the measurement of fatigue parameters should be done with tests employing realistic crack sizes, environments, and the applicable load histories. As a result, the development of standardized static and cyclic fatigue test methods has revolved around the use of small, inherent flaws.

Fatigue Testing of Brittle Solids

J.A. Salem, Glenn Research Center at Lewis Field; M.G. Jenkins, University of Washington

References

1. C. Gurney and S. Pearson, Fatigue of Mineral Glass under Static and Cyclic Loading, *Proc. R. Soc. A.*, Vol 192, 1948, p 537–543
2. E.B. Shand, Experimental Study of Fracture of Glass, Part I: The Fracture Process, *J. Ceram. Soc.*, Vol 37, 1954, p 52–60
3. S. Pearson, Delayed Fracture of Sintered Alumina, *Proc. Physiol Soc.*, Vol 69, Part 12, Section B, Dec 1956, p 1293–1296
4. R.E. Mould and R.D. Southwick, Strength and Static Fatigue of Abraded Glass under Controlled Ambient Conditions, Part II: Effect of Various Abrasions and the Universal Fatigue Curve, *J. Am. Ceram. Soc.*, Vol 42, 1959, p 582–592
5. S.M. Weiderhorn, Influence of Water Vapor on Crack Propagation in Soda-Lime Glass, *J. Am. Ceram. Soc.*, Vol 50, 1967, p 407–414
6. A.G. Evans and F.F. Lange, Crack Propagation and Fracture in Silicon Carbide, *J. Mater. Sci.*, Vol 10 (No. 10), 1975, p 1659–1664
7. J.E. Ritter and J.N. Humenik, Static and Dynamic Fatigue of Polycrystalline Alumina, *J. Mater. Sci.*, Vol 14 (No. 3), 1979, P 626–632

8. S.M. Weiderhorn and L.H. Boltz, Stress Corrosion and Static Fatigue of Glass, *J. Am. Ceram. Soc.*, Vol 62 (No. 7–8), 1970, p 547–548
9. B.J.S. Wilkins and E. Dutton, Static Fatigue Limit with Particular Reference to Glass, *J. Am. Ceram. Soc.*, Vol 59 (No. 3–4), 1976, p 108–112
10. T.A. Michalske, The Stress Corrosion Limit: Its Measurement and Implications, *Fracture Mechanics of Ceramics*, Vol 5, R.C. Bradt, A.G. Evans, D.P.H. Hasselman, and F.F. Lange, Ed., Plenum Publishing Corp., 1983
11. T. Fett, K. Germerdonk, A. Grossmuller, K. Keller, and D. Munz, Subcritical Crack Growth and Threshold in Borosilicate Glass, *J. Mater. Sci.*, Vol 26, 1991, p 253–257
12. S.M. Wiederhorn, Moisture Assisted Crack Growth in Ceramics, *Int. J. Fract. Mech.*, Vol 4 (No. 2), 1968, p 171–177
13. S.M. Wiederhorn, B.J. Hockey, and D.E. Roberts, Effect of Temperature on the Fracture of Sapphire, *Philos. Mag.*, Vol 28 (No. 4), 1973, p 783–796
14. T.A. Michalske, B.C. Bunker, and S.W. Freiman, Stress Corrosion of Ionic and Mixed Ionic/Covalent Solids, *J. Am. Ceram. Soc.*, Vol 69 (No. 10), 1986, p 721–724
15. DD ENV 843-3 Advanced Technical Ceramics—Monolithic Ceramics—Mechanical Properties at Room Temperature, Part 3: Determination of Subcritical Crack Growth Parameters from Constant Stressing Rate Flexural Strength Tests, British Standards Institution, London, 1997
16. “Testing Method for Bending Fatigue of Fine Ceramics,” JIS R 1621, Japanese Standards Association, Tokyo, Japan, 1996
17. “Standard Test Method for Determination of Slow Crack Growth Parameters of Advanced Ceramics by Constant Stress-Rate Flexural Testing at Ambient Temperature,” C 1368, *Annual Book of ASTM Standards*, ASTM, Vol 15.01, 1999, p 706–714
18. “Test Methods for Static Bending Fatigue of Fine Ceramics,” JIS R 1632, Japanese Standards Association, Tokyo, Japan, Dec 1998
19. Standard Practice for Constant-Amplitude, Axial Tension-Tension Cyclic Fatigue of Advanced Ceramics at Ambient Temperatures,” C1361, *Annual Book of ASTM Standards*, ASTM
20. J.A. Salem, N.N. Nemeth, L.M. Powers, and S.R. Choi, Reliability Analysis of Uniaxially Ground Brittle Materials, *J. Eng. Gas Turbines Power (Trans. ASME)*, Vol 118, 1996, p 863–871
21. D.H. Roach and A.R. Cooper, “Etching of Soda Lime Glass—Another Look,” in the third proceedings of a symposium sponsored by the Etel Institute for Silicate Research/The University of Toledo and the Northwestern Ohio Section of the Am. Ceram. Soc., W. Kneller, Ed., March 1983, p 1–7
22. F. Gigu, Cyclic Fatigue of Polycrystalline Alumina in Direct Push-Pull, *J. Mater. Sci. Lett.*, Vol 13 (No. 6), 1978, p 1357–1361
23. M.V. Swain, Lifetime Prediction of Ceramic Materials, *Mater. Forum*, Vol 9 (No. 1–2), 1st and 2nd Quarter 1986, p 34–44
24. H. Kawakubo and K. Komeya, Static and Cyclic Fatigue Behavior of a Sintered Silicon Nitride at Room Temperature, *J. Am. Ceram. Soc.*, Vol 70 (No. 6), 1987, p 400–405

25. R.H. Dauskardt, W. Yu, and R.O. Ritchie, Fatigue Crack Propagation in Transformation Toughened Zirconia, *J. Am. Ceram. Soc.*, Vol 70 (No. 10), 1987, p C-248–C-252
26. G. Grathwohl, Fatigue of Ceramics under Cyclic Loading, *Mater. Sci. Technol.*, Vol 19 (No. 4), April 1988, p 113–124 (in German)
27. M.J. Reece, F. Guiu, and M.F.R. Sammur, Cyclic Fatigue Crack Propagation in Alumina under Direct Tension-compression Loading, *J. Am. Ceram. Soc.*, Vol 72 (No. 2), 1989, p 348–352
28. Y. Mutoh, M. Takahashi, T. Oikawa, and H. Okamoto, Fatigue Crack Growth of Long and Short Cracks in Silicon Nitride, *Fatigue of Advanced Materials*, R.O. Ritchie, R.H. Dauskardt, and B.N. Cox, Ed., Material and Component Engineering Publications, Ltd., Edgbaston, U.K., 1991, p 211–225
29. S. Horibe and H. Hirahara, Cyclic Fatigue of Ceramics Materials: Influence of Crack Path and Fatigue Mechanisms, *Acta Metall. Mater.*, Vol 39 (No. 6), 1991, p 1309–1317
30. M. Okazaki, A.J. McEvily, and T. Tanaka, On the Mechanism of Fatigue Crack Growth in Silicon Nitride, *Metall. Trans. A*, Vol 22A, 1991, p 1425–1434
31. T. Tanaka, N. Okabe, H. Nakayama, and Y. Ishimaru, Fatigue Crack Growth of Silicon Nitride with Crack Wedging by Fine Fragments, *Fatigue Fract. Eng. Mater. Struct.*, Vol 17 (No. 7), 1992, p 643–653
32. R.O. Ritchie, C.J. Gilbert, and J.M. McNaney, Mechanics and Mechanisms of Fatigue Damage and Crack Growth in Advanced Materials, *Int. J. Solids Struct.*, Vol 37, 2000, p 311–329
33. R. Dauskardt, Cyclic Fatigue-Crack Growth in Grain Bridging Ceramics, *J. Eng. Mater. Technol. (Trans. ASME)*, Vol 115, 1993, p 115–251
34. T.A. Michalske and B.C. Bunker, Slow Fracture Based on Strained Silicate Structures, *J. Appl. Phys.*, Vol 56 (No. 10), 1984, p 2686–2694
35. T. Yishio and K. Oda, Aqueous Corrosion and Pit Formation of Si_3N_4 under Hydrothermal Conditions, *Ceram. Trans.*, Vol 10, 1990, p 367–386
36. M.K. Ferber, H.T. Lin, and J. Keiser, Oxidation Behavior of Non-Oxide Ceramics in a High-Pressure, High-Temperature Steam Environment, *Mechanical, Thermal and Environmental Testing and Performance of Ceramic Composites and Components*, STP 1392, M.G. Jenkins, E. Lara-Curzio, and S. Gonczy, Ed., ASTM, 2000
37. G. Vekinis, M.F. Ashby, and P.W. Beaumont, R-Curve Behaviour of Al_2O_3 Ceramics, *Acta Metall. Mater.*, Vol 38 (No. 6), 1990, p 1151–1162
38. D.A. Krohn and D.P.H. Hasselman, Static and Cyclic Fatigue Behavior of a Polycrystalline Alumina, *J. Am. Ceram. Soc.*, Vol 55 (No. 4), 1972, p 208–211
39. M. Masuda, T. Soma, M. Matsui, and I. Oda, Fatigue of Ceramics, Part 1: Fatigue Behavior of Sintered Silicon Nitride under Tension-Compression Cyclic Stress, *J. Ceram. Soc. Jpn. Int. Ed.*, Vol 96, 1988, p 275–280
40. A. Steffen, R.H. Dauskardt, and R.O. Ritchie, Cyclic Fatigue Life and Crack Growth Behavior of Microstructural Small Cracks in Magnesia-Partially-Stabilized Zirconia Ceramics, *J. Am. Ceram. Soc.*, Vol 74 (No. 6), 1991, p 1259–1268

41. S.M. Wiederhorn and J.E. Ritter, Application of Fracture Mechanics Concepts to Structural Ceramics, *Fracture Mechanics Applied to Brittle Materials*, STP 678, S.W. Frieman, Ed., ASTM, 1979, p 202–214
42. K. Jakus, J.E. Ritter, and J.M. Sullivan, Dependency of Fatigue Predictions on the Form of the Crack Velocity Equation, *J. Am. Ceram. Soc.*, Vol 64 (No. 6), 1981, p 372–374
43. S.M. Weiderhorn, Prevention of Failure in Glass by Proof-Testing, *J. Am. Ceram. Soc.*, Vol 56 (No. 4), 1973, p 227–228
44. G. Evans and S.M. Weiderhorn, Proof Testing of Ceramic Materials-An Analytical Basis for Failure Prediction, *In. J. Fract.*, Vol 10 (No. 3), 1974, p 379–392
45. A.G. Evans and E.R. Fuller, Crack Propagation in Ceramic Materials under Cyclic Loading Conditions, *Metall. Trans. A*, Vol 5 (No. 1), 1974, p 27–33
46. B.J.S. Wilkins and L.A. Simpson, Errors in Estimating the Minimum Time-to-Failure in Glass, *J. Am. Ceram. Soc.—Discussion and Notes*, Dec 1974, p 505
47. W.P. Minnear and R.C. Bradt, (K-V) Diagrams for Ceramic Materials, *J. Am. Ceram. Soc.—Discussion and Notes*, Vol 58 (No. 7–8), 1975, p 345–346
48. G. Sines, Rationalized Crack Growth and Time-to-Fracture of Brittle Materials, *Am. Ceram. Soc.—Discussion and Notes*, Vol 59 (No. 7–8), 1976, p 370–371
49. S. Hillig and R.J. Charles, Surfaces, Stress-Dependent Surface Reactions and Strength, *High Strength Materials*, V.F. Zackay, Ed., John Wiley & Sons, 1965, p 682–705
50. B.R. Lawn, An Atmospheric Model of Kinetic Crack Growth in Brittle Solids, *J. Mater. Sci.*, Vol 10, 1975, p 469–480
51. E.M. Lenoë and D.M. Neil, “Assessment of Strength Probability-Time Relationships in Ceramics,” AMMRC Tech. Report 75-13, ARPA Order No. 2181, Army Mater. and Mech. Res. Center, Watertown, MA, 1975
52. “Standard Test Method for Plane Strain Fracture Toughness of Metallic Materials,” E 399, *Annual Book of ASTM Standards*, Vol 03.01, ASTM, 1998
53. W.G. Clark, Jr., Fracture Mechanics and Nondestructive Testing of Brittle Materials, *J. Eng. Ind. (Trans. ASME)*, Feb 1972, p 291–298
54. J.N. Masters, “Cyclic and Sustained Load Flow Growth Characteristics in 6Al-4V Titanium,” NASA-CR-92231, NASA, 1968
55. J.E. Ritter, Jr., K. Jakus, and D.S. Cooke, Predicting Failure of Optical Glass Fibers, Environmental Degradation of Engineering in Aggressive Environments, *Proceedings of the 2nd International Conference on Environmental Degradation of Engineering Materials*, Va. Polytech Inst. and State Univ., NASA Lewis Res. Center, NACE, and Va. Polytech Inst., Lab for the Study of Environ. Degrad. of Eng. Mater., 1981, p 565–575
56. “Test Method for Flexural Strength (Modulus of Rupture) of Fine Ceramics,” JIS R 1601, Japanese Standards Association, Tokyo, Japan, 1995

57. J.E. Ritter, Jr., Assessment of Reliability of Ceramic Materials, *Fracture Mechanics of Ceramics*, Vol 6, R.C. Bradt et al., Ed., Plenum Press, 1983, p 227–251
58. J.E. Ritter, Jr., Engineering Design and Fatigue Failure of Brittle Materials, *Fracture Mechanics of Ceramics*, Vol 4, R.C. Bradt et al., Ed., Plenum Press, 1978, p 667–685
59. E.B. Haugen, *Probabilistic Mechanical Design*, John Wiley & Sons, 1980
60. N.N. Nemeth, L.M. Powers, L.A. Janosik, and J.P. Gyekenyesi, “Durability Evaluation of Ceramic Components Using CARES/LIFE,” ASME Paper 94-GT-362 and NASA-TM 106475, ASME/IGTI Gas Turbine Conference, June 1994
61. A.D. Peralta, D.C. Wu, P.J. Brehm, J.C. Cuccio, and M.N. Menon, Strength Prediction of Ceramic Components under Complex Stress States, *Proceedings of the International Gas Turbine and Aeroengine Congress and Exposition*, 5–8 June 1995 (Houston, TX), American Society of Mechanical Engineers, 1995; Allied Signal Document 31-12637, 1995
62. “Fatigue Crack Growth Program NASA/Flagro 2.0,” JSC 22267A, NASA Johnson Space Flight Center, May 1994
63. J.E. Ritter, N. Bandyopadhyay, and K. Jakus, *Am. Ceram. Soc. Bull.*, Vol 60, 1981, p 798
64. “Standard Test method for Flexural Strength of Advanced Ceramics at Ambient Temperature,” C 1161, *Annual Book of ASTM Standards*, ASTM, Vol 15.01, 1999, p 309–315
65. H.A. Linders and B. Caspers, Method for Determining Life Diagrams of Mechanoceramic Materials DKG/DKM-Joint Experiment, *Ceramics in Science and Practice, Mechanical Properties of Ceramic Construction Materials*, G. Grathwohl, Ed., DGM Information Association, Verlag, Germany, 1993, p 191–195 (in German)
66. S. Freiman, “Pre-Standardization and Standardization Activities in the USA in Mechanical Property Testing of Advanced Structural Ceramics,” presentation at the 7th CIMTEC World Ceramics Congress, Montecatini Terme, Italy, 23 June 1990
67. S.W. Freiman and E.R. Fuller, Versailles Project on Advanced Materials and Standards, VAMAS TWA 3 Bulletin 8, July 1988
68. W.P. Byrn and R. Morrell, “Results of the UK Interlaboratory Strength Test Exercise,” NPL Report DMM (D) 72, National Physical Laboratory, Teddington, Middlessex, U.K., Crown Copyright, Dec 1990
69. “Standard Test Method for Tensile Strength of Monolithic Advanced Ceramics at Ambient Temperatures,” C 1273, *Annual Book of ASTM Standards*, Vol 15.01, ASTM, 1999, p 671–678
70. Cyclic Fatigue Testing of Silicon Nitride, *Ceramics* (newsletter), Ceramics Division of IIT Research Institute, Chicago, IL, 42, March 1978; *Ceram. Eng. and Sci. Proc. of the 18th Annual Conference on Composites and Advanced Ceram. Mater.-A*, Part 1 of 2, 9–14 Jan 1994, Vol 15 (No. 4), July–Aug 1994 (Cocoa Beach, FL), *Am. Ceram. Soc.*, Westerville, OH, 1994, p 32–39
71. H.N. Ko, Cyclic Fatigue Behavior of Ceramics under Rotary Bending, *Materials Research Society International Meeting on Advanced Materials*, Materials Research Society, Vol 5, 1989, p 43–48
72. H.N. Ko, Cyclic Fatigue Behavior of Sintered Al₂O₃ under Rotary Bending, *J. Mater. Sci. Lett.*, Vol 6, 1987, p 801–805

73. R. Kossowsky, "Cyclic Fatigue of Hot Pressed Silicon Nitride," *J. Am. Ceram. Soc.*, Vol 56, 1973, p 10, 531–535
74. Y. Matsuo, Y. Hattori, Y. Katayama, and I. Fukuura, Cyclic Fatigue Behavior of Ceramics, *Progress in Nitrogen Ceramics*, F.L. Riley, Ed., Martinus Nijhoff, 1983, p 515–522
75. K. Ohya, K. Ogura, and M. Takatsu, Effect of Loading Waveform on Cyclic Fatigue Behavior of PSZ, *J. Soc. Mater. Sci., Jpn.*, Vol 38 (No. 425), 1989, p 144–148
76. K. Ohya, K. Ogura, and M. Takatsu, Cyclic Fatigue Testing Device for Fine Ceramics by Using Piezo-Electric Bimorph Actuator, *J. Soc. Mater. Sci., Jpn.*, Vol 38 (No. 424), 1989, p 44–48
77. J.A. Salem, L.J. Ghosn, and M.G. Jenkins, A Strain Gage Technique to Measure Stable Crack Extension in Ceramics, *Post Conference Proceedings of the 1997 SEM Spring Conference on Experimental Mechanics*, Society for Experimental Mechanics, Bethel, CT, 1997, p 1–8
78. J.A. Salem, L.J. Ghosn, and M.G. Jenkins, Back-Face Strain as a Method for Monitoring Stable Crack Extension in Ceramics, *Ceram. Eng. Sci. Proc.*, Vol 19 (No. 3), 1998, p 587–594
79. J.O. Outwater and D.J. Gerry, "On the Fracture Energy of Glass," NRL Interim Contract Report, Contract NONR 3219(01)(x), AD 640848, University of Vermont, Burlington, VT, Aug 1966
80. J.O. Outwater and D.J. Gerry, "On the Fracture Energy, Rehealing Velocity and Fracture Energy of Cast Epoxy Resin," Paper 13-D, presented at the 22nd Society of Plastic Industry Conference, 1967; also, *J. Adhes.*, Vol 1, 1969, p 290–298
81. G.W. Weidmann and D.G. Holloway, Slow Crack Propagation in Glass, *Phys. Chem. Glasses*, Vol 15 (No. 5), Oct 1974, p 116–122
82. C.D. Beacham, J.A. Kies, and B.F. Brown, A Constant K Specimen for Stress Corrosion Cracking Testing, *Mater. Res. Standards*, Vol 11, 1970, p 30
83. A.G. Evans, Method For Evaluating the Time-Dependent Failure Characteristics of Brittle Material and Its Application to Polycrystalline Alumina, *J. Mater. Sci.*, Vol 7 (No. 10), 1972, p 1137–1146
84. A.G. Evans and S.M. Wiederhorn, Crack Propagation and Failure Prediction in Silicon Nitride at Elevated Temperatures, *J. Mater. Sci.*, Vol 9, 1974, p 270–278
85. A.G. Evans, L.R. Russel, and D.W. Richerson, Slow Crack Growth in Ceramic Materials at Elevated Temperatures, *Metall. Trans. A*, Vol 6A (No. 14), 1975, p 707–716
86. K.R. McKinney and H.L. Smith, Method of Studying Subcritical Cracking of Opaque Materials, *J. Am. Ceram. Soc.*, Vol 56 (No. 1), 1973, p 30–32
87. P.N. Thornby, Experimental Errors in Estimating Times to Failures, *J. Am. Ceram. Soc.*, Vol 59 (No. 11–12), 1976, p 514–517
88. E.R. Fuller, Jr., an Evaluation of Double Torsion Testing: Analysis, *Fracture Mechanics Applied to Brittle Materials*, STP 678, S.W. Frieman, Ed., ASTM, 1979, p 3–18
89. B.J. Pletka, E.R. Fuller, Jr., and B.G. Koepke, An Evaluation of Double Torsion Testing: Experimental, *Fracture Mechanics Applied to Brittle Materials*, STP 678, S.W. Frieman, Ed., ASTM, 1979, p 19–37

90. C.G. Annis and J.S. Cargill, Modified Double Torsion Method for Measuring Crack Velocity in NC-132 Si₃N₄, *Fracture Mechanics of Ceramics*, Vol 4, R.C. Bradt et al., Ed., Plenum Press, 1978, p 737–744
91. D.P. Williams and A.G. Evans, A Simple Method for Studying Slow Crack Growth, *J. Test. Eval.*, Vol 1 (No. 4), 1973, p 264–270
92. K.R. Linger and D.G. Holloway, Fracture Energy of Glass, *Philos. Mag.*, Vol 18 (No. 156), 1968, p 1269–1280
93. J.A. Salem, M.G. Jenkins, M.K. Ferber, and J.L. Shannon, Jr., Effects of Pre-Cracking Method on Fracture Properties of Alumina, *Proceedings of Society of Experimental Mechanics Conference on Experimental Mechanics*, 10–13 June 1991 (Milwaukee, WI), Society for Experimental Mechanics, Bethel, CT, 1991, p 762–769
94. S.W. Freiman, D.R. Mulville, and P.W. Mast, *J. Mater. Sci.*, Vol 8 (No. 11), 1973, p 1527–1533
95. S. Mostovoy, P.B. Crosley, and E.J. Ripling, Use of Crack-Line-Loaded Specimens for Measuring Plane-Strain Fracture Toughness, *J. Mat.*, Vol 2 (No. 3), Sept 1967, p 661–681
96. A.G. Evans and H. Johnson, The Fracture Stress and Its Dependence on Slow Crack Growth, *J. Mater. Sci.*, Vol 10, 1975, p 214–222
97. T. Sadahiro, Transverses Rupture Strength and Fracture Toughness of WC-Co Alloys, *J. Jpn. Inst. Met.*, Vol 45, 1981, p 291–295
98. D.J. Martin, K.W. Davido, and W.D. Scott, Slow Crack Growth Measurement Using an Electric Grid, *Am. Ceram. Soc. Bull.*, Vol 65 (No. 7), 1986, p 1052–1156
99. P.K. Liaw, H.R. Hartmann, and W.A. Lodgson, A New Transducer to Monitor Fatigue Crack Propagation, *J. Test Eval.*, Vol 11 (No. 3), 1983, p 202–207
100. R.H. Dauskardt, R.O. Ritchie, J.K. Takemoto, and A.M. Brendzel, Cyclic Fatigue in Pyrolytic Carbon-Coated Graphite Mechanical Heart-Valve Prostheses: Role of Small Cracks in Life Prediction, *J. Biomed. Mater. Res.*, Vole 28, 1994, p 791–804
101. R.H. Dauskardt, M.R. James, J.R. Porter, and R.O. Ritchie, Cyclic Fatigue-Crack Growth in a SiC-Whisker-Reinforced Alumina Ceramic Composite: Long- and Small-Crack Behavior, *J. Am. Ceram. Soc.*, Vol 75 (No. 4), 1992, p 759–771
102. “Standard Test Methods for Fracture Toughness of Advanced Ceramics,” C 1421, *Annual Book of ASTM Standards*, ASTM, Vol 15.01, 2000, p 631–662
103. L. Ewart and S. Suresh, Dynamic Fatigue Crack Growth in Polycrystalline Alumina under Cyclic Compressive Loads, *J. Mater. Sci.*, Vol 5, 1986, p 774–778
104. L. Ewart and S. Suresh, Crack Propagation in Ceramics under Cyclic Loads, *J. Mater. Sci.*, Vol 22, 1987, p 1173–1192
105. F. Sudreau, C. Olagnon, and G. Fantozzi, Lifetime Prediction of Ceramics: Importance of Test Method, *Ceram. Int.*, Vol 10, 1994, p 125–135
106. E.M. Rockar and B.J. Pletka, Fracture Mechanics of Alumina in a Simulated Biological Environment, *Fracture Mechanics of Ceramics*, Vol 4, R.C. Bradt et al., Ed., Plenum Press, 1978, p 725–735

Multiaxial Fatigue Testing

Yukitaka Murakami, Kyushu University, Japan

Introduction

TESTS for combined-stress fatigue and multiaxial fatigue have been conducted since the early stages in the history of fatigue testing. In particular, the combined-stress fatigue test for cylindrical specimens has been used by many researchers. The main objective for classical studies of combined-stress fatigue was to obtain fatigue data for axles and to find the criterion for the fatigue limit under combined stress. Although recent studies still use essentially the same testing method, the main objective is to elucidate the factors that control the fatigue mechanism and particularly the behavior of small fatigue cracks.

The influence of loading history and phases is also a topic of recent studies. Cylindrical specimens or tubular specimens are mostly used for these studies. Perhaps the most important recent topic in multiaxial fatigue studies is the behavior of cracks. The threshold condition of macrocracks and crack propagation paths in large structures have been investigated by many researchers.

Although cracks mostly propagate by mode I (the opening tension mode), even under mixed mode loading, the propagation behavior is affected by mixed mode loadings due to various factors such as the size of the yield zone at the crack tip, crack closure, and friction between crack surfaces.

On the other hand, a crack seldom grows by pure mode II (sliding or shear mode) or mode III (tearing mode) in real structures. Some examples of mode II fatigue are contact fatigue damage in rolls of steelmaking mills, contact fatigue of rails and bearings, and fretting fatigue. In these cases, the criteria for the threshold condition for mode II cracks and the resistance to mode II crack growth are needed. Crack growth by mode III is the form studied in the torsional fatigue test of circumferentially notched specimens. Thus, the fatigue testing method, specimen geometries, and stress intensity factors are all important factors in the study of multiaxial fatigue.

Many factors of multiaxiality make the testing method more complicated than mode I fatigue testing, and, accordingly, many researchers, working independently, have developed their own original methods. This article first explains stress states of combined stress and stress fields near crack tips and then describes various multiaxial fatigue testing methods.

Multiaxial Fatigue Testing

Yukitaka Murakami, Kyushu University, Japan

Stress States

Most engineering designs and/or failure analyses involve three-dimensional combinations of stress and strain (multiaxiality) in the vicinity of surfaces and notches, which can be limiting in fatigue applications. This section provides a brief review of these stress states. Additional information is provided in the article “Multiaxial Fatigue Strength” in *Fatigue and Fracture*, Volume 19 of *Asm Handbook*.

Two dimensional stress states without cracking are defined in Fig. 1, where the basic relations are:

$$\sigma_1, \sigma_2 = \frac{(\sigma_x + \sigma_y) \pm \sqrt{(\sigma_x - \sigma_y)^2 + 4\tau_{xy}^2}}{2} \quad (\text{Eq 1})$$

where σ_1, σ_2 are the principal stresses. $\sigma_x = \sigma_0$ and $\sigma_y = -\sigma_0$ in Fig. 1(d), and this is equivalent to the case shown in Fig. 1(b) if $\tau_{xy} = \sigma_0$.

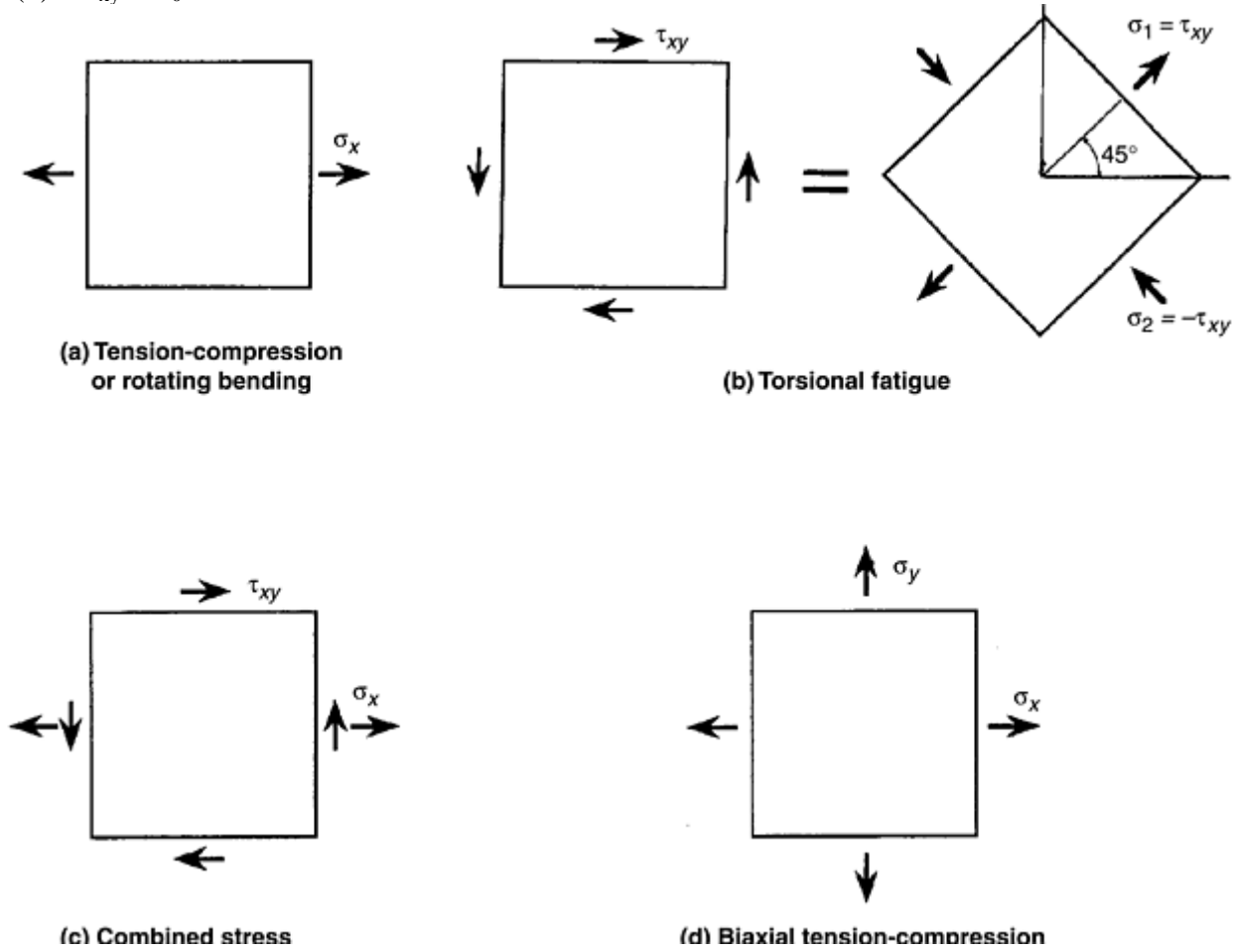


Fig. 1 Two-dimensional stress states without cracking

The yield criterion or yield stress, σ_Y , is:

$$\text{Tresca: } \sigma_1 - \sigma_2 = \sigma_Y \quad (\text{Eq 2})$$

$$\text{Von Mises: } \sigma_x^2 - \sigma_x \sigma_y + \sigma_y^2 + 3\tau_{xy}^2 = \sigma_Y^2 \quad (\text{Eq 3})$$

Stress states at the tip of a crack in combined mode I and mode II are defined by stress-intensity factors. K_I is the mode I stress intensity factor, and K_{II} is the mode II stress intensity factor. Radial stress (σ_r), normal stress (σ_θ), and shear stress ($\tau_{r\theta}$) in polar coordinate (r, θ) in the vicinity of the crack tip are given as follows (Fig. 2):

$$\sigma_r = \frac{1}{\sqrt{2\pi r}} \cos \frac{\theta}{2} \left[K_I \left(1 + \sin^2 \frac{\theta}{2} \right) + \frac{3}{2} K_{II} \sin \theta - 2 K_{II} \tan \frac{\theta}{2} \right] \quad (\text{Eq 4})$$

$$\sigma_\theta = \frac{1}{\sqrt{2\pi r}} \cos \frac{\theta}{2} \left[K_I \cos^2 \frac{\theta}{2} - \frac{3}{2} K_{II} \sin \theta \right] \quad (\text{Eq 5})$$

$$\tau_{r\theta} = \frac{1}{2\sqrt{2\pi r}} \cos \frac{\theta}{2} [K_I \sin \theta + K_{II} (3 \cos \theta - 1)] \quad (\text{Eq 6})$$

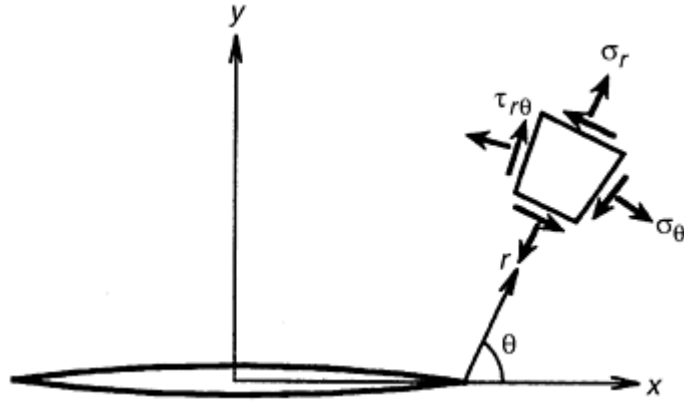


Fig. 2 Stress state near a crack in a polar coordinate

The direction (θ_0) where σ_θ has the maximum value is given by:

$$K_I \sin\theta_0 + K_{II} (3 \cos\theta_0 - 1) = 0 \quad (\text{Eq 7})$$

$$\tan \frac{\theta_0}{2} = \frac{1 \pm \sqrt{1 + 8\gamma^2}}{4\gamma}, \quad \gamma = \frac{K_{II}}{K_I} \quad (\text{Eq 8})$$

This equation gives $\theta_0 = \pm 70.5^\circ$ for pure mode II ($K_I = 0$).

The stress intensity factor that prescribes σ_θ is defined by:

$$\begin{aligned} K_{\theta \max} &= \sigma_{\theta \max} \sqrt{2\pi r} \\ &= \cos \frac{\theta_0}{2} \left[K_I \cos^2 \frac{\theta_0}{2} - \frac{3}{2} K_{II} \sin \theta_0 \right] \end{aligned} \quad (\text{Eq 9})$$

The maximum value ($K_{\theta \max}$) of K_θ for pure mode II is derived, substituting $\theta_0 = \pm 70.5^\circ$ into Eq 9. Thus:

$$K_{\theta \max} = 1.155 K_{II} \quad (\text{Eq 10})$$

Stress State at the Tip of a Crack in Mode III. If there is a semielliptical surface crack and the crack is subjected to pure shear (Fig. 3), the condition at the deepest point of crack front, *A*, is pure mode III, and the condition at surface corner points, *B* and *C*, is pure mode II, which means the branching angle at *B* and *C* by mode I crack growth is 70.5° under reversed torsion (Ref 1). (There have been some discussions among researchers about the irregular singularity close to the corner point where a crack meets the free surface. It is known that a mode I stress component in tension has a singularity different from $-\frac{1}{2}$. If $K_{III} \neq 0$ at the surface point, it means that there exists a shear stress τ_{yz} on the free surface. Therefore, K_{III} must be zero at points *B* and *C*.)

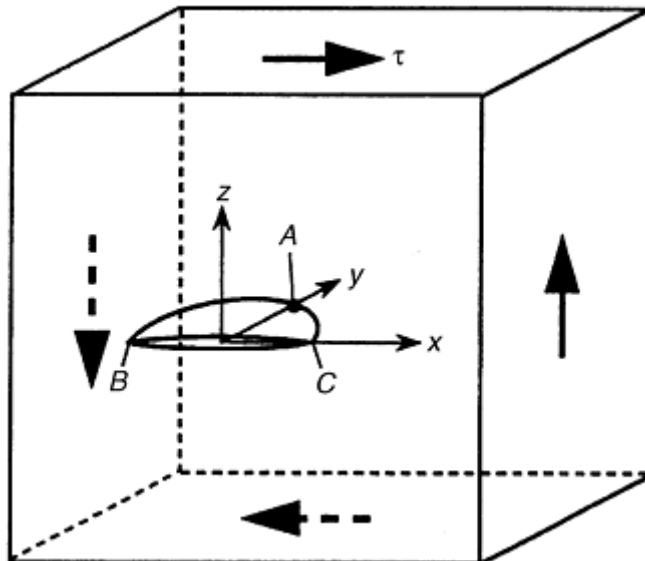


Fig. 3 A semielliptical surface crack under shear. A, pure mode III; B, C, pure mode II

Reference cited in this section

1. Y. Murakami and K. Takahashi, Torsional Fatigue of a Medium Carbon Steel Containing an Initial Small Surface Crack Introduced by Tension-Compression Fatigue: Crack Branching, Non-Propagation and Fatigue Limit, *Fatigue Fract. Eng. Mater. Struct.*, Vol 21, 1998, p 1473–1484

Multiaxial Fatigue Testing

Yukitaka Murakami, Kyushu University, Japan

Testing of Cylindrical Specimens

Torsion-Rotating Bending Fatigue. In a classical type of torsion-rotating bending fatigue test, cylindrical specimens similar to those for rotating bending fatigue are used (Ref 2). A static twisting moment is applied through the axis of the specimen. In this type of machine, the normal stress in the rotating test piece is continuously varied between positive and negative stress of equal magnitudes. Furthermore, the steady shearing stress is simultaneously induced in the specimen by connecting the testing machine with an electric absorption dynamometer, which consists of a small direct-current dynamo placed on an iron frame suspended by ball bearing. The specimen geometry for this type of fatigue testing is essentially similar to those for rotating bending except for the special grip shape. This type of testing machine has still been used in recent studies (Ref 3). In another classical test, bending moment is coupled with twisting moment, which is loaded by the reversed motion of a fly wheel. The specimen geometry for this test is shown in Fig. 4.

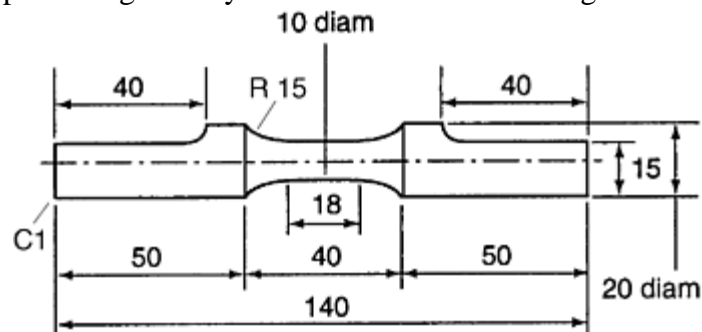


Fig. 4 Specimen for conventional reversed torsion test. Dimensions are in mm. Source: Ref 4

Torsion Coupled with Tension Compression. Biaxial fatigue testing machines of the closed-loop type in which torsion can be coupled with tension-compression are now commonly used. In the closed-loop type of testing machine, torsion and tension-compression can be loaded independently in phase or out of phase. Figure 5 shows a biaxial fatigue testing machine of this type. Figure 6 shows the extensometer used to measure axial and angular displacement. A cylindrical specimen (Fig. 7) is the standard geometry for this type of testing machine.

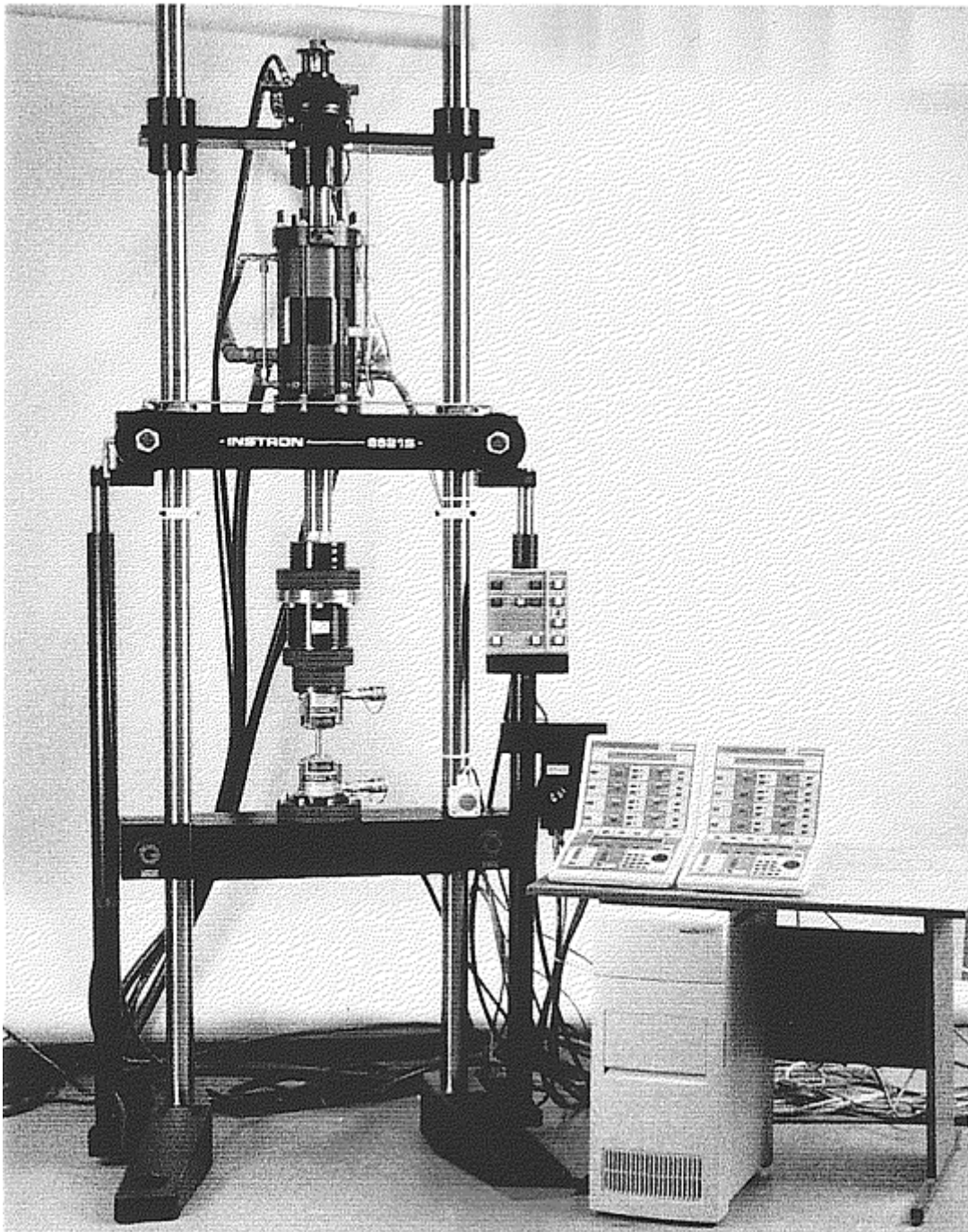


Fig. 5 Biaxial fatigue testing machine. Courtesy of Instron Corporation

Fig. 8 Tubular specimen for triaxial fatigue test; dimensions are in mm. D , diameter; ID , inside diameter; R , radius. Source: Ref 5

References cited in this section

1. Y. Murakami and K. Takahashi, Torsional Fatigue of a Medium Carbon Steel Containing an Initial Small Surface Crack Introduced by Tension-Compression Fatigue: Crack Branching, Non-Propagation and Fatigue Limit, *Fatigue Fract. Eng. Mater. Struct.*, Vol 21, 1998, p 1473–1484
2. A. Ono, “Fatigue of Steel under Combined Bending and Torsion,” Mem. Coll. Eng., Kyushu Imp. Univ., Vol 2, 1921, p 117–145
3. M.A. Fonte and M.M. Freitas, Semi-Elliptical Crack Growth Under Rotating or Reversed Bending Combined with Steady Torsion, *Fatigue Fract. Eng. Mater. Struct.*, Vol 20, 1997, p 895–906
4. M. Endo and Y. Murakami, Effects of an Artificial Small Defect on Torsional Fatigue Strength of Steels, *J. Eng. Mater. Technol. (Trans. ASME)*, Vol 109, 1987, p 124–129
5. M.W. Brown and K.J. Miller, Biaxial Cyclic Deformation Behavior of Steels, *Fatigue Eng. Mater. Struct.*, Vol 1, 1979, p 93–106

Multiaxial Fatigue Testing

Yukitaka Murakami, Kyushu University, Japan

Testing of Specimens Containing Notches or Cracks

Rectangular plate specimens containing an inclined central or edge crack are used for crack propagation tests in mixed-mode loading (Ref 6, 7, and 8). The axial load is applied through the pins attached to the holes at the grips. A notch or crack is introduced by a saw or razor. If a fatigue crack is introduced in a wide plate by preliminary tension-compression fatigue, a specimen such as that shown in Fig. 9 can be prepared by cutting the plate (Ref 6, 7, and 8).

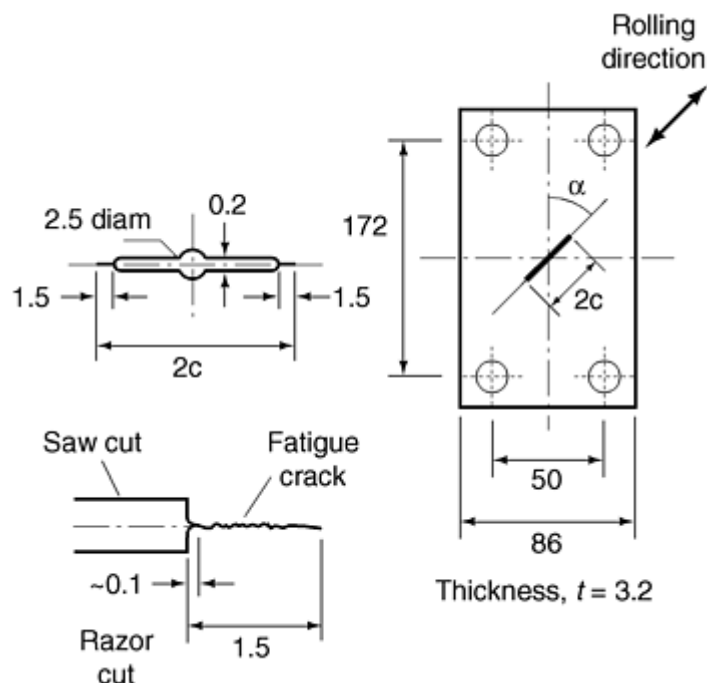


Fig. 9 Rectangular plate specimens containing an inclined center crack. Dimension are in mm. Source: Ref 7

Cruciform Specimen. The type of specimen shown in Fig. 10 is used to investigate the effect of plastic zone size or yielding at the tip of a crack. The stress intensity factor has the same value under the combination of an identical stress, σ_y , and a different stress, σ_x . However, the size of the yield zone at the crack tip is dependent on the value of the stress, σ_x , in the direction of the crack line.

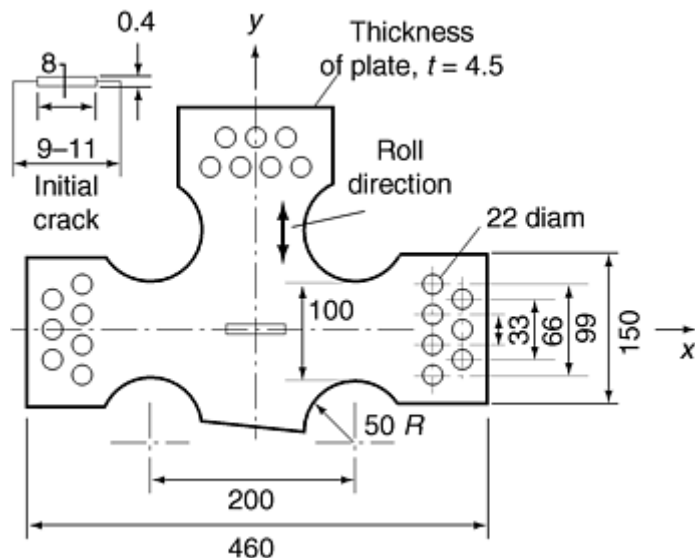


Fig. 10 Cruciform specimen containing a central crack. Dimension are in mm. Source: Ref 9

Three-Point and Four-Point Bending Specimens with a Crack. In three-point bending (Fig. 11a), not only shear force but also bending moment is always induced at the crack and, accordingly, we have both K_I and K_{II} . On the other hand, in four-point bending, one can control the magnitude of bending moment at the crack by changing the location of loads. This can be done in such a way that there is only a K_{II} stress state at the crack tip (Ref 10).

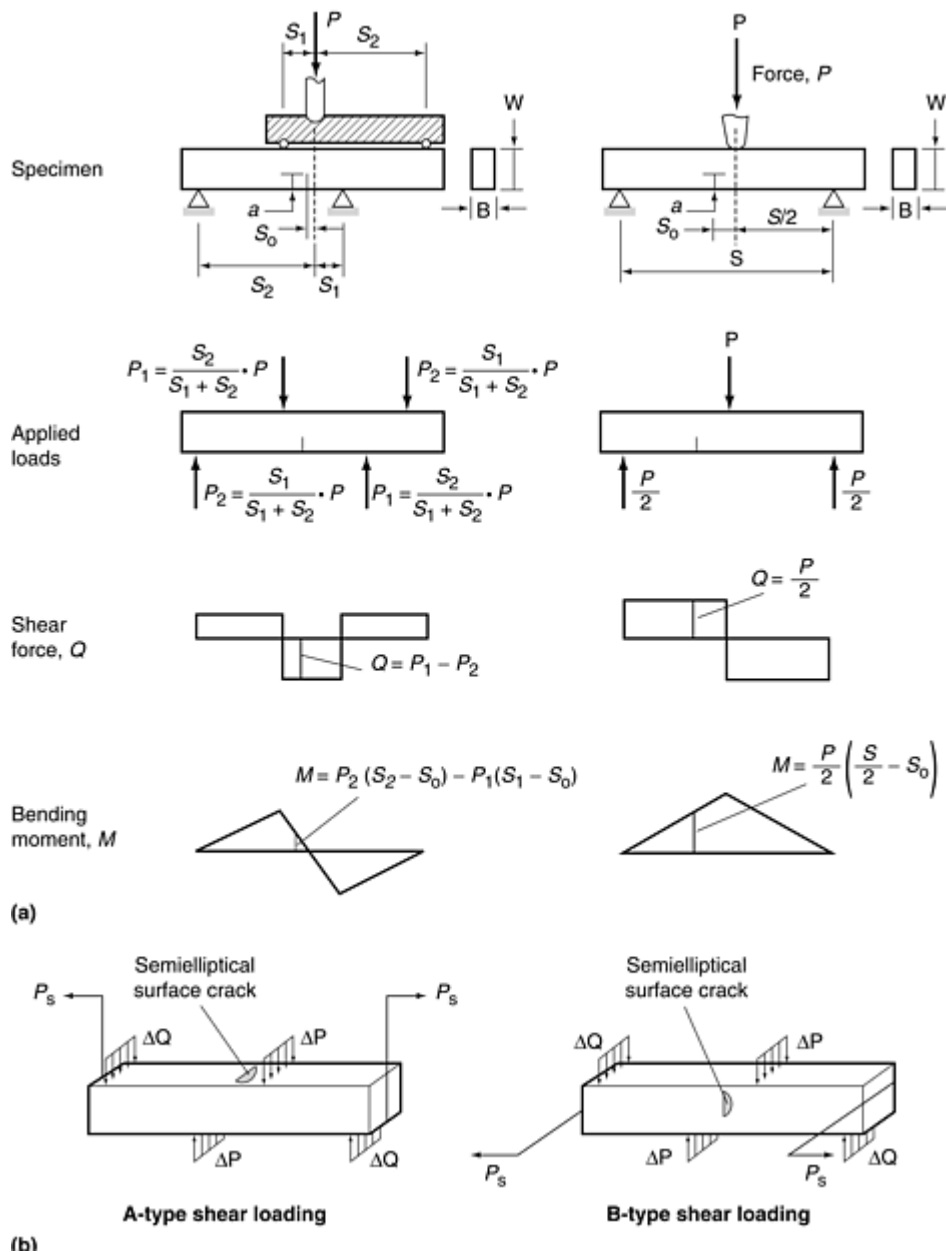


Fig. 11 Three-point and four-point bending specimens, (a) Three-point and four-point bending specimens with an offset crack. Source: Ref 10. (b) Four-point bending specimens with a semielliptical edge crack. Source: Ref 11

The specimens shown in Fig. 11(b) are variations of four-point bending specimens with edge cracks (Ref 11). However, it must be noted that the shear stress component is always zero at the free surface.

Compact Tension Shear Specimen. The compact tension specimen shown in Fig. 12 is used in combination with a jig that can control the direction of loadings and thus the combination of K_I and K_{II} (Fig. 13) (Ref 12).

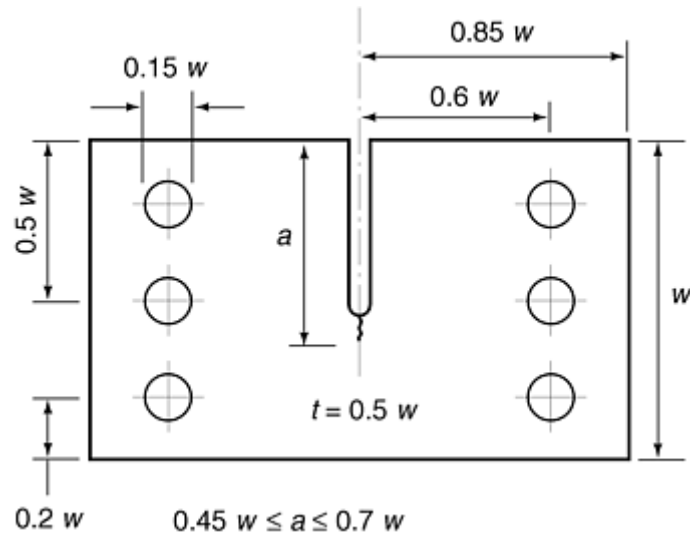


Fig. 12 Shape and dimension of compact tension shear specimen. w , width; t , thickness; a , crack length. Source: Ref 12

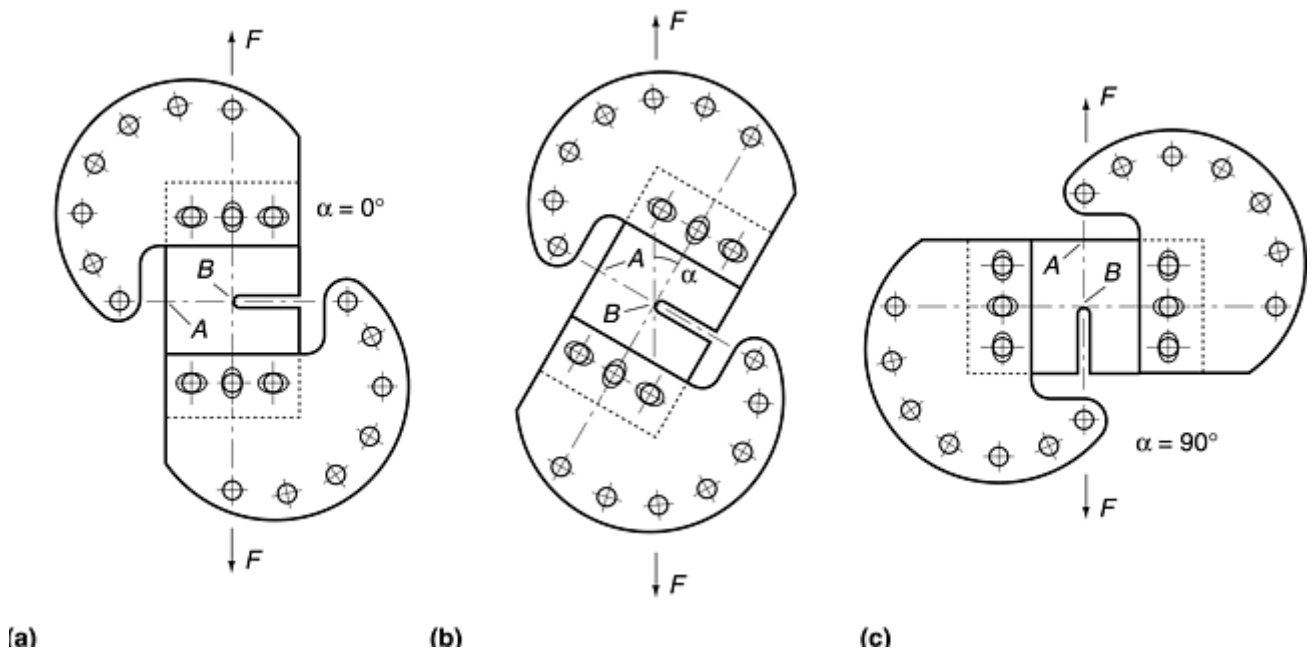


Fig. 13 Position of loading device. (a) Mode I ($\alpha = 0^\circ$), (b) Mixed mode ($0^\circ < \alpha < 90^\circ$), (c) Mode II ($\alpha = 90^\circ$). F , force. Source: Ref 12

Compact Shear Specimen. The compact shear specimen (Ref 13, 14) shown in Fig. 14 is used in the equilibrium loading system (Fig. 15a), though the mode is not pure mode II. If the distance between the pins of load application is small, the component of mode I is relatively small compared to the component of mode II. The specimen of the type in Fig. 15(b) is for the mode III test, but it also has a problem in that the mode I component is always induced in the system.

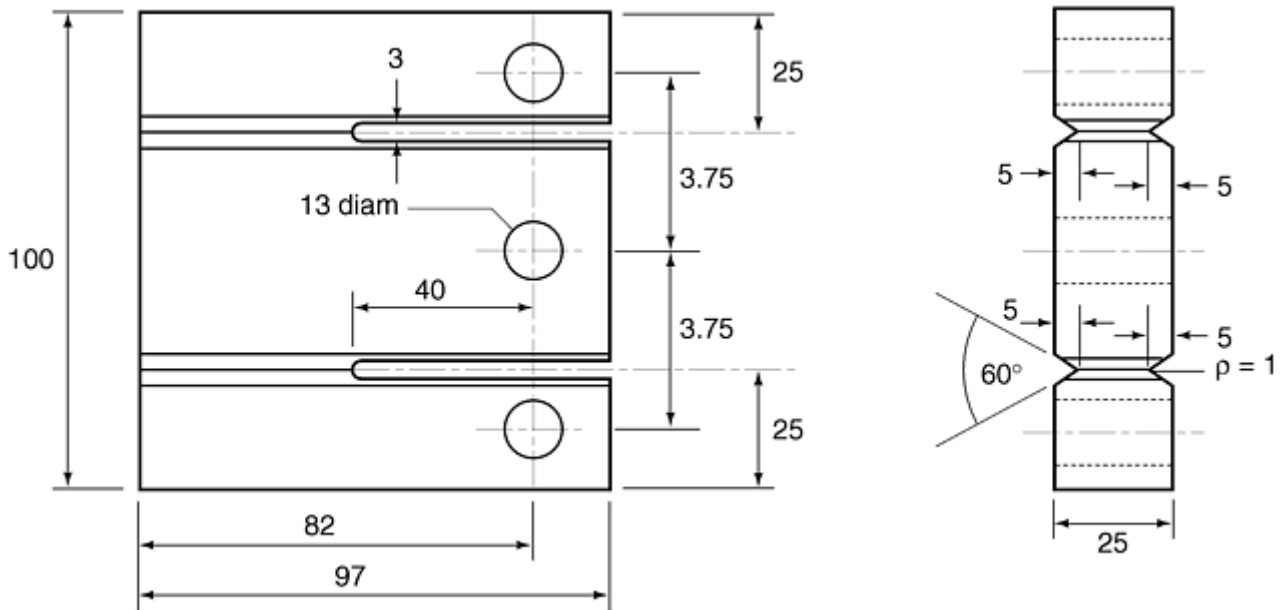


Fig. 14 Shape and dimension of compact shear specimen. Dimension are in mm. ρ , notch root radius. Source: Ref 14

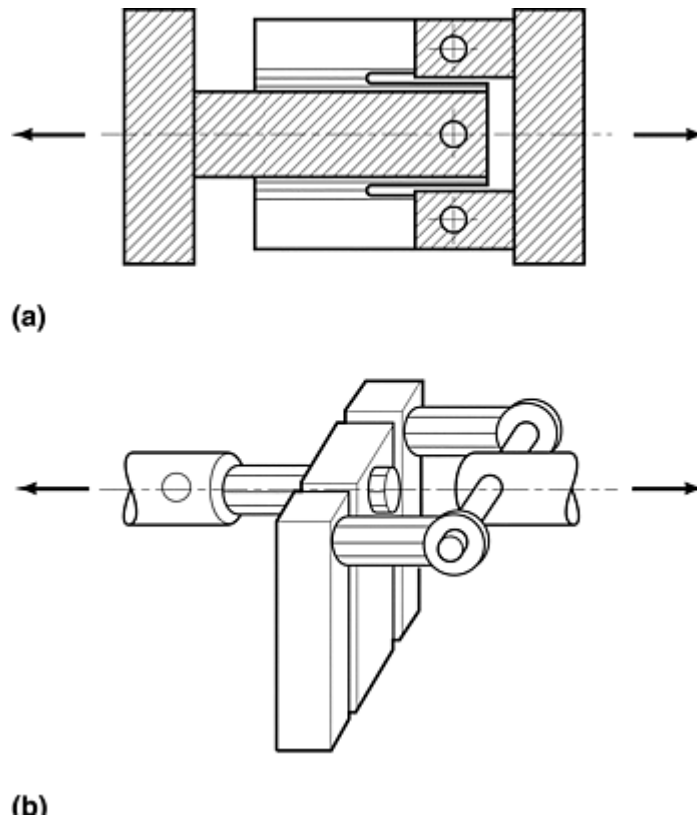


Fig. 15 Loading apparatus. (a) Mode II type, (b) Mode III type. Source: Ref 14

Mode II Crack Growth Specimen (Ref 15, 16). The mode II threshold stress intensity factor range, ΔK_{IIth} , is an important material property with respect to rolling contact fatigue resistance. However, the measurement of ΔK_{IIth} in the laboratory is very difficult because a crack that has been growing in mode II can easily switch to mode I growth during the test. A method of measuring ΔK_{IIth} has been developed and applied to various steels (Ref 15, 16).

Figure 16 shows the basic model of measurement method in which a specially designed double-cantilever specimen is used. Figure 16 shows stress distributions and the normal and shear stress at the position without a slit. In principle, neither tensile nor compressive stress of σ_x exists on the neutral axis, and so a mode II fatigue crack is expected to grow along this section. The specimen (Fig. 17) has a chevron notch and side grooves.

Figure 18(a) shows the setup for the mode II fatigue crack growth test. In this test, two identical specimens are used as a pair so that a conventional closed-loop type tension-compression servomechanical fatigue machine can be used. Figure 18(b) shows the detail of attaching one specimen to the testing machine. Ceramic cylinders are inserted between cantilevers to share the applied load equally to each lever.

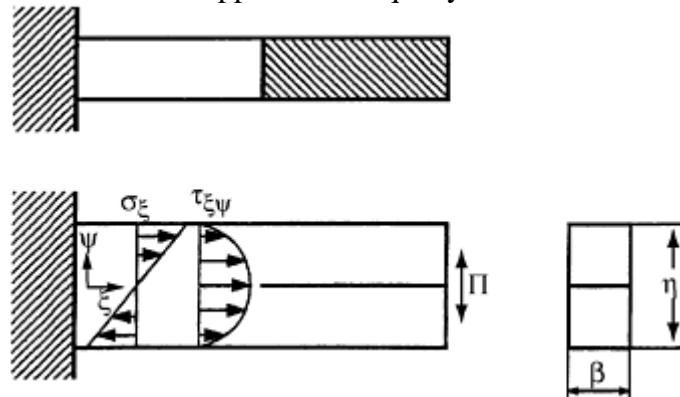


Fig. 16 Basic model of mode II crack growth test. P , force

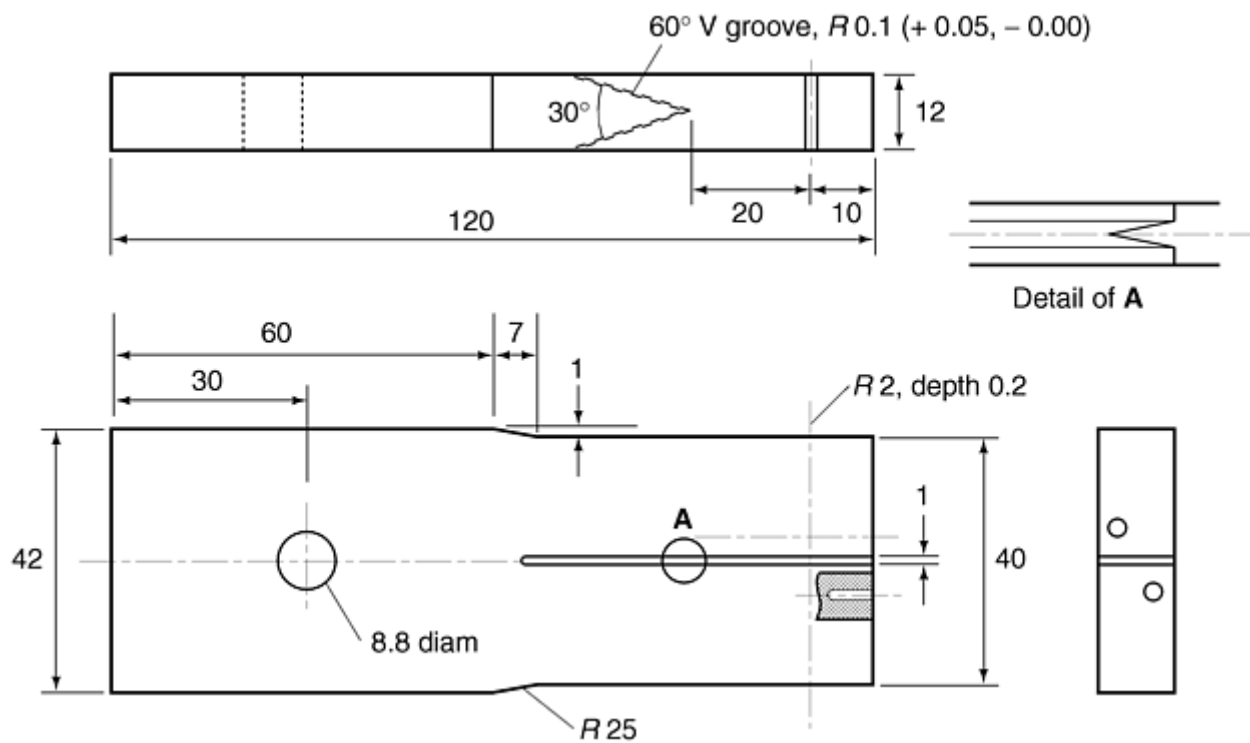


Fig. 17 Shape and dimension of mode II crack growth specimen. Dimensions are in mm

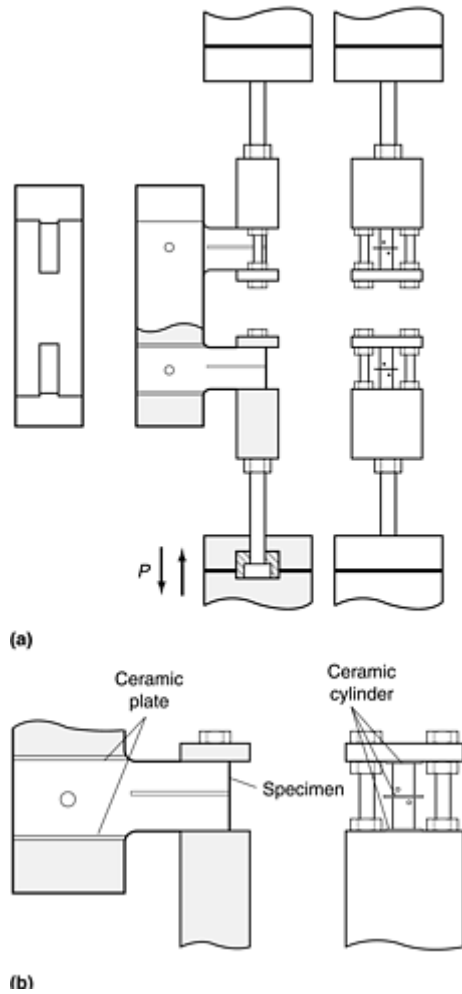


Fig. 18 Mode II crack growth testing machine, (a) Setup of mode II crack growth testing machine. (b) Detail of mode II crack growth testing machine with one specimen in place

Circumferentially Notched Cylindrical Specimen. This type of specimen is used to investigate the behavior of mode III crack growth under torsional loading (Fig. 19). Although the nominal stress intensity factor, K_{III} , is known, the exact value is difficult to estimate due to the friction between mating crack surfaces. A typical morphology of the fracture surface under these conditions is termed “factory roof” morphology (Ref 17).

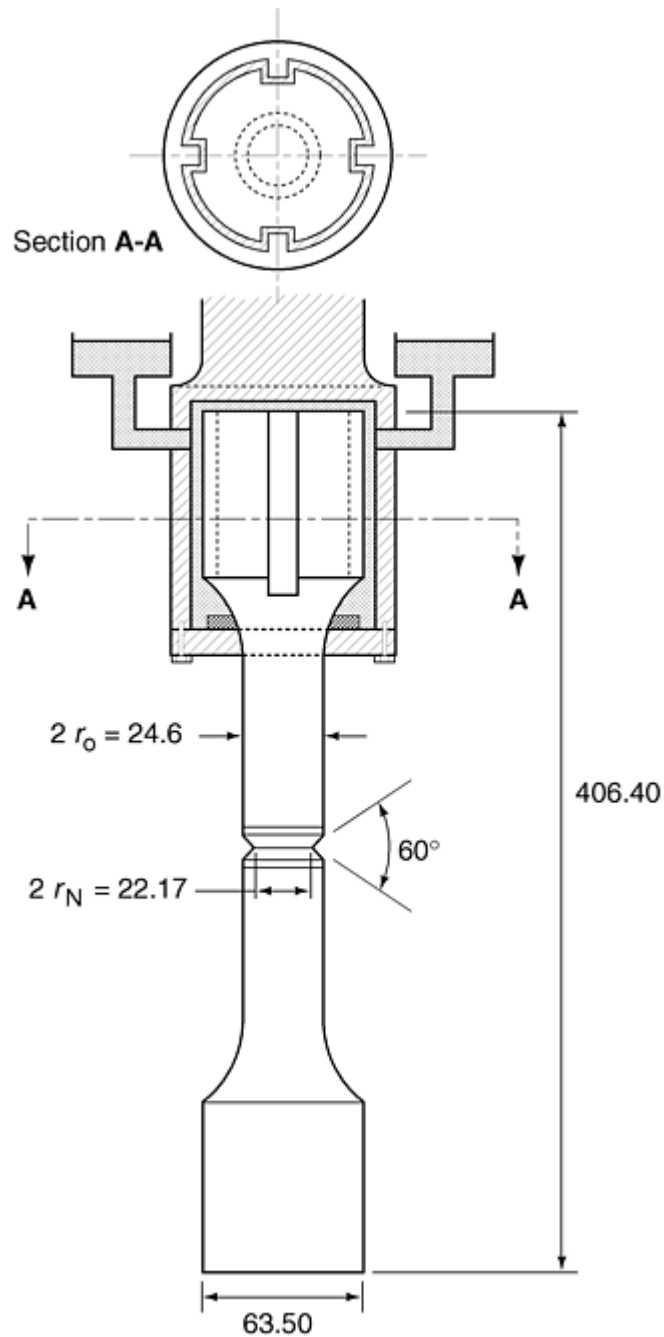


Fig. 19 Circumferentially notched torsion specimen for mode III fatigue crack propagation. Dimensions are in mm. r_o , outer radius; r_N , radius of notch. Source: Ref 17

Tubular Specimen Containing a Slit. This type of specimen is used to investigate the fatigue crack growth behavior and approximately two-dimensional, mixed-mode stress condition under torsion coupled with tension-compression. A typical initial notch (Fig. 20) is usually introduced. The width of slit must be very small, because the initial geometry of the slit strongly influences the initial direction of crack growth.

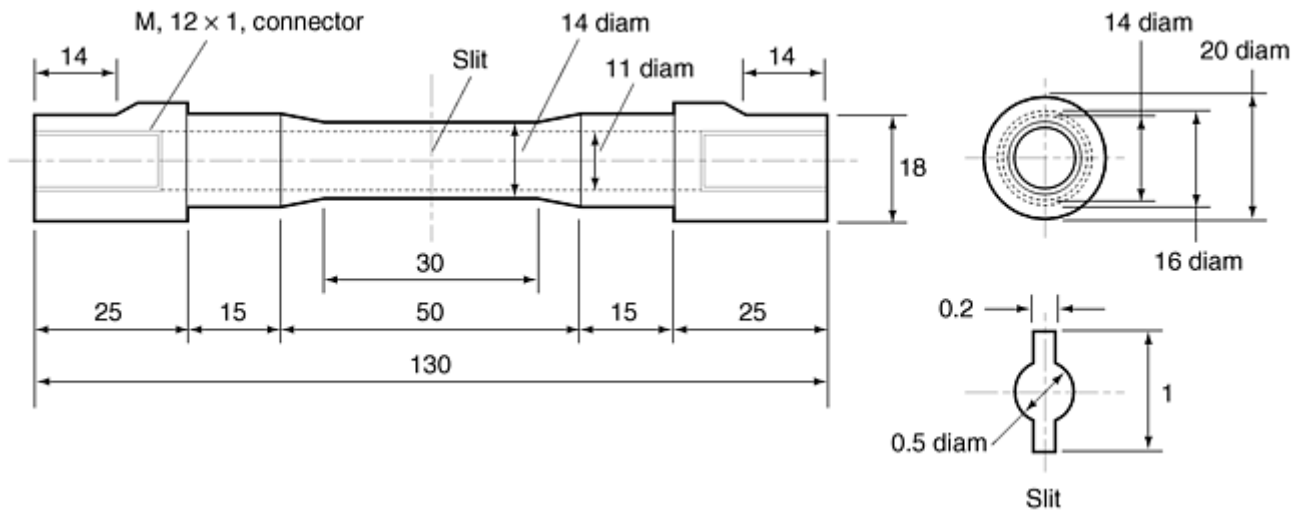


Fig. 20 Tubular specimen containing a slit for combined torsion and tension-compression fatigue test. Dimensions are in mm. Source: Ref 18

Solid Cylindrical Specimen Containing a Small Hole or Initial Crack. The effects of artificial small defects on torsional fatigue strength can be studied by introducing an artificial small hole (Ref 4). Figure 21 shows the shape and dimension of a drilled hole.

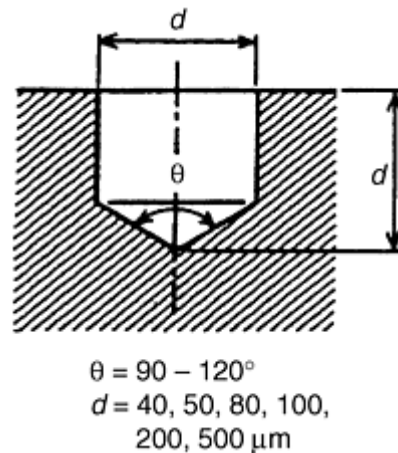


Fig. 21 Shape and dimension of a small hole introduced on the surface of torsional fatigue test specimen. (Geometry of specimen is shown in Fig. 4.) d , diameter. Source: Ref 4

If a fatigue crack is introduced by a preliminary tension-compression fatigue test, crack growth behavior and threshold condition under mixed-mode loading can be studied. Initial small semielliptical cracks ranging from 200 to 1000 μm in length are introduced by preliminary tension-compression fatigue using a specimen containing holes of 40 μm diameter (Fig. 22). Crack growth behavior from the initial small crack, such as crack branching (Ref 1) and kinking (Ref 19), can be investigate. The threshold condition of a small crack can be studied based on the mixed-mode fracture mechanics analysis of a semielliptical crack (Fig. 3).

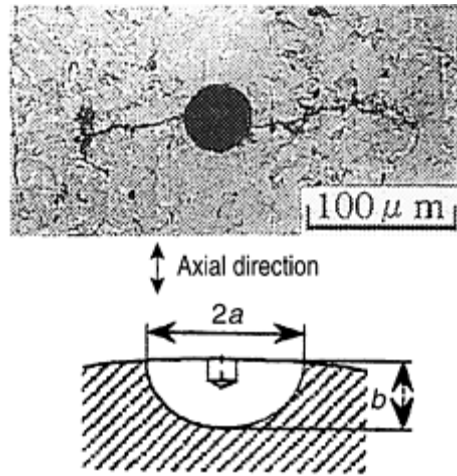


Fig. 22 Initial small surface crack introduced by tension-compression fatigue test using the specimens containing holes of 40 μm . (Geometry of specimen is shown in Fig. 7.) Source: Ref 1

References cited in this section

1. Y. Murakami and K. Takahashi, Torsional Fatigue of a Medium Carbon Steel Containing an Initial Small Surface Crack Introduced by Tension-Compression Fatigue: Crack Branching, Non-Propagation and Fatigue Limit, *Fatigue Fract. Eng. Mater. Struct.*, Vol 21, 1998, p 1473–1484
4. M. Endo and Y. Murakami, Effects of an Artificial Small Defect on Torsional Fatigue Strength of Steels, *J. Eng. Mater. Technol. (Trans. ASME)*, Vol 109, 1987, p 124–129
6. S. Iida and A.S. Kobayashi, Crack-Propagation Rate in 7075-T6 Plates under Cyclic Tensile and Transverse Shear Loadings, *J. Bas. Eng. (Trans. ASME), Ser. D*, Vol 91, 1969, p 764–769
7. K. Tanaka, Fatigue Crack Propagation from a Crack Inclined to the Cyclic Tensile Axis, *Eng. Fract. Mech.*, Vol 6, 1974, p 493–507
8. A. Otsuka, K. Mori, and T. Miyata, The Condition of Fatigue Crack Growth in Mixed-Mode Condition, *Eng. Fract. Mech.*, Vol 7, 1975, p 429–439
9. H. Kitagawa, R. Yuuki, and K. Tohgo, A Fracture Mechanics Approach to High-Cycle Fatigue Crack Growth Under In-Plane Biaxial Loads, *Fatigue Eng. Mater. Struct.*, Vol 2, 1979, p 195–206
10. H. Gao, M.W. Brown, and K.J. Miller, Mixed-Mode Fatigue Thresholds, *Fatigue Eng. Mater. Struct.*, Vol 5, 1982, p 1–17
11. K. Tohgo, A. Otsuka, and M. Yoshida, Fatigue Behavior of a Surface Crack under Mixed Mode Loading, *Fatigue '90, Proc. of the 4th International Conf. on Fatigue and Fatigue Thresholds*, Vol 1, Materials and Component Engineering Publication, 1990, p 567–572
12. H.A. Richard and K. Benitz, A Loading Device for the Creation of Mixed Mode in Fracture Mechanics, *Int. J. Fract.*, Vol 22, 1983, p R55–R58
13. D.L. Jones and D.B. Chisholm, An Investigation of the Edge-Sliding Mode in Fracture Mechanics, *Eng. Fract. Mech.*, Vol 7, 1975, p 261–270
14. K. Komai and E. Usuki, Fractographic Study on Mode II and Mode III SCC Crack Growth in Al-Zn-Mg Alloy, *J. Soc. Mater. Sci., Jpn.*, Vol 33, 1984, p 921–926

15. Y. Murakami and S. Hamada, New Method for the Measurement of Mode II Fatigue Threshold Stress Intensity Factor Range ΔK_{IIth} , *Fatigue Fract. Eng. Mater. Struct.*, Vol 20, 1997, p 863–870
16. Y. Murakami, C. Sakae, and S. Hamada, Mechanism of Rolling Contact Fatigue and Measurement of ΔK_{IIth} for Steels, *Proc. of Engineering Against Fatigue*, A.A. Balkema, Rotterdam, 1999
17. H. Nayeb-Hashemi, F.A. McClintock, and R.O. Ritchie, Effect of Friction and High Torque on Fatigue Crack Propagation in Mode III, *Metal. Trans. A*, Vol 13A, 1982, p 2197–2204
18. A.T. Yokobori, Jr., T. Yokobori, K. Sato, and K. Syoji, Fatigue Crack Growth under Mixed Mode I and II, *Fatigue Fract. Eng. Mater. Struct.*, Vol 8, 1985, p 315–325
19. Y. Murakami and K. Takahashi, Crack Branching and Threshold Conditions of Small Cracks in Biaxial Fatigue, *Proc. of the 12th Biennial Conf. on Fracture, ECF 12*, EMAS Publishing, Vol 1, 1998, p 67–72

Multiaxial Fatigue Testing

Yukitaka Murakami, Kyushu University, Japan

Summary

Since no standard testing method exists, it is important to choose a testing method suitable for a purpose of each testing. Various testing methods available for biaxial and multiaxial fatigue testing are summarized as follows. Biaxial fatigue testing machines, in which cyclic torsion is coupled with tension-compression loading, have been widely used because these testing machines can be applied to study the following:

- Mode III crack growth behaviors under cyclic torsion by using circumferentially notched cylindrical specimens
- Crack growth behaviors under approximately two-dimensional mode I and by using a tubular specimen with a slit
- Effects of small fatigue crack or defect under biaxial loading if an initial small crack is introduced by preliminary tension-compression fatigue testing

Triaxial Testing. In addition, biaxial fatigue testing (cyclic torsion with tension-compression) can be combined with the application of internal or external pressure for tubular specimens or cylindrical specimens. The influence of complex three-dimensional stress conditions can be investigated. However, these triaxial testing machines are very complicated and expensive.

Notched Plate and Precracked Bending Specimens. Rectangular plate specimens with an inclined notch or a crack and three-point or four-point bending specimens with a crack are used to investigate crack growth under mixed mode I and II. It must be noted that the stress intensity factors cannot be kept constant during the test, because crack growth mode shifts from mode II or III to mode I.

The cruciform specimen permits a wide variation of stress intensity factors, K_I and K_{II} . However, testing machines for this type of specimen are complex, and preparation of specimens is not easy. High compressive loads cannot be applied to the specimen because of the possibility of buckling.

Compact Specimen. The compact tension-shear (CTS) specimen is used to investigate the crack growth under mixed mode I and II, including pure mode II, loadings. The compact shear (CS) specimen is also used to investigate the crack growth under mode II and mode III. However, it is very difficult to achieve pure mode II crack growth by these specimens because crack growth mode easily switches from mode II to mode I. Thus, mode of loading is not necessarily the same as mode of crack growth.

Double Cantilever Specimen. Mode II crack growth plays an important role in crack growth under rolling contact fatigue. The values of ΔK_{Ith} for various steels can be measured using the specially designed double cantilever specimen. A conventional closed-loop tension-compression fatigue testing machine can be used in the system.

Multiaxial Fatigue Testing

Yukitaka Murakami, Kyushu University, Japan

References

1. Y. Murakami and K. Takahashi, Torsional Fatigue of a Medium Carbon Steel Containing an Initial Small Surface Crack Introduced by Tension-Compression Fatigue: Crack Branching, Non-Propagation and Fatigue Limit, *Fatigue Fract. Eng. Mater. Struct.*, Vol 21, 1998, p 1473–1484
2. A. Ono, “Fatigue of Steel under Combined Bending and Torsion,” Mem. Coll. Eng., Kyushu Imp. Univ., Vol 2, 1921, p 117–145
3. M.A. Fonte and M.M. Freitas, Semi-Elliptical Crack Growth Under Rotating or Reversed Bending Combined with Steady Torsion, *Fatigue Fract. Eng. Mater. Struct.*, Vol 20, 1997, p 895–906
4. M. Endo and Y. Murakami, Effects of an Artificial Small Defect on Torsional Fatigue Strength of Steels, *J. Eng. Mater. Technol. (Trans. ASME)*, Vol 109, 1987, p 124–129
5. M.W. Brown and K.J. Miller, Biaxial Cyclic Deformation Behavior of Steels, *Fatigue Eng. Mater. Struct.*, Vol 1, 1979, p 93–106
6. S. Iida and A.S. Kobayashi, Crack-Propagation Rate in 7075-T6 Plates under Cyclic Tensile and Transverse Shear Loadings, *J. Bas. Eng. (Trans. ASME), Ser. D*, Vol 91, 1969, p 764–769
7. K. Tanaka, Fatigue Crack Propagation from a Crack Inclined to the Cyclic Tensile Axis, *Eng. Fract. Mech.*, Vol 6, 1974, p 493–507
8. A. Otsuka, K. Mori, and T. Miyata, The Condition of Fatigue Crack Growth in Mixed-Mode Condition, *Eng. Fract. Mech.*, Vol 7, 1975, p 429–439
9. H. Kitagawa, R. Yuuki, and K. Tohgo, A Fracture Mechanics Approach to High-Cycle Fatigue Crack Growth Under In-Plane Biaxial Loads, *Fatigue Eng. Mater. Struct.*, Vol 2, 1979, p 195–206
10. H. Gao, M.W. Brown, and K.J. Miller, Mixed-Mode Fatigue Thresholds, *Fatigue Eng. Mater. Struct.*, Vol 5, 1982, p 1–17
11. K. Tohgo, A. Otsuka, and M. Yoshida, Fatigue Behavior of a Surface Crack under Mixed Mode Loading, *Fatigue '90, Proc. of the 4th International Conf. on Fatigue and Fatigue Thresholds*, Vol 1, Materials and Component Engineering Publication, 1990, p 567–572
12. H.A. Richard and K. Benitz, A Loading Device for the Creation of Mixed Mode in Fracture Mechanics, *Int. J. Fract.*, Vol 22, 1983, p R55–R58
13. D.L. Jones and D.B. Chisholm, An Investigation of the Edge-Sliding Mode in Fracture Mechanics, *Eng. Fract. Mech.*, Vol 7, 1975, p 261–270

14. K. Komai and E. Usuki, Fractographic Study on Mode II and Mode III SCC Crack Growth in Al-Zn-Mg Alloy, *J. Soc. Mater. Sci., Jpn.*, Vol 33, 1984, p 921–926
15. Y. Murakami and S. Hamada, New Method for the Measurement of Mode II Fatigue Threshold Stress Intensity Factor Range ΔK_{IIth} , *Fatigue Fract. Eng. Mater. Struct.*, Vol 20, 1997, p 863–870
16. Y. Murakami, C. Sakae, and S. Hamada, Mechanism of Rolling Contact Fatigue and Measurement of ΔK_{IIth} for Steels, *Proc. of Engineering Against Fatigue*, A.A. Balkema, Rotterdam, 1999
17. H. Nayeb-Hashemi, F.A. McClintock, and R.O. Ritchie, Effect of Friction and High Torque on Fatigue Crack Propagation in Mode III, *Metal. Trans. A*, Vol 13A, 1982, p 2197–2204
18. A.T. Yokobori, Jr., T. Yokobori, K. Sato, and K. Syoji, Fatigue Crack Growth under Mixed Mode I and II, *Fatigue Fract. Eng. Mater. Struct.*, Vol 8, 1985, p 315–325
19. Y. Murakami and K. Takahashi, Crack Branching and Threshold Conditions of Small Cracks in Biaxial Fatigue, *Proc. of the 12th Biennial Conf. on Fracture, ECF 12*, EMAS Publishing, Vol 1, 1998, p 67–72

Introduction to Mechanical Testing of Components

Introduction

TESTING OF COMPONENTS requires an understanding of service conditions and mechanical testing and design. While there are many types of components tests for a multitude of products, the articles in this Section focus primarily on the basic principles for some common types of engineering components. These articles provide an overview of the typical test methodology, developed by national organizations such as ASTM, as well as industry-specific organizations, test apparatus, procedures, test sample preparation, data collection, and interpretation. Using standard test methods provides for consistent test results.

The mechanical evaluation of components requires an engineer to use many sources of information. It also requires an understanding of service conditions, design, and manufacturing variables. All these variables can make it difficult to validate components. The following overviews briefly summarize some general factors in the design and manufacture of components. Additional information is also provided in the article "Overview of Mechanical Properties and Testing for Design" in this Volume. The remaining articles in this Section describe tests for common types of fabricated components and the modeling of metal deformation.

Introduction to Mechanical Testing of Components

Overview of Component Testing

Brian Klotz, Component Test Resources, General Motors Corporation

Testing of components involves a series of processes to validate the product for usage. Computer systems are playing a dominating role in the design of components and simulating how they react under different environments. Design engineers use three-dimensional modeling software to design components. This software allows the engineer to create a three-dimensional image of the component to scale. He or she can then manipulate the image to identify design concerns, match to models of mating parts to check for interference, and manufacture the component right from the model. This design model can also be used to generate a finite-element analysis (FEA) model. The FEA model can show an engineer how the design reacts under various loading conditions. If areas of the design are suspect, design changes can be made and reevaluated easily. While FEA models provide an engineer the ability to improve component designs without making a physical part, further test simulations to evaluate durability need to be developed to accurately predict the total capability of a component. The use of physical tests is required to develop these simulations.

An understanding of the operating environment in which the component must function establishes the basis for testing the component. The environment may include cyclic or static loading, vibration concerns, thermal variations, or many others. Duplicating or simulating this environment becomes a challenge at a component level. While elaborate test systems can be produced to incorporate multiple environments, in most instances the basic component design functionality is all that need be evaluated. Developing tests to perform the evaluations typically involves developing a set of fixtures to hold the component and impart the loading into the part on some type of test stand. Design of fixtures is critical to the repeatability of the overall testing. The loading characteristics the component experiences in its application must be understood in order for a test to be developed.

Once the test environment is understood, fixtures developed, and the component design manufactured, a test can be performed on the component. The testing is done either to correlate the output of the FEA model or validate the component design and manufacturing. Testing done to compare the results from math-based FEA models to real-life test results allows engineers the ability to further develop the capability of the models to predict design concerns. This type of testing typically requires less samples and can provide long-term cost

benefits to an organization. This iterative process of design analysis and testing ultimately leads to product designs that may require no component testing, only testing as part of an assembly to validate the system. Testing done to validate the component design and manufacturing requires knowledge of the duty cycle in which the component must operate. In order to develop component-level validation tests, test procedures and methods must be correlated to this duty cycle, and the test stand must be able to duplicate these load inputs. Validation tests require multiple samples to be subjected to duty-cycle loading. Results of these tests are then evaluated using statistical methods in order to determine whether they meet the product design requirements. This method of testing can be very costly if several redesigns must be done.

Introduction to Mechanical Testing of Components

Overview of Mechanical Properties for Component Design

Henry E. Fairman, MQS Inspection, Inc.

The ultimate result of performing mechanical tests is to provide information that may be used in the design and manufacture of components. Design of components requires an understanding of the materials properties and how they will be used by the component. The manufacturing process that is used to produce the part also must be considered during the design process because manufacturing methods influence materials properties and the selection of appropriate mechanical testing methods to ensure that the component will meet its required life cycle.

This overview briefly reviews the relationship of mechanical properties in the process of mechanical design. As previously noted, detailed materials properties and design methodologies are required for a wide variety of applications that encompass factors such as:

- Load-bearing capability to meet the desired service condition
- Capability of the design to meet the required lifetime
- Effect of service (environmental) conditions on the design
- Performance requirements such as minimum weight, stiffness, and life-cycle cost
- Size and shape factors

A significant part of the design process is also the experience based on the performance of similar components. The design process also uses predictive models, which may be a simple model or a more complex model developed by the FEA method.

Introduction to Mechanical Testing of Components

General Mechanical Behavior

One key aspect of product and process design is a basic understanding of fundamental mechanical behavior, which is described in the first two articles of this Volume (“Introduction to the Mechanical Behavior of Metals” and “Introduction to the Mechanical Behavior of Nonmetallic Materials”). In general, fine-grained materials have better mechanical and fatigue properties than coarse-grained materials. Components that have a mixture of fine- and coarse-grained materials will generally have properties similar to those of the coarse-grained material. Coarse-grained materials exhibit the lowest properties with the exception of creep and stress rupture, where single-grained materials have exhibited superior properties at elevated temperature.

Nonuniform microstructures will affect the mechanical properties of the material or component. For example, the center of 8 in. carbon or alloy bar produced by the strand casting process will exhibit different mechanical

properties than samples taken from the center, midradius, and outer diameter when tested in the longitudinal direction. Samples taken from the transverse direction will also have different properties than the longitudinal samples will have. Impact and fracture testing results are significantly impacted by the sample direction.

Mechanical working such as the rolling or drawing of materials can significantly improve the mechanical properties of the materials, raising the yield and ultimate strengths along with reducing the ductility values. Age hardening of metals generally raises the yield and ultimate strengths of materials. The fatigue properties are not generally significantly improved by age hardening.

Heat treating processes that result in transformation hardening, such as occurs with carbon and alloy steels, will raise the mechanical and fatigue properties of these alloys. It changes the creep properties by only a small degree because the principal effect is in the initial stage of creep deformation.

Introduction to Mechanical Testing of Components

Properties and Design for Static Loads

Tension and compression testing are common test methods as described in detail in the articles “Uniaxial Tension Testing” and “Uniaxial Compression Testing” in this Volume. Property data present in the literature are normally based on specimens machined from raw materials and represent ideal data for the materials. Typical stress-strain data for a variety of alloys are provided in Fig. 1. In the elastic region, stress and strain are proportional by Hooke's law ($\sigma = E\varepsilon$). In the plastic region, work hardening is described by a power law:

$$\sigma = Ke^n \quad (\text{Eq 1})$$

where K is the strength coefficient and n is the strain-hardening exponent. Typical stress-strain properties values are shown in Tables 1 and 2 (Ref 1) for selected steels and aluminum alloys, respectively, for monotonic loads. Tables 1 and 2 also list cyclic stress-strain properties, as described later. General properties related to monotonic stress-strain behavior are described briefly here.

Table 1 Monotonic and cyclic stress-strain properties of selected steels

Alloy	Condition ^(a)	Elastic modulus (E)		Yield strength (S_y)		Tensile strength (S_u)		Strength coefficient (K)		Strain hardening exponent (n)	Reduction in area, %	True fracture stress (σ_f)		True fracture strain (ϵ_f)
		MPa	10 ⁶ ksi	MPa	ksi	MPa	ksi	MPa	ksi			MPa	ksi	
Monotonic properties^(b)														
A136	As-received	207	30	321	46.5	556	80.6	993	144.0	0.21	67	990	143.6	1.06
A136	150 HB	207	30	317	46.0	565	81.9	0.21	69	1000	145.0	1.19
SAE950X	As-received, 137 HB	207	30	432	62.6	523	75.8	654	94.9	0.11	54
SAE950X	As-received, 146 HB	207	30	391	56.7	510	74.0	800	116.0	0.15	74	978	141.8	1.34
SAE980X	Prestrained, 225 HB	193	28	576	83.5	695	100.8	992	143.9	0.13	68	1219	176.8	1.15
1006	Hot rolled, 85 HB	207	30	248	36.0	318	46.1	414	60.0	0.14	73
1020	Annealed, 108 HB	186	27	254	36.8	392	56.9	399	57.9	0.07	64	661	95.9	1.02
1045	225 HB	200	29	516	74.8	751	108.9	1047	151.8	0.12	44	998	144.7	...
1045	Q&T, 390 HB	200	29	1274	184.8	1343	194.8	0.04	59	1860	269.8	0.89
1045	Q&T, 500 HB	200	29	1728	250.6	1956	283.7	2351	341.0	0.04	38	2306	334.4	...
1045	Q&T, 705 HB	200	29	1825	264.7	2067	299.8	0.19	2	2135	309.6	0.02
10B21	Q&T, 320 HB	200	29	999	144.9	1048	152.0	1294	187.7	0.05	67	1499	217.4	1.13
1080	Q&T, 421 HB	207	30	978	141.8	1349	195.6	2227	323.0	0.15	32	1645	238.6	...
4340	Q&T, 350 HB	200	29	1178	170.8	1240	179.8	1580	229.2	0.07	57	1653	239.7	0.84
4340	Q&T, 410 HB	207	30	1371	198.8	1467	212.8	38	1557	225.8	0.48
5160	Q&T, 440 HB	207	30	1487	215.7	1586	230.0	1940	281.4	0.05	39	1931	280.0	0.51
8630	Q&T, 254 HB	207	30	709	102.8	785	113.9	1061	153.9	0.08	16	840	121.8	0.17
Alloy	Condition ^(a)	Cyclic yield strength (S'_y)		Cyclic strength exponent (K')		Cyclic strain hardening exponent (n')	Cyclic true fracture stress (σ'_f)		b	Cyclic true fracture strain (ϵ'_f)	c			
		MPa	ksi	MPa	ksi		MPa	ksi						
Cyclic properties^(c)														
A136	As-received	330	47.9	1026	148.8	0.18	799	115.9	- 0.09	0.22	- 0.46			
A136	150 HB	337	48.9	1151	167.0	0.2	846	122.7	- 0.08	0.20	- 0.42			
SAE950X	As-received, 137 HB	353	51.2	957	138.8	0.16	772	112.0	- 0.08	0.34	- 0.52			
SAE950X	As-received,	409	59.3	939	136.2	0.13	824	119.5	-	0.42	-			

	146 HB								0.08		0.57
SAE980X	Prestrained, 225 HB	569	82.5	2658	385.5	0.25	1185	171.8	- 0.10	0.09	- 0.48
1006	Hot rolled, 85 HB	236	34.2	1351	196.0	0.28	802	116.3	- 0.12	0.48	- 0.52
1020	Annealed, 108 HB	233	33.8	1206	174.9	0.26	850	123.3	- 0.12	0.44	- 0.51
1045	225 HB	402	58.3	1178	170.8	0.17	960	139.2	- 0.08	0.50	- 0.52
1045	Q&T, 390 HB	842	122.1	1492	216.4	0.09	1408	204.2	- 0.07	1.51	- 0.85
1045	Q&T, 500 HB	1303	189.0	4634	672.1	0.2	2888	418.9	- 0.09	0.23	- 0.56
1045	Q&T, 705 HB	2255	327.0	4264	618.4	0.1	2416	350.4	- 0.07	0.002	- 0.47
10B21	Q&T, 320 HB	691	100.2	990	143.6	0.06	1036	150.3	- 0.04	4.33	- 0.85
1080	Q&T, 421 HB	870	126.2	3177	460.8	0.21	2364	342.9	- 0.10	0.51	- 0.59
4340	Q&T, 350 HB	797	115.6	1863	270.2	0.14	1944	282.0	- 0.10	1.22	- 0.73
4340	Q&T, 410 HB	876	127.0	1950	282.8	0.13	1898	275.3	- 0.09	0.67	- 0.64
5160	Q&T, 440 HB	1070	155.2	2432	352.7	0.13	2068	300.0	- 0.08	9.56	- 1.05
8630	Q&T, 254 HB	603	87.5	961	139.4	0.08	1049	152.1	- 0.11	0.21	- 0.86

(a) Q&T, quenched and tempered.

(b) E , elastic modulus; S_y , yield strength; S_u , tensile strength; σ_f , true fracture stress; ϵ_f , true fracture strain; %RA, percent reduction in area. K and n per Eq 1.

(c) S'_y cyclic yield strength; K' cyclic strength coefficient; n' cyclic strain hardening exponent; see also Eq 3 for definitions of b and c .

Source: Ref 1

Table 2 Monotonic and cyclic stress-strain properties of selected aluminum alloys

Alloy	Condition	Elastic modulus (E)		Yield strength (S_y)		Tensile strength (S_u)		Strength coefficient (K)		Strain hardening exponent (n)	Reduction in area, %	True fracture stress (σ_f)		True fracture strain (ϵ_f)
		GPa	10 ⁶ ksi	MPa	ksi	MPa	ksi	MPa	ksi			MPa	ksi	
Monotonic properties ^(a)														
1100	As received	69	10	97	14	110	16	88	2.1
2014	T6 temper	73	10.6	462	67	510	74	35	627	91	0.42
2024	T351 temper	70	10.2	303	44	476	69	807	117	0.20	35	634	92	0.38
2024	T4 temper	73	10.6	T 688 C 303	T 55 C 44	469	68	T 455 C 634	T 66 C 92	T 32 C 0.17	25	558	81	0.43
2219	T851 temper	71	10.3	359	52	469	68	0.28
5086	F temper	70	10.1	207	30	310	45	0.36
5182	O temper	72	10.5	L 110 T 131	L 16 T 19	L 303 T 338	L 44 T 49	L 37 T 44	393	57	L 0.46 T 0.58
5454	O Temper	69	10	138	20	248	36	44	365	53	0.58
5454	10% cold rolled	69	10
5454	20% cold rolled	69	10
5456	H311 temper	69	10	234	34	400	58	35	524	76	0.42
6061	T651 temper	69	10	290	42	310	45	365	53	0.042	58	469	68	0.86
7075	T6 temper	71	10.3	469	68	579	84	827	120	0.113	33	745	108	0.41
7075	T73 temper	72	10.4	414	60	483	70	...	86	0.054	23	579	84	0.26
Alloy	Condition	Cyclic yield strength (S'_y)		Cyclic strength exponent (K')		Cyclic strain hardening exponent (n')	Cyclic true fracture stress (σ'_f)		b	Cyclic true fracture strain (ϵ'_f)	c			
		MPa	ksi	MPa	ksi		MPa	ksi						
Cyclic properties ^(b)														
1100	As received	55	8	159	23	0.17	193	28	-0.106	1.8	-0.69			
2014	T6 temper	448	65	703	102	0.073	786	114	-0.081	0.85	-0.86			
2024	T351 temper	448	65	786	114	0.09	1014	147	-0.11	0.21	-0.52			
2024	T4 temper	427	62	655	95	0.065	1103	160	-0.124	0.22	-0.59			
2219	T851 temper	331	48	793	115	0.14	834	121	-0.11	1.33	-			

											0.079
5086	F temper	296	43	600	87	0.11	572	83	-0.092	0.69	-0.75
5182	O temper	296	43	469	68	0.075	841	122	-0.137	1.76	-0.92
5454	O temper	234	34	400	58	0.084	565	82	-0.116	1.78	-0.85
5454	10% cold rolled	234	34	427	62	0.098	565	82	-0.108	0.48	-0.67
5454	20% cold rolled	255	37	407	59	0.081	565	82	-0.103	1.75	-0.80
5456	H311 temper	352	51	600	87	0.086	724	105	-0.11	0.46	-0.67
6061	T651 temper	296	43	538	78	0.096	634	92	-0.099	0.92	-0.78
7075	T6 temper	517	75	965	140	0.10	1317	191	-0.126	0.19	-0.52
7075	T73 temper	400	58	510	74	0.032	800	116	-0.098	-0.26	-0.73

(a) K and n as defined in Eq 1; L, longitudinal; T, transverse. See Table 1 for remaining symbol definitions.

(b) See Eq 3.

Source: Ref 1

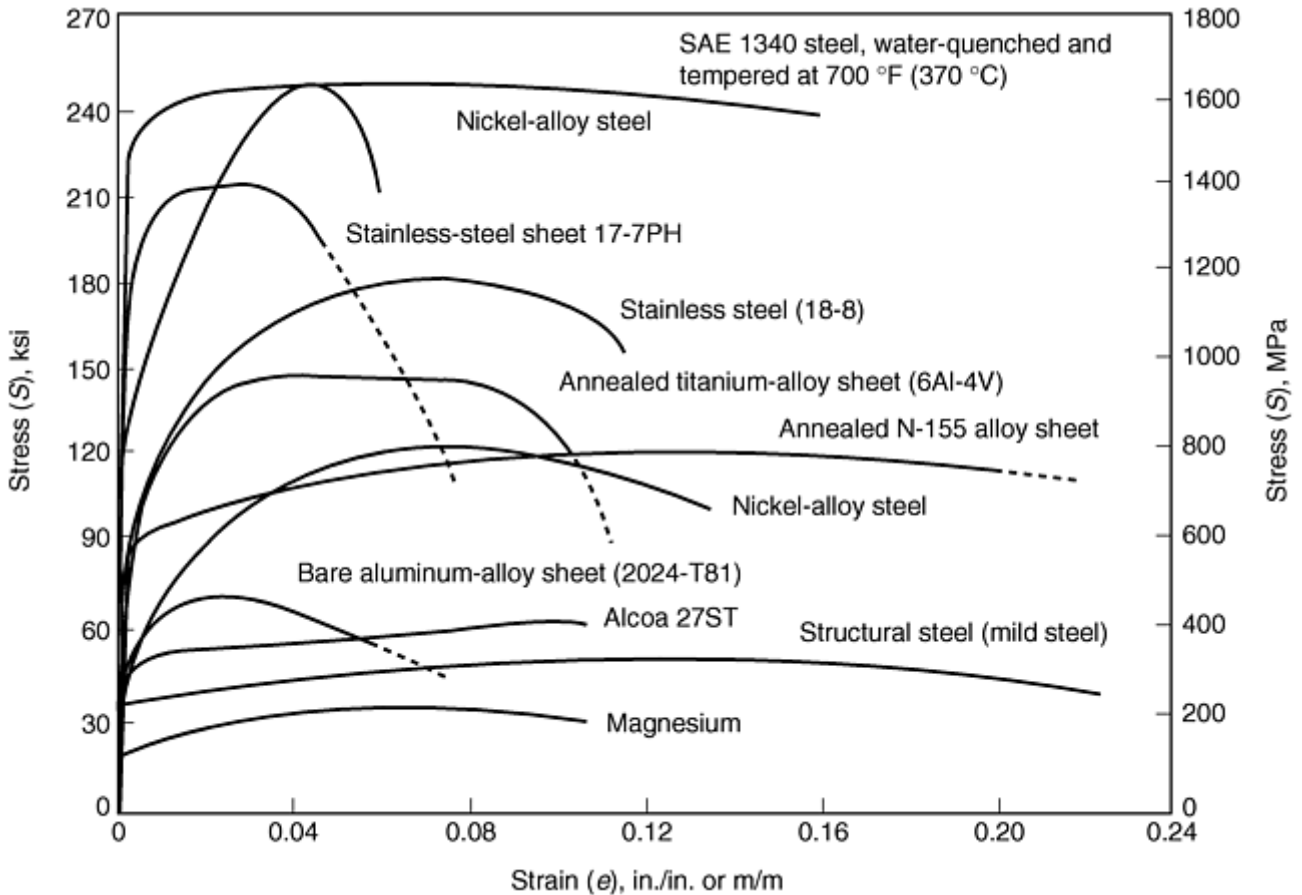


Fig. 1 Typical stress-strain curves for selected metals

Ultimate strength refers to the maximum stress that a material can withstand before failure occurs. The ultimate strength is related to the materials composition, mechanical working, and heat treatment. The term *ultimate tensile strength* is synonymous with tensile strength, which is the accepted ASTM term for the maximum stress obtainable before fracture of the specimen.

Yield strength is commonly defined as the load at which a given amount of plastic strain has occurred. The yield strength is related to the materials composition, mechanical working, and heat treatment.

Elastic limit (or proportional limit) is the load at which plastic deformation begins to take place. Removal of the load allows the material to return to its initial shape. This property of materials is not commonly used in the design of components.

Modulus of elasticity is the ratio of stress to strain below the elastic limit. The modulus is a measure of material rigidity or stiffness for loading under tension, compression, or shear. The tensile modulus of elasticity (E), in principle, is roughly equivalent to the modulus in compressive. The shear modulus (or the modulus of rigidity, G) is related to the tensile modulus as follows:

$$G = \frac{E}{2}(1 + \mu) \quad (\text{Eq 2})$$

where μ is Poisson's ratio.

The moduli are usually characteristic for a given materials family such as aluminum, steel, and so on. Table 3 (Ref 2) provides data on the relative stiffness of a number of materials. Tensile moduli range from 45 to 207 GPa (6.5×10^6 to 30×10^6 psi) for common metallic materials.

Table 3 Comparison of the stiffness of selected engineering materials

Material	Modulus of elasticity (E), GPa	Density (ρ), mg/m ³	$E/\rho \times 10^{-5}$	$E1/2/\rho \times 10^{-2}$	$E1/3/\rho$
Steel (carbon and low alloy)	207	7.825	26.5	5.8	35.1
Aluminum alloys (average)	71	2.7	26.3	9.9	71.2
Magnesium alloys (average)	40	1.8	22.2	11.1	88.2
Titanium alloys (average)	120	4.5	26.7	7.7	50.9
Epoxy-73% E-glass fibers	55.9	2.17	25.8	10.9	81.8
Epoxy-70% S-glass fibers	62.3	2.11	29.5	11.8	87.2
Epoxy-63% carbon fibers	158.7	1.61	98.6	24.7	156.1
Epoxy-62% aramid fibers	82.8	1.38	60	20.6	146.6

Source: Ref 2

Dynamic Modulus. Modulus can also be determined from resonant vibrations with piezoelectric or electromagnetic transducers. ASTM standards C 1198 and C 1259 describe test method for determining the dynamic elastic module of advanced ceramics. These standards also form the basis for two recent additions to ASTM standards:

- ASTM E 1875-98; Standard Test Method for Dynamic Young's Modulus, Shear Modulus, and Poisson's Ratio by Sonic Resonance
- ASTM E 1876-98; Standard Test Method for Dynamic Young's Modulus, Shear Modulus, and Poisson's Ratio by Impulse Excitation

These two standards are almost verbatim versions of C 1198 and C 1259, which are generic and need not be confined to advanced ceramics, but are applicable to all elastic materials.

In resonant methods, Young's modulus, sheer modulus, and Poisson's ratio can all be computed from the resonant frequencies of prismatic bar, rods, or slabs. Dynamic methods of measuring elastic moduli are related to adiabatic conditions; whereas, static methods are isothermal. For ceramic materials (Ref 3), the adiabatic values can be of the order of 0.1% higher than isothermal values (Ref 4).

ASTM C 1198 is a clone of two earlier ASTM standards (C 848 and C 623) that are suitable for ceramic whitewares, and glass and glass-ceramics, respectively. Rather than using the tables and graphs in the earlier standards, the newer standard C 1198 uses the original equations for relating the elastic constants to the resonance frequencies. Although recommended sizes for flat and round specimens are given, the equations are sufficiently general that a wide size range can be used. The equations include the conventional polynomial correction factors to reflect the finite specimen thicknesses, but simplified equations are also provided for instances where the length-to-thickness ratio of the specimens is greater than 20. Specimen flatness and parallelism are critical; but, with proper care, accuracies and precisions of better than 1% are feasible. C 1198 is

primarily intended to be used with monolithic, or whisker-or particulate-reinforced ceramics. There is some potential for its use on continuous-fiber reinforced ceramics.

ASTM C 1259 describes a similar but more modern methodology for measuring the same properties as C 1198 except that impulse rather than continuous excitation is used to resonate the specimen. The fundamental resonant frequency of a rectangular-shaped specimen is measured following mechanical excitation by a singular elastic strike with an impulse tool. The resulting vibrations are monitored and transformed into electrical signals. The signals are analyzed and the properties calculated with a knowledge of the mass and dimensions of the specimen.

JIS Standard R 1602 also uses the resonance frequency method, but goes further by incorporating several alternate procedures. These include measurements of the static deflection of a beam in bending (with proper corrections for machine compliance), the strain in a strain-gauged specimen loaded in flexure, or the longitudinal-wave velocity in an ultrasonically pulsed specimen. The elevated temperature standard JIS R 1605 incorporates the resonance frequency or ultrasonic pulse methods to compute dynamic elastic moduli. Both Japanese standards prescribe specimen length to thickness ratios of 20 or greater. The same simplified formulas as given in ASTM C 1198 are used.

Elongation and reduction of area are ductility measurements determined during static mechanical testing and are related to the plastic deformation that takes place between the elastic limit and the ultimate strength of a material. These properties are useful when evaluating ductility during deformation such as extrusion, forging, or drawing.

Poisson's ratio, μ , is the ratio between axial strain to lateral strain during tensile loading. It usually has a value of approximately 0.3 for most metallic materials. For some materials with anisotropic crystal structures (such as the hcp structure of titanium α or α - β alloys with a preferred or textured crystal orientation), Poisson's ratio may depend on orientation.

Design of components for tensile loads normally uses the "fail-safe" concept of design in which a safety factor is applied to either the yield strength or the ultimate strength of the material. Design using cast materials typically uses the ultimate strength, whereas design using wrought materials uses the yield strength. Design that anticipates rapid loading often utilizes the ratio of yield strength to ultimate strength. A material having a ratio above 0.75 often will fail due to its inability to undergo plastic deformation under load.

Flexural Modulus and Strength. For ceramics and polymer materials, modulus and strength is often evaluated by flexural testing. In the case of ceramics, bend testing eliminates the gripping problems associated with the tension testing of ceramics.

Flexural testing by either three-point or four-point loading is the traditional method for evaluating the uniaxial strength ceramics. The method is applicable for purposes of material development, and sometimes design. However, for design purposes, tension testing is generally preferred (Ref 5).

Standards for the flexural testing of ceramics include:

- ASTM C 1161-90 Standard Test Method for Flexural Strength of Advanced Ceramics at Ambient Temperature
- ASTM C 1211-92 Standard Test Method for Flexural Strength of Advanced Ceramics at Elevated Temperature
- MIL STD 1942 Flexural Strength of Advanced Ceramics at Ambient Temperatures
- JIS R 1601 Testing Method for Flexural Strength (Modulus of Rupture) of High-Performance Ceramics
- JIS R 1604 Elevated Temperature Testing Method for Flexural Strength
- EN 843-1 Monolithic Ceramics, Mechanical Properties at Room Temperature, Part 1: Determination of Flexural Strength.

The latter standard has been adopted by the European Community and supercedes previous European Standards (DIN 51-110 Part 1 and AFNOR B41-104). There are many similarities between these standards. The specimen and fixture sizes are quite comparable and many tolerances and specifications are identical. Nevertheless, there are some differences that are of concern as discussed in Ref 5. For example, the U.S. and European standards require the load rollers to be free to rotate to eliminate friction error, but the JIS standard does not.

Although the flexure test is a simple method, significant errors (>5%) can occur from twisting, misalignment, and frictional constraints (Ref 3). Flexure testing of continuous-fiber, ceramic matrix composites must be

viewed with considerable caution because the failure mode could be tension fracture, shear fracture, compression failure, or buckling.

Hardness testing is a very common mechanical test applied to materials. Hardness testing is used extensively in quality control, where data can be collected that relate the mechanical properties of a given material, its microstructure, and processing methods.

Over the years, many researchers have endeavored to relate hardness values obtained from mechanical testing to the properties of the material. This has proved to be difficult because the shape of the indenters, loads, and rate of loading interact with each material in a different manner. For example, an annealed material will work harden during the test differently than the same material that has received various degrees of cold work. Materials such as carbon and alloy steels, which are strengthened by different processes (such as annealing, normalizing, and hardening), have different work-hardening behavior that influences indentation results. Likewise, cast aluminum alloys have similar hardness values to the wrought alloys yet possess significant different mechanical properties. Therefore, the correlation of strength and hardness (much like the conversion of hardness readings for different hardness scales) depends on the material, its condition, and the underlying strengthening mechanisms.

More information on the factors and variation of strength-hardness correlations are discussed in the article "Selection and Industrial Applications of Hardness Tests" in this Volume. In fact, Fig. 15(b) in that article illustrates an example of an inverse correlation of tensile strength and hardness for a line pipe steel. The explanation of this unexpected result is not clear, but it demonstrates the need for caution and empirically derived analysis when estimating mechanical strength from hardness.

References cited in this section

1. M.R. Mitchell, Fundamentals of Modern Fatigue Analysis for Design, *Fatigue and Fracture*, Vol 19, *ASM Handbook*, ASM International, 1996, p 231
2. M.M. Farag, Properties Needed for the Design of Static Structures, *Materials Selection and Design*, Vol 20, *ASM Handbook*, ASM International, 1997, p 510
3. C.R. Brinkman and G.D. Quinn, Standardization of Mechanical Properties Tests for Advanced Ceramics, in *Mechanical Testing Methodology for Ceramic Design and Reliability*, Marcel Dekker, 1998, p 353–386
4. R. Morrell, *Handbook of Properties of Technical and Engineering Ceramics*, Vol 1, Her Majesty's Stationary Office, London, 1989
5. G.D. Quinn and R. Morrell, "Design Data for Engineering Ceramics: A Review of the Flexure Test," *J. Am. Ceram. Soc.*, Vol 74 (No. 9), 1991, p 2037–2066

Introduction to Mechanical Testing of Components

Properties and Design for Dynamic Loads

Mechanical design is commonly based on static loading of a component. However, there are many components that see an initial dynamic load followed by static or cyclic loading. Typical examples are explosive fasteners driven into concrete walls, the torsion spring used in overhead door mechanisms, dies for metal-forming operations, and aircraft landing gears. Impact tests and fracture toughness tests are the most common tests performed to demonstrate how materials behave under dynamic loads. These types of tests are performed to use standard test specimens and often bear no relationship to the complex shapes present in components. The rate of loading is also kept to standard conditions.

Impact testing of materials provides information on how a material will perform under dynamic loading. The data obtained from impact testing provide no values that can be used in the designing of components. The data do provide comparative information between different materials as well as the difference between lots of materials and/or heat treatment. The data are often plotted as a function of temperature because many materials exhibit a loss in impact strength as the temperature is lowered. This point is defined as the *transition* temperature (Fig. 2).

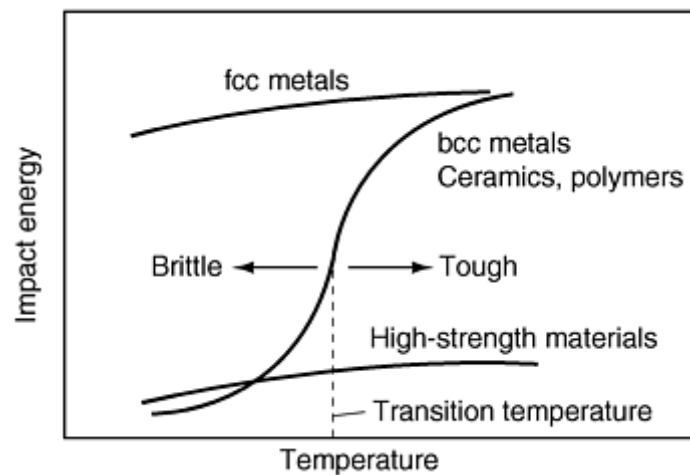


Fig. 2 Ductile-brittle temperature transition. bcc, body-centered cubic; fcc, face-centered cubic

The most common impact tests are the Charpy and Izod tests, in which the notched specimen is struck by a hammer. The notch concentrates the stresses so that plastic flow is minimized, and almost all of the energy is used to fracture the specimen. Other less-common impact tests are the tensile and torsional impact tests, which measure the performance of materials under these conditions.

The tensile impact test provides comparative information on the differences between various materials and lots of materials. It also can be used to predict the forming characteristics of materials being fabricated by high-energy forming methods. The torsional impact test provides information on how tubular cross sections of various materials will perform under load. The most common application of these data is for shafts that are rapidly brought up to an operating speed and supplement the torsional fatigue data on these sections. The test is rarely performed on solid specimens due to the more complex stress state that exists in this geometry.

Fracture toughness testing evaluates the ability of a material to withstand fracture in the presence of cracks. When fracture toughness is used as design criteria, the designer must be aware that the failure of the component will occur at nominal stresses below the design stresses for the given material. Cracks, discontinuities, and microscopic features such as inclusions and other anomalies are often present in components and should be accounted for in the design process.

The design philosophy for fracture toughness falls into four categories:

- *Infinite-life design*: This philosophy assumes that the component has no defects that will affect the life of the component. This philosophy incorporates the traditional design method that uses the fatigue (endurance) limit of the material.
- *Safe-life design*: This approach uses a design stress based on the number of cycles at the working stress that the component must carry to perform its task.
- *Fail-safe design*: This design philosophy assumes that the structure will continue to support its load after the failure of a single component of the structure. Fail-safe designs often include the presence of cracks.
- *Damage-tolerant design*: This approach was developed by the U.S. Air Force and incorporates the detection of cracks along with the crack growth rate of the material. Based on life histories, the remaining life of the component is determined.

Properties and Design for Cyclic Loads

In the real world, very few components are subject to static tensile, compression, and bending loads. The common approach for design of components in fatigue is the design-life approach, where data obtained from cyclic testing are presented as an $S-N$ curve. The data from $S-N$ testing are often combined in a constant-life fatigue diagram, which combines the alternating stress conditions with the cycles to failure. One of the advantages of such a diagram is that the effect of different loading conditions is easily seen in this type of diagram. Figure 3 (Ref 6) shows a typical constant-life diagram for alloy steel. This type of diagram can be used to construct $S-N$ diagrams for the expected loading of the component.

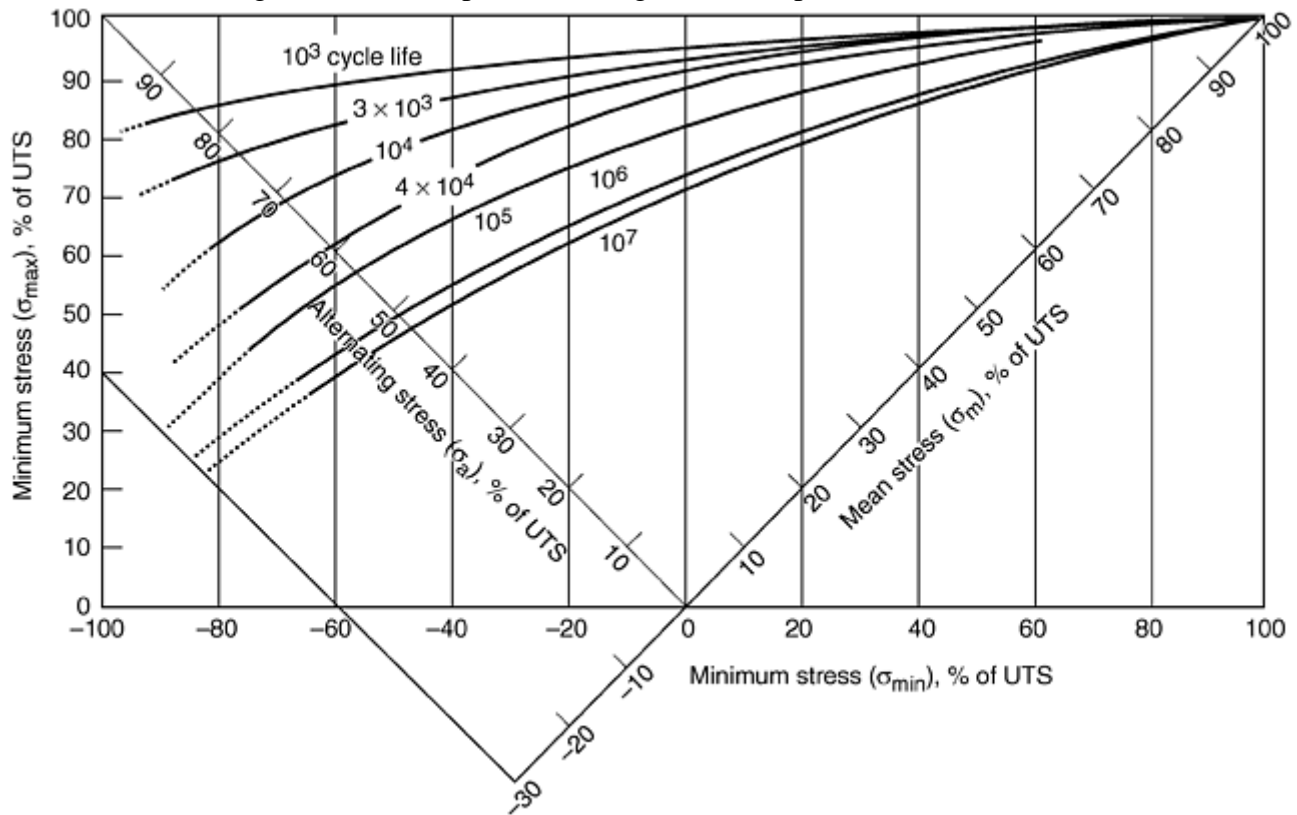


Fig. 3 Constant-life diagram for alloy steels. The data in this type of representation can be used to create an $S-N$ curve for any level of mean stress. Note the presence of safe-life, finite-life lines on this plot. This plot. This diagram is for average test data for axial loading of polished specimens of AISI 4340 steel (ultimate tensile strength, UTS, 125 to 180 ksi) and is applicable to other steel (e.g., AISI 2330, 4130, and 8630). Source: Ref 6

External and internal notches significantly reduce the fatigue properties of materials. For example, precipitation-hardened metals exhibit lower fatigue properties than would be expected from their yield/tensile properties. Ceramics and glasses contain internal defects, which reduce their expected fatigue strengths. The operating environment can produce external defects such as corrosion pits or stress corrosion cracks, which can serve as initiation sites for fatigue to occur.

Fatigue life data are also expressed in terms of a strain-based fatigue, which is divided into an elastic (high-cycle) component and a plastic (low-cycle) component as follows (Ref 1):

$$\frac{\Delta \epsilon}{2} = \underbrace{\frac{\sigma'_f}{E} (2N_f)^b}_{\text{Elastic}} + \underbrace{\epsilon'_f (2N_f)^c}_{\text{Plastic}} \quad (\text{Eq 3})$$

where N_f is the number of cycles to failure, σ'_f is the cyclic true fracture, ϵ'_f is the true fracture strain, and b and c are constants for a given material. Values for selected steels and aluminum alloys are listed in Tables 1 and 2, respectively.

Use of published fatigue data and stress concentrations combined with appropriate calculations and rate of loading provide only an approximation of the useful life of a component. If repeated failures of a component occur, a statistically designed, factorial test program should perform to validate the design assumptions. Data obtained from strain gage measurements are useful in the design of the experiment.

Tension-tension (axial) fatigue commonly occurs in press frames, bolted assemblies, and components subjected to thermal stresses. In the case of a press frame, it would be a zero to maximum tensile loading condition. The bolted joint normally has a preload applied so that the loading of the bolt is between a mean and maximum tensile stress. A bridge that undergoes thermal expansion will have both compressive and tensile loading, with the mean stress being that of the ambient temperature at time of construction. Many materials exhibit a good correlation of axial fatigue strength with their yield and/or ultimate strengths and typically have a ratio of 0.3 to 0.5 to these properties.

Bending fatigue results in the outer surface being subjected to alternating tensile and compressive stresses in varying ratios with the limiting strength being in the tensile direction. Common components subjected to bending fatigue include flapper-type valves and gear teeth. The stresses are given by:

$$\sigma = (Mc)/I \quad (\text{Eq 4})$$

where M is the bending moment, c is the distance from the center of the section to the outside surface, and I is the moment of inertia of the section.

Since the maximum stress is at the surface, processes such as shot peening and carburizing that produce compressive stresses are often used to improve the properties of the material.

Rotating bending fatigue tests have been performed for many years, and the bulk of fatigue data presented in the literature were produced by the R.R. Moore rotating bending fatigue machine. In this type of loading, a given point on the outside diameter of the specimens is subjected to alternating tensile or tensile-compressive stress each time it undergoes a 360° rotation. The effects of various stress concentrations on rotating bending endurance limits are also readily available. These data are widely used for shafts that are subjected to varying degrees of misalignment and are the predominate failure modes for these components.

Torsional fatigue data are less commonly reported in the literature. These are the predominate failure modes of compression springs and shafts that are connected to drive gears. For steels, the ratio between rotating bending and torsional endurance limits is typically 0.8.

Fatigue crack growth rates are directly related to the material's crystal structure, stress level, rate of loading, and stress concentrations present in the component. The field of fracture mechanics has provided significant data on the growth rate of fatigue cracks under axial loading where fracture toughness (K_{Ic}) has been determined for a wide variety of materials.

References cited in this section

1. M.R. Mitchell, Fundamentals of Modern Fatigue Analysis for Design, *Fatigue and Fracture*, Vol 19, *ASM Handbook*, ASM International, 1996, p 231
6. D.W. Cameron and D. Hoepfner, Fatigue Properties in Engineering, *Fatigue and Fracture*, Vol 19, *ASM Handbook*, ASM International, 1996, p 19

Introduction to Mechanical Testing of Components

Mechanical Properties and Design for High Temperature

Creep properties of materials are those in which a material continues to elongate under constant load at the working temperature of a component. Creep damage usually results in fracture, and creep properties of metallic materials are significant in such diverse applications as a toaster heating element, automobile exhaust system

components, high-temperature steam lines, furnaces and burners, and jet engine turbine components. It is of major importance for polymers, which exhibit creep at or just above room temperature.

Stress-rupture testing is also used to evaluate the creep resistance of materials. In this test, the sample is subjected to a constant load, and the time to fracture is measured as it varies with stress and temperature. It is often used as an acceptance test for high-temperature materials since it can be performed more rapidly than creep testing can. Creep fatigue results when cyclic loading occurs at elevated temperatures where creep damage can occur. It is directly related to the crack growth properties of the material, and is discussed in the article "Creep Crack Growth Testing" in this Volume. In general, materials are classed as being either creep-ductile materials (iron-base materials fall within this group) or creep-brittle materials (this group includes high-temperature aluminum alloys, titanium alloys, nickel-base high-temperature alloys, and ceramics).

Creep of Ceramics. Ceramics also exhibit creep behavior. Use of advanced ceramics for elevated temperature applications may involve the need for constitutive laws in order to predict deformation or strain up to a specified limit as established by design. Similarly creep-rupture models may also be required. Bending test data obtained at temperatures within the creep range are not suitable for establishing these laws because of difficulties in interpretation of specimen behavior (Ref 5). Therefore, to formulate these laws, data must be generated in both pure tension or compression in accordance with established standards.

ASTM C 1291 is a new standard that covers determination of the elevated-temperature time-dependent deformation tensile (creep) and stress-rupture properties of monolithic ceramics. Creep time-to-failure is also included in this test method. This method is only suitable for monolithic ceramics. This test is not suitable for continuous fiber-reinforced ceramic composites, which do not behave as isotropic, homogeneous materials. Specimens (dogbone flats or rounds) are subjected to uniform stress in the gage area, where creep deformation is measured by either optical or mechanical extensometers (Ref 7, 8, and 9). Optical extensometers provide good stability, while mechanical devices may have advantages in terms of accuracy and ease of use.

References cited in this section

5. G.D. Quinn and R. Morrell, "Design Data for Engineering Ceramics: A Review of the Flexure Test," *J. Am. Ceram. Soc.*, Vol 74 (No. 9), 1991, p 2037–2066
7. H. Pih and K.C. Liu, "Laser Diffraction Methods for High Temperature Strain Measurements," *Exp. Mech.*, March 1991, p 60–64
8. K.C. Liu and J.L. Ding, "A Mechanical Extensometer for High Temperature Tensile Testing of Ceramics," *J. Test. Eval.*, Sept 1993, p 406–413
9. J.Z. Gyekenyesi and P.A. Bartolotta, "An Evaluation of Strain Measuring Devices for Ceramic Composites," *J. Test. Eval.*, Vol 20, 1992, p 285–295

Introduction to Mechanical Testing of Components

Applications Factors in Mechanical Performance

Application of materials properties along with the operating stresses calculated from traditional mechanics yields only a best-case scenario for the performance of a component. Design shape, environmental effects and surface degradation, the manufacturing method, and the condition of the material all play significant roles in the design process.

Part Shape. In almost all cases, engineering components and machine elements have to incorporate design features that introduce changes in their cross section. For example, shafts must have shoulders to take thrust loads at the bearings and must have keyways or splines to transmit torques to or from pulleys and gears mounted on them. Under load, such changes cause localized stresses that are higher than those based on the

nominal cross section of the part. Figures 4 , 5 , 6 , and 7 (Ref 10) show the effects of notches on the stress field in tension, compression, torsion, and bending, respectively.

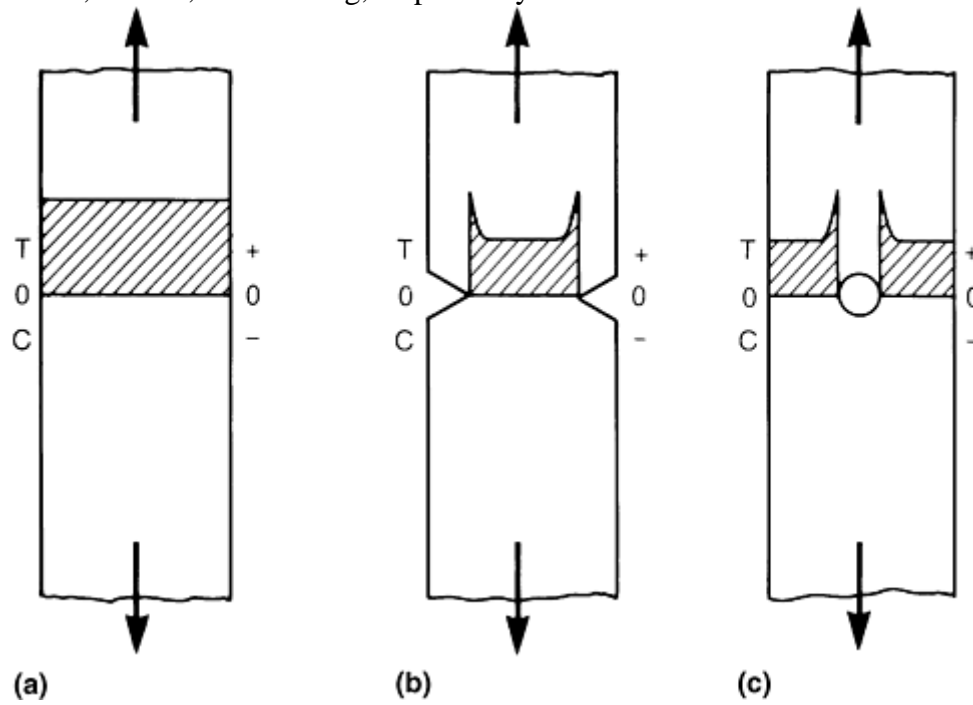


Fig. 4 Effect of stress concentrations in tension. (a) No stress concentration. (b) Surface stress concentrations. (c) Transverse hole stress concentration.

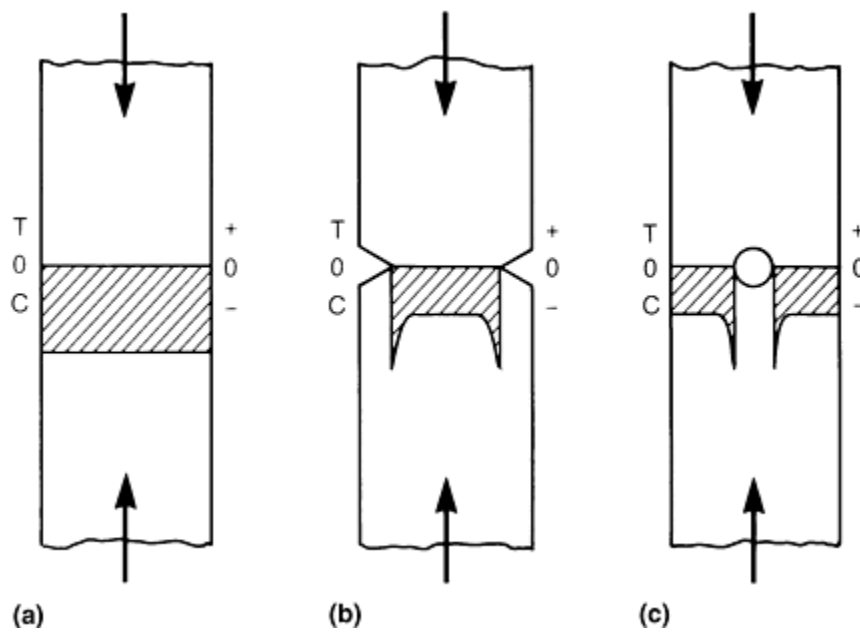


Fig. 5 Effect of stress concentrations in compression. (a) No stress concentration. (b) Surface stress concentrations. (c) Transverse hole stress concentration. Source: Ref 4

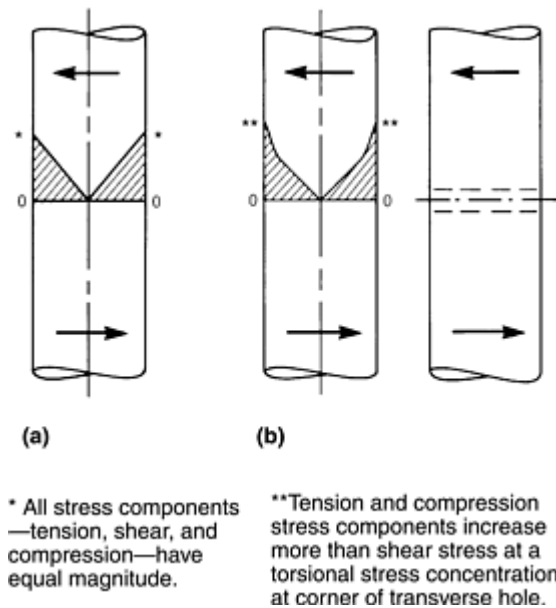


Fig. 6 Effect of stress concentrations in torsion. (a) No stress concentration. (b) Transverse hole stress concentration. Source: Ref 4

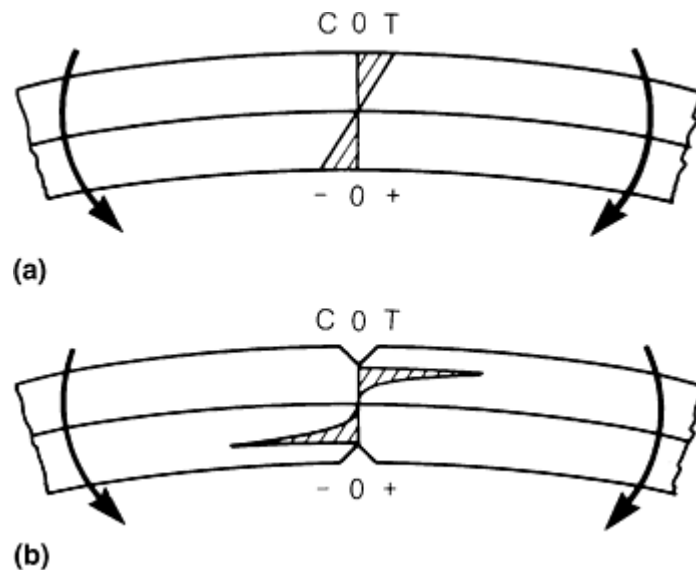


Fig. 7 Effect of stress concentrations in bending. (a) No stress concentration. (b) Transverse surface stress concentrations. Source: Ref 4

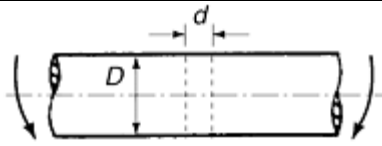
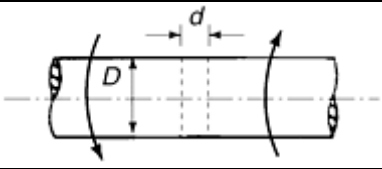
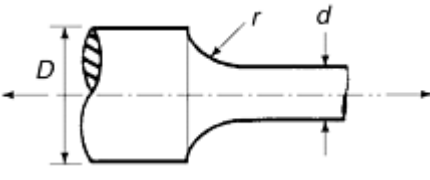
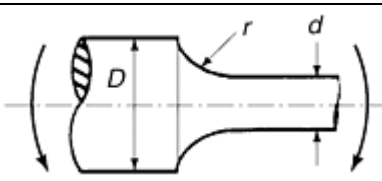
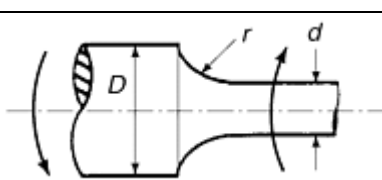
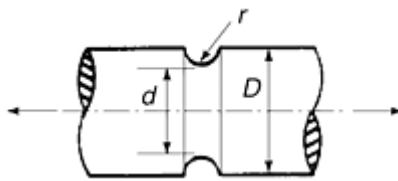
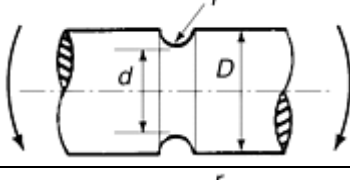
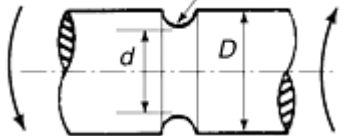
The severity of the stress concentration depends on the geometry of the discontinuity and the nature of the material. A geometric, or theoretical, stress concentration factor, K_t , is usually used to relate the maximum stress, σ_{max} , at the discontinuity to the nominal stress, σ_{av} , according to the relationship:

$$K_t = \sigma_{max} / \sigma_{av}$$

Stress concentration factors have been published for many years in references such as *Peterson's Stress Concentration Factors*, originally published in 1950 with a new edition recently published (Ref 11). The value of K_t depends on the geometry of the part and can be determined from stress concentration charts such as those given in Ref 11 and 12. Table 4 (Ref 2) also gives some typical values of K_t .

Table 4 Values of the stress concentration factor, K_t

Component shape		Value of critical parameter, K_t	
Round shaft with transverse hole			
Bending		$d/D = 0.025$	2.65

		= 0.05	2.50
		= 0.10	2.25
		= 0.20	2.00
Torsion		$d/D = 0.025$	3.7
		= 0.05	3.6
		= 0.10	3.3
		= 0.20	3.0
Round shaft with shoulder			
Tension		$d/D = 1.5, r/d = 0.05$	2.4
		$r/d = 0.10$	1.9
		$r/d = 0.20$	1.55
		$d/D = 1.1, r/d = 0.05$	1.9
		= 0.10	1.6
		= 0.20	1.35
Bending		$d/D = 1.5, r/d = 0.05$	2.05
		$r/d = 0.10$	1.7
		$r/d = 0.20$	1.4
		$d/D = 1.1, r/d = 0.05$	1.9
		$r/d = 0.10$	1.6
		$r/d = 0.20$	1.35
Torsion		$d/D = 1.5, r/d = 0.05$	1.7
		$r/d = 0.10$	1.45
		$r/d = 0.20$	1.25
		$d/D = 1.1, r/d = 0.05$	1.25
		$r/d = 0.10$	1.15
		$r/d = 0.20$	1.1
Grooved round bar			
Tension		$d/D = 1.1, r/d = 0.05$	2.35
		$r/d = 0.10$	2.0
		$r/d = 0.20$	1.6
Bending		$d/D = 1.1, r/d = 0.05$	2.35
		$r/d = 0.10$	1.9
		$r/d = 0.20$	1.5
Torsion		$d/D = 1.1, r/d = 0.05$	1.65
		$r/d = 0.10$	1.4
		$r/d = 0.20$	1.25

Source: Ref 2

Other methods of estimating K_t for a certain geometry include photoelasticity, brittle coatings, and finite-element techniques. Experience shows that under static loading, K_t gives an upper limit to the stress concentration value and applies it to high-strength, low-ductility materials. With more ductile materials, local yielding in the very small area of maximum stress causes some relief in the stress concentration. Generally, the following design guidelines should be observed if the deleterious effects of stress concentration are to be kept to a minimum (Ref 2):

- Abrupt changes in cross section should be avoided. If they are necessary, generous fillet radii or stress-relieving grooves should be provided.
- Slots and grooves should be provided with generous run-out radii and with fillet radii in all corners.
- Stress-relieving grooves or undercuts should be provided at the ends of threads and splines.
- Sharp internal corners and external edges should be avoided.
- Oil holes and similar features should be chamfered and the bore should be smooth.
- Weakening features such as bolt and oil holes, identification marks, and part numbers should not be located in highly stressed areas.
- Weakening features should be staggered to avoid the addition of their stress-concentration effects.

Pin Bearing Testing. Special geometric conditions or configurations may also have specially designed tests for strength evaluation. One example of this is the pin bearing test conducted on metal products that must sustain loads that are applied when the material is riveted, bolted, or similarly mechanically fastened. The purpose of the test is to determine the bearing strength properties and to indicate the bearing stress versus the deformation of the hole. The bearing load is applied to the specimen through a cylindrical pin, which is fitted into a hole normal to the surface of the specimen. The data obtained by this test procedure are used to calculate minimum properties that can be used in the design of structural members used in the aerospace industry.

The properties of primary concern in pin bearing tests are bearing yield strength and bearing ultimate strength. The bearing yield strength is the bearing stress at which a material exhibits a specified limiting deviation from the proportionality of bearing stress to bearing strain. The bearing ultimate strength is the maximum bearing stress a material is capable of sustaining. These values are normally determined at edge-distance ratios (e/D) of 1.5 and 2.0, where the edge-distance ratio is the ratio of the edge distance, e , to the pin diameter, D . Edge distance, e , is the distance from the edge of a bearing specimen to the center of the hole in the direction of the applied force. Bearing area is the product of the pin diameter and specimen thickness. The bearing loads are divided by the bearing area to yield the bearing stress or strength, which is the force per unit of bearing area.

Although a standard method for the pin-type bearing test is covered in ASTM E 238, "Standard Test Method for Pin-Type Bearing Test of Metallic Materials," it is oriented to testing aluminum and magnesium. Consequently, problems with pin distortion or failure may be encountered when testing higher-strength materials such as titanium and high-strength steel at ultimate strengths of 1860 to 2070 MPa (270 to 300 ksi). Much of ASTM E 238 is aimed toward obtaining consistent results among laboratories. Consequently, it must be recognized that values obtained under laboratory-type conditions will not be representative of those achieved under actual loading conditions of a part or structure.

Cleaning of the specimen and pin is also necessary to provide consistent, comparable results. However, cleaning produces test results that are higher than in actual service (where fasteners may have platings, sealants, or lubricants to facilitate installation). In aluminum and magnesium alloys, lubrication can cause reductions of up to 15% in bearing yield strength values obtained in tests with clean, dry bearing surfaces. This includes the unintentional application of oil from human fingers during handling of the specimens and test fixtures.

Pin bearing tests typically are conducted on sheet-type specimens, using the full thickness of the material when possible. If the specimen is too thick in relation to the pin diameter, the test pin may bend or break before the bearing strength can be achieved. Conversely, buckling may occur if the specimen is too thin in relation to the pin diameter. To avoid pin deformation or failure and specimen buckling, a pin diameter to specimen thickness ratio (D/t) of 2 to 4 is recommended in ASTM E 238. Most testing of aluminum is conducted using a D/t ratio of 2. To test high-strength steel, D/t ratios up to 4 may be necessary. Using a higher D/t ratio, however, increases the possibility of buckling.

Stress-Corrosion Cracking (SCC) occurs in a variety of materials as a result of internal and external stress conditions in the component in conjunction with the operating environment. After completion of stress analysis in the design process, a designer normally has a list of materials suitable for a given environment. However, SCC and other environmentally assisted cracking (EAC) are complex problems that warrant careful attention at the materials selection stage. Unexpected causes, such as the use of cleaning agents on high-strength or stainless steels, can be a factor. More details on the standards and tests associated with SCC and hydrogen embrittlement are described in the article "Evaluation of Environmentally Assisted Crack Growth" in this Volume.

Wear can occur by a variety of mechanisms depending on the properties of the material and the service condition. Wear resistance is, therefore, not a materials property as are strength, elastic modulus, endurance limit, or fracture toughness. Wear and its corollary, wear resistance, are systems properties or responses. A

summary of designing for wear resistance is provided in the article “Design for Wear Resistance” in *Materials Selection and Design*, Volume 20 of the *ASM Handbook*. Comprehensive information on the wear properties of materials is provided in *Friction, Lubrication, and Wear Technology*, Volume 18 of the *ASM Handbook*.

The properties of castings vary widely as a function of the section thickness due to the differences in the cooling rate and the specific characteristics of the alloy being cast. The reported properties of cast materials are normally obtained from test bars, which have solidified under ideal conditions. Properties can be specified at selected areas based on the expected design stress at these locations.

Forgings are often selected as the material form for components since the grain flow can be controlled to produce directional properties that improve the performance of the component. For example, if the grain flow is aligned with the direction of the maximum tensile stress, maximum properties can be realized. Gears are often forged with the grain flow normal to the applied load in order to improve the resistance to crack initiation and propagation.

Rolling and extrusion of metals also produce directional properties. For example, a strip of 1095 carbon steel having a hardness of 58-60 HRC will tear like a piece of paper when loaded parallel to the rolling direction and will be almost impossible to fracture in the transverse condition.

Powder metallurgy (P/M) parts must be carefully considered by designers. The mechanical properties and fatigue performance of press-and-sintered P/M parts generally do not match those obtained by cast or wrought materials of the same composition. Porosity is an integral part of castings and P/M materials. The net effect of porosity on mechanical properties is a combination reduced cross-sectional area along with internal notches, which reduces the ultimate strength and elongation of the component.

References cited in this section

2. M.M. Farag, Properties Needed for the Design of Static Structures, *Materials Selection and Design*, Vol 20, *ASM Handbook*, ASM International, 1997, p 510
4. R. Morrell, *Handbook of Properties of Technical and Engineering Ceramics*, Vol 1, Her Majesty's Stationary Office, London, 1989
10. D. Wulpi, *Understanding How Components Fail*, 2nd ed., ASM International, 1999, p 51–53
11. W.D. Pilkey, *Peterson's Stress Concentration Factors*, 2nd ed., John Wiley & Sons, 1997
12. J.E. Shigley and L.D. Mitchell, *Mechanical Engineering Design*, 4th ed., McGraw-Hill, 1983

Introduction to Mechanical Testing of Components

References

1. M.R. Mitchell, Fundamentals of Modern Fatigue Analysis for Design, *Fatigue and Fracture*, Vol 19, *ASM Handbook*, ASM International, 1996, p 231
2. M.M. Farag, Properties Needed for the Design of Static Structures, *Materials Selection and Design*, Vol 20, *ASM Handbook*, ASM International, 1997, p 510
3. C.R. Brinkman and G.D. Quinn, Standardization of Mechanical Properties Tests for Advanced Ceramics, in *Mechanical Testing Methodology for Ceramic Design and Reliability*, Marcel Dekker, 1998, p 353–386

4. R. Morrell, *Handbook of Properties of Technical and Engineering Ceramics*, Vol 1, Her Majesty's Stationary Office, London, 1989
5. G.D. Quinn and R. Morrell, "Design Data for Engineering Ceramics: A Review of the Flexure Test," *J. Am. Ceram. Soc.*, Vol 74 (No. 9), 1991, p 2037–2066
6. D.W. Cameron and D. Hoepfner, Fatigue Properties in Engineering, *Fatigue and Fracture*, Vol 19, *ASM Handbook*, ASM International, 1996, p 19
7. H. Pih and K.C. Liu, "Laser Diffraction Methods for High Temperature Strain Measurements," *Exp. Mech.*, March 1991, p 60–64
8. K.C. Liu and J.L. Ding, "A Mechanical Extensometer for High Temperature Tensile Testing of Ceramics," *J. Test. Eval.*, Sept 1993, p 406–413
9. J.Z. Gyekenyesi and P.A. Bartolotta, "An Evaluation of Strain Measuring Devices for Ceramic Composites," *J. Test. Eval.*, Vol 20, 1992, p 285–295
10. D. Wulpi, *Understanding How Components Fail*, 2nd ed., ASM International, 1999, p 51–53
11. W.D. Pilkey, *Peterson's Stress Concentration Factors*, 2nd ed., John Wiley & Sons, 1997
12. J.E. Shigley and L.D. Mitchell, *Mechanical Engineering Design*, 4th ed., McGraw-Hill, 1983

Testing for Deformation Modeling

Dan Zhao, Johnson Controls, Inc.

Introduction

COMPUTER MODELING OF DEFORMATION has become a popular engineering tool and is used with considerable success in the metal forming industry. The popularity of deformation modeling has increased with the rapid advancement of computer hardware and software technology. However, one of the key factors in successfully employing deformation modeling is accurate and adequate input of material properties. Various mechanical, thermal, and interfacial properties are required depending on the particular material and process being modeled.

The mechanical properties required for deformation modeling include flow stress, Young's modulus, Poisson's ratio, and anisotropic properties. The most important property is flow stress, and it is usually required as a function of strain, strain rate, and temperature.

Forming processes can be divided into three major categories: bulk forming, sheet-metal forming, and special forming processes. Bulk forming includes forging, extrusion, drawing, and rolling. Sheet-metal forming consists of stamping, deep drawing, blanking, punching, spinning, and superplastic forming. Semisolid forming and polymer extrusion are some of the special forming processes. In this article, each processing category is introduced with a brief description of the constitutive models. The required properties for process modeling are outlined, and the test methods for determining these properties are described. Special attention is given to the accuracy of data. Additional information on bulk workability testing and sheet formability is also contained in *ASM Handbook, Volume 14, Forming and Forging*.

Testing for Bulk Forming

As the name implies, bulk forming usually involves workpieces that are bulky compared with sheet metal. Because bulk forming usually involves large plastic deformation, the most important mechanical input for modeling is stress-strain data. For warm and hot forming processes, data may be needed over a range of temperatures and strain rates. Several efforts have been made to make such data available for a number of alloys (Ref 1, 2, and 3). In this section, both compression and tension tests are discussed in detail. In addition to stress-strain curves, other properties such as Young's modulus and workability data can also be obtained from these tests. Data reduction procedures, such as temperature correction and fitting to constitutive equations, are provided. Finally, testing for interfacial properties such as the friction coefficient and heat-transfer coefficient are described briefly.

Constitutive Equations

The general form of the constitutive equation for deformation processing is:

$$\bar{\sigma} = f(\bar{\epsilon}, \bar{\dot{\epsilon}}, T) \quad (\text{Eq 1})$$

where $\bar{\sigma}$ is equivalent true stress, $\bar{\epsilon}$ is equivalent true strain, $\bar{\dot{\epsilon}}$ is equivalent true strain rate, and T is processing temperature.

Most software packages for bulk forming modeling have options to input the testing data in a tabular form or as a constitutive equation. The tabular form is easy to use, but is not based on any fundamental metallurgical principles, as with some of the constitutive equations. The most frequently used constitutive equation is:

$$\bar{\sigma} = K\bar{\epsilon}^n\bar{\dot{\epsilon}}^m + Y \quad (\text{Eq 2})$$

where n is the strain-hardening exponent, m is the strain-rate sensitivity, and Y and K are constants.

Strain-rate sensitivity is important at elevated temperatures, while it has little influence at room temperature for most metallic materials. In contrast, the importance of the strain-hardening exponent increases with decreasing temperature. The values of m and n can be found in Ref 4 for a number of metals and alloys.

The equation above does not reflect the influence of temperature. For each temperature, there is a set of constants. A more fundamentally sound equation was proposed by Sellars and Tegart (Ref 5) by assuming material flow during deformation as a thermally activated process:

$$\dot{\epsilon} = A(\sinh \alpha\bar{\sigma})^{n'} \exp\left(-\frac{Q}{RT}\right) \quad (\text{Eq 3})$$

where A , α , and n' are constants determined by fitting the empirical data, and Q is the apparent activation energy. At low stresses ($\alpha\bar{\sigma} < 0.8$), Eq 3 reduces to a power law:

$$\dot{\epsilon} = A_1\bar{\sigma}^{n'} \exp\left(-\frac{Q}{RT}\right) \quad (\text{Eq 4})$$

At high stresses ($\alpha\bar{\sigma}$ is greater than 1.2), and Eq 3 reduces to an exponential relation:

$$\begin{aligned} \dot{\epsilon} &= A_2 \exp(\alpha n' \bar{\sigma}) \exp\left(-\frac{Q}{RT}\right) \\ &= A_2 \exp(\beta \bar{\sigma}) \exp\left(-\frac{Q}{RT}\right) \end{aligned} \quad (\text{Eq 5})$$

where β is a material parameter.

Other constitutive relations have been proposed to describe dynamic recovery and dynamic recrystallization, such as the Laasroui-Jonas model (Ref 6) and internal variable model (Ref 7). Those relationships have not

been implemented in commercially available software packages and can only be used as user-defined subroutines. The testing and data reduction procedures for these models were documented by Thirukkonda, Zhao, and Male (Ref 8).

Fracture Criteria

One of the most useful predictions that can be made from computer modeling is failure of parts during processing. To predict failure, ductile-fracture criteria must be incorporated in modeling. The most popular fracture criterion is the Cockcroft-Latham criterion, which states that fracture occurs when the integration of the maximum principal stress over equivalent strain exceeds a constant (Ref 9):

$$\bar{\epsilon}_f \int_0^{\bar{\epsilon}_f} \sigma_1 d\bar{\epsilon} \geq C_2 \quad (\text{Eq 6})$$

where σ_1 is the maximum principal stress, $\bar{\epsilon}_f$ is equivalent strain at fracture, and C_2 is a constant representing the workability of the workpiece material. If $\sigma_1 < 0$, there are only compressive stresses, and no fracture occurs. Zhao, Bandstra, and Kuhn (Ref 10) developed a new fracture criterion that can be directly related to the bulk workability test (Ref 11):

$$\sigma_{1f} \frac{\bar{\epsilon}}{\bar{\sigma}} \geq C' \quad (\text{Eq 7})$$

where σ_{1f} is the maximum principal stress at fracture, and C' is a workability constant. For incremental loading, Bandstra (Ref 12) proved the criterion can be expressed as:

$$\int_0^{\bar{\epsilon}_f} \frac{\sigma_1}{\bar{\sigma}} d\bar{\epsilon} \geq C' \quad (\text{Eq 8})$$

A review of fracture criteria can be found in Ref 10.

Testing for Deformation Processing

It must be understood that testing for deformation processing is very different from testing for static mechanical properties. Testing for static mechanical properties, such as tensile strength, yield strength, and elongation, needs to be conducted at a very low loading rate, and according to standards such as those published by ASTM (Ref 13, 14, 15, and 16). For example, the conventional strain rate specified in the standards for compression testing is $8.33 \times 10^{-5} \text{ s}^{-1}$, and the rapid strain rate is only $8.33 \times 10^{-3} \text{ s}^{-1}$ (Ref 14). Testing for deformation processing must be conducted to cover the range of strain rates experienced by the workpiece, which can reach 1000 s^{-1} . In addition, large strains, such as true strain of 120%, are common in metal forming processes. Such high strains may not be needed when testing for static properties.

Compression Test

Compression tests are normally used to determine stress-strain curves for bulk forming, because most bulk forming processes involve mainly compressive stresses. The test is also relatively easy to perform, and the specimen geometry is usually simple.

Testing Apparatus. The testing machine can be either a servohydraulic or mechanical screw-driven machine. A schematic of a testing apparatus is shown in Fig. 1. The capacity of the loading frame is rated in units of kilonewtons (kN) or kilopounds (kip). Selection of loading capacity depends on the material being tested. In general, a 300 kN servohydraulic machine is capable of testing most metallic materials over a wide range of temperatures and strain rates. High-speed testing machines can also be ordered with custom design from manufacturers.

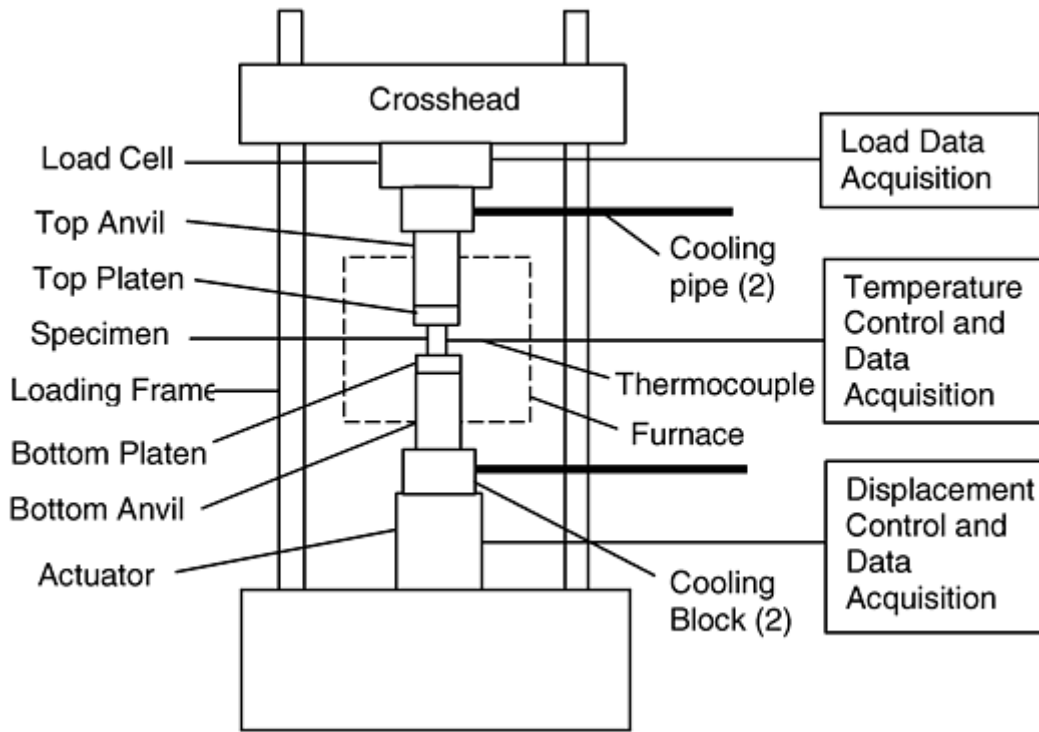


Fig. 1 Schematic of a compression-testing system

Load cells are rated for load capacity. Several load cells may be needed to cover different load ranges and provide accurate readings. There are two kinds of load cells: static and dynamic. Hydraulic machines usually come with dynamic load cells. Dynamic load cells can be used for both static and dynamic loading.

For elevated-temperature testing, a furnace is mounted on the testing machine, usually on the loading frame. The furnace can also be mounted on a cart to be pushed in or out. Four types of furnaces are commonly used: resistance heating, radiant heating, induction heating, and vacuum. A resistance-heating furnace is slower compared to radiant and induction-heating furnaces, but usually has three heating zones and better temperature control. A radiant-heating furnace is fast and has good temperature control, but the life of the radiant bulbs is short, which increases maintenance cost. An induction-heating furnace is very rapid, but its temperature control is poor. In addition, specimens may not be heated uniformly in such a furnace. A vacuum furnace or environmental chamber is needed for specimens, such as titanium alloys, that can oxidize at elevated temperatures. Quenching may be performed to retain microstructures at testing temperatures. For the first three types of furnaces, quenching can be performed by opening the furnace and dropping the specimen in a quenching medium such as water. For a vacuum furnace, quenching has to be performed with an inert gas, such as helium, inside the furnace. The furnace door can only be opened after the furnace temperature is low enough (below 300 °C, or 570 °F, for a tungsten heating element) to prevent damage to the heating element.

Cooling blocks must be installed between the load cell and the top anvil, and between the bottom anvil and the actuator. Aluminum alloys can be used to construct cooling blocks. Several water channels are drilled through the cooling blocks and connected with copper tubing to circulate cold water through the blocks.

The top and bottom anvils can be made of stainless steel, superalloys, Ti-Zr-Mo alloy (TZM), or graphite. For temperatures below 1000 °C (1830 °F), stainless steel can be used. For temperatures below 1350 °C (2460 °F), TZM can be used. For temperatures above 1350 °C (2460 °F), graphite can be used. The diameter of the anvils should be at least three times that of the specimen. TZM and graphite are suitable in a vacuum furnace. In air, alternative materials for TZM would be Inconel 718, stainless steel 17-7PH, or Haynes 188. However, the temperature limits for these materials are not as high as for TZM.

The compression platens can be made of several materials. Table 1 shows the materials and their applicable temperatures and strain rates. In most cases, TZM anvils and platens are used for temperatures of 800–1350 °C (1470–2460 °F). For testing below 1000 °C (1830 °F), tungsten carbide (WC) platens can be used, especially when testing steel specimens. D2 steel is good enough to test nonferrous alloys, such as aluminum and copper. For testing above 1000 °C (1830 °F), silicon carbide (SiC), silicon nitride (SiN), and alumina can be used. However, if high-speed impact is encountered, such as when testing with strain rates higher than 1 s⁻¹, TZM or ceramic composite (Al₂O₃ + SiC) platens should be used. If the specimen is a high-strength heat-resistant alloy,

only the ceramic composite platens can sustain the impact. In general, when choosing tooling materials, one should consider the hardness of the material being tested and the impact strength and thermal conductivity of platens. For example, a high-strength heat-resistant alloy, such as Udimet 720, would damage TZM platens when tested at high strain rates and provide invalid testing data. In addition, high heating rates can explode the ceramic composite platens because the thermal conductivity of alumina is low.

Table 1 Platen materials for different temperatures and strain rates

Strain rate, s^{-1}	Temperature			
	RT-400 °C (RT-750 °F)	<1000 °C (<1830 °F)	1000–1350 °C (1830–2460 °F)	>1350 °C (>2460 °F)
<1	D2 Steel	WC	TZM, SiC, SiN, Al ₂ O ₃ + SiC	Graphite
1–60	D2 Steel	WC, TZM	TZM, Al ₂ O ₃ + SiC	Al ₂ O ₃ + SiC

The flat and parallel tolerance of platens should be within 0.0002 (Ref 13). To improve parallelism, adjustable platens (such as bearing blocks) may be used. A drawing of such blocks is shown in Ref 13. Using a subpress is suggested in the ASTM standards (Ref 13, 14), but it is very difficult with the limited space inside the furnace. Specimen Geometry. The simplest specimen geometry is a cylinder, as shown in Fig. 2. The height-diameter aspect ratio (H/d) is usually between 1 and 2. An aspect ratio that is too high can cause the specimen to buckle, while one that is too low can increase friction even if lubricant is applied. Excellent results have been obtained using $H/d = 1.25$ for high-strength steel specimens (Ref 8). Typical specimen diameter is 10 to 15 mm (0.4–0.6 in.), depending on microstructure. For a cast alloy with a coarse grain structure, larger specimens may be necessary. Subscale specimens can also be used for materials with a fine grain structure. In general, the specimen size must be representative of the material being tested.

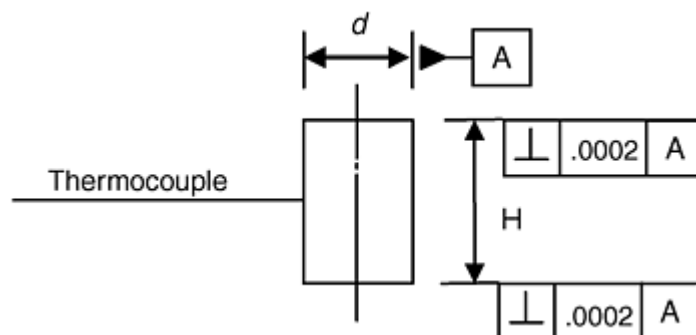


Fig. 2 Cylindrical compression specimen geometry

The parallelism of the top and the bottom of specimens should be 0.0005 or better. The surface finish of specimens should be 1.6 μm (63 $\mu in.$) or better, which usually requires turning or grinding. A typical specimen with friction looks like Fig. 3 (Ref 17). The specimen shown in Fig. 3 exhibits bulging due to friction between the platens and the top and bottom surfaces of the specimen. Ideally, the test is frictionless, and the specimen is compressed homogeneously, as shown in Fig. 4. Shear banding may occur during compression testing, as shown in Fig. 5 (Ref 17). It can be caused by localized flow (Ref 18) or unparallel platens or specimens.

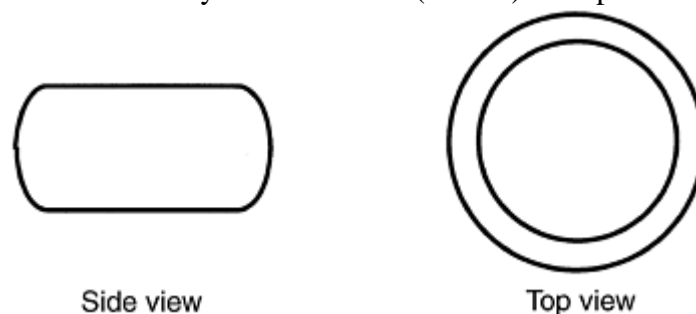


Fig. 3 Schematics of a regularly tested specimen

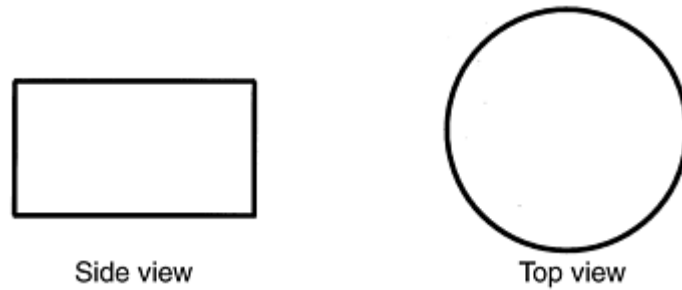


Fig. 4 Schematics of an ideally tested specimen



Fig. 5 Schematics of a tilted (sheared) tested specimen

Temperature Measurement. Temperature measurement using a thermocouple that just touches the specimen is not accurate until the specimen is soaked at the set testing temperature for a long time. To accurately measure the temperature of the specimen, thermocouples can be either welded to the specimen or inserted into a small hole drilled into the specimen. Hole drilling is not recommended for workability testing because the hole may induce premature cracking. To determine the uniformity of temperature within the specimen, three thermocouples may be used to measure the top, bottom, and center temperatures of a dummy specimen as a function of time. If the temperatures are identical, only one thermocouple is necessary during testing. If it takes some time for the entire specimen to reach the set temperature, this procedure can also be used to determine the necessary soaking time. To obtain the microstructure right before the compression testing begins, a specimen soaked at the testing temperature for the specified time should be quenched and examined. Some other detailed precautions for temperature measurement are specified in Ref 14.

It is essential that the platens be at the same temperature as the specimen. Temperature difference between the platens and the specimen results in a deformation gradient and, therefore, barreling of the deformed specimen (Ref 19).

Lubrication. When the specimen is compressed homogeneously, as shown in the ideal case (Fig. 4), the resulting stress calculations are accurate. For most tests, deformed specimens look like the one in Fig. 3 due to friction, even with lubrication. For testing at room temperature, TFE-fluorocarbon sheet and molybdenum disulfide can be used (Ref 13, 20). For testing at elevated temperatures, water-base graphite, graphite sheet, boron-nitride solution, glass-base lubricant, and molybdenum disulfide may be used (Ref 8, 21).

To retain lubricant on the ends of the specimens, various end designs have been developed (Ref 7, 21, and 22). One such design is shown in Fig. 6. The procedure for applying lubricant solutions on the ends of the specimens is also very important. The lubricant needs to be applied twice on each end. The second application can only be made after the first application dries.

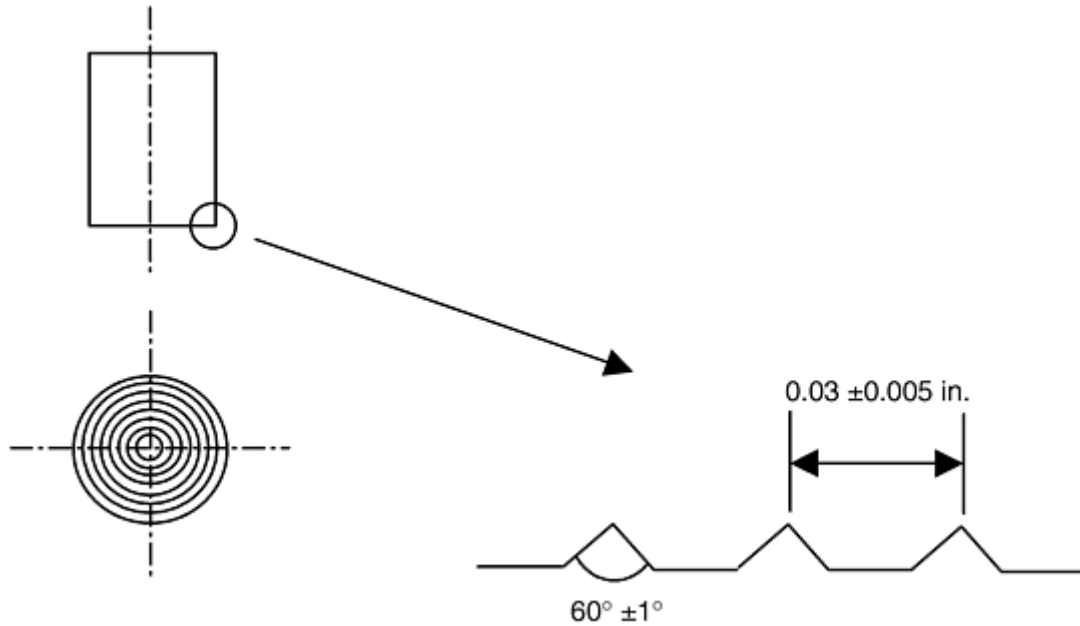


Fig. 6 A typical groove design for the ends of compression test specimens

Machine Stiffness. Because the testing train consists of a number of components, as shown in Fig. 1, the stiffness of the system needs to be quantified. The easiest way to quantify is to bring the top and bottom platens together and record the displacement at a number of load levels. This procedure needs to be performed at each testing temperature. For high-strain compression tests, for instance, 60 to 80%, it is not possible to attach an extensometer to the specimen. The displacement data must be subtracted by the intrinsic displacement that resulted from the system. The subtraction can be incorporated into a data acquisition program.

Machine Control. The testing machine should be controlled to generate constant strain rates during testing. To do so, the motion of the crosshead must follow exponential curves. The true strain is expressed as a function of specimen height as follows:

$$\varepsilon = \ln \frac{h}{h_0} = \ln \left(1 - \frac{\Delta h}{h_0} \right) \quad (\text{Eq 9})$$

where ε is true strain (in the case of compression or tension, if the deformation is homogeneous, $\varepsilon = \bar{\varepsilon}$), and h_0 and h are the initial and instantaneous height of the specimen, respectively. $\Delta h = h_0 - h$ is the distance the crosshead has traveled since the compression test commenced.

For a constant strain-rate test, the instantaneous strain is simply the product of strain rate and time:

$$\varepsilon = \dot{\varepsilon}t \quad (\text{Eq 10})$$

Combining Eq 9 and 10 yields:

$$\Delta h = h_0[1 - \exp(-\dot{\varepsilon}t)] \quad (\text{Eq 11})$$

For hydraulic machines, the distance of crosshead travel is controlled by the voltage input as a function of time. For a mechanical machine, the crosshead is controlled by the motor speed. In general, Eq 11 is the governing equation for machine control for constant strain-rate compression tests. The equation for tension tests can be derived similarly with the exception of $\Delta h = h - h_0$. Software to control the machine for constant strain-rate tests has recently become commercially available (Ref 23).

Data Reduction and Temperature Correction. Load and stroke (displacement) data are acquired from testing. To reduce the data into true stress and true strain, deformation is assumed homogeneous. True strain is calculated using Eq 9. Of course, the correction for the elastic deflection of the machine needs to be considered (Ref 24). True stress is simply the load divided by instantaneous cross-sectional area, which can be calculated by assuming a constant volume of the specimen.

Deformation heating occurs inevitably during testing, especially at high strain rates. Because isothermal stress-strain curves are desired for analysis, correction for deformation heating is necessary. The commonly used equation for calculating temperature rise during deformation is (Ref 25):

$$\Delta T = \frac{\alpha \int_0^\epsilon \sigma d\epsilon}{\rho C} = \frac{\alpha \sigma_a \epsilon}{\rho C} \quad (\text{Eq 12})$$

where σ_a is the average stress value over the strain range of testing, ρ is density, C is mass heat capacity of the specimen, and α is the fraction of deformation energy transformed into heat. Usually α is equal to 0.98.

As shown in Eq 12, the temperature rises continuously as the test continues. A typical stress-strain curve obtained after testing and deformation heating correction would look like the curves in Fig. 7. Deformation heating is most severe at low temperatures and high strain rates, where the stress level is high. At high strain rates, higher than, for instance, 1 s^{-1} , there is not much time for heat to dissipate, and the specimen is basically under adiabatic conditions. Equation 12 applies under these conditions. In contrast, when strain rates are very slow, such as 10^{-3} s^{-1} , heat generated from deformation is transferred to tooling and the environment, and deformation heating is negligible. However, Eq 12 does not reflect the effect of strain rate, and still provides a finite temperature increase. In addition, the equation does not apply at even intermediate strain rates. To solve these problems, Zhao (Ref 26) developed an equation for calculating temperature increase due to deformation heating at all strain rates, which also includes the heat generated by friction at the platen/specimen interface:

$$\Delta T = \frac{h_a \sigma_a}{h_T} \left(\alpha \dot{\epsilon} + \frac{f v_a}{h_a} \right) \left[1 - \exp\left(-\frac{h_T t}{C \rho h_a} \right) \right] \quad (\text{Eq 13})$$

where h_a is the average height of the specimen, h_T is the heat-transfer coefficient between the platen and the specimen, f is the friction coefficient between the platen and the specimen, t is time, and v_a is the average velocity at the platen/specimen interface. If lubrication is excellent and friction is negligible, Eq 13 can be reduced to:

$$\Delta T = \frac{h_a \sigma_a \alpha \dot{\epsilon}}{h_T} \left[1 - \exp\left(-\frac{h_T t}{C \rho h_a} \right) \right] \quad (\text{Eq 14})$$

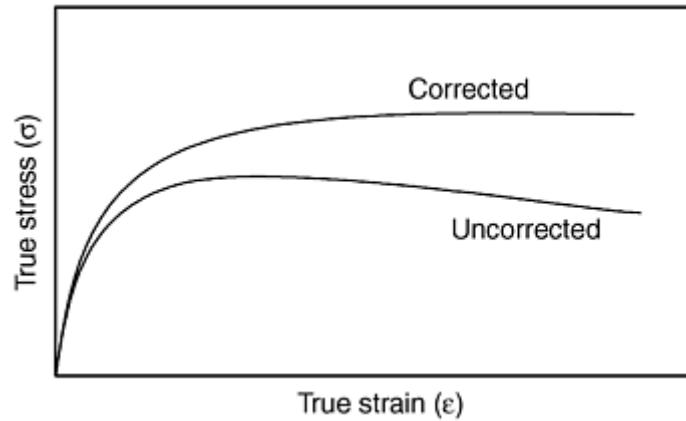


Fig. 7 A schematic of stress-strain curves before and after correction for deformation heating

The purpose of determining temperature increase is to obtain isothermal stress-strain curves. Strength loss of the specimen due to deformation heating can be expressed in terms of the derivative of stress by temperature (Ref 27):

$$\Delta \sigma = \Delta T \left. \frac{d\sigma}{dT} \right|_{\epsilon, \dot{\epsilon}} \quad (\text{Eq 15})$$

The way to determine the derivative is to plot stress data at constant strain and strain rate, and at corrected temperatures ($T = T_{\text{test}} - \Delta T$), as shown in Fig. 8. The derivative is usually a function of temperature.

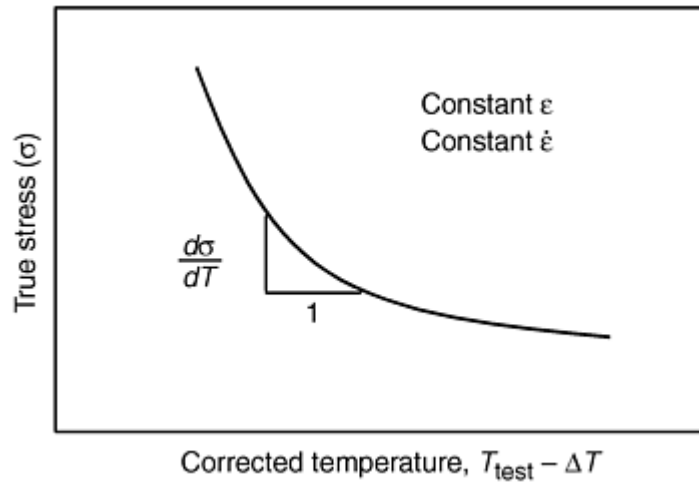


Fig. 8 A schematic showing determination of derivative of stress in terms of temperature

The step-by-step procedure for reducing load-stroke data is:

1. Convert load-stroke data to true stress-versus-true strain data, including correction for machine elastic deflection.
2. Calculate ΔT for every data point using Eq 13 or 14.
3. Plot true stress-versus-corrected temperature at each strain rate and at a number of constant strains.
4. Obtain the slope of the plotted curves in step 3 using $d\sigma/dT$.
5. Calculate the stress increase when temperature is corrected to the nominal testing temperature.
6. Generate isothermal stress-strain curves by adding the stress increase to the true stress obtained in the first step.

Figure 9 shows both uncorrected and corrected stress-strain curves for HY-100 steel at 1000 °C (1830 °F) and at various strain rates.

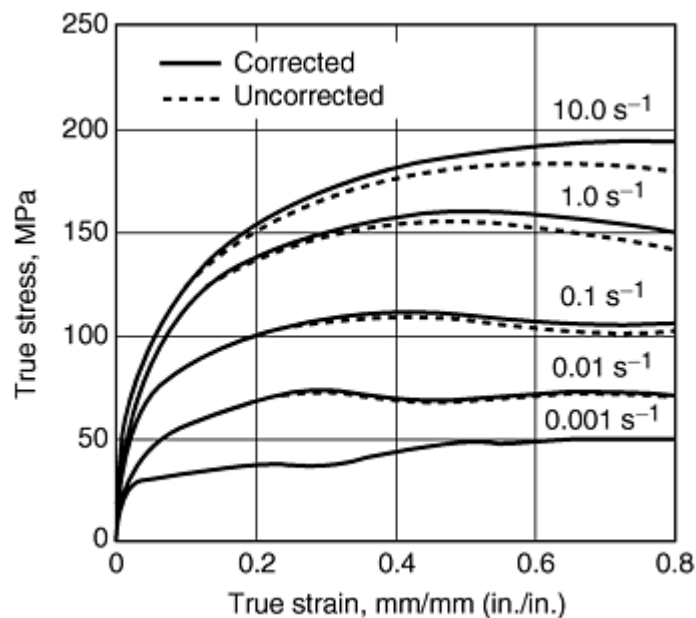


Fig. 9 Stress-strain curves before and after temperature corrections for HY-100 steel at 1000 °C (1830 °F) and various strain rates. Source: Ref 8

Tension Test

When compression-testing equipment is not available, or the deformation process experiences more tension than compression, tensile testing can be used to obtain stress-strain curves. Tensile testing can be especially

useful for sheet-metal forming applications. Constant strain-rate tensile tests should follow an exponential curve, as shown in Fig. 10.

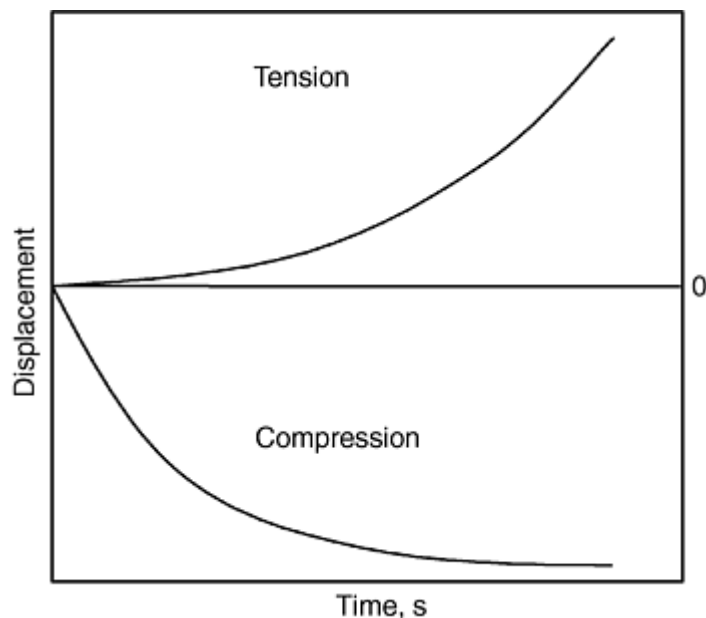


Fig. 10 Displacement as a function of time for tension and compression tests at constant strain rate

The setup of high-temperature tensile-testing equipment is similar to compression testing. The difference is that tensile testing does not need anvils and platens. Instead, it uses pulling bars and grips. Figure 11 shows a typical setup of high-temperature tensile loading train.

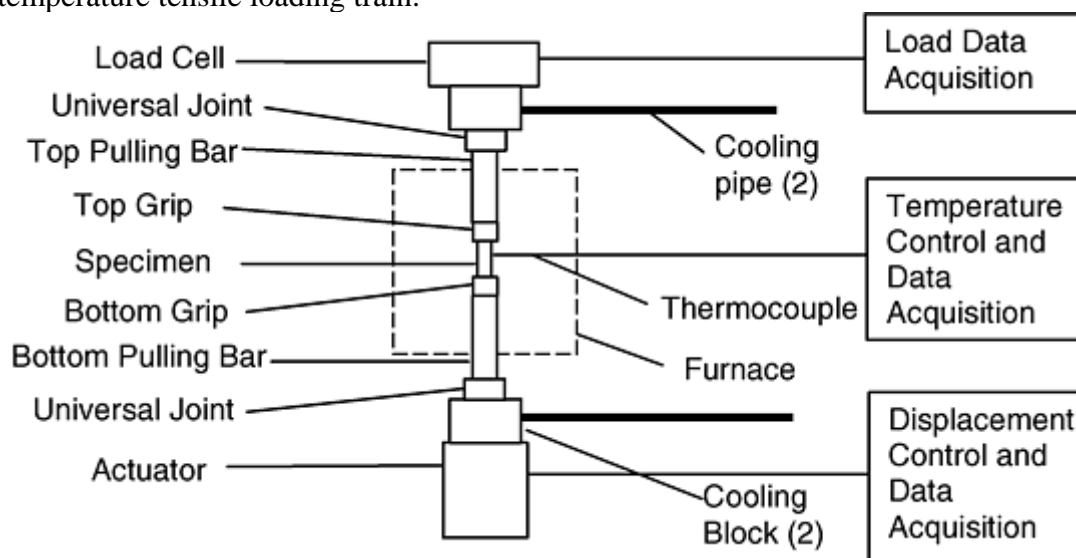


Fig. 11 Loading train for high-temperature tensile testing

The grips can be either of the screw type or the split-ring type; both are commercially available. Split-ring grips provide for a quick removal of the specimen if quenching immediately after testing is desirable and has to be performed outside the furnace.

Universal joints are necessary to align the loading train. In any case, the maximum bending strain should not exceed 10% of the axial strain. One way to check the bending strain is to use strain gages on a specimen at the middle of the gage length. If the maximum (or minimum) bending strain is within the limit at room temperature, the alignment should be fine at elevated temperatures. Care must be taken not to affect the alignment of the loading train with the furnace and its accessories. The alignment needs to be tested periodically.

Because tensile specimens usually have longer gage lengths than compression specimens, more than one thermocouple may be needed to monitor the temperature of the gage length. Thermocouples should very closely contact the reduced section. Shielding the thermocouple is necessary unless the difference in indicated

temperature from an unshielded bead and a bead inserted in a hole in the specimen has been shown to be less than one half the variation listed here (Ref 16):

Up to and including 1000 °C (1800 °F)	±3 °C (5 °F)
Above 1000 °C (1800 °F)	±6 °C (10 °F)

Thermocouples need to be calibrated as specified in Ref 16. Thermocouple wire exposed to a hot zone should be cut off after each test, and a new bead should be formed. During the entire test, temperature variation should not exceed the ranges indicated in the previous table for the entire gage length.

One of the advantages of a tensile test compared to a compression test is that the tensile test does not have a friction effect, and an extensometer can be used to measure true strain up to the maximum loading. The true stress would have to be corrected due to the reduction of cross-sectional area. Stress-strain data may not be useful beyond the maximum load point due to necking. Attachment of the extensometer should be carried out very carefully because it may affect alignment (Ref 28). Attaching extensometers on opposite sides and averaging the readings can reduce the error. When feasible, extensometers should be attached directly to the reduced section (Ref 16).

One important parameter that can be determined from tensile tests is the strain-hardening exponent, n , which is important for both bulk and sheet-metal forming. The procedure used to determine n -values is quite simple and is explained well in Ref 29.

Young's modulus can also be determined by tensile tests with accurate extensometers. Temperature control during the test is very important. The average temperature over the specimen gage length should not deviate from the indicated nominal test temperature by more than ±1.5 °C (2.5 °F) for test temperatures up to and including 900 °C (1650 °F), and ±3 °C (5.5 °F) for above 900 °C (1650 °F) (Ref 30). The loading rate should also be slow in order to avoid the thermal effect of adiabatic expansion or contraction. However, the test speed should not be so slow that creep effects are not negligible (Ref 30).

Data Reduction for Workability

Workability is an important issue in deformation modeling. For bulk workability, Kuhn developed the testing technique described in Ref 11. The workability constant C for a particular material at certain testing temperature and strain rate can be determined by a simple plane-strain bending test. The constant C is related to the constant C' in Eq 7 and 8 as follows:

$$C = 0.75C' \quad (\text{Eq 16})$$

It also relates to the constant C_2 in Eq 6 (Ref 31):

$$C_2 = \frac{2K}{3(n+1)} C^{n+1} \left(\frac{2}{\sqrt{3}} \right)^n \quad (\text{Eq 17})$$

assuming that the constitutive equation $\bar{\sigma} = K\bar{\epsilon}^n$ applies.

Fitting Testing Data to Constitutive Models

If one uses the tabular input form for modeling, the interpolation of data is left to the finite element modeling (FEM) software after stress-strain data have been obtained. Care must be taken to ensure that the temperature and strain-rate ranges in the data cover every possible case in the simulation for convergence.

If a constitutive model is being used, data needs to be fit to the equation. Equation 2 is not difficult to fit. However, Eq 3 has four constants: A , α , n' , and Q , and the procedure to fit it is somewhat complex. There are many ways to fit the data; some may lead to significant errors. A description of a general procedure to determine the constants follows.

Equation 3 can also be written as:

$$Z = A[\sinh(\alpha\sigma)]^{n'} \quad (\text{Eq 18})$$

where Z is the Zener-Hollomon parameter, defined as:

$$Z = \dot{\epsilon} \exp\left(\frac{Q}{RT}\right) \quad (\text{Eq 19})$$

To determine parameter α , we need to determine the strain-rate sensitivity, m , and another material parameter, β . At high stresses, the following relationship holds:

$$\alpha = m\beta \tag{Eq 20}$$

When n' is replaced approximately by $1/m$, the following equations result:

$$m = \left. \frac{\partial \log \sigma}{\partial \log \dot{\epsilon}} \right|_{T,\epsilon} \tag{Eq 21}$$

and

$$\beta = \left. \frac{\partial \ln \dot{\epsilon}}{\partial \sigma} \right|_{T,\epsilon} \tag{Eq 22}$$

Steady-state stresses are plotted for each temperature-versus-strain rate example on a log-log scale, as shown in Fig. 12. The slope of the straight lines is the strain-rate sensitivity, m . At high stresses, the lines are parallel. The parameter β can be determined from the slope of stress versus the natural log of strain rate, as shown in Fig. 13. From the m and β values, α can be determined using Eq 20.

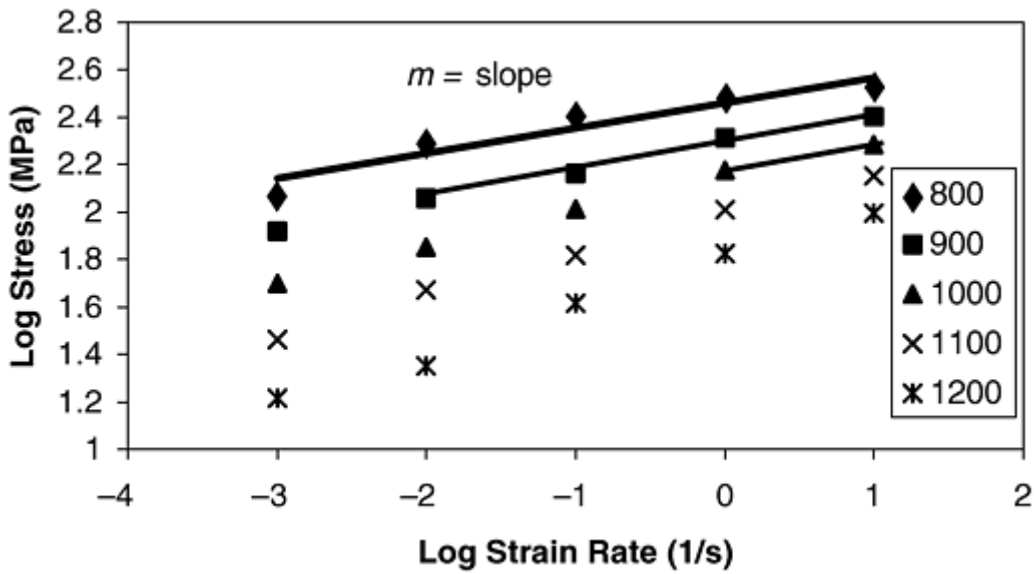


Fig. 12 Steady-state stresses versus strain rate at different temperatures (°C) on a log-log scale for HY-100 steel

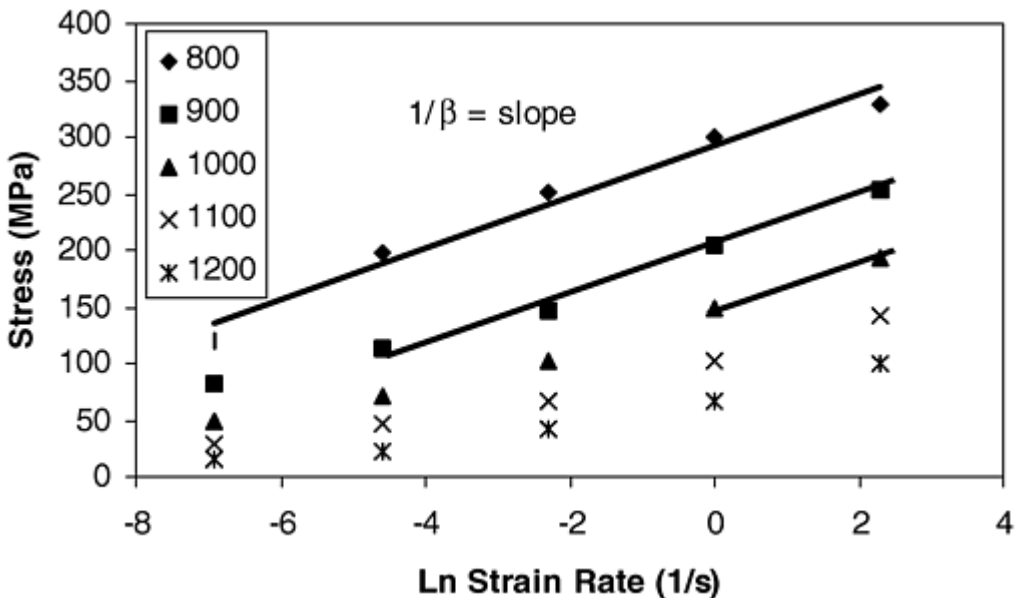


Fig. 13 Steady-state stresses versus natural log of strain rate at different temperatures (°C) for HY-100 steel

Equation 4 yields:

$$Q = \frac{R}{0.4343m} \left. \frac{\partial \log \sigma}{\partial (1/T)} \right|_{\dot{\epsilon}, \epsilon} \quad (\text{Eq 23})$$

Again, n' is approximately replaced by $1/m$. However, this time the m value is determined from the low stresses, as shown in Fig. 14. The apparent activation energy, Q , can be determined by plotting log stress versus $1/T$ at low stresses, as shown in Fig. 15. In Eq 23, R is the gas constant.

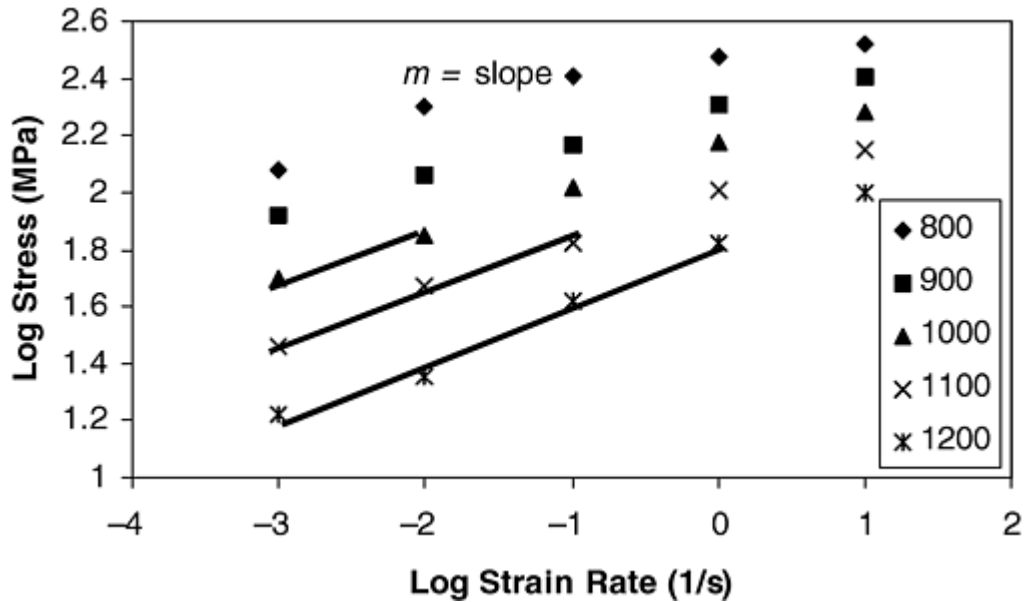


Fig. 14 Steady-state stresses versus strain rate at different temperatures (°C) on a log-log scale for HY-100 steel

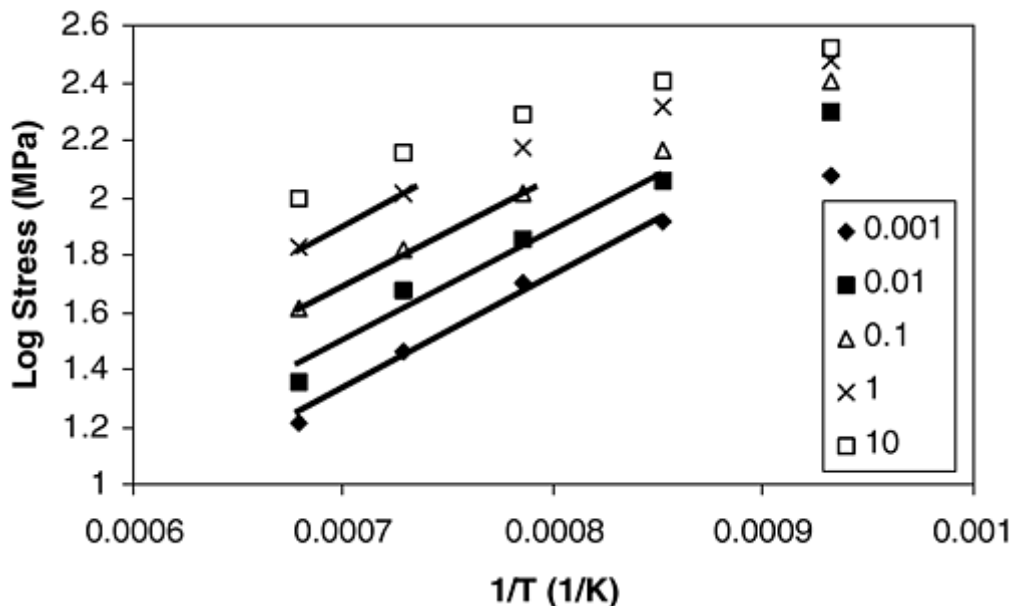


Fig. 15 Log stress versus 1/T at different strain rates (in 1/s) for HY-100 steel

After obtaining the values of α and Q , the natural log of Z (Zener-Hollomon parameter) is plotted versus the natural log of $\sinh(\alpha\sigma)$ to determine the values of n' and A . If the deformation behavior is governed by Eq 18, the plot can be well fit by a linear equation, as shown in Fig. 16. The slope would be equal to n' , and the intercept would be $\ln A$. The final results for HY-100 steel are shown here:

m at high σ	0.1059
m at low σ	0.2089
β	0.0441
α , MPa ⁻¹ (ksi ⁻¹)	4.671×10^{-3} (6.775×10^{-4})
Q , kJ/mol	368.67
n'	5.8417
A , s ⁻¹	1.2519×10^{16}

See Eq 3

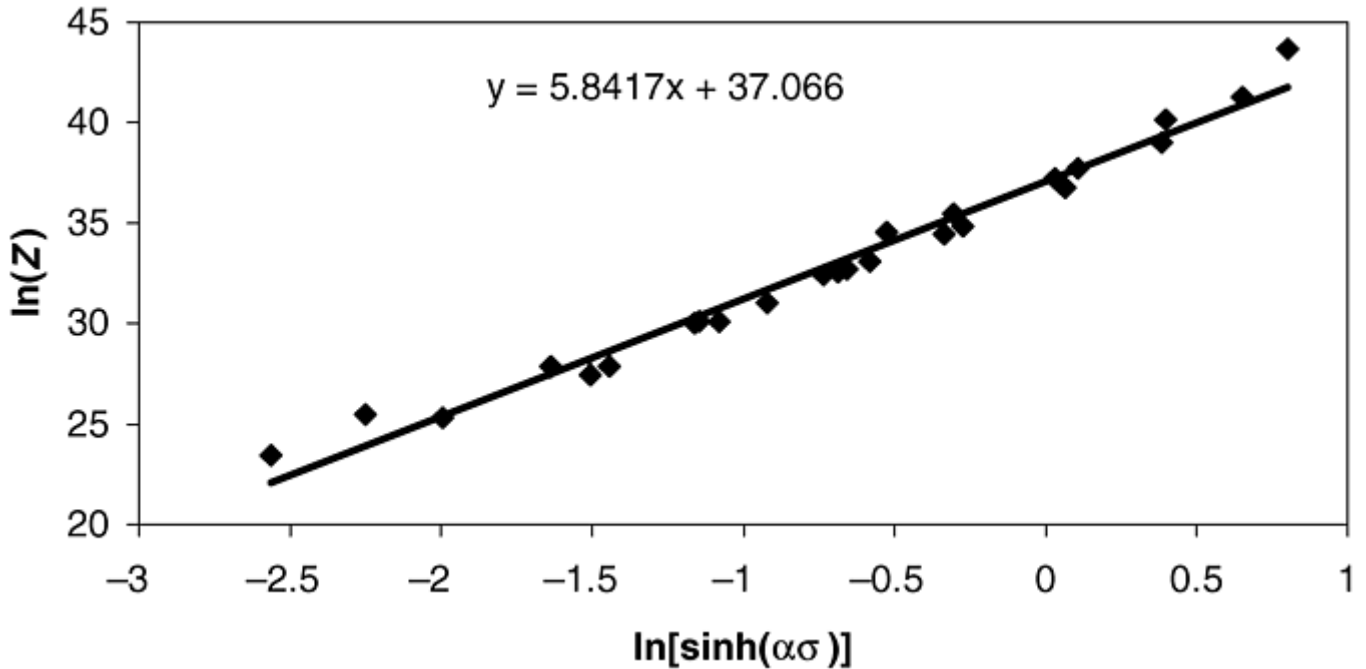


Fig. 16 Plot of $\ln(Z)$ versus $\ln[\sinh(\alpha\sigma)]$ to determine the values of n' and A

Testing for the Friction Coefficient

For bulk forming, the friction coefficient can be measured by a ring compression test (Ref 32). The principle of this test is that when a ring is compressed, the inner diameter of the ring either increases or decreases depending on the friction condition at the ring/platen interface. As shown in Fig. 17, measurements of the inside diameters of the ring specimens provide a sensitive means to determine the friction coefficient because the inside diameter increases if the friction is low and decreases if the friction is high.

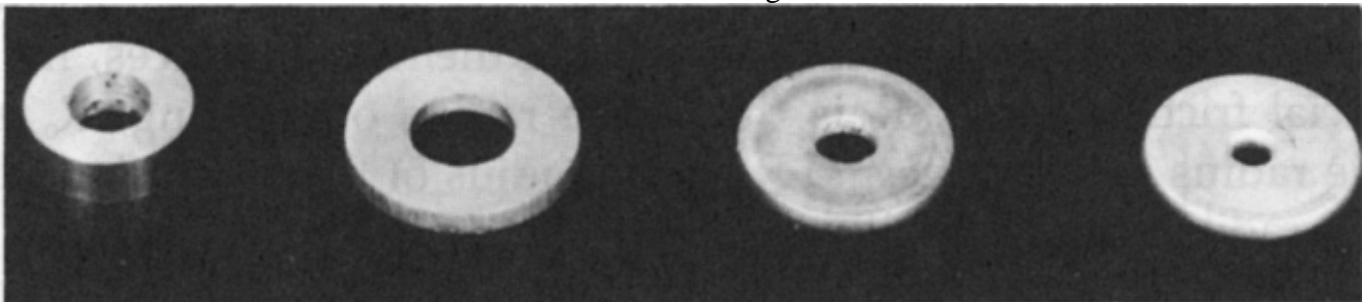


Fig. 17 Variation in shape of ring specimen under different friction conditions. (a) Undeformed. (b) Low friction. (c) Medium friction. (d) High friction. 50% deformation for (b), (c), and (d). Source: Ref 32

The specimen, as shown in Fig. 18, is usually made with a specific geometry ratio. The ratio of outer diameter to inner diameter to thickness ($D_o:D_i:T$) is 6:3: x , where x can be 0.5, 1, or 2. The analysis of this test is based on homogeneous deformation. To avoid error introduced by bulging or for high friction, the x -value 0.5 should be used. For medium friction, the x -value 1 should be used, and for low friction, the x -value 2 should be used. Analytical treatment that takes into account bulging for the specimens 6:3:2 was provided by DePierre, Gurney,

and Male (Ref 33). Before testing, lubricant is applied to the surface of the ring specimen. The testing is conducted the same way as compression testing at a certain temperature and strain rate. After a certain amount of deformation (reflecting the forming operation reduction), the test is ended, and the inner diameter of the tested ring specimen is measured. The measured value and percent reduction are then compared to a set of calibration curves (Fig. 19) to determine the friction coefficient (Ref 4, 32, 34, and 35).

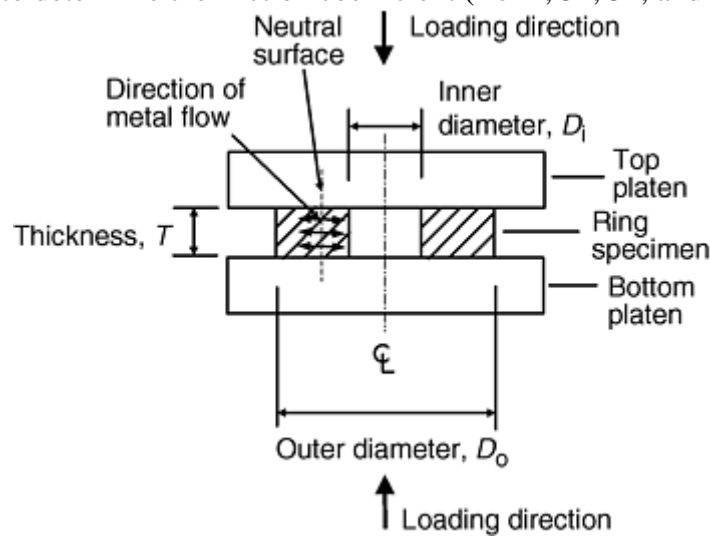


Fig. 18 Schematic of ring compression test. Revised from Ref 4

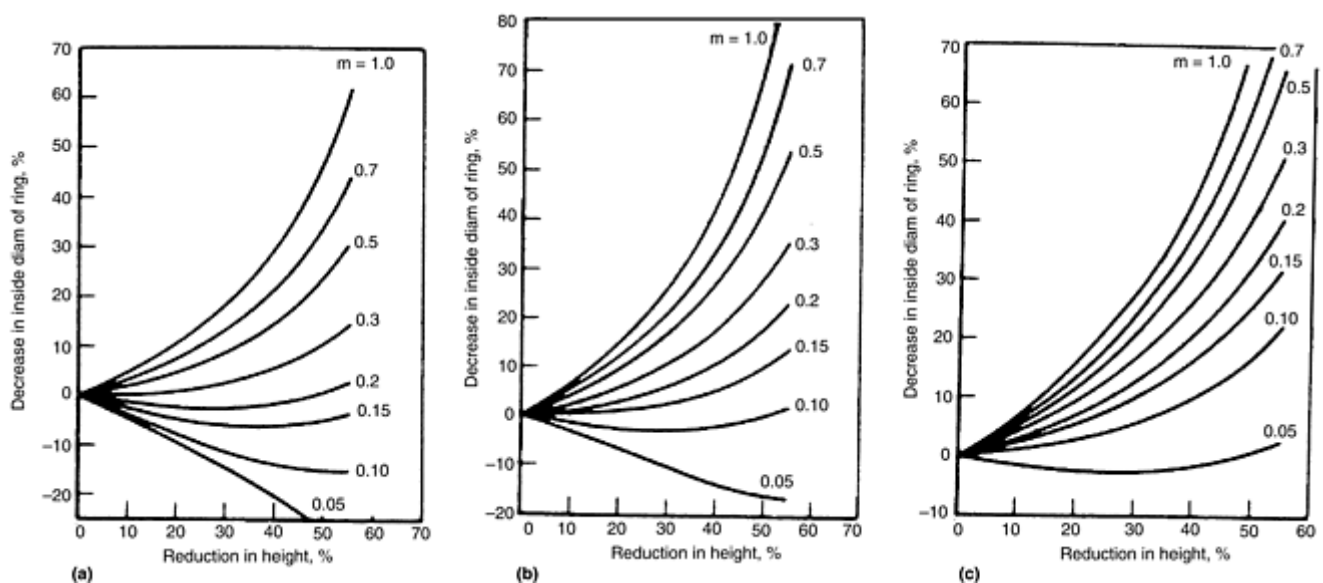


Fig. 19 Theoretical calibration curves for ring compression test. The ratio is for outside diameter:inside diameter:thickness. (a) 6:3:2 ratio. (b) 6:3:1 ratio. (c) 6:3:0.5 ratio. Source: Ref 4

Testing for the Heat-Transfer Coefficient

Deformation processing often involves heat transfer. One of the difficulties in modeling is determining the input value of the heat-transfer coefficient. The most commonly used method of determining the heat-transfer coefficient is the inverse method. In this method, the temperatures of the workpiece and tooling are measured at different locations as a function of time. Subsequently, the process is modeled with trial values of the heat-transfer coefficient to match the temperature measured in the experiments. The trial-and-error method for determining the heat-transfer coefficient can be programmed to loop the simulations until an optimum value of the coefficient is determined.

Chen, Samarasekera, and Hawbolt (Ref 36) performed such work on the hot rolling of steels. Figure 20 shows the workpiece geometry and the position of thermal couples. Three thermocouples were used in this case to measure the temperatures at different locations. Figure 21 shows how the experimental equipment was

configured. The tube furnace was positioned right in front of the rolling mill to ensure an accurate starting temperature. During rolling, temperature data was acquired continuously by a computer. The thermal responses of the thermocouples are presented in Fig. 22. When the workpiece entered the roll gap, the temperature dropped immediately. As it came out of the roll gap, the temperature recovered to a level lower than the initial temperature. Figure 23 shows the detailed temperature reading for thermocouple 2 inside the roll gap.

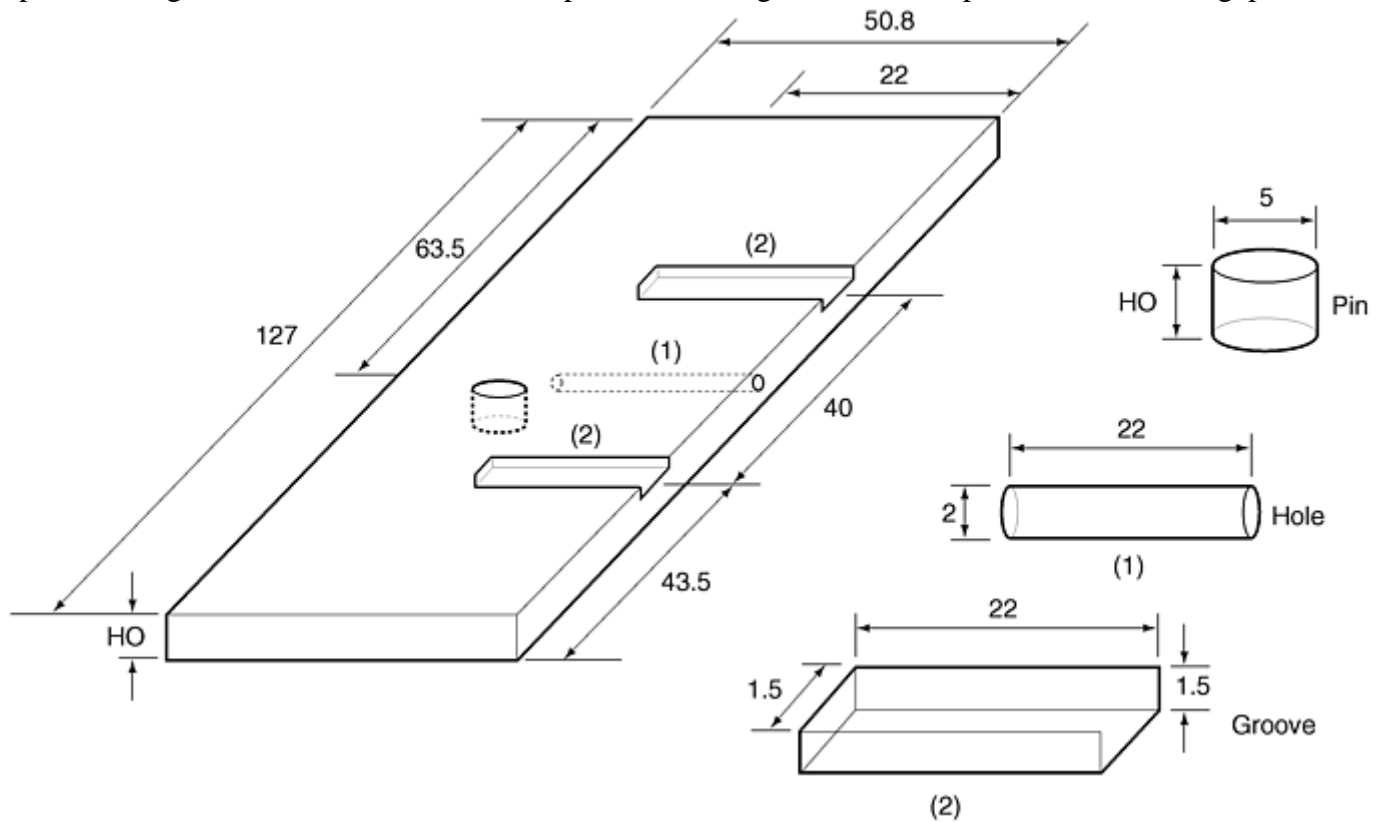


Fig. 20 The workpiece used to measure temperature during hot rolling, showing the positions of the thermocouples. Source: Ref 36

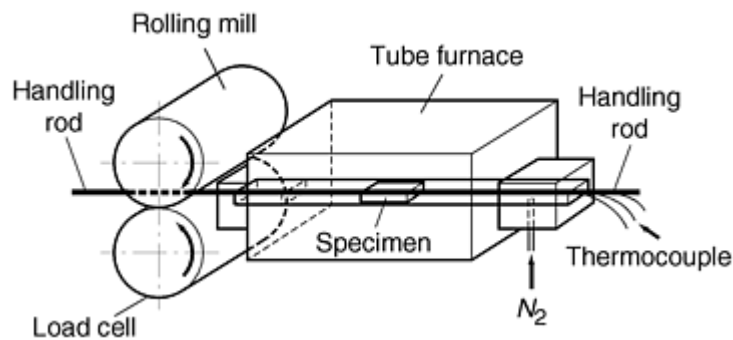


Fig. 21 Experimental setup for temperature measurement during hot rolling. Source: Ref 36

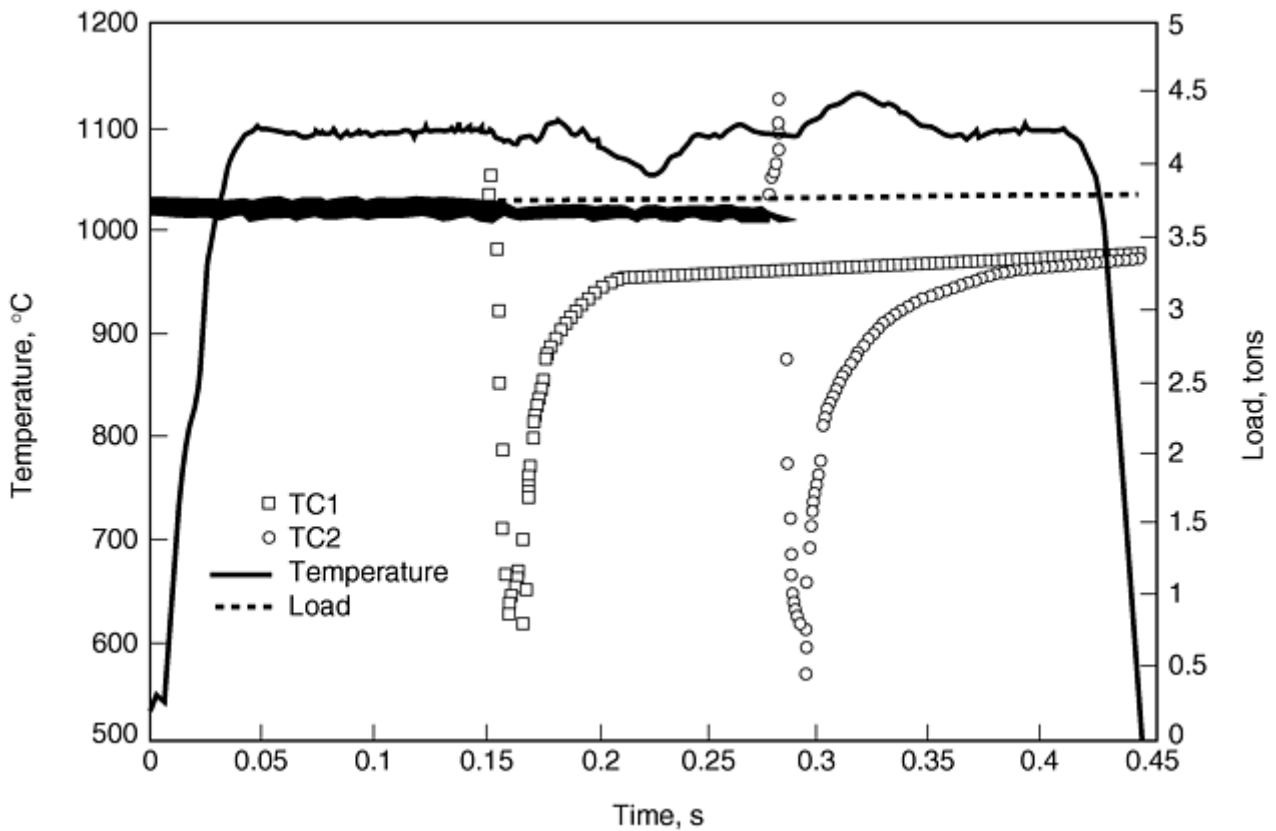


Fig. 22 Thermal responses of two thermocouples (TC1 and TC2) in the workpiece during hot rolling. Source: Ref 36

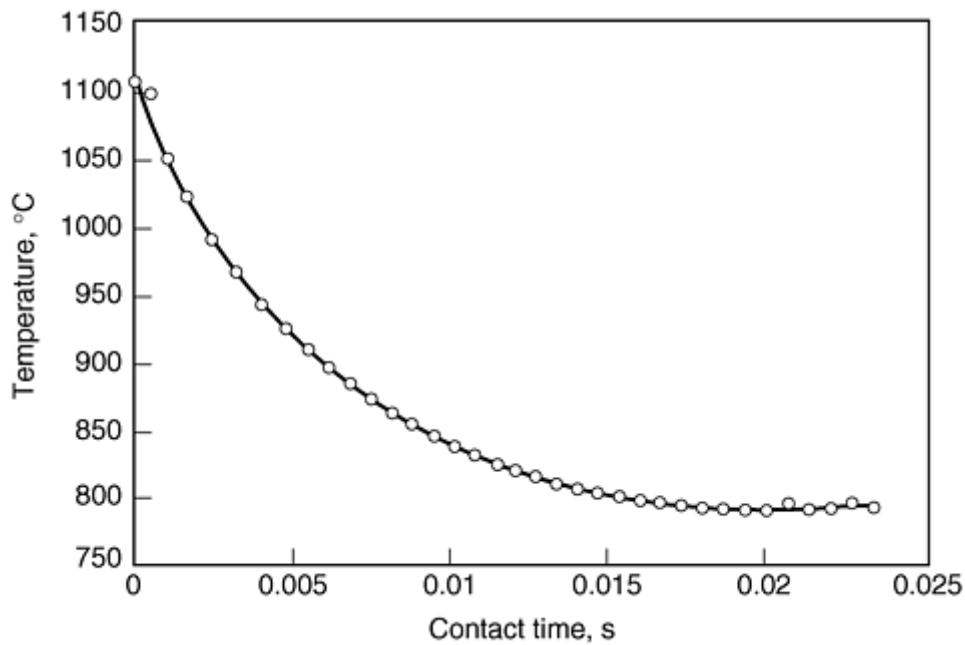


Fig. 23 Detailed temperature reading for thermocouple 2 in the roll gap. Source: Ref 36

The rolling process was then modeled. The contact time of the workpiece in the roll gap is divided into a number of time steps. For each time step, the calculated temperature with the trial heat-transfer coefficient is compared to the measured temperature. When the two temperature values are close enough—for instance, within 1 to 2 °C (1.75–3.5 °F)—the assumed heat-transfer coefficient is accepted as the real heat-transfer coefficient. The calculation process is then repeated for the next time step. Results of the heat-transfer coefficient at two different rolling temperatures are shown in Fig. 24.

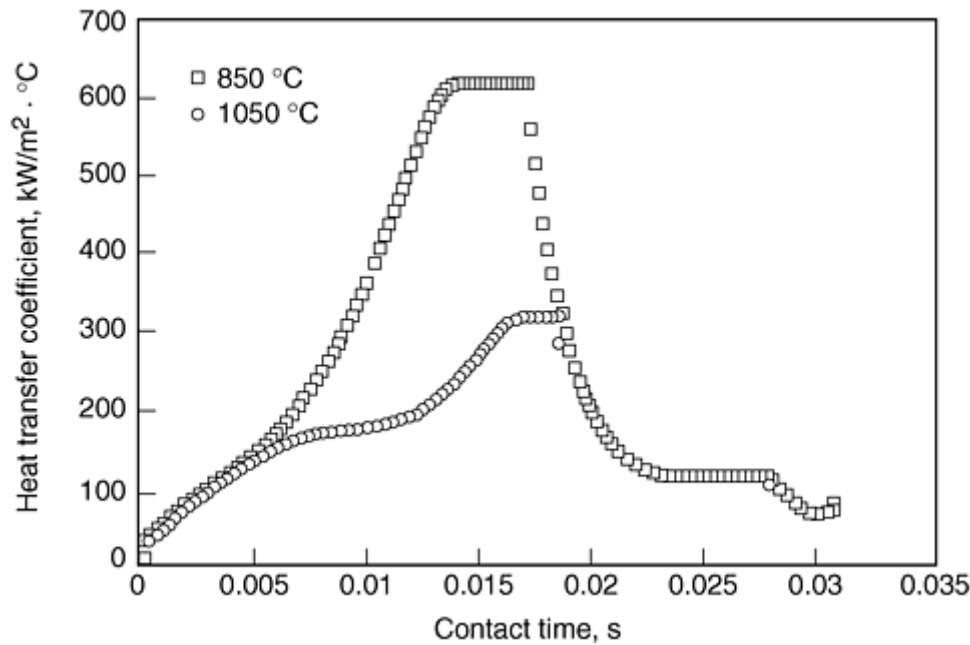


Fig. 24 Inversely calculated results of the heat-transfer coefficient during contact. Source: Ref 36

References cited in this section

1. H.E. Boyer, *Atlas of Stress-Strain Curves*, ASM International, 1987
2. Y.V.R.K. Prasad and S. Sasidhara, *Hot Working Guide: A Compendium of Processing Maps*, ASM International, 1997
3. *Atlas of Formability Bulletins*, National Center for Excellence in Metalworking Technology (NCEMT), Johnstown, PA
4. T. Altan, S. Oh, and H. Gegel, *Metal Forming: Fundamentals and Applications*, ASM International, 1983, p 86
5. C.M. Sellars and W.J.McG. Tegart, *Mem. Sci. Rev. Metall.*, Vol 63, 1966, p 731
6. A. Laasroui and J.J. Jonas, Prediction of Steel Flow Stresses at High Temperatures and Strain Rates, *Metall. Trans. A*, Vol 22, 1991, p 1545–1558
7. S.B. Brown, K.H. Kim, and L. Anand, An Internal Variable Constitutive Model for Hot Working of Metals, *Int. J. Plast.*, Vol 5, 1989, p 95–130
8. M. Thirukkonda, D. Zhao, and A.T. Male, “Materials Modeling Effort for HY-100 Steel,” Technical Report TR 96-027, NCEMT, Johnstown, PA, March, 1996, p 27
9. M.G. Cockcroft and D.J. Lahtam, Ductility and the Workability of Metals, *J. Inst. Met.*, Vol 96, 1968, p 33–39
10. D. Zhao, J.P. Bandstra, H.A. Kuhn, A New Fracture Criterion for Fracture Prediction in Metalworking Processes, *Concurrent Engineering Approach to Materials Processing*, S.N. Dwivedi, A.J. Paul, and F. R. Dax, Ed., TMS, 1992, p 107–119
11. H.A. Kuhn, Workability Theory and Application in Bulk Forming Processes, *Forming and Forging*, Vol 14, *Metals Handbook*, ASM International, 1988, p 388–404

12. J.P. Bandstra, "3D Extension of Kuhn Surface Fracture Criterion," *CTC memorandum CTC/JPB-M0469-95*, Johnstown, PA, 1995
13. "Standard Test Methods of Compression Testing of Metallic Materials at Room Temperature," ASTM E 9, *Annual Book of ASTM Standards*, 1994
14. "Standard Practice for Compression Tests of Metallic Materials at Elevated Temperatures with Conventional or Rapid Heating Rates and Strain Rates," ASTM E 209, *Annual Book of ASTM Standards*, 1994
15. "Standard Test Methods for Tension Testing of Metallic Materials," ASTM E 8, *Annual Book of ASTM Standards*, 1994
16. "Standard Test Methods for Elevated Temperature Tension Tests of Metallic Materials," ASTM E 21, *Annual Book of ASTM Standards*, 1994
17. D. Zhao and H. Dong, unpublished technical report, Concurrent Technologies Corporation, Johnstown, PA, 1996
18. S.L. Semiatin and J.J. Jonas, *Formability and Workability of Metals: Plastic Instability and Flow Localization*, American Society for Metals, 1984
19. M.C. Mataya, Simulating Microstructural Evolution during the Hot Working of Alloy 718, *JOM*, Jan 1999, p 18–26
20. R. Chait and C.H. Curll, "Evaluating Engineering Alloys in Compression," ASTM STP 608, *Recent Developments in Mechanical Testing*, 1976, p 3–19
21. M.L. Lovato and M.G. Stout, Compression Testing Techniques to Determine the Stress/Strain Behavior of Metals Subject to Finite Deformation, *Metall. Trans. A*, Vol 23, 1992, p 935–951
22. O. Alnik, D.D. Murphy, T. Terada, A.K. Koul, and J.-P. Immarigeon, "Modeling of Deformation and Microstructural Changes in P/M Rene 95 Under Isothermal Forging Conditions," Conf. Proc. No. 426 presented at Aerospace Materials Process Modeling, Oct 2–4, 1987 (Cesme, Turkey), AGARD
23. Merlin IV Test Application Package, Instron Corporation, Canton, MA, 1998
24. J.F. Thomas, Jr. and R. Srinivasan, Constitutive Equations for High Temperature Deformation, *Computer Simulation in Materials Science*, R.J. Arsenault, J. R. Beeler, Jr., and D.M. Esterling, Ed., ASM International, 1988, p 269–290
25. W.F. Hosford and R.M. Caddell, *Metal Forming: Mechanics and Metallurgy*, Prentice-Hall, Inc., 1983
26. D. Zhao, Temperature Correction in Compression Tests, *J. Mater. Process. Technol.*, Vol 36, 1993, p 467–471
27. H.L. Gegel, J.C. Malas, S.M. Doraivelu, and V.A. Shende, Acquisition of Data for Forging Process Design, *Forming and Forging*, Vol 14, *ASM Handbook*, ASM International, 1988, p 439–442
28. D.N. Tishler and C.H. Wells, An Improved High-Temperature Extensometer, *Mater. Res. Stand.*, Vol 6 (No. 1), ASTM, MTRSA, 1966, p 20–22
29. "Standard Test Method for Tensile Strain-Hardening Exponents (n -Values) of Metallic Sheet Materials," ASTM E 646, *Annual Book of ASTM Standards*, 1994

30. "Standard Test Method for Young's Modulus, Tangent Modulus, and Chord Modulus," ASTM E 111, *Annual Book of ASTM Standards*, 1994
31. H.A. Kuhn, P.W. Lee, and T. Erturk, A Fracture Criterion for Cold Forming, *J. Eng. Mater. Technol (Trans. ASME)*, Oct 1973, p 213–217
32. A.T. Male and G.E. Dieter, Hot Compression Testing, *Workability Testing Techniques*, G.E. Dieter, Ed., American Society for Metals, 1984, p 51–72
33. V. DePierre, F.J. Gurney, and A.T. Male, Mathematical Calibration of the Ring Test with Bulge Formation, Technical Report AFML-TR-37, U.S. Air Force Materials Lab, March 1972
34. A.T. Male and V. DePierre, *Proc. 10th Int. Machine Tool Design and Research Conf.*, Pergamon Press, 1969, p 537
35. A.T. Male and V. DePierre, *J. Lubr. Technol. (Trans. ASME)*, Vol 92, 1970, p 389
36. W.C. Chen, I.V. Samarasekera, and E.B. Hawbolt, Fundamental Phenomena Governing Heat Transfer During Rolling, *Metall. Trans. A*, Vol 24, June 1993, p 1307–1320

Testing for Deformation Modeling

Dan Zhao, Johnson Controls, Inc.

Testing for Sheet-Metal Forming

Sheet-metal forming comprises deep drawing, stamping, stretching, drape forming, spin forming, coining, ironing, bending, blanking, and superplastic forming. Sheet metals are usually produced by rolling, and so mechanical properties vary along different directions in relation to the rolling direction (RD). Figure 25 shows a schematic of a sheet-metal specimen and its directions relative to the rolling direction. In addition, spring-back is significant for sheet metals, and elastic properties are much more important than in bulk forming.

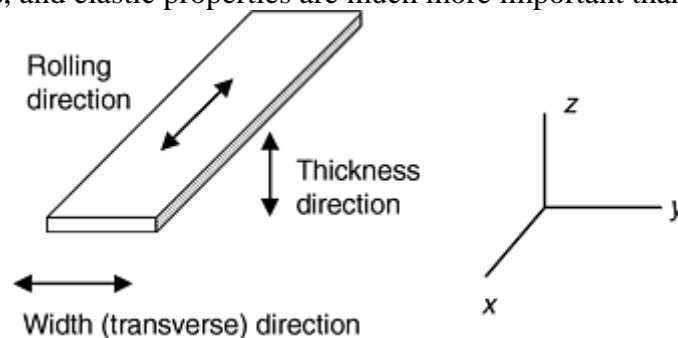


Fig. 25 Schematic of a sheet-metal specimen and its directions relative to the rolling direction

A very important parameter for sheet metal is the ratio (R) of plastic strains in width (transverse) and thickness directions:

$$R = \frac{\epsilon_w}{\epsilon_t} = \frac{\epsilon_y}{\epsilon_z} \quad (\text{Eq 24})$$

Because the strains in thickness direction are difficult to measure, they are usually calculated by using volume constancy:

$$\varepsilon_t = -(\varepsilon_l + \varepsilon_w) \quad (\text{Eq 25})$$

R -values vary in different directions on the plane of the sheet metal, and are usually denoted by the angle (in degrees) to rolling direction. In the rolling direction, R is denoted as R_0 , and in the transverse direction, as R_{90} . Most sheet-metal forming operations, such as deep drawing and stamping, are performed at room temperature. However, sheet forming in the aerospace industry with titanium alloys and superalloys almost always are done at elevated temperatures. Forming at elevated temperatures is also done to achieve the desirable benefits of superplastic behavior, which is described in more detail in the article “Superplastic Deformation at Elevated Temperatures” in this Volume.

Constitutive Equations

For elastic deformation, generalized Hooke's law holds (Ref 37):

$$\sigma_i = C_{ij}\varepsilon_j \quad i, j = 1, \dots, 6 \quad (\text{Eq 26})$$

where σ_i is the stress component, C_{ij} is the stiffness matrix, and ε_j is the strain component. Due to symmetry, C_{ij} has a maximum number of 21 independent constants. Table 2 lists the independent constants for different types of materials. For orthotropic material, there are nine independent constants; for transversely isotropic materials, there are five independent constants; and for isotropic materials, there are only two independent constants. The elastic constants can be measured using nondestructive testing techniques (Ref 38). Once these constants are determined, they can be directly input into modeling software.

Table 2 Independent constants in stiffness matrix for different types of materials

Material	Independent constants
Orthotropic	$C_{11}, C_{12}, C_{13}, C_{22}, C_{23}, C_{33}, C_{44}, C_{55}, C_{66}$
Transversely isotropic	$C_{11}, C_{12}, C_{13}, C_{33}, C_{44}$
Isotropic	C_{11}, C_{12}

For plastic deformation, Hill's anisotropic yield criterion (Ref 39) has wide recognition:

$$2f(\sigma_{ij}) = F(\sigma_y - \sigma_z)^2 + G(\sigma_z - \sigma_x)^2 + H(\sigma_x - \sigma_y)^2 + 2L\tau_{yz}^2 + 2M\tau_{zx}^2 + 2N\tau_{xy}^2 = 1 \quad (\text{Eq 27})$$

where $F, G, H, L, M,$ and N are constants that characterize the anisotropy. Tensile tests can be used to determine constants $F, G,$ and H , and shear tests can be used to evaluate constants $L, M,$ and N .

A tensile test in the x -direction provides the yield strength X . Similarly, tensile tests in the y - and z -directions provide yield strengths Y and Z . Inputting these yield strengths into Eq 27 solves $F, G,$ and H (Ref 26):

$$2F = \frac{1}{Y^2} + \frac{1}{Z^2} - \frac{1}{X^2}$$

$$2G = \frac{1}{Z^2} + \frac{1}{X^2} - \frac{1}{Y^2} \quad (\text{Eq 28})$$

$$2H = \frac{1}{X^2} + \frac{1}{Y^2} - \frac{1}{Z^2}$$

However, a tensile test in the thickness direction (z -direction) is very difficult. R -values in rolling and width directions can be used to obtain Z (Ref 26):

$$Z = Y \sqrt{\frac{R_0(1 + R_{90})}{(R_{90} + R_0)}} \quad (\text{Eq 29})$$

The plastic constitutive behavior for anisotropic material can also be described by Eq 2 for different directions. Tensile tests can be conducted in the rolling direction, width direction, and the direction 45° from the rolling direction. Yield strength, tensile strength, uniform elongation, total elongation, the strain-hardening exponent (n), K -values, R -values, and the strain-rate sensitivity (m) are recorded or calculated. The data can subsequently be input into commercial software for deformation modeling (Ref 40).

Failure of Sheet Metal

Failure of sheet metals can be caused by either fracture or plastic instability. A general way of describing the failure is a forming-limit diagram (FLD) (Ref 41). A typical FLD for a low carbon steel is shown in Fig. 26 (Ref 25, 42). If the combination of major and minor strains is above the solid line, failure is likely to occur. If this combination is under the line, the forming process is safe. Theoretical equations for calculating critical major strain (ϵ_1^*) have also been developed, including an equation for local necking (Ref 25):

$$\epsilon_1^* = \frac{n}{1 + \rho} \quad (\text{Eq 30})$$

where n is strain-hardening exponent, provided that $\sigma_1 = K \epsilon_1^n$ is followed; and ρ is the ratio of minor strain to major strain, ϵ_2/ϵ_1 . For diffuse necking, the critical major strain (ϵ_1^*) is (Ref 43):

$$\epsilon_1^* = \frac{2n(1 + \rho + \rho^2)}{(\rho + 1)(2\rho^2 - \rho + 2)} \quad (\text{Eq 31})$$

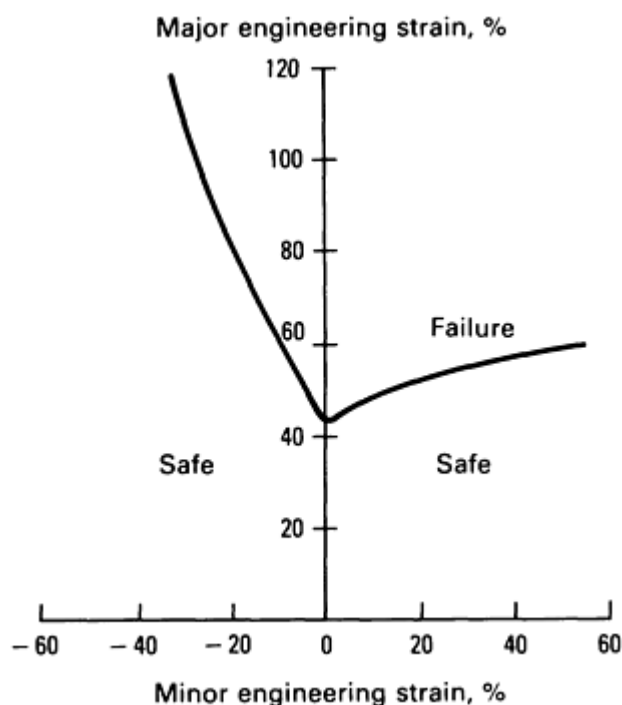


Fig. 26 Typical forming-limit diagram for steel

Tensile Test

Tensile tests for sheet metal are specified in ASTM standards (Ref 15, 16, 29, and 44). Several special issues for sheet metals are discussed in the following sections.

Specimen Preparation. Specimens can be rectangular with or without reduced section. The specimens can be either machined or sheared. Sawing is also permitted by the applicable ASTM standard (Ref 44), but may not provide good dimensional control. Shearing with a precise punch and die is the most efficient way of making specimens. Computer numerical control machining, though slower than punching, is very precise and introduces little deformation along the machined surfaces. Specimens should be made along different directions to reflect anisotropy. Figure 27 shows the orientation of specimens on a piece of sheet metal.

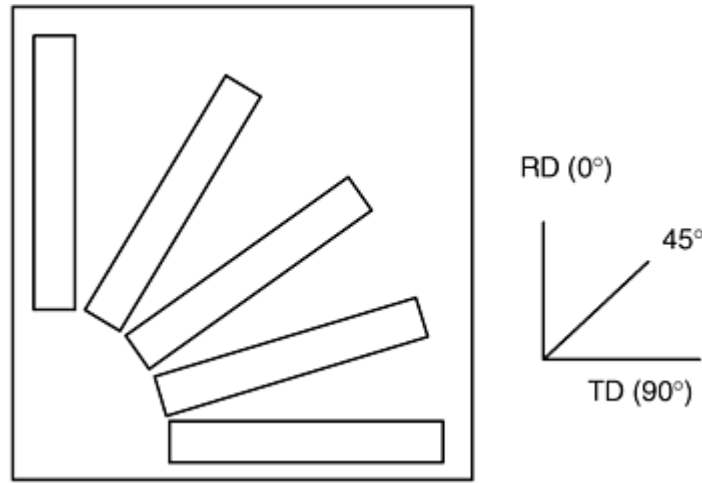


Fig. 27 Sheet-metal specimen orientations for tensile testing. RD, rolling direction; TD, transverse direction

Commercial extensometers are available for strain measurement. To measure local strains, grid patterns can be put on the specimen surface over the gage length, as shown in Fig. 28. The patterns can be inscribed on a layer of paint (Ref 45, 46), photoetched, or thermally transferred from printed transparencies. Thermally transferred patterns printed with a laser printer can stand testing temperatures up to 1200 °C (2190 °F). The size of the grid can be 1 to 2 mm (0.04–0.08 in.) to permit accurate local measurement.

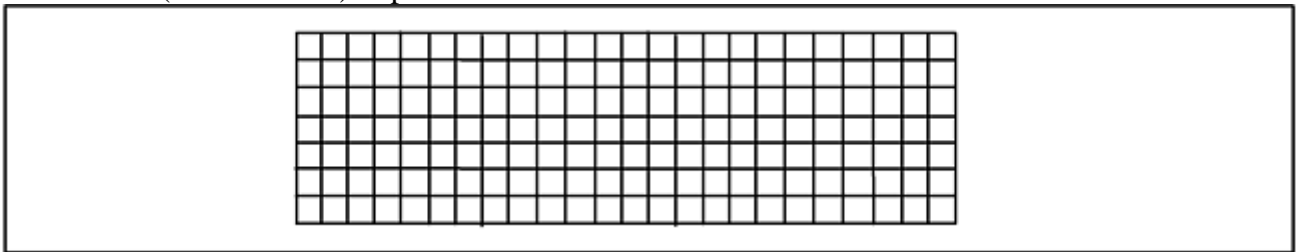


Fig. 28 Grid pattern on the specimen gage length

Alignment of the Specimen. Special care should be taken to ensure the alignment of the specimen with a gripping apparatus. Improper gripping results in bending of the specimen, especially in the width direction. It is helpful to mark the specimen with gripping lines for reference.

Measurement of Strain. Displacement of the grid on the specimen can be recorded with a high-speed camera for calculation of instantaneous strains (Fig. 29). If a camera is not available, displacement can be measured manually. However, manual measurement is difficult at elevated temperatures. The fracture strains can always be measured manually with a microscope. Some specialized three-dimensional displacement-measurement systems, as shown in Fig. 30, are also available (Ref 45, 46).

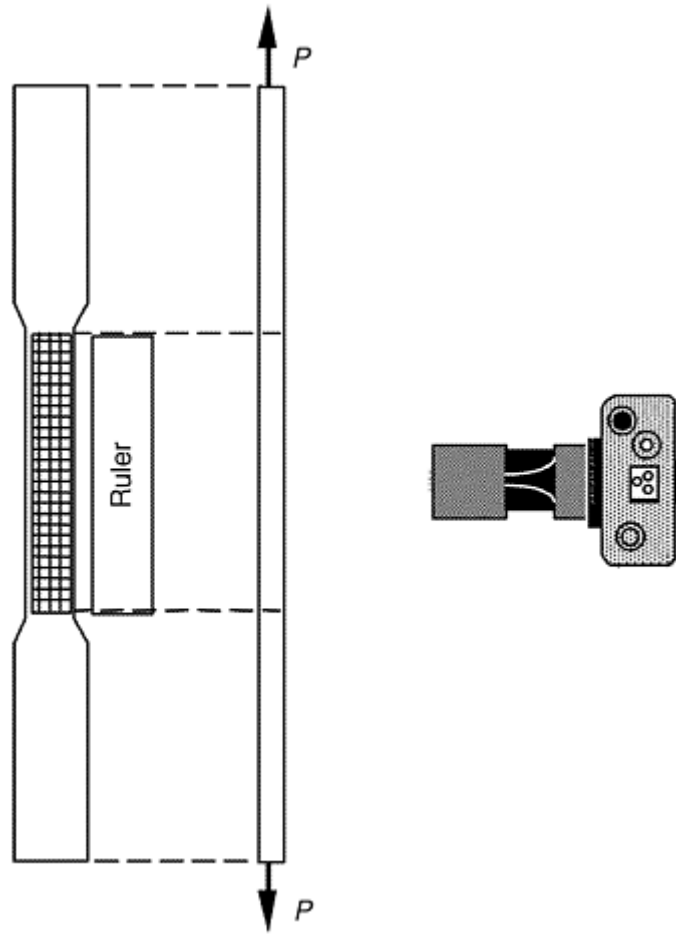


Fig. 29 Strain recording with a camera during a tensile test of a sheet-metal specimen. Source: Ref 46

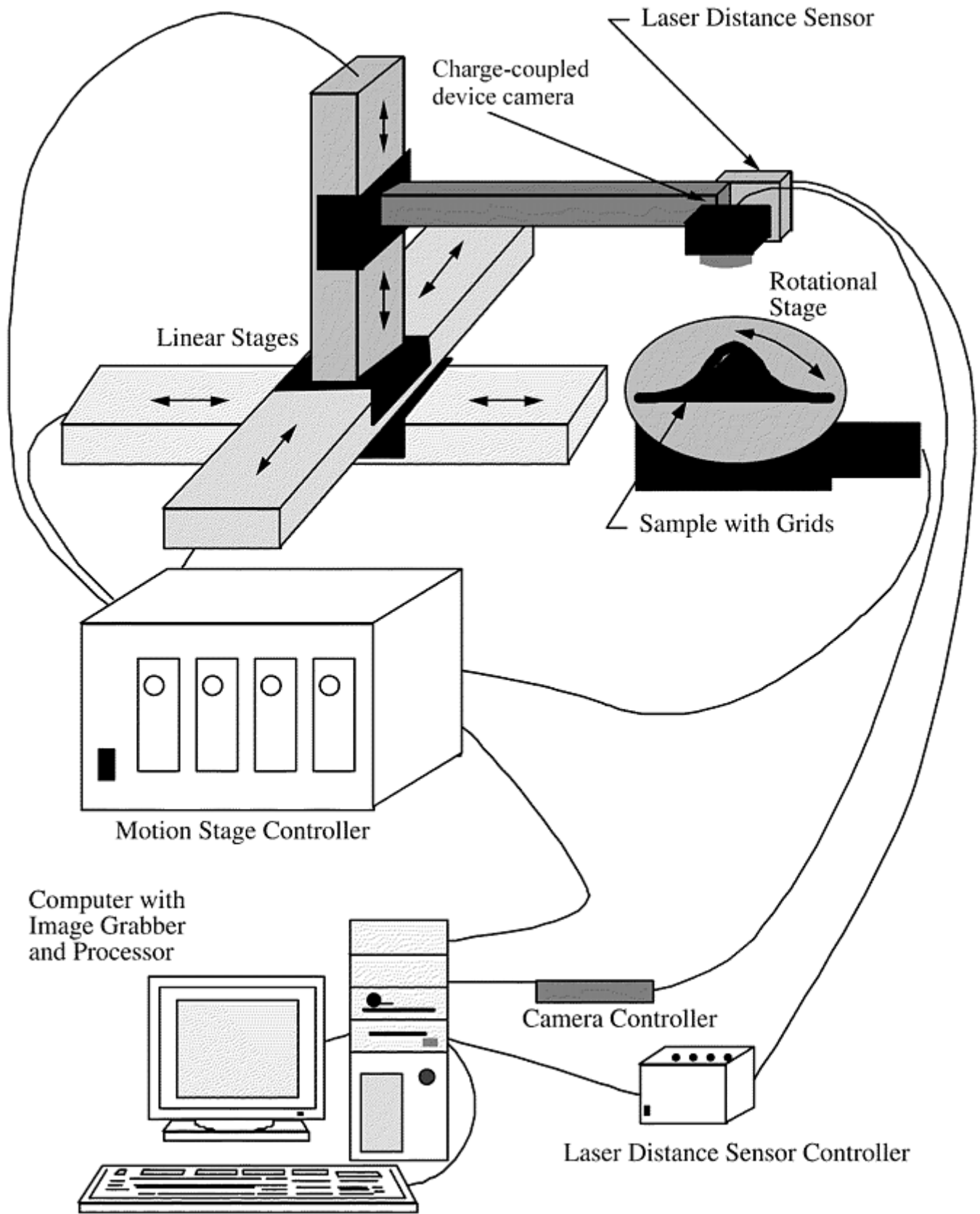


Fig. 30 Automatic noncontact 3-D surface-deformation measuring system. Source: Ref 46

Punch Testing

The punch test is used to obtain data for constructing FLDs of sheet metals. A schematic is shown in Fig. 31 for a punch-test apparatus. Punch testing can also be used to measure the workability for deep drawing. An

important parameter for drawability is the limiting dome height (LDH). In addition to the fracture data from punch testing, data from biaxial stretching and tensile tests can also be used for constructing FLDs.

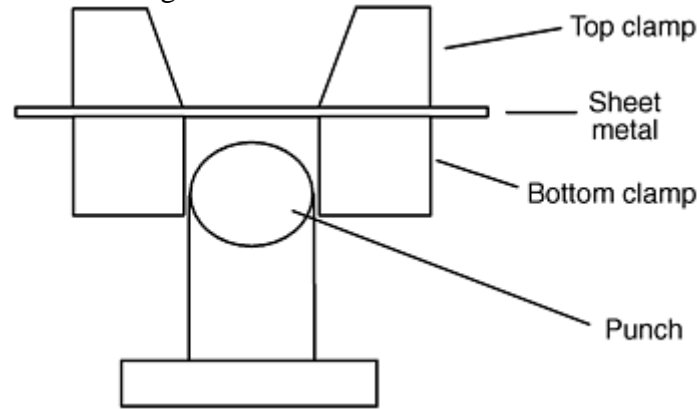


Fig. 31 Schematic of a punch-test device

The specimen can be round or rectangular for the full-size punch test. The specimen is clamped around the edge. The punch moves at a specified speed (usually between 0.08 and 0.4 mm/s, or 0.003 and 0.015 in./s, unless simulating a specific operation at a different speed). When the specimen starts necking severely or fractures, a load drop stops the punch. A hydraulic sheet-metal testing machine has options to vary the clamping force and program the movement of the punch.

The punch should be lubricated with petroleum jelly. Clamping should be conducted carefully to ensure it does not cause the specimen to crack at the clamping site. Specimens with grids on them help determine fracture strains. Circular grids also help identify the directions of major and minor strains after deformation. However, if a three-dimensional digital measurement system is available, the strains can be calculated automatically, and square grids are as useful as circular grids.

Different widths of specimens are needed to cover the wide range of major and minor strain combinations. However, the width can change in the transverse direction or rolling direction, and FLDs constructed with the two different groups of specimens are different.

References cited in this section

15. "Standard Test Methods for Tension Testing of Metallic Materials," ASTM E 8, *Annual Book of ASTM Standards*, 1994
16. "Standard Test Methods for Elevated Temperature Tension Tests of Metallic Materials," ASTM E 21, *Annual Book of ASTM Standards*, 1994
25. W.F. Hosford and R.M. Caddell, *Metal Forming: Mechanics and Metallurgy*, Prentice-Hall, Inc., 1983
26. D. Zhao, Temperature Correction in Compression Tests, *J. Mater. Process. Technol.*, Vol 36, 1993, p 467–471
29. "Standard Test Method for Tensile Strain-Hardening Exponents (n -Values) of Metallic Sheet Materials," ASTM E 646, *Annual Book of ASTM Standards*, 1994
37. R.M. Jones, *Mechanics of Composite Materials*, Taylor & Francis Ltd., New York, 1975, p 32–45
38. C.J. Yu and T. Prucher, Measuring Young's Modulus and Shear Modulus—A Comparison of Dynamic and Mechanical Techniques, *Proc. of the 1993 Powder Metallurgy & Particulate Materials*, Vol 1, 1993, p 273–286
39. R. Hill, *Mathematical Theory of Plasticity*, Oxford University Press, 1950

40. J.K. Lee, G.L. Kinzel, and R.H. Wagoner, Ed., *NUMISHEET '96, Proc. of 3rd Int. Conf.: Numerical Simulation of 3-D Sheet-metal forming Processes—Verification of Simulations with Experiments*, Sep 29–Oct 3 (Dearborn, MI), 1996
41. S.P. Keeler, Understanding Sheet Metal Formability, parts IV and VI, *Mach. Mag.*, May and July 1968
42. S.S. Hecker, *Sheet Met. Ind.*, Vol 52, 1975, p 671–675
43. H.W. Swift, Plastic Instability Under Plane-Stress, *J. Mech. Phys. Sol.*, Vol 1, 1952, p 1–18
44. “Standard Test Method for Plastic Strain Ratio r for Sheet Metal,” ASTM E 517, *Annual Book of ASTM Standards*, 1994
45. S.Y. Lin, R. Czarnek, and P.K. Chaudhury, Modified Grid Method for Plastic-Strain-Ratio Measurement in Sheet Metal, *Proc. of the VIII Int. Congress on Experimental Mechanics* (Nashville, TN), June 1996, p 469–470
46. S.Y. Lin, Plastic-Strain-Ratio Measurement for Sheet Metal Using Modified Grid Method, unpublished technical report, Concurrent Technologies Corporation, Johnstown, PA, 1998, p 4–5

Testing for Deformation Modeling

Dan Zhao, Johnson Controls, Inc.

Testing for Sheet-Metal Forming

Sheet-metal forming comprises deep drawing, stamping, stretching, drape forming, spin forming, coining, ironing, bending, blanking, and superplastic forming. Sheet metals are usually produced by rolling, and so mechanical properties vary along different directions in relation to the rolling direction (RD). Figure 25 shows a schematic of a sheet-metal specimen and its directions relative to the rolling direction. In addition, spring-back is significant for sheet metals, and elastic properties are much more important than in bulk forming.

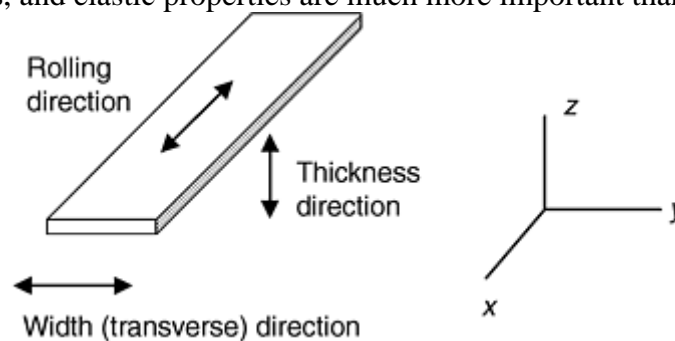


Fig. 25 Schematic of a sheet-metal specimen and its directions relative to the rolling direction

A very important parameter for sheet metal is the ratio (R) of plastic strains in width (transverse) and thickness directions:

$$R = \frac{\epsilon_w}{\epsilon_t} = \frac{\epsilon_y}{\epsilon_z} \quad (\text{Eq 24})$$

Because the strains in thickness direction are difficult to measure, they are usually calculated by using volume constancy:

$$\varepsilon_t = -(\varepsilon_l + \varepsilon_w) \quad (\text{Eq 25})$$

R -values vary in different directions on the plane of the sheet metal, and are usually denoted by the angle (in degrees) to rolling direction. In the rolling direction, R is denoted as R_0 , and in the transverse direction, as R_{90} . Most sheet-metal forming operations, such as deep drawing and stamping, are performed at room temperature. However, sheet forming in the aerospace industry with titanium alloys and superalloys almost always are done at elevated temperatures. Forming at elevated temperatures is also done to achieve the desirable benefits of superplastic behavior, which is described in more detail in the article “Superplastic Deformation at Elevated Temperatures” in this Volume.

Constitutive Equations

For elastic deformation, generalized Hooke's law holds (Ref 37):

$$\sigma_i = C_{ij}\varepsilon_j \quad i, j = 1, \dots, 6 \quad (\text{Eq 26})$$

where σ_i is the stress component, C_{ij} is the stiffness matrix, and ε_j is the strain component. Due to symmetry, C_{ij} has a maximum number of 21 independent constants. Table 2 lists the independent constants for different types of materials. For orthotropic material, there are nine independent constants; for transversely isotropic materials, there are five independent constants; and for isotropic materials, there are only two independent constants. The elastic constants can be measured using nondestructive testing techniques (Ref 38). Once these constants are determined, they can be directly input into modeling software.

Table 2 Independent constants in stiffness matrix for different types of materials

Material	Independent constants
Orthotropic	$C_{11}, C_{12}, C_{13}, C_{22}, C_{23}, C_{33}, C_{44}, C_{55}, C_{66}$
Transversely isotropic	$C_{11}, C_{12}, C_{13}, C_{33}, C_{44}$
Isotropic	C_{11}, C_{12}

For plastic deformation, Hill's anisotropic yield criterion (Ref 39) has wide recognition:

$$2f(\sigma_{ij}) = F(\sigma_y - \sigma_z)^2 + G(\sigma_z - \sigma_x)^2 + H(\sigma_x - \sigma_y)^2 + 2L\tau_{yz}^2 + 2M\tau_{zx}^2 + 2N\tau_{xy}^2 = 1 \quad (\text{Eq 27})$$

where $F, G, H, L, M,$ and N are constants that characterize the anisotropy. Tensile tests can be used to determine constants $F, G,$ and $H,$ and shear tests can be used to evaluate constants $L, M,$ and $N.$

A tensile test in the x -direction provides the yield strength $X.$ Similarly, tensile tests in the y - and z -directions provide yield strengths Y and $Z.$ Inputting these yield strengths into Eq 27 solves $F, G,$ and H (Ref 26):

$$2F = \frac{1}{Y^2} + \frac{1}{Z^2} - \frac{1}{X^2}$$

$$2G = \frac{1}{Z^2} + \frac{1}{X^2} - \frac{1}{Y^2} \quad (\text{Eq 28})$$

$$2H = \frac{1}{X^2} + \frac{1}{Y^2} - \frac{1}{Z^2}$$

However, a tensile test in the thickness direction (z -direction) is very difficult. R -values in rolling and width directions can be used to obtain Z (Ref 26):

$$Z = Y \sqrt{\frac{R_0(1 + R_{90})}{(R_{90} + R_0)}} \quad (\text{Eq 29})$$

The plastic constitutive behavior for anisotropic material can also be described by Eq 2 for different directions. Tensile tests can be conducted in the rolling direction, width direction, and the direction 45° from the rolling direction. Yield strength, tensile strength, uniform elongation, total elongation, the strain-hardening exponent (n), K -values, R -values, and the strain-rate sensitivity (m) are recorded or calculated. The data can subsequently be input into commercial software for deformation modeling (Ref 40).

Failure of Sheet Metal

Failure of sheet metals can be caused by either fracture or plastic instability. A general way of describing the failure is a forming-limit diagram (FLD) (Ref 41). A typical FLD for a low carbon steel is shown in Fig. 26 (Ref 25, 42). If the combination of major and minor strains is above the solid line, failure is likely to occur. If this combination is under the line, the forming process is safe. Theoretical equations for calculating critical major strain (ϵ_1^*) have also been developed, including an equation for local necking (Ref 25):

$$\epsilon_1^* = \frac{n}{1 + \rho} \quad (\text{Eq 30})$$

where n is strain-hardening exponent, provided that $\sigma_1 = K \epsilon_1^n$ is followed; and ρ is the ratio of minor strain to major strain, ϵ_2/ϵ_1 . For diffuse necking, the critical major strain (ϵ_1^*) is (Ref 43):

$$\epsilon_1^* = \frac{2n(1 + \rho + \rho^2)}{(\rho + 1)(2\rho^2 - \rho + 2)} \quad (\text{Eq 31})$$

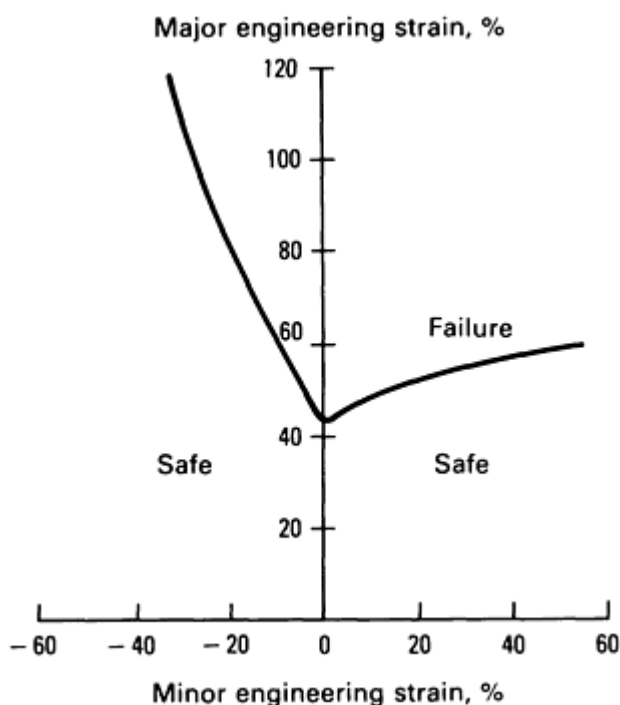


Fig. 26 Typical forming-limit diagram for steel

Tensile Test

Tensile tests for sheet metal are specified in ASTM standards (Ref 15, 16, 29, and 44). Several special issues for sheet metals are discussed in the following sections.

Specimen Preparation. Specimens can be rectangular with or without reduced section. The specimens can be either machined or sheared. Sawing is also permitted by the applicable ASTM standard (Ref 44), but may not provide good dimensional control. Shearing with a precise punch and die is the most efficient way of making specimens. Computer numerical control machining, though slower than punching, is very precise and introduces little deformation along the machined surfaces. Specimens should be made along different directions to reflect anisotropy. Figure 27 shows the orientation of specimens on a piece of sheet metal.

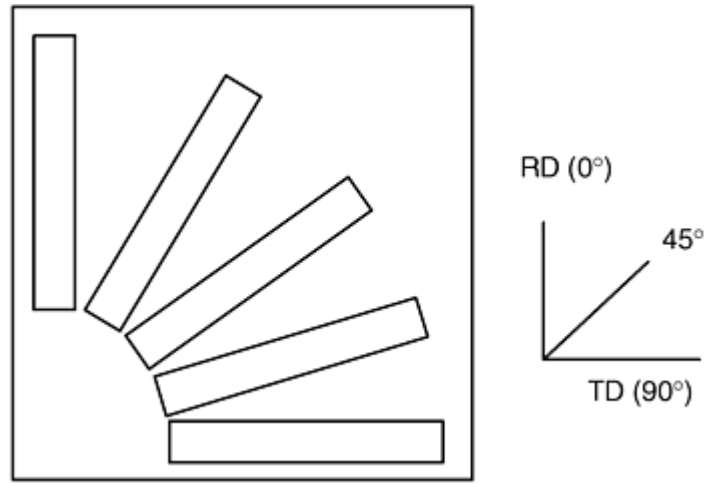


Fig. 27 Sheet-metal specimen orientations for tensile testing. RD, rolling direction; TD, transverse direction

Commercial extensometers are available for strain measurement. To measure local strains, grid patterns can be put on the specimen surface over the gage length, as shown in Fig. 28. The patterns can be inscribed on a layer of paint (Ref 45, 46), photoetched, or thermally transferred from printed transparencies. Thermally transferred patterns printed with a laser printer can stand testing temperatures up to 1200 °C (2190 °F). The size of the grid can be 1 to 2 mm (0.04–0.08 in.) to permit accurate local measurement.

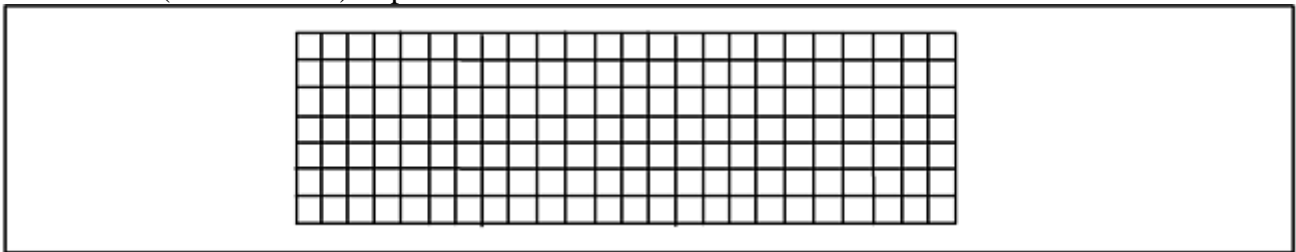


Fig. 28 Grid pattern on the specimen gage length

Alignment of the Specimen. Special care should be taken to ensure the alignment of the specimen with a gripping apparatus. Improper gripping results in bending of the specimen, especially in the width direction. It is helpful to mark the specimen with gripping lines for reference.

Measurement of Strain. Displacement of the grid on the specimen can be recorded with a high-speed camera for calculation of instantaneous strains (Fig. 29). If a camera is not available, displacement can be measured manually. However, manual measurement is difficult at elevated temperatures. The fracture strains can always be measured manually with a microscope. Some specialized three-dimensional displacement-measurement systems, as shown in Fig. 30, are also available (Ref 45, 46).

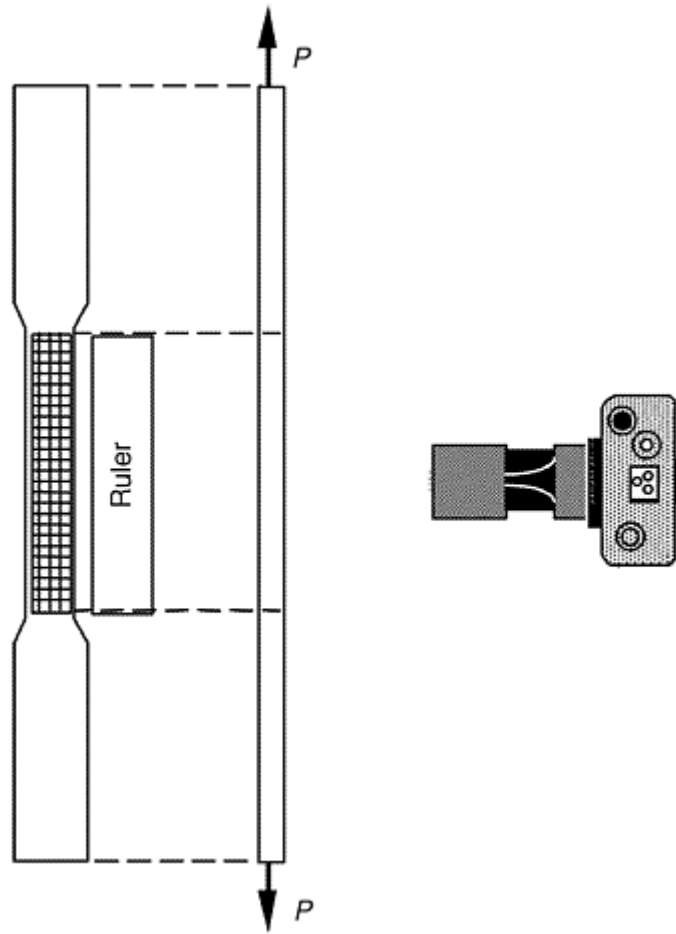


Fig. 29 Strain recording with a camera during a tensile test of a sheet-metal specimen. Source: Ref 46

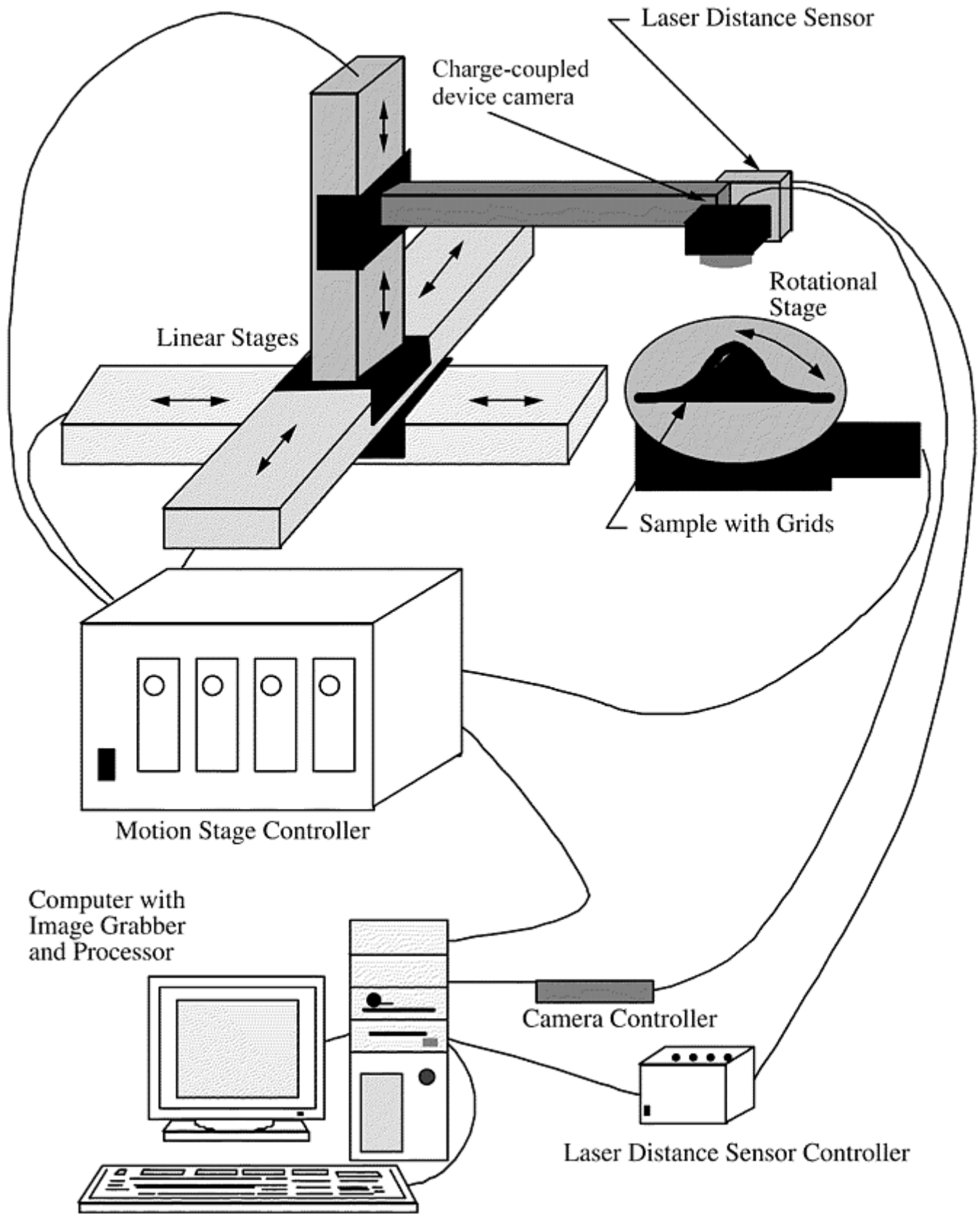


Fig. 30 Automatic noncontact 3-D surface-deformation measuring system. Source: Ref 46

Punch Testing

The punch test is used to obtain data for constructing FLDs of sheet metals. A schematic is shown in Fig. 31 for a punch-test apparatus. Punch testing can also be used to measure the workability for deep drawing. An

important parameter for drawability is the limiting dome height (LDH). In addition to the fracture data from punch testing, data from biaxial stretching and tensile tests can also be used for constructing FLDs.

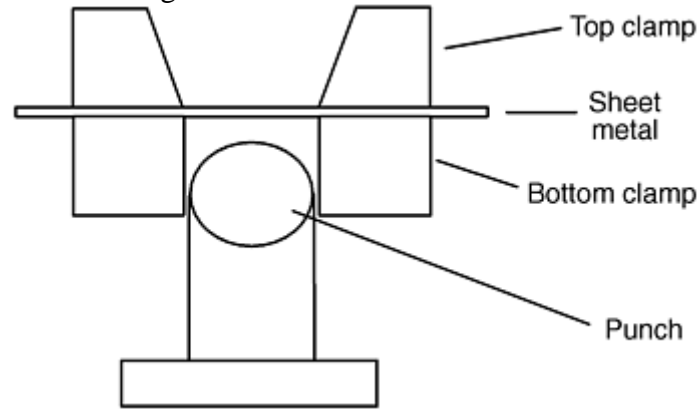


Fig. 31 Schematic of a punch-test device

The specimen can be round or rectangular for the full-size punch test. The specimen is clamped around the edge. The punch moves at a specified speed (usually between 0.08 and 0.4 mm/s, or 0.003 and 0.015 in./s, unless simulating a specific operation at a different speed). When the specimen starts necking severely or fractures, a load drop stops the punch. A hydraulic sheet-metal testing machine has options to vary the clamping force and program the movement of the punch.

The punch should be lubricated with petroleum jelly. Clamping should be conducted carefully to ensure it does not cause the specimen to crack at the clamping site. Specimens with grids on them help determine fracture strains. Circular grids also help identify the directions of major and minor strains after deformation. However, if a three-dimensional digital measurement system is available, the strains can be calculated automatically, and square grids are as useful as circular grids.

Different widths of specimens are needed to cover the wide range of major and minor strain combinations. However, the width can change in the transverse direction or rolling direction, and FLDs constructed with the two different groups of specimens are different.

References cited in this section

15. "Standard Test Methods for Tension Testing of Metallic Materials," ASTM E 8, *Annual Book of ASTM Standards*, 1994
16. "Standard Test Methods for Elevated Temperature Tension Tests of Metallic Materials," ASTM E 21, *Annual Book of ASTM Standards*, 1994
25. W.F. Hosford and R.M. Caddell, *Metal Forming: Mechanics and Metallurgy*, Prentice-Hall, Inc., 1983
26. D. Zhao, Temperature Correction in Compression Tests, *J. Mater. Process. Technol.*, Vol 36, 1993, p 467–471
29. "Standard Test Method for Tensile Strain-Hardening Exponents (n -Values) of Metallic Sheet Materials," ASTM E 646, *Annual Book of ASTM Standards*, 1994
37. R.M. Jones, *Mechanics of Composite Materials*, Taylor & Francis Ltd., New York, 1975, p 32–45
38. C.J. Yu and T. Prucher, Measuring Young's Modulus and Shear Modulus—A Comparison of Dynamic and Mechanical Techniques, *Proc. of the 1993 Powder Metallurgy & Particulate Materials*, Vol 1, 1993, p 273–286
39. R. Hill, *Mathematical Theory of Plasticity*, Oxford University Press, 1950

40. J.K. Lee, G.L. Kinzel, and R.H. Wagoner, Ed., *NUMISHEET '96, Proc. of 3rd Int. Conf.: Numerical Simulation of 3-D Sheet-metal forming Processes—Verification of Simulations with Experiments*, Sep 29–Oct 3 (Dearborn, MI), 1996
41. S.P. Keeler, Understanding Sheet Metal Formability, parts IV and VI, *Mach. Mag.*, May and July 1968
42. S.S. Hecker, *Sheet Met. Ind.*, Vol 52, 1975, p 671–675
43. H.W. Swift, Plastic Instability Under Plane-Stress, *J. Mech. Phys. Sol.*, Vol 1, 1952, p 1–18
44. “Standard Test Method for Plastic Strain Ratio r for Sheet Metal,” ASTM E 517, *Annual Book of ASTM Standards*, 1994
45. S.Y. Lin, R. Czarnek, and P.K. Chaudhury, Modified Grid Method for Plastic-Strain-Ratio Measurement in Sheet Metal, *Proc. of the VIII Int. Congress on Experimental Mechanics* (Nashville, TN), June 1996, p 469–470
46. S.Y. Lin, Plastic-Strain-Ratio Measurement for Sheet Metal Using Modified Grid Method, unpublished technical report, Concurrent Technologies Corporation, Johnstown, PA, 1998, p 4–5

Testing for Deformation Modeling

Dan Zhao, Johnson Controls, Inc.

Testing for Semisolid Forming and Polymer Extrusion

Semisolid forming has become popular due to improved mechanical properties of the parts compared to those made by casting. Polymer extrusion has flow characteristics very similar to those of semisolid forming.

Constitutive Equations

The deformation of a semisolid is significantly affected by temperature and strain rate, as with a solid. The only difference is that the deformation of a semisolid is characterized by shear rate instead of strain rate.

Newton's law of viscosity states (Ref 47, 48):

$$\tau_{yx} = -\eta \frac{dv_x}{dy} = \eta \dot{\gamma} \quad (\text{Eq 32})$$

where τ_{yx} , is shear stress, η is viscosity, v_x is velocity, and $\dot{\gamma}$ is shear rate.

For Newtonian fluid, viscosity is only a function of temperature, and does not depend on shear rate. Most liquid metals and alloys are Newtonian. However, semisolid alloys, as well as polymeric materials, exhibit Non-Newtonian behavior. The viscosity of those materials varies with shear rate; in most cases, it decreases with increasing shear rate—so-called shear thinning. Figure 32 shows the viscosity behavior of Newtonian and Non-Newtonian fluids (Ref 47).

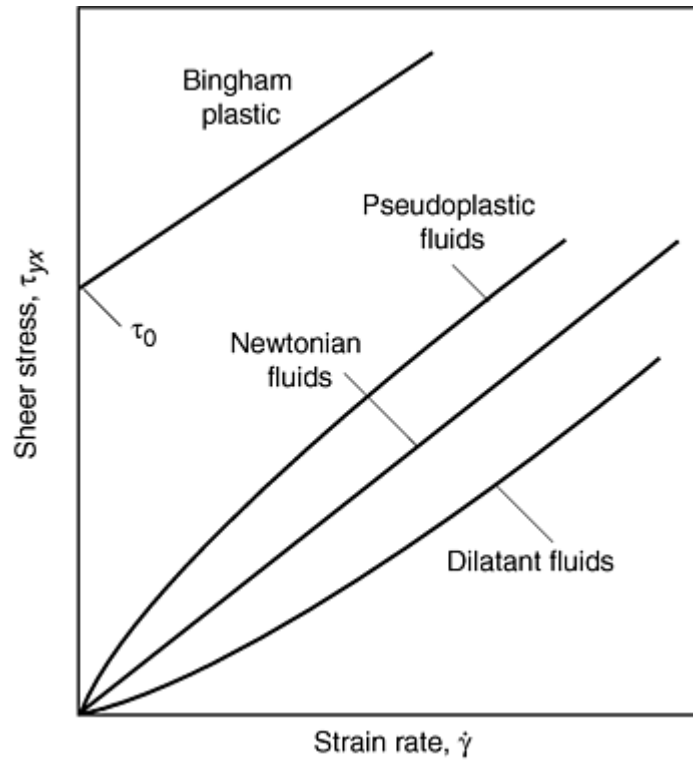


Fig. 32 Stress-strain rate curves for time-independent fluids. Source: Ref 47

For semisolid materials, viscosity is a function of temperature, shear rate, and fraction of solid. Figure 33 shows the viscosity of an Al-Si-Mg alloy with 0.45 and 0.55 solid fractions (Ref 49). Figure 34 shows viscosity variation as a function of temperature and shear rate for a polymer compound.

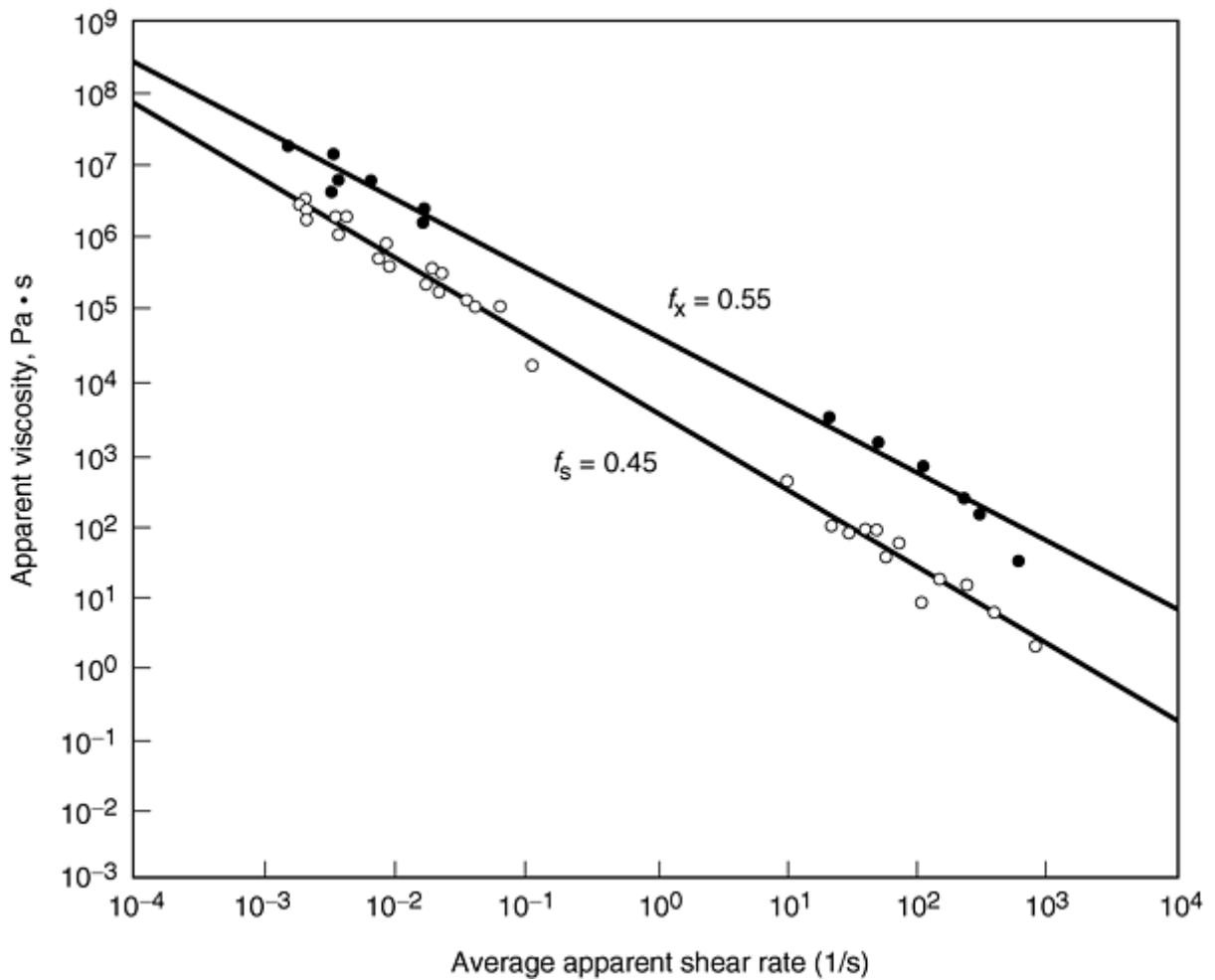


Fig. 33 Apparent viscosity of partially remelted Al-Si-Mg alloys with solid fraction 0.45 and 0.55.
 Source: Ref 49. (See also Ref 48.)

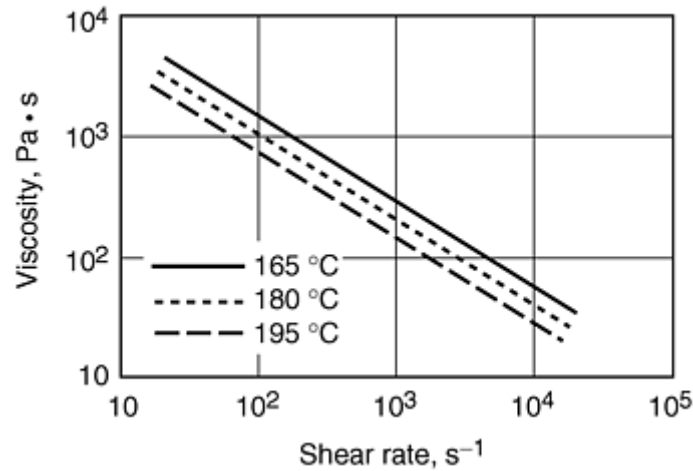


Fig. 34 Viscosity for a polymer material as a function of shear rate at several temperatures

The variation of viscosity as a function of shear rate can be described by a power law (Ref 50):

$$\eta = k \dot{\gamma}^{n-1} \quad (\text{Eq 33})$$

where k and n are empirically determined constants. More complicated equations have been suggested when viscosity data is not a straight line on a log-log scale, as shown in Fig. 33 and 34. One of the equations is the Carreau model (Ref 51):

$$\eta = \eta_0 [1 + (\lambda \dot{\gamma})^2]^{1/2n} \quad (\text{Eq 34})$$

where η_0 is the viscosity at zero shear rate, and λ and n are again empirical constants.

Viscosity is measured by various viscometers. Descriptions of three types of viscometers follow (Ref 50, 51).

Coaxial Cylinder Viscometer

The coaxial cylinder viscometer approximates the classic parallel-plate drag flow problem. As shown in Fig. 35, a cylinder is filled with the fluid with a viscosity to be measured. A coaxial cylinder rotates inside the cylinder with the fluid. The torque, T_0 , and the rotational speed, n , (in rpm) are recorded. The viscosity is given as:

$$\eta = \frac{15T_0 h}{\pi^2 r^3 n L} \quad (\text{Eq 35})$$

where h is the distance between the two cylinders, r is the radius of the inside cylinder, and L is the length of the inside cylinder.

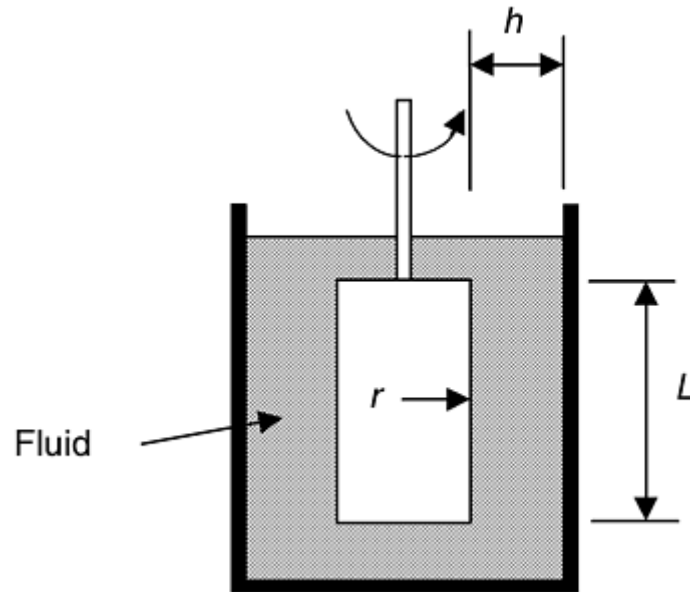


Fig. 35 A schematic of the coaxial cylinder viscometer. Source: Ref 51

Cone-and-Plate Viscometer

The cone-and-plate viscometer, depicted in Fig. 36, is also called a Weissenberg rheogoniometer. It also approximates the parallel-plate drag flow with the flow in the gap between a plate and a cone at very small angles (a couple of degrees). This test also records the torque and the rotational speed. However, the rotational speed here is in rad/s, and it is denoted as Ω . The viscosity is calculated as:

$$\eta = \frac{3\alpha T_0}{2\pi R^3 \Omega} \quad (\text{Eq 36})$$

where α is the angle between the cone and the plate and R is the radius of the cone or plate.

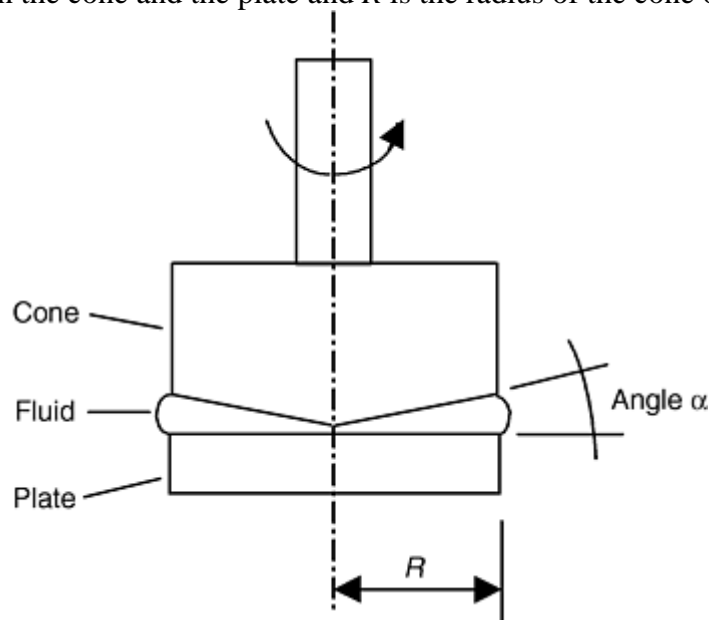


Fig. 36 Schematic of the cone-and-plate instrument. Source: Ref 51

This instrument works well for shear-rate ranges of 10^{-2} to 10^5 s^{-1} . At higher shear rates, flow in the radial direction develops, and the sample may fly out.

Capillary Viscometer

This instrument, depicted in Fig. 37, is good for shear rates of 10 to 1000 s⁻¹. In this test, the fluid is extruded through a tube by applying pressure. The shear stress is related to the pressure drop over the length of the tube:

$$\tau = -\frac{\Delta P R}{2L} \quad (\text{Eq 37})$$

where ΔP is the pressure drop. When the reservoir is large, the gradient of pressure in the reservoir is negligible, and, therefore, ΔP is negligible as well.

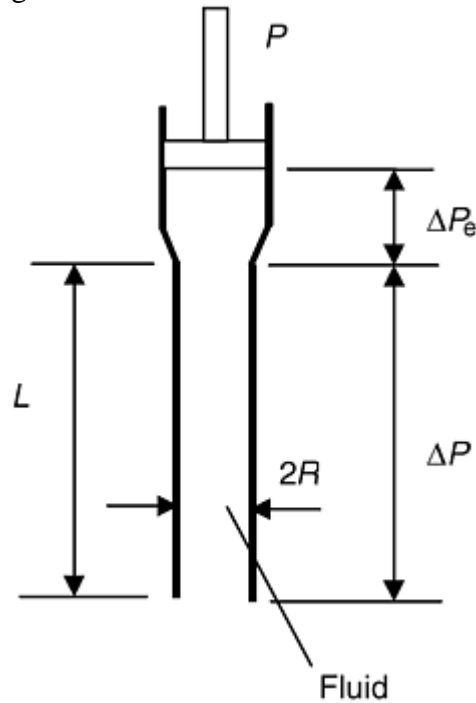


Fig. 37 Schematic of a capillary viscometer. Source: Ref 51

The apparent shear rate is:

$$\dot{\gamma}_a = \frac{4Q}{\pi R^3} \quad (\text{Eq 38})$$

where Q is the volume flow rate (mass flow rate over density).

There is a correction for the shear rate, which takes into account the resistance to stretching at the entrance of the tube. The resistance is small for Newtonian fluid, but large for polymer melts. With this correction (Rabinowitsch correction), shear rate becomes:

$$\dot{\gamma} = \frac{4Q}{\pi R^3} \left(\frac{3}{4} + \frac{d \ln Q}{4 d \ln \tau} \right) \quad (\text{Eq 39})$$

and the viscosity is:

$$\eta = \frac{\tau}{\dot{\gamma}} \quad (\text{Eq 40})$$

Figure 38 provides the ranges of viscosity suitable for different viscometers. In general, cone-and-plate viscometers are good for low shear rates, and capillary viscometers are good for medium to high shear rates.

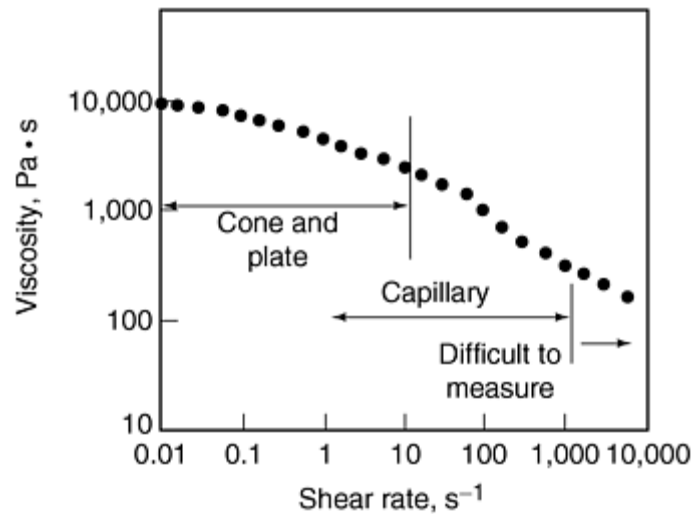


Fig. 38 Viscosity ranges for different viscometers. Source: Ref 51

The control of temperature and structural changes of fluid being tested present difficulty in testing for viscosity. For semisolid materials, local segregation of solid fractions and interaction of particles can affect viscosity significantly. In the forming of semisolid parts, induction heating, which is difficult to control, is usually employed. A few degrees variation in temperature can cause a large difference in the solid fraction. For polymer materials, nonuniform heating and localized curing also greatly influence the data. In general, 10% error in viscosity data is not unusual.

References cited in this section

47. D.R. Poirier and G.H. Geiger, *Transport Phenomena in Materials Processing*, TMS, 1994, p 30
48. G.K. Sigworth, Rheological Properties of Metal Alloys in the Semisolid State, *Can. Metall. Q.*, Vol 35 (No. 2), 1996, p 101–122
49. W.R. Loue, Ph.D. dissertation, Institute National Polytechnique de Grenoble, 1992
50. J. Vlachopoulos, *Polymer Rheology and Extrusion*, Polydynamics, Inc., Hamilton, Ontario, Canada, June 1998
51. J. Vlachopoulos, *Introduction to Plastic Processing*, Center for Advanced Polymer Processing and Design, Department of Chemical Engineering, McMaster University, Hamilton, Ontario, Canada, May 1997, p 2.49–2.52

Testing for Deformation Modeling

Dan Zhao, Johnson Controls, Inc.

References

1. H.E. Boyer, *Atlas of Stress-Strain Curves*, ASM International, 1987
2. Y.V.R.K. Prasad and S. Sasidhara, *Hot Working Guide: A Compendium of Processing Maps*, ASM International, 1997

3. *Atlas of Formability Bulletins*, National Center for Excellence in Metalworking Technology (NCEMT), Johnstown, PA
4. T. Altan, S. Oh, and H. Gegel, *Metal Forming: Fundamentals and Applications*, ASM International, 1983, p 86
5. C.M. Sellars and W.J.McG. Tegart, *Mem. Sci. Rev. Metall.*, Vol 63, 1966, p 731
6. A. Laasroui and J.J. Jonas, Prediction of Steel Flow Stresses at High Temperatures and Strain Rates, *Metall. Trans. A*, Vol 22, 1991, p 1545–1558
7. S.B. Brown, K.H. Kim, and L. Anand, An Internal Variable Constitutive Model for Hot Working of Metals, *Int. J. Plast.*, Vol 5, 1989, p 95–130
8. M. Thirukkonda, D. Zhao, and A.T. Male, “Materials Modeling Effort for HY-100 Steel,” Technical Report TR 96-027, NCEMT, Johnstown, PA, March, 1996, p 27
9. M.G. Cockcroft and D.J. Lahtam, Ductility and the Workability of Metals, *J. Inst. Met.*, Vol 96, 1968, p 33–39
10. D. Zhao, J.P. Bandstra, H.A. Kuhn, A New Fracture Criterion for Fracture Prediction in Metalworking Processes, *Concurrent Engineering Approach to Materials Processing*, S.N. Dwivedi, A.J. Paul, and F. R. Dax, Ed., TMS, 1992, p 107–119
11. H.A. Kuhn, Workability Theory and Application in Bulk Forming Processes, *Forming and Forging*, Vol 14, *Metals Handbook*, ASM International, 1988, p 388–404
12. J.P. Bandstra, “3D Extension of Kuhn Surface Fracture Criterion,” CTC memorandum CTC/JPB-M0469-95, Johnstown, PA, 1995
13. “Standard Test Methods of Compression Testing of Metallic Materials at Room Temperature,” ASTM E 9, *Annual Book of ASTM Standards*, 1994
14. “Standard Practice for Compression Tests of Metallic Materials at Elevated Temperatures with Conventional or Rapid Heating Rates and Strain Rates,” ASTM E 209, *Annual Book of ASTM Standards*, 1994
15. “Standard Test Methods for Tension Testing of Metallic Materials,” ASTM E 8, *Annual Book of ASTM Standards*, 1994
16. “Standard Test Methods for Elevated Temperature Tension Tests of Metallic Materials,” ASTM E 21, *Annual Book of ASTM Standards*, 1994
17. D. Zhao and H. Dong, unpublished technical report, Concurrent Technologies Corporation, Johnstown, PA, 1996
18. S.L. Semiatin and J.J. Jonas, *Formability and Workability of Metals: Plastic Instability and Flow Localization*, American Society for Metals, 1984
19. M.C. Mataya, Simulating Microstructural Evolution during the Hot Working of Alloy 718, *JOM*, Jan 1999, p 18–26
20. R. Chait and C.H. Curll, “Evaluating Engineering Alloys in Compression,” ASTM STP 608, *Recent Developments in Mechanical Testing*, 1976, p 3–19

21. M.L. Lovato and M.G. Stout, Compression Testing Techniques to Determine the Stress/Strain Behavior of Metals Subject to Finite Deformation, *Metall. Trans. A*, Vol 23, 1992, p 935–951
22. O. Alnik, D.D. Murphy, T. Terada, A.K. Koul, and J.-P. Immarigeon, “Modeling of Deformation and Microstructural Changes in P/M Rene 95 Under Isothermal Forging Conditions,” Conf. Proc. No. 426 presented at Aerospace Materials Process Modeling, Oct 2–4, 1987 (Cesme, Turkey), AGARD
23. Merlin IV Test Application Package, Instron Corporation, Canton, MA, 1998
24. J.F. Thomas, Jr. and R. Srinivasan, Constitutive Equations for High Temperature Deformation, *Computer Simulation in Materials Science*, R.J. Arsenault, J. R. Beeler, Jr., and D.M. Esterling, Ed., ASM International, 1988, p 269–290
25. W.F. Hosford and R.M. Caddell, *Metal Forming: Mechanics and Metallurgy*, Prentice-Hall, Inc., 1983
26. D. Zhao, Temperature Correction in Compression Tests, *J. Mater. Process. Technol.*, Vol 36, 1993, p 467–471
27. H.L. Gegel, J.C. Malas, S.M. Doraivelu, and V.A. Shende, Acquisition of Data for Forging Process Design, *Forming and Forging*, Vol 14, *ASM Handbook*, ASM International, 1988, p 439–442
28. D.N. Tishler and C.H. Wells, An Improved High-Temperature Extensometer, *Mater. Res. Stand.*, Vol 6 (No. 1), ASTM, MTRSA, 1966, p 20–22
29. “Standard Test Method for Tensile Strain-Hardening Exponents (n -Values) of Metallic Sheet Materials,” ASTM E 646, *Annual Book of ASTM Standards*, 1994
30. “Standard Test Method for Young's Modulus, Tangent Modulus, and Chord Modulus,” ASTM E 111, *Annual Book of ASTM Standards*, 1994
31. H.A. Kuhn, P.W. Lee, and T. Erturk, A Fracture Criterion for Cold Forming, *J. Eng. Mater. Technol (Trans. ASME)*, Oct 1973, p 213–217
32. A.T. Male and G.E. Dieter, Hot Compression Testing, *Workability Testing Techniques*, G.E. Dieter, Ed., American Society for Metals, 1984, p 51–72
33. V. DePierre, F.J. Gurney, and A.T. Male, Mathematical Calibration of the Ring Test with Bulge Formation, Technical Report AFML-TR-37, U.S. Air Force Materials Lab, March 1972
34. A.T. Male and V. DePierre, *Proc. 10th Int. Machine Tool Design and Research Conf.*, Pergammon Press, 1969, p 537
35. A.T. Male and V. DePierre, *J. Lubr. Technol. (Trans. ASME)*, Vol 92, 1970, p 389
36. W.C. Chen, I.V. Samarasekera, and E.B. Hawbolt, Fundamental Phenomena Governing Heat Transfer During Rolling, *Metall. Trans. A*, Vol 24, June 1993, p 1307–1320
37. R.M. Jones, *Mechanics of Composite Materials*, Taylor & Francis Ltd., New York, 1975, p 32–45
38. C.J. Yu and T. Prucher, Measuring Young's Modulus and Shear Modulus—A Comparison of Dynamic and Mechanical Techniques, *Proc. of the 1993 Powder Metallurgy & Particulate Materials*, Vol 1, 1993, p 273–286
39. R. Hill, *Mathematical Theory of Plasticity*, Oxford University Press, 1950

40. J.K. Lee, G.L. Kinzel, and R.H. Wagoner, Ed., *NUMISHEET '96, Proc. of 3rd Int. Conf.: Numerical Simulation of 3-D Sheet-metal forming Processes—Verification of Simulations with Experiments*, Sep 29–Oct 3 (Dearborn, MI), 1996
41. S.P. Keeler, Understanding Sheet Metal Formability, parts IV and VI, *Mach. Mag.*, May and July 1968
42. S.S. Hecker, *Sheet Met. Ind.*, Vol 52, 1975, p 671–675
43. H.W. Swift, Plastic Instability Under Plane-Stress, *J. Mech. Phys. Sol.*, Vol 1, 1952, p 1–18
44. “Standard Test Method for Plastic Strain Ratio r for Sheet Metal,” ASTM E 517, *Annual Book of ASTM Standards*, 1994
45. S.Y. Lin, R. Czarnek, and P.K. Chaudhury, Modified Grid Method for Plastic-Strain-Ratio Measurement in Sheet Metal, *Proc. of the VIII Int. Congress on Experimental Mechanics* (Nashville, TN), June 1996, p 469–470
46. S.Y. Lin, Plastic-Strain-Ratio Measurement for Sheet Metal Using Modified Grid Method, unpublished technical report, Concurrent Technologies Corporation, Johnstown, PA, 1998, p 4–5
47. D.R. Poirier and G.H. Geiger, *Transport Phenomena in Materials Processing*, TMS, 1994, p 30
48. G.K. Sigworth, Rheological Properties of Metal Alloys in the Semisolid State, *Can. Metall. Q.*, Vol 35 (No. 2), 1996, p 101–122
49. W.R. Loue, Ph.D. dissertation, Institute National Polytechnique de Grenoble, 1992
50. J. Vlachopoulos, Polymer Rheology and Extrusion, Polydynamics, Inc., Hamilton, Ontario, Canada, June 1998
51. J. Vlachopoulos, Introduction to Plastic Processing, Center for Advanced Polymer Processing and Design, Department of Chemical Engineering, McMaster University, Hamilton, Ontario, Canada, May 1997, p 2.49–2.52

Mechanical Testing of Threaded Fasteners and Bolted Joints

Ralph S. Shoberg, RS Technologies, Ltd.

Introduction

FASTENER ENGINEERING and the mechanical testing of threaded fasteners and bolted joints is an important specialty within the field of mechanical engineering. With the wide variety of fasteners and bolted joints available for use, no one set of tests can be specified to cover all applications. The guidelines and examples presented in this article are intended to introduce technical testing concepts and necessary theoretical background subjects. With this introduction as a guide, the interested reader can select and perform practical tests that can help confirm strength and reliability factors for fasteners and bolted-joint assemblies.

All testing and analysis efforts must begin with an understanding of the behavior of individual fasteners. A proper overview recognizes the complex interaction of the materials properties of the fastener, clamped components, and internally threaded components, as well as the influence of coatings, lubricants, and adhesives

on the performance of fasteners in bolted joints. The test methods and procedures that yield the most informative data will test the threaded fastener in the same manner in which it is actually installed.

Test methods for mechanical properties such as hardness, tensile strength, and torsional strength, as well as corrosion and hydrogen embrittlement, are covered in other articles of this Volume and in more detail in the various referenced SAE, ISO, DIN, and ASTM testing standards. These tests provide the baseline information necessary for proper interpretation of the torque-tension tests and testing methods for evaluation of bolted joints presented in this article.

This article outlines test procedures for obtaining useful data for understanding details critical to reliable threaded-fastener applications. Some tests described herein are based on versions of published testing standards. Users should study the referenced standards prior to beginning a testing program. For example, by following the standard test methods and procedures according to ASTM F 606M, the basic mechanical strength properties of threaded fasteners can be determined, and by following the procedures specified in DIN 946, thread and underhead friction coefficients for threaded fasteners can be determined.

Combining basic materials strength and friction coefficient information leads to the development of a powerful method called torque-angle signature analysis. This method provides valuable information on joint strength and performance when applied to testing fasteners in bolted joints. By careful review of an applied torque versus angle-of-turn plot, signature analysis can be used to evaluate bolted joints for loss of preload due to settling, creep, and relaxation, or vibration and dynamic loading. In addition, joint strength problems, such as thread strip and embedment of bearing surfaces and material yield within the bolted joint, are easily identified.

Mechanical Testing of Threaded Fasteners and Bolted Joints

Ralph S. Shoberg, RS Technologies, Ltd.

Torque, Angle, Tension, and Friction

A proper amount of tension, or clamping force, must be developed to ensure that a bolted assembly will function in a safe and reliable manner. The most common attempt to indirectly estimate fastener tension is to take torque measurements either dynamically as the fastener is tightened or with a breakaway audit after the fact. The torque that is required to produce the desired tension in a fastener is dependent on several factors, with frictional characteristics being the most important. Angle-of-turn measurements combined with torque measurements can help overcome the unknown friction-induced variability in the torque-tension relationship. This section provides a brief overview of the relationships between torque, angle-of-turn, tension, and friction and how they are measured and evaluated. This background information is the foundation of the testing methods described in subsequent sections of this article.

Tension

The tension that is created in a threaded fastener when it is tightened represents the clamping force that holds the assembly together. Once the assembly is brought together, the fastener responds like a tension spring, and the assembly acts like a compression spring. The interaction between the fastener and the assembly is illustrated in Fig. 1. As the fastener is turned and load is applied, the fastener is stretched, and the parts are compressed. This compression results in an elastic joint in which the fastener is normally the more flexible member, and the assembly is the more rigid member.

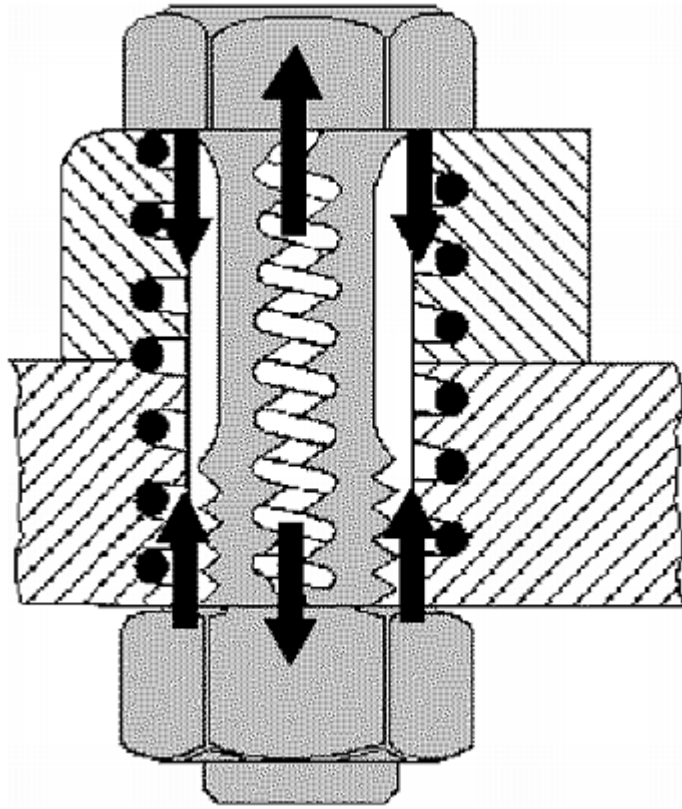


Fig. 1 Spring effect of fastener and assembly under load

The amount of clamping force that the fastener must provide to hold the assembly together must be sufficient to both maintain preloading and prevent slipping of the parts or opening of the joint when the service loads are applied. The factors that primarily establish the preload requirement are the stiffness of the materials in the joint and the loads that are placed on the assembly.

Fastener tension can be measured using different devices, such as strain-gaged bolts or fastener force washers, or by using special techniques, such as ultrasonic bolt measurement. Although these devices and methods are useful in research and engineering efforts, they are often impractical or costly for evaluating fastener tension in production quality-control efforts.

Torque

The most common way to estimate clamping force is to observe the amount of torque applied to the fastener, either as the fastener is tightened or with a breakaway audit of the tightened fastener. This procedure assumes that the relationship between torque and tension is known, such that, for example, the nut factor, or K , from the simple equation $T = KDF$ (where T is torque, D is diameter, and F is clamping force) is established and known to have acceptable variability. The truth of the matter is that if torque alone is measured, it can never be known with certainty whether the desired tension has been achieved. Thus, unfortunately, it must be concluded that torque is a highly unreliable, totally inaccurate measurement for evaluation of the preload on a threaded fastener. However, for many noncritical fasteners, where safety or the functional performance of an assembly is not compromised, it may be acceptable to specify and monitor torque alone. The most common measurement tools are hand torque wrenches that are used for installation and torque audit measurements and rotary torque sensors that are used to measure installation torque dynamically.

In order for tension to be developed, the torque applied to a fastener must overcome friction under the head of the fastener and in the threads, and the fastener or nut must turn. Because the friction may absorb as much as 90 to 95% of the energy applied to the fastener, as little as 5 to 10% of the energy is left for generating fastener tension as shown in Fig. 2. If the amount of friction varies greatly, wide variations in clamping force are produced, which can mean loose or broken bolts leading to assembly failures. To ensure proper assembly of critical fasteners, more than torque must be measured.

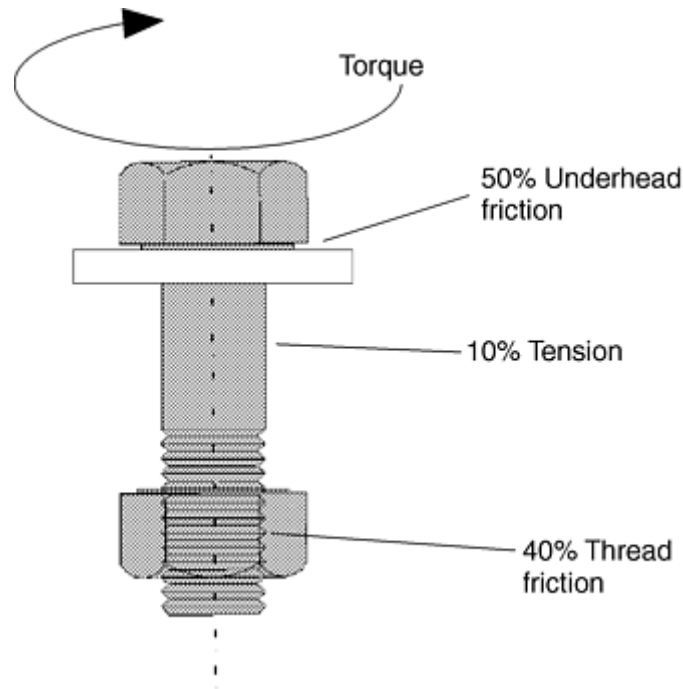


Fig. 2 Typical distribution of energy from torque applied to a bolted assembly

Angle

The amount of fastener tension can be correlated to fastener rotation once the parts of an assembly are drawn firmly together. The clamping force that is developed in this zone of the assembly process, called the elastic tightening region, has been proven to be proportional to the angle of turn. This proportional relationship is based on the helix of the threads and is not influenced by the frictional characteristics of the joint once sufficient clamping force has been produced to firmly align the components such that a linear torque-angle signature slope is attained. Many years ago, in one of his books on the fundamentals of threaded fasteners, John Bickford wrote, “If we knew where to start measuring angle, it would be easy to get uniform tension results.” For the benefit of all, that problem has been solved for many applications using the torque-angle analysis method described in detail in the section “Torque-Angle Signature Analysis” in this article. Practical application of this concept requires that the user learn how to locate what is called the elastic origin.

The basic procedure for locating the elastic origin involves the following steps:

1. A rotary torque sensor equipped with an angle encoder is used to measure the applied torque and fastener rotation.
2. After the tension-versus-angle signature is plotted, a line is drawn tangent to the straight-line elastic tightening section of the plot.
3. The tangent line is extended until it intersects the torque axis. The point where the tangent line intersects the torque axis locates the elastic origin (Fig. 3).
4. The amount of fastener rotation from the elastic origin to where the fastener stops turning can be used to estimate the clamp load that was developed in the joint.

A number of practical signature analysis techniques are presented in detail in the section “Torque-Angle Signature Analysis” in this article.

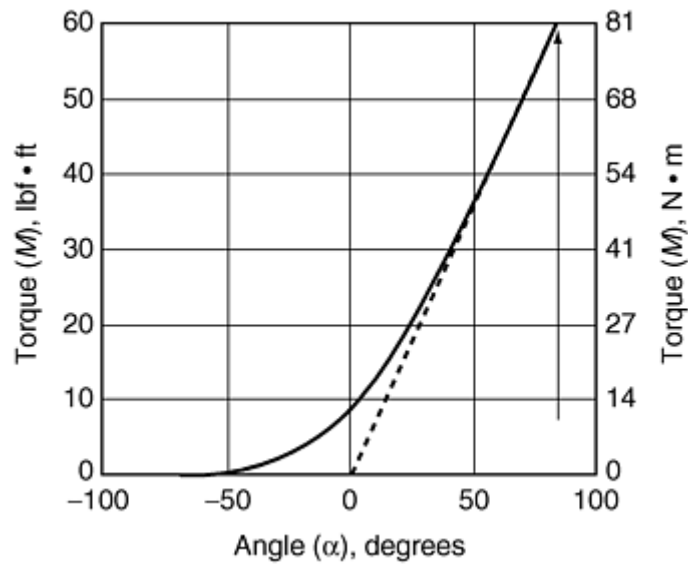


Fig. 3 Location of elastic origin using torque vs. angle signature

Thread and Underhead Friction Measurements

Whereas fastener engineering analysis of threaded fasteners must consider material strength, surface finishes, plating, and coatings to ensure reliable performance, for predictable and repeatable assemblies it is also necessary to understand, measure, and control the frictional characteristics in both the thread and underhead regions. This is particularly true when developing fastener-locking devices such as locknuts, serrated underheads, special thread forms, and thread-locking adhesives and friction patches. Achieving a specific clamp force during installation is always the desired result, and the roles of thread friction and underhead friction must be analyzed and understood to ensure joint integrity.

To determine both thread friction and underhead friction, measurements are taken using a torque-tension research head, as shown in Fig. 4. This device is a special load cell designed to simultaneously measure both thread torque and clamp load. When used with torque sensors that measure the input torque, it is possible to determine the underhead friction torque and the thread friction torque. With this measurement equipment, the fastener can then be tested to establish and maintain standards for friction performance.

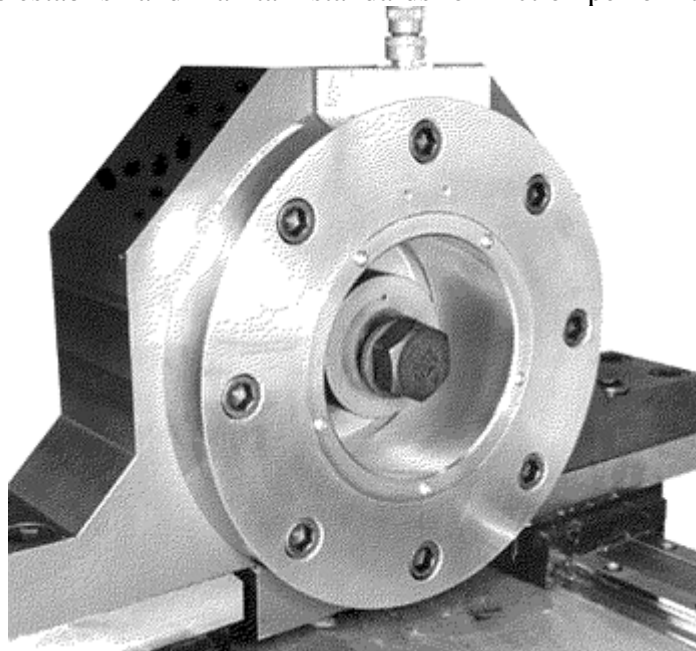


Fig. 4 Torque-tension research head, 800 kN capacity

For example, in the test plot illustrated in Fig. 5, a locknut is initially driven onto a bolt. The thread friction torque is equal to the input torque until contact with the underhead-bearing surface is made. Once contact is made with the underhead area, the underhead friction torque is measured as the difference between the total input torque and the thread torque. As clamp force is developed, the pitch torque is calculated and subtracted from the thread torque to compute the thread-friction torque. Note that for prevailing torque locknuts, the elastic origin is located at the prevailing torque level as shown in Fig. 5, not at the zero torque level used for fasteners without prevailing torque characteristics.

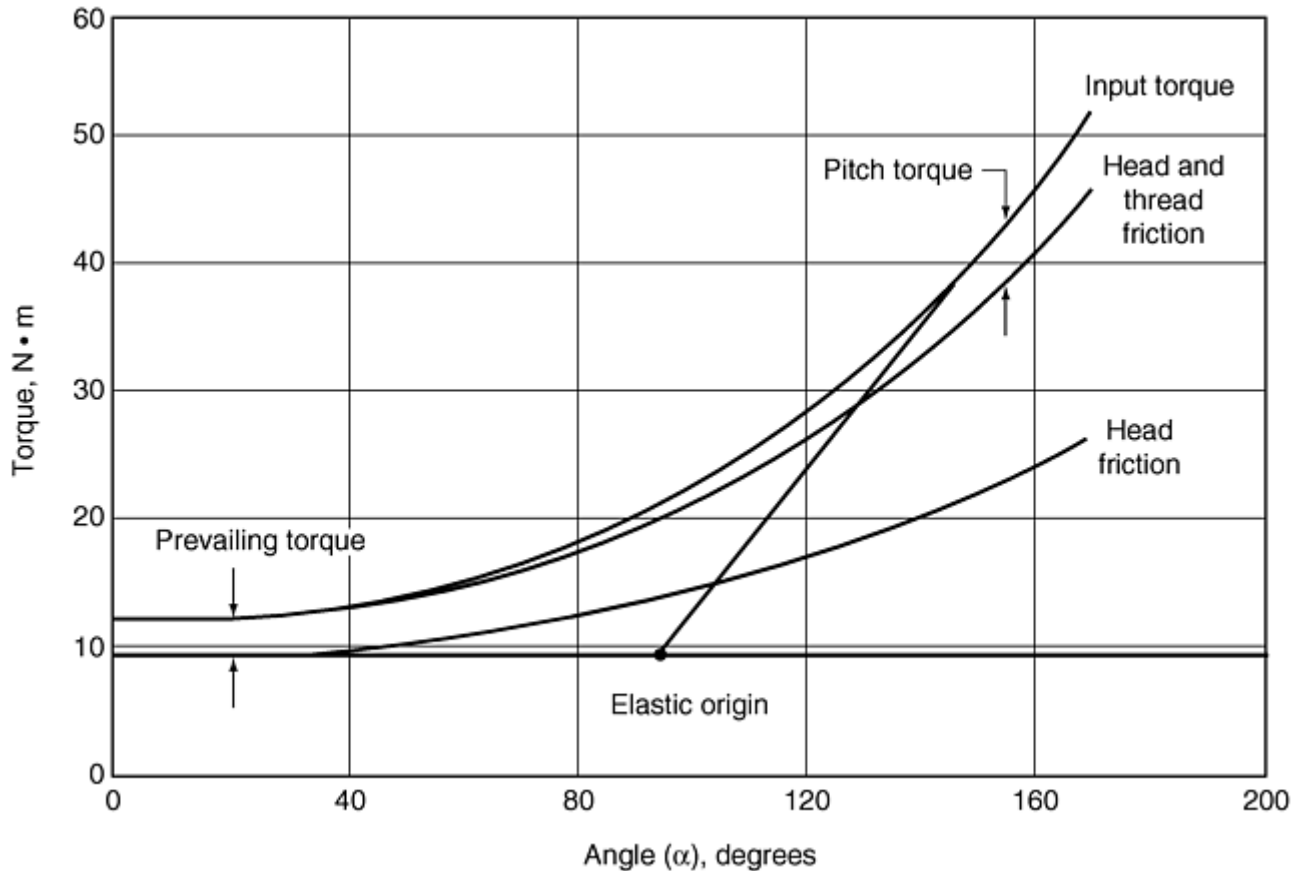


Fig. 5 Determining friction forces for prevailing torque locknut

Considerations in Testing

There are a number of factors that can affect the tension created in a bolt when torque is applied. Depending on the fastener and joint configuration, direct measurement of tension is not always practical or even possible by any means. Fortunately, torque and angle measurements can be taken for most bolted joints and then analyzed to assist in determination of important characteristics and properties related to strength and reliability.

When tightening a threaded fastener, it is almost always important to know both how much torque is applied and how far the fastener is turned. Similarly, it is always important to fully understand how friction affects the relationship of torque, angle, and tension.

To ensure that critical joints are tightened properly, it must be kept in mind that it is the control of tension that is most important, not the control of torque. This fact must always be considered when choosing and setting up tools, when monitoring production, and when performing quality control audits. The fastener-tightening process is dependent upon the energy transfer from the tightening tool into the fastener and bolted joint. The integrated area under the torque-angle signature curve is a measure of the energy absorbed by the assembly.

The purpose of this chapter is to review basic methods and fundamental principles for mechanical testing of threaded fasteners and bolted joints. All fastener engineering applications must start with the assumption of the magnitude of the service loads to which a fastener or assembly will be subjected. Where the service load information is incomplete, the engineer responsible for the design or testing should always at least document assumed loading conditions for analysis and testing. Such assumptions can often be used to great advantage when, in the future, more precise service load information is obtained.

Standard Test Methods for Determining Materials Properties of Fasteners

The materials properties of the fastener must be known before a more detailed analysis of the bolted joint is possible. Many standards exist for the testing of fasteners. ASTM F 606M, a specification developed through the procedures of ASTM for metric fasteners, is considered to be one of the most complete. The corresponding standard for English threaded fasteners is ASTM F606. More complete descriptions of the methods can be found in the standard. The text following in this section is a summary of the basic test methods according to ASTM F 606M.

The test methods described in ASTM F 606M establish procedures for conducting mechanical tests to determine the materials properties of externally and internally threaded fasteners. For externally threaded fasteners, the following test methods are described:

- Product hardness
- Proof load by length measurement, yield strength, or uniform hardness
- Axial tension testing of full-sized products
- Wedge tension testing of full-sized products
- Tension testing of machined test specimens
- Total extension at fracture testing

For internally threaded fasteners, the following test methods are described:

- Product hardness
- Proof load
- Cone proof-load test

Test methods are also provided in the standard for washers and rivets. This article concentrates on the portions applicable to threaded fasteners.

Test Methods for Externally Threaded Fasteners

Product Hardness. The hardness of fasteners and studs can be determined on the ends, wrench flats, or unthreaded shanks after removal of any oxide, decarburization, plating, or other coating material. Rockwell or Vickers hardness standards may be used at the option of the manufacturer. Hardness is determined at midradius of a transverse section of the product taken at a distance of one diameter from the point end of the product. The reported hardness is the average of four hardness readings located at 90° to one another. Acceptable alternative methods of determining hardness for bolts are either at midradius, one diameter from the end, or on the side of the head of a hex-head or square-head product of all property classes after adequate preparation to remove any decarburization.

Tension Tests. Fasteners and studs should be tested at full-size and to a minimum ultimate load in kilonewtons (kN) or stress in megapascals (MPa). Such testing includes proof-load tests (by length measurement, yield strength, or uniform hardness), axial tension tests, wedge tension tests, and total extension-at-fracture tests.

Proof-Load Tests. The basic proof-load test consists of stressing the product with a specified load that the product must withstand without any measurable permanent set and evaluating the fastener in terms of any change in length. Alternative tests to determine the ability of a fastener to pass the proof-load test are the yield-strength test and the uniform hardness test. Although any of the alternative test methods described may be used, the proof-load test is the arbitration method used in case of any dispute.

Method 1, Length Measurement. The overall length of the specimen is measured at its true centerline with an instrument capable of measuring changes in length of 0.0025 mm with an accuracy of 0.0025 mm in any 0.025

mm range. Measuring the length between conical centers on the centerline of the fastener or stud with mating centers on the measuring anvils is preferred. The head or body of the fastener or stud should be marked so that it can be placed in the same position for all measurements.

The product is assembled in the fixture of the tension-testing machine so that six complete threads are exposed between the grips. Tests for heavy hex structural bolts are based on four threads. This is obtained by freely running the nut or fixture to the thread runout of the specimen and then unscrewing the specimen six full turns. For continuous threaded fasteners, at least six full threads should be exposed. The fastener should be loaded axially to the proof load specified in the product specification. The speed of testing, as determined with a free-running cross head, should not exceed 3 mm/min, and the proof load should be maintained for a period of 10 s before releasing the load. Upon release of this load, the length of the fastener or stud should be measured again to determine permanent elongation. A tolerance (for measurement error only) of ± 0.013 mm is allowed between the measurements made before loading and that made after loading.

Variables, such as straightness, thread alignment, or measurement error, could result in apparent elongation of the product when the specified proof load is initially applied. In such cases, the product may be retested using a 3% greater load and is considered acceptable if there is no difference in the length measurement after this loading within a 0.013 mm measurement tolerance as outlined.

Method 2, Yield Strength. The product is assembled in the testing equipment as described for method 1. As the load is applied, the total elongation of the product or any part of it that includes the exposed threads should be measured and recorded to produce a load-elongation diagram. The load or stress at an offset equal to 0.2% of the length of fastener occupied by six full threads is determined, as shown in Fig. 6.

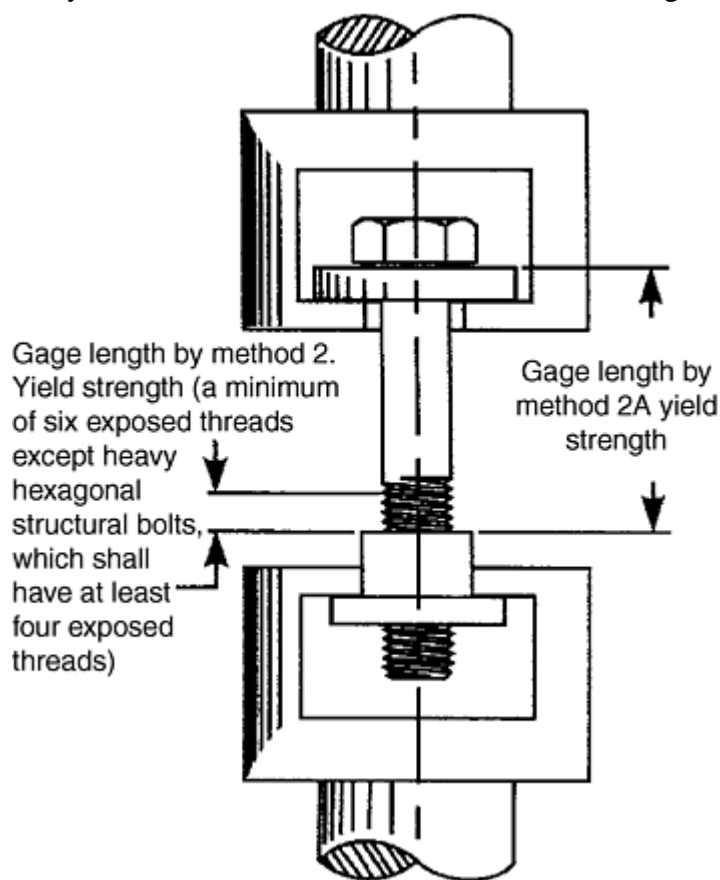


Fig. 6 Tension testing of full-size fastener (typical set-up). Source: Ref 1

Method 2A, Yield Strength for Austenitic Stainless Steel and Nonferrous Materials. The product is assembled in the testing equipment as described in method 1. As the load is applied, the total elongation of the product should be measured and recorded in order to produce a load-elongation diagram. The load or stress at an offset equal to 0.2% strain should be determined based on the length of the bolt between the holders as shown in Fig. 6, which will be subject to elongation under load by using the yield-strength method described in the section “Tension Testing of Machined Test Specimens.”

Method 3, Uniform Hardness. The fasteners are tested for hardness as described previously, and in addition, the hardness is determined in the core. The difference between the midradius and core hardness should be not more than three points on a Rockwell C scale, and both readings must be within product specification.

Short Fasteners and Studs. Fasteners with lengths less than those shown in Table 1, or that do not have sufficient threads for proper engagement, are deemed too short for tension testing. Acceptance is then based on a hardness test. If tests other than product hardness are required, their requirements are referenced in the product specification.

Table 1 Required minimum length of fasteners for tension testing

Nominal product diam (<i>D</i>), mm	Min length, mm
5	12
6	14
8	20
10	25
12	30
14	35
16	40
20	45
Over 20	3D

Source: Ref 1

Axial Tension Testing of Full-Sized Products. Fasteners are tested in a holder with a load axially applied between the head and a nut or in a suitable fixture as shown in Fig. 6. Sufficient thread engagement must exist to develop the full strength of the product. The nut or fixture should be assembled on the product, leaving six complete fastener threads exposed between the grips. Studs are tested by assembling one end of the threaded fixture to the thread runout. If the stud has unlike threads, the end with the finer pitch thread, or with the larger minor diameter, is used. The other end of the stud is assembled in the threaded fixture, leaving six complete threads exposed between the grips. For continuous studs, at least six complete threads are exposed between the fixture ends.

The maximum speed of the free-running cross head should not exceed 25 mm/min. When reporting the tensile strength of the product, the thread stress area is calculated as follows:

$$A_s = 0.7854(D - 0.9382P)^2 \quad (\text{Eq 1})$$

where A_s is the thread stress area, mm²; D is the nominal diameter of the fasteners or stud, mm; and P is thread pitch, mm.

The product should support a load prior to fracture not less than the minimum tensile strength specified in the product specification for its size, property class, and thread series. In addition, failure should occur in the body or in the threaded section with no fracture at the juncture of the body and head.

Wedge Tension Testing. The wedge tensile strength of a hex or square-head fastener, socket-head cap screw, or stud is the tensile load that the product is capable of sustaining when stressed with a wedge under the head. The purpose of this test is to obtain the tensile strength and to demonstrate the head quality and ductility of the product.

Wedge Tension Testing of Fasteners. The ultimate load of the fastener is determined as described previously under “Axial Tension Testing of Full-Sized Products,” except to place a wedge under the fastener head. When both wedge and proof-load testing are required by the product specification, the proof-load-tested fastener for wedge testing should be used. The wedge must have a minimum hardness of 45 HRC for fasteners having an ultimate tensile strength of 1035 MPa or less, and a minimum of 55 HRC for fasteners having a tensile strength in excess of 1035 MPa. Additionally, the wedge should have the following:

- A thickness of one-half the nominal fastener diameter (measured at the thin side of the hole as shown in Fig. 7)
- A minimum outside dimension such that at no time during the test will any corner loading of the head of the product occur adjacent to the wedge
- An included angle as shown in Table 2 for the product type being tested

The hole in the wedge should have a clearance over the nominal size of the fastener and have its edges top and bottom rounded as specified in Table 3.

Table 2 Wedge angles for tension testing of fasteners

Nominal product diam, mm	Degrees	
	Fasteners ^(a)	Studs and flange fasteners
5–24	10	6
Over 24	6	4

(a) For heat-treated fasteners that are threaded one diam or closer to the underside of the head, a wedge angle of 6° for sizes 5 to 24 mm and 4° for sizes over 24 mm should be used.

Source: ASTM F 606M

Table 3 Requirements for wedge-hole clearance and radius for tension testing of fasteners

Nominal product diam, mm	Nominal clearance in hole, mm	Nominal radius on corners of hole, mm
To 6	0.50	0.70
Over 6–12	0.80	0.80
Over 12–20	1.60	1.30
Over 20–36	3.20	1.60
Over 36	3.20	3.20

Source: ASTM F 606M

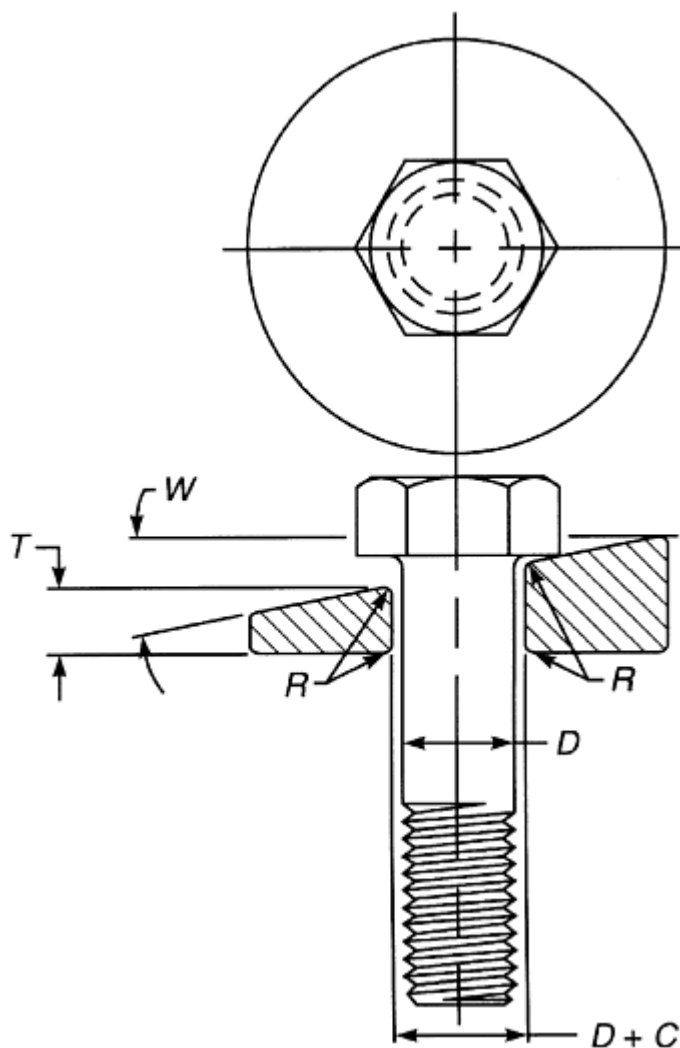


Fig. 7 Wedge-test details for fasteners. D , diameter of bolt; C , clearance of wedge hole; R , radius; T , thickness of wedge at short side hole; W , wedge angle

The fastener is then tension tested to failure. The fastener must support a load prior to fracture not less than the minimum tensile strength specified in the product specification for the applicable size, property class, and thread series. In addition, the fracture should occur in the body or threaded portion with no fractures at the junction of the head and the shank.

Wedge-Tension Testing of Studs. When both wedge-tension and proof-load testing are required, one end of the same stud previously used for proof-load testing is assembled in a threaded fixture to the thread runout. For studs having unlike threads, the end with the finer-pitch thread or with the larger minor diameter is used. The other end of the stud should be assembled in a threaded wedge to the runout and then unscrewed six full turns, leaving six complete threads exposed between the grips as shown in Fig. 8. For continuous threaded studs, at least six full threads are exposed between the fixture ends. The angle of the wedge for the stud size and property class is as specified in Table 2.

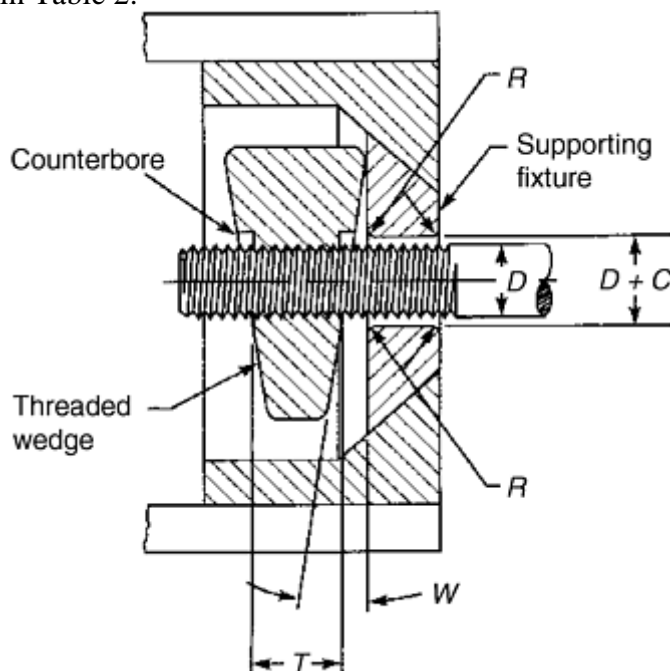


Fig. 8 Wedge-test details for studs. D , diameter of stud; C , clearance of wedge hole; R , radius; T , thickness of wedge at short side hole; W , wedge angle

The stud should be assembled in the testing machine and tension tested to failure, as described previously under “Axial Tension Testing of Full-Sized Products.” The minimum hardness of the threaded wedge is 45 HRC for products having an ultimate tensile strength of less than 1035 MPa and 55 HRC for product lines having an ultimate tensile strength in excess of 1035 MPa. The length of the threaded section of the wedge must be equal to at least the diameter of the stud. To facilitate removal of the broken stud, the wedge can be counterbored. The thickness of the wedge at the thin side of the hole is equal to the diameter of the stud plus the depth of the counterbore. The thread in the wedge should have class 4H6H tolerance, except when testing studs having an interference fit thread, in which case the wedge will have to be threaded to provide a finger-free fit. The supporting fixture should have a hole clearance over the nominal size of the stud, and the top and bottom edges should be rounded or chamfered to the same limits specified for the hardened wedge in Table 3.

The stud must support a load prior to fracture of not less than the minimum tensile strength specified in the product specification or its size, property class, and thread series.

Tension Testing of Machined Test Specimens. Where fasteners and studs cannot be tested at full-size, tests are conducted using test specimens machined from the fastener or stud. Fasteners and studs should have their shanks machined to the dimensions shown in Fig. 9. The reduction of the shank diameter of heat-treated fasteners and studs with nominal diameters larger than 16 mm should not exceed 25% of the original diameter of the product. Alternatively, fasteners 16 mm in diameter or larger may have their shanks machined to a test specimen with the axis of the specimen located midway between the axis and outside surface of the fastener as

shown in Fig. 10. In either case, machined test specimens should exhibit tensile strength, yield strength (or yield point), elongation, and reduction of area equal to or greater than the values of these properties specified for the product size in the applicable product specification when tested in accordance with this section.

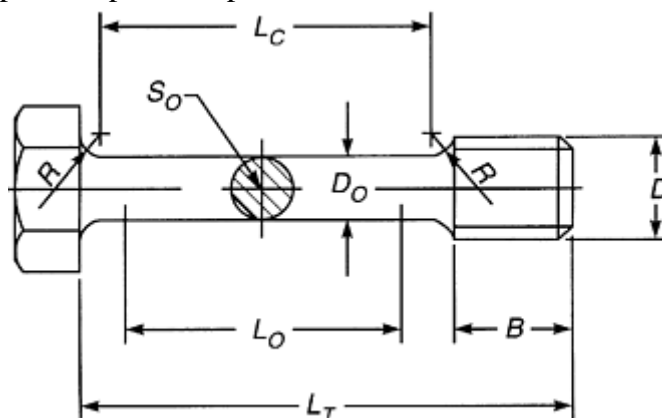


Fig. 9 Tension-test specimen with turned-down shank. Source: Ref 1

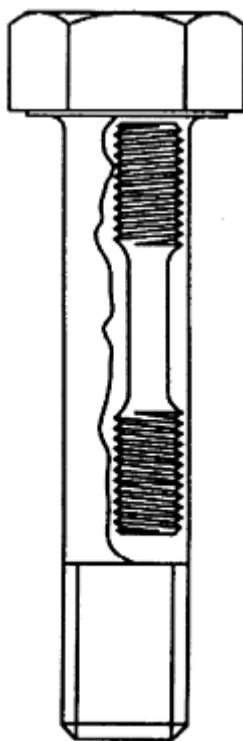


Fig. 10 Location of standard tension-test specimen when turned from large sized fastener. Source: Ref 1

Tensile Properties: Yield Point. Yield point is the first stress in a material, less than the maximum obtainable stress, at which an increase in strain occurs without an increase in stress. Yield point is intended for application only for materials that may exhibit the unique characteristic of showing an increase in strain without an increase in stress. A sharp knee or discontinuity characterizes the stress-strain diagram. The yield point can be determined by one of the following methods:

- *Drop-of-the-beam or halt-of-the-pointer method:* In this method, an increasing load is applied to the specimen at a uniform rate. When a lever and poise machine is used, the beam is kept in balance by running out the poise at an approximately steady rate. When the yield point of the material is reached, the increase of the load will stop, but the poise should be run a small amount beyond the balance position, and the beam of the machine will drop for a brief interval of time. When a machine equipped with a load-indicating dial is used, there is a halt or hesitation of the load-indicating pointer, which

corresponds to the drop of the beam. The load is recorded at the drop of the beam or the halt of the pointer. This point is the yield point of the fastener or stud.

- *Autographic diagram method:* When a sharp-kneed stress-strain diagram is obtained by an autographic device, the yield point is taken as either the stress corresponding to the top of the knee, as shown in Fig. 11, or as the stress at which the curve drops, as shown in Fig. 12.
- *Total extension-under-load method:* When testing material for yield point, the test specimens may not exhibit the well-defined disproportionate deformation that characterizes a yield point as measured by the previous methods. In these cases, the following method can be used to determine a value equivalent to the yield point in its practical significance that may be recorded as the yield point. A class C or better extensometer is attached to the specimen. When the load producing a specified extension is reached, the stress corresponding to the load as the yield point is recorded and the extensometer removed (Fig. 13).

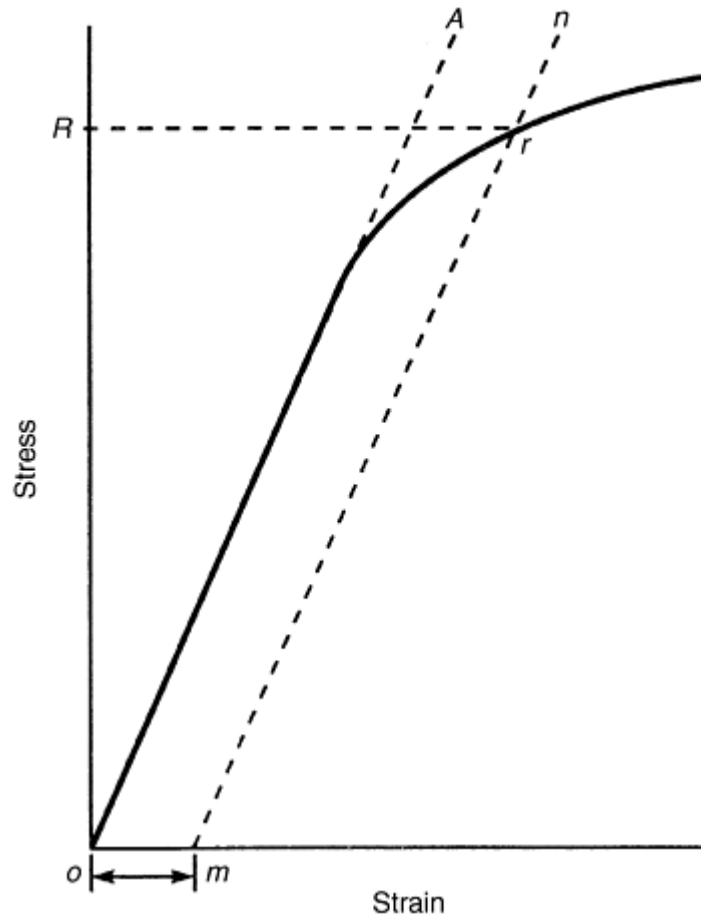


Fig. 11 Stress-strain diagram for determination of yield strength by the offset method. $o-m$ is the specified offset. To determine offset yield strength, draw line $m-n$ parallel to the line $o-A$. From the intersection point r , draw a horizontal line to determine the offset yield strength, R .

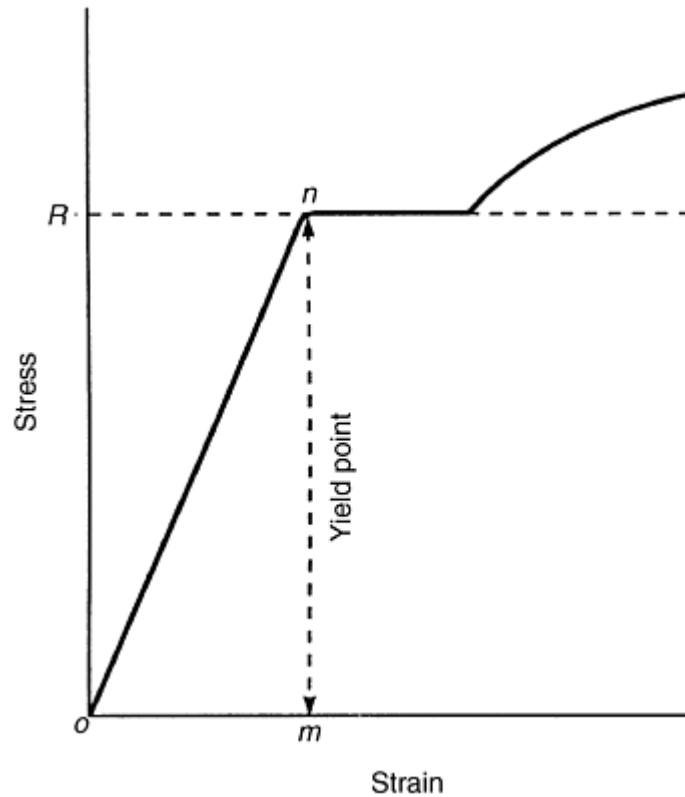


Fig. 12 Stress-strain diagram showing yield point corresponding with top of knee. $o-m$, offset to yield point. Source: Ref 1

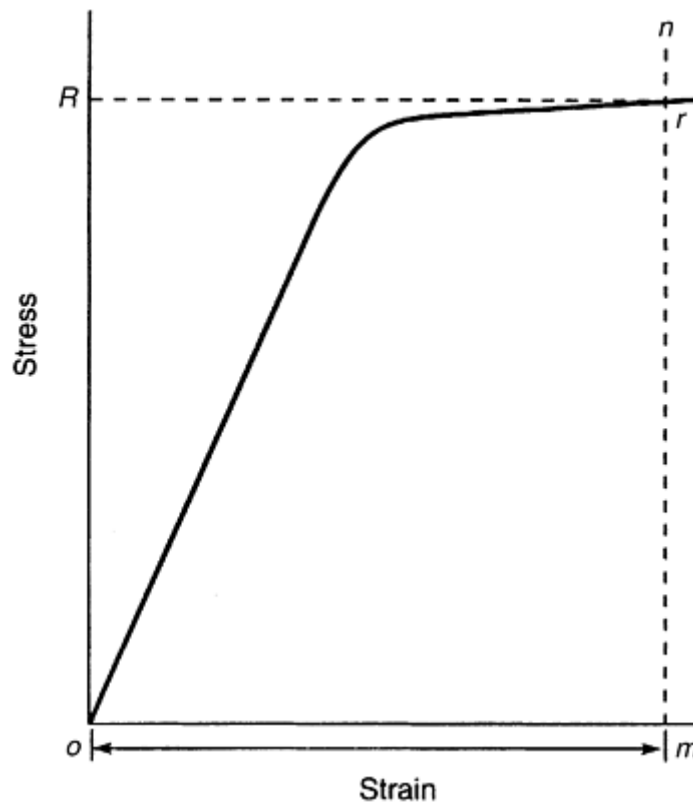


Fig. 13 Stress-strain diagram showing yield point or yield strength by extension-under-load method. $o-m$, specified extension under load. Line $m-n$ is vertical, and the intersection point, r , determines yield strength value, R . Source: Ref 1

Yield Strength. Yield strength is the stress at which a material exhibits a specified limiting deviation from the proportionality of stress to strain. The deviation is expressed in terms of strain, percentage of offset, total

extension under load, and so on. Yield strength may be determined by the offset method or the extension-under-load method.

To determine the yield strength by the offset method, it is necessary to secure data (autographic or numerical) from which a stress-strain diagram may be drawn. Then, on the stress-strain diagram layoff, $o-m$, as shown in Fig. 11, equal to the specified value of the offset, $m-n$ should be drawn parallel to $o-A$ and thus locate r . The yield-strength load, R , is the load corresponding to the highest point of the stress-strain curve before or at the intersection of $m-n$ and r . In reporting values of yield strength obtained by this method, the specified value of the offset used should be stated in parenthesis after the term yield strength, thus:

$$\text{Yield strength (0.2\% offset)} = 360 \text{ MPa}$$

In using this method, a minimum extensometer magnification of 250 to 1× is required. A class B1 extensometer meets this requirement.

The extension-under-load method is used to determine the acceptance or rejection of materials whose stress-strain characteristics are well known from previous tests of similar materials in which stress-strain diagrams are plotted. For these tests, the total strain corresponding to the stress at which the specified offset occurs should be known as within satisfactory limits. The stress on the specimen, when total strength is reached, is the value of the yield strength. The total strain can be obtained satisfactorily by the use of a class B1 extensometer. The extension under load (mm/mm of gage length) can be determined as follows:

$$YS/E = R \tag{Eq 2}$$

where YS is the specified yield strength, MPa; E is the modulus of elasticity, MPa; and r is the limiting plastic strain, mm/mm.

Tensile strength is calculated by dividing the maximum load the specimen sustains during a tension test by the original cross-sectional area of the specimen.

Elongation. The ends of the fractured specimen are fitted together carefully and the distance between the gage marks measured to the nearest 0.25 mm for gage lengths of 50 mm or under, and to the nearest 0.5 mm of the gage length for gage lengths over 50 mm. A percentage scale reading to 0.5% of the gage length may be used. The elongation is the increase in length of the gage length, expressed as a percentage of the original gage length. In reporting elongation values, both the percentage increase and the original gage length should be given.

If any part of the fracture takes place outside the middle half of the gage length or in a punched or scribed mark with the reduced section, the elongation value obtained may not be representative of the material. If the elongation so measured meets the minimum requirements specified, no further testing is indicated, but if the elongation is less than the minimum requirements, the test should be discarded and performed again.

Reduction of Area. The ends of the fractured specimen are fitted together and the mean diameter or the width and thickness at the smallest cross section measured to the same accuracy as the original dimensions. The difference between the area thus found and the area of the original cross section expressed as a percentage of the original area is the reduction in area.

Total Extension at Fracture Test. The test to determine extension at fracture, A_L , is carried out on stainless steel and nonferrous products in the finished condition with the length equal to or in excess of those minimums listed in Table 1. The products to be tested are measured for total length, L_1 , described as follows and shown in Fig. 14.

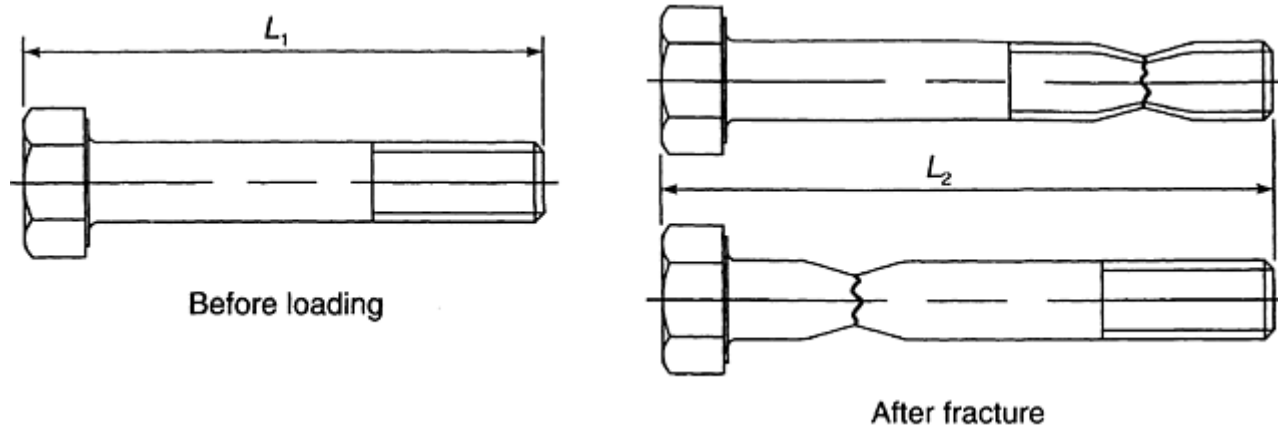


Fig. 14 Determination of total extension at fracture (A_L) for a screw product. Source: Ref 1

Both ends of the fastener or stud are marked using a permanent marking substance, such as bluing, so that the measuring reference points for determining total lengths, L_1 and L_2 , are established. An open-end caliper and steel rule or other device capable of measuring to within 0.25 mm are used to determine the total length of the product (Fig. 14).

The product under test is screwed into the threaded adapter to a depth of one diameter (Fig. 6) and load applied axially until the product fractures. The maximum speed of the freerunning cross head should not exceed 25 mm/min.

After the product has been fractured, the two broken pieces are fitted closely together, and the overall length, L_2 , is measured. The total extension at fracture, A_L , is then calculated as follows:

$$A_L = L_2 - L_1 \quad (\text{Eq 3})$$

The value obtained should equal or exceed the minimum values shown in the applicable specification for the product and material type.

Test Methods for Internally Threaded Fasteners

Product Hardness. For routine inspection, hardness of nuts may be determined on the bearing face or wrench flats after removal of any plating or coating. Rockwell or Vickers hardness testing may be used at the option of the manufacturer, taking into account the size and property class of the nut. The reported hardness is a minimum of two hardness readings taken 180° apart, halfway between the major diameter of the thread and one corner or, if applicable, on a wrench face one-third of the distance from a corner to the center of the wrench face. In preparation of the surface, sufficient material is removed to ensure elimination of any oxide, decarburization, coating, or other surface irregularities. The preparation of test specimens and the performance of hardness tests for Rockwell or Vickers testing are in conformity with the requirements of ASTM E 18 and E 92, respectively. For the purpose of arbitration, hardness is taken on a longitudinal section through the nut axis with readings taken as closely as possible to the nominal major diameter of the nut thread.

Proof-Load Test. The nut to be tested is assembled on a hardened threaded mandrel or a test bolt using the tension method (Fig. 15a) or the compression method (Fig. 15b). The hardened test mandrel and the tension method shown in Fig. 15(a) is mandatory as a reference if arbitration is necessary. The specified proof load is applied for the nut against the nut. The nut should resist this load without stripping or rupture and should be removable from the test bolt or mandrel by the fingers after the load is released. Occasionally, it may be necessary to use a manual wrench or other means to start the nut in motion. Use of such means is permissible, provided the nut is removable by the fingers following the initial loosening of not more than one-half turn of the nut. If the threads of the mandrel or test bolt are damaged during the test, the test should be discarded.

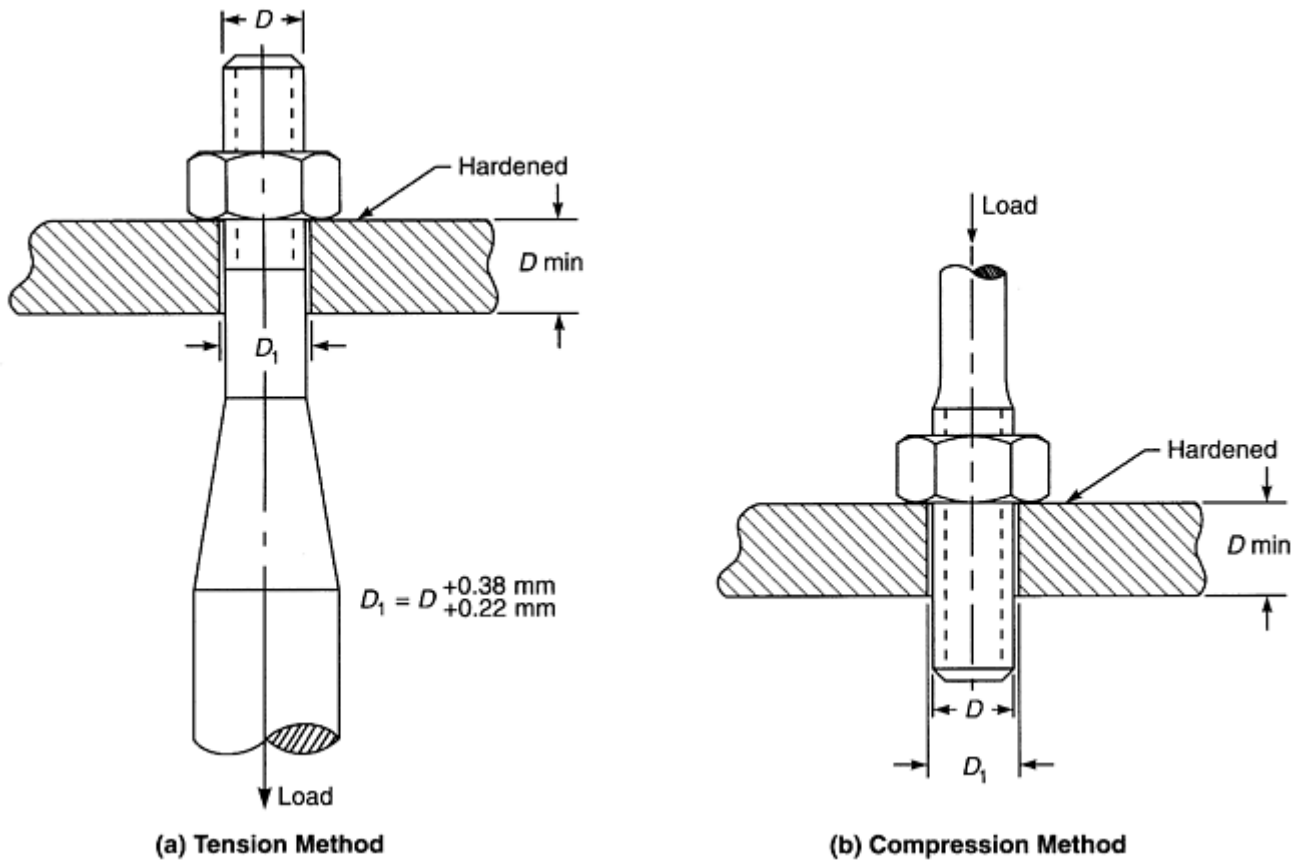


Fig. 15 Proof-load testing of nuts. Source: Ref 1

The test fastener should be appropriate to the standard specified for the nut being tested and should have a yield strength in excess of the specified proof load of the nut being tested. Mandrels should have a hardness of 45 HRC minimum; the mandrel should have threads conforming to the same standards as those specified for the nut being tested, except that the maximum major diameter is the specified minimum major diameter for class 4H6H threads and the maximum major diameter plus 0.25 times the major diameter tolerance of class 4H6H threads.

The proof load is determined at a free-running cross head not exceeding 25 mm/min and is held at load for a minimum of 10 s.

Cone proof-load tests should be performed by the use of a conical washer and threaded mandrel (Fig. 16) to determine the influence of surface discontinuities (forging cracks and seams) on the load-carrying ability of hardened steel nuts through 36 mm in diameter by introducing a simultaneous dilation and stripping action of the nut. The conical washer should have a hardness of 57 HRC minimum and a hole diameter of the mandrel +0.05 mm and -0.00 mm. The contact point of the cone should be sharp for nut sizes 12 mm or less. For sizes greater than 12 mm, the point should be flat and 0.38 ± 0.03 mm in width. The nut and the conical washer are assembled on the mandrel and the cone proof load applied for the nut against the nut. The speed of testing as determined with a free-running cross head should be a maximum of 3 mm/min. Apply the proof load for 10 s. The proof load of the nut is computed as follows:

$$CPL = (1 - 0.012D)f \times A_s \times 0.001 \quad (\text{Eq 4})$$

where CPL is the cone proof load, kN; D is the nominal diameter of the nut, mm; f is the specified proof stress of the nut, MPa; A_s is the tensile stress area of the nut, mm^2 , equal to $0.7854 [D - (0.9382P)]^2$; and P is the thread pitch, mm.

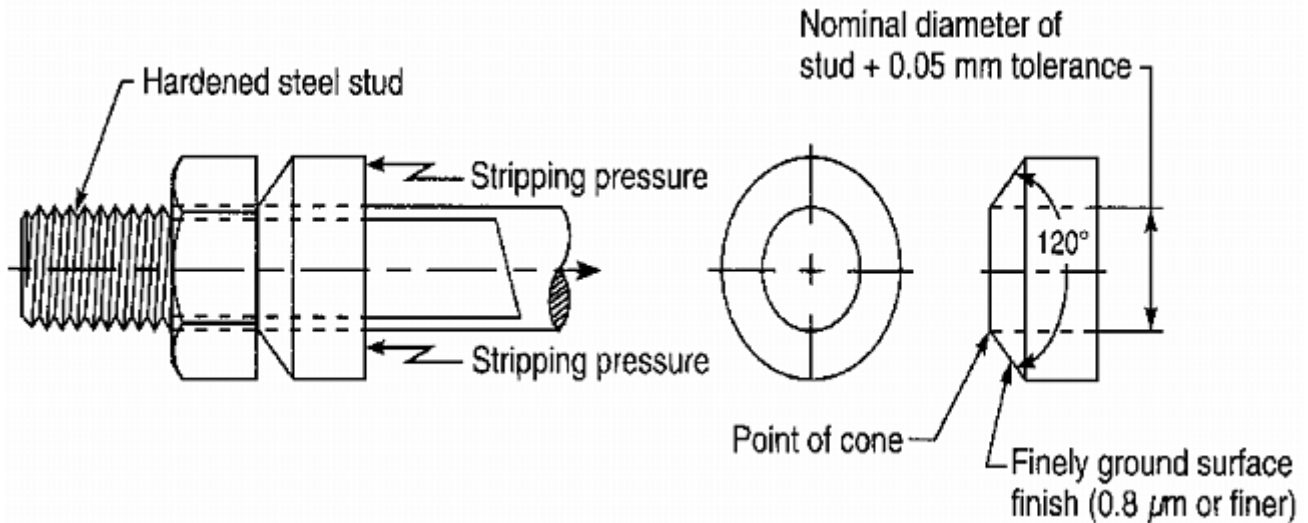


Fig. 16 Cone-proof test. Source: Ref 1

To meet the requirements of the cone proof-load test, the nut should support its specified cone proof load without stripping or rupture.

Reference cited in this section

1. "Standard Test Methods for Determining the Mechanical Properties of Externally and Internally Threaded Fasteners, Washers, and Rivets (Metric)," F 606M, *Annual Book of ASTM Standards*, ASTM

Mechanical Testing of Threaded Fasteners and Bolted Joints

Ralph S. Shoberg, RS Technologies, Ltd.

Friction Coefficient Testing

This section describes the testing method for a tightening test to determine the coefficients of friction of assemblies using threaded fasteners under specified conditions. A standardized measurement and analysis procedure is presented for comparison of assemblies with different surface finishes or for cases where different coatings, plating processes, or lubricants are used.

The results of testing in accordance with this test specification can provide valuable insights as to the expected behavior of actual bolted-joint assemblies. Additional testing and analysis, including computer modeling, is necessary to confirm the influence of frictional components of torque in actual assemblies. Torque-angle signatures plotted from tests on actual assemblies can be best understood if accurate friction coefficient data are available for modeling the bolted-joint-tightening process.

The frictional coefficient data obtained are necessary for the design and testing of bolted assemblies. *In the final analysis, it is impossible to accurately model or calculate a bolted-joint design if correct friction coefficient information is not known.*

Principle

A tightening torque is steadily applied to a bolted-joint assembly at ambient temperature. In the range of elastic deformation, there is a linear relationship between torque and clamping load. This relationship is expressed by the following equation applicable to bolted-joint assemblies with ISO metric threads and to other screw threads

with triangular profiles and a 60° pitch angle as specified in ISO 68:1973 or ASME B1.13M-1995 (“Metric Screw Threads—M Profile”):

$$T_A = F_V \left(0.159 \cdot P + 0.578 \cdot d_2 \cdot \mu_G + \frac{D_{Km}}{2} \cdot \mu_K \right) \quad (\text{Eq 5})$$

where terms on the right side are defined in Eq 6, 7, 8, 9, 10, 11, and 12. The applied torque, T_A , is composed of a component acting in the thread and serving to both apply the proofing load and to overcome thread-friction torque, T_G . It also comprises a component acting at the bolt head or nut-bearing face, termed underhead friction torque, T_K .

$$T_A = T_G + T_K \quad (\text{Eq 6})$$

where

$$T_G = F_V (0.159 \cdot P + 0.578 \cdot d_2 \cdot \mu_G) \quad (\text{Eq 7})$$

where d_2 is the bolt thread pitch diameter, and where

$$T_K = F_V \frac{D_{Km}}{2} \cdot \mu_K \quad (\text{Eq 8})$$

The mean diameter required for measuring the coefficient of friction acting at the bearing face of the bolt head or nut is calculated from the following equation:

$$D_{Km} = \frac{d_w + d_h}{2} \quad (\text{Eq 9})$$

where d_w is the external diameter of the bearing face for frictional torque, and d_h is the clearance hole diameter. Equation 9 applies to plane-bearing surfaces located vertically to the bolt axis. In other cases, such as in the case of screws with a conical bearing face, D_{Km} is the nominal mean diameter of the conical contact area. Suitable allowance should be made for bearing faces that differ in form, such as countersunk heads or spherical faces.

Determination of the coefficients of friction are based on the relationships obtained when transforming Eq 7 and 8, such as the following thread friction coefficient:

$$\mu_G = \frac{T_G / F_V - 0.159 \cdot P}{0.578 \cdot d_2} \quad (\text{Eq 10})$$

and the following underhead friction coefficient:

$$\mu_K = \frac{2 \cdot T_K}{D_{Km} \cdot F_V} \quad (\text{Eq 11})$$

where the test apparatus does not permit a separate measurement of T_G and T_K , a reference coefficient of friction may be calculated from the following equation (reference friction coefficient):

$$\mu_{ges} = \frac{T_A / F_V - 0.159 \cdot P}{0.578 \cdot d_2 + (D_{Km} / 2)} \quad (\text{Eq 12})$$

This equation is derived from Eq 10 and 11 assuming $\mu_G = \mu_K$. The above coefficient can be used only for assessment of the overall friction behavior of bolted joint assemblies and is not suitable for the design of bolted connections in general. Because the test results are influenced by a variety of parameters, minimum requirements for the test procedure have been specified in the sections “Test Equipment” and “Procedure.”

The statement of this principle can be extended to cover determination of K , which is often referred to as the nut factor and is a function of thread and underhead friction coefficients as well as thread pitch and diameter. Basic threaded-fastener theory states that the torque required to tighten the joint is the product of the friction in the joint, K , the diameter of the fastener, D , and the applied force, F_V . This theory is represented by the following formula:

$$T = K \cdot D \cdot F_V \quad (\text{Eq 13})$$

Because the applied torque is the result of the torque required to overcome friction in the threads, T_G , and the torque required to overcome friction in the underhead area, T_K , the basic equation can be restated as

$$T_A = K \cdot d \cdot F_V = T_G + T_K \quad (\text{Eq 14})$$

By substituting the expressions for T_G and T_K from Eq 3 and 4, we obtain the following equation:

$$K \cdot d \cdot F_V = F_V(0.159 \cdot P + 0.578 \cdot d_2 \cdot \mu_G) + F_V \left(\frac{D_{Km}}{2} \right) \mu_K \quad (\text{Eq 15})$$

Placing the equation in terms of K , we obtain the following:

$$K = \frac{1}{d}(0.159 \cdot P) + \frac{1}{d}(0.578 \cdot d_2 \cdot \mu_G) + \frac{1}{d} \left(\frac{D_{Km}}{2} \cdot \mu_K \right) \quad (\text{Eq 16})$$

Simplifying terms results in the following equation:

$$K = \frac{1}{d} \left[(0.159 \cdot P) + (0.578 \cdot d_2 \cdot \mu_G) + \left(\frac{D_{Km}}{2} \cdot \mu_K \right) \right] \quad (\text{Eq 17})$$

The three elements in the above equation represent the components of K as related to pitch, thread, and underhead friction torque. When tightening nut and bolt assemblies, it should be understood that, depending on the frictional torque factors, the value of K could be different during tightening when either the nut or bolt is turned. For a given tension, the thread torque will always be the same, while the underhead torque depends on which element (nut or bolt) is turned. The value for K can be best understood and accurately represented only if the thread and underhead friction coefficients are determined. Simple torque-tension tests without friction coefficient determination capability do not provide enough information to precisely locate the source of variability in k -factors.

Test Equipment

The test equipment should be capable of fixturing the test bolt, nut, and washer. This equipment must also be capable of recording the torque- and force-related data. Care should be taken to ensure that whichever part (bolt or nut) is not moved during tightening of the assembly and the washer are both held firmly in place. Figure 17 shows an illustration of a typical test setup using a thread torque and fastener tension load cell.

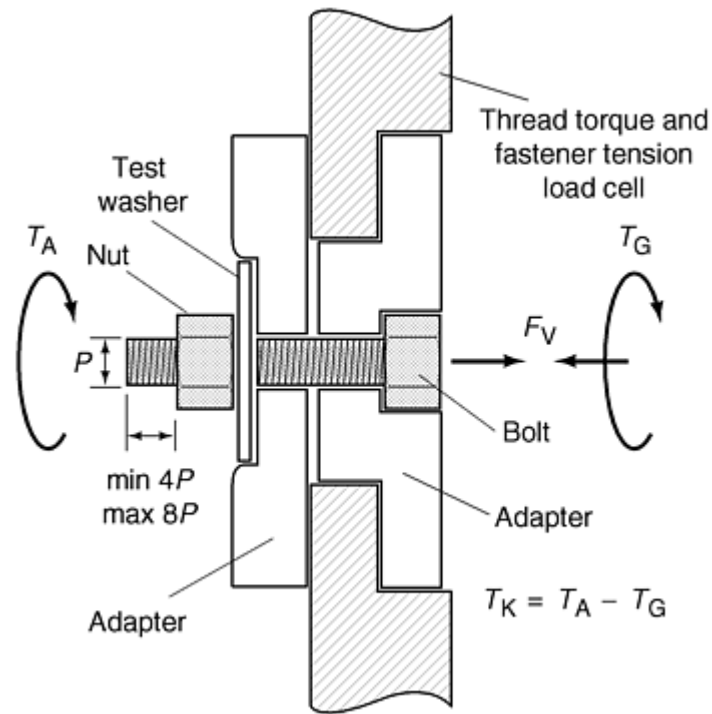


Fig. 17 Cutaway of typical test setup using torque-tension research head. T_A , tightening torque for generating load F_V ; T_G , component of tightening torque acting in threads; T_K , frictional torque acting at bearing face of bolt head or nut; P , thread pitch

In cases of arbitration, only such coefficients of friction may be compared that have been determined using the same apparatus, the same washer, and a bolt and nut with the same thread. The measuring system should permit determination of T_A , T_G , T_K , and F_V with a limit of error of $\pm 3\%$ at the point of measurement (a discussion can be found in the section “Measurement Accuracy” in this article).

Procedure

Each test should be carried out with a set of new bolts, nuts, and washers with the property classes of bolt and nut being compatible.

When investigating the effect of lubricants on the tightening process, a special test setup may be specified, which then may be used for a series of tightening tests. In such cases, the bolt, nut, and washer all have the status of reference components.

Mounting of Bolt and Nut. The bolt and nut assembly to be tested should be clamped into the apparatus so that the bolt end projects beyond the surface of the nut when fitted for a maximum number of eight turns of thread. On the shank side of the nut, there should be at least two complete turns of thread not engaged.

The test washer should be constructed with material properties and finish representative of the bearing surface for which friction coefficient data are to be obtained. Where no particular agreements have been made as to the condition of the washer or type under that part of the assembly, which is rotated in the tightening process, steel washers can be used. The washers are required to have the following characteristics (DIN 946 contains further details):

- Polished lengthwise with surface roughness average, R_a , of 0.8 to 1.6 μm
- Flatness tolerance and parallelism tolerance, each of 0.04 mm
- Bright and degreased
- Minimum thickness of 0.5 d
- Hardness 38 to 42 HRC or 380 to 420 HV20
- Clearance hole diameter, $d_h = d_a$ (max), maximum internal bearing diameter (tolerance H 13), not countersunk

This list is intended as a sample specification that can be used as a model for definition of test washers in general. For simulation of production, component sections of actual parts can be made into washer coupons. Fixtures can often be fabricated to permit mounting unmodified components on the research head for efficient testing of as-manufactured surfaces.

Thread Tolerance for and Surface Finish of Reference Components. The surface finish and thread tolerance for reference components should comply with the following specifications appropriate to the parts to be evaluated. For example, DIN 946 suggests the following specifications for bolts and nuts used to evaluate lubricants and coatings:

- Where bolts are to be tested, nuts with a bright finish should be used as reference components, degreased and capable of being fully loaded with thread manufactured to a tolerance of 6 H. If the bolt cannot be easily screwed in by hand, nuts with thread manufactured to a larger tolerance should be used.
- Where nuts are to be tested, zinc-phosphated bolts should be used as reference components, degreased and with thread manufactured to a tolerance of 6 g. The coated bolt should permit the nut to be easily mounted by hand.
- When investigating the effects of lubricants, bolts and nuts that comply with the requirements specified under the preceding two items should be used.

In general, it is necessary that finishes and tolerances of test components be adequately defined to permit replication of test conditions.

Tightening Rate Specification (rpm). In order to standardize testing conditions, it is necessary to closely control tightening speed (rpm). Maintenance of a constant turning rate is essential to obtaining comparable results. The recommended tightening rate of the assembly is 30 rpm as specified by DIN 946. Certain locknut testing standards require 100 rpm. In general, larger fasteners must be run at slower speeds to achieve uniform, predictable results. Depending on the surface coatings, lubricants, and size of fasteners, testing speeds as low as 5 to 10 rpm may be necessary to ensure repeatable results. Because production tools are often selected improperly, based upon high speed capability, extreme caution must be taken to verify tension obtained on actual assemblies.

Evaluation

The coefficients of friction are determined from Eq 9, 10, 11, and 12, making allowance for the geometry of bolt, nut, and washer for the torque applied and the proofing load generated.

Using Eq 9, 10, 11, and 12, the following parameters are entered: nominal sizes of d_2 , P , and d_h , and the size of d_w in accordance with the relevant product standard.

Evaluation of the test results may best be made by reading the coefficients of friction from the diagrams plotted on the basis of Eq 7 and 8. Normally, the minimum value of d_w as specified in the relevant product standard is to be entered in these equations. The maximum hole size or chamfer diameter is used for d_h .

The test results should be plotted, where possible, in a single graph for ease of comparison. Where bolt and nut assemblies are to be subjected to repeated tightening and loosening cycles, the results for each assembly may be plotted separately to minimize confusion. Evaluation should be based on a proofing load obtained for an average value of μ_G , μ_K , or μ_{ges} as determined by testing as specified in VDI 2230, Part 1.

By way of simplification, for normal values of μ , from 0.10 to 0.16, evaluation may be based on a value of F_V equal to $0.7 \cdot F_{0.2}$ (nominally, 70% of yield load).

Outliers are ignored only if they can be definitely assigned to abnormal influences, such as a chip caught in a thread and so on. As a rule, the evaluation should be based on 12 tests. A different number of tests may be agreed upon between the concerned parties.

Test Report

It is recommended that test results reported include maximum, mean, and minimum values and the standard deviation based upon $n-1$ sample calculation, assuming a normal distribution. In the test report, the coefficients of friction, normally minimum and maximum values, should be given together with details of the test conditions as itemized in the section "Procedure," stating any deviations from these conditions. The test report

also should include any graphic data that the test equipment is capable of providing. For example, Fig. 18 shows the breakdown of the torque measurements. Figure 19 shows the calculated friction coefficients relating to thread and underhead torque. Figure 20 shows the k -factor as a function of the achieved force.

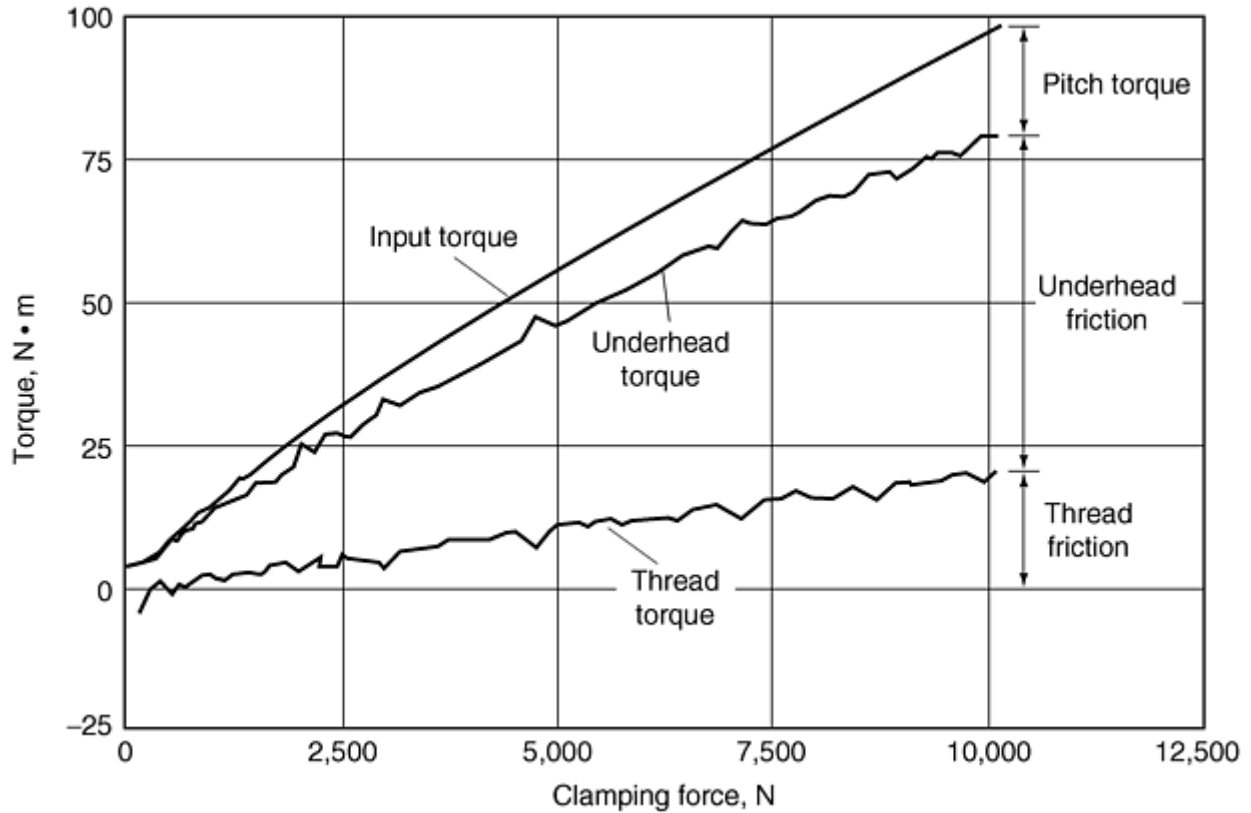


Fig. 18 Torque measurements for friction determination

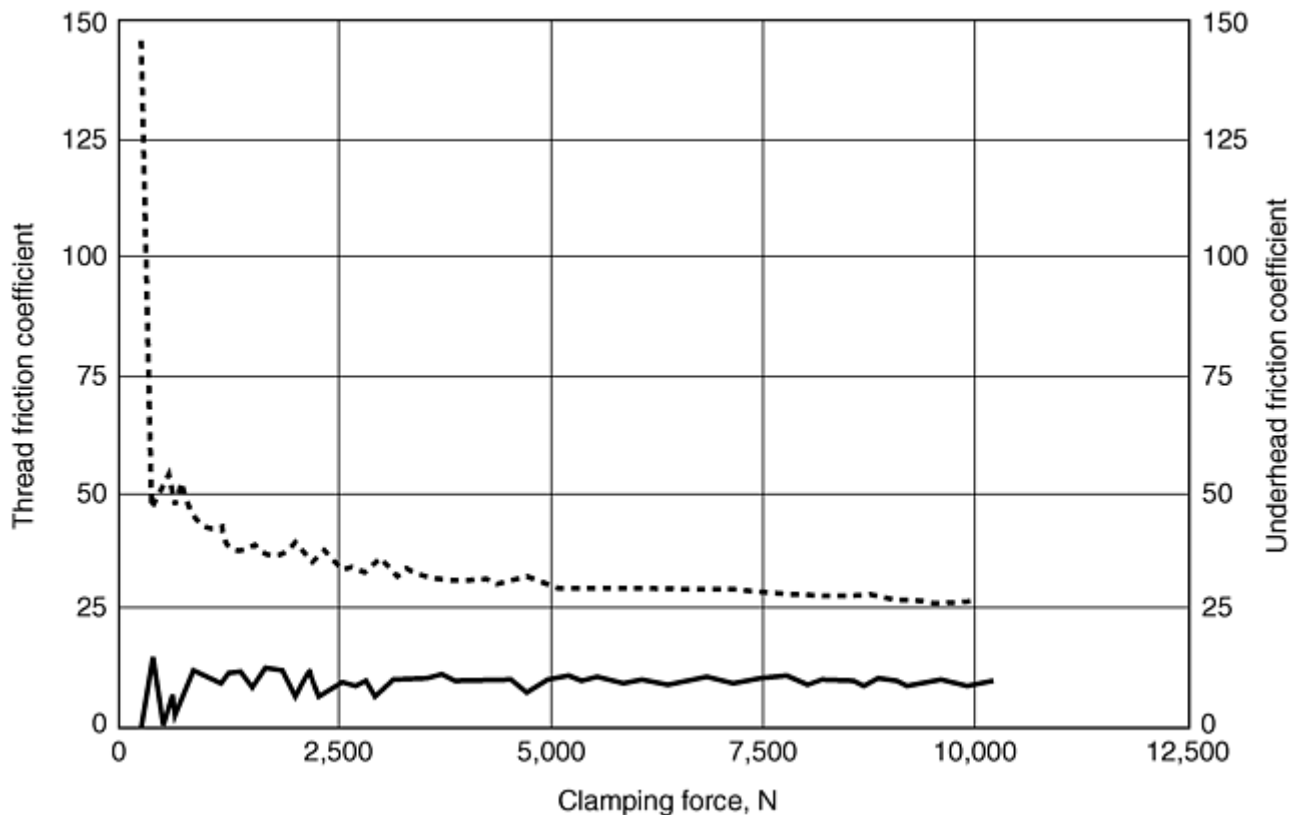


Fig. 19 Calculated thread and underhead friction coefficients

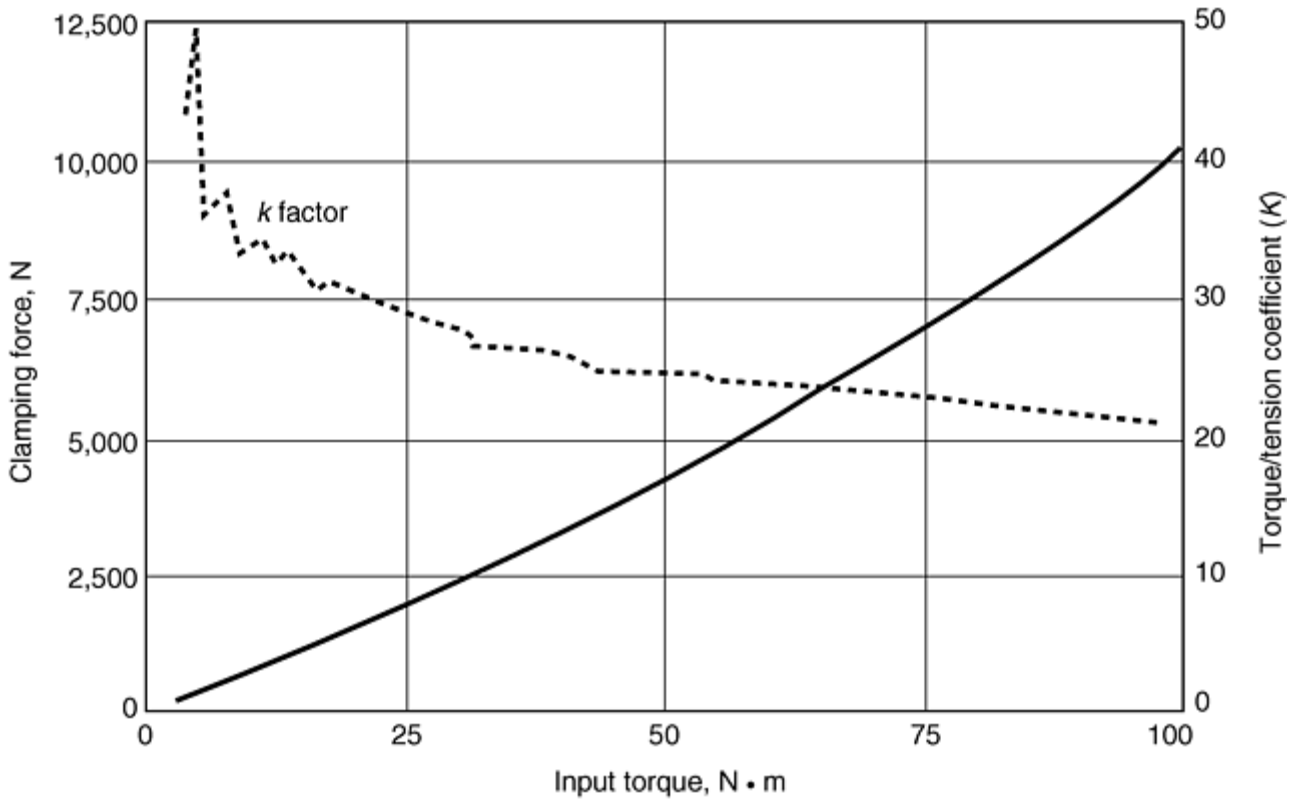


Fig. 20 K-factor plot

Mechanical Testing of Threaded Fasteners and Bolted Joints

Ralph S. Shoberg, RS Technologies, Ltd.

Torque Tension Testing

The amount of tension or clamping force exerted by a fastener when it is tightened is what actually holds the assembly together. Once the assembly is brought together, the fastener responds like a tension spring, and the assembly acts like a compression spring. As the fastener is turned and load is applied, the fastener is stretched, and the parts are compressed. The effect of this interaction between the fastener and the assembly is illustrated in Fig. 21. This response results in an elastic joint in which the fastener is the flexible member, and the assembly is the rigid member.

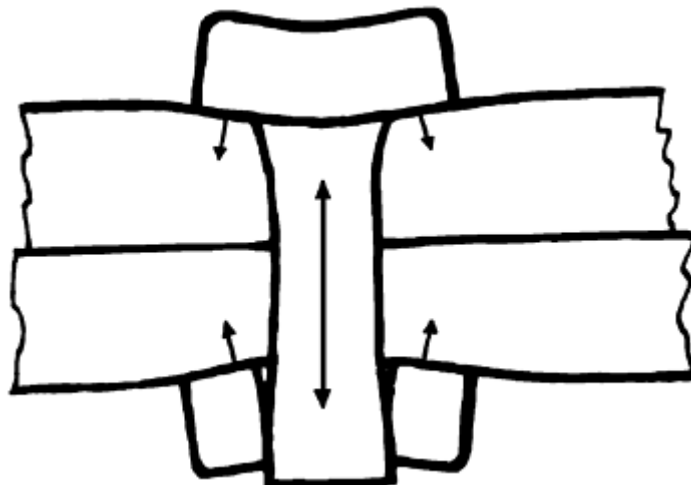


Fig. 21 Response of components in a bolted joint to applied load

The torque-tension testing procedure specifies a generic method for evaluating the effect of different surface finishes, coatings, or manufacturing processes on the torque versus tension characteristics of threaded fasteners. Test specifications published by standards organizations and engineering societies are identified in the section “Selected References.”

Test Equipment

Test Bolts, Nuts, and Washers. Test bolts should be of sufficient length so as to be easily fixtured into the adapters that are used with the test equipment. Test bolts should have a uniform application of finish, coatings, or both.

Test nuts should be plated, coated, and lubricated according to the test plan or experimental design.

Test washers should be square torque-tension test washers corresponding to the bolt size being tested. They should be appropriately hardened, finished, plated, or coated according to the test plan. The test washer provides the reference surface for contact with the underhead of the nut or bolt element to which torque is applied. The square shape provides means to prevent the washer from slipping on the test plate when the friction coefficient between the washer and plate is less than that between the bolt or nut and washer.

Test Equipment. A fixtured direct-current (dc) electric nutrunner or other drive system capable of maintaining the required constant test speed is used to tighten and remove the test bolt or nut. The nutrunner should have the capability of producing a torque output greater than the torque values specified for the size and grade of bolts to be tested and should be capable of reaching the continuous speed required by the test specification. Test specifications generally require 25 to 100 rpm for most fasteners. For tests that require torque application above 250 N · m, the continuous speed may be reduced to the range of 5 to 25 rpm. Speed should be held constant within 10% of the specified test rpm. For valid comparison to be made between results obtained by two or more laboratories, the testing speeds must be specified and controlled.

Torque Transducer. A strain-gage torque sensor is used to measure the torque required for the installation of the bolt being tested. The torque sensor should have an accuracy of $\pm 2\%$ at the point of measurement (more information can be found in the section “Measurement Accuracy”). A torque sensor equipped with an angle encoder is recommended in the event that additional analysis is desired.

Tension Load Cell. A tension load cell is used to hold the test bolt, nut, and washer in position and to measure the tension generated in the bolt as the test nut is tightened. The recommended accuracy of the tension load cell is $\pm 2\%$ at the point of measurement. A tension load cell with thread torque measurement capability is recommended in the event that additional analysis, such as frictional characteristics, is desired.

Data Acquisition and Control Equipment. A multiple channel recorder capable of recording the torque, tension, and angle and thread torque (if required) data during the entire test cycle should be used. Equipment that can control the dc electric nutrunner, calculate statistics, and provide graphic plots of the test is highly recommended.

Procedure

The following procedure can be used as a reference for conducting torque-tension testing. This procedure assumes that the bolt is secured and the nut is tightened. Some test evaluations of bolt underhead characteristics require that the nut be secured and the bolt rotated. In that case, the position of the nut and bolt should simply be reversed:

1. Determine the torque and tension loads that are appropriate for the size of the fastener to be tested. These are typically specified by the required test standard or special requirements of the customer.
2. Select an appropriately sized nut and test washer. A new nut and test washer should be used with each bolt that will be tightened.
3. Place the bolt being tested through the test fixture (load cell and adapters) and test washer so that the bolt extends beyond the test nut approximately six threads after bolt rundown. Make sure that the test washer is secured so that it does not rotate during testing (Fig. 17).
4. Assemble the nut onto the bolt approximately two threads.

5. Place the nutrunner tool on the bolt and tighten to the specified torque or tension value. Simultaneously record the torque that is applied and the tension that is achieved.
6. Loosen the nut, and return to the original starting position.
7. Repeat steps 5 and 6 for the specified number of bolts to obtain data that can be statistically analyzed to produce torque at tension to 3 sigma limits. A new nut and washer is to be used for each test bolt.

Note: In addition to obtaining torque-tension data for previously unused bolts and nuts as described, it is often desirable to tighten and loosen the same bolt-nut-washer combination multiple times to evaluate the effect of repeated tightening and loosening on the torque-tension relationship.

Test Report

The test report for torque-tension testing generally requires a multiple graphic plot of torque versus tension for the prescribed number of rundowns, as shown in Fig. 22. A statistical graphic plot of torque at tension also is desirable. This testing can be further documented by a report of the numerical data to which statistics can be added.

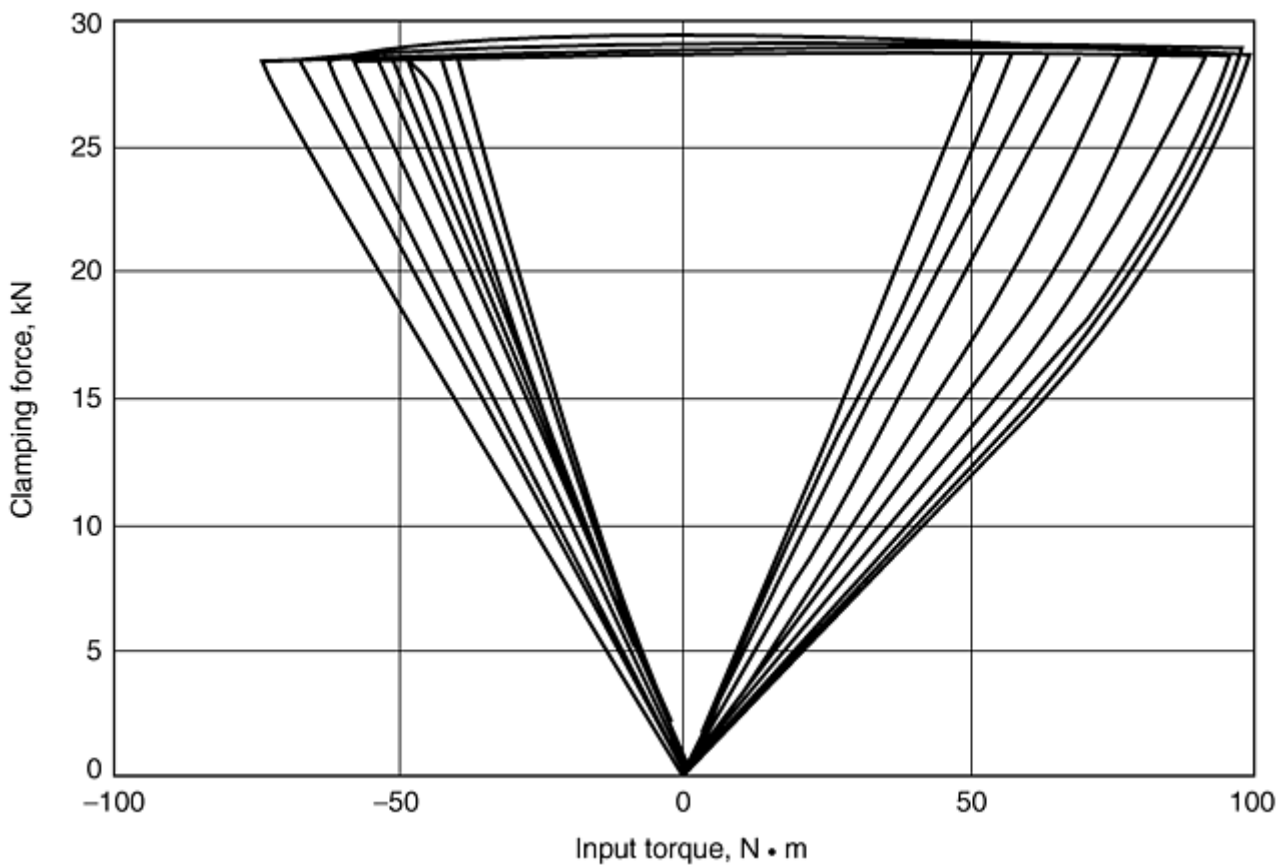


Fig. 22 Multiple rundown torque-tension plot

Locknut Testing

A locknut is a device that provides extra resistance to vibration loosening beyond that produced by proper preload, either by providing some form of prevailing torque or, in free-spinning locknuts, by deforming,

crimping, or biting into mating parts when fully tightened. A locknut counters the back-off torque created by the inclined planes of the thread. Locknuts and locking mechanisms take many forms. Such forms include thread interference locknuts, also known as prevailing torque locknuts, that use several different forms, such as nuts with out-of-round holes, a nylon locking collar in the nut, a nylon patch, or mechanically deformed dimples or crimps. Another form of locking devices are free-spinning locknuts, such as springhead nuts, beam-type nuts, and serrated nut bearing surfaces.

Because of the particular characteristics of prevailing torque locknuts, a unique testing process is required for them. In the past, there has been a wide range of equipment available for prevailing torque locknut testing from basic hand tool and indicator systems to various semiautomated systems. Test results for locknut prevailing torque are particularly sensitive to control of testing speed or a lack thereof. Automated testing systems have been developed with the capability to conduct multiple tightening cycles on production lots or research and development samples of locknuts, with tests preprogrammed according to Industrial Fasteners Institute (IFI) 100/107 for inch, ISO 2320 and ANSI B818.61.1 for metric, and other common test specifications. Precisely controlling test speeds, tension shut-off points, and cycle timing is necessary to ensure repeatability of test results.

The locknut testing procedure specifies a generic method for evaluating the effectiveness of prevailing torque-locking devices. Test specifications published by standards organizations and others that may apply to these types of fasteners are listed in the section “Selected References.”

Principle

There are several published standards for testing and evaluating prevailing torque locknut devices. The standards all generally attempt to determine how well the prevailing torque element works the first time it is used and how well it holds up when reused a specified number of times. The Industrial Fasteners Institute (IFI) publishes well-known and widely accepted test specifications. The IFI test is often referred to as a “first-on, fifth-off” test. In this test, the locknut is torqued on and off the bolt five times. Torque is measured and recorded the first time on and the fifth time off. On the first cycle, the locknut is tightened to a specified clamp load. The second through fifth cycles involve installation and removal without achieving clamp load.

Multiple locknut and bolt samples are tested to develop a summary report. On completion of the test batch, statistical data are generated for the breakthrough torque, where the locking device is first penetrated, the first-on maximum prevailing torque, the torque to reach the specified clamp load, and the fifth-off minimum prevailing torque.

Figure 23 shows a graph of a typical locknut test tightening cycle. The clamp-force-versus-angle curve is superimposed on the torque curve. The graph indicates the breakthrough torque, prevailing on-torque, prevailing off-torque, and the clamp force attained.

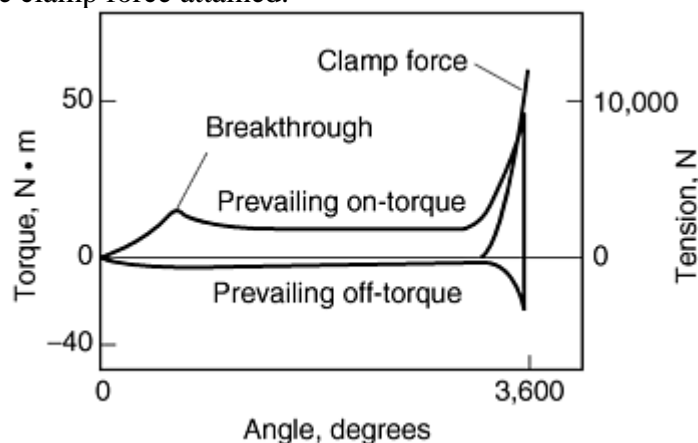


Fig. 23 Prevailing torque locknut testing cycle

Variations of the IFI test have been developed by other organizations and include the following differences (users may also specify their own variations):

- Tighten, but do not attain clamp-load cycle test, up to 30 cycles

- Tighten to clamp load each of three or five times on
- Standard torque versus tension cycles, from one time up to 30 cycles

When multiple tightening cycles are required, the user can specify dwell times after each tightening-and-loosening cycle to permit cooling of the test specimen. This procedure helps to ensure uniform testing conditions, which are particularly important when testing certain prevailing torque locknuts.

Test Equipment

Test Bolts. Test bolts should be specified to meet the strengths and finish characteristics of the fasteners intended to be used with the locking device being tested. Bolt length must be sufficient so that at least two threads are projecting past the nut after tightening. Test bolts should have a uniform application of finish, coatings, or both. If an applied adhesive is the locking device, its application must be uniform and consistent throughout the test sample. When production conditions are to be simulated, the maximum thread projection found in the production assembly must be replicated in the test assembly.

Test Nuts. The test nuts used in this type of testing generally contain the locking device described previously. However, if the locking device is an adhesive applied to the bolt, the bolt should have the same surface finish and be of the same size and grade as the bolt normally used in production.

Test Washers. Test washers should be hardened, finish-plated, or coated square torque-tension test washers corresponding to the surface conditions related to the application for which the locking device is being tested.

Nutrunner. A fixtured nutrunner is used to tighten and remove the test bolt or nut. The nutrunner should have a capability for producing a torque output greater than the torque values specified for the size and grade of nuts and bolts to be tested and should be capable of reaching and maintaining the continuous speed required by the test specification. Test specifications for prevailing torque testing are typically slower than those for torque-tension testing, around 25 rpm, ± 5 . However, a number of standards require tests to be run at 100 rpm.

Torque Transducer. A strain gage torque sensor is used to measure the torque required for the installation of the locknut being tested. The recommended accuracy of the torque sensor is $\pm 2\%$ at the point-of-measurement. A torque sensor equipped with an angle encoder is required so that the position of the locknut can be used to establish certain windows of measurement to obtain prevailing on- and off-torque values, as well as the breakthrough torque value, if required.

Tension Load Cell. A tension load cell is used to hold the test bolt, nut, and washer in position and to measure the tension generated in the bolt as the test nut is tightened. The recommended accuracy of the tension load cell is $\pm 2\%$ at the point of measurement.

A tension load cell with thread-torque measurement capability is recommended in the event that additional analysis, such as thread and underhead frictional characteristics, is desired. The use of a torque-tension research head is mandatory if the separation of underhead friction torque from thread friction torque is to be achieved for control of manufacturing tolerances for thread-loading friction.

Data Acquisition and Control Equipment. A multiple-channel recorder capable of recording the torque, tension, and angle and thread torque (if required) data during the entire test cycle should be used. Equipment that can control the dc electric nutrunner as well as calculate statistics and provide graphic plots of the test is highly recommended. Since achieving a specified clamping load is normally a part of the test, the test nutrunner drive should be capable of being stopped with no more than 2% overshoot once the target tension is achieved. Excessive overshoot of assembly torque can be a major source of variation in test results.

Procedure

The following procedure can be used as a reference for conducting prevailing torque locknut testing. This procedure assumes that the test bolt is secured, and the test nut is tightened:

1. Determine the torque and tension loads that are appropriate for the size of the fastener to be tested. These loads are typically specified by the required test standard or special requirements of the customer.
2. Select an appropriately sized bolt and test washer. A new bolt and test washer should be used with each locknut that will be tested.

3. Place the bolt being tested through the test fixture (load cell and adapters) and test washer so that the bolt will extend beyond the test nut approximately six threads after bolt rundown. Be sure the test washer is secured so that it does not rotate during testing (Fig. 17).
4. Assemble the nut onto the bolt approximately two threads so that the locking device will be ready to engage the threads.
5. Place the nutrunner tool on the bolt and tighten to the specified torque or tension value. Simultaneously record the torque that is applied and the tension that is achieved.
6. Loosen the nut and return it to the original position. Simultaneously record the removal torque that is required and the tension such that once the clamp load has been released, the prevailing off-torque can be measured in the specified window as the nut is loosened to the starting position.
7. Repeat steps 5 and 6 the indicated number of times to obtain the specified data.

Evaluation

The locknuts are inspected to determine conformance to the specific standard. Inspection procedures may be designated by the purchaser or may be agreed upon between the purchaser and the supplier prior to the acceptance of the order.

Test Report

As an example, the illustration in Fig. 24 shows a representative printed locknut analysis according to IFI specifications. The upper chart indicates the following:

- Measurements for five samples of breakthrough torque for the first cycle (initial angle window specified)
- Maximum on-torque for the first cycle (generally after the breakthrough is achieved and recorded in a 360° window before any clamp force is generated)
- Clamp load for the first cycle at a verified tension shut-off point
- Maximum off-torque for the first cycle (measured in a 360° window of turn after the clamp force has been released)
- Minimum off-torque for the first cycle (measured the same as maximum off-torque)
- Maximum off-torque for the fifth cycle (same window as first cycle)
- Minimum off-torque for the fifth cycle (same window as first cycle)

The lower chart provides statistics for the above values including high, mean, low, range, standard deviation, ± 3 sigma, and the process capability index, C_{pk} .

ANALYSIS: STANDARD										
RUN	DATE	TIME	Pk Torque (Nm)	Ang @ Pk (deg)	Final Ang (deg)	Pk Tension (N)	42000 (Nm)	52000 (Nm)	62000 (Nm)	72000 (Nm)
1	04-18-98	10:10:16	163.1	1299.17	1299.70	72612	106.79	125.24	144.92	162.15
2	04-18-98	10:10:31	155.5	1242.50	1244.50	72798	102.11	121.30	138.53	155.01
3	04-18-98	10:10:48	154.7	1266.33	1267.50	72798	104.32	122.29	138.77	154.27
4	04-18-98	10:11:03	153.0	1279.83	1279.83	72612	102.60	120.32	137.05	152.55
5	04-18-98	10:12:35	161.4	1271.17	1274.00	72798	108.75	127.45	144.68	160.92

STATISTICS: 5 Samples										
Std Dev based on N-1 formula.										
HI:	163.13	1299.17	1299.17	72798	108.75	127.45	144.92	162.15		
Mean:	157.57	1271.80	1273.00	72724	104.92	123.32	140.79	156.98		
Low:	153.04	1242.50	1244.50	72612	102.11	120.32	137.05	152.55		
Range:	10.09	56.67	54.67	185	6.64	7.14	7.87	9.60		
Std Dev:	4.42	20.63	19.84	102	2.82	2.95	3.72	4.27		
+ 3 Sigma:	170.84	1333.69	1332.53	73029	113.37	132.18	151.95	169.80		
- 3 Sigma:	144.30	1209.91	1213.47	72419	96.46	114.46	129.63	144.16		
CpK:	11.88	20.55								

ANALYSIS: LOCKNUT-STANDARD							
Run	BrkThruTq (Nm)	MaxONTq (Nm)	Clamp 1 st (Nm)	MaxOFF Tq 1 st (Nm)	MinOFF Tq 1 st (Nm)	MaxOFF Tq 5 th (Nm)	MinOFF Tq 5 th (Nm)
1	0.0	20.18	162.15	13.29	11.96	9.60	8.06
2	0.0	18.70	155.01	13.99	11.10	10.15	8.12
3	0.0	20.21	154.27	14.33	10.33	9.60	6.64
4	0.0	16.79	152.55	13.04	10.09	9.10	7.47
5	0.0	18.21	160.92	14.27	11.23	10.43	8.86

STATISTICS: 5 Samples							
Std Dev based on N-1 formula.							
HI:	0.0	20.21	162.15	14.33	11.96	10.43	8.86
Mean:	0.0	18.82	156.98	13.78	10.94	9.77	7.83
Low:	0.0	16.79	152.55	13.04	10.09	9.10	6.64
Range:	0.0	3.41	9.60	1.29	1.88	1.32	2.21
Std Dev:	0.0	1.44	4.27	0.59	0.79	0.52	0.83
+3 Sigma:	0.0	23.13	169.80	15.55	13.19	11.33	10.31
-3 Sigma:	0.0	14.51	144.16	12.02	8.69	8.22	5.35
CpK:	0.00	2.82	6.09	-2.86	-3.38	-1.34	

Fig. 24 Representative printed locknut analysis according to IFI specifications

Other test specifications may require that the on- and off-torque be reported for cycles other than those required by IFI. A common variation of the IFI 101/107 locknut test is to require that the specified clamp force be achieved on each of three or five loading cycles. The maximum and minimum off-torques are specified and checked on the last off cycle.

Mechanical Testing of Threaded Fasteners and Bolted Joints

Ralph S. Shoberg, RS Technologies, Ltd.

Angular Ductility and Rotational Capacity Tests

The ability of a fastener to provide additional clamping load after it has been taken into yield has been used to advantage in certain assemblies. The critical challenge has been to determine the point at which the fastener begins to yield. By measuring and recording torque and clamp load versus angle of turn as a fastener is taken to failure, the resulting signature can be analyzed to determine the angular ductility or rotational capacity of the fastener, which is an additional measurement indicative of the overall energy-absorbing capacity of the fastener. Angular ductility measurements are the torque-tension test equivalents to the reduction-in-area or elongation measurements made in stress-strain tensile testing.

This section describes a generic method for determining the clamp load at the torque-tension yield point and the angular ductility of threaded fasteners. Test specifications published by standards organizations and engineering societies are identified in the section "Selected References."

Principle

This testing quantifies the ductility of the fastener as it relates to rotational capacity. It locates the point of yield and determines the fastener rotation from yield to failure. This measurement can then be used to establish the relative toughness of the fastener.

The yield point may be located by offsetting the slope of the elastic tightening curve by an amount established by the following equation:

$$\alpha_{0.2} = \frac{L_e \cdot 0.002}{P} \cdot 360^\circ \quad (\text{Eq 18})$$

where L_e is the effective grip length of the fastener, and P is the pitch of the thread. The constant, 0.002, relates the angular yield point to the 0.2% offset often used in tensile testing to establish the yield point. For example, to calculate the offset angle for a $\frac{1}{2}$ -20 \times 1 English fastener, the effective grip length is 1 in., and the pitch of the fastener is $\frac{1}{20}$ or 0.050. Thus, the calculation would appear as follows:

$$\begin{aligned} \alpha_{0.2} &= \frac{1 \cdot 0.002}{0.050} \cdot 360^\circ = \frac{0.002}{0.050} \cdot 360^\circ \\ &= \frac{360^\circ}{25} = 14.4^\circ \end{aligned} \quad (\text{Eq 19})$$

Test Equipment

Test Bolts, Nuts, and Washers. Test bolts should be selected from a representative production lot with all dimensions, finishes, and coatings certified according to the appropriate manufacturing specification.

Test nuts or drilled and threaded test bars should be plated, coated, and lubricated according to the testing plan or experimental design.

Test washers should be square torque-tension test washers or suitably prepared test bars with holes prepared corresponding to the bolt size being tested. Test washers should be appropriately hardened, finished, plated, or coated according to the testing plan.

Nutrunner. A fixtured dc electric nutrunner or other drive system capable of predictable control of test speed and torque is used to tighten the test bolt or nut. The nutrunner should have a capability for producing a torque output sufficient to bring the test bolts to failure. Test specifications generally require 25 to 100 rpm, $\pm 10\%$, for most fasteners. For tests that require torque application above 250 N \cdot m, the continuous speed may be reduced to the range of 10 to 25 rpm, $\pm 10\%$.

Torque Transducer. A strain-gage torque sensor is used to measure the torque required to fail the bolt being tested. The torque sensor should have an accuracy of $\pm 2\%$ at the point of measurement (more information can be found in the section "Measurement Accuracy"). The measurement system must be equipped with an angle encoder with sufficient resolution for determining the yield point and plotting the torque and tension versus angle of turn.

Tension Load Cell. A tension load cell is used to hold the test bolt, nut, and washer in position and to measure the tension generated in the bolt as the test nut is tightened. The recommended accuracy of the tension load cell is $\pm 2\%$ at the point of measurement.

Data Acquisition and Control Equipment. A multiple-channel recorder capable of recording the torque, tension, and angle data during the test should be used. Equipment that can control the dc electric nutrunner and construct the required offset for yield determination in graphic form is highly recommended.

Procedure

The following procedure can be used as a reference for conducting angular ductility testing. This procedure assumes that the nut is secured and the bolt is tightened. Some test evaluations require that the bolt be secured and the nut rotated. In that case, the position of the nut and bolt are simply reversed:

1. Determine the torque and tension loads that are appropriate for the size of the fastener to be tested. These loads are typically specified by the required test standard or special requirements of the customer.
2. Select an appropriately sized nut and test washer.
3. Place the bolt being tested through the test fixture (load cell and adapters) and test washer so that the bolt extends beyond the test nut approximately six threads after bolt rundown. Be sure the test washer is secured so that it does not rotate during testing (Fig. 17).
4. Assemble the nut onto the bolt approximately two threads.
5. Place the dc nutrunner tool on the bolt and tighten to failure. Simultaneously record the torque that is applied, the angle of turn, and the tension that is achieved.
6. Repeat steps 3 to 5 for the statistically agreed-upon sample of fasteners.
7. Construct a plot of the data as torque or force versus angle of turn.
8. Using the test-reporting software or by hand, draw a straight-line tangent to the elastic tightening slope of the curve back to zero torque or force.
9. Draw a line parallel to the line drawn in step 8 at the offset calculated using Eq 18, extending the line upward so that it intersects the plotted curve. This intersection locates the point of yield in the fastener.
10. Calculate the angular ductility by determining the angle of turn from the yield point to the point of fracture (Fig. 25).

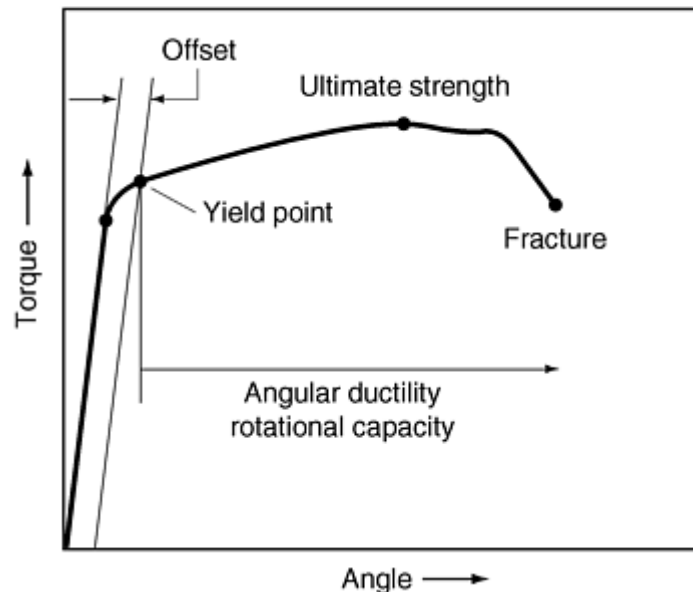


Fig. 25 Angular ductility calculation

Test Report

The test report for angular ductility generally requires a multiple graphic plot of torque or force versus angle of turn for the prescribed number of rundowns, as shown in Fig. 26. This testing can be further documented by a report of the numerical data to which statistics can be added.

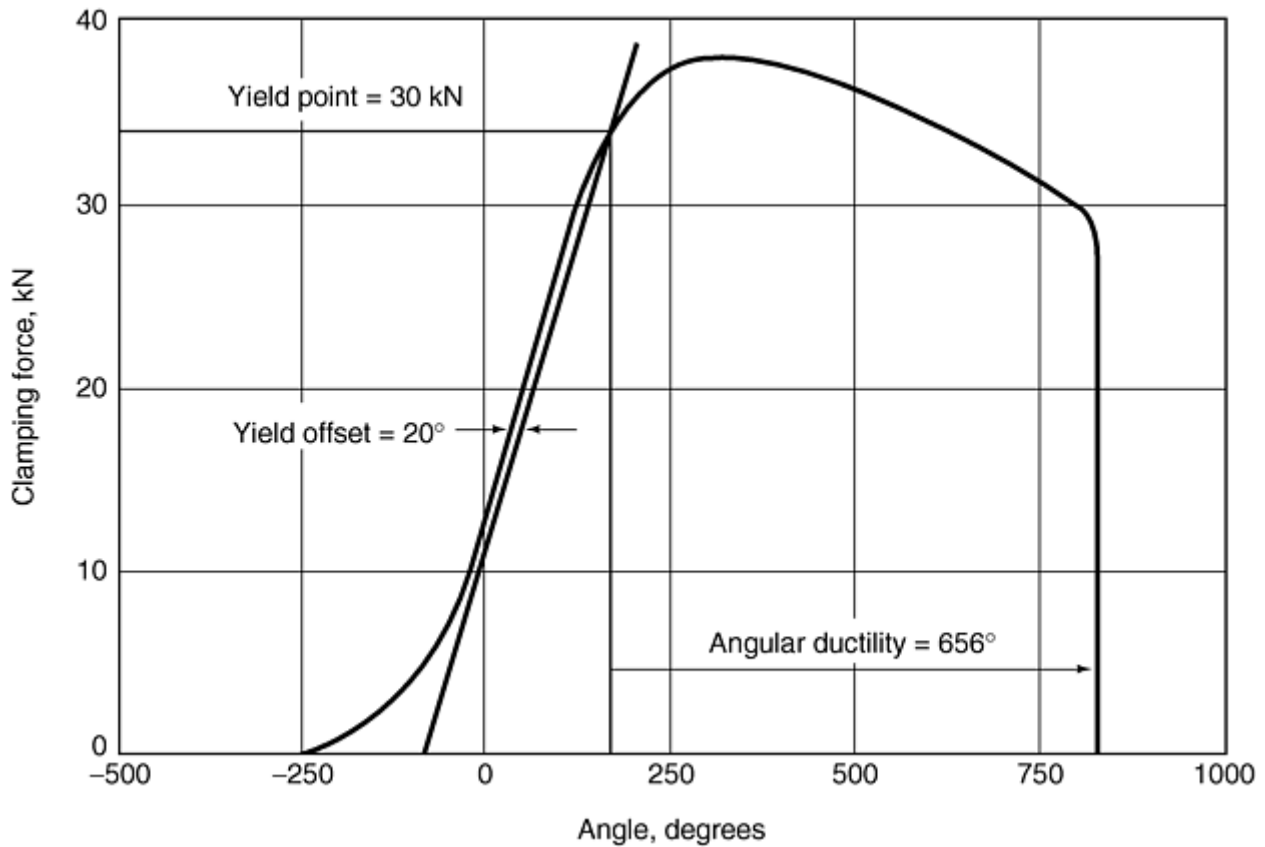


Fig. 26 Angular ductility report

Mechanical Testing of Threaded Fasteners and Bolted Joints

Ralph S. Shoberg, RS Technologies, Ltd.

Torque-Angle Signature Analysis

The factors that must be considered when establishing a threaded-fastener, bolted-joint analysis program are described in this section. Included are methods for modeling the joint, experimental testing of components and assemblies, and procedures conducting postassembly audits.

The basic torque-angle signature is used as a starting point for all analysis. As a first example, it can be used to illustrate the influence of underhead and thread friction on the tightening process. An increase in friction, in either the thread or underhead regions, results in a proportional increase in the slope of the torque-angle signature. The study of the slope of the elastic tightening zone is an important element in analyzing the performance of threaded fasteners in bolted joints.

To apply torque-angle signature analysis, a torque-angle transient recorder is used for measurement and curve plotting. The transient recorder can provide curves onscreen for analysis as well as print them out for detailed study. Tightening, audit, and release-angle signatures for a given fastener can be simultaneously displayed and printed.

Classical Design Concepts: Modeling the Tightening Process

When developing a testing program to correlate the design of a bolted joint and the actual assembly, it is necessary to document the relationship between torque and turn in the development of tension. Before control of a tightening process can be gained, it is necessary to become familiar with what actually happens when the

fastener is tightened. The process of tightening a fastener involves turning, advancing the lead screw, and torque, or the turning moment, so that preload, or tension, is produced in the fastener. The desired result is a clamping force that holds the components together. A torque-versus-angle signature correlated to the clamp force-versus-angle plot offers the best model that can be used to explain this process. The most general model of the torque-turn signature for the fastener tightening process has four distinct zones, as illustrated in Fig. 27.

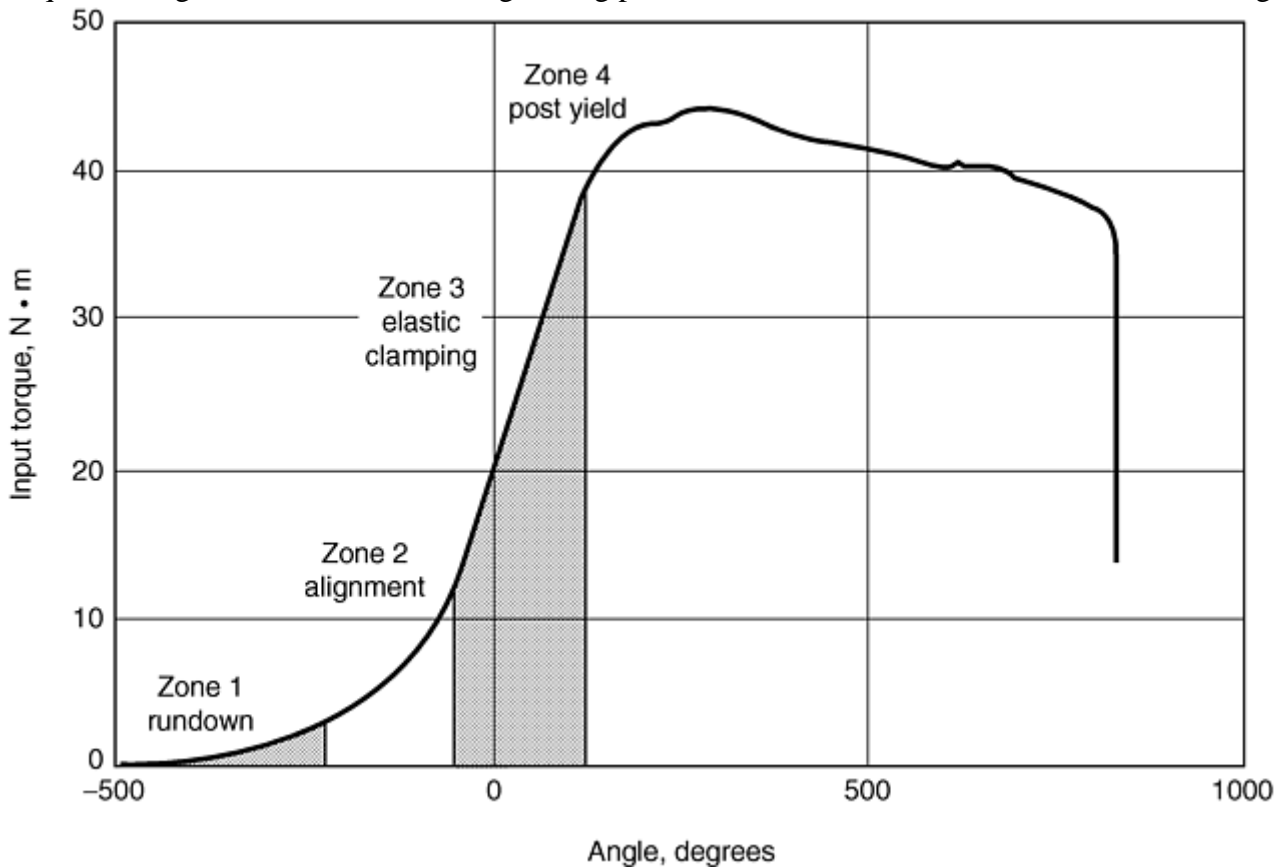


Fig. 27 Four zones of torque-angle tightening

Zone 1: Rundown. The first zone is the rundown, or prevailing torque, zone that occurs before the fastener or nut contacts the bearing surface. Prevailing torque, due to thread-locking features, such as nylon inserts or deformed threads, will show up in the rundown zone. Frictional drag on the shank or threads due to misalignment of parts, chips, or foreign material in the threads, as well as unintended interference due to out-of-tolerance threads, are additional causes of prevailing torque in the rundown zone.

Zone 2: Alignment. The second zone is the alignment, or snugging, zone wherein the fastener and joint mating surfaces are drawn into alignment, or a stable, clamped condition. The nonlinear alignment zone is a complex function of the process of drawing together the mating parts and bending of the fastener as a result of nonparallelism of the bearing surface to the fastener underhead surface. In addition to the macroeffects related to the alignment of parts, there are microeffects within the alignment zone. The microeffects include contact stress-induced deformations of plating and coatings as well as local surface roughness and thread deformations. These macroeffects and microeffects are illustrated in Fig. 28.

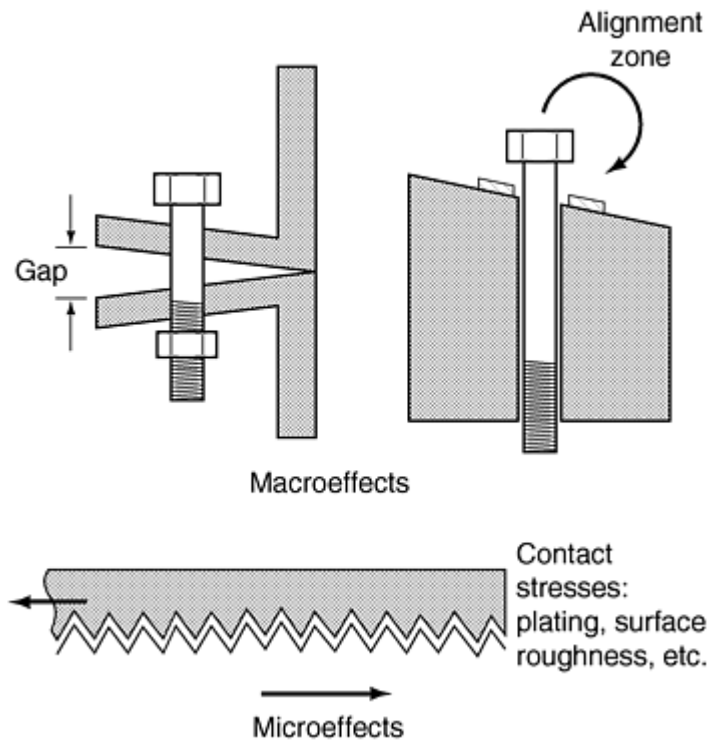


Fig. 28 Macroeffects and microeffects in the alignment zone

Zone 3: Elastic Clamping Range. In this zone, the slope of the torque-angle curve is essentially constant. The elastic-clamping-zone torque-angle slope is a very important characteristic of each bolted joint. This slope can be projected backward to zero torque to locate the elastic origin. For joints with prevailing torque in the rundown zone, the elastic origin is located at the intersection of the prevailing torque level and the backward projection of the tangent to the elastic clamping zone. If the angle of turn is measured from the elastic origin to the point where torquing was stopped in the elastic clamping zone, the tension in the fastener is directly proportional to that angle of turn. In this elastic zone, the compression of the parts and the stretching of the fastener are occurring in a linear fashion from the projected elastic origin. Even if friction between threads or in the underhead region of the fastener is varied, it still will be found that, within the elastic zone, the tension generated is always proportional to the angle of turn from the elastic origin. The angle of turn from the elastic origin to the point where the torque is removed can be multiplied by the angle-tension coefficient to estimate the tension that has been created by the tightening process.

To further illustrate the concept of the elastic origin, the torque-angle signatures in Fig. 29 show the increased slope, induced by increased friction, in the elastic tightening zone. It can be noted that as friction increases, the torque required to bring the bolt to yield is also increased. The curves in Fig. 30 show that, as friction increases, the clamp force at the yield point is reduced, while the torque that is required to reach the yield point increases. This illustrates the fact that for a given fastener size, the torque required to yield the bolt is a function of the material yield strength and the thread-friction coefficient.

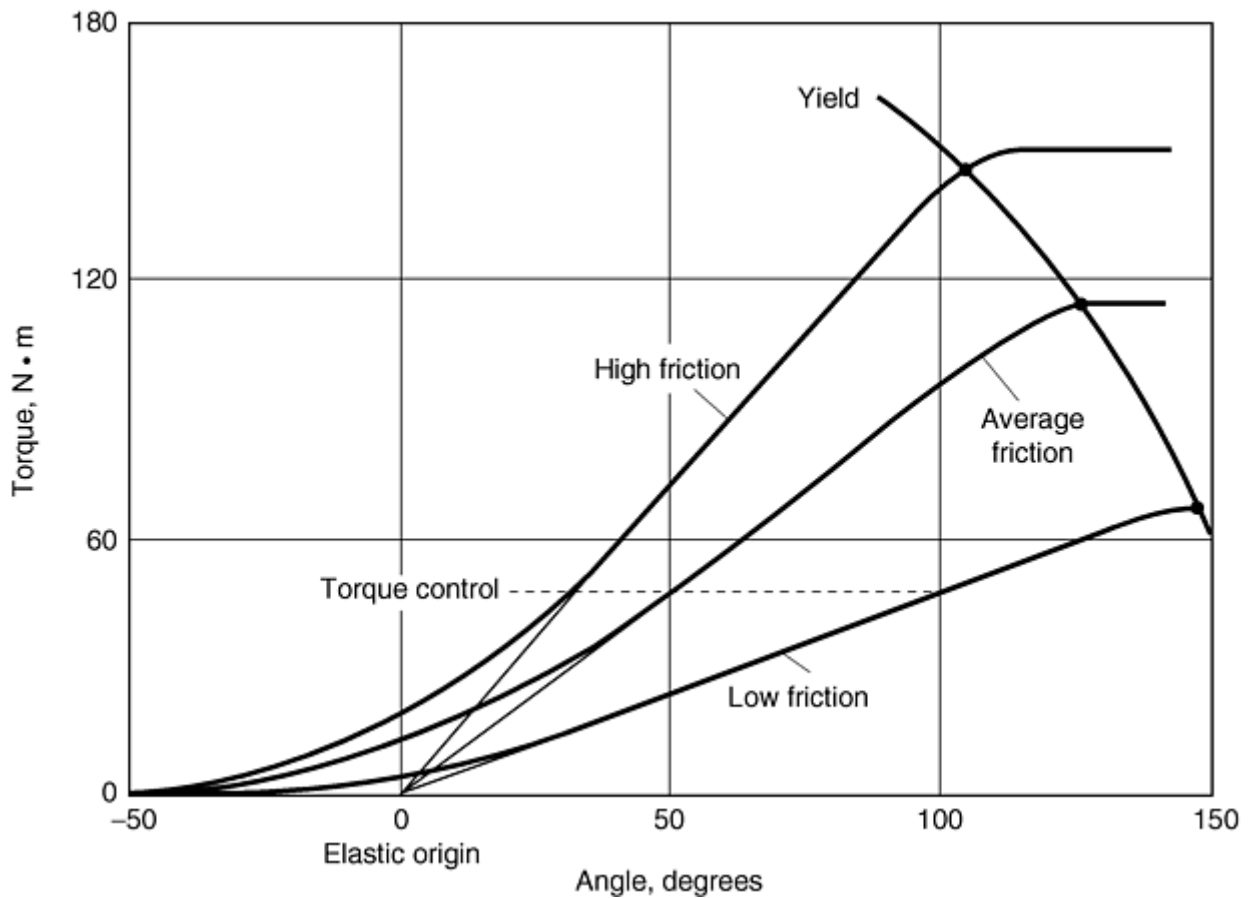


Fig. 29 Friction effects on yield point

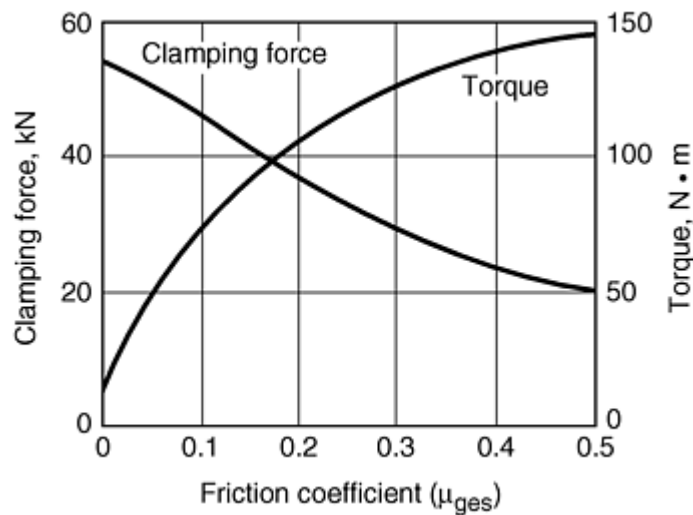


Fig. 30 Friction effects on applied torque and clamping force at yield for class 9.8 M12 × 1.75 bolts

Zone 4: Post Yield. The post-yield zone begins with an inflection point at the end of the elastic clamping range. Yielding can occur in the bolt or in the joint assembly as a result of underhead embedment or as thread strip in the bolt or mating threads. This fourth zone can be due to yielding in the joint or gasket or due to yield of the threads in the nut or clamped components or nut, rather than to yield of the fastener. The yield point of the bolt can be used to approximate the angle-tension coefficient for the tightening process.

The yield clamp load of a torqued fastener is less than the tensile yield due to the combined tension and thread torque. Because the thread friction coefficient is unknown, an initial assumption could be that the clamp load at yield torque is about 90% of the tensile-yield load. This calculation would be approximately correct for an average friction coefficient, μ_{ges} , of 0.1.

Torque-Angle (M -Alpha) Diagram

The torque-angle (M -alpha) diagram is a powerful tool for use in joint analysis. As shown in Fig. 31, it is a straight-line projection of the tangent to the torque-angle assembly curve projected backward from the predicted yield point through the elastic tightening point to zero torque. This tangent projection is used to locate the elastic origin. Because the M -alpha diagrams in this discussion were developed using SR1, a bolted-joint stress calculation software program based on the well-known German design standard, VDI 2230, terminology native to VDI is used in this discussion, such as M for torque, from the German word *Drehmoment* (torque moment).

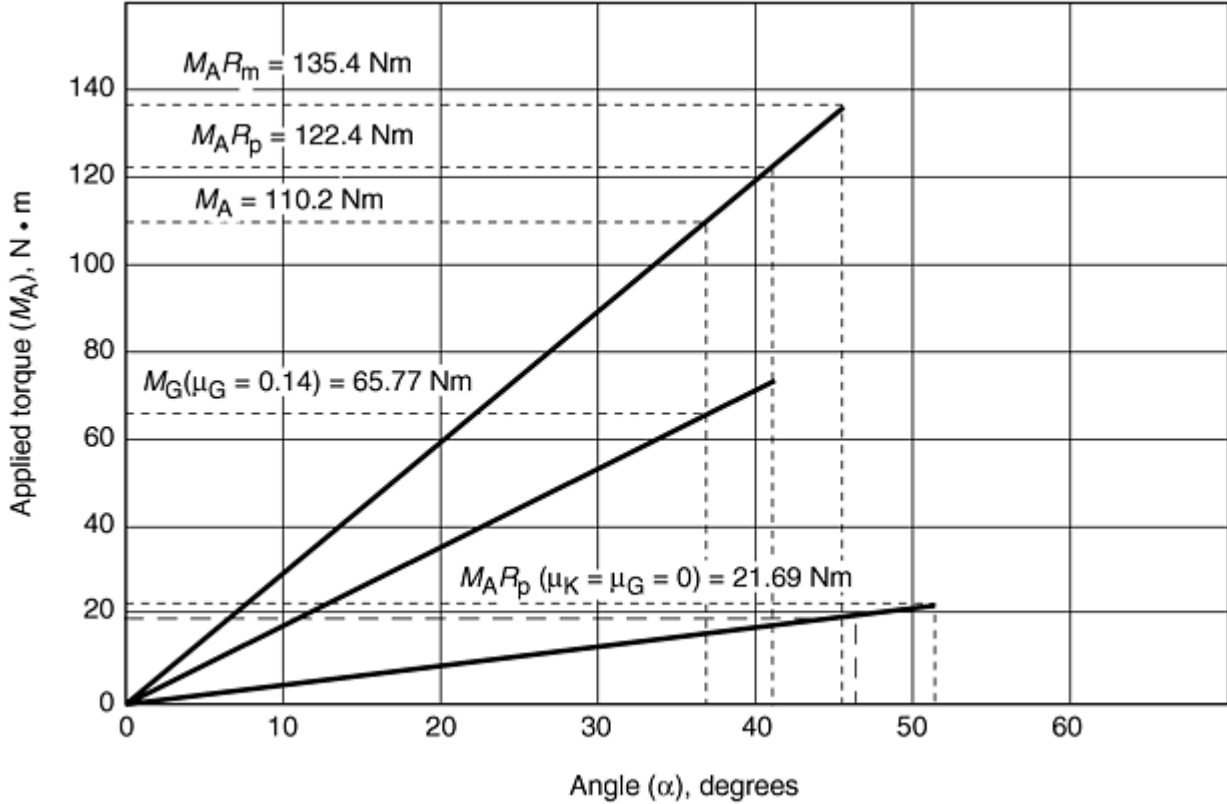


Fig. 31 Torque-angle diagram

In addition to the applied torque, M_A , the torque-angle diagram has projections from the elastic origin for both the thread torque, M_G , and the pitch torque, M_{G0} (where $\mu = 0$). A very useful feature of the torque-angle diagram is the manner in which the diagram clearly illustrates the distribution of the torque in a tightening process. With M_A showing the total input torque, M_G represents the thread torque that is the thread friction plus the pitch torque, which creates the clamp force. The difference between the M_A and M_G curves represents the underhead-friction torque. The difference between the pitch torque curve, M_{G0} , and the M_G curve represents the thread-friction torque.

The torque-angle diagram is a straight line projected from the elastic origin to the yield point. By changing the coefficients for thread friction, μ_G , and underhead friction, μ_K , assumed for the VDI 2230 analysis, the effect of friction on the tightening process can be clearly seen. In the diagram shown in Fig. 32, the torque values required to reach the assembly preload and the yield point are lower because the assumed friction coefficients are lower.

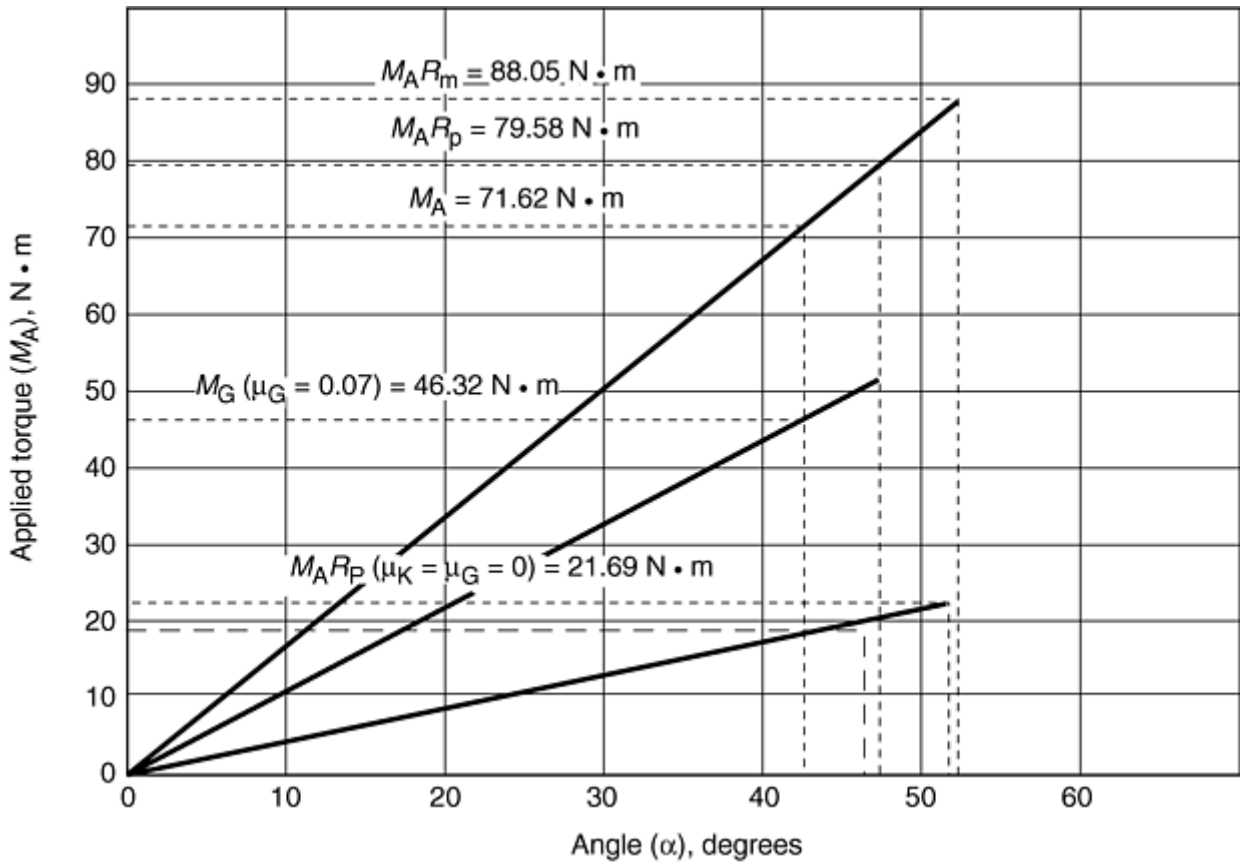


Fig. 32 Torque-angle diagram with low friction coefficients

Strength Considerations

The clamp force and preload requirements for a bolted joint are determined by the static and dynamic loads that the assembly is expected to see in service. The bolted-joint design must be completely engineered with regard to the axial (concentric), eccentric, and shear loads to which the assembly will be subjected. This design is the first step in any fastener-engineering project.

After the external working loads have been defined, the necessary bolt preload can be calculated. Next, the safety factors against embedment and thread strip must be checked to ensure that yielding in the bearing areas or threads will not limit the preload to less than the required amount. Safety factors for shear slip, fatigue, loss of preload, and overelongation due to combined loads must also be evaluated.

The safety factors for embedment and thread strip are important both for the initial installation of the fastener and for long-term reliability with regard to both loosening and fatigue resistance. The illustration in Fig. 33 shows some of the strength factors that should be evaluated with regard to expected service loads and preload requirements.

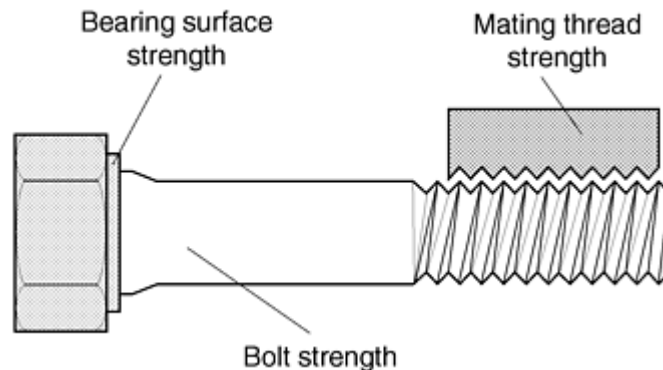


Fig. 33 Basic clamping force and material strength considerations

Bolt Yield

Tightening a fastener beyond the yield point is a means of achieving the maximum preload possible for a given size and strength. This tightening method is commonly used in automotive engine assembly for connecting rod bolts, crankshaft bearing cap bolts, and engine head bolts. When bolts first replaced rivets in the construction of bridges and buildings, tightening beyond the yield point quickly proved to be a reliable method of assembly. The preload obtained by tightening beyond the yield point is proportional to the material yield strength and inversely proportional to the thread friction coefficient, μ_G . The thread friction coefficient is important because the yield point during tightening results from combined tensile loads plus the torsional load due to the thread friction and pitch torque.

After the yield load is reached, the clamping force will continue to increase in proportion to the increase in torque. In the elastic tightening zone, tension is proportional to the angle of turn from the elastic origin located on the torque-angle signature. When tightening beyond the yield point, the clamping force can be estimated by the procedure illustrated in Fig. 34.

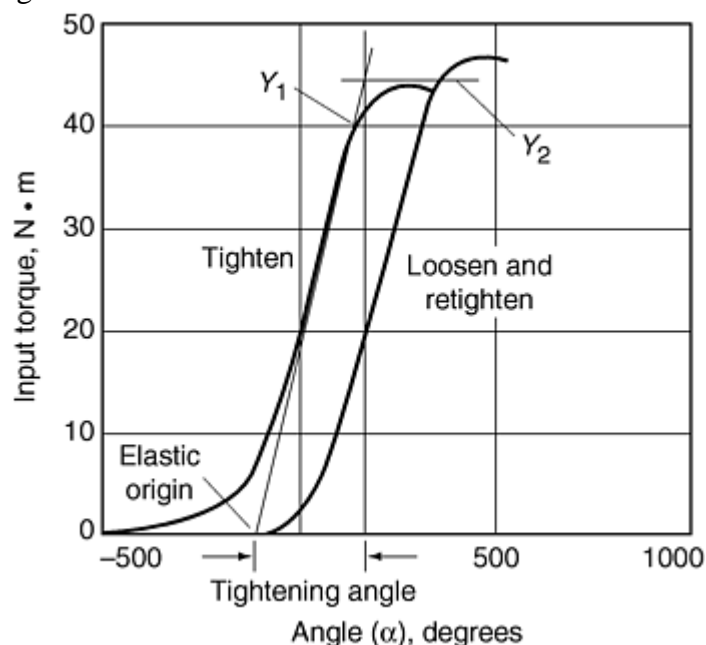


Fig. 34 Bolt yield from initial tightening (Y_1) and from loosening and retightening (Y_2)

The tangent line to the elastic straight-line tightening section of the signature is projected beyond the yield point, and the final torque value is projected to the tangent line. The angle of turn from the elastic origin to the intercept of the backward projection from the final torque can be used to estimate the tension. This procedure can be seen as related to the strain-hardening phenomena observed when working materials beyond the yield point.

After the material is first loaded beyond yield, Y_1 , the yield point is found to be at a higher level, Y_2 , on the next tightening cycle. After yielding, when the load is released, the release curve is offset and parallel to the elastic tightening curve.

Thread Strip

In general, a properly designed bolted joint will not fail by stripping of the threads either during installation or if the assembly is overloaded in tension. As a matter of good design practice, failure should always be due to fracture of the bolt.

The thread-stripping areas for internal and external threads can be approximately calculated using the formulas expressed in Eq 20 and 21. The geometric configurations that define the formulas are shown in Fig. 35.

$$AS_B = \pi \left(\frac{d_3}{P} \right) \cdot L_e [0.5P + 0.577(d_2 - d_3)] \quad (\text{Eq 20})$$

where AS_B is the shear area of the bolt; L_e is the effective thread engagement; d_2 is the pitch diameter, external thread; d_3 is the minor diameter, internal thread; and D_3 is the maximum diameter, internal thread.

$$AS_N = \pi \left(\frac{D_3}{P} \right) \cdot L_e \cdot [0.5P + 0.577(D_3 - D_2)] \quad (\text{Eq 21})$$

where AS_N is the shear area of the nut thread; L_e is the effective thread engagement (grip length of the fastener); D_2 is the maximum pitch diameter, internal thread; D_3 is the major diameter, external thread; and d_3 is the minimum diameter, external thread.

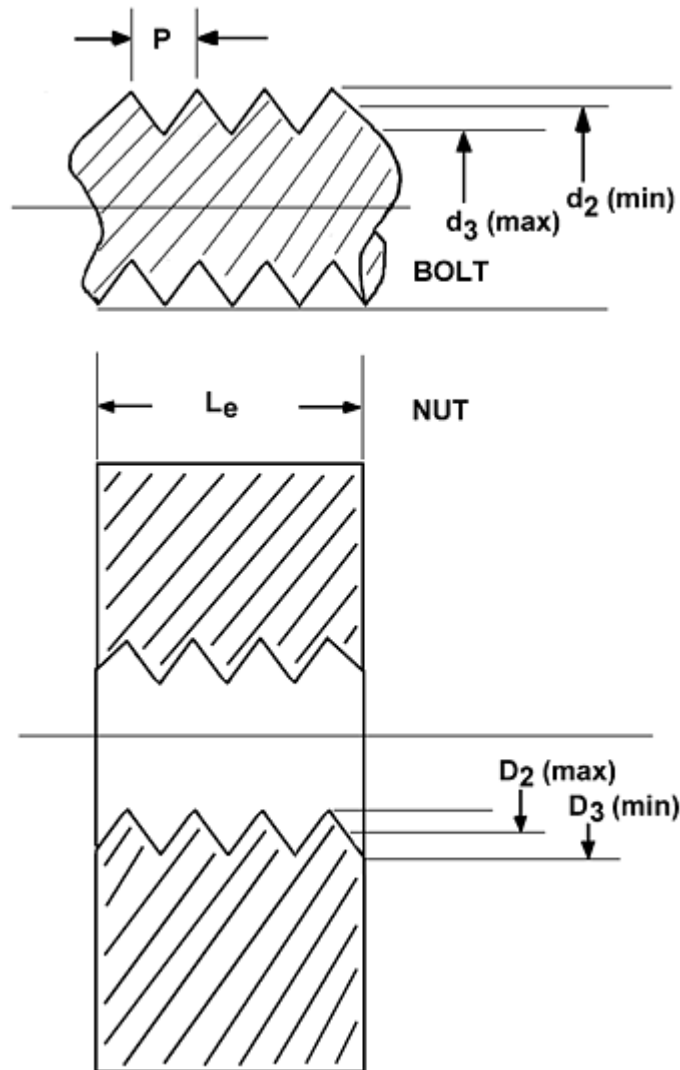


Fig. 35 Thread-stripping areas in bolted assemblies. P , pitch; L_e , effective grip length of the fastener; d_2 , bolt pitch diameter; d_3 , bolt root diameter; D_2 , nut pitch diameter; D_3 , nut root diameter

Assuming that the maximum shear strength of the bolt material equals half of the tensile strength (ductile material, maximum shear stress failure mode), the bolt load to strip the threads can be estimated by multiplying the calculated shear area times the shear strength of the bolt or nut. This formula is a simplified calculation that assumes the loading is uniformly distributed on all engaged threads. In actual practice, due to the elastic coupling between threads, the first engaged thread carries a higher-than-average load, while remaining threads carry progressively lower loads as the load is transferred between the bolt and nut, or internally threaded hole.

When evaluating a bolted-joint, torque-angle assembly signature, the onset of thread stripping appears as a yield point, or a change of slope in the elastic portion of the tightening curve (Fig. 36). The thread-strip signature is similar to the signature for embedment of the fastener into the bearing surface. Both embedment (described in the following section) and thread strip lead to creep of materials within the loaded surface areas of the assembly. Over a period of time, embedment and excessive thread-stripping loads cause loss of preload as the high-stress regions relax and redistribute the loads.

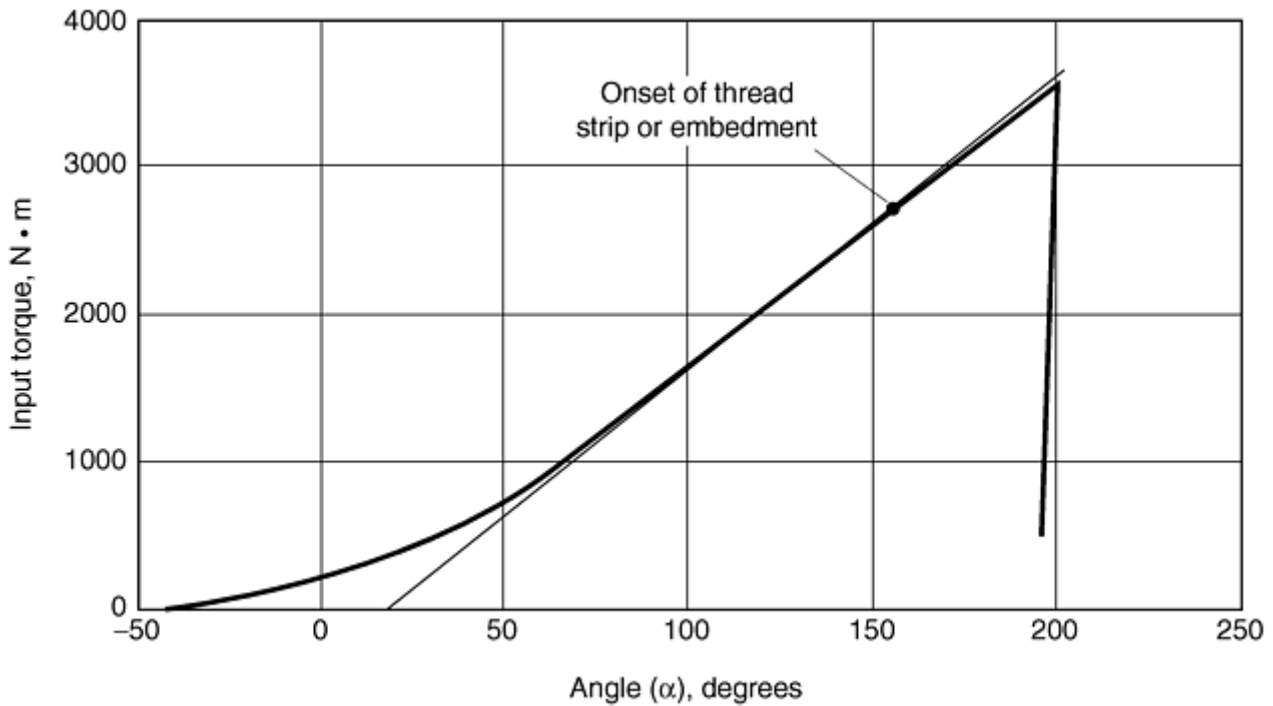


Fig. 36 Test plot of fastener with stripped threads

In service, thread-strip failure can be progressive in nature, gradually transferring the load from thread to thread. Loss of preload due to thread strip can occur over many hours or days and is a cause of fastener loosening that is often difficult to diagnose.

Embedment or Loss of Preload

The release-angle method has been successfully used to study fastener-loosening problems. The basic procedure involves recording and analysis of the torque-angle signatures for tightening and then loosening the fasteners that are to be tested.

First, the torque-angle-tightening curve is plotted, the elastic origin is located, and the amount of angle of turn from the elastic origin is determined. After the assembly has been allowed to relax, for example, to sit overnight or run on a dynamic field test, the fastener is loosened and the loosening curve is analyzed. The release angle is determined, compared to the tightening angle, and if not equal, evaluated to see how much tension was lost by relaxation or loosening.

In one release-angle study, a fastener had a tightening angle of 120°. After 10 to 12 h, the release angle was 20°. The manufacturer was already aware there was a major problem because the parts were literally falling apart somewhere between the assembly factory and the automotive plant where they were delivered for final assembly in vehicles. The signature-analysis study showed that creep or relaxation in the threads was causing an approximately 80% loss in clamp force over a 12 h period. The release-angle method provided a quantitative answer as to the amount of clamp force lost and clearly showed that the parts needed to be redesigned.

The release angle method is particularly valuable for studying short-grip-length fasteners holding composite or plastic parts. These parts are generally too small to allow for use of strain gages or ultrasonic stretch measurements to confirm fastener preload.

For these applications, a torque-angle signature curve for tightening is recorded, and the parts are then put in an environmental chamber and load/temperature cycled.

Following the test-load cycle, the release-angle signature is recorded. Analysis of the release-angle signature in comparison to the tightening signature is used to directly estimate the percentage of initial clamp load lost due to embedment or creep of the plastic part in response to applied loads or temperature cycles. By changing geometric shapes and washer size, the effects can be quantitatively measured and compared. The section “Torque-Angle Tension Audits” describes an audit method that can be used along with the release-angle method to help audit relatively fastener tension values.

Estimating the Angle-Tension Coefficient

A number of different methods can be used to determine the angle-tension coefficient for the bolted joint. A basic assumption is that as the fastener is turned to develop preload in the joint, the fastener stretches, and the clamped parts compress elastically according to the effective spring rates of the fastener and the clamped parts. After the angle-tension coefficient is determined for elastic clamping through analysis of the torque-angle signature, it is relatively easy to estimate the tension achieved when tightening beyond the bolt-yield point.

The angle-tension coefficient for each bolted joint must be determined in order to establish the control parameters for torque-angle-tension control. By shutting off the assembly tool at a specified angle of turn after the threshold torque is attained, the scatter in achieved tension will be much less than the scatter observed for the same fasteners tightened with torque-only control. For this process to work reliably, it is necessary that the threshold torque level for starting angle counting be set at a level above the alignment zone of the tightening process.

The curves in Fig. 37 show how the process control limits are determined to achieve torque-turn-tension control for an application. Three examples are shown:

- With torque-angle control (110°) under normal friction, the clamping tension force achieved is 60 kN.
- With torque control of $60 \text{ N} \cdot \text{m}$ under high friction, the clamping tension achieved is 28.25 kN.
- With an angle count threshold of about $20 \text{ N} \cdot \text{m}$ and 110° torque-angle control, the clamping tension achieved is 56.15 kN.

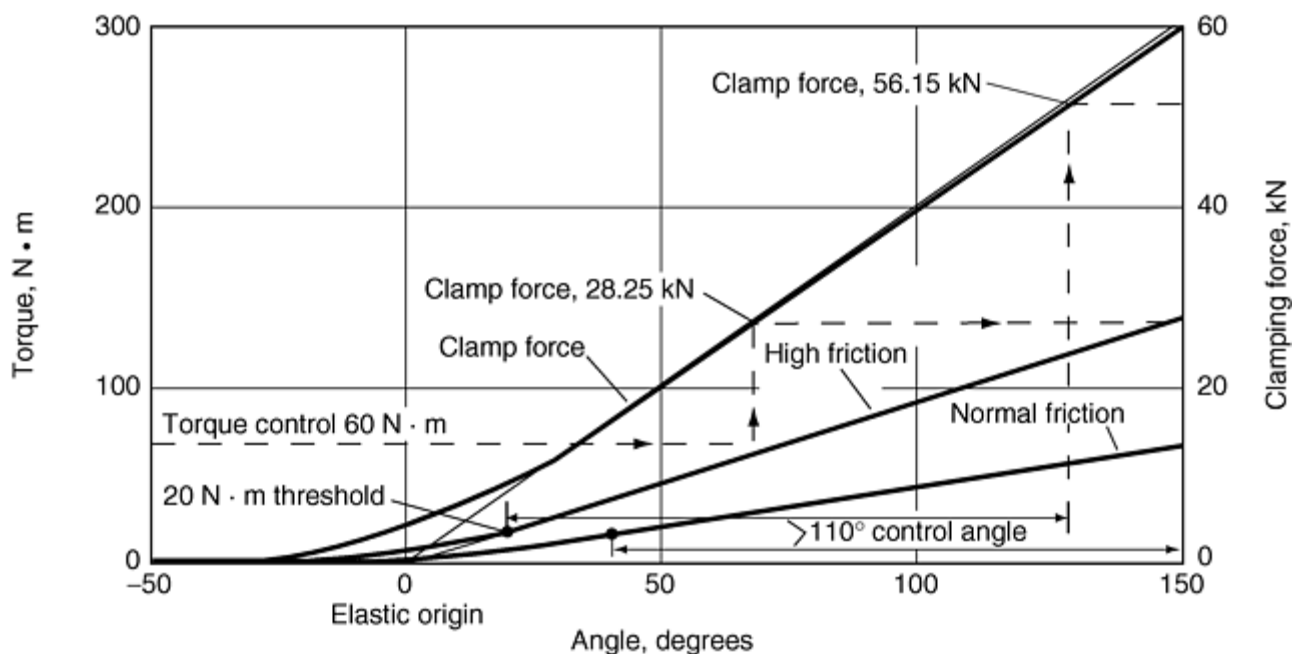


Fig. 37 Torque-turn-tension control principles. Three examples are shown; see text for discussion.

After the installation process has been defined and implemented, methods must be specified to audit the results in order to verify that the process has achieved the desired fastener preload. Process audit procedures, including the release-angle measurement method and hand-torque breakaway audits, are presented later.

Release Angle Analysis

The complete analysis of a fastener involves looking at both the tightening and the loosening torque-angle curves as the fastener is first installed and then loosened. These curves are studied initially in the elastic tightening region where the fastener has not gone beyond yield, such as the assembly torque-angle signature shown in Fig. 38. When the fastener is loosened, a torque-angle-loosening signature, as shown in Fig. 39, can be recorded. The release signature shows the release of the fastener stretch as well as the release of the compression in the clamped parts. Analysis of this signature provides a direct method for verification of preload

or tightness. First, the line tangent to the elastic-release portion of the curve is projected to zero torque to locate the elastic origin. The release angle, measured from the point where loosening starts to the projected elastic origin, is a direct measure of the tension released from the bolted joint.

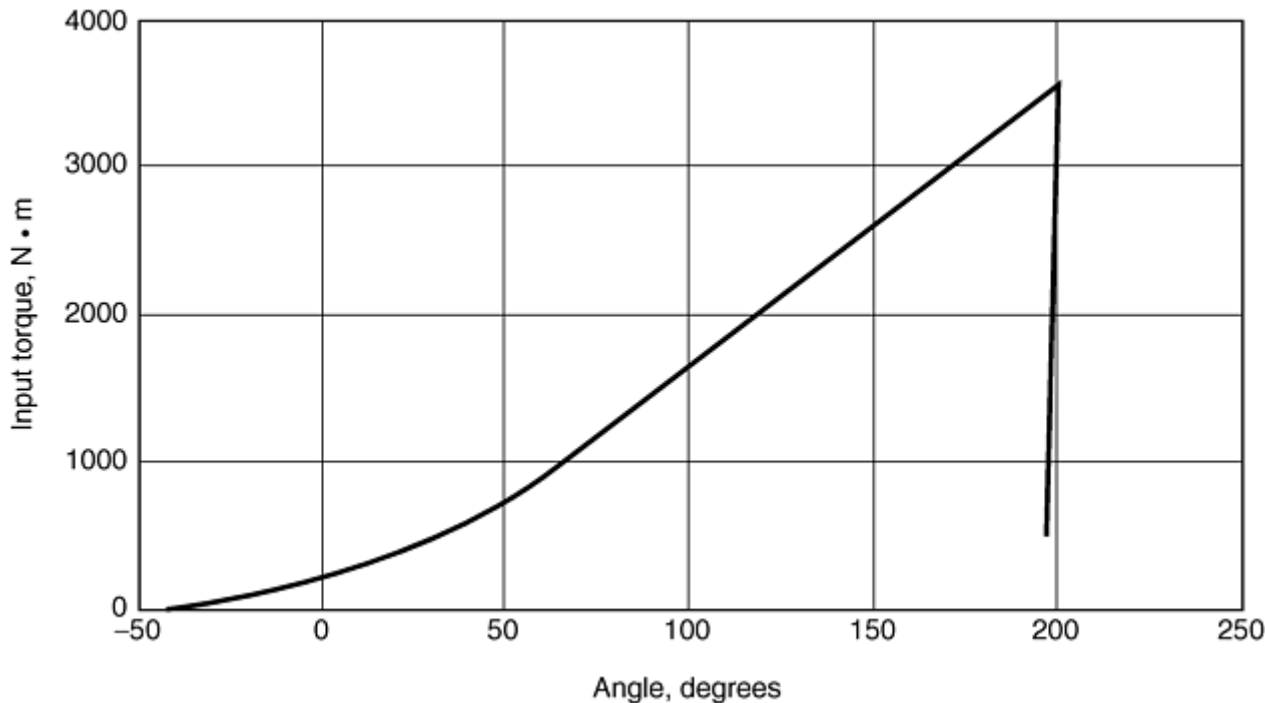


Fig. 38 Torque-angle assembly signature

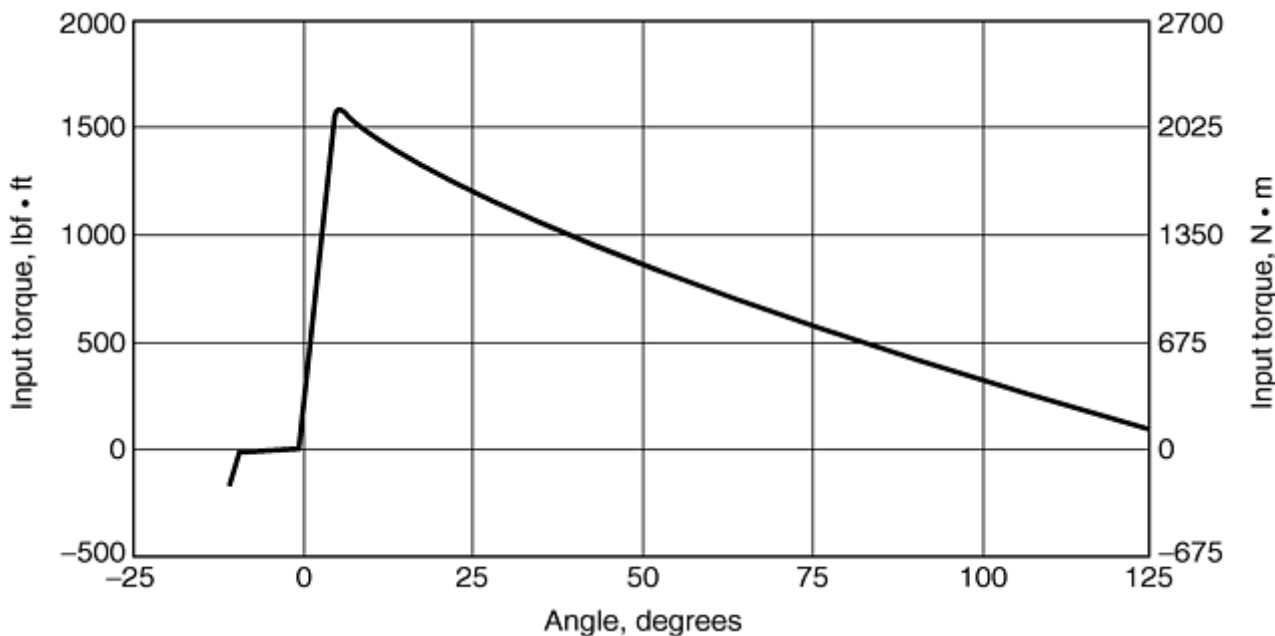


Fig. 39 Torque-angle loosening signature

The tangent line must be drawn on the straight-line portion of the curve after the initial peak release torque due to static friction or thread-locking adhesive that has been broken free. The starting point is the angle where initial loosening motion begins. The total release angle is measured from the initial loosening point to the projected elastic origin. Note that if a significant prevailing torque is present after loosening the fastener, the elastic origin must be located at the prevailing level, not zero torque.

The torque-angle signature shown in Fig. 40 has been plotted as an *M*-alpha diagram with the tangent line, locating the elastic origin, drawn at 50% of the maximum torque to set the elastic tightening slope below the onset of embedment of the nut. The bolt is an M30 × 3.5 with a strength of class 11.9. The corresponding clamp force signature, plotted as an *F*-alpha (tension-angle) diagram confirms that the clamp force increases linearly

with the angle of turn from the projected elastic origin. In the example shown in Fig. 41, the elastic-tightening angle is approximately 125° .

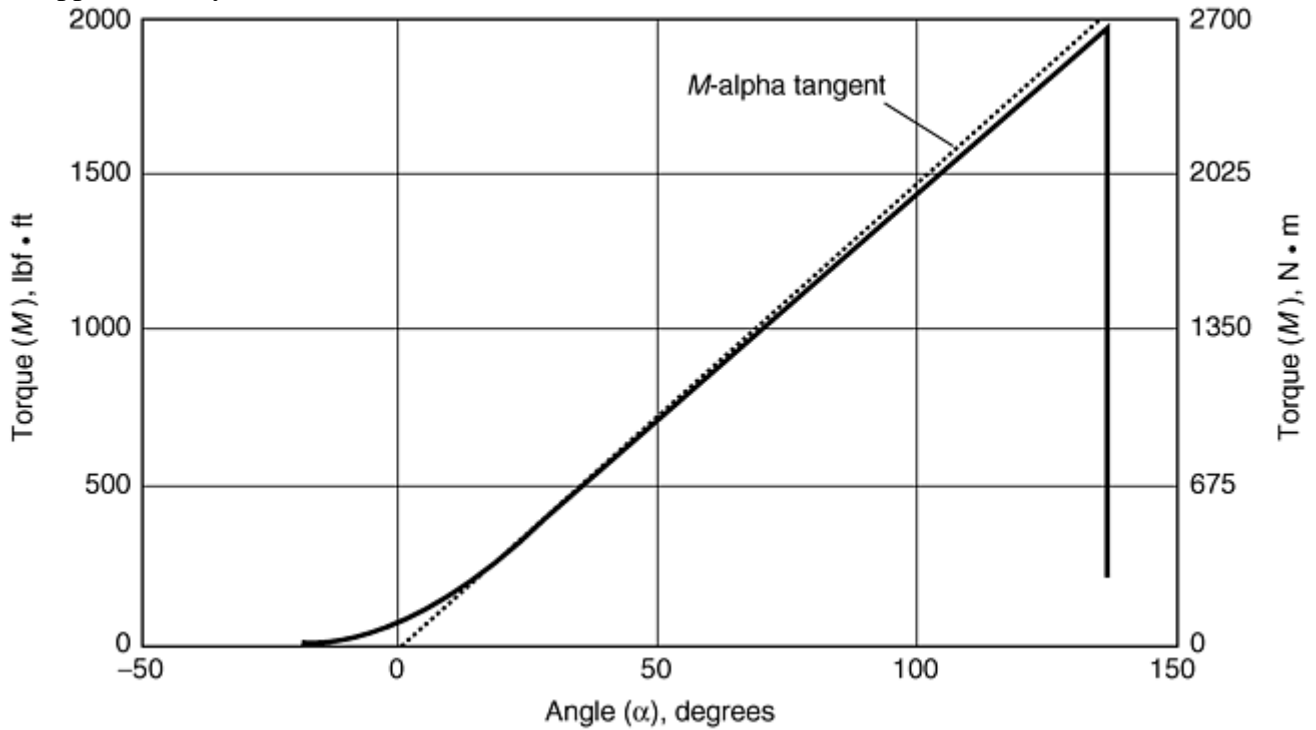


Fig. 40 Torque-angle signature showing embedment

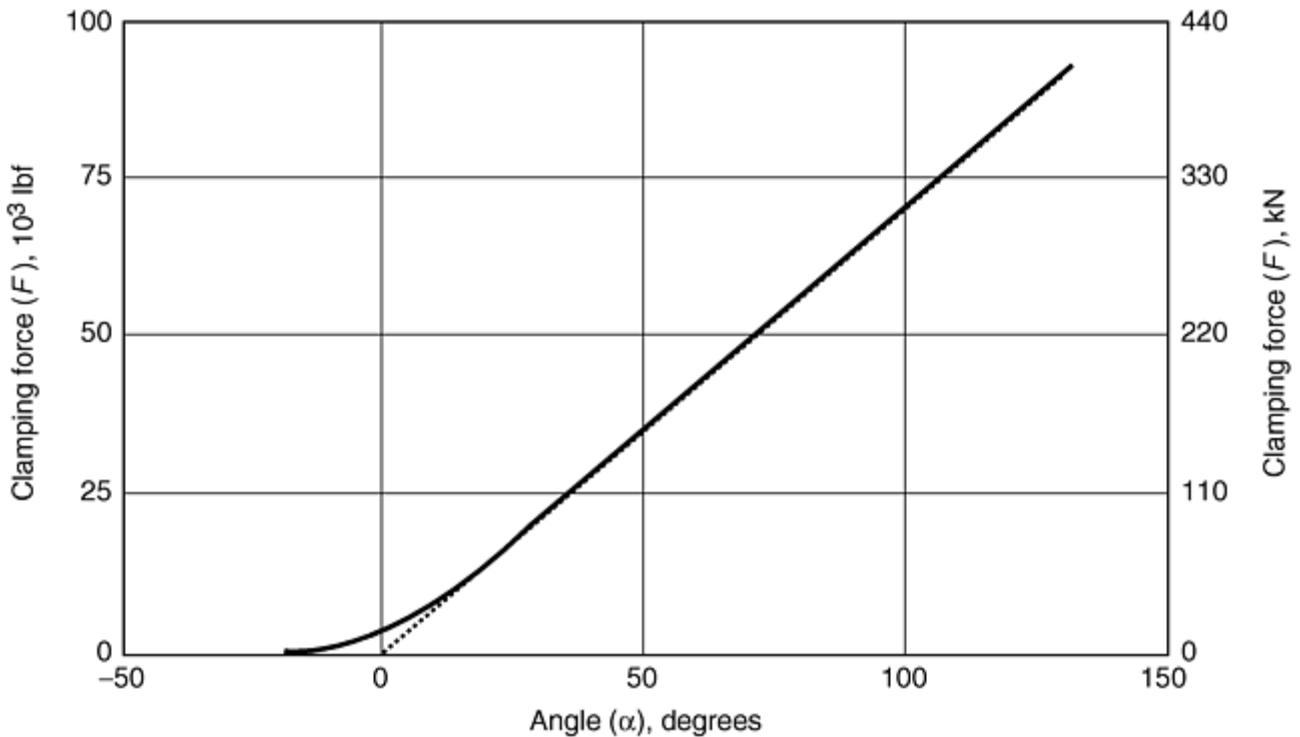


Fig. 41 Clamp force vs. angle of turn from elastic origin

The loosening torque-angle signature (Fig. 39) also has a projected release angle of approximately 125° . The tension-angle diagram (Fig. 41) confirms the fact that, even after embedment occurs, the clamp force increases in direct proportion to the angle of turn from the elastic origin. Similar to the analysis of added tension achieved after yield of the bolt, for embedment or thread strip, the backward projection to the extended tangent to the curve before thread strip or embedment is used to locate the effective tightening angle. Experiments with strain-

gage bolts or force washers, where the clamp force is measured along with the torque and angle during tightening, verify that this theory is correct for a given fastener.

Figure 42 shows a release-angle study performed on an automotive wheel nut. A tool with a torque and angle sensor connected to a transient recorder is used to loosen the nut, record the torque and angle values, and plot the data. The resulting printed curve shows an extremely high release torque. The high initial breakaway loosening peak torque region is disregarded because it is simply an indication of the static torque required to start loosening motion. The high value of release torque is significant from the point of view that it illustrates the high thread friction due to thread-pitch distortion on the wheel nut, a factor that helps prevent vibratory loosening on typical wheel nuts.

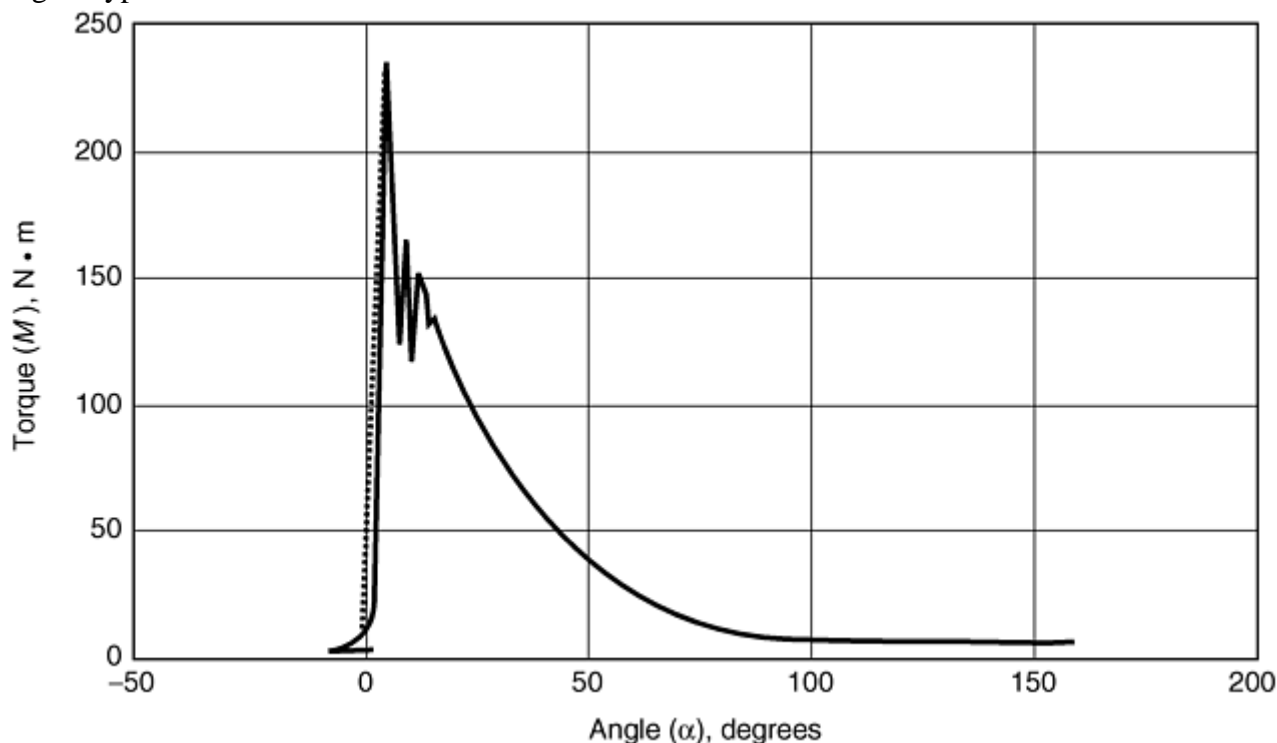


Fig. 42 Wheel nut-loosening signature

The elastic release angle for the wheel nut shown in Fig. 42 is approximately 40°. The nut had been tightened to a peak torque of 206 N · m (152 lbf · ft), which is 75 N · m (52 lbf · ft) greater than the vehicle manufacturer specification. The wheel nut was originally tightened to a torque of 160 N · m (118 lbf · ft), which did not appear to get past the tightening alignment zone as illustrated by the signature shown in Fig. 43. In this example, high underhead friction limited the tension on the stud, which for normal friction conditions, would have resulted in stud yield or fracture due to overelongation.

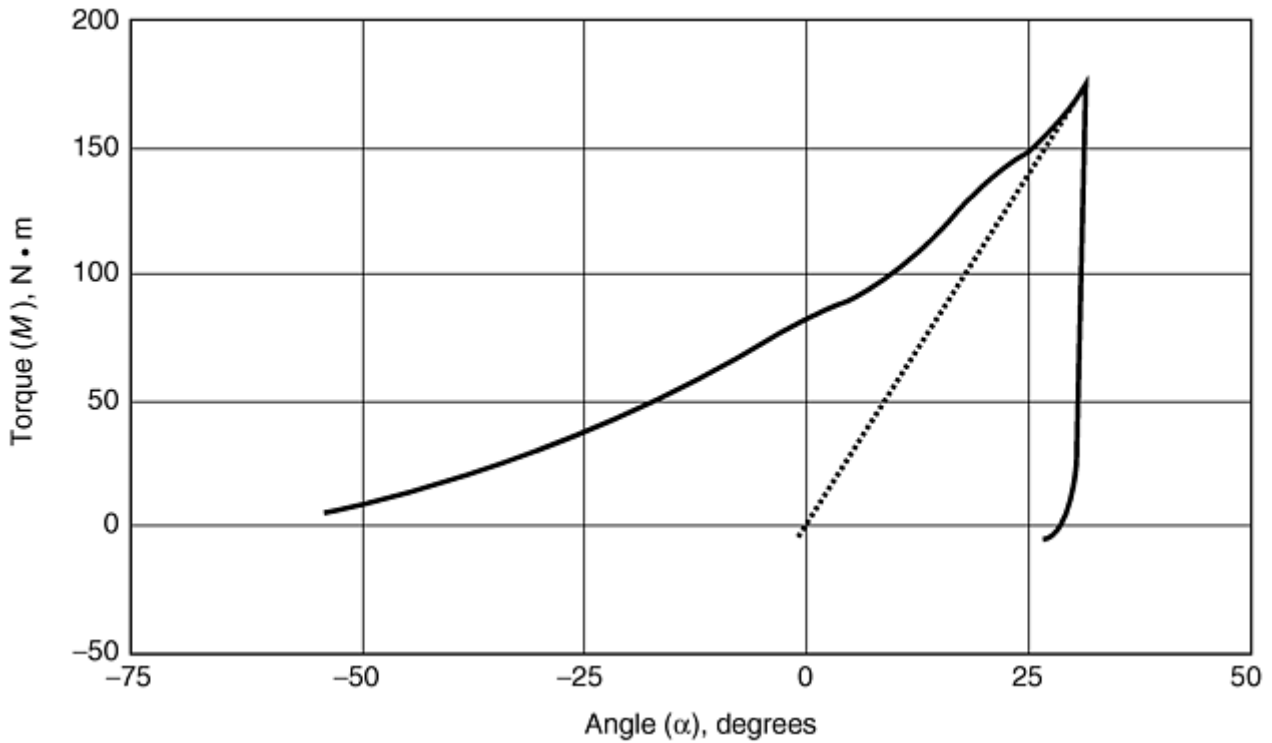


Fig. 43 Wheel nut-installation signature

The installation was followed by a hand-torque breakaway audit where the nut was advanced about 7 or 8° in the tightening direction, as shown in Fig. 44. The torque-angle diagram for the audit shows that the final torque was about 206 N · m (152 lbf · ft), with a projected elastic-tightening angle of 40°.

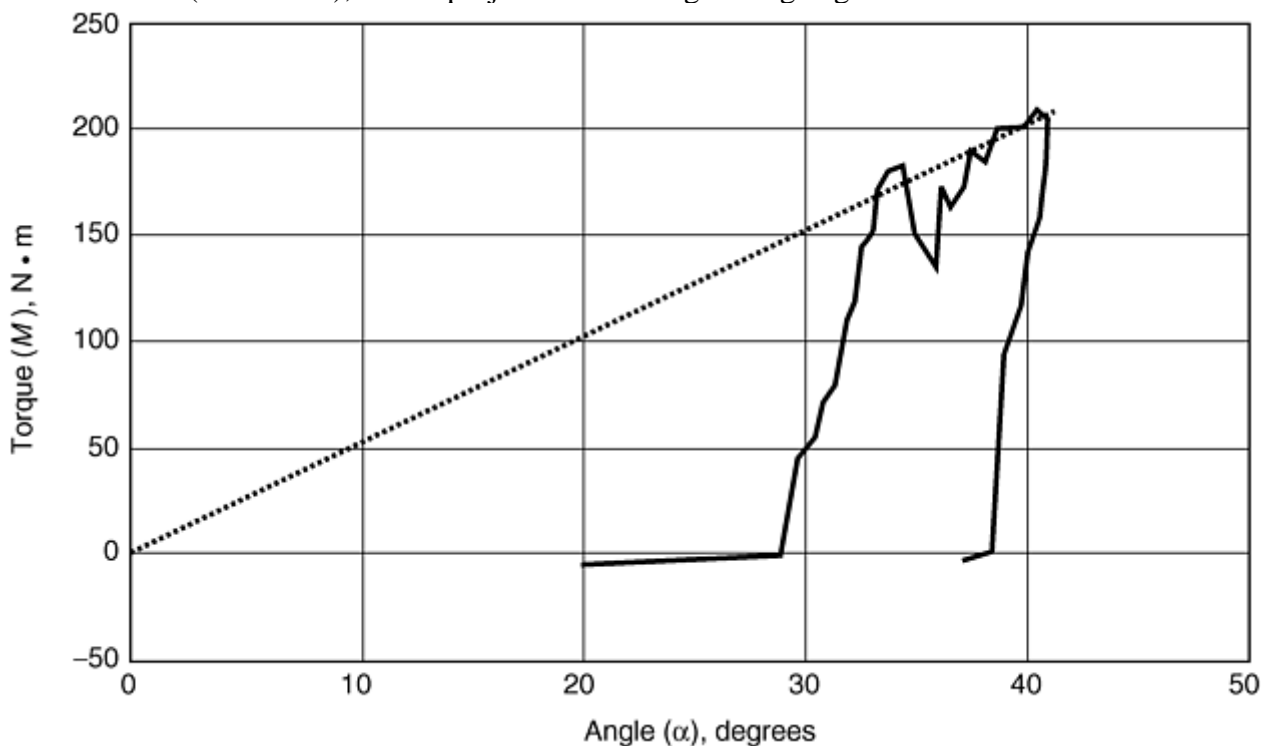


Fig. 44 Wheel nut-torque audit signature

Applying the release-angle method, a line is projected tangent to the elastic release portion of the curve to zero torque. This release angle, measured from the release-torque point to the point where the tangent line crosses the zero torque or prevailing torque level, is directly proportional to the tension or clamp force released. In comparing Fig. 44 with Fig. 42, a significant correlation is seen to exist between the release angle determined

by loosening the fastener and the torque-angle diagram as applied to the torque-angle signature for the breakaway audit. The loosening signature in Fig. 42 was recorded after the audit plotted in Fig. 44.

Torque-Angle Tension Audits

Torque-angle signature analysis is particularly useful for studying all critical fastener assemblies where, in terms of safety or reliability, it is important that proper preload is initially obtained and maintained throughout the operating life of an assembly. In addition to analyzing fastener problems, such as loosening and embedment, torque-angle signature analysis can also be used to evaluate the performance of tightening tools in applying the desired clamp force on fasteners. This technique is particularly applicable for evaluating processes that employ pulse tools and impact tools.

Due primarily to ergonomic considerations, pulse tools have recently been widely specified for use in high-volume assembly operations. Unfortunately, the limitations of these tools related to their energy transfer characteristics are not generally well understood. Pulse and impact tools are particularly sensitive to joint rate and friction variations. Because friction coefficients are a function of velocity as well as surface pressure, tightening results with pulse, and high-rpm tools must be carefully evaluated to ensure suitable tightening process capability.

For example, pulse and impact tools move fasteners at high speeds with a great deal of stick-slip, chatter, and unique frictional characteristics that are not seen with steady, continuous tightening processes. These factors can lead to a deceptively high torque reading but with minimal clamp force created. By checking the assembled joint with an audit method that can correlate angle of turn and clamp load, the user can ensure that the assembly is securely tightened.

The following series of tightening, breakaway-torque audits and release signatures illustrate the basic concepts of torque and tension audit using torque-angle signatures. Understanding of the engineering mechanics of threaded fasteners is greatly enhanced through the use of the concept of the elastic origin and the application of torque-angle (M - α) and tension-angle (F - α) diagrams to the audit process.

Tightening Curve Analysis. In the example illustrated in Fig. 45, an $M12 \times 1.75$ fastener was tightened to $80 \text{ N} \cdot \text{m}$ ($60 \text{ lbf} \cdot \text{ft}$). The signature was recorded with a recording threshold of $27 \text{ N} \cdot \text{m}$ ($20 \text{ lbf} \cdot \text{ft}$). The plot shows both torque and tension versus angle of turn, with zero angle located at the threshold.

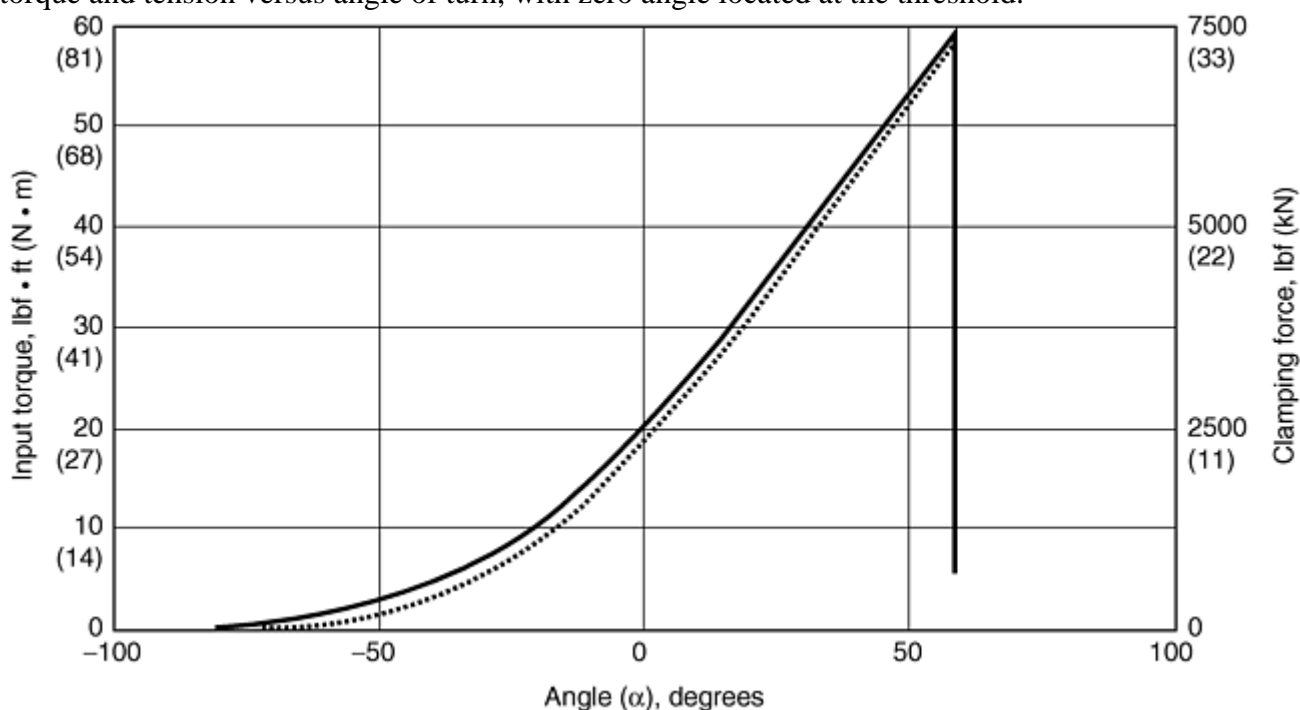


Fig. 45 Torque and clamp load vs. angle

The signature analysis software used in this analysis can automatically locate the elastic origin on the torque-angle diagram by projecting a tangent line from the final point on the torque-angle curve to the zero torque level. The torque-angle diagram for the installation-tightening signature, shown in Fig. 46, illustrates that the

torque resulted in a projected elastic tightening angle of approximately 85° . The corresponding tension-angle curve, shown in Fig. 47, confirms the relationship between torque and angle with the concept of the elastic origin. Note that the 85° elastic tightening angle for the bolt results in a clamping force of approximately 33.4 kN (7500 lbf).

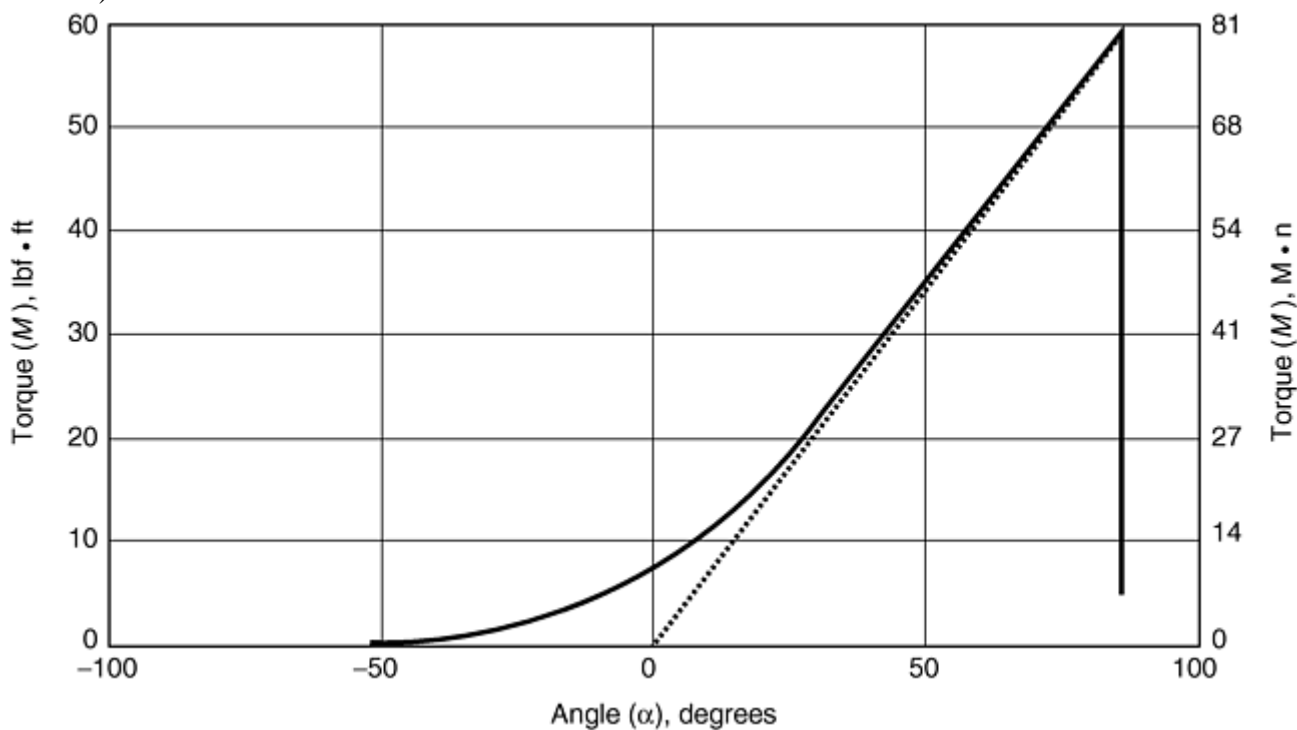


Fig. 46 Torque-angle diagram for installation tightening signature

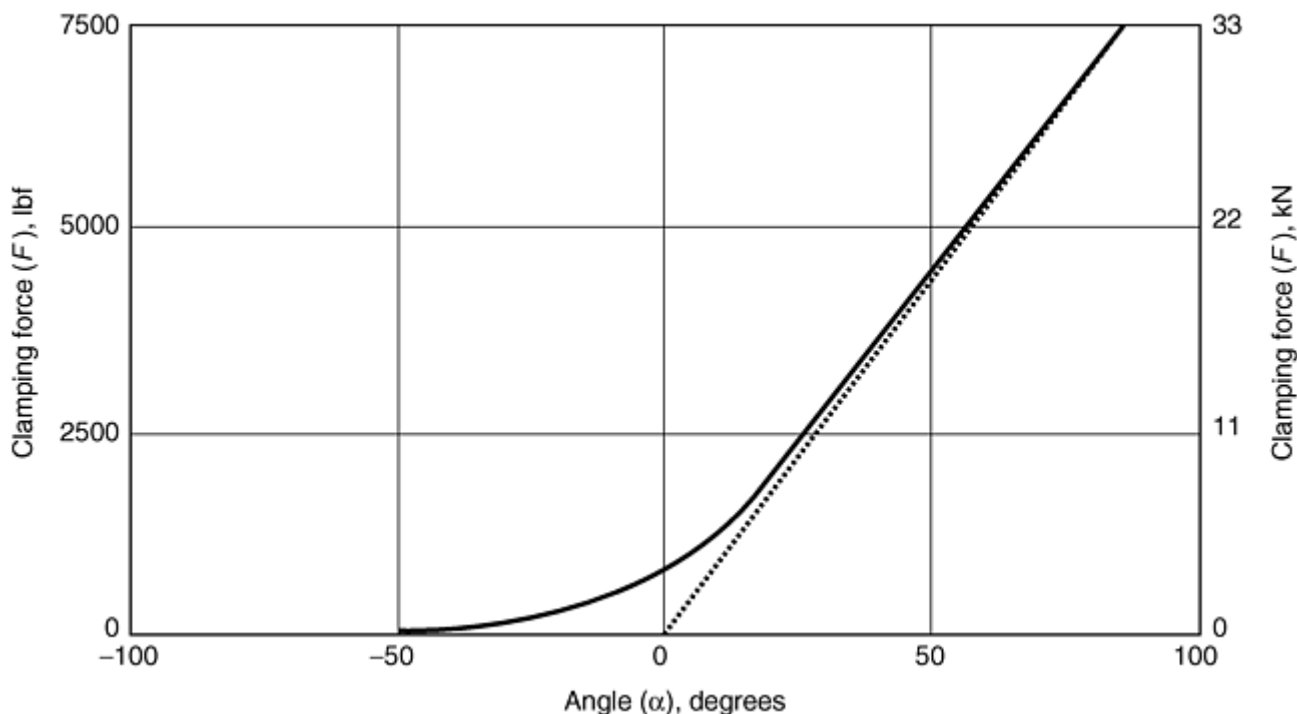


Fig. 47 Clamp force vs. angle diagram corresponding to the torque-angle diagram in Fig. 46

Breakaway Analysis. The next signature is the breakaway torque audit (Fig. 48) on the bolted joint tightened for the example shown in Fig. 43 44 45. Breakaway hand-torque audits are often used in an attempt to correlate the dynamic installation torque with the measured breakaway point. In this example, the fastener was torqued in the tightening direction until an additional angle of turn of approximately 12 to 13° was attained. Note that the head of the fastener started to move at approximately $74.5 \text{ N} \cdot \text{m}$ ($55 \text{ lbf} \cdot \text{ft}$). The actual breakaway point and

continuation of the tightening process occurred at approximately 88 N · m (65 lbf · ft) of applied torque. These observations confirm the installation torque of 81 N · m (60 lbf · ft) as is normally done for a breakaway torque audit.

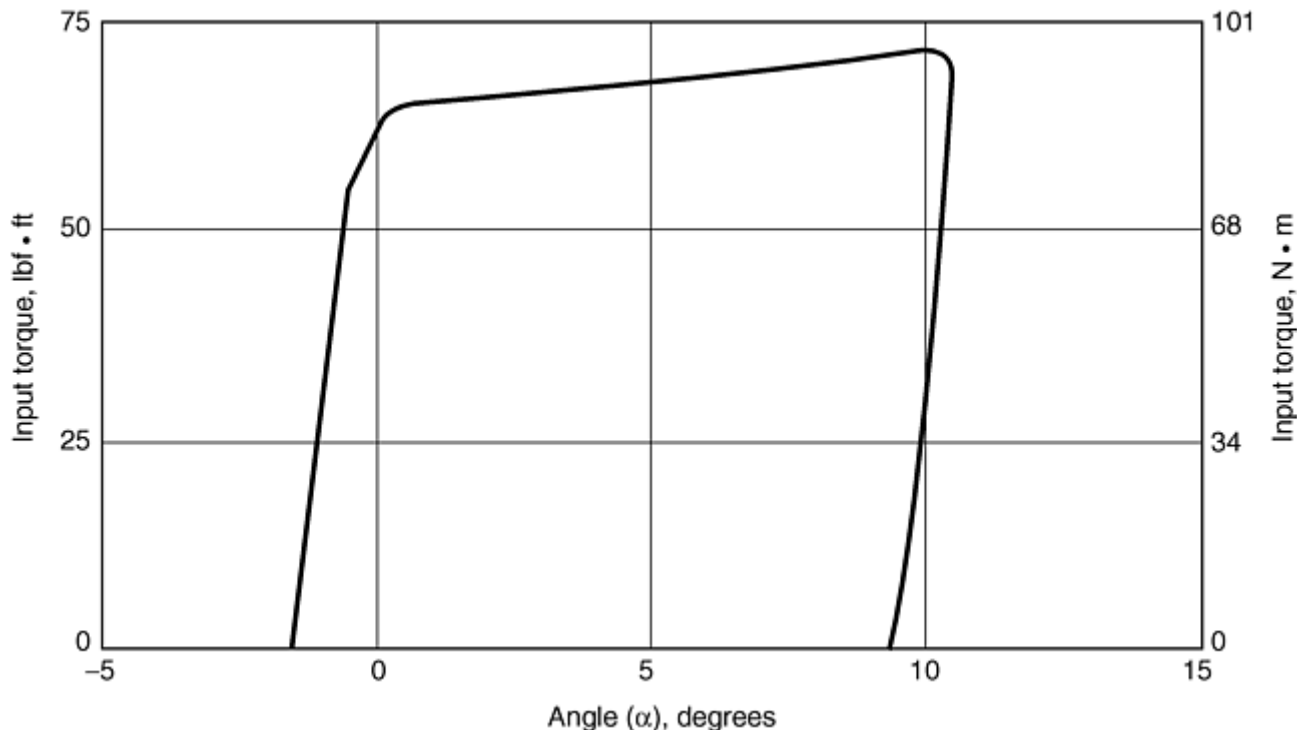


Fig. 48 Breakaway torque audit on the bolted joint tightened for the example shown in Fig. 43 44 45

The signature analysis diagram shown in Fig. 49 is one of the most significant analysis tools developed in the past 10 years. This diagram shows how it is possible to audit both the installation torque and correlate the signature of the audit curve directly with fastener tension. The projection of the tangent to the torque-angle signature curve that locates the elastic origin is the key to significant improvement of the hand-torque audit process. The torque-angle diagram for this audit signature clearly shows the torque breakaway point related to the installation torque, as well as the 85° initial tightening angle, which correlates with a preload of 33.4 kN (7500 lbf) clamping force. Note that the breakaway audit increased the tightening angle to approximately 95 to 100° projected from the elastic origin, with an expected proportionate increase in preload.

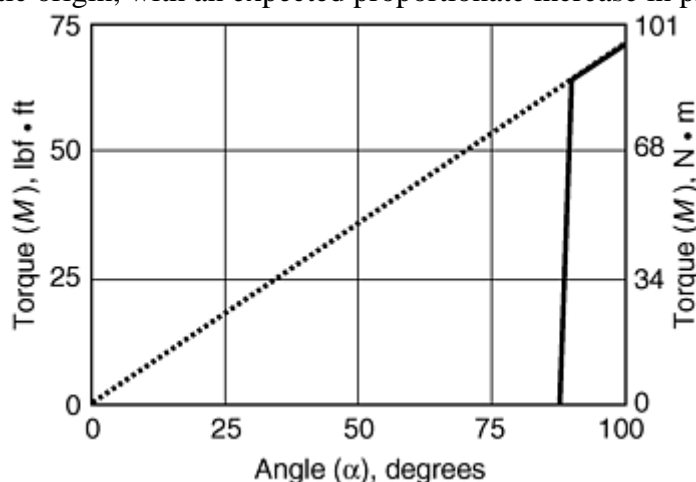


Fig. 49 Breakaway torque audit showing the torque breakaway point related to the installation torque

Release-Angle Audit. If the torque-angle signature is recorded when a fastener is loosened, as shown in Fig. 50, the resulting release-angle graph can be used to determine the elastic tightening angle and, thus, directly estimate the approximate fastener tension that was released, provided the tension-angle slope for the joint has been established.

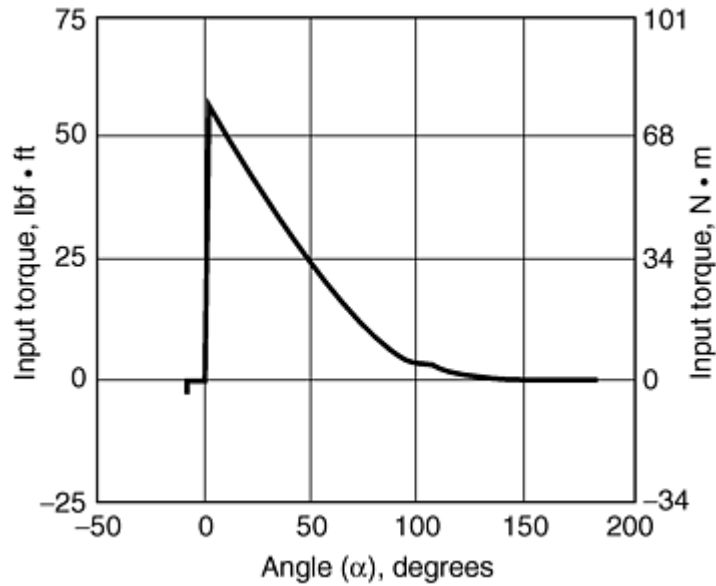


Fig. 50 Release angle signature

Torque-angle plots and release-angle plots can be used to directly estimate bolt tension, or preload, which is the ultimate goal of the fastener-tightening process. The release angle of approximately 95° in the example shown in Fig. 50 confirms the tightening angle measured on the torque-angle diagram for the hand-torque audit. Clearly, the release-angle method of audit provides a direct measure of the capability of a given tool to develop tension in the tightened fastener.

Frictional Analysis Audits. To provide an example of how audit techniques can be used to the effect of differences in frictional characteristics, the fastener type used in the previous examples (Fig. 43, 44, 45, 46, 47, and 48) was stripped of all thread and underhead lubricants to create higher friction coefficients in the thread and underhead regions. The torque-angle diagram for tightening to $81 \text{ N} \cdot \text{m}$ ($60 \text{ lbf} \cdot \text{ft}$), shown in Fig. 51, indicates a tightening angle of only 25° projected from the elastic origin. Compared with the lubricated fastener, where the tightening angle was 85° , the predicted preload of 9786 N (2200 lbf) was confirmed by the clamp-force measurement. The breakaway audit for the dry-tightened fastener (Fig. 52), confirms that the installation torque was approximately $81 \text{ N} \cdot \text{m}$ ($60 \text{ lbf} \cdot \text{ft}$) and also reveals the expected very low angle of turn from the elastic origin.

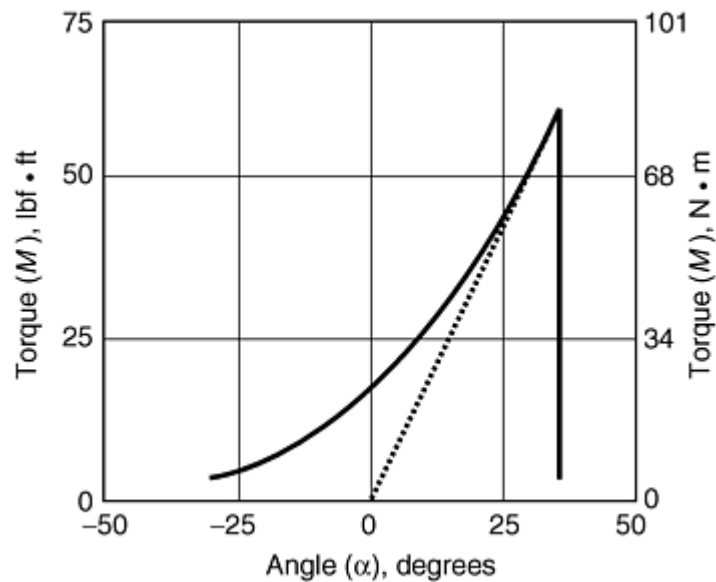


Fig. 51 Torque-angle diagram for a fastener stripped of all thread and underhead lubricants, tightened dry

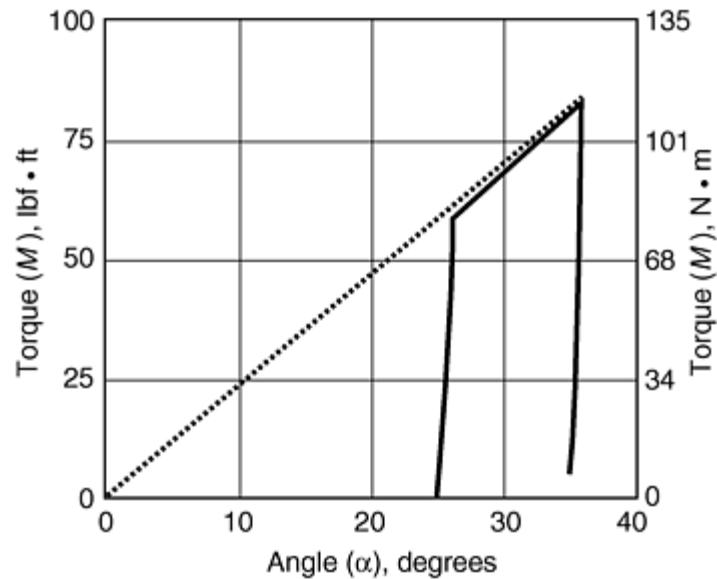


Fig. 52 Breakaway torque-angle audit for the dry-tightened fastener

Application of Torque-Angle Signature Analysis

The torque-angle signature method of analysis applied to tightening and loosening curves is plain, simple, and straightforward. It is a basic engineering analysis technique using fundamental stress, deflection, and material strength properties to model and measure the bolted-joint tightening process. Torque angle signatures can be analyzed to determine installation torque, thread strip, underhead embedment, bolt yield, and most importantly, fastener tension. While there are many factors that can alter the tightness of a given bolted joint, the torque-angle signature analysis method provides a practical method for direct verification of clamp force to assure a quality fastener assembly. The technique can be applied to fasteners of all sizes and all grip lengths.

The release-angle signature, when compared to the installation-torque angle, can be used to evaluate the clamp load retained after a dynamic test. Material creep and embedment phenomena, which lead to loss of preload, are readily analyzed and quantitatively evaluated through the use of release-angle analysis methods. The results of release-angle audits, being directly related to the achieved tension, are significantly more meaningful than the torque magnitudes obtained from breakaway torque audits. An improved version of the breakaway torque audit, which uses the torque-angle signature of the audit, can be used to directly estimate fastener tension. This analysis process correlates precisely with the release-angle-signature method. The only limitation is that the breakaway audit must be conducted in the elastic tightening region for the bolted joint where bolt yield or thread strip are not present.

Measurement Accuracy

It is important that all standards for fasteners be reviewed in regard to the specification for measurement accuracy. The specification of measurement accuracy for torque and clamp force should be in compliance with the ISO 25 methods used by the American Association for Laboratory Accreditation (A2LA) in the certification of laboratories. Both torque and clamp-force measurement specifications should refer to accuracy at the point of measurement. It is desirable to certify the accuracy and uncertainty of dynamic measurements at the real-time testing speeds (i.e., rpm) that are required by each test specification.

The following paragraphs of this section illustrate some examples of the accuracy specifications found in current standards that need to be reviewed and perhaps changed or revised. It is hoped that future revised editions of existing standards and all new standards will give proper attention to understanding the science of measurements and the capability of current state-of-the-art measurement equipment. From a practical point of view, it is also important to consider the true need of accuracy so that unnecessarily tight tolerances are not specified. This is especially true where broader tolerances that are capable of properly meeting the desired end result can be demonstrated as sufficient to qualify the measurement with regard to its intended purpose.

Defining the Measurement

All measurements are comparisons to standards, and practically no measurement is without a degree of uncertainty. To be valid, a measurement must have an unbroken chain of traceability to well-defined, established primary standards. Each step of the traceability chain introduces additional uncertainty, which has a cumulative effect on the accuracy and uncertainty of the final measurement.

It should be recognized that the accuracy of a measurement cannot be any better than the resolution of the measurement system. For most practical purposes, the measurement system resolution is defined as the smallest increment displayed on the measurement dial, such as the scale on a torque wrench or the pressure read on a hydraulic load-indicating gage. In digital electronic measurement systems, the smallest increment for the analog-to-digital (A/D) converter establishes the basic measurement resolution.

U.S. Standards

The American Society of Mechanical Engineers (ASME), the Society of Automotive Engineers (SAE), ASTM, the American National Standards Institute (ANSI), and the Industrial Fasteners Institute (IFI) all have established fastener standards in the United States. However, to meet the needs of a global economy where products manufactured in the United States can be marketed worldwide, it is important to recognize that a large amount of effort may be necessary to align U.S. testing standards with the international marketplace.

Significant progress has been made in the conversion of U.S. manufacturing to the metric (*Système International d'Unites*) (SI) system. Recognizing the United States' continued slow progress in this matter, the European commission has recently delayed the mandatory metric-only labeling requirement from 31 Dec 1999 to the year 2010.

International Standards

The European Committee for Standardization (CEN) centralizes the establishment of standards for the European Union (EU) member nations. By coordinating U.S. testing standards with those approved by CEN, it will then be possible to avoid or at least minimize any costly duplicate testing on products intended for sale to customers in EU member countries.

One area in which the United States needs to address serious deficiencies is in its method of definition of accuracy with regard to the test measurement procedures specified by U.S. standards. A number of U.S.

standards contain specifications that are obsolete, impractical, or not precise enough to be acceptable when subjected to the qualifying analysis applied to European testing methods.

For a number of years, many U.S. companies have been striving to become world class manufacturers with certification to ISO 9002. Fastener testing that meets the requirements of ISO/International Electrotechnical Commission (IEC) 25, titled “General Requirements for the Technical Competence of Calibration and Testing Laboratories,” would qualify to meet the requirements of ISO 9002. Failure to specify accuracy and uncertainty of measurements in a manner consistent with ISO 25 requirements will very likely make testing unacceptable for product sales to the European community.

Definitions of Accuracy

Accuracy can be defined only in terms of the entire measuring system and the environment, pertaining to both the instrumentation and the physical nature of the phenomena to be measured. Measurement accuracy is dependent on the capability of the measuring system to dynamically track the signal (frequency response) and provide sufficient resolution to permit comparison to be made between readings. Because a measurement reading is always an approximation of the true value, the uncertainty quantifies the limits of accuracy that can be expected. In the example illustrated in Fig. 53, the stated accuracy is 1% of the reading.

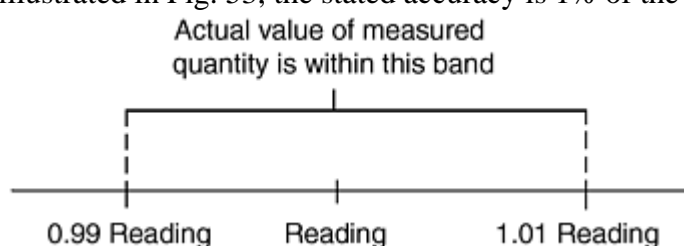


Fig. 53 Range of accuracy

Measurement Error

There are two general components of measurement error, bias and random. Bias is a constant value, such as a zero offset of a transducer or measuring amplifier, or a digital reference point. The random component is a complex function of system noise or the least-bit resolution in digital systems (Fig. 54).

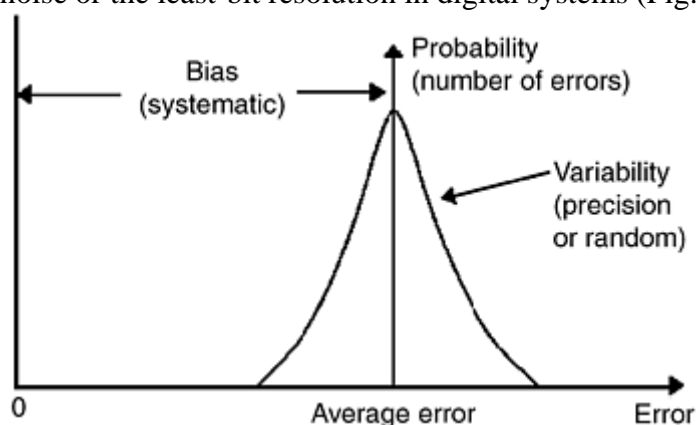


Fig. 54 Nature-of-measurement error

Frequency response effects where the phenomena measured may occur dynamically in a region beyond the flat response of the measurement system are not random errors. Such errors are the result of poor measurement system performance resulting from improper understanding of the engineering physics of the process being measured.

Measurement Error Observations. Measurement errors of a random nature typically have a normal distribution as shown in Fig. 55. To evaluate a measurement system, it is necessary to input constant known values and determine the scatter in the measurements over a number of samples. Statistics, such as sample standard

deviation, can be used to quantify the probability function for the readings that define the uncertainty for the test conditions simulated.

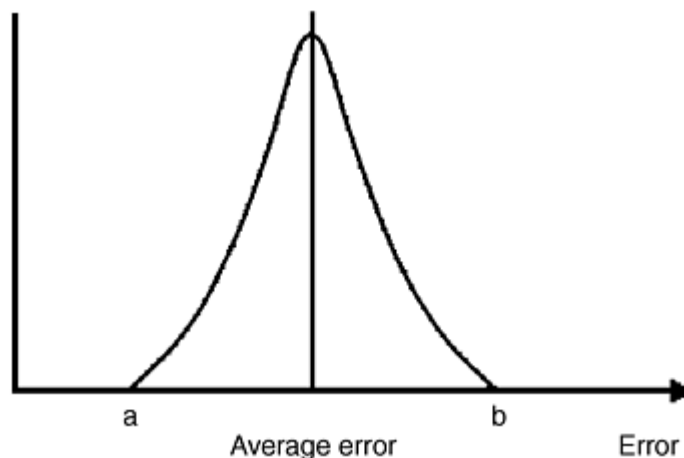


Fig. 55 Measurement error observations

Allowable Uncertainty Versus Percent Full-Scale Reading

A number of currently used standards specify the accuracy of readings in terms of “percent full scale.” As shown in Fig. 56, the 2% full-scale accuracy specification results in a 4% error at a point of reading taken at 50% of the full scale of the measuring device range (in this case, a force transducer). Similarly, the error would extrapolate to 8% of the reading at 25% of measurement-transducer range. In an attempt to limit the error in measurement, this standard stipulates that “transducers cannot be used below 50% of their full-scale range.” If this stipulation is followed closely for locknut testing, the tester would need to use one set of transducers to obtain prevailing on-torque and clamp-load values, then stop the test and use a higher capacity set of sensors to obtain the torque at clamp load. This process would be followed by a return to the lower-range sensor to obtain the prevailing off-torque data to complete the test. This situation is impractical at the least and impossible in most cases. Fortunately, with properly calibrated and qualified modern testing systems and specifications based on accuracy at the point of measurement, the complicated process described is rendered totally unnecessary.

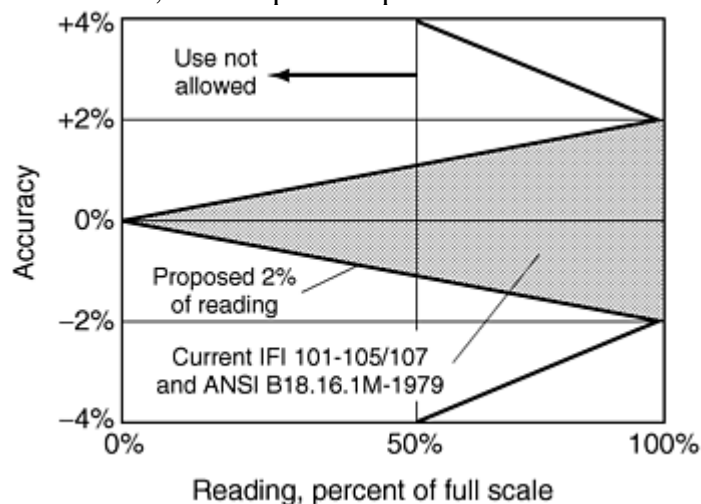


Fig. 56 Allowable uncertainty

It is far more practical and consistent with modern testing procedures according to ISO 25 that accuracy be specified at the point of measurement. In this example, it would be proposed that the accuracy specification be changed to “within 2% of reading.” Taking a modern approach in revising this standard, the totally impractical and unnecessary limitation on the use of the transducer below 50% of its full-scale range would be eliminated. There are a number of test procedures where accuracy specifications can be adjusted to different values at various points within the test, thus permitting a valid comparison of samples while using a single transducer over a broad measurement range. One possible example would be testing of prevailing torque locknuts where

the accuracy of torque measured for achieving clamp load could be 2% of the reading ($50 \text{ N} \cdot \text{m}$) and a fifth off-torque accuracy of 5% ($1.1 \text{ N} \cdot \text{m}$). In this case, testing could be done with a single transducer for all torque measurements.

Frequency Response Analysis

All test specifications should call for accuracy of measurements at the speeds at which the test is run rather than contain statements that specify reading rates or 3 dB points on filters, which can introduce errors as high as 30%.

A typical example is shown in Fig. 57, where a 30° hard joint is used to evaluate fastening tools according to ISO 5393. With a 100 rpm tool and the filter specified in the standard, an error of about 30% would be expected because the filter will have reduced the measured signal at least 30% for equivalent waveforms above 500 Hz. To properly capture the peak torque for a 1000 rpm tool, the system needs to be flat to 500 Hz, not down 3 dB in response at 500 Hz.

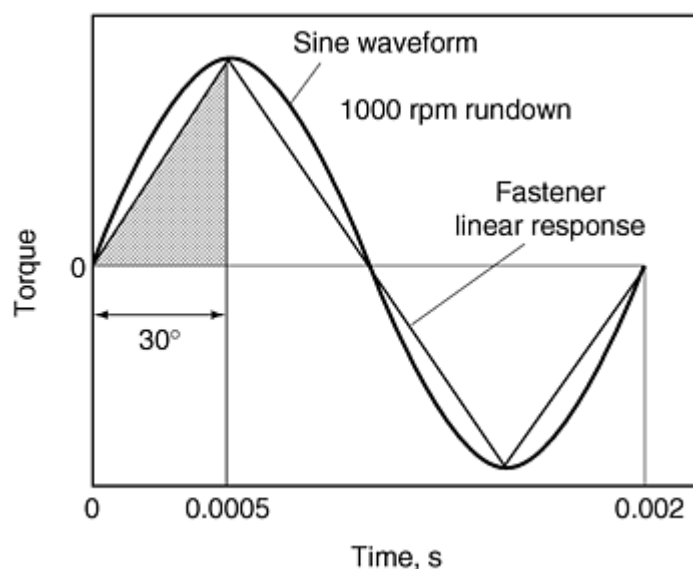


Fig. 57 Frequency response analysis

In this case, the intent of the standard was to minimize errors due to electrical noise and perhaps due to a perception that higher-frequency components did not contribute to the tightening process. The 3 dB point specified at 500 Hz in the standard clearly places a limitation on the upper rpm for the testing of tools.

Measurement Resolution

The measurement resolution and accuracy for a test should be verified at the specified testing speed. The example shown in Fig. 58 illustrates several important features verifying measurement capability. In the following test, two torque transducers in series are driving an M12 prevailing nut at 100 rpm. The initial position of the nut is such that the nylon patch is not engaged. The transducers have full-scale ranges of 68 and $9 \text{ N} \cdot \text{m}$.

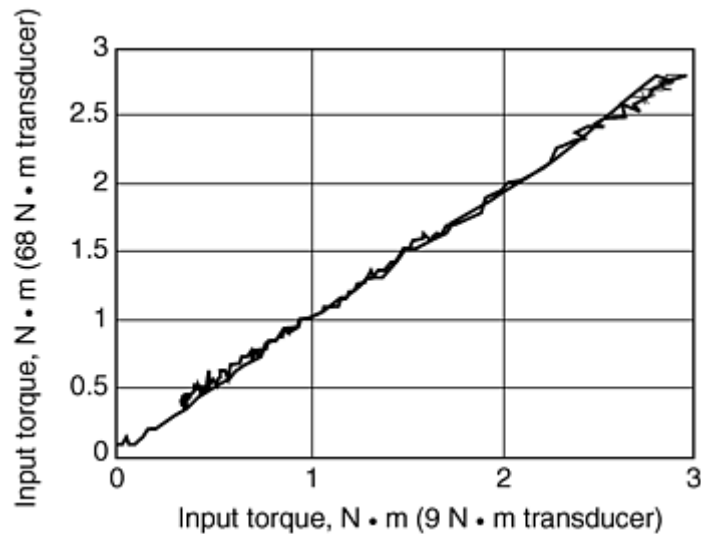


Fig. 58 Measurement resolution using transducers with full-scale ranges of 68 and 9 N · m

The maximum applied torque is slightly less than 3 N · m, or about 2%, of full scale on the larger capacity unit and 30% of full scale on the smaller-capacity unit. It is clear from the recorded data plot that at 100 rpm, the transducers are reading precisely the same torque values.

This test verifies that the measurement system is capable of simultaneously capturing readings at the 100 rpm test speed. It also illustrates the possibility of the use of the high-capacity torque sensor to make valid measurements in the range of 2% of full-scale capacity when used with this measuring system.

ISO 9000 Registration Versus Laboratory Accreditation

There are significant differences between laboratory accreditation using ISO 25 and quality system registration. The key difference can be summarized in that the essence of ISO 25 is to ensure the validity of test data, whereas technical credibility is not addressed in ISO 9000.

ISO 9000 and QS 9000 registrations require that procedures are in place, well documented, and followed. ISO 25 goes further in that it requires the science of the laboratory measurements be understood and that the tester is capable of demonstrating that valid measurements are the product of his or her testing procedures.

All testing procedures should be evaluated to account for certain basic considerations. American testing standards for fasteners may not receive international recognition unless they can be shown to meet the basic requirements of ISO 25. The most important questions to answer when reviewing standards are the following:

- Will the procedure produce accurate results?
- How have the procedures been validated to ensure accuracy?
- Does the tester understand the science behind the test procedures?
- Are the limitations of the procedures known?

The science of measurement engineering is a critical area of technology needed to properly qualify both the specifications and the measurement systems used to verify the quality of threaded fasteners. The pure acquisition of data for its own sake is one of the greatest technical crimes of this era. All measurements must reflect a technical knowledge of the testing process, as well as a full understanding of the capability and limitations of the measuring system.

Reference

1. “Standard Test Methods for Determining the Mechanical Properties of Externally and Internally Threaded Fasteners, Washers, and Rivets (Metric),” F 606M, *Annual Book of ASTM Standards*, ASTM

Mechanical Testing of Threaded Fasteners and Bolted Joints

Ralph S. Shoberg, RS Technologies, Ltd.

Selected References

Fastener Design and Application Engineering

- J.H. Bickford, *An Introduction to the Design and Behavior of Bolted Joints*, 3rd ed., Marcel Dekker, Inc., New York, 1995
- A. Blake, *Design of Mechanical Joints*, Marcel Dekker, Inc., New York, 1985
- A. Blake, *What Every Engineer Should Know about Threaded Fasteners: Materials and Design*, Marcel Dekker, Inc., New York, 1986
- V. Moring Faires, *Design of Machine Elements*, 3rd ed., The Macmillan Co., 1955
- P.G. Forrest, *Fatigue of Metals*, Pergamon Press, Addison-Wesley Publishing Co., Inc., 1962
- *Fastener Standards*, 5th ed., Industrial Fasteners Institute, Cleveland, OH, 1970
- *Metric Fastener Standards*, 2nd ed., Industrial Fasteners Institute, Cleveland, OH, 1983
- R.C. Juvinall, *Engineering Consideration of Stress, Strain, and Strength*, McGraw-Hill Book Co., 1967
- R.C. Juvinall and K.M. Marshek, *Fundamentals of Machine Component Design*, 3rd ed., John Wiley & Sons, 1999
- G.L. Kulak, J.W. Fisher, and J.H.A. Struik, *Guide to Design Criteria for Bolted and Riveted Joints*, 2nd ed., John Wiley & Sons, 1987
- J.E. Shigley, *Mechanical Engineering Design*, 5th ed., McGraw-Hill Book Co., 1989
- R.S. Shoberg, Torque-Angle Signature Analysis, *Fastener Technology International*, Vol 19 (No. 1), 1996
- R.S. Shoberg, Engineering Fundamentals of Torque-Turn Tightening, *Fastening Technology 1996*, March 1996 (Cleveland, OH), Clemson University College of Engineering & Science, 1996
- R.S. Shoberg, Analyzing Torque-Angle Signatures For Reliable Bolted Joints, *Assembly Technology Expo '96* (Chicago, IL), Sept 1996
- R.S. Shoberg, Coordination of Bolted Joint Design and Test Methods, *Fastening Design & Application Engineering Conference* (Novi, MI), Oct 1996

Fastener Testing

- “Metric Screw Threads—M Profile,” B1.13M-1995, American Society of Mechanical Engineers
- “Standard Test Methods for Determining the Mechanical Properties of Externally and Internally Threaded Fasteners, Washers, and Rivets,” F 606, *Annual Book of ASTM Standards*, ASTM
- *Determination of Coefficient of Friction of Bolt/Nut Assemblies under Specified Conditions*, DIN 946, *Deutsches Institut für Normung e.V.*, Berlin, Germany, 1990
- “Steel Metric Threaded Fasteners Torque/Clamping Force Performance,” Ford WZ100, Ford Motor Co., 1993
- “Torque Tension Test,” GM 9064P, General Motors Corp., 1998
- IFI 101, 100/107, and 543 standards (drafts), Industrial Fastener Institute, Cleveland, OH
- “Torque-Tension Test Procedure for Steel Threaded Fasteners—Inch Series,” SAE J 174, Society of Automotive Engineers, 1996

- “Systematic Calculation of High Duty Bolted Joints, Part I,” VDI 2230, Translation of the German Edition 7/1986, C. Junker and J. Newnham, SPS Laboratories, Naas, Ireland, 1988

Measurement Accuracy

- “Rotary Tools for Threaded Fasteners—Performance Test Method,” ISO 5393, 2nd ed., 1994-0501, Ref No. ISO 5393:1994(E), International Organization for Standardization
- “Guidelines for Evaluating and Expressing the Uncertainty of NIST Measurement Results,” NIST Technical Note 1297, 1994
- F.R. Schraff, Defining Data Accuracy, *Sensors*, Vol 15 (No. 6), 1998
- R.S. Shoberg, “Special Report: Measurement Resolution for Locknut Testing,” RS Technologies, Ltd., April 1994
- P.K. Stein, *Measurement Engineering*, Vol 1, Stein Engineering Services, Inc., 1962
- J.L. Taylor, *Measurement Uncertainty: A Basis for Assessing and Improving the Quality of Measurement Processes*, Sverdrup Technology, May 1998
- P.S. Unger, *ISO/IEC Guide 25 Versus ISO 9000 for Laboratories*, American Association for Laboratory Accreditation, 1995
- “Test for Evaluating the Torque-Tension Relationship of Both Externally and Internally Metric Threaded Fasteners,” USCAR Fastener Strategic Standards Technical Committee, draft, May 1998
- C.P. Wright, *Applied Measurement Engineering*, Prentice Hall, 1995

Testing of Adhesive Joints

K.L. DeVries and Paul Borgmeier, University of Utah

Introduction

MOST ENGINEERING DESIGNS require the connecting or joining of component parts. Means available to accomplish these goals can be broadly classified as mechanical connections, welding, and adhesives. Mechanical connections such as bolts, pins, and rivets have the advantages of being easy to install, they can be inspected often, and they can be repaired or replaced. On the other hand, such connections require making holes in the component members, which act as stress risers (with typical stress concentration factors of 3 or greater). Structures that experience dynamic loading, such as airframes, often fail from fatigue cracks originating at their stress concentrations. The heads of connections such as nuts and bolts can affect aesthetics, streamlining, and other parameters. Another type of mechanical connection that is becoming increasingly popular is the “snap” connector. These connections are wedge-like tabs and grooves that, when forced together, snap into place to hold containers or housings together. Snap connectors greatly facilitate assembly but have limited strength, are easily damaged in assembly (or even more likely during disassembly), and may deteriorate with time and wear. In welding, the joining segments of the component parts are locally melted, brought together, and fused (additional material may be supplied from a welding rod). Welded joints have the advantage of being relatively continuous, resulting in high strength. They have the disadvantage of requiring a relatively expensive process. The required heating can damage other parts of the structure or its contents. Not all combinations of materials can be welded. Most metals and plastics can be welded only to themselves or to a limited number of other similar materials. Some materials do not lend themselves to welding at all.

Adhesive joints involve joining parts by bonding component parts together with an adhesive. In some plastic applications, one of the parts may act as the adhesive, and in some cases, a solvent may be used to dissolve/soften the materials, which are then bonded by diffusion of the polymer chains into the respective parts, forming essentially one material. Examples of this type of bonding include the solvent bonding of polyvinyl chloride (PVC) pipe and acrylic materials. Very dissimilar materials can, in principle, be joined by

adhesives, for example, wood to plastic, metal to ceramics, and aluminum to steel. Likewise, it appears that the “load” could be distributed over a larger area compared with joining materials with, for example, bolts. This aspect can be even further enhanced by appropriate design as, for example, in the familiar finger-scarf joint used to increase the length of lumber. This type of joint design accomplishes several beneficial goals: it increases the bonded area, changes what for a butt joint would be largely tensile stresses to more shear stress, and produces a smooth, attractive (almost invisible) joint.

Along with their advantages, adhesive joints pose their own design problems. Prediction of load-carrying capacity is often neither straightforward nor reliable. Adhesive joints also have problems with inspection because the bonded surfaces are usually not visible after assembly. Stresses in an adhesive joint are generally not uniformly distributed on the bonded surfaces, and in fact, elastic stress analysis often exhibits singularities analogous to the stress risers associated with the other methods of joining already mentioned. Because adhesive joints usually involve very dissimilar materials in the adherends and adhesives, cure stresses, thermostresses, deformation mismatches, and so on may cause problems.

Despite these drawbacks, the advantages and positive features of adhesive joints are so attractive that the use of adhesives has enjoyed phenomenal growth over the last 50 years. One compilation of adhesives lists more than 5000 different commercial adhesives available to the U.S. designer (Ref 1). Adhesive selection, testing, use in design, and application is a very complex subject covered in a variety of large reference books (for example, Ref 2, 3, 4, 5, 6 and *Adhesives and Sealants*, Volume 3 of the *Engineered Materials Handbook* published by ASM International) and literally thousands of journal articles; dedicated journals include the *Journal of Adhesion* and the *International Journal of Adhesion Science and Technology*. Articles on adhesives and adhesion also appear in journals or publications of the following organizations: American Society for Testing and Materials, Society for Experimental Mechanics, American Society of Mechanical Engineers, Materials Research Society, and many others. The Society for Adhesion, the Gordon Research Conferences, and the American Chemical Society hold annual or periodic conferences dedicated to the subject of adhesives. Despite this extensive research and study, there is still much to be done, and adhesive joint design is still as much art as it is science.

Brazing and soldering are methods of joining that have similarities to adhesives and welding. These methods might be viewed as falling between welding and adhesive bonding. Brazing is closer to welding in that, while it uses a different material for “bonding” the “adherends,” its application typically involves extensive heating and perhaps some interpenetration of the brazing and host materials. The material used for brazing is melted in a puddle, in which there may be some alloying with the host material(s) on fusion. In soldering, on the other hand, usually only the solder material melts, and if it wets the host material(s), it attaches by adhering to the joined pieces. It might be viewed as a metallic form of hot-melt adhesive.

Adhesive science and technology remains an important area of active research. New adhesives continue to be developed, and work continues on the understanding of stresses; methods of analyzing stresses, strains, displacement, and load-carrying capacity; improved experimental techniques; and so on.

References cited in this section

1. *Adhesives*, Edition 6, D.A.T.A. Digest International Plastics Selector, 1991
2. R.L. Patrick, Ed., *Treatise on Adhesion and Adhesives*, Vol 1–6, Marcel Dekker, 1966–1988
3. G.P. Anderson, S.J. Bennett, and K.L. DeVries, *Analysis and Testing of Adhesive Bonds*, Academic Press, 1977
4. A.J. Kinlock, *Adhesion and Adhesives*, Chapman and Hall, 1987
5. A. Pizzi and K.L. Mittal, Ed., *Handbook of Adhesive Technology*, Marcel Dekker, 1994
6. K.L. Mittal, *Adhesive Joints*, Plenum Press, 1984

Purpose of Testing Adhesive Joints

In no area of materials is testing more important than it is for adhesives. In the United States, the largest organization devoted to standardizing test procedures is the American Society for Testing and Materials (ASTM). ASTM and its counterparts in other countries work through the International Organization of Standardization (ISO) in an effort to coordinate testing on an international scale. All these activities are very important and time consuming, entailing countless hours of volunteer efforts in the United States alone. Other organizations, besides ASTM, have established testing procedures that relate to the testing of adhesive joints. Such organizations include the military (MIL specs), other professional societies, such as the Society of Automotive Engineers (SAE), the American Society of Mechanical Engineers (ASME), and industrial organizations.

Many examples of the wide variety of standardized tests for adhesives can be found in the *Annual Book of ASTM Standards*, Volume 15.06, which is updated and republished annually (Ref 7). Except where specifically noted, the standards and practices listed in this treatise can be found in this volume. There are also many other less formalized tests used by various organizations and a few specialized tests for adhesives found in other ASTM volumes. ASTM practices, specifications, and test methods cover a wide variety of topics ranging from measurements of shelf life and pot life through resistance to mold or insect attack to determination of viscosity and various aspects of strength. This article concentrates on tests and methods used in the measurement of adhesive joint strength. A logical question in the discussion relative to the selection of the specific adhesive might be “How strong is it compared with the other available adhesives?” The answer to such a query is neither as simple nor as straight-forward as might be assumed. The reasons for this complexity are addressed in this article.

Testing of adhesive joint strength might be conducted for a number of reasons, including the following:

- *Quality control*: To ensure that changes such as adhesive age, mix method, and surface preparation that will affect bond quality have not been introduced
- *Comparative analyses*: To determine which of a series of adhesives, primers, surface preparations, cure methods, and so on is best suited for a given bond application
- *Generation of engineering design data*: To predict the load-carrying capability of a given bonded joint

The geometry of the test specimen selected is very important even for quality control tests. In fact, an adhesive that exhibits “high strength” in a tensile test may have poor peel strength and vice versa. In fact, many variables may affect bond strength. Each variable may affect the bond strength in a different manner, and the manner in which the bond strength is affected may be different for each test geometry. The amount of adhesive used in a mixing batch and the delay time between mixing and casting will likely affect strength and may affect peel strength differently than it affects tensile strength. As another example, bond thickness often affects lap shear strength in a different way than it affects tensile button strength. If a series of lap shear joint test are completed for various adhesive thickness is optimum for a given joint unless the geometry, adhesive, and loading are nearly identical to those of the lap shear joints tested. Thus, even for comparative analyses, a great deal of care must be used in applying laboratory test data to joints whose geometries differ in even subtle ways from that of the laboratory test specimens.

There are many standard adhesive tests available to the engineer for determining the strength of adhesive joints. In the example just discussed, reference was made to tensile and peel specimens. Indeed, most standard tests for adhesive joints fall within three general categories, namely, peel tests, lap shear tests, and tensile tests. It is important to recognize, however, that the stresses at the tip of the debond region are not necessarily of the character implied by the name. In fact, the stresses are usually of mixed character. For example, as discussed in the section “Lap Shear Tests”, the stress in the critical region of the so-called lap shear specimens are apt to be more crack opening (tensile) in nature than shear.

One purpose for obtaining adhesive joint engineering data is in an effort to ensure that a bonded joint will withstand the loads for which it was designed. This might be accomplished by “proof testing” every joint, that is, by loading every joint manufactured to its design load. However, this approach has its problems. First, such procedures are apt to be very costly. Furthermore, the joint may withstand such loading but be damaged by the loading such that it subsequently fails when subjected to aging, creep, and fatigue loading or the environment. In addition, when a joint is in place in a structure, it is often difficult to apply the actual or even a simulated load. The load may be prohibitively large and/or in an awkward location, making testing difficult, very expensive, or even impossible. There is also a danger that applying such proof loads might damage neighboring or adjoining parts of the structure.

For these reasons, an engineer is generally required to obtain data from laboratory size samples and use this data to infer the strength of a given “practical” joint. For many of the standard adhesive joint tests, the results are reported as the load at failure divided by bonded area. In one straightforward design approach, this stress is then compared with the average stress that exists in the joint being evaluated when its maximum load is applied. However, if the joint geometry, loading time, and other conditions are not identical to the laboratory test conditions, the direct comparison can lead to unsafe joint designs. This problem is discussed in subsequent sections (“Lap Shear Tests” and “Adhesive Fracture Mechanics Tests”).

Reference cited in this section

7. Adhesives, *Annual Book of ASTM Standards*, Vol 15.06, ASTM (updated annually)

Testing of Adhesive Joints

K.L. DeVries and Paul Borgmeier, University of Utah

Factors Influencing Mechanical Strength of Adhesive Joints

Before proceeding with a description of specific tests, a few general comments might be helpful. The strength of an adhesive joint should not be viewed as being essentially (or even largely) an inherent property of a given adhesive. Typically, strength depends on many factors. The nature of the adherends may have a dramatic effect on joint strength. A given adhesive may not even “adhere” to some potential substrates. Even where the inherent adhesion may be good, its quantitative value is typically highly dependent on proper cleaning, surface treatment, and details of curing. The presence of coupling agents and surface roughness can affect strength. Thickness of adhesive and adherends and other geometric factors also play strong roles in the strength of a joint. In short, it is safe to say that the strength of an adhesive joint is a system property that depends on many factors beyond the chemical and physical nature of the adhesive per se.

Some ASTM and other standards and practices address these other factors. For example, the following ASTM standards cover surface treatments for various materials:

- D 2093, “Standard Practice for Preparation of Surfaces of Plastics Prior to Adhesive Bonding”
- D 2651, “Standard Guide for Preparation of Metal Surfaces for Adhesive Bonding”
- D 2674, “Standard Test Method for Analysis of Sulfochromate Etch Solution Used in Surface Preparation of Aluminum”
- D 3933, “Standard Guide for Preparation of Aluminum Surfaces for Structural Adhesives Bonding (Phosphoric Acid Anodizing)”

Coupling agents such as silanes, titanates, zirconates, and chrominates are sometimes applied to the surface before application of the adhesive. The agents are also sometimes incorporated into the adhesive. In at least some cases, they are thought to form covalent bonds between the adhesive and the adherend surfaces (Ref 8).

As with most materials, aging can affect the properties of an adhesive and the strength of an adhesive joint. It is often not convenient (or possible) to simply wait to see how time and exposure to the elements might cause deterioration. Accelerated aging tests are an effort to infer from short-term tests, usually under very harsh conditions, how well materials might hold up under longer-term, more realistic service conditions. A comparison of how different adhesive joints in wood exposed to boiling water for several hours or days might, for example, be used to estimate their relative weatherability (ASTM D 3434, D 5572). While the comparisons might not be perfect, they are likely better than nothing. Several other standards that address accelerated testing of adhesives include ASTM D 1101, D 1183, D 2559, D 3632, and D 4502.

Reference cited in this section

8. E.P. Plueddemann, *Silane Coupling Agents*, Plenum Press, 1982

Testing of Adhesive Joints

K.L. DeVries and Paul Borgmeier, University of Utah

Qualitative Tests

Most “adhesive strength tests” are quantitative in nature. The test results are typically given as “average stress” at failure (tensile and lap joints) or force per unit width (peel tests). The preparation and testing of quantitative samples are expensive and time consuming. It would often be advantageous to have a means of making a qualitative determination of adherence to ascertain if the cost of conducting the quantitative tests would likely be justified. Such quick screening of candidate adhesive/adherend pairs might result in significant time and cost savings by eliminating unlikely candidates and assisting in selecting those worthy of further study.

The first effort along this line with which the authors are familiar is found in the patent literature (U.S. Patent 4,025,159, Cellular Retroreflective Sheeting). In this patent, Dr. J.M. McGrath of 3M Corporation explores means of increasing the bond strength between the cover sheet and the base sheet (polymer binder with embedded reflective glass spheres) in retroreflective sheeting. This sheeting is used in stop signs and other reflective signs. To accomplish this goal, McGrath proposes curing (cross linking or chain extension) the sheeting after the thermoforming operation. He points out that the proposed process does not work for all potential pairs of cover sheet and base materials. As an aid in selecting materials for further study, he suggests casting a small amount of candidate base materials on potential cover sheets and curing them in place. After curing, McGrath proposes a single-edged razor blade be used to lift, scrape, or otherwise separate the base material from the cover sheet. The relative effort required to facilitate this separation is assessed and used as guide in the selection of candidates for further study.

More recently, Committee D-14 of ASTM formalized and adopted ASTM D 3808 “Standard Test Method for Qualitative Determination of Adhesion of Adhesives to Substrates by Spot Adhesion.” The stated purpose of the document is to provide “a simple qualitative procedure for quickly screening whether an adhesive will, under recommended application conditions, bond to a given substrate without actually making bonded assemblies.” In this test method, spots of adhesive are placed onto a substrate using the application procedure and curing conditions acceptable to the user and supplier of the adhesive. To test adhesion, the document recommends the use of “a thin stainless steel spatula or similar probe” as a prying lever. It states “If the results are acceptable, then standard quantitative adhesive test procedures can be used to obtain quantitative measurement of the adhesive’s performance.” The authors believe such methods of preliminary screening are certainly worthy of consideration in many instances. They can often save time and testing costs.

Peel Tests

Peel tests are easy to visualize albeit their analysis and the interpretation of peel test results is neither so easy nor straightforward. When a strip of adhesive tape is placed partially on paper or on another substrate and then removed by pulling the free end (the portion of the tape that is not attached), in essence, a peel test is being conducted, as shown schematically in Fig. 1. Several quantitative observations might readily be made from such a test (it is important to note that the tape is a very flexible material). The force required to propagate the peel failure is a strong function of the angle at which the peel force is applied. If the angle is small (i.e., close to the direction of the substrate surface), large peel surfaces are required. As the angle increases to the point where the peel angle is 90° , perpendicular to the surface, the force is reduced significantly. As the angle is further increased, it reaches a limit at 180° (ASTM D 903 describes a 180° peel test for a “flexible” peel specimen). The force per unit width required to facilitate peel is called the peel force or the stripping strength. It can also be observed that the forces required to sustain peeling depend on the rate of peel. For tapes bonded with pressure-sensitive adhesives, very slow peel rates require relatively small peel forces, while at extremely high rates, the peel forces are much more substantial. It can also be noted in this simple peel test that the force required to initiate the peel may differ from that required to sustain the peel once it has started. It may also be observed that the force required to peel the tape from the substrate depends on the nature of the surface to which the tape is attached. For example, it may adhere very tightly to a clean glass surface but hardly at all to moist or oily glass.

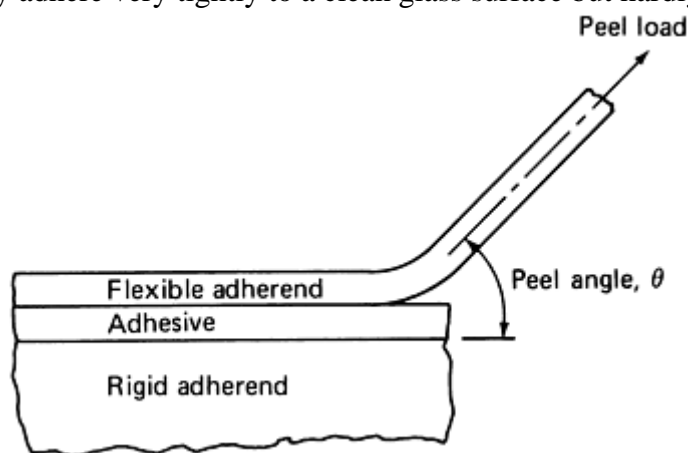


Fig. 1 Schematic of the peel test

ASTM has formalized a variety of different peel tests in its *Annual Book of ASTM Standards*, Volume 15.06. Several of the standard peel test geometries (described in detail in ASTM D 903, D 3167, and D 1876) are illustrated in Fig. 2 (Ref 7). ASTM D 1781 describes the climbing drum peel test, which is used to determine the peel resistance of adhesive bonds between a relatively flexible adherend and a rigid adherend.

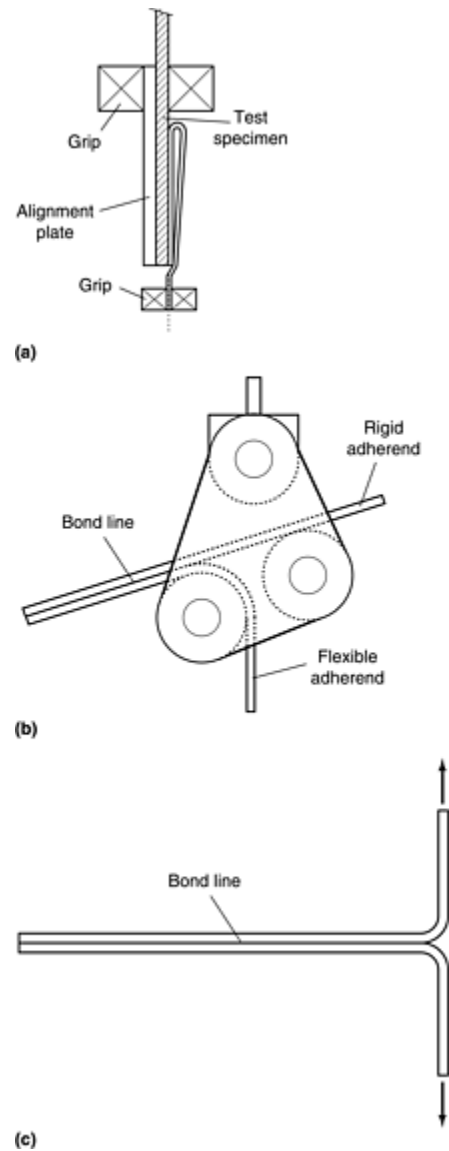


Fig. 2 Typical peel test specimens. (a) Stripping strength specimen (ASTM D 903). (b) Roller drum peel test specimen (ASTM D 3167). (c) T-peel test specimen (ASTM D 1876). Source: Ref 7

Several other peel tests are in common usage that have not been standardized by organizations such as ASTM. For example, the authors have found a test they have adopted from researchers at 3M Corporation to be very useful for measuring peel strength. This method makes use of a test jig incorporating a platform that uses rollers that allow the platform to move horizontally with extremely low friction. It is used to test the adhesion between two thin flexible sheets. For testing, one of the sheets is bonded to a thin aluminum sheet with a strong adhesive. A region of debond along the adhesive between the thin flexible sheets is initiated with a razor blade or by other means, leaving a loose tab. The aluminum sheet with the attached bilayer sheeting is inserted into slots on the jig platform, or otherwise held fixed to it. The jig is then attached to the lower crosshead of a universal-testing machine such that the platform is horizontal. The loose tab is then attached by a grip to the upper crosshead. During testing, motion between the two crossheads then peels the upper sheet from the lower. The peel angle is maintained at very nearly 90° as the platform moves horizontally (facilitated by the low friction rollers), keeping the peel region directly below the upper grip. In some cases where the adherence between the sheetings is high and the sheeting cohesive strength is relatively low, it has been helpful to reinforce the upper sheet by applying strapping tape that is gripped and peeled along with the upper sheet. It is important to note, however, that even though the peel failure may follow the same path, it would not be anticipated that the peel force would be the same as for the nonreinforced sheet. Adhesive joint strength is a “system property,” and the addition of another layer can modify the energy absorption during the peel process, thereby altering the associated peel forces. It is, therefore, important to compare the results from tests on reinforced materials with those of other materials that are similarly reinforced and vice versa.

All peel tests have the common characteristic that failure propagates from an initially debonded area. They also generally involve large displacements/deformations. For these and other reasons, linear elastic stress analysis is often not well suited to peel tests. The stresses and strains in the peel configuration are complex and seldom well understood. Test results are generally not given in terms of stress but rather as force per unit length required to peel the specimen. It is, therefore, generally difficult to compare the results from a peel test with those from other testing methods.

Because of the large deformations involved in peel tests, the analysis of such geometries is very difficult except under certain simplifying assumptions (Ref 3, 4, 6, 9, and 10). Some very interesting and informative observations can be made on the basis of simplifying assumptions and approximations. Indeed, considerable useful work has been completed using peel tests. The informative work of Gardon (Ref 10) and Kaelble (Ref 11) is noteworthy. The polymer research group at The University of Akron, under the direction of Professor A. Gent, has been particularly adroit in applying peel techniques and the concepts of fracture mechanics (see the section "Adhesive Fracture Mechanics Tests" in this article) to obtain critical information and insight into the behavior of adhesive joints (Ref 12, 13). The peel specimen is, in principle, a very versatile geometry for obtaining adhesive fracture energy because various combinations of mode I and mode II loadings can be applied by varying the peel angle (Ref 3). The stress analyses of Adams and Crocombe (Ref 14) have provided additional insight into the peeling mechanisms. They examined the stress distributions in peel specimens using elastic large-displacement, finite-element analysis techniques.

References cited in this section

3. G.P. Anderson, S.J. Bennett, and K.L. DeVries, *Analysis and Testing of Adhesive Bonds*, Academic Press, 1977
4. A.J. Kinlock, *Adhesion and Adhesives*, Chapman and Hall, 1987
6. K.L. Mittal, *Adhesive Joints*, Plenum Press, 1984
7. Adhesives, *Annual Book of ASTM Standards*, Vol 15.06, ASTM (updated annually)
9. G.P. Anderson and K.L. DeVries, Predicting Strength of Adhesive Joints from Test Results, *Int. J. Fract.*, Vol 39, 1989, p191–200
10. J.L. Gardon, Peel Adhesion, I. Some Phenomenological Aspects of the Test, *J. Appl. Polym. Sci.*, Vol 7, 1963, p 654
11. D.H. Kaelble, Theory and Analysis of Peel Adhesion: Mechanisms and Mechanics, *Trans. Soc. Rheol.*, Vol 3, 1959, p 161
12. A.N. Gent and G.R. Hamed, Peel Mechanics, *J. Adhes.*, Vol 7, 1975, p 91
13. A.N. Gent and G.R. Hamed, *J. Appl. Polym. Sci.*, Vol 21, 1977, p 2817
14. R.D. Adams and A. Crocombe, *J. Adhes.*, Vol 12, 1981, p 127

Testing of Adhesive Joints

K.L. DeVries and Paul Borgmeier, University of Utah

Lap Shear Tests

The most popular test geometry for testing adhesive joints is the lap shear specimen. Its appeal is probably based on the fact that it closely duplicates the geometry used in many practical joints. These lap joints are popular for several reasons:

- They facilitate use of larger contact areas than, for example, a butt joint.
- They are easier to make and align than butt joints.
- The adhesive is not exposed to “direct” tensile stresses. Direct tensile stresses are known to have deleterious effects on adhesives.

Typical lap shear test specimens for which ASTM standards have been written are presented in Fig. 3 (Ref 7). The specimens shown in this figure conform most closely to ASTM Standards D 1002, D 3163, D 3164, D 3165, and D 3528 for testing adhesives used to bond metals, plastics, and laminates. These represent only a small sampling of the more than two dozen standards in the *Annual Book of ASTM Standards*, Volume 15.06, that relate to shear testing. These other standards range from descriptions of block-type sample configurations for testing lumber and wood bonding in shear by compression loading, through descriptions of devices to simultaneously expose samples to lap shear stresses and extremes in temperature. Still others describe apparatus for exposing lap joints to sustained loads (using springs) to measure long-term creep or time to failure.

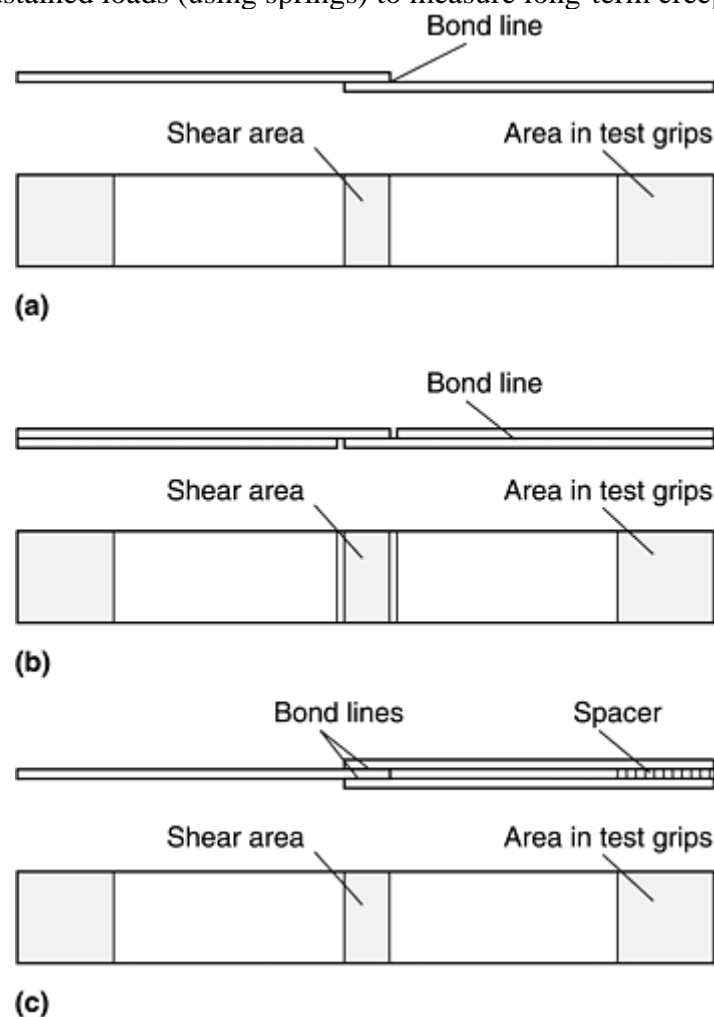


Fig. 3 Typical lap shear geometries. (a) ASTM D 1002, D 3163, and D 3164. (b) ASTM D 3165. (c) ASTM D 3528. Source: Ref 7

The results from lap shear tests are generally reported as the force at failure divided by the bonded area (overlap area). Such values are listed in a number of reference books and manufacturers' literature for a wide variety of adhesives. The reference book on types of adhesives (Ref 1) lists typical lap shear strength values for literally thousands of commercial adhesives. Such tables of “shear strength” values are without doubt of considerable utility for comparison and other purposes. However, their use also can lead to faulty expectations and

conceptions. Otherwise knowledgeable designers might logically assume from the tabulations that these average stress values could, in a straightforward manner, be used to design an adhesive joint.

For example, the tabulated shear stress value for a given adhesive from an ASTM D 1002 test might be given as 3000 psi. It might be assumed that this adhesive is to be used to bond two 25 mm (1 in.) wide by 3 mm (0.12 in.) thick 7075-T6 aluminum pieces together to carry a tensile load of 3200 lb with a safety factor of two. First, the designer must ascertain whether the aluminum pieces can carry such a load. Typically, 7075-T6 aluminum has a yield strength slightly in excess of 65 ksi for an allowable stress of 32.5 ksi. The pieces in question would have an allowable load of 4000 lb, which is more than the 3200 lb required in the design. The “straightforward” method to design the joint would be to assume that the allowable shear strength for the adhesive used in the joint would be $3000/2 = 1500$ psi, suggesting that an overlap of $3200/1500 = 2.13$ in. would be sufficient to support the load. This is, in fact, the approach taught by a variety of otherwise very good texts on material science and mechanical design. However, doubling the length of a lap joint almost never doubles its load-carrying capacity, and the increased joint strength is usually much less than doubled. The length of overlap recommended in ASTM D 1002 is 12.7 mm (0.50 in.). Typically, quadrupling the amount of overlap does not increase the load at failure by anywhere near a factor of four. For reasons given in the next few paragraphs, it is likely that it is not even the value of the maximum shear stress that determines the failure of the “lap shear joint.” As this article reveals, joint failure is more likely determined by the value of secondary induced cleavage stresses.

The stresses along the bond line of lap specimens are not constant. The bond stress distribution is highly dependent on the thickness of the adherends and the adhesive as well as the length of overlap. As a consequence, the load to initiate failure also varies markedly with both the adherend(s) and adhesive-bond thicknesses. The failure load increases very nearly linearly with width of the overlap but increases in a very nonlinear manner with length of the overlap. As the load is increased in a lap shear test, the debonding generally initiates at or near one of the bond terminations. Elastic stress analysis generally indicates that the stresses are singular at these termination points. Debond initiation in lap shear specimens can perhaps, therefore, be best characterized in terms of fracture mechanics parameters, which are discussed in the section “Adhesive Fracture Mechanics Tests” in this article. In addition, it has been demonstrated that for debonds after initiation, crack propagation is dominated by crack-opening mode displacements (mode I). For this reason and reasons given in the next couple of paragraphs, the word *shear* in the test titles and generally reported in test results may, therefore, be a misnomer.

It has been known for many years that the shear stresses in the bond line of lap specimens are accompanied by tensile stresses. Many analyses have been completed for lap shear geometries, almost all of which have clearly demonstrated the presence of induced tensile stresses in so-called lap shear specimens under load. In 1938, Volkersen (Ref 15) obtained expressions for the stresses in a lap shear joint by considering the differential displacements of the adherends and neglecting bending. This study was followed in 1944 by the now classical treatment of Goland and Reissner (Ref 16) who used standard beam theory and strength of materials concepts to obtain expressions for the joint stresses. Plantema (Ref 17) combined the results of these two earlier investigations to include shear effects in the system.

Because the stress state of the lap shear joint is so complex and does not lend itself to closed-form solutions, it is only logical that as numerical methods became available, researchers would apply them to analyze adhesive joints. Wooley and Carver (Ref 18), for example, used finite-element methods to calculate the joint stresses. They compared their results with the results obtained by Goland and Reissner and reported very good agreement. Adams and Peppiatt (Ref 19) used a two-dimensional finite-element code to analyze the stresses in a standard lap shear joint and also reported good agreement with Goland and Reissner. These authors also investigated the effect of a spew (triangular adhesive fillet) on the calculated stresses. A nonlinear finite-element analysis of the single lap joint was completed by Cooper and Sawyer (Ref 20) in 1979.

Anderson and DeVries conducted a linear elastic stress analysis of a typical single lap joint (Ref 21) making use of plane-strain finite-element computer programs using elements as small as 0.00025 cm (0.0001 in.). They considered steel (modulus of elasticity, 207 GPa; Poisson's ratio, 0.30) adherends of various thicknesses bonded with a 0.25 mm (0.01 in.) thick epoxy (modulus of elasticity, 2.76 GPa; Poisson's ratio, 0.34). The overlap region was taken as 13 mm (0.5 in.) long. The results of these analyses are shown in Fig. 4. Note that both the shear and tensile stresses are distributed very nonlinearly over the length of the bond region. Reference 21 reports stresses resulting from other adherend thicknesses. As the bond termini is approached, both shear and normal stresses appear to become singular. Careful analysis in this region suggests that the local mode I stresses

(tensile or crack opening) are significantly higher than mode II stresses (shear). Perhaps even more importantly, the mode I energy release rate is greater than that for mode II. From these results, it might be concluded that lap shear specimens fail by mode I crack growth. Therefore, the failure of lap shear specimens is usually governed by tensile stress rather than shear stresses. This is true for double lap joints as well as single lap joints (Ref 22, 23).

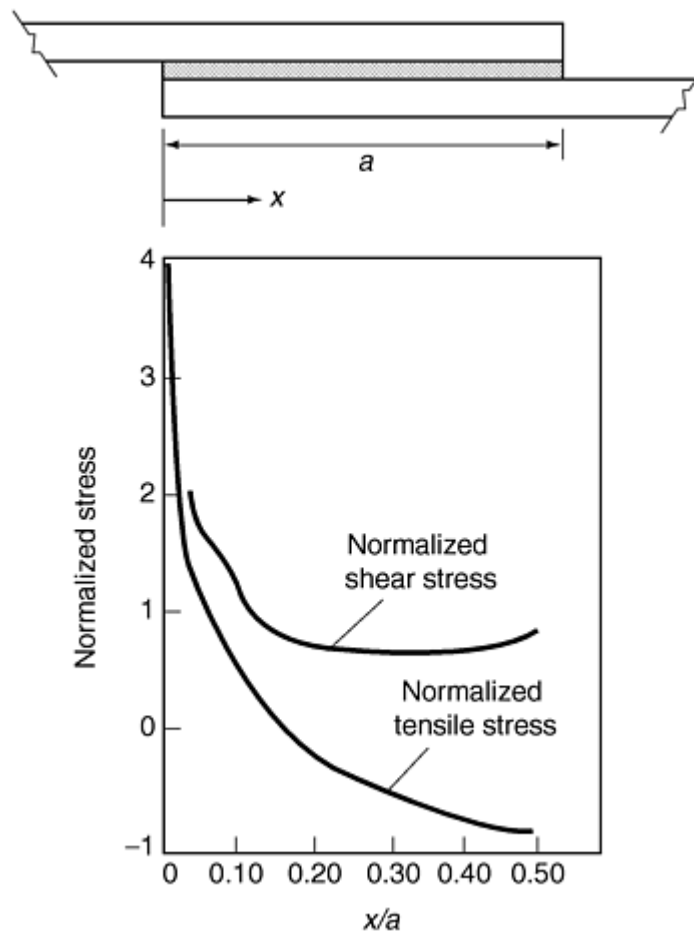


Fig. 4 Bond line tensile and shear stresses in lap shear specimen (adherend thickness = 1.6 mm, or 0.06 in.)

As noted, the end(s) of the overlap on bond termini on lap shear specimens are points of stress concentration and of large induced tensile stresses. While this closely simulates many practical situations, some have suggested that for determination of intrinsic adhesive properties, it would be useful if these termini could be eliminated. ASTM E 229 “Standard Test Method for Shear Strength and Shear Modulus of Structural Adhesives” is a test designed specifically for this purpose. In this test, the adhesive is applied in the form of a thin annulus ring bonded between two relatively rigid adherends in circular disc form. Torsion shear forces are applied to the adhesive through this circular specimen, which produces a peripherally uniform stress distribution. The maximum stress in the adhesive at failure is taken to represent the shear strength of the adhesive. By measuring the angle of twist experienced by the adhesive and having knowledge of sample geometry, it is possible to calculate the strain. A stress- strain curve can then be established from which the adhesive's effective shear modulus can be determined.

References cited in this section

1. *Adhesives*, Edition 6, D.A.T.A. Digest International Plastics Selector, 1991
7. *Adhesives, Annual Book of ASTM Standards*, Vol 15.06, ASTM (updated annually)
15. O. Volkersen, Die Nietraftverteilung in Zugbeanspruchten Nietverblendungen mit Knastaten Laschenquerschnittlen, *Luftfahrt forsch.*, Vol 15, 1938, p 41

16. M. Goland and E. Reissner, The Stresses in Cemented Joints, *J. Appl. Mech.*, Vol 11, 1944, p 17
17. J.J. Plantema, "De Schuifspanning in eme Limjnaad," Rep. M1181, Nat. Luchtvaart-laboratorium, Amsterdam, 1949
18. G.R. Wooley and D.R. Carver, *J. Aircr.*, Vol 8 (No. 19), 1971, p 817
19. R.D. Adams and N.A. Peppiatt, Stress Analysis of Adhesive-Bonded Lap Joints, *J. Strain Anal.*, Vol 9 (No. 3), 1974, p 185
20. P.S. Cooper and J.W. Sawyer, "A Critical Examination of Stresses in an Elastic Single Lap Joint," NASA Tech. Rep. 1507, NASA Scientific and Technical Information Branch, 1979
21. G.P. Anderson and K.L. DeVries, Analysis of Standard Bond-Strength Tests, *Treatise on Adhesion and Adhesives*, Vol 6, R.L. Patrick, K.L. DeVries, and G.P. Andersen, Ed., Marcel Dekker, 1989
22. J.K. Strozier, K.J. Ninow, K.L. DeVries, and G.P. Anderson, *Adhes. Sci. Rev.*, Vol 1, 1987, p 121
23. G.P. Anderson, D.H. Brinton, K.J. Ninow, and K.L. DeVries, A Fracture Mechanics Approach to Predicting Bond Strength, *Advances in Adhesively Bonded Joints, Proceedings of a Conference at the Winter Annual Meeting of ASME*, 27 Nov-2 Dec 1988 (Chicago), S. Mall, K.M. Liechti, and J.K. Vinson, Eds., ASME, 1988, p 98-101

Testing of Adhesive Joints

K.L. DeVries and Paul Borgmeier, University of Utah

Tensile Tests

Generally, the idea of mechanical failure produces a vision of an object being pulled apart by tensile force. As noted previously, most practical adhesive joints are designed to avoid (or at least reduce) direct tensile forces across the bond line. Examples of such joints are lap joints and scarf joints. It was also pointed out that for many joints, where it appears that the primary loading is shear, failure might be initiated by the induced secondary tensile stresses. There are, therefore, reasons why an adhesive's or adhesive joint's tensile strength might be of interest. Accordingly, the third most common type of adhesive joint strength test is the tensile test. ASTM has also formalized this type of test.

The geometries of several tensile tests for which there are specific ASTM test procedures are shown in Fig. 5 (Ref 7). Some of these test geometries seem relatively simple; however, it has been demonstrated that the stresses along the bond line have a rather complex dependence on geometric factors and adhesive and adherent properties (adhesive thickness and its variation across the bonded surface, modulus, Poisson's ratio, and so on) (Ref 21).

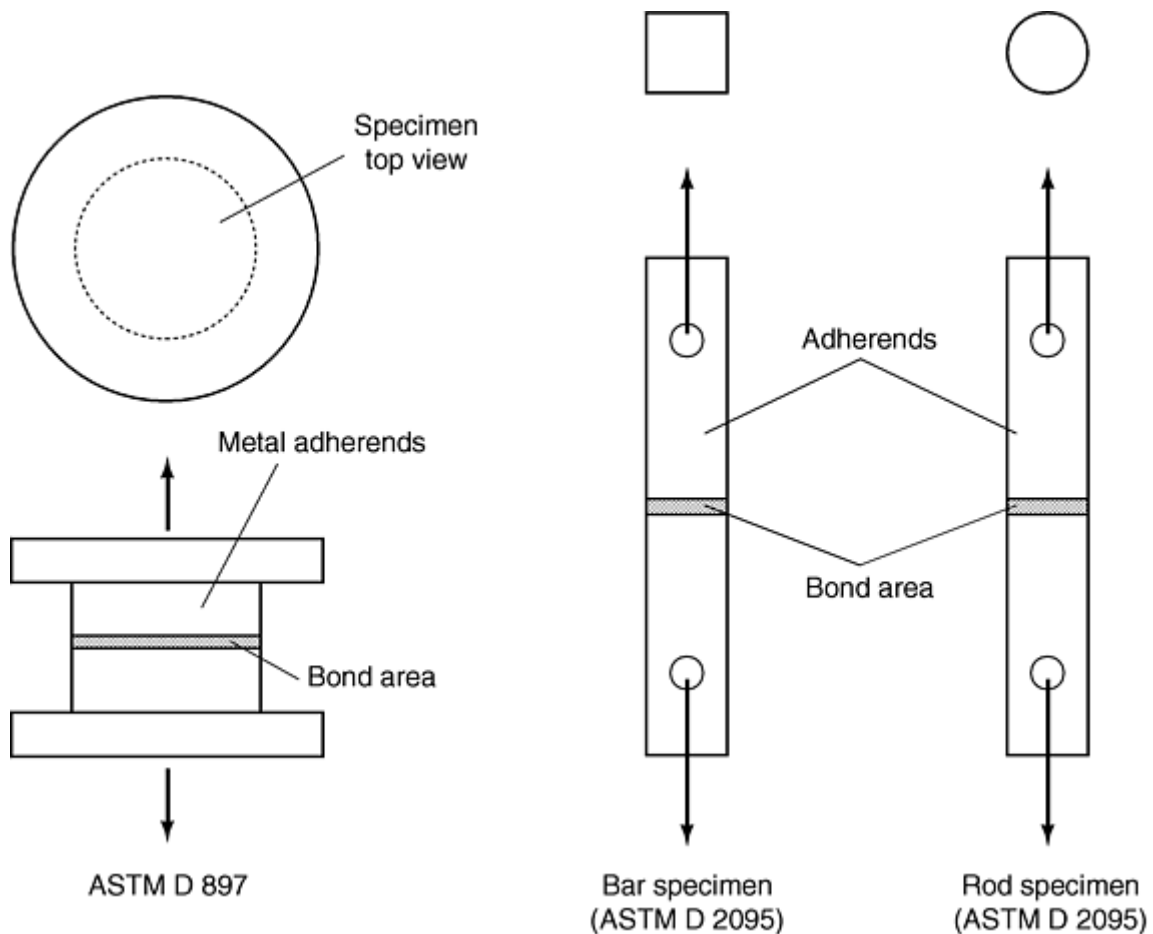


Fig. 5 Typical specimen geometries for testing the tensile strength of adhesive joints. Source: Ref 7

It is almost always difficult to load tensile adhesion specimens in an axisymmetric manner, even if the sample itself is axisymmetric. Nonaxisymmetric loads have been shown to reduce the bond failure load capability and to cause large scatter in the resulting failure data. Superficially, the geometry for standard tensile adhesion tests is deceptively simple. The result of the tensile adhesion test, as normally reported by experimentalists, is simply the failure load divided by the cross-sectional area of the adhesive (Ref 22). Such average stress at failure can be very misleading. Because of the differences in mechanical properties of the adhesive and adherend, the stresses may become singular at the bond edges when analyzed using linear elastic analysis (Ref 21, 23). Even if the edge singularity is neglected, the stress field in the adhesive is very complex and nonuniform, with maximum values differing markedly from the average value (Ref 21, 23).

Some sense of the complex nature of the stresses can be obtained by visualizing a butt joint of a low modulus polymer (e.g., a rubber) between two steel cylinders. As these are pulled apart, the rubber elongates much more readily than the steel. Poisson's effect will cause a tendency for the rubber to contract laterally. However, if it is tightly bound to the metal, it is restrained from contracting, and shear stresses are induced at the bond line. Reference 9 provides the results of a finite element analysis that demonstrates how these stresses vary across the sample. As noted, for an elastic analysis, both the shear and tensile stresses are singular (tending to infinity) at the outer periphery.

For the tensile specimen configurations considered to this point, the applied loading is intended to be axisymmetric. There is another class of specimen in which the dominant stress is deliberately tensile but in which the loading is obviously "off center." At least four ASTM standards describe so-called cleavage specimens and tests. These tests are a logical preface to the next section in this article, "Adhesive Fracture Mechanics Tests". The reader familiar with cohesive fracture mechanics will see a similarity between the test specimen in ASTM D 1062 (Fig. 6) and the compact tensile specimen commonly used in fracture mechanics testing. ASTM D 1062 specifies reporting the test results as force required, per unit width, to initiate failure in the specimen, while in fracture mechanics, the results are given as G_c with units of J/m^2 , which might be interpreted as the energy required to create a unit surface. A knowledgeable and enterprising reader may want to adapt the D 1062 specimen for obtaining fracture mechanics parameters. ASTM D 3807, "Standard Test

Method for Strength Properties of Adhesives in Cleavage Peel by Tension Loading,” uses a different geometry to measure the cleavage strength. In this case, two 25.4 mm (1 in.) wide by 6.35 mm (0.25 in.) thick plastic strips 177 mm (7 in.) long are bonded over a length of 76 mm (3 in.) on one end, leaving the other ends free and separated by the thickness of the adhesive. Approximately 25 mm (1 in.) from the end of each of these free segments, a “gripping wire” is attached as shown in Fig. 7. During testing, these wires are clamped in the jaws of a universal testing machine and the sample pulled to failure. The results are reported as load per unit width (kg/m or lb/in.). Again, it would be possible to analyze this sample in terms of fracture mechanics, but it is unnecessary because, as the next section explains, this analysis is done in ASTM D 3433 for a very similar beam geometry.

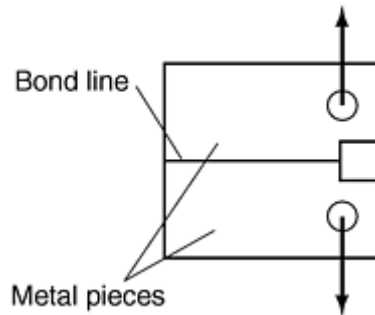


Fig. 6 Specimen for testing the cleavage strength of metal-to-metal adhesive bonds (ASTM D 1062)

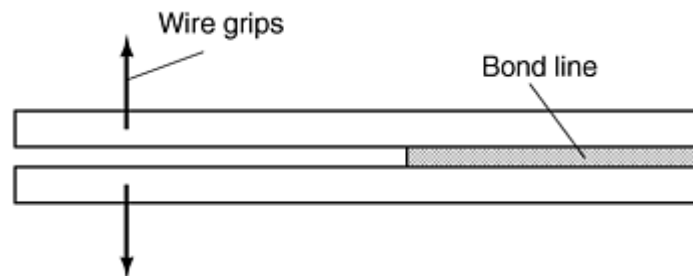
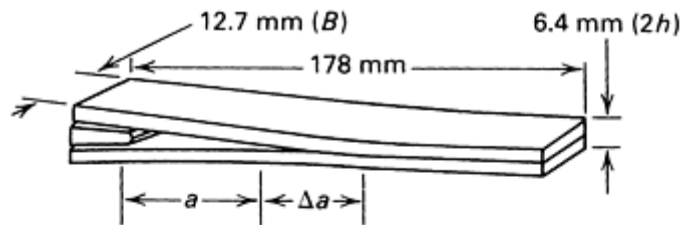


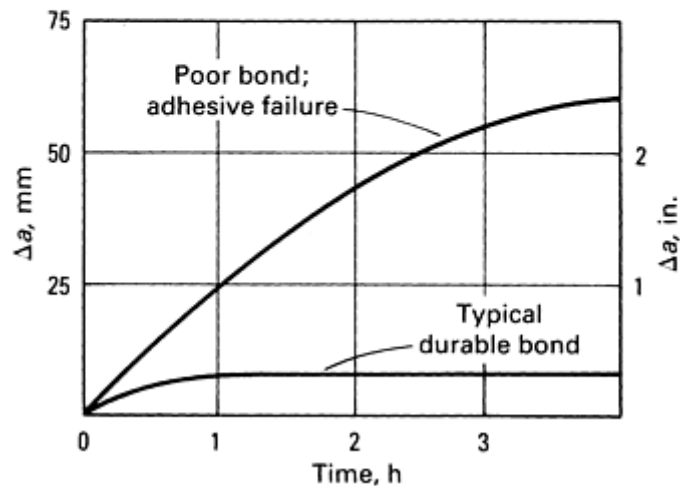
Fig. 7 Specimen for testing cleavage peel (by tension loading) (ASTM D 3807)

ASTM D 5041 also makes use of a sample composed of two thin sheets bonded together over part of their length. In this case, forcing a wedge (45° angle) between the unbonded portion of the sheets facilitates the separation. The results are typically given as “failure initiation energy” or “failure propagation energy” (i.e., areas under the load deformation curve).

This latter test is similar to another test, formalized as ASTM D 3762, that has been found very useful for studying time-environmental effects on adhesive bonds. This test is called by various names, but the authors prefer the name “Boeing Wedge Test” (Ref 24, 25). The test has been used by personnel at this and other aerospace companies to screen various adhesives, surface treatment, and so on for long-term loading at high temperatures and humidities. For testing, two long, slender strips of candidate structural materials are first treated with the prescribed surface treatment(s) and bonded over part of their length with a candidate adhesive (Fig. 8). As in the test described in the previous paragraph, the free ends are forced apart by a wedge. The amount of separation by the wedge (determined by wedge thickness and depth of insertion) determines the value of the stresses in the adhesive. These stresses can, of course, be adjusted and the values calculated from mechanics of material concepts. When the wedge is in place, the sample is placed in an environmental chamber. At periodic time intervals, the length of the crack is measured, and a plot of crack length versus time is constructed. The more satisfactory adhesives and/or surface treatments are those for which the crack is arrested or grows very slowly. While the environmental chamber typically contains hot, humid air, there is no reason why other environmental agents cannot be studied by the same method, including immersion in liquids.



(a)



(b)

Fig. 8 Boeing wedge test (ASTM D 3762) (a) Test specimen. (b) Typical crack propagation behavior at 49 °C (120 °F) and 100% relative humidity. a , distance from load point to initial crack tip; Δa , growth during exposure. Source: Ref 49

References cited in this section

7. Adhesives, *Annual Book of ASTM Standards*, Vol 15.06, ASTM (updated annually)
9. G.P. Anderson and K.L. DeVries, Predicting Strength of Adhesive Joints from Test Results, *Int. J. Fract.*, Vol 39, 1989, p191–200
21. G.P. Anderson and K.L. DeVries, Analysis of Standard Bond-Strength Tests, *Treatise on Adhesion and Adhesives*, Vol 6, R.L. Patrick, K.L. DeVries, and G.P. Andersen, Ed., Marcel Dekker, 1989
22. J.K. Strozier, K.J. Ninow, K.L. DeVries, and G.P. Anderson, *Adhes. Sci. Rev.*, Vol 1, 1987, p 121
23. G.P. Anderson, D.H. Brinton, K.J. Ninow, and K.L. DeVries, A Fracture Mechanics Approach to Predicting Bond Strength, *Advances in Adhesively Bonded Joints, Proceedings of a Conference at the Winter Annual Meeting of ASME*, 27 Nov-2 Dec 1988 (Chicago), S. Mall, K.M. Liechti, and J.K. Vinson, Eds., ASME, 1988, p 98–101
24. V.L. Hein and F. Erodogan, Stress Singularities in a Two-Material Wedge, *Int. J. Fract.*, Vol 7, 1971, p 317
25. J.A. Marceau, Y. Moji, and J.C. McMillan, A Wedge Test for Evaluating Adhesive Bonded Surface Durability, *21st SAMPE Symposium*, Vol 21, 6–8 April 1976
49. J.C. McMillan, *Developments in Adhesives in Engineering*, 2nd ed., Applied Science, London, 1981, p 243

Adhesive Fracture Mechanics Tests

Fracture mechanics originated with the pioneering efforts of A.A. Griffith in the early 1920s. The field remained relatively dormant until the late 1940s when it was developed into a very effective and valuable design tool to describe and predict “cohesive” crack growth. Interested readers are referred to a number of excellent texts on fracture mechanics (e.g., Ref 26 and *Fatigue and Fracture*, Volume 19 of the *ASM Handbook*).

In the 1960s and 1970s, researchers began exploring the use of the concepts of fracture mechanics in adhesive joint analysis as reviewed in Ref 3. These methods have the potential to use the results from a test joint to predict the strength of other joints with different geometries.

In a common fracture mechanics approach (including Griffith's papers), the conditions for failure are calculated by equating the energy lost from the strain field as a “crack” grows to the energy consumed in creating the new crack surface. This energy per unit area, G_c , determined from standard tests, is called by various names, including the Griffith fracture energy, the specific fracture energy, the fracture toughness, or the energy release rate.

In 1975, ASTM Committee D-14 adopted a test configuration and testing method with fracture mechanics ramifications based on the pioneering efforts of Mostovoy and Ripling (Ref 27, 28). The method is described in ASTM D 3433 “Standard Test Method for Fracture Strength in Cleavage of Adhesives in Bonded Joints.” Figure 9 shows the shape and dimensions for one specimen type recommended for use in this standard. The specimen is composed of two “beams” adhesively bonded over much of their length as shown. Testing is accomplished by pulling the specimen apart by means of pins passing through the holes shown near the sample's left end. This adhesive sample configuration and loading to failure gives rise to the sample's nickname, “split-cantilever beam.” Another recommended geometry in ASTM D 3433 is similar except the adherends are not tapered.

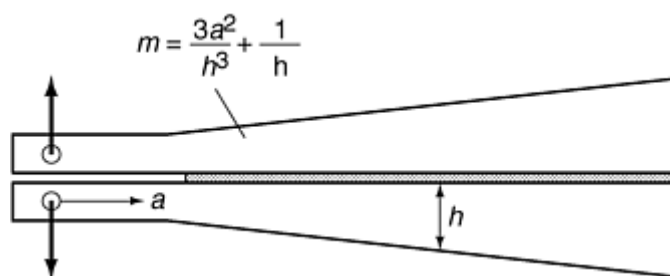


Fig. 9 Specimen for the contoured double-cantilever-beam test (ASTM D 3433)

It should now be clear that the stress distribution in adhesive joints is generally complex. Furthermore, the details of this distribution are highly dependent on specific details of the joint system. The maximum stresses in the bond almost always differ markedly from the average value, and elastic analyses often exhibit mathematical singularities at geometric or material discontinuities. From these observations, it should be clear that the use of the conventionally reported results from most tests (i.e., values of the average stress at failure) would be of little use in designing joints that differ in any significant detail from the sample test configuration.

For the resolution of this problem, the concepts of fracture mechanics have much to offer. One of the more popular and graphically appealing approaches to fracture mechanics views the joint as a system in which failure (often considered as the growth of a crack) of a material (or joint) requires the stresses at the crack tip to be sufficient to break bonds and an energy balance. It is hypothesized that even if the stresses are very large (often theoretically infinite), a crack can grow only if sufficient energy is released from the stress field to account for the energy required to create the new crack (or adhesive debond) surface as the fractured region enlarges. The specific value of this energy (J/m^2 , or $in. \cdot lbf/in.^2$, of crack area) for the adhesive bonding problem uses the same basic titles as given previously but prefaced with the term *adhesive*. Hence, *adhesive fracture toughness*

might be used to distinguish adhesive failure from tests of cohesive fracture. The word adhesion is dropped from the comparable term when cohesive failure is being considered. The cohesive and adhesive embodiments of fracture mechanics both involve a stress-strain analysis and an energy balance.

The analytical methods of fracture mechanics (both cohesive and adhesive) are described in Ref 3 and 25. These are not repeated here other than a few comments on the concepts and a brief outline of a numerical approach that can be applied where analytical solutions are tedious or impossible. Inherent in fracture mechanics is the concept that natural cracks or other stress risers exist in materials and that final failure of an object often initiates at such points. For a crack (or region of debond) situated in an adhesive layer, modern computation techniques are available (most notably, finite element methods) that facilitate the computation of stresses and strains throughout a body, even if analytical solutions may not be possible. The stresses and strains are calculated throughout the entire adhesive system (adhesive and all adherends), including the effects of a crack in the bond. These can then be used to calculate the strain energy, U_1 , stored in the body for the particular crack size, A_1 . Next, the hypothetical crack is allowed to grow to a slightly larger area, A_2 , and the preceding process is repeated to determine the strain energy, U_2 . This approach to fracture mechanics assumes that at critical crack growth conditions, the energy loss from the stress-strain field goes into the formation of the new fracture energy. The quantity $\Delta U/\Delta A$ is called the energy release rate, where $\Delta U = U_2 - U_1$ and $\Delta A = A_2 - A_1$. The so-called critical energy release rate $(\Delta U/\Delta A)_{crit}$ is that value of the energy release rate that will cause the crack to grow. Loads that result in energy release rates lower than this critical value will not cause failure to proceed from the given crack, while loads that produce energy release rates greater than this value will cause it to accelerate. This critical energy release rate value is equivalent to the adhesive fracture energy, or work of adhesion, previously noted. While the model just described is conceptually useful, computer engineers have devised other convenient ways of computing the energy required to “create” the new surface, such as the crack closure method (Ref 29, 30).

It is hoped that this simple model of fracture mechanics will help the reader who is unfamiliar with fracture mechanics to visualize the concepts of fracture mechanics. The molecular mechanisms responsible for the fracture energy or fracture toughness are not completely understood. They generally involve more than simply the energy required to rupture a plane of molecular bonds. In fact, for most practical adhesives, the energy to rupture these bonds is a small but essential fraction of the total energy. The total energy includes energy that is lost because of viscous, plastic, and other dissipation mechanisms at the tip of the crack. As a result, linear elastic stress analyses are inexact.

While fracture mechanics has found extensive use in cohesive failure considerations, its use for analyzing failure of adhesive systems is more recent. There has, however, been a significant amount of research and development in the adhesive fracture mechanics area. To review it all, even superficially, would take more space than is allocated for this article. A small sampling of publications in this extensive and rich area of research is listed as Ref 12, 13, 26, 27, 28, and 31, 32, 33, 34, 35, 36, 37, 38, 39, 40, 41, 42, 43, 44, 45, 46, 47, 48, 49, 50, 51, 52, 53, 54, 55, 56, 57, 58. Not only is this listing incomplete, but also many of the researchers listed have scores of other publications. It is hoped that the one or two listed for each investigator will provide the reader with a starting point from which more details can be found from reference cross listings, searching of citation indexes, abstracting services, and so on. These investigators have treated such subjects as theory; mode dependence, effects of shape, thickness, and other geometric dependence; plasticity and other nonlinearities; numerical methods; testing techniques; different adhesive types; rate and temperature effects; fatigue; and failure of composites, as well as a wide variety of other factors and considerations in adhesion.

Modern finite element or other numerical methods have no difficulty in treating nonlinear behavior. Physical understanding of material behavior at such levels is lacking, and effective use of the capabilities of such computer codes depends, to a large extent, on the experimental determination of these properties. For many problems, it has become conventional to lump all dissipative effects together into the fracture energy and not be overly concerned with separating this quantity into its individual energy-absorbing components. Another fracture mechanics approach, called the J -integral, has some advantages in treating nonlinear as well as elastic behavior (Ref 51, 52, 59, and 60).

It was noted previously that most adhesive systems are not linearly elastic up to the failure point. Nevertheless, researchers have shown that elastic analyses of many systems can be very informative and useful. Several adhesive systems are sufficiently linear so that it is possible to lump the plastic deformation and other energy dissipative mechanisms at the crack tip into the adhesive fracture energy (critical energy release rate) term. There has recently been some significant success in explaining many aspects of adhesive performance and

predicting the strength of a bond from tests on other, quite different, joints by using linear elastic fracture mechanics.

As noted, in principle, fracture mechanics lends itself to using test results from one test in the design of other joints that have significantly different geometries. A number of adhesive geometries have been proposed to measure fracture toughness in addition to the split-cantilever beam, but to date, it is the only one formalized by ASTM (Ref 3, 4, 6, 12, 36, 47, and 48). A recent paper by the authors (Ref 61) has demonstrated how such factors as end rotation (at the cantilever point assumed rigidly fixed in the original ASTM analysis) shear, and presence of the adhesive and its thickness (also neglected in the original analysis) affect the energy release rate. It is shown that inclusion of these effects can dramatically affect the results and greatly reduce test scatter. Furthermore, this paper demonstrates how fracture mechanics may be used to predict the locus of adhesive crack growth. To accomplish this, various crack paths were assumed, and using finite element methods, the energy release rate calculated for each path.

References cited in this section

3. G.P. Anderson, S.J. Bennett, and K.L. DeVries, *Analysis and Testing of Adhesive Bonds*, Academic Press, 1977
4. A.J. Kinlock, *Adhesion and Adhesives*, Chapman and Hall, 1987
6. K.L. Mittal, *Adhesive Joints*, Plenum Press, 1984
12. A.N. Gent and G.R. Hamed, Peel Mechanics, *J. Adhes.*, Vol 7, 1975, p 91
13. A.N. Gent and G.R. Hamed, *J. Appl. Polym. Sci.*, Vol 21, 1977, p 2817
25. J.A. Marceau, Y. Moji, and J.C. McMillan, A Wedge Test for Evaluating Adhesive Bonded Surface Durability, *21st SAMPE Symposium*, Vol 21, 6–8 April 1976
26. D. Broek, *The Practical Use of Fracture Mechanics*, Kluwer Acad. Press, Dordrecht, NL, 1989
27. S. Mostovoy and E.J. Ripling, *J. Appl. Polym. Sci.*, Vol 15, 1971, p 661
28. S. Mostovoy and E.J. Ripling, *J. Adhes. Sci. Technol.*, Vol 9B, 1975, p 513
29. E.F. Rybicki and M.F. Kanninen, *Eng. Fract. Mech.*, Vol 9, 1974, p 921
30. G.P. Anderson and K.L. DeVries, *J. Adhes.*, Vol 23, 1987, p 289
31. E.H. Andrews, T.A. Khan, and H.A. Majid, *J. Mater. Sci.*, Vol 20, 1985, p 3621
32. E.H. Andrews, H.A. Majid, and N.A. Lockington, *J. Mater. Sci.*, Vol 19, 1984, p 73
33. D.W. Aubrey and M. Sherriff, *J. Polym. Sci. Polym. Chem. Ed.*, Vol 18, 1980, p 2597
34. W.D. Bascom and J. Oroshnik, *J. Mater. Sci.*, Vol 10, 1978, p 1411
35. W.D. Bascom and D.L. Hunston, Fracture of Epoxy and Elastomer-Modified Epoxy Polymers, *Treatise on Adhesion and Adhesives*, Vol 6, R. L. Patrick, K.L. DeVries, and G.P. Anderson, Ed., Marcel Dekker, 1988, p 123
36. H.F. Brinson, J.P. Wightman, and T.C. Ward, *Adhesives Science Review 1*, VPI Press, 1987
37. J.D. Burton, W.B. Jones, and M.L. Williams, *Trans. Soc. Rheol.*, Vol 15, 1971, p 39

38. G. Danneberg, *J. Appl. Polym. Sci.*, Vol 5, 1961, p 125
39. F. Erdogan, *Eng. Fract. Mech.*, Vol 4, 1972, p 811
40. T.R. Guess, R.E. Allred, and F.P. Gerstle, *J. Test. Eval.*, Vol 5 (No. 2), 1977, p 84
41. G.R. Hamed, Energy Conservation During Peel Testing, *Treatise on Adhesion and Adhesives*, Vol 6, R. L. Patrick, K. L. DeVries, and G. P. Anderson, Eds., Marcel Dekker, 1988, p 233
42. R.W. Hertzberg and J.A. Manson, *Fatigue of Engineering Plastics*, Academy, 1980
43. G.R. Irwin, Fracture Mechanics Applied to Adhesive Systems, *Treatise on Adhesion and Adhesives*, Vol 1, R. L. Patrick, Ed., Marcel Dekker, 1966, p 233
44. W.S. Johnson, *J. Test. Eval.*, Vol 15 (No. 6), 1987, p 303
45. D.H. Kaelble, *Physical Chemistry of Adhesion*, Wiley-Interscience, 1971
46. H.H. Kaush, *Polymer Fracture*, Springer-Verlag, Berlin, 1978
47. W.G. Knauss and K.M. Liechti, Interfacial Crack Growth and Its Relation to Crack Front Profiles, *ACS Organic Coatings and Applied Polymer Science Proceedings*, Vol 47, American Chemical Society, Washington, DC, 1982, p 481
48. K.M. Liechti and C. Lin, *Structural Adhesives in Engineering*, Institute of Mechanical Engineering, London, 1986, p 83
49. J.C. McMillan, *Developments in Adhesives in Engineering*, 2nd ed., Applied Science, London, 1981, p 243
50. D.R. Mulville, D.L. Hunston, and P.W. Mast, *J. Eng. Mater. Technol.*, Vol 100, 1978, p 25
51. J.R. Rice and G.C. Sih, *J. Appl. Mech.*, Vol 32, 1965, p 418
52. E.F. Rybicki and M.F. Kanninen, *Eng. Fract. Mech.*, Vol 9, 1974, p 921
53. G.B. Sinclair, *Int. J. Fract.*, Vol 16, 1980, p 111
54. J.D. VENABLES, D.K. McNamara, J.M. Chen, T.S. Sun, and R.L. Hopping, *Appl. Surf. Sci.*, Vol 3, 1979, p 88
55. S.S. Wang, J.F. Mandell, and F.J. McGarry, *Int. J. Fract.*, Vol 14, 1978, p 39
56. J.G. Williams, *Fracture Mechanics of Polymers*, Ellis Horwood, Chichester, 1984
57. M.L. Williams, *J. Adhes.*, Vol 5, 1973, p 81
58. R.J. Young, in *Structural Adhesives: Developments in Resins and Primers*, A.J. Kinlock, Ed., Applied Science, London, 1986, p 163
59. J.R. Rice, A Path Independent Integral and the Approximate Analysis of Strain Concentration by Notches and Cracks, *J. Appl. Mech.*, 1979, p 379–386h

60. J.W. Hutchinson and P.C. Paris, *Stability of J-Controlled Crack Growth*, STP 668, ASTM, 1979, p 37–64
61. K.L. DeVries and P.R. Borgmeier, *Fracture Mechanics Analyses of the Behavior of Adhesion Test Specimens*, *Mittal Festschrift*, W.J. Van Ooij and H.R. Anderson, Jr., Ed., 1998, p 615–640

Testing of Adhesive Joints

K.L. DeVries and Paul Borgmeier, University of Utah

Conclusions

The adhesive researcher or technologist has many standard test methods from which to choose. These techniques are designed with various goals and objectives in mind. Many of these methods are useful for the purposes of comparing different adhesives and substrates, investigating the effects of different loading, investigating chemical or physical attacks on adhesives, exploring aging phenomena, determining the effects of radiation and moisture combined with sustained loading on adhesive properties, and so on. On the other hand, care should always be exercised not to use the test results for purposes for which they are not well suited. Results from many of the adhesive strength tests are conventionally reported as the failure force divided by the bond area. Such average stress at failure results cannot, in general, be consistently and reliably used to predict failure of other joints that differ even slightly from the test geometry. Fracture mechanics approaches, on the other hand, show promise and have been used to predict the strength of joints that differ considerably from the reference joint. ASTM D 3433 and Ref 27 and 28 describe a standard adhesive fracture mechanics joint in the form of a tapered double-cantilever beam. The specimen dimensions are shown in Fig. 9. It is important to note, however, that fracture mechanics is not limited to this or any other specific testing geometry. In principle, any geometry for which the described energy balance (or alternatively, calculation of the stress intensity factor, J -integral, and so on) can be accomplished might be used as an adhesive test.

Sometimes, circumstances dictate the use of a nonstandard test geometry. For example, a few years ago, the authors were given the problem of measuring the quality of natural barnacle adhesive. The barnacle dictated the exact form of the joint between the barnacle's shell and the plastic sheets that were placed in the ocean. This form did not lend itself to tensile, lap shear, or split-cantilever testing. It was, however, possible to predrill holes in the plate and to fill these holes with dental waxes that were solid and hard at the ocean temperatures near San Francisco, CA, where the barnacle growth experiments were conducted. The wax was later easily removed at a moderately elevated temperature. The base of the barnacle covering this hole was thereby exposed and could be tested by application of fluid pressure, thus forming a blister. Measurement of the pressurization at failure allowed the determination of the adhesive fracture energy (Ref 3, 62).

Once the adhesive fracture energy is determined by testing, fracture mechanics points the way that it, along with a knowledge of the flaw size and a stress-strain analysis of the joint, can be used to predict the performance of other joints. Modern computational techniques greatly facilitate the application of these methods.

Finally, it is noted that the stresses, strains, fracture energy, and other such parameters used in the adhesive analysis depend on loading rate, mode of stress at the crack tip, temperature, environment, and other factors. Development of means for incorporating these parameters into joint design has been, and continues to be, an area of active research. Such concepts and methodology can be found in the references cited previously in this section.

References cited in this section

3. G.P. Anderson, S.J. Bennett, and K.L. DeVries, *Analysis and Testing of Adhesive Bonds*, Academic Press, 1977

27. S. Mostovoy and E.J. Ripling, *J. Appl. Polym. Sci.*, Vol 15, 1971, p 661

28. S. Mostovoy and E.J. Ripling, *J. Adhes. Sci. Technol.*, Vol 9B, 1975, p 513

62. R.R. Despain, R.D. Luntz, K.L. DeVries, and M.L. Williams, *J. Dental Res.*, Vol 52, 1973, p 742

Testing of Adhesive Joints

K.L. DeVries and Paul Borgmeier, University of Utah

Acknowledgments

Major portions of the authors' research has been supported by The National Science Foundation, most recently under grant No. CMS-9522743.

Testing of Adhesive Joints

K.L. DeVries and Paul Borgmeier, University of Utah

References

1. *Adhesives*, Edition 6, D.A.T.A. Digest International Plastics Selector, 1991
2. R.L. Patrick, Ed., *Treatise on Adhesion and Adhesives*, Vol 1–6, Marcel Dekker, 1966–1988
3. G.P. Anderson, S.J. Bennett, and K.L. DeVries, *Analysis and Testing of Adhesive Bonds*, Academic Press, 1977
4. A.J. Kinlock, *Adhesion and Adhesives*, Chapman and Hall, 1987
5. A. Pizzi and K.L. Mittal, Ed., *Handbook of Adhesive Technology*, Marcel Dekker, 1994
6. K.L. Mittal, *Adhesive Joints*, Plenum Press, 1984
7. *Adhesives*, *Annual Book of ASTM Standards*, Vol 15.06, ASTM (updated annually)
8. E.P. Plueddemann, *Silane Coupling Agents*, Plenum Press, 1982
9. G.P. Anderson and K.L. DeVries, Predicting Strength of Adhesive Joints from Test Results, *Int. J. Fract.*, Vol 39, 1989, p191–200
10. J.L. Gardon, Peel Adhesion, I. Some Phenomenological Aspects of the Test, *J. Appl. Polym. Sci.*, Vol 7, 1963, p 654
11. D.H. Kaelble, Theory and Analysis of Peel Adhesion: Mechanisms and Mechanics, *Trans. Soc. Rheol.*, Vol 3, 1959, p 161

12. A.N. Gent and G.R. Hamed, Peel Mechanics, *J. Adhes.*, Vol 7, 1975, p 91
13. A.N. Gent and G.R. Hamed, *J. Appl. Polym. Sci.*, Vol 21, 1977, p 2817
14. R.D. Adams and A. Crocombe, *J. Adhes.*, Vol 12, 1981, p 127
15. O. Volkersen, Die Nietraftverteilung in Zugbeanspruchten Nietverblendungen mit Knastaten Laschenquerschnitten, *Luftfahrtforsch.*, Vol 15, 1938, p 41
16. M. Goland and E. Reissner, The Stresses in Cemented Joints, *J. Appl. Mech.*, Vol 11, 1944, p 17
17. J.J. Plantema, "De Schuifspanning in eme Limjnaad," Rep. M1181, Nat. Luchtvaart-laboratorium, Amsterdam, 1949
18. G.R. Wooley and D.R. Carver, *J. Aircr.*, Vol 8 (No. 19), 1971, p 817
19. R.D. Adams and N.A. Peppiatt, Stress Analysis of Adhesive-Bonded Lap Joints, *J. Strain Anal.*, Vol 9 (No. 3), 1974, p 185
20. P.S. Cooper and J.W. Sawyer, "A Critical Examination of Stresses in an Elastic Single Lap Joint," NASA Tech. Rep. 1507, NASA Scientific and Technical Information Branch, 1979
21. G.P. Anderson and K.L. DeVries, Analysis of Standard Bond-Strength Tests, *Treatise on Adhesion and Adhesives*, Vol 6, R.L. Patrick, K.L. DeVries, and G.P. Andersen, Ed., Marcel Dekker, 1989
22. J.K. Strozier, K.J. Ninow, K.L. DeVries, and G.P. Anderson, *Adhes. Sci. Rev.*, Vol 1, 1987, p 121
23. G.P. Anderson, D.H. Brinton, K.J. Ninow, and K.L. DeVries, A Fracture Mechanics Approach to Predicting Bond Strength, *Advances in Adhesively Bonded Joints, Proceedings of a Conference at the Winter Annual Meeting of ASME*, 27 Nov-2 Dec 1988 (Chicago), S. Mall, K.M. Liechti, and J.K. Vinson, Eds., ASME, 1988, p 98-101
24. V.L. Hein and F. Erodogan, Stress Singularities in a Two-Material Wedge, *Int. J. Fract.*, Vol 7, 1971, p 317
25. J.A. Marceau, Y. Moji, and J.C. McMillan, A Wedge Test for Evaluating Adhesive Bonded Surface Durability, *21st SAMPE Symposium*, Vol 21, 6-8 April 1976
26. D. Broek, *The Practical Use of Fracture Mechanics*, Kluwer Acad. Press, Dordrecht, NL, 1989
27. S. Mostovoy and E.J. Ripling, *J. Appl. Polym. Sci.*, Vol 15, 1971, p 661
28. S. Mostovoy and E.J. Ripling, *J. Adhes. Sci. Technol.*, Vol 9B, 1975, p 513
29. E.F. Rybicki and M.F. Kanninen, *Eng. Fract. Mech.*, Vol 9, 1974, p 921
30. G.P. Anderson and K.L. DeVries, *J. Adhes.*, Vol 23, 1987, p 289
31. E.H. Andrews, T.A. Khan, and H.A. Majid, *J. Mater. Sci.*, Vol 20, 1985, p 3621
32. E.H. Andrews, H.A. Majid, and N.A. Lockington, *J. Mater. Sci.*, Vol 19, 1984, p 73
33. D.W. Aubrey and M. Sherriff, *J. Polym. Sci. Polym. Chem. Ed.*, Vol 18, 1980, p 2597

34. W.D. Bascom and J. Oroshnik, *J. Mater. Sci.*, Vol 10, 1978, p 1411
35. W.D. Bascom and D.L. Hunston, Fracture of Epoxy and Elastomer-Modified Epoxy Polymers, *Treatise on Adhesion and Adhesives*, Vol 6, R. L. Patrick, K.L. DeVries, and G.P. Anderson, Ed., Marcel Dekker, 1988, p 123
36. H.F. Brinson, J.P. Wightman, and T.C. Ward, *Adhesives Science Review 1*, VPI Press, 1987
37. J.D. Burton, W.B. Jones, and M.L. Williams, *Trans. Soc. Rheol*, Vol 15, 1971, p 39
38. G. Danneberg, *J. Appl. Polym. Sci.*, Vol 5, 1961, p 125
39. F. Erdogan, *Eng. Fract. Mech.*, Vol 4, 1972, p 811
40. T.R. Guess, R.E. Allred, and F.P. Gerstle, *J. Test. Eval.*, Vol 5 (No. 2), 1977, p 84
41. G.R. Hamed, Energy Conservation During Peel Testing, *Treatise on Adhesion and Adhesives*, Vol 6, R. L. Patrick, K. L. DeVries, and G. P. Anderson, Eds., Marcel Dekker, 1988, p 233
42. R.W. Hertzberg and J.A. Manson, *Fatigue of Engineering Plastics*, Academy, 1980
43. G.R. Irwin, Fracture Mechanics Applied to Adhesive Systems, *Treatise on Adhesion and Adhesives*, Vol 1, R. L. Patrick, Ed., Marcel Dekker, 1966, p 233
44. W.S. Johnson, *J. Test. Eval.*, Vol 15 (No. 6), 1987, p 303
45. D.H. Kaelble, *Physical Chemistry of Adhesion*, Wiley-Interscience, 1971
46. H.H. Kaush, *Polymer Fracture*, Springer-Verlag, Berlin, 1978
47. W.G. Knauss and K.M. Liechti, Interfacial Crack Growth and Its Relation to Crack Front Profiles, *ACS Organic Coatings and Applied Polymer Science Proceedings*, Vol 47, American Chemical Society, Washington, DC, 1982, p 481
48. K.M. Liechti and C. Lin, *Structural Adhesives in Engineering*, Institute of Mechanical Engineering, London, 1986, p 83
49. J.C. McMillan, *Developments in Adhesives in Engineering*, 2nd ed., Applied Science, London, 1981, p 243
50. D.R. Mulville, D.L. Hunston, and P.W. Mast, *J. Eng. Mater. Technol.*, Vol 100, 1978, p 25
51. J.R. Rice and G.C. Sih, *J. Appl. Mech.*, Vol 32, 1965, p 418
52. E.F. Rybicki and M.F. Kanninen, *Eng. Fract. Mech.*, Vol 9, 1974, p 921
53. G.B. Sinclair, *Int. J. Fract.*, Vol 16, 1980, p 111
54. J.D. Venable, D.K. McNamara, J.M. Chen, T.S. Sun, and R.L. Hopping, *Appl. Surf. Sci.*, Vol 3, 1979, p 88
55. S.S. Wang, J.F. Mandell, and F.J. McGarry, *Int. J. Fract.*, Vol 14, 1978, p 39
56. J.G. Williams, *Fracture Mechanics of Polymers*, Ellis Horwood, Chichester, 1984

57. M.L. Williams, *J. Adhes.*, Vol 5, 1973, p 81
58. R.J. Young, in *Structural Adhesives: Developments in Resins and Primers*, A.J. Kinlock, Ed., Applied Science, London, 1986, p 163
59. J.R. Rice, A Path Independent Integral and the Approximate Analysis of Strain Concentration by Notches and Cracks, *J. Appl. Mech.*, 1979, p 379–386h
60. J.W. Hutchinson and P.C. Paris, *Stability of J-Controlled Crack Growth*, STP 668, ASTM, 1979, p 37–64
61. K.L. DeVries and P.R. Borgmeier, Fracture Mechanics Analyses of the Behavior of Adhesion Test Specimens, *Mittal Festschrift*, W.J. Van Ooij and H.R. Anderson, Jr., Ed., 1998, p 615–640
62. R.R. Despain, R.D. Luntz, K.L. DeVries, and M.L. Williams, *J. Dental Res.*, Vol 52, 1973, p 742

Mechanical Testing of Welded Joints

William Mohr, Edison Welding Institute

Introduction

IN WELDED STRUCTURES, the welds typically have a mechanical purpose. Loads must be carried across the weld joint. Standard mechanical tests have been devised to demonstrate that not only the base metals but also the entire welded joint can fulfill this mechanical purpose (Ref 1, 2). This article primarily discusses standard test methods that can be applied to many types of welds. These include tension, bending, impact, and toughness testing.

Residual stress measurement techniques and weldability testing also are discussed. Residual stress can be imposed by the welding itself, as well as by cutting and forming processes. The presence of high-tension or compression residual stresses can affect the ability of the welded structure to carry the mechanical loading. Cracking due to welding can also affect the load-carrying capacity of welded joints, and weldability testing techniques that combine welding and mechanical loading to test the resistance to cracking are available. Many other testing techniques can be applied to weld joints and welded structures. Fatigue and creep are both important areas where mechanical tests on welded joints have indicated properties different from those of the base metal. Testing of welded structure properties can also be done on structures that more closely model the service structure than the standard specimens described below.

References cited in this section

1. “Standard Welding Terms and Definitions,” AWS 3.0, American Welding Society
2. L.P. Connor, Ed., *Welding Handbook*, 8th ed., Vol 1, American Welding Society, 1991

Reasons to Measure Properties of Welds

The mechanical properties of welded joints, the properties related to stress and strain, are most often measured to show that such a weld and other similar welds will serve their purpose under loading. More rarely, several welds are compared to see which welding techniques, processes, or chemistries provide the best combination of mechanical properties.

Four stages in the qualification process for the weld joint can use standard mechanical test methods. The weld metal can be chosen based on the mechanical properties from standard tests. The base metal, in some situations, may also need to be qualified to demonstrate that its mechanical properties will not be substantially degraded by welding. Once base metal and weld metal are chosen, the other weld process parameters, such as weld shape or heat input, can be qualified by standard mechanical testing. Finally, after the weld is made, it may require qualification by mechanical testing.

Each of the four qualification stages requires different types of tests and different approaches. These approaches are described in the next four sections.

Weld Material Qualification

Weld metals are qualified by making welds that pass mechanical property tests on the weld metal itself. Such tests can be used to qualify filler materials, such as welding wire or electrodes. Mechanical tests for such qualification are described in the individual specifications of the filler metals, such as those in American Welding Society (AWS) Specification A5.1 (Ref 3) and others of the AWS A5 series.

Mechanical property tests applied to weld qualification are designed to determine a small number of standard values to check whether the weld metal passes or fails. This approach will not reveal the entire range of properties that the weld metal can achieve. For instance, weld metal toughness in AWS A5.1 is measured by a Charpy test specimen taken from the weld centerline. Other locations, which may have different toughnesses, are not checked.

Base Material Qualification for Welded Service

The heat of welding will modify the structure and properties of the region of the base metal adjacent to the weld in the heat-affected zone (HAZ). To prevent this modification in properties from causing service failures, some standards require that a sample of the base material be tested after undergoing a representative heat treatment.

American Petroleum Institute standard (API) RP2Z is an example of a standard that requires base-material qualification for welded service (Ref 4). Multipass welding provides the heat treatment. The welding parameters are chosen to represent the most severe heat treatment of the base material that may occur during fabrication. The parameter of interest is the fracture toughness, commonly measured by crack tip opening displacement (CTOD). Particular regions of the HAZ are the most likely to show low toughness (the local brittle zones, or LBZs), so there is also a requirement that the crack sample the required portion of that kind of microstructure.

Weld Procedure Qualification

Weldment properties are dependent not only on the materials used to make the joint but also on the other parameters of the welding process. Weld metal properties may be modified by the admixture of base material melted by the heat of welding. The region where the base metal was only partially melted, at the fusion line, may have local mechanical properties differing from those of the neighboring weld metal and HAZ regions. In addition, the welding processes and procedures may induce specific imperfections, such as slag inclusions, blowholes, or cracks.

Because the issues described cannot be resolved by either weld metal or base material tests alone, test procedures that use specimens containing weld metal, base metal, and HAZ are used to determine mechanical properties of welded joints in weldment procedure qualifications.

Weld procedure qualification tests may be less quantitative than weld metal qualification tests and often provide only a “yes-or-no” answer. They are often capable of being completed in a shop floor environment rather than a testing laboratory with calibrated equipment.

While many of the weld procedure qualification tests in wide use are discussed subsequently in this article, several are not, because they are not properly mechanical tests; that is, neither a loading parameter, such as stress, or a displacement parameter, such as strain, is measured. This group includes visual examination for surface flaws and the breaking of fillet welds to examine the weld root.

Weld Service Assessment

Assessment of existing welds to determine if they meet the needs of future service may require that material properties be obtained from representative weldments. In some cases, new weldments can be made with the same materials and process parameters, so that sections from these weldments can be tested to find representative properties for the existing welds. Generally, neither the original materials nor full information is available to allow replication of existing weldments. Instead, a sample must be taken from the existing weldments.

Taking a sample requires trading the advantage of obtaining mechanical property data for the disadvantage of damaging the existing structure. Choices often are made that limit the damage to the existing structure by limiting the amount of material to be tested. Tests such as macrohardness or microhardness, which damage a small surface volume, may be appropriate. Smaller-scale test specimens may also be used, for instance, subsize Charpy specimens. Alternatively, specimens can be taken from regions where subsequent repair is easiest or from an area that is being removed as part of a modification.

References cited in this section

3. “Specification for Carbon Steel Electrodes for Shielded Metal Arc Welding,” ANSI/AWS A5.1-91, American National Standards Institute/American Welding Society, Miami, 1991
4. “Recommended Practice for Preproduction Qualification for Steel Plates for Offshore Structures,” API 2Z, 2nd ed. (includes November 1998 addenda), American Petroleum Institute, Washington DC, 1998

Mechanical Testing of Welded Joints

William Mohr, Edison Welding Institute

Mechanical Testing for Weldment Properties

Tensile Strength and Ductility of Weldments

Testing for mechanical properties of strength and ductility for welded joints is somewhat more complicated than it is for base metal, because these properties vary across the weld metal, the adjacent HAZ, and the base metal. Several different tests may be used or combined to assess the strength of the overall welded joints. Tensile testing is widely used to measure the strength and ductility of the weld metal alone. Tensile testing of welds in place, with weld metal, HAZ, and base metal, allows an overall strength to be determined but usually cannot provide the strengths of the individual parts of the weldment.

Tensile tests of welds can also measure elastic modulus. However, except in rare cases of dissimilar metal joining, the elastic modulus is not sensitive to the differences between weld, HAZ, and base metal. So,

measurement during weld tensile tests is not usually required. Also, most tensile testing procedures for weld joints cannot be relied upon to provide accurate values of elastic modulus. The specific procedures for testing of elastic modulus distributed by ASTM should be used if required (Ref 5).

Testing of Weld Material. Deposited weld metal can be tested for the mechanical properties of strength and ductility using the same test methods used for base metals (Ref 6, 7). However, a sufficient volume of deposited weld metal is required to remove a test specimen made entirely of weld metal. Often, arc welds are long only in one direction (the longitudinal direction), while the through-thickness and cross-weld directions are much smaller. This encourages all-weld-metal tensile test specimens to be removed with the long direction of the specimen corresponding to the longitudinal direction of the weld. Such longitudinal tensile test specimens are standard for all-weld-metal tests.

All-weld-metal tests are most commonly done on specimens with round cross section. The diameter of the specimen may need to be reduced from that used for base metal so that the specimen can be taken entirely from weld metal. Rectangular cross-section specimens also are used occasionally.

Ultimate tensile strength, yield strength (usually based either on yield point or a specified offset), elongation, and reduction of area are all commonly recorded.

While the specimen surface should be smooth, without deep machining marks, imperfections within the gage length due to welding should not be removed. This requirement may increase the variability of results within a group of similar specimens.

If the data required are for a class of weld material such as an electrode lot, the material can be taken from specimens that reduce the possibility of dilution of base metal into the weld, such as a built-up weld pad. If the data required are for a particular weldment, the geometry as well as the welding process and procedure should model those of the weldment as closely as possible. Some modifications of the weldment may be allowed, such as increasing the root opening by 6 mm ($\frac{1}{4}$ in.) or buttering the groove faces with the weld metal to be tested.

The surface of the tested section, in the gage length, is recommended to be 3 mm ($\frac{1}{8}$ in.) or more from the fusion line.

Testing of Welds in Place. When the weld metal extends over only part of the tested gage length, tensile tests can be performed similar to those performed on the round and rectangular specimen tests of weld metal. The nonuniformity of deformation or stresses of the weld, HAZ, and base metal combination limits the information normally recorded.

For transverse tests, ultimate strength and the location of fracture are the only commonly recorded parameters, because strength, elongation, and reduction in area will all be affected by the constraint of the adjacent differing materials. If the weld is undermatched, the yield strength tends to be higher than it is for an all-weld-metal specimen, while the elongation over the gage length and reduction in area are smaller. If the weld yield strength exceeds that of the base material, that is, it is overmatched, the failure tends to occur not in the adjacent HAZ, but in the base material closer to the end of the gage length, because of the constraint provided by the high-strength weld metal.

Local strain measurements, such as those made by strain gages, can add useful information to the results of transverse testing. The local strain information can be correlated to the load and displacement information to allow local strengths to be determined.

For longitudinal tests, the strain will be nearly uniform across the weld metal, HAZ, and base metal. Differences in response to the applied strain may result in stresses varying across the cross section. Only ultimate strength is commonly measured.

Testing standards may need to be varied for some specific geometries. For instance, girth welded tubes of less than 75 mm (3 in.) diameter are commonly tested in the form of tubes with central plugs at the grips. The weld is placed at the center of the gage length between the grips. The additional constraint induced by the hoop direction continuity tends to increase the measured strengths and decrease the measured ductilities for tube welds tested in this manner compared to a similar joint between flat sheets.

Shear Testing of Fillet Welds

Shear strength tests for fillet welds are described in AWS B4.0 for two orientations of fillet welds (transverse to the tension loading and longitudinal to the tension loading) (Ref 8, 9). The transverse specimen is a double lap specimen with loaded fillet welds, as shown in Fig. 1. The longitudinal specimen is a combination of two

lapped shear plates that are tack welded back to back, as shown in Fig. 2. These geometries are chosen to avoid rotation during loading. The longitudinal specimen requires machining of grooves after the fillet welds are made. The base plate is cut under the center of the lapped plate. The lapped plate is cut near each end so that each length of weld connecting the base plate to the lapped plate across the gap in the base plate is 38 mm ($1\frac{1}{2}$ in.).

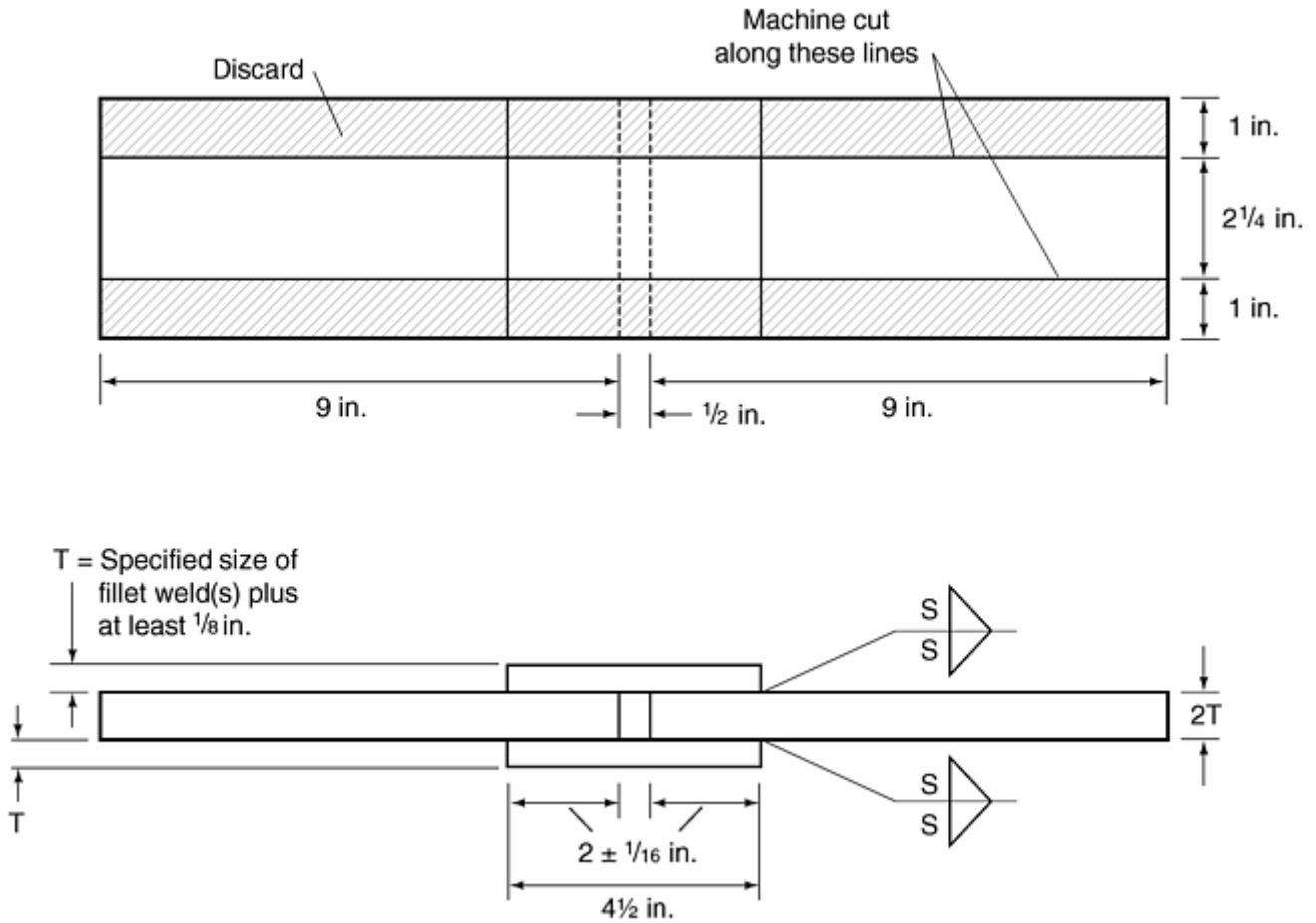


Fig. 1 Transverse fillet weld shear test specimen. Source: Ref 9

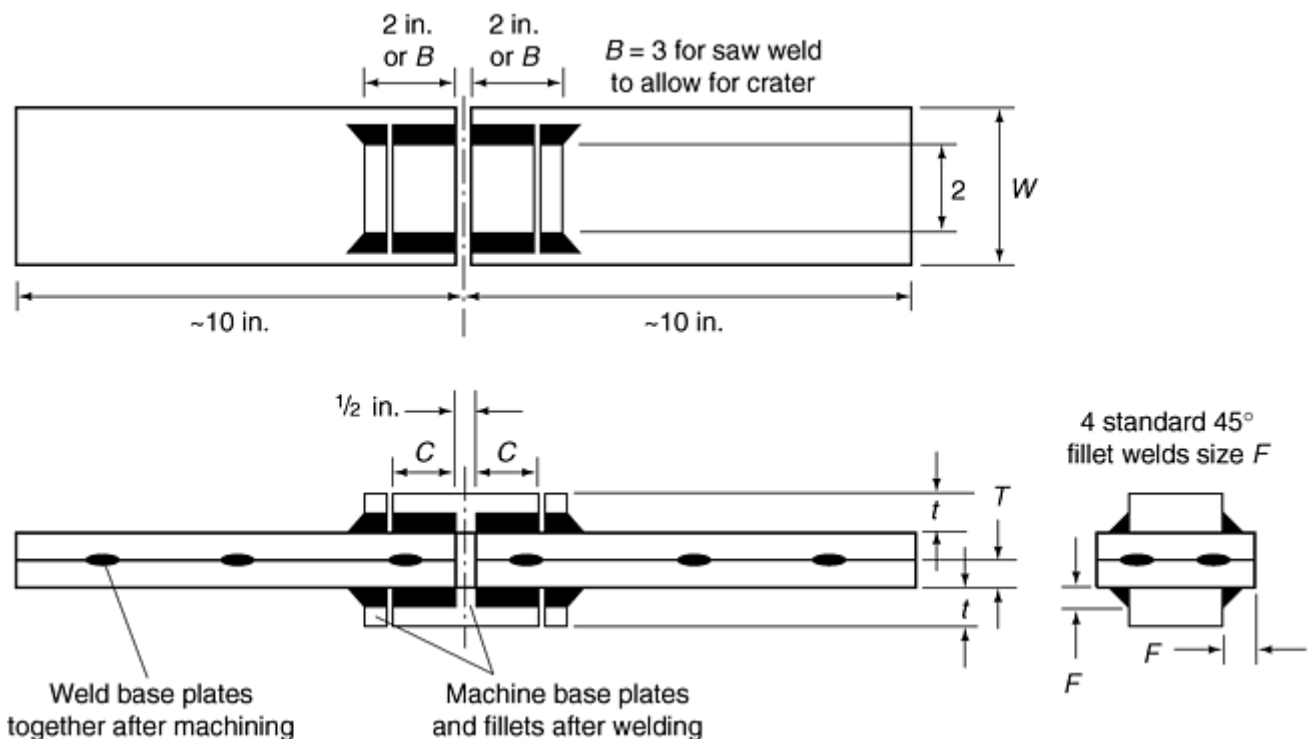


Fig. 2 Longitudinal fillet weld shear test specimen. Source: Ref 8

Fillet-weld strength tests are sensitive to surface contour of the welds and to the condition of the weld root. Excessive gaps between the lapped plates should be avoided, because these tend to magnify stresses at the weld root. The specimens are also sensitive to underbead cracking and undercut. Fillet size is most accurately measured after failure in the test. The stress is calculated based on assuming uniform stress across the entire weld throat.

Bending Strength and Ductility

Bend tests are commonly used to evaluate the acceptability of weld procedures for providing sound welds (Ref 10). They allow rapid determination of strength and ductility on a specimen substantially simpler than the standard tensile specimen. Bend tests tend to provide vivid demonstrations of difference between welds with surface or near-surface flaws and welds without flaws adjacent to the convex surface of the bend. Bend tests are further described in the article “Bend Testing” in this Volume.

Bending ductility can be calculated by determining the radius of the outer surface of the bend specimen at the completion of the test. This ductility is usually smaller than that measured in a uniaxial tensile test. The bend ductility is localized at the outer surface of the specimen, and the constraint is more severe because of the shear stresses generated through the thickness of the bend specimen.

The thickness of the specimens and the size of the plunger or mandrel determine the outer surface ductility requirement. Table 1 provides a summary of the radii of plungers or mandrels and the maximum test specimen thicknesses for several groups of materials as required by the American Society of Mechanical Engineers (ASME) Boiler and Pressure Vessel Code (Ref 11).

Table 1 Bend test geometry for testing based on material thickness and material type

Radius of plunger or mandrel	Maximum test thickness	Materials
$2t$	$\frac{1}{8}$ in.	With >20% elongation
$(3 + \frac{1}{3})t$	$\frac{1}{8}$ in.	Alloy steels with <20% elongation High strength Al alloys
$4t$	$\frac{1}{8}$ in.	Ti or Ti alloy with strength <65 ksi
$5t$	$\frac{1}{8}$ in.	Ti or Ti alloy with strength ≥ 65 ksi Zr or Zr alloy
$(8 + \frac{1}{4})t$	$\frac{1}{8}$ in.	4000 series Al alloy Al alloy welded with 4000 series electrodes Cu base alloys with Al and <20% elongation
(a)	(a)	Other alloys with <20% elongation

t , material thickness.

(a) Radius of plunger or mandrel and maximum test thickness chosen to achieve the required minimum elongation from a base metal tensile test at the outer fiber of the convex surface of the bent specimen

Increasing specimen width can increase the constraint and reduce the likelihood of achieving the required bend test radius without cracking. Face bends for welds in plates of greater than 38 mm ($1\frac{1}{2}$ in.) thickness may require multiple specimens.

Root, Side, and Face Bends. The primary geometries for bend test specimens place the butt weld so that the bending stress is transverse to the weld axis. Different areas of the welds reach the highest bending stress in transverse root bends, transverse face bends, and transverse side bends. Root bends put the weld-root side of the tested butt weld on the convex side of the bend specimen. Face bends put the weld-cap side of the tested butt weld on the convex side of the bend specimen. Side bends put a cross section of the weld on the convex side of the bend specimen.

Longitudinal bend tests may sometimes be used to replace transverse tests, particularly when the strengths of the regions within the specimen differ greatly. However, longitudinal side bends are not possible since the weld cross section does not include the longitudinal direction. Longitudinal root bends, with the convex side of the bent specimen on the weld-root side, and longitudinal face bends, with the convex side of the bent specimen on the weld-cap side, can both be made and tested.

Longitudinal tests are less likely than transverse tests to fail from flaws that are long in the same direction as the weld.

Wrap-Around Bend Testing. While the plunger-type bend fixtures are by far the most widely used for guided bend testing, some circumstances require a fixture that creates a different distribution of strain. The most common is a wrap-around testing fixture. Both the plunger type and the wrap-around type force the material into a specified radius. However, the wrap-around fixture moves the points of bending load application around a mandrel rather than using a fixed location for the central force, as shown in Fig. 3.

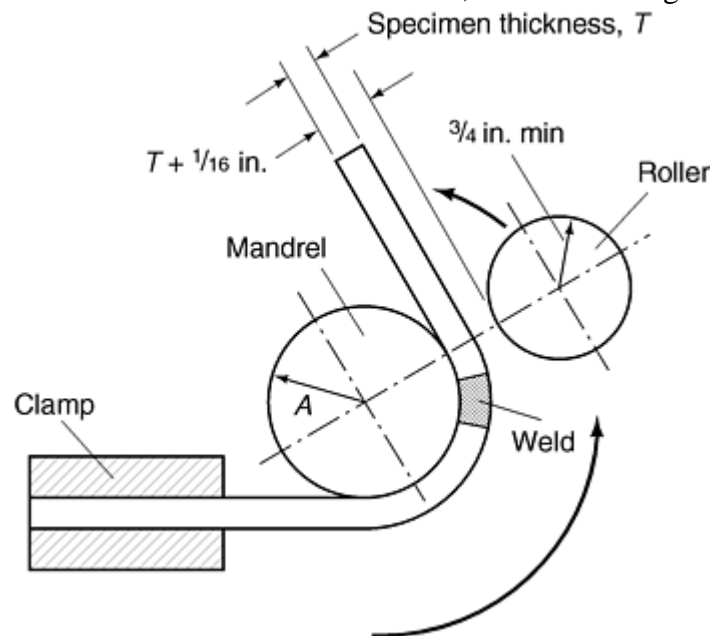


Fig. 3 Wrap-around bend testing. Source: Ref 9

The wrap-around fixture is most commonly used for welds that have significant mismatch between base metal strengths, between base metal and weld metal strengths, or where the HAZ strength differs greatly from the weld or base metal. If such welds are tested in a plunger-type fixture, the strain can be concentrated into the lower-strength material, leaving a sharper bend in that material and much less bending in the higher-strength material. The wrap-around fixture forces a more uniform strain into the materials because the loading point in the center of the specimen moves across the weld.

Wrap-around test fixtures are commonly used for aluminum alloys where the strength of the weld metal and HAZ may be chosen to be lower than the base metal. For instance, 6061-T6 aluminum base metal that is welded with 4043 electrodes has a minimum yield strength of 240 MPa (35 ksi) in the base metal but only 100 MPa (15 ksi) for cross-weld tensile specimens (Ref 12). Wrap-around testing can limit the localization of the strain at the weld.

Hardness

Hardness testing of welded joints is widely used as a rapid measurement of mechanical properties across the varying microstructures of the welded region. It allows local regions and individual microstructures to be compared for strength, because strength is correlated to hardness. A further discussion of hardness testing can be found in the Section “Hardness Testing” in this Volume.

Hardness has been primarily related to the tensile strength rather than to the yield strength or the ductility. Standard conversion charts are available for conversion of one hardness measurement to another and from hardness to tensile strength measurement. Such converted information should be used with caution, because the

variation of weld microstructure may cause the average hardness to correspond to values that cannot be obtained in larger scale specimens.

Macrohardness testing of welds requires preparation of a small region of the surface. The major techniques are Brinell testing, which uses a spherical indenter, and Rockwell testing, which uses a diamond penetrator or a sphere. The Brinell indentation is typically 2 to 6 mm in diameter while the Rockwell indentation is much smaller but still is visible, unaided. Rockwell methods use several different loads for different hardness scales, so it is possible for a weld to require different hardness scales for different regions.

Macrohardness testing results can be limited by the microstructural gradients around the welds. A result of 240 HB may represent a hardness for one uniform microstructure or an average over the regions deformed by the indenter. Welds and HAZs often have gradients of microstructure and chemistry that can cause variations in hardness across the indentation. Interpretation of the hardness from the impression may be made more difficult if there is a large gradient in the hardness of the material under the indenter. This can result in noncircular Brinell impressions and Rockwell tests with the deepest point not under the deepest point of the indenter.

Microindentation hardness testing using an indenter requires an even smaller region of the surface to be used than macrohardness testing, but the surface preparation requirements are more stringent. Thus the Knoop and Vickers microindentation hardness tests are primarily applied to ground and polished cross sections or to ground, polished, and etched cross sections. Microindentation hardness traverses are often used to determine the variation of hardness within the weld, across the fusion line, and across the HAZ.

Impact Toughness

Several methods are available for measuring the material resistance to starting and growing cracks that can be applied to welded joints. This section discusses test methods that cause a crack to grow from a notch under the rapid load of an impact. Methods that use sharp crack tips and thus can apply the loading more slowly are discussed in the next section on fracture toughness.

Charpy. The Charpy V-notch impact test is the most common measurement method for fracture toughness of welded joints. Specifications for the test are given in ASTM E 23 (Ref 13) and AWS B4.0. The test uses a pendulum hammer to rapidly fracture a notched bar with dimensions of 55 mm by 10 mm by 10 mm (2.165 in. by 0.394 in. by 0.394 in.).

Several measures of toughness can be obtained from a Charpy test. Absorbed energy, measured in ft · lbf or joules, is the most commonly reported, but the percent shear fracture and the lateral expansion in inches or millimeters are also sometimes reported. Greater toughness material will have higher values of each of these three parameters. Occasionally, percent fibrous fracture, which is 100% minus the percent shear fracture, is reported.

Many metals, including carbon and alloy steels, have toughnesses that vary strongly with temperature. So tests on welded joints are often conducted at several temperatures, and the absorbed energy or other parameter is plotted as a function of temperature. Material specifications and weld qualifications that include Charpy V-notch testing normally require a minimum absorbed energy at a particular temperature. In this case, testing is routinely conducted only at the temperature of interest.

The choice of minimum absorbed energy and test temperature are often varied between standards or within a standard, based on service conditions. For instance, welded joints on bridges to be used in cold climates are qualified to lower temperatures than those used in warm climates.

The absorbed energy in a Charpy V-notch test includes both the energy to start the crack from the 0.25 mm (0.010 in.) radius notch and the energy to propagate the crack across the Charpy specimen. For many cases, including constructional steels, these two parts are of comparable magnitude. In fact, the popularity of the Charpy V-notch test was originally based on its ability to predict both crack initiation and crack arrest in ship steel plates. This means that both the metal microstructure at the notch tip and through the specimen thickness contribute to the reported toughness. For welded joints with heterogeneous microstructures, the position of the notch tip will be important in determining the measured absorbed energy. The absorbed energy, however, will also depend on the microstructures through which the fracture passes.

The dependence of Charpy impact test results on microstructure for many metals causes weld joints with heterogeneous microstructures to have a range of Charpy values depending on specimen orientation in the weld and notch position. Often weld centerline values are reported or compared with standards. Sometimes the HAZ is tested at a particular location, such as 1 mm from the fusion line. These tests cannot determine a toughness

appropriate to all microstructures in the weld or HAZ. Additional tests of a greater variety of specimens may reveal zones of lower toughness, such as unrefined columnar weld metal or coarse-grained HAZ, or zones of higher toughness, such as reheated weld metal or fine-grained HAZ.

Subsize Charpy specimens are sometimes taken from thin material or areas where the geometry prevents a full-size specimen. Only one dimension is reduced, the distance from the notched face to the unnotched surface opposite. Reductions of this dimension can be from 10 mm (0.394 in.) to 7.5 mm (0.296 in.), called three-quarter size; to 5 mm (0.197 in.), called half-size; and to 2.5 mm (0.099 in.), called quarter-size. These are the most common reductions. Reduced thickness Charpy tests can be used to test the toughness of the root or cap regions of fillet welds.

Charpy toughness test specimens can be taken from welded joints in several orientations. These orientations can be given two-letter designations to show the orientation. The first letter is the direction normal to the crack plane (the long direction of the Charpy specimen), while the second letter is the direction in which the crack will propagate. The letter designations are L, longitudinal direction; T, long transverse direction (the weld width direction); and S, short transverse direction (the through thickness direction). The letter designations are shown for compact tension specimens in Fig. 4. Care should be taken that the orientation letters describe the weld area, because different combinations of these letters may apply to the same orientation of specimen in base metal. For instance, in a girth weld in a pipe, the long direction of the weld is the hoop direction of the pipe, not the longitudinal or axial direction of the pipe.

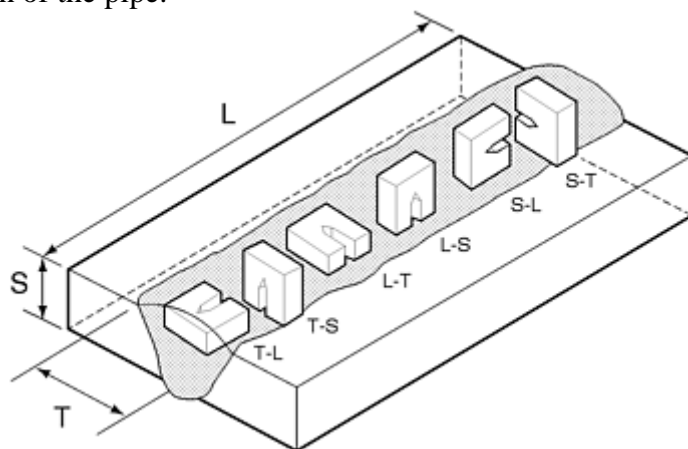


Fig. 4 Orientations of toughness specimens in relation to welds. L, longitudinal direction; T, long transverse direction (weld width direction); S, short transverse direction (weld thickness direction). In the two-letter code for specimen designation, the first letter designates the direction normal to the crack plane, and the second letter designates the expected direction of the crack plane. Source: Ref 9

Nil-Ductility Temperature. Drop weight tests use a notched weld bead as the starting point for a crack. The test determines the ability of the base metal to arrest the crack running from an overlay of brittle weld metal. The test results do not describe the properties of the overlay weld metal, so the overlay weld metal is standardized. A brittle hard-facing alloy with good surface adhesion is used as the crack starter.

ASTM E 208 describes the test procedure (Ref 14). A standard weight is dropped onto test specimens at different temperatures. The lowest temperature without full-section fracture is determined as the nil-ductility temperature (NDT).

Weld metal can be tested for crack arrest by placing the notched weld overlay across a machined butt weld of the weld metal of interest. The notch is typically placed so its long direction is above the longitudinal direction of the butt weld.

Fracture Toughness

Fracture toughness testing of welded joints introduces several complications to standard fracture toughness measurement as described in the Section “Impact Toughness Testing and Fracture Mechanics” in this Volume. The weld and adjacent HAZ will have heterogeneous microstructures that can have widely varying strength and toughness. In addition, welding residual stresses may be retained.

Fracture initiation testing, using slow loading and a crack tip sharpened by precracking, allows determination of only the crack initiation portion of the fracture toughness. Charpy testing determines a combination of crack initiation and arrest properties. Fracture initiation testing of welded joints thus is even more sensitive to the local microstructure around the tip of the precrack than Charpy tests are to the microstructure at the notch.

Weld heterogeneity also causes welds to be particularly sensitive to the rules for data interpretation for fracture initiation tests. Fatigue precracks are less likely to be straight in a heterogeneous material. Tests may have multiple events of crack initiation and arrest in local areas (“pop-ins”). Varying strengths may cause validity criteria based on yield strength and specimen size to give ambiguous results. Each of these issues must be accounted for in a test protocol appropriate to welds.

Fracture toughness specimens can be taken from welded joints in several orientations. These orientations can be given two-letter designations to show the orientation. The first letter is the direction normal to the crack plane, while the second letter is the direction in which the crack will propagate. The letter choices are L, longitudinal direction; T, long transverse direction (the weld width direction); and S, short transverse direction (the through thickness direction). The letter designations are shown for compact tension specimens in Fig. 4, but the same designations can be used for other shapes of test specimen. Care should be taken that the orientation letters describe the weld area, because different combinations of these letters may apply to the same orientation of specimen in base metal. For instance, in a girth weld in a pipe, the long direction of the weld is the hoop direction of the pipe, not the longitudinal or axial direction of the pipe.

Fracture toughness testing to measure the fracture resistance of weld HAZs presents particular problems, because several different microstructures can cluster within the HAZ, based on the different histories of heating from the welding in different locations. A fracture toughness measured from the HAZ is likely to be affected both by the properties of the several HAZ microstructures that the crack tip passes through and by the properties of the adjacent weld metal and base material.

Fracture initiation toughness is measured most commonly using the stress intensity factor, K ; the J -integral, J ; or the crack tip opening displacement (CTOD). All of these are regularly applied to welded joints. CTOD measurements are somewhat more commonly specified in welded regions than in base metal, because the test was originally developed for welded joints. Conversions between K , J , and CTOD are routinely performed but should be noted, because the correlations have limited precision.

Test Modifications for Welds. Fracture toughness testing of welds may require precise positioning of the notch to test the microstructure of interest. Testing of welds may also require modification of the test specimen. Two methods of modification, local compression and gull-winging (Ref 15), are described in the following section. Local compression counteracts the effects of welding residual stress. Gull-winging allows a curved piece with a weld to be tested as a full-thickness specimen.

Local Compression. The sharp crack tip needed for a fracture toughness test to determine initiation toughness is commonly provided by fatigue precracking at low levels of stress. In welds, fatigue precracking may produce a crack front that is not straight across the specimen. This is particularly likely when the specimen is thick and was removed from a weld with as-welded residual stresses. The crack tip of the fatigue precrack can deviate from the average straight line so much that the fracture toughness test results are invalidated because the crack depth is poorly described by a single average value.

Determining valid or invalid precracks is part of the standard to which the testing is done, such as ASTM E 1290 for CTOD testing (Ref 16) or ASTM E 1737 for J -integral testing (Ref 17).

A local compression treatment can be applied before precracking to avoid excessive deviation of the precrack from a straight line. Compression is applied in circular regions around the points where the notch tip reaches the surface, as shown in Fig. 5. Local compression can be applied to the most common fracture test specimen shapes, including compact tension specimens and single-edge notched bend bars.

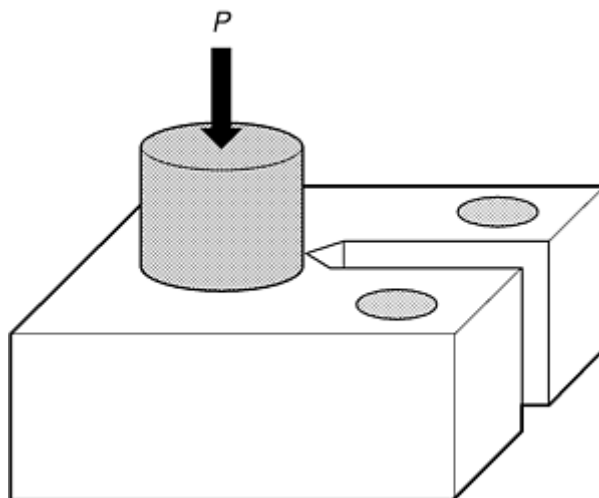


Fig. 5 Local compression of fracture specimens before fatigue precracking, P , load. Source: Ref 15

Gull-Winging. Some geometries of weld may be difficult to test for fracture toughness because the shape of the base metal around the weld limits the thickness or area of any standard geometry specimen, such as a compact tension specimen or a three-point bend bar. Welds in curved shapes, such as spheres and cylinders, can be particularly difficult.

As shown in Fig. 6(a), a flat specimen taken for fracture toughness testing from a curved part may be limited in dimension by both the inside surface and the outside surface of the curved part. This could force the use of small specimens preferentially determining the toughness near the inside or concave surface of the weld. Gull-winging is a mechanical bending process that allows the full thickness of the curved part to be used for fracture testing.

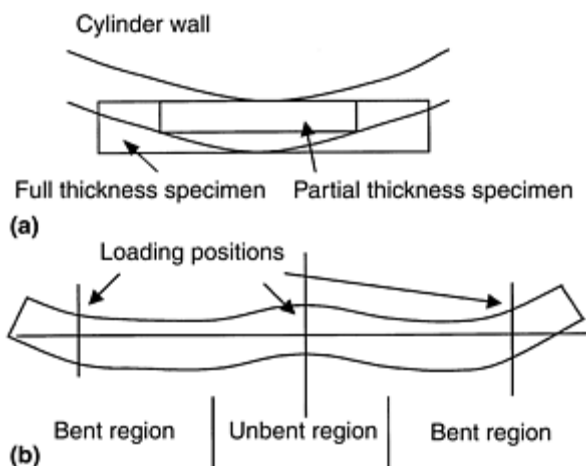


Fig. 6 Gull-winging of single-edge notched-bar weld fracture toughness specimen. (a) Small scale of specimen that can be obtained from a longitudinal weld in a cylinder compared to full thickness. (b) Gull-winged specimen at full cylinder thickness ready to be loaded. Source: Ref 15

Full-thickness transverse tests using a modified three-point bend bar geometry may be used for geometries where the weld is straight but the curvature is transverse to the weld by gull-winging. The gull wings are introduced by plastically bending the base material away from the weld. These bends must allow the three locations of loading to be the same as if the specimen were flat, as shown in Fig. 6(b). During gull-winging, the area adjacent to the weld must be supported to prevent plastic deformation of the weld or the area directly adjacent to it.

Gull-winged specimens should have limited deviation from the flat centerline of the equivalent flat specimen. Greater deviation may allow plastic deformation during testing at the point of greatest deviation.

References cited in this section

5. "Standard Test Method for Young's Modulus, Tangent Modulus, and Chord Modulus," E 111, *Annual Book of ASTM Standards*, Vol 3.01, ASTM, 1999
6. "Standard Methods of Tension Testing of Metallic Materials," E 8, *Annual Book of ASTM Standards*, Vol 3.01, ASTM, 1999
7. "Standard Methods of Tension Testing Wrought and Cast Aluminum, and Magnesium Alloy Products," B 557, *Annual Book of ASTM Standards*, Vol 3.01, ASTM, 1999
8. B4 Committee on Mechanical Testing of Welds, Mechanical Testing of Welds, Part 1: Summary of Tension Testing of Welds, *Weld. J.*, Jan 1981, p 33–37
9. "Standard Methods for Mechanical Testing of Welds," ANSI/AWS B4.0-98, American National Standards Institute/American Welding Society, Miami, 1998
10. B4 Committee on Mechanical Testing of Welds, Mechanical Testing of Welds, Part 2: Bend Testing of Welds. A Summary, *Weld. J.*, Feb 1981, p 34–37
11. *ASME Boiler and Pressure Vessel Code*, Section IX, American Society of Mechanical Engineers
12. *Aluminum Design Manual*, The Aluminum Association, 1994
13. "Standard Test Methods for Notched Bar Impact Testing of Metallic Materials," E 23, *Annual Book of ASTM Standards*, Vol 3.01, ASTM
14. "Standard Method for Conducting Drop-Weight Test to Determine Nil-Ductility Transition Temperature of Ferritic Steels," E 208, *Annual Book of ASTM Standards*, Vol 3.01, ASTM
15. M.G. Dawes, H.G. Pisarski, and S. J. Squirrell, Fracture Mechanics Tests on Welded Joints, *Nonlinear Fracture Mechanics Vol II: Elastic-Plastic Fracture*, STP 995, J.D. Landes, A. Saxena, and J.G. Merkle, Ed., ASTM, 1989, p 191–213
16. "Standard Test Method for Crack-Tip Opening Displacement (CTOD) Fracture Toughness Measurement," E 1290, *Annual Book of ASTM Standards*, Vol 3.01, ASTM
17. "Standard Test Method for *J*-Integral Characterization of Fracture Toughness," E 1737, *Annual Book of ASTM Standards*, Vol 3.01, ASTM

Mechanical Testing of Welded Joints

William Mohr, Edison Welding Institute

Residual Stress Measurement

Residual stress measurement on welded joints must take account of the characteristics of the welded joint. Welds usually have gradients of residual stress through the weld area and have these residual stress gradients in the same regions as gradients in microstructure. These features may limit the amount of information that can be obtained from some techniques. Some residual stress measurement techniques, for instance, work by comparing the distances between atoms in the crystal structure from an unstressed area to the stressed area of interest. If no

unstressed area is available with the same crystal structure as the weld, the zero stress level for that weld region would be uncertain.

Two general types of measurements for residual stress in welds are most common: locally destructive techniques and nondestructive techniques. The locally destructive techniques include hole drilling, chip machining, groove machining, and block sectioning. These measure changes in strain as a new surface is created and determine residual stresses most sensitively around the area where the machining took place. The nondestructive techniques measure the local strain of the material by inputting a physical change, receiving a signal based upon that change and the residual stress, and then decoding the part of the signal induced by the residual stress. These techniques include x-ray diffraction, neutron diffraction, Barkhausen noise analysis, and ultrasonic propagation analysis.

Both groups of techniques do not measure stress directly. Both measure strain. Both groups have limitations for measuring rapidly varying residual stress fields because they need to sample a volume of material to get sufficient signal to determine the residual stresses with precision.

Sectioning Methods

One extreme way of imagining a residual stress measurement of a welded region is that many tiny pieces of the weldment could all be separated simultaneously from neighboring pieces and allowed to change shape to reach zero residual stress. The shape change in each tiny piece could be measured and that change correlated using the elastic properties of the material to the residual stress originally in each piece of the weldment.

Sectioning methods can come close to this extreme case, but each cut cannot happen simultaneously. So analysis techniques for determining residual stress by multiple cuts need to include calculations of the effects of previous cuts on the residual stress to find the original stress rather than the stress determined for an individual cut.

Block sectioning and block layering and sectioning are significantly more destructive than hole drilling. The part for which the residual stresses will be determined is cut into sections and layers while surface strain gages are monitored. These techniques can provide distributions of residual stress in multiple dimensions.

Hole Drilling and Similar Local Measurements

Hole drilling techniques, often called center-hole drilling or blind-hole drilling, measure the change in strain on the adjacent surface as the residual stress field is disturbed by the machining of a hole from that surface (Ref 18). The hole depth is generally between 1 and 2 mm (0.04 and 0.08 in.), although several organizations make residual stress measurements as a function of hole depth as the hole is drilled.

The drilling techniques should cause as little as possible additional stress around the hole, so techniques are commonly used that avoid contact of the walls of the hole as the bottom is drilled. Air turbine and air abrasion systems can provide holes with close dimensional tolerance and little machining-induced surface stress on the hole. Specialized strain gage rosettes are available for measurement, both with the hole placed in the center of the rosette and with the rosette on one side of the hole. The rosette on one side of the hole is used for cases where the surface is obstructed on one side of the measurement position, as may happen adjacent to a weld toe. The measured strain must be converted to a local residual stress in the area where the hole was drilled. This conversion can be done most simply by assuming a uniform residual stress distribution. Only components of the residual stress that are parallel to the surface are measured by this technique, giving two directions of axial stress and one of shear stress.

Chip machining has been used similarly to hole drilling to determine near-surface residual stresses. In this case, a small region of the surface is removed with the strain gage rosette on the surface of the chip rather than attached to the base material. The advantage is that the small chip can be assumed to reach essentially zero residual stress, so the change of strain measured on the chip can be directly correlated to the stress in the chip region. However, the chip must be larger than the most common size of drilled hole to carry the strain gage. The chip machining method will average the strains over a larger volume of material.

Other shapes of local machining can be used, including deep holes and partial thickness slits (Ref 19). These methods can measure residual strains either with surface strain gages or with measurements of post-cut displacement. As with hole drilling, only part of the residual stress tensor is obtained by these methods, but the direction of cutting can be oriented to find the residual stresses of most interest.

Nondestructive Techniques

Nondestructive techniques for measuring residual strains in welded joints use a variety of inputs, including x-rays, neutrons, magnetic signals, and ultrasonic waves. Each of these inputs can induce different outputs, depending on the residual strains in the welded joint area, but also depending on other parameters, such as the crystal structure or grain size. Nondestructive techniques thus are best applied where a standard for comparison without residual strains but with the same microstructure is available. The comparison of test material with an unstrained standard may be easiest in base metal outside the HAZ and much more difficult for HAZ or weld metal (Ref 20).

X-ray diffraction determines the residual strains by measuring the average distances between atoms. X-rays, being limited in surface penetration in metallic materials, can be used for detection of residual strains only within approximately 0.5 mm (0.02 in.) of the surface on which they impinge. The surfaces of welds may be more difficult locations than smooth surfaces of base material for measurement of residual strains. The rough surface of the weld cap and notches at weld toes may cause some of the area of interest for residual strain measurement to be hidden from residual stress detection by x-rays.

Neutron diffraction uses an input that is much more difficult and costly to generate than x-rays but has the advantage of penetrating much further into metallic materials. Neutrons can be used for detection of residual strains in steel thicknesses beyond 25 mm (1 in.). Average values of the residual strains are determined in a volume approximately 1 mm^3 ($6 \times 10^{-4} \text{ in.}^3$). The power of the source, the efficiency of the detector, and the time of exposure all influence the volume required for residual stress detection. Neutron diffraction is easiest when the grain size is significantly smaller than the detection volume and the grains are oriented randomly. Large grains and highly oriented microstructures can eliminate the diffracted neutron signal.

Barkhausen noise analysis uses an external varying magnetic field as input and monitors the magnetic response of the area of interest. The response comes from the jumps in magnetization as magnetic domain walls move within the metal. This response is a surface response, so the surface condition of the part is important.

Ultrasonic propagation analysis inputs ultrasonic waves and then monitors the response of the time taken for the waves to travel through the metal and reach the detector. Since the residual stress distribution can change the speed of propagation all along the path of the ultrasound, the resulting effect is summed over the entire path. Multiple path analysis can provide local results.

Barkhausen noise and ultrasonic propagation analysis both are limited by the microstructural variations around welds. The combination of welding induced changes cannot be easily deconvoluted, because both techniques are comparing unstressed areas to stressed areas and also are sensitive to microstructural variation.

References cited in this section

18. N.J. Rendler and I. Vigness, Hole-Drilling Strain-Gage Method of Measuring Residual Stresses, *Experimental Mechanics*, Vol 6, 1966, p 577–586
19. W. Cheng and I. Finnie, A Method for Measurement of Axisymmetric Axial Residual Stresses in Circumferentially Welded Thin-Walled Cylinders, *J. Eng. Mater. Technol. (Trans. ASME)*, Vol 107, July 1985, p 181–185
20. D.S. Kim and J.D. Smith, Residual Stress Measurements of Tension Leg Platform Tendon Welds, *Proc. of the Offshore Mechanics and Arctic Engineering Conference 1994*, Vol 3, American Society of Mechanical Engineers, 1994

Mechanical Testing of Welded Joints

William Mohr, Edison Welding Institute

Weldability Testing

Weldability, while sometimes defined in the general sense as the measure of the compatibility of base metal and any added filler metal with the heating cycles used for welding, is more commonly defined as the measure of the resistance of the materials to the formation of cracks during welding. Methods are available for assessing both hot cracking, at or near the solidification temperature, and cold cracking, at or near room temperature. Test methods do not check for all types of cracking at once, but, instead, each test checks for the susceptibility to a certain type of crack.

Weldability tests have been designed to allow small-scale specimens to mimic the cracking behavior of large, rigid welded structures. These tests either use specimen geometry to force the shrinkage of the weldment as it cools to be counteracted by plastic extension of the weld and HAZ, or they use additional loading to achieve plastic extension of weld and HAZ in addition to that caused by weld shrinkage. The bulk of this section will discuss the types of tests where additional loadings are required, because these are properly mechanical tests. A limited discussion of some test methods without additional loading is also provided for comparison.

The techniques that include welding and loading to measure weldability have been designed primarily for hot cracking at temperatures at or just below that for the last solidification of weld metal. The loading augments the shrinkage strains. Cracking when the weld has cooled, such as cracks due to hydrogen, is usually tested using welding without additional loading.

Varestraint Testing

Varestraint testing uses a cantilever beam specimen that is bent downward by a rapid application of force while a weld is being made on the top surface of the beam (Ref 21, 22). The weld is made parallel to the direction of tension once the force is applied with the welding torch moving toward the support point, as shown in Fig. 7. A die block 51 mm (4 in.) long is placed beneath the specimen to force it to a limiting value of augmented strain. The radius of the die block can be varied to examine the dependence of cracking on augmented strain, or a single radius can be used to examine the effect of other welding variables such as base metal chemistry or weld heat input. Common values of the augmented strain are between 0 and 4%. Standard varestraint testing methods are discussed in AWS B4.0.

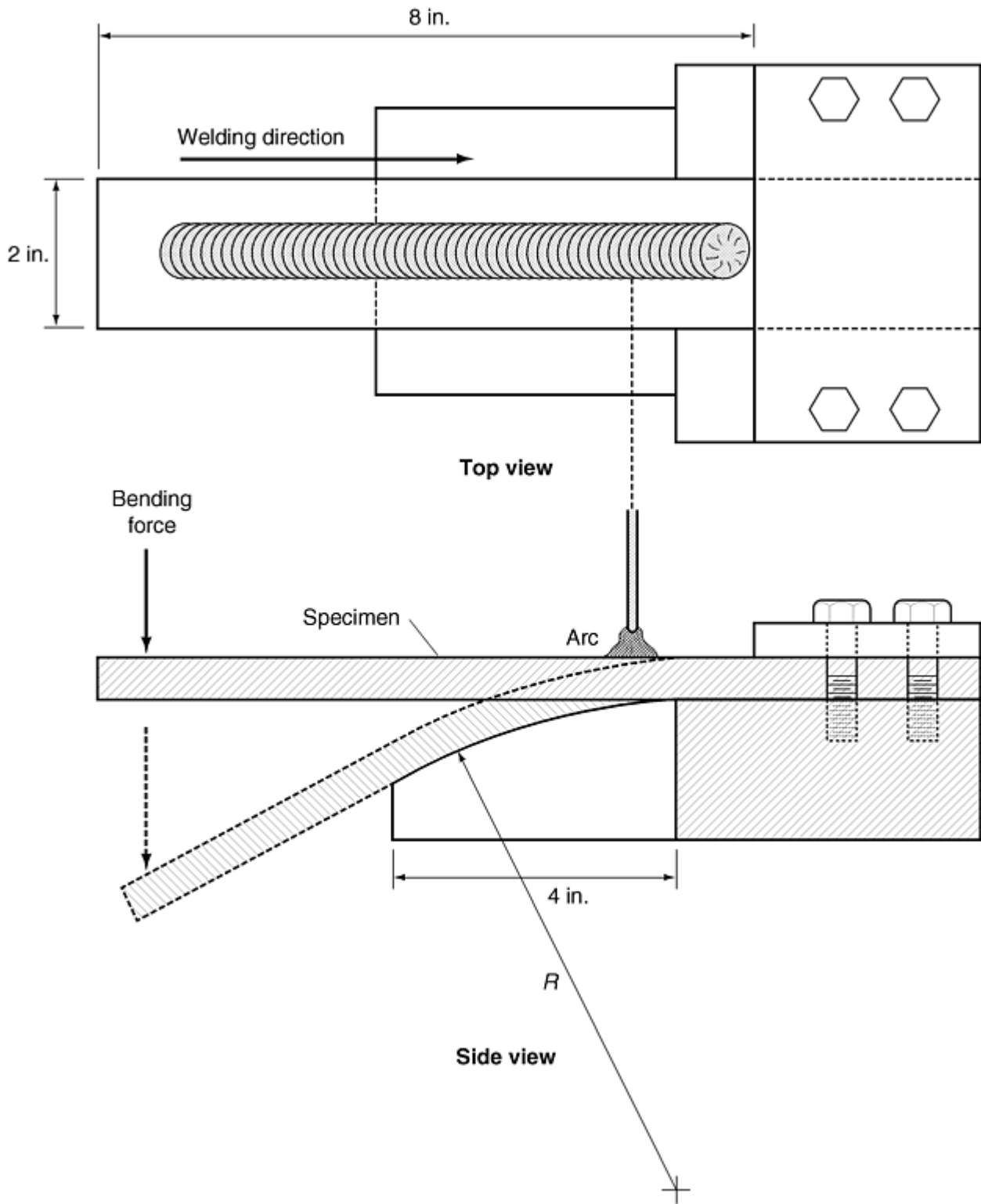


Fig. 7 Varestraint test fixture and specimen. Source: Ref 9

The specimen size is usually 305 mm (12 in.) long and 51 mm (2 in.) wide with a thickness of either 6 or 12.5 mm ($\frac{1}{4}$ or $\frac{1}{2}$ in.), although minivarestraint specimens are sometimes tested, which reduce all dimensions by a factor of 2. To prevent local kinking of the specimen, auxiliary plates are bent along with the test plate. The auxiliary plates, rolled steel 305 mm by 51 mm by 12.5 or 6 mm (12 in. by 2 in. by $\frac{1}{2}$ or $\frac{1}{4}$ in.), are clamped to the edges of the test plate. A minimum of three specimens are tested for any experimental condition. The weld on the top surface is produced by gas tungsten arc welding (GTAW). Measurements are based on crack length of cracks found in the HAZ or fusion zone. Hot cracks typically form radially along the trailing edge of the weld pool and in the HAZ. Either the length of the longest crack or the total combined crack length of all cracks is the measured parameter. Cracks are counted and sized on the

surface under a low power microscope (40 to 80×). One parameter of interest is the maximum augmented strain without cracks. However, because only one augmented strain is measured per specimen, the value is most closely estimated by extrapolating to zero the crack length measured at higher augmented strains. Transvarestraint testing also uses welding on the top surface on a piece that is bent over a die block (Ref 23). However, the force is applied so that tension is rapidly applied across the direction of welding rather than along it. This method detects cracking sensitivity in weld metal more effectively than the original varestraint method. Cracks in weld metal are more likely to be subsurface, so weld cross sections or nondestructive methods, such as radiography, are required to observe the subsurface cracks. One problem with transvarestraint tests is that cracks formed during the rapid loading may continue to propagate after the specimen has been bent.

Spot Varestraint Testing

The spot varestraint test, or TIG-A-MA-JIG test, is a modification of the varestraint test. This test uses a stationary welding torch (Ref 24). The torch is shut off at the instant of bending of the specimen or a specified short time before.

The size of the weld pool should remain relatively constant between tests that are to be compared. This may require changes of welding current or arc time when materials of differing thicknesses are compared.

The die block for the spot varestraint test is curved in only one direction, that is, it is shaped like the surface of a cylinder. Cracking, thus, will be primarily found transverse to the tension above the highest part of the surface of the die block. Radii for the die block have ranged from 44.5 to 1270 mm (1.75 to 50 in.).

Like the varestraint test, cracks are measured visually on the surface using a low-power microscope. Because this test is primarily used to test for HAZ liquation cracks, crater cracks in the center of the weld metal are ignored.

A measure of the relative susceptibility to HAZ liquation cracks that is not available in the varestraint test is the shortest time from torch shut-off to bending that produces no cracks.

Weldability Testing without Augmented Strain

Weldability testing without augmented strain requires that the weld be made in a highly restrained specimen. Highly restrained geometries prevent weld shrinkage in more than one direction. Cracking is typically from the root of the weld, either at a fillet weld or a partial penetration butt weld. Specimen shapes sometimes surround the weld metal with base metal, as in the Lehigh restraint test. Other test geometries, such as the oblique Y-groove test, join two plates with welds at the ends and then put the test weld in the center.

References cited in this section

9. "Standard Methods for Mechanical Testing of Welds," ANSI/AWS B4.0-98, American National Standards Institute/American Welding Society, Miami, 1998
21. W.F. Savage and C.D. Lundin, The Varestraint Test, *Weld. J.*, October 1965, p 433s-442s
22. C.D. Lundin, A.C. Lingenfelter, G.E. Grotke, G.G. Lessmann, and S.J. Matthews, *The Varestraint Test*, Bulletin 280, Welding Research Council, August 1982
23. B.F. Dixon, R.H. Phillips, and J.C. Ritter, Cracking in the Transvarestraint Test, Part 1: A New Procedure for Assessment of Cracking, *Met. Constr.*, Feb 1984 and *Aust. Weld. J.*, Vol 28 (No. 4), summer 1983
24. W. Lin, J.C. Lippold, and W.A. Baeslack III, An Evaluation of Heat-Affected Zone Liquation Cracking Susceptibility, Part I: Development of a Method for Quantification, *Weld. J.*, Vol 72 (No. 4), 1993, p 135s-153s

Weldability Testing

Weldability, while sometimes defined in the general sense as the measure of the compatibility of base metal and any added filler metal with the heating cycles used for welding, is more commonly defined as the measure of the resistance of the materials to the formation of cracks during welding. Methods are available for assessing both hot cracking, at or near the solidification temperature, and cold cracking, at or near room temperature. Test methods do not check for all types of cracking at once, but, instead, each test checks for the susceptibility to a certain type of crack.

Weldability tests have been designed to allow small-scale specimens to mimic the cracking behavior of large, rigid welded structures. These tests either use specimen geometry to force the shrinkage of the weldment as it cools to be counteracted by plastic extension of the weld and HAZ, or they use additional loading to achieve plastic extension of weld and HAZ in addition to that caused by weld shrinkage. The bulk of this section will discuss the types of tests where additional loadings are required, because these are properly mechanical tests. A limited discussion of some test methods without additional loading is also provided for comparison.

The techniques that include welding and loading to measure weldability have been designed primarily for hot cracking at temperatures at or just below that for the last solidification of weld metal. The loading augments the shrinkage strains. Cracking when the weld has cooled, such as cracks due to hydrogen, is usually tested using welding without additional loading.

Varestraint Testing

Varestraint testing uses a cantilever beam specimen that is bent downward by a rapid application of force while a weld is being made on the top surface of the beam (Ref 21, 22). The weld is made parallel to the direction of tension once the force is applied with the welding torch moving toward the support point, as shown in Fig. 7. A die block 51 mm (4 in.) long is placed beneath the specimen to force it to a limiting value of augmented strain. The radius of the die block can be varied to examine the dependence of cracking on augmented strain, or a single radius can be used to examine the effect of other welding variables such as base metal chemistry or weld heat input. Common values of the augmented strain are between 0 and 4%. Standard varestraint testing methods are discussed in AWS B4.0.

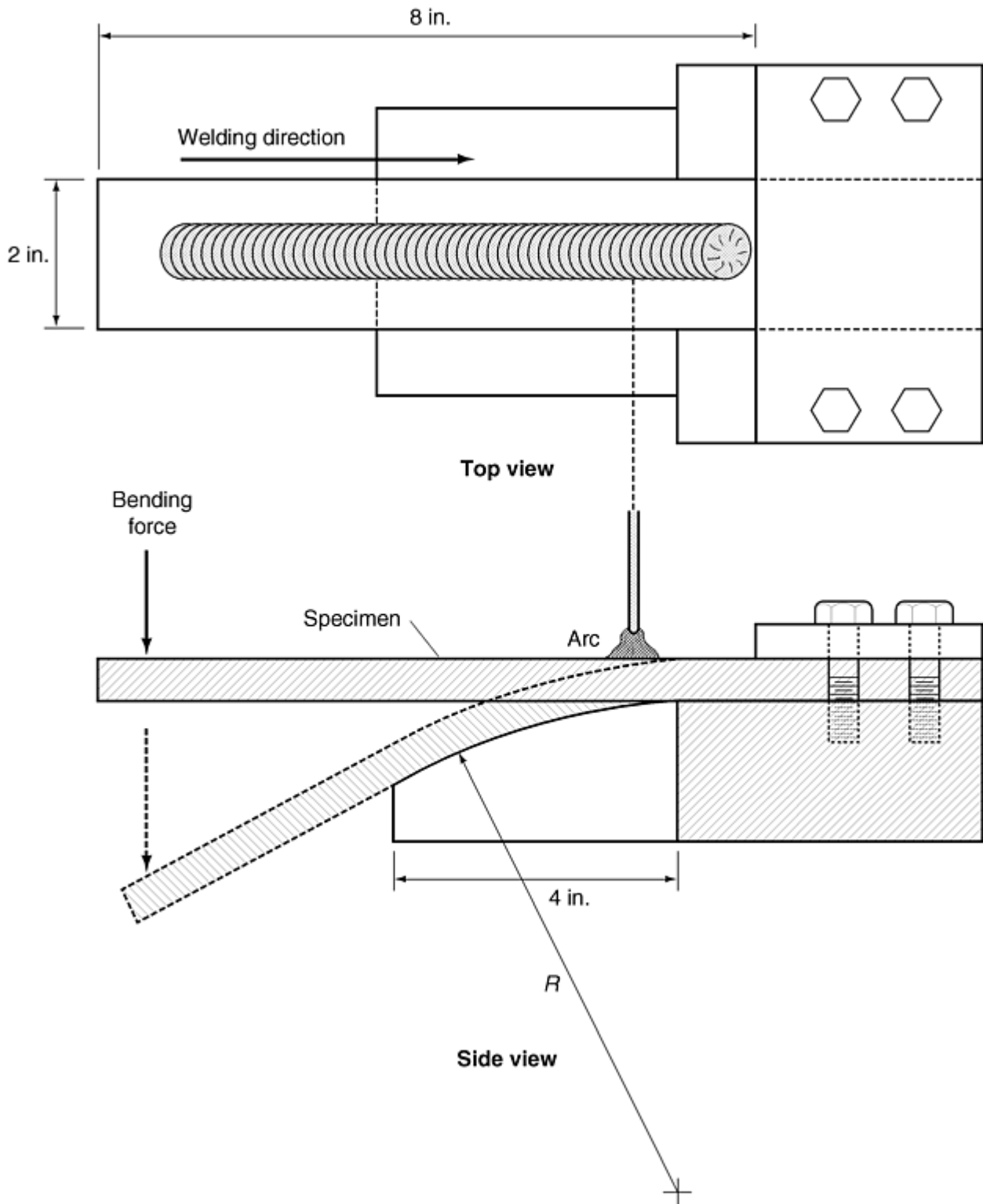


Fig. 7 Restraint test fixture and specimen. Source: Ref 9

The specimen size is usually 305 mm (12 in.) long and 51 mm (2 in.) wide with a thickness of either 6 or 12.5 mm ($\frac{1}{4}$ or $\frac{1}{2}$ in.), although minirestraint specimens are sometimes tested, which reduce all dimensions by a factor of 2. To prevent local kinking of the specimen, auxiliary plates are bent along with the test plate. The auxiliary plates, rolled steel 305 mm by 51 mm by 12.5 or 6 mm (12 in. by 2 in. by $\frac{1}{2}$ or $\frac{1}{4}$ in.), are clamped to the edges of the test plate. A minimum of three specimens are tested for any experimental condition. The weld on the top surface is produced by gas tungsten arc welding (GTAW).

Measurements are based on crack length of cracks found in the HAZ or fusion zone. Hot cracks typically form radially along the trailing edge of the weld pool and in the HAZ. Either the length of the longest crack or the total combined crack length of all cracks is the measured parameter. Cracks are counted and sized on the surface under a low power microscope (40 to 80 \times). One parameter of interest is the maximum augmented strain

without cracks. However, because only one augmented strain is measured per specimen, the value is most closely estimated by extrapolating to zero the crack length measured at higher augmented strains.

Transvarestraint testing also uses welding on the top surface on a piece that is bent over a die block (Ref 23). However, the force is applied so that tension is rapidly applied across the direction of welding rather than along it. This method detects cracking sensitivity in weld metal more effectively than the original varestraint method. Cracks in weld metal are more likely to be subsurface, so weld cross sections or nondestructive methods, such as radiography, are required to observe the subsurface cracks.

One problem with transvarestraint tests is that cracks formed during the rapid loading may continue to propagate after the specimen has been bent.

Spot Varestraint Testing

The spot varestraint test, or TIG-A-MA-JIG test, is a modification of the varestraint test. This test uses a stationary welding torch (Ref 24). The torch is shut off at the instant of bending of the specimen or a specified short time before.

The size of the weld pool should remain relatively constant between tests that are to be compared. This may require changes of welding current or arc time when materials of differing thicknesses are compared.

The die block for the spot varestraint test is curved in only one direction, that is, it is shaped like the surface of a cylinder. Cracking, thus, will be primarily found transverse to the tension above the highest part of the surface of the die block. Radii for the die block have ranged from 44.5 to 1270 mm (1.75 to 50 in.).

Like the varestraint test, cracks are measured visually on the surface using a low-power microscope. Because this test is primarily used to test for HAZ liquation cracks, crater cracks in the center of the weld metal are ignored.

A measure of the relative susceptibility to HAZ liquation cracks that is not available in the varestraint test is the shortest time from torch shut-off to bending that produces no cracks.

Weldability Testing without Augmented Strain

Weldability testing without augmented strain requires that the weld be made in a highly restrained specimen. Highly restrained geometries prevent weld shrinkage in more than one direction. Cracking is typically from the root of the weld, either at a fillet weld or a partial penetration butt weld. Specimen shapes sometimes surround the weld metal with base metal, as in the Lehigh restraint test. Other test geometries, such as the oblique Y-groove test, join two plates with welds at the ends and then put the test weld in the center.

References cited in this section

9. "Standard Methods for Mechanical Testing of Welds," ANSI/AWS B4.0-98, American National Standards Institute/American Welding Society, Miami, 1998
21. W.F. Savage and C.D. Lundin, The Varestraint Test, *Weld. J.*, October 1965, p 433s-442s
22. C.D. Lundin, A.C. Lingenfelter, G.E. Grotke, G.G. Lessmann, and S.J. Matthews, *The Varestraint Test*, Bulletin 280, Welding Research Council, August 1982
23. B.F. Dixon, R.H. Phillips, and J.C. Ritter, Cracking in the Transvarestraint Test, Part 1: A New Procedure for Assessment of Cracking, *Met. Constr.*, Feb 1984 and *Aust. Weld. J.*, Vol 28 (No. 4), summer 1983
24. W. Lin, J.C. Lippold, and W.A. Baeslack III, An Evaluation of Heat-Affected Zone Liquation Cracking Susceptibility, Part I: Development of a Method for Quantification, *Weld. J.*, Vol 72 (No. 4), 1993, p 135s-153s

References

1. "Standard Welding Terms and Definitions," AWS 3.0, American Welding Society
2. L.P. Connor, Ed., *Welding Handbook*, 8th ed., Vol 1, American Welding Society, 1991
3. "Specification for Carbon Steel Electrodes for Shielded Metal Arc Welding," ANSI/AWS A5.1-91, American National Standards Institute/American Welding Society, Miami, 1991
4. "Recommended Practice for Preproduction Qualification for Steel Plates for Offshore Structures," API 2Z, 2nd ed. (includes November 1998 addenda), American Petroleum Institute, Washington DC, 1998
5. "Standard Test Method for Young's Modulus, Tangent Modulus, and Chord Modulus," E 111, *Annual Book of ASTM Standards*, Vol 3.01, ASTM, 1999
6. "Standard Methods of Tension Testing of Metallic Materials," E 8, *Annual Book of ASTM Standards*, Vol 3.01, ASTM, 1999
7. "Standard Methods of Tension Testing Wrought and Cast Aluminum, and Magnesium Alloy Products," B 557, *Annual Book of ASTM Standards*, Vol 3.01, ASTM, 1999
8. B4 Committee on Mechanical Testing of Welds, Mechanical Testing of Welds, Part 1: Summary of Tension Testing of Welds, *Weld. J.*, Jan 1981, p 33–37
9. "Standard Methods for Mechanical Testing of Welds," ANSI/AWS B4.0-98, American National Standards Institute/American Welding Society, Miami, 1998
10. B4 Committee on Mechanical Testing of Welds, Mechanical Testing of Welds, Part 2: Bend Testing of Welds. A Summary, *Weld. J.*, Feb 1981, p 34–37
11. *ASME Boiler and Pressure Vessel Code*, Section IX, American Society of Mechanical Engineers
12. *Aluminum Design Manual*, The Aluminum Association, 1994
13. "Standard Test Methods for Notched Bar Impact Testing of Metallic Materials," E 23, *Annual Book of ASTM Standards*, Vol 3.01, ASTM
14. "Standard Method for Conducting Drop-Weight Test to Determine Nil-Ductility Transition Temperature of Ferritic Steels," E 208, *Annual Book of ASTM Standards*, Vol 3.01, ASTM
15. M.G. Dawes, H.G. Pisarski, and S. J. Squirrell, Fracture Mechanics Tests on Welded Joints, *Nonlinear Fracture Mechanics Vol II: Elastic-Plastic Fracture*, STP 995, J.D. Landes, A. Saxena, and J.G. Merkle, Ed., ASTM, 1989, p 191–213
16. "Standard Test Method for Crack-Tip Opening Displacement (CTOD) Fracture Toughness Measurement," E 1290, *Annual Book of ASTM Standards*, Vol 3.01, ASTM

17. "Standard Test Method for J -Integral Characterization of Fracture Toughness," E 1737, *Annual Book of ASTM Standards*, Vol 3.01, ASTM
18. N.J. Rendler and I. Vigness, Hole-Drilling Strain-Gage Method of Measuring Residual Stresses, *Experimental Mechanics*, Vol 6, 1966, p 577–586
19. W. Cheng and I. Finnie, A Method for Measurement of Axisymmetric Axial Residual Stresses in Circumferentially Welded Thin-Walled Cylinders, *J. Eng. Mater. Technol. (Trans. ASME)*, Vol 107, July 1985, p 181–185
20. D.S. Kim and J.D. Smith, Residual Stress Measurements of Tension Leg Platform Tendon Welds, *Proc. of the Offshore Mechanics and Arctic Engineering Conference 1994*, Vol 3, American Society of Mechanical Engineers, 1994
21. W.F. Savage and C.D. Lundin, The Vareststraint Test, *Weld. J.*, October 1965, p 433s–442s
22. C.D. Lundin, A.C. Lingenfelter, G.E. Grotke, G.G. Lessmann, and S.J. Matthews, *The Vareststraint Test*, Bulletin 280, Welding Research Council, August 1982
23. B.F. Dixon, R.H. Phillips, and J.C. Ritter, Cracking in the Transvareststraint Test, Part 1: A New Procedure for Assessment of Cracking, *Met. Constr.*, Feb 1984 and *Aust. Weld. J.*, Vol 28 (No. 4), summer 1983
24. W. Lin, J.C. Lippold, and W.A. Baeslack III, An Evaluation of Heat-Affected Zone Liquation Cracking Susceptibility, Part I: Development of a Method for Quantification, *Weld. J.*, Vol 72 (No. 4), 1993, p 135s-153s

Testing of Bearings

Charles A. Moyer, The Timken Company (Retired)

Introduction

BEARINGS can be divided into two major classes: rolling bearings, which include rolling elements (balls, rollers, or needle rollers) between the inner and outer raceways, and sliding, or plain, bearings, which have motion from one surface directly imposed on a stationary support.

Rolling bearings include radial, thrust, and angular contact designs. A review of the many versions of these bearings can be found in the article "Friction and Wear of Rolling-Element Bearings" in *Friction, Lubrication, and Wear Technology*, Volume 18 of the *ASM Handbook* (Ref 1). The primary requirement of rolling bearings is proper and adequate lubricant that provides separation of the moving surfaces under all conditions, maintains appropriate temperature, and provides an operating environment so that bearings will achieve their expected lives.

Sliding bearings include sleeve and thrust bearings of various designs. Based on designs and materials selection, plain bearings operate under dry or boundary lubrication conditions, partial film or mixed lubricant film conditions, or a full film, which means the "rubbing" surfaces are essentially separated. More details of sliding bearings can be found in the article "Friction and Wear of Sliding Bearings" in *Friction, Lubrication, and Wear Technology*, Volume 18 of the *ASM Handbook* (Ref 2) and in Ref 3.

References cited in this section

1. T.A. Harris, Friction and Wear of Rolling-Element Bearings, *Friction, Lubrication, and Wear Technology*, Vol 18, *ASM Handbook*, ASM International, 1992, p 499
2. R. Pike and J.M. Conway-Jones, Friction and Wear of Sliding Bearings, *Friction, Lubrication, and Wear Technology*, Vol 18, *ASM Handbook*, ASM International, 1992, p 515–521
3. M.M. Khonsari and J.Y. Jang, Chapters 61, 62, and 63, *Tribology Data Handbook*, E.R. Booser, Ed., CRC Press, LLC, 1997, p 669–707

Testing of Bearings

Charles A. Moyer, The Timken Company (Retired)

Rolling Element Bearings

Rolling bearings date back to the Neolithic period, or the new Stone Age (Ref 4). When heavy materials needed to be moved, or when primitive vehicles had wheels, someone devised bronze or wood “bearings,” with or without oils or fats. Archaeologists have found bronze balls, cylindrical rollers, and wooden tapered roller bearings dating back to 300 to 500 B.C.

Considering the different materials used, it is clear that finding the proper material, shapes, and sizes was then, and continues to be, important and is the core of testing to determine what performance can be expected from rolling element bearings. Advancements continued over the years, but bearings that resemble those in use today did not appear until the late 19th century. Modern rolling bearings developed gradually from 1850 to 1925 (Ref 4). One driving force was the need for bearings in bicycles.

While working in Berlin, Germany, Professor Richard Stribeck undertook early bearing tests, the results of which were published in 1901 and 1902 (Ref 5, 6). His goal was to determine safe ball loads statically and in complete bearings over different speed ranges. He made use of Hertz's work covering elastic bodies in contact (Ref 7) and started with a press arrangement with three hardened steel balls in contact, two steel balls with a steel plate between them, and finally, a single ball between two short cylinders set on end with cup shapes to fit the ball. He found the relation of load P on the ball diameter d to be:

$$P = Kd^2 \quad (\text{Eq 1})$$

K was a constant based on steel type and contact geometry. Based on the materials he used, Stribeck established that Eq 1 held to the elastic limit and somewhat beyond. He also ran tests on complete bearings and established the way balls shared loads under radial load conditions. Using bearings with 10 to 20 balls and no clearance between balls and rings, he determined that the most heavily loaded ball (P_0) was related to the total load P by:

$$P_0 = 4.37/Z \cdot P \quad (\text{Eq 2})$$

where Z is the number of balls in the bearing. To be conservative, Stribeck changed 4.37 to 5.0.

In 1912, Professor John Goodman published in England studies on rolling element bearings (Ref 8), covering life, friction, and wear. He knew of Stribeck's work and determined reductions in bearing load capacity based on bearing speed (N). Goodman's equation for this reduction was:

$$P = Kd^2/ND + Ad \quad (\text{Eq 3})$$

where D is the ball-race path diameter; A is a constant; and P, K , and d are the same as in Eq 1.

Studies of bearings and bearing materials (primarily steel) were followed by the emergence of the first manufacturing companies to patent and produce rolling element bearings. Bearing lubrication at this time was greatly influenced by the Reynold's equation (Ref 9) and the successes experienced in the hydrodynamic films generated in conformal bearings. It was assumed that the nonconformal contacts in “antifriction” bearings generated much thinner and, thus, less protective films for the contact region. The actual lubricating means for rolling bearings was thus a puzzle.

However, in 1949, Grubin (Ref 10) considered the elastic behavior of the contact materials and the pressure characteristics of the viscosity under the high stresses in the contact region in an equation that gave lubricant films one or two orders thicker than with the usual rigid cylinders assumption used for determining lubricant films as in hydrodynamic bearings. For rolling bearings, elastohydrodynamic lubrication came to be recognized as an important factor in determining life expectancy under a wide range of operating conditions. Tallian (Ref 11) described the stages of rolling element bearings as an empirical state until late 1920. A classical period then emerged that saw the engineering inclusion of Hertz's elasticity theory, the Weibull function, and statistics leading to worldwide bearing standards. Finally, the modern period began in the 1950s. The advancements in bearing technology allowed the new era to develop meaningful testing for rolling bearings.

References cited in this section

4. D. Dowson, *History of Tribology*, 2nd ed., Professional Eng. Pub., Ltd., London, Edmunds, U.K., 1998
5. R. Stribeck, Kugellager für beliebige Belastungen, *Z. Ver. dt. Ing.*, Vol 45 (No. 3), 1901, p 73–125
6. R. Stribeck, Die Wesentlichen Eigenschaften der Gleit und Rollenlager, *Z. Ver. dt. Ing.*, Vol 46 (No. 38), 1902, p 1341–8, 1432–8; (No. 39), 1463–70
7. H. Hertz, On the Contact of Elastic Solids, *J. reine und angew, Math.*, Vol 92, 1881, p 156–71
8. J. Goodman, (1) Roller and Ball Bearings, (2) The Testing of Antifriction Bearing Materials, *Proc. Inst. Civ. Engrs.*, clxxxix, Session 1911-2, Pt. 111, 1912, p 4–88
9. O. Reynolds, On the Theory of Lubrication and Its Application to Mr. Beauchamp Tower's Experiments, Including an Experimental Determination of the Viscosity of Olive Oil, *Philos. Trans. R. Soc.*, 177, 1886, p 157–234
10. A.N. Grubin and I.E. Vinogradova, *Investigation of the Contact of Machine Components*, Book No. 30 (DSIR Trans. No. 337), Kh. F. Ketova, Ed., Central Scientific Research Institute for Technology and Mechanical Engineering, Moscow, 1949
11. T.E. Tallian, "Progress in Rolling Contact Technology," Report AL 690007, (SKF) Industries, King of Prussia, PA, 1969

Testing of Bearings

Charles A. Moyer, The Timken Company (Retired)

Sliding Bearings

There is evidence from potters' wheels and ancient vehicles that plain bearings date back more than 5,000 years (Ref 1). Materials were stone or primarily wood for wheels of vehicles. It is assumed that the axles were stationary and the wheels rotated. Changes of material and "design" brought plain bearings to the point that scientific studies were underway in the mid 1800s by people such as Gustov Hirn (Ref 12), who, by empirical means, provided information about fluid film lubrication.

Others, such as Robert Thurston (Ref 13), who studied journal bearing friction and lubrication; Nikolai Petrov, who explained the hydrodynamic characteristics of journal bearing friction (Ref 14); and Beauchamp Tower (Ref 15), who discovered the pressure that developed within an operating journal bearing and that a bearing with sufficient lubrication floated on a film of oil, followed Hirn's studies. Although the studies first

concentrated on understanding bearing friction, the important findings covering the mechanism of lubrication were profound.

These empirical findings, combined with the theory of fluid-film lubrication developed by Osborne Reynolds (Ref 9), have provided much of the understanding of what is required to successfully operate and test plain bearings working today. Unlike rolling bearings, sliding bearings went from simple journal bearings to a variety of designs of journal bearings and thrust bearings with various tilting pads, pivoted pads, and other thrust bearing designs made with a wide range of bearing materials, such as tin- or lead-based babbit, porous bronze, Teflon (E.I. DuPont de Nemours & Co., Inc., Wilmington, DE) fabric, and reinforced Teflon (i.e., a wide range of material aimed for specific applications and performance). In addition, the operating fluid for these bearings, depending on design, can be oil, grease, or gas, or the bearings can run when completely dry (Ref 16, 17).

References cited in this section

1. T.A. Harris, Friction and Wear of Rolling-Element Bearings, *Friction, Lubrication, and Wear Technology*, Vol 18, *ASM Handbook*, ASM International, 1992, p 499
9. O. Reynolds, On the Theory of Lubrication and Its Application to Mr. Beauchamp Tower's Experiments, Including an Experimental Determination of the Viscosity of Olive Oil, *Philos. Trans. R. Soc.*, 177, 1886, p 157–234
12. G. Hirn, Sur les principaux Phénomènes qui présentent les frottements médiats, *Bull. Soc. ind Mulhouse*, Vol 26, 1854, p 188–277
13. R.H. Thurston, *A Treatise on Friction and Lost Work on Machinery and Millwork*, 7th ed., Wiley, 1885, 1903
14. N.P. Petrov, *Friction in Machines and the Effect of the Lubricant*, *Inzh. Zh.*, St. Petersburg, 1883, (1) 71–140, (2) 227–79, (3) 377–436, (4) 533–64
15. B. Tower, Second Report on Friction Experiments (Experiments on the Oil Pressure in a Bearing), *Proc. Inst. Mech. Eng.*, Jan 1885, p 58–70
16. E.R. Booser, *Rolling vs Sliding Bearings*, *Product Eng.*, McGraw Hill, 1964, p 731
17. G.R. Kingsbury, Friction and Wear of Sliding Bearing Materials, *Friction, Lubrication, and Wear Technology*, Vol 18, *ASM Handbook*, ASM International, 1992, p 741–757

Testing of Bearings

Charles A. Moyer, The Timken Company (Retired)

Role of Lubrication

One area of importance to both bearing types (fluid film and rolling contact) is the relationship of the operating oil film thickness between the contacting surfaces to bearing performance as this relates to the coefficient of friction or expected length of life. For plain bearings, the variation in operating conditions within the contact is often expressed by the Stribeck curve as illustrated in Fig. 1. As shown, the variation in coefficient of friction (μ) is related to the Sommerfeld number that ranges from 0.001 to over 1.0, going from left to right in Fig. 1. The lubricant condition goes from boundary (minimal film) to mixed- to full-film lubrication, also going left to right in Fig. 1, indicating how the actual oil film relates to μ .

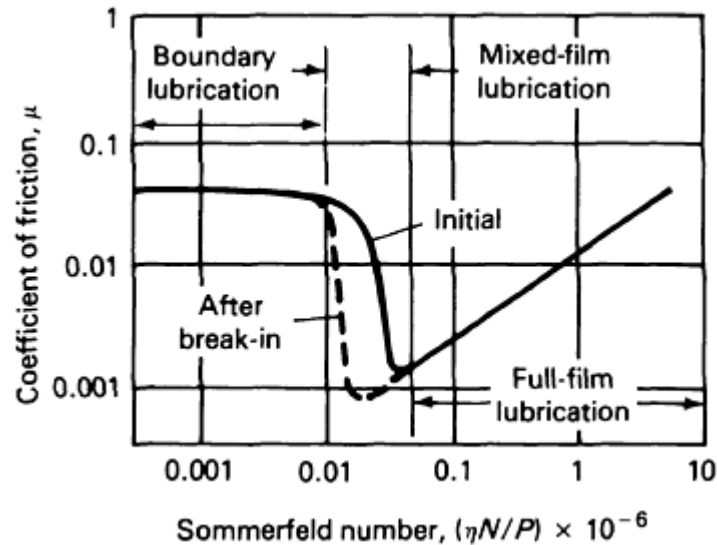


Fig. 1 Stribeck curve of coefficient of friction versus Sommerfeld number, S , where $S = \eta N/P$. N , shaft speed; P , average pressure between shaft and bearing due to applied load; η , lubricant viscosity. Source: Ref 2

For rolling bearings, the variation in operating conditions is related to the minimum oil film thickness between the rolling surfaces by dividing the film thickness by the composite asperity height of the moving surfaces. This ratio, known as lambda, or η , gives an estimate of the actual operating conditions based on the lubricant condition of boundary, mixed- to full-film separation as shown in Fig. 1. Rather than Sommerfeld numbers, the curve for rolling bearings is expressed in η values. These are, going from right to left, above 1.0 (full lubricant film) to just under 1.0 (mixed film or intermittent contact) to η much less than 1.00, perhaps down to 0.05 (continuous contact of the two surfaces). The shape of the curve for η versus is somewhat the same as shown in Fig. 1, but for η versus rolling bearing relative life, the curve drops down toward the thinner film, boundary lubrication section, and the rise on the left of Fig. 1 does not occur (an example of η versus relative life can be found in Ref 4, p 558). Such curves appear in many tribology texts with considerable variation in shape.

Unfortunately, boundary lubrication can mean both minimal lubricating conditions and surface protection from films formed by chemical reaction (that is, adsorption, chemisorption, or chemical reaction, along with reaction with metal oxide films). Therefore, the appropriate η value that applies for contacting surfaces may need minimum reactivity and comparisons with topographies, microstructures, and lubricants that are known. Thus, η is very much used, but in reality, it may be only a general tool for estimating operating conditions for values between 3.0 to approximately 0.05 (Ref 18) unless one fully understands the specifics of the lubricant, related microstructures, and surface reactions that are part of a test.

References cited in this section

2. R. Pike and J.M. Conway-Jones, Friction and Wear of Sliding Bearings, *Friction, Lubrication, and Wear Technology*, Vol 18, *ASM Handbook*, ASM International, 1992, p 515–521
4. D. Dowson, *History of Tribology*, 2nd ed., Professional Eng. Pub., Ltd., London, Edmunds, U.K., 1998
18. K.C. Ludema, *Friction, Wear, Lubrication: A Textbook in Tribology*, CRC Press, LLC, 1996, p 161–176

Testing of Bearings

Charles A. Moyer, The Timken Company (Retired)

Testing of Rolling Bearings

From the 1910s to about 1945, bearing testing was primarily based on the use of test machines designed and built by the bearing manufacturer and in some universities. Enough information developed in this time period for a symposium on the testing of bearings (Ref 19). Thomas Barish covered fatigue test machines for ball and roller bearings (Ref 20). The rigs described were primarily large machines for testing full-sized bearings. Fafnir Bearing Company, The New Departure Division of General Motors, Marlin Rockwell Corporation, Timken Roller Bearing Company, and Tinius Olsen Testing Machine Company were represented.

It was stated that ball and roller bearings were fatigue tested primarily for product improvement but also for proposed changes in material, heat treatment, or mechanical limits. In the event of a field problem, specific tests might have been run but under conditions that would reproduce the failure or problem in the field. Loads were heavier than in service with the aim to reduce testing life to 100 to 500 h. Problems of increased deflection, misalignment, machine wear, and special lubrication system requirements, such as to handle excessive heat removal, were recognized. These considerations are still important and clearly more challenging than they were over 50 years ago when the early machines were operating. Figures 2 and 3 show typical roller and ball test machines from this era.

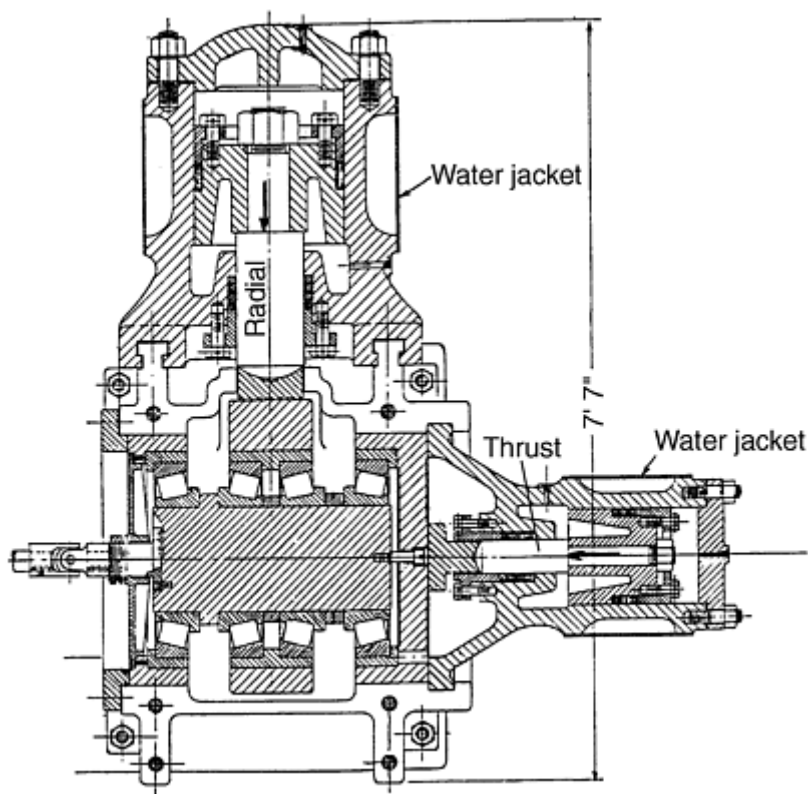


Fig. 2 Tapered roller bearing 24 in. radial and thrust load machine. Source: Ref 19

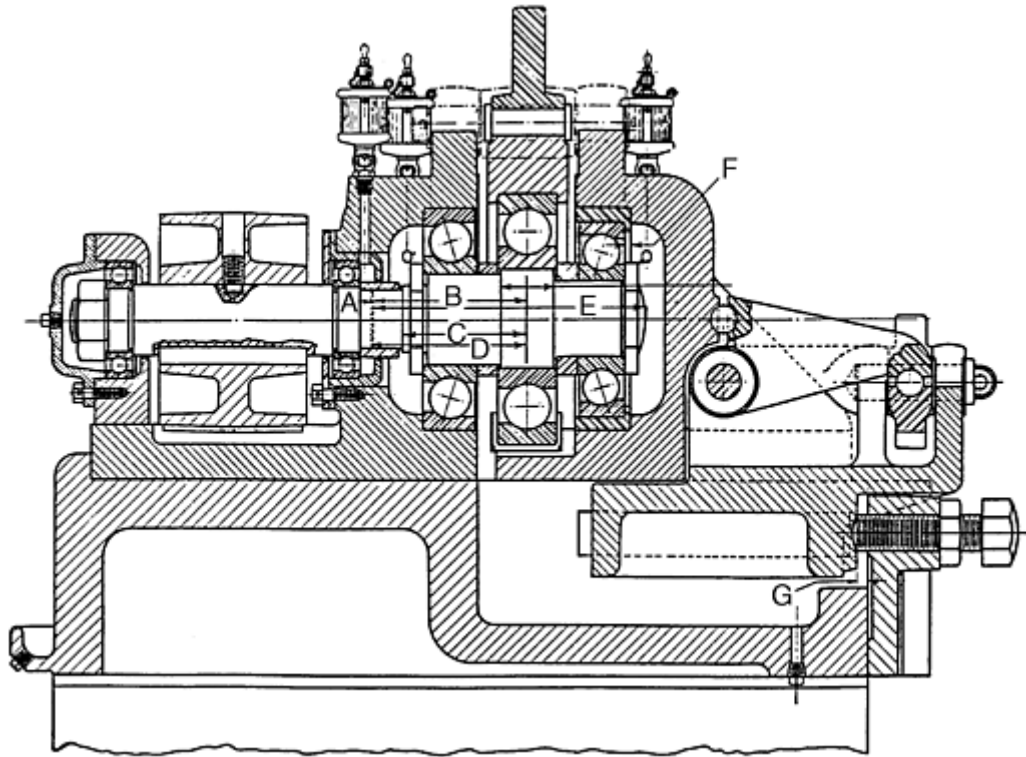


Fig. 3 Ball bearing combined load machine, A, $\frac{3}{32}$ in.; B, $\frac{9}{32}$ in.; C, $\frac{15}{16}$ in.; D, $\frac{3}{8}$ in.; E, $\frac{19}{32}$ in.; F, $\frac{7}{32}$ in.; G, $\frac{5}{16}$ in. Source: Ref 19

Because of these problems and the extreme scatter in life when rolling bearings are tested, there have been continuous attempts to find simpler test machines that can separately evaluate specific improvements. Such rigs might assess the merits of cleaner steels, closer tolerances, levels of surface roughness, and even special manufacturing processes or special design. Table 1 summarizes rolling contact fatigue (RCF) test methods that ASTM published in STP 771 (Ref 22). The table represents the variety of element testing machines in which balls only, balls against a flat washer, ball-rod combination, cylinder to ball, cylinder to cylinder, or ring against ring have been developed. Numerous variations of all these machines are available commercially or are specifically designed as one-of-a-kind units built for one purpose. Figures 4 5 6 7 8 9 10 11 12 13 14 illustrate test rigs described in Table 1.

Table 1 Summary of rolling contact test methods

Method	Description
NASA five-ball testing apparatus (Fig. 4)	Four lower balls, freely rotating 90° apart in a separator; simulates the kinematics of a thrust-loaded bearing; the contact angle can be varied; vibration sensor detects failure in unattended tests; low- (cryo) and high-temperature testing (to 1000 °C, or 1830 °F). (Ref 22, p 5–45)
Flat-washer testing apparatus (Fig. 5)	16 retained balls rolling in a circle on a flat washer with a 75 mm (3 in.) OD, 50 mm (2 in.) bore, and 6.4 mm ($\frac{1}{4}$ in.) thickness; 4.17 GPa (605 ksi) contact stress; 1500 rev/min; filtered lubricant delivery system; piezo sensor detects vibration. (Ref 22, p 46–66)
Unisteel testing apparatus (Fig. 6)	Flat washer on retained balls; hanging dead-weight load; contact stress approximately 4.5 GPa (650 ksi); 1500rev/min; drip feed of lubricant; vibration detection system; thermocouples monitor temperature (typically 50–60 °C, or 120–140 °F). (Ref 22, p 67–84)
Rolling contact testing apparatus	Two hemispherically ground, toroidal rollers loaded against a round bar; 40:1 ratio of roller diameter to bar diameter; 2.7–5.5 Gpa (390–880 ksi) contact stress; 12,500

(Fig. 7)	rev/min; drip-feed lubrication; velocity-vibration sensor. (Ref 22, p 85–106)
Ball-rod testing apparatus (Federal Mogul) (Fig. 8)	Three 12.5 mm ($\frac{1}{2}$ in.) balls loaded against a rotating 9.5 mm ($\frac{3}{8}$ in.) OD center rod; 3600 rev/min; spring load on opposing tapered retaining rings; accelerometer coupled with a shutdown device; drip-feed lubrication; stress per ball typically 6 GPa (870 ksi). (Ref 22, p 107–124)
Cylinder-to-ball testing apparatus (Fig. 9)	Symmetrical arrangement of two 19 mm ($\frac{3}{4}$ in.) balls rolling on a 12.5 mm ($\frac{1}{2}$ in.) OD captive cylinder; coiled-spring load through a multiplying lever; small cylinder rev/min = 22,677; splash lubrication; maximum contact stress, 5.8 GPa (840 ksi). (Ref 22, p 125–135)
Cylinder-to-cylinder testing apparatus (Fig. 10)	Symmetrical arrangement of two 12.5 mm ($\frac{1}{2}$ in.) cylinders on two 20 mm (0.8 in.) OD captive cylinders; coiled-spring load through a multiplying lever; small cylinder, cpm = 20,400; splash lubrication; maximum contact stress less than 4.4 GPa (640 ksi); vibration sensor terminates test. (Ref 22, p 136–149)
Ring-on-ring testing apparatus (Fig. 11)	Crowned rings rolling on their peripheries; ring diameters of 50 and 53 mm (2 and 2.1 in.) provide no-slip” condition, but various degrees of slip are possible by changing ring diameters; typically 2000 rev/min; contact ratio measured by electrical resistance; contact stress range typically 0.98–3.9 GPa (140–570 ksi). (Ref 22, p 150–165)
Various types	See review article of rolling contact fatigue and full-scale bearing testers. (Ref 22, p 169–189)
Multiple bearing testing apparatus (Fig. 12)	Deep-groove ball bearing design; typically 3000 rev/min; four bearings on a single center shaft; maximum contact stress, 2.9 GPa (420 ksi); accelerometers on the outer housing monitor failure. (Ref 22, p 206–218)
Rolling four-ball testing apparatus (Fig. 13)	Top ball drives three lower balls in a tetragonal arrangement; lower balls free to rotate in the cup; all balls 12.5 mm ($\frac{1}{2}$ in.) diam; upper ball spindle speed, 1500 rev/min; 5.9 kN (1325 lbf) load applied vertically. (Ref 22, p 219–236)
High-speed four-ball testing apparatus (Fig. 13)	Same arrangement as above, but speeds of 15,000–20,000 rev/min; operating temperatures often exceed 100 °C (210 °F) (Plint machine). (Ref 22, p 219–236)
“AOL” vertical testing apparatus (not shown)	11 retained balls clamped between two flat washers; thrust load; recirculating lubricant system. (Ref 22, p 219–236)
Inclined ball-on-disk testing apparatus (Fig. 14)	Spindle-held 20.5 mm (0.8 in.) ball rolling on a disk; up to 800 °C (1470 °F); ball speed up to 7200 rev/min; disk speed up to 3600 rev/min; variable slide/roll ratios; traction measurements; designed for ceramics. (Ref 26)

OD, outside diameter.

Source: Ref 21

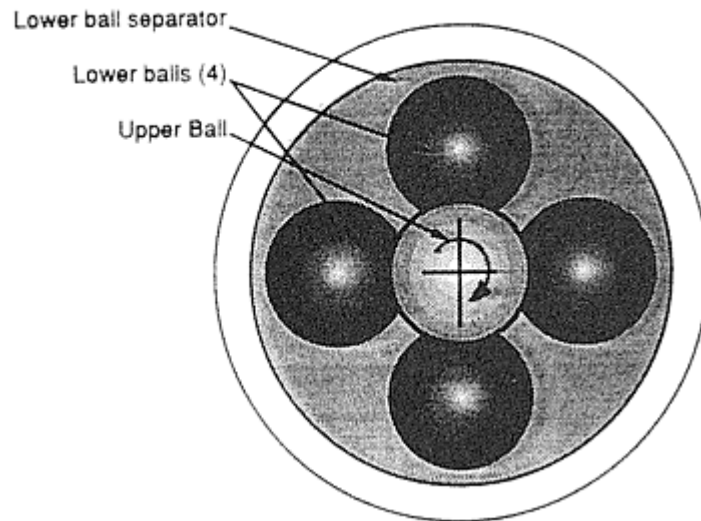


Fig. 4 NASA five-ball RCF testing apparatus. (See Table 1.) Source: Ref 22

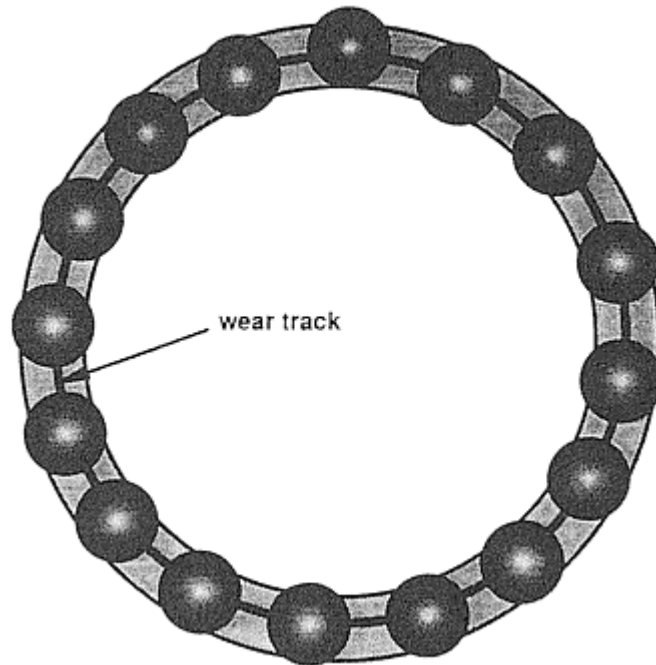


Fig. 5 Flat washer RCF testing apparatus. (See Table 1.) Source: Ref 22

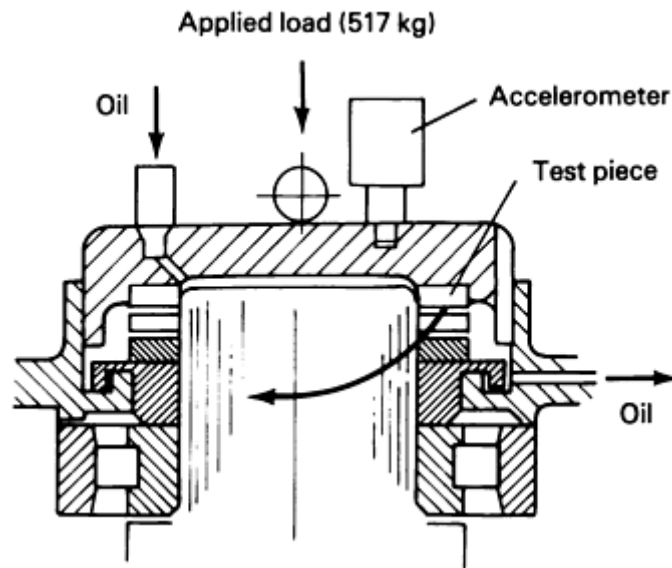


Fig. 6 Unisteel RCF testing apparatus. (See Table 1.) Source: Ref 22

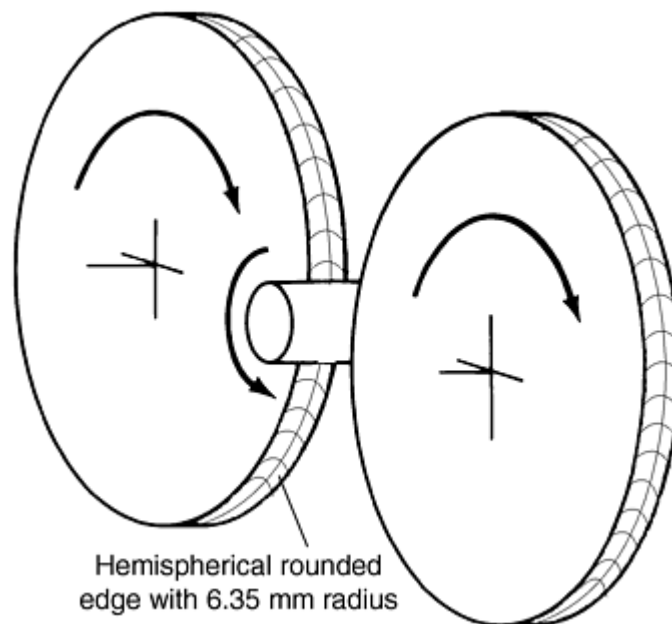


Fig. 7 Rolling contact testing apparatus. (See Table 1.) Source: Ref 22

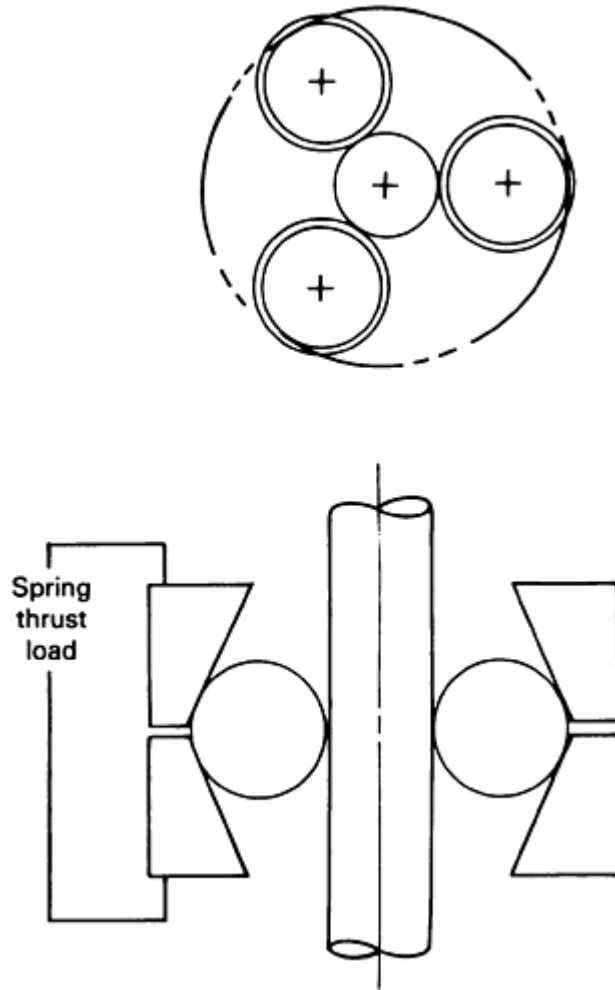


Fig. 8 Ball-rod RCF testing apparatus. (See Table 1.) Source: Ref 22

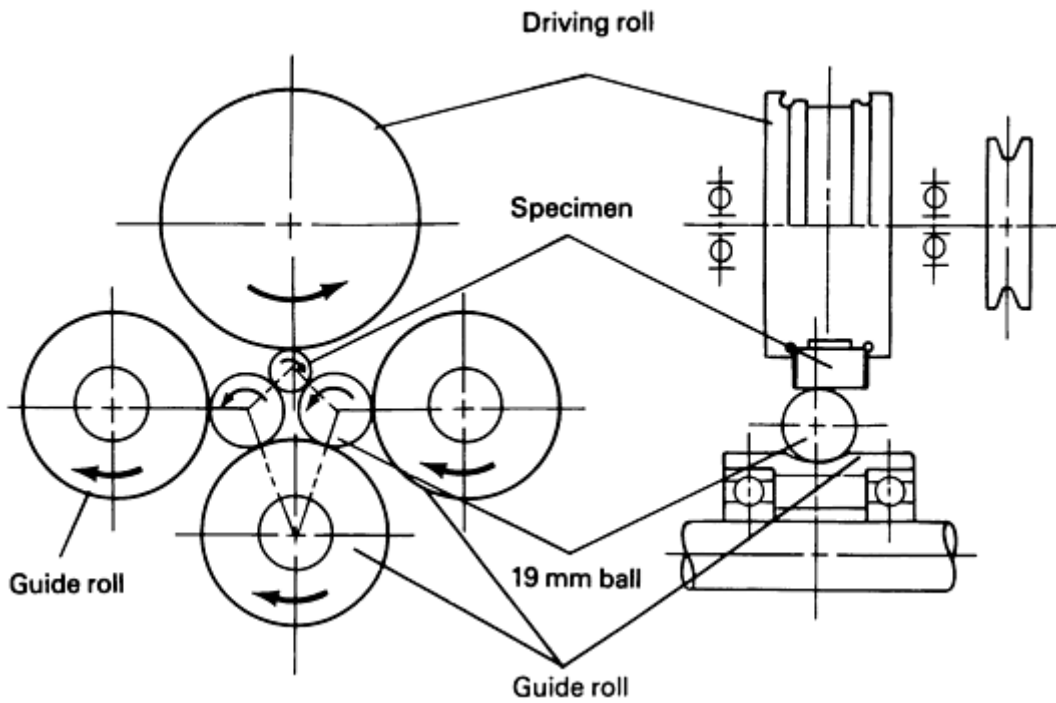


Fig. 9 Cylinder-to-ball RCF testing apparatus. (See Table 1.) Source: Ref 22

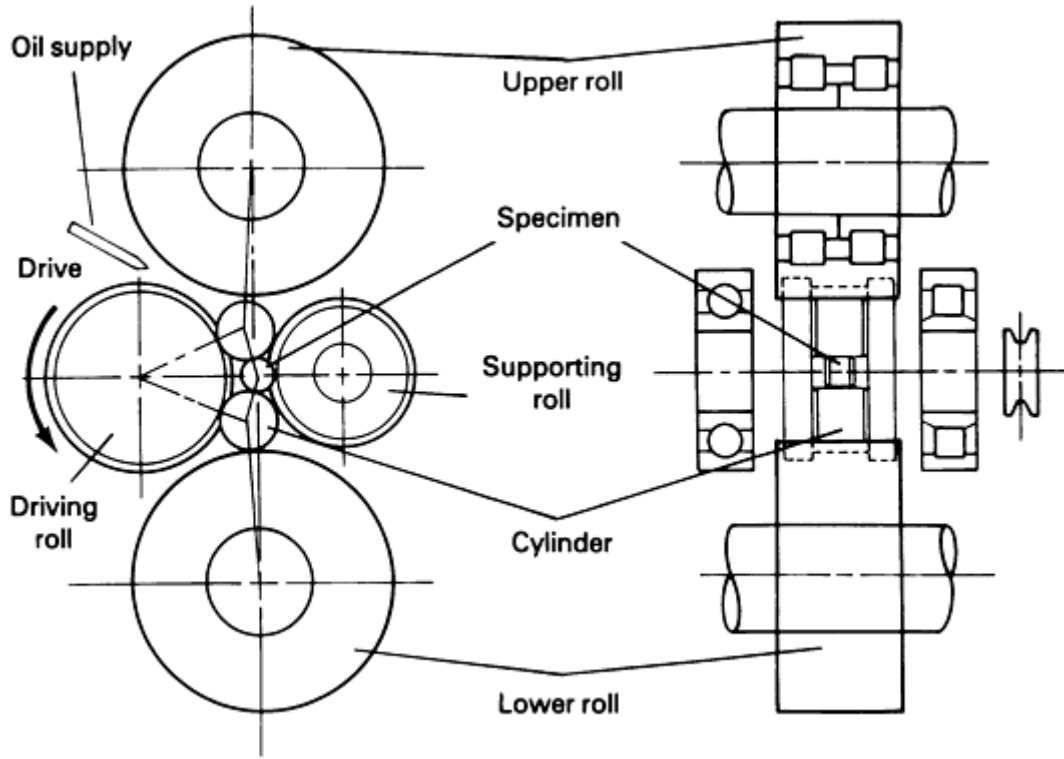


Fig. 10 Cylinder-to-cylinder testing apparatus. (See Table 1.) Source: Ref 22

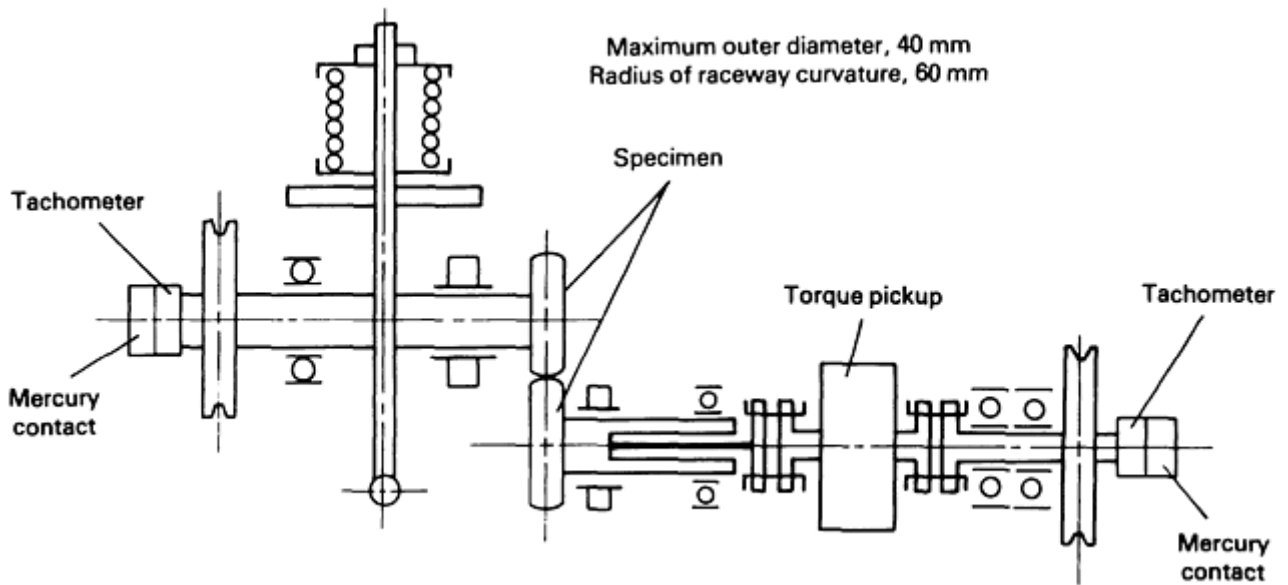


Fig. 11 Ring-on-ring RCF testing apparatus. (See Table 1.) Source: Ref 22

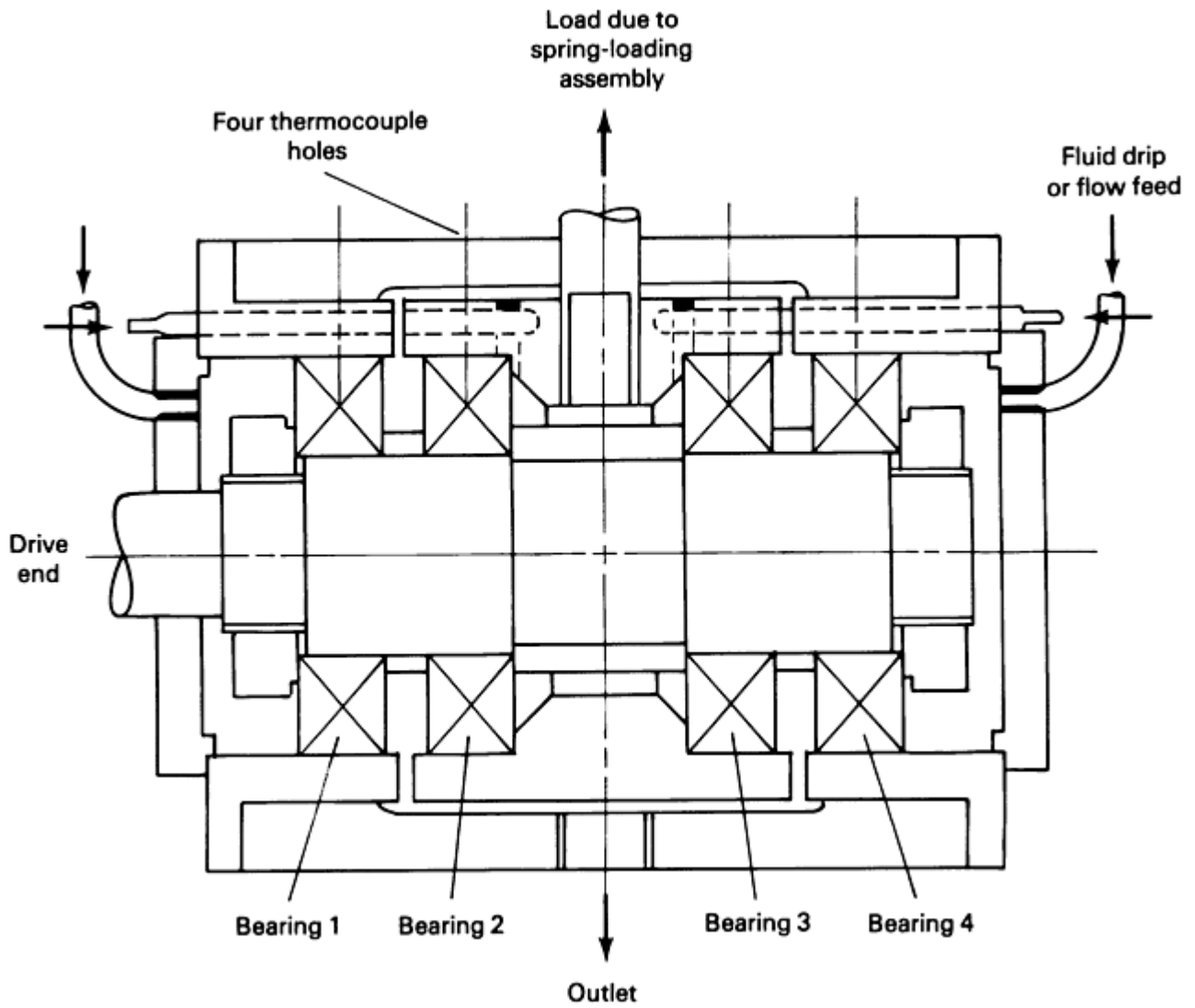


Fig. 12 Four-bearing RCF test rig smaller than those shown in Fig. 2 and 3. (See Table 1.) Source: Ref 22

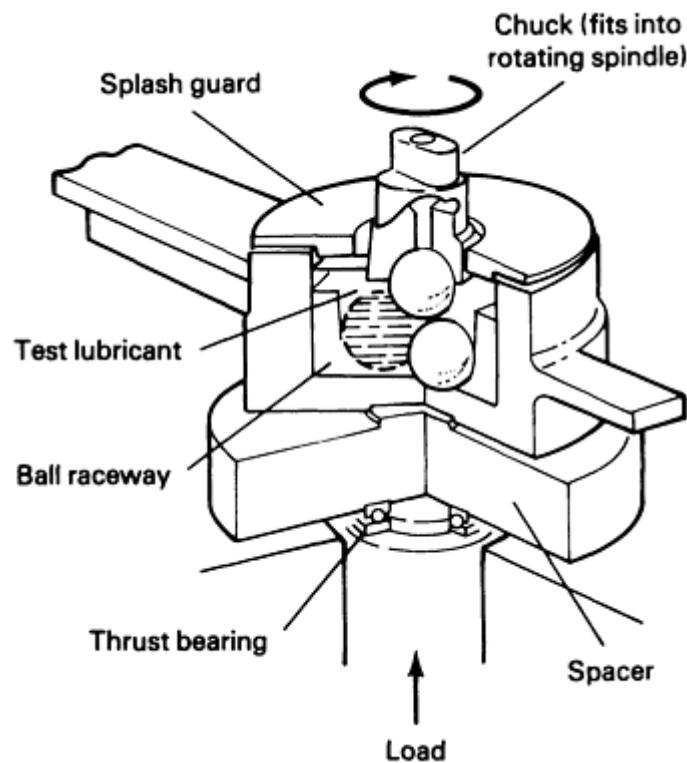


Fig. 13 Four-ball RCF testing apparatus. (See Table 1.) Source: Ref 22

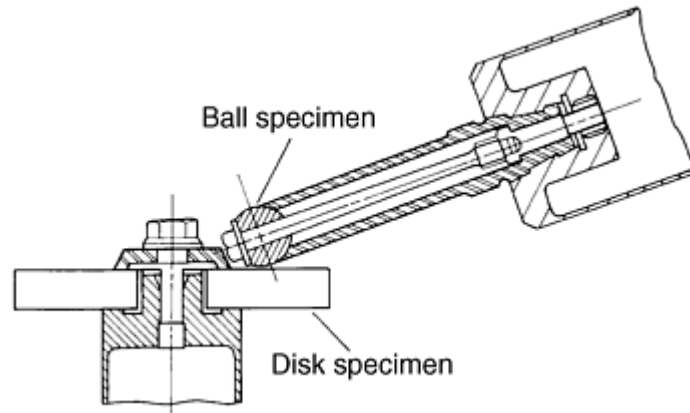


Fig. 14 Ball-on-disk RCF testing apparatus. (See Table 1.) Source: Ref 26

The chapter from STP 771 (Ref 23) that covered NASA John Glenn (Lewis) Research Center's over 20 years of rolling contact research spans early tests with the fatigue spin rig (Ref 24) developed by NASA to the NASA five-ball fatigue tester that provided over 500,000 test hours by 1981. Data developed included hardness effects, influence of compressive residual stress, lubricant types, elastohydrodynamic film thickness influence on life, along with traction fluids and many other factors with qualitative correlation between the fatigue tester and full-scale bearing tests (Ref 23).

Unfortunately, G.B. Johnston et al. (Ref 25) revealed different findings in their chapter in STP 771. They had run full-scale bearing tests (6,309 deep-groove ball bearings and then radial ball bearings with cylindrical inner rings) and flat washer tests somewhat like the Unisteel rig. Their results from the two last element test methods did not correlate well with full-scale bearing performance. Their experience does not rule out simpler, single-element rolling contact rigs but does indicate the need to verify element or simple rig machine data by also running full-sized related bearing tests. The newer specialized rigs, such as the ball-on-disk machine listed at the bottom of Table 1 (and shown in Fig. 12), has been able to simulate very specific contact, load/traction conditions and determine wear difference for rolling with incipient sliding using silicon nitride against different materials (Ref 26).

The very high contact stresses used in many rig tests can produce different modes of failure. Microstructures may be altered. Surface coatings and modifications may be destroyed. Failures may be initiated by internal and surface stress-raising features too small to be of consequence in normal bearing operation. In rigs, the volume tested may be too small to encounter statistically the macro flaws that often determine bearing life. Rig test results must be evaluated with careful examination of failures and attention to all tribological conditions.

At the end of this text there are 17 selected references that describe a wide range of rolling contact machines from recent work to those that started the modern era. These machines and others supply data to the goal of providing an accelerated test that could contribute to better defining the limits of material, manufacture, and the environment so that significantly longer life could occur in the real applications.

References cited in this section

19. Symposium on Testing of Bearings, *American Society for Testing and Materials 49th Annual Meeting*, 24–28 June 1946 (Buffalo, NY), American Society for Testing and Materials, p 22–23
20. T. Barish, *Fatigue Testing Machines for Ball and Roller Bearings*, Symposium on Testing of Bearings, *American Society for Testing and Materials 49th Annual Meeting*, 24–28 June 1946 (Buffalo, NY), American Society for Testing and Materials, 1947, p 19–34
21. P.J. Blau, *Rolling Contact Wear*, *Friction, Lubrication, and Wear Technology*, Vol 18, *ASM Handbook*, ASM International, 1992, p 258
22. *Rolling Contact Fatigue Testing of Bearing Steels*, STP 771, J.J.C. Hoo, Ed., ASTM, 198

23. E.V. Zaretsky, R.J. Parker, and W.J. Anderson, NASA Five-Ball Fatigue Tester—Over 20 Years of Research, *Rolling Contact Fatigue Testing of Bearing Steels*, STP 771, J.J.C. Hoo, Ed., ASTM, 1982, p 5–45
24. E.F. Macks, The Fatigue Spin Rig, *STLE Lub. Eng.*, Oct 1953, p 254–258
25. G.B. Johnston, T. Andersson, E.V. Amerongen, and A. Voskamp, Experience of Element and Full-Bearing Testing of Materials over Several Years, *Rolling Contact Fatigue Testing of Bearing Steels*, STP 771, J.J.C. Hoo, Ed., ASTM, 1982, p 190–205
26. L.D. Wedeven and N.C. Miller, Material and Tribological Considerations for Turbopump Bearings, *STLE Lub. Eng.*, Vol 47 (No. 12), Dec 1991, p 1009–1017

Testing of Bearings

Charles A. Moyer, The Timken Company (Retired)

Testing of Sliding Bearings

The 1946 American Society for Testing and Materials symposium also included testing of plain bearings for automotive engines under a range of operating conditions. These conditions included higher-than-service loads, constant loads or shock loads, shaft irregularities, and others aimed at shorter duration testing without the interference of other component failures that might happen in an actual engine. Figure 15 shows a diagram of the automotive plain bearing test machine. Results achieved included fatigue failure of linings (such as lead-based babbitt), seizure of the lining or corrosion damage, for example, corroded copper lead bearing (Ref 27). Duplicate bearing tests seemed to show closer agreement, especially for fatigue failures, so that mortality curves for groups of tests did not seem necessary. The difference between sleeve bearings and rolling bearings was thought to be primarily due to the ability of sleeve bearing flow under high local stress, thus providing some stress equalization for sleeve bearings (Ref 27).

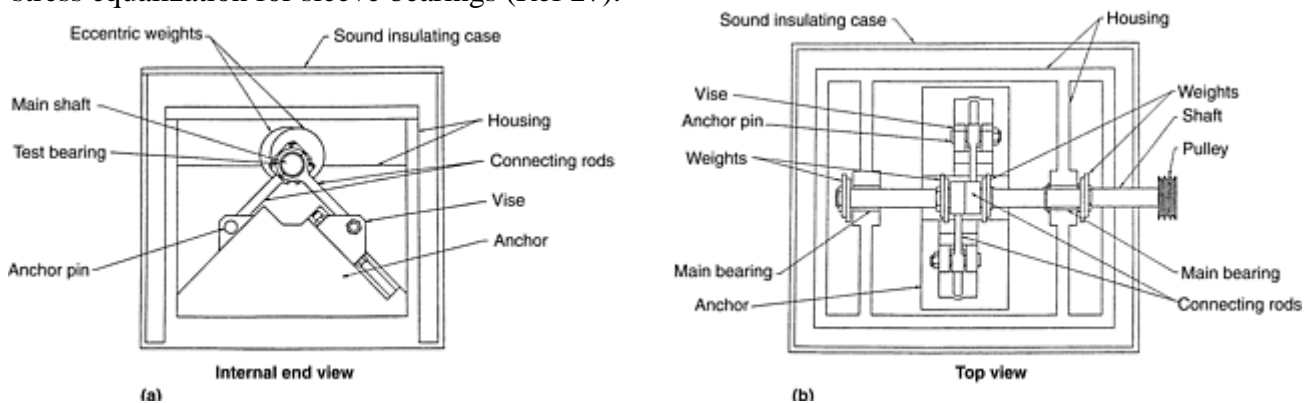


Fig. 15 Schematic of sliding bearing test machine. Source: Ref 27

References 28 and 29 came from the same time period as the 1946 symposium and featured hydrodynamic journal bearings tested under cyclical loading or high-speed operation. The aim of these studies was to provide experimental data as a check to the theoretical Reynold's number of other theoretical curves. From the numerous discussions of these papers, it is obvious that the technical community sought worthwhile data to help explain the dynamic behavior of journal bearings.

In 1968, the Institution of Mechanical Engineers in England had a symposium on experimental methods in tribology that primarily considered testing methods and measurement techniques. Reference 30, *Basic Principles of Bearing Testing-Machine Design* includes simulation ideas for journal and thrust bearings.

References 31, 32, 33, and 34 contain designs and/or explanations of additional rigs for assessing loading systems, friction, local film pressure, and thickness measurement, stress distributions, merits of rig testing of materials, and fatigue strength assessment of plain bearings.

Measurement and testing of sliding bearing materials are reviewed in Ref 17. The article covers a wide range of materials and materials systems, both single metals, such as commercial bronze or porous metal bronze, and bimetal and trimetal bearing materials systems. Bearing alloy designations and nominal compositions are described in considerable detail. Because bearing testing aims to expose a specific bearing to similar but more rigorous conditions than are encountered in service, either speed, load, lubricant amount, or cleanliness and temperature, or several of these parameters, is degraded to cause failures in shorter time. Figure 16 shows two types of engine bearing test machines that are used to evaluate sliding bearings. As has been stated, in order to know how such accelerated tests match real world conditions, periodic full-scale bearing tests are still required.

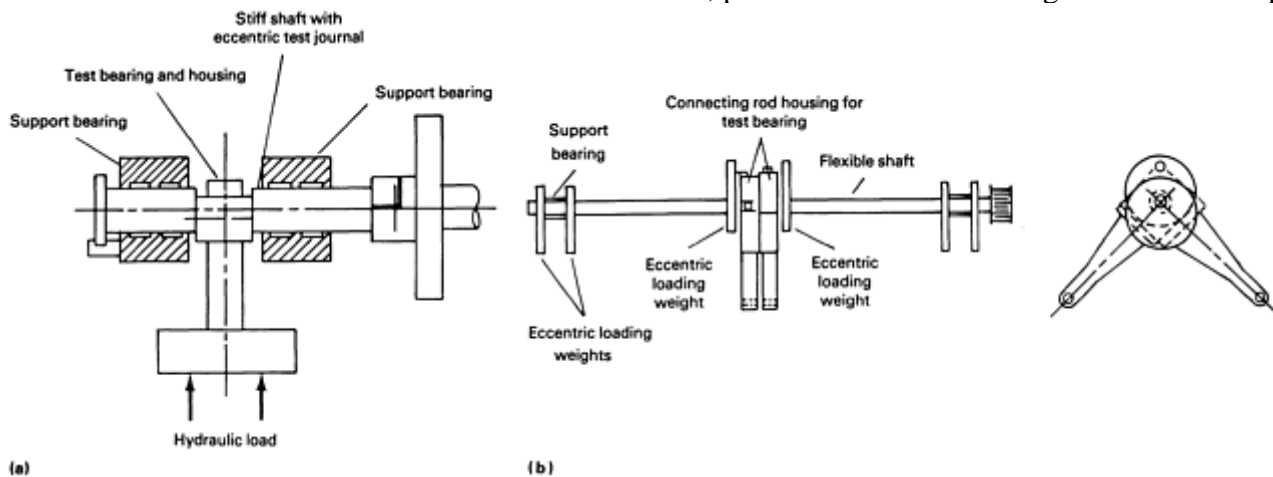


Fig. 16 Schematic showing key components of two types of engine bearing test machines. (a) “Sapphire” hydraulically loaded machine. (b) Front (left) and side (right) views of Underwood centrifugally loaded machine. Source: Ref 1

Additional sources that provide experimental plain bearing test rig development and test data are listed in the Selected References.

References cited in this section

1. T.A. Harris, Friction and Wear of Rolling-Element Bearings, *Friction, Lubrication, and Wear Technology*, Vol 18, *ASM Handbook*, ASM International, 1992, p 499
17. G.R. Kingsbury, Friction and Wear of Sliding Bearing Materials, *Friction, Lubrication, and Wear Technology*, Vol 18, *ASM Handbook*, ASM International, 1992, p 741–757
27. E.T. Johnson, Life Testing of Plain Bearings for Automotive Engines, Symposium on Testing of Bearings, *American Society for Testing and Materials 49th Annual Meeting*, 24–28 June 1946 (Buffalo, NY), American Society for Testing and Materials, Jan 1947, p 2–18
28. E.M. Simons, *The Hydrodynamic Lubrication of Cyclically Loaded Bearings (Trans. ASME)*, Aug 1950, p 805–816
29. D.F. Wilcock, *Turbulence in High-Speed Journal Bearings (Trans. ASME)*, Aug 1950, p 825–834
30. P.B. Neal, Basic Principles of Bearing Testing-Machine Design, *Experimental Methods in Tribology Proc.*, 1967–68, Vol 182 (Pt 3G), March 1968, p 24–32
31. C.C.M. Ettles, A Comparison of Some Instrumental Methods for Hydrodynamic Bearings, *Experimental Methods in Tribology Proc.*, 1967–1968, Vol 182 (Pt 3G), March 1968, p 53–55

32. R.W.T. Preater, Photoelastic Analysis of Journal Bearings: Preliminary Investigations, *Experimental Methods in Tribology Proc.*, 1967–1968, Vol 182 (Pt 3G), March 1968, p 90–94
33. S.W.E. Earles and D.G. Powell, Considerations in the Design of Plain Sliding Test Rigs, *Experimental Methods in Tribology Proc.*, 1967–1968, Vol 182 (Pt 3G), March 1968, p 118–121
34. W.H. Wilson, A Test Machine for Assessing the Fatigue Properties of Impulsively Loaded Plain Bearings, *Experimental Methods in Tribology Proc.*, 1967–1968, Vol 182 (Pt 3G), March 1968, p 129–131

Testing of Bearings

Charles A. Moyer, The Timken Company (Retired)

References

1. T.A. Harris, Friction and Wear of Rolling-Element Bearings, *Friction, Lubrication, and Wear Technology*, Vol 18, *ASM Handbook*, ASM International, 1992, p 499
2. R. Pike and J.M. Conway-Jones, Friction and Wear of Sliding Bearings, *Friction, Lubrication, and Wear Technology*, Vol 18, *ASM Handbook*, ASM International, 1992, p 515–521
3. M.M. Khonsari and J.Y. Jang, Chapters 61, 62, and 63, *Tribology Data Handbook*, E.R. Booser, Ed., CRC Press, LLC, 1997, p 669–707
4. D. Dowson, *History of Tribology*, 2nd ed., Professional Eng. Pub., Ltd., London, Edmunds, U.K., 1998
5. R. Stribeck, Kugellager für beliebige Belastungen, *Z. Ver. dt. Ing.*, Vol 45 (No. 3), 1901, p 73–125
6. R. Stribeck, Die Wesentlichen Eigenschaften der Gleit und Rollenlager, *Z. Ver. dt. Ing.*, Vol 46 (No. 38), 1902, p 1341–8, 1432–8; (No. 39), 1463–70
7. H. Hertz, On the Contact of Elastic Solids, *J. reine und angew. Math.*, Vol 92, 1881, p 156–71
8. J. Goodman, (1) Roller and Ball Bearings, (2) The Testing of Antifriction Bearing Materials, *Proc. Inst. Civ. Engrs.*, clxxxix, Session 1911-2, Pt. 111, 1912, p 4–88
9. O. Reynolds, On the Theory of Lubrication and Its Application to Mr. Beauchamp Tower's Experiments, Including an Experimental Determination of the Viscosity of Olive Oil, *Philos. Trans. R. Soc.*, 177, 1886, p 157–234
10. A.N. Grubin and I.E. Vinogradova, *Investigation of the Contact of Machine Components*, Book No. 30 (DSIR Trans. No. 337), Kh. F. Ketova, Ed., Central Scientific Research Institute for Technology and Mechanical Engineering, Moscow, 1949
11. T.E. Tallian, “Progress in Rolling Contact Technology,” Report AL 690007, (SKF) Industries, King of Prussia, PA, 1969
12. G. Hirn, Sur les principaux Phénomènes qui présentent les frottements médiats, *Bull. Soc. ind Mulhouse*, Vol 26, 1854, p 188–277

13. R.H. Thurston, *A Treatise on Friction and Lost Work on Machinery and Millwork*, 7th ed., Wiley, 1885, 1903
14. N.P. Petrov, *Friction in Machines and the Effect of the Lubricant*, *Inzh. Zh.*, St. Petersburg, 1883, (1) 71–140, (2) 227–79, (3) 377–436, (4) 533–64
15. B. Tower, Second Report on Friction Experiments (Experiments on the Oil Pressure in a Bearing), *Proc. Inst. Mech. Eng.*, Jan 1885, p 58–70
16. E.R. Booser, *Rolling vs Sliding Bearings*, *Product Eng.*, McGraw Hill, 1964, p 731
17. G.R. Kingsbury, Friction and Wear of Sliding Bearing Materials, *Friction, Lubrication, and Wear Technology*, Vol 18, *ASM Handbook*, ASM International, 1992, p 741–757
18. K.C. Ludema, *Friction, Wear, Lubrication: A Textbook in Tribology*, CRC Press, LLC, 1996, p 161–176
19. Symposium on Testing of Bearings, *American Society for Testing and Materials 49th Annual Meeting*, 24–28 June 1946 (Buffalo, NY), American Society for Testing and Materials, p 22–23
20. T. Barish, Fatigue Testing Machines for Ball and Roller Bearings, *Symposium on Testing of Bearings, American Society for Testing and Materials 49th Annual Meeting*, 24–28 June 1946 (Buffalo, NY), American Society for Testing and Materials, 1947, p 19–34
21. P.J. Blau, Rolling Contact Wear, *Friction, Lubrication, and Wear Technology*, Vol 18, *ASM Handbook*, ASM International, 1992, p 258
22. *Rolling Contact Fatigue Testing of Bearing Steels*, STP 771, J.J.C. Hoo, Ed., ASTM, 1982
23. E.V. Zaretsky, R.J. Parker, and W.J. Anderson, NASA Five-Ball Fatigue Tester—Over 20 Years of Research, *Rolling Contact Fatigue Testing of Bearing Steels*, STP 771, J.J.C. Hoo, Ed., ASTM, 1982, p 5–45
24. E.F. Macks, The Fatigue Spin Rig, *STLE Lub. Eng.*, Oct 1953, p 254–258
25. G.B. Johnston, T. Andersson, E.V. Amerongen, and A. Voskamp, Experience of Element and Full-Bearing Testing of Materials over Several Years, *Rolling Contact Fatigue Testing of Bearing Steels*, STP 771, J.J.C. Hoo, Ed., ASTM, 1982, p 190–205
26. L.D. Wedeven and N.C. Miller, Material and Tribological Considerations for Turbopump Bearings, *STLE Lub. Eng.*, Vol 47 (No. 12), Dec 1991, p 1009–1017
27. E.T. Johnson, Life Testing of Plain Bearings for Automotive Engines, *Symposium on Testing of Bearings, American Society for Testing and Materials 49th Annual Meeting*, 24–28 June 1946 (Buffalo, NY), American Society for Testing and Materials, Jan 1947, p 2–18
28. E.M. Simons, *The Hydrodynamic Lubrication of Cyclically Loaded Bearings (Trans. ASME)*, Aug 1950, p 805–816
29. D.F. Wilcock, *Turbulence in High-Speed Journal Bearings (Trans. ASME)*, Aug 1950, p 825–834
30. P.B. Neal, Basic Principles of Bearing Testing-Machine Design, *Experimental Methods in Tribology Proc.*, 1967–68, Vol 182 (Pt 3G), March 1968, p 24–32

31. C.C.M. Ettles, A Comparison of Some Instrumental Methods for Hydrodynamic Bearings, *Experimental Methods in Tribology Proc.*, 1967–1968, Vol 182 (Pt 3G), March 1968, p 53–55
32. R.W.T. Preater, Photoelastic Analysis of Journal Bearings: Preliminary Investigations, *Experimental Methods in Tribology Proc.*, 1967–1968, Vol 182 (Pt 3G), March 1968, p 90–94
33. S.W.E. Earles and D.G. Powell, Considerations in the Design of Plain Sliding Test Rigs, *Experimental Methods in Tribology Proc.*, 1967–1968, Vol 182 (Pt 3G), March 1968, p 118–121
34. W.H. Wilson, A Test Machine for Assessing the Fatigue Properties of Impulsively Loaded Plain Bearings, *Experimental Methods in Tribology Proc.*, 1967–1968, Vol 182 (Pt 3G), March 1968, p 129–131

Testing of Bearings

Charles A. Moyer, The Timken Company (Retired)

Selected References

Rolling Bearings (1996 to 1951)

- Y.P. Chiu, P.K. Pearson, M. Dezzani, and H. Daverio, Fatigue Life and Performance Testing of Hybrid Ceramic Ball Bearings, *STLE Lub. Eng.*, Vol 52 (No. 3), March 1996, p 198–204
- T.N. Ying and S.M. Hsu, Asperity-Asperity Friction as Measured by a Two-Ball Collision Apparatus, *Trans. STLE Trib.*, Vol 39 (No. 1), 1996, p 32–42
- J.F. Braza, Ceramic Roller Evaluation in Valve Train Tests, *Trans. STLE Trib.*, Vol 38 (No. 1), 1995, p 146–152
- W. Cheng and H.S. Cheng, Effect of Surface Roughness Orientation on Pitting Resistance of Lubricated Rollers, *Trans. STLE Trib.*, Vol 38 (No. 2), 1995, p 396–402
- R. Wei, P.J. Wilbur, and F.M. Kustas, A Rolling Contact Fatigue Study of Hard Carbon Coated M-50 Steel, *J. Tribology (Trans. ASME)*, Vol 114, April 1992, p 298–303
- V.A. Dikshit and P. Clayton, A Simple Material Model for Water-Lubricated Rolling Contact Fatigue of Eutectoid Steels, *STLE Lub. Eng.*, Vol 48 (No. 7), July 1992, p 606–614
- D.J. Carre, P.D. Fleischauer, C.G. Kalogeras, and H.D. Marten, Comparison of Lubricant Performance in an Oscillating Spacecraft Mechanism, *J. Tribology (Trans. ASME)*, Vol 113, April 1991, p 308–312
- G. Dalmaz and R. Nantua, An Evaluation of Grease Behavior in Rolling Bearing Contacts, *STLE Lub. Eng.*, Vol 43 (No. 12), Dec 1987, p 905–915
- H. Czichos, S. Becker, and J. Lexow, Multilaboratory Tribotesting: Results from the Versailles Advanced Materials and Standards Program on Wear Test Methods, *Wear*, Vol 114, 1987, p 109–130
- A.H. Nahm and E.N. Bamberger, Rolling Contact Fatigue Life of AISI M-50 as a Function of Specific Film Thickness Ratio Using a High Speed RC Rig, *J. Lubr. Technol. (Trans. ASME)*, Vol 102, Oct 1980, p 534–538
- P.M. Ku, E.L. Anderson, and H.J. Carper, Some Considerations in Rolling Fatigue Evaluation, *ASLE Trans.*, Vol 15 (No. 2), 1972, p 113–129
- C.A. Foord, C.G. Hingley, and A. Cameron, Pitting of Steel Under Varying Speeds and Combined Stresses, *J. Lubr. Technol.*, April 1969, p 282–293
- J.W. Kannel, J.A. Walowit, J.C. Bell, and C.M. Allen, The Determination of Stresses in Rolling-Contact Elements, *J. Lubr. Technol.*, Oct 1967, p 453–465
- J. Morrow, Correlation of the Pitting Fatigue Life of Bearings with Rolling Contact Rig Data, *JBE (Trans. ASME)*, Sept 1966, p 583–588

- W.J. Greenert, The Toroid Contact Roller Test as Applied to the Study of Bearing Materials, *JBE (Trans. ASME)*, Vol 84 (No. 1), March 1962, p 181–191
- F. Hirano and S. Yamamoto, Four-Ball Test on Lubricating Oils Containing Solid Particles, *Wear*, Vol 2, 1958–1959, p 349–363
- H. Styri, Fatigue Strength of Ball Bearing Races and Heat-Treated 52100 Steel Specimens, *ASTM Proc.*, Vol 51, 1951, p 682–700

Sliding Bearings (1998 to 1993)

- R. Bassani, E. Ciulli, and P. Forte, An Investigation on Thrust Bearing Tilting Pads, *Proc. Inst. Mech. Eng. E, J. Eng. Tribol.*, Vol 212 (No. J4), 1998, p 271–277
- S. Taniguchi, T. Makino, Y. Ozawa, and T. Ichimura, A Thermohydrodynamic Lubrication Analysis to Design Large Two-Pad Journal Bearing with Cooling Ditches, *J. Tribology (Trans. ASME)*, Vol 120 (No. 2), April 1998, p 214–220
- P. Monmousseau, M. Fillon, and J. Fréne, Transient Thermoelastohydrodynamic Study of Tilting-Pad Journal Bearings—Application to Bearing Seizure, *J. Tribology (Trans. ASME)*, Vol 120 (No. 2), April 1998, p 319–324
- Q. (Jane) Wang, Fanghui Shi, and S.C. Lee, A Mixed-Lubrication Study of Journal Bearing Conformal Contacts, *J. Tribology (Trans. ASME)*, Vol 119 (No. 3), July 1997, p 456–461
- N.V. Walton and L.S. Andres, Measurements of Static Loading Versus Eccentricity in a Flexure-Pivot Tilting Pad Journal Bearing, *J. Tribology (Trans. ASME)*, Vol 119 (No. 2), April 1997, p 297–305
- H. Heshmat and D.E. Brewster, Performance of a Powder Lubricated Journal Bearing with WS₂ Powder: Experimental Study, *J. Tribology (Trans. ASME)*, Vol 118 (No. 3), July 1996, p 484–491
- A.K. Tieu and Z.L. Qiu, Experimental Study of Freely Alignable Journal Bearings, Part 1: Static Characteristics; Part 2: Dynamic Characteristics, *J. Tribology (Trans. ASME)*, Vol 118 (No. 3), July 1996, p 498–508
- J.D. Summers-Smith and G. Taylor, Screw Compressor Bearing Failures on Process Plant: A Case Study and Some General Lessons, *Proc. Inst. Mech. Eng. E, J. Eng. Tribol.*, Vol 209 (No. J2), 1995, p 77–83
- D.J. Hargreaves, Predicted Performance of a Tri-Taper Journal Bearing Including Turbulence and Misalignment Effects, *Proc. Inst. Mech. Eng. E, J. Eng. Tribol.*, Vol 209 (No. J2), 1995, p 85–97
- D. Ashman, Investigation of the Failure of Heavily Loaded Journal Bearings, *Proc. Inst. Mech. Eng. E, J. Eng. Tribol.*, Vol 208 (No. J3), 1994, p 167–171
- D. Sheeja and B.S. Prabhu, Thermohydro-dynamic Analysis of Journal Bearings Lubricated by Non-Newtonian Fluids—Theory and Experiments, *Proc. Inst. Mech. Eng. E, J. Eng. Tribol.*, Vol 208 (No. J3), 1994, p 173–181
- L. O'Connor, Fluid-Film Foil Bearings Control Engine Heat, *ASME, Mech. Eng.*, May 1993, p 72–75

Mechanical Testing of Gears

Douglas R. McPherson and Suren B. Rao, Applied Research Laboratory, The Pennsylvania State University

Introduction

MECHANICAL TESTS are performed to evaluate the durability of gears under load. One of the primary uses of gear testing is to generate performance data, which are used to develop design-allowable stresses. Design-allowable stresses are used as a guide for determining the size, geometry, material, manufacturing process, and process conditions for new designs during the design process. Gear testing is also used to compare the performance of a new attribute or characteristic introduced in the gear to a baseline, which defines the part

performance with the old or existing attribute or characteristics. These new attributes or characteristics may be related to tooth geometry, gear material, manufacturing processes, and even process parameters used to manufacture the gear. In the aerospace industry, gear testing forms the minimum basis for accepting a change in these characteristics and is usually termed “qualification” of a proposed or recommended change.

Mechanical testing of gears is conducted under different scenarios. The first scenario is termed *rig testing*, which is extensively discussed and defined in this article. In rig testing, the gear is subjected to simulated loading that exercises a distinct mode of gear failure. While this simulation may not always be successful for a variety of reasons, data on the resistance of the gear to a distinct mode of failure allow the analysis of the specific characteristics that need to be altered to change its performance.

After rig testing is complete, it is customary to incorporate the gear into a transmission and subject the transmission to *bench testing*. In bench testing, the input and output of the transmission under test are simulated using various devices for power input and absorption. After bench testing, it is not unusual to subject the transmission to *full-scale testing*, where the transmission is subjected to controlled but actual operating conditions to determine the performance of the specific gear. Both bench and full-scale testing represent very specific application-oriented testing and are usually carried out by the organization manufacturing a specific product. It is obvious that rig testing, bench testing, and full-scale testing represent increasing orders of cost. Consequently, in most situations, extensive rig testing is followed by limited bench testing and even more limited full-scale testing. While the testing methods described in this article are particularly applicable to carburized and hardened steel gears, the described techniques are applicable to through-hardened steel and gears fabricated from other materials, with modifications.

Mechanical Testing of Gears

Douglas R. McPherson and Suren B. Rao, Applied Research Laboratory, The Pennsylvania State University

Common Modes of Gear Failure

Gear tooth failures occur in two distinct regions, the tooth flank and the root fillet. The mechanisms of failure in these two regions are distinct and are discussed separately. While much more detailed information on the subject is available elsewhere (Ref 1, 2, 3, 4, 5, and 6), only the essentials are covered in this section.

Failure Modes on Tooth Flanks

In order to understand the common modes of failure on tooth flanks, it is important to study the kinematics of a gear mesh, illustrated in Fig. 1 for a pair of spur gears. For the direction of rotation shown, contact starts at the left side of the figure and progresses to the right. Initial contact occurs well below the pitch diameter of the driving tooth and well above the pitch diameter of the driven tooth. There is significant sliding along with rolling contact at this point. Sliding on the surface of the driving gear is in the same direction as rolling. As rotation continues, the point of contact moves toward the tip of the driving gear and toward the root of the driven gear. Sliding decreases as the point of contact moves toward the pitch diameter, reaching zero (pure rolling) at the pitch diameter. As the point of contact moves above the pitch diameter of the driving gear, the direction of sliding reverses. At the end of contact, significant sliding again occurs. Tests have shown that sliding in the same direction as rolling (as occurs below the pitch diameter of the driving gear) has a more severe effect on the surface durability of the material.

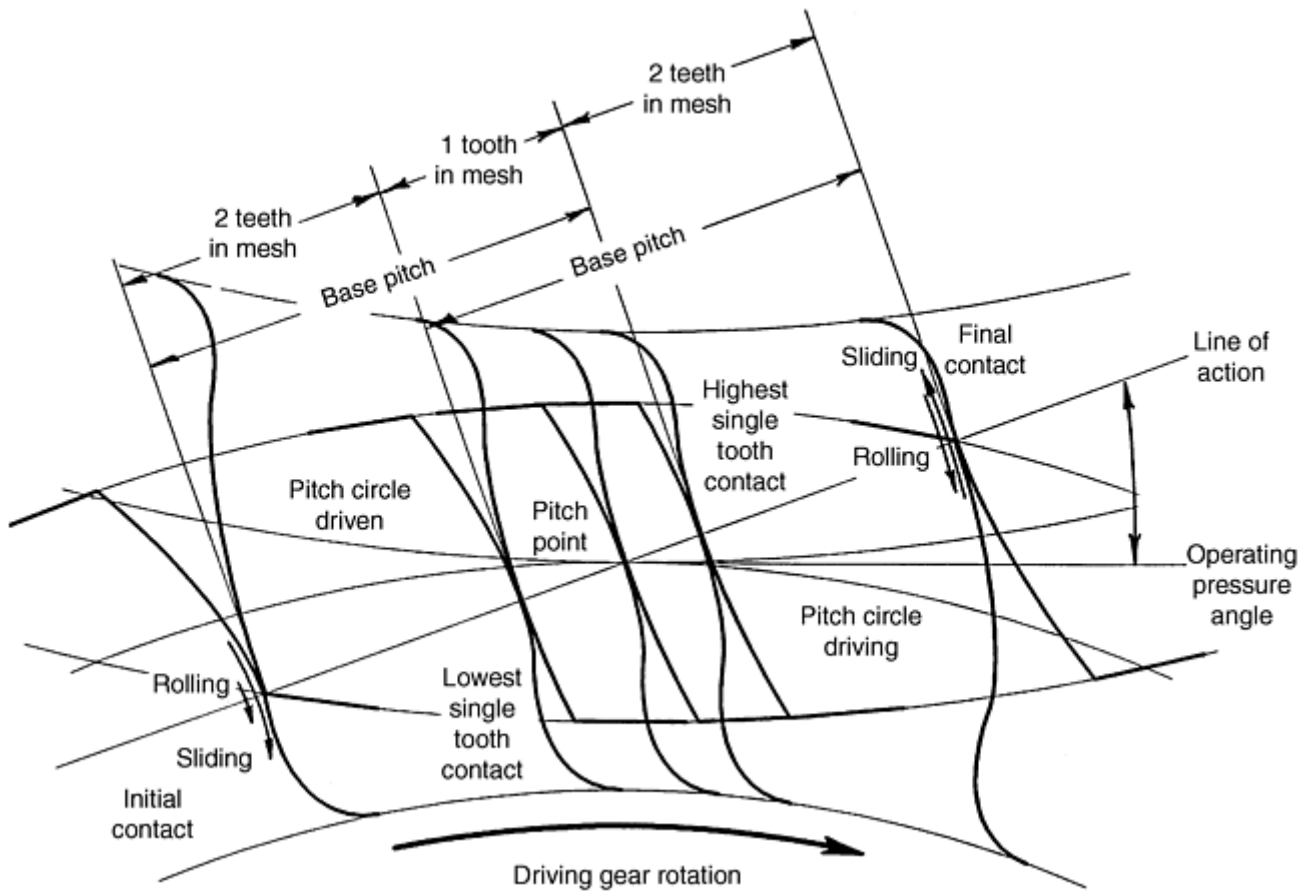


Fig. 1 Kinematics of a gear mesh

Failure modes on tooth flanks are caused by this combination of rolling and sliding. The more common failure modes are *scoring* (or *scuffing*), *wear*, and *pitting*. These modes are discussed briefly in this article. Additional information on these failure modes is provided in *Friction, Lubrication, and Wear Technology*, Volume 18 of the *ASM Handbook*.

Scoring (or Scuffing). This phenomenon is a lubrication failure, frequently brought on by an increase in the operating temperature. The lubricant film breaks down, allowing metal-to-metal contact at high spots (asperities) on the flank surfaces. Under sufficient conditions of load and temperature, this metal-to-metal contact causes asperities to weld together and then tear apart as the motion continues. The surface is characterized by torn or furrowed markings in the direction of sliding. Figure 2 shows a typical scored gear. The terms scoring and scuffing are used interchangeably in the literature, even though the term scoring is more prevalent in the aerospace industry, and the term scuffing is more commonly used in the automotive and other industries. Similar damage can occur without the instantaneous welding of the contact surfaces. This damage is sometimes caused by foreign material being carried through the mesh but is more frequently caused by high asperities on one contacting surface plowing through the other. This damage is termed *cold scoring* (or *scuffing*), or *burnishing*, and is differentiated from that described previously by the absence of tearing.

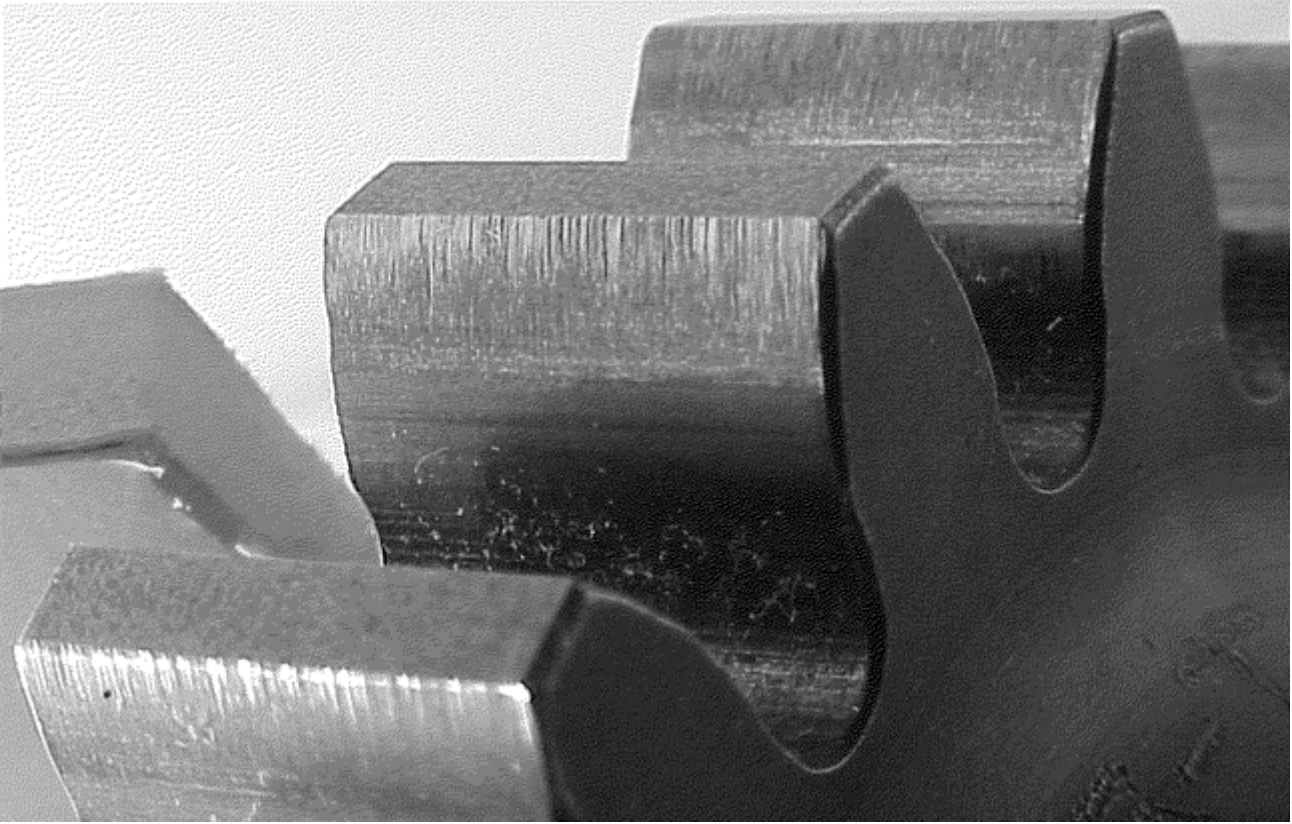


Fig. 2 Specimen gear with scoring (scuffing) failure

Wear generally describes the phenomenon that results in the gradual removal of material from the tooth flank. It can be accelerated by significant metal-to-metal contact, the presence of abrasive particles in the lubricant, or by chemical deterioration of the surface (corrosion) related to additives in the lubricant. A small amount of initial wear is sometimes desirable and is achieved by the process of “break-in” or “run-in.” This wear is generally accomplished by gradually loading the gears to their full load, thus allowing the individual tooth surfaces to interact and gently polish off the peaks of asperities. It is usually assumed that break-in enables the gears to last longer. Wear is hard to detect visually, frequently requiring measurement of tooth geometry to detect changes in profile or lead to confirm its occurrence. Wear will generally be more severe on portions of the tooth flank that experience greater sliding. This wear ultimately changes the shape of the tooth surface and increases dynamic loads. Thus, wear can be detected by an increase in noise or vibration. Obviously, the presence of metal particles in the lubrication oil is one sure sign of wear occurring, and this presence forms the basis of many diagnostic monitoring systems for gearbox applications.

Pitting is a fatigue failure brought on by the cyclical rolling contact load and aggravated by the surface traction forces due to sliding. Pitting failures are divided into three categories based on the location of the origin. *Surface origin pitting* is the result of interaction of asperities as tooth surfaces slide against each other. *Subsurface origin pitting* is the result of fatigue below the surface in the region of highest shear stress. The third category results from fatigue at the case/core interface, which should be well below the region of highest shear stress, and is termed *case crushing* or *spalling*. This third category represents parts that have been improperly manufactured and is not discussed here.

For most surface vehicle gearing and low-speed drives in general, surface origin pitting is the predominant flank failure mode. When tooth surfaces slide against each other, asperities on the opposing surfaces interact, resulting in very high, localized, shear stresses. This interaction produces a series of cracks at about 45° to the surface to a depth of up to 25 μm (0.001 in.). The cracks arrest at this point because the shear stresses produced in the bulk of the material by the contact load are not high enough to promote further propagation. When many such cracks occur on a localized area, the surface acquires a gray-etched appearance. This condition is termed *gray staining* or *microfissuring*. After continued cyclical loading, some of the surface material between the cracks may break away, leaving cavities up to 15 μm (0.0006 in.) deep. This condition is termed *exfoliation* or *frosting*. These conditions are not usually considered failure.

After continued running, some of the cracks may propagate further into the surface. The exact mechanism that allows some cracks to propagate, while most remain arrested, is probably related to nonmetallic inclusions providing stress risers, but it could also be related to more severe interaction of the surfaces in localized areas (scuffing) or the action of the lubricant. As cracks progress further into the surface, larger chunks of material can break away, leaving larger cavities. When cavities have grown from the size of exfoliation up to about 100 μm (0.004 in.) deep, the condition is termed *micropitting*. The term frosting sometimes is applied to this condition as well. For critical applications, the occurrence of micropitting over a significant area is considered failure. A gear in this condition is shown in Fig. 3.

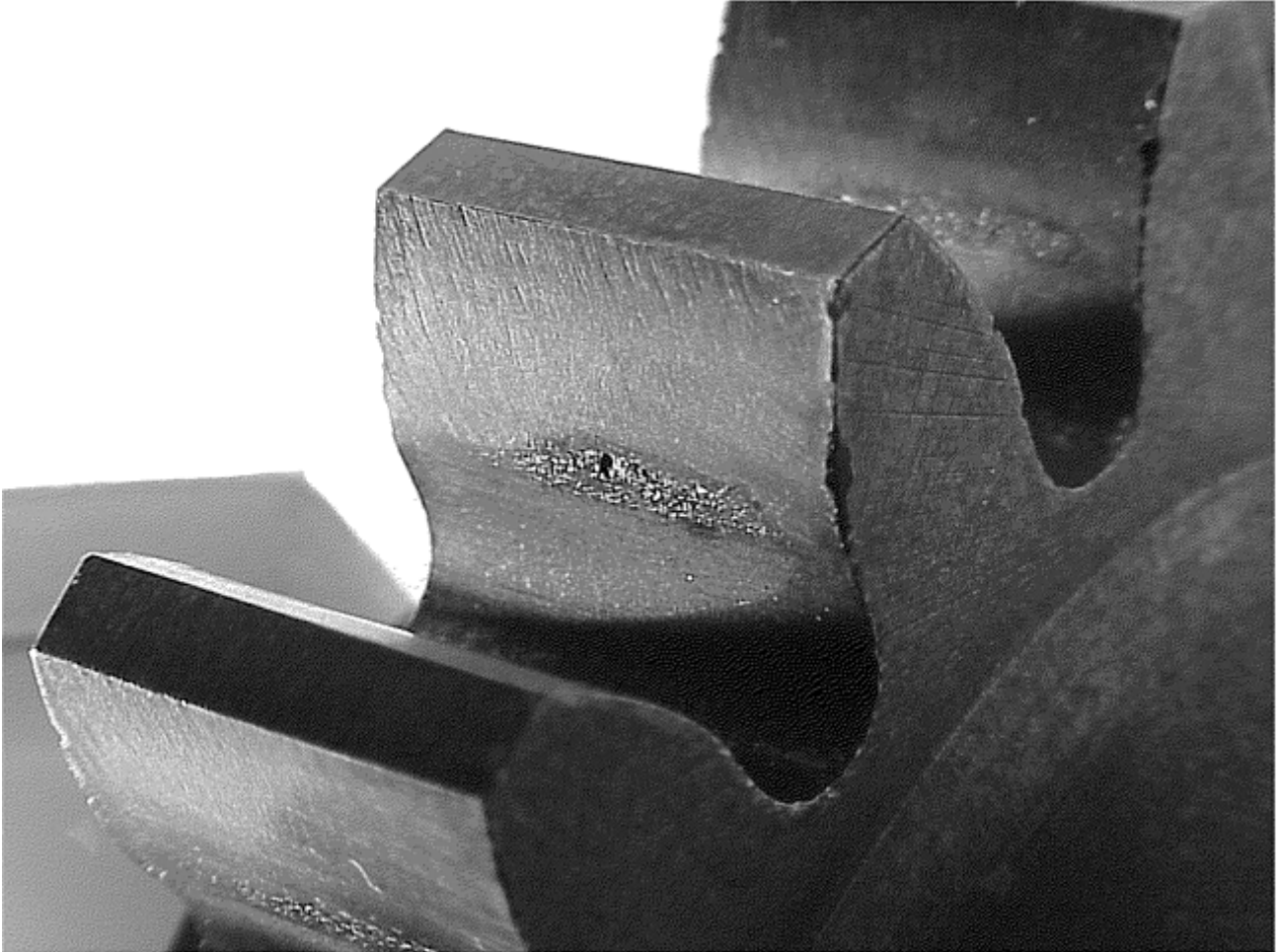


Fig. 3 Specimen gear with micropitting (frosting) failure

As cracks progress further into the surface, the rate of propagation increases. This increase is related in part to lubricant (under contact pressure) being forced into the crack and wedging it further open, but it mostly is due to the higher shear stresses produced by the contact load. At some point below the surface, in the region of 100 to 500 μm (0.004 to 0.020 in.) or deeper, depending on contact geometry, shear stresses produced by the contact loading become high enough to promote rapid crack propagation. Progressively larger pieces break away from the surface, leaving yet larger cavities. This condition is termed *pitting* or *macropitting*. The material is torn away from the damaged area by the relative motion of the contacting part; thus, the cavity becomes wider and deeper in the direction opposite to sliding, leading to an arrow shape. Figure 4 illustrates a gear with an arrow-shaped surface origin pit at this stage. As pits become larger, they eventually cause a readily detectable increase in dynamic loads. A loss of material that reaches this level is frequently termed *spalling* and is considered failure.



Fig. 4 Specimen gear with arrow-shaped surface origin pit

Subsurface origin pitting typically occurs only in cases where the elastohydrodynamic lubricant film thickness is great enough to prevent significant asperity interaction. This pitting occurs in high-speed power gearing and in aerospace power drives. It is also typical in antifriction bearings (which operate with pure rolling as at the pitch diameter on spur gears). The origin is typically a nonmetallic inclusion or discontinuity in the structure, in the area of highest shear stress (about 100 to 500 μm , or 0.004 to 0.020 in.) below the surface. Crack propagation is initially quite slow, until a crack penetrates the surface, allowing lubricant to enter. It can be difficult to tell the difference between surface and subsurface origin pits, although subsurface origin pits often do not have the arrow shape typical of surface origin pits. As with surface origin pits, when the pit becomes large enough to cause a readily detectable increase in noise and vibration, it is considered a failure. Because most pits start small and progressively grow large, some critical high-speed drives incorporate a chip detector in the lubrication system to provide advance warning of imminent failure.

Failure Modes in Root Fillets

Failure of the gear tooth also can occur in the root fillet. This failure is primarily due to bending fatigue but can be precipitated by sudden overloading (impact). Sudden overloads can be caused by a large foreign object (e.g., a broken tooth) being drawn through the mesh, the driving or driven shafts suddenly stopping, or sudden loss of alignment (failure of an adjacent bearing).

Bending Fatigue. The origins of bending fatigue failures typically are imperfections in the surface of the root fillet (e.g., tooling “witness” marks) or nonmetallic inclusions near the surface. Cracks slowly propagate around the origin until they reach the critical size for the case material at the prevailing stress level. For hardened high-carbon material typically used for gears, when the crack reaches this critical size, it “pops” through the case (i.e., the entire case fractures). At this point, the rigidity of the tooth is reduced (compliance increases), and dynamic load increases significantly. This produces a readily detectable increase in noise and vibration and represents failure.

In many rig tests it is impossible to stop the rig quickly enough, once cracking is detected, to prevent complete fracture of the tooth and potential jamming of the test rig. This limitation causes some reluctance to conduct bending fatigue tests in high-speed power-circulating gear test rigs. However, with some transmission designs there is enough time between the onset of increased vibration and catastrophic failure for a vibration monitoring system to give sufficient warning to permit an orderly shutdown of the equipment. The mechanism that allows this shutdown is the reduced compliance of the cracked tooth, which transfers some of the load to adjacent teeth. The lower load and the lower hardness of the core results in slower crack propagation, allowing a brief

interval between the occurrence of detectable cracking and fracture of the tooth. This feature notwithstanding, tooth fracture is a potential catastrophic form of gear failure, and a substantial portion of gear test programs are dedicated to obtaining sufficient data to minimize its occurrence in service. In some gear designs (such as thin rims), cracks can propagate into the rim area. Rim fracture is the most catastrophic form of gear failure and should always be avoided.

Impact fracture of a gear tooth occurs in one loading cycle. The impetus for studying impact properties of gear steels is to ensure that steels used in gears have enough impact resistance to prevent failure when gears are subjected to normal spike loads.

References cited in this section

1. E.E. Shipley, "Failure Modes in Gears," presented at Forum on Gear Manufacture and Performance, 19 Oct 1973 (Detroit), American Society of Mechanical Engineers
2. D.W. Dudley, Gear Wear, *Wear Control Handbook*, M. Peterson and W. Winer, Ed., American Society of Mechanical Engineers, 1980
3. G. Niemann and H. Winter, Getriebeschäden und Abhilfe, Entwicklungstendenzen, *Maschinenelemente*, Vol 2, 2nd ed., Springer-Verlag (Berlin), 1983
4. "Appearance of Gear Teeth—Terminology of Wear and Failure," ANSI/AGMA 1010-E95, American National Standards Institute/American Gear Manufacturers Association
5. R. Errichello, Friction, Lubrication, and Wear of Gears, *Friction, Lubrication, and Wear Technology*, Vol 18, *ASM Handbook*, ASM International, 1992, p 535–545
6. L. Alban, *Systematic Analysis of Gear Failures*, American Society for Metals, 1985

Mechanical Testing of Gears

Douglas R. McPherson and Suren B. Rao, Applied Research Laboratory, The Pennsylvania State University

Stress Calculations for Test Parameters

Gear-rating standards, such as American National Standards Institute (ANSI)/American Gear Manufacturers Association (AGMA) 2001-C95 ("Fundamental Rating Factors and Calculation Methods for Involute Spur and Helical Gear Teeth") and International Organization for Standardization (ISO) 6336, base gear performance on contact and bending stresses. Nominal stresses are determined from first principles and are then modified to allow for the realities of manufactured gears running in actual gearboxes. This modification approximates a reasonable upper limit for the range of stress variation.

ANSI/AGMA 2001-C95 contains factors in the fundamental stress formulas for contact and bending to address overload, gear dynamics, size, load distribution, surface condition (contact only), and rim thickness (bending only). Design-allowable stress numbers are modified by further factors that address intended life, operating temperature, reliability, safety factor, and hardness ratio (contact only). It is normal practice in determining stresses to be reported with rig test results to take all of these factors as unity. The intent of rig testing is to compare the effect of various attributes or characteristics on performance. Thus, it is reasonable to determine the actual stress based on a value of unity for each factor, then determine suitable values for the factors based on test results.

The factors that are in essence being ignored by this approach represent real phenomena that occur as gears operate. It is critical to address this fact in the design of test rigs and in their day-to-day operation. For example,

it is important to conduct tests in a manner that precludes overloading; in a set of tests intended to evaluate the effect of overloading, only controlled overloads can be permitted. Most of the other factors can be handled in the same manner. However, gear dynamics and load distribution need to be addressed in a more direct fashion because they both can introduce uncontrolled variation in a set of test results.

Gear dynamics present a problem in determining the proper stress to be related to performance. Rating standards provide guidance on dynamic load variations in normal gearboxes. Gear test rigs, as described here, load one gearbox against another to keep power requirements to a minimum. Thus, there are two or more sets of dynamic variations, plus their interactions, to be considered. If the shafts connecting the gearboxes are quite rigid, the dynamic loading can be greater than the applied loading, even when precision gears are tested. Owing to the complexity of the situation, stresses for rig tests are computed making no allowance for dynamics. The fact that the dynamics of gear test rigs are not the same as real machines that use gears is a principal reason that bench testing and full-scale testing are required before a given gear design is adopted for critical applications.

The load distribution factor accounts for variations in alignment due to deflections of teeth, gearbox, and so on for variations in axial alignment of gear teeth, and for variations in load sharing between teeth. Much of the variation in load distribution can be minimized by straddle mounting test gears between bearings so their axes remain parallel under loading, modifying the profiles of test gears to optimize load sharing and so on. However, concentration of contact load at one end of a gear tooth (due to a small variation in axial alignment) produces a bending stress concentration. To avoid this condition, one or both test gears can be crowned to keep the load at the center of the face width. In this condition, the load-distribution factor is taken as unity for bending stress, and a suitable factor is estimated as shown in the following section for contact stress. However, crowning adds an additional variable that could affect test repeatability. It may be more expensive to accurately crown (and measure for verification) these test gears. Many times it may be more feasible to use high-accuracy standard test gears and very stiff (lateral) mounting to ensure uniform load distribution.

Contact Stress Computations for Gear Tooth Flank. Contact stresses on the surfaces of gear teeth are determined using Hertz's solution for the stress between contacting cylinders. The equation for contact stress taken from this solution, reduced to the simplest form applicable to spur gear teeth, is:

$$\text{Contact stress} = (P' \times B)^{1/2} \times EF \quad (\text{Eq 1})$$

where the contact force per unit width, P' , is:

$$\frac{\text{Pinion torque}}{\text{Pinion base radius} \times \text{effective face width}} \quad (\text{Eq 2})$$

and

$$B = \frac{R_1 + R_2}{R_1 \times R_2} \quad (\text{Eq 3})$$

where B is the geometry factor, R_1 is the radius of the pinion contact surface at the point of interest, and R_2 is the radius of the gear contact surface at the point of interest.

$$EF = \left[\pi \left(\frac{1 - \nu_1^2}{E_1} + \frac{1 - \nu_2^2}{E_2} \right) \right]^{-1/2} \quad (\text{Eq 4})$$

where EF is the elasticity factor, E_1 is the pinion modulus of elasticity, ν_1 is the pinion Poisson's ratio, E_2 is the gear modulus of elasticity, and ν_2 is the gear Poisson's ratio. For pinion and gear (both steel), the EF is 2290 in U.S. customary units (P' in lb/in., B in in.⁻¹, and stress in psi), and EF is 190.2 in Système International d'Unités (SI) units (P' in N/mm, B in mm⁻¹, and stress in MPa).

The most critical combination of contact load and sliding in spur gears occurs on the flank of the driving gear at the lowest point of contact with one pair of teeth in mesh (the location labeled "lowest single tooth contact" in Fig. 1). The radii of the contact surfaces at this point can be determined from the corresponding roll angles for the gear and pinion. The radius of curvature is the roll angle (in radians) times the base radius. The radii used in determining the geometry factor are thus:

$$R_1 = (OR_p^2 - BR_p^2)^{1/2} - \frac{2 \times \pi \times BR_p}{N_p} \quad (\text{Eq 5})$$

$$R_2 = \sin(OPA) \times OCD - (OR_p^2 - BR_p^2)^{1/2} + \frac{2 \times \pi \times BR_G}{N_G} \quad (\text{Eq 6})$$

where OR_p is the pinion outside the radius, BR_p is the pinion base radius, N_p is the number of pinion teeth, OCD is the operating center distance, BR_G is the gear base radius, N_G is the number of gear teeth, and OPA is the operating pressure angle, equal to $\cos^{-1} (BR_p + BR_G)/OCD$.

The contact stress returned by Eq 1 is a nominal stress and assumes uniform distribution of load. With crowned gears this uniform distribution will not be the case. The contact area becomes an ellipse, or in most cases, the center portion of an ellipse, with the highest contact stress at the center of the face width and progressively lower contact stress toward the ends. The proportions of the ellipse can be determined from a more complex form of Hertz's solution to the contact stress problem. A second geometry factor, A , related to the radius of curvature along the lead of the gears is needed:

$$A = \frac{R'_1 + R'_2}{R'_1 \times R'_2} \text{ or } A = \frac{1}{R'} \quad (\text{Eq 7})$$

where R'_1 is the radius of curvature along the pinion lead, R'_2 is the radius of curvature along the gear lead, and R' is the radius of curvature along the lead (only one gear crowned).

The amount of crown is usually a very small proportion of the face width; thus, the radius of curvature is large, and the section that can be measured represents an infinitesimal angular segment of the circle. This geometry makes it difficult for coordinate measuring machines (CMMs) to determine the crown radius. A useable crown radius can be determined from lead traces and Eq 8:

$$\frac{(\text{effective face width})^2}{8 \times (\text{average drop at ends of effective face})} \quad (\text{Eq 8})$$

The following equations regarding the contact ellipse are empirical in nature and assume that the ratio B/A is appreciably greater than 20, which will be the case with most crowned gears. If this is not the case, a thorough presentation of Hertz's contact solution, such as Ref 7, should be consulted.

$$k = \left(\frac{B}{A} \right)^{-0.62} \quad (\text{Eq 9})$$

where k is the ratio of ellipse minor to major axis.

$$\left[1 + \frac{B \times (\pi \times k \times EF \times \text{effective face width})^2}{48 \times (1 + k) \times P'} \right]^{1/2} \quad (\text{Eq 10})$$

If the crown radii are small enough in proportion to the contact load and effective face width, the contact area will be an ellipse narrower than the effective face width. The width of the elliptical contact area and the corresponding contact stress for this case can be determined from Eq 11, 12, and 13.

$$\text{contact force} = \frac{\text{pinion torque}}{\text{pinion base radius}} \quad (\text{Eq 11})$$

Width of contact ellipse, EW , is determined by:

$$2 \times \left[\frac{3 \times \text{contact force}}{B \times (\pi \times k \times EF)^2} \right]^{1/3} \quad (\text{Eq 12})$$

$$\text{contact stress (crowned)} = \frac{6 \times \text{contact force}}{\pi \times k \times EW^2} \quad (\text{Eq 13})$$

These formulas can compute contact stresses for rig test specimen gears far higher than would be predicted by the load distribution factors presented in gear-rating standards. The formulas are presented here to permit comparison of performance on a stress basis between gears with differing crown. Stresses determined in this manner should be reduced by a typical load distribution factor before being used to develop allowable design stresses.

In most cases, there will be variation in contact stress between specimen gears in the same lot (and from tooth to tooth on each gear) tested at the same load. The edge break at the ends of teeth is frequently applied in a manual operation; thus, the effective face width can vary. Crown can vary from tooth to tooth on each gear. Center distance can vary due to radial runout in shafts and bearings. The outside diameter of gears can vary (as required for manufacturing tolerance). It is important, therefore, to determine the mean contact stress and the probable range of variance.

Bending stress computations for root fillets are computed based on the assumption that the gear tooth is a cantilever beam with a stress concentration at its supported end. AGMA rating standards determine the form of the cantilever beam from the solution presented by Lewis and use a corresponding stress concentration factor. ISO and Deutsche Industrie-Normen (German Industrial Standards) (DIN) use different proportions for the beam and determine the stress concentration factor in a different manner. Only the AGMA approach is discussed here.

Figure 5 shows a spur gear tooth with a point load applied at the highest point of single-tooth contact. This point of loading corresponds to the highest bending stress when there is effective load sharing between gear teeth. Specimen gears used in rig tests should have effective load sharing, so this is the appropriate point of loading for determining bending stress in rig tests. For gears tested in single-tooth bending fatigue, the actual point of loading established by the test fixture should be used in calculating bending stresses.

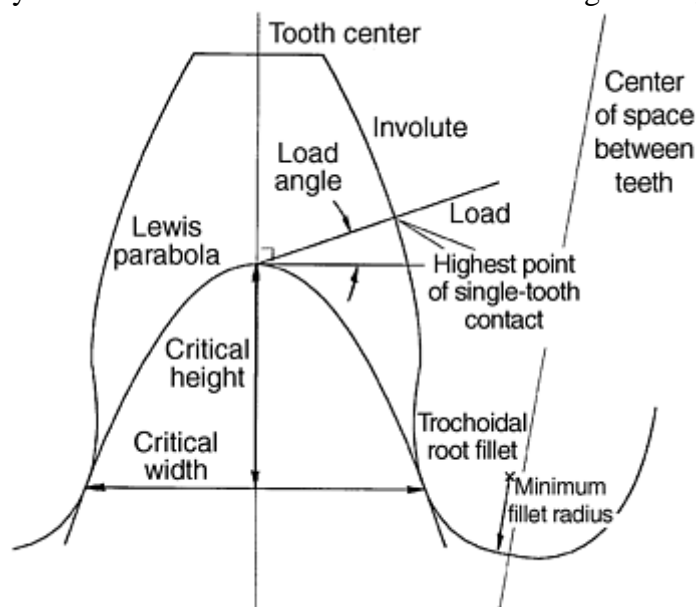


Fig. 5 Layout of Lewis parabola for tooth-bending stress calculation

The Lewis parabola is drawn from the point at which the load line intersects the center of the gear tooth and is tangent to the root fillet. Methods used to lay out this parabola depend on how the root form is generated, the particulars of which are presented in detail elsewhere (Ref 8). The critical height and width are determined from the Lewis parabola as shown in Fig. 5. The angle between the load line and a normal-to-the-tooth center is termed the *load angle* (it differs from the pressure angle at the point of loading because of the thickness of the tooth). The bending stress is thus:

$$\frac{\text{load} \times \cos(\text{load angle})}{\text{face width}} \left[\frac{6 \times h}{s^2} - \frac{\tan(\text{load angle})}{s} \right] K_f \quad (\text{Eq 14})$$

where s is the critical width from the Lewis Parabola, h is the critical height from the Lewis Parabola, and K_f is the stress concentration factor:

$$H + \left(\frac{s}{r} \right)^L \left(\frac{s}{h} \right)^M \quad (\text{Eq 15})$$

where r is the minimum fillet radius, H is equal to $0.331 - 0.436 \times$ (nominal pressure angle, in radians), L is equal to $0.324 - 0.492 \times$ (nominal pressure angle, in radians), and M is equal to $0.261 + 0.545 \times$ (nominal pressure angle, in radians).

Equation 14 is derived from first principles but also can be derived from AGMA standards by taking the forms of relevant formulas pertinent to spur gears and setting all design factors at unity. While a similar formula could be developed for helical gears, testing them usually represents a step between rig testing and bench testing, and such tests are negotiated between the client and the testing laboratory.

References cited in this section

7. A.P. Boresi and O.M. Sidebottom, *Advanced Mechanics of Materials*, 4th ed., John Wiley & Sons, 1985
8. “Information Sheet: Geometry Factors for Determining the Pitting Resistance and Bending Strength of Spur, Helical, and Herringbone Gear Teeth,” AGMA 908-B89 (R1995), American Gear Manufacturers Association, 1995

Mechanical Testing of Gears

Douglas R. McPherson and Suren B. Rao, Applied Research Laboratory, The Pennsylvania State University

Specimen Characterization

Specimen characterization is a critical part of any fatigue test program because it enables meaningful interpretation of the results. It is important to know that the specimens to be tested meet specifications, where key parameters fall in the specified range, and what the variations are. Characterizations fall into four areas: dimensional, surface finish/texture, metallurgical, and residual stress.

Dimensional Characterization. Basic dimensional checks include size and alignment of mounting surfaces, size and alignment of test surfaces relative to mounting surfaces, and size and uniformity of edge breaks at the edges of test surfaces. These checks ensure that the specimens will fit into the test rig and either ensures that stresses will be consistent or provides data to determine variations.

The important dimensions to check on rolling contact fatigue (RCF) specimens are diameters of mounting trunnions and test surface, total indicator reading (TIR) test surface-to-mounting trunnions, and overall length. The important dimensions to check on the mating load rollers are inside and outside diameters, TIR inside to outside, crown radius and location of high point of crown, and thickness. In the case of nonstandard specimens where the entire width of the test surface is intended to make contact, the size and uniformity of the edge break needs to be checked.

The important dimensions to check on gear specimens fall into the areas of mounting surfaces, gear functional charts, and other specific features impacting stress. All of the gear specimens described in the following sections are mounted on their inside diameter. Thus, inside diameter, length between end faces, and perpendicularity of end faces to inside diameter need to be checked. For specimens with a splined bore, the pitch diameter, or inside diameter if so specified, counts as the inside diameter for alignment checks. The gear functional charts are developed with the gear mounted on the test mounting surfaces. Typical measurements include lead, profile, spacing, index, and runout. Other specific items to check include diameter over wires, root diameter, and size and uniformity of edge break at tooth ends and along the tip.

Surface Finish/Texture Characterization. It has been standard practice to specify surface finish and texture in terms of arithmetic average surface roughness (R_a). Because it is possible to manufacture surfaces with widely varying load capacity, all with the same R_a , more information than R_a is needed to interpret data. At a minimum, R_z (a measure of “average” peak roughness) should also be measured. A preferable method would be to examine surfaces with an optical interference system that maps the contour of an area rather than the traditional line contact. Test surfaces to be subject to contact fatigue should also be examined at 10× to ensure they are free of corrosion, dings, scratches, and so on.

Metallurgical Characterization. Both surface hardness and hardness gradients are to meet specification. For gear specimens, hardness should be checked at the tooth half height and at the root fillet. Details of the

microstructure should be characterized at the same locations as hardness. Typical practice has been to prepare and document photomicrographs of the etched structure at 400× to 600×.

Residual Stress Measurement. Residual stresses vary among a lot of parts; therefore, enough measurements should be made to permit a statistical analysis. Residual stress gradients provide more useful information than surface measurements but at a much higher price. A complete study should include some residual stress gradient data. Typical practice is to measure surface residual stress at six points per variant and measure the residual stress gradient at one or two of these points. Contact fatigue specimens should be measured at the center of the contact surface. Gear specimens should be measured at the tooth half height (or lowest point of single-tooth contact) for surface durability tests and at the midpoint of the root fillet for bending strength tests.

Mechanical Testing of Gears

Douglas R. McPherson and Suren B. Rao, Applied Research Laboratory, The Pennsylvania State University

Tests Simulating Gear Action

Tests that simulate gear action are the RCF test, the single-tooth fatigue test, the single-tooth single-overload test, and the single-tooth impact test.

Rolling Contact Fatigue (RCF) Test

The RCF test simulates the rolling/sliding action that occurs in a gear mesh, and depending on the test parameters employed, it can simulate the most severe condition in the mesh. Because the specimens are cylindrical, this test is the least expensive to run in both cost and time. Hence, it is frequently used as a screening test, and its results are used to plan further gear testing.

Test Equipment. Figure 6 shows a schematic of the rolling/sliding contact fatigue test. The specimen and load rollers are cylindrical. The outside diameter of the load roller is crowned to concentrate the load at the center of contact and eliminate the possibility of concentrated loading at the edge of contact due to misalignment. A normal load is applied by air pressure. Phasing gears, attached to the shafts on which the specimen and load rollers are mounted, control the extent of sliding at the specimen/load roller interface. The amount of sliding is determined by the gear ratio and can be fixed at any value (21 and 43% are commonly selected), simulating the rolling/sliding action at any desired location on gear teeth. This test is primarily intended to evaluate the resistance of candidate material systems to surface origin pitting, but other modes of surface failure can be studied. The surfaces of the specimen and load roller are sliding against each other, with lubrication, under high load. Therefore, some indication of the lubricated wear resistance of the material being tested can be obtained. In addition, the resistance of the material/surface finish/lubricant system to scuffing can be studied. Tests are conducted at very high overload to promote failure in real time; thus, it is possible to introduce plastic deformation (rippling) on the contact surface. With specially adapted equipment, these tests can be conducted at different temperatures up to 400 °F. Specimens and load rollers can be designed for a variety of testing requirements, depending on the exact material and objective of the test.

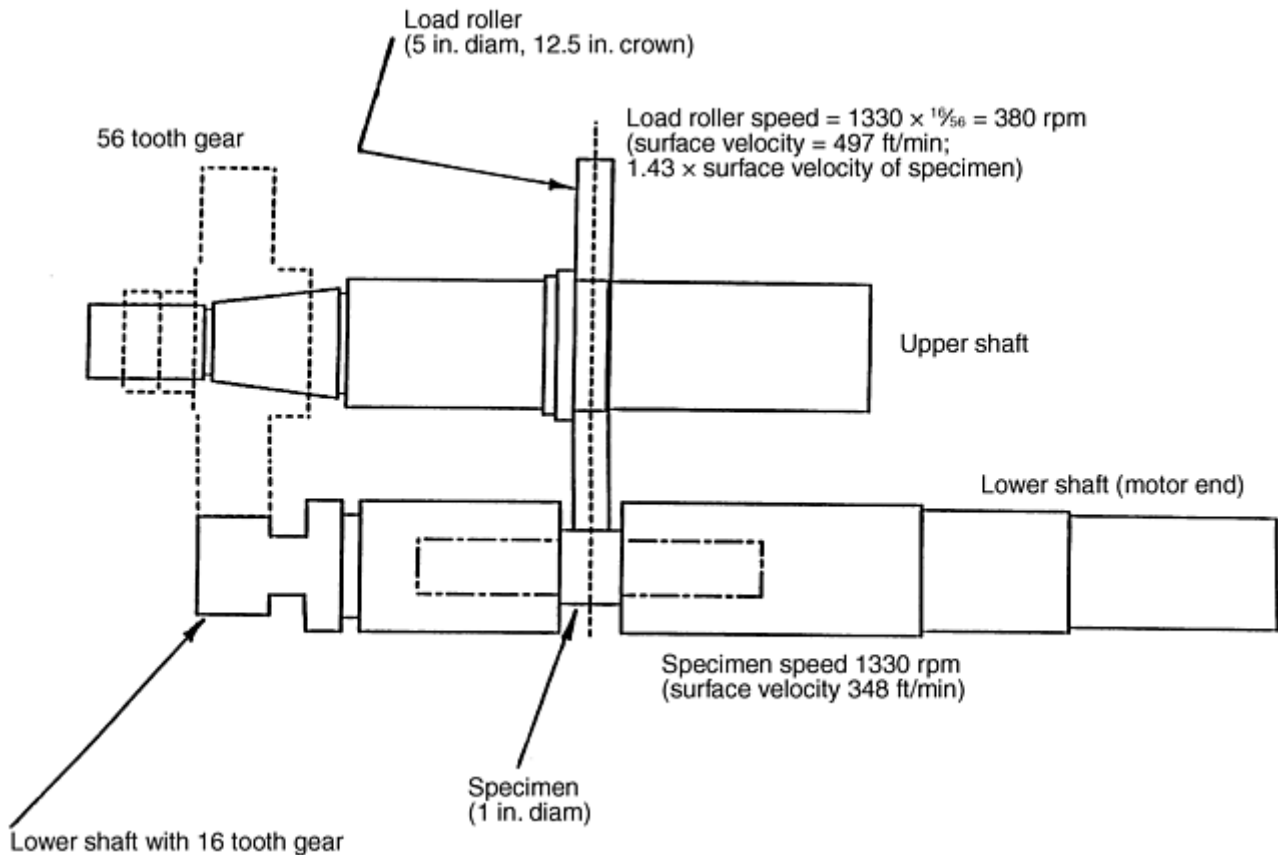


Fig. 6 Schematic of a rolling/sliding contact fatigue (RCF) test

Test Procedure. The lubricant stream to the specimen/load roller interface is aimed at the discharge side of the mesh (to cool the surfaces after contact). The lubricant flow rate is adjusted (typically to about 2 L/min, or as specified for the project), with the lubricant at test temperature.

Alignment of the specimen and load roller is checked as each test is set up. One method often used is to coat the surface of the load roller with a thin layer of layout blue and ensure that contact occurs uniformly at the center of the load roller. Before the start of testing at load, a break-in run is typically conducted. This procedure is accomplished by running the machine for 10 min at each of a series of increasing loads up to the full test load. The intent of the break-in run is to gently polish away asperities on the contacting surfaces that might cause scuffing (i.e., localized scoring), burnishing, or wear to occur under full load.

Tests are stopped periodically, and the contacting surfaces of the specimen and load roller are inspected for signs of surface distress. The diameter at the center of the specimen is also measured to provide an indication of wear. The formation of large, progressing pits produces a strong vibration signal, which, in turn, shuts down the test. Lubricant temperature, lubricant pressure, and air pressure (to apply the contact load) are also monitored, and the test is stopped if irregularities are detected.

The results of contact fatigue tests exhibit more scatter than is typical with other fatigue tests. One gage of scatter is the Weibull slope, a measure of the increase in rate of failure with increasing life. For many fatigue tests, a Weibull slope of six or more is typical. A Weibull slope of six can be roughly translated into practical terms as follows. If 20 samples were randomly selected from a large group of theoretically identical parts and tested to failure under identical conditions, the longest test would, on the average, last about twice as long as the shortest. For contact fatigue testing with current ultraclean steels, a Weibull slope of 1.5 is typical. In this example, if the Weibull slope were 1.5, the longest of the 20 tests would last approximately 20 times as long as the shortest. The impact on test programs is that many tests have to be conducted to develop enough data to make statistically meaningful comparisons. The minimum number of tests with each variant (at each load) to enable reasonable comparisons has typically been considered to be six. With six tests for each of two variants and Weibull slopes of 1.5, the G50 life of one variant would have to be twice that of the other to conclude that it is better. If the comparison were made on the basis of G10 life, the ratio would have to be 5 to 1.

Specimen Results. An example set of data, representative of the results of rolling/sliding contact fatigue testing, is shown in Table 1. In addition to specimen identification, load, and life to failure, other information is

reported to aid in the interpretation of results. Several test parameters can be varied as needed; thus, the actual values are reported with the results. These parameters include lubricant, lubricant bulk temperature, nominal filter size, test speed, and phasing gear set/slide ratio. Also reported for each test are data regarding surface roughness, ratio of elastohydrodynamic lubricant film thickness to composite roughness, wear, and wear rate. A Weibull statistical analysis of this set of results is shown graphically in Fig. 7. Comparisons between variants are made on either a G10 life or a G50 life basis.

Table 1 Example of rolling/sliding contact fatigue test data

Lubricant, automatic transmission fluid. Bulk temperature, 90 °C (194 °F). Filter, 10 µm (nominal). Test speed, 1330 rpm. Phasing gear set, 16 tooth/56 tooth. Slide/roll ratio, 43%. Contact stress, 400 ksi. Load, 3000 lb.

Test No.	Specimen No.	Test duration		$R_a^{(a)}$		$\lambda^{(b)}$	Wear ^(c) , in.	Wear rate ^(d)	Comments
		10 ⁶ cycles	h	Specimen	Load roller				
		1.173	14.7	13.5	3.8				
3	10-9/LR 1	1.603	20.2	8.5	...	0.58	0.0002	12	Surface origin pitting
8	10-11/LR 5	7.332	92.3	9.3	...	0.56	0.0001	1.4	Surface origin pitting
12	10-4/LR 13	7.565	95.3	...	5.0	0.57	0.0008	12	Surface origin pitting. Severe exfoliation and wear at center of wear track
18	10-2/LR 17	5.267	66.3	9.0	6.8	0.51	0.0002	3.8	Surface origin pitting
22	10-3/LR 22	6.322	79.7	...	5.0	0.56	0.0003	4.7	Surface origin pitting

(a) R_a , arithmetic average surface roughness measured in axial direction, µin.

(b) λ , ratio of elastohydrodynamic film thickness to composite surface roughness. In cases where surface roughness was not measured for a particular specimen or load roller, λ is based on average surface roughness for group.

(c) Diametral wear (i.e., change in diameter) on specimen.

(d) Change in diameter, in. $\times 10^{-5}$ /cycles $\times 10^6$

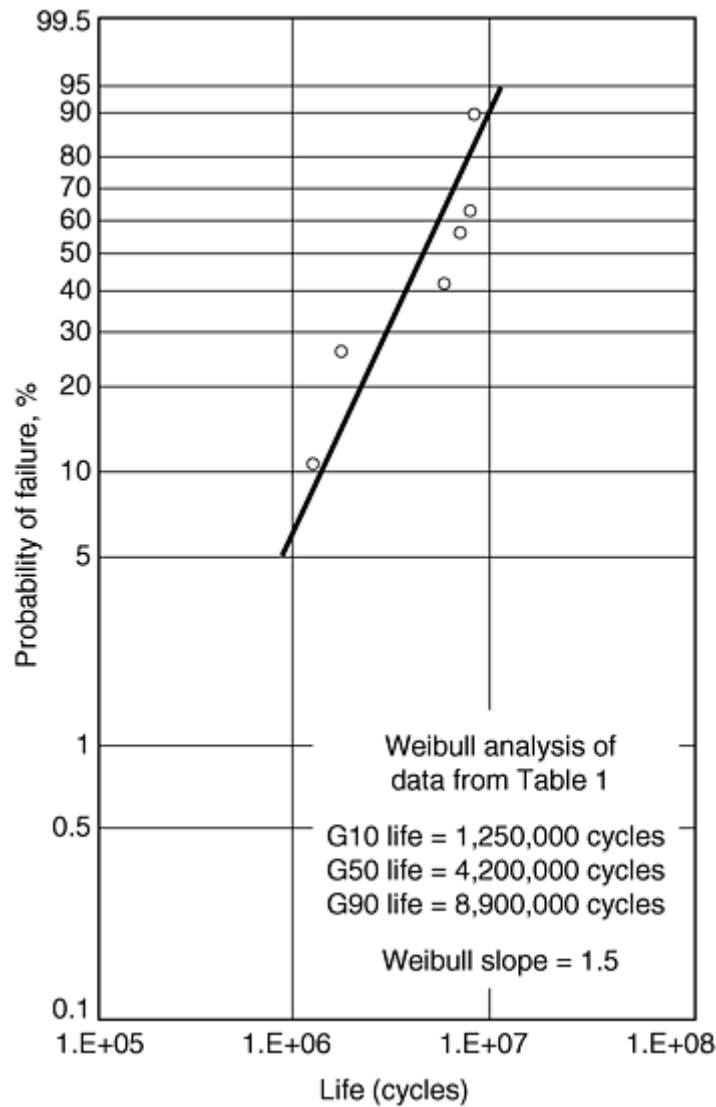


Fig. 7 Weibull analysis with RCF test data

Single-Tooth Fatigue (STF) Test

The STF test is used to generate a statistically significant quantity of bending fatigue data at a comparatively low price. Teeth are tested one at a time with a fixed loading point, allowing the generation of bending fatigue data at comparatively high cycles without risk of losing tests to other modes of failure. Another cost-saving measure is that four or more tests can be conducted with each gear specimen.

Test Equipment. A gear is placed in a fixture so that one tooth at a time can be loaded while another tooth supports the reaction. The test is usually done in an electrohydraulic, servocontrolled universal test machine. The primary object of this test is to determine fatigue properties in bending. However, the same setup can be used to determine single overload properties (ultimate bending strength) as well. Frequently, enough teeth are tested to develop a stress-cycles diagram to define the bending fatigue characteristics of the material system.

Several arrangements for loading can be considered. One fixture arrangement is shown in Fig. 8. This illustration shows the Boeing flexural design, which appears to have found favor with the aerospace sector. This

fixture is designed for a 32 tooth, 5.333 diametral pitch (DP), 8 mm ($\frac{3}{8}$ in.) face width spur gear with several teeth removed to provide access to test and reaction teeth. The gear is rigidly supported on a shaft. Load is applied through a carbide block contacting the test tooth at the highest point of single-tooth contact. The loading block is held in the specified orientation to the gear by a flexural loading arm. This flexural design ensures accurate loading of the gear tooth with minimal migration of the point of loading. Reaction is carried through a block contacting the reaction tooth at the lowest point of single-tooth contact. Load is cycled from the specified test load to a minimum load high enough to keep the slack in the system taken up (usually 10% of the test load). While most testing is conducted at 20 Hz, other frequencies also are possible. The fatigue test

machine is instrumented to monitor instantaneous loads and tooth deflections. Changes in compliance can be used for monitoring crack initiation and propagation in the root fillet region. In addition, a crack wire can be incorporated to monitor catastrophic tooth failure. Typical fatigue load capacity of such types of equipment is in the range of 10 to 20 kips, although higher loads, up to 110 kips, can be used for single overload tests.

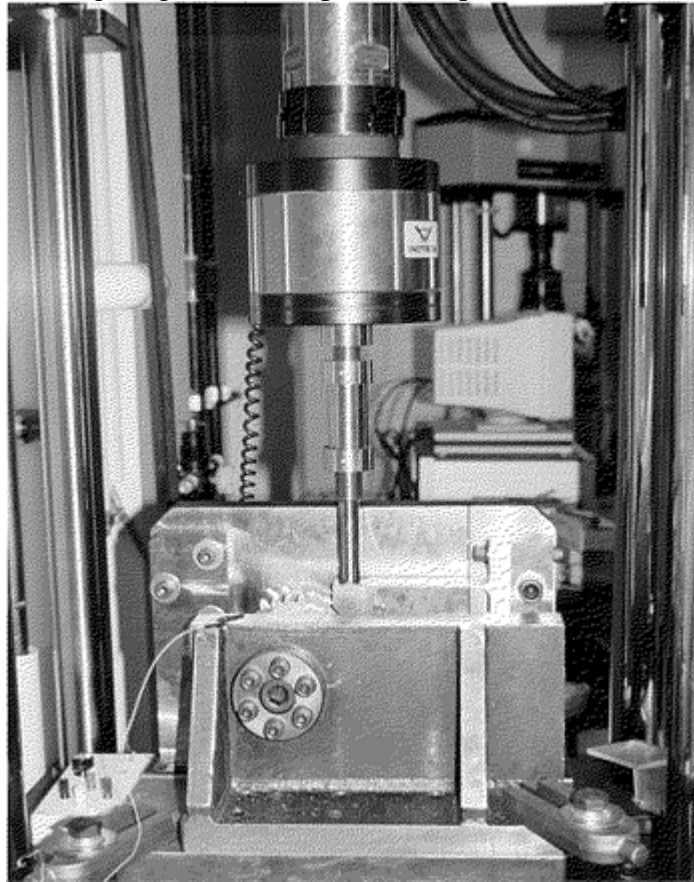


Fig. 8 Flexure arm single-tooth fatigue (STF) test fixture

A second fixture arrangement (Fig. 9) appears to have found favor with many other industry segments. This fixture utilizes a 34 tooth, 6 DP, 25 mm (1 in.) face width spur gear and is derived directly from the Society of Automotive Engineers (SAE) Division 33 STF fixture. Fatigue test loads up to about 15 kips are feasible with this fixture, and single overload tests up to about 50 kips can be accommodated. These STF fixtures are compact enough to be immersed in heated fluid; thus, fatigue testing can be conducted at elevated temperatures (up to 400 °F).

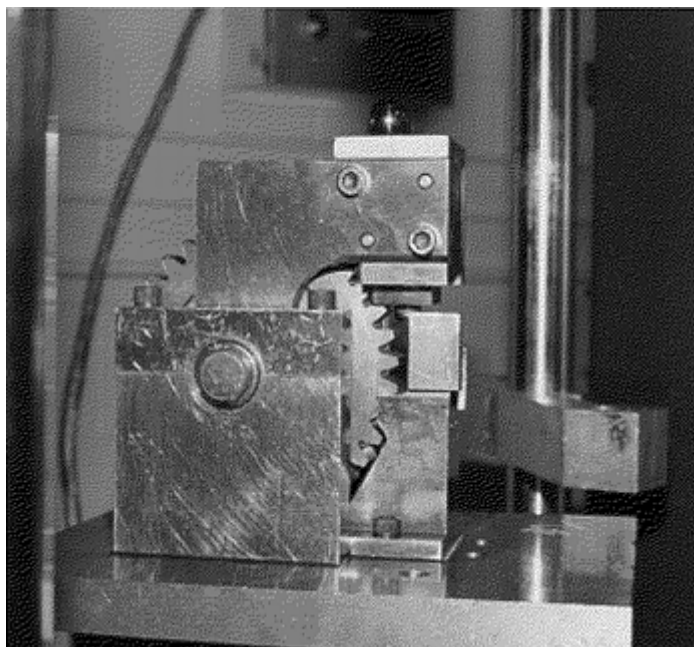


Fig. 9 SAE division 33 single-tooth fatigue (STF) test fixture

Test Procedure. Special concern must be taken with regard to safety in conducting the STF test (in addition to general lab safety procedures). Setting up the test requires moving the hydraulic load ram while lining up the fixture, bypassing safety features, such as a light curtain to stop the machine, and so on, and considerable caution needs to be exercised during setup. Periodic calibration of the test fixture is important because there are many closely fitted parts that can wear and change the bending stress in specimen gears. A calibration gear is made from a standard specimen with strain gages fit at key points in the root fillets. This calibration gear is installed in the fixture and loaded to set loads periodically to ensure consistent loading. If specimens for a specific test program differ from the standard design established for the fixture, one of these specimens should also be fitted with strain gages, and calibrations should be conducted with both gears. Typical calibration intervals are from every six to every thirty tests, or any time the fixture is cleaned and repaired.

Other set-up items that can affect test results are mounting of the fixture on the universal test stand, tuning of the test-stand controller, and test frequency. If the SAE type fixture is used, it is important to ensure that the fixture floats freely on an oil film before starting each test. Other fixture designs can be bolted to the machine base, provided proper alignment between the load ram and loading point on the load arm is maintained. The feedback control should be tuned to suit test fixture and specimen compliance. Some systems do this automatically each time the machine is turned on; with others, this tuning may have to be done manually. At a minimum, tuning should be verified as often as fixture calibration. Some systems provide a feature to automatically adjust tuning as compliance changes. This feature should be turned off when running STF tests—a significant change in compliance is proof of failure. The maximum frequency for STF testing is limited by the capacity of the system to maintain a satisfactory load waveform. An inability to maintain peaks on the unload side of the wave at the specified value is a sign of testing at too high a frequency. All of the tests for a given project should be conducted at the same frequency, which is usually set at slightly less than the maximum for the highest anticipated load.

The other procedural item that can affect test results is the method used to detect failure and stop the test (and stop counting cycles). All systems can be set up to stop if the load goes out of the specified range. This deviation will happen when compliance changes, usually as a result of a crack in the root fillet. Many systems incorporate a linear variable differential transformer and can be set up to stop if the load ram moves beyond the specified range (also an indication of tooth failure). A limit switch can be set to trip when the load ram moves too far. Other failure detection devices, such as a crack wire bonded near the root fillet so that it will break when the tooth cracks, or an ultrasonic system to detect cracking, can be used to stop the test. At least two of these methods should be employed to ensure that the machine stops cycling load when the tooth breaks. If a computer is used to control loading during tests, one of the failure detection systems should be connected directly to the universal test-stand controller to guarantee that the machine stops if the computer crashes.

Specimen Results. Table 2 summarizes results from a typical set of STF tests. Testing was conducted in three phases. Initial searching tests were conducted to establish loads that would result in failure in reasonable time. A “modified staircase sequence” of tests was conducted to develop data at a series of loads representing zero to 100% failure. Further tests were conducted to fill in the stress cycles relationship. Searching tests are started at a high load to ensure starting with a failure, then stepped down until the tooth survives the specified number of cycles (here, 5 million cycles has been selected as a run-out limit). The modified staircase sequence is conducted by testing three specimen gears in sequence. If the tested tooth breaks before the specified limit, the next test is conducted one load step lower. If it does not break by the specified limit, the next test is conducted one load step higher. After the modified staircase sequence is completed, additional tests are conducted to ensure that all the specimen gears are tested at the lowest load. More tests are conducted to develop enough data for Weibull analysis at two loads resulting in 100% failure.

Table 2 Results from a typical set of gear single-tooth fatigue tests showing overall testing sequence, including modified staircase (“up and down”) tests

Legend: X, failure; O, runout. Specimen serial numbers 2, 4, and 6. Specimens cut from bar stock, hobbled roots. *R*, loading; *R* = 0.1. Frequency, 25 Hz

The load-cycles diagram shown in Fig. 10 was developed from the data in Table 2. Results at 9000 and 8500 lb were analyzed via Weibull statistical analyses (similar to that shown in Fig. 7) to determine lives to 10, 50, and 90% failure. The failure rates at 5 million cycles for loads from 6500 to 8500 lb were analyzed using normal probability concepts to determine 10, 50, and 90% failure loads. The curves labeled G10, G50, and G90 were then fit visually using the results of these analyses as a guide. Results are reported in terms of load versus cycles, and load can be converted to stress using the method discussed previously. Comparisons can be made between groups of gears with the same geometry on a load-cycles basis or between gears with differing geometry on a stress-cycles basis. When converting to stress for comparison with running gear data, consideration must be given to the different stress ranges applied to STF gears and running gears. Also, consideration must be given to the statistical difference between four, eight, or more data points from a single STF specimen gear compared with one data point from a running gear specimen set.

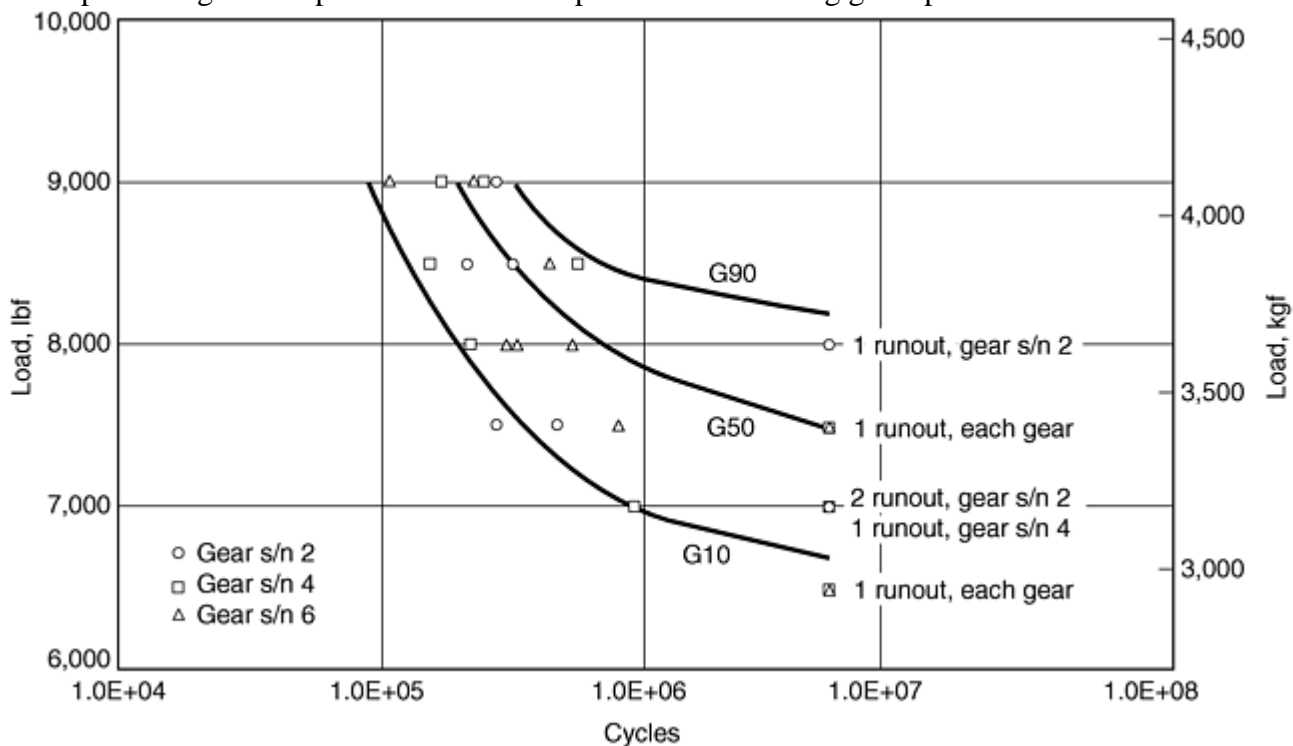


Fig. 10 Load cycles diagram constructed from STF data. See Table 2 for load-cycles relationship for data

Single-Tooth Single-Overload and Impact Testing

The single-tooth impact test is used to investigate impact strength of gear steels. Impact strength is an important property for steels to be used in high-speed gear drives or transmissions for off-highway equipment, which can be subjected to significant shock loading. It has been suggested that fatigue strength can be related to impact strength; however, results of tests to support this suggestion have been mixed.

Single overload tests are used to investigate the ultimate strength of gear materials. The results are useful in selecting loads for fatigue tests and in constructing allowable stress-range diagrams (e.g., for use in comparing STF results with bending fatigue data developed from running gear tests).

Test Equipment. Figure 11 shows a closeup of the test area of a 4.5 m (15 ft) drop tower for single-tooth impact testing. A single-tooth fatigue test fixture, without loading block, load arm, and so on, is placed on a load cell and arranged so that the striking surface of the drop weight hits the load point on the test gear tooth. Stops are provided to prevent the forces required to stop the drop weight after the test tooth fractures passing through the load cell. A high-speed digital oscilloscope captures the signal from the load cell.

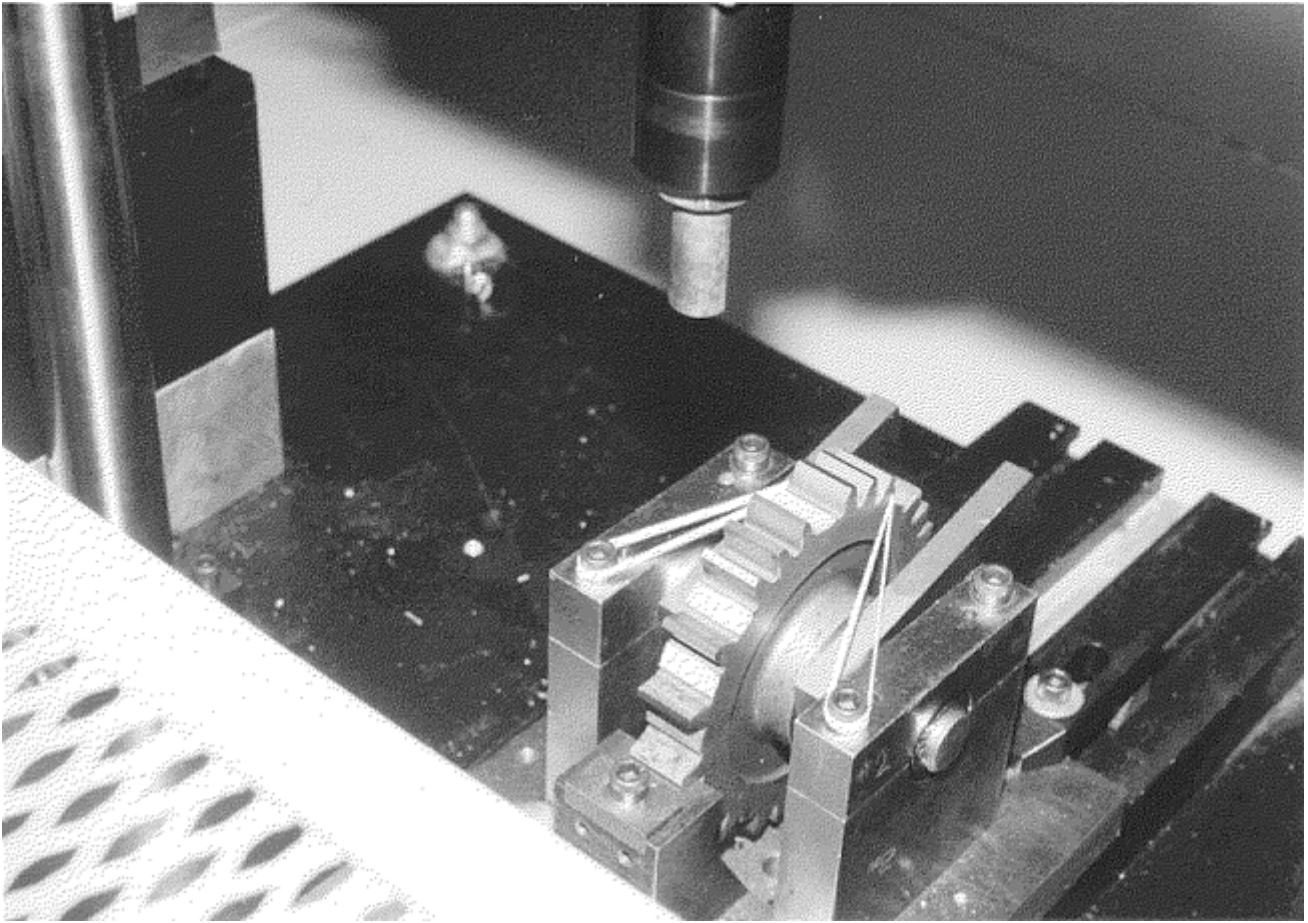


Fig. 11 Test area of an impact test tower

Single-tooth, single-overload tests are accomplished with the same equipment used in STF testing. The only change is that a high-speed digital oscilloscope captures the signal from the single event.

Test Procedure. The single-tooth fatigue test fixture, without loading block, loading arm, and so on, is placed on a load cell and installed under the drop weight. The striking surface on the drop weight is adjusted to the correct angle to strike the test tooth at the load point. This point is verified by coating the tooth with a thin layer of layout blue and allowing the drop weight assembly to contact the tooth statically. The digital oscilloscope is set up to record a single event using a change in signal as a trigger. Usually three to six tests per variant are conducted.

For single-overload tests, the STF fixture is installed in the universal test stand as for fatigue testing, and a preload is applied. For the SAE fixture, 1800 kg (4000 lb) is used, and for other fixtures the load should be high enough to take the slack out of the system. The function generator is set up to ramp up the load to break the tooth in approximately 30 s for slow bend tests and in approximately 0.050 s for fast bend tests. One slow bend and three fast bend tests usually are conducted per variant.

Specimen Results. A load deflection trace for a single-tooth impact test is shown in Fig. 12. Results from fast and slow bend tests are similar. This trace shows load increasing linearly with deflection up to 5900 kg (13,000 lb), then increasing at a slower rate until tooth breakage at 9000 kg (20,000 lb). This result is typical for many materials and is possibly related to the onset of plastic flow prior to fracture. Based on this, the stress corresponding to the change in slope of the load deflection (or load time) trace corresponds to the ultimate bending strength of the material at the critical point in the case. Maximum load, or energy required to break the tooth, represents the strength of the core rather than the strength of the case.

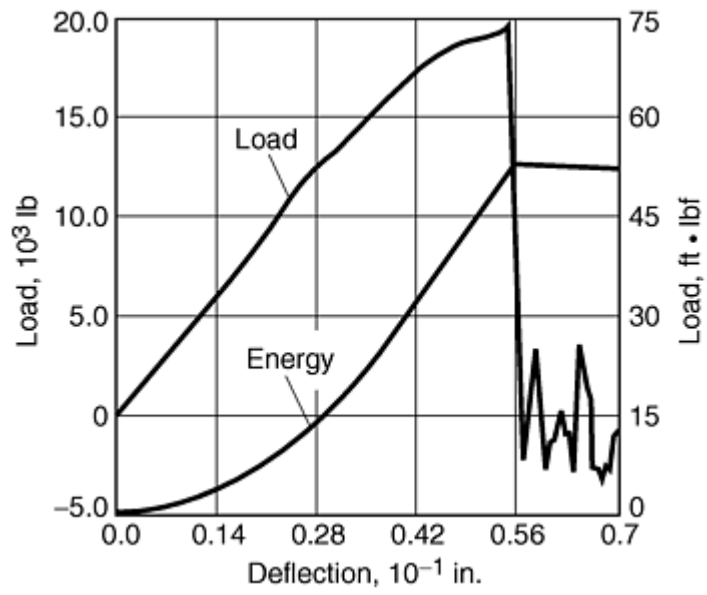


Fig. 12 Load deflection trace from single-tooth impact test

Gear Power-Circulating (PC), or Four-Square, Tests

A gear failure map is shown in Fig. 13. This map indicates that by varying load and speed, failure by any of several different modes can be induced. Thus, PC gear tests can be used to evaluate bending fatigue strength, surface durability with regard to pitting, or scoring resistance. A limiting factor is that tests targeted at one of the failure modes may have to be terminated because of failure by another mode. For example, bending fatigue tests conducted at a comparatively low load, targeting failure in several million cycles, may have to be terminated due to pitting failure. Consequently, PC gear testing is more expensive than the tests simulating gear action previously discussed. It is, however, less expensive than bench testing, and several standard specimen designs are available to allow tests targeted at particular failure modes.

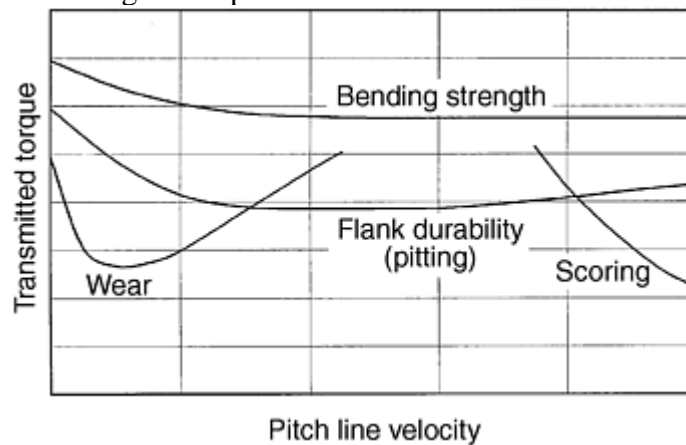


Fig. 13 Gear failure map

Test Equipment. A test and a torque-reversing gear set are mounted at opposite ends of the test bed. One shaft connects the test and torque-reversion pinions, and another connects the torque-reversing and test gears. One gearbox is loaded against the other by twisting the shafts to lock in torque. This rig is known as a power (re-) circulating, or four-square, test rig and is schematically illustrated in Fig. 14. The locked-in torque, which is fixed at various values to create the required tooth load, can be generated mechanically or hydraulically. The entire loaded arrangement is driven by an electric motor at the required speed, and the motor need only supply the friction losses. Significant transmitted power can be simulated in this system with comparatively little power input. Data from these tests can be directly translated for design use.

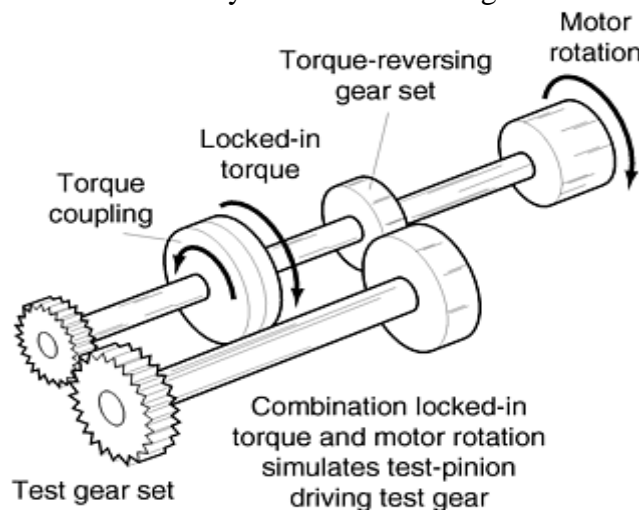


Fig. 14 Schematic of a power (re-) circulating (PC) test rig

In a four-square test rig, the tooth accuracy of the torque-reversing gears, and their transmission error, has a significant impact on the dynamic loads on the test-gear pair. These dynamic loads due to torque reversing gear inaccuracy can be further amplified or attenuated by the longitudinal and torsional frequency response characteristics of the four-square-test rig. This intensification is of particular significance in high-speed testing where operating frequencies will be close to or at torsional and/or longitudinal natural frequencies of the four-square system. However, high-accuracy torque-reversing gears are expensive. Consequently, the PC test rigs can be classified into two categories. The first category of PC test rigs have low power, operate at low speeds, and generally have AGMA quality class Q9 or Q10 gears in the torque-reversing gearbox that are quite adequate for many industry segments. The second category of PC test rigs operate at high power, high speed, and incorporate high-accuracy torque-reversing gears that are essential for gear testing in certain industry segments, such as the aerospace industry. Testing costs associated with each of the two categories of test rigs are significantly different.

The low-speed PC test rigs illustrated in Fig. 15 nominally operate at 900 rpm but can be adapted to operate at 1500 rpm. The standard center distance is 100 mm (4 in.), which can be modified if necessary, although there are some costs associated with doing so. These test rigs can simulate the transmission of up to 100 hp when driven with a 3 hp motor. Load is applied via a mechanical loading arm and locked in with a special coupling that can be set at any angle. Thus, load cannot be varied as the rig is running. Depending on specimen design, contact stresses of up to 450 ksi at the lowest point of single-tooth contact and bending stresses up to 160 ksi can be generated. Splash lubrication is standard, and spray lubrication to either side of the mesh can be provided. These rigs can be adapted to conduct scoring tests.

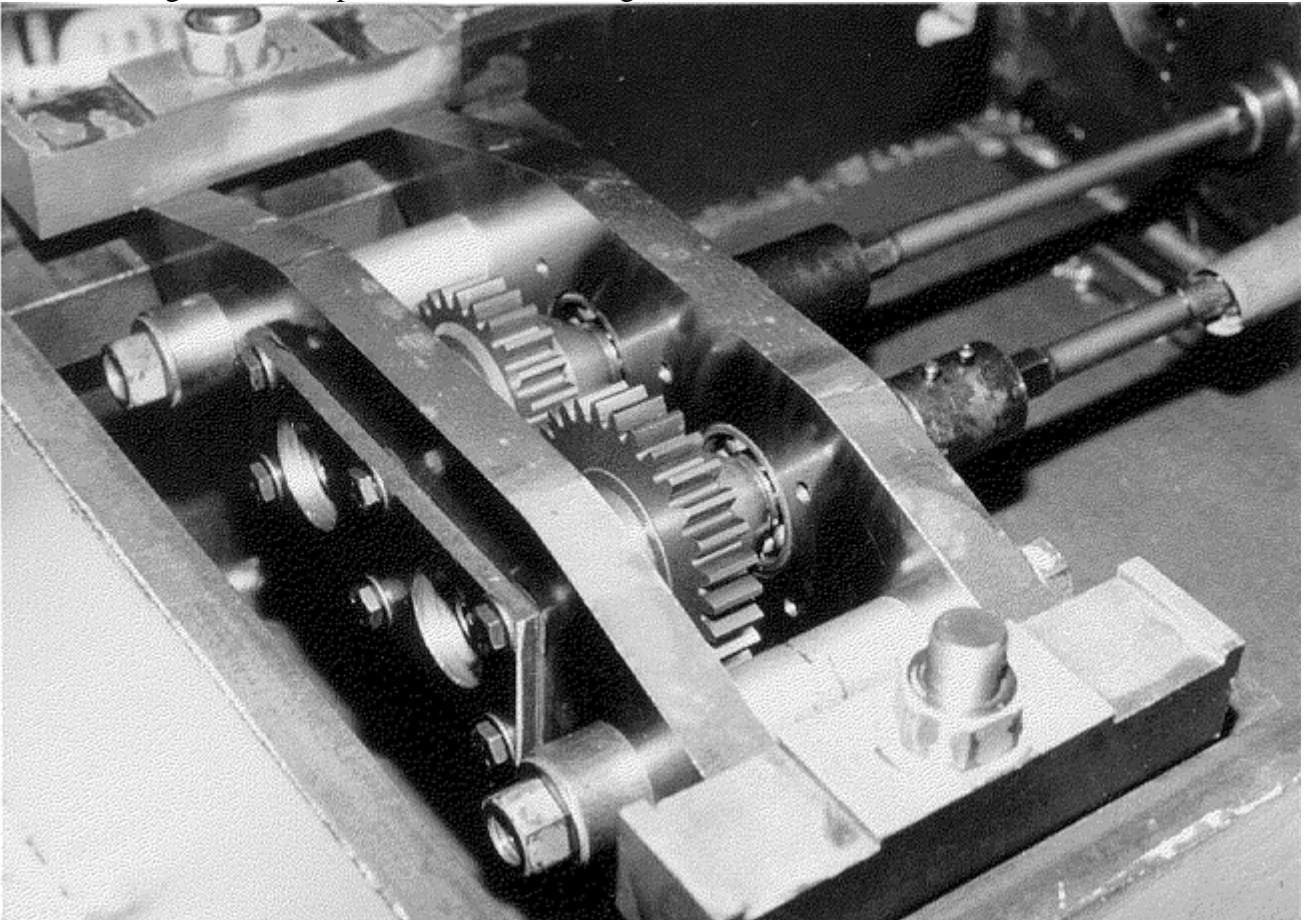


Fig. 15 Low-speed (4 in. center distance) PC test rig

Figure 16 shows a PC test rig with a 155 mm (6 in.) center distance that can operate up to 8000 rpm and simulate the transmission of up to 1400 hp. This test rig has two test gearboxes so that two pairs of gears can be tested simultaneously. In programs to evaluate materials for aerospace gearing, runout can be set as high as 400 million cycles for surface durability tests, making the project a lengthy exercise. In this case, obtaining two data points in one run can be a significant benefit. Figure 17 shows another PC test rig with a 90 mm (3.5 in.) center distance, capable of operating at 10,000 rpm and simulating transmission of up to 700 hp. Torque-reversing

gears in these high-power rigs are in AGMA quality class Q13 and Q14. Load is applied via a servocontrolled hydraulic system and can be varied as required during tests. Torque is monitored continuously by a noncontact torque cell. This monitoring permits interpretation of test results in light of the actual load signature. Based on input lubricating oil temperature and load, surface durability (pitting), bending, and scoring tests can be conducted on these PC test rigs. Spray lubrication, to either side of the mesh, is standard; oil-mist lubrication can be provided.

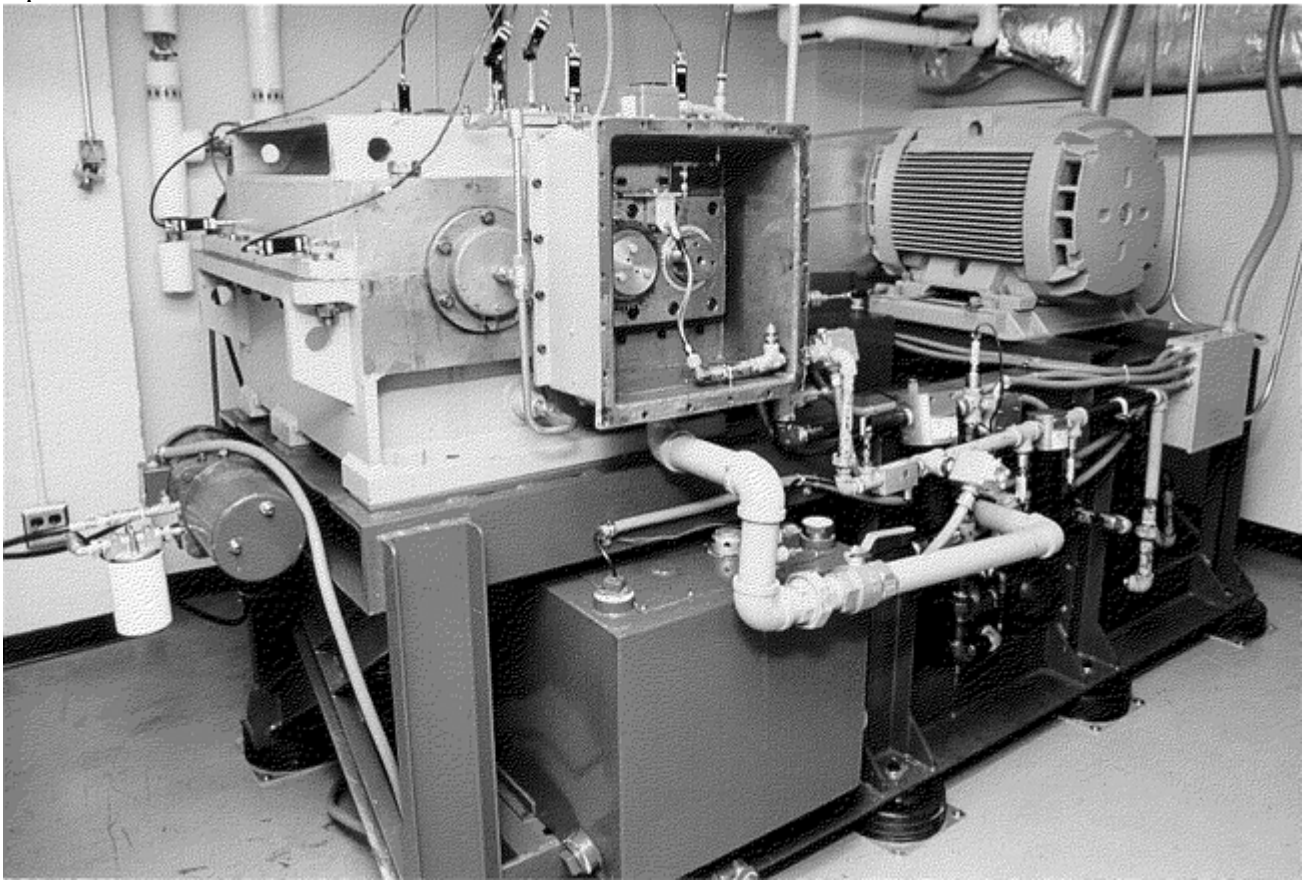


Fig. 16 High-speed (6 in. center distance) PC test rig

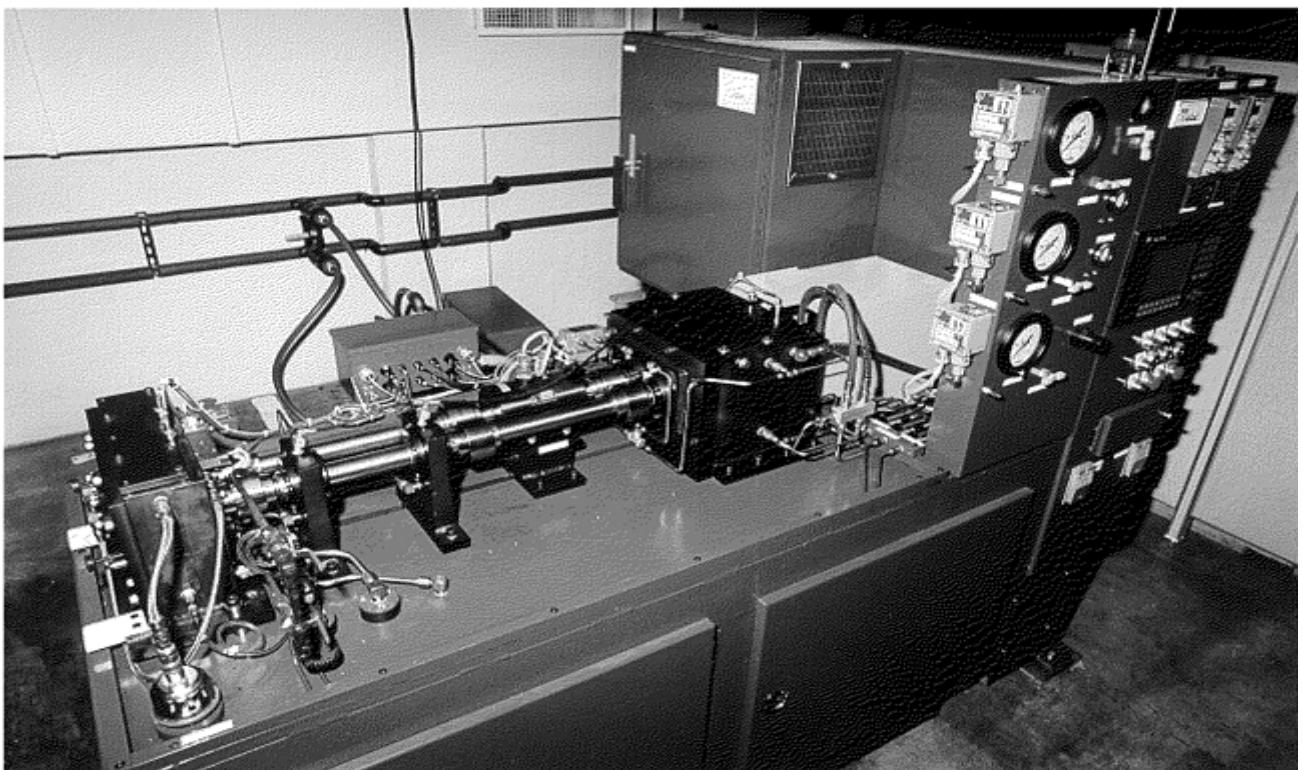


Fig. 17 High-speed (3.5 in. center distance) PC test rig

Test Procedures for Surface Durability (Pitting) and Root Strength (Bending) Testing. One or both gears in the specimen set are coated with a thin layer of layout blue prior to installation in the test machine. After the gears are installed, they are run briefly at low load with room-temperature lubricant to determine the contact pattern. The low-speed test rigs allow some alignment adjustment to optimize contact pattern. The specimen mountings in the high-speed test rigs are rigid, so the only remedy for nonuniform contact is to change specimen gear sets. A break-in run is generally conducted before the start of the test run. On the low-speed machines this run is

accomplished by applying one-half of the test load and running for $\frac{1}{2}$ h at test speed starting with room-temperature lubricant. The friction of the meshing gears warms the lubricant to near test temperature in this time. On the high-speed machines, load and speed are increased in a set pattern to accomplish break-in. As described previously, break-in is expected to increase the life of the gears. Thus, all specimens tested in a given project should be broken in using the same method. For root strength (bending fatigue) tests, break-in may not affect bending fatigue life but may delay the onset of pitting long enough to allow the gear to fail in bending.

In general, the main difference in surface durability (pitting) and root strength (bending) tests is the load. Most of the standard specimen gear sets are designed to allow surface durability testing at loads high enough to produce failure in less than 10 million cycles. Root strength tests, therefore, have to be conducted at loads high enough to produce failure in less than 1 million cycles to avoid surface durability failures. Thus, unless specially designed specimens are tested, the results of this test can only be compared to the lower-life portion of the stress-cycles relationship developed in the STF test.

Surface durability gear tests have similar problems with scatter as those previously described for RCF tests. However, each specimen gear has 18 or more teeth; therefore, the result of a single PC surface durability test represents the lowest performance of 18 or more items tested. This statistical difference causes the results of PC surface durability tests to exhibit less scatter than those of RCF tests, and Weibull slopes are generally three or higher. Six tests are still generally conducted with each variant at each load, the reduced scatter being used to allow more statistically reliable comparison of the results rather than to reduce the number of tests. A similar statistical difference exists between the results of STF tests and PC bending tests, and this difference must be considered when comparing STF and PC bending results.

Specimen Results. The end point of a surface-durability test may be somewhat ambiguous. The section regarding pitting in the discussion of failure modes indicates several points in the development of surface origin pitting that may be considered failure. Figures 3 and 4 show gear teeth with different stages of pitting, both of which were considered failures. Test gear teeth are also subject to wear and localized scoring, both of which can affect the appearance of the contact surface in ways similar to some of the stages of pitting development. A composite failure criterion has to be adopted that specifies the level of damage in each of these categories that

constitutes failure. A typical failure criterion for pitting is one pit 4 mm ($\frac{1}{16}$ in.) wide or several smaller pits with slightly greater total area. Typical failure criteria for micropitting is micropitting over half of the contact width of all the teeth and for wear, a loss of 12 μ m (0.0005 in.) at any point on the profile.

A test program evaluating bending and surface durability performance of candidate materials would include 24 tests with each material. Six tests would be conducted at each of two loads intended to result in bending failure; the balance of the tests would be conducted at two loads intended to result in pitting failure. The results of tests at each of the four loads are analyzed with Weibull statistical analysis (as illustrated in Fig. 7). A load-cycles diagram is then constructed showing loads corresponding to 10, 50, and 90% failures at various lives for both bending and surface durability. Comparisons are made on the basis of life to 50% (or 10%) failures at a given load, or the load corresponding to 50% failures at a given life. It is useful to construct a stress-cycles diagram (determining contact stress as described here) to compare surface durability results obtained from specimens having differing crown.

Test Procedures for Scoring (or Scuffing) Testing. Scoring is typically most severe in the dedendum of the driving gear (at the start of contact) and at the tip of the driven gear. Therefore, to facilitate observation of scoring, the gears and loading are set up so that the specimen is the driven gear. Scoring is more probable at high speed, high load, and/or high-lubricant temperature. Because of this probability, the test machine is set up to run at high speed and high-lubricant temperature. Resistance to scoring is then measured by the load that will precipitate scoring. Load is increased in comparatively small steps until scoring starts. Because small variations in lead or crown can produce as much variation in unit loading at the most heavily loaded area as one or more

load steps, specimens used for scoring should be those with the most consistent geometry that can be selected from the lot to minimize scatter. Gear alignment should be adjusted, if possible, to obtain the best contact pattern.

Break-in is a particularly critical part of this test. Therefore, all specimens should be broken in using an identical process, and control specimens should be included in the project test matrix to benchmark the results for comparison with prior tests. Typically, break-in is started at low load in room-temperature oil and run-in one to four load steps lasting 20,000 to 50,000 loading cycles each. The lubricant temperature is allowed to slowly rise due to the friction of the meshing gears during break-in. The condition of the lubricant also can affect the outcome of the test; thus, lubricant should be changed prior to the start of each test.

Specimen Results. After break-in, the surface roughness (R_a) is measured in the axial direction at the tips of several teeth on the specimen gear, and the surface condition is documented. The load is increased, and the lubricant temperature is raised to test temperature. The gear set is run 20,000 to 50,000 loading cycles for each load step. After each load step, surface roughness and surface condition are examined and recorded. The appearance of score marks, or an abrupt increase in surface roughness, indicates scoring failure. The gear shown in Fig. 2 illustrates a typical failure in this test. Typically, three tests are conducted per variant. Comparisons between variants are made on the basis of the load that precipitates scoring. Contact stress considered alone has little influence on scoring; consequently, comparisons made on the basis of contact stress may be misleading.

Mechanical Testing of Gears

Douglas R. McPherson and Suren B. Rao, Applied Research Laboratory, The Pennsylvania State University

References

1. E.E. Shipley, "Failure Modes in Gears," presented at Forum on Gear Manufacture and Performance, 19 Oct 1973 (Detroit), American Society of Mechanical Engineers
2. D.W. Dudley, Gear Wear, *Wear Control Handbook*, M. Peterson and W. Winer, Ed., American Society of Mechanical Engineers, 1980
3. G. Niemann and H. Winter, Getriebeschäden und Abhilfe, Entwicklungstendenzen, *Maschinenelemente*, Vol 2, 2nd ed., Springer-Verlag (Berlin), 1983
4. "Appearance of Gear Teeth—Terminology of Wear and Failure," ANSI/AGMA 1010-E95, American National Standards Institute/American Gear Manufacturers Association
5. R. Errichello, Friction, Lubrication, and Wear of Gears, *Friction, Lubrication, and Wear Technology*, Vol 18, *ASM Handbook*, ASM International, 1992, p 535–545
6. L. Alban, *Systematic Analysis of Gear Failures*, American Society for Metals, 1985
7. A.P. Boresi and O.M. Sidebottom, *Advanced Mechanics of Materials*, 4th ed., John Wiley & Sons, 1985
8. "Information Sheet: Geometry Factors for Determining the Pitting Resistance and Bending Strength of Spur, Helical, and Herringbone Gear Teeth," AGMA 908-B89 (R1995), American Gear Manufacturers Association, 1995

Testing of Pressure Vessels, Piping, and Tubing

E. Roos, K.-H. Herter, and F. Otremba, Staatliche Materialpruefungsanstalt (MPA), University of Stuttgart

Introduction

THE MECHANICAL EVALUATION OF PIPE FAILURES has evolved over time. An initial purpose of such analysis was to determine the causes of large breaks occurring in oil and gas pipelines. The development of commercial nuclear power plants initiated the need for additional tools to assess the reliability and the failure behavior of pressurized vessels and pipes under different loading and environmental conditions. The results of these efforts have been transferred to other relevant industrial branches as well.

The main effort in evaluating the mechanical and structural behavior of pressurized components started about 1950. Since that time, numerous investigations have been performed to assess the loading capacity and the failure behavior of pressure vessels, piping, and tubing. Investigations have also focused on determining failure loads and quantifying the margins of safety.

Testing of Pressure Vessels, Piping, and Tubing

E. Roos, K.-H. Herter, and F. Otremba, Staatliche Materialpruefungsanstalt (MPA), University of Stuttgart

Safety Aspects and Integrity Concepts

The license and operation of pressure vessels and piping in the different countries throughout the world are subject to national laws, special regulations, and safety criteria. Pressure vessels and piping are designed according to the relevant national technical codes and standards that contain detailed rules regarding materials, construction, design and calculation, manufacture, and quality assurance. These codes require that state-of-the-art technology is applied to the safe operation and maintenance of this equipment.

The relevant national technical codes and standards for pressure vessels and piping include the following:

- In the United States, the American Society of Mechanical Engineers (ASME) Boiler and Pressure Vessel Code—for example, Section III for nuclear power plant components (Ref 1) and Section VIII for the construction of pressure vessels (Ref 2)—and the ASME Code for Pressure Piping (B31) (Ref 3)
- In Germany, the Technical Rules for Steam Boilers (TRD) (Ref 4), the Technical Rules for Pressure Vessels (AD-Rules) (Ref 5), and the Safety Standards of the Nuclear Safety Standards Commission (e.g., KTA 3201 and KTA 3211) (Ref 6)
- In France, the code for the Construction of Pressure Vessels (CODAP) (Ref 7), the Industrial Piping Code (CODETI) (Ref 8), and the Design and Construction Rules for Mechanical Components of Nuclear Power Plants (RCC-M and RCC-MR) (Ref 9, 10)
- In the United Kingdom, the standards of the British Standards Institution related to Boilers and Pressure Vessels (BS 5500) (Ref 11)

For a general or a component-specific design of pressure vessels and piping according to the technical codes and standards, it has to be demonstrated that all stresses resulting from mechanical and/or thermal as well as environmental loadings are within the allowable stress limits, and the usage factor developed by a fatigue analysis is well below the limiting value.

This article describes general concepts related to the evaluation of pressurized components without or with defects. The reliability of these concepts is demonstrated by tests of full-scale components with and without

defects under internal pressure loading and, in some cases, with an external bending load superimposed at the relevant temperatures.

Integrity Concept

The integrity concept for pressure vessels, piping, and tubing is demonstrated in the following example for pressurized components of nuclear power plants. Requirements for nuclear power plants take into account not only the stresses resulting from operational loads, but also extreme loading conditions that could be caused by accidents (for example, water hammer, aircraft crash, earthquake, and postulated pipe rupture). For such loads it must be demonstrated that, on the one hand, catastrophic failures of the components can be excluded, or, on the other hand, sequential damages will not lead to critical sequences for the plant.

The engineering of high-performance steam-generating plants and chemical plants (including design and construction, selection of material, manufacture, and quality assurance of ductile steel components and systems) has evolved over decades. The ongoing advances in science and technology have increased the standards for the construction and operation of the plants, especially concerning the safety against catastrophic failure of pressurized components and systems (Ref 12).

Safety principles and approaches, especially for nuclear power plants, vary somewhat from country to country. However, a generally accepted standard requires that the possibility of catastrophic failure from double-ended guillotine breaks (DEGB) must be completely excluded for pressure vessels and piping. A leak-before-break (LBB) assessment is used to show the likelihood of detectable crack sizes, which allows countermeasures to be taken before a large break occurs (Ref 13, 14, 15, 16, and 17).

Analyses of the operational behavior of high-quality pressurized components and systems as well as flaw and damage analyses have shown that proven and well-defined principles exist to reliably attain and maintain high quality. In Germany, these principles have been codified as the basis safety concept (BSC) and break preclusion concept (Ref 12). These concepts require that the quality of components must be guaranteed during the production process. Furthermore, the BSC requires the existence of redundancies to ensure that any possible deviation from optimization is sufficiently unimportant and unlikely to cause catastrophic failure. One redundancy of considerable importance relies on verification and validation using calculation codes and fracture mechanics as well as nondestructive testing technologies. Testing and evaluation are indispensable to provide the knowledge basis for the validation of codes and standard. The validation work is done mainly based on the results of the uniquely large full-scale quasi-static and dynamic testing of components with and without degraded sections to demonstrate their load-bearing capacity and their failure behavior, for example, Ref 18, 19, 20, 21, 22, 23, 24, 25, and 26.

References cited in this section

1. "Rules for Construction of Nuclear Power Plant Components," ASME Boiler and Pressure Vessel Code, Section III, American Society of Mechanical Engineers, 1998
2. "Rules for Construction of Pressure Vessels," ASME Boiler and Pressure Vessel Code, Section VIII, Divisions 1 and 2, American Society of Mechanical Engineers, 1998
3. ASME Code for Pressure Piping, B31, An American National Standard, The American Society of Mechanical Engineers, 1989
4. German Technical Rules for Steam Boilers (Technische Regeln für Dampf-kessel, TRD), Carl Heymanns Verlag KG, Cologne, 1998
5. German Technical Rules for Pressure Vessels (Arbeitsgemeinschaft Druckbehälter, AD-Merkblätter), Carl Heymanns Verlag KG, Cologne, 1998
6. German Safety Standards of the Nuclear Safety Standards Commission (Sicherheitstechnische Regeln des Kerntechnischen Ausschusses, KTA), KTA Rule 3201 and KTA Rule 3211, Carl Heymanns Verlag KG, Cologne, latest edition

7. French Code for the Construction of Pressure Vessels (CODAP), Association Francaise des Ingénieurs en Appareils à Pression (AFIAP), Paris
8. French Code for the Construction of Industrial Piping Components (CODETI)
9. French Design and Construction Rules for Mechanical Components of PWR Nuclear Islands (RCC-M), Association Francaise pour la Construction des Ensembles Nucleaires (AFCEN)
10. French Design and Construction Rules for Mechanical Components of Fast Breeder Reactors (RCC-M), Association Francaise pour la Construction des Ensembles Nucleaires (AFCEN)
11. “Unfired Fusion Weld Pressure Vessels,” BS 5500, British Standard Institution
12. K. Kussmaul, German Basis Safety Concept Rules Out Possibility of Catastrophic Failure, *Nucl. Eng. Int.*, Vol 12, 1984, p 41–46
13. R. Wellein and G. Preußner, “State of Engineering of the Leak-Before-Break Procedure in Germany,” Seventh German-Japanese Joint Seminar, 29–30 Sept 1997, MPA Stuttgart
14. K. Kussmaul, D. Blind, E. Roos, and D. Sturm, The Leak-Before-Break Behavior of Pipes, *VGB Kraftwerkstech.*, Vol 70 (No. 7), July 1990, p 465–477
15. G.M. Wilkowski, R.J. Olson, and P.M. Scott, “State -of-the-Art Report on Piping Fracture Mechanics,” Report NUREG/CR-6540, BMI-2196, Jan 1998
16. Y. Asada, K. Takumi, H. Hata, and Y. Yamamoto, Development of Criteria for Protection against Pipe Breaks in LWR Plants, *Int. J. Pressure Vessels Piping.*, Vol 43, 1990, p 95–111
17. C. Faidy, P. Jamet, and S. Bhandari, “Developments in Leak-Before-Break Approaches in France,” NUREG/CP-0092, March 1988, p 69–82 (available from U.S. NRC)
18. D. Sturm, W. Stoppler, and J. Schiedermaier, The Behavior of Dynamically Loaded Pipes with Circumferential Flaws under Internal Pressure and External Bending Loads, *Nucl. Eng. Des.*, Vol 96, 1986, p 99–113
19. E. Roos, K.-H. Herter, P. Julisch, G. Bartholome, and G. Senski, Assessment of Large Scale Pipe Tests by Fracture Mechanics Approximation Procedures with Regard to Leak-Before-Break, *Nucl. Eng. Des.*, Vol 112, 1989, p 183–195
20. Y. Asada, K. Takumi, N. Gotoh, T. Umemoto, and K. Kashima, Leak-Before-Break Verification Test and Evaluations of Crack Growth and Fracture Criterion for Carbon Steel Piping, *Int. J. Pressure Vessels Piping*, Vol 43, 1990, p 379–397
21. K. Kashima, N. Miura, S. Kanno, K. Miyazaki, M. Ishiwata, and N. Gotoh: A Research Program for Dynamic Fracture Evaluation of Japanese Carbon Steel Pipes, *Nucl. Eng. Des.*, Vol 174, 1997, p 33–39
22. D. Moulin and P. Le Delliou, French Experimental Studies of Circumferential Through Wall Cracked Austenitic Pipes under Static Loading, *Int. J. Pressure Vessels Piping*, Vol 65, 1996, p 343–352
23. P. Scott et al., “IPIRG-2 Task 1—Pipe System Experiments with Circumferential Cracks in Straight Pipe Location,” NUREG/CR-6389, Feb 1997 (available from U.S. NRC)
24. K. Shibata, T. Isozaki, S. Ueda, R. Kurihara, K. Onziawa, and A. Kohsaka, “Results of Reliability Test Program on Light Water Reactor Piping,” *Nucl. Eng. Des.*, Vol 153, 1994, p 71–86

25. G.M. Wilkowski et al., “Degraded Piping Program—Phase II, Summary of Technical Results and Their Significance to Leak-Before-Break and In-Service Flaw Acceptance Criteria,” March 1984-Jan 1989, NUREG/CR-4082, Vol 8, March 1989 (available from U.S. NRC)
26. G. Yagawa, Y. Takahashi, N. Kato, M. Saito, K. Hasegawa, and T. Umemoto, Fracture Behavior of Cracked Type 304 Stainless Steel Pipes under Tensile and Thermal Loadings, *Int. J. Pressure Vessels Piping*, Vol 19, 1985, p 247–281

Testing of Pressure Vessels, Piping, and Tubing

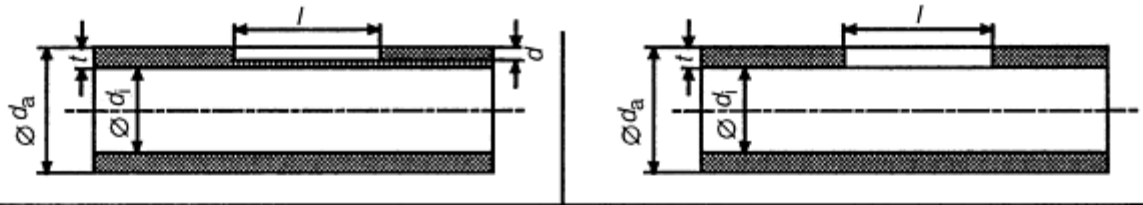
E. Roos, K.-H. Herter, and F. Otremba, Staatliche Materialpruefungsanstalt (MPA), University of Stuttgart

Fracture Mechanics Analysis

Fracture mechanics approaches are used to validate components with longitudinal cracks and with circumferential cracks and to analyze crack growth behavior under cyclic loading.

Components with Longitudinal Cracks

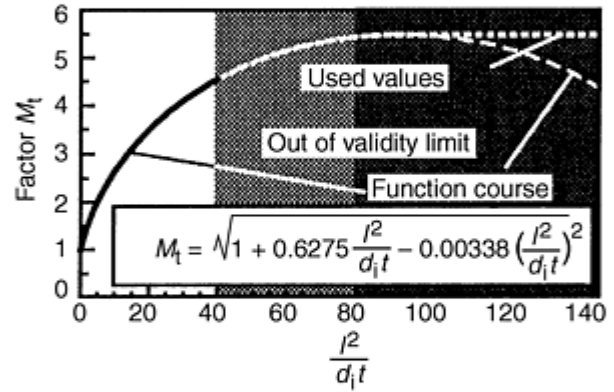
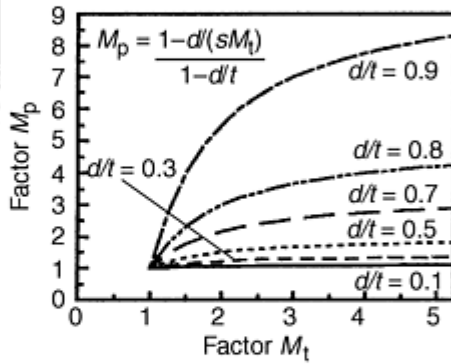
The well-known methods for the validation of pressurized components with longitudinal part-through or through-wall cracks (slots) were developed on the basis of a huge number of experimental results, for example, Ref 14, 27, and 28, 29. These semiempirical engineering methods (Fig. 1) require major plastic deformation to occur in the region around the crack tip. In one of the methods, the behavior of a material is expressed solely by the flow stress, $\sigma_{fl} = (R_{p0.2} + R_m)/2$ (yield strength and tensile strength dependent method). In another method, the toughness values of the material, expressed by the Charpy energy impact toughness (C_v) in the upper shelf, are also considered (toughness-dependent approach). In Fig. 2, the influence of different toughness values of the material used is shown with respect to the critical length of through-wall cracks (for the same pipe dimension and corresponding material strength data). In the tensile load (σ_t) range of interest, $\sigma_t/\sigma_{fl} \leq 0.4$, the critical crack length for through-wall cracks increases with increasing Charpy energy.



Theory	Net section collapse concept					
Criterion	Toughness		Flow stress	Toughness		Flow stress
Formula burst pressure $P_B =$	$\frac{2t \sigma_{fl}}{d_i M_p}$	$\frac{2}{\pi} \arccos \left(\exp \left[\frac{-3.1 C_V E \pi}{k \sigma_{fl}^2} \right] \right)$	$\frac{2t \sigma_{fl}}{d_i M_p}$	$\frac{2t \sigma_{fl}}{d_i M_p}$	$\frac{2}{\pi} \arccos \frac{-3.1 C_V E \pi}{(e k \sigma_{fl}^2)}$	$\frac{2t \sigma_{fl}}{d_i M_t}$

Factors

$$\sigma_f = (R_{p0.2} + R_m)/2$$



Validity limit

$$\frac{l^2}{d_i t} < 40$$

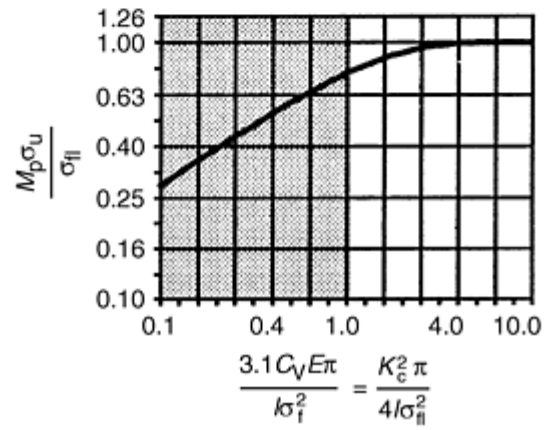
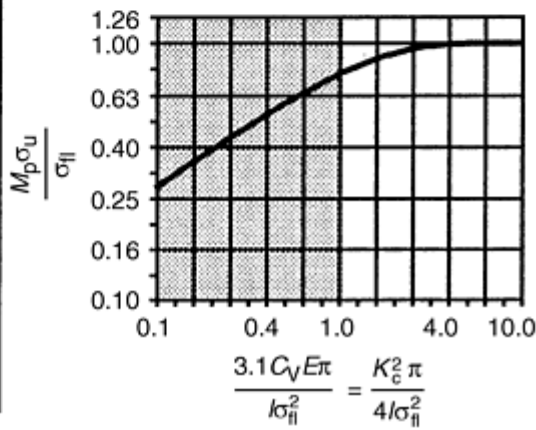


Fig. 1 Methods for calculating maximum loads for piping with longitudinal cracks. Note: $\exp [A] = e^A$

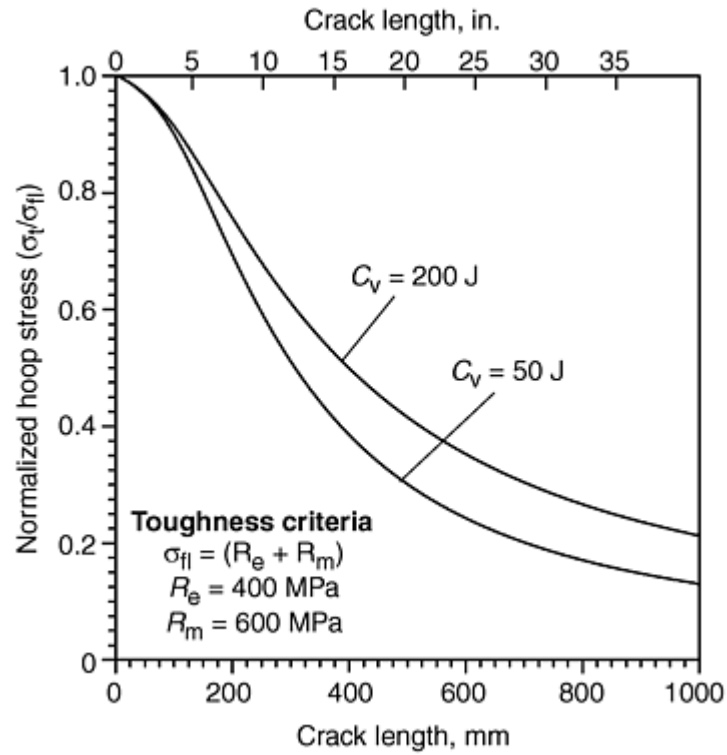


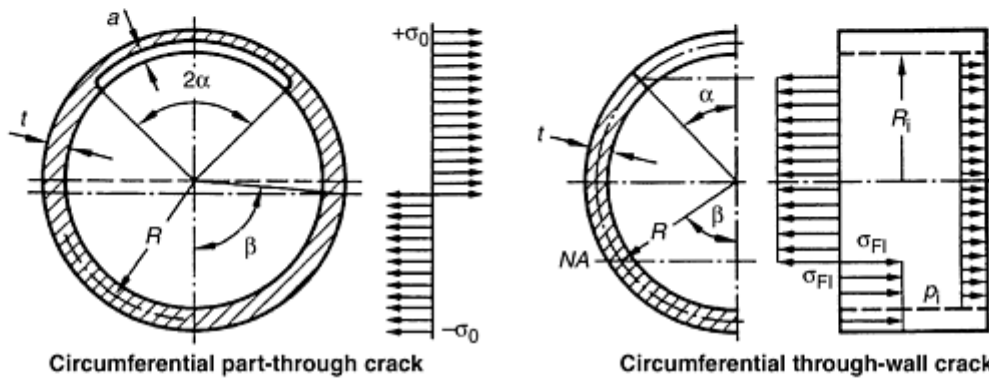
Fig. 2 Toughness-dependent critical crack length for longitudinal crack in a pipe with an outer diameter of 800 mm (31.5 in.), wall thickness of 47.2 mm (1.86 in.), internal pressure of 20 MPa (2.9 ksi), and a ratio of crack depth to wall thickness of 1.0

Components with Circumferential Cracks

For pressurized cylindrical components with circumferential part-through or through-wall cracks, there are several methods available to determine the failure load for the degraded component. In piping systems, the relevant loads are external bending moments in addition to the internal pressure. Consequently, the methods for the validation of pressurized components with circumferential defects take into account not only the internal pressure, but also, in particular, the external bending moment.

Plastic Limit Load Concept. For pipes made of ductile materials, local yielding in the region of the crack tips can propagate until, under limit load conditions, the entire pipe cross section is subjected to plastic deformation. If linear-elastic/ideal-plastic material behavior is assumed, the stress distribution over the cracked cross section is as shown in Fig. 3 (Ref 30).

	Circumferential part-through crack	Circumferential through-wall crack
Criterion	Flow stress	Flow stress
Bending moment, $M_b =$	$2 \sigma_f R^2 t (2 \sin \beta - f \sin \alpha)$	$2 \sigma_f R^2 t (2 \sin \beta - \sin \alpha)$
Factors	$\beta = \frac{\pi - f\alpha}{2} - \frac{\pi p_i R_i^2}{4 \sigma_f R t}$	$\beta = \frac{\pi - \alpha}{2} - \frac{\pi p_i R_i^2}{4 \sigma_f R t}$
	$\sigma_f = \frac{1}{2} (R_m + R_{p0.2})$	$\sigma_f = \frac{1}{2} (R_m + R_{p0.2})$
	$f = \frac{a}{t}$	
Scope of application	Thin-walled vessels	Thin-walled vessels



	Circumferential part-through crack	Circumferential through-wall crack
Criterion	Flow stress	Flow stress
Bending moment, $M_b =$	$2 \sigma_f R^2 t (2 \sin \beta - f \sin \alpha)$	$2 \sigma_f R^2 t (2 \sin \beta - \sin \alpha)$
Factors	$\beta = \frac{\pi - f\alpha}{2} - \frac{\pi p_i R_i^2}{4 \sigma_f R t}$	$\beta = \frac{\pi - \alpha}{2} - \frac{\pi p_i R_i^2}{4 \sigma_f R t}$
	$\sigma_f = \frac{1}{2} (R_m + R_{p0.2})$	$\sigma_f = \frac{1}{2} (R_m + R_{p0.2})$
	$f = \frac{a}{t}$	
Scope of application	Thin-walled vessels	Thin-walled vessels

Fig. 3 Procedure and designations for failure moment of pipes with circumferential cracks according to the plastic limit load concept, p_i , internal pressure; NA, neutral axis

The shift of the neutral axis within the cracked-pipe cross section can be determined according to the balance of the forces in axial direction, with the flow stress σ_{fI} acting uniformly on the tension side of the cross section up to the neutral axis and the compressive flow stress $-\sigma_{fI}$ acting on the compression side. To allow for work hardening of the material, the assumption made in Ref 30 is, for example, $\sigma_{fI} = 0.5 (R_{p0.2} + R_m)$.

Compared with experimental results, the calculated failure loads for degraded pipes under internal pressure and superimposed external bending moment are conservative when using the flow stress as $\sigma_f = (R_{p0.2} + R_m)/2.4$. A more conservative assessment of the failure loads or the corresponding critical crack sizes is achieved by using flow stress of $\sigma_f = R_{p0.2}$.

Two-Criteria Approach (R_6 -Method). This section describes a calculation method for which the strength values determined by tensile testing are required as material characteristics as well as fracture toughness values. This is demonstrated using the R_6 -method and the R -curve method. It is indeed possible in fracture mechanics procedures to include not only the strength but also the fracture mechanics characteristics of the material in the failure analysis.

The *R6*-method is based on the idea that, depending on the material characteristics, failure of a component can occur from brittle fracture up to full plastic deformation with the transition between these two extreme conditions assumed to be continuous.

The limit curve is defined as:

$$K_r = (1 - 0.14 L_r^2) [0.3 + 0.7 \exp(-0.65 L_r^6)]$$

and

$$L_r(\max) = \sigma_{fl}/R_{p0.2}$$

where:

$$\sigma_{fl} = (R_{p0.2} + R_m)/2$$

The loading parameters of the components are given by:

$$L_r = F/F_K$$

as the ratio of the actual load F to the plastic limit load F_K and

$$K_r = K_I/K_{Ic} = \sqrt{J/J_i}$$

as the ratio of the actual stress-intensity factor K_I as a function of crack size and load, and the fracture mechanics material characteristic K_{Ic} for linear-elastic and J_i for elastic-plastic conditions (Ref 31).

In the above equation, the J_i values are derived from the linear-elastic K_{Ic} values. According to this concept, onset of stable crack extension occurs when the load point developed by L_r and K_r is on the limit curve. Instability is derived from the load path, which forms a tangent to the limit curve, taking into consideration the stable crack extension. A schematic of the application of this procedure is shown in Fig. 4. For this purpose, the constant load F acting in L_r is normalized to the crack-length-dependent limit load $F_K(a + \Delta a)$ and in K_I the applied K_I value, calculated with regard to the crack growth ($K_I = a + \Delta a$) is converted to J and normalized with the crack resistance curve of the material, which is usually represented by the J_R -curve ($J_R + (\Delta a)$), (a = crack depth).

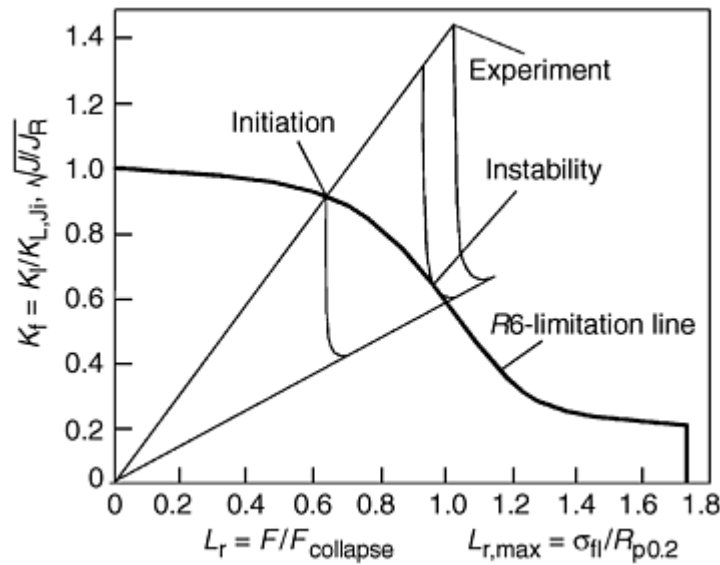


Fig. 4 Application of the two-criteria approach (*R6*-method, Rev 3)

R-Curve Method. The *R*-curve method combines the crack driving force calculated for the component with the material characteristics (evaluated from the crack resistance curve), especially the fracture mechanics characteristics. The crack driving force is calculated in terms of the J -integral by superposition of the elastic and the plastic part, which is, according to Ref 32, 33, and 34:

$$J = J_{el} + J_{pl}$$

with

$$J_{el} = \frac{K_I^2}{E}$$

and

$$J_{pl} = \sigma_0 \varepsilon_0 \alpha h_1 \left(\frac{a}{W}, n \right) \left(\frac{F}{F_K} \right)^{n+1}$$

where K_I is the linear elastic stress-intensity factor, which is available for different geometries and loading conditions in the literature, and σ_0 , ε_0 , α , and n are parameters developed by the Ramberg-Osgood approximation of the true stress-strain curve of the material. The load, F_K , is the plastic limit load, and $h_1(a/W, n)$ is a calibration function evaluated from finite element analyses. Both are given for different geometries (e.g., Ref 33, 34).

Initiation occurs at the load at which the crack driving force curve intersects the J_R -curve of the material at the initiation value J_i . The instability load is given by the curve of the crack driving force that forms a tangent to the J_R -curve (Fig. 5).

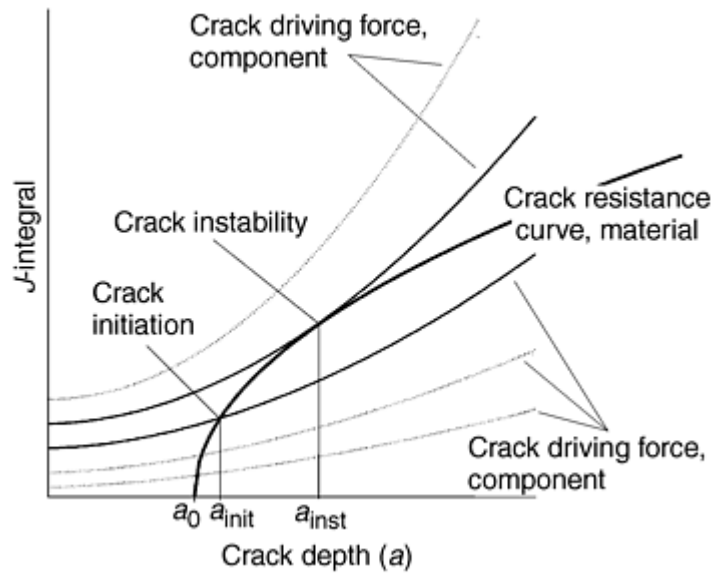


Fig. 5 Application of the R-curve method

Crack Growth Behavior under Cyclic Loading

For components operating under alternating loads, the crack growth under these loading conditions should be known. The crack growth in a component under alternating loads can be calculated from the loading amplitude, the number of cycles, and the crack geometry. From the crack size and the loading amplitude, the range of the stress-intensity factor $\Delta K/2$ can be calculated as follows:

$$\Delta K = f(\Delta\sigma, a, f)$$

The crack propagation rate da/dN for ΔK -values greater than the threshold value ΔK_{th} can be calculated by the well-known Paris law (Ref 35), which has the general form:

$$da/dN = C (\Delta K)^m$$

A typical curve of fatigue crack propagation is shown in Fig. 6. There are three regions within the curve. Region I may be referred to as the near-threshold area. Table 1 lists threshold values for selected materials. If ΔK is smaller than ΔK_{th} then da/dN is assumed to be zero. If ΔK is greater than the threshold value ΔK_{th} , there is a crack growth under alternating loads (region II). The Paris law is a good approach, especially for this region II. In region III, the crack propagation is very progressive. With increasing crack size, the stress intensity increases and the crack growth rate accelerates until the remaining ligament fails due to instability. Forman's equation (Ref 36) could describe the fatigue propagation behavior in regions II and III (see Fig. 6) and also consider the stress ratio. Forman's empirical approach is:

$$\frac{da}{dN} = \frac{C(\Delta K)^m}{(1-R)K_{Ic} - \Delta K}$$

where C , m , ΔK_{th} , and ΔK_{Ic} are material characteristics determined with standardized test methods (Ref 37). Environmental conditions and the load range ratio R affect these values. For example, the ASME Boiler and Pressure Vessel Code (Ref 1) contains some C and m values for different R -ratios of typical steels of light water reactors.

Table 1 Threshold stress-intensity values for selected materials

Material	ASTM designation	German designation	Threshold stress-intensity value ($R = 0.1$)	
			MPa \sqrt{m}	ksi $\sqrt{in.}$
Carbon steel plate	A 573	St 52-3	11.5	10.5
High-strength low-alloy steel	A 633, grade C	StE 355	9.3	8.5
High-strength low-alloy niobium-vanadium structural steel	A 572	StE 47	9.1	8.3
Titanium alloy Ti-6Al-4V	B 265	TiAl6V4	8.3	7.6
High-strength manganese carbon steel pressure vessel plate	A 455	16 Mn	8.1	7.4
Chromium steel	...	30CrMnSiNi2A	3.3	3.0
Aluminum alloys	2.5	2.3

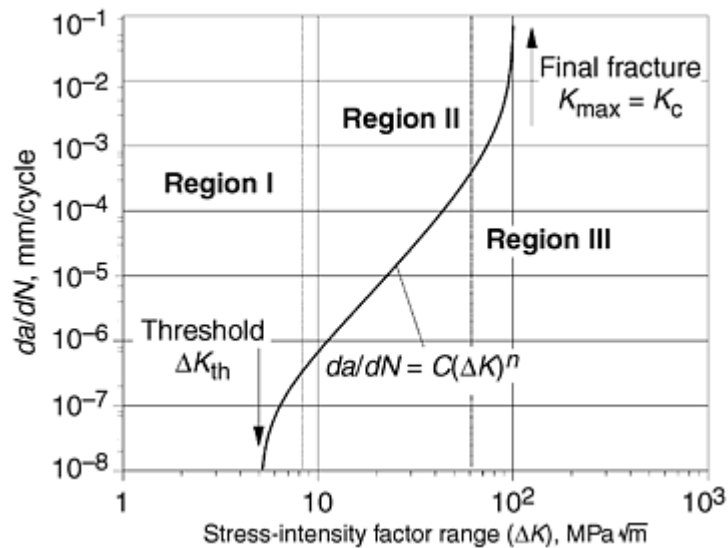


Fig. 6 Cyclic crack growth

References cited in this section

1. "Rules for Construction of Nuclear Power Plant Components," ASME Boiler and Pressure Vessel Code, Section III, American Society of Mechanical Engineers, 1998
14. K. Kussmaul, D. Blind, E. Roos, and D. Sturm, The Leak-Before-Break Behavior of Pipes, *VGB Kraftwerkstech.*, Vol 70 (No. 7), July 1990, p 465–477
27. G.T. Hahn, M. Sarrate, and A.R. Rosenfield, Criteria for Crack Extension in Cylindrical Pressure Vessels, *Int. J. Fract. Mech.*, Vol 8, 1969, p 187–210

28. R.J. Eiber et al., "Investigations of the Initiation and Extent of Ductile Pipe Rupture," Final report, Task 17, BMI-1866, 1966, and BMI-1908, 1971, Battelle Memorial Institute, Columbus
29. W.A. Maxey, "Fracture Initiation, Propagation and Arrest," Fifth Symposium on Line Pipe Research, 1974
30. M.F. Kanninen et al., "Instability Predictions for Circumferentially Cracked Type 304 Stainless Steel Pipes under Dynamic Loading," EPRI report NP-2347, Vol 1, 2, Electric Power Research Institute, April 1982
31. I. Milne, R.A. Ainsworth, A.R. Dowling, and A.T. Stuart, "Background to and Validation of CEGB Report R/H/R6," CEGB R/HR6-Rev. 3, Validation, Central Electricity Generating Board (CEGB), Jan 1987
32. V. Kumar, M.D. German, and C.F. Shih, "An Engineering Approach for Elastic-Plastic Fracture Analysis," EPRI NP-1931, topical report, Electric Power Research Institute, July 1981
33. V. Kumar, M.D. German, W.W. Wilkening, A.R. Andrews, H.G. deLorenzi, and D.F. Mowbray, "Advances in Elastic-Plastic Fracture Analysis," EPRI NP-3607, Project 1237-1, final report, Electric Power Research Institute, Aug 1984
34. A. Zahoor, Circumferential Through Wall Cracks, *Ductile Fracture Handbook*, Vol 1, EPRI NP-6301-D, research project 1757-69, Electric Power Research Institute, June 1989
35. P.C. Paris and F. Erdogan, A Critical Analysis of Crack Propagation Laws, *J. Basic Eng. (Trans. ASME D)*, Vol 85, 1963, p 528-534
36. R.G. Forman, V.E. Kearney, and R.M. Engle, Numerical Analysis of Crack Propagation in Cyclic Loaded Structures, *J. Basic Eng. (Trans. ASME)*, Vol 89, 1967, p 459
37. "Standard Test Method for Measurement of Fatigue Crack Growth Rates," E 647-95a, ASTM

Testing of Pressure Vessels, Piping, and Tubing

E. Roos, K.-H. Herter, and F. Otremba, Staatliche Materialpruefungsanstalt (MPA), University of Stuttgart

Transferability of Mechanical Properties

The generally used material characteristics in the design phase and in safety analysis are the strength properties (yield strength and tensile strength) of the material. Normally, requirements are given in standards and material specifications for the materials used. Additionally, toughness properties are used for characterizing the material. Toughness properties are reduction of area and maximum elongation derived from the tensile test and Charpy V-notch impact energy.

Besides these properties for the assessment of critical crack sizes, fracture mechanics characteristics also have to be evaluated. The fracture mechanics properties very much depend on the material behavior.

Unlike the calculation of the failure loads by the plastic limit load equations, which are based on the strength values evaluated from the tensile test, the calculations using fracture mechanics procedures are more distinguishing because the crack initiation as well as the maximum or instability load can be determined. The indispensable premise is the transferability of the fracture mechanics characteristics from small-scale

(laboratory) specimens to the components. This could be checked by the parameter that describes the event of the crack initiation with the same value for the specimen and for the component as well.

Numerous large-scale tests were conducted at MPA Stuttgart to investigate this issue of transferability (Ref 38, 39, and 40). The crack resistance curves were evaluated using large-scale specimens. Crack initiation values were consequently determined analogous to small-scale specimen tests. The results were verified for the effective crack initiation value J_i . The evaluation of this transferable fracture mechanics materials characteristic is only given in European standards ESIS P1-92 (Ref 41) and ESIS P2-92 (Ref 42).

The transferability, however, cannot be validated for all crack resistance curves (Ref 43). Figure 7 shows crack resistance curves determined from large specimens of different geometry and size made of the ferritic material 22NiMoCr-3-7 mod. The test temperature was 80 °C (175 °F); that is, the tests were performed at the onset of the upper-shelf regime of the C_v - T curve. The crack initiation values J_i of all specimens fall within a narrow scatterband, whereas the crack resistance curves demonstrate a significantly divergent behavior with increasing crack growth Δa . This is due to the distinct difference in the degree of multiaxiality of the stress state because of the different geometry and size of the specimens. The multiaxiality of the stress state could be quantified with coefficient of triaxiality (Ref 43):

$$q = \sigma_e / (\sqrt{3} \sigma_m)$$

where σ_e is the von Mises equivalent stress and $\sigma_m = (\sigma_1 + \sigma_2 + \sigma_3)/3$.

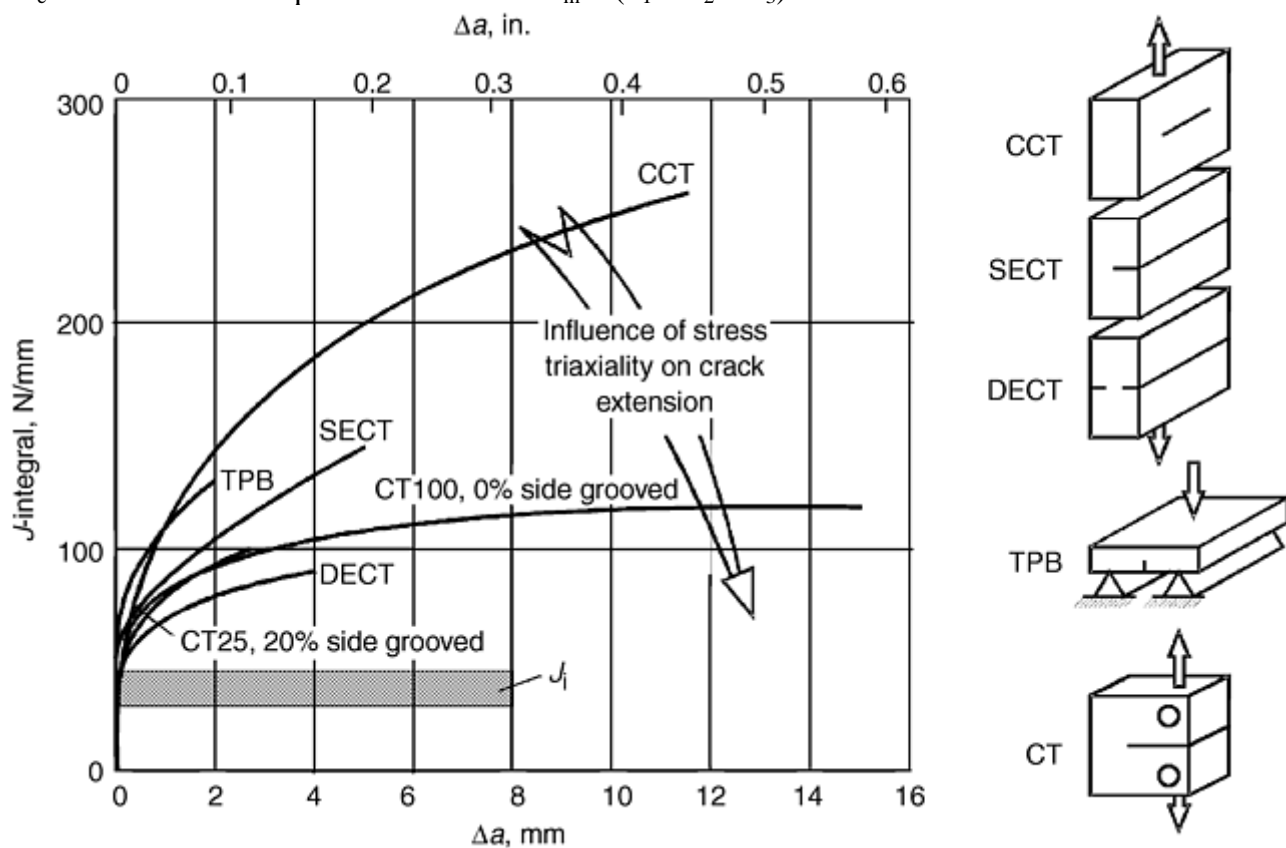


Fig. 7 Influence of stress triaxiality on J_R -curves above initiation J_I . Material: 22NiMoCr-3-7 mod; test temperature 80 °C (175 °F); ratio of crack length (a) to specimen width (W), 0.5

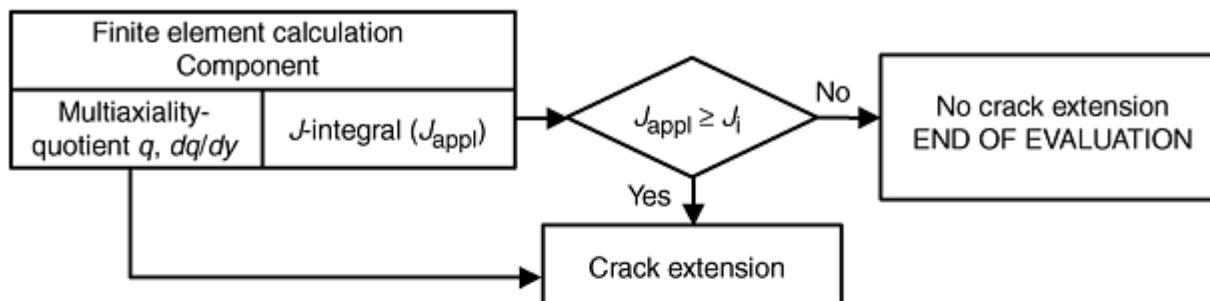
Therefore, crack resistance curves cannot be regarded as generally valid material characteristics, but instead are specimen- or component-specific characteristics. The failure process after crack initiation in terms of stable crack extension is very strongly dependent on and controlled by the stress state, especially by the multiaxiality of the stress state.

The transferability of the J_R -curve from a laboratory specimen to a component and the use of the J_R -curve within a fracture mechanics concept to calculate the failure behavior (e.g., instability load) is only possible if the distribution of q values across the ligament is comparable. The process of evaluating the initiation and instability load is represented in Fig. 8.

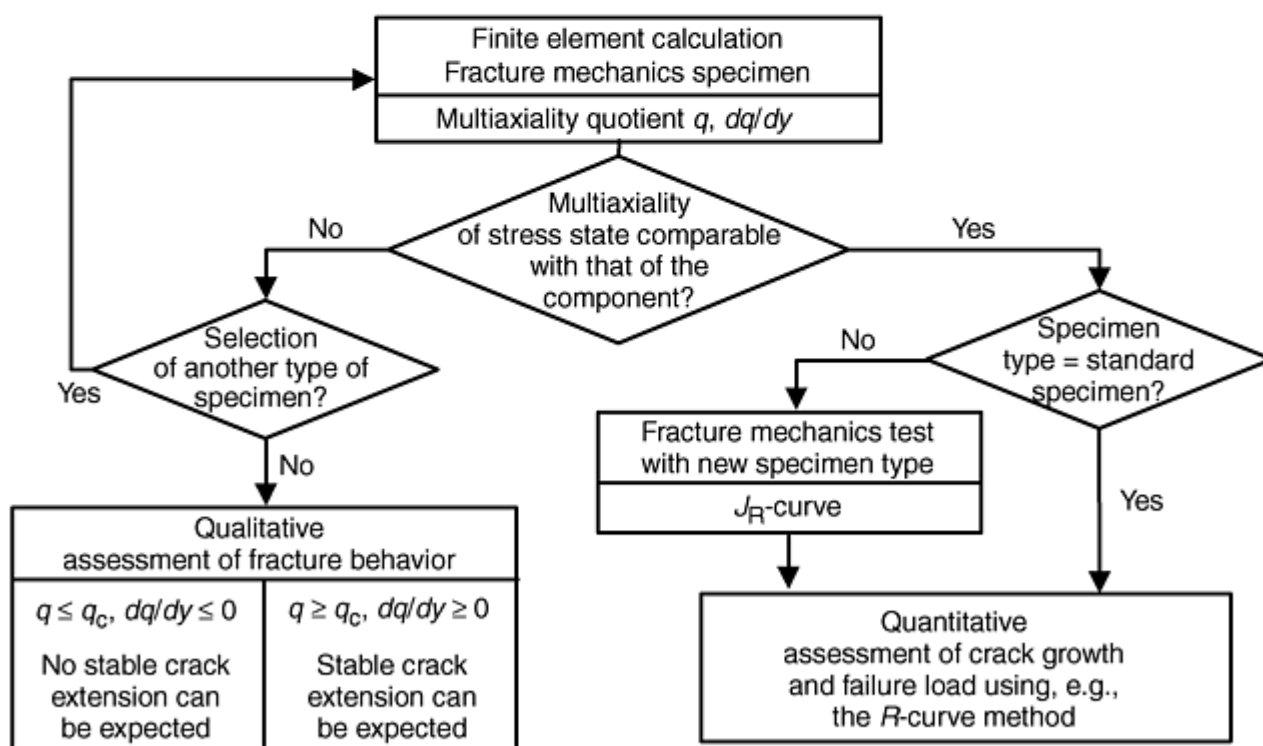
1 Material characterization



2 Evaluation of crack initiation $J_{appI} = J_I$



3 Evaluation of ductile crack growth $J_{appI} \geq J_I$



Multiaxiality quotient $q : q = f(\text{geometry, flaw depth, load, material})$
 Gradient of $q : dq/dy = f(\text{geometry, flaw depth, load, material})$
 Crack initiation value $J_I : J_I = f(\text{material})$
 Crack resistance curve : J_R -curve = $f(\text{geometry, flaw depth, load, material})$
 Critical q -value : $q_c \cong 0.3$ (for steel)

Fig. 8 Flow chart for the evaluation of degraded components

The quality of analytical and numerical approaches is highly dependent on the transferability of data developed by small-scale laboratory tests to the full-scale components. Within the scope of research programs performed by MPA Stuttgart, large-scale specimen and full-scale components with dimensions similar to the original components in power plants were investigated to demonstrate the transferability of material data. The following section describes some specific selected large-scale and full-scale tests and their results relevant to the topic of this article.

References cited in this section

38. Research Project 150 0270, "Phenomenological Pipe and Vessel Burst Tests, Phase I und II," Final Report 150 0279, MPA Stuttgart, Abschlußberichte 1985 und 1987 (final reports in German)
39. Research Project 150 0304, "Integrity of Components, Phase I und II," Final Report 150 0304, MPA Stuttgart, Abschlußberichte 1983 and 1989 (final reports in German)
40. Research Project 150 0618, "Pressure Vessels Subjected to Pressurized Thermal Shock Loading," Final Report 150 0618, MPA Stuttgart, Abschlußbericht 1990 (final report in German)
41. "Recommendations for Determining the Fracture Resistance of Ductile Materials," ESIS P1-92, European Structural Integrity Society (ESIS), Jan 1992
42. "Procedure for Determining the Fracture Behavior of Materials," ESIS P2-92, European Structural Integrity Society (ESIS), Jan 1992
43. H. Clausmeyer, K. Kussmaul, and E. Roos, Influence of Stress State on the Failure Behavior of Cracked Components Made of Steel, *Appl. Mech. Rev.*, Vol 44 (No. 2), Feb 1991, p 77–92

Testing of Pressure Vessels, Piping, and Tubing

E. Roos, K.-H. Herter, and F. Otremba, Staatliche Materialprüfungsanstalt (MPA), University of Stuttgart

Full-Scale Testing

The overall objective for full-scale testing of pressure vessels, piping, and tubing is the proof of integrity and the leak-before-break behavior. Full-scale testing also provides verification and validation of structural analyses and fracture mechanics calculations. In the following section, some full-scale testing facilities are described briefly as an introduction on general capabilities of the facilities. This is followed by a description of typical test results for various applications.

Requirements and Test Facilities

Quasi-Static (Monotonic Increase) Internal Pressure Loading (Burst Test). Straight pipe sections with an internal diameter of 700 mm (28 in.) and a wall thickness of 47.5 mm (1.87 in.) and closed on both ends were used as full-scale test components (Ref 44, 45, and 46). Regarding internal pressure and temperature, the test conditions were related to the operating conditions of pressurized water reactors. Water was mainly used as the pressurizing medium and had already been filled in the pipe during the heating process. The internal pressure was controlled in parallel with the heating temperature so that no steam could develop inside the pipes (for safety). After reaching the test temperature, the pressure was raised monotonically by further injection of water. In order to control the time-dependent decay of pressure during the fracture or failure process, the test could also be carried out under main steam line conditions or those similar to the conditions of boiling water reactors. Therefore, the test facility was additionally designed for the use of air as a compressible pressurizing medium in some tests.

Quasi-Static (Monotonic Increase) External Loading. In the case of straight pipes, different types of test equipment were used for static external bending moment loading:

- A four-point bending device with a capacity of 10 MN · m for pipe dimensions up to nominal diameter 800 mm (31.5 in.) and 50 mm (2 in.) wall thickness (Ref 47) and with a capacity of 3 MN · m for pipe

dimensions up to nominal diameter 400 mm (15.75 in.) and 15 mm (0.6 in.) wall thickness (Ref 48). To guarantee constant loading conditions in the phase of crack initiation and crack propagation, as well as to realize a testing system with high stored energy, air was used as a compressible pressurizing medium in the hydraulic actuators and as a reservoir in the test pipes.

- A constant-moment loading bending device with a capacity of 2 MN · m bending for pipe dimensions up to nominal diameter 300 mm (11.8 in.) and 35 mm (1.4 in.) wall thickness (Fig. 9), and with a capacity of 40 kN · m for pipe dimensions up to nominal diameter 80 mm (3.1 in.) and 10 mm (0.4 in.) wall thickness

The test temperature was ambient (room) temperature up to operational temperature (e.g., 300 °C, or 570 °F). The pipes were loaded under specified constant internal pressure and a superimposed monotonic increasing external bending moment.

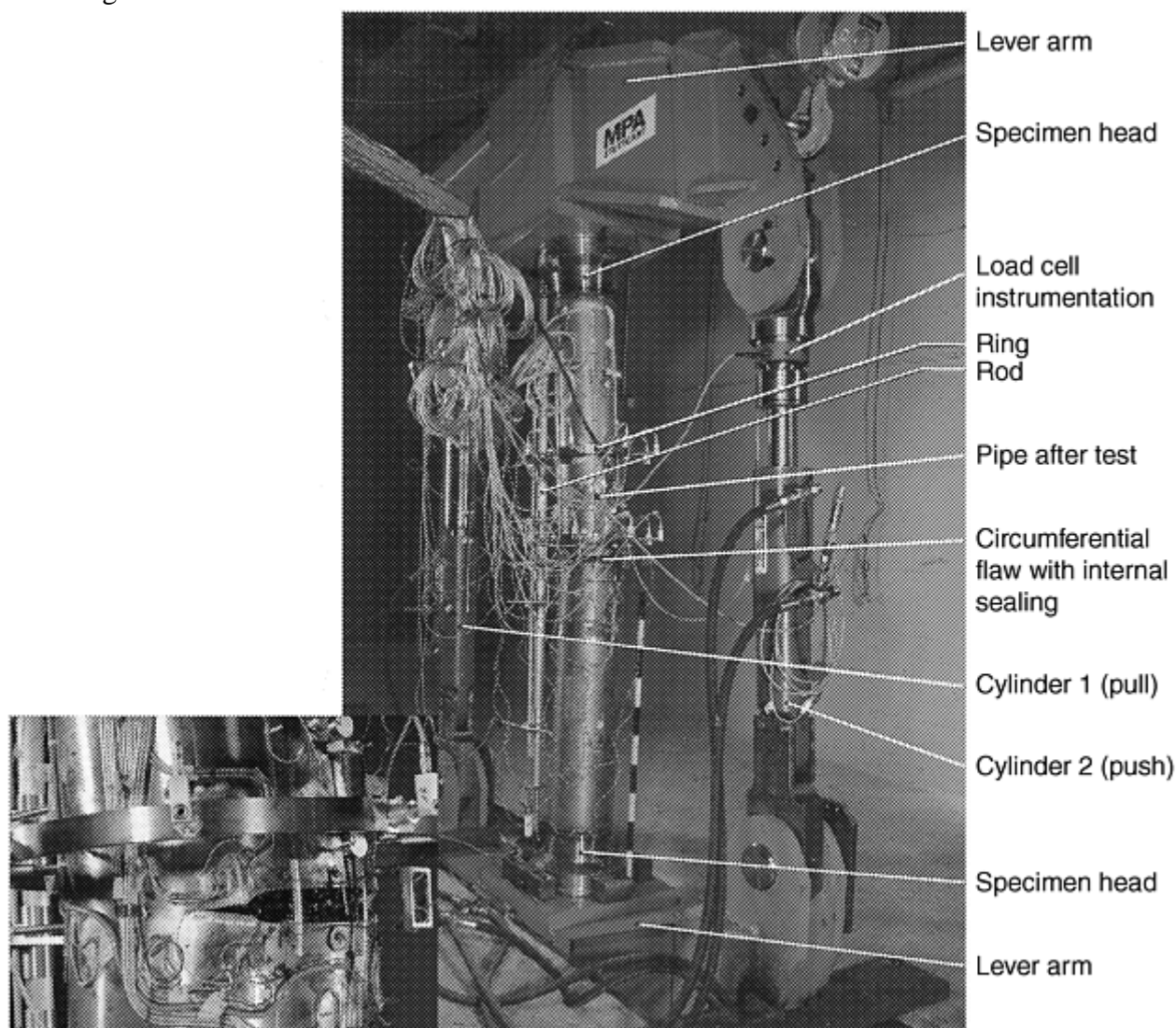


Fig. 9 Constant moment loading bending device with capacity of 2 MN · m. Inset shows instrumented pipe after the test

In the case of elbows (pipe bends) depending on the loading mode (in-plane opening or closing, out-of-plane) different types of test equipment were used for quasi-static external bending moment loading:

- Moment loading for the elbows with nominal diameter 400 mm (15.75 in.) and 30 mm (1.2 in.) wall thickness was realized by transverse forces at the end of long pipe sections adjacent to the elbows (Ref 49). For the in-plane opening mode, the load was imposed by a 15 MN horizontal-testing device, which exerted a force combination of normal and lateral force on the pipe together with a bending moment; however, the long pipe leg meant that the bending moment imposed the dominant stress in the elbow

(Fig. 10). A similar test setup was used for the in-plane closing mode. Out-of-plane loading was realized by a combined torsional moment and a lateral force. The testing device was set up horizontally (Fig. 11). A hydraulic cylinder was imposed vertically at the long end of the two adjacent straight pipe sections of different length. A special fixpoint had to balance the forces resulting from the applied transverse forces of the loading point. In all the different loading cases, the elbow mid-sections were dominantly stressed by moment loading.

- Elbows with nominal diameter 800 mm (31.5 in.) and 50 mm (2 in.) wall thickness and degraded by longitudinal flaws on both bend flanks were loaded by constant internal pressure and superimposed bending moment with in-plane closing mode (Ref 50, 51, 52) (Fig. 12).

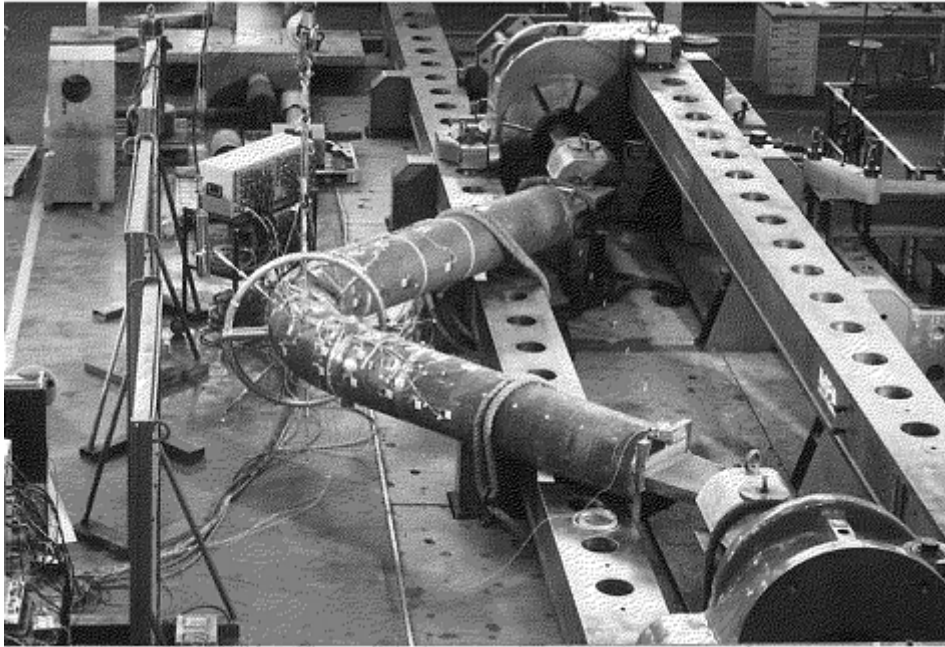


Fig. 10 Bending device for elbows (in-plane opening mode)

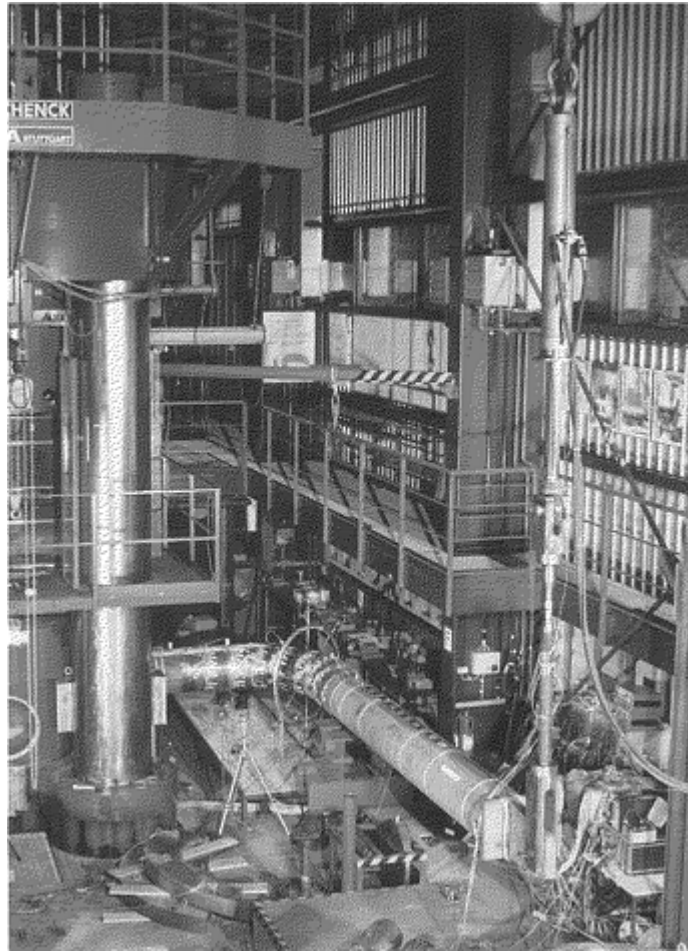
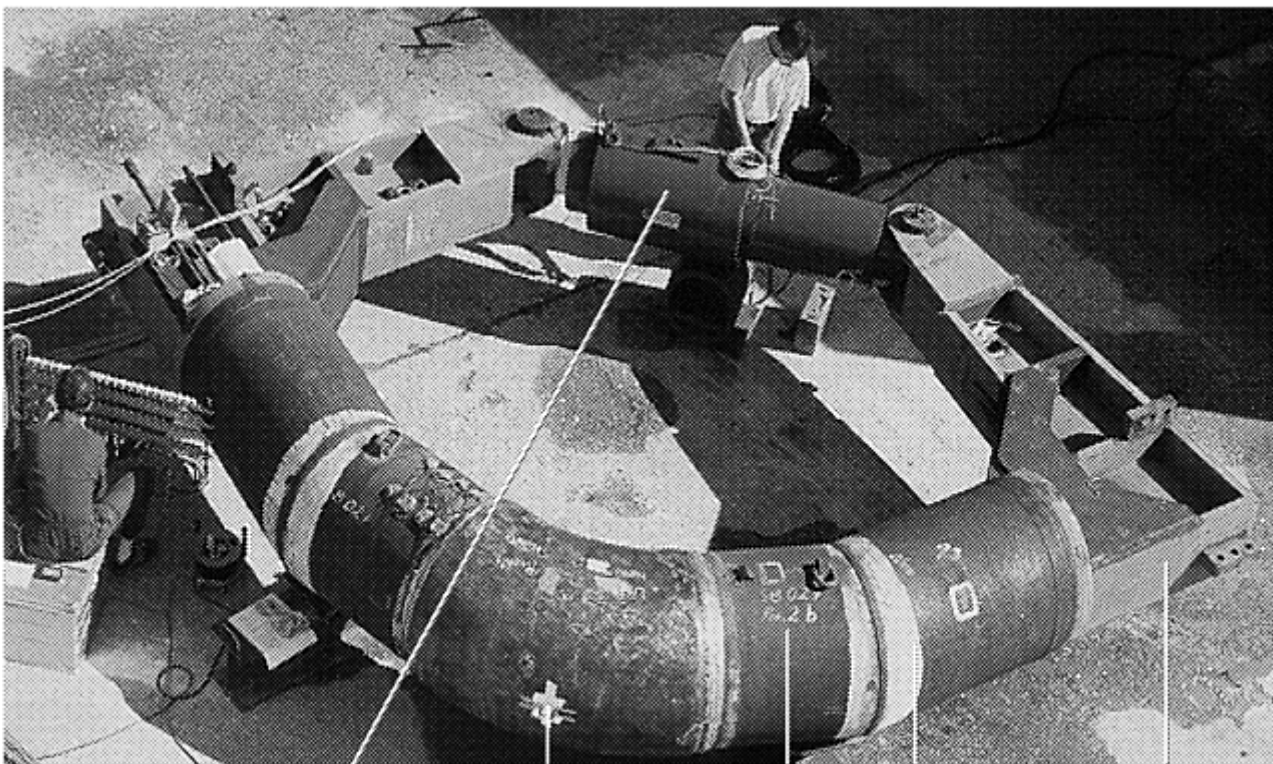


Fig. 11 Bending device for elbows (out-of-plane opening mode)



Hydraulic cylinder

Pipe bend

Extension pipes

Lever arms

Fig. 12 Bending device for elbows with nominal diameter 800 mm (31.5 in.) and wall thickness 50 mm (2 in.)

Dynamic Loading (High-Loading-Rate Tensile Testing). For high-loading-rate tensile testing, several concepts that differ mainly in the function of the testing equipment and especially in the attained load and maximum velocity as well as in the velocity history can be used for dynamic tensile tests. Hydraulic and hydropneumatic testing machines cover the range up to a maximum velocity of about 12 m/s (39 ft/s). Cable-loaded testing facilities or machines driven by a propellant charge attain 50 to 60 m/s (165–200 ft/s), whereas on rotary impact machines the velocity goes up to 80 m/s (260 ft/s) (Fig. 13). The velocity of hydropneumatic, cable-loaded testing machines and rotary impact machines is nearly constant during the test procedure, and full loading is applied instantaneously. The machines driven by a propellant charge attain the maximum velocity after a certain stroke, depending on the type and quantity of the propellant charge used, on the volume of the combustion chamber, and on the masses to be accelerated. This peculiarity allows a more realistic simulation of actual dynamic loading cases. The mode of operation of a propellant-driven 12 MN high-loading-rate tensile testing machine (Fig. 14) is shown schematically in Fig. 15 together with an idealized energy diagram. The energy that is released on combustion of the propellant divides into acceleration energy and deformation energy until fracture of the test specimen occurs. Subsequent to the fracture, the remaining energy of the accelerated components is absorbed by deformation of an aluminum damping element.

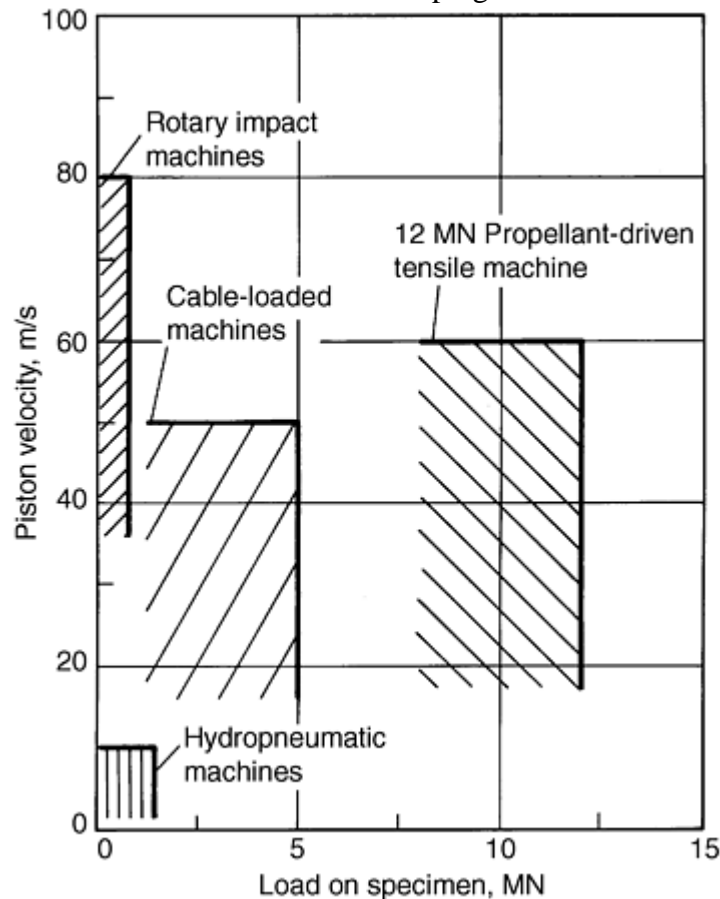


Fig. 13 Load capabilities of different high loading rate tensile testing equipment

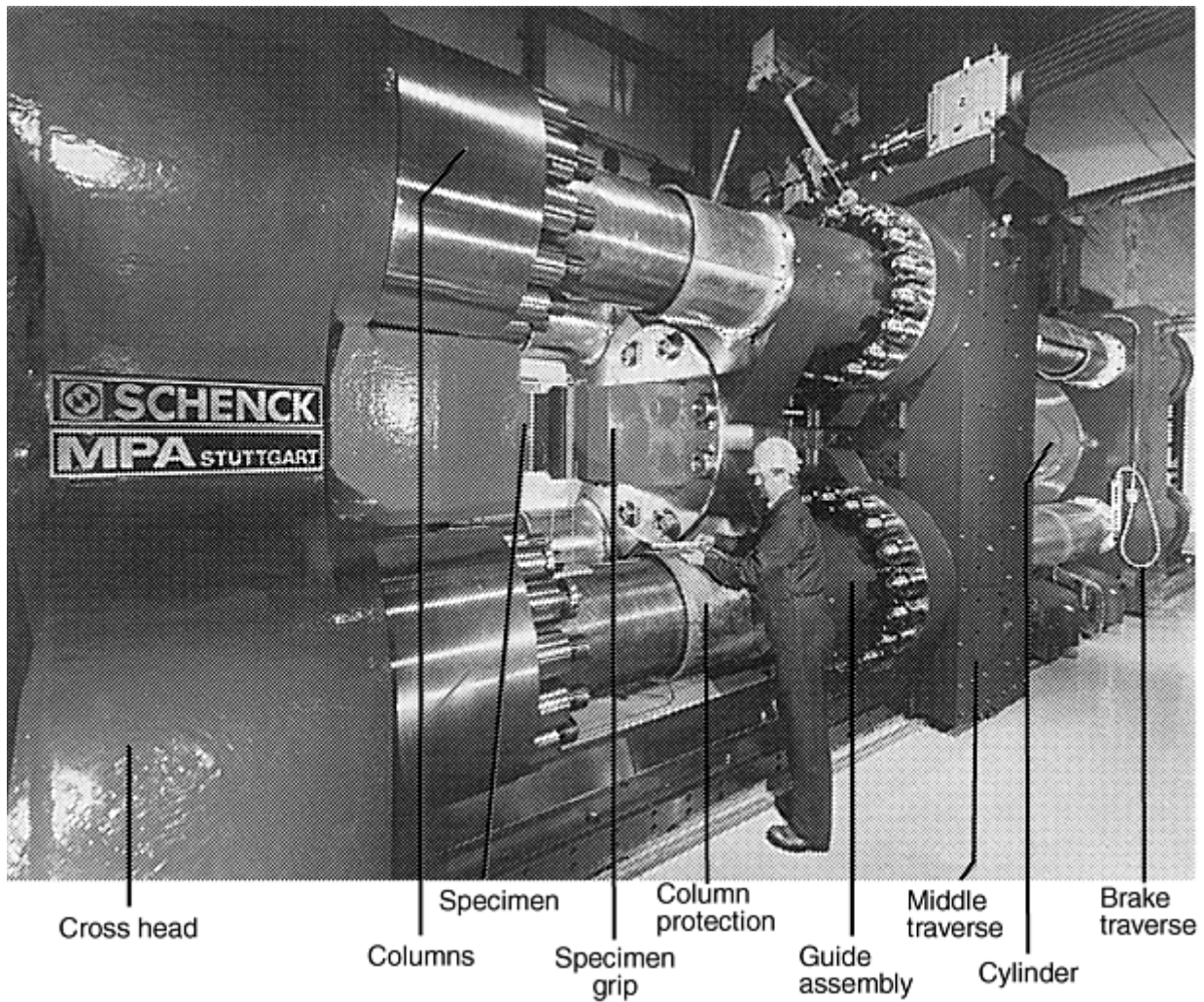


Fig. 14 High-loading-rate tensile testing machine (12 MN capacity)

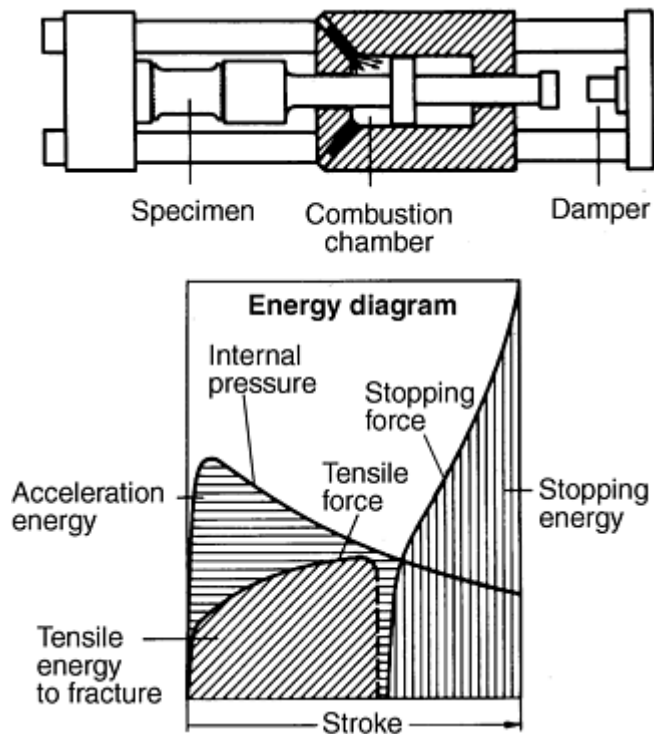


Fig. 15 Test configuration and energy diagram for high-loading-rate propellant-driven tensile testing machines

Tests were carried out on unwelded and welded wide plate specimens (e.g., 960 mm, or 37.8 in., long; 500 mm, or 19.7 in., wide; and 40 mm, or 1.6 in., thick) with and without different flaw positions as well as for pipe sections (e.g., 406 mm, or 16 in., outer diameter and 12.5 mm, or 0.5 in., wall thickness; 168 mm, or 6.6 in., outer diameter and 4.5 mm, or 0.18 in., wall thickness; or 220 mm, or 8.6 in., outer diameter and 16 mm, or 0.6 in., wall thickness) with and without circumferential cracks. Austenitic and ferritic materials were investigated (Ref 53, 54).

Cyclic/Repeated Loading. Different types of test equipment were used for cyclic/repeated external bending moment loading on straight pipes and elbows:

- Bending device for resonance excitation in which fast-alternating external bending loads with high acceleration can be generated (Ref 55) (Fig. 16).
- 12 MN · m bending device for low-cycle, load-controlled, bending loads for pipe dimensions up to 800 mm (31.5 in.) nominal diameter and 50 mm (2 in.) wall thickness (Ref 55).
- The deformation and failure behavior of thick-walled elbows made of austenitic material was investigated in Ref 56. The dimensions of the elbow were 108 mm (4.25 in.) outer diameter and 12 mm (0.47 in.) wall thickness. The bend angles were 60° and 90°.

Numerous piping experiments have also been performed at the German Heissdampfreaktor (HDR) Test Facility (Ref 57). It was built in the period 1965 to 1969 for a prototype superheated steam reactor, but was shut down in 1971 after only 2000 h of operation. After extensive decommissioning and conversion work, it was used from 1974 until 1991 by the HDR Safety Project of the Kernforschungszentrum Karlsruhe to perform vibrational/seismic, thermal hydraulic, blowdown, and other experiments related to the safety and design of nuclear power plants. The load-bearing capacity margins of a piping system with different pipe dimensions and degraded pipe sections under operating conditions were demonstrated for earthquake-type loads (Ref 58). Experiments were also performed to demonstrate the behavior of a full-size feedwater piping system under operational conditions (Ref 59) (Fig. 17).

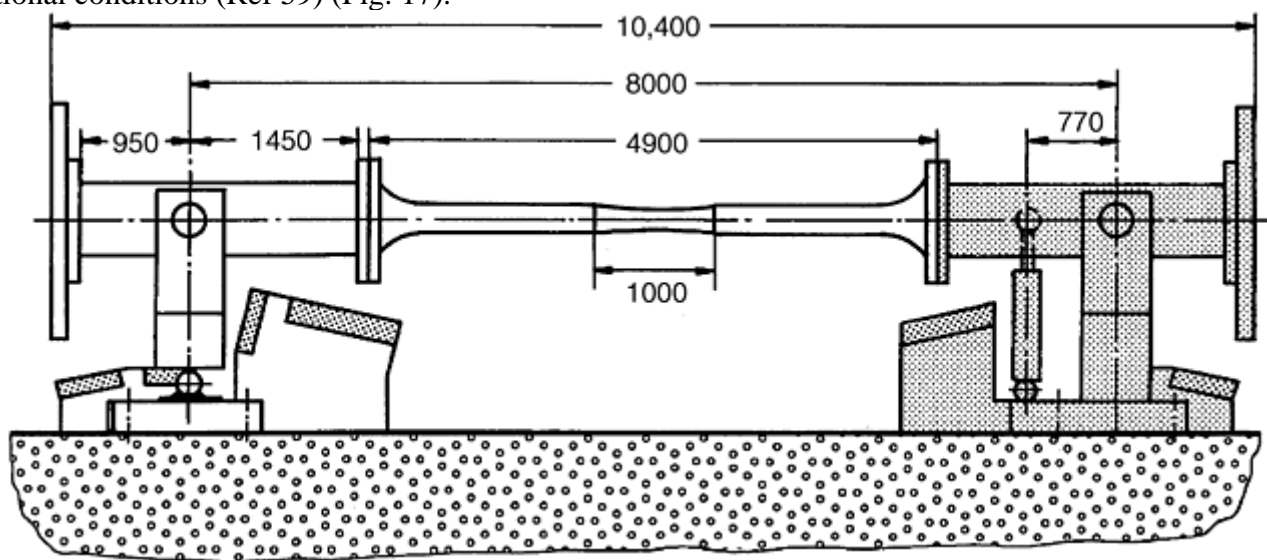


Fig. 16 Resonance bending device. Dimensions are in millimeters.

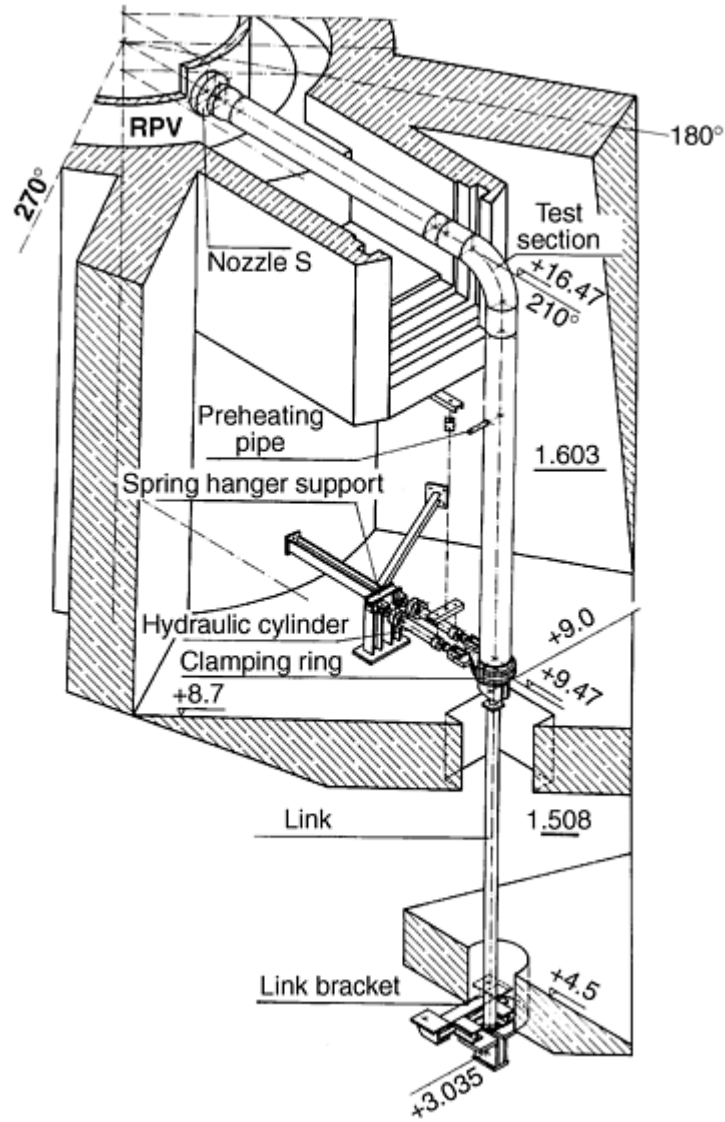


Fig. 17 Reactor pressure vessel (RPV) piping system with degraded elbow

High-Temperature Loading. A pipe component test (700 mm, or 27.6 in., inside diameter and 47 mm, or 1.9 in., wall thickness) to verify the failure behavior postulated from small-specimen tests was carried out to simulate specific accident conditions (Ref 60). Under constant internal pressure of 16.3 MPa (2.4 ksi) using air as pressurizing medium, the pipe was heated up to about 700 °C (1300 °F) to determine the time to failure (Fig. 18).

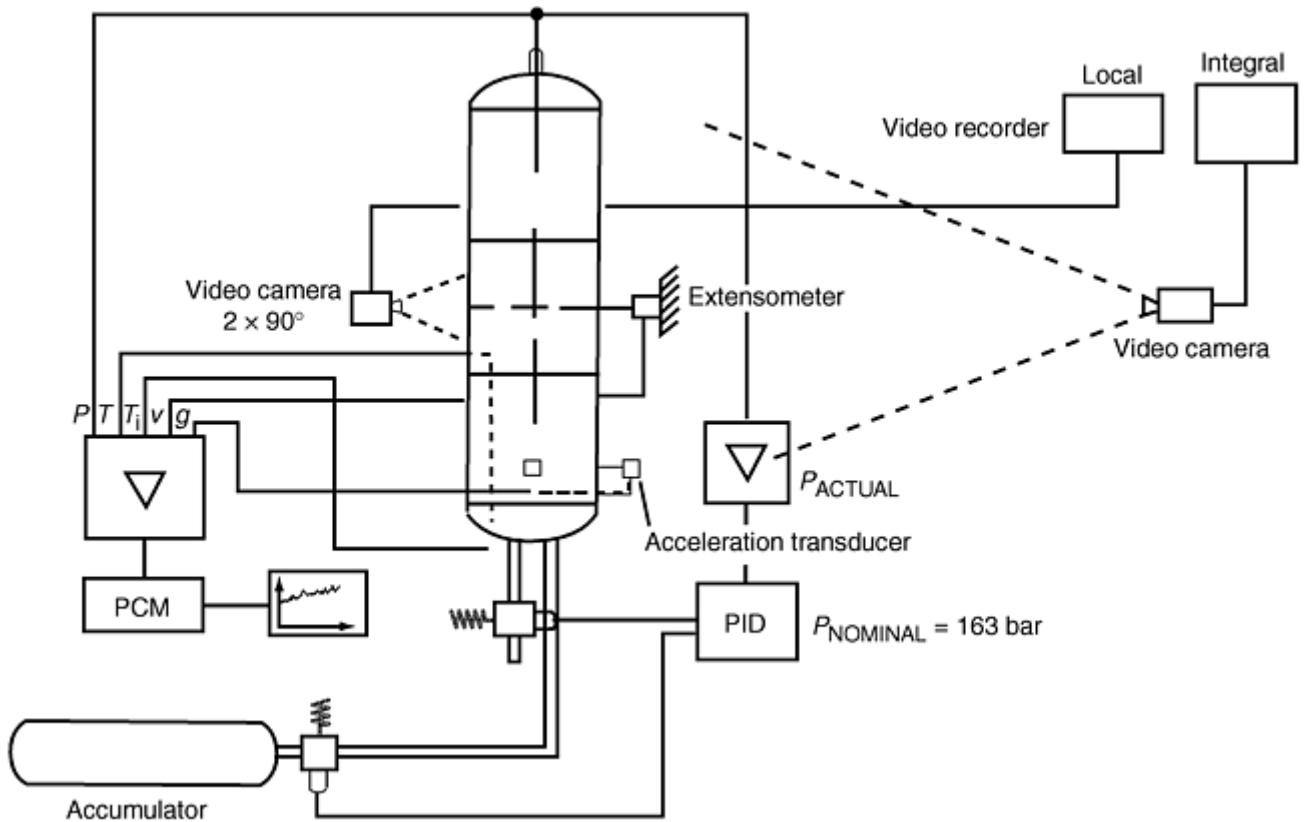


Fig. 18 Test assembly and measurement data collection for testing pipe components under high-temperature loading. PCM, pulse code modular (data acquisition unit); PID, pressure controller; p , pressure; T , outside temperature; v , displacement; g , acceleration; T_i , inside temperature

Creep damage had been observed in elbows (235 mm, or 9.3 in., outer diameter and 25 and 30 mm, or 1 and 1.2 in., wall thickness) in steam piping of fossil-fired power plants. It was assumed that the reasons for this damage were additional forces and moments and also geometrical effects (Ref 61). For that reason, the creep damage and failure behavior of a low-alloy 0.6% Mo steel elbow and a high-alloy 12% Cr steel elbow under internal pressure and a superimposed static bending moment at 550 °C (1000 °F) were investigated in experiments. The test configuration is shown in Fig. 19.

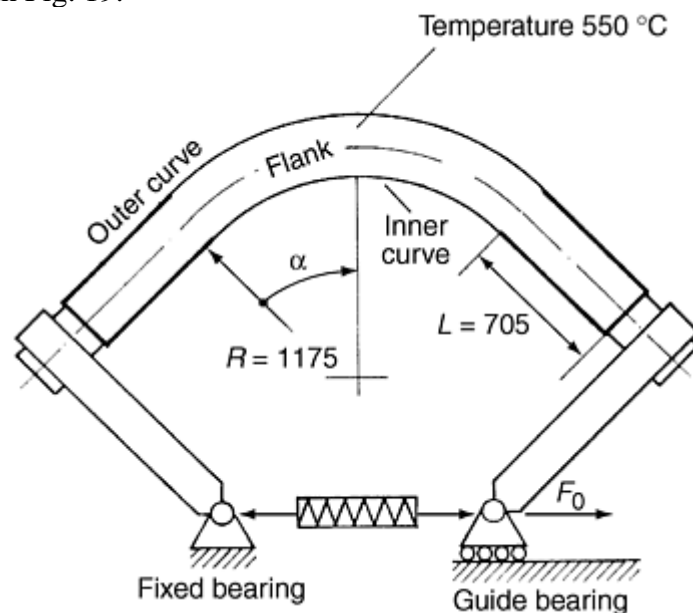


Fig. 19 Test configuration for evaluating long-term creep failure behavior of pipe elbows. F_0 , external static force; R , pipe elbow radius; L , length of the straight ends of the elbow

During all the tests, the variation with time of internal pressure, bending moment, crack opening displacement, crack extension, bending deflection (load-line displacement, strain measurement), and ovalization should be measured to monitor the loading conditions as well as the deformation behavior. Based on the results of the measurements, a comparison between experimental and numerical calculated data is possible. That is why a detailed plan of instrumentation before the tests was developed. In all of the tests mentioned above, the requirements on data acquisition systems and measuring parameters throughout the tests required high-performance data acquisition units.

Some of the specific and interesting test results achieved by running experiments with the above-mentioned test facilities are discussed in the following sections.

Examples of Test Results

Longitudinally Cracked Components. Figure 20 is an example of catastrophic failure from a full-scale internal pressure test (using air as the pressurizing medium) of a feedwater vessel. For crack initiation, a brittle disk was welded in the feedwater tank with a longitudinal notch to initiate the crack (Ref 45). The vessel was completely destroyed because of the compressibility of air. This test shows the influence of stored energy on the failure behavior.



Fig. 20 Catastrophic failure at internal pressure of a feedwater tank

Table 2 summarizes test results for straight pipe with longitudinal defects. The pipes are made of ferritic material having different toughness values, and the failure loads are calculated on the safe side by means of the toughness-dependent approximation technique (Ref 14, 45) (Fig. 21).

Table 2 Test results for longitudinally cracked piping under internal pressure loading

Test No.	Crack length		Crack depth		a/t	Temperature		Burst pressure		Stress at failure		Hoop stress		Normalized crack opening area	Remarks
	mm	in.	mm	in.		°C	°F	MPa	ksi	MPa	ksi	MPa	ksi		
Pipe with $C_v > 150$ J															
BVZ010	650	25.6	1.00	20	68	23.8	3.5	187	27.1	178	25.8	0.02	...
BVZ011	1102	43.4	1.00	20	68	14.8	2.1	117	17.0	111	16.0	0.05	...
BVZ012	1105	43.5	1.00	20	68	14.4	2.1	113	16.4	108	15.6	0.16	...
BVZ022	782	30.8	38.3	1.5	0.81	305	581	21.9	3.2	173	25.1	164	23.7	0.04	Leakage
BVZ030	1500	59.1	36.2	1.4	0.77	300	572	19.5	2.8	155	22.5	146	21.1	>2	Large break
BVZ080	1500	59.1	36.2	1.4	0.77	17	63	20.4	3.0	164	23.8	152	22.1	0.12	Leakage
BVZ070	700	27.6	38.2	1.5	0.81	265	509	22.4	3.2	177	25.7	167	24.3	0.01	Leakage
BVZ060	1500	59.1	36.0	1.4	0.76	305	581	18.0	2.6	143	20.7	135	19.5	0.16	Large break
Pipe with $C_v = 50$ J															
BVS010	800	31.5	1.00	155	311	17.5	2.5	137	19.9	131	19.0	0.1	...
BVS020	709	27.9	37.3	1.5	0.79	320	608	14.8	2.1	117	17.0	111	16.0	0.02	Limited break
BVS030	1100	43.3	35.0	1.4	0.74	305	581	13.1	1.9	103	14.9	98	14.2	0.11	Large break
BVS042	709	27.9	38.3	1.5	0.81	245	473	16.8	2.4	132	19.1	126	18.2	>2	Large break

(a) Pipe outer diameter: 800 mm (31.5 in.), wall thickness: 47.2 mm (1.86 in.)

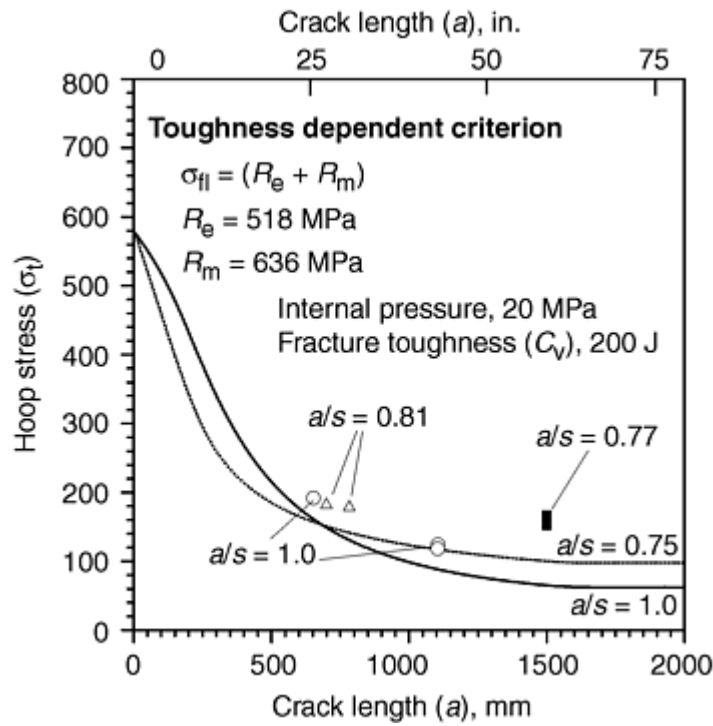


Fig. 21 Test results for longitudinally cracked straight pipes (outer diameter, 800 mm, or 31.5 in.; wall thickness, 47.2 mm, or 1.86 in.) under internal pressure (burst test). R_e , yield strength; R_m , tensile strength; a , crack depth; s , wall thickness

Tests were also performed on large-diameter pipe elbows and pipe T-joints under internal pressure and superimposed quasi-static external bending moment loading.

Circumferentially Cracked Components (Straight Pipes). The experimental results of more than 330 tests with circumferentially cracked pipes with both austenitic and ferritic material are shown in Fig. 22 as normalized experimental moment versus the normalized crack length. It has to be supposed by the test facilities that in the cracked cross section of the pipes the loading condition is constant, especially in moment loading (Fig. 23).

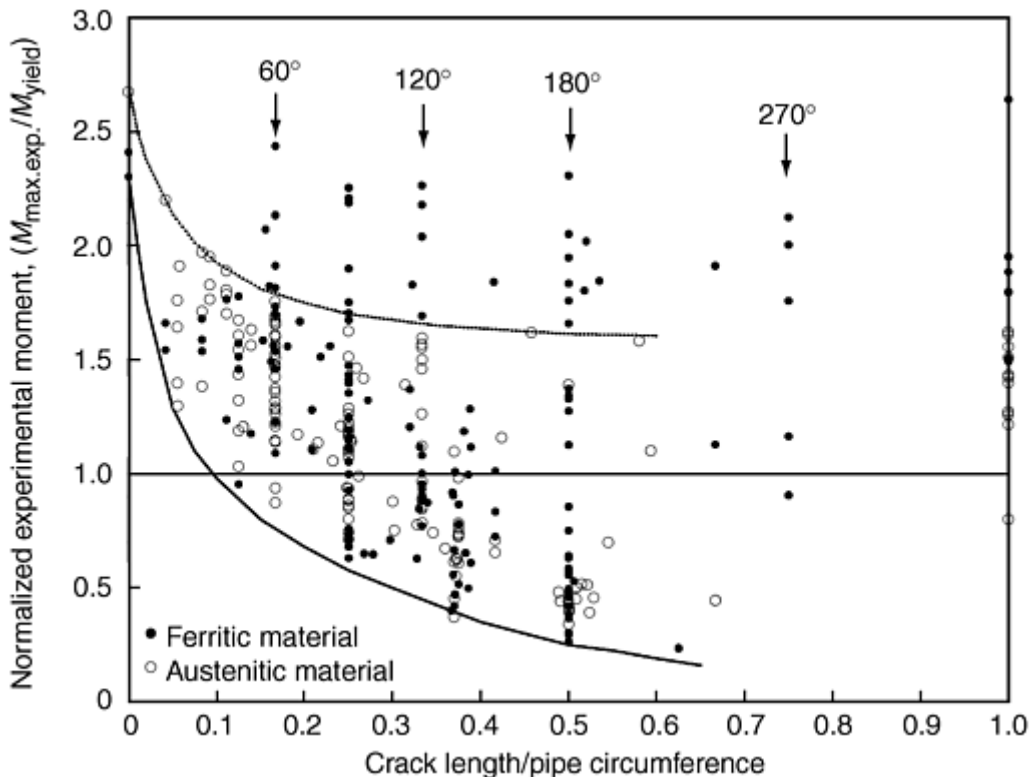


Fig. 22 Results of experimental moment versus crack length for tests for circumferentially cracked pipes (333 full-scale pipe tests)

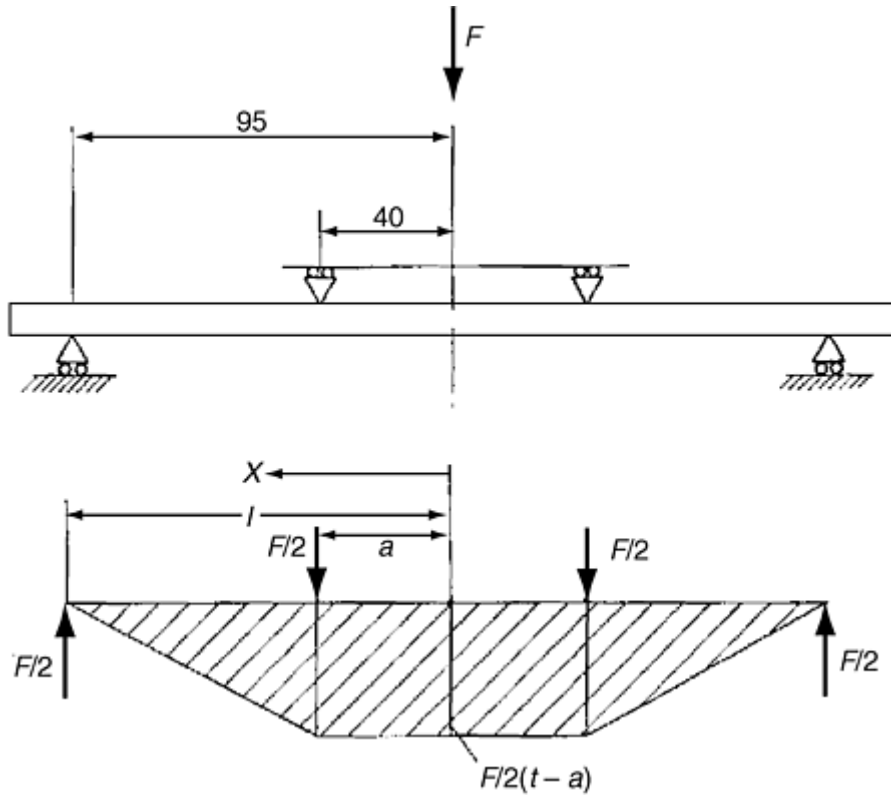


Fig. 23 Constant-moment loading for straight pipes

With the engineering methods (plastic limit load calculation) used and an appropriate flow stress, the experimental maximum moment can be estimated with some accuracy if the expression to calculate the flow stress is adjusted to experimental results. This is demonstrated in Fig. 24 using plastic limit load calculations based on different flow stress assumptions in comparison with experimental results. More precise calculations of the failure course (for example, initiation and instability loads) are possible with the fracture mechanics approximation methods like the two criteria approach or the R -curve method. The results based on J_i demonstrate the transferability of this initiation value to components. The greater differences in the calculated results of the failure load depend on the J_R -curve that could be used only if the triaxiality of the stress state in the ligament in front of the crack tip is comparable to the specimen from which the J_R -curve is evaluated and the component. This is shown in Fig. 25 and 26.

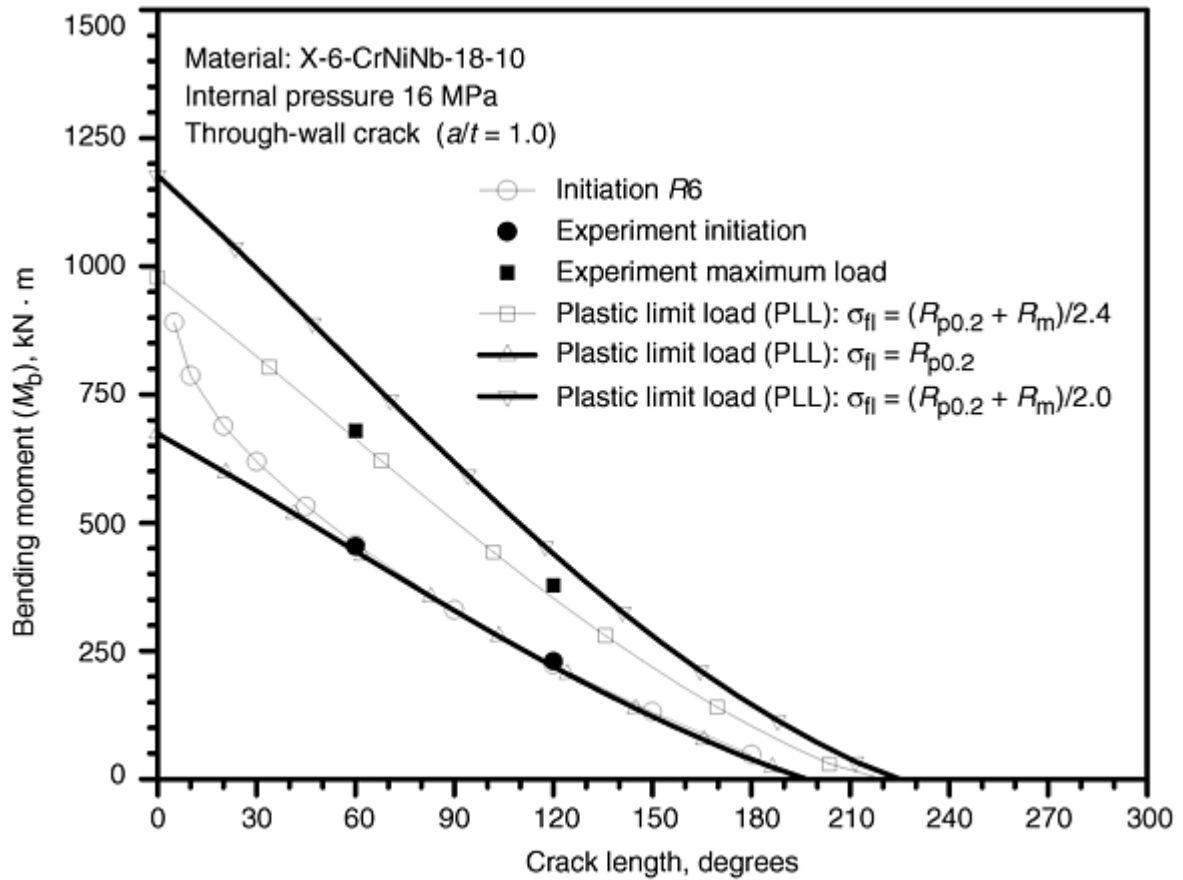


Fig. 24 Comparison of experimental and calculated loads versus the crack length for pipe with outer diameter of 331 mm (13 in.) and wall thickness of 32 mm (1.3 in.)

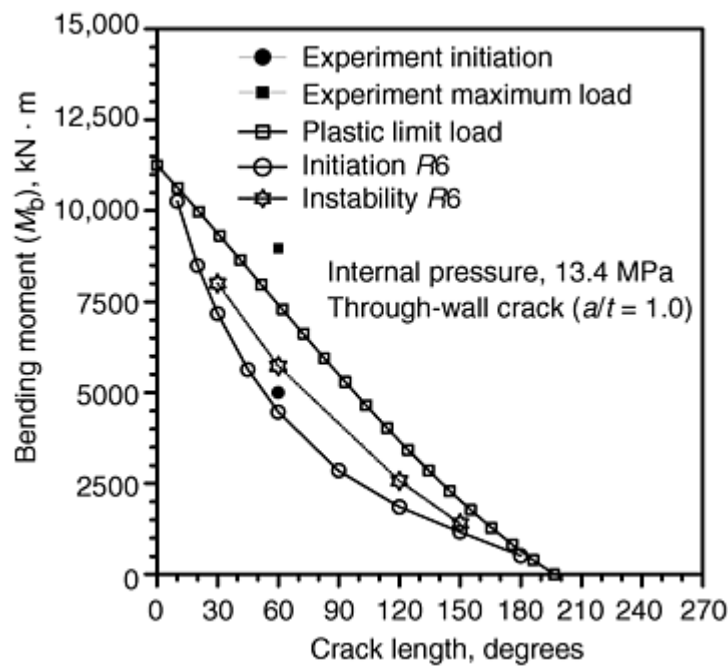


Fig. 25 Comparison of experimental and calculated loads versus the crack length for pipe with outer diameter 800 mm (31.5 in.), wall thickness 50 mm (2 in.); ferritic material, through-wall crack, $\sigma_{fl} = (R_{p0.2} + R_m)/2.4$

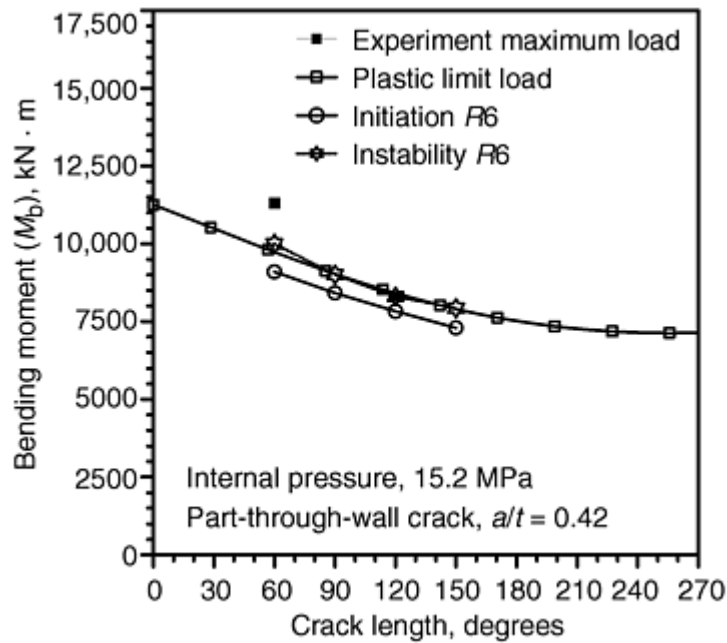


Fig. 26 Comparison of experimental and calculated loads versus the crack length for pipe with outer diameter 800 mm (31.5 in.), wall thickness 50 mm (2 in.); ferritic material, part-through-wall crack, $\sigma_{II} = (R_{p0.2} + R_m)/2.4$

Figure 27 shows the distribution of the coefficient of triaxiality q across the ligament of a fracture mechanics compact tension (CT) specimen compared with q values calculated for a circumferentially cracked pipe. This comparison shows that the transferability of the crack resistance curve determined on a CT specimen to the pipe with circumferential crack is not direct. However, because of the much steeper q gradients and the higher q values in the investigated pipes, it is not surprising to be on the safe side when calculating the failure load of the pipes. In all cases, however, this has to be proven.

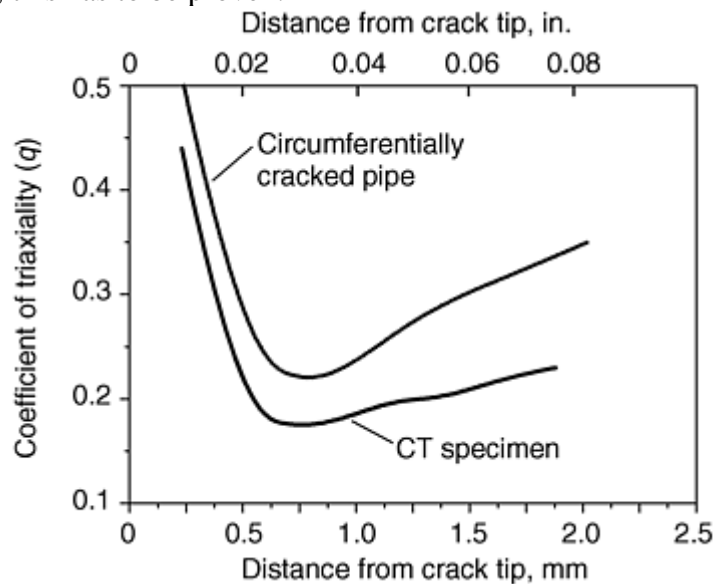


Fig. 27 Distribution of q value across the ligament at the plane of symmetry of a compact tension (CT) specimen and a circumferentially cracked pipe

Based on an extensive program of high-speed tensile tests with large-diameter pipes (406 mm, or 16 in., outer diameter; 12.5 mm, or 0.5 in., wall thickness; material with low upper-shelf Charpy impact energy), no indications of unfavorable material behavior resulting from the dynamic loading conditions up to transients of $\dot{\epsilon} = 6/s$ (Fig. 28, 29) were found. The tests show increasing loadability with increasing strain rate.

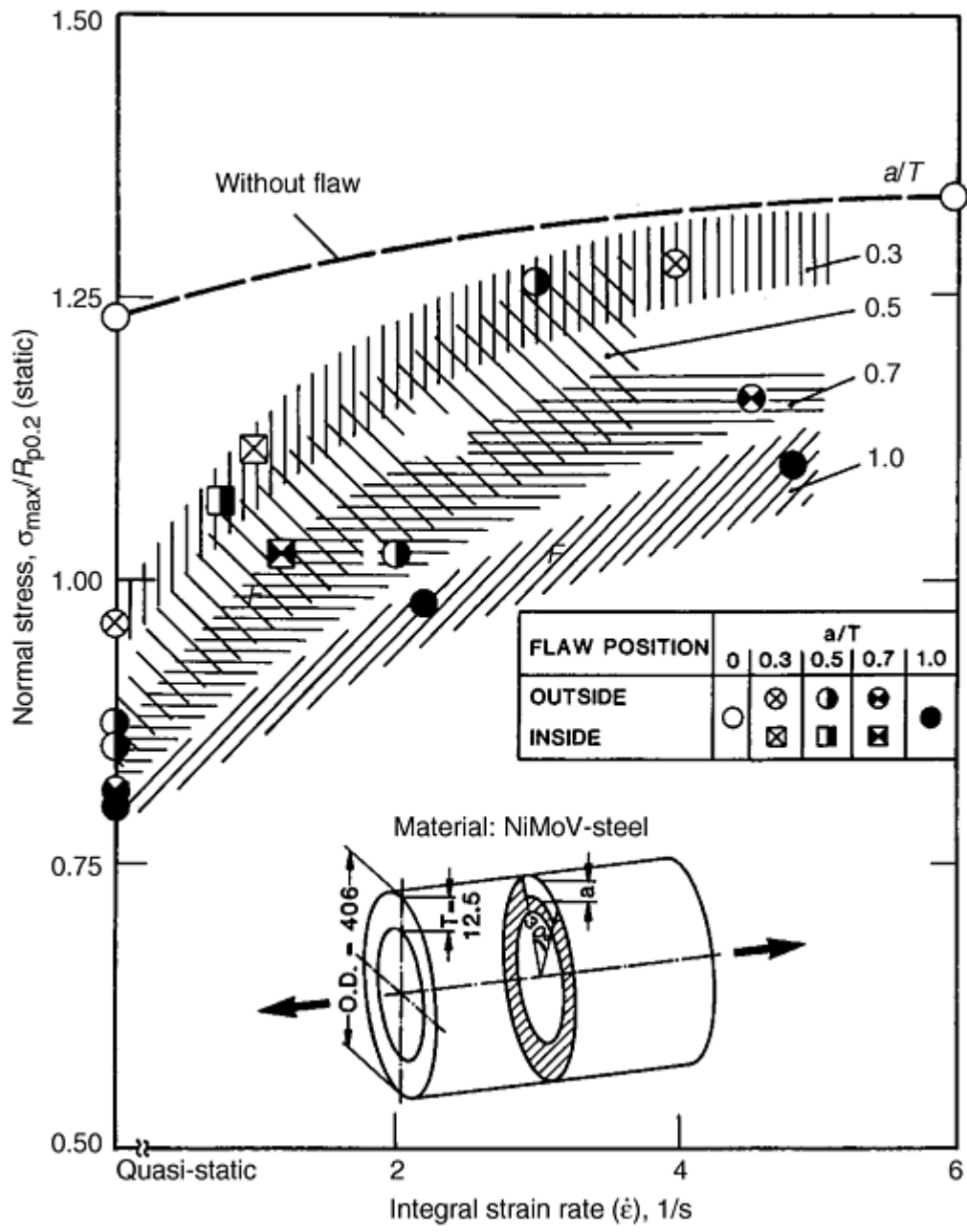


Fig. 28 Dependence of load-bearing capacity on strain rate for large-diameter pipes at room temperature

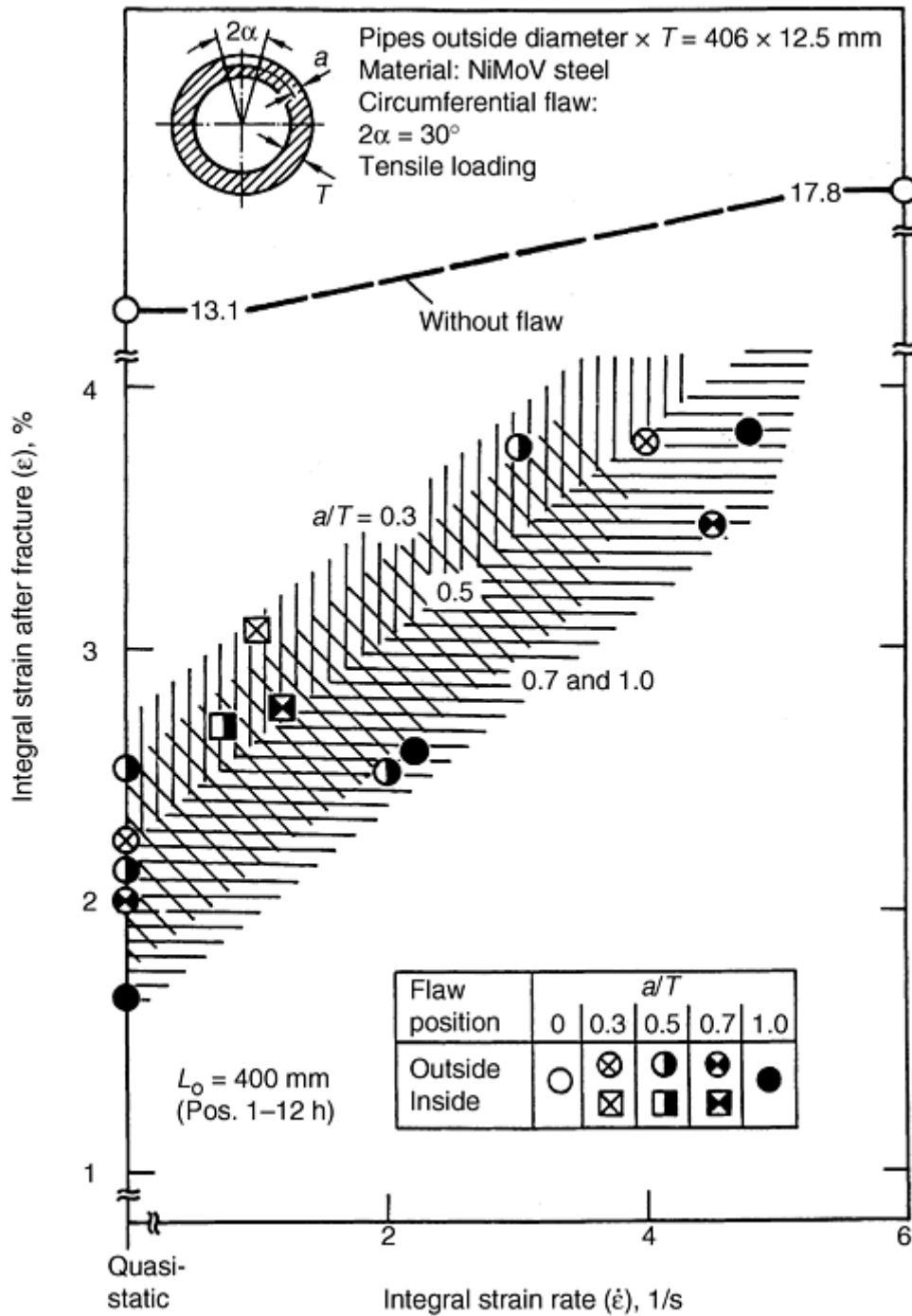


Fig. 29 Dependence of maximum elongation on strain rate for large-diameter pipes at room temperature

Test Results of Piping Systems. Incipient cracks were generated on the inner surface around the bend flanks by cyclic bending (Ref 59). In various phases of the test characterized by sinoidal and sawtooth modes of loading and different load frequencies, the cracks were further extended. At the end of the phases of cyclic testing a macrocrack was embedded in a crack field. In the final load test with monotonously rising bending moment, the pipe bend failed by leakage (Fig. 30).

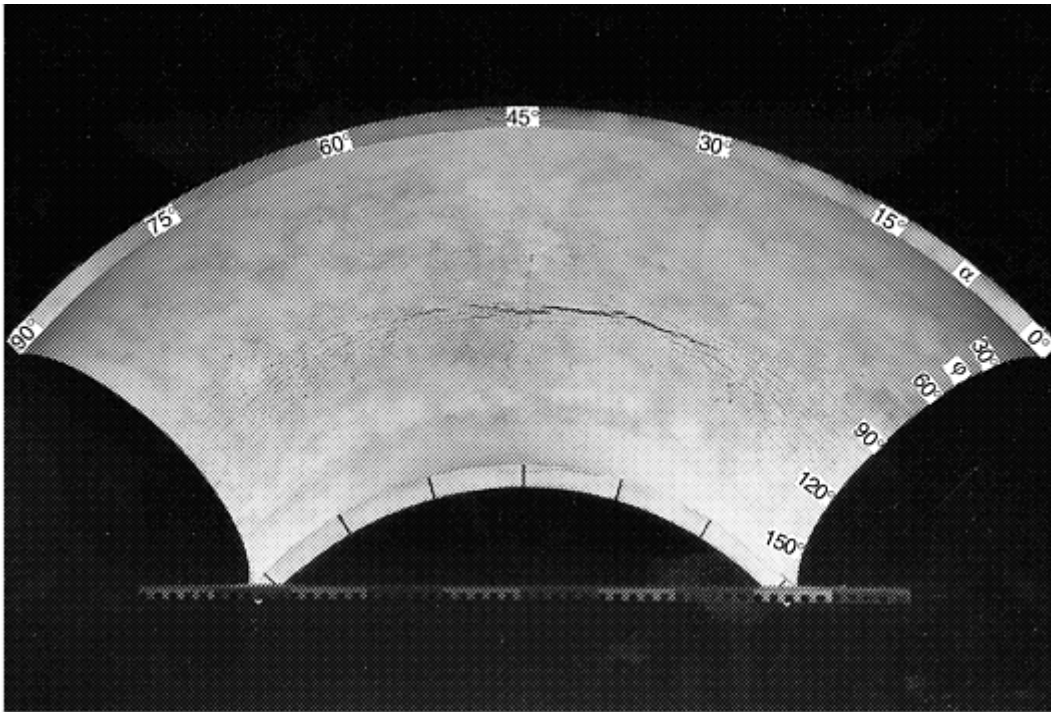


Fig. 30 Multiple crack field pipe elbow

For a piping system (see Fig. 17) under real loading conditions and for a real loading history, the calculated number of load cycles up to failure based on the crack propagation law of ASME XI (wet conditions) was compared with the experimental values (Fig. 31). The actual number of cycles up to failure of the piping system was underestimated (estimated on the safe side) by all crack propagation analyses carried out.

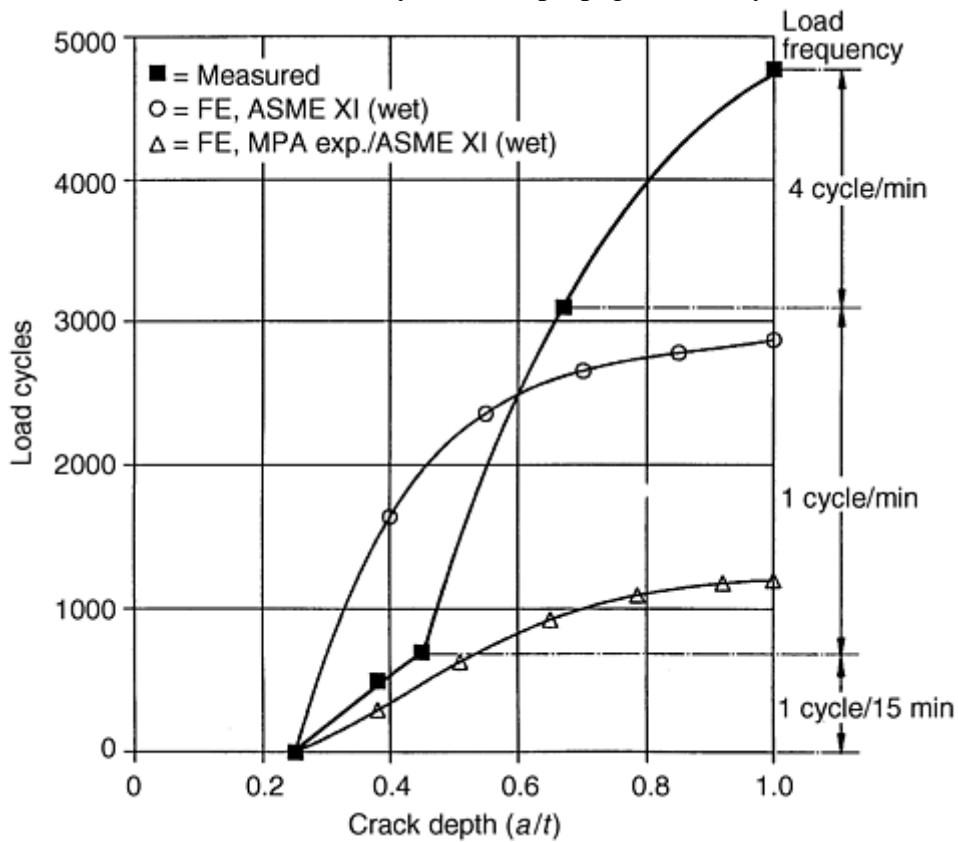


Fig. 31 Measured and calculated number of load cycles to failure for a piping system under real loading conditions. FE, finite element

Test Results of High-Temperature Tests. The material behavior of components in the primary circuit of pressurized water reactors under conditions beyond design criteria (that is, temperature increases considerably and system pressure reaches a maximum level) was examined by means of a component test and small-scale specimen tests (Ref 60). A comparison of the heating test of small-scale specimens (without hold time) with the component test is shown in Fig. 32 as well as the relationship between temperature to failure and time to rupture.

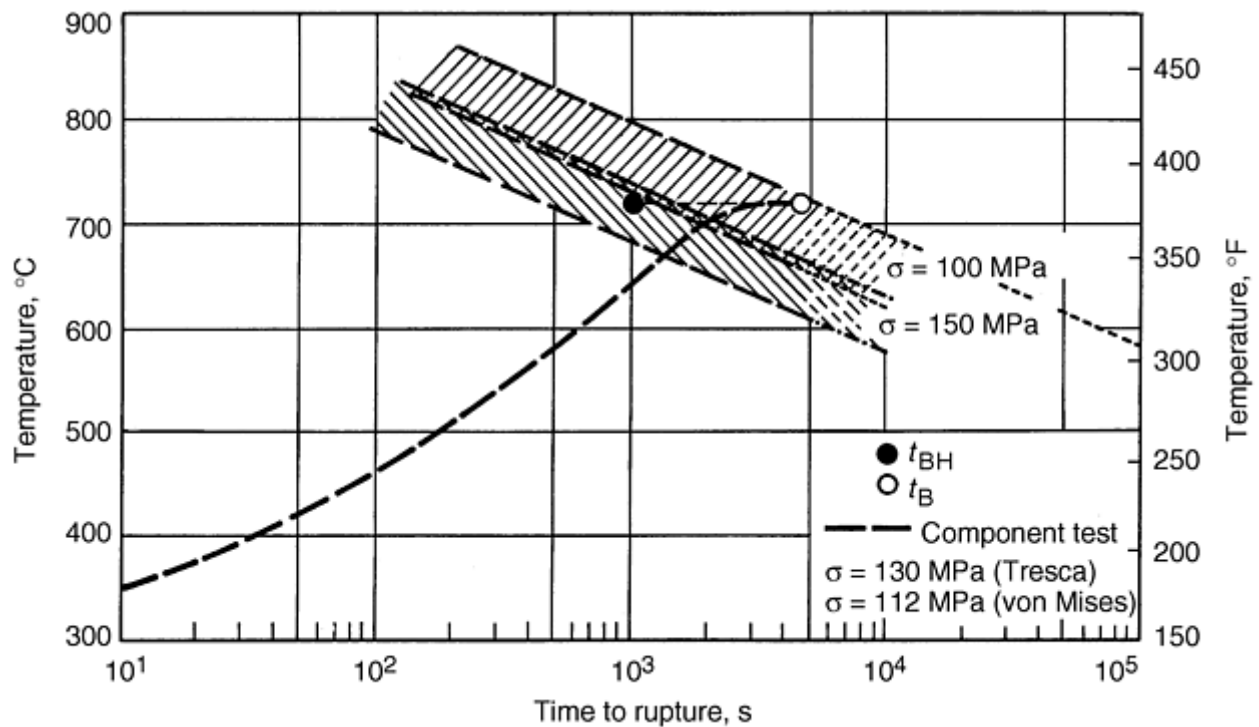


Fig. 32 Failure temperature versus time to rupture for components in a pressurized water reactor. t_{BH} , time to failure of small specimen; t_B , time to failure of small specimen without heating time

For the long-term creep tests on elbows (Ref 61), the comparison of calculated and measured local creep deformation is shown in Fig. 33. It could be demonstrated that realistic stresses and strains can be expected if the constants of the creep law within the inelastic finite element calculation had been fitted using data from uniaxial creep specimen of the same material heat as the component under consideration.

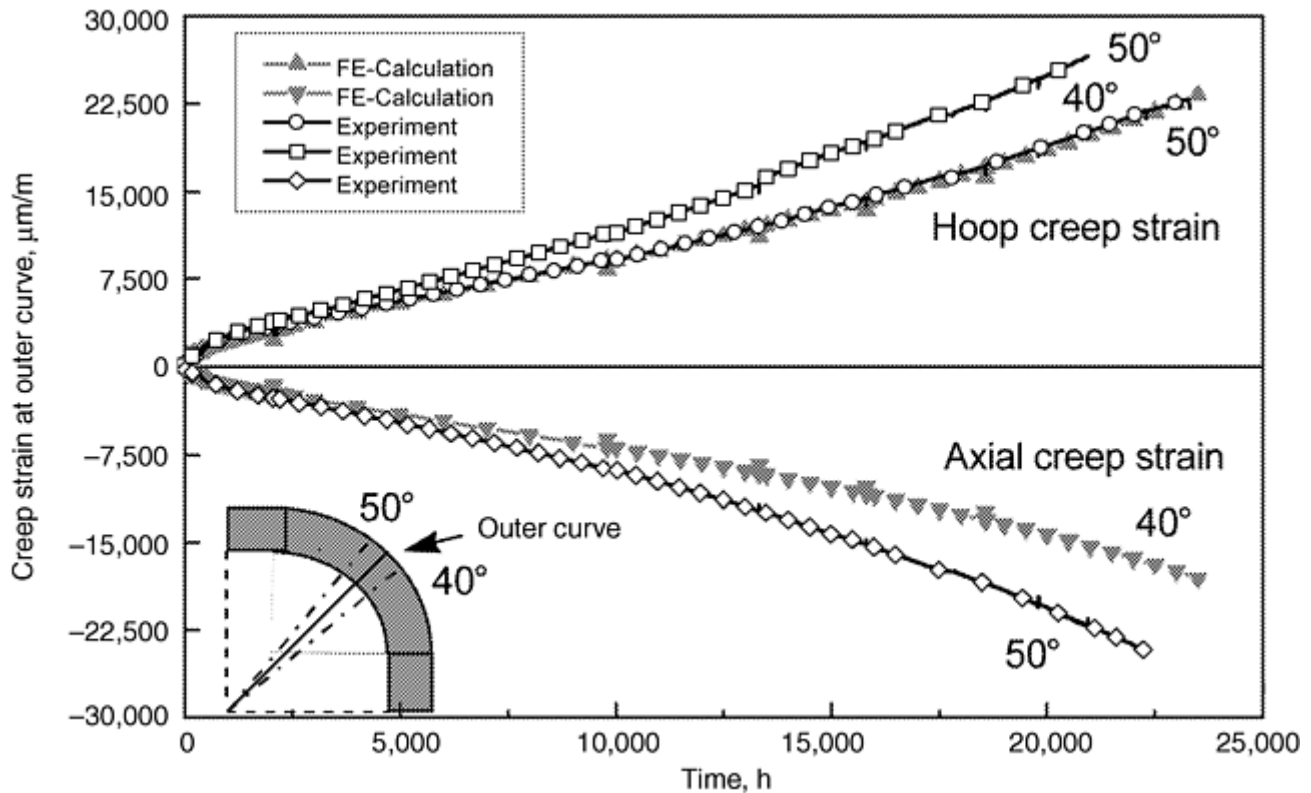


Fig. 33 Comparison of calculated and experimental local creep deformation for pipe elbows. FE, finite element

References cited in this section

14. K. Kussmaul, D. Blind, E. Roos, and D. Sturm, The Leak-Before-Break Behavior of Pipes, *VGB Kraftwerkstech.*, Vol 70 (No. 7), July 1990, p 465–477
44. K. Kussmaul, D. Sturm, W. Stoppler, and D. Müller-Ecker, “Experimental Investigation on the Crack Opening Behavior of Cylindrical Vessels under Light Water Reactor Service Conditions,” PVP-Vol 62, 1982, American Society of Mechanical Engineers, p 97–134
45. D. Sturm, W. Stoppler, P. Julisch, K. Hippelein, and J. Muz, Fracture Initiation and Fracture Opening under Light Water Reactor Conditions, *Nucl. Eng. Des.*, Vol 72, 1982, p 81–95
46. K. Kussmaul, W. Stoppler, D. Sturm, and P. Julisch, “Ruling-Out of Fractures in Pressure Boundary Piping; Part 1: Experimental Studies and Their Interpretation,” IAEA-SM-269/7, International Atomic Energy Agency (IAEA), 1983, p 211–235
47. D. Sturm, W. Stoppler, K. Hippelein, J. Schiedermaier, and H. Zhu, “Experimental Investigation on the Strength and Fracture Behavior of Circumferentially Cracked Piping under Internal Pressure and Outer Bending Loading,” PVP-Vol 120, 1987, American Society of Mechanical Engineers, p 73–81
48. P. Julisch, D. Sturm, and J. Wiedemann, Exclusion of Rupture for Welded Piping Systems of Power Stations by Component Tests and Failure Approaches, *Nucl. Eng. Des.*, Vol 158, 1995, p 191–201
49. K. Kussmaul, H. Diem, D. Uhlmann, and E. Kobes, Pipe Bend Behavior at Load Levels Beyond Design, *Trans. SMiRT-13*, Vol II, 1995, p 187–198
50. Th. Schwarz, K.-H. Herter, P. Julisch, and W. Stoppler, Experimental Investigation on the Strength and Fracture Behavior of Degraded Piping Components, *Trans. SMiRT-12*, Vol F, 1993, p 87–92

51. X. Schuler, D. Blind, U. Eisele, K.-H. Herter, and W. Stoppler, Fracture Mechanics Evaluation of Cracked Components with Consideration of Multiaxiality of Stress State, *Nucl. Eng. Des.*, Vol 151, 1994, p 291–305
52. X. Schuler, D. Blind, U. Eisele, and K.-H. Herter, Extension of Fracture Mechanics Evaluation Methods by Consideration of Multiaxiality of Stress State for Piping Components, *Nucl. Eng. Des.*, Vol 158, 1995, p 227–240
53. P. Julisch, H.-J. Hädrich, W. Stadtmüller, and D. Sturm, “High Speed Tensile Tests with Large Pipes to Cover Dynamic Loading Transients,” PVP-Vol 187, American Society of Mechanical Engineers, 1990, p 87–93
54. P. Julisch, H.-J. Hädrich, W. Stadtmüller, and D. Sturm, Load Bearing and Deformation Behavior of Dynamically Loaded Wide Plate Specimens, *Nucl. Eng. Des.*, Vol 112, 1993, p 93–103
55. W. Stoppler, D. Sturm, K. Hippelein, and A. de Boer, Crack Initiation, Crack Growth and Fracture Behavior of Large Diameter Pipes with Circumferential Defects under Internal Pressure and Superimposed Alternating Bending Load, *Nucl. Eng. Des.*, Vol 160, 1996, p 137–152
56. H. Diem, D. Blind, E. Roos, O. Wachter, and E. Tolksdorf, Failure Behavior of Thick-Walled Austenitic Pipe Bends under Bending Loading at Constant Internal Pressure, *Nucl. Eng. Des.*, Vol 151, 1994, p 269–289
57. G. Katzenmeier, K. Kussmaul, H. Diem, and E. Roos, “The HDR Project—Validation Tests for Structural Integrity Assessment of LWR Components,” SMiRT Post Conference Seminar No. 2, Taiwan, Aug 1991
58. H. Diem, L. Malcher, D. Schrammel, and H. Steinhilber, Load Bearing Capacity of an Intact and a Degraded Pipe System under Repeated Simulated Earthquake Loading, *Nucl. Eng. Des.*, Vol 130, 1991, p 435–450
59. K. Kussmaul, H. Diem, D. Uhlmann, and H. Hunger, Fatigue and Failure Behavior of a Mechanically Loaded Ferritic Pipe Bend in High Temperature Water with Elevated Oxygen Content, *Trans. SMiRT-11*, Vol F, 1991, p 213–217
60. K. Maile, A. Klenk, V. Obst, and D. Sturm, Load Carrying Behavior of the Primary System of PWR's for Loads beyond the Design Limits, *Nucl. Eng. Des.*, Vol 119, 1990, p 131–137
61. K. Kussmaul, and K. Maile, “Large Scale High Temperature Testing of Specimens and Components—An Essential Tool for Structural Integrity Engineering,” International HIDA Conf., Paris, Commissariat à l’Energie Atomique (CEA)/INSTN, Saclay/Paris, 15–17 April 1998, p 119–124

Testing of Pressure Vessels, Piping, and Tubing

E. Roos, K.-H. Herter, and F. Otremba, Staatliche Materialprüfungsanstalt (MPA), University of Stuttgart

Summary

The safe and reliable operation of systems including pressure vessels, piping, and tubing with high stored energies has to be guaranteed under all loading conditions. The basis for this are design rules and material

requirements, given in applicable standards. However, the failure behavior of these components cannot be assessed on this basis; such assessment is only possible using fracture mechanics concepts. These concepts can be verified using numerous tests on straight pressurized pipes, elbows, T-branches, and nozzles with different dimensions and made of different materials. The tests have to be conducted with regard to the loading and environmental conditions and the measuring devices have to be adjusted to the expected damage mechanism. It can be demonstrated that the assessment of the failure behavior is in good agreement with the experimental results if the fracture mechanics procedures on the basis of the fracture toughness K_{Ic} in the linear-elastic regime and of the initiation value J_i in the elastic-plastic regime are used. The calculational procedures based on strength values of the material lead also to results to the safe side, if the procedure is fitted to the experiments that have to cover the boundary conditions under consideration.

Testing of Pressure Vessels, Piping, and Tubing

E. Roos, K.-H. Herter, and F. Otremba, Staatliche Materialprüfungsanstalt (MPA), University of Stuttgart

References

1. "Rules for Construction of Nuclear Power Plant Components," ASME Boiler and Pressure Vessel Code, Section III, American Society of Mechanical Engineers, 1998
2. "Rules for Construction of Pressure Vessels," ASME Boiler and Pressure Vessel Code, Section VIII, Divisions 1 and 2, American Society of Mechanical Engineers, 1998
3. ASME Code for Pressure Piping, B31, An American National Standard, The American Society of Mechanical Engineers, 1989
4. German Technical Rules for Steam Boilers (Technische Regeln für Dampf-kessel, TRD), Carl Heymanns Verlag KG, Cologne, 1998
5. German Technical Rules for Pressure Vessels (Arbeitsgemeinschaft Druckbehälter, AD-Merkblätter), Carl Heymanns Verlag KG, Cologne, 1998
6. German Safety Standards of the Nuclear Safety Standards Commission (Sicherheitstechnische Regeln des Kerntechnischen Ausschusses, KTA), KTA Rule 3201 and KTA Rule 3211, Carl Heymanns Verlag KG, Cologne, latest edition
7. French Code for the Construction of Pressure Vessels (CODAP), Association Francaise des Ingénieurs en Appareils à Pression (AFIAP), Paris
8. French Code for the Construction of Industrial Piping Components (CODETI)
9. French Design and Construction Rules for Mechanical Components of PWR Nuclear Islands (RCC-M), Association Francaise pour la Construction des Ensembles Nucleaires (AFCEN)
10. French Design and Construction Rules for Mechanical Components of Fast Breeder Reactors (RCC-M), Association Francaise pour la Construction des Ensembles Nucleaires (AFCEN)
11. "Unfired Fusion Weld Pressure Vessels," BS 5500, British Standard Institution
12. K. Kussmaul, German Basis Safety Concept Rules Out Possibility of Catastrophic Failure, *Nucl. Eng. Int.*, Vol 12, 1984, p 41–46

13. R. Wellein and G. Preußer, "State of Engineering of the Leak-Before-Break Procedure in Germany," Seventh German-Japanese Joint Seminar, 29–30 Sept 1997, MPA Stuttgart
14. K. Kussmaul, D. Blind, E. Roos, and D. Sturm, The Leak-Before-Break Behavior of Pipes, *VGB Kraftwerkstech.*, Vol 70 (No. 7), July 1990, p 465–477
15. G.M. Wilkowski, R.J. Olson, and P.M. Scott, "State -of-the-Art Report on Piping Fracture Mechanics," Report NUREG/CR-6540, BMI-2196, Jan 1998
16. Y. Asada, K. Takumi, H. Hata, and Y. Yamamoto, Development of Criteria for Protection against Pipe Breaks in LWR Plants, *Int. J. Pressure Vessels Piping.*, Vol 43, 1990, p 95–111
17. C. Faidy, P. Jamet, and S. Bhandari, "Developments in Leak-Before-Break Approaches in France," NUREG/CP-0092, March 1988, p 69–82 (available from U.S. NRC)
18. D. Sturm, W. Stoppler, and J. Schiedermaier, The Behavior of Dynamically Loaded Pipes with Circumferential Flaws under Internal Pressure and External Bending Loads, *Nucl. Eng. Des.*, Vol 96, 1986, p 99–113
19. E. Roos, K.-H. Herter, P. Julisch, G. Bartholome, and G. Senski, Assessment of Large Scale Pipe Tests by Fracture Mechanics Approximation Procedures with Regard to Leak-Before-Break, *Nucl. Eng. Des.*, Vol 112, 1989, p 183–195
20. Y. Asada, K. Takumi, N. Gotoh, T. Umamoto, and K. Kashima, Leak-Before-Break Verification Test and Evaluations of Crack Growth and Fracture Criterion for Carbon Steel Piping, *Int. J. Pressure Vessels Piping*, Vol 43, 1990, p 379–397
21. K. Kashima, N. Miura, S. Kanno, K. Miyazaki, M. Ishiwata, and N. Gotoh: A Research Program for Dynamic Fracture Evaluation of Japanese Carbon Steel Pipes, *Nucl. Eng. Des.*, Vol 174, 1997, p 33–39
22. D. Moulin and P. Le Delliou, French Experimental Studies of Circumferential Through Wall Cracked Austenitic Pipes under Static Loading, *Int. J. Pressure Vessels Piping*, Vol 65, 1996, p 343–352
23. P. Scott et al., "IPIRG-2 Task 1—Pipe System Experiments with Circumferential Cracks in Straight Pipe Location," NUREG/CR-6389, Feb 1997 (available from U.S. NRC)
24. K. Shibata, T. Isozaki, S. Ueda, R. Kurihara, K. Onziawa, and A. Kohsaka, "Results of Reliability Test Program on Light Water Reactor Piping," *Nucl. Eng. Des.*, Vol 153, 1994, p 71–86
25. G.M. Wilkowski et al., "Degraded Piping Program—Phase II, Summary of Technical Results and Their Significance to Leak-Before-Break and In-Service Flaw Acceptance Criteria," March 1984-Jan 1989, NUREG/CR-4082, Vol 8, March 1989 (available from U.S. NRC)
26. G. Yagawa, Y. Takahashi, N. Kato, M. Saito, K. Hasegawa, and T. Umamoto, Fracture Behavior of Cracked Type 304 Stainless Steel Pipes under Tensile and Thermal Loadings, *Int. J. Pressure Vessels Piping*, Vol 19, 1985, p 247–281
27. G.T. Hahn, M. Sarrate, and A.R. Rosenfield, Criteria for Crack Extension in Cylindrical Pressure Vessels, *Int. J. Fract. Mech.*, Vol 8, 1969, p 187–210
28. R.J. Eiber et al., "Investigations of the Initiation and Extent of Ductile Pipe Rupture," Final report, Task 17, BMI-1866, 1966, and BMI-1908, 1971, Battelle Memorial Institute, Columbus

29. W.A. Maxey, "Fracture Initiation, Propagation and Arrest," Fifth Symposium on Line Pipe Research, 1974
30. M.F. Kanninen et al., "Instability Predictions for Circumferentially Cracked Type 304 Stainless Steel Pipes under Dynamic Loading," EPRI report NP-2347, Vol 1, 2, Electric Power Research Institute, April 1982
31. I. Milne, R.A. Ainsworth, A.R. Dowling, and A.T. Stuart, "Background to and Validation of CEGB Report R/H/R6," CEGB R/HR6-Rev. 3, Validation, Central Electricity Generating Board (CEGB), Jan 1987
32. V. Kumar, M.D. German, and C.F. Shih, "An Engineering Approach for Elastic-Plastic Fracture Analysis," EPRI NP-1931, topical report, Electric Power Research Institute, July 1981
33. V. Kumar, M.D. German, W.W. Wilkening, A.R. Andrews, H.G. deLorenzi, and D.F. Mowbray, "Advances in Elastic-Plastic Fracture Analysis," EPRI NP-3607, Project 1237-1, final report, Electric Power Research Institute, Aug 1984
34. A. Zahoor, Circumferential Through Wall Cracks, *Ductile Fracture Handbook*, Vol 1, EPRI NP-6301-D, research project 1757-69, Electric Power Research Institute, June 1989
35. P.C. Paris and F. Erdogan, A Critical Analysis of Crack Propagation Laws, *J. Basic Eng. (Trans. ASME D)*, Vol 85, 1963, p 528-534
36. R.G. Forman, V.E. Kearney, and R.M. Engle, Numerical Analysis of Crack Propagation in Cyclic Loaded Structures, *J. Basic Eng. (Trans. ASME)*, Vol 89, 1967, p 459
37. "Standard Test Method for Measurement of Fatigue Crack Growth Rates," E 647-95a, ASTM
38. Research Project 150 0270, "Phenomenological Pipe and Vessel Burst Tests, Phase I und II," Final Report 150 0279, MPA Stuttgart, Abschlußberichte 1985 und 1987 (final reports in German)
39. Research Project 150 0304, "Integrity of Components, Phase I und II," Final Report 150 0304, MPA Stuttgart, Abschlußberichte 1983 and 1989 (final reports in German)
40. Research Project 150 0618, "Pressure Vessels Subjected to Pressurized Thermal Shock Loading," Final Report 150 0618, MPA Stuttgart, Abschlußbericht 1990 (final report in German)
41. "Recommendations for Determining the Fracture Resistance of Ductile Materials," ESIS P1-92, European Structural Integrity Society (ESIS), Jan 1992
42. "Procedure for Determining the Fracture Behavior of Materials," ESIS P2-92, European Structural Integrity Society (ESIS), Jan 1992
43. H. Clausmeyer, K. Kussmaul, and E. Roos, Influence of Stress State on the Failure Behavior of Cracked Components Made of Steel, *Appl. Mech. Rev.*, Vol 44 (No. 2), Feb 1991, p 77-92
44. K. Kussmaul, D. Sturm, W. Stoppler, and D. Müller-Ecker, "Experimental Investigation on the Crack Opening Behavior of Cylindrical Vessels under Light Water Reactor Service Conditions," PVP-Vol 62, 1982, American Society of Mechanical Engineers, p 97-134
45. D. Sturm, W. Stoppler, P. Julisch, K. Hippelein, and J. Muz, Fracture Initiation and Fracture Opening under Light Water Reactor Conditions, *Nucl. Eng. Des.*, Vol 72, 1982, p 81-95

46. K. Kussmaul, W. Stoppler, D. Sturm, and P. Julisch, "Ruling-Out of Fractures in Pressure Boundary Pippings; Part 1: Experimental Studies and Their Interpretation," IAEA-SM-269/7, International Atomic Energy Agency (IAEA), 1983, p 211–235
47. D. Sturm, W. Stoppler, K. Hippelein, J. Schiedermaier, and H. Zhu, "Experimental Investigation on the Strength and Fracture Behavior of Circumferentially Cracked Piping under Internal Pressure and Outer Bending Loading," PVP-Vol 120, 1987, American Society of Mechanical Engineers, p 73–81
48. P. Julisch, D. Sturm, and J. Wiedemann, Exclusion of Rupture for Welded Piping Systems of Power Stations by Component Tests and Failure Approaches, *Nucl. Eng. Des.*, Vol 158, 1995, p 191–201
49. K. Kussmaul, H. Diem, D. Uhlmann, and E. Kobes, Pipe Bend Behavior at Load Levels Beyond Design, *Trans. SMiRT-13*, Vol II, 1995, p 187–198
50. Th. Schwarz, K.-H. Herter, P. Julisch, and W. Stoppler, Experimental Investigation on the Strength and Fracture Behavior of Degraded Piping Components, *Trans. SMiRT-12*, Vol F, 1993, p 87–92
51. X. Schuler, D. Blind, U. Eisele, K.-H. Herter, and W. Stoppler, Fracture Mechanics Evaluation of Cracked Components with Consideration of Multiaxiality of Stress State, *Nucl. Eng. Des.*, Vol 151, 1994, p 291–305
52. X. Schuler, D. Blind, U. Eisele, and K.-H. Herter, Extension of Fracture Mechanics Evaluation Methods by Consideration of Multiaxiality of Stress State for Piping Components, *Nucl. Eng. Des.*, Vol 158, 1995, p 227–240
53. P. Julisch, H.-J. Hädrich, W. Stadtmüller, and D. Sturm, "High Speed Tensile Tests with Large Pipes to Cover Dynamic Loading Transients," PVP-Vol 187, American Society of Mechanical Engineers, 1990, p 87–93
54. P. Julisch, H.-J. Hädrich, W. Stadtmüller, and D. Sturm, Load Bearing and Deformation Behavior of Dynamically Loaded Wide Plate Specimens, *Nucl. Eng. Des.*, Vol 112, 1993, p 93–103
55. W. Stoppler, D. Sturm, K. Hippelein, and A. de Boer, Crack Initiation, Crack Growth and Fracture Behavior of Large Diameter Pipes with Circumferential Defects under Internal Pressure and Superimposed Alternating Bending Load, *Nucl. Eng. Des.*, Vol 160, 1996, p 137–152
56. H. Diem, D. Blind, E. Roos, O. Wachter, and E. Tolksdorf, Failure Behavior of Thick-Walled Austenitic Pipe Bends under Bending Loading at Constant Internal Pressure, *Nucl. Eng. Des.*, Vol 151, 1994, p 269–289
57. G. Katzenmeier, K. Kussmaul, H. Diem, and E. Roos, "The HDR Project—Validation Tests for Structural Integrity Assessment of LWR Components," SMiRT Post Conference Seminar No. 2, Taiwan, Aug 1991
58. H. Diem, L. Malcher, D. Schrammel, and H. Steinhilber, Load Bearing Capacity of an Intact and a Degraded Pipe System under Repeated Simulated Earthquake Loading, *Nucl. Eng. Des.*, Vol 130, 1991, p 435–450
59. K. Kussmaul, H. Diem, D. Uhlmann, and H. Hunger, Fatigue and Failure Behavior of a Mechanically Loaded Ferritic Pipe Bend in High Temperature Water with Elevated Oxygen Content, *Trans. SMiRT-11*, Vol F, 1991, p 213–217
60. K. Maile, A. Klenk, V. Obst, and D. Sturm, Load Carrying Behavior of the Primary System of PWR's for Loads beyond the Design Limits, *Nucl. Eng. Des.*, Vol 119, 1990, p 131–137

Residual Stress Measurements

Clayton O. Ruud, The Pennsylvania State University

Introduction

MANY METHODS and techniques have been proposed for the measurement of residual stresses. A classification of techniques is provided in *Welding, Brazing, and Soldering*, Volume 6 of the *ASM Handbook* (Ref 1), and this list is shown in Table 1. However, only a few of these techniques may be applied generally in practice on items ranging from small components, such as bearing balls and rods, to very large structures, such as bridges and aircraft. For some of the methods described herein, the component in which residual stresses are to be measured must be brought to the measuring instrument. For others, the measurement devices are portable and may be brought to the component (Fig. 1). In some cases it may be feasible to remove a section from the component and bring that section to the residual stress measuring device. However, great caution must be observed in sectioning a component, because it will change the stress field by relieving and/or inducing stresses. The relieved stresses must be accounted for by the assumptions and reconstruction methods described in the section "Stress Field Condition Assumptions and Reconstruction" in this article.

Table 1 Classification of techniques for measuring residual stress

A-1 Stress relaxation techniques using electric and mechanical strain gages

- **Plate**
 - **Section technique using electric resistance strain gages**
 - **Gunnert technique**
 - **Mathar-Soete drilling technique**
 - **Stablein successive milling technique**
- **Solid cylinders and tubes**
 - **Heyn-Bauer successive machining technique**
 - **Mesnager-Sachs boring-out technique**
- **Three-dimensional solids**
 - **Gunnert drilling technique**
 - **Rosenthal-Norton sectioning technique**

A-2 Stress relaxation techniques using apparatus other than electric and mechanical strain gages

- **Grid system-dividing technique**
- **Brittle coating-drilling technique**
- **Photoelastic coating-drilling technique**

B X-ray diffraction technique

- **X-ray film technique**
- **X-ray diffractometer technique**

C Techniques using stress-sensitive properties

- **Ultrasonic techniques**
 - **Polarized ultrasonic wave technique**
 - **Ultrasonic attenuation technique**
 - **Hardness techniques**

D Cracking techniques

- **Hydrogen-induced cracking technique**
- **Stress-corrosion cracking technique**



Fig. 1 Measurement of residual stresses on a gas pipeline in the field using a portable x-ray diffraction instrument. (Courtesy of Proto Manufacturing)

Any manufacturing process that changes the shape of a solid, or where severe temperature gradients exist during the process, causes residual stresses. These processes include the preparation of a specimen for testing as might be performed for other tests described in this Volume. Fatigue testing is especially sensitive to surface residual stresses, and specimens must be prepared with known, consistent residual stress conditions.

By their very nature, processes that change the shape of a solid cause nonuniform plastic deformation in the solid, which leads to residual stresses. These processes include forging, rolling, drawing, machining, and so on. Also, processes that produce high thermal gradients in a solid often lead to residual stresses. These processes include quenching, casting, welding, and so forth. Further, processes that induce localized phase changes produce residual stresses. These processes include martensitic hardening.

The residual stresses caused by manufacturing processes usually show very steep residual stress to distance gradients as illustrated in Fig. 2. The steep gradients typical of residual stresses induced by manufacturing processes may be cited as the cause of disagreement between residual stress measurements made by stress relaxation techniques and those made by x-ray diffraction (XRD) techniques. The disagreement is nearly always because the volume of the component in which the stress is measured is not the same in the two

methods, and, thus, a different portion of the stress gradient is measured by each. Ruud et al. (Ref 2) showed that the hole drilling method resulted in measured stresses approaching those measured at the surface by XRD when the hole drilling results were extrapolated to the surface. Further, because of the steep gradients, stress measurements must be performed at many locations in the manufactured solid in order to establish the magnitude and distribution of the stress field of interest. Many researchers in XRD residual stress techniques have focused on enhancing the accuracy of residual stress measurement and have ignored the fact that from a practical standpoint, tens to hundreds of stress measurements are needed to define the stress field of interest. Thus, many of the residual stress measurement techniques require too much time to perform and, thus, are impractical. These include some of the techniques developed for XRD, strain gaging, and other methods. Measurement times on the order of a second are available with XRD and some other methods, and automated stress mapping has been performed with such techniques (Ref 3). Another concern in the measurement of residual stresses in manufactured components is that the area or volume over which the stresses are resolved must often be on the order of 1 mm (0.04 in.) or less. This is because the residual stress gradients are usually quite steep, and measurement resolution larger than this tends to average the stresses to such an extent that the high stresses are not detected.

$$\left(\frac{d\sigma}{dx} > \frac{200 \text{ MPa}}{\text{mm}} \right)$$

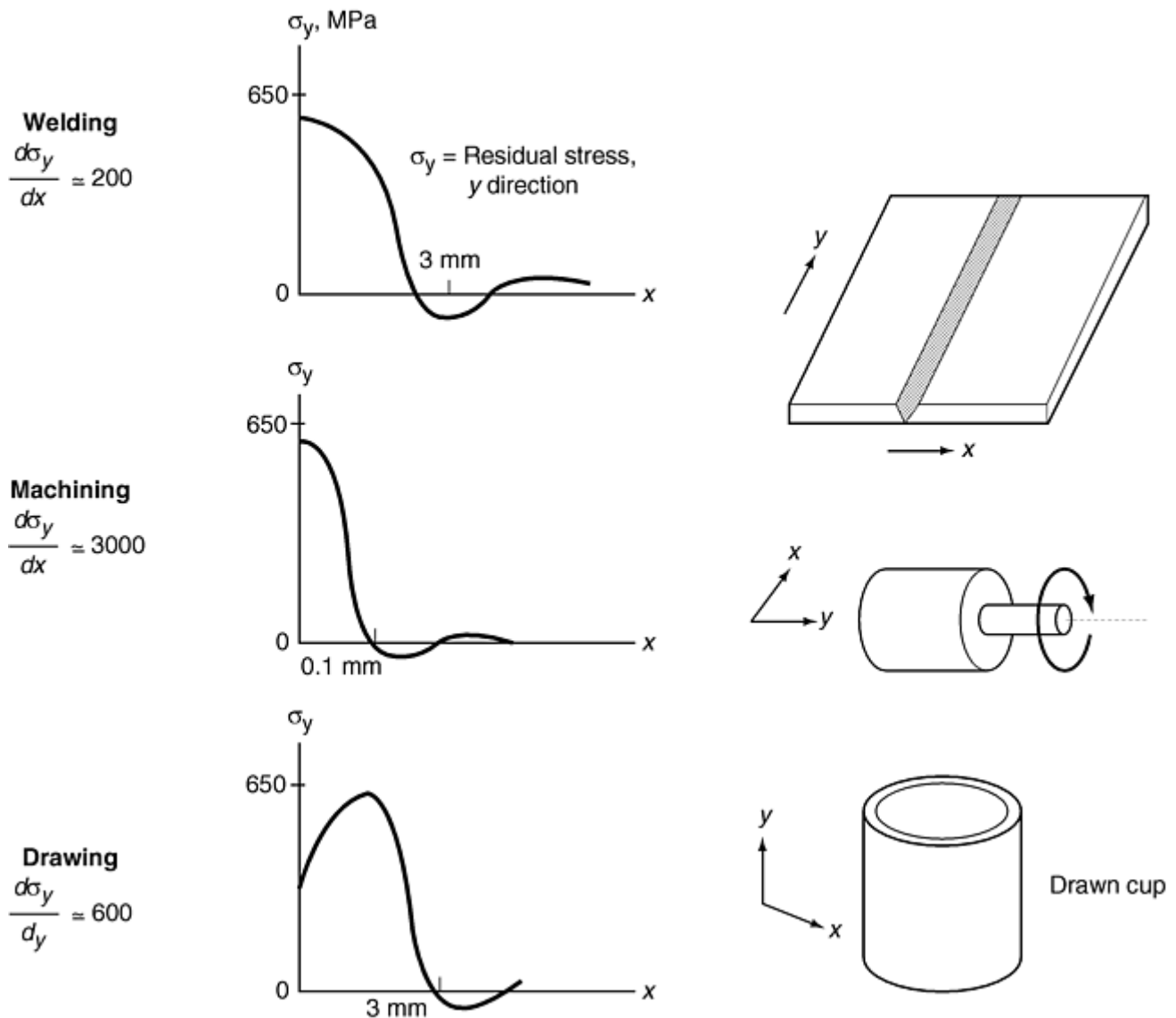


Fig. 2 The residual stress magnitudes and distributions typical of a 650 MPa yield strength metal. For example, in machining it is not unusual for the residual stress at the surface of the machined part to be near the yield strength of the cold worked material.

Some characteristics of metals that can cause error in residual stress measurement by the methods described herein include phase composition, plastic strain, grain size, crystallographic texture, and others. For example, in a mixed ferrite/austenitic structure, the residual stresses in the ferrite are invariably different than those in the austenite (Table 2). Also, Wimpory et al. (Ref 4) described the influence of varying amounts of cementite in a ferrite matrix. The possibility of one or more of these microstructural characteristics causing error in residual stress measurements performed by the methods described herein should be assessed by an expert in the method selected. Details of the errors and their causes are not discussed in this article.

Table 2 Sample of residual stress readings from a 316 stainless steel pipe weldment

Distance from the weld fusion line		Stress ^(a)			
		In austenite		In ferrite	
mm	in.	MPa	ksi	MPa	ksi
1.02	0.04	-145	-21	-315	-46
1.80	0.07	-130	-19	-460	-67
2.80	0.11	-110	-16	-425	-62
3.80	0.15	-115	-17	-450	-65

(a) The precision of these measurement was ± 3.0 ksi. Note that the ferrite places tensile stresses on the lattice of the austenite while the austenite tends to compress the ferrite. Therefore, the more compressive the stress in the ferrite, the less compressive the stress in the austenite.

The subsequent sections of this article discuss and describe the following:

- The need for measurement—the problem the engineer or metallurgist is trying to solve by obtaining information about the residual stress field
- The nature of the residual stress fields in metals—examples of the magnitudes and distributions
- The strain basis for residual stress measurements—elastic strain measured, not stresses
- The destructive methods of residual stress measurement. These procedures are all based on sectioning or removal of material to cause a redistribution of the residual stress, which is measured as a strain change. These include most of the techniques listed under A-1, A-2, and D in Table 1.
- The semidestructive methods of residual stress measurement. These procedures are based on the same principle as the destructive methods or on the perturbation of the residual stress field by other means, but the extent of deformation is very small and usually repairable with little or no degradation in the usefulness of the component. Semidestructive methods include some of the drilling and trepanning techniques under A-1 and A-2, as well as the hardness techniques under C in Table 1.
- The nondestructive methods of residual stress measurement. These procedures do not permanently disturb the residual stress field but directly measure the atomic lattice strain caused by the stress or measure some physical property perturbed by the lattice strain. The nondestructive methods include the techniques listed under B as well as ultrasonic methods, under C, and others to be described.

The purpose of this article is to provide an insight into the principles, practice, and limitations of residual stress measurement procedures for metals. The article is not meant to provide sufficient detail for the performance of the various methods described, but references are cited where such procedural details may be found, for example, Gunnert (Ref 5), Moore and Evans (Ref 6), Constantinescu and Ballard (Ref 7), the SAE Handbook Supplement (Ref 8), and Ref 9.

References cited in this section

1. K. Masubuchi, Residual Stresses and Distortion, *Welding, Brazing, and Soldering*, Vol 6, *ASM Handbook*, 10th ed., 1993, p 1094–1102
2. C.O. Ruud, P.S. DiMascio, and J.J. Yavelak, Comparison of Three Residual Stress Measurement Methods on a Mild Steel Bar, *Exp. Mech.*, Vol 25 (No. 4), Sept 1985, p 338–343

3. J. Pineault and M. Brauss, Automated Stress Mapping—A New Tool for the Characterization of Residual Stress and Stress Gradients, *Proc. 4th International Conf. on Residual Stresses*, Society for Experimental Mechanics, Bethel, CT, 1994, p 40–44
4. R. Wimpory, G.M. Swallow, and P. Lukas, Neutron Diffraction Residual Stress Measurements in Carbon Steels, *The Fifth International Conference on Residual Stresses*, Vol 2, Institute of Technology, Linkopings University, Sweden, 1997, p 676–681
5. R. Gunnert, “Method for Measuring Triaxial Residual Stresses,” Document No. X-184057-OE, *Commission X of the International Institute of Welding*, 1957, and *Weld. Res. Abroad*, Vol 4 (No. 10), 1958, p 1725
6. M.G. Moore and W.P. Evans, Mathematical Corrections in Removal Layers in X-Ray Diffraction Residual Stress Analysis, *SAE Trans.*, Vol 66, 1958, p 340–345
7. A. Constantinescu and P. Ballard, On the Reconstruction Formulae of Subsurface Residual Stresses after Matter Removal, *The Fifth International Conf. on Residual Stresses*, Vol 2, Institute of Technology, Linkopings University, Sweden, 1997, p 703–708
8. Residual Stress Measurement by X-Ray Diffraction-SAE J784a, *Society of Automotive Engineers Handbook Supplement*, Warrendale, PA, 1971
9. A.J. Bush and F.J. Kromer, “Residual Stresses in a Shaft after Weld Repair and Subsequent Stress Relief,” Paper No. A-16 presented at Society for Experimental Stress Analysis (SESA) Spring Meeting, 1979 (Westport, CT), 1979

Residual Stress Measurements

Clayton O. Ruud, The Pennsylvania State University

Need for Residual Stress Measurements

Before committing to measuring residual stresses in some component or workpiece, the engineer or metallurgist must be sure that the reason for the need for measurement is clearly understood. The major reasons that residual stresses are of concern are these:

- Failures that are suspected to be due to fatigue, stress corrosion, corrosion fatigue, or hydrogen embrittlement
- Assessment for the continued serviceability of a component, for example, life assessment. This is usually focused on a concern for in-service failure.
- Inconsistent test results on a machined or otherwise manufactured test specimen, especially in fatigue testing
- Distortion occurring during processing of a component
- Distortion of components during storage or in-service

In the first three situations (where failure is of concern), surface stresses are usually of greatest interest, and surface measuring procedures and techniques that provide optimum spatial resolution are needed. These are required in order to identify the location and magnitude of the highest tensile residual stress, because those stresses and locations are likely to dominate the failure conditions. In the last two situations, where distortion is of concern, the stress field contour through the cross section of the component is usually most relevant and not

the location or magnitude of the maximum tensile residual stress. In these cases, procedures or methods that provide measurement of stresses through the cross section are more relevant than spatial resolution.

It is extremely important that the investigator understand the mechanism for the inducement of the residual stress field of concern. Most cases of suspected harmful residual stress fields are induced by manufacturing processing or repair procedures, although sometimes abusive service conditions or an accident may have caused them (Ref 10). When manufacturing processes or sometimes repair procedures are judged the most likely sources of the residual stresses, it is often possible to predict the magnitude and distribution of the residual stresses. Such information may be obtained through consulting the literature or applying computer modeling (Ref 11, 12, 13, 14, 15, 16, 17, 18, and 19). A preconceived model of the residual-stress field will aid the investigator in determining the best method for residual stress measurement and the location and number of measurements that need to be made.

Nevertheless, sometimes the source and cause of the residual stress field is not evident, and the investigator is compelled to perform measurements as a means to determine the cause. In such cases, measurement methods and location must be selected without the aid of a priori knowledge of the stress field, and it is prudent to consult the literature and experts in the field of residual stress measurement and manufacturing processes.

References cited in this section

10. M.E. Brauss and J.A. Pineault, Residual Strain Measurement of Steel Structures, *NDE for the Energy Industry*, NDE Vol 13 (Book No. H00930-1995), D.E. Bray, Ed., American Society of Mechanical Engineers, 1995
11. C.O. Ruud and P.S. DiMascio, A Prediction of Residual Stress in Heavy Plate Butt Weldments, *J. Mater. Eng. Sys.*, Vol 31 (No. 1), Jan 1981, p 62–65
12. C.O. Ruud and M.E. Jacobs, Residual Stresses Induced by Slitting Copper Alloy Strip, *NDC of Materials VI*, Plenum Press, 1994, p 413–424
13. E.F. Rybicki and R.B. Stonesifer, Computation of Residual Stresses Due to Multipass Welds in Piping Systems, *ASME*, 78-PVP-104, 1978
14. M. Ehlers, H. Muller, and D. Loke, Simulation of Stresses and Residual Stresses Due to Immersion Cooling of Tempering Steel, *The Fifth International Conf. on Residual Stresses*, Vol 1, Institute of Technology, Linkopings University, Sweden, 1997, p 400–405
15. K. Masubuchi, *Analysis of Welded Structures: Residual Stresses, Distortion, and Their Consequences*, 1st ed., Pergamon Press, 1980
16. M. Bijak-Zochowski, P. Marek, and M. Tracz, On Subsurface Distributions of Residual Stress Created by Elasto-Plastic Rolling Contact, *The Fifth International Conf. on Residual Stresses*, Vol 1, Institute of Technology, Linkopings University, Sweden, 1997, p 430–445
17. D. Green and S. Bate, Calculation of Residual Stresses Using Simplified Weld Bead Modelling Technique, *Fifth International Conf. on Residual Stresses*, Vol 1, Institute of Technology, Linkopings University, Sweden, 1997, p 508–513
18. H. Michaud, F. Mechi, and T. Foulquies, Three Dimensional Representation of the Residual Stress Distribution in Steel Wires or Bars, *The Fifth International Conf. on Residual Stresses*, Vol 1, Institute of Technology, Linkopings University, Sweden, 1997, p 534–538
19. K.W. Mahin, W.S. Winters, T. Holden, and J. Root,, Measurement and Prediction of Residual Elastic Strain Distributions in Stationary and Traveling Gas Tungsten Arc Welds, *Practical Applications of Residual Stress Technology*, ASM, 1991, p 103–109

Residual Stress Measurements

Clayton O. Ruud, The Pennsylvania State University

Nature of Residual Stresses

Residual stresses are the inevitable consequence of thermal-mechanical processing of metals. The resulting stress fields usually are nonuniform and show high stress gradients. For example, Fig. 2 illustrates the residual stress magnitudes and distributions typical of a metal with a 650 MPa (94 ksi) yield strength. Because of the high stress gradients, tens to hundreds of residual stress measurements with resolution on the order of 1 mm (0.04 in.) may be required in order to precisely identify the maximum stress and its location.

The characteristically nonuniform, high stress gradient nature of residual stresses requires that either the induced stress field is well understood and predictable or many residual stress measurements are performed on one or more components in order to reveal the nature of the stress fields. Often scientists attempt to gain an understanding of a residual stress field by making a few measurements on one or two components, and, from this, they often derive erroneous conclusions regarding the nature of the stress field.

A few measurements may be useful if the scientist or engineer knows the distribution of the stresses a priori. However, this is seldom the case, and tens to hundreds of measurements are required on a single component or many samples to really understand the residual stresses induced by a given manufacturing process. This means that the method of measurement must be as rapid and as labor-efficient as possible. Some of the new, semidestructive hole drilling procedures, XRD, and ultrasonic instrumentation methods (for special cases) meet this criteria. Stress mapping is offered with some XRD instruments to map stresses over the surface of a component (Ref 3). Also, because the stress gradients are often very high, the method of measurement must be able to resolve the stresses in dimensions on the order of a millimeter or less. Here some of the hole drilling procedures and recently developed XRD instruments can offer the best resolution.

Finally, often the component in which residual stresses are to be determined is too large to be brought to a laboratory, and removing sections is not a rational solution. Note that sectioning often disturbs the existing stress field to the extent that it is not possible to reconstruct the original stress field from the residual stress measured in pieces removed from the original whole. Hole-drilling, XRD, and ultrasonic instrumentation are available as portable devices, which may be brought to the component in the field (Ref 10, 20, 21, 22).

References cited in this section

3. J. Pineault and M. Brauss, Automated Stress Mapping—A New Tool for the Characterization of Residual Stress and Stress Gradients, *Proc. 4th International Conf. on Residual Stresses*, Society for Experimental Mechanics, Bethel, CT, 1994, p 40–44
10. M.E. Brauss and J.A. Pineault, Residual Strain Measurement of Steel Structures, *NDE for the Energy Industry*, NDE Vol 13 (Book No. H00930-1995), D.E. Bray, Ed., American Society of Mechanical Engineers, 1995
20. M. Brauss, J. Pineault, S. Teodoropol, M. Belassel, R. Mayrbaur, and C. Sheridan, Deadload Stress Measurement on Brooklyn Bridge Wrought Iron Eye Bars and Truss Sections Using X-ray Diffraction Techniques, *Proc. of 14th Annual International Bridge Conf. and Exhibition*, Engineering Society of Western Pennsylvania, Pittsburgh, ICB-97-51, 1997, p 457–464
21. M.G. Carfagno, F.S. Noorai, M.E. Brauss, and J.A. Pineault, “X-Ray Diffraction Measurement of Stresses in Post-Tensioning Tendons,” International Association for Bridge and Structural Engineering (IABSE) Symposium, 1995 (San Francisco), “Extending the Life Span of Structures,” IABSE, ETH Honggerberg, Zurich, Switzerland, Vol. 71/1, 1995, p 201–206

22. J.A. Pineault and M.E. Brauss, In Situ Measurement of Residual and Applied Stresses in Pressure Vessels and Pipeline Using X-ray Diffraction Techniques, Determining Material Characterization: *Residual Stress and Integrity with NDE*, PUP-Vol 276, NDE-Vol 12, American Society of Mechanical Engineers, New York, 1994

Residual Stress Measurements

Clayton O. Ruud, The Pennsylvania State University

Stress Measurement

A number of procedures and methods have been applied to determining the residual stresses extant in a metallic component, usually as a result of manufacturing processing. However, stress is never the quantity measured, because stress is a quantity that is applied to a metal and can only be measured in the process of its application. What is invariably measured to determine residual stress is elastic strain—either the elastic strain resulting directly from the existing residual stress in the metal or the elastic strain change resulting from relief of some portion or all of the existing residual stress. The stress that is causing, or has caused, the strain is then calculated using the applicable elastic constants for the metal.

The methods described in the section “Nondestructive Procedures” in this article directly or indirectly measure the strain response of metals to the residual stress in situ, while the destructive and semidestructive methods described in the following sections measure the strain change caused in relieving some or all of the residual stress in the metal.

Residual Stress Measurements

Clayton O. Ruud, The Pennsylvania State University

Destructive Measurement Procedures (Stress-Relaxation Techniques)

The first concern in selecting a destructive residual stress measurement procedure is whether it is reasonable to destroy one or more components or samples in order to determine the residual stresses. Usually this implies that one or a few of the components are a small portion of the total number produced. Also coupled to this decision is whether the one or more components in which the residual stresses are to be measured are representative of all the others. In other words, how great is the expected variation of the residual stress field from part to part?

As mentioned at the beginning of this article, the need for the residual stress information on a component must be clearly understood. This includes whether the triaxial stress field must be established or if the uniaxial or biaxial condition of the stress field along specific directions is sufficient. Examples of these three situations are illustrated in this subsection. However, in any case, the fact that residual stresses are usually not uniform in any direction and show high stress gradients must be kept in mind when stress measurement criteria are selected.

Destructive methods of residual stress measurement are fundamentally stress-relaxation procedures (techniques A-1 and A-2 in Table 1). That is, the information is obtained by relaxing the residual stress in some finite volume element of the component and measuring the resulting strain change. The strain change is then used, along with applicable assumptions about the nature of the stress field, to reconstruct the original stress field. Assumptions about the nature of the stress field include the magnitudes and gradients in the stress field and whether it is sufficient to assume that the gradients are one-dimensional, two-dimensional, or three-dimensional. In particular, the gradients that exist will dictate the size of the element that is to be isolated and made stress-free, in that the higher the stress gradient, the smaller the finite element must be in the direction of

that gradient. It must be emphasized that the larger the element and the higher the stress gradient, the less quantitative and more qualitative are the measurement results. Electrical resistance strain gage technologies will be emphasized as the dominant method of strain change measurement for destructive and semidestructive stress relaxation methods due to their economic, procedural, and precision advantages over other methods. However, modern XRD stress measurement instrumentation (instruments designed specifically for stress measurement and not conventional XRD instruments modified with stress measurement accessories) has all of these advantages as well and can be used to measure the stresses existing before and after sectioning.

A generic destructive stress relief procedure will first be described along with the issues generally involved in each procedural step. A summary of destructive residual stress measurement procedures is provided in Table 3. This section on destructive methods concludes with discussion of qualitative chemical methods of residual stress measurement, which are listed in Table 1 under D.

Table 3 Summary of destructive residual stress measurement procedures

Component shape	Stress field condition assumptions	Stress direction measured	Method	Reference
Rods, cylinders, tubes	Uniaxial stresses; axial symmetry	Longitudinal	Bauer-Heyn	23
Rectangular cross section, bar	Uniaxial stresses varying through thickness	Longitudinal	Stablein	24
Rods, cylinders, tubes	Biaxial stresses; axial symmetry	Longitudinal, radial	Mesnager-Sachs	25, 26
Plate, sheet	Homogeneous planar; biaxial stresses varying through thickness	Biaxial in the plane of the component	Trenting and Read	27
Plate, sheet	Homogeneous planar; biaxial stresses uniform through thickness	Biaxial in the plane of the component	Gunnert	28
Plate, sheet	Homogeneous planar; biaxial stresses varying through thickness	Biaxial in the plane of the component	Gunnert	5, 29
Plate, sheet	Planar biaxial stresses varying through thickness	Biaxial in the plane of the component	Rosenthal and Norton	30
Plate, sheet	Planar biaxial stresses varying through thickness	Biaxial in the plane of the component	Moore and Evans	6
Plate, sheet	Triaxial	All	Chen	31
Cylinder, plate	Various	All	Moore and Evans	6
Plate, weldment	Triaxial	All	Johanssen	32

Generic Destructive Procedure

Once the decision to destructively measure the residual stresses is made, the following steps are usually applied in a typical stress-relief technique for residual stress measurement.

Stress Field Conditions. The engineering problem for which the residual stress information to be derived destructively is needed must be analyzed. This need is often generated by failures of the component in service, anticipated failures due to problems with similar components, or inconsistent mechanical test results, especially in fatigue testing. Distortion of a product in storage or during manufacturing can also be a concern. The shape of the component, that is, cylinder, disc, plate, and so on, or some irregular shape, must be considered. This consideration, along with the process or processes by which residual stresses were introduced, must be analyzed. From these considerations, the justification for assumptions regarding the condition of the residual stress field can be established. This may lead to simplifying assumptions about the stress field condition, such as axial symmetry for a cylinder in which the dominant residual stress field is due to quenching during heat treat processing or stress uniformity in the surface plane of a plate where stress gradient with depth is the major concern (see Fig. 3).

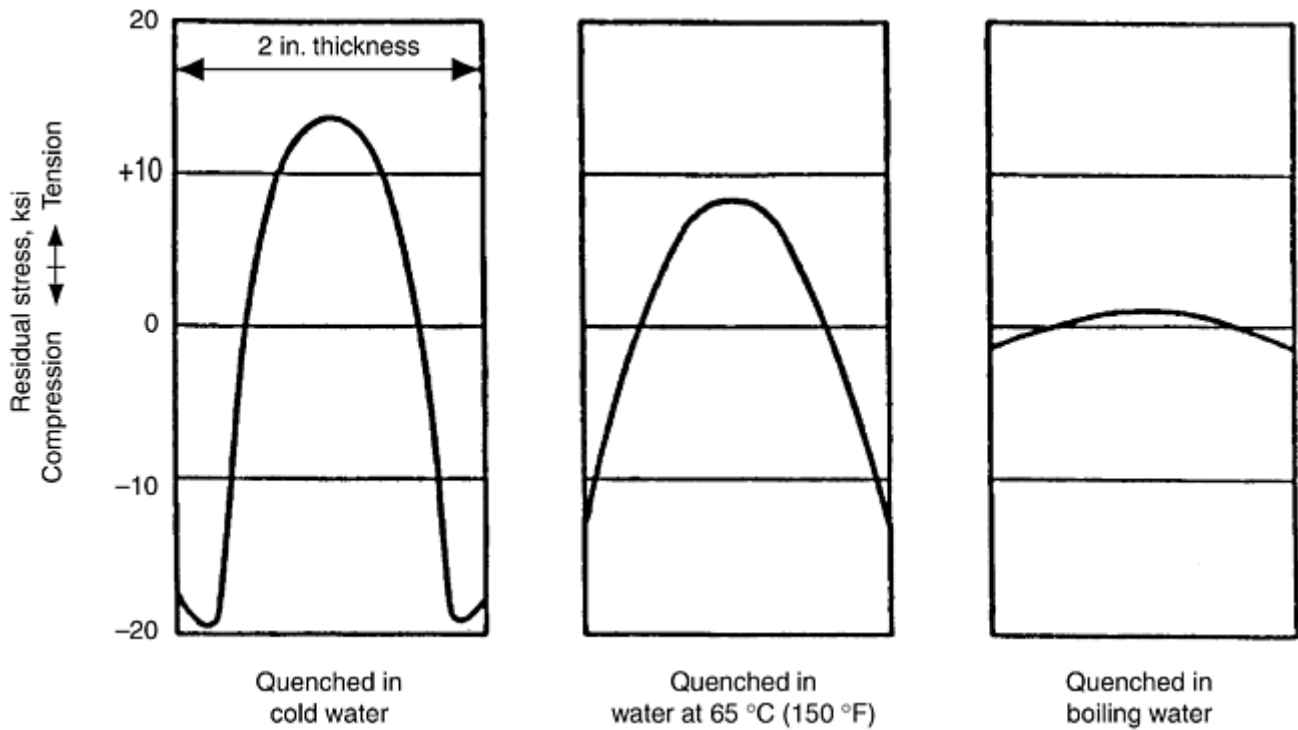


Fig. 3 Residual stresses in 7075-T6 plate specimens quenched in water at different temperatures

These assumptions and considerations lead to the methodology, that is, equations, to be used for computational reconstruction of the stress fields from the measured strains for the destructive methods.

Strain Measurement Technique. With the stress reconstruction approach established, the method of strain measurement and, consequently, the number and/or spatial frequency of measurements can be determined. The strain measurement technique selected will greatly affect the resolution of the stress measurement because of the spatial precision inherent in the technique.

There are a number of techniques that have been used to measure the strain induced by the relief of stresses due to sectioning or material removal in destructive residual stress measurement. These include mechanical gages, often dial gages, employed with specially made jigs and fixtures, reflected light schemes, photoelastic coatings, and electrical resistance strain gages. However, over the last few decades, the use of the latter has become dominant due to the variety, availability, and precision of these gages. They are available as uniaxial, biaxial, and rosette gages of many sizes. The section "Strain Measurement Methods" of this article provides some detail regarding these methods. Also, in the last several decades, extensive use of XRD to provide rapid and numerous stress measurements on sectioned components so as to provide information regarding the internal stress field has been applied (Ref 6, 32, 33, 34, and 35).

Preparation for Strain Measurement. With the strain measurement technique selected, the measurement location must be established and the component and/or element prepared for the measurement by, for example, attaching strain gages. A pre-stress-relaxation reading must be made before stress relaxation and isolation of the element is initiated.

Isolation of Gaged Element. With the measurement technique in place, material removal to isolate the gaged volume must be performed. The technique for material removal or sectioning must be carefully considered, because mechanical chip removal processes such as lathe turning, milling, sawing, grinding, and so forth introduce surface residual stresses that can be as great as the yield strength of the strain hardened material and tens of micrometers (several thousandths of an inch) in depth (Ref 36, 37). The section "Sectioning and Material Removal Methods" in this article discusses methods used to isolate the gaged element.

Post-Stress-Relaxation Measurement. After the residual stresses have been relaxed and, thus, the elements isolated, strain measurements are repeated, and the final reading is subtracted from the initial one to obtain the strain change resultant from the residual stress relaxation. The resultant quantities are then used in the residual stress reconstruction equations to obtain the original stress state of the component. The stress reconstruction equations were selected as a result of the assumptions made in the section "Stress Field Conditions" and described in detail in following sections.

Stress Field Condition Assumptions and Reconstruction

Engineers and research scientists have approached the measurement of residual stresses using destructive methods with the aid of assumptions about the stress field conditions, including that the stresses in only one axis are of interest, in order to simplify the measurement and reconstruction of the stress field. These have included certain uniaxial, biaxial, and triaxial stress field assumptions.

Uniaxial Conditions. A procedure applicable only to the measurement of residual stresses in rods, cylinders, and tubes, that is, components with axial symmetry, was reported by Heyn (Ref 23). In this work, it was assumed that the stresses were axially symmetric and that only the longitudinal stresses were of interest. Thus, the changes in length of the components (cylinders, rods, and tubes) were measured after removal of an axially symmetric layer from the outside radius or boring out from an inside radius. The length of the component was measured after each layer removal process, and this measurement was entered into various equations described in the article. This procedure is called the Bauer-Heyn or Heyn-Bauer method (Ref 23) and is applicable only to measuring longitudinal stresses in axially symmetric components. It does not measure radial or circumferential stresses.

A second procedure assuming a uniaxial stress field, or that only the stresses in one axis are of interest, was proposed by Stablein (Ref 24). Here the component was a bar with a rectangular cross section, and the residual stresses acting along its length and varying through its thickness (smallest dimension) were measured. The material from one face of the bar (one of the two faces with the largest area) was removed by milling. Equations used to reconstruct the original stress field are described in the article. The depth of the removed layer must be significantly greater than the depth of plastic deformation caused by the milling (see the section “Sectioning and Material Removal Methods” in this article) and sufficient to cause a measurable bend in the material. The length of the opposite face of the bar from where the material was removed is measured before and after layer removal to determine the effect of the removal of the stressed layer. Presently this is usually done using electrical resistance strain gages (see the section “Strain Measurement Methods”), but in the past it was done by sensitive mechanical gaging techniques. This measurement can also be accomplished by measuring the bend in the bar with suitable mechanical gages and fixtures; for example, a cantilever beam approach. This procedure is applicable only to components of rectangular cross section where the stresses parallel to the length are to be measured as they vary through the thickness.

Biaxial Conditions. A procedure applicable to axially symmetric components is the Mesnager-Sachs boring-out technique (Ref 25, 26). The technique is applicable to cylindrical components with an axially symmetric distribution of stresses. Here the change in length and diameter of the component is measured as material is removed by axially boring-out material from the inside to produce a hollow cylinder. Presently biaxial electrical resistance strain gages are usually attached to the outside of the component to measure the dimensional changes in the axial and tangential directions. The strain change results are entered into equations described in two articles (Ref 25, 26).

A procedure applicable to measuring biaxial residual stresses homogeneous over the planar surface of a flat metal plate or sheet was proposed by Trenting and Read (Ref 27). It was based on uniformly removing thin layers of the metal on one side of the sheet or plate and measuring the changes in curvature as the layers were removed. It was assumed that the stresses were constant over the plane of the sheet or plate and varied only through the thickness. Electrical resistance strain gages or mechanical gaging may be used to measure the change in curvature.

Another procedure for measuring biaxial stresses homogeneous over the planar surface of a metal plate was developed by Gunnert (Ref 28). This procedure assumes that a biaxial stress condition was uniform throughout the depth of a circular groove that was milled around an elemental volume of material (trepanning) to render it stress free. Thus, the strain change on only one surface was measured. The mechanical gaging technique involved measuring the distance between each of four sets of shallow holes drilled in the element before the groove was milled into the surface using a core drill. The distance between each set of holes was measured before and after the groove was produced and provided the information necessary to calculate the original, assumed biaxial residual stress condition parallel to the surface of the plate. Theoretically, only three sets of holes are required to measure the biaxial stresses, but Gunnert used a fourth set to improve the accuracy. A mechanical gage, termed an *extensometer*, was used to measure the distance between each set of holes. It should be noted that this technique could be used to measure the gradient in the biaxial stress condition by pausing in the milling operation at selected depths and measuring the distance between the holes at each groove

depth. Also, as with many of the older techniques, which originally applied mechanical strain gage apparatus, electrical resistance strain gages or modern XRD stress instrumentation (instruments designed specifically for stress measurement and not conventional XRD instruments modified with stress measurement accessories) could be used. A procedure involving the drilling of a blind hole and electrical resistance strain gage is somewhat similar to Gunnert's original technique and is described under semidestructive methods.

A more accurate procedure was later used to measure residual stresses in pipe weldments. Here the component (pipe) was divided into a network (grid) of squares, and biaxial electrical strain gages were placed in the center of each grid square on the outside diameter of the pipe (Ref 38). The pipe was then sectioned as shown in Fig. 4 into elements assumed to be stress-free, and the strain induced by the stress relief was read from the gages. In placing the gages only on the outside diameter, the biaxial stress field was assumed to be uniform with depth; however, had gages been placed on the inside and outside diameter, a more complete measurement of the stress field could have been obtained, albeit assuming a linear variation in the residual stress from the outside to the inside surface.

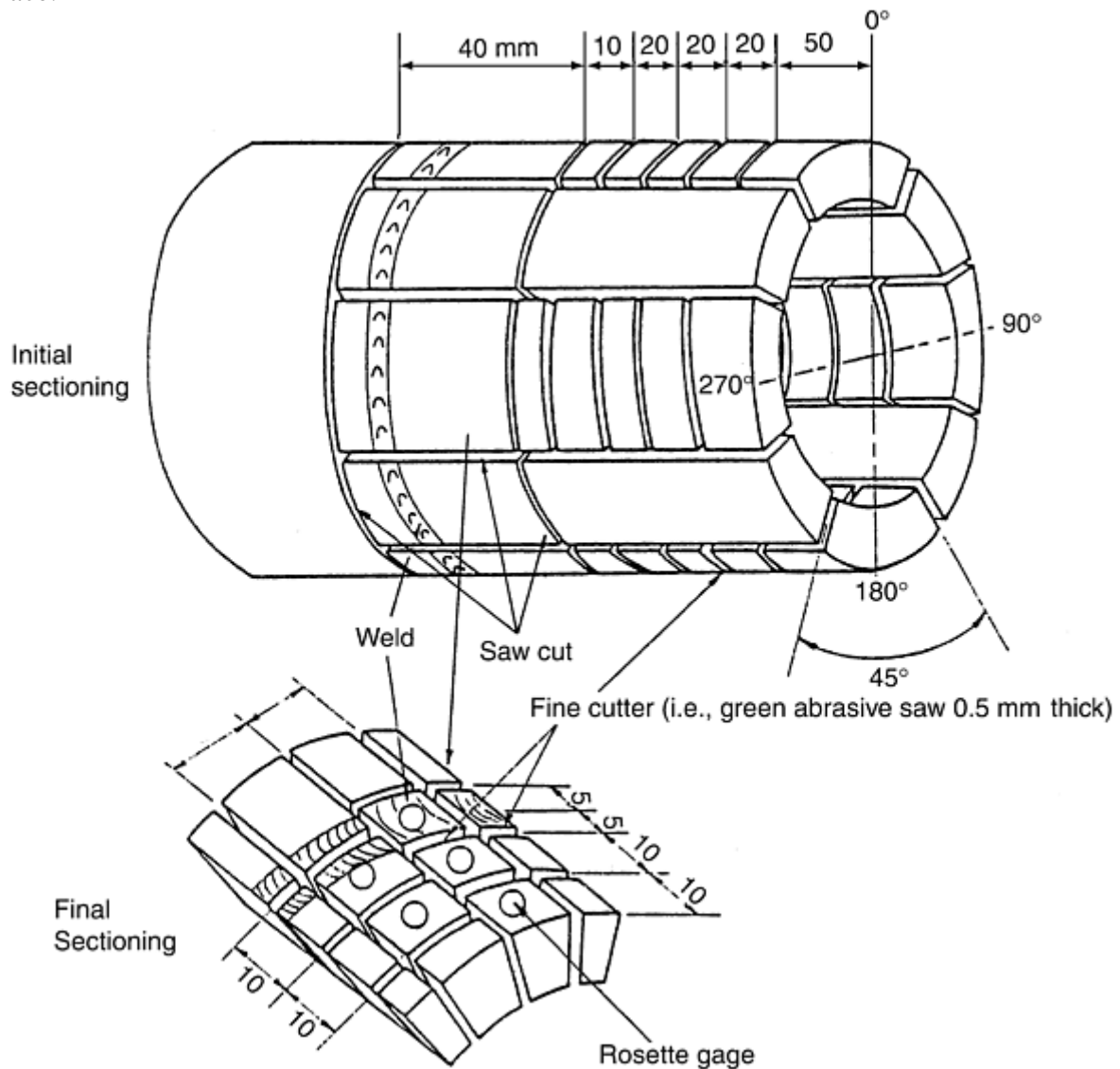


Fig. 4 Residual stress measurement of a girth welded pipe by strain gaging and sectioning. Note that strain gages shown in the final sectioning should be placed on the pipe prior to initial sectioning. For a more complete analysis, several of the layer sections detailed in the final sectioning step should be strain gaged and sectioned (Ref 38).

A variation on the Gunnert procedure described in a previous paragraph was later published (Ref 5, 29). This variation also was for application to plates and implied that the triaxial stress field could be measured by the technique. It assumed that a homogeneous residual biaxial stress field, which varied with depth through the plate thickness, existed. Four holes in a square pattern were drilled through the plate thickness. The distances between all of the holes were then measured at selected hole depths. Next, a circular groove is milled in steps

of, for example, 2 mm around the drilled holes using a core drill as in Gunnert's original procedure (Ref 28). The distance between the holes at the various depths was then measured at each core depth until the core was milled completely through the plate. The cored plug was then assumed to be completely free of residual stresses. The measured distances were then used to reconstruct the original biaxial stress condition of the plug at each cored depth. A similar mechanical measuring gage was used in this technique as was used in Gunnert's first technique (Ref 28).

Another approach to measuring residual stresses that has a broader application with respect to the shape of the component and the stress field distribution was proposed by Rosenthal and Norton (Ref 30). It is applicable to plates and plate-shaped weldments.

The procedure involved cutting two narrow blocks having the full thickness of the plate, each with its long axis parallel to one of the assumed biaxial, principal residual stress directions in the surface of the plate (see the near side of Fig. 5). Thus, the long axes of the blocks are perpendicular to each other and parallel to the face, the largest area surface of the plate. The smallest dimension of the block should be several times smaller than the thickness of the plate, and the largest dimension of the block should be at least twice the thickness. The block then can be further sectioned in order to determine the biaxial stress variation through the thickness of the component. This proceeds first by cutting the block at the location representing the midthickness of the component plate and then by removing thin slices parallel to the original surface and from the bisected block as shown in the upper part of Fig. 5.

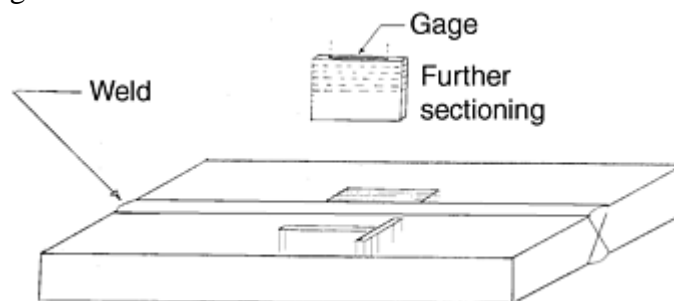


Fig. 5 A welded steel plate, the near side of which shows the two narrow blocks suggested in Rosenthal and Norton's (Ref 30) procedure. The far side shows several blocks sectioned to reveal the stresses parallel to the weld with a gradient transverse to the weld.

The change in strain of the blocks is measured using shallow holes or dimples in the original surfaces of the component. These gage points are located along the long axis of the block on the original faces of the plate (see Fig. 5). The distance between these gage marks is measured before and after removal of the blocks from the plate and after each sectioning of the block (Ref 30).

This procedure assumes a constant biaxial stress field over the length of the blocks, which is not the case in welded plates in the direction transverse to the weld. The far side of the block in Fig. 5 shows a sectioning procedure that would reveal the stresses parallel to the weld along a gradient transverse to the weld. Also, electrical resistance strain gages could be used instead of measuring the distance between shallow holes or dimples.

Another approach to a constant biaxial stress field in a flat plate, varying only through thickness, was described by Moore and Evans (Ref 6). They relied on XRD for the measurement of the strains from which the stress was calculated, and the procedure consisted of removing layers from the surface of the plate and measuring the strains existing at each layer. The process assumed that the stress perpendicular to the surface was zero. It should be noted that in order for this procedure to be valid, the XRD-measured areas would have to be free of plastic deformation caused by layer removal (see the section "Sectioning and Material Removal Methods" in this article).

Triaxial Conditions. In reality, in most components in which residual stresses have been induced, usually due to manufacturing processes, the stress field is triaxial and varies from point to point (element to element) in all three directions. Thus, a number of destructive procedures and stress field condition assumptions have been applied in order to measure the three-dimensional residual stress field condition existing in most components of practical engineering interest. Two of these are described in this section as follows.

Chen (Ref 31) revised Rosenthal and Norton's (Ref 30) approach to deriving the triaxial residual stress condition. The typical method of residual stress measurement is by mechanically removing part of a body and measuring the change of stress in the rest of the body. The method of Rosenthal and Norton instead deals only with a small element that has been cut free from a plate. The sectioning procedure consists of removal of a narrow block from a plate with gages attached, followed by splitting the block in half with gages attached on the top and bottom surface of the block and successive slicing of both halves from the midsection to the outer surface as shown in Fig. 5.

When the half-block is sliced to a thickness of 2.5 mm (0.1 in.), gages are removed and stresses are measured (at at least two points) on the surface by XRD techniques. The basic assumptions of Rosenthal and Norton are these: (a) partial relief of stress occurs in the direction of the long axis of the block, and a total relief of stress occurs in the direction transverse to the long axis, (b) the small amount of stress relaxed in the remainder of the block follows a linear law through the thickness when a thin slice of metal is removed, and (c) variation of transverse stress along the axis of the weld is small in the middle portion of the plate weldment. The determination of residual stresses may be divided into the steps described in the following paragraphs.

Determination is made of ϵ'_1 and ϵ'_t , which represent the amount of strain relaxed in longitudinal and transverse directions respectively, by cutting one longitudinal and one transverse block free from the plate. This is done by determining the strain relief between two indentations on the top and bottom surface of each block using a mechanical gage (see Fig. 5) and subtracting the gage readings on the blocks from the initial reading from the plate. Note that this measurement also can be performed using electrical resistance strain gages or XRD (Ref 22, 33).

Determination is made of ϵ'_1 ϵ'_t the strain relaxed on the top and bottom surfaces by splitting each block in half and then successively slicing the blocks. Here again, measurements of the change are made by using mechanical or electrical resistance strain gages or XRD.

Determination is made of the strain relieved (using at least two points) on the top and bottom surface using sensitive mechanical gages to measure the distance between indentations and XRD after the thickness of the top and bottom halves of the blocks has been reduced to 2.5 mm (0.1 in.). Note that the strain mechanical gages were used because Rosenthal and Norton used conventional scanning x-ray instrumentation. With modern XRD stress instrumentation (designed specifically for stress measurement, and not conventional XRD instruments modified with stress measurement accessories), measurements can be made on any size of specimen (Ref 20, 22, 34, and 39).

Determination of the residual stress remaining in the top and bottom slices is made using XRD (an enhancement of the Rosenthal and Norton procedure as suggested by Chen) (Ref 31). Here, the lattice strain was measured in the remaining slices in at least two places near the gage points using XRD, and the absolute residual stress remaining in the transverse and longitudinal directions respectively, S^*_t and S^*_l , was calculated as described in the section "X-Ray Diffraction" in this article. These x-ray diffraction determined stresses measured for each block were averaged and designated S^*_t or S^*_l for that face. The original stress S'' , present before slicing was determined by the following equations:

$$S''_t = S^*_t + E\epsilon''_t \quad (\text{Eq 1})$$

$$S''_l = S^*_l + E\epsilon''_l$$

The total strain, ϵ'' , may be obtained by dividing S''_t or S''_l by the modulus of elasticity, E .

Computation of Stress Relaxed by Cutting the Blocks from the Plate. Using the values of ϵ' and ϵ'' obtained in previous steps, the amount of longitudinal and transverse stress, S'_1 and S'_t relaxed by cutting the blocks from the plate was computed by means of the following equations:

$$S'_1 = \frac{E}{1-\nu^2}(\epsilon'_1 + \nu\epsilon'_t) + \frac{\nu E}{1-\nu^2}(\epsilon''_1 + \nu\epsilon''_t) \quad (\text{Eq 2})$$

$$S'_t = \frac{E}{1-\nu^2}(\epsilon'_t + \nu\epsilon'_1) + \frac{\nu E}{1-\nu^2}(\epsilon''_t + \nu\epsilon''_1)$$

where ν is Poisson's ratio. Equation 2 is valid for the case where the length of the block is at least twice the thickness of the block. In case of shorter blocks, the following equations are used:

$$S'_1 = \frac{E}{1-\nu^2}(\epsilon'_1 + \nu\epsilon'_t) + \frac{E}{1-\nu^2} \times \left(\nu\epsilon''_t + \frac{\nu^2 - \beta^2}{1-\beta} \epsilon''_1 \right) \quad (\text{Eq 3})$$

$$S'_t = \frac{E}{1-\nu^2}(\epsilon'_t + \nu\epsilon'_1) + \frac{E}{1-\nu^2} \times \left(\nu\epsilon''_1 + \frac{\nu^2 - \beta^2}{1-\beta} \epsilon''_t \right)$$

where β is the correction factor for a shorter block.

These values, when plotted for the top and bottom faces of the block and joined by a straight line, give the stress, S' , relaxed by cutting the block from the plate.

Computation of Stress S'' Relieved by Splitting and Slicing the Blocks. This is done by means of the following equations:

$$(S''_\alpha)_t = E \left[\frac{1}{2} \frac{d\epsilon''_t}{d\alpha} (1-\alpha) - 2(\epsilon''_t - \epsilon''_t^0) + 3(1-\alpha) \int_{0.5}^{\alpha} \frac{\epsilon''_t - \epsilon''_t^0}{(1-\mu)^2} d\mu + (5\alpha - 4)\epsilon''_t^0 + (1-\alpha)\epsilon''_b^0 \right] \quad (\text{Eq 4})$$

$$(S''_\alpha)_b = E \left[\frac{1}{2} \frac{d\epsilon''_b}{d\alpha} (1-\alpha) - 2(\epsilon''_b - \epsilon''_b^0) + 3(1-\alpha) \int_{0.5}^{\alpha} \frac{\epsilon''_b - \epsilon''_b^0}{(1-\mu)^2} d\mu + (5\alpha - 4)\epsilon''_b^0 + (1-\alpha)\epsilon''_t^0 \right] \quad (\text{Eq 5})$$

where α = fraction of the total thickness removed; $\epsilon''_t, \epsilon''_b$ = relaxed strain measured on top and bottom surface for position; and $\epsilon''_t^0, \epsilon''_b^0$ = relaxed strain on the top and bottom surface when splitting the block in half.

Determination of total stresses relaxed across the thickness of the block in the longitudinal and transverse directions is made by the following equations:

$$S_l = S'_l + S''_l \quad (\text{Eq 6})$$

$$S_t = S'_t + S''_t$$

Determination of shearing stresses in the longitudinal and transverse directions is made by the use of the following equation:

$$\tau_{xy} = \tau_{yx} = \frac{S_w - S_v}{2} \quad (\text{Eq 7})$$

where S_w and S_v are the stresses measured in the direction w and v making angles $+45^\circ$ and -45° with the longitudinal axis. However, if the biaxial stress condition is assumed, only the strain relief in one 45° direction need be determined because the strain relief values would be equal. This requires that either a block at a 45° angle to the longitudinal block be removed or that electric residual strain gage rosettes or XRD measuring at the 45° angle be used.

Determination of Stress in the Thickness Direction. The equilibrium equations may be written as the following:

$$\frac{\partial S_x}{\partial x} + \frac{\partial \tau_{xy}}{\partial y} + \frac{\partial \tau_{xz}}{\partial z} + X = 0 \quad (\text{Eq 8})$$

$$\frac{\partial S_y}{\partial y} + \frac{\partial \tau_{xy}}{\partial x} + \frac{\partial \tau_{yz}}{\partial z} + Y = 0 \quad (\text{Eq 9})$$

$$\frac{\partial S_z}{\partial z} + \frac{\partial \tau_{xz}}{\partial x} + \frac{\partial \tau_{yz}}{\partial y} + Z = 0 \quad (\text{Eq 10})$$

Differentiation of Eq 8, 9, and 10 with respect to x , y , z , respectively, yields:

$$\frac{\partial^2 S_x}{\partial x^2} + \frac{\partial^2 \tau_{xy}}{\partial x \partial y} + \frac{\partial^2 \tau_{xz}}{\partial x \partial z} = 0 \quad (\text{Eq 11})$$

$$\frac{\partial^2 S_y}{\partial y^2} + \frac{\partial^2 \tau_{xy}}{\partial x \partial y} + \frac{\partial^2 \tau_{yz}}{\partial y \partial z} = 0 \quad (\text{Eq 12})$$

$$\frac{\partial^2 S_z}{\partial z^2} + \frac{\partial^2 \tau_{xz}}{\partial x \partial z} + \frac{\partial^2 \tau_{yz}}{\partial y \partial z} = 0 \quad (\text{Eq 13})$$

Subtracting the summation of Eq 11 and 12 from Eq 13, results in:

$$\frac{\partial^2 S_z}{\partial z^2} = \frac{\partial^2 S_x}{\partial x^2} + \frac{\partial^2 S_y}{\partial y^2} + 2 \frac{\partial^2 \tau_{xy}}{\partial x \partial y} \quad (\text{Eq 14})$$

Variation of S_x along the x -axis is small in the middle portion of the plate; therefore, the first term in Eq 14 can be neglected. Equation 14 can be approximated using the following:

$$\frac{\partial^2 S_z}{\partial z^2} = \frac{2}{\Delta y_1^2} (S_{y1} - S_{y0}) + \frac{2}{\Delta x_2 \Delta y_2} \tau_{x_2 y_2} \quad (\text{Eq 15})$$

where S_{y0} = value of S_y at the axis; S_{y1} = value of S_y at a distance Δy_1 on either side of the x axis; and $\tau_{x_2 y_2}$ = value of τ_{xy} at a distance Δx_2 and Δy_2 from the y axis and x axis respectively.

Therefore the stress in the thickness direction S_z can be obtained through double integration with the boundary condition that S_z vanishes at both the top and bottom surfaces. In this way the entire triaxial residual stress state was determined. Note that this procedure assumes that the residual stresses are uniform along the length of each block.

A variation on Rosenthal and Norton's (Ref 30) method using electrical resistance strain gages or a nondestructive technique such as XRD is as follows. The largest face of the blocks (described by the thickness of the component or plate and the longest dimension of the blocks, Fig. 5) is divided into a two-dimensional grid of elements. An electrical resistance strain gage is placed on each element, or a nondestructive measurement such as XRD is performed. The block is sectioned along the grid lines to produce elements that are assumed to be stress free. Note that if a nondestructive technique such as XRD is used, the plastically deformed surface created by removing the block from the original component must be removed. This is best done using electropolishing (see the section of this article "Sectioning and Material Removal Methods"). If electropolishing of these cut faces is done to remove the plastic deformation and resultant residual stress induced by a mechanical cutting procedure and XRD is applied, then the blocks need not be sectioned. The measured XRD stress will provide the absolute residual stress field condition in the block, and, coupled with the strain relieved by the original removal of the block from the plate, the entire triaxial residual stress condition of the plate may be obtained.

This variation on Rosenthal and Norton's (Ref 30) method provides the information necessary to derive the biaxial stress condition of each block, which can in turn be used to derive the triaxial condition of the original plate. The stresses on each of the measured faces of the blocks must be measured in three directions to provide the information necessary to obtain the principal stresses in the block faces in each element. Note that the strain change caused by the sectioning of the blocks must be added to the strains measured in each element.

This procedure may be applied to a weldment with a single weld through its center as described by Rosenthal and Norton (Ref 30), or to a more elaborate stress field, for example, where two orthogonal welds existed in the component (plate). With a single weld, only the block-intersecting weld needs to be sectioned into elements,

because the residual stress field in the block parallel to the weld is likely to be constant along the direction parallel to the weld.

Moore and Evans (Ref 6) proposed mathematical procedures for the reconstruction of the original three-dimensional residual stress fields in cylindrical and flat plate components, and Constantinescu and Ballard (Ref 7) recently proposed a modification of Moore and Evans's work. They proposed using XRD as the measurement technique and presented stress reconstruction equations for the following conditions: (a) solid cylinder bar with rotationally symmetric stresses; (b) solid cylinder bar without rotationally symmetric stresses; (c) hollow cylinder bar with rotationally symmetric stresses; and (d) flat plate with biaxial stresses.

The Moore and Evans procedures are described in the *Society of Automotive Engineers Handbook Supplement* (Ref 8) and summarized in the following paragraphs.

Solid Cylinder Bar with Rotationally Symmetric Stresses. It was presumed that the residual stress distribution had both rotational and longitudinal symmetry, except near the ends where measurements were avoided. Stresses were therefore functions of the radius, r , and did not depend on the angle, θ , measured around the cylinder, nor the distance, z , taken parallel to the axis. With repeated removal of thin concentric shells, the stresses on the exposed surface in depth were obtainable. The circumferential and longitudinal measures of stress, $\sigma_{\theta m}(r)$ and $\sigma_{zm}(r)$, respectively, were then used to calculate the original stresses, $\sigma_{\theta}(r)$ and $\sigma_z(r)$, as well as the radial stress, $\sigma_r(r)$.

The theory of elasticity provides nine partial differential equations—the three equations of equilibrium and the six equations of compatibility. Unique solutions are possible, depending on boundary conditions. For the case considered, the nine equations give the following working formulas:

$$\sigma_r(r_1) = \int_{r_1}^R \frac{\sigma_{\theta m}(r)}{r} dr \quad (\text{Eq 16})$$

$$\sigma_z(r_1) = \sigma_{zm}(r_1) - 2 \int_{r_1}^R \frac{\sigma_{zm}(r)}{r} dr \quad (\text{Eq 17})$$

$$\sigma_{\theta}(r_1) = \sigma_{\theta m}(r_1) + \sigma_r(r_1) \quad (\text{Eq 18})$$

where r is the original radius, and r_1 is the radius at the depth of interest.

Solid Cylinder Bar without Rotationally Symmetric Stresses. Stresses were again assumed independent of z but allowed to vary in the circumferential, θ , direction. Complex variable methods gave general solutions for stresses in the radial, $\sigma_r(r_1, \theta)$ circumferential, $\sigma_{\theta}(r_1, \theta)$; and axial, $\sigma_z(r_1, \theta)$, directions as well as the shear stress, $\tau_{r\theta}(r_1, \theta)$. Details of the equations used may be found in the references (Ref 6 or 8).

Hollow Cylinder Bar with Rotationally Symmetric Stresses. With the inside radius included in the equations used to calculate $\sigma_r(r_1)$, $\sigma_z(r_1)$, and $\sigma_{\theta}(r_1)$, the general solutions for these stresses are developed (Ref 6, 8).

Flat Plate with Biaxial Stresses. It was assumed that the residual stresses in a flat plate of uniform thickness depended only on the distance from one of the flat surfaces of the plate, except, of course, near the edges. It was also assumed that the principal stresses are σ_x and σ_y , lying in the plane of the flat surfaces, and that the stress normal to the flat surfaces, σ_z , was zero at all points sufficiently distant from the edges.

From the assumptions and conditions of equilibrium, the true stresses $\sigma_x(z_1)$ at depth z_1 could be expressed in terms of the measured stress $\sigma_{xm}(z_1)$ by the relation:

$$\sigma_x(z_1) = \sigma_{xm}(z_1) + 2 \int_{z_1}^H \frac{\sigma_{xm}(z)}{z} dz - 6z_1 \int_{z_1}^H \frac{\sigma_{xm}(z)}{z^2} dz \quad (\text{Eq 19})$$

where H = original thickness of the plate and z_1 = distance from lower surface to uncovered depth of interest.

A similar expression holds for the y direction. Equation 19 holds, even if σ_x and σ_y are not principal stresses, but in this case a shear stress also exists, expressed by:

$$\tau_{xy}(z_1) = \tau_{xy_m}(z_1) + 2 \int_{z_1}^H \frac{\tau_{xy_m}(z)}{z} dz - 6z_1 \int_{z_1}^H \frac{\tau_{xy_m}(z)}{z^2} dz \quad (\text{Eq 20})$$

$\tau_{xym}(z)$ is determined from:

$$\begin{aligned} \sigma_{\alpha m}(z_1) = & \sigma_{xm}(z_1) \cos^2 \alpha + \sigma_{ym}(z_1) \sin^2 \alpha \\ & + 2\tau_{xym}(z_1) \sin \alpha \cos \alpha \end{aligned} \quad (\text{Eq 21})$$

where α is the acute angle that the measured stress $\sigma_{\alpha m}(z_1)$ makes with the x axis. When measurements are taken 45° apart, $\tau_{xym}(z_1)$ becomes:

$$\begin{aligned} \tau_{xym}(z_1) = & \sigma_{45 \text{ deg}}(z_1) - \frac{1}{2}(\sigma_{xm}(z_1) \\ & + \sigma_{ym}(z_1)) \end{aligned} \quad (\text{Eq 22})$$

meaning that three x-ray stress measurements are required after each layer is removed.

Johanssen (Ref 32) proposed a procedure for the determination of the three-dimensional residual stress field in thick plate (plate weldments) components using XRD techniques to measure the strains on the surfaces of the plate and plate sections and on removal of layers of surfaces. The procedure included the measurement of the biaxial stress field existing on the top surface of the component (Fig. 6), assuming that the stress perpendicular to the surface is zero. Material was removed from this surface by, for example, milling and electropolishing or by electropolishing alone (see the section "Sectioning and Material Removal Methods"), and the biaxial stresses were remeasured at the new depth. Each time material was removed, the forces that the removed layer exerted on the remaining component had to be accounted for, and the subsequent measurements required correction for this change in the stress field. Johanssen based his method on the following assumptions:

- When a layer of material is removed, the resulting changes in the stress condition will be linear elastic; that is, Hooke's law is applicable.
- The residual stress distribution is constant in the z -direction, except at the surface, and σ_z is a principal stress in the z -direction (Fig. 6).
- On material removal, it is assumed that the strain, ϵ_z , remains unchanged. Together with the previous assumption, this implies that the change in stresses can be treated as a plane problem.
- It is assumed that the stresses are symmetrical with respect to the y - z plane. This assumption is, however, not necessary. The procedure can be developed to include asymmetrical stress states.

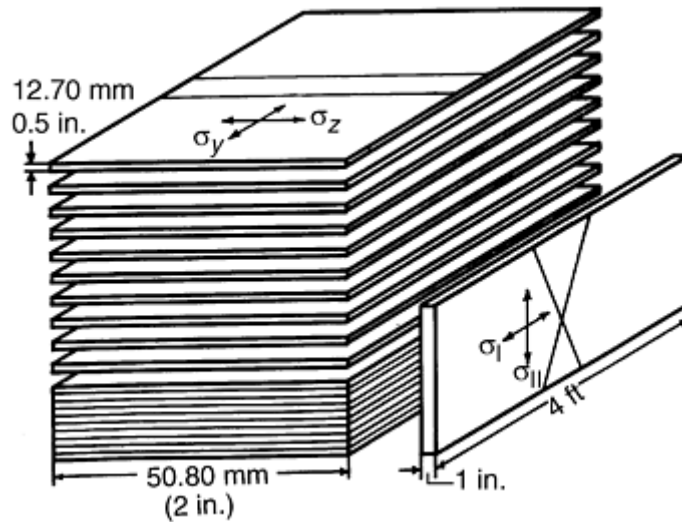


Fig. 6 A 2 ft by 2 ft by 4 ft weldment showing the layers proposed by Johanssen (Ref 32) where the thickness (T) of the layers are 12.70 mm (0.5 in.) and $\sigma_I = \sigma_y$, $\sigma_{II} = \sigma_x$, and $\sigma_{III} = \sigma_z$

Johanssen's (Ref 32) justification for his procedure to measure the three-dimensional stress field in the weldment shown in Fig. 6 is as follows.

Johanssen showed that the change in stresses resulting from the removal of material can be determined by $\Delta\sigma(x)$ and $v(x)$ shown in Fig. 7. These were to be measured at a number of positions x_i , $i = 1, \dots, N$, on the lower side of the plate. $\Delta\sigma_x(x)$ and $v(x)$ are the differences between the stress and deformation measured prior to

and following the removal of material. Changes in the internal stress conditions are thus calculated directly and need not be calculated as accumulated stress changes resulting from several layers of material being removed. The development of equations for the stress reconstruction may be found in Ref 32.

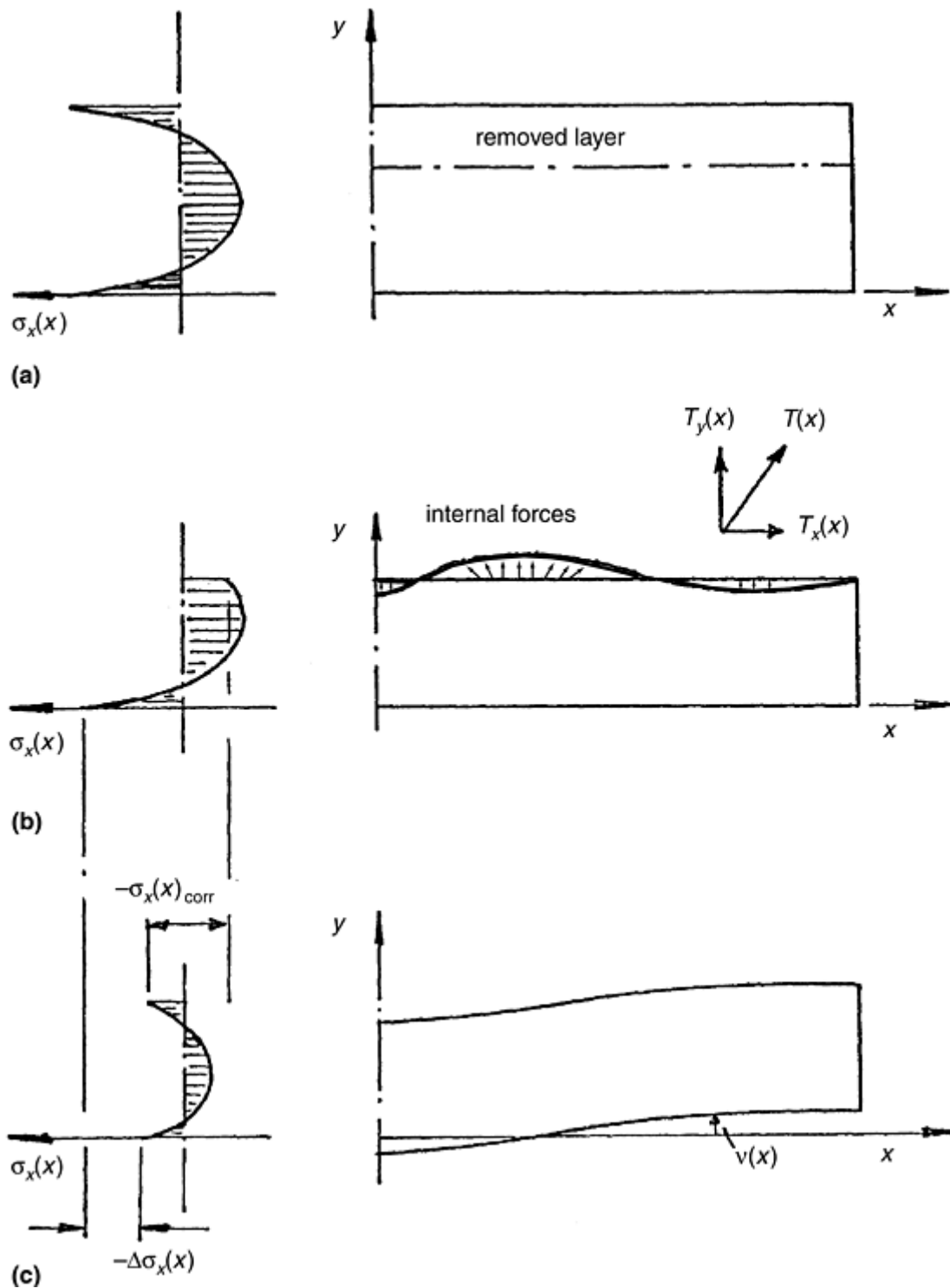


Fig. 7 Residual stress distributions, forces, and distortion of a plate before and after layer removal. (a) Residual stress distribution in the x -direction in the center of the plate in the x - z plane. (b) Same as (a) after removal of a layer with the forces $T_i(j)$ caused by the residual stresses tending to distort the plate. (c) Same as (b) with the distortion displacement shown (Ref 32)

Pickel (Ref 40) described a method for analytical solution of problems with similar boundary conditions to Johanssen's, using infinite, related series, but in this instance, an approximate method was used with trial solutions that were more convenient and numerically more stable than those used by Johanssen.

Sikarskie (Ref 41) proposed a stress reconstruction procedure (series method) when thin layers were removed from the surface of a component. He described procedures applicable to flat plates and solid cylinders. The procedure works well for shallow depths (a few percent of specimen diameter or thickness) or in instances where the stress gradient over the total depth removed does not change too rapidly and is of essentially one sign. The practicality of this method depends on the fit of the measured stresses in depth by a Taylor's series referred to the surface values of stress and successive derivatives at the surface. When the method is applicable, very convenient relations are obtained, which describe the stress correction in terms of the influencing factors; for example, layer depth, stress magnitude, stress gradient, and specimen size. Judgment is necessary, however, in using the series approximation, which does not arise when using the exact equations of the previous sections. The method is summarized for two of the previous cases as follows.

Flat Plate. (See the previous discussion "Flat Plate, Biaxial Stress" for the Moore and Evans procedures.) A generalized solution is written:

$$\begin{aligned} \sigma(z_1) = & \sigma_m(z_1) + 2 \int_{z_1}^H \frac{\sigma_m(z)}{z} dz \\ & - 6z_1 \int_{z_1}^H \frac{\sigma_m(z)}{z^2} dz \end{aligned} \quad (\text{Eq 23})$$

The subscripts x , y , or xy have been dropped, because the form of Eq 19 and 20 are exactly the same. $\sigma(z_1)$ represents the true stress in any direction at depth, z_1 , before a layer was removed, and $\sigma_m(z_1)$ represents the measured value at that depth.

The correction in stress, $c(z_1)$, at z_1 is the difference between the true and measured values, given by:

$$\begin{aligned} c(z_1) = & \sigma(z_1) - \sigma_m(z_1) = 2 \int_{z_1}^H \frac{\sigma_m(z)}{z} dz \\ & - 6z_1 \int_{z_1}^H \frac{\sigma_m(z)}{z^2} dz \end{aligned} \quad (\text{Eq 24})$$

The integrands are then expanded in a Taylor's series referred to the surface values, after which the integration is performed term by term. The final form for the correction is:

$$\begin{aligned} c(z_1) = & -4\sigma_m(H) \left(\frac{H-z_1}{H} \right) \\ & + [\sigma_m(H) + 2H\sigma'_m(H)] \left(\frac{H-z_1}{H} \right)^2 + \frac{1}{3} \\ & \times [2\sigma_m(H) + H\sigma'_m(H) - 2H^2\sigma''_m(H)] \\ & \times \left(\frac{H-z_1}{H} \right)^3 + \dots \end{aligned} \quad (\text{Eq 25})$$

where $\sigma_m(H)$, $\sigma'_m(H)$ are true surface stress and successive derivatives with respect to z at the surface. For shallow depths only, the first terms of the series may be used and:

$$c(z_1) = -4\sigma_m(H) \frac{\Delta z_1}{H} \quad (\text{Eq 26})$$

where $\Delta z_1 = H - z_1$. This correction is seen to be approximately proportional to the magnitude of the surface stress and thickness of the removed layer (Fig. 8). It is inversely proportional to the specimen thickness.

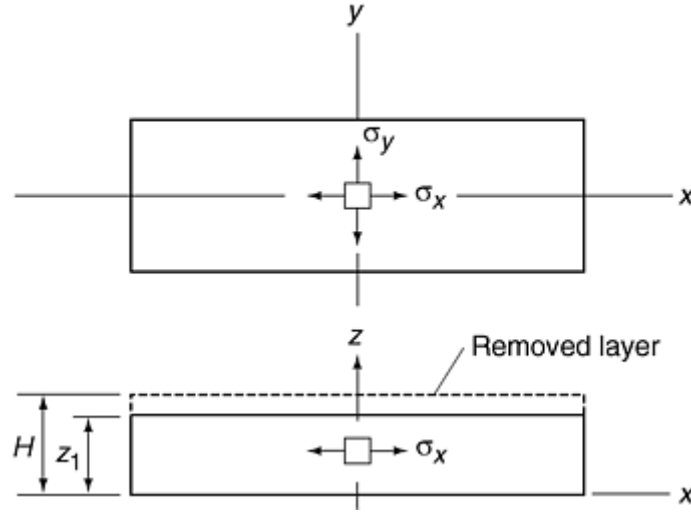


Fig. 8 Stresses in flat plate after layer removal

By solving for Δz_1 , the question of proper slice is given by:

$$\Delta z_1 = -\frac{1}{4} \frac{Hc(z_1)}{\sigma_m(H)} \quad (\text{Eq 27})$$

Thus, for example, if the measured stress is to be in error by less than 5%, $-c(z_1)/\sigma_m(H) = 0.05$, and the appropriate slice depth is:

$$\Delta z_1 = \frac{1}{4}(0.05)H \quad (\text{Eq 28})$$

For a plate 102 mm (4.0 in.) thick, for example, the slice depth is 1.3 mm (0.050 in.).

If the stress gradient is high, then the next term in the correction series should be included, and a quadratic in Δz_1 should be solved. This requires an estimate of $\sigma'_m(H)$ based on experience.

Solid Cylinder. (See the previous discussion "Solid Cylinder Bar with Rotationally Symmetric Stresses" for the Moore and Evans procedures.) A generalized solution from Eq 16 and 17 is written:

$$\sigma(r_1) = \sigma_m(r_1) - k \int_{r_1}^R \frac{\sigma_m(r)}{r} dr \quad (\text{Eq 29})$$

where, again, the subscripts r , θ , and z have been dropped because the form is the same.

When $\sigma_r(r_1)$ is desired:

$$\sigma(r_1) = \sigma_r(r_1)$$

$$\sigma_m(r_1) = 0$$

$$k = 1$$

$$\sigma_m(r) = \sigma_{\theta m}(r)$$

When $\sigma_z(r_1)$ is desired:

$$\sigma(r_1) = \sigma_z(r_1)$$

$$\sigma_m(r_1) = \sigma_{zm}(r_1)$$

$$k = 2$$

$$\sigma_m(r) = \sigma_{zm}(r)$$

$\sigma_{\theta}(r_1)$ is calculated from $\sigma_{\theta m}(r_1)$ using Eq 18.

The correction term in stress, $c(r_1)$, is written as before:

$$(\text{Eq 30})$$

$$(\text{Eq 31})$$

$$c(r_1) = \sigma(r_1) - \sigma_m(r_1) \quad (\text{Eq 32})$$

Again, expanding the integrand of Eq 29 in a Taylor's series and integrating term by term, a final form for the correction is obtained:

$$\begin{aligned} c(r_1) = & -k \left\{ \sigma_m(R) \left(\frac{R-r_1}{R} \right) \right. \\ & + \frac{1}{2} [\sigma_m(R) - R\sigma'_m(R)] \left(\frac{R-r_1}{R} \right)^2 \\ & + \frac{1}{6} [2\sigma_m(R) - 2R\sigma'_m(R) + R^2\sigma''_m(R)] \\ & \left. \times \left(\frac{R-r_1}{R} \right) + \dots \right\} \end{aligned} \quad (\text{Eq 33})$$

where $\sigma_m(R)$, $\sigma'_m(R)$ and so on, are the surface stress and successive derivatives with respect to z at the surface. Insights into the factors that influence the correction apply exactly as previously discussed, as do the limitations of the method.

Ruud et al. (Ref 33, 34) applied a modification of the Johanssen method to measure the triaxial stress condition of thick plate $\frac{1}{4}$ Cr-1 Mo plate weldments. They actually measured the strains in all directions and calculated the stresses but did not correct for layer removal due to the complex nature of the stress field.

Ruud et al. also measured the residual stress condition of expanded tubing including 304 stainless steel tubing (Ref 35) but focused on the residual stresses on the inside surface of the heat exchanger tube components. Table 3 summarizes the destructive residual stress measurement procedure described in this section of this article.

Sectioning and Material Removal Methods

As discussed in the previous sections on destructive measurement procedures, many procedures require that the component (sample or part) be sectioned and/or some material be removed from it to measure the residual stresses. This is especially true for the measurement of internal residual stress fields where the component nearly always must be sectioned to reveal the internal stress field. There are two exceptions to the necessity of sectioning and material removal, and these are neutron diffraction and ultrasonic methods, which will be described in the section "Nondestructive Procedures."

Sectioning or material removal may be required by a particular residual stress measurement procedure or method. Mechanical chip removal processes are usually applied because of their economy and speed. All chip removal processes, including lathe turning, drilling, milling, sawing, grinding, and so forth, introduce surface residual stresses that can be as high as the yield strength of the strain hardened metal and several thousandths of an inch (tens of microns) in depth (Ref 36, 42, 43, 44, and 45). Figures 9 10 11 show the residual stresses in steels caused by various machining processes. Further, some steels are especially prone to strain hardening, for example, austenitic stainless steels, and extra care must be used with these materials when selecting a material removal technique. Figure 12 shows plots of the residual stresses in 304 austenitic stainless steel caused by various grinding methods. Note that these plots are only samples and may not be typical. If the size of the element in which the strain change is measured is smaller, or thinner in the case of surface depth gradients, than about 2 to 3 mm ($\frac{1}{10}$ in.), then a chemical or electrochemical material removal technique must be used to remove the surface residual stresses caused by mechanical chip removal. These techniques may be used solely or in conjunction and after the chip removal method. It should be noted that material removal techniques such as electrical discharge machining (EDM) induce residual stresses (Ref 46) as do chip removal methods. Other methods, such as laser, flame, or plasma cutting, which cause heating of the element, must be applied with caution because they may reduce the stress field to be measured by annealing before measurement.

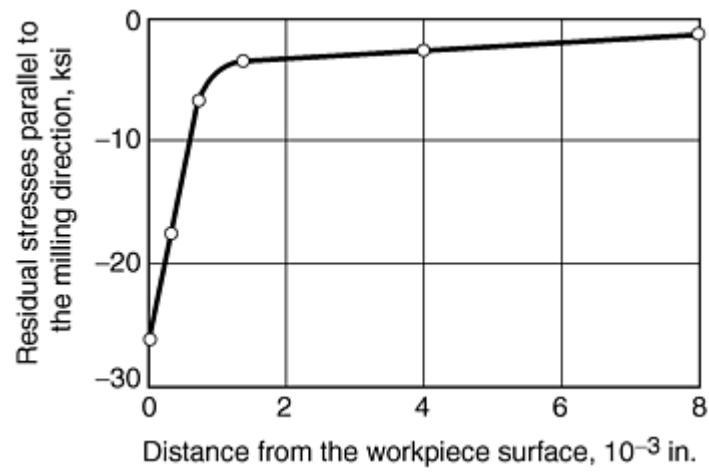


Fig. 9 Residual stresses at the surface and near the surface due to milling a medium carbon steel workpiece

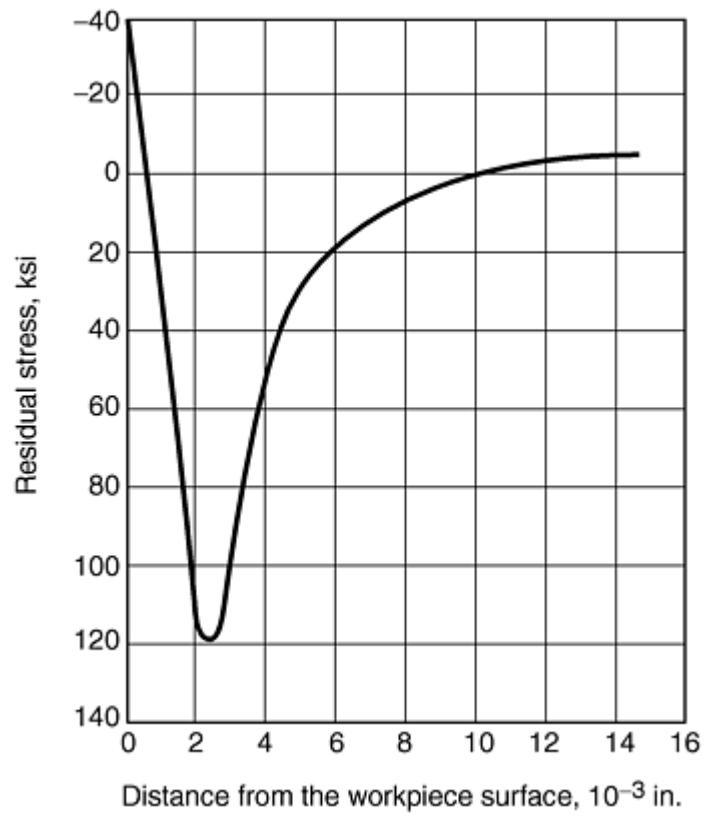


Fig. 10 Residual stresses in a 440C stainless steel workpiece induced by facing

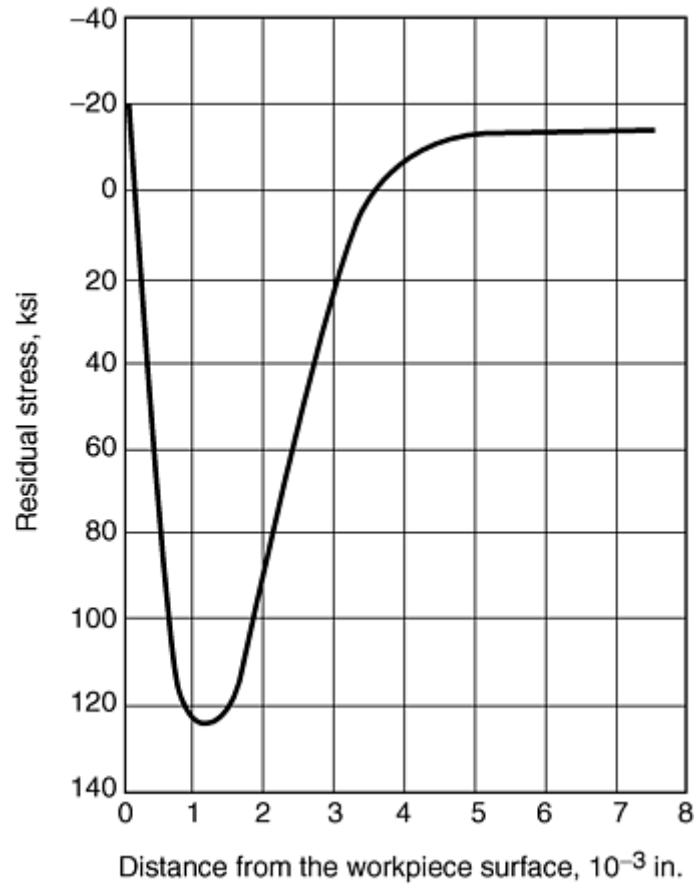


Fig. 11 Residual stresses in an alloy steel workpiece induced by turning

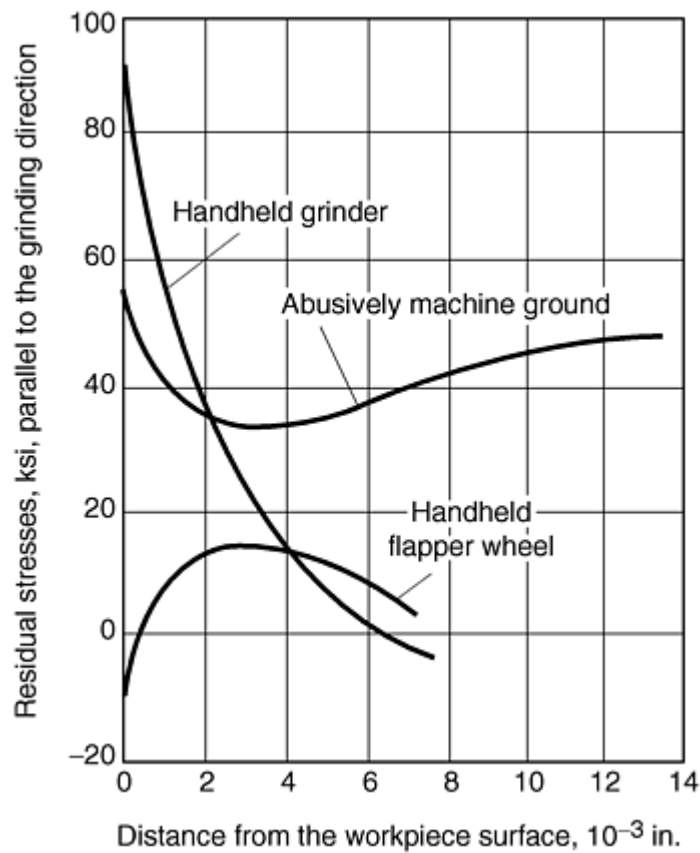


Fig. 12 Samplings of residual stress distributions induced in 304 stainless steel workpieces by common grinding procedures

Thus, the only methods for material removal from a component surface that do not induce residual stresses are electrolytic or chemical polishing. Electropolishing is described in some detail in *Surface Cleaning, Finishing, and Coating*, Volume 5, 9th ed., of *Metals Handbook* (Ref 47), and guidelines are provided for application to various alloys on Table 1 of that publication. In electropolishing, the electrolyte and operating conditions depend on the alloy being polished as shown in the *Metals Handbook* (Ref 47) and the *SAE Handbook Supplement* (Ref 8). Electropolishing combined with XRD is used extensively to reveal residual stress gradients on machined, ground, and hardened surfaces.

However, application of these techniques requires that the subsurface stresses be corrected for the removal of prior surface layers (Ref 8).

Another concern when reducing components to a more convenient, smaller size when it is necessary in order to place them on or in a measurement device is that the stresses of interest are likely changed by the sectioning. Generally plates should be cut to a length and width of at least three times the thickness to avoid end effects. Cylinders, both thin-walled and solid, should be a minimum of three diameters in length.

Where the manufacturing process affects the entire thickness of a component, such as heat treatment or forging, it might not be advisable to section without means of measuring the stress change extensively over the entire component before sectioning. In other words, selection of the stress measurement procedure and methods should avoid sectioning unless techniques to measure the effects of sectioning are applied before sectioning is initiated.

On the other hand, when the processes that have induced the residual stress produce only shallow stress fields, then the three times rule suggested above is applicable.

Strain Measurement Methods

As discussed in the section “Stress Measurement” in this article, all residual stress determination methods measure elastic strain, not stress, and the residual stress is calculated from the strain values. Several methods for the measurement of strain have been applied in residual stress studies, and some have been mentioned previously. These methods include mechanical gages, electrical resistance gages, brittle coatings, optical gages, laser methods, birefringent methods, diffraction methods (x-ray and neutron), ultrasonic methods, and magnetic methods. The last three methods will be discussed in the section “Nondestructive Procedures” in this article.

Mechanical Gages. The application of mechanical gages such as those described by Heyn (Ref 23), Stablein (Ref 24), Gunnert (Ref 27), and others generally preceded the availability of electrical resistance strain gages and are not discussed here due to their general lack of precision, poor spatial resolution, and inefficiency.

Electrical Resistance Strain Gages. Most bonded electrical resistance strain gages are made from either metallic wire or foil materials. There are also the recently developed semiconductor gages. A variety of sizes, shapes, and configurations are available, including single-element gages and rosettes with two, three, or four elements. Electrical resistance strain gages are available in sizes as small as about 1 mm and thus provide a resolution of strain measurement on that order. Information on electrical strain gages is available in numerous sources, including the *Handbook of Experimental Stress Analysis* (Ref 48) and in reviews by Crites (Ref 49) and Masubuchi (Ref 15) as well as by suppliers.

Changes in temperature tend to cause an apparent strain. Some type of temperature compensation, therefore, is needed. Frequently, a dummy gage, which is not subjected to the strain, is exposed to the same temperature as the actual gage to provide a basis for comparison. A temperature-compensated gage can also be used.

Gages must be bonded securely to the specimen. Various types of cements have been developed. Sometimes gages must be protected from metal chips produced during machining as well as from the oil or water. A number of systems have been devised for protecting gages under various conditions.

Brittle Coatings. A simple inexpensive strain gage that will only provide qualitative indications of residual stress is used for brittle coatings. Here a brittle lacquer is applied to the area where the stresses are to be measured by a material removal method. After the lacquer has cured (dried), a change in the stress field is induced, and if the change is sufficient, strain will be produced in the lacquer, causing it to crack. If the material removal is in the form of a hole drilled in the lacquer, radial cracks indicate a tensile residual stress in the plane of the component surface, and circular cracks indicate compressive stress.

Optical Gages. In a well-fixtured component that is held securely in place during material removal to change the stress field and, therefore, induce strain change, light reflective methods can be used to magnify the movement of a reflective surface. Also, this method can be used if the component can be removed and replaced

precisely in a fixture and if the position of the reflected light can be measured before and after removal and replacement, during which a change in the residual stress field is induced.

Laser Methods. Other techniques applying laser light have been proposed as well. These have included shearography (Ref 50), interferometry (Ref 51), speckle-correlation interferometry (Ref 52), and others. Vikram et al. (Ref 52) suggested that a small volume of the material could be stress relieved by heating via a laser to induce a change in the stress field and the strain change measured by an optical technique to reveal the residual stresses existing in the volume before heating. However, it must be recognized that heating a volume of metal sufficiently to change the residual stress field will result in tensile residual stresses in the heated volume, as observed by Cullity (Ref 53, p 471–472), and this would likely be detrimental to the component in which stresses were being measured.

Birefringent Methods. Under the action of stresses, transparent materials become doubly refracting (birefringent), and if a beam of a polarized light is passed through a model (under stress) made of such a material, a colored image is obtained from which the stress distribution can be determined. This technique is called the photoelastic technique (Ref 48). A practical variation on this technique is to coat a metal component in which the residual stress is to be measured with a photoelastic polymer. When residual stress changes are induced in the component, strain changes are caused and transmitted to the polymer coating, which then becomes birefringent. This can be observed and measured using a reflection polariscope (Ref 15). Instructions for analyzing fringe patterns in this application (nearly the same as those obtained in ordinary photoelasticity) are provided by the manufacturer of the polariscope.

The photoelastic coating may be applied by brushing a liquid polymer on the surface of the specimen and polymerizing it by applying heat. Alternatively, a prefabricated flat or contoured sheet of polymer may be bonded to the part at room temperature (Ref 54). The maximum strain that can be measured ranges between 3 and 50%, depending on the type of polymer used; the strain sensitivity usually decreases with the increase in the maximum measurable strain.

Chemical Methods

A number of qualitative methods to detect residual stresses that may lead to stress corrosion or hydrogen-induced cracking (HIC) in metals have been applied to specimens representing components to be manufactured. Magnesium chloride solutions have been applied extensively to the study of stress corrosion in nickel alloys and austenitic stainless steels, including some recent work by Bouzina et al. (Ref 55).

Masabuchi and Martin (Ref 56) studied the susceptibility of SAE 4340 steel weldments to hydrogen-induced stress cracking. The test procedure was to immerse the weldment specimens in a 4% H₂SO₄ (sulfuric acid) aqueous solution charged with H₂ and to which two drops of a 5% phosphorus (P) solution of CS₂ was dissolved. A direct current (dc) was applied between a specimen and a lead anode to provide a current density of 0.5 to 1.2 mA/mm² (0.35 to 0.8 A/in.²). The crack patterns that developed were related to the surface tensile residual stress distribution in each specimen.

Stress corrosion cracking (SCC) induced by residual stresses in carbon and low-alloy high-strength steels have been investigated by several researchers (Ref 56, 57, and 58). One procedure consisted of immersing the specimens in a boiling aqueous solution of 60% Ca(NO₃)₂ and 4% NH₄NO₃ for 31 h. The crack patterns that developed were related to the surface tensile residual stress distributions in the specimen.

A number of standard practices for testing the susceptibility of metals to SCC have been published by ASTM, including the following:

ASTM No.	Title
G 38	Standard Recommended Practice for Making and Using C-Ring Stress Corrosion Test Specimens
G 58	Standard Practice for the Preparation of Stress Corrosion Test Specimens for Weldments
G 39	Standard Practice for the Preparation and Use of the Bent-Beam Stress Corrosion Test Specimens
G 30	Standard Recommended Practice for Making and Using U-Bend Stress Corrosion Test Specimens
STP 425	Stress Corrosion Testing

However, these tests for the most part do not reveal the residual stress but the susceptibility of the metal to cracking under known stresses in the specified corrosion medium—not residual stress.

References cited in this section

5. R. Gunnert, "Method for Measuring Triaxial Residual Stresses," Document No. X-184057-OE, *Commission X of the International Institute of Welding*, 1957, and *Weld. Res. Abroad*, Vol 4 (No. 10), 1958, p 1725
6. M.G. Moore and W.P. Evans, Mathematical Corrections in Removal Layers in X-Ray Diffraction Residual Stress Analysis, *SAE Trans.*, Vol 66, 1958, p 340–345
7. A. Constantinescu and P. Ballard, On the Reconstruction Formulae of Subsurface Residual Stresses after Matter Removal, *The Fifth International Conf. on Residual Stresses*, Vol 2, Institute of Technology, Linkopings University, Sweden, 1997, p 703–708
8. Residual Stress Measurement by X-Ray Diffraction-SAE J784a, *Society of Automotive Engineers Handbook Supplement*, Warrendale, PA, 1971
15. K. Masubuchi, *Analysis of Welded Structures: Residual Stresses, Distortion, and Their Consequences*, 1st ed., Pergamon Press, 1980
20. M. Brauss, J. Pineault, S. Teodoropol, M. Belassel, R. Mayrbaurl, and C. Sheridan, Deadload Stress Measurement on Brooklyn Bridge Wrought Iron Eye Bars and Truss Sections Using X-ray Diffraction Techniques, *Proc. of 14th Annual International Bridge Conf. and Exhibition*, Engineering Society of Western Pennsylvania, Pittsburgh, ICB-97-51, 1997, p 457–464
22. J.A. Pineault and M.E. Brauss, In Situ Measurement of Residual and Applied Stresses in Pressure Vessels and Pipeline Using X-ray Diffraction Techniques, Determining Material Characterization: *Residual Stress and Integrity with NDE*, PUP-Vol 276, NDE-Vol 12, American Society of Mechanical Engineers, New York, 1994
23. E. Heyn, Internal Strains in Cold Wrought Metals, and Some Troubles Caused Thereby, *J. Inst. Met.*, Vol 12, 1914, p 1–37
24. E. Stablein, Stress Measurements on Billets Quenched from One Side," *Stahl and Eisen*, Vol 52, 1932, p 15–17
25. M. Mesnager, Methods for the Determination of Stresses Existing in a Circular Cylinder, C.R. Hebd. Seances Acad. Sci., 1926, Vol 169
26. G. Sacks, Evidence of Residual Stresses in Rods and Tubes, *Feitschrift fur Metallkunde*, Vol 19, 1927, p 352–357
27. T.G. Trenting and W.T. Read, Jr., *J. Appl. Phys.*, Vol 22 (No. 2), Feb 1951, 130–134
28. R. Gunnert, *Residual Welding Stresses, Method of Measuring Residual Stresses and Its Application to a Study of Residual Welding Stresses*, Alquist E. Wicksell, Stockholm, 1955
29. R. Gunnert, "Method for Measuring Residual Stresses in the Interior of a Material," Document No. X-162-57, *Commission X of the International Institute of Welding*, 1957, and *Weld. Res. Abroad*, Vol 6, 1960, p 10–24

30. D. Rosenthal and J.T. Norton, A Method for Measuring Triaxial Residual Stresses in Plates, *Weld. J.*, Vol 24 (No. 5), Research Supplement, 194 295s–307s
31. R. J-S. Chen, “Determination of Residual Stresses in a Thick Weldment,” M.S. thesis, The Pennsylvania State University, November 1983
32. P. Johansson, “Determination of Residual Stresses in Thick Welded Plated Utilizing X-Rays and Layer Removal Techniques, Part 1: Theory for Reconstruction of Original Stress State,” Internal Report, Department of Materials and Solid Mechanics, The Royal Institute of Technology, S100, 44, Stockholm, April 1978
33. C.O. Ruud, R.N. Pangborn, P.S. DiMascio, and P.J. Snoha, Residual Stress Measurement on Thick Plate Low-Alloy Steel Narrow Gap Weldments by X-Ray Diffraction, *ASME*, 84-PVP-128, 1984
34. C.O. Ruud, J.A. Josef, and D.J. Snoha, “Residual Stress Characterization of Thick-Plate Weldments Using X-ray Diffraction,” *Weld. Res. J. Supplement*, AWS, March 1993, p 875–915
35. A.R. McIlree, C.O. Ruud, and M.E. Jacobs, The Residual Stresses in Stress Corrosion Performance of Roller Expanded Inconel 600 Steam Generator Tubing, *Proc. of the International Conf. on Expanded and Rolled Joint Technology*, Canadian Nuclear Society, 1993, p 139–148
36. Y.W. Park, P.H. Cohen, and C.O. Ruud, The Development of a Model for Plastic Deformation in Machined Surface, *Mater. Manuf. Process.*, Vol 8 (No. 5), 1994
37. E. Schreiber and H. Schlicht, Residual Stresses After Turning of Hardened Components, *Residual Stresses in Science and Technology*, Vol 2, DGM Informationsgesellschaft, Verlag, Germany, 1987, p 853–860
38. W.J. Shack, W.A. Ellingson, and L.E. Pahis, “Measurements of Residual Stresses in Type-304 Stainless Steel Piping Butt Welds,” EPRI NoP-1413, R.P. 449-1, Electric Power Research Institute, Palo Alto, CA, June 1980
39. C.O. Ruud, P.S. DiMascio, and D.J. Snoha, A Miniature Instrument for Residual Stress Measurement, *Adv. X-Ray Anal.*, Vol 27, Plenum Press, 1984, p 273–283
40. G. Pickel, Application of the Fourier Method to the Solution of Certain Boundary Problems in the Theory of Elasticity, *J. Appl. Mech.*, 1944, p 176–182
41. D.L. Sikarskie, On a Series Form of Correction to Stresses Measured Using X-Ray Diffraction, *AIME Trans.*, Vol 39, 1967, p 577–580
42. Y.W. Park, P.H. Cohen, and C.O. Ruud, Sensitivity of Shear Process on Metal Cutting to the Development of Residual Stress, *Rev. Prog. in NDE*, Vol 14, 1995, p 1183–1188
43. Y.C. Shin, S.J. Oh, and C.O. Ruud, Investigation of Residual Stresses of Machined Surfaces by an X-Ray Diffraction Technique, *NDC of Materials IV*, Plenum Press, 1992, p 408–418
44. J.E. Hoffman, D. Lohe, and E. Macherauch, Influence of Machining Residual Stresses on the Bending Fatigue Behaviors of Notched Specimens of Ck45 in Different Heat Treating States, *Residual Stresses in Science and Technology*, Vol 2, p 801–814, DGM Informationsgesellschaft, Verlag, Germany, 1987
45. E. Brinksmier, Residual Stressed in Hard Metal Cutting, *Residual Stresses in Science and Technology*, Vol. 2, DGM Informationsgesellschaft, Verlag, Germany, 1987, p 839–846

46. F. Ghanem, H. Dishom, C. Braham, R. Fatallak, and J. Leider, An Engineering Approach to the Residual Stresses Due to Electric-Discharge Machining Process, *Proc. The Fifth International Conf. on Residual Stresses (ICRS-5)*, Vol 1, Ericson, Oden, and Anderson, Ed., Institute of Technology, Linkopings University, Sweden, 1977, p 157–163
47. Electropolishing, *Surface Cleaning, Finishing, and Coating*, Vol 5, *Metals Handbook*, 9th ed., American Society for Metals, Vol 5, 1982, p 303–309
48. M. Hetenyi, Ed., *Handbook of Experimental Stress Analysis*, John Wiley & Sons, Inc., 1950
49. N.A. Crites, Your Guide to Today's Strain Gages, *Prod. Eng.*, Vol 33 (No. 4), 17 Feb 1962, p 69–81, and Equipment and Application-Today's Strain Gages, *Prod. Eng.*, Vol 33 (No. 6), 19 March 1962, p 85–93
50. Y.Y. Hung, Shearography: A New Optical Method for Strain Measurement and Nondestructive Testing, *Opt. Eng.*, Vol 21 (No. 3), 1982, p 391–394
51. K. Li, Interferometric Strain/Slope Rosette Technique for Measuring Displacements/Slopes/Strains/Residual Stresses, *Proc. of the 1997 NSF Design and Manufacturing Grantees Conf.*, University of Washington, Seattle, National Science Foundation (NSF), 1997, p 571–572
52. C.S. Vikram, M.J. Pedensky, C. Feng, and D. Englehaupt, Residual Stress Analysis by Local Laser Heating and Speckle-Correlation Interferometry, *Exp. Tech.*, Nov/Dec 1996, p 27–30
53. B.D. Cullity, *Elements of X-Ray Diffraction*, 2nd ed., Addison-Wesley Publishing Co., Inc., 1978, p 469–472
54. C.O. Ruud, “Residual and Applied Stress Analysis of an Alloy 600 Row 1 U-Bend,” NP-5282, R.P 5303-3, Elect. Power Res. Inst., Palo Alto, CA 1987, p 2–11
55. A. Bouzina, C. Braham, and J. Ledion, Evaluation and Prediction of Real Stress State Stress Corrosion Cracking Specimens, *The Fifth International Conf. on Residual Stresses*, Vol 2, Institute of Technology, Linkopings University, Sweden, 1997, p 1060–1065
56. K. Masubuchi and D.C. Martin, Investigation of Residual Stresses by Use of Hydrogen Cracking, *Weld. J.*, Vol 40 (No. 12), Research Supplement, 1961, p 553s–556s
57. C.E. McKinsey, Effect of Low-Temperature Stress Relieving on Stress Corrosion Cracking, *Weld. J.*, Vol 33 (No. 4), 1954, Research Supplement p 161s–166s
58. W. Radeker, A New Method for Proving the Existence of Internal Stress Caused by Welding, *Schneissen Schneider*, Vol 10 (No. 9), 1958, p 351–358

Residual Stress Measurements

Clayton O. Ruud, The Pennsylvania State University

Semidestructive Procedures

Nondestructive methods of residual stress measurement are characterized as methods that in no way affect the serviceability or reduce the mechanical strength or other properties of the component in which stresses are

measured. Between the nondestructive and destructive methods, which have a severe effect on the serviceability, strength, and properties, are the semidestructive methods. These are methods that have a small to negligible effect on the components in which stresses are measured or methods for which the component may be repaired after the measurement.

The methods that are considered semidestructive are those that require small holes to be drilled, rings to be trepanned in the component, or indentations to be made in the surface. The first two methods provide quantitative data, and the third produces only qualitative data.

Blind Hole Drilling and Ring Coring. The hole-drilling method was proposed nearly seven decades ago (Ref 59) and is based on measurement of the change in surface strain caused by stresses relieved by machining a shallow hole in the test piece. The principle is that stressed material, on being removed, results in the surrounding material readjusting its stress state to attain equilibrium. The method has been standardized in ASTM E 837 (Ref 60). The ring core method (Ref 61) is also based on the strain caused by redistributing the stress field, but in this case a relatively stress-free island of material is isolated by making a shallow ring around a strain gage. This method is also called trepanning. These two methods are the least destructive mechanical stress relief techniques and are relatively simple and economical. They, as by and large all stress relief techniques do, rely on electrical resistance strain gages to measure the strain change due to metal removal. Rosettes of strain gages are available especially for hole drilling. The size of the rosettes has been progressively reduced over the last few decades, and rosettes are now available in sizes less than about 10 mm from a number of manufacturers.

As with most residual stress techniques, hole drilling and ring coring have been applied mostly to steels. Most applications have been done on flat plate or cylindrically round parts (Ref 9, 62, 63). Stresses can be determined at various depths into the surface of the material, down to a depth equal to the diameter of the hole or core (Ref 64, 65). Kelsey (Ref 66), however, observed that stresses with depth cannot be measured accurately to greater than half the hole diameter. The thickness of the layers in which stresses may be resolved is about 10 to 20% of the hole or core diameter.

The equipment necessary to perform the measurement is reasonably inexpensive, portable, and can be used in a manufacturing shop environment. However, experienced technologists are necessary to perform many tasks in taking the readings—from selecting the area in which stresses are to be measured to preparing the surface, applying the strain gages, and reading and interpreting the data. Due to the possibility of residual stresses being induced by the hole drilling or coring technique, prior calibration of the application is recommended in all cases, with the possible exception of certain applications where holes are produced by abrasive jet machining (Ref 67).

Rendler and Vigness (Ref 68) developed calibration constants for cold-rolled steel, which they proposed as generally applicable to all metals, provided that the elastic constants were known. However, they seem to have overlooked variations in the strain hardening coefficients and the accompanying residual stress, which exist between alloys and even between tempers of the same alloy. Dini et al. (Ref 69) showed that direct experimental determination of the necessary constants for any isotropic material with known elastic constants can be eliminated by using data available for cold-rolled steel and calculating these constants using a formula presented. Despite the success that some researchers have claimed in circumventing the development of calibration constants, experimental calibration is strongly recommended. This is best done by applying strain gages and drilling the holes in test pieces prior to stressing them known amounts (Ref 67, 68). The abrasive jet machining (AJM) technique should be applied to any material with high propensity to work hardening during machining, for example, austenitic stainless steel (Ref 70).

The following are general limitations and/or concerns of hole drilling and ring coring:

- Areas of high stress gradients should be avoided because the stress gradient must be assumed to be constant across the hole or ring diameter.
- Areas where stresses are greater than one-third the yield strength of the material are likely to produce erroneous results due to local plastic yielding during metal removal.
- The thickness of the part or specimen must be at least four times the hole or core diameter.
- Strain hardening of the metal in the vicinity of the hole may result during metal removal, which can result in tens of ksi (69 MPa) error.
- Heating may result during the metal removal.
- Holes or cores must be spaced at least eight times their diameter apart.

- The area in which stresses are to be measured must be accessible to a rather bulky drilling or coring alignment device.
- Preparation of the surface for strain gage adherence may induce residual stresses that introduce substantial error to the subsequent measurement (Ref 71).

In conclusion, the drilling and ring coring methods are nearly nondestructive variations of the destructive mechanical stress relief techniques and require only rather simple equipment and instrumentation. The state-of-the-art is relatively well developed compared to many nondestructive methods, some of which require considerable research and development work before they will ever be suitable to general application in terms of alloys and stress field conditions. Technological advancements in hole drilling and ring coring have largely been due to advancements in the more general areas of mechanical stress relief methods and research in new metal removal techniques for metal fabrication.

Indentation Methods. For more than six decades, engineers and scientists have proposed the use of indentors, such as those used to perform hardness measurements, as a means to measure or detect surface residual stresses. Kokubo in 1932 reported that stresses applied under bending load changed the apparent Vickers hardness values in carbon steel rolled sheets, both as rolled and annealed. He showed that tensile stresses tended to decrease the apparent hardness, and compressive stresses tended to increase the hardness. The stresses applied in tension and compression were sufficient to cause 0.3% strain.

Two decades later Sines and Carlson (Ref 72) proposed a method that required various amounts of external loads to be applied to the component in which residual stresses were to be measured while hardness measurements were made. The loads were made to cause both tensile and compressive applied stresses. The quality—that is, whether the residual stress was compressive or tensile—was then revealed by comparing the effect of the applied stress and whether the applied stress was tensile or compressive on the hardness measurement. At about the same time, Pomey et al. (Ref 73) proposed that residual stresses could be measured by pressing a ball-shaped penetrator into the component in which residual stresses were to be measured and establishing the relationship between the pressing load while it was progressively increased and the electrical resistance at the interface between the penetration and the component. He maintained that a smaller decrease in electrical resistance indicated that portions of material under the ball were plastically yielding and that the corresponding load on the ball could be related to the existing residual stress.

Later, Chiang et al. (Ref 74) provided a critique of several existing indentation analyses and proposed an interpretation of indentations exhibiting hemispherical plasticity. Nevertheless, the applications illustrated in this article were focused on brittle materials and not metals.

There have been numerous papers published proposing various approaches to interpreting the indentation loads and shapes so as to estimate the residual stress field on the surface and near-surface regions of materials. However, indentation methods have not earned the degree of confidence of XRD or hole drilling methods for general applications and, thus, are rarely applied.

Spot Annealing. Another semidestructive method that has been proposed to measure residual stresses in metal surfaces is to reduce the residual stresses in a small volume by annealing the metal in the volume. It has been proposed that this annealing be performed by intense laser light (Ref 52). This technique was envisioned to be similar to relief of residual stresses by removal of the material as accomplished in the hole drilling techniques. However, as Cullity discussed (Ref 53), such localized heating would induce high surface residual tensile stresses in the heat-affected region, and this would be detrimental to the component being tested.

References cited in this section

9. A.J. Bush and F.J. Kromer, “Residual Stresses in a Shaft after Weld Repair and Subsequent Stress Relief,” Paper No. A-16 presented at Society for Experimental Stress Analysis (SESA) Spring Meeting, 1979 (Westport, CT), 1979
52. C.S. Vikram, M.J. Pedensky, C. Feng, and D. Englehaupt, Residual Stress Analysis by Local Laser Heating and Speckle-Correlation Interferometry, *Exp. Tech.*, Nov/Dec 1996, p 27–30
53. B.D. Cullity, *Elements of X-Ray Diffraction*, 2nd ed., Addison-Wesley Publishing Co., Inc., 1978, p 469–472

59. J. Mathar, Determination of Initial Stresses by Measuring Deformation Around Drilled Holes, *Arch. Eisenhüttenwes.*, Vol 6, p 277–281 and *Trans. ASME*, Vol 56 (No. 4), 1934, p 249–254
60. “Determining Residual Stresses by the Hole Drilling Strain-Gage Method,” E 837, ASTM, 1983
61. H. Wolf and D.C. Sauer, “New Experimental Technique to Determine Residual Stresses in Large Turbine-Generator Components,” presented at the American Power Conf., (Chicago, IL), 1 May 1974
62. H. Wolf and W. Bohn, Origin, Measurement and Assessment of Residual Stresses in Large Forging for Turbines and Generators, *Arch. Eisenhüttenwes.*, Vol 42 (No. 7) 1971, p 509–511 (in German)
63. H. Wolf, E. Stucker, and H. Nowack, “Investigations of Residual Stresses in the Turbine and Generator Industry,” *Arch. Eisenhüttenwes.*, Vol 48 (No. 3), March 1977, p 173–178
64. J. Lu and J.F. Flavenot, “Applications of the Incremental Hole-Drilling Method for Measurement of Residual Stress Distributions—Experimental Techniques, paper presented at the Society for Experimental Mechanics (SEM) Spring Conference,” 5–10 June 1988 (Portland, OR), SEM
65. M.T. Flaman and B.H. Manning, Determination of Residual Stress Variation with Depth by the Hole-Drilling Method, *Exp. Mech.*, Vol 25, 1985, p 205–207
66. R.A. Kelsey, Measuring Nonuniform Residual Stresses by the Hole Drilling Method, *Proc. Society for Experimental Stress Analysis*, Vol 14 (No. 1), 1956, p 181–184
67. A.J. Bush and F.J. Kromer, Simplification of the Hole-Drilling Method of Residual Stress Measurement, *ISA Transactions*, Vol 12 (No. 3), 1973, p 249–259
68. N.J. Rendler and I. Vigness, Hole-Drilling Strain-Gage Method of Measuring Residual Stress, *Exp. Mech.*, Vol 6 (No. 12), Dec 1966, p 577–586
69. J.W. Dini, G.A. Beneditti, and H.R. Johnson, Residual Stresses in Thick Electro-deposits of a Nickel-Cobalt Alloy, *Exp. Mech.*, February 1976, p 56–60
70. F. Witt, F. Lee, and W. Rider, A Comparison of Residual Stress Measurements Using Blind-Hole, Abrasive-Jet and Trepanning Methods, *Exp. Tech.*, Vol 7, Feb 1983, p 41–45
71. P.S. Prevey, “Residual Stress Distribution Produced by Strain Gage Surface Preparations,” *1986 SEM Conference on Experimental Mechanics*, 1986
72. G. Sines and R. Carlson, “Hardness Measurements for the Determination of Residual Stresses,” *ASTM Bulletin* 180, Feb 1952, p 35–37
73. J. Pomey, F. Goratel, and L. Abel, “Determination des Cartraintes Residuelles dans les Pieces Einentees,” *Publication Scientifiques et Techniques du Ministere de l'air*, 1950, p 263
74. S.S. Chiang, D.B. Marshall, and A.G. Evans, The Response of Solids to Elastic/Plastic Indentations I: Stresses and Residual Stresses, *J. Appl. Phys.*, Vol 53 (No. 1), 1982, p 298–311

Nondestructive Procedures

The methods for strain measurement described previously all measure the change in some dimension (strain) of the component produced by the removal of a finite volume of stressed metal from that component. Thus, these methods measure the strain induced by removing material so as to perturb the residual stress field. On the other hand, the nondestructive procedures measure a dimension in the crystal lattice of the metal or some physical parameter affected by the crystal lattice dimension. Whenever a mechanical force resulting in stress that is less than the yield strength is placed on a solid metal component, that component distorts (strains) elastically. That elastic strain results in a change in the atomic lattice dimension, and this dimension, or change, is measured by a nondestructive stress measurement procedure. For example, the diffraction methods, x-ray and neutron, measure an actual crystal dimension, and this dimension can be related to the magnitude and direction of the stress that the metal is subject to, whether that stress is residual or applied. Subsequently in this section, the following methods of nondestructive stress measurement are described: XRD, neutron diffraction, ultrasonic velocity, and magnetic Barkhausen noise.

X-ray diffraction techniques exploit the fact that when a metal is under stress (applied or residual), the resulting elastic strains cause the atomic planes in the metallic crystal structure to change their spacings. X-ray diffraction can directly measure this interplanar atomic spacing; from this quantity, the total stress on the metal can then be obtained.

Because metals are composed of atoms arranged in a regular three-dimensional array to form a crystal, most metal components of practical concern consist of many tiny crystallites (grains), randomly oriented with respect to their crystalline arrangement and fused together to make a bulk solid. When such a polycrystalline metal is placed under stress, elastic strains are produced in the crystal lattice of the individual crystallites. In other words, an externally applied stress or one residual within the material, when below the yield strength of the material, is taken up by interatomic strain. X-ray diffraction techniques can actually measure the interatomic spacings, which are indicative of the elastic strain in the specimen. Stress values are obtained from these elastic strains in the crystals by knowing the elastic constants of the material and assuming that stress is proportional to strain, a reasonable assumption for most metals and alloys of practical concern. An article published in *Journal of Metals* describes the XRD method and instrumentation in some detail. References 8 and 75 are excellent sources of practical, more detailed information on XRD stress measurement.

There are three basic techniques for measuring stresses, based on the XRD method. They are the double exposure (or two-angle) technique (DET), the single exposure (or one-angle) technique (SET), and the sin-square-psi (or multiangle) technique. The angle of exposure referred to is that between the incident x-ray beam and the specimen surface normal. It should be noted that in any XRD stress measurement technique, x-ray peaks in the far back-reflection range, that is, peaks with Bragg (θ) angles of near 90° , are much preferred because they show the greatest effect with a given amount of applied or residual stress. This is illustrated in the following equation:

$$\sigma_\phi = (2\theta_1 - 2\theta_2) \frac{\cot\theta_1}{2} \left[\frac{E}{1+\nu} \right] \frac{1}{\sin^2 \psi} \left[\frac{\pi}{180} \right] \quad (\text{Eq 34})$$

In Eq 34, θ_1 is the Bragg angle of the planes diffracting at ψ_1 ; θ_2 is the Bragg angle of the planes diffracting at ψ_2 . In Fig. 13, it can be seen that as θ_1 increases, its cotangent decreases; therefore, a larger difference ($2\theta_1 - 2\theta_\psi$) would result from a given σ_ϕ to maintain an equality.

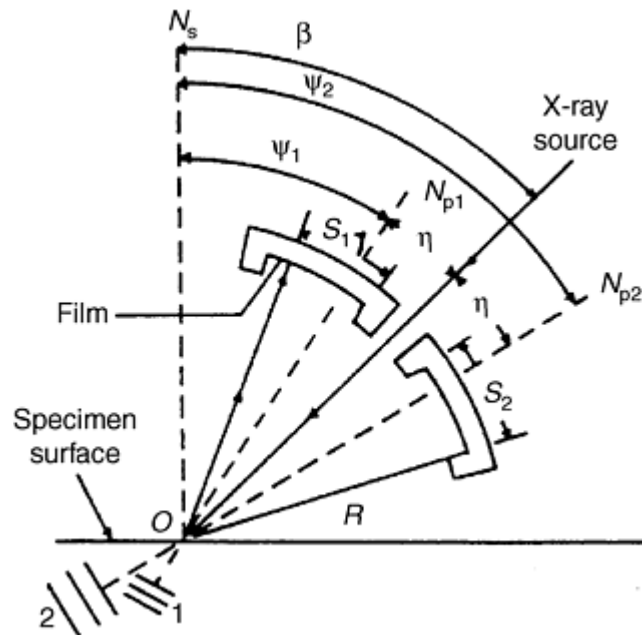


Fig. 13 One-angle arrangement or the single exposure technique (SET). N_s is the specimen normal, and β is the angle that the incident beam makes with N_s . N_{p1} and N_{p2} are the normals to the diffracting planes 1 and 2 respectively, and ψ_1 and ψ_2 are the angles between N_s , N_{p1} , and N_{p2} respectively. η is the angle between the incident beam and the diffracting plane normals. R_0 is the camera radius, and O is the point of incidence of the x-ray beam of the specimen. 1 and 2 represent the diffracting planes at various attitudes to the specimen surface. S_1 and S_2 are the measured parameters representing the distance from a reference point of known distance from the incident beam and the diffracted x-ray beam position. S_1 and S_2 are directly related to the Bragg angles, θ_1 and θ_2 . The stress being measured is parallel to the specimen surface and in the plane containing the x-ray source vector and the specimen surface normal, N_s .

For a residual stress measurement, the diffracting angle, θ , of interatomic planes of at least two different psi (ψ) angles with respect to the surface normal must be measured (Fig. 13). These planes are crystallographically equivalent (same Miller indices, hkl) and in the unstressed state of the metal would have the same interatomic, d , spacing for the planes labeled 1 and 2 in Fig. 13 (Ref 53, 76, 77). In a stressed material, however, the two or more orientations of diffracting planes are selected so that they are at different angles to the surface; thus their normals are at different (ψ) angles to the surface normal. Then, depending on the angle of these planes to the stress vector, their interplanar atomic spacing is increased or decreased by varying amounts.

The most common sources of errors and misapplications in stress measurements by x-rays are related to stress constant selection, focusing geometry, diffracted peak location, and cold-working, crystallographic texture, grain size, microstructure, and surface condition. The source, significance, and correction techniques for these errors are not elaborated on here; details may be found in an article by Ruud and Farmer (Ref 78) and (Ref 8).

A point of interest in the error sources listed above concerns cold working and microstresses. Microstresses are usually considered to be those manifested by strain variation across single metallic grain. This strain variation is detected in the XRD method as broadening of the x-ray peak—a distinctly different phenomenon from the peak shift caused by residual stresses. However, microstrain variation can be measured simultaneously with stress. This microstrain phenomenon has been proposed as a means of judging cold work, dislocation density, and fatigue damage (Ref 79).

Despite the facts that x-rays provide stress readings only to a depth of less than 0.025 mm. (0.001 in.) and that the error sources listed above must be considered, the noncontact XRD method is presently the only time-proven, generally applicable, truly nondestructive method for measuring residual stresses. Its reliability has been proved and documented by thousands of engineers and scientists over the past four decades beginning with the classic work of Bolstad et al. at Boeing using x-ray film cameras (Ref 80). This documentation includes measurement of stresses in the Brooklyn Bridge (Ref 20) and tempering evaluation of carburized steels. The Society of Automotive Engineers (SAE) considers the method of sufficient practical importance to have printed three handbook supplements on the subject (Ref 8), and another supplement is under revision.

Even so, this nondestructive technology has been largely restricted to the laboratory because of the general lack of knowledge regarding the state-of-the-art instruments and the limitations of the more widely known and available conventional scanning XRD equipment. Instrumentation for bringing this technology into the field and manufacturing area has advanced rapidly in the last two decades, especially toward increased portability, compactness, and speed of operation.

As shown in Fig. 14, instrumentation has been developed and is commercially available for stress measurement in situ on the inside diameter of 10 mm (4 in.) diameter pipe (Ref 39). Position sensitive x-ray detectors have been largely responsible for these improvements to both laboratory-based and field deployable residual stress measuring instruments (Ref 10, 21, 22, 39, 81, 82, and 83). Also, with the speed of data collection being less than 0.1 s with conventional x-ray tube sources in some applications, XRD stress measurement can be performed on moving components (Ref 12). Nevertheless, many engineers have been frustrated in applying XRD to residual stress measurement. This has been largely due to crystallographers inexperienced in residual stress measurement, attempting to apply conventional scanning x-ray diffractometers and techniques to residual stress measurement. For example, in conventional XRD analysis and crystallography, sharp resolution of the diffracted spectra is very beneficial. However, in XRD stress measurement, the need to measure (ψ) angles that are not zero defocuses the beam, and attempts to refocus lead to significant error in the stresses read (Ref 84). In XRD stress measurement, what is more important than sharp resolution is the repeatable ability to measure the position of a defocused diffracted x-ray peak (Ref 85). Thus, it is recommended in most cases that XRD residual stress measurement be performed by trained technologists using x-ray instrumentation specifically designed and built for stress measurement, not conventional scanning diffractometers. Software packages specifically for residual stress measurement used with conventional scanning diffractometers do not in most cases eliminate the mechanical and focusing problems of applying these instruments to residual stress measurement. It is necessary to mount the component (or specimen) in which stresses are to be measured on the conventional scanning diffractometer, which usually requires sectioning of the component and which complicates and adds error to the measurement procedure.



Fig. 14 Photograph of a miniature x-ray diffractometer for the one angle technique arrangement of XRD stress measurement. This device incorporates a Ruud-Barrett position sensitive scintillation detector and is capable of being inserted in a 101.60 mm (4 in.) inside diameter for measuring residual stress (Ref 39).

Neutron diffraction (ND) allows measuring the elastic strains induced by residual stresses throughout the volume of relatively thick steel components with a spatial resolution as small as 1 mm^3 . Such capability provides for the measurement of residual stress inside of components without the necessity of sectioning or layer removal. Principal ND methods, like the XRD methods, measure the spacing between crystallographic planes in a component, and this spacing is affected by residual and applied stress. The spacing between a selected set of crystallographic planes (ϕ) is related to the angle of incidence and diffraction of the neutron radiation, θ , which are equal, and the wavelength of the monochromatic radiation (λ) by Bragg's law:

$$\lambda = 2 d \sin \theta \quad (\text{Eq 35})$$

The elastic strain, ε , induced by the residual stress perpendicular to the diffracting crystallographic plane then is related to d by:

$$\varepsilon = \frac{d - d_0}{d_0} = \left(\frac{\sin \theta_0}{\sin \theta} \right)^{-1} \quad (\text{Eq 36})$$

where d_0 is the distance between the unstressed crystallographic planes. If the orientation of principal stresses is known in the component, the stress in any principal direction may be calculated by:

$$\sigma_A = \frac{E}{(1 + \nu)} \left[\varepsilon_A + \frac{\nu}{(1 - 2\nu)} (\varepsilon_A + \varepsilon_B + \varepsilon_C) \right] \quad (\text{Eq 37})$$

where σ_A , σ_B , and σ_C are the principal stresses and ε_A , ε_B , and ε_C are the strains measured in the corresponding principal stress directions. E and ν are the Young's modulus and Poisson's ratio, respectively. If the principal stress directions are not known, strains in at least six directions must be measured to determine the residual stresses acting on the volume of material in which strains are being measured.

For residual stress measurement in most alloys, the unstressed spacing (d_0) between crystallographic planes at the exact point of strain measurement is not known and not easily measured. This means that d_0 or θ_0 in Eq 36 cannot be precisely established, and this leads to various degrees of error in the accuracy and precision of ND residual stress measurements. This condition is aggravated by the fact that the elemental composition, and thus d_0 , vary considerably within a component and markedly within the phase (e.g., martensite, austenite, and ferrite for steel) of the alloy at various locations. Additional limitations are that the component must be brought to a nuclear reactor, each strain measurement requires over an hour, a single stress determination in one small volume of the component requires at least three strain measurements, and the measurements are very costly.

Nevertheless, the ND methods have been applied to residual stress measurements in weldments (Ref 86), cylindrical forgings (Ref 87), plastically deformed plate (Ref 88), rocket case forgings (Ref 86), and many other types of components.

Ultrasonic Velocity. The principle underlying the measurement of stress and thus elastic strain by ultrasonic (acoustic) techniques is the phenomenon of an approximately linear change in ultrasound velocity with applied stress. It has been shown that under certain restricted conditions, residual stress can be measured by exploiting this phenomenon. Stress is measured by inducing a sound wave in the frequency of several megahertz in the metal specimen and measuring the time of flight or some other velocity-related parameter. Because many other characteristics of metals besides stress-induced elastic strain affect velocity, their effect must be sorted out, but neither the technology nor the fundamental knowledge for such sorting is usually available. The great interest in ultrasonic techniques for residual stress measurement stems from their promise for three-dimensional nondestructive measurements within the material.

Principle. A number of velocity-related phenomena have been used in various methods to measure stress effects by ultrasound. All utilize the deviation of the reaction of the metal from the linearity of Hooke's law of elasticity, $\sigma = M\varepsilon$, where σ = stress, ε = strain, and M = elastic modulus. This has been referred to as the anharmonic property of the solid and may be represented by a power series $\sigma = M\varepsilon + C\varepsilon^2 + D\varepsilon^3 + \dots$, where C = third order anharmonic constant, D = fourth, and so on. Most research done for stress measurement has used expressions in which terms past the third order constant, C , are dropped. Of the several anharmonic property effects that may be used to measure stress, the following are probably the most exploited: velocity dependence on the elastic modulus; dispersion of frequency amplitudes in surface waves; birefringence of orthogonally polarized shear waves; and harmonic generation in surface waves.

A very simplified form of the anharmonic stress strain law has been written as $\sigma = M\varepsilon + C\varepsilon^2$ and rewritten as $\sigma = \varepsilon(M + C\varepsilon)$. The term in parentheses is approximately related to the velocity of sound as $\rho V^2 \cong M + C\varepsilon$, where ρ is the density of the medium and V is the velocity of sound. This may be approximately rewritten in terms of velocity dependence on strain as:

$$V = \sqrt{\frac{M}{\rho} \left[1 + \frac{C}{2M} \varepsilon \right]} \quad (\text{Eq 38})$$

Then, to solve for strain, $\varepsilon = 2(V\sqrt{M\rho} - 2M)/C$ (Ref 89).

A simple view of the dependency of ultrasonic velocity on the elastic modulus and density may be shown by rewriting the equation $\pi V^2 = M + C\varepsilon$ in terms of V , differentiating and dividing by V to yield an expression for $\Delta V/V$. The result will readily show that a fractional change in elastic modulus or density would affect the velocity. The density of metal, for which the Poisson ratio is near 0.3, obviously changes as a compressive or tensile stress is placed on the specimen, and it is reasonable that the speed of sound would then change.

Limitations and Applications. Ultrasonic technology offers a number of types of wave modes in which to probe metals; these include bulk waves, such as longitudinal and shear, and surface waves, usually confined to Rayleigh type. Each mode offers many unique parameters for extracting information. As has been discussed, the primary effect of stress—induced strain on ultrasonic propagation in metals—is on velocity. This may be detected in a number of ways, including measurements of wave velocity, shear wave birefringence, and dispersion. However, there are other characteristics of metals that affect the ultrasonic velocity to the same degree as stress. These include crystallographic texture, microstresses, multiple phases, coherent precipitates, composition gradients, and dislocation density and distribution.

Crecraft (Ref 90) discussed velocity effects, manifested as texture, induced birefringence, and the marked change seen with ultrasonic frequency. He also reported birefringence due to cold work in nickel-steel specimens but did not attempt to separate the cold-work effects in terms of texture, dislocation density, and so on. In the early 1950s, Bradfield and Pursey (Ref 91) and Pursey and Cox (Ref 92) reported showing the influence of small degrees of texture on ultrasonically measured elasticity in polycrystalline bars. They showed how the true isotropic elastic constants can be determined by using measurements of both longitudinal and shear wave speeds along several directions. They presented stereographic charts that illustrated the relationship between elastic behavior of cubic crystals and results of x-ray texture determinations.

McGonagle and Yun (Ref 93) noted the cold-work effects in an article comparing x-ray diffraction results with Rayleigh wave velocity measurements. Boland et al. (Ref 94) also recognized that other material properties can affect ultrasonic velocity and recommended that methods be developed to distinguish stress-induced velocity changes from those from other sources.

James and Buck (Ref 95) pointed out that since the third order elastic constants for most structural materials are not readily available from the literature, ultrasonic stress measurement must be calibrated relative to the particular material being investigated. In the same paper they discounted the possible effect of mobile dislocations on the sound velocity in structural engineering metals with high yield strengths due to the short dislocation loop lengths prevalent. However, they did mention that crystallographic preferred orientation (texture) during deformation or fatigue is capable of severely modifying the elastic constants on which the sound velocity depends.

Papadakis (Ref 96) noted marked velocity changes for ultrasonic waves in various steel microstructures, and Moro et al. (Ref 97) measured the effect of microstructural changes caused by tempering on the ultrasonic velocity in low-alloy steel.

Tittman and Thompson (Ref 98) evaluated the near-surface hardness of case-hardened steel with Rayleigh waves; because hardness in this case is a combination of composition, microstress, and macrostress, the velocity change was due to a combined effect.

The temperature sensitivity of ultrasonic stress measurements has also been cited as an important source of error. Salma et al. (Ref 99, 100) proposed that this dependence be used as a means to measure stress but also noted the marked effect of dislocations and did not address a methodology of separating the stress from the dislocation effect.

Much of the work cited above is concerned with attempts to measure the effects of a variety of material properties on the changes in ultrasonic velocity. However, there apparently is no comprehensive study that demonstrates the capability of quantitatively separating stress effects on ultrasonic propagation from other variables found in structural metals, such as dislocation density or crystallographic texture. Furthermore, most of the studies cited observed velocity changes in bulk waves. Velocity measurements on these waves must be measured through the thickness of a component and, as most metallurgists recognize, obtaining uniform properties through thicknesses greater than a few millimeters, especially in steels, is difficult. The subtle property variations to which ultrasound velocity is sensitive, the inherent lack of homogeneity in engineering metals, and the high residual stress gradients often found in manufactured components present additional serious problems for through-thickness stress measurements.

In spite of the microstructural variations in manufactured steel products, success in the application of ultrasonic methods to residual stress measurement has been achieved in specific cases. One is in the measurement of hoop

stresses in railroad wheels (Ref 101). Here changes or variations of the residual stress in the hoop direction is of concern, while that in the radial or axial direction can often be assumed to be constant or negligible. Some techniques, then, for the measurement of the residual hoop stresses have relied on normalizing the hoop velocity against the axial velocity (Ref 102). Also, European railroads have monitored ultrasonic velocity along the wheel rims during use and attributed changes to residual stress changes (Ref 103). Schramm in his article mentioned a number of approaches for the application of ultrasound to the measurement of residual stresses in railroad wheels, and these examples may find application in the measurement of residual stress in other axially symmetric shapes (Ref 101). Ultrasonic residual stress measurements have also been applied to rails as reported by Egle and Bray (Ref 104) and Bray and Leon-Salamanca (Ref 105).

Magnetic Barkhausen Noise. The Barkhausen noise analysis technique (BNA) is concerned with measuring the number and magnitude of abrupt magnetic reorientations made by expansion and contraction of the magnetic domains in a ferromagnetic metal. These reorientations are observed as pulses somewhat random in amplitude, duration, and temporal separation, and therefore roughly described as noise.

Applications. A few applications of BNA to ferromagnetic metallic components have been made. Gardner (Ref 106) mentions a number of applications, which include helicopter rotor blade spans, autofrettaged gun tubes, gas turbine engine components, and rolling element antifriction bearing components. In these examples the change in residual stresses caused by known service histories was measured.

Chait (Ref 107) qualitatively measured the residual stress condition of a high-hardness laminar composite steel weldment and compared some of the BNA data with XRD stress readings. Sundstrom and Torronen (Ref 108) applied their BNA method to a number of microstructural measurements, including evaluation of grain size measurement for low-carbon ferritic and ferritic-pearlitic steels, evaluation of anisotropy in deep drawing and textured steels for electrical applications, measurement of the degree of aging in rimmed carbon steels, and pearlite morphology in steel wires. These researchers have also measured iron loss in magnetic material used for transformers and have proposed using BNA for residual stress measurements, pointing out that quantitative results can be obtained if the material and its fabrication history are known and calibration is possible.

Most studies and applications of BNA to stress measurement have focused on the uniaxial stress state. However, Sundstrom and Torronen (Ref 108) implied that the instrumentation they used could simultaneously measure stress in two directions to give biaxial stress conditions for magnetic inspection of roller bearing components, including BNA for monitoring residual stress change.

The BNA method certainly has been demonstrated to be sensitive to the stress condition in ferromagnetic materials (Ref 109). Nevertheless, its possibilities for application are limited by the condition that the material must be ferromagnetic, the narrow total range of stress sensitivity (i.e., ± 40 ksi, or 275 MPa), and the shallow depth of measurement. The latter condition might be relieved by using magnetomechanical-acoustic emission (MAE) (Ref 110), an ultrasound analog to BNA. However, the sensitivity of either of these techniques to other characteristics of metallic components and the consequent need for calibration with a nearly identical specimen severely restricts the general applicability of BNA and MAE. Many misapplications have been made that have severely damaged the reputation of the BNA methods (Ref 107, 111). Such restrictions can be removed only if the basic phenomena responsible for the effect of microstructural properties on BNA and MAE are understood and quantified in terms of the signal.

BNA is not recommended where variations in elemental composition, phase composition, grain size, strain hardening, crystallographic texture, grain shape, grain orientation, carbide size and distribution, and other microstructural characteristics accompany variations in residual stress. A recent evaluation of BNA by Allison and Hendricks (Ref 112) confirms the uncertainty of BNA residual stress measurements.

References cited in this section

8. Residual Stress Measurement by X-Ray Diffraction-SAE J784a, *Society of Automotive Engineers Handbook Supplement*, Warrendale, PA, 1971
10. M.E. Brauss and J.A. Pineault, Residual Strain Measurement of Steel Structures, *NDE for the Energy Industry*, NDE Vol 13 (Book No. H00930-1995), D.E. Bray, Ed., American Society of Mechanical Engineers, 1995

12. C.O. Ruud and M.E. Jacobs, Residual Stresses Induced by Slitting Copper Alloy Strip, *NDC of Materials VI*, Plenum Press, 1994, p 413–424
20. M. Brauss, J. Pineault, S. Teodoropol, M. Belassel, R. Mayrbaur, and C. Sheridan, Deadload Stress Measurement on Brooklyn Bridge Wrought Iron Eye Bars and Truss Sections Using X-ray Diffraction Techniques, *Proc. of 14th Annual International Bridge Conf. and Exhibition*, Engineering Society of Western Pennsylvania, Pittsburgh, ICB-97-51, 1997, p 457–464
21. M.G. Carfaguo, F.S. Noorai, M.E. Brauss, and J.A. Pineault, “X-Ray Diffraction Measurement of Stresses in Post-Tensioning Tendons,” International Association for Bridge and Structural Engineering (IABSE) Symposium, 1995 (San Francisco), “Extending the Life Span of Structures,” IABSE, ETH Honggerberg, Zurich, Switzerland, Vol. 71/1, 1995, p 201–206
22. J.A. Pineault and M.E. Brauss, In Situ Measurement of Residual and Applied Stresses in Pressure Vessels and Pipeline Using X-ray Diffraction Techniques, Determining Material Characterization: *Residual Stress and Integrity with NDE*, PUP-Vol 276, NDE-Vol 12, American Society of Mechanical Engineers, New York, 1994
39. C.O. Ruud, P.S. DiMascio, and D.J. Snoha, A Miniature Instrument for Residual Stress Measurement, *Adv. X-Ray Anal.*, Vol 27, Plenum Press, 1984, p 273–283
53. B.D. Cullity, *Elements of X-Ray Diffraction*, 2nd ed., Addison-Wesley Publishing Co., Inc., 1978, p 469–472
75. C.O. Ruud, X-Ray Analysis and Advances in Portable Field Instrumentation, *J. Met.*, Vol 31 (No. 6), 10–15 June 1979
76. H.P. Klug and L.E. Alexander, *X-Ray Diffraction Procedures*, 2nd ed., New York, John Wiley & Sons, 1974, p 768–770
77. C.S Barrett and T.B. Massalski, *Structure of Metals*, 3rd ed., McGraw-Hill, 1966, p 474–476
78. C.O. Ruud and G.D. Farmer, Residual Stress Measurement by X-rays: Errors, Limitations, and Applications, *Nondestructive Evaluation of Materials*, J.J. Burke and V. Weiss, Ed., Plenum Press, 1979, p 101–116
79. R.N. Pangborn, S. Weissman, and I.R. Kramer, Dislocation Distribution and Prediction of Fatigue Damage, *Metall. Trans. A*, Vol 12 (No. 1) 1981, p 109–120
80. D.A. Bolstad, R.A. Davis, W.E. Quist, and E.C. Roberts, Measuring Stress in Steel Parts by X-Ray Diffraction, *Metals Progress*, 1963, p 88–92
81. D.S. Kurtz, P.R. Moran, K.J. Kozaczek, and M. Brauss, Apparatus for Rapid Psi Squared Stress Measurement and Its Applications to Titanium Alloy Jet Engine Fan Blades, *The Fifth International Conference on Residual Stresses*, Vol 2, Institute of Technology, Linkopings University, Sweden, 1997, p 744–749
82. B.B. He and K.L. Smith, Strain and Stress Measurements with Two-Dimensional Detector, *Adv. X-Ray Anal.*, Vol 41, 1977
83. M.R. James and J.B. Cohen, The Application of a Position-Sensitive X-Ray Detector to the Measurements of Residual Stresses, *Adv. X-Ray Anal.*, Vol 19, Gould, Barnett, Newkirk, and Ruud, Ed., 1976, p 695–708

84. H. Zantopoulou and C.F. Jateczak, Systematic Errors in Residual Stress Measurement Due to Specimen Geometry, *Adv. in X-Ray Anal.*, New York, Plenum Press, Vol 14, 1970
85. C.O. Ruud, D.J. Snoha, and D.P. Ivkovich, Experimental Methods for Determination of Precision and Estimation of Accuracy in XRD Residual Stress Measurement, *Adv. X-Ray Anal.*, Vol 30, 1987, p 511–522
86. J.H. Root, R.R. Hosbaus, and T.M. Holden, Neutron Diffraction Measurements of Residual Stresses Near a Pin Hole in a Solid-Fuel Booster Rocket Casing, *Practical Applications of Residual Stress Technology*, C.O. Ruud, Ed., ASM International, 1991, p 83–93
87. R.C. Donmarco, K.J. Kozaczek, P.C. Bastias, G.T. Hahn, and C.A. Rubin, Residual Stress and Retained Austenite Distribution and Evaluation in SAE 52100 Steel under Rolling Contact Loading, PVP-Vol 322, NDE-Vol 15, *NDE Engineering Codes and Standards and Materials Characterization*, J.S. Cook, Sr., C.D. Cowfer, and C.C. Monahan, Ed., American Society of Mechanical Engineers, 1996, p 63–70
88. M. Hayashi, S. Ohkido, N. Minakawa, and Y. Murii, Residual Stress Distribution Measurement in Plastically Bent Carbon Steel by Neutron Diffraction, *The Fifth International Conf. on Residual Stresses*, Vol 2, Institute of Technology, Linkopings University, Sweden, 1997, p 762–769
89. G.A. Alers, Ultrasonic Methods—Overview, *Proc. of a Workshop on Nondestructive Evaluation of Residual Stress*, NTIAC-76-2, 1975, p 155–161
90. D.I. Crecraft, Ultrasonic Measurement of Stresses, *Ultrasonics*, 1968, p 117–121
91. G. Bradfield and H. Pursey, *Philos. Mag.*, Vol 44 (No. 295), 1953
92. H. Pursey and H.L. Cox, *Philos. Mag.*, Vol 45, 1954, p 295
93. W.J. McGonagle and S.S. Yun, Measurement of Surface-Residual Stress by Nondestructive Methods, *Proc. of the 5th International Conf. on Nondestructive Testing*, 1967, p 159–164
94. A.J. Boland et al., “Development of Ultrasonic Tonography for Residual Stress Mapping,” Final Report, EPRI RP 504-2, Electric Power Research Institute, 1980
95. M.R. James and O. Buck, Quantitative Nondestructive Measurement of Residual Stresses, *Crit. Rev. Solid State Mater. Sci.*, August 1980, p 61–105
96. E.P. Papadakis, Ultrasonic Attenuation and Velocity in Three Transformation Products of Steel, *J. Appl. Phys.*, Vol 35 (No. 5), 1964, p 1474–1482
97. A. Moro, C. Farina, and F. Rossi, Measurement of Ultrasonic Wave Velocity of Steel for Various Structures and Degrees of Cold-Working, *Nondestruct. Test. Int.*, Aug 1980, p 169–175
98. B.R. Tittman and R.B. Thompson, Measurement of Physical Property Gradients with Elastic Surface Wave Dispersion, *Proc. Ninth Symposium on NDE*, 1980, p 20–28
99. K. Salama and C.K. Ling, The Effect of Stress on The Temperature Dependence of Ultrasound Velocity, *J. Appl. Phys.*, Vol 51 (No. 3) March 1980, 1505–1509
100. K. Salama and G.A. Alers, Third-Order Elastic Constants of Copper at Low Temperature, *Phys. Rev.*, Vol 161 (No. 3), Sept 1967, p 673–680

101. R.E. Schramm, J. Szelazek, and A. Van Clark, Jr., Ultrasonic Measurement of Residual Stress in the Rims of Inductively Heated Railroad Wheels, *Mater. Eval.*, August 1996, p 929–933
102. H. Fukuaka, H. Tada, K. Hirakawa, H. Sakawoto, and Y. Toyo, Acoustoelastic Measurements of Residual Stresses in the Rim of Railroad Wheels, *Wave Propagation in Inhomogenous Media and Ultrasonic Nondestructive Evaluation*, Vol 6, G.C. Johnson, Ed., American Society of Mechanical Engineers, 1984, p 185–193
103. E.R. Schneider, R. Harzer, D. Bruche, and H. Frotscher, Reliability Assurance of Railroad Wheels by Ultrasonic Stress Analysis, *Proc. of Third European Conf. on Residual Stress Analysis*, 4–6 Nov 1992, DGM Informationsgesellschaft mbH
104. D.M. Egle and D.E. Bray, Ultrasonic Measurement of Longitudinal Rail Stresses, *Mater. Eval.*, Vol 378 (No. 4), March 1979, p 41–46
105. D.E. Bray and T. Leon-Salamanca, Zero-Force Travel-Time Parameters of Ultrasonic Head-Waves in Railroad Rail, *Mater. Eval.*, Vol 43 (No. 7), June 1985, p 854–858
106. C.G. Gardner, Barkhausen Noise Analysis, *Proc. of a Workshop on Nondestructive Evaluation of Residual Stress*, NTIAC-76-2, 1975, p 211–217
107. R. Chait, “Residual Stress Pattern in a High Hardness Laminar Composite Steel Weldment,” *Proc. of a Workshop on Nondestructive Eval. of Residual Stress*, NTIAC-76-2, 1975, p 237–245
108. O. Sundstrom and K. Torronen, The Use of Barkhausen Noise Analysis in Nondestructive Testing, *Mater. Eval.*, Feb 1979, p 51–56
109. J.R. Barton, F.N. Kusenberger, R.E. Beissner, and G.A. Matskanin, Advanced Quantitative Magnetic Nondestructive Evaluation Methods, Theory and Experiment, *Nondestructive Evaluation of Materials*, J.J. Burke and V. Weiss, Ed., Plenum Press, 1979, p 461–463
110. K. Ono, M. Shibata, and M.M. Kwan, “Determination of Residual Stress by Magnetomechanical Acoustic Emission,” ONR Technical Report 80-01, April 1980
111. R.R. King and V.D. Smith, “Residual Stress Measurements in Structural Steels,” Final Report SWRI Project 15-4600, Contract DOT-FH-11-9133, January 1978
112. H.D. Allison and R.W. Hendricks, Correlation of Barkhausen Noise Signal and X-Ray Residual Stress Determinations in Grinding-Burned 52100 Steel,” *The Fifth International Conference on Residual Stresses*, Vol 2, Institute of Technology, Linkopings University, Sweden, 1997, p 640–645

Residual Stress Measurements

Clayton O. Ruud, The Pennsylvania State University

Summary

Only the destructive stress relief, semidestructive hole drilling, or nondestructive XRD methods of residual stress measurement are generally reliable over a broad range of alloys displaying residual stress fields induced by the various manufacturing processes. By and large, failures on metallic components caused or aided by

residual stresses are due to surface stresses and can be measured by surface measuring methods including XRD and, for some cases, hole drilling. In these cases good spatial resolution and identification of the magnitude and location of the highest stresses is of primary importance. On the other hand, when distortion of metallic components presents a problem, the distribution and magnitude of residual stresses through the bulk of the component are of most interest, and high resolution and identification of areas of high stress magnitude are not of primary concern. In either case, stress measurement precision on the order of 5 ksi (35 MPa) is usually sufficient. Measurement of residual stresses can be very expensive and time consuming, and it is often worthwhile to consult experts in the field before deciding on a measurement method. Before an engineer or scientist not experienced in residual stress measurement selects a method and attempts to measure stresses, consultation with an expert experienced in residual stress measurement and analysis should be sought.

Residual Stress Measurements

Clayton O. Ruud, The Pennsylvania State University

References

1. K. Masubuchi, Residual Stresses and Distortion, *Welding, Brazing, and Soldering*, Vol 6, *ASM Handbook*, 10th ed., 1993, p 1094–1102
2. C.O. Ruud, P.S. DiMascio, and J.J. Yavelak, Comparison of Three Residual Stress Measurement Methods on a Mild Steel Bar, *Exp. Mech.*, Vol 25 (No. 4), Sept 1985, p 338–343
3. J. Pineault and M. Brauss, Automated Stress Mapping—A New Tool for the Characterization of Residual Stress and Stress Gradients, *Proc. 4th International Conf. on Residual Stresses*, Society for Experimental Mechanics, Bethel, CT, 1994, p 40–44
4. R. Wimpory, G.M. Swallow, and P. Lukas, Neutron Diffraction Residual Stress Measurements in Carbon Steels, *The Fifth International Conference on Residual Stresses*, Vol 2, Institute of Technology, Linkopings University, Sweden, 1997, p 676–681
5. R. Gunnert, “Method for Measuring Triaxial Residual Stresses,” Document No. X-184057-OE, *Commission X of the International Institute of Welding*, 1957, and *Weld. Res. Abroad*, Vol 4 (No. 10), 1958, p 1725
6. M.G. Moore and W.P. Evans, Mathematical Corrections in Removal Layers in X-Ray Diffraction Residual Stress Analysis, *SAE Trans.*, Vol 66, 1958, p 340–345
7. A. Constantinescu and P. Ballard, On the Reconstruction Formulae of Subsurface Residual Stresses after Matter Removal, *The Fifth International Conf. on Residual Stresses*, Vol 2, Institute of Technology, Linkopings University, Sweden, 1997, p 703–708
8. Residual Stress Measurement by X-Ray Diffraction-SAE J784a, *Society of Automotive Engineers Handbook Supplement*, Warrendale, PA, 1971
9. A.J. Bush and F.J. Kromer, “Residual Stresses in a Shaft after Weld Repair and Subsequent Stress Relief,” Paper No. A-16 presented at Society for Experimental Stress Analysis (SESA) Spring Meeting, 1979 (Westport, CT), 1979

10. M.E. Brauss and J.A. Pineault, Residual Strain Measurement of Steel Structures, *NDE for the Energy Industry*, NDE Vol 13 (Book No. H00930-1995), D.E. Bray, Ed., American Society of Mechanical Engineers, 1995
11. C.O. Ruud and P.S. DiMascio, A Prediction of Residual Stress in Heavy Plate Butt Weldments, *J. Mater. Eng. Sys.*, Vol 31 (No. 1), Jan 1981, p 62–65
12. C.O. Ruud and M.E. Jacobs, Residual Stresses Induced by Slitting Copper Alloy Strip, *NDC of Materials VI*, Plenum Press, 1994, p 413–424
13. E.F. Rybicki and R.B. Stonesifer, Computation of Residual Stresses Due to Multipass Welds in Piping Systems, *ASME*, 78-PVP-104, 1978
14. M. Ehlers, H. Muller, and D. Loke, Simulation of Stresses and Residual Stresses Due to Immersion Cooling of Tempering Steel, *The Fifth International Conf. on Residual Stresses*, Vol 1, Institute of Technology, Linkopings University, Sweden, 1997, p 400–405
15. K. Masubuchi, *Analysis of Welded Structures: Residual Stresses, Distortion, and Their Consequences*, 1st ed., Pergamon Press, 1980
16. M. Bijak-Zochowski, P. Marek, and M. Tracz, On Subsurface Distributions of Residual Stress Created by Elasto-Plastic Rolling Contact, *The Fifth International Conf. on Residual Stresses*, Vol 1, Institute of Technology, Linkopings University, Sweden, 1997, p 430–445
17. D. Green and S. Bate, Calculation of Residual Stresses Using Simplified Weld Bead Modelling Technique, *Fifth International Conf. on Residual Stresses*, Vol 1, Institute of Technology, Linkopings University, Sweden, 1997, p 508–513
18. H. Michaud, F. Mechi, and T. Foulquies, Three Dimensional Representation of the Residual Stress Distribution in Steel Wires or Bars, *The Fifth International Conf. on Residual Stresses*, Vol 1, Institute of Technology, Linkopings University, Sweden, 1997, p 534–538
19. K.W. Mahin, W.S. Winters, T. Holden, and J. Root, Measurement and Prediction of Residual Elastic Strain Distributions in Stationary and Traveling Gas Tungsten Arc Welds, *Practical Applications of Residual Stress Technology*, ASM, 1991, p 103–109
20. M. Brauss, J. Pineault, S. Teodoropol, M. Belassel, R. Mayrbaur, and C. Sheridan, Deadload Stress Measurement on Brooklyn Bridge Wrought Iron Eye Bars and Truss Sections Using X-ray Diffraction Techniques, *Proc. of 14th Annual International Bridge Conf. and Exhibition*, Engineering Society of Western Pennsylvania, Pittsburgh, ICB-97-51, 1997, p 457–464
21. M.G. Carfagno, F.S. Noorai, M.E. Brauss, and J.A. Pineault, “X-Ray Diffraction Measurement of Stresses in Post-Tensioning Tendons,” International Association for Bridge and Structural Engineering (IABSE) Symposium, 1995 (San Francisco), “Extending the Life Span of Structures,” IABSE, ETH Honggerberg, Zurich, Switzerland, Vol. 71/1, 1995, p 201–206
22. J.A. Pineault and M.E. Brauss, In Situ Measurement of Residual and Applied Stresses in Pressure Vessels and Pipeline Using X-ray Diffraction Techniques, Determining Material Characterization: *Residual Stress and Integrity with NDE*, PUP-Vol 276, NDE-Vol 12, American Society of Mechanical Engineers, New York, 1994
23. E. Heyn, Internal Strains in Cold Wrought Metals, and Some Troubles Caused Thereby, *J. Inst. Met.*, Vol 12, 1914, p 1–37

24. E. Stablein, Stress Measurements on Billets Quenched from One Side," *Stahl and Eisen*, Vol 52, 1932, p 15–17
25. M. Mesnager, Methods for the Determination of Stresses Existing in a Circular Cylinder, C.R. Hebd. Seances Acad. Sci., 1926, Vol 169
26. G. Sacks, Evidence of Residual Stresses in Rods and Tubes, *Feitschrift fur Metallkunde*, Vol 19, 1927, p 352–357
27. T.G. Trenting and W.T. Read, Jr., *J. Appl. Phys.*, Vol 22 (No. 2), Feb 1951, 130–134
28. R. Gunnert, *Residual Welding Stresses, Method of Measuring Residual Stresses and Its Application to a Study of Residual Welding Stresses*, Alquist E. Wicksell, Stockholm, 1955
29. R. Gunnert, "Method for Measuring Residual Stresses in the Interior of a Material," Document No. X-162-57, *Commission X of the International Institute of Welding*, 1957, and *Weld. Res. Abroad*, Vol 6, 1960, p 10–24
30. D. Rosenthal and J.T. Norton, A Method for Measuring Triaxial Residual Stresses in Plates, *Weld. J.*, Vol 24 (No. 5), Research Supplement, 194 295s–307s
31. R. J-S. Chen, "Determination of Residual Stresses in a Thick Weldment," M.S. thesis, The Pennsylvania State University, November 1983
32. P. Johanssen, "Determination of Residual Stresses in Thick Welded Plated Utilizing X-Rays and Layer Removal Techniques, Part 1: Theory for Reconstruction of Original Stress State," Internal Report, Department of Materials and Solid Mechanics, The Royal Institute of Technology, S100, 44, Stockholm, April 1978
33. C.O. Ruud, R.N. Pangborn, P.S. DiMascio, and P.J. Snoha, Residual Stress Measurement on Thick Plate Low-Alloy Steel Narrow Gap Weldments by X-Ray Diffraction, *ASME*, 84-PVP-128, 1984
34. C.O. Ruud, J.A. Josef, and D.J. Snoha, "Residual Stress Characterization of Thick-Plate Weldments Using X-ray Diffraction," *Weld. Res. J. Supplement*, AWS, March 1993, p 875–915
35. A.R. McIlree, C.O. Ruud, and M.E. Jacobs, The Residual Stresses in Stress Corrosion Performance of Roller Expanded Inconel 600 Steam Generator Tubing, *Proc. of the International Conf. on Expanded and Rolled Joint Technology*, Canadian Nuclear Society, 1993, p 139–148
36. Y.W. Park, P.H. Cohen, and C.O. Ruud, The Development of a Model for Plastic Deformation in Machined Surface, *Mater. Manuf. Process.*, Vol 8 (No. 5), 1994
37. E. Schreiber and H. Schlicht, Residual Stresses After Turning of Hardened Components, *Residual Stresses in Science and Technology*, Vol 2, DGM Informationsgesell Schaft, Verlag, Germany, 1987, p 853–860
38. W.J. Shack, W.A. Ellingson, and L.E. Pahis, "Measurements of Residual Stresses in Type-304 Stainless Steel Piping Butt Welds," EPRI NoP-1413, R.P. 449-1, Electric Power Research Institute, Palo Alto, CA, June 1980
39. C.O. Ruud, P.S. DiMascio, and D.J. Snoha, A Miniature Instrument for Residual Stress Measurement, *Adv. X-Ray Anal.*, Vol 27, Plenum Press, 1984, p 273–283

40. G. Pickel, Application of the Fourier Method to the Solution of Certain Boundary Problems in the Theory of Elasticity, *J. Appl. Mech.*, 1944, p 176–182
41. D.L. Sikarskie, On a Series Form of Correction to Stresses Measured Using X-Ray Diffraction, *AIME Trans.*, Vol 39, 1967, p 577–580
42. Y.W. Park, P.H. Cohen, and C.O. Ruud, Sensitivity of Shear Process on Metal Cutting to the Development of Residual Stress, *Rev. Prog. in NDE*, Vol 14, 1995, p 1183–1188
43. Y.C. Shin, S.J. Oh, and C.O. Ruud, Investigation of Residual Stresses of Machined Surfaces by an X-Ray Diffraction Technique, *NDC of Materials IV*, Plenum Press, 1992, p 408–418
44. J.E. Hoffman, D. Lohe, and E. Macherauch, Influence of Machining Residual Stresses on the Bending Fatigue Behaviors of Notched Specimens of Ck45 in Different Heat Treating States, *Residual Stresses in Science and Technology*, Vol 2, p 801–814, DGM Informationsgesellschaft, Verlag, Germany, 1987
45. E. Brinksmier, Residual Stressed in Hard Metal Cutting, *Residual Stresses in Science and Technology*, Vol. 2, DGM Informationsgesellschaft, Verlag, Germany, 1987, p 839–846
46. F. Ghanem, H. Dishom, C. Braham, R. Fatallak, and J. Leider, An Engineering Approach to the Residual Stresses Due to Electric-Discharge Machining Process, *Proc. The Fifth International Conf. on Residual Stresses (ICRS-5)*, Vol 1, Ericson, Oden, and Anderson, Ed., Institute of Technology, Linkopings University, Sweden, 1977, p 157–163
47. Electropolishing, *Surface Cleaning, Finishing, and Coating*, Vol 5, *Metals Handbook*, 9th ed., American Society for Metals, Vol 5, 1982, p 303–309
48. M. Hetenyi, Ed., *Handbook of Experimental Stress Analysis*, John Wiley & Sons, Inc., 1950
49. N.A. Crites, Your Guide to Today's Strain Gages, *Prod. Eng.*, Vol 33 (No. 4), 17 Feb 1962, p 69–81, and Equipment and Application-Today's Strain Gages, *Prod. Eng.*, Vol 33 (No. 6), 19 March 1962, p 85–93
50. Y.Y. Hung, Shearography: A New Optical Method for Strain Measurement and Nondestructive Testing, *Opt. Eng.*, Vol 21 (No. 3), 1982, p 391–394
51. K. Li, Interferometric Strain/Slope Rosette Technique for Measuring Displacements/Slopes/Strains/Residual Stresses, *Proc. of the 1997 NSF Design and Manufacturing Grantees Conf.*, University of Washington, Seattle, National Science Foundation (NSF), 1997, p 571–572
52. C.S. Vikram, M.J. Pedensky, C. Feng, and D. Englehaupt, Residual Stress Analysis by Local Laser Heating and Speckle-Correlation Interferometry, *Exp. Tech.*, Nov/Dec 1996, p 27–30
53. B.D. Cullity, *Elements of X-Ray Diffraction*, 2nd ed., Addison-Wesley Publishing Co., Inc., 1978, p 469–472
54. C.O. Ruud, “Residual and Applied Stress Analysis of an Alloy 600 Row 1 U-Bend,” NP-5282, R.P 5303-3, Elect. Power Res. Inst., Palo Alto, CA 1987, p 2–11
55. A. Bouzina, C. Braham, and J. Ledion, Evaluation and Prediction of Real Stress State Stress Corrosion Cracking Specimens, *The Fifth International Conf. on Residual Stresses*, Vol 2, Institute of Technology, Linkopings University, Sweden, 1997, p 1060–1065

56. K. Masubuchi and D.C. Martin, Investigation of Residual Stresses by Use of Hydrogen Cracking, *Weld. J.*, Vol 40 (No. 12), Research Supplement, 1961, p 553s–556s
57. C.E. McKinsey, Effect of Low-Temperature Stress Relieving on Stress Corrosion Cracking, *Weld. J.*, Vol 33 (No. 4), 1954, Research Supplement p 161s–166s
58. W. Radeker, A New Method for Proving the Existence of Internal Stress Caused by Welding, *Schneissen Schneider*, Vol 10 (No. 9), 1958, p 351–358
59. J. Mathar, Determination of Initial Stresses by Measuring Deformation Around Drilled Holes, *Arch. Eisenhüttenwes.*, Vol 6, p 277–281 and *Trans. ASME*, Vol 56 (No. 4), 1934, p 249–254
60. “Determining Residual Stresses by the Hole Drilling Strain-Gage Method,” E 837, ASTM, 1983
61. H. Wolf and D.C. Sauer, “New Experimental Technique to Determine Residual Stresses in Large Turbine-Generator Components,” presented at the American Power Conf., (Chicago, IL), 1 May 1974
62. H. Wolf and W. Bohn, Origin, Measurement and Assessment of Residual Stresses in Large Forging for Turbines and Generators, *Arch. Eisenhüttenwes.*, Vol 42 (No. 7) 1971, p 509–511 (in German)
63. H. Wolf, E. Stucker, and H. Nowack, “Investigations of Residual Stresses in the Turbine and Generator Industry,” *Arch. Eisenhüttenwes.*, Vol 48 (No. 3), March 1977, p 173–178
64. J. Lu and J.F. Flavenot, “Applications of the Incremental Hole-Drilling Method for Measurement of Residual Stress Distributions—Experimental Techniques, paper presented at the Society for Experimental Mechanics (SEM) Spring Conference,” 5–10 June 1988 (Portland, OR), SEM
65. M.T. Flaman and B.H. Manning, Determination of Residual Stress Variation with Depth by the Hole-Drilling Method, *Exp. Mech.*, Vol 25, 1985, p 205–207
66. R.A. Kelsey, Measuring Nonuniform Residual Stresses by the Hole Drilling Method, *Proc. Society for Experimental Stress Analysis*, Vol 14 (No. 1), 1956, p 181–184
67. A.J. Bush and F.J. Kromer, Simplification of the Hole-Drilling Method of Residual Stress Measurement, *ISA Transactions*, Vol 12 (No. 3), 1973, p 249–259
68. N.J. Rendler and I. Vigness, Hole-Drilling Strain-Gage Method of Measuring Residual Stress, *Exp. Mech.*, Vol 6 (No. 12), Dec 1966, p 577–586
69. J.W. Dini, G.A. Beneditti, and H.R. Johnson, Residual Stresses in Thick Electro-deposits of a Nickel-Cobalt Alloy, *Exp. Mech.*, February 1976, p 56–60
70. F. Witt, F. Lee, and W. Rider, A Comparison of Residual Stress Measurements Using Blind-Hole, Abrasive-Jet and Trepanning Methods, *Exp. Tech.*, Vol 7, Feb 1983, p 41–45
71. P.S. Prevey, “Residual Stress Distribution Produced by Strain Gage Surface Preparations,” *1986 SEM Conference on Experimental Mechanics*, 1986
72. G. Sines and R. Carlson, “Hardness Measurements for the Determination of Residual Stresses,” *ASTM Bulletin 180*, Feb 1952, p 35–37
73. J. Pomey, F. Goratel, and L. Abel, “Détermination des Contraintes Résiduelles dans les Pièces Élévées,” *Publication Scientifiques et Techniques du Ministère de l'air*, 1950, p 263

74. S.S. Chiang, D.B. Marshall, and A.G. Evans, The Response of Solids to Elastic/Plastic Indentations I: Stresses and Residual Stresses, *J. Appl. Phys.*, Vol 53 (No. 1), 1982, p 298–311
75. C.O. Ruud, X-Ray Analysis and Advances in Portable Field Instrumentation, *J. Met.*, Vol 31 (No. 6), 10–15 June 1979
76. H.P. Klug and L.E. Alexander, *X-Ray Diffraction Procedures*, 2nd ed., New York, John Wiley & Sons, 1974, p 768–770
77. C.S Barrett and T.B. Massalski, *Structure of Metals*, 3rd ed., McGraw-Hill, 1966, p 474–476
78. C.O. Ruud and G.D. Farmer, Residual Stress Measurement by X-rays: Errors, Limitations, and Applications, *Nondestructive Evaluation of Materials*, J.J. Burke and V. Weiss, Ed., Plenum Press, 1979, p 101–116
79. R.N. Pangborn, S. Weissman, and I.R. Kramer, Dislocation Distribution and Prediction of Fatigue Damage, *Metall. Trans. A*, Vol 12 (No. 1) 1981, p 109–120
80. D.A. Bolstad, R.A. Davis, W.E. Quist, and E.C. Roberts, Measuring Stress in Steel Parts by X-Ray Diffraction, *Metals Progress*, 1963, p 88–92
81. D.S. Kurtz, P.R. Moran, K.J. Kozaczek, and M. Brauss, Apparatus for Rapid Psi Squared Stress Measurement and Its Applications to Titanium Alloy Jet Engine Fan Blades, *The Fifth International Conference on Residual Stresses*, Vol 2, Institute of Technology, Linkopings University, Sweden, 1997, p 744–749
82. B.B. He and K.L. Smith, Strain and Stress Measurements with Two-Dimensional Detector, *Adv. X-Ray Anal.*, Vol 41, 1977
83. M.R. James and J.B. Cohen, The Application of a Position-Sensitive X-Ray Detector to the Measurements of Residual Stresses, *Adv. X-Ray Anal.*, Vol 19, Gould, Barnett, Newkirk, and Ruud, Ed., 1976, p 695–708
84. H. Zantopoulou and C.F. Jaczak, Systematic Errors in Residual Stress Measurement Due to Specimen Geometry, *Adv. in X-Ray Anal.*, New York, Plenum Press, Vol 14, 1970
85. C.O. Ruud, D.J. Snoha, and D.P. Ivkovich, Experimental Methods for Determination of Precision and Estimation of Accuracy in XRD Residual Stress Measurement, *Adv. X-Ray Anal.*, Vol 30, 1987, p 511–522
86. J.H. Root, R.R. Hosbaus, and T.M. Holden, Neutron Diffraction Measurements of Residual Stresses Near a Pin Hole in a Solid-Fuel Booster Rocket Casing, *Practical Applications of Residual Stress Technology*, C.O. Ruud, Ed., ASM International, 1991, p 83–93
87. R.C. Donmarco, K.J. Kozaczek, P.C. Bastias, G.T. Hahn, and C.A. Rubin, Residual Stress and Retained Austenite Distribution and Evaluation in SAE 52100 Steel under Rolling Contact Loading, PVP-Vol 322, NDE-Vol 15, *NDE Engineering Codes and Standards and Materials Characterization*, J.S. Cook, Sr., C.D. Cowfer, and C.C. Monahan, Ed., American Society of Mechanical Engineers, 1996, p 63–70
88. M. Hayashi, S. Ohkido, N. Minakawa, and Y. Murii, Residual Stress Distribution Measurement in Plastically Bent Carbon Steel by Neutron Diffraction, *The Fifth International Conf. on Residual Stresses*, Vol 2, Institute of Technology, Linkopings University, Sweden, 1997, p 762–769

89. G.A. Alers, Ultrasonic Methods—Overview, *Proc. of a Workshop on Nondestructive Evaluation of Residual Stress*, NTIAC-76-2, 1975, p 155–161
90. D.I. Crecraft, Ultrasonic Measurement of Stresses, *Ultrasonics*, 1968, p 117–121
91. G. Bradfield and H. Pursey, *Philos. Mag.*, Vol 44 (No. 295), 1953
92. H. Pursey and H.L. Cox, *Philos. Mag.*, Vol 45, 1954, p 295
93. W.J. McGonagle and S.S. Yun, Measurement of Surface-Residual Stress by Nondestructive Methods, *Proc. of the 5th International Conf. on Nondestructive Testing*, 1967, p 159–164
94. A.J. Boland et al., “Development of Ultrasonic Tonography for Residual Stress Mapping,” Final Report, EPRI RP 504-2, Electric Power Research Institute, 1980
95. M.R. James and O. Buck, Quantitative Nondestructive Measurement of Residual Stresses, *Crit. Rev. Solid State Mater. Sci.*, August 1980, p 61–105
96. E.P. Papadakis, Ultrasonic Attenuation and Velocity in Three Transformation Products of Steel, *J. Appl. Phys.*, Vol 35 (No. 5), 1964, p 1474–1482
97. A. Moro, C. Farina, and F. Rossi, Measurement of Ultrasonic Wave Velocity of Steel for Various Structures and Degrees of Cold-Working, *Nondestruct. Test. Int.*, Aug 1980, p 169–175
98. B.R. Tittman and R.B. Thompson, Measurement of Physical Property Gradients with Elastic Surface Wave Dispersion, *Proc. Ninth Symposium on NDE*, 1980, p 20–28
99. K. Salama and C.K. Ling, The Effect of Stress on The Temperature Dependence of Ultrasound Velocity, *J. Appl. Phys.*, Vol 51 (No. 3) March 1980, 1505–1509
100. K. Salama and G.A. Alers, Third-Order Elastic Constants of Copper at Low Temperature, *Phys. Rev.*, Vol 161 (No. 3), Sept 1967, p 673–680
101. R.E. Schramm, J. Szelazek, and A. Van Clark, Jr., Ultrasonic Measurement of Residual Stress in the Rims of Inductively Heated Railroad Wheels, *Mater. Eval.*, August 1996, p 929–933
102. H. Fukuaka, H. Tada, K. Hirakawa, H. Sakawoto, and Y. Toyo, Acoustoelastic Measurements of Residual Stresses in the Rim of Railroad Wheels, *Wave Propagation in Inhomogenous Media and Ultrasonic Nondestructive Evaluation*, Vol 6, G.C. Johnson, Ed., American Society of Mechanical Engineers, 1984, p 185–193
103. E.R. Schneider, R. Harzer, D. Bruche, and H. Frotscher, Reliability Assurance of Railroad Wheels by Ultrasonic Stress Analysis, *Proc. of Third European Conf. on Residual Stress Analysis*, 4–6 Nov 1992, DGM Informationsgesellschaft mbH
104. D.M. Egle and D.E. Bray, Ultrasonic Measurement of Longitudinal Rail Stresses, *Mater. Eval.*, Vol 378 (No. 4), March 1979, p 41–46
105. D.E. Bray and T. Leon-Salamanca, Zero-Force Travel-Time Parameters of Ultrasonic Head-Waves in Railroad Rail, *Mater. Eval.*, Vol 43 (No. 7), June 1985, p 854–858
106. C.G. Gardner, Barkhausen Noise Analysis, *Proc. of a Workshop on Nondestructive Evaluation of Residual Stress*, NTIAC-76-2, 1975, p 211–217

107. R. Chait, "Residual Stress Pattern in a High Hardness Laminar Composite Steel Weldment," *Proc. of a Workshop on Nondestructive Eval. of Residual Stress*, NTIAC-76-2, 1975, p 237–245
108. O. Sundstrom and K. Torronen, The Use of Barkhausen Noise Analysis in Nondestructive Testing, *Mater. Eval.*, Feb 1979, p 51–56
109. J.R. Barton, F.N. Kusenberger, R.E. Beissner, and G.A. Matskanin, Advanced Quantitative Magnetic Nondestructive Evaluation Methods, Theory and Experiment, *Nondestructive Evaluation of Materials*, J.J. Burke and V. Weiss, Ed., Plenum Press, 1979, p 461–463
110. K. Ono, M. Shibata, and M.M. Kwan, "Determination of Residual Stress by Magnetomechanical Acoustic Emission," ONR Technical Report 80-01, April 1980
111. R.R. King and V.D. Smith, "Residual Stress Measurements in Structural Steels," Final Report SWRI Project 15-4600, Contract DOT-FH-11-9133, January 1978
112. H.D. Allison and R.W. Hendricks, Correlation of Barkhausen Noise Signal and X-Ray Residual Stress Determinations in Grinding-Burned 52100 Steel," *The Fifth International Conference on Residual Stresses*, Vol 2, Institute of Technology, Linkopings University, Sweden, 1997, p 640–645

Mechanical Testing of Fiber-Reinforced Composites*

Dale Wilson, The Johns Hopkins University, Leif A. Carlsson, Florida Atlantic University

Introduction

THE CHARACTERIZATION of engineering properties is a complex issue for fiber-reinforced composites (FRC) due to their inherent anisotropy and inhomogeneity. In terms of mechanical properties, advanced composite materials are evaluated by a number of specially designed test methods. These test methods are mechanically simple in concept but extremely sensitive to specimen preparation and test-execution procedures, often requiring complex data reduction analysis. The rigor of specimen fabrication and testing practices employed determine the quality and cost of the resulting mechanical property data. It is important to define the purpose of mechanical characterization prior to conducting tests. The purpose determines the type of testing program, specimen fabrication, testing rigor, and, ultimately, the cost of characterization. Costs are controlled and time is saved by matching quality and accuracy requirements to the intended materials usage.

Footnote

* The section "Interlaminar Shear Properties of Fiber-Reinforced Composites at High Strain Rates" was written by John Harding and Stephen Hallett, Oxford University. The section "Fatigue Testing and Behavior of Fiber-Reinforced Composites" was written by W. Steven Johnson and Ramesh Talreja, Georgia Institute of Technology.

Mechanical Testing of Fiber-Reinforced Composites

Dale Wilson, The Johns Hopkins University, Leif A. Carlsson, Florida Atlantic University

General Concepts

Before describing the principal tests used for mechanical characterization of composites, the authors offer a review of the purposes of such tests and general considerations related to the mechanical properties of anisotropic systems, specimen fabrication, equipment and fixturing, environmental conditioning, and analysis of test results.

Purposes of Mechanical Characterization

The three most common purposes of mechanical property characterization are research and development, quality control (QC), and design data generation. Various levels of rigor are practiced within each category, but, in general, design data generation is the most rigorous. Rigor, as applied here, refers to the process of strictly following processing, fabrication, testing, and data reduction standards and specifications on statistically significant sample sets made from commercially standard materials.

Testing in support of research and development serves a variety of purposes and, by definition, must be flexible. Research and development testing is used to develop and assess the validity of the test methods, to aid in exploring materials science and mechanics concepts, and to support scientific discovery in materials development and applications research. In the materials industry, research and development testing supports the study of materials performance in comparison to program objectives, competitive materials, or other developmental materials. Once a material is developed, the tests can also be used to produce the first generation of property data used to market the new material. The goal of most industrial research and development testing is to control costs, keep turnaround times short, and develop data with accuracy and repeatability sufficient for comparisons. Often this is achieved by using small sample sizes, less rigor in specimen preparation, and minimal levels of test instrumentation. Testing is defined by internal procedures for specimen fabrication, test execution, and data reduction. Flexibility exists to modify specimen preparation and test procedures or to create new test methods, as required to meet research and development objectives.

Quality control characterization is defined primarily by customer acceptance of test methods and/or product specifications. The specimen sampling, specimen preparation, and test procedures must rigorously follow documented specifications. Sample sizes are statistically specified, but reduced levels are often allowed to control costs once production history is demonstrated to be consistent. Quality control tests usually characterize a couple of the most critical characteristics that define a product and strive for comparison against historical values rather than absolute properties. Many QC tests do not measure absolute mechanical properties. For example, flexural strength and modulus do not in general coincide with the strength and modulus of a material tested in uniaxial tension.

Design data generation strives to produce absolute property data. The data must represent the actual mechanical performance of the material under loading conditions like those that will be encountered in service. The tests used must be capable of measuring the material property desired, and specimen preparation must rigorously conform to the standards specified in the test methods. Sample sizes must meet the statistical requirements for A-basis or B-basis design allowables. The number of test-specimen replicates is usually greater than in either of the two previous types of testing. Also, specimen inspection, test instrument calibration, and test method execution are very rigorous.

In summary, different testing approaches are appropriate to meet the range of objectives that one may encounter in materials characterization. The cost of the testing and the time required to generate the results increase with increasing rigor of the characterization process. In order to strike the proper balance in addressing testing needs, the test engineer must fully understand the cause-effect relationships of all aspects of the specimen preparation and testing procedures on the quality and the cost of the results. To that end, this article provides a condensed yet concise presentation of the key concepts of mechanical characterization of composite materials.

Mechanical Properties of Anisotropic Systems

In order to focus on testing, the authors assume that the reader has an understanding of the various types of composite material systems and their special characteristics. If background in laminate mechanics is required, the reader is referred to (Ref 1, 2, 3). Methods for measuring properties of fiber and matrix constituents are not covered, although it is important that the reader understand the relationship that constituent properties, volume

fraction, and void content have to engineering property development in composite systems. This article focuses, thus, exclusively on measuring the engineering and structural performance of laminates and composite structures.

Mechanical properties of a composite material refer to the elastic and strength properties of the material under tensile, shear, or compression loading. Other properties, such as fracture toughness and flexural strength and stiffness, are also useful in characterizing the performance of a composite material. Finally, thermomechanical and hydromechanical properties are of importance under changing temperature and moisture environments. The homogeneity assumption that microstructural features of the material are small enough to be inconsequential to the average behavior of the material on a macroscale may not apply to composites, especially when strength and fracture are considered. Fabrics and laminates are very inhomogeneous in character. The scale of homogeneity of a composite system must be taken into account for fixture design, instrumentation decisions, and in data analysis.

The fundamental description of the engineering properties for a lamina under tension, compression, and shear loading is given in terms of the lamina coordinate system shown in Fig. 1. The strength and stiffness properties are defined in Table 1. If the material is transversely isotropic, then the indicated properties need not be determined. The fracture toughness is sometimes measured as part of durability assessment of a material system. These properties are the mode I and II critical strain energy release rates (G_{Ic} and G_{IIc} , respectively). Flexural properties are also determined routinely and result from bending the material to produce tension, compression, and shear stresses. The result is more a structural property than an intrinsic material property, but it is very useful in materials screening and quality control.

Table 1 Listing of mechanical properties typically determined for composite materials

Symbol	Property
E_1^t	Tensile modulus in the fiber direction
E_2^t	Tensile modulus transverse to the fiber
E_3^t	Tensile modulus transverse through the thickness^(a)
E_1^c	Compression modulus in the fiber direction
E_2^c	Compression modulus transverse to the fiber
E_3^c	Compression modulus transverse through the thickness^(a)
G_{12}	Shear modulus in the 1–2 plane
G_{13}	Shear modulus in the 1–3 plane^(a)
G_{23}	Shear modulus in the 2–3 plane
X_1^t	Tensile strength in the fiber direction
X_2^t	Tensile strength transverse to the fiber
X_3^t	Tensile strength through the thickness^(a)
X_1^c	Compression strength in the fiber direction
X_2^c	Compression strength transverse to the fiber
X_3^c	Compression strength through the thickness^(a)
S_{12}	Shear strength in the 1–2 plane
S_{13}	Shear strength in the 1–3 plane^(a)
S_{23}	Shear strength in the 2–3 plane
ν_{12}	Poisson's ratio in the 1–2 plane
ν_{13}	Poisson's ratio in the 1–3 plane
ν_{23}	Poisson's ratio in the 2–3 plane
ϵ_1^t	Ultimate tensile strain in fiber direction
ϵ_2^t	Ultimate tensile strain transverse to the fiber
ϵ_3^t	Ultimate tensile strain through the thickness^(a)
ϵ_1^c	Ultimate compression strain in the fiber direction
ϵ_2^c	Ultimate compression strain transverse to the fiber
ϵ_3^c	Ultimate compression strain through the thickness^(a)

(a) This property does not need to be determined if the 2–3 plane is transversely isotropic.

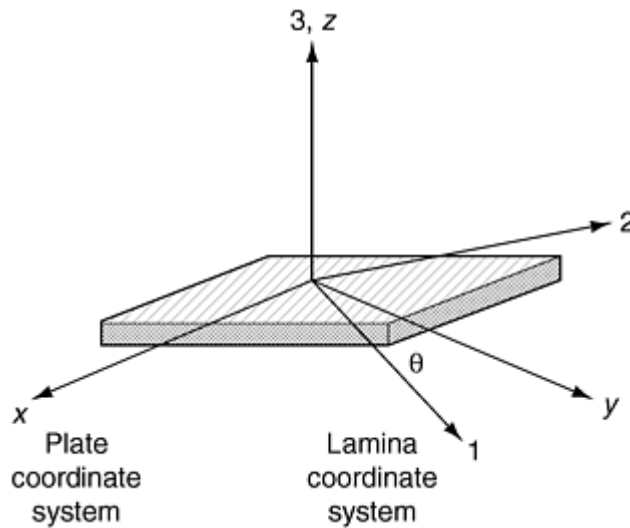


Fig. 1 Lamina and plate coordinate designation system for composites. Plate coordinates are labeled x , y , and z . Lamina coordinates are labeled 1, parallel to the fiber axis; 2, perpendicular to the fiber axis; and 3, normal to the fiber plane.

Properties of laminated composites are defined similarly to those for the lamina, except a laminate coordinate system (x , y , z) is employed. The subscripts 1, 2, 3 on the properties defined in Table 1 are respectively changed to x , y , and z , and the properties become the effective laminate properties. The word “effective” is very important because it signifies that the measured response is an average response through the material thickness. In reality, the stresses in a composite are nonuniform. It should also be noted that composites may behave differently in compression and tension; the elastic and strength properties must be characterized in both tension and compression to fully characterize the material.

Role of Specimen Fabrication

The test results from any characterization are critically dependent on material and specimen integrity. Material processing and specimen machining strongly influence the quality and reproducibility of test results. The recently issued ASTM D 5687, “Guide for Preparation of Flat Composite Panels with Processing Guidelines for Specimen Preparation,” provides descriptions of current practices for autoclave processed composites. Machining of test specimens influences the cost of characterization, and trade-offs must often be weighed between machining tolerance (program costs) and the requirements on the end use of that data.

Specific specimen geometry and laminate configuration requirements are defined for each test type and are associated with the discussion of the test methods. Materials for the test specimens are either cast, molded to shape, pultruded, filament wound, or machined from plaques or plates fabricated using autoclave or other processing methods. For laminates, a reference edge must be established, and each ply must be oriented accurately with respect to the reference edge. Before cure, the laminate reference edge is accurately scribed with a reference line that is used to maintain alignment when the cured plate is trimmed. The fiber volume fraction, void content, and the uniformity of fiber wetout in the part are controlled by the processing of the test panel or specimen. All of these factors strongly influence the mechanical properties of the material. Relationships between processing conditions and material microstructure must be understood and controlled to produce valid test specimens that are representative of the actual material being characterized (i.e., specimens that have the same microstructure and properties that the material will have in a structure). The specimen must be fabricated or machined so that the material axes align properly with the test axes.

Specimen Machining. When fabricated from panels, specimens are normally machined using a diamond wafering saw. A cut is first made along the reference edge, and then all subsequent cuts are made relative to the reference edge to preserve the accuracy of the fiber orientation in the panel. When machining specimens to final geometry, make allowances for scrap, and machine specimens from the heart of the material away from edges. A diamond saw blade produces a very smooth surface along the cut edges, and no further finishing is required usually. In specimens requiring holes, a diamond core bit provides satisfactory hole quality. Other methods

include ultrasonic drilling, or drilling with special drill bits in conjunction with templates to guard against punch-through delamination.

If a specimen is designed to have tabs, the tabs are bonded into place before the specimen is machined to its final shape. The tab material is typically 3.2 mm (0.13 in.) thick [0/90°] glass/epoxy or a woven fabric glass/epoxy material, although steel or aluminum can be used. When required, bevels are machined onto the tab, and then the tab is bonded onto the test panel using special jigs to ensure alignment of the tabs with the specimen reference edge. Individual specimens are cut from the tabbed panel, again taking care to maintain alignment with the reference edge (test axis).

Good quality composite specimens should be of uniform dimensions, have a precise fiber alignment, and possess high-quality finish on machined edges. There should be no evidence of delamination along machined edges. The laminate should contain no dry fiber regions, voids, or other obvious flaws. If available, ultrasonic C-scan should be employed to nondestructively evaluate composite panels for flaws prior to specimen fabrication and testing. Flawed panels or flawed regions within panels should be discarded.

Test Equipment and Fixturing Considerations

The availability of suitable, well-maintained, and accurately calibrated testing equipment is essential for reliable characterization of composite materials. Standard test instrumentation is used for load introduction and strain measurement of composite materials, but test fixturing must be specially designed to meet the specific requirements of the composite tests. The drawings and specifications for standard composite test fixtures are available for most test standards, and many fixtures are now available commercially. Testing is usually performed in a screw-driven or a servo-hydraulic universal test machine.

The test machine must have sufficient stiffness and load capacity to insure accurate load application and deformation measurement. A universal test machine with a load capacity greater than or equal to 110 kN (25×10^3 lbf) is recommended to test composite materials. Longitudinal tension and compression properties of some composite specimens require this capacity. Fiber tests, transverse tension, and flex properties require much lower load capacity. Universal test machines allow interchangeability of load cells to accommodate different testing requirements, and, when needed, small capacity load cells can be used in a 110 kN frame. The load cell must be properly matched to the loading requirements of the specimen in order to ensure required levels of accuracy and sensitivity.

Fixturing Issues. Proper fixturing is critically important to composite testing. The special fixtures for each test are designed to perform two important functions: (a) to transfer loads or displacements from the test machine to the test specimen, and (b) to achieve load introduction such that the desired stress state and deformation are produced in the specimen test section. The quality of test results is governed by proper fixture design, accurate machining to design specifications, and meticulous maintenance of the fixture.

No fixture functions perfectly in generating required states of uniform stress in test specimens; good tests closely approximate desired stress states and minimize stress concentrations in the test section. Mechanically, fixtures must provide reproducible alignment of the specimen in the test machine, and specimens should be easy to insert and remove after testing. The fixture must be strong and stiff enough not to change the characteristics of the state of stress in the specimen during the test. It must also be constructed of hardened materials that will not wear excessively with repeated use. Mating surfaces designed to slip relative to each other must be polished to stringent flatness-finish requirements to minimize friction binding during testing. Fixture functionality must conform to specifications in all required test environments.

All fixtures should be inspected routinely before testing to ensure that they are not worn or damaged in any way that will affect the test results. With use, all fixtures wear and eventually decrease the reliability of test results.

Electronic Transducers for Strain Measurement. Strain and deformation measurements are performed on composites using methods and instruments similar to those used for metals (Ref 4, 5, 6). A few issues must be addressed when using standard, bondable-foil strain gages on composites.

Gage heating is a problem that must be addressed when using bondable-foil strain gages on polymeric matrix composites because the polymer does not conduct heat very well. This allows heat to build up in the gage, and the resulting temperature change causes a resistance change, which is falsely recorded as an apparent strain. The use of 350 Ω (or greater) strain gages is recommended for composite testing, and the excitation voltage should be between 2 and 5 V. Measurement sensitivity is related to the excitation voltage, and 2 V is the lowest voltage that will ensure sufficient sensitivity.

Composites, especially woven fabrics and braided structures, have very coarse microstructure. The size of the strain-gage grid area must be large enough to average deformation over a representative area of the specimen. If the material is heterogeneous, such as a woven fabric, the grid must be large enough to cover at least one unit cell of the structure. A comprehensive discussion of this issue is covered by Masters and Ifju (Ref 6), based on their extensive survey of experimental results using strain gages of varying size on different types of fabric and braided composite structures.

The third problem that can occur when using bondable-foil strain gages for testing composites is that transverse strain sensitivity can influence strain measurements. This is especially prevalent for certain types of angle-ply lay-ups, such as the $[\pm 45^\circ]$ laminate. Correction factors must be applied to achieve accurate longitudinal readings measured under such conditions.

Environmental Conditioning

Environmental conditioning is perhaps one of the most controversial aspects of composites testing. It is not just the temperature at which the material is to be tested that is important. The entire temperature and moisture histories of the specimen influence the properties. Specimens should be preconditioned before testing by exposure to the specified temperature and humidity conditions. Specimens to be tested under standard laboratory conditions ($21 \pm 1.0^\circ\text{C}$, $50\% \pm 20\%$ relative humidity) can be conditioned in the laboratory for a period of 24 h prior to testing. Specimens designed to evaluate effects of environmental exposure must be conditioned by using conventional environmental chambers or temperature-controlled baths using the procedures outlined below.

Moisture conditioning is covered under a relatively new method (ASTM D 5229) and is usually specified in one of three ways:

- Exposure at a specific temperature and relative humidity or in a water bath to attain a target percentage weight gain
- Exposure for a specified time duration
- Exposure to attain equilibrium weight gain

Diffusion constants for composites are often very small, and sometimes accelerated conditioning practices are employed. A specimen can be soaked in water for short durations and attain a certain moisture content instead of being conditioned for months at 95% relative humidity to attain the same moisture content. Increase of temperature greatly increases the diffusion rate.

Accelerated conditioning is usually not equivalent to normal conditioning. The aging of the material is a rate process that depends on path; thus, specimens may not yield the same properties when conditioned using accelerated processes. Accelerated conditioning is considered a conservative approach, because accelerated conditioning typically yields larger degradation of properties than tests that are more representative of actual service conditions.

Prior to conditioning, polymeric matrix composites should ideally be fully characterized using infrared spectroscopy, thermomechanical analysis, and differential scanning calorimetry to determine the state of cure, moisture content, and glass transition temperature (T_g) of the matrix material. This information defines the preconditioned state of the material. The material can then be subjected to the specified environmental conditioning regimen. Once conditioned, specimens should again be characterized by analytical equipment. This is best done on travelers, which are dummy specimens conditioned along with the test specimens for this purpose. The test specimen cannot be used, since the analytical tests will influence the conditioning of the specimen and render it useless for testing.

Metal matrix and ceramic matrix composites also have requirements for environmental conditioning. The key difference is that these types of composites have less sensitivity to moisture uptake, because metallic or ceramic materials do not exhibit moisture-induced “aging” phenomena.

Analysis of Test Results

Statistical principles should be employed in test program design and analysis of test results (Ref 7). Variability is normal in all testing, and proper statistical treatment of data ensures that variability is handled properly in

deducing conclusions about the meaning and trends of the measured data. To start, typical variability of a given test should be used to determine the sample sizes needed to meet statistical significance requirements. Sample means, medians, and standard deviations are useful but may not be sufficient if the population is not normally distributed or if variance is large. Analysis of variance techniques may need to be employed to determine significance in comparisons of results.

Many investigators conduct parametric experiments changing one variable at a time to determine relationships among experimental variables. This approach results in huge, costly test matrices and often produces poor results. Design of experiments is a rigorous, statistically based method for testing the relationship of experimental variables. The design minimizes the number of tests necessary to determine the relationships between the test variables to a desired level of statistical significance. Consultation with an expert is advised, since this can save money and produce more reliable results. Several software packages are available to support statistical analysis and design of experiments.

In any experimental test program, failure modes must be carefully noted. Specimen failures should be the proper mode for the test being conducted and be consistent. Improper failures are an indication that the test is poorly designed, the specimen is flawed, or the test fixture or setup is improper. Failed specimens should always be saved, and typical failures should be photographed and documented.

Footnote

* The section "Interlaminar Shear Properties of Fiber-Reinforced Composites at High Strain Rates" was written by John Harding and Stephen Hallett, Oxford University. The section "Fatigue Testing and Behavior of Fiber-Reinforced Composites" was written by W. Steven Johnson and Ramesh Talreja, Georgia Institute of Technology.

References cited in this section

1. R.M. Jones, *Mechanics of Composite Materials*, 2nd ed., Taylor and Francis, Philadelphia, 1999
2. S.W. Tsai, and H.T. Hahn, *Introduction to Composite Materials*, Technomic, Lancaster, 1980
3. J.R. Vinson, and T.W. Chou, *Composite Materials and Their Use in Structures*, Halstead Press, Applied Science Publishers, Barking, 1975
4. J.M. Whitney, I.M. Daniel, and R.B. Pipes, *Experimental Mechanics of Fiber Reinforced Composite Materials*, revised ed., Society for Experimental Mechanics; Prentice-Hall, Englewood Cliffs, 1984
5. R.B. Pipes, Test Methods, *Delaware Composites Design Encyclopedia*, Vol 6, (L.A. Carlsson and J.W. Gillespie, Jr., Ed.), Technomic, Lancaster, 1990, p 3
6. J.E. Masters and P.G. Ifju, Strain Gage Selection Criteria for Textile Composite Materials, *J. Compos. Technol. Res.*, Vol 19 (No. 3), 1997, p 152
7. H.M. Wadsworth, *Handbook of Statistical Methods for Engineers and Scientists*, McGraw-Hill, New York, 1990

Characterization of Mechanical Properties

The basic building block of laminated composites is the unidirectional lamina (Fig. 1). Specific test methods are available to measure lamina mechanical properties. The unidirectional lamina is highly anisotropic, which complicates mechanical testing. Alignment of the test specimen in the test frame is an important requirement for obtaining adequate test results, and undesirable transverse failures are a common occurrence in such materials. For these reasons, a number of investigators propose to back out unidirectional properties from laminate tests, but no acceptable standards have yet emerged, except for the $[\pm 45^\circ]$ laminate coupon subjected to uniaxial tension for the generation of lamina shear stress-strain response (ASTM D 3518). There exists a host of test fixtures, specimen geometries, and test procedures for the generation of mechanical property data for composite materials. Reviews and further information on the subject are provided in Ref 4, 5, and 8–10. Space limitations prohibit discussion of each test method. Only test methods accepted by the community as ASTM standards or as candidates for ASTM standardization are considered in this article. In cases where more than one method is discussed, the differences are clearly brought out, and guidelines are given about the use of each method.

Tension Testing

The most basic mechanical test is the tension test. For most structural materials, the tensile properties are essential elements of the material design allowables. The tension test is used to measure Young's modulus, Poisson's ratio, tensile strength, and ultimate strain to failure for composites. The properties reduced from tension tests on composite materials are effective (averaged) properties. The test method applies to unidirectional composites but can also be performed on laminates, woven fabrics, or discontinuous fiber composites. For asymmetric and/or unbalanced laminates, extension/bending coupling and extension/shear coupling effects produce nonuniform stress states in the test section. Under these conditions, effective properties cannot be accurately determined from the test results using the standard data reduction methods.

The adequate gripping of the test specimen is the major issue in tension tests. Any tension test specimens (Fig. 2) require gripping regions where loads are introduced through the specimen surfaces, a transition region, and a gage section region that may be of reduced cross-sectional area to promote failures away from the grips. Sufficient volume should be involved in the gage section to achieve adequate sampling of the material being tested.

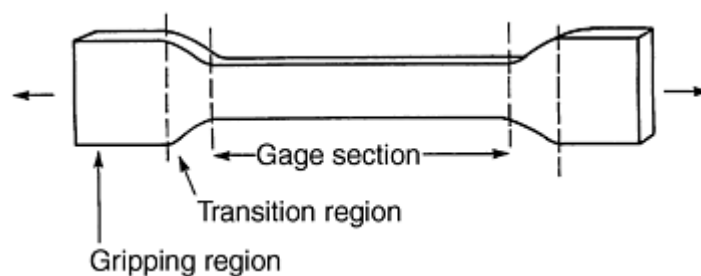


Fig. 2 Generic tension test specimen

The widthwise tapering popular with metals (Fig. 2) usually leads to splitting failures of highly anisotropic composites in the gripping region prior to ultimate failure of the material in the gage section. This problem is avoided by using uniform width (rectangular) test specimens (Ref 10). The grips of the tension test frame introduce large clamping forces that can cause splitting failures or surface damage in the gripped region. These forces, coupled with normal stress concentrations induced by load introduction, can lead to anomalous failures. Tabs with tapered (beveled) ends, therefore, are bonded on each side of the specimen. The load is transferred into the specimen test section through shear (see Fig. 3). When tabs are used, the properties of the adhesive

must be carefully chosen to meet the strength and elongation requirements of the composite under the temperature and moisture conditions imposed by the test. Figure 4 shows the geometry of the ASTM D 3039 tension test specimen. Stress analysis of tabbed specimens (Ref 11, 12) indicates that intense out-of-plane peel and shear stress exist at the tip of the bevel and that the axial tensile stress in the specimen is increased. Consequently, tabbed specimens may fail at the tab ends or inside the tabs, but low bevel angles will reduce the stress concentration (Ref 11). Typically, bevel angles in the range of 15 to 30° are used because tabs with small taper angles occupy too much of the gage section.

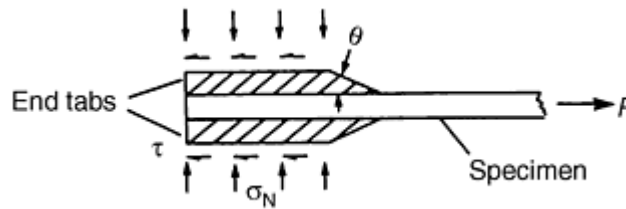


Fig. 3 Load transfer in gripping region of tension test specimen through end tabs

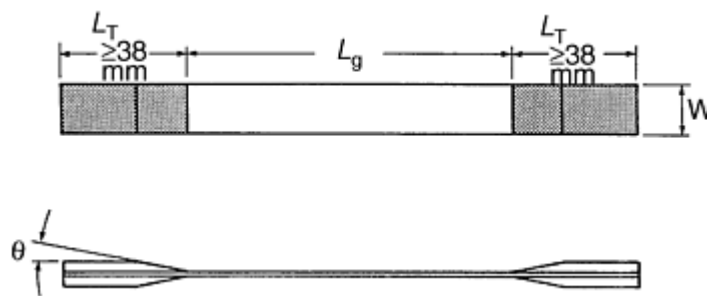


Fig. 4 Specimen for tension testing of composites as defined in ASTM D 3039, L_g = gage length; L_T = tab length; θ = tab bevel angle; w = width

To characterize the tensile response of the unidirectional lamina, 0° and 90° specimens are employed to determine longitudinal and transverse properties. The [±45°] laminate tension test measures shear properties of the lamina and is discussed under shear testing. When characterizing multidirectional laminates, the tabs are sometimes replaced by emery paper inserted between the grips and specimen surface to avoid slippage and minimize surface damage, but in composite laminates with 0° surface plies, fiber damage is likely to occur in the gripping region if tabs are not used.

Specimen Machining and Instrumentation. For unidirectional composites of 0° fiber orientation, a specimen width of 12.7 mm (0.5 in.) and a thickness of 6 plies are common. Unidirectional 90° specimens are typically 25 mm (1 in.) wide and 8 to 16 plies thick. Laminates and sheet molding compound use the same geometry as the 90° specimen and have the specimen thickness defined by laminate configuration or fundamental sheet thickness. Loading eccentricity may arise due to variations in tab and specimen thickness. As proposed in ASTM standard D 3039, tolerances for tab and specimen thicknesses are ±1 and 4%, respectively (Ref 10). Tabs should be made from [±45°] or [0/90°] glass/epoxy or woven fabric composites. Printed circuit board (NVF Co., Kennett Square, PA) is often used because of its tight thickness tolerances. Laminates and sheet molding compound can be tested with or without tabs, although tabs are recommended for thin specimens. Gage length (L_g), (Fig. 4) is commonly 125 to 150 mm (5 to 6 in.).

It is common to bond continuous end tabs on the panels prior to machining the specimens. After careful surface preparation of the bonding surfaces of the specimens and end tabs (Ref 8), the end tabs are attached with an adhesive, typically Hysol 9309, 934 or 929 (Hysol Division, The Dexter Corporation, Pittsburg, CA) or similar epoxy adhesive appropriate to the test conditions specified. The tab length, L_T in Fig. 4, should be at least 38 mm (1.5 in.), and the tab material should be 1.6 to 3.2 mm (0.06 to 0.13 in.) thick. As pointed out in Ref 10 and 13, strips of beveled tab material of similar or slightly larger length than the width of the uncut composite panel should be bonded on both ends of the composite panel prior to machining the specimens. It is desirable to use a special tab-fixturing jig to symmetrically secure the position of the four strips of tabs on the composite panel to maintain positive alignment between the tabs and composite panel. Such fixtures are available commercially, (e.g., Ref 14).

Resin matrix composites are typically machined using a slitting saw or a water-cooled diamond saw (Ref 8). Polishing of the edges has been found to increase the strength, but the finish produced by diamond sawing meets the requirements of ASTM methods and is the commonly accepted industry practice. Alignment of the specimen axis with respect to the fiber direction is an important issue in machining of composites (Ref 8, 15). Hart-Smith (Ref 15) found that specimens cut with 1° of misalignment may cause as much as a 30% decrease in strength due to reduced effective width of the specimen. The variations of the specimen width should not exceed 1% (ASTM D 3039). If Poisson's ratio is desired, a $0/90^\circ$ strain gage rosette should be bonded in the center-gage-section region of the specimen. If only Young's modulus and strength are desired, a longitudinal strain gage or an extensometer attached to the specimen can be used. When load eccentricity is of concern, back-to-back strain gages may be used to detect bending of the specimen. When using strain gages on woven fabric materials, one must select the strain gage size to average deformation over a representative portion of the fabric structure. Failure to use a sufficiently large strain gage will result in large variability in the measured strain.

The specimen geometry and dimensions discussed so far are strictly valid for polymeric resin matrix composites but also apply to other types of composites, after some modifications. Johnson et al. (Ref 16) for example, who studied metal matrix composites containing unidirectional silicon-carbide fibers, found that laminates containing 0° fibers required reduction of the gage-section cross-sectional area (as shown in Fig. 5) so that the specimen would fail in the gage section without slipping or failing in the grips.

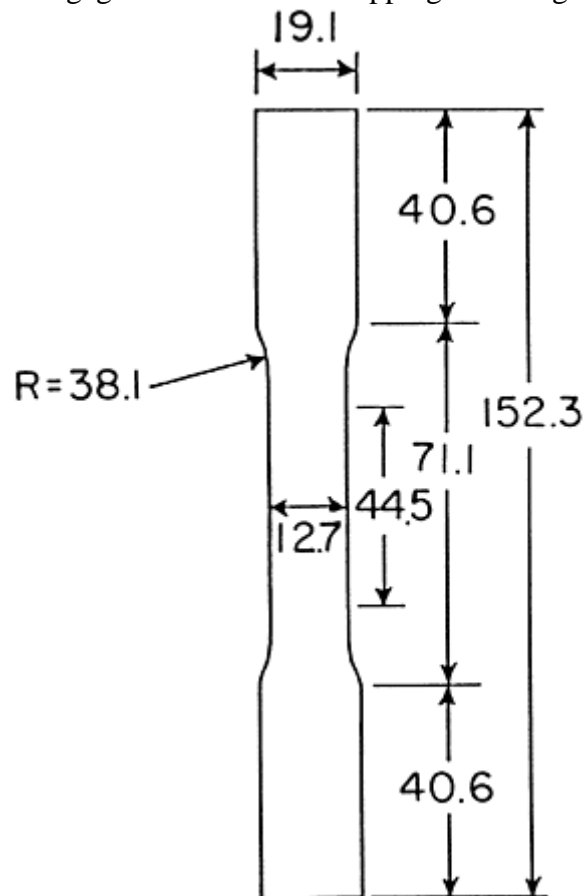


Fig. 5 Dog-bone specimen used for tension strength testing of fiber-dominated metal matrix composites. All dimensions are in millimeters. Source: Ref 16

Test Procedure. Use of standard wedge-action grips with hardened steel serrated jaws is the common practice. With such grips, the clamping pressure increases in proportion to the axial load acting on the specimen. Hydraulic grips provide means to adjust the clamping pressure to avoid crushing of the specimen ends at high loads. Alignment of the test specimen is especially important for unidirectional composites. The specimen is tested monotonically to failure while recording load, crosshead displacement, and strain. Normally, the test is run at a crosshead speed of 2 mm/min (0.08 in./min). Failure mode and location should be noted for each test along with ultimate failure load. A failure located outside the test section justifies rejection of the result. Figure

6 shows acceptable and common failure modes for 0 and 90° carbon fiber composites. Some 0° specimens literally explode. Safety glasses and a protective shield are recommended during tension testing.



Fig. 6 Commonly observed, acceptable failure modes of (a) 0°, and (b) 90° carbon/epoxy unidirectional composites

Figure 7 shows a representative example of stress-strain curves for a 0° glass/polyphenylene sulfide (PPS) composite, that is, stress σ_1 versus longitudinal and transverse strains, strains ϵ_1 and ϵ_2 . The stress σ_1 is defined as load divided by cross-sectional area in the test section. Based on the data collected from the test, the modulus E_1 was reduced using a least squares linear fit to the linear initial portion of the curve σ_1 versus ϵ_1 . Poisson's ratio, ν_{12} , was determined from the ratio of the initial slopes of σ_1 versus ϵ_1 and σ_1 versus $-\epsilon_2$, with $\nu_{12} = -\epsilon_2/\epsilon_1$. The ultimate strength in tension $\sigma_1^{\text{ult}} = X_1^T$ is the maximum value of σ_1 . Values of E_1 , ν_{12} and X_1^T are given in Fig. 7.

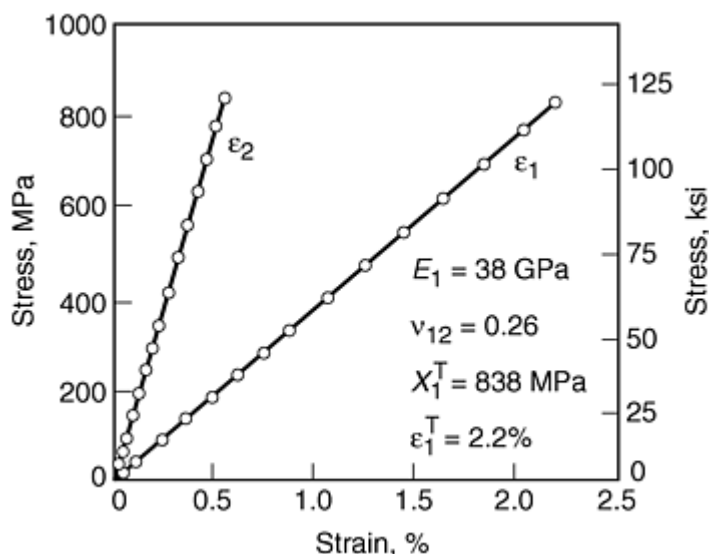


Fig. 7 Stress-strain response for a unidirectional [0]₈ glass/polyphenylene sulfide (PPS) specimen

Compression Testing

Compression testing is performed by subjecting a test specimen to an increasing compressive load until the specimen fails in a failure mode that is representative of that in an actual structure. As discussed in Ref 10, however, compressive failure is triggered by phenomena on the microlevel that are very difficult to observe, and detailed study is required to reach a clear definition of valid failure modes. It is clear, however, that strength degradation due to stress concentrations in the specimen arising from load introduction or slight eccentricities in load-specimen alignment should be minimized and that failure caused by global specimen buckling must be suppressed. Buckling and kinking of the fibers within the composite are features regarded as representative for the material and should not be inhibited.

To avoid buckling instability, relatively short gage lengths are necessary, but short gage lengths generally tend to amplify sensitivities due to clamping. Thus, for very short gage lengths, the apparent compressive strength tends to decrease (Ref 17, 18, 19). It is likely that nonuniformities in specimen thickness or in the bond or tab thicknesses result in nonuniform loading in the short gage section, leading to premature failure. Figure 8 shows

some typical failure modes. The failure modes shown in Fig. 8(a–c) are acceptable, but the column buckling failure (Fig. 8d) is clearly unacceptable, although difficult to visually observe. Because of the stress concentration at the tab ends, it is common to observe failure at the tabbed region (Ref 20). Such failures are not acceptable in tensile testing but are usually accepted in compression testing, because they rarely can be avoided (Ref 10).

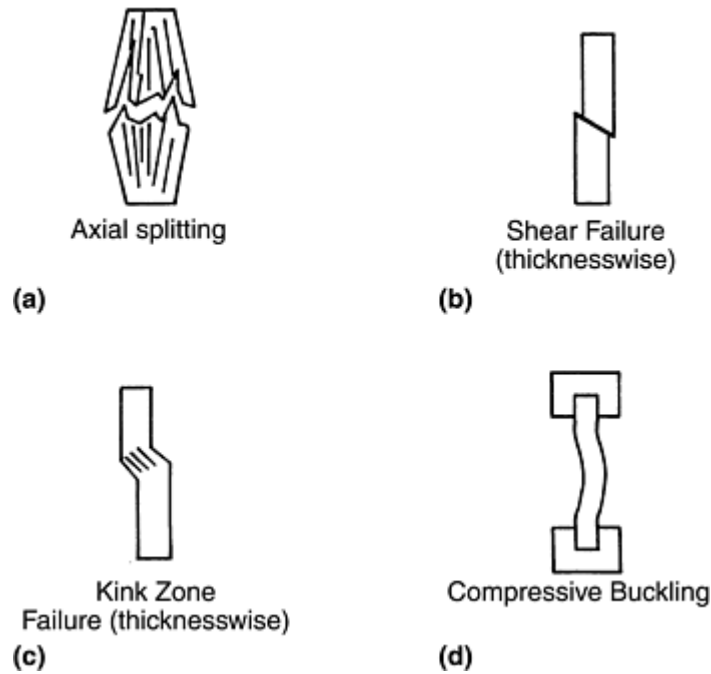


Fig. 8 Typical failure modes for composite compression specimens

Several compression test methods have emerged during the past twenty years, and much confusion exists on their relative virtues. The methods may be grouped into three categories based on load introduction and specimen design: shear loading, end-loading, and sandwich beam specimen testing (Fig. 9). The sandwich beam specimen (Fig. 9c), may be tested in flexure or axial compression. Chatterjee et al. (Ref 10) presented a thorough review of currently available compression test methods and rated the methods according to problems associated with load introduction, uniformity of stress field, sensitivity to imperfections, simplicity, acceptability of failure modes, adequacy of data reduction, specimen preparation and fixture requirements, and consistency of results. Table 2 summarizes the various test methods and their ratings (1, 2, and 3). The test methods included in Table 2 are essentially based on polymer matrix composites but should be applicable to metal matrix and ceramic matrix composites as well. According to Ref 10, the Illinois Institute of Technology Research Institute (IITRI) test method (ASTM standard D 3410) is the most reliable and versatile. Because of space limitations, only the methods with the highest rating (1) are described here with the exception of the Boeing-modified ASTM D 695 method, which has been adopted as a recommended method (SRM 1-88) by the (Suppliers of Advanced Composite Materials Association) (SACMA). It should be emphasized that while all the methods provide adequate measures of modulus, the “true” composite strength may not be determined.

Table 2 Compression test methods for fiber-reinforced composites

Method	Description	Rating ^(a)
Shear-loaded specimen test methods		
Celanese (ASTM D 3410)	Long-established ASTM standard. Results are very sensitive to accuracy of fixture and test procedure.	2
Wyoming-modified Celanese	Cone grips replaced by tapered cylindrical grips. Post and bearing alignment replaces sleeve. Reduced fixture cost. Wider specimen	1
IITRI (Illinois Institute of Technology Research Institute) (ASTM D 3410)	An ASTM standard since 1987. Tapered flat wedges. Post and bearing alignment. Massive, relatively expensive fixture. Wide, thick specimen can be tested.	1

Wyoming-modified IITRI	Smaller, more simply fabricated version of standard IITRI fixture.	2
End-loaded specimen test methods		
ASTM D 695	Designed for unreinforced plastics. Not very suitable for composites.	3
Modified ASTM D 695	Currently a Boeing and SACMA recommended method. Deviates extensively from the ASTM standard. Short (4.8 mm) gage length	2
Wyoming end-loaded, side supported	Very simple fixture. Standard gage length. Limited by end crushing to low and medium-strength materials unless end tabs are used	2
RAE (Royal Aircraft Establishment)	Thickness-tapered specimen. Simple fixture. Few detailed results available	2
Block compression	Limited by end crushing to low-strength composites unless end reinforcement is used	3
Sandwich beam specimen test methods		
ASTM D 3410 Method C-flexure	Large specimen. Expensive to fabricate. Simple fixture. Reliable results if specimen is properly designed to prevent core failure	3
Sandwich column, axial loading	Must fabricate sandwich laminate. End crushing a problem	3
Mini-sandwich column, axial loading	Newly developed. Few data available. Promise of high measured strengths	2

(a) As rated in Ref 10; see text for general description of rating criteria.

Source: Ref 10

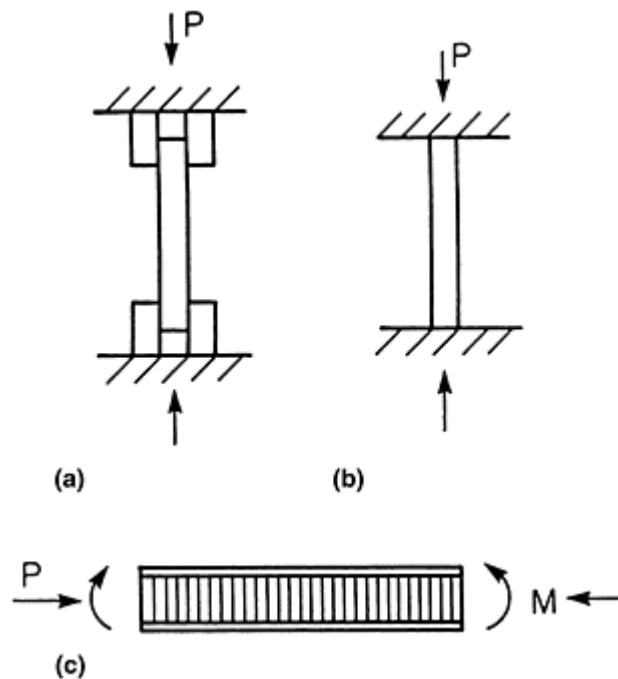


Fig. 9 Generic types of compression test methods. (a) Shear loaded. (b) End-loaded. (c) Sandwich beam specimen.

IITRI Compression Test Method. Figure 10 is a schematic of the IITRI test fixture (ASTM Standard D 3410) (see also Ref 10 and 21). The upper block of the fixture is bolted to the crosshead of the testing machine. The lower block rests on the base of the test machine. The wedge grips have flat surfaces that rest in the end block cavities. Large diameter (19 mm, or 0.75 in.) rods and linear bearings are used to maintain alignment during linear motion of the upper block during testing. The standard IITRI test specimen is 140 mm (5.5 in.) long and has a width dependent on the design of the wedge grips. The maximum width reported is 38.1 mm (1.5 in.) (Ref 10). Figure 11 shows the specimen geometry and dimensions for unidirectional composites. For laminates and

short-fiber composites, 25 mm (1 in.) wide specimens are recommended (Ref 9). Variations in specimen width and thickness should be within ± 0.03 mm (± 0.001 in.). Untapered tabs are specified (Ref 20). Thickness, materials, and bonding procedures for the end tabs are the same as for the tension test. Extreme care should be taken to achieve tab surfaces parallel within 0.08 mm (0.003 in.).

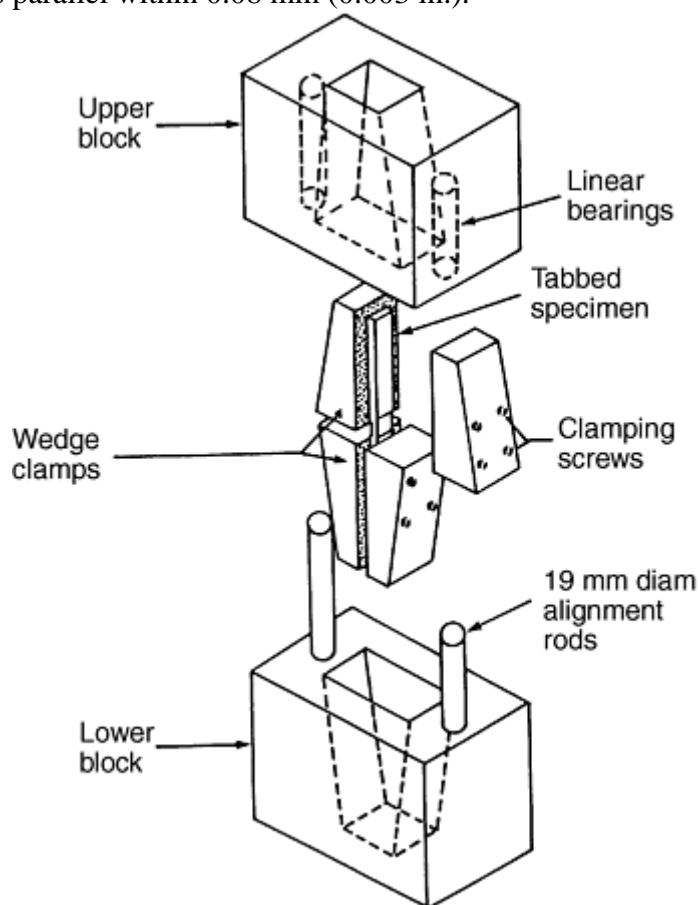
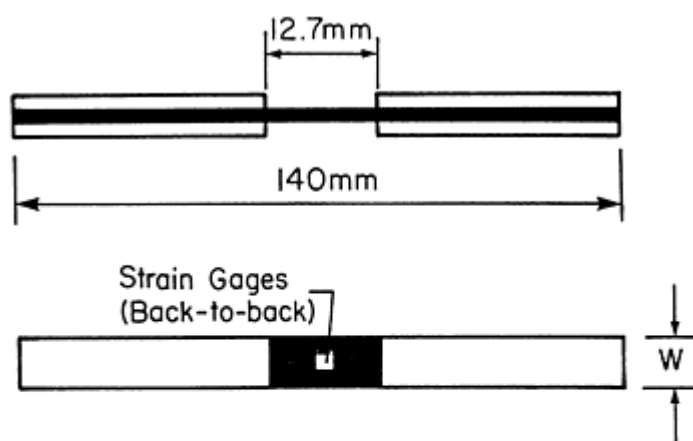


Fig. 10 Compression test fixture developed at the Illinois Institute of Technology Research Institute (IITRI). Source: Ref 10



Fiber Orientation	width (w) mm	#Plies*
0°	6.4	16 - 20
90°	12.7	30-40

* Based on 0.127mm ply thickness

Fig. 11 Dimensions for unidirectional specimens for the IITRI compression test

As with any compression test, concern about specimen buckling exists, and back-to-back strain gages should be attached to the specimen surfaces in the gage region (Fig. 11). By monitoring the stress-strain response for each gage, loading eccentricity and buckling instability can be detected. For a well-aligned, precisely machined specimen, the strains from both surfaces will be in close agreement (Fig. 12). Bending caused by loading eccentricity will cause the strains to diverge with increasing load until instability causes strain reversal (Fig. 12). When buckling instability occurs, the gage on the convex side will be relieved of some of its compressive stress and the corresponding magnitude of strain will decrease. The gage on the concave side (A in Fig. 12) will correspondingly experience an increased compressive strain. As a result of buckling, the apparent strength is decreased, and the compression test is invalidated.

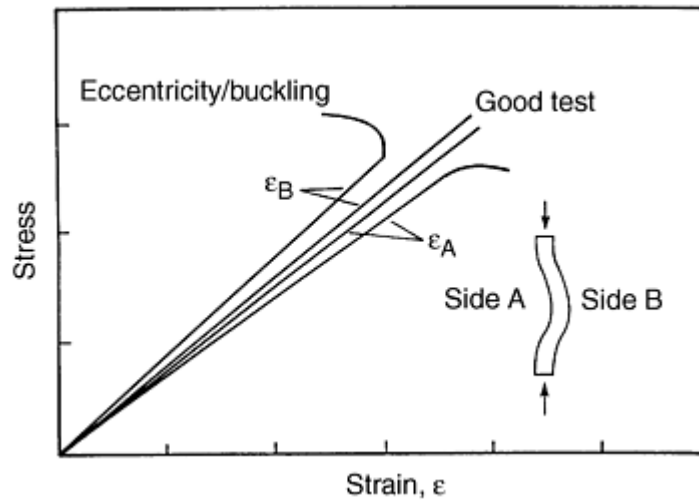


Fig. 12 Schematic of stress-strain responses for well aligned (good test) and eccentrically loaded (bad test) compression test specimens

Since the compressive load is introduced in the specimen through shear (Fig. 9a) via tabs, there are stress concentrations in the regions at the ends of the end tabs at the beginning of the gage section. Consequently, failures are commonly observed close to the ends of the end tabs, but, as mentioned previously, such failures are difficult to avoid and are commonly accepted.

Test Procedure. Measure the width and thickness of the specimen to within 0.03 mm (0.001 in.) at several locations, and calculate the cross-sectional area. Attach strain gages on both sides of the specimen. Mount the specimen in the grips and place the grips in the fixture, which should be placed between the crosshead and the base on the centerline of the test machine. Set the crosshead speed at 0.59 to 1.2 mm/min (0.02 to 0.05 in./min). The strain readings may be recorded continuously or at discrete load intervals. If discrete data are taken, the strain readings should be captured at small load intervals in order to get at least 25 points in the linear response region. A total of 40 to 50 points is desirable to establish the total stress-strain response. Monitor all specimens to failure. Plot the data for reduction and inspect the stress-strain curves for signs of global bending of the specimen. To obtain the ultimate strain, the response curve may need to be extrapolated, assuming linear elastic behavior or curve fitting to the available stress-strain data. The modulus should be established by a least squares fit of the initial slope and, once established, the procedure should be consistently employed for modulus calculation.

Wyoming Modified Celanese Compression Test Method. The Wyoming-modified Celanese fixture is shown in Fig. 13. This fixture was developed at the University of Wyoming and avoids several shortcomings of the original Celanese fixture (ASTM standard D 3410). The fixture has wedge grips with a constant radius and does not require the troublesome alignment sleeve of the Celanese fixture (see Ref 10, 22). The fixture is much smaller than the IITRI fixture and weighs only about 4.5 kg, (10 lb), compared to about 40 kg (88 lb) for the IITRI. The low weight provides for easier handling and requires less time for reaching thermal equilibrium in nonambient temperature testing. The grips can, like the IITRI fixture (Fig. 10), be pretightened onto the test specimen and allow alignment of each pair of wedges with respect to each other.

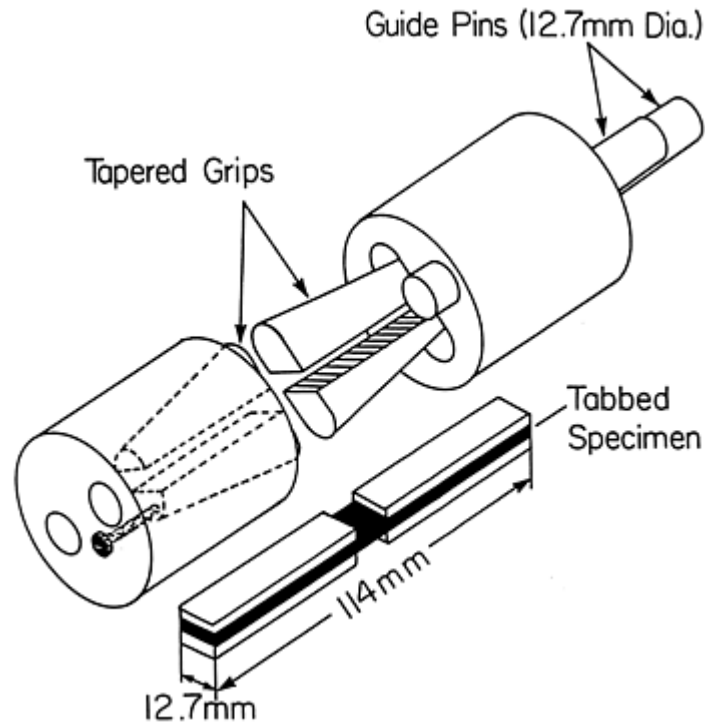
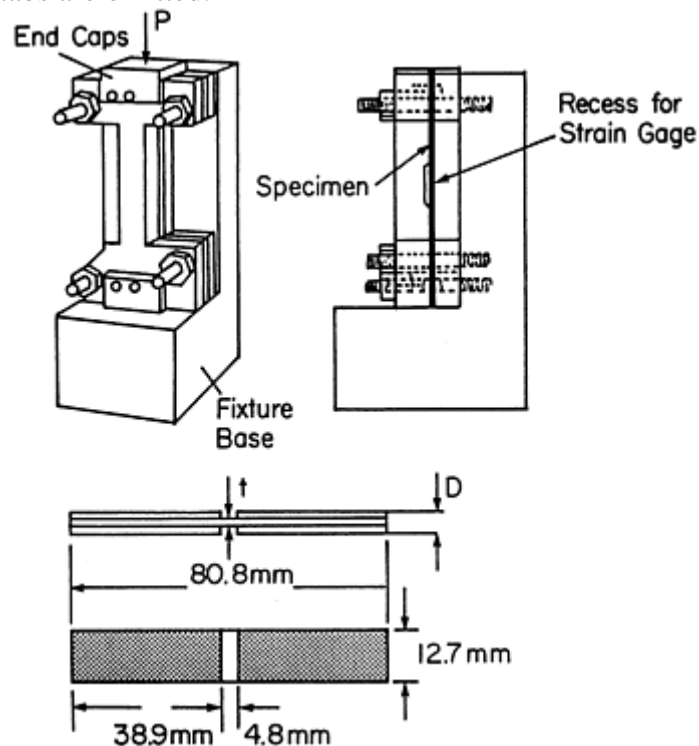


Fig. 13 Wyoming-modified Celanese compression test fixture. Source: Ref 10

The test specimen is 114 mm (4.5 in.) long and 12.7 mm (0.5 in.) wide. The gage length is 12.7 mm (0.5 in.). The fixture can accommodate specimens that are between 3.8 and 6.4 mm (0.15 and 0.25 in.) thick in the tab region. Specimen fabrication, bonding of end tabs, tolerances, and testing and failure modes are equivalent to those outlined for the IITRI test.

Boeing Modified ASTM D 695 Test. The ASTM D 695 method as modified by Boeing (Ref 23) is illustrated in Fig. 14. The test method was adopted by SACMA as a recommended test method (SRM 1-88, April 1989) and is also under consideration for adoption by ASTM. As shown in Fig. 14, the specimen is end-loaded and face-supported with a 0° orientation; the test is predominantly used to measure longitudinal properties. To obtain both modulus and strength data, two tests are required. For strength measurement, tabs are bonded onto the specimen, increasing the bearing area in the end-loaded regions. For modulus determination, the specimen is not tested to failure, and the tabs are omitted.



Material	t, mm	D, mm
0° Uni tape	1.00	3.00
90° Uni tape	2.50	7.50
Fabric	2.50	7.50

Fig. 14 Boeing-modified ASTM D 695 compression test fixture. Source: Ref 10

The standard specimen is 80.8 mm (3.2 in.) long and 12.7 mm (0.5 in.) wide. Specimen thickness recommendations are given in the table in Fig. 14. A thin, tabbed specimen subjected to compression is face-supported along its length, except for the 4.8 mm (0.19 in.) long gage section, and buckling is commonly not a problem. For compressive strength determination, two continuous lateral supports without the strain gage recess are used. Typically, untapered [0/90°] or plain-weave fabric tabs made from the same type of material as that being tested are used. To determine the modulus, a strain gage is bonded at the center of an untabbed specimen, and a lateral support with a central cutout to provide clearance for the strain gage and its connections is used. As an alternative, continuous supports may be used with an extensometer attached to the specimen edge. The specimen should be deformed at least to 0.3% (Ref 10).

The end-load introduction can cause axial splitting or bearing failures on the loaded ends. This must be prevented and has prompted the use of tabs and end caps. Another problem is alignment. Alignment depends on the machining precision of the specimen ends; that is, on the parallelism between opposing ends and the perpendicularity of these ends to the specimen loading axis. Not only must the specimen be precise, but the test machine platens must also be precisely parallel and aligned with the axis of the test machine. Tolerances for specimen thickness and thickness of the tabbed region (t and D in Fig. 14) are ± 0.1 mm (± 0.004 in.). Tabs must be flat, parallel, and of equal thickness to within 0.05 mm (0.002 in.). Ends must be surface ground flat to within 0.03 mm (0.001 in.) and perpendicular to the reference axis. The third source of alignment error is specimen insertion. Much of the fixture-design complexity revolves around the preservation of specimen alignment in the test machine.

Because of the end loading, severe stress concentrations exist at the loaded ends. For the untabbed specimens used to measure modulus, this is not considered a problem because the central region is far away from the loaded edges. For the tabbed strength specimen, the use of tabs prevents failure at the loaded ends. For valid strength tests, failure modes and strength values similar to those seen with other compression test methods have been observed (Ref 10). Specimen fabrication, bonding of end tabs, and testing are equivalent to those specified for the IITRI test.

A number of studies have been conducted exploring the use of [0/90°] laminate configurations to obtain better strength results (Ref 24, 25). Results have shown that the highest strengths and lowest variability are measured using [90/0₂/90°]s laminates. Work by Welsh and Adams (Ref 26) confirmed the benefit of using [90/0°] laminate subgroupings to achieve higher strengths for either IITRI or modified ASTM D 695 test configurations. This is one area where serious consideration is being given to develop a standard based on laminate tests for determination of lamina properties.

Extending this concept, Adams and Welsh (Ref 27) have developed a new test method that uses combined loading to measure compression strength. The method uses both shear and end loading to test the [90/0°] laminate specimen and has been shown to produce results that are consistent with properly conducted tests using existing ASTM methods. An advantage of the method is the ease of testing and very consistent (low scatter) results. The method is currently under review for ASTM standardization.

Flexure Testing

Flexure, or bending, tests have emerged because of the simplicity of specimen preparation and testing. Figure 15 shows stresses developed in the three-point flexure test. It is readily observed that gripping, buckling, and end-tapping are not issues for this test and that testing is very simple. Analysis of the test reveals that the bending moment is balanced by a distribution of normal stress, σ_x . The top side is under compression while the bottom surface is under tension. Theoretically, the neutral axis is identically at the midplane where the shear stress, τ_{xy} , is maximum (see, e.g., Ref 28). In practice, differences in the tension and compression moduli exhibited by many composites invalidate this assumption, moving the neutral axis off the midplane of the beam and, unless corrected, making standard data reduction calculations erroneous. Depending on the span-to-

thickness ratio (L/h) and the strengths in tension, compression, and shear, the beam may fail in tension, compression, or shear. It can be shown that shear failure occurs at very short spans, and that failure in tension and compression occurs for longer spans. The three-point bend test for interlaminar shear strength determination is discussed in the section “Shear Testing” in this article. In this section it is assumed that the beam span is long enough to promote failure in tension or compression. Flexure tests are not recommended for determination of design data because deformation and failure of the material occurs under a combined stress state, and stress concentrations at load introduction points and supports may trigger failure (Ref 29). Consequently, the flexural modulus and strength are combinations of the corresponding tensile and compressive properties of the material. The flexure tests, however, may be used as a reference to previously obtained tensile and compressive data.

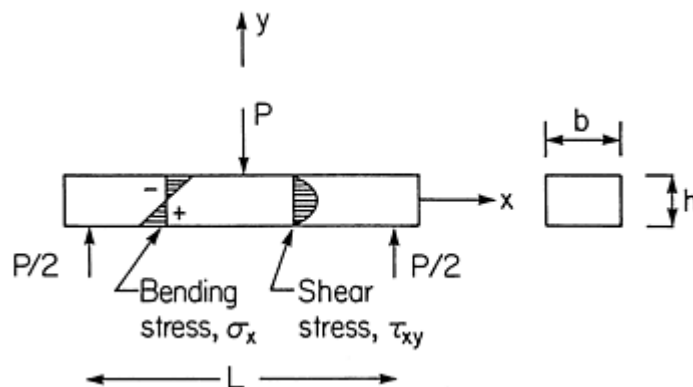


Fig. 15 Illustration of bending and shear stresses in the three-point flexure test

The flexure test is generally limited to unidirectional materials with the fibers aligned parallel or perpendicular to the beam axis. For laminates, interpretation of the results requires laminated beam theory (Ref 30).

Flexure Test Methods. Flexure testing utilizes the three-point or four-point methods (Fig. 16). The four-point flexure test is commonly performed with load noses located at the quarter-span points (Fig. 16b) but is sometimes configured with the loading at the third span ($L/3$) locations. Flexure tests are most commonly used to generate flexural modulus and strength for the purpose of quality control. Proper testing and data reduction may render the test data of more value than just a quality check. The span-to-thickness ratio, L/h , should be large for materials with a large ratio between the tensile and interlaminar shear strengths. For glass/epoxy tested along the fiber direction and graphite/epoxy tested perpendicular to the fiber direction, $L/h = 16$ is appropriate. For high tensile strength composites such as graphite/epoxy tested along the fiber direction, $L/h = 32$ is recommended (Ref 4). The diameter of the load noses and support pins should, according to ASTM standard D 790, be at least 6.4 mm (0.25 in.). The maximum diameter is three times the specimen thickness.

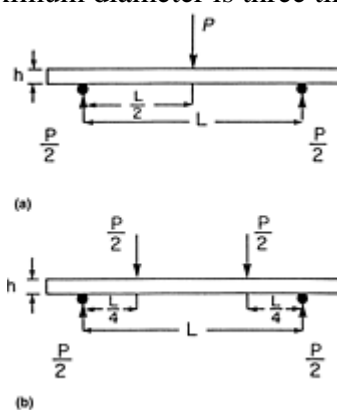


Fig. 16 Schematic of flexure tests. (a) Three-point loading. (b) Four-point loading

Specimen Preparation and Flexure Testing. The specimen is nominally 130 mm (5.1 in.) long, although longer span lengths would require longer specimens (see ASTM standard D 790). Although the ASTM standard D 790 does not indicate tolerances for the width, the ASTM D 3039 standard for tension testing specifies variations within $\pm 1\%$, which would amount to ± 0.13 mm (± 0.005 in.) for the flexure specimen. The accuracy of the total

length is less critical. Typically, 0° specimens use 12 to 16 plies, and 90° specimens use 16 to 30 plies (0.127 mm or 0.005 in., ply thickness).

Measure the cross-sectional dimensions of the test specimens to obtain an average of six measurements and check for parallelism of the edges. If a strain gage is to be used, bond one longitudinal strain gage at the geometrical center on the intended tension side of the specimen. The flexure fixture should be mounted in a properly aligned and calibrated test fixture. Determine the support span according to the beam thickness and material specifications as discussed previously, and set the support and load spans within 1% of their desired values. The crosshead rate, \dot{x} , should be selected so that the maximum strain rate (for a surface fiber) is $\dot{\epsilon} = 0.01/\text{min}$. For both the three-point and four-point methods (at quarter points), this leads to (Ref 4):

$$\dot{x} = \dot{\epsilon} L^2 / 6h \quad (\text{Eq 1})$$

Commonly, a crosshead rate in the range 1 to 5 mm/min (0.05 to 0.2 in./min) is selected. For three-point loading, place the specimen in the fixture with the strain gage on the tension side centered directly under the central loading pin. For four-point loading, the strain gage may be on either the top (compression) or bottom (tension) surface. If the vertical beam deflection, δ , is measured, place a calibrated linear voltage differential transformer (LVDT) or extensometer at the beam midspan. The vertical displacement may be approximated as the crosshead travel if the additional displacement due to the machine compliance is subtracted. The strain or displacement readings may be recorded continuously or at discrete load intervals. If discrete data are recorded, take the load and strain/displacement readings at small load intervals with at least 25 points in the linear response region. A total of at least 40 points is desirable for description of the response up to failure.

Data Reduction for Three-Point Loading. The flexural stress at the specimen surface at beam midspan is calculated from:

$$\sigma = 3PL/2bh^2 \quad (\text{Eq 2})$$

where P is the applied load, L is the span, b is the specimen width, and h is the specimen thickness.

If specimens with greater than a 16 to 1 span-to-thickness ratio are used, a correction factor must be used to compensate for the geometric nonlinearity caused by the large deflections that occur. By calculating the stress from the load data and plotting it versus the strain gage readings, a stress-strain plot for flexure can be constructed, and flexural modulus, E_f , is evaluated from the initial slope of the curve, and flexural strength, X_f , from the maximum stress. For the case that the specimen is not strain gaged, the flexural modulus is determined from the deflection δ according to (Ref 30):

$$E_f = \frac{PL^3}{4bh^3\delta} \left(1 + \frac{6h^2 E_x}{5L^2 G_{xz}} \right) \quad (\text{Eq 3})$$

where G_{xz} is the interlaminar shear modulus in the x - z plane. The last term in Eq 3 is a shear correction factor that may be significant for high axial modulus specimens with a low interlaminar shear modulus, that is, beams with the fibers along the beam axis.

For beams with the fibers perpendicular to the beam axis, shear deformation is generally not significant in bending, and the flexural modulus is given by the first term only:

$$E_f = PL^3/4bh^3\delta \quad (\text{Eq 4})$$

A problem with the shear correction according to Eq 3 is that the extensional and shear moduli (E_x and G_{xz}) must be known beforehand. For the purpose of correction, the extensional modulus E_x is equivalent to the tension modulus, E_1^t , and the shear modulus can be approximated by the in-plane shear modulus, G_{12} , if the fibers are along the beam axis. If the shear correction factor cannot be determined, the flexural modulus can be evaluated from Eq 4 at increasing span lengths until a constant value is achieved (see Fig. 17).

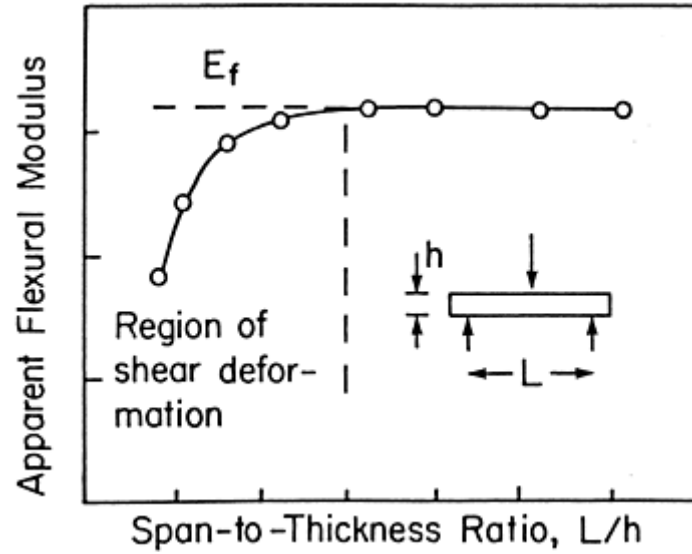


Fig. 17 Illustration of graphical method to determine flexural modulus free of influence of shear deformation

Data Reduction for Four-Point Loading (Quarter Point). The flexural stress at the specimen surface in the region between the inner load noses is given by:

$$\sigma = 3PL/4bh^2 \quad (\text{Eq 5})$$

If a strain gage is used, calculation of the stress from the load data and plotting stress versus strain allow determination of flexural modulus and strength exactly as previously outlined for three-point loading. If load and midspan deflection are measured, the flexural modulus is evaluated from:

$$E_f = \frac{PL^3}{64bh^3\delta} \left(11 + \frac{48h^2 E_x}{5L^2 G_{xz}} \right) \quad (\text{Eq 6})$$

where the symbols have the meaning as in Eq 3.

If the beam deflection is measured at the quarter points, which would be equal to the crosshead travel compensated for test machine compliance, the flexural modulus is (Ref 30):

$$E_f = \frac{PL^3}{8bh^3\delta_q} \left(1 + \frac{6h^2 E_x}{5L^2 G_{xz}} \right) \quad (\text{Eq 7})$$

where δ_q is the deflection at quarter points. Since the shear correction is proportionally larger for the quarter-point deflection formula Eq 7 than for the center deflection formula, Eq 6, shear deformation is less a factor for a test conducted with center-deflection measurement.

Shear Testing

A shear test is performed to determine shear modulus and shear strength of a composite material. The response of a material subjected to shear is commonly nonlinear, and full characterization requires the entire stress-strain curve. The tests may be grouped as in-plane tests that relate to the structural response of plates and shells, and interlaminar tests that relate to the behavior of local details such as joints. Figure 18 defines in-plane shear stress, τ_{xy} , and out-of-plane (interlaminar) shear stresses τ_{xz} and τ_{yz} . The corresponding shear moduli are denoted by G_{xy} , G_{xz} and G_{yz} and the corresponding shear strengths, S_6 , S_5 and S_4 , according to contracted stress notation.

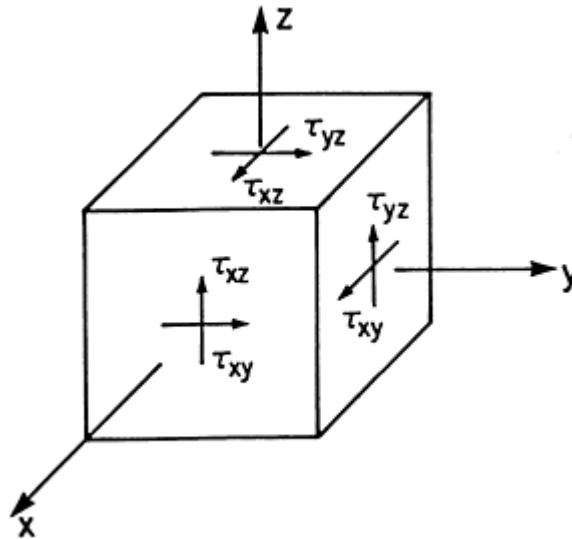


Fig. 18 Definition of shear stress components. τ_{xy} is the in-plane shear stress, and τ_{xz} and τ_{yz} are out-of-plane shear stresses.

The ideal shear test method should provide a region of pure, uniform shear stress. It is also required that the shear stress and strain can be straightforwardly evaluated from the applied load and deformation measurements. The major difficulty in designing shear tests for composite materials is attaining a uniform state of pure shear stress in the test section. Many shear test methods exist as documented by Chatterjee et al. (Ref 10). Chatterjee et al. (Ref 10) ranked the various shear test methods using the same criteria as for the previously discussed compression test methods. Table 3 presents the various shear tests and their rankings. In this section, only the methods with the highest ranking (1) are discussed except for the $[\pm 45^\circ]_{ns}$ tension test because of its popularity in industry.

Table 3 Shear test methods for fiber-reinforced composites

Method	Description	Rating ^(a)
In-plane shear		
$[\pm 45^\circ]_{ns}$, tension, ASTM D 3518, SACMA SRM 7-88	Ultimate strength and strain not acceptable for thin specimens. Study required for effects of tabs and thickness. Effects of transverse tension may be important in some cases.	2
Iosipescu, ASTM D 5379	Acceptable. Correction factor and measurement of all strains with rosettes and back-to-back gages may be required.	1
Rail shear rectangular or parallelogram, ASTM Guide D 4255	Controlled 0° test required. 90° tests appear to yield good data. Measurement of all strains may be required for $[0/90^\circ]$ lay-ups.	1
Torsion-circular bar	Acceptable, but ultimate strains appear to be lower than Iosipescu and rail shear. Data reduction procedure is simple but needs approval from composites community. Machining required. Damage progression needs study.	2
Torsion-rectangular bar	Acceptable, but ultimate strains appear to be lower than Iosipescu and rail shear. Data reduction procedure is complicated. Damage progression needs study.	2
Torsion tube, ASTM standard under development	Excellent but expensive. Ultimate stress and strain levels high for fibers parallel to longitudinal axis of tube. Effects of this and other fiber orientations (hoop and slightly off from hoop) should be compared.	1
Off-axis tension	Acceptable only for modulus; correction factors based on aspect ratio required	...
Picture frame or cross	May be acceptable but more studies required. Tests are highly	...

beam	complicated.	
Slotted shear, ASTM D 3846	Not acceptable for material property testing, possibly useful for quality control.	...
Interlaminar shear		
Iosipescu, ASTM D 5379	Thick specimens with bonded layers required. Appears to be the best choice for unidirectional and fabric composites. Laminates may suffer from free-edge effects because of small width.	1
Short beam shear, ASM D 2344, SACMA SRM 8-88	Three-point loaded specimens not acceptable because of local failure near loading points and strong influence of bending stresses. Four-point loaded specimens with optimized dimensions may perform better.	...

(a) As rated in Ref 10; see discussion of Table 2 in text for general description of rating criteria.

Source: Ref 10

Short Beam Shear Test. The short beam shear test (ASTM D 2344) is a three-point flexure test with a span-to-thickness ratio constrained to 4 to 1, forcing shear failure prior to tension or compression failure. The specimen is all 0° lay-up, and the beam is usually 6.35 mm (0.25 in.) wide and between 2 and 3.5 mm (0.08 and 0.14 in.) thick. The specimen length should be approximately $4h + 16$ mm ($4h + 0.6$ in.), where h is the thickness. The apparent shear strength is calculated as:

$$\tau_{xz}^{\text{ult}} = 3P^{\text{ult}}/4bh \quad (\text{Eq 8})$$

The test does not always yield a pure shear failure and is not recommended for anything more than a quick and inexpensive QC test of fiber/matrix adhesion.

$[\pm 45^\circ]_{\text{ns}}$ Tension Test. The test geometry for the $[\pm 45^\circ]_{\text{ns}}$ tension specimen is shown in Fig. 19. The ASTM standard D 3518 suggests the same specimen geometry as for the ASTM D 3039 tension test. The specimen width typically ranges between 13 and 25 mm (0.5 and 1 in.). End tabs may not be required for polymer matrix composites. The test measures the in-plane shear stress-strain response in the fiber coordinate system and is only applicable for continuous fiber composites. Commonly, a $[\pm 45^\circ]_{\text{ns}}$ laminate is instrumented with a $0/90^\circ$ strain gage rosette as shown in Fig. 19. The specimen is prepared and tested in tension to ultimate failure following the procedures outlined for the tension test.

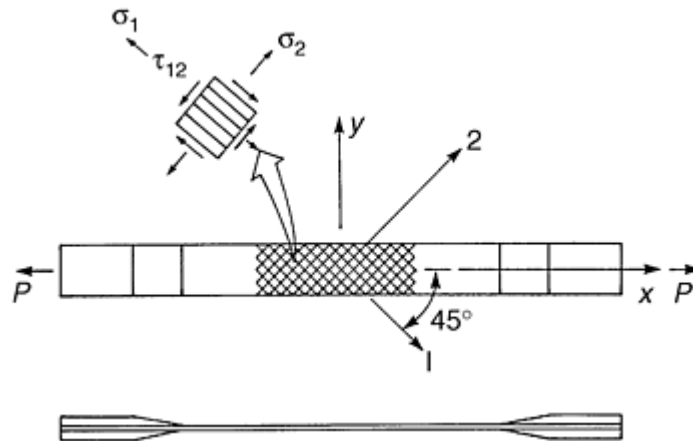


Fig. 19 ASTM D 3518 $[\pm 45^\circ]_{\text{ns}}$ tension test specimen for evaluation of in-plane shear stress-strain response of unidirectional composites

Determination of the lamina shear properties from the tension test requires stress analysis of the $[\pm 45^\circ]_{\text{ns}}$ specimen. Using laminated plate theory, Rosen (Ref 31) showed that the shear stress τ_{12} (see Fig. 19), is simply given by:

$$\tau_{12} = \sigma_x/2 \quad (\text{Eq 9})$$

where σ_x is the axial stress (P/A), and the shear strain is given by:

$$\gamma_{12} = \epsilon_x - \epsilon_y \quad (\text{Eq 10})$$

where ϵ_x and ϵ_y are the axial and transverse strains, respectively ($\epsilon_y < 0$). A sample calculation is provided in ASTM D 3518.

Stress State and Failure Modes. In addition to the shear stress τ_{12} , there exist normal stresses, σ_1 and σ_2 , as shown in Fig. 19. Because the stresses σ_1 and σ_2 are tensile, the apparent shear stress at failure may be reduced. It has furthermore been shown that thin $[\pm 45^\circ]_{ns}$ specimens with $n \leq 2$ may fail at load and strain levels that are too low and not representative for the shear strength of the material (Ref 32, 33). The thickness effect is attributed to multiple ply cracks that tend to be more localized and, thus, more detrimental in thinner specimens. V-Notch (Iosipescu) Shear Test (ASTM standard D 5379). The V-notch (Iosipescu) test method shown in Fig. 20 is based on modifications of the original test (Ref 34) by the composites group at the University of Wyoming (Ref 35, 36). Analysis of the specimen under compressive loading reveals that a state of relatively uniform shear stress exists in the center of the notched specimen (Ref 35, 36, 37, 38, 39). Because of the small specimen size and opportunity for interlaminar shear testing, the test has become popular. Figure 21 shows the specimen configuration for measuring shear response of unidirectional composites, but the test has also successfully been used for laminated, woven fabric, and chopped fiber composites.

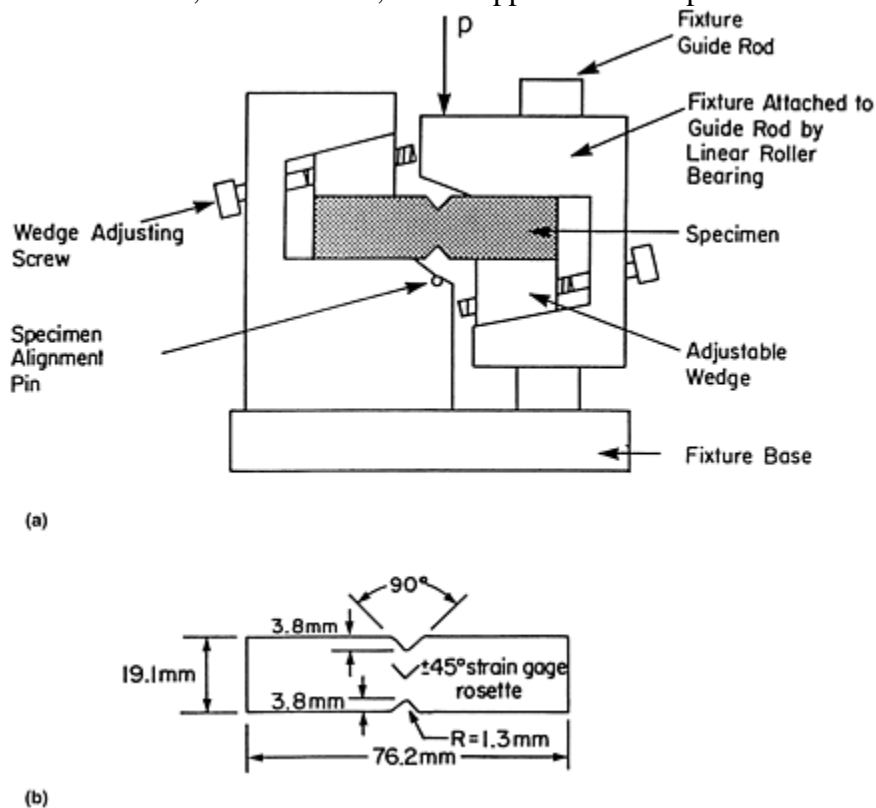


Fig. 20 Iosipescu shear test. (a) Testing configuration. (b) Specimen

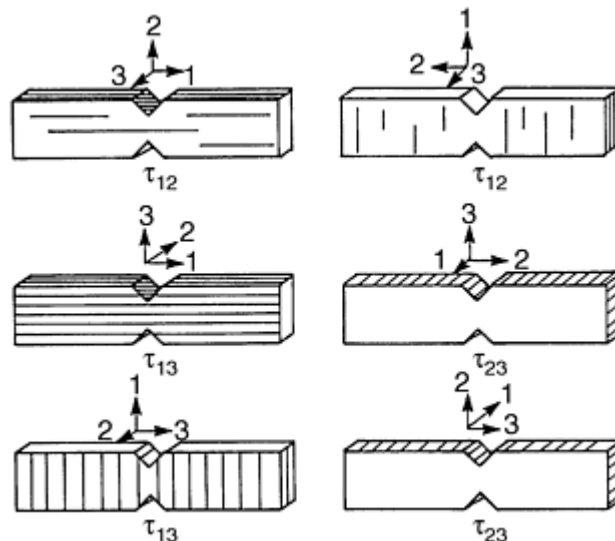


Fig. 21 Iosipescu test specimen configurations and active shear stresses

The specimen (Fig. 20b) should be carefully machined. The loading faces should be ground smooth and parallel to avoid out-of-plane bending and twisting. Good quality notches with rounded tips are required to minimize stress concentrations at the notch tips and the occurrence of early failures, such as splitting in unidirectional, 0° specimens. Specimen thickness is nominally 2.5 mm (0.1 in.). A $\pm 45^\circ$ strain gage rosette should be attached to the center test section. If bending and twisting are of concern, the use of back-to-back strain gages has been suggested (Ref 39).

The specimen should be carefully centered and clamped in the test fixture using the specimen alignment pin (see Fig. 20a). Compressive load should be delivered by the crosshead at a rate of 1.5 mm/min (0.05 in./min) while monitoring the load and strain signals until the specimen fails. Determination of the shear stress-strain response of the material is based on shear stress calculated from:

$$\tau_{xy} = P/A \quad (\text{Eq 11})$$

where A is the test-section cross-sectional area in the notched region of the specimen. For 0° specimens, detailed stress analysis (Ref 39) has revealed a nonuniform stress state. Shear stress calculation incorporating a correction factor is suggested below:

$$\tau_{12} = 0.84P/A \quad (\text{Eq 12})$$

for a specimen with 90° angle notches. After early initiation of notch-tip damage, however, the stress becomes more uniform, and the use of the correction factor of 0.84 may be unwarranted (Ref 10). Shear strain, γ_{xy} , is simply calculated from the $\pm 45^\circ$ strain gage readings as:

$$\gamma_{xy} = |\epsilon_{45}| + |\epsilon_{-45}| \quad (\text{Eq 13})$$

or, if only a 45° gage is used:

$$\gamma_{xy} = 2|\epsilon_{45}| \quad (\text{Eq 14})$$

Failure Modes. Damage in the form of longitudinal matrix cracks initiating from the notches is a common occurrence in 0° unidirectional specimens. Load drops are observed when the cracks propagate, but the splits eventually arrest. The specimen can carry further load until final failure occurs, which involves multiple matrix cracks. 90° specimens fail early due to matrix cracking and do not produce a representative failure stress. Cross-ply $[0/90^\circ]$ lay-ups show distributed microcracking, which is representative for laminated composites. $[\pm 45^\circ]$ and quasi-isotropic lay-ups are difficult to test because of the high loads required for failure.

Rail Shear Test. The rail shear test is described in ASTM D 4255. The in-plane shear properties of unidirectional, laminated, and discontinuous fiber composites are determined by imposing axial load on a fixture consisting of two pairs of tensile loaded rails or three pairs of compressive loaded rails (see Fig. 22). Usually the specimen is bolted to the rails, but slippage is common at increasing loads for some composites. Adhesive bonding of the specimen to the rails has been suggested (Ref 40). Figure 23 shows the specimen geometries for the two-rail and three-rail tests. The diameter of the holes in the specimens exceeds that of the fasteners so that load is only transferred through shear. The specimens should be instrumented with $\pm 45^\circ$ strain gage rosettes as indicated in Fig. 22 and 23. To alleviate stress concentrations and cracking, especially in 0° unidirectional specimens at free edges at loaded corners, different specimen designs have been suggested (Ref 40), but such cracking may not be critical in 90° and $[0/90^\circ]$ lay-ups. The specimen thicknesses should be between 1.3 and 3.2 mm (0.05 and 0.13 in.) to avoid shear buckling while failing at reasonable loads. Tolerances for specimen and fixture dimensions are not provided in the ASTM D 4255 guide, but the dimensions are listed within 0.1 mm (0.04 in.), which should indicate the necessary accuracy.

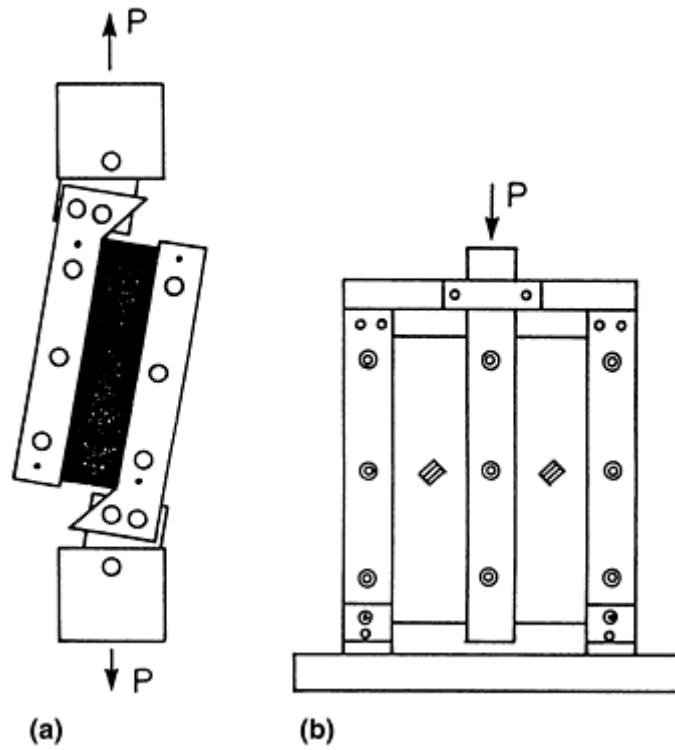


Fig. 22 Rail shear test. (a) Two-rail configuration. (b) Three-rail configuration

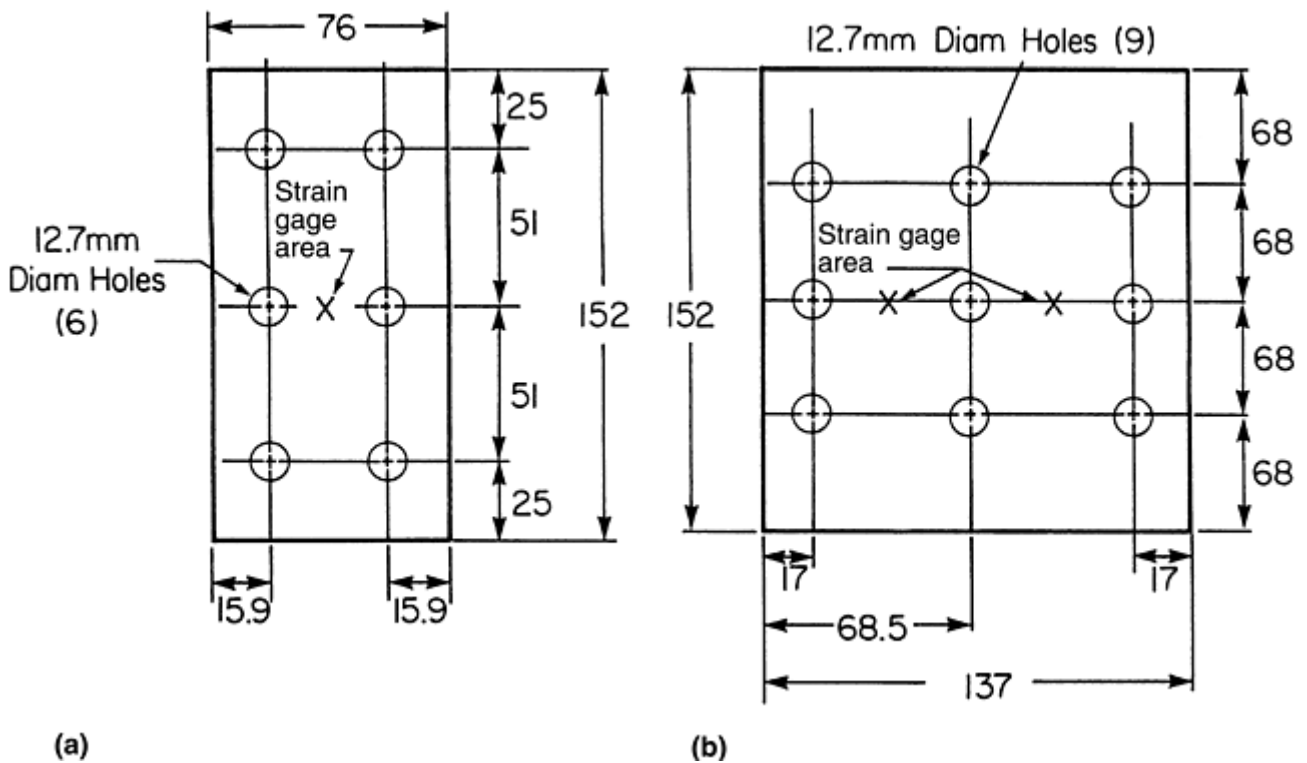


Fig. 23 Specimen geometries for rail shear tests. (a) Two-rail test. (b) Three-rail test. All dimensions are in millimeters.

The test specimen should be bolted to the test fixture using a torque wrench (see ASTM D 4255). The crosshead speed should be 1.5 mm/min. (0.06 in./min), and load and strains should be monitored until the specimen fails. The shear stress is calculated from:

$$\tau_{xy} = P/bh \text{ (two rail)} \tag{Eq 15a}$$

$$\tau_{xy} = P/2bh \text{ (three rail)} \tag{Eq 15b}$$

where b and h are specimen length and thickness, respectively. The shear strain is determined from:

$$\gamma_{xy} = |\epsilon_{45}| + |\epsilon_{-45}| \quad (\text{Eq 16})$$

A stress-strain curve can thus be constructed, which enables shear modulus, G_{xy} , to be determined from the initial slope of the curve and the shear strength, S_{xy} , to be determined from the maximum stress.

Failure Modes. Due to stress concentrations at the corners formed at the intersection of the steel rails and the specimen, damage is likely to initiate at these locations. Such damage is usually in the form of matrix cracks that propagate along the fibers in a unidirectional ply. In a 0° lay-up, such cracks cause a large scatter in shear strength (Ref 40, 41). Tests with the fibers perpendicular to the rails or cross-ply $[0/90^\circ]$ laminates produce many ply cracks, but such cracking may not be detrimental and is often considered acceptable. Hussain and Adams (Ref 42) have developed a modification of the two-rail shear test that eliminates the need for holes, thus improving the stress distribution in the specimen. The simplification reduces the cost of fabrication significantly while producing results consistent with expectations from other tests. Tests on quasi-isotropic and $[\pm 45^\circ]$ lay-ups using the standard method have revealed delamination, and the results are not conclusive. The Wyoming-modified method (Ref 42) produced much better results on the $[\pm 45^\circ]$ lay-ups.

Torsion Tube Test. The torsion tube test (Fig. 24), is especially suited for in-plane shear testing of filament-wound structural parts, and has been recognized as an excellent shear test (Table 3) considered for ASTM standardization. The specimen, however, is difficult to fabricate from prepreg and can obviously not be used to test materials in the form of flat sheets. The specimen is bonded to the end fixtures using potting compound, instrumented with at least two three-element strain gage rosettes ($-45/0/45^\circ$) with the reference direction being the tube axis (Ref 43). The gage length-to-inner diameter ratio is unity (see Fig. 24), and wall thickness-to-diameter ratio is 0.02. This small ratio leads to minor variations in the shear stress across the wall, and the tube may be considered as “thin-walled.”

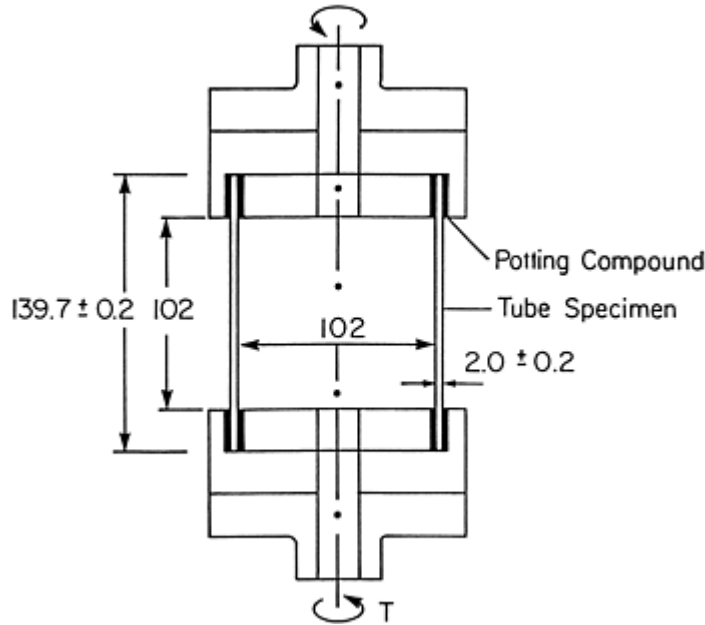


Fig. 24 Torsion tube shear test. All dimensions are in millimeters.

The shear stress is calculated from:

$$\tau_{xy} = Tr/I_p \quad (\text{Eq 17})$$

where T is the torque applied, r is the mean radius, and I_p is the polar moment of inertia. For a thin-walled tube, I_p is given by (Ref 28):

$$I_p = 2\pi r^3 t \quad (\text{Eq 18})$$

where t is the wall thickness. Equation (17) then becomes:

$$\tau_{xy} = T/2\pi r^2 t \quad (\text{Eq 19})$$

Shear strain, γ_{xy} , is evaluated from the gages at 45° and -45° :

$$\gamma_{xy} = |\epsilon_{45}| + |\epsilon_{-45}| \quad (\text{Eq 20})$$

An axial gage may be used to verify the absence of axial strains, that is, for a good shear test, $\epsilon(0^\circ) \sim 0$. Failure Modes. The tube specimen configuration under torque load produces a pure state of shear stress over most of the test specimen volume except near the grips. Hoop wound tubes fail perpendicular to the tube axis, away from the grips at low stress levels. Failure stresses and strains in tubes with axial fiber orientation or cross-ply [0/90°] lay-ups are larger than those for 90° tubes and comparable to other tests, but such tubes are difficult to make. Buckling is a possible failure mode for thin-walled tubes when the shear strength is large (Ref 44), such as in tubes containing $\pm 45^\circ$ angle plies. Such failures invalidate the shear test.

Footnote

* The section "Interlaminar Shear Properties of Fiber-Reinforced Composites at High Strain Rates" was written by John Harding and Stephen Hallett, Oxford University. The section "Fatigue Testing and Behavior of Fiber-Reinforced Composites" was written by W. Steven Johnson and Ramesh Talreja, Georgia Institute of Technology.

References cited in this section

4. J.M. Whitney, I.M. Daniel, and R.B. Pipes, *Experimental Mechanics of Fiber Reinforced Composite Materials*, revised ed., Society for Experimental Mechanics; Prentice-Hall, Englewood Cliffs, 1984
5. R.B. Pipes, Test Methods, *Delaware Composites Design Encyclopedia*, Vol 6, (L.A. Carlsson and J.W. Gillespie, Jr., Ed.), Technomic, Lancaster, 1990, p 3
8. L.A. Carlsson and R.B. Pipes, *Experimental Characterization of Advanced Composite Materials*, 2nd ed., Technomic, Lancaster, 1987
9. D.W. Wilson and L.A. Carlsson, Mechanical Characterization of Composite Materials, *Physical Methods of Chemistry*, 2nd. ed., Vol VII, B.W. Rossiter and R.B. Baetzold, Ed., John Wiley & Sons, 1991, p 139
10. S. Chatterjee, D.F. Adams, and D.W. Oplinger, "Test Methods for Composites - A Status Report," (Vol I, Tension Test Methods; Vol II, Compression Test Methods; Vol III. Shear Test Methods), DOT/FAA/CT-93/17-I, II, III, FAA Technical Center, Atlantic City International Airport, NJ, June 1993
11. D.W. Oplinger, K.R. Gandhi, and B.S. Parker, "Studies of Tension Test Specimens for Composite Material Testing," AMMRC TR 82-27, Army Materials and Mechanics Research Center, Watertown, MA, 1982
12. M.H. Kural and D.L. Flaggs, A Finite Element Analysis of Composite Tension Specimens, *Compos. Technol. Rev.*, Vol 3, 1983, p 11
13. M.G. Abdallah and R.L. Westberg, Effect of Tab Design of the ASTM D 3039 Tension Specimen on Delivered Strength of HMS¹3501-6 Graphite/Epoxy Materials, *Proc. 1987 SEM Spring Conf. on Experimental Mechanics*, 1987, p 362
14. Product Catalog, Wyoming Test Fixtures, Laramie, Wyoming, 1992
15. L.J. Hart-Smith, "Some Observations About Test Specimens and Structural Analysis for Fibrous Composites," ASTM STP 1059, 1988, p 86
16. W.S. Johnson, S.J. Lubowinski, and A.L. Highsmith, Mechanical Characterization of Unnotched SCS/Ti-15-3 Metal S₆ Matrix Composites at Room Temperature, ASTM STP 1080, 1990, p 193

17. R. Walsh, private communication
18. K.F. Port, "The Compressive Strength of Carbon Fiber Reinforced Plastics," Technical Report 82083, Royal Aircraft Establishment, Farnborough, England, Aug 1982
19. D.F. Adams and E.Q. Lewis, Influence of Specimen Gage Length and Loading Method on the Axial Compressive Strength of a Unidirectional Composite Material, *Exp. Mech.*, Vol 31, 1991, p 14
20. E.M. Odom and D.F. Adams, Failure Modes of Unidirectional Carbon/Epoxy Composite Specimens, *Composites*, Vol 21, 1990, p 289
21. K.E. Hofer, Jr. and P.N. Rao, A New Static Testing Compression Fixture for Advanced Composite Materials, *J. Testing Eval.*, Vol 5, 1977, p 278
22. M.N. Irion and D.F. Adams, Compression Creep Testing of Unidirectional Composites, *Composites*, Vol 12, 1981, p 117
23. "Advanced Composite Compression Tests", Boeing Specification Support Standard BSS 7260, The Boeing Company, Seattle, WA, Dec 1988
24. L.J. Hart-Smith, Backing Out Equivalent Unidirectional Strengths from Tests on Cross-Plied Laminates, *Proc. 3rd International SAMPE Symposium and Exhibition*, 1992, p 977
25. D.W. Wilson, V. Altstadt, M. Maier, J. Prandy, K. Thoma, and D. Vinckier, An Analytical and Experimental Evaluation of 0/90 Laminate Tests for Compression Characterization, *J. Compos. Technol. Res.*, Vol 16 (No. 2), Apr 1994, p 146–153
26. J.S. Welsh and D.F. Adams, "Unidirectional Composite Compression Strengths Obtained by Cross-Ply Laminates," *J. Compos. Technol. Res.*, Vol 18 (No. 4), Oct 1996, p 241
27. D.F. Adams and J.S. Welsh, The Wyoming Combined Loading Compression (CLC) Test Method, *J. Compos. Technol. and Res.*, Vol 19 (No. 3), 1997, p 123
28. J.M. Gere and S.P. Timoshenko, *Mechanics of Materials*, 2nd. ed., PWS Eng., Boston, 1984
29. J.M. Whitney and C.E. Browning, On Short-Beam Shear Tests for Composite Materials, *Exp. Mech.*, Vol 25, 1985, p 294
30. J.M. Whitney, *Structural Analysis of Laminated Anisotropic Plates*, Technomic, Lancaster, 1987
31. B.W. Rosen, A Simple Procedure for Experimental Determination of the Longitudinal Shear Modulus of Unidirectional Composites, *J. Compos. Mater.*, Vol 6, 1972, p 552
32. S. Kellas and J. Morton, "Scaling Effects in Angle-Ply Laminates," NASA CR 4423, Feb 1992
33. S. Kellas, J. Morton, and K. E. Jackson, An Evaluation of the ± 45 Tensile Test for the Determination of the In-Plane Shear Strength of Composite Materials, *Proc. of the ICCM-8 Conf.*, Honolulu, July 1991
34. N. Iosipescu, New Accurate Procedure for Single Shear Testing of Metals, *J. Mater.*, Vol 2, 1967, p 537
35. D.E. Walrath and D.F. Adams, The Iosipescu Shear Test as Applied to Composite Materials, *Exp. Mech.*, March 1983, p 105–110

36. D.E. Walrath and D.F. Adams, "Verification and Application of the Iosipescu Shear Test Method," UWME-DR-401-103-1, University of Wyoming, Laramie, June 1984
37. M.G. Abdallah, D.S. Gardener, and H.E. Gascoigne, An Evaluation of Graphite/Epoxy Iosipescu Shear Specimen Testing Methods with Optical Techniques, *Proc. of the 1985 SEM Spring Conf. on Experimental Mechanics*, Society of Experimental Mechanics, June 1985, p 833
38. H. Ho, M.Y. Tsai, J. Morton, and G.L. Farley, "An Evaluation of the Iosipescu Specimen for Composite Materials Shear Property Measurement," VPI & SU Report CCMS-91-18, Center for Composite Materials and Structures, Aug 1991
39. S.N. Chatterjee, E.C.J. Wung, C.F. Yen, V. Ramnath, J.A. Kessler and D.F. Adams, "Composite Specimen Design Analysis," MTL Report TR-91-5, Vol I and II, 1991
40. R. Garcia, T.A. Weisshar, and R.R. McWhitney, "An Experimental and Analytical Investigation of the Rail Shear Test Method as Applied to Composite Materials," *Exp. Mech.*, Vol 20, 1980, p 273
41. R.J. Butler, P.M. Barnard, and P.T. Curtis, The Development of a Satisfactory, Simple, Shear Fatigue Test for Unidirectional E-Glass/Epoxy, ASTM STP 972, 1988, p 227
42. A. Hussain and D.F. Adams, "The Wyoming-Modified Two-Rail Shear Test Fixture for Composite Materials," *J. Compos. Technol. Res.*, Vol 21 (No. 4), 1999, p 215
43. R. Bucinell, "Interim JANNAF Test Method for In-Plane Shear Properties of Unidirectional Fiber/Resin Composite Cylinders," Interim Report for MIL-HDBK-17, AMTL Contract DAAL04-89-C-0023, 1991
44. G.A. Foley, M.E. Roylance, and W.W. Houghton, "Use of Torsion Tubes to Measure In-Plane Shear Properties of Filament Wound Composites," STP 1003, ASTM 1989, p 208

Mechanical Testing of Fiber-Reinforced Composites

Dale Wilson, The Johns Hopkins University, Leif A. Carlsson, Florida Atlantic University

Structural Laminate Properties

The lamina and laminate tests fail to address the effect of holes or cutouts in laminates, a critical requirement for structural design. Also, designers need experimental data quantifying the effect of impact induced damage on laminates. Of particular concern is the compression strength of impact damaged laminates, since sublaminates formed by delamination are susceptible to buckling that can produce failures at substantially lower failure loads than undamaged laminates. Open hole tension, open hole compression, and compression after impact tests have been developed to characterize the behavior of composite laminates with cutouts or damage. Methods have been written for these tests but none are currently standardized. Data from the open hole tests is routinely used in design analysis. The compression after impact test is used primarily in screening candidate materials.

Open Hole Tension Test

Cutouts and holes are requirements in many structural applications. The effect of cutouts in composite laminates is greater than the effect caused by the reduction in load-carrying area alone. Stress concentrations are produced in the laminate adjacent to cutout boundaries that substantially reduce load-carrying capacity.

Stress concentrations are a function of laminate anisotropy and cutout geometry. Sharp notches produce higher stress concentration factors than circular cutouts. However, the notch sensitivity of laminates is significantly influenced by laminate stacking sequence and a host of microstructural materials characteristics like matrix toughness, matrix stiffness, and fiber to matrix adhesion. High stress concentrations produce complex damage zones, which in turn redistribute the stress and increase the energy required to produce failure significantly above that predicted from the stress concentration factor alone. It has been shown that larger notches produce lower strengths, because the stress concentrations involve a larger volume, increasing the probability of failure due to a critical flaw (Ref 45). The stress distribution illustrated in Fig. 25 is the basis for the point stress criterion for notched strength prediction (Ref 46), which states that failure occurs when the stress at some characteristic distance d_0 reaches the unnotched tensile strength of the composite.

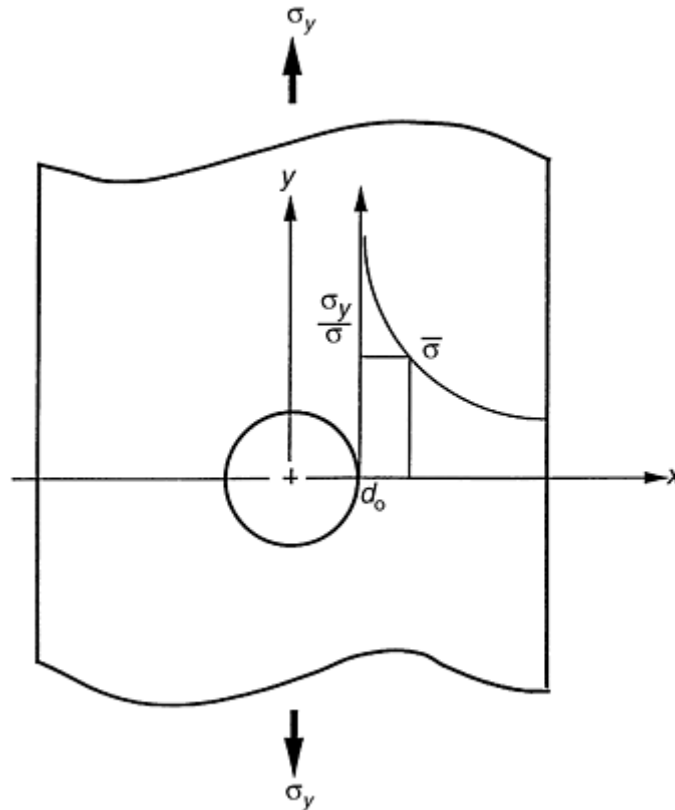


Fig. 25 Stress concentration adjacent to a hole in a composite laminate subjected to uniaxial loading

The test method for open hole tension uses a circular cutout in a test specimen (Fig. 26). The method is now standardized as test method ASTM D 5766. It employs a 305 mm long by 38 mm wide (12 in. by 1.5 in.) specimen containing a 6.35 mm (0.25 in.) hole. Quasi-isotropic laminate configurations are specified to be $(+45/0/-45/90^\circ)_{2s}$ for tape or $(\pm 45/(0/90^\circ))_{2s}$ for fabric prepregs. While other laminate configurations and geometries are possible, it is recommended that the width-to-hole diameter ratio of 6 be maintained.

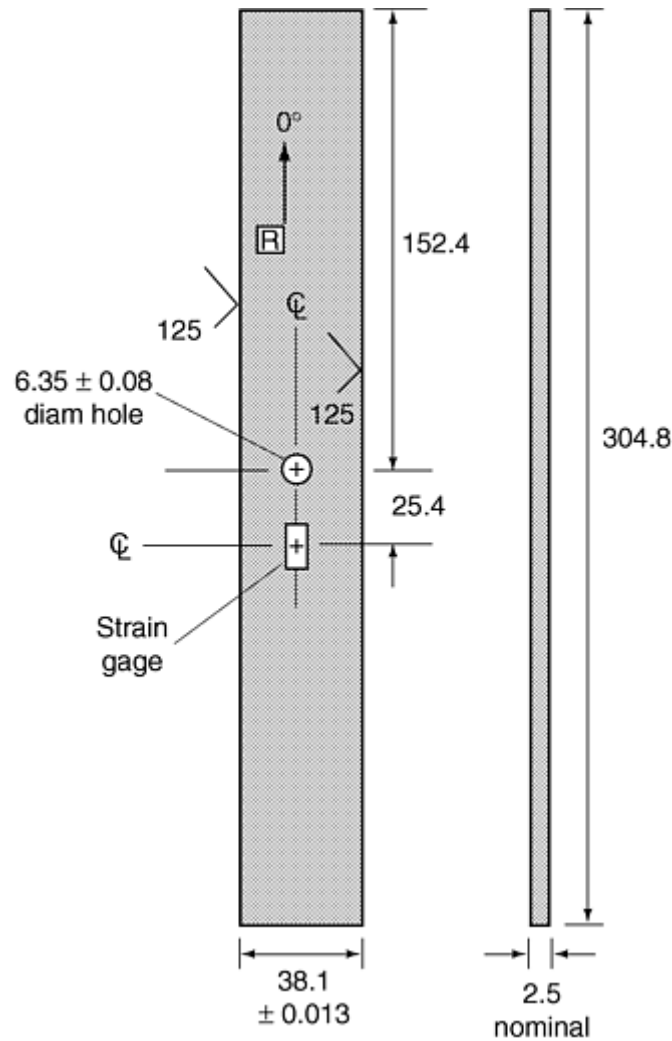


Fig. 26 Open hole tension test specimen geometry. All dimensions are in millimeters.

The specimen should be machined to the specification shown in Fig. 26. Tolerance on the hole location relative to the specimen centerline is critical, since eccentricity can significantly decrease strengths. Specimens can be tabbed or untabbed, although untabbed specimens reduce cost. If ultimate strain and modulus are desired, specimens may be instrumented with a strain gage located on the specimen centerline 25 mm (1 in.) from the hole center. ASTM D 5766, however, covers only notched strength and does not contain provisions for strain measurement.

The test is performed as a uniaxial tension test following ASTM D 3039. The specimen is loaded until tension failure occurs through the notch. If failure occurs outside the notch, the test result should be discarded, since the failure was caused by a flaw in the material. If failures consistently fall outside the notch area, the naturally occurring flaws in the material are larger than the notch (this is possible with some sheet molding compounds). Then, the specimen design must be scaled to reflect the material inhomogeneity level. At least five specimens should be tested per test condition.

The notched strength σ_N is calculated as the tensile strength of the laminate based on the far-field stress:

$$\sigma_N = P/bd \quad (\text{Eq 21})$$

where P is the maximum load, b is the specimen width, and d is the specimen thickness. If the specimen is instrumented, the modulus is determined as:

$$E_x = \frac{P_3 - P_1}{0.002 bd} \quad (\text{Eq 22})$$

where P_1 and P_3 are the loads at 1000 and 3000 microstrain, respectively. The strain at failure is determined from the stress-strain curve.

Notched strength data is typically used for materials screening and for determining design allowables. For design, it is necessary to generate empirical data based on the material, the laminate configuration, and the hole

sizes required. In lieu of generating empirical data for every conceivable material, laminate, and hole size combination, it is possible to use the point stress criterion (PSC) analysis to interpolate notched strength over a range of hole diameters by testing a series of three different notch sizes for the material and laminate construction of interest (Ref 8, 47).

Open Hole Compression Test

Aside from the added complexity associated with specimen loading, much of what was described for the open hole tension test applies to the open hole compression test. Damage develops differently, and the failure mode reflects sensitivity to the microbuckling failure mechanisms that contribute to compression failure in composite materials. Gynn and Bradley (Ref 48) studied the damage mechanisms in open hole compression specimens and found that matrix stiffness plays a significant role in the development of a damage zone and the type of fiber failure mechanism that leads to ultimate failure. In ductile matrix composites, fiber kinking leads to the formation of a shear crippling zone across the net section of the hole, eventually leading to catastrophic failure. Brittle systems fail quickly and catastrophically, without evidence of the shear crippling behavior.

The open hole compression strength can be measured using the same specimen as the open hole tension test. One difference (shown in Fig. 27) is that more stringent tolerances are specified for the machining of the specimen ends. For end loaded compression tests the perpendicularity of the specimen ends with the loading direction is critical. The quality of the hole and the location of the hole relative to the loading centerline are also important. The compression test commonly employs the SACMA fixture shown in Fig. 28. The specimen is face supported during testing (see Fig. 28). The fixture incorporates a cutout around the specimen hole so as not to constrain damage propagation and artificially increase the failure load. It also provides a milled out section located 25 mm (1 in.) from the specimen cutout to accommodate a strain gage.

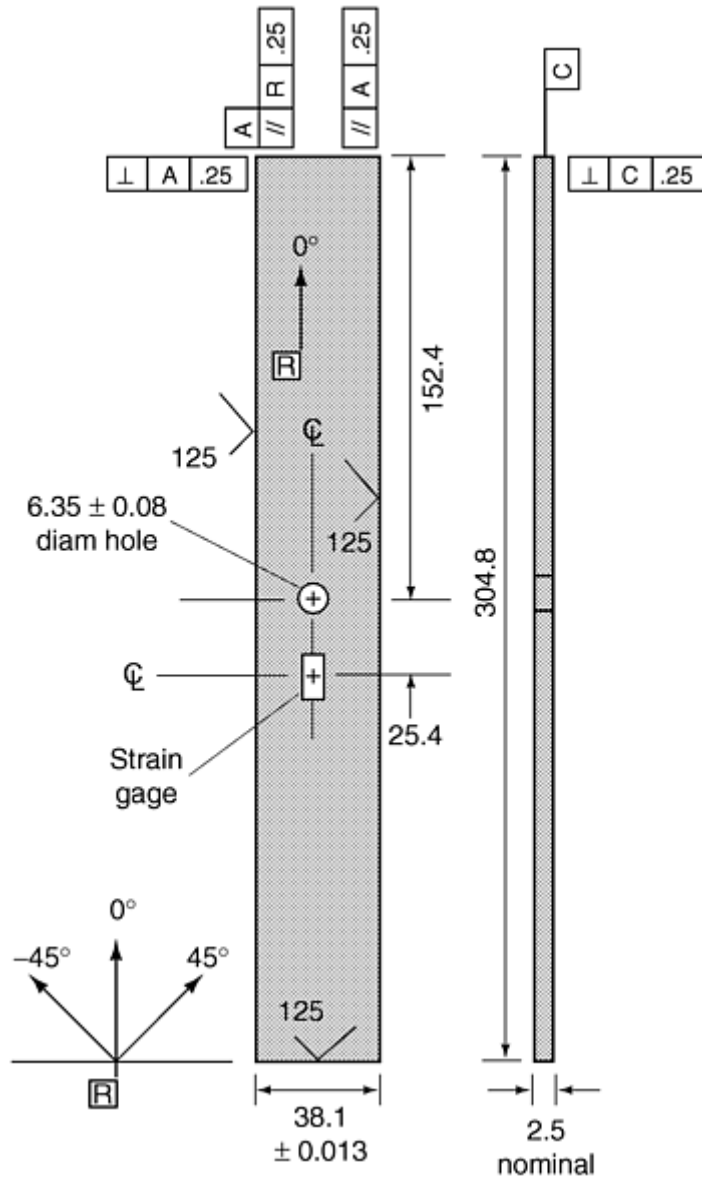


Fig. 27 Open hole compression test specimen geometry. All dimensions are in millimeters.

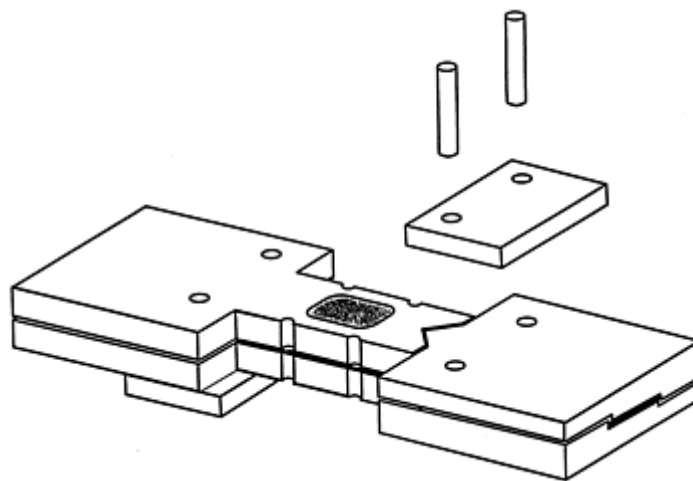


Fig. 28 Test fixture for the SACMA SRM-3 open hole compression test

Loading can be accomplished through two methods. The fixture halves can be bolted together, and the specimen is end loaded between compression platens after verifying that the specimen and fixture are perpendicular to the platens. The other method uses hydraulic grips that can simultaneously grip the fixture to

hold the specimen and apply compression through shear developed by friction between the fixture and specimen. This method is preferred but is often not available. The specimen is tested until failure and the following data reduction analysis applied to determine the open hole compression strength:

$$\sigma^{\text{ult}} = P/bd \quad (\text{Eq 23})$$

where P is the maximum load, b is the specimen width, and d is the specimen thickness.

Gripping pressure, a controllable test parameter with hydraulic grips, can influence the strengths measured if carried to an extreme. High clamping pressures induce transverse normal constraint that may raise the compression failure load. Since such transverse normal constraints are not present in most structural applications, the use of high clamping forces to increase open hole compression strength is nonconservative and ill-advised.

If strain is measured, the elastic modulus can be determined using the following equation:

$$E_x = \frac{P_3 - P_1}{0.002bd} \quad (\text{Eq 24})$$

where b and d are the specimen dimensions and P_3 and P_1 are the loads at 3000 and 1000 microstrain. The ultimate open hole compression strain is found from the stress-strain plot.

Another test method is based on the “Northrop specimen and fixture” (Fig. 29), which uses a smaller test specimen than that shown in Fig. 27. It is also end-loaded and face-supported, but due to different geometry and boundary constraints it gives different strength than the SACMA method. There is no technical basis at this time to recommend one method over the other, but the Northrop specimen and fixture are less expensive and the method is easier to use than the SACMA method. Because of its lower mass, it is easier to use for testing under variable temperature and moisture conditions.

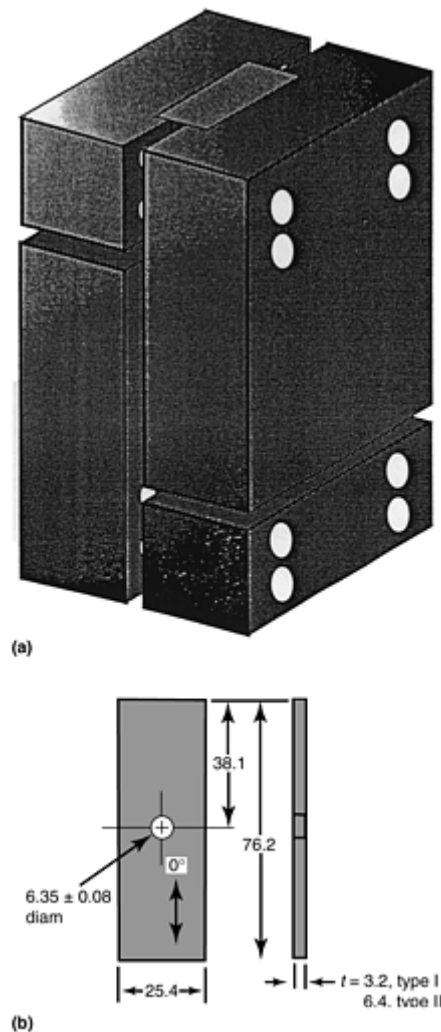


Fig. 29 Northrop test fixture and specimen geometry for the open hole compression test

Compression-after-Impact (CAI) Test

Concerns about damage tolerance of composites in primary load bearing aircraft structures prompted the development of test methods to measure fracture toughness and damage tolerance. Fracture mechanics test methods have been adapted to measure interlaminar crack growth resistance and are covered in the next section of this article, "Interlaminar Fracture." Damage tolerance tests have been developed that simulate foreign object impact and then measure residual strength properties of the "damaged" laminates.

The tests are quite complex since they involve two separate and distinct events, damage generation by impact and compression strength testing of impacted specimens that involves post-impact damage propagation. Damage is imparted by striking a test laminate with a projectile or instrumented impact tup having a specified energy. During impact, the test panel, usually a quasi-isotropic laminate, is held by a fixture capable of consistently applying defined boundary conditions. During impact the specimen can be loaded or unloaded. Depending on the geometry of the impactor, the energy applied, and the toughness and lay-up of the test panel, damage can range from through-penetration to nonvisible internal delamination. It is important to have a nondestructive method to assess the level of damage sustained by the specimen before testing for residual strength. While either tension or compression loading can be applied to determine residual strength, compression is most common. Under tension loading, the strength tends to be reduced by an amount equivalent to the laminate having a hole similar in size to the primary damage zone. In compression, sublaminar buckling occurs as a result of the delaminations in the damage zone, amplifying the reduction in strength.

A method popularized by Boeing in specification BSS 7260 became, by virtue of widespread use, a defacto industry standard for materials screening. The method was formalized by publication of SACMA SRM-2 and is currently under development as an ASTM standard test method. This method covers both the impact and compression after impact testing of a composite laminate. The impact is produced by a falling weight with a 15.9 mm (0.625 in.) diameter hemispherical tup dropped from a height so as to produce 170 Nm (1500 lbf · in.) of energy per 25.4 mm (1 in.) of laminate thickness. The test panel is nominally 152 by 102 mm (6 by 4 in.) wide by 5 mm (0.2 in.) thick and is held during impact by mechanical clamps on a steel fixture with a 76 by 127 mm (3 in. by 5 in.) opening (Fig. 30). Subsequent to impact, the laminate is ultrasonically scanned to reveal the extent of damage imparted and then subjected to compression testing. The panel is not loaded during impact and is used to assess damage tolerance due to low-velocity, nonpenetrating impact.

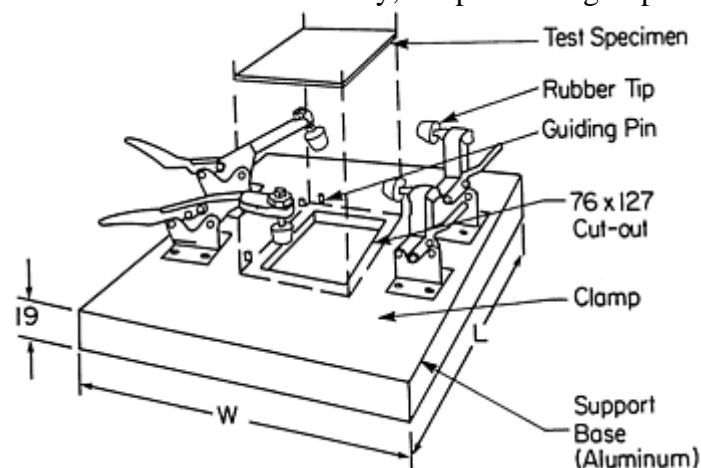


Fig. 30 Fixture used to support the test specimen during impact for the compression-after-impact (CAI) test. Dimensions are in millimeters.

A quasi-isotropic $[45/0/-45/90]_{3s}$ laminate machined to the specifications summarized in Fig. 31 is used as a test specimen. The number of repeating units should be adjusted for different grades of prepreg in order to keep the laminate in the 4 to 6 mm (0.16 to 0.24 in.) cured thickness range. It is highly recommended that the test panel be instrumented with four strain gages located as indicated in Fig. 31 to characterize any eccentricity in loading and to indicate the onset of any excessive delamination growth in the test specimen under compression loading.

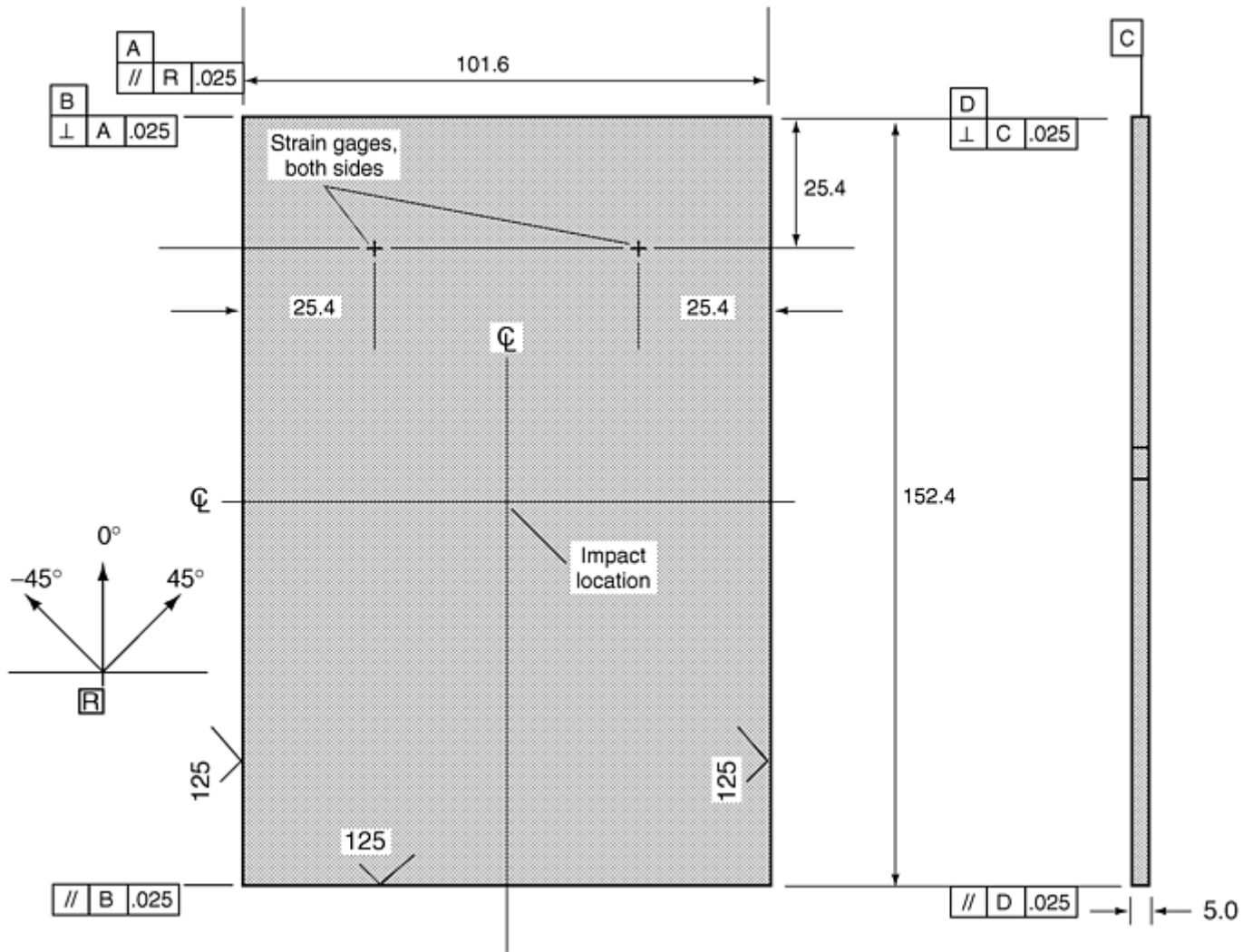


Fig. 31 Specimen geometry for the compression-after-impact test

The compression test is carried out using the fixture shown in Fig. 32. The vertical edges of the specimen are lightly supported by knife edges to simulate simply supported conditions, and the specimen is clamped along the top and bottom edges. The clamping along the top and bottom help constrain brooming failures at the load introduction boundaries. The test is carried out at a loading rate of 1.5 mm/min (0.05 in./min) in a load frame of at least 250 kN capacity until failure occurs as indicated by a drop in the load deflection curve.

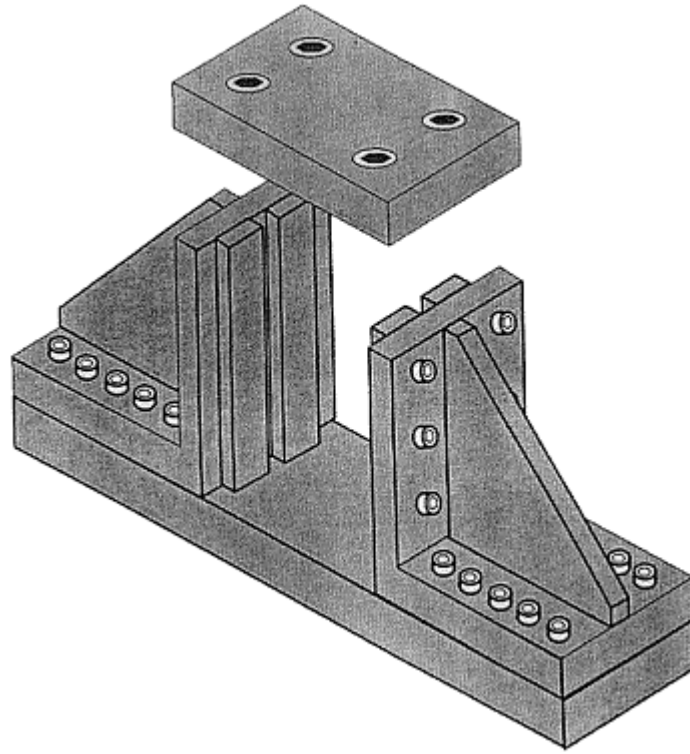


Fig. 32 The test fixture used to conduct compression-after-impact testing

Typical stress-strain results are shown in Fig. 33. Ideally, the four strain gages will track closely with each other. Separation is an indication of eccentricity in load introduction. Divergence near the failure load indicates the onset of global buckling, and early divergence is an indication of sublaminar delamination growth and buckling instability. The compression after impact strength, σ^{ult} , is calculated by dividing the failure load by the cross-sectional area:

$$\sigma^{\text{ult}} = P^{\text{ult}}/bd \quad (\text{Eq 25})$$

where P^{ult} is the failure load, and b and d are the specimen width and thickness respectively. The test results are not considered valid if the impact damage area extends to the edge of the test plaque; these specimens are normally removed from the test matrix. Indication of excessive eccentricity during loading, normally caused by improper specimen machining, and failure of the specimen at a location outside the impact damage zone are reasons to invalidate test results. It is important to examine and record failure location and mode as part of the test results.

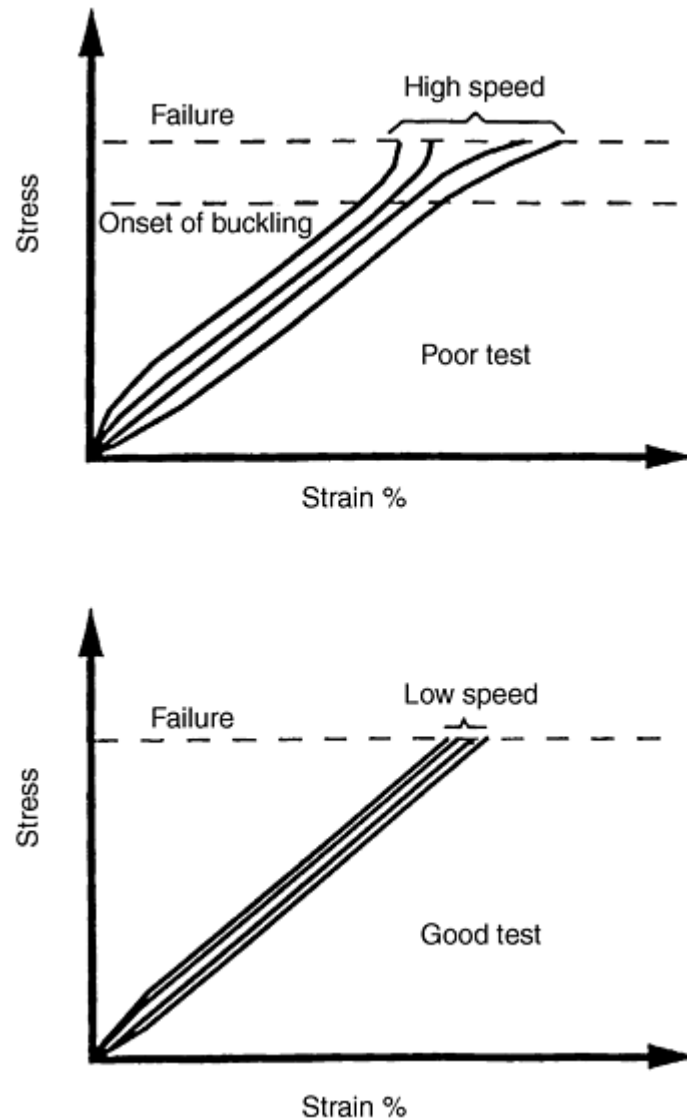


Fig. 33 Typical stress-strain behavior in a compression-after-impact test

A number of factors pertaining to the impact and compression test can influence the test results. A single impact is specified, and rebound impacts must be prevented. The weight of the tup assembly and the velocity of the impact can influence the type and amount of damage generated. The stiffness of the base assembly holding the specimen during impact affects the energy transfer, and, hence, the damage imparted to the specimen. A study by Fallabella et al. (Ref 49) showed this effect by comparing the plywood base originally employed by Boeing and the steel base specified by SACMA. Specimens impacted on the steel base incurred greater damage and exhibited lower compression-after-impact (CAI) strengths.

The compression test is sensitive to the amount of clamping pressure used to constrain the specimen during testing. The test specifies light constraint. Heavy clamping pressures can produce higher failure loads by changing the boundary conditions along the edges of the plate. Alignment is critical to prevent premature failures due to bending induced by loading eccentricity. Both the fixture and the specimen can be sources of misalignment and eccentric load introduction. Most fixtures have alignment features, so lack of specimen conformance to machining tolerances is the most common source of variability in load introduction.

Compression-after-impact test results from the SACMA method allow comparison of material performances under the specific conditions imparted by this test. The CAI data alone do not completely characterize a materials damage tolerance or toughness properties. CAI strength must be combined with other fracture toughness and mechanical property results to draw significant conclusions about the capabilities of a material. Design allowables should not be based on CAI test results. Subscale component tests must be used to provide the type of data required to assess a material's performance under design conditions.

Footnote

* The section “Interlaminar Shear Properties of Fiber-Reinforced Composites at High Strain Rates” was written by John Harding and Stephen Hallett, Oxford University. The section “Fatigue Testing and Behavior of Fiber-Reinforced Composites” was written by W. Steven Johnson and Ramesh Talreja, Georgia Institute of Technology.

References cited in this section

8. L.A. Carlsson and R.B. Pipes, *Experimental Characterization of Advanced Composite Materials*, 2nd ed., Technomic, Lancaster, 1987
45. J.M. Ogonowski, Analytical Study of Finite Geometry Plates with Stress Concentrations, *AIAA Paper 80-0778*, American Institute of Aeronautics and Astronautics, New York, 1980, p 694
46. J.M. Whitney and R.J. Nuismer, Stress Fracture Criteria for Laminated Composites Containing Stress Concentrations, *J. Compos. Mater.*, Vol 8, 1974, p 253
47. R.B. Pipes, R.C. Wetherhold, and J.W. Gillespie, Jr., Notched Strength of Composite Materials, *J. Compos. Mater.*, Vol 13, 1979, p 148
48. E.G. Gynn, W.L. Bradley, and W. Elber, Micromechanics of Compression Failures in Open Hole Composite Laminates, *ASTM STP 1012*, 1989, p 118
49. R. Falabella, K.A. Olesen, and M.A. Boyle, Variations in Impact Test Methods for Tough Composites, *Proc. of the 35th International SAMPE Symposium*, 2–5 April 1990, p 1454

Mechanical Testing of Fiber-Reinforced Composites

Dale Wilson, The Johns Hopkins University, Leif A. Carlsson, Florida Atlantic University

Interlaminar Fracture

With the introduction of composite materials into primary structures, defect and damage tolerance have become important issues for design and materials selection. While damage tolerance testing such as compression after impact testing is performed on substructure specimens or on prototype parts, the use of fracture tests has become popular for materials screening and qualification programs. Of particular interest is the characterization of interlaminar fracture resistance of laminated composites.

The short beam shear test is one of the methods most commonly applied to determine interlaminar properties, but it has many deficiencies. The fracture mechanics approach to interlaminar fracture characterization has evolved as a more fruitful approach. Fracture mechanics of composites is commonly based on the strain energy release rate, and fracture toughness is expressed as the work of fracture. Some background will be given in support of the description of the fracture tests.

It is generally recognized that the resistance to delamination is minimum at the interface between two unidirectional plies of the same fiber orientation. In composites with angle plies, the delamination may be deflected away from the desired midplane through matrix cracks, which invalidates the test. In composites with a tough matrix interleaf film at the midplane, the crack may deflect into an adjacent composite ply due to less crack growth resistance within the ply than between the plies, which would complicate the interpretation of the test results. Woven fabric composites possess resin pockets at the crack plane and may show significant variation in fracture toughness as the delamination grows. Composites with significant interlaminar strength and toughness, such as metal matrix composites and three-dimensional reinforced composites, may not fail in the desired delamination mode. Interlaminar testing of such composites would require specialized fixtures and

specimens. Consequently, the interlaminar fracture test procedures described here are strictly limited to unidirectional single-resin matrix composites.

Strain Energy Release Rate

The most commonly employed approach to characterize interlaminar fracture resistance of composites is by the strain energy release rate. The energy release rate, G , is a thermodynamic parameter that quantifies the energy available for crack growth. The fracture criterion based on G simply states that fracture (crack growth) will occur if the energy available for crack growth exceeds the work required to create a unit of new crack area (Ref 50). The energy approach does not require a detailed analysis of the stress state at the crack tip, where a stress singularity exists. Several delamination fracture tests employ beam specimens, and analysis of the energy release rate is based on simplified beam theory and strength of materials approaches for the calculation of the energy release rate of the fracture specimen.

For a specimen of width w containing a crack of length a , the condition for crack growth is:

$$\frac{d(W - U)}{dA} = \frac{dS}{dA} \quad (\text{Eq 26})$$

where W is the work performed by external forces, U is the elastic strain energy stored in the body, and S is the energy for crack formation (Ref 50). dA is the increment of new crack area, and $dA = wda$. The quantity $d(W - U)/dA$ is the net driving force for crack extension and is denoted by G . dS/dA is the crack growth resistance. If the crack growth resistance is independent of crack length, dS/dA is a material constant denoted by G_c , and is called “fracture toughness.”

The energy release rate can be related to the rate of change in specimen compliance with change in crack length (Ref 50). The specimen compliance, C , is defined as:

$$C = \delta/P \quad (\text{Eq 27})$$

where δ is the relative displacement of the points of load application, and P is the magnitude of applied load. It may be shown (Ref 50) that the strain energy release rate is:

$$G = \frac{P^2}{2w} \frac{dC}{da} \quad (\text{Eq 28})$$

Crack extension can occur through three distinct fracture modes, as shown in Fig. 34. Mode I is the crack opening mode, mode II is a shearing mode, and mode III is a tearing mode. Fracture may occur as a result of any one or a combination of these modes. In this article, only mode I and mode II and mixed mode (I and II) fracture test methods are covered, although Mode III test methods are being examined (Ref 51, 52).

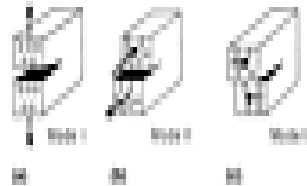


Fig. 34 Modes of crack surface displacements. (a) Mode I (opening). (b) Mode II (forward shear). (c) Mode III (antiplane shear)

Several delamination fracture tests have been proposed (Ref 51, 52, 53, 54). This article restricts attention to only one test of each type. The double cantilever beam (DCB) and end-notched-flex (ENF) test and the mixed-mode bending (MMB) test methods have been recognized by ASTM Committee D-30 as promising interlaminar fracture tests.

Mode I Fracture

The DCB specimen for mode I fracture is now an ASTM standard (ASTM D 5528). The purpose of the test is to determine the opening mode I (Fig. 34a) interlaminar fracture toughness, G_{IC} , of continuous fiber composite materials with a polymer matrix. First developed in a tapered form by Bascom (Ref 55), the specimen has evolved to a straight-sided geometry, as shown in Fig. 35. The analysis developed for data reduction in the

subsequent sections applies only to the straight-sided specimen. The DCB specimen contains a nonadhesive film insert at the midplane to define a precrack of length a_0 , as shown in Fig. 35. Load is applied to the DCB specimen via the adhesively bonded hinges until the crack begins to propagate. Load, displacement, and crack length are monitored during the fracture test.

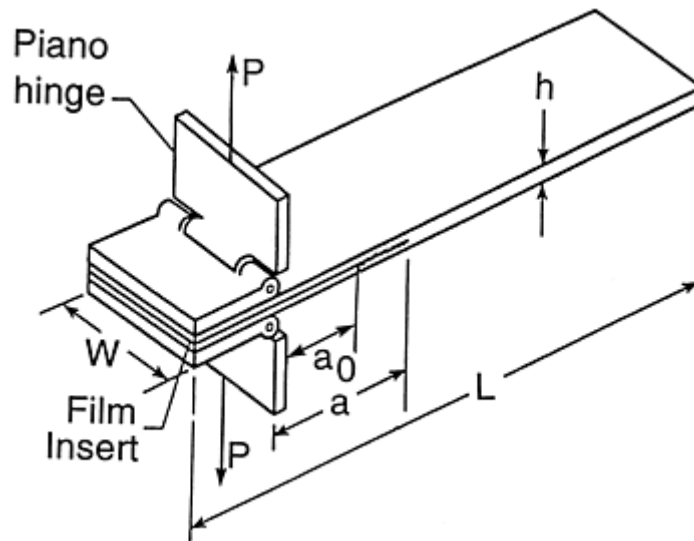


Fig. 35 Double cantilever beam (DCB) specimen geometry

DCB Specimen Preparation and Testing. The DCB specimen should be at least 125 mm (5 in.) long and between 20 and 25 mm (0.8 and 1.0 in.) wide. Panels should be manufactured with a nonadhesive Teflon or Kapton film at the laminate midplane. The film thickness should be less than 13 μm , and the film may be sprayed with a mold release agent before it is inserted between the plies. The insert length should extend approximately 63 mm (2.5 in.) from the front edge of the specimen to achieve an approximately 50 mm (2 in.) long precrack ($a_0 \sim 50$ mm), (Fig. 35). Because it is difficult to detect a thin insert film from the edge of a cut specimen, it is recommended that the end of the insert be carefully marked on the panel before cutting the specimens.

The laminate should contain an even number of plies, and the thickness, h , should be between 3 and 5 mm. Variations in thickness should not exceed 0.1 mm. For thin specimens of large fracture resistance, large deflections may lead to nonlinear response, and thicker specimens may be selected. After appropriate surface preparation of the hinges and the composite (see Ref 8), the hinges should be carefully aligned with the specimen axis and loading line and bonded with a room temperature curing adhesive, such as the adhesives recommended for the end tabs or cyanoacrylate (superglue).

Thickness and width of the specimen are measured at three points along the specimen length, close to the ends and at the center, and the results are averaged. The specimen edges are painted with a thin, white coating or typewriter correction fluid to enhance visualization of crack growth. To aid in recording of crack length, the first 5 mm (0.2 in.) from the insert are marked with thin vertical lines 1 mm (0.04 in.) apart. The remaining 20 mm (0.8 in.) of test length is marked every 5 mm (0.2 in.). Crack length, a , is the distance from the line of load application to the crack tip (see Fig. 35).

The DCB specimen is mounted in the grips of a properly calibrated test machine with a sensitive load cell (5 kN, or 1125 lbf, maximum load capacity). The delamination front is observed as the specimen is being loaded. Load is applied at a crosshead rate of 0.5 mm/min (0.02 in./min), and load versus crosshead displacement is recorded on an x - y recorder for real time visual inspection of the load-displacement response. Displacement of the loaded ends, δ in Fig. 36, is estimated from the crosshead travel, provided that the machine and load cell are stiff enough not to deform more than 2% of the total opening displacement.

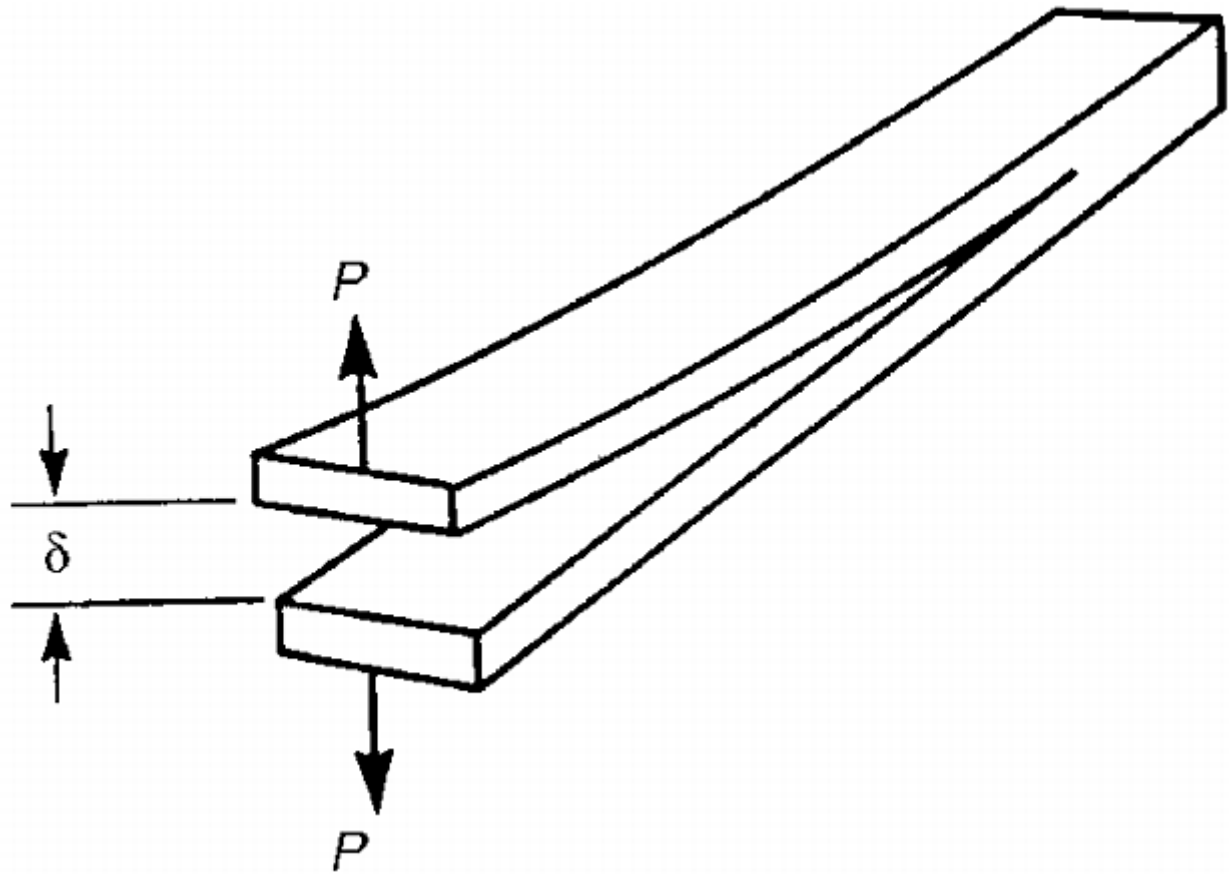


Fig. 36 Definition of crack opening displacement for a double cantilever beam test

The crack front may not grow uniformly across the width of the specimen, so growth must be monitored on both edges of the specimen. A traveling optical microscope located on one side of the specimen with approximately 10 \times magnification and a crosshair can be used to monitor the crack tip location during the fracture test. A mirror is employed to observe the delamination front on the edge of the specimen away from the scope. The accuracy of crack length measurement should exceed ± 0.5 mm (± 0.02 in.). Prior to loading the specimen, the delamination crack front must be located and marked; this defines the precrack length, a_0 , shown in Fig. 35. On loading, when the delamination grows from the end of the insert, a_0 is used to mark the load on the chart recording as indicated in Fig. 37. This process is continued for each new increment of the crack growth, labeling chart points as 1, 2, 3 ... (see Fig. 37). For the first 5 mm (0.2 in.) of crack growth, the loads associated with each 1 mm (0.04 in.) increment should be marked on the chart. After 5 mm of crack extension, the crosshead rate may be increased to 1.5 mm/min (0.06 in./min) or higher, and load is marked at 5 mm increments of crack length extension. The difference in crack length between the two edges should be less than 2 mm (0.08 in.) at all times during the test. When the delamination has been extended about 25 mm (1 in.), the specimen may be unloaded while recording the unloading load-displacement response. This procedure should result in a load-displacement chart such as the one in Fig. 37.

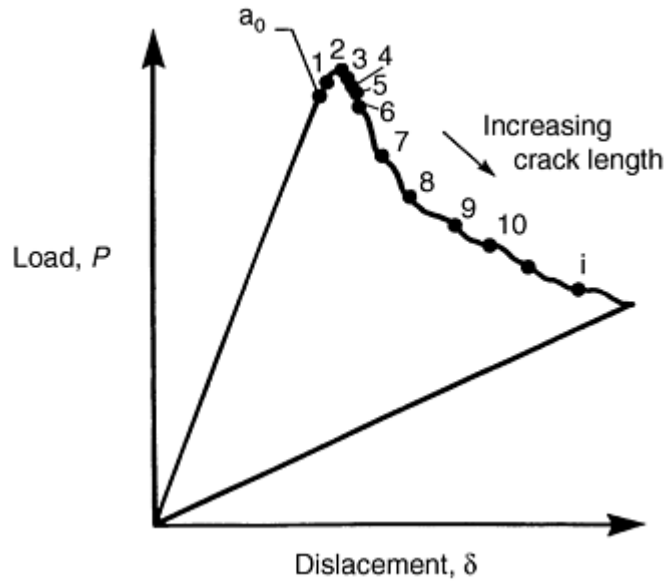


Fig. 37 Schematic load-displacement record during crack growth for a double cantilever beam test

DCB Data Reduction. As the delamination grows from the insert, a resistance curve may be constructed by calculating and plotting the fracture toughness, G_{Ic} , versus crack extension, Δa , or crack length, a . A common occurrence in DCB testing is “fiber bridging,” which refers to debonded fibers bridging the fracture surfaces as illustrated in Fig. 38. The fiber bridging increases the apparent fracture toughness as a result of the fiber debonding process. This phenomenon may not occur at interfaces between dissimilar ply orientations in laminates used in composite structures. Fiber bridging is thus considered as an artifact I, and the significance of G_{Ic} values incorporating contributions from fiber bridging is questionable. It has been suggested that the only significant G_{Ic} value is the initial value associated with crack extension from the film insert, because fiber bridging occurs only after some crack extension (Ref 56).

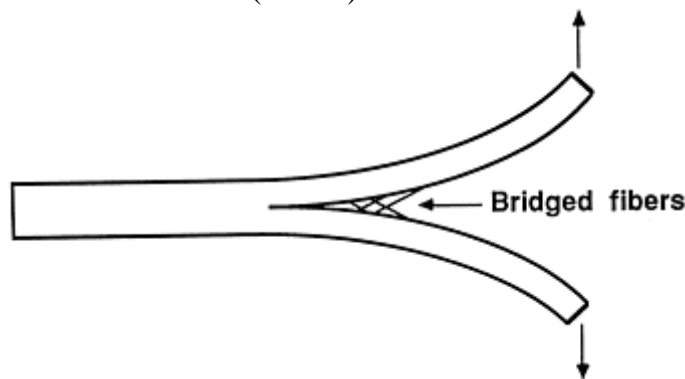


Fig. 38 Fiber bridging in DCB testing of unidirectional laminates

Several data reduction methods for evaluating G_{Ic} have been proposed (e.g., Ref 4, 8, 9, 53, 54) (see also ASTM D 5528). The compliance calibration method based on the empirical compliance expression suggested by Berry (Ref 57) has gained substantial acceptance. In this method the beam compliance, $C = \delta/P$, is expressed as:

$$C = a^n/H \quad (\text{Eq 29})$$

where a is the crack length and parameters n and H are determined experimentally. Compliance values, $C_i = \delta_i/P_i$, corresponding to each crack length marked on the DCB specimen are evaluated from the data in Fig. 37. A plot of $\log C$ versus $\log a$ is generated using all data points, and a least squares analysis is used to fit a straight line to the data. The exponent n is obtained as magnitude of the slope of the straight line. Substitution of Eq 29 into Eq 28 yields at fracture:

$$G_{Ic} = nP_c\delta_c/2wa \quad (\text{Eq 30})$$

in which P_c and δ_c are the critical load and displacement associated with each crack length, a , and w is the specimen width.

Three toughnesses corresponding to crack growth from the insert may be defined (Ref 56). $G_{Ic}(NL)$ refers to the critical load and displacement associated with the deviation from linear response (Fig. 37). The second definition of G_{Ic} (visible) refers to the visual observance of crack growth measured with the traveling microscope. The third definition of G_{Ic} (5%) considers the load and displacement corresponding to a 5% increase in compliance or where the load has reached its maximum value. $G_{Ic}(NL)$ is typically the most conservative estimate of the fracture toughness. For subsequent crack growth, G_{Ic} is calculated from the recorded loads and crack lengths (Fig. 37) and Eq 30.

Figure 39 shows an example of a resistance curve R -curve for a graphite/polyetheretherketone composite. At the first loading increment, the delamination grows from the tip of the thin film insert starter crack without any influence from fiber bridging. The three fracture toughnesses, $G_{Ic}(NL)$, $G_{Ic}(\text{visible})$ and $G_{Ic}(5\%)$ are illustrated in Fig. 39. As the crack grows, the crack surfaces become more and more separated and bridged fibers may fracture or become pulled out from the matrix, which causes the apparent fracture toughness to increase. With further crack extension, a steady-state toughness is usually reached, $G_{Ic}(\text{prop.})$, corresponding to an equilibrium number of bridged fibers per unit crack area.

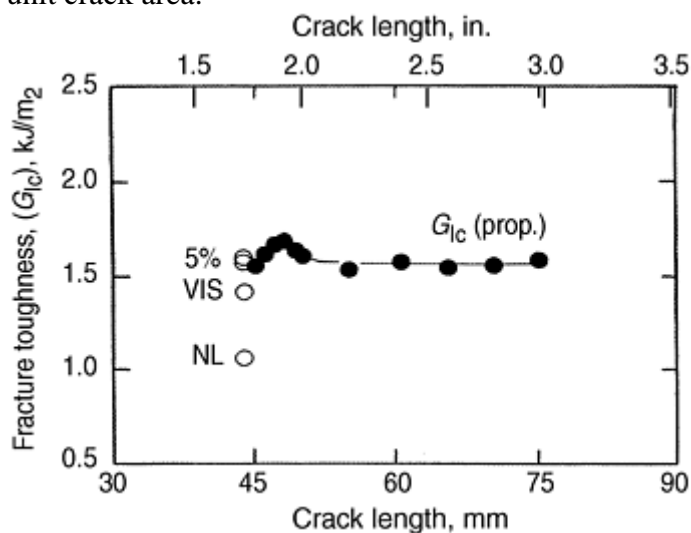


Fig. 39 R -curve describing mode I interlaminar fracture resistance of graphite/PEEK with a 13 μm insert. Source: Ref 56

Mode II Fracture

The end-notched flexure (ENF) beam specimen has emerged as a popular mode II test method since its introduction to the composite community by Russell and Street in 1982 (Ref 58). The purpose of the test is to determine the interlaminar fracture toughness, G_{IIc} , of polymer matrix continuous fiber composites in the forward shear mode (mode II) (see Fig. 34b). Pure shear loading of the crack tip is achieved by loading a cracked three-point flexure specimen (Fig. 40) until the crack propagates. The test has been used primarily with unidirectional laminates. The ENF specimen, like the DCB specimen, has been studied extensively by the ASTM D-30 Committee but the unstable crack growth experienced has delayed ASTM standardization.

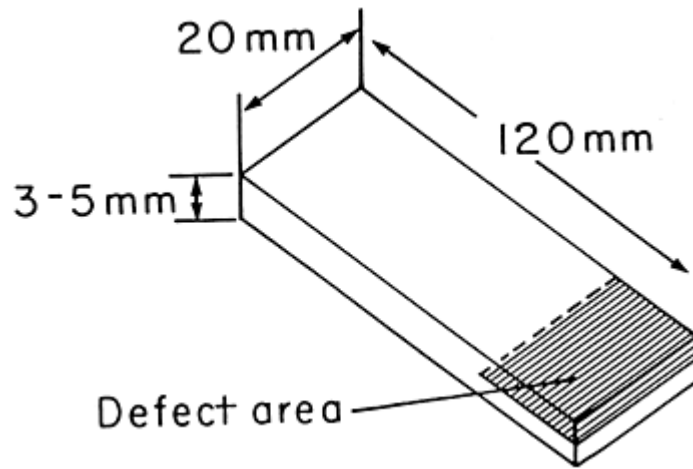


Fig. 40 End-notched flexure (ENF) specimen geometry and dimensions

ENF Specimen Preparation and Testing. The ENF specimen (Fig. 40) is typically 120 mm (4.7 in.) long and 20 mm (0.8 in.) wide. Specimen thicknesses for unidirectional graphite and glass fiber composites are typically 3 and 5 mm (0.12 and 0.20 in.), respectively. The specimen is loaded in a three-point bend fixture (Fig. 41) with a distance between the supports, $2L$, of 100 mm (4 in.). The diameter of the loading and support pins should be about 5 mm (0.2 in.). The ratio of crack length to half-span, a/L , should be 0.5 prior to propagation of the crack. Panels should be manufactured with a nonadhesive Teflon or Kapton (i.e., DuPont de Nemours and Co., Wilmington, DE) film of thickness equal to or less than $13\ \mu\text{m}$ placed at the midplane to define a starter crack. As with the mode I test, the exact location of the precrack must be determined.

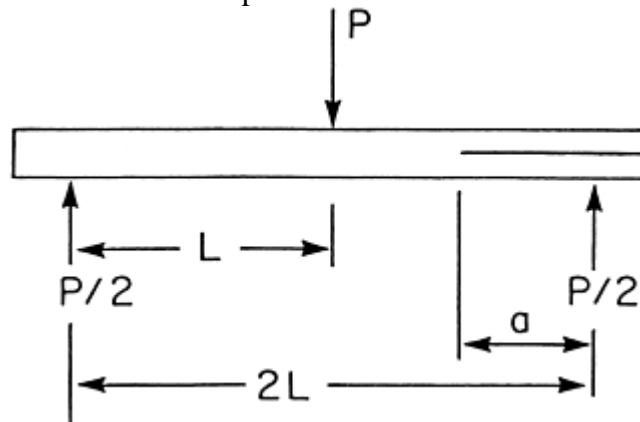


Fig. 41 End-notched flexure test configuration

After specimens have been cut from the panel, the width and thickness are measured at the center and 1 cm (0.4 in.) from each end. The thickness variations should not exceed 0.1 mm (0.004 in.). Prior to testing, the edges should be painted white. There is presently no consensus on whether or not precracking away from the starter film should be performed.

Precracking in mode I is likely to create fiber bridging and is not recommended (Ref 59). A shear precrack may be achieved by using a long specimen (length $> 150\ \text{mm}$, or 6 in.) with a long insert film ($a > 50\ \text{mm}$, or 2 in.), positioning the specimen so that a crack length of about 40 mm (1.6 in.) is achieved and loading the specimen until a short, stable extension of the crack occurs. The shear crack front, however, is not visible on the fracture surfaces of a broken-apart specimen, and accuracy of crack length measurement may suffer. Therefore, propagation of the crack directly from the insert film is recommended.

ENF Testing. The ENF specimen should be placed in a standard three-point bend fixture, so that a crack length, a , of 25 mm (1 in.) is achieved (see Fig. 41). Mark the support location on the specimen edge for subsequent measurement of crack length. The center beam deflection (load point displacement), δ , should be measured with a linear variable differential transformer (LVDT) or may be obtained from the crosshead displacement corrected for the machine compliance. The specimen is loaded at a crosshead rate in the range of 0.5 to 1 mm/min (0.02 to 0.04 in./min), while the load-displacement response is monitored on a chart recorder. Both

loading and unloading paths should be recorded. Observe the crack tip with the traveling microscope during loading to detect any stable crack propagation prior to fast fracture. Slow crack propagation preceding fast fracture is commonly observed in ductile matrix composites (Ref 60). If this occurs, mark this event on the load deflection curve. Brittle-matrix composites tend to show linear response (see the load-deflection curve for a brittle graphite/epoxy composite in Fig. 42). For such systems, fast fracture tends to occur without noticeable stable crack extension.

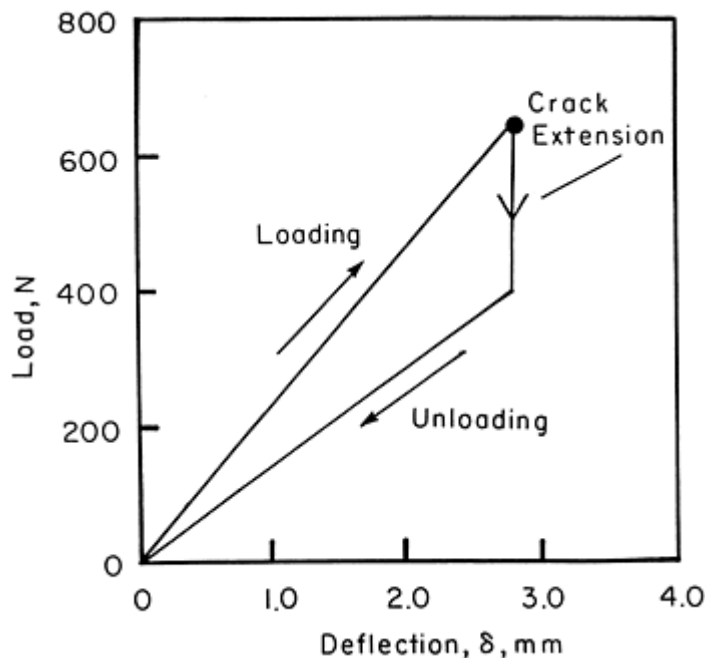


Fig. 42 End-notched flexure test load-deflection curve for brittle graphite/epoxy (AS4/3501-6). $L = 50.8$ mm (2 in.), $w = 25.4$ mm (1 in.) and $a = 27.9$ mm (1.1 in.)

After testing, the initial crack length can be verified by cracking the failed specimen in two parts and measuring the distance between the support pin (marked on the specimen edge) and the crack front defined by the insert film. Commonly the outer support pin leaves an imprint on the specimen surface that can be used to further verify the crack length measurements.

ENF Data Reduction. To evaluate the critical strain energy release rate (mode II fracture toughness), G_{IIc} , the load-displacement curve, shown in Fig. 43, is needed. Several toughness values may be determined, namely, $G_{IIc}(NL)$, $G_{IIc}(\text{visible})$ and $G_{IIc}(\text{max})$ referring to the loads at onset of nonlinearity, visual stable crack extension, and maximum load, respectively, as illustrated in Fig. 43. For calculation of G_{IIc} the initial crack length is required. For the specimen with no precrack, the initial crack length is measured directly from the tip of the starter film as already described.

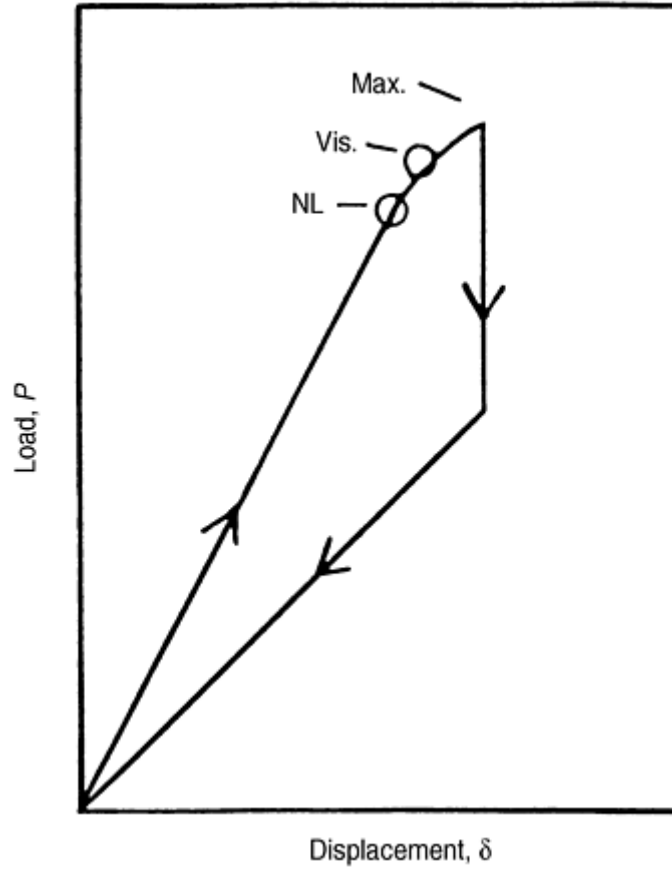


Fig. 43 Schematic load-displacement curve for the end-notched flexure fracture test. $P(NL)$, $P(\text{visible})$ and $P(\text{max})$ denote loads at onset of nonlinearity, onset of visible stable crack growth, and onset of fast fracture, respectively.

The fracture toughness, G_{IIc} , is calculated from the following expression:

$$G_{IIc} = \frac{9a^2 P^2 (C - C_{SH})}{4wL^3 [1 + 1.5(a/L)^3]} \quad (\text{Eq 31})$$

where

$$C_{SH} = \frac{6L + 3a - L^3 / a^2}{20whG_{13}} \quad (\text{Eq 32})$$

The inplane shear modulus G_{12} can be used as an approximation to the interlaminar shear modulus G_{13} . To calculate $G_{IIc}(NL)$, $G_{IIc}(\text{visible})$, and $G_{IIc}(\text{max})$, the loads $P(NL)$, $P(\text{visible})$, and $P(\text{max})$, defined in Fig. 43 are substituted along with the initial crack length in Eq 31.

Mixed Mode Fracture

In most practical situations, delaminations in composite materials tend to grow in mixed-mode stress fields, that is, under combinations of tension and shear stresses ahead of the crack front. Experimental studies, (Ref 61, 62), have shown that the delamination toughness depends on the mode of loading. Consequently, delamination characterization requires mixed mode fracture testing. Several mixed mode fracture specimens exist, but most suffer from complicated test fixturing, a small range of mode mixities (G_{II}/G_I), and varying mode mixity as the crack grows (Ref 63). The most promising mixed mode test specimen for delamination toughness testing is the mixed mode bending (MMB) test (Fig. 44) proposed by Reeder and Crews (Ref 64, 65). The MMB test is currently a candidate for becoming an ASTM standard because of simplicity of testing and the wide range of mode mixities.

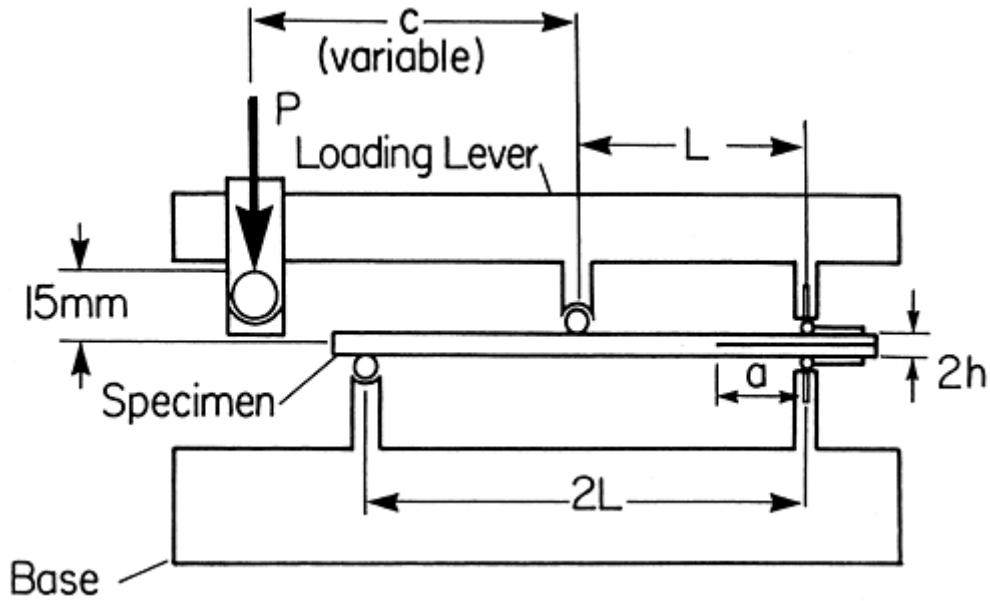


Fig. 44 Mixed mode bending (MMB) specimen and loading.

Figure 44 depicts the geometric parameters of the specimen. The MMB test is a superposition of the DCB and ENF tests discussed previously. As shown in Fig. 44, the loading lever adds an opening load to the midspan-loaded ENF specimen. The adjustable distance, c , between the point of load application and the midspan determines the ratio of the downward force to upward force and, hence, the mode mix. Pure mode II corresponds to $c = 0$ with the ratio G_{II}/G_I decreasing with increasing distance c .

MMB Testing. The MMB test employs a 150 mm (6 in.) long, hinged specimen prepared as the DCB specimen discussed above (no precrack). The specimen width, w , and nominal thickness, $2h$, considered by Reeder and Crews (Ref 64, 65) were 25.4 and 3 mm (1.0 and 0.12 in.), respectively. The initial delamination length, a , was 25 mm (1 in.), and the half-span length, L , was 50 mm (2 in.) (Fig. 44). A set of desired mode mixes $G_{II}/G_I = 0.25$ (2 in.), 1, and 4 can be obtained by proper setting of the distance, c .

A crosshead rate in the range of 0.5 to 1 mm/min (0.02 to 0.04 in./min) should be used for consistency with the DCB and ENF tests discussed above. A real time record of the load displacement response should be obtained using an x - y recorder, and the crack tip should be monitored by a low magnification traveling microscope. The occurrence of slow, stable crack growth should be marked on the load-displacement curve. The load-displacement record is principally similar to that for the ENF specimen (Fig. 43) which allows $G(NL)$, $G(\text{visible})$, and $G(\text{max})$ to be evaluated.

MMB Data Reduction. Reeder and Crews (Ref 64, 65) derived the following expressions for the mode I and mode II components of the energy release rate:

$$G_I = \frac{3P^2(3c-L)^2}{4w^2h^3L^2E_1} \times \left(a^2 + \frac{2a}{\lambda} + \frac{1}{\lambda^2} + \frac{h^2E_1}{10G_{13}} \right) \quad (\text{Eq 33a})$$

$$G_{II} = \frac{3P^2(c-L)^2}{16w^2h^3L^2E_1} \left(a^2 + \frac{h^2E_1}{5G_{13}} \right) \quad (\text{Eq 33b})$$

where

$$\lambda = \frac{1}{h} \left(\frac{6E_2}{E_1} \right)^{1/4} \quad (\text{Eq 34})$$

These expressions are quite accurate for the finite beam geometries employed in the MMB test. Study of Eq 33b reveals that the ratio G_{II}/G_I is only slightly dependent on crack length. An approximate equation for the mode mixity is obtained from the asymptotic beam analysis presented in Ref 65:

$$\frac{G_{II}}{G_I} = \frac{3}{4} \left(\frac{c+L}{3c-L} \right)^2 \quad c \geq \frac{L}{3} \quad (\text{Eq 35})$$

For $c < L/3$, crack face contact may occur, which invalidates the analysis above. Equation (35) may be used for initial (approximate) calculation of the mode mix, which ultimately should be calculated using Eq 33b.

The preceding sections of this article have presented a practical overview of the characterization methods used to measure the fundamental mechanical properties of advanced composite materials. Methods for determining basic engineering strength and elastic properties of lamina, structural properties of laminates, including open-hole and damage tolerance performance, and the material fracture properties have been presented. Understanding these static engineering properties and structural performance characteristics is crucial for making material selection decisions and for preliminary design development. While necessary, these properties are not the complete set of data required to design a structure. Design engineers must address numerous other issues, such as environmental effects, fatigue behavior, creep, and behavior under extreme dynamic loading. Two articles that follow provide valuable insights into how high strain rate and fatigue behavior of composites are characterized.

Footnote

* The section “Interlaminar Shear Properties of Fiber-Reinforced Composites at High Strain Rates” was written by John Harding and Stephen Hallett, Oxford University. The section “Fatigue Testing and Behavior of Fiber-Reinforced Composites” was written by W. Steven Johnson and Ramesh Talreja, Georgia Institute of Technology.

References cited in this section

4. J.M. Whitney, I.M. Daniel, and R.B. Pipes, *Experimental Mechanics of Fiber Reinforced Composite Materials*, revised ed., Society for Experimental Mechanics; Prentice-Hall, Englewood Cliffs, 1984
8. L.A. Carlsson and R.B. Pipes, *Experimental Characterization of Advanced Composite Materials*, 2nd ed., Technomic, Lancaster, 1987
9. D.W. Wilson and L.A. Carlsson, Mechanical Characterization of Composite Materials, *Physical Methods of Chemistry*, 2nd. ed., Vol VII, B.W. Rossiter and R.B. Baetzold, Ed., John Wiley & Sons, 1991, p 139
50. H.L. Ewalds and R.J.H. Wanhill, *Fracture Mechanics*, Edward Arnold, London, 1989
51. S.-M. Lee, An Edge Crack Torsion Method for Mode III Delamination Fracture Testing, *J. Compos. Technol. Res.*, Vol 15, 1993, p 193
52. P. Davies, B.R.K. Blackman, and A.S. Brunner, “Standard Test Methods for Delamination Resistance of Composite Materials: Current Status, *Appl. Compos. Mater.*, Vol 5, 1998, p 345
53. J.W. Gillespie, Jr. and L.A. Carlsson, Interlaminar Fracture of Laminated Composite Materials, *Delaware Composites Design Encyclopedia*, Vol 6, Technomic, Lancaster, 1990, p 113
54. Z. Suo, Delamination Specimens for Orthotropic Materials, *J. Appl. Mech.*, Vol 57, 1990, p 627
55. W.B. Bascom, R.J. Bitner, R.J. Moulton, and A.R. Siebert, The Interlaminar Fracture of Organic-Matrix Woven Reinforced Composites, *Composites*, Vol 11, 1980, p 9
56. T.K. O'Brien and R.H. Martin, Results of ASTM Round Robin Testing for Mode I Interlaminar Fracture Toughness of Composite Materials, *J. Compos. Technol. Res.*, Vol 15, 1993, p 327

57. J.P. Berry, Determination of Fracture Energies by the Cleavage Technique, *J. Appl. Phys.*, Vol 34, 1963, p 62
58. A.J. Russell and K.N. Street, Factors Affecting the Interlaminar Fracture Energy of Graphite/Epoxy Laminates, *Progress in Science and Engineering of Composites*, T. Hayashi, K. Kawata, and S. Omekawa, Ed., ICCM-IV, American Society for Metals, 1982, p 279
59. T.K. O'Brien, G.B. Murri, and S.A. Salpekar, "Interlaminar Shear Fracture Toughness and Fatigue Thresholds for Composite Materials," ASTM STP 1012, 1989, p 222
60. L.A. Carlsson, J.W. Gillespie, Jr., and B.R. Trethewey, Mode II Interlaminar Fracture of Graphite/Epoxy and Graphite/PEEK," *J. Reinf. Plast. Compos.*, Vol 5, 1986, p 170
61. W.S. Johnson and P.D. Mangalgiri, Influence of the Resin on Interlaminar Mixed Mode Fracture, ASTM STP 937, 1987, p 295
62. S. Hashemi, A.J. Kinloch, and J.G. Williams, The Effects of Geometry, Rate and Temperature on the Mode I, Mode II, and Mixed Mode I/II Interlaminar Fracture of Carbon-Fiber/Poly (ether-ether ketone) Composites, *J. Compos. Mater.*, Vol 24, 1990, p 918
63. L.A. Carlsson, Fracture of Fiber Composites, *Structure and Properties of Composites*, T-W. Chow, Ed., VCH, Weinheim, 1993, p 533
64. J.R. Reeder and J.H. Crews, Jr., "A Mixed Mode Bending Method for Delamination Testing," AIAAJ, Vol 28, 1990, p 1270
65. J.R. Reeder and J.H. Crews, Jr., Redesign of the Mixed Mode Bending Delamination Test to Reduce Nonlinear Effects, *J. Compos. Technol. Res.*, Vol 14, 1992, p 12

Mechanical Testing of Fiber-Reinforced Composites

Dale Wilson, The Johns Hopkins University, Leif A. Carlsson, Florida Atlantic University

Interlaminar Shear Properties of Fiber-Reinforced Composites at High Strain Rates

John Harding and Stephen Hallet, Oxford University

Delamination damage in composite materials frequently occurs as a result of transverse impact loading. A significant parameter in determining the ability of the composite to resist delamination is its interlaminar shear strength. It is important, therefore, to be able to measure the interlaminar shear strength under impact. However, even at quasi-static rates of loading, the design of a specimen in which interlaminar failure occurs under pure shear is a significant problem. Under impact loading there is an added constraint in that quasi-static equilibrium must be achieved within the specimen well before it fails if the results are to be capable of meaningful interpretation.

Footnote

* The section “Interlaminar Shear Properties of Fiber-Reinforced Composites at High Strain Rates” was written by John Harding and Stephen Hallett, Oxford University. The section “Fatigue Testing and Behavior of Fiber-Reinforced Composites” was written by W. Steven Johnson and Ramesh Talreja, Georgia Institute of Technology.

Mechanical Testing of Fiber-Reinforced Composites

Dale Wilson, The Johns Hopkins University, Leif A. Carlsson, Florida Atlantic University

Types of Interlaminar Shear Test

In practice, the split Hopkinson pressure bar (SHPB) technique, as described in the Section “High Strain Rate Testing” in this Volume, is probably the best established for producing reliable data at impact rates of strain. Several different types of interlaminar shear specimen have been developed for use with this technique (Ref 66, 67) but all have some limitations. Although very inconvenient to manufacture, thin-walled tubular specimens cut with the axis perpendicular to the interlaminar plane and tested in the torsional SHPB would seem to offer a good chance of success, and excellent results have been obtained this way for a plain-weave glass fiber reinforced plastic (GFRP) (Ref 68). However, the continuous variation of shear direction in relation to the directions of reinforcement leads to problems in specimens with a cross-ply lay-up (Ref 69), problems that are likely to be equally if not more severe with unidirectionally reinforced specimens. This difficulty is overcome by the use of a double-lap design of specimen tested in the tensile SHPB (Ref 70). In these tests, however, the shear stress on the interlaminar failure planes shows some considerable variation, and significant normal stresses are present at the ends of the failure plane. More recently an improved single-lap design of shear specimen has been developed for testing in a modified-compression SHPB. This was first used by Bouette et al. (Ref 71) to determine shear modulus at high rates of strain and later by Bouette et al. (Ref 72) and by Dong and Harding (Ref 73) to determine interlaminar shear strength. This type of specimen has the advantage that the shear stress on the central interlaminar plane is close to uniform and the normal (peeling) stress is very small. More recently, the most commonly used design of single-lap specimen has been the subject of a detailed analysis by Hallett et al. (Ref 74) who have shown that with a cross-ply lay-up, failure may not initiate on the central plane but in a region of stress concentration adjacent to the central interlaminar plane. Nevertheless this remains the best documented and probably the most versatile technique for composites of different lay-ups and so will be the one presented in more detail here.

Footnote

* The section “Interlaminar Shear Properties of Fiber-Reinforced Composites at High Strain Rates” was written by John Harding and Stephen Hallett, Oxford University. The section “Fatigue Testing and Behavior of Fiber-Reinforced Composites” was written by W. Steven Johnson and Ramesh Talreja, Georgia Institute of Technology.

References cited in this section

66. S.M. Werner and C.K.H. Dharan, The Dynamic Response of Graphite Fiber/Epoxy Laminate at High Shear Strain Rate, *J. Compos., Mater.*, Vol 20, 1986, p. 365–374
67. C.Y. Chiem and Z.G. Liu, Modelling of Dynamic Behavior of Composite Materials, *Proc. IMPACT 87, Impact Loading and Dynamic Behavior of Materials*, C.Y. Chiem, H.-D. Kunze, and L.W. Meyer, Ed., DGM Informationsgesellschaft mbH, Oberursel, 1988, Vol 2, p 579–586

68. H. Leber and J.M. Lifshitz Interlaminar Shear Behavior of Plain-Weave GRP at Static and High Rates of Strain, *Compos. Sci. Technol.*, Vol 56,1996, p 391–405
69. T. Parry and J. Harding, The failure of Glass-Reinforced Composites under Dynamic Torsional Loading, Colloque Int. Du CNRS No. 319, *Plastic Behaviour of Anisotropic Solids*, J.P. Boehler, Ed., (CNRS, Paris, 1988) p 271–288
70. J. Harding and Y.L. Li, Determination of Interlaminar Shear Strength for Glass/Epoxy and Carbon/Epoxy Laminates at Impact Rates of Strain, *Compos. Sci. Technol.*, Vol 45, 1992, p 161–171
71. B. Bouette, C. Cazeneuve, and C. Oytana, Shear in Carbon/Epoxy Laminates at Various Strain Rates, *Proc. ECCM-4, Developments in the Science and Technology of Composite Materials*, J. Fuller et al., Ed., (Elsevier Applied Science, London and New York) 1990, p 937–942
72. B. Bouette, C. Cazeneuve, and C. Oytana, Effect of Strain Rate on Interlaminar Shear Properties of Carbon/Epoxy Composites, *Compos. Sci. Technol.*, Vol 45, 1992, p 313–321
73. L.M. Dong and J. Harding, A Single-Lap Shear Specimen for Determining the Effect of Strain Rate on the Interlaminar Shear Strength of Carbon-Fiber Reinforced Laminates, *Composites*, Vol 25, 1994, p 129–138
74. S.R. Hallett, C. Ruiz, and J. Harding, The Effect of Strain Rate on the Interlaminar Shear Strength of a Carbon/Epoxy Cross-Ply Laminate: Comparison between Experiment and Numerical Prediction, *Compos. Sci. Technol.*, Vol 59, 1999, p 749–758

Mechanical Testing of Fiber-Reinforced Composites

Dale Wilson, The Johns Hopkins University, Leif A. Carlsson, Florida Atlantic University

Split-Hopkinson Pressure Bar Test

Specimen Design. The optimum design of a single-lap specimen and the Hopkinson-bar arrangement in which it is tested are shown in Fig. 45. This design has been used successfully in tests on unidirectional carbon fiber reinforced plastic (CFRP) (Ref 73) but, because of difficulties in fixing the specimen to the loading bars, it could not be used when testing unidirectional carbon/polyetheretherketone (PEEK). A modified design of specimen was therefore developed with a slightly different fixing to the loading bars (see Fig. 46). This has been used successfully in tests on both unidirectional and cross-ply carbon/epoxy and carbon/PEEK specimens and on woven reinforced carbon/epoxy and glass/epoxy specimens (Ref 75). Since very similar results were obtained in tests on carbon/epoxy specimens using the optimum and the modified geometries (Ref 73), the modified geometry is now most commonly used. The specimen is intended to fail on the central interlaminar plane where the shear stress is highest and most uniform and the normal stresses are lowest. In practice, the position of the failure plane will be constrained by the lay-up of the composite. For example, in a cross-ply specimen (see Fig. 46), the positions of the interfaces between the 0 and 90° layers with respect to the centerline between the notches will determine the failure plane.

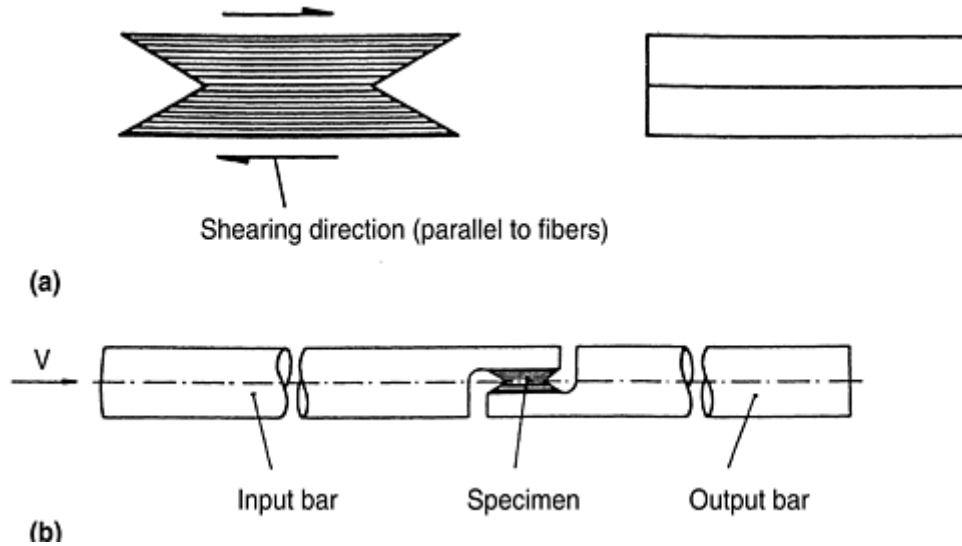


Fig. 45 Split-Hopkinson pressure bar testing to determine the interlaminar shear properties of composites. (a) Optimum design of a single lap specimen. (b) Arrangement of the Hopkinson loading bars.

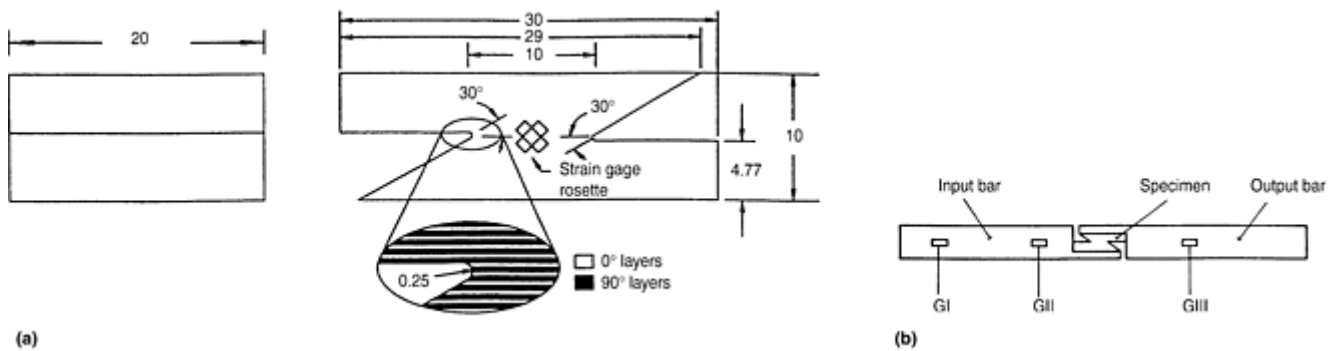


Fig. 46 Modified single-lap specimen for Hopkinson pressure bar testing of composites. (a) Specimen dimensions (in millimeters) and ply lay-up arrangement. (b) Arrangement of loading bars.

Test Details. Impact tests may be performed in a standard compression SHPB apparatus where a cylindrical projectile fired from the high-pressure gas gun strikes the input loading bar. The force transmitted through the specimen is recorded on the output bar strain gages, gage station GIII in Fig. 46. In analyzing the data, it is assumed that the specimen central plane is the interlaminar failure plane and that the shear force is uniformly distributed over this plane. Then the interlaminar shear stress may be determined directly from the output bar strain gages.

The shear strain in the region of failure is measured using $\pm 45^\circ$ strain gage rosettes mounted on either side of the specimen, as shown in Fig. 46. Signals from the specimen strain gage rosettes for an impact test on a plain-weave carbon fiber reinforced plastic CFRP specimen are compared in Fig. 47 (Ref 75). In general, signals of equal magnitude and opposite sign, $\epsilon_{+45} = -\epsilon_{-45}$, are obtained, indicating that on this scale the specimen is indeed in a state of pure shear, the engineering shear strain being given by $\gamma = 2\epsilon_{+45} = -2\epsilon_{-45}$. A divergence between the signals from the $+45^\circ$ and the -45° gages in the later stages of the test is apparent in Fig. 47, while at the end of the test the $+45^\circ$ gages fail while the -45° gages unload. This is probably due to the failure plane not being the central interlaminar plane. However a reasonable estimate of the engineering shear strain close to the failure plane may be made from the algebraic sum of ϵ_{+45} and ϵ_{-45} . The average shear stress on the interlaminar plane may be derived from the output bar strain gages so that, with allowance for the time delay for the stress wave to travel between the specimen gages and the output bar gages, a shear stress-strain curve may be obtained. Quasi-static and intermediate rate tests may be performed on the same design of specimen using shorter loading bars and conventional testing machines to apply the load.

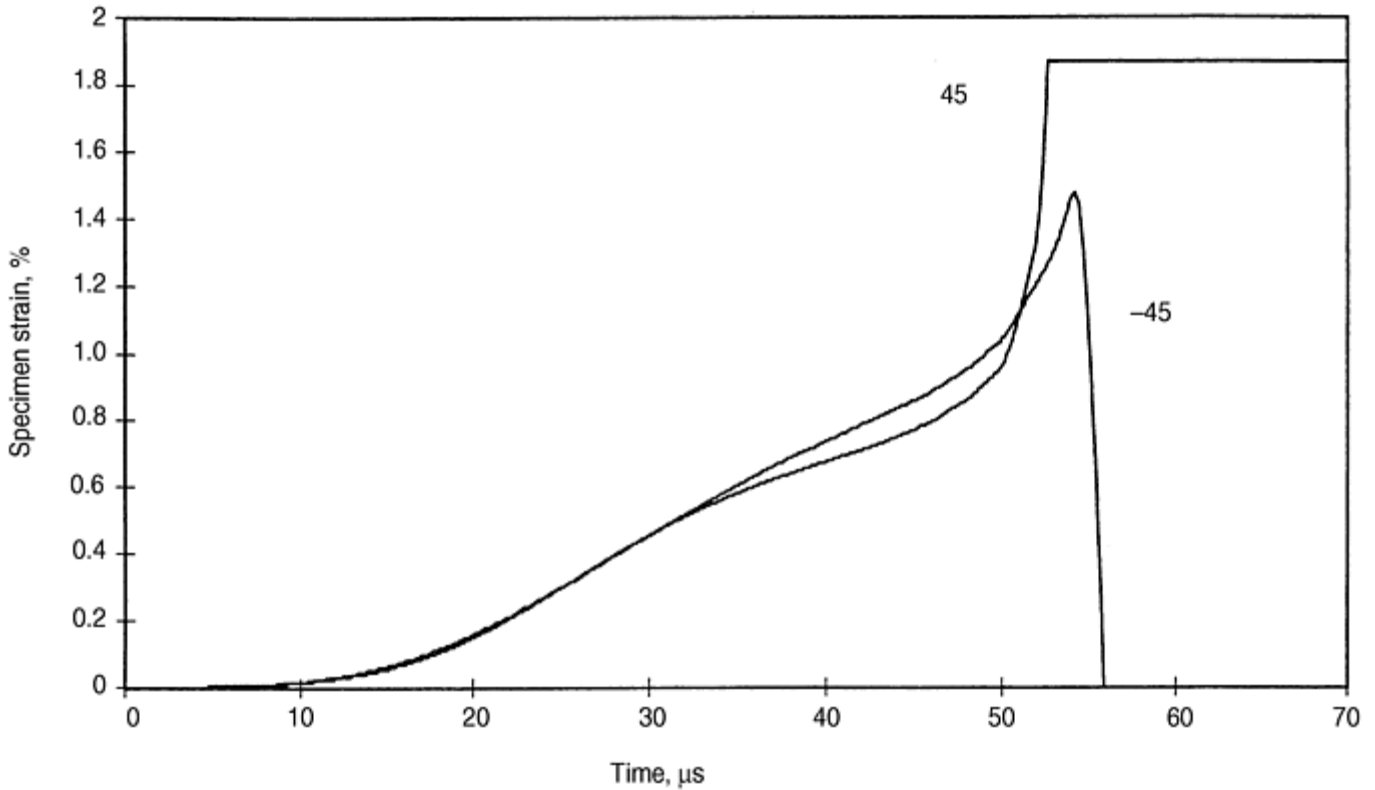


Fig. 47 Strain-time signals from specimen strain gages in impact testing of a plain-weave carbon-fiber reinforced plastic single-lap specimen

Example Test Results. Stress-strain curves obtained in this way for cross-ply CFRP at a quasi-static, an intermediate, and an impact rate of strain are shown in Fig. 48. The variation in interlaminar failure stress and strain with strain rate, obtained from a set of five tests at each rate, are shown in Fig. 49. A marked increase in interlaminar failure stress and strain with strain rate is apparent. It is clear from Fig. 48 that the shear modulus is independent of strain rate. In an earlier study (Ref 73) where only the interlaminar failure stress was measured, a somewhat smaller increase with strain rate was generally observed except for carbon/PEEK, where no increase or a slight reduction was seen.

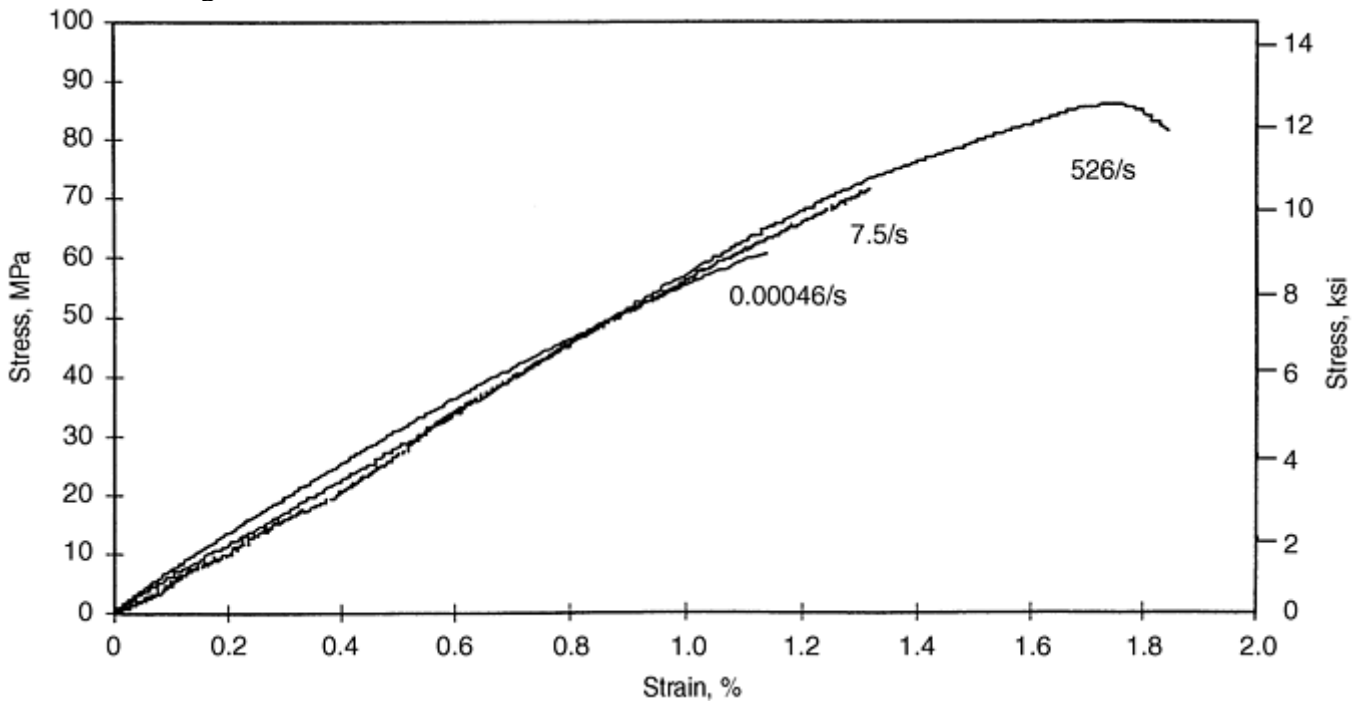


Fig. 48 Effect of strain rate on interlaminar shear stress strain curves for cross-ply carbon-fiber reinforced plastic

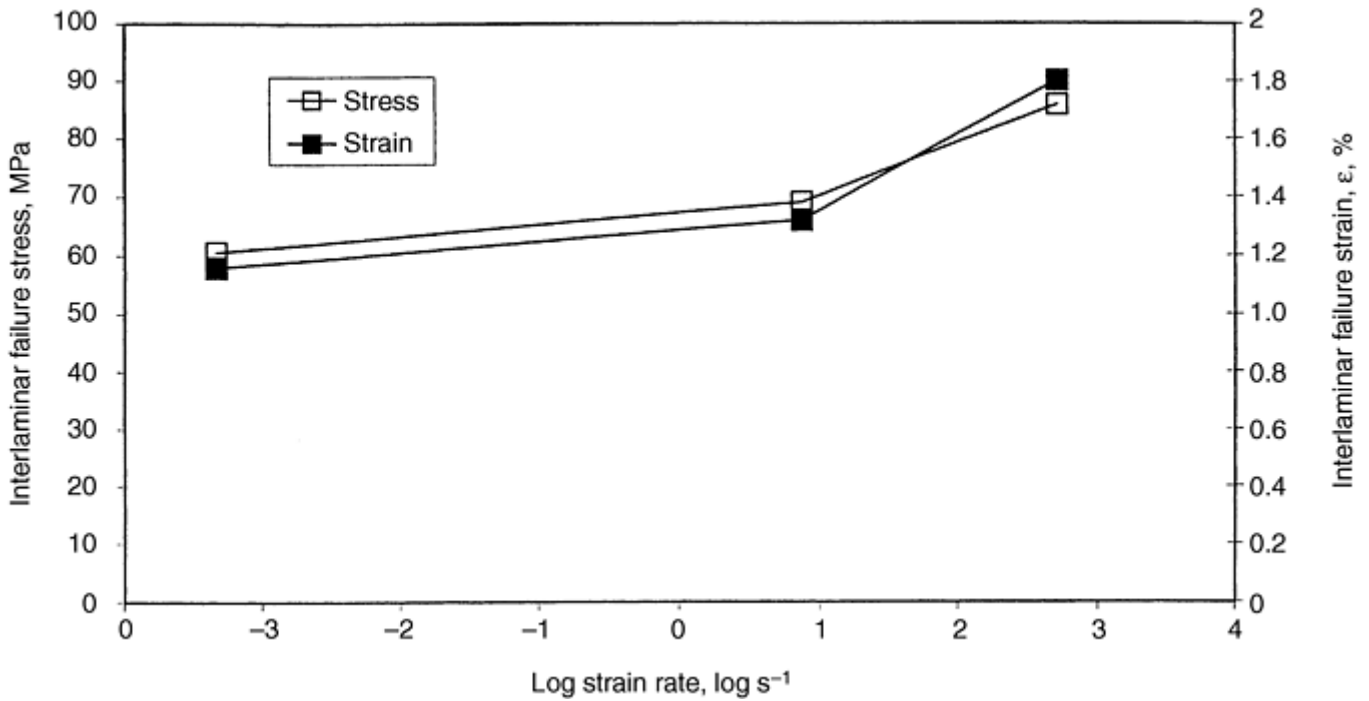


Fig. 49 Effect of strain rate on the interlaminar failure stress and strain

An impact test on a cross-ply CFRP specimen (Ref 74) has shown that failure does not occur on the interlaminar plane nearest to the centerline between the notches but, rather on a neighboring plane, which lies closer to the point where the notch tip radius on the input end meets the horizontal section of the notch. Since each reinforcing ply has a finite thickness, the exact position of the plane on which failure occurs will clearly depend on the precise position of the notch with respect to the lay-up. Nevertheless, the same result, that is failure on a plane slightly offset from the centerline in this manner, was also observed in the earlier work on unidirectional carbon/PEEK (Ref 76) where there was less constraint on the position of the failure plane.

Numerical Modeling of the Shear Test. In light of the experimental observation that failure does not occur on the central interlaminar plane, a numerical analysis was performed (Ref 76) to investigate the shear and normal stress distribution on the actual failure plane. For the cross-ply lay-up of Fig. 46, but simplified such that only a single ply that, on the central plane, had the 90° orientation, the highest shear stress concentration was found in the element where the notch tip radius joined the horizontal section of the notch, that is, at the input end of the experimentally observed failure plane. The numerically predicted shear and normal stresses on this plane are shown in Fig. 50. The mean shear stress in this figure corresponds to that which is measured experimentally. The implication of the numerical analysis, therefore, is that failure actually initiates at a shear stress that is approximately twice the mean shear stress determined experimentally and in the presence of a significant normal compressive stress.

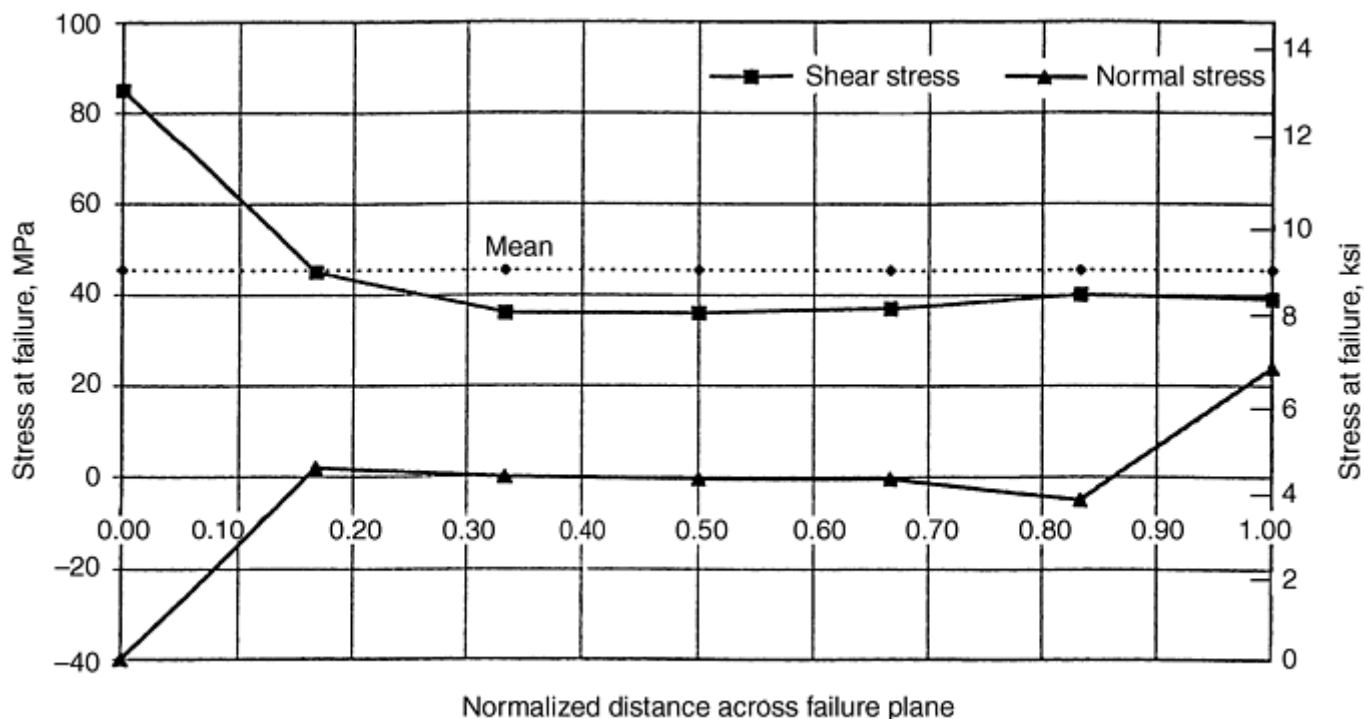


Fig. 50 Numerically predicted shear and normal stresses on actual failure plane

However, using a modification form of Chang-Chang failure criteria (Ref 77), we found it possible to predict the initiation and growth of damage by delamination. This was predicted to start in the region of the shear stress concentration at the input end of the failure plane, followed almost immediately by similar damage in the corresponding element at the other end of the specimen and propagation from each end towards the center on the two interlaminar planes, which are then joined by a step in the middle. Such a step has been seen experimentally in unidirectionally reinforced specimens (Ref 76) but was not found in these tests on cross-ply material. In similar tests on woven GFRP (Ref 75), complete failure on the first of these planes was mirrored by extensive damage on the second.

Footnote

* The section "Interlaminar Shear Properties of Fiber-Reinforced Composites at High Strain Rates" was written by John Harding and Stephen Hallett, Oxford University. The section "Fatigue Testing and Behavior of Fiber-Reinforced Composites" was written by W. Steven Johnson and Ramesh Talreja, Georgia Institute of Technology.

References cited in this section

73. L.M. Dong and J. Harding, A Single-Lap Shear Specimen for Determining the Effect of Strain Rate on the Interlaminar Shear Strength of Carbon-Fiber Reinforced Laminates, *Composites*, Vol 25, 1994, p 129-138
74. S.R. Hallett, C. Ruiz, and J. Harding, The Effect of Strain Rate on the Interlaminar Shear Strength of a Carbon/Epoxy Cross-Ply Laminate: Comparison between Experiment and Numerical Prediction, *Compos. Sci. Technol.*, Vol 59, 1999, p 749-758
75. J. Harding and J.L. Medina, Oxford University Engineering Department, Solid Mechanics Group, Unpublished data, August 1999

76. M.J. Hiley, L. Dong, and J. Harding, Effect of Strain Rate on the Fracture Process in Interlaminar Shear Specimens of Carbon Fiber-Reinforced Laminates, *Composites*, Vol 28A, 1997, p 171–180

77. F. Chang and K. Chang, *J. Compos. Mater.*, Vol 21, 1987, p 834–855

Mechanical Testing of Fiber-Reinforced Composites

Dale Wilson, The Johns Hopkins University, Leif A. Carlsson, Florida Atlantic University

Summary

While the single-lap shear test using the modified specimen geometry (Fig. 46), allows the effect of strain rate on the interlaminar shear failure of laminated composites to be determined, the shear stress on the failure plane is not completely uniform, and failure initiates under a combination of stress concentrations in both shear and normal compression. A similarly detailed analysis has not been performed for the optimum specimen geometry (Fig. 45), so it is possible that the stress concentrations are less severe in this case. However, since in all practical applications, interlaminar shear failure almost certainly initiates in the presence of stress concentrations, the use of numerical analysis in conjunction with experimental testing becomes a necessity if the results obtained are to be capable of useful application. It is encouraging, therefore, that by the use of a modified Chang-Chang failure criterion, features actually observed in the single-lap shear test under impact loading, in particular the initiation and growth of delamination damage associated with the failure plane, have been successfully modeled numerically (Ref 74).

Footnote

* The section “Interlaminar Shear Properties of Fiber-Reinforced Composites at High Strain Rates” was written by John Harding and Stephen Hallett, Oxford University. The section “Fatigue Testing and Behavior of Fiber-Reinforced Composites” was written by W. Steven Johnson and Ramesh Talreja, Georgia Institute of Technology.

Reference cited in this section

74. S.R. Hallett, C. Ruiz, and J. Harding, The Effect of Strain Rate on the Interlaminar Shear Strength of a Carbon/Epoxy Cross-Ply Laminate: Comparison between Experiment and Numerical Prediction, *Compos. Sci. Technol.*, Vol 59, 1999, p 749–758

Fatigue Testing and Behavior of Fiber-Reinforced Composites

W. Steven Johnson and Ramesh Talreja, Georgia Institute of Technology

From the preceding discussions, one can see that the mechanical behavior of composites is complex and varied. The mechanisms of fatigue damage are also complex. This section gives an overview of fatigue testing and fatigue damage mechanisms for several classes of composite materials. Several types of mechanical measurements that can be made during the course of testing to assess fatigue damage are reviewed. In addition, some other destructive techniques that can be used to assess fatigue damage are described.

Footnote

* The section “Interlaminar Shear Properties of Fiber-Reinforced Composites at High Strain Rates” was written by John Harding and Stephen Hallett, Oxford University. The section “Fatigue Testing and Behavior of Fiber-Reinforced Composites” was written by W. Steven Johnson and Ramesh Talreja, Georgia Institute of Technology.

Fatigue Damage Mechanisms

Before attempting to predict life of composite components in service under cyclic loads, one should understand the mechanisms of damage that govern the material behavior. For this purpose, posing the following questions is useful:

- How does the material state (properties of constituents and interfaces) change from the initial to the instant when the first maximum load is applied?
- On reversal of the load from maximum to the initial value, does the material return to its initial state, and if not, what are the irreversible changes?
- How do the irreversible changes affect the response of the material to the next application of the load?
- What are the factors governing the progressiveness in the irreversible changes?
- What is the critical material state (failure), and how is it attained?

For metals, these questions have been addressed for many years, and the knowledge generated forms the basis for safe and reliable structural design as well as for the development of fatigue resistant metals. For composites, much remains to be done to reach the same level of progress. The problems faced for composites are complex due to the roles of constituents and interfaces and the many possible configurations in which composites can be made. It is inevitable that multiple fatigue mechanisms operate simultaneously with differing rates of progression. To facilitate a systematic interpretation of the mechanisms, fatigue life diagrams have been useful for polymer-matrix composites (PMCs) (Ref 78), ceramic-matrix composites (CMCs) (Ref 79), and metal-

matrix composites (MMCs) (Ref 80). In the following sections, the fatigue mechanisms for these material systems are reviewed with the aid of these diagrams.

Fatigue Life Diagram. The basic construction of a fatigue life diagram is shown in Fig. 51 for a unidirectional, continuous fiber reinforced PMC of standard materials (such as carbon/epoxy) subjected to cyclic tension in the fiber direction. Consider first a load cycle in which the maximum strain attained is within the scatter band of the composite failure strain. At the first application of the maximum load in this cycle, a certain number of fibers will fail, assuming the composite survives. The locations of fiber breaks will be determined by the points at which the fiber stress exceeded the fiber strength. A distributed pattern of fiber breaks will result (see Fig. 52, $N = 1$), and the matrix around broken fibers will experience higher stresses than elsewhere and will likely become inelastic. On reversal of the load to its minimum value, the inelastic strains will irreversibly change the material state from the virgin state. In the next and subsequent load cycles, the axial stress in unbroken fibers will progressively change. However, all cross sections containing broken fiber ends will not experience the same rate of growth of fiber breaks, because of the variability of the fiber strength, and failure will result from a cross section that can form a core of fiber failures of a critical size (see Fig. 52, $N = N_f$).

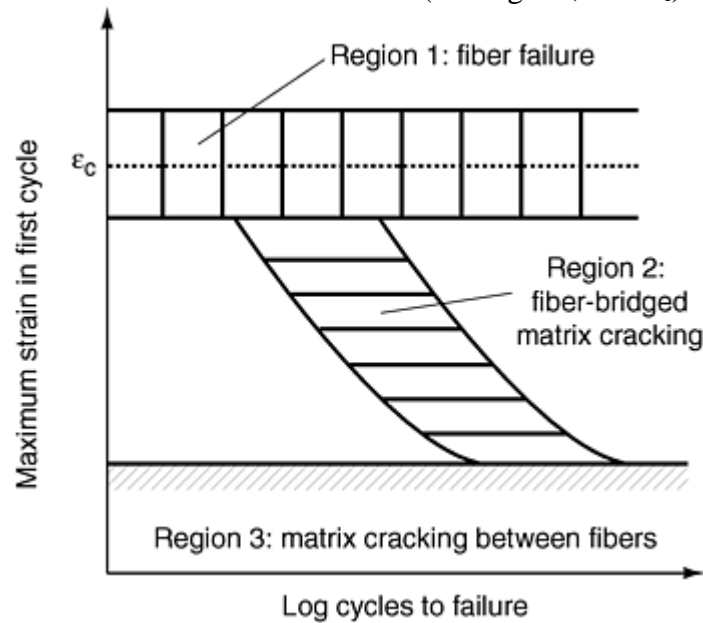


Fig. 51 Fatigue life diagram of a unidirectional composite under cyclic tension in the fiber direction

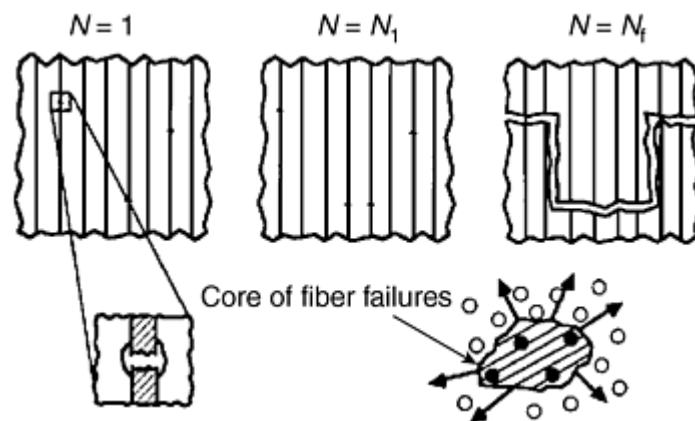


Fig. 52 Mechanism of fiber failure in region I of the fatigue life diagram

It can now be imagined that the number of cycles to failure, N_f depends on the fiber strength distribution, the geometric distribution of fibers, the matrix deformation characteristics, and the critical size of the core of fiber failures. For stiff and brittle fibers, the critical core size is expected to be small and the number of cycles needed to reach it could vary from a few to several millions, depending on how the initial pattern of broken fibers is formed. This extreme sensitivity to the first-cycle failure pattern overshadows the cycle-by-cycle progression of the fiber failure process. Thus, region 1 in the fatigue life diagram (Fig. 51), where fiber failure is the dominant

mechanism, is viewed as a nonprogressive failure region. The scatter band here is centered about the fiber failure strain, which is also the composite failure strain, and extends to infinite number of cycles.

Consider now a load cycle where the first application of load gives a maximum strain less than the lower limit of the composite failure scatter band. The number of fibers failed in this cycle will be insignificant. In the next and subsequent load cycles, the stress redistribution in the unbroken fibers due to matrix inelasticity would not increase the number of fiber breaks significantly. The inelastic cyclic deformation of matrix will, however, initiate fatigue cracks in the matrix, assuming that the local matrix strain exceeds its fatigue limit. The fatigue crack thus produced will grow progressively as a fiber-bridged crack, breaking some (weak) fibers while debonding others and growing around them (Fig. 53). At a critical crack size, depending on the maximum load applied, unstable crack growth will occur, resulting in composite failure.

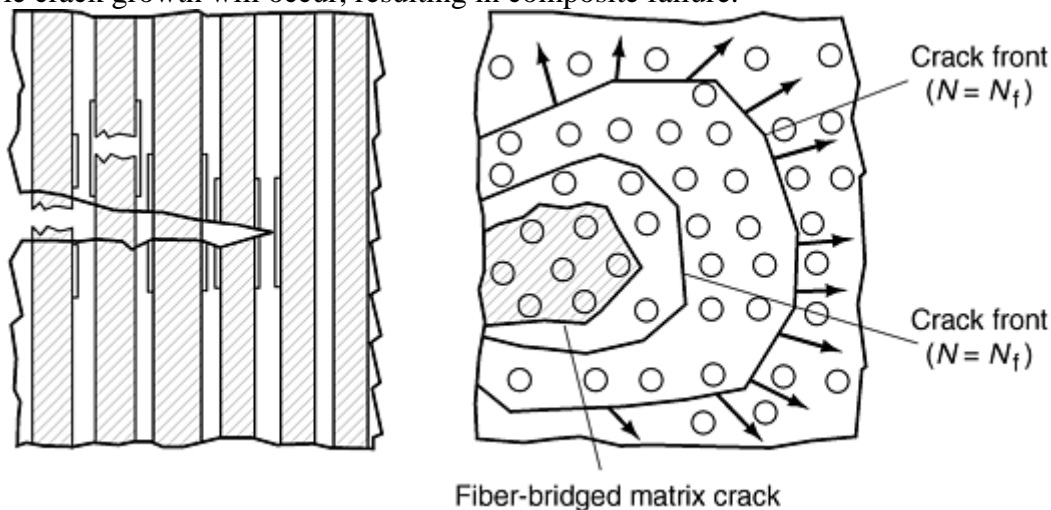


Fig. 53 Mechanism of fiber-bridged matrix cracking in region II of the fatigue life diagram

This postulated sequence of events has been documented (Ref 78) for two PMC systems (Ref 81), and the sloping scatter band in Fig. 51 (marked as region 2) represents this progressive mechanism. The rate of progression of this mechanism depends on the maximum strain applied in the first load cycle. It is natural to expect that a threshold value of the maximum strain exists, below which the mechanism either does not progress (e.g., matrix cracks are not able to overcome the resistance given by fibers, Fig. 54) or does not cause further damage (i.e., unstable growth) in a great number of cycles. The region in the fatigue life diagram below such a threshold value is called the composite fatigue limit (region 3 in Fig. 51). It is expected that this threshold value for a given composite will depend on the matrix fatigue limit, the fiber stiffness and strength, the interface strength, and the distribution of fibers in the composite.

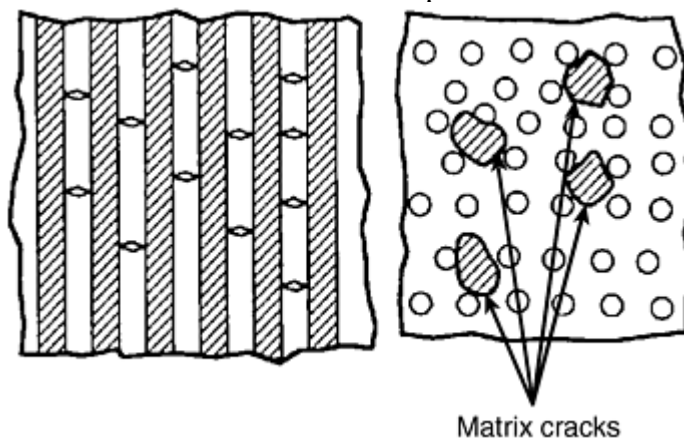


Fig. 54 Mechanism of matrix cracking arrested by fibers corresponding to region III of the fatigue life diagram

Effects of Constituents on Fatigue Damage. The fatigue life diagram described for Fig. 51 is based on the mechanisms expected to occur in standard PMCs such as glass/epoxy and graphite/epoxy. When the properties of the constituents are varied, for example, by changing the fiber stiffness, fiber strain to failure, or matrix

ductility, the mechanisms are affected and the resultant effects on the fatigue life can be easily understood by observing changes in the fatigue life diagrams. For instance, an increase in the fiber failure strain will displace region 1 upwards, while increasing fiber stiffness will delay matrix crack growth, shifting region 2 to the right as indicated in Fig. 55. On the other hand, increasing matrix ductility will enlarge the crack-tip plastic zone, thereby increasing crack-tip opening displacement and straining the bridging fibers further. The detrimental effect on fatigue life by this change in the mechanism will shift region 2 (Fig. 51) to the left (Fig. 55). Finally, improved fatigue properties of the matrix material and reduced fiber stiffness will raise the composite fatigue limit, reducing thereby the range of strain in which fatigue failure can occur.

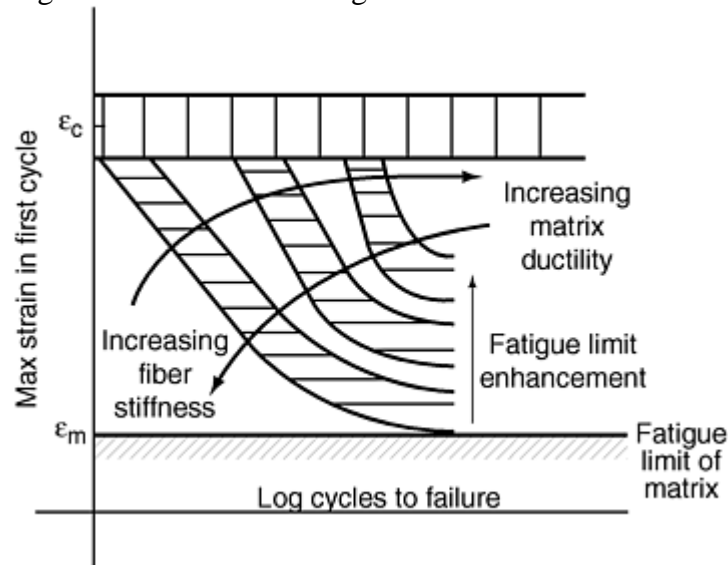


Fig. 55 Trends in the fatigue life diagram induced by fiber stiffness and matrix ductility

In high temperature materials, such as MMCs and CMCS, the residual stresses can be large. For instance, in SCS-6/Ti-15-3, the residual stress on cooldown to the room temperature is compressive in the fibers. The inelastic cyclic deformation can relieve this stress and thereby increase the probability of fiber failure. This changes region 1 of the fatigue life diagram from having a horizontal scatter band of nonprogressive fiber failure to a sloping scatter band of cycle-dependent progressive failure. At high temperatures, the residual compressive stress in fibers decreases while the matrix inelastic deformation increases. These two effects render the fiber failure mechanism of region 1 even more progressive. The slope of region 1, thus, increases with increasing temperature (Ref 80).

In CMCs, where both constituents are brittle, the source of irreversibility in cyclic loading is provided primarily by friction at the debonded fiber/matrix interfaces. The fiber stress redistribution with cycles is caused by load transfer between matrix and fibers through the frictional shear stress at the interface. At room temperature, at which the matrix behaves in a brittle manner, its role in the fatigue process is not significant. Region 1 and region 2 of the fatigue life diagram are then not as easily separable as in PMCs and MMCs. The dominant mechanism in both regions is fiber failure, whose progression is governed by the fiber/matrix interface. A fatigue limit still exists but is not governed by the matrix. As discussed in (Ref 81), the fatigue limit in this case is given by the threshold below which the rate at which fibers are broken in a cycle is exceeded by the rate at which fibers bridge the matrix crack.

Effects of Fiber Architecture. In multidirectional laminates, other mechanisms in addition to those previously described come into play. These additional mechanisms consist primarily of multiple intralaminar cracking of off-axis plies and interlaminar cracking (delamination). These mechanisms can be viewed as subcritical, while those associated with failure of on-axis plies should be viewed as critical. The role of the subcritical mechanisms is thus seen as effecting stress transfer from off-axis plies to on-axis plies. This stress transfer occurs progressively, and failure occurs when the on-axis plies are stressed to their limiting value.

The progression of intralaminar cracking in off-axis plies is conveniently described by the evolution of the average number of cracks per unit length normal to the crack planes (or inverse of the average crack spacing). This crack density parameter is shown plotted against the number of load cycles of different maximum load value for a glass/epoxy cross ply laminate in Fig. 56. The evolution rate of this parameter depends on the

laminates geometry, that is, the thickness of the off-axis plies and the stacking sequence of the laminate, and the relative stiffness of the off-axis plies with respect to the on-axis plies.

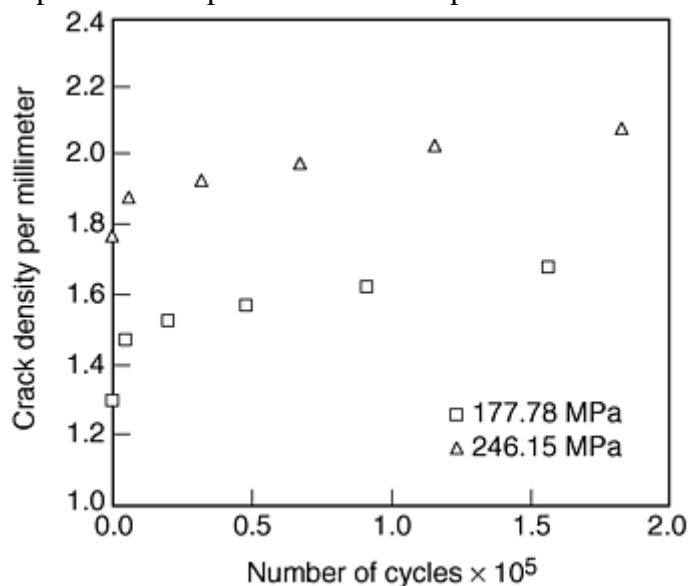


Fig. 56 Evolution of transverse cracking under fatigue in a glass/epoxy cross-ply laminate at two stress amplitude. Data from Ref 82

The interlaminar cracking, that is, delamination, results from the local failure of the ply/ply interface due to the high (and complex) stress accompanying the fronts of the intralaminar cracks and by diversion of these fronts into the interlaminar planes. These distributed delaminations grow under cyclic loading and are thought to be responsible for altering the stress states in the plies, giving rise to the progressive cracking of the off-axis plies. In woven fabric composites, the fiber bundles develop multiple cracks in much the same way as intralaminar cracks in laminates. The interbundle planes crack in the crossover regions of the bundles and presumably play a role similar to that of delaminations in laminates.

Footnote

* The section “Interlaminar Shear Properties of Fiber-Reinforced Composites at High Strain Rates” was written by John Harding and Stephen Hallett, Oxford University. The section “Fatigue Testing and Behavior of Fiber-Reinforced Composites” was written by W. Steven Johnson and Ramesh Talreja, Georgia Institute of Technology.

References cited in this section

78. R. Talreja, Fatigue of Composite Materials: Damage Mechanisms and Fatigue Life Diagrams, Proc. R. Soc. (London), Vol A378, 1981, p 461–475
79. R. Talreja, “Fatigue of Fiber-Reinforced Ceramics”, *Structural Ceramics—Processing, Manufacture and Properties*, J.J. Bentzen, et al., Ed., Riso National Laboratory, Roskilde, Denmark, 1990, p 145–159
80. R. Talreja, A Conceptual Framework for Interpretation of MMC Fatigue, Mater. Sci. Eng., Vol A200, 1995, p 21–28
81. E.K. Gamstedt and R. Talreja, Fatigue Damage Mechanisms in Unidirectional Carbon-Fiber-Reinforced Plastics, *J. Mater. Sci.*, 1999, in press
82. A.L. Highsmith and K.L. Reifsnider, Stiffness Reduction Mechanisms in Composite Laminates, *Damage in Composite Materials*, K.L. Reifsnider, Ed., ASTM STP 775, 1982, p 103–117

Fatigue Testing

Strain gages are commonly used to measure the strain response of the specimens. However, strain gages only measure local strains. In general, fatigue damage in unnotched composite laminates may be quite random. Unless the strain gage is quite large, the measured strain may or may not reflect the random damage. O'Brien (Ref 83) has discussed the effect of gage-section size on composite stiffness measurements. In most cases, strain measurement over a 25 mm (1.0 in.) gage section is recommended. This will result in a global measurement of the effect of damage on laminate moduli. There is a trade-off, however; too large a gage length will not be sensitive to local damage, and too small a gage length will miss local damage.

In lieu of strain gages, clip-on extensometers can also provide excellent accuracy without the difficulty of bonding a strain gage in place. Most extensometers only give the strain in the axial direction of the specimen, although there are some special extensometers that can measure the transverse strain in the laminate as well. Since most extensometers are at least 13 mm (0.5 in.) in gage length, they will measure the global deformation of the composite. Extensometers are available for operation at a wide variety of temperatures.

As an example, the cyclic stress-strain response of a boron/aluminum laminate presented in Fig. 57 can be analyzed to yield several mechanical properties. These properties include the following:

- Initial elastic modulus (tangent modulus)
- Stiffness (secant modulus)
- Permanent plastic deformation (strain)
- Elastic unloading modulus after N number of cycles
- Stiffness after N number of cycles
- Cyclic strain
- Number of cycles to fatigue failure
- Strain to static failure
- Residual strength after a set number of cycles

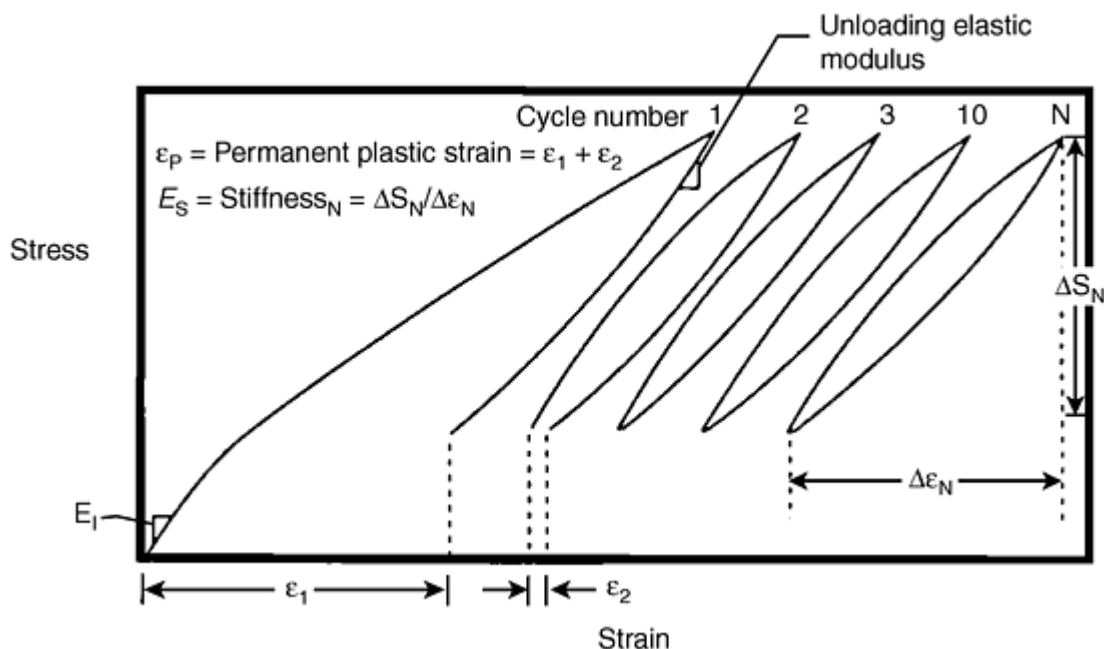


Fig. 57 Schematic of the cyclic stress-strain behavior of a quasi-isotropic laminate of boron/aluminum as a function of number of cycles. Source: Ref 84

A detailed definition of each property along with the physical significance is presented next.

Initial Elastic Modulus. The elastic modulus E is the tangent modulus of the initial linear portion of the loading curve. The initial elastic modulus E_1 is measured on the first loading cycle as shown in Fig. 57. E_1 usually correlates with elastic modulus predicted by lamination theory for an undamaged composite. The initial elastic modulus is significant in that all later measurements of elastic modulus at N cycles will be compared to this initial modulus to give an indication of the amount of fatigue damage accumulated by the composite laminate.

Stiffness. The stiffness E_S is defined as the secant modulus of the loading cycle as indicated in Fig. 58. In order to eliminate permanent plastic deformation from the stiffness measurement, the stiffness is defined utilizing the unloading portion of the cycle (the stress range, ΔS , divided by the unloading strain range, $\Delta \epsilon$). The initial stiffness can be compared to measurements of stiffness at N cycles and is therefore significant.

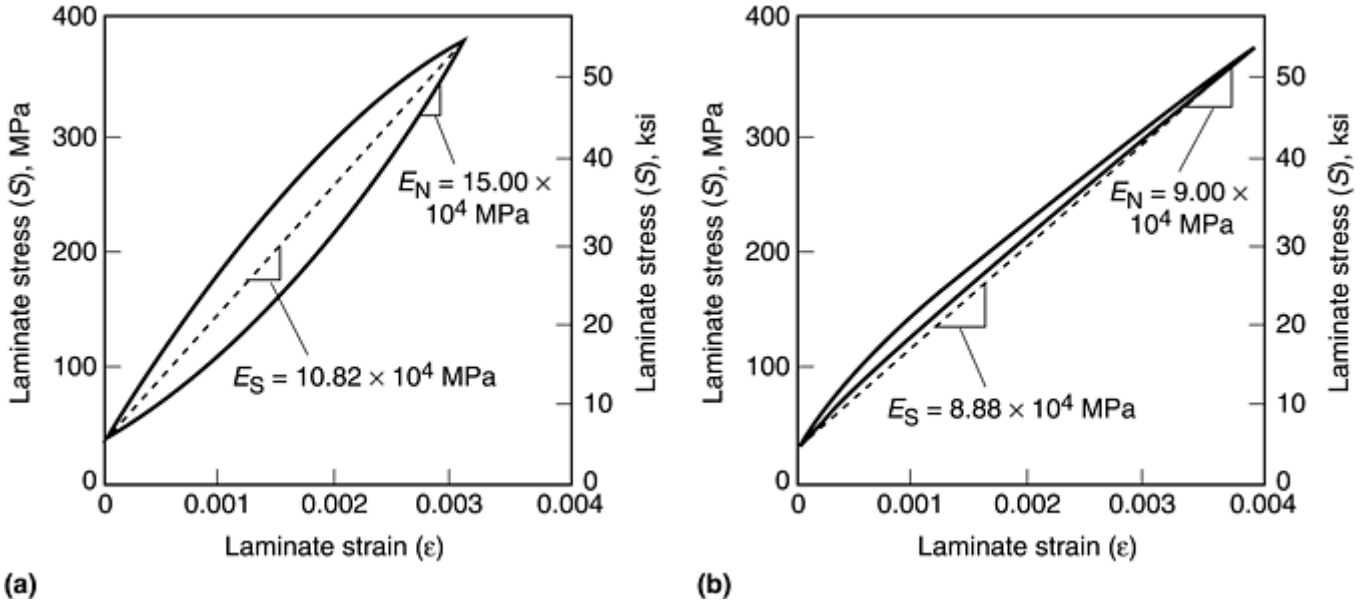


Fig. 58 The cyclic stress-strain response of a boron/aluminum ($[0/\pm 45/90/0/\pm 45/\overline{90}]_s$, $V_f = 0.45$) composite showing a dramatic change due to fatigue damage and cyclic hardening of the matrix material. (a) After 4 cycles. (b) After 500,000 cycles

The stiffness may be a useful measurement to design engineers since this is the total strain of the material in response to an applied load. (This is after no additional permanent plastic strain occurs during cyclic loading.) The stiffness is a combination of the elastic properties of the laminate as well as the plastic behavior of the metal matrix.

The stiffness is, therefore, a function of the matrix yield stress. The matrix may cyclically harden and the stiffness increase during the time damage initiates. (In some metals/heat treat conditions, the material may even cyclically soften. The properties of polymer matrix materials can also change with cycling and time/environmental dependent aging.) However, as the fatigue damage in the laminate grows, the stiffness decreases. Therefore, one cannot determine the onset and extent of fatigue damage in a metal matrix composite using a stiffness (secant modulus) criterion alone.

Permanent Plastic Strain. The permanent plastic strain, ϵ_p , is measured directly from the stress-strain curve. The permanent strain is usually accumulated in the first three or four cycles with little additional permanent strain accumulating thereafter. The accumulated permanent strain gives a good indication of the amount of residual stress in the 0° fibers since all the constituents in the composite are assumed to strain the same.

Elastic Unloading Modulus after N Number of Cycles. The elastic unloading modulus E_N is measured directly from the stress-strain curve at intervals throughout the life of the composite (Fig. 58). The percentage of the elastic unloading modulus at N cycles E_N as divided by the initial elastic modulus:

$$E_N/E_1 \times 100 = \%E_1$$

can be plotted against the number of fatigue cycles N in order to present fatigue damage as a function of constant amplitude cycling at a prescribed stress ratio and maximum stress.

Stiffness After N Number of Cycles. The stiffness (secant modulus) is measured as the stress range divided by the unloading strain range. The percentage of the initial stiffness is calculated by dividing the stiffness at N cycles E_{NS} by the initial stiffness E_{iS} $E_{NS}/E_{iS} \times 100 = \%E_{iS}$.

The $\% E_{iS}$ can be plotted against N in order to compare a “stiffness” and “elastic modulus” criteria for assessing fatigue damage.

Cyclic Strain. The cyclic strain $\Delta\epsilon$ is measured directly from the stress-strain curve. This strain range can be used to examine the possible correlation between the composite strain and fatigue endurance. The cyclic strain can also be multiplied by the elastic fiber modulus to calculate the cyclic fiber stress in the 0° plies.

Number of Cycles to Fatigue Failure. The number of cycles to fatigue failure N_F plotted against the maximum cyclic stresses for a given value of stress ratio is the traditional $S-N$ curve. This type of data can be used to determine the fatigue endurance limit stress and the maximum cyclic stress at a given stress ratio at which the composite laminate can be expected to survive beyond some endurance life. The $S-N$ curve does not, however, indicate the physical condition of the laminate at the established endurance limit other than the fact that the laminate can survive the endurance stress.

Residual Static Strength. Fatigue specimens that survive a given number of cycles without failure can be tested for residual strength to correlate fatigue damage and residual strength. The stress at failure, which is the maximum stress from the stress-strain curve, is defined as the residual static strength S_F .

Strain to Static Failure. For static strength tests, unfatigued composite specimens are loaded to failure. Thus, the strain to static failure $\epsilon_{f\text{tot}}$ is used to estimate the 0° fiber ultimate stress.

Footnote

* The section “Interlaminar Shear Properties of Fiber-Reinforced Composites at High Strain Rates” was written by John Harding and Stephen Hallett, Oxford University. The section “Fatigue Testing and Behavior of Fiber-Reinforced Composites” was written by W. Steven Johnson and Ramesh Talreja, Georgia Institute of Technology.

References cited in this section

83. T.K. O'Brien, Effect of Gage-Section Size on Composite Stiffness Measurements, *Compos. Technol. Rev.*, Vol 1 (No. 4), 1979, p 5–6
84. W.S. Johnson, Fatigue Testing and Damage Development in Continuous Fiber Reinforced Metal Matrix Composites, ASTM STP 1032, 1989, p 194–221

Mechanical Testing of Fiber-Reinforced Composites

Dale Wilson, The Johns Hopkins University, Leif A. Carlsson, Florida Atlantic University

Damage Assessment

The common methods of assessing the extent and type of damage can be divided into those techniques that are nondestructive and those that are destructive. The manual edited by Pendleton and Tuttle (Ref 85) is an excellent reference for several of the techniques, which are described further in the following.

Nondestructive Techniques

Edge Replica Technique. In the edge replica technique, a permanent impression of the specimen edge is produced in a cellulose acetate film. The advantage of this technique is that the replica can be taken while the specimen is under load in the test machine. The replica can then be examined later for details of damage, such

as matrix cracks, split fibers, or fiber/matrix separation. This technique can be easily used for replicating any surface for microstructural detail.

A softened acetate film is held against the desired surface to be replicated. Acetone is applied to the face of the film to soften it. The acetone serves to polymerize the acetate, making it viscous enough to flow into the microstructural cavities present on the surface. Pressure is applied to the backside of the film to aid in the flow process. The acetate film is allowed to dry in place for 3 to 5 min and then is carefully peeled from the surface. The replica can now be sputtered with gold (a thin layer of gold-palladium alloy) and viewed in a scanning electron microscope (SEM).

Radiography. As discussed earlier, much of the damage that develops in composite materials is of an internal nature (i.e., not readily observable from the surface). One of the more popular techniques to assess this internal damage is radiography. There has been much written about this technique, and a good summary paper can be found in Ref 85.

Depending on the differences in the x-ray absorptivity between the fiber and matrix, differing details of damage can be determined. Most fibers do not show well in radiographs, and it is nearly impossible to see individual fiber failures in graphite/epoxy composites. However, solutions for penetrant enhancement can allow for clear identification of matrix cracks and delaminations. The penetrant has a significantly higher opacity than the composite, so areas into which it penetrates show up well in the radiograph. For example, zinc-iodine solution enhanced the display of ply cracking and delamination in the radiograph of a composite after static testing (Ref 86). With penetrants, damage must come to a free surface (the specimen edge or radiate from a notch) so that the penetrant can wick into the damage areas. This is usually never a problem since most damage does start at the free edge or from a notch.

Several laboratories have special rooms set up such that specimens can be radiographed while under load in the testing machine (Ref 86). This makes the study of damage progression much more efficient.

Acoustic Emissions. This technique can be used real time to “listen” to damage occurring. Each noise emission has an energy level associated with it. Through much experience with a given composite system, the energy level of a given event can be associated with a damage mode (See Ref 87). The number of events or acoustic emission counts is also used to correlate with the extent of damage. This technique is very indirect, requiring a lot of experience and interpretation of data. Once again, Ref 86 has a good description of this technique.

C-scans. Ultrasonic through transmission C-scans are very popular for assessing initial quality of composite materials and components. They are an excellent way to assess the presence of delaminations, air pockets, or significant changes in density (for example, resin rich areas). The initial quality as indicated by C-scans may provide a good indicator of how the particular laminate will behave under fatigue loading (Ref 88). This technique is a little less useful for monitoring damage evolution since the part or specimen must be removed from the machine/structure and placed into the C-scan tank.

Destructive Techniques

Micrographs. After the specimen fails, the fracture surfaces and interface characteristics can be examined using SEM and energy dispersive x-ray analysis (EDXA). A SEM can be used to distinguish fatigue striation markings from dimple fracture patterns in order to determine if a portion of the fracture surface failed because of fatigue or static fracture. The SEM is also very useful for close-up viewing of any type of microstructural damage. The EDXA is useful for the determination of the chemical composition of the failure surface. This is especially useful for determining whether the failure occurred in the fiber, matrix, or in some reaction zone between the fiber and the matrix. Taking photographs through a 30 to 60 power optical microscope has also been used with considerable success to document damage, such as matrix cracking.

Matrix Etching. After a MMC specimen has been statically or fatigue loaded, matrix etching can be used to reveal two types of composite damage. First, etching away the matrix material will expose the fibers. The fibers can then be inspected for breaks. Second, by carefully etching away the matrix in the outer ply and then removing the exposed fibers, the next layer can be examined for matrix cracking and fiber damage. This technique can be used to systematically examine the damage of each ply in a laminate.

For 6061 aluminum matrix composites, a 30% hydrochloric acid (HCl) solution in distilled water was found to be effective for etching away the matrix without detectable damage to either boron or silicon-carbide fibers. The actual etching process must be carefully controlled if one wishes to remove one layer at a time to inspect the matrix in the underlying layers. Enough matrix material must be etched away to allow the surface layer of

fibers to be removed; however, if too much matrix material is removed, the matrix damage in the underlying ply will be etched away. This process is a trial and error operation at best and often requires several attempts before a satisfactory result is obtained.

Laminate Deply. The specimen-deply technique is a simple destructive-examination method whereby the individual plies of a polymer matrix laminate are separated for easy examination (Ref 85). This technique is excellent for determining the laminate-stacking sequence, studying the details of broken fibers, and determining the extent and precise interface location of delaminations. The interlaminar-bond strength is broken down by a partial pyrolysis of the matrix resin between the plies of the laminate. This allows for the separation (unstacking) of the individual plies, provided the adjacent plies have different fiber angles. The individual plies may then be microscopically examined to study the details of broken fibers. Furthermore, by using a marking agent prior to the pyrolysis, delaminations are clearly visible and matrix cracks in the adjacent ply may also be visible. This procedure is well suited to general angle-ply laminates of graphite/epoxy. The procedure for deplying graphite/epoxy composites was originally developed by S.M. Freeman (Ref 89).

Footnote

* The section "Interlaminar Shear Properties of Fiber-Reinforced Composites at High Strain Rates" was written by John Harding and Stephen Hallett, Oxford University. The section "Fatigue Testing and Behavior of Fiber-Reinforced Composites" was written by W. Steven Johnson and Ramesh Talreja, Georgia Institute of Technology.

References cited in this section

85. Manual on Experimental Methods for Mechanical Testing of Composites, R.L. Pendleton and M.E. Tuttle, Ed., Society for Experimental Mechanics, Galion, 1989, p 170
86. G.A. Etheridge, W.S. Johnson, and S. Reeve, Effect of Lay-Up and Constraint on Tensile Notch Strength, *Proc. of the American Society of Composites 13th Annual Technical Conf. on Composite Materials*, A.J. Vizzini, Ed., 1998, p 489–504
87. J.G. Bakuckas Jr., W.H. Prosser, and W.S. Johnson, Monitoring Damage Growth in Titanium Matrix Composites Using Acoustic Emission, *J. Compos. Mater.*, Vol 28 (No. 24), 1994, p 305–328
88. W.S. Johnson, Screening Metal Matrix Composites Using Ultrasonic C-SCANS, *ASTM J. Compos. Technol. Res.*, Vol 11 (No. 1), Spring 1989, p 31–34
89. S.M. Freeman, Characterization of Lamina and Interlaminar Damage in Graphite-Epoxy Composites by Deply Technique, *ASTM STP 787*, 1982, p 50–62

Mechanical Testing of Fiber-Reinforced Composites

Dale Wilson, The Johns Hopkins University, Leif A. Carlsson, Florida Atlantic University

References

1. R.M. Jones, *Mechanics of Composite Materials*, 2nd ed., Taylor and Francis, Philadelphia, 1999
2. S.W. Tsai, and H.T. Hahn, *Introduction to Composite Materials*, Technomic, Lancaster, 1980

3. J.R. Vinson, and T.W. Chou, *Composite Materials and Their Use in Structures*, Halstead Press, Applied Science Publishers, Barking, 1975
4. J.M. Whitney, I.M. Daniel, and R.B. Pipes, *Experimental Mechanics of Fiber Reinforced Composite Materials*, revised ed., Society for Experimental Mechanics; Prentice-Hall, Englewood Cliffs, 1984
5. R.B. Pipes, Test Methods, *Delaware Composites Design Encyclopedia*, Vol 6, (L.A. Carlsson and J.W. Gillespie, Jr., Ed.), Technomic, Lancaster, 1990, p 3
6. J.E. Masters and P.G. Ifju, Strain Gage Selection Criteria for Textile Composite Materials, *J. Compos. Technol. Res.*, Vol 19 (No. 3), 1997, p 152
7. H.M. Wadsworth, *Handbook of Statistical Methods for Engineers and Scientists*, McGraw-Hill, New York, 1990
8. L.A. Carlsson and R.B. Pipes, *Experimental Characterization of Advanced Composite Materials*, 2nd ed., Technomic, Lancaster, 1987
9. D.W. Wilson and L.A. Carlsson, Mechanical Characterization of Composite Materials, *Physical Methods of Chemistry*, 2nd. ed., Vol VII, B.W. Rossiter and R.B. Baetzold, Ed., John Wiley & Sons, 1991, p 139
10. S. Chatterjee, D.F. Adams, and D.W. Oplinger, "Test Methods for Composites - A Status Report," (Vol I, Tension Test Methods; Vol II, Compression Test Methods; Vol III. Shear Test Methods), DOT/FAA/CT-93/17-I, II, III, FAA Technical Center, Atlantic City International Airport, NJ, June 1993
11. D.W. Oplinger, K.R. Gandhi, and B.S. Parker, "Studies of Tension Test Specimens for Composite Material Testing," AMMRC TR 82-27, Army Materials and Mechanics Research Center, Watertown, MA, 1982
12. M.H. Kural and D.L. Flagg, A Finite Element Analysis of Composite Tension Specimens, *Compos. Technol. Rev.*, Vol 3, 1983, p 11
13. M.G. Abdallah and R.L. Westberg, Effect of Tab Design of the ASTM D 3039 Tension Specimen on Delivered Strength of HMS¹3501-6 Graphite/Epoxy Materials, *Proc. 1987 SEM Spring Conf. on Experimental Mechanics*, 1987, p 362
14. Product Catalog, Wyoming Test Fixtures, Laramie, Wyoming, 1992
15. L.J. Hart-Smith, "Some Observations About Test Specimens and Structural Analysis for Fibrous Composites," ASTM STP 1059, 1988, p 86
16. W.S. Johnson, S.J. Lubowinski, and A.L. Highsmith, Mechanical Characterization of Unnotched SCS/Ti-15-3 Metal S₆ Matrix Composites at Room Temperature, ASTM STP 1080, 1990, p 193
17. R. Walsh, private communication
18. K.F. Port, "The Compressive Strength of Carbon Fiber Reinforced Plastics," Technical Report 82083, Royal Aircraft Establishment, Farnborough, England, Aug 1982
19. D.F. Adams and E.Q. Lewis, Influence of Specimen Gage Length and Loading Method on the Axial Compressive Strength of a Unidirectional Composite Material, *Exp. Mech.*, Vol 31, 1991, p 14

20. E.M. Odom and D.F. Adams, Failure Modes of Unidirectional Carbon/Epoxy Composite Specimens, *Composites*, Vol 21, 1990, p 289
21. K.E. Hofer, Jr. and P.N. Rao, A New Static Testing Compression Fixture for Advanced Composite Materials, *J. Testing Eval.*, Vol 5, 1977, p 278
22. M.N. Irion and D.F. Adams, Compression Creep Testing of Unidirectional Composites, *Composites*, Vol 12, 1981, p 117
23. "Advanced Composite Compression Tests", Boeing Specification Support Standard BSS 7260, The Boeing Company, Seattle, WA, Dec 1988
24. L.J. Hart-Smith, Backing Out Equivalent Unidirectional Strengths from Tests on Cross-Plied Laminates, *Proc. 3rd International SAMPE Symposium and Exhibition*, 1992, p 977
25. D.W. Wilson, V. Altstadt, M. Maier, J. Prandy, K. Thoma, and D. Vinckier, An Analytical and Experimental Evaluation of 0/90 Laminate Tests for Compression Characterization, *J. Compos. Technol. Res.*, Vol 16 (No. 2), Apr 1994, p 146–153
26. J.S. Welsh and D.F. Adams, "Unidirectional Composite Compression Strengths Obtained by Cross-Ply Laminates," *J. Compos. Technol. Res.*, Vol 18 (No. 4), Oct 1996, p 241
27. D.F. Adams and J.S. Welsh, The Wyoming Combined Loading Compression (CLC) Test Method, *J. Compos. Technol. and Res.*, Vol 19 (No. 3), 1997, p 123
28. J.M. Gere and S.P. Timoshenko, *Mechanics of Materials*, 2nd. ed., PWS Eng., Boston, 1984
29. J.M. Whitney and C.E. Browning, On Short-Beam Shear Tests for Composite Materials, *Exp. Mech.*, Vol 25, 1985, p 294
30. J.M. Whitney, *Structural Analysis of Laminated Anisotropic Plates*, Technomic, Lancaster, 1987
31. B.W. Rosen, A Simple Procedure for Experimental Determination of the Longitudinal Shear Modulus of Unidirectional Composites, *J. Compos. Mater.*, Vol 6, 1972, p 552
32. S. Kellas and J. Morton, "Scaling Effects in Angle-Ply Laminates," NASA CR 4423, Feb 1992
33. S. Kellas, J. Morton, and K. E. Jackson, An Evaluation of the ± 45 Tensile Test for the Determination of the In-Plane Shear Strength of Composite Materials, *Proc. of the ICCM-8 Conf.*, Honolulu, July 1991
34. N. Iosipescu, New Accurate Procedure for Single Shear Testing of Metals, *J. Mater.*, Vol 2, 1967, p 537
35. D.E. Walrath and D.F. Adams, The Iosipescu Shear Test as Applied to Composite Materials, *Exp. Mech.*, March 1983, p 105–110
36. D.E. Walrath and D.F. Adams, "Verification and Application of the Iosipescu Shear Test Method," UWME-DR-401-103-1, University of Wyoming, Laramie, June 1984
37. M.G. Abdallah, D.S. Gardener, and H.E. Gascoigne, An Evaluation of Graphite/Epoxy Iosipescu Shear Specimen Testing Methods with Optical Techniques, *Proc. of the 1985 SEM Spring Conf. on Experimental Mechanics*, Society of Experimental Mechanics, June 1985, p 833

38. H. Ho, M.Y. Tsai, J. Morton, and G.L. Farley, "An Evaluation of the Iosipescu Specimen for Composite Materials Shear Property Measurement," VPI & SU Report CCMS-91-18, Center for Composite Materials and Structures, Aug 1991
39. S.N. Chatterjee, E.C.J. Wung, C.F. Yen, V. Ramnath, J.A. Kessler and D.F. Adams, "Composite Specimen Design Analysis," MTL Report TR-91-5, Vol I and II, 1991
40. R. Garcia, T.A. Weissnar, and R.R. McWhitney, "An Experimental and Analytical Investigation of the Rail Shear Test Method as Applied to Composite Materials," *Exp. Mech.*, Vol 20, 1980, p 273
41. R.J. Butler, P.M. Barnard, and P.T. Curtis, The Development of a Satisfactory, Simple, Shear Fatigue Test for Unidirectional E-Glass/Epoxy, ASTM STP 972, 1988, p 227
42. A. Hussain and D.F. Adams, "The Wyoming-Modified Two-Rail Shear Test Fixture for Composite Materials," *J. Compos. Technol. Res.*, Vol 21 (No. 4), 1999, p 215
43. R. Bucinell, "Interim JANNAF Test Method for In-Plane Shear Properties of Unidirectional Fiber/Resin Composite Cylinders," Interim Report for MIL-HDBK-17, AMTL Contract DAAL04-89-C-0023, 1991
44. G.A. Foley, M.E. Roylance, and W.W. Houghton, "Use of Torsion Tubes to Measure In-Plane Shear Properties of Filament Wound Composites," STP 1003, ASTM 1989, p 208
45. J.M. Ogonowski, Analytical Study of Finite Geometry Plates with Stress Concentrations, *AIAA Paper 80-0778*, American Institute of Aeronautics and Astronautics, New York, 1980, p 694
46. J.M. Whitney and R.J. Nuismer, Stress Fracture Criteria for Laminated Composites Containing Stress Concentrations, *J. Compos. Mater.*, Vol 8, 1974, p 253
47. R.B. Pipes, R.C. Wetherhold, and J.W. Gillespie, Jr., Notched Strength of Composite Materials, *J. Compos. Mater.*, Vol 13, 1979, p 148
48. E.G. Gynn, W.L. Bradley, and W. Elber, Micromechanics of Compression Failures in Open Hole Composite Laminates, ASTM STP 1012, 1989, p 118
49. R. Falabella, K.A. Olesen, and M.A. Boyle, Variations in Impact Test Methods for Tough Composites, Proc. of the 35th International SAMPE Symposium, 2-5 April 1990, p 1454
50. H.L. Ewalds and R.J.H. Wanhill, *Fracture Mechanics*, Edward Arnold, London, 1989
51. S.-M. Lee, An Edge Crack Torsion Method for Mode III Delamination Fracture Testing, *J. Compos. Technol. Res.*, Vol 15, 1993, p 193
52. P. Davies, B.R.K. Blackman, and A.S. Brunner, "Standard Test Methods for Delamination Resistance of Composite Materials: Current Status," *Appl. Compos. Mater.*, Vol 5, 1998, p 345
53. J.W. Gillespie, Jr. and L.A. Carlsson, Interlaminar Fracture of Laminated Composite Materials, *Delaware Composites Design Encyclopedia*, Vol 6, Technomic, Lancaster, 1990, p 113
54. Z. Suo, Delamination Specimens for Orthotropic Materials, *J. Appl. Mech.*, Vol 57, 1990, p 627
55. W.B. Bascom, R.J. Bitner, R.J. Moulton, and A.R. Siebert, The Interlaminar Fracture of Organic-Matrix Woven Reinforced Composites, *Composites*, Vol 11, 1980, p 9

56. T.K. O'Brien and R.H. Martin, Results of ASTM Round Robin Testing for Mode I Interlaminar Fracture Toughness of Composite Materials, *J. Compos. Technol. Res.*, Vol 15, 1993, p 327
57. J.P. Berry, Determination of Fracture Energies by the Cleavage Technique, *J. Appl. Phys.*, Vol 34, 1963, p 62
58. A.J. Russell and K.N. Street, Factors Affecting the Interlaminar Fracture Energy of Graphite/Epoxy Laminates, *Progress in Science and Engineering of Composites*, T. Hayashi, K. Kawata, and S. Omekawa, Ed., ICCM-IV, American Society for Metals, 1982, p 279
59. T.K. O'Brien, G.B. Murri, and S.A. Salpekar, "Interlaminar Shear Fracture Toughness and Fatigue Thresholds for Composite Materials," ASTM STP 1012, 1989, p 222
60. L.A. Carlsson, J.W. Gillespie, Jr., and B.R. Trethewey, Mode II Interlaminar Fracture of Graphite/Epoxy and Graphite/PEEK," *J. Reinf. Plast. Compos.*, Vol 5, 1986, p 170
61. W.S. Johnson and P.D. Mangalgiri, Influence of the Resin on Interlaminar Mixed Mode Fracture, ASTM STP 937, 1987, p 295
62. S. Hashemi, A.J. Kinloch, and J.G. Williams, The Effects of Geometry, Rate and Temperature on the Mode I, Mode II, and Mixed Mode I/II Interlaminar Fracture of Carbon-Fiber/Poly (ether-ether ketone) Composites, *J. Compos. Mater.*, Vol 24, 1990, p 918
63. L.A. Carlsson, Fracture of Fiber Composites, *Structure and Properties of Composites*, T-W. Chow, Ed., VCH, Weinheim, 1993, p 533
64. J.R. Reeder and J.H. Crews, Jr., "A Mixed Mode Bending Method for Delamination Testing," AIAAJ, Vol 28, 1990, p 1270
65. J.R. Reeder and J.H. Crews, Jr., Redesign of the Mixed Mode Bending Delamination Test to Reduce Nonlinear Effects, *J. Compos. Technol. Res.*, Vol 14, 1992, p 12
66. S.M. Werner and C.K.H. Dharan, The Dynamic Response of Graphite Fiber/Epoxy Laminate at High Shear Strain Rate, *J. Compos., Mater.*, Vol 20, 1986, p. 365–374
67. C.Y. Chiem and Z.G. Liu, Modelling of Dynamic Behavior of Composite Materials, *Proc. IMPACT 87, Impact Loading and Dynamic Behavior of Materials*, C.Y. Chiem, H.-D. Kunze, and L.W. Meyer, Ed., DGM Informationsgesellschaft mbH, Oberursel, 1988, Vol 2, p 579–586
68. H. Leber and J.M. Lifshitz Interlaminar Shear Behavior of Plain-Weave GRP at Static and High Rates of Strain, *Compos. Sci. Technol.*, Vol 56, 1996, p 391–405
69. T. Parry and J. Harding, The failure of Glass-Reinforced Composites under Dynamic Torsional Loading, Colloque Int. Du CNRS No. 319, *Plastic Behaviour of Anisotropic Solids*, J.P. Boehler, Ed., (CNRS, Paris, 1988) p 271–288
70. J. Harding and Y.L. Li, Determination of Interlaminar Shear Strength for Glass/Epoxy and Carbon/Epoxy Laminates at Impact Rates of Strain, *Compos. Sci. Technol.*, Vol 45, 1992, p 161–171
71. B. Bouette, C. Cazeneuve, and C. Oytana, Shear in Carbon/Epoxy Laminates at Various Strain Rates, *Proc. ECCM-4, Developments in the Science and Technology of Composite Materials*, J. Fuller et al., Ed., (Elsevier Applied Science, London and New York) 1990, p 937–942

72. B. Bouette, C. Cazeneuve, and C. Oytana, Effect of Strain Rate on Interlaminar Shear Properties of Carbon/Epoxy Composites, *Compos. Sci. Technol.*, Vol 45, 1992, p 313–321
73. L.M. Dong and J. Harding, A Single-Lap Shear Specimen for Determining the Effect of Strain Rate on the Interlaminar Shear Strength of Carbon-Fiber Reinforced Laminates, *Composites*, Vol 25, 1994, p 129–138
74. S.R. Hallett, C. Ruiz, and J. Harding, The Effect of Strain Rate on the Interlaminar Shear Strength of a Carbon/Epoxy Cross-Ply Laminate: Comparison between Experiment and Numerical Prediction, *Compos. Sci. Technol.*, Vol 59, 1999, p 749–758
75. J. Harding and J.L. Medina, Oxford University Engineering Department, Solid Mechanics Group, Unpublished data, August 1999
76. M.J. Hiley, L. Dong, and J. Harding, Effect of Strain Rate on the Fracture Process in Interlaminar Shear Specimens of Carbon Fiber-Reinforced Laminates, *Composites*, Vol 28A, 1997, p 171–180
77. F. Chang and K. Chang, *J. Compos. Mater.*, Vol 21, 1987, p 834–855
78. R. Talreja, Fatigue of Composite Materials: Damage Mechanisms and Fatigue Life Diagrams, Proc. R. Soc. (London), Vol A378, 1981, p 461–475
79. R. Talreja, “Fatigue of Fiber-Reinforced Ceramics”, *Structural Ceramics—Processing, Manufacture and Properties*, J.J. Bentzen, et al., Ed., Riso National Laboratory, Roskilde, Denmark, 1990, p 145–159
80. R. Talreja, A Conceptual Framework for Interpretation of MMC Fatigue, *Mater. Sci. Eng.*, Vol A200, 1995, p 21–28
81. E.K. Gamstedt and R. Talreja, Fatigue Damage Mechanisms in Unidirectional Carbon-Fiber-Reinforced Plastics, *J. Mater. Sci.*, 1999, in press
82. A.L. Highsmith and K.L. Reifsnider, Stiffness Reduction Mechanisms in Composite Laminates, *Damage in Composite Materials*, K.L. Reifsnider, Ed., ASTM STP 775, 1982, p 103–117
83. T.K. O'Brien, Effect of Gage-Section Size on Composite Stiffness Measurements, *Compos. Technol. Rev.*, Vol 1 (No. 4), 1979, p 5–6
84. W.S. Johnson, Fatigue Testing and Damage Development in Continuous Fiber Reinforced Metal Matrix Composites, ASTM STP 1032, 1989, p 194–221
85. Manual on Experimental Methods for Mechanical Testing of Composites, R.L. Pendleton and M.E. Tuttle, Ed., Society for Experimental Mechanics, Galion, 1989, p 170
86. G.A. Etheridge, W.S. Johnson, and S. Reeve, Effect of Lay-Up and Constraint on Tensile Notch Strength, *Proc. of the American Society of Composites 13th Annual Technical Conf. on Composite Materials*, A.J. Vizzini, Ed., 1998, p 489–504
87. J.G. Bakuckas Jr., W.H. Prosser, and W.S. Johnson, Monitoring Damage Growth in Titanium Matrix Composites Using Acoustic Emission, *J. Compos. Mater.*, Vol 28 (No. 24), 1994, p 305–328
88. W.S. Johnson, Screening Metal Matrix Composites Using Ultrasonic C-SCANS, *ASTM J. Compos. Technol. Res.*, Vol 11 (No. 1), Spring 1989, p 31–34

89. S.M. Freeman, Characterization of Lamina and Interlaminar Damage in Graphite-Epoxy Composites by Deply Technique, ASTM STP 787, 1982, p 50–62

Footnote

* The section “Interlaminar Shear Properties of Fiber-Reinforced Composites at High Strain Rates” was written by John Harding and Stephen Hallett, Oxford University. The section “Fatigue Testing and Behavior of Fiber-Reinforced Composites” was written by W. Steven Johnson and Ramesh Talreja, Georgia Institute of Technology.

Property Comparison Tables: Hardness and Tensile Properties

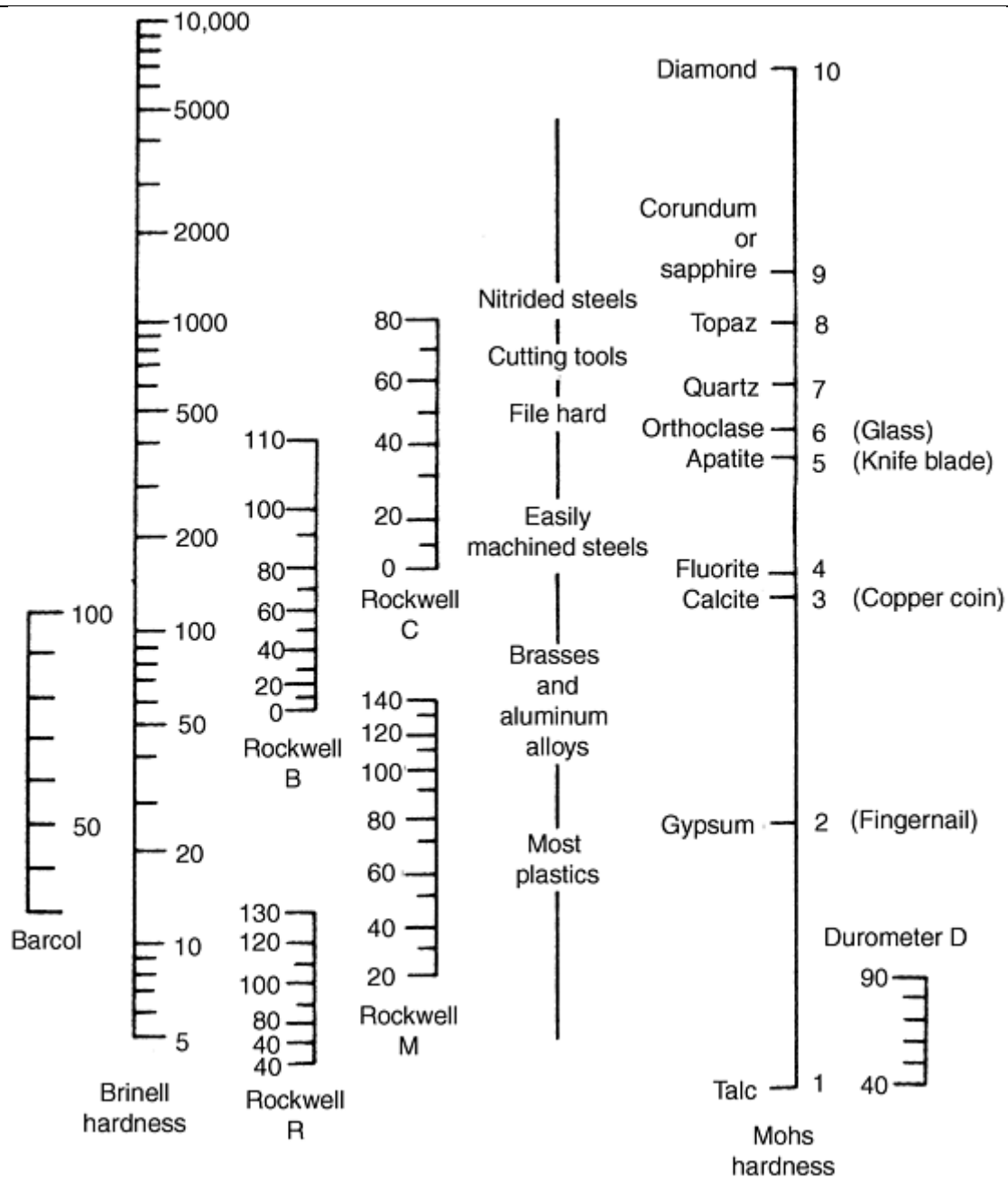


Fig. 1 General comparison of hardness scales

Table 1 Hardness of plastics (Rockwell R scale)

Material	High	Low
Melamine, cellulose electrical	125	115
Polyphenylene sulfide; unreinforced	124	...
Polyphenylene sulfide; 40% glass reinforced	123	...
Chlorinated polyvinyl chloride	122	111
Nylon, mineral reinforced	121	119
Polyester, thermoplastic, PBT; unreinforced	120	117

Polyester, thermoplastic, PET, 45 and 30% glass reinforced	120	...
Polyester, thermoplastic, PBT/PET blend, 30 and 15% glass reinforced	120	119
Cellulose acetate	120	49
Nylons, general purpose	120	111
PVC, PVC-acetate; rigid	120	110
Polysulfone; unreinforced	120	...
Phenylene oxide-based resins; unreinforced	119	115
Polyester, thermoplastic, PBT, 45 and 35% glass/minimal reinforced	119	114
Polyester, thermoplastic, PBT, 30% glass reinforced	119	118
Polyester, thermoplastic, PBT, 30 and 10% mineral filled	118	112
ABS/polycarbonate	117	...
ABS/polysulfone (polyaryl ether)	117	...
ABS	115	75
Polypropylene; glass reinforced	115	90
Cellulose acetate butyrate	114	23
Fluorocarbon, PVF ₂	110	...
Cellulose acetate propionate	109	57
ABS/PVC	102	...
Polypropylene, general purpose	100	80
Fluorocarbon, ETFE and ETCFE, unreinforced	95	...
ABS/polyurethane	82	70
Fluorocarbon, PTFE	55	35

PBT, polybutylene terephthalate; PET, polyethylene terephthalate; PVC, polyvinyl chloride; ABS, acrylonitrile-butadiene-styrene; PVF, polyvinyl formal; ETFE, ethylene tetrafluoroethylene; ECTFE, ethylene chlorotrifluoroethylene; PTFE, polytetrafluoroethylene.

Source: Adapted from Guide to Engineering Materials, *Advanced Materials and Processes*, Dec 1999

Table 2 Hardness of rubber and elastomers (Shore A scale)

Material	High	Low
Thermoplastic elastomers	100	35
Urethane, polyether and polyester	100	80
Styrene butadiene	100	40
Natural rubber	100	30
Chlorinated polyethylene	95	40
Chloroprene	95	40
Chlorosulfonated polyethylene	95	50
Silicone	90	25
Polyacrylate	90	40
Nitrile	90	20
Fluorocarbon	90	65
Ethylene propylene, ethylene propylene diene	90	30
Epichlorohydrin	80	40
Isobutylene-isoprene	80	40
Polybutadiene	80	45
Polysulfide	80	20
Propylene oxide	80	40
Synthetic isoprene	80	40

Table 3 Hardness of ceramics (Mohs scale)

Material	High	Low
Mullite	18	14
Niobium carbide	10	9
Beryllium carbide	9+	...
Tantalum carbide	9+	...
Beryllia	9	...
Alumina	9	...
Titanium carbide	9	8
Zirconium carbide	9	8
Zirconia	8	7
Zircon	8	...
Steatite	7.5	...
Thoria	7	...
Magnesia	6	...
Porcelain enamel	6	3.5
Calcia	6.0	3.3
Boron and aluminum nitrides	2	...

Table 4 Hardness of metals (Brinell scale)

Material	High	Low
White and alloy irons; cast	700	130
Osmium	670	300
Low-alloy steels, wrought; normalized, quenched and tempered	627	202
Stainless steels, wrought martensitics hardened and tempered	580	180
Rhenium	555	331
Molybdenum and its alloys	555	179
Nickel and its alloys	534	75
Stainless steels, cast	470	130
Tungsten	443	330
Low-alloy steels, wrought; carburized, quenched and tempered	429	212
Copper casting alloys	415	35
Alloy steels, cast; quenched and tempered	401	262
Rhodium	401	100
Iridium	351	200
Gray irons; cast	350	140
Ruthenium	350	200
Nickel-base superalloys	341	302
Titanium and its alloys	331	...
Ductile (nodular) irons; cast	300	140
Hafnium	285	277
Malleable irons, pearlitic grades; cast	269	163
Stainless steels, standard martensitic grades, wrought; annealed	260	150
Ductile (nodular) austenitic cast irons	240	130
Tantalum and its alloys	237	...
Alloy steels, cast; normalized and tempered	217	137
High-strength low-alloy steels, 290–450 MPa (42–65 ksi) yield stress, wrought; as rolled	190	149
Depleted uranium	187	...
Zirconium and its alloys	179	112
Stainless steels, standard austenitic grades, wrought; annealed	170	143
Aluminum alloys, 7000 series	160	60

Malleable ferritic cast irons	156	110
Aluminum casting alloys	145	40
Aluminum alloys, 2000 series	135	45
Zinc foundry alloys	125	85
Aluminum alloys, 4000 series	120	...
Aluminum alloys, 6000 series	120	25
Palladium	118	40
Niobium and its alloys	114	...
Platinum	106	40
Aluminum alloys, 5000 series	105	28
Zinc die-casting alloys	91	82
Silver	90	26
Magnesium alloys, wrought	82	46
Magnesium alloys, cast	80	50
Aluminum alloys, 3000 series	77	28
Rare earths	77	17
Gold	66	25
Aluminum alloys, 1000 series	44	19
Tin and its alloys	29	5
Lead and its alloys	17	4.7
Indium	0.9	...

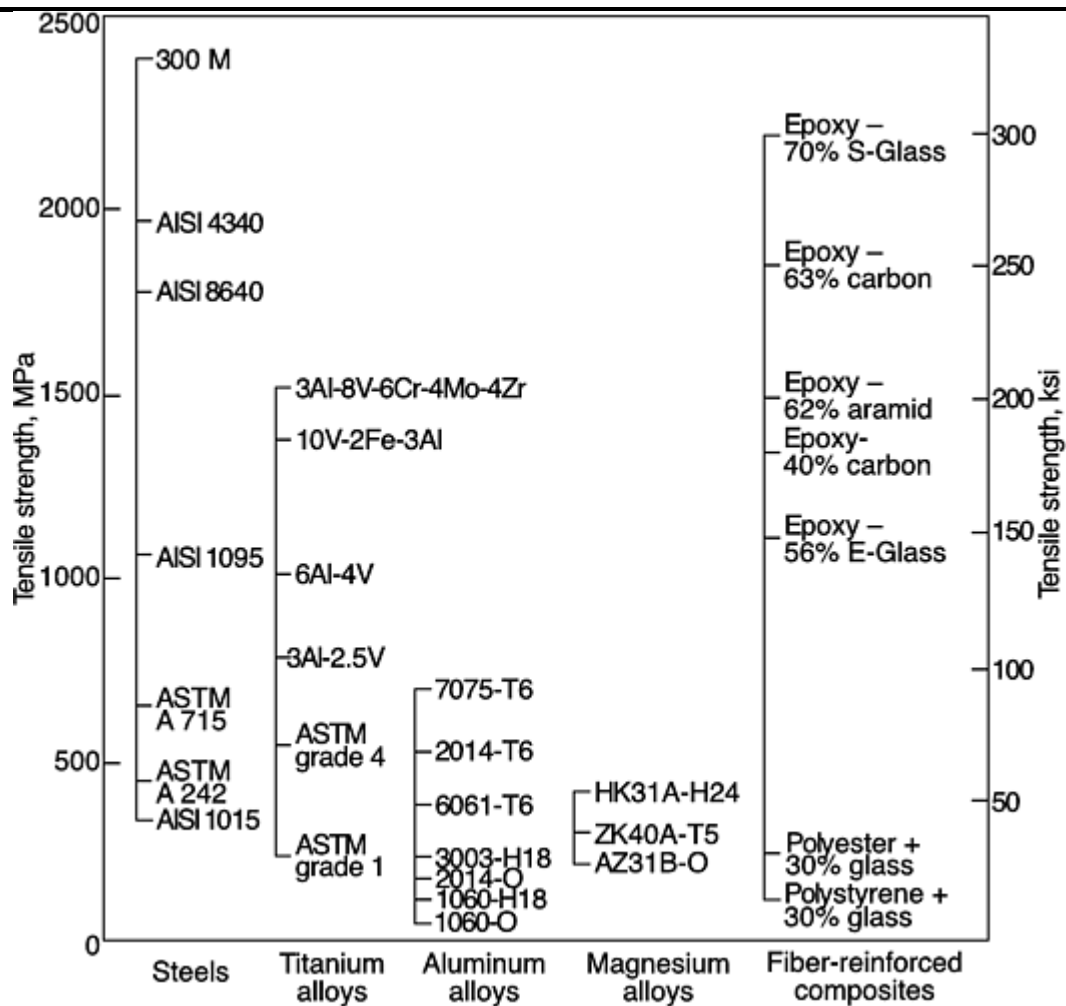


Fig. 2 Comparison of various engineering materials on the basis of tensile strength. Source: *ASM Handbook, Volume 20, Materials Selection and Design*, p 513

Table 5 Tensile yield strength of metals and plastics at room temperature

Material	Tensile yield strength			
	High		Low	
	MPa	ksi	MPa	ksi
Cobalt and its alloys	1999	290	179	26
Low-alloy hardening steels; wrought, quenched and tempered	1986	288	524	76
Stainless steels, standard martensitic grades; wrought, heat treated	1896	275	414	60
Rhenium	1862	270
Ultrahigh strength steels; wrought, heat treated	1862	270	1172	170
Stainless steels, age hardenable; wrought, aged	1634	237	724	105
Nickel and its alloys	1586	230	69	10
Stainless steels, specialty grades; wrought, 60% cold worked	1558	226	703	102
Tungsten	1517	220
Molybdenum and its alloys	1448	210	565	82
Titanium and its alloys	1317	191	186	27
Carbon steels, wrought; normalized, quenched and tempered	1296	188	400	58
Low-alloy carburizing steels; wrought, quenched and tempered	1227	178	427	62
Nickel-base super alloys	1186	172	276	40
Alloy steels, cast; quenched and tempered	1172	170	772	112
Stainless steels; cast	1138	165	214	31
Tantalum and its alloys	1089	168	331	48
Steel P/M parts; heat treated	1062	154	517	75
Ductile (nodular) irons, cast	1034	150	276	40
Copper casting alloys ^(a)	965	140	62	9
Stainless steels, standard austenitic grades; wrought, cold worked	965	140	517	75
Niobium and its alloys	931	135	241	35
Iron-base superalloys; cast, wrought	924	134	276	40
Cobalt-base superalloys, wrought	800	116	241	35
Bronzes, wrought ^(a)	786	114	97	14
Heat treated low-alloy constructional steels; wrought, mill heat treated	758	110	621	90
High-copper alloys, wrought ^(a)	758	110	62	9
Stainless steels, standard martensitic grades; wrought, annealed	724	105	172	25
Cobalt-base superalloys, cast	689	100	517	75
Heat treated carbon constructional steels; wrought, mill heat treated	690	100	290	42
Hafnium	662	96	221	32
Brasses, wrought ^(a)	638	92.5	69	10
Aluminum alloys, 7000 series	627	91	97	14
Alloy steels, cast; normalized and tempered	627	91	262	38
Copper-nickel-zinc, wrought ^(a)	620	90	124	18
Copper nickels, wrought ^(a)	586	85	90	13
Malleable irons, pearlitic grades; cast	552	80	310	45
High-strength low-alloy steels; wrought, as-rolled	552	80	290	42
Stainless steels, specialty grades; wrought, annealed	552	80	186	27
Stainless steels, standard ferritic grades; wrought, cold worked	552	80	310	45
Carbon steels, wrought; carburized, quenched and tempered	531	77	317	46
Carbon steel, cast; quenched and tempered	517	75
Stainless steel (410) P/M parts; heat treated	517	75
Steel P/M parts; as-sintered	517	75	207	30
Coppers, wrought ^(a)	496	72	69	10
Aluminum alloys, 2000 series	455	66	69	10
Ductile (nodular) austenitic irons, cast	448	65	193	28
Zinc foundry alloys	441	64	207	30

Zinc alloys, wrought	421	61	159	23
Stainless steels, standard ferritic grades; wrought, annealed	414	60	241	35
Aluminum alloys, 5000 series	407	59	41	6
Aluminum alloys, 6000 series	379	55	48	7
Aluminum casting alloys	379	55	55	8
Carbon steels, cast; normalized and tempered	379	55	331	48
Stainless steels, standard austenitic grades; wrought, annealed	379	55	207	30
Stainless steel P/M parts, as sintered	372	54	276	40
Rare earths	365	53	66	9.5
Zirconium and its alloys	365	53	103	15
Depleted uranium	345	50	241	35
Aluminum alloys, 4000 series	317	46
Thorium	310	45	179	26
Magnesium alloys, wrought	303	44	90	13
Silver	303	44	55	8
Carbon steels, cast; normalized	290	42	262	38
Beryllium and its alloys	276	40	34	5
Aluminum alloys, 3000 series	248	36	41	6
Carbon steel, cast; annealed	241	35
Malleable ferritic cast irons	241	35	221	32
Palladium	207	30	34	5
Gold	207	30
Magnesium alloys, cast	207	30	83	12
Polyimides, reinforced	193	28	34	5
Platinum	186	27	14	2
Iron P/M parts; as-sintered	179	26	76	11
Aluminum alloys, 1000 series	165	24	28	4
Polyphenylene sulfide, 40% glass reinforced	145	21
Polysulfone, 30–40% glass reinforced	131	19	117	17
Acetal, copolymer, 25% glass reinforced	128	18.5
Styrene acrylonitrile, 30% glass reinforced	124	18
Phenylene oxide based resins, 20–30% glass reinforced	117	17	100	14.5
Polyamide-imide	117	17	92	13.3
Polystyrene, 30% glass reinforced	97	14
Zinc die-casting alloys	96	14
Polyimides, unreinforced	90	13	52	7.5
Nylons, general purpose	87	12.6	49	7.1
Polyethersulfone	84	12.2
Polyphenylene sulfide, unreinforced	76	11
Polysulfone, unreinforced	70	10.2
Acetal, homopolymer, unreinforced	69	10
Nylon, mineral reinforced	69	10	62	9
Polypropylene, glass reinforced	69	10	41	6
Polystyrene, general purpose	69	10	34	5.0
Phenylene oxide based resins, unreinforced	66	9.6	54	7.8
Acetal, copolymer, unreinforced	61	8.8
ABS/polycarbonate	55	8.0
Lead and its alloys	55	8	11	1.6
Polyarylsulfone	55	8
ABS/polysulfone (polyarylether)	52	7.5
Acrylic/PVC	48	7.0	45	6.5

Tin and its alloys	45	6.6	7	1.3
ABS/PVC, rigid	41	6.0
Polystyrene, impact grades	41	6.0	19	2.8
Polypropylene, general purpose	36	5.2	33	4.8
ABS/polyurethane	31	4.5	26	3.7
Polypropylene, high impact	30	4.3	19	2.8

At 0.2% offset for metals, unless otherwise noted; tensile strength at yield for plastics, per ASTM D 638. P/M, powder metallurgy; ABS, acrylonitrile-butadiene-styrene; PVC, polyvinyl chloride.

(a) At 0.5% offset. Adapted from Guide to Engineering Materials, *Advanced Materials and Processes*, Dec 1999

Table 6 Tensile modulus of elasticity in tension at room temperature

Material	Tensile modulus			
	High		Low	
	GPa	10 ⁶ psi	GPa	10 ⁶ psi
Silicon carbide	655	95	90	13
Tungsten carbide-base cermets	650	94.3	425	61.6
Tungsten carbide	648	94	448	65
Osmium	551	80
Iridium	545	79
Titanium, zirconium, hafnium borides	503	73	490	71
Ruthenium	469	68
Rhenium	469	68
Boron carbide	448	65	290	42
Boron	441	64
Tungsten	406	59.0
Beryllia	399	58	270	39
Titanium carbide-base cermets	393	57	290	42
Rhodium	379	55
Titanium carbide	379	55	248	36
Molybdenum and its alloys	365	53	317	46
Tantalum carbide	365	53
Magnesia	345	50	241	35
Alumina ceramic	345	50	207	30
Niobium carbide	338	49
Beryllium carbide	317	46	207	30
Chromium	289	42
Beryllium and its alloys	289	42.0	186	27.0
Graphite-epoxy composites	276	40	134	20
Cobalt-base superalloys	248	36.0	199	29.0
Zirconia	241	35	158	23
Nickel and its alloys	234	34.0	131	19.0
Cobalt and its alloys	231	33.6	207	30.0
Nickel-base superalloys	231	33.5	126	18.3
Iron-base superalloys; cast and wrought	214	31	193	28
Silicon nitride	214	31	62	9
Alloy steels; cast	207	30	200	29
Boron-epoxy composites	207	30
Carbon steels; cast	207	30
Carbon steel, carburizing grades; wrought	207	30	200	29

Carbon steels, hardening grades; wrought	207	30	200	29
Depleted uranium	207	30	138	20
Stainless steels, age hardenable; wrought	207	30	193	28
Stainless steels, specialty grades; wrought	207	30	186	27
Ultrahigh strength steels; wrought	207	30	186	27
Stainless steels; cast	200	29	165	24
Stainless steels, standard austenitic grades; wrought	200	29	193	28
Stainless steels, standard ferritic grades; wrought	200	29
Stainless steels, standard martensitic grades; wrought	200	29
Boron-aluminum composites	193	28
Malleable irons, pearlitic grades; cast	193	28	179	26
Tantalum and its alloys	186	27.0	144	21.0
Ductile (nodular) irons; cast	172	25	152	22
Malleable ferritic cast irons	172	25
Platinum	172	25
Gray irons; cast	165	24	66	9.6
Copper nickels, wrought	151	22.0	124	18.0
Mullite	145	21
Zircon	145	21
Ductile (nodular) austenitic irons; cast	138	20	90	13
Hafnium	138	20
Copper casting alloys	133	19.3	76	11.0
Vanadium	131	19	124	18
High-copper alloys, wrought	131	19.0	117	17.0
Coppers, wrought	129	18.7	117	17.0
Titanium and its alloys	127	18.5	76	11.0
Copper-nickel-zinc; wrought	124	18.0	124	18.0
Palladium	124	18.0
Brasses; wrought	124	18.0	103	15.0
Bronzes; wrought	120	17.5	110	16.0
Polycrystalline glass	119	17.3	86	12.5
Niobium and its alloys	110	16.0	79	11.5
Silicon	107	15.5
Zirconium and its alloys	96	14.0	95	13.8
Zinc alloys; wrought	96	14.0	43	6.2
Rare earths	84	12.2	15	2.2
Gold	82	12.0
Aluminum alloys, 4000 series	79	11.4
Silver	76	11.0
Boron nitride	76	11	48	7
Aluminum alloys, 2000 series	74	10.8	70	10.2
Silica	72	10.5
Aluminum alloys, 7000 series	72	10.4	71	10.3
Aluminum alloys, 5000 series	71	10.3	69	10.0
Thorium	71	10.3
Aluminum alloys, 1000 series	69	10.0	69	10.0
Aluminum alloys, 3000 series	69	10.0	69	10.0
Aluminum alloys, 6000 series	69	10.0	69	10.0
Thorium	69	10.0
Tin and its alloys	53	7.7	41	6.0
Cordierite	48	7

Magnesium alloys; wrought	45	6.5	41	6.0
Magnesium alloys; cast	45	6.5	45	6.5
Polyesters, thermoset, pultrusions, general purpose	41	6.0	16	2.3
Epoxy, glass laminates	40	5.8	23	3.3
Glass fiber-epoxy composites	34	5
Bismuth	32	4.6
Polyimides; glass reinforced	31	4.5
Carbon graphite	28	4.0	4	0.6
Graphite, pyrolytic	28	4.0
Phenolics; reinforced	23	3.3	2.4	0.35
Alkyds	20	2.9	13	1.9
Graphite; recrystallized	19	2.7	5.5	0.8
Hickory (shag bark)	15	2.2
Locust (black)	14	2.1
Polyester, thermoplastic, PET; 45 and 30% glass reinforced	14	2.1	9	1.3
Birch (yellow)	13	2.0
Douglas fir (coat type)	13	2.0
Lead and its alloys	13	2.0
Pine (long needle, ponderosa)	13	2.0	9	1.3
Polyesters, thermoset, reinforced moldings	13	2.0	8.3	1.2
Ash (white)	12	1.8
Graphite, general purpose	12	1.8	3.4	0.5
Maple (sugar)	12	1.8
Oak (red, white)	12	1.8
Styrene acrylonitrile; 30% glass reinforced	12	1.8
Beech	11	1.7
Carbon and graphite, fibrous reinforced	12	1.8	2	0.3
Graphite, premium	11.7	1.7	4.8	0.7
Walnut (black)	11.7	1.7
Polycarbonate, 40% glass reinforced	11.7	1.7	5.9	0.86
Spruce (sitka)	11.0	1.6
Poplar (yellow)	11.0	1.6
Carbon, petroleum coke base	11.0	1.6	15.8	2.3
Indium	10.8	1.57
Basswood	10.3	1.5
Elm (rock)	10.3	1.5
Polysulfone, 30–40% glass reinforced	10.3	1.5	7.6	1.1
Cypress (Southern bald)	9.6	1.4
Nylons; 30% glass reinforced	9.7	1.4	6.9	1.0
Polyester, thermoplastic, PBT; 40 and 15% glass reinforced	9.7	1.4	5.5	0.8
Cedar (Port Orford)	8.9	1.3
Cottonwood (black)	8.9	1.3
Phenylene oxide based resins; 20–30% glass reinforced	9.0	1.3	6.4	0.93
Redwood (virgin)	8.9	1.3
Acetal, copolymer; 25% glass reinforced	8.6	1.25
Carbon, anthracite coal base	8.2	1.2	4.1	0.6
Diallyl phthalates, reinforced	8.3	1.2	4.1	0.6
Fir (balsam)	8.3	1.2
Hemlock (Eastern, Western)	8.3	1.2	10.3	1.5
Pine (Eastern white)	8.3	1.2
Polybutadienes	8.3	1.2	2.8	0.4

Polystyrene, 30% glass reinforced	8.3	1.2
Polyphenylene sulfide, 40% glass reinforced	7.7	1.12
Fluorocarbon, ETFE and ECTFE; glass reinforced	7.6	1.1
Melamines, cellulose electrical	7.6	1.1	6.9	1.0
Cedar (Eastern red)	6.2	0.9
Polyimides, unreinforced	4.8	0.70	3.1	0.45
Polyesters, thermoset, cast, rigid	4.5	0.65	1.0	0.15
Acetal, homopolymer; unreinforced	3.6	0.52
Acrylics, cast, general purpose	3.4	0.50	2.4	0.35
Acrylics, moldings	3.4	0.50	1.6	0.23
Nylon, mineral reinforced	3.4	0.5
Polystyrene, general purpose	3.4	0.50	3.2	0.46
Styrene acrylonitrile; unreinforced	3.4	0.50	2.8	0.40
Nylons; general purpose	3.3	0.48	1.9	0.28
Polyphenylene sulfide, unreinforced	3.3	0.48
Polystyrene, impact grades	3.2	0.47	1.0	0.15
Epoxies, cast	3.1	0.45	0.3	0.05
Polycarbonate, unreinforced	3.1	0.45	2.3	0.34
ABS	2.9	0.42	2.0	0.29
Acetal, copolymer; unreinforced	2.8	0.41
Phenylene oxide based resins; unreinforced	2.6	0.38	2.5	0.36
ABS/polycarbonate	2.6	0.37
Acrylic/PVC	2.6	0.37	2.3	0.34
Polyaryl sulfone	2.6	0.37
Polysulfone; unreinforced	2.5	0.36
Polyether sulfone	2.4	0.35
ABS/PVC, rigid	2.3	0.33
ABS/polysulfone (polyaryl ether)	2.2	0.32
Allyl diglycol carbonate	2.1	0.30
Fluorocarbon, PTFCE	2.1	0.30	1.3	0.19
Fluorocarbon, ETFE and ECTFE; unreinforced	1.7	0.24
ABS/polyurethane	1.5	0.22	1.1	0.16
Polypropylene, general purpose	1.5	0.22	1.1	0.16
Polymethylpentene	1.4	0.21
Fluorocarbon, PVF	1.4	0.2	1.2	0.17
Vinylidene chloride copolymer; oriented	1.38	0.20
Polypropylene, high impact	0.9	0.13
Polyethylene, high molecular weight	0.69	0.1
Fluorocarbon, FEP	0.5	0.07	0.3	0.05
Fluorocarbon, PTFE	0.5	0.07	0.3	0.04
Vinylidene chloride copolymer; unoriented	0.48	0.07
Polybutylene, homopolymer	0.25	0.036	0.23	0.034
Polybutylene, copolymer	0.23	0.034	0.08	0.012
Polyacrylate, unfilled	0.20	0.29
Polyethylenes, low density	0.19	0.027	0.14	0.020
PVC, PVC-acetate, nonrigid	0.021	0.003	0.0027	0.0004

PET, polyethylene terephthalate; ECTFE, ethylene tetrafluoroethylene; ETCFE, ethylene chlorotrifluoroethylene; PVC, polyvinyl chloride; PVF, polyvinyl formal; FEP, fluorinated ethylene propylene; PTFE, polytetrafluoroethylene

Glossary of Terms

A

A-basis

Mechanical property value above which at least 99% of the population of values is expected to fall, with a confidence of 95%. Also called A-allowable. See also B-basis, S-basis, and typical basis.

abrasion

Roughening or scratching of a surface due to abrasive wear.

abrasive wear

The removal or displacement of material from a surface when hard particles slide or roll across the surface under pressure. The particles may be loose or may be part of another surface in contact with the surface being worn. Contrast with adhesive wear.

accepted reference value

A value that serves as an agreed-on reference for comparison and which is derived as the following: (1) a theoretical or established value, based on scientific principles, (2) an assigned value, based on experimental work of some national or international standards organization, or (3) a consensus value, based on collaborative experimental work under the auspices of a scientific or engineering group. When the accepted reference value is the theoretical value, it is sometimes referred to as the “true” value.

accuracy

(1) The agreement or correspondence between an experimentally determined value and an accepted reference value for the material undergoing testing. The reference value may be established by an accepted standard (such as those established by ASTM), or, in some cases, the average value obtained by applying the test method to all the sampling units in a lot or batch of the material may be used. (2) The extent to which the result of a calculation or the reading of an instrument approaches the true value of the calculated or measured quantity. Compare with precision.

adhesive wear

The removal or displacement of material from a surface by the welding together and subsequent shearing of minute areas of two surfaces that slide across each other under pressure. In advanced stages, may lead to galling. Contrast with abrasive wear.

alligator skin

See preferred term orange peel.

angle of bend

The angle between the two legs of a specimen after bending is completed. It is measured before release of the bending force, unless otherwise specified.

anisotropy

The characteristic of exhibiting different values of a property in different directions with respect to a fixed reference system in the material. See also planar anisotropy

apparent area of contact

In tribology, the area of contact between two solid surfaces defined by the boundaries of their macroscopic interface.

arbitration bar

A test bar, cast with a heat of material, used to determine chemical composition, hardness, tensile strength, and deflection and strength under transverse loading in order to establish the state of acceptability of the casting.

asperity

In tribology, a protuberance in the small-scale topographical irregularities of a solid surface.

average linear strain

See engineering strain.

axial strain

See uniaxial strain.

B

batch

A definite quantity of some product or material produced under conditions that are considered uniform. A batch is usually smaller than a lot.

Bauschinger effect

The phenomenon by which plastic deformation increases yield strength in the direction of plastic flow and decreases it in other directions.

B-basis

Mechanical property value above which at least 90% of the population of values is expected to fall, with a confidence of 95%. See also A-basis, S-basis, and typical-basis.

bearing area

The product of the pin (or hole) diameter and specimen thickness in a bearing test. See also bearing stress.

bearing strain

The ratio of the deformation of the bearing hole, in the direction of the applied force, to the pin diameter in a bearing test.

bearing strength

The maximum bearing stress that a material is capable of sustaining.

bearing stress

The force per unit of bearing area.

bearing test

A method of determining the response to stress (load) of metal products that are subjected to riveting, bolting, or a similar fastening procedure. The purpose of the test is to determine the bearing strength of the material and to measure the bearing stress versus the deformation of the hole created by a pin or rod of circular cross section that pierces the sheet perpendicular to the surface.

bearing yield strength

The bearing stress at which a material exhibits a specified limiting deviation from the proportionality of bearing stress to bearing strain in a bearing test.

bend radius

(1) The inside radius of a bent section. (2) The radius of a tool around which metal is bent during testing or fabrication.

bend test

A test for determining the relative ductility of metal that is to be formed (usually sheet, strip, plate, or wire) or for determining soundness and toughness of metal (after welding, for example). The specimen is usually repeatedly bent over a specified diameter through a specified angle and then unbent for a specified number of cycles. There are four general types of bend tests, named according to the manner in which the forces are applied to the specimen to make the bend: free bend, guided bend, semiguided bend, and wrap-around bend.

biaxial stress

See principal stress (normal).

blanking shear test

A method used to determine the through-thickness shear strength of sheet material that involves blanking a disk out of flat strip using a simple punch-and-die method. Also known as punching shear test.

breaking load

The maximum load (or force) applied to a test specimen or structural member loaded to rupture.

breaking stress

The stress at failure. Also known as rupture stress. See also fracture stress.

Brinell hardness number, HB

A number related to the applied load and to the surface area of the permanent impression made by a ball indenter computed from the equation:

$$HB = \frac{2P}{\pi D \left(D - \sqrt{D^2 - d^2} \right)}$$

where P is applied load, kgf; D is diameter of ball, mm; and d is mean diameter of the impression, mm.

Brinell hardness test

A test for determining the hardness of a material by forcing a hard steel or carbide ball of specified diameter into it under a specified load. The result is expressed as the Brinell hardness number.

brittle crack propagation

A very sudden propagation of a crack with the absorption of no energy except that stored elastically in the body. Microscopic examination may reveal some deformation not noticeable to the unaided eye. Contrast with ductile crack propagation.

brittle fracture

Separation of a solid accompanied by little or no macroscopic plastic deformation. Typically, brittle fracture occurs by rapid crack propagation with less expenditure of energy than for ductile fracture.

buckling

A compression phenomenon that occurs when, after some critical level of load, a bulge, bend, bow, kink, or other wavy condition is produced in a beam, column, plate, bar, or sheet structural element.

bulk modulus

See bulk modulus of elasticity.

bulk modulus of elasticity (K)

The measure of resistance to change in volume; the ratio of hydrostatic stress to the corresponding unit change in volume. This elastic constant can be expressed by the equation:

$$K = \frac{\sigma_m}{\Delta} = \frac{-p}{\Delta} = \frac{1}{\beta}$$

where K is bulk modulus of elasticity, σ_m is hydrostatic or mean stress tensor, p is hydrostatic pressure, and β is the coefficient of compressibility. Also known as bulk modulus, compression modulus, hydrostatic modulus, and volumetric modulus of elasticity.

button

That part of a weld, including all or part of the weld nugget, that tears out in the destructive testing of a spot, seam, or projection welded specimen.

C

capacity

In tensile testing machines, the maximum load and/or displacement for which a machine is designed. Some testing machines have more than one load capacity. These are equipped with accessories that allow the capacity to be modified as desired.

catastrophic wear

Rapidly occurring or accelerating surface damage, deterioration, or change of shape caused by wear to such a degree that the service life of a part is appreciably shortened or its function is destroyed.

caustic cracking

A form of stress-corrosion cracking most frequently encountered in carbon steels or iron-chromium-nickel alloys that are exposed to concentrated hydroxide solutions at temperatures of 200 to 250 °C (400 to 480 °F). Also known as caustic embrittlement.

caustic embrittlement

See preferred term caustic cracking.

cavitation damage

Erosion of a solid surface through the formation and collapse of cavities or bubbles in an adjacent liquid that contains vapor and/or gas.

cavitation erosion

See preferred term cavitation damage.

central tendency of data

In statistics this is described by the central limit theorem. This theorem states the fact that if one draws samples of size n from the population and calculates the mean of these samples, the means will form a distribution that tends toward normality regardless of the form of the original sample distribution.

chafing fatigue

Fatigue damage initiated in a surface damaged by rubbing against another body. See also fretting.

Charpy test

An impact test in which a V-notched, keyhole-notched, or U-notched specimen, supported at both ends, is struck behind the notch by a striker mounted at the lower end of a bar that can swing as a pendulum. The energy that is absorbed in fracture is calculated from the height to which the striker would have risen had there been no specimen and the height to which it actually rises after fracture of the specimen.

Contrast with Izod test.

chevron pattern

A fractographic pattern of radial marks (shear ledges) that looks like nested letters "V," sometimes called a herringbone pattern. Chevron patterns are typically found on brittle fracture surface in parts whose widths are considerably greater than their thicknesses. The points of the chevrons can be traced back to the fracture origin.

chord modulus

The slope of the chord drawn between any two specific points on a stress-strain curve. Compare with secant modulus. See also modulus of elasticity.

cleavage

The tendency of a material to cleave or split along definite crystallographic planes.

cleavage fracture

A fracture, usually of a polycrystalline metal, in which most of the grains have failed by cleavage, resulting in bright reflecting facets. It is one type of crystalline fracture and is associated with low-energy brittle fracture. Contrast with shear fracture.

coefficient of compressibility

See bulk modulus of elasticity.

coefficient of friction (μ)

The dimensionless ratio of the force (F) between two bodies to the normal force (N) pressing these bodies together: μ (or f) = (F/N)

coefficient of thermal expansion

(1) Change in unit of length (or volume) accompanying a unit change of temperature, at a specified temperature. (2) The linear or volume expansion of a given material per degree rise of temperature, expressed at an arbitrary base temperature or as a more complicated equation applicable to a wide range.

compression modulus

See bulk modulus of elasticity.

compression test

A method for assessing the ability of a material to withstand compressive loads.

compressive modulus

The ratio of compressive stress to compressive strain below the proportional limit. Theoretically equal to Young's modulus determined from tensile experiments.

compressive strength

Maximum compressive stress a material is capable of developing. With a brittle material that fails in compression by fracturing, the compressive strength has a definite value. For ductile, malleable, or semiviscous materials (which do not fail in compression by a shattering fracture), the value obtained for compressive strength is an arbitrary value dependent on the degree of distortion that is regarded as effective failure of the material.

compressive stress

A stress that causes an elastic body to deform (shorten) in the direction of the applied load. Contrast with tensile stress.

compressometer

Instrument for measuring change in length over a given gage length caused by application or removal of a force. Commonly used in compression testing of metal specimens.

constant-life fatigue diagram

A plot (usually on rectangular coordinates) of a family of curves, each of which is for a single fatigue life (number of cycles), relating alternating stress, maximum stress, minimum stress, and mean stress. The constant-life fatigue diagram is generally derived from a family of *S-N* curves, each of which represents a different stress ratio for a 50% probability of survival. See also nominal stress, maximum stress, minimum stress, S-N curve, fatigue life, and stress ratio.

continuous use temperature

The maximum temperature at which material may be subjected to continuous use without fear of premature thermal degradation.

conventional strain

See engineering strain.

conventional stress

See engineering stress.

corrosion fatigue

Cracking produced by the combined action of repeated or fluctuating stress and a corrosive environment at lower stress levels or fewer cycles than would be required in the absence of a corrosive environment.

corrosive wear

Wear in which chemical or electrochemical reaction with the environment is significant. Compare with oxidative wear.

covalent bond

A bond in which two atoms share a pair of electrons. Contrast with ionic bond.

crack arrest

The temporary or permanent cessation of crack extension.

crack extension (Δ_a)

An increase in crack size. See also crack length (depth), effective crack size, original crack size, and physical crack size.

crack-extension force (G)

The elastic energy per unit of new separation area that would be made available at the front of an ideal crack in an elastic solid during a virtual increment of forward crack extension. See also J-integral.

crack-extension resistance (K_R)

A measure of the resistance of a material to crack extension, expressed in terms of the stress-intensity factor, the crack-extension force, or values of J derived using the J-integral concept.

crack-growth rate

Rate of propagation of a crack through a material due to statically or dynamically applied load.

crack length (depth) (a)

In fatigue and stress corrosion cracking, the physical crack size used to determine the crack growth rate and the stress-intensity factor. For the compact-type specimen, crack length is measured from the line connecting the bearing points of load application. For the center-cracked-tension specimen, crack length is measured from the perpendicular bisector of the central crack.

crack-mouth-opening displacement (CMOD)

See crack-opening displacement.

crack-opening displacement (COD)

On a K_{Ic} specimen, the opening displacement of the notch surfaces at the notch and in the direction perpendicular to the plane of the notch and the crack. The displacement at the tip is called the crack-tip-opening displacement (CTOD); at the mouth, it is called the crack-mouth-opening displacement (CMOD).

crack-plane orientation

An identification of the plane and direction of a fracture in relation to product geometry. This identification is designated by a hyphenated code, the first letter(s) representing the direction normal to the crack plane and the second letter(s) designating the expected direction of crack propagation.

crack size (a)

A lineal measure of a principal planar dimension of a crack. This measure is commonly used in the calculation of quantities descriptive of the stress and displacement fields. In practice, the value of crack size is obtained from procedures for measurement of physical crack size, original crack size, or effective crack size, as appropriate to the situation under consideration. See also crack length.

crack-tip-opening displacement (CTOD)

See crack-opening displacement.

crack-tip plane strain

A stress-strain field, near a crack-tip, that approaches plane strain to the degree required by an empirical criterion.

crazing

Region of ultrafine cracks, which may extend in a network on or under the surface of a resin or plastic material. May appear as a white band. Often found in a filament-wound pressure vessel or bottle. In many plastics, craze growth precedes crack growth, often generating additional strength because crazes are load bearing.

creep

Time-dependent strain occurring under stress. The creep strain occurring at a diminishing rate is called primary or transient creep; occurring at a minimum and almost constant rate, secondary or steady-rate creep; that occurring at an accelerating rate, tertiary creep.

creep rate

The slope of the creep-time curve at a given time determined from a Cartesian plot.

creep recovery

The time-dependent decrease in strain in a solid, following the removal of force. Recovery is usually determined at a constant temperature.

creep-rupture strength

The stress that will cause fracture in a creep test at a given time in a specified constant environment. Also known as stress-rupture strength.

creep-rupture test

A method of evaluating elevated temperature durability in which a tension specimen is stressed under constant load until it breaks. Data recorded commonly include initial stress, time to rupture, initial extension, creep extension, and reduction in area at the fracture. Also known as stress-rupture test.

creep strain

The time-dependent total strain (extension plus initial strain) produced by applied stress during a creep test.

creep strength

The stress that will cause a given creep strain in a creep test at a given time in a specified constant environment.

creep stress

The constant load in a creep test divided by the original cross-sectional area of the specimen.

creep test

A method of determining the extension of metals under a given load at a given temperature. The determination usually involves the plotting of time-elongation curves under constant load.

cross linking

With thermosetting and certain thermoplastic polymers, the setting up of chemical links between the molecular chains. When extensive, as in most thermosetting resins, cross linking makes an infusible supermolecule of all the chains. In rubbers, the cross linking is just enough to join all molecules into a network.

crushing test

(1) A radial compressive test applied to tubing, sintered-metal bearings, or other similar products for determining radial crushing strength (maximum load in compression). (2) An axial compressive test for determining quality of tubing, such as soundness of weld in welded tubing.

crystalline

That form of a substance comprised predominantly of (one or more) crystals, as opposed to glassy or amorphous.

crystalline defects

The deviations from a perfect three-dimensional atomic packing that are responsible for much of the structure-sensitive properties of the materials. Crystal defects can be point defects (dislocations) or surface defects (vacancies), line defects (dislocations), or surface defects (grain boundaries).

crystalline fracture

A pattern of brightly reflecting crystal facets on the fracture surface of a polycrystalline metal, resulting from cleavage fracture of many individual crystals. Contrast with fibrous fracture and silky fracture, See also granular fracture.

cup fracture (cup-and-cone fracture)

A mixed-mode fracture, often seen in tensile-test specimens of a ductile material, where the central portion undergoes plane-strain fracture and the surrounding region undergoes plane-stress fracture. One of the mating fracture surfaces looks like a miniature cup; it has a central depressed flat-face region surrounded by a shear lip. The other fracture surface looks like a miniature truncated cone.

cupping test

A mechanical test used to determine the ductility and drawing properties of sheet metal. It consists of measuring the maximum depth of bulge that can be formed before fracture. The test is commonly carried out by drawing the test piece into a circular die by means of a punch with a hemispherical end. See also Erichsen cup test, Olsen cup test, and Swift cup test.

cycle

In fatigue, one complete sequence of values of applied load that is repeated periodically. The symbol N represents the number of cycles. See also S-N curve.

cyclic loads

Loads that change value by following a regular repeating sequence of change.

D

decarburization

Loss of carbon from the surface layer of a carbon-containing alloy due to reaction with one or more chemical substances in a medium that contacts the surface.

deflection temperature under load (DTUL)

The temperature at which a simple cantilever beam deflects a given amount under load. Formerly called heat distortion temperature.

deformation

A change in the form of a body due to stress, thermal change, change in moisture, or other causes. Measured in units of length.

deformation curve

See stress-strain diagram.

deformation energy

See strain energy.

density

The mass per unit volume of a solid material.

design of experiments (DOE)

A methodology involving statistically designed experiments in which the character and sequence of individual experiments are planned in advance so that data are taken in a way that will provide the most unbiased and precise results commensurate with the available time and money. The chief classes of statistically designed experiments are: (1) blocking designs to remove the effect of background variables from the experimental error, (2) factorial designs, in which all levels of each factor in an experiment are combined with all levels of every other factor, and (3) response surface designs, which determine the empirical relation between the factors (independent variables) and the response (performance variable).

diamond pyramid hardness test

See Vickers hardness test

dilatometer

An instrument for measuring length or volume changes in a solid during heating and subsequent cooling or isothermal holding.

dimensional stability

Ability of a plastic part to retain the precise shape in which it was molded, fabricated, or cast.

dimpled rupture

A fractographic term describing ductile fracture that occurs through the formation and coalescence of microvoids along the fracture path. The fracture surface of such a ductile fracture appears dimpled when

observed at high magnification and usually is most clearly resolved when viewed in a scanning electron microscope. See also ductile fracture.

discontinuous yielding

The nonuniform plastic flow of a metal exhibiting a yield point in which plastic deformation is inhomogeneously distributed along its length. Under some circumstances, it may occur in metals not exhibiting a distinct yield point, either at the onset of or during plastic flow.

dislocation

A linear imperfection in a crystalline array of atoms. Two basic types are recognized: (1) an edge dislocation corresponds to the row of mismatched atoms along the edge formed by an extra, partial plane of atoms within the body of a crystal; (2) a screw dislocation corresponds to the axis of a spiral structure in a crystal, characterized by a distortion that joins normally parallel planes together to form a continuous helical ramp (with a pitch of one interplanar distance) winding about the dislocation. Most prevalent is the so-called mixed dislocation, which is any combination of an edge dislocation and a screw dislocation.

dislocation density

The total length of dislocation lines per unit volume, or the number of dislocation lines that cut through a unit cross-sectional area.

displacement

The distance that a chosen measurement point on a cracked specimen displaces normal to the crack plane as the crack grows. See also crack-opening displacement and crack plane orientation.

distortion

Any deviation from an original size, shape, or contour that occurs because of the application of stress or the release of residual stress.

double-shear test

A shear test having two stationary, shear blades and one moving one and that uses solid round bars as test specimens.

ductile crack propagation

Slow crack propagation that is accompanied by noticeable plastic deformation and requires energy to be supplied from outside the body. Contrast with brittle fracture.

ductile fracture

Fracture characterized by tearing of metal accompanied by appreciable gross plastic deformation and expenditure of considerable energy. Contrast with brittle fracture.

ductility

The ability of a material to deform plastically before fracturing. Measured by elongation or reduction in area in a tensile test, by height of cupping in a cupping test, or by the radius or angle of bend in a bend test. See also malleability.

durometer hardness

Measure of the indentation hardness of plastics. It is the extent to which a spring-loaded steel indenter protrudes beyond the pressure foot into the material.

dynamic mechanical measurement

A technique in which either the modulus and/or damping of a substance under oscillatory load or displacement is measured as a function of temperature, frequency, or time, or a combination thereof.

dynamic modulus

The ratio of stress to strain under cyclic conditions (calculated from data obtained from either free or forced vibration tests, in shear, compression, or tension).

dynamic recovery

A process occurring in hot working of metals in which a fine subgrain structure forms within the elongated grains due to annihilation of dislocations due to easy cross slip and climb. It results in a lowering of the flow stress. Dynamic recovery, as opposed to dynamic recrystallization that occurs in hot working, occurs in metals of high stacking fault energy such as aluminum, iron, and most bcc metals.

dynamic strain aging

A behavior in metals in which solute atoms are sufficiently mobile to move toward and interact with dislocations. This results in strengthening over a specific range of elevated temperature and strain rate.

E

edge distance

The distance from the edge of a bearing specimen to the center of the hole in the direction of applied force. See also bearing test.

edge distance ratio

The ratio of the edge distance to the pin diameter in a bearing test.

edge strain

Transverse strain lines or Lüders lines ranging from 25 to 300 mm (1 to 12 in.) in from the edges of cold rolled steel sheet or strip.

effective crack size (a_e)

The physical crack size augmented for the effects of cracking plastic deformation. Sometimes the effective crack size is calculated from a measured value of a physical crack size plus a calculated value of a plastic-zone adjustment. A preferred method for calculation of effective crack size compares compliance from the secant of a load-deflection trace with the elastic compliance from a calibration for the type of specimen.

effective yield strength

An assumed value of uniaxial yield strength that represents the influence of plastic yielding on fracture-test parameters.

elastic calibration device

A device for use in verifying the load readings of a testing machine consisting of an elastic member(s) to which loads may be applied, combined with a mechanism or device for indicating the magnitude (or a quantity proportional to the magnitude) of deformation under load.

elastic constants

The factors of proportionality that relate elastic displacement of a material to applied forces. See also modulus of elasticity, bulk modulus of elasticity, shear modulus, and Poisson's ratio.

elastic deformation

A change in dimensions directly proportional to and in phase with an increase or decrease in applied force.

elastic energy

The amount of energy required to deform a material within its elastic range of behavior, neglecting small heat losses due to internal friction. The energy absorbed by a specimen per unit volume of material contained within the gage length being tested. It is determined by measuring the area under the stress-strain curve up to a specified elastic strain. See also modulus of resilience and strain energy.

elastic hysteresis

See preferred term mechanical hysteresis.

elastic limit

The maximum stress which a material is capable of sustaining without any permanent strain (deformation) remaining on complete release of the stress. Compare with proportional limit.

elastic recovery

Amount the dimension of a stressed elastic material returns to its original (unstressed) dimension on release of an applied load. In hardness testing, the shortening of the original dimensions of the indentation upon release of the applied load.

elastic resilience

The amount of energy absorbed in stressing a material up to the elastic limit; or, the amount of energy that can be recovered when stress is released from the elastic limit.

elastic strain

See elastic deformation.

elastic strain energy

The energy expended by the action of external forces in deforming a body elastically. Essentially, all the work performed during elastic deformation is stored as elastic energy, and this energy is recovered upon release of the applied force.

elasticity

The property of a material by virtue of which deformation caused by stress disappears on removal of the stress. A perfectly elastic body completely recovers its original shape and dimensions after release of stress.

elongation

A term used in mechanical testing to describe the amount of extension of a test piece when stressed. See also elongation, percent.

elongation, percent

The extension of a uniform section of a specimen expressed as percentage of the original gage length:

$$\text{Elongation, \%} = \frac{L_x - L_o}{L_o} = 100$$

where L_o is original gage length, and L_x is final gage length.

endurance

The capacity of a material to withstand repeated application of stress.

endurance limit

The maximum stress below which a material can presumably endure an infinite number of stress cycles.

The value of the maximum stress and the stress ratio also should be stated. Compare with fatigue limit.

engineering strain (e)

A term sometimes used for average linear strain or conventional strain in order to differentiate it from true strain. In tension testing it is calculated by dividing the change in the gage length by the original gage length.

engineering stress (s)

A term sometimes used for conventional stress in order to differentiate it from true stress. In tension testing, it is calculated by dividing the breaking load applied to the specimen by the original cross-sectional area of the specimen.

environmentally assisted cracking

Brittle fracture of a normally ductile material in which the corrosive effect of the environment is a causative factor. Environmental cracking is a general term that includes corrosion fatigue, high-temperature hydrogen attack, hydrogen blistering, hydrogen embrittlement, liquid metal embrittlement, solid metal embrittlement, stress-corrosion cracking, and sulfide stress cracking.

equiaxed grain structure

A structure in which the grains have approximately the same dimensions in all directions.

Erichsen cup test

A cupping test used for assessing the ductility of sheet metal. The method consists of forcing a conical or hemispherical-ended plunger into the specimen and measuring the depth of the impression at fracture. Compare with Olsen cup test and Swift cup test.

erosion

Progressive loss of original material from a solid surface due to mechanical interaction between that surface and a fluid, a multicomponent fluid, or impinging liquid or solid particles.

error

Deviation from the correct value. For a testing machine, the difference obtained by subtracting the load indicated by the calibration device from the load indicated by the testing machine.

extensometer

An instrument for measuring changes in length over a given gage length caused by application or removal of a force. Commonly used in tension testing of metal specimens.

F

fatigue

The phenomenon leading to fracture under repeated or fluctuating stresses having a maximum value less than the ultimate tensile strength of the material. Fatigue failure generally occurs at loads that, applied statically, would produce little perceptible effect. Fatigue fractures are progressive, beginning as minute cracks that grow under the action of the fluctuating stress.

fatigue crack growth rate (da/dN)

The rate of crack extension caused by constant-amplitude fatigue loading, expressed in terms of crack extension per cycle of load application.

fatigue failure

Failure that occurs when a specimen undergoing fatigue completely fractures into two parts or has softened or been otherwise significantly reduced in stiffness by thermal heating or cracking.

fatigue life (N)

The number of cycles of stress or strain of a specified character that a given specimen sustains before failure occurs.

fatigue life for p % survival

An estimate of the fatigue life that $p\%$ of the population would attain or exceed at a given stress level. The observed value of the median fatigue life estimates the fatigue life for 50% survival. Fatigue life for $p\%$ survival values, where p is any number, such as 95, 90, etc., may also be estimated from the individual fatigue life values.

fatigue limit

The maximum stress that presumably leads to fatigue fracture in a specified number of stress cycles. The value of the maximum stress and the stress ratio also should be stated. Compare with endurance limit.

fatigue limit for p % survival

The limiting value of fatigue strength for $p\%$ survival as the number of stress cycles becomes very large; p may be any number, such as 95, 90, etc.

fatigue notch factor (K_f)

The ratio of the fatigue strength of an unnotched specimen to the fatigue strength of a notched specimen of the same material and condition; both strengths are determined at the same number of stress cycles.

fatigue notch sensitivity (q)

An estimate of the effect of a notch or hole of a given size and shape on the fatigue properties of a material; measured by $q = (K_f - 1)/(K_t - 1)$, where K_f is the fatigue notch factor and K_t is the stress-concentration factor. A material is said to be fully notch sensitive if q approaches a value of 1.0; it is not notch sensitive if the ratio approaches 0.

fatigue strength

The maximum stress that can be sustained for a specified number of cycles without failure. The value of the maximum stress and the stress ratio also should be stated.

fatigue strength at N cycles (S_N)

A hypothetical value of stress for failure at exactly N number of cycles as determined from an S-N curve. The value of S_N thus determined is subject to the same conditions as those which apply to the $S-N$ curve. The value of S_N that is commonly found in the literature is the hypothetical value of maximum stress, S_{max} , minimum stress, S_{min} , or stress amplitude, S_a , at which 50% of the specimens of a given sample could survive N number of stress cycles in which the mean stress, S_m , = 0. This is also known as the median fatigue strength at N cycles .

fatigue strength for $p\%$ survival at N cycles

An estimate of the stress level at which $p\%$ of the population would survive N number of cycles; p may be any number, such as 95, 90, etc. The estimates of the fatigue strengths for $p\%$ survival values are derived from particular points of the fatigue-life distribution because there is no test procedure by which a frequency distribution of fatigue strengths at N cycles can be directly observed.

fatigue striations

Parallel lines frequently observed in electron microscope fractographs or fatigue-fracture surfaces. The lines are transverse to the direction of local crack propagation; the distance between successive lines represents the advance of the crack front during the one cycle of stress variation. Compare with Wallner lines.

fatigue test

A method for determining the range of alternating (fluctuating) stresses a material can withstand without failing.

fatigue wear

Wear of a solid surface caused by fracture arising from material fatigue.

fibrous fracture

A gray and amorphous fracture surface that results when a metal is sufficiently ductile for the crystals to elongate before fracture occurs. When a fibrous fracture is obtained in an impact test, it may be regarded as definite evidence of toughness of the metal. Contrast with crystalline fracture and silky fracture.

fibrous structure

(1) In forgings, a structure revealed as laminations, not necessarily detrimental, on an etched section or as a ropy appearance on a fracture. It is not to be confused with the ductile fracture of a clean metal. (2) In wrought iron, a structure consisting of slag fibers embedded in ferrite. (3) In rolled steel plate stock, a uniform, fine-grained structure on a fractured surface, free of laminations or shale-type discontinuities. As contrasted with (1), it is virtually synonymous with ductile fracture.

file hardness

Hardness as determined by the use of a steel file of standardized hardness on the assumption that a material that cannot be cut with the file is as hard as, or harder than, the file. Files covering a range of hardnesses may be employed. See also scratch hardness test.

fixed-load or fixed-displacement crack-extension-force curves

Curves obtained from a fracture mechanics analysis for the test configuration, assuming a fixed applied load or displacement and generating a curve of crack-extension force versus the effective crack size as the independent variable.

flare test

A test applied to tubing, involving tapered expansion over a cone. Similar to pin expansion test.

flattening test

A quality test for tubing in which a specimen is flattened to a specified height between parallel plates.

flexibility

The quality or state of a material that allows it to be flexed or bent repeatedly without undergoing rupture. See also flexure.

flexural modulus

Within the elastic limit, the ratio of the applied stress on a test specimen in flexure to the corresponding strain in the outermost fiber of the specimen. Flexural modulus is the measure of relative stiffness.

flexural strength

The maximum stress in the outer fiber at the moment of crack or break.

flexure

A term used in the study of strength of materials to indicate the property of a body, usually a rod or beam, to bend without fracture. See also flexibility.

flow

Movement (slipping or sliding) of essentially parallel planes within an element of a material in parallel directions; occurs under the action of shear stress. Continuous action in this manner, at constant volume and without disintegration of the material, is termed yield, creep, or plastic deformation.

flow lines

Texture showing the direction of metal flow during hot or cold working. Flow lines often can be revealed by etching the surface or a section of a metal part.

flow stress

The stress required to produce plastic deformation in a solid metal.

forged roll Scleroscope hardness number (HFRSc or HFRSd)

A number related to the height of rebound of a diamond-tipped hammer dropped on a forged steel roll. It is measured on a scale determined by dividing into 100 units the average rebound of a hammer from a forged steel roll of accepted maximum hardness. See also Scleroscope hardness number and Scleroscope hardness test.

formability

The ease with which a metal can be shaped through plastic deformation. The evaluation of the formability of a metal involves measurement of strength and ductility, as well as the amount of deformation required to cause fracture. Workability is used interchangeably with formability; however, formability refers to the shaping of sheet metal, while workability refers to shaping materials by bulk deformation (i.e., forging or rolling).

forming limit diagram (FLD)

A diagram on which the major strains at the onset of necking in sheet metal are plotted vertically and the corresponding minor strains are plotted horizontally. The onset-of-failure line divides all possible strain combinations into two zones: the “safe” zone, in which failure during forming is not expected, and the “failure” zone, in which failure during forming is expected.

fractography

Descriptive explanation of a fracture process, especially in metals, with specific reference to photographs of the fracture surface. Macrofractography involves photographs at low magnification; microfractography, at high magnification.

fracture surface

The irregular surface produced when a piece of metal is broken. See also fracture test, granular fracture, fibrous fracture, silky fracture, and crystalline fracture.

fracture mechanics

See linear-elastic fracture mechanics.

fracture stress

The true normal stress on the minimum cross-sectional area at the beginning of fracture. This term usually applies to tension tests of unnotched specimens.

fracture test

A test in which a specimen is broken and its fracture surface is examined with the unaided eye or with a low-power microscope to determine such factors as composition, grain size, case depth, or internal discontinuities.

fracture toughness

A generic term for measures of resistance to extension of a crack. The term is sometimes restricted to results of fracture mechanics tests, which are directly applicable in fracture control. However, the term commonly includes results from simple tests of notched or precracked specimens not based on fracture-mechanics analysis. Results from tests of the latter type are often useful for fracture control, based on either service experience or empirical correlations with fracture mechanics tests. See also stress-intensity factor.

frame

A list, compiled for sampling purposes, that designates the items(units) of a population or universe to be considered in a study.

free bend

The bend obtained by applying forces to the ends of a specimen without the application of force at the point of maximum bending. In making a free bend, lateral forces first are applied to produce a small amount of bending at two points. The two bends, each a suitable distance from the center, are both in the same direction. Compare with guided bend and semiguided bend.

frequency distribution

The way in which the frequencies of occurrence of members of a population, or a sample, are distributed according to the values of the variable under consideration.

fretting

A type of wear that occurs between tight-fitting surfaces subjected to oscillation at very small amplitude. This type of wear can be a combination of oxidative wear and abrasive wear. See also fretting corrosion.

fretting corrosion

(1) The accelerated deterioration at the interface between contacting surfaces as the result of corrosion and slight oscillatory movement between the two surfaces. (2) A form of fretting in which chemical reaction predominates. Fretting corrosion is often characterized by the removal of particles and subsequent formation of oxides, which are often abrasive and so increase the wear. Fretting corrosion can involve other chemical reaction products, which may not be abrasive.

fretting fatigue

(1) Fatigue fracture that initiate at a surface area where fretting has occurred. The progressive damage to a solid surface that arises from fretting. Note: If particles of wear debris are produced, then the term fretting wear may be applied.

fretting wear

Wear resulting from fretting. See also fretting fatigue.

G

gage length

The original length of the portion of a specimen over which strain, change of length, or other characteristics are determined.

galling

(1) A condition whereby excessive friction between high spots results in localized welding with subsequent spalling and a further roughening of the rubbing surfaces of one or both of two mating parts.
(2) A severe form of scuffing associated with gross damage to the surfaces or failure. Galling has been used in many ways in tribology; therefore, each time it is encountered its meaning must be ascertained from the specific context of the usage. See also scoring, scuffing, and spalling.

glide

See slip.

grain growth

An increase in the average size of the grains in polycrystalline metal, usually as a result of heating at elevated temperature. See also grain size.

grain size

A measure of the areas or volumes of grains in a polycrystalline metal, usually expressed as an average when the individual sizes are fairly uniform. In metals containing two or more phases, the grain size refers to that of the matrix unless otherwise specified. Grain size is reported in terms of number of grains per unit area or volume, average diameter, or as a grain-size number derived from area measurements.

granular fracture

A type of irregular surface produced when metal is broken that is characterized by a rough, grainlike appearance, rather than a smooth or fibrous one. It can be subclassified as transgranular or intergranular. This type of fracture is frequently called crystalline fracture; however, the inference that the metal broke because it “crystallized” is not justified, because all metals are normally crystalline when in the solid state. Contrast with fibrous fracture and silky fracture.

group

The specimens tested at one time, or consecutively, at one stress level. A group may comprise one or more specimens.

guided bend

The bend obtained by use of a plunger to force the specimen into a die in order to produce the desired contour of the outside and inside surfaces of the specimen. Compare with free bend.

guided-bend test

A test in which the specimen is bent to a definite shape by means of a punch (mandrel) and a bottom block.

H

Hall-Petch relationship

A general relationship for metals that shows that the yield strength is linearly related to the reciprocal of the square root of the grain diameter.

hardness

A measure of the resistance of a material to surface indentation or abrasion; may be thought of as a function of the stress required to produce some specified type of surface deformation. There is no absolute scale for hardness; therefore, to express hardness quantitatively, each type of test has its own scale of arbitrarily defined hardness. Indentation hardness can be measured by Brinell hardness test, Rockwell hardness test, Vickers hardness test, Knoop hardness test, and the Scleroscope hardness test.

Hartmann lines

See Lüders lines.

heat distortion temperature (HDT)

See deflection temperature under load (DTUL).

herringbone pattern

See chevron pattern.

hole-expansion test

A simulative test in which a flat sheet specimen with a circular hole in its center is clamped between annular die plates and deformed by a punch, which expands and ultimately cracks the edge of the hole.

Hooke's law

Observation that, in the elastic region of solid material, stress is directly proportional to strain and can be expressed as:

$$\frac{\text{Stress}}{\text{Strain}} = \frac{\sigma}{\epsilon} = \text{constant} = E$$

where E is the modulus of elasticity, or Young's modulus. The constant relationship between stress and strain applies only below the proportional limit. See also modulus of elasticity.

hydrogen damage

A general term for the embrittlement, cracking, blistering, and hydride formation that can occur when hydrogen is present in some metals.

hydrogen embrittlement

A condition of low toughness, low ductility or cracking in metals resulting from the absorption of hydrogen.

hydrogen-induced delayed cracking

A term sometimes used to identify a form of hydrogen embrittlement in which a metal appears to fracture spontaneously under a steady stress less than the yield stress. There is usually a delay between the application of stress (or exposure of the stressed metal to hydrogen) and the onset of cracking. Also referred to as static fatigue.

hydrostatic modulus

See bulk modulus of elasticity.

hysteresis

The phenomenon of permanently absorbed or lost energy that occurs during any cycle of loading or unloading when a material is subjected to repeated loading.

I

ideal crack

A simplified model of a crack used in elastic-stress analysis. In a stress-free body, the crack has two smooth surfaces that are coincident and join within the body along a smooth curve called the crack front; in two-dimensional representations, the crack front is called the crack tip.

ideal-crack-tip stress field

The singular stress field, infinitesimally close to the crack front, that results from the dominant influence of an ideal crack in an elastic body that is deformed. In a linear-elastic homogeneous body, the significant stress components vary inversely as the square root of the distance from the crack tip. In a linear-elastic body, the crack-tip stress field can be regarded as the superposition of three component stress fields called modes.

impact energy

The amount of energy required to fracture a material, usually measured by means of an Izod test or Charpy test. The type of specimen and test conditions affect the values and therefore should be specified.

impact loads

Especially severe shock loads such as those caused by instantaneous arrest of a falling mass, shock meeting of two parts (in a mechanical hammer, for example), or by explosive impact, in which there can be an exceptionally rapid build-up of stress.

impact strength

The resiliency or toughness of a solid as measured by impact energy.

impact test

A test for determining the energy absorbed in fracturing a test piece at high velocity, as distinct from static test. The test may be carried out in tension, bending, or torsion, and the test bar may be notched or unnotched. See also impact energy, Charpy test, and Izod test.

indentation hardness

The resistance of a material to indentation as determined by hardness testing. The indenter, which may be spherical or diamond shaped, is pressed into the surface of a metal under specified load for a given time. See also Brinell hardness test, Knoop hardness test, Rockwell hardness test, and Vickers hardness test.

initial recovery

The decrease in strain in a solid during the removal of force before any creep recovery takes place, usually determined at constant temperature. Sometimes referred to as instantaneous recovery.

initial strain

The strain in a specimen immediately upon achieving the given loading conditions in a creep test (before creep occurs). Sometimes referred to as instantaneous strain.

initial stress

The stress produced by strain in a specimen immediately on achieving the given constant-strain conditions in a stress-relaxation test before stress-relaxation occurs. Sometimes referred to as instantaneous stress.

initial tangent modulus

The slope of the stress-strain curve at the beginning of loading. See also modulus of elasticity.

initiation of stable crack growth

The initiation of slow stable crack advance from the blunted crack tip.

instantaneous recovery

See initial recovery.

instantaneous strain

See initial strain.

instantaneous stress

See initial stress.

instrumented impact test

An impact test in which the load on the specimen is continually recorded as a function of time and/or specimen deflection prior to fracture.

interval estimate

The estimate of a parameter given by two statistics, defining the end points of an interval.

ionic bond

(1) A type of chemical bonding in which one or more electrons are transferred completely from one atom to another, thus converting the neutral atoms into electrically charged ions. These ions are approximately spherical and attract each other because of their opposite charges. (2) A primary bond arising from the electrostatic attraction between two oppositely charged ions. Contrast with covalent bond.

item

(1) An object or quantity of material on which a set of observations can be made. (2) An observed value or test result obtained from an object or quantity of material.

Izod test

A type of impact test in which a V-notched specimen, mounted vertically, is subjected to a sudden blow delivered by the weight at the end of a pendulum arm. The energy required to break off the free end is a measure of the impact strength or toughness of the material. Contrast with Charpy test.

J

J-integral

A mathematical expression describing a line or surface integral that encloses the crack front from one crack surface to the other, used to characterize the fracture toughness of a material having appreciable plasticity before fracture. The *J*-integral eliminates the need to describe the behavior of the material near the crack tip by considering the local stress-strain field around the crack front; J_{Ic} is the critical value of the *J*-integral required to initiate crack extension from a preexisting crack.

K

keel block

A standard test casting, for steel and other high-shrinkage alloys, consisting of a rectangular bar that resembles the keel of a boat, attached to the bottom of a large riser, or shrinkhead. Keel blocks that have only one bar are often called Y-blocks; keel blocks having two bars, double keel blocks. Test specimens are machined from the rectangular bar, and the shrinkhead is discarded.

keyhole specimen

A type of specimen containing a hole-and-slot notch, shaped like a keyhole, usually used in impact and bend tests. See Charpy test.

Knoop hardness number (HK)

A number related to the applied load and to the projected area of the permanent impression made by a rhombic-based pyramidal diamond indenter having included edge angles of $172^{\circ} 30'$ and $130^{\circ} 0'$ computed from the equation:

$$HK = \frac{P}{0.07028d^2}$$

where P is applied load, kgf; and d is long diagonal of the impression, mm. In reporting Knoop hardness numbers, the test load is stated.

Knoop hardness test

An indentation-hardness test using calibrated machines to force a rhombic-based pyramidal diamond indenter having specified edge angles, under specified conditions, into the surface of the material under test and to measure the long diagonal after removal of the load.

L

least count

The smallest value that can be read from an instrument having a graduated scale. Except on instruments provided with a vernier, the least count is that fraction of the smallest division which can be conveniently and reliably estimated; this fraction is ordinarily one-fifth or one-tenth, except where the graduations are very closely spaced. Also known as least reading.

least reading

See least count.

limiting dome height (LDH) test

A mechanical test, usually performed unlubricated on sheet metal, that simulates the fracture conditions in a practical press-forming operation. The results are dependent on the sheet thickness.

linear-elastic fracture mechanics

A method of fracture analysis that can determine the stress (or load) required to induce fracture instability in a structure containing a cracklike flaw of known size and shape. See also stress-intensity factor.

linear (tensile or compressive) strain

The change per unit length due to force in an original linear dimension. An increase in length is considered positive.

load

For testing machines, a force applied to a test piece that is measured in units such as pound-force, newton, or kilogram-force.

load range, P

In fatigue, the algebraic difference between the maximum and minimum loads in a fatigue cycle.

load ratio, R

In fatigue, the algebraic ratio of the minimum to maximum load in a fatigue cycle, that is, $R = P_{\min}/P_{\max}$. Also known as stress ratio.

longitudinal direction

The principal direction of flow in a worked metal. See also normal direction and transverse direction.

long transverse direction

See transverse direction.

lot

A definite quantity of a product or material accumulated under conditions that are considered uniform for sampling purposes. Compare with batch.

lubricant

Any substance interposed between two surfaces for the purpose of reducing the friction or wear between them.

Lüders lines

Elongated surface markings or depressions, often visible with the unaided eye, that form along the length of sheet metal or a tension specimen at an angle of approximately 45° to the loading axis. Caused by localized plastic deformation, they result from discontinuous (inhomogeneous) yielding. Also known as Lüders bands, Hartmann lines, Piobert lines, or stretcher strains. See also edge strain.

M

macrostrain

The mean strain over any finite gage length of measurement large in comparison with interatomic distances. Macrostrain can be measured by several methods, including electrical-resistance strain gages and mechanical or optical extensometers. Elastic macrostrain can be measured by x-ray diffraction. Compare with microstrain.

malleability

The characteristic of metals that permits plastic deformation in compression without fracture. See also ductility.

maximum load (P_{\max})

(1) The load having the highest algebraic value in the load cycle. Tensile loads are considered positive and compressive loads negative. (2) Used to determine the strength of a structural member; the load that can be borne before failure is apparent.

maximum strength

See ultimate strength.

maximum stress (S_{\max})

The stress having the highest algebraic value in the stress cycle, tensile stress being considered positive and compressive stress negative. The nominal stress is used most commonly.

maximum stress-intensity factor (K_{\max})

The maximum value of the stress-intensity factor in a fatigue cycle.

mean stress (or steady component of stress) (S_m)

The algebraic average of the maximum and minimum stresses in one cycle, that is, $S_m = (S_{\max} + S_{\min})/2$.

mechanical hysteresis

Energy absorbed in a complete cycle of loading and unloading within the elastic limit and represented by the closed loop of the stress-strain curves for loading and unloading. Sometimes called elastic hysteresis.

mechanical metallurgy

The science and technology dealing with the behavior of metals when subjected to applied forces.

median fatigue life

The middle value when all of the observed fatigue life values of the individual specimens in a group tested under identical conditions are arranged in order of magnitude. When an even number of specimens are tested, the average of the two middlemost values is used. Use of the sample median rather than the arithmetic mean (that is, the average) is usually preferred.

median fatigue strength at N cycles

An estimate of the stress level at which 50% of the population would survive N cycles. The estimate is derived from a particular point of the fatigue life distribution, because there is no test procedure by which a frequency distribution of fatigue strengths at N cycles can be directly observed. See also fatigue strength at N cycles.

microhardness test

See preferred term microindentation hardness test.

microindentation hardness test

Hardness test using a calibrated machine to force a diamond indenter of specific geometry, under a test load of 1 to 1000 gramforce, into the surface of the test material and to measure the diagonal or diagonals of the indentation optically.

microstrain

The strain over a gage length comparable to interatomic distances. These are the strains being averaged by the macrostrain measurement. Microstrain is not measurable by currently existing techniques. Variance of the microstrain distribution can, however, be measured by x-ray diffraction.

minimum load (P_{\min})

In fatigue, the least algebraic value of applied load in a cycle.

minimum stress (S_{\min})

In fatigue, the stress having the lowest algebraic value in the cycle, tensile stress being considered positive and compressive stress negative.

minimum stress-intensity factor (K_{\min})

In fatigue, the minimum value of the stress-intensity factor in a cycle. This value corresponds to the minimum load when the load ratio is 0 and is taken to be 0 when the load ratio is ≤ 0 .

modes

The three classes of crack (surface) displacements adjacent to the crack tip. These displacement modes are associated with stress-strain fields around the crack tip and are designated I, II, and III and represent opening, sliding, and tearing displacements, respectively. See also crack-tip plane strain and crack opening displacement.

modulus of elasticity (E)

The measure of rigidity or stiffness of a metal; the ratio of stress, below the proportional limit, to the corresponding strain. In terms of the stress-strain diagram, the modulus of elasticity is the slope of the stress-strain curve in the range of linear proportionality of stress to strain. Also known as Young's modulus. For materials that do not conform to Hooke's law throughout the elastic range, the slope of either the tangent to the stress-strain curve at the origin or at low stress, the secant drawn from the origin to any specified point on the stress-strain curve, or the chord connecting any two specific points on the stress-strain curve is usually taken to be the modulus of elasticity. In these cases, the modulus is referred to as the tangent modulus, secant modulus, or chord modulus, respectively.

modulus of resilience

The amount of energy stored in a material when loaded to its elastic limit. It is determined by measuring the area under the stress-strain curve up to the elastic limit. See also elastic energy, resilience, and strain energy.

modulus of rigidity

See shear modulus.

modulus of rupture

Nominal stress at fracture in a bend test or torsion test. In bending, modulus of rupture is the bending moment at fracture divided by the section modulus. In torsion, modulus of rupture is the torque at fracture divided by the polar section modulus. See also modulus of rupture in bending and modulus of rupture in torsion.

modulus of rupture in bending (S_b)

The value of maximum tensile or compressive stress (whichever causes failure) in the extreme fiber of a beam loaded to failure in bending computed from the flexure equation:

$$S_b = \frac{Mc}{I}$$

where M is maximum bending moment, computed from the maximum load and the original moment arm; c is initial distance from the neutral axis to the extreme fiber where failure occurs; and I is initial moment of inertia of the cross section about the neutral axis. See also modulus of rupture.

modulus of rupture in torsion (S_s)

The value of maximum shear stress in the extreme fiber of a member of circular cross section loaded to failure in torsion computed from the equation:

$$S_s = \frac{Tr}{J}$$

where T is maximum twisting moment, r is original outer radius, and J is polar moment of inertia of the original cross section. See also modulus of rupture.

modulus of toughness

The amount of work per unit volume of a material required to carry that material to failure under static loading. See also toughness.

Mohs hardness test

A scratch hardness test for determining comparative hardness using 10 standard minerals—from talc (the softest) to diamond (the hardest).

monotron hardness test

An obsolete method of determining indentation hardness by measuring the load required to force a spherical penetrator into a metal to a specified depth.

multiaxial stress

See principal stress (normal).

m-value

See strain-rate sensitivity.

N

natural strain

See true strain.

necking

(1) Reducing the cross-sectional area of metal in a localized area by stretching. (2) Reducing the diameter of a portion of the length of a cylindrical shell or tube.

nominal strain

See strain.

nominal strength

See ultimate strength.

nominal stress

The stress at a point calculated on the net cross section by simple elasticity theory without taking into account the effect on the stress produced by stress raisers such as holes, grooves, fillets, etc.

normal direction

Direction perpendicular to the plane of working in a worked metal. See also longitudinal direction and transverse direction.

normal stress

The stress component perpendicular to a plane on which forces act. Normal stress may be either tensile stress or compressive stress.

notch brittleness

Susceptibility of a material to brittle fracture at points of stress concentration. For example, in a notch tensile test, the material is said to be notch brittle if the notch strength is less than the tensile strength of an unnotched specimen. Otherwise, it is said to be notch ductile.

notch depth

The distance from the surface of a notched test specimen to the bottom of the notch. In a cylindrical test specimen, the percentage of the original cross-sectional area removed by machining an annular groove.

notch ductility

The percentage reduction in area after complete separation of the metal in a tensile test of a notched specimen.

notch strength

The maximum load on a notched tensile-test specimen divided by the minimum cross-sectional area (the area at the root of the notch). Also known as notch tensile strength.

n-value

See strain hardening exponent.

O

observed value

The particular value of a characteristic determined as a result of a test or measurement.

offset

The distance along the strain coordinate between the initial portion of a stress-strain curve and a line parallel to the initial portion that intersects the stress-strain curve at a value of stress (commonly 0.2%) that is used as a measure of the yield strength. Used for materials that have no obvious yield point.

offset modulus

The ratio of the offset yield stress to the extension at the offset point (plastics).

offset yield strength

The stress at which the strain exceeds by a specified amount (the offset) an extension of the initial proportional portion of the stress-strain curve. Expressed in force per unit area.

Olsen cup test

A cupping test in which a piece of sheet metal, restrained except at the center, is deformed by a standard steel ball until fracture occurs. The height of the cup at time of fracture is a measure of the ductility. Compare with Erichsen cup test and Swift cup test.

orange peel

A surface roughening in the form of a pebble-grained pattern where a metal of unusually coarse grain is stressed beyond its elastic limit. Also known as pebbles and alligator skin.

original crack size (a_0)

The physical crack size at the start of testing

oxidative wear

A type of wear resulting from the sliding action between two metallic components that generates oxide films on the metal surfaces. These oxide films prevent the formation of a metallic bond between the sliding surfaces, resulting in fine wear debris and low wear rates. Compare with corrosive wear.

P

parameter

In statistics, a constant (usually unknown) defining some property of the frequency distribution of a population, such as a population median or a population standard deviation.

pebbles

See preferred term orange peel.

percent error

For testing machines, the ratio, expressed as a percentage, of the error to the correct value of the applied load.

permanent set

The deformation or strain remaining in a previously stressed body after release of load.

permissible variation

For testing machines, the maximum allowable error in the value of the quantity indicated. It is convenient to express permissible variation in terms of the percent error.

physical crack size (a_p)

The distance from a reference plane to the observed crack front. This distance may represent an average of several measurements along the crack front. The reference plane depends on the specimen form, and it is normally taken to be either the boundary or a plane containing either the load line or the centerline of a specimen or plate.

physical properties

Properties of a material the determination of which does not involve the deformation or destruction of the specimen—for example, density, electrical conductivity, coefficient of thermal expansion, magnetic permeability, and lattice parameter. Does not include chemical reactivity or the properties more appropriately regarded as mechanical properties.

physical testing

Methods used to determine the entire range of physical properties of a material. In addition to density and thermal, electrical, and magnetic properties, physical testing methods can be used to assess simple fundamental physical properties such as color, crystalline form, and melting point.

pin expansion test

A test for determining the ability of a tube to be expanded or for revealing the presence of cracks or other longitudinal weaknesses in it, made by forcing a tapered pin into the open end of the tube, similar to flare test.

pin or mandrel

In bend testing, the plunger or tool used in making semiguided, guided, or wrap-around tests to apply the bending force to the inside surface of the bend. In free bends or semiguided bends to an angle of 180°, a shim or block of the proper thickness may be placed between the legs of the specimen as bending is completed. This shim or block is also referred to as a pin or mandrel.

pin shear test

See shear test.

Piobert lines

See Lüders lines.

pitting

In tribology, a type of wear characterized by the presence of small, sharp surface cavities formed by processes such as fatigue, local adhesion, wear, corrosion, or cavitation.

planar anisotropy

A variation in physical and/or mechanical properties with respect to direction within the plane of material in sheet form. See also plastic strain ratio.

plane strain

The stress condition in linear-elastic fracture mechanics in which there is zero strain in a direction normal to both the axis of applied tensile stress and the direction of crack growth (i.e., parallel to the crack front); most nearly achieved in loading thick plates along a direction parallel to the plate surface. Under plane-strain conditions, the plane of fracture instability is normal to the axis of the principal tensile stress.

plane-strain fracture toughness (K_{Ic})

The crack extension resistance under conditions of crack-tip plane strain. See also stress-intensity factor.

plane stress

The stress condition in linear-elastic fracture mechanics in which the stress in the thickness direction is zero; most nearly achieved in loading very thin sheet along a direction parallel to the surface of the sheet. Under plane-stress conditions, the plane of fracture instability is inclined 45° to the axis of the principal tensile stress.

plane-stress fracture toughness (K_c)

In linear-elastic fracture mechanics, the value of the crack-extension resistance at the instability condition determined from the tangency between the R-curve and the critical crack-extension force curve of the specimen. See also stress intensity factor.

plastic deformation

The permanent (inelastic) distortion of a material under applied stress that strains the material beyond its elastic limit.

plastic flow

See yielding.

plastic instability

The stage of deformation in a tensile test where the plastic flow becomes nonuniform and necking begins.

plasticity

The property that enables a material to undergo permanent deformation without rupture.

plastic strain

Dimensional change that does not disappear when the initiating stress is removed. Usually accompanied by some elastic deformation.

plastic strain ratio (r -value)

The ratio of the true width strain to the true thickness strain in a tensile test, $r = \epsilon_w/\epsilon_t$. Because of the difficulty in making precise measurement of thickness strain in sheet material, it is more convenient to express r in terms of initial and final length and width dimensions. It can be shown that

$$r = (\ln W_o W_f) - (\ln L_f W_f / L_o W_o)$$

where L_o and W_o are initial length and width of gage section, respectively; and L_f and W_f are final length and width, respectively.

plastic-zone adjustment, r_Y

An addition to the physical crack size to account for plastic crack-tip deformation enclosed by a linear-elastic stress field.

plowing

In tribology, the formation of grooves by plastic deformation of the softer of two surfaces in relative motion.

point estimate

The estimate of a parameter given by a single statistic.

Poisson's ratio (ν)

The absolute value of the ratio of transverse (lateral) strain to the corresponding axial strain resulting from uniformly distributed axial stress below the proportional limit of the material.

population

The hypothetical collection of all possible test specimens that could be prepared in the specified way from the material under consideration. Also known as universe.

precision

The closeness of agreement between the results of individual replicated measurements or tests. The standard deviation of the error of measurement may be used as a measure of “imprecision.”

principal stress (normal)

The maximum or minimum value of the normal stress at a point in a plane considered with respect to all possible orientations of the considered plane. On such principal planes the shear stress is zero. There are three principal stresses on three mutually perpendicular planes. The state of stress at a point may be: (1) uniaxial, a state of stress in which two of the three principal stresses are zero; (2) biaxial, a state of stress in which only one of the three principal stresses is zero; or (3) triaxial, a state of stress in which none of the principal stresses is zero. Multiaxial stress refers to either biaxial or triaxial stress.

proof stress

(1) The stress that will cause a specified small permanent set in a material. (2) A specified stress to be applied to a member or structure to indicate its ability to withstand service loads.

proportional limit

The greatest stress a material is capable of developing without a deviation from straight-line proportionality between stress and strain. Compare with elastic limit. See also Hooke's law.

punching shear test

See blanking shear test.

R

radial marks

Lines on a fracture surface that radiate from the fracture origin and are visible to the unaided eye or at low magnification. Radial lines result from the intersection and connection of brittle fractures propagating at different levels. Also known as shear ledges. See also chevron pattern.

radius of bend

The radius of the cylindrical surface of the pin or mandrel that comes in contact with the inside surface of the bend during bending. For free or semiguided bends to 180° in which a shim or block is used, the radius of bend is one-half the thickness of the shim or block.

range of stress (S_r)

The algebraic difference between the maximum and minimum stress in one cycle—that is,

$$S_r = S_{\max} - S_{\min}$$

ratchet marks

Lines on a fatigue fracture surface that result from the intersection and connection of fatigue fractures propagating from multiple origins. Ratchet marks are parallel to the overall direction of crack propagation and are visible to the unaided eye or at low magnification.

rate of creep

See creep rate.

R-curve

In linear-elastic fracture mechanics, a plot of crack-extension resistance as a function of stable crack extension, which is either the difference between the physical crack size, or the effective crack size, and the original crack size. *R*-curves normally depend on specimen thickness and, for some materials, on temperature and strain rate.

reduction in area (RA)

The difference between the original cross-sectional area of a tensile specimen and the smallest area at or after fracture as specified for the material undergoing testing. Also known as reduction of area.

relaxation curve

A plot of either the remaining, or relaxed, stress as a function of time. See also relaxation rate.

relaxation rate

The absolute value of the slope of a stress-relaxation curve at a given time.

relaxed stress

The initial stress minus the remaining stress at a given time during a stress-relaxation test. See also stress relaxation.

remaining stress

The stress remaining at a given time during a stress-relaxation test. See also stress relaxation.

repeatability

A term used to refer to the test-result variability associated with a limited set of specifically defined sources of variability within a single laboratory.

reproducibility

A term used to describe test-result variability associated with specifically defined components of variance obtained both from within a single laboratory and between laboratories.

residual stress

Stresses that remain within a body as the result of thermal or mechanical treatment or both.

resilience

The ability of a material to absorb energy when deformed elastically and return to its original shape on release of load. See also modulus of resilience.

response curve for *N* cycles

In fatigue-data analysis, a curve fitted to observed values of percentage survival at *N* number of cycles for several stress levels, where *N* is a preassigned number such as 10^6 , 10^7 , etc. It is an estimate of the relationship between applied stress and the percentage of the population that would survive *N* cycles. See also S-N curve.

Rockwell hardness number (HR)

A number derived from the net increase in the depth of impression in a Rockwell hardness test as the load on an indenter is increased from a fixed minor load to a major load and then returned to the minor load. Rockwell hardness numbers are always quoted with a scale symbol representing the penetrator, load, and dial used.

Rockwell hardness test

An indentation-hardness test using a calibrated machine that utilizes the depth of indentation, under constant load, as a measure of hardness. Either a 120° diamond cone with a slightly rounded point, or a $\frac{1}{16}$ or $\frac{1}{8}$ in. diameter steel ball is used as the indenter.

Rockwell superficial hardness number

See Rockwell hardness number.

Rockwell superficial hardness test

Same as Rockwell hardness test, except that smaller minor and major loads are used.

rosette

Strain gages arranged to indicate, at a single position, strain in three different directions.

rupture stress

The stress at failure. Also known as breaking stress. See also fracture stress.

r-value

See plastic-strain ratio.

S

sample

- (1) One or more units of product (or a relatively small quantity of a bulk material) that are withdrawn from a lot or process stream and that are tested or inspected to provide information about the properties, dimensions, or other quality characteristics of the lot or process stream. Not be confused with specimen.
- (2) A portion of a material intended to be representative of the whole.

sample average

The sum of all the observed values in a sample divided by the sample size. It is a point estimate of the population mean. Also known as arithmetic mean.

sample median

The middle value when all observed values in a sample are arranged in order of magnitude. If an even number of samples are tested, the average of the two middlemost values is used. It is a point estimate of the population median, or 50% point.

sample percentage

The percentage of observed values between two stated values of the variable under consideration. It is a point estimate of the percentage of the population between the same two stated values. (One stated value may be $-\infty$ or $+\infty$.)

sample standard deviation (s)

The square root of the sample variance. It is a point estimate of the population standard deviation, a measure of the “spread” of the frequency distribution of a population. This value of s provides a statistic that is used in computing interval estimates and several test statistics. For small sample sizes, s underestimates the population standard deviation.

sample variance (s^2)

The sum of the squares of the differences between each observed value and the sample average divided by the sample size minus one. It is a point estimate of the population variance.

S-basis

Minimum property value specified by the appropriate federal, military, Society of Automotive Engineers, American Society for Testing and Materials, or other recognized and approved specifications for the material. See also A-basis, B-basis, and typical basis.

Scleroscope hardness number (HSc or HSd)

A number related to the height of rebound of a diamond-tipped hammer dropped on the material being tested. It is measured on a scale determined by dividing into 100 units the average rebound of the hammer from a quenched (to maximum hardness) and untempered AISI W5 tool steel test block.

Scleroscope hardness test

A dynamic indentation-hardness test using a calibrated instrument that drops a diamond-tipped hammer from a fixed height onto the surface of the material being tested. The height of rebound of the hammer is a measure of the hardness of the material. Also known as Shore hardness test.

scoring

In tribology, a severe form of wear characterized by the formation of extensive grooves and scratches in the direction of sliding.

scratch hardness test

A form of hardness test in which a sharp-pointed stylus or corner of a mineral specimen is traversed along a surface so as to determine the resistance of that surface to cutting or abrasion. See also file hardness and Mohs hardness test.

scratching

In tribology, the mechanical removal or displacement, or both, of material from a surface by the action of abrasive particles or protuberances sliding across the surfaces. See also plowing.

scuffing

A form of adhesive wear that produces superficial scratches or a high polish on the rubbing surfaces. It is observed most often on inadequately lubricated parts.

secant modulus

The slope of the secant drawn from the origin to any specified point on a stress-strain curve. Compare with chord modulus. See also modulus of elasticity.

semiguided bend

The bend obtained by applying a force directly to the specimen in the portion that is to be bent. The specimen is either held at one end and forced around a pin or rounded edge, or is supported near the ends and bent by a force applied on the side of the specimen opposite the supports and midway between them. In some instances, the bend is started in this manner and finished in the manner of a free bend.

set

See permanent set.

sharp-notch strength

The notch tensile strength measured using specimens with very small notch root radii (approaching the limit for machining capability); values of sharp-notch strength usually depend on notch root radius.

shear

The type of force that causes or tends to cause two contiguous parts of the same body to slide relative to each other in a direction parallel to their plane of contact.

shear fracture

A ductile fracture in which a crystal (or a polycrystalline mass) has separated by sliding or tearing under the action of shear stresses. Contrast with cleavage fracture.

shear lip

A narrow, slanting ridge along the edge of a fracture surface. The term sometimes also denotes a narrow, often crescent-shaped, fibrous region at the edge of a fracture that is otherwise of the cleavage type, even though this fibrous region is in the same plane as the rest of the fracture surface.

shear modulus (G)

The ratio of shear stress to the corresponding shear strain for shear stresses below the proportional limit of the material. Values of shear modulus are usually determined by torsion testing. Also known as modulus of rigidity.

shear strain

The tangent of the angular change, as a response to force, between two lines originally perpendicular to each other through a point in a body. Also known as shearing strain.

shear strength

The maximum shear stress that a material is capable of sustaining. Shear strength is calculated from the maximum load during a shear or torsion test and is based on the original dimensions of the cross section of the specimen.

shear stress

(1) A stress that exists when parallel planes in metal crystals slide across each other. (2) The stress component tangential to the plane on which the forces act. Also known as tangential stress.

shear test

Any of several tests to obtain shear strength of a metal. Common tests used on mill products include the double-shear test, single-shear test, the blanking shear test (also known as the punching shear test) and the torsion test.

shock load

The sudden application of an external force that results in a very rapid build-up of stress.

Shore hardness test

See Scleroscope hardness test.

short transverse

See transverse direction.

significance level

The stated probability (risk) that a given test of significance will reject the hypothesis that a specified effect is absent when the hypothesis is true.

significant

Statistically significant. An effect of difference between populations is said to be present if the value of a test statistic is significant, that is, lies outside predetermined limits. See also population.

silky fracture

A metal fracture in which the broken metal surface has a fine texture, usually dull in appearance. Characteristic of tough and strong metals. Contrast with crystalline fracture and granular fracture.

single-shear test

(1) A shear test similar to the double-shear test used for round-bar specimens, but that uses only one stationary shear blade. (2) A shear test that uses a sheet or thin-plate specimen.

size effect

Effect of the dimensions of a piece of metal on its mechanical and other properties and on manufacturing variables such as forging reduction and heat treatment. In general, the mechanical properties are lower for a larger size.

slant fracture

A type of fracture appearance, typical of plane-stress fractures, in which the plane of metal separation is inclined at an angle (usually about 45°) to the axis of the applied stress.

slenderness ratio

The effective unsupported length of a uniform column divided by the least radius of gyration of the cross-sectional area.

slip

Plastic deformation by the irreversible shear displacement (translation) of one part of a crystal relative to another in a definite crystallographic direction and usually on a specific crystallographic plane. Sometimes called glide.

slip band

A group of parallel slip lines so closely spaced as to appear as a single line when observed under an optical microscope. See also slip line.

slip line

The trace of the slip plane on a viewing surface; the trace is usually observable only if the surface has been polished before deformation. The usual observation on metal crystals (under the light microscope) is of a cluster of slip lines known as a slip band.

S-N curve

A plot of stress, S , against the number of cycles to failure, N . The stress can be the maximum stress, S_{\max} , or the alternating stress amplitude, S_a . The stress values are usually nominal stresses; i.e., there is no adjustment for stress concentration. The curve indicates the *S-N* relationship for a specified value of the mean stress, S_m or the stress ratio, A , or R and a specified probability of survival. For N , a log scale is almost always used. For S , a linear scale is used most often, but a log scale is sometimes used. Also known as *S-N* diagram.

S-N curve for 50% survival

A curve fitted to the median value of fatigue life at each of several stress levels. It is an estimate of the relation between applied stress and the number of cycles-to-failure that 50% of the population would survive.

S-N curve for $p\%$ survival

A curve fitted to the fatigue life for $p\%$ survival values at each of several stress levels. It is an estimate of the relationship between applied stress and the number of cycles-to-failure that $p\%$ of the population would survive. p may be any number, such as 95, 90, and so forth.

spalling

The separation of macroscopic particles from a surface in the form of flakes or chips.

specimen

A test object, often of standard dimensions or configuration, that is used for destructive or nondestructive testing. One or more specimens may be cut from each unit of a sample.

springback

The extent to which metal tends to return to its original shape or contour after undergoing a forming operation.

standard deviation

The most usual measure of the dispersion of observed values or results expressed as the positive square root of the variance.

static fatigue

A term referring to a time-dependent reduction in strength with a static (noncyclic) load. The term may refer to hydrogen-induced delayed cracking or the effect of creep on the strength of plastics.

statistic

A summary value calculated from the observed values in a sample.

steady loads

Loads that do not change in intensity or that change so slowly they may be regarded as steady.

stiffness

(1) The ability of a metal or shape to resist elastic deflection.(2) The rate of stress increase with respect to the rate of increase in strain induced in the metal or shape; the greater the stress required to produce a given strain, the stiffer the material is said to be.

strain

The unit of change in the size or shape of a body due to force. Also known as nominal strain. See also engineering strain, linear strain, and true strain.

strain-age embrittlement

A loss in ductility accompanied by an increase in hardness and strength that occurs when low-carbon steel (especially rimmed or capped steel) is aged following plastic deformation. The degree of embrittlement is a function of aging time and temperature, occurring in a matter of minutes at about 200°C (400 °F), but requiring a few hours to a year at room temperature.

strain aging

The changes in ductility, hardness, yield point, and tensile strength that occur when a metal or alloy that has been cold worked is stored for some time. In steel, strain aging is characterized by a loss of ductility and a corresponding increase in hardness, yield point, and tensile strength.

strain energy

A measure of the energy absorption characteristics of a material determined by measuring the area under the stress-strain diagram. Also known as deformation energy. See also elastic energy, resilience, and toughness.

strain gage

A device for measuring small amounts of strain produced during tensile and similar tests on metal. A coil of fine wire is mounted on a piece of paper, plastic, or similar carrier matrix (backing material), which is rectangular in shape and usually about 25 mm (1.0 in.) long. This is glued to a portion of metal under test. As the coil extends with the specimen, its electrical resistance increases in direct proportion. This is known as bonded resistance-strain gage. Other types of gages measure the actual deformation. Mechanical, optical, or electronic devices are sometimes used to magnify the strain for easier reading. See also rosette.

strain hardening

An increase in hardness and strength caused by plastic deformation at temperatures below the recrystallization range. Also known as work hardening.

strain-hardening coefficient

See strain-hardening exponent.

strain-hardening exponent (*n* value)

The value *n* in the relationship $\sigma = K\varepsilon^n$, where σ is the true stress, ε is the true strain, and *K*, the strength coefficient, is equal to the true stress at a true strain of 1.0. The strain hardening exponent is equal to the slope of the true stress/true strain curve up to maximum load, when plotted on log-log coordinates. The *n*-value relates to the ability of a sheet of material to be stretched in metalworking operations. The higher the *n*-value, the better the formability(stretchability). Also known as the strain-hardening coefficient.

strain rate

The time rate of straining for the usual tensile test. Strain as measured directly on the specimen gage length is used for determining strain rate. Because strain is dimensionless, the units of strain rate are reciprocal time.

strain-rate sensitivity (*m* value)

The increase in stress (σ) needed to cause a certain increase in plastic-strain rate ($\dot{\varepsilon}$) at a given level of plastic strain (ε) and a given temperature(*T*).

$$\text{Strain -rate sensitivity} = m = \left(\frac{\Delta \log \sigma}{\Delta \log \dot{\varepsilon}} \right)_{\varepsilon T}$$

strength

The maximum nominal stress a material can sustain. Always qualified by the type of stress (tensile, compressive, or shear).

strength coefficient

See strain-hardening exponent (n -value).

stress

The intensity of the internally distributed forces or components of forces that resist a change in the volume or shape of a material that is or has been subjected to external forces. Stress is expressed in force per unit area and is calculated on the basis of the original dimensions of the cross section of the specimen. Stress can be either direct (tension or compression) or shear. See also engineering stress, mean stress, nominal stress, normal stress, residual stress, and true stress.

stress amplitude

One-half the algebraic difference between the maximum and minimum stress in one cycle of a repetitively varying stress.

stress-concentration factor (K_t)

A multiplying factor for applied stress that allows for the presence of a structural discontinuity such as a notch or hole; K_t equals the ratio of the greatest stress in the region of the discontinuity to the nominal stress for the entire section. Also known as theoretical stress-concentration factor.

stress-corrosion cracking (SCC)

A time-dependent process in which a metallurgically susceptible material fractures prematurely under conditions of simultaneous corrosion and sustained loading at lower stress levels than would be required in the absence of a corrosive environment. Tensile stress is required at the metal surface and may be a residual stress resulting from heat treatment or fabrication of the metal or the result of external loading. Cracking may be intergranular or transgranular, depending on the combination of alloy and environment.

stress cycle

The smallest segment of the stress-time function that is repeated periodically.

stress cycles endured (N)

The number of cycles of a specified character (that produce fluctuating stress and strain) that a specimen has endured at any time in its stress history.

stress-intensity calibration

A mathematical expression, based on empirical or analytical results, that relates the stress-intensity factor to load and crack length for a specific specimen planar geometry. Also known as K calibration.

stress-intensity factor

A scaling factor, usually denoted by the symbol K , used in linear-elastic fracture mechanics to describe the intensification of applied stress at the tip of a crack of known size and shape. At the onset of rapid crack propagation in any structure containing a crack, the factor is called the critical stress-intensity factor, or the fracture toughness. Various subscripts are used to denote different loading conditions or fracture toughnesses:

stress-intensity factor range (ΔK)

The variation in the stress-intensity factor in a fatigue cycle, that is, $K_{\max} - K_{\min}$.

stress raisers

Changes in contour or discontinuities in structure that cause local increases in stress.

stress ratio (A or R)

The algebraic ratio of two specified stress values in a stress cycle. Two commonly used stress ratios are the ratio of the alternating stress amplitude to the mean stress, $A = S_a/S_m$, and the ratio of the minimum stress to the maximum stress, $R = S_{\min}/S_{\max}$.

stress relaxation

The time-dependent decrease in stress in a solid under constant strain at constant temperature due to creep. The stress-relaxation behavior of a metal is usually shown in a stress-relaxation curve.

stress-relaxation curve

A plot of the remaining, or relaxed, stress in a stress-relaxation test as a function of time. The relaxed stress equals the initial stress minus the remaining stress. Also known as a stress-time curve.

stress-rupture strength

See creep-rupture strength.

stress-rupture test

See creep-rupture test.

stress-strain curve

See stress-strain diagram.

stress-strain diagram

A graph in which corresponding values of stress and strain are plotted against each other. Values of stress are usually plotted vertically (ordinates or y-axis) and values of strain horizontally (abscissas or x-axis). Also known as deformation curve and stress-strain curve.

stress-time curve

See stress-relaxation curve.

stretch-bending test

A simulative test for sheet metal formability in which a strip of sheet metal is clamped at its ends in lock beads and deformed in the center by a punch. Test conditions are chosen so that fracture occurs in the region of punch contact.

stretcher strains

See Lüders lines.

striation

A fatigue fracture feature, often observed in electron micrographs, that indicates the position of the crack front after each succeeding cycle of stress. The distance between striations indicates the advance of the crack front across that crystal during one stress cycle, and a line normal to the striation indicates the direction of local crack propagation.

Swift cup test

A simulative cupping test in which circular blanks of various diameters are clamped in a die ring and deep drawn into cups by a flat-bottomed cylindrical punch. Compare with Erichsen cup test and Olsen cup test.

T

tangent modulus

The slope of the stress-strain curve at any specified stress or strain. See also modulus of elasticity.

temper embrittlement

Brittleness that results when certain steels are held within, or are cooled slowly through, a certain range of temperature below the transformation range. The brittleness is manifested as an upward shift in ductile-to-brittle transition temperature but only rarely produces a low value of reduction in area in a smooth-bar tension test of the embrittled material.

tensile strength

In tension testing, the ratio of maximum load to original cross-sectional area. Also known as ultimate strength. Compare with yield strength.

tensile stress

A stress that causes two parts of an elastic body, on either side of a typical stress plane, to pull apart. Contrast with compressive stress.

tensile testing

See tension testing.

tension

The force or load that produces elongation.

tension testing

A method of determining the behavior of materials subjected to uniaxial loading, which tends to stretch the metal. A longitudinal specimen of known length and diameter is gripped at both ends and stretched at a slow, controlled rate until rupture occurs. Also known as tensile testing.

testing machine (load-measuring type)

A mechanical device for applying a load (force) to a specimen.

theoretical stress concentration factor

See stress-concentration factor.

thermal fatigue

Fatigue resulting from the presence of temperature gradients that vary with time in such a manner as to produce cyclic stresses in a structure.

thermocouple

A device for measuring temperature, consisting of lengths of two dissimilar metals or alloys that are electrically joined at one end and connected to a voltage-measuring instrument at the other end. When one junction is hotter than the other, a thermal electromotive force is produced that is roughly proportional to the difference in temperature between the hot and cold junctions.

threshold stress for stress-corrosion cracking (σ_{th})

An experimentally determined critical gross-section stress below which stress-corrosion cracking will not occur under specified test conditions.

tolerance limits

The extreme values (upper and lower) that define the range of permissible variation in size or other quality characteristic of a part.

torsion

A twisting deformation of a solid body about an axis in which lines that were initially parallel to the axis become helices.

torsion test

A test designed to provide data for the calculation of the shear modulus, modulus of rupture in torsion, and yield strength in shear.

torsional stress

The shear stress on a transverse cross section resulting from a twisting action.

total elongation

A total amount of permanent extension of a test piece broken in a tensile test. See also elongation, percent.

total-extension-under-load yield strength

See yield strength.

toughness

The ability of a metal to absorb energy and deform plastically before fracturing.

transgranular

Through or across crystals or grains. Also known as intracrystalline or transcrystalline.

transition temperature

(1) An arbitrarily defined temperature that lies within the temperature range in which metal fracture characteristics (as usually determined by tests of notched specimens) change rapidly, such as from primarily fibrous (shear) to primarily crystalline (cleavage) fracture. (2) Sometimes used to denote an arbitrarily defined temperature within a range in which the ductility changes rapidly with temperature.

transverse direction

Literally, the "across" direction, usually signifying a direction or plane perpendicular to the direction of working. In rolled plate or sheet, the direction across the width is often called long transverse, and the direction through the thickness, short transverse.

transverse strain

Linear strain in a plane perpendicular to the loading axis of a specimen.

triaxial stress

See principal stress (normal).

tribology

The science and technology concerned with interacting surfaces in relative motion.

true strain

(1) The ratio of the change in dimension, resulting from a given load increment, to the magnitude of the dimension immediately prior to applying the load increment. (2) In a body subjected to axial force, the natural logarithm of the ratio of the gage length at the moment of observation to the original gage length. Also known as natural strain. Compare with engineering strain.

true stress

The value obtained by dividing the load applied to a member at a given instant by the cross-sectional area over which it acts. Compare with engineering stress.

typical basis

The typical property value is an average value. No statistical assurance is associated with this basis. See also A-basis, B-basis, and S-basis.

U

ultimate strength

The maximum stress (tensile, compressive, or shear) a material can sustain without fracture, determined by dividing maximum load by the original cross-sectional area of the specimen. Also known as nominal strength or maximum strength.

uniaxial strain

Increase (or decrease) in length resulting from a stress acting parallel to the longitudinal axis of the specimen.

uniaxial stress

See principal stress (normal).

uniform elongation

The elongation at maximum load and immediately preceding the onset of necking in a tension test.

uniform strain

The strain occurring prior to the beginning of localization of strain (necking); the strain to maximum load in the tension test.

V

variance

A measure of the squared dispersion of observed values or measurements expressed as a function of the sum of the squared deviations from the population mean or sample average.

verification

Checking or testing an instrument to ensure conformance with a specification.

verified loading range

For testing machines, the range of indicated loads for which the testing machine gives results within the permissible variation specified.

vernier

A short auxiliary scale that slides along the main instrument scale to permit more accurate fractional reading of the least main division of the main scale. See also least count.

Vicat softening point

The temperature at which a flat-ended needle of 1 mm²(0.0015 in.²) circular or square cross section will penetrate a thermoplastic specimen to a depth of 1 mm (0.040 in.) under a specified load, using a uniform rate of temperature rise.

Vickers hardness number (HV)

A number related to the applied load and the surface area of the permanent impression made by a square-based pyramidal diamond indenter having included face angles of 136°, computed from the equation:

$$HV = 2P \sin \frac{\alpha}{2} = \frac{1.8544P}{d^2} \quad (\text{Eq 1})$$

where P is applied load, kgf; d is mean diagonal of the impression, mm; and α is face angle of diamond, 136°.

Vickers hardness test

An indentation hardness test employing a 136° diamond pyramid indenter (Vickers) and variable loads, enabling the use of one hardness scale for all ranges of hardness—from very soft lead to tungsten carbide. Also known as diamond pyramid hardness test.

viscoelasticity

A property involving a combination of elastic and viscous behavior. A material having this property is considered to combine the features of a perfectly elastic solid and a perfect fluid. A phenomenon of time-dependent, in addition to elastic, deformation (or recovery) in response to load.

volumetric modulus of elasticity

See bulk modulus of elasticity.

W

Wallner lines

A distinct pattern of intersecting sets of parallel lines, usually producing a set of V-shaped lines, sometimes observed when viewing brittle fracture surfaces at high magnification in an electron microscope. Wallner lines are attributed to interaction between a shock wave and a brittle crack front propagating at high velocity. Sometimes Wallner lines are misinterpreted as fatigue striations.

wear

Damage to a solid surface, generally involving progressive loss of material, due to relative motion between that surface and a contacting surface or substance.

wear rate

The rate of material removal or dimensional change due to wear per unit of exposure parameter—for example, quantity of material removed (mass, volume, thickness) in unit distance of sliding or unit time.

welding

In tribology, the bonding between metallic surfaces in direct contact, at any temperature.

Widmanstätten structure

A structure characterized by a geometrical pattern resulting from the formation of a new phase along certain crystallographic planes of the parent solid solution. The orientation of the lattice in the new phase is related crystallographically to the orientation of the lattice in the parent phase. The structure is readily produced in many alloys by appropriate heat treatment.

workability

See formability.

work hardening

See strain hardening.

wrap-around bend

The bend obtained when a specimen is wrapped in a closed helix around a cylindrical mandrel. This term is sometimes applied to a semiguided bend of 180° or less.

wrinkling

A wavy condition obtained in deep drawing of sheet metal, in the area of the metal between the edge of the flange and the draw radius. Wrinkling may also occur in other forming operations when unbalanced compressive forces are set up.

Y

yielding

Evidence of plastic deformation in structural materials. Also known as plastic flow or creep. See also flow.

yield point

The first stress in a material, usually less than the maximum attainable stress, at which an increase in strain occurs without an increase in stress. Only certain metals—those which exhibit a localized, heterogeneous type of transition from elastic to plastic deformation—produce a yield point. If there is a decrease in stress after yielding, a distinction may be made between upper and lower yield points. The load at which a sudden drop in the flow curve occurs is called the upper yield point. The constant load shown on the flow curve is the lower yield point.

yield-point elongation

During discontinuous yielding, the amount of strain measured from the onset of yielding to the beginning of strain hardening.

yield strength

The stress at which a material exhibits a specified deviation from proportionality of stress and strain. An offset of 0.2% is used for many metals. Compare with tensile strength.

yield stress

The stress level of highly ductile materials, such as structural steels, at which large strains take place without further increase in stress.

Young's modulus

A term used synonymously with modulus of elasticity. The ratio of tensile or compressive stresses to the resulting strain.

Z

zero time

The time when the given loading or constraint conditions are initially obtained in creep or stress-relaxation tests, respectively.

Glossary of Terms

Selected References

- *Compilation of ASTM Standard Definitions*, 8th ed., ASTM, 1994
- H.E. Davis, G.E. Troxell, and G.F.W. Hauck, *The Testing of Engineering Materials*, 4th ed., McGraw Hill, 1982
- J.R. Davis, Ed., *ASM Materials Engineering Dictionary*, ASM International, 1992
- G.E. Dieter, *Mechanical Metallurgy*, 2nd ed., McGraw Hill, New York, 1976
- *Glossary of Metallurgical Terms and Engineering Tables*, American Society for Metals, 1979
- D.N. Lapedes, Ed., *Dictionary of Scientific and Technical Terms*, 2nd ed., McGraw Hill, 1974
- A.D. Merriman, *A Dictionary of Metallurgy*, Pitman Publishing, London, 1958
- "Metal Test Methods and Analytical Procedures," *Annual Book of ASTM Standards*, Vol 03.01 and 03.02, ASTM, 1984
- J.G. Tweeddale, *Mechanical Properties of Metals*, American Elsevier, 1964